JANUARY/FEBRUARY 2006
Volume 17, Number 1

© Copyright 2006 by the American Chemical Society

Bioconjugate Chemistry

EDITORIAL: No More Hardcopy Submissions

As of January 1, 2006, the journal will no longer accept hardcopy submissions of manuscripts and Supporting Information. All must be submitted through the ACS Paragon System. This change should have little effect on our authors, who have overwhelmingly migrated to Web submission already. Other, minor changes in procedure are described in the new *Bioconjugate Chemistry* Guidelines for Authors, available on the journal Web page and in this print issue.

Thanks to Our Reviewers

It is a pleasure to acknowledge the contributions of the reviewers of manuscripts submitted in 2005 for publication in *Bioconjugate Chemistry*. Their unselfish service has been essential in the shaping of the sixteenth volume of the journal. The scientific community is fortunate that its members are willing to share their time and specialized knowledge in this way. The reviewers are listed on the following page.

Claude F. Meares

Editor-in-Chief

10.1021/bc050420j CCC: $33.50 © 2006 American Chemical Society
Published on Web 01/18/2006

List of Reviewers

Michael Abrams
Samuel Achilefu
Roger Alberto
Nancy Allbritton
Steve Alley
Thomas Anchordoquy
Carolyn Anderson
David Andreu
Yasushi Arano
Paola Arimondo
Bruce Armitage
Don Axworthy
Marina Backer
Christian Bailly
Marcel Bally
Jacqueline Barton
Amit Basu
Hagan Bayley
Annette Beck-Sickinger
Jean-Paul Behr
Leonie Beljaars
Dennis Benjamin
Gary Bignami
Philip Blower
Otto Boerman
Alexei A. Bogdanov
Elijah Bolotin
Darryl Bornhop
Line Bourel-Bonnet
M. Boyle
Martin Brechbiel
Marcel Bruchez
Cynthia Burrows
Paolo Caliceti
Britton Chance
Chien-Hsing Chang
Arabinda Chaudhuri
Chongsu Cho
Moo Cho
Yun Choe
Mary Cloninger
Patrick Couvreur
Mark Davis
Clemens Decristoforo
Eric Defranq
W. Denny
Bauke Dijkstra
Adriano Duatti
Gene Dubowchik
Pascal Dumy
Ramon Eritja
Virginie Escriou
Dan Feldheim
M. G. Finn
Nicholas Flinn
Nigel Forrow
Catherine Foulon
Keith Fox
Mati Fridkin
Shiroh Futaki
Michael Gait
Mike Gelb
Juri Gelovani
Kieran Geoghegan
J. Gerig
Mauro Ginanneschi
Malcolm Gilchrist
Aaron Goldstein
David Goodwin
Gilles Gosselin
Mark Green
Mark Greenberg
Gary Griffiths
Hermann Gruber
Boyd Haley
Hideyoshi Harashima
Ken-ichi Hatanaka
T. Alan Hatton
Piet Herdewijn
Greg Hermanson
Jean Herscovici
Donald Hnatowich
Robert Hider
Thomas Horn
Jari Hovinen
Ferenc Hudecz
Gerard Jaouen
Scott Jeffrey
Shougu Jin
Lee Josephson
Sylvia Jurisson
Robert Kane
Ravi Kane
Kazunori Kataoka
Yoshiki Katayama
Shigeo Katoh
John Katzenellenbogen
Haruma Kawaguchi
John Keana
Michael Keller
David Kessel
Marek Kwiatkowski
Sung Wan Kim
Thomas Kissel
Toni Kline
Beate Kloesgen
Ronald Kluger
Linda Knight
Hisataka Kobayashi
Thomas Kodadek
Robert Kok
Gerben Koning
Kenji Kono
Eric Kool
Jindrich Kopecek
Heinz-Bernhard Kraatz
Felix Kratz
Paul Kremer
Andrei Kutateladze
Marek Kwiatkowski
Kit Lam
Ulo Langel
Robert Langer
Peter Laverman
Christopher Leamon
Bernard Lebleu
Robert Lee
Hakon Leffler
Jean-Christophe Leroux
Robert Lever
Chun Li
Xingguo Liang
Kai Licha
Jonathan Lindner
David Liu
Guozheng Liu
Shuang Liu
Harri Lonnberg
Weiyue Lu
Helmut Maecke
Hiroshi Maeda
Ralph Mason
Hideki Masuda
Jules Mattes
Heather Maynard
Thomas McMurry
Kamran Melikov
Oleg Melnyk
Andre Merbach
Nils Metzler-Nolte
Jim Mixson
Hong Moulton
Robert Muller
Yukio Nagasaki
Katsumi Nakao
Dario Neri
Edward Neuwalt
Francesco Nicotra
Takuro Niidome
Hiroaki Okada
Nicole Okeley
Chris Orvig
David Oupicky
Daniel Pack
Chang Paik
Ravindra Pandey
Keykavous Parang
Tae Gwan Park
Joop Peters
Blake Peterson
Hans-Jurgen Pietzsch
Glenn Prestwich
Suzi Pun
Tariq Rana
Kenneth Raymond
Steven Regen
Theresa Reineke
Ralph Reisfeld
Kevin Rice
Steven Roffler
Buck Rogers
Keith Rose
Mary Rosendahl
Vincent Rotello
Hideo Saji
Yogesh Sanghvi
Markus Sauer
Ajit Sharma
Roger Schibli
Wolfgang Schramm
Gideon Schreiber
Francis Schuber
Ralph Schwall
Joachim Seelig
Michael Seidman
Ajit Sharma
Dean Sherry
John Shively
Zbigniew Skrzypczynski
Stan Slomkowski
Kevin Smith
Caroline Springer
Pat Stayton
David Thompson
Ignacio Tinoco, Jr.
Werner Tjarks
Brian Toki
Don Tomalia
Pam Trail
Eishun Tsuchida
Thomas Tullius
Ching-Hsuan Tung
Hiroshi Uyama
Ganesan Vaidyanathan
Lai-Xi Wang
Ralph Weissleder
Michael Welch
Hans-Jurgen Wester
Eric Wickstrom
D. Scott Wilbur
Meir Wilchek
Chris Wilds
Itamar Willner
Dieter Woehrle
Karen L. Wooley
Andrew Woolley
Anna Wu
Kazushige Yamana
Masayuki Yokoyama
Janusz Zakrzewski
Samuel Zalipsky
Michael Zalutsky
Matteo Zanda
Jon Zubieta

BC050420J

COMMUNICATIONS

Synthesis and Characterization of a Head−Tail Type Polycation Block Copolymer as a Nonviral Gene Vector

Atsushi Harada,* Masanori Kawamura, Takashi Matsuo, Toshinari Takahashi, and Kenji Kono

Department of Applied Chemistry, Graduate School of Engineering, Osaka Prefecture University, 1-1 Gakuen-cho, Sakai, Osaka 599-8531, Japan . Received September 29, 2005; Revised Manuscript Received December 5, 2005

A head−tail type polycation block copolymer, which is composed of the polyamidoamine (PAMAM) dendron and poly(L-lysine) (PLL) blocks, was newly designed as a nonviral gene vector in this study. This block copolymer (PAMAM dendron-PLL) was successfully synthesized in two steps: the synthesis of the PAMAM dendron block and the polymerization of the PLL block from the PAMAM dendron block. PAMAM dendron and PLL blocks in block copolymer showed independent deprotonation behavior, and their pK_a were determined to be 6.8 and 9.0, respectively. The complexation with pDNA was evaluated by gel retardation assay and dye exclusion assay, and both assays indicated that pDNA was selectively complexed with PLL block of block copolymer. Also, the PAMAM dendron-PLL poplyplexes showed 10^2 fold higher transfection efficiency to HeLa cells as that for PLL polyplexes. This might be due to the buffering effect of the PAMAM dendron block. This block copolymer could produce a function share in each block, i.e., tail block complexed with pDNA and head block showed a buffering effect. This molecular design of the head−tail type block copolymer might provide a new approach for realizing in vivo gene therapy.

The delivery of nucleic acids to cells as well as the instability in blood are important subjects for successful in vivo gene therapies. The design of synthetic polycation as nonviral gene vectors has received considerable attention for the purpose of realizing in vivo gene therapy (*1*−*4*). Although numerous polycations have been designed and synthesized, the rational design of polymers as in vivo gene vector systems has not yet been established. The use of polycations with relatively low pK_a values are mentioned as one of the guidelines. Polycations with low pK_a values, such as polyethyleneimine (PEI) and polyamidoamine (PAMAM) dendrimer, exhibit a high transfection efficiency due to the buffering effect (*5*−*8*), and PEI and PAMAM dendrimer are marketed under the trade names of ExGene and SuperFect, respectively. However, these have relatively weak affinity to DNA compared with cationic polymers, such as poly(L-lysine) (PLL) having a high pK_a value. One looks forward to the design of polycations, which combines stable complex formation under physiological conditions and a buffering effect. Recently, Kataoka et al. reported the polyplex vectors from A−B−C type triblock copolymers with spatially ordered layering of the condensed pDNA and buffering units for enhanced intracellular gene delivery (*9*). Such a molecular design, which produces a function share in each block of the copolymer, could be effective in realizing in vivo gene therapy. Here, we have newly designed a head−tail type polycation block copolymer, which is composed of the PAMAM dendron as the head block and PLL as the tail block, as a nonviral gene vector (Figure 1). In the design of the block copolymer composed of polycation blocks with different pK_a values as the gene vector, it is important that the pK_a values of the polycation block with a relatively low pK_a value be maintained even after the block copolymerization with different kind of polycations as well as the complexation with the pDNA. Consequently, the PAMAM dendron was selected as a buffering block with a low pK_a value, since the tertiary amino groups in the interior of the PAMAM dendron cannot be easily influenced by another polycation block due to steric hindrance. It was expected that the head and tail blocks exhibit a buffering action and complexation with pDNA, respectively.

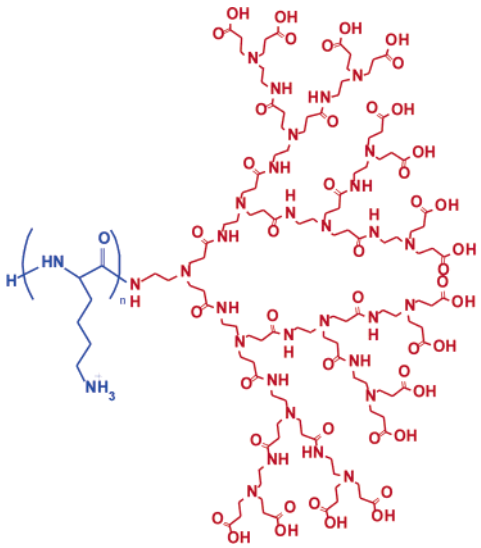

Figure 1. The chemical structure of head−tail type polycation block copolymer.

The head−tail type polycation block copolymer was synthesized in two steps, i.e., the synthesis of the PAMAM dendron

* To whom correspondence should be addressed. Tel and Fax: +81-72-254-9328, e-mail: harada@chem.osakafu-u.ac.jp.

10.1021/bc0502863 CCC: $33.50 © 2006 American Chemical Society
Published on Web 12/22/2005

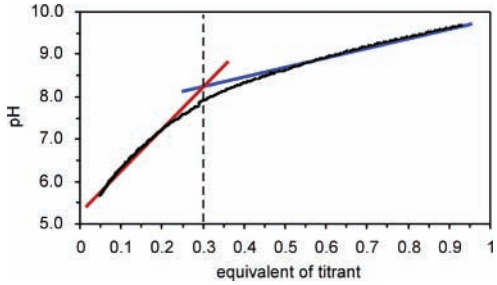

Figure 2. Titration curve of PAMAM dendron-PLL. 150 mg of PAMAM dendron-PLL in 45 mL of 0.01 M HCl was titrated with 0.01 M NaOH. The titrant was added in 0.1 mL quantities at 25 °C.

block and the polymerization of the PLL block from the PAMAM dendron block. Briefly, the PAMAM dendron block was synthesized by the repetitive exhaustive Michael addition with methyl acrylate using *tert*-butyl *N*-(2-aminoethyl)carbamate], for which one amino group of ethylenediamine is protected by a *tert*-butoxycarbonyl (Boc) group, as the starting reagent and subsequent exhaustive amidation with ethylenediamine (*10*). With four repetitions of the Michael addition and three amidations, the PAMAM dendron (Boc-PAMAM dendron) was made. To polymerize the PLL block from the PAMAM block, the Boc group at the root of the PAMAM dendron was removed by CF_3COOH treatment. The polymerization of the ϵ-benzyloxycarbonyl L-lysine *N*-carboxy anhydride [Lys(Z)-NCA], which was synthesized by the Fuchs−Farthing method using triphosgene (*11*), was then initiated from the primary amino group at the root of the PAMAM dendron in DMF at 40 °C. The obtained PAMAM dendron-PLL(Z) was converted to the PAMAM dendron-PLL by acid treatment using 30% HBr/AcOH in TFA. Also, the peripherial group of the PAMAM dendron block (methyl ester group) was removed by alkali treatment and converted to a carboxylate group. The finally obtained PAMAM dendron-PLL had 16 carboxylate groups at the periphery of the head block, 15 tertiary amino groups in the interior of the head block, and 70 primary amino groups in the tail block.

The deprotonation behavior of the PAMAMA dendron-PLL was important for determining the properties as a gene vector. The change in the ionization state vs the pH change was evaluated by an acid−base titration. Figure 2 shows the acid−base titration curve, pH vs equivalent of titrant, of the PAMAMA dendron-PLL. Obviously, two independent deprotonation processes were observed bound at equivalents of titrant = 0.3. The deprotonation at equivalents of titrant < 0.3 was due to the deprotonation of the tertiary amino groups in the interior of the PAMAM dendron block and carboxylate groups at the periphery of the PAMAM dendron block, and the deprotonation at equivalents of titrant > 0.3 was due to the primary amino groups of the PLL block. This might be a reasonable quantity for deprotonation, since the numbers of ionizable groups were 70 for the PLL block and 31 for the PAMAM dendron block. The pK_a values for each block were 9.0 for the PLL block and 6.8 for the PAMAM dendron block. Such a property vs the pH change (independent deprotonation behavior) as shown in Figure 2 was quite important in the design of the polycation block copolymer which makes a function share in each block. In the case of the design of polyelectrolytes having different kinds of weakly ionizable groups with different pK_a values, it is difficult to maintain the pK_a values for each ionizable group, because the pK_a value of a weakly ionizable group is shifted by the effect of the neighboring groups (*12*). Also, by pH change from physiological pH (7.4) to endsomal pH (less than 6.0), equivalents of titrant changed from 0.23 to 0.08. This suggests that the PAMAM dendron block exhibits a proton sponge nature in the uptake process into the cells.

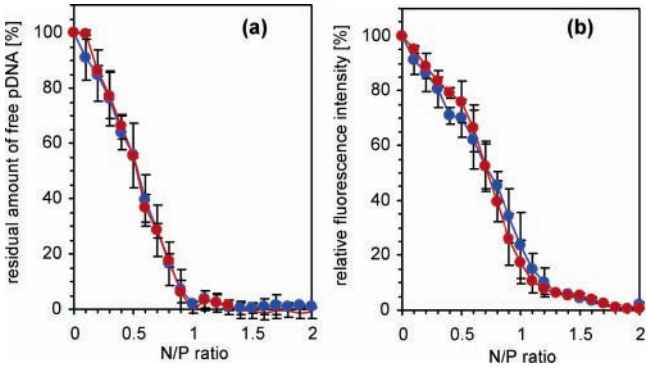

Figure 3. Complexation of pDNA with PAMAM dendron-PLL (red) and PLL (blue) evaluated by gel retardation assay (a) and dye exclusion assay (b). In part a, the gel electrophoresis was carried out at 100 V/cm for 30 min with 0.6 w/w% agarose gel, and residual amounts of free pDNA was determined by analyzing the magnitude of ethidium bromide-stained bands for free pDNA. In part b, fluorescence intensities for the polyplex solutions containing 10 μg of pDNA/mL and 2.5 μg of ethidium bromide (EtBr)/mL were measured. The excitation and emission wavelengths were 510 and 590 nm, respectively. For both experiments, the N/P ratio was defined as the number of ϵ-amino groups of PLL vs the number of phosphate groups of pDNA, and the data are presented as the average of three experiments ± SD.

The polyplex solutions were prepared by mixing pDNA and polycation solutions, after pDNA and polycations, PAMAM dendron-PLL or PLL, were separately dissolved in 20 mM Tris-HCl buffer (pH 7.4). The complexation of the PAMAM dendron-PLL with pDNA was evaluated by two assays, i.e., the dye exclusion assay and gel retardation assay (Figure 3). For both assays, the PAMAM dendron-PLL and PLL showed identical profiles with the change in the N/P ratios, in which the N/P ratio was defined as the number of ϵ-amino groups of PLL vs the number of phosphate groups of pDNA, nevertheless, the PAMAM dendron-PLL has tertiary amino groups in the PAMAM dendron block. Also, the addition of the Boc-PAMAM dendron to pDNA did not induce any complexation, since the tertiary amino groups in the interior was not protonated at pH 7.4. The protonation of the tertiary amino groups in the PAMAM dendron block was not facilitated by the complexation with pDNA via electrostatic interactions between pDNA and PLL. It was expected that the tertiary amino groups of the PAMAM dendron block in the PAMAM dendron-PLL might show a buffering effect.

From the transfection efficiency toward the culture cells (HeLa cells), it was indirectly evaluated whether the PAMAM dendron-PLL vector exhibits the buffering effect. It was known that the polyplexes of pDNA with the PLL homopolymer required the use of a lysosomotropic reagent such as chloroquine in order to express a sufficient transfection efficiency. Indeed, the PLL polyplexes showed a very low transfection efficiency to HeLa cells in the absence of the lysosomotropic reagent (Figure 4). On the other hand, the PAMAM dendron-PLL system showed a considerably high transfection efficiency compared with the PLL polyplex. Comparing the transfection efficiency at N/P = 3.5, at which PAMAM dendron-PLL polyplexes showed highest transfection efficiency, PAMAM dendron-PLL polyplexes showed 10^2 times as high transfection efficiency as PLL polyplexes, suggesting a buffering effect during endosomal/lysosomal processes. Also, when pDNA was complexed with the mixture of PLL and the Boc-PAMAM dendron, the complexes did not exhibit a sufficient transfection efficiency, and there was no difference with as significant their transfection efficiency as transfection efficiency of PLL polyplexes in the evaluated N/P ratio range. That is, the block copolymerization with the PAMAM dendron was required for expressing the buffering effect. Further, it should be noted the

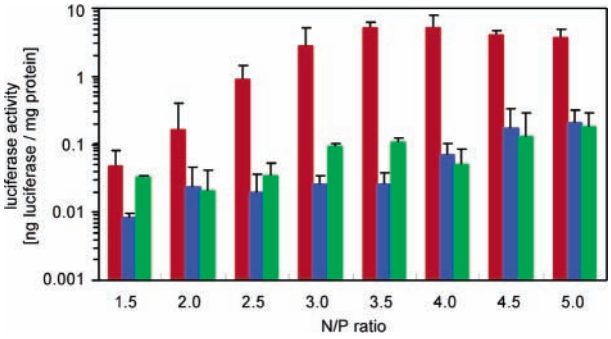

Figure 4. Transfection efficiency of PAMAM dendron-PLL polyplexes (red), PLL polyplexes (blue), and the mixture of PAMAM dendron and PLL (green) to HeLa cells. The cells (5×10^4) were treated with the polyplexes including 1 μg of pDNA. The N/P ratio was defined as the number of ϵ-amino groups of PLL vs the number of phosphate groups of pDNA. The data are presented as the average of three experiments $\pm$ SD.

difference in the effect of N/P ratio between the complexation (Figure 3) and transfection efficiency (Figure 4). The transfection efficiency of PAMAM dendron-PLL was increasing to N/P = 3.5, although both residual amounts of free pDNA and relative fluorescence intensity were almost no change at N/P > 1. This might worry the influence of free PAMAM dendron-PLL, i.e., uncomplexed PAMAM dendron-PLL, to an increase in transfection efficiency. To confirm the change in the property of polyplexes, the zeta-potential measurements were carried out for the PAMAM dendron-PLL polyplexes prepared at varying N/P ratios. The zeta-potentials of the complexes of PAMAM dendron-PLL with pDNA changed in this N/P ratio range ($1 < N/P < 3.5$), and the zeta-potentials of pDNA/PAMAM dendron-PLL at N/P = 1.0, 1.5, 2.0 and 3.5 were -20.9 ± 1.7, 9.1 ± 0.7, 15.8 ± 0.9 and 24.7 ± 2.4 mV, respectively. This indicates that the properties of pDNA/PAMAM dendron-PLL changed with an increase in N/P ratio even at $1.0 < N/P < 3.5$. Consequently, the increase in transfection efficiency at $1.5 < N/P < 3.5$ shown in Figure 4 might be induced by the effect of increasing the relative number of PAMAM dendron block, which exhibit a buffering effect, against pDNA and the effect of the change in the complex properties including zeta-potentials.

In conclusion, a head−tail type polycation block copolymer, which is composed of a PAMAM dendron as the head block and PLL as the tail block, was newly designed as a nonviral gene vector. The head−tail type block copolymer complexed with pDNA is driven by electrostatic interactions between pDNA and PLL block. Also, the polyplexes of the head−tail type block copolymer showed a sufficient transfection efficiency due to the buffering effect of the PAMAM dendron block even in the absence of a lysosomotropic reagent. This molecular design of the head−tail type block copolymer might provide a new approach to the realization of in vivo gene therapy.

ACKNOWLEDGMENT

This work was financially supported by a Grant-in-aid for Scientific Research form the Ministry of Education, Science, Sports, and Culture in Japan.

Supporting Information Available: The detailed procedure and characterization of block copolymer synthesis and the experimental procedure of dye exclusion assay, gel retardation assay, the transfection to HeLa cells, and zeta-potential measurements. This material is available free of charge via the Internet at http://pubs.acs.org.

LITERATURE CITED

(1) Felgner, P. L. (1990) Particulate systems and polymers for in vitro and in vivo delivery of polynucleotides. *Adv. Drug Delivery Rev. 5*, 163−187.

(2) Behr, J. P. (1994) Gene transfer with synthetic cationic amphiphiles: Prospects for gene therapy. *Bioconjugate Chem. 5*, 382−389.

(3) Kabanov, A. V., and Kabanov, V. A. (1995) DNA complexes with polycations for the delivery of geneticmaterial into cells. *Bioconjugate Chem. 6*, 7−20.

(4) Stull, R. A., and Szoka, F. (1995) Antigen, ribozyme and aptamer nucleic-acid drugs − progress and prospects. *Pharm. Res. 12*, 465−483.

(5) Boussif, O., Lezoualæh, F., Zanta, M. A., Mergny, M. D., Scherman, D., Demeneix, B., and Behr, J. P. (1995) A versatile vector for gene and oligonucleotide transfer into cells in culture and in-vivo − polyethyleneimine. *Proc. Natl. Acad. Sci. U.S.A. 92*, 7297−7301.

(6) Behr, J. P. (1997) The proton sponge: A trick to enter cells the viruses did not exploit. *Chemia 51*, 34−36.

(7) Tang, M., Redemann, C. T., and Szoka, F. C. Jr. (1996) In vitro gene delivery by degraded polyamidoamine dendrimers. *Bioconjugate Chem. 7*, 703−714.

(8) Kukowska-Latallo, J. F., Bielinska, A. U., Johnson, J., Spindler, R., Tomalia, D. A., and Baker, J. R., Jr. (1996) Efficient transfer of genetic material into mammalian cells using starburst polyamidoamine dendrimers. *Proc. Natl. Acad. Sci. U.S.A. 93*, 4897−4902.

(9) Fukushima, S., Miyata, K., Nishiyama, N., Kanayama, N., Yamasaki, Y., and Kataoka, K. (2005) PEGylated polyplex micelles from triblock catiomers with spatially ordered layering of condensed pDNA and buffering units for enhanced intracellular gene delivery. *J. Am. Chem. Soc. 127*, 2810−2811.

(10) Tomalia, D. A., Baker, H., Dewald, J., Hall, M., Kallos, G., Martin, S., Roeck, J., Ryder, J., and Smith, P. (1985) A new class of polymers − starburst-dendritic macromolecules. *Polym. J. 17*, 117−132.

(11) Harada, A., and Kataoka, K. (1995) Formation of polyion complex micelles in an aqueous milieu from a pair of oppositely charged block copolymers with poly(ethylene glycol) segments. *Macromolecules 28*, 5294−5299.

(12) Morawetz, H. *Macromolecules in solution*; Interscience Publishers, New York, 1985.

BC0502863

ARTICLES

Water-Soluble Dendrigrafts Bearing Saccharidic Moieties: Elaboration and Application to Enzyme Linked OligoSorbent Assay (ELOSA) Diagnostic Tests

Julien Bernard,[†] Michel Schappacher,[†] Alain Deffieux,*[,†] Pascal Viville,[‡] Robert Lazzaroni,[‡] Marie-Hélène Charles,[§] Marie-Thérèse Charreyre,*[,§] and Thierry Delair[§]

Laboratoire de Chimie des Polymères Organiques, UMR 5629 CNRS-ENSCPB-Université Bordeaux I, 16 Avenue Pey Berland, 33607 Pessac, France, Unité Mixte CNRS-bioMérieux, UMR-2714, ENS-Lyon, 46, Allée d'Italie 69364 Lyon Cedex 07, France, and Service de Chimie des Matériaux Nouveaux, Université de Mons-Hainault, Mons, Belgium. Received December 7, 2004; Revised Manuscript Received September 15, 2005

The synthesis of a series of water-soluble galactopyranose-functionalized polystyrene−polyvinyl ether dendrigrafts and their characterization (in solution and thin solid deposits) have been achieved. The presence of external galactopyranose groups on dendritic polymers has been exploited to prepare dendrigraft−oligonucleotide conjugates using a simple one-step coupling procedure with amino-ended oligonucleotides (ODNs). Several parameters such as the peripherical density of hydrophilic branches, the polymerization degree of polystyrene or poly(hydroxyethyl vinyl ether) blocks, and the number of galactopyranose groups were tuned. A capture test with short labeled complementary ODNs (25 bases) confirmed the presence of covalently bound ODNs on various kinds of dendrigrafts. The ability of the dendritic polymers to enhance the sensitivity of enzyme-linked oligosorbent assay (ELOSA) diagnostic tests (detection of hepatitis B virus, DNA target of 2400 bases) was then evaluated, especially the influence of the macromolecular architecture and the impact of the structural parameters. The dendrigraft−ODN conjugate with the lower saccharide external density was found to lead to a very significant amplification of the fluorescence signal, corresponding to a limit of sensitivity of 10^9 DNA copies per milliliter (instead of 10^{11} DNA copies per milliliter without using dendrigrafts). Conversely, the dendrigrafts exhibiting a very high number of branches and galactopyranose groups at their periphery were not able to induce a better sensitivity due to steric hindrance generated by the peripheral congestion on these polymers.

INTRODUCTION

Contrary to the traditional ELISA[1] diagnostic tests, ELOSA tests are based on the capture and detection of nucleic acids and provide a direct and specific detection of genetic or infectious diseases. The principle of these tests lies, first, in the capture of a target material (single-stranded DNA sequences) by oligonucleotide probes anchored onto a solid support and, second, in the detection and quantification of the captured DNA target (colorimetric or fluorescent signal). As the quantities of target material are typically very low, this strategy generally includes either amplification of the target sequence (*1*) or signal amplification, to enhance the sensitivity of the test. Since the target amplification strategy gives rise to numerous drawbacks such as cross-contamination or poor reproducibility, attention has then been paid to the second approach.

Several signal amplification strategies have been proposed, either based on the introduction of multiple reporter groups such as biotin (*2*), fluorophores (*3*), or 2,4-dinitrophenyl (*4*) in the ODN used for the detection or focusing on the use of branched oligonucleotides (*5*, *6*) in combination with detection probes labeled with an enzyme. However, the increase of sensitivity obtained by these routes is still limited.

An alternative way consists of the preparation of (co)-polymer−ODN amplification structures (conjugates). With this aim, a number of new polymer supports, consisting of functional (co)polymers bearing different reactive groups (activated ester, anhydride, aldehyde), have been developed to immobilize ODNs (*7*−*17*). The conjugates were typically prepared either by binding amino-ended single-stranded oligonucleotide probes (synthesized via automated synthesis with an $-NH_2$ group at the 5′ position) onto reactive (co)polymers via amination or amidation reaction (*7*−*15*) or by direct synthesis of the ODNs from the polymer backbone (*16*−*17*). Both kinds of conjugates enable the capture of complementary DNA targets through hybridization and lead to an increase in the sensitivity of the ELOSA test.

[†] Université Bordeaux I.

[‡] Unité Mixte CNRS-bioMérieux.

[§] Université de Mons-Hainault.

[1] List of abbreviations: DLS, dynamic light scattering; DMF, dimethyl formamide; DMSO, dimethyl sulfoxide; EGP, 1,2:3,4-di-*O*-isopropylidene-6-*O*-epoxypropyl-D-galactopyranose; ELISA, enzyme-linked immunosorbent assay; ELOSA, enzyme-linked oligosorbent assay; DiGVE, 1,2:3,4-di-*O*-isopropylidene-6-*O*-(2-vinyloxy ethyl)-D-galactopyranose; Gal, galactose; HBV, hepatitis B virus; NMP, *N*-methylpyrrolidone; ODN, oligonucleotide; PCEVE, poly(chloroethyl vinyl ether); PDiPGVE, poly(1,2:3,4-di-*O*-isopropylidene-6-*O*-(2-vinyloxy ethyl)-D-galactopyranose); PEO, poly(ethylene oxide); PEGP, poly(1,2:3,4-di-*O*-isopropylidene-6-*O*-epoxypropyl-D-galactopyranose); PGVE, poly(6-*O*-(2-vinyloxy ethyl)-D-galactopyranose); PHEVE, poly(hydroxyethyl vinyl ether); PS, polystyrene; PSiVE, poly(*tert*-butyldimethylsilyloxyethyl vinyl ether); PVE, poly(vinyl ether); SEC, size exclusion chromatography; SiVE, 5,10,15,20-((*tert*-butyldimethylsilyl)oxy)ethyl vinyl ether; SLS, static light scattering; THF, tetrahydrofuran; TMAFM, tapping mode atomic force microscopy; VPO, vapor pressure osmometry

10.1021/bc049708j CCC: $33.50 © 2006 American Chemical Society
Published on Web 12/24/2005

Scheme 1. Reaction Pathways for the Elaboration of Hydrophobic Hyperbranched Precursors [PCEVE-*g*-(PS-*b*-PCEVE) or PCEVE-*g*-(PS-*b*-(PCEVE-*g*-PS))] and Amphiphilic Dendrigrafts [PCEVE-*g*-(PS-*b*-(PCEVE-*g*-(PEO-*b*-PEGP))) or PCEVE-*g*-(PS-*b*-(PCEVE-*g*-(PS-*b*-PHEVE-*b*-PGVE)))]

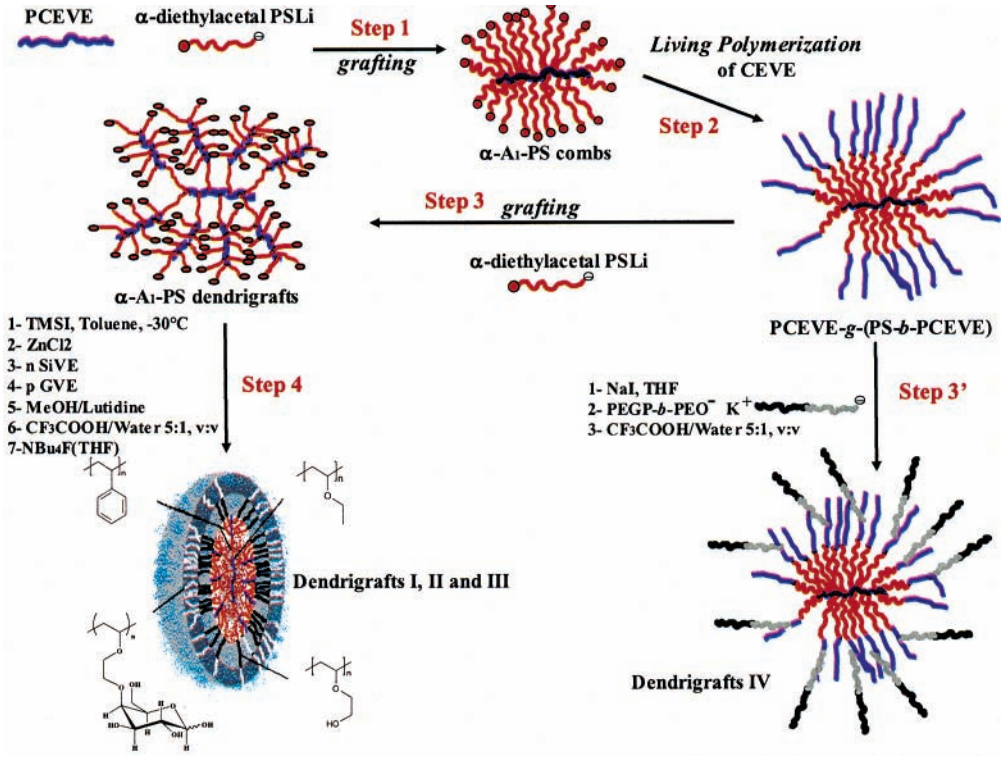

Concerning polymer−ODN conjugate properties desirable for an effective enhancement of the signal, it was shown that accessibility of the immobilized ODNs (rather than their number) was a major issue. Among the above-mentioned functional (co)polymers, various architectures have been designed such as (i) linear (co)polymers, namely poly(maleic anhydride-*co*-methyl vinyl ether) (*8*), poly(*N*-vinylpyrrolidone-*co*-*N*-acryloxysuccinimide) (*7*, *10*), poly(*N*-(2,2-dimethoxyethyl)-*N*-methyl acrylamide) (*11*), and synthetic glycopolymers (*9*, *12*, *13*), (ii) graft (co)polymers (*14*, *15*), and (iii) latex particles (*18*, *19*). However, to our knowledge, no study describing the use of dendrigrafts as supports for ODN immobilization has been previously reported.

In a recent article, we described the synthesis of hydrosoluble amphiphilic dendrigrafts bearing saccharide groups located at the periphery (*20*). These polymers were prepared from functional arborescent PS precursors (*21*) by taking advantage of the presence of terminal acetal functions on every PS branch to grow poly(vinyl ether) blocks of poly(*tert*-butyldimethylsilyloxyethyl vinyl ether) and poly(1,2:3,4-di-*O*-isopropylidene-6-*O*-(2-vinyloxyethyl)-D-galactopyranose) via living cationic polymerization. After deprotection, the dense hydrophilic PVE shell (PHEVE and PGVE) surrounding the PS core ensured the solubilization of the dendrigrafts in water. The presence of both PHEVE blocks (acting as hydrophilic spacers) and PGVE external blocks (bearing galactopyranose groups with the potential ability to covalently immobilize amino-ended oligonucleotides (*13*, *15*)) on these dendritic polymers encouraged us to evaluate their efficiency as supports for ELOSA diagnostic tests. In addition, we also developed a second route to galactopyranose-functionalized water-soluble dendrigrafts based on the coupling of living polyoxirane chains onto PCEVE-*g*-(PS-*b*-PCEVE) precursors during this work.

In this article, we report the synthesis and the characterization of a series of galactopyranose-functionalized dendrigrafts. Several parameters such as the peripheral density of branches, the polymerization degree of PS or PHEVE blocks, and the number of Gal groups were tuned. The ability of these polymers to enhance the sensitivity of ELOSA tests was then evaluated, especially the influence of the macromolecular architecture and the impact of the structural parameters on the results of the test.

EXPERIMENTAL PROCEDURES

Materials. Toluene (99.5%, J. T. Baker, Deventer, The Netherlands) was purified by distillation over calcium hydride and stored over polystyryllithium seeds. Tetrahydrofuran (99%, J. T. Baker, Deventer, The Netherlands) was purified by distillation over calcium hydride and stored over potassium/benzophenone. Ethylene oxide (99.5%, Sigma Aldrich Chimie, St Quentin Fallavier, France) was purified and stored over calcium hydride. Dimethyl sulfoxide (99.9%, Sigma Aldrich Chimie, St Quentin Fallavier, France), dimethyl formamide (99.9%, Sigma Aldrich Chimie, St Quentin Fallavier, France), *N*-methylpyrrolidone (99.9%, Sigma Aldrich Chimie, St Quentin Fallavier, France), epichlorhydrine (99%, Sigma Aldrich Chimie, St Quentin Fallavier, France), 2-hydroxyethyl vinyl ether, 1,2:3,4-di-*O*-isopropylidene-α-D-galactopyranose, and potassium (98%, Sigma Aldrich Chimie, St Quentin Fallavier, France) were used as received. SiVE was prepared as described previously by Fukui et al. (*22*) from 2-hydroxyethyl vinyl ether and distilled over calcium hydride twice before use. DiGVE was prepared as recently described by D'Agosto et al. (*13*). EGP was synthesized from epichlorhydrine and 1,2:3,4-di-*O*-isopropylidene-α-D-galactopyranose according to the procedure reported by Koell et al. (*23*).

Synthesis of the PCEVE/PS Dendrigraft Precursors. The dendrigraft precursors 200/50/50/$A_1$50 (A) ($\overline{DP}_{n\mathrm{PCEVE1}}/\overline{DP}_{n\mathrm{PS1}}/\overline{DP}_{n\mathrm{PCEVE2}}/\overline{DP}_{n\mathrm{A1-PS2}}$, A_1 = α-acetal group), 200/50/50/$A_1$5 (B), and 200/120/40 (C) used in this work were elaborated according to a previously reported procedure (*21*, *24*) (Scheme 1).

PCEVE/PS dendrigraft precursor properties. A: $\overline{M}_w$ = 3.8×10^7 g·mol^{-1}; PDI = 1.05; R_g = 34.5 nm; R_h = 34 nm. **B**:

$\overline{M_w} = 0.6 \times 10^7 g \cdot mol^{-1}$; PDI = 1.18; R_g = 22.5 nm; R_h = 25 nm. **C**: $\overline{M_w} = 0.3 \times 10^7 g \cdot mol^{-1}$; PDI = 1.13.

Synthesis of Amphiphilic Dendrigrafts (I, II, III) with a Hydrophilic PVE Shell. The dendrigrafts were prepared as previously described (*20*) via a "grafting from" procedure: initiation of living cationic polymerization of SiVE and DiGVE from the diethylacetal ends of PS branches of the PCEVE/PS hyperbranched cores, using trimethylsilyl iodide and zinc dichloride as a catalytic system. Typically, the chain extension was carried out under nitrogen in toluene at −30 °C in a 250 mL baked flask with a double-way stopcock equipped with a magnetic stirring bar. The PS precursor (200/50/50/$A_1$50, 5 g, 1 mmol acetal termini) was dissolved in anhydrous toluene and vacuum-dried to remove traces of moisture. The polymer and SiVE (19 g, 93 mmol) were subsequently dissolved in anhydrous toluene (100 mL) under nitrogen. Trimethylsilyl iodide (0.17 mL, 1.2 mmol) was then added to the solution and vigorously stirred for 1 h. A $ZnCl_2$ solution (1 mL, 3 mmol·L^{-1} in diethyl ether) was added to initiate the polymerization of SiVE. After complete conversion of SiVE (12 h), DiGVE (5 g, 15 mmol) was added to the living polymer solution to grow a third block and generate external PS-*b*-PSiVE-*b*-PDiGVE branches. After 10 h, the polymerization was stopped by adding a methanol/lutidine mixture. The polymer was washed several times with potassium thiosulfate aqueous solution (2 wt %) and then with water. The solvent was evaporated, and the polymer was precipitated in methanol. The deprotection of the saccharidic moieties was achieved by treatment with a trifluoroacetic acid/water mixture (v/v, 5/1, 3 h, room temperature), and the hydroxyl functions on PSiVE were regenerated via a treatment with NBu_4F in THF (3 h, room temperature). After deprotection of the hydroxyl groups of SiVE and DiGVE, the dendrigrafts were purified by dialysis against pure water (I, II) or methanol (III) for 3 days (membrane Spectra/Por 7).

On the basis of the previously measured PS precursor characteristics ($\overline{M_w}$, $\overline{DP_{n\mathrm{PS2}}}$, number of external branches) and assuming quantitative initiation from the precursor acetal ends, PSiVE and PDiGVE degrees of polymerization were evaluated by ^{1}H NMR, from the relative integration of PS aromatic (5H), *tert*-butyldimethylsilyl group (15H), and saccharidic protons (1H, H1 or H2). The molecular weight of the dendrigrafts was calculated with the following equation: $\overline{M_{n\mathrm{RMN}}} = \overline{M_n}(\mathrm{precursor}) + (\overline{DP_{n\mathrm{PSiVE\ (RMN)}}} \times m_{\mathrm{SiVE}} + \overline{DP_{n\mathrm{PDiGVE\ (RMN)}}} \times m_{\mathrm{DiGVE}})$, with *n* equal to the number of branches in the precursor. The number of galactopyranose groups per dendrigraft was determined from the number of PS_2 external branches and the degree of polymerization of PDiGVE (Nber of Gal = Nber of external branches × $\overline{DP_{n\mathrm{PDiGVE}}}$).

^{1}H NMR ($CDCl_3$) δ (ppm): −0.1−0.2 (−Si−CH_3), 0.7−1.1 (−Si−C−CH_3), 1−2.2 (PSiVE and PDiGVE backbones: −CH_2−CH−O−; PS backbone: −CH_2−CH−; PDiGVE: CH_3−C−O), 3−3.8 (PSiVE and PDiGVE backbones: −CH_2−CH−O−; PSiVE and PDiGVE pendent groups: O−CH_2−CH_2−O; PDiGVE pendent groups: O−CH_2−CH−), 3.8−4 (PDiGVE, H5), 4.1−4.3 (PDiGVE, H3 and H4), 4.5−4.7 (PDiGVE, H2), 5.4−5.6 (PDiGVE, H1), 6.2−7.2 (PS, Ph).

Synthesis of Amphiphilic Dendrigrafts (IV) with a Hydrophilic Polyoxirane Shell. *(a) Preparation of the PEGP-b-PEO−K^+ Diblocks.* The synthesis of PEGP-*b*-PEO chains was carried out by living anionic polymerization. The potassium alcoholate salt of 1,2:3,4-di-*O*-isopropylidene-D-galactopyranose was first prepared under vacuum by addition of 1 g of 1,2:3,4-di-*O*-isopropylidene-α-D-galactopyranose (3.8 mmol) dissolved in 150 mL of distilled THF in a flask containing an excess of potassium (0.3 g, 7.7 mmol, ∼2 equiv). After reacting for 24 h at room temperature, the slightly yellow solution of alcoholate was filtered under vacuum to eliminate residual potassium. Polymerization of EGP was carried out in THF at 50 °C in a 500 mL flask equipped with a magnetic stir bar after addition to the potassium alcoholate solution of 6 g of EGP (19 mmol) dissolved in 50 mL of dry THF. After reacting for 24 h, an aliquot of the solution was collected and analyzed by size exclusion chromatography in THF, confirming the complete polymerization of EGP. Ethylene oxide (15 g, 0.34 mol) was then added to the "living" polymer solution at room temperature in order to grow the second block. After 24 h of reaction, an aliquot of PEGP-*b*-PEO^- K^+ block copolymer solution was deactivated by addition of degassed methanol and then analyzed by SEC in THF, ^{1}H NMR in $CDCl_3$, and VPO in toluene.

Copolymer characteristics: $\overline{DP_n}$(PEGP) = 5; $\overline{DP_n}$(PEO) = 90 (calculated from ^{1}H NMR spectrum and VPO measurement of PEGP-*b*-PEO); $\overline{M_{w\mathrm{GPC}}}$ = 4200 g·mol^{-1}; $\overline{M_{w\mathrm{VPO}}}$ = 5880 g·mol^{-1}; PDI = 1.14.

(b) Synthesis of Amphiphilic Dendrigrafts IV by the Grafting onto Procedure. The synthesis of the amphiphilic dendrigrafts bearing a polyoxirane shell was performed by grafting the living PEGP-*b*-PEO^- K^+ chains onto the $PCEVE_2$ blocks of ($PCEVE_1$-*g*-(PS_1-*b*-$PCEVE_2$)) comblike precursors.

Typically, the comb copolymer (C, 1.1 g, 3.2 mmol of chloroethyl functions) and NaI (20 mg, 0.13 mmol) were dissolved in 25 mL of anhydrous THF in a 500 mL flask equipped with a double-way stopcock and a magnetic stir bar. To remove traces of moisture, the solvent was evaporated under vacuum and the polymer was vacuum dried for 1 h at 60 °C. This operation was repeated twice. The polymer was then redissolved in 20 mL of anhydrous THF, and the solution containing the "living" oxanionic polyoxirane chains was then slowly added. After 3 weeks, the reaction was deactivated by addition of degassed methanol and 250 mL of CH_2Cl_2 was introduced. The polymer solution was washed several times with potassium thiosulfate/water (2 wt %), to eliminate iodine, and then with water. The organic solution was then dried with magnesium sulfate, filtered, and precipitated in diethyl ether and redissolved in acetone. The dendrigraft was isolated from unreacted polyoxirane chains by selective precipitation in an acetone/diethyl ether mixture. The pure arborescent polymer was then characterized by SEC (THF), SLS (THF), DLS (THF), and ^{1}H NMR ($CDCl_3$). Deprotection of the saccharidic groups (1 g of polymer in 10 mL of THF) was achieved by acidic treatment with a 5:1, v:v CF_3COOH/H_2O mixture (10 mL) for 3 h. After neutralization of the solution by addition of aqueous NaOH (1 M), the polymer was purified by dialysis against pure water (membrane Spectra/Por7, molecular weight cutoff ca. 1000) for a week.

^{1}H NMR ($CDCl_3$) δ (ppm): 1−2.2 (PCEVE backbone: −CH_2−CH−O−; PS backbone: −CH_2−CH−Ph; PEGP: CH_3−C−O), 3.4−3.8 (PCEVE backbone: −CH_2−CH−O−; PCEVE: −O−CH_2−CH_2−Cl, −O−CH_2−CH_2−Cl; PEO backbone: −CH_2O−; PEGP backbone: O−CH_2−CH−O−, O−CH_2−CH−O−), 3.9−4.1 (PEGP, H5), 4.2−4.4 (PEGP, H3 and H4), 4.5−4.7 (PEGP, H2), 5.4−5.6 (PEGP, H1), 6.2−7.2 (PS, Ph).

Binding of ODN onto Galactopyranose-Functionalized Dendrigrafts. NH_2-terminated oligonucleotides were synthesized by standard DNA cyanoethyl *N*,*N*-di-isopropylamino phosphoramidite chemistry. They were modified at their 5′ positions with an aminohexyl spacer arm for coupling to the polymer. The following sequence was used (given from the 5′ to 3′ position): 5′-TCA-ATC-TCG-GGA-ATC-TCA-ATG-TTA-G-3′.

To optimize the conditions for ODN coupling onto the dendrigrafts, several organic solvents (DMF, DMSO, and NMP), different aqueous buffer to organic solvent ratios, and various pH and ionic strength values of the aqueous buffer were tested.

Typically, 10.2 μL of an aqueous solution of oligonucleotides (5 nmol) and 27 μL of borate buffer (20 mM, pH = 7.2) were introduced in an Eppendorf tube. After removing water under reduced pressure (speed-vac), the pellet (ODNs and salts) was redissolved in 21.7 μL of pure water. Next, 5.3 μL of an aqueous solution of dendrigrafts IV (100 nmol of galactopyranose moieties) and 243 μL of DMF was introduced in the tube (run 11, total volume 270 μL, 10/90 v/v aqueous buffer/DMF). The tube was finally placed under stirring at 50 °C for 5 days.

Capture Test: Dendrigraft−ODN Conjugate Characterization. The binding of ODNs onto the dendrigraft was indirectly confirmed by evaluating the ability of the dendrigraft−ODN conjugates to capture short complementary ODN sequences labeled with an enzyme (alkaline phosphatase). These capture tests were performed on bioMérieux's Vidas immunoanalysis system. The dendrigraft−ODN conjugates (300 μL, 15 nmol) were first physically adsorbed onto the Vidas solid-phase receptacle. After a washing step, the capture step was performed over a period of 1 h with complementary labeled ODNs (300 μL, 10 nmol). After another wash and addition of the enzyme substrate (methyl umbelliferyl phosphate), the emitted signal was measured and expressed by the Vidas detector in relative fluorescence units (RFU). Each series of tests included one control sample without conjugate (labeled ODNs only).

ELOSA Tests. Complete ELOSA tests were performed as previously described (*9*, *10*) with the conjugates providing a significant signal in the capture tests. The dendrigraft−ODN conjugates (300 μL, 15 nmol) were first physically adsorbed onto the Vidas solid phase (coating step). After a washing step, the capture step was carried out with increasing concentrations of HBV DNA target (2339 base pairs) (0, 10^7, 10^8, 10^9, 10^{10}, and 10^{11} DNA copies per mL, 200 μL). Intermediate detection probes (called Mix) ensured the link between the captured DNA targets and the polymer−ODN detection conjugate (300 μL, 15 nmol). This detection conjugate was based on a saccharidic graft copolymer (AF 112) (*15*). The fluorescent signal (RFU) was finally produced by labeled ODNs hybridized on the polymer−ODN detection conjugate.

Polymer Characterization. ^{1}H NMR spectra were recorded in $CDCl_3$ or in D_2O on a Bruker AC 200 FT apparatus. Size exclusion chromatography (SEC) measurements of PVE amphiphilic dendrigrafts (I, II, III) before deprotection were performed in tetrahydrofuran at 25 °C (flow rate 0.7 mL/min) on a Varian apparatus equipped with refractive index (Varian) and laser light scattering (Wyatt Technology) dual detection, and fitted with four TSK gel HXL columns (250, 1500, 10^4, and 10^5 Å). For the light scattering measurements, the d*n*/d*c* values of the different PVE and polyoxirane dendrigrafts were determined in THF at 25 °C with a laser source operating at 633 nm.

Size exclusion chromatography analyses of PEO-*b*-PEGP blocks, dendrigrafts IV, and deprotected PVE dendrigrafts I, II, and III were performed at 25 °C in a water/methanol mixture (v/v 80/20) containing $NaNO_3$ (1.27 g/L) on a Varian apparatus equipped with a refractive index detector and four TSK PWXL columns (300 × 7.7 mm; 250, 1500, 10^4, and 10^5 Å), at a flow rate of 1 mL/mn.

Dynamic light scattering measurements were performed at 25 °C in THF and in water on a Malvern apparatus (Zetasizer 3000HS) equipped with a laser source (633 nm). Correlation functions were analyzed by the Contin method. Latex particles were used as calibration standards.

VPO measurements were performed on a Gonotec Osmomat 090 in toluene. Samples for AFM of the dendrigrafts and their precursors were prepared by solvent casting at ambient conditions on substrates, starting from either MeOH solutions of dendrigrafts or THF solutions for the precursors. Typically, 20 μL of a dilute solution (0.002−0.1 wt %) was cast on a 1 × 1 cm^2 freshly cleaved mica substrate. Samples were analyzed after complete evaporation of the solvent at room temperature. All AFM images were recorded in air with a Nanoscope IIIa microscope operated in tapping mode. The probes were commercially available silicon tips with a spring constant of 24−52 N/m, a resonance frequency lying in the 264−339 kHz range, and a typical radius of curvature in the 10−15 nm range. Both the topography and the phase signal images were recorded with the highest sampling resolution available, i.e., 512 × 512 data points.

Table 1. Dimensions and Solution Characteristics of Amphiphilic PVE-Based Dendrigrafts I, II, and III

	I	II	III
	A	B	B
$\overline{DP_n}_{PS_2}$[a]	50	5	5
$\overline{DP_n}_{PSiVE}$[a]	90	110	11
$\overline{DP_n}_{PDiGVE}$[a]	12	4	3
$\overline{M_w}_{RMN} \times 10^{-7}$[a]	14.4	20.3	3.1
$\overline{M_w} \times 10^{-7}$[b]	14.8	16.3	2.8
$\overline{M_w}/\overline{M_c}$[c]	1.03	1.16	1.35
R_g[b]	56	51	37
R_h (THF)[d]	55 (34[f])	44 (25[f])	36 (25[f])
R_h after deprotection (water)[d]	56	58	- - -
(Nb of Gal units/dendrigraft)[e]	96 000	33 400	25 000

[a] Determined by ^{1}H NMR in $CDCl_3$. [b] Measured by SLS in THF at 25 °C. [c] Measured by SEC in THF. [d] Measured by DLS at 25 °C. [e] Nb of Gal units/dendrigraft = (experimental number of branches of A (I) or B (II and III) × $\overline{DP_n}_{PDiGVE}$). [f] R_h of PCEVE$_1$-*g*-(PS-*b*-(PCEVE$_2$-*g*-A$_1$PS)) precursors measured by DLS in THF at 25 °C.

RESULTS AND DISCUSSION

The hydrosoluble dendritic polymers were synthesized from functional PCEVE/PS dendrigraft (A, B) or comb (C) precursors. As previously reported, these monodispersed polymers were prepared by covalently assembling elementary macromolecular blocks by repeated grafting of α-end-functionalized polystyryllithium onto chloroethyl vinyl ether units of linear or comblike chains (obtained via living cationic polymerization) as described in Scheme 1, steps 1, 2, and 3. Two strategies have been developed to prepare hydrosoluble dendritic polymers suitable for DNA immobilization, from these hydrophobic precursors.

Synthesis of the Water-Soluble Dendrigrafts I, II, and III. The first route (*20*) was based on the use of acetal-terminated PCEVE$_1$-*g*-(PS$_1$-*b*-(PCEVE$_2$-*g*-A$_1$PS$_2$)) (precursors A and B) as multifunctional initiators to grow a surrounding hydrophilic shell with galactopyranose units available at the periphery. As previously described, this was achieved by initiation—from the terminal acetal groups—of the living cationic polymerization of two types of poly(vinyl ether) blocks (see Scheme 1, step 4**)**: the PSiVE block that ensured the solubilization of the dendrigrafts in aqueous solution after deprotection of hydroxyl groups (PHEVE) and the PDiGVE block that enabled the binding of NH_2-ended oligonucleotides after deprotection of the saccharidic moieties. To evaluate the influence of parameters such as the length of the hydrophilic spacer (PHEVE) or the number of the GVE units on the immobilization of ODNs and on the ability of the resulting conjugates to provide an amplification enhancement, we prepared three different dendrigrafts tuning the degree of polymerization of the external PS ($\overline{DP_n}_{PS2}$ = 5 or 50), PSiVE, and PDiGVE blocks. The dimensions and the main characteristics of dendrigrafts I, II, and III are indicated in Table 1. The growth of the PVE blocks was confirmed by ^{1}H NMR. The increase of the hydrodynamic

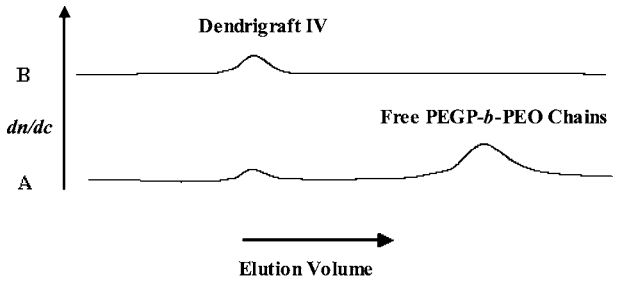

Figure 1. SEC chromatograms of dendrigraft IV (SEC water/methanol 80/20 v/v): (A) crude product; (B) dendrigraft IV after fractionation and elimination of unreacted PEGP-*b*-PEO.

Scheme 2. Synthesis of PEGP-*b*-PEO Living Chains via Anionic Polymerization

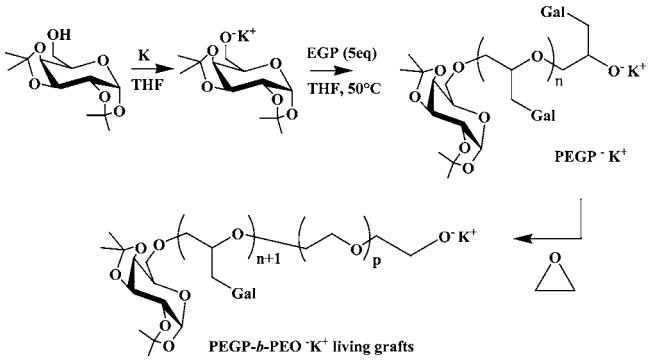

radii (in THF) from 34 nm (A) to 55 nm (I**)**, and from 25 nm (B) to 44 (II) and 36 nm (III**)** corroborated the successful chain extension from the acetal termini. Consistent with a living polymerization process, the resulting polymers exhibited unimodal and narrow molar mass distributions. The molecular weights of the dendrigrafts (evaluated by ^{1}H NMR and SLS) were ranging from 2.8 to 16.3 $\times$ 10^7 g·mol^{-1}, and the number of galactopyranose groups introduced on each dendrigraft scaled from 25 $\times$ 10^3 (III) to 96 $\times$ 10^3 (I). It is worth noting that the number of Gal per macromolecule is significantly higher than the values reported with linear or graft saccharidic copolymers (typically less than 2000 Gal/macromolecule) (*14*, *15*).

After regeneration of the hydroxyl functions, I and II were soluble in water while III could only be dissolved in MeOH, likely due to the presence of short PHEVE and PGVE blocks. Dynamic light scattering analysis confirmed that the unprotected dendrigrafts behave as unimeric macromolecules in water (I and II).

Synthesis of the Water-Soluble Dendrigrafts IV. The second approach aimed at the preparation of water-soluble dendrigrafts with PEO-*b*-PEGP external branches, considering that the PEGP blocks bearing the reactive saccharidic groups would enable the binding of NH_2-terminated oligonucleotides, while the PEO blocks would ensure the water solubility of the dendrigraft and improve, as spacers, the accessibility of the Gal units. The synthesis of these amphiphilic dendrigrafts was achieved by grafting living polyoxirane chains onto the activated chloroethyl functions of PCEVE external blocks of $PCEVE_1$-*g*-(PS_1-*b*-$PCEVE_2$) precursors (C: 200/120/40).

Living PEGP-*b*-PEO^- K^+ diblock copolymers were first obtained by anionic polymerization (Scheme 2). SEC analysis clearly established the preparation of narrow dispersed diblock chains (PDI = 1.14). The exact composition and molar mass of the copolymer were determined by ^{1}H NMR and VPO analysis of PEGP-*b*-PEO: $\overline{DP}_{n\mathrm{PEGP}} = 5$; $\overline{DP}_{n\mathrm{PEO}} = 90$.

Amphiphilic dendrigrafts IV were subsequently prepared by grafting living PEGP-*b*-PEO^- K^+ oxanionic species onto $PCEVE_1$-*g*-(PS_1-*b*-$PCEVE_2$) precursors (C) in the presence of NaI as activator (see Scheme 1**,** step 3′). After reaction, the hyperbranched polymer was separated from free PEGP-*b*-PEO chains by selective precipitation. The SEC analysis of the dendrigrafts (Figure 1) confirmed the unimodal and narrow molar mass distribution of IV. The main dimensional characteristics of IV are collected in Table 2. The previous characterization of C enabled us to calculate, by ^{1}H NMR, the yield of PEGP-*b*-PEO grafting, the final molar mass of dendrigraft IV, and the number of Gal units per dendrigraft. The poor reactivity of the oxanionic species resulted in low efficiency of grafting (15%), giving birth, after deprotection of the hydroxyl groups, to water-soluble dendrigrafts displaying a low peripheral density and bearing about 6100 Gal units each. In contrast to the cases of dendrigrafts I and II, the dynamic light scattering analysis revealed the presence of a few aggregates (constituted of two to three dendrigrafts) in aqueous solution (see Figure 2).

Table 2. Dimensional and Solution Characteristics of the Amphiphilic Polyoxirane-Based Dendrigraft IV Synthesized from Precursor C

ref	IV
PEGP-*b*-PEO grafting yield (%)	15
$\overline{M}_{n\mathrm{RMN}} \times 10^{-6}$ (g·mol^{-1})[a]	8.8
$\overline{M}_{w\mathrm{LS}} \times 10^{-6}$ (g·mol^{-1}) (THF)[a]	10.6
PDI	1.16
R_h[b] (THF) (nm)	30
R_h[c] (water) (nm)	39
Nb of Gal/dendrigraft	6120

[a] Protected dendrigraft. [b] Measured by DLS at 25 °C. [c] Measured by DLS at 25 °C on the unprotected dendrigraft.

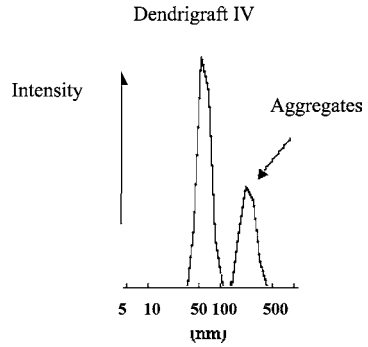

Figure 2. Hydrodynamic radius of deprotected dendrigraft IV in water measured by dynamic laser light scattering.

Characterization by Tapping-Mode Atomic Force Microscopy (TMAFM). TMAFM characterization of PHEVE- and PGVE-functionalized dendrigrafts (especially I) with a high grafting density of PVE hydrophilic blocks has been described in a previous paper (*20*). In this case, individual molecules can be easily observed as unique olivelike shaped objects with a diameter of about 100 nm (Figure 3, left). In this work, we mainly focused on the molecular characteristics of dendrigraft IV with PEO_{90}-*b*-$PEGP_5$ external hydrophilic blocks, which exhibits a lower peripheral grafting density (15%). The typical morphology of submonolayer deposits obtained by drop casting of 0.02 wt % MeOH solutions on mica is shown in Figure 3, right. Deposits of IV exhibit both globular and wormlike structures. The globular structures, more clearly seen in the topographic image inset (c) of Figure 3, correspond to unimeric dendrigrafts exhibiting a narrow size distribution (diameter = 22 nm $\pm$ 2 nm), in agreement with the low polydispersities measured in solution by SEC. The much reduced size of IV measured here by AFM, compared to the DLS data of Table 2 (diameter 22 nm as solid deposit vs 60 nm in THF), most probably arises from the fact that AFM measurements are performed in the dry state while the DLS values in a good

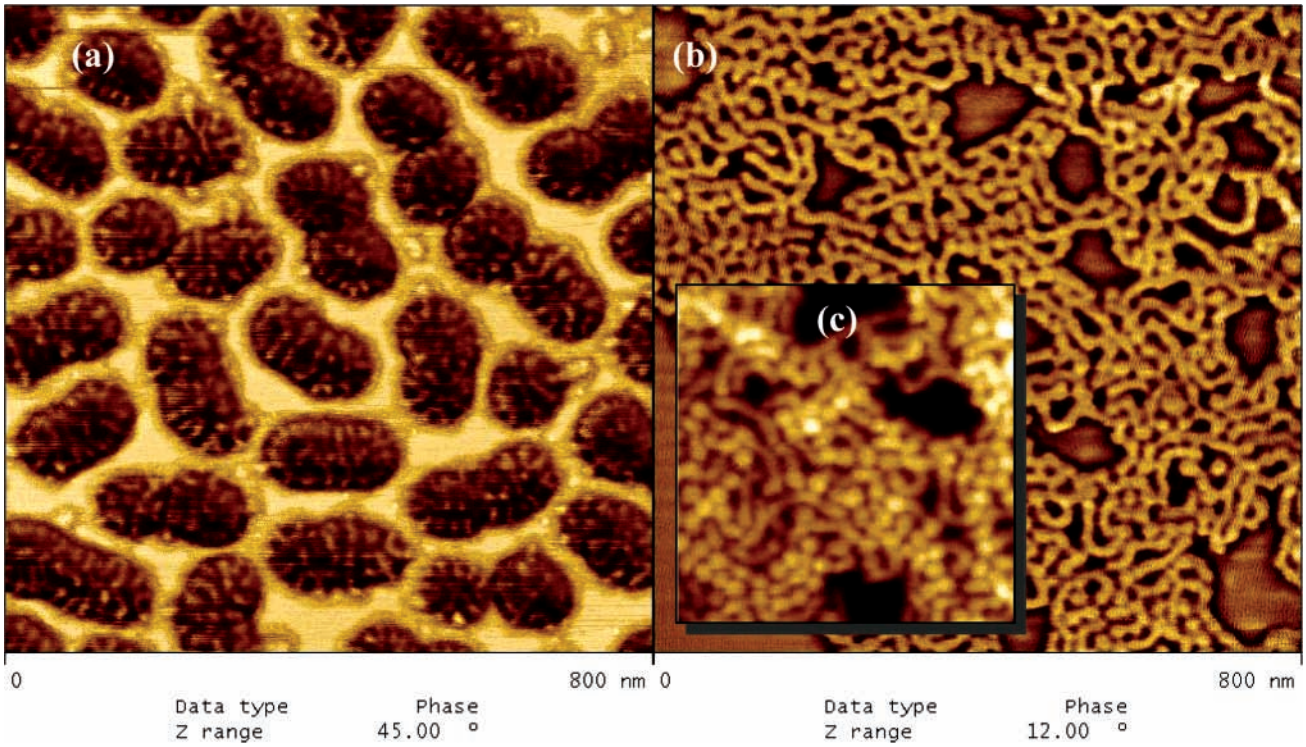

Figure 3. Tapping mode AFM (800 × 800 nm^2) phase image of a monolayer of the dendrigraft IV obtained from a 0.002 wt % methanol solution deposited on mica (b). The inset (c) shows a higher resolution (400 × 400 nm^2) topographic image. The left image (a) shows, as a comparison, the morphology of the dendrigraft I deposited from a 0.01 wt % THF solution on mica.

Scheme 3. Preparation of Dendrigraft−ODN Capture Conjugates Using a Simple One-Step Coupling Procedure (Schiff Base) with Amino-Ended ODNs

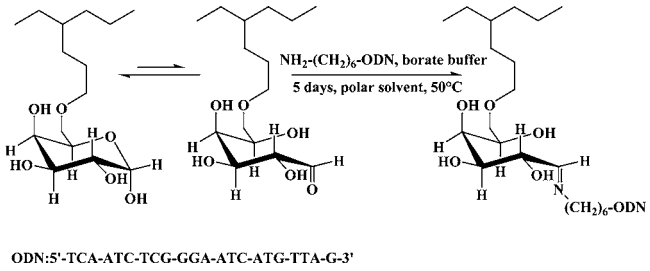

ODN:5'-TCA-ATC-TCG-GGA-ATC-ATG-TTA-G-3'

solvent correspond to swollen molecules. This is in contrast with the close diameter observed for I in the dry state and in solution (100 nm as solid vs 110 nm in THF). The presence of wormlike structures for IV, with a length up to 300 nm and a constant width corresponding to the diameter of unimeric dendrigrafts, clearly results from unidirectional assemblies of a large number of dendrigrafts. This organization also strongly contrasts to the one observed for dendrigraft I. Such an intermolecular organization and the size reduction of IV could be interpreted as the consequence of the quite low density of peripheral branches, which allows hydrophobic (PCEVE, PS) and hydrophilic domains of several dendrigrafts to interpenetrate, whereas the much higher lateral grafting density in I makes it much more compact, avoiding swelling and interpenetration phenomena.

Preparation of Dendrigraft−ODN Conjugates and ELOSA Tests. The covalent binding of DNA sequences on the dendrigraft surface was performed in aprotic polar solvent (DMSO, DMF, or NMP)/(aqueous buffer) mixtures, by reaction of the primary amine at the 5′-end of the ODNs with the aldehyde function at the anomeric position of the galactopyranose residues (formation of a Schiff base) as shown in Scheme 3. Various parameters such as the Gal/ODN molar ratio, the (organic solvent)/(aqueous buffer) volume ratio, the nature of the solvent, the ionic strength, and the pH of the aqueous buffer were tuned to optimize the coupling reaction. Due to the size of the dendrigraft−ODN conjugates and their tendency to form aggregates in organic/aqueous mixtures, it was not possible to follow the coupling reaction by SEC as previously reported (*7*, *9*, *10*) by comparing the relative peak areas of the bound ODNs and the unreacted ODNs. Formation of aggregates during the coupling reaction had already been reported for polymer−ODN conjugates (*7*) and had been attributed to possible side reactions from heterocyclic base amino groups and/or hydrogen bondings between the polymer and the ODNs. Finally, the presence of covalently bound ODNs on the dendrigrafts was indirectly evaluated by a capture test.

The ability of the prepared dendrigraft−ODN conjugates to capture short complementary ODNs (25 bases) through hybridization was studied on the Vidas instrument. As these complementary ODNs were labeled with an alkaline phosphatase enzyme, addition of methylumbelliferyl phosphate substrate led to the appearance of a fluorescence signal (Scheme 4A). The main results of the capture tests performed with I, II, III, and IV dendrigraft−ODN conjugates are reported in Table 3.

Except III, the dendrigrafts were all suitable for the elaboration of dendrigraft−ODN capture conjugates, as revealed by the high fluorescence signal obtained under specific coupling conditions. The nature of the organic solvent, the (organic solvent)/(aqueous buffer) volume ratio, and the Gal/ODN molar ratio appeared to be the main parameters of the coupling reaction. In contrast, no influence of the buffer ionic strength or pH was observed.

To estimate the proportion of ODNs immobilized on the dendrigrafts by physical adsorption, a run was carried out using an ODN without an amino spacer arm (run 6 to be compared with run 4). This test indicated that the amount of adsorbed ODNs was low (the signal was of the same order of magnitude as that of the control run performed without dendrigrafts). Although partially due to adsorption phenomena, the fluorescence signals obtained with I−ODN, II−ODN, or IV−ODN capture conjugates clearly confirmed the presence of ODNs

Table 3. Preparation Conditions of the Dendrigraft−ODN Conjugates and Performance of the Capture Tests

run	dendrigraft	solvent	org/aq v/v ratio	pH of borate buffer	Gal/ODN ratio (nmol)	optimal signal (RFU) capture test
1	I	NMP	97/3	9.2	∼60	1100
2	I	DMF	97/3	9.2	∼60	9400
3	II	DMF	50/50	7.2	20	2200
4	II	DMF	50/50	7.2	100	6800
5	II	DMF	50/50	7.2	300	8700
6	II	DMF	50/50	7.2	100	1900[a]
7	III	DMSO	96/4	7.2	100	2600
8	III	DMSO	96/4	7.2	100	2900[a]
9	IV	DMF	90/10	9.2	4	10500
10	IV	DMF	90/10	9.2	10	10500
11	IV	DMF	90/10	9.2	20	10500
12[b]						2600

[a] "Coupling reaction" performed using ODNs without NH_2-ended spacer arm. [b] Control run without dendrigrafts (labeled ODNs only).

Scheme 4. Principles of the Capture Test (A, top) and of the Complete Sandwich Hybridization Assay (ELOSA Diagnostic Test) with Capture and Detection Amplification (B, bottom)

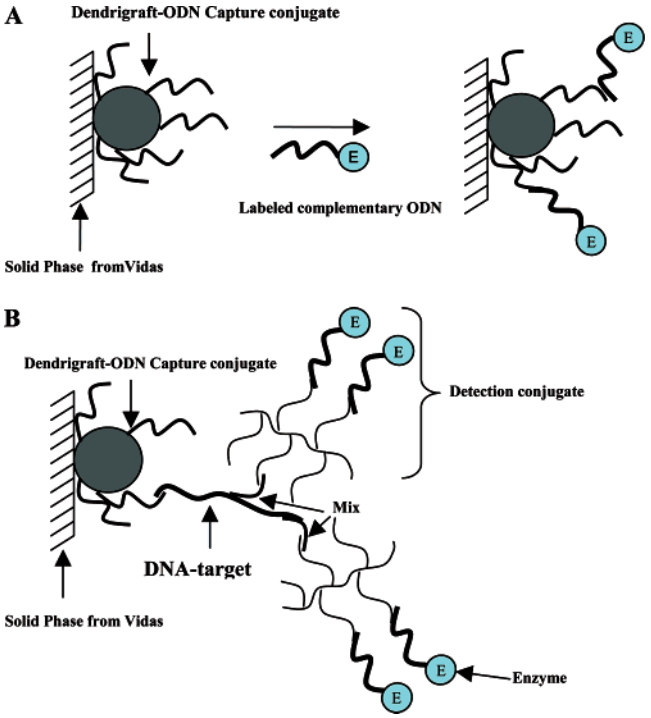

bound at the periphery of the dendrigrafts and their availibility for hybridization. In contrast, concerning III−ODN conjugates (run 7), the detected signal was attributed only to the presence of some adsorbed ODNs, since the run performed using ODNs without an amino spacer arm produced a similar fluorescence signal (run 8). This result clearly underlines the influence of the hydrophilic spacer block (PHEVE) on the ODN coupling reaction and the necessity to grow long PHEVE blocks (III: $\overline{DP}_{n\mathrm{PHEVE}} = 11$; I and II: $\overline{DP}_{n\mathrm{PHEVE}} = 90$ and 110, respectively) to improve the accessibility of the Gal moieties and consequently to favor the binding of ODNs.

The conjugates synthesized from I and IV provided high fluorescence signals with moderate Gal/ODN ratios (4−60) (see runs 2, 9, 10, and 11) whereas in the case of II it was necessary to perform the coupling reactions with high Gal/ODN ratios (∼100−300) to obtain a significant signal (runs 4 and 5). Although it remains difficult to draw conclusions, this unexpected trend could be correlated to the short saccharidic block ($\overline{DP}_n = 4$) at the periphery of dendrigraft II. In addition, in opposition to the case of I or IV, the ODN coupling reaction with II was more efficient at a higher water content (50% v/v instead of 10% v/v).

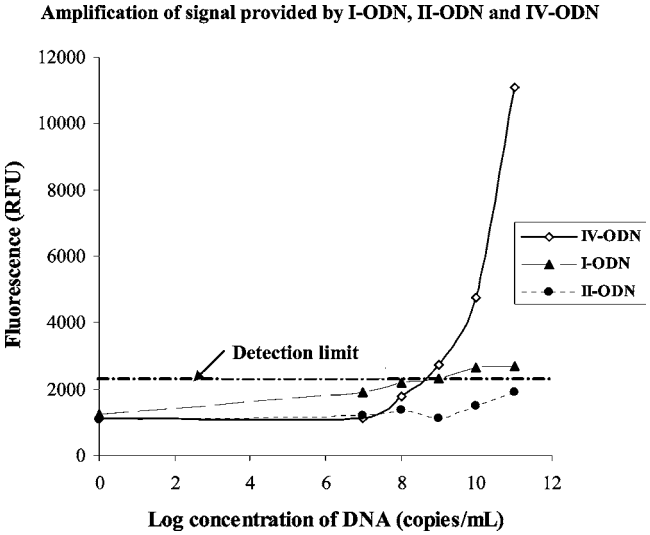

Figure 4. Complete sandwich hybridization assays (ELOSA tests) with capture and detection amplification (I−ODN, II−ODN, and IV−ODN, runs 2, 5, and 11).

Finally, IV appeared to have the best structure to favor the binding of ODNs, since a Gal/ODN ratio of 4 was enough to give a saturation signal (run 9). In comparison with I, IV is smaller ($R_h = 30$ instead of 55 nm in THF) and thus has a much higher specific area (1086 instead of 155 m^2 per gram). In addition, each dendrigraft IV bears an average of 6100 Gal residues (instead of 96 000 for dendrigraft I) and thus a lower saccharidic density at the surface which favors accessibility (0.32 and 2.52 Gal/nm^2 for IV and I, respectively). Consequently, the more favorable structure for the binding of ODNs seems to correspond to dendrigrafts of 60 nm diameter bearing a moderate number of Gal residues located at the end of long hydrophilic spacer arms.

Complete sandwich hybridization assays (ELOSA tests) with capture and detection amplification were further performed with a HBV DNA target (∼2400 bases) (Scheme 4B). Each dendrigraft−ODN capture conjugate which had provided a high fluorescence signal in the capture test was evaluated (I−ODN, II−ODN, and IV−ODN, runs 2, 5, and 11, respectively). The different dendrigraft−ODN capture conjugates were independently compared in the presence of a detection conjugate prepared from a saccharidic graft copolymer (AF112) (*14*, *15*). The results of the different tests are presented in Figure 4.

Despite the presence of ODNs on each conjugate, the results clearly showed that the conjugates made from IV (the dendrigraft of lowest external branch density) were the only ones leading to an increase in sensitivity. I- and II-based conjugates did not provide a significant increase in sensitivity since the signal/noise ratio remained very low (≤2) even at high

Table 4. Amplification Performances of IV−ODN Conjugates in Complete Sandwich Hybridization Assays (ELOSA Diagnostic Tests) with Capture and Detection Amplification

polymer−ODN capture conjugate	signal/noise ratio (10^{11} DNA copies/mL)	signal/noise ratio (10^9 DNA copies/mL)
AF112−ODN[a]	13.5	2.9
IV−ODN (run 9)	7.6	1.7
IV−ODN (run 11)	10	2.5
capture ODN[b]	1.4	1

[a] Polymer−ODN capture conjugate made from a saccharidic graft copolymer (AF112) (*15*) bearing an average of 650 Gal residues per copolymer. [b] Control run without dendrigraft−ODN capture conjugate (ODNs alone).

concentrations of DNA (10^{11} copies/mL). The difference of behavior between I−ODN, II−ODN, and IV−ODN conjugates was correlated with the relative steric hindrance induced by the external structure of conjugates I and II. In comparison with the case of IV−ODN, the high external density of saccharidic residues could affect the availability of the immobilized capture ODNs and/or prevent either the approach or the hybridization of the target of 2400 nucleic bases and/or prevent the approach or the hybridization of the detection conjugate. It was not possible to determine which of these steps was finally responsible for the low resulting signal.

In the case of IV−ODN, the signal/noise ratio was equal to 8−10 at 10^{11} DNA copies per mL and was still superior to 2 (which is the detection limit) at 10^9 DNA copies per mL (Table 4). In comparison, the same test without dendrigrafts (with capture ODNs alone) reached the same detection limit for 10^{11} DNA copies per mL and thus was 100 times less sensitive. Moreover, the background signal provided by the IV−ODN conjugate was relatively low (1000 RFU, a value similar to that of linear copolymers) (*9*).

Finally, it was interesting to compare these dendrigraft−ODN conjugates (IV−ODN) with a capture conjugate based on a saccharidic graft copolymer, AF112−ODN, bearing on average 650 ODNs per copolymer chain. In both cases, the sensitivity of the test reached 10^9 DNA copies per mL (Table 4), confirming the interest of the less crowded dendrigrafts bearing a moderate number of external branches and Gal residues for such diagnostic tests.

In summary, two families of amphiphilic water-soluble dendrigrafts exhibiting well controlled dimensions and bearing saccharidic moieties have been synthesized. The presence of external galactopyranose groups on these polymers has been exploited to prepare dendrigraft−oligonucleotide capture conjugates via a simple one-step coupling procedure (Schiff base) using amino-ended ODNs. A capture test with short labeled complementary ODNs (25 bases) confirmed the presence of covalently bound ODNs on various kinds of dendrigrafts (I, II, and IV) except for the dendrigraft (III) displaying short hydrophilic spacer blocks, which led exclusively to some ODN adsorption.

The conjugates made from I, II, and IV were finally evaluated in a nucleic acid detection test with a real DNA target from hepatitis B virus, HBV DNA with 2400 nucleic bases. The IV−ODN conjugate which possesses a low saccharidic external density (6120 Gal per dendrigraft) was the only capture conjugate leading to a significant amplification of the fluorescence signal, corresponding to a limit of sensitivity of 10^9 DNA copies per mL (instead of 10^{11} DNA copies per mL without using dendrigrafts) and a low background signal. Conversely, despite the large number of galactopyranose groups located at their periphery (respectively 96 000 and 33 000), I and II were not able to induce a better sensitivity of the test, probably due to the steric hindrance generated by the peripheral congestion of these polymers.

ACKNOWLEDGMENT

The authors would like to thank Arnaud Favier (Unité Mixte CNRS-bioMérieux) for the sample of the saccharidic graft copolymer AF112 and Aude Dassonville (Unité Mixte CNRS-bioMérieux) for some help with the ELOSA tests. We would also like to acknowledge the cooperation agreement (Tournesol) between France (LCPO) and the Communauté Française de Belgique (Mons) for financial support.

LITERATURE CITED

(1) Abramson, R., and Myers, T. W. (1993) Nucleic acid amplification technologies. *Curr. Opin. Biotechnol. 4*, 41−47.

(2) Nelson, P. S., Sherman-Gold, R., and Leon, R. (1989) A new and versatile reagent for incorporating multiple primary aliphatic amines into synthetic oligonucleotides. *Nucleic Acids Res. 17*, 7179−7186.

(3) Haralambidis, J., Duncan, L., Angres, K., and Tregear, G. W. (1990) The synthesis of polyamide-oligonucleotide conjugate molecules. *Nucleic Acids Res. 18*, 493−499.

(4) Grzybowski, J., Will, D. W., Randall, R. E., Smith, C. A., and Brown, T. (1993) Synthesis and antibody-mediated detection of oligonucleotides containing multiple 2,4-dinitrophenyl reporter groups. *Nucleic Acids Res. 21*, 1705−1712.

(5) Horn, T., Werner, B. D., Running, J. A., Downing, K., Clyde, J., and Urdea, M. S. (1989) The synthesis of branched oligonucleotides as signal amplication multimers for use in nucleic acid assays. *Nucleosides Nucleotides 8*, 875−877.

(6) Chang, C. A., Horn, T., Ahle, D., and Urdea, M. S. (1991) Improved methods for the synthesis of branched DNAb(DNA) for use as amplification multimers in bioassays. *Nucleosides Nucleotides 10*, 389−392.

(7) Erout, M. N., Troesch, A., Pichot, C., and Cros, P. (1996) Preparation of conjugates between oligonucleotides and N-vinylpyrrolidone/N-acryloxysuccinimide copolymers and applications in nucleic acid assays to improve sensitivity. *Bioconjugate Chem. 7*, 568−575.

(8) Ladaviere, C., Veron, L., Delair, T., Domard, A., Pichot, C., and Mandrand, B. (1997) Reactive polymers in diagnostics: synthesis and characterizations of nucleic acid probes and maleic anhydride-*co*-methyl vinyl ether polymers. *J. Appl. Polym. Sci. 65*, 2567−2577.

(9) Delair, T., Badey, B., Charles, M. H., Laayoun, A., Domard, A., Pichot, C., and Mandrand, B. (1997) Conjugation of nucleic acid probes to 6-aminoglucose-based homo and copolymers. II. Application to diagnostics. *Polym. Adv. Technol. 8*, 545−555.

(10) Delair, T., Charles, M. H., Cros, P., Laayoun, A., Mandrand, B., and Pichot, C. (1998) Synthesis and characterization of nucleic acid-(co)polymer conjugates: application to diagnostics. *Polym. Adv. Technol. 9*, 349−361.

(11) Véron, L., de Bignicourt, M. C., Delair, T., Pichot, C., and Mandrand, B. (1996) Synthesis of poly[N-(2,2-dimethoxyethyl)-N-methacrylamide] for the immobilization of oligonucleotides. *J. Appl. Polym. Sci. 60*, 235−244.

(12) Badey, B., Boullanger, P., Domard, A., Cros, P., Delair, T., and Pichot, C. (1996) Radically initiated polymerization of a methacryloylamido-terminated saccharide. Part 1. Monomer synthesis, homopolymerization and characterizations. *Macromol. Chem. Phys. 197*, 3711−3728.

(13) D'Agosto, F., Charreyre, M. T., Pichot, C., and Mandrand, B. (2002) Polymer of controlled chain length carrying hydrophilic galactose moieties for immobilization of DNA probes. *Macromol. Chem. Phys. 203*, 146−154.

(14) D'Agosto, F., Charreyre, M. T., Melis, F., Pichot, C., and Mandrand, B. (2003) High molecular weight hydrophilic functional copolymers by free radical copolymerization of acrylamide and of N-acryloylmorpholine with N-acryloxysuccinimide: Applications to the synthesis of a graft copolymer. *J. Appl. Polym. Sci. 88*, 1808−1816.

(15) Favier, A. (2002) Ph.D. Thesis, Claude Bernard University, Lyon I.

(16) Minard-Basquin, C., Chaix, C., Pichot, C., and Mandrand, B. (2000) Oligonucleotide-polymer conjugates: Effect of the method of synthesis on their structure and performance in diagnostic assays. *Bioconjugate Chem. 11*, 795−804.
(17) Minard-Basquin, C., Chaix, C., D'Agosto, F., Charreyre, M. T., and Pichot, C. (2004) Oligonucleotide synthesis onto poly(N-acryloylmorpholine-*co*-N-acryloxysuccinimide): Assessement of the resulting conjugates in a DNA sandwich hybridization. *J. Appl. Polym. Sci. 92*, 3784−3795.
(18) Charreyre, M. T., Hiver, A., Delair, T., Cros, P., Pichot, C., Mandrand, B., Tcherkasskaya, O., and Winnik, M. A. (1997) Fluorescence energy transfer study of the conformation of oligonucleotides covalently bound to polystyrene latex particles. *Langmuir 13*, 3103−3110.
(19) Elaissari, A., Chevalier, Y., Ganachaud, F., Delair, T., and Pichot, C. (2000) Structure of adsorbed and grafted single-stranded DNA fragments on aminated latex particles. *Langmuir, 16*, 1261−1269.
(20) Schappacher, M., Deffieux, A., Putaux, J. L., Viville, P., and Lazzaroni, R. (2003) Synthesis and characterization of water-soluble amphiphilic polystyrene-based dendrigrafts. *Macromolecules 36*, 5776−5783.
(21) Muchtar, Z., Schappacher, M., and Deffieux, A. (2001) Hyperbranched nanomolecules: Regular polystyrene dendrigrafts. *Macromolecules 34*, 7595−7600.
(22) Fukui, H., Yoshihashi, S., Sawamoto, M., and Higashimura, T. (1996) Multifunctional coupling agents for living cationic polymerization. 7. Synthesis of amphiphilic tetraarmed star block polymers with α-methylstyrene and 2-hydroxyethyl vinyl ether segments by coupling reactions with tetrafunctional silyl enol ether. *Macromolecules 29*, 1862−1866.
(23) Koell, P., Saak, W., Pohl, S., Steiner, B., and Koos, M. (1994) Preparation and crystal and molecular structure of 6-O-[(2S)-2,3-epoxypropyl]-1,2:3,4-di-O-isopropylidene-galactopyranose. Pyranoid ring conformation in 1,2:3,4-di-O-isopropylidene-galactopyranose and related systems. *Carbohydr. Res. 265*, 237−248.
(24) Schappacher, M., Bernard, J., and Deffieux, A. (2003) Functional polystyrene combs and dendrigrafts, 1- Selective introduction of dihydroxymethyl functions at their periphery. *Macromol. Chem. Phys. 204*, 762−769.

BC049708J

Unilamellar Liposomes with Enhanced Boron Content

Tiejun Li, Julie Hamdi, and M. Frederick Hawthorne*

Department of Chemistry and Biochemistry, University of California, Los Angeles, 607 Charles E. Young Drive East, Los Angeles, California 90095. Received May 5, 2005; Revised Manuscript Received October 20, 2005

A new type of boron-rich, DSPC-free, unilamellar liposomes was formed using the novel dual-chain, ionic, *nido*-carborane lipid, K[nido-7-($C_{16}H_{33}OCH_2$)$_2$CHOCH$_2$-7,8-$C_2B_9H_{11}$] (DAC-16), and cholesterol for encapsulation of an aqueous buffer core. Since DSPC was not necessary for the formation of stable DAC-16 liposomes, the boron concentration of these vesicles was increased dramatically to approximately 8.8 wt % in the dry lipid; these liposomes had a high bilayer boron incorporation efficiency of 98%. DSPC-free liposomes exhibited a size distribution pattern of 40−60 nm, which was in the range normally associated with selective tumor uptake. This size distribution was maintained throughout storage at room temperature for several months. Additionally, optimized liposome formulations incorporating DAC-16, DSPC, and cholesterol were identified having stable size distribution patterns after storage for more than two months at a variety of temperatures. Although animal studies indicate that DAC-16 liposomes are toxic, this new ionic *nido*-carborane lipid allows the formation of liposomes of high boron content for in vitro applications that require the delivery of large amounts of boron.

INTRODUCTION

Unilamellar liposomes have been studied as drug delivery agents for more than 30 years because of their many unique properties, most notably the ability to selectively deliver large quantities of a wide variety of encapsulated agents to tumor sites (*1*, *2*). Rapidly growing tumors have leaky vasculature and immature capillary endothelia through which small liposomes (<100 nm) can pass (*3*). Because liposomes provide this tumor-targeting property, it is not necessary for the incorporated agent to have its own tumor-seeking capability. Additionally, liposome-encapsulated drugs have longer circulation life spans than the free drug, making it possible to achieve the same therapeutic level of treatment using a lower injected dose (*4*). At the same time, the toxic side-effects of some drugs are markedly reduced when the drug is encapsulated by liposomes that maintain their structural integrity in blood (*5*). Currently, there are several FDA-approved liposomal drugs available commercially and many more are in clinical trials (*6*).

In addition to their proven role as drug carriers, liposomes provide a promising solution to a major obstacle in the continued development of boron neutron capture therapy (BNCT), the selective delivery of therapeutic quantities of ^{10}B atoms to tumor cells (*7*−*9*). Nearly 30 years before the identification of liposomes as encapsulating drug carriers, BNCT was first proposed by Locher (*10*). BNCT is a binary cancer treatment based on the nuclear reaction of two essentially nontoxic species, ^{10}B and thermal neutrons. The neutron capture reaction produces $^7Li^{3+}$ and $^4He^{2+}$ ions together with 2.4 MeV of kinetic energy and a 480 keV photon. With a range of only one cell-diameter, these highly energetic ions are cytotoxic to the cell in which they are generated, allowing for the selective destruction of cells containing a minimum number of ^{10}B atoms (10^9 ^{10}B atoms per cell, representing approximately 30 mg ^{10}B per kg of tumor). The limited investment in the thorough evaluation of boron delivery agents has been one of the major limitations of the clinical development of BNCT. Another contributing factor has been the clinical preoccupation with glioblastoma multiforme, a fatal type of brain cancer. Over the past decades, various boron delivery methods have been explored in small animals, including boronated porphyrins, monoclonal antibodies, nucleosides, amino acids, oligomers, and liposomes (*11*−*13*), with varying degrees of success. The utilization of liposomes as ^{10}B delivery agents is a promising approach to meet the requirements of BNCT of tumors other than gliomas (*4*, *14*, *15*).

Liposomes for Use as Potential BNCT Agents. Small unilamellar liposomes, because of their tumor-targeting ability and biphasic nature (*1*, *2*), are ideal carriers for the transport of large quantities of both lipophilic and hydrophilic boron-containing species. Two distinct methods of boron localization in liposomes are possible: incorporation of lipophilic molecules into lipid bilayers and/or entrapment of hydrophilic compounds into a liposome's aqueous core. Previous work (*7*−*9*, *16*−*19*) has demonstrated this in the formation of three types of unilamellar liposomes (identified as liposome types A, B, and C) for the delivery of therapeutic quantities of boron (30 μg ^{10}B per gram of tumor tissue, or 10^9 ^{10}B atoms per tumor cell) (*20*) to tumor cells with high tumor/blood ratios using low injected doses. Liposomes of type A involved the encapsulation of hypertonic solutions of soluble borane salts within a distearoylphosphatidylcholine (DSPC)/cholesterol bilayer (*7*, *8*, *16*, *17*), while type B liposomes utilized a DSPC/cholesterol bilayer doped with boron-containing lipids to encapsulate an isotonic buffer solution (*9*, *18*), and type C liposomes represented a combined approach: the encapsulation of either a hyper- or isotonic aqueous solution of a borane salt within a bilayer composed of DSPC, cholesterol, and lipophilic borane compounds (*9*, *19*).

Type A liposomes were prepared from a lipid mixture containing equimolar quantities of DSPC and cholesterol to achieve enhanced serum stability while encapsulating an aqueous solution of borane salts such as $Na_3B_{20}H_{17}NH_3$ (TAC) (*7*, *8*, *16*, *17*). The size of the resultant liposomes is regulated by the liposome-formation method chosen: the reverse-phase evaporation method results in larger vesicles than are obtained by probe sonication. Although it was found that liposomes of up to 400 nm in diameter could still penetrate the tumor cell wall (*21*), liposomes created by probe sonication resulted in small unilamellar vesicles less than 100 nm in diameter that displayed

* To whom correspondence should be addressed. Fax: (310) 825-5490, E-mail: mfh@chem.ucla.edu.

10.1021/bc0501350 CCC: $33.50 © 2006 American Chemical Society
Published on Web 12/23/2005

selective uptake by tumor tissue and had a longer half-life in circulation than those with a larger diameter (*22*, *23*). Many water-soluble boron compounds encapsulated within these smaller type A liposomes were tested as BNCT agents (injected does of approximately 15 μg B per gram body weight), resulting in selective delivery of up to 47 μg of boron per g of tumor in BALB/c mice bearing EMT6 tumors without serious toxicity problems (*7*, *8*). Uptake of liposomes by the liver and spleen was normally observed and paralleled tumor uptake with time. Maximum boron content in tumor tissue was usually observed near 30 h postinjection (*8*, *17*).

In contrast to the many water-soluble borane ions investigated, only a few amphiphiles have been studied as bilayer addends to create type B liposomes that encapsulated a hyper- or isotonic saline or HPS (10 mM HEPES/375 mM NaCl, pH 7.4) buffer solution. The first amphiphilic carborane compound incorporated into a lipid bilayer, K[*nido*-7-$CH_3(CH_2)_{15}$-7,8-$C_2B_9H_{11}$] (referred to as MAC-16) (**1**), was synthesized and evaluated in biodistribution studies reported in 1994 (*9*, *18*). The compound had a high incorporation efficiency of 70% in liposome bilayers composed of DSPC and cholesterol. Biodistribution studies of these lipsomes in BALB/c mice bearing EMT6 tumors indicated that, 30 h postinjection, tumor-boron concentrations of up to 35 ppm were maintained following injected doses ranging from 99 to 188 μg of boron, while only very slight uptake by the liver and spleen was noted (*9*, *18*).

Further work revealed that in addition to incorporating lipophilic boron-containing species in the bilayer, it was also possible to create type C liposomes that encapsulated salts such as TAC within the aqueous cores of DSPC/cholesterol liposomes doped with **1** (*9*, *19*). These stable liposomes (**1**:DSPC: cholesterol ratio equals 1:3:3) displayed good biodistribution properties resulting in significantly enhanced boron delivery of up to 71 μg of boron per g of tumor in BALB/c mice bearing EMT6 tumors. Liposomes constructed with smaller molar proportions of DSPC and cholesterol stabilizer resulted in lower observed incorporation efficiencies and decreased physical stabilities. This restriction limited the amount of boron that could be incorporated into liposomes using **1** as a bilayer addend in type B and C liposomes. To improve the performance of these liposomes, the boron content of the amphiphilic bilayer addend could be increased while maintaining the necessary structural components, or alternatively, the DSPC and cholesterol might be removed and the bilayer formed completely from an amphiphilic boron derivative.

To pursue this concept, the synthesis and liposome-forming characteristics of a new amphiphilic addend composed of a *nido*-carborane anion appended to a dual hydrocarbon chain (**2**, see below) was reported (*24*) which formed liposomes of type B. In this paper the properties of the resulting liposomes and preliminary information obtained from initial animal toxicity studies is presented.

Recently, Nakamura and co-workers also reported the synthesis of a dual-chain *nido*-carborane compound, **3** (*25*), as illustrated in Figure 1. Similar to the results we report, liposomes formed from this compound showed suitable stability and addend incorporation properties, demonstrating that such *nido*-carborane species possess satisfactory liposome-forming properties and further support the results presented here. Unfortunately, biodistribution and in vivo toxicity data are not reported (*25*) for these liposomes.

EXPERIMENTAL SECTION

General. All reactions were performed under N_2 or Ar using Schlenk techniques. All reagents were purchased from commercial suppliers and used without further purification, while solvents were dried and distilled before use. Silica gel was obtained from Sorbent Technologies (60 Å, 32−63 μm).

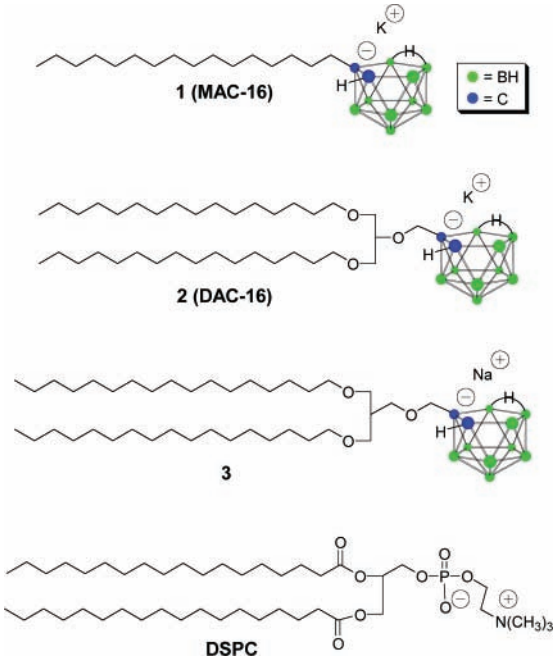

Figure 1. Structures of **1**, **2**, **3**, and DSPC.

The ^{11}B NMR spectra were obtained with a Bruker ARX500 spectrometer at 160 MHz and were externally referenced to BF_3·Et_2O; peaks upfield of the reference are designated as negative. The ^{1}H and ^{13}C NMR spectra were acquired at 500 and 126 MHz with Bruker ARX500 and AVANCE500 spectrometers, respectively. Mass spectra were obtained at the UCLA Pasarow Mass Spectrometry Laboratory. High-resolution EI spectra were acquired using a Micromass GCT EI Time-of-Flight Instrument; MALDI and electrospray spectra were acquired on an Ionspec 7.0 Ultima FTMS utilizing MALDI and ESI sources. The ICP-AES analysis of boron was performed at Idaho National Engineering and Environmental Laboratory (INEEL, Idaho Falls, ID) using a Thermo Iris instrument. The toxicity evaluation was performed at Washington State University.

1,3-Bis-hexadecyloxy-propan-2-ol (4). According to previously reported literature precedent (*26*), sodium hydride (60% in mineral oil, 2.1 g, 53 mmol) was added in small portions to 1-hexadecanol (26.5 g, 109 mmol) at 100 °C. After stirring for 0.5 h, epichlorohydrin (1.0 mL, 12.8 mmol) was added dropwise to the hot mixture and maintained at 100 °C overnight, after which water (2 mL) was added to quench the reaction. The filtrate (obtained in ether after extraction of the crude reaction mixture) was washed with water (3 × 100 mL) and dried with anhydrous $MgSO_4$ before the ether was removed under reduced pressure. Excess 1-hexadecanol was removed by vacuum distillation. The crude product was recrystallized from ethyl acetate at 4 °C to yield a white solid (6.16 g, 89.0%) that was isolated by filtration and dried under vacuum. Mp 54−55.2 °C. ^{1}H NMR (500 MHz, $CDCl_3$): δ 0.88 (t, 6H, ^3J = 6.9, CH_3), 1.25 (br, 52H) ($(CH_2)_n$), 1.55 (m, 4H, OCH_2CH_2), 2.47 (d, ^{1}H, ^3J = 4.1, O*H*), 3.45 (m, 8H, OCH_2), 3.93 (m, 1H, C*H*). ^{13}C-{^{1}H} NMR (500 MHz, $CDCl_3$): δ 14.0 (CH_3), 22.6 (CH_3CH_2), 26.0 ($OCH_2CH_2CH_2$), 29.2−29.6 ($(CH_2)_n$), 31.8 (OCH_2CH_2), 69.4 (CH), 71.6 (OCH_2), 71.7 (OCH_2). IR: 3481.44 cm^{-1} (OH stretch), 2957.91−2849.30 cm^{-1} (sp^3-CH stretch), 1471.64 cm^{-1} (sp^3-CH bend), 1126.41 cm^{-1} (C−O stretch), and 719.62 cm^{-1} (CH_2 long-chain band).

1,3-Bis-hexadecyloxy-2-(prop-2-ynyloxy)-propane (5). Into a 25 mL round-bottom flask were added 1,3-bis-hexadecyloxy-propan-2-ol (1.0 g, 1.8 mmol), NaOH (4.0 g, 100 mmol), NBu_4HSO_4 (0.4 g, 1.2 mmol), water (3 mL), and benzene (12 mL). After stirring for 5 min, propargyl bromide (80% in toluene,

0.23 mL, 2.1 mmol) was added dropwise. The reaction mixture was stirred at room temperature for 3 days and then extracted with ether and brine. The organic layer was collected, and the solvent was removed under reduced pressure. Purification by column chromatography on silica gel (5% ether in pentane) yielded the pure product as a white solid (0.44 g, 41%). Mp 43.8−45.5 °C. ^{1}H NMR (500 MHz, $CDCl_3$): δ 0.87 (t, 6H, ^3J = 7.0, CH_3), 1.25 (br, 52H) ((CH_2)$_n$), 1.55 (m, 4H, OCH_2CH_2), 2.39 (t, 1H, ^4J = 2.4, CCH), 3.41−3.54 (m, 8H, OCH_2), 3.83 (m, 1H, C*H*), 4.33 (d, 2H, ^4J = 2.4, $CHCCH_2$). ^{13}C{^{1}H} NMR (126 MHz, $CDCl_3$): δ 14.0 (CH_3), 22.7 (CH_3CH_2), 26.1 ($OCH_2CH_2CH_2$), 29.4−29.7 ((CH_2)$_n$), 31.9 (OCH_2CH_2), 57.6 ($CHCCH_2$), 70.8 (OCH_2), 71.7 (OCH_2), 73.9 (*C*HC), 76.6 (*C*H), 80.3 (CH*C*). HRMS (EI+): calculated for $C_{38}H_{74}O_3$ (M^+): 578.5638, found: 578.5634 (Δ = 0.7 ppm). IR: 3241.86 cm^{-1} (sp-CH stretch), 2953.46−2847.59 cm^{-1} (sp^3-CH stretch), 2113.98 cm^{-1} (sp-CC stretch), 1472.56 cm^{-1} (sp^3-CH bend), 1122.87 cm^{-1} (C−O stretch), and 716.75 cm^{-1} (CH_2 long-chain band).

***closo*-1-($C_{16}H_{33}OCH_2$)$_2$CHOCH_2-1,2-$C_2B_{10}H_{11}$ (6).** Decaborane (0.211 g, 1.7 mmol) was dissolved in toluene (15 mL) and acetonitrile (5 mL), and the mixture was heated at reflux for 5 h. To this solution was added **5** (1.0 g, 1.7 mmol) in toluene (10 mL) at room temperature. After refluxing for 3 d, the reaction mixture was cooled to room temperature followed by the addition of a 5% NaOH solution (20 mL) with continued stirring for an additional 3 h. Upon completion, the reaction mixture was extracted with ether. The organic fractions were collected, and the solvent was removed under reduced pressure. The crude product was purified by column chromatography on silica gel (10% ether in pentane) to yield the product as a white solid (0.623 g, 51.7%). Mp 33−34.5 °C. ^{1}H NMR (500 MHz, $CDCl_3$): δ 0.88 (t, 6H, ^3J = 7.0, C*H*$_3$), 1.26 (br, 52H) ((CH_2)$_n$), 1.54 (m, 4H, OCH_2CH_2), 3.38 (m, 8H, OCH_2), 3.66 (m, 1H, C*H*), 4.09 (s, 2H, CCH_2), 4.44 (br, 1H, BC*H*). ^{13}C{^{1}H} NMR (126 MHz, $CDCl_3$): δ 14.1 (*C*H$_3$), 22.7 (CH_3CH_2), 26.1 ($OCH_2CH_2CH_2$), 29.4−29.7 ((CH_2)$_n$), 31.9 (OCH_2CH_2), 57.6 (B*C*H), 71.1 (OCH_2), 71.7 (OCH_2), 71.7 ($OCHCH_2$), 73.5(B*C*), 80.4 (*C*H). ^{11}B{^{1}H} NMR (160 MHz, $CHCl_3$): δ −3.1, −4.7, −8.8, −11.4, −13.0. HRMS (electrospray): calculated for $C_{38}H_{83}O_3B_{10}$ ($M - H^-$): 696.7338, found: 696.7349 (Δ = 1.5 ppm). IR: 3018.15 cm^{-1}, 2919.12−2850.58 cm^{-1} (sp^3-CH stretch), 2593.05 cm^{-1} (B−H stretch), 1471.00 cm^{-1} (sp^3-CH bend), 1152.17−1087.17 cm^{-1} (C−O stretch), and 716.39 cm^{-1} (CH_2 long-chain band).

K[*nido*-7-($C_{16}H_{33}OCH_2$)$_2$CHOCH_2-7,8-$C_2B_9H_{11}$] (2). *closo*-1-($C_{16}H_{33}OCH_2$)$_2$CHOCH_2-1,2-$C_2B_{10}H_{11}$ (1.0 g, 1.4 mmol) and KOH (0.5 g, 8.9 mmol) were added to absolute ethanol (30 mL), and the mixture was heated at reflux for 10 h. Completion of the reaction was confirmed by TLC, after which a stream of CO_2 gas was injected into the solution to precipitate K_2CO_3. The precipitate was removed by filtration, and the solvent was removed from the filtrate under reduced pressure. The pure product was obtained as a white solid after recrystallization from benzene (1.0 g, 96.2%). ^{1}H NMR (500 MHz, $CDCl_3$): δ −3.0 (br, 1H, B*H*B), 0.88 (t, 6H, ^3J = 7.0, C*H*$_3$), 1.26 (br, 52H) ((CH_2)$_n$), 1.56 (m, 4H, OCH_2CH_2), 2.07 (br 1H, BC*H*), 3.37−3.65 (m, 11H). ^{13}C{^{1}H} NMR (126 MHz, $CDCl_3$): δ 14.1 (*C*H$_3$), 22.7(CH_3CH_2), 26.0 ($OCH_2CH_2CH_2$), 29.4−29.7 ((CH_2)$_n$), 31.9 (OCH_2CH_2), 69.3 (B*C*H), 70.5 ($CHCH_2O$), 72.0−72.1 (CCH_2O-, OCH_2CH_2), 77.1 (B*C*), 78.5 (*C*H). ^{11}B{^{1}H} NMR (160 MHz, $CHCl_3$): δ −10.8, −14.5, −16.7, −18.0, −19.4, −21.9, −33.1, −37.5. HRMS (MALDI): calculated for $C_{38}H_{84}O_3B_9$ (M^{1-}): 686.7321, found: 686.7307 (Δ = 2.0 ppm). IR: 2917.96−2849.71 cm^{-1} (sp^3-CH stretch), 2543.25 cm^{-1} (B−H stretch), 2488.52 cm^{-1} (BH_2 stretch), 1611.28 cm^{-1}, 1460.90 cm^{-1} (sp^3-CH bend), 1127.10 cm^{-1} (C−O stretch), and 718.65 cm^{-1} (CH_2 long-chain band).

Vesicle Preparation. Suspensions of DSPC-free liposomes were prepared by probe sonication of a dried film composed of an equimolar ratio of **2** and cholesterol (195.9 mg **2**, 104.1 mg cholesterol, 300 mg total weight) in PBS buffer solution (6 mL) at room temperature for 0.5 h. After sonication, the liposome suspensions were eluted with buffer solution through Sephadex G-25 (medium) columns to remove any unincorporated impurities. The eluent was diluted with blank buffer solution (∼12 mL) to a lipid concentration of 23−24 mg/mL and sterilized by filtration through a 0.22-μm Millipore membrane. The boron content of the liposome suspensions was determined by ICP-AES and reported in ppm (μg boron per g of suspension). The liposomal size distribution was determined by dynamic light scattering, with typical volume-weight mean vesicle diameters (m_v) averaging 40 nm.

The incorporation efficiency of **2** was determined separately using a second liposome sample prepared in a manner similar to that described above. After sonication, the unincorporated DAC-16 was separated from the lipid mixture by centrifugal filtration with Centricon membrane instead of elution with a Sephadex column. After centrifugation, the retentate contained the pure lipid mixture, while the filtrate contained the unincorporated compound, the quantity of which was determined by ICP-AES. In this manner the incorporation efficiency was determined to be 98% for DSPC-free liposomes that were 8.8% boron by weight in the dry lipid, resulting in a liposome suspension with a boron concentration of 1600 ppm (measured by ICP-AES).

Other liposome formulations from lipid mixtures containing DSPC (see Table 3) were prepared as described above, with the exception that the sonication temperature was raised from 23 to 60 °C. The workup and sterilization of these liposomes follows the procedure described above using Sephadex G-25 (medium) columns and 0.22-μm Millipore membranes.

Partition Coefficient Measurement of 2, 1, DSPC, and Phenylboronic Acid. The water and 1-octanol used in this study were mutually presaturated with each other prior to use. Stock solutions of the compounds (1.00×10^{-3} M) were prepared in 1-octanol. A mixture of each 1-octanol solution (10 mL) in water (40 mL) was shaken for 2 h to reach equilibrium before the emulsion that formed was broken by centrifugation. The concentration of the solute in the 1-octanol and water layers was measured by ICP-AES to determine the partition coefficient.

Preliminary in Vivo Evaluation of 2. The toxicity assessment of **2** was performed at Washington State University with BALB/c and normal mice according to their availability. Five sets of experiments were performed using liposomes composed of **2**, DSPC, and cholesterol in varying proportions to create vesicles with boron content ranging from 0 to 8.8% in the dry lipid (see Table 3). Serial dilution of each liposome suspension with PBS buffer was used to obtain diluted samples ranging in concentration from 300 to 1525 ppm. Samples of liposome suspensions (0.2 mL, representing injected doses of 6.0−30. mg B/kg mouse) were introduced through the tail vein and the behaviors of the mice were monitored over 2 days. With the exception of mice injected with the control formulation (1:1 ratio of DSPC:cholesterol), all mice injected with liposomes incorporating the potassium salt of **2** were dead within 24 h of the injection. Mice injected with liposomes incorporating the sodium salt of **2** appeared to be in shock after 24 h and were dead within 48 h.

RESULTS AND DISCUSSION

Lipidic DSPC is a commonly used structural component in the formulation of synthetic unilamellar liposomes. Like most phospholipids, DSPC consists of a zwitterionic choline-based headgroup in addition to the two hydrocarbon chains that make

Scheme 1. The Synthesis of 2

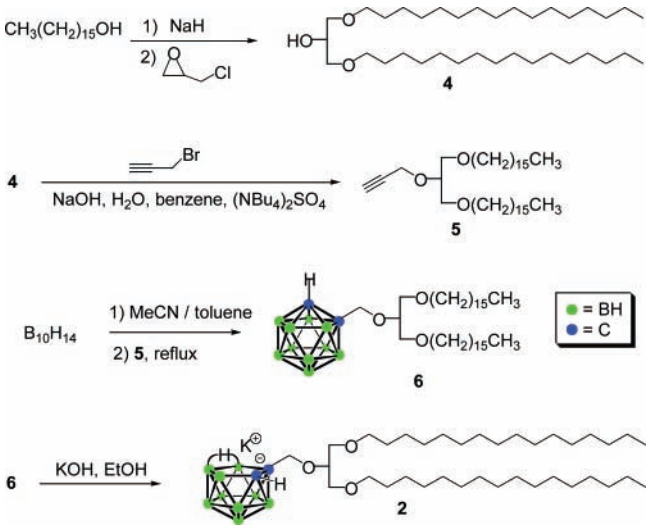

up the lipophilic tail moiety. The facile incorporation of **1** into phospholipid bilayers can be explained by its physical similarity to DSPC (Figure 1). Characterized by a 16-carbon alkyl chain appended to a negatively charged *nido*-carborane, **1** effectively mimics amphiphilic phospholipids leading to successful bilayer incorporation with an efficiency of about 70% (*8*, *9*). The negative surface charge of MAC-16 liposomes could also lead to better delivery efficiency of the encapsulated species, enhanced tumor selectivity, and increased stability (*27*) of these small unilamellar liposomes. These encouraging results led to the design of an anionic *nido*-carborane derivative to even more accurately imitate the structure of phospholipids such as DSPC. The species K[*nido*-7-$(C_{16}H_{33}OCH_2)_2CHOCH_2$-7,8-$C_2B_9H_{11}$] (referred to as DAC-16) (**2**) was synthesized in fulfillment of this goal (Figure 1). It was hoped that structurally sound boron-containing liposomes of increased boron content could be prepared from **2** and cholesterol in the absence of DSPC.

K[*nido*-7-$(C_{16}H_{33}OCH_2)_2CHOCH_2$-7,8-$C_2B_9H_{11}$] (DAC-16, 2). The synthesis of **2** began by reaction of the alkoxide ion derived from 1-hexadecanol and NaH with epichlorohydrin, according to the procedure described in the literature (*28*), to give 1,3-bis-hexadecyloxy-propan-2-ol (**4**) in 89% yield. Upon addition of propargyl bromide to the two-phase system comprised of benzene and aqueous 50% NaOH in the presence of NBu_4^+, **4** was converted (*29*) to 1,3-bis-hexadecyloxy-2-(prop-2-ynyloxy)-propane (**5**) in 41% yield. The reaction of $B_{10}H_{12}(CH_3CN)_2$, formed from the reaction of decaborane with acetonitrile in toluene, with the alkyne **5** (*30*−*32*) produced *closo*-1-$(C_{16}H_{33}OCH_2)_2CHOCH_2$-1,2-$C_2B_{10}H_{11}$ (**6**) in moderate yield (52%). Deboronation of **6** to form the corresponding anionic *nido*-derivative, **2**, was easily accomplished with potassium hydroxide in hot ethanol (*33*), and the product was purified by recrystallization from benzene (Scheme 1). The ^{11}B NMR spectrum of **2** contained resonances at −33.1 ppm and −37.5 ppm, which unequivocally confirmed the presence of the anionic *nido*-carborane derivative.

Liposome Formation. Species **2** and DSPC have comparable structural features, the most obvious similarity being the dual alkyl chains comprising their lipophilic regions. Like **1**, the ionic *nido*-carborane moiety of **2** serves as a hydrophilic group. On the basis of these features and the previously published work regarding MAC-16 and DSPC/cholesterol bilayer formation (*4*, *9*, *18*), **2** and DSPC/cholesterol were expected to display similar liposome-forming properties.

An assortment of Type B liposomes, composed of DSPC, cholesterol, and **2** in varying proportions, was prepared by probe sonication of the components in PBS buffer. The resulting small unilamellar liposomes incorporating isotonic saline buffer all exhibited excellent stability and size distribution patterns. The volume-weighted mean vesicle diameters (m_v) ranged from 40 to 60 nm, with all vesicles in the size range of 20 to 100 nm. In addition, DSPC-free liposomes composed of equimolar quantities of **2** and cholesterol were also prepared. Interestingly, the absence of DSPC did not inhibit bilayer formation, and resulted in liposomes with a markedly increased boron concentration that were stable for several months at room temperature. DSPC-free liposomes incorporating **2** (**2**:cholesterol ratio of 1:1) consisted of 8.8% boron by weight in the dry lipid mixture, a nearly 4-fold increase in boron concentration over the previous report (*18*) of optimized liposomes incorporating **1**, which contained 2.5% boron by weight in the dry lipid component (**1**:DSPC:cholesterol in a ratio of 1:3:3).

Table 1. Partition Coefficients of 2, 1, DSPC,[a] and $PhB(OH)_2$

	2	**1**	DSPC	$PhB(OH)_2$
[B] in 1-octanol[b]	64.63	47.58	25.47	49.53
[B] in water[b]	3.379	4.058	0.541	1.178
log P[c]	1.282	1.069	1.673	1.623 (1.58) (*37*)

[a] The concentration of phosphorus in the solution was measured by ICP-AES. [b] μg of B/mL. [c] $\log P = \log([B_{octanol}]/[B_{water}])$.

Before conducting in vivo studies, the hydrophobicity of **2** was investigated in an attempt to determine the effect of the additional hydrocarbon chain on the liposome incorporation efficiency. The relative hydrophobicity of **2** was determined by measuring the partition coefficient (log P_{oct}) of **2** in a biphasic 1-octanol/water system (*34*, *35*) using inductively coupled plasma-atomic emission spectroscopy (ICP-AES). In 1998 Gulati outlined four classes of molecules, categorized by their solubility and hydrophobicity, and defined the characteristics of each group (*36*). In general, compounds with log $P_{oct} < -0.3$ are highly hydrophilic and are likely to be found in a liposome's aqueous core, while those with log $P_{oct} > 5$ are very hydrophobic and will be located almost exclusively in the lipid bilayer. Amphiphilic molecules, with log P_{oct} between 1.7 and 4, have lower bilayer incorporation efficiencies than lipophilic species, and they are more easily lost from the bilayer because their biphasic nature allows for rapid transfer between the lipid and aqueous phases.

The partition coefficients of **2**, **1**, DSPC, and phenylboronic acid were determined by measuring the concentration of boron or phosphorus present in each of the 1-octanol and water layers after equilibrium was reached. The previously studied phenylboronic acid (*37*) was included to validate the method when using ICP-AES boron analyses. As expected, the results (Table 1) indicated that **2** (log $P = 1.282$) was more hydrophobic than **1** (log $P = 1.069$), while less lipophilic than DSPC (log $P = 1.673$). Because of its increased hydrophobic character, lipids incorporating **2** are expected to do so with higher efficiency than lipids incorporating **1**.

After formation of the liposomes by sonication, the unincorporated DAC-16 was separated from the lipid mixture through centrifugal filtration with Centricon membranes. The incorporation efficiency for DSPC-free DAC-16 liposomes (1:1 ratio of **2**:cholesterol) was determined by ICP-AES analysis of the unincorporated DAC-16 in the filtrate and was found to be 98% for the DSPC-free liposomes, compared to the previously observed (*18*) average incorporation efficiency for **1** of 70% in the optimized formulation. This remarkably high incorporation efficiency indicates that, in the absence of DSPC, almost all of the DAC-16 carborane derivative is incorporated by the bilayer membrane of the liposomes.

Because of applications in drug delivery the long-term stability of liposomes is another important property for consid-

Table 2. Size Distribution Data of DSPC-free Liposomes (1:1 ratio of 2:cholesterol)

storage temp	24 hours	1 week	2 weeks	4 weeks	2 months
23 °C	38.5[a]	39.3	42.3	38.9	39.8
4 °C	-	40.4	38.1	37.5	40.1

[a] m_v values reported in nm.

Table 3. Preliminary in Vivo Evaluation of Liposomes Containing 2

liposome composition (DSPC:**2**:CH)	m_v (nm)	%B in bilayer (dry lipid)	B concn[b] of injected suspension (ppm)	injected dose (mg B/kg mouse)	mortality (hours until mouse death)
0:1:1	40.1	8.8	1525	30	24
			763	15	24
1:1:2	60.9	4.2	750	15	24
			325	6.0	24
1:2:3	56.1	5.7	1000	20	24
			700	14	24
			300	6.0	24
1:1:2[a]	56.4	4.3	750	15	48[c]
			325	6.5	48[c]
1:0:1	55.4	-	-	-	-

[a] Sodium salt of **2** was employed rather than the corresponding potassium salt. [b] Serial dilution of the concentrated liposome suspension was used to obtain the diluted samples. [c] Mice appeared to be in shock after 24 h.

eration, the ideal liposomes must have a long shelf life throughout which structural integrity is maintained. The stability of liposomes incorporating **2** into DSPC/cholesterol vesicles was tested by storing two different samples for two months, one at room temperature and the other at 4 °C. The size distribution pattern of the two samples was monitored frequently throughout this time interval, with no obvious changes in vesicle diameters (m_v) observed during this period (Table 2).

Studies of 2 in Vivo. Liposomes formed from *nido*-carborane, **2**, have a much higher boron content than liposomes incorporating *nido*-carborane, **1**; the enhanced incorporation efficiency of **2** into lipid bilayers is likely due to the increased hydrophobicity of the DAC-16 lipid. The increased boron content resulting from incorporation of **2** could also affect the biological behavior of the consequent liposomes. The biodistribution studies of such liposomes, containing **2**, DSPC, and cholesterol in varied proportions, were performed at Washington State University using male BALB/c mice (about 10 g body weight) bearing small EMT-6 tumors. Typically 200 μL of each liposome suspension was injected into the tail vein, and the behavior of the mice was followed for up to 48 h. Unfortunately, in each case, the liposomes were found to be very toxic: no mouse survived longer than 48 h following injection of doses ranging from 6 to 30 mg of boron per kg of body weight. Since high potassium ion concentrations present in **2** could have been the cause of the observed toxicity, one liposome formulation contained the sodium salt of **2**, but these liposomes also proved to be lethal (Table 3). A control formulation, containing only DSPC and cholesterol, clearly proved that the toxicity was attributable to **2**, since mice injected with the control liposomes showed no adverse effects well past 48 h. Because of this result, further biodistribution tests were halted and no data were obtained on DAC-16 tumor boron concentration or tumor:blood ratio prior to animal death.

For evaluation purposes, this information was compared to previously unpublished biodistribution data (*38*) obtained for the free uncomplexed DAC-16 compound, performed under similar conditions as reported above for the lipidic DAC-16. These results indicated acceptable tumor boron uptake with good tumor:blood ratios early in the trial period. Tumor boron values steadily increased over the course of the study, reaching 4.8 μg of B per gram of tumor tissue 50 h postinjection with a tumor:blood ratio of greater than 3 upon injected dose of 61 μg of B. Though the free DAC-16 did not indicate the same degree of toxicity seen for the compound in the complexed lipidic-version, all BALB/c mice involved in the study were clearly affected and barely survived. Attempts to minimize this toxicity are under investigation. Although liposomes containing DAC-16 cannot be used as boron delivery vehicles for BNCT, the use of DAC-16 does provide a method of preparing liposomes of high boron content that may be suitable for other applications.

CONCLUSION

A new family of liposomes is reported here, assembled with DSPC, cholesterol, and a novel dual-chain *nido*-carborane amphiphilic lipid of high boron content, **2**. The resulting small liposomes exhibit satisfactory stability and size distribution with m_v in the range of 40−60 nm. Also, the new lipid component exhibited very high bilayer incorporation efficiency (98%) during liposome formation. A DSPC-free liposome was produced when using a lipid mixture containing only equimolar ratios of **2** and cholesterol. Because DSPC was not required, the boron content of the resulting liposomes is markedly increased compared to previously synthesized DSPC-containing liposomes (*9*, *18*). Although the animal studies showed liposomes derived from **2** to be too toxic for use in BNCT, these liposomes contain a new type of bilayer constituent of high boron content, and they may prove to be suitable for applications involving boron delivery in vitro.

ACKNOWLEDGMENT

This research was performed under the auspices of the Department of Energy (DOE) under contract DE-FG03-95ER61975 with the additional assistance of a grant-in-aid from U.S. Borax, Inc. Support for equipment was provided by the National Science Foundation under equipment grant numbers CHE-9974928 and CHE-0092036.

Supporting Information Available: Full experimental details and characterization data. This material is available free of charge via the Internet at http://pubs.acs.org.

LITERATURE CITED

(1) Bangham, A. D., Standish, M. M., and Watkins, J. C. (1965) Diffusion of Univalent Ions across the Lamellae of Swollen Phospholipids. *J. Mol. Biol. 13*, 238−252.

(2) Gregoriadis, G. (1976) The Carrier Potential of Liposomes in Biology and Medicince (Second of Two Parts). *N. Engl. J. Med. 295*, 765−770.

(3) Yuan, F., Leunig, M., Huang, S. K., Berk, D. A., Papahadjopoulos, D., and Jain, R. K. (1994) Microvascular Permeability and interstitial Penetration of Sterically Stabilized (Stealth) Liposomes in a Human Tumor Xenograft. *Cancer Res. 54*, 3352−3356.

(4) Hawthorne, M. F., and Shelly, K. (1997) Liposomes as drug delivery vehicles for boron agents. *J. Neuro-Oncology 33*, 53−58.

(5) Massing, U., and Fuxius, S. (2000) Liposomal formulations of anticancer drugs: selectivity and effectiveness. *Drug Resist. Updates 3*, 171−177.

(6) Barenholz, Y. (2001) Liposome application: problems and prospects. *Curr. Opin. Colloid Interface Sci. 6*, 66−77.

(7) Shelly, K., Feakes, D. A., Hawthorne, M. F., Schmidt, P. G., Krisch, T. A., and Bauer, W. F. (1992) Model studies directed toward the boron neutron-capture therapy of cancer: Boron deleivery to murine tumors with liposomes. *Proc. Natl. Acad. Sci. U.S.A. 89*, 9039−9043.

(8) Feakes, D. A., Shelly, K., Knobler, C. B., and Hawthorne, M. F. (1994) *Proc. Natl. Acad. Sci. U.S.A. 91*, 3029.

(9) Feakes, D. A., Shelly, K., and Hawthorne, M. F. (1995) *Proc. Natl. Acad. Sci. U.S.A. 92*, 1367.

(10) Locher, G. L. (1936) Biological Effects and Therapeutic Possibilities of Neutrons. *J. Roentgenol. Radium Ther. 36*, 1−13.

(11) Paxton, R. J., Beatty, B. G., Hawthorne, M. F., Varadarajan, A., Williams, L. E., Curtis, F. L., Knobler, C. B., Beatty, J. D., and Shively, J. E. (1991) A Transition Metal Complex (Venus Flytrap Cluster) for Radioimmunodetection and Radioimmunotherapy. *Proc. Natl. Acad. Sci. U.S.A. 88*, 3387.

(12) Hawthorne, M. F. (1993) The Role of Chemistry in the Development of Boron Neutron Capture Therapy of Cancer. *Angew. Chem., Int. Ed. Engl. 32*, 950−984.

(13) Hawthorne, M. F. (1998) New horizons for therapy based on the boron neutron capture reaction. *Mol. Med. Today 4*, 174−181.

(14) Hawthorne, M. F., Feakes, D. A., and Shelly, K. (1996) Recent results with liposomes as boron delivery vehicles for boron neutron capture therapy, in *Cancer Neutron Capture Therapy* (Mishima, Y., Ed.) pp 27−36, Plenum Press, New York.

(15) Shelly, K., Georgiev, E. M., Watson-Clark, R., and Hawthorne, M. F. (1997) Boron delivery to tumors for BNCT: recent murine results with liposomes, in *Advances in Neutron Capture Therapy* (Larsson, B., Crawford, J., and Weinreich, R., Eds.) pp 357−361, Elsevier Science, New York.

(16) Shelly, K., Hawthorne, M. F., and Schmidt, P. G. (1992) (Allen, B. J., et al., Ed.) pp 259−264, Plenum Press: New York.

(17) Feakes, D. A., Shelly, K., Hawthorne, M. F., Schmidt, P. G., Elstad, C. A., Meadows, G. G., and Bauer, W. F. (1993) (Soloway, A. H., et al., Ed.), Plenum Press: New York.

(18) Shelly, K., Feakes, D. A., and Hawthorne, M. F. (1994) in *Current Topics in the Chemistry of Boron* (Kabalka, G. W., Ed.), Royal Society of Chemistry, Cambridge.

(19) Watson-Clark, R., Banquerigo, M. L., Shelly, K., Hawthorne, M. F., and Brahn, E. (1998) Model studies directed toward the application of boron neutron capture therapy to rheumatoid arthritis: Boron delivery by liposomes in rat collagen-induced arthritis. *Proc. Natl. Acad. Sci. U.S.A. 95*, 2531−2534.

(20) Fairchild, R. G., and Bond, V. P. (1985) Current status of boron-10-neutron capture therapy: enhancement of tumor dose via beam filtration and dose rate, and the effects of these parameters on minimum boron content: a theoretical evaluation. *J. Radiat. Oncol. Biol. Phys. 11*, 831−840.

(21) Yuan, F., Dellian, M., Fukumura, D., Leunig, M., Berk, D. A., Torchilin, V. P., and Jain, R. K. (1995) Vascular Permeability in a Human Tumor Xenograft: Molecular Size Dependence and Cutoff Size. *Cancer Res. 55*, 3752−3756.

(22) Huang, S. K., Lee, K.-D., Hong, K., Friend, D. S., and Papahadjopoulos, D. (1992) Microscopic Localization of Sterically Stabilized Liposomes in Colon Carcinoma-bearing Mice. *Cancer Res. 53*, 5135−5143.

(23) Nagayasu, A., Uchiyama, K., and Kiwada, H. (1999) The size of liposomes: a factor which affects their targeting efficiency to tumors and therapeutic activity of liposomal antitumor drugs. *Adv. Drug Delivery Rev 40*, 75−87.

(24) Li, T., Thomas, J., and Hawthorne, M. F. (2003) Liposomes from novel carborane-containing lipids for boron neutron capture therapy. *Abstract of Papers*, 225th National Meeting of the American Chemical Society, New Orleans, pp INOR 161, American Chemical Society, Washington, DC.

(25) Nakamura, H., Miyajima, Y., Takei, T., Kasaoka, S., and Maruyama, K. (2004) Synthesis and vesicle formation of a nido-carborane cluster lipid for boron neutron capture therapy. *Chem. Commun.* 1910−1911.

(26) Minamikawa, H., Murakami, T., and Hato, M. (1994) Synthesis of 1,3-di-O-alkyl-2-O−(beta-glcosyl)glycerols bearing oligosaccharides as hydrophilic groups. *Chem. Phys. Lipids 72*, 111−118.

(27) Sharma, A., and Sharma, U. S. (1997) Liposomes in drug delivery: progress and limitations. *Int. J. Pharm 154*, 123−140.

(28) Boullanger, P., Sancho-Camborieux, M.-R., Bouchu, M.-N., Marron-Brignone, L., Morelis, R. M., and Coulet, P. R. (1997) Synthesis and interfacial behavior of three homologous glycero neoglycolopids with various chain lengths. *Chem. Phys. Lipids 90*, 63−74.

(29) Yeo, S.-K., Hatae, N., Sieki, M., and Kanematsu, K. (1995) Enantioselective Synthesis of an Oxa-Taxane Derivative *via* Tandem Intramolecular [2+2] Cycloaddition and [3,3]-Sigmatropic Rearrangement of Allenyl Ether. *Tetrahedron 51*, 3499−3506.

(30) Fein, M. M., Grafstein, D., Paustian, J. E., Bobinski, J., Lichstein, B. M., Mayes, N., Schwartz, N., and Cohen, M. (1963) Carboranes. II. The Preparation of 1- and 1,2-Substituted Carboranes. *Inorg. Chem. 6*, 1115−1119.

(31) Fein, M. M., Bobinski, J., Mayes, N., Schwartz, N., and Cohen, M. (1963) Carboranes. I. The Preparation and Chemistry of 1-Isopropenylcarborane and its Derivatives (a new Family of Stable Clovoboranes). *Inorg. Chem. 6*, 1111−1115.

(32) Heying, T. L., Ager, J. W., Jr., Clark, S. L., Mangold, D. J., Goldstein, H. L., Hillman, M., Polack, R. J., and Szymanski, J. W. (1963) A New Series of Organoboranes. I. Carboranes from the Reaction of Decaborane with Acetylenic Compounds. *Inorg. Chem. 2*, 1089−1092.

(33) Wiesboeck, R. A., and Hawthorne, M. F. (1964) Dicarbaundecaborane(13) and Derivatives. *J. Am. Chem. Soc. 86*, 1642−1643.

(34) Hansch, C., and Anderson, S. M. (1967) The Effect of Intramolecular Hydrophobic Bonding on Partition Coefficients. *J. Org. Chem. 32*, 2583−2586.

(35) Hansch, C., Leo, A., and Hoekman, D. (1995) Exploring QSAR: Vol. 2: Hydrophobic, Electronic, and Steric Constants, (Hansch, C., Leo, A., and Hoekman, D., Eds.) American Chemical Society, Washington, DC.

(36) Gulati, M., Grover, M., Singh, S., and Singh, M. (1998) Lipophilic drug derivatives in liposomes. *Int. J. Pharm. 165*, 129−168.

(37) Iwasa, J., Fujita, T., and Hansch, C. (1964) Substituent Constants for Aliphatic Functions Obtained from Partition Coefficients. *J. Med. Chem. 8*, 150−153.

(38) Shelly, K., Hawthorne, M. F. Unpublished Biodistribution Data involving BALB/c mice injected with DAC-16. 2001.

BC0501350

Generic Bioaffinity Silicone Surfaces

Hong Chen,[†,‡,§] Michael A. Brook,*[,‡] Heather D. Sheardown,*[,†] Yang Chen,[‡] and Bettina Klenkler[†]

Department of Chemical Engineering and Department of Chemistry, McMaster University, 1280 Main Street W., Hamilton ON Canada, L8S 4M1. Received June 18, 2005; Revised Manuscript Received October 17, 2005

Synthetic polymer surfaces require surface modification to improve biocompatibility. A generic route to biocompatible silicone elastomers is described involving high yield surface functionalization of standard silicones with hydrosilanes, hydrosilylation using asymmetric, allyl-, NSC-terminated PEO of narrow molecular weight, and covalent modification in one step with amine-containing biological molecules including oligopeptides (YIGSR, RGDS), proteins (EGF, albumin, fibrinogen, mucin), and glycosaminoglycans (heparin). Efficient, high-density binding (e.g., 0.2 EGF molecules/nm^2) was demonstrated using radiolabeling studies. The resulting surfaces were demonstrated to be biocompatible by further reaction with biomolecules, for example, thrombosis suppression on surfaces modified by heparin + ATIII, and the formation of confluent corneal epithelial cell layers on EGF, RGDS, or YIGSR surfaces.

INTRODUCTION

When synthetic biomaterials are implanted, they are met with a complex and aggressive biological system that ultimately passivates the material or creates a fibrotic capsule, essentially walling the material off from the system. Various synthetic strategies have made impressive inroads to the problems of preparing compatible biomaterials (*1*). One promising approach exploits the plasma polymerization of hydrophilic monomers such as alkylamines or tetraglyme onto an existing polymer surface (*2*−*4*). However, the most general and powerful methods (*5*) involve the formation of layers of hydrophilic polymers on the surface, of which oligo- (*6*−*8*) and poly(ethylene glycol) (*9*−*12*) are exemplary. The polymers either bloom from polymer blends to an aqueous interface or are covalently grafted onto an activated polymer surface (*13*, *14*). While promising, it is clear that more biocompatible surfaces can be produced when constituents of the local biology are harnessed to "bioactivate" or "biopassivate" the surface (*15*), either alone or in combination with hydrophilic polymers. Such approaches include modification with amino acids, cell adhesion peptides, proteins, and glycosaminoglycans. These materials have traditionally been tethered at multiple sites, reducing the mobility of the linking chain. The specific spacing of the tethered biomolecules from the polymer interface is not normally controllable.

Silicone polymers offer many advantages as biocompatible supports, including their very high oxygen transmissibility and the ease with which a variety of different substrates can be conformally coated using several chemically different cross-linking processes. Silicones suffer, however, from an extremely high surface hydrophobicity to which biomolecules readily adhere (*16*, *17*) generally resulting, in the case of proteins, in the subsequent mediation of biological reactions (*15*, *18*). Herein we describe the development of a flexible, narrow molecular weight range, asymmetric linker that provides a facile route to convert hydrophobic silicones into activated ester-terminated, PEO-modified surfaces. These surfaces react effectively with alcohols and particularly amines and thus serve as key intermediates in the preparation of saccharide-, amino acid-, peptide-, and nucleotide-modified surfaces. We report on the preparation of high density films on silicone of biomolecules including the cell adhesion peptides, RGDS and YIGSR, proteins (EGF, lysozyme, albumin, fibrinogen, and mucin), and the glycosaminoglycan heparin, to which ATIII was complexed. The resulting surfaces are thus tailored to be selectively repellent or adherent to biomolecules and, as a result, biocompatible in a variety of environments.

EXPERIMENTAL PROCEDURES

Reagents. Poly(ethylene glycol) monoallyl ether (average MW 500) was obtained as a gift from JuTian Chemical Co. (Nanjing, China). It was dried by azeotropic distillation with toluene before use. *N*,*N*′-Disuccinimidyl carbonate, *o*-xylene (97%, anhydrous), triethylamine (99%), acetonitrile (99%, anhydrous), Karstedt's Pt catalyst (2−3 wt % in xylene, $[(Pt)_2(H_2C{=}CH{-}SiMe_2OSiMe_2CH{=}CH_2)_3]$), 2-mercaptoethanol, and CF_3SO_3H were purchased from Aldrich Chemical Co. Sylgard 184 (a platinum cured silicone rubber $H_2C{=}CH{-}$silicone + HSi-silicone → silicone-CH_2CH_2Si-silicone) and DC1107 $(Me\text{-}HSiO)_n$ were purchased from Dow Corning (Midland, MI). Human serum albumin (HSA), Tyr-Ile-Gly-Ser-Arg (YIGSR), Arg-Gly-Asp-Ser (RGDS), and Sephadex G-25 columns were obtained from Sigma. Epidermal growth factor (EGF) was obtained from Research Diagnostics Incorporated. Fibrinogen was obtained from Enyzme Research Laboratories. Toluene was dried by refluxing over Na prior to distillation, and MeOH was dried by refluxing over Mg and was distilled before use.

Materials Characterization. ^{1}H and ^{13}C NMR spectra were recorded at 30 °C on a Bruker AC-200 spectrometer (at 200 and 50.3 MHz for ^{1}H and ^{13}C, respectively). Attenuated total reflection Fourier transform IR spectroscopy (ATR-FTIR) measurements were carried out on a Bruker VECTOR 22 Fourier transform infrared spectrometer (Bruker Instruments, Billerica, MA) equipped with a Harrick ATR accessory MUP with GeS crystal; 200 scans were collected for each sample. Electrospray mass spectra (ESI-MS) were recorded on a Micromass Quattro Ultima LC, triple quadruple MS.

Water Contact Angle. Advancing and receding sessile drop contact angles were measured on PEO-grafted surfaces using

* To whom correspondence should be addressed. E-mail: mabrook@mcmaster.ca, sheardow@mcmaster.ca.

† Department of Chemical Engineering.

‡ Department of Chemistry.

§ Current address: Wuhan University of Technology, Institute of Materials Science and Engineering, 133 Luoshird, 430070 Wuhan, PR China.

10.1021/bc050174b CCC: $33.50 © 2006 American Chemical Society
Published on Web 12/23/2005

Scheme 1: Synthesis of 3 and NMR Assignments of 2

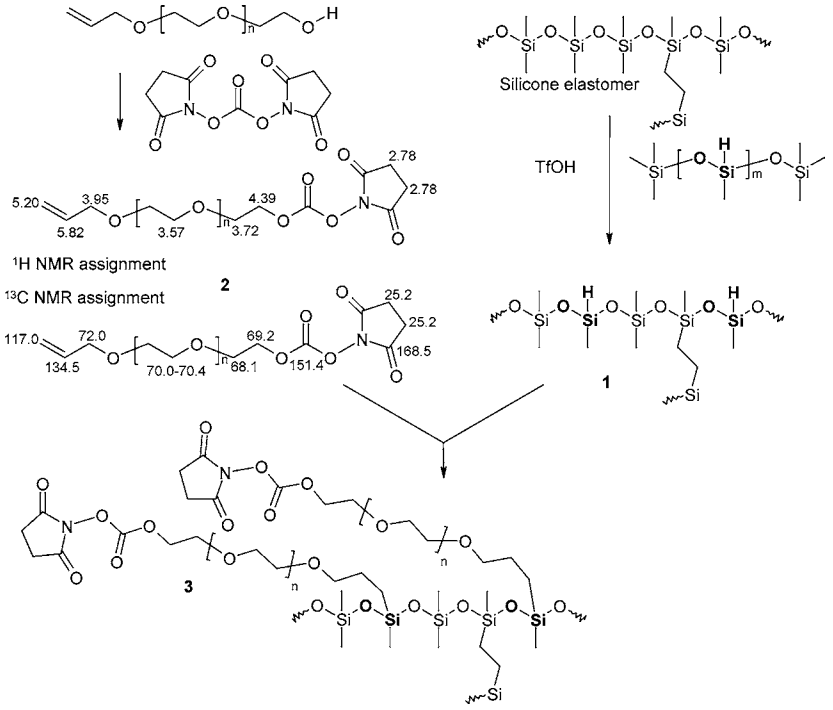

Ramé Hart NRL C.A. goniometer (Mountain Lakes, NJ). Milli-Q water (18 MΩ/cm) was used with a drop volume of approximately 0.02 mL. Results are presented as an average of 18 measurements or more on at least three different surfaces. Contact angles were also measured using the captive bubble method, where an air bubble was injected from a syringe onto an inverted sample surface immersed into Milli-Q water. Results are presented as the average of at least 10 measurements on three different surfaces.

X-ray photoelectron spectroscopy (XPS) was performed at Surface Interface Ontario, University of Toronto, using a Leybold Max 200 X-ray photoelectron spectrometer with a MgK-α nonmonochromatic X-ray source.

Preparation of *N*-Succinimidyl Carbonate PEG-Grafted PDMS Surfaces. *Synthesis of* α*-Allyl-*ω*-*N*-succinimidyl Carbonate−Poly(ethylene glycol),* ***2.*** To a solution of poly(ethylene glycol) monoallyl ether (2.0 g, 4.0 mmol) and triethylamine (1.62 g, 16 mmol) in CH_3CN (10 mL) was added *N*,*N*′-disuccinimidyl carbonate (4.1 g, 16 mmol). The mixture was allowed to stir at room temperature over 10 h under N_2. After removal of the solvent in vacuo, the residue was dissolved in dry toluene (25 mL), and the solution was cooled to 0 °C. A pale brown precipitate was filtered off. The toluene was removed under reduced pressure. This procedure was repeated three times. The resultant compound **2** was a yellow oil (1.2 g, 60% yield). IR (neat): 1739 (N*C*═*O*), 1788 (O*C*═*O*). ^{1}H NMR (200.2 MHz, $CDCl_3$, Scheme 1, see also Suppporting Information): δ 2.78 (s, 4H, O═CCH_2CH_2C═O), 3.57 (bs, 40H, PEO's OCH_2), 3.72 (bs, 2H, OCH_2CH$_2$OC═O), 3.95 (d, 2H, J = 5.6 Hz, CH$_2$═CHCH_2O), 4.39 (m, 2H, OCH$_2$CH_2OC═O), 5.20 (m, 2H, CH_2═CHCH$_2$O), 5.82 (m, 1H, CH$_2$═C*H*CH$_2$O) ppm. ^{13}C NMR (50.3 MHz, $CDCl_3$): δ 25.2 (O═C*C*H$_2$*C*H$_2$C═O), 68.1 (O*C*H$_2$CH$_2$-OC═O), 69.2 (O═CO*C*H$_2$CH$_2$O), 70.4 (PEG's O*C*H$_2$), 72.0 (CH$_2$═CH*C*H$_2$O), 117.0 (*C*H$_2$═CHCH$_2$O), 134.5 (CH$_2$═*C*HCH$_2$O), 151.4 (O*C*═OO), 168.5 (N*C*═OCH$_2$) ppm. MS (ESI): m/z = 745.6 (M + NH_4^+, n = 12 100).

Elastomer Preparation. Silicone elastomers were prepared according to the procedure provided by Dow Corning. Sylgard 184 PDMS prepolymer and catalyst was mixed thoroughly with its cross-linker in a 10:1 ratio (w/w) in a plate mold and degassed under vacuum. Films were allowed to cure at room temperature for 48 h. After being cured, the silicone elastomer films were punched into disks, approximately 5 mm in diameter and 0.5 mm thick. The disks were washed with hexane and then dried under vacuum for further use.

Si−H Surface Functionalization 1. For Si−H functionalization of the surface, 20 silicone elastomer disks were immersed in a mixture of DC1107 (3 mL) and methanol (5 mL). To this was added F_3CSO_3H (0.02 mL, 0.26 mmol). After being stirred at room temperature for 30 min, the functionalized surfaces were rinsed with methanol and hexane and dried under vacuum (for surface characterization, see below).

Addition of PEG Derivative, 3. Si−H modified silicone surfaces **1** were incubated in a solution of 2-methoxyethyl ether solvent and **2** (80:20 wt %:wt %, 3 mL). Pt-catalyst (platinum-divinyltetramethyldisiloxane complex, 1 drop) was added, and the mixture was stirred for 15 h at room temperature. Following modification, the PEG-modified surfaces **3** were washed thoroughly with dry acetone and dried under vacuum.

Characterization of NSC and Modified Surfaces. *ATR-FTIR.* As described above, *N*,*N*′-disuccinimidyl carbonate was used to activate the hydroxy-terminal of α-allyl-ω-poly(ethylene glycol). The desired compound **2** was characterized by ^{1}H NMR, with the resonance of the CH_2CH_2 on the NHS (2.78 ppm) being particularly diagnostic. Two types of C═O groups were observed on the NSC-activated termini (O−C(O)−O and imide) by ^{13}C NMR (168.8 and 151.7 ppm, respectively). Assignments of the FT-IR spectrum of the NSC-activated PEO are shown in Figure 1. The band at 1739 cm^{-1}, representing the C═O stretch of the NHS group, can be further used to diagnose the succinimidyl carbonate PEG grafting process.

H−Si-functionalized silicone surfaces **1** were obtained by acid-catalyzed equilibration of a silicone elastomer in the presence of $(MeHSiO)_n$ as noted above. The ATR-FTIR spectra of the resulting surfaces exhibited a band at 2166 cm^{-1} due to the Si−H stretch.

Succinimidyl carbonate PEO **2** was grafted onto the silicone rubber surfaces via a hydrosilylation reaction with the H−Si groups. In the ATR-FTIR spectrum of the succinimidyl carbonate PEG-grafted surfaces **3**, the band at 2166 cm^{-1} due to H−Si

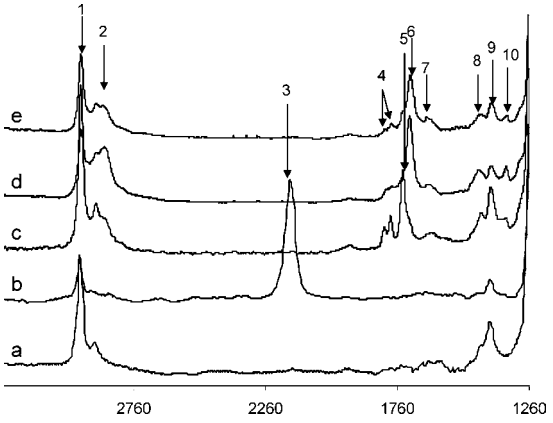

Figure 1. FT-IR spectra of (a) PDMS, (b) Si−H-modified PDMS, (c) succinimidyl carbonate PEO-modified PDMS surfaces **3**, (d) RGD-modified **4**, and (e) YIGSR-modified **5** PDMS surfaces, respectively.

Table 1. XPS Surface Analysis of Unmodified PDMS, Succinimidyl Carbonate PEO-Modified 3, RGDS−PEO-Modified 4, and YIGSR−PEO-Modified 5 PDMS Surfaces

elemental at. %	control PDMS	NSC−PEO **3**	RGDS−PEO **4**	YIGSR−PEO **5**
C1s	46	52.2	54.6	55.4
N1s	0	0.9	1.9	2.7
O1s	26.5	26.3	25.2	26.5
Si2p	27.4	20.6	18.4	15.5

was no longer visible following the reaction. There were two C═O stretches at 1741 and 1789 cm^{-1}, respectively, which were assigned to the C═O groups at the succinimidyl carbonate termini, and the O−C(O)−O linkage, which was also present in the starting material. The PEO CH_2 scissoring band at 1454 cm^{-1}, the antisymmetric stretch mode of the CH_2-O-CH_2 chain at 1351 cm^{-1}, and the symmetric stretch mode of the CH_2-O-CH_2 chain at 1258 cm^{-1} indicated the presence of PEO chains on the resulting surface.

XPS. NSC−PEO binding to the surface **3** was further confirmed by the presence of an N1s signal in the XPS survey scan due to the amine groups in the NSC−PEO polymer (Table 1, see Supporting Information). The C1s high-resolution spectrum shows a distinct peak at 286.4 eV which corresponds to the C−C−O bond in PEO repeat unit.

Conjugation of Various Molecules to the NSC-Modified Surface. *Peptide Conjugation.* The covalent conjugation of peptides to the functionalized surfaces was carried out in a phosphate-buffered saline (PBS) buffer solution (pH 7.5). The *N*-succinimidyl carbonate PEG-grafted surfaces **3** were immersed in PBS buffer containing the peptide RGDS or YIGSR, (10 μg/mL) for 12 h to give **4** or **5**, respectively.

Washing Protocol. All samples were rinsed three times with PBS for 10 min, for a total of 30 min, and the surfaces were dried under vacuum. For radioactive samples, residual adherent buffer was removed by wicking onto filter paper and transferred to clean tubes, and the surface radioactivity was determined by counting using a gamma counter. Radioactivity counts were converted to surface protein concentrations. One milliliter of a 2% sodium dodecyl sulfate (SDS) solution was then added to each tube and left at room temperature for 4 h and overnight at 4 °C. After three PBS rinses, the surfaces were transferred to clean tubes and radioactivity was measured to determine the levels of the protein remaining after the SDS treatment, which indicated that the growth factor was covalently immobilized to the surface (Table 2).

Characterization. The IR spectra of modified surfaces **3**−**5**, respectively, are presented in Figure 1 (see also Supporting Information). Distinct bands at 1652 and 1656 cm^{-1} due to amides were observed on both the RGDS- and YIGSR-modified surfaces: the C═O stretch mode at 1741 cm^{-1}, due to the NHS group, disappeared in both cases following modification. These spectral changes indicated the coupling of the succinimidyl carbonate PEG to the peptides. Peptide immobilization was further demonstrated by an increase in the XPS N1s signal to 1.9 and 2.7% for RGDS and YIGSR, respectively, due to the amine groups in the peptides and a decrease in the Si2p signal (Table 1, see Supporting Information). Note that the starting succinimidyl carbonate PEO-modified PDMS **3** showed a very weak nitrogen peak due to the presence of a single nitrogen in NHS. The nitrogen intensity, postmodification, was much higher.

EGF Conjugation 6. EGF was first labeled with ^{125}I (ICN Pharmaceuticals, Irvine CA) using the iodogen method. The *N*-succinimidyl carbonate PEG-grafted surface **3** was immersed in a PBS buffer (pH 7.4) containing radiolabeled EGF (10 μg/mL) for 2 and 24 h and rinsed three times with PBS for 10 min each (Table 2).

Human Serum Albumin Conjugation 7. Human serum albumin was labeled with ^{125}I (ICN Pharmaceuticals, Irvine CA) using the ICl method. The labeled protein was passed through an AG 1-X4 column (Bio-Rad Laboratories, Hercules, CA) to remove any free iodide. For measurement of nonspecific adsorption of protein from buffer and covalent coupling of albumin to the surfaces, a mixture of labeled and unlabeled protein (1:20) at a total concentration of 1 mg/mL was prepared. NSC−PEO-modified surfaces **3** were incubated with albumin for 2 h at room temperature, rinsed three times with PBS for 10 min, (250 μL per rinse per disk, 30 min total).

The modification of surfaces by albumin, via adsorption or covalent grafting, is shown in Figure 3B. Figure 3D also shows the results of fibrinogen adsorption on the albumin pretreated surfaces.

Fibrinogen Adsorption 11. Fibrinogen was labeled with ^{131}I (ICN Pharmaceuticals, Irvine CA) using the ICl method. The labeled protein was passed through an AG 1-X4 column (Bio-Rad Laboratories, Hercules, CA) to remove any free iodide. The untreated control (PDMS elastomer) surface, ^{125}I-albumin-pretreated control surface, and ^{125}I-albumin-pretreated NSC−PEG-modified surfaces **7** were incubated in PBS solution containing the radiolabeled fibrinogen at a concentration of 1

Table 2. Efficiency of Protein Binding to 3

	onto control surfaces		onto **3**	
	before washing with SDS ng/cm^2	after washing with SDS ng/cm^2	before washing with SDS ng/cm^2	after washing with SDS ng/cm^2 (surface)
YIGSR	n/a	n/a	19	n/a (**5**)
EGF	116	26	190	180 (**6**)
albumin	220	50	180	170 (**7**)
fibrinogen	580	200[a]		45 (**11**)
lysozyme	200	40	460	402 (**9**)
heparin				680 (**10**)

[a] Adsorption on to albumin-coated control surface; i.e., 220 ng/cm^2 is displaced by 200 ng/cm^2 fibrinogen.

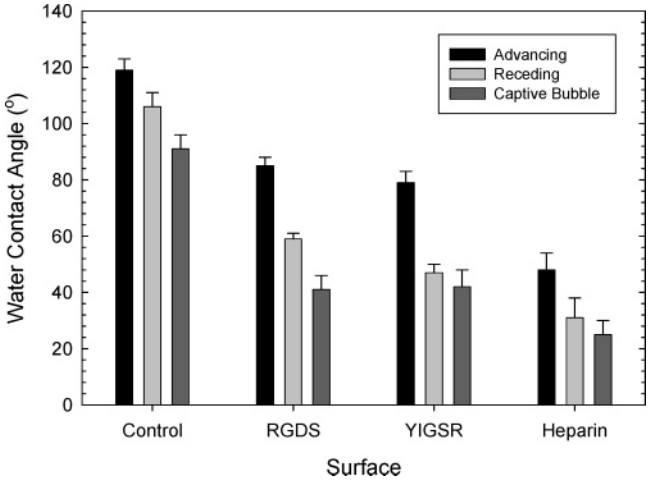

Figure 2. Water contact angle of control, RGDS **4**-, YIGSR **5**-, and heparin **10**-modified surfaces.

mg/mL for 2 h. The fibrinogen amounts on various surfaces were determined radioactively as described above (Figure 3D).

Conjugation of Mucin 8. NSC surfaces **3** were incubated in 5 mg/mL solution of mucin from bovine (submaxillary glands, Type I-S, Sigma) in PBS buffer (pH = 8.0) for 6 h. Surfaces were subsequently rinsed three times with fresh PBS.

Conjugation of Lysozyme 9, 12. Lysozyme adsorption and conjugation to various surfaces was carried out in a phosphate-buffered saline (PBS, pH 7.4). Lysozyme was labeled with ^{125}I (ICN Pharmaceuticals, Irvine CA) using the ICl method. The *N*-succinimidyl carbonate PEG-grafted surface **3**, PEG350-grafted surface, mucin-modified surface **8**, and control surface, respectively, were immersed in a PBS buffer (pH 7.4) containing (unlabeled:radiolabeled = 9:1) lysozyme (1 mg/mL) for 3 h and rinsed three times with PBS (Table 2).

Heparin Conjugation 10. NSC surfaces **3** were incubated in 10 mg/mL solution of heparin (Sigma Aldrich) in PBS buffer (pH = 8.0) for 6 h. Surfaces were subsequently rinsed three times with fresh PBS. The density of heparin on the NSC surface **10** was 0.68 μg/cm^2, as shown by a toludine blue assay (see next section).

For the assay, a series of heparin standard solutions with concentrations varying from 0 to 20 μg/mL were prepared by diluting a stock solution. The stock solution was obtained by dissolving 10 mg heparin in an aqueous 0.2 wt % NaCl solution.

Toluidine blue (Sigma-Aldrich Canada, 50 mg) was dissolved in HCl (1 mL, 0.01 N solution), in which 0.2 wt % NaCl had been previously added and dissolved. The 50 mg/mL toluidine blue solution was diluted with deionized water to give a 0.005 mg/mL (0.0005%) solution. The solution (1.0 mL) was added to a 5 mL tube, followed by 0.1 mL of the above heparin 10 mg/mL standard solution. The mixed solution was vortexed for 30 s. *n*-Hexane (Aldrich-Sigma Canada, 1 mL) was added, and the solution was vigorously mixed for 30 s and then allowed to separate into two phases over 5 min. The heparin−toluidine blue complex was extracted into the upper transparent organic layer. After the organic layer was removed, the absorbance of the aqueous layer at 631 nm was measured on a Beckman DU640UV/VIS spectrophotometer. A linear standard calibration curve was obtained by plotting absorbance at 631 nm versus concentration of heparin in the aqueous NaCl solution. The amount of heparin immobilized on the polymer surfaces was determined using this calibration curve.

Prior to testing, polymer samples were incubated in 0.05 M Tris-buffered saline (TBS) with pH 7.4 at room-temperature overnight to hydrate the surfaces. For each experiment, 0.1 mL of 0.2% NaCl solution and 1.0 mL of 0.005 mg/mL (0.0005%) toluidine blue solution were mixed in a 5 mL polypropylene test tube. The heparin-modified (polymer) surfaces **10** (0.77 cm^2

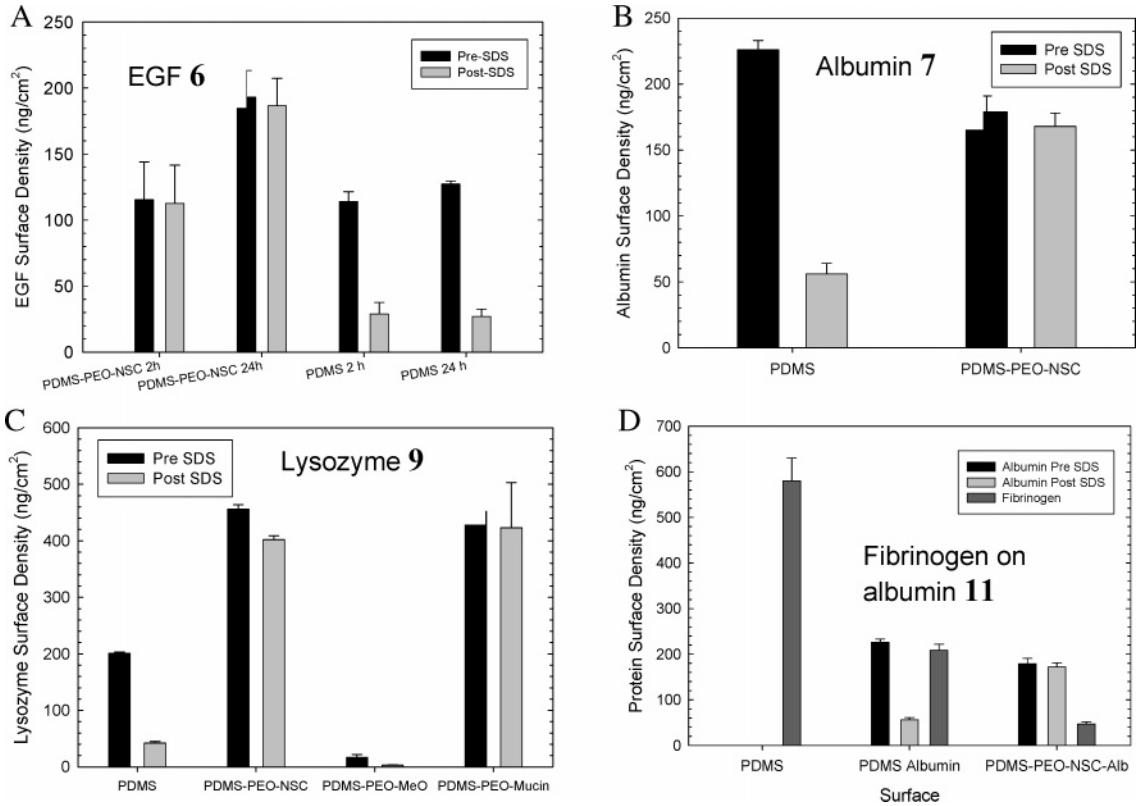

Figure 3. A: Binding EGF to the surfaces: PDMS = control, PDMS−PEO−NSC → **6**. B: Covalent and physical association of albumin on PDMS and PDMS−PEO−NSC surfaces → **7**, including the effect of SDS washing. C: Adsorption of lysozyme with PDMS (control), PDMS−PEO−NSC → **9**, PDMS−PEO-MeO and PDMS−PEO-mucin → **12** surfaces before and after SDS exposure. D: Adsorption of fibrinogen (Fg) onto albumin-coated control or onto **7** giving **11**.

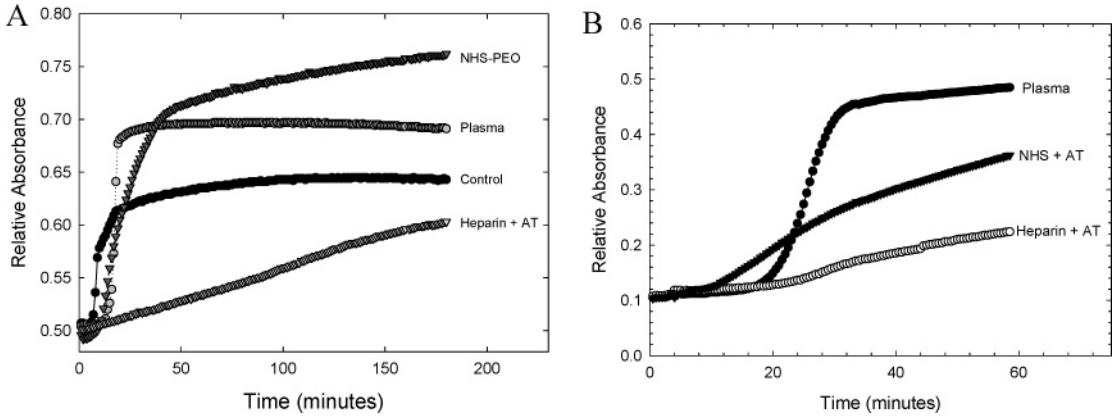

Figure 4. A: Ability of thrombin to process *N*-*p*-tosyl-gly-pro-arg *p*-nitroanilide under various conditions. B: Thrombin inactivation by AT bound to heparin surface **10** and versus AT directly bound to **3**.

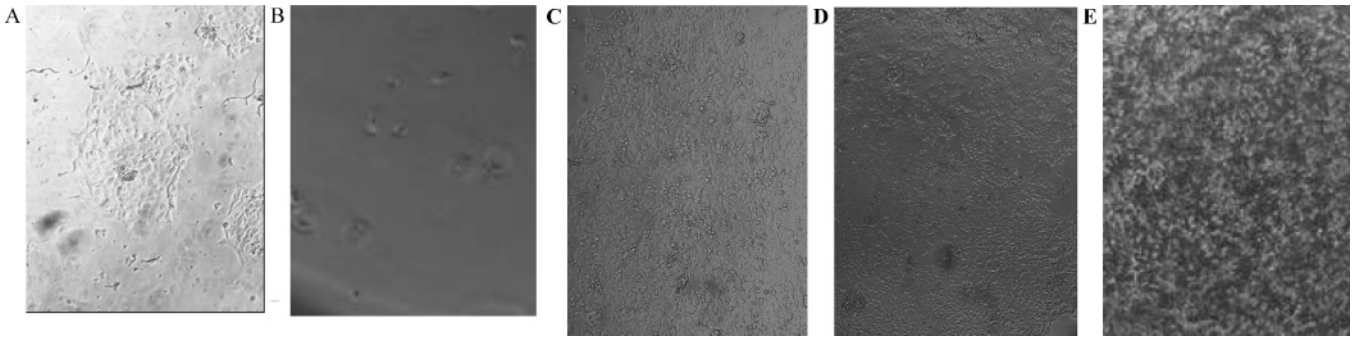

Figure 5. Human corneal epithelial cells (HCEC) grown on A: control PDMS, B: PDMS−PEO−NSC **3**, C: RGDS **4**, D: YIGSR **5**, and E: EGF **6**-modified surfaces (5 days).

area) were immersed in the solution, which was vortexed for 30 s. Then, 1 mL *n*-hexane was added and shaken well. The mixture was allowed to phase-separate for 5 min after removal of the surfaces. As above, the upper organic layer was removed and the absorbance of the aqueous layer at 631 nm was investigated on a Beckman DU640 UV/vis spectrophotometer. The density of total heparin immobilized on the surfaces was calculated from the above calibration curve. For each surface, the heparin density was expressed by mass per unit surface area (μg/cm^2).

Thromboresistant Properties. Platelin was obtained from Organon Teknila Corp., Durham, NC (No. 35501). TBS/Ca^{2+}/Platelin (0.1 M $CaCl_2$ with a 1:10 dilution of platelin) buffer solution was made by dissolving $CaCl_2$ (1.11 g) and four standard vials of Platelin in 10 mL of Milli-Q water (10 mL). The volume was then brought to 100 mL with TBS (0.05 M, pH = 7.4). Thrombin substrate *N*-*p*-tosyl-gly-pro-arg *p*-nitroanilide (Sigma-Aldrich) (5 mg) was dissolved in TBS (10 mL) to give a solution with a final concentration of 0.5 mg/mL.

To passivate the walls of the 96-well microtitration plate, the wells were exposed to human serum albumin in TBS (10 mg/mL) overnight at 4 °C. The albumin solution was then withdrawn from the wells, and the wells were aspirated and washed three times with fresh TBS (0.3 mL/well/time) before adding the unmodified and heparin-modified silicone surfaces. The heparin-modified surface **10** was incubated in antithrombin III in TBS buffer solution (0.25 mg/mL) for 30 min before testing.

The disks were placed vertically in the wells, and 10% diluted pooled human citrated plasma (200 μL) was added to the wells. After the plate was warmed to 37 °C, TBS/Ca^{2+}/platelin buffer solution (20 μL) and thrombin substrate (30 μL of 0.5 mg/mL) were added. The release of *p*-nitroaniline by thrombin was measured as a function of time by recording the optical density at 405 nm and 37 °C using a UV−vis plate reader (Figure 4).

Cell Culture on Peptide-Modified-Surfaces. Surfaces (~5 mm disks) **4** or **5** as well as controls were washed three times with PBS supplemented with antibiotics (penicillin, streptomycin, and gentamycin) and subsequently stored overnight at 4 °C in Keratinocyte Serum Free Medium (KSFM, Invitrogen, Grand Island, NY) medium containing antibiotics. Under sterile conditions, the surfaces were transferred to a 24-well plate and plated with human corneal epithelial cells (HCECs, 10^4 cells per well) in KSFM supplemented with penicillin, streptomycin, gentamycin, and EGF. Surfaces **6** were cultured under identical conditions except the cells were grown in medium only; no exogenous EGF or antibiotics were added. The cells were cultured at 37 °C in a 5% CO_2 atmosphere. Samples were imaged regularly. All images were taken at 100× magnification (Figure 5). Epithelial cell morphology was confirmed by AE5 staining.

RESULTS

Unlike most polymers, silicones can be readily formed and degraded under thermodynamic control (*19*). Thus, treatment of monomers and/or polymers with endcapping molecules in the presence of acid or base allows the preparation of homo- or copolymers of various molecular weights. By carefully controlling the swelling conditions using relatively poor solvents for silicone, such as methanol, it was possible to preferentially introduce Si−H functional groups at the surfaces of a variety of pre-cured silicone elastomer by a redistribution polymerization with triflic acid (*20*), giving **1**, as shown by the characteristic strong IR absorption at 2166 cm^{-1} (Scheme 1, Figure 1, see also Supporting Information). The Si−H group underwent efficient hydrosilylation with a series of olefins, including allyl-PEO (*13*, *14*) and, more importantly, allyl-PEO−NSC **2**, prepared by the reaction of allyl-PEO-OH with bis-*N*-hydroxysuccinimidyl carbonate to give a high density, reactive NSC

Scheme 2: Generic Route to Biomolecule Attachment to Silicone Surfaces

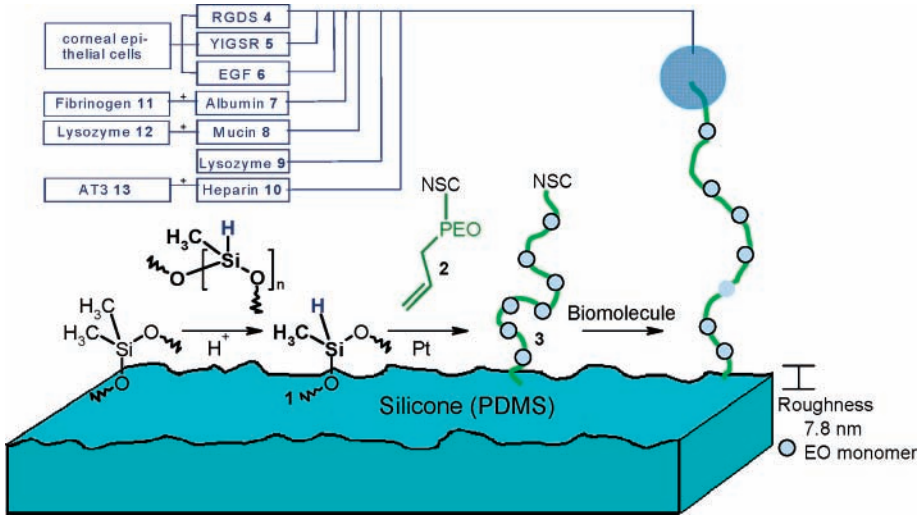

surface **3**. Surface properties (ATR-IR, Figure 1, Table 1, XPS, see also Suporting Information) were determined using traditional methods. It should be noted that, unlike model systems prepared on flat gold films (*21*), these functional surfaces can be prepared from any dimethylsilicone elastomer, and on objects with both simple and complex shapes.

Surface **3** was modified, in phosphate-buffered saline (PBS) solutions (pH = 8.0), with a series of peptides and proteins, respectively, including the cell adhesion peptides Arg-Gly-Asp-Ser **4** (RGDS)and Tyr-Ile-Gly-Ser-Arg **5** (YIGSR), epidermal growth factor **6** (EGF), human serum albumin **7** (HSA), mucin **8**, lysozyme **9**, and the glycosaminoglycan heparin **10**. Selected modified surfaces were further exposed to additional proteins. Thus, the HSA surface **7** was modified with fibrinogen **11**, a mucin-modified surface **8** was treated with lysozyme **12**, and heparin surface **10** was exposed to antithrombin III **13** (Scheme 2).

The biologically modified silicones were characterized by IR, XPS, and contact angle (Figure 1, Figure 2, Table 1, see also Supporting Information). The total quantities of the surface linked and adsorbed peptides or proteins were determined by radioactivity assays before and after exhaustively washing the modified surface with sodium dodecyl sulfate (SDS) (Table 2). This method also provided a minimum estimate of the total graft density of the surface. For example, after 24 h of reaction of surface **3** with EGF, the resulting surface **6** exhibited a surface concentration of 190 ng/cm^2 (ca. 0.2 EGF molecules/nm^2): after washing with SDS, the control surface showed only 26 ng/cm^2 while the EGF-*g*-PEO surface was essentially unchanged (Figure 3A). The smaller molecule YIGSR was found at a surface concentration of 19 ng/cm^2, also about 0.2 molecules/nm^2. Larger molecules, such as lysozyme (MW ca. 14400), also efficiently grafted, 402 ng/cm^2 (0.15 molecules/nm^2), to the surface to give **9** after extensive washing with SDS. Similarly, heparin bound to the surface **10** with a graft density of 0.68 μg/cm^2 (see below).

The silicone surfaces are not molecularly flat, and thus it is not possible make direct comparison of EO surface packing on these silicones with model systems, such as planar self-assembled monolayer-modified gold surfaces (*21*). The cross-sectional area of an anhydrous EO oligomer when coiled in a helix is on the order of 0.2 nm^2. Thus, an ideal PEO brush, rarely achieved with the exception of self-assembled monolayers on noble metal surfaces (*9*), could pack about 20−25 anhydrous EO chains/nm^2 (*22*). Water-swollen PEO chains occupy significantly more space (*23*). We did not directly assess the packing density of PEO on these surfaces. . However, as noted above, approximately 0.2 molecules/nm^2 of peptides and EGF, and 0.15 molecules/nm^2 of the larger lysozyme, were bound to the surface, surface densities which approach a monolayer (the diameter of lysozyme is approximately 3.0 nm (*24*)). These molecules cast a larger shadow on the surface than a PEO helix, and therefore efficiency of surface binding is more dependent on the size of the biomolecules to be tethered than on the PEO density: multiple attachments to the surface are anticipated. We note that the ability to tether biomolecules in high density in active form to rough, instead of smooth model, surfaces is a major advantage of the method: any silicone surface can be functionalized.

Albumin, the most abundant protein in blood, can be used to passivate implanted synthetic surfaces (*25*). Less protein was initially found on the NSC-modified surface **7** than on the control (0.22 vs 0.18 μg/cm^2, Figure 3B). However, the control surface was mostly washed free of the ^{125}I-labeled protein with SDS (0.05 μg/cm^2 remained), while more than 90%, 0.17 μg/cm^2, remained on the functionalized surface. These data are consistent with initial, patchy, protein physisorption that changed to chemisorption **7** before the protein could migrate across the NSC surface to form a coherent monolayer. That is, the albumin binds on contact, leaving a noncoherent film and accessible interstitial areas. Attempts to form a coherent albumin film prior to covalent linkage, by controlling the rate of surface binding, have not so far been successful.

The ability to displace the albumin by ^{131}I-labeled fibrinogen, from control and **7** surfaces, respectively, was examined. Fibrinogen adsorbed effectively to the control surface (0.58 μg/cm^2). However, much less fibrinogen was able to contact and bind to the albumin adsorbed surface (0.20 μg/cm^2), and even less was found on the albumin-passivated NSC surface **11**, Figure 3D (0.045 μg/cm^2). This is consistent with a control surface in which albumin can be "nudged aside" by fibrinogen, but a covalently linked surface **7** in which only a few interstitial spaces are sufficiently large to accommodate the large fibrinogen molecule (340 kD) giving **11**.

Lysozyme, one of the proteins responsible for ophthalmic disinfection, was exposed to a variety of modified silicones. Significantly more lysozyme was adsorbed to the pregrafted mucin **8** (post SDS, 423 ng/cm^2) and NSC surfaces **3** (post SDS, 402 ng/cm^2) than to the control silicone (post SDS, 42 ng/cm^2) or simple methoxy PEO-modified (post SDS, 0.3 ng/cm^2) silicone surfaces (Figure 3C) (*13*, *26*, *27*). The natural surface with which lysozyme interacts in the eye is mucin (*28*). Thus, this modified polymer may prove useful as a model system to examine surface fouling by lysozyme in ophthalmic applications.

Heparin, a highly sulfonated, anionic polysaccharide that is a well-known antithrombotic agent was analogously grafted to the surface **3** in high density (0.68 μg/cm^2) giving **10**. The surface was subsequently exposed to thrombin, via the interaction of $CaCl_2$ with plasma, in the presence of the chromogenic substrate *N*-*p*-tosyl-gly pro-arg *p*-nitroanilide. Release of the *p*-nitroaniline hydrolysis product was followed over 3 h (Figure 4A). Although nitroaniline was formed in the presence of **10**, it did so at a significantly lower rate and with a significantly longer half-life than observed with plasma alone, or in the presence of the control silicone surface or the NSC−PEO-modified surface **3**. The heparinized surface was demonstrably less thrombogenic than the other surfaces examined and was comparable to those previously described (*29*). Also of interest was the observation that antithrombin III (ATIII) covalently linked to the heparin surface **10**, giving **13**, was far more efficient at inhibiting thrombin than ATIII directly bound to the surface (after reaction with **3**, Figure 4B).

The most important criterion for any biomedical surface is the degree to which it is accepted by the local biological environment. To test the hypothesis that cell-compatible surfaces could be prepared using this method, human corneal epithelial cells (HCEC) were cultured on NSC surfaces modified with the cell adhesion peptides RGDS and YIGSR, **4** and **5**, respectively, under serum-free conditions as well as on surfaces modified with EGF cultured under serum-free and exogenous EGF-free conditions. In this case, unlike other studies in which various proteins including EGF and a bovine pituitary extract are added back to the medium, potential exogenous stimulatory effects of adsorbed and soluble proteins in the medium were eliminated. As shown in Figure 5C,D, cells readily adhere to, spread, and mitose on the peptide-modified surfaces **4** and **5**, respectively, to give confluent monolayers in less than 96 h. Significantly lower levels of confluence were observed on both the control and on the PEO-modified silicone surfaces (*13*), respectively (Figure 5A,B; see also Supporting Information).

The lack of cell adhesion on the PEO-modified surfaces in particular is not surprising given that PEO has been widely described as cell and protein repellent. In fact, under conditions where there were no exogenous factors present in the medium, the surfaces were completely cell-free after 5 days of culture. Confluent epithelial cell monolayers could be formed on the EGF-modified surfaces **8** as rapidly in as rapidly as 5 days, demonstrating that the tethered EGF was active and able to stimulate the production of extracellular matrix proteins (Figure 5E, see also Supporting Information).

DISCUSSION

The NSC group, related to NHS esters, has become one of the 'workhorse' functional groups for the attachment of biological molecules to various supports because it is mild and selective for amines over alcohols, and it reacts with both groups faster than with water (*30*). PEO is a polymer widely exploited by the biomaterials community because of the water-swollen layer it forms that is known, particularly in in vitro assays, to passivate surfaces from adsorption by various biomolecules (*8*). We chose to combine these two elements in the development of our generic surfaces **3**. In this regard, we have borrowed from a key finding of Castner, who described the use of polyfunctional silanes, including NHS groups, for the preparation of well-defined gold surfaces on to which protein absorption could be studied (*21*). The preparation of NHS surfaces as self-assembled monolayers on gold surfaces are excellent model systems. However, these surfaces are not readily adaptable to complex devices themselves or to coatings on devices composed of other polymers.

There are important distinctions between this work and previous reports. First, an advantage of this method is that any silicone elastomer will suffice for the biological surface modification described. Thus, one can exploit the ability of silicone materials to form complex shapes, for example, in various molding applications, or their ability to form conformal films on a variety of substrates.

Second, a network is not formed on the surface. Instead, a series of monofunctional PEO chains, of approximately the same length (dependent on the original PEO polydispersity), are grafted onto a silicone. That is, the NSC functional PEO chains act as a brush to which biological molecules can covalently adhere. The concentration of these groups is enhanced by the absence of water in the brush-forming process, such that PEO swelling is reduced (*9*). These monofunctional species provide a more predictable distribution of functional groups along the surface than can a network system and, of course, the functional groups are only arrayed across the surface XY plane.

The generic utility of these modified silicone surfaces **3** to create biologically modified surfaces is amply demonstrated by the wide variety of biomolecules that can be readily grafted to them, in high density (ca.0.1−0.2 molecules/nm^2), to give **6**−**10**, and the maintenance of the bioreactivity of the tethered molecules after modification (**11**−**13**), which can make the surface compatible and/or render it usefully bioactive.

A simple two-step synthetic process, hydrosilylation of NSC−PEO onto a Si−H functional silicone and reaction of the NSC group with a biomolecule, permits generic modification of silicone substrates or conformal silicone coatings. The density of groups can be varied as can the nature of groups to facilitate rejection or attraction of available biomolecules. Proteins including enzymes, peptides, or polysaccharides are readily attached in stable form to give biocompatible, PEO-stabilized surfaces.

ACKNOWLEDGMENT

We acknowledge with gratitude the financial support by the Natural Sciences and Engineering Research Council of Canada.

Supporting Information Available: XPS data for surfaces **3**, **4**, and **5**; IR data for **1**−**5**. This material is available free of charge via the Internet at http://pubs.acs.org.

LITERATURE CITED

(1) Ratner, B., Hoffman, A., Schoen, F., and Lemons, J. (1996) Biomaterials Science. Academic, New York.

(2) Nicolson, P. C., Baron, R. C., Chabrecek, P., Court, Jo., Domschke, A., Griesser, H. J., Ho, A., and Hopken, J., et al. (1999) Extended wear ophthalmic lens. US Patent 5,965,631 (CIBA Vision and CSIRO).

(3) Shen, M., Wagner, M. S., Castner, D. G., Ratner, B. D., and Horbett, T. A. (2004) Multivariate Surface Analysis of Plasma-Deposited Tetraglyme for Reduction of Protein Adsorption and Monocyte Adhesion. *Langmuir 19*, 1692−1699.

(4) Shen, M., Martinson, L., Wagner, M. S., Castner, D. G., Ratner, B. D., and Horbett, T. A. (2002) PEO-like plasma polymerized tetraglyme surface interactions with leukocytes and proteins: in vitro and in vivo studies. *J. Biomater. Sci. Polym. Ed. 13*, 367−390.

(5) Gray, J. J. (2004) The interaction of proteins with solid surfaces. *Curr. Opin. Struct. Biol. 14*, 110−115.

(6) Ostuni, E., Chapman, R. G., Holmlin, R. E., Takayama, S., and Whitesides, G. M. (2001) A survey of structure−property relationships of surfaces that resist the adsorption of protein. *Langmuir 17*, 5605−5620.

(7) Chapman, R. G., Ostuni, E., Liang, M. N., Meluleni, G., Kim, E., Yan, L., Pier, G., Warren, H. S., and Whitesides, G. M. (2001) Polymeric thin films that resist the adsorption of proteins and the adhesion of bacteria. *Langmuir 17*, 1225−1233.

(8) Harris, J. M., and Zalipsky, S. (1997) *Polyethylene glycol: chemistry and biological applications*, American Chemical Society: Washington, DC.

(9) Kingshott, P., Thissen, H., and Griesser, H. J. (2002) Effects of cloud-point grafting, chain length, and density of PEG layers on competitive adsorption of ocular proteins. *Biomaterials 23*, 2043−2056.
(10) Wagner, M. S., Pasche, S., Castner, D. G., and Textor, M. (2004) Characterization of Poly(L-lysine)-graft-Poly(ethylene glycol) Assembled Monolayers on Niobium Pentoxide Substrates Using Time-of-Flight Secondary Ion Mass Spectrometry and Multivariate Analysis. *Anal. Chem. 76*, 1483−1492.
(11) Elbert, D. L., and Hubbell, J. A. (1996) Surface Treatments of Polymers for Biocompatibility. *Annu. Rev. Mater. Sci. 26*, 365−394.
(12) Kingshott, P., and Griesser, H. J. (1999) Surfaces that resist bioadhesion. *Curr. Opin. Solid State Mater. Sci. 4*, 403−412.
(13) Brook, M. A., Chen, H., and Sheardown, H. (2004) Silicone elastomers for reduced protein adsorption. *Biomaterials 25*, 2273.
(14) Ragheb, A., Brook, M. A., and Hrynyk, M. (2003) Highly activated, silicone entrapped, lipase. *Chem. Commun.* 2314−15.
(15) Brash, J. L. (2000) Exploiting the current paradigm of blood−material interactions for the rational design of blood-compatible materials. *J. Biomater. Sci. Polym. ed. 11*, 1135−1146.
(16) Bartzoka, V., McDermott, M. R., and Brook, M. A. (1999) Protein-Silicone Interactions. *Adv. Mater. 11*, 257−259.
(17) Anderson, J. M., Ziats, N. P., Azeez, A., Brunstedt, M. R., Stack, S., and Bonfield, T. L. (1995) Protein adsorption and macrophage activation on polydimethylsiloxane and silicone rubber. *J. Biomater. Sci. Polym. Edn. 7*, 159−170.
(18) This problem can be exacerbated by the leaching of untethered constituents, particularly small cyclic silicones. However, carefule vacuum stripping of the precursors and appropriately functionalized prepolymer constituents (i.e., those that ensure an excess of either vinyl or Si−H groups such that each chain will have multiple tethers to the network) can obviate these problems.
(19) Chojnowski, J. (1993) Polymerization. In *Siloxane Polymers* (Clarson, S. J., Semlyen, J. A., Eds.) pp 1−17, Chapter 1, PTR Prentice Hall, Englewood Cliffs, NJ.
(20) Kossmehl, G., Quast, D., and Schafer, H. (1982) Process for rendering silicone rubber contact lenses hydrophilic. US Patent 4,-332,922 (to Titmus Eurocon).
(21) Xia, N., Hu, Y., Grainger, D. W., and Castner, D. G. (2002) Functionalized Poly(ethylene glycol)-Grafted Polysiloxane Monolayers for Control of Protein Binding. *Langmuir 18*, 3255−3262.
(22) Harder, P., Grunze, M., Dahint, R., Whitesides, G. M., and Laibinis, P. E. (1998) Molecular Conformation in Oligo(ethylene glycol)-Terminated Self-Assembled Monolayers on Gold and Silver Surfaces Determines Their Ability To Resist Protein Adsorption. *J. Phys. Chem. B 102*, 426−436.
(23) Irvine, D. J., Mayes, A. M., Satija, S. K., Barker, J. G., Sofia-Allgor, S. J., and Griffith, L. G. (1998) Comparison of tethered star and linear poly(ethylene oxide) for control of biomaterials surface properties. *J. Biomed. Mater. Res. 40*, 498−509.
(24) Grigsby, J. J., Blanch, H. W., and Prausnitz, J. M. (2001) Cloud-point temperatures for lysozyme in electrolyte solutions: effect of salt type, salt concentration and pH. *Biophys. Chem. 91*, 231−243.
(25) Lawrence, C. C., Yuan, W., and Shanafelt, A. B. (2003) Particles for immunoassays and methods for treating the same. US Patent Appl. 20030092201.
(26) Chen, H., Brook, M. A., Chen, Y., and Sheardown, H. (2005) Surface properties of PEO-silicone composites: reducing protein adsorption. *J. Biomater. Sci., Polym. Ed. 16*, 531−548.
(27) Chen, H., Zhang, Z., Chen, Y., Brook, M. A., and Sheardown, H. (2005) Protein Repellant Silicone Surfaces by Covalent Immobilization of Poly(Ethylene Oxide). *Biomaterials 26*, 2391−2399.
(28) Davidson, H. J., and Kuonen, V. J. (2004) The tear film and ocular mucins. *Vet. Ophthalmol. 7*, 71−78.
(29) Sefton, M. V., Sawyer, A., Gorbet, M., Black, J. P., Cheng, E., Gemmell, C., and Pottinger-Cooper, E. (2001) Does surface chemistry affect thrombogenicity of surface modified polymers? *J. Biomed. Mater. Res. 55*, 447−59.
(30) Hermanson, G. T. (1996) Bioconjugate Techniques. Academic, New York.

BC050174B

Synthesis and Evaluation of Novel Dendrimers with a Hydrophilic Interior as Nanocarriers for Drug Delivery

Renu Singh Dhanikula and Patrice Hildgen*

Faculty of Pharmacy, University of Montreal, Montreal, Québec, Canada, H3C 3J7. Received June 27, 2005; Revised Manuscript Received August 9, 2005

Novel polyester-*co*-polyether dendrimers consisting of a hydrophilic core were synthesized by a combination of convergent and divergent syntheses. The core was synthesized from biocompatible moieties, butanetetracarboxylic acid and aspartic acid, and the dendrons from PEO (poly(ethylene oxide)), dihydroxybenzoic acid or gallic acid, and PEG monomethacrylate. The dendrimers, Den-1-(G 2) (second generation dendrimer-1) and Den-2-(G 2) (second generation dendrimer-2) consisting of 16 and 24 allyl surface groups, respectively, were obtained by coupling the dendrons to the core. The dendrimer (Den-1-(G 2)-OH) with hydroxyl groups at the surface was synthesized by oxidation of the allyl functional groups of Den-1-(G 2), which was divergently coupled to the dendrons to obtain the third generation dendrimer Den-1-(G 3) consisting of 32 surface groups. The modifications in surface groups and generation of dendrimers were shown to influence the shape of dendrimers in the AFM studies. The aggregation as well as self-assembly of dendrimers was observed at high concentration in water by light scattering studies; however, it was reduced on dilution and in the presence of sodium chloride. Dendrimers demonstrated good ability to encapsulate the guest molecule, with loading of 15.80 and 6.47% w/w for rhodamine and β-carotene, respectively. UV spectroscopy proved the absence of any $\pi-\pi$ complexation between the dendrimer and encapsulated compounds. ^{1}H NMR and FTIR studies showed that the physical entrapment and/or hydrogen bonding by PEO in the interior and branch of the dendrimer are the mechanisms of encapsulation. The release of the encapsulated compounds was found to be slow and sustained, suggesting that these dendrimers can serve as potential drug delivery vehicles.

INTRODUCTION

The discovery and development of new and potent drug molecules is time-consuming and a costly process. It is estimated that every new drug takes 12 to 15 years to develop, at an approximate cost of $800 million (*1*, *2*). A more economical and viable strategy is to devise effective delivery systems for drugs that have failed to provide optimum therapeutic benefit. It is stated that controlled release of drug at specific target can significantly improve the effectiveness of a drug and thereby increase the therapeutic benefit (*3*). The two most common delivery systems that have been explored for this purpose are liposomal and polymeric systems. The poor stability of liposome-based delivery systems has limited their applicability and market potential. On the other hand, polymeric systems remain one of the most widely sought delivery vehicles by virtue of their high stability. Furthermore, advances in the polymer chemistry have constantly provided avenues to the drug delivery scientists to explore these polymeric architectures for providing more efficient drug delivery. Various categories of polymeric materials that have been discovered in the past century include linear, cross-linked, branched, and dendritic polymers (*4*). Among these polymeric scaffolds, dendrimers have well defined nanoscopic dimensions, with highly branched structure and a discrete number of end functional groups. These characteristics endow them with many intriguing properties such as globular shape (resembling proteins), monodisperse size, and presence of internal cavities. By virtue of these properties, evaluation and application of dendrimers in drug delivery is becoming one of the most lucrative areas of drug research.

* Author for correspondence: Dr. Patrice Hildgen, Associate Professor, Pavillon Jean-Coutu C.P. 6128, Succursale Centre-ville Montréal (Québec) H3C 3J7 Canada, Tel: 1−514-343-6448, Fax: 514-343-2102, E-mail: patrice.hildgen@umontreal.ca.

Dendrimers can be used to deliver drugs either by encapsulating the drug in an internal cavity or by conjugating it to surface functionalities *(5)*. Since the conjugation of drugs to polymers is a time-consuming process and could sometimes result in decreased therapeutic benefit (due to failure of conversion to parent drug or decreased permeability of the conjugate) (*6*, *7*), the encapsulation of the drug by dendrimers seems to be the more attractive approach. Recent studies have shown that they can act as potential carriers for small guest molecules (*8*−*11*). However, the biocompatibility and cytotoxicity of these polymers are the major concerns for drug delivery application. The most widely used dendrimers, such as PAMAM, poly(propylene imine) and poly(aryl ether) dendrimers, are rendered cytotoxic by virtue of the presence of aromatic rings or amino groups at the periphery. The covalent attachment of poly(ethylene glycol) (PEG) to the PAMAM dendrimers has shown to reduce the cytotoxicity (*12*). PEGylation of dendrimers can also significantly reduce immunogenecity and antigenecity by shielding the system from recognition by the defense mechanism of the body. It also prevents sequestration and uptake by reticuloendothelial system (*13*) and thereby prolongs circulation time in the body. Another major concern on application of these dendrimers to drug delivery is the presence of amidoamine and ether linkages that are inherently resistant to degradation and hence limits their biodegradability. Incorporation of hydrolyzable linkages such as the ester bond is of particular interest to increase biodegradability of these delivery vehicles (*14*).

It is a rationale in drug delivery that the presence of a hydrophobic core is essential for encapsulating hydrophobic drug molecules, and, in general, polymeric micelles are tailored based on this concept. However, recently Ooya et al. synthesized polyglycerol dendritic polymers and reported a 3-fold increase in the water solubility of paclitaxel (*10*). Due to the absence of

10.1021/bc050184c CCC: $33.50 © 2006 American Chemical Society
Published on Web 11/30/2005

the hydrophobic region in the dendrimer, hydrotropic solubilization was proposed to be the probable mechanism of solubilization of paclitaxel. PEG is a biocompatible polymer, utilized as a *cosolvent* or hydrotropic agent (*15*) to enhance the solubility of poorly water soluble drugs (*16*). There are a number of reports in the literature on the use of PEG grafts of various dendrimers to increase the encapsulation of drugs (*8, 17*−*19*). It is also reported that PEG 400 increases the aqueous solubility of β-estradiol by 4- to 5-fold at high concentrations (*20*). On the basis of these observations, we hypothesized that introduction of poly(ethylene oxide) (PEO) in the cavity of the dendrimer will not only increase the size of the cavity but also will provide the dendrimers ability to encapsulate both water soluble and poorly water soluble compounds, in contrast to drug carriers with a hydrophobic core, which preferentially encapsulate hydrophobic compounds. Thus, we devised a new approach to enhance the solubility of compounds as well as the encapsulation of drugs by using PEO in the dendrimer cavity.

The aim of this study was to synthesize dendritic nanocarriers with a hydrophilic interior/cavity composed of PEO as drug delivery vehicles. Dendrimers were synthesized using butanetetracarboxylic acid as core molecule and composed of allyl or hydroxyl groups as surface functionalities. The synthesized dendrimers were characterized for their chemical and physical properties. Their ability to act as drug carrier was evaluated by encapsulating rhodamine and β-carotene as model hydrophilic and hydrophobic compounds, respectively. Further, the mechanism of encapsulation of compounds by dendrimers was also studied.

EXPERIMENTAL SECTION

Materials. Rhodamine, β-carotene, 1,2,3,4 butanetetracarboxylic acid, L-aspartic acid, PEG (M_n 400), PEG monomethacrylate (M_n 360), 3,5-dihydroxybenzoic acid (DHBA), 4-(dimethylamino)pyridine (DMAP), 1-ethyl-3-[3-(dimethylamino)-propyl]carbodiimide hydrochloride (EDC), gallic acid, hydroxybenztriazole (HOBT), borane−tetrahydrofuran complex (BH_3−THF, IM), *p*-toluenesulfonic acid monohydrate (TsOH), chromium trioxide (CrO_3), hydrogen peroxide (H_2O_2), triethylamine, sodium chloride, sodium hydroxide (NaOH), urea, activated carbon 4−14 mesh granular, and filter aid Celite521 were purchased from Sigma-Aldrich Inc., (St. Louis, MO). Anhydrous pyridine, *N*,*N*-dimethylformamide (DMF), dimethyl sulfoxide-d_6 (99.9% D) (DMSO-d_6), and $CDCl_3$ (99.9% D) were supplied from Aldrich Chemicals Inc. (Milwaukee, WI). Acetone, dichloromethane, methanol, chloroform, anhydrous diethyl ether, tetrahydrofuran (THF), sulfuric acid, and silica gel (70−230) were purchased from Laboratoire Mat. (Montreal, Québec), and thionyl chloride was purchased from A & C Chemicals Ltd. (Montreal, Québec). THF was dried over sodium while dichloromethane was dried with molecular sieves; all other solvents were used without purification unless specified otherwise.

Characterization Techniques. ^{1}H NMR and ^{13}C NMR spectra were recorded with Bruker ARX400 NMR spectrometer (Bruker Biospin, Billerica, MA) at 400 MHz using tetramethylsilane (TMS) as internal reference. FTIR spectroscopy was performed using a Bruker vector 22 spectrometer (Bruker Optik GmbH, Ettlingen, Germany), and the matrix-associated laser desorption ionization-time-of-flight (MALDI-TOF) mass spectroscopy of dendrimers was performed on a Bruker Autoflex (Bruker Daltonik GmbH, Bremen, Germany) in linear, positive ion mode using dithranol as matrix and sodium iodide as cationizing agent. The molecular weights of dendrimers were also determined by gel permeation chromatography (GPC) with Waters system (Waters, Milford, MA) equipped with refractive index detector, using DMF as mobile phase at a flow rate of 1 mL/min.

Synthesis of Core (3). Butane-1,2,3,4-tetracarboxylic acid (**1**) (5.00 g, 0.021 mol) was dried under vacuum for 24 h. Thionyl chloride (5 mL) was added dropwise to the reactant over a period of 15 min, followed by reflux at 50 °C for 6 h under nitrogen atmosphere. Subsequently, thionyl chloride was removed by evaporation under reduced pressure, and the product was dried under vacuum for 48 h to obtain compound **2**.

L-Aspartic acid (7.71 g, 0.058 mol) was added to compound **2** (4.50 g, 0.0144 mol), and the flask was purged with nitrogen for 15 min to displace any moisture. Anhydrous pyridine (20 mL) was added dropwise at room temperature under nitrogen atmosphere. The above solution was refluxed at 60 °C for 12 h. Pyridine was evaporated by rotavaporation, and the white product obtained was purified by column chromatography using dichloromethane:acetone:water (1:2:0.5). The solvents were evaporated under reduced pressure, and product obtained was dried under vacuum for 48 h. Yield: 90%; ^{1}H NMR (δ, ppm, D_2O): 5.52 (q, 4H, C*H*NH), 4.93 (d, 2H, N*H*CO), 4.91 (d, 2H, N*H*CO), 3.92 (q, 2H, C*H*CO), 3.30 (d, 8H, CH_2COOH), 2.85 (d, 4H, CH_2CO); ^{13}C NMR (δ, ppm, D_2O): 174.94, 174.11, 173.44, 42.83, 34.15, 33.87, 14.75; Anal. calculated (%): C (41.51), H (4.35), N (8.07); observed (%): C (41.53), H (4.80), N (8.65).

Synthesis of Poly(oxyethylene) (POE) Monomethacrylate Carboxylic Acid (4). PEG monomethacrylate (20 g, 0.055 mol) was dissolved in 200 mL of acetone at room temperature. The solution was cooled to 0 °C by placing the flask in ice bath. Later, 9 mL of Jones reagent (containing 0.02 M CrO_3) was added dropwise over a period of 15 min. The flask was removed from ice bath after 30 min, and the reaction was allowed to occur at room temperature for 18 h. The reaction was quenched by adding 5 mL of isopropyl alcohol. Subsequently, 2 g of finely powdered activated carbon (10% w/w) was added and stirred for 2 h. This was filtered over wet Celite, and the filtrate was evaporated on a rotavapor. The viscous liquid obtained was dissolved in water and extracted with dichloromethane, and the extracts were combined and evaporated to obtain the product which was dried under vacuum for 48 h. Yield: 95%; ^{1}H NMR (δ, ppm, DMSO): 6.02 (s, 1H, trans CH_2═CH), 5.64 (s, 1H, cis CH_2═CH), 4.18 (t, 2H, CH_2), 3.62 (t, 2H, CH_2), 3.46 (m, 24H, OCH_2CH_2O), 1.83 (s, 3H, CH_3); ^{13}C NMR (δ, ppm, DMSO): 167.15, 159.40, 73.45, 70.80, 69.28, 64.70, 61.70, 18.18. Anal. calculated (%): C (51.66), H (8.39); observed (%): C (51.65), H (8.88). FTIR (neat) ν_{max} cm^{-1}: 2883, 1753, 1467, 1358, 1279, 1239, 1145, 1101, 1062, 967, 842, 528.

Synthesis of POE−DHBA (6). Compound **4** (11.00 g, 0.029 mol) was purged with nitrogen for approximately 15 min, and thionyl chloride was added dropwise at room temperature. It was then refluxed at 50 °C for 7 h. Thionyl chloride was evaporated under reduced pressure, and the viscous liquid obtained was dried under vacuum to obtain compound **5**.

Compound **5** (11.00 g, 0.028 mol) was dissolved in pyridine under nitrogen atmosphere, and to this solution was added DHBA (1.96 g, 0.0127 mol). Reactants were refluxed at 50 °C for 18 h. Thereafter, pyridine was evaporated by rotavaporation and product was precipitated in diethyl ether. It was further purified by gel chromatography (Sepharose CL-4B) using water at pH 7.4 as eluent. The product was recovered as a viscous liquid by freeze-drying. Yield: 93%; ^{1}H NMR (δ, ppm, DMSO): 6.77 (d, 2H, C*H*-aromatic), 6.40 (t, 1H, C*H*-aromatic), 6.00 (s, 2H, trans CH_2═CH), 5.65 (s, 2H, cis CH_2═CH), 4.15 (t, 4H, CH_2), 3.63 (t, 8H, CH_2), 3.50 (m, 54H, OCH_2CH_2O), 3.42 (t, 4H, CH_2), 3.39 (t, 4H, CH_2), 3.37 (t, 4H, CH_2), 1.85 (s, 6H, CH_3); ^{13}C NMR (δ, ppm, DMSO): 168.41, 167.55, 159.44, 147.13, 142.80, 136.80, 133.41, 128.29, 108.31, 73.33, 70.78, 69.26, 64.76, 61.19, 18.99. Anal. calculated (%): C (53.75), H (7.51); observed (%): C (54.29), H (7.43). FTIR (neat) ν_{max}

cm^{-1}: 2936, 2872, 1713, 1599, 1540, 1453, 1296, 1097, 1004, 944, 860, 772, 682, 608, 519.

Synthesis of Dendron 1, POE−DHBA−PEG (7). Compound **6** (5 g, 5.77 mmol) was dissolved in dichloromethane, followed by addition of PEG (400) (2.8 g, 7.00 mmol) and TsOH (1.14 g, 5.99 mmol). A Dean−Stark trap was placed on the mouth of the flask, and it was connected to refluxed condenser. The reaction was carried out at 50 °C for 24 h. Solvent was evaporated under reduced pressure, and the product was precipitated in diethyl ether. Subsequently, it was purified by column chromatography using a mobile phase composed of dichloromethane, ethanol, and acetic acid (2:1:0.05). The product was further purified by dialysis against deionized water for 72 h (Spectra/Por no.1 dialysis tubing, MWCO 1000 Da). The dialysate was freeze-dried to obtain the product (79% yield).

Another method was also employed to synthesize dendron 1. In this method, compound **6** (8 g, 0.0092 mol) was dissolved in dichloromethane. Later, PEG (400) (4.4 g, 0.011 mol), EDC (2.76 g, 0.014 mol), DMAP (0.15 g, 0.0012 mol), and HOBT (0.2025 g, 0.0015 mol) were added to the flask. The reaction was allowed to occur for 24 h at room temperature. The precipitate of EDCU (1-ethyl-3-[3-(dimethylamino)propyl]carbodiimide urea) was removed by filtration, and solvent was evaporated. The precipitate was purified by using the same procedure as mentioned in the previous method and was freeze-dried to obtain the product (88% yield). The later method was found to improve the product yield as well as purity; thus, it was used for other synthetic steps. ^{1}H NMR (δ, ppm, DMSO): 6.81 (d, 2H, C*H*-aromatic), 6.48 (t, 1H, C*H*-aromatic), 6.01 (s, 2H, trans CH_2═CH), 5.67 (s, 2H, cis CH_2═CH), 4.42 (s, 4H, CH_2), 4.15 (t, 4H, CH_2), 3.69 (t, 4H, CH_2), 3.65 (t, 8H, CH_2), 3.49 (m, 98H, OCH_2CH_2O), 3.45 (t, 4H, CH_2), 3.43 (t, 4H, CH_2), 2.07 (t, 1H, OH), 1.85 (s, 6H, CH_3); ^{13}C NMR (δ, ppm, DMSO): 168.41, 167.54, 159.45, 146.94, 142.92, 136.81, 133.41, 128.24, 108.31, 73.34, 70.79, 69.26, 64.76, 64.61, 62.99, 61.19, 53.95, 51.93, 18.19. Anal. calculated (%): C (53.99), H (8.11); observed (%): C (53.09), H (8.39). FTIR (neat) ν_{max} cm^{-1}: 2933, 2873, 1716, 1598, 1540, 1453, 1295, 1185, 1128, 1003, 946, 862, 815, 771, 680, 597.

Synthesis of Dendrimer-1-(G 2) (8). Dendrimer was synthesized by coupling the core with dendron 1. Briefly, compound **7** (2.02 g, 1.60 mmol) was dissolved in DMF. To this were added compound **3** (0.124 g, 0.18 mmol), EDC (0.35 g, 1.83 mmol), and DMAP (0.18 g, 1.48 mmol). The reaction was allowed to occur for 96 h at room temperature. The EDCU precipitate was filtered, and the filtrate was precipitated in diethyl ether. The product obtained was dialyzed (Fisher Scientific dialysis tubing, MWCO 3500 Da) against deionized water for 72 h, and the dialysate was freeze-dried. Yield: 75%; ^{1}H NMR (δ, ppm, DMSO): 8.27 (d, 16H, C*H*, aromatic), 7.02 (t, 8H, C*H*, aromatic), 6.03 (s, 16H, trans CH_2═CH), 5.69 (s, 16H, cis CH_2═CH), 4.36 (s, 2H, N*H*CO, core), 4.34 (s, 2H, N*H*CO, core), 4.19 (t, 32H, CH_2), 4.14 (t, 32H, CH_2), 4.07 (t, 64H, CH_2), 3.93 (s, 4H, C*H*-NH, core), 3.79 (t, 32H, CH_2), 3.65 (m, 32H, CH_2), 3.42 (m, 386H, OCH_2CH_2O), 3.19 (t, 32H, CH_2), 2.95 (2H, C*H*CO, core), 2.20 (s, 8H, CH_2CO, core), 2.17 (s, 4H, CH_2, core), 1.88 (s, 6H, CH_3); ^{13}C NMR (δ, ppm, DMSO): 165.39, 165.31, 164.64, 164.58, 159.76, 159.68, 152.60, 152.19, 131.69, 131.24, 126.85, 122.41, 115.83, 108.76, 71.57, 70.80, 69.21, 64.76, 61.91, 61.22, 44.61, 26.91, 19.01. Anal. calculated (%): C (52.61), H (7.88), N (0.70); observed (%): C (51.97), H (8.34), N (0.80). FTIR (neat) ν_{max} cm^{-1}: 2935, 2870, 1728, 1649, 1540, 1454, 1350, 1100, 947, 878, 771.

Synthesis of Dendrimer-1-(G 2)-OH (9). The allyl surface functional groups in dendrimer (Den-1-(G 2)) were oxidized to the hydroxyl group to obtain den-1-(G 2)-OH. For this purpose, compound **8** (0.1 g, 12.9 μmol) was dissolved in a mixture of DMF and THF (1:20; dried over molecular sieves) at room temperature. Later, the solution was cooled to 0 °C by placing the flask in ice bath. Thereafter, BH_3−THF (12.9 μmol) was added dropwise over a period of 5 min, and the contents were stirred at 0 °C for another 15 min. The reaction was allowed to occur at room temperature for 18 h. The excess reagent was hydrolyzed by addition of water, and 3 N NaOH (11.6 μmol) was added. After 15 min, 30% H_2O_2 (25.8 μmol) was added dropwise, and the solution was stirred for another 5 h. The product was purified by dialysis (MWCO 3500 Da) against deionized water for 72 h. Yield: 85%; ^{1}H NMR (δ, ppm, DMSO): 7.67 (d, 16H, C*H*, aromatic), 7.18 (s, 8H, C*H*, aromatic), 4.47 (s, 16H, OH), 3.90, 3.79 (m, 379H, OCH_2CH_2O), 3.61 (s, 4H, C*H*NH, core), 3.57 (t, 64H, CH_2), 2.91 (s, 2H, C*H*CO, core), 2.90 (s, 8H, CH_2CO, core), 2.13 (s, 4H, CH_2, core), 1.37 (d, 48H, CH_3); ^{13}C NMR (δ, ppm, CD_3OD and pyridine-d_5): 164.73, 160.23, 159.97, 153.05, 15.84, 145.14, 131.78, 114.91, 104.43, 79.87, 75.84, 70.92, 68.06, 65.08, 59.11, 54.65, 30.93, 30.11, 23.72. Anal. calculated (%): C (50.78), H (7.99), N (0.67); observed (%): C (50.91), H (8.07), N (1.30). FTIR (neat) ν_{max} cm^{-1}: 3280, 2949, 2873, 2360, 1917, 1868, 1835, 1732, 1649, 1599, 1543, 1513, 1451, 1291, 1188, 1132, 1083, 1000, 947, 867, 807, 770, 673.

Synthesis of Dendrimer-1-(G 3) (10). Compound **9** (0.10 g, 0.013 mmol) was dissolved in DMF, and compound **6** (0.22 g, 0.28 mmol), EDC (0.07 g, 0.36 mmol), and DMAP (0.028 g, 0.23 mmol) were added to this solution. Reaction was allowed to occur for 96 h at room temperature. The EDCU precipitate was filtered, and the filtrate was dialyzed (MWCO 3500 Da) against deionized water for 72 h. The product obtained by precipitation of dialysate in diethyl ether was dried under reduced pressure. Yield: 81%; ^{1}H NMR (δ, ppm, DMSO): 6.97 (d, 32H, C*H*, aromatic), 6.51 (t, 32H, C*H*, aromatic), 6.00 (s, 64H, trans CH_2═CH), 5.66 (s, 64H, cis CH_2═CH), 4.35 (t, 64H, CH_2), 4.16 (t, 64H, CH_2), 3.61 (t, 128H, CH_2), 3.44 (m, 1239H, OCH_2CH_2O), 3.01 (t, 64H, CH_2), 1.84 (s, 192H, CH_3); ^{13}C NMR (δ, ppm, DMSO): 163.18, 163.16, 162.15, 158.27, 158.25, 144.33, 130.18, 130.16, 121.91, 107.25, 89.43, 87.79, 75.30, 69.38, 67.76, 64.25, 49.98, 23.92, 17.52. Anal. calculated (%): C (54.05), H (7.63), N (0.27); observed (%): C (55.47), H (6.15), N (0.60). FTIR (neat) ν_{max} cm^{-1}: 3334, 2949, 2874, 2361, 2335, 1916, 1867, 1835, 1792, 1738, 1648, 1598, 1549, 1514, 1452, 1341, 1289, 1187, 1130, 1082, 1000, 948, 863, 810, 770, 672, 585, 514.

Synthesis of POE-Gallate (11). Gallic acid (1.44 g, 0.0085 mol) was added to compound **5** (11 g, 0.028 mol), and the flask was purged with nitrogen to remove any moisture. Pyridine was added dropwise to the flask under nitrogen atmosphere, and the contents were refluxed at 50 °C for 18 h. Pyridine was evaporated under reduced pressure after completion of the reaction, and product was precipitated in diethyl ether. Finally, the product was dried in a vacuum for 48 h. Yield: 92%; ^{1}H NMR (δ, ppm, DMSO): 6.92 (s, 2H, C*H*-aromatic), 6.02 (s, 3H, trans CH_2═CH), 5.67 (s, 3H, cis CH_2═CH), 4.18 (t, 6H, CH_2), 3.81 (t, 6H, CH_2), 3.62 (m, 70H, OCH_2CH_2O), 1.86 (s, 9H, CH_3); ^{13}C NMR (δ, ppm, DMSO): 167.60, 146.39, 145.96, 143.98, 136.80, 128.75, 127.83, 126.87, 109.85, 71.55, 70.79, 69.26, 65.31, 64.76, 61.21, 18.96. Anal. calculated (%): C (52.96), H (7.69); observed (%): C (51.23), H (7.12). FTIR (neat) ν_{max} cm^{-1}: 2871, 1714, 1634, 1488, 1451, 1349, 1318, 1297, 1247, 1171, 1097, 1037, 945, 851, 775, 684, 579, 523.

Synthesis of Dendron 2, POE-Gallate-PEG (12). Compound **11** (5 g, 4.1 mmol) was dissolved in dichloromethane, followed by addition of PEG (400) (1.85 g, 4.6 mmol), EDC (1.33 g, 6.9 mmol), DMAP (0.55 g, 4.5 mmol), and HOBT (0.061 g, 0.45 mmol). Reaction was allowed to occur for 48 h at room temperature. Afterward, the EDCU precipitate was

filtered and filtrate was concentrated by rotavaporation. The product obtained was precipitated in a hexane and diethyl ether mixture (1:1). Finally, it was subjected to dialysis against deionized water for 72 h (MWCO 1000 Da). The product was obtained by freeze-drying of dialysate. Yield: 86%; ^{1}H NMR (δ, ppm, DMSO): 6.89 (s, 2H, C*H*-aromatic), 6.00 (s, 3H, trans CH_2═CH), 5.66 (s, 3H, cis CH_2═CH), 4.19 (t, 4H, CH_2), 4.03 (t, 6H, CH_2) 3.77 (t, 12H, CH_2), 3.46 (m, 106H, OCH_2CH_2O), 1.85 (s, 9H, CH_3); ^{13}C NMR (δ, ppm, DMSO): 167.36, 151.53, 149.53, 147.46, 146.51, 143.31, 136.55, 126.74, 110.13, 72.05, 70.62, 69.08, 64.92, 64.60, 64.51, 62.89, 61.08, 52.82, 50.80, 26.32. Anal. calculated (%): C (52.34), H (7.43); observed (%): C (52.51), H (7.42). FTIR (neat) ν_{max} cm^{-1}: 2870, 1715, 1635, 1540, 1507, 1488, 1456, 1349, 1297, 1096, 1032, 944, 844, 757, 682, 567.

Synthesis of Dendrimer-2-(G 2) (13). For the synthesis of den-2-(G 2), compound **12** (1.8 g, 1.11 mmol) was dissolved in DMF, and compound **3** (0.083 g, 0.12 mmol) was added to it. Later, EDC (0.27 g, 1.41 mmol) and DMAP (0.12 g, 0.98 mmol) were added. The reaction was allowed to occur at room temperature for 96 h. Subsequently, EDCU precipitate was filtered and the filtrate was dried under reduced pressure. The product obtained was precipitated in diethyl ether and dried under reduced pressure. It was later dialyzed (MWCO 3500 Da) against deionized water for 72 h, and the dialysate was freeze-dried to obtain the dendrimer. Yield: 73%; ^{1}H NMR (δ, ppm, DMSO): 7.29 (s, 16H, C*H*-aromatic), 5.57 (s, 24H, trans CH_2═CH), 5.52 (s, 24H, cis CH_2═CH), 3.48 (t, 16H, CH_2), 3.33 (m, 755 H, OCH_2CH_2O), 2.87 (s, 8H, CH_2CO, core), 2.71 (s, 4H, C*H*CH$_2$CO, core), 1.85 (s, 4H, CH_2, core), 1.69 (s, 2H, C*H*, core), 1.47 (t, 72H, CH_3). ^{13}C NMR (δ, ppm, DMSO): 167.56, 165.32, 163.44, 163.65, 151.66, 149.48, 147.26, 146.31, 143.45, 136.61, 126.82, 72.25, 70.82, 69.11, 65.02, 64.73, 64.65, 63.00, 61.16, 53.05, 50.95, 26.75, 18.93. Anal. calculated (%): C (52.34), H (7.17), N (0.55); observed (%): C (52.41), H (7.25), N (1.11). FTIR (neat) ν_{max} cm^{-1}: 2932, 2361, 1715, 1677, 1560, 1508, 1453, 1319, 1262, 1175, 1082, 1029, 947, 890, 754, 647, 540.

Determination of Acid Value of Core. The acid value of the core was determined by classical titration method. In brief, approximately 0.2 g of the compound was dissolved in 50 mL of water. The solution was titrated with 0.1 N NaOH using phenolphthalein as an indicator. The method was standardized using monocarboxylic acid (hexanoic acid), dicarboxylic acid (oxalic acid, succinic acid), and tetracarboxylic acid (butanetetracarboxylic acid) prior to determination of acid value of the core.

Acid value represents milliequivalents of NaOH per milligram of compound; it was calculated using the following equation:

$$\text{acid value} = (\text{mg of acid})/(\text{normality of NaOH}) \times (\text{mL of NaOH used in titration})$$

The theoretical acid value for a compound was obtained by normalizing molecular weight of compound by number of carboxylic groups.

Determination of the Hydroxyl Value of Dendrimer-1-(G 2)-OH. Pyridine-catalyzed acetylation and phthalation are standard methods for the determination of the hydroxyl value, which is the indicator of the number of hydroxyl groups in the compound. DMAP-catalyzed acetylation with acetic anhydride, reported to have specific catalytic activity 10^4 times greater than that of pyridine-catalyzed reactions (*21*), was utilized in this study. Approximately, 5−6 mequiv of the dendrimer (lyophilized to remove traces of moisture) was transferred to a dried stoppered tube under nitrogen atmosphere and was dissolved in 1 mL of pyridine (anhydrous). To this solution, 1 mL of freshly prepared acetic anhydride solution consisting of acetic anhydride and pyridine (1:4) was added. This was followed by the addition of 0.5 mL of a catalyst solution (2% w/v of DMAP in anhydrous pyridine). The reaction was carried out in strictly anhydrous conditions. The stoppered tubes were maintained at 50 °C for 18 h, because shorter reaction times have yielded incomplete acetylation of the dendrimer. After 18 h, 5 mL of water was added to the tube, and contents were brought to room temperature. Later, 25 mL of water was added to the solution (to ascertain complete hydrolysis of excess of acetic anhydride), and samples were incubated for approximately 15 min. All the samples were titrated with 0.1 N NaOH using phenolphthalein as indicator. A blank determination was carried out in exactly the same way. The hydroxyl value was calculated as follows:

$$\text{hydroxyl value} = ((V_{sample} - V_{blank}) \times N \times 1.701)/W_{sample}$$

where, V_{sample} is volume of 0.1 N NaOH used for sample, V_{blank} is volume of 0.1 N NaOH used for blank, N is normality of NaOH, and W_{sample} is the weight of sample used.

Particle Size Measurements. The size of the dendrimers was determined by Coulter Nanosizer, N4 plus (Coulter Corporation, Hialeah, Florida) and ALV/LSE−5003 (ALV-GmbH, Langen, Germany). Dendrimers were suspended in water (filtered through 0.22 μm) to obtain a concentration of 0.1 mg/mL. The samples were vigorously agitated and subsequently filtered through a 0.22 μm or 0.1 μm filter (wherever specified) to remove dust particles. Each experiment was performed in triplicate at 25 °C and at angle of 90°.

Differential Scanning Calorimetry (DSC). The thermal properties of dendrimers were determined by employing DSC as a tool. The experiments were performed in triplicate on Metler TA 4000 (Metler Toledo, Switzerland) which was calibrated by using indium as a reference. Samples weighing between 3 and 5 mg were placed in a standard aluminum pan with a pinhole and were scanned in the temperature range of −70 °C to 380 °C at a heating rate of 10 °C/min under nitrogen atmosphere.

Atomic Force Microscopy (AFM). AFM was done with Nanoscope IIIa, Dimension 3100 (Digital Instruments, Santa Barbara, CA) in tapping mode. In this mode, the tip spends less time on the sample surface, and as a result the lateral forces on the sample are reduced. Thus, it provides an opportunity to image delicate samples without severe distortion. Samples were prepared by dissolving the dendrimers in DMF at room temperature and later diluting with water. These were deposited on a freshly cleaved mica surface by spin coating (WS,-400A-6NPP/LITE, Laurell Tech Corporation, North Wales, PA) at 2000 rpm for a period of 1 min. The samples were allowed to dry at room temperature. Subsequently, they were imaged in air at ambient conditions using etched silicon probes with a tip radius of 5−10 nm and spring constant in the range of 20−100 N/m, oscillated at its fundamental resonant frequency (200−400 kHz).

Encapsulation Studies. The ability of the dendrimers to act as host for the molecules was determined by encapsulating rhodamine and β-carotene as hydrophilic and hydrophobic model compounds, respectively. The weighed amount of dendrimer was transferred to screw-capped vials and was dissolved in DMF. Later, a defined weight of compound to be encapsulated was added to the vials and stirred at room temperature. The unencapsulated drug was removed by dialysis of the solution against deionized water for approximately 18 h. The sink conditions for removal of β-carotene were maintained by increasing volume of water and addition of ethanol (10% v/v) in the dialysis medium. The dialysate was lyophilized to obtain freeze-dried dendrimer with encapsulated compounds. For the determination of the loading and encapsulation efficiency, a weighed amount of freeze-dried dendrimer was dissolved in

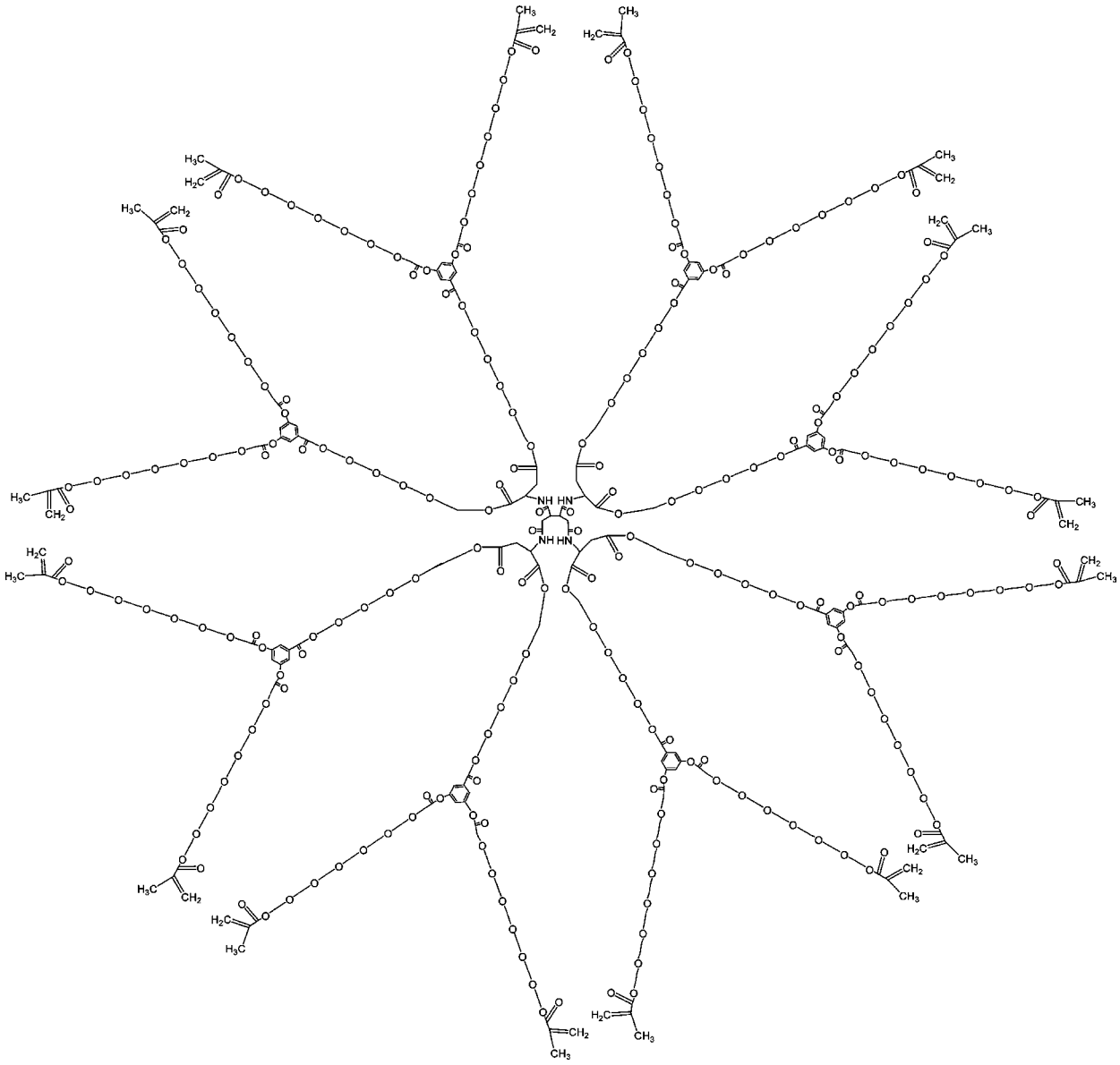

Figure 1. Structure of dendrimer-1 (den-1(G 2)).

DMF, and samples were analyzed with appropriate blank corrections for the dendrimer. Rhodamine was assayed fluorimetrically (excitation and emission wavelength 550 and 625 nm) using a SAFIRE microplate reader (Tecan, Salzburg, Austria), while β-carotene was determined at 460 nm (λ_{max}) using a UV spectrophotometer U-2001 (Hitachi High Technologies, Orlando, FL).

Release Studies. The release of encapsulated compounds from the dendrimers was studied using vertical, jacketed Franz diffusion cells with an area of 0.79 cm^2 (Permgear). The experiments were carried out at 37 °C, and phosphate buffer (0.1 M, pH 7.4) was used as the release medium for studying rhodamine release while ethanol and 0.1 M phosphate buffer (2:1) were used to maintain the sink conditions for β-carotene release experiments. A definite amount of dendrimer with encapsulated compound was added to 800 μL of respective release medium and was transferred into the donor compartment. It was separated from the receptor compartment containing 5 mL of release medium by a dialysis membrane MWCO of 3500 Da (equilibrated overnight with release medium at 37 °C). The samples were taken with replacement from the receptor compartment at each predetermined time point (1, 2, 3, 4, 6 h and later, after every 24 h) and assayed as mentioned in the previous section.

RESULTS AND DISCUSSION

Dendrimers can be synthesized by an iterative sequence of steps using either a divergent or convergent procedure (*22*). The divergent approach is reported to lead to structural defects and some difficulties in purification of the final product. However, the convergent approach is stated to minimize these synthetic problems, but it seems that steric hindrance in coupling of the dendron to the core molecule limits the synthesis of a higher generation of dendrimer by this approach. Thus, in the present work, dendrimers were synthesized using a strategic combination of both approaches, i.e., the core molecule was grown divergently to obtain multifunctional core, and this was then coupled to the dendron synthesized convergently, to obtain the final dendrimer. The higher generation dendrimer was synthesized by divergently coupling lower generation dendrimer to the dendrons. To the best of our knowledge, this is the first report on the combination of these two synthetic approaches for the synthesis of these dendrimers.

Synthesis and Characterization of Dendrimers. The polyester-*co*-polyether dendrimers containing PEO in the cavity were

Scheme 1. Synthesis of the Core

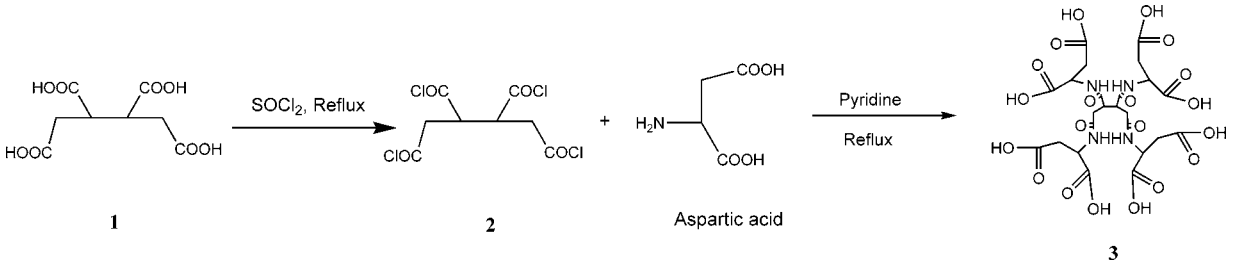

Scheme 2. Synthesis of Den-1-(G 2), Den-1-(G 2)-OH, and Den-1-(G 3)

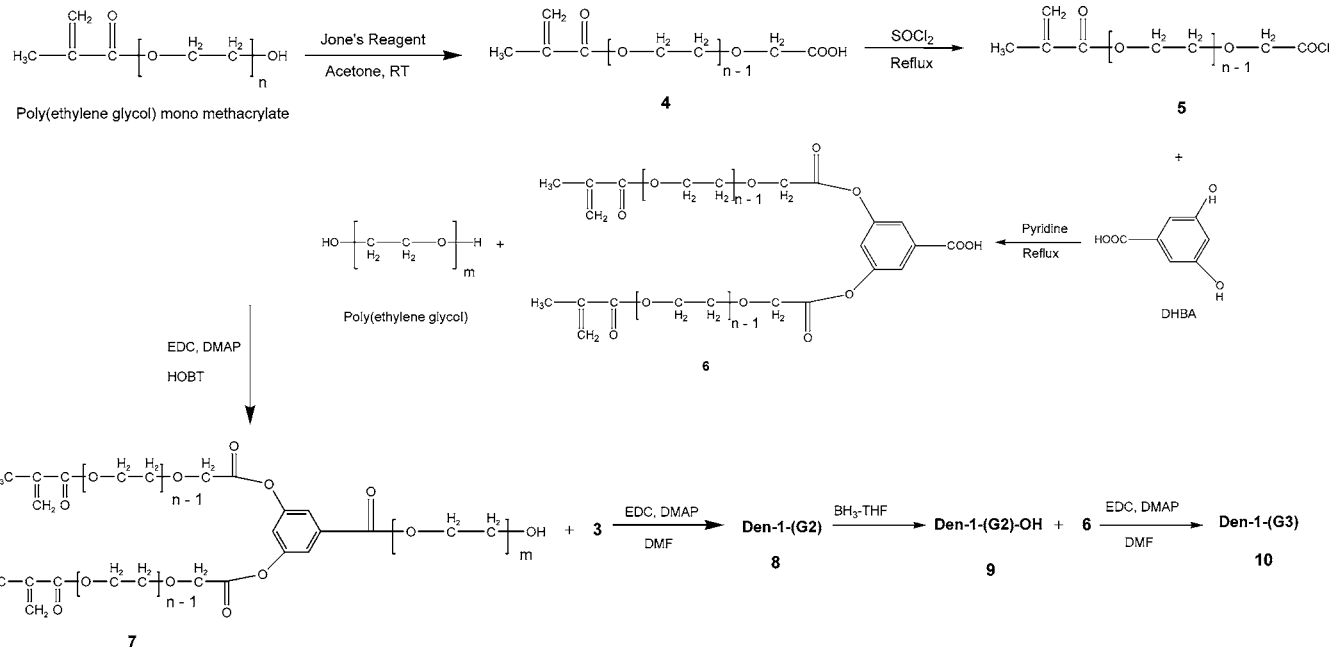

Scheme 3. Synthesis of Den-2-(G 2)

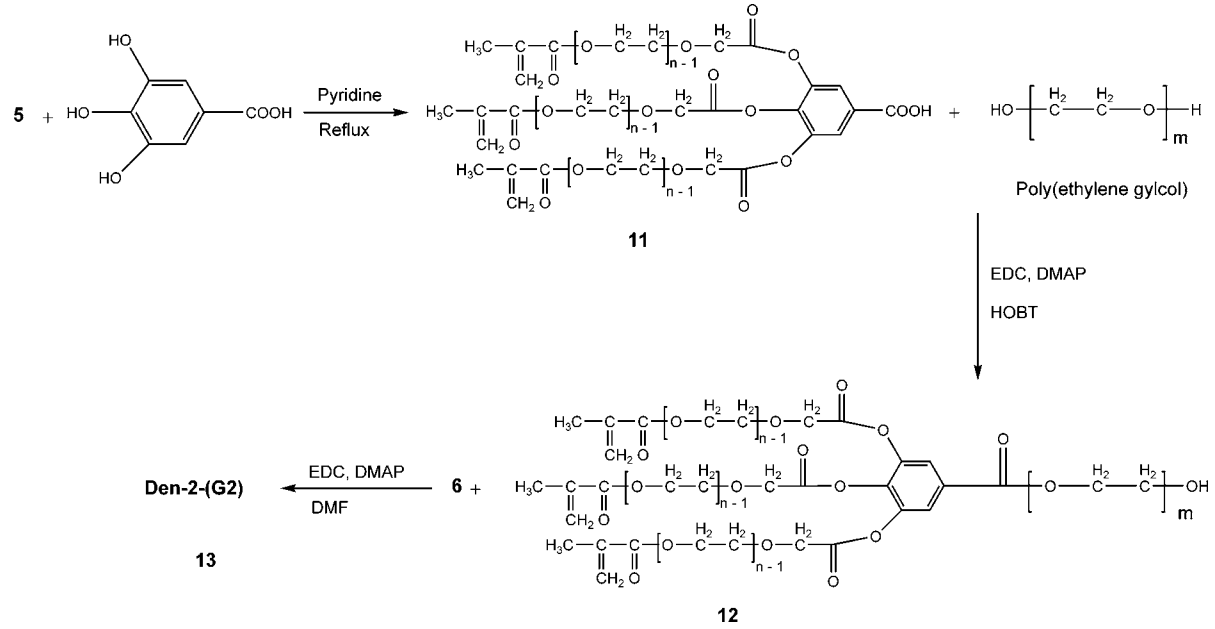

synthesized using a simple synthetic scheme by which den-1-(G 2) (Figure 1) could be obtained in seven reaction steps (Schemes 1 and 2). The use of PEO as a major building block helped in obtaining the desired molecular architecture in less synthetic steps. Trollsås et al. have also reported a similar strategy to obtain high molecular weight dendrimers of specific architecture by using poly(ϵ-caprolactone) as the building block (*23*). The synthesis was initiated by esterification of butanetetracarboxylic acid with an amino acid, aspartic acid, to obtain the core. The ^{1}H NMR, ^{13}C NMR, and elemental analysis showed successful synthesis of the core. To estimate the number of carboxylic acid groups in the core, the acid value/neutralization equivalent was determined (Table 1). The acid value for the core obtained by the titration method was within the

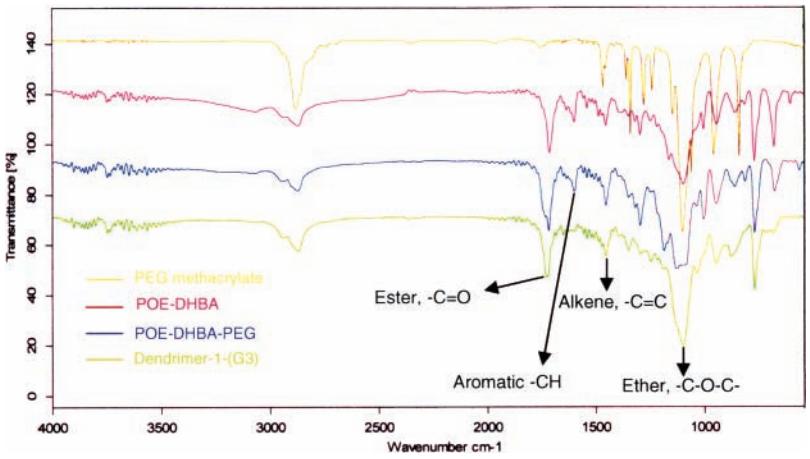

Figure 2. FTIR spectra of PEG monomethacrylate, POE-DHBA, dendron 1, and dendrimer (den-1-(G 2)).

Table 1. Acid Value of the Core Determined by the Titration Method

	sample	theoretical acid value	observed acid value[a]	calcd no. of carboxylic groups[b]
1	butane-tetracarboxylic acid	58.50	60.60 ± 0.26	3.86
2	core	86.75	88.58 ± 0.58	7.83

[a] Data are mean value ± SD ($n = 4$). [b] Average acid value was used for calculation.

experimental error of the method. Since the acid value is specific for each compound, it can be used as a derivative to identify it. This parameter can also be used to back calculate the number of carboxyl groups if the molecular weight is known. For the core, an acid value of 7.8 was obtained, substantiating that the synthesized core has eight carboxylic groups at the surface.

The dendron was synthesized convergently by esterification of compound **5** with DHBA for the synthesis of den-1-(G 2) and to gallic acid for the synthesis of den-2-(G 2) (Scheme 3), followed by esterification with PEG 400. The esterification was monitored by FTIR spectroscopy; the appearance of the ester C═O peak in the FTIR spectra of compound **6** (Figure 2) gave the evidence about the formation of an ester bond. In addition, the characteristic stretch of the alkene group at 1540 cm^{-1}, PEO between 1300 and 1500 cm^{-1}, and the C−O−C stretch at 1000−1200 cm^{-1} proved the incorporation of PEG monomethacrylate in compound **6**. Further esterification of compound **6** by PEG 400 was supported by the splitting of ester C═O and C−O ether peaks in the spectra of compound **7**, which confirmed the synthesis of a new ester bond as well as introduction of new ether bonds in the dendron.

It is reasonable to speculate that the methacrylate ester present in PEG monomethacrylate could be cleaved during the synthesis. To circumvent this probability, the reactions were carried out in the mildest possible conditions, and the peaks due to the allyl group of PEG methacrylate were followed throughout the synthesis as the marker. The existence of peaks due to cis and trans protons of the allyl group of PEG methacrylate in FTIR and ^{1}H NMR spectra (Figure 3 and 4) of compounds **5**−**8** indicated that the methacrylate moiety was not cleaved during the synthesis. Additionally, the relative integration area of allyl proton and benzyl protons showed the presence of two PEG methacrylate units per dendron in case of compound **6**, **7**, and **8** and three units in case of **11**, **12**, and **13**, respectively. Summarizing these observations, it was concluded that polyester-co-polyether dendrons with two and three allyl surface functionalities have been synthesized. Later, dendrons **7** and **12** were coupled to the multifunctional core to build dendrimers den-1-(G 2) and den-2-(G 2), respectively.

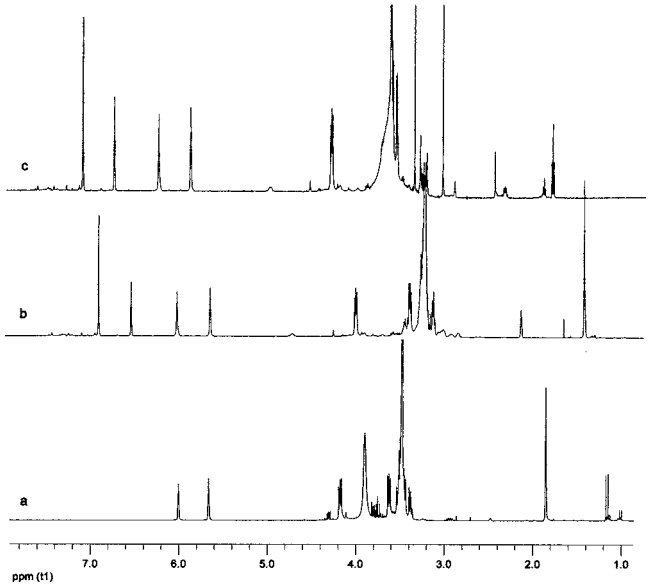

Figure 3. ^{1}H NMR spectra of (a) PEG-methacrylate, (b) POE-DHBA, (c) POE-DHBA-PEG in DMSO at 400 MHz.

The dendrimer den-1-(G 2)-OH was synthesized by hydroboration of dendrimer den-1-(G 2) (Scheme 2). The conversion of allyl functional group to hydroxyl was monitored by disappearance of the peak in the ^{1}H NMR spectra due to allylic protons (Figure 5) as well as by determination of hydroxyl value of the product. Initial incubation of 18 h was allowed to ensure complete addition of BH_3 to the allyl groups, and further reaction time of 5 h was found to be adequate to convert all allyl groups to hydroxyl groups.

It was previously reported that steric hindrance offered by hyperbranched polymers could lead to incomplete acetylation of hydroxyl groups and thus result in lower than expected hydroxyl values (*24*). Thus, to minimize the possibility of this experimental limitation, acetylation was performed at higher temperature and for a longer duration of time. Further, it was also reported that the presence of ethylene oxide units in the polymer could lead to erroneous results, and often hydroxyl values obtained are overestimated (*25*). Keeping this factor in consideration, dendrimers without any hydroxyl groups (i.e. den-1-(G 2)) were always titrated under similar conditions and were used to correct the final values obtained. The experimental hydroxyl value determined by titration was found to be 4.12 ± 0.57, which is in close agreement with the calculated value of 3.63 (calculated on the basis of molecular weight (M_n) of the dendrimer), thus confirming that all the allyl groups have been oxidized.

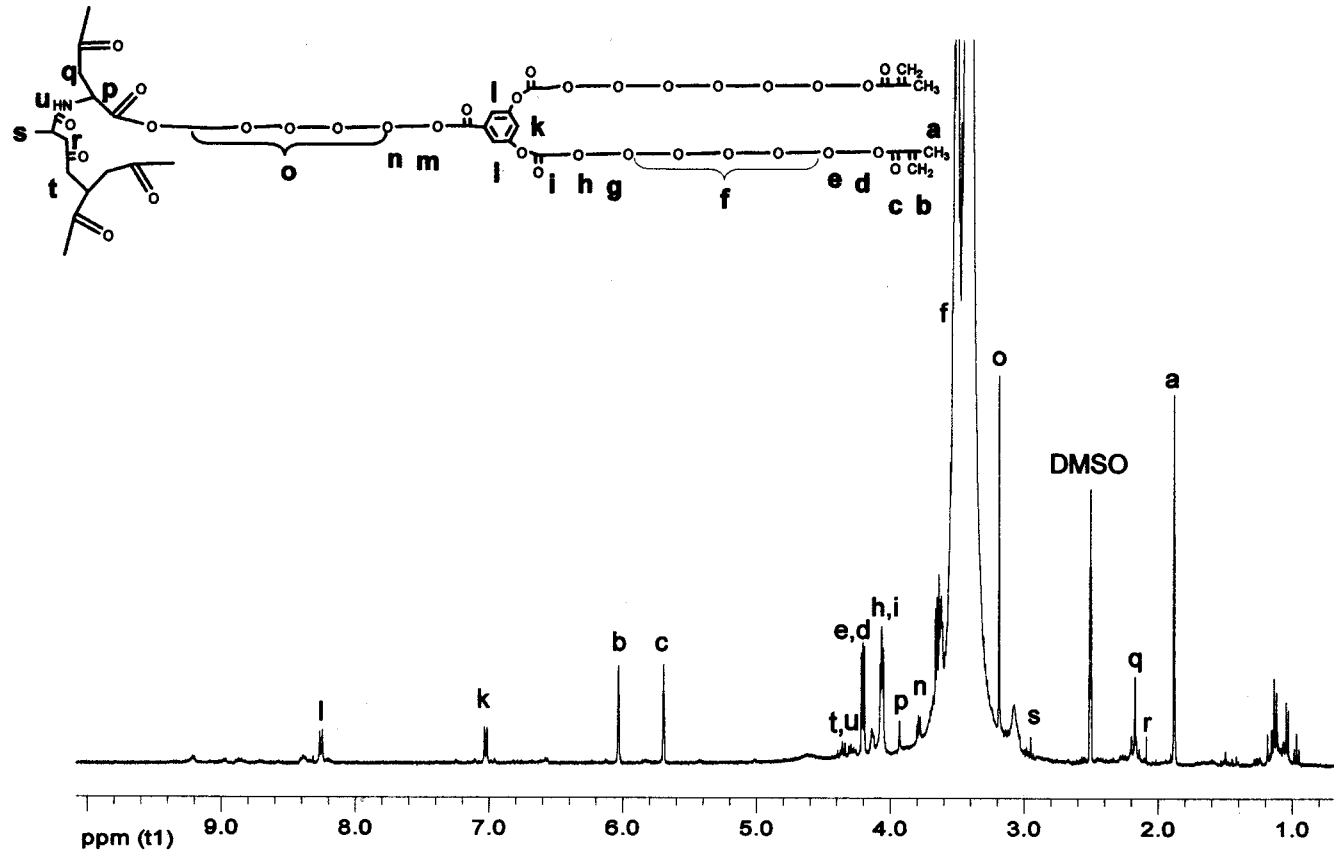

Figure 4. [1]H NMR spectrum of the dendrimer (Den-1-(G 2)) in DMSO at 400 MHz.

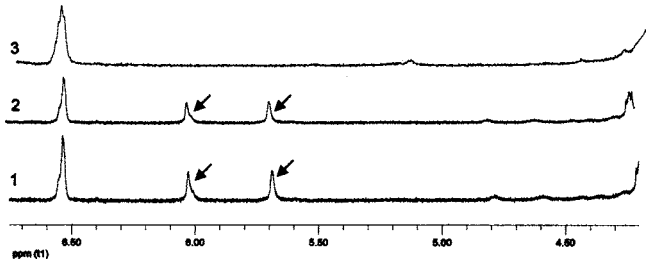

Figure 5. [1]H NMR spectra showing the disappearance of allylic cis and trans protons during oxidation to hydroxyl groups (1) with out any oxidation, (2) after approximately 50% oxidation, (3) after complete oxidation.

The higher generation dendrimer, den-1-(G 3), was synthesized by divergently coupling den-1-(G 2)-OH to POE-DHBA (**6**) in the presence of EDC and DMAP (Scheme 2). Characterization of den-1-(G 3) by routine instrumental techniques showed successful synthesis.

The characteristics of all the synthesized dendrimers are presented in Table 2. The M_n of dendrimers was determined by [1]H NMR, GPC, and MADLI-TOF. The M_n values determined by GPC are less than the expected theoretical values. This deviation is due to differences in hydrodynamic volume between dendrimers and linear PEG standards.

Particle Size Measurements. The size of the dendrimers was determined in water at various concentrations (data not shown). At a concentration of 1 mg/mL, size of about 200 nm was observed which indicated a high aggregation of the dendrimers. At lower concentrations (0.5 mg/mL), bimodal size distribution with an average size of 200 nm and a small population with an approximate size between 10 and 30 nm was observed for all dendrimers. It was also found that even after filtration through a 0.10 μm membrane, a dendrimer population with a size around 200 nm was obtained (data not shown), which indicated self-assembly of dendrimer after filtration of the sample. Percec et al. and Wang et al. have also reported self-assembly of dendrimers, which they explained to be mediated by various nondirectional forces such as hydrophobic, electrostatic interactions, and Coulombic forces, etc. (*26*, *27*). To overcome this problem, experiments were performed at a lower concentration (0.1 mg/mL), and the effect of various additives such as triethylamine, NaOH, HCl, DMF, methanol, acetone, urea, and sodium chloride was examined. Although triethylamine and methanol were found to reduce aggregation of dendrimers, they had no significant influence on self-assembly. Sodium chloride (0.25−0.35 M) inhibited not only aggregation but also the self-assembly phenomenon. Thus, hydrodynamic sizes of all the dendrimers were determined in sodium chloride solution, and results are shown in Table 2. Even though dendrimers showed aggregation under in vitro conditions, it is speculated that after in vivo administration, these aggregates will breakdown due to high dilution as well as presence of various biological substances (*28*). The absence of aggregates is significantly important for improved in vivo efficacy because the size of the drug carrier influences not only the circulation time in blood but also the endocytosis or uptake by the cells. The smaller particles are rapidly taken up by cells; thus, they can provide intracellular delivery and thereby increase the therapeutic efficacy.

Thermal Properties. It is reported that polymeric carriers undergo glass−rubber transition during the penetration of water, and this influences the drug release profile (*29*). Thus, thermal properties of polymers not only influence the stability but also the release of drug (*30*). All the synthesized dendrimers were investigated for their thermal properties and, in particular, glass transition temperature (T_g) by DSC. The T_g for PEG-methacrylate (**1**) was observed to be −67.50 °C which is close to the reported value of −65 °C. The T_g values for POE-DHBA and POE-DHBA-PEG were found to be −31.10 °C and −21.45 °C, respectively (Table 3), indicating an increase in the transition

Table 2. Characteristics of Dendrimers

	dendrimer	surface functional group	number of functional group	M_n (NMR)[a]	M_n (GPC)[b]	M_n (MALDI-TOF)	particle size (nm) (AFM)[c]	particle size (nm) (DLS)
1	dendrimer-1-(G 2)	$CH{=}CH_2$	16	8130	6909 (1.00)	7743	5.39	4.7 ± 0.4
2	dendrimer-1-(G 3)	$CH{=}CH_2$	32	16978	-	15072	11.13	8.5 ± 0.3
3	dendrimer-2-(G 2)	$CH{=}CH_2$	24	10096	-	11922	9.85	7.2 ± 0.4
4	dendrimer-1-(G 2) OH	OH	16	8024	6795 (1.01)	7325	9.05	5.3 ± 0.6

[a] Calculated based on the relative integration ratio of peaks with respect to the peak of the $CH{=}CH_2$ cis/trans proton or aromatic proton (in case of Den-1-(G 2)-OH). [b] Determined using PEG standards and DMF as mobile phase at a flow rate of 1 mL/min; value in brackets is polydispersity index. [c] Data are the mean value, determined by ≥30 measurements. [d] Data are the mean ± SD ($n = 3$).

Table 3. Details of Thermal Events for Various Dendrons and Dendrimers Obtained by DSC

	sample	T_g (°C)	T_m (°C)
1	PEG methacrylate	−67.50	-
2	POE-DHBA	−31.10	234.60
3	POE-DHBA-PEG	−21.45	293.20
4	dendrimer-1-(G 2)	−12.52	311.90
5	dendrimer-1-(G 3)	−10.89	308.30
6	dendrimer-1-(G 2)-OH	−13.50	300.60
7	POE-gallate	−45.50	218.50
8	POE-gallate-PEG	−41.70	231.60
9	dendrimer-2-(G 2)	−21.37	298.20

temperature. Further, the transition temperature for den-1-(G 2) (−12.52 °C) is higher than that of POE−DHBA−PEG. These increases in transition temperature could be explained by an increase in molecular weight as well as by the decrease in chain flexibility as the branching increases (*31*, *32*). A similar trend was observed for in POE-gallate, POE-gallate−PEG, and den-2-(G 2); however, the T_g values were always less than that for the den-1-(G 2) series. This is probably due to a higher number of PEG chains present per dendron (POE-DHBA has two PEG chains, while POE-gallate has three PEG chains) in the later case. Interestingly, only one T_g was observed for all the polymers analyzed, which suggests that all the polymers had no unreacted monomers, and also there was no nanophase separation due to clustering of the polar groups as reported by Sunder et al. for hyperbranched polymers (*24*). Minor melting peaks were also observed for all the polymers, which indicate the existence of amorphous as well as crystalline nature.

Atomic Force Microscopy. AFM is a versatile technique which offers the opportunity to obtain high resolution topographic images of nanoscale polymeric materials. All the dendrimers were imaged in tapping mode after depositing the sample by spin coating on a freshly cleaved mica surface. The spin coating results in the formation of monolayer of polymer at low concentrations; in addition, the centrifugal forces operating during the process aids in breaking the aggregates.

A dendrimer height between 1.39 and 3.55 nm was observed on the mica surface, which indicates the absence of pillarlike aggregation. The scope trace of the surface as well as the topographical view showed the presence of few aggregates, but a majority of the dendrimers were present as isolated molecules. All the dendrimers appeared flattened on the substrate in the surface plot as has been reported for other hydrophilic dendrimers (*33*). However, as seen in Figure 6, den-1-(G 2) and den-2-(G 2) were approximately spherical in shape, while den-1-(G 2)-OH was slightly oval in shape and den-1-(G 3) showed a spherical shape with floral pattern, which indicates that the shape of dendrimer is influenced not only by surface groups but also by the generation (each scan was repeated 3−4 times to ascertain the reproducibility). This observation is in agreement with various simulations and molecular modeling reports of dendrimers (*34*−*36*) where the shape of dendrimer was found to be influenced by surface groups, solvents, and generation.

AFM was also exploited as a tool to determine the size of the dendrimers. For this purpose, all the images were treated offline by using a particle size analysis function, which is designed for analyzing the lateral and vertical dimensions of isolated particles on the substrate surface based on the height of pixel data. The dimensions obtained slightly deviate from that observed by DLS (Table 2). Müller et al. found that residual water in the sample that remained after the drying procedure can lead to overestimation of dendrimer size by AFM (*37*). Further, it is also reported (*33*, *38*−*40*) that hydrophilic and flexible dendrimers (such as PAMAM) flatten and laterally expand on hydrophilic substrates such as mica. This flattening and lateral expansion is enhanced by the large forces exerted by residual water on absorbed species (*37*). All these factors could contribute to overestimation of the diameter of these hydrophilic dendrimers.

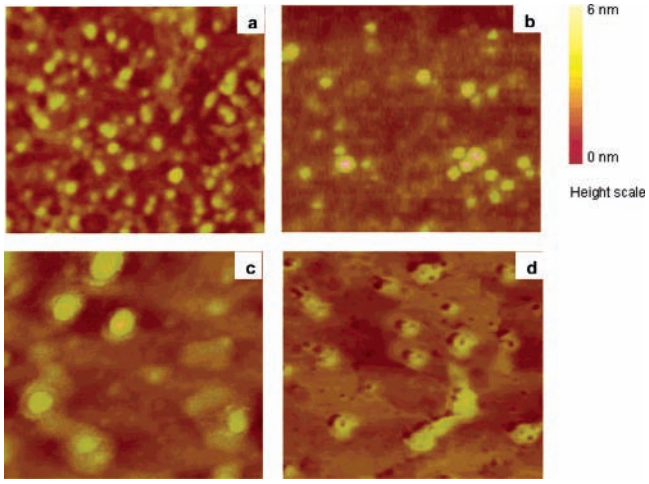

Figure 6. Topographical tapping mode AFM images of (a) den-1-(G 2), (b) den-2-(G 2), (c) den-1-(G 2)-OH, and (d) den-1-(G 3), spin coated on a freshly cleaved mica surface. The scan area is 200 × 200 nm.

Table 4. Encapsulation of Rhodamine and β-Carotene in Dendrimer-1 (Den-1-(G 2))

		drug:dendrimer feed ratio (1:4.5)[a]		drug:dendrimer feed ratio (1:3.6)[b]	
	compound	loading (% (w/w))	encapsulation efficiency (%)	loading (% (w/w))	encapsulation efficiency (%)
1	rhodamine	10.76 ± 1.06	63.27 ± 0.75	15.80 ± 0.14	64.52 ± 0.58
2	β-carotene	5.86 ± 0.24	33.49 ± 0.68	6.47 ± 0.02	33.66 ± 1.08

[a] Mean ± SD ($n = 3$). [b] Mean ± SD ($n = 2$).

Encapsulation and Release Studies. Rhodamine, a hydrophilic fluorescent compound, and β-carotene, a highly hydrophobic compound, were encapsulated in a dendrimer (den-1-(G 2)). As shown in Table 4, at the drug/dendrimer feed ratio of 1:4.5, loading of 10.76% w/w was achieved for rhodamine and 5.86% w/w for β-carotene. It was observed that upon increasing the drug/dendrimer feed ratio to 1:3.6, rhodamine loading increased to 15.80% w/w and that of β-carotene was increased to 6.47% w/w. Further increase in drug/dendrimer feed ratio had no increase in loading for either of the compounds. Kojima et al. also reported a similar observation where an increase in drug/dendrimer feed ratio resulted in an increase in

the drug loading (mol/mol), which reached a maximum value at a certain feed ratio (*8*). The lower loading of β-carotene could be due to the highly hydrophobic nature as well as linear shape of the molecule. It was reported by Namazi and Adeli that size and polarity of the guest molecule affect the ability of dendrimers to encapsulate drug (*11*). They also reported that the encapsulation of pyridine, mefanamic acid, and acetylsalicylic acid in second generation citric acid dendrimers on dendrimer/drug ratio basis was 20, 32, and 49 mol % (i.e. 0.8, 3.8, and 4.4% w/w), respectively. In another study, PMAM dendrimers with PEG grafts had shown maximum encapsulation of 6.5 mol/mol (drug/dendrimer mole ratio) i.e., 2.7% w/w for doxorubicin and 26 mol/mol (10.9% w/w) for methotrexate (*8*). As seen above, drug loading is dependent upon of the size and solubility of the molecule: a lower solubility results in lower loading, and a smaller size increases the loading for molecules with comparable polarity. Although pyridine (79 Da), mefanamic acid (241 Da), and acetylsalicylic acid (180 Da) are smaller and more soluble than β-carotene (537 Da), the loading obtained for β-carotene in this study is much higher. Further, comparatively the loading of rhodamine (479 Da) is higher than that of methotrexate (454 Da). This clearly indicates significantly improved drug loading by these dendrimers and thus substantiates that incorporation of PEO in the interior of the dendrimer increased the size of the internal cavity and thereby increased the encapsulation. Furthermore, it also provided a favorable environment to encapsulate hydrophilic as well as large and hydrophobic molecules. Thus, incorporation of PEO in the core of drug carriers can provide an attractive approach to deliver both water soluble and poorly water soluble compounds.

Since the dendrimer employed for encapsulation studies had no ionizable surface group, it was speculated that encapsulation is largely due to hydrogen bonding by PEO in the cavity and branch (*9*) and/or physical entrapment of molecule in the cavity, rather than being a complexation phenomenon as has been reported for PAMAM dendrimers (*41*). To provide evidence for this hypothesis, the mechanism that involved the encapsulation of these compounds in the dendrimer was investigated. The absorbance spectra of both the compounds before and after encapsulation in dendrimer were recorded and are presented in Figure 7. No shift in absorption maxima was observed for either compounds. The absence of shift in absorption maxima indicates absence of any $\pi-\pi$ complexation, because such complex formation is evidenced by formation of a new chromophore (*42, 43*). NMR spectroscopy is reported to furnish important information on direct interaction between compound and dendrimers (*10, 41, 44*). Thus, the ^{1}H NMR spectra of rhodamine and β-carotene encapsulated in dendrimer were acquired, and the chemical shifts of rhodamine as well as β-carotene in DMSO before and after encapsulation in dendrimer were determined. No significant shift in the peaks of the aromatic rings as well as ethyl amino group was observed in spectra of rhodamine encapsulated in the dendrimer, but a few peaks were suppressed (Figure 8), which implies that the compound is physically encapsulated. To further investigate the mechanism of encapsulation and interactions between encapsulated compound and dendrimer, FTIR spectroscopy was employed as a tool. The FTIR spectra of rhodamine alone, den-1(G 2), and rhodamine encapsulated in den-1(G 2) were acquired as neat samples. The spectrum of den-1(G 2) was subtracted from that of rhodamine encapsulated in den-1(G 2) to obtain the spectral features of rhodamine after encapsulation in dendrimer. It was observed that the carboxylic OH which appears in the region of 3300−2500 cm^{-1} and is overlapped by the C−H stretch (*45*) had increased in intensity as well as broadened after encapsulation in the dendrimer. The absence of peak splitting around 1372−1344 cm^{-1} was also seen (Figure 9). These peaks in the range of 1370−1310 cm^{-1} are assigned to the aromatic tertiary amine C−N stretch. Further, the shift in the peak at 1223 cm^{-1}, attributed to the aromatic C−O stretch, was also seen. Since these changes are associated with OH, C−N, and C−O stretching frequencies, they are generally attributed to hydrogen bonding interactions. Thus, weak hydrogen bonding between dendrimer and rhodamine is postulated to exist. In addition, the significant decrease in intensity of peaks in the region of 1650−1500 cm^{-1} (aromatic ring stretch) was observed, indicating either that the aromatic region is surrounded by the PEO chain of the dendrimer or there are dipole−dipole/induced dipole interactions. The changes in FTIR spectral features of rhodamine after encapsulation indicated the presence of weak hydrogen bonding or dipole−dipole/induced dipole interactions. Thus, hydrogen bonding of the molecule by PEO together with physical entrapment of molecule in the dendrimer is the probable mechanism of encapsulation. It was previously reported that at high concentration, PEG 400 self-associates by hydrogen bonding and disrupts the water structure to a certain extent (*46*). Since these dendrimers have a high density of PEO, it is possible that self-association of PEO chains could also occur, resulting in hydrotropic solubilization of the compounds.

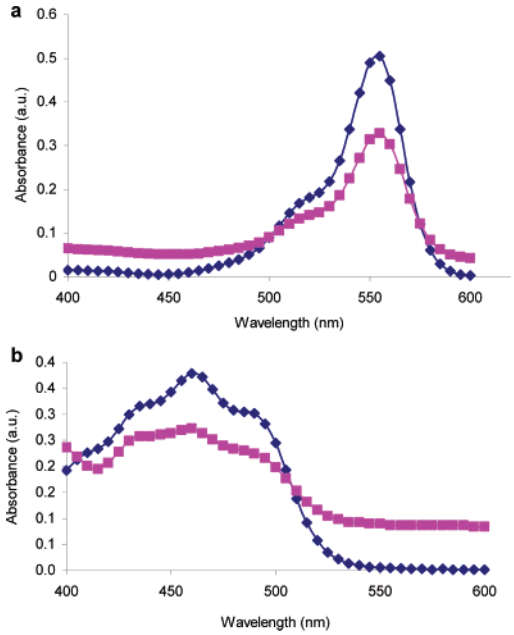

Figure 7. Absorbance spectra of (a) rhodamine and (b) β-carotene before and after encapsulation in the dendrimer, determined to study the effect of encapsulation on the fluorophore and chromophore. Key: ◆ before encapsulation; ■ after encapsulation.

The release of drug molecules from polymeric carriers occurs by either diffusion and/or degradation of the polymer. Approximately 90% of both encapsulated compounds was released in 172 h, i.e. 7 days (Figure 10), and the preliminary in vitro biodegradation studies have shown that degradation of den-1(G 2) ensues after 10 days of incubation. Therefore, in vitro release of both compounds under will be mainly governed by diffusion. The release of rhodamine was slow and almost linear till 120 h, after which it reached a plateau phase. Approximately 82% of rhodamine was released from the dendrimer in 120 h, and 90% was released after 172 h. Since rhodamine is a water soluble compound, the slow release profile demonstrates the ability of these dendrimers to provide sustained release of even water soluble drugs.

β-Carotene is practically insoluble in water, and hence ethanol was added to the release medium to obtain necessary sink conditions. In the absence of necessary sink conditions the hydrophobic compounds exhibit a slow release profile. Thus,

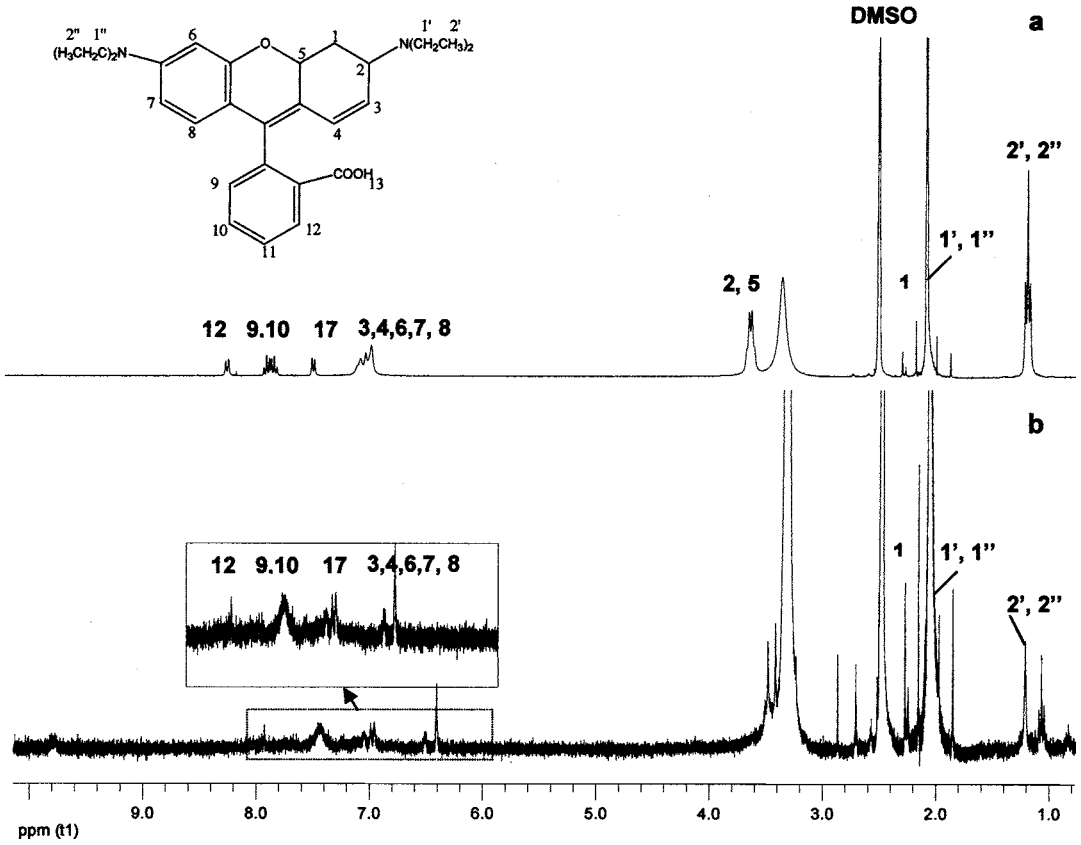

Figure 8. ^{1}H NMR spectra of (a) rhodamine (10 μM) and (b) rhodamine encapsulated in dendrimer (Den-1-(G 2)) (4 μM) measured in DMSO at 400 MHz.

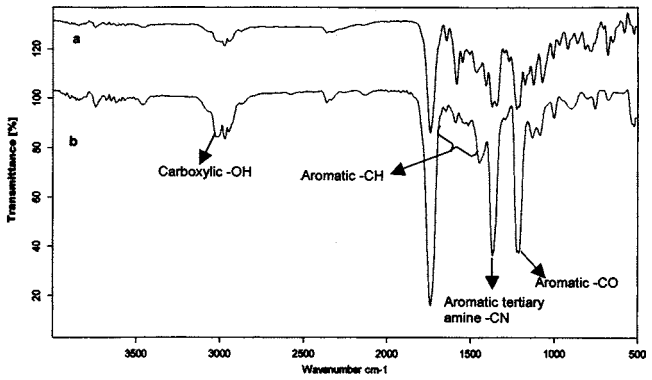

Figure 9. FTIR spectra of (a) free rhodamine and (b) encapsulated rhodamine (obtained by subtracting spectrum of den-1-(G 2) from spectrum of rhodamine encapsulated in den-1-(G 2)).

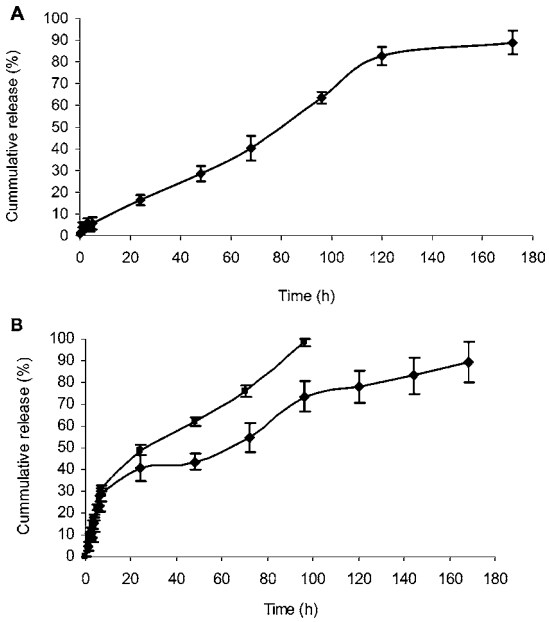

Figure 10. Cumulative release profile of (A) rhodamine encapsulated in den-1-(G 2) and (B) β-carotene encapsulated in den-1-G 2 (diamonds) and β-carotene suspension (squares). Data are mean ± SD.

the slow release of the drug from the carrier could be due to the absence of sink conditions and not due to the influence of drug delivery vehicle. To overrule the factor that slow release of β-carotene is due to an absence of sink conditions or slow dissolution of drug, release of β-carotene from suspension was performed under the same conditions but at 10 times higher amount. It also allowed comparison of the release characteristics of drug from dendrimer and suspension. Even though drug concentration in suspension was much higher, approximately 100% of the drug was released from suspension in 96 h as compared to 70% from dendrimers, indicating sustained release of drug encapsulated from the dendritic architecture. A triphasic release profile was observed in the case of dendrimers, with an initial rapid release phase during which 30% of drug was released in 7 h, followed by a slower release with drug release up to 70% in 96 h and another slow release with 90% of encapsulated drug being released in 168 h. The absence of burst release in the case of both rhodamine and β-carotene also ascertains the nonexistence of surface-bound drug. Comparatively, release of rhodamine was slower than that of β-carotene; this is in contrast to the general trend where hydrophobic compounds exhibit slower release as compared to hydrophilic compounds. This slower release of rhodamine is due to the hydrogen boding interaction of the former with the PEO, which retards the diffusion and hence release of the drug. This interesting observation highlights the ability of these dendrimers

to prolong the release of encapsulated drugs and thus demonstrates their potential to act as carriers for sustained release of both hydrophilic and hydrophobic drugs. The ability to encapsulate both hydrophilic and hydrophobic drugs is advantageous because it eliminates the need to tailor polymeric architectures specifically for hydrophilic or hydrophobic drugs. Further, it provides an opportunity for combination therapy, wherein drugs with different solubilities can also be encapsulated simultaneously and delivered to the target site.

These dendrimers have hydrolyzable ester linkages and are composed of mainly PEG, a biocompatible polymer that has shown to reduce the cytotoxicity, immunogenecity, and antigenecity of various dendrimers as well as other drug delivery vehicles (*12, 13*). Further, due to the absence of cationic groups at the surface, it is speculated that the synthesized dendrimers will be biodegradable and biocompatible.

CONCLUSIONS

Novel polyester-*co*-polyether second and third generation dendrimers were synthesized by simple synthetic schemes using butanetetracarboxylic acid as the core molecule by combination of divergent and convergent synthesis. PEO was incorporated in the interior of the dendrimers to increase the size of the cavity as well as to provide a hydrophilic interior region. The dendrimers demonstrated the ability to encapsulate both hydrophilic and hydrophobic model compounds, with sufficiently high drug loading. Further, the release of both rhodamine and β-carotene was found to be slow and sustained, with approximately 90% of drug being released in 170 h. The study indicates that polymeric architectures with a PEO interior can potentially be used for delivery of hydrophobic and hydrophilic drugs, which provides an advantage over drug carriers with hydrophobic core that have preferential ability to deliver hydrophobic compounds. It is postulated that by virtue of their small size and slow release characteristics these dendrimers can be used as nanocarriers for intracellular drug delivery.

ACKNOWLEDGMENT

The authors thank Dr. Françoise Winnik for providing the DLS and FTIR facility. Renu Singh also expresses sincere thanks to Julie Boivin for help provided throughout the MALDI-TOF experiments.

LITERATURE CITED

(1) Bolten, B. M., and Degregorio, T. (2002) Trends in development cycles. *Nature Rev. Drug Discovery 1,* 335−336.

(2) Dimasi, J. A., Hansen, R. W., and Grabowski, H. G. (2003) The price of innovation: new estimates of drug development costs. *J. Health Economics 22,* 151−185.

(3) Langer, R. (1998) Drug delivery and targeting. *Nature 392,* 5−10.

(4) Tomalia, D. A., and Frechet, J. M. (2002) Discovery of dendrimers and dendritic polymers: A brief historical perspective. *J. Polym. Science: Part A: Polym. Chem. 40,* 2719−2728.

(5) Esfand, R., Tomalia, D. A. (2001) Poly(amidoamine) (PAMAM) dendrimers: from biomimicry to drug delivery and biomedical applications. *Drug Discovery Today 6,* 427−436.

(6) Fix, J. A., Alexander, J., Cortese, M., Engle, M., Leppert, P., and Repta, A. J. (1990) A comparison of oral and rectal absorption of L-Dopa esters in rats and mice. *Pharm. Res. (NY) 7,* 384−387.

(7) Denny, W. A. (2004) The Design of Drugs that Target Tumour Hypoxia. *Aust. J. Chem. 57,* 821−828.

(8) Kojima, C., Maruyama, K., and Takagishi, T. (2000) Synthesis of polyamidoamine dendrimers having poly(ethylene glycol) grafts and their ability to encapsulate anticancer drugs. *Bioconjugate Chem. 11,* 910−917.

(9) Liu, M., Kono, K., and Frechet, J. M. (2000) Water soluble dendritic unimolecular micelles: their potential as drug delivery agents. *J. Controlled Release 65,* 121−131.

(10) Ooya, T., Lee, J., and Park, K. (2004) Hydrotropic dendrimers of generation 4 and 5: Synthesis, characterization, and hydrotropic solubilization of paclitaxel. *Bioconjugate Chem. 15,* 1221−1229.

(11) Namazi, H., and Adeli, M. (2005) Dendrimers of citric acid and poly(ethylene glycol) as the new drug-delivery agents. *Biomaterials 26,* 1175−1183.

(12) Jevapresphant, R., Penny, J., Jalal, R., Attwood, D., Mckeown, N. B., and D′Emanuele, A. (2003) The influence of surface modification on cytotoxicity of PAMAM dendrimers. *Int. J. Pharm. 252,* 263−266.

(13) Bhadra, D., Bhadra, S., Jain, P., and Jain, N. K. (2002) Pegnology: a review of PEGylated systems. *Pharmzie* 57, 5−29.

(14) Padilla De Jesus, O. L., Ihre, H. R., Gagne, L., Frechet, J. M., and Szoka Jr., F. C. (2002) Polyester dendritic systems for drug delivery applications: in vitro and in vivo evaluation. *Bioconjugate Chem. 13,* 453−461.

(15) Mora, P. C., Cirri, M., Guenther, S., Allolio, B., Carli, F., Mura, P. (2003) Enhancement of dehydroepiandrosterone solubility and bioavailability by ternary complexation with alpha-cyclodextrin and glycine. *J. Pharm. Sci. 92,* 2177−2184.

(16) Sugimoto, M., Okagaki, T., Narisawa, S., Koida, Y., and Nakajima, K. (1998) Improvement of dissolution characteristics and bioavailability of poorly water soluble drugs by novel co-grinding methods using water soluble polymers. *Int. J. Pharm. 160,* 11−19.

(17) Liu, M., Kono, K., and Frechet, J. M. (1999) Water soluble dendrimer-poly(ethylene glycol) star like conjugates as potential drug carriers. *J. Polym. Sci. 37,* 3492−3503.

(18) Bhadra, D., Bhadra, S., Jain, S., and Jain, N. K. (2003) A pegylated dendritic nanoparticulate carrier of fluorouracil. *Int. J. Pharm. 257,* 111−124.

(19) Yang, H., Moris, J. J., and Lopina, S. T. (2004) Polyethylene glycol-polyamidoamine dendritic micelle as solubility enhancer and the effect of the length of poly(ethylene glycol) arms on the solubility of pyrene in water. *J. Colloid Interface Sci. 273,* 148−154.

(20) Groves, M. J., Bassett, B., and Sheth, V. (1984) The solubility of 17 β-estradiol in aqueous poly(ethylene glycol). *J. Pharm. Pharmacol. 36,* 799−802.

(21) Connors, K. A., and Albert, K. S. (1973) Determination of hydroxyl compounds by 4-dimethyl amino pyridine-catalyzed acetylation. *J. Pharm. Sci. 62,* 845−846.

(22) Klajnert, B., and Bryszewska, M. (2001) Dendrimers: properties and applications. *Acta Biochim. Pol. 48,* 199−208.

(23) Trollsås, M., Atthof, B., Würsch, A., and Hedrick, J. L. (2000) Constitutional isomers of dendrimer-like star polymers: design, synthesis, and conformational and structural properties. *Macromolecules 33,* 6423−6438

(24) Sunder, R., and Mülhaupt, H. F. (2000) Hyperbranched polyether-polyols based on polyglycerol: Polarity design by block copolymerization with propylene oxide. *Macromolecules 33,* 309−314.

(25) Yamamoto, K., Kakita, R., Suzuki, C., Meno, M., and Nozawa, Y. (2003) Simultaneous determination of hydroxyl value, ethylene oxide content, and primary hydroxyl content for polyetherpolyol by near-infrared spectroscopy. *Appl. Spectrosc. 57,* 353−355.

(26) Percec, V., Golde, M., Bera, T. K., Miura, Y., Shiyanovskaya, T., Singer, K. D., Balagurusamy, V. S. K., Heiney, P. A., Schnell, T., Rapp, A., Spiess, H. W., Hudson, S. D., and Duan, H. (2002) Self-organization of supramolecular helical dendrimers into complex electronic materials. *Nature 419,* 384−387.

(27) Wang, B. B., Zhang, X., Jia, X. R., Luo, Y. F., Sun, Z., Yang, L., Ji, Y., and Wei, Y. (2004) Poly(amidoamine) dendrimers with phenyl shells: fluorescence and aggregation behavior. *Polymer 45,* 8395−6402.

(28) Allen, C., Maysinger, D., and Eisenberg, A. (1999) Nano-engineering block copolymer aggregates for drug delivery. *Colloids Surfaces B: Biointerfaces 16,* 3−27.

(29) Omelczuk, M. O., and McGinity, J. W. (1992) The influence of polymer glass transition temperature and molecular weight on drug release from tablets containing poly(DL-lactic acid). *Pharm. Res. 9,* 26−32.

(30) Liggins, R. T., and Burt, H. M. (2004) Paclitaxel-loaded poly-(L-lactic acid) microspheres 3: blending low and high molecular weight polymers to control morphology and drug release. *Int. J. Pharm. 282,* 61−71.

(31) Stevens, M. P. (1999) *Polymer Chemistry: An Introduction,* 3rd ed., Oxford Univ. Press, NewYork.

(32) Tadlaoui, K., Michel, A., Pietrasanta, Y., Verney, V. (1991) Influence of molecular weight on the glass transition temperature and the melt rheological behaviour of methyl methacrylate telomers. *Polymer 32*, 2234−2237.

(33) Betley, T. A., Banaszak Holl, M. M., Orr, B. J., Swanson, D. R., Tomalia, D. A., and Baker Jr., J. R. (2001) Tapping Mode Atomic Force Microscopy investigation of poly(amidoamine) dendrimers: Effects of substrate and pH on dendrimer deformation. *Langmuir 17*, 2768−2773.

(34) Rathgeber, S., Pakula, T., and Urban, V. (2004) Structure of star burst dendrimers: A comparison between small-angle X-ray scattering and computer simulation results. *J. Chem. Phys. 121*, 3840−3853.

(35) Ballauff, M., and Likos, C. N. (2004) Dendrimers in solution: Insight from theory and simulation. *Angew. Chem. 43*, 2998−3020.

(36) Maiti, P. K., Cagin, T., Lin, S. T., and Goddard, W. A. (2005) Effect of solvent and pH on the structure of PAMAM dendrimers. *Macromolecules 38*, 979−991.

(37) Müller, T., Yablon, D. G., Karchner, R., Knapp, D., Kleinman, M. H., Fang, H., Durning, C. J., Tomalia, D. A., Turro, N. J., and Flynn, G. W. (2002) AFM studies of high generation PAMA dendrimers at the liquid/solid interface. *Langmuir 18*, 7452−7455.

(38) Hierlemann, A., Cambell, J. K., Baker, l. A., Crooks, R. M., and Ricco, A. J. (1998) Structural Distortion of Dendrimers on Gold Surfaces: A Tapping-Mode AFM Investigation. *J. Am. Chem. Soc. 120*, 5323−5324.

(39) Lackowsi, W. M., Cmapbell, J. K., Edwards, G., Chechik, V., and Crooks, R. M. (1999) Time dependent phase-segregation of dendrimer/*n*-alkylthiol mixed-monolayers on Au(111): an atomic force microscopy study. *Langmuir 15*, 7632−7638.

(40) Li, J., Piehler, L. T., Qin, D., Baker Jr., J. R., Tomalia, D. A., and Meier, D. J. (2000) Visualization and characterization of poly(amidoamine) dendrimers by Atomic Force Microscopy. *Langmuir 16*, 5613−5616.

(41) Kohle, P., Misra, E., Kannan, R. M., Kannan, S., and Lieh-Lai, M. (2003) Drug complexation, in vitro release and cellular entry of dendrimers and hyperbranched polymers. *Int. J. Pharm. 259*, 143−160.

(42) Coffman, R. E., and Kildsig, D. A. (1996) Hydrotropic solubilization − mechanistic studies. *Pharm. Res. 13*, 1460−1463.

(43) Agrawal, S., Pancholi, S. S., Jain, N. K., and Agrawal, C. P. (2004) Hydrotropic solubilization of nimesulide for parenteral administration. *Int. J. Pharm. 274*, 149−155.

(44) Morgan, M. T., Carnahan, M. A., Immos, C. E., Ribeiro, A. A., Finkelstrin, S., Lee, S. J., and Grinstaff, M. W. (2003) Dendritic molecular capsules for hydrophobic compounds. *J. Am. Chem. Soc. 125*, 15485−15489.

(45) Coates, J. (2000) Interpretation of Infrared spectra, a practical approach. *Encyclopedia of analytical chemistry* (Meyers, R. A., Ed.) pp 10815−10837, John Wiley and Sons Ltd., Chichester.

(46) Sato, T., Niwa, H., and Chiba, A. (1998) Dynamical structure of oligo ethylene glycols-water solutions studied by time domain reflectometry. *J. Chem. Phys. 108*, 4138−4147.

BC050184C

Synthesis and Characterization of HE-24.8: A Polymeric Contrast Agent for Magnetic Resonance Angiography

Fabian Kiessling,*[,†,#] Melanie Heilmann,[†,#] Twan Lammers,[‡,§] Karel Ulbrich,[||] Vladimir Subr,*[,||] Peter Peschke,[‡] Bjoern Waengler,[†] Walter Mier,[Δ] Hans-Herrmann Schrenk,[⊥] Michael Bock,[†] Lothar Schad,[†] and Wolfhard Semmler[†]

Divisions of Medical Physics in Radiology and Radiation Oncology, Molecular Toxicology, German Cancer Research Center, Heidelberg, Germany, Department of Nuclear Medicine, University Heidelberg, Germany, Department of Pharmaceutical Technology, Utrecht University, Utrecht, The Netherlands, and Institute of Macromolecular Chemistry, Academy of Sciences of the Czech Republic, Prague, Czech Republic. Received June 30, 2005; Revised Manuscript Received October 28, 2005

The physical and biological properties of a water-soluble polymeric contrast agent based on a complex of *N*-(2-hydroxypropyl)methacrylamide copolymer with gadolinium (HE-24.8) were investigated, and its potential for experimental magnetic resonance (MR) angiography was assessed. Relaxivities of Gd-DTPA-BMA, Gd-DTPA-HSA (human serum albumin), and HE-24.8 were determined at 1.5 T. Thermic stability and biocompatibility of HE-24.8 were assessed in vitro and by analyzing kinetics and organ distribution in rats for up to 2 weeks. For comparison, HE-24.8- and Gd-DTPA-HSA-enhanced micro-MR angiographies of brain, chest, and subcutaneous tumors in rats were performed. T_1 relaxivity of HE-24.8 (21.3 ± 1.1 mM^{-1} s^{-1}) was 5-fold higher than that of Gd-DTPA-BMA (4.1 ± 0.1 mM^{-1} s^{-1}) and twice as high as that of Gd-DTPA-HSA (12.4 ± 0.2 mM^{-1} s^{-1}). Varying the molecular weight of the polymer (15−46 kDa) did not significantly change the T_1 relaxivity. In rats, 20 and 10% of the injected dose of HE-24.8 was detected at 24 and 168 h postinjection, respectively. Upon a relatively rapid initial renal clearance, no specific retention in any organ was noted, with some exception for the reticulo-endothelial system. No measurable release of gadolinium from the polymer−Gd complex or cell toxicity was observed during its incubation in aqueous environment. Excellent display of rat and tumor vascularization was achieved with Gd-DTPA-HSA and HE-24.8; however, contrast of vessels was higher in HE-24.8-enhanced scans. HE-24.8 is considered a macromolecular contrast agent highly suited for experimental MR studies.

INTRODUCTION

Clinically approved contrast agents for magnetic resonance imaging (MRI) are small chelates of gadolinium often complexed with diethylenetriaminepentaacetic acid (DTPA)[1] (*1*, *2*). They are characterized by an early extravasation, a fast renal clearance, and a low toxicity (*1*, *2*). This makes them suitable for many clinical implementations such as the detection and delineation of pathologically altered tissue (*3*−*5*) or first-pass angiographies of larger vessels (*6*−*8*). However, their use for studying micro-vascularization often is problematic: For visualizing microvessels, long scanning times are required to achieve a suitable signal-to-noise ratio, and these are not compatible with the kinetics of small gadolinium chelates. Furthermore, in functional experiments on tissue vascularization, the fast extravasation may not allow it to catch differences in vessel permeability in a reliable manner (*9*, *10*).

Therefore, numerous attempts have been undertaken to design contrast agents with larger molecular sizes to circumvent these limitations (*11*, *12*). First attempts included the labeling of plasma proteins such as albumin with gadolinium complexes (*13*, *14*). These gadolinium-labeled albumin compounds were marked by long circulation times and a high degree of hepatic metabolism of the altered proteins, which make clinical implementation questionable. As a consequence, with the outlook to a clinical assessment, dendrimeric contrast agents with a medium molecular size like Gadomer (*15*) and contrast agents with affinity to plasma proteins such as MS325 (*16*) were designed, which show a moderate intravascular half-life of several minutes and are largely cleared by the kidneys (*11*, *15*). Indeed, these contrast agents show the potential to improve functional studies on tumor vascularization including the assessment of vessel permeability during anti-angiogenic treatments (*10*, *17*) and to visualize microvessels in vivo (*18*, *19*). An alternative is the use of labeled polymers such as the PGC-derivates (*20*). As an advantage, these can be synthesized with variable configurations and molecular sizes, thus enabling optimization of their pharmacokinetic properties to the biological target (*20*). Furthermore, contrast-giving agents can easily be connected to these molecules and double or triple labeling for example with a fluorescence dye, a radioactive isotope and a lanthanide or superparamagnetic agent can be performed (*21*, *22*). Furthermore, they can be used as a matrix for molecular contrast agents by connecting them with one or more ligands

* Corresponding author: Fabian Kiessling, MD, German Cancer Research Center, Division of Medical Physics in Radiology, Im Neuenheimer Feld 280, 69120 Heidelberg, Germany. Tel. +49 6221 422533. E-mail: F.Kiessling@dkfz.de.

[#] These authors contributed equally to this work.

[†] Division of Medical Physics in Radiology, German Cancer Research Center.

[‡] Division of Radiation Oncology, German Cancer Research Center.

[⊥] Division of Molecular Toxicology, German Cancer Research Center.

[Δ] University Heidelberg.

[§] Utrecht University.

[||] Academy of Sciences of the Czech Republic.

[1] Abbreviations: DTPA, diethylenetriaminepentaacetic acid; HSA: human serum albumin; HPMA: *N*-(2-hydroxypropyl)methacrylamide; THF: tetrahydrofurane; DCC: *N*,*N*′-dicyclohexylcarbodiimide; AIBN: 2,2′-azobis(isobutyronitrile); TFA: trifluoroacetic acid; HEP-G2: hepatocarcinoma cell line; MSU: human fibroblast cell line; PBS: phosphate buffered saline; FBS: fetal bovine serum; ICP-MS: inductively coupled plasma-mass spectrometry; MRI: magnetic resonance imaging; TR: relaxation time; TE: echo time; SI: signal intensity; MIP: maximum intensity projection

10.1021/bc0501909 CCC: $33.50 © 2006 American Chemical Society
Published on Web 12/23/2005

to the biological target and the signal-enhancing molecules as described above (*22*).

Copolymers based on *N*-(2-hydroxypropyl)methacrylamide (HPMA) are water-soluble, biocompatible, and nonimmunogenic macromolecular carriers that have been studied as potential drug delivery systems for a variety of low-molecular-weight drugs such as doxorubicin (*23*), campthotecin (*24*), paclitaxel (*25*), and platinates (*26*). Conjugates of this highly biocompatible polymer with cytotoxic drugs have already been used in early clinical trials (*27*−*29*). At this, it was shown that the uptake of HPMA-based copolymers in tumors depends on the molecular weight of the copolymer molecule (*29*−*31*). In contrast, in the molecular weight range between 23 and 60 kDa, the distribution of HPMA copolymer in normal organs was quite similar (*31*). Synthesis and properties of the HPMA copolymer labeled with ^{99m}Tc used for scintigraphic imaging were described in ref *32*, and the HPMA copolymer-linked nitroxides were already studied as potential MR agents (*33*). It was shown that organ biodistribution of the copolymer significantly depends on its molecular weight, that the ^{99m}Tc complexes are relatively stable, and that polymer nitroxides exhibit higher relaxivity than does Gd-DTPA-BMA.

Taking the advantages of the high flexibility in polymer synthesis and the existing preclinical and clinical experiences with HPMA polymers, the aim of this study was to use HPMA copolymers as carriers of gadolinium-based MR contrast agents. As compared with the results of Wang (*34*), who had already presented initial results with Gd-containing HPMA copolymers, in this study an alternative way of integrating gadolinium into the polymer structure was chosen. Several Gd-containing HPMA polymers with different molecular weights were synthesized. Of those, a Gd-HPMA polymer with an intermediate molecular weight of 24.8 kDa (named HE-24.8) was used to collect the first experiments addressing its cell toxicity in vitro, the blood half-life in rats, and the organ distribution during 2 weeks. Furthermore, first results using HE-24.8 as a MR contrast agent are presented including the determination of the T_1 and T_2 relaxation times and its in vivo use as a contrast agent for micro-MR angiography. The HE-24.8-enhanced MR angiographies were also compared with those performed after administration of Gd-DTPA-HSA (human serum albumin), the latter being a standard experimental contrast agent with a long blood half-life.

EXPERIMENTAL PROCEDURES

Chemicals. Methacryloyl chloride, 1-aminopropan-2-ol, 6-aminohexanoic acid, L-aspartic acid, di-*tert*-butyl dicarbonate ($(Boc)_2O$), thionyl chloride, triethylamine (Et_3N) *N*,*N*′-dicyclohexylcarbodiimide (DCC), isobutyl chloroformate, 2,2′-azobis-(isobutyronitrile) (AIBN), and trifluoroacetic acid (TFA) were purchased from Fluka (Czech Republic), and L-tyrosinamide was from Sigma-Aldrich s.r.o. (Czech Republic). All other chemicals and solvents were of analytical grade.

Synthesis of Monomers and Copolymers. *N-(2-Hydroxypropyl)methacrylamide (HPMA)* was synthesized as described earlier (*35*). *N*-Methacryloyl tyrosinamide ($Ma\text{-}TyrNH_2$) was prepared by reaction of methacryloyl chloride with tyrosinamide in distilled water as described earlier (*36*).

Synthesis of Ma-Acap-Asp-[(Asp-(OMe)$_2$]$_2$. *Synthesis of N-tert-Butyloxycarbonyl-L-aspartic Acid, Boc-Asp-OH.* L-Aspartic acid (10 g, 0.075 mol) and sodium hydroxide (6.0 g, 0.15 mol) were dissolved in distilled water (100 mL). The solution was cooled to 0 °C, and dioxane (100 mL) was added. $(Boc)_2O$ (18.0 g, 0.083 mol) was added dropwise during 1 h. The reaction mixture was stirred in an ice bath for 2 h and then for another 2 h at room temperature. The reaction mixture was concentrated on a vacuum evaporator. The unreacted $(Boc)_2O$ was removed by extraction into diethyl ether. The aqueous layer was separated and acidified to pH 2 with a saturated solution of sodium hydrogen sulfate, and the product was extracted into ethyl acetate. The organic phase was separated, dried with sodium sulfate, and concentrated on a vacuum evaporator. Boc-L-Asp-OH was crystallized from a mixture of ethyl acetate/hexane. Yield: 13.4 g (76.5%), mp 116−118 °C.

Synthesis of L*-Aspartic Acid Bis-methylester Hydrochloride HCl·Asp-(OMe)$_2$.* Methanol (100 mL), dried with calcium hydride, was put into a 250-mL two-neck round-bottom flask equipped with a stirrer and condenser. Methanol was cooled to −10 °C, and the thionyl chloride (16.4 mL, 0.225 mol) was added dropwise during 30 min. L-Aspartic acid (15.0 g, 0.112 mol) was added, and a reaction mixture was stirred and refluxed for 5 h. The reaction mixture was cooled to room temperature and concentrated on a vacuum evaporator. The final product was crystallized from a mixture methanol/diethyl ether. Yield: 18.3 g (82.5%), mp 115−117 °C.

Synthesis of TFA·Asp-[Asp-(OMe)$_2$]$_2$. Boc-Asp-OH (1.475 g, 6.33 mmol), HCl.Asp-$(OMe)_2$ (2.5 g, 12.66 mmol), and Et_3N (1.77 mL, 6.33 mmol) were mixed in 50 mL of tetrahydrofurane (THF), and the suspension was cooled to −10 °C. DCC (3.12 g, 15.1 mmol) was dissolved in 20 mL of THF, and the solution was cooled to −10 °C. The cool solution of DCC was added to the suspension, and the reaction mixture was kept for 1 h at −10 °C and then overnight at 5 °C without mixing. The reaction mixture was warmed to room temperature, acetic acid (0.1 mL) was added, and the mixture was stirred for 30 min at room temperature. Precipitated *N*,*N*′-dicyclohexylurea (DCU) and triethylamine hydrochloride (Et_3N·HCl) were filtered off, and the filtrate was concentrated on a vacuum evaporator. The resulting oily residue was diluted with ethyl acetate (100 mL) and gradually extracted with 2 wt % aqueous sodium hydrogen carbonate (50 mL), 0.5 wt % citric acid (50 mL), and water (50 mL) in a last step. The organic layer was dried with sodium sulfate, and the product was crystallized from a mixture ethyl acetate/hexane. Yield: 2.1 g (64.5%), mp 115−116 °C, TLC: (silica gel, ethyl acetate, $R_f = 0.54$). Elemental analysis: calcd/found C = 48.55/48.85, H = 6.40/6.50, N = 8.09/8.05. The Boc protection group was removed by TFA. Boc-Asp-[Asp-$(OMe)_2]_2$ (2.0 g) was dissolved in TFA (8.0 mL) and stirred for 30 min at room temperature. The excess TFA was evaporated, the mixture was diluted three times with dry methanol, and the solvent was evaporated again. The oily residue was triturated with diethyl ether to form crystals of TFA·Asp-[Asp-$(OMe)_2]_2$. Yield 1.6 g (77.9%).

Synthesis of N-methacryloyl-6-amino Hexanoic Acid, Ma-Acap-OH (Ma = methacryloyl). The Schotten-Baumann acylation method with methacryloyl chloride in an aqueous alkaline medium was used for methacryloylation of 6-aminohexanoic acid (*37*). (mp 52−53 °C, elemental analysis: calcd/found C 60.28/60.43, H 8.60/8.37, N 7.03/6.98).

Synthesis of Ma-Acap-Asp-[(Asp-(OMe)$_2$]$_2$. N-Methacryloyl 6-aminohexanoic acid (0.5 g, 2.51 mmol) and Et_3N (0.385 mL, 2.76 mmol) were dissolved in THF (5 mL). The solution was cooled to −10 °C, and isobutyl chloroformate (0.36 mL, 2.76 mmol) was added. After 10 min, the reaction mixture was added to a cooled mixture of TFA·Asp-[Asp-$(OMe)_2]_2$ (1.47 g, 2.76 mmol) and Et_3N (0.424 mL, 3.04 mmol) in THF (5 mL). The reaction mixture was stirred for 4 h at room temperature. The precipitated Et_3N·HCl was filtered off, and THF was evaporated in a vacuum. The residue was dissolved in ethyl acetate (20 mL) and gradually extracted with 2 wt % aqueous sodium hydrogen carbonate (5 mL), 0.5 wt % citric acid (5 mL), and water (5 mL). The organic layer was dried with sodium sulfate, and the product was crystallized from a mixture of ethyl acetate/

hexane. Yield 0.5 g (33%), mp 110−113 °C, elemental analysis: Calcd/found C = 51.99/50.31, H = 6.71/6.34, N = 9.33/8.93.

Synthesis and Characterization of the Copolymer P-Acap-Asp-[(Asp-(OH)$_2$]$_2$. The copolymer was prepared by solution radical copolymerization of HPMA with Ma-Acap-Asp-[(Asp-(OMe)$_2$]$_2$ in methanol at 60 °C. HPMA (1.0 g, 6.98 mmol) and Ma-Acap-Asp-[(Asp-(OMe)$_2$]$_2$ (0.221 g, 0.368 mmol) were dissolved in methanol (7.0 mL), and initiator AIBN (0.068 g, 0.41 mmol) was added. The solution was transferred into a glass ampule and bubbled with nitrogen. The ampule was sealed, and polymerization was carried out at 60 °C for 24 h. The polymer was isolated by precipitation into a mixture of acetone and diethyl ether (3:1), filtered off, washed with acetone, and diethyl ether, and dried in a vacuum. Yield: 0.998 g (81.7%).

The HPMA copolymer used for kinetic and biodistribution studies (HE-radiolabel) was prepared by terpolymerization of HPMA (1.0 g, 6.98 mmol), Ma-TyrNH$_2$ (0.037 g, 0.15 mmol), Ma-Acap-Asp-[(Asp-(OMe)$_2$]$_2$ (0.221 g, 0.368 mmol), and AIBN (0.070 g, 0.42 mmol) in methanol (7.0 mL) at 60 °C for 24 h.

The methyl ester groups from both copolymers mentioned above were removed by alkaline hydrolysis. Briefly, the copolymer (0.8 g) was dissolved in distilled water, and the pH of the solution was maintained at 11.5 with addition of 0.1 M NaOH for 6 h at room temperature. Then, the pH was lowered to 2 with diluted hydrochloric acid, and the copolymer was dialyzed in a Visking dialysis tube with a molecular weight cut off of 3500 for 2 days and lyophilized. Yield: 0.75 g.

The weight-average molecular weight M_w and polydispersity M_w/M_n were determined by size exclusion chromatography on the HPLC system ÄKTA explorer (Amersham Biosciences) equipped with RI and multiangle light scattering detectors DAWN DSP-F (Wyatt Technol. Corp., USA) on Superose 6 column.

The side chain (amino acids) content was determined after hydrolysis of polymers HE 24.8 and HE-radiolabel with 6 N HCl at 115 °C for 16 h using a HPLC amino acid analyzer (LDC Analytical, USA) with a reverse-phase column Nucleosil 120-3 C_{18} (Macherey-Nagel, 125 × 4 mm) using precolumn derivatization with phthaldialdehyde, and detection with a fluorescence detector (excitation at 229 nm, emission at 450 nm). Gradient elution: 0−100% of solvent B within 65 min and flow rate 0.5 mL min^{-1} (solvent A: 0.05 M sodium acetate buffer, pH 6.5; solvent B: 300 mL of 0.17 M sodium acetate and 700 mL of methanol).

HPMA copolymers differing in chemical composition and molecular weight characteristics could be easily prepared by changing monomers ratio (HPMA: Ma-Acap-Asp-[(Asp-(OMe)$_2$]$_2$), initiator concentration, concentration of monomers in the polymerization mixture, and polymerization temperature. Several copolymers with a content of Ma-Acap-Asp-[(Asp-(OMe)$_2$]$_2$ up to 30% and molecular weights between 15 and 200 kDa could be prepared. From these, gadolinium-containing HPMA polymers with an average weight of 16.2, 21.7, 22.2, 24.8, 27.7, 43.9, and 45.6 kDa were used for comparison of T_1 relaxivities.

Synthesis of P-Acap-Asp-[Asp-(OH)$_2$]$_2$ Gadolinium Complex HE-24.8 (P Means HPMA Copolymer Chain). HPMA copolymer P-Acap-Asp-[Asp-(OH)$_2$]$_2$ (0.45 g) was dissolved in distilled water, and gadolinium chloride (0.045 g) was added. The pH of the solution was gradually increased to 6.0 by addition of 0.1 M NaOH during 1 h. The excess of gadolinium was removed from a complex by dialysis using a Visking dialysis tube with a cut off of 3500 for 48 h in water. The polymer−gadolinium complex was lyophilized. The yield was 0.41 g of the complex.

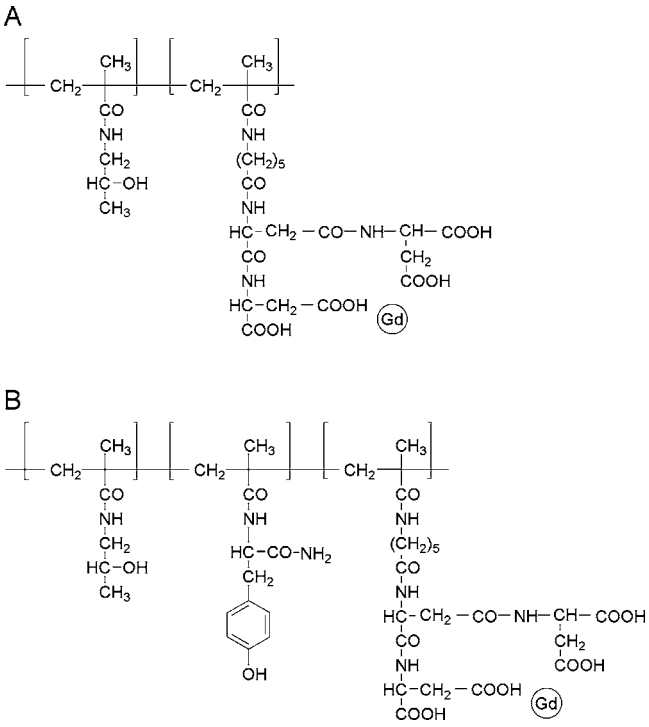

Figure 1. Chemical structures of the 24.8 kDa HPMA copolymer-based contrast agent HE-24.8 (A) and HE-radiolabel (B), the latter being used for the scintigraphic pharmacokinetic analysis in vivo.

The gadolinium content in the polymer complexes was 5.2 ± 0.3 as determined by inductively coupled plasma-mass spectrometry (ICP-MS).

Structures and characteristics of the HPMA copolymer−Gd complexes are given in Figure 1 and Table 1.

Determination of the Thermic Stability. A total of 1 μmol of the Gd-HPMA polymers and 100 μmol of tri-sodium-citrate were diluted in 11 mL of PBS (pH7.4). Samples of the stock solution with 1 mL each were incubated at 60 °C for 1, 5, and 25 h, respectively. At each time point, 100 μL were removed and diluted with 900 μL of PBS, then filtered (5 kDa MW filter, Millipore, Billerica, USA) to remove free gadolinium. The citrate complexed Gd-content was determined by plasma mass spectrometry.

Gd-DTPA-human Serum Albumin (Gd-DTPA-HSA). Gadolinium-DTPA-labeled albumin conjugates were synthesized at the German Cancer Research Center (DKFZ, Heidelberg, Germany) as described previously (*13*), by covalently binding gadolinium-DTPA to albumin.

In Vitro Determination of Cell Toxicity. Human fibroblasts (MSU) and human hepatoma cells (HEP-G2) were used. MSU and HEP-G2 cell lines were obtained from the German Cancer Research Center, Heidelberg, Germany.

Cells were grown in 75 cm^2 plastic culture flasks (TPP, Switzerland) in 10 mL of medium at 37 °C and in a humidified 5% CO_2 atmosphere. Human fibroblasts were maintained in Dulbecco's MEM-medium (Biochrom. AG, Berlin) supplemented with 10% fetal bovine serum (FBS), 1% sodium pyruvate, and 100 U penicillin/streptomycin. HEP-G2 cells were grown in RPMI 1640-medium (GIBCO, UK) with 5% FBS, 1% glutamine, and 100 U penicillin/streptomycin. Media were replaced every 4 days, and cells were split upon confluence at a split ratio of 1:5. For incubations, 24-bottom well plates with plastic cover slips of 13-mm diameter (Nalge Nunc International, Denmark) were used. A total of 500 μL of cell suspension was added to each well.

To investigate toxicity, cells were incubated with either HE-24.8 or Gd-DTPA-BMA (Omniscan, Amersham Health, Prin-

Table 1. Characteristics of HPMA Copolymer−Gd Complexes

sample	comonomer[a] in monomer mixture (mol %)	Ma-Tyr-NH_2 in monomer mixture (mol %)	comonomer[a] in polymer (mol %)	Ma-Tyr-NH_2 in polymer (mol %)	M_w	M_w/M_n
HE-24.8	5	0	3.3	0	24800	1.92
HE-radiolabel	5	2	3.2	0.8	26900	1.76

*Ma-Acap-Asp-[Asp-$(OMe)_2$]$_2$.

ceton, USA) in equimolar gadolinium concentrations (0.05 and 0.5 mmol of Gd/L) for 24 and 48 h. Cells grown in unmodified medium served as controls.

Viability was determined by Trypan blue (GIBCO, Gland Island, NY) exclusion following the manufacturer's instructions. The fraction of nonviable cells was determined using a Neubauer's counting chamber by analyzing five vision fields and calculating means and standard deviations (SD).

Cell survival was compared using the Student's t-test and $p < 0.05$ was considered to indicate a significant difference.

Animals and Tumors. All experiments were approved by the governmental review committee on animal care. Four healthy Copenhagen rats were used to study kinetics, biodistribution, and tolerability of HE-24.8. To perform tumor micro-angiographies, five Copenhagen rats with subcutaneous Dunning R3327-AT1 prostate tumors were used. Tumors were induced in the right upper thigh by injection of 2×10^5 cells in 1 mL of 0.9% NaCl. Tumors were grown for 3 weeks.

Kinetics, Biodistribution, and in Vivo Toxicity. To assess circulation time, organ accumulation and elimination, an analogous HPMA copolymer−Gd complex to HE-24.8 containing tyrosinamide in its side chain was synthesized, to allow radio labeling with ^{131}I (HE-radiolabel). The radiolabeled conjugate was injected into the tail vein of four healthy Copenhagen rats. Blood samples and scintigraphic images were taken at indicated time points. Two weeks after intravenous injection, the animals were sacrificed, and their organs were removed. Residual activity was corrected for radioactive decay. During the two-week follow-up period, the animals were monitored for signs of toxicity.

MR Imaging. Magnetic resonance imaging (MRI) was performed on a clinical 1.5 T whole-body MR system (Siemens Symphony, Erlangen, Germany) using a custom-made radio frequency-(rf) coil for rf excitation and signal reception. The rf coil was designed as a cylindrical volume resonator with an inner diameter of 83 mm and a useable length of 120 mm. To optimize the available signal-to-noise ratio, manual tuning and matching of the coil's resonance circuitry was performed for each measurement individually.

Determination of the Relaxivity of HE-24.8, Gd-DTPA-HSA, and Gd-DTPA-BMA. Relaxivity measurements of HE-24.8, Gd-DTPA-HSA, and Gd-DTPA-BMA were performed using a 1.5 T MR scanner (Magnetom Vision, Siemens Erlangen, Germany) and a standard head coil (Siemens Erlangen, Germany). Increasing concentrations of contrast medium (0.0, 0.01, 0.05, 0.1, 0.5, 1.0 mmol of Gd/L of 0.9% NaCl) were transferred to phantom vials and placed in the isocenter of the coil. T_1 times were determined with a saturation-recovery turbo FLASH-sequence (TR/TE = 10 ms/4 ms, flip-angle: 12°, T_{rec} = 53−9000 ms). The relaxation rates were plotted against concentrations and fitted by linear regression to achieve the relaxivity.

High-Resolution MR Angiography. For MR examination and catheterization, rats were anaesthetized by inhalation of a mixture of isofluorane (1.5%), N_2O (35%), and O_2 (60%). A tail vein was catheterized using a 24 G indwelling cannula (Introcan, B. Braun Melsungen AG, Melsungen, Germany), which was connected with a 1 mL syringe (Braun Melsungen AG, Melsungen, Germany) filled with 1 mL of the contrast agent (0.05 mmol of Gd/kg of body weight for both HE-24.8 and Gd-DTPA-HSA).

MR examinations of the rats were initiated by a T_2 weighted turbo spin−echo sequence: TR = 4000 ms, TE = 96 ms, 1 acquisition, echo train length = 7, TA = 1 min 49 s, field of view = 50 × 37.5 mm, matrix = 140 × 256, slice thickness = 2 mm, voxel size = 2.0 × 0.36 × 0.15 mm^3.

Four animals were examined with HE-24.8-enhanced scans, one after administration of Gd-DTPA-HSA. The contrast agent was injected before the first MR angiography scan. In three of four rats, which were examined with HE-24.8-enhanced scans and in the animal with Gd-DTPA-HSA at first the tumors were investigated using a three-dimensional gradient echo pulse sequence (TR/TE = 28.0/8.6 ms, flip-angle = 70°, field of view = 12.8 × 30 × 50 mm^3, matrix = 128 × 317 × 512, reconstructed voxel size = 100 × 98 × 98 μm^3, 2 acquisitions, total scan time = 24 min). Subsequently, the chest was imaged using again a three-dimensional gradient echo pulse sequence with the following parameters: TR/TE = 10.2/3.8 ms, flip-angle = 70°, field of view = 30 × 55 × 110 mm^3, matrix = 60 × 256 × 512, reconstructed voxel size = 500 × 215 × 215 μm^3, 4 acquisitions, total scan time = 5.18 min. In the remaining animal, which was scanned with HE-24.8, a high resolved examination of the brain was performed using the first men-

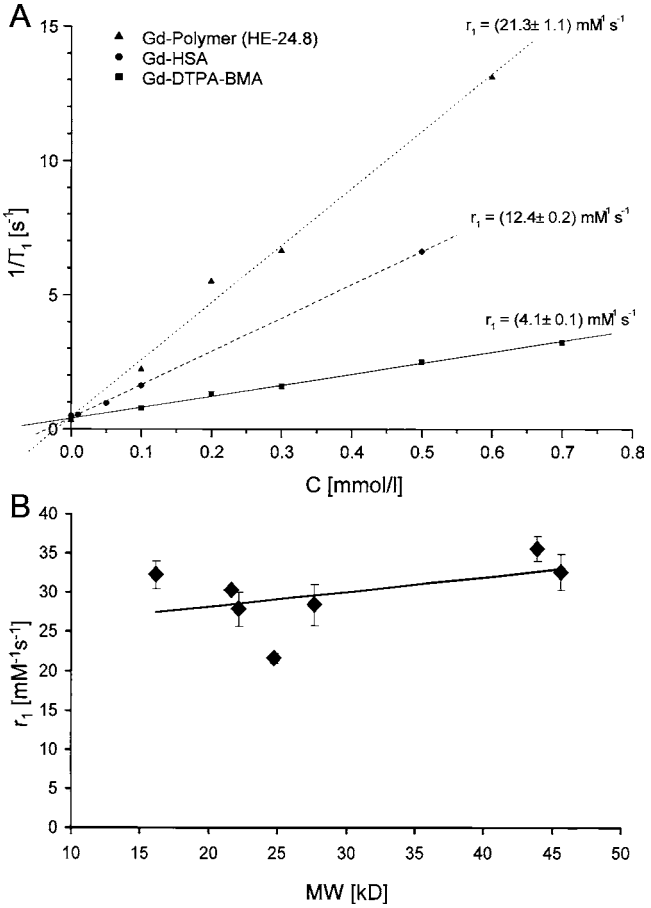

Figure 2. (A) Results of the T_1 relaxivity (r_1) measurements of Gd-DTPA-BMA, Gd-DTPA-HSA, and HE-24.8 measured at 1.5 T. (B) T_1 relaxivity (r_1) of HPMA copolymer−Gd complexes with different sizes (16.2, 21.7, 22.2, 24.8, 27.7, 43.9, and 45.6 kDa; $n = 5 \pm$ SD).

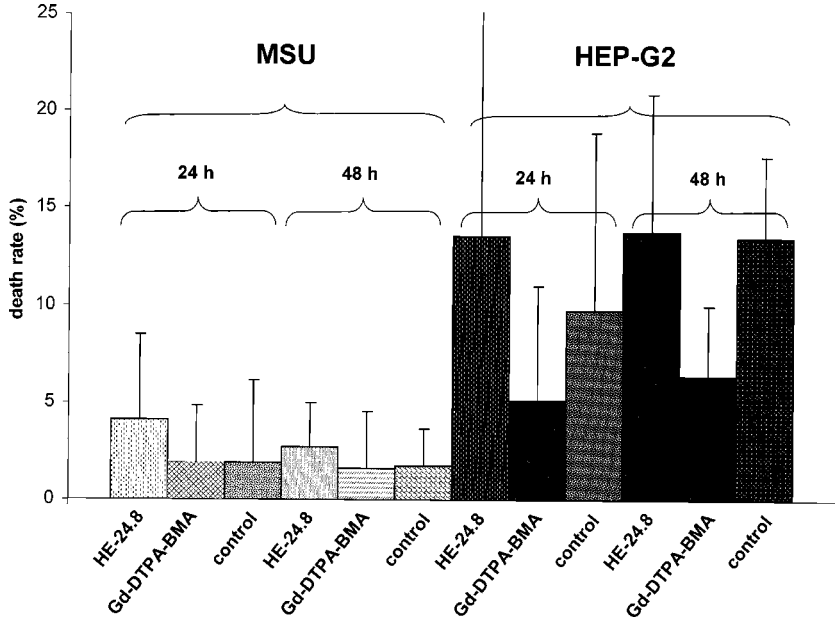

Figure 3. Death rates of human fibroblasts (MSU) and hepatocarcinoma cells (HEP-G2) after incubation with HE-24.8 and Gd-DTPA-BMA in dosages of 0.5 mmol of Gd/L of growth medium. Incubation times were 24 and 48 h. Data presented as mean ($n = 10 \pm$ SD).

tioned gradient echo pulse sequence. Afterward, the tumor was investigated as described previously.

Comparison of Vessel Contrast in HE-24.8- and Gd-DTPA-HSA-Enhanced Scans. To compare the in vivo contrast of vessels in HE-24.8- and Gd-DTPA-HSA-enhanced scans circular ROIs ($n = 5$) were placed in the left ventricle of the heart, the aorta, the caval vein, the brachial vein, and the neck musculature. Signal intensities (SI) of vessels and heart were normalized to the mean SI of the muscle. Data were compared using the Student's t-test, and $p < 0.05$ was considered to indicate a significant difference.

Histological and Immunofluorescence Examination. For histological diagnosis and assessment of vital tissue and its vascularization, tumors were dissected, covered with "tissue tek" (Sacura, Zoeterwoude, Netherlands), and frozen in liquid nitrogen vapor. 5-μm-thick sections were cut with a Reichert-Jung Frigocut 2700 microtome. For histology, sections were stained with hematoxilin and eosin (HE). Blood vessels were visualized by immunofluorescence using a polyclonal antibody against collagen IV (Progen, Heidelberg, Germany) and a Cy3-labeled secondary anti-rabbit IgG antibody (Dianova, Hamburg, Germany). Tissue sections were viewed by fluorescence microscopy using an Olympus AX-70 microscope. Images were captured with a digital camera at ×4 magnification and composed using the Soft-Imaging-System analysis software. From immunofluorescence images, the mean diameters of the 10 largest vessels either tumor periphery or center were analyzed to obtain information about the minimal vessel diameters, which were resolved by MR-angiography using Gd-DTPA-HSA or HE-24.8, respectively.

RESULTS

In Vitro Experiments: Thermic Stability, Relaxivity, and Toxicity. *Chemical Characterization of the Polymers.* New polymeric MRI contrast agents based on HPMA copolymers bearing in the side chains aspartic acid residues complexed with Gd were synthesized. Structures and characteristics of the HPMA copolymer−Gd complexes are given in Scheme 1 and Table 1.

Thermic Stability of HE-24.8. The gadolinium content of nonfiltered samples containing the Gd−HPMA polymers in PBS was 11.6 ± 0.1 μg of Gd/mL. After the polymers were removed

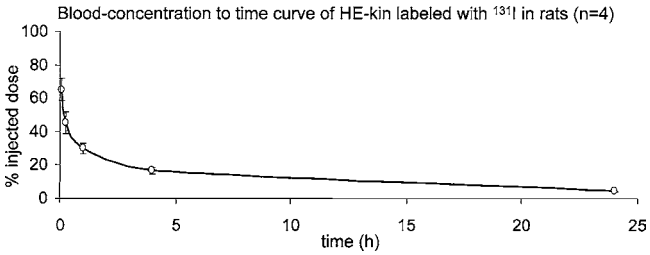

Figure 4. Blood concentration to time curve of HE-radiolabel (^{131}I) in rats ($n = 4$). After 15 min, less than 50% and after 24 h less than 5% of the injected dose was found in the blood.

by filtration with a 5 kD MW filter 0.07 ± 0.01 μg of Gd/mL were left in the probe. Incubation of the polymer at 60 °C did not increase the amount of filtered gadolinium significantly. A constant level of 0.05 ± 0.01 μg of Gd/mL was determined after 1, 5, and 25 h, respectively.

Relaxivity. HE-24.8 showed a T_1 relaxivity of 21.3 ± 1.1 mM^{-1} s^{-1} at 1.5 T, which was higher than the relaxivity of Gd-DTPA-HSA (12.4 ± 0.2 mM^{-1} s^{-1}) and Gd-DTPA-BMA (4.1 ± 0.1 mM^{-1} s^{-1}). In consequence, a higher T_1 contrast was achieved in MR angiography (Figure 2A). T_2 relaxivity of HE-24.8 at 1.5 T was 29.4 ± 0.3 mM^{-1} s^{-1}. When comparing Gd-labeled HPMA copolymers of different sizes, it was observed that the T_1 relaxivity of the different compounds was similar in the used molecular size range (Figure 2B), which is desirable when using such substances for studying vessel permeability in vivo.

Cell Toxicity. Cell survival experiments were performed to study toxicity and stability of the HPMA copolymer−Gd complex HE-24.8. No increased cell death rates were observed after incubation of the cells with HE-24.8 or Gd-DTPA-BMA at concentrations of 0.05 and 0.5 mmol of Gd/L in growth medium. After 24 h incubation of the cells with 0.5 mmol of Gd/L the ratio of nonviable MSU cells was lower than 5% for both contrast agents and thus comparable to the control cells in which the death rate was 2%. Also after incubation times of 48 h mean death rates were always lower than 5% (Figure 3).

The excellent tolerance of HE-24.8 was underlined by toxicity experiments with HEP-G2 cells, where no significantly increased death rates were observed, although the baseline rate of dead cells was higher for all incubation conditions (Figure 3).

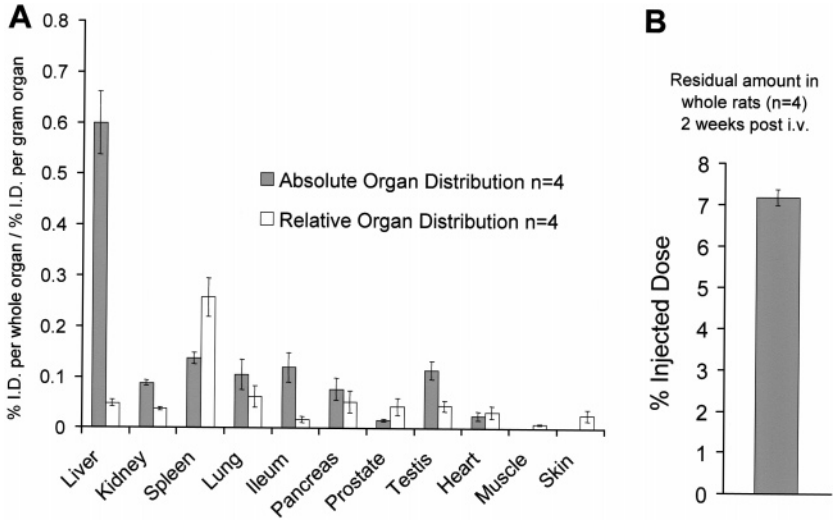

Figure 5. Radioactive counts representing the absolute and relative organ concentrations of HE-radiolabel in rats 14 days after administration (A). The mean absolute concentration for the entire animal ($n = 4$) is shown in B.

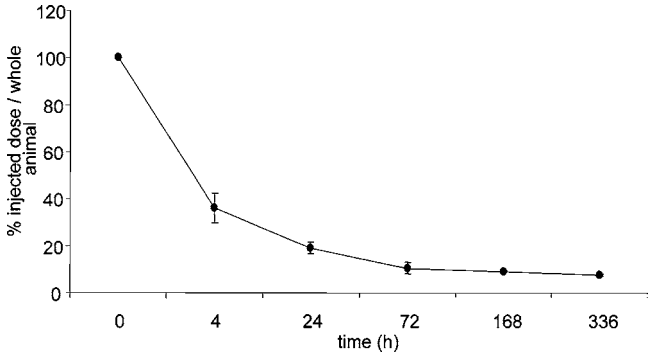

Figure 6. The mean relative number of counts in rats ($n = 4$) from scintigraphic detection of HPMA copolymer−Gd complex labeled with ^{131}I is shown during a two-week follow up. The total number of counts after 1 h measured in rats, which were kept under continuous anesthesia, was set at 100%.

Kinetics, Biodistribution, and in Vivo Toxicity. Lack of toxicity in cell culture experiments encouraged us to initiate animal studies.

As shown in Figure 4, HE-radiolabel circulates for significantly prolonged periods of time as compared with data known from the literature about low-molecular-weight gadolinium chelates. After 15 min, less than 50% of the injected dose (ID) was left in the systemic circulation. Four hours postintravenous injection, the concentration in the systemic circulation had decreased to 16.9% ID. A total of 24, 168, and 336 h after injection, 4.67, 0.36, and 0.15% ID could be attributed to the vascular compartment, respectively (Figure 4).

Two weeks after intravenous injection of HE-radiolabel, animals were sacrificed, organs were removed, and radioactive counts were analyzed. HE-radiolabel did not accumulate in any organ specifically, when expressed as a percentage of ID. Relatively, the largest fraction of contrast agent accumulated in the spleen, with 0.25% ID/g of tissue (Figure 5). In most other tissues, retention rates were comparable with approximately 0.05% ID/g of tissue. Absolutely, i.e., when taking organ weight into account, at 336 h postinjection, most of the conjugate ended up in the liver. Hepatic uptake was very acceptable, with only 0.6% per whole liver.

At the level of the entire animal, 37.6, 20.0, and 8.0% ID were still detected by scintigraphic imaging at 4, 24, and 336 h postinjection, respectively (Figure 6).

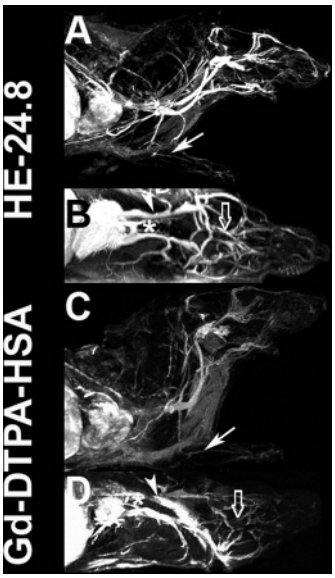

Figure 7. MR angiography scans of the chest of rats using HE-24.8 (A, B) and Gd-DTPA-HSA (C, D). Images give sagittal (A, C) and coronal (B, D) views of the animal. Both contrast agents give an excellent display of larger veins of the chest (arrowheads) and the brain (open arrow: jugular vein) as well as of the heart with its ventricles. While the contrast of larger vessels is better in the He-24.8-enhanced scan, in smaller vessels such as the brachial vein (arrow) the vessel contrast is comparable. *: aortic arc.

No decreased overall activity, no reduction in food intake, and no substantial signs of weight loss were observed during the experiments.

MR Angiography. To get an idea of the in vivo contrast characteristics of HE-24.8, micro-MR angiographies of rats and experimental tumors were performed and compared with images of Gd-DTPA-HSA-enhanced MR angiographies. Both contrast agents showed an excellent display of larger veins of the chest and the brain as well as of the heart with its ventricles (Figure 7). However, as expected from the higher T_1 relaxivity, the contrast of heart ventricles, larger arteries, and veins was more than 70% higher using HE-24.8 (Figures 7 and 8). For smaller peripheral veins such as the brachial vein no significant differences in vessel contrast was found (Figure 8). In the subcutaneous tumors (Figure 8), both contrast agents showed the potential to visualize the small and fragile tumor neovascularization. However, vessel architecture of tumors was not displayed in higher detail in HE-24.8-enhanced scans, which

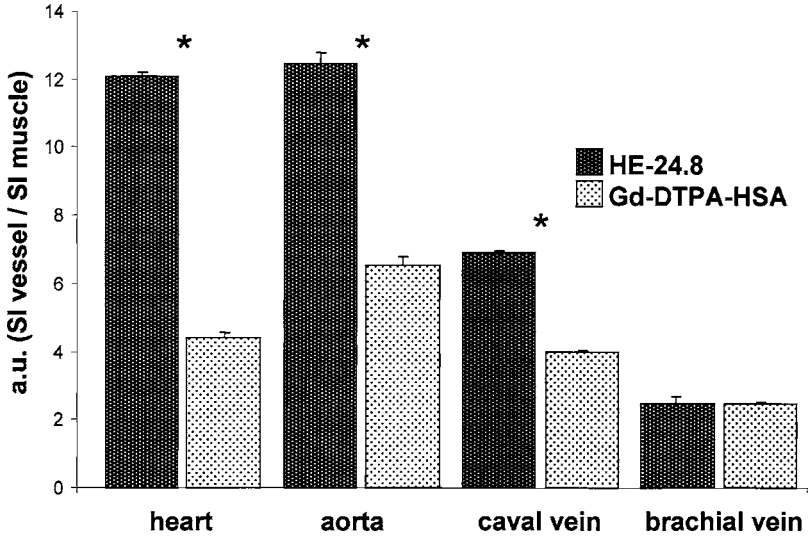

Figure 8. Comparison of vessel contrast in HE-24.8- and Gd-DTPA-HSA-enhanced scans. Using HE-24.8, significantly higher vessel contrast was found in the heart, aorta, and caval vein. In contrast, vessel contrast in the brachial vein was not significantly different. Data presented as mean of 5 ROI analyses + SD. *$p < 0.05$.

was most probably reasoned by the limited resolution and signal-to-noise ratio of the clinical 1.5 T MR scanner. Predominantly larger vessels localized at the tumor periphery were visualized by MR angiography and reconstructed three-dimensionally (Figure 9). Determining the mean diameters of peripheral vessels on histological images, it was clearly shown that these had diameters of 96 ± 51 μm, which is in line with vessel sizes resolved by other groups using 1.5 T MR angiography (*18,19*). The small vessels found in the tumor center with a mean diameter of 12 ± 5 μm (SD) were not depicted by MRI either using Gd-DTPA-HSA or HE-24.8.

Also in the brain HE-24.8 proved its potential as an excellent experimental angiographic contrast agent by clearly visualizing the vascular network with the feeding carotic artery, the draining jugular vein, and the basal cerebral arteries of the circulus arteriosus cerebri. Even the middle cerebral artery and some of its branches could be detected at 1.5 T using HE-24.8 (Figure 10).

DISCUSSION

In this paper, an MR contrast agent based on an HPMA copolymer−Gd complex is presented. In this context, the synthesis of a new comonomer Ma-Acap-Asp-[(Asp-$(OMe)_2$]$_2$ and its two copolymers with HPMA is described. The synthesis enables preparation of a broad range of copolymers differing in molecular weight and copolymer composition. The copolymers after deprotection of carboxylic groups form complexes with gadolinium exhibiting an excellent thermostability in aqueous solutions, which was tested for a temperature of up to 60 °C. The copolymer HE-radiolabel contains small amount of tyrosinamide in its structure enabling radiolabeling and the use of this copolymer for pharmacokinetic studies. Copolymer HE-24.8 consists of HPMA and Ma-Acap-Asp-[(Asp-$(OH)_2$]$_2$-Gd units. In both polymer complexes, Gd was embedded in side chains of the hydrophilic polymer formed by three aspartic acid residues extending four carboxylic groups for complexation with Gd. As a basis for further studies, the biological behavior of HE-24.8 was examined in vitro and in vivo. Furthermore, initial results are presented using this contrast agent to visualize tumor microvasculature, and the contrast of vessels was compared between HE-24.8- and Gd-DTPA-HSA-enhanced scans.

Embedding the gadolinium atoms in a HPMA copolymer results in a high T_1 relaxivity, which is superior to those of Gd-DTPA-BMA and Gd-DTPA-HSA. The high T_1 relaxivity can be attributed to the new type of structure of the Gd complex leading to an improved interaction of the gadolinium with surrounding protons. It may be further supported by the integration of the gadolinium into a highly hydrophilic HPMA copolymer, which is also known to increase T_1 relaxivity of contrast agents, where gadolinium compounds were coupled or bound to proteins (*38*−*40*) and other tracers (*11*, *15*, *20*). Relaxivity of Gd-DTPA-HSA may also increase when binding more Gd-DTPA molecules to the albumin or by modifying the way of binding (*41*). However, the low number of Gd-DTPA molecules bound to HSA was chosen to reduce hepatic elimination, which is highly influenced by the loading rate of albumin (*42*).

It is a further advantage of the HPMA copolymer−Gd complexes that the T_1 relaxivities of compounds with molecular sizes between 15 and 46 kDa were not significantly different. This predetermines the HPMA copolymer−Gd complexes for studies on vessel permeability in vivo, e.g., to find optimal polymer sizes to visualize neoplastic tissue.

There were no indications of release of free gadolinium in the in vitro experiments, which would result in high cell toxicity. Likewise, no toxic effects were observed in vivo. However, studies with higher animal numbers and monitoring over longer periods of time are necessary to confirm this preliminary result. Although the HPMA polymer carrier is not immunogenic, it is also important to exclude immunogenic reactions, which may be induced by the gadolinium chelate derivates and which are for example known from Gd-DOTA.

For visualization of microvessels using a clinical 1.5 T MR scanner, long acquisition times are required to reveal a sufficiently high signal-to-noise ratio. In this study, extended acquisition times could be chosen due to the longer intravasal persistence of HE-24.8 as compared to the clinically used small Gd-chelates. On the other hand, long circulation times go along with a delayed systemic elimination of the compound.

Comparable with native and cytostatic drug-loaded HPMA copolymers (*30*, *31*), and other uncharged polymeric drug and tracer carriers such as PEG, HPMA copolymer−Gd complex did not accumulate in any organ specifically. In general, such carriers are initially cleared by the kidneys, and later on more dominantly by the reticulo-endothelial system. Thus, it is plausible that the highest uptake of HE-24.8 per gram of tissue was found in the spleen, where the substance was most probably accumulated by macrophages via phagocytosis.

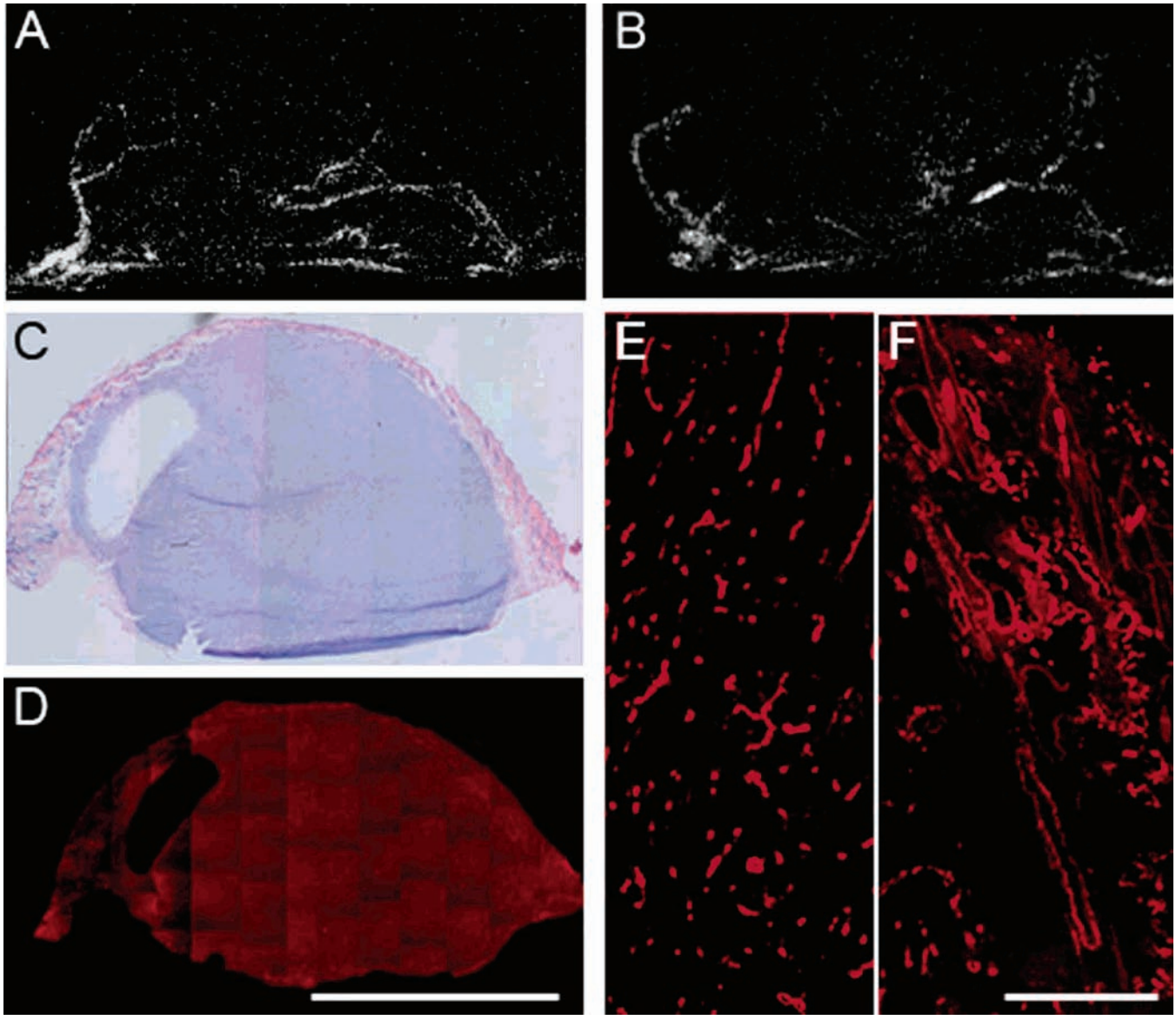

Figure 9. Maximum intensity projections (MIP) of a subcutaneous Dunning prostate carcinoma in rats using HE-24.8 (A) and Gd-DTPA-HSA (B). Histological compound images of the tumor shown in A are demonstrated using a hematoxilin and eosin stain (C) and an immunofluorescence stain against the vessel collagen type IV (D), respectively. Magnifications of the immunofluorescence image taken from representative areas of the tumor periphery (E) and center (F) show the differences in vessel architecture with larger vessels of approximately 91 ± 51 μm at the tumor periphery and small capillary vessels of less than 12 ± 5 μm diameter in the center. Bars: 5 mm (D), 0.4 mm (F).

When comparing HE-24.8 with comparable macromolecules (*13*, *20*), it is a great advantage that the liver does not accumulate HE-24.8 in higher amounts. Only 0.6% of the injected dose was found in liver two weeks postinjection. Thus, we conclude that the hydrophilic nature of the HPMA polymer chain, neutral loading, the absence of structural inhomogeneities, e.g., as present in liposomes and the random coil configuration, reduce the immunological detection of HE-24.8.

We are aware that for clinical use the intracorporal persistence of approximately 7.6% of HE-24.8 after 14 days is still too high. The molecular weight of approximately 25 kDa was chosen for the synthesis of HE-24.8 to be in the size range of HPMA copolymer constructs loaded with cytostatic drugs. Currently, at least six HPMA copolymer-based drug conjugates of comparable size are being evaluated in various clinical stages (*43*). Ultimate goal of these studies was, however, to increase circulation time and tumor accumulation of the delivered drug and to better control its side effects by substantially altering biodistribution. Because the nature of the polymers allows us to flexibly modify its size, structure, and stability, there is still room for further developments. Currently, we are evaluating conjugates of significantly smaller size, and in the future we may try to establish comparable, but biodegradable, contrast-enhancing conjugates (*44*, *45*), to boost elimination in the first two weeks after injection.

MR angiographies showed a detailed display of rat and tumor vasculature even for vessels with relatively slow blood flow like most of the tumor vessels. For these vessels, the signal enhancement by flow effects is considerably low, and as a consequence the vessel contrast is more dependent on the contrast agent. Compared with Gd-DTPA-HSA, the contrast of vessels was higher, while the amount of vessels was not increased. The lack of displaying smaller vessels, however, can be attributed to the voxel sizes, which could not be chosen smaller at an acceptable signal-to-noise ratio with the clinical 1.5 T MR-scanner. In the extremities, the difference in vessel contrast between HE-24.8- and Gd-DTPA-HSA-enhanced scans was reduced as compared with larger central vessels of the chest. This may be because if only a part of the voxel contains the vessel, the signal intensity change after application of contrast

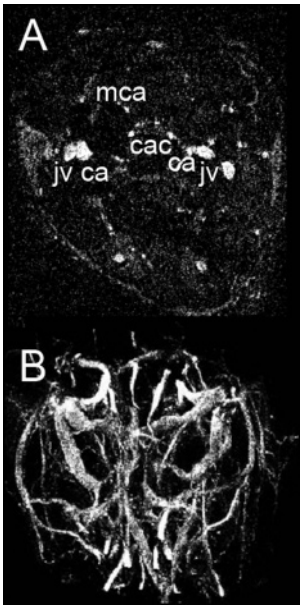

Figure 10. Coronal image (A) and MIP (B) of HE-24.8-enhanced scans of the rat head. The carotic artery (ca) and the jugular vein (jv) are clearly shown on both images. Also smaller vessels as those of the circulus arteriosus cerebri (cac) or the middle cerebral artery (mca) with some of its larger branches are visualized.

agent becomes lower. Thus, the signal enhancement, which is achieved with contrast agents with higher or lower T_1 relaxivity, equalizes. The advantages of HE-24.8 to image smaller vessels would most probably become more evident at higher field strength (>1.5 T), where differences in T_1 relaxivity between Gd-DTPA-BMA, Gd-DTPA-HSA, and HE-24.8 become more important (own unpublished results), and the voxel sizes of the MR angiography sequence could be chosen smaller.

In summary, a new polymeric contrast agent is presented, which can be synthesized with flexible molecular weight and structure. Besides its suitability for experimental studies on micro-MR angiography, the independency of the T_1 relaxivity of the Gd-labeled HPMA compounds on the polymer sizes makes it an interesting tool to study vessel permeability in tumors. For a future clinical approach, however, further chemical refinement seems necessary to fasten the corporal elimination.

ACKNOWLEDGMENT

The work was supported by the Grant Agency of the Academy of Sciences of the Czech Republic (Grant No. IAA 4050201 and Ministry of Education, Youth and Sports, through the program "Research Centers" (IM 4635608802) and the EU Framework Program 6 (project LSHC-CT-2003-503297).

LITERATURE CITED

(1) Felix, R., Semmler, W., Schorner, W., and Laniado, M. (1985) Contrast media in magnetic resonance tomography. A review. 1. Physicochemical and pharmacological bases of MR contrast media using gadolinium-DTPA as an example. *Rofo 142*, 641−646.

(2) Wolf, G. L., Burnett, K. R., Goldstein, E. J., and Joseph, P. M. (1985) Contrast agents for magnetic resonance imaging. *Magn. Reson. Annu.* 231−266.

(3) Semelka, R. C., and Helmberger, T. K. (2001) Contrast agents for MR imaging of the liver. *Radiology 218*, 27−38.

(4) Padhani, A. R. (2002) Dynamic contrast-enhanced MRI in clinical oncology: current status and future directions. *J. Magn. Reson. Imaging 16*, 407−422.

(5) Roberts, T. P., Chuang, N., and Roberts, H. C. (2000) Neuroimaging: do we really need new contrast agents for MRI? *Eur. J. Radiol. 34*, 166−178.

(6) Krinsky, G. (1998) Gadolinium-enhanced three-dimensional magnetic resonance angiography of the thoracic aorta and arch vessels. A review. *Invest. Radiol. 33*, 587−605.

(7) Rofsky, N. M., and Adelman, M. A. (2000) MR angiography in the evaluation of atherosclerotic peripheral vascular disease. *Radiology 214*, 325−338.

(8) Spinosa, D. J., Kaufmann, J. A., and Hartwell, G. D. (2002) Gadolinium chelates in angiography and interventional radiology: a useful alternative to iodinated contrast media for angiography. *Radiology 223*, 319−325.

(9) Kiessling, F., Farhan, N., Lichy, M. P., Vosseler, S., Heilmann, M., Krix, M., Bohlen, P., Miller, D. W., Mueller, M. M., Semmler, W., Fusenig, N. E., and Delorme, S. (2004) Dynamic contrast-enhanced magnetic resonance imaging rapidly indicates vessel regression in human squamous cell carcinomas grown in nude mice caused by VEGF receptor 2 blockade with DC101. *Neoplasia 6*, 213−223.

(10) Turetschek, K., Preda, A., Novikov, V., Brasch, R. C., Weinmann, H. J., Wunderbaldinger, P., and Roberts, T. P. (2004) Tumor microvascular changes in antiangiogenic treatment: Assessment by magnetic resonance contrast media of different molecular weights. *J. Magn. Reson. Imaging 20*, 138−144.

(11) Kobayashi, H., and Brechbiel, M. W. (2003) Dendrimer-based macromolecular MRI contrast agents: characteristics and application. *Mol. Imaging 2*, 1−10.

(12) Brasch, R., and Turetschek, K. (2000) MRI characterization of tumors and grading angiogenesis using macromolecular contrast media: status report. *Eur. J. Radiol. 34*, 148−155.

(13) Kiessling, F., Fink, C., Hansen, M., Bock, M., Sinn, H., Schrenk, H. H., Krix, M., Egelhof, T., Fusenig, N. E., and Delorme, S. (2002) Magnetic resonance imaging of nude mice with heterotransplanted high-grade squamous cell carcinomas: use of a low-loaded, covalently bound Gd−Hsa conjugate as contrast agent with high tumor affinity. *Invest. Radiol. 37*, 193−198.

(14) Dafni, H., Gilead, A., Nevo, N., Eilam, R., Harmelin, A., and Neeman, M. (2003) Modulation of the pharmacokinetics of macromolecular contrast material by avidin chase: MRI, optical, and inductively coupled plasma mass spectrometry tracking of triply labeled albumin. *Magn. Reson. Med. 50*, 904−914.

(15) Misselwitz, B., Schmitt-Willich, H., Ebert, W., Frenzel, T., and Weinmann, H. J. (2001) Pharmacokinetics of Gadomer-17, a new dendritic magnetic resonance contrast agent. *MAGMA 12*, 128−134.

(16) Lauffer, R. B., Parmelee, D. J., Dunham, S. U., Ouellet, H. S., Dolan, R. P., Witte, S., McMurry, T. J., and Walovitch, R. C. (1998) MS-325: albumin-targeted contrast agent for MR angiography. *Radiology 207*, 529−538.

(17) Marzola, P., Farace, P., Calderan, L., Crescimanno, C., Lunati, E., Nicolato, E., Benati, D., Degrassi, A., Terron, A., Klapwijk, J., Pesenti, E., Sbarbati, A., and Osculati, F. (2003) In vivo mapping of fractional plasma volume (fpv) and endothelial transfer coefficient (Kps) in solid tumors using a macromolecular contrast agent: correlation with histology and ultrastructure. *Int. J. Cancer 104*, 462−468.

(18) Fink, C., Kiessling, F., Bock, M., Lichy, M. P., Misselwitz, B., Peschke, P., Fusenig, N. E., Grobholz, R., and Delorme, S. (2003) High-resolution three-dimensional MR angiography of rodent tumors: morphologic characterization of intratumoral vasculature. *J. Magn. Reson. Imaging 18*, 59−65.

(19) Kobayashi, H., Sato, N., Kawamoto, S, Saga, T., Hiraga, A., Ishimori, T., Konishi, J., Togashi, K., and Brechbiel, M. W. (2001) 3D MR angiography of intratumoral vasculature using a novel macromolecular MR contrast agent. *Magn. Reson. Med. 46*, 579−585.

(20) Weissleder, R., Bogdanov, A., Tung, C. H., and Weinmann, H. J. (2001) Size optimization of synthetic graft copolymers for in vivo angiogenesis imaging. *Bioconjugate Chem. 12*, 213−219.

(21) Callahan, R. J., Bogdanov, A., Fischman, A. J., Brady, T. J., and Weissleder, R. (1998) Preclinical evaluation and phase I clinical trial of a 99mTc-labeled synthetic polymer used in blood pool imaging. *Am. J. Roentgenol. 171*, 137−143.

(22) Bremer, C., Tung, C. H., and Weissleder, R. (2001) In vivo molecular target assessment of matrix metalloproteinase inhibition. *Nat. Med. 7*, 743−748.

(23) Říhová, B., Strohalm, J., Kubáčková, K., Jelinkova, M., Rozprimova, L., Sirova, M., Plocova, D., Mrkvan, T., Kovar M., Pokorna,

J., Etrych, T., and Ulbrich, K. (2003) Drug-HPMA-HuIg conjugates effective against human solid cancer. *Adv. Exp. Med. Biol. 519*, 125−143.

(24) Caiolfa, V. R., Zamai, M., Fiorino, A., Frigerio, E., Pellizzoni, C., d'Argy, R., Ghiglieri, A., Castelli, M. G., Farao, M., Pesenti, E., Gigli, M., Angelucci, F., and Suarato, A. (2000) Polymer-bound camptothecin: initial biodistribution and antitumour activity studies. *J. Control. Release 65*, 105−119.

(25) Meerum-Terwogt, J. M., ten Bokkel Huinink, W. W., Schellens, J. H., Schot, M., Mandjes, I. A., Zurlo, M. G., Rocchetti, M., Rosing, H., Koopman, F. J., and Beijnen, J. H. (2001) Phase I clinical and pharmacokinetic study of PNU166945, a novel water-soluble polymer-conjugated prodrug of paclitaxel. *Anti-Cancer Drugs 12*, 315−323.

(26) Gianasi, E., Buckley, R. G., Latigo, J., Wasil, M., and Duncan, R. (2002) HPMA copolymers platinates containing dicarboxylato ligands. Preparation, characterisation and in vitro and in vivo evaluation. *J. Drug Targeting 10*, 549−556.

(27) Rihova, B., and Kubackova, K. (2004) Clinical implications of *N*-(2-hydroxypropyl)methacrylamide copolymers. *Curr. Pharm. Biotechnol. 4*, 311−322.

(28) Searle, F., Gac-Breton, S., Keane R., Dimitrijevic, S., Brocchini, S., Sausville, E. A., and Duncan, R. (2001) *N*-(2-hydroxypropyl)-methacrylamide copolymer-6-(3-aminopropyl)-ellipticine conjugates. Synthesis, in vitro, and preliminary in vivo evaluation. *Bioconjugate Chem. 12*, 711−718.

(29) Noguchi, Y., Wu, J., Duncan, R., Strohalm, J., Ulbrich, K., Akaike, T., and Maeda, H. (1998) Early phase tumor accumulation of macromolecules: a great difference in clearance rate between tumor and normal tissues. *Jpn. J. Cancer Res. 89*, 307−314.

(30) Shiah, J. G., Dvorak, M., Kopeckova, P., Sun, Y., Peterson, C. M., and Kopecek, J. (2001) Biodistribution and antitumour efficacy of long-circulating *N*-(2-hydroxypropyl)methacrylamide copolymer-doxorubicin conjugates in nude mice. *Eur. J. Cancer 37*, 131−139.

(31) Kissel, M., Peschke, P., Šubr, V., Ulbrich, K., Schuhmacher, J., Debus, J., and Friedrich, E. (2001) Synthetic macromolecular drug carriers: biodistribution of poly[(N-2-hydroxypropyl)methacrylamide] copolymers and their accumulation in solid rat tumors. *PDA J. Pharm. Sci. Technol. 55*, 191−201.

(32) Mitra, A., Nan, A. J., Ghandehari, H., McNeill, E., Mulholland, J., and Line, B. R. (2004) Technetium-99m-labeled *N*-(2-hydroxypropyl) methacrylamide copolymers: Synthesis, characterization, and in vivo biodistribution. *Pharm. Res. 21*, 1153−1159.

(33) Huang, Y., Nan, A. J., and Rosen, G. M. (2003) *N*-(2-hydroxypropyl)methacrylamide (HPMA) copolymer-linked nitroxides: Potential magnetic resonance contrast agents. *Macromol. Biosci. 3*, 647−652.

(34) Wang, D., Miller, S. C., Sima, M., Parker, D., Buswell, H., Doodrich, K., C., Kopeckova, P., and Kopecek J. (2004) The arthrotropism of macromolecules in adjuvant-induced arthritis rat model: a preliminary study. *Pharm. Res. 21*, 1741−1749.

(35) Ulbrich, K., Šubr, V., Strohalm, J., Plocová, D., Jelínková, M., and Říhová, M. (2000) Polymeric drugs based on conjugates of synthetic and natural macromolecules I. Synthesis and physicochemical characterisation. *J. Control. Release 64*, 63−79.

(36) Kissel, M., Peschke, P., Šubr, V., Ulbrich, K., Strunz, A. M., Kuhnlein, R., Debus, J., and Friedrich, E. (2002) Detection and cellular localisation of the synthetic soluble macromolecular drug carrier pHPMA. *Eur. J. Nucl. Med. 29*, 1055−1062.

(37) Drobník, J., Kopeček, J., Labský, J., Reimanova, P., Exner, J., Saudek, V., and Kalal, J. (1976) Enzymatic cleavage of side chains of synthetic water-soluble polymers. *Makromol. Chem. 177*, 2833−2848.

(38) Stanisz, G. J., and Henkelman, R. M. (2000) Gd-DTPA relaxivity depends on macromolecular content. *Magn. Reson. Med. 44*, 665−667.

(39) McMurry, T. J., Parmelee, D. J., Sajiki, H., Scott, D. M., Ouellet, H. S., Walovitch, R. C., Tyeklar, Z., Dumas, S., Bernard, P., Nadler, S., Midelfort, K., Greenfield, M., Troughton, J., and Lauffer, R. B. (2002) The effect of a phosphodiester linking group on albumin binding, blood half-life, and relaxivity of intravascular diethylenetriaminepentaacetato aquo gadolinium(III) MRI contrast agents. *J. Med. Chem. 45*, 3465−3474.

(40) Aime, S., Chiaussa, M., Digilio, G., Gianolio, E., and Terreno, E. (1999) Contrast agents for magnetic resonance angiographic applications: 1H and 17O NMR relaxometric investigations on two gadolinium(III) DTPA-like chelates endowed with high binding affinity to human serum albumin. *J. Biol. Inorg. Chem. 4*, 766−774.

(41) Stehle, G., Sinn, H., Wunder, A., Schrenk, H. H., Schutt, S., Maier-Borst, W., and Heene, D. L. (1997) The loading rate determines tumor targeting properties of methotrexate-albumin conjugates in rats. *Anti-Cancer Drugs 8*, 677−685.

(42) Caravan, P., Greenfield, M. T., Li, X., and Sherry, A. D. (2001) The Gd(3+) complex of a fatty acid analogue of DOTP binds to multiple albumin sites with variable water relaxivities. *Inorg. Chem. 40*, 6580−6587.

(43) Duncan, R. (2003) The dawning era of polymer therapeutics. *Nat. Rev. Drug Discov. 2*, 347−360.

(44) Jabbari, E., Wang, S., Lu, L., Gruetzmacher, J. A., Ameenuddin, S., Hefferan, T. E., Currier, B. L., Windebank, A. J., and Yaszemski, M. J. (2005) Synthesis, material properties, and biocompatibility of a novel self-cross-linkable poly(caprolactone fumerate) as an injectable tissue engeneering scaffold. *Biomacromolecules 6*, 2503−2511.

(45) Mohs, A. M., Wang, X., Goodrich, K. C., Zong, Y., Parker, D. L., and Lu, Z. R. (2004) PEG-*g*-poly(GdDTPA-*co*-L-cystine): a biodegradable macromolecular blood pool contrast agent for MR imaging. *Bioconjugate Chem. 15*, 1424−1430.

BC0501909

Carbohydrate and Protein Immobilization onto Solid Surfaces by Sequential Diels−Alder and Azide−Alkyne Cycloadditions

Xue-Long Sun,*[,†] Cheryl L. Stabler,[†] Chrystelle S. Cazalis,[†] and Elliot L. Chaikof*[,†,‡]

Departments of Surgery and Biomedical Engineering, Emory University, Atlanta, Georgia 30322, and School of Chemical and Biomolecular Engineering, Georgia Institute of Technology, Atlanta, Georgia 30332. Received July 29, 2005; Revised Manuscript Received December 6, 2005

We demonstrate the applicability of sequential Diels−Alder and azide−alkyne [3 + 2] cycloaddition reactions (click chemistry) for the immobilization of carbohydrates and proteins onto a solid surface. An α,ω-poly(ethylene glycol) (PEG) linker carrying alkyne and cyclodiene terminal groups was synthesized and immobilized onto an *N*-(ϵ-maleimidocaproyl) (EMC)-functionalized glass slide via an aqueous Diels−Alder reaction. In the process, an alkyne-terminated PEGylated surface was provided for the conjugation of azide-containing biomolecules via click chemistry, which proceeded to completion at low temperature and in aqueous solvent. As anticipated, alkyne, azide, cyclodiene, and EMC are independently stable and do not react with common organic reagents nor functional groups in biomolecules. Given an appropriate PEG linker, sequential Diels−Alder and azide−alkyne [3 + 2] cycloaddition reactions provide an effective strategy for the immobilization of a wide range of functionally complex substances onto solid surfaces.

INTRODUCTION

Robust immobilization techniques that preserve the activity of biomolecules have many potential applications. For example, microarrays, microbeads, and biosensor chips play increasingly important roles in characterizing the function and interaction of biomolecules, purification schemes, and point-of-care diagnostics (*1*). In addition, appropriate surface functionalization remains a critical variable for the optimal performance of a wide range of implantable medical devices (*2*). The design of solid-phase-based assays and bioactive implant surfaces often requires the immobilization of proteins and carbohydrates in their native state. Current immobilization techniques have relied on adsorption, direct covalent immobilization to chemically activated surfaces, or on the biosynthetic expression of a polypeptide 'tag' that mediates immobilization on an appropriately derivatized surface (*3*). Although appropriate for many applications, these schemes can, at times, be limited by the reduction in biomolecular activity due to protein denaturation, unintended reactions at or near the 'active' domain, or random orientation at the solid−liquid interface that reduces access to molecular recognition sites.

Diels−Alder cycloaddition has been recognized as an exceedingly useful bioconjugation procedure (*4*). The reaction takes place between an electronically matched pair of a double bond (dienophile) and a conjugated diene to form a six-membered unsaturated ring. Recently, this scheme has been applied to the immobilization of biomolecules onto a solid surface (*5*). Crucial to the selection of Diels−Alder cycloaddition as a preferential strategy for surface immobilization of biomolecules is (i) the recognition that water has an extraordinary rate-accelerating effect on the reaction process; (ii) the reaction occurs efficiently at room temperature; and (iii) cyclodiene and *N*-(ϵ-maleimidocaproyl) (EMC) are independently stable and easy to introduce.

The Cu(I)-catalyzed 1,3-dipolar cycloaddition of azide and alkyne to form a triazole, termed 'click' chemistry, has been recently established as an important tool for chemically and biologically modifying biomolecules (*6*). The reactants, alkyne and azide, are convenient to introduce, independently stable, and do not react with common organic reagents or functional groups in biomolecules. Triazole formation is irreversible and usually quantitative. In addition, this reaction benefits from an extremely mild and regioselective copper(I) catalyst system that is surprisingly indifferent to solvent and pH. Thus, the potential for this reaction to modify a wide range of functionally complex substances is significant. The unique properties of this reaction appears transferable to surface-bound reactants and will likely provide access to a growing variety of novel functionalized surfaces (*7*). Indeed, azide-containing compounds have been successfully captured to alkynes via the Cu(I)-catalyzed 1,3-dipolar cycloaddition reaction (*8*). Therefore, azide/alkyne-based click chemistry can be expected to provide a robust strategy for uniform, high-density biomolecular surface immobilization using a conjugation scheme that is both covalent and displays a high degree of selectivity.

Poly(ethylene glycol) (PEG) is widely used as an inert and biocompatible linker in surface engineering and in the modification of proteins and peptides for drug delivery (*9*). Monofunctional PEG coupled to proteins is known to prolong circulation half-life and reduce immunogenicity (*10*). Moreover, PEG-modified liposomes have been used for cell targeting applications (*11*). While carboxyl or amine-terminated PEGs are widely available, they remain expensive and require further chemical modification to convert their corresponding groups. Further, these functional PEGs are available mainly as higher molecular weight compounds (>3400 Da), which under many conditions may limit grafting density onto solid surfaces due to steric repulsive effects. In this report, we describe the synthesis of a bifunctional short PEG linker with alkyne and cyclodiene groups at opposite chain termini to facilitate surface bioconjugation based upon sequential Diels−Alder and azide−alkyne cycloadditions. We demonstrate that this linker is suitable for the immobilization of biomolecules onto solid surfaces in a chemi-

* Address correspondence to Xue-Long Sun or Elliot L. Chaikof, Emory University, 101 Woodruff Circle, Rm 5105, Atlanta, GA 30322, Tel: (404) 727-8413, Fax: (404)-727−3660, E-mail: xsun@emory.edu or echaiko@emory.edu.

† Emory University.

‡ Georgia Institute of Technology.

10.1021/bc0502311 CCC: $33.50 © 2006 American Chemical Society
Published on Web 12/21/2005

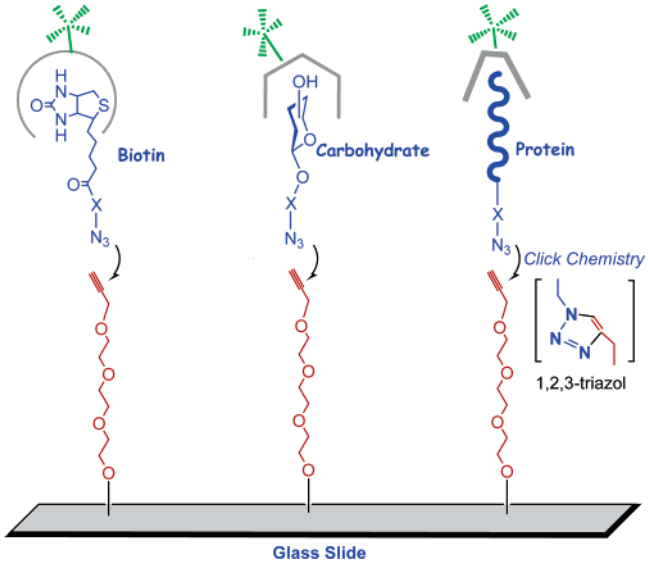

Figure 1. Schematic illustration of test substrates produced by sequential Diels−Alder and azide−alkyne cycloadditions of azide-derivatized biomolecules.

cally and biologically orthogonal fashion (Figure 1). Specifically, the alkyne and cyclodiene moieties are capable of conjugating under aqueous conditions and in a selective fashion to azide and EMC groups, respectively. As a covalent conjugation scheme that is orthogonal to diverse functionalities intrinsic to biological systems, this approach provides an attractive alternative to other currently available immobilization protocols.

EXPERIMENTAL PROCEDURES

General Methods. Thin-layer chromatography (TLC) was performed on Whatman silica gel aluminum backed plates of 250 μm thickness on which spots were visualized by UV light or by charring the plate after dipping in 10% H_2SO_4 in methanol. ^{1}H NMR spectra were recorded at 400 MHz at room temperature using a Varian INOVA 400 spectrometer. Fluorescence images were acquired using a Zeiss LSM 510 epifluorescence microscope under 10× magnification and illuminated using an argon ion laser at 485 nm. Images were acquired using eight co-added scans in line mode on air-dried glass slides stained with FITC-labeled proteins. Post-image processing was not performed.

Materials. All solvents and reagents were purchased from commercial sources and were used as received, unless otherwise noted. Amino PEG_4 azide **7** was prepared, as reported in the literature (*12*). 2-Azide-ethyl-*O*-lactoside **9** was synthesized, as previously reported (*18*). *N*-Hydroxsuccinimidobiotin and the lectin (*Arachis hypogaea*)-FITC were purchased from Sigma. The recombinant thrombomodulin construct (*r*TM-N_3) with an azide group and S-tag at the C- and N-termini, respectively, was prepared as previously reported (*21*). The FITC-conjugated S-protein and FITC-conjugated streptavidin, which specifically bind to S-Tag and biotin, respectively, were obtained from Novagen. EMC functionalized glass slides were purchased from XENOPORE Corp.

Synthesis of Bifunctional PEG Spacers. *O-Propargyl-tetra(ethylene glycol) (2).* To a solution of tetra(ethylene glycol) (**1**, 2 g, 5.30 mmol) in 20 mL of THF was added NaH (60% w/w in mineral oil, 272 mg, 11.34 mmol, 1.1 equiv.) at 0 °C with frequent venting. After stirring for 15 min, propargyl bromide (80% in toluene, 1.68 mL, 11.34 mmol, 1.1 equiv) was added slowly, and the mixture was stirred at 0 °C for 2 h and then 23 °C for an additional 2 h. The reaction mixture was passed through a silica gel column eluted with ethyl acetate to give the purified product **2** (1.552 g, 65%) as a clear oil. ^{1}H NMR ($CDCl_3$) δ: 4.16 (d, 2 H, J = 2.4 Hz, $OCH_2C{\equiv}CH$), 3.65−3.61 (m, 14 H, $-(OCH_2CH_2)O-$), 3.56 (t, 2 H, J = 4.4 Hz, OCH_2CH_2OH), 2.75 (br. s, 1 H, −OH), 2.40 (t, 1 H, J = 2.4 Hz, $OCH_2C{\equiv}CH$).

O-Propargyl-tetra(ethylene glycol) tosylate (3). *p*-Toluenesulfonyl chloride (1 g, 5.4 mmol) and DMAP (25 mg, 0.2 mmol) were added to a solution of **2** (1.044 g, 4.5 mmol) in 1:1 pyridine-dichloromethane (10 mL). After 5 h, the solution was poured into ice−water (20 mL), and the aqueous phase was extracted with dichloromethane (3 × 20 mL). The combined organic phases was washed with NH_4Cl (20 mL) and brine (20 mL), dried over anhydrous Na_2SO_4, and concentrated. The yellow oil was chromatographed on silica gel (EtOAc:hexane 3:1) to yield **3** (1.404 g, 81%) as a clear oil. ^{1}H NMR ($CDCl_3$) δ: 7.75 (d, 2 H, J = 8.4 Hz, Ph), 7.26 ((d, 2 H, J = 8.4 Hz, Ph), 4.19 (d, 2 H, J = 2.4 Hz, $OCH_2C{\equiv}CH$), 4.16 (t, 2 H, J = 7.8 Hz, OCH_2CH_2OTs), 3.70−3.55 (m, 14 H, $(OCH_2CH_2)O$), 2.54 (s, 3 H, Ph-CH_3), 2.52 (t, 1 H, J = 2.4 Hz, $OCH_2C{\equiv}CH$).

2-O-Propargyl-8-O-cyclopentadieneethyl tri(ethylene glycol) (4). Sodium cyclopentadienylide (0.75 mL, 2 M solution in THF) was added dropwise to a solution of **3** (390 mg, 1.01 mmol) in THF (10 mL) at −78 °C. The reaction mixture was stirred at −78 °C for 30 min and at room temperature for an additional 4 h. The solution was filtered through a pad of Celite, and the salts were washed thoroughly with THF. Evaporation of the filtrate and subsequent silica gel chromatography (EtOAc:hexane 1:1) afforded **4** (172 mg, 61%) as a clear oil. ^{1}H NMR ($CDCl_3$) δ: 6.44−6.05 (m, 3 H, cyclodiene), 4.18 (d, 2 H, J = 2.4 Hz, $OCH_2C{\equiv}CH$), 3.70−3.55 (m, 12 H, $(OCH_2CH_2)O$), 2.91 (dd, 2 H, J = 1.4, 9.8 Hz, OCH_2CH_2-cyclodiene), 2.66 (m, 2 H,-OCH_2CH_2-cyclodiene), 2.42 (t, 1 H, J = 2.4 Hz, $OCH_2C{\equiv}CH$).

Azidoethyl-di(ethylene glycol) ethylamine (7) was synthesized from tetra(ethylene glycol) **1** as reported in the literature (*12*).

Azidoethyl-di(ethylene glycol) ethylamino biotin (8). Triethylamine (0.1 mL, 0.71 mmol) was added to a solution of **7** (200 mg, 0.917 mmol) in DMF (5 mL). After the solution was stirred for 30 min, a solution of *N*-hydroxsuccinimidobiotin (375 mg, 1.10 mmol) was added. The reaction mixture was stirred for 12 h at room temperature and then concentrated in a vacuum to give a residue, which was purified by silica gel column chromatography using acetone:hexane (4:1) as eluent to afford **8** (345 mg, 85%). ^{1}H NMR (CD_3OD) δ: 4.51 (m, 1 H, C*H*-1-Biotin), 4.32 (m, 1 H, C*H*-4-Biotin), 3.70−3.63 (m, 8 H, $O(CH_2CH_2O)$-PEG), 3.39 (m 4 H, CH_2NH and CH_2N_3-PEG), 3.20 (m 1 H, C*H*-3-Biotin), 2.93 (dd, 1 H, J = 4.8, 12.8 Hz, CH-2a-Biotin), 2.71 (m 1 H, CH-2b-Biotin), 2.23 (t, 1 H, J = 7.6 Hz, CH_2CO-Biotin), 1.76−1.43 (m, 6 H, $(CH_2)_3$-Biotin).

Aqueous Diels−Alder Alkyne PEGylation of EMC Solid Surface. An EMC functionalized glass slide (0.5 cm^2) was placed in a glass vial and incubated overnight on a shaker at room temperature in a solution of alkyne PEG cyclodiene **4** (0.5 mg) in 500 μL of H_2O-*tert*-BuOH (1:1). The PEG solution was removed, and the slide was washed three times with 1 mL of H_2O-*tert*-BuOH (1:1). The unreacted EMC groups were blocked by incubation in a 500 μL solution of cysteine (10 mg/L in PBS pH 7.4) for 1 h at room temperature, followed by three washes with dd water.

Click Biotinylation of an Alkyne PEGylated Glass Slide. A total of 75 μL of biotin PEG azide **8** (0.2 mg) in PBS was added to a glass vial containing an alkyne PEGylated glass slide (0.5 cm^2). This was followed by the sequential addition of 5 μL of *tert*-BuOH, 10 μL of 2 mM ligand (tris(triazolyl)amine) solution in PBS, 10 μL of 1 mM $CuSO_4$ solution, and 2 mM TCEP in PBS. The vial was shaken at 4 °C for 12 h. The reaction solution was removed and the slide washed three times with 1 mL of dd water.

Scheme 1. Synthesis of Bifunctional PEG Linkers

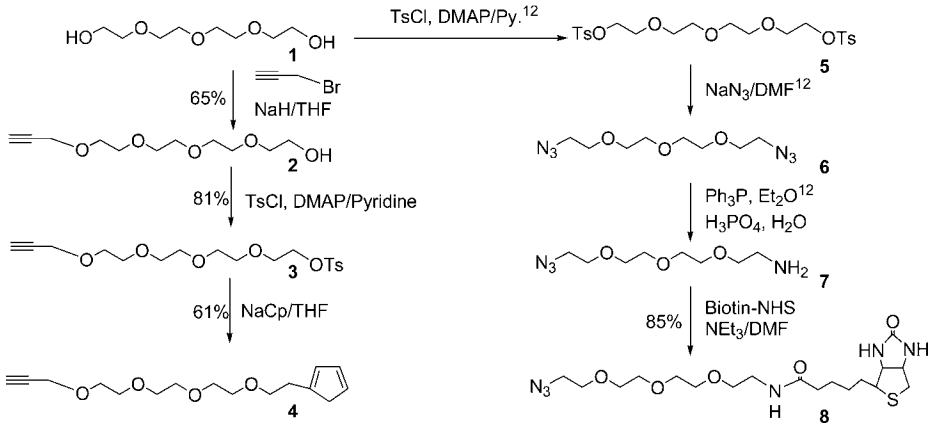

FITC-conjugated streptavidin (Novagen) was diluted 1:50 in PBST. The biotin-PEG immobilized slide was incubated in 500 μL of the diluted streptavidin solution (0.02 mg/mL) for 2 h at 4 °C and then washed three times with 1 mL of dd water.

Click Immobilization of Azide Lactose onto a Glass Slide. A total of 75 μL of lactose azide **9** (*18*) (0.2 mg) in PBS was added to a glass vial containing an alkyne PEGylated glass slide (0.5 cm^2). This was followed by the sequential addition of 5 μL of *tert*-BuOH and then 10 μL of 2 mM tris(triazolyl)amine solution in PBS, and 10 μL of 1 mM $CuSO_4$ and 2 mM TCEP solution in PBS. The vial was shaken at 4 °C for 14 h. The reaction solution was removed and the slide washed three times with 1 mL of dd water.

The lactose-PEG immobilized slide was incubated in 500 μL of a FITC-conjugated galactose binding lectin (*Arachis hypogaea*, Sigma) solution (0.5 mg/mL) in PBST for 5 h at 4 °C and then washed three times with 1 mL of dd water.

Click Immobilization of *r*TM-N_3 onto a Glass Slide. A total of 75 μL of *r*TM-N_3 (0.1 mg) in PBS was added to a glass vial containing an alkyne PEGylated glass slide (0.5 cm^2). This was followed by the sequential addition of 5 μL of *tert*-BuOH, 10 μL of 2 mM tris(triazolyl)amine solution in PBS, and 10 μL of 1 mM $CuSO_4$ solution in PBS. A small piece of Cu wire was placed in contact with the above mixture. The vial was incubated at 4 °C for 72 h without shaking. The reaction solution and the wire, which has become black due to oxidation, were removed and the slide washed three times with 1 mL of dd water.

The *r*TM-N_3 immobilized slide was incubated overnight at 4 °C in 500 μL of the diluted FITC-conjugated S-protein solution (1: 500 diluted commercial sample from Novagen as manufacture protocol in PBST) and then washed three times with 1 mL of dd water.

RESULTS AND DISCUSSION

1. Synthesis of Bifunctional PEG Spacers. The alkyne PEG_4 cyclodiene (**4**) was synthesized from tetra(ethylene glycol) (**1**, PEG_4) as shown in Scheme 1. First, PEG_4 **1** was converted to *mono*-alkyne-PEG_4 **2** by reacting with 1.1 equivalent of propargyl bromide in the presence of sodium hydride. Treatment of **2** with *p*-toluenesulfonyl chloride followed by reaction with sodium cyclopentadienylide afforded alkyne-PEG_4-cyclodiene **4** in good yield. For further functionalization of an alkyne-derivatized surface, biotin PEG_4 azide **8** was synthesized by biotinylation of amino PEG_4 azide **7** (*12*) with commercial available *N*-hydroxsuccinimidobiotin in good yield.

2. Alkyne PEG Surface Functionalization via an Aqueous Diels−Alder Reaction. An EMC-functionalized glass slide (XENOPORE Corp.) was incubated with alkyne-PEG_4-cyclodiene **4** in H_2O-*tert*-BuOH (1:1) at room temperature for 12 h, followed by three washes in H_2O-*tert*-BuOH (1:1) to provide an alkyne-PEG functionalized surface (Figure 2B). The unreacted EMC groups on the slide were blocked with cysteine by incubation in PBS solution at room temperature, followed by three washes with dd water.

A biotin PEG azide was used as a model compound to assess both the extent of Diels−Alder driven surface PEGylation and the capacity of this surface to be further functionalized via click chemistry. Biotin exhibits high affinity binding to strept(avidin) and has been widely used in bioconjugation (*13*) and surface immobilization applications (*14*). As shown in Figure 2, alkyne-PEG functionalized glass slides were treated with biotin-PEG-azide **8** in the presence of $CuSO_4$, tris(carboxethyl)phosphine (TCEP), and tris(triazolyl)amine in PBS (pH 7.0)-*tert*-BuOH (1:1) at 4 °C for 12 h followed by PBS and water washes. In this reaction, Cu(I) is the direct catalyst and is prepared in situ by reduction of inexpensive and air-stable Cu(II) salt $CuSO_4$ with TCEP, and tris(triazolyl)amine is used as ligand to enhance the reaction rate greatly and inhibit oxidative alkyne coupling. Notably, the low temperature condition was investigated for later protein immobilization since many proteins are thermally sensitive. The success of alkyne PEGylation and the capacity of this surface to participate in click immobilization chemistry are evident by confocal fluorescence images that demonstrate FITC-labeled streptavidin specifically binds to a biotinylated surface (C), with no binding to either untreated EMC-glass slides (A) or slides functionalized with alkyne-PEG alone (B) (Figure 2). In addition, binding was not observed upon incubation with either a biotin-saturated FITC-labeled streptavidin to biotinylated surfaces or to EMC slides deactivated with cysteine prior to PEG immobilization (data not show).

3. Immobilization of an Azide-Containing Sugar. Cells universally carry a sugar coating formed by glycoproteins, proteoglycans, and glycolipids, which are involved in highly specific recognition events between cells and proteins, hormones, antibodies, and toxins (*15*). Understanding the mechanism of these processes may lead to the development of new antimicrobial, anticancer, and antiinflammatory therapies. Therefore, simple and readily accessible methods for high-throughput analysis, such as carbohydrate microarrays or glycoarrays, are an area of active investigation (*16*). We investigated the click immobilization of carbohydrates onto alkyne-PEG-functionalized glass slides using lactose-N_3 as a model ligand (*17*).

As depicted in Figure 3, an alkyne-PEG functionalized glass slide was treated with an azide-derivate lactose **9** (*18*) in the presence of $CuSO_4$, TCEP, and tris(triazolyl)amine in PBS (pH 7.0)-*tert*-BuOH (1:1) at 4 °C for 14 h. Binding of a fluorescently labeled lectin confirmed the effectiveness of sugar immobilization. Specifically, uniform fluorescence was noted upon incubation of glycosylated test surfaces with FITC-lectin from *Arachis hypogaea* that binds to terminal β-galactose, but was not

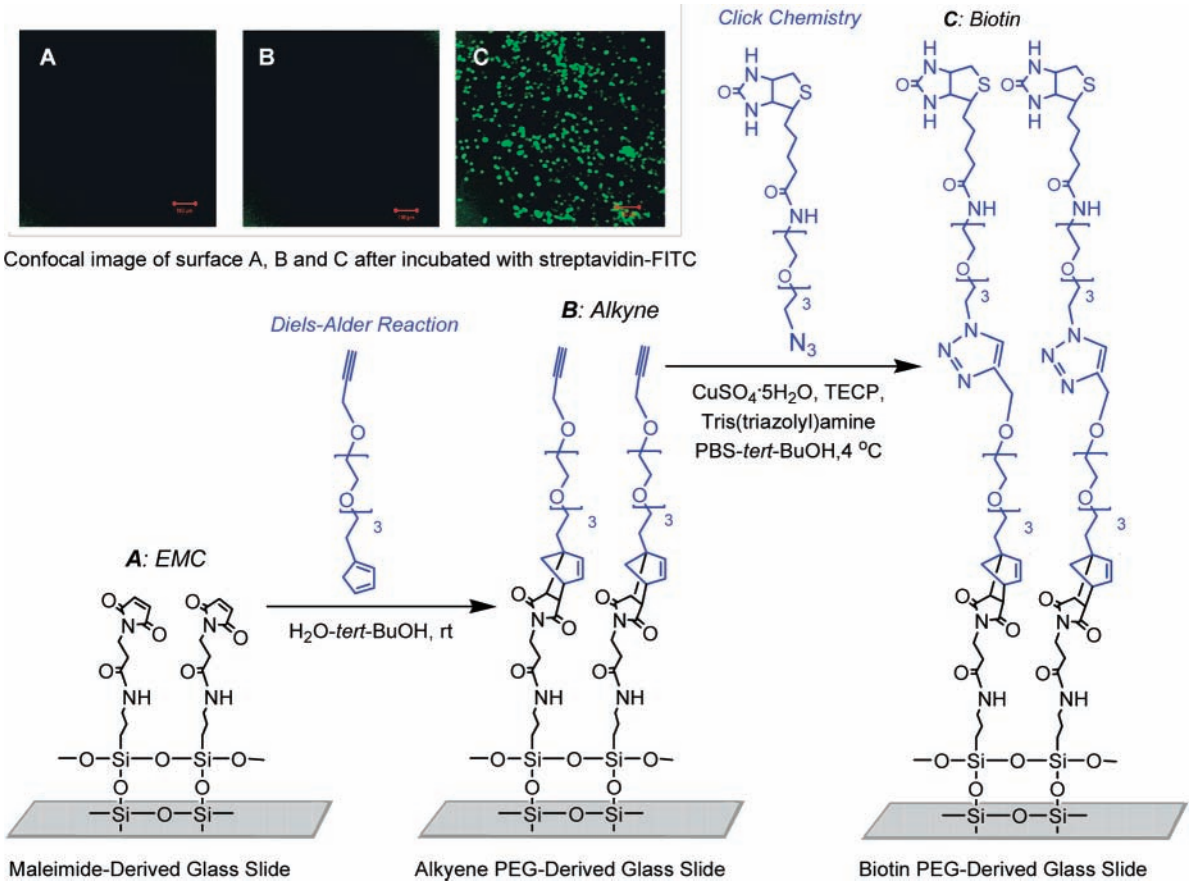

Figure 2. Diels−Alder cycloaddition was used to modify an EMC-derivatized substrate with an alkyne-terminated PEG linker, which was followed by surface biotinylation via click chemistry. Representative confocal image of initial EMC surface incubated with streptavidin-FITC (A); alkyne-derivatized surface incubated with streptavidin-FITC (B); and a biotinylated surface produced by sequential Diels−Alder and azide−alkyne cycloadditions incubated with streptavidin-FITC (C). Bar size: 100 μm.

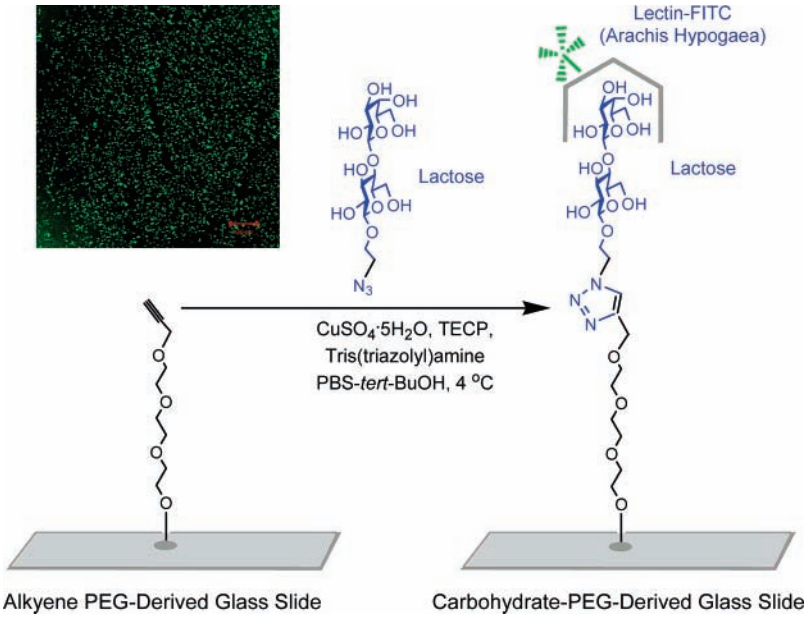

Figure 3. Immobilization of lactose-N_3 onto an alkyne-PEG-functionalized glass substrate via azide−alkyne cycloaddition. Representative confocal image of a lactose-derivatized surface after incubation with FITC-labeled *Arachis hypogaea*. Bar: 100 μm.

observed when untreated EMC or alkyne-derivatized glass substrates were used. Furthermore, binding was not observed when a glucose/mannose specific lectin, concavalian A was used (data not show).

4. Immobilization of a Recombinant Protein with a C-Terminal Azide Group. The immobilization of a protein onto a solid surface in the correct orientation is imperative for optimal interaction with other species in which it may form a functional complex. However, most current surface conjugation schemes offer somewhat limited control over the three-dimensional presentation of bound proteins due to their reliance on functional groups that are often abundantly present within the protein of interest. Falsey et al. has recently reported chemoselective N-terminal attachment of peptides onto glyoxylic

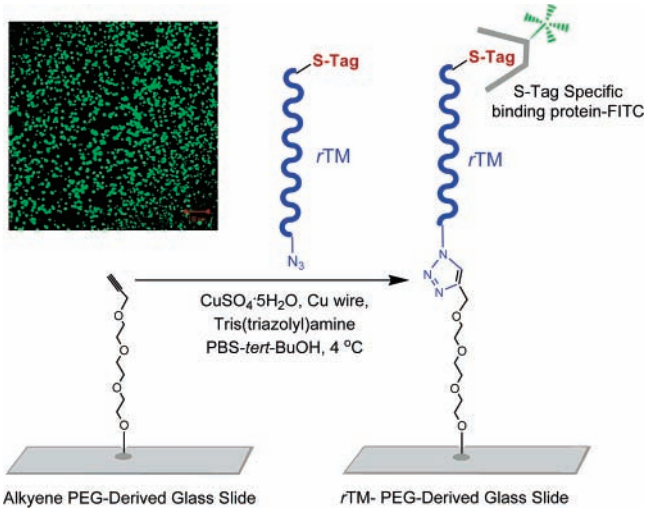

Figure 4. Immobilization of recombinant thrombomodulin (*r*TM-N_3) containing an N-terminal S-tag peptide seuqence onto an alkyne-PEG-functionalized glass surface via azide−alkyne cycloaddition. Representative confocal image of a thrombomodulin-derivatized surface after incubation with an S-tag binding FITC-labeled S-protein. Bar: 100 μm.

acid functionalized slides via oxime-bond or thiazolidine-ring ligation reaction (*19*). Although elegantly designed for site-specific coupling of peptides, the oxime bond is relatively unstable and its formation less selective. Zhu et al. has reported a method for site-specific immobilization of His-tag proteins on slides functionalized with Ni−NTA (*20*). Although an appropriate strategy for protein purification in which elution of the bound protein is required, the binding between His-tag proteins and the Ni−NTA complex is not very strong and is incompatible with many common chemicals such as DTT, SDS, and EDTA. Specifically, decoupling occurs outside pH 4−10 or when the buffer contains high concentrations of common salts. In the current report, the use of a recombinant protein containing a nonnatural azide-containing amino acid at the C-terminus provides an example of site-specific and regiospecific protein immobilization to an alkyne-derivatized surface.

We have recently reported a strategy for site-specific PEGylation of a truncated thrombomodulin (*r*TM-N_3) mutant through an azide group located at the C-terminus. The thrombomodulin (TM) construct was expressed in *E. coli* and contains epidermal growth factor (EGF)-like domains 4−6 and an azido-functionalized alanine analogue as a C-terminal linker (*21*). As shown in Figure 4, alkyne-PEG functionalized glass slides were treated with *r*TM-N_3 in the presence of $CuSO_4$, Cu wire, and tris-(triazolyl)amine in PBS (pH 7.0)-*tert*-BuOH (95:5) at 4 °C for 72 h. Cu wire was used for reduction of Cu(II) to Cu(I) and to avoid the risk of cleavage of the dithiosulfide bonds in the protein (6c and 6d). The recombinant TM also contains an N-terminal peptide sequence, referred to as an S-Tag that was used to qualitatively assess the extent of surface immbolization. As shown in Figure 4, the TM-functionalized surface was incubated with a FITC-labeled S-protein that specifically binds the S-tag (*22*) and examined by confocal microscopy. S-Tag binding was consistent with the production of a surface grafted at a high density with *r*TM-N_3. S-Protein binding was not observed for either untreated EMC-glass slides or for those functionalized with alkyne-PEG alone (data not show). On inspection of Figures 2−4, differences in surface domain size and morphology are noted, which likely reflects varying steric effects attributed to the use of ligands and binding proteins of varying size.

In conclusion, sequential Diels−Alder cycloaddition and azide−alkyne [3 + 2] cycloaddition reactions were successfully applied to the functionalization of EMC-derivatized glass slides with a diverse series of ligands, including biotin, lactose, and a recombinant thrombomodulin protein. This approach was enabled by the synthesis of a bifunctional poly(ethylene glycol) (PEG) linker carrying alkyne and cyclodiene groups at opposite chain termini. Significantly, azide, alkyne, cyclodiene, and EMC groups were stable under bioconjugation conditions and did not appear predisposed to unintended side reactions. In principle, the potential to immobilize a wide range of functionally complex substances onto solid surfaces can be achieved, which will likely extend design schemes directed at the fabrication of microarrays and medical devices whose performance is dictated by precisely defined surface molecular engineering.

ACKNOWLEDGMENT

This work was supported by awards from the University Research Committee of Emory University and the AHA (X.-L.S.) and by grants from the NIH (E.L.C.). C. L. Stabler is supported by a JDRF Postdoctoral Fellowship.

Supporting Information Available: Experimental details. This material is available free of charge via the Internet at http://pubs.acs.org.

LITERATURE CITED

(1) (a) Wilson, D. S., and Nock, S. (2002) Functional protein microarrays. *Curr. Opin. Chem. Biol. 6*, 81−85. (b) MacBeath, G. (2002) Protein microarrays and proteomics. *Nat. Genet. 32 Suppl 2*, 526−532.

(2) Ratner, B. D., Hoffman, A. S., Schoen, F. J., and Lemons, J. E. (1996) *Biomaterials science: an introduction to materials in medicine*, Academic Press, San Diego, CA.

(3) (a) Lee, K. B., Park, S. J., Mirkin, C. A., Smith, J. C., and Mrksich, M. (2002) Protein nanoarrays generated by dip-pen nanolithography. *Science 295*, 1702−1705. (b) MacBeath, G., and Schreiber, S. L. (2000) Printing proteins as microarrays for high-throughput function determination. *Science 289*, 1760−1763. (c) Zhu, H., Bilgin, M., Bangham, R., Hall, D., Casamayor, A., Bertone, P., Lan, N., Jansen, R., Bidlingmaier, S., Houfek, T., Mitchell, T., Miller, P., Dean, R. A., Gerstein, M., and Snyder, M. (2001) Global analysis of protein activities using proteome chips. *Science 293*, 2101−2105. (d) Hodneland, C. D., Lee, Y. S., Min, D. H., and Mrksich, M. (2002) Supramolecular chemistry and self-assembly special feature: selective immobilization of proteins to self-assembled monolayers presenting active site-directed capture ligands. *Proc. Natl. Acad. Sci. U.S.A. 99*, 5048−5052. (e) Lesaicherre, M. L., Lue, R. Y., Chen, G. Y., Zhu, Q., and Yao, S. Q. (2002) Intein-mediated biotinylation of proteins and its application in a protein microarray. *J. Am. Chem. Soc. 124*, 8768−8769.

(4) (a) Pozsgay, V., Vieira, N. E., and Yergey, A. (2002) A method for bioconjugation of carbohydrates using Diels−Alder cycloaddition. Org. Lett. 4, 3191−3194. (b) Kumar, A. (2001) Salt effects on Diels−Alder reaction kinetics**.** *Chem. Rev. 101*, 1−19. (c) Garner, P. P. (1998) Diels−Alder reactions in aqueous media. In *Organic synthesis in water* (Grieco, P. A., Ed.) pp 1−46, Blackie Academic and Professional: London. (d) Breslow, R., and Rideout, D. C. (1980) Hydrophobic acceleration of Diels−Alder reactions. *J. Am. Chem. Soc. 102*, 7816−7817.

(5) (a) Houseman, B. T., Huh, J. H., Kron, S. J., and Mrksich, M. (2002) Peptide chips for the quantitative evaluation of protein kinase activity. *Nature Biotechnol. 20*, 270−274. (b) Houseman, B. T., and Mrksich, M. (2002) Carbohydrate arrays for the evaluation of protein binding and enzymatic modification. *Chem. Biol. 9*, 443−454.

(6) (a) Rostovtsev, V. V., Green, L. G., Fokin, V. V., and Sharpless, K. B. (2002) A stepwise Huisgen cycloaddition process: Copper (I)-catalyzed regioselective Ligation of azides and terminal alkynes. *Angew. Chem., Int. Ed. 41*, 2596−2599. (b) Lewis, W. G., Green, L. G., Grynszpan, F., Radic, Z., Carlier, P. R., Taylor, P., Finn, M. G., and Sharpless, K. B. (2002) Click chemistry in situ: acetylcholinesterase as a reaction vessel for the selective assembly of a femtomolar inhibitor from an array of building blocks. *Angew.*

Chem., Int. Ed. 41, 1053−1055. (c) Wang, Q., Chan, T. R., Hilgraf, R., Fokin, V. V., Sharpless, K. B., and Finn, M. G. (2003) Bioconjugation by Copper (I)-catalyzed azide−alkyne [3 + 2] cycloaddition. *J. Am. Chem. Soc. 125*, 3192−3193. (d) Speers, A. E., Adam, G. C., and Cravatt, B. F. (2003) Activity-based protein profiling in vivo using a Copper (I)-catalyzed azide−alkyne [3 + 2] cycloaddition. *J. Am. Chem. Soc. 125*, 4686−4687. (d) Deiters, A., Cropp, T. A., Mukherji, M., Chin, J. W., Anderson, J. C., and Schultz, P. G. (2003) Adding amino acids with novel reactivity to the genetic code of Saccharomyces Cerevisiae. *J. Am. Chem. Soc. 125*, 11782−11783. (e) Link, A. J., and Tirrell, D. A. (2003) Cell surface labeling of *Escherichia coli* via Copper (I)-catalyzed [3 + 2] cycloaddition. *J. Am. Chem. Soc. 125*, 11164−11165.

(7) (a) Devaraj, N. K., Miller, G. P., Ebina, W., Kakaradov, B., Collman, J. P., Kool, E. T., and Chidsey, C. E. D. (2005) Chemoselective covalent coupling of oligonucleotide probes to self-assembled monolayers. *J. Am. Chem. Soc. 127*, 8600−8601. (b) Collman, J., Devaraj, N. K., and Chidsey, C. E. D. (2004) "Clicking" functionality onto electrode surfaces. *Langmuir 20*, 1051−1053. (c) Lummerstorfer, T., and Hoffmann, H. (2004) Click chemistry on surfaces: 1,3-dipolar cycloaddition reactions of azide-terminated monolayers on silica. *J. Phys. Chem. B 108*, 3963−3966.

(8) Fazio, F., Bryan, M. C., Blixt, O., Paulson, J. C., and Wong, C. H. (2002) Synthesis of sugar arrays in microtiter plate. *J. Am. Chem. Soc. 124*, 14397−14402.

(9) (a) Harris, J. M. (1992) *Poly(ethylene glycol) chemistry: Biotechnical and biomedical applications*, Plenum Press, New York. (b) Zalipsky, S. (1995) Chemistry of poly(ethylene glycol) conjugates with biologically active molecules. *Adv. Drug Delivery Rev. 16*, 157−182.

(10) Yang, Z. J., Wang, J. H., Lu, Q., Xu, J. B., Kobayashi, Y., Takakura, T., Takimoto, A., Yoshioka, T., Lian, C. G., Chen, C. M., Zhang, D. D., Zhang, Y., Li, S. K., Sun, X. H., Tan, Y. Y., Yagi, S., Frenkel, E. P., and Hoffman, R. M. (2004) PEGylation confers greatly extended half-life and attenuated immunogenicity to recombinant methioninase in primates. *Cancer Res. 64*, 6673−6678.

(11) Klibanov, A. L., Karuyama, K., Torchilin, V. P., and Huang, L. (1990) Amphipathic poly(ethylene glycol)s effectively prolong the circulation time of liposomes. *FEBS Lett. 268*, 235−238.

(12) Schwabacher A. W., Lane, J. W., Schiesher, M. W., Leigh, K. M., and Johnson, C. W. (1998) Desymmetrization reactions: efficient preparation of unsymmetrically substituted linker molecules. *J. Org. Chem. 63*, 1727−1729.

(13) Wilchek, M., and Bayer, E. A. (1990) Introduction to avidin−biotin technology. *Methods Enzymol. 184*, 5−9.

(14) (a) Pande, R., Kamtekar, S., Ayyagari, M. S., Kamath, M., Marx, K. A., Kumar, J., Tripathy, S. K., and Kaplan, D. L. (1996) A Biotinylated undecylthiophene copolymer bioconjugate for surface immobilization: creating an alkaline phosphatase chemiluminescence-based biosensor. *Bioconjug Chem. 7*, 159−64. (b) Liebermann, T., Knoll, W., Sluka, P., and Herrmann, R. (2000) Complement hybridization from solution to surface-attached probe-oligonucleotides observed by surface-plasmon-field-enhanced fluorescence spectroscopy. *Colloids Surf. A 169*, 337−350.

(15) (a) Sodetz, J. M., Paulson, J. C., and McKee, P. A. (1979) Carbohydrate composition and identification of blood group A, B, and H oligosaccharide structures on human Factor VIII/von Willebrand factor. *J. Biol. Chem. 254*, 10754−10760. (b) Varki, A. (1993) Biological roles of oligosaccharides: all of the theories are correct. *Glycobiology 3*, 97−130. (c) Karlsson, K. A. (1995) Microbial recognition of target-cell glycoconjugates. *Curr. Opin. Struct. Biol. 5*, 622−635.

(16) Shin, I., Park, S., and Lee, M. (2005) Carbohydrate microarrays: an advanced technology for functional studies of glycans. *Chem. Eur. J. 11*, 2894−22901 and references therein.

(17) (a) Kobayashi, A., Kobayashi, K., and Akaike, T. (1994) Culturing hepatocytes on lactose-carrying polystyrene layer via asialoglycoprotein receptor-mediated interactions. *Methods Enzymol. 247*, 409−418. (b) Pohl, N. L., and Kiessling, L. L. (1999) Scope of multivalent ligand function: lactose-bearing neoglycopolymers by ring-opening metathesis polymerization. *Synthesis* 1515−1519. (c) Tietze, L. F., Bothe, U., and Schuberth, I. (2000) Preparation of a new carboranyl lactoside for the treatment of cancer by boron neutron capture therapy: Synthesis and toxicity of fluoro carboranyl glycosides for in vivo ^{19}F NMR spectroscopy. *Chem. Eur. J. 6*, 836−842.

(18) Sun, X.-L., Grande, D., Baskaran, S., Hanson, S. R., and Chaikof, E. L. (2002) Glycosaminoglycan mimetic biomaterials. 4. Synthesis of sulfated lactose-based glycopolymers that exhibit anticoagulant activity. *Biomacromolecules 3*, 1065−1070.

(19) Falsey, J. R., Renil, R., Park, S., Li, S., and Lam, K. S. (2001) Peptide and small molecule microarray for high throughput cell adhesion and functional assays. *Bioconjugate Chem. 12*, 346−353.

(20) Zhu, H., Bigin, M., Bangham, R., Hall, D., Casamayor, A., Bertone, P., Lan, N., Jansen, R., Bidlingmaier, S., Houfek, T., Mitchell, T., Miller, P., Dean, R. A., Gerstein, M., and Snyder, M. (2001) Global analysis of protein activities using proteome chips. *Science 293*, 2101−2105.

(21) Cazalis, C. S., Haller, C. A., Sease-Cargo, L., and Chaikof, E. L. (2004) *C*-Terminal site-specific PEGylation of a truncated thrombomodulin mutant with retention of full bioactivity. *Bioconjugate Chem. 15*, 1005−1009.

(22) McCormick, M., and Mierendorf, R. (1994) S•Tag: A multipurpose fusion peptide for recombinant proteins. *Innovations 1*, 4−6.

BC0502311

Bright Oligothiophene *N*-Succinimidyl Esters for Efficient Fluorescent Labeling of Proteins and Oligonucleotides

Giovanna Barbarella,*,§ Massimo Zambianchi,§ Alfredo Ventola,† Eduardo Fabiano,‡ Fabio Della Sala,‡ Giuseppe Gigli,‡ Marco Anni,‡ Andrea Bolognesi,|| Letizia Polito,|| Marina Naldi,§ and Massimo Capobianco§

Consiglio Nazionale Ricerche (ISOF), Mediteknology srl, Area Ricerca CNR, Via Gobetti 101, I-40129 Bologna, Italy, National Nanotechnology Laboratory (NNL), Distretto Tecnologico, Via Arnesano, I-73100 Lecce, Italy, and Dipartimento di Patologia Sperimentale, Università di Bologna, Via San Giacomo, 14, I-40126 Bologna, Italy. Received August 14, 2005; Revised Manuscript Received October 27, 2005

The synthesis of multicolor fluorescent oligothiophene *N*-succinimidyl esters (TSEs) is reported, and their optical properties are discussed with the aid of ab initio calculations. The esters were coupled to proteins and to 3′-amino-modified oligonucleotides in mild conditions and with similar modalities. A comparative study of the bioconjugate of IgG_1 anti-CD3 antibody labeled with a blue fluorescent TSE and with fluorescein isothiocyanate (FITC) is reported, showing that the former achieves higher photoluminescence intensity and optical stability than the latter. Fluorescence resonance energy transfer experiments with TSE-labeled oligonucleotides and examples of cellular imaging via TSE-labeled proteins are reported.

INTRODUCTION

Fluorescence techniques are currently of wide use and are progressively replacing radioisotopes in analyses and clinical tests, while new optical imaging methodologies are being developed; see for example the application of optical tomography for breast cancer diagnosis based on a near-infrared-emitting indocyanine (*1*−*3*). The increasing use of fluorescence techniques for immunological labeling and pathological diagnosis generates new demands and user-oriented characteristics for the fluorophores, the instrumentation, and the light sources. Moreover, in vivo applications, which also entail the injection of solutions of the fluorophores (*1*), make the issue of fluorophore toxicity very stringent.

In recent years numerous families of organic and inorganic compounds have been developed as fluorescent labels for proteins, oligonucleotides, DNA, and live cells (*1*−*8*). In particular, many investigations have concerned quantum dots of cadmium selenide, i.e., semiconductor nanocrystals, characterized by great brightness, optical stability, and sharp fluorescence emission independent of the excitation wavelength (*4*−*8*). The use of nanocrystals as probes for biological molecules requires that they are encapsulated with a transparent organic polymer bearing functional groups capable to bind biomolecules, as shown, for example, in a recent study aimed to monitor in vivo tumor growth in rats (*7*). However, even polymer-protected cadmium selenide nanoparticules may be toxic to cells, and the issue of their toxicity and in vivo metabolism still lacks a definitive answer (*8*).

The characteristics that a good family of fluorescent probes should have are numerous and include photostability, sharp spectral emission, high absorbance, high fluorescence quantum yield, large differences between absorption and emission wavelengths, color tunability from blue to near-infrared, easy modalities for binding to biomolecules, lack of toxicity, and low preparation costs. A single family of small, suitably functionalized, organic dyes with fluorescence colors tunable by minor structural changes would ensure the easy binding to biomolecules and the standardization of staining methodologies, while low molecular weights would allow easy cell membrane permeability for multicolor live cell imaging. No family presenting simultaneously all the required properties has been described as yet, which justifies the continuous search for improvement.

Among the newcomers as optical sensors to monitor events of biological importance are conjugated semiconducting polymers, for which combined electrical and fluorimetric detection of biomolecules can also be envisaged. Single nucleotide mismatches between two DNA strands have been detected, both in solution and with the polymer patterned on a surface, by using a zwitterionic polythiophene electrostatically interacting with the negatively charged phosphate DNA groups (*9*). More recently, the specific detection in solution of zemptomolar amounts of genetic material using a positively charged polythiophene has been described (*10*).

Our group has focused its attention on short thiophene oligomers which have displayed a variety of useful properties, from white electroluminescence (*11*) to easy nanopatterning via nanoimprint lithography (*12*). The photostability and fluorescence color tunability of thiophene oligomers, mainly known for their semiconducting properties (*13*−*15*), suggested that they could also be fruitfully employed as fluorescent markers for biopolymers. Thus, we started an investigation aimed to explore this possibility and reported initial studies showing that, indeed, thiophene oligomers functionalized with the isothiocyanate group can be covalently bound to monoclonal antibodies via the ϵ-NH_2 lysine sites (*16*−*18*). We have now found that oligothiophenes functionalized with the *N*-succinimidyl group (TSEs) are easier to prepare and to conjugate to proteins, in agreement with previous studies on fluorescein-based fluorophores (*19*). Moreover, they can also be conjugated to oligonucleotides in similar conditions and be used to prepare fluorescent oligonucleotide probes.

We describe here the synthesis and the electronic and optical characterization of oligothiophene *N*-succinimidyl esters and demonstrate that they are optically stable and can achieve high

* To whom correspondence should be adressed. E-mail: barbarella@isof.cnr.it.

§ Consiglio Nazionale Ricerche (ISOF).

† Mediteknology srl.

‡ National Nanotechnology Laboratory (NNL).

|| Università di Bologna.

10.1021/bc050250a CCC: $33.50 © 2006 American Chemical Society
Published on Web 12/27/2005

fluorescence sensitivity when bound to proteins and oligonucleotides (*20*). We also show for the first time that thiophene oligomers can be used for cell staining as well as for fluorescence resonance energy transfer experiments with oligonucleotides.

MATERIALS AND METHODS

Synthesis. General Details. 5-Bromo-2-thiophenecarboxaldehyde (**1**), 2-(tributylstannyl)thiophene (**4**), 2-(2-thienyl)ethanol (**6a**), 2-(methylthio)thiophene (**8a**), *N*-hydroxysuccinimide (HOSu), *N*,*N*′-dicyclohexylcarbodiimide (DCC), 2-methoxylethoxylmethyl chloride (MEMCl), *N*,*N*-diisopropylethylamine, 4-(dimethylamino)pyridine (DMAP), *N*-bromosuccinimide (NBS), *n*-butyllithium, tributyltin chloride, tris(dibenzylideneacetone)-dipalladium(0)−chloroform adduct, and triphenylarsine are commercially available compounds.

The syntheses of compounds **2**, **3**, **6d**, **8b**, **10**, and **14** are reported as Supporting Information.

General Procedure for the Preparation of Oligothiophene *N*-Succinimidyl Esters. To a 10 mL toluene solution containing 0.015 mmol of tetrakis(triphenylarsine)palladium(0) prepared in situ was added the desired thienyl bromide (0.5 mmol). The mixture was then heated to 80 °C and the appropriate thienyl stannane (0.5 mmol) dissolved in 3 mL of toluene added dropwise. The mixture was stirred for 2 h at this temperature, and then the solvent was evaporated under reduced pressure. The crude product was purified by flash chromatography (silica gel, petroleum ether/ethyl acetate 1:1). The analytical data for the specific compounds are given below.

2,2′-Bithiophenyl-5-carboxylic Acid 2,5-Dioxopyrrolidin-1-yl Ester, **5**. Yield: 83%. Microcrystalline white solid, mp 159−160 °C; EI-MS *m*/*z* 307 (M^+). ^{1}H NMR ($CDCl_3$, TMS/ppm) δ 7.91 (d, ^3J = 4.0 Hz, 1H), 7.36 (dd, ^3J = 5.0 Hz, ^4J = 0.8 Hz, 1H), 7.33 (dd, ^3J = 3.6 Hz, ^4J = 0.8 Hz, 1H), 7.21 (d, ^3J = 4.0 Hz, 1H), 7.07 (dd, ^3J = 3.6 Hz, ^3J = 5.0 Hz, 1H), 2.89 (s, 4H); ^{13}C NMR ($CDCl_3$, TMS/ppm) δ 169.14, 157.09, 147.71, 137.52, 135.41, 128.32, 127.13, 126.19, 124.26, 124.05, 25.58. Anal. Calcd for $C_{13}H_9NO_4S_2$ (307.34): C, 50.80; H, 2.95. Found: C, 50.92; H, 3.02.

5′-[2-(2-Methoxyethoxymethoxy)ethyl]-[2,2′]bithiophenyl-5-carboxylic Acid 2,5-Dioxopyrrolidin-1-yl Ester, **7**. Yield: 82%. Pale yellow oil, EI-MS *m*/*z* 439 (M^+). ^{1}H NMR ($CDCl_3$, TMS/ppm) δ 7.89 (d, ^3J = 4.0 Hz, 1H), 7.15 (d, ^3J = 4.0 Hz, 1H), 7.12 (d, ^3J = 4.0 Hz, 1H), 6.80 (d, ^3J = 4.0 Hz, 1H), 4.75 (s, 2H), 3.81 (t, ^3J = 6.0 Hz, 2H), 3.67 (m, 2H), 3.53 (m, 2H), 3.37 (s, 3H), 3.09 (t, ^3J = 6.0 Hz, 2H), 2.88 (s, 4H); ^{13}C NMR ($CDCl_3$, TMS/ppm) δ 169.14, 157.06, 148.09, 144.12, 137.48, 133.67, 126.57, 125.91, 123.59, 123.41, 95.43, 71.61, 67.70, 66.85, 58.89, 30.70, 25.52. Anal. Calcd for $C_{19}H_{21}NO_7S_2$ (439.50): C, 51.92; H, 4.82. Found: C, 51.95; H, 4.96.

5′-Methylsulfanyl-[2,2′]bithiophenyl-5-carboxylic Acid (2,5-Dioxopyrrolidin-1-yl) Ester, **9**. Yield: 81%. Microcrystalline light yellow solid, mp 181−182 °C; EI-MS *m*/*z* 353 (M^+). ^{1}H NMR ($CDCl_3$, TMS/ppm) δ 7.90 (d,, ^3J = 4.0 Hz, 1H), 7.18 (d, ^3J = 4.0 Hz, 1H), 7.15 (d, ^3J = 4.0 Hz, 1H), 6.99 (d, ^3J = 4.0 Hz, 1H), 2.90 (s, 4H), 2.55 (s, 3H); ^{13}C NMR ($CDCl_3$, TMS/ppm) δ 169.08, 157.09, 147.21, 140.57, 137.53, 136.60, 130.84, 126.37, 124.08, 124.02, 25.63, 21.44. Anal. Calcd for $C_{14}H_{11}NO_4S_3$ (353.44): C, 47.58; H, 3.14. Found: C, 47.76; H, 3.26.

2,2′;5′,2″-Terthiophene-5-carboxylic Acid 2,5-Dioxopyrrolidin-1-yl Ester, **11**. Yield: 95%. Amorphous light yellow solid, mp 223−224 °C; EI-MS *m*/*z* 389 (M^+). ^{1}H NMR ($CDCl_3$, TMS/ppm) δ 7.92 (d, ^3J = 4.0 Hz, 1H), 7.28 (dd, ^3J = 5.2 Hz, ^4J = 1.2 Hz, 1H), 7.26 (d, ^3J = 4.0 Hz, 1H), 7.23 (dd, ^3J = 4.0 Hz, ^4J = 1.2 Hz, 1H), 7.20 (d, ^3J = 4.0 Hz, 1H), 7.13 (d, ^3J = 4.0 Hz, 1H), 7.05 (dd, ^3J = 4.0 Hz, ^3J = 5.2 Hz, 1H), 2.90 (s, 4H); ^{13}C NMR ($CDCl_3$, TMS/ppm) δ 169.14, 157.08, 147.41, 139.22, 137.61, 136.31, 133.89, 128.07, 126.93, 125.43, 124.63, 124.54, 124.05, 123.95, 25.62. Anal. Calcd for $C_{17}H_{11}NO_4S_3$ (389.47): C, 52.43; H, 2.85. Found: C, 52.54; H, 2.98.

5″-[2-(2-Methoxyethoxymethoxy)ethyl]-[2,2′;5′,2″]terthiophene-5-carboxylic Acid 2,5-Dioxopyrrolidin-1-yl Ester, **12**. Yield: 209 mg (80%). Polycrystalline yellow-orange solid, mp 119−120 °C; EI-MS *m*/*z* 521 (M^+). ^{1}H NMR ($CDCl_3$, TMS/ppm) δ 7.88 (d, ^3J = 4.0 Hz, 1H), 7.21 (d, ^3J = 4.0 Hz, 1H), 7.16 (d, ^3J = 4.0 Hz, 1H), 7.02 (d, ^3J = 4.0 Hz, 2H), 6.77 (d, ^3J = 3.6 Hz, 1H), 4.74 (s, 2H), 3.80 (t,^3J = 6.2 Hz, 2H), 3.66 (m, 2H), 3.52 (m, 2H), 3.36 (s, 3H), 3.07 (t, ^3J = 6.2 Hz, 2H), 2.87 (s, 4H); ^{13}C NMR ($CDCl_3$, TMS/ppm) δ 169.14, 157.02, 147.47, 142.08, 139.54, 137.55, 134.54, 133.32, 126.88, 126.24, 124.17, 123.97, 123.87, 123.70, 95.46, 71.66, 67.91, 66.85, 58.95, 30.70, 25.58. Anal. Calcd for $C_{23}H_{23}NO_7S_3$ (521.63): C, 52.96; H, 4.44. Found: C, 52.98; H, 4.49.

5″-Methylsulfanyl-[2,2′;5′,2″]terthiophene-5-carboxylic Acid 2,5-Dioxopyrrolidin-1-yl Ester, **13**. Yield: 126 mg (58%). Amorphous yellow-orange solid, mp 206−207 °C, EI-MS *m*/*z* 435 (M^+). ^{1}H NMR ($CDCl_3$, TMS/ppm) δ 7.92 (d, ^3J = 4.0 Hz, 1H), 7.24 (d, ^3J = 4.0 Hz, 1H), 7.20 (d, ^3J = 4.0 Hz, 1H), 7.07 (d, ^3J = 4.0 Hz, 1H), 7.06 (d, ^3J = 3.6 Hz, 1H), 6.99 (d, ^3J = 3.6 Hz, 1H), 2.91 (s, 4H), 2.53 (s, 3H); ^{13}C NMR ($CDCl_3$, TMS/ppm) δ 169.12, 157.05, 147.23, 138.73, 138.03, 137.93, 137.58, 133.99, 131.44, 126.94, 124.61, 124.52, 124.11, 124.05, 25.62, 21.86. Anal. Calcd for $C_{18}H_{13}NO_4S_4$ (435.56): C, 49.64; H, 3.01. Found: C, 49.54; H, 2.98.

2,2′;5′,2″;5″,2‴-Quaterthiophene-5-carboxylic Acid 2,5-Dioxopyrrolidin-1-yl Ester, **15**. Yield: 188 mg (80%). Amorphous orange solid, mp 263−264 °C; EI-MS *m*/*z* 471 (M^+). ^{1}H NMR ($CDCl_3$, TMS/ppm) δ 7.93 (d, ^3J = 4.0 Hz, 1H), 7.26 (d, ^3J = 4.0 Hz, 1H), 7.24 (dd, ^3J = 4.0 Hz, ^4J = 1.2 Hz, 1H), 7.21(d, ^3J = 4.0 Hz, 1H), 7.20 (dd, ^3J = 5.2 Hz, ^4J = 1.2 Hz, 1H), 7.12 (m, 3H), 7.04 (dd, ^3J = 4.0, ^3J = 5.2, 1H), 2.90 (s, 4H); ^{13}C NMR ($CDCl_3$, TMS/ppm) δ 169.10, 157.08, 147.32, 138.93, 137.60, 137.45, 137.39, 136.76, 134.97, 133.97, 127.97, 127.02, 125.17, 124.91, 124.53, 124.49, 124.10, 124.07, 25.64. Anal. Calcd for $C_{27}H_{25}NO_7S_4$ (471.59): C, 53.48; H, 2.78. Found: C, 53.54; H, 2.83.

5‴-[2-(2-Methoxyethoxymethoxy)ethyl]-[2,2′;5′,2″;5″,2‴]-quaterthiophene-5-carboxylic Acid 2,5-Dioxopyrrolidin-1-yl Ester, **16**. Yield: 260 mg (86%). Amorphous orange solid, mp 141−142 °C; EI-MS *m*/*z* 603 (M^+). ^{1}H NMR ($CDCl_3$, TMS/ppm) δ 7.91 (d, ^3J = 4.0 Hz, 1H), 7.24 (d, ^3J = 4.0 Hz, 1H), 7.19 (d, ^3J = 4.0 Hz, 1H), 7.09 (m, 2H), 7.01 (m, 2H), 6.77 (d, ^3J = 4.0, 1H), 4.75 (s, 2H), 3.81 (t,^3J = 6.6 Hz, 2H), 3.68 (m, 2H), 3.54 (m, 2H), 3.38 (s, 3H), 3.08 (t, ^3J = 6.6 Hz, 2H), 2.89 (s, 4H); ^{13}C NMR ($CDCl_3$, TMS/ppm) δ 169.10, 157.06, 147.34, 141.52, 139.03, 137.74, 137.59, 135.03, 134.45, 133.79, 127.00, 126.18, 125.13, 124.37, 124.04, 123.98, 123.87, 123.72, 95.55, 71.74, 68.05, 66.92, 59.00, 30.78, 25.63. Anal. Calcd for $C_{27}H_{25}NO_7S_4$ (603.05): C, 53.71; H, 4.17. Found: C, 53.82; H, 4.23.

5‴-Methylsulfanyl-[2,2′;5′,2″;5″,2‴]quaterthiophene-5-carboxylic Acid 2,5-Dioxopyrrolidin-1-yl Ester, **17**. Yield: 145 mg (56%). Microcrystalline red-orange solid, mp 253−254 °C; EI-MS *m*/*z* 517 (M^+). ^{1}H NMR (DMSO-d_6, TMS/ppm) δ 8.14 (d, ^3J = 4.0 Hz, 1H), 7.71 (d, ^3J = 4.0 Hz, 1H), 7.63 (d, ^3J = 4.0 Hz, 1H), 7.48 (d, ^3J = 4.0 Hz, 1H), 7.46 (d, ^3J = 4.0 Hz, 1H), 7.35 (d, ^3J = 4.0 Hz, 1H), 7.33 (d, ^3J = 4.0, 1H), 2.92 (s, 4H), 2.59 (s, 3H). Anal. Calcd for $C_{22}H_{15}NO_4S_5$ (517.68): C, 51.04; H, 2.92. Found: C, 51.54; H, 2.83.

Synthesis of Oligonucleotides. Oligonucleotides were synthesized in our laboratory using a Gene Assembler II plus synthesizer using manufacturer protocols and commercial reagents. The 3′-amino modification was obtained using 3′-PT Amino-Modifier C6 CPG (Glenn Research). Dabcyl was linked at the 5′ position using dabcyl phosphoramidite (Chem Genes).

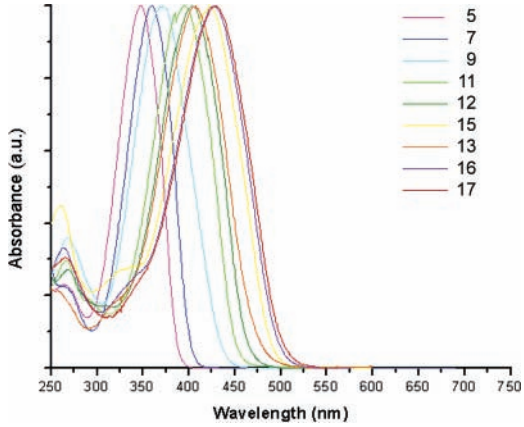

Figure 1. Normalized absorption spectra of compounds **5**, **7**, **9**, **11**−**13**, and **15**−**17** in CH_2Cl_2.

At the end of the synthesis, the oligonucloetides, DMTr off, were deprotected with 30% aqueous ammonia at 50 °C for 16 h and then lyophilized. The 3′-amino-modified oligonucleotides were purified by chromatography using a DEAE-Sephacell column (Pharmacia), eluting with a gradient of triethylammonium bicarbonate, and lyophilized. The dabcyl-oligonucleotide was purified by reversed phase chromatography on RP-18 silica gel with a gradient of CH_3CN in 0.1M triethylammonium acetate and then lyophilized. The lyophilized compounds were stored at −18 °C.

Protein Labeling. *Conjugation of Bithiophene N-Succinimidyl Ester* **9** *and FITC with anti-CD3 Antibody.* Anti-CD3 antibody dissolved in phosphate buffer saline solution (pH 7.4) was dialyzed (v:v = 1:1000) vs a 0.05 M carbonate buffer (pH 9.0) containing a non ionic detergent, and the dialysis was allowed to run for about 16 h at 4 °C. Then the solution was concentrated by microcon membrane (Amicon) with 50 kD cut off. Four vials containing a 2.6 mg/mL of anti-CD3 were prepared. To three of these aliquots was added **9** dissolved in DMSO (10 mg/mL) in the amounts needed to reach protein: fluorophore 1:10, 1:25, 1:50 molar ratios. The solutions were incubated for 3 h at room T under stirring. To the fourth vial of anti-CD3 was added a 10 mg/mL FITC solution in DMSO (protein:fluorophore 1:50 molar ratio), and the incubation was carried out in the dark. Afterward each conjugate was chromatographed on a desalting 1.0 mL G25 column in PBS pH 7.4. In the case of fluorophore **9** the separation of the labeled protein from the free dye could be followed by irradiating with a 15 mW lamp (see Figure 11 in the Supporting Information). The degree of labeling, namely F:P the average number of fluorophore molecules for protein, was obtained by absorption spectroscopy according to standard procedures (*2*). The absorbance of the protein at 280 nm was corrected for a factor corresponding to the contribution of the fluorophore at this wavelength (see Figure 1). The estimated F:P ratios varied from 2.5 to 6.7 for the mAb marked with **9**. For mAb marked with FITC the F:P ratio amounted to 7. The absorption spectra for the different experiments are given as Supporting Information.

Conjugation of Bithiophene N-Succinimidyl Ester **9** *with Saporin.* The plant toxin saporin (*21*) was conjugated with **9** as described above for anti-CD3 mAb.

Cells. HeLa cells, derived from a human cervical carcinoma, and Jurkat cells, derived from a human T-cell lymphoma, were cultured in RPMI 1640 medium supplemented with 10% FCS and antibiotics. HeLa cells were seeded on four-chambered culture slides (Falcon BD) (5000 cells/well) in complete medium. After 24 h cells were incubated with 10 μM saporin−**9** for 1 h at 37 °C. After treatment, cells were washed twice with PBS and then fixed with cold methanol at −20 °C for 15 min. Jurkat cells (10^7 cells/ml) were incubated at 4 °C for 30 min with the anti-CD3 mAb labeled with compound **13** (dilution 1:100). The reaction was carried out at 4 °C, to allow the specific binding of the anti-CD3 mAb to the corresponding antigen on cell surface while preventing the internalization of the immunocomplex. After treatment, cells were washed twice with PBS at 0 °C and fixed with 4% formaldehyde pH 7.5 for 30 min at room temperature. Drops of fixed Jurkat cells were dried on the slides.

Oligonucleotide Labeling. The oligothiophene *N*-succinimidyl ester (1 mg) was first dissolved in 60 μL of DMF in a microvial, and then about 10 OD (∼300 μg) of 3′-amino-modified oligonucleotide dissolved in 12 μL of a 0.1 mM buffered solution (pH 7.4) were added to the solution. The mixture was kept at 40 °C overnight. The reaction was checked by HPLC and diluted with 500 μL of deionized H_2O and the excess of fluorophore repeatedly extracted with a 1:4 methanol: methylene chloride solution using a syringe. The conjugated oligonucleotide was recovered from the aqueous phase by reversed phase chromatography, exploiting the lipophilicity of the conjugated dye. Up to 7 OD of pure conjugated oligonucleotide were recovered (70% yield).

Fluorescence Microscopy. Fluorescence microscopy was performed with a Nikon Eclipse E600W fluorescence microscope equipped with a 100× objective. Color photomicrographs were obtained using a Nikon-dedicated digital camera.

Absorption and Photoluminescence Measurements. Absorption and photoluminescence spectra in methylene chloride were obtained using 10^{-4}−10^{-6} M solutions (spectroscopic grade). Photoluminescence measurements were performed by exciting the solutions at optimum wavelengths for absorbances 0.1−0.2.

Theoretical Calculations. Calculations were carried out with the quantum-chemistry program package TURBOMOLE V5.7 (*22*, *23*). In particular, the RICC22 (*24*−*26*) module was used. In the CC2 calculations, core orbitals were removed from the active space. In addition, for the calculation of excitation energies, virtual orbitals with energies above 150 eV were freezed. All calculations were performed on an HP rx8620 Itanium-2 server.

RESULTS

I. Synthesis. Despite the great number of functionalization types realized for oligo and polythiophenes, the functionalization with the succinimidyl group has not yet been reported. To prepare oligothiophene *N*-succinimidyl esters we followed the synthetic pattern reported in Scheme 1, starting from commercial 5-bromo-2-thiophenecarboxaldehyde (**1**). It consists of repeated sequences of bromination and Stille coupling reactions (*27*) occurring in good yields. Generally, on increasing the oligomer size, the yield of the Stille coupling decreases, owing to the increased number of side reactions related to metal−halogen exchange. However, in this case, we did not observe the formation of side products ascribable to the presence of slow metal−halogen exchange equilibria, probably due to the high rate of the cross coupling reaction. As a consequence, the crude products were much easier to purify and the yields higher than generally observed in the preparation of conventional oligothiophenes. The $CH_2OCH_2CH_2OCH_3$ group (MEM) was used to increase the solubility in polar solvents.

II. Optical Properties. The maximum wavelength absorption, λ_{max} (nm), and emission, λ_{PL} (nm), and molar absorption coefficients, ϵ (cm^{-1} mol^{-1}), of oligothiophene succinimidyl esters **5**, **7**, **9**, **11**−**13**, and **15**−**17** are given in Table 1, while the normalized absorption and emission spectra of all compounds are shown in Figures 1 and 2. The emission colors vary from blue to deep orange, within a range of 160 nm, almost

Scheme 1[a]

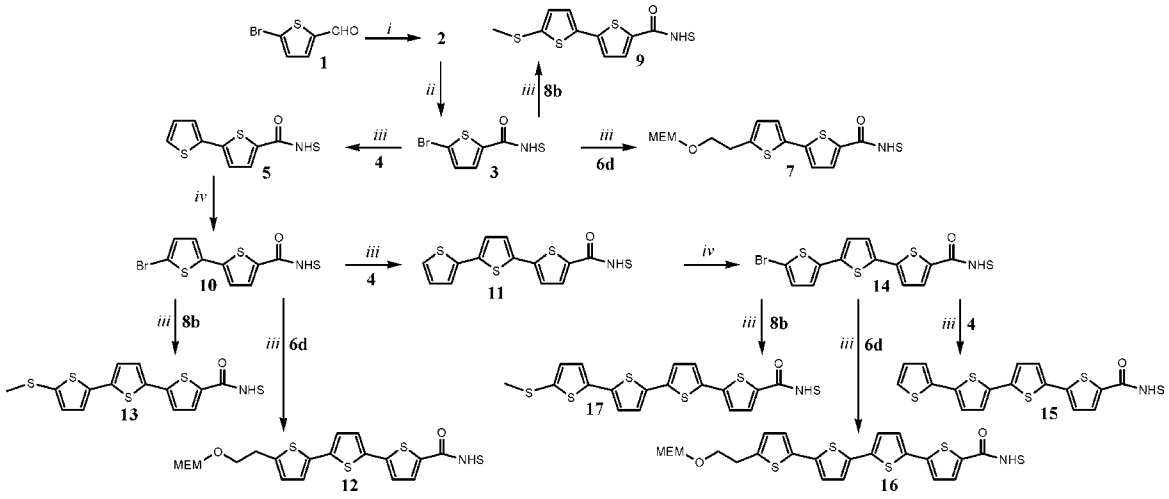

[a] Reagents and conditions: NHS = *N*-hydroxysuccinimide; MEM = $CH_2OCH_2CH_2OCH_3$. (i) Jones reagent, acetone, 15 min, 0 °C; (ii) HOSu, DCC, THF, 2 h, r.t.; (iii) $Pd(AsPh_3)_4$, toluene, 2 h, 80 °C; (iv) NBS, CH_2Cl_2, 12 h, r.t.

Table 1. Maximum Absorption (λ_{max})[a] and Emission (λ_{PL})[a] Wavelengths and Molar Absorption Coefficients (ϵ)[b]of Compounds 5, 7, 9, 11−13, and 15−17

compound	λ_{max}	λ_{PL}	$\Delta(\lambda_{PL} - \lambda_{max})$[c]	ϵ
5	347	418	4.895	24.000
7	359	432	4.707	26.700
9	370	479	6.150	27.300
11	395	482	4.570	36.900
12	404	498	4.672	33.700
13	407	545	6.221	29.900
15	421	536	5.096	45.100
16	427	552	5.333	61.900
17	432	577	5.817	39.000[d]

[a] nm, in CH_2Cl_2. [b] In cm^{-1} mol^{-1}. [c] In cm^{-1}. [d] In DMSO.

twice that of the absorption range (85 nm). All compounds are characterized by very large differences between absorption and emission wavelengths, much greater than those measured for the most commonly used markers such as fluorescein and its derivatives (*2*). As already shown for oligothiophene isothiocyanates (*16*−*18*), TSEs can also undergo repeated irradiation cycles without any appreciable change in fluorescence intensity (see section IV, Figure 4D).

An estimate of fluorescence quantum yields of the compounds of Table 1 in methylene chloride was obtained using various dithienothiophene *S,S*-dioxides (*28*) as the standards. For **5**, **7**, and **9**, values of 63%, 36%, and 28%, respectively, were obtained using 3,5-dimethyldithieno[3,2-*b*;2′,3′-*d*]thiophene 4,4-dioxide (*28*) as the standard, for compounds **11** (21%), **12** (24%), and **13** (32%) using 3,5-dimethyl-2,3-bis(phenyl)dithieno[3,2-*b*;2′,3′-*d*]thiophene 4,4-dioxide (*28*), and for compounds **15** (5%) and **16** (3%) using 3,5-dimethyl-2,3′-bis(3-methylthiophene)-dithieno[3,2-*b*;2′,3′-*d*]thiophene 4,4-dioxide (*28*). The fluorescence quantum yields obtained in this way are approximate values, and measurements of absolute quantum yields of free fluorophores in organic solvents and of the fluorophores bound to biopolymers in water are currently under way using an integrating sphere.

Apparently, and contrary to what is observed for unsubstituted thiophene oligomers (*29*−*31*), the increase in size of TSEs is not accompanied by the increase in fluorescence efficiency, indicating that the decay relaxation mechanisms from the excited state in these compounds should be different.

III. Theoretical Calculations. To investigate the optical properties of TSEs, ab initio calculations on the smallest term of the series, namely compound **5**, were first carried out. Afterward, calculations on a model system, consisting of 2,2′-bithiophene bearing the $CONH(CH_2)_3CH_3$ group at one of the terminal positions and supposed to simulate the oligothiophene after the covalent binding to the biomolecule (see sections IV and V), were performed. We refer to this system as **AT2** (amide-bound bithiophene).

As it will be clear in the following, a density-functional theory approach is not accurate enough to study these systems. Thus, we choose a correlated method, namely the approximate coupled-cluster singles and doubles method (CC2) with the resolution of identity, which is a size-consistent method well suited to calculate excitation energies of large systems (*32*−*35*). The geometries of **5** and **AT2** were optimized with the CC2 method using a cc-pVDZ basis set (*22*−*26*).

The presence of several local minima very close in energy (about 0.20 kcal/mol) to the global minimum required a highly correlated ab initio method and a large basis set to identify the global minimum. In the optimized structures the two thiophene rings are in a s-trans configuration. In **5**, the plane of the succinimide group is almost perpendicular to the plane of its nearest neighboring thiophene ring. In **AT2**, the terminal group is turned from the sulfur side. As shown in Figure 3, in this system the bithiophene structure is slightly modified by the inclusion of the terminal group: the inter-ring distance between the two thiophene rings is 1.45 Å and the dihedral angle between the two rings is 29°.

Excitation energies of **5** and **AT2** were computed by the CC2 method, using the triple-ζ valence basis set with polarization functions (cc-pVTZ) (*24*−*26*). The results are summarized in Table 2. The calculations show that in compound **5** the lowest singlet state (S_1 at 3.57 eV) is almost optically forbidden. The optically active state, S2, is an admixture of HOMO → LUMO (52%) and HOMO−LUMO+1 (41%) transition, and it is calculated to be at 4.00 eV. As can be seen in Figure 3a, the HOMO is completely localized on the bithiophene, whereas the LUMO is completely localized on the succinimidyl group. Thus, the S2 state of **5** is mainly of charge transfer in character, so the excitation energies can be expected to be strongly dependent on the environment. In addition such charge-transfer excitation cannot be described by density functional theory due to the well known limitations of the current exchange-correlation functionals (*22*−*26*). The calculated excitation energy of the optically active state overestimates the experimental value (3.58 eV), due to basis-set effects, approximations of the CC2 method, and the omission of solvent polarization.

The first optically active state of the unsubstituted bithiophene at the same level of calculation is at 4.40 eV. Thus, the inclusion

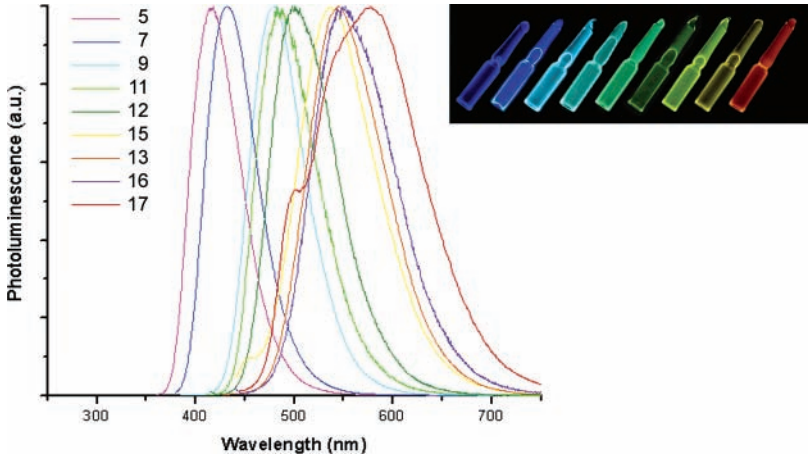

Figure 2. Normalized photoluminescence spectra of compounds **5**, **7**, **9**, **11**−**13**, and **15**−**17** in CH_2Cl_2. The emission colors on the right were obtained by irradiating with a single light source, a 15 W lamp with $\lambda = 364$ nm.

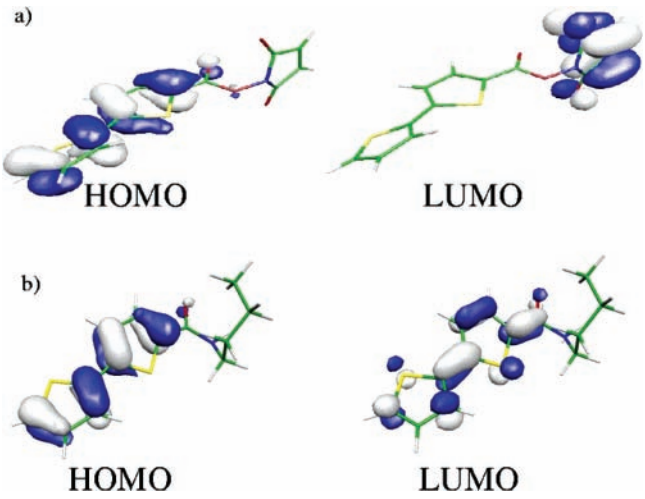

Figure 3. (a) HOMO and LUMO wave functions for *N*-succinimidyl ester **5**. (b) HOMO and LUMO wave functions for the model compound **AT2**.

Table 2. Lowest Two CC2 Singlet Excitation Energies (eV) and Oscillator Strengths (OS) for 5 and the Model Compound AT2

	state	energy	OS
5	S1	3.57	$2.1\ 10^{-4}$
	S2	4.00 (3.58)	$7.1\ 10^{-1}$
AT2	S1	4.11	$5.9\ 10^{-1}$
	S2	4.35	$4.2\ 10^{-2}$

[a] Experimental value.

of the succinimide group causes a red-shift of 0.40 eV. This value is in complete agreement with the experimental one of 0.47 eV. The latter value is obtained by comparing the experimental absorption peak energy of **5** (i.e. 3.58 eV) with the experimental absorption peak energy of the unsubstituted bithiophene (4.05 eV (*36*)).

In the model compound **AT2** the optically active state is S1 which is mainly a HOMO → LUMO (88.3%) transition, i.e., the charge-transfer character of the transition is not present. As can be seen by inspection of Figure 3b, this is essentially a transition localized on bithiophene. The inclusion of the CONH-$(CH_2)_3CH_3$ group does not induce a strong perturbation on the bithiophene HOMO and LUMO orbitals, so the photophysical properties of bithiophene should be almost unaltered upon the binding to the biological system.

IV. Coupling to Proteins and in Vitro Cell Imaging. It is known that the fluorophores functionalized with the *N*-succinimidyl ester functionality react with the ϵ-NH_2 lysine groups of proteins forming a stable amide bond (*2*, *19*).

The coupling of oligothiophene *N*-succinimidyl esters, TSEs, to proteins was carried out at slightly basic pH according to the modalities described in the Experimental Section, which are very similar to those already reported for the coupling of oligothiophene isothiocyanates to monoclonal antibodies (*16*).

Figure 4 compares the photoluminescence spectra of the bioconjugate of anti-CD3 monoclonal antibody, a IgG1 isotype antibody which reacts with CD3, a 20 kDa molecular weight antigen normally expressed on the surface of T-lymphocyte cells (*37*), labeled with bithiophene succinimidyl ester **9** (Figure 4A,B), with that (Figure 4 C) of the same antibody marked with fluorescein isothiocyanate (FITC, the most commonly used fluorescent marker (*2*)). The corresponding absorption spectra are reported as Supporting Information.

The conjugation reaction was carried out using anti-CD3 to **9** molar ratios of 1:10, 1:25, and 1:50. At the end of each reaction and after the first UV measurements, the bioconjugate was stabilized with a solution of phosphate buffer saline containing 0,5% (w/v) of bovine serum albumine (BSA) and 0.1% (w/v) of sodium azide. The presence of BSA avoided the normal aggregation of IgG's biopolimeres at low concentration, keeping the total protein concentration at 4−5 mg/mL.

Owing to the photostability of **9**, the separation of the conjugated fraction from the free fluorophore could be followed by irradiation with an UV lamp (see the Experimental Section). The F/P (fluorophore-to-protein ratio) was determined on the basis of the relative absorbances of the fluorophore and the antibody, corrected for a factor corresponding to the weak absorption band around 270−280 nm present in the spectrum of **9** (see Figure 1) and overlapping the absorbance of the protein. The conjugation of FITC with the anti-CD3 antibody was carried out with the same modalities and using a 1:50 mAb: FITC molar ratio. The measured F/P values for the bioconjugate of **9** varied from a minimum of 2.5 to a maximum of 6.7, with a proportional increase in fluorescence intensity. The bioconjugate of anti-CD3 with FITC afforded a F/P value of nearly 7. The biological activity of the anti-CD3 antibody marked with **9** was checked for all dilutions by cytofluorimetry through indirect detection using a GAM IgG-FITC and found unaltered, as in the case of the antibodies marked with oligothiophene isothiocyanates (*16*).

Figures 4A and 4B show the photoluminescence spectra of the anti-CD3 antibody labeled with **9** and obtained using 1:50 and 1:10 molar ratios and corresponding to 6.7 and 2.5 F/P values, respectively. The figures show that decreasing the F/P ratio leads to a proportional decrease in photoluminescence

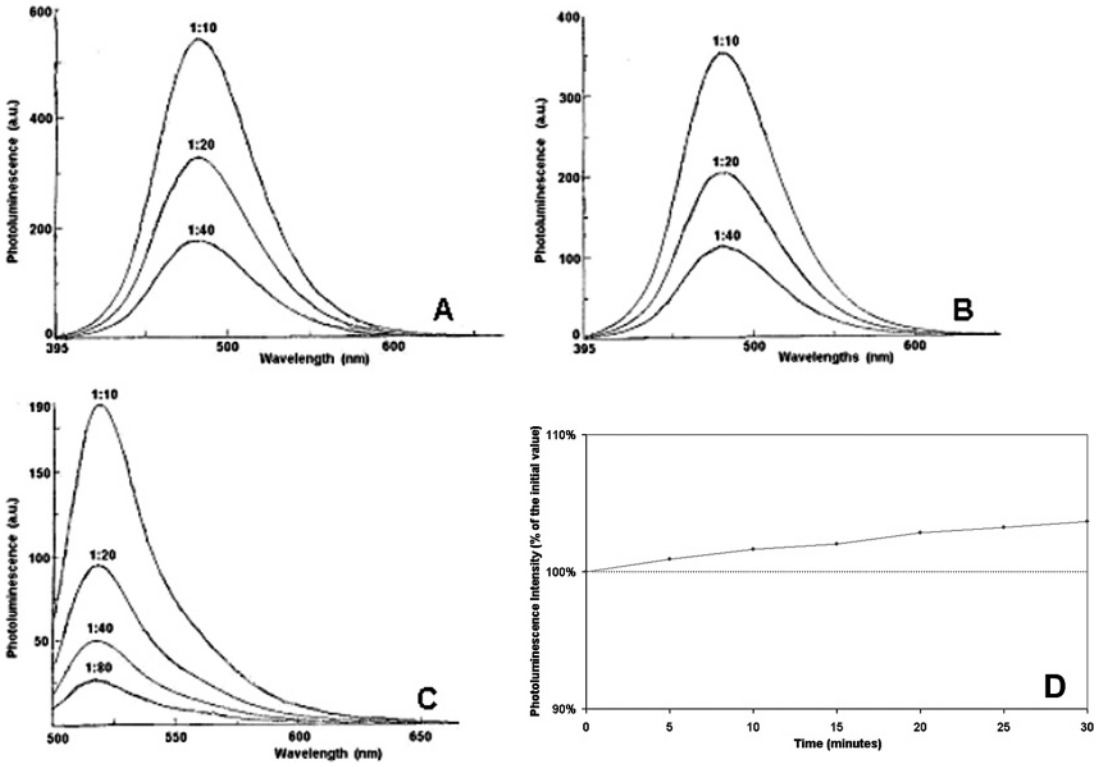

Figure 4. Photoluminescence of the IgG_1 anti-CD3 monoclonal antibody labeled with compound **9** (A, B, D) and with fluorescein isothiocyanate (C). A. PL spectra of anti-CD3:**9** bioconjugate with fluorophore-to-protein ratio 6.7. B. PL spectra of anti-CD3:**9** bioconjugate with fluorophore-to-protein ratio 2.5. C. PL spectra of anti-CD3: FITC bioconjugate with fluorophore-to-protein ratio 7. The different plots of each figure are the spectra corresponding to different dilutions of the bioconjugates (1:10, 1:20, 1:40, and 1:80 v:v). D. Photoluminescence intensity, in % of the starting value, of the bioconjugate of part A as a function of time under continuous excitation at a frequency corresponding to maximum absorption wavelength.

intensity. Figure 4C shows the photoluminescence spectra of the anti-CD3 antibody labeled with FITC. The different plots of each figure are the spectra corresponding to different dilutions of the bioconjugate (1:10, 1:20, 1:40, 1:80 v/v).

Comparison of Figures 4A and 4C shows that despite the sligthly lower F/P ratio and lower absorbance (see the Supporting Information), the photoluminescence intensity of the anti-CD3 antibody marked with **9** is higher than that of the antibody marked with fluorescein. Figure 4D shows the photoluminescence of the anti-CD3 antibody marked with **9** as a function of time, under continuous irradiation with the spectrofluorimeter lamp at a frequency corresponding to the maximum absorption wavelength. It is seen that after 30 min the PL intensity is slightly increased. On the contrary, and in agreement with what is already known (*2*), the photoluminescence signal of the bioconjugate with fluorescein faded quickly and after a few minutes of continuous irradiation at optimum wavelength became undetectable.

The slight fluorescence increase reported in Figure 4 is either due to photoactivation phenomena similar to those observed for quantum dots in cells (*38*) or phenomena related to the reorganization of the solvent cage (*19*). The phenomenon is currently under investigation.

To evaluate the suitability of oligothiophene *N*-succinimidyl esters for in vitro cells imaging, the anti-CD3 monoclonal antibody (mAb) labeled with compounds **9** and **13** were employed. The conjugation of the anti-CD3 mAb to **13** was carried out with the same modalities described above for **9**, using mAb to fluorophore molar ratios of 1:25 and 1:50.

To evaluate the cell binding, human T-lymphoma Jurkat cells were incubated at 4 °C for 30 min with the anti-CD3 mAb labeled with **13**. The reaction was carried out at $T = 4$ °C, to allow the specific binding of the anti-CD3 mAb to the corresponding antigen on cell surface while preventing the internalization of the immuno-complex. The resulting fluorescence microscopy image is shown in Figure 5A. The image shows the membrane fluorescence of the labeled cells.

To evaluate the cell binding and endocytosis, adherent human cervical carcinoma HeLa cells were treated with the plant toxin saporin, one of the type 1 ribosome-inactivating proteins most used to construct immunotoxin, chimeric proteins with specific efficacy (*21, 39*−*41*). Cells were incubated at 37 °C for 60 min with saporin, previously conjugated with fluorophore **9** as detailed in the Experimental Section. The binding was carried out at $T = 37$ °C in order to allow endocytosis. Since saporin has not a membrane receptor, the diffusion into the cells is not specific and occurs prevalently via pinocytosis. The corresponding fluorescence microscopy image is reported in Figures 5B, showing a brilliant fluorescence despite the bioconjugate widespread diffusion into the cell.

Figures 5A,B indicate that fluorophores TSEs are bright enough for effective cell labeling and, owing to the high excitation intensity at the focus of the objective of the microscope, also characterized by high photostability. Some blinking phenomena, namely fluorescence intermittency (*42*−*43*), were however observed, which are currently under investigation. Nevertheless, labeled cells observed after a few days showed no sign of decline of the optical characteristics.

V. Coupling to Oligonucleotides. Oligonucleotides functionalized at the 3′-position with the NH_2 group were coupled to oligothiophene *N*-succinimidyl esters in buffered solution at pH 7.4 (see the Experimental Section). As an example, the conjugates of oligothiophene *N*-succinimidyl esters **5** and **15** with the molecular beacons $^{5'}$GCGGTAGTGTGGTTCGAAGG-GTGGTACCGC$-(CH_2)_6NH_2{}^{3'}$ and $^{5'}$dabcyl-GCGGTAGTGTG-GTTCGAAGGGTGGTACCGC$-(CH_2)_6NH_2{}^{3'}$ are described.

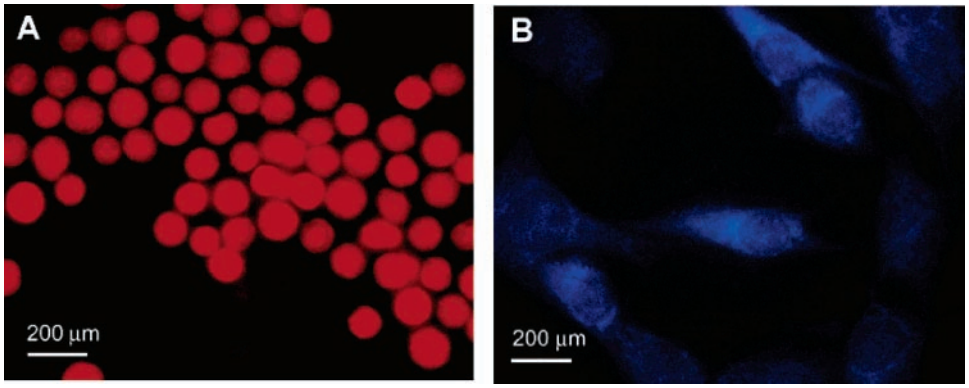

Figure 5. A: Immunofluorescent staining of Jurkat cells using the anti-CD3 monoclonal antibody labeled with fluorophore **13**. B: Binding and endocytosis of **9**-labeled saporin by HeLa cells.

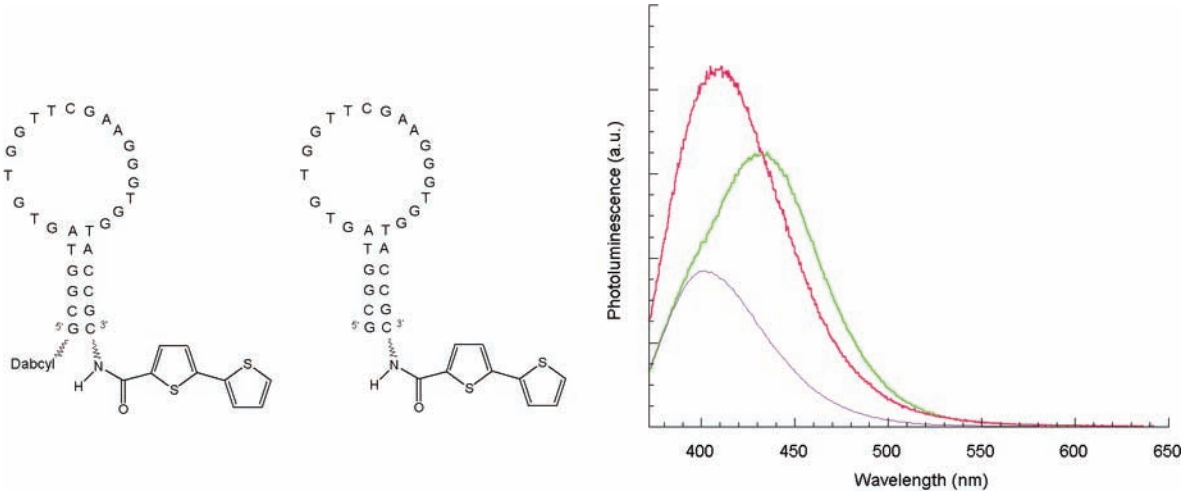

Figure 6. Left: 3′-Amino-terminated molecular beacon sequence coupled to oligothiophene *N*-succinimidyl ester **5** with and without the quencher dabcyl at the 5′-end. Right: Photoluminescence spectrum of free **5** (green, 10^{-7} M in H_2O), of the molecular beacon−**5** conjugate (red) and of the molecular beacon−**5** conjugate with dabcyl at the 5′-end (violet).

Molecular beacons (MB) (*44*) are single stranded oligonucleotides possessing a complementary set of bases at both ends of the sequence, thus enabling the formation of a hairpin conformation as shown in the scheme of Figure 6. Dabcyl is a well-known quencher used to probe nucleic acid structures, which is nonfluorescent and acts as energy acceptor in conjunction with fluorophores such as fluorescein (*45*). The emission spectra of **5** and **15** overlap the absorption spectrum of dabcyl (λ_{max} = 475 nm)**,** permitting energy transfer between the fluorophores and the quencher to occur when they are at appropriate distance (*44*−*47*). Thus, some fluorescence quenching is expected following the intramolecular interaction of the fluorophores with dabcyl in the molecular beacon bearing the fluorophore and dabcyl at the opposite ends.

Figure 6 compares the photoluminescence spectra of free **5** with that of the MB sequence labeled with **5** and the MB sequence labeled with both **5** and dabcyl at the 3′- and 5′-positions, respectively. It is seen that upon conjugation with MB, the photoluminescence of **5** increases by about 30% and undergoes a blue shift of about 20 nm. However, in the presence of dabcyl at the opposite end of the MB sequence, the quenching of the emission of **5** takes place and the PL intensity decreases to nearly half the value observed for the **5**-labeled oligonucleotide lacking dabcyl at the opposite end.

Figure 7 (red plot) illustrates the effect of the addition of a complementary strand to the photoluminescence of the MB sequence labeled with oligothiophene *N*-succinimidyl ester **15** at the 3′-end and with dabcyl at the 5′-end. The shape of the PL spectrum of the MB sequence bearing **15** at the 3′-end and dabcyl at the 5′-end (black plot) indicates that the intramolecular interactions of dabcyl with the tetrameric **15** are more complex than those observed for the dimeric fluorophore **5** and deserve deeper investigations to be fully understood. However, for the present purposes, what is significant is that upon addition of a complementary strand, i.e., of the probe sequence $^{3'}$CACAC-CAAGCTTCCCACCA$^{5'}$ (see the scheme of Figure 7), a sizable alteration of the emission of the fluorescent label is observed. Indeed, Figure 7 shows that upon addition of 3 equiv of the complementary oligonucleotide, the PL intensity is remarkably increased and the PL maximum wavelength blue shifted to 440−450 nm. This indicates that the presence of the complementary strand allows the opening of the loop, the removal of dabcyl from the proximity of the fluorophore, and the formation of a duplex with a significantly higher PL intensity and a large blue shift of the fluorophore.

The results reported in Figures 6 and 7 indicate that oligothiophene-based fluorophores are able to transfer the energy absorbed upon excitation to nearby molecules and are then worth testing in a variety of experiments for nucleic acid detection.

DISCUSSION

The most significant result reported here is that small and simple systems, such as bithiophene *N*-succinimidyl ester **9**, can behave as robust ‘nanolamps’ emitting even more light than fluorescein when bound to proteins, such as monoclonal antibodies, and with an incomparably greater optical stability. The result is important not only in view of the possible applications but also from a fundamental point of view. Indeed,

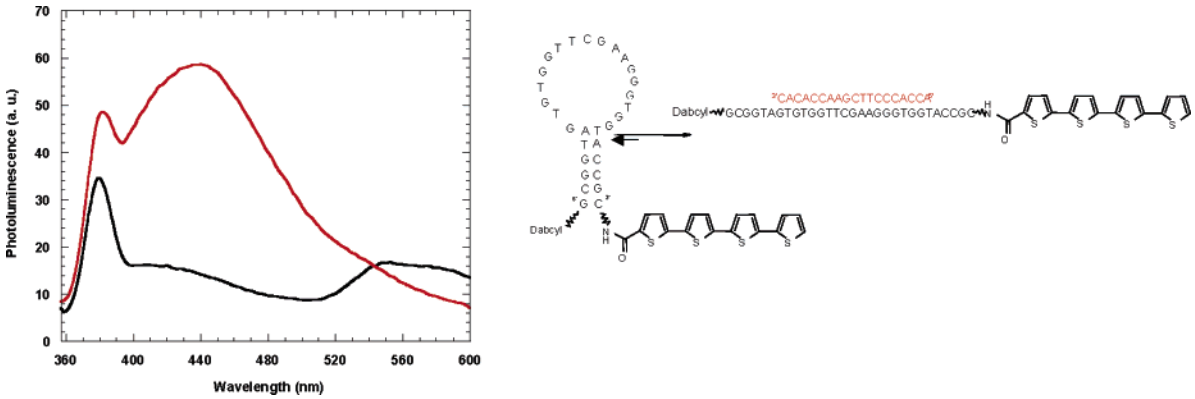

Figure 7. Effect of hybridization on the PL intensity of the MB sequence labeled with **15** at the 3′-end and dabcyl at the 5′- end in the presence of 3 equiv of the complementary strand. Black plot: before addition of the complementary sequence. Red plot: after duplex formation.

despite the large body of experimental data on the fluorescence properties of thiophene oligomers, with oligomers that emit in solution but not in solid, in solid but not in solution, or both in solution and in solid (*28, 48, 49*), there are still very few data on the relative importance of radiative and nonradiative de-excitation mechanisms in these systems (*29*−*31, 50*−*52*).

Compound **9** is a bithiophene bearing a donor (SCH_3) and an acceptor (−COO−*N*-succinimidyl) group at the terminal positions. It is poorly soluble in water but acquires high water solubility upon binding to proteins or oligonucleotides. There are a few experimental data indicating that molecules with donor−acceptor substituents increase their photoluminescence when the solvent polarity increases (*53*). This suggests that a possible explanation for the high fluorescence of **9** in water, when bound to biopolymers, could be related to its nature of donor−acceptor system, and we are currently investigating the phenomenon both theoretically and experimentally.

Theoretical calculations on bithiophene **5** show that *N*-succinidimyl esters are charge transfer compounds with the LUMO completely delocalized on the substituent and the lowest singlet S1 state almost optically forbidden. These results make oligothiophene *N*-succinimidyl esters interesting compounds in themselves. For the present purposes, however, it is important that when the −COO−*N*-succinidimyl substituent is replaced by the −CONH− linker that is formed upon reaction with the biopolymer, the characteristics of bithiophene are recovered. The optically active state becomes singlet S1 which is mainly a HOMO → LUMO transition, essentially localized on bithiophene. Figure 3 shows that there is still a large charge separation in the LUMO with an excess of negative charge on the thienyl ring bearing the linker. It is likely that this charge separation is accentuated by the presence of an electron donor at the opposite side of the molecule, such as the methylsulfanyl group of compounds **9**, **13**, and **17**.

As shown in Figure 2, dimers have narrow (60−70 nm at half-height) and symmetric PL spectra while trimers (∼70−90 nm at half-height) and tetramers (∼90−140 nm at half-height) have broader emission lines. The absorption spectra follow the same trend, albeit less accentuated. The fact that the absorption spectra vary within a much narrower range than the emission one is a favorable factor for multilabeling multicolor experiments using a single irradiation source. On the other hand, the fluorescence colors shown in Figure 2 were obtained by irradiation with a single UV 15 W lamp at $\lambda = 364$ nm, of those used for product revelation in thin layer chromatography.

Table 1 shows that the absorpitivities of the *N*-succinimidyl esters in methylene chloride are between 24.000 and 61.000 cm^{-1} mol^{-1} and increase with the oligomer size, as in the case of unsubstituted oligothiophenes. However, on the basis of our first approximate estimates, the fluorescence efficiency decreases on increasing the oligomer size, contrary to unsubstituted oligothiophenes (*29*−*31*). While this result needs to be confirmed by more accurate, absolute, fluorescence quantum yield measurements, we recall that the balance of factors affecting the radiative and nonradiative de-excitation patterns in thiophene oligomer changes on changing the nature of the substituents grafted to the aromatic backbone and needs accurate elucidation case by case.

The bioconjugates of *N*-succinimidyl esters with monoclonal antibodies are characterized by very clean photoluminescence spectra, as shown in Figures 4A,B for the bioconjugate of compound **9** with anti-CD3 antibody. The emission band is symmetric for all concentrations, contrary to the bioconjugate of the same antibody with FITC, which displays the presence of weak tails at red wavelegths (Figure 4C). The optical stability of the bioncojugates is documented in Figure 4D, showing the PL intensity of the bioconjugate of **9** with anti-CD3 antibody monitored for 30 min under continuous irradiation with the spectrofluorimeter light source. This result is in agreement with what was found for oligothiophene isothiocyanates (*16*). The photoluminescence intensity of the anti-CD3-**9** bioconjugate undergoes even a slight increase with time, a further phenomenon currently under investigation.

To our knowledge, the fluorescence microscopy images shown in Figure 5 are the first ones obtained using thiophene-based fluorophores. We used two different cell lines, Jurkat cells derived from a T lymphoma and HeLa cells derived from a carcinoma, in order to show different applications of fluorescence, in suspension and in adherent growing cells. Jurkat cells were used to evaluate specific membrane fluorescence by the binding of an anti-CD3 antibody whereas HeLa cells were used to evaluate a non specific fluorescence, due to a toxin (saporin) entering in vivo in the cells. Images 5A and 5B indicate that oligothiophene *N*-succinimidyl esters are valuable photostable probes for cell detection.

What we have still to demonstrate is that the esters allow multicolor tagging of cells for the simultaneous tracking of multiple biological events. We are currently planning such kind of experiments with the oligothiophene *N*-succinimidyl esters described here, since the absorption and emission spectra of Figures 1 and 2 show that at least one couple of well separated colors is available. Moreover, we are pursuing our synthetic effort to get better emission colors particularly for the red wavelengths, taking advantage of the easy functionalization of thiophene oligomers with a great variety of substituents. This objective demands a parallel effort to explore in more detail the relationship between the molecular structure and the optical characteristics of oligothiophenes, even with the aid of theoretical calculations, since the optical behavior of these compounds is so far scarcely predictable.

The results concerning the labeling of oligonucleotides with oligothiophene *N*-succinimidyl esters, shown in Figures 6 and 7, indicate that these fluoropores allow experiments that are generally carried out using FITC and its derivatives, with the non-negligeable advantage of a much greater optical stability. In particular, we have demonstrated the feasibility of fluorescence resonance energy transfer (FRET) experiments (*44*−*47*); see for example Figure 6 showing that the fluorescence is partially quenched when the oligonucleotide sequence bears dabcyl at the 5′-end. These kinds of experiments are commonly employed for monitoring hybridization of a fluorescent oligonucleotide probe to a complementary single-stranded DNA target (*44*−*47, 54*). When hybridization occurs, the markers at the opposite ends (the reporter and the quencher) are separated and the fluorescence signal increases again. In our case, Figure 7 shows that the expected changes in fluorescence upon hybridization are indeed observed with our fluorophores. Figure 7 also illustrates the complexity of the optical patterns associated to the intra- and intermolecular interactions of the longer oligothiophenes, a complexity that contains much information but that requires, once again, a great deal of further experimental and theoretical work to be elucidated.

CONCLUSION

For the easy synthesis, fluorescence sensitivity, optical stability, color tuning, large shifts between absorption and emission wavelengths, and the easy conjugation modalities to proteins and oligonucleotides, oligothiophene *N*-succinimidyl esters are among the best classes of organic fluorescent markers described so far. They also represent a remarkable improvement with respect to the family of oligothiophene isothiocyanates previously described (*16*), particularly regarding fluorescence intensities and absorption and emission bandwidths of the bioconjugates. The conjugates of oligothiophene *N*-succinimidyl esters with proteins and oligonucleotides display high water solubility and do not show any sign of photobleaching even after hours of continuous irradiation. The fact that they can even achieve fluorescence intensities higher than those of the same bioconjugates with fluorescein indicates that they have the potential to replace the most commonly used markers for detection and quantitation of biopolymers in clinical diagnostics, molecular biology, environment analysis, etc. Furthermore, the first examples reported here of cell imaging by fluorescence microscopy using oligothiophene *N*-succinimidyl esters are greatly encouraging regarding the possibility of multicolor experiments for the simultaneous tracking of different cell events.

Finally, it is worth noting that the optical stability and color tunability of thiophene-based fluorophores would also be of great interest for monoclonal antibodies and DNA cytofluorimetric analyses. Unfortunately, the flow cytometry currently in use, mainly developed for fluorescein and its derivatives (*2*), employs the argon laser at 488 nm as irradiation source, while thiophene oligomers absorb around 400 nm and would require instrumentation with a very expensive blue laser as excitation source. Owing to the recent great interest in polythiophenes as optical sensors (*9*−*10, 55*−*57*), it cannot be excluded that cheaper blue lasers and instrumentation will rapidly be developed. As an alternative, there is the engineering of thiophene-based light emitters with the appropriate characteristics for detection with the currently used instrumentation. Considering the increasing importance of fluorescence detection techniques, the large place left for fundamental research in order to understand the photophysics of thiophene-based fluorophores and the versatility of thiophene chemistry, this is a challenge that it is worth accepting.

ACKNOWLEDGMENT

This work was partially supported by the project FIRB RBNE01YSR8 NanObioMoleculAr Devices (NOMADE), and by the University of Bologna, Funds for Selected Research Topics, the Ministry of Instruction, University and Research, the Ministry of Welfare and the Pallotti's Legacy for Cancer Research. Thanks are also due to R. Ahlrichs for providing the TURBOMOLE program package and G. Aloisio for his support.

Supporting Information Available: Synthesis of compounds **2**, **3**, **6d**, **8b**, **10**, and **14**, absorption spectra of the bioconjugates of anti-CD3 antibody with **9** and FITC, and a photograph of the separation by size exclusion chromatography of the bioconjugate of anti-CD3 antibody with **9** from the free fluorophore under UV irradiation. This material is available free of charge via the Internet at http://pubs.acs.org/BC.

LITERATURE CITED

(1) Ntziachristos, V. A., Yodh, G., Schnall, M., and Chance, B. (2000) Concurrent MRI and diffuse optical tomography of breast after indocyanine green enhancement. *Proc. Natl. Acad. Sci. U.S.A. 97*, 2767−2772.

(2) Haugland, R. P. (2001) *Handbook of Fluorescent Probes and Research Products*, 9th ed., Molecular Probes Inc., Eugene, OR.

(3) Powe, A. M., Fletcher, K. A., St. Luce, N. N., Lowry, M., Neal, S., McCarroll, M. E., Oldham, P. B., McGown, L. B., and Warner, I. M. (2004) Molecular Fluorescence, Phosphorescence, and Chemiluminescence Spectrometry. *Anal. Chem. 76*, 4614−4634.

(4) Bruchez, M., Jr., Moronne, M., Gin, P., Weiss, S., and Alivisatos, A. P. (1998) Semiconductor Nanocrystals as Fluorescent Biological Labels. *Science 281*, 2013−2016.

(5) Wu, X., Liu, H., Liu, J., Haley, K. N., Treadway, J. A., Larson, J. P., Ge, N., Peale, F., and Bruchez, M. P. (2003) Immunofluorescent labeling of cancer marker Her2 and other cellular targets with semiconductor quantum dots. *Nat. Biotechnol. 21*, 41−46.

(6) Jaiswal, J. K., Mattoussi, H., Mauro, J. M., and Simon, S. M. (2003) Long-term multiple color imaging of live cells using quantum dot bioconjugates. *Nat. Biotechnol. 21*, 47−51.

(7) Gao, X., Cui, Y., Levenson, R. M., Chung, L. W. K., and Nie, S. (2004) In vivo cancer targeting and imaging with semiconductor quantum dots. *Nat. Biotechnol. 22*, 969−976.

(8) Derfus, A. M., Chan, W. C.,and Bhatia, S. N. (2004) Probing the Cytotoxicity of Semiconductor Quantum Dots. *Nano Lett. 4*, 11−18.

(9) Nilsson, K. P. R.,and Inganas, O. (2003) Chip and solution detection of DNA hybridization using a luminescent zwitterionic polythiophene derivative. *Nat. Mater. 2*, 419−424.

(10) Doré, K., Dubus, S., Ho, H. A., Lévesque, I., Brunette, M., Corbeil, M., Boissinot, M., Boivin, G., Bergeron, M. G., Boudreau, D., and Leclerc, M. (2004) Fluorescent Polymeric Transducer for the Rapid, Simple, and Specific Detection of Nucleic Acids at the Zeptomole Level. *J. Am. Chem. Soc. 126*, 4240−4244.

(11) Mazzeo, M., Vitale, V., Della Sala, F., Anni, M., Barbarella, G., Favaretto, L., Sotgiu, G., Cingolani, R., and Gigli, G. (2005) Bright White Organic Light-Emitting Devices from a Single Active Molecular Material. *Adv. Mater. 17*, 34−39.

(12) Pisignano, D., Persano, L., Visconti, P., Cingolani, R., and Gigli, G. (2003) Oligomer-based organic distributed feedback lasers by room-temperature nanoimprint lithography. *Appl. Phys. Lett. 83*, 2545−2547

(13) Fichou, D. (1999) *Handbook of oligo and polythiophenes*, Wiley-VCH, New York.

(14) Müllen, K., and Wegner, G. (1998) *Electronic Materials: The Oligomer Approach*, Wiley-VCH, New York.

(15) (c) Nalwa, H. S. (1997) *Handbook of Organic Conductive Molecules and Polymers*, J. Wiley & Sons, Chichester.

(16) Barbarella, G., Zambianchi, M., Pudova, O., Paladini, V., Ventola, A., Cipriani, F., Gigli, G., Cingolani, R., and Citro, G. (2001) Oligothiophene Isothiocyanates as a New Class of Fluorescent Markers for Biopolymers. *J. Am. Chem. Soc. 123*, 11600−11607.

(17) Barbarella, G. (2002) Oligothiophene Isothiocyanates as Fluorescent Markers *Chem. Eur. J. 8*, 5072−5077.
(18) Sotgiu, G., Zambianchi, M., Barbarella, G., Aruffo, F., Cipriani, F., and Ventola, A. (2003) Rigid-Core Fluorescent Oligothiophene-S,S-dioxide Isothiocyanates. Synthesis, Optical Characterization, and Conjugation to Monoclonal Antibodies. *J. Org. Chem. 68*, 1512−1520.
(19) Banks, P. R., and Paquette, D. M. (1995) Comparison of Three Common Amine Reactive Fluorescent Probes Used for Conjugation to Biomolecules by Capillary Zone Electrophoresis. *Bioconjugate Chem. 6*, 447−458.
(20) Patent pending.
(21) Barbieri, L., Bolognesi, A, and Stirpe, F. (2001) Purification and conjugation of type 1 ribosome-inactivating proteins. *Methods Mol. Biol. 166*, 71−85.
(22) Dunning, T. H., Jr. (1989) Gaussian basis sets for use in correlated molecular calculations. I. The atoms boron through neon and hydrogen. *J. Chem. Phys. 90*, 1007−1023.
(23) Woon, D. E, and Dunning, T. H., Jr. (1993) Gaussian basis sets for use in correlated molecular calculations. III. The atoms aluminum through argon. *J. Chem. Phys. 98*, 1358−1371.
(24) Casida, M. E., Gutierrez, F., Guan, J., Gadea, X., Salahub, D, and Daudey, J. P. (2000) Charge-transfer correction for improved time-dependent local density approximation excited-state potential energy curves: Analysis within the two-level model with illustration for H_2 and LiH. *J. Chem. Phys. 113*, 7062−7071.
(25) Gritsenko, O., and Baerends, E. J. Asymptotic correction of the exchange-correlation kernel of time-dependent density functional theory for long-range charge-transfer excitations. *J. Chem. Phys. 121*, 655−660.
(26) Drew, A., and Gordon, M. H. (2004) Failure of Time-Dependent Density Functional Theory for Long-Range Charge-Transfer Excited States: The Zincbacteriochlorin-Bacteriochlorin and Bacteriochlorophyll-Spheroidene Complexes. *J. Am. Chem. Soc. 126*, 4007−4016.
(27) Espinet, P., and Echavarren, P. M. (2004) The Mechanisms of the Stille Reaction. Angew. *Chem., Int. Ed. 43*, 4704−4734.
(28) Barbarella, G., Favaretto, L., Sotgiu, G., Antolini, L., Gigli, G., Cingolani, R., and Bongini, A. (2001) Rigid-Core Oligothiophene-S, S-dioxides with High Photoluminescence Efficiencies Both in Solution and in the Solid State. *Chem. Mater. 13*, 4112−4122.
(29) Kanemitsu, Y., Suzuki, K., Masumoto., Y., Tomiuchi, Y., Shiraishi, Y., and Kuroda, M. (1994) Optical properties of quasi-one-dimensional thiophene-based oligomers. *Phys. Rev. B 150*, 2301−2305.
(30) Brédas, J. L., Beljonne, D., Coropceanu, V., and Cornil, J. (2004) Charge-Transfer and Energy-Transfer Processes in ŏ-Conjugated Oligomers and Polymers: A Molecular Picture. *Chem. Rev. 104*, 4971−5003.
(31) Brédas, J. L., Cornil, J., Beljonne, D., Dos Santos, D. A., Shuai Z. (1999) Excited-State Electronic Structure of Conjugated Oligomers and Polymers: A Quantum-Chemical Approach to Optical Phenomena. *Acc. Chem. Res. 32*, 267−276.
(32) Christiansen, O., Koch, H., and Jørgensen, P. (1995) The second-order approximate coupled cluster singles and doubles model CC2. *Chem. Phys. Lett. 243*, 409−418.
(33) Hättig, C., and Weigend, F. (2000) CC2 excitation energy calculations on large molecules using the resolution of the identity approximation. *J. Chem. Phys. 113*, 5154−5161.
(34) Hättig, C. (2003) Geometry optimizations with the coupled-cluster model CC2 using the resolution-of-the-identity approximation. *J. Chem. Phys. 118*, 7751−7761.
(35) Hättig, C., and Kohn, A. (2002) Transition moments and excited-state first-order properties in the coupled-cluster model CC2 using the resolution-of-the-identity approximation. *J. Chem. Phys. 117*, 6939−6951.
(36) Lap, D. V., Grebner, D., and Rentsh, S. J. (1997) Femtosecond Time-Resolved Spectroscopic Studies on Thiophene Oligomers. *J. Phys. Chem. A 101*, 107−112.
(37) Thibault, G., and Bardos, P. (1995) Compared TCR and CD3 epsilon expression on alpha beta and gamma delta T cells. Evidence for the association of two TCR heterodimers with three CD3 epsilon chains in the TCR/CD3 complex. *J. Immunol. 154*, 3814−3820.
(38) Silver, J., and Ou, W. (2005) Photoactivation of Quantum Dot Fluorescence Following Endocytosis. *Nano Lett. 5*, 1445−1449.
(39) Bolognesi, A., Tazzari, P. L., Olivieri, F., Polito, L., Falini, B., and Stirpe, F. (1996) Induction of apoptosis by ribosome-inactivating proteins and related immunotoxins. *Int. J. Cancer 68*, 349−55.
(40) Stirpe, F. (2004) Ribosome-inactivating proteins. *Toxicon 44*, 371−83.
(41) Bolognesi, A., and Polito, L. (2004) Immunotoxins and other conjugates: pre-clinical studies. *Mini Rev. Med. Chem. 4*, 563−583.
(42) Kuno, M., Fromm, D. P., Hamann, H. F., Gallagher, A., and Nesbitt, D. J. (2000) Nonexponential "blinking" kinetics of single CdSe quantum dots: A universal power law behavior. *J. Chem. Phys. 112*, 3117−3120.
(43) Koberling, F., Mews, A., and Bascḧy, T. (2001) Oxygen-Induced Blinking of Single CdSe Nanocrystals. *Adv. Mater. 13*, 672−676.
(44) Tyagi, S., and Kramer, F. R. (1996) Molecular Beacons: Probes that Fluoresce upon Hybridization. *Nat. Biotechnol. 14*, 303−308.
(45) Marras, S. A., Kramer, F. R., and Tyagi, S. (2002) Efficiencies of fluorescence resonance energy transfer and contact-mediated quenching in oligonucleotide probes. *Nucleic Acids Res. 30*, e122.
(46) Wu, P., and Brand, L. (1994) Resonance Energy Transfer: Methods and Applications. *Anal. Biochem. 218*, 1−13.
(47) Pakhurst, K. M., and Parkhurst, L. J. (1995) Kinetic Studies by Fluorescence Resonance Energy Transfer Employing a Double-Labeled Oligonucleotide: Hybridization to the Oligonucleotide Complement and to Single-Stranded DNA. *Biochemistry 34*, 285−292.
(48) Gigli, G., Barbarella, G., Favaretto, L., Cacialli, F., and Cingolani, R. (1999) High-efficiency oligothiopene-based light-emitting diodes. *Appl. Phys. Lett. 75*, 439−441.
(49) Barbarella, G., Favaretto, L., Sotgiu, G., Zambianchi, M., Bongini, A., Arbizzani, C., Mastragostino, M., Anni, M., Gigli, G., and Cingolani, R. (2000) Tuning Solid-State Photoluminescence Frequencies and Efficiencies of Oligomers Containing One Central Thiophene-S, S-dioxide Unit. *J. Am. Chem. Soc. 122*, 11971−11978.
(50) Lanzani, G., Cerullo, C., De Silvestri, S., Barbarella, G., and Sotgiu, G. (2001) Influence of the environment on the excited-state deactivation in functionalized quinque-thienyls. *J. Chem. Phys. 115*, 1623−25.
(51) Rubio, M. Merchán, M., Pou-AméRigo, R., and Ortí, E. (2003) The Low-Lying Excited States of 2,2′-Bithiophene: A Theoretical Analysis. *ChemPhysChem 4*, 1308−1315.
(52) Tedesco, E., Della Sala, F., Favaretto, L., Barbarella, G., Albesa-Jové, D., Pisignano, D., Gigli, G., Cingolani, R., and Harris, K. D. M. (2003) Solid-State Supramolecular Organization, Established Directly from Powder Diffraction Data, and Photoluminescence Efficiency of Rigid-Core Oligothiophene-S,S-dioxides. *J. Am. Chem. Soc. 125*, 12277−12283.
(53) Ikemoto, N., Esteves, I., Nakanishi, K., and Berova, N. (1997) Fluorescent bithiophene chromophores: synthesis and application in CD exciton chirality studies. *Heterocycles 46*, 489−501.
(54) Davies, M. J., Shah, A., and Bruce, I. J. (2000) Synthesis of fluorescently labelled oligonucleotides and nucleic acids. *Chem. Soc. Rev. 29*, 97−107.
(55) Nilsson, K. P. R., Rydberg, J., Baltzer, L., and Inganäs, O. (2004) Twisting macromolecular chains: Self-assembly of a chiral supermolecule from nonchiral polythiophene polyanions and random-coil synthetic peptides. *Proc. Natl. Acad. Sci. U.S.A. 101*, 11197−11202.
(56) McQuade, D. T., Pullen, A. E., and Swager, T. M. (2000) Conjugated Polymer-Based Chemical Sensors. *Chem. Rev. 100*, 2537−2574
(57) Kilbinger, A. F. M., and Feast, W. J. (2000) Solution processable alternating oligothiophene-PEO-block-co-polymers: synthesis and evidence for solvent dependent aggregation. *J. Mater. Chem. 10*, 1777−1784.

BC050250A

Improved Biodistribution and Radioimmunoimaging with Poly(ethylene glycol)-DOTA-Conjugated Anti-CEA Diabody

Lin Li,[†] Paul J. Yazaki,[‡] Anne-Line Anderson,[‡] Desiree Crow,[‡] David Colcher,[‡] Anna M. Wu,[§] Lawrence E. Williams,[||] Jeffrey Y. C. Wong,[⊥] Andrew Raubitschek,[‡] and John E. Shively[†,*]

Division of Immunology, Beckman Research Institute of the City of Hope, Duarte, California 91010, Division of Cancer Immunotherapy and Tumor Immunology, City of Hope National Medical Center, Duarte, California 91010, Department of Molecular and Medical Pharmacology, Crump Institute for Molecular Imaging, University of California School of Medicine, Los Angeles, California 90095, Division of Diagnostic Radiology, City of Hope National Medical Center, Duarte, California 91010, and Division of Radiation Oncology, City of Hope National Medical Center, Duarte, California 91010

Received August 25, 2005; Revised Manuscript Received November 20, 2005

Diabodies are single chain antibody fragments (scFvs) that spontaneously form bivalent dimers of molecular size 50−55000. Radiolabeled diabodies are almost ideal tumor targeting agents due to their high avidity (bivalent) binding to tumor antigens and small size (50−55000) that leads to improved tumor-to-blood ratio compared to intact antibodies (150000). However, due to their high retention and metabolism in the kidney, radioiodine is the current radiolabel of choice for diabodies since radioiodine is rapidly excreted from the kidney once metabolized. We have previously shown that ^{111}In-DOTA-diabody gives higher tumor uptake in nude mouse xenografts than ^{125}I-diabody, but has extremely high kidney retention since its ^{111}In-labeled metabolites are retained by and only slowly excreted from the kidney. When a diabody is conjugated to a bifunctional PEG-3400 derivative followed by reaction with cysteinyl-DOTA, the resulting product has an apparent molecular size of 75000 and a Stokes radius of 35 Å on size exclusion chromatography, compared to a Stokes radius of 25 Å for intact diabody. When radiolabeled, the conjugate gives high yields of ^{111}In-labeled product, retains high immunoreactivity, and gives improved biodistributions (30−40%ID/g, 12−48 h) compared to ^{111}In-DOTA-diabody (12−13%ID/g, 6−12 h). We show that the improved biodistribution is due to an increase in Stokes radius caused by the linear PEG-3400 since conjugation of diabody with multiple $(PEG)_{12}$ linkers followed by reaction with cysteinyl-DOTA does not reduce kidney accumulation. We also show that ^{111}In-cysteinyl-DOTA-PEG3400-diabody gives excellent tumor images in the nude mouse xenograft model and that ^{125}I-PEG3400-diabody gives equivalent images to ^{125}I-minibody (molecular size, 80000), but improved tumor-to-liver ratios, suggesting that this imaging agent can be used to image liver metastases.

INTRODUCTION

To be effective tumor imaging agents, tumor-targeted radiolabeled antibodies must give both high tumor uptake and high tumor-to-blood ratios (*1*). At one extreme, monoclonal antibodies (150 kda) have a relatively slow blood clearance ($t_{1/2\ \beta}$ = 48−72 h), allowing ample time for high accumulation in the tumor, but suffer from low tumor-to-blood ratios. At the other extreme, single chain (sc) Fv recombinant antibodies (25 kDa) are rapidly cleared from the blood ($t_{1/2\ \beta}$ = 0.5−2.0 h) resulting in high tumor-to-blood ratios but low overall accumulation of radioactivity in the tumor. To predict optimal tumor imaging, one must account for both parameters using pharmacokinetic analytic indicators such as the Imaging Figure of Merit (IFOM). The IFOM indicator was derived by us by comparing the biodistributions (%ID/g over time) of a series of radioiodinated recombinant anti-CEA antibodies of molecular sizes 25000, 50000, 80000, and 150000 in a nude mouse xenograft model (*1*). From these studies we concluded that the best combination of high tumor uptake and high tumor-to-blood ratio requires at least a bivalent antibody of size 50−80000. However, a drawback to radioiodinated antibodies is that they may be rapidly metabolized in tissues, including the tumor, especially if the antigen undergoes internalization upon antibody binding. Although most anti-CEA antibodies undergo negligible internalization, we and others have observed higher tumor uptake and persistence at the tumor site for radiometal-labeled anti-CEA antibodies compared to radioioinated anti-CEA antibodies (*2*). For radiometal-labeled recombinant antibody fragments, this improvement is offset by high kidney retention, indicating that the radiometal-labeled antibody was filtered, reabsorbed, and metabolized by the kidney, but the radiometal metabolic products are retained or only slowly excreted compared to radioiodine metabolic products. Indeed, we have identified ^{111}In-DOTA-ϵ-lysine as the ultimate metabolic product in the kidney when anti-CEA antibody fragments are conjugated to the NHS-active ester of DOTA and radiolabeled with $^{111}InCl_3$ (*3*).

In light of these findings, we and others have sought to improve the utility of radiometal-labeled recombinant antibody fragments by decreasing kidney retention. In one approach kidney uptake is partially blocked by the administration of intravenous L- or D-lysine (*4*, *5*). In a second approach, we have designed unique metabolizable linkers between the antibody and DOTA that have decreased kidney retention by up to 4-fold

* To whom correspondence should be addressed. Tel: 626-359-8111 ext 62601, E-mail: jshively@coh.org.

[†] Division of Immunology, Beckman Research Institute of the City of Hope.

[‡] Division of Cancer Immunotherapy and Tumor Immunology, City of Hope National Medical Center.

[§] University of California School of Medicine.

[||] Division of Diagnostic Radiology, City of Hope National Medical Center.

[⊥] Division of Radiation Oncology, City of Hope National Medical Center.

10.1021/bc0502614 CCC: $33.50 © 2006 American Chemical Society
Published on Web 12/24/2005

over NHS-DOTA conjugates (*6*). A third approach is to increase the blood retention of antibody fragments by increasing their molecular weight through conjugation to poly(ethylene glycol) (PEG) polymers (*7*). This approach was successfully applied to recombinant cytokines such as IL-2 where the increase in the beta phase of blood clearance was greater than 8-fold (*8*). In the case of anti-CEA F(ab′) fragment A5B7 conjugated to MPEG6000, tumor retention increased by 5.7-fold and serum half-life by 5-fold (*9*). In the case of anti-mucin scFv CC49/218 conjugated to PEG-5000, a 14-fold increase in serum half was observed (*10*). In the latter study, the authors conclude that greater improvements were observed with increasing size of PEG polymers rather than total amount of PEG, which in addition, often led to decreased immunoreactivity of the conjugate. In this respect, recombinant antibodies have been designed to allow site-specific attached of PEG to prevent alterations in immunoreactivity (*11*). As yet, no biodistributions have been published on site-specific PEG- antibody conjugates.

In this study we selected a commercially available bifunctional PEG3400 for conjugation to an anti-CEA diabody that we have previously characterized (*2*). This linear polymer has an NHS-active ester at one end and vinyl sulfone at the other end. Reaction conditions were adjusted to conjugate approximately 1 PEG3400 per diabody molecule (at lysine residues), followed by reaction with cysteinyl-DOTA, a chelate with high metal complex stability that we have previously described (*12*). The resulting cys-DOTA-PEG3400-diabody conjugate had an apparent molecular size of 75000 and a Stokes radius of 35 Å, compared to an apparent molecular size of 50000 and a Stokes radius of 25 Å for intact diabody, demonstrating a net gain of 50% in its Stokes radius. The conjugate was radiolabeled with high efficiency (>90%) to high specific activity (2−4 μCi/ug) with $^{111}InCl_3$, retained high immunoreactivity (90%), and showed improved tumor uptake and blood retention compared to ^{111}In-DOTA-diabody. In addition, kidney retention was decreased by over 4-fold compared to ^{111}In-DOTA-diabody, and excellent tumor images were obtained. We also conjugated PEG3400 to a site-specific cys-diabody, a diabody with C-terminal cysteines (*13*) that were reduced and conjugated to DO3A-vinyl sulfone to chemically separate DOTA from PEG3400. This conjugate also gave high efficiency labeling to high specific activity and gave identical biodistributions compared to cys-DOTA-PEG3400-diabody. Since cys-DOTA-PEG3400-diabody has an apparent molecular size similar to a "minibody" construct (scFv-hinge-C_H3) made from the same parent antibody (*14*), we decided to compare the two radioiodine-labeled antibodies in the same animals. Within experimental error, the two constructs behaved identically and gave similar images. Since most scFv antibodies are easily expressed as diabodies in bacteria or yeast, while minibodies are best expressed in myeloma cells, we conclude that diabodies conjugated to this bifunctional PEG3400 offer a simple route to the rapid generation of useful imaging agents. A potential drawback is that, due to their small size, conjugation of PEG3400 to a diabody may reduce immunoreactivity.

EXPERIMENTAL PROCEDURES

Materials, Radiolabeling, Immunoreactivity, and Mass Spectrometry. NHS-PEG3400-VS (Cat No 4M5B0F02) was obtained from Nektar (San Carlos, CA). MAL-dPEG12-NHS ester (Cat No 10284) was obtained from Quanta Biodesign Ltd. (Powell, OH). The synthesis of cysteinyl-DOTA (cys-DOTA) and DO3A-VS were previously described (*12*, *15*). All other reagents were obtained from Aldrich-Sigma (St. Louis, MO). LS-174T cells were obtained from ATCC and maintained in maintained in sterile growth media consisted of Eagle's Minimal Essential Media 1X (EMEM) (Cellgro, Herndon, VA) supplemented with 10% heat inactivated fetal bovine serum (FBS) (Omega Scientific, Tarzana, CA), and 1% L-glutamine, 10 mM sodium pyruvate, 0.1 mM nonessential AA. The production and purification of anti-CEA T84.66 diabody, Cys-Diabody, and Minibody have been previously described (*13*, *16*). Chelate-conjugated antibodies were radiolabeled either with ^{111}In (Amersham, 2−3 mCi/mg of protein) as previously described (*17*) or with ^{125}I or ^{131}I by the iodogen method (*2*). Percent labeling was determined by ITLC or by size exclusion chromatography (SEC) on a Superose 6 column (1 × 30 cm, Amersham). Radiolabeled antibody was purified by SEC on the same column (in saline, flow rate 0.5 mL/min, fraction size was 0.5 mL). Immunoreactivity was determined by mixing the radiolabeled sample with a 20-fold excess by mass of CEA and running the sample over a Superose 6 column. Percent immunoreactivity was calculated as counts in CEA conjugate complex/ total counts × 100. MALDI-MS was performed on Perkin-Elmer-Sciex prOTOF 2000 using sinapinic acid (10 mg/mL in TFA/water/acetonitrile (0.1/99/100 v/v/v) as a matrix. Prior to mixing with matrix the sample was desalted on a Sephadex G25 spin column (100−200 mg in a 250 μL pipet tip), equilibrated in water.

Cys-DOTA-PEG3400-Diabody Conjugate. The reaction conditions for a molar ratio of 20:1 NHS-PEG3400-VS to diabody at pH 6.0 are given here. NHS-PEG3400-VS (3.0 mg, 0.8 μmol) was mixed with 2 mg (0.04 μmol) of diabody in 0.62 mL of pH 7.0 PBS, the pH was adjusted to 6.0 with 0.1 M NaOH, and allowed to react for 2 h at RT. In other reactions, the molar ratios and reaction pH were varied (see Results). When the reaction was monitored by SDS gels, it appeared to be >70% complete at the end of 2 h. At the end of 2 h the entire reaction mixture was applied to a Superdex 75 column (1 × 30 cm, Pharmacia), monitored at 214 and 280 nm, and eluted at a flow rate of 0.5 mL/min with PBS. The first peak that eluted at 18 min was the conjugate followed by unconjugated diabody at 22 min and free NHS-PEG3400-VS at 35−40 min (see Results). The conjugate (4 mL) was concentrated to 0.3 mL in a Amicon Ultra-4 (Millipore, Bedford, MA) and mixed with 1.0 mg (2 μmol) of cys-DOTA, the pH adjusted to 8.5, and reaction continued on a sample rotator for 17 h at RT. The product was dialyzed vs 3 × 1.5 L of PBS containing 1.5 g Chelex 100, followed by 2 × 1.5 L of 0.9% NaCl or 0.25 M ammonium acetate, pH 7.0. The dialysate was concentrated to 2−4 mg/L on a Centricon 10 and sterile filtered. The conjugate was characterized by both SDS and IEF gel electrophoresis (see Results).

Cys-DOTA-Mal-PEG$_{12}$-Diabody Conjugate. Diabody (0.5 mL of 4 mg/mL; 0.04 μmol)) in PBS was mixed with 0.93 mg (0.8 μmol) of NHS-PEG$_{12}$-maleimide, the pH was adjusted to 6.0 with 0.1 M NaOH, reacted for 2.5 h at RT, and the conjugate purified by SEC on a Superdex 75 column as above. The major peak (see Results) was collected and concentrated to 0.7 mL by centrifugation on an Amicon Ultra-4. The conjugate was mixed with 1 mg (1.0 μmol) of cys-DOTA, the pH adjusted to 8.3, and reaction continued overnight at RT. The product was characterized by SDS and IEF gel electrophoresis (see Results) and dialyzed vs PBS (1.5 L), saline (1.5 L) and then concentrated to 0.3 mL (3.6 mg/mL) on an Amicon Ultra-4.

DO3A-VS-cys-Diabody-PEG3400 Conjugate. Cys-diabody (2 mg, 0.04 μmol) in 0.38 mL of pH 7.5 PBS was reduced with 6 μL of freshly made 0.2 M TCEP (tris-carboxyethylphosphine, 0.12 μmol) for 2 h at 37 °C. The sample was run through a 1 mL spin column (Sephadex G25 in PBS) to remove excess TCEP and run on a nonreducing SDS gel to verify complete reduction from 50 kDa to 25 kDa. The reduced sample was mixed with 0.9 mg (2.0 μmol) of DO3A-VS and reacted at 25 °C for 2 h. Reaction with DO3A-VS was verified by running

an IEF gel where the conjugate was shifted to a lower pI (see Results). The conjugate was reacted with 3.0 mg (0.8 μmol) of NHS-PEG3400-VS at pH 6.0 for 2 h at RT and purified on a Superdex 75 column as described above. The final product (0.28 mL) was dialyzed into 0.25 M, pH 7.0 ammonium acetate and concentrated to 2.0 mg/mL.

Determination of Stokes Radius of Cys-DOTA-PEG3400-Diabody Conjugate. The elution volumes (V_e) of proteins of known Stokes radii were measured by SEC on a Superdex 75 column (1 × 30 cm, Pharmacia) in PBS with a flow rate of 0.5 mL/min. The standards were catalase (250000, 52 Å), alcohol dehydrogenase (150000, 46 Å), bovine serum albumin (65000, 35 Å), carbonic anhydrase (29000, 24 Å), myogobin (19000, 19 Å), and cytochrome *c* (17000, 12.4 Å). Stokes radii were plotted vs $K_d^{1/3}$ where $K_d = (V_e - V_o)/(V_t - V_g - V_o)$ (*18*). The void volume (V_o) was determined as 7.71 mL using Dextran Blue. The values for V_t (24 mL) and V_g (0.84 mL) were obtained from Pharmacia. The V_e for diabody was 11.0 mL, corresponding to a Stokes radius of 25 Å, and 9.8 mL for Cys-DOTA-PEG3400-diabody conjugate, corresponding to a Stokes radius of 35 Å.

LS-174T Xenograft Model. Female, athymic nu/nu mice (Charles River), 10−12 weeks old, were injected with LS-174T cells (5×10^6) sc in the flank. Tumors were established within 7−10 days postinjection. Athymic mice bearing LS-174T xenografts were tail vein injected with 200 μL of 4 μCi/2−3 μg ^{111}In-labeled DOTA-conjugates, 4 μCi/2 μg I-labeled minibody, or 4 μCi/1 μg of ^{125}I-labeled PEG3400 diabody. Five mice per time point were sacrificed at 0, 2, 4, 6, and 18 h postinjection and biodistributions performed (blood, liver, spleen, kidneys, lungs, tumor, and carcass). Results were calculated as percent injected dose per gram (%ID/g) vs time. For radioimaging, mice were injected with 40 μCi/20 μg ^{111}In-labeled DOTA conjugates or 20 μCi/5μg of ^{125}I PEG3400 diabody and imaged using a BIOSPACE γ Imager instrument with settings of 154−188 keV and 220−270 keV, respectively.

RESULTS

Optimization of Cys-DOTA-PEG3400-Diabody Conjugate. PEG-antibody conjugates have demonstrated the ability for improved blood retention over their unconjugated cognates but have the drawback of reducing immunoreactivity if over-conjugated (*10*). We searched for a commercially available PEG reagent of moderate size that could be both conjugated to diabody and to a chelate without over-derivatizing the diabody. We chose the bifunctional reagent NHS-PEG3400-VS because, in theory, it could first be conjugated to the ϵ-amino group of lysines in the diabody, followed by reaction with a chelate possessing a free thiol group (Scheme 1). Indeed, we had such a chelate (cysteinyl DOTA) in hand that previously had been shown to have high metal binding stability when conjugated via linkers to antibody (*12*). We were further interested in the use of vinyl sulfone as a functional group because its reaction toward thiols is rather pH specific (*15*) and the products are more stable than maleimide derivatives (*12*) which are also commercially available. The bifunctional reagent NHS-PEG3400-VS was first reacted with diabody over a range of conditions to determine the optimal reaction conditions to retain maximal immunoreactivity (Table 1). From these studies we determined that a NHS-PEG3400-VS to diabody ratio of 20:1 at pH 6.0 was a good compromise since >80% of the diabody reacted under these conditions (Figure 1) retaining 90% of its immunoreactivity (Table 1). At higher ratios (e.g., 50:1), more PEG3400 reacted with diabody resulting in lowered immunoreactivity (e.g., 40−54%, Table 1). In addition, we found that the reaction products of the first step must be purified by SEC and not by dialysis because NHS-PEG3400-VS remained in the dialysate (10 kDa cutoff) and interfered with the subsequent reaction with cys-DOTA. Although the diabody-PEG3400-VS conjugate could not be completely separated from unreacted diabody by SEC at this ratio (Figure 1A vs 1C), we were able to estimate the apparent molecular size of the conjugate as 75000 with a Stokes radius of 35 Å by SEC. In contrast, intact diabody has an apparent molecular weight of 50000 with a Stokes radius of 25 Å. Since SDS gel electrophoresis revealed that the PEG3400 conjugated diabody was >90% monosubstituted (Figure 1B and 1D), and the predicted molecular size of the monosubstituted product was only 28400 (diabody plus PEG3400), we conclude that the addition of the linear PEG polymer to the diabody led to a dramatic change in its Stokes radius as analyzed by SEC. The final product was also characterized by MALDI-MS. In this analysis intact diabody gave three peaks corresponding to monomer, dimer, and trimer species in the gas phase (Figure 1E). The PEG3400-modified monomer peak increased in mass from 25771 Da to 29944 Da, an increase in agreement with the addition of PEG3400 and Cys-DOTA (507 Da).

Table 1. Optimization of Reaction Conditions on the Formation of Diabody-PEG Conjugates[a]

conjugate	conj pH	conj ratio	labeling ratio	mCi/mg	% IR
Cys-DOTA-VS-PEG3400-DB	7	50:1	97	3	40
Cys-DOTA-VS-PEG3400-DB	6	50:1	96	3	54
Cys-DOTA-VS-PEG3400-DB	6	20:1	60−70	2−3	83−95
Cys-DOTA-VS-PEG3400-DB	6	10:1	70−94	3	88
Cys-DOTA-Mal-PEG_{12}-DB	6	20:1	95	2−3	85
DO3A-VS-cys-DB-PEG3400	6	20:1	95−98	2−8	90−97

[a] Reaction conditions include pH and molar ratio of PEG bifunctional reagent to diabody. The products were compared after further conjugation to cys-DOTA by labeling efficiency, labeling ratio (mCi/mg), and % immunoreactivity (IR).

Cys-DOTA-PEG3400-diabody (pH 6.0, 20:1 ratio) was radiolabeled with $^{111}InCl_3$ in good yield (60−90% efficiency, 2−3 mCi/mg labeling ratio, and immunoreactivity 83−95%, Table 1), suitable for biodistribution studies. Stability studies performed by radiolabeling the sample (stored at 4 °C) and remeasuring immunoreactivity and molecular size over a 3 month interval demonstrated no loss in activity or aggregation over this period (data not shown).

Biodistribution and Imaging of ^{111}In-Cys-DOTA-PEG3400-Diabody Conjugate in a Nude Mouse LS174T Xenograft Model. The cys-DOTA-PEG3400-diabody conjugate obtained from the pH 6.0, 20:1 ratio reaction was radiolabeled with $^{111}InCl_3$, purified by SEC, and injected into nude mice bearing LS174T (CEA positive) xenografts. The results of the biodistributions shown in Figure 2 demonstrate high tumor uptake, reaching a maximum of about 40% ID/g at 12 h that is sustained through 48 h. Over the same period blood levels drop to about 10% ID/g at 12 h, and to about 2% ID/g by 48 h. Thus, the tumor-to-blood ratios increase from 5:1 at 12 h to 25:1 at 48 h. The combination of high tumor uptake and high tumor-to-blood ratios gives exceptionally high IFOM values (see below). As expected, the uptake in kidney is high but, unlike unmodified ^{111}In-DOTA-diabody (*2*), is similar to tumor levels at all time points tested. Kidney reaches a maximum of about 50% ID/g at 24 h and remains high at 48 h. Thus, the tumor-to-kidney ratio at 24 h is about 0.8, a significant improvement over that seen for ^{111}In-labeled DOTA-diabody at 12 h (0.08, see ref 2). Importantly, low liver levels (<10% ID/g) are seen throughout the biodistribution, suggesting that this agent may be used to image liver metastases. Finally, we performed radioimmunoimaging on several of the mice that were injected with larger amounts of radiolabeled conjugate (Figure 3). Tumor is

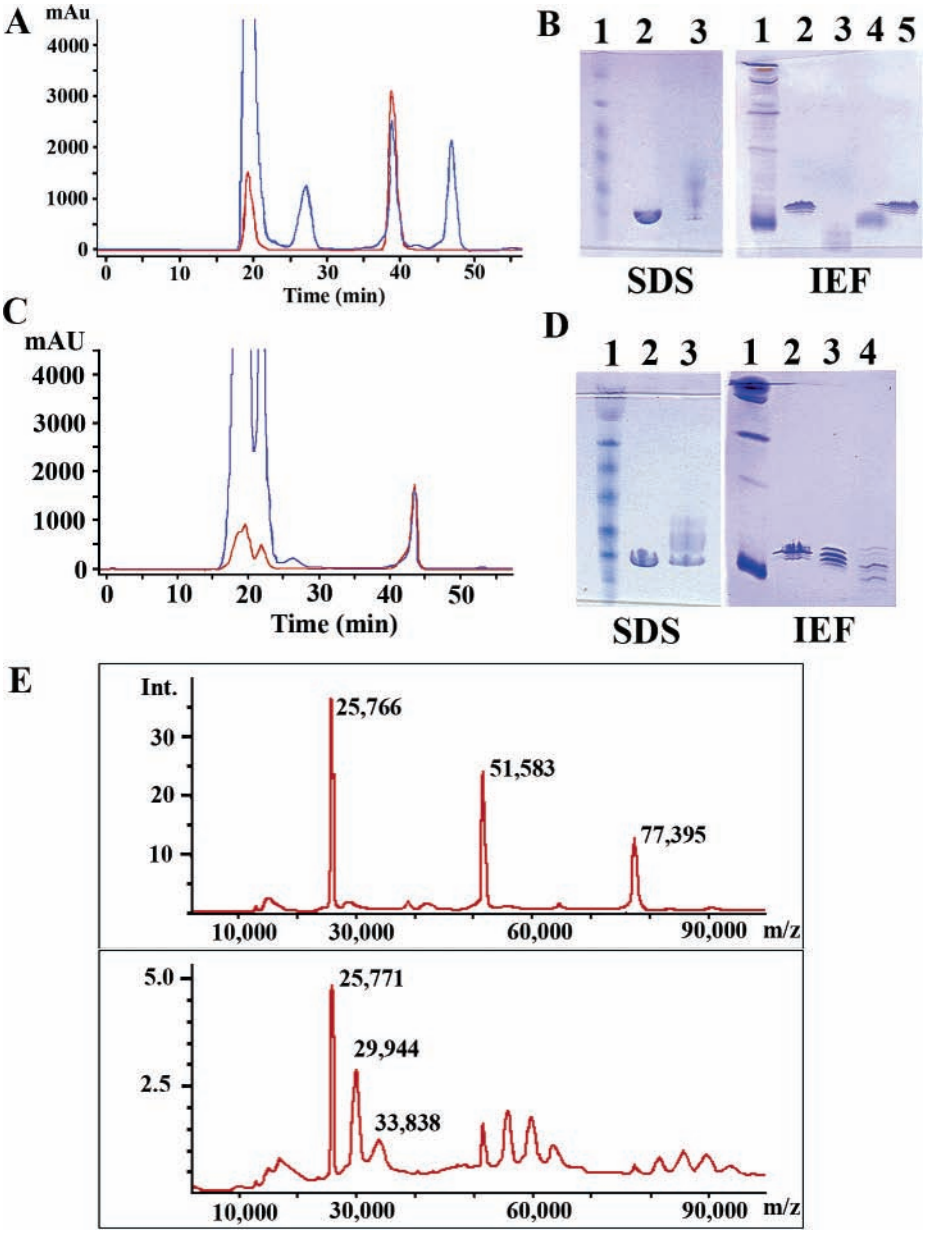

Figure 1. Characterization of cys-DOTA-PEG3400-diabody conjugates. A. SEC profile of PEG3400-diabody, for a conjugation ratio of PEG3400 to diabody of 50:1 at pH 6. Prior to reaction with cys-DOTA, the product was purified on Superdex 75 and monitored at 214 nm (blue) and 280 nm (red). B. Analysis of conjugation products by SDS and IEF gel electrophoresis. SDS: 1 = MW markers, 2 = diabody, 3 = PEG3400-diabody. IEF: 1 = IEF markers, 2 = diabody, 3 = cys-DOTA-PEG3400-diabody, 4= PEG3400-diabody, 5= diabody. C. SEC profile of PEG3400-DB, for ratio of PEG3400 to diabody of 20:1 at pH 6. Prior to reaction with cys-DOTA, the product was purified on Superdex 75 and monitored at 214 nm (blue) and 280 nm (red). D. Analysis of the conjugation products by SDS and IEF gel electrophoresis. SDS: 1 = MW markers, 2 = diabody, 3 = PEG3400-diabody. IEF: 1 = IEF markers, 2 = diabody, 3 = PEG3400-diabody, 4 = cys-DOTA-PEG3400-diabody conjugation. E. MALDI-TOF analysis of cys-DOTA-PEG3400-diabody. Upper: diabody control. Lower: cys-DOTA-PEG3400-diabody conjugated at the ratio of 20:1 (PEG3400 to diabody) at pH 6.

positively imaged as early as 2 h and is of similar intensity to kidneys over the period 12−48 h, in agreement with the biodistribution studies.

Comparison of ^{125}I-PEG3400-Diabody Conjugate with ^{131}I-Minibody in a Nude Mouse LS174T Xenograft Model. The high tumor uptake and apparent molecular size of 75000 of the PEG3400-diabody conjugate compares well with that of the scFv-hinge-C_H3 "minibody" construct engineered from the same parent T84.66 anti-CEA antibody (*2*). Thus, it was of interest to directly compare the two in the same mouse model and preferably in the same animals. Comparisons of this sort can be performed by labeling one antibody with ^{125}I and the other with ^{131}I. The results shown in Figure 4 indicate that the biodistributions are essentially identical, thus confirming the idea that the apparent molecular size of the antibody fragment dominates the biodistribution, as long as both have the same relative affinities and immunoreactivities. This experiment also demonstrates that radioiodine-labeled antibodies have low kidney and liver accumulations at all time points due to rapid removal of metabolized products in these organs. To a lesser extent, the same is true for the tumor where we observe about a 50% in reduction in tumor uptake at 12−48 h compared to the radiometal-labeled antibodies (Figure 3 and ref 2). In addition, animals were imaged with ^{125}I-PEG3400-diabody, demonstrating excellent tumor imaging results with no normal organ activity from 19 to 43 h (Figure 5).

Although we did not compare the two radiometal-labeled antibodies in the same animals, we have compared our previously published data for ^{111}In-DOTA minibody (*2*) to the results obtained in this study. At 12 h ^{111}In-DOTA minibody has an

Scheme 1. Schematic Model of Diabody (top left) Showing the Cross Pairing of V_L (green) and V_H (purple) Domains[a]

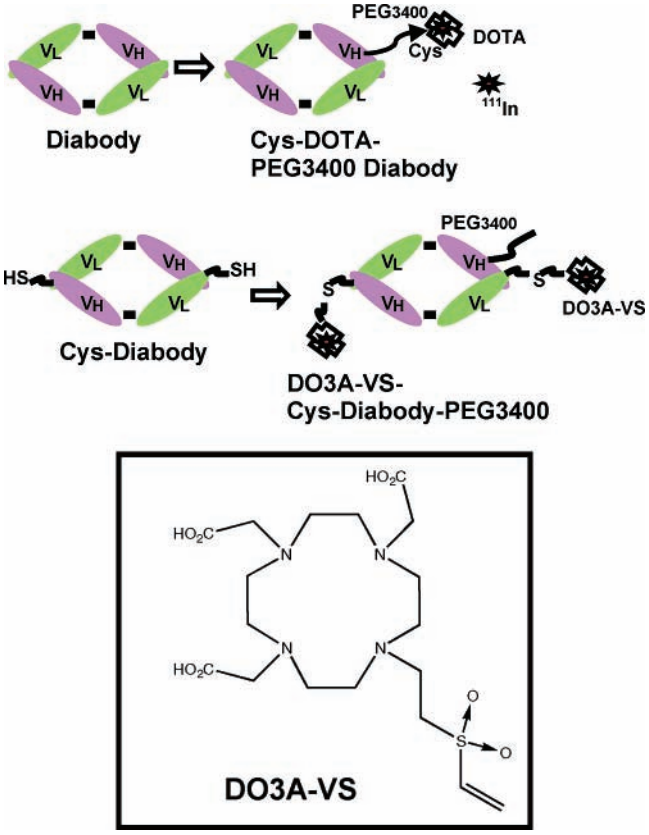

[a] NHS-PEG3400-VS is randomly conjugated to lysines on the surface of the diabody via the NHS active ester of NHS-PEG3400-VS, followed by reaction with Cys-DOTA via the vinyl sulfone (VS) moiety of NHS-PEG3400-VS (top right). The final conjugate is radiolabeled with ^{111}In (top right). In a control reaction, Cys-diabody (bottom left), that has C-terminal cysteine residues on V_H domains, is first reacted with DO3A-VS (inset) and then NHS−PEG3400 to physically separate the chelate from the PEG3400 (bottom right).

absolute uptake of 24(± 6) %ID/g in the tumor with a T/B ratio of 6.8, compared to the ^{111}In-cys-DOTA-PEG3400 diabody which had 49(±3) %ID/g in the tumor with a T/B ratio of 5.4. At 48 h ^{111}In-DOTA minibody gives 11(±1) %ID/g for tumor uptake and a T/B ratio of 66 compared to 50 (±30) %ID/g tumor uptake and a T/B ratio of 25 for ^{111}In-cysDOTA-PEG3400-diabody. On the basis of these comparisons alone, it is necessary to calculate IFOMs (a measure of both tumor-to-tissue ratio and absolute uptake over time) for both to determine which would be the better imaging agent in the mouse model. At 20−24 h the tumor to blood IFOMs are 25 for ^{111}In-cys-DOTA-PEG3400 diabody and 15 for ^{111}In-DOTA minibody (Figure 6). The results are even more impressive when comparing tumor to liver IFOMs where ^{111}In-cys-DOTA-PEG3400 diabody performs as well as the tumor to blood IFOM for minibody. The tumor to liver IFOM for ^{111}In-DOTA minibody (not shown) is similar to the tumor to kidney IFOM for ^{111}In-cys-DOTA-PEG3400 diabody (Figure 6), predicting that tumors cannot be positively imaged with ^{111}In-DOTA minibody in these organs. On the basis of these considerations, both imaging agents have certain drawbacks. On one hand ^{111}In-DOTA minibody has high liver uptake (19%ID/g at 12 h) compared to ^{111}In-cys-DOTA-PEG3400-diabody (9%ID/g at 12 h). On the other hand ^{111}In-cysDOTA-PEG3400-diabody has high kidney uptake (50%ID/g at 12 h) compared to ^{111}In-DOTA minibody (12%ID/g at 12 h). The final choice of imaging agent must take into account the potential interference of uptake in either the kidney or the liver, thus offering one the choice of agents.

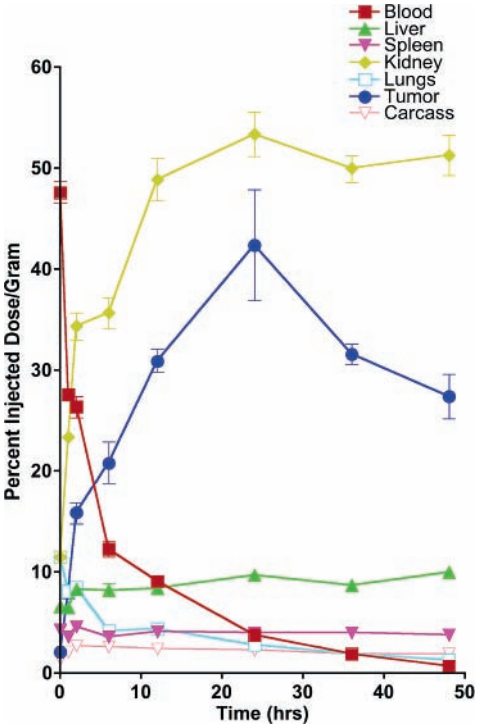

Figure 2. Biodistribution of ^{111}In-cys-DOTA-PEG3400-diabody in nude mice bearing LS174T xenografts. The average %ID/g (± std dev) of five animals per tissue analyzed is shown.

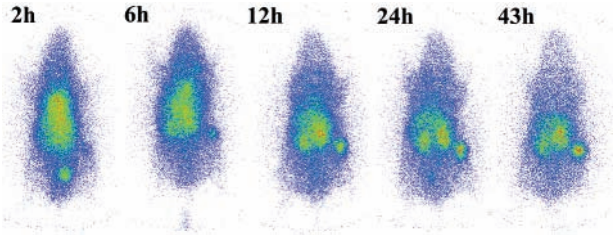

Figure 3. Radioimmunoimaging of ^{111}In-cys-DOTA-PEG3400-diabody in nude mice bearing LS174T xenografts. The time points are shown. The tumor is on the right flank. At 2 h. the large central mass is blood pool, liver, and kidneys: bladder is also imaged. By 12 h, the central mass is mostly kidneys and tumor is seen on the right side.

Control Experiments. Since the concept of attaching a chelate to an engineered antibody fragment via a bifunctional PEG linker is novel, we felt obligated to run several controls. First, we injected ^{111}In-cys-DOTA-PEG3400 into tumor bearing animals to demonstrate that tumor uptake was not due to cleavage of the linker from the diabody in some organ and redistribution into the tumor. As can be seen in Figure 7, ^{111}In-cysDOTA-PEG3400 is rapidly cleared from the blood with little or no accumulation in tumor or other organs counted. Next we considered the possibility that the conjugation of multiple PEGs of smaller size, rather than the conjugation of one larger sized PEG would lead to equivalent results. To explore this possibility, we conjugated commercially available NHS-PEG_{12}-Mal to diabody (Table 1). While this bifunctional linker has a maleimide rather than a vinyl sulfone moiety, it is otherwise homologous to NHS-PEG3400-VS in terms of chemical reactivity, but has a molecular weight of only 865 Da. The cys-DOTA conjugated product gave high efficiency labeling, high specific activity, and good immunoreactivity (Table 1). When the product was analyzed by SDS gel electrophoresis, the apparent size was only slightly largely than the monomeric size of diabody (25−27 kDa), a result in agreement with the predicted mass of the addition of several PEG_{12} adducts. However, when run on a Superdex 75 column, the apparent molecular size (Figure 8)

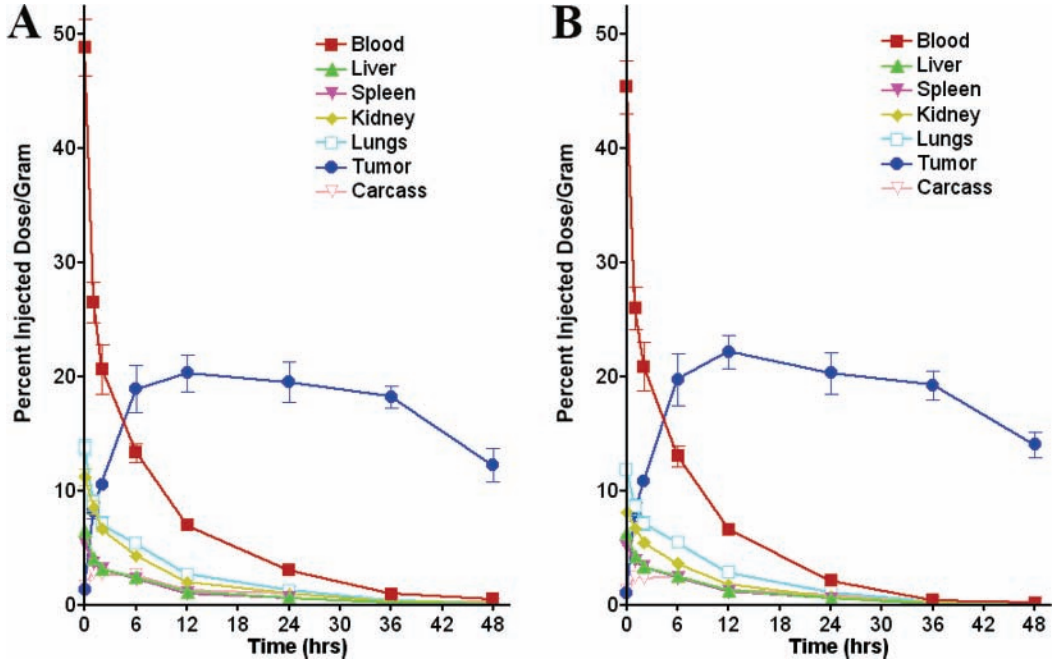

Figure 4. Biodistribution of ^{125}I-PEG3400-diabody and ^{131}I-minbody in nude mice bearing LS174T xenografts. The average %ID/g (± std dev) of five animals per tissue analyzed is shown. A: ^{125}I-labeled PEG3400 diabody. B: ^{131}I-labeled minibody.

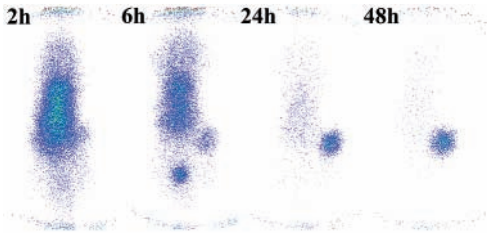

Figure 5. Radioimmunoimaging of ^{125}I-PEG3400-diabody in nude mice bearing LS174T xenografts. The time points shown. The tumor is on the right flank. At 2 h the large central mass is blood pool. By 6 h, tumor is visible on the right side, as well as bladder at the bottom of the image. By 48 h, only tumor is imaged.

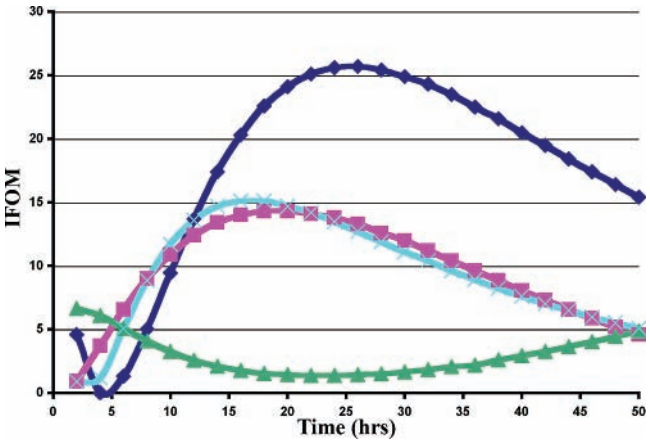

Figure 6. IFOM values for ^{111}In-DOTA minibody vs ^{111}In-cys-DOTA-PEG3400-diabody. IFOM (imaging figure of merit) values were calculated according to Williams et al. (*1*) and plotted vs time for both ^{111}In-DOTA minibody vs ^{111}In-cys-DOTA-PEG3400-diabody. The values take into account both absolute uptake in %ID/g and the tumor-to-tissue ratio vs time. Dark blue (diamonds)= cys-DOTA-PEG3400-diabody tumor/blood. Magenta (squares) = cys-DOTA-PEG3400-diabody tumor/liver. Light blue (X) = minibody tumor/blood. Green (triangles)= cys-DOTA-PEG3400-diabody tumor/kidney. Data for ^{111}-In-DOTA minibody was taken from Yazaki et al. (*2*).

was similar to that of cysDOTA-PEG3400-diabody (Figure 1), suggesting the presence of noncovalent trimers or tetramers. When the ^{111}In-labeled product was injected into nontumor bearing nude mice it showed high kidney uptake (ca. 50%D/g) and rapid blood clearance ($t_{1/2}$ of 7 h) (Figure 9), suggesting that its biodistribution was intermediate between that of ^{111}In-DOTA-diabody and ^{111}In-cysDOTA-PEG3400-diabody.

Finally, we separated the chelate from the bifunctional PEG linker by first conjugating the bifunctional chelate DO3A-VS to reduced site-specific cys-diabody which has C-terminal cysteine residues and then reaction with NHS-PEG3400-VS (Scheme 1) When run on Superdex 75, the apparent size of the conjugate is similar to cys-DOTA-PEG3400-diabody (Figure 10). When radiolabeled with $^{111}InCl_3$, the % labeling, specific activity, and immunoreactivity were uniformly high (Table 1). When ^{111}In-DO3A-VS-cys-diabody-PEG3400 was injected into tumor bearing animals the biodistributions (Figure 11) were essentially identical to those seen for ^{111}In-Cys-DOTA-PEG3400-diabody (Figure 2).

DISCUSSION

Although much progress has been made in designing radiolabeled antibodies for tumor targeting, many challenges still exist. In this study, we explored the use of a bifunctional PEG reagent for fine-tuning the biodistributions of an ^{111}In-labeled anti-CEA diabody. We chose the diabody construct because it is the smallest bivalent (high affinity) recombinant antibody that can be produced in multigram quantities in the lab (*16*). However, its molecular size (50 kDa) lies just below the kidney filtration threshold, creating a problem of high kidney retention due to the reabsorption process in the kidney glomeruli. While this problem is not observed for radioiodine-labeled diabody due to metabolism of the radiolabel within the glomeruli, it is a major problem for the nonmetabolizable radiometal-chelate conjugated antibodies. As a first approach to solving this problem, we conjugated our anti-CEA diabody to NHS-PEG3400-vinyl sulfone, purified the product, and then conjugated it to cys-DOTA, a macrocyclic chelate that we had previously shown to bind radiometals ($^{111}InCl_3$ and $^{90}YCl_3$) with the same relative strength as to unconjugated DOTA. In the first step, the NHS active ester of the bifunctional PEG was reacted with surface lysines on the diabody at pH 6 while preserving the vinyl sulfone moiety. In the second step, the pH

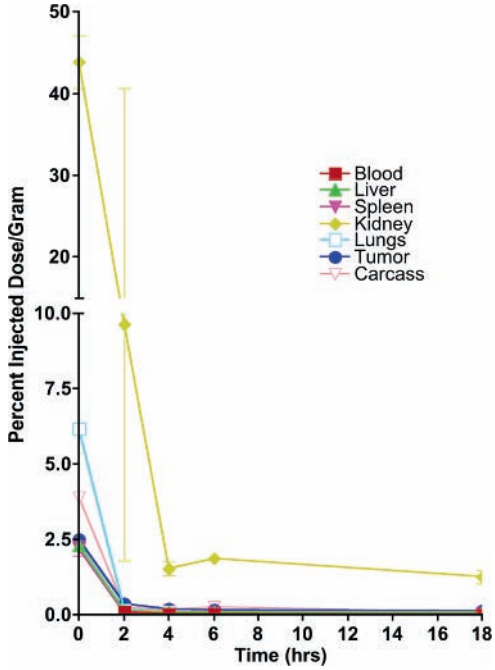

Figure 7. Biodistribution of ^{111}In-cys-DOTA-PEG3400 in nude mice bearing LS174T xenografts. The average %ID/g (± std dev) of five animals per tissue analyzed is shown. The large standard deviation for kidney at 2 h is due to a single animal, otherwise all standard deviations are within 10%.

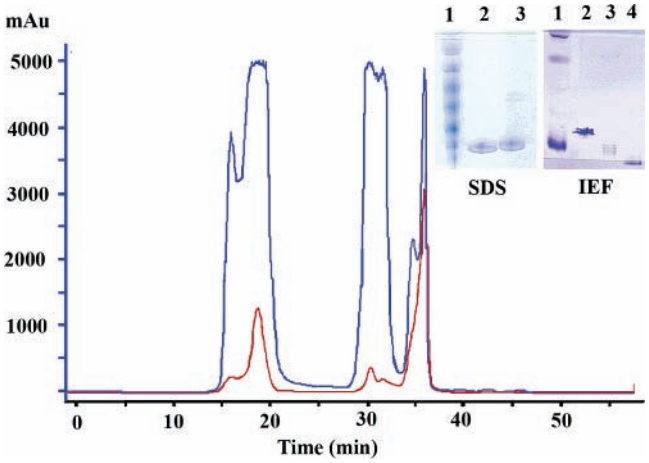

Figure 8. Characterization of cys-DOTA-Mal-PEG$_{12}$-diabody. SEC profile of Mal-PEG$_{12}$-diabody conjugate for a conjugation ratio of Mal-PEG$_{12}$ to diabody of 20: 1 at pH 6. Prior to reaction with cys-DOTA, the product was purified on Superdex 75 and monitored at 214 nm (blue) and 280 nm (red). The inset shows the conjugates run on SDS and IEF gels. SDS: 1 = MW markers, 2 = diabody, 3 = Mal-PEG$_{12}$-diabody. IEF: 1 = IEF markers, 2 = diabody, 3 = Mal-PEG$_{12}$-diabody, 4 = cys-DOTA-Mal-PEG$_{12}$-diabody.

was raised and the vinyl sulfone moiety of the bifunctional PEG was reacted with the thiol group on cys-DOTA. Thus, we were able to place the DOTA moiety at the end of a very long linker, namely PEG3400, perhaps allowing ^{111}In to react preferentially with DOTA rather than the diabody protein surface. We were able to demonstrate that the final product retained high immunoreactivity, but only if the conjugation ratio of bifunctional PEG to diabody was strictly controlled. Although we can routinely conjugate 3−4 DOTA moieties to the lysines of this diabody without affecting immunoreactivity (*2*), it appears that attachment of more than one PEG3400 to the diabody adversely affects its immunoreactivity. Since this problem has been observed by others (*7*, *9*−*11*), it appears that it is a general feature of conjugating high molecular weight, linear PEGs to

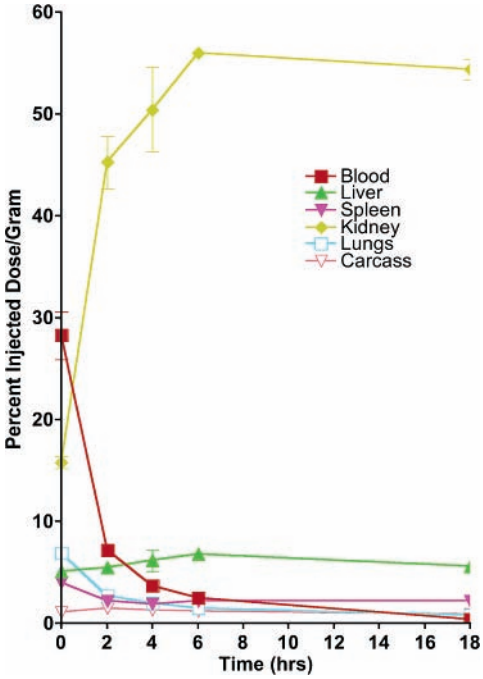

Figure 9. Biodistribution of ^{111}In-cys-DOTA-Mal-PEG$_{12}$-diabody in nontumor bearing nude mice. The average %ID/g (± std dev) of five animals per tissue analyzed is shown.

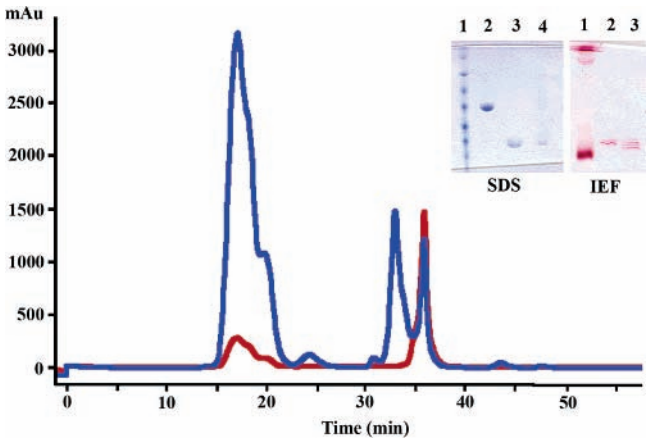

Figure 10. Characterization of DO3A-VS-cys-Diabody-PEG3400. SEC profile of DO3A-VS-cys-Diabody-PEG3400. Cys-diabody was reduced with TCEP, desalted on a Spehadex G25 spin column, and reacted with DO3A-VS at a ratio of 50:1 (DO3A-VS to cys-diabody). The intermediate conjugate was analyzed by SDS and IEF gel electrophoresis and then reacted with NHS-PEG3400-VS at a ration of 20:1 (PEG to diabody ratio) at pH 6 for 2h. The final conjugate was purified by SEC on Superdex 75 to remove excess PEG3400 (monitored at 214 nm (blue) and 280 nm (red)). The inset shows the conjugates analyzed by SDS (nonreducing) and IEF gel electrophoresis. SDS: 1 = MW markers, 2 = cys-diabody, 3 = TCEP reduced cys-diabody, 4 = DO3A-VS-cys-diabody-PEG3400. IEF: 1 = IEF markers, 2 = TCEP reduced cys-diabody, 3 = DO3A-VS-cys-diabody.

antibody fragments. As expected the product had an increased molecular size (75000) due to an increase in its Stokes radius (35 Å) compared to intact diabody (25 Å). Thus, this approach can be successfully used to fine-tune the apparent molecular size of a recombinant antibody fragment.

The final conjugate, cys-DOTA-PEG3400-diabody was radiolabeled with $^{111}InCl_3$ with high efficiency (>90% labeling) to suitably high specific activities (2−3 mCi/mg) for both biodistribution and radioimmunoimaging studies in nude mice bearing CEA-positive xenografts. Although the radiolabeled conjugate contains up to 20% unconjugated diabody, the presence of unconjugated diabody was not expected to adversely

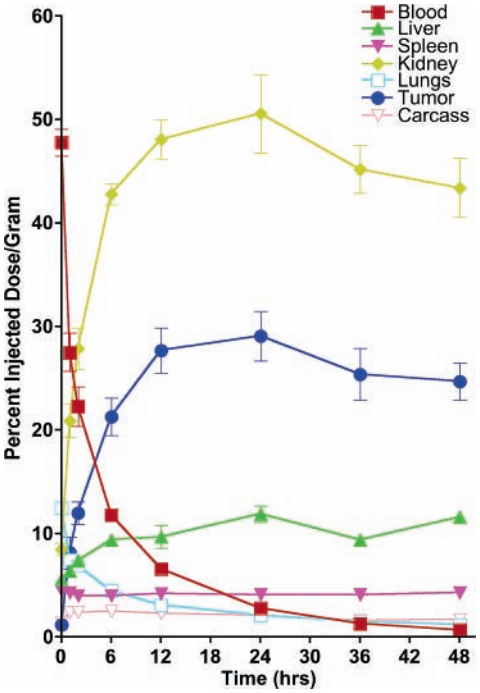

Figure 11. Biodistribution of ^{111}In-DO3A-VS-cys-diabody-PEG3400 in nude mice bearing LS174T xenografts. The average %ID/g (± std dev) of five animals per tissue analyzed is shown.

affect tumor targeting because nonsaturating amounts of total diabody were injected into animals and intact diabody was expected to clear more rapidly from the blood than conjugated diabody. The results were very encouraging in that tumor accumulation was higher than that seen for ^{111}In-DOTA-diabody and essentially equivalent to that seen for ^{111}In-DOTA minibody which has a molecular mass of 80 kDa. Since the molecular masses of the minibody and PEG3400-diabody are almost equivalent, we decided to compare their biodistributions side by side in the same animals. In this comparison, one was radiolabeled with ^{125}I and the other with ^{131}I to take advantage of discriminatory counting and the wealth of data (including IFOM analysis) we have on our radioiodine-labeled recombinant antibody fragments. As expected, the biodistributions were essentially equivalent. However, the question remained as to whether the radiometal-labeled conjugates were equivalent. This was an important question since ^{111}In-DOTA minibody has a problem with high liver uptake and ^{111}In-cys-DOTA-PEG3400-diabody has a problem with high kidney uptake. When the IFOM analysis was performed on the two, the ^{111}In-cys-DOTA-PEG3400-diabody was clearly superior to ^{111}In-DOTA minibody, in fact, the tumor to liver IFOMs of ^{111}In-cys-DOTA-PEG3400-diabody at 24 h were equivalent to the tumor to blood IFOMs of ^{111}In-DOTA minibody at 24 h. Since our experience with imaging tumors in patients with ^{111}In-DOTA minibody have been excellent (unpublished data), based on these IFOM calculations, we expect that ^{111}In-cys-DOTA-PEG3400-diabody will be superior to ^{111}In-DOTA minibody in areas both outside and inside the liver. Since a nude mouse, liver metastasis model is available for CEA positive LS174T cells (*19*), we are currently testing this hypothesis. If these predictions are verified in the clinic, then ^{111}In-cys-DOTA-PEG3400-diabody will be a decided improvement as a radioimmunoimaging agent over all the agents we have tested so far and may permit us to positively image liver metastases with a radiometal-labeled imaging agent for the first time. The remaining problem with the high kidney uptake should not be an issue with imaging CEA positive colorectal or breast cancer patients where kidney metastases are rarely observed. Since the kidney uptake is roughly equivalent to tumor uptake, the problem is somewhat lessened compared to the use of ^{111}In-DOTA diabody where kidney uptake is roughly 10-fold higher than tumor uptake at 12 h (*2*). Nonetheless, we are committed to further reducing the kidney uptake by combining other approaches such as the use of metabolizable linkers (*6*) and adminstration of intravenous lysine (*20*). If successful, we may have a fully optimized approach to radioimmunoimaging with radiometal-labeled antibody fragments.

ACKNOWLEDGMENT

This research was supported by NCI grant CA43904.

LITERATURE CITED

(1) Williams, L. E., Wu, A. M., Yazaki, P. J., Liu, A., Raubitschek, A. A., Shively, J. E., and Wong, J. Y. (2001). Numerical selection of optimal tumor imaging agents with application to engineered antibodies. *Cancer Biother. Radiopharm. 16*, 25−35.

(2) Yazaki, P. J., Wu, A. M., Tsai, S. W., Williams, L. E., Ikler, D. N., Wong, J. Y., Shively, J. E., and Raubitschek, A. A. (2001). Tumor targeting of radiometal-labeled anti-CEA recombinant T84.66 diabody and t84.66 minibody: comparison to radioiodinated fragments. *Bioconjugate Chem. 12*, 220−228.

(3) Tsai, S. W., Li, L., Williams, L. E., Anderson, A.-L., Raubitschek, A. A., and Shively, J. E. (2001). Metabolism and renal clearance of 111In-labeled DOTA conjugated antibody fragments. *Bioconjugate Chem. 12*, 264−270.

(4) Olafsen, T., Kenanova, V. E., Sundaresan, G., Anderson, A. L., Crow, D., Yazaki, P. J., Li, L., Press, M. F., Gambhir, S. S., Williams, L. E., Wong, J. Y., Raubitschek, A. A., Shively, J. E., and Wu, A. M. (2005). Optimizing radiolabeled engineered anti-p185HER2 antibody fragments for in vivo imaging. *Cancer Res. 65*, 5907−5916.

(5) Behr, T. M., Goldenberg, D. M., and Becker, W. (1998). Reducing the renal uptake of radiolabeled antibody fragments and peptides for diagnosis and therapy: present status, future prospects and limitations. *Eur. J. Nucl. Med. 25*, 201−212.

(6) Li, L., Olafsen, T., Anderson, A. L., Wu, A., Raubitschek, A. A., and Shively, J. E. (2002). Reduction of kidney uptake in radiometal-labeled peptide linkers conjugated to recombinant antibody fragments. Site-specific conjugation of DOTA-peptides to a Cys-diabody. *Bioconjugate Chem. 13*, 985−995.

(7) Yang, K., Basu, A., Wang, M., Chintala, R., Hsieh, M. C., Liu, S., Hua, J., Zhang, Z., Zhou, J., Li, M., Phyu, H., Petti, G., Mendez, M., Janjua, H., Peng, P., Longley, C., Borowski, V., Mehlig, M., and Filpula, D. (2003). Tailoring structure−function and pharmacokinetic properties of single-chain Fv proteins by site-specific PEGylation. *Protein Eng. 16*, 761−770.

(8) Bailon, P., Palleroni, A., Schaffer, C. A., Spence, C. L., Fung, W. J., Porter, J. E., Ehrlich, G. K., Pan, W., Xu, Z. X., Modi, M. W., Farid, A., Berthold, W., and Graves, M. (2001). Rational design of a potent, long-lasting form of interferon: a 40 kDa branched poly(ethylene glycol)-conjugated interferon alpha-2a for the treatment of hepatitis C. *Bioconjugate Chem. 12*, 195−202.

(9) Delgado, C., Pedley, R. B., Herraez, A., Boden, R., Boden, J. A., Keep, P. A., Chester, K. A., Fisher, D., Begent, R. H., and Francis, G. E. (1996). Enhanced tumour specificity of an anti-carcinoembrionic antigen Fab′ fragment by poly(ethylene glycol) (PEG) modification. *Br. J. Cancer 73*, 175−182.

(10) Lee, L. S., Conover, C., Shi, C., Whitlow, M., and Filpula, D. (1999). Prolonged circulating lives of single-chain Fv proteins conjugated with poly(ethylene glycol): a comparison of conjugation chemistries and compounds. *Bioconjugate Chem. 10*, 973−981.

(11) Natarajan, A., Xiong, C. Y., Albrecht, H., DeNardo, G. L., and DeNardo, S. J. (2005). Characterization of site-specific ScFv PEGylation for tumor-targeting pharmaceuticals. *Bioconjugate Chem. 16*, 113−121.

(12) Lewis, M. R., and Shively, J. E. (1998). Maleimidocysteineamido-DOTA derivatives: new reagents for radiometal chelate conjugation to antibody sulfhydryl groups undergo pH-dependent cleavage reactions. *Bioconjugate Chem. 9*, 72−86.

(13) Olafsen, T., Cheung, C. W., Yazaki, P. J., Li, L., Sundaresan, G., Gambhir, S. S., Sherman, M. A., Williams, L. E., Shively, J. E., Raubitschek, A. A., and Wu, A. M. (2004). Covalent disulfide-linked anti-CEA diabody allows site-specific conjugation and radiolabeling for tumor targeting applications. *Protein Eng. Des. Sel. 17*, 21−27.

(14) Hu, S., Shively, L., Raubitschek, A., Sherman, M., Williams, L. E., Wong, J. Y., Shively, J. E., and Wu, A. M. (1996). Minibody: A novel engineered anti-carcinoembryonic antigen antibody fragment (single-chain Fv-CH3) which exhibits rapid, high-level targeting of xenografts. *Cancer Res. 56*, 3055−3061.

(15) Li, L., Tsai, S. W., Anderson, A. L., Keire, D. A., Raubitschek, A. A., and Shively, J. E. (2002). Vinyl sulfone bifunctional derivatives of DOTA allow sulfhydryl- or amino-directed coupling to antibodies. Conjugates retain immunoreactivity and have similar biodistributions. *Bioconjugate Chem. 13*, 110−115.

(16) Yazaki, P. J., Shively, L., Clark, C., Cheung, C. W., Le, W., Szpikowska, B., Shively, J. E., Raubitschek, A. A., and Wu, A. M. (2001). Mammalian expression and hollow fiber bioreactor production of recombinant anti-CEA diabody and minibody for clinical applications. *J. Immunol. Methods 253*, 195−208.

(17) Lewis, M. R., Raubitschek, A. A., and Shively, J. E. (1994). A facile, water-soluble method for modification of proteins with DOTA. Use of elevated temperature and optimized pH to achieve high specific activity and high chelate stability in radiolabeled immunoconjugates. *Bioconjugate Chem. 5*, 565−576.

(18) Siegel, L. M., and Monty, K. J. (1966). Determination of molecular weights and frictional ratios of proteins in impure systems by use of gel filtration and density gradient centrifugation. Application to crude preparations of sulfite and hydroxylamine reductases. *Biochim. Biophys. Acta 112*, 346−362.

(19) Giavazzi, R., Jessup, J. M., Campbell, D. E., Walker, S. M., and Fidler, I. J. (1986). Experimental nude mouse model of human colorectal cancer liver metastases. *J. Natl. Cancer Inst. 77*, 1303−1308.

(20) Behr, T. M., Becker, W. S., Sharkey, R. M., Juweid, M. E., Dunn, R. M., Bair, H. J., Wolf, F. G., and Goldenberg, D. M. (1996). Reduction of renal uptake of monoclonal antibody fragments by amino acid infusion. *J. Nucl. Med. 37*, 829−833.

BC0502614

Tunable DNA Release from Cross-Linked Ultrathin DNA/PLL Multilayered Films

Kefeng Ren, Jian Ji,* and Jiacong Shen

Department of Polymer Science and Engineering, Zhejiang University, Hangzhou 310027, China. Received August 28, 2005; Revised Manuscript Received November 6, 2005

A novel ultrathin enzymatically degradable multilayered film using DNA as building blocks was fabricated by the layer-by-layer (LbL) technique. The UV−vis spectrometry and AFM experiments showed that the buildup of DNA and poly-L-lysine (PLL) was a kind of "exponentially growing films". The dye adsorption experiment suggested that the DNA molecules in the multilayered films were effectively protected by PLL. The films were further cross-linked by glutaraldehyde (GA). The cross-linking density of the films was modulated through the simple controlling of the time of the GA incubation process. An *in vitro* enzymatic degradation was carried out to investigate the DNA release profiles. The UV−vis spectrometry and fluorescence measurements indicated that the DNA release profiles were accordingly changed with the cross-linking density of the films. The nanoscale, easily processed enzymatically biodegradable PLL/DNA film with the ability to precisely control DNA release profiles may serve as a novel DNA delivery system, which may have great potential for gene therapy applications in implantable materials and biomedical devices.

INTRODUCTION

Gene therapy, which can be defined as a method to efficiently transfer the genetic material into the somatic cells of individual patients to produce specific therapeutic proteins to prevent, diagnose, correct, or modulate disease has been increasingly clinically applied in the field of severe diseases such as cancer (*1*, *2*). Safe and effective gene delivery is the main objective in gene therapy. Therefore, driven by the development of new methods to provide precisely controlled gene delivery, numerous strategies are developed and have become a major concern over the past few decades. Naked DNA was first used and directly transferred into the mouse muscle (*3*). Then, controlled delivery of DNA from hydrogel (*4*, *5*), tissue engineering scaffolds (*6*), and nanoparticles (*7*, *8*) have been developed. These gene delivery systems can localize and sustain the presence of a therapeutic gene at targeted cells relative to traditional delivery methods such as injection. Recently, a growing interest has been focused on the sustained release or delivery of DNA from ultrathin films or coatings. For example, Levy et al. have demonstrated the controlled release of DNA from a thin polymer coating, and it could be useful as delivery systems for candidate vectors for gene therapy of cardiovascular diseases (*9*). They also investigated a gene delivery system through the surface attachment of replication-defective adenoviruses using an anti-adenovirus antibody tethering mechanism for local gene therapy of heart-valve disease and vascular disorders (*10*). Lynn et al. recently reported an ultrathin film constructed by hydrolytically degradable polymer and DNA. Such film sustained the release of DNA and localized delivery DNA to cells (*11*, *12*).

Polyelectrolyte multilayered films, which are formed by layer-by-layer (LbL) deposition of polyanions and polycations from aqueous solutions, have raised considerable interest (*13*, *14*). This technique allows nanoscale control over the deposition of a large variety of functionalized materials including proteins (*15*, *16*), DNA (*17*−*19*), dyes (*20*), and nanoparticles (*21*, *22*) into several 10−100 nm films. A variety of architectures and properties of films such as thickness, roughness, molecular structure, surface wettability, and surface charge can be precisely engineered (*13*, *14*, *23*). Consequently, the versatility of the LbL technique presents biotechnical applications such as the construction of cytophilic/cytophobic films (*24*) and procoagulation/anticoagulation films (*25*).

Recently, we have constructed DNA multilayered films through LbL deposition of DNA and poly-L-lysine (PLL) (*26*, *27*). The PLL/DNA ultrathin films have demonstrated to be sensitive to the enzyme and degraded under 5 units/mL α-chymotrypsin in phosphate-buffered saline (PBS) at 37 °C. It is known that, during some biological events such as tumor angiogenesis and metastasis, wound healing, and coronary artery restenosis, a number of enzymes will be secreted or locally activated to degrade and remodel extracelluar matrix or targeted proteins (*28*−*30*). With the feature of sensitizing to enzymatic activities, the PLL/DNA film may be very useful as a DNA delivery system for gene therapy in those diseases. Furthermore, taking the advantages of the LbL technique, the PLL/DNA ultrathin film can be deposited onto any kind and shape of material surface such as implantable materials and biomedical devices including vascular stents, intervention catheters, and tissue engineering scaffold (*31*, *32*). The films thickness, namely, the amount of DNA, can be controlled with a nanoscale by simply adjusting the number of PLL/DNA bilayers.

The objective of the present study is to assess the possibility of protecting the DNA structure via the multilayered polyelectrolyte complexes and controlled release of DNA through cross-linking of the PLL/DNA film. PLL is one of the first research polycations served as a gene carrier (*33*). It can interact with DNA to form complexes in aqueous solution. The complexes can effectively reduce the degradation of DNA by DNase, resulting in a more efficient gene expression *in vivo*. It is found that, during the LbL deposition of PLL and DNA, the PLL/DNA complexes will also form, and such complexes could serve as a mechanism to protect the DNA from DNase attack. It is known that the aim from the gene delivery system varies according to the application. For example, the disease of gene dysfunction like hypercholesterolemia needs a prolonged and sustained gene expression, while in the case of most cancer gene therapy strategies, a short period of gene expression is sufficient

* To whom correspondence should be addressed. Present address: Department of Polymer Science and Engineering, Zhejiang University, Hangzhou, 310027, China. Telephone: +86-571-87953729. Fax: +86-571-87953729. E-mail: jijian@zju.edu.cn.

10.1021/bc050264g CCC: $33.50 © 2006 American Chemical Society
Published on Web 12/22/2005

(*34*). Thus, a DNA delivery system with controllable DNA release kinetics can play a more important role in clinical application. In this study, we demonstrate that the DNA molecules in the multilayered films were effectively protected by PLL and the ultrathin PLL/DNA film with 150 nm thickness (10 bilayers) is able to be cross-linked by glutaraldehyde (GA). The density of cross-linking can be modulated by simply controlling the time of the cross-linking process. More importantly, different DNA release profiles are observed, which suggest that the DNA release kinetics can be precisely modulated by the GA cross-linking method.

EXPERIMENTAL PROCEDURES

Materials. Poly-L-lysine (PLL, MW of 83 000) and bisBENZIMIDE (Hoechest 33258) were purchased from Sigma. Deoxyribonucleic acid (DNA, fish sperm, sodium salt), *N*-[2-hydroxyethyl] piperazine-*N*′-[2-ethanesulfonic acid] (HEPES, free acid, high-purity grade), and trypsin (250 N.F. units/mg of protein) were purchased from AMRESCO. GA (25% water solution) was purchased from Shanghai Chemical Reagent Factory, China. Ethidium bromide (EtBr) was purchased from BBI. The water used was distilled 3 times. All reagents were used as received.

PLL/DNA Films Fabrication. Alternating PLL/DNA films were LbL-deposited onto quartz substrates (10 × 20 mm). The first layer of PLL was adsorbed onto the quartz surface by immersing the quartz substrate in a 0.5 mg/mL PLL/HEPES buffer (20 mM HEPES with 20 mM NaCl) at pH 7.4 for 10 min. Substrates were then dipped in water 5 times, followed by drying under a stream of N_2. DNA was then attached to the PLL layer by immersing the quartz substrate in a 0.5 mg/mL DNA/HEPES buffer (20 mM HEPES with 20 mM NaCl) at pH 7.4 for 10 min, followed by the water wash and N_2 drying. The process was repeated until a desired number of bilayers had been deposited. Before the measurements, all samples were dried in a vacuum desiccator under room temperature for at least 12 h.

Characterization of PLL/DNA Films. The growth of the PLL/DNA bilayer was followed by UV−vis spectrometry on a UV−vis spectrophotometer (CARY 100 BIO). The surface topographic feature of the films was monitored on an atomic force microscope (AFM, SPA400, Seiko, Japan) in tapping mode in air. The root-mean-square (rms) roughness values were obtained from the software. For an experiment designed to visually observe the film, a $(PLL/DNA)_{10}$ film was embedded by epoxy resin for microtome and then the cross-section of the film was investigated by a transmission electron microscope (TEM, Jem-1230 at 80 kV, JEOL, Japan). For an experiment designed to characterize the DNA in the film, a $(PLL/DNA)_9$-PLL (PLL is the outmost layer) and a $(PLL/DNA)_{10}$ film (DNA is the outmost layer) were immersed into a EtBr aqueous solution (0.5 mg/mL) for 12 h. After that, the samples were pulled out from the EtBr solution, rinsed sufficiently with water, and then measured by a UV−vis spectrophotometer. All measurements were carried out under room temperature.

GA Cross-Linking of PLL/DNA Films. The $(PLL/DNA)_{10}$ films were immersed into a GA aqueous solution (1 wt %) for varying times under room temperature. After that, the samples were pulled out from the GA solution and immersed into aqueous solution overnight to remove free GA. Before the measurements, all samples were dried in a vacuum desiccator under room temperature for at least 12 h.

***In Vitro* Enzymatic Degradation of PLL/DNA Films.** An enzymatic degradation study was carried out, and trypsin was selected as the model protease to investigate the DNA release profiles from cross-linked PLL/DNA films. Unless stated, the $(PLL/DNA)_{10}$ film was selected as the degradation samples.

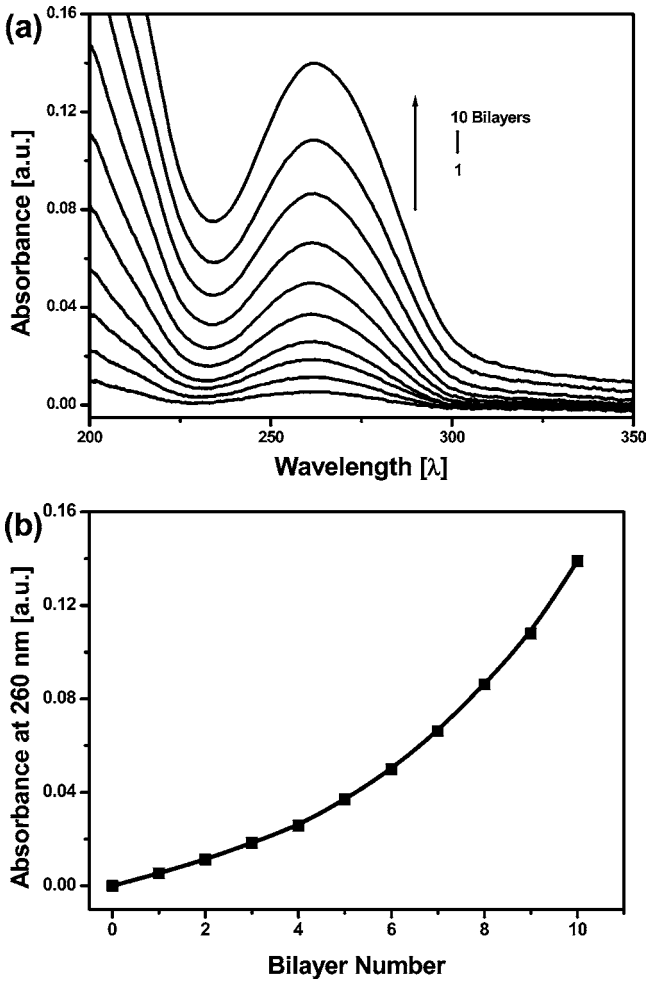

Figure 1. UV−vis absorption spectra of PLL/DNA films and a plot of DNA absorption at 260 nm as a function of the bilayer number are shown in a and b, respectively.

Films were exposed to a trypsin solution (0.1 mg/mL trypsin in PBS at pH 7.4) at 37 °C. The samples were removed from the incubation solution at appropriate time intervals, washed, and then dried in a vacuum desiccator under room temperature for at least 12 h.

Characterization of DNA Release Kinetics. A UV−vis absorption spectrum change of the PLL/DNA films was measured on a UV−vis spectrophotometer. The incubation solution that contained released DNA was added (1:2, vol %) Hoechest 33258 solution (0.15 μg/mL, pH 7.4) and then incubated for 10 min in darkness under room temperature. After that, the solutions were measured on a spectrofluorophotometer (RF-5301PC, Shimadzu, Japan) with an excitation wavelength of 346 nm, a 5 nm slit, and an emission wavelength of 460 nm with a 5 nm slit. All measurements were carried out under room temperature.

RESULTS AND DISCUSSION

Characterization of PLL/DNA Films. LbL film growth on quartz slides can be easily monitored by UV−vis absorption spectrometry. The UV−vis absorption spectra of PLL/DNA film 1−10 bilayers are shown in Figure 1a. DNA contributes a characteristic absorption band at 260 nm. The plot of absorbance at 260 nm shows an increase curve with the bilayer number, as can be seen in Figure 1b, which means that DNA has been successively incorporated into the films. The data are similar to our previously reports (*26*−*27*); however, the absorbance of data points are slightly decreased. It may mainly be due to a

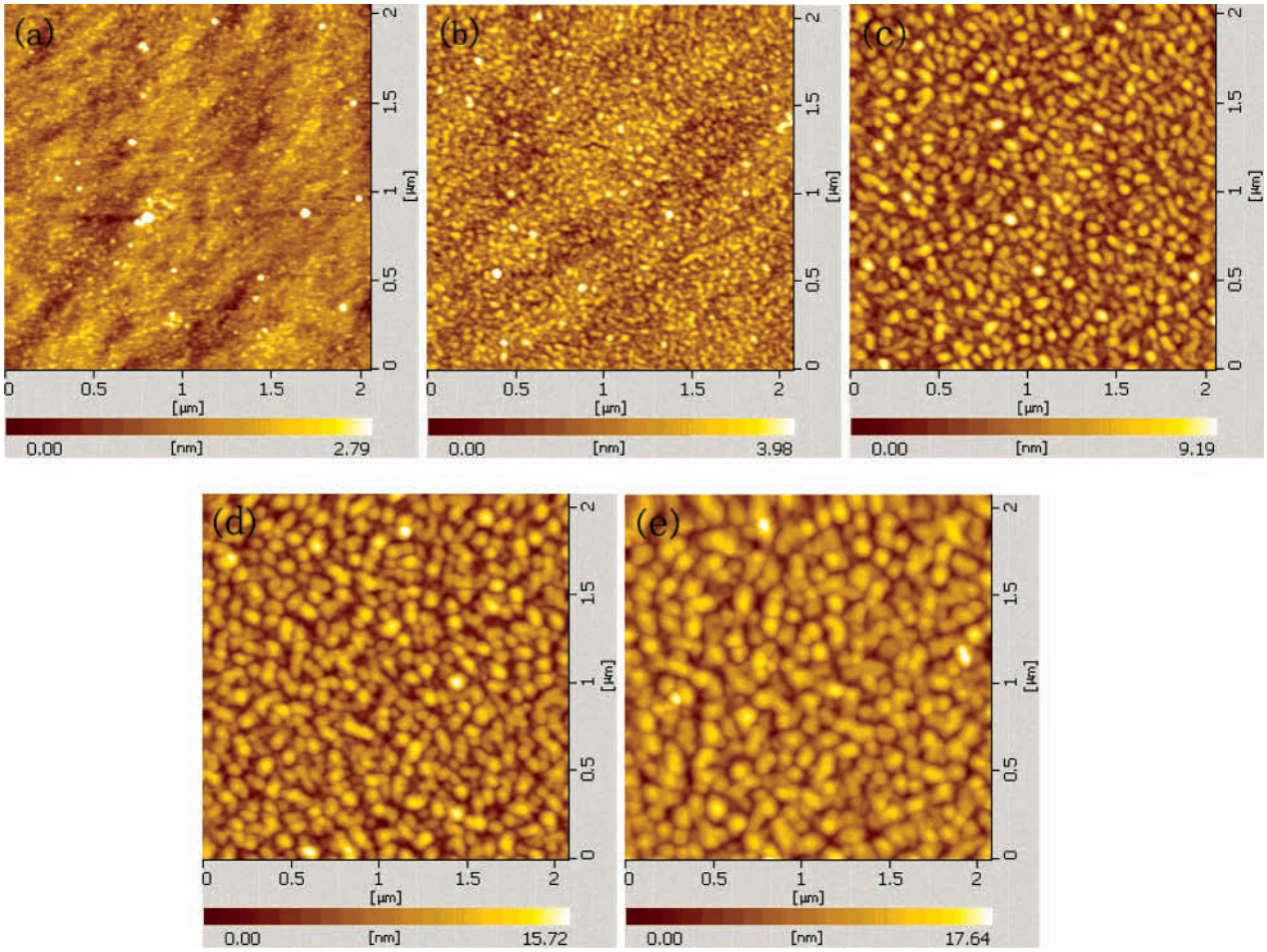

Figure 2. Topographical AFM micrographs of (a) 1 bilayer, (b) 2 bilayers, (c) 3 bilayers, (d) 4 bilayers, and (e) 5 bilayers film. The outmost layer is DNA.

decrease of the NaCl concentration of the aqueous solution (20 mM for this work and 75 mM for previous work), because the salt concentration can affect the polyelectrolytes adsorption during the LbL deposition. In general, a decrease of the salt concentration will lead to low polyelectrolyte adsorption. The data also show that the buildup of the films is followed as an exponential growth (the data are fitted well by an exponential growth curve, with $R^2 = 0.99$), rather than the linear relationship observed for some other DNA films, such as DNA/poly(allylamine hydrochloride) (PAH) (*17*), DNA/poly(ethylenimine) (PEI) (*18*), and DNA/poly(dimethyldiallylammonium chloride) (PDDA) (*19*). Several explanations have been presented for the exponential growth, including the diffusion of polyelectrolytes "in" and "out" of the film during the deposition steps, the formation of polyelectrolyte complexes, and the increase of film surface roughness with the layer number (*35*−*37*). Exponentially growing films are mainly observed in polypeptide or polysaccharide systems. In our case, the PLL (typical polypeptides with MW of 83 000) might play a key role in the exponentially growth of the PLL/DNA film. The ability to form thicker films is important, because the exponential growth could be beneficial to a greater amount of DNA incorporated into the films.

AFM is used to characterize the surface topographic feature of the PLL/DNA film. The AFM micrographs of PLL/DNA films 1, 2, 3, 4, and 5 bilayers with the topmost layer of DNA are shown in Figure 2. There are a lot of island-like domains on the film surface. It is mainly attributing to PLL/DNA complexes during the layer deposition. The complexes may coalesce and grow with the LbL deposition. At the early stages of the deposition, for $(PLL/DNA)_1$, small islands are seen with a characteristic height of 2−3 nm. Such a value is consistent with the width of a double-stranded DNA molecule (*38*). As the number of deposited bilayers increase, the islands become larger, which made the surface of the film rougher. Correspondingly, rms roughness increased from 0.40 (1 bilayer) to 2.82 nm (5 bilayers). This is very close to the observation made by Picart et al. (*37*) on the PLL/HA multilayer system and Richert et al. (*39*) on the HA/chitosan multilayer system. Rigoberto et al. (*40*) also demonstrated that the roughness and feature size of the multilayered films changed with an increasing thickness and that the thicker layers tended to produce larger feature sizes with increased roughness. Meanwhile, we find that the dimension of islands in the present work is smaller than that of our previous paper (*27*). It is reported that the salt concentration could dramatically affect the size of complexes in aqueous solution, and a low salt concentration generally lead to a small size of complexes (*33*). Thus, the relatively small islands should attribute to a low NaCl concentration. The island-like domains and rough surface might be the explanation for the exponential growth of the PLL/DNA film observed in the UV−vis measurement (*35*−*37*). The AFM micrographs indirectly indicate the LbL buildup again.

To further directly observe the PLL/DNA film, TEM is employed to investigate the $(PLL/DNA)_{10}$ film. Figure 3 presents a cross-section of the film. The micrograph clearly shows an ultrathin film fabricated by alternate deposits of the PLL and DNA layer. The TEM micrograph also indicates that the thickness of the $(PLL/DNA)_{10}$ film is about 150 nm, from which the average bilayer thickness of PLL/DNA is about 15 nm. Here, we should mention that, when we take the exponential growth of the films into account, the thickness of each bilayer may different and each bilayer may be thicker than the previous one.

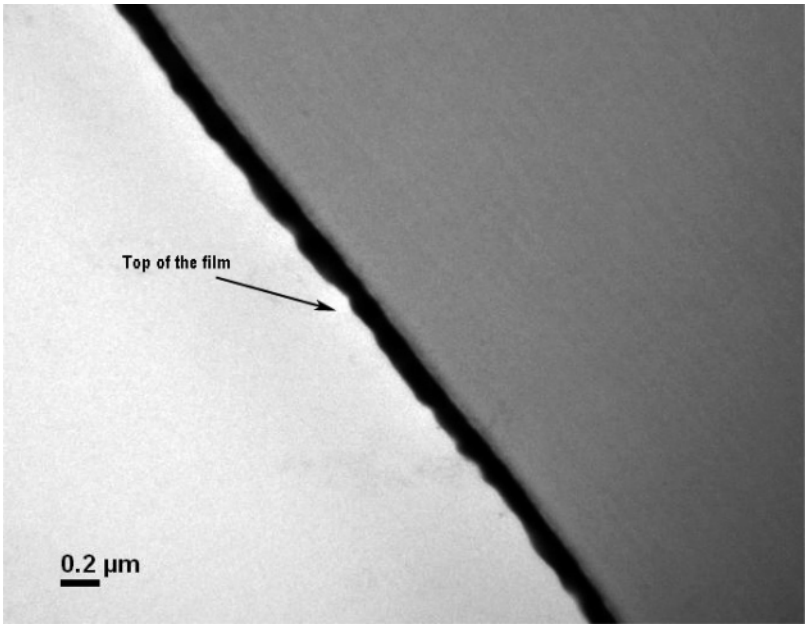

Figure 3. TEM micrograph shows a cross-section of the $(PLL/DNA)_{10}$ film.

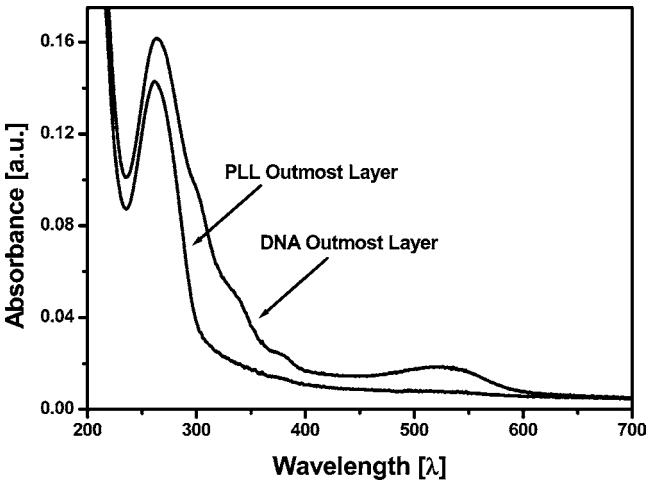

Figure 4. UV−vis absorption spectra of $(PLL/DNA)_9$-PLL (PLL as the outmost layer) and $(PLL/DNA)_{10}$ (DNA as the outmost layer) films interacting with EtBr aqueous solution.

The film is much thicker than some "linearly growing films" [40 nm for the $(DNA/PAH)_{10}$ film (*17*), 44 nm for the $(DNA/PEI)_{10}$ film (*18*), and 59 nm for the $(DNA/PDDA)_{10}$ film (*19*)]. These data suggest that, in our case, PLL/DNA is a kind of "exponentially growing film", and much larger amount of DNA can be obtained by a few numbers of LbL depositions. The observation is consistent with the conclusion drawn from the UV−vis spectrometric and AFM experiments. Because the polyelectrolytes in the film are penetrated by each other, there is not the absolutely layered structure in the film, while it is reasonable that the PLL/DNA film could be served as an ultrathin microgel film.

The fluorescence enhancement of EtBr is the most commonly used in nucleic acid stain. It can produce a strong fluorescence signal upon intercalation with double-stranded DNA (*41*). Here, we chose an EtBr stain assay to characterize two kinds of film: $(PLL/DNA)_9$-PLL (PLL as the outmost layer) and $(PLL/DNA)_{10}$ (DNA as the outmost layer). As shown in Figure 4, the UV−vis absorption spectra of $(PLL/DNA)_9$-PLL and $(PLL/DNA)_{10}$ are totally different. For the film with PLL as the outmost layer, the absorption band is found only at 260 nm, which characterized the DNA absorption. However, for the film with DNA as the outmost layer, the absorption band is found at 260 and 530 nm, which can be attributed to DNA and EtBr/DNA complex absorptions, respectively. It is reported that the absorption maximum of EtBr in aqueous solution appears at 480 nm (*42*). The shift of the peak from 480 to 530 nm is related to the intercalation of EtBr with DNA in solution (*43*). Therefore, it indicates that the EtBr/DNA complexes are formed on the surface of the $(PLL/DNA)_{10}$ film. However, almost no EtBr/DNA complexes are recorded on the surface of the $(PLL/DNA)_9$-PLL film. With the data of the AFM experiment, the PLL/DNA complexes are formed during the deposition of PLL and DNA. Similar complexes are found in other LbL films (*35*, *44*). Such complexes can effectively protect the DNA from the intercalation of EtBr. In brief, the UV−vis data suggest that (1) DNA can be effectively adsorbed onto the PLL layer and (2) the PLL layer can effectively protect the DNA layer from intercalation of EtBr molecules, which might serve as a mechanism to the protection of DNA from the degradation by DNase *in vivo*.

Characterization of DNA Release Kinetics. Previously, we have demonstrated that the PLL/DNA film is a kind of enzymatically biodegradable film (*26*, *27*). The film can be degraded by enzymes, and simultaneously, DNA that is incorporated into the film can be released. However, because the formation of the film is mainly driven by an electrostatic attractive force, the interaction between PLL and DNA molecules in the original (no cross-linked) PLL/DNA film is not very strong, which leads to a relatively quick and uncontrolled DNA release kinetics. As a novel DNA delivery system, the DNA release kinetics should have the ability to be controlled for a variety of clinical applications. Toward this goal, the PLL/DNA films are cross-linked by GA. GA gets many medical uses including tissue examinations, clinical diagnoses, and developmental studies based on its highly reactive chemical properties. It can react with the amino group of PLL and has almost no damage to DNA (*45*, *46*). We hypothesize that the DNA release kinetics might depend upon the cross-linking density, because it directly affects the degradation rate of the film. Thus, the cross-linking density of the film is modulated by controlling the time of the cross-linking process to achieve different DNA release profiles.

First, a $(PLL/DNA)_{10}$ film, which is cross-linked by GA for 30 min, is incubated in a trypsin solution to investigate the

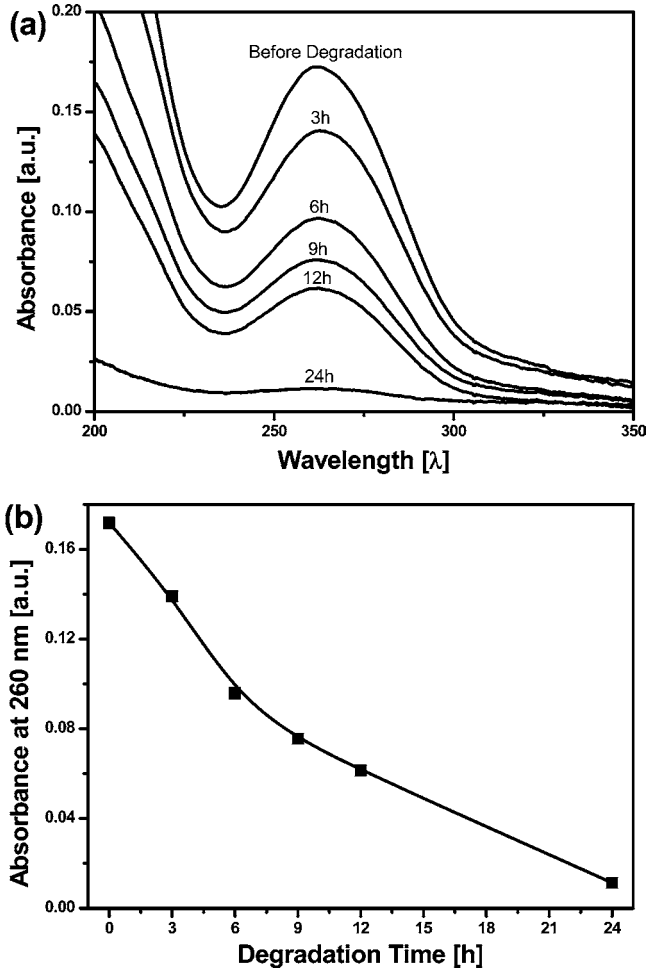

Figure 5. UV−vis absorption spectra of $(PLL/DNA)_{10}$ film and a plot of DNA absorption at 260 nm as a function of the bilayer number, shown in a and b, respectively, showing a degradation of the film. The film was cross-linked by GA for 30 min and then incubated in a trypsin solution at 37 °C. The films were removed from the incubation solution at appropriate time intervals for characterization.

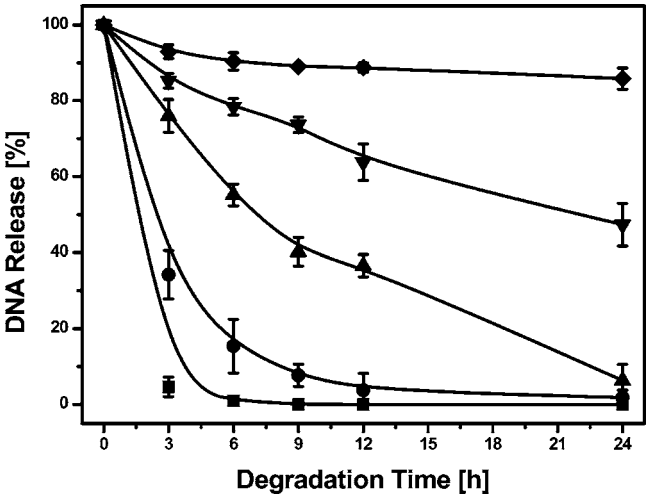

Figure 6. DNA release kinetics in a trypsin solution at 37 °C from PLL/DNA films with varying cross-linking time: (■) original film; (●) 10 min; (▲) 30 min; (▼) 60 min; and (◆) 180 min. A relative absorbance of 100% represents the absorbance of original PLL/DNA film, while 0% designates the absorbance of bare quartz substrates. Values are given as mean ± standard deviation ($n = 3$).

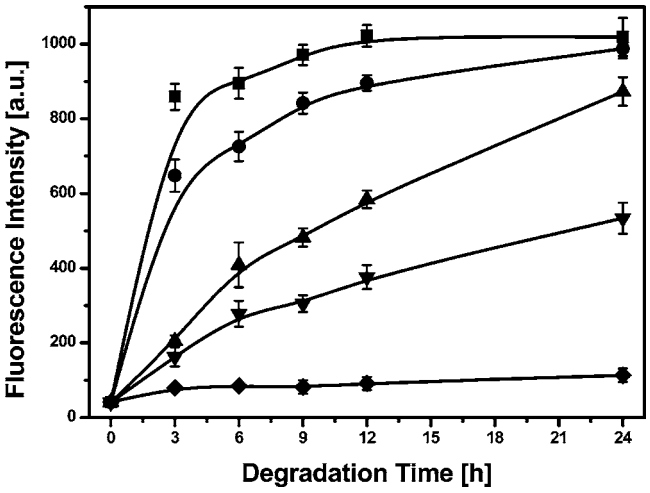

Figure 7. Fluorescence intensity of the incubation solution, in which incubated PLL/DNA films with varying cross-linking time: (■) original film; (●) 10 min; (▲) 30 min; (▼) 60 min; and (◆) 180 min. Values are given as mean ± standard deviation ($n = 3$).

degradation. As can be seen in Figure 5a, the DNA absorption band of 260 nm is decreased gradually with the degradation time over a period of 24 h, showing a deconstruction process, which means that DNA has been successively released from the films. The absorbance of the film at a band of 260 nm before degradation is 0.17. The value is then decreased to 0.01 after 24 h of degradation, as shown in Figure 5b. After that, the films with varying cross-linking density are recorded by the UV−vis measurement. DNA release profiles from the PLL/DNA film with varying cross-linking density are shown in Figure 6. The films are cross-linked for 10, 30, 60, and 180 min, respectively. Different DNA release profiles are observed. For the original film, the DNA releases very fast in an early incubation stage. Almost 95% of incorporated DNA is released within 3 h. Such a burst release is mainly attributed to the formation of a relatively weak interaction between PLL and DNA, because this interaction is mainly driven by electrostatic attractive forces. Thus, the enzymatic degradation of PLL would lead to fast bulk deconstruction of the film. However, the DNA release rates are significantly decreased with the cross-linking density. For example, from the 12 h of incubation in the trypsin solution, the amount of DNA that remains in the films that cross-linked for 0, 10, 30, 60, and 180 min is 0, 3.75 ± 4.47, 36.57 ± 2.92, 63.75 ± 4.8, and 88.72 ± 1.24%, respectively. These data suggest that the DNA release kinetics mainly depends upon the density of cross-linking. The more extent of cross-linking, the more difficult is the enzymatic degradation, which lead to a decreased DNA release rate.

The measurement of the amount of DNA that released into the incubation solution can probe the deconstruction behavior and the DNA release profiles. Hoechest 33258 is a bisBENZIMIDE DNA intercalator. It has been used to stain and to quantitate DNA (*47*). Here, we chose a Hoechest 33258 fluorescence assay to measure qualitatively the amount of DNA contained in the incubation solution. Throughout the 24 h of degradation experiments, as shown in Figure 7, the fluorescence intensity of the incubation solution, in which incubated PLL/DNA films with a varying density of cross-linking, increases gradually with time when the films are exposed to the trypsin solution. However, the films with a varying density of cross-linking lead to a different DNA release rate; the original PLL/DNA film achieves almost maximal fluorescence intensity within the first 3 h. A further increase in the incubation time does not increase the intensity, which means that the amount of DNA in the incubation solution is stable. The cross-linked films show the slower DNA release rate. Especially, the film that cross-linked for 180 min leads to a significant low

fluorescence intensity. These data suggest that the DNA release kinetics can be precisely controlled by GA cross-linking. The observation is consistent with the conclusion drawn from the UV−vis spectrometry experiment.

CONCLUSIONS

The ultrathin PLL/DNA film was successfully constructed by the LbL technique. The UV−vis spectrometry and AFM experiments showed the successful buildup of PLL and DNA with a kind of exponential growth. The TEM micrograph showed clearly an ultrathin film with a thickness value of 150 nm (10 bilayers). Furthermore, the EtBr adsorption experiment suggested that the DNA molecules in the film are being effectively protected by PLL.

The PLL/DNA film was able to be cross-linked by GA. The cross-linking density of the film can be modulated by controlling the time of the GA incubation process. The GA cross-linking procedure can effectively slow the enzymatic degradation of the film, which lead to the various DNA release profiles. Thus, the PLL/DNA film with the ability of precise controllable DNA release profiles could serve as a novel DNA delivery system in gene therapy applications in tissue engineering, medical implants, etc.

ACKNOWLEDGMENT

This research work is supported by the Natural Science Foundation of China (50373036), Fok Ying Tung Education Foundation (J20040212), and Key Project of Natural Science Foundation of Zhejiang Province, China (Z404114).

LITERATURE CITED

(1) Meager, A. (1999) *Gene Therapy Technologies, Applications, and Regulations*; John Wiley and Sons, Ltd.: U.K.

(2) Curiel, D. T., Gerritsen, W. R., and Krul, M. R. (2000) Progress in cancer gene therapy. *Cancer Gene Ther. 7*, 1197−1199.

(3) Wolff, J. A., Malone, R. W., Williams, P., Chong, W., Acsadi, G., Jani, A., and Felgner, P. L. (1990) Direct gene transfer into mouse muscle *in vivo*. *Science 247*, 1465−1468.

(4) Palasis, M., Luo, Z., Barry, J. J., and Walsh, K. (2000) Analysis of adenoviral transport mechanisms in the vessel wall and optimization of gene transfer using local delivery catheters. *Hum. Gene Ther. 11*, 237−246.

(5) Isner, J. M., Walsh, K., Symes, J., et al. (1996) Arterial gene transfer for therapeutic angiogenesis in patients with peripheral artery disease. *Hum. Gene Ther. 7*, 959−988.

(6) Shea, L. D., Smiley, E., Bonadio, J., and Mooney, D. J. (1999) Controlled DNA delivery from three-dimensional polymer matrices for tissue engineering. *Nat. Biotechnol. 17*, 551−554.

(7) Prabha, S., Zhou, W., Panyam, J., and Labhasetwar, V. (2002) Size-dependency of nanoparticle-mediated gene transfection: Studies with fractionated nanoparticles. *Int. J. Pharm. 244*, 105−115.

(8) Walter, E., Dreher, D., Kok, M., Thiele, L., et al. (2001) Hydrophillic poly(D,L-lactide-co-glycolide) microspheres for the delivery of DNA to human-derived macrophages and dendritic cells. *J. Controlled Release 76*, 149−168.

(9) Klugherz, B. D., Jones, P. L., Cui, X., Chen, W., Meneveau, N. F., DeFelice, S., Connolly, J., Wilensky, R. L., and Levy, R. J. (2000) Gene delivery from a DNA controlled-release stent in porcine coronary arteries. *Nat. Biotechnol. 18*, 1181−1184.

(10) Stachelek, S. J., Song, C., Alferiev, I., Defelice, S., Cui, X., Connolly, J. M., Bianco, R. W., and Levy, R. J. (2004) Localized gene delivery using antibody tethered adenovirus from polyurethane heart valve cusps and intra-aortic implants. *Gene Ther. 11*, 15−24.

(11) Zhang, J., Chua, L. S., and Lynn, D. M. (2004) Multilayered thin films that sustain the release of functional DNA under physiological conditions. *Langmuir 20*, 8015−8021.

(12) Jewell, C. M., Zhang, J., Fredin, N. J., and Lynn, D. M. (2005) Multilayered polyelectrolyte films promote the direct and localized delivery of DNA to cells. *J. Controlled Release 106*, 214−223.

(13) Decher, G. (1997) Fuzzy nanoassemblies: Toward layered polymeric multicomposites. *Science 277*, 1232−1237.

(14) Hammond, P. T. (2000) Recent explorations in electrostatic multilayer thin film assembly. *Curr. Opin. Colloid Interface Sci. 4*, 430−442.

(15) Lvov, Y., Ariga, K., Ichinose, I., and Kunitake, T. (1995) Assembly of multicomponent protein films by means of electrostatic layer-by-layer adsorption. *J. Am. Chem. Soc. 117*, 6117−6123.

(16) Jin, W., Shi, X. Y., and Caruso, F. (2001) High activity enzyme microcrystal multilayer films. *J. Am. Chem. Soc. 123*, 8121−8122.

(17) Lvov, Y., Decher, G., and Sukhorukov, G. (1993) Assembly of thin films by means of successive deposition of alternate layers of DNA and poly(allylamine). *Macromolecules 26*, 5396−5399.

(18) Sukhorukov, G., Möhwald, H., Decher, G., et al. (1996) Assembly of polyelectrolyte multilayer films by consecutively alternating adsorption of polynucleotides and polycations. *Thin Solid Films 284*, 220−223.

(19) Pei, R., Cui, X., Yang, X., and Wang, E. (2001) Assembly of alternating polycation and DNA multilayer films by electrostatic layer-by-layer adsorption. *Biomacromolecules 2*, 463−468.

(20) Yoo, D., Wu, A. P., Lee, J., and Rubner, M. F. (1997) New electroactive self-assembled multilayer thin films based on alternately adsorbed layers of polyelectrolytes and functional dye molecules. *Synth. Met. 85*, 1425−1426.

(21) Feldheim, D. L., Grabar, K. C., Natan, M. J., and Mallouk, T. E. (1996) Electron transfer in self-assembled inorganic polyelectrolyte/metal nanoparticle heterostructures. *J. Am. Chem. Soc. 118*, 7640−7641.

(22) Lvov, Y., Ariga, K., Onda, M., Ichinose, I., and Kunitake, T. (1997) Alternate assembly of ordered multilayers of SiO_2 and other nanoparticles and polyions. *Langmuir 13*, 6195−6203.

(23) Steitz, R., Leiner, V., Siebrecht, R., and Klitzing, R. V. (2000) Influence of the ionic strength on the structure of polyelectrolyte films at the solid−liquid interface. *Colloids Surf., A 163*, 63−70.

(24) Mendelsohn, J. D., Yang, S. Y., Hiller, J., Hochbaum, A. I., and Rubner, M. F. (2003) Rational design of cytophilic and cytophobic polyelectrolyte multilayer thin films. *Biomacromolecules 4*, 96−106.

(25) Serizawa, T., Yamaguchi, M., and Akashi, M. (2002) Alternating bioactivity of polymeric layer-by-layer assemblies: Anticoagulation vs procoagulation of human blood. *Biomacromolecules 3*, 724−731.

(26) Ren, K., Ji, J., and Shen, J. (2004) Construction of biodegradable multilayer films via layer-by-layer self-assembly as gene delivery system. *Chem. Res. Chin. Univ.* (Chinese) *25*, 1576−1578.

(27) Ren, K., Ji, J., and Shen, J. (2006) Construction and enzymatic degradation of multiayered poly-L-lysine/DNA films. *Biomaterials*, in press.

(28) Ekblom, P., and Timpl, R. (1996) Cell-to-cell contact and extracellular matrix. A multifaceted approach emerging. *Curr. Opin. Cell Biol. 8*, 599−601.

(29) Rabbani, S. A. (1998) Metalloproteases and urokinase in angiogenesis and tumor progression. *In Vivo 12*, 135−142.

(30) Galis, Z. S., and Khatri, J. J. (2002) Matrix metalloproteinases in vascular remodeling and atherogenesis: The good, the bad, and the ugly. *Circ. Res. 90*, 251−262.

(31) Tan, Q., Ji, J., Barbosa, M. A., Fonseca, C., and Shen, J. (2003) Constructing thromboresistant surface on biomedical stainless steel via layer-by-layer deposition anticoagulant. *Biomaterials 24*, 4699−4705.

(32) Zhu, H., Ji, J., and Shen, J. (2004) Biomacromolecules electrostatic self-assembly on 3-dimensional tissue engineering scaffold. *Biomacromolecules 5*, 1933−1939.

(33) Vijayanathan, V., Thomas, T., and Thomas, T. J. (2002) DNA nanoparticles and development of DNA delivery vehicles for gene therapy. *Biochemistry 41*, 14085−14094.

(34) El-Aneed, A. (2004) An overview of current delivery systems in cancer gene therapy. *J. Controlled Release 94*, 1−14.

(35) Elbert, D. L., Herbert, C. B., and Hubbell, J. A. (1999) Thin polymer layers formed by polyelectrolyte multilayer techniques on biological surfaces. *Langmuir 15*, 5355−5362.

(36) Picart, C., Mutterer, J., Richert, L., Luo, Y., Prestwich, G. D., Schaaf, P., Voegel, J. C., and Lavalle, P. (2002) Molecular basis

for the explanation of the exponential growth of polyelectrolyte multilayers. *Proc. Natl. Acad. Sci. U.S.A. 99*, 12531−12535.
(37) Picart, C., Lavalle, P., Hubert, P., Cuisinier, F. J. G., Dether, G., Schaaf, P., and Voegel, J. C. (2001) Buildup mechanism for poly-(L-lysine)/hyaluronic acid films onto a solid surface. *Langmuir 17*, 7414−7424.
(38) Shi, X. Y., Sanedrin, R. J., and Zhou, F. M. (2002) Structural characterization of multilayered DNA and polylysine composite films: Influence of ionic strength of DNA solutions on the extent of DNA incorporation. *J. Phys. Chem. B 106*, 1173−1180.
(39) Richert, L. R., Lavalle, P., Payan, E., et al. (2004) Layer by layer buildup of polysaccharide films: Physical chemistry and cellular adhesion aspects. *Langmuir 20*, 448−458.
(40) Rigoberto, A., Park, M., Baba, A., and Kaneko, F. (2003) Photoalignment in ultrathin films of a layer-by-layer deposited water-soluble azobenzene dye. *Langmuir 19*, 654−665.
(41) Dutton, M. D., Varhol, R. J., and Dixon, D. G. (1995) Technical considerations for the use of ethidium bromide in the quantitative analysis of nucleic acids. *Anal. Biochem. 230*, 353−355.
(42) Lang, J., and Liu, M. (1999) Layer-by-layer assembly of DNA films and their interactions with dyes. *J. Phys. Chem. B 103*, 11393−11397.
(43) Porumb, H. (1978) The solution spectroscopy of drugs and the drug−nucleic acid interactions. *Prog. Biophys. Mol. Biol. 34*, 175−195.
(44) Thierry, B., Winnik, F., Merhi, Y., Bilodean, L., and Tabrizian, M. (2004) Non-viral transfection of the vasculature though self-assembled nanocoatings. 7th World Biomaterials Congress 1820.
(45) Douglas, M. P., and Rogers, S. O. (1998) DNA damage caused by common cytological fixatives. *Mutat. Res. 401*, 77−88.
(46) Fukunaka, Y., Iwanaga, K., Morimoto, K., Kakemi, M., and Tabata, Y. (2002) Controlled release of plasmid DNA from cationized gelatin hydrogels based on hydrogel degradation. *J. Controlled Release 80*, 333−343.
(47) Rago, R., Mitchen, J., and Wilding, G. (1990) DNA fluorometric assay in 96-well tissue culture plates using Hoechst 33258 after cell lysis by freezing in distilled water. *Anal. Biochem. 191*, 31−34.

BC050264G

Ferrocene-Assisted Stabilization of Collagen Mimetic Triple Helices: Solid-Phase Synthesis and Structure

Subrata K. Dey and Heinz-Bernhard Kraatz*

Department of Chemistry, University of Saskatchewan, 110 Science Place, Saskatoon, Canada. Received September 5, 2005; Revised Manuscript Received November 8, 2005

A series of ferrocene-containing collagen models Fc-CO-(Pro-Hyp-Gly)$_n$-Cys (n = 4 (**1**), 6 (**2**), 7 (**3**), 8 (**4**), 9 (**5**)) were synthesized by solid-phase synthesis. Biophysical studies using circular dichroism (CD) show that these collagen analogues form triple-helical conformations, and the peptides showed a range of thermal stabilities ((T_m), 38−74 °C). Results also indicate that the ferrocene (Fc)-labeled collagen models possesses a higher triple-helical propensity than the unlabeled collagen models as demonstrated by the higher melting temperatures and thermodynamic parameters, and we conclude that the Fc group at the *N*-terminal position of the peptide strands increases the stability of the triple helix.

INTRODUCTION

The design of collagens with a high melting temperature (T_m) is a formidable task, which has attracted significant attention over the past few years. It has been well-known that the collagen molecule consists of three polypeptide chains; each undergoes a transition to a single coil state as the temperature increases (*1*). The thermal stability of the collagen triple helix depends on the identity and sequence of the amino acid residues Xaa and Yaa in the Gly-Xaa-Yaa sequence. H-Bonding on the interior of the triple helix holds the triple helix together. The imino acids, proline (Pro) and hydroxyproline (Hyp), are both stabilizing factors, so that the melting temperature T_m of collagen from many animals is proportional to the imino acid content (*2*). In general, the higher the Hyp content in the Yaa position, the higher the T_m. In addition, it was shown that amino acids such as 4-fluoroproline or 4-aminoproline influence the T_m, causing it to increase due to electronic effects (*3*). This may have interesting application for the formation of biomaterials that exhibit a higher stability under biological conditions (*4*). On the basis of the biophysical studies on (Gly-Pro-Pro)$_{10}$, Bhatnagar and co-workers suggested that the major stabilizing force in the Gly-Pro-Pro triple-helix is the interchain and/or interresidue nonbonded interactions, including close van der Waals contacts and hydrophobic interactions (*5*). Goodman and co-workers demonstrated that template-assembled collagen residues greatly enhance the conformational stability of the collagen triple helix, and recently they also reported the incorporation of an Fe^{3+}−catechol complex as a scaffold to assemble peptide chains into triple helices (*6*). As a part of our ongoing study into the electron transfer properties of peptides chemically linked to gold surfaces, we synthesized a series of Fc-labeled collagen mimetic structures composed of Pro-Hyp-Gly sequences (Scheme 1) equipped with a C-terminal Cys residue and began to assess the propensity for triple helix formation by variable temperature circular dichroism (CD) spectroscopy, thermodynamic studies, and molecular modeling. Here we present the results of this study indicating that Fc, a simple organometallic molecule, attached to the N-terminal end of the collagen helix enhances the stability of the triple helix.

* To whom correspondence should be addressed. Fax: 306-966-4730; Tel: 306-966-4660. E-mail: kraatz@sask.usask.ca.

Scheme 1

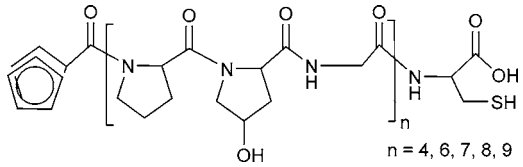

MATERIALS AND METHODS

All chiral amino acids were of the L configuration. Amino acids, SPPS resins, and HOBt were purchased from SynPep. EDC was purchased from Novabiochem. DIEAP, TFA (HPLC-grade), TIS, piperidine, phenol, and ferrocene were purchased from Aldrich Chem. DMF (BDH; ACS grade) was used for synthesis. Acetone, CH_2Cl_2, diethyl ether (BDH; ACS grade), CH_3CN (Fischer; HPLC grade), and CH_3OH (Fisher, for electrochemistry, spectra-grade) were used for the purpose of purification. Reagents were used as provided. All solutions (for biophysical studies and HPLC purification) were prepared using deionized Millipore water (18.2 MΩ·cm) obtained from a Milli-Q water system.

General Procedure. A series of collagen models (both the modified model with ferrocene and unmodified model) were synthesized by the standard *N*-(9-fluorenyl)methoxycarbonyl (Fmoc)-based solid-phase protocol on a Quest Organic Synthesizer. Couplings were carried out on Fmoc-L-cysteine(trityl) Wang resin (Syn Pep, 0.50 mmol/g) using Fmoc amino acids (Fmoc-Gly-OH, Fmoc-Hyp-OH, and Fmoc-Pro-OH, 2 equiv each) in the presence of 1-ethyl-3-[3-(dimethylamino)propyl]-carbodiimide (EDC) (2.2 equiv) and *N*-hydroxybenzotriazole (HOBt) (2.2 equiv) as activating agents and diisopropylethylamine (4 equiv). To prepare ferrocene-attached collagen-like polypeptides, the specific peptide chains were built up on resin, and the ferrocene monocarboxylic acid was directly coupled to the N-termini of these chains before removal from the resin. The synthetic route is described in Scheme 2.

Coupling efficiency was monitored with Kaiser test (*7*), except for N-terminal proline residues where the chloranil test (*8*) was applied. The desired peptides were cleaved from the resin with trifluoroacetic acid (TFA) containing phenol (2.5% v/v) and triethylsilane (TIS; 2.5% v/v) and then precipitated with diethyl ether.

10.1021/bc050268l CCC: $33.50 © 2006 American Chemical Society
Published on Web 12/31/2005

Scheme 2

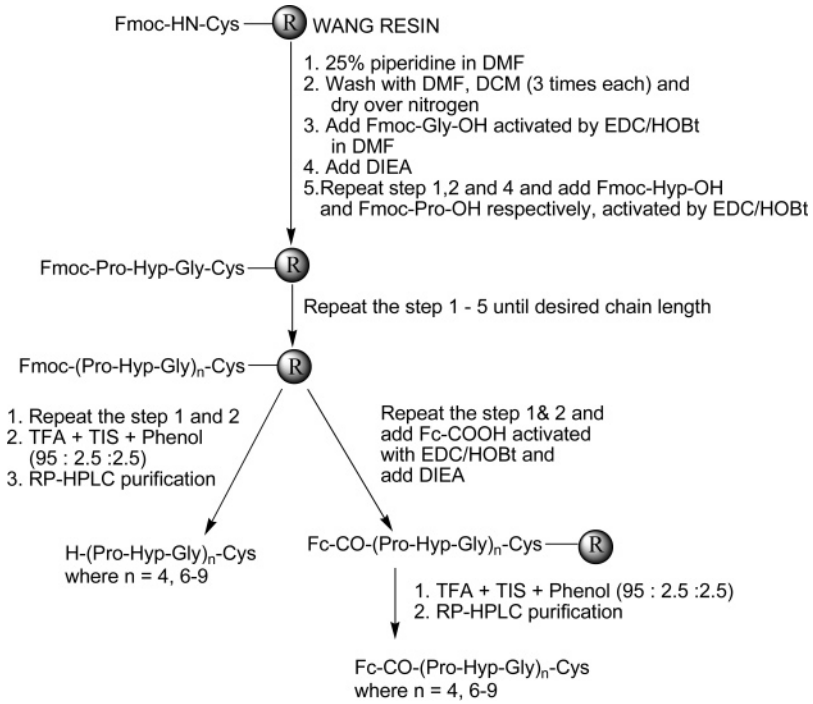

Peptides are purified by reversed-phase high performance liquid chromatography (RP-HPLC) (Varian, Inc.) using a water−acetonitrile system and Vydac C-18, 25 × 2.2 cm preparatory column. Peptides were eluted with a gradient of aqueous acetonitrile containing TFA (0.1%, v/v) at a flow rate of 16.6 mL/min. Purified peptides were obtained by collecting the major peak with absorbance at 215 nm, which occurred between 32 and 77% acetonitrile. HPLC-purified peptides were analyzed by electrospray mass spectrometry using a QSTAR XL-MS/MS ionspray source.

Synthesis and Purification. The Fmoc-protected Wang-Cys resin (loaded: 0.50 mmol/g, taken 0.1 mmol) was treated with 25% piperidine in DMF (1 × 20 min, 1 × 10 min) and then washed successively with DMF (3 × 1 min), MeOH (3 × 1 min), and CH_2Cl_2 (3 × 1 min). Coupling of the first amino acid (Fmoc-Gly-OH) was performed with Fmoc-Gly-OH/EDC/HOBt/DIEA (2 equiv, 1:1.1:1.1:2) in DMF (2.5h) followed by washing with DMF (3 × 1 min), MeOH (3 × 1 min), and CH_2Cl_2 (3 × 1 min). Chain elongation was performed with Fmoc-Hyp-OH/EDC/HOBt/DIEA (2 equiv, 1:1.1:1.1:2) and Fmoc-Pro-OH/EDC/HOBt/DIEA (2 equiv, 1:1.1:1.1:2) sequentially up to the desired length. Fmoc cleavage from Fmoc-Pro-Peptidyl resin was carried out with 25% piperidine and 1% DBU in DMF (2 × 15 min) and washings with DMF (3 × 1 min), MeOH (3 × 1 min), and CH_2Cl_2 (3 × 1 min). In the final step, half of the polypeptide resin beads were taken out, the desired polypeptides were cleaved from the resin with trifluoroacetic acid (TFA) containing phenol (2.5% v/v) and triisopropylsilane (TIS; 2.5% v/v), and with the remainder of the beads, an additional Fc-coupling step was carried out. Fc-COOH/EDC/HOBt/DIEA (2 equiv, 1:1.1:1.1:2) was added to the remaining beads. The Fc-labeled collagen polypeptides were also cleaved from the resin using the same cleaving agent. All modified and unmodified collagen models were purified by RP-HPLC using a water−acetonitrile gradient and characterized by ESI-MS spectra. For the spectroscopic and electrochemical measurements, a portion of the material was further purified by preparative HPLC (ESI).

CD Spectroscopy. Circular dichroism (CD) spectra were recorded on a π*-180 spectrometer (Applied Photophysics Ltd, UK) equipped with a model 3016 isotemp refrigerator circulator (Fisher Scientific), interfaced to an Acorn PC. A rectangular 2 mm-path length cell was used. The spectrometer was routinely calibrated with an aqueous solution of (1*S*)-(+)-10-camphorsulfonic acid. Mean residue molar ellipticities were calculated according to the following equation:

$$[\theta] = [\theta]_{obs}/10 \times lcn$$

where $[\theta]_{obs}$ is the observed ellipticity measured in degrees, l is the path length of the cell in centimeters, c is the molar peptide concentration, and n is the number of amino acid residues in the peptide. The spectra for both modified and unmodified polypeptides were obtained as an average of eight scans using a slit width of 0.5 nm. The thermal denaturation results were obtained by measuring the ellipticity at 223 nm as a function of temperature using a 120 s thermal equilibration time between data points.

RESULTS AND DISCUSSION

In addition to nonnatural amino acids, one can expect that increasing the hydrophobicity at the N-terminal side of the collagens may also influence the melting behavior. In our efforts toward the design of collagen conjugates, we have synthesized a series of Fc-labeled collagen mimetic structures composed of Pro-Hyp-Gly sequences (Scheme 1) to assess their triple helical propensities and the role of Fc in triple helix stability by variable temperature circular dichroism (CD) spectroscopy, thermodynamic studies, and molecular modeling.

Fc-collagen conjugates Fc-CO-(Pro-Hyp-Gly)$_n$-Cys (n = 4 (**1**), 6 (**2**), 7 (**3**), 8 (**4**), 9 (**5**)) of increasing peptide length were synthesized by solid-phase synthesis on Wang resin using EDC/HOBt, cleaved off the resin by TFA, phenol, and triethylsilane (95:2.5:2.5), and then purified by preparative RP-HPLC on C18. All compounds were characterized by mass spectroscopy. The synthesis, purification, and characterization of the unlabeled collagens (lacking the Fc group) were carried out in the same fashion (Scheme 2). In water/methanol (99/1), compounds **1**−**5** exhibit a single broad absorbance in the visible region with a λ_{max} between 430 and 445 nm. For all of the complexes excitation within the region of 200−240 nm, the peptide bond

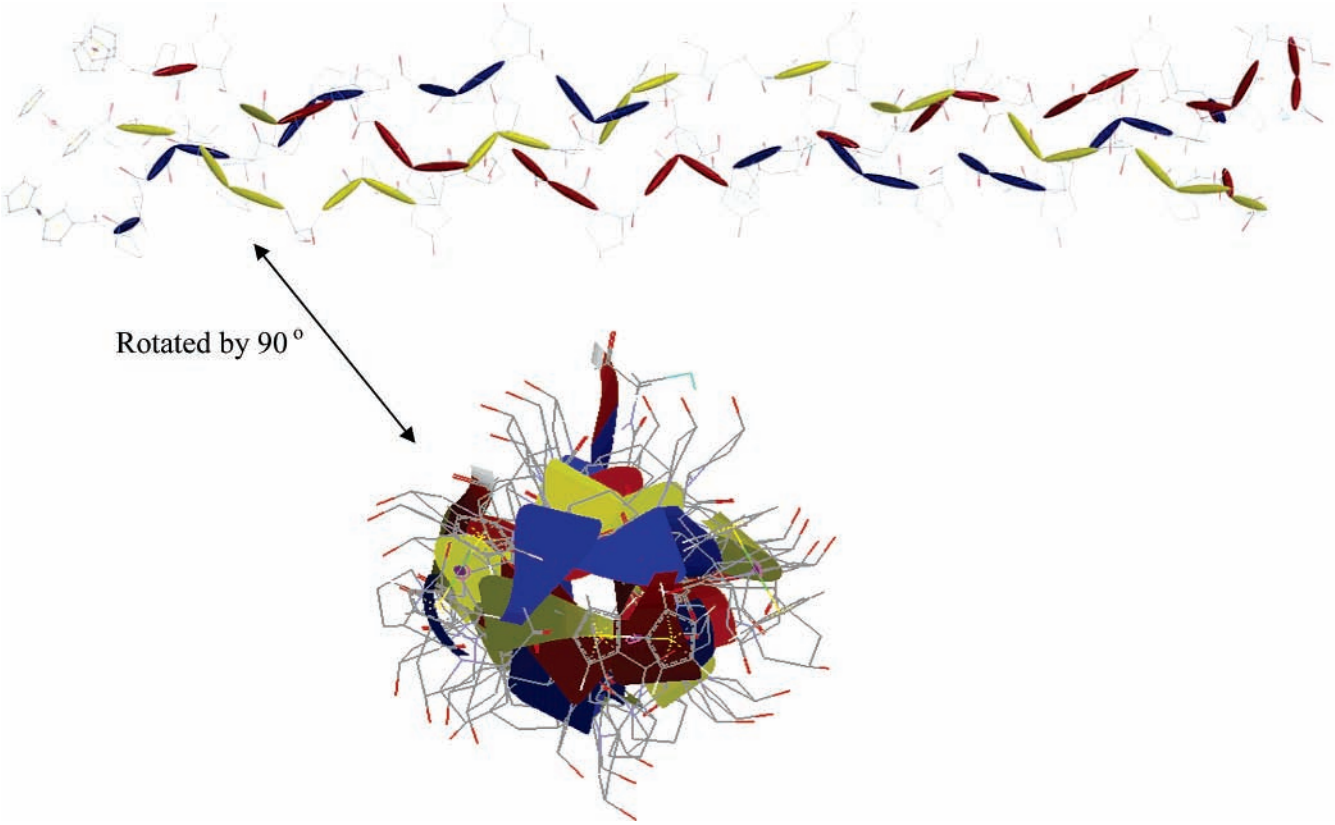

Figure 1. Modeling of the Fc-labeled collagen mimics (for compound **5**).

due to the n → π * transitions yields UV spectra dominated by the peptide bond absorptions. The solution electrochemistry in water/methanol (99/1) for compounds **1**−**5** shows a fully reversible oxidation wave of the Fc group with a half-wave potential $E_{1/2}$ at about 560 mV, a peak separation of 70 mV, and a ratio of anodic to cathodic peak currents close to unity (ESI, Table S1).

Molecular Modeling. Molecular models of triple-helical ferrocene-labeled compounds were created by modifying the structure of crystalline collagen (PDB entry 1CGD (*9*)). The side chain methyl group of the three alanine residues was replaced by a hydrogen atom. The one (Pro-Hyp-Gly) unit was deleted from the C-terminus (for **5**, Figure 1). This section was subjected to energy minimization for equilibrium geometry using Hartree−Fock method. Three Fc-CO groups were added to the N-terminal proline residues, and three Cys groups were added to the C-terminal glycine residues. The whole section was subjected to energy minimization, locking all the entire amide bonds by Hartree−Fock method except the cysteine amide group.

The molecular modeling of ferrocene-labeled triple helices includes two basic steps. First, the backbones of three Fc-CO-[Pro-Hyp-Gly]$_n$-Cys (where n = 4, 6−9) chains have to be assembled into a triple-helical assembly. Second, the conformational space accessible to the ferrocene group needs to be searched for minimum energy structures. The first step concerns only the chain backbone and simplifies the process of triple-helical assembly. The three Fc-CO-[Pro-Hyp-Gly]$_n$-Cys molecules were constrained to have the same backbone torsions as the structure proposed by Scheraga (*10*) for (Gly-Pro-Hyp)$_n$. This conformation has been shown to be very stable with respect to the unsubstituted compounds and is therefore possibly a good candidate to use as starting backbone conformation for minimizations. On the basis of our present study, we conclude that the Fc−collagen conjugates have an enhanced stability toward denaturation.

Determination of Triple-Helical Conformation in Solution. The solution conformation of compounds **1**−**5** was investigated by CD spectroscopy. Natural collagen has a CD spectrum exhibiting a low intensity maximum at 220 nm, a crossover at 213 nm, and a minimum at 197 nm (*11*). Using these data, the helicity of any collagen can be determined. The CD spectra for compounds **1**−**5** are shown in Figure 2. All compounds display a spectrum typical of collagen with a maximum at 223, a minimum at 201 nm, and a crossover at 218 nm. The spectral data is listed in Table 1 and is comparable to known collagen models, (Gly-Pro-Hyp)$_{10}$-NH$_2$ (*11*, *12*). As the length of the peptide increases in compounds **1**−**5**, the helical content increases up to the reported value for (Gly-Pro-Hyp)$_{10}$-OH (*12c*). The entire unmodified system also demonstrates a similar type

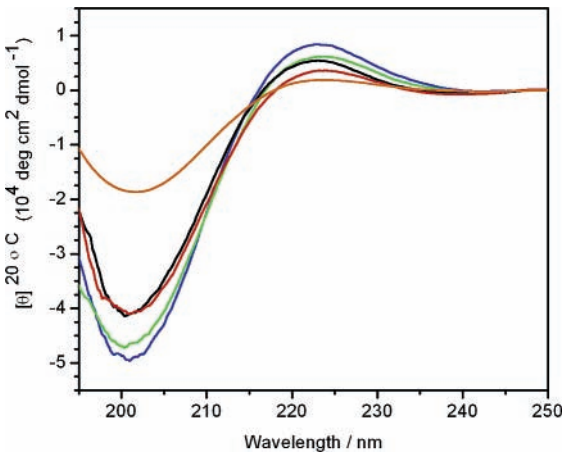

Figure 2. CD spectra of Fc-CO-(Pro-Hyp-Gly)$_n$-Cys where n = 4, 6−9 in water/methanol, 99/1, at pH 7.2 at 20 °C. Blue line for n = 9, green for n = 8, black for n = 7, red for n = 6, and orange for n = 4. The samples were kept in a refrigerator (4 °C) for at least 1 week so they would reach the equilibrium of triple-helix formation.

Table 1. Circular Dichroism Data for the Synthesized Fc-attached Collagen-Based Polypeptides Composed of (Pro-Hyp-Gly) Sequences[a]

compound	λ_{min} (nm)	cross (nm)	λ_{max} (nm)	R_{pn}	T_m (°C)	T_m (°C, unmodified)	ΔH_m, kJ mol^{-1}	ΔS_m, kJ mol^{-1} K^{-1}	length (Å)
1	202 (-1.96×10^4)	219	223 (0.22×10^4)	0.11	38 ± 3	31 ± 1	10	0.03	32
2	201 (-4.06×10^4)	218	223 (0.37×10^4)	0.09	48 ± 1	38 ± 2	34	0.10	48
3	200 (-4.06×10^4)	216	223 (0.63×10^4)	0.14	50 ± 2	39 ± 1	72	0.22	56
4	201 (-4.11×10^4)	217	223 (0.63×10^4)	0.14	70 ± 1	51 ± 3	103	0.30	64
5	201 (-4.93×10^4)	216	223 (0.87×10^4)	0.17	73 ± 1	66 ± 2	154	0.45	72
collagen[b]	198 (-5.4×10^4)	213	220 (0.71×10^4)	0.13					
(G-P-O)$_{10}$-OH [c]	198 (-3.4×10^4)	218	225 (0.43×10^4)	0.13					

[a] CD spectra were obtained at 20 °C using a peptide concentration of 0.01 mM (water/methanol, 99/1). The peak intensities are indicated in the parentheses. [b,c] Estimated from published CD spectra: ref 12b,c.

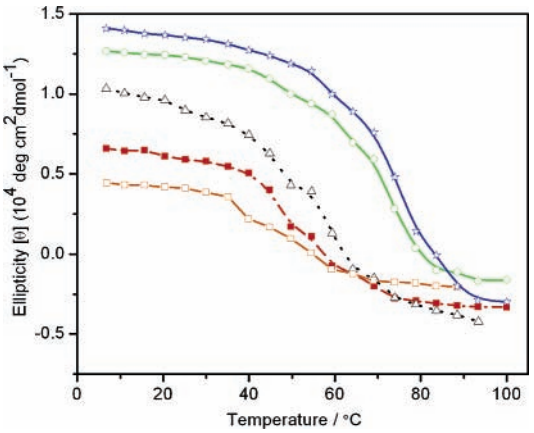

Figure 3. Thermal denaturation of ferrocene-labeled collagen triple helices at 223 nm (blue line for $n = 9$, green for $n = 8$, black for $n = 7$, red for $n = 6$, and orange for $n = 4$). The critical triple-helical concentration is ca. 0.01 mM (methanol/water). Ellipticities at 223 nm were monitored by circular dichroism spectroscopy as the temperature was increased by increments of 5 °C with 2-min equilibrium.

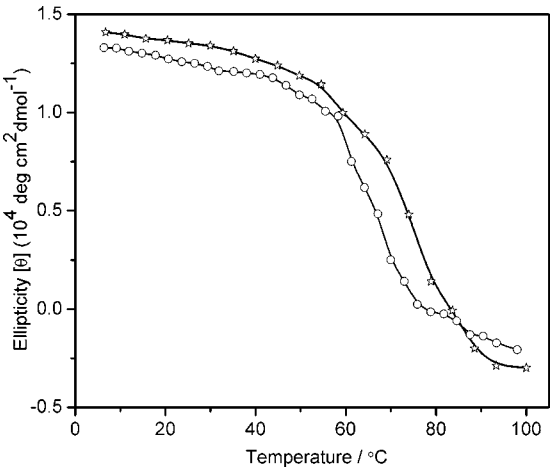

Figure 4. Thermal denaturation of ferrocene-labeled collagen triple helices at 223 nm ((☆) for modified system, Compd. **5**, and (○) for unmodified system of same length). The critical triple-helical concentration is ca. 0.01 mM (methanol/water). Ellipticities at 223 nm were monitored by circular dichroism spectroscopy as the temperature was increased by increments of 5 °C with 2-min equilibrium in both cases.

of spectrum with a maximum at 222 nm and a minimum at around 200 nm (e.g., compound **5**, modified and unmodified systems, ESI, Figure S1). To establish the triplex formation we have used the ratio of the positive peak intensity over negative peak intensity, R_{pn} (*12c*, *13*). For the synthetic Fc-collagen conjugates **1**−**5**, the R_{pn} values are summarized in Table **1**, including the values for the natural collagen (*13*) and for (Gly-Pro-Hyp)$_{10}$−OH (*11c*). On the basis of these R_{pn} values, the presence of triple-helical conformations is established for our ferrocene-labeled systems **1**−**5** at 20 °C and a concentration of 0.01 mM at pH 7.2. As the solution temperature was gradually increased from 5 to 100 °C, the CD spectrum for compounds **1**−**5** change gradually, showed a pattern featuring the triple-helix polypeptide with slight damage to the triple helix at higher temperatures. The positive Cotton effect disappeared at 223 nm (ESI, Fig. S2), which reflects the loosening of the triple helix and dissociation to single helical strands having polyproline-II conformations.

The resulting T_m value provides an indication of the conformational stability of a triple helix (Figure 3). The key result of our study is that the temperature of the triplex-to-singlex transition is higher for the Fc−collagen conjugates **1**−**5** than for the collagens lacking the N-terminal Fc group, indicating that the Fc group is stabilizing the triplex. The resulting T_m values, along with those of triple helices of same number of amino acids (lengths (in Å) for all of complexes were calculated from molecular modeling) without the Fc moiety are tabularized in Table 1 and compared in Figure 4 and Figure 5. This indicates that the modification of collagen by the Fc group stabilizes the triple helix, which can be due to changes in the local chemical environment, such as the additional hydrogen bond and/or hydrophobic interaction or the overall conformational change

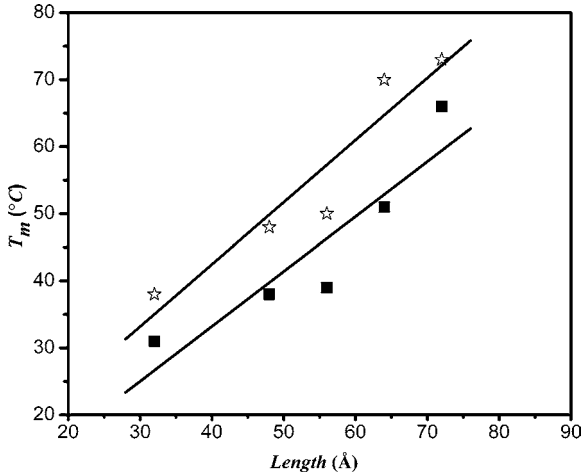

Figure 5. Comparison of thermal denaturation values of ferrocene-labeled collagen triple helices with unlabeled systems at 223 nm (star for the Fc-labeled systems, block for unlabeled systems).

including the whole Pro-Hyp-Gly moiety, which is induced by attachment of the hydrophobic Fc group.

Importantly, we observe a small hysteresis of the melting behavior, shown in Figure 6. Although, the overall features in the CD spectra recovered after heating and cooling of aqueous solutions of compounds **1**−**5**, the intensities of the bands were diminished. However, the positive and negative Cotton effects did not completely recover their intensities, but it proves that the conformational change in the triple helices was nearly reversible in aqueous solution.

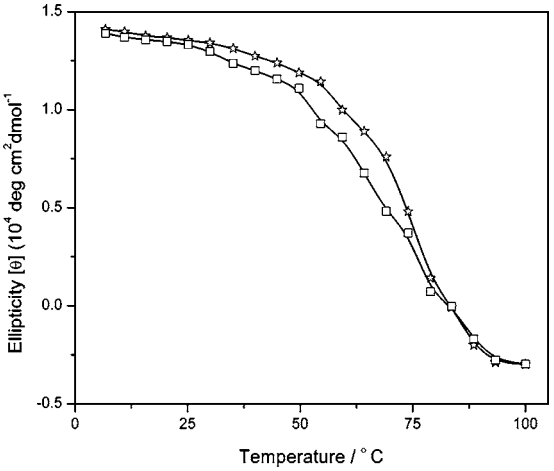

Figure 6. Thermal unfolding (☆) and refolding (□) of ferrocene-labeled collagen model (**5**) at 0.01 mM concentration in aqueous solution (pH 7.2) as monitored by CD at 223 nm. Melting and formation of the triple helix are virtually reversible.

Thermodynamic parameters are also estimated from CD transition profiles at 223 nm to understand the overall nature of the thermal stability of our Fc-labeled systems (ESI, Figures S3, S4). In thermal unfolding experiments, the thermodynamic parameters of the compounds **1**−**5** were calculated assuming two-state denaturation process (*14*) using Levenberg−Marquardt nonlinear least-squares method. The van't Hoff enthalpy, ΔH_m, was calculated by nonlinear least-squares fitting of the CD transition profile. The entropy change of the transition at T_m, ΔS_m, was calculated by dividing ΔH_m by T_m (see Table 1). Expectedly, ΔH_m increases with increasing the collagen chain length, which indicates an increase in stability as the collagen chain length increases. It is noteworthy to point out that this trend is reflected also in ΔH_m for Fc-labeled and unlabeled collagens (see ESI, Table S2, for $n = 9$), which again emphasizes that Fc-collagens appear stabilized compared to the corresponding unlabeled collagens in different ways. However, it should be noted that errors higher than 10% seem to be unavoidable for parameters derived from the van't Hoff equation.

CONCLUSION

We have presented the results of our comparative study showing that the attachment of an Fc group to the N-terminus of a collagen peptide stabilizes the formation of the collagen triple helix. These findings open an unexpected path for the design of stable and redox active collagen mimics and in the use of collageneous peptides for the studies on collagen structure, folding, and biochemistry. We are currently synthesizing some Fc-labeled collagen models in which individual amino acids are replaced. We are also investigating the possibility of electron-transfer reactions in Fc-labeled collagen films containing redox entities with a cysteine linker.

ACKNOWLEDGMENT

The Natural Science and Engineering Research Council of Canada supported this research. H.-B.K. is the Canada Research Chair in Biomaterials. Our thanks are also extended to Mr. Somenath Choudhury, Dr. Yitao Long, and Dr. Todd Sutherland Department of Chemistry, University of Saskatchewan, for their valuable discussion in the circular dichroism studies.

Supporting Information Available: HPLC traces and ESI-MS, solution CVs of Fc-labeled collagens and the CD spectrum of a modified and unmodified collagen system, the CD spectrum at different temperatures, table for thermodynamic data, details of thermal unfolding, data analysis (e.g., compound **5**). This material is available free of charge via the Internet at http://pubs.acs.org.

LITERATURE CITED

(1) Baum, J., and Brodsky, B. (2000) In *Mechanisms of Protein Folding*, 2nd ed. (Pain, R. H., Ed.) pp 330−351, Oxford University Press, Oxford.

(2) (a) Rich, A., and Crick, F. H. C. (1961) The Molecular Structure of Collagen. *J. Mol. Biol. 3*, 483−506. (b) Ramachandran, G. N. (1964) *In Treatise on Collagen* (Ramachandran, G. N., Ed.) pp 103−183, Academic Press: New York. (c) Radmer, R. J., and Klein, T. E. (2004) Severity of Osteogenesis Imperfecta and Structure of a Collagen-like Peptide Modeling a Lethal Mutation Site. *Biochemistry 43*, 5314−5323. (d) Persikov, A. V., Ramshaww, J. A. M., Kirkpatrick, A., and Brodsky, B. (2003) Triple-Helix Propensity of Hydroxyproline and Fluoroproline: Comparison of Host−Guest and Repeating Tripeptide Collagen Models. *J. Am. Chem. Soc. 125*, 11500−11501. (e) Hodges, J. A., and Ranies, R. T. (2003) Stereoelectronic Effects on Collagen Stability: The Dichotomy of 4-Fluoroproline Diastereomers. *J. Am. Chem. Soc. 125*, 9262−9263. (f) Doi, M., Nishi, Y., Uchiyama, S., Nakazawa, T., Ohkubo, T., and Kobayashi, Y. (2003) Characterization of Collagen Model Peptides Containing 4-Fluoroproline; (4(*S*)-Fluoroproline-Pro-Gly)$_{10}$ Forms a Triple Helix, but (4(*R*)-Fluoroproline-Pro-Gly)$_{10}$ Does Not. *J. Am. Chem. Soc. 125*, 9922−9923. (g) Berisio, R., Granata, V., Vitagliano, L., and Zagari, A. (2004) Imino Acids and Collagen Triple Helix Stability: Characterization of Collagen-like Polypeptides Containing Hyp-Hyp-Gly Sequence Repeats. *J. Am. Chem. Soc. 126*, 11402−11403.

(3) (a) Holmgren, S. K., Taylor, K. M., Brestscher, L. E., and Ranies, R. T. (1998) Code for collagen's stability deciphered. *Nature 392*, 666−667. (b) Umashankara, M., Babu, I. R., and Ganesh, K. N. (2003) Two prolines with a difference: contrasting stereoelectronic effects of 4*R*/*S*-aminoproline on triplex stability in collagen peptides [Pro(X)-Pro(Y)-Gly]$_n$. *Chem. Commun.* 2606−2607.

(4) Koide, T., Yuguchi, M., Kawakita, M., and Konno, H. (2002) Metal-Assisted Stabilization and Probing of Collagenous Triple Helices. *J. Am. Chem. Soc. 124*, 9388−9399.

(5) Bhatnagar, R. S., and Gough, C. A. (1996) in *Circular Dichroism and the Conformational Analysis of Biomolecules* (Fasman, G. D., Ed.) pp 183−199, Plenum Press, New York.

(6) (a) Feng, Y., Melacini, G., Taulane, J. P., and Goodman, M. (1996) Acetyl-Terminated and Template-Assembled Collagen-Based Polypeptides Composed of Gly-Pro-Hyp Sequences. 2. Synthesis and Conformational Analysis by Circular Dichroism, Ultraviolet Absorbance, and Optical Rotation. *J. Am. Chem. Soc. 118*, 10351−10358. (b) Feng, Y., Melacini, G., and Goodman, M. (1997) Collagen-Based Structures Containing the Peptoid Residue *N*-Isobutylglycine (Nleu): Synthesis and Biophysical Studies of Gly-Nleu-Pro Sequences by Circular Dichroism and Optical Rotation. *Biochemistry 36*, 8716−8724. (c) Cai, W., Kwok, S. W., Taulane, J. P., and Goodman, M. (2004) Metal-assisted Assembly and Stabilization of Collagen-like Triple Helices. *J. Am. Chem. Soc. 126*, 15030−15031.

(7) Kaiser, E., Colescott, R. L., Bossinger, C. D., and Cook, P. I. (1970) Color test for detection of free terminal amino groups in the solid-phase synthesis of peptides. *Anal. Biochem. 34*, 595−598.

(8) Christensen, T. (1979) Peptides, Structure and Biological Functions. *Proceedings of the 6th American Peptide Symposium* (Gross, E., Meienhofer, J., Eds.) pp 385−388, Pierce Chemical Co., Rockford, IL.

(9) Bella, J., Brodsky, B., and Bermanm, H. M. (1995) Hydration Structure of a Collagen Peptide. *Structure 3*, 893−906.

(10) Miller, M. H., Nemethy, G., and Scheraga, G. H. A. (1980) Calculations of the Structures of Collagen Models. Role of Interchain Interactions in Determining the Triple-Helical Coiled-Coil Conformation. 2. Poly(glycyl-prolyl-hydroxyprolyl). *Macromolecules 13*, 470−478.

(11) (a) Sakakibara, S., Kishida, Y., Okuyama, K., Tanaka, N., Ashida, T., and Kakudo, M. (1972) Single crystals of (Pro-Pro-Gly)$_{10}$, a synthetic polypeptide model of collagen. *J. Mol. Biol. 65*, 371−

372. (b) Brown, F. R., III, Corato, A. Di, Lorenzi, G. P., and Blout, E. R. (1972) Synthesis and structural studies of two collagen analogues: Poly (L-prolyl-L-seryl-glycyl) and poly (L-prolyl-L-alanyl-glycyl). *J. Mol. Biol. 63*, 85−99. (c) Toumadje, A., and Johnson, W. C., Jr. (1995) Systemin has the characteristics of a poly-(L-proline) II type helix. *J. Am. Chem. Soc. 117*, 7023−7024.

(12) (a) Jenkins, C. L., and Ranies, R. T. (2002) Insights on the conformational stability of collagen. *Nat. Prod. Rep. 19*, 49−59. (b) Periskov, A. V., Ramshaw, J. A. M., and Brodsky, B. (2000) Collagen model peptides: Sequence dependence of triple-helix stability. *Pept. Sci. 55*, 436−450. (c) Venugopal, M. G., Ramshaw, J. A. M., Braswell, E., Zhu, D., and Brodsky, B. (1994) Electrostatic Interactions in Collagen-like Triple-Helical Peptides. *Biochemistry 33*, 7948−7956.

(13) (a) Brown, F. R., III, Carver, J. P., and Blout, E. R. (1969) Low temperature circular dichroism of poly (glycyl-L-prolyl-L-alanine). *J. Mol. Biol. 39*, 307−313. (b) Brown, F. R., III, Hopfinger, A. J., and Blout, E. R. (1972) The collagen-like triple helix to random-chain transition: Experiment and theory. *J. Mol. Biol. 63*, 101−115.

(14) Kizhakkedathu, A. K. J. P., Nazeerunnisa, M., and Behere, D. V. (2002) Thermal Unfolding of Soybean Peroxidase. *J. Biol. Chem. 277*, 40717−40721.

BC050268L

Intracellular Traffic and Fate of Protein Transduction Domains HIV-1 TAT Peptide and Octaarginine. Implications for Their Utilization as Drug Delivery Vectors

Saly Al-Taei,[†,⊥] Neal A. Penning,[†,⊥] Jeremy C. Simpson,[‡] Shiroh Futaki,[§,||] Toshihide Takeuchi,[§] Ikuhiko Nakase,[§] and Arwyn T. Jones*[,†]

Welsh School of Pharmacy, Cardiff University, Cardiff, CF10 3XF, Wales, United Kingdom, Cell Biology and Biophysics, EMBL-Heidelberg, 69117 Heidelberg, Germany, Institute for Chemical Research, Kyoto University, Uji, Kyoto 611-0011, Japan, and PRESTO, Japan Science and Technology Agency (JST), Kawaguchi, Saitama 332-0012, Japan. Received September 10, 2005; Revised Manuscript Received November 17, 2005

Transduction domains such as those derived from the HIV-TAT protein are candidate vectors for intracellular delivery of therapeutic macromolecules such as DNA and proteins. The mechanism by which they enter cells is controversial, and very little spatial information regarding the downstream fate of these peptides from the plasma membrane is available. We studied endocytic traffic of fluorescent conjugates of HIV-TAT peptide and octaarginine in human hematopoietic cell lines K562 ($CD34^-$) and KG1a ($CD34^+$) and substantiated our findings in epithelia cells. Both peptides were efficiently internalized to endocytic pathways of both hematopoietic cell lines; however, comparative analysis of the intracellular location of the peptides with endocytic probes revealed major differences in spatial organization of their endocytic organelles and their interaction with the peptides at low temperatures. Double labeling confocal microscopy demonstrates that prelabeled lysosomes of all the tested cells are accessible to internalized peptides within 60 min of endocytic uptake. Incubation of cells with nocodazole and cytochalasin D inhibited peptide traffic from early to late endosomal structures, demonstrating a cytoskeletal requirement for lysosomal delivery. Disruption of Golgi and endoplasmic reticulum dynamics was without effect on peptide localization, suggesting that endosomes and lysosomes rather than these organelles are the major acceptor compartments for these molecules.

INTRODUCTION

Peptides derived from a number of proteins are able to enter cells and gain access to the cytosol and nucleus, thus generating much interest in their potential use as vectors for intracellular delivery of therapeutic molecules (*1*−*4*). To date, the most studied include cationic peptides derived from proteins such as the HIV transcription factor TAT, the *Drosophila melanogaster* homeobox protein Antennapedia (penetratin), and the herpes simplex virus protein VP22. These have been classified as cell penetrating peptides or protein transduction domains (PTD).[1] Predominantly in cell models, these peptides have been shown to have potential as cellular delivery vectors for enhancing the activities of their associated cargo, whether they be small molecules such as cytotoxic drugs or macromolecules such as genes and proteins (*1*, *2*, *5*−*7*). Transition of their use from cell culture systems to animal disease models has been slow, but the ability of TAT conjugates to protect mice against ischemia, to inhibit tumor growth, and enhance gene delivery in aerosol formulations suggests that these offer wide ranging pharmaceutical applications for treating a range of diseases (*2*, *7*−*9*).

Much research has been directed toward understanding how the peptides, either alone or in conjugation with other molecules, traverse biological barriers such as the plasma membrane and those lining endocytic organelles and the nucleus. Recently a number of cellular localization and uptake observations, documented for PTDs in cell culture models, were found to be due to artifacts caused by fixation and extensive nonspecific binding of the peptides to the plasma membrane at physiological and low temperatures (*10*, *11*). Recent data suggest a major role for endocytosis in PTD uptake but an agreed mechanism for their intracellular traffic, following internalization, is yet to emerge (*10*, *12*−*17*).

On the classical endocytic pathway, TAT peptides have been shown to colocalize with markers of early/recycling endosomes such as transferrin and FM4-64 (*10*, *18*). Since TAT−DNA conjugates or complexes have the capacity to modify gene expression, a fraction of the peptides therefore escape, presumably from the endocytic pathway or associated organelles, in an undefined mechanism to the cytosol. Internalized TAT peptides have also been shown to colocalize with the Golgi marker BODIPY-ceramide and in agreement with direct traffic from early endosomes to the Golgi complex, no peptide was visualized in Lysotracker-labeled late endosomes and lysosomes (*14*). These data suggest that the peptides could utilize the retrograde secretory pathway via the Golgi complex and enter the cytosol from the endoplasmic reticulum. Earlier reports have demonstrated that TAT peptide fusion proteins enter neutral caveosomes via plasma membrane caveolae (*13*), but more recent reports suggest that caveolae are not required for uptake

* To whom correspondence should be addressed: Welsh School of Pharmacy, Redwood Building, Cardiff University, Cardiff, CF10 3XF, Wales, United Kingdom. Tel: +44 (0) 2920876431, Fax: +44 (0) 2920874536; E-mail: jonesat@cardiff.ac.uk.

† Cardiff University.

‡ EMBL-Heidelberg.

§ Kyoto University.

|| PRESTO.

⊥ Both authors contributed equally to this work

[1] Abbreviations: BFA, Brefeldin A; CytD, Cytochalasin D; EEA1, Early Endosome Antigen 1; EIPA, 5-(*N*-ethyl-*N*-isopropyl)amiloride; PI 3-kinase, phosphatidylinositol 3-kinase, PTD, protein transduction domains; TFA, trifluoroacetic acid; TGN, *trans*-Golgi network; TMR, tetramethylrhodamine; TxR-Tf, Texas-Red-transferrin.

10.1021/bc050274h CCC: $33.50 © 2006 American Chemical Society
Published on Web 12/27/2005

(*16*). Conversely, TAT-conjugated liposomes were recently shown to enter acidic Lysotracker-positive compartments (*19*), and full-length TAT protein also entered acidic late endocytic structures containing the mannose 6-phosphate receptor (*20*). Indeed the ability of TAT protein to translocate to the cytosol was dependent on it reaching acidic organelles. For utilization of PTDs as cellular vectors for delivery of lysosome-fragile entities such as proteins and DNA, it is imperative that the trafficking route of these molecules downstream from the plasma membrane is delineated.

New nonviral systems for the delivery of macromolecules into hematopoietic cells are required for phenotype manipulation of precursor stem cells and for improved therapy against drug resistant leukemias (*21*). Green Fluorescent Protein conjugated to a TAT derivative and an alternate PTD were both found to be internalized into a number of primary hematopoietic cells, suggesting that this may be a promising avenue for delivery of macromolecular entities into these cells (*22*). In addition, overcoming multidrug resistance in leukemia cells via conjugation of a PTD to the anthracycline doxorubicin has also been demonstrated (*23*).

Overall it is clear that a greater understanding of PTD trafficking is a key requisite for extending their potential use in therapy. To address this we investigated and compared the intracellular traffic of fluorescent conjugates of TAT and octaarginine (R8) peptides in human leukemia KG1a-CD34$^+$ and K562-CD34$^-$ cells, that serve as models for primary hematopoietic stem cells and myeloid leukemia. In this report we show that despite the fact that the two cell lines have major differences in their interaction with PTDs at different temperatures and distinct organization of their endocytic pathways, they both deliver TAT-peptide and R8 to lysosomes. We extend these studies to adherent cells and demonstrate that lysosomal sequestration may be a common cellular fate following endocytic capture. Finally, the significance of these findings with respect to their potential as drug delivery vectors is discussed.

EXPERIMENTAL PROCEDURES

Reagents. Wortmannin, Cytochalasin D (CytD), 5-(*N*-ethyl-*N*-isopropyl)amiloride (EIPA), brefeldin A (BFA), nocodazole, and porcine intestinal mucosa heparin were from Sigma. Sheep anti-TGN46 was from Serotec, Oxford, UK, mouse anti-Lamp-II and anti-EEA1 antibodies were from DSHB, and BD Biosciences, Oxford, UK, respectively. Texas Red (TxR) (10000 Mw) and tetramethylrhodamine (TMR)−dextran conjugates, lysine fixable TxR-dextran (10000 Mw), TxR-transferrin (TxR-Tf), and Alexa594 and 488 labeled anti-sheep and anti-mouse antibodies were from Molecular Probes, Paisley, UK. Mounting medium containing 1.5 μg/mL 4′,6-diamidino-2-phenylindole dihydrochloride (DAPI) was from Vector Laboratories, Burlingame, CA. All cell culture reagents were from Invitrogen, Paisley, UK.

Peptide Synthesis. All the peptides used in this study were chemically synthesized as described below, and their structures are shown in Figure 1. All peptides were purified by high performance liquid chromatography (HPLC), and the molecular masses were confirmed by matrix-assisted laser desorption ionization time-of-flight mass spectrometry (MALDI-TOFMS).

TxR-labeled R8 peptide: The peptide chain was constructed by Fmoc (= 9-fluorenylmethyloxycarbonyl)-solid-phase peptide synthesis on a Rink amide resin (*24*) as previously reported (*25, 26*). After removal of the N-terminal Fmoc group, the N-terminus of the peptide resin was fluorescently labeled by treatment with TxR-X succinimidyl ester mixed isomer (Molecular Probes) (*27*). The fluorescently labeled peptide resins were then treated with trifluoroacetic acid (TFA)−ethanedithiol (EDT) (95:5) at 25 °C for 2 h to yield TxR−(Arg)$_8$-amide.

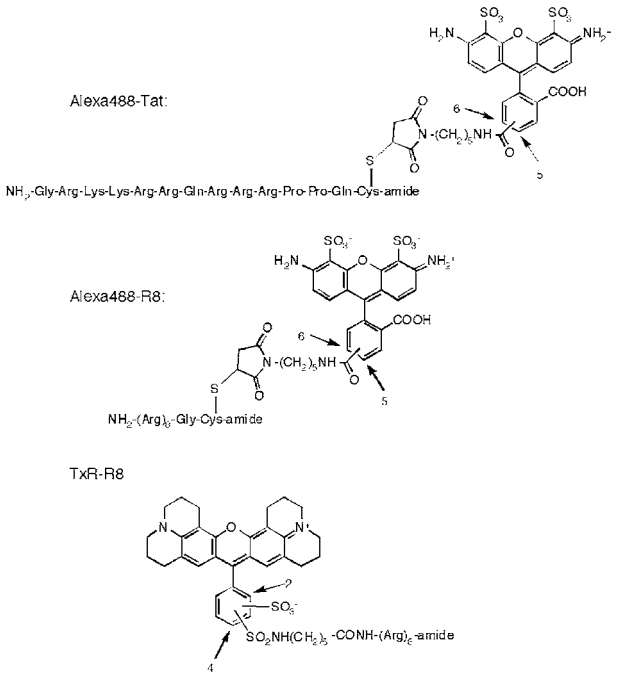

Figure 1. Structures of the fluorescently labeled peptides. In Alexa488-Tat and -R8, the linker is connected to the phenyl moiety at position 5 or 6, and in TxR-R8 the (sulfonamide) linker is connected at position 2 or 4 of the phenyl ring.

MALDI-TOFMS: 1969.0 [calcd for (M + H)$^+$: 1969.4]. Retention time in HPLC was 17.4 min [Column: Cosmosil 5C4-AR-300 (4.6 × 150 mm); Gradient: 5−95% B in A (A = H_2O containing 0.1% CF_3COOH, B = CH_3CN containing 0.1% CF_3COOH) over 40 min; Flow: 1 mL/min; Detection: 215 nm].

Alexa-labeled peptides (Alexa488-TAT or Alexa488-R8): The peptide segments bearing extra cysteine or glycylcysteine residues at the C-terminus of the arginine segments were prepared by Fmoc-solid-phase peptide synthesis followed by the treatment in TFA−EDT and HPLC purification. Peptides were then treated with Alexa488 C_5 maleimide sodium salt (Molecular Probes) and purified by HPLC. The sequences of the synthesized peptides are Alexa488-TAT, NH_2-Gly-Arg-Lys-Lys-Arg-Arg-Gln-Arg-Arg-Arg-Pro-Pro-Gln-Cys(Alexa)-amide; Alexa488-R8, NH_2-(Arg)8-Gly-Cys(Alexa)-amide. MALDI-TOFMS; Alexa-TAT: 2521.1 [calcd for (M + H)$^+$: 2520.9]; Alexa-R8: 2126.81 [calcd for (M + H)$^+$: 2126.4]. Retention time in HPLC: 3.1 min (Alexa488-Tat) and 3.0 min (Alexa488-R8) [Column: Chromolith Performance (4.6 × 100 mm); Gradient: 5−85% B in A (A = H_2O containing 0.1% CF_3COOH, B = CH_3CN containing 0.1% CF_3COOH) over 10 min; Flow: 4 mL/min; Detection: 215 nm].

Cell Culture. Cells were maintained at 37 °C in a humidified 5% CO_2 incubator. K562 cells, a gift from Dr. Paul Brennan (Cardiff University), and KG1a cells (ECACC 91030101) were maintained at a confluency of (0.5−5) × 10^6 in RPMI 1640 media supplemented with 10% fetal calf serum (FCS), 100 IU/mL penicillin, and 100μg/mL streptomycin. HeLa cells were maintained in D-MEM supplemented with 10% FCS, 100 IU/mL penicillin, and 100μg/mL streptomycin.

Fluorescence Microscopy. Images were acquired on either a Leica DMIRB inverted fluorescent microscope or a Leica SP2 RS confocal laser rapid scanning microscope as previously described (*28*). For double label live cell imaging, cells were loaded with endocytic markers or peptides as described below and washed in imaging medium, and aliquots were placed in eight-chambered coverglass slides (Nalgene Nunc International) prior to confocal microscopy. For this the cells were maintained at 37 °C/5% CO_2 and imaged at between 1.0 and 3.0 frames

s^{-1} using an UltraView RS real-time confocal system (Perkin-Elmer) consisting of a Zeiss Axiovert 200 microscope equipped with a 1.3 NA PlanFluar 100× objective and a three line Argon−Krypton laser. Images were merged and stacked using NIH ImageJ version 1.33 software, and the background fluorescence was removed using the 'despeckle' filter.

Transferrin Labeling in K562 and KG1a Cells. Cells (5×10^5) were incubated with 25 ng/mL TxR-Tf in 0.5 mL serum free media for 1 min at 37 °C prior to addition of 1 mL of ice cold 10 mM phosphate buffered serum, pH 7.4 (PBS). The cells were centrifuged for 1 min (1500*g*) at 4 °C and washed 4× in ice cold PBS containing 0.2% w/v BSA. The final cell pellet was resuspended in 70 μL of imaging medium (DMEM lacking Phenol Red containing 25 mM HEPES pH 7.4) and analyzed within 2 min by fluorescence microscopy.

For colocalization experiments of peptides with TxR-Tf, K562 cells were incubated with 3 μM Alexa488-TAT for 90 min prior to a further incubation in peptide free medium for 120 min. The cells were washed and incubated for 6 min at 37 °C with 50 ng/mL TxR-Tf in serum free medium containing 25 mM HEPES, pH 7.4. The cells were washed 3× in PBS and 1× in imaging medium prior to analysis by confocal microscopy.

Dextran Uptake and Distribution in K562 and KG1a Cells. For initial localization studies, 5×10^5 cells in 0.5 mL of complete medium were incubated for 60 min at 37 °C with 0.5 mg/mL TMR-dextran (*29*). The cells were then washed 4× in PBS and analyzed by fluorescence microscopy in imaging medium as described.

Peptide Uptake and Distribution in K562 and KG1a Cells. Cells (5×10^5) in 0.5 mL complete medium were incubated for 60 min at 37 °C with 1μM TxR-R8, Alexa488-R8 or 3μM Alexa-488 TAT. The cells were then washed 4× in PBS and analyzed by fluorescence microscopy in imaging medium as described. For BFA experiments cells were allowed to internalize the fluorescent peptides as above, washed and then incubated for 30 min at 37 °C in 5μg/mL BFA or control diluent. The cells were then analyzed by fluorescence microscopy.

Dextran and Peptide Uptake and Distribution in K562 and KG1a Cells. Cells (5×10^5) were incubated with TxR-dextran for 120 min as described, and the label was then chased into lysosomes via a further incubation in dextran-free medium for 300 min (chase) (*29*). At 120 and 180 min chase, the cells were washed to remove any recycled label. At the end of the chase period, the cells were washed and incubated with either 3 μM Alexa488-TAT or 1 μM Alexa488-R8 in complete medium for 60 min at 37 °C. The cells were washed 3× in PBS and analyzed by live-cell confocal microscopy as previously described. For analysis of the effects of pharmacological inhibitors of endocytic processes, dextran was internalized and chased as described prior to preincubation for 15 min at 37 °C with either 50 μM CytD or 10 μM nocodazole. In the continued presence of the drug the cells were then incubated at 37 °C for 60 min with Alexa488 peptides as described. The inhibitors were also present during the subsequent washing processes and confocal imaging.

Dextran and Peptide Uptake and Distribution in HeLa Cells. HeLa cells (1.2×10^5) were seeded on glass bottomed 35 mm culture dishes (MatTek Corporation, Ashland) and allowed to adhere for 15 h. The cells were then incubated for 120 min at 37 °C in complete medium containing 0.5 mg/mL TxR-dextran (*29*). Cells were washed and incubated for 240 min in complete medium prior to a further 60 min incubation in complete medium containing 2 μM Alexa488-TAT. The cells were washed and analyzed by confocal microscopy at 37 °C/5% CO_2.

Quantification of Alexa488-peptide Uptake by Flow Cytometry. K562 cells (5×10^5) were washed 2× in PBS and resuspended in 200 μL of RPMI 1640 medium supplemented with 10% FCS and containing either 10 μM EIPA, 150 nM wortmannin, 10 μM nocodazole, or their respective diluents. The cells were incubated for 15 min at 37 °C prior to the addition of 3 μM Alexa488-Tat or 1 μM Alexa488-R8 and incubated for 60 min in the continued presence of the drug. Equivalent aliquots of cells were precooled to 4 °C and incubated with the peptides on ice. Following all peptide incubations, the cells were washed 3× in PBS prior to incubation in 0.25 g/L trypsin for 5 min at 37 °C. Trypsinization was stopped by addition of an excess of ice cold PBS and cells were washed 2× in PBS, 3× in 15 μg/mL heparin/PBS and a further two washes in ice cold PBS. The cells were finally resuspended in 200 μL of PBS, and fluorescence was measured immediately on a Becton Dickinson FACSCalibur analyzer. The fluorescence of 10000 viable cells was acquired. Each experiment was performed at least two times, each condition was analyzed in triplicate, and statistical significance was assessed by analysis of variance (ANOVA), followed by Dunnett's multiple comparison between means.

Immunostaining. K562/KG1a cells: 1×10^6 cells were washed in PBS, fixed in 2% paraformaldehyde (PFA) in PBS for 15 min, and washed, and aliquots were transferred to wells on a multispot microscope slide (Hendley, UK). For some experiments, the lysosomes were preloaded as described with lysine fixable TxR-dextran prior to fixing. The cells were dried on to the slide and permeabilized with 0.1% Triton X-100 in PBS (for TGN46, EEA1 labeling) or acetone (for Lamp-II labeling) before blocking nonspecific binding sites with 10% v/v fetal calf serum/PBS for 10 min. Cells were then incubated with anti-TGN46, Lamp-II or EEA1 antibodies for 30 min in a humidified box at 37 °C. Cells were washed 3× with 0.1% Triton X-100 in PBS (TGN46, EEA1) or PBS alone (Lamp-II) and then incubated for 30 min with Alexa594 or Alexa488 conjugated secondary antibodies. The cells were washed as before and overlaid with 5 μL of mounting medium containing DAPI. The wells were covered with a coverslip and sealed with nail polish prior to analysis by confocal fluorescence microscopy. To test the effect of BFA on TGN46 labeling, cells were incubated with 5 μg/mL BFA in complete medium for 30 min at 37 °C prior to fixation and immunolabeling. HeLa cells: BFA treated (as above) or control cells were washed in PBS and processed for immunofluorescence microscopy as previously described (*28*) and labeled with antibodies against TGN46 or Lamp-II.

RESULTS

Distribution of TAT and R8 in Hematopoietic Cells. Numerous recent reports have provided strong evidence that endocytosis is a major entry route for PTDs such as TAT and penetratin. The ability to monitor and resolve traffic downstream of the plasma membrane in adherent cell culture models, using fluorescence microscopy, is hampered by the extensive binding of these peptides to the plasma membrane and tissue culture surfaces. We therefore investigated the uptake of two fluorescently conjugated PTD peptides TAT and R8 in nonadherent leukemia cell lines K562 and KG1a. For this, both cell lines were initially incubated with 3 μM Alexa488-TAT for 120 min at 37 °C, and after washing, the cellular localization of the peptide was analyzed by fluorescence microscopy. As fixing has been shown to cause major artifacts in the intracellular localization of PTDs, all fluorescence microscopy studies, unless otherwise specified, were performed in live cells. Figure 2 shows that although both cell lines contained internalized peptide, there were major differences in its subcellular distribution. In K562

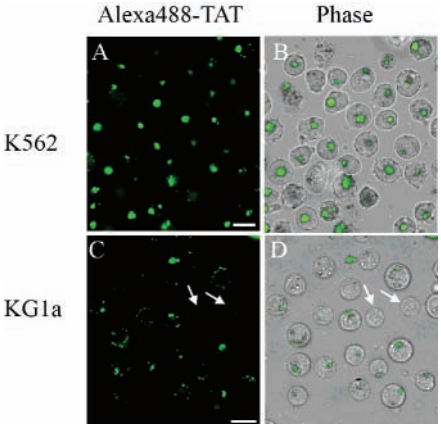

Figure 2. Distribution of Alexa488-TAT in myeloid leukemia cell lines. K562 (A,B) and KG1a (C,D) cells were incubated with 3μM Alexa488-TAT for 120 min at 37 °C prior to washing and analysis by fluorescence and bright field microscopy. Arrows denote KG1a cells containing very low amounts of fluorescence. Scale bars 25 μm.

cells, labeling was enriched in the perinuclear region; however, in KG1a cells, the peptide was predominantly localized in small disperse cytoplasmic vesicular structures. The majority of the cells contained labeled structures, but within each cell line there was variation in the intensity of labeling. Under these conditions, we could not detect significant nuclear or cytosolic labeling.

In view of these data and the paucity of information on the subcellular organization of organelles at specific locations on the endocytic pathway in these cell lines, especially KG1a, we labeled distinct endocytic structures of both cell lines with fluorescent probes whose intracellular fate following endocytic capture is well defined. Transferrin enters cells via clathrin-coated vesicles after binding to the transferrin receptor and traffics through early and recycling endosomes en route for return to the plasma membrane (*30*). In this study we generally define early endosomes as organelles containing internalized probe after 0−10 min of uptake, late endosomes (10−30 min), lysosomes (30+ min) (*30, 31*). Plasma membrane derived vesicles and early endosomes were labeled in both cell lines by internalizing TxR-Tf for only 1 min, followed by immediate microscopic analysis. In both cell lines the plasma membrane was labeled, in addition to distinct punctate structures (Figure 3A−D). Endocytosis of dextran is also well characterized in terms of its fluid phase uptake into early endosomes, through late endosomes, and finally to lysosomes (*32, 33*). K562 and KG1a cells were incubated with TMR-dextran for 60 min, thus allowing labeling of early and late endosomal compartments. Similar to observations with Alexa488-TAT (Figure 2), dextran-labeled vesicles were strongly enriched in the perinuclear region of K562 cells (Figure 3E,F); however, in KG1a cells the dextran-labeled structures were distributed throughout the peripheral cytoplasm (Figure 3G,H). The subcellular distribution profiles of fluorescent TAT and R8 after internalization at 37 °C for 60 min were then compared. As shown in Figure 3I−P, the distribution patterns of both peptides were similar to each other in each respective cell line, indicative of trafficking to the same structures. We observed minimal plasma membrane labeling of the peptides at 37 °C, and the labeling was predominantly confined to internal punctate structures. Cells treated with peptides had normal morphologies, and using an apoptosis assay utilizing YO−PRO-1 and propidium iodide dyes followed by flow cytometry, we found no increase in permeability to these agents in either cell line when they were incubated with 3 μM TAT or R8 for up to 4 h (data not shown).

Effect of Endocytosis Inhibitors on Peptide Uptake. The contribution of endocytosis to peptide uptake was then investigated by flow cytometry after treating cells with pharmacological agents that disrupt endocytic processes. K562 cells were pretreated with wortmannin, nocodazole, or EIPA prior to addition of the peptides for 60 min in the continued presence of the drug. The PI 3-kinase inhibitor wortmannin affects uptake at the plasma membrane and several downstream trafficking events (*34, 35*), nocodazole depolymerizes microtubules and also affects numerous endocytic processes including uptake at the plasma membrane and delivery through the endocytic pathway (*36*), while the amiloride analogue EIPA has been shown to inhibit macropinocytosis (*37*). We observed, in most cases, similar effects on uptake of both TAT and R8 in the presence of these agents (Figure 4A). The addition of 10 μM EIPA resulted in only a minimal decrease in peptide uptake, with only the uptake of R8 being statistically significant. We also performed experiments at higher EIPA concentrations, but toxicity issues possibly related to increases in intracellular pH and apoptosis (*38*) predominated over uptake effects (data not shown). Microtubule depolymerization inhibited uptake of both peptides by ∼30%, and cells treated with wortmannin had significantly lower (∼50%) fluorescence. The effect of incubating cells with CytD and methyl-β-cyclodextrin to compare the requirements of the actin cytoskeleton and lipid rafts, respectively, on peptide uptake (*39*) was also investigated. However, even the relatively mild treatments that we used for reducing plasma membrane labeling following internalization led to a significant enhancement of minimal effects of CytD that were observed in the absence of trypsinization, and in the case of methyl-β-cyclodextrin, trypsinization led to significant increases in dead cells identified via trypan blue staining.[2]

Finally to determine whether peptide internalization in these cells is an energy-dependent process, the effects of reducing incubation temperature was examined. Incubating K562 cells with peptides on ice resulted in a >88% decrease in fluorescence compared to cells incubated with the peptide at 37 °C (Figure 4A). In KG1a cells, however, the fluorescence of cells incubated with peptide on ice was often equal to or even higher than those incubated at 37 °C. Using flow cytometry, we compared cell numbers versus fluorescence intensity profiles of K562 and KG1a cells after incubation with both peptides at 4 °C and 37 °C and for 5 and 60 min (Figure 4B). After 5 min there was a clear difference between the 37 °C and 4 °C profiles for both peptides in the two cell lines, with the expected increased fluorescence at the higher temperature. However, after 60 min there was significant fluorescence in KG1a cells incubated at 4 °C, and the mean fluorescence of a large population of these cells was often higher than those incubated at 37 °C. These experiments were performed three times with two batches of peptides, and although there was much higher variation in cell-associated fluorescence at 4 °C, the value was always at least 50% of the control 37 °C value and in some cases was 2-fold higher.

Peptide distribution in KG1a cells after incubation at the two temperatures was then analyzed by fluorescence microscopy. The left panel of Figure 4C shows that after incubating the cells with R8 peptide on ice for 60 min followed by trypsinization and heparin washes, cell-associated fluorescence was still clearly evident, but rather than being located in distinct punctate structures, as previously observed (see Figure 3O), the peptide diffusely labeled and outlined the entire cell. Although the staining pattern was the same in all cells, we observed a high degree of heterogeneity with respect to fluorescence intensity, as some cells were very bright and others had much lower fluorescence. This heterogeneity is clearly observed by comparing the fluorescence of the three cells in Figure 4C. In cells incubated with the peptide at 37 °C, and then treated with trypsin and heparin, the peptide was predominantly localized in

[2] A.T.J., personal communication.

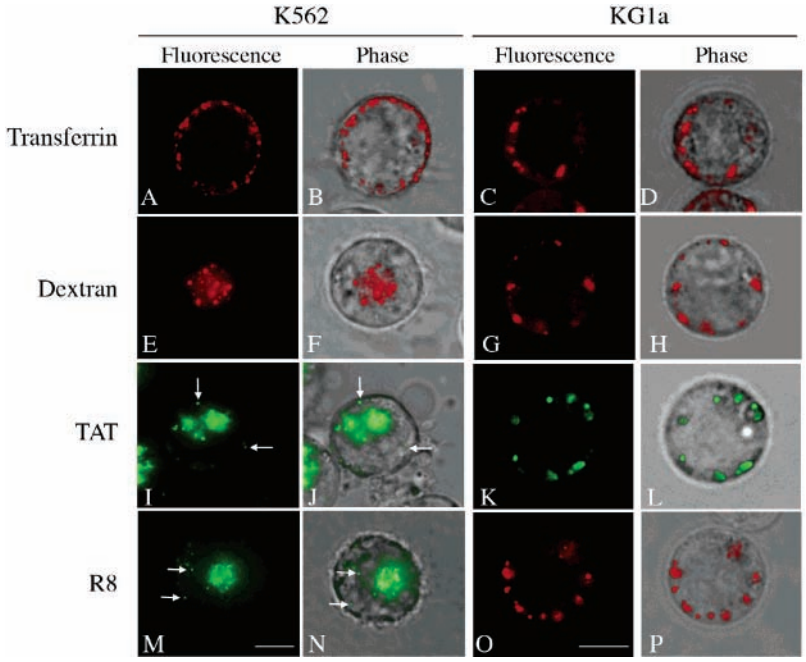

Figure 3. Comparison of cellular localization of endocytic probes with TAT and R8. (A−H) K562 (A,B, E,F) and KG1a (C,D, G,H) cells were incubated with Texas-red transferrin for 1 min (A−D) or TMR-dextran for 60 min (E−H) prior to washing and analysis by fluorescence and bright field microscopy. (I−P) K562 (I,J, M,N) and KG1a (K,L, O,P) cells were incubated with 3 μM Alexa488-TAT (I−L), 1 μM Alexa488-R8 (M,N) or 1 μM TxR-R8 (O,P) for 60 min prior to washing and analysis by fluorescence and bright field microscopy. Arrows show peptide-positive vesicles peripheral to the perinuclear structures. Scale bars 10 μm.

vesicular structures, similar to that seen in untreated cells. Increasing the trypsin concentration 2-fold, the length of the heparin washes to 5 min and the heparin concentration to 50 μg/mL did not significantly diminish the amount of peptide bound to the cells (data not shown).

Identification of Peptide Labeled Structures. Previous analysis of the intracellular traffic of TAT peptide in HeLa cells suggested that it bypasses late endosomal and lysosomal structures and traffics to the Golgi (*14*). We therefore further characterized the peptide labeled vesicles, initially in leukemia cells, and investigated whether they were morphologically sensitive to agents that disrupt membrane traffic on endocytic and secretory pathways. Cells treated with the phosphoinositide 3-kinase inhibitor wortmannin are characterized by the appearance of swollen vacuole-like endosomes (*35*, *40*). This is primarily due to inhibition of hVPS34 protein that is required for formation of phosphatilylinositol 3-phosphate on endosome membranes and vesicles within the lumen of the endosome (*41*). We therefore analyzed the localization pattern of Alexa488-TAT after uptake into cells pretreated with 150 nM wortmannin. Only minor wortmannin effects were observed in K562 cells (Figure 5A−D), but this was difficult to visualize, as the peptide, despite the presence of the drug, still accumulated in the perinuclear region. In KG1a cells a dramatic wortmannin-induced redistribution of both TxR-R8 and Alexa488-TAT into enlarged vacuole-like structures was observed (Figure 5E−J).

To investigate whether TAT and R8 peptides traffic to the Golgi, cells were incubated with either Alexa488-TAT or -R8 for 120 min and then incubated for 60 min in the presence of the Golgi-disrupting agent brefeldin A (BFA) (*42*). Figure 5A-D shows that in K562 cells, there was no visible difference in the Alexa488-TAT labeling pattern in the presence or absence of BFA. This experiment was also performed in KG1a cells, and they yielded the same results (data not shown). To analyze the localization of the Golgi in these cell lines and to assess the activity of BFA, cells incubated in the absence or presence of the drug were fixed and immunolabeled with antibodies against the *trans*-Golgi marker TGN46. Previous studies have shown that BFA collapses the *cis/medial* Golgi cisterna into the endoplasmic reticulum and causes the relocation of the *trans*-Golgi network (TGN) to a compact centrosomal location with some diffuse staining of the cytoplasm (*43*−*45*). In untreated K562 cells, TGN46 labeling was almost exclusively confined to a perinuclear region that was, as previously shown, conspicuous in cells incubated with the fluorescent peptides (Figure 6E,F). However, on treatment with BFA, a relocation of a significant fraction of the protein to diffuse cytoplasmic vesicles and reticular networks was observed (Figure 6G,H). The Golgi was also prominent in untreated KG1a cells (Figure 6I,J) and unlike in K562 cells which harbor both TGN46, TAT, and R8 in a perinuclear region, the TGN distribution in KG1a cells was markedly different to that of the internalized peptides (Figure 3O,P). TGN46 labeling in KG1a cells was also markedly sensitive to BFA (Figure 6K,L). Together, the data strongly suggest that the major fraction of internalized TAT and R8 does not traffic to the Golgi.

These data prompted us to design further experiments to characterize the organelles enriched with endocytosed TAT and R8. K562 cells were incubated with TxR-dextran for 120 min prior to washing and a further incubation in dextran-free medium for 5 h to allow the label to empty from early endosomes and traffic (chase) to lysosomal compartments (*29*, *33*, *46*, *47*). By this method, the label would be depleted from early and late endosomes, and the potential re-entry of recycled label was minimized by washing during the chase period. Dextran-loaded cells were then incubated for 60 min with Alexa488-TAT or -R8, and the subcellular location of both labels was analyzed by double-labeling confocal microscopy. We observed extensive colocalization of both R8 and TAT with dextran in highly motile perinuclear structures of the K562 cells (Figure 7A−C; Movie 1, Supporting Information). Some single-labeled structures were observed, possibly representing peptide that had not yet reached the dextran-loaded compartment; tubulation of TAT-labeled structures was also apparent. A similar degree of high colocalization was also observed when dextran-loaded cells were incubated with Alexa488-R8 (Figure 7D−F; Movie 2, Supporting Information).

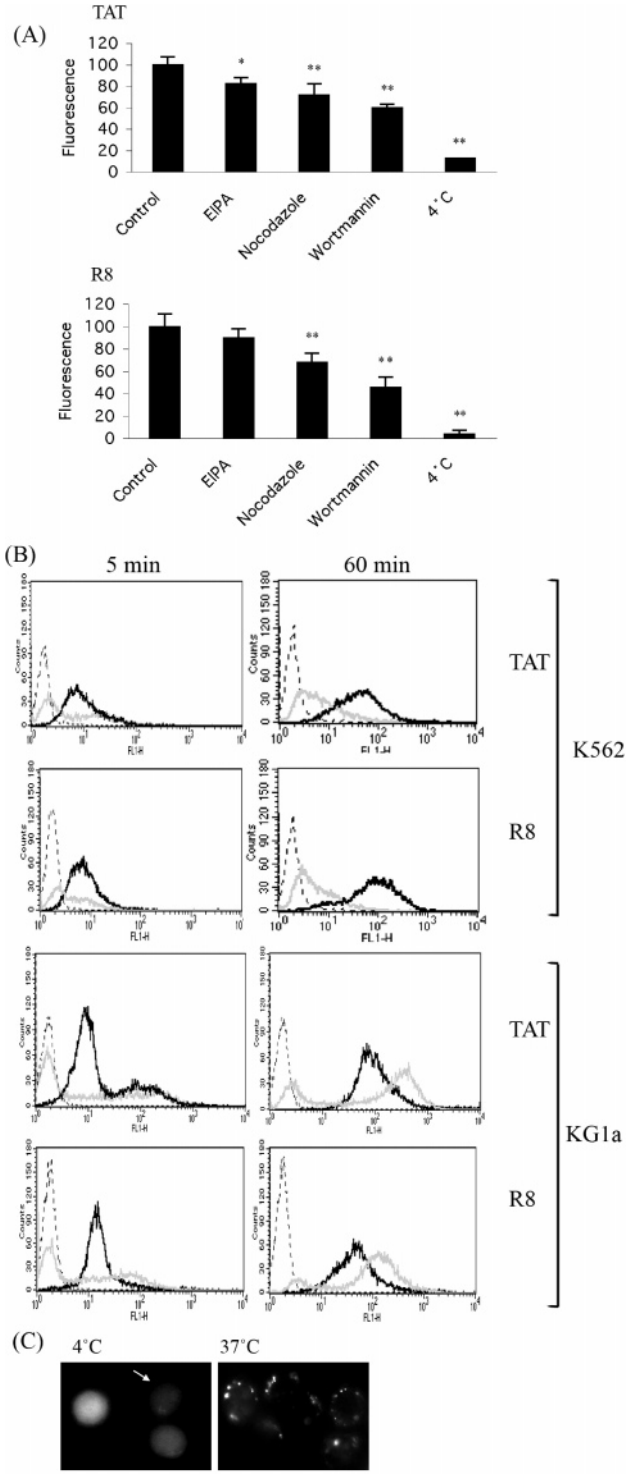

Figure 4. Effects of temperature and pharmacological inhibitors of endocytosis on uptake of TAT and R8. (A) K562 cells preincubated with diluent (control) or 10 μM EIPA, 10 μM nocodazole, and 150 nM wortmannin were incubated, in the continued presence of the drug, with 1 μM Alexa488-TAT (upper panel) or 3 μM Alexa488-R8 (lower panel) for 60 min prior to trypsin/heparin treatment and analysis by flow cytometry as described in Materials and Methods. Equivalent aliquots of cells were incubated with the peptides on ice (4 °C). (B) K562 and KG1a cells were incubated with 3 μM Alexa488-TAT or 1 μM Alexa488-R8 for either 5 or 60 min at 37 °C or 4 °C prior to trypsin/heparin treatment and analysis by flow cytometry. The number of cells (*y*-axis) is plotted against the fluorescence signal of cells (*x*-axis); 37 °C (black line), 4 °C (grey line) untreated cells dotted line. (C) KG1a cells were incubated with 1 μM Alexa488-R8 for 60 min at either 4 °C (left panel) or 37 °C (right panel) to prior to trypsin/heparin treatment and after by fluorescence microscopy. Arrow denotes cell with low fluorescence. * Statistically significant * $p < 0.05$, ** $p < 0.01$.

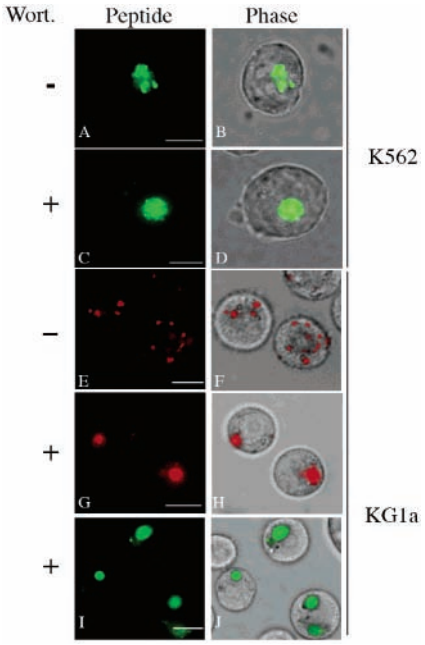

Figure 5. TAT and R8 distribution in wortmannin treated cells. K562 (A−D) or KG1a (E−J) cells were incubated for 15 min in control media (A,B, E,F) or media containing 150 nM wortmannin (C,D, G−J). The cells were then incubated with 3 μM Alexa488-TAT (A−D), 1 μM TxR-R8 (E−H) or 3 μM Alexa488-TAT (I,J) for 60 min in the continued presence of the drug or DMSO equivalent. The cells were washed and analyzed by fluorescence and bright field microscopy. Scale bars 10 μm.

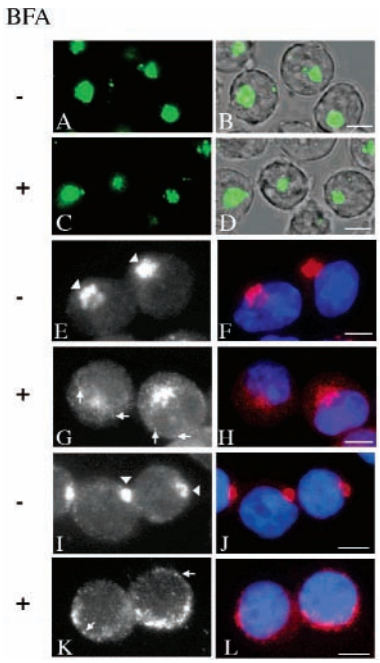

Figure 6. Cellular distribution of Alexa488-TAT in BFA treated K562 and KG1a cells. (A−D) K562 cells were incubated with 3 μM Alexa488-TAT for 60 min prior to washing and a further incubation for 30 min in control medium or medium containing (5 μg/mL) BFA. The cells were washed and analyzed by fluorescence and bright field microscopy. (E−L) K562 (E−H) or KG1a (I−L) cells were incubated in the absence or presence of 5 μg/mL BFA for 30 min prior to fixing and labeling with anti-TGN46 antibodies followed by secondary Alexa594 anti-sheep antibodies and analysis by fluorescence microscopy. Arrowheads denote compact Golgi staining in control cells, arrows denote TGN46-positive vesicles in BFA-treated cells. Scale bars 10 μm.

We then investigated whether the peptides, in a fashion similar to dextran, could be depleted from early endosomes and

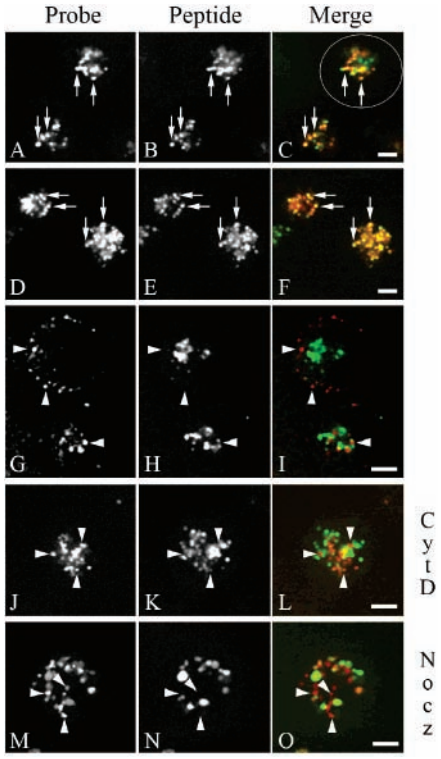

Figure 7. Colocalization of TAT and R8 with dextran in lysosomes of K562 cells. (A−F) K562 cells were incubated in the presence of TxR-dextran for 120 min and then washed and further incubated in dextran-free medium (chase) for 300 min. The cells were then allowed to internalize 3 μM Alexa488-TAT (A−C) or 1 μM Alexa488-R8 (D−F) for 60 min prior to washing and analysis by live-cell confocal microscopy. (G−I) K562 cells were allowed to internalize Alexa488-TAT for 90 min prior to washing and incubating in peptide free medium for 120 min. Cells were then incubated in 50 ng/mL TxR-Tf for 6 min prior to washing and analysis by live-cell confocal microscopy. (J−O) Cells were incubated with TxR-dextran as in A−F and following the chase period the cells were preincubated for 15 min with 50 μM CytD (J−L) or 10 μM nocodazole (M−O) and then incubated with 3 μM Alexa488-TAT in the continued presence of the drug. The cells were washed and analyzed by live-cell confocal microscopy. Arrows denote colocalization of peptide with dextran in the perinuclear region, and arrowheads denote uniquely labeled structures. The circle in C represents the plasma membrane of the cell. The data in A−O show the first frame of the accompanying movies: Movie 1 Image C, Movie 2 Image F, Movie 3 Image I, Movie 4 Image L, and Movie 5 Image O. Scale bars 10 μm.

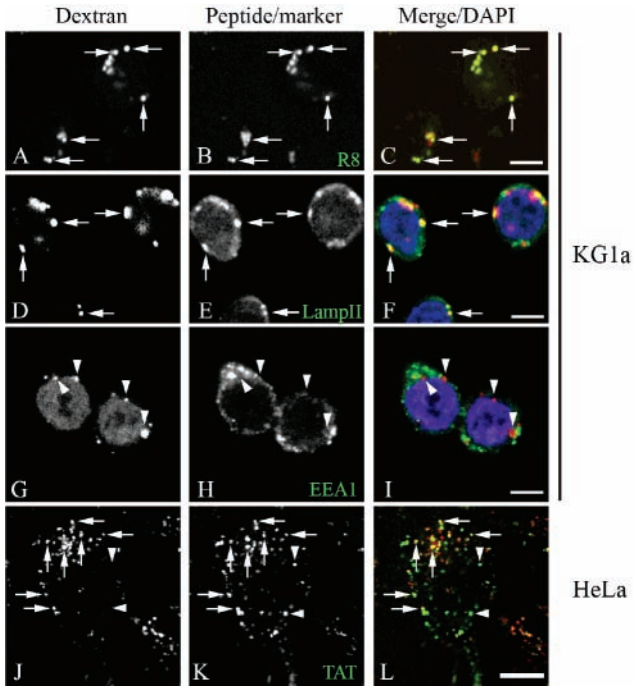

Figure 8. Colocalization of Alexa488-TAT and dextran in lysosomes of KG1a and HeLa cells. KG1a (A−I) and HeLa cells (J−L) were incubated in the presence of TxR-dextran (A−C, J−L) or (D−I) lysine fixable TxR-dextran for 120 min and then washed and further incubated in dextran-free medium (chase) for 300 min. (A−C, J−L). Cells were then incubated with 1 μM Alexa488-R8 (A−C) or 3 μM Alexa488-TAT (J−L) for 60 min prior to washing and analysis by live-cell confocal microscopy or immediately fixed and labeled with antibodies against Lamp-II (D−F) or EEA1 (G−I) and secondary Alexa488 conjugated anti-mouse antibodies and analyzed by confocal fluorescence microscopy. Arrows in A−C and J−L denote colocalization of TxR-dextran with Alexa488 peptides and arrowheads denote peptide unique structures. Arrows in D−F show colocalization of dextran with Lamp-II and arrowheads in G−I show dextran positive EEA1 negative structures. A−C, J−L show the first frame of the movies: Movie 6 Image C and Movie 7 Image L. Scale bars 10 μm.

chased into lysosomal structures. For this, K562 cells were allowed to internalize Alexa488-TAT for 120 min prior to washing and chasing the label through the endocytic pathway via a further 90 min incubation in peptide-free medium. Early endosomes were then labeled by a 6 min incubation with 50 ng/mL TxR-Tf prior to washing and live cell imaging. TxR-Tf was mainly localized to peripheral cytoplasmic structures, but interestingly in this short incubation time and during the imaging process a fraction of the ligand had traversed into a perinuclear location (Figure 7G−I; Movie 3, Supporting Information). The perinuclear staining is more prominent in the lower cell in Figure 7G; however, both peripheral and perinuclear structures were distinct from TAT-labeled structures with very little colocalization between the two labels. We next investigated whether actin disruption inhibited the delivery of TAT to dextran-labeled lysosomes. TxR-dextran was first chased into K562 lysosomes as previously described, and then the cells were preincubated with 50 μM CytD for 15 min prior to adding 3 μM Alexa488-TAT and incubating for a further 60 min in the continued presence of the drug. Figure 7J−L and Movie 4 (Supporting Information) show that there is very little colocalization of TAT and dextran in these cells with both probes labeling distinct vesicles. The distribution of peptide labeling was quite variable, but peptide-labeled structures were often peripheral to the lysosomes, the distribution of which were relatively unaffected by CytD. These observations strongly suggest that the traffic of TAT to lysosomes has a requirement for the actin cytoskeleton.

Lysosomes have been shown to be associated with microtubules, and loss of microtubule integrity has been shown to affect lysosome distribution, and delivery of material to late endocytic structures (*48, 49*). We therefore used the microtubule-disrupting agent nocodazole to investigate the involvement of microtubules in peptide traffic. K562 lysosomes were labeled with dextran as described, and then Alexa488-TAT was incubated in nocodazole pretreated cells in the continued presence of the drug. There was very little colocalization of the two probes in these cells (Figure 7M−O; Movie 5, Supporting Information), and both peptide and dextran were localized in vesicular structures that were scattered throughout the cytoplasm. In these experiments nocodazole appeared to inhibit traffic of the peptide to the perinuclear region and also to dissipate the perinuclear lysosomes. The movie also demonstrates that compared to control cells there was very little overall vesicular movement in cells treated with nocodazole. Large swollen TAT-labeled vesicles of the type shown in Figure 7N were observed in many cells but this was not a universal feature.

Colocalization of dextran with the two peptides in lysosomes was also investigated in KG1a cells, and Figure 8A−C and

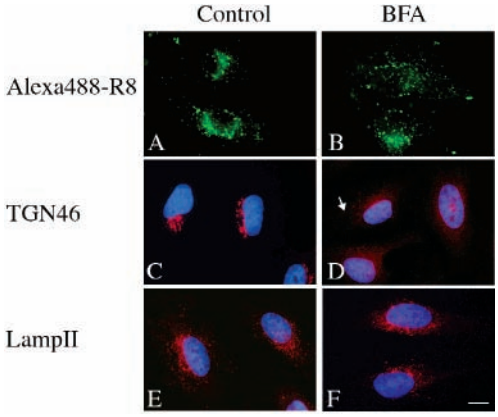

Figure 9. BFA does not affect the subcellular distribution of Alexa488-R8 in HeLa cells. (A−B) HeLa cells were incubated for 120 min with 1 μM Alexa488-R8 prior to incubation for 60 min in control diluent or 5 μg/mL BFA. The cells were then washed visualized by fluorescence microscopy. (C−F) HeLa cells were incubated for 60 min with control diluent or 5 μg/mL BFA prior to fixing and immunostaining with antibodies against TGN46 (C−D) or Lamp-II (E−F) and secondary Alexa594 conjugated anti-sheep (C−D) or anti mouse (E−F) antibodies. The cells were then analyzed by fluorescence microscopy. Arrow denotes BFA induced TGN46 positive tubule. Scale bar 10 μm.

Movie 6 (Supporting Information) show that Alexa488-R8 and dextran both labeled the same more diffusely labeled vesicles. Alexa488-TAT similarly colocalized with dextran in KG1a cells (data not shown). Together, these results demonstrate that TAT and R8 are delivered to lysosomal structures, and this process requires functional actin and microtubular networks.

To confirm that the dextran/peptide-positive organelles were conventional late endosomes and lysosomes, we fixed and labeled KG1a cells containing previously internalized and chased Lysine fixable TxR-dextran with antibodies against the early endosomal marker EEA1 and the late endosome/lysosome marker Lamp-II (*28, 50*). Figure 8D-I shows extensive colocalization between TxR-dextran and Lamp-II but minimal colocalization between EEA1 and dextran. Thus, a 5-h chase period is sufficient to deplete early endocytic organelles of internalized dextran and deliver the ligand to late endocytic, Lamp-II-positive, structures. Similar observations were observed in K562 cells (data not shown).

In view of the fact that we predominantly observed lysosome labeling as opposed to Golgi labeling in leukemia cells, we performed similar experiments in epithelial cells. For this, HeLa lysosomes were similarly labeled with TxR-dextran prior to incubation for 60 min with 3 μM Alexa488-TAT. A representative cell is shown in Figure 8J−L, and this together with Movie 7 (Supporting Information) demonstrates that both labels are located in mobile vesicular structures and short tubules. In agreement with the data from the K562 and KG1a cells, there are numerous examples of vesicles containing both labels, thus demonstrating that a significant fraction of TAT can be delivered to lysosomes within 1 h of incubation. As expected, there were also examples of vesicular structures positive for only one label.

To determine whether peptide distribution in HeLa cells is sensitive to Golgi disruption, cells were incubated with Alexa488-TAT for 120 min prior to a further 60 min incubation in the presence of 5 μg/mL BFA; separate control and BFA treated cells were also fixed and labeled with antibodies against TGN46. In agreement with the data in leukemia cells, BFA had no major effect on the distribution of Alexa488-R8 or -TAT (Figure 9A,B and data not shown). In the presence of BFA, the peptides remained localized in a typical vesicular pattern, enriched to differing extents in the perinuclear region. TGN46 labeling in these cells was highly sensitive to BFA treatment, and the protein dissipated from the perinuclear location to diffuse reticular and tubular structures (Figure 9C,D). We did not find similar TAT peptide-labeled structures in cells treated with BFA. Finally, HeLa cells were incubated with BFA for 60 min and then fixed and labeled with antibodies against Lamp-II and in agreement with our earlier findings, and concordant with other studies (*45*), we observed that the distribution of late endosomes and lysosomes was also predominantly unaffected by BFA treatment (Figure 9E,F).

DISCUSSION

The mechanism of entry and subsequent cellular location of cationic peptides such as those derived from HIV-TAT has received much focus due to their considerable potential as delivery vectors for a range of therapeutic entities. Based on a number of recent observations, there is now widespread acceptance that a large fraction of the material that crosses the plasma membrane does so by an endocytic mechanism. Whether uptake is mediated via a specific plasma membrane domain or receptors is unresolved, as agents that disrupt lipid rafts, macropinocytosis, and clathrin-mediated endocytic events can all inhibit peptide uptake to various extents.

Numerous reports also show that trypsinization and heparin washing can remove a significant fraction of cell-associated peptide confined to the plasma membrane. We and others have however shown that differences in cell-associated fluorescence between peptide incubations performed at 4 °C and 37 °C may be less than 50% (*27, 51*). The latter study also suggested that this is highly dependent on the sequence of the peptide, and that generally the extent of peptide binding at 4 °C is more heterogeneous compared with cells incubated with peptides at 37 °C. In agreement with other studies in HeLa cells (*52*), we observe in both K562 and KG1a cells some heterogeneity in the fluorescent intensities at 37 °C; however, the majority of peptide was confined to vesicular structures. There was very little cell-associated peptide in K562 cells incubated at 4 °C, but this was not the case for KG1a cells, suggesting that they have a very different repertoire of lipids and proteins at the plasma membrane; this may be a reflection of their more primitive differentiation status. Peptide distribution in KG1a cells was highly temperature specific, suggesting that distinct cellular interaction mechanisms operate at low and physiological temperatures.

Though 10 μM amiloride was shown to inhibit approximately 60% of TAT peptide in Namalwa cells (*39*), we previously showed in HeLa cells that 70% R8 uptake occurs in an amiloride insensitive manner (*27*). Here we show that TAT and R8 uptake in K562 cells was relatively insensitive to this drug; together these suggest that macropinocytosis is not the sole entry mechanism for these peptides. K562 cells do not express caveolin 1 and are phenotypically devoid of plasma membrane caveolae (*53*), and therefore, together with the data in HeLa cells, this supports previous observations that caveolae are not required for uptake of TAT and R8 (*16, 54*).

TAT-derived peptides have been localized to vesicular structures containing internalized transferrin, and these could either be early and/or recycling endosomes (*10, 52*). Thus, delivery from the plasma membrane is conventional inasmuch as an early endosome is the first peptide acceptor compartment. The downstream fate of the peptides from these early organelles was, previous to this study, unknown, but increased Antennapedia accumulation in cells treated with the endosomal acidification inhibitor bafilomycin A1 suggested this drug was protecting the peptide from degradation in late endosomes and lysosomes; however, little colocalization of peptides in late endosomes and lysosomes was observed (*14*). TAT uptake was later shown to be dependent on clathrin-coated vesicles and was then transported to an unspecified acidic component (*54*). Since

differential pH quenching experiments with fluorescein and Alexa488 were utilized in this study, it is possible that the peptide-positive organelles could be early or late endosome-like compartments, lysosomes, or possibly even the TGN, a compartment known to have an acidic pH of 6−6.2 (*55*). It was suggested, based on colocalization of BODIPY-ceramide with internalized TAT in HeLa cells and a corresponding lack of colocalization in Lysotracker-positive acidic compartments, that the peptide bypasses late endosomes and lysosomes and traffics to the Golgi. K562 cells have also been utilized for characterizing the uptake of cationic peptides that were shown to be internalized via endocytosis and localized to a perinuclear region, postulated to be of endosomal origin (*56*). Here we show comparable R8 and TAT distribution in K562 cells but extend the observations to show in this cell line and two others that these organelles are most likely lysosomes.

We were initially able to study peptide traffic by virtue of an ability to analyze their subcellular localization in leukemia cells using live cell confocal microscopy and dual labeling. These experiments were aided by the fact that we observed very little plasma membrane labeling at 37 °C, as they were removed from the original peptide-incubation container prior to microscopic analysis. This negated the usual problems of imaging peptide-loaded adherent cells by fluorescence microscopy and allowed for high-resolution spatial analysis of the peptides in organelles.

Internalization of endocytic probes for various time points allowed us to profile distinct subpopulations of endosomes, initially, in the two leukemia cell lines. This revealed major differences in the localization of late endosomes, lysosomes, and peptide-loaded vesicles. There was, however, similar extensive colocalization of dextran with the fluorescent peptides in these cells, after the former was initially allowed to traffic through the endocytic compartment for a minimum of 6 h and a maximum of 8 h. These dextran-labeled organelles should be regarded predominantly as lysosomes, as a number of studies have shown that late endosomes and lysosomes are accessible to plasma membrane-derived molecules within 10−30 min, and typically the half-life for delivery of a fluid phase label or one that is receptor internalized is between 90 and 120 min (*46, 47*). We confirmed this by showing that in fixed cells the dextran-positive compartments are labeled with antibodies against late endosomes and lysosomes but distinct from early endosomes. Previous studies have shown that the perinuclear region in a number of cell lines including K562 is enriched in recycling endosomes (*57*). Although we find transferrin in this region after ∼6 min internalization (Figure 7H and data not shown), it does not colocalize to any major extent with TAT that has previously been chased from early endosomes to late endosomes and lysosomes. In agreement with previous observations suggesting a role for microtubules in endosome to lysosome delivery in a number of cell lines, including K562 cells, (*58*), delivery of TAT to dextran-positive lysosomes was inhibited by nocodazole. The drug also caused a redistribution and scattering of lysosomes from the compact perinuclear region, and this is similar to SynB3 peptide labeling in nocodazole-treated K562 cells (*56*). The ability of this drug to inhibit the uptake of cationic peptides in K562 cells was highly sequence specific (*56*), and we observed only a 30% inhibition in nocodazole-treated cells. Cytochalasin D treatment also inhibited the delivery of peptides to lysosomes, suggesting that both an intact actin and microtubule network is required for delivery of these peptides to late endocytic structures.

To refute the possibility that lysosomal labeling of TAT was unique in these leukemia cells, dextran chase experiments were repeated in epithelia cells, and again we found a significant albeit reduced colocalization of the peptides with the lysosomal probe. This reduction in colocalization may reflect obvious differences in endosome dynamics between the cell lines and the possibility in HeLa cells that a greater fraction of the peptide is yet to reach the lysosomes or is trafficked to an alternative compartment(s). Both peptide and dextran were localized together or separately in distinct vesicles rather than in any larger or reticular organelles such as the Golgi and endoplasmic reticulum, respectively. In agreement with our findings that peptides are prevalent only in vesicles, there was a concordant insensitivity of peptide localization to the effects of BFA and a lack of overlap between peptide distribution and Golgi resident proteins. This was clearly shown by us in this study in the leukemia models, most notably in KG1a cells, and in our previous studies in HeLa cells (*28*). It therefore seems unlikely that the Golgi is a major acceptor compartment for these peptides. Fluorescence microscopy utilized in this way does not differentiate between intact and degraded conjugates in any subcellular organelle or the cytosol. As a large fraction of these peptides are delivered to lysosomes, the possibility exists for these and other studies that a heterogeneous population of peptide fragments and possibly free fluorophore are analyzed. Previous studies have shown that R8 and TAT are susceptible to degradation (*14, 59*); however, we previously established that R8 colocalizes extensively with its less proteinase-sensitive D form (*27*). Analysis of peptide stability in these cells lines is now a focus of our research.

Despite our finding of peptide traffic to lysosomes in the three cell lines, it may be as previously mentioned (*54*) that only a very small fraction is required to escape from the endocytic pathway or conceivably enter via a nonendocytic mechanism to elicit a cellular response. The intracellular traffic of these peptides in immature blood cells and epithelia cells as demonstrated in our study mirrors that of the full length HIV TAT protein in T-cells. In Jurkat T-cells the full length TAT protein was shown to be delivered to late endosomes and possibly lysosomes, and of particular significance was that translocation of this protein from the endocytic pathway was dependent on delivery to these late endocytic structures (*20*). Of note in the context of our data with BFA was their observation of very little colocalization of internalized full length TAT with Golgi proteins. On the basis of our observations, we favor a model where peptide translocation to the cytosol also occurs from an endocytic organelle; whether this occurs from an early endosome or a downstream compartment still remains to be determined.

ACKNOWLEDGMENT

The authors would like to thank Birgit Schramm, Brigitte Joggerst-Thomalla (EMBL), and Maria Manunta (Cardiff University) for technical assistance, and Randy Mrsny, Cardiff University, for critical reading of the manuscript. We also thank PerkinElmer and Leica Microsystems for continuous support of the EMBL Advanced Light Microscopy Facility.

Supporting Information Available: Legends for supplemental movies: Movie1. Colocalization (yellow) of TxR-dextran (red) with Alexa488-TAT (green) in lysosomes of K562 cells. Movie 2. Colocalization (yellow) of TxR-dextran (red) with Alexa488-R8 (green) in lysosomes of K562 cells. Movie 3. Localization of TxR-Tf (red) in early/recycling endosomes and Alexa488-R8 (green) in lysosomes of K562 cells. Movie 4. Localization of Alexa488-TAT (green) and lysosomal TxR-dextran (red) in cytochalasin D-treated cells. Movie 5. Localization of Alexa488-TAT (green) and lysosomal TxR-dextran (red) in nocodazole-treated cells. Movie 6. Colocalization (yellow) of TxR-dextran (red) with Alexa488-R8 (green) in lysosomes of KG1a cells. Movie 7. Colocalization (yellow) of TxR-dextran (red) and Alexa488-TAT (green) in lysosomes of HeLa cells. This

material is available free of charge via the Internet at http://pubs.acs.org.

LITERATURE CITED

(1) Joliot, A., and Prochiantz, A. (2004) Transduction peptides: from technology to physiology. *Nat. Cell Biol. 6*, 189−96.

(2) Snyder, E. L., and Dowdy, S. F. (2004) Cell penetrating peptides in drug delivery. *Pharm. Res. 21*, 389−93.

(3) Deshayes, S., Morris, M. C., Divita, G., and Heitz, F. (2005) Cell-penetrating peptides: tools for intracellular delivery of therapeutics. *Cell. Mol. Life Sci. 62*, 1839−49.

(4) Fischer, R., Fotin-Mleczek, M., Hufnagel, H., and Brock, R. (2005) Break on through to the Other Side-Biophysics and Cell Biology Shed Light on Cell-Penetrating Peptides. *Chembiochem*, in press.

(5) Beerens, A. M., Al Hadithy, A. F., Rots, M. G., and Haisma, H. J. (2003) Protein transduction domains and their utility in gene therapy. *Curr. Gene Ther. 3*, 486-94.

(6) Wadia, J. S., and Dowdy, S. F. (2003) Modulation of cellular function by TAT mediated transduction of full length proteins. *Curr. Protein Pept. Sci. 4*, 97−104.

(7) Wadia, J. S., and Dowdy, S. F. (2005) Transmembrane delivery of protein and peptide drugs by TAT-mediated transduction in the treatment of cancer. *Adv. Drug Delivery Rev. 57*, 579−96.

(8) Green, I., Christison, R., Voyce, C. J., Bundell, K. R., and Lindsay, M. A. (2003) Protein transduction domains: are they delivering? *Trends Pharmacol. Sci. 24*, 213−5.

(9) Rudolph, C., Schillinger, U., Ortiz, A., Tabatt, K., Plank, C., Muller, R. H., and Rosenecker, J. (2004) Application of novel solid lipid nanoparticle (SLN)-gene vector formulations based on a dimeric HIV-1 TAT-peptide in vitro and in vivo. *Pharm. Res. 21*, 1662−9.

(10) Richard, J. P., Melikov, K., Vives, E., Ramos, C., Verbeure, B., Gait, M. J., Chernomordik, L. V., and Lebleu, B. (2003) Cell-penetrating peptides. A reevaluation of the mechanism of cellular uptake. *J. Biol. Chem. 278*, 585−90.

(11) Vives, E., Richard, J. P., Rispal, C., and Lebleu, B. (2003) TAT peptide internalization: seeking the mechanism of entry. *Curr. Protein Pept. Sci. 4*, 125−32.

(12) Lundberg, M., Wikstrom, S., and Johansson, M. (2003) Cell surface adherence and endocytosis of protein transduction domains. *Mol. Ther. 8*, 143−50.

(13) Ferrari, A., Pellegrini, V., Arcangeli, C., Fittipaldi, A., Giacca, M., and Beltram, F. (2003) Caveolae-mediated internalization of extracellular HIV-1 tat fusion proteins visualized in real time. *Mol. Ther. 8*, 284−94.

(14) Fischer, R., Kohler, K., Fotin-Mleczek, M., and Brock, R. (2004) A stepwise dissection of the intracellular fate of cationic cell-penetrating peptides. *J. Biol. Chem. 279*, 12625−35.

(15) Tkachenko, A. G., Xie, H., Liu, Y., Coleman, D., Ryan, J., Glomm, W. R., Shipton, M. K., Franzen, S., and Feldheim, D. L. (2004) Cellular trajectories of Peptide-modified gold particle complexes: comparison of nuclear localization signals and Peptide transduction domains. *Bioconjugate Chem. 15*, 482−90.

(16) Wadia, J. S., Stan, R. V., and Dowdy, S. F. (2004) Transducible TAT-HA fusogenic peptide enhances escape of TAT-fusion proteins after lipid raft macropinocytosis. *Nat. Med. 10*, 310−5.

(17) Brooks, H., Lebleu, B., and Vives, E. (2005) Tat peptide-mediated cellular delivery: back to basics. *Adv. Drug Delivery Rev. 57*, 559−77.

(18) Fischer, P. M., Krausz, E., and Lane, D. P. (2001) Cellular delivery of impermeable effector molecules in the form of conjugates with peptides capable of mediating membrane translocation. *Bioconjugate Chem. 12*, 825−41.

(19) Fretz, M. M., Koning, G. A., Mastrobattista, E., Jiskoot, W., and Storm, G. (2004) OVCAR-3 cells internalize TAT-peptide modified liposomes by endocytosis. *Biochim. Biophys. Acta 1665*, 48−56.

(20) Vendeville, A., Rayne, F., Bonhoure, A., Bettache, N., Montcourrier, P., and Beaumelle, B. (2004) HIV-1 Tat enters T cells using coated pits before translocating from acidified endosomes and eliciting biological responses. *Mol. Biol. Cell 15*, 2347−60.

(21) Norgaard, J. M., Olesen, L. H., and Hokland, P. (2004) Changing picture of cellular drug resistance in human leukemia. *Crit. Rev. Oncol. Hematol. 50*, 39−49.

(22) Lea, N. C., Buggins, A. G., Orr, S. J., Mufti, G. J., and Thomas, N. S. (2003) High efficiency protein transduction of quiescent and proliferating primary hematopoietic cells. *J. Biochem. Biophys. Methods 55*, 251−8.

(23) Mazel, M., Clair, P., Rousselle, C., Vidal, P., Scherrmann, J. M., Mathieu, D., and Temsamani, J. (2001) Doxorubicin-peptide conjugates overcome multidrug resistance. *Anticancer Drugs 12*, 107−16.

(24) Rink, H. (1987) Solid-phase synthesis of protected peptide fragments using a trialkoxy-diphenyl-methylester resin. *Tetrahedron Lett. 28*, 3787−3790.

(25) Atherton, E., and Sheppard, R. C. (1989) *Solid-Phase Peptide Synthesis: A Practical Approah*, RL Press, Oxford.

(26) Futaki, S., Ishikawa, T., Niwa, M., Kitagawa, K., and Yagami, T. (1997) Embodying a stable alpha-helical protein structure through efficient chemical ligation via thioether formation. *Bioorg. Med. Chem. 5*, 1883−91.

(27) Nakase, I., Niwa, M., Takeuchi, T., Sonomura, K., Kawabata, N., Koike, Y., Takehashi, M., Tanaka, S., Ueda, K., Simpson, J. C., Jones, A. T., Sugiura, Y., and Futaki, S. (2004) Cellular uptake of arginine-rich peptides: roles for macropinocytosis and actin rearrangement. *Mol. Ther. 10*, 1011−22.

(28) Simpson, J. C., Griffiths, G., Wessling-Resnick, M., Fransen, J. A., Bennett, H., and Jones, A. T. (2004) A role for the small GTPase Rab21 in the early endocytic pathway. *J. Cell Sci. 117*, 6297−311.

(29) Kauppi, M., Simonsen, A., Bremnes, B., Vieira, A., Callaghan, J., Stenmark, H., and Olkkonen, V. M. (2002) The small GTPase Rab22 interacts with EEA1 and controls endosomal membrane trafficking. *J. Cell Sci. 115*, 899−911.

(30) Maxfield, F. R., and McGraw, T. E. (2004) Endocytic recycling. *Nat. Rev. Mol. Cell Biol. 5*, 121−32.

(31) Mellman, I. (1996) Membranes and sorting. *Curr. Opin. Cell Biol. 8*, 497−8.

(32) Baravalle, G., Schober, D., Huber, M., Bayer, N., Murphy, R. F., and Fuchs, R. (2005) Transferrin recycling and dextran transport to lysosomes is differentially affected by bafilomycin, nocodazole, and low temperature. *Cell Tissue Res. 320*, 99−113.

(33) Bright, N. A., Gratian, M. J., and Luzio, J. P. (2005) Endocytic delivery to lysosomes mediated by concurrent fusion and kissing events in living cells. *Curr. Biol. 15*, 360−5.

(34) Shpetner, H., Joly, M., Hartley, D., and Corvera, S. (1996) Potential sites of PI-3 kinase function in the endocytic pathway revealed by the PI-3 kinase inhibitor, wortmannin. *J. Cell Biol. 132*, 595−605.

(35) Backer, J. M. (2000) Phosphoinositide 3-kinases and the regulation of vesicular trafficking. *Mol. Cell Biol. Res. Commun. 3*, 193−204.

(36) Murray, J. W., and Wolkoff, A. W. (2003) Roles of the cytoskeleton and motor proteins in endocytic sorting. *Adv. Drug. Delivery Rev. 55*, 1385−403.

(37) West, M. A., Bretscher, M. S., and Watts, C. (1989) Distinct endocytotic pathways in epidermal growth factor-stimulated human carcinoma A431 cells. *J. Cell Biol. 109*, 2731−9.

(38) Rich, I. N., Worthington-White, D., Garden, O. A., and Musk, P. (2000) Apoptosis of leukemic cells accompanies reduction in intracellular pH after targeted inhibition of the Na(+)/H(+) exchanger. *Blood 95*, 1427−34.

(39) Kaplan, I. M., Wadia, J. S., and Dowdy, S. F. (2005) Cationic TAT peptide transduction domain enters cells by macropinocytosis. *J. Controlled Release 102*, 247−53.

(40) Bright, N. A., Lindsay, M. R., Stewart, A., and Luzio, J. P. (2001) The relationship between lumenal and limiting membranes in swollen late endocytic compartments formed after wortmannin treatment or sucrose accumulation. *Traffic 2*, 631−42.

(41) Fernandez-Borja, M., Wubbolts, R., Calafat, J., Janssen, H., Divecha, N., Dusseljee, S., and Neefjes, J. (1999) Multivesicular body morphogenesis requires phosphatidyl-inositol 3- kinase activity. *Curr. Biol. 9*, 55−8.

(42) Lippincott-Schwartz, J., Yuan, L. C., Bonifacino, J. S., and Klausner, R. D. (1989) Rapid redistribution of Golgi proteins into the ER in cells treated with brefeldin A: evidence for membrane cycling from Golgi to ER. *Cell 56*, 801−13.

(43) Doms, R. W., Russ, G., and Yewdell, J. W. (1989) Brefeldin A redistributes resident and itinerant Golgi proteins to the endoplasmic reticulum. *J. Cell Biol. 109*, 61−72.

(44) Lippincott-Schwartz, J., Donaldson, J. G., Schweizer, A., Berger, E. G., Hauri, H. P., Yuan, L. C., and Klausner, R. D. (1990) Microtubule-dependent retrograde transport of proteins into the ER

in the presence of brefeldin A suggests an ER recycling pathway. *Cell 60*, 821−36.

(45) Reaves, B., and Banting, G. (1992) Perturbation of the morphology of the trans-Golgi network following Brefeldin A treatment: redistribution of a TGN-specific integral membrane protein, TGN38. *J. Cell Biol. 116*, 85−94.

(46) Green, S. A., Zimmer, K. P., Griffiths, G., and Mellman, I. (1987) Kinetics of intracellular transport and sorting of lysosomal membrane and plasma membrane proteins. *J. Cell Biol. 105*, 1227−40.

(47) Griffiths, G., Back, R., and Marsh, M. (1989) A quantitative analysis of the endocytic pathway in baby hamster kidney cells. *J. Cell Biol. 109*, 2703−20.

(48) Collot, M., Louvard, D., and Singer, S. J. (1984) Lysosomes are associated with microtubules and not with intermediate filaments in cultured fibroblasts. *Proc. Natl. Acad. Sci. U.S.A. 81*, 788−92.

(49) Gruenberg, J., Griffiths, G., and Howell, K. E. (1989) Characterization of the early endosome and putative endocytic carrier vesicles in vivo and with an assay of vesicle fusion in vitro. *J. Cell Biol. 108*, 1301−16.

(50) Kuronita, T., Eskelinen, E. L., Fujita, H., Saftig, P., Himeno, M., and Tanaka, Y. (2002) A role for the lysosomal membrane protein LGP85 in the biogenesis and maintenance of endosomal and lysosomal morphology. *J. Cell Sci. 115*, 4117−31.

(51) Saalik, P., Elmquist, A., Hansen, M., Padari, K., Saar, K., Viht, K., Langel, U., and Pooga, M. (2004) Protein cargo delivery properties of cell-penetrating peptides. A comparative study. *Bioconjugate Chem. 15*, 1246−53.

(52) Potocky, T. B., Menon, A. K., and Gellman, S. H. (2003) Cytoplasmic and nuclear delivery of a TAT-derived peptide and a beta-peptide after endocytic uptake into HeLa cells. *J. Biol. Chem. 278*, 50188−94.

(53) Scherer, P. E., Lewis, R. Y., Volonte, D., Engelman, J. A., Galbiati, F., Couet, J., Kohtz, D. S., van Donselaar, E., Peters, P., and Lisanti, M. P. (1997) Cell-type and tissue-specific expression of caveolin-2. Caveolins 1 and 2 co-localize and form a stable hetero-oligomeric complex in vivo. *J. Biol. Chem. 272*, 29337−46.

(54) Richard, J. P., Melikov, K., Brooks, H., Prevot, P., Lebleu, B., and Chernomordik, L. V. (2005) Cellular uptake of unconjugated TAT peptide involves clathrin-dependent endocytosis and heparan sulfate receptors. *J. Biol. Chem. 280*, 15300−15306.

(55) Weisz, O. A. (2003) Organelle acidification and disease. *Traffic 4*, 57−64.

(56) Drin, G., Cottin, S., Blanc, E., Rees, A. R., and Temsamani, J. (2003) Studies on the internalization mechanism of cationic cell-penetrating peptides. *J. Biol. Chem. 278*, 31192−201.

(57) Green, E. G., Ramm, E., Riley, N. M., Spiro, D. J., Goldenring, J. R., and Wessling-Resnick, M. (1997) Rab11 is associated with transferrin-containing recycling compartments in K562 cells. *Biochem. Biophys. Res. Commun. 239*, 612−6.

(58) Jin, M., and Snider, M. D. (1993) Role of microtubules in transferrin receptor transport from the cell surface to endosomes and the Golgi complex. *J. Biol. Chem. 268*, 18390−7.

(59) Gammon, S. T., Villalobos, V. M., Prior, J. L., Sharma, V., and Piwnica-Worms, D. (2003) Quantitative analysis of permeation peptide complexes labeled with Technetium-99m: chiral and sequence-specific effects on net cell uptake. *Bioconjugate Chem. 14*, 368−76.

BC050274H

Poly(glycoamidoamine)s for Gene Delivery: Stability of Polyplexes and Efficacy with Cardiomyoblast Cells

Yemin Liu and Theresa M Reineke*

Department of Chemistry, University of Cincinnati, Cincinnati, Ohio 45221-0172. Received September 12, 2005; Revised Manuscript Received October 24, 2005

Polymeric vectors have potential as nucleic acid delivery vehicles for novel gene therapy and oligonucleotide treatments for cardiovascular disease. In this report, poly(glycoamidoamine)s that contain four secondary amines and either two or four hydroxyl units in the repeat unit with D-glucarate (**D4**), *meso*-galactarate (**G4**), D-mannarate (**M4**), and L-tartarate (**T4**) stereochemistry have been investigated for their pDNA-binding affinity, DNase protection effect, and polyplex stability in the presence of salt and serum. Also, the luciferase gene delivery and cellular internalization of polyplexes formed with these polymers have been investigated with rat cardiomyoblast [H9c2(2-1)] cells. The results demonstrate that the number of hydroxyl groups and the stereochemistry affect the biological properties. Polymers **T4** and **G4** have higher pDNA binding affinity, protect pDNA from nuclease degradation, and do not release pDNA in the presence of serum. Polymers **D4** and **M4** bind pDNA with lower affinity, which allows for some pDNA degradation and release in the presence of serum. Although **T4** forms the most stable polyplexes, vector **G4** reveals the highest luciferase gene expression in serum-free media and the greatest cellular internalization of fluorescein-labeled pDNA both in serum-free and serum-supplemented media. The results of these studies indicate that the polymer−DNA binding affinity, nuclease protection capability, and polyplex stability are important parameters to facilitate effective pDNA delivery with poly(glycoamidoamine)s in cultured cardiomyoblast cells. The carbohydrate type also plays an important role to increase cellular uptake and gene expression where the polymer with the galactarate stereochemistry (in **G4**) is found to be the most effective vector for pDNA delivery to cardiomyoblast cells in vitro.

INTRODUCTION

Gene therapy is actively being studied as a therapeutic option to treat cardiovascular disease (*1*). The development of suitable vectors that facilitate in vivo gene transfer is a large challenge facing the clinical application of this technique (*2*). The use of "naked" DNA (not complexed with a vector) has been significant in cardiovascular gene therapy trials in contrast to non-cardiovascular applications (*1*, *3*−*5*); however, delivery of naked DNA is inefficient and untargeted. Many current studies have focused on the use of viral vectors because of their promise to increase the magnitude and/or duration of gene expression (*1*). Unfortunately, severe problems associated with viral vectors in cardiovascular trials, such as irreproducible administration (*1*), insertional mutagenesis (*5*), and inflammatory and/or immune response (*3*), have hindered their further use in clinical trials. For myocardial gene transfer, specifically, replication-deficient adenoviruses are among the most efficient vectors that can vastly improve the tissue penetration and transgene expression in contrast to the use of naked DNA (*5*). Cytotoxicity (*6*) and humoral response (*7*) are associated with the first generation of replication-deficient adenoviruses, while the second and third generations require supplemental viral systems to facilitate their amplification (*8*) and can be difficult to purify, which can cause problems in vivo. Investigations of nonviral delivery vectors demonstrate that developing both nontoxic and highly efficient nonviral alternatives with clinical potential has become an urgent and important issue facing cardiovascular gene therapy.

Synthetic polymers have been increasingly proposed as practical nonviral vectors because of their numerous advantages such as the ease of synthesis (*9*), tissue-specific targeting (*10*−*13*), low immune response (*9*), and ability to complex an unrestricted amount of DNA (*14*). For example, polyethylenimine (PEI) (*15*), water-soluble lipopolymers (*15*), and Terplex (*4*) have been investigated for myocardial gene delivery. However, little is known about how specific chemical traits affect the biological properties of polymeric vectors (*16*−*19*). In an effort to understand such structure−bioactivity relationships, our lab has designed a library of poly(glycoamidoamine)s with secondary amine densities between chitosan (low nitrogen density, low cytotoxicity, and low delivery efficiency) and linear polyethylenimine (high nitrogen density, high cytotoxicity, and high delivery efficiency) (*16*, *20*−*24*). Previous investigations have shown that the poly(glycoamidoamine) structures containing four secondary amines between the carbohydrate repeat units deliver plasmid DNA (pDNA) containing the firefly luciferase reporter gene with high efficacy into a variety of mammalian cell lines (BHK-21, HeLa, and HepG2 cells) in a nontoxic manner (*16*, *20*, *21*). In addition, we have found that the biological properties, particularly the delivery efficiency of these polymers are cell-type dependent and are affected by the hydroxyl stereochemistry within the polymer repeat unit. We have chosen to further investigate the properties of poly(glycoamidoamine)s containing four amine groups in the repeat unit (named **D4**, **G4**, **M4**, and **T4)** to enhance our understanding of the structural effects of this polymer class on the observed biological properties. Here, we discover that the pDNA binding affinity, protection of pDNA against nuclease degradation, and the polyplex stability in the presence of salt and serum contribute greatly to the differences observed between these seemingly similar polymeric vectors. Also, the efficiency of both cellular uptake and gene expression of polyplexes formed with these polymers as a function of carbohydrate type are investigated via flow cytometry and luciferase gene expression experiments

* To whom correspondence should be addressed. E-mail: Theresa.Reineke@uc.edu.

10.1021/bc050275+ CCC: $33.50 © 2006 American Chemical Society
Published on Web 12/27/2005

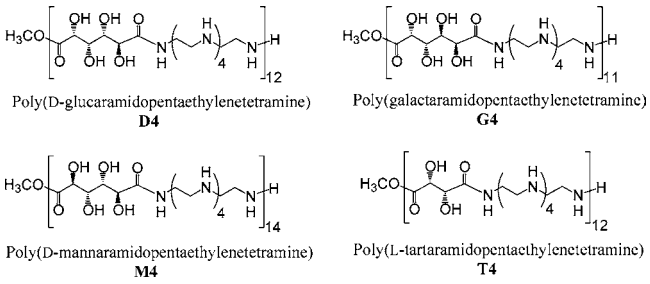

Figure 1. Poly(glycoamidoamine)s containing four secondary amines and either two or four hydroxyl groups per repeat unit with differing stereochemistry.

Table 1. Number Average Molecular Weight (M_n), Weight Average Molecular Weight (M_w), Polydispersity (M_w/M_n), and Degree of Polymerization (n) Data for the Poly(glycoamidoamine)s

polymer	M_n (kDa)	M_w (kDa)	M_w/M_n	n
D4	3.1	4.9	1.6	12
G4	3.1	4.6	1.5	11
M4	4.7	5.6	1.2	14
T4	3.6	4.3	1.2	12

with rat cardiomyoblast cells [H9c2(2-1) cells]. This model cell line was chosen due to its similarity to myocardial cells. This study represents our initial efforts to utilize these poly(glycoamidoamine)s to optimize the protocols for delivery of DNA to myocardial cells and to understand the chemical structure−biological property of polymeric vectors for cardiovascular targets.

EXPERIMENTAL PROCEDURES

Materials. The poly(glycoamidoamine)s (Figure 1) were synthesized through condensation polymerization of esterified D-glucaric acid (**D**), dimethyl *meso*-galactarate (**G**), D-mannaro-1,4:6,3-dilactone (**M**), or dimethyl L-tartarate (**T**) with pentaethylenehexamine (**4**) under conditions previously described (*16*, *20*, *21*). The molecular weight (M_n and M_w), polydispersity (M_w/M_n), and degree of polymerization (n) data are listed in Table 1. Media, supplements, nuclease-free water, and phosphate-buffered saline (PBS) were purchased from Gibco BRL (Carlsbad, CA). Plasmid DNA gWiz-Luc and pCMVβ were purchased from Aldevron (Fargo, ND) and PlasmidFactory (Bielefeld, Germany), respectively. Fluorescein-labeled pDNA was purchased from Mirus (Madison, WI). Heparin was purchased from Sigma (St. Louis, MO) as heparin ammonium salt from porcine intestinal mucosa. H9c2(2-1) cells, a cardiac-like myoblast cell line derived from BD1X rat heart tissue that exhibits properties of skeletal muscle, was purchased from ATCC (Rockville, MD). All reagents and polyplexes were prepared in nuclease-free water unless otherwise specified. N/P ratios (the ratio of the number of amines/phosphates from pDNA) were calculated by using the secondary amines in the polymer repeat unit only (not the amide nitrogens).

Heparin Competitive Displacement Assay. This experiment was performed as previously described for **D4**, **G4**, and **M4** (*21*). In brief, **T4** (10 μL) was mixed with pCMVβ (1 μg in 10 μL of H_2O) to form polyplexes at N/P = 20. The polyplexes were allowed to incubate for 30 min. A series of heparin solutions (400−600 μg/mL) were prepared by diluting aliquots of a heparin stock solution (2700 μg/mL). The polyplex solutions were incubated in 10 μL of each heparin solution above for 15 min. After the addition of loading buffer (1 μL), an aliquot (10 μL) of each sample was subjected to electrophoresis.

DNase Protection Assay. The experimental procedure used to measure DNase protection was modified from a reported method (*25*). One microgram of pCMVβ (in 5 μL) was complexed with 5 μL of **D4**, **G4**, **M4**, or **T4** at N/P = 5. Samples of the complexes were then incubated with 5 μL of fetal bovine serum (FBS) at 37 °C for 0, 1, 2, 4, and 6 h. After incubation, 1.5 μL of sodium dodecyl sulfate (SDS, 10% w/v) and 1.5 μL of loading buffer were added to the samples. SDS is used to release the pDNA from the polymers to evaluate the DNase protection capability of each poly(glycoamidoamine). The treated samples were incubated at 4 °C until gel electrophoresis was performed on an agarose gel (0.6% w/v) containing 60 μg of ethidium bromide/100 mL TAE buffer (40 mM Trisacetate, 1 mM EDTA). FBS only and DNA only were the negative controls in this experiment.

Measurement of Polyplex Size by Dynamic Light Scattering. Polyplex sizes were measured at 633 nm on a Zetasizer (Nano ZS) dynamic light scattering instrument (Malvern Instruments, Malvern, UK). pCMVβ (150 μL, 0.02 μg/μL in H_2O) was incubated with polymers **D4**, **G4**, **M4**, and **T4** (150 μL in H_2O) at N/P = 30 for 1 h to form the polyplexes. Each sample was then diluted to 900 μL with either Opti-MEM or supplemented DMEM (10% FBS) to determine the salt and serum stability of the polyplexes. The particle sizes were then measured at 37 °C and at time intervals of 0, 20, 40, and 60 min after dilution using a detection angle of 173°. The intensity-averaged particle size of each sample was reported as an average of 12 measurements.

Luciferase Reporter Gene Transfection and Cell Viability Assays. H9c2(2-1) cells were cultured according to ATCC specifications in Dulbecco's Modified Eagle medium (DMEM, supplemented with 10% FBS, 100 units/mg penicillin, 100 μg/mL streptomycin, and 0.25 μg/mL amphotericin) in 5% CO_2 at 37 °C. Prior to transfection, H9c2(2-1) cells were seeded at 4 $\times$ 10^4 cells/well in 24-well plates and were incubated for 24 h. **D4**, **G4**, **M4**, and **T4** (150 μL of an aqueous solution) were incubated with gWiz-Luc (150 μL, 0.02 μg/μL) at N/P ratios of 5, 10, 15, 20, 25, and 30 at room temperature for 1 h to form the polyplexes. The mixtures were then diluted to 900 μL with serum-free media (Opti-MEM, pH 7.2) or supplemented DMEM (10% FBS). Each well of cells was transfected with 300 μL of the polyplex solution containing 1 μg of gWiz-Luc. Untransfected cells and cells transfected with naked gWiz-Luc (1 μg) were used as negative controls. Four hours after transfection, 800 μL of the supplemented DMEM was added to each well. Twenty-four hours after transfection, the media was replaced with fresh supplemented DMEM (1 mL). Forty-seven hours after initial transfection, the media was removed and the cells were washed with 500 μL of PBS and treated with cell culture lysis buffer (Promega, Madison, WI). The amount of protein in the cell lysates (as milligrams of protein) was determined against a standard curve of bovine serum albumin (98%, Sigma, St. Louis, MO), using a Bio-Rad DC protein assay kit (Hercules, CA).

Cell lysates were analyzed for luciferase activity with Promega's luciferase assay reagent (Madison, WI). For each sample, luminescence was measured over 10 s in duplicate with a luminometer (GENios Pro, TECAN US, Research Triangle Park, NC), and the average was utilized. The gene delivery efficiency of each sample was characterized by firefly luciferase expression in H9c2(2-1) cells and denoted as relative light units (RLU)/mg of protein. The toxicity profiles were characterized by the amount of protein in the cell lysates. The protein level of untransfected cells was used to normalize the data obtained for the protein levels of the cells transfected with naked pDNA and polyplexes formed with **D4**, **G4**, **M4**, and **T4**.

Flow Cytometry. H9c2(2-1) cells were seeded on six-well plates at 2 $\times$ 10^5 cells/well and allowed to incubate in supplemented DMEM at 37 °C and 5% CO_2 for 24 h. The polyplexes were prepared by combining 250 μL of fluorescein-labeled pDNA (0.02 μg/μL) and 250 μL of **D4**, **G4**, **M4**, or **T4**

at N/P = 30. The cells were then transfected with 0.5 mL of polyplex solution (5 μg of pDNA/well) in 1 mL of serum-free media (OPTI-MEM) or 1 mL of advanced DMEM (2% FBS). The cells were incubated with each solution for 4 h to allow endocytosis and internalization of the polyplexes. After transfection, the cells were rinsed with PBS multiple times to remove the cell surface bound polyplexes. Supplemented DMEM was then added, and the cells were incubated for another 2 h to allow further polyplex internalization. Six hours after initial transfection, the cells were trypsinized, pelleted, and resuspended in PBS containing 2% FBS for fluorescent activated cell sorting (FACS) analysis. A FACSCalibur (Becton Dickenson, San Jose, CA) equipped with an argon ion laser to excite fluorescein (488 nm) was used. From 20 000 to 50 000 events were collected for each sample. The positive fluorescence level was established by visual inspection of the histogram of negative control cells such that less than 1% appeared in the positive region.

RESULTS AND DISCUSSION

The poly(glycoamidoamine)s examined in this study (**D4**, **G4**, **M4**, and **T4**) differ by the number and stereochemistry of hydroxyl groups, and each structure contains four secondary amine groups along the polymer chain (Figure 1). These polycations have been created with similar degrees of polymerization (11−14) (*16*, *20*, *21*) so that the chemical structure−biological property relationships of the polymers can be accurately compared (*24*). As previously shown, these polycations all complexed and compacted pDNA into small nanoparticles in water (in the proper range to be endocytosed) and displayed promising transfection efficiency and cell viability values with BHK-21, HeLa, and HepG2 cell lines (*16*, *20*, *21*). Here, we further investigated these poly(glycoamidoamine)s for their pDNA binding affinity, their ability to protect nucleic acids from nuclease degradation, and their stability in the presence of salt and serum. These investigations, along with analysis of the cellular uptake and gene expression properties of the polyplexes, were conducted to understand the efficacy difference between these similar polymer structures and to optimize their pDNA delivery with cardiomyoblast cells [H9c2(2-1) cells] for future in vivo myocardial delivery studies.

Structural Effects on pDNA Binding and Compaction. Previous studies with **D4**, **G4**, and **M4** found that the hydroxyl stereochemistry played a role in the polymer binding affinity to pDNA, which appeared to influence the transfection efficiency (*21*). It was found that **G4** demonstrated the strongest binding affinity and generally the best transfection and **M4** the weakest binding affinity and the lowest transfection; however, the results differed slightly with each cell line. Here, poly(L-tartaramidopentaethylenetetramine) (**T4**) was created to examine the biological effects of decreasing the amount of hydroxyl groups in the polymer repeat unit. In this polymer, the distance between the oligoamine moieties is shorter, which leads to an increase in amine density. A gel electrophoretic shift assay revealed that complete retardation of pDNA migration in electrophoresis field by **T4** started at N/P = 1, which was lower than the other three analogues **D4**, **G4**, and **M4** (these polymers retarded the migration of pDNA at N/P = 2, 2, and 3, respectively) (*21*). This indicates that the polymer−pDNA binding may become stronger by decreasing the hydroxyl number (in **T4**). The binding affinity of **T4** to pDNA was further investigated using a heparin competitive displacement assay. As previous reported (*21*), polyplexes formed between pDNA and **D4**, **G4**, and **M4** started to dissociate at heparin concentrations of 340, 440, and 240 μg/mL, respectively. Here, we have found that polyplexes formed with **T4** dissociate at a heparin concentration of 560 μg/mL (Figure 2b) and that the order of binding affinity is **T4** > **G4** > **D4** > **M4**. This result further suggests that decreasing the hydroxyl number (and thus increasing the amine density) along the backbone of poly(glycoamidoamine)s promotes stronger pDNA binding.

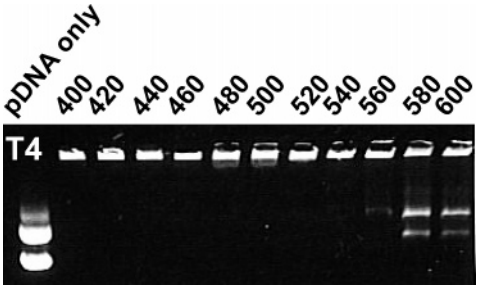

Figure 2. Heparin competitive displacement assay of **T4**. The first lane is uncomplexed pDNA. The numbers shown above the gel are the heparin concentrations tested to displace pDNA from the polyplexes.

Protection of pDNA from DNase Degradation. The ability of each poly(glycoamidoamine) to protect pDNA against DNase (present in FBS) degradation was investigated using a gel electrophoretic shift assay. It is important to determine the ability of the different polymers to protect pDNA from nuclease degradation to fully understand why the chemical and structural characteristics affect the cellular uptake and gene expression profiles. We performed the degradation experiments at a low N/P ratio (N/P = 5) to "simulate" the endosomal environment. During endocytosis, the polyplexes are exposed to an environment that contains a high concentration of negatively charged cell surface proteins, such as heparin. These polyanions can bind up excess polycations in the polyplexes and dissociate the polyplex slightly (this effect is shown in Figure 2; heparin competes with pDNA for polycation binding and dissociates the polyplexes, releasing the pDNA). This decreases the "effective" polyplex N/P ratio that is available for protection from DNase during cellular uptake. After incubation of the polyplexes with FBS, SDS was used to release the pDNA from the polyplexes to inspect the integrity of the pDNA and to assess and compare the protection effect of each polymer. As shown in Figure 3, degraded pDNA was visualized by the presence of band 5 and by a decrease in the intensity of bands 2 and 3. Plasmid DNA complexed with **M4** and **D4** began to degrade after 1 and 4 h of incubation with FBS, respectively. In addition, a decrease in the intensity of the pDNA bands (2 and 3) was also noticed after incubation of **D4** and **G4** polyplexes for 2 and 4 h with FBS, possibly indicating some pDNA degradation at these time points. When the four polymers were compared, **G4** and **T4** offered better pDNA protection from nuclease degradation. Particularly, **T4** completely protected pDNA after 6 h of exposure to FBS at 37 °C (a decrease in the intensity of pDNA bands was not observed). Again, this result shows that the hydroxyl number and stereochemistry affect the ability of the polymers to protect pDNA from nuclease degradation. The order of the ability of each polymer to protect pDNA from nuclease degradation is **T4** > **G4** > **D4** > **M4**, which is the same trend and likely related to the pDNA binding affinity of these polymers.

Effect of Salt and Serum on Polyplex Size. The stability of polyplexes formed with pDNA and **D4**, **G4**, **M4**, and **T4** was studied in the presence of media containing salt (serum-free Opti-MEM) and serum (DMEM supplemented with 10% FBS). This study is significant to understand how the polymer structure affects the polyplex stability under the conditions of the transfection experiments. After the polyplexes were formed in nuclease-free water, Opti-MEM or serum-supplemented DMEM was added for further incubation, and the polyplex solutions were analyzed at various time points (0, 20, 40, and 60 min) for the size measurements. As shown in Figure 4a, in

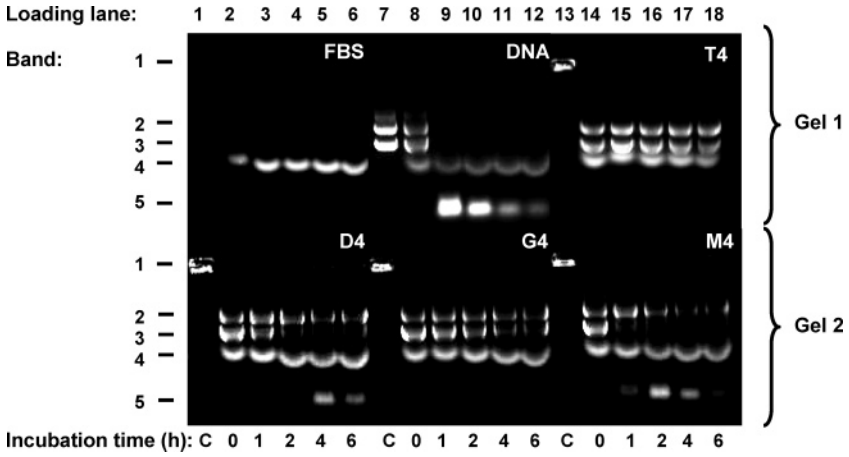

Figure 3. DNase protection of plasmid DNA by **T4** (lanes 13−18 of gel 1), **D4** (lanes 1−6 of gel 2), **G4** (lanes 7−12 of gel 2), and **M4** (lanes 13−18 of gel 2) complexed at N/P = 5. Fetal bovine serum (FBS, lanes 1−6 of gel 1) and naked pDNA (lanes 7−12 of gel 1) were used as controls. Control samples of FBS only (gel 1, lane 1, no band under UV), pDNA (gel 1, lane 7), and polyplexes formed with **T4** (gel 1, lane 13), **D4** (gel 2, lane 1), **G4** (gel 2, lane 7), and **M4** (gel 2, lane 13) without addition of FBS and SDS were also analyzed (labeled as C for the incubation time). Band 1 is the position of sample loading (polyplexes without FBS and SDS treatment). Bands 2 and 3 are relaxed and supercoiled pDNA forms. Band 4 results from combining both FBS and SDS. Band 5 is degraded pDNA.

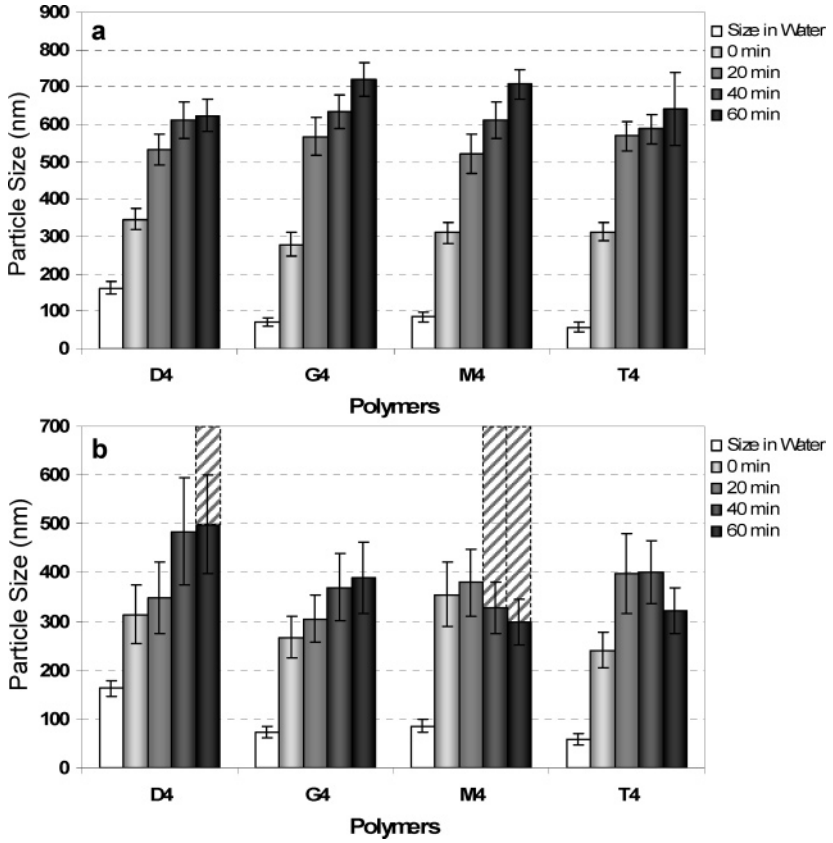

Figure 4. Polyplex stability of the poly(glycoamidoamine)s in the presence of salt and serum at N/P = 30. (a) Polyplex sizes in Opti-MEM at certain time intervals (0, 20, 40, and 60 min). (b) Polyplexes sizes in DMEM supplemented with 10% FBS at certain time intervals (0, 20, 40, and 60 min). The cross-hatched bars (shown behind **D4** at 60 min and **M4** at 40 and 60 min) indicate that a bimodal distribution is observed at these time points, where between 15 to 30% of the samples (by light scattering intensity) consist of particles around 3 μm.

Opti-MEM, all the polyplexes had similar particle sizes, and their sizes also increased in a similar manner with the incubation time. When the polyplexes were initially formulated in water, particles between 60 and 160 nm were formed. Upon addition of Opti-MEM, the polyplexes immediately aggregated to about 300 nm. After 20 min, the polyplexes further increased in size to 530−570 nm. After exposure to the salt solution for 40 and 60 min, the particle sizes continued to grow to 600−720 nm. Flocculation of **D4** polyplexes appeared to level off at 40 min (600 nm); however, **G4**, **M4**, and **T4** polyplexes continued to grow upon salt exposure.

In serum-containing DMEM (Figure 4b), the polyplexes formed with the poly(glycoamidoamine)s also aggregated but followed a different trend than that observed in the salt conditions. Polyplexes formed with **D4** aggregated rapidly and yielded the largest particles, where after 60 min, **D4** polyplexes were about 500 nm. In addition, a small amount of larger aggregates (around 3 μm) was observed in this sample (approximately 20% by light scattering intensity). Polyplexes formed with **M4** also aggregated, and a bimodal distribution of particles was also observed after 40 min of exposure to serum-containing DMEM, where about 15% of the sample at 40 min

and 30% of the sample at 60 min (percentages by light scattering intensity) contained aggregates larger than 3 μm. These large particles were also detected when measuring naked pDNA in FBS-supplemented DMEM, but they were not seen when the media only (the FBS-supplemented DMEM control) was measured. This result suggests that these particles may arise from the aggregation between naked pDNA and components in serum-containing media, which has also been observed by Moret et al. (*26*). Polyplexes formed with pDNA and polymers **G4** and **T4** did not reveal these large 3 μm aggregates but did flocculate to some degree (to about 400 nm), which was significantly smaller than the particle sizes observed in salt only conditions. This finding is again likely related to the binding affinities of these poly(glycoamidoamine)s with pDNA. The weaker-binding polymers, **D4** and **M4**, may release some pDNA into the media (due to competitive binding of negative serum proteins with the polycations). The pDNA then forms larger aggregates (around 3 μm) with positively charged serum proteins (*27*, *28*). However, the stronger pDNA binding polymers, **G4** and **T4**, do not appear to release pDNA, and polyplexes formed with these polymers are more stable in serum-containing media, which may help to increase pDNA delivery efficiency.

Luciferase Reporter Gene Expression with H9c2(2-1) Cells. The transfection efficiency of **D4**, **G4**, **M4**, and **T4** were characterized by firefly luciferase expression with H9c2(2-1) cells both in serum-free and serum-supplemented (10% FBS) media. Untransfected cells and naked gWiz-Luc were used as the negative controls. Previous studies with poly(glycoamidoamine)s have shown that gene expression is enhanced with an increase in N/P ratio (*20*, *21*), which is a common characteristic of low molecular weight polymeric vectors (*14*). Figure 5 reveals the luciferase expression values of polyplexes formed with pDNA and **D4**, **G4**, **M4**, and **T4** as a function of N/P ratio (between 5 and 30) in serum-free media with rat cardiomyoblast cells. The maximum luciferase expression of polyplexes formed with all four polymers occurred at N/P = 30. As shown in Figure 1, the carbohydrate moieties in **D4**, **G4**, and **M4** all have four hydroxyls that only differ by their stereochemistry. By comparing the transfection efficiencies of these three polymers, it was noticed that **G4** facilitated higher luciferase expression under serum-free transfection conditions. The increase in efficacy of **G4** over **D4** and **M4** may be due to the stronger pDNA binding affinity as demonstrated by the competitive displacement experiments with heparin (*21*). If the binding affinity is relatively weak, cell surface proteoglycans (such as heparin sulfate) may prematurely release the pDNA from the polyplex before cellular internalization. Also, **G4** protected pDNA better against DNase (Figure 3), which increased the pDNA resistance to enzymatic damage in the endocytotic pathway, thus resulting in higher pDNA delivery.

It is generally believed that enhancing the amine density improves gene expression (*16*, *21*, *29*). However, at higher N/P ratios, **T4** did not generally facilitate higher gene expression values than the other three polymer analogues (containing four hydroxyl groups), although at lower N/P ratios it was noticed that **T4** did have a higher expression profile. At N/P = 5, **D4**, **G4**, and **M4** did not transfect H9c2(2-1) cells higher than naked pDNA (N/P = 0 in Figure 5). However, **T4** presented a significant enhancement in gene expression at N/P = 5. This could be due to the higher binding affinity and DNase protection offered by **T4** as compared with **D4**, **G4**, and **M4** (Figure 3) at N/P = 5, which would allow more pDNA to survive the cellular uptake and intracellular trafficking events from nuclease degradation at this low N/P ratio. At N/P = 10, **T4** still exhibited slightly higher gene expression. When the N/P ratios were increased further (15 to 30), **G4** clearly displayed the highest transfection efficiency with H9c2(2-1) cells. These results imply

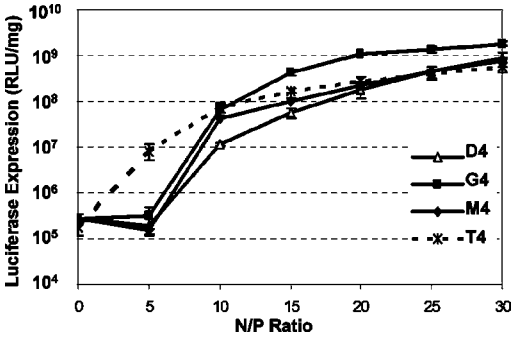

Figure 5. Luciferase gene expression (RLU/mg) in H9c2(2-1) cells with polyplexes formed with **D4**, **G4**, **M4**, and **T4** at N/P ratios between 0 (pDNA only) and 30. Transfections were performed in serum-free media (Opti-MEM) for the first four hours.

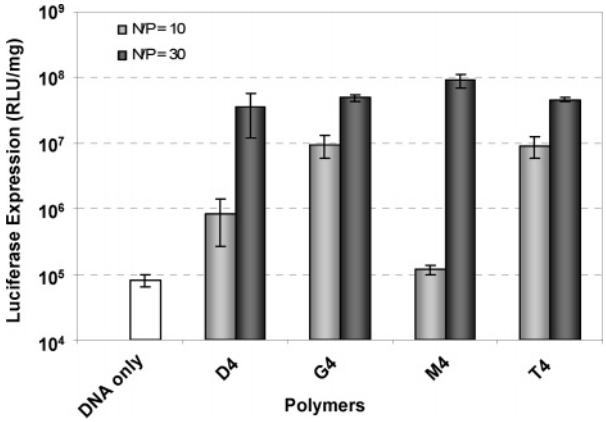

Figure 6. Luciferase gene expression (RLU/mg) in H9c2(2-1) cells with polyplexes formed with **D4**, **G4**, **M4**, and **T4** at N/P ratios 10 and 30 with DMEM containing 10% serum.

that both the number and the stereochemistry of the hydroxyl groups and the N/P ratio affect the gene delivery efficiency of polyplexes formed with the poly(glycoamidoamine)s with H9c2(2-1) cells. The carbohydrate type appears to play a role in the efficacy of gene transfection, and this effect is not clearly understood.

The luciferase expression with polyplexes formed with **D4**, **G4**, **M4**, and **T4** in the presence of serum was lower than that obtained in serum-free media. This is commonly observed with most nonviral vectors due to interaction of these systems with serum proteins (*30*−*32*). The maximum luciferase expression of polyplexes formed with all four polymers occurred at N/P = 30 under serum conditions. As shown in Figure 6, at N/P = 10, **G4** and **T4** polyplexes yielded gene expression values significantly higher than that of **D4** and **M4** polyplexes. This effect may again be attributed to the better DNase protection ability of **G4** and **T4** (Figure 3), which would allow more pDNA to survive the harsh extra- and intracellular degradative environment. However, at N/P = 30, gene expression values were higher, and similar values were obtained with all of the polymers. To our surprise, **M4** displayed slightly higher gene expression (at N/P = 30), which is not clearly understood.

Toxicity. All of the polyplexes revealed low toxicity profiles in H9c2(2-1) cells even at the high N/P ratio required for maximum gene expression (as shown in Figure 7, N/P = 30). The viability values with H9c2(2-1) cells, characterized by the cellular protein concentration (fraction of cell survival was normalized to untransfected cells), were all greater than 85% with **D4**, **G4**, **M4**, and **T4** in both serum-free and serum-supplemented transfection conditions. These results were similar to the high cell viability profiles generally observed with chitosan and uncomplexed DNA (*9*, *22*). As shown, **T4** exhibited

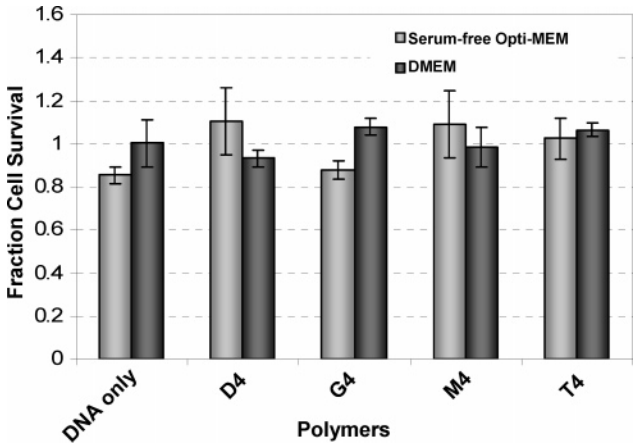

Figure 7. The fraction of cell survival of H9c2(2-1) cells transfected with naked DNA and polyplexes formed with **D4**, **G4**, **M4**, and **T4** and N/P=30. The toxicity values are normalized to untransfected cells (fraction of cell survival = 1.0).

the same toxicity profile as the other three poly(glycoamidoamine)s. These data indicate that the toxicity in H9c2(2-1) cells does not increase with the increase of amine density (by decreasing the hydroxyl number) along the polymer chain. This study demonstrates that by systematically incorporating monosaccharide units into a PEI-like backbone, the polymer biocompatibility can be greatly enhanced while retaining high delivery efficacy with H9c2(2-1) cells.

Cellular Uptake of the Polyplexes. Flow cytometry was performed to quantify the cellular uptake efficiency of fluorescein-labeled pDNA complexed with polymers **D4**, **G4**, **M4**, or **T4** at the N/P ratio of maximum luciferase gene expression (N/P = 30). This experiment yields the number of cells that uptake pDNA, as well as the average intensity of fluorescence (relative amount of pDNA) in the cells. The cells were incubated with each polyplex solution for 4 h in either Opti-MEM or FBS-supplemented DMEM to allow endocytosis. After removal of the cell surface bound polyplexes and further incubation with supplemented DMEM for 2 h, the cells were trypsinized and isolated for FACS analysis. The flow histograms of H9c2(2-1) cells transfected in serum-free media and supplemented DMEM are shown in Figure 8a,b. The mean fluorescence intensity and the percentage of positive cells are shown in Figure 8c. In this experiment, only 8% of H9c2(2-1) cells in serum-free media and less than 1% of cells in supplemented DMEM were transfected with the control, naked fluorescein-labeled pDNA. As shown, the poly(glycoamidoamine) delivery vehicles greatly improved the cellular uptake of the labeled pDNA. Greater than 90% of cells (with the exception of **T4** in supplemented DMEM, where about 88% cellular uptake was observed) were positive for fluorescence after 6 h of incubation with polyplexes formed with fluorescein-labeled pDNA and polymers **D4**, **G4**, **M4**, or **T4** (Figure 8c).

It is generally believed that the binding affinity between polymers and pDNA plays a significant role in the internalization of polyplexes via cell surface interaction (e.g., proteoglycans) (*21*, *33*, *34*). When the polyplex comes into contact with the cell surface, negatively charged proteoglycans may compete with polycation binding and disassemble the polyplex if the polymer−pDNA binding affinity is not strong enough. This would decrease the amount of polyplexes (and pDNA) that are internalized and/or decrease the protection of pDNA from nuclease degradation (both outside and inside the cells). As shown in Figure 8a,c, polyplexes formed with **D4** and **G4** revealed very similar cellular uptake efficacy in serum-free Opti-MEM, and both vectors transfected more cells than **M4**. These data are consistent with their binding affinity to pDNA (**G4** > **D4** > **M4**). However, to our surprise, the mean fluorescence intensities of these three polymers were higher than that of **T4**, which has an even stronger binding affinity for pDNA. This result is consistent with the luciferase expression results and suggests that polymer−pDNA binding affinity is not the only parameter that controls the cellular internalization of polyplexes formed with poly(glycoamidoamine)s in serum-free conditions. As shown in Figure 4a, polyplexes formed with **D4**, **G4**, **M4**,

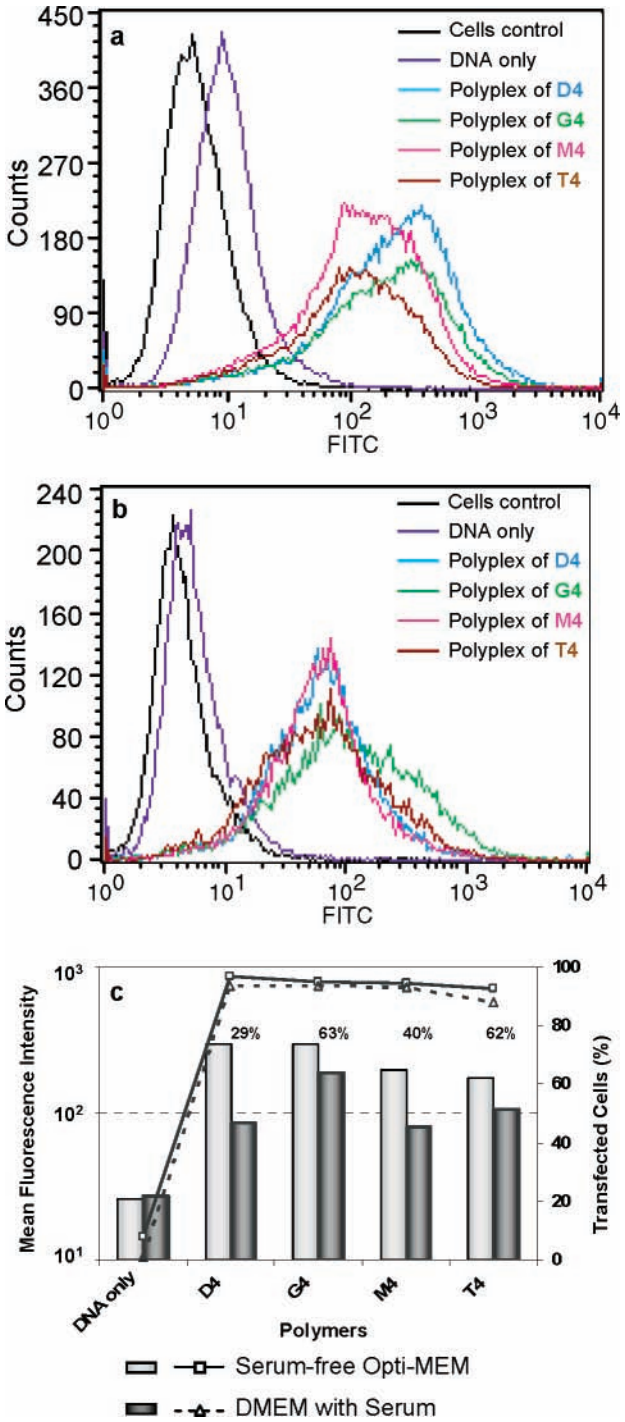

Figure 8. Cellular uptake of fluorescein-labeled pDNA complexed with **D4**, **G4**, **M4**, and **T4**. (a) Flow histogram of H9c2(2-1) cells after transfection in serum-free media. (b) Flow histogram of H9c2(2-1) cells after transfection in supplemented DMEM. (c) Mean fluorescence intensity (bars) and the percentage of cells positive for fluorescein (lines). The values shown above the bars are the percentages of the fluorescence intenisty retained for each vector in serum conditions as compared to the fluorescence intensity obtained in the serum-free conditions (= 100%).

and **T4** all aggregated similarly in serum-free media, and therefore the polyplex size should not contribute to this discrepancy. It is possible that the number and stereochemistry of the hydroxyl groups within the carbohydrate moieties may affect polyplex−cell surface binding and certain linear hydroxyl stereochemistries may increase signaling of cellular internalization via endocytosis with cardiomyocytes.

The percentage of cells that internalized the pDNA in the presence of serum (Figure 8b,c) did not significantly decrease as compared to the serum-free results. Also, the trend was similar to the Opti-MEM results where **D4**, **G4**, and **M4** polyplexes were all uptaken by the same number of cells and **T4** transfected the lowest number of cells. However, the mean fluorescence intensity (the amount of pDNA internalized) did decrease to a large degree as compared to the results in serum-free media, and an interesting trend was observed. As shown in Figure 8c, polyplexes formed with **G4** and **T4** retained greater than 60% of their respective fluorescence intensity values obtained in serum-free media. However, **D4** and **M4** polyplexes only retained 29 and 40%, respectively, of their fluorescence values obtained in serum-free media.

As highlighted in Figure 8c, **G4** polyplexes yielded the greatest fluorescence intensity in serum-containing media and therefore facilitated the greatest amount of pDNA to be internalized. Also, it was noticed that the cellular internalization in the presence of serum with polyplexes formed with the poly(glycoamidoamine)s followed an interesting trend (**G4** > **T4** > **D4** > **M4**), which is consistent with the luciferase gene expression results obtained with serum at N/P = 10. This trend could be due to a combined effect of the binding affinity, DNase protection ability, polyplex stability in serum, and the carbohydrate type within the polymer. Vectors **G4** and **T4** appear to yield the greatest efficacy in serum conditions with H9c2(2-1) cells. Polymers **G4** and **T4** both have high binding affinities (Figure 2) and DNase protection capabilities (Figure 3) with pDNA. Also, the polyplexes formulated with these two vectors do not form large aggregates with serum (Figure 4b), which suggests that they do not release pDNA from the polyplex in the presence of serum. **G4** delivers pDNA with the greatest efficacy, and this effect is not clearly understood. However, it is likely due to the hydroxyl number and/or stereochemistry along the polymer backbone where the hydroxyl stereochemistry in the linear galactose residues seems to facilitate greater cell surface interaction that triggers endocytosis with this cell line. **D4** and **M4** yield the lowest cellular internalization, and may be due to the fact that these vectors have a weaker binding affinity, do not protect pDNA from nuclease degradation, and also form large aggregates (possibly due to the release of some pDNA in the presence of serum). An interesting observation was that although **M4** facilitated the lowest cellular internalization in the presence of serum (Figure 8c), it demonstrated the highest luciferase gene expression at N/P = 30 (shown in Figure 6). Thus, it appears that on a per plasmid basis (luciferase expression/mean fluorescence intensity) **M4** is more efficient than the other systems. This indicates that **M4** could be more effective after cellular internalization, where this vector may facilitate higher endosomal and pDNA release than the other polymers. The low binding affinity of **M4** to pDNA may cause easier dissociation of the polyplexes within the endosome and cytoplasm, where the released pDNA can be expressed more readily. In addition, the dissociated **M4** polycations may chelate the proteoglycans on the interior of the endosomes causing endosomal membrane leakage and increased cytoplasmic pDNA release (thus enhancing gene expression). These phenomena are currently being investigated via confocal microscopy and flow cytometry experiments in our lab.

CONCLUSION

The poly(glycoamidoamine) nucleic acid delivery vectors **D4**, **G4**, **M4**, and **T4** have been investigated for their pDNA-binding affinity, DNase protection ability, and polyplex stability in the presence of salt and serum. Also, the luciferase gene delivery, cell viability, and the capacity of these vectors to promote cellular internalization of fluorescein-labeled pDNA have been studied with a rat cardiomyoblast cell line. We have found that both the number and the stereochemistry of the hydroxyl units significantly affect the biological properties. The results demonstrate that **T4** and **G4** have a stronger binding affinity and enhanced DNase protection ability. Also, the polyplexes formed with these vectors are more stable in the presence of serum, where they do not appear to release pDNA. Polyplexes formed with **D4** and **M4** reveal weaker pDNA binding, allow pDNA degradation in the presence of serum, and appear to release some pDNA in the presence of serum-containing media. Particularly, **G4** is found to promote the highest luciferase gene expression in serum-free media and higher cellular internalization of pDNA both in serum-free and serum-containing media than the other analogues. These results are likely an effect of more pDNA surviving the cellular uptake and intracellular trafficking events due to increased polyplex stability from pDNA release and degradation. Although **T4** reveals the highest pDNA binding affinity and DNase protection when compared to **D4**, **G4**, and **M4**, it does not show higher cell internalization and luciferase gene expression. It seems that both the distance of the amine functionalities and the carbohydrate type affect the gene delivery efficiency, where the carbohydrate residues, particularly with the linear galactarate stereochemistry, promote higher delivery efficacy with this cardiomyoblast cell line. This study presents our first step to facilitate the use of nucleic acid drugs for cardiovascular aliments by further examining the chemical properties of these new synthetic polymers and developing their potential as novel vectors for myocardial targets. PEGylation of these polymers to further stabilize the polyplexes from aggregation and examination of these vectors for in vivo myocardial gene delivery are currently being investigated.

ACKNOWLEDGMENT

The authors gratefully acknowledge funding of this work by the National Institutes of Health (1-R21-EB003938-01) and the UC Institute for Nanoscale Science and Technology. Yemin Liu thanks University of Cincinnati for the Chemical Sensors and Laws-Stecker graduate fellowships.

LITERATURE CITED

(1) Isner, J. M. (2002) Myocardial gene therapy. *Nature 415*, 234−239.

(2) Nable, E. G. (1995) Gene therapy for cardiovascular disease. *Circulation 91*, 541−548.

(3) Symes, J. F. (2001) Gene therapy for ischemic heart disease. *Am. J. Cardiovasc. Drugs 1*, 159−166.

(4) Affkeck, D. G., Yu, L., Bull, D. A., Bailey, S. H., and Kim, S. W. (2001) Augmentation of myocardial transfection using TerplexDNA: a novel gene delivery system. *Gene Ther. 8*, 349−353.

(5) Alexander, M. Y., Webster, K. A., McDonald, P. H., and Prentice, H. M. (1999) Gene transfer and models of gene therapy for the myocardium. *Clin. Exp. Pharmacol. Physiol. 26*, 661−668.

(6) Wells, K. E., Maule, J., Kingston, R., Foster, K., McMahon, J., Damien, E., Poole, A., and Wells, D. J. (1997) Immune responses, not promoter inactivation, are responsible for decreased long-term expression following plasmid gene transfer into skeletal muscle. *FEBS Lett. 407*, 164−168.

(7) Gilgenkrantz, H., Duboc, D., Juillard, V., Couton, D., Pavirani, A., Guillet, J. G., Briand, P., and Kahn, A. (1995) Transient expression of genes transferred in vivo into heart using first-

generation adenoviral vector: Role of the immune response. *Hum. Gene Ther. 6*, 1265−1274.
(8) Kochanek, S., Clemens, P. R., Mitani, K., Chen, H.-H., Chan, S., and Caskey, C. T. (1996) A new adenoviral vector: Replacement of all viral coding sequences with 28 kb of DNA independently expressing both full-length dystrophin and beta-galactosidase. *Proc. Natl. Acad. Sci. U.S.A. 93*, 5731−5736.
(9) Anwer, K., Rhee, B. G., and Mendiratta, S. K. (2003) Recent progress in polymeric gene delivery systems. *Crit. Rev. Ther. Drug Carrier Syst. 20*, 249−293.
(10) Kircheis, R., Schüller, S., Brunner, S., Ogris, M., Heider, K.-H., Zauner, W., and Wagner, E. (1999) Polycation-based DNA complexes for tumor-targeted gene delivery in vivo. *J. Gene Med. 1*, 111−120.
(11) Puls, R. L., and Minchin, R. F. (1999) Gene transfer and expression of a non-viral polycation-based vector in CD4+ cells. *Gene Ther. 6*, 1774−1778.
(12) Nishikawa, M., Takemura, S., Yamashita, F., Takakura, Y., Meijer, D. K., Hashida, M., and Swart, P. J. (2000) Pharmacokinetics and in vivo gene transfer of plasmid DNA complexed with mannosylate poly(L-lysine) in mice. *J. Drug Target. 8*, 29−38.
(13) Mahato, R. I., Takamura, S., Akamatsu, K., Nishikawa, M., Takakura, Y., and Hashida, M. (1997) Physicochemical and disposition characterization of antisense oligonucleotides complexed with glycosylated poly(L-lysine). *Biochem. Phamacol. 53*, 887−895.
(14) Garnett, M. C. (1999) Gene-delivery systems using cationic polymers. *Crit. Rev. Ther. Drug Carrier Syst. 16*, 147−207.
(15) Turunen, M. P., Hiltunen, M. O., Ruponen, M., Virkamäki, L., Szoka, F. C., Urtti, A., and Ylä-Herttuala, S. (1999) Efficient adventitial gene delivery to rabbit carotid artery with cationic polymer-plasmid complexes. *Gene Ther. 6*, 6−11.
(16) Liu, Y., Wenning, L., Lynch, M., and Reineke, T. M. (2004) New poly(D-glucaramidoamine)s induce DNA nanoparticle formation and efficient gene delivery into mammalian cells. *J. Am. Chem. Soc. 126*, 7422−7423.
(17) Reineke, T. M., and Davis, M. E. (2003) Structural effects of carbohydrate-containing polycations on gene delivery. 2. Charge center type. *Bioconjugate Chem. 14*, 255−261.
(18) Reineke, T. M., and Davis, M. E. (2003) Structural effects of carbohydrate-containing polycations on gene delivery 1. Carbohydrate size and its distance from charge centers. *Bioconjugate Chem. 14*, 247−254.
(19) Han, S.-O., Mahato, R. I., Sung, Y. K., and Kim, S. W. (2000) Development of biomaterials for gene therapy. *Mol. Ther. 2*, 302−317.
(20) Liu, Y., Wenning, L., Lynch, M., and Reineke, T. M. (2005) Gene delivery with novel poly(L-tartaramidoamine)s, in *Polymeric Drug Delivery Volume I − Particulate Drug Carriers* (Svenson, S., Ed.) American Chemical Society, Washington, DC.
(21) Liu, Y., and Reineke, T. M. (2005) Hydroxyl stereochemistry and amine number within poly(glycoamidoamine)s affect intracellular DNA delivery. *J. Am. Chem. Soc. 127*, 3004−3015.
(22) MacLaughlin, F. C., Mumper, R. J., Wang, J., Tagliaferri, J. M., Gill, I., Hinchcliffe, M., and Rolland, A. P. (1998) Chitosan and depolymerized chitosan oligomers as condensing carriers for in vivo plasmid delivery. *J. Control. Release 56*, 259−272.
(23) Boussif, O., Lezoualch, F., Zanta, M. A., Mergny, M. D., Scherman, D., Demeneix, B., and Behr, J. P. (1995) A versatile vector for gene and oligonucleotide transfer into cells in culture and in vivo: Polyethylenimine. *Proc. Natl. Acad. Sci. U.S.A. 92*, 7297−7301.
(24) Godbey, W. T., Wu, K. K., and Mikos, A. G. (1999) Size matters: Molecular weight affects the efficiency of poly(ethylenimine) as a gene delivery vehicle. *J. Biomed. Mater. Res. 45*, 268−275.
(25) Gao, X., and Huang, L. (1996) Potentiation of cationic liposome-mediated gene delivery by polycations. *Biochemistry 35*, 1027−1036.
(26) Moret, I., Peris, J. E., Guillem, V. M., Benet, M., Revert, F., Dası, F., Crespo, A., and Alino, S. F. (2001) Stability of PEI-DNA and DOTAP-DNA complexes: effect of alkaline pH, heparin and serum. *J. Control. Release 76*, 169−181.
(27) Dash, P. R., Read, M. L., Barret, L. B., Wolfert, M. A., and Seymour, L. W. (1999) Factors affecting blood clearance and in vivo distribution of polyelectrolyte complexes for gene delivery. *Gene Ther. 6*, 643−650.
(28) Yang, J.-P., and Huang, L. (1997) Overcoming the inhibitory effect of serum on lipofection by increasing the charge ratio of cationic liposome to DNA. *Gene Ther. 4*, 950−960.
(29) Plank, C., Tang, M. X., Wolfe, A. R., and Szoka, F. C. (1999) Branched cationic peptides for gene delivery: role of type and number of cationic residues in formation and in vitro activity of DNA polyplexes. *Hum. Gene Ther. 10*, 319−332.
(30) Eliyahu, H., Makovitzki, A., Azzam, T., Zlotkin, A., Joseph, A., Gazit, D., Barenholz, Y., and Domb, A. J. (2005) Novel dextran-spermine conjugates as transfecting agents: comparing water-soluble and micellar polymers. *Gene Ther. 12*, 494−503.
(31) Wagner, E. (2004) Strategies to improve DNA polyplexes for in vivo gene transfer: Will "artificial viruses" be the answer? *Pharm. Res. 21*, 8−14.
(32) Escriou, V., Ciolina, C., Lacroix, F., Byk, G., Scherman, D., and Wils, P. (1998) Cationic lipid-mediated gene transfer: effect of serum on cellular uptake and intracellular fate of lipopolyamine/DNA complexes. *Biochim. Biophys. Acta Biomembr. 1368*, 276−288.
(33) Ruponen, M., Ylä-Herttuala, S., and Urtti, A. (1999) Interactions of polymeric and liposomal gene delivery systems with extracellular glycosaminoglycans: physicochemical and transfection studies. *Biochim. Biophys. Acta Biomembr. 1415*, 331−341.
(34) Mislick, K. A., and Baldeschwieler, J. D. (1996) Evidence for the role of proteoglycans in cation-mediated gene transfer. *Proc. Natl. Acad. Sci. U.S.A. 93*, 12349−12354.

BC050275+

Development of Nanoparticle Libraries for Biosensing

Eric Yi Sun, Lee Josephson, Kim A. Kelly, and Ralph Weissleder*

Center for Molecular Imaging Research, Massachusetts General Hospital, Harvard Medical School, Boston, Massachusetts 02129-2060. Received October 4, 2005; Revised Manuscript Received December 5, 2005

Magnetic and magnetofluorescent nanoparticles have become important materials for biological applications especially for sensing, separation, and imaging. To achieve target specificity, these nanomaterials are often covalently modified with binding proteins such as antibodies or proteins. Here we report on the creation of nanoparticle libraries that achieve specificity through multivalent modification with small molecules. We explore different synthetic routes to attach small molecules with anhydride, amine, hydroxyl carboxyl, thiol, and epoxy handles. We show that the derived nanomaterials have unique biological functions, possess different behaviors in cell screens, and can be used as substrates for biological screens.

INTRODUCTION

To use emerging nanomaterials more efficiently in biological applications, it is often essential to functionalize them with organic ligands to impart precise biological functions (*1*−*3*). Conversely, the creation of entire libraries of nanomaterials could greatly accelerate screening for use in biomedical applications. Magnetic and magnetofluorescent nanoparticles (MNPs and MFNPs) have become important materials in biomedicine for sensing (*4*), magnetic separation, and/or in vivo imaging (*5*). While prior research has focused on the design of specific nanoparticles (*6*, *7*, *20*) or polymers (*9*), detailed procedures for the synthesis and evaluation of surface-modified nanoparticle libraries using different conjugation strategies has not been described. The goal of this study was to develop, optimize, and characterize parallel conjugation chemistries for the creation of magnetofluorescent nanoparticle libraries.

We describe methods of attaching different types of small molecules with reactive handles (anhydride, amino, hydroxyl, carboxyl, thiol, and epoxy) to an aminated magnetofluorescent nanoparticle (amino-CLIO-FITC (*9*)). Although a variety of antibodies and proteins have been conjugated to this nanoparticle, small molecules of nonbiological origin were employed to avoid cost and regulatory issues if a member of the library is subsequently selected for scale-up and clinical use. Small molecules (<2 kDa) can also be separated from the nanoparticle (∼1000 kDa) easily. For each of the chemistries, a method of ensuring that modified particles have been produced is provided. This is particularly important when large numbers of surface-functionalized nanoparticles are made and screened for activity, since an unsuccessful nanoparticle modification cannot be readily distinguished from successful nanoparticle modification with inactivity due to a lack of recognition by a biomolecule. The presence of these types of errors in a database can thus lead to erroneous conclusions regarding structure activity relationships and the misdesign of subsequent libraries. We also show how modified nanoparticles can be used for library screens, analyte sensing, and microarray printing.

EXPERIMENTAL PROCEDURES

Materials. 1-Ethyl-3-(3-dimethylaminopropyl) carbodiimide hydrochloride (EDC), sulfosuccinimidyl ester (sulfo-NHS), and Tris(2-carboxyethyl)phosphine hydrochloride (TCEP) were purchased from Pierce. *N*-Succinimidyl 3-(2-pyridyldithio) propionate (SPDP) and succinimidyl iodo acetate (SIA) were purchased from Molecular Biosciences. All other chemicals were purchased from Sigma Aldrich and used as received.

Magnetic Nanoparticle. The superparamagnetic nanoparticle used in this study consisted of an iron oxide core (5 nm diameter, 2064 Fe per average nanoparticle) with a thick shell of dextran (*10*). Amino-CLIO nanoparticles were synthesized by cross-linking the dextran coating with epichlorohydrin and reacting it with ammonia to provide primary amine groups (*11*). The number of amines per nanoparticle was determined using the SPDP method described previously (*12*). To attach FITC to amino-CLIO, a 2.0 mL DMSO fluorescein isothiocyanate (FITC, 5.0 mg, 12.8 mol) solution, 10 mL of amino-CLIO (10 mg/mL Fe) in 0.01 M sodium citrate buffer, pH 8.0 was added. Subsequently 100 μL of *N*,*N*-diisopropylethylamine (0.57 mmol) was added as catalyst. The mixture was incubated at room temperature overnight, and unreacted FITC was separated by gel filtration (Sephadex G-25), equilibrated, and eluted with PBS buffer, pH 7.4 (Cambrex, Rockland, ME). The number of FITC conjugated to CLIO was determined spectrophotometrically (extinction coefficient of 73 000 M^{-1} cm^{-1} at 494 nm). All batch syntheses were characterized by determining size by laser light scattering (38 nm), magnetic relaxivities (R1 of 21 mM s^{-1}, an R2 of 62 mM s^{-1}), magnetic susceptibility, and number of amines (n = 62 per 2000 Fe) and FITC (n = 2) conjugated.

Surface Modification of Nanoparticles. *Modification by Anhydrides.* To a 100 μL anhydride (50 mM, 5 μmol) DMSO solution, 200 μL of amino-CLIO (5.0 mgFe /mL, 0.4 μmol of amine) in 0.1 M bicarbonate buffer, pH 8.5 was added. The mixture was incubated at room temperature for 2 h with gentle shaking. Unreacted anhydride was separated with Sephadex G-25 column and eluted with PBS buffer, pH 7.4.

Modification by Amine Groups. We first converted amine groups on amino-CLIO to carboxyl groups by reaction with succinic anhydride at the conditions described above for the anhydride/CLIO surface modification. After purification of the sample, carboxylated CLIO was stored in MES buffer (50 mM MES, 0.1 M NaCl), pH 6.0 at a concentration of 5.0 mg/mL Fe. To react with amine molecules, a 200 μL COOH-CLIO solution was first reacted with EDC (0.96 mg, 5 μmol) and sulfo-NHS (1.1 mg, 5 μmol) at room temperature for 60 min. The mixture was then purified through Sephadex G-25 column eluted with PBS buffer, pH 7.4. Subsequently 100 μL of amine

* Corresponding author: R. Weissleder, M.D., Ph.D., Center for Molecular Imaging Research, Massachusetts General Hospital, Building 149, 13th St., Room 5403, Charlestown, MA, 02129. Phone: 617-726-8226. E-mail: weissleder@helix.mgh.harvard.edu.

10.1021/bc050290e CCC: $33.50 © 2006 American Chemical Society
Published on Web 12/30/2005

compound in DMSO (50 mM) was added to the above CLIO solution and reacted for 2 h at room temperature. Unreacted amines were separated by a Sephadex G-25 column eluted with PBS buffer, pH 7.4.

Modification by Hydroxyl Groups. Amino groups on the amino-CLIO nanoparticle were first converted to hydroxyl groups by reaction with SIA. Two milligrams of amino-CLIO was reacted with SIA (1.0 mg, 3.5 μmol) in PBS buffer, pH 7.4. The mixture was incubated at room temperature for overnight to allow displacement of iodine by hydroxyl groups. Hydroxylated CLIO was purified by a Sephadex 25 column eluted with PBS buffer, pH 7.4. Purified OH-CLIO was subsequently precipitated and washed with cold acetone for several times. One milligram of precipitated OH-CLIO was resuspended in 200 μL of anhydrous DMSO and activated by $SOCl_2$ (5 μL, 68.5 μmol). After 5 min reaction at room temperature, a drop of H_2O was added to decompose the excess $SOCl_2$. Subsequently, 200 μL of alcohol (50 mM) in DMSO was added with *N*,*N*-diisopropylethylamine (10 μL, 50 μmol) as catalyst. The mixture was incubated at room temperature for 3 h, and hydroxylated CLIO conjugates were purified by a Sephadex G-25 column eluted with PBS buffer, pH 7.4.

Modification by Carboxyl Groups. Amino-CLIO in PBS buffer, pH 7.4 was first exchanged with MES buffer (50 mM MES hydrate, 0.1 M NaCl), pH 6.0, and the solution was concentrated to 5.0 mg/mL. 100 μL (50 mM) of carboxylic compound in DMSO was added to 200 μL of amino-CLIO (5.0 mg/mL Fe) in MES solution, pH 6.0. This was followed by the addition of excess EDC (0.96 mg, 5 μmol) and sulfo-NHS (1.1 mg, 5 μmol) in 100 μL of DMSO. The reaction proceeded at room temperature for 2 h, and the product was purified by a Sephadex G-25 column and eluted with PBS buffer, pH 7.4.

Modification by Thiols. Amino-CLIO was first reacted with SPDP.[7] After purification of the sample, 200 μL of SPDP derived CLIO (5.0 mg/mL Fe) in PBS buffer, pH 7.4 was mixed with 100 μL of thiol compounds (50 mM) in DMSO. The reaction proceeded for 2 h at room temperature. The CLIO conjugate was separated by a Sephadex G-25 column and eluted with PBS buffer, pH 7.4. For the MRS assays, thiolated influenza hemagglutinin (HA) peptide with a cysteine terminus (YPYDVPDVAGGC) was synthesized by using Fmoc chemistry on Rink amide resin (Calbiochem, NovaBiochem) and was purified by reverse phase HPLC. The molecular weight of HA was confirmed by MALDI-TOF.

Modification by Epoxide Groups. Amino-CLIO in PBS buffer, pH 7.4 was first exchanged to a 0.15 M sodium bicarbonate buffer, pH 8.5, and the solution was concentrated to 5.0 mg/mL. To 200 μL above solution, 100 μL (50 mM) of epoxide compound in DMSO was added. The reaction proceeded at 80 °C for 4 h, and the product was purified by a Sephadex G-25 column and eluted with PBS buffer, pH 7.4.

Surface Characterization. *Surface Modification by Amine Loss.* The loss of amines on anhydrides or carboxyl reacted amino-CLIO was determined using with SPDP as reagent (*12*). SPDP is preferred as a reagent for amine group analysis over more conventional amine assay methods because after treatment with dithiothreitol the pyridine-2-thione (P2T) can be separated from iron based on size. Iron absorbs strongly in the ultraviolet region, a feature that interferes with many amine determining reagents. After reaction with SPDP, the nanoparticle is treated with a reducing agent (TCEP) and the released P2T separated from the nanoparticle by a spin column. P2T absorption can now be determined without the strong nanoparticle absorption at the wavelength of the P2T (343 nm). In a typical experiment, 150 μL of 50 mM SPDP solution in DMSO was added to 50 μL (2 mg Fe) of CLIO in PBS, pH 7.4. The mixture was allowed to react at room temperature for 1 h and purified by Sephadex 25 column. This solution was subsequently added with 50 μL of TCEP (Pierce) and UV-Vis absorption was read at 343 nm. The number of amines was calculated based on an extinction coefficient of 8080 M^{-1} cm^{-1} for P2T.

Magnetic Relaxation Switch Assay. The bioactivity of surface-modified CLIO nanoparticles was examined by their interaction with their corresponding binding molecules, a process that can be monitored by the change in the proton spin−spin relaxation time (T2) (*4*). When nanoparticles bind to their corresponding binding proteins, nanoscale aggregation occurs and the T2 decreases (Figure 2). Control samples were prepared with unmodified nanoparticles. Surface-modified nanoparticles at 10 μg/mL iron in PBS buffer, pH 7.4 were mixed with their binding protein at concentrations, which induced maximal T2 changes determined on a minispec MR spectrometer. Imaging was performed after a 30 min incubation of surface-modified nanoparticles with their corresponding binding proteins at 37 °C. T2 was measured by NMR imaging acquired in a 49 well plate using a 4.7 T superconducting magnet (Brucker, Karlsruhe, Germany). Imaging sequences included multi-echo T2-weighted spin−echo sequences with echo times (TE) ranging from 20−160 ms in increments of 20 ms and a repetition time (TR) of 2000 ms.

Array Printing and Imaging. Two strategies were used to print modified nanoparticles to glass slides. The first method utilized epoxy-modified glass slides. In this method, CLIO compounds were dissolved in 0.1 M carbonate buffer, pH 9.6 at a concentration of 0.1 mg/mL Fe. Each compound was spotted on epoxy glass slides in quadruplicate using a 0.5 μL pipet. Spotted slides were incubated at 80 °C in a humid chamber for 30 min. The alternative method used carboxylated glass slides, which were first activated with EDC and NHS in MES buffer (50 mM MES, pH 6.0) for 30 min followed by drying. Nanoparticles in 0.1 M bicarbonate buffer, pH 8.5 were spotted in quadruplicate using a 0.5 μL pipet. Spotted slides were allowed to dry under inert gas and stored at 4 °C for further use.

To reveal the binding of corresponding proteins to modified nanoparticles, slides were first washed for 2 h with DMF, and 1 h each with 2-propanol and PBS buffer (pH 7.4, containing 0.1% Tween-20). The slides were then blocked for 1 h by incubation with 0.1 M carbonate buffer containing 3% BSA, pH 8.5. After a brief rinse with PBS, fluorescently labeled target proteins (streptavidin-rhodamine, anti-IgG-Cy5.5) were then added at a concentration of 0.1 mg/mL in PBS supplemented with 1% BSA. The slides were incubated for 30 min and then washed 10 times with PBS. The slides were then dried at ambient temperature and imaged with a fluorescence imager. The following filter sets were employed: 680/700 nm excitation/emission filter set (2 s exposure); 560/590 nm excitation/emission filter set (1 s exposure).

Cell Uptake Experiments. U937 cells were obtained from the American Type Tissue Culture Collection (ATCC) and maintained according to ATTCC protocol. For differentiation into macrophages, the nonadherent monocyte-like undifferentiated U937 cells were induced to differentiate by a 48-h exposure to 40 nM PMA (Sigma). After addition of PMA, cells were plated onto gelatin-coated 96-well tissue culture plates. Cells were incubated with 0.1 mg/mL Fe of the indicated CLIO derivatives for 4 h at 37 °C in the presence of 5% CO_2. Following incubation, wells were washed 3× with PBS/0.1%BSA/0.05%Tween-20 wash buffer to remove any surface-bound materials. Cells were then analyzed via an immunoassay to quantitate FITC concentrations (*13*). All experiments were performed in triplicate. For each screening experiment, the uptake of FITC (pM) was log10 transformed, and the mean was determined for each cell line.

Table 1. Summary of Surface Modification

type	reagents	examples	binder	modification[a]	MRSW[b]
anhydride	direct	1,8-naphthalic anhydride	lysozyme	24	23 ms
amine	EDC, NHS	D-glucosamine	concavalin A	36	69 ms
alcohol	SIA, $SOCl_2$	digoxigenin	MAB to dig	30	65 ms
acid	EDC, NHS	folic acid	MAB to folate	32	63 ms
thiol	SPDP	HA peptide	MAB to HA	34	81 ms
epoxide	direct	glycidoxypropyltrimethoxy silane	glass slide	40	NA

[a] Refers to average number of small molecule bound per nanoparticle as determined analytically and assuming an average core of 2,064 Fe/nanoparticle. [b] T2 were measured in PBS buffer, pH 7.4, 37 °C, 0.47 T at an iron concentration of 10 μg/mL. Data are expressed as change in T2 relaxation times.

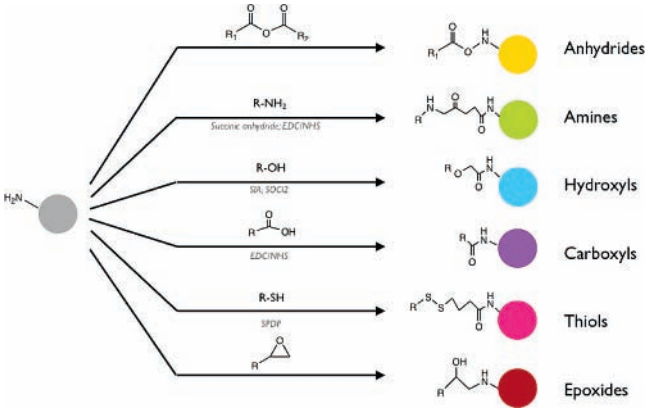

Figure 1. Conjugation strategies. Aminated magnetofluorescent nanoparticles (amino-CLIO-FITC) were reacted with small molecules with different reactivities. Reactions were analyzed by determining loss of amines[12] and the magnetic relaxation switch assay (see Figure 2).

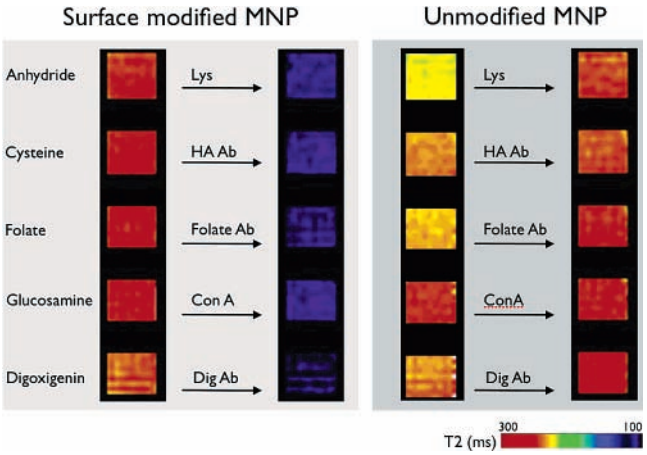

Figure 2. MRS assay confirms bioactivity of derivatized nanoparticles. Nanoparticle preparations modified according to Table 1 (left) or unmodified (right) were incubated with their corresponding binding protein that induces nanoparticle clustering and thus T2 decreases. It is clearly shown that T2 decreases dramatically when modified nanoparticles react with corresponding binding proteins (second column), while nonmodified nanoparticles did not show any visible binding interactions (third and fourth columns).

RESULTS AND DISCUSSION

The first step toward creation of libraries was to optimize the conjugation of six types of small molecules with "reactive handles" to a magnetofluorescent nanoparticle: anhydrides, amines, hydroxyls, carboxyls, thiols, and epoxides (Figure 1). The starting material consisted of a cross-linked dextran coated aminated magnetic nanoparticle of 38-nm diameter that had been reacted with two molecules of FITC (*9*). Each nanoparticle contained 62 amines and a magnetic core containing 2064 Fe per nanoparticle (*14*). For the specific task at hand, we chose representative examples of each class of small molecules to optimize conjugation protocols. The representative examples included diglycolic anhydride, glucosamine, digoxigenin, folic acid, cystein-containing HA peptide, and glycidoxypropyltrimethoxy silane. These specific molecules were chosen because each has a corresponding binding protein, which can be used to examine the bioactivity of the surface-functionalized nanoparticle.

The conjugation of anhydride molecules to amino CLIO was performed in bicarbonate buffer at pH 8.6. Higher pH facilitates the reaction of anhydride group and amino group on CLIO. There were an average of 24 modified amines per nanoparticle. To efficiently attach amine groups to amino-CLIO, we first converted primary amines on the nanoparticle to carboxylic groups. Subsequently, EDC and sulfo-NHS were used to conjugate carboxylate CLIO to amine compounds. To link hydroxyl groups to CLIO, we first treated amino CLIO with succimidyl iodoacetate (SIA). Hydrolysis of SIA-treated CLIO resulted in the conversion of amine groups on CLIO to hydroxyl groups. Hydroxylated CLIO was first precipitated by cold acetone and then resuspended in anhydrous DMSO. Subsequently, $SOCl_2$ was added to activate hydroxyl groups. Excess $SOCl_2$ was decomposed by a small amount of water. The alcohol molecules were added to chlorinated CLIO with the addition of a small quantity of NaOH as catalyst. With respect to carboxyl conjugation, we compared several conjugation methods and found that EDC conjugation was the most efficient. In this

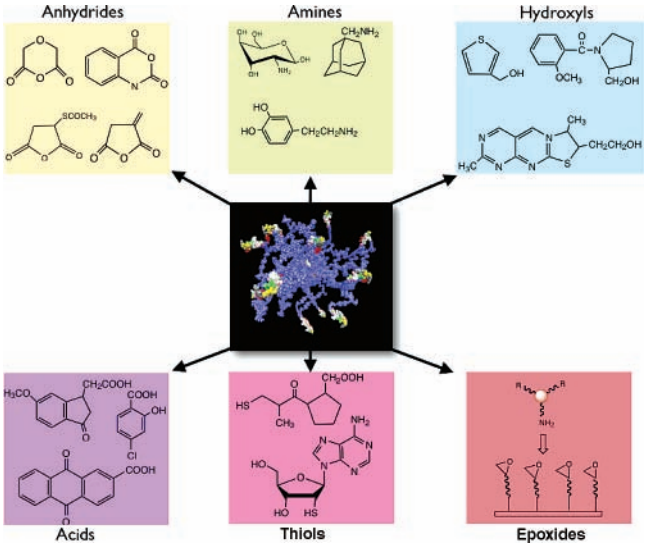

Figure 3. Nanoparticle library. Examples of small molecules attached to amino-CLIO to create a 96-member library (to fill one microtiter plate) that was subsequently used (see Figures 4 and 5).

reaction, the carboxylic molecule (in DMSO) was first activated by EDC in MES buffer, and the reaction to amino-CLIO was accomplished in room temperature in 3 h. Unreacted molecules were separated by a PD-10 column eluted with PBS buffer, pH 7.4. For the reaction of thiol molecules, CLIO was first activated with SPDP, and subsequently thiol molecules were conjugated. Attachment to epoxides was performed in 0.15 M sodium bicarbonate buffer, pH 8.5 by adding epoxides in DMSO. Reaction proceeded for 4 h, and the product was purified by Sephadex G-25 column chromatography.

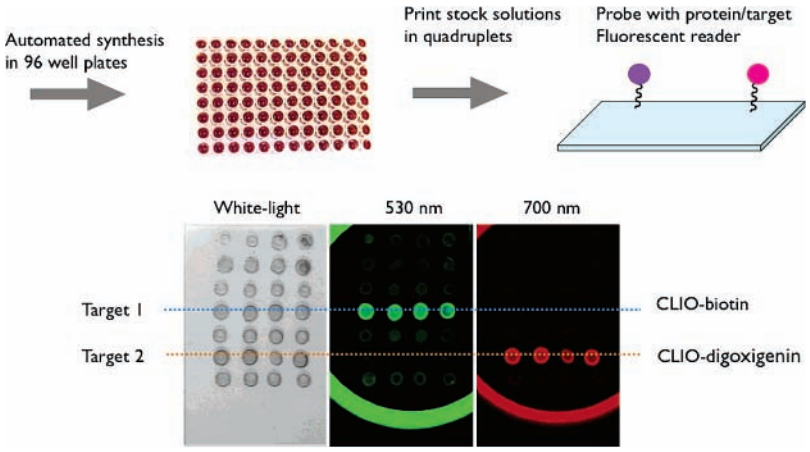

Figure 4. Microarray feasibility experiments. Surface-functionalized nanoparticles of different types were printed onto epoxy glass slides and then washed. Fourth row from top: CLIO-biotin; sixth row from top: CLIO-digoxigenin; remaining rows contained unmodified nanoparticles. Slides were incubated with a mixture of the binding proteins, streptavidin-rhodamine, and anti-digoxigenin, revealed by anti-IgG-Cy5.5, and scanned using a fluorescent reader. Note that the targets are clearly separated in the different channels. All experiments were performed in quadruplicate.

Surface modification of nanoparticles was monitored by two different assays, specifically developed for MFNP: (a) an assay for the modification of amines (amine loss) using SPDP as a reagent (*12*) and (b) a magnetic relaxation switch assay to demonstrate that both surface modification and the activity of the surface with a biological molecule (*4*). The strong absorption from iron oxide between 250 and 450 nm, nanoparticle superparamagnetism, and the presence of both the oxidizing ferrous ion and reducing ferric ions, mean that the nanoparticle interferes with many analytical methods that work well with other materials. The use of SPDP for amine determination permits separation of P2T, released from the nanoparticle with a reducing agent, from iron before quantitation. Second, biomolecules when attached to surfaces can interact with the surface and lose bioactivity (surface denaturation). On average, small molecule modification resulted in the attachment of 20−40 functional groups per nanoparticle. Table 1 summarizes the overall chemical conjugation and characterization conditions. The magnetic relaxation switch assay (MRS) was used to verify the bioactivity of a surface-functionalized CLIO made with each of the conjugation chemistries. This assay is based on the fact that water proton spin−spin relaxation time (T2) are altered upon self-assembly when surface-functionalized CLIO nanoparticles react with a biomolecule in solution (*4*, *15*−*17*). As can be seen from Figure 2, each representative example of a surface-modified nanoparticle showed a significant decrease in T2 relaxation time, whereas unmodified nanoparticles did not. Thus, each of the surface modification reactions employed was capable of producing a bioactive surface.

We next set out to develop a larger diverse library set based on the optimized conjugation strategies discussed above. Figure 3 lists some of the representative examples of each of the classes of small molecules bound to the nanoparticle. Overall, we created a nanoparticle library consisting of 96 compounds (Figure 4). This library was used to perform two different sets of biological experiments: (a) microarray screen after compounds were printed on glass slides and (b) fluid-phase experiments to determine nanoparticle uptake into macrophages (Figure 5). We first wished to determine if the nanoparticles could be printed onto glass slides to ultimately allow high-throughput screening against purified target proteins. We experimented with two different conjugation schemes: attachment of nanoparticles to epoxide-coated glass slides and to carboxylated glass slides. Either method resulted in visible attachment of nanoparticles to the glass surface, both by pipet spotting (Figure 4) as well as a by pin-printing. To determine whether functionalized nanoparticles would retain the ability

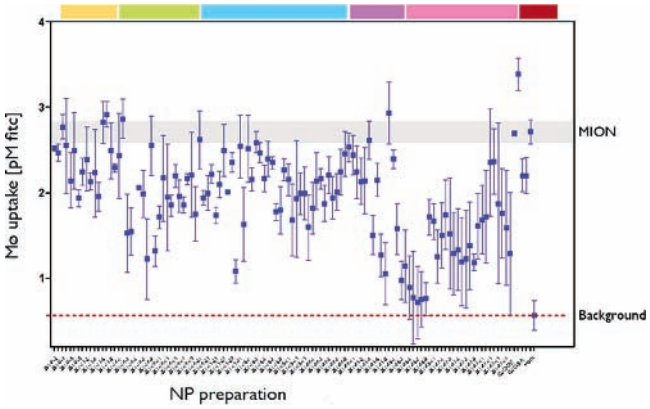

Figure 5. Screening of nanoparticle library in macrophages. Small molecule modified nanoparticle preparations were incubated with U937 macrophages, and cellular uptake was determined by a FITC-mediated immuno ELISA assay.[13] Note the variability in uptake upon small molecule modification compared to base material (MION).

to interact with binding proteins, we tested biotinylated and digoxigenated nanoparticles against fluorescent streptavidin-Cy3 and anti-digoxigenin-Cy5.5, respectively. As is shown in Figure 4, there was good distinction between the signals from the different fluorochromes.

We and others have previously shown that macrophages represent a prime target for systemically injected nanomaterials (*2*, *18*). To develop functionalized nanomaterials targeted to other cell types, it would therefore be desirable to minimize macrophage uptake of the parent compound. We therefore performed a cell-based screen of all synthesized nanoparticle preparations and compared binding/uptake to preparations currently in clinical use (MION-like dextran-coated compounds). As is apparent in Figure 5, several nanoparticle preparations had lower macrophage uptake than starting materials. More in-depth screens in primary human isolated macrophages are currently ongoing to identify novel nanomaterials with limited a priori macrophage affinity.

In conclusion, we have developed a series of highly general methods to modify the surface of magnetofluorescent nanoparticles with small molecules and demonstrated that these nanoparticles achieve specific interactions with protein targets. Analytical methods have been developed to ensure that the desired surface modification of nanoparticles has occurred, and magnetic relaxation switch assays have been used to demonstrate bioactivity, as the reaction of surface-modified nanoparticles with their corresponding binding protein. All materials used for

the modification of nanoparticles were low molecular weight and of nonbiological origin. The current approach has the potential to generate a larger and more diverse library of functional nanomaterials toward numerous biological targets. Moreover, these methods are readily adapted to automated synthesis and suitable for high-throughout screening of the interaction of surface-modified nanoparticles with specific types of cells or molecular targets.

ACKNOWLEDGMENT

The authors would like to acknowledge the help of Dr. Sergeyev for synthesizing CLIO. We also thank Rabi Upadhyay and Sarah Rhee for technical assistance with imaging. Part of this research was supported by P50 CA86355, P01 CA69246, R24 CA92782 and a grant from the Reynolds Foundation.

LITERATURE CITED

(1) Whitesides, G. M. (2003) The 'right' size in nanobiotechnology. *Nat. Biotechnol. 21*, 1161−1165.

(2) Akerman, M. E., Chan, W. C., Laakkonen, P., Bhatia, S. N., and Ruoslahti, E. (2002) Nanocrystal targeting in vivo. *Proc. Natl. Acad. Sci. U.S.A. 99*, 12617−12621.

(3) Ferrari, M. (2005) Cancer nanotechnology: opportunities and challenges. *Nat. Rev. Cancer 5*, 161−171.

(4) Perez, J. M., Josephson, L., O'Loughlin, T., Hogemann, D., and Weissleder, R. (2002) Magnetic relaxation switches capable of sensing molecular interactions. *Nat. Biotechnol. 20*, 816−820.

(5) Jaffer, F. A., and Weissleder, R. (2005) Molecular imaging in the clinical arena. *JAMA 293*, 855−862.

(6) Kelly, K. A., Allport, J. R., Tsourkas, A., Shinde-Patil, V. R., Josephson, L., and Weissleder, R. (2005) Detection of vascular adhesion molecule-1 expression using a novel multimodal nanoparticle. *Circ. Res. 96*, 327−336.

(7) Schellenberger, E. A., Reynolds, F., Weissleder, R., and Josephson, L. (2004) Surface-functionalized nanoparticle library yields probes for apoptotic cells. *ChemBioChem 5*, 275−279.

(8) Anderson, D. G., Lynn, D. M., and Langer, R. (2003) Semi-automated synthesis and screening of a large library of degradable cationic polymers for gene delivery. *Angew. Chem., Int. Ed. 42*, 3153−3158.

(9) Josephson, L., Kircher, M. F., Mahmood, U., Tang, Y., and Weissleder, R. (2002) Near-infrared fluorescent nanoparticles as combined MR/optical imaging probes. *Bioconjugate Chem. 13*, 554−560.

(10) Shen, T., Weissleder, R., Papisov, M., Bogdanov, A., Jr., and Brady, T. (1993) Monocrystalline iron oxide nanocompounds (MION): physicochemical properties. *J. Magn Reson. Med. 29*, 599−604.

(11) Lewin, M., Carlesso, N., Tung, C. H., Tang, X. W., Cory, D., Scadden, D. T., and Weissleder, R. (2000) Tat peptide-derivatized magnetic nanoparticles allow in vivo tracking and recovery of progenitor cells. *Nat. Biotechnol. 18*, 410−414.

(12) Zhao, M., Kircher, M. F., Josephson, L., and Weissleder, R. (2002) Differential conjugation of tat peptide to superparamagnetic nanoparticles and its effect on cellular uptake. *Bioconjugate Chem. 13*, 840−844.

(13) Kelly, K. A., Reynolds, F., Weissleder, R., and Josephson, L. (2004) Fluorescein isothiocyanate-hapten immunoassay for determination of peptide-cell interactions. *Anal. Biochem. 330*, 181−185.

(14) Reynolds, F., O'loughlin, T., Weissleder, R., and Josephson, L. (2005) Method of determining nanoparticle core weight. *Anal. Chem. 77*, 814−817.

(15) Perez, J. M., O'Loughin, T., Simeone, F. J., Weissleder, R., and Josephson, L. (2002) DNA-based magnetic nanoparticle assembly acts as a magnetic relaxation nanoswitch allowing screening of DNA-cleaving agents. *J. Am. Chem. Soc. 124*, 2856−2857.

(16) Perez, J. M., Josephson, L., and Weissleder, R. (2004) Use of magnetic nanoparticles as nanosensors to probe for molecular interactions. *ChemBioChem 5*, 261−264.

(17) Perez, J. M., Simeone, F. J., Saeki, Y., Josephson, L., and Weissleder, R. (2003) Viral-induced self-assembly of magnetic nanoparticles allows the detection of viral particles in biological media. *J. Am. Chem. Soc. 125*, 10192−10193.

(18) Weissleder, R., Elizondo, G., Wittenberg, J., Rabito, C. A., Bengele, H. H., and Josephson, L. (1990) Ultrasmall superparamagnetic iron oxide: Characterization of a new class of contrast agents for MR imaging. *Radiology 175*, 489−493.

(19) Tsourkas, A., Shinde-Patil, V. R., Kelly, K. A., Patel, P., Wolley, A., Allport, J. R., and Weissleder, R. (2005) In vivo imaging of activated endothelium using an anti-VCAM-1 magnetooptical probe. *Bioconjugate Chem. 16*, 576−581.

(20) Weissleder, R., Kelly, K., Sun, E. Y., Shtatland, T., and Josephson, L. (2005) Cell-specific targeting of nanoparticles by multivalent attachment of small molecules. *Nat. Biotechnol. 23*, 1418−1423.

BC050290E

Enhanced Activity of Monomethylauristatin F through Monoclonal Antibody Delivery: Effects of Linker Technology on Efficacy and Toxicity

Svetlana O. Doronina,* Brian A. Mendelsohn, Tim D. Bovee, Charles G. Cerveny, Stephen C. Alley, Damon L. Meyer, Ezogelin Oflazoglu, Brian E. Toki, Russell J. Sanderson, Roger F. Zabinski, Alan F. Wahl, and Peter D. Senter

Seattle Genetics, Inc., 21823 30th Drive SE, Bothell, Washington 98021. Received October 4, 2005; Revised Manuscript Received October 19, 2005

We have previously shown that antibody−drug conjugates (ADCs) consisting of cAC10 (anti-CD30) linked to the antimitotic agent monomethylauristatin E (MMAE) lead to potent in vitro and in vivo activities against antigen positive tumor models. MMAF is a new antimitotic auristatin derivative with a charged C-terminal phenylalanine residue that attenuates its cytotoxic activity compared to its uncharged counterpart, MMAE, most likely due to impaired intracellular access. In vitro cytotoxicity studies indicated that mAb−maleimidocaproyl-valine-citrulline-*p*-aminobenzyloxycarbonyl−MMAF (mAb−L1−MMAF) conjugates were >2200-fold more potent than free MMAF on a large panel of CD30 positive hematologic cell lines. As with cAC10−L1−MMAE, the corresponding MMAF ADC induced cures and regressions of established xenograft tumors at well tolerated doses. To further optimize the ADC, several new linkers were generated in which various components within the L1 linker were either altered or deleted. One of the most promising linkers contained a noncleavable maleimidocaproyl (L4) spacer between the drug and the mAb. cAC10−L4−MMAF was approximately as potent in vitro as cAC10−L1−MMAF against a large panel of cell lines and was equally potent in vivo. Importantly, cAC10−L4−MMAF was tolerated at >3 times the MTD of cAC10−L1−MMAF. LCMS studies indicated that drug released from cAC10−L4−MMAF was the cysteine−L4−MMAF adduct, which likely arises from mAb degradation within the lysosomes of target cells. This new linker technology appears to be ideally suited for drugs that are both relatively cell-impermeable and tolerant of substitution with amino acids. Thus, alterations of the linker have pronounced impacts on toxicity and lead to new ADCs with greatly improved therapeutic indices.

INTRODUCTION

In recent years, the impact that monoclonal antibodies (mAbs)[1] have had in the clinical treatment of cancer has been pronounced. There are now several approved therapeutic antibodies, including trastuzumab (Herceptin), rituximab (Rituxan), cetuximab (Erbitux), and bevacizumab (Avastin), and many others are in late-stage development (reviewed in refs 1, 2). While these agents display significant activities through such mechanisms as antibody-dependent cellular cytotoxicity, complement-dependent cytotoxicity, and signal transduction, the activities are generally suboptimal, even when combined with conventional cancer chemotherapeutic agents. Consequently, significant attention has turned toward the use of mAb-based immunoconjugates, in which the mAb carries a toxic payload to tumor cells (reviewed in refs 3, 4). Three such agents are now clinically approved: ibritumomab tiuxetan (Zevalin), a ^{90}Y labeled anti-CD20 mAb; tositumomab (Bexxar), an ^{131}I labeled anti-CD20 mAb; and gemtuzumab ozogamicin (Mylotarg), an anti-CD33−calicheamicin conjugate. The activities of these conjugated mAbs provide validation for the concept, and a basis for developing other such agents for cancer therapy.

The goal of targeted therapy with mAb−drug conjugates is to achieve high degrees of therapeutic activity, while sparing normal tissues from chemotherapeutic damage. Toward this end, several critical parameters have been identified that must be addressed. These include the barriers to mAb extravasation, conjugate immunogenicity, widespread expression of the target antigen on normal tissue, metabolism at nontarget sites, low drug potency, and efficient release of the drug in forms that do not impair activity (*3*−*6*). Consequently, the focus in many laboratories has been to use chimeric or humanized mAbs against highly selective tumor-associated antigens, attached to potent drugs through linkers that allow for efficient drug release once the antibody−drug conjugate (ADC) has bound to the target and has undergone internalization. Examples of some advanced agents include C242-DM1 (cantuzumab mertansine), an anticarcinoma mAb linked to a derivative of maytansine (*7*), MLN2704, an anti-prostate cancer mAb attached to maytansine (*5*), and an anti-CD22−calicheamicin conjugate for the treatment of B-cell lymphomas (*8*).

In developing highly active agents that address the issues described for targeted therapy, we have focused considerable attention on the drug payload, the linker used for drug attachment, and the method by which the antibody is modified. This has led to the development of mAb−auristatin conjugates

* To whom correspondence should be addressed. E-mail: sdoronina@seagen.com

[1] Abbreviations: ADC, antibody−drug conjugate; cAC10−linker−drug$_{4\ or\ 8}$, cAC10 ADC with four or eight drugs/mAb; Cit, L-citrulline; Cys, L-cysteine; Dap, dolaproine; DEPC, diethyl cyanophosphonate; DIEA, *N*,*N*-diisopropylethylamine; Dil, dolaisoleuine; DMF, dimethylformamide; DTNB, 5,5′-dithio-bis(2-nitrobenzoic acid); DTT, dithiothreitol; Fmoc, 9-fluorenylmethoxycarbonyl; HATU, *O*-(7-azabenzotriazol-1-yl)-*N*,*N*,*N*′,*N*′-tetramethyluronium hexafluorophosphate; HRP, horseradish peroxidase; IC_{50}, dose that inhibits cell growth by 50%; L1−4, linkers 1−4 (Table 1); MeVal, *N*-methyl valine; mAb, monoclonal antibody; MDR, multidrug resistance; MMAE, monomethylauristatin E; MMAF, monomethylauristatin F; MMAF-OMe, monomethylauristatin F methyl ester; MTD, maximum tolerated dose; PAB, *p*-aminobenzyl; PABC, *p*-aminobenzyloxycarbonyl; PABOH, *p*-aminobenzyl alcohol; PBS, phosphate-buffered saline; Phe, L-phenylalanine; pNP, *p*-nitrophenyl; TFA, trifluoroacetic acid; Val, L-valine.

10.1021/bc0502917 CCC: $33.50 © 2006 American Chemical Society
Published on Web 12/22/2005

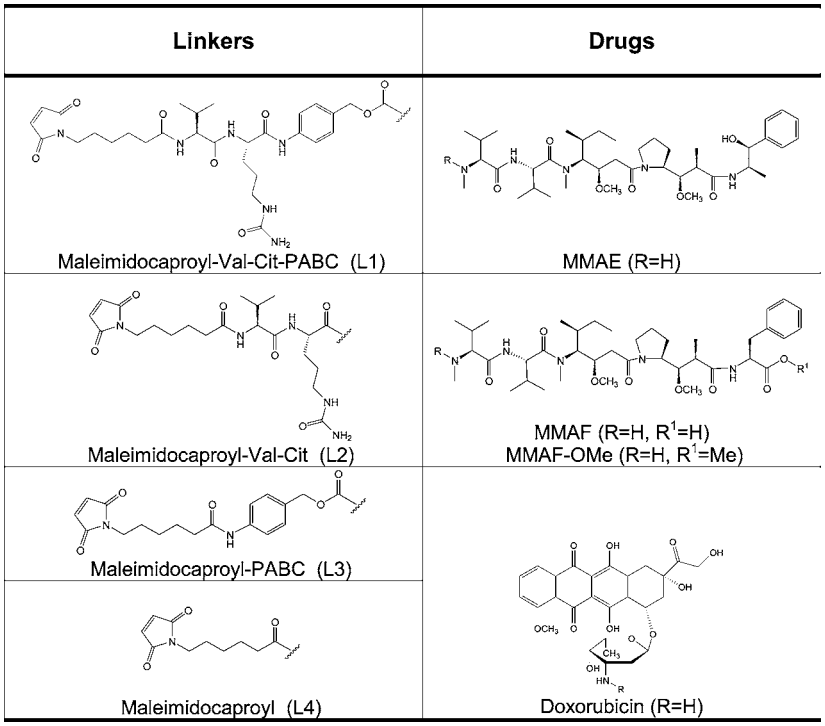

Figure 1. Structures of drugs and linkers.

that include a highly potent and totally synthetic drug attached to mAb cysteine residues through a proteolytically cleavable linker (*3, 6, 9*−*12*). The most advanced agent that we have described (*12*−*15*) is cAC10−maleimidocaproyl-valine-citrulline-*p*-aminobenzyloxycarbonyl-monomethylauristatin E (cAC10−maleimidocaproyl-Val-Cit-PABC−MMAE, or cAC10−L1−MMAE, shown in Figure 1). This is comprised of the highly potent antimitotic agent MMAE, attached to mAb−cysteines through the L1 linker that is cleaved by intracellular proteases such as cathepsin B. The optimal number of drugs/mAb was found to be four (*14*), where pronounced activities at well tolerated doses were obtained in CD30 positive hematologic malignancies.

Here, we describe the properties of a new auristatin, MMAF, that was designed to be much more active when actively delivered inside cells with a mAb, compared to treatment in the untargeted form. We viewed such an approach to targeted delivery as advantageous compared to that of drugs that have high potency in the untargeted form, since any drug that is systemically released would not be expected to contribute to toxic side-effects. Several linker technologies were evaluated to optimize the delivery of MMAF to target cells. In this report, we demonstrate that targeted MMAF is much more potent than the free drug, and that cAC10 conjugates of MMAF display pronounced activities, both in vitro and in vivo. In addition, conjugates of MMAF circumvent a common form of multidrug resistance (MDR). The development of this drug, together with the biological activities of ADCs derived from it, are described for the first time.

EXPERIMENTAL PROCEDURES

General. Unless otherwise noted, materials were obtained from commercial suppliers in the highest purity grade available and used without further purifications. Anhydrous DMF and CH_2Cl_2 were purchased from Aldrich. *N*-Fmoc-L-[ring-$^{13}C_6$]-Phenylalanine was obtained from Cambridge Isotope Laboratories, Inc. (Andover, MA). 2-Chlorotrityl chloride resin was purchased from Advanced ChemTech and loaded with *N*-Fmoc-L-[ring-$^{13}C_6$]-phenylalanine according to manufacturer's specifications. Phenylalanine-2-chlorotrityl resin was purchased from Novabiochem. Phenylalanine loading level of the resin was determined (0.55 mmol/gram) by extensive acylation with Fmoc-Cl followed by spectrophotometric Fmoc-quantitation assay. Solid-phase synthesis was performed in plastic syringes (National Scientific Company) fitted with a filter cut out of fritware PE medium grade porous sheet (Scienceware). Burrell wrist action shaker (Burrell Scientific, Pittsburgh, PA) was used for agitation. All solid-phase yields reported are based upon the initial phenylalanine substitution level of the resin and constitute a mass balance of isolated pure material from support, unless otherwise stated. Fmoc-Dap was custom synthesized by Albany Molecular Research, Inc. (Albany, NY).

HPLC assays were performed using C12 Phenomenex Synergy MAX-RP 4μ, 80 Å reversed-phase column, 150 × 2.0 mm. The eluent was a linear gradient of acetonitrile from 5% to 95% in 5 mM aqueous ammonium phosphate, pH 7.0, in 10 min, then 95% acetonitrile for 10 min, flow rate 1 mL/min, 215 nm detection. Preparative HPLC purifications were performed on Varian instrument equipped with C12 Phenomenex Synergy MAX-RP 4μ reversed phase column, 250 × 21.2 mm, eluting with 0.1% TFA in a water−acetonitrile gradient. Flash chromatography was carried out using Whatman 60 Å 230−400 mesh ASTM silica gel.

Low resolution mass spectra (LCMS) were recorded on a ZMD-Micromass Single Quadrupole Mass Spectrometer equipped with an electrospray ion source (45 eV) coupled with HP1100 HPLC system (reverse phase C12 Phenomenex column, 4 μ, 100 Å, 150 × 2.0 mm. The eluent was a linear gradient of acetonitrile from 5% to 95% in water in the presence of 0.1% formic acid in 10 min, then 95% acetonitrile for 5 min, flow rate 400 μL/min). High resolution (exact mass, HRMS) electrospray ionization (ESI) data were obtained at the University of Washington Medicinal Chemistry Mass Spectrometry Center on a Bruker APEXIII 47e [FT(ICR)]MS. NMR data were recorded on Varian Mercury 400 MHz Instrument. Chemical shifts (δ) are reported in ppm downfield from an internal solvent peak, and *J* values are in hertz.

The chimeric IgG_1 cAC10 (*16*) and cBR96 (*17*) mAbs recognize the CD30 and Lewis Y antigens, respectively. The human lymphoma cell lines Karpas 299, SUP-M2, SU-DHL-1, SR-786, DEL, HDLM-2, L428, KMH-2, and WSU-NHL were obtained from the DSMZ (Braunschweig, Germany). 786-O and Caki-1 renal cell carcinoma and HH lymphoma cell lines were purchased from the ATCC (Manassas, VA). H3396 breast carcinoma cells were obtained as described earlier (*16*). The parent/drug resistant cell line pair NCI-H69, NCI-H69/LX4 were obtained from the ECACC (Salisbury, England), and the Hodgkin's disease cell line L540cy has been previously described (*18*). All cell lines were grown according to the manufacturers' recommendations and routinely checked for mycoplasma contamination.

Maleimidocaproyl−MMAE (L4−MMAE). To a solution of MMAE (*12*) (72 mg, 0.1 mmol) in anhydrous CH_2Cl_2 (2 mL) 6-maleimidocaproic acid (30 mg, 0.15 mmol, 1.5 equiv) was added followed by DEPC (36 μL, 0.2 mmol, 2 equiv) and DIEA (55 μL, 0.3 mmol, 3 equiv). The reaction mixture was stirred at room temperature for 2 h. CH_2Cl_2 (30 mL) was added, and the mixture was washed with 10% aqueous citric acid (2 × 20 mL), water (20 mL), and brine (20 mL) and concentrated to near dryness. Product was isolated by flash chromatography on silica gel eluting with 5% MeOH in CH_2Cl_2 to give a white solid, 32 mg (35%). Reversed-phase HPLC analysis: 98% at 9.48 min. ^{1}H NMR (DMSO-d_6): δ 0.70−0.89 (18H, m), 0.95−1.05 (6H, m), 1.19−1.34 (m), 1.44−1.55 (m), 1.66−1.84 (m), 1.88−2.02 (m), 2.06−2.16 (m), 2.22−2.46 (m), 2.81 (s), 2.86 (s), 2.90 (s), 2.93 (s), 2.97 (d), 3.01−3.08 (m), 3.12 (d), 3.17 (d), 3.20 (d), 3.23 (dd), 3.35−3.40 (m), 3.42−3.50 (m), 3.52−3.59 (m), 3.77 (d), 3.93−4.04 (m), 4.37−4.54 (m), 4.59−4.64 (m), 4.70−4.78 (m), 5.36 (d), 5.43 (d), 7.01−7.02 (2H, m), 7.14−7.31 (5H, m), 7.65 (d), 7.74 (d), 7.78 (d), 7.89−7.92 (m), 8.56−8.61 (m). HRMS (ESI) calcd for $C_{49}H_{79}N_6O_{10}$ $(MH)^+$ 911.5858; found, *m*/*z* 911.5839.

Fmoc-MMAF-OMe. Fmoc-MeVal-Val-Dil (*12*) (0.50 g, 0.78 mmol) and Dap-Phe-OMe·HCl (*12*) (0.30 g, 0.78 mmol) were dissolved in CH_2Cl_2 (5 mL) followed by the addition of DIEA (0.30 mL, 1.71 mmol, 2.2 equiv). DEPC (0.20 mL, 1.17 mmol, 1.5 equiv) was added next while the contents stirred under Ar. Reaction was complete according to HPLC analysis after 1 h. The mixture was concentrated and purified on silica gel eluting with a step gradient of ethyl acetate (from 50% to 100%) in hexane to provide a white foam, 0.65 g (87%). Reversed-phase HPLC analysis: 95% at 16.2 min. ^{1}H NMR (DMSO-d_6): δ 0.71−0.95 (20H, m), 1.01−1.07 (3H, dd), 1.22−1.30 (m), 1.34−1.52 (m), 1.60−1.83 (m), 1.92−2.11 (m), 2.16−2.28 (2H, m), 2.31−2.42 (m), 2.79−2.89 (m), 2.96−3.07 (m), 3.15−3.16 (m), 3.19 (s), 3.24 (s), 3.29 (d), 3.42−3.55 (m), 3.63 (1.5H, s), 3.66 (1.5H, s), 3.75 (0.5H, d), 3.96 (1H, m), 4.09−4.11 (m), 4.21−4.51 (m), 4.61−4.74 (m), 7.15−7.23 (5H, m), 7.31 (2H, t), 7.41 (3H, t), 7.62 (2H, d), 7.89 (2H, d), 8.05 (0.5H, d), 8.11 (0.5H, d), 8.29 (0.5H, d), 8.51 (0.5H, d). LCMS (ESI): *m*/*z* 968.35 $(MH)^+$ (eluted at 14.84 min).

MMAF-OMe. Fmoc-MMAF-OMe (140 mg, 0.14 mmol) in CH_2Cl_2 (5 mL) was treated with diethylamine (2 mL). After 2 h, the reaction was concentrated and purified by preparative HPLC to give a TFA salt of MMAF-OMe as a white solid, 126 mg (98%). Reversed-phase HPLC analysis: 94% at 11.25 min.^{1}H NMR (DMSO-d_6): δ 0.77 (3H, m), 0.87−1.07 (19H, m), 1.22−1.32 (m), 1.37−1.52 (m), 1.60−1.88 (m), 1.96−2.12 (m), 2.18−2.29 (m), 2.32−2.54 (m), 2.83−2.90 (m), 2.99 (s), 3.07 (s), 3.16−3.20 (m), 3.26 (s), 3.42−3.58 (m), 3.64 (s), 3.66 (s), 3.75 (d), 3.98 (m), 4.43−4.52 (m), 4.55−4.76 (m), 7.17−7.58 (5H, m), 8.30 (0.5H, d), 8.56 (0.5H, d), 8.83−8.93 (3H, m). HRMS (ESI) calcd for $C_{40}H_{68}N_5O_8$ $(MH)^+$ 746.5068; found, *m*/*z* 746.5037.

Maleimidocaproyl-Val-Cit-PABC−MMAF-OMe (L1−MMAF-OMe). MMAF-OMe·TFA (110 mg, 0.13 mmol, 1.0 equiv), maleimidocaproyl-Val-Cit-PAB-OCO-pNP (*10*) (103 mg, 0.14 mmol, 1.1 equiv), and 1-hydroxybenzotriazole (HOBt, 3.4 mg, 26 μmol, 0.2 equiv) were dissolved in pyridine (0.5 mL) and DMF (2 mL) under Ar. To this mixture was added DIEA (22.5 μL, 0.13 mmol, 1.0 equiv). The resulting solution stirred for 3 h before more DIEA (22.5 μL) was added. After stirring for 40 h total, the mixture was concentrated, taken up in DMSO (2 mL). Preparative HPLC purification followed by precipitation from CH_2Cl_2 (2 mL) with ether resulted in 90 mg (52%) of white solid. Reversed-phase HPLC analysis: 95% at 9.48 min. ^{1}H NMR (DMSO-d_6): δ 0.72−0.94 (28H, m), 1.02−1.06 (3H, dd), 1.14−1.52 (m), 1.54−1.82 (m), 1.90−2.38 (m), 2.28−2.46 (m), 2.85 (br s), 2.97 (s), 3.04 (s), 3.16 (s), 3.18 (s), 3.20 (s), 3.25 (s), 3.28−3.30 (m), 3.42−3.58 (m), 3.63 (s), 3.66 (s), 3.75 (d), 3.96 (m), 4.17−4.21 (m), 4.23−4.28 (m), 4.32−4.42 (m), 4.44−4.55 (m), 4.60−4.74 (m), 4.94−5.12 (m), 6.01 (1H, br s), 7.01 (2H, s), 7.18−7.32 (9H, m), 7.58 (2H, m), 7.81 (1H, d), 8.07−8.12 (1.5H, m), 8.29 (1H, m), 8.51 (0.5H, d), 10.0 (1H, d). HRMS (ESI) calcd for $C_{69}H_{106}N_{11}O_{16}$ $(MH)^+$ 1344.7819; found, *m*/*z* 1344.7776.

Maleimidocaproyl-PAB-OCO-pNP. To a suspension of 6-maleimidocaproic acid (1.0 g, 4.52 mmol) in CH_2Cl_2 (13.0 mL) was added *p*-aminobenzyl alcohol (PABOH, 1.11 g, 9.04 mmol, 2.0 equiv) and 2-ethoxy-1-ethoxycarbonyl-1,2-dihydroquinoline (EEDQ, 2.24 g, 9.04 mmol, 2.0 equiv). The reaction mixture was stirred at ambient temperature for 16 h, and then concentrated to near dryness. The residue was purified by flash chromatography on silica gel, eluting with a step gradient from 25 to100% ethyl acetate in hexane, to give 1.38 g (96%) of maleimidocaproyl-PABOH as a white solid. Maleimidocaproyl-PABOH (0.85 g, 2.69 mmol) was then activated by reaction with bis *p*-nitrophenyl carbonate (2.45 g, 8.07 mmol, 3 equiv) and DIEA (0.94 mL, 5.38 mmol, 2 equiv) in DMF (10 mL). After 1 h, HPLC analysis indicated complete consumption of starting material. Solvent was removed under reduced pressure, and the residue was triturated with diethyl ether (5 × 20 mL) resulting in 1.25 g (96%) of an off white solid. Reversed-phase HPLC analysis: 99% at 9.98 min. ^{1}H NMR ($CDCl_3$): δ 1.37 (2H, m), 1.64 (2H, m), 1.77 (2H, m), 2.37 (2H, t, J = 7.6), 3.54 (2H, t, J = 7.2), 6.68 (2H, s), 7.37 (2H, d, J = 9.2), 7.41 (2H, d, J = 8.8), 7.57 (2H, d, J = 8.8), 8.27 (2H, d, J = 9.2).

MeVal-Val-Dil-Dap-Phe-2-chlorotrityl Resin. Fmoc-Dap (450 mg, 1.1 mmol) and HATU (418 mg, 1.1 mmol, 2 equiv) were dissolved in anhydrous DMF (8 mL), and DIEA (384 μL, 2.2 mmol, 4 equiv). The resulting solution was added to the 20 mL syringe containing Phe-2-chlorotrityl resin (1 g, 0.55 mmol). Mixture was agitated for 3 h. Reaction completion was determined by LCMS analysis of material cleaved off a small amount of resin. The resin was filtered, washed with DMF (6 × 10 mL), CH_2Cl_2 (6 × 10 mL), ethyl ether (6 × 10 mL), and dried in vacuo for 2 h. A 20% piperidine in DMF solution (5 mL) was added to the syringe, and the mixture was agitated for 2 h. The resin was then filtered, rinsed with DMF (6 × 10 mL), CH_2Cl_2 (6 × 10 mL), and ethyl ether (6 × 10 mL), and dried in vacuo. In a separate flask Fmoc-MeVal-Val-Dil tripeptide (*12*) (702 mg, 1.1 mmol) and HATU (418 mg, 1.1 mmol, 2 equiv) were dissolved in anhydrous DMF (8 mL) followed by the addition of DIEA (384 μL, 2.2 mmol, 4 equiv). The solution was then transferred to the syringe containing the resin, and the mixture was agitated for 3 h. LCMC analysis of material cleaved from a small amount of resin was used to determine reaction completion. The resin was filtered, washed with DMF (6 × 10 mL), CH_2Cl_2 (6 × 10 mL), and ethyl ether (6 × 10 mL), and dried in vacuo for 2 h. A 20% piperidine solution in DMF (5 mL) was added to the resin, and the mixture

was agitated for 2 h. The resin was then filtered, washed with DMF (6 × 10 mL), CH_2Cl_2 (6 × 10 mL), and ethyl ether (6 × 10 mL), and dried in vacuo.

MMAF (MeVal-Val-Dil-Dap-Phe). MeVal-Val-Dil-Dap-Phe-2-chlorotrityl resin (100 mg, 0.044 mmol) in a 5 mL syringe was treated with 2% TFA in CH_2Cl_2 (4 mL) for 5 min at ambient temperature. Preparative HPLC purification provided 27 mg (73%) of white solid. Reversed-phase HPLC analysis: 95% at 5.74 min. ^{1}H NMR (DMF-d_7): δ 0.78 (3H, t), 0.90−1.15 (19H, m), 1.28−1.44 (m), 1.46−1.62 (m), 1.75−2.00 (m), 2.03−2.12 (m), 2.14−2.23 (m), 2.24−2.48 (m), 2.50−2.61 (m), 2.78−2.82 (m), 2.97−3.09 (m), 3.12 (s), 3.18−3.21 (m), 3.26 (d), 3.30 (s), 3.34 (s), 3.41−3.46 (m), 3.49 (d), 3.53−3.60 (m), 3.61−3.69 (m), 3.72−3.78 (m), 3.93 (d), 4.10 (2H, br d), 4.12−4.38 (1H, br), 4.64−4.92 (3H, m), 7.21−7.35 (5H, m), 8.12 (0.5H, d), 8.40 (0.5H, d), 8.78−8.83 (1H, m), 9.03 (1H, br s), 9.63 (1H, br s). HRMS (ESI) calcd for $C_{39}H_{66}N_5O_8$ $(MH)^+$ 732.4911; found, *m*/*z* 732.4890.

Maleimidocaproyl-Val-Cit-PABC−MMAF (L1−MMAF). MeVal-Val-Dil-Dap-Phe-2-chlorotrityl resin (120 mg, 0.053 mmol) in a 5 mL syringe was treated with a solution of maleimidocaproyl-Val-Cit-PAB-OCOpNP (313 mg, 0.42 mmol, 8 equiv), 1-hydroxy-7-azabenzotriazole (HOAt, 2 mg, 0.015 mmol, 0.3 equiv), and DIEA (148 μL, 0.84 mmol, 16 equiv) in DMF (4 mL) for 16 h. The resin was then filtered and washed with DMF (6 × 3 mL), CH_2Cl_2 (6 × 3 mL) and ethyl ether (6 × 3 mL). Cleavage from resin by treatment with 2% TFA in CH_2Cl_2 (4 mL) for 5 min and preparative HPLC purification of the released material generated 15 mg (21%) of white solid that was 98% pure by reversed-phase HPLC analysis (retention time 7.20 min).^{1}H NMR (DMSO-d_6): δ 0.75−0.95 (28H, m), 1.05 (3H, t), 1.14 (m), 1.22−1.53 (m), 1.53−1.80 (m), 1.80−2.40 (m), 2.80 (br s), 2.96 (d), 3.11 (s), 3.13 (s), 3.20 (s), 3.62−3.70 (d), 3.83−3.94 (m), 4.08−4.24 (m), 4.28−4.5 (m), 4.50−4.68 (m), 4.90−5.10 (m), 5.35 (s), 5.96 (1H, t), 7.02 (2H, s), 7.08−7.32 (9H, m), 7.54 (2H, d), 7.80 (d), 8.04−8.12 (m), 8.16−8.33 (m), 10.0 (1H, br s). HRMS (ESI) calcd for $C_{68}H_{104}N_{11}O_{16}$ $(MH)^+$ 1330.7663; found, *m*/*z* 1330.7665.

Maleimidocaproyl-Val-Cit−MMAF (L2−MMAF). Fmoc-Cit (140 mg, 0.352 mmol) and Fmoc-Val (60 mg, 0.176 mmol) were coupled sequentially to MeVal-Val-Dil-Dap-Phe-2-chlorotrityl resin (200 mg, 0.088 mmol) using HATU coupling chemistry as described above for MeVal-Val-Dil-Dap-Phe-2-chlorotrityl resin. Then, to the dry Val-Cit-MeVal-Val-Dil-Dap-Phe-2-chlorotrityl resin a solution of 6-maleimidocaproic acid *N*-hydroxysuccinimide ester (54 mg, 0.176 mmol) in DMF (3 mL) was added. The mixture was shaken at room temperature for 4 h. Cleavage from resin by treatment with 2% TFA in CH_2Cl_2 (4 mL) for 5 min provided 28 mg (27%) of white solid after preparative HPLC purification. Reversed-phase HPLC analysis: 98% at 6.16 min. ^{1}H NMR (DMF-d_7): δ 0.69−0.92 (28H, m), 1.01−1.06 (3H, m), 1.17 (m), 1.42−1.53 (m), 1.53−1.68 (m), 1.70−2.28 (m), 2.28−2.46 (m), 2.74−2.88 (m), 2.89−3.00 (m), 3.04−3.06 (m), 3.15 (s), 3.18 (s), 3.24 (s), 3.40−3.47 (m), 3.48−3.58 (m), 3.59−3.68 (m), 3.71−3.76 (d), 3.96 (m), 4.14 (t), 4.23 (m), 4.38−4.52 (m), 4.58−4.76 (m), 4.89 (m), 5.95 (m), 7.01 (2H, s), 7.17−7.28 (5H, m), 7.77 (m), 7.89 (m), 7.96 (m), 8.04 (m), 8.17 (m), 8.28 (m), 8.38 (d), 8.47 (m). HRMS (ESI) calcd for $C_{60}H_{97}N_{10}O_{14}$ $(MH)^+$ 1181.7186; found, *m*/*z* 1181.7164.

Maleimidocaproyl-PABC−MMAF (L3−MMAF). MeVal-Val-Dil-Dap-Phe-2-chlorotrityl resin (100 mg, 0.044 mmol) was treated with a solution of maleimidocaproyl-PAB-OCO-pNP (42 mg, 0.088 mmol, 2 equiv), 1-hydroxybenzotriazole (HOBt, 1 mg, 9 μmol, 0.1 equiv), and DIEA (30 μL, 0.176 mmol, 4 equiv) in DMF (3 mL) for 16 h. The resin was then filtered and washed with DMF (6 × 3 mL), CH_2Cl_2 (6 × 3 mL), and ethyl ether (6 × 3 mL). Cleavage from resin by treatment with 2% TFA in CH_2Cl_2 (4 mL) for 5 min followed by preparative HPLC purification provided 31 mg (66%) of white solid which was 99% pure by reversed-phase HPLC analysis (retention time 7.14 min).^{1}H NMR (DMF-d_7): δ 0.76−0.98 (18H, m), 1.04 (2H, d), 1.12 (3H, m), 1.25−1.40 (m), 1.51−1.61 (m), 1.63−1.69 (m), 1.76−1.90 (m), 1.94−2.40 (m), 1.35−2.38 (m), 2.50−2.60 (m), 2.96 (s), 3.10 (s), 3.23 (s), 3.27 (s), 3.30 (s), 3.34 (s), 3.41−3.50 (m), 3.50−3.80 (m), 3.90−4.20 (m), 4.33−4.48 (m), 4.54−4.62 (m), 4.63−4.77 (m), 4.82−4.93 (m), 5.06−5.20 (m), 7.02 (2H, s), 7.36−7.21 (9H, m), 7.70 (2H, d), 8.11 (0.5H, d), 8.36 (0.5H, d), 10.00 (1H, br s). HRMS (ESI) calcd for $C_{57}H_{84}N_7O_{13}$ $(MH)^+$ 1074.6127; found, *m*/*z* 1074.6095.

Maleimidocaproyl−MMAF (L4−MMAF). 6-Maleimidocaproic acid (37 mg, 0.176 mmol, 2 equiv) and HATU (67 mg, 0.176 mmol, 2 equiv) were dissolved in anhydrous DMF (3 mL), followed by the addition of DIEA (62 μL, 0.35 mmol, 4 equiv). The solution was then transferred to a 5 mL syringe containing MeVal-Val-Dil-Dap-Phe-2-chlorotrityl resin (200 mg, 0.088 mmol), and the mixture was agitated for 3 h. The resin was filtered, washed with DMF (6 × 3 mL), CH_2Cl_2 (6 × 3 mL), and ethyl ether (6 × 3 mL), and dried in vacuo. Drug−linker was cleaved off the resin by treatment with 2% TFA in CH_2Cl_2 (4 mL) for 5 min and then purified by preparative HPLC to give 57 mg (70%) of white solid. Reversed-phase HPLC analysis: 98% at 6.72 min. ^{1}H NMR (DMF-d_7): δ 0.78−0.96 (18H, m), 1.04 (2H, t), 1.12 (3H, m), 1.25−1.36 (m), 1.41 (2H, d), 1.46−1.65 (m), 1.73−1.87 (m), 1.88−2.07 (m), 2.08−2.26 (m), 2.32−2.48 (m), 2.48−2.67 (m), 2.79−2.84 (m), 2.96 (d), 3.02 (d), 3.10 (d), 3.23 (d), 3.27 (s), 3.30 (s), 3.34 (s), 3.45 (t), 3.52−3.61 (m), 3.62−3.80 (m), 3.93 (d), 4.09−4.28 (m), 4.54−4.78 (m), 4.82−4.91 (2H, m), 7.03 (2H, s), 7.21−7.35- (5H, m), 7.51 (0.5H, d), 8.11 (0.5H, d), 8.36 (0.5H, d), 8.48 (0.5H, d), 13.0 (br s). HRMS (ESI) calcd for $C_{49}H_{77}N_6O_{11}$ $(MH)^+$ 925.5650; found, *m*/*z* 925.5636.

Maleimidocaproyl−[^{13}C]MMAF (L4−[^{13}C]MMAF) was prepared as described above starting from *N*-Fmoc-L-[ring-$^{13}C_6$]-phenylalanine-2-chlorotrityl resin. LCMS (ESI): *m*/*z* 931.62 $(MH)^+$.

Preparation of Antibody−Drug Conjugates. The conjugates with eight drug molecules per antibody were prepared as described previously (*12*, *19*). Briefly, cBR96 or cAC10 (5−15 mg/mL) were mixed with DTT (10 mM, final) at 37 °C for 30 min, and the buffer was exchanged by elution through Sephadex G-25 resin with PBS containing 1 mmol/L diethylenetriaminepentaacetic acid. PBS containing 1 mmol/L diethylenetriaminepentaacetic acid was added to the reduced mAb bringing its final concentration to 2.5 mg/mL. The thiol concentration was ∼8.4 thiols/mAb as measured by Ellman's reagent, DTNB. A 9.5-fold molar excess of linker−drug (L1−MMAF, L1−Dox (*10*), L1−MMAE (*12*), or L4−MMAE) was added to the reduced antibody at 4 °C for 1 h, and the conjugation reaction was quenched by adding a 20-fold excess of cysteine. The reaction mixture was concentrated by centrifugal ultrafiltration and buffer-exchanged through Sephadex G-25 equilibrated with PBS at 4 °C. The conjugate was then sterile filtered through a 0.2-μm filter.

cAC10 antibody−drug conjugates with four drugs per antibody were prepared by partial reduction of the mAb (*14*, *20*) followed by reaction with desired linker−drug (L1−MMAF, L2−MMAF, L3−MMAF, or L4−MMAF). The antibody cAC10 (10 mg/mL) was partially reduced by addition of 3.0 molar equivalents of DTT at pH 8.0, followed by incubation at 37 °C for ∼2 h. The reduction reaction was then chilled to ∼10 °C and the excess DTT removed via diafiltration. The thiol concentration was determined by DTNB, and the SH/Ab ratio was found to be in the range of 3.8−4.5. The linker−drug was

then added to a linker−drug/thiol molar ratio of ∼1.15. The conjugation reaction was carried out in the presence of 15% v/v of DMSO. After conjugation, excess free cysteine (2 mol/L cysteine per mol/L linker−drug) was added to quench unreacted linker−drug to produce the cysteine−linker−drug adduct. The reaction mixture was purified and buffer-exchanged into PBS by diafiltration to obtain the partially loaded cAC10−linker−$drug_4$ conjugate. The molar ratio of drug substitution was determined according to previously published methods (*14, 20*).

Released Drug Identification. Lysosomal extracts of L540cy cells were prepared by swelling 2.4×10^8 cells in 9 mL of 0.25 M sucrose, 1 mM EDTA, and 10 mM HEPES (4-(2-hydroxyethyl)piperazine-1-ethansulfonic acid), pH 7.4. After 30 min on ice, cells were Dounce homogenized until >95% were broken as measured by Trypan Blue dye exclusion. Homogenates were centrifuged (3000*g*, 10 min, 4 °C) to pellet cellular debris, and the supernatant (4×10^7 cell equivalents per tube) was transferred to polyallomar ultracentrifuge tubes (13 × 51 mm) and centrifuged (17000*g*, 15 min, 4 °C) in a TLA100.3 rotor to isolate the lysosome-containing light mitochondrial pellet. Pellets were stored at −80 °C. The pellets were thawed and resuspended in 500 μL of 50 mM sodium acetate pH 5.0 and 2 mM DTT. cAC10−L4-[^{12}C]$MMAF_4$, cAC10−L4-[^{13}C]-$MMAF_4$, and cAC10−L4-[$^{12/13}$C]$MMAF_4$ (50 μg/mL) were independently added to one pellet. After three freeze/thaw cycles to break open lysosomes, samples were incubated for 24 h at 37 °C. Cold methanol (2 vol) was added to precipitate protein, the samples were centrifuged at 14000*g* to pellet debris, and 100 μL of supernatant was analyzed by low resolution mass spectrometry as described above. Authentic cysteine−L4−MMAF was prepared by treating 100 μM L4−MMAF with 1 mM cysteine in PBS at room temperature for 10 min.

In Vitro Growth Inhibition. Log phase cultures of cells were collected and cells plated at seeding densities ranging from 500 to 10000 cells/well according to predetermined conditions. After incubating 24 h to allow surface protein reconstitution, serial dilutions of test molecules were added and cultures incubated a further 4−6 days depending on cell line. Assessment of cellular growth and data reduction to generate IC_{50} values was done using Alamar Blue (Biosource International, Camarillo, CA) dye reduction assay as previously described, according to previously published methods (*12, 14, 15, 19*). Briefly, a 40% solution (wt/vol) of Alamar Blue was freshly prepared in complete media just before cultures were added. Ninety-two hours after drug exposure, Alamar Blue solution was added to cells to constitute 10% culture volume. Cells were incubated for 4 h, and dye reduction was measured on a Fusion HT fluorescent plate reader (Packard Instruments, Meriden, CT).

In Vivo Therapy Experiments. For the localized, subcutaneous disease model of anaplastic large cell lymphoma, 5×10^6 Karpas 299 cells were implanted into the right flanks of C.B.-17 SCID mice. Therapy was initiated when the tumor size in each group of six animals averaged approximately 100 mm^3. Treatments consisted of a single injection of solutions of the conjugates or controls in PBS intravenously (tail vein). Tumor volume was determined using the formula $(L \times W^2)/2$. For the disseminated ALCL model, 1×10^6 Karpas 299 were injected in the tail vein into C. B.-17 SCID mice**.** Single dose injection treatment was performed at 9 days after tumor injection. Mice that developed hind limb paralysis or other signs of significant disease were euthanized in accordance with Animal Care and Use Committee guidelines.

In Vivo Localization of Antibodies via Immunohistochemistry. When subcutaneous Karpas 299 tumor size reached 300 mm^3, three animals per group received one injection of 10 mg antibody component/kg body weight of either cAC10−L1−$MMAF_4$ or cBR96−L1−$MMAF_4$ intravenously. Tumors were then removed and placed in optimal cutting temperature (OCT) compound (Sakura Finetec, Torrence, CA), and 5 μm-thin frozen tissue sections were stained using immunohistochemistry evaluation. Briefly, frozen tissues on the slides were air-dried then fixed in 4% paraformaldehyde for 15 min at room temperature. Endogenous peroxidase activity was blocked using 0.6% H_2O_2 for 15 min. Additional blocking for endogenous biotin was done using the Avidin−Biotin Blocking kit (Vector Labs). Biotinylated-anti-human-Fc and biotinylated-anti-drug antibodies (both Seattle Genetics) were incubated on tissues at 2 μg/mL concentration for 1 h at room temperature. Following incubation of slides with avidin conjugated to HRP (Vectastatin Elite ABC kit, Vector Labs), 3,3′-diabenzidine (DAB) was used as a substrate for HRP. Tissues were counterstained using hematoxylin, slides were dehydrated, and slips were applied. Images were taken using the Zeiss Axiovert light microscope.

TUNEL Assay. Apoptosis was evaluated by TUNEL Staining (In Situ Cell Death Detection Kit, TR Red, Roche Applied Science, Germany) according to the manufacturer's instructions. TUNEL staining was carried out on sections of frozen specimens embedded in OCT. Labeling was visualized by Zeiss Axiovert fluorescence microscopy.

Table 1. In Vitro Cytotoxicity of Auristatins

		IC_{50} (nM)[a]		
cell line	type	MMAE	MMAF	MMAF-OMe
Karpas 299	anaplastic large cell lymphoma	0.5	119	<0.001
H3396	breast carcinoma	0.1	105	<0.001
786-O	renal cell carcinoma	2.0	257	0.01
Caki-1	renal cell carcinoma	0.7	200	<0.001

[a] Cells were exposed to the drugs, and the cytotoxic activities were determined 96 h later using Alamar Blue dye conversion as a measure of cell viability.

RESULTS

Development of MMAF-Based Conjugates. The structure of the antimitotic agent MMAE is shown in Figure 1. This drug has previously displayed IC_{50} values in the range of 1−5 nM on hematologic cell lines (*12, 15*) and was designed for mAb-based targeted delivery using peptide-based linkers appended to the N-terminal methylvaline residue (*12, 19*). The synthesis of MMAE proceeded through a solution-phase route involving the coupling of the amino-protected N-terminal trimer to the C-terminal dimer. Due to the convergent nature of the process, it was possible for us to produce a large number of auristatins with varied solubilities, potencies, and pharmacokinetic properties. One molecule that emerged was MMAF-OMe (Figure 1), a C-terminal phenylalanine containing auristatin that remains one of the most potent drugs we have ever made (Table 1). We regarded MMAF-OMe as a prodrug of MMAF (Figure 1), with the potential of having facilitated intracellular uptake due to the presence of a neutral C-terminus. In addition, intracellular ester hydrolysis of MMAF-OMe should rapidly generate MMAF, a C-terminally charged molecule expected to have impaired membrane translocation capabilities. Therefore, MMAF was synthesized using solid-phase synthetic methodology and as expected was much less potent than MMAE on all cell lines tested (Table 1). In addition, the maximum tolerated dose in mice of MMAF (>16 mg/kg) was much higher than MMAE (1 mg/kg). Thus, MMAF was of great interest for targeted delivery, since the free drug had attenuated potency, lower toxicity, and much higher aqueous solubility compared to MMAE. Facilitated intracellular transport was expected to greatly enhance its activity.

Conjugates of MMAF were produced using the maleimidocaproyl-Val-Cit-PABC linker (L1, Figure 1) as described

Table 2. In Vitro Cytotoxicity of cAC10−MMAF ADCs and Free MMAF on a Panel of CD30$^+$ and CD30$^-$ Cell Lines

		IC_{50} (nM)[a]		
cell line tumor	type	cAC10−L1−$MMAF_4$	cAC10−L4−$MMAF_4$	MMAF
Karpas 299	anaplastic large cell lymphoma	0.057	0.059	119
SUP-M2	anaplastic large cell lymphoma	0.023	0.024	79.7
SU-DHL-1	anaplastic large cell lymphoma	0.007	0.045	34.7
SR-786	anaplastic large cell lymphoma	0.010	0.016	38.1
DEL	anaplastic large cell lymphoma	0.038	0.046	69.0
HH	cutaneous T-cell lymphoma	0.016	0.022	30.7
L540cy	Hodgkin's disease	0.060	0.085	70.4
HDLM-2	Hodgkin's disease	0.080	0.210	66.0
L428	Hodgkin's disease	0.021	0.058	68.0
KMH-2	Hodgkin's disease	0.009	0.068	45.4
RPMI 6666	Hodgkin's disease	0.091	0.180	164
WSU-NHL	Non-Hodgkin's lymphoma, CD30$^-$	>25[b]	>25[b]	60.3
	mean (all lines)	0.034[c]	0.066[d]	70.4

[a] Cytotoxicity was measured as indicated in Table 1. Concentrations of the ADCs are represented by the drug component. [b] Represents 1000 ng/mL mAb component. [c] Represents 1.36 ng/mL mAb component. [d] Represents 2.64 ng/mL mAb component.

earlier for MMAE (*12, 19*). The mAbs used were BR96 (*17*) and AC10 (*19*), chimeric IgG1 mAbs that bind to the LewisY antigen on human carcinomas, and the CD30 antigen on hematologic malignancies, respectively. Initial studies were undertaken with conjugates that had eight drugs/mAb, but more recent data demonstrating improved pharmacokinetic and toxicologic properties of conjugates having lower drug loadings (*14*) prompted us to investigate the activities of conjugates with fewer drugs/mAb. These were obtained through carefully controlled mAb disulfide reduction with limiting amounts of DTT sufficient to produce an average of four thiol groups/mAb. Alkylation with drugs bearing thiol-reactive maleimide functionalities led to the formation of conjugates having an average of four drugs/mAb. The resulting distributions of species were as previously described (*20*). It was found that the ability of the parent unmodified mAb to bind to cell-surface receptors was maintained in conjugates (*12*), and aggregate (<5%) and free drug levels (0.5%) were very low.

In Vitro Growth Inhibition. cAC10−L1−$MMAF_4$ was tested on a panel of both CD30 positive and negative cell lines as shown in Table 2. Cells were exposed to the ADCs continuously for 96 h, and the cytotoxic effects, as determined by Alamar Blue conversion, were compared to those of free MMAF. On a molar basis, the cAC10−L1−$MMAF_4$ was an average of >2200-fold more potent than free MMAF and was active on all the CD30-positive cell lines tested. The effects were immunologically specific, since WSU-NHL cells, which do not express detectable levels of the CD30 antigen, were unaffected by the conjugate. Limited studies were also undertaken with the cAC10−L1−MMAF-OMe_4-based conjugates, and it was found that they displayed IC_{50} values on Karpas 299 (0.04 nM) and L540cy (0.11 nM) cells that were comparable to those of cAC10−L1−$MMAF_4$ (Table 2). This is consistent with the assumption stated earlier that the active form of MMAF-OMe is the free acid MMAF.

Further studies were undertaken with MMAF and the cBR96−L1−$MMAF_8$ conjugate on a LewisY positive human small cell lung carcinoma cell line (H69) and its P-glycoprotein-overexpressing counterpart H69/LX4 (*18*). The results were compared to doxorubicin and cBR96−L1−$doxorubicin_8$, a previously described conjugate with eight doxorubicin molecules/mAb (*17, 21*). H69/LX-4 cells were approximately 100-times less sensitive to doxorubicin compared to the parental cell (Figure 2A), while there was only a 3-fold difference with MMAF (Figure 2B). This trend extended to the conjugates, in that the drug resistant cell line was refractory to BR96−L1−$doxorubicin_8$ (Figure 2C), but quite sensitive to the corresponding MMAF conjugate (Figure 2D). These results have been confirmed on several MDR positive cell lines (data not shown), in which it has been found that MMAF and MMAF-based immunoconjugates circumvent common forms of the MDR phenotype.

New Linker Technologies. The linker joining the drug to the mAb carrier plays a critical role in conjugate potency (*3, 21−24*). We applied our peptide linker technology to MMAF, based on its successful application with MMAE (*12, 14, 15, 19, 20*) and other drug classes (*6, 9−11*). To expand our understanding of the role that the linker plays in drug release and cytotoxicity, we made truncated linker−MMAF derivatives lacking the *p*-aminobenzyloxycarbonyl (PABC) self-immolative group (L2, Figure 1), the peptide (L3), and both the peptide and the PABC group (L4). The resulting modified drugs were attached to cAC10, forming ADCs with approximately four drugs/mAb. As expected from earlier work with related doxorubicin ADCs (*6, 9−11*), cAC10−L2−$MMAF_4$ was devoid of activity on Karpas 299 cells (Table 3). In contrast, both cAC10−L3−$MMAF_4$ and cAC10−L4−$MMAF_4$ were highly active, and were as active as the full-length construct (cAC10−L1−$MMAF_4$). Interestingly, ADCs with truncated linkers (L2, L3, and L4) were not substrates for human cathepsin B, which was a critical design element in forming the original proteolytically cleavable linker technology for doxorubicin (*6, 9−11*). The effects of the truncated linkers were drug-dependent, in that cAC10−L4−$MMAE_8$ had no cytotoxic activity above 50 nM (1000 ng/mL) on Karpas 299 cells.

The results prompted us to test cAC10−L4−$MMAF_4$ on the broad panel of hematologic cell lines shown in Table 2. The conjugate was active against all CD30 positive cell lines tested and had approximately half the activity of cAC10−L1−$MMAF_4$. In addition, the effects were immunologically specific, as CD30 negative SU-NHL cells were not affected by cAC10−L4−$MMAF_4$. Thus, MMAF can be attached to cAC10 through linkers not designed for proteolytic cleavage, without significant loss in potency.

The high potency and broad reactivity of cAC10−L4−$MMAF_4$ conjugates raised the question of precisely what drug related molecule might be released from the conjugate, since the L4 linker would appear to be noncleavable. To elucidate this, ^{13}C-phenylalanine substituted L4−MMAF was synthesized and conjugated to cAC10. ^{12}C, ^{13}C, and a 1:1 mixture of ^{12}C and ^{13}C cAC10−L4−$MMAF_4$ were then incubated in lysosomal extracts of L540cy cells. Low molecular weight products were separated from proteins and were analyzed by LCMS. The identification of released drugs was based on the 6 mass unit shifts between the ^{12}C and ^{13}C derivatives of the drug. After inspection of mass spectra for such shifts, the only detectable drug-related molecule that was found was the cysteine adduct of maleimidocaproyl−MMAF (Figure 3). To confirm this, an

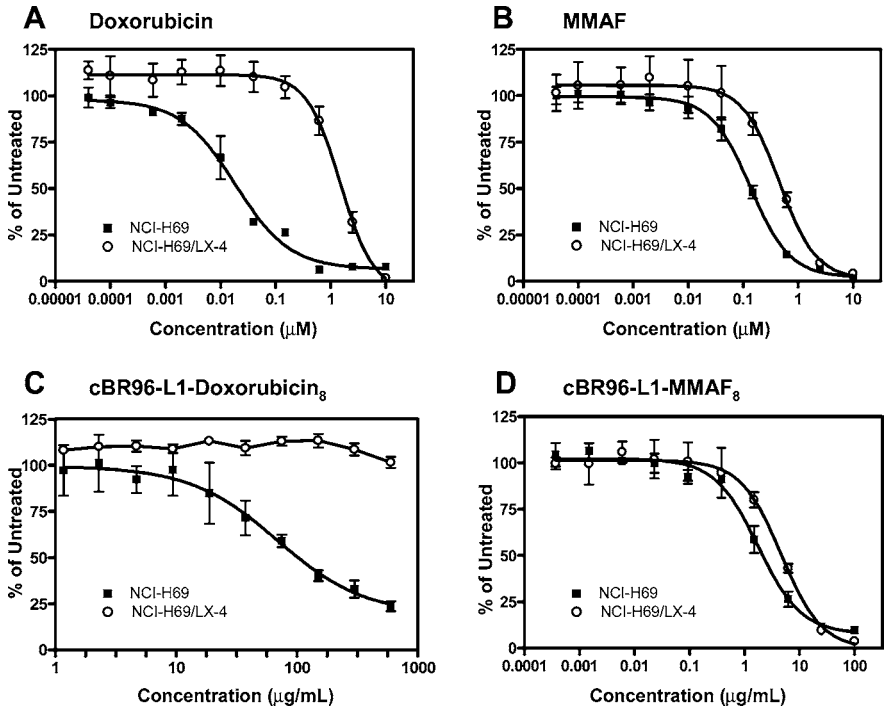

Figure 2. Cytotoxic effects of drugs (A, B) and cBR96-drug conjugates (C, D) on human small cell lung carcinoma cell line H69 (-■-) and its P-glycoprotein-overexpressing counterpart H69/LX-4 (-○-). Both cell lines are Lewis Y positive. The cells were incubated with either the drugs or the conjugates for 6 days, and the cytotoxic effects were determined by metabolism of Alamar Blue during the last 24 h of incubation.

Table 3. In Vitro Cytotoxicity of Drug−Linker Combinations

conjugate	target antigen	IC_{50} (nM) Karpas 299 cells[a]
cAC10−L1−$MMAF_4$	CD30	0.03
cAC10−L2−$MMAF_4$	CD30	>25
cAC10−L3−$MMAF_4$	CD30	0.055
cAC10−L4−$MMAF_4$	CD30	0.065
cAC10−L1−$MMAE_8$	CD30	0.18
cAC10−L4−$MMAE_8$	CD30	>50
cBR96−L1−$MMAF_4$	Lewis Y	>25
cBR96−L4−$MMAF_4$	Lewis Y	>25

[a] Karpas 299 cells are CD30 positive, Lewis Y negative. Cytotoxicity was measured as indicated in Table 1. Concentrations of the ADCs are represented by the drug component. The numbers reported are representative of at least two independent experiments.

authentic sample of cysteine−L4−MMAF was synthesized and was shown to have the same elution and LCMS profile as the drug released from the cAC10−L4−$MMAF_4$ ADC (data not shown). The mAb is the likely source for cysteine in cysteine−L4−MMAF, since this was the residue to which the drug was attached. Thus, drug release takes place through mAb degradation. Studies are currently ongoing to identify other products that might also be formed and to establish the rates and extent of drug release.

Maximum Tolerated Doses. The maximum tolerated doses (MTDs) of the cAC10−MMAF conjugates were determined in BALB/c mice and in Sprague−Dawley rats and are defined as the highest dose that did not induce >20% weight loss, distress, or overt toxicities in any of the animals. This dose was generally within 20% of doses where such events took place. cAC10−L1−$MMAF_4$ has an MTD of 50 mg/kg in mice and 15 mg/kg in rats. The corresponding cAC10−L4−$MMAF_4$ ADC was much less toxic, having MTDs in mice and rats of >150 mg/kg (the highest dose tested, which resulted in no apparent toxicity) and 90 mg/kg in rats, respectively. This clearly indicates that the method by which the drug is attached to the mAb can have a pronounced effect on ADC tolerability, and the ADC lacking the peptide spacer within the linker was much less toxic than the peptide-based ADC.

Immunohistochemical Analyses. Studies were undertaken to determine if cAC10−L1−$MMAF_4$ localized into subcutaneous Karpas 299 tumors in nude mice. Animals were injected intravenously with cAC10−L1−$MMAF_4$ or cBR96−L1−$MMAF_4$ at 10 mg antibody component/kg body weight. Tumors were removed 24 h later, and frozen sections were evaluated for the presence of the mAb and drug components using immunohistochemistry with biotinylated anti-human-Fc and anti−MMAF mAbs as secondary antibodies, respectively. Figures 4A and 4C show that cAC10−L1−$MMAF_4$ accumulated much more efficiently within Karpas 299 tumors compared to the cBR96 nonbinding control ADC (Figure 4B and 4D). Since both the mAb (Figure 4A) and drug (Figure 4C) moieties were detected throughout the tumor, we conclude that the ADC is delivered as an intact molecule.

Additional studies were undertaken to determine the effects of ADC localization on apoptosis. Figure 4E demonstrates that there were significant levels of fragmented DNA in tumors of animals that received cAC10−L1−$MMAF_4$. This was established by TUNEL analysis, which measures bromodeoxyuridine incorporation into fragmented DNA. A nonbinding control ADC (Figure 4F) did not induce nearly this level of fragmentation, which is consistent with the localization data.

In Vivo Therapy Studies. The therapeutic effects of the ADCs were determined in nude mice with subcutaneous or disseminated Karpas 299 tumors. In animals with subcutaneous tumors, significant antitumor effects were obtained with a single injection of either cAC10−L1−$MMAF_4$ or cAC10−L4−$MMAF_4$, which were indistinguishably potent and active (Figure 5A). Nearly all animals that received single ADC injections at 2 mg antibody component/kg body weight were cured. In lowering the dose to 1 mg/kg, efficacy for both ADCs, dropped off in an apparently equal manner. At this dose, there were still two of six and three of six animals cured with the cAC10−L1−$MMAF_4$ and cAC10−L4−$MMAF_4$ ADCs, respectively.

To establish disseminated tumors, Karpas 299 cells were injected intravenously and allowed to distribute and become established before therapy was initiated 9 days later. In the

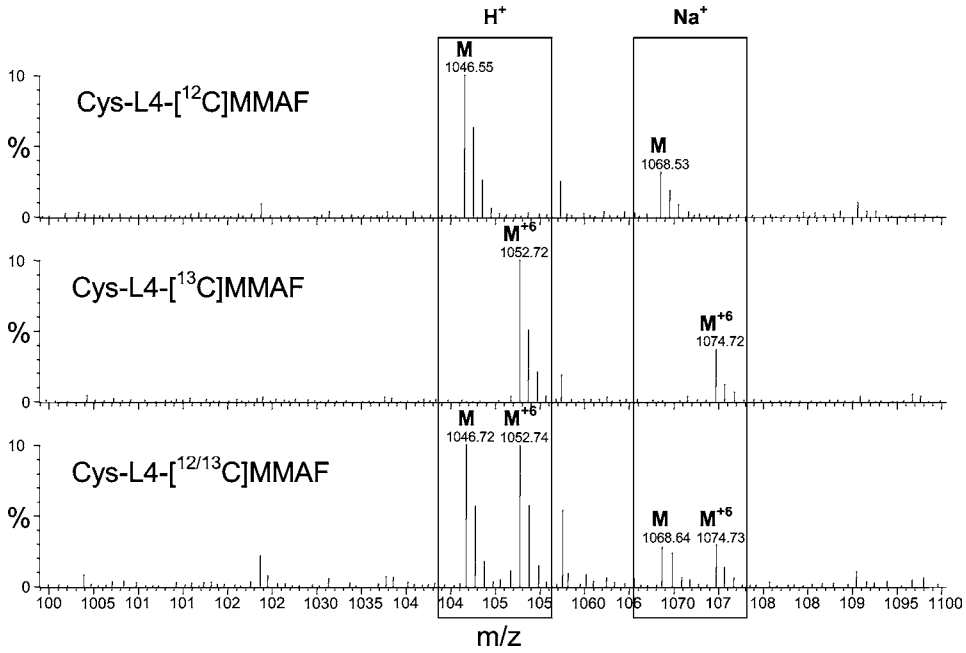

Figure 3. LCMS analysis of products released in lysosomal extracts of L540cy cells from cAC10−L4−MMAF$_4$ conjugate composed of [$^{12}C_6$-Phe]−MMAF (top), [$^{13}C_6$-Phe]−MMAF (middle), and a 1:1 mixture of these two conjugates (bottom). The fragments obtained from the co-mixture of the conjugates were analyzed for (M) and (M + 6) molecular ion clusters. Cysteine−L4−MMAF, *m*/*z* 1046/1052, was the only identifiable MMAF component.

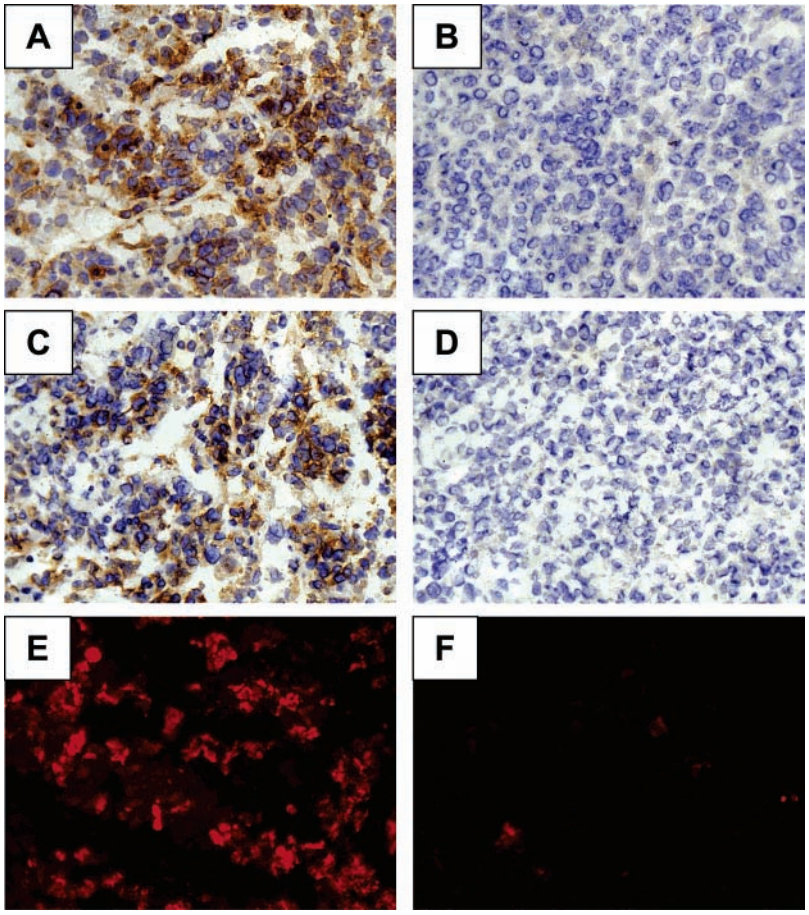

Figure 4. In vivo localization and activities of mAb−L1−MMAF$_4$ ADCs. Nude mice with subcutaneous Karpas 299 human tumors (cAC10 antigen positive, cBR96 antigen negative) were injected either with cAC10−L1−MMAF$_4$ (A, C, E) or with cBR96−L1−MMAF$_4$ (B, D, F) to investigate the localization and the induction of apoptosis on tumor xenografts. The presence of intratumoral mAb (A, B) and intratumoral MMAF (C, D) were determined by immunohistochemistry using either biotinylated anti-human-Fc or biotinylated anti-MMAF mAbs, respectively, as secondary antibodies. The tumors were excised and sectioned 24 h postconjugate administration. The apoptotic effect on Karpas 299 (E, F) were investigated using the TUNEL assay. The images were taken using 20× objectives on a Zeiss microscope.

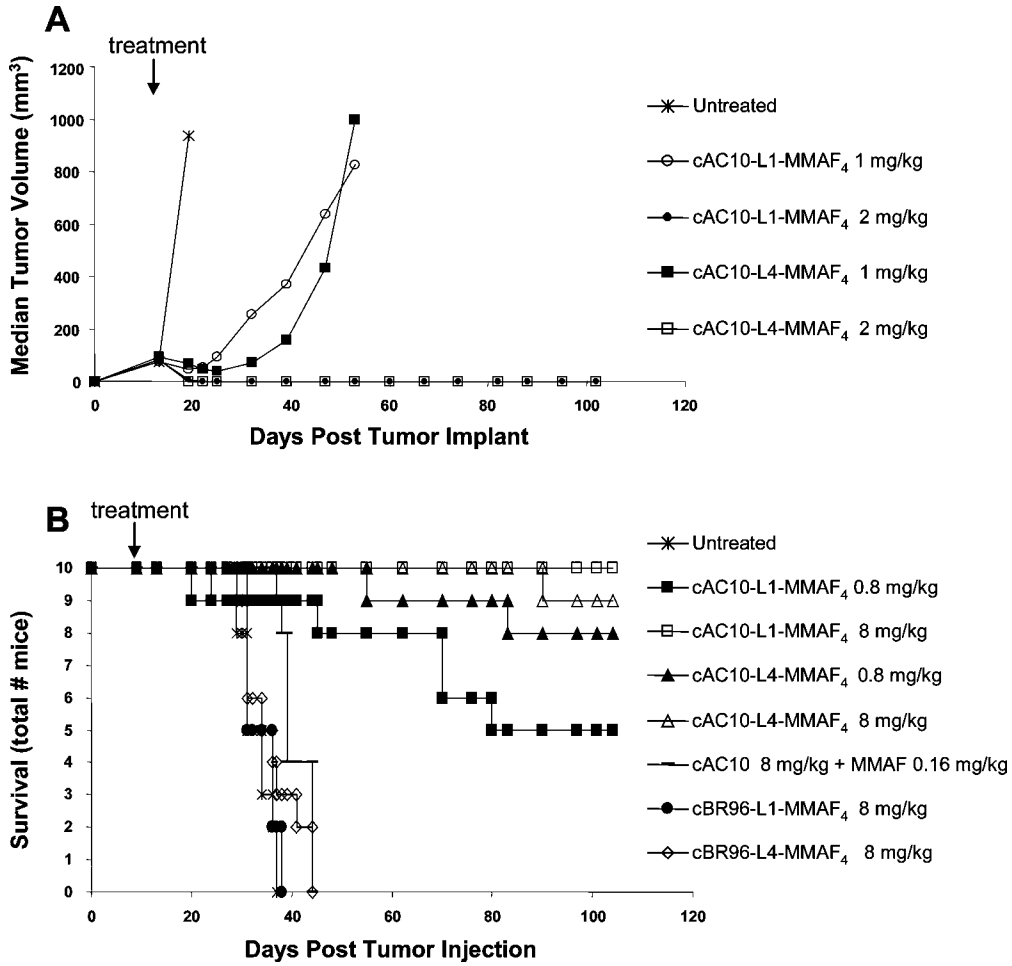

Figure 5. In vivo therapeutic efficacy of the conjugates in SCID mice. The data reported are representative of a number of independent studies. (A) Groups of mice (six/group) with subcutaneous Karpas 299 human ALCL tumors (cAC10 Ag^+) of approximately 100 mm^3 average in size were treated with cAC10−L1−$MMAF_4$ or cAC10−L4−$MMAF_4$ at 1 mg and 2 mg mAb component/kg. Cures: 1 mg/kg cAC10−L1−$MMAF_4$, two out of six; 1 mg/kg cAC10−L4−$MMAF_4$, three out of six; 2 mg/kg cAC10−L4−$MMAF_4$, five out of six; 2 mg/kg cAC10−L1−$MMAF_4$, six out of six. (B) Groups of mice (ten/group) with disseminated Karpas 299 ALCL tumor model (cAC10 Ag^+, cBR96 Ag^-) were treated on day 9 after tumor injection with cAC10−L1−$MMAF_4$, cAC10−L4−$MMAF_4$, cAC10 + unconjugated MMAF, cBR96−L1−$MMAF_4$, or cBR96−L4−$MMAF_4$ at the doses indicated.

absence of any treatment, all of the animals succumbed to disseminated disease by day 45. A single administration with either cAC10−L1−$MMAF_4$ or cAC10−L4−$MMAF_4$ was sufficient to cure most of the animals, with a slight dose response between 0.8 mg/kg and 8 mg/kg. The differences between the L1 and L4 linkers were not significant in this tumor model. One of the noteworthy findings in this experiment was the level of specificity. The nonbinding control ADCs, cBR96−L1−$MMAF_4$ and cBR96−L1−$MMAF_4$ were inactive, even at 8 mg/kg, which is 10-times the effective dose of the corresponding cAC10 ADCs. Thus, the MMAF conjugates exhibit pronounced activity at very well tolerated doses and are highly immunologically specific. Furthermore, the therapeutic window of cAC10−L4−$MMAF_4$ is measurably greater than that of cAC10−L1−$MMAF_4$, indicating that the linker technology plays a critical role in the design of effective ADCs that can be safely administered.

DISCUSSION

In this paper, we describe the synthesis and properties of MMAF, a new auristatin antimitotic agent designed for attachment to mAbs through the secondary amino terminus. MMAF has much lower cytotoxic activity than MMAE (*12, 14, 15, 19*), presumably owing to the charged C-terminal phenylalanine group that impairs intracellular access. This hypothesis is supported by the pronounced activity of MMAF-OMe, one of the most potent auristatins that we have developed. To further understand the precise cause of the attenuated activity of MMAF compared to the other drugs, studies are currently underway to measure intracellular concentrations in MDR positive and negative cell lines.

ADCs comprised of MMAF are distinct from those of other drugs, including MMAE. We show that the activities of MMAF are potentiated an average of 2200-fold when the drug is attached through the L1 linker to cAC10, a mAb that is efficiently taken up within the lysosomes of target cells (Table 2). With one exception that is likely cell line dependent (*25*), broad-scale drug potentiation through ADC formation is generally not seen, as evidenced by the in vitro results of MMAE (*12*) and other drug-containing ADCs (*23, 24, 26, 27*). The significance of this finding will become evident though detailed toxicological analyses, in which MMAE- and MMAF-based ADCs should be quite distinct if systemically released drug contributes to ADC toxicity.

One of the most striking results from this work surrounds the unexpected activity of cAC10−L4−$MMAF_4$, an ADC that has no built-in provision for drug release. Purified human enzymes that we have tested were unable to facilitate release of MMAF or any identifiable MMAF fragments, yet cAC10−L4−$MMAF_4$ is highly potent, both in vitro and in vivo. We

propose that the mechanism of drug release involves complete degradation of the mAb, based on the identification of the cysteine adduct of L4−MMAF. The finding that the released drug from the L4 linker is highly modified might explain why such truncated linker technology is not uniformly applicable, since many drugs lose activity as a result of derivatization. Indeed, MMAE was not tolerant of such modification (Table 3), and corresponding doxorubicin ADCs have also proven to be inactive (data not shown). The data in Table 3 also demonstrate that the various linkers within the MMAF ADC family provide a range of cytotoxic activities. The fact that cAC10−L2−$MMAF_4$ was inactive suggests that the released agent from the L2−MMAF ADC is highly attenuated in activity. We focused on cAC10−L4−$MMAF_4$ for further work rather than cAC10−L3−$MMAF_4$, since the PABC group in the L3 linker is hydrophobic and apparently unnecessary for activity.

The objective of the investigations with various linkers was to determine if the mode of drug release could affect ADC therapeutic index. We found that cAC10−L4−$MMAF_4$ differed from cAC10−L1−$MMAF_4$ by an average of only 2-fold on a large panel of hematologic cell lines (Table 2) although L1 linker cleavage is quite facile through enzymes such as cathepsin B, while drug release through the L4 linker requires antibody degradation. This provided the basis for in vivo experiments, since we anticipated that the different pathways required for drug elimination could strongly influence the therapeutic windows of the ADCs. Indeed, it was found that cAC10−L4−$MMAF_4$ was tolerated at significantly higher doses in rodents than cAC10−L1−$MMAF_4$ but was equally efficacious in vivo. Our results suggest that the therapeutic window is increased by at least 3-fold through the L4 linker system.

We are in the process of assessing several aspects of MMAF linker technology. Current studies include the application of mAb−L4−MMAF ADCs directed against antigens on an array of tumor types. Our preliminary data suggest that such ADCs are broadly active against hematologic malignancies but are only sporadically effective in the carcinomas we have evaluated. We are gaining insight into the factors that influence activity by assessing bound and unbound drug both inside and outside target cells. In addition, we are characterizing the mechanisms of drug release in target and nontarget cells in order to further understand the principles that influence activity and toxicity.

Supporting Information Available: Synthetic schemes for all linker−drugs. This material is available free of charge via the Internet at http://pubs.acs.org/BC.

LITERATURE CITED

(1) Adams, G. P., and Weiner, L. M. (2005) Monoclonal antibody therapy of cancer. *Nat. Biotechnol. 23*, 1147−57.

(2) Baker, M. (2005) Upping the ante on antibodies. *Nat. Biotechnol. 23*, 1065−72.

(3) Wu, A. M., and Senter, P. D. (2005) Arming antibodies: prospects and challenges for immunoconjugates. *Nat. Biotechnol. 23*, 1137−46.

(4) Lambert, J. M. (2005) Drug-conjugated monoclonal antibodies for the treatment of cancer. *Curr. Opin. Pharmacol. 5*, 543−9.

(5) Payne, G. (2003) Progress in immunoconjugate cancer therapeutics. *Cancer Cell 3*, 207−12.

(6) Dubowchik, G. M., and Walker, M. A. (1999) Receptor-mediated and enzyme-dependent targeting of cytotoxic anticancer drugs. *Pharmacol. Ther. 83*, 67−123.

(7) Smith, S. V. (2004) Technology evaluation: cantuzumab mertansine, ImmunoGen. *Curr. Opin. Mol. Ther. 6*, 666−74.

(8) DiJoseph, J. F., Popplewell, A., Tickle, S., Ladyman, H., Lawson, A., Kunz, A., Khandke, K., Armellino, D. C., Boghaert, E. R., Hamann, P., Zinkewich-Peotti, K., Stephens, S., Weir, N., and Damle, N. K. (2005) Antibody-targeted chemotherapy of B-cell lymphoma using calicheamicin conjugated to murine or humanized antibody against CD22. *Cancer Immunol. Immunother. 54*, 11−24.

(9) Dubowchik, G. M., and Firestone, R. A. (1998) Cathepsin B-sensitive dipeptide prodrugs. 1. A model study of structural requirements for efficient release of doxorubicin. *Bioorg. Med. Chem. Lett. 8*, 3341−6.

(10) Dubowchik, G. M., Firestone, R. A., Padilla, L., Willner, D., Hofstead, S. J., Mosure, K., Knipe, J. O., Lasch, S. J., and Trail, P. A. (2002) Cathepsin B-labile dipeptide linkers for lysosomal release of doxorubicin from internalizing immunoconjugates: model studies of enzymatic drug release and antigen-specific in vitro anticancer activity. *Bioconjugate Chem. 13*, 855−69.

(11) Dubowchik, G. M., Mosure, K., Knipe, J. O., and Firestone, R. A. (1998) Cathepsin B-sensitive dipeptide prodrugs. 2. Models of anticancer drugs paclitaxel (Taxol), mitomycin C and doxorubicin. *Bioorg. Med. Chem. Lett. 8*, 3347−52.

(12) Doronina, S. O., Toki, B. E., Torgov, M. Y., Mendelsohn, B. A., Cerveny, C. G., Chace, D. F., DeBlanc, R. L., Gearing, R. P., Bovee, T. D., Siegall, C. B., Francisco, J. A., Wahl, A. F., Meyer, D. L., and Senter, P. D. (2003) Development of potent monoclonal antibody auristatin conjugates for cancer therapy. *Nat. Biotechnol. 21*, 778−84.

(13) Sanderson, R. J., Hering, M. A., James, S. F., Sun, M. M., Doronina, S. O., Siadak, A. W., Senter, P. D., and Wahl, A. F. (2005) In vivo drug-linker stability of an anti-CD30 dipeptide-linked auristatin immunoconjugate. *Clin. Cancer Res. 11*, 843−52.

(14) Hamblett, K. J., Senter, P. D., Chace, D. F., Sun, M. M., Lenox, J., Cerveny, C. G., Kissler, K. M., Bernhardt, S. X., Kopcha, A. K., Zabinski, R. F., Meyer, D. L., and Francisco, J. A. (2004) Effects of drug loading on the antitumor activity of a monoclonal antibody drug conjugate. *Clin. Cancer Res. 10*, 7063−70.

(15) Law, C. L., Cerveny, C. G., Gordon, K. A., Klussman, K., Mixan, B. J., Chace, D. F., Meyer, D. L., Doronina, S. O., Siegall, C. B., Francisco, J. A., Senter, P. D., and Wahl, A. F. (2004) Efficient elimination of B-lineage lymphomas by anti-CD20-auristatin conjugates. *Clin. Cancer Res. 10*, 7842−51.

(16) Wahl, A. F., Klussman, K., Thompson, J. D., Chen, J. H., Francisco, L. V., Risdon, G., Chace, D. F., Siegall, C. B., and Francisco, J. A. (2002) The anti-CD30 monoclonal antibody SGN-30 promotes growth arrest and DNA fragmentation in vitro and affects antitumor activity in models of Hodgkin's disease. *Cancer Res. 62*, 3736−42.

(17) Trail, P. A., Willner, D., Lasch, S. J., Henderson, A. J., Hofstead, S., Casazza, A. M., Firestone, R. A., Hellstrom, I., and Hellstrom, K. E. (1993) Cure of xenografted human carcinomas by BR96-doxorubicin immunoconjugates. *Science 261*, 212−5.

(18) Reeve, J. G., Rabbitts, P. H., and Twentyman, P. R. (1989) Amplification and expression of mdr1 gene in a multidrug resistant variant of small cell lung cancer cell line NCI-H69. *Br. J. Cancer 60*, 339−42.

(19) Francisco, J. A., Cerveny, C. G., Meyer, D. L., Mixan, B. J., Klussman, K., Chace, D. F., Rejniak, S. X., Gordon, K. A., DeBlanc, R., Toki, B. E., Law, C. L., Doronina, S. O., Siegall, C. B., Senter, P. D., and Wahl, A. F. (2003) cAC10-vcMMAE, an anti-CD30-monomethyl auristatin E conjugate with potent and selective antitumor activity. *Blood 102*, 1458−65.

(20) Sun, M. M., Beam, K. S., Cerveny, C. G., Hamblett, K. J., Blackmore, R. S., Torgov, M. Y., Handley, F. G., Ihle, N. C., Senter, P. D., and Alley, S. C. (2005) Reduction-alkylation strategies for the modification of specific monoclonal antibody disulfides. *Bioconjugate Chem. 16*, 1282−90.

(21) Trail, P. A., Willner, D., Knipe, J., Henderson, A. J., Lasch, S. J., Zoeckler, M. E., TrailSmith, M. D., Doyle, T. W., King, H. D., Casazza, A. M., Braslawsky, G. R., Brown, J., Hofstead, S. J., Greenfield, R. S., Firestone, R. A., Mosure, K., Kadow, K. F., Yang, M. B., Hellstrom, K. E., and Hellstrom, I. (1997) Effect of linker variation on the stability, potency, and efficacy of carcinoma-reactive BR64-doxorubicin immunoconjugates. *Cancer Res. 57*, 100−5.

(22) Chari, R. V., Martell, B. A., Gross, J. L., Cook, S. B., Shah, S. A., Blattler, W. A., McKenzie, S. J., and Goldmacher, V. S. (1992) Immunoconjugates containing novel maytansinoids: promising anticancer drugs. *Cancer Res. 52*, 127−31.

(23) Hamann, P. R., Hinman, L. M., Beyer, C. F., Greenberger, L. M., Lin, C., Lindh, D., Menendez, A. T., Wallace, R., Durr, F. E., and Upeslacis, J. (2005) An anti-MUC1 antibody-calicheamicin conjugate for treatment of solid tumors. Choice of linker and overcoming drug resistance. *Bioconjugate Chem. 16*, 346−53.

(24) Hamann, P. R., Hinman, L. M., Beyer, C. F., Lindh, D., Upeslacis, J., Shochat, D., and Mountain, A. (2005) A calicheamicin conjugate with a fully humanized anti-MUC1 antibody shows potent antitumor effects in breast and ovarian tumor xenografts. *Bioconjugate Chem. 16*, 354−60.

(25) Hamann, P. R., Hinman, L. M., Hollander, I., Beyer, C. F., Lindh, D., Holcomb, R., Hallett, W., Tsou, H. R., Upeslacis, J., Shochat, D., Mountain, A., Flowers, D. A., and Bernstein, I. (2002) Gemtuzumab ozogamicin, a potent and selective anti-CD33 antibody-calicheamicin conjugate for treatment of acute myeloid leukemia. *Bioconjugate Chem. 13*, 47−58.

(26) Miller, M. L., Roller, E. E., Wu, X., Leece, B. A., Goldmacher, V. S., Chari, R. V., and Ojima, I. (2004) Synthesis of potent taxoids for tumor-specific delivery using monoclonal antibodies. *Bioorg. Med. Chem. Lett. 14*, 4079−82.

(27) Ojima, I., Geng, X., Wu, X., Qu, C., Borella, C. P., Xie, H., Wilhelm, S. D., Leece, B. A., Bartle, L. M., Goldmacher, V. S., and Chari, R. V. (2002) Tumor-specific novel taxoid-monoclonal antibody conjugates. *J. Med. Chem. 45*, 5620−3.

BC0502917

Linear Polyethyleneimine Grafted to a Hyperbranched Poly(ethylene glycol)-like Core: A Copolymer for Gene Delivery

Pallab Banerjee,* Ralph Weissleder, and Alexei Bogdanov, Jr.*

Center for Molecular Imaging Research, Massachusetts General Hospital, Building 149, 13th Street, Charlestown, Massachusetts 02129. Received March 18, 2005; Revised Manuscript Received November 21, 2005

A block copolymer of a hyperbranched poly(ethylene glycol)-like core and linear polyethylenimine (HBP) was synthesized by a facile synthetic route that included (1) a single-step cationic copolymerization of diepoxy and polyhydroxyl monomers, (2) derivatization of hydroxyl groups of the core HBPEG copolymer with either tosyl or chloromethylbenzoyl chlorides resulting in a corresponding macroinitiator, and (3) synthesis of HBPEG-*block*-poly(alkyl oxazolines). HBPEG-*block*-linear polyethyleneimine (HBP) was obtained by hydrolysis of HBPEG-*block*-poly(alkyl oxazolines). Linear PEI-bearing hyperbranched polycations (HBP) had lower inherent toxicity in cell culture than PEG-grafted linear polyethyleneimines (PEGLPEI). PEGLPEI formed a complex with DNA with an average diameter of 250 nm. The complexes were loosely condensed and formed aggregates and precipitates during storage. By contrast, hyperbranched polycations (HBP) formed ∼50 nm nanocomplexes with DNA that were stable for several weeks and showed resistance to DNAse I-mediated degradation. The 'inverted' block copolymers showed several orders of magnitude higher transfection efficiency than PEGLPEI in vitro. Because of the biocompatibility and higher transfection efficiency, the 'inverted' block copolymer merits further investigation as a gene carrier.

INTRODUCTION

Polyionic complexes between polycations (e.g. branched polyethyleneimine (BPEI) (*1*), "fractured" polyamidoamine (PAMAM) dendrimer fragments (*2, 3*)), and plasmid DNA were shown to transfect cells in vitro with high efficiency. Unfortunately, positively charged complexes with DNA induce acute inflammatory toxicity in vivo associated with the release of TNFα, complement activation, and erythrocyte aggregation (*4, 5*). Covalent modification of BPEI and PAMAM with poly(ethylene glycol) (*2, 6, 7*) for providing nonionic shells has been previously used to address the above problem and resulted in an overall lower systemic toxicity (*8*−*11*). Since poly(ethylene glycol) (PEG) partially shields a polycation's positive charge (*8*−*11*), large amounts of PEG-grafted polymers are usually required to obtain complexes with DNA for efficient cell transfection (*2*). Recently, Petersen et al. (*12*) reported synthesis and DNA-condensing properties of a block copolymer of low molecular weight branched polyethyleneimine grafted to a *star*-poly(ethylene glycol) core. The grafting of such low molecular mass PEI by block copolymerization enhanced the transfection efficacy of PEI which otherwise shows poor or low transfection (*12*). An alternative strategy of polycationic hydrophilic core-first polymer synthesis (*13*) has been also reported but the efficacy of resultant polymers for DNA delivery is yet to be explored. Our earlier work suggested that although PEG-grafted poly-L-lysine (protected graft copolymer, PGC) (*14*) showed a long blood circulation time in vivo, low cytotoxicity, and immunogenicity, its efficacy for in vivo gene transfer was limited (*15*). One potential explanation of this is in that grafted PEG chains provide shielding of the positive charge of the core polycation (*10*) and thus usually has limited use for in vivo gene delivery due to low binding to cells (*16*). However, the lack of efficacy in vitro does not preclude the potential use of PEG-grafted polycations for targeted delivery of expression vectors in vivo. To facilitate higher structural diversity of the "inverted", core-first polycationic gene delivery carriers, we extended the above studies by devising a hyperbranched PEG-like core polymer (HBPEG) and using the core as a macroinitiator for grafting it with linear polyethyleneimine obtained by using cationic polymerization of 2-alkyl-2-oxazolines.

Here we report a comparative study of two classes of polymers: (1) graft copolymers of PEI and PEG and (2) the above novel polycationic block copolymer-hyperbranched polycations (HBP). We compared their ability to form complexes with plasmid DNA, thus providing protection of DNA from nuclease degradation and cell transfection.

MATERIALS AND METHODS

Materials. Branched polyethyleneimine (BPEI) (M_n 10 kDa), linear polyethyleneimine (LPEI) (22 kDa) were obtained from Polyscience (Warrington, PA). Other chemicals were from Aldrich or Fisher Scientific. Detailed polymer syntheses are described in Supporting Information.

Characterization. Gel permeation chromatography (GPC) was performed by using PL aquagel-OH 40 8mm column (Polymer Laboratories Inc, Amherst, MA) coupled with two detectors, UV/vis, and differential refractive index (RI) at 30 °C. The column was eluted with 100 mM ammonium acetate (pH 7). Molecular mass was measured using poly(ethylene oxide) standards (5−920 kDa Polysciences, Inc, Warrington, PA). The weight average molecular mass was computed using refractive index data. Proton and ^{13}C NMR spectra were recorded in solutions (Spectral Data Service, Champaign, IL) at 400 MHz for ^{1}H and 100 MHz for ^{13}C spectra, respectively.

* Correspondence should be addressed to S2-804, Department of Radiology, University of Massachusetts Medical School, 55 Lake Avenue North, Worcester, MA 01655, Tel. (508) 856-5571, Fax (508) 856-1860. E-mail: Alexei.Bogdanov@umassmed.edu.

[1] Abbreviations: PEG, poly(ethylene glycol); LPEI, linear polyethyleneimine; BPEI, branched polyethyleneimine; HBPEG, hyperbranched poly(ethylene glycol); HBPEOX, hyperbranched poly(ethylene glycol) block poly(ethyl oxazoline); HBPMOX, hyperbranched poly(ethylene glycol) block poly(methyl oxazoline); HBP, hyperbranched poly(ethylene glycol) block linear polyethyleneime.

10.1021/bc050083e CCC: $33.50 © 2006 American Chemical Society
Published on Web 12/22/2005

The quantitative ^{13}C spectra were acquired in DMSO-d_6 using inverse gated decoupling pulse sequences. The spectra were obtained by using 0.5 g/mL polymer solutions at 30 °C. The data were acquired with an 80° pulse and 10 s recycle delay.

Cell Culture. COS-1 cells were propagated in DMEM supplemented with 4 mM L-glutamine, 1% penicillin−streptomycin, and 10% fetal bovine serum at 37 °C in 5% CO_2.

Reporter Gene Plasmid. pCMV-Luc (3.2 MDa, 5.12 kb) plasmid vector encoding firefly luciferase was propagated in *E. coli* DH5α and using Megaprep kit (Qiagen, Valencia, CA). Plasmid integrity was confirmed by gel electrophoresis in agarose. DNA concentration and purity were determined by measuring absorbance at 260 nm and 280 nm.

Polymer−DNA Complexes. To prepare complexes of each individual polymer with plasmid DNA, polymer solutions were added to DNA solutions (20 μg DNA/mL in 25 mM HEPES/5% glucose buffer, pH 5.5), mixed by vortexing, and incubated for 20 min at room temperature before use, unless stated otherwise. Polymer stock solutions were diluted with the same buffer as above to desired concentration. Hydrodynamic diameters of complexes were measured daily for four weeks by using Zetasizer 1000HSA (Malvern Instruments Inc, Southborogh, MA), at a fixed angle of 90° at room temperature. All complexes were stored at 4 °C.

An ethidium bromide exclusion experiment was performed with a F-4500 fluorescence spectrophotometer (Hitachi, Danbury, CT) at $\lambda_{ex} = 366$ nm and $\lambda_{em} = 591$ nm, respectively. Briefly, 10 μg of DNA and 2 μL of ethidium bromide solution (0.4 mg/mL) were mixed in 2 mL of TE buffer (pH 7.1). Polymer solution was added in 4-5 μL aliquots (1.1 mg/mL).The mixture was incubated at room temperature for 6 min, and the fluorescence intensity was measured. Two consecutive measurements were performed, and intensity values were averaged and corrected for dilution.

Cytotoxicity Assay. Cells were plated at a density 10000 cells/well of 96-well plates in 150 mL of medium 24 h before the experiment. Medium was replaced by fresh 150 μL of serum-containing media before the addition of polymers. Polymer solutions in 50 μL were then added to each well and incubated at 48 h, 37 °C. Cytotoxicity assays ($n = 4$ experiments) were performed using CytoTox 96 assay (Promega, Madison, WI), as described by the manufacturer. Nontreated cells were used as controls.

Cell Transfection. Transfections with polymer−plasmid DNA complexes were performed, and the results were analyzed using standard assay for luciferase activity expression. Various amounts of polymer in 5% glucose, 25 mM HEPES, were added to the plasmid solution (0.5 μg pCMV-luc plasmid in 30 μL of 0.1 TE buffer), mixed, and incubated at room temperature for 30 min. Cells were plated at a density of 10000 cells/well in 96-well plates, 24 h prior to transfection. Before the addition of complexes, medium was replaced by fresh 100 μL of serum containing media. The complexes were then added to each well. The total volume did not exceed 150 μL/ well. The transfection was carried out for 24 h at 37 °C. The luciferase activity in cell lysates was determined using Microlumat LB96P (EG&G Berthold), by adding 50 μL of luciferin (Promega, Madison, WI) to 25 μL of cell lysate in each well using an automated injector ($n = 3$ independent experiments for each transfection reagent). Luciferase activity was integrated over 10 s with 2 s intervals. The protein concentration was measured in the rest of 25 μL cell lysate using standard protein assay reagent Pierce-Endogen, Rockford, IL). Results were expressed in relative light units per mg of cell protein. The significance of differences between data sets (here and below) was determined by using Student's unpaired, two-tailed test with Welch's correction.

DNAse I Protection Assay. DNA was prelabeled with Cy3 by using Label IT Cy3 kit (Mirus, Madison, WI) as described by the manufacturer. Labeled DNA was mixed with unlabeled pCMV−Luc at 1:6 w/w. The final concentration of DNA was 1 μg/μL. HBP and Cy3-labeled pCMV−Luc complexes were prepared at the best transfection efficiency ratio using 1.8 μg of DNA in 10 mM Tris buffer (pH 7.5). The DNA/polymer complex was first incubated for 20 min at room temperature. Various amounts of DNAse I were then added to either "naked" pCMV−Luc or to polymer complexes, and the samples were incubated at room temperature for 150 min. Samples were analyzed by 0.8% agarose gel electrophoresis. Gels were imaged using 530 nm excitation filter (Kodak 440CF) followed by staining with ethidium bromide.

RESULTS

Graft Copolymer Synthesis. To prepare a linear PEI backbone polymer (LPEI, Supporting Information, Figure S1A) commercially available poly(2-ethyl 2-oxazoline) was hydrolyzed as described (*17*). Proton NMR results suggested that hydrolysis was 90% complete. Two graft copolymers were prepared by grafting PEG chains onto linear polyethyleneimine (LPEI) as well as onto the branched polyethyleneimine (BPEI) (Supporting Information, Figure S1). The linear polyethyleneimine graft MPEG (PEGLPEI) was obtained by reacting the MPEG chloroformate with LPEI (Supporting Information, Figure S1A). The graft copolymer contained 5% PEG by weight (i.e. 2−3 PEG chains per molecule of LPEI), as calculated from ^1H NMR using the ratio of peak intensity of PEG ($-CH_2O-$, 3.57 ppm) to ethyleneimine peak intensity ($NHCH_2CH_2$, 3.0−3.3 ppm). Branched PEI (BPEI, M_n 10 kDa) was reacted with monomethoxy PEG carboxy-*N*-hydroxysuccinimide. The corresponding graft-copolymer obtained using BPEI as a backbone contained approximately 10 wt % of PEG calculated from ^1H NMR using the ratio of peak intensity of PEG ($-CH_2O$, 3.57 ppm) to ethyleneimine proton peak intensity ($NHCH_2CH_2$, 2.9−3.2 ppm).

Synthesis of Hyperbranched PEG-like Core Polymers (HBPEG). Cationic copolymerization of poly(ethylene glycol) diglycidyl ether (bearing two reactive epoxy groups) and pentaerithrytol ethoxylate (containing four hydroxyl groups) was accomplished by using boron trifluoride as a catalyst (Supporting Information, Figure S2). By varying the catalyst concentration, polymers with different molecular masses ranging from 25 to 35 kDa were obtained. Upon the omission of the polyol (pentaerithrytol ethoxylate), the formation of a gel instead of a soluble polymer was observed. The use of methylene chloride instead of THF as copolymerization solvent resulted in polymers with a lower molecular mass. Quantitative ^{13}C NMR showed incorporation of butylene ether moiety within the HBPEG composition (Figure 1B). The butylene ether moiety was absent from ^{13}C NMR spectra if the copolymerization was carried out in methylene chloride. The hyperbranched PEG-like polymers were isolated as semisolids that had excellent solubility in water and various organic solvents (e.g. methylene chloride, tetrahydrofuran). The obtained HBPEG polymers were analyzed by using a size-exclusion chromatography (Figure 1A, Table 1). Due to the fact that size exclusion chromatography (SEC) tends to underestimate the true molecular mass of branched polymers (*18*), the true molecular masses of branched polymers were likely to be higher than those suggested by SEC if linear polymers were used as standards. The polydispersity of obtained products was low due to the removal of low molecular weight polymer fraction during the dialysis. The presence of hydroxyl groups was determined by titration method as described (*19*). Titration of available hydroxyls in HBPEG gave a value of approximately 100 hydroxyl groups/HBPEG molecule. The

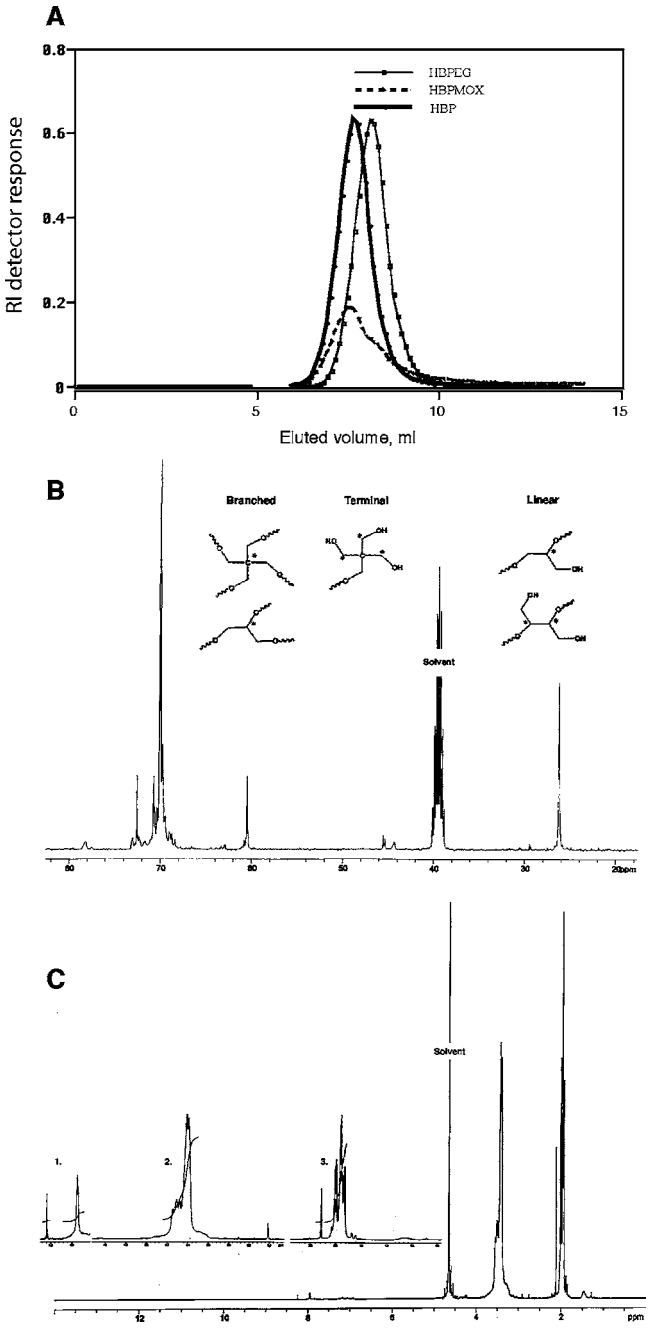

Figure 1. A. Gel permeation chromatography of HBPEG2 (M_n 24.7 kDa); "inverted" precursor, a block copolymer HBPMOX1 (M_n 56.2 kDa), and the hydrolyzed product (HBP1) (M_n 42.6kDa). B. Structural units of hyperbranched poly(ethylene glycol)-like core (HBPEG2, Table 1) predicted from quantitative ^{13}C NMR data in DMSO-d_6. Linear monomeric unit (l) 44.3 and 72.5−78.2 ppm; branch (t) peaks at 30.4, 44.5, 60.4−60.8, and 62.9 ppm; dendritic core (d) peaks at 29.4 and 72.4 ppm. C. ^1H NMR spectra of HBPMOX1 in D_2O. Inserts: enlarged view of spectras in the following ranges (1) 1.2−2.2 ppm; (2) 2.6−4.2 ppm; and (3) 7.9−8.2 ppm.

observed high content of terminal hydroxyl groups argues for the formation of extensive branching structure. To calculate the degree of branching, quantitative ^{13}C NMR data were used. We assigned the 44.3, 72.5−78.2 ppm peaks to the linear monomeric unit (l), whereas peaks corresponding to 30.4, 44.5, 60.4−60.8, and 62.9 ppm were assigned to the termini of branches (t). The peaks at 29.4 and 72.4 ppm correspond to the dendritic core (d). The degree of branching was calculated using the following formula as described in (*20*). The degree of branching, DB = $(N_d + N_t)/(N_d + N_t + N_l)$, where N is the integrated value of the peak; d, l, t are dendritic, linear, and terminal units, respectively (Figure 1B). The calculated DB values were 0.68 (HBPEG1) and 0.59 (HBPEG2). Both polymers were synthesized using identical conditions and various amounts of the catalyst (Table 1). According to published data, in hyperbranched polymers the degree of branching is approximately 0.5 (*21*).

HBP Block Copolymer Synthesis. We synthesized a cationic block copolymer (HBP) with grafted polyethyleneimine chains using hyperbranched PEG (HBPEG) as the inner core. First, we performed activation of surface hydroxyl groups of HBPEG using either 4-chloromethylbenzoyl chloride or *p*-toluenesulfonyl chloride. The above chlorides catalyze ring-opening polymerization of 2-oxazoline groups (*22*, *23*) (Supporting Information, Figure S3). The purified chloromethyl or tosyl derivative of HBPEG was characterized by ^{13}C NMR data that showed the presence of a sulfonyl derivative (δ 127.9 (aromatic ortho carbon $(CH)_2-C-SO_2^-$) and chloromethyl derivative (δ 128.4 (aromatic ortho carbon, $ClCH_2C(CH)_2$), respectively. The block copolymer prepared by reacting ethyl oxazoline with the tosyl derivative of HBPEG (HBPEOX) was precipitated in ethyl ether, dried in a vacuum, and characterized (Table 1). ^1H NMR peaks at 3.2−3.44 ppm ($(-CH_2CH_2NCOCH_2CH_2-$) and 1.49 ppm (CH_3CH_2CO-) confirmed the presence of poly(2-ethyl 2-oxazoline). The polymer was then hydrolyzed as described earlier (*23*), using sodium hydroxide in ethanol/ethylene glycol and purified by dialysis. The disappearance of peak at 3.2−3.4 ppm and the new peak at 2.59−3.09 ppm ($-NHCH_2CH_2-$) suggested that hydrolysis of the block copolymer proceeded efficiently and that the "inverted" block copolymer (HBP4) was formed (Table 1). The block copolymer of the chloromethyl derivative of HBPEG was prepared by the cationic polymerization method, using 2-methyl 2-oxazoline monomer in benzonitrile and potassium iodide as a coinitiator. Potassium iodide was used for exchanging chloride anion with iodide, that resulted in high efficacy of conversion into HBPEG−poly(methyl oxazoline) (Supporting Information, HBPMOX, Figure S3). Upon varying the reaction composition and time of polymerization we prepared different molecular weight HBPMOX (Table 1). We further analyzed the obtained polymers using GPC (Figure 1A) before and after the alkaline hydrolysis that demonstrated the progressive increase of the average mass of the polymer after the extension of poly(2-ethyl 2-oxazoline) chains and their hydrolysis (Table 1). Figure 1C depicts the ^1H NMR spectrum of HBPMOX1. The observed peak at 7.95 ppm (aromatic ortho hydrogen, $-NCH_2(CH)_2(CH)_2-$) pointed to the extension of the poly(2-methyl 2-oxazoline) block from the chloromethyl derivative HBPEG core as the reaction scheme (Supporting Information, Figure S3) suggested. The methyl protons of the acetyl group (1.9 ppm) were undetectable after the hydrolysis, whereas methylene protons adjacent to nitrogen shifted from 3.4 to 2.7 ppm.

Complex Formation with DNA. The formation of complexes between DNA and HBP polymers was monitored by fluorometry using the ethidium bromide displacement method. Control PEG-grafted polymers (PEGLPEI and PEGBPEI) showed a gradual decrease of fluorescence that reached 50% of the initial relative fluorescence intensity value in the presence of large polymer amounts (concentration exceeded 50 μg/mL, Figure 2). In the case of hyperbranched block copolymer (HBP), linear polyethyleneimine LPEI, and commercially available branched polyethyleneimine BPEI (Figure 2), a 50% decrease of fluorescence intensity was observed in the presence of much lower polymer amounts (approximately 10−13 μg/mL). DNA condensing properties of polymers were tested in parallel by measuring hydrodynamic radii of polymers and the complex with negatively charged DNA (Table 1). Initially, we measured

Table 1. A Characterization of Hyperbranched and Graft Copolymers and Their Precursors

polymer	M_n (K)	M_W (K)	PDI (M_w/M_n)	yield (%)	HD[a] (nm)	CHD[b] (nm)	CHD4W[k] (nm)	Zeta Pl[m] (mV)
HBPEG1[c]	38.1	72.1	1.89	92	30.9 ± 3.9	-	-	-
HBPEG2[d]	24.7	41.3	1.67	90	24.7 ± 5.6	-	-	-
HBPEOX	67.3	120	1.78	44	48.7 ± 4.8	-	-	-
HBPMOX1	56.2	97.5	1.73	82	39.8 ± 3.9	-	-	-
HBPMOX2[e]	49.3	81.5	1.65	90	32.8 ± 6.3	-	-	-
HBPMOX3[f]	43.6	69.5	1.59	89	27.8 ± 5.7	-	-	-
HBP1[g]	42.6	69.4	1.63	-	46.1 ± 5.8	35.9 ± 5.3	36.9 ± 3.7	-
HBP2[h]	37.5	59.6	1.59	-	31.2 ± 3.4	56.2 ± 8.5	54.2 ± 4.3	11.72
HBP3[i]	29.3	48.9	1.67	-	17.2 ± 2.7	56.1 ± 6.7	61.3 ± 6.2	4.69
HBP4[j]	49.3	75.9	1.54	-	60.9 ± 6.2	44.6 ± 3.4	43.7 ± 4.1	-
PEGLPEI	36.8	78.0	2.12	-	273.4 ± 5.8	195 ± 10.9		-
PEGBPEI	20.4	45.5	2.23	-	256.7 ± 12.3	73.4 ± 8.7		-

[a] Hydrodynamic diameter; measured at 50 μg polymer/mL. [b] Hydrodynamic diameter of DNA complex prepared by mixing 25 μg of plasmid DNA and 50 μg of polymer in 1 mL 5% glucose solution. [c] 0.01 mol boron trifluoride etherate. [d] 0.02 mol boron trifluoride etherate. [e] 10 mL of 2-methyl 2-oxazoline, polymerization time 24 h. [f] 7 mL 2-methyl 2-oxazoline, polymerization time 24 h. [g] Synthesized from hydrolyzed HBPMOX1. [h] Synthesized from hydrolyzed HBPMOX2. [i] Synthesized from hydrolyzed HBPMOX3. [j] Synthesized from hydrolyzed HPPEOX. [k] Hydrodynamic diameter of the DNA complex after 4 weeks of storage. [l] Size exclusion chromatography was performed in 0.1 M ammonium acetate using poly(ethylene oxide)s as molecular weight standards. [m] Complex was prepared by mixing 25 μg of DNA and 50 μg of polymer in 1 mL of 5% glucose solution.

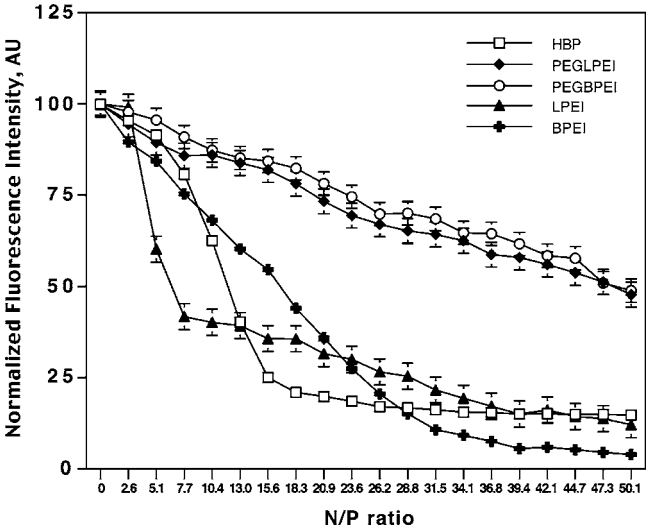

Figure 2. DNA-bound ethidium bromide displacement as a result of complex formation with polycations. The legend denotes complexes formed with BPEI (closed circles), LPEI (closed triangles), PEGBPEI (open circles), PEGLPEI (diamonds), and HBP1 (squares). The *y*-axis represents the normalized fluorescence intensity. Results of three independent experiments are shown as mean ± SD.

the hydrodynamic diameter of the HBPEG core (approximately 25 nm). After block copolymerization with the formation of the LPEI "corona", the diameter increased by ~10 nm. Further, we observed that complexes between the plasmid DNA and HBP formed in nonionic, isotonic solution (5% glucose in water) were small, ~50 nm in diameter, and that particle size did not change for at least 30 days. We further performed measurements of zeta potentials of complexes prepared using 25 μg of DNA and 50 μg of hyperbranched block copolymer (HBP2 or HBP3). Zeta potential of complexes was affected by changing the density of cationic residues in the polymer. We used two different molecular weight polymers for zeta potential measurement and established that higher molecular weight polymer (HBP2) yields more positive zeta potential of the complex than the low molar mass polymer HBP3 (Table 1).

The ability of the HBP to protect the nucleic acids from enzymatic cleavage was tested by using DNAse I treatment, and the data were compared to that obtained using LPEI and the conventional graft copolymer (PEGLPEI). The complex composition corresponded to that with the highest transfection efficiency in cell culture (see below). HBPs were able to protect DNA from degradation by DNAse I for at least 2 h (Figure 3), and only traces of DNA fragments were present at the highest concentrations of DNAse I used. The control "naked" DNA as well as PEGLPEI complex with DNA was completely degraded at concentrations of DNAse I exceeding 2.5 U/mL. In the case of the complex prepared using LPEI, ethidium bromide staining of the complex is much higher than the in the complexes prepared using HBPs.

Cell Transfection. Cell transfection efficacy was compared in COS-1 cell culture. Prepared in identical conditions, all complexes gave very different levels of luciferase expression. In case of both types of "conventional" graft copolymers transfection efficiency was low even when higher amounts of polymer were used for complex preparation (Figure 4A). The transfection efficacy observed in the case of HBP block copolymers was compared against linear polyethylneimine (LPEI). The resultant luciferase activity expressed in transfected cells was at least 5 orders of magnitude higher than any of PEGLPEI or PEGBPEI while the amount of hyperbranched block copolymer needed for transfection was less (at least 50 times). Used at similar weight ratio, hyperbranched block copolymers showed at least two orders higher transfection efficiency than that of positive control Superfect reagent (Figure 4A and Figure 4B). At slightly higher concentrations, hyperbranched block copolymer showed higher transfection efficiency than LPEI.

Cytotoxicity. Cytotoxicity of polymers was investigated in COS-1 cells at 48 h after the addition of polymers (Figure 4C). The highest molecular mass HBP had a very low cytoxicity even at a very high concentration (0.5 mg/mL). Although at lower concentration the toxicity of HBP was lower than that of LPEI, the observed differences were not significant.

DISCUSSION

It is well-known that upon mixing positively charged block copolymers with DNA, polycationic blocks induce DNA binding and condensation while PEG blocks provide steric protection for condensed DNA−polycation cargo (*7*, *24*). The major goal of our research was to compare "conventional" copolymers composed of polycationic PEI- and PEG-based blocks with HBPs, based on hyperbranched PEG-like polymer block surrounded with PEI blocks, i.e. "inverted" design. The "conventional" copolymers contained between 5 and 10% of PEG2000 by weight, respectively, which appears to prevent binding of the DNA−polymer complex to the cell (*16*, *25*), resulting in at least 4 orders of magnitude lower transfection efficiency than that of its 22 kDa PEG-free LPEI counterpart at all concentrations (*26*). Our experiments with similar copolymers also showed that even at very high concentrations of graft copolymers (1.5 mg/mL), the highest achieved transfection efficiency

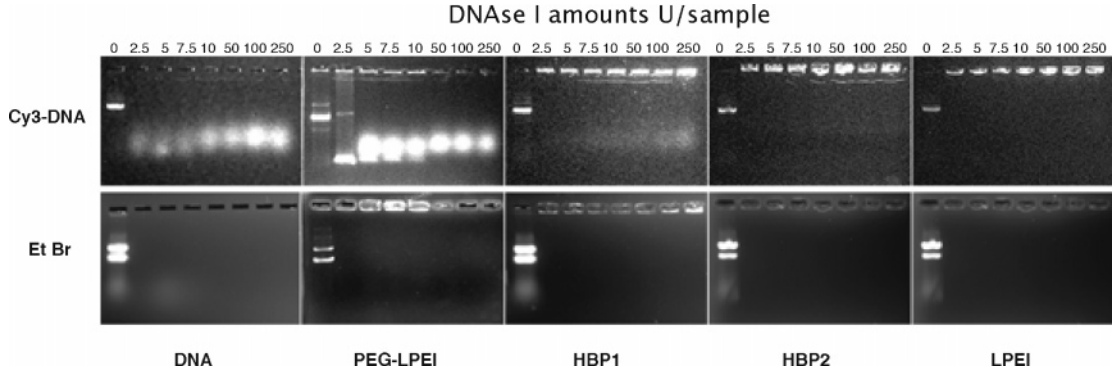

Figure 3. DNAse I protection assay. Lane 1 shows control pCMV−Luc/Cy3-pCMV−Luc mixture (6:1 by weight, 1.5 μg of DNA was loaded per lane). Lane 2−7 shows the same mixture at different amounts of DNAse I present: 2.5U, 5U, 7.5U, 10U, 50U, 100U, and 250U, respectively. DNAse I was incubated with DNA and polycation-containing samples for 2.5 h at room temperature followed by 0.8% agarose gel electrophoresis and imaging using Kodak 440CF equipped with Cy3 fluorescence filters (upper row), staining with ethidium bromide, and imaging (lower row). A typical result is shown.

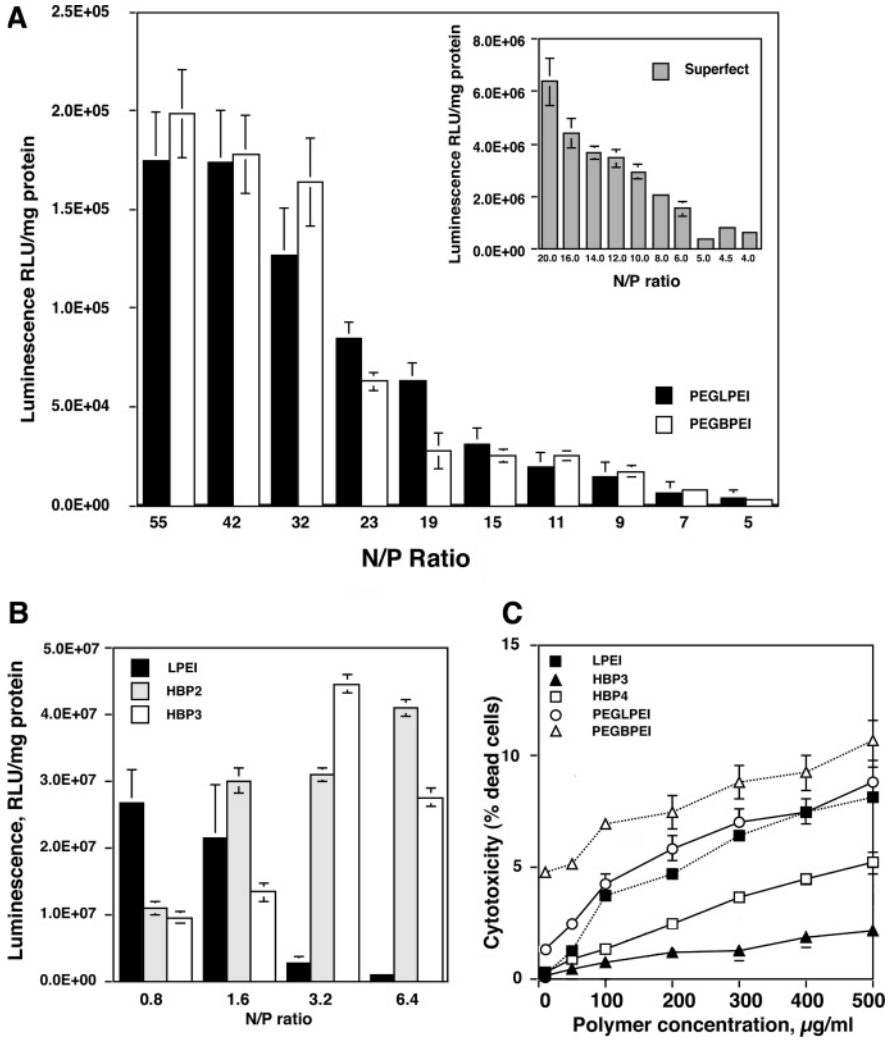

Figure 4. A. Luciferase expression in COS 1 cells after a 24 h transfection in serum-containing medium: transfection efficiency of PEGLPEI (solid bars), PEGBPEI (open bars) at various N/P ratios. Transfection results obtained using various concentrations of Superfect reagent are shown in the inset. Polymer complex with plasmid DNA was prepared by mixing 0.5 μg of pCMV-luc in 30 μL solvent with polymers at different concentrations. B. Luciferase expression in COS-1 cells after a 24 h transfection in serum-containing medium: transfection efficiency of LPEI (solid bars), HBP3 (shaded bars), and HBP2 (open bars). The complex was prepared by mixing 0.5 μg of pCMV-luc plasmid DNA with various polymer amounts (shown in *x*-axis). C. Cytotoxicity profiles of linear polyethyleneimine (closed squares) and hyperbranched block copolymers: HBP3 (closed triangles), HBP4 (open squares), PEGLPEI (open circles), and PEGBPEI (open triangles) in COS-1 cell culture after 48 h incubation. Results of four independent experiments are shown as mean ± SD.

was still at least 3 orders of magnitude lower than that of LPEI (Figure 4A,B). Ethidium bromide displacement results suggested that for the purposes of cell transfection, "conventional" PEG-grafted polymers are effectively shielded by PEG, resulting in only partial availability of positive charges of the polymer for complex formation with the DNA (Figure 2).

In choosing HBP architecture, we hypothesized that the PEG-based polymer core could still provide protection to bound DNA

while the polycationic "shell" could be fully functional in DNA binding. Thus, we expected that upon the formation of complexes with negatively charged DNA, the cationic residues would get neutralized and that the formation of nanosized complexes could be achieved.

We devised the synthesis of the above hyperbranched molecule using a mixture of poly(ethylene glycol) diglycidyl ether and pentaerythritol ethoxylate upon cationic polymerization. The method enabled us to obtain high molecular mass hydroxyl-terminated, hyperbranched PEG-like polymer (HBPEG) in a single step. The available hydroxyl groups in hyperbranched polymer could be easily modified using chloromethyl benzoyl chloride or *p*-toluene sulfonyl chloride, yielding a hyperbranched macroinitiator that enabled synthesis of a block copolymer with poly(2-alkyl 2-oxazoline). The molar mass of block copolymer (Mn) could be controlled by changing the reaction parameters (Table 1). By treating polyoxazoline blocks in mild alkaline conditions, we obtained final HBPEG−LPEI (HBP).

Unlike PEGylated PEI (e.g. PEGLPEI or PEGBPEI), HBP-mediated condensation of DNA appeared not to be affected by hyperbranched PEG-like core blocks, because the concentration of HBP required to achieve a half-maximal displacement of ethidium bromide initially bound to DNA in the complex was low (Figure 2). Consequently, the DNA condensing properties of the "inverted" block copolymer was superior to that of graft copolymers used in this study. At the same time, particle size and stability data suggested that HBP behaved differently from PEGBPEI, since the complex with plasmid DNA was very stable during the storage and was at least two times smaller than DNA complexes obtained using "conventional" PEG-grafted PEI (Table 1, see also ref 24). The observed lack of core interference with the complex formation was also apparent in experiments which investigated DNA-protective properties of HBP. We observed that ethidium bromide-negative, i.e., highly condensed complexes, were highly resistant to DNAse I degradation (Figure 3).

We further measured cytotoxicity as well as transfection efficacy of the resultant block copolymer and compared them with the PEG-grafted PEI and LPEI (22 kDa). Due to the presence of hyperbranched HBPEG core, a higher amount of block copolymer was required to achieve optimal cell transfection (Figure 4A) at the concentration that was less toxic than that of LPEI (Figure 4C). It is known that PEG-grafted BPEI always show less toxicity than BPEI alone (*10*). In our case, i.e., when PEG-like polymer comprised the inner core of the molecule, the effect of lesser toxicity was achieved in a manner similar to that of the "conventional" PEG coating (Figure 4C). This suggests that the presence of HBPEG inner core indeed reduced cytotoxicity, whereas complex condensation by "inverted" block copolymer HBPs was superior to that of PEG grafted PEI (*26*). The latter effect could be explained by the lack of interference with DNA binding to PEI.

In conclusion, we report here synthesis and properties of hyperbranched block copolymers based on PEG-like hyperbranched core-first design. We demonstrated that "inverted" block copolymers (HBPs) obtained using grafting of linear PEI showed low toxicity in vitro and formed stable nanosized complexes with plasmid vectors that were protected from degradation with DNAse I. Furthermore, these nanocomplexes showed high transfection efficacy in vitro. Since in vitro transfection efficacy is not ideal in predicting the ability of a polycation to deliver expression or silencing vectors in vivo, the latter properties of hyperbranched polycations with PEG-like cores are currently under investigation.

ACKNOWLEDGMENT

This work has been supported in part by 1P50CA86355-01 (Project 2).

Supporting Information Available: Experimental details. This material is available free of charge via the Internet at http://pubs.acs.org.

LITERATURE CITED

(1) Boussif, O., Lezoualch, F., Zanta, M. A., Mergny, M. D., Scherman, D., Demeneix, B., and Behr, J. P. (1995) A versatile vector for gene and oligonucleotide transfer into cells in culture and in-vivo − polyethylenimine. *Proc. Natl. Acad. Sci. U.S.A. 92*, 7297−7301.

(2) Luo, D., Haverstick, K., Belcheva, N., Han, E., and Saltzman, W. M. (2002) Poly(ethylene glycol)-conjugated pamam dendrimer for biocompatible, high-efficiency DNA delivery. *Macromolecules 35*, 3456−3462.

(3) Tang, M. X., Redemann, C. T., and Szoka, F. C. (1996) In vitro gene delivery by degraded polyamidoamine dendrimers. *Bioconjugate Chem. 7*, 703−714.

(4) Ogris, M., Brunner, S., Schuller, S., Kircheis, R., and Wagner, E. (1999) Pegylated DNA/transferrin-pei complexes: Reduced interaction with blood components, extended circulation in blood and potential for systemic gene delivery. *Gene Ther. 6*, 595−605.

(5) Plank, C., Mechtler, K., Szoka, F. C., Jr., and Wagner, E. (1996) Activation of the complement system by synthetic DNA complexes: A potential barrier for intravenous gene delivery. *Hum. Gene Ther. 7*, 1437−46.

(6) Choi, J. S., Joo, D. K., Kim, C. H., Kim, K., and Park, J. S. (2000) Synthesis of a barbell-like triblock copolymer, poly(l-lysine) dendrimer-*block*-poly(ethylene glycol)-*block*-poly(l-lysine) dendrimer, and its self-assembly with plasmid DNA. *J. Am. Chem. Soc. 122*, 474−480.

(7) Bronich, T. K., Cherry, T., Vinogradov, S. V., Eisenberg, A., Kabanov, V. A., and Kabanov, A. V. (1998) Self-assembly in mixtures of poly(ethylene oxide)-graft- poly(ethyleneimine) and alkyl sulfates. *Langmuir 14*, 6101−6106.

(8) Kabanov, A. V., Vinogradov, S. V., Suzdaltseva, Y. G., and Alakhov, V. Y. (1995) Water-soluble block polycations as carriers for oligonucleotide delivery. *Bioconjugate Chem. 6*, 639−643.

(9) Katayose, S., and Kataoka, K. (1997) Water-soluble polyion complex associates of DNA and poly(ethylene glycol)-poly(l-lysine) block copolymer. *Bioconjugate Chem. 8*, 702−707.

(10) Petersen, H., Fechner, P. M., Fischer, D., and Kissel, T. (2002) Synthesis, characterization, and biocompatibility of polyethylenimine-graft-poly(ethylene glycol) block copolymers. *Macromolecules 35*, 6867−6874.

(11) Kircheis, R., Wightman, L., and Wagner, E. (2001) Design and gene delivery activity of modified polyethylenimines. *Adv. Drug Delivery Rev. 53*, 341−358.

(12) Petersen, H., Kunath, K., Martin, A., Stolnik, S., Roberts, C., Davies, M., and Kissel, K. (2002) Star-shaped poly(ethylene glycol)-*block*-polyethylenimine copolymers enhance DNA condensation of low molecular weight polyethylenimines. *Macromolecules 3*, 926−936.

(13) Koç, F., Wyszogrodzka, M., Eilbracht, P., and Haag, R. (2005) Highly regioselective synthesis of amino-functionalized dendritic polyglycerols by a one-pot hydroformylation/reductive amination sequence. *J. Org. Chem. 70*, 2021−2025.

(14) Bogdanov, A. A., Weissleder, R., Frank, H. W., Bogdanova, A. V., Nossif, N., Schaffer, B. K., Tsai, E., Papisov, M. I., and Brady, T. J. (1993) A new macromolecule as a contrast agent for mr-angiography − preparation, properties, and animal studies. *Radiology 187*, 701−706.

(15) Bogdanov, A., Kayne, L., and Weissleder, R. (1998) in *The 25th International Symposium on Controlled Release of Bioactive Materials* (Controlled Release Society, Intl., Ed.) pp 91−92, Controlled Release Society, Inc., Las Vegas, NV.

(16) Nguyen, H. K., Lemieux, P., Vinogradov, S. V., Gebhart, C. L., Guerin, N., Paradis, G., Bronich, T. K., Alakhov, V. Y., and Kabanov, A. V. (2000) Evaluation of polyether-polyethyleneimine graft copolymers as gene transfer agents. *Gene Ther. 7*, 126−138.

(17) Jeong, J. H., Song, S. H., Lim, D. W., Lee, H., and Park, T. G. (2001) DNA transfection using linear poly(ethylenimine) prepared by controlled acid hydrolysis of poly(2-ethyl-2-oxazoline). *J. Controlled Release 73*, 391−399.

(18) Feast, W. J., and Stainton, N. M. (1995) Synthesis, structure and properties of some hyperbranched polyesters. *J. Mater. Chem. 5*, 405−411.

(19) Sunder, A., Turk, H., Haag, R., and Frey, H. (2000) Copolymers of glycidol and glycidyl ethers: Design of branched polyether polyols by combination of latent cyclic ab(2) and abr monomers. *Macromolecules 33*, 7682−7692.

(20) Hawker, C. J., Lee, R., and Frechet, J. M. J. (1991) One-step synthesis of hyperbranched dendritic polyesters. *J. Am. Chem. Soc. 113*, 4583−4588.

(21) Radke, W., Litvinenko, G., and Muller, A. H. E. (1998) Effect of core-forming molecules on molecular weight distribution and degree of branching in the synthesis of hyperbranched polymers. *Macromolecules 31*, 239−248.

(22) Kobayashi, S. (1990) Ethylenimine polymers. *Prog. Polym. Sci. 15*, 751−823.

(23) Akiyama, Y., Harada, A., Nagasaki, Y., and Kataoka, K. (2000) Synthesis of poly(ethylene glycol)-*block*-poly(ethylenimine) possessing an acetal group at the peg end. *Macromolecules 33*, 5841−5845.

(24) Petersen, H., Fechner, P. M., Martin, A. L., Kunath, K., Stolnik, S., Roberts, C. J., Fischer, D., Davies, M. C., and Kissel, T. (2002) Polyethylenimine-graft-poly(ethylene glycol) copolymers: Influence of copolymer block structure on DNA complexation and biological activities as gene delivery system. *Bioconjugate Chem. 13*, 845−854.

(25) Erbacher, P., Bettinger, T., Belguise-Valladier, P., Zou, S. M., Coll, J. L., Behr, J. P., and Remy, J. S. (1999) Transfection and physical properties of various saccharide, poly(ethylene glycol), and antibody-derivatized polyethylenimines (pei). *J. Gene. Med. 1*, 210−222.

(26) Kichler, A., Chillon, M., Leborgne, C., Danos, O., and Frisch, B. (2002) Intranasal gene delivery with a polyethylenimine-peg conjugate. *J. Controlled Release 81*, 379−388.

BC050083E

RNAi Silencing of Exogenous and Endogenous Reporter Genes Using a Macrocyclic Octaamine as a "Compact" siRNA Carrier. Studies on the Nonsilenced Residual Activity

Kazuki Matsui, Shohei Horiuchi, Shinsuke Sando, Takashi Sera, and Yasuhiro Aoyama*

Department of Synthetic Chemistry and Biological Chemistry, Graduate School of Engineering, Kyoto University, Katsura, Nishikyo-ku, Kyoto 615-8510, Japan. Received April 14, 2005; Revised Manuscript Received August 26, 2005

A macrocyclic octaamine **1** having a covalently linked lipid-bundle structure was introduced as a new type of siRNA carrier. Gel electrophoresis, DLS, and SPR results indicate that it strongly binds to a luciferase-targeting 21-mer (42P) siRNA with a ratio of **1**/P ≅ 0.3 (**1**/N ≅ 2.4) to give remarkably compact **1**−siRNA complexes with an average size of ∼10 nm. The **1**-mediated siRNA silencing of the exogenous luciferase gene occurs with a 90−95% efficiency. The overall suppression−[siRNA] profile with a 5−10% residual activity in the saturation region is commonly observed irrespective of the cell type (HeLa, HepG2, or HEK293), the order, or timing (stepwise or simultaneous) of supply of the siRNA and that of the luciferase-encoding plasmid, the level of mRNA transcribed, or the type of carriers (**1** vs lipofectamine 2000). The silencing of the endogenous DsRed2 gene stably incorporated in the genome of HeLa cells also has a similar overall profile. These results suggest that (1) the cellular uptake of the plasmid and that of the siRNA are basically independent of each other and (2) the incomplete silencing is not due to insufficient siRNA delivery. Implication of item 2 is briefly discussed.

INTRODUCTION

RNA interference (RNAi) is the posttranscriptional gene silencing process mediated by a 21−23-mer duplex siRNA (si = small or short interfering) which is homologous in sequence with the silenced gene (*1*−*5*). The siRNA taken up in the cells forms the so-called RISC (RNA-induced silencing complex) containing the antisense strand; consequently the complex then attacks the sense mRNA to result in degradation and hence silencing of the latter (*6*, *7*). The activity of synthetic siRNA was demonstrated for the first time by Tuschl et al., in terms of siRNA-dependent suppression of an exogenous reporter gene provided in the form of plasmid (*8*). This simple analysis was based on the assumption that a substantial portion of the plasmid-transfected cells also contains siRNA. Actually, the suppression, in this pioneering work, of pGL3 luciferase was complete (∼100%) in Drosophila cells but less complete (90−95%) in mammalian cells (*8*). Efficient but incomplete silencing has been generally observed in many subsequently studies using mammalian cells (*9*−*15*).

We are concerned here about two matters. One is the nonsilenced "residual" ≥5% gene-expression activity. Does it simply reflect incomplete siRNA delivery or is it a consequence of essential incompleteness of RNAi? The other is size control of carrier−siRNA complexes, particularly in view of their in vivo performance. As is often a problem in artificial (nonviral) gene delivery, huge particles cannot simply diffuse into vascular periphery (*16*). Small particles, on the other hand, may be selectively taken up in malignant tissues by the so-called EPR (enhanced permeation and retention) effect (*17*). The size we aim at is ≤50 nm, which has not been precedented before for the siRNA complexes to the best of our knowledge.

We introduced a cone-shaped macrocyclic octaamine **1** of an amphiphilic character as siRNA carrier. We report here that it forms an unprecedented compact (∼10 nm) complex with siRNA and mediates effective gene silencing but not completely regardless of the cell type, transfection order (siRNA vs plasmid), extent of gene transcription, carrier type (**1** vs lipofectamine 2000), or gene type (exogenous vs endogenous). This led us to suggest that the incomplete silencing should be interpreted in terms of intrinsic incompleteness of RNAi.

EXPERIMENTAL PROCEDURES

Materials and General Analysis. Octaamine **1** in the form of octa(hydrochloride) was obtained from the corresponding free-base, prepared as described (*18*), upon treatment with HCl. Thus, 2 mL of concentrated hydrochloric acid was added to an ethanol solution (200 mL) of the free-base (200 mg). Most of the ethanol was removed and the white precipitates that separated were collected and dried in vacuo to give 225 mg (94%) of the octa(hydrochloride). Plasmids (pGL3, pGL2, and pGL3-Promoter), siRNAs, and lipofectamine were commercial products of Promega, TAKARA BIO, and Invitrogen, respectively. HeLa (Riken Cell Bank, RCB0007), HepG2 (Dainippon Pharmaceutical Co. Ltd., HB8-65), and HEK293 (Riken Cell Bank, RCB1637) cells were cultivated in DMEM (Dulbecco's modified Eagle's medium) containing 10% FCS (fetal calf serum) and antibiotics (penicillin−streptomycin, 50 μg/mL) with (HepG2) or without (HeLa, HEK293) 1% NEAA (nonessential amino acids) at 37 °C in a humidified atmosphere containing 5% CO_2. HeLa cells stably expressing DsRed2 were provided by Prof. Kazunari Taira and Dr. Yutaka Ikeda (Tokyo University) and were cultivated in a similar manner as above. Gel electrophoresis was performed with 0.7% agarose gel in Tris-acetate buffer and 20% polyacrylamide gel in Tris-borate-EDTA buffer for pGL3 and siRNA, respectively. Size distribution profiles (histograms) in reference to number of particles were obtained by NICOMP analysis of dynamic light scattering (DLS) data for solutions of pGL3 or siRNA (2 μM P) in water in the presence of varying amounts of octaamine **1** at 23 °C using a Particle Sizing Systems NICOMP 380 ZLS zeta potential/particle sizer at 100 mW green laser (532 nm). DLS measure-

* To whom correspondence should be addressed. Tel: +81-75-383-2766, Fax: +81-75-383-2767. E-mail: aoyamay@sbchem.kyoto-u.ac.jp.

10.1021/bc050112l CCC: $33.50 © 2006 American Chemical Society
Published on Web 12/17/2005

ments were also carried out for solutions of **1** with or without siRNA in the transfection medium Opti-MEM. However, the formation of big (≥50 nm) particles as a result of siRNA-independent aggregation processes prohibited detailed analysis of the **1**−siRNA complexes. Surface plasmon resonance (SPR) response curves were recorded on a BIAcore X system docked with a hydrophobized (HPA) sensor chip by repeated injection of an aqueous solution of octaamine **1** (100 μM, 25 μL) or siRNA (100 μM P, 25 μL) under the flow of degassed water (10 μL/min). Microscopic images were taken with an Olympus IX70 microscope.

Transfection and Subsequent Analysis. Cells (Hela, HepG2, or HEK293) were seeded at a density of 1.0×10^4 cells/well in a 96-well plate and cultivated. After 24 h, the cells became ~60% confluent and were washed with 100 μL of PBS(−) (magnesium/calcium-free phosphate buffer). To the cells in each well was added under cotransfection conditions a transfection medium (100 μL of Opti-MEM (GIBCO)) containing 200 ng of pGL3 (625 μM P) and 0, 2, 10, 42, or 126 ng of siRNA (0, 6, 30, 125, or 372 μM P) in the absence or presence of a carrier, octaamine **1** (1088 ng; **1**/P = 1.0 (N/P = 8.0) with respect to pGL3) or lipofectamine (500 ng, according to the manufacturer's protocol). After incubation for 6 h at 37 °C, the medium was replaced by 100 μL of fresh DMEM containing 10% FCS, and the cells were further incubated for 48 h. Under pretransfection conditions, the cells were first treated with an Opti-MEM solution (100 μL) containing siRNA (0, 2, 10, 42, or 126 ng) and octaamine **1** (1088 ng) or lipofectamine 2000 (500 ng) for 6 h, washed with 100 μL of PBS(−), and then transfected with pGL3 (200 ng) and lipofectamine (500 ng) in 100 μL of Opti-MEM. After 6 h, the medium was replaced by DMEM and incubation was continued for 48 h as above.

Luciferase assay was performed by the conventional chemiluminescence method using a Lumat LB5907 luminometer (Berthold Detection System) and the luciferase assay kit (Promega). Luciferase relative light units (RLU) integrated over 10 s are normalized for the total protein content of the cell lysate, obtained by the Bradford assay (Bio-Rad Laboratories) using bovine serum albumin as a standard. For MTT assay of lively cells, 20 μL of a solution of the MTT reagent (3-(4,5-dimethyl-2-thiazolyl)-2,5-diphenyl-2*H*-tetrazolium bromide) in PBS(−) (5 mg/mL) was added to each transfection mixture in a well. After incubation for 3 h, the medium was removed, a 10% SDS solution (200 μL) was added, and the absorbance at 570 nm of the resulting homogeneous solution was measured.

Gene silencing in HeLa cells stably expressing DsRed2 was carried out in essentially the same manner as above. After washing with PBS(−), the cells were dissolved in 25 μL of PLB (passive lysis buffer, Promega). The resulting solution was divided into two parts; one (2.5 μL) was analyzed for the total proteins and the other (20 μL) for the fluorescence intensity at 580 nm (excitation at 563 nm) after dilution with 380 μL of PBS(−).

RESULTS AND DISCUSSION

Complexation Behavior. The new carrier introduced here is a cone-shaped macrocyclic octaamine **1** (Figure 1), having four long alkyl (undecyl) chains and eight amino groups on the opposite sides of the calix[4]resorcarene macrocycle. It is obtained as octaammonium octachloride. Because of its amphiphilic structure, it is what may be called a covalently linked lipid bundle. The free-base compound served as precursor of glycocluster compounds (*18*, *19*) capable of stoichiometric gene coating to give transfectious "glycoviruses" (*16*, *20*). Cationic lipid aggregates (cationic liposomes) and polymers have so far been extensively used as nonviral gene carriers (*21*−*23*). While being a small molecule (mw, 1740), compound **1** unimolecularly

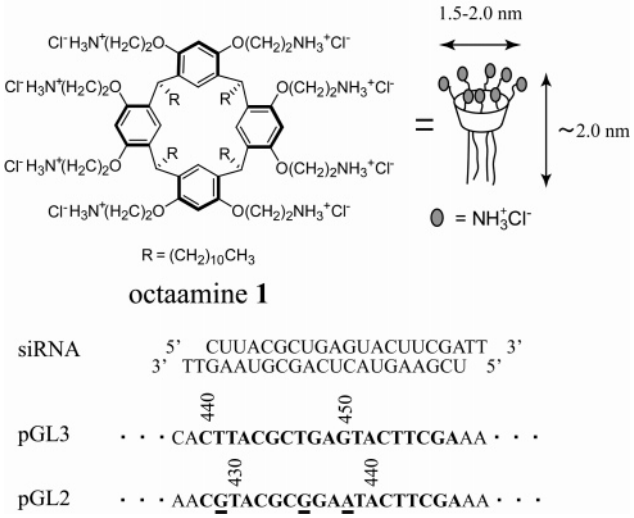

Figure 1. Structures of octaamine **1**, siRNA, and siRNA-relevant sequences (only sense strands are shown) of the luciferase genes in plasmids pGL3 and pGL2.

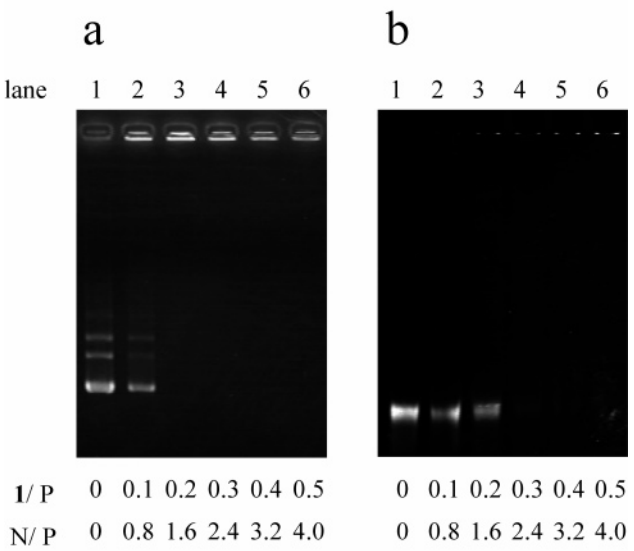

Figure 2. Electrophoretic gel shifts for pGL3 (a) and siRNA (b) in the absence (lane 1) and presence (lanes 2−6) of increasing amounts of octaamine **1** using 0.7% agarose gel in Tris-acetate buffer (a) or 20% polyacrylamide gel in Tris-borate-EDTA buffer (b); N and P stand for an ammonium group of octamine **1** and a phosphate moiety of the plasmid, respectively.

presents a characteristic amine/ammonium cluster motif with a well-defined geometry.

RNAi experiments were carried out using the same set of plasmid and siRNA (Figure 1) as used before (*8*). The plasmid is pGL3 (5256 base pairs) encoding a firefly protein luciferase under control of an SV40 promoter and an SV40 enhancer. The siRNA is a 21-mer duplex having two-nucleotide overhangs at the 3′-ends, the sense strand copying the 440−458 nucleotide sequence (shown in bold letters) of that of the luciferase gene in pGL3.

The complexation of octaamine **1** with pGL3 (a) and with siRNA (b) was monitored by gel (agarose and polyacrylamide, respectively) electrophoresis (Figure 2). The huge plasmid DNA duplex (pGL3) and the short linear RNA duplex (siRNA) are rendered completely immobile at a ratio of **1**/P in the range 0.1−0.2 (N/P 0.8−1.6) or 0.2−0.3 (N/P 1.6−2.4), respectively (N and P stand for an ammonium group of **1** and a phosphate moiety of DNA/RNA, respectively). Dynamic light scattering (DLS) also confirmed the complexation. When alone, octaamine

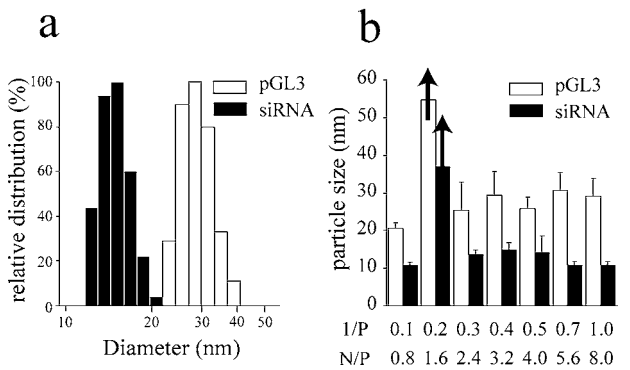

Figure 3. Typical size-distribution profiles (histograms) for the **1**−pGL3 and **1**−siRNA complexes at **1**/P = 0.4 (2 μM P) (a) and variation in the mean sizes thereof as a function of **1**/P or N/P (b) in reference to number of particles as evaluated by NICOMP analysis of the DLS data taken after 1 h from mixing of components. N and P stand for an ammonium group of octaamine **1** and a phosphate moiety of the plasmid, respectively.

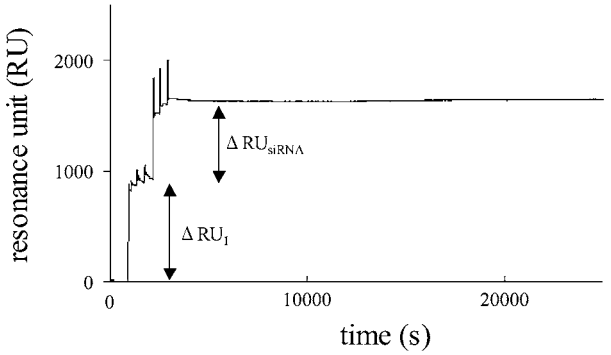

Figure 4. SPR response curve for the immobilization of octaamine **1** on a hydrophobized sensor chip and further adsorption of siRNA on the resulting monolayer of **1**. An aqueous solution of **1** (100 μM, 25 μL) or siRNA (100 μM P, 25 μL) was injected successively three times for immobilization of **1** or adsorption of siRNA, respectively, in the flow of water at a flow rate of 10 μL/min.

1 shows no tendency of forming aggregates of a size of ≥10 nm. However, in the presence of pGL3 or siRNA (2 μM P), the formation of particles (**1**-pGL3 or **1**−siRNA complexes) in that size range with a well-behaved size−distribution profile can be readily detected. In Figure 3a are shown typical histograms for the pGL3 and siRNA complexes at **1**/P = 0.4 (N/P = 3.2), both having a polydispersity index of 1.02. The mean sizes are plotted in Figure 3b as a function of **1**/P (N/P). The particle sizes are changeable and time-dependently grow at **1**/P = 0.2 (N/P = 1.6) probably as a result of cross-linking but are rendered time-stable and leveled off upon further increase in the amount of **1**. Saturation occurs at **1**/P ≅ 0.3 (N/P ≅ 2.4), and the saturation sizes for the **1**-pGL3 and **1**−siRNA complexes are d_{DLS} ≅ 30 and 10 nm, respectively, the latter being remarkably smaller than the size of cationic liposome−siRNA complexes (>100 nm) (*15*). The saturation ratio of **1**/P ≅ 0.3 or N/P ≅ 2.4 suggests that the complexation is primarily electrostatic in origin and that each siRNA molecule (42P) binds ∼12 molecules of **1**, having a width of 1.5−2.0 nm and a height of ∼2 nm (Figure 1). Amphiphile **1** in the cone shape may form small micelle-like nanoparticles but not huge vesicular/liposomal aggregates (*18*, *19*), and this may be at least partly why the present **1**−siRNA complex can be kept exceptionally compact (∼10 nm).

Surface plasmon resonance (SPR) shed more light on the **1**−siRNA interaction. Octaamine **1** (molecular weight, 1456) having four long alkyl chains can be readily immobilized on a hydrophobized (alkanethiol-coated) sensor chip (HPA) of SPR with an increase in resonance unit of ΔRU_1 = 960 (Figure 4). The latter, in light of the known relationship that ΔRU = 1000 corresponds to 1 ng/mm^2 of adsorbate, indicates that compound **1** is adsorbed with a packing density of 0.40 molecules/nm^2 or an occupation area of 2.5 nm^2/molecule, which is very close to the expected area of the octaammonium macrocycle with a diameter of 1.5−2.0 nm (Figure 1). Compound **1** must thus form a closely packed monolayer on the surface with its alkyl chains embedded in the hydrophobic forest of the sensor chip and the arrayed ammonium groups exposed to bulk water, as has been confirmed for the **1**-derived glycocluster compounds (*24*).

Treatment of the resulting **1**-coated sensor chip with siRNA gave a further increase in RU (Figure 4) as a result of adsorption of the siRNA (molecular weight per P or nucleotide, 320) via interaction with the ammonium groups on the surface. The interaction is strong or practically irreversible, since no notable dissociation of siRNA adsorbed was observed even after 24 h (ΔRU ≤ 20). The increase in RU of ΔRU_{siRNA} = 700 corresponds to a packing density of 1.3 P/nm^2 or an occupation area of 0.76 nm^2/P. These values, taken in conjunction with the corresponding values for octaamine**1** shown above, reveal the stoichiometry of **1**/P = 0.40/1.3 ≅ 0.3, which is in excellent agreement with that (**1**/P ≅ 0.3) evaluated from the DLS results. Neighboring phosphate groups in each strand of B-type duplex polynucleotides are separated by ∼0.7 nm from each other (*25*). The open conformation of the octaammonium motif of **1** has a diameter of ∼2 nm (Figure 1). Each molecule of **1** could thus cover three (2/0.7) P or nucleotide moieties with a stoichiometry of P/**1** ≅ 3. This is indeed what was observed (**1**/P ≅ 0.3). While the actual structure of complex **1**−siRNA is still not ready to be imaged, the present results and analysis suggest that (1) the anionic surface of siRNA is effectively coated with the cyclic array of the ammonium groups of rigid macrocycle **1** which is possibly micellized in small nanoparticles, (2) the coating stoichiometry is governed by steric factors, and (3) the resulting **1**−siRNA complex with insulated negative charges is free from further electrostatic aggregation.

Cotransfection. Cotransfection of cell culture was carried out by incubating HeLa (a human uterine cell line), HepG2 (a human hepatic cell line), or HEK293 (a human embryo kidney cell line) cells for 6 h in a transfection medium (Opti-MEM, 100 μL) containing a fixed amount (200 ng; 0.6 nM or 6.2 μM P) of pGL3 and a varying amount of siRNA in the presence of octaamine **1** as a carrier of both pGL3 and siRNA, followed by further incubation of the cells for 48 h in a fresh medium of DMEM (100 μL). The amount of carrier **1** (1088 ng per well) was set at **1**/P = 1.0 (N/P = 8) with respect to pGL3 to ensure complete complexation thereof. Each transfection mixture was analyzed for luciferase expression efficiency and for cytotoxicity. The cytotoxicity in reference to cell morphology and cell viability (Supporting Information) turned out to be slightly more pronounced than that of widely used lipofectamine 2000. In Figure 5 are shown the yields of luciferase, in terms of chemiluminescence relative light units (RLU) per mg total protein (top) or relative percentages (bottom), as a function of the amounts of siRNA (0, 2, 10, 42, and 126 ng; 0, 1.8, 7.0, 29, and 88 nM or 0, 0.08, 0.3, 1.2, or 3.7 μM P) for HeLa (a), HepG2 (b), or Hek293 (c) cells. The saturation-type yield-[siRNA] profile indicates that octaamine **1** acts as carrier for both pGL3 and siRNA. The **1**-mediated expression of luciferase becomes sharply suppressed with increasing amounts of siRNA but not perfectly. Thus, the suppression is evident at 2 ng of siRNA, reaches a plateau at ≥ 10 ng with 90−95% silencing, and remains in that level upon further increase in the amount of siRNA up to 126 ng. The suppression profiles with a 5−10% residual activity are remarkably similar or even superimposable for the three independent cell lines.

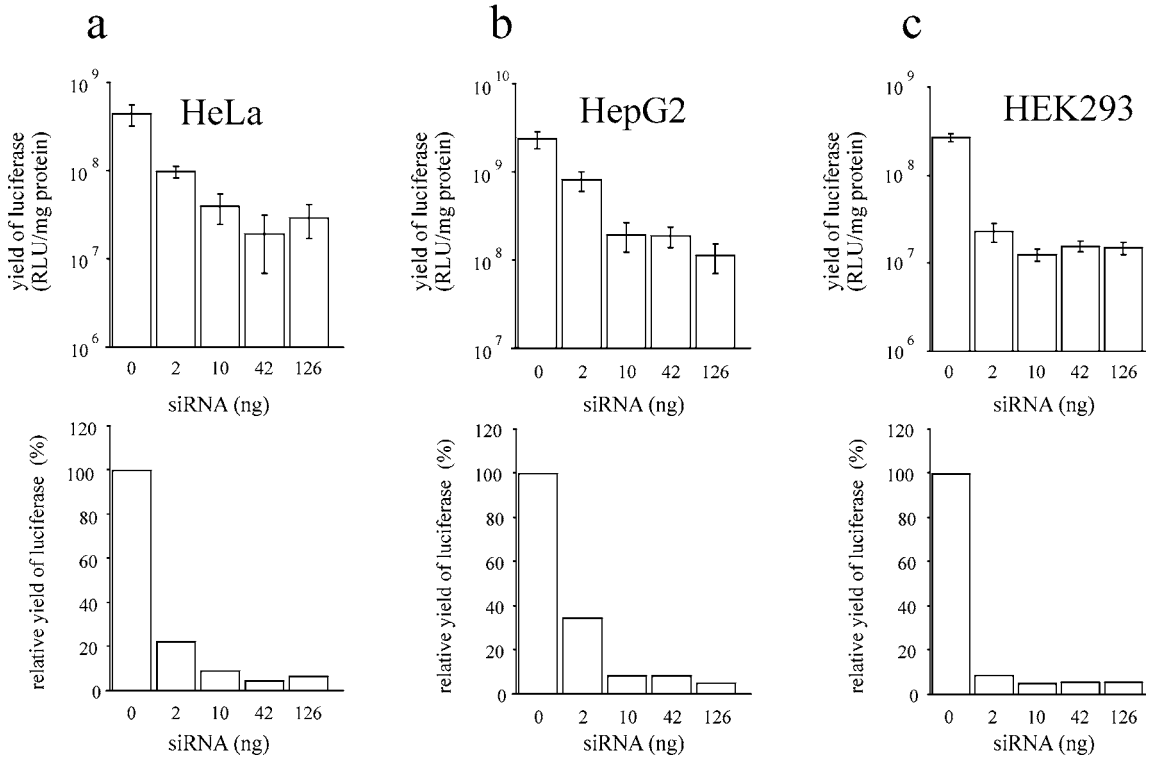

Figure 5. Transfection of HeLa (a), HepG2 (b), and HEK293 (c) cells under cotransfection conditions with siRNA and pGL3 (200 ng) as mediated by octaamine **1** (1088 ng). Yields of luciferase in terms of chemiluminescence relative light units (RLU) per mg total protein (top) or percentages relative to siRNA-free runs (bottom) are plotted as a function of the amounts of siRNA. Data are averages of about five experiments and error bars represent standard deviations.

Pretransfection. There are many conceivable explanations for the incomplete silencing. A simple one would assume that a small fraction (5−10%) of the cells cotreated with plasmid and siRNA actually incorporates only the plasmid and no siRNA for a statistical reason or as a result of competition between plasmid and siRNA. There is no way of efficient suppression in such plasmid(+)siRNA(− or Δ) cells. The question in a more general term is if or not the residual 5−10% activity arises anyhow from insufficient delivery of siRNA. If this is the case, the performance of the silencer siRNA might be improved when it is introduced in advance to enhance its population in the cells and to *wait* for its target, i.e., the mRNA coming from the plasmid taken afterward. If this pretransfection method is to work, the siRNA should be amply stable in the cells and should not seriously inhibit subsequent cellular uptake of the plasmid.

Thus, under the pretransfection conditions, the cells (HeLa, HepG2, or HEK293) were treated first with a mixture of siRNA (0−126 ng) and octaamine **1** (1088 ng) in Opti-MEM for 6 h, medium was removed, and the cells were washed for 1 h and then treated with a mixture of pGL3 (200 ng) and lipofectamine 2000 (500 ng) in Opti-MEM for 6 h, followed by further incubation for 48 h in a fresh medium of DMEM. It was in order to make the siRNA-delivery and plasmid-delivery steps distinguishable that we used different carriers for the plasmid and siRNA. We also used a reference gene contained in plasmid pGL2 (6047 base pairs) (Figure 1) (*8*). This also encodes luciferase but the key siRNA-relevant sequence (shown in bold letters) is different from that in pGL3 at three points underlined. Thus, the mRNA transcribed from pGL2 cannot be a target of the present siRNA. Each transfection mixture was analyzed for luciferase expression efficiency (Figure 6) and for cytotoxicity (Supporting Information), as above. An inspection of Figures 5 and 6 immediately shows that the overall feature remains unchanged as regards the general saturation profile and particularly the persisting 5−10% activity even at 126 ng of siRNA for the three different types of the cells. The siRNA introduced in the cells prior to the plasmid may competitively inhibit the uptake of the latter in a [siRNA]-dependent manner. This could explain the decreasing yields of luciferase with increasing [siRNA], but this cannot be the case. This is because the uptake of, and hence the expression of luciferase from, the RNAi-irrelevant pGL2 is not inhibited at all by the siRNA even at the highest 126 ng level (Figure 6, black bars). In this context, the [siRNA]-dependent suppression of pGL3 under the present pretransfection conditions should be ascribed to specific RNAi as in the case of cotransfection.

The similar suppression profiles under the cotransfection and pretransfection conditions can be interpreted as suggesting that cellular uptake of the plasmid and that of the siRNA are basically independent of (orthogonal with) each other. There is no evidence that the preintroduced siRNA notably inhibits subsequent uptake of the plasmid. There is no evidence either that the siRNA can be taken in the cells much more efficiently when alone under the pretransfection conditions than when in combination with the plasmid under the cotransfection conditions. Thus, the siRNA and the plasmid are not competitors with each other.

Control Runs. A couple of control runs were carried out. In one set of experiments, we used the pGL3-Promoter vector in place of pGL3; the former lacks the SV40 enhancer sequence which is present in the latter. With pGL3-Promoter, the nonsuppressed yields of luciferase at siRNA = 0 ng were one- or two-orders of magnitude lowered than those with the enhancer-containing pGL3 vector. Nevertheless, the general siRNA-suppression profile with a 5−10% residual activity under both cotransfection and pretransfection conditions (Supporting Information) remained remarkably the same as that shown in the bottom panels of Figures 5 and 6. In the other control, we carried out the same set of cotransfection and pretransfection experiments using lipofectamine 2000 in place of octaamine **1** under the otherwise identical conditions. All the results (shown in Supporting Information) not only reproduce the ∼90%

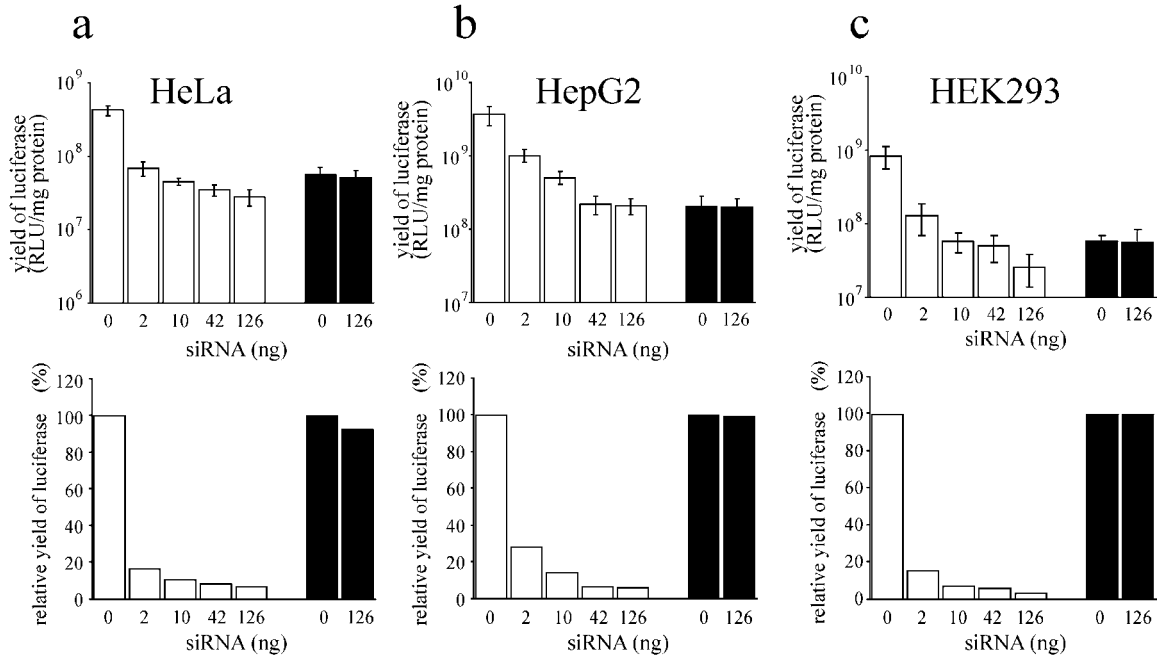

Figure 6. Transfection of Hela (a), HepG2 (b), and HEK293 (c) cells under pretransfection conditions with successive introduction of siRNA by the aid of octaamine **1** (1088 ng) followed by that of pGL3 (white bars) or pGL2 (black bars) (200 ng) by the aid of lipofectamine (500 ng). Yields of luciferase in terms of chemiluminescence relative light units (RLU) per mg total protein (top) or percentages relative to siRNA-free runs (bottom) are plotted as a function of the amounts of siRNA. Data are averages of about five experiments, and error bars represent standard deviations.

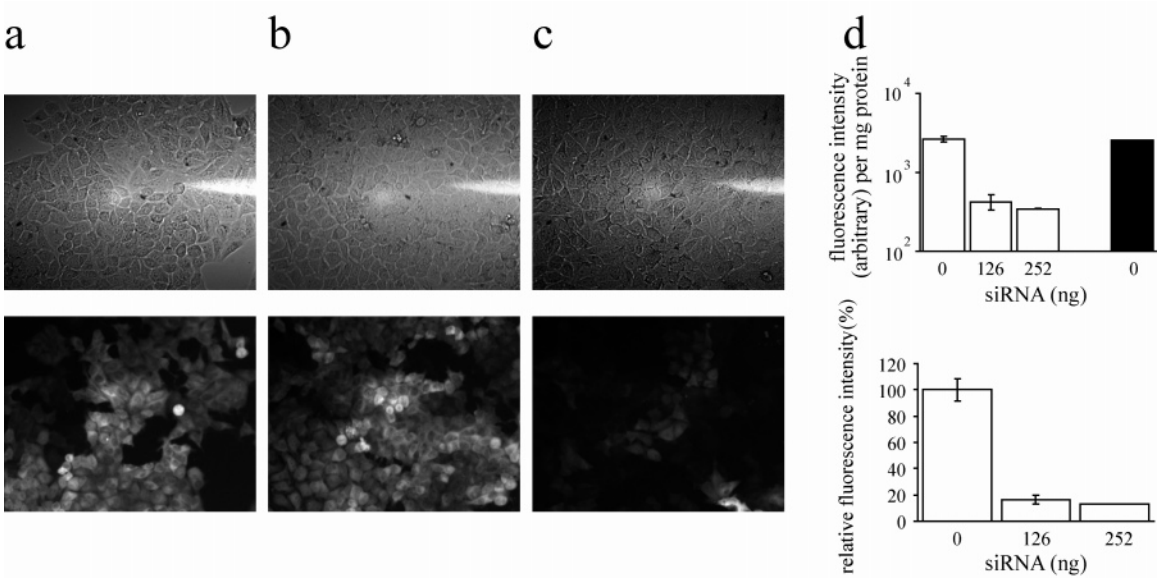

Figure 7. Optical micrographs (top) and their fluorescence images (bottom) of the DsRed2-expressing HeLa cells treated in Opti-MEM (100 μL) for 6 h. (a) In the presence of neither octaamine **1** nor siRNA, (b) in the presence of **1** (500 ng) without siRNA, and (c) in the presence of **1** (500 ng) and siRNA (126 ng). The fluorescence intensities (in arbitrary unit) normalized by the total protein content of the cell lysate (top) or as relative percentages (bottom) are plotted as a function of the amounts of siRNA in panel d. The black bar shows the reference intensity in the presence of neither **1** nor siRNA.

suppression previously reported (*8*) but also reveal that the overall feature with a saturation profile (*8, 12*) is essentially the same as that for octaamine **1** (Figures 5 and 6). Thus, the surviving 5−10% activity in the saturation range is neither cell-sensitive nor carrier-dependent, in accord with a previous report (*15*).

Silencing of Endogenous Gene. Silencing of endogenous gene is practically more significant and allows more direct evaluation of the performance of siRNA. The target gene here is that for fluorescent protein DsRed2 stably incorporated in the genome of HeLa cells. The latter constantly fluoresces at 580 nm when excited at 563 nm (Figure 7a). In the presence of the DsRed2-targeting siRNA (126 ng) conjugated with octaamine **1**, the otherwise fluorescent $HeLa_{DsRed2}$ cells were rendered remarkably nonfluorescent (Figure 7c) as a result of siRNA-silencing of the endogenous DsRed2 gene. The suppression is 84% or 87% in the saturation range of siRNA = 126 ng or 252 ng, as evaluated by referring to relative fluorescence intensities (Figure 7d). The residual activity of 13−16% of the present endogenous gene is slightly higher than that of 5−10% observed above in case of exogenous luciferase but the overall features (Figures 5 and 6 vs 7d) are quite similar to each other.

Residual Gene-Expression Activity. We have so far investigated the siRNA silencing of the exogenous luciferase gene using three cell lines, two expression vectors with or without

an enhancer, and two carriers under cotransfection and pretransfection conditions. Different cells have different transfectabilities, giving rise to different yields of luciferase at siRNA = 0 ng. The amounts of mRNA transcribed can be more directly changed by changing the expression vectors for a given cell type. The two carriers have different size properties. Octaamine **1** forms small particles which coat the plasmid or siRNA into a compact size (~30 or ~10 nm, respectively), while lipofectamine forms huge liposomes to which the plasmid or siRNA is attached (*26*). Nevertheless, the effects of increasing amounts of siRNA turned out to be essentially identical, leaving a 5−10% nonsuppressed gene-expression activity. Similar profiles are found in the literature (*9*−*15*). One report shows that the delivery efficacy of siRNA is not affected by the particle size (*15*). As far as residual activity is concerned, there is no essential difference between the exogenous luciferase and the endogenous DsRed2 genes to be silenced. The common profile should be interpreted as reflecting something essential rather than accidental.

It is beyond the scope of this work to go into the mechanistic aspect of RNAi. Obviously, however, the incomplete silencing should not be ascribed to insufficient (relative to mRNA in concern) siRNA delivery. Therefore, it is not a fault of the siRNA carrier. Formally, the mRNA transcribed would be captured either by the ribosome to get decoded into protein or by the RISC (RNA-induced silencing complex containing the antisense strand of siRNA) to give the mRNA−RISC adduct for cleavage. In terms of ribosome−RISC competition, the present results should be interpreted as suggesting that the competition is 90−95% in favor of the RISC pathway and 5−10% of the ribosome route irrespective of the cell type. Another possibility is that the mRNA is well saturated with the RISC, and it is the mRNA−RISC adduct itself that is responsible for the incomplete silencing. There has been considerable recent discussion on the formulation and functions of the RISCs (*26*). On the basis of the type of constituent proteins, these complexes can be divided into two general types, a cleaving RISC and a noncleaving RISC, which direct the complementary target mRNA either for cleavage or for translational repression, respectively. Even the cleaving RISC has such dual functions, depending on the base-pairing features between the small RNA and the target mRNA (*27*, *28*). It is tempting, although by no means convincing, to attribute the present 90−95/5−10 selectivity to the selectivity of the cleaving/noncleaving pathways.

CONCLUDING REMARKS

This work may be summarized as follows. (1) Cone-shaped quadruple-chain/octaammonium amphiphile **1** serves as a nonliposomal lipid capable of complexing plasmid DNA and siRNA in compact sizes of ~30 and ~10 nm, respectively. Its performance in vivo will be a subject of future work. (2) The carrier-mediated siRNA-silencing of reporter genes in the present type of cells is generally 90−95% at best. The residual ≥5% nonsilenced activity is most likely not a fault of the carrier but a fault of the RNAi process itself, where the choice of ~20-nucleotide target sequences of a given mRNA would be of a primary importance (*10*, *11*, *29*−*32*). The abilities of siRNA carriers should be judged in terms of such factors as minimal effective quantity (*8*), speed of action, maximal possible toxicity (*15*), versatility/selectivity (*33*), and particularly in vivo performance. (3) The plasmid and the siRNA are independent in their cellular uptake. The stepwise or pretransfection method works equally as the simultaneous or cotransfection procedure. Such a plasmid/siRNA orthogonality poses a new question. Is that because they are remarkably different in size, because one is DNA and the other RNA, or because the cellular uptake of nucleic acids is reversible to such an extent as to make the timing of supply less important? These remain to be better answered. From a practical point of view, controlled timing of introduction of siRNAs may find its unique application in the sequential knockdown of multiple genes, although possible interference between similarly sized plasmids and/or siRNAs should be kept in mind.

ACKNOWLEDGMENT

This work was supported by Grant-in-Aids for Scientific Research on Priority Areas (no. 16023230 and 16041222), Scientific Research (no. 16350087), and for 21st COE on Kyoto University Alliance for Chemistry from the Ministry of Education, Culture, Sports, Science, and Technology, Japan. We thank Prof. K. Taira and Dr. Y. Ikeda of Tokyo University for the generous gift of HeLa cells stably expressing DsRed2.

Supporting Information Available: Suppression profiles for lipofectamine 2000 as a carrier (Figures S1 and S2) and pGL3-Promoter as a control expression-vector (Figure S3), cell morphology (Figure S4), and cytotoxicity (Figure S5). This material is available free of charge via the Internet at http://pubs.acs.org/BC.

LITERATURE CITED

(1) Fire, A. (1999) RNA-triggered gene silencing. *Trends Genet. 15*, 358−363.

(2) Sharp, P. A. (2001) RNA interference 2001. *Genes Dev. 15*, 485−490.

(3) Tuschl, T. (2001) RNA Interference and small Interfering RNAs. *Chem. BioChem. 2*, 239−245.

(4) Hannon, G. J. (2002) RNA interference. *Nature 418*, 244−251.

(5) Wadhwa, R, Kaul, S. C., Miyagishi, M., and Taira, K. (2004) Vectors for RNA interference. *Curr. Opin. Mol. Ther. 6*, 367−372.

(6) Hammond, S. M., Bernstein, E., Beach, D., and Hannon, G. J. (2000) An RNA-directed nuclease mediates post-transcriptional gene silencing in Drosophila cells. *Nature 404*, 293−296.

(7) Hammond, S. M., Boettcher, S., Caudy, A. A., Kobayashi, R., and Hannon, G. J. (2001) Argonaute2, a link between genetic and biochemical analyses of RNAi. *Science 293*, 1146−1150.

(8) Elbashir, S. M., Harborth, J., Lendeckel, W., Yalcin, A., Weber, K., and Tuschl, T. (2001) Duplexes of 21-nucleotide RNAs mediate RNA interference in cultured mammalian cells. *Nature 411*, 494−498.

(9) Elbashir, S. M., Harborth, J., Weber, K., and Tuschl, T. (2002) Analysis of gene function in somatic mammalian cells using small interfering RNAs. *Methods 26*, 199−213.

(10) Kumar, R., Conklin, D. S., Mittal, and V. (2003) High-throughput selection of effective RNAi probes for gene silencing. *Genome Res. 13*, 2333−2340.

(11) Ui-Tei, K., Naito, Y., Takahashi, F., Haraguchi, T., Ohki-Hamazaki, H., Juni, A., Ueda, R., and Saigo, K. (2004) Guidelines for the selection of highly effective siRNA sequences for mammalian and chick RNA interference. *Nucleic Acids Res. 32*, 936−948.

(12) Chiu, Y.-L., and Rana, T. (2003) siRNA function in RNAi: a chemical modification analysis. *RNA 9*, 1034−1048.

(13) Ohnishi, Y., Tokunaga, K., and Hohjoh, H. (2005) Influence of assembly of siRNA elements into RNA-induced silencing complex by fork-siRNA duplex carrying nucleotide mismatches at the 3′- or 5′-end of the sense-stranded siRNA element. *Biochem. Biophys. Res. Commun. 329*, 516−521.

(14) Liu, J., Carmell, M. A., Rivas, F. V., Marsden, C. G., Thomson, M., Song, J.-J., Hammond, S. M., Joshur-Tor, L., and Hannon, G. J. (2004) Argonaute2 is the catalytic engine of mammalian RNAi. *Science 305*, 1437−1441.

(15) Spagnou, S., Miller, A. D., and Keller, M. (2004) Lipidic carriers of siRNA: differences in the formulation, cellular uptake, and delivery with plasmid DNA. *Biochemistry 43*, 13348−13356.

(16) Nakai, T., Kanamori, T., Sando, S., and Aoyama, Y. (2003) Remarkably size-regulated cell invasion by artificial viruses. Sac-

charide-dependent self-aggregation of glycoviruses and its consequence in glycoviral gene delivery. *J. Am. Chem. Soc. 125*, 8465−8475.
(17) Maeda, H., Wu, J., Sawa, T., Matsumura, Y., and Hori, K. (2000) Tumor vascular permeability and the EPR effect in macromolecular therapeutics: a review. *J. Controlled Release 65*, 271−284.
(18) Hayashida, O. Mizuki, K., Akagi, K., Matsuo, A., Kanamori, Y., Nakai, T., Sando, S., and Aoyama, Y. (2003) Macrocyclic glycoclusters. Self-aggregation and phosphate-induced agglutination behaviors of calix[4]resorcarene-based quadruple-chain amphiphile with a huge oligosaccharide pool. *J. Am. Chem. Soc. 125*, 3455−3457.
(19) Aoyama, Y. (2004) Macrocyclic glycoclusters. From amphiphiles through nanoparticles to glycoviruses. *Chem. Eur. J. 10*, 588−593.
(20) Aoyama, Y., Kanamori, T., Nakai, T., Sasaki, T., Horiuchi, S., Sando, S., and Niidome, T. (2003) Artificial viruses and their application to gene delivery. Size-controlled gene coating with glycocluster nanoparticles. *J. Am. Chem. Soc. 125*, 3455−3457.
(21) Felgner, P. L., Gadek, T. R., Holm, M., Roman, R., Chan, H. W., Wenz, M., Northrop, J. P., Ringold, G. M., and Danielsen, M. (1987) Lipofection: a highly efficient, lipid-mediated DNA-transfection procedure. *Proc. Nat. Acad. Sci. U.S.A. 84*, 7413−7417.
(22) Behr, J.-P. (1993) Synthetic gene-transfer vectors. *Acc. Chem. Res. 26*, 274−278.
(23) Kabanov, A. V., Felgner, P. L., and Seymour, L. W., Eds. (1998) Self-Assembling Complexes for Gene Delivery. *From Laboratory to Clinical Trial*, Wiley, Chichester.
(24) Hayashida, O., Shimizu, T., Fujimoto, T., and Aoyama, Y. (1998) Surface Plasmon Resonance Study on the Interaction of Immobilized Macrocyclic Sugar Clusters with Lectins and Water-Soluble Polymers. *Chem. Lett.* 13−14.
(25) Saenger, W. (1983) *Principles of Nucleic Acid Structure*, Springer-Verlag, New York, Chapter 9.
(26) Tang, G. (2005) siRNA and miRNA: an insight into RISCs. *Trends Biochem. Sci. 30*, 106−114.
(27) Hutvagner, G., and Zamore, P. D. (2002) A microRNA in a multiple-turnover RNAi enzyme complex. *Science 297*, 2056−2060.
(28) Tang, G., Reinhart, B. J., Bartel, D. P., and Zamore, P. D. (2003) A biochemical framework for RNA silencing in plants. *Genes Dev. 17*, 49−63.
(29) Kawasaki, H., Suyama, E., Iyo, M., and Taira, K. (2003) siRNAs generated by recombinant human Dicer induce specific and significant but target site-independent gene silencing in human cells. *Nucleic Acids Res. 31*, 981−987.
(30) Amarzguioui, M., and Prydz, H. (2004) An algorithm for selection of functional siRNA sequences**.** *Biochem. Biophys. Res. Commun 316*, 1050−1058.
(31) Saxena, S., Jonsson, Z. O., and Dutta, A. (2003) Small RNAs with imperfect match to endogenous mRNA repress translation: implications for off-target activity of small inhibitory RNA in mammalian cells. *J. Biol. Chem 278*, 44312−44319.
(32) Reynolds, A., Leake, D., Boese, Q., Scaringe, S., Marshall, W. S., and Khvorova, A. (2004) Rational siRNA design for RNA interference. *Nature Biotech. 22*, 326−330.
(33) Oishi, M., Nagasaki, Y., Itaka, K., Nishiyama, N., and Kataoka, K. (2005) Lactosylated poly(ethylene glycol)-siRNA conjugate through acid-labile β-thiopropionate linkage to construct pH-sensitive polyion complex micelles achieving enhanced gene silencing in hepatoma cells. *J. Am. Chem. Soc. 127*, 1624−1625.

BC050112L

Biodegradable Nanoparticles for Direct or Two-Step Tumor Immunotargeting

Leila Nobs,[†] Franz Buchegger,[‡] Robert Gurny,*[,†] and Eric Allémann[†,§]

Department of Pharmaceutical Technology and Biopharmaceutics, School of Pharmaceutical Sciences, Ecole de Pharmacie Genève-Lausanne, University of Geneva, Quai Ernest-Ansermet 30, 1211 Geneva 4, Switzerland, and Service of Nuclear Medicine, University Hospital of Geneva, Rue Micheli-du-Crest 24, 1211 Geneva 14, Switzerland. Received May 11, 2005; Revised Manuscript Received September 9, 2005

In this study, selective cancer cell targeting of biodegradable poly(lactic acid) (PLA) nanoparticles (NPs) has been investigated in vitro. SKOV-3 (HER2 positive) ovarian cancer and Daudi (CD20 positive) lymphoma cell targeting was mediated by anti-HER2 (trastuzumab, Herceptin) and anti-CD20 (rituximab, Mabthera) monoclonal antibodies (mAbs), respectively. The mAb against nonexpressed antigen serving on each cell as isotype matched irrelevant control. Two different targeting approaches have been studied, a direct method using antibody-labeled NPs (mAb-NPs) and a pretargeting method using the avidin−biotin technology. For the direct protocol, fluorescent PLA-NPs were prepared including 10% 1-pyrenebutanol (PB)-labeled PLA in the NP-preparation (PB-NP). Thiol groups were covalently bound to the PB-NP, and the resulting thiolated PB-NP were coupled with the two mAbs using a bifunctional cross-linker. The effective targeting of cells by mAb-PB-NP was shown by flow cytometry analysis. Clearly anti-HER2-PB-NP specifically bound to the SKOV-3 cells and not to the Daudi cells, while anti-CD20-PB-NPs bound to Daudi cells but not to SKOV-3 cells. Specific mAb-PB-NP binding to tumor cells produced a mean 10-fold or higher signal increase compared to irrelevant IgG-PB-NPs. For the pretargeting protocol, plain PLA-NPs were also thiolated and NeutrAvidin-Rhodamine Red-X (NAR) coupled to the functionalized PLA-NPs with sulfo-MBS. The two-step method was evaluated in vitro by incubating SKOV-3 cells first with biotinylated mAbs followed by NAR-NPs. The relative fluorescence associated to the specific binding of NPs produced a 6-fold increase in flow cytometry signal compared to nonspecific binding. In conclusion, these experiments have shown that NPs covalently coupled with antibodies or NAR can specifically and efficiently bind to cancer cells in both a pretargeting and a direct approach, suggesting that functionalized NPs may be a useful drug carrier for tumor targeting.

INTRODUCTION

One of the major problems facing cancer chemotherapy is the undesirable side effects. These are mainly of nonspecific nature due to distribution of the chemotherapeutic drugs to tissues other than tumor. To overcome the undesirable side effects and to increase local concentration of the drug at the target site, several drug-delivery systems have been investigated, such as drug−polymer conjugates (*1*), liposomes (*2*, *3*), micelles (*4*, *5*), and polymeric nanoparticles (NPs)[1] (*6*, *7*). Colloidal carrier systems, such as liposomes and NPs, present some relevant advantages over other drug carriers: (a) a high drug loading capacity; (b) the possibility to control size and permeability of the carrier; (c) the protection of the encapsulated drug from metabolism or early excretion. Among the different carriers, biodegradable NPs emerged as suitable means of carrying bioactive molecules to tissues of interest, especially due to their long shelf life, to the potential for control of release rate of the drug, and to the well established methods of preparation (*8*, *9*). Furthermore, long circulating "stealth" nanoparticles such as poly(ethylene glycol)-coated NP (PEG-NP) have proved to greatly enhance the therapeutic index of the drug (*10*−*12*). In fact, owing to their prolonged circulation time in blood, they more readily accumulate in areas with leaky vasculature, such as tumors, than plain NPs. However, a long-circulation time of NPs might be insufficient to obtain tumor control since a specific interaction with tumor cells does not occur. A promising strategy to achieve direct drug delivery is the development of active targeting of cancer cells via interactions mediated by ligands such as antibodies, lectins, and peptides, as presented with liposomes (*13*, *14*).

Active tumor targeting of NPs may be achieved with either direct targeting or the pretargeting-multistep method. In direct targeting, NPs should be covalently coupled with the ligand and the resulting drug carrier be administered at once. In the pretargeting approach, the therapeutic molecule is not coupled with the ligand and is administered after an appropriate delay time following the targeting ligand. This delay allows time for the antibody to localize and concentrate in the tumor. Commonly, pretargeting protocol involves an avidin−biotin system (*15*) or bispecific antibodies (*16*).

In this study, we explored the two approaches to target biodegradable poly(lactic acid) (PLA) NPs to tumor cells. Anti-HER2 mAbs (trastuzumab, Herceptin) and anti-CD20 mAbs (rituximab, Mabthera) were used as targeting ligands. Two cell lines were used, SKOV-3 human ovarian cancer cells expressing HER2 antigen, and Daudi lymphoma cells, expressing CD20 antigen. On each cell line, the antibody directed against the nonexpressed antigen served as isotype-matched irrelevant control immunoglobulin. In the direct approach, NPs exposing mAbs at their surface were incubated with the two tumor cell

* Corresponding author: Robert Gurny, Phone: +41 22 379 61 46. Fax: +41 22 379 65 67. E-mail: Robert.Gurny@pharm.unige.ch.

[†] University of Geneva.

[‡] University Hospital of Geneva.

[§] Current address: Bracco Research SA, Route de la Galaise 31, 1228 Plan-les-Ouates, Geneva, Switzerland.

[1] Abbreviations: PLA, poly(lactic acid); FACS, fluorescence-activated cell sorting; NAR, NeutrAvidin Rhodamine Red-X.; NP, nanoparticle; mAb, monoclonal antibody; mAb-NP, mAb labeled nanoparticle; NAR-NPs, NeutrAvidin-labeled NP.; PB-NP, 1-pyrenebutanol loaded NP.; mAb-biot, biotinylated mAb; sulfo-MBS, *m*-maleimidobenzoyl-*N*-hydroxysulfosuccinimide ester.

10.1021/bc050137k CCC: $33.50 © 2006 American Chemical Society
Published on Web 12/02/2005

lines. In the pretargeting protocol, tumor cells were pretargeted with biotinylated mAbs prior to the administration of avidin-labeled NPs. Cell interaction of fluorescence-labeled NPs was measured by flow cytometry.

EXPERIMENTAL PROCEDURES

Materials. Poly(DL-lactic acid) (PLA) (100DL 4A, Mw 57 kDa) was a gift from Alkermes (Cincinnati, OH). 4-Hydroxyazobenzene-2-carboxylic acid (HABA) and phosphate-buffered saline (PBS) were from Sigma (Buchs, Switzerland). *m*-Maleimidobenzoyl-*N*-hydroxysulfosuccinimide ester (sulfo-MBS), sulfosuccinimidyl 6-(biotinamido)hexanoate (sulfo-NHS-LC-biotin), BCA protein assay kit, and D-Salt dextran plastic desalting columns were supplied by Pierce (Rockford, IL). NeutrAvidin Rhodamine Red-X (NAR) was from Molecular Probes (Leiden, The Netherlands).

Cell Lines. SKOV-3, human ovarian carcinoma cells expressing HER2, and Daudi, human B lymphoma cells expressing CD20 (American Type Culture Collection ATCC, Manassas, VA), were cultured in 75-cm^2 culture flasks in RPMI-1640 with Glutamax I (Gibco, Grand Island, NY) supplemented with 10% fetal calf serum (FCS) (Brunschwig, Basle Switzerland), 100 units/mL of penicillin, and 100 μg/mL of streptomycin (Gibco) in an atmosphere of 95% humidified air and 5% CO_2 at 37 °C. Cells were maintained in exponential growth using adequate splitting and renewal of medium. SKOV-3 cells were maintained as a monolayer, and for all the experiments, cells were harvested from subconfluent cultures using trypsin-EDTA (Gibco) and were resuspended in fresh complete medium. Unless stated otherwise, all in vitro studies were performed at 37 °C under gentle rotation in tubes containing phosphate-buffered saline (PBS) with 0.1% bovine serum albumin.

Biotinylated Antibodies. Antibodies for targeting assay included the anti-HER2 mAb (trastuzumab, Herceptin) and anti-CD20 mAb (rituximab, Mabthera) (Roche, Basle, Switzerland). Prior to the coupling reactions, the antibodies were purified by size exclusion chromatography using a D-Salt dextran plastic desalting column.

For the pretargeting approach, anti-HER2 and anti-CD20 mAbs were biotinylated as follows: 1 mL of purified mAbs (5 mg/mL) was mixed with sulfo-NHS-LC-biotin in bicarbonate buffer (pH 8.3) at a molar reaction ratio of 5 molecules of biotins per mAb molecule. After incubation for 1 h at room temperature, the unconjugated sulfo-NHS-LC-biotin molecules were removed from the mixture by size exclusion chromatography using a D-Salt dextran plastic desalting column. The fractions containing mAb were pooled, and the mAb concentration was determined by absorbance at 280 nm assuming an extinction coefficient of 1.4 M^{-1} cm^{-1} $(mg/mL)^{-1}$. The molar ratio of mAb-to-biotin was assessed by the colorimetric method using the dye 4-hydroxyazobenzene-2-carboxylic acid (HABA) (*17*). The biotinylated mAbs (mAb-biot) were stored at 4 °C until use.

The capacity of biotinylated mAbs to bind to cells was assessed in vitro on both SKOV-3 and Daudi cells using a two-step targeting protocol. SKOV-3 or Daudi cells in suspension (5×10^5 cells/mL) in PBS were incubated with 100 μg/mL of either biotinylated anti-HER2 or biotinylated anti-CD20 mAbs during 2 h. Unbound antibodies were removed by three successive centrifugations (400*g*, 5 min). Thereafter, 4 μL of NAR (1 mg/mL) were added to the cells and incubated for 1 h. The cells were rinsed with cold PBS three times before being analyzed by flow cytometry as described below.

Nanoparticles Coupled with NeutrAvidin Rhodamine Red-X. Plain NPs were prepared by a salting-out method according to a previously described method (*18*). Thiol functions were covalently bound to the surface of the plain nanoparticles to allow the subsequent covalent binding of ligands to the NPs. Optimization of the reaction conditions and characterization of the thiolated NPs has been presented elsewhere (*19*). Briefly, carboxylic acid groups of PLA NPs were activated with 1-Ethyl-3-(3-dimethylaminopropyl)carbodiimide (EDAC) to allow the covalent binding of cystamine. Thereafter, disulfide bonds of cystamine were reduced using Tris(2-carboxyethyl)phosphine (TCEP). Thiolated NPs were subsequently used to covalently bind mAbs for the direct approach or NeutrAvidin Rhodamine Red-X (NAR) for the pretargeting protocol. The preparation and characterization of NAR-labeled NPs (NAR-NPs) has been described previously (*20*).

Antibody Coupling to Fluorescent Nanoparticles for Direct Targeting. Fluorescent NPs were prepared by the salting-out process with 10% (w/w) of 1-pyrenebutanol-labeled PLA and 90% of unlabeled PLA (*21*). The fluorescent polymer, 1-pyrenebutanol-labeled PLA, was used in this experiment as a fluorescent tracer for flow cytometry analysis. The fluorescence excitation and emission spectra of 1-pyrenebutanol contained in the NPs were determined in PBS (FluoroMax spectrofluorometer, Spec Indutries, NJ). The mean Z size of the labeled NPs was determined by dynamic light scattering (Malvern Instruments, Ltd, UK).

Thiol functions were covalently bound to fluorescent NPs as described above and the resulting thiolated PB-NP were coupled to purified Herceptin or Mabthera using the bifunctional cross-linker, sulfo-MBS. mAbs (2 mg/mL) were incubated over 45 min at room temperature with sulfo-MBS in PBS (pH 7.4) at four different molar ratios, 1:5; 1:10; 1:20; 1:40 (mAb:sulfo-MBS). The excess of sulfo-MBS was removed from the mixture by size exclusion chromatography using the desalting columns. The fractions containing the maleimide-activated mAbs were collected, and their concentration was determined. Thereafter, 500 μL of mAb (1 mg/mL) was incubated with 500 μL of thiolated PB-NP (20 mg/mL) and gently shaken for 60 min at room temperature. Subsequently, the uncoupled mAbs were removed by four cycles of centrifugation (20000*g*, 10 min). The supernatant of the centrifugation step was used for the determination of uncoupled mAb by a BCA assay (microplate procedure). Finally, mAb-conjugated NPs (mAb- PB-NP) were stored in PBS at 4 °C. Trials were carried out on plain PB-NP (without thiol functions) to determine the fraction of noncovalently attached mAb on the surface of the NPs.

Nanoparticle Binding. For the direct targeting, 100 μL of a 1 mg/mL suspension of specific or irrelevant mAb-PB-NP was incubated for 45 min with 5×10^5 SKOV-3 or Daudi cells. Cells were rinsed with three successive centrifugation steps (400*g*, 5 min) with cold PBS to remove unbound nanoparticles, and the mean relative fluorescence was measured by cytometry analysis.

For pretargeting experiments, SKOV-3 cells (5×10^5 cells/ml) were incubated for 2 h with 100 μg/mL of biotinylated anti-HER-2 or anti-CD20 mAbs (negative control). PBS containing unbound mAb was removed, and cells were washed with two cycles of successive centrifugations (400*g*, 5 min). Subsequently, 100 μL of a 1 mg/mL suspension of NAR-NPs was added, and cells wrer incubated for 1 h. Three successive centrifugation steps (400*g*, 5 min) with cold PBS were carried out to remove unbound NAR-NPs and resuspended in PBS for flow cytometry analysis.

For both targeting approaches, parallel incubations were performed with unlabeled NPs and with irrelevant mAbs to assess the nonspecific interaction of the nanoparticles with cells. Other controls included the incubation during 45 min of free mAb (100 μg) prior to the incubation of mAb-PB-NP or NAR-NPs.

Flow Cytometry Analysis. The capacity of mAb-NP−BPs and of biotinylated mAbs to bind cells was analyzed using flow

cytometry. The cells were suspended in 500 μL of cold PBS prior the measurements. For the pretargeting protocol, mean fluorescence intensity of 10000 cells was analyzed using a FACSfits cytometer (Becton Dickinson, San Jose, CA) equipped with an argon-ion laser adjusted to 488 nm. For the direct targeting method, the mean fluorescence intensity was measured using a FACSVAntage flow cytometer (Becton Dickinson, San Jose, CA). The excitation of 1-pyrenebutanol (PB-NP) was performed using an UV laser with two wavelengths at 351 and 364 nm (Coherent Laser, Inc. Santa Clara, CA) set at 20 mW. The emission signal was analyzed using the reading channel FL5-H corresponding to wavelengths ranging from 383 to 407 nm. Median fluorescence *F* was calculated using Cellquest software (Becton Dickinson) with the results presented as relative cell number versus log fluorescence intensity. Cells incubated with only PBS were used for background fluorescence calibration.

RESULTS

Fluorescent, Thiolated Nanoparticles. Plain NPs and fluorescent NPs were obtained by a salting-out procedure (18). For the fluorescent labeling of NP, the 1-pyrenebutanol-PLA conjugate was used at 10% of unconjugated PLA. Both plain NPs and fluorescent NPs (PB-NP) showed very similar characteristics in terms of particle size and redispersibility. The mean size of the plain NPs and PB-NP was 265 and 270 nm, respectively. After freeze-drying the NPs or PB-NPs, complete redispersion of all formulations could be achieved in water. Spectofluorimetric assay revealed that the PB-NP were efficiently loaded with 1-pyrenebutanol-PLA (results not shown). Further results suggested that notably no subsequent spontaneous release occurred. The maximum for the excitation and emission wavelengths of 1-pyrenebutanol NPs was found at 375 and 390 nm, respectively.

The thiolation reaction was very reproducible on both fluorescent and nonfluorescent NPs with an incorporation of 104 $\pm$ 2 mmol of thiol functions per mol of PLA, for nonfluorescent NPs and 89 $\pm$ 10 mmol for PB-NP. The average size of plain NPs and PB-NP after the thiolation reaction was 278 and 297 nm, respectively, corresponding to a size increase of 5 to 10% only compared to the original size.

Direct Coupling with Antibodies. The coupling reaction between the two different mAbs and the thiolated PB-NP was carried out in the presence of the bifunctional cross-linker sulfo-MBS. Four different molar ratios of sulfo-MBS to mAbs were evaluated. An equal concentration of maleimide-mAb was used for all the coupling reactions with thiolated PB-NP. Figure 1 summarizes the results of the coupling reaction between maleimide-mAbs and thiolated PB-NP. For both anti-CD20 and anti-HER2 mAbs the amount of mAbs bound to the surface of the PB-NP increased when an increased molar ratio between mAbs and sulfo-MBS was used. Amounts of 1.5, 2.5, and 5.6 mmol of mAbs per mol of PLA were bound to the PB-NP using a mAbs to sulfo-MBS molar ratio of 1:10, 1:20, and 1:40, respectively. These three formulations were retained for the in vitro studies. At the lowest molar ratio between sulfo-MBS and mAbs (1:5), no coupling of mAbs to the surface of the nanoparticles could be demonstrated. Between 2500 and 2700 mAbs (25 to 27% of total mAb) were coupled to the thiolated PB-NP surface at the highest molar ratio of sulfo-MBS. This corresponds to coupling of approximately 19% of the total measurable thiol functions on the surface of NPs. Control reactions on PB-NP lacking thiol functions showed that only a minor amount of mAbs (2.8%) bound nonspecifically to the particles. The average size of the mAb-PB-NP after the coupling reaction was ranging from 340 to 410 nm, depending on the amount of mAbs bound to the particles.

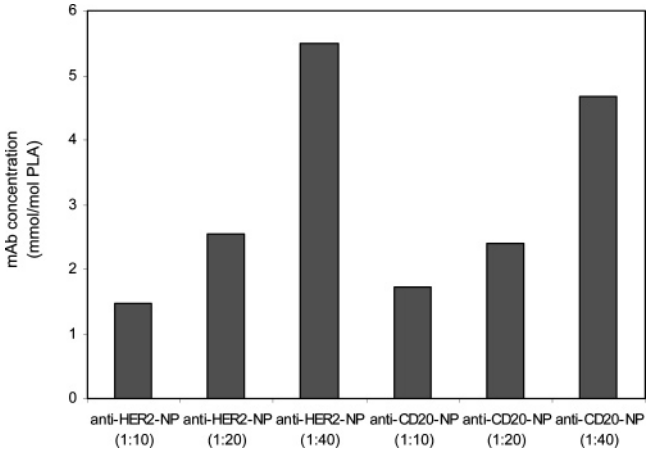

Figure 1. Summary of the coupling reaction between thiolated NPs and mAbs (anti-HER2 and anti-CD20 mAbs). Influence of the molar ratio (mAb:sulfo-MBS, values given in parentheses) on the coupling reaction on the ratio of mAbs obtained at the surface of the NPs.

NeutrAvidin-Rhodamine Red-X-Coupled NPs. After activation of NAR with sulfo-MBS, 500 μL of the activated NAR solution (360 μg/mL) was used for the coupling reaction with an equal volume of NPs (20 mg/mL). The quantification of the fluorescent Neutravidin on the NP surface revealed that 5.0 mmol of NAR per mol of PLA was covalently attached to the surface of the NAR-NP, corresponding to approximately 1300 molecules of NAR per NP. In control reactions the concentration of activated NAR nonspecifically bound to nonthiolated NPs was as low as 0.6 mmol of NAR per mol of PLA. The mean particle size increased from 278 nm before coupling to 320 nm after the coupling reaction.

Biotinylation of Antibodies. The water-soluble NHS-LC-biotin was chosen due to its extended spacer arm that limits steric hindrance and provides optimal reactivity with avidin and permits the biotin to reach the lysine groups (*22*). Starting with a NHS-LC-biotin-to-antibody molar ratio of 5:1, an average of three molecules of biotin was introduced per antibody molecule, as determined in the colorimetric assay with HABA reagent. The ability of biotinylated mAbs to bind to specific antigens was assessed in vitro with a two step-targeting protocol using free NAR. Anti-HER2 bound specifically to SKOV-3 cells but not to Daudi cells. On the contrary, anti-CD20 interacted with Daudi cells, but not with SKOV-3 cells (Figures 2A and 2B). Results of a competition assay with radiolabeled Rituximab indicated that the immunoreactivity of Rituximab coupled with 3 to 4 NHS-LC-biotin per antibody molecule as measured with the HABA assay was only slightly impaired with loss of about 25% compared with native Rituximab. Higher biotinylation degrees of the antibody resulted in stronger impairment of the immunoreactivity in this assay (data not shown).

Direct Targeting. The three retained PB-NP formulations were tested for each type of mAb. The targeting of SKOV-3 showed that all anti-HER2 formulations bound specifically to the cells. Whereas, when anti-CD20-PB-NP were incubated with SKOV-3 cells only little cell interaction was observed compared with plain NPs and no significant difference was observed among the three anti-CD20-PB-NP formulations (Figures 3A and 4A).

The binding efficiency of targeted NP to the cells was dependent on the mAb:sulfo-MBS ratio, since increased fluorescence was observed for the 1:20 molar ratio compared with 1:10. However, the highest ratio of sulfo-MBS (1:40) that resulted in the highest amount of antibody coupled per NP showed the lowest binding among the three NP formulations, suggesting that this formulation resulted in significant inactivation of antibody. Based on these results, the optimum molar

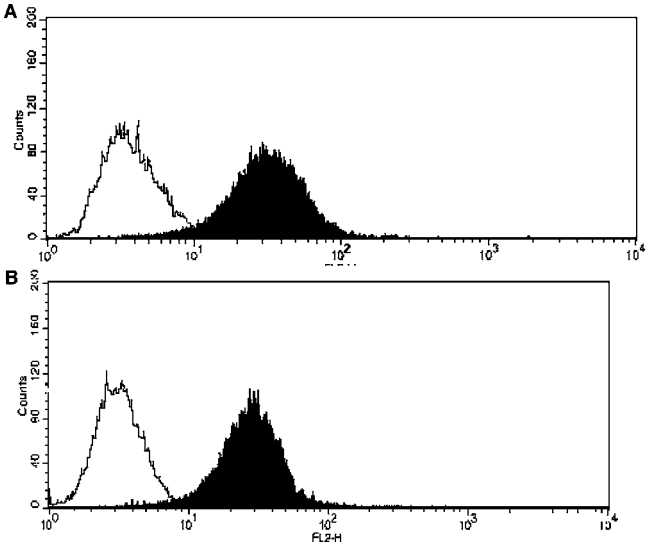

Figure 2. Flow cytometry analysis of biotinylated mAbs biding to SKOV-3 and Daudi cells. (A) SKOV-3 cells were preincubated with biotinylated anti-HER2 (black peak) or biotinylated anti-CD20 (white peak) followed by NAR. B) Daudi cells were preincubated with biotinylated anti-CD20 (black peak) or biotinylated anti-HER2 (white peak) followed by NAR.

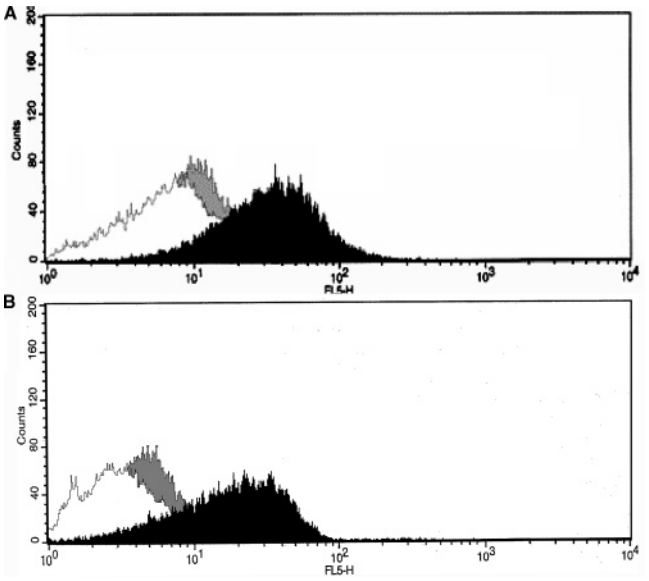

Figure 3. Direct targeting protocol. Flow cytometry analysis of targeted PB-NP binding to SKOV-3 and Daudi cells. (A) SKOV-3 cells were incubated with either anti-HER2−PB-NP (black peak) or anti-CD20-PB-NP (grey peak) during 45 min. (B) Daudi cells were incubated with either anti-CD20-PB-NP (black peak) or anti-HER2−PB-NP (grey peak) during 45 min. Cells incubated alone were used as background fluorescence (white peak).

ratio used was 1:20 (mAb:sulfo-MBS). This anti-HER2−PB-NP formulation showed significantly higher binding activity up to 13-fold than the equivalent anti-CD20-NPs formulation.

The targeting ability of the same mAb-PB-NP reagents was also assessed on Daudi cells. A very similar result as on SKOV-3 was again observed on Daudi cells with strong interaction of the specific mAb-coupled NPs and low background activity with irrelevant mAb. At the 1:20 molar ratio of activation with sulfo-MBS, binding impairment was also observed with rituximab (Figures 3B and 4B). The 1:20 anti-CD20-NP formulation showed up to 10-fold higher binding activity than anti-HER2-NPs in cells expressing CD20 antigens. No significant difference was observed among the three anti-HER2-NP formulations.

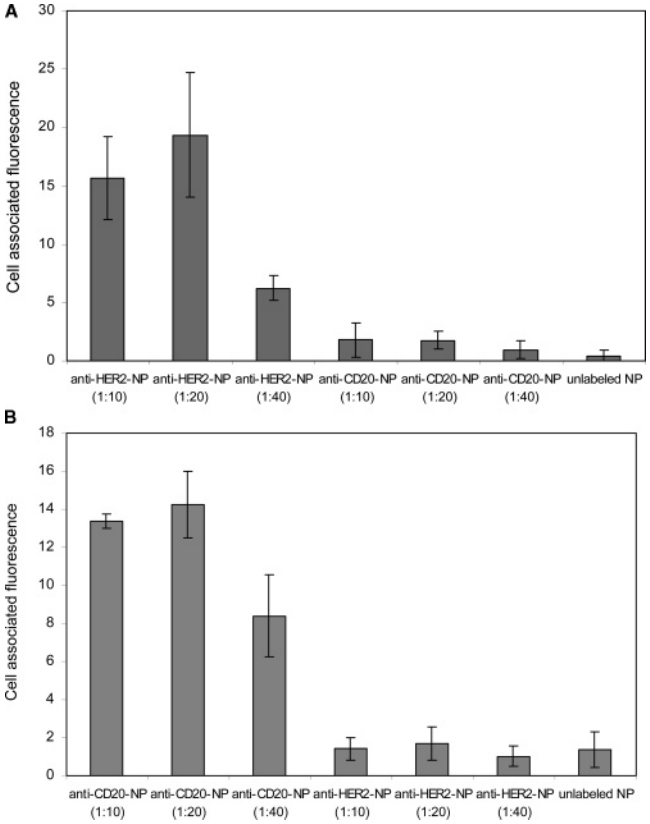

Figure 4. Direct targeting protocol. Effect of mAb:sulfo-MBS ratio on the binding capacity of mAbs-NPs to specific antigens expressed on the surface of the cells. (A) Anti-HER2-NPs incubated with SKOV-3 cells using anti-CD20-NPs and unlabeled NPs as negative controls. Data are mean of four independent experiments ± SD. (B) Anti-CD20-NPs incubated with Daudi cells using anti-HER2−PB-NP and unlabeled PB-NP as negative controls. Data are mean of three independent experiments ± SD. Values in parentheses indicate initial molar ratios mAb:sulfo-MBS.

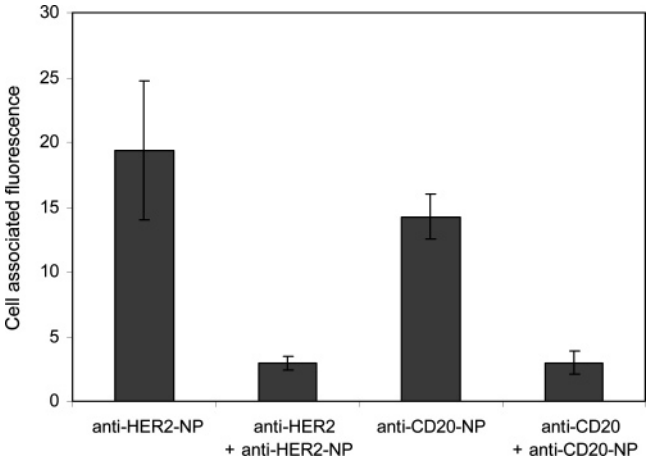

Figure 5. Direct targeting protocol. Study of the influence of free mAbs on the interaction between cells and targeted-NPs. Cells were incubated either with targeted-NPs for 45 min (1st and 3rd bar) or with free mAbs for 45 min followed by the incubation of targeted-NPs over 45 min (2nd and 4th bar). Data are mean of four independent experiments ± SD for anti-HER2-NPs on SKOV-3 cells and mean of three independent experiments ± SD for anti-CD20-NPs on Daudi cells.

As a further demonstration of the specificity of mAb-PB-NP interaction with cells, flow cytometry analyses were also carried out on both cells incubated with free mAbs followed by the treatment of mAb-NPs. As illustrated in Figure 5, the association of anti-HER-NPs with SKOV-3 could be competitively inhibited by the preincubation of free anti-HER2, indicating that the cell-

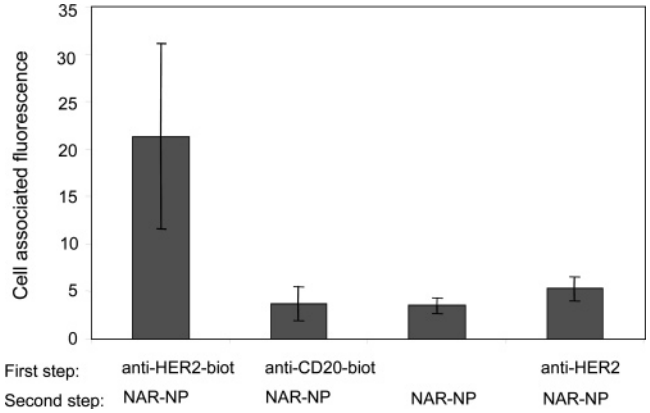

Figure 6. Pretargeting protocol. Study of the interaction between SKOV-3 cells prelabeled with biotinylated mAbs anti-HER2-biot and anti-CD20-biot followed by the incubation of NAR-NPs. First step: preincubation with mAbs during 2 h; second step: interaction with NAR-NPs during 60 min. Two control experiments were performed with free anti-HER2 (not biotin conjugated) or NAR-NPs without antibody. Data are mean of three independent experiments ± SD.

association with NPs was mediated through the HER2 antigens on SKOV-3 cells. Similar results were obtained with Daudi cells (Figure 5).

Two-Step Targeting. The cell association of NAR-NPs with the two-step approach was evaluated on SKOV-3 cells. Results shown in Figure 6 demonstrated that the cells preincubated with biotinylated anti-HER2 mAb showed significantly higher fluorescence intensity compared with those treated with biotinylated anti-CD20 mAbs.

The mean fluorescence of cell-associated NPs measured with biotinylated anti-HER2 was 6-fold higher that obtained with biotinylated anti-CD20 using equivalent concentrations of NAR-NPs. Cells incubated with NAR-NPs in the absence of mAbs confirmed that the specific binding of the NPs to the cells was mediated by the biotinylated-anti-HER2. When anti-HER2 mAbs without biotin were used to pretarget the cells, only a small amount of NAR-NPs interacted with the cells, demonstrating that the association between NPs and cells is due to the strong affinity between NAR and biotin.

DISCUSSION

Nanoparticle Fluorescence Labeling and Activation for Covalent Ligand Coupling. The use of biodegradable NPs for drug delivery of therapeutic agents is now well established (*23, 24*). Among different carrier systems, and particularly with respect to liposomes, NPs have proved to be suitable candidates for antitumor drug therapy. NPs present notably a high drug loading capacity and a variety of well-defined biodegradable polymers, allow the controlled release rate of the drug, and finally show a high storage and in vivo stability. To further improve the therapeutic index of anticancer agent, NPs must be designed to target cancer cells. The reliable way to achieve this goal is the tumor targeting mediated by ligands such as antibodies. To our knowledge, there are very few reports regarding tumor targeting using mAb-labeled biodegradable NPs (*25*−*27*) and no study at all on the multistep targeting approach. Hence, the main goal of the present study was the development of a novel concept of functionalized biodegradable NPs designed to specifically target antigen receptors on tumor cells. In the course of development of the NP-targeting, we made several unexpected observations. We previously described the evaluation and selection, among three different methods, of the NP thiolation used here based on EDAC and cystamine that provided low nonspecific reaction with the NPs (*19*). An unexpected difficulty was observed with the fluorescence labeling of the NPs. Initially, nile red loaded NPs had been selected for flow cytometry studies. Nile red is commercially available highly hydrophobic fluorescent marker. It has been used previously to label NPs for in vitro investigations (*28, 29*). However, in the setting presented here, nile red staining of NPs was unstable; the dye leaked out and labeled cells even in the absence of NP targeting. As an alternative, we coupled commercially available NeutrAvidin Rhodamine Red-X onto the NPs. In this reagent, biotin binding sites remain available (*20*), providing double function as fluorescent dye and two-step reagent for binding to biotinylated antibodies. As a drawback, however, the fluorescence labeling is not independent from the NP-targeting function in this approach. Even though we did not observe release of this reagent from the NPs, we cannot exclude that this happened at low level. 1-Pyrenebutanol coupled to PLA chains appeared finally as optimal fluorescence labeling. The use of 10% of 1-pyrenebutanol-PLA for the preparation PLA-NPs was efficient and gave a stable fluorescent labeling, well adapted for flow cytometry. The other functions of the NPs, such as solubility and particle size, were not altered in the presence of this fluorescent PLA.

The coupling reaction carried out on both fluorescent and nonfluorescent NPs were highly efficient leading to the formation of covalent thioether bonds. In this study, it was demonstrated that NPs can be easily labeled by two types of mAbs, anti-HER2 and anti-CD20 mAbs, and that by varying the molar ratio of the cross-linker, the mAb density on the particles be tailored.

Cancer Cell Association. The ability of NPs to specifically bind tumor cells was shown with the direct and two-step targeting approaches on two different cancer cell lines, SKOV-3 and Daudi. For direct targeting, mAbs were covalently bound to the surface of the PB-NP, and it was demonstrated that the antigen binding activity of the mAbs was dependent on the density of the mAb on the PB-NP surface. In fact, the amount of total cell-associated PB-NP decreased when a high molar ratio was used (1:40), suggesting that inactivation of the antigen binding domain had occurred. Increased sulfo-MBS substitution on mAbs resulted in a higher cell targeting capacity until a maximum was reached. Nevertheless, further studies must be carried out, particularly in vivo, to determine the most favorable mAb density, taking into account that excessive mAb densities on particles may induce rapid clearance from plasma, as shown with immunoliposomes (*30*). For the two types of cells, only minor NP−cell interaction was observed in the absence of mAbs, demonstrating that PB-NP bound specifically to the cells via the antigen−antibody interaction. This was also confirmed by the incubation of cells with NPs labeled with irrelevant mAbs.

The second approach investigated in this study was the pretargeting approach. Multistep targeting is promising since it has the potential of increasing tumor-to-normal-tissue ratios, and as a result, to enhance the therapeutic index of pretargeted drug compared with the use of direct targeting. Frequently, pretargeting protocols involve the use of the avidin−biotin system. Avidin−biotin presents the advantage of dose amplification, since avidin can bind four molecules of biotin. In this study, NeutrAvidin, a chemically deglycosylated avidin, has been preferred to avidin. NeutrAvidin is similar to avidin with respect to its biotin binding affinity but it present less nonspecific binding to cells and has an increased circulation time in the blood compartment. To allow FACS analysis, a fluorescent labeled NeutrAvidin has been chosen: NeutrAvidin Rhodamine Red-X (NAR). It has been shown in this study that NAR-NPs recognized and bound specifically to cells preincubated with biotinylated specific mAbs, demonstrating that the pretargeting approach is feasible with NPs. NAR-NP can be potentially used

for the conjugation of any biotinylated ligand. Furthermore, it may also be possible to simultaneously target different antigens with the same avidin-labeled formulation.

A surprising result, however, was observed in the use of the biotin−avidin reagents in single step targeting. The successful use of these reagents in the two-step NP-targeting had shown that they were perfectly operational, as indicated also by the quality controls. However, when trying to use the same reagents in a one-step targeting whereby the NAR-NPs were first precoated with the biotinylated antibodies, washed, and then incubated with cells, no targeting was observed. When trying to explain the apparent difference between the two- and one-step targeting result, we remained essentially with three hypotheses. First, the immunoreactivity of the antibodies coupled with a mean of three biotins per antibody molecule was conserved when used as soluble agent, but might be strongly reduced when reacted first with the NAR-NPs due to sterical hindrance on the NP surface. Second, when used as two-step reagent, antibodies with conserved immunoreactivity might be positively selected, while, when first reacted with the avidin-NPs, selection of antibodies might occur for the number of available biotin sites (from the Gaussian distribution) and therefore a higher probability of reduced immunoreactivity. Finally, in the two-step reaction, the number of reaction sites on the cell surface might become amplified by the three biotins per antibody molecule, while in the NAR-NP precoating, any loss of immunoreactivity due to sterical hindrance would result in a reduced number of potential binding sites for the cells. These different effects might possibly occur in combination and could explain the loss of binding capacity of the two-step reagents in a one-step targeting in combination with NPs.

Despite the numerous advantages of the pretargeting approach and the promising results in preclinical (*31*−*33*) and clinical studies (*34*, *35*), there are some points that must be considered. Avidin, like streptavidin, is a foreign protein for humans and, therefore, has shown considerable immunogenicity in vivo, thus limiting the number of times that it can be administered. As an alternative to both avidin and streptavidin, chemically modified avidins, such as NeutrAvidin, have been proposed, but their efficacy and their potential low immunogenicity remains to be demonstrated in vivo. Furthermore, it is not yet known to what extent the presence of endogenous biotin or biotinases can interfere in the pretargeting approach (*36*), even though clinical results have shown the feasibility of this multistep targeting. An important condition for good targeting results in pretargeting systems is the relatively slow internalization or even absence of internalization of the mAbs after binding the antigens. In fact, it has to be kept in mind that the antibodies should remain available for a sufficient period of time after binding to the target to allow the avidin−biotin interaction to take place. On the other hand, it has been proven that internalizing antibodies can be necessary for improved efficacy of certain therapeutic agents (*37*). In this study internalizing target HER2 and the noninternalizing target CD20 were used as models. Other internalizing mAbs can be coupled to the NPs for the therapy of lymphoma, such as anti-CD22, a humanized mAb (Epratuzumab) that is presently in clinical phase II study (*38*).

At the present stage of the work, it is not possible to define which targeting strategy is preferred to deliver NPs to tumor cells. More work has to be accomplished, especially in vivo studies have to be undertaken using different tumor models (solid and hematopoietic). Nevertheless, the proof-of-concept of cancer cell targeting with NPs has been demonstrated on two cell lines using two mAbs as models. Universal NPs have been designed to target specific antigens, and these targeted PLA NPs can be applied to other target antigens.

ACKNOWLEDGMENT

This work was supported by a grant from Cancer Research Switzerland (#938-09-1999) and from the Geneva Cancer League. The authors thank D. Wohlwend for technical assistance with regard to cytofluorometric experiments, Mrs. C. Grannavel and C. Paschoud for assistance in the preparation of particular reagents, and C. Nguyen for kindly supplying the 1-pyrenebutanol-labeled poly(lactic acid).

LITERATURE CITED

(1) Satchi-Fainaro, R., Puder, M., Davies, J. W., Tran, H. T., Sampson, D. A., Greene, A. K., Corfas, G., and Folkman, J. (2004) Targeting angiogenesis with a conjugate of HPMA copolymer and TNP-470. *Nat. Med. 10*, 255−261.

(2) Crosasso, P., Ceruti, M., Brusa, P., Arpicco, S., Dosio, F., and Cattel, L. (2000) Preparation, characterization and properties of sterically stabilized paclitaxel-containing liposomes. *J. Controlled Release 63*, 19−30.

(3) Martin, F. J. (1998) Clinical pharmacology and antitumor efficacy of DOXIL (pegylated liposomal doxorubicin). *Medical Applications of Liposomes* (Lasic, D. D., and Papahadjopoulos, D., Eds.) pp 635−688, Elsevier Science BV, New York.

(4) Greish, K., Sawa, T., Fang, J., Akaike, T., and Maeda, H. (2004) SMA-doxorubicin, a new polymeric micellar drug for effective targeting to solid tumours. *J. Controlled Release 97*, 219−230.

(5) Nishiyama, N., Okazaki, S., Cabral, H., Miyamoto, M., Kato, Y., Sugiyama, Y., Nishio, K., Matsumura, Y., and Kataoka, K. (2003) Novel cisplatin-incorporated polymeric micelles can eradicate solid tumors in mice. *Cancer Res. 63*, 8977−8983.

(6) Allémann, E., Rousseau, J., Brasseur, N., Kudrevich, S. V., Lewis, K., and Van Lier, J. E. (1996) Photodynamic therapy of tumours with hexadecafluoro zinc phthalocynine formulated in PEG-coated poly(lactic acid) nanoparticles. *Int. J. Cancer 66*, 821−824.

(7) Verdun, C., Brasseur, F., Vranckx, H., Couvreur, P., and Roland, M. (1990) Tissue distribution of doxorubicin associated with polyisohexylcyanoacrylate nanoparticles. *Cancer Chemother. Pharmacol. 26*, 13−18.

(8) Soppimath, K. S., Aminabhavi, T. M., Kulkarni, A. R., and Rudzinski, W. E. (2001) Biodegradable polymeric nanoparticles as drug delivery devices. *J. Controlled Release 70*, 1−20.

(9) Sakhalkar, H. S., Dalal, M. K., Salem, A. K., Ansari, R., Fu, J., Kiani, M. F., Kurjiaka, D. T., Hanes, J., Shakesheff, K. M., and Goetz, D. J. (2003) Leukocyte-inspired biodegradable particles that selectively and avidly adhere to inflamed endothelium in vitro and in vivo. *Proc. Natl. Acad. Sci. U.S.A. 100*, 15895−15900.

(10) Leroux, J.-C., Allémann, E., De Jaeghere, F., Doelker, E., and Gurny, R. (1996) Biodegradable nanoparticles-from sustained release formulations to improved site specific drug delivery. *J. Controlled Release 39*, 339−350.

(11) Gref, R., Minamitake, Y., Peracchia, M. T., Trubetskoy, V., Torchilin, V., and Langer, R. (1994) Biodegradable long-circulating polymeric nanospheres. *Science 263*, 1600−1603.

(12) Allémann, E., Brasseur, N., Benrezzak, O., Rousseau, J., Kudrevich, S. V., Boyle, R. W., Leroux, J. C., Gurny, R., and Van Lier, J. E. (1995) PEG-coated poly(lactic acid) nanoparticles for the delivery of hexadecafluoro zinc phthalocyanine to EMT-6 mouse mammary tumours. *J. Pharm. Pharmacol. 47*, 382−387.

(13) Mamot, C., Drummond, D. C., Greiser, U., Hong, K., Kirpotin, D. B., Marks, J. D., and Park, J. W. (2003) Epidermal growth factor receptor (EGFR)-targeted immunoliposomes mediate specific and efficient drug delivery. *Cancer Res. 63*, 3154−3161.

(14) Forssen, E., and Willis, M. (1998) Ligand-targeted liposomes. *Adv. Drug Delivery Rev. 29*, 249−271.

(15) Goodwin, D. A., and Meares, C. F. (2001) Advances in pretargeting biotechnology. *Biotechnol. Adv. 19*, 435−450.

(16) Sharkey, R. M., McBride, W. J., Karacay, H., Chang, K., Griffiths, G. L., Hansen, H. J., and Goldenberg, D. M. (2003) A universal pretargeting systems for cancer detection and therapy using bispecific antibody. *Cancer Res. 63*, 354−363.

(17) Green, N. M. (1968) Spectrophotomertic determination of avidin and biotin. *Methods Enzymol. 18*, 418−424.

(18) De Jaeghere, F., Allémann, E., Feijen, J., Kissel, T., Doelker, E., and Gurny, R. (2000) Freeze-drying and lyopreservation of diblock and triblock poly(lactic acid)-poly(ethylene oxide) (PLA-PEO) copolymer nanoparticles. *Pharm. Dev. Technol. 5*, 473−483.

(19) Nobs, L., Buchegger, F., Gurny, R., and Allémann, E. (2003) Surface modification of poly(lactic acid) nanoparticles by covalent attachment of thiol groups by means of three methods. *Int. J. Pharm. 250*, 327−337.

(20) Nobs, L., Buchegger, F., Gurny, R., and Allémann, E. (2004) Poly-(lactic acid) nanoparticles labled with biologically active NeutrAvidin for active targeting. *Eur. J. Pharm. Biopharm. 58*, 483−490.

(21) Nguyen, C. A., Allemann, E., Schwach, G., Doelker, E., and Gurny, R. (2003) Synthesis of a novel fluorescent poly(D,L-lactide) end-capped with 1-pyrenebutanol used for the preparation of nanoparticles. *Eur. J. Pharm. Sci. 20*, 217−222.

(22) De Jong, M. O., Rozemuller, H., Bauman, J. G. J., and Visser, J. W. M. (1995) Biotinylation of interleukin-2 (IL-2) for flow citometric analysis of IL-2 receptor expression. *J. Immunol. Methods 184*, 101−112.

(23) Konan, Y. N., Chevallier, J., Gurny, R., and Allemann, E. (2003) Encapsulation of p-THPP into nanoparticles: cellular uptake, subcellular localization and effect of serum on photodynamic activity. *Photochem. Photobiol. 77*, 638−644.

(24) Fonseca, C., Simoes, S., and Gaspar, R. (2002) Paclitaxel-loaded PLGA nanoparticles: preparation, physicochemical characterization and in vitro anti-tumoral activity. *J. Controlled Release 83*, 273−286.

(25) Rolland, A., Bourel, D., Genetet, B., and Le Verge, R. (1987) Monoclonal antibodies covalently coupled to polymethacrylic nanoparticles: in vitro specific targeting to human T lymphocytes. *Int. J. Pharm. 39*, 173−180.

(26) Akasaka, Y., Ueda, H., Takayama, K., Machida, Y., and Nagai, T. (1988) Preparation and evaluation of bovine serum albumin nanospheres coated with monoclonal antibodies. *Drug Des. Delivery 3*, 85−97.

(27) Bourel, D., Rolland, A., Le Verge, R., and Genetet, B. (1988) A new immunoreagent for cell labeling CD3 monoclonal antibody covalently coupled to fluorescent polymethacrylic nanoparticles. *J. Immunol. Methods 106*, 161−167.

(28) De Jaeghere, F., Allémann, E., Leroux, J.-C., Stevels, W., Feijen, J., Doelker, E., and Gurny, R. (1999) Formulation and lyoprotection of poly(lactic acid-*co*-ethylene oxide) nanoparticles: influence on physical stability and in vitro cell uptake. *Pharm. Res. 16*, 859−866.

(29) Leroux, J. C., Gravel, P., Balant, L., Volet, B., Anner, B. M., Allémann, E., Doelker, E., and Gurny, R. (1994) Internalization of poly(D,L-lactic acid) nanoparticles by isolated human leukocytes and analysis of plasma proteins adsorbed onto the particles. *J. Biomed. Mater. Res. 28*, 471−481.

(30) Allen, T. M., Brandeis, E., Hansen, C. B., Kao, G. Y., and Zalipsky, S. (1995) A new strategy for attachment of antibodies to sterically stabilized liposomes resulting in efficient targeting to cancer cells. *Biochim. Biophys. Acta 127*, 99−108.

(31) Moro, M., Pelagi, M., Fulci, G., Paganelli, G., Dellabona, P., Casorati, G., Siccardi, A. G., and Corti, A. (1997) Tumor cell targeting with antibody-avidin complexes and biotinylated tumor necrosis factor a1. *Cancer Res. 57*, 1922−1928.

(32) Goshorn, S., Sanderson, J., Axworthy, D., Lin, Y., Hylarides, M., and Schultz, J. (2001) Preclinical evaluation of a humanized NR-LU-10 antibody-streptavidin fusion protein for pretargeted cancer therapy. *Cancer. Biother. Radiopharm. 16*, 109−123.

(33) Zhang, M., Zhang, Z., Garmestani, K., Schultz, J., Axworthy, D. B., Goldman, C. K., Brechbiel, M. W., Carrasquillo, J. A., and Waldmann, T. (2003) Pretarget radiotherpy with an anti-CD25 antibody-streptavidin fusion protein was effective in therapy of leukemia/lymphoma xenografts. *Proc. Natl. Acad. Sci. U.S.A. 100*, 1891−1895.

(34) Paganelli, G., Bartomomei, M., Ferrari, M., Cremonesi, M., Broggi, G., Maira, G., Sturiale, C. C., Prisco, G., Gatti, M., Caliceti, P., and Chinol, M. (2001) Pre-targeted locoregional radioimmunotherapy with 90Y-biotin in glioma patients: phase I study and preliminary therapeutic results. *Cancer. Biother. Radiopharm. 16*, 227−235.

(35) Knox, S. J., Goris, M. L., Tempero, M., Weiedn, P. L., Gentner, L., Breitz, H., Adams, G. P., Axworthy, D., Gaffigan, S., Bryan, K., Fisher, D. R., Colcher, D., Horak, I., and Weiner, L. M. (2000) Phase II trial of yttrium-90-DOTA-biotin pretargeted by NR-LU-10 antibody/streptavidin in patients with metastatic colon cancer. *Clin. Cancer Res. 6*, 406−414.

(36) Rusckowski, M., Fogarasi, M., Fritz, B., and Hnatowich, D. J. (1997) Effect of endogenous biotin on the applications of streptavidin and biotin in mice. *Nucl. Med. Biol. 24*, 263−268.

(37) Sapra, P., and Allen, T. M. (2002) Internalizing antibodies are necessary for improved therapeutic efficacy of antibody-targeted liposomal drugs. *Cancer Res. 62*, 7190−7194.

(38) Mavromatis, B. H., and Cheson, B. D. (2004) Novel therapies for chronic lymphocytic leukemia. *Blood Rev. 18*, 137−148.

BC050137K

Human Serum Albumin Hybrid Incorporating Tailed Porphyrinatoiron(II) in the α,α,α,β-Conformer as an O_2-Binding Site

Akito Nakagawa, Teruyuki Komatsu,* Makoto Iizuka, and Eishun Tsuchida*

Advanced Research Institute for Science and Engineering, Waseda University, 3-4-1 Okubo, Shinjuku-ku, Tokyo 169-8555 Japan. Received June 1, 2005; Revised Manuscript Received October 30, 2005

We have found that recombinant human serum albumin (HSA) incorporating tailed porphyrinatoiron(II) in the α,α,α,β-conformer can reversibly bind and release O_2 under physiological conditions (pH 7.3, 37 °C) like hemoglobin and myoglobin. β-2-Methylimidazolyl-tailed porphyrinatoirons (**6a**, **6b**) are synthesized via four steps from the atropisomers of tetrakis(*o*-aminophenyl)porphyrin. The stereochemistry of the α,α,α,β-conformer has been determined by NMR spectroscopy. **6a** and **6b** form stable O_2-adduct complexes in toluene solution at room temperature. The association rate constants of O_2 are 3.1- and 1.9-fold lower than those of the corresponding α,α,α,α-conformers (**1a**, **1b**), indicating that the three substituents (cyclohexanamide or pivalamide groups) are close to each other on the porphyrin platform and construct a narrow encumbrance around the O_2-coordination site. Although **6a** and **6b** are incorporated into the hydrophobic domains of HSA to produce the albumin−heme hybrid, only HSA-**6a** can bind O_2 in aqueous medium. The cyclohexanamide fences are necessary for the tailed porphyrinatoiron to form a stable O_2-adduct complex under physiological conditions. The O_2-binding affinity ($P_{1/2}$) of HSA-**6a** is 45 Torr (37 °C), and the O_2 transporting efficiency between lungs and muscle tissues in the human body is estimated to be identical to that of human red blood cells. The HSA-**6a** solution will become one of the most promising materials for red blood cell substitutes, which can be manufactured on an industrial scale.

INTRODUCTION

To reproduce the O_2-binding ability of hemoglobin (Hb) and myoglobin (Mb), numerous numbers of model hemes have been synthesized over the past decades (*1*). These continuous approaches, aimed at understanding the precise mechanism of the O_2-binding reaction, have been mostly accomplished in organic solvents, and tetrakis(phenyl)porphyrin (TPP) was widely used as a molecular scaffold. We have also synthesized tetrakis{α,α,α,α-*o*-(1-methylcyclohexanamido)phenyl}porphinatoiron(II) bearing a covalently linked proximal imidazole (**1a**, Figure 1)[1] that forms a stable O_2-adduct complex in toluene solution at ambient temperature (*2*). The four cyclohexanamide fences on the distal-side (α-side) of the porphyrin plane are bulky enough to prevent μ-oxo dimer formation, and the 2-methylimidazolyl arm intramolecularly coordinated to the Fe^{2+} center from the proximal-side (β-side) modulates the O_2-binding affinity.

Some substantial efforts have been directed to prepare an artificial O_2 carrier involving a synthetic heme under physiological conditions (pH 7.3, 37 °C), which may become a red blood cell substitute (*1a, 3*). We have successfully incorporated **1a** into the hydrophobic domains of recombinant human serum albumin (HSA) and found that the albumin−heme hybrid (HSA−**1a**) could reversibly absorb O_2 in aqueous medium (*1a, 2, 4*). This red-colored albumin solution showed a long shelf life of over two years without precipitation. More recently, exchange transfusion experiments with HSA−**1a** into anesthetized rats demonstrated that it effectively rescitates the hemorrhagic shock state and transports O_2 to the muscle tissues (*5*). We are now developing this albumin−heme hybrid as an entirely synthetic red blood cell substitute that can be extensively used in a variety of medical situations (*6*).

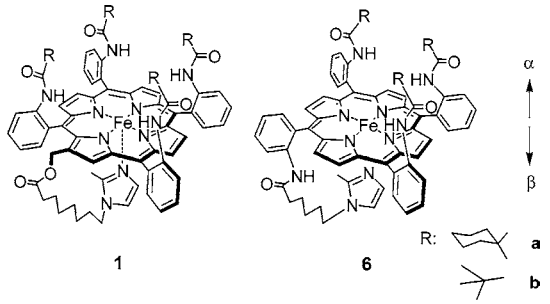

Figure 1. Structures of porphyrinatoiron derivatives in the α,α,α,α-conformer and α,α,α,β-conformer (tailed porphyrinatoiron).

The only disadvantage of this synthetic heme **1a** is that a great deal of labor is required to make the α,α,α,α (α^4)-conformer and to introduce the imidazolylalkyl arm at the porphyrin periphery via the Vilsmeier reaction (*2*). The starting material, tetrakis(α,α,α,α-*o*-aminophenyl)porphyrin (TAPP), is in a statistical mixture of the four possible atrop isomers (α,α,α,α, α,α,α,β, α,β,α,β, α,α,β,β; the ratio is 1:4:2:1), and the variable α^4-conformer used to be isolated by Lindsey's procedure with a silica gel column separation (*7*). The number of total steps for the synthesis of **1a** is, therefore, eight from TAPP.

In this study, we first incorporated a "tailed porphyrinatoiron" with the $\alpha^3\beta$-conformer as an O_2-binding site of the albumin−heme. A series of tailed porphyrins as the model compound of Hb and Mb were synthesized by Collman and co-worker (*8*). There are two advantages of the tailed porphyrin: (i) the statistical content of the $\alpha^3\beta$-conformer of TAPP is maximum

* Corresponding authors: (E.T.) Tel: +81-3-5286-3120. Fax: +81-3-3205-4740. E-mail: eishun@waseda.jp. (T.K.) E-mail: teruyuki@waseda.jp.

[1] Abbreviations: **1a**: 2-[8-{*N*-(2-methyl-1-imidazolyl)octanoyloxy]-methyl]-5,10,15,20-tetrakis{(α,α,α,α-o-(1-methylcyclohexanamido)-phenyl}porphinatoiron; **1b**: 2-[8-{*N*-(2-methyl-1-imidazolyl)octanoyl oxymethyl]-5,10,15,20-tetrakis{α,α,α,α-*o*-(pivalamido)phenyl}porphinatoiron; **6a**: 5,10,15-Tris {α,α,α-*o*-(1-methylcyclohexanamido)-phenyl}-20-mono[β-*o*-[6-{*N*-(2-methyl-1-imidazolyl)}hexanamido]phenyl]-porphinatoiron; **6b**: 5,10,15-Tris(α,α,α-*o*-(pivalamido)phenyl)-20-mono[β-*o*-[6-{*N*-(2-methyl-1-imidazolyl)}hexyramido]phenyl]-porphinatoiron.

10.1021/bc050154+ CCC: $33.50 © 2006 American Chemical Society
Published on Web 12/21/2005

Scheme 1. Synthesis of Tailed Porphyrinatoirons

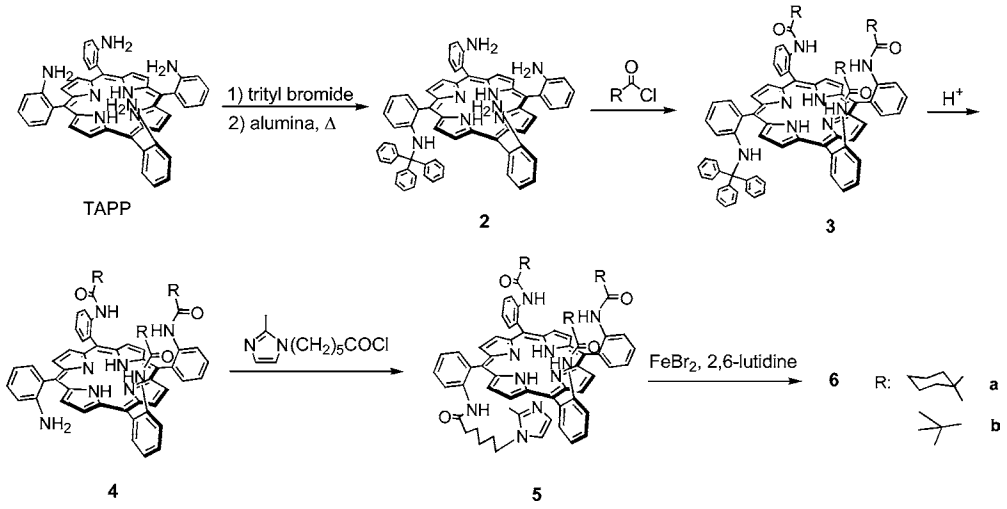

(50%), and (ii) there is no need to modify the porphyrin ring because the proximal base is attached to the fourth β-*o*-NH_2 group of the phenyl ring. This convenient synthetic procedure is a great advantage for the industrial scale-up of the manufacturing of the albumin−heme solution. However, we were not certain of the stability of the O_2-adduct complex of the tailed porphyrinatoiron(II) in an aqueous medium. It has been postulated that the four substituents were essential for preventing an unfavorable proton-driven oxidation of the central ferrous ion of the Fe^{2+}TPP derivatives in water (*1a*, *3*).

First, we describe the synthesis and stereochemistry of the 2-methylimidazole-tailed porphyrinatoirons (**6a**, **6b**) and compare their O_2-binding properties in toluene solution. The effects of the substituents on the O_2-binding parameters are discussed. Furthermore, the O_2-binding property of the albumin−heme hybrid including the tailed porphyrinatiron(II) **6a** has been characterized under physiological conditions. The 5 wt % albumin−heme solution involving the easily prepared **6a** could be the most promising artificial O_2 carrier suitable for mass production.

EXPERIMENTAL SECTION

Synthesis of Tailed Porphyrinatoirons. Experimental details of the synthesis and spectra (^{1}H NMR, IR, UV−Vis, HR-MS) are supplied as Supporting Information.

Reduction of Ferric Complex to Ferrous Complex in Toluene. Reduction to the porphyrinatoiron(II) was carried out using toluene-aq $Na_2S_2O_4$ in a heterogeneous two-phase system under an N_2 atmosphere as previously reported (*9*). After separation of the two phases, the organic layer containing the ferrous complex was transferred to a 1-cm quartz cuvette under an N_2 atmosphere. The UV−Vis absorption spectra were recorded by a JASCO V-570 spectrophotometer.

Preparation of Albumin−Heme Hybrid. The HSA (Albrec, 25 wt %) was obtained from the NIPRO Corp. (Osaka). Aqueous ascorbic acid (15 mM, 20 μL) was added to an ethanol solution of the porphyrinatoiron(III) derivative (37.5 μM, 4 mL) under CO. After complete reduction of the central ferric ion, the UV−Vis absorption spectrum showed the formation of the six-coordinated carbonyl complex. This ethanol solution was slowly injected into the phosphate buffered solution (pH 7.3, 8 mL) of HSA (9.38 μM) through a Teflon tube under a pressure of CO stream. The mixture was dialyzed using a cellulose membrane against phosphate buffer (pH 7.3) for 2 and 15 h at 4 °C. The ethanol concentration should be reduced to less than 100 ppm. Finally, the total volume was adjusted to 15 mL, thus producing the carbonyl albumin−heme solution (heme/HSA = 4 (mol/mol), [Fe]: 20 μM). The water was deionized using an ADVANTEC GS-200 system.

O_2-Coordination Equilibria and Kinetics. The O_2-binding affinity ($P_{1/2}$) of the porphyrinaoitron(II) in organic solvents or their albumin−hemes in aqueous solution were determined by the spectral changes at various partial pressures of O_2 in previous reports (*2*, *10*). The heme concentrations of 20 μM were normally used for the UV−Vis absorption spectroscopy. The spectra were recorded within the range of 350−700 nm. The O_2-association and -dissociation rate constants (k_{on}, k_{off}) were measured by a competitive rebinding technique (*11*, *12*) using a Unisoku TSP-1000WK-WIN time-resolved spectrophotometer with a Spectron Laser system SL803G-10 Q-switched Nd:YAG laser, which generated a 532 nm pulse of 6-ns duration (10 Hz).

Magnetic Circular Dichroism (MCD). The MCD for the phosphate buffered solutions (pH 7.3) of HSA−**6a** (20 μM) under N_2, O_2, and CO atmospheres were measured using a JASCO J-820 circular dichrometer fitted with a 1.5 T electromagnet at 25 °C. The accumulation times were normally five, and each spectra were subtracted by ones without the electromagnetic as a baseline.

RESULTS AND DISCUSSION

Synthesis of Tailed Porphyrinatoiron. The tailed porphyrinatoirons, **6a** and **6b**, can be synthesized via four reaction steps from TAPP with 6-{*N*-(2-methyl-1-imidazolyl}hexanoic acid (Scheme 1), and their structures were determined by IR, UV, mass and NMR (^{1}H NMR, H−H COSY, Nuclear Overhauser effect (NOE) experiment) spectroscopies. First, TAPP was monotritylated using tritylbromide at room temperature. Statistically, six atrop isomers of the monotritylated compound are formed. Collman and co-workers reported the superior synthesis of tris(α,α,α-aminopheny)-mono(β-tritylaminophenyl)porphyrin (**2**) using the alumina absorption technique in the dark (*13*). We isolated two major components from the reaction mixture according to the procedure with the R_f values (chloroform/ethyl acetate = 1:1 (v:v)) of 0.75 (compound **A**) and 0.90 (compound **B**). The coupling reaction of compound **A** with pivaloyl chloride gave a single product, tris(pivalamido)phenyl-monotritylphenyl-porphyrin (compound **A1**). On the other hand, the same coupling reaction of compound **B** provided two products (compounds **B1** and **B2**) with R_f values (chloroform/ethyl acetate = 2:1 (v/v)) of 0.68 and 0.62, respectively. The mass spectra of the above three compounds exactly demonstrated the same value (calcd. for $C_{78}H_{73}N_8O_3$: 1169.5806), indicating that **A1**, **B1**, and **B2** are atrop isomers. In ^{1}H NMR spectra of **A1** and **B1**, the peaks derived from the CH_3 protons in the pivalamide groups were

Scheme 2. Atropisomers of 2 and Their Pivalamide Derivatives

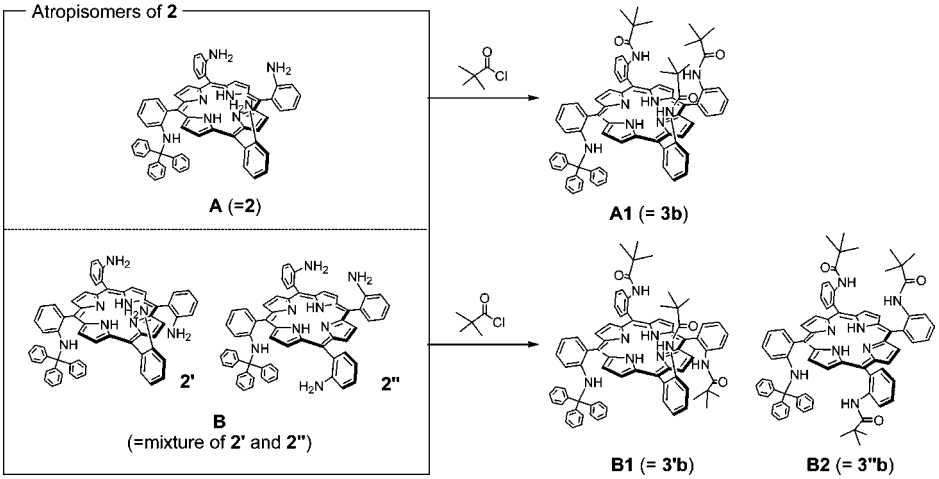

clearly separated into two peaks, and the patterns resembled those of the other $\alpha^3\beta$-structured TAPP derivatives (*14*, *15*) (see Figures ESI1−ESI3, Supporting Information). The differences in the chemical shift between the two peaks were 0.12 (**A1**) and 0.15 (**B1**) ppm, respectively. The CH_3 peaks of **B2** were also splited, but the peak separation was rather small, 0.01 ppm.

To clarify the stereochemistry of these atrop isomers and the geometry of the substituents, we employed the NOE differential spectra (*16*) (see Figures ESI1−ESI3, Supporting Information). In porphyrin **A1**, three pivalamide groups are directed toward the same side and a trityl group is directed only toward the other side, which means **A1** is the target compound **3b**. In **B1**, one of the pivalamide groups is in the same plane with the trityl group, but they do not interact with each other. This result suggests the formation of the $\alpha,\beta,\alpha,\beta$-conformer **3′b**. In **B2**, at least one pivalamide group is on the same side with the trityl group. In this case, there are four atrop isomers expected, but we concluded **B2** would be the $\alpha,\alpha,\beta,\beta$-structure (**3′′b**) because the parent compound **B** was less polar than compound **A** in the $\alpha^3\beta$-conformer. In summary (Scheme 2), (i) compound **A** is porphyrin **2** in the $\alpha^3\beta$-conformer, (ii) compound **B** is a mixture of **2′** ($\alpha,\beta,\alpha,\beta$-conformer) and **2′′** ($\alpha,\alpha,\beta,\beta$-conformer). Our attempts to perform the same NOE experiment on **3a** unfortunately failed because it was difficult to saturate only the peak of the 1-methyl group at the bottom of cyclohexane ring. The coupling reaction of **2** with 1-methylcyclohexanoyl chloride gave the desired **3a** (yield: 53%).

After detritylation under acidic conditions, 6-(2-methylimidazole-1-yl)hexanoic acid chloride was reacted with the β-*o*-NH_2 group of **4**. Iron insertions of these free base porphyrins were performed with an excess of $FeBr_2$ with 2,6-lutidine as the base. The total yields of **6a** and **6b** were 15 and 10% from the atrop-isomeric mixture of TAPP. All these compounds are now available in gram quantities.

During the synthesis of the tailed porphyrinatoiron, we are always careful to prevent the atrop isomerizations of the products. The bulky pivalamide or 1-methylcyclohexanamide substituted phenyl rings did not rotate with respect to the porphyrin plane by the ambient light and heating even at 100 °C in toluene for 2 h (*8*). However, the same heating of the detritylated porphyrin **4** afforded two components, the unchanged original **4** and the new one with a lower R_f value. They both showed identical molecular weights. The newly appearing compound is suspected to be the porphyrin **4′** in the α^4-conformer. Tritylation of **4′** again by the same procedure for TAPP with tritylbromide did not proceed at all due to the steric hindrance of the fence groups next to the NH_2 group.

Table 1. Absorption Maxima (λ_{max}) of Tailed Porphyrinatoiron(II) in Toluene

	λ_{max}		
	under N_2	under O_2	under CO
6a	438, 535, 558	426, 550	424, 535
6b	435, 535, 555	422, 546	421, 534
1a	441, 539, 558	424, 552	425, 534
1b[a]	439, 535, 561	422, 550	422, 534

[a] Reference 10b.

Table 2. O_2-Binding Parameters of Tailed Porphyrinatoiron(II) in Toluene at 25°C

	k_{on} ($M^{-1}\,s^{-1}$)	k_{off} (s^{-1})	$P_{1/2}$ (Torr)
6a	5.8×10^7	5.1×10^4	67
6b	8.6×10^7	5.6×10^4	50
1a[a]	1.8×10^8	4.7×10^4	20
1b[a]	1.6×10^8	7.9×10^4	38

[a] Reference 2.

O_2-Binding Properties of Tailed Porphyrinatoiron(II) in Toluene Solution. UV−Vis absorption spectra of ferrous **6a** and **6b** in toluene solution under an N_2 atmosphere were very similar to those of the five-N-coordinate complexes of **1a** and **1b** (Table 1). This indicates that **6a** and **6b** are also five-N-coordinate high-spin Fe^{2+} complex with an intramolecularly coordinated imidazole tail. Upon bubbling of O_2 gas into these solutions, the absorption spectra immediately changed to that of the well-characterized O_2 adduct complex of the Fe^{2+}TPP derivative. After passing the CO gas, the spectral pattern was converted to the typical carbonyl complex. There is no significant difference in the λ_{max} values of **6a**, **6b**, **1a**, and **1b** within 6 nm.

The binding affinities ($P_{1/2}$), association and dissociation rate constants (k_{on}, k_{off}) of O_2 to the tailed porphyrinatoiron(II)s, **6a** and **6b**, were determined (Table 2). We thought that the reduction of the fence numbers on the porphyrin ring plane from four to three unfastens the steric hindrance around the O_2-coordination site and enhanced the association rate constant of O_2. It is generally recognized that the k_{on} value increases with the relaxing distal steric encumbrance (*1*, *11*, *12*, *15*). However, the reverse was the case. In contrast to our assumption, the k_{on} values of the tailed porphyrinatoirons, **6a** and **6b**, were 3.1- and 1.9-fold lower than the corresponding α^4-conformers (**1a** and **1b**), respectively, while their k_{off} values were nearly the same. This result suggests that the steric hindrances for the O_2 association to **6a** and **6b** are greater than those of **1a** and **1b**. Most probably, three fences on the amide bonds in the $\alpha^3\beta$-

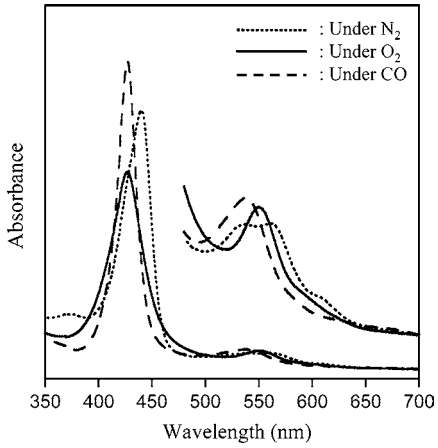

Figure 2. UV−Vis absorption spectral change of HSA−**6a** hybrid in phosphate buffered solution (pH 7.3).

Table 3. Absorption Maxima (λ_{max}) of HSA−Tailed Porphinatoiron (II) Hybrid in Phosphate Buffered Solution (pH 7.3)

	λ_{max}		
	under N_2	under O_2	under CO
HSA-**6a**	440, 536, 559	427, 550	427, 539
HSA-**6b**	−	−	424, 537
HSA-**1a**[a]	445, 543, 567	428, 555	429, 545
HSA-**1b**[a]	443, 542, 567	426, 552	427, 539

[a] Reference 2.

conformer can easily move on the porphyrin platform compared to the crowded four fences of the α^4-conformer. These flexible geometries of the substituents, if anything, narrowed the encumbrance around the O_2-coordination site relative to the α^4 arrangement.

O_2-Binding Properties of HSA-Tailed Porphyrinatoiron in Aqueous Medium. The tailed porphyrinatoirons, **6a** and **6b**, in the $\alpha^3\beta$-conformer could be incorporated into hydrophobic domains of HSA, providing the corresponding albumin−heme hybrids. Their maximum binding numbers to HSA were determined to be approximately 8 (mol/mol), which is identical to those of **1a** and **1b** (*2, 10a*). It is known that HSA binds porphyrin derivatives and their binding sites largely depend on the chemical structures, hydrophobicity, and electrostaticity. Crystal structure analysis of HSA complexed with natural Fe^{3+} protoporphyrin IX, namely, hemin, revealed that hemin is accommodated into subdomain IB of HSA (*17*). On the other hand, hematoporphyrin is incorporated into subdomain IIIA (*18*), and tetrakis(*p*-sulfonatophenyl)porphyrin binds to subdomain IIA or IIIA (*19*). On the basis of the competitive binding inhibition, we supposed that the some of the binding sites of **1a** are subdomains IB, IIA, and IIIB (*10a*). Attempts to crystallize HSA−**6a** hybrid are now underway, but the porphyrin **6a** dissociated from albumin during the crystallization process due to the relatively low binding constants of **6a** to HSA (10^6−10^4 M^{-1}) and coexistence of poly(ethylene glycol) in the media. We suspect that the binding sites of **6a** and **6b** are the same places of **1a**. The isoelectric point ($pI = 4.8$) and circular dichroism spectral patterns of HSA−**6a** and HSA−**6b** were similar to those of HSA itself, indicating that the surface and conformation of albumin were unaltered after bindings of the tailed porphyrinatoirons.

UV−Vis absorption spectra of the freshly prepared ferrous HSA−**6a** showed λ_{max} values at 424 and 537 nm (Figure 2, Table 3). This spectrum was almost identical to that of the CO coordinated low-spin **6a** in toluene solution, implying that the incorporated tailed porphyrinatoiron(II) is still the CO adduct complex in HSA. Light irradiation to this aqueous HSA−**6a** using a 500-W halogen lamp under an O_2 atmosphere leads to

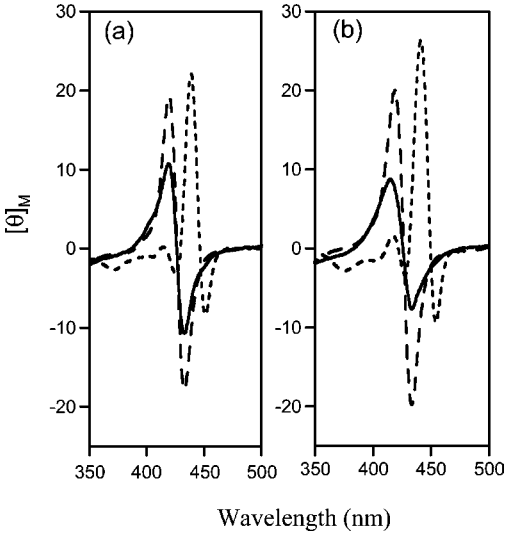

Figure 3. MCD spectral changes of (a) HSA−**6a** and (b) HSA−**1a** hybrids in phosphate buffered solution (pH 7.3). Solid line: under O_2; dotted line: under N_2; dashed line: under CO.

Table 4. O_2-Binding Parameters of HSA−Tailed Porphinatoiron (II) Hybrid in Phosphate Buffered Solution (pH 7.3) at 25°C

	k_{on} (M^{-1} s^{-1})		k_{off} (s^{-1})		
	fast	slow	fast	slow	$P_{1/2}$ (Torr)[a]
HSA−**6a**	2.9×10^7	4.4×10^6	1.1×10^3	1.6×10^2	22 (45)[b]
HSA−**1a**[c]	4.6×10^7	7.3×10^6	9.8×10^2	1.6×10^2	13 (35)[b]

[a] $P_{1/2} = (k_{on}/k_{off})^{-1}$. [b] At 37 °C in parentheses. [c] Reference 2.

CO dissociation, giving a typical spectral pattern of the O_2 adduct complex. Upon exposure of the dioxygenated HSA−**6a** to N_2, the absorption spectrum changed to that of the five-N-coordinated ferrous complex with an intramolecularly coordinated axial imidazole. This O_2 binding and releasing were found to be reversible.

In contrast, the ferrous HSA−**6b** was irreversibly oxidized during the CO dissociation process under an O_2 atmosphere. We concluded that the bulky and hydrophobic substituent like the 1-methylcyclohexanamide fences are necessary for the tailed porphyrinatoiron(II) in the $\alpha^3\beta$-conformer to form a stable O_2 adduct complex under physiological conditions (pH 7.3, 37 °C).

The magnetic circular dichloisim (MCD) spectra of HSA−**6a** showed almost the same pattern as those of HSA−**1b** (Figure 3) (*20*). Under an N_2 atmosphere, the MCD spectrum of HSA−**6a** showed the formation of the five-coordinate ferrous high-spin complex of **6a** with the intramolecular coordinated proximal imidazole. This result showed no ligation of the amino acid residues of the protein, e.g., histidine, tyrosine, cysteine, to the sixth coordination site of the heme. The bulky fences on the porphyrin plane could prevent access of the neighboring peptide residues to the sixth coordination site of **6a**. Upon exposure of this solution to O_2, the spectrum immediately changed and showed an S-shaped A-term MCD in the Soret region, which indicates a transformation to the ferrous low-spin complex (*8, 21*). The CO adduct complex of HSA−**6a** also exhibited a similar A-term MCD band in the same region with a much stronger intensity. The wavelength where the value of $[\theta]_M$ is zero for the O_2 and CO adduct complex coincided well with the absorption maxima in their corresponding UV−Vis spectra.

The $P_{1/2}$ of the HSA−**6a** was determined by measuring the UV−Vis absorption spectral changes during the O_2 titration. The laser flash photolysis experiments provided the k_{on} and k_{off} values of the O_2 binding to HSA−**6a** (Table 4). The absorption decays accompanying the O_2 recombination were composed of two-phases of the first-order kinetics. The curve was fitted by

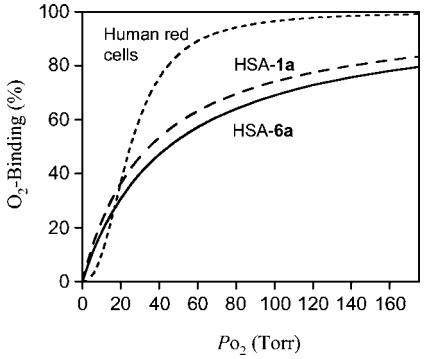

Figure 4. O_2-binding equilibrium curve of HSA−**6a** under physiological conditions (pH 7.3, 37 °C).

a double exponential equation, which was assigned to the fast and slow rebindings [k_{on}(fast) and k_{on}(slow)] of O_2. The k_{on}(fast) values were 7 times greater than k_{on}(slow), and the concentration ratio of the fast and slow reactions was 2:1. This is presumably because the O_2 association to **6a** in HSA is influenced by the molecular microenvironment in the hydrophobic domains (steric hindrance of the amino acid residue and difference in polarity). This behavior was similarly observed in HSA−**1a** and HSA−**1b** (*2*, *22*). The k_{on} values of HSA−**6a** are again 1.6−1.7-fold lower than those of HSA−**1a** in aqueous medium as observed in toluene solution. This is also caused by the narrow encumbrance on the porphyrin ring plane constructed by the three 1-methlcyclohexanamide fences of **6a**.

The HSA−**6a** did not show a cooperative O_2-binding profile like Hb; the Hill coefficient was 1.0 (Figure 4). Although the O_2-binding affinity of HSA−**6a** at 37 °C is relatively low ($P_{1/2}$ value (45 Torr) is high) compared to those of HSA−**1a** (35 Torr) and human red blood cells (28 Torr), the O_2-transporting efficiency of HSA−**6a** between the lungs (Po_2: 110 Torr) and muscle tissues (Po_2: 40 Torr) is estimated to be 22%, which is identical to human red blood cells and HSA−**1a**.

CONCLUSIONS

Tailed porphyrinatoirons have been first employed as an O_2-binding site of the synthetic hemoprotein, albumin−heme. **6a** and **6b** with a β-*o*-(2-methylimidazolyl)hexyramide tail have been easily synthesized via four steps from the TAPP scaffold compared to the eight steps of **1a**. The stereochemistry of the $\alpha^3\beta$-conformer was confirmed by NOE experiments. The association rates of O_2 were slower than for the corresponding α^4-conformers, which indicates that three substituents are close to the porphyrin platform and narrowed the encumbrance space around the O_2-coordination site. As an active site for the albumin−heme hybrid, **6a** was effective, but **6b** was rapidly oxidized. It can be concluded that bulky and hydrophobic substituents like the 1-methylcyclohexanamide fences are necessary for obtaining a stable O_2 adduct complex. The O_2 transporting ability of the HSA−**6a** was almost the same as human red blood cells. Currently, since HSA is manufactured on a large scale by yeast expression (*23*), the 5 wt % albumin−heme solution involving **6a** as O_2 binding site is the most promising material as a red blood cell substitute and O_2-carrying therapeutic reagent, which would be mass produced on an industrial scale.

ACKNOWLEDGMENT

This work was partially supported by Grant-in-Aid for Scientific Research (No. 16350093) from JSPS, Grantin-Aid for Exploratory Research (No. 16655049) from MEXT Japan, and Health Science Research Grants (Regulatory Science) from MHLW Japan.

Supporting Information Available: Synthetic procedure of the tailed porphyrinatoirons (**6a**, **6b**); ^{1}H NMR and NOE differential spectra of compounds **A1**, **B1**, and **B2**. These materials are available free of charge via the Internet at http://pubs.acs.org.

LITERATURE CITED

(1) (a) Collman, J. P., Boulatov, R., Sunderland, C. J., and Fu, L. (2004) Functional analogues of cytochrome *c* oxidase, myoglobin, and hemoglobin. *Chem. Rev. 104*, 561−588. (b) Momenteau, M., and Reed, C. A. (1994) Synthetic heme-dioxygen complexes. *Chem. Rev. 94*, 659−698 and references therein.

(2) Komatsu, T., Matsukawa, Y., and Tsuchida E. (2002) Effect of heme structure on O_2-binding properties of human serum albumin-heme hybrids: Intramolecular histidine coordination provides a stable O_2-adduct complex. *Bioconjugate Chem. 13*, 397−402.

(3) Komatsu, T., Moritake, M., Nakagawa, A., and Tsuchida, E. (2002) Self-organized lipid-porphyrin bilayer membranes in vesicular form: Nanostructure, photophysical properties and dioxygen coordination. *Chem. Eur. J. 8*, 5469−5480.

(4) Komatsu, T., Oguro, Y., Teramura, Y., Takeoka, S., Okai, J., Anraku, M., Otagiri, M., and Tsuchida, E. (2004) Physicochemical characterization of cross-linked human serum albumin dimer and its synthetic heme hybrid as an oxygen carrier. *Biochim. Biophys. Acta 1675*, 21−31.

(5) (a) Huang, Y., Komatsu, T., Yamamoto, H., Horinouchi, H., Kobayashi, K., and Tsuchida, E. (2004) Safety evaluation of an artificial O_2 carrier as a red blood cell substitute by blood biochemical tests and histopathology observations, *ASAIO J. 50*, 525−529. (b) Komatsu, T., Huang, Y., Yamamoto, H., Horinouchi, H., Kobayashi, K., and Tsuchida, E. (2004) Exchange transfusion with synthetic oxygen-carrying plasma protein "albumin-heme" into an acute anemia rat model after seventy-percent hemodilution. *J. Biomed. Mater. Res. 71A*, 644−651. (c) Huang, Y., Komatsu, T., Yamamoto, H., Horinouchi, H., Kobayashi. K., and Tsuchida, E. (2004) Exchange transfusion with entirely synthetic red-cell substitute albumin-heme into rats: physiological responses and blood biochemical tests. *J. Biomed. Mater. Res. 71A*, 63−69.

(6) Kobayashi, K., Komatsu, T., Iwamaru, A., Matsukawa, Y., Horinouchi, H., Watanabe, M., and Tsuchida, E. (2002) Oxygenation of hypoxic region in solid tumor by administration of human serum albumin incorporating synthetic hemes. *J. Biomed. Mater. Res. 64A*, 48−51.

(7) Lindsey, J. (1980) Increased yield of a desired isomer by equilibriums displacement on binding to silica gel, applied to meso-tetrakis(o-aminophenyl)porphyrin. *J. Org. Chem. 45*, 5215−5215.

(8) Collman, J. P., Brauman, J. I., Doxsee, K. M., Halbert, T. R., Bunnenberg, E., Linder, R. E., LaMar, G. N., Gaudio, J. D., Lang, G., and Spartalian, K. (1980) Synthesis and characterization of "tailed picket fence" porphyrins. *J. Am. Chem. Soc. 102*, 4182−4192.

(9) Tsuchida, E., Hasegawa, E., Komatsu, T., Nakata, T., Nakao, K., and Nishide, H. (1991) Synthesis and coordination behaviors of new double-sided porphyrinatoiron(II) complexes: effect of the pocket size for imidazole on dioxygen binding. *Bull. Chem. Soc. Jpn. 64*, 888−894.

(10) (a) Komatsu, T., Hamamatsu, K., Wu, J., and Tsuchida, E. (1999) Physicochemical properties and O_2-coordination structure of human serum albumin incorporating tetrakis-(*o*-pivalamido)phenylporphyrinatoiron(II) derivatives. *Bioconjugate Chem. 10*, 82−86. (b) Tsuchida, E., Komatsu, T., Kumamoto, S., Ando, K., and Nishide, H. (1995) Synthesis and O_2-binding properties of tetraphenylporphyrinatoiron(II) derivatives bearing a proximal imidazole covalently bound at the β-pyrrolic position. *J. Chem. Soc., Perkin Trans. 2*. 747−753.

(11) Collman, J. P., Brauman, J. I., Iverson, B. L., Sessler, J. L., Morris, R. M., and Gibson, Q. H. (1983) O_2 and CO binding to iron(II) porphyrins: A comparison of the "picket fence" and "pocket" porphyrins. *J. Am. Chem. Soc. 105*, 3052−3064.

(12) Traylor, T. G., Tsuchiya, S., Campbell, D., Mitchell, M., Stynes, D., and Koga, N. (1985) Anthracene heme cyclophanes. Steric Effects in CO, O_2 and RNC Binding. *J. Am. Chem. Soc. 107*, 604−614.

(13) Collman, J. P., Broring, M., Fu, L., Rapta, M., Schwenninger, R., and Straumanis, A. (1998) Novel protecting strategy for the synthesis of porphyrins with different distal and proximal superstructures. *J. Org. Chem. 63*, 8082−8083.

(14) Inaba, Y., and Kobuke, Y. (2004) Synthesis of a complementary dimer from mono(imidazolyl)-substituted cobalt(II) porphyrin as a new artificial T-form hemoglobin. *Tetrahedron 60*, 3097−3107.
(15) Wuenschell, G. E., Tetreau, C., Lavalette, D., and Reed, C. A. (1992) Hydrogen-bonded oxyhemoglobin models with substituted picket-fence porphyrins: the model compound equivalent of site-directed mutagenesis. *J. Am. Chem. Soc. 114*, 3346−3355.
(16) Collman, J. P., Sunderland, C. J., and Boulatov, R. (2002) Biomimetic studies of terminal oxidases: trisimidazole picket metalloporphyrins. *Inorg. Chem. 41*, 2282−2291.
(17) Zunszain, P. A., Ghuman, J., Komatsu, T., Tsuchida, E., and Curry, S. (2003) Crystal structural analysis of human serum albumin complexes with hemin and fatty acid, *BMC Struct. Biol. 3*, 6.
(18) Cohen, S., and Margalit, R. (1990) Binding of porphyrin to human serum albumin, structure−activity relationship. *Biochem. J. 270*, 325−330.
(19) Andrade, S. M., and Costa, S. M. B. (2002) Spectroscopic studies on the interaction of a water soluble porphyrin and two drug carrier proteins. *Biophys. J. 82*, 1607−1619.
(20) Tsuchida, E., Nakagawa, A., and Komatsu, T. (2003) Coordination structure of active site in synthetic hemoprotein (albumin-heme) with dioxygen and carbon monoxide. *Macromol. Symp. 195*, 275−280.
(21) (a) Collman, J. P., Brauman, J. I., Collins, T. J., Iverson, B. L., Lang, G., Pettman, R. B., Sessler, J. L., and Walters, M. A. (1983) Synthesis and characterization of the "pocket" porphyrins. *J. Am. Chem. Soc. 105*, 3038−3052. (b) Collman, J. P., Basolo, F., Bunnenberg, E., Collins, T. C., Dawson, J. H., Ellis, P. E., Marrocco, M. L., Moscowitz, A., Sessler, J. L., and Szymanski, T. (1981) Use of magnetic circular dichroism to determine axial ligation for some sterically encumbered iron(II) porphyrin complexes. *J. Am. Chem. Soc. 103*, 5636−5648.
(22) Komatsu, T., Matsukawa, Y., and Tsuchida, E. (2000) Kinetics of CO and O_2 binding to human serum albumin-heme hybrid. *Bioconjugate Chem. 11*, 772−776.
(23) Sumi, A., Ohtani, W., Kobayashi, K., Ohmura, T., Yokoyama, K., Nishida, M., and Suyama, T. (1993) Purification and physico-chemical properties of recombinant human serum albumin. *Biotechnology of Blood Proteins* (Rivat, C., Stoltz, J.-F., Eds.) Vol. 227, pp 293−298, John Libbey Eurotext, Montrouge.

BC050154+

PEI-g-chitosan, a Novel Gene Delivery System with Transfection Efficiency Comparable to Polyethylenimine in Vitro and after Liver Administration in Vivo

Kokhou Wong,[†] Guobin Sun,[†] Xueqing Zhang,[‡] Hui Dai,[‡] Ye Liu,*[,†] Chaobin He,[†] and Kam W. Leong[‡,§]

Institute of Materials Research and Engineering, 3 Research Link, Singapore 117602, Division of Johns Hopkins in Singapore, Singapore 138669, and Department of Biomedical Engineering, Johns Hopkins University School of Medicine, Baltimore, Maryland 21205. Received June 5, 2005; Revised Manuscript Received November 21, 2005

Polyethylenimine-graft-chitosan (PEI-g-chitosan) was synthesized by performing cationic polymerization of aziridine in the presence of water-soluble oligo-chitosan ($M_n = 3400$). The absolute molecular weight and chemistry of the PEI-g-chitosan obtained were characterized using GPC, ^{13}C and ^{1}H NMR, respectively. The results indicated that all the amines of chitosan were grafted with oligo-PEI, and the average length of the oligo-PEI side chains was determined by the feed molar ratio of aziridne/amine in chitosan. PEI-g-chitosan of $M_n = 7400$ with a polydispersity index (PDI) of 1.50, and PEI side chains of $M_n = 206$ was prepared for gene delivery. Gel electrophoresis showed that DNA migration was retarded completely at a N/P ratio of 2.5/1, indicating good DNA condensation capability of PEI-g-chitosan. The sizes and the ζ-potentials of the complexes of PEI-g-chitosan/DNA were characterized. The cytotoxicity of PEI-g-chiotsan was evaluated, and the results reflected that PEI-g-chitosan had a lower cytotoxicity than PEI (25 K). Gene transfection efficiency of PEI-g-chitosan in HepG2, HeLa, and primary hepatocytes cells and after administration in the common bile duct of rat liver was determined. Remarkably, PEI-g-chitosan showed a higher transfection efficiency than that of PEI (25 K) both in vitro and in vivo. The systematic distribution and the distribution in liver of the gene expression of the complexes of PEI-chitosan/DNA were determined as well.

INTRODUCTION

Gene therapy is promising for curing various inherited or acquired diseases. However, lack of safe and efficient carriers for DNA currently is a main hurdle to the success of gene therapy. Great concerns about the safety of viral vectors make nonviral vectors more and more attractive. The good DNA delivery properties of polyethylenimines (PEI) initiated interests in applying polymers for preparing nonviral vectors due to improved safety, ease of synthesis, and adjustable structures of polymers (*1*−*3*). PEI of a certain high molecular weight is necessary for efficient delivery of DNA; however, a high molecular weight PEI is cytotoxic, and its long-term safety is problematic because of its nonbiodegradability (*3*). Other polymers have also been exploited for gene delivery, including natural products such as cyclodextrins (*4*) and chitosan (*5*, *6*), and synthetic polymers such as polyesters, polyphosphoesters, and polysaccharides with side amine groups (*7*−*12*), poly(amino ester)s (*13*−*18*). Recently, polymer-functionalized carbon nanotubes also have been explored for DNA delivery (*19*). Nevertheless, PEI is still one of the most efficient synthetic materials for gene delivery.

The cytotoxicity of PEI is dependent on its molecular weight. A lower molecular weight PEI has a lower cytotoxicity (*20*), e.g., PEI (5 K) was reported to have lower cytotoxicity and show DNA transfection efficiency comparable to PEI (25 K) in vitro, but no in vivo results were reported (*21*). One rational way was suggested to combine low molecular weight PEIs together using degradable links to form combined PEIs with suitable high molecular weights. It was expected that the toxicity should be reduced, and the long-term safety should be improved because those combined PEIs should be degraded to much less toxic low molecular weight PEIs after delivering DNA into cells; meanwhile, those combined PEIs should have good transfection efficiency for gene delivery for the high enough molecular weights (*22*−*25*). Some of those combined PEIs showed good transfection efficiency and low cytotoxicity (*22*, *25*), but gelation might occur easily in those reactions of the multifunctional low molecular weight PEIs with the degradable linkers (*26*). Even though soluble products could be obtained through carefully adjusting the reaction conditions, it was difficult to control the structures of the products such as the molecular weights and constitutions, and the reproducibility was inevitably very poor.

With the aim to prepare well-defined novel polymers with structures similar to the combined low molecular weight PEIs in a reproducible and controllable way, we prepared PEI-g-chitosan by performing cationic polymerization of aziridine in the presence of chitosan. As described in Scheme 1, oligo-PEI was combined together via grafting to biocompatible and biodegradable chitosan through the chain transfer reaction. The advantages of this approach is that no gelation occurred and the PEI length could be well controlled by adjusting the feed molar ratio of aziridine to amine of chitosan. PEI-g-chitosan showed good DNA condensation capability and lower cytotoxicity than PEI (25 K) but higher transfection efficiency for DNA delivery both in vitro and in vivo.

MATERIALS AND METHOD

General Characterization. ^{1}H NMR and ^{13}C NMR were performed on a Bruker DRX-400 spectrometer. Gel permeation chromatography (GPC) was implemented on a Waters 2690 apparatus with a Waters 410 refractive index detector and a miniDAWN light scattering detector and two columns in series (Waters Ultrahydrogel 250 and 200). 0.5 M acetic acid/0.5 M sodium acetate was used as eluent.

* To whom correspondence should be addressed. E-mail: ye-liu@imre.a-star.edu.sg.

[†] Institute of Materials Research and Engineering.

[‡] Division of Johns Hopkins in Singapore.

[§] Department of Biomedical Engineering, Johns Hopkins University School of Medicine.

10.1021/bc0501597 CCC: $33.50 © 2006 American Chemical Society
Published on Web 12/27/2005

Scheme 1. Mechanism of Preparation of PEI-g-chitosan

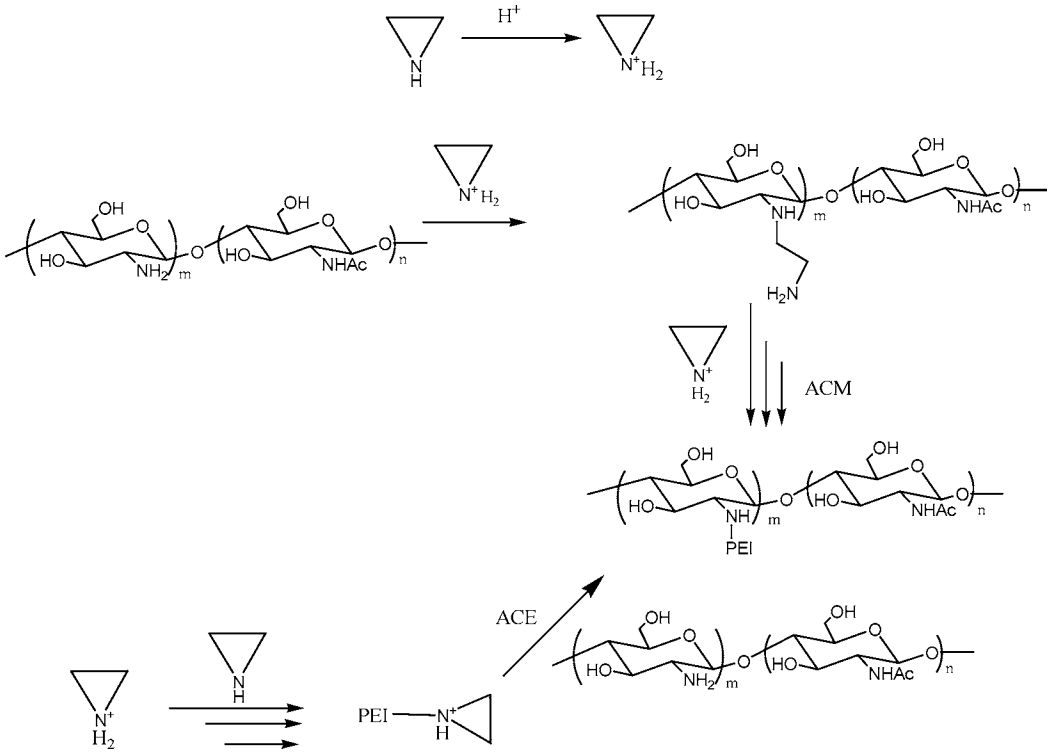

Materials. Water-soluble chitosan was prepared by degradation of commercially available chitosan of a 80% deacetylation degree (Aldrich). Twenty-five grams of chitosan powder was dispersed in 500 mL of 0.5% H_2O_2 in an autoclave vessel. After the sample was purged with argon for 5 min, the vessel was sealed. Then the reaction was performed under 90 °C and 100 psi for 1 h. The filtered solution was precipitated in acetone. The precipitated oligo-chitosan was collected and purified by dissolving in water followed by lyophilization. Aziridine was synthesized from ethanolamine as reported (*27*).

(3-(4,5-Dimethyl-thiazol-2-yl)-2,5-diphenyl tetrazolium bromide (MTT) was from Aldrich (Milwaukee, WI). The other materials and solvents were used as received without further purification.

Synthesis and Characterization of PEI-g-chitosan. Typically, 0.4 g of water-soluble oligo-chitosan powder was dissolved in 5 mL of deionized water, and 3 M hydrochloric acid (HCl) was added with the molar ratio of HCl to the amine of chitosan to be 1:10. Then aziridine was added dropwise into the solution under stirring with the molar ratio of EI to amine of chitosan to be 5:1. The polymerization was performed at ambient temperature for 5 days. Finally, the temperature was increased to 60 °C for 1 day. After being purified by dialysis in water, the solution was lyophilized to give a light yellow powder.

Cytotoxicity Assay of PEI-g-chitosan. HepG2 cells (8000 cells/well), HeLa cells (8000 cells/well), and primary hepatocytes cells (4000 cells/well) were seeded in 96-well plates, respectively. The cells were incubated for 4 h with 200 μL of complete DMEM containing PEI-g-chitosan, or PEI at different concentrations. The medium in each well was replaced with 100 μL of fresh complete medium 4 h later. After 25 μL of MTT solution in PBS (5 mg/mL) was added, the cells were incubated for another 2 h. Then 100 μL of the extraction buffer (20% SDS in 50% DMF, PH 4.7) was added to the wells, and the cells were incubated overnight. The optical intensity was measured at 550 nm using a microplate reader (model 550, Bio-Rad Lab, Hercules, CA). The cell viability was expressed as a percentage of the intensity to that of the control experiment without polymers. The results were reported for triplicate samples.

Formation and Characterization of DNA/PEI-g-chitosan Complexes. A 1 mg/mL aqueous solution of plasmid DNA (pCMV-Luc) (Elim Biopharmaceuticals, California) was diluted to designed concentration (usually 0.5−2.0 μg/μL) using pure water under vortexing. Various amounts of aqueous solution of PEI-g-chiotosan of designed concentrations were added slowly to the DNA solutions. The amount of polymer added was calculated based on the chosen N/P ratios of PEI-g-chitosan/DNA. After the solution was incubated at ambient temperature for 30 min under gentle vortexing, the formed PEI-g-chiotosan/DNA complexes was mixed with a loading buffer and loaded onto a 1% agarose gel containing ethidium bromide. Gel electrophoresis was run at room temperature in TBE buffer at 80 V for 60 min. DNA bands were visualized by an UV (254 nm) illuminator. The particle sizes and ζ-potentials of the complexes of DNA/polymer were measured at 25 °C using a ZetaPALS dynamic light scattering detector (Brookhaven Instruments Corporation, Holtsville, NY, 15 mW laser, incident beam = 676 nm).

Transfection Efficiency in Vitro. The in vitro transfection efficiency of PEI-graft-chitosan was evaluated in HepG2, HeLa, and primary hepatocytes cells, using the complexes formed from PEI-g-chitosan and pVR 1255 DNA. Cells were seeded 24 h prior to transfection into 24-well plates (Becton-Dickinson, Lincoln Park, N.J) at densities of 8×10^4 per well for HepG2 cells and HeLa cells, and 4×10^4 per well for primary hepatocytes cells with 1 mL of indicated medium, respectively. At the time of transfection, the medium in each well was replaced with 300 μL of Opti-MEM. The complexes of polymer/DNA were incubated with the cells for 4 h at 37 °C. The medium was replaced with 1 mL of fresh complete medium, and the cells were further incubated for 44 h. After the incubation, cells were permeabilized with 200 μL of cell lysis buffer (Promega Co., Wis.). After two cycles of freezing and thawing, the lysate was transferred into microtubes and centri-

fuged for 5 min. Then the luciferase activity of the supernatants were measured using 100 μL of luciferase assay reagent (Promega Co., Madison, WI) on a single-well luminometer (Berthold Lumat LB 9507, Germany) for 10 s. The light units (LU) measured using a protein assay kit (Bio-Rad Labs, Hercules, California) were normalized against protein concentration in the cell extracts. Luciferase activity was expressed as relative light units (RLU ng/mg of protein). The data were reported for triplicate samples.

Transfection Efficiency in Vivo. Wistar rats (male, 200−250 g, 20−24 per group) were used for the in vivo transfection efficiency evaluation. Six- to eight-week-old male Wistar rats were obtained and housed in National University of Singapore Animal Holding Unit. Rats were maintained on ad libitum rodent feed and water at room temperature under 40% humidity. All animal procedures were approved by the Animal Care and Use Committee of Faculty of Medicine, National University of Singapore.

First the optimal N/P ratio for PEI-g-chitosan was screened. Four complexes of PEI-chitosan and VR1255 plasmid encoding firefly luciferase driven by CMV promoter were prepared with N/P ratios of 5:1; 10:1; 20:1, and 40:1 and evaluated in one rat, respectively. After identifying the optimal N/P ratio to be 10/1, the transfection efficiency of the complex of the optimal N/P ratio was compared with these of the complexes of chitosan and DNA (N/P = 3:1), PEI (25 K), and DNA (N/P ratio = 10:1), and naked DNA. The results were obtained from three rats.

Animals were laparotomized under general anesthesia, and the livers were then surgically isolated from the surrounding tissue. The complexes of polymers and DNA or naked DNA were administered at a dose equivalent to 200 μg of plasmid (~0.8 mg/kg of body weight) in 4 mL of medium into the common bile duct over 20 min (0.2 mL/min) using a syringe pump and 33-gauge needles. The needle was inserted into the common bile duct and a tie was used to secure the needle. A tie was then placed around the bile duct between the liver and the point of infusion to prevent back flow before the needle was withdrawn. After 30 min, all ties were removed. The needle hole in the bile duct might require a single 10-O nylon (Ethicon) stitch to prevent bile leakage. Rats were kept on normal diet if necessary. After 3 days, the rat from each group was sacrificed, and major organs (liver, heart, lung, spleen, and kidney) were harvested and stored at −80 °C. Each liver was divided into four sections composed of median, left, right, and caudate lobes. A total of 2 mL of lysis buffer (0.1% Triton X-100, 2 mmol/L ethylenediamine tetraacetic acid, and 0.1 mol/L Tris-HCl pH 7.8) per gram of organ was used on each sample, and the major organs were homogenized and then subjected to two cycles of freezing and thawing. The mixtures were centrifuged at 14 000 rpm for 10 min. The samples protein concentration in the supernatant was determined using a luciferase protein assay kit (Pierce, Rockford, IL). A total of 10 μL of supernatant was analyzed for luciferase activity. Luminescence was measured for 10 s of incubation, and the luciferase activity for each assay was presented as RLU per gram of tissue. The mean of luciferase activity of the liver was the sum of the values obtained by timing the RULs per gram of each lobe with the weight percentage of each lobe relative to the total liver weight.

RESULTS AND DISCUSSION

Synthesis and Characterization of PEI-g-chitosan. PEI-g-chitosan was prepared by performing the cationic polymerization of aziridine in the presence of chitosan. As described in Scheme 1, PEI was grafted onto chitosan through two mechanisms, i.e., by transferring of the iminium ion of a protonated aziridine monomer to amines of chitosan (activated monomer mechanism (AMM)) or by transferring of the iminium ion at the end of a propagation chain to the amines of chitosan (activated chain mechanism (ACM)) (*19*, *28*−*30*). To obtain PEI-g-chitosan with a homogeneous constitution, a water-soluble oligo-chitosan was adopted as a chain transfer reagent in the cationic polymerization of aziridine. The molar ratio of hydrochloride acid to the amine of chitosan was kept to be ca. 1:10. When the feed molar ratio of aziridine to amine of chitosan was 5:1, GPC results as shown in Figure 1a indicate that PEI-g-chitosan with a molecular weight of ca. 7400 (M_n) and a polydispersity index (PDI) of 1.50 was obtained. M_n of the water-soluble oligo-chiotsan adopted was ca. 3400 with a PDI of 1.36.

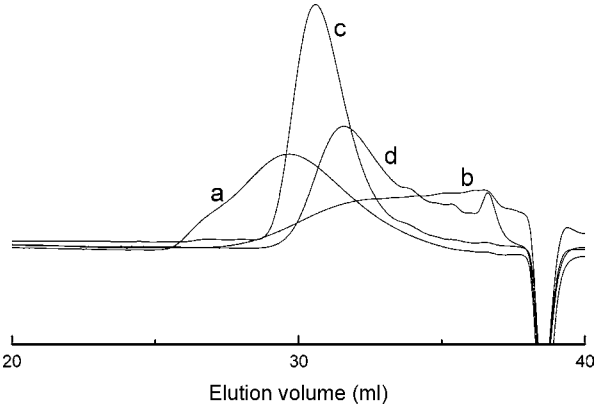

Figure 1. GPC profiles of (a) PEI-g-chitosan, (b) degraded PEI-g-chitosan obtained by treatment with 1% aqueous solution of H_2O_2 at 90 °C for 16 h, (c) PEI (2 K), and (d) degraded PEI (2 K) obtained by treatment with 1% aqueous solution of H_2O_2 at 90 °C for 16 h.

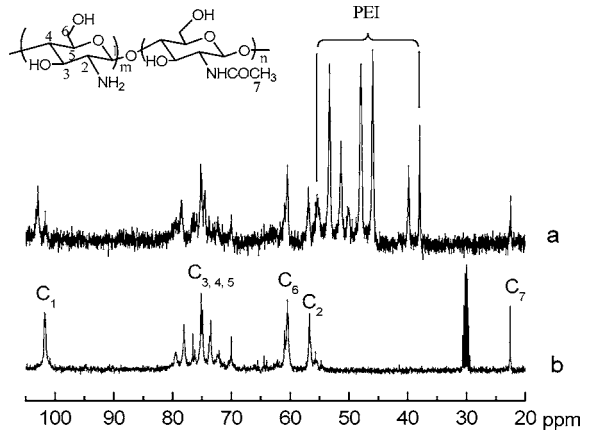

Figure 2. Comparison of ^{13}C NMR spectra of (a) PEI-g-chitosan and (b) water-soluble oligo-chitosan.

The chemistry of PEI-g-chiotsan was analyzed using ^{13}C NMR. On the basis of the ^{13}C NMR spectrum (INVGATE) as shown in Figure 2, the deacetylation degree was determined to be ca. 75% (deacetylation degree = $I_{22.5}/I_{60.5} \times 100\%$, where $I_{22.5}$ and $I_{60.46}$ stand for the integral intensity of the peaks at 22.5 and 60.5 ppm attributed to the carbon in acetyl units and C-6 in the β-(1-4)-2-amino-2-deoxy-D-glucopyranose repeating units of chitosan). Further, there was only one peak located at ca. 101.8 ppm ascribed to C-1 in the β-(1-4)-2-amino-2-deoxy-D-glucopyranose repeating units of chitosan, so acetylation/deacetylation might have little effect on the position of C-1 peak in ^{13}C NMR (*31*). However, after PEI was grafted onto chitosan, a new peak appeared at ca. 103.1 ppm as shown in Figure 2a, probably caused by the inductive effect of the grafted PEI. The integral intensity of the peak at ca. 103.1 and 101.8 ppm was ca. 71:28, therefore, almost all the amines of chitosan were grafted with PEI. The amine constitution could be determined

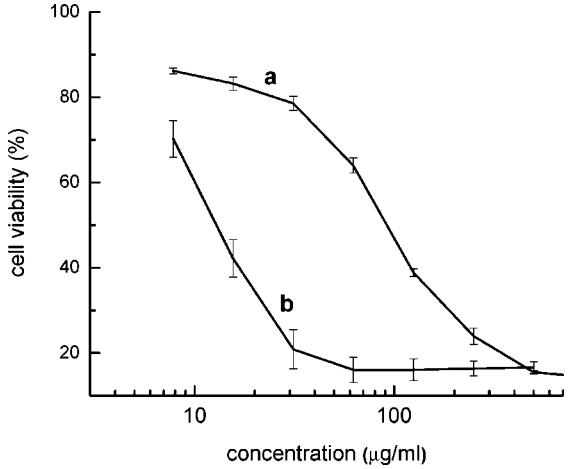

Figure 3. Comparison of the cytotoxicity of (a) PEI-g-chitosan with (b) PEI (25 K) in HeLa cells. Mean ± standard derivation ($n = 3$).

as well (*32*). The molar ratio of primary/secondary/tertiary amine was calculated to be around 1:1.97:1.23 based on the integral intensities of the corresponding peaks in Figure 2a. In addition, the ratio of PEI/chitosan unit was calculated to be around 4.8:1 based on the integral intensities of peaks located at 2.5−3.0 and 3.2−4.2 ppm in ^{1}H NMR ascribed to proton in PEI and attached to C2−6 in chitosan, which is close to the feed molar ratio. Therefore, one PEI side chain should contain around five ethylenimine units with a molecular weight of ca. 206 on average, which is in agreement with the GPC results.

To clarify whether PEI-g-chitosan was contaminated with high molecular weight PEIs, which were not expected due to the high toxicity and poor long-term safety, the degradation behavior of polymer obtained and PEI (2 K) in a 1% aqueous solution of H_2O_2 at 90 °C for 16 h was monitored using GPC. As shown in Figure 1, the degradation degree of PEI (2 K) was limited as shown by a still existing sharp elution peak with a shifting of the peak position from 2678 to 2074 and almost the same starting point of the elution peak. In comparison, the degradation of PEI-g-chitosan was significant as indicated by a very widening peak of the degraded product, the shifting of the whole peak to a much lower position, and the remarkable delay in the starting point of the elution peak. Hence, no high molecular weight PEI coexisted with PEI-g-chitosan.

Cytotoxicity of PEI-g-chitosan. MTT assay was carried out to determine the cytotoxicity of PEI-g-chitosan. Figure 3 shows that PEI-g-chitosan had a lower cytotoxicity as compared to PEI (25 K) in HeLa cells, as indicated by a IC_{50} of 97.3 μg/mL being around six times higher than 13.5 μg/mL for PEI (25 K). The cytotoxicity of cationic polymers was probably caused by polymer aggregation on cell surfaces impairing the important membrane functions (*33*). Also polymers may interfere with critical intracellular processes of cells; in particular, primary amine was reported to disrupt PKC function through disturbance of protein kinase activity (*34*). PEI-g-chitosan has an amine constitution similar to PEI (25 K); therefore, its low cytotoxicity should be caused by the lower molecular weight as reported for lower molecular weight PEI (*20*) and the lower amine content. In addition, PEI-g-chitosan may degrade in cells resulting in lower cytotoxicity as well. PEI-g-chitosan should degrade into chitosan units and nontoxic low molecular weight PEI (the average molecular weight of PEI side chain was 206); therefore, the biocompatibility and long-term safety of PEI-g-chitosan should be improved significantly as compared to PEI (25 K). In addition, here the cytotoxicity of the pure polymers was evaluated. When used for gene delivery, polymers would be complexed with DNA, and the complexes generally showed less toxicity than pure polymers.

Complexes of PEI-g-chitosan and DNA. The condensation capability of PEI-g-chitosan with DNA was evaluated using agarose gel electrophoresis. Figure 4 demonstrates that the migration of DNA was retarded completely when the N/P ratios of PEI-g-chitosan/DNA was around 2.5/1. Chitosan used for the preparation of PEI-g-chitosan with a M_n of ca. 3400 could not form stable complexes with DNA; even the N/P ratios were higher than 140, which was consistent with the reported result that only chitosan with a molecular weight higher than 4056 could form stable complexes with DNA (*35*). The condensation capability of PEI is also related to its molecular weight. For example, two times higher N/P ratio is needed to form stable complexes with DNA for PEI (5 K) as compared to PEI (25 k) (*21*). Herein M_n of PEI-g-chitosan was determined to be around 7400, but the stable complexes with DNA can be formed with the N/P ratio of 2.5/1 close to that of PEI (25 K). Probably the extended conformation of the hyperbranched PEI-g-linear chiotsan contributed to the good DNA condensation capability.

Figure 5 shows the sizes and ζ-potentials of the complexes with different N/P ratios. When the N/P was 10/1, the largest complex with a diameter of 2433.7 nm was formed. Under this condition, the complex was almost neutrally charged, so aggregation probably occurred. The complexes were negatively charged when the N/P ratio was below 10:1, and positively charged complexes were obtained when the N/P ratio was higher than 10:1. The charged complex surfaces hindered aggregation; therefore, the smaller complexes with diameters ranging from 182 to 403 nm were produced.

DNA Delivery in Vitro. DNA transfection efficiency of PEI-g-chitosan was evaluated in HepG2, HeLa, and primary hepatocytes cells. As shown in Figure 6, the complexes with N/P of 40:1 displayed the highest transfection efficiency in the three kinds of cells. Under this condition, PEI-g-chitosan showed DNA transfection efficiency being ca. 5.2-, 4.3-, and 1.5-fold higher than PEI (25 K) and much higher than naked DNA.

The higher transfection efficiency of PEI-g-chitosan should be attributed to a higher amine content of the complexes with a N/P ratio of 40:1. The higher amine content and an amine constitution similar to PEI make the complexes escape endosome easily due to a higher buffer capability. In addition, the low molecular weight PEI-g-chitosan may have a weaker

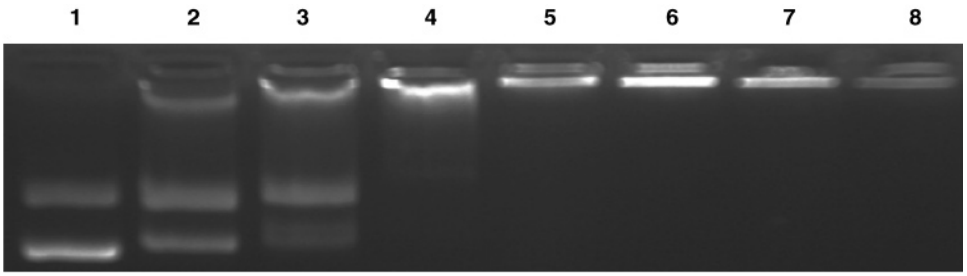

Figure 4. Agarose gel electrophoresis retardation of DNA (pCMV-Luc) by PEI-g-chitosan. Lane numbers correspond to different N/P ratios of PEI-g-chitosan/DNA as follows: (1) 0:1 (DNA only), (2) 0.6:1, (3) 0.8:1, (4) 1:1, (5) 1.5:1, (6) 2:1, (7) 3:1, (8) 4:1.

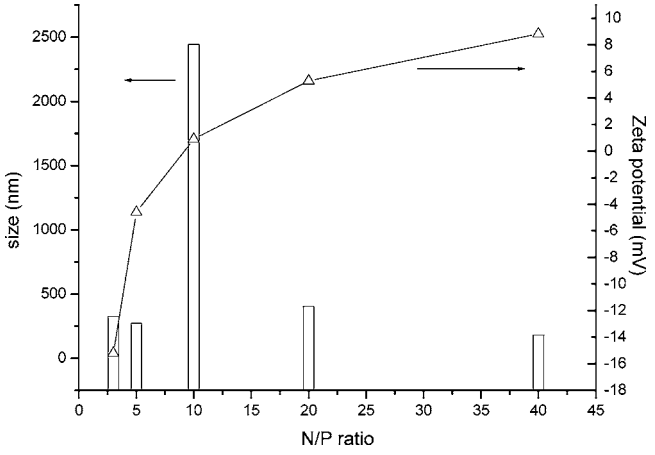

Figure 5. Effect of the N/P ratio on the diameter and ζ-potential of the complex formed from DNA (pCMV-Luc) and PEI-g-chitosan.

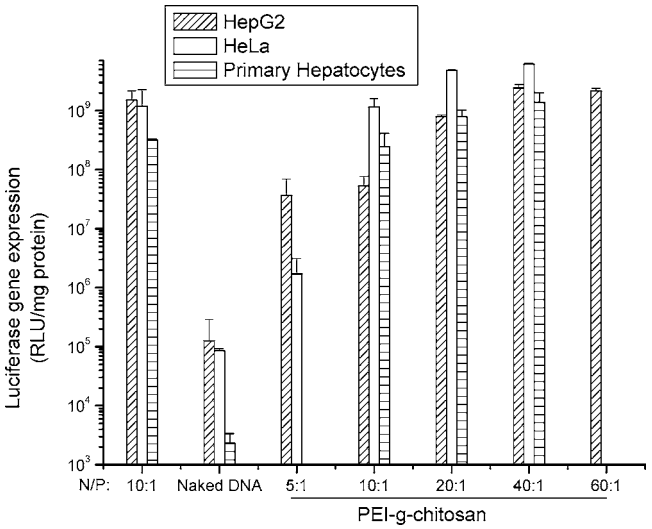

Figure 6. In vitro transfection efficiency of the complexes of PEI-g-chitosan/DNA in HepG2, HeLa, and primary hepatocytes cells in comparison with that of PEI (25 kDa). The transfection efficiency of PEI (25 K) was obtained with an optimal N/P ratio of 10:1. Mean ± standard derivation ($n = 3$).

condensation capability than PEI (25 K), which resulted in an easy release of DNA from the complexes after entering cells. This also would facilitate a higher transfection efficiency of DNA.

DNA Delivery in Vivo. The in vitro transfection efficiency of the complexes of PEI-g-chitosan/DNA was evaluated through administration in common bile duct in rat liver. A VR1255 plasmid encoding firefly luciferase driven by CMV promoter was used. The complexes of DNA and PEI-g-chitosan with N/P ratios of 5:1, 10:1, 20:1, and 40:1 were administered to screen the optimal N/P ratio for in vivo transfection. The results indicated that the complex of PEI-g-chitosan/DNA showed the highest transfection efficiency when the N/P ratio was 10:1. Then the transfection efficiency of the complexes of the optimal N/P ratio from PEI-g-chitosan was compared with these from the chitosan/DNA complexes of (N/P 3:1), PEI (25 K)/DNA (N/P 10:1), and naked DNA. Figure 7 reflects that under this condition the transfection efficiency in liver was ca. 141 times higher than that of naked DNA, 58 times higher than that of PEI (N/P 10:1), and 3 times higher than chitosan (N/P 3:1) after 3 days.

There is no relationship between the in vitro and in vivo transfection efficiency for PEI-g-chitosan in terms of the optimal N/P ratio. The complexes of the biggest size with an N/P ratio of 10:1 showed the highest transfection efficiency after admin-

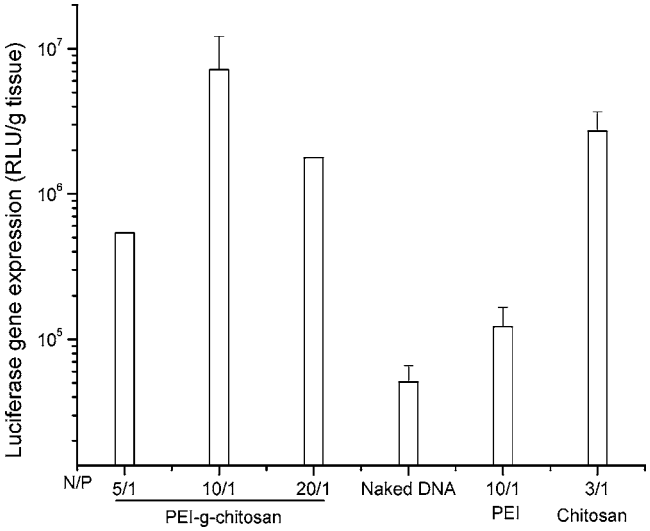

Figure 7. In vivo transfection efficiency of the complexes of PEI-g-chitosan/DNA in comparison with that of PEI (25 kDa) (N/P = 10:1) and chitosan (N/P = 3:1) after administration into common bile duct in rat liver. For the complexes of PEI-g-chitosan with N/P ratios of 5/1 and 10/1, the values were obtained from one rat. For the other samples, the values were mean ± standard derivation ($n = 3$).

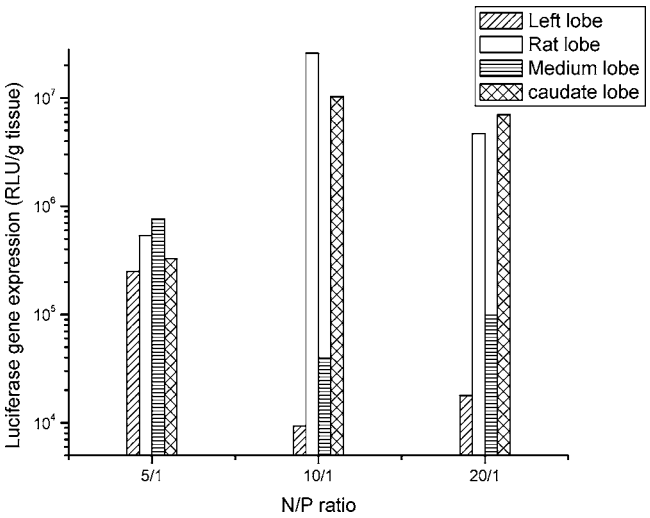

Figure 8. Gene expression in the different parts of rat liver after administration of the complexes of PEI-g-chitosan/DNA of different N/P ratios in the common bile duct in rat liver.

istration in liver. In contrast, the optimal N/P ratio for in vitro transfection was 40:1. The discrepancy may be because more stable complexes of PEI-g-chitosan/DNA are needed for efficient uptake by cells in vitro as compared to the in vivo transfection when a more concentrated suspension of the complexes was injected directly to the common bile duct.

PEI-g-chiotan still could protect pDNA from degradation efficiently with the N/P of 10:1; therefore, the complexes showed transfection efficiency still much higher than naked DNA. But factors other than the protection function should contribute to the transfection efficiency higher than PEI (25 K) and chitosan. Probably the weaker association of DNA and the low molecular weight PEI-g-chitosan would result in the ease of DNA release from the complexes, which would facilitate the transfection of DNA, together with the good buffer capability of PEI-g-chitosan. Similar results have been observed in transfection efficiency in vivo mediated by oligo-chitosan of suitable chain lengths (5).

Further, Figure 8 shows the distribution of the transgene product in different lobes of the transfected rat livers. Luciferase

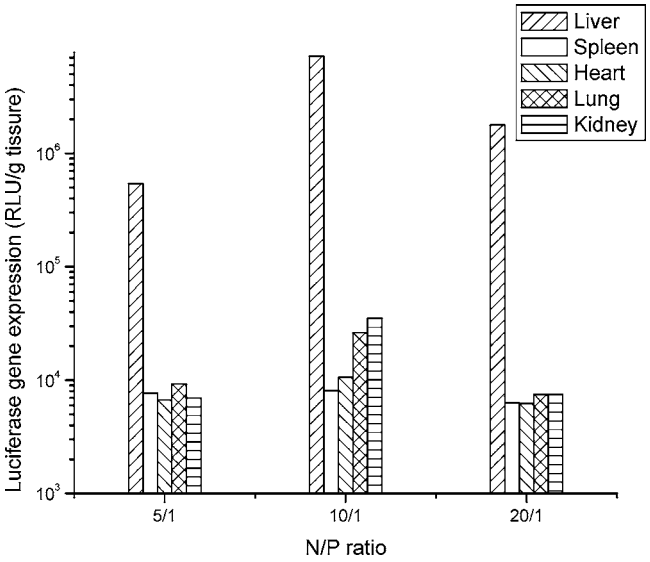

Figure 9. Gene expression in the different tissues after administration of the complexes of PEI-g-chitosan/DNA of different N/P ratios in common bile duct in rat liver.

expression in the left and medium lobes were about 5−1000-fold lower than that of the other lobes at the early time points for the complexes with N/P ratios of 10:1 or 20:1. In contrast, the expression levels were similar in different lobes for the complexes with an N/P ratio of 5: 1. Moreover, Figure 9 shows that the gene expression in kidney, lung, heart, and spleen were negligible in comparison with that in liver for the complexes of different N/P ratios.

In conclusion, PEI-g-chitosan, a kind of combined oligo-PEI, was synthesized by performing cationic polymerization of aziridine in the presence of chitosan. The length of the grafted PEI side chain could be controlled well through the feed molar ratio of aziridine/amine in chitosan. The obtained PEI-g-chiotsan has amine constitution similar to hyperbranched PEI. PEI-g-chitosan of a $M_n = 7400$ and PEI side chains of $M_n = 206$ showed good DNA condensation capability, much lower cytotoxicity, and transfection efficiency for DNA delivery higher than those of PEI (25 K) both in vitro and after administration in a rat liver. Improved biocompatibility and long-term safety could be expected for PEI-g-chitosan due to the degradable chitosan main chain and the short PEI ($M_n = 206$) side chains. So PEI-g-chitosan should be a promising nonviral gene carrier.

ACKNOWLEDGMENT

We are grateful to Mr. Wu Decheng for his help in measurement of the sizes and ζ-potentials of the complexes.

LITERATURE CITED

(1) Boussif, O., Lezoualc'h, F., Zanta, M. A., Mergny, M. D., Scherman, D., Demeneix, B., and Behr, J. P. (1995) A versatile vector for gene and oligonucleotide transfer into cells in culture and in vivo: polyethylenimine. *Proc. Natl. Acad. Sci. U.S.A. 92*, 7297−7301.

(2) Behr, J. P. (1997) The proton sponge: A trick to enter cells the viruses did not exploit. *Chimia 1*, 34−36.

(3) Kircheis, R., Wightman, L., and Wagner, E. (2001) Design and gene delivery activity of modified polyethylenimines. *Adv. Drug Delivery Rev. 53*, 341−358.

(4) Pun, S. H., and Davis, M. E. (2002) Development of a nonviral gene delivery vehicle for systemic application. *Bioconjugate Chem. 13*, 630−639.

(5) Koping-Hoggard, M., Varum, KM., Issa, M., Danielsen, S., Christensen, B. E., Stokke, B. T., and Artursson, P. (2004) Improved chitosan-mediated gene delivery based on easily dissociated chitosan polyplexes of highly defined chitosan oligomers. *Gene Therapy 11*, 1441−1452.

(6) Borchard, G. (2001) Chitosans for gene delivery. *Adv. Drug Delivery Rev. 52*, 145−150.

(7) Lim, Y. B., Kim, C. H., Kim, W., Kim, S. W., and Park, J. S. (2000) Development of a safe gene delivery system using biodegradable polymer, poly[alpha-(4-aminobutyl)-L-glycolic acid]. *J. Am. Chem. Soc. 122*, 6524−6525.

(8) Lim, Y. B., Han, S. Q., Kong, H. U., Lee, Y., Park, J. S., Jeong, B., and Kim, S. W. (2000) Biodegradable polyester, poly[alpha-(4 aminobutyl)-L-glycolic acid], as a nontoxic gene carrier. *Pharm. Res. 17*, 811−816.

(9) Wang, J., Mao, H. Q., Leong, K. W. (2001) A novel biodegradable gene carrier based on polyphosphoester. *J. Am. Chem. Soc. 123*, 9480−9481.

(10) Wang, J., Mao, H. Q., and Leong, K. W. (2002) Enhanced gene expression in mouse muscle by sustained release of plasmid DNA using PPE-EA as a carrier. *Gene Therapy 9*, 1254−1261.

(11) Azzam, T., Raskin, A., Makovitzki, A., Brem, H., Vierling, P., Lineal, M., and Domb, A. J. (2002) Cationic Polysaccharides for Gene Delivery. *Macromolecules 35*, 9947−9953.

(12) Eliyahu, H., Makovitzki, A., Azzam, T., Zlotkin, A., Joseph, A., Gazti, D., Barenholz, Y., and Domb, A. J. (2005) Novel dextran-spermine conjugates as transfecting agents: comparing water-soluble and micellar polymers. *Gene Therapy 12*, 494−503.

(13) Lynn, D. M., and Langer, R. (2000) Degradable poly(beta-amino esters): Synthesis, characterization, and self-assembly with plasmid DNA. *J. Am. Chem. Soc. 122*, 10761−10768.

(14) Akinc, A., Lynn, D. M., Anderson, D. G., and Langer, R. (2003) Parallel synthesis and biophysical characterization of a degradable polymer library for gene delivery. *J. Am. Chem. Soc.* **2003**, *125*, 5316−5323.

(15) Lim, Y. B., Kim, S. M., Lee, Y, Lee, W. K., Yang, T. G., Lee, M. J., Suh, H., and Park, J. S. (2001) Cationic hyperbranched poly-(amino ester): A novel class of DNA condensing molecule with cationic surface, biodegradable three-dimensional structure, and tertiary amine groups in the interior. *J. Am. Chem. Soc. 123*, 2460−2461.

(16) Lim, Y. B., Kim, S. M., Suh, H., and Park, J. S. (2002) Biodegradable, endosome disruptive, and cationic network-type polymer as a highly efficient and nontoxic gene delivery carrier. *Bioconjugate Chem. 13*, 952−957.

(17) Liu, Y., Wu, D. C., Ma, Y. X., Tang, G. P., Wang, S., He, C. B., Chung, T. S., and Goh, S. H. (2003) Novel poly(amino ester)s obtained from Michael addition polymerizations of trifunctional amine monomers with diacrylates: safe and efficient DNA carriers. *Chem. Commun.* 2630−2631.

(18) Wu, D. C., Liu, Y., Jiang, X., Chen, L., He, C. B., Goh, S. H., Leong, Kam W. (2005) Evaluation of hyperbranched poly(amino ester)s of amine constitutions similar to polyethylenimine for DNA delivery, *Biomacromolecules 6*, 3166.

(19) Liu, Y., Wu, D. C., Zhang W.-D., Jiang X., He, C. B., Chung, T. S., Goh, S. H., Kam W. Leong (2005) Polyethylenimine (PEI)-grafted multiwalled carbon nanotubes for secure noncovalent immobilization and efficient delivery of DNA. *Angew. Chem., Int. Ed. 44*, 4782.

(20) Fischer, D., Bieber, T., Li, Y. X., Elsasser, H. P., and Kissel, T. (1999) A novel nonviral vector for DNA delivery based on low molecular weight, branched polyrthylenimine: effect of molecular weight on transfection efficiencyand cytotoxicity. *Pharm. Res. 16*, 1273−1279.

(21) Kunath, K., Harpe, A. v., Fischer, D., Peterson, H., Bickel U., Voigt, K., and Kissel, T. (2003) Low-molecular-weight polyethylenimine as a nov-viral vector for DNA delivery: comparison of physicochemical properties, transfection efficiency and in vivo distribution with high-molecular-weight polyethylenimine. *J. Controlled Release 89*, 113−125.

(22) Gosselin, M. A., Guo, W. J., and Lee, R. J. (2001) Efficient gene transfer using reversibly cross-linked low molecular weight polyethylenimine. *Bioconjugate Chem. 12*, 989−994.

(23) Petersen, H., Merdan, T., Kunath, K., Fischer, D., and Kissel, T. (2002) Poly(ethylenimin-*co*-lactamide-*co*-L-succinamide): A bio-

degradable polyethylenimine derivatives with an advantageous pH-dependent hydrolytic degradation for gene delivery. *Bioconjugate Chem. 13*, 812−821.
(24) Ahn, C. H., Chae, S. Y., Bae, Y. H., and Kim, S. W. (2002) Biodegradable poly(ethylenimine) for plasmid DNA delivery. *J. Controlled Release 80*, 273−282.
(25) Forrest, M. L., Koerber, J. T., and Pack, D. W. (2003) A degradable polyethylenimine derivative with low toxicity for highly efficient gene delivery. *Bioconjugate Chem. 14*, 934−940.
(26) Flory, P. J. (1953) *Principles of Polymer Chemistry*, Chapter 9, Cornell University Press: New York.
(27) Wenker H. (1930) The preparation of ethylene imine from monoethanolamine. *J. Am. Chem. Soc. 52*, 2328.
(28) Liu, Y., Wang, H. B., and Pan, C. Y. (1997) Study on the cationic polymerization mechanism of 1,3-dioxepane in the presence of ethylene glycol. *Macromol. Chem. Phys. 198*, 2613−2622.
(29) Oh, S. J., Cho, S. J., Kim, C. O., and Park, J. W. (2002) Characteristics of DNA microarrays fabricated on various aminosilane layers. *Langmuir 18*, 1764−1769.
(30) Petersen, H., Martin, A. L., Stolnik, S., Roberts, C. J., Davies, M. C., and Kissel, T. (2002) The macrostopper route: A new synthesis concept leading exclusively to diblock copolymers with enhanced DNA condensation potential. *Macromolecules 35*, 9854−9856.
(31) Nah, J.-W., and Jang, M.-K. (2002) Spectroscopic characterization and preparation of low molecular, water-soluble chitosan with free-amine group by novel method. *J. Polym. Sci.: Polym. Chem. Ed. 40*, 3796−3803.
(32) Harpe, A. v., Peterson, H., Li, Y. X., and Kissel, T. (2003) Characterization of commercially available and synthesized polyethylenimines for gene delivery. *J. Controlled Release 69*, 309−322.
(33) Ryser, H. J.-P. (1967) A membrane effect of basic polymers dependent on molecular size. *Nature 215*, 934.
(34) Bottega, R., and Epand, R. M. (1992) Inhibition of protein-kinase-c by cationic amphiphiles. *Biochemistry 31*, 9025−9030.
(35) Koping-Hoggard, M., Mel'nikova, Y. S., Varum, K. M., Lindman, B., and Artursson, P. (2003) Relationship between the physical shape and the efficiency of oligomeric chitosan as a gene delivery system in vitro and in vivo. *J. Gene Med. 5* (2), 130−141.

BC0501597

In Vitro Gene Transfer Efficacies and Serum Compatibility Profiles of Novel Mono-, Di-, and Tri-Histidinylated Cationic Transfection Lipids: A Structure−Activity Investigation

Priya Prakash Karmali,[†] Bharat Kumar Majeti,[†] Bojja Sreedhar,[‡] and Arabinda Chaudhuri*[,†]

Division of Lipid Science and Technology, and Inorganic and Physical Chemistry Division, Indian Institute of Chemical Technology, Hyderabad-500 007, India. Received July 2, 2005; Revised Manuscript Received November 25, 2005

Recently, we demonstrated that covalent grafting of an endosome-disrupting single histidine functionality in the headgroup region imparts high gene transfer properties to cationic amphiphiles (Kumar, V. V., et al. *Gene Ther.* **2003**, *10,* 1206−1215). However, whether covalent attachment of multiple histidine functionalities in the headgroup region are capable of further enhancing the gene transfer efficacies of cationic amphiphiles remains to be explored. To this end, herein, we report on the design, syntheses, physicochemical characterizations, in vitro gene transfer properties, and serum compatibilites of three novel nontoxic cationic transfection amphiphiles containing mono-, di-, and tri-histidine functionalities in their headgroup regions (lipids **1**−**3**) in multiple cultured cells**.** Significantly, findings in both the reporter gene expression assay and the whole cell histochemical X-gal staining assay support the notion that there is no linear correlation between the in vitro transfection efficacies and the number of histidine functionalities in the polar headgroup regions for histidinylated cationic amphiphiles. The relative gene transfer efficiencies, as well as the serum compatibilities, of the present histidinylated cationic amphiphiles were found to be strikingly dependent on the medium of lipoplex formation. Most importantly, high serum compatibilities (up to 50% added serum) of the lipoplexes of lipids **1** and **3** make them promising nonviral transfection vectors for future systemic applications.

INTRODUCTION

Body cells are supplemented with normal functioning copies of the malfunctioning genes in gene therapy, the modality to combat myriads of inherited diseases, dreadful viral infections, and cancer. However, since both genes (DNA) and the biological cell surfaces are negatively charged, entry of genes into our body cells is not an efficient and spontaneous process. In other words, clinical success of gene therapy critically depends on the availability of safe, efficacious, and serum-compatible gene transfer reagents. Contemporary gene transfer reagents are broadly classified into two major categories: viral and nonviral. Despite their high gene transfer efficacies, serious biosafety concerns associated with the clinical uses of viral vectors have been raised (*1*−*5*). Viral vectors have a low insert-size limit (for the therapeutic genes they can pack inside) and are capable of generating: (a) inflammatory immunogenic responses against their structural components and (b) replication-competent virus through recombination events with the host genome (*6*−*10*). Such biosafety-related issues associated with the use of viral vectors have led to much effort in developing synthetic nonviral gene carriers. Contemporary major nonviral gene delivery reagents are mainly of two types: cationic polymers and cationic lipids. Cationic polymers, polylysines (*11, 12*), poly(ethylene imines) (PEI) (*13*), etc., are good in transfecting cells due to their abilities of condensing and thereby protecting DNA from the attack of DNase. However, such cationic polymers can be significantly cytotoxic (*11*) and may not be readily biodegradable (*14*). Because of their less immunogenic nature, ability to deliver large pieces of DNA, and ease of handling and preparation, cationic lipids are increasingly being demonstrated as the nonviral transfection vectors of choice for delivering genes into body cells (*15*−*22*). Detailed structure−activity investigations using libraries of cationic amphiphiles with varying headgroups, hydrophobic anchor chain lengths, linker functionalities, etc. are being actively pursued with a view to find more efficacious cationic transfection lipids for use in nonviral gene delivery (*23*−*34*).

Currently believed intracellular pathways involved in cationic lipid mediated gene transfer (lipofection) include (a) endocytotic cellular uptake of the lipid−DNA complex (lipoplex), (b) release of DNA from endosomes to cell cytoplasm, and (c) the nuclear transport of the endosomally released DNA followed by transcription and gene expression (*35*−*38*). Recently, toward enhancing gene transfer properties of cationic amphiphiles through use of endosome-disrupting headgroups (i.e., through improving the efficacies of step b mentioned above), we designed and synthesized two efficacious cationic amphiphiles containing a covalently grafted endosome-pH-sensitive single histidine functionality in their polar headgroup regions (*26, 32*). In the present structure−activity investigation, we address the issue of whether covalent grafting of increasing numbers of histidine functionalities in the polar headgroup region of cationic amphiphiles leads to further enhancement of their in vitro gene transfer efficacies. To this end, we have designed and synthesized three novel histidinylated cationic lipids containing mono-, di-, and tri-histidine functionalities in the polar headgroup regions (lipids **1**, **2**, and **3**, respectively, Schemes 1−3) and evaluated their efficacies in transfecting multiple cultured cells including COS-1 (African green monkey kidney cells), CHO (Chinese hamster ovarian cells), HepG2 (human hepatocarcinoma cells), and the highly transfectable HEK293T (SV-40 T-antigen transformed human embryonic kidney) cells both in the presence and in the absence of added serum. As described below, our present findings shows an absence of any linear correlation between the in vitro transfection efficacies and the

* Corresponding author. Tel: 91-40-27193201. Fax: 91-40-27160757. E-mail: arabinda@iict.res.in.

‡ Inorganic and Physical Chemistry Division.

† Division of Lipid Science and Technology.

10.1021/bc050194d CCC: $33.50 © 2006 American Chemical Society
Published on Web 12/20/2005

Scheme 1. Synthesis of Lipids: Lipid 1[a]

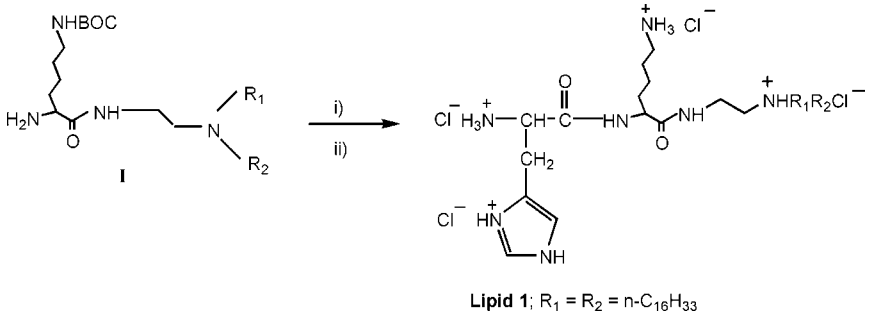

[a] Reagents: (i) N^{α},N^{im}-di-BOC-histidine, DCC, HOSu, DMAP(cat); (ii) 2 N HCl, MeOH.

Scheme 2. Synthesis of Lipids: Lipid 2[a]

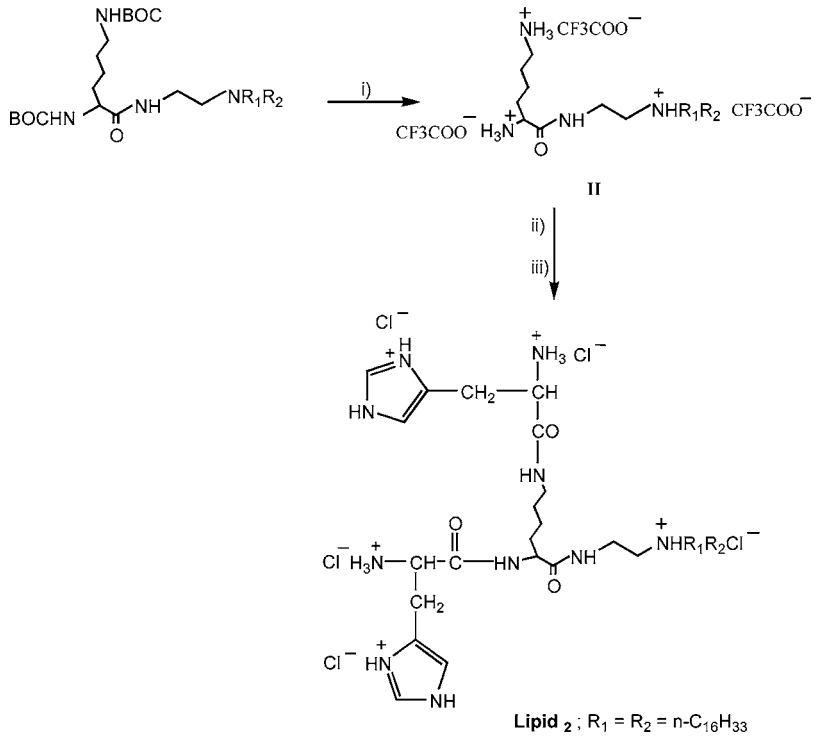

[a] Reagents: (i) TFA, DCM; (ii) N^{α},N^{im}-di-BOC-histidine, DCC, HOSu, NEt_3; (iii) 2 N HCl, MeOH.

number of histidine functionalities in the polar headgroup regions for histidinylated cationic amphiphiles. Our findings also demonstrate that the relative in vitro gene transfer efficacies of the presently described histidinylated cationic amphiphiles are remarkably sensitive to the nature of the buffer used in preparing lipoplexes. In addition, in sharp contrast to serum incompatibilities of many cationic amphiphiles, the lipoplexes of both mono- and tri-histidinylated lipids **1** and **3** when prepared in HEPES[1] buffer remained remarkably transfection efficient in the presence of up to 50% (v/v) added serum at lipid/DNA charge ratios of 8:1 and 4:1.

[1] Abbreviations: BOC, *tert*-butyloxycarbonyl; Chol, cholesterol; DCC, dicyclohexylcarbodiimide; DCM, dichloromethane; DMAP, 4-(dimethylamino)pyridine; DMEM, Dulbecco's modified Eagle's medium; DMF, *N*,*N*-dimethylformamide; DOPE, 1,2-dioleoyl-*sn*-glycero-3-phosphoethanolamine; DOTAP, *N*-[1-(2,3-dioleoyloxy)propyl]-*N*,*N*,*N*-trimethylammonium methyl sulfate FBS, fetal bovine serum; HOSu, *N*-hydroxysuccinimide; HEPES, [*N*-(2-hydroxyethyl)] piperazine-*N*′-[2-ethanesulfonic acid]; ONPG, *o*-nitrophenyl-β-D-galactopyranoside; PBS, phosphate-buffered saline; TFA, trifluoroacetic acid; Z, benzyloxycarbonyl: NP-40, nonylphenylpoly(ethylene glycol).

EXPERIMENTAL PROCEDURES

General Procedures and Materials. The FABMS data were acquired by the liquid secondary ion mass spectrometry (LSIMS) technique using *meta*-nitrobenzyl alcohol as the matrix. LSIMS analysis was performed in the scan range 100−1000 amu at the rate of 3 scans/s. ^{1}H NMR spectra were recorded on a Varian FT 200 MHz, AV 300 MHz, or Varian Unity 400 MHz. 1-Bromohexadecane, *n*-hexadecylamine, and 10% Pd/C were procured from Lancaster (Morecambe, England); L-lysine and N^{α}-*Z*-L-lysine used were a product of Aldrich (St. Louis, MO). The progress of the reactions was monitored by thin-layer chromatography on 0.25 mm silica gel plates. Column chromatography was performed with silica gel (Acme Synthetic Chemicals, India, 60−120 and 100−200 mesh). pCMV-SPORT-β-gal plasmid was a generous gift from Dr. Nalam Madhusudhana Rao (Centre for Cellular and Molecular Biology, Hyderabad, India). Lipofectamine was purchased from Invitrogen Life Technologies (Carlsbad, CA). Cell culture media, fetal bovine serum, 3-(4,5-dimethylthiazol-2-yl)-2,5-diphenyltetrazolium bromide (MTT), poly(ethylene glycol) 8000, *o*-nitrophenyl-β-D-galactopyranoside, cholesterol, and bafilomycin A1 were pur-

Scheme 3. Synthesis of Lipids: Lipid 3[a]

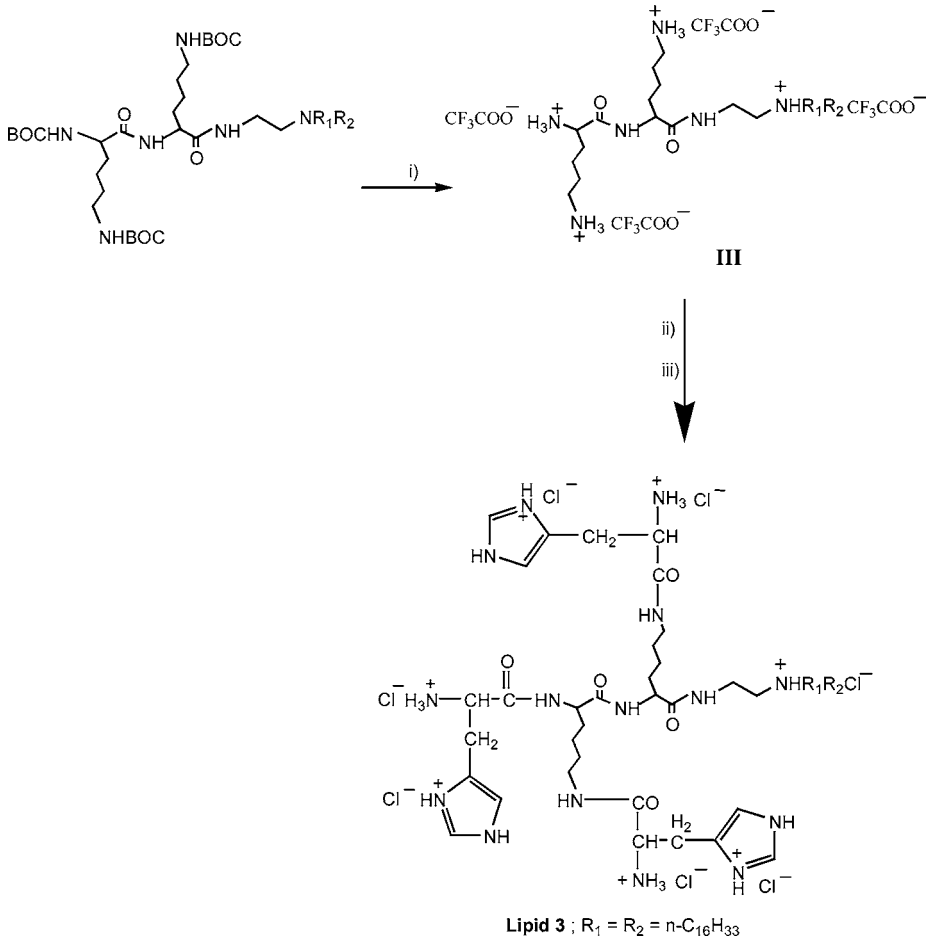

[a] Reagents: (i) TFA, DCM; (ii) N^{α},N^{im}-di-BOC-histidine, DCC, HOSu, NEt_3; (iii) 2 N HCl, MeOH.

chased from Sigma, St. Louis, MO. NP-40, antibiotics, and agarose were purchased from Hi-media, India. DOPE was purchased from Fluka (Switzerland). Unless otherwise stated, all the other reagents purchased from local commercial suppliers were of analytical grades and were used without further purification. COS-1 (SV-40 transformed African green monkey kidney), CHO (Chinese hamster ovary), and HepG2 (human hepatocarcinoma) cell lines were procured from the National Centre for Cell Sciences (NCCS), Pune, India. HEK293T cells (SV-40 T-antigen transformed human embryonic kidney) were a generous gift from Dr. V. Radha (Centre for Cellular and Molecular Biology, Hyderabad, India). Purity of all the final lipids (**1**−**3**) was determined by analytical HPLC (Shimadzu model LC10A) using a PARTISIL 5 ODS-3 WCS analytical column (4.6 mm × 250 mm, Whatman Inc., Clifton, NJ) in two different mobile phases. One solvent system (A) was methanol (100%) for 20 min with a flow rate of 1.2 mL/min. The other (B) was methanol/water/trifluoroacetic acid in the ratio 98:2:0.05 (v/v) for 20 min with a flow rate of 1.3 mL/min. Peaks were detected by UV absorption at 219 nm. All the target lipids (**1**−**3**) showed more than 95% purity. Retention times in mobile phase A and B were 2.25 and 2.22 min for lipid **1**; 2.14 and 2.24 min for lipid **2**, and 2.01 and 2.41 min for lipid **3**, respectively.

Synthesis. Lipids **1**−**3** were synthesized following strategies depicted in Schemes 1−3. ^{1}H NMR spectra for all the intermediates, as well as for the final lipids **1**−**3**, are provided in the Supporting Information. The final lipids **1**−**3** were further characterized by the molecular ion peaks in their FABMS, and their purities were confirmed by reverse phase analytical HPLC using two different mobile phases (Supporting Information).

Synthesis of lipid 1 (Scheme 1). *Step a.* Solid HOSu (0.125 g, 1.09 mmol) and DCC (0.23 g, 1.09 mmol) were added sequentially to an ice cold and stirred solution of N^{α},N^{im}-di-*tert*-butyloxycarbonyl-L-histidine (0.39 g, 1.09 mmol) in 10 mL of dry DCM/dry DMF (9:1, v/v). After half an hour, *N*-2-[*N*′-(N^{ϵ}-BOC-L-lysyl)]aminoethyl-*N*,*N*-di-*n*-hexadecylamine (**I**, 0.8 g, 1.09 mmol, prepared as described in ref *29*) and DMAP (catalytic) dissolved in dry DCM were added to the reaction mixture. The resulting solution was left stirring at room temperature for 24 h, solid DCU was filtered, and the solvent was evaporated from the filtrate. The residue was taken up in ethyl acetate (100 mL) and washed sequentially with ice-cold 1 N HCl (3 × 100 mL), saturated sodium bicarbonate (3 × 100 mL), and water (3 × 100 mL). The organic layer was dried over anhydrous sodium sulfate and filtered, and the solvent was removed from the filtrate by rotary evaporation. The residue upon column chromatographic purification with 60−120 mesh silica gel using 2.5−3% methanol−chloroform (v/v) as eluent afforded 0.28 g (24% yield) of the pure intermediate *N*-2-[*N*′-(N^{α},N^{im}-di-BOC-L-histidyl-N^{ϵ}-BOC-L-lysyl)]aminoethyl-*N*,*N*-di-*n*-hexadecylamine (R_f = 0.4, 5% methanol−chloroform, v/v).

Step b. The intermediate obtained in step a (0.28 g, 0.26 mmol) was dissolved in 1 mL of 2 N HCl in methanol at 0 °C. The resulting solution was left stirring at room temperature for 4 h to ensure complete deprotection. Excess HCl was removed by flushing with nitrogen to give the title compound as a chloride salt. Repeated crystallization from dry acetone/dichloromethane/methanol (8:1:1, v/v) afforded 0.175 g (overall yield of about 18%) of *N*,*N*-di-*n*-hexadecyl-*N*-2-[*N*′-(L-histidyl-L-lysyl)]aminoethylammonium chloride, lipid **1** (R_f = 0.1, 40% methanol in chloroform, v/v).

Synthesis of lipid 2 (Scheme 2). *Step a.* *N*-2-[*N*′-(*N*$^{\alpha}$,*N*$^{\epsilon}$-Di-BOC-L-lysyl)]aminoethyl-*N*,*N*-di-*n*-hexadecylamine (1.05 g, 1.26 mmol, prepared as described in ref *29*) was dissolved in 10 mL of dry DCM, and 5 mL of TFA was added at 0 °C. The resulting solution was left stirring at room temperature for 4 h to ensure complete deprotection. Excess TFA was removed by flushing with nitrogen followed by recrystallization of the resulting trifluoroacetate salt from methanol/diethyl ether (1:4 v/v) to afford 1.09 g (88% yield) of *N*,*N*-di-*n*-hexadecyl-*N*-2-[*N*′-(L-lysyl)]aminoethylammonium trifluoroacetate (R_f = 0.2, 20% methanol in chloroform, v/v).

Step b. *N*$^{\alpha}$,*N*^{im}-Di-*tert*-butyloxycarbonyl-L-histidine (0.73 g, 2.06 mmol) was coupled with the intermediate prepared in step a (1.0 g, 1.02 mmol) in the presence of solid HOSu (0.24 g, 2.06 mmol), DCC (0.47 g, 2.06 mmol), and triethylamine (0.85 mL, 6.14 mmol) following essentially the same protocol as described in step a of the lipid **1** synthesis. The resulting crude product upon column chromatographic purification with 60−120 mesh silica gel using 25% acetone in petroleum ether (v/v) as eluent afforded 0.32 g (50% yield) of *N*-2-[*N*′-{*N*$^{\alpha}$,*N*$^{\epsilon}$-di-(*N*$^{\alpha}$,*N*^{im}-di-*tert*-butyloxycarbonyl-L-histidyl)-L-lysyl}]aminoethyl-*N*,*N*-di-*n*-hexadecylamine intermediate as a white gummy solid (R_f = 0.41, 35% acetone in petroleum ether, v/v).

Step c. The intermediate obtained in step b (0.2 g, 0.15 mmol) was dissolved in 1 mL of 2 N HCl in methanol at 0 °C. The resulting solution was left stirring at room temperature for 4 h to ensure complete deprotection. Excess HCl was removed by flushing with nitrogen to give the title compound as a chloride salt. Repeated crystallization from dry acetone/dichloromethane/methanol (8:1:1) afforded 0.15 g (90% yield) of *N*,*N*-di-*n*-hexadecyl-*N*-2-[*N*′-{*N*$^{\alpha}$,*N*$^{\epsilon}$-di-(L-histidyl)-L-lysyl}]aminoethylammonium chloride, lipid **2** (R_f = 0.14, 40% methanol in chloroform, v/v).

Synthesis of lipid 3 (Scheme 3). *Step a.* *N*-2-[*N*′-(*N*$^{\alpha}$,*N*$^{\epsilon}$-Di-BOC-L-lysyl-*N*$^{\epsilon}$-BOC-L-lysyl)]aminoethyl-*N*,*N*-di-*n*-hexadecylamine {0.5 g, 0.47 mmol, prepared as described previously (*29*)}was dissolved in 4 mL of dry DCM, and TFA (2 mL) was added at 0 °C. The resulting solution was left stirring at room temperature for 4 h to ensure complete deprotection. Excess TFA was removed by flushing with nitrogen. Repeated crystallization of the resulting trifluoroacetate salt from methanol/diethyl ether (1:4, v/v) afforded 0.3 g (84% yield) of *N*,*N*-di-*n*-hexadecyl-*N*-2-[*N*′-(L-lysyl)$_2$]aminoethylammonium chloride as a white gummy solid (R_f = 0.15, 40% methanol in chloroform, v/v).

Step b. *N*$^{\alpha}$,*N*^{im}-Di-*tert*-butyloxycarbonyl-L-histidine (0.84 g, 2.35 mmol) was coupled with intermediated otained in step a (0.3 g, 0.39 mmol) in the presence of solid HOSu (0.27 g, 2.35 mmol), DCC (0.49 g, 2.35 mmol), and triethylamine (0.32 mL, 3.12 mmol) following essentially the same protocol as described in step a of the lipid **1** synthesis. The resulting crude product upon column chromatographic purification with 100−200 mesh silica gel using 4.5−5% methanol in chloroform (v/v) as eluent afforded 0.18 g (26% yield) of *N*-2-[*N*′-{*N*$^{\alpha}$,*N*$^{\epsilon}$-di-(*N*$^{\alpha}$,*N*^{im}-di-*tert*-butyloxycarbonyl-L-histidyl)-L-lysyl-*N*$^{\epsilon}$-(*N*$^{\alpha}$,*N*^{im}-di-*tert*-butyloxycarbonyl-L-histidyl)-L-lysyl}]aminoethyl-*N*,*N*-di-*n*-hexadecylamine as a gummy solid (R_f = 0.5, 10% methanol in chloroform, v/v).

Step c. The intermediate obtained in step b (0.17 g, 0.1 mmol) was dissolved in 1 mL of 2N HCl in methanol at 0 °C. The resulting solution was left stirring at room temperature for 4 h to ensure complete deprotection. Excess HCl was removed by flushing nitrogen to give the title compound as a chloride salt. Repeated crystallization from dry acetone/dichloromethane/methanol (8:1:1, v/v) afforded 0.062 g (45% yield) of *N*,*N*-di-*n*-hexadecyl-*N*-2-[*N*′-{*N*$^{\alpha}$,*N*$^{\epsilon}$-di-(L-histidyl)-L-lysyl-*N*$^{\epsilon}$-(L-histidyl)-L-lysyl}]aminoethylammonium chloride, lipid **3** (R_f = 0.1, 50% methanol in chloroform, v/v).

Cell Culture. COS-1 (SV-40 transformed African green monkey kidney), CHO (Chinese hamster ovary), HepG2 (Human hepatocarcinoma), and HEK293T (SV-40 T-antigen transformed human embryonic kidney) cell lines were cultured at 37 °C in Dulbecco's modified Eagle's medium (DMEM) with 10% fetal bovine serum, 50 μg/mL penicillin, 50 μg/mL streptomycin, and 20 μg/mL kanamycin in a humidified atmosphere containing 5% CO_2.

Preparation of Liposomes. The cationic lipids (**1**−**3**) and 1,2-di-oleoyl-*sn*-glycero-3-phosphatidyl ethanolamine (DOPE) in 1:1 mole ratio were dissolved in a mixture of chloroform and methanol (3:1, v/v) in a glass vial. The solvent was removed with a thin flow of moisture-free nitrogen gas, and the dried lipid film was then kept under high vacuum for 8 h. One milliliter of sterile deionized water was added to the vacuum-dried lipid film, and the mixture was allowed to swell overnight. The vial was then vortexed for 2−3 min at room temperature and occasionally sonicated in a bath sonicator to produce multilamellar vesicles (MLVs). MLVs were then sonicated in an ice bath until clarity using a Branson 450 sonifier at 100% duty cycle and 25 W output power to give a final lipid concentration of 1 mM. These resulting clear aqueous liposomes were used in forming lipoplexes.

Plasmid DNA. pCMV-SPORT-β-gal plasmid was amplified in the DH5α strain of *Escherichia coli*, isolated by the alkaline lysis procedure, and finally purified by PEG-8000 precipitation as described previously (*39*). The purity of the plasmid was checked by A_{260}/A_{280} ratio (around 1.9) and 1% agarose gel electrophoresis.

Transfection of Cells. Cells were seeded at a density of 15 000 (for COS-1) and 20 000 cells (for CHO, HepG2, and HEK293T) per well in a 96-well plate 18−24 h before the transfection. Plasmid DNA (0.3 μg) was complexed with varying amounts of lipids (to give ± charge ratios of 1:1, 2:1, 4:1, and 8:1) in plain DMEM or 10 mM HEPES buffer, pH 7.4 (total volume made up to 100 μL), for 30 min. When the complexation was carried out in HEPES buffer, the total volume of the lipoplexes was made up to 150 μL with 50 μL of DMEM, and the NaCl concentration was adjusted to 0.15 M with 5 M NaCl after the 30 min incubation period. Immediately prior to the addition of lipoplexes, cells plated in the 96-well plate were washed with PBS (2 × 100 μL). When the transfection efficacy was evaluated in the presence of serum, 100 μL of DMEM (or 150 μL of DMEM when the complexation was carried out in HEPES) containing 20%, 60%, or 100% FBS was added to cells to give an effective serum concentration of 10%, 30%, and 50%, respectively. After 4 h of incubation, the medium was changed to 10% complete medium. The medium was again replaced with 10% complete medium after 24 h, and the reporter gene activity was estimated after 48 h. The cells were washed with PBS (2 × 100 μL) and lysed in 50 μL of lysis buffer [0.25 M Tris-HCl (pH 8.0) and 0.5% NP-40]. Care was taken to ensure complete lysis. The β-galactosidase activity per well was estimated by adding 50 μL of 2×-substrate solution [1.33 mg/mL of ONPG, 0.2 M sodium phosphate (pH 7.3) and 2 mM magnesium chloride] to the lysate in a 96-well plate. Absorbance of the product ortho-nitrophenol at 405 nm was converted to β-galactosidase units by using calibration curve constructed using pure commercial β-galactosidase enzyme. Each transfection experiment was repeated two times on three different days. The transfection values reported here are average values from duplicate experiments performed on the same day. The values of β-galactosidase units in replicate plates assayed on the same day varied by less than 20%. The day to day variation in transfection efficiency values for identically treated transfection

plates was mostly within 2−3-fold and was dependent on the cell density and condition of the cells. When bafilomycin A1 was used, the cells were pretreated for 30 min at 37 °C with bafilomycin A1 (25 or 50 nM), and the transfection was carried out in the presence of the drug. After 4 h at 37 °C, the medium was replaced with fresh complete medium without bafilomycin A1, and the transfection activity was evaluated after 48 h as described above.

X-Gal Staining. Cells expressing β-galactosidase were histochemically stained with the substrate 5-bromo-4-chloro-3-indolyl-β-D-galactopyranoside (X-gal) as described previously (*27*). Briefly, 48 h after transfection with lipoplexes in 96 well plates, the cells were washed (2 × 100 μL) with PBS (137 mM NaCl, 2.7 mM KCl, 10 mM Na_2HPO_4, 2 mM KH_2PO_4, pH 7.4) and fixed with 0.5% glutaraldehyde in PBS (225 μL). After 15 min incubation at room temperature, the cells were washed again with PBS (3 × 250 μL) and, subsequently, were stained with 1.0 mg/mL X-gal in PBS containing 5.0 mM $K_3[Fe(CN)_6]$, 5.0 mM $K_4[Fe(CN)_6]$ and 1 mM $MgSO_4$ for 2−4 h at 37 °C. Blue colored cells were identified by light microscopy (Leica, Germany).

Toxicity Assay. Cytotoxicities of the lipids **1**−**3** were assessed by the 3-(4,5-dimethylthiazol-2-yl)-2,5-diphenyltetrazolium bromide (MTT) reduction assay as described earlier (*40*). The cytotoxicity assay was performed in 96-well plates by maintaining the ratio of number of cells to amount of cationic lipid the same as that used in the transfection experiments. MTT was added 3 h after addition of cationic lipid to the cells. Results were expressed as percent viability = [(A_{540}(treated cells) − background)/(A_{540}(untreated cells) − background)] × 100.

Size Measurements. The sizes of liposomes and lipoplexes were measured by photon correlation spectroscopy on a Zeta sizer 3000HS_A (Malvern, U.K.) in DMEM and HEPES buffer, pH 7.4, using a sample refractive index of 1.59 and a viscosity of 0.89. The system was calibrated by using the 200 ± 5 nm polystyrene polymer (Duke Scientific Corps., Palo Alto, CA). The diameters of liposomes and lipoplexes were calculated by using the automatic mode.

Gel Retardation Assay. The DNA binding ability of the cationic lipids **1**−**3** was assessed by gel retardation assay on a 1% agarose gel. pCMV-β-gal (0.30 μg) was complexed with varying amounts of cationic lipids (using the indicated lipid/DNA charge ratios in Figure 8A) in a total volume of 20 μL in HEPES buffer, pH 7.40, and incubated at room temperature for 20−25 min. Four microliters of 6× loading buffer (0.25% bromophenol blue, 40% sucrose) was added to it, and 20 μL of the resultant solution was loaded in each well. The samples were electrophoresed at 80 V for approximately 2 h, and the DNA bands were visualized by staining for 30 min with ethidium bromide solution.

DNase 1 Sensitivity Assay. Briefly, in a typical assay pCMV-β-gal (0.6 μg) was complexed with varying amounts of the cationic lipids (using the indicated lipid/DNA charge ratios in Figure 8B) in a total volume of 20 μL in HEPES buffer, pH 7.40, and incubated at room temperature for 30 min on a rotary shaker. Subsequently, the complexes were treated with 5 μL of DNase I (at a final concentration of 1 μg/mL) in the presence of 20 mM $MgCl_2$ in a final volume of 50 μL and incubated for 20 min at 37 °C. The reactions were then halted by adding EDTA (to a final concentration of 50 mM) and incubated at 60 °C for 10 min in a water bath. The aqueous layer was washed with 50 μL of phenol/chloroform/isoamyl alcohol (25:24:1mixture, v/v) and centrifuged at 10 000 rpm for 5 min. The aqueous supernatants (30 μL) were separated, 6 μL of 6× loading buffer (0.25% bromophenol blue, 40% sucrose) was added to it, and 20 μL of the resultant solution was loaded in each well on a 1% agarose gel and electrophoresed at 80 V for 2 h. The DNA bands were visualized by staining for 30 min with ethidium bromide solution.

Transmission Electron Microscopy. Transmission electron microscopy was performed on a FEI Tecnai 12 TEM apparatus operated at 100 kV. Lipoplex samples were transferred onto an ultrathin carbon-coated copper grid by placing the grid on top of a 10 μL drop of the sample for 1 min. After removing the excess fluid from one side, the grid was placed on a 20 μL water drop for a 30 s wash. The excess fluid was removed, and the grid was placed for 1 min on a 20 μL drop of freshly filtered uranyl acetate (1.33%). Once again, the excess fluid was wicked away, and the grid was air-dried.

RESULTS

Chemistry. The mono-histidinylated lipid **1** was synthesized by DCC coupling of N^{α},N^{im}-di-BOC-L-histidine with the N^{ϵ}-BOC-L-lysinyl tertiary amine precursor **I**, a commonly available precursor in our laboratory prepared as described previously (*29*), followed by acid deprotection of the resulting intermediate in 2 N HCl in methanol (Scheme 1). The di-histidinylated cationic lipid **2** was synthesized by DCC coupling of N^{α},N^{im}-di-BOC-L-histidine with the L-lysinyl tertiary amine precursor **II** {obtained by acid deprotection of *N*-2-[*N*′-(N^{α},N^{ϵ}-di-BOC-L-lysyl)]aminoethyl-*N*,*N*-di-*n*-hexadecylamine (*29*) with TFA}, followed by acid deprotection of the resulting intermediate (Scheme 2). Similarly, the tri-histidinylated cationic lipid **3** was prepared by DCC coupling of the dilysinylated precursor **III** {prepared by acid deprotection of *N*-2-[*N*′-(N^{α},N^{ϵ}-di-BOC-L-lysyl-N^{ϵ}-BOC-L-lysyl)]aminoethyl-*N*,*N*-di-*n*-hexadecylamine (*29*) with TFA}, followed by acid deprotection of the resulting intermediate in 2 N methanolic HCl (Scheme 3). Structures of all the synthetic intermediates and the final histidinylated cationic lipids **1**−**3** shown in Schemes 1−3 were confirmed by ^{1}H NMR and FABMS, and the purity of the final lipids was confirmed by quantitative reversed phase HPLC analysis using two different mobile phases (detailed spectral data for all the intermediates and the final lipids, as well as the HPLC chromatograms for all the final lipids are provided in the Supporting Information).

Transfection Biology. Figures 1 and 2 summarize the representative relative in vitro efficiency profiles of lipids **1**−**3** (in combination with equimolar amounts of DOPE as the colipid) in transfecting COS-1 and CHO cells, respectively. Similar transfection profiles for lipids **1**−**3** were also observed in HepG2 and HEK293T cells (Figures S1 and S2, Supporting Information). pCMV-SPORT-β-gal plasmid DNA was used as the reporter gene across the lipid/DNA charge ratios of 8:1 to 1:1. Interestingly, cholesterol, the other commonly used colipid in liposomal gene delivery, was found to be significantly less efficient in imparting gene transfer properties to lipids **1**−**3** (data not shown). The in vitro transfection profiles of lipids **1**−**3** in combination with equimolar amounts of DOPE were found to be remarkably influenced by the complexation medium used in preparing lipoplexes. Only the mono-histidinylated cationic lipid **1** was found to be transfection efficient, whereas the di- and tri-histidinylated lipids **2** and **3** were essentially incompetent in transfecting all the four cells when lipoplexes were prepared in the culture medium, DMEM. The relative transfection profiles in representative COS-1 and CHO cells are shown in part A of Figures 1 and 2. The corresponding transfection results for HepG2 and HEK293T cells are provided in the Supporting Information (part A, Figures S1 and S2, respectively). In contrast, when lipoplexes were prepared in HEPES buffer, the optimal gene transfer efficacies of the tri-histidinylated lipid **3** became comparable to (in COS-1, CHO, and HEK293T cells) or better than (in HepG2 cells) that of lipid **1**. Part B of Figures 1 and 2 summarizes the relative transfection profiles of the

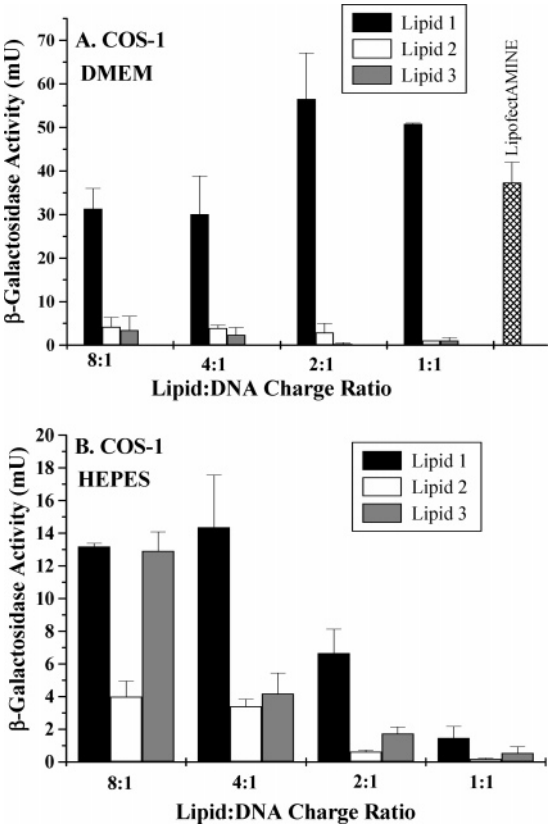

Figure 1. In vitro transfection efficiencies of lipids **1**, **2**, and **3** using reporter gene expression assays in COS-1 cells in combination with equimolar DOPE as colipid at lipid/DNA charge ratios of 8:1−1:1 with DMEM (A) and HEPES buffer (B) as complexing medium for preparing lipoplexes. Units of β-galactosidase activity were plotted against the varying lipid/DNA charge ratios. The transfection values shown are average of duplicate experiments performed on the same day. Details of the transfection assays are as described in the text.

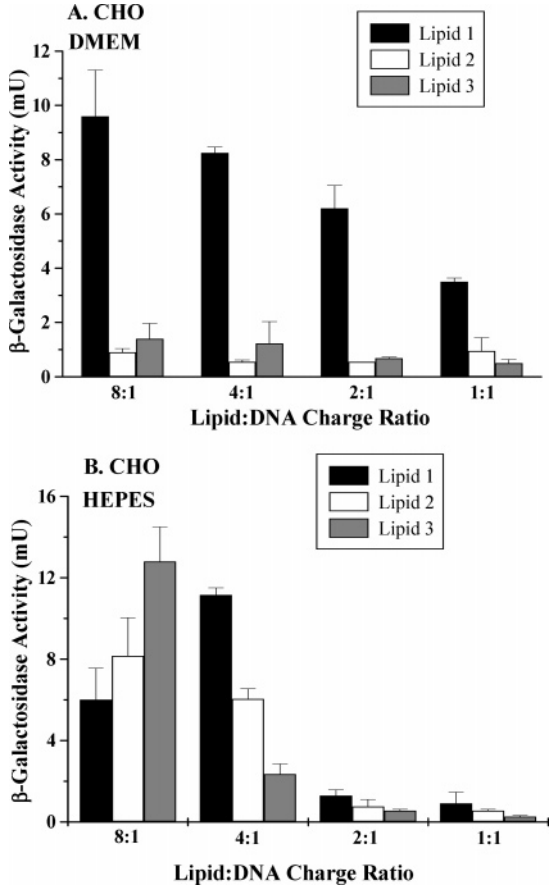

Figure 2. In vitro transfection efficiencies of lipids **1**, **2**, and **3** using reporter gene expression assays CHO cells in combination with equimolar DOPE as colipid at lipid/DNA charge ratios of 8:1−1:1 with DMEM (A) and HEPES buffer (B) as complexing medium for preparing lipoplexes. Units of β-galactosidase activity were plotted against the varying lipid/DNA charge ratios. The transfection values shown are average of duplicate experiments performed on the same day. Details of the transfection assays are as described in the text.

lipoplexes **1**−**3** prepared in HEPES buffer in representative COS-1 and CHO cells. The transfection profiles in HepG2 and HEK293T cells for the lipoplexes prepared in HEPES buffer are provided in the Supporting Information (part B, Figures S1 and S2, respectively).

The above-mentioned complexation-medium-dependent transfection profiles for lipids **1**−**3** observed in the reporter gene expression assays (Figures 1 and 2) were further confirmed by the whole cell histochemical X-gal staining assay in representative CHO cells. Consistent with the findings in the reporter gene expression assay (Figure 2, part A), the number of X-gal stained CHO cells transfected with the efficacious mono-histidinylated lipoplex prepared in DMEM at a representative lipid/DNA charge ratio of 4:1was found to be remarkably higher than those transfected by the lipoplexes of lipids **2** and **3** (Figure S3, part A, Supporting Information). Similarly, at the representative lipid/DNA charge ratio of 8:1, consistent with the higher transfection properties of lipid **3** measured by the reporter gene expression assay in CHO cells for lipoplexes prepared in HEPES buffer (Figure 2, part B), the number of X-gal stained CHO cells transfected with lipoplexes of lipid **3** prepared in HEPES buffer was found to be significantly higher than those transfected by lipid **1** lipoplexes prepared in HEPES buffer medium (Figure S3, part B, Supporting Information).

As to the possible component of the culture medium behind the compromised transfection efficacies of the lipoplexes **2** and **3** (parts A, Figures 1 and 2) (*41*), we suspected mainly two major components, namely, sodium chloride and sodium bicarbonate, used in preparing the culture medium (the molar concentrations of these two components in DMEM are about 150 mM and 44 mM, respectively). To find out which of these two major components (present in DMEM and absent in 10 mM HEPES buffer) might play some role in abolishing the transfection efficacies of lipids **2** and **3** in DMEM (parts A, Figures 1 and 2), we separately evaluated the relative gene transfer efficacies of the lipoplexes **1**−**3** prepared in 10 mM HEPES buffer containing 150 mM NaCl and those for the lipoplexes **1**−**3** prepared in 10 mM HEPES buffer containing 44 mM sodium bicarbonate (bringing the final pHs of the complexing medium to 7.4 in both the cases). The transfection efficacies of the lipoplexes **1**−**3** prepared in 10 mM HEPES buffer containing 150 mM NaCl were found to be either unaffected or enhanced compared with those for the lipoplexes **1**−**3** prepared in 10 mM HEPES buffer alone (data not shown). In contrast, the transfection efficacies of the lipoplexes **2** and **3** prepared in 10 mM HEPES buffer containing 44 mM sodium bicarbonate were found to be adversely affected compared with those of the lipoplexes prepared in 10 mM HEPES buffer alone (Figure 3, parts B and C).

Serum compatibilities for the presently described histidinylated cationic transfection lipids were evaluated across the lipid/DNA charge ratios 8:1−1:1 by measuring transfection efficacies of the lipids in the presence of increasing concentrations of added serum (10−50%, v/v). Several interesting features were revealed. At lipid/DNA charge ratios lower than 4:1, all three lipids failed to transfect (data not shown). However, at higher

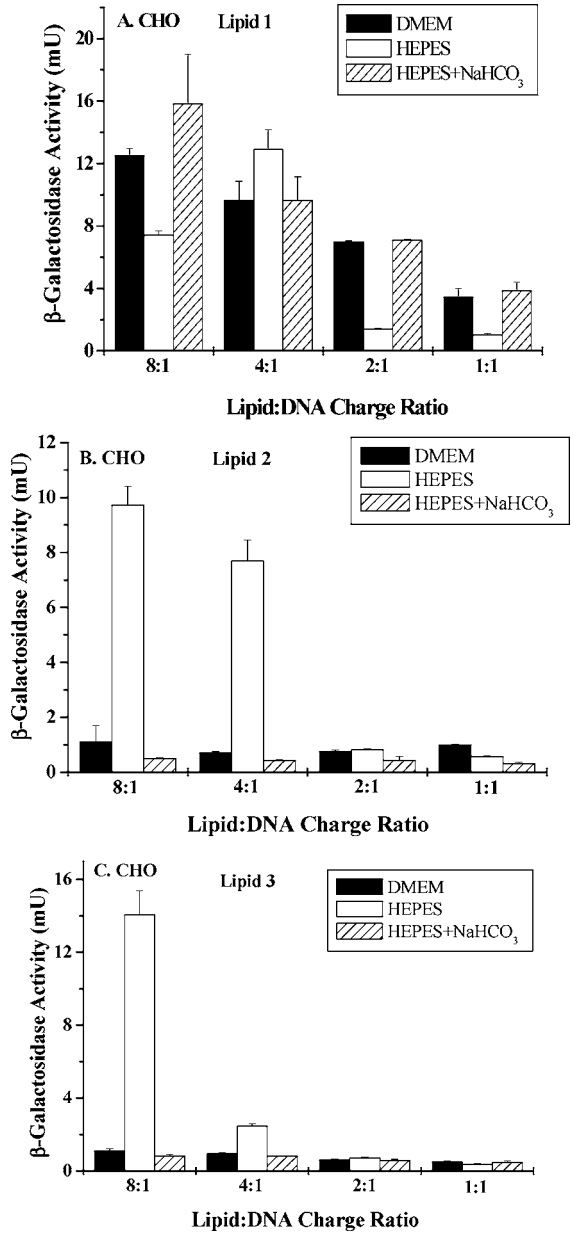

Figure 3. In vitro transfection efficiencies of lipids **1** (A), **2** (B), and **3** (C) using reporter gene expression assays in CHO cells in combination with equimolar DOPE as colipid at lipid/DNA charge ratios of 8:1−1:1 with DMEM, HEPES buffer, and HEPES buffer containing sodium bicarbonate (44 mM) as complexing medium for preparing lipoplexes. Units of β-galactosidase activity were plotted against the varying lipid/DNA charge ratios. The transfection values shown are average of duplicate experiments performed on the same day. Details of the transfection assays are as described in the text.

lipid/DNA charge ratios of 4:1 and 8:1, consistent with the in vitro transfection profiles of lipids **1**−**3** in the absence of added serum for lipoplexes prepared in culture medium (Figures 1 and 2, part A), only lipoplexes of lipid **1** prepared in DMEM were found to be efficient in transfecting all four cell lines in the presence of up to 50% added serum. Figures 4 and 5 (parts A−D) summarize the serum compatibility profiles of the lipoplexes **1**−**3** prepared both in DMEM and in 10 mM HEPES buffer in the representative COS-1 and CHO cells. The serum compatibility profiles of the lipoplexes **1**−**3** in HepG2 and HEK293T cells are provided in the Supporting Information (Figures S4 and S5, respectively). Interestingly, except in CHO cells where transfection efficacies of lipoplex **1** prepared in DMEM decreased with increasing serum content (Figure 5, parts A and C), the transfection efficacies of lipid **1** lipoplexes prepared in DMEM were comparable, improved (Figure 4, parts A and C; Figure S4, parts A and C), or significantly enhanced (Figure S5, parts A and C) with increasing concentrations of added serum (up to 50% v/v). Notably, at the highest lipid/DNA charge ratio of 8:1, the transfection efficiencies of the lipoplexes of both the di- and tri-histidinylated cationic lipids (**2** and **3**, respectively) prepared in HEPES buffer were either comparable to or better than those of the mono-histidine lipid **1** up to 50% added serum (parts B and D, Figures 4 and 5 and Figures S4 and S5).

Involvement of acid-mediated endosomal escape of DNA was assessed by measuring transfection properties of lipids **1**−**3** in representative CHO cells in the presence of bafilomycin A1, which is known to prevent endosomal acidification by inhibiting the vacuolar ATPase endosomal proton pump (*42*). The reporter gene expression efficacies of the lipoplexes prepared in HEPES buffer were inhibited by about 90% for lipid **1** and the lipoplexes prepared in HEPES buffer with lipids **2** and **3** became essentially transfection inefficient in the presence of 25 nM bafilomycin A1 (Figure 6). In presence of 50 nM bafilomycin A1, the transfection of all three lipoplexes prepared in HEPES buffers were completely abolished (data not shown). Such remarkable inhibition of gene transfer efficacies of lipids **1**−**3** in the presence of bafilomycin A1 (Figure 6) are consistent with the involvement of endosomal acidification as a crucial mechanistic event for the present class of histidinylated cationic amphiphiles.

Cell Viabilities. MTT-based cell viability assays were performed in representative CHO cells to gain insights into possible influence of the complexation medium on the percent cell viabilities for the lipoplexes of lipids **1**−**3**. The percent cell viabilities were found to be remarkably high (more than 80%) for lipoplexes prepared in DMEM and somewhat lower (more than 70%) for lipoplexes prepared in HEPES buffer across the entire lipid/DNA charge ratios used in the actual transfection experiments (Figure S6, Supporting Information). Thus, the contrasting complexation-medium-dependent transfection profiles of lipids **1**−**3** (Figures 1 and 2) cannot originate from varying cell cytotoxicity profiles of the present lipoplexes.

Physicochemical Characterizations of Liposomes and Lipoplexes. Sizes and ζ Potentials. With a view to gaining insights into whether the above-mentioned complexation-medium-dependent transfection profiles of lipids **1**−**3** could be related to varying lipoplex sizes, we measured the sizes of the lipoplexes prepared both in DMEM and in HEPES buffers using a dynamic laser light scattering technique. The sizes of the lipoplexes prepared in DMEM remained within the range 300−500 nm across the entire lipid/DNA charge ratios 1:1−8:1, and interestingly, the lipoplexes prepared in DMEM were significantly larger than those prepared in HEPES buffer throughout the lipid/DNA charge ratios 1:1−8:1 (Table 1). Transmission electron microscopic studies revealed similar spherical morphological features as well as similar sizes (around 500−1000 nm) for the lipoplexes prepared in DMEM and HEPES buffer containing 44 mM added sodium bicarbonate for the representative lipid **3** (Figure 7, parts A and B). Interestingly, lipoplexes of **3** prepared in HEPES buffer alone were found to be somewhat smaller in size (Figure 7, part C).

Lipid/DNA Binding Interactions and DNase I Sensitivities. The electrostatic binding interactions between the plasmid DNA and lipids **1**−**3** at varying lipid/DNA charge ratios were measured by both conventional electrophoretic gel retardation assay and DNase I sensitivity assays. The electrophoretic gel patterns in simple gel retardation assay (Figure 8, part A) revealed some interesting features. All three lipids were capable of completely inhibiting the electrophoretic mobility of plasmid DNA from lipoplexes prepared at a high lipid/DNA charge ratio

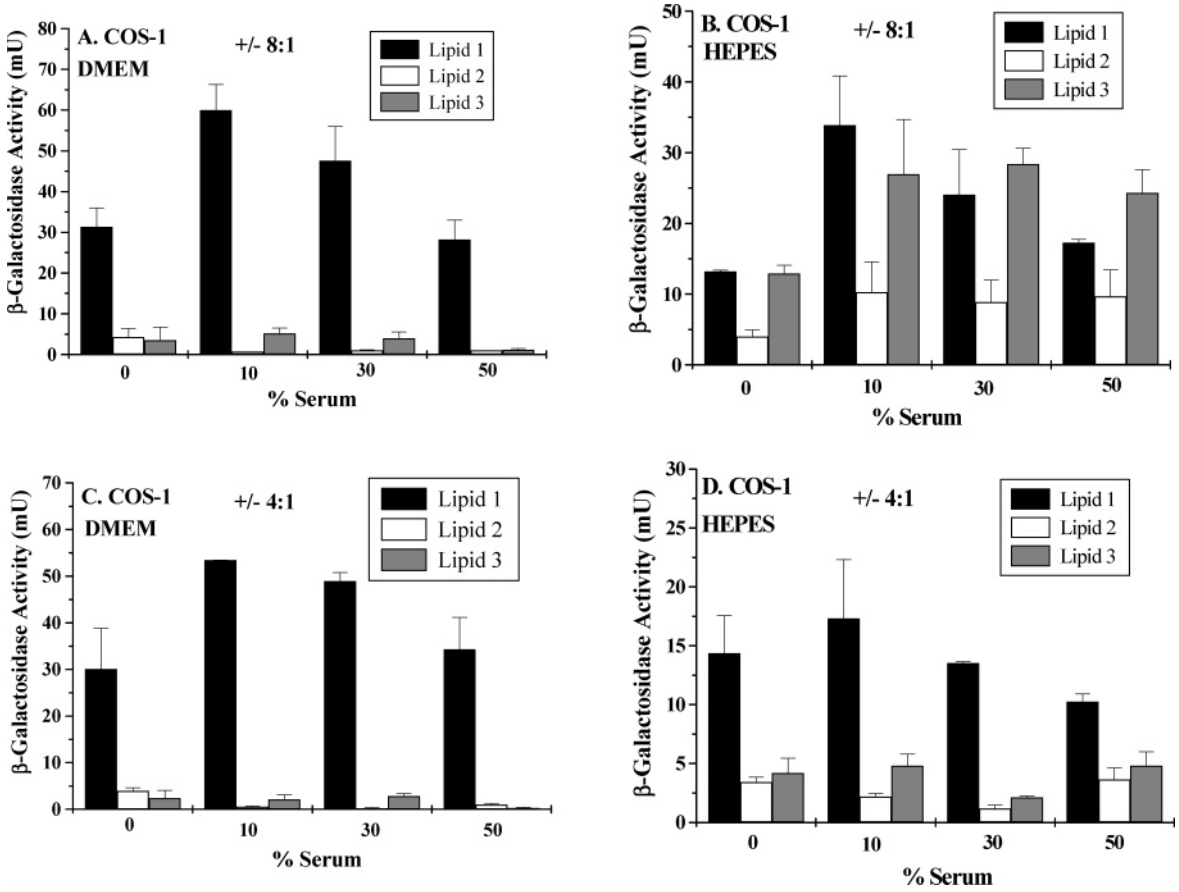

Figure 4. In vitro transfection efficiencies of lipids **1**, **2**, and **3** using reporter gene expression assays in the presence of 10%, 30%, and 50% added serum in COS-1 cells in combination with equimolar DOPE as colipid at lipid/DNA charge ratio of 8:1 (A and B) and 4:1 (C and D) with DMEM (A and C) and HEPES (B and D) as complexing medium for preparing lipoplexes. Units of β-galactosidase activity were plotted against the varying serum concentrations. The transfection values shown are average of duplicate experiments performed on the same day. Details of the transfection assays are as described in the text.

of 8:1 (Figure 8, part A). At lipid/DNA charge ratios of 4:1, all three lipids exhibited moderately strong DNA-binding properties, and at lipid/DNA charge ratios lower than 4:1, all the lipids showed poor DNA binding (Figure 8, part A). Such gel patterns are consistent with the notion that suboptimal lipid/DNA binding interactions could play some major role in abolishing the in vitro gene transfer efficacies of lipids **2** and **3** at lipid/DNA charge ratios lower than 4:1. However, this gel pattern (Figure 8, part A) is not consistent with the high gene transfer properties of lipid **1** at lower lipid/DNA charge ratios of 2:1 and 1:1 (Figures 1 and 2). The most surprising was the gel pattern found in the DNase I sensitivity assay. With a view to obtaining insights into the accessibilities of the lipoplex associated DNA to DNase I, DNase I sensitivity assays were carried out across the lipid/DNA charge ratios 1:1−8:1. After the free DNA digestion by DNase I, the total DNA (both digested and inaccessible DNA) was separated from the lipid and DNase I (by extracting with organic solvent) and loaded onto a 1% agarose gel. Across the entire range of lipid/DNA charge ratios 1:1−8:1, the band intensities of inaccessible and therefore undigested DNA were almost undetectable (Figure 8, part B).

DISCUSSION

One of the major mechanistic factors impeding the transfection efficacies of cationic liposomes is suboptimal release of plasmid DNA from endosome into cell cytoplasm. In the area of cationic polymer-mediated gene delivery, significantly improved transfection efficacies have been achieved through covalent grafting of endosome-disrupting multiple histidine functionalities in the molecular architecture of cationic polymers (*43*). Chen et al. succeeded in enhancing transfection efficacies of cationic liposomes by using them in combination with copolymers of histidine and lysine (*44*, *45*). In a recent collaborative research, we have demonstrated that covalent grafting of a single endosome-disrupting histidine functionality in the headgroup region imparts high gene transfer properties to cationic amphiphiles (*26*). In the present study, we have addressed the issue of how the presence of multiple histidine functionalities in the polar headgroup regions of cationic amphiphiles affects their in vitro transfection efficacies. To this end, we have designed and synthesized three novel cationic amphiphiles containing one, two, and three histidine functionalities in their polar headgroup region through use of lysine linkers (lipids **1**−**3**, Schemes 1−3) and have evaluated their in vitro gene transfer efficacies in multiple cultured cells.

Surprisingly, the relative in vitro gene transfection profiles of lipids **1**−**3** were found to be dependent on the medium of lipid/DNA complexation. In the absence of serum, the trihistidinylated lipid **3** showed higher or comparable transfection efficacies to lipid **1** only when lipoplexes were prepared in HEPES buffer at the highest lipid/DNA charge ratios of 8:1 (Figures 1 and 2). Size measurements by dynamic laser light scattering technique did not reveal any meaningful insights into the possible origin of the severely compromised transfection efficacies of lipids **2** and **3** (compared with that of lipid **1**) when lipoplexes were prepared in DMEM. Although the lipoplexes of lipids **1**−**3** prepared in DMEM were all relatively large (within the approximate range of 300−700 nm across the lipid/DNA charge ratios of 8:1−1:1, Table 1), only lipid **1** was transfection efficient (Figures 1 and 2, parts A). In other words,

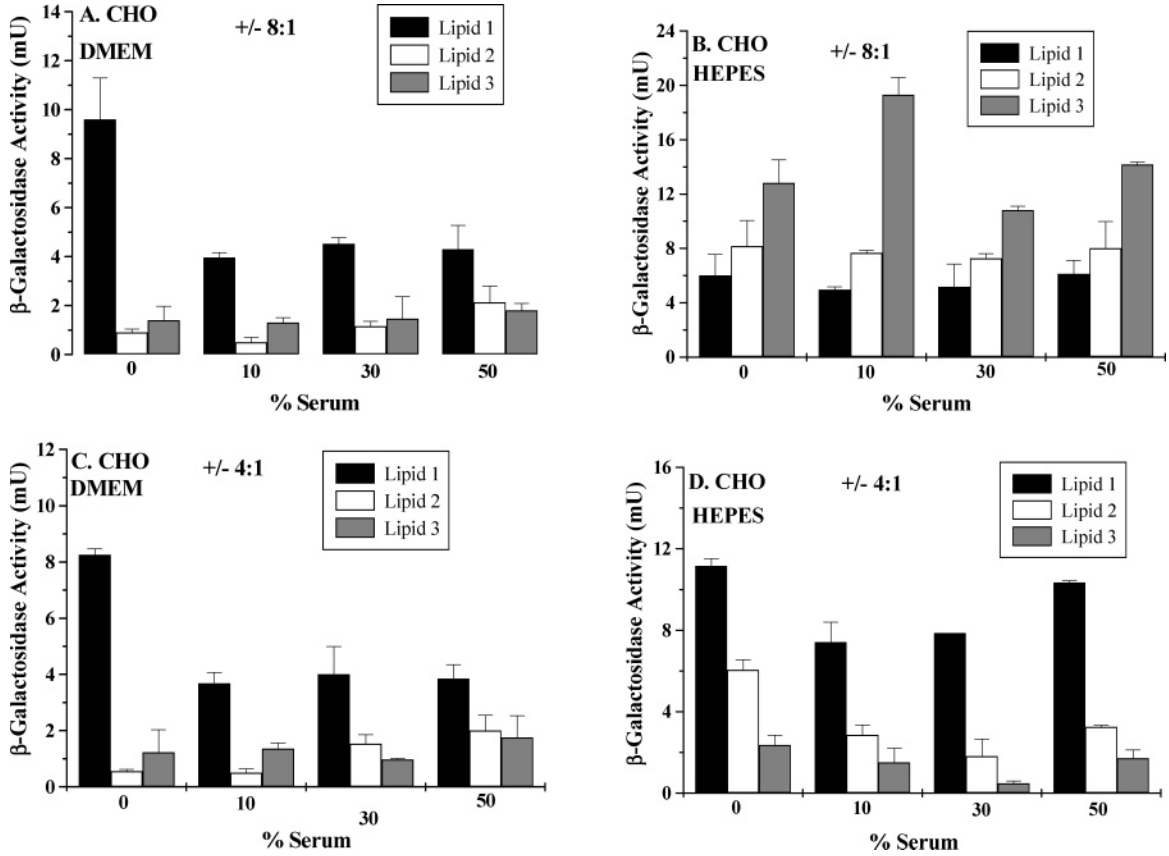

Figure 5. In vitro transfection efficiencies of lipids **1**, **2**, and **3** using reporter gene expression assays in the presence of 10%, 30%, and 50% added serum in CHO cells in combination with equimolar DOPE as colipid at lipid/DNA charge ratio of 8:1 (A and B) and 4:1 (C and D) with DMEM (A and C) and HEPES (B and D) as complexing medium for preparing lipoplexes. Units of β-galactosidase activity were plotted against the varying serum concentrations. The transfection values shown are average of duplicate experiments performed on the same day. Details of the transfection assays are as described in the text.

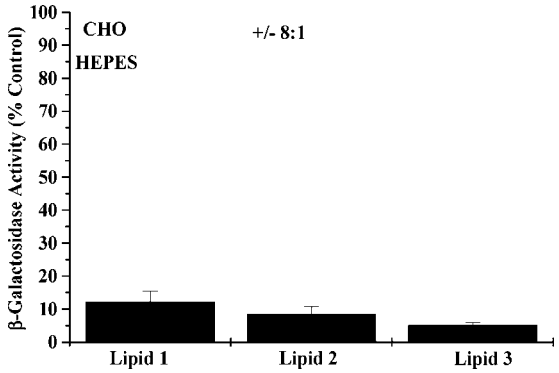

Figure 6. In vitro transfection efficiencies of lipids **1**, **2**, and **3** using reporter gene expression assays in representative CHO cells in the presence of bafilomycin A1 (25 nM) at lipid/DNA charge ratios of 8:1 with HEPES buffer as the complexing medium for preparing lipoplexes. Details of the treatment are as described in the text.

the similar size ranges for lipoplexes prepared in DMEM hint that the higher gene transfection efficacies of the lipoplexes prepared from lipid **1** compared with those of the lipoplexes prepared from lipids **2** and **3** in DMEM (Figures 1 and 2, parts A) are unlikely to originate from any grossly different endocytotic cellular uptake profiles. Interestingly, the sizes of all three lipoplexes prepared in HEPES buffer were smaller (170−350 nm, Table 1) than those prepared in DMEM across the entire range of lipid/DNA charge ratios 8:1−1:1. Such larger sizes for lipid/DNA complexes prepared in DMEM (compared with the corresponding lipoplexes prepared in HEPES) have also been reported previously for DOTAP−oligonucleotide complexes (46). Previously reported physicochemical and morphological characteristics of the cationic liposomes and oligonucleotide complexes (*47*) indicate that the larger sizes of the lipoplexes prepared in cell growth medium may originate from aggregation and fusion of liposomes after adding them to culture medium. Thus, the overall improved transfection efficacies of the lipoplexes of lipids **2** and **3** prepared in HEPES buffer in all four cell lines (Figures 1 and 2, part B; Figures S1 and S2, part B) may partly originate from their smaller lipoplex sizes.

The significantly reduced transfection efficacies of the lipoplexes **2** and **3** prepared in DMEM compared with the transfection efficiencies of the corresponding lipoplexes prepared in HEPES buffer might originate from some transfection inhibitory component of DMEM that is not present in HEPES buffer (*41*). Careful compositional analysis revealed that the two major DMEM components absent in 10 mM HEPES buffer are 150 mM sodium chloride and 44 mM sodium bicarbonate. Toward understanding which of these two components might play some role in the compromised transfection efficacies of the lipoplexes **2** and **3** prepared in DMEM (Figures 1 and 2, Figures S1 and S2), we measured the relative transfection profiles of the lipoplexes **1**−**3** prepared in four different media, namely, DMEM, HEPES buffer, HEPES buffer containing 44 mM sodium bicarbonate, and HEPES buffer containing 150 mM sodium chloride. Transfection efficacies of lipoplexes **2** and **3** in 10 mM HEPES buffer containing 150 mM NaCl either remained unaffected or were enhanced compared with their transfection efficacies in 10 mM HEPES buffer alone (data not shown). However, the transfection properties of the lipoplexes **2** and **3** prepared in 10 mM HEPES buffer were found to be severely compromised when the lipoplexes **2** and **3** were prepared in 10 mM HEPES buffer containing 44 mM sodium

Table 1. Hydrodynamic Diameters of Liposomes and Lipoplexes[a]

	size (nm)				
lipids	lipid/DNA (1:0)	lipid/DNA (1:1)	lipid/DNA (2:1)	lipid/DNA (4:1)	lipid/DNA (8:1)
lipid **1**/DOPE (1:1)	729.1 ± 39.7	332.0 ± 11.3	298.4 ± 11.7	338.5 ± 4.8	444.0 ± 8.4
	(141.2 ± 2.6)	(177.6 ± 3.3)	(171.7 ± 1.8)	(176.1 ± 4.7)	(284.2 ±24.5)
lipid **2**/DOPE (1:1)	630.1 ± 119.2	401.5 ± 78.5	396.9 ± 18.7	268.2 ± 53.8	445.6 ± 24.9
	(116.7 ± 1.6)	(170.3 ± 3.7)	(164.0 ± 2.0)	(189.0 ± 5.0)	(335.4 ± 42.9)
lipid **3**/DOPE (1:1)	479.1 ± 115.6	450.6 ± 24.9	506.7 ± 77.0	335.5 ± 21.7	320.4 ± 27.8
	(118.7 ± 2.3)	(186.4 ± 3.1)	(162.2 ± 3.4)	(194.0 ± 1.4)	(248.2 ± 7.9)

[a] Sizes of liposomes and lipoplexes in plain DMEM and HEPES buffer, pH 7.40 (values within parentheses), were measured by a laser light scattering technique using Zetasizer 3000A (Malvern Instruments, U.K.). Values shown are the averages obtained from three measurements.

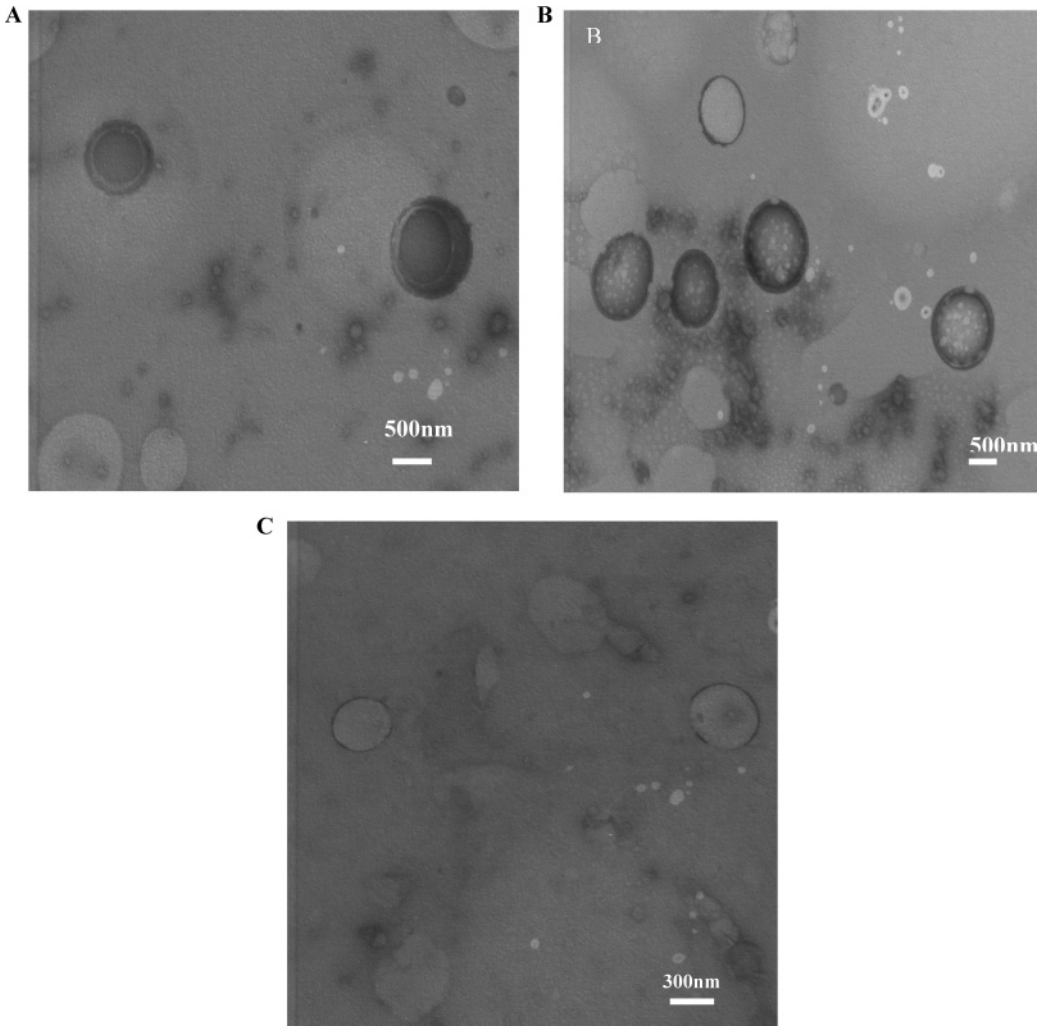

Figure 7. Transmission electron micrographs for lipoplexes **3** prepared in combination with equimolar DOPE as colipid at lipid/DNA charge ratios of 8:1 in DMEM (A), HEPES buffer containing 44 mM sodum bicarbonate (B), and HEPES buffer alone (C) as complexing medium for preparing lipoplexes. Bars correspond to 300 (A) and 500 nm (B and C).

bicarbonate (Figure 3). Thus, the transfection results summarized in Figure 3 are consistent with the notion that the sodium bicarbonate component of the culture medium might be responsible for the compromised transfection properties of lipoplexes **2** and **3** prepared in DMEM (part A, Figures 1and 2). Transmission electron microscopy studies revealed that the sizes of the lipoplexes prepared in the three different media (DMEM, 10 mM HEPES buffer alone, and 10 mM HEPES buffer containing 44 mM sodium bicarbonate) are within the range 300−1000 nm. Figure 7 shows the TEM pictures for the representative lipoplex **3**. Thus, sizes are unlikely to play any key role in modulating the in vitro gene transfer efficiencies of the present class of mono-, di-, and tri-histidinylated cationic amphiphiles.

In general, in cationic lipid mediated gene delivery, the gene transfer efficacies of libraries of novel cationic amphiphiles are evaluated either in the complete absence of added serum or in the presence of only 10% (v/v) serum as reported in many prior investigations (*15*−*22*), including our own (*23*−*31*). However, serum incompatibility still remains one of the major setbacks retarding clinical success of cationic transfection lipids. Quite often, the high in vitro gene transfer efficacies of cationic amphiphiles have been found to be adversely affected in the presence of serum (*48*−*58*). The usual serum incompatibility of cationic transfection lipids is believed to begin via adsorption of negatively charged serum proteins onto the positively charged cationic liposome surfaces preventing their efficient interaction with the cell surface or internalization (*54*, *59*−*62*). Clearly,

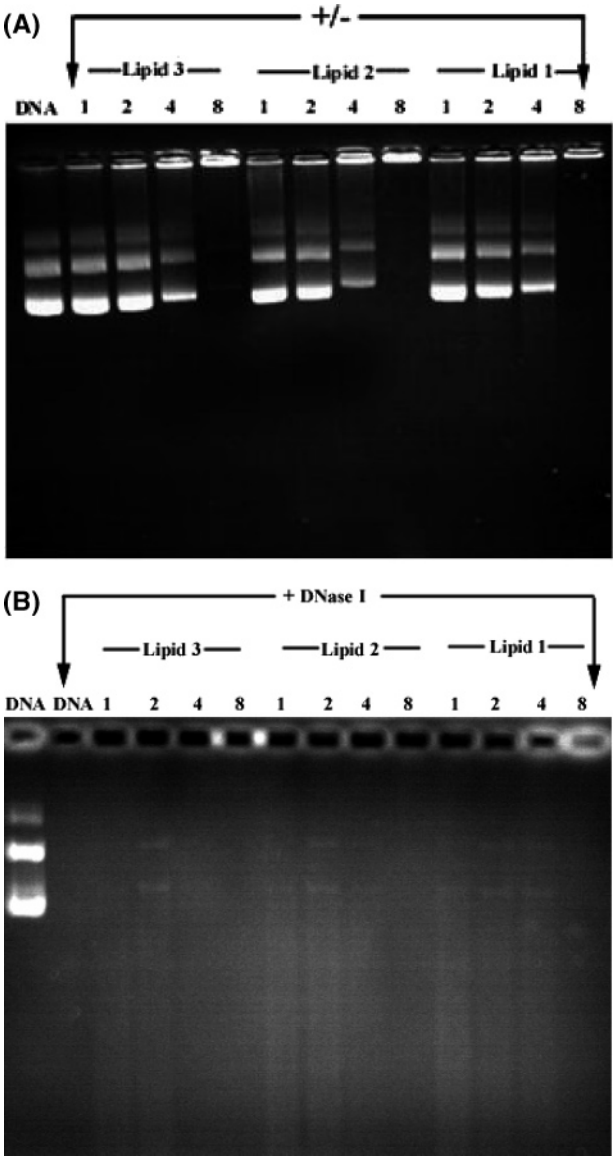

Figure 8. Electrophoretic gel patterns for DNA associated with lipoplexes of lipids **1**, **2**, and **3** (A) and DNase I sensitivity assay for DNA associated with lipoplexes of lipids **1**, **2**, and **3** (B) prepared with equimolar DOPE as colipid. The lipid/DNA charge ratios are indicated at the top of each lane. The details of treatment are as described in the text.

evaluation of gene transfer efficacies across a range of lipid/DNA charge ratios in multiple cultured cells in the presence of increasing concentrations of added serum is needed for obtaining meaningful systemic potential of any in vitro efficient cationic transfection lipid. To this end, we finally evaluated the serum compatibility of lipids **1**−**3** across the entire lipid/DNA charge ratios 8:1−1:1. Several interesting features on the relative serum compatibility issues for the present class of histidinylated cationic lipids were revealed. Below lipid/DNA charge ratios of 4:1, the gene transfer efficacies of all three lipids were found to be highly incompatible with the presence of added serum irrespective of whether the lipoplexes were prepared in the presence of DMEM or HEPES buffer (data not shown). Such serum incompatibility of the present lipids at lower lipid/DNA charge ratios are consistent with the previously reported findings of Yang and Huang in which it was shown that the inhibitory effect of serum in lipofection could be overcome by increasing the charge ratios of cationic liposome−DNA lipoplexes (*57*). However, given that serum contains nucleases, the striking DNase I sensitivities of the plasmid DNA associated with lipids **1**−**3** across the entire lipid/DNA charge ratios of 8:1−1:1 (Figure 8, part B) are clearly inconsistent with the high gene transfer properties of lipids **1**−**3** particularly for lipoplexes prepared in HEPES buffer at lipid/DNA charge ratios of 4:1 and 8:1 in the presence of up to 50% added serum (Figures 4 and 5, parts B and D). It has been previously demonstrated that incubation of lipoplexes prepared from either lipofectin or SAINT-2 (a dialkyl pyridinium cationic amphiphile)/DOPE with serum resulted in the binding of the same serum proteins to either complex (*63*). However, in the presence of serum, the transfection efficiencies of only lipofectin were found to be adversely affected and those of SAINT-2 were not. Such findings (*63*) indicated that parameters other than simple adsorption of negatively charged serum protein components onto the lipoplex surfaces are likely to be involved in modulating transfection efficacies of cationic amphiphiles in the presence of serum. Most significantly, when the lipoplexes were prepared in HEPES buffer using the high lipid/DNA charge ratio of 8:1, the gene delivery efficacies of all three lipids were highly serum compatible (up to 50% added serum). Perhaps adsorption of the negatively charged components of HEPES buffer on the lipoplexes prepared at high lipid/DNA charge ratios can prevent adsorption of negatively charged serum protein components to the lipoplex surfaces thereby enhancing their serum compatibilities.

The compromised transfection efficacies of the lipoplexes of lipids **2** and **3** prepared in HEPES buffer at lipid/DNA charge ratios lower than 4:1 (Figures 1 and 2, part B) could be partly related to the poor lipid/DNA binding interactions at lower lipid/DNA charge ratios as was revealed in the conventional gel retardation assay (Figure 8, part A). However, the findings in the gel retardation assay did not explain why lipid **1** despite having poor DNA binding at lipid/DNA charge ratios lower than 4:1 (Figure 8, part A) showed significant transfection efficacies at such lower lipid/DNA charge ratios (Figures 1 and 2, part A). Dramatic reduction of the transfection efficacies of all three lipids in the presence of bafilomycin A1 (Figure 6) are consistent with the involvement of endosomal protonation as an important mechanistic event in the intracellular transfection pathways for the presently described lipoplexes. In other words, the cytosolic release step of the endosomally trapped DNA complexed with the presently described cationic amphiphiles containing weakly basic histidine functionalities in their headgroup regions are likely to be mediated by protonation of the histidine headgroups in the acidic lumen (pH 5.5−6.5) of endosomes (*22*). The electrophoretic gel patterns observed in the DNase I sensitivity assays turned out to be the most puzzling result. In general, the gel pattern in such DNase I senstivity assays provides a useful hint of whether the compromised transfection efficacies of any cationic amphiphile could be related to the high DNase I accessibility of the lipoplex-associated DNA. However, for the present lipoplexes, the electrophoretic gel pattern in the DNase I protection experiment (Figure 8, part B) is consistent with the notion that the reporter genes associated with the present lipids are highly accessible to DNase I even at high lipid/DNA charge ratios of 8:1. Such extreme DNase I sensitivities is inconsistent particularly with the high gene transfer properties of lipid **1**, whose in vitro gene transfer efficacies are comparable to or better than those of LipofectAmine, a widely used commercially available liposomal transfection kit. One possibility is that the release kinetics from endosomes into cell cytoplasm for DNA associated with lipid **1** could be significantly faster than those for DNA associated lipids **2** and **3** thereby imparting overall higher gene delivery efficacies to lipid **1**.

To conclude, the findings of the present structure−activity investigation involving the use of three novel histidinylated

cationic amphiphiles (**1**−**3**, Schemes 1−3) demonstrate that the relative in vitro gene transfection profiles of mono-, di-, and tri-histidinylated cationic amphiphiles are remarkably dependent on the medium of lipoplex formation. Most importantly, the high serum compatibilities of the lipoplexes of lipids **1** and **3** make them promising nonviral transfection vectors for future systemic applications.

ACKNOWLEDGMENT

Financial support received from the Department of Biotechnology, Government of India (to A.C.), is gratefully acknowledged. P.P.K. and B.K.M acknowledge the Senior Research Fellowships received from the University Grant Commission and Council of Scientific and Industrial Research, Government of India, respectively.

Supporting Information Available: ^{1}H NMR and mass spectral data for all the final lipids **1**−**3** and their synthetic intermediates, transfection results for lipids **1**−**3** in HepG2 and HEK293T in the absence and presence of serum, histochemical whole cell X-gal staining of CHO cells with lipids **1**−**3**, results in the MTT-based cell viability assays for lipids **1**−**3** in CHO cells, and reverse phase HPLC chromatograms for the lipids **1**−**3** in two mobile phases with details of used HPLC parameters. This material is available free of charge via the Internet at http://pubs.acs.org.

LITERATURE CITED

(1) Raper, S. E., Chirmule, N., Lee, F. S., Wivel, N. A., Bagg, A., Gao, G. P., Wilson, J. M., and Batshaw, M. L. (2003) Fatal systemic inflammatory response syndrome in a ornithine transcarbamylase deficient patient following adenoviral gene transfer. *Mol. Genet. Metab. 80*, 148−158.

(2) Hacein-Bey-Abina, S., Von Kalle, C., Schimdt, M., et al. (2003) A serious adverse event after successful gene therapy fro X-linked severe combined immunodeficiency. *N. Engl. J. Med. 348*, 255−256.

(3) Verma, I. M., and Somina, M. (1997) Gene Therapy-Promises, Problems and Prospects. *Nature 389*, 239−242.

(4) Anderson, W. F. (1998) Human Gene Therapy. *Nature 392*, 25−30.

(5) Yla-Herttuala, S., and Martin, J. F. (2000) Cardiovascular Gene Therapy. *Lancet 355*, 213−222.

(6) Yang, Y., Nunes, F. A., Berencsi, K., Furth, E. E., Gonczol, E., and Wilson, J. M. (1994) Cellular Immunity to Viral Antigens Limits E1-Deleted Adenoviruses for Gene Therapy. *Proc. Natl. Acad. Sci. U.S.A. 91*, 4407−4411.

(7) Knowles, M. R., Hohneker, K. W., Zhou, Z., Olsen, J. C., Noah, T. L., Hu, P. C., Leigh, M. W., Engelhardt, J. F., Edwards, L. J., Jones, K. R., and Boucher, R. A. (1995) Controlled Study of Adenoviral-Vector mediated Gene Transfer in the Nasal Epithelium of Patients with Cystic Fibrosis. *N. Engl. J. Med. 333*, 823−831.

(8) Crystal, R. G., McElvaney, N. G., Rosenfeld, M. A., Chu, C. S., Mastrangeli, A., Hay, J. G., Brody, S. L., Jaffe, H. A., Eissa, N. T., and Danel, C. (1994) Administration of an Adenovirus containing the Human CFTR cDNA to the Respiratory Tract of Individuals with Cystic Fibrosis. *Nat. Genet. 8*, 42−51.

(9) Yang, Y., Nunes, F. A., Berencsi, K., Gonczol, E., Engelhardt, J. F., and Wilson, J. (1994) Inactivation of E2a in Recombinant Adenoviruses Improves the Prospect for Gene Therapy in Cystic Fibrosis. *Nat. Genet. 7*, 362−369.

(10) Lehrman, S. (1999) Virus Treatment Questioned after Gene Therapy Death. *Nature 401*, 517−518.

(11) Wagner, E., Ogris, M., and Zauner, W. (1998) Polylysine-based transfection systems utilizing receptor-mediated delivery. *Adv. Drug Delivery Rev. 30*, 97−113.

(12) Kabanov, A. V., and Kabanov, V. A. (1995) DNA complexes with polycations for the delivery of genetic material into cells. *Bioconjugate Chem. 6*, 7−20.

(13) Boussif, O., Lezoulac' H. F., Zanta, M. A., Mergny, M. D., Scherman, D., Demeneix, B., and Behr, J. P. (1995) A versatile vector for gene and oligonucleotide transfer into cells in culture and in vivo: polyethylenimine. *Proc. Natl. Acad. Sci. U.S.A. 92*, 7297−7301.

(14) Uhrich, K. (1997) In vitro bone biocompatibility of poly (anhydride-*co*-imides) containing pyromellitylimidoalanine. *Trends Polym. Sci. 5*, 388−393.

(15) McGregor, C., Perrin, C., Monck, M., Camilleri, P., and Kirby, A. J. (2001) Rational approaches to the design of cationic gemini surfactants for gene delivery *J. Am. Chem. Soc. 123*, 6215−6220.

(16) Prata, C. A. H., Zhao, Y., Barthelemy, P., Li, Y., Luo, D., McIntosh, T. J., Lee, S. J., and Grinstaff, M. W. (2004) Charge-reversal amphiphiles for gene delivery. *J. Am. Chem. Soc. 126*, 12196−12197.

(17) Bell, P. C., Bergsma, M., Dolbnya, I. P., Bras, W., Stuart, M. C. A., Rowan, A. E., Feiters, M. C., and Engberts, J. B. F. N. (2003) Transfection mediated by gemini surfactants: engineered escape from the endosomal compartment *J. Am. Chem. Soc. 125*, 1551−1558.

(18) Majeti, B. K., Singh, R. S., Yadav, S. K., Reddy, S. B., Ramkrishna, S., Diwan, P. V., Madhavendra, S. S., and Chaudhuri, A. (2004) Enhanced Intravenous Transgene Expression in Mouse Lung using Cyclic-head Cationic Lipids. *Chem. Biol. 11*, 427−437.

(19) Kumar, V. V., Singh, R. S., and Chaudhuri, A. (2003) Cationic transfection lipids in gene therapy: successes, setbacks, challenges and promises. *Curr. Med. Chem. 10*, 1297−1306 and references therein.

(20) Zhu, J., Munn, R. J., and Nantz, M. H. (2000) Self-Cleaving Ortho Ester Lipids: A New Class of pH-Vulnerable Amphiphiles. *J. Am. Chem. Soc. 122*, 2645−2646.

(21) Guenin, E., Herve, A. C., Floch, V., Loisel, S., Yaounac, J. J., Clement, J. C., Ferec, C., and des Abbayas, H. (2000) Cationic Phosphonolipids Containing Quaternary Phosphonium and Arsonium Groups for DNA Transfection with Good Efficiency and Low Cellular Toxicity. *Angew. Chem., Int. Ed. . 39*, 629−631.

(22) Miller, A. D. (1998) Cationic Liposomes in Gene Therapy. *Angew. Chem., Int. Ed. 37*, 1768−1785 and the references therein.

(23) Banerjee, R., Mahidhar, Y. V., Chaudhuri, A., Gopal, V., and Rao, N. M. (2001) Design, Synthesis and Transfection Biology of Novel Cationic Glycolipids for Use in Liposomal Gene Delivery. *J. Med. Chem. 44*, 4176−4185.

(24) Banerjee, R., Das, P. K., Srilakshmi, G. V., Chaudhuri, A., and Rao, N. M. (1999) A Novel Series of Nonglycerol based Cationic Transfection Lipids for Use in Liposomal Gene Delivery. *J. Med. Chem. 42*, 4292−4299.

(25) Singh, R. S., Mukherjee, K., Banerjee, R., Chaudhuri, A., Hait, S. K., Moulik, S., Ramadas, Y., Vijayalakshmi, A., and Rao, N. M. (2002) Anchor-dependency for Non- glycerol based Cationic Lipofectins: Mixed Bag of Regular and Anomalous Transfection Profiles. *Chem.—Eur. J. 8*, 900−909.

(26) Kumar, V. V., Pichon, C., Refregiers, M., Guerin, B., Midoux, P., and Chaudhuri, A. (2003) Single Histidine Residue in Head-group Region is Sufficient to Impart Remarkable Gene Transfection Properties to Cationic Lipids: Evidence for Histidine-mediated Membrane Fusion at Acidic pH. *Gene. Ther. 10*, 1206.

(27) Singh, R. S., and Chaudhuri, A. (2004) Single Additional Methylene Group in the Head-group Region Imparts High Gene Transfer Efficacy to a Transfection-Incompetent Cationic Lipid. *FEBS Lett. 556*, 86−90.

(28) Mahidhar, Y. V., Rajesh, M., and Chaudhuri, A. (2004) Spacer-arm modulated gene delivery efficacy of novel cationic glycolipids: design, synthesis, and in vitro transfection biology. *J. Med. Chem. 47*, 3938−3948.

(29) Karmali, P. P., Kumar, V. V., and Chaudhuri, A. (2004) Design, syntheses and in vitro gene delivery efficacies of novel mono-, di-, and trilysinated cationic lipids: a structure−activity investigation. *J. Med. Chem. 47*, 2123−2132.

(30) Sen, J., and Chaudhuri, A. (2005) Design, syntheses, and transfection biology of novel non- cholesterol-based guanidinylated cationic lipids. *J. Med. Chem. 48*, 812−820.

(31) Majeti, B. K., Karmali, P. P., Reddy, B. S., and Chaudhuri, A. (2005) In vitro Gene Transfer Efficacies of N, N.-Dialkylpyrrolidinium Chlorides: A structure−Activity Investigation. *J. Med. Chem. 48*, 3784−3795.

(32) Singh, R. S., Goncalves, C., Sandrin, P., Pichon, C., Midoux, P., and Chaudhuri, A. (2004) On the gene delivery efficacies of pH-

sensitive cationic lipids via endosomal protonation: a chemical biology investigation. *Chem. Biol. 11*, 713−723.
(33) Heyes, J. A., Duvaz, D. N., Cooper, R. G., and Springer, C. J. (2002) Synthesis of Novel Cationic Lipids: Effect of Structural Modification on the Efficiency of Gene Transfer. *J. Med. Chem. 45*, 99−114.
(34) Fichert, T., Regelin, A., and Massing, U. (2000) Synthesis and Transfection Properties of Novel Nontoxic Monocationic Lipids: Variations of Lipid Anchor, Spacer and Headgroup Structure. *Bioorg. Med. Chem. Lett. 10*, 787−791.
(35) Bally, M. B., Harvie, P., Wong, F. M., Kong, S., Wasan, E. K., and Reimer, D. L. (1999) Biological barriers to cellular delivery of lipid-based DNA carriers. *Adv. Drug Delivery Rev. 38*, 291−315.
(36) Zabner, J., Fasbender, A. J., Moninger, T., Poellinger, K. A., and Welsh, M. J. (1995) Cellular and molecular barriers to gene transfer by a cationic lipid. *J. Biol. Chem. 270*, 18997−19007.
(37) Friend, D. S., Papahadjopoulos, D., and Debs, R. J. (1996) Endocytosis and Intracellular Processing accompanying Transfection Mediated by Cationic Liposomes. *Biochim. Biophys. Acta 1278*, 41−50.
(38) Xu, Y., and Szoka, F. C., Jr. (1996) Mechanism of DNA release from Cationic Liposome/DNA Complexes used in Cell Transfection. *Biochemistry 35*, 5616−5623.
(39) Sambrook, J., Fritsch, E. F., and Maniatis, T. (1989) *Molecular Cloning: A Laboratory Manual*, 2nd ed., Cold Springer Harbor Laboratory Press: Cold Spring Harbor, NY.
(40) Hansen, M.-B., Neilson, S. E., and Berg, K. (1989) Reexamination and further development of a precise and rapid dye method for measuring cell growth/cell kill. *J. Immunol. Methods 119*, 203−210.
(41) We sincerely thank the reviewer for bringing this important issue to our notice.
(42) Bowman, E. J., Siebers, A., and Altendorf, K. (1988) Bafilomycins: a class oh inhibitors of membrane ATPases from microorganisms, animal cells, and plant cells. *Proc. Natl. Acad. Sci. U.S.A. 85*, 7972−7976.
(43) Pichon, C., Gonçalves, C., and Midoux, P. (2001) Histidine-rich peptides and polymers for nucleic acids delivery. *Adv. Drug Delivery Rev. 53*, 75−94.
(44) Chen, Q.-R., Zhang, L., Stass, S. A., and Mixon, A. J. (2000) Copolymer of Histidine and Lysine markedly Enhances Transfection Efficiency of Liposomes. *Gene Ther. 7*, 1698−1705.
(45) Chen, Q.-R., Zhang, L., Luther, P. W., and Mixson, A. J. (2002) Optimal transfection with the HK polymer depends on its degree of branching and the pH of endocytic vesicles. *Nucleic Acids Res. 30*, 1338−1345.
(46) Jaaskelainen, I., Peltola, S., Honkakoski, P., Monkkonen, J., and Urtti, A. (2000) A lipid carrier with a membrane active component and a small complex size are required for efficient cellular delivery of anti-sense phosphorothioate oligonucleotides. *Eur. J. Pharm Sci. 10*, 187−193.
(47) Jaaskelainen, I., Sternberg, B., Monkkonen, J., and Urtti, A. (1998) Physicochemical and morphological properties of complexes made of cationic liposomes and oligonucleotides. *Int. J. Pharm. 167*, 191−203.
(48) Wasan, E. K., Harvey, P., Edwards, K., Karlsson, G., and Bally, M. B. (1999) A multi-step lipid mixing assay to model structural changes in cationic lipoplexes used for in vitro transfection. *Biochim. Biophys. Acta 1461*, 27−46.
(49) Escriou, V., Ciolina, C., Lacroix, F., Byk, G., Scherman, D., and Wils, P. (1998) Cationic lipid-mediated gene transfer: effect of serum on cellular uptake and intracellular fate of lipopolyamine/DNA complexes. *Biochim. Biophys. Acta 1368*, 276−288.
(50) Vitiello, L., Bockhold, K., Joshi, P. B., and Worton, R. G. (1998) Transfection of cultured myoblasts in high serum concentration with DODAC: DOPE liposomes. *Gene Ther. 5*, 1306−1313.
(51) Turek, J., Dubertret, C., Jaslin, G., Antonakis, K., Scherman, D., and Pitard, B. (2000) Formulations which increase the size of lipoplexes prevent serum-associated inhibition of transfection. *J. Gene Med. 2*, 32−40.
(52) Thierry, A, R., Rabinovich, P., Peng, B., Mahan, L. C., Bryant, J. L., and Gallo, R. C. (1997) Characterization of liposome-mediated gene delivery: expression, stability and pharmacokinetics of plasmid DNA. *Gene Ther. 4*, 226−237.
(53) Trivedi, R. A., and Dickson, G. (1995) Liposome-mediated gene transfer into normal and dystrophin-deficient mouse myoblasts. *J. Neurochem. 64*, 2230−2238.
(54) Zelphati, O., Uyechi, L. S., Barron, L. G., and Szoka, F. C., Jr. (1998) Effect of serum components on the physicochemical properties of cationic lipid/oligonucleotide complexes and on their interactions with cells. *Biochim. Biophys. Acta 1390*, 119−133.
(55) Farhood, H., Bottega, R., Epand, R. M., and Huang, L. (1992) Effect of cationic cholesterol derivatives on gene transfer and protein kinase C activity. *Biochim. Biophys. Acta 1111*, 239−246.
(56) Yang, J. P., and Huang, L. (1998) Time-dependent maturation of cationic liposome-DNA complex for serum resistance. *Gene Ther. 5*, 380−387.
(57) Yang, J. P., and Huang, L. (1997) Overcoming the inhibitory effect of serum on lipofection by increasing the charge ratio of cationic liposome to DNA. *Gene Ther. 4*, 950−960.
(58) Li, S., Tseng, W. C., Stolz, D. B., Wu, S. P., Watkins, S. C., and Huang L. (1999) Dynamic changes in the characteristics of cationic lipidic vectors after exposure to mouse serum: implications for intravenous lipofection. *Gene Ther. 6*, 585−594.
(59) Gao, X., and Huang, L (1995) Cationic liposome-mediated gene transfer. *Gene Ther. 2*, 710−722.
(60) Li, S., Rizzo, M. A., Bhattacharya, S., and Huang L. (1998) Characterization of cationic lipid-protamine-DNA (LPD) complexes for intravenous gene delivery. *Gene Ther. 5*, 930−937.
(61) Crook, K., Stevenson, B. J., Dubouchet, M., and Porteous, D. J. (1998) Inclusion of cholesterol in DOTAP transfection complexes increases the delivery of DNA to cells in vitro in the presence of serum. *Gene Ther. 5*, 137−143.
(62) Lewis, J. G., Lin, K. Y., Kothavale, A., Flanagan, W. M., Matteucci, M. D., DePrince, R. B., Mook, R. A., Jr., Hendren, R. W., and Wagner, R. W. (1996) A serum-resistant cytofectin for cellular delivery of antisense oligodeoxynucleotides and plasmid DNA. *Proc. Natl. Acad. Sci. U.S.A. 93*, 3176−3181.
(63) Audouy, S., Molema, G., de Leij L., and Hoekstra, D. (2000) Serum as a modulator of lipoplex-mediated gene transfection: dependence of amphiphile, cell type and complex stability. *J. Gene Med. 2*, 465−476.

BC050194D

Dendrons with Spermine Surface Groups as Potential Building Blocks for Nonviral Vectors in Gene Therapy

John G. Hardy,[†] Mauri A. Kostiainen,[†] David K. Smith,*[,†] Nathan P. Gabrielson,[‡] and Daniel W. Pack[‡]

Department of Chemistry, University of York, Heslington, York, YO10 5DD, UK, and
Department of Chemical and Biomolecular Engineering, University of Illinois at Urbana Champaign, Urbana, Illinois 61801. Received July 20, 2005; Revised Manuscript Received September 29, 2005

This paper investigates a series of dendrons based on the Newkome dendritic scaffold that displays a naturally occurring polyamine (spermine) on their surface. These dendrons have previously been shown to interact with DNA in a generation dependent manner with the more highly branched dendrons exhibiting a strong multivalency effect for the spermine surface groups. In this paper, we investigate the ability of these dendrons to transfect DNA into cells (human breast carcinoma cells, MDA-MB-231, and murine myoblast cells, C2C12) as determined by the luciferase assay. Although the dendrons are unable to transfect DNA in their own right, they are capable of delivering DNA in vitro when administered with chloroquine, which assists with escape from endocytic vesicles. The cytotoxicity of the dendrons was determined using the XTT assay, and it was shown that the dendrons were nontoxic either alone or in the presence of DNA. However, when administered with DNA and chloroquine, the most highly branched dendron did exhibit some cytotoxicity. This paper elucidates the relationship between in vitro transfection efficiency and toxicity. While transfection efficiencies are modest, the low toxicity of the dendrons, both in their own right, and in the presence of DNA, provides encouragement that this type of building block, which has a relatively high affinity for DNA, will provide a useful starting point for the further synthetic development of more effective gene transfection agents.

INTRODUCTION

The introduction of genetic material into cells (gene transfection) (*1*) has the potential to treat a wide variety of diseases such as those that are characterized by a single mutation at a well-defined position on the genome, for example muscular dystrophy (*2*) and cystic fibrosis (*3*). Gene therapy is also being investigated to treat a range of other diseases, including cancer (*4*) and AIDS (*5*), with the aim being to introduce genetic material into the affected cells and ultimately lead to their destruction. The key problem in gene therapy is the delivery of genetic material to the required cells within a patient. Ex vivo methods involve the removal, genetic modification, and re-administration of the patient's cells. The ex vivo approach enables well controlled localized delivery but has a number of limitations such as being labor intensive, requiring special production facilities, and only being applicable for accessible and robust cells. More interesting, however, is the development of in vivo gene therapies, and with this goal in mind, the development of novel vectors for gene delivery capable of navigating a series of extra- and intracellular barriers is of crucial importance.

Vectors fall into two main categories, viral and nonviral (synthetic) vectors. Viruses are naturally evolved vectors, in which part of the virus' genome is replaced with therapeutic genetic material (*6*). Although viral vectors are efficient gene delivery systems and have been utilized in the majority of clinical trials, there have been a number of problems with their application in human gene therapy, including poor targeting to cells, expensive production, and immunogenic and pathogenic responses. Nonviral vectors rely on the ability of synthetic systems to bind and condense the genetic material effectively (*7*). Cationic liposomes (*8*) (normally used in the presence of a helper lipid) are quite efficient, even in vivo, and there is good potential for synthetic modification of this class of delivery agent. However, they tend to be relatively unstable and toxic and often lack cell-specific targeting ability. Cationic polymers (*9*) are cheap and simple to modify in order to impart desirable properties such as degradation under certain conditions and cell-specific targeting.

In the last 10 years, there has been an explosion of interest in using dendrimers (*10*) (highly branched monodisperse polymers) as vectors. Their transfection ability is comparable to polymers, but many of them exhibit reduced toxicity. The commercially available spherical poly(amidoamine) (PAMAM) dendrimers have been extensively studied. It has been shown that fractured (i.e., partially degraded) PAMAMs can be more effective at gene transfection, potentially as a consequence of their greater flexibility and ability to compact DNA (*11*). PAMAM dendrimers have also been synthetically modified in order to improve solubility and cell membrane fusion and reduce toxicity (*12*). Other spherical dendritic polyamine scaffolds have also been investigated as gene delivery systems, such as those based on a poly(propyleneimine) (PPI) framework (*13*). Dendritic L-lysine derivatives have been widely exploited (*14*), and in a number of these cases, dendrons (individual dendritic branches) have been used as DNA binding and gene delivery agents, rather than fully formed spherical dendrimers. The inherent asymmetry of the dendron structure facilitates simple structural modification in a precisely controlled fashion, either at the surface, or at the focal point. This is not possible to the same extent with polymers or spherical dendrimers. The typical 'dendron strategy' is to use a branched molecule with a polycationic surface capable of interacting with the anionic phosphates on DNA and then subsequently functionalize the focal point with a unit capable of either hydrophobic groups

* To whom correspondence should be addressed. E-mail: dks3@york.ac.uk.
[†] University of York.
[‡] University of Illinois at Urbana Champaign.

10.1021/bc050212r CCC: $33.50 © 2006 American Chemical Society
Published on Web 11/04/2005

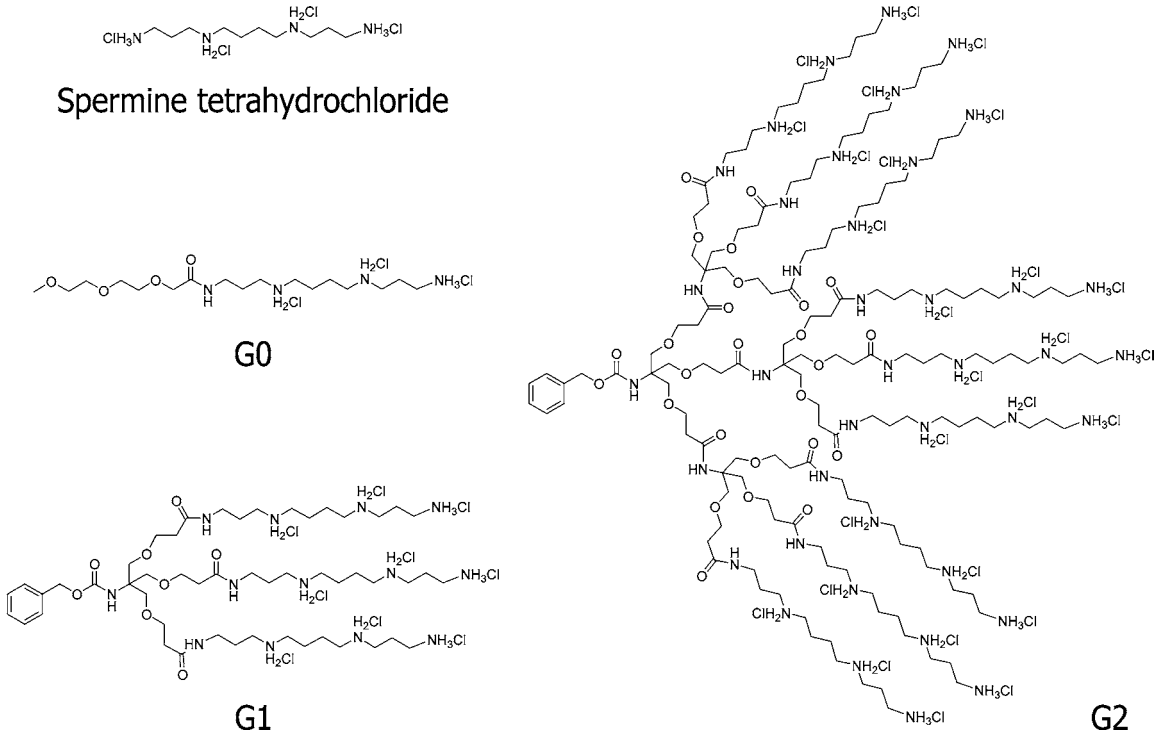

Figure 1. Polyamines based on spermine investigated in this paper for their transfection potential, including dendritic multivalent spermines, **G1** and **G2**.

which assist the process of membrane fusion (*15*) or polar groups assisting water solubility and biocompatibility (e.g., poly(ethylene glycol), PEG) (*12e*).

Spermine, a naturally occurring linear polyamine, is often utilized as the DNA binding portion of nondendritic vectors (*16*). Indeed, some commercially useful vectors (e.g. Transfectam (*17*), Genzyme Lipid #67 (*18*), and RPR-120535 (*19*)) incorporate spermine units. Biology itself makes use of simple tetraamines, such as spermine, to achieve DNA binding (*20*). Although spermine is significantly better than an isolated amine for binding DNA, however, the interaction is still relatively weak and generates a mobile complex. Consequently, spermine struggles to compete with DNA-bound inorganic cations (*21*).

We have recently reported (*22*) a series of dendrons utilizing the Newkome dendritic scaffold (*23*) which display multiple spermine groups on the dendritic surface (Figure 1). We demonstrated that these dendrons bind DNA in a generation dependent manner (i.e., **G0** < **G1** < **G2**), with higher generation dendrons exhibiting binding strengths which were independent of salt concentration. Dendron G2 showed very strong DNA binding, and we could ascribe this to a clear multivalency effect. Some multivalent arrays had been previously reported in which multiple spermine groups were grafted onto dextran polymers (*24*). However, we wanted to develop multivalent DNA binders with well-defined molecular structures, to enable the construction of structure−activity relationships, as well as developing monodisperse systems, with relatively low molecular weights, which have a greater chance of being licensed for therapeutic use in the longer term. In this new paper, we explore the in vitro transfection efficiency (as determined by luciferase assay) and the toxicity (as determined by XTT assay), using human breast carcinoma cells (MDA-MB-231) and murine myoblast cells (C2C12). Most importantly, using this approach, we identify the optimum unit (G1) which exhibits the greatest potential for future synthetic development as a nonviral vector.

MATERIALS AND METHODS

Polyamine Dendrons. The polyamine dendrons with spermine surface groups were synthesized using methods previously reported by us and fully characterized; all data were in agreement with those previously published (*22*).

Cells and Plasmid DNA. The MDA-MB-231 human breast carcinoma cell line was purchased from the American Type Culture Collection, and the C2C12 murine myoblast cell line was a gift from Prof. Stephen Kaufman (University of Illinois at Urbana Champaign, IL). All cell lines were maintained according to their respective ATCC protocols at 37 °C and 5% CO_2 but were adapted from fetal bovine serum to heat-inactivated horse serum. The 5.3 kilobase pair expression vector, pGL3 (Promega, Madison, WI), containing the luciferase gene driven by the SV40 promoter and enhancer, was grown in DH5α E. Coli (Gibco BRL, Rockville, MD) and purified using a commercial plasmid purification kit (Bio-Rad, Hercules, CA). Plasmids were further purified by ethanol precipitation; the ratio of absorbances at 260 and 280 nm was 1.8 or greater.

Gel Retardation Studies. Appropriate amounts of polyamine and DNA plasmid solutions in 150 mM NaCl (pH 7.3, 20 mM PIPES as buffer) were added to a further 10 μL of 150 mM NaCl (pH 7.3, 20 mM PIPES as buffer) to achieve the desired polyamine/DNA ratio. The resultant complexes were incubated at 4 °C for 15 min. Then, 3 μL Blue/Orange 6X loading dye (Promega, Madison, WI) was added, and the mixtures were incubated at 4 °C for a further 5 min. After this time, 15 μL was electrophoresed on a 0.75% agarose gel (70 V, 1 h). DNA was visualized with ethidium bromide staining (Bio-Rad, Hercules, CA). Samples were run in duplicate.

Dynamic Light Scattering Studies. DNA−polyamine complexes were prepared at room temperature, by the titration of polyamine solution into a solution of plasmid DNA (1 μg) in PBS-buffered Millipore water (500 μL) to achieve the desired mass ratios. The volume of polyamine solution added to the DNA solution did not exceed 5% of the total volume of the solution. Complex size determination was performed by dynamic light scattering on a DynaPro-MS800 particle sizer (Protein Solutions, Lakewood, NJ), and the data were analyzed with Dynamics v6.3 software (Protein Solutions).

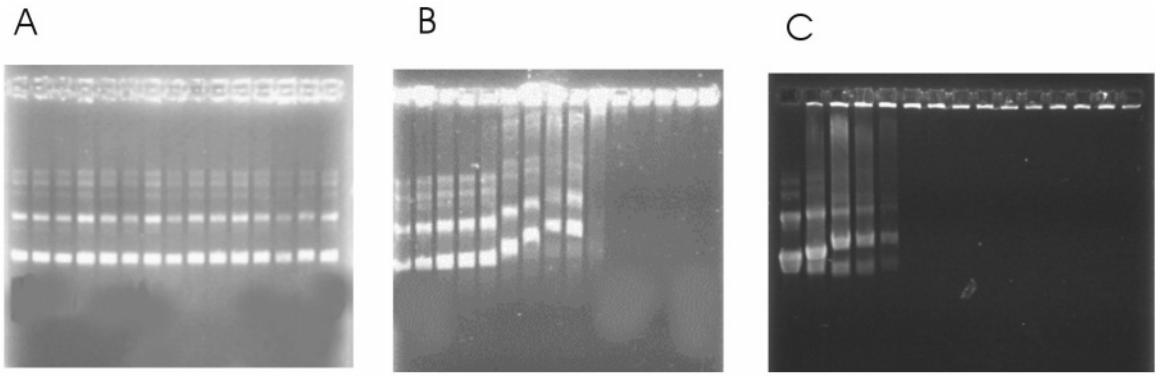

Figure 2. Agarose gel electrophoresis of polyamine/DNA complexes. (A) G0 (polyamine:DNA, w:w): lane 1, 0:1; lane 2, 6:1; lane 3, 7:1; lane 4, 8:1; lane 5, 9:1; lane 6, 10:1; lane 7, 20:1; lane 8, 30:1; lane 9, 40:1; lane 10, 50:1; lane 11, 60:1; lane 12, 70:1; lane 13, 80:1; lane 14, 90:1; lane 15, 100:1. (B and C) G1 and G2 respectively (polyamine:DNA, w:w): lane 1, 0:1; lane 2, 0.1:1; lane 3, 0.2:1; lane 4, 0.3:1; lane 5, 0.4:1; lane 6, 0.5:1; lane 7, 0.6:1; lane 8, 0.7:1; lane 9, 0.8:1; lane 10, 0.9:1; lane 11, 1:1; lane 12, 2:1; lane 13, 3:1; lane 14, 4:1; lane 15, 5:1.

Complex Formation and Transfection. DNA−polyamine complexes were prepared at room temperature in 150 mM NaCl (pH 7.3, 20 mM PIPES as buffer) by addition of 250 μL of polyamine solution to an equal volume of 10 μg of plasmid to achieve the desired polyamine/DNA ratio. The resultant complexes were incubated at 4 °C for 15 min. Cells were cultured in standard growth medium (DMEM supplemented according to ATCC protocols with 10% horse serum and 1% penicillin−streptomycin) and plated in 12-well plates at 1×10^5 cells per well 24 h before transfection. Immediately before transfection, the growth medium was replaced with serum-free medium, and 50 μL of complex (1 μg of plasmid per well) was added to each well (either with or without chloroquine at a final concentration of 100 μM). Transfection medium was replaced with growth medium 4 h after transfection. Luciferase expression was quantified 20 h later using a Promega luciferase assay system ($n \geq 6$) according to the manufacturer's protocol. Luciferase activity was measured in relative light units (RLU) using a Lumat LB9507 luminometer (Berthold, GMBH, Germany) and converted to luciferase concentration by comparison with recombinant luciferase standards (Promega). Results were normalized to total cell protein as determined using a Bio-Rad protein assay kit.

Cytotoxicity Determinations. Cytotoxicity was characterized as a decrease in metabolic activity using the XTT assay (*25*). Cells were placed in 96-well plates at an initial density of 5000 cells per well in 100 μL of growth medium for 24 h, after which time the growth medium was replaced with fresh serum-free medium. At this point a solution of: polyamine alone (5 μg of polyamine per well), polyamine/DNA complexes (1 μg of DNA and 5 μg of polyamine per well), or polyamine/DNA complexes with chloroquine (effective transfection conditions: 0.2 μg of DNA, 1.0 μg of polyamine per well, chloroquine at a final concentration of 100 μM), in 150 mM NaCl (pH 7.3, 20 mM PIPES as buffer) was added (volume equal to or less than 10 μL). Cells were incubated for 4 h, and the medium was replaced with complete growth medium for 16 h. Fresh XTT (1 mg/mL) and the coenzyme Q_0 (80 mg/mL) stock were prepared each day in PBS (0.5 μg/μL XTT and 0.04 μg/μL coenzyme Q_0), and 25 μL aliquots were added to each well. The samples were incubated for a further 4 h at 37 °C, and the absorbance was read at 450 nm relative to blank well prepared without cells ($n = 16$).

RESULTS

Gel Retardation Studies. As outlined in the Introduction, we have previously shown the dendrons to be capable of binding plasmid DNA and condensing it into well-defined nanoscale particles. The formation of these polyplexes can be observed as a reduction of mobility in gel electrophoresis (Figure 2). DNA was mixed with increasing amounts of polyamine in order to determine the ability of the polyamine to form complexes with the DNA. Both spermine and the **G0** model compound failed to retard the migration of DNA, even at mass ratios of 1:100 (DNA:polyamine). In contrast, however, dendritic spermine derivatives **G1** and **G2** both effectively retarded the migration of DNA at mass ratios of 1:1 (DNA:polyamine) and above. This highlights the cooperativity of the DNA binding afforded by using a dendritic scaffold for the placement of multiple spermine groups, as discussed in more detail in our previous publication (*22*).

Dynamic Light Scattering Studies. Polyplex size can be a crucial factor for efficient cell uptake, and we therefore investigated the effect of charge ratio on complex size. Complexes with polyamine/DNA ratios of 0:1 to 40:1 (w/w), typical of transfection experiments, were formed, and dynamic light scattering was used to measure complex size. Assuming that spherical aggregates were formed (as observed for **G1** and **G2** with plasmid DNA by transmission electron microscopy [TEM] methods), allowed us to calculate approximate diameters for the aggregates. These studies were performed with plasmid DNA alone, and in the presence of spermine, **G0**, **G1**, and **G2**. In each case, the experiments were performed at different polyamine:DNA mass ratios in order to see the effect of molar ratio on the aggregate formed. The data are presented in Figure 3.

In the absence of DNA, a diameter of 66 nm was determined for the DNA. Spermine and **G0** had little effect on the dimensions of the system − the diameter of the aggregate remained constant at around 40−50 nm, irrespective of the ratio of polyamine to DNA employed. This is in agreement with previous studies (*20a*). Dendron **G1** formed significantly larger aggregates in the presence of plasmid DNA. This was particularly true at higher polyamine:DNA mass ratios, where nanoscale complexes of around 100 nm were present in solution. Previous reports have indicated that complexes in this size range are efficiently endocytosed during transfection (*26*). The size of the aggregates formed between **G2** and plasmid DNA was significantly larger than that formed between **G1** and DNA, in agreement with the previous TEM studies (*22*). Once again, on increasing the polyamine:DNA mass ratio, the diameter of these complexes increased significantly (to over 200 nm).

Complex Formation and Transfection. Our groups are interested in the utilization of gene therapy for the treatment of cancer (*4*) and muscular dystrophy (*2*); hence, we investigated the efficacy of the polyamine dendrons in gene delivery to human breast carcinoma cells (MDA-MB-231) and murine myoblasts (C2C12). Both cell lines were transfected in vitro

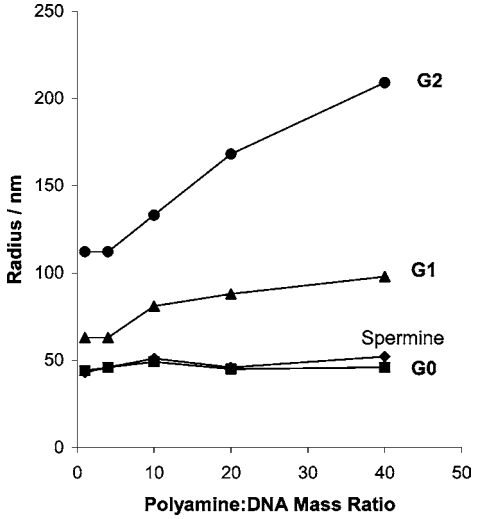

Figure 3. Dynamic light scattering results indicating the polyamine:DNA mass ratio and the approximate dimensions (nm) of the aggregate formed in each case. In the absence of polyamine, light scattering indicated a diameter of 66 nm.

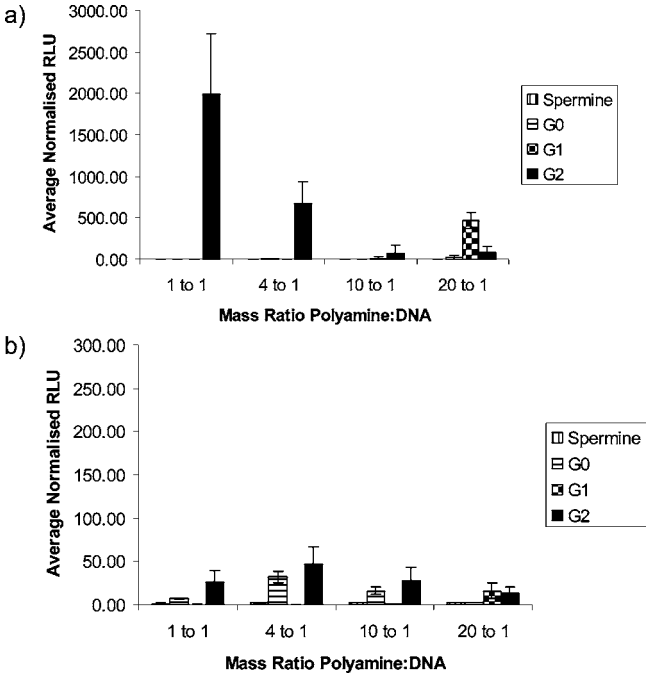

Figure 4. Transfection efficiency of spermine, the nondendritic model (**G0**), and the dendrons displaying spermine on the surface (**G1** and **G2**) in (a) C2C12 and (b) MDA-MB-231 cells. Luciferase expression was normalized by total cellular protein, i.e., data are given in RLU/mg of protein. ($N = 6$, error bars represent standard deviation). Transfection is performed in the presence of chloroquine (100 μM).

with 1 μg of plasmid DNA per 100 000 cells. In each case, the DNA was complexed with varying amounts of different polyamines. Gene transfection efficiency was measured as luciferase enzyme activity and normalized to total cell protein. Initially, the dendrons were investigated in their own right to determine their ability to transfect DNA into cells and allow expression of luciferase. However, no measurable transfection could be observed in any case.

However, in the presence of chloroquine (at a final concentration of 100 μM) measurable gene transfection was observed with some of the spermine derivatives (Figure 4). Chloroquine is widely used as a 'helper molecule' for gene transfection (*27*). Although the mechanism of action is not fully understood, it has been argued that chloroquine is a weak endosomotropic buffer, raising the endosomal pH, resulting in an increase in osmolarity and consequent endosome lysis. In this way chloroquine assists the escape of transfected DNA from the endosome. The nondendritic molecules (i.e., spermine and **G0**) induced no measurable gene expression over the range of polyamine:DNA mass ratios investigated (1:1 and 4:1). However, some transfection and subsequent luciferase expression was observed for the dendritic spermine derivatives in combination with chloroquine. At low polyamine:DNA mass ratios (1:1 and 4:1), the second generation dendron was significantly better at transfection than the first generation analogue. However, at higher polyamine:DNA mass ratios (10:1 and 20:1) the transfection efficiency of the second generation dendron was observed to decrease sharply. Under equivalent conditions, the transfection efficiency of the first generation analogue **G1** increased dramatically. Indeed, **G1** became more effective at transfection than **G2** at high polyamine:DNA mass ratios. A similar trend was observed for both cell lines, although the transfection into murine myoblasts C2C12 was higher than that for the human breast carcinoma cells (MDA-MB-231).

Cytotoxicity Determination. Polycationic molecules have been reported to damage cell membranes as a result of the electrostatic attraction of polycations to the plasma membrane, whereas neutral and anionic polymers cause minimal damage to cellular membranes. With this potential drawback of polycationic vectors firmly in mind, we assayed the cytotoxicity of our dendrons using an XTT assay (*25*). Human breast carcinoma cells (MDA-MB-231) and murine myoblasts (C2C12) were exposed to various conditions (i.e., polyamine, polyamine+DNA, polyamine+DNA+chloroquine) for 4 h, and metabolic activity was assayed 20 h later. The results of these studies are collected in Table 1.

No reduction in metabolic activity was observed when the polyamine alone was added at a concentration of 1 μg per 1000 cells. The one exception to this was when a polyamine control (25 kDa poly(ethyleneimine)) was employed, in which case the observed metabolic activity was reduced by 30% for the C2C12 cells. This is important as it indicates that our dendrons are significantly less cytotoxic than PEI. Similarly, when a combination of polyamine and DNA was added to the cells (0.2 μg DNA and 1 μg polyamine per 1000 cells), our dendrons (**G1** and **G2**) had no observable cytotoxicity. However, once again, the 25 kDa PEI control reduced metabolic activity, this time by 20% for the C2C12 cells.

Significant cytotoxicities, however, were observed in the presence of chloroquine, under experimental conditions identical to those in which transfection had been performed (i.e., 0.01 μg DNA and 0.1 μg polyamine per 1000 cells, and chloroquine at a final concentration of 100 μM). Under these conditions, chloroquine and DNA reduced metabolic activity by 50% (even in the absence of polyamines). In the presence of chloroquine, DNA, and either spermine, **G0**, or **G1**, the cells actually exhibited greater metabolic activities than they did in the absence of the polyamine. Indeed, in the presence of **G0** or **G1**, the metabolic activity of the cells was effectively normal. However, using chloroquine and DNA in the presence of **G2** gave rise to a marked reduction in metabolic activity (ca. 70% for C2C12 cells). In all cases, the MDA-MB-231 cells were found to be more robust, and the polyamines and chloroquine were found to have smaller effects on the metabolic activity than they do for C2C12 cells.

DISCUSSION

For effective transfection, plasmid DNA must be effectively bound and condensed under biological conditions (i.e., high salt concentrations, relevant pH values). We have previously shown that dendritic molecules **G1** and **G2** can do this very effectively.

Table 1. Cytotoxicity of Spermine, the Nondendritic Model (G0), and First (G1) and Second (G2) Generation Dendrons, as well as Poly(ethyleneimine) (PEI) in Murine Myoblast C2C12 and Human Breast Carcinoma MDA-MB-231 Cells[a]

		metabolic activity (relative to 1.000)					
cell line	conditions	spermine	G0	G1	G2	PEI	CQ[b]
C2C12	no polyamine						0.512
C2C12	polyamine alone	0.980	1.000	1.070	1.006	0.705	
C2C12	polyamine + DNA	1.659	1.032	1.032	1.015	0.808	
C2C12	polyamine + DNA + chloroquine	0.758	0.968	1.238	0.305		
MDA-MB-231	no polyamine						0.678
MDA-MB-231	polyamine alone	1.022	1.070	1.003	0.997	0.878	
MDA-MB-231	polyamine + DNA	1.099	1.063	1.011	1.034	0.954	
MDA-MB-231	polyamine + DNA + chloroquine	0.886	0.979	0.988	0.398		

[a] Cytotoxicity is reported as the effective metabolic activity, using an XTT assay. In each case, the metabolic activity of a blank sample of cells (i.e. untreated by polyamine, DNA, or chloroquine) was taken as 1.000 [b] CQ = chloroquine; concentration = 100 μM.

We previously used ethidium bromide displacement assays to determine that the DNA binding strength was very low for the nondendritic systems (i.e., spermine and **G0**) and significantly higher for **G1** and **G2**. Indeed, for **G2** the binding of DNA was independent of salt concentration. The detailed gel retardation assays reported in this paper indicate that condensation of the DNA occurs from polyamine:DNA mass ratios of 1:1 and greater for **G1** and **G2**. Our previous TEM studies indicated that the G1:DNA complexes were approximately spherical and 100−150 nm in diameter. The G2:DNA complexes, however, were significantly larger (ca. 400 nm). In this paper, we have used light scattering methods to provide further evidence for the dimensions of the polyplexes formed between polyamines and DNA in solution. The results from these studies are in approximate agreement with the dimensions as visualized using TEM methods. Assuming the formation of spherical polyplexes, **G1** was calculated to form a polyplex with a diameter of up to 100 nm, while **G2** once again formed larger polyplexes up to approximately 210 nm.

The results from the in vitro tests reported in this paper indicate that the dendrons are ineffective transfection agents in their own right. This is clearly not due to an inability to condense the DNA effectively, and we postulate that transfection may fail due to an inability of the polyplex to escape from endocytic vesicles. This postulate is supported by the observation that in the presence of chloroquine the transfection efficiencies improved significantly. Spermine itself is almost completely protonated at physiological pH, and it is therefore possible that these constructs have limited capacity to act as proton sponges and buffer the endosome (a process associated with endosomal escape). Therefore chloroquine is required to enable the escape process. In this way, we propose that these dendritic spermine derivatives behave more like polylysine than proton sponge polymers such as PEI or PAMAM. One aspect of future work will focus on improving the ability of these dendritic constructs to cross cell membranes and escape from endosomes even in the absence of chloroquine. It should also be noted that an alternative postulate is that the polyplexes are so strongly bound that they are unable to release the DNA once within the cell.

In the presence of chloroquine, the nondendritic molecules (spermine and **G0**) are ineffective nonviral vectors for DNA. This is presumably because they fail to bind and condense DNA effectively (as shown by our previous ethidium bromide displacement assays and the gel electrophoresis reported in this paper). Dendron **G1** generally improved in its transfection efficiency on increasing the polyamine:DNA mass ratio. At low mass ratios, dendron **G2** was significantly more effective than **G1**. However, on increasing the mass ratio, the transfection efficiency achieved by **G2** was observed to drop significantly, and **G1** became the more effective transfection agent. We argue that this decrease in transfection efficiency observed with **G2** is a consequence of its toxicity when administered in the presence of chloroquine (Table 1). Dendron **G1** on the other hand has no significant toxicity in the presence of chloroquine and therefore became more effective than **G2** at high polyamine:DNA mass ratios. In this way, the results from our toxicity assay support the observed delivery results.

It must be noted here that even in the presence of chloroquine, the transfection efficiencies observed are too low for these structures to have clinically significant activity in vivo. In fact, transfection efficiencies would need to be improved by several orders of magnitude. The observed efficiencies are in line with low molecular weight poly(amidoamine) (PAMAM) dendrimers (*11*), which only form complexes with DNA at high N/P ratios. In general terms, an increase in molecular weight for PAMAMs yields a significant increase in transfection efficiency, and the same trend may be expected for higher molecular weight analogues of our dendrons. However, it is also possible to make other significant structural modifications to the structure of dendrons **G1** and **G2** which might be expected to enhance transfection efficiencies and would avoid the tedious and time-consuming syntheses required for higher generation dendritic molecules. Work to generate simple synthetically modified versions of our nontoxic dendrons is currently underway.

CONCLUSIONS

In summary, this paper has investigated the ability of our new simple dendron structures, functionalized on the surface with multiple spermine groups, to act as vectors in gene therapy. It has been shown that the dendrons can transfect DNA in the presence of chloroquine (which assists membrane permeation). The transfection efficiencies can be understood in terms of both the DNA affinities of the dendrons (**G2** > **G1** > **G0**) and the fact that **G2** shows some toxicity when administered in combination with DNA *and* chloroquine. The development of structure−activity relationships in the area of gene transfection is a goal of considerable importance in the field of gene therapy (*28*).

However, perhaps the most important observation from this study is that the dendrons exhibit negligible toxicities, either in their own right, or in the presence of DNA. This is an important first step in the development of potential vectors for application in gene therapy. It is also encouraging that the dendritic systems can be encouraged to transfect under certain conditions (i.e., addition of chloroquine to enable endosomal escape). We therefore believe that these systems have significant potential for application as the DNA binding subunit within more complex constructs designed for targeted gene therapy. However, this study has made clear that further synthetic modification of the basic dendron structure will be required, to enhance the transfection efficiencies of the nontoxic dendritic building blocks. Work targeting this goal is currently in progress within our laboratories, and we hope to report dendritic vectors for gene therapy applications, with significantly enhanced transfection efficiencies, in due course.

ACKNOWLEDGMENT

We gratefully acknowledge financial support from the EPSRC and Syngenta (J.G.H.) and a generous scholarship from the Worldwide Universities Network (WUN) which allowed J.G.H. to visit the laboratories in Illinois. Finally, we acknowledge financial support from the Erasmus-Socrates scheme (M.A.K.).

LITERATURE CITED

(1) (a) Verma, I. M., and Somia, N. (1997) Gene therapy − promises, problems and prospects. *Nature 389*, 239−242. (b) Luo, D., and Saltzman, W. M. (2000) Enhancement of transfection by physical concentration of DNA at the cell surface. *Nature Biotechnol. 18*, 33−37. (c) Demeneix, B., Hassani, Z., and Behr, J.-P. (2004) Towards multifunctional synthetic vectors. *Curr. Gene Ther. 4*, 445−455.

(2) (a) Gregorevic, P., and Chamberlain, J. S. (2003) Gene therapy for muscular dystrophy − a review of promising progress. *Exp. Opin. Biol. Ther. 3*, 803−814.

(3) (a) Ferrari, S., Geddes, D. M., and Alton, E. W. F. W. (2002) Barriers to and new approaches for gene therapy and gene delivery in cystic fibrosis. *Adv. Drug. Delivery Rev. 54*, 1373−1393. (b) Sangiuolo, F., D'Apice, M. R., Gambardella, S., Di Daniele, N., and Novelli, G. (2004) Toward the pharmacogenomics of cystic fibrosis − an update. *Pharmacogenomics 5*, 861−878. (c) Kinsey, B. M., Densmore, C. L., and Orson, F. M. (2005) Nonviral gene delivery to the lungs. *Curr. Gene Ther. 5*, 181−194.

(4) (a) Hunt, K. K., and Vorburger, S. A. (2002) Hurdles and hopes for cancer treatment. *Science 297*, 415−416. (b) Fang, B. L., and Roth, J. A. (2003) Tumor-suppressing gene therapy. *Cancer Biol. Ther. 2*, S115−S121. (c) Scanlon, K. J. (2004) Cancer gene therapy: Challenges and opportunities. *Anticancer Res. 24*, 501−504. (d) Vassaux, G., and Martin-Duque, P. (2004) Use of suicide genes for cancer gene therapy: Study of the different approaches. *Exp. Opin. Biol. Ther. 4*, 519−530. (e) Schatzlein, A. G. (2001) Nonviral vectors in cancer gene therapy: Principles and progress. *Anticancer Drugs 12*, 275−304.

(5) (a) Fanning, G., Amado, R., and Symonds, G. (2003) Gene therapy for HIV/AIDS: The potential for a new therapeutic regimen. *J. Gene Med. 5*, 645−653. (b) Wolkowicz, R., and Nolan, G. P. (2005) Gene therapy progress and prospects: Novel gene therapy approaches for AIDS. *Gene Ther. 12*, 467−476.

(6) Tomanin, R., and Scarpa M. (2004) Why do we need new gene therapy viral vectors? Characteristics, limitations and future perspectives of viral vector transduction. *Curr. Gene Ther. 4*, 357−372.

(7) Behr, J.-P. (1993) Synthetic Gene-Transfer Vectors. *Acc. Chem. Res. 26*, 274−278.

(8) Martin, B., Sainlos, M., Aissaoui A., Oudrhiri, N., Hauchecorne, M., Vigneron, J.-P., Lehn, J.-M., and Lehn, P. (2005) The design of cationic lipids for gene delivery. *Curr. Pharm. Des. 11*, 375−394.

(9) (a) Han, S., Mahato, R. I., Sung, Y. K., and Kim, S. W. (2000) Development of biomaterials for gene therapy. *Mol Ther. 2*, 302−317. (b) Merdan, T., Kopecek, J., and Kissel, T. (2002) Prospects for cationic polymers in gene and oligonucleotide therapy against cancer. *Adv. Drug. Delivery Rev.* 54, 715−758. (c) Pack, D. W., Hoffman, A. S., Pun, S., and Stayton, P. S., Design and development of polymers for gene delivery. (2005) *Nature Rev. Drug Discovery 4*, 581−593.

(10) (a) Dennig, J. (2003) Gene transfer in eukaryotic cells using activated dendrimers. *Top. Curr. Chem. 228*, 227−236. (b) Stiriba, S. E., Frey, H., and Haag, R. (2002) Dendritic polymers in biomedical applications: From potential to clinical use in diagnostics and therapy. *Angew. Chem., Int. Ed. 41*, 1329−1334. (c) Smith, D. K., Hirst, A. R., Love, C. S., Hardy, J. G., Brignell, S. V., and Huang, B. (2005) Self-assembly using dendritic building blocks − towards controllable nanomaterials. *Prog. Polym. Sci. 30*, 220−293.

(11) (a) Haensler, J., and Szoka, F. C. (1993) Polyamidoamine cascade polymers mediate efficient transfection of cells in culture. *Bioconjugate Chem. 4*, 372−379. (b) Kukowska-Latallo, J. F., Bielinska, A. U., Johnson, J., Spindler, R., Tomalia, D. A., and Baker, J. R. (1996) Efficient transfer of genetic material into mammalian cells using Starburst polyamidoamine dendrimers. *Proc. Natl. Acad. Sci. U.S.A. 93*, 4897−4902. (c) Tang, M. X., Redemann, C. T., and Szoka Jr, F. C. (1996) In vitro gene delivery by degraded polyamidoamine dendrimers. *Bioconjugate Chem. 7*, 703−714. (d) Tang, M. X., and Szoka, F. C. (1997) The influence of polymer structure on the interactions of cationic polymers with DNA and the morphology of the resulting complexes. *Gene Ther. 4*, 823−828. (e) Turunen, M. P., Hiltunen, M. O., Ruponen, M., Virkamaki. L., Szoka, F. C., Urtti, A., and Yla Herttuala, S. (1999) Efficient adventitial gene delivery to rabbit carotid artery with cationic polymer-plasmid complexes. *Gene Ther. 6*, 6−11. (f) Ottaviani, M. F., Furini, F., Casini, A., Turro, N. J., Jockusch, S., Tomalia, D. A., and Messori, L. (2000) Formation of supramolecular structures between DNA and starburst dendrimers studied by EPR, CD, UV, and melting profiles. *Macromolecules 33*, 7842−7851. (g) Bielinska, A. U., Chen, C. L., Johnson, J., and Baker, J. R. (1999) DNA complexing with polyamidoamine dendrimers: Implications for transfection. *Bioconjugate Chem. 10*, 843−850.

(12) (a) Luo, D., Haverstick, K., Belcheva, N., Han, E., and Saltzman, W. M. (2002) Poly(ethylene glycol)-conjugated PAMAM dendrimer for biocompatible, high-efficiency DNA delivery. *Macromolecules 35*, 3456−3462. (b) Lee, J. H., Lim, Y. B., Choi, J. S., Lee, Y., Kim, T.-i., Kim, H. J., Yoon, J. K., Kim, K., and Park, J. S. (2003) Polyplexes assembled with internally quaternized PAMAM-OH dendrimer and plasmid DNA have a neutral surface and gene delivery potency. *Bioconjugate Chem. 14*, 1214−1221.

(13) (a) Zinselmeyer, B. H., Mackay, S. P., Schatzlein, A. G., and Uchegbu, I. F. (2002) The lower-generation polypropyleneimine dendrimers are effective gene-transfer agents. *Pharm. Res. 19*, 960−967. (b) Lim, Y. B., Kim, T., Lee, J. W., Kim, S. M., Kim, H. J., Kim, K., and Park, J. S. (2002) Self-assembled ternary complex of cationic dendrimer, cucurbituril, and DNA: Noncovalent strategy in developing a gene delivery carrier. *Bioconjugate Chem. 13*, 1181−1185.

(14) (a) Ohsaki, M., Okuda, T., Wada, A., Hirayama, T., Niidome, T., and Aoyagi, H. (2002) In vitro gene transfection using dendritic poly(L-lysine). *Bioconjugate Chem. 13*, 510−517. (b) Okuda, T., Kidoaki, S., Ohsaki, M., Koyama, Y., Yoshikawa, K., Niidome, T., and Aoyagi, H. (2003) Time-dependent complex formation of dendritic poly(L-lysine) with plasmid DNA and correlation with in vitro transfection efficiencies. *Org. Biomol. Chem. 1*, 1270−1273. (c) Okuda, T., Sugiyama, A., Niidome, T., and Aoyagi, H. (2004) Characters of dendritic poly(L-lysine) analogues with the terminal lysines replaced with arginines and histidines as gene carriers in vitro. *Biomaterials 25*, 537−544. (d) Vlasov, G. P., Korol'kov, V. I., Pankova, G. A., Tarasenko, I. I., Baranov, A. N., Glazkov, P. B., Kiselev, A. V., Ostapenko, O. V., Lesina, E. A., and Baranov, V. S. (2004) Lysine dendrimers and their starburst polymer derivatives: Possible applications for DNA compaction and *in vitro* delivery of genetic constructs. *Russ. J. Bioorg. Chem. 30*, 12−20. (e) Choi, J. S., Lee, E. J., Choi, Y. H., Jeong, Y. J., and Park, J. S. (1999) Poly(ethylene glycol)-*block*-poly(L-lysine) dendrimer: Novel linear polymer/dendrimer block copolymer forming a spherical water-soluble polyionic complex with DNA. *Bioconjugate Chem. 10*, 62−65. (f) Choi, J. S., Joo, D. K., Kim, C. H., Kim, K., and Park, J. S. (2000) Synthesis of a barbell-like triblock copolymer, poly(L-lysine) dendrimer-*block*-poly(ethylene glycol)-*block*-poly(L-lysine) dendrimer, and its self-assembly with plasmid DNA. *J. Am. Chem. Soc. 122*, 474−480.

(15) Joester, D., Losson, M., Pugin, R., Heinzelmann, H., Walter, E., Merkle, H. P., and Diederich, F. (2003) Amphiphilic dendrimers: Novel self-assembling vectors for efficient gene delivery. *Angew. Chem., Int. Ed. 42*, 1486-1490.

(16) (a) Blagborough, I. S., Geall, A. J., and Neal, A. P. (2003) Polyamines and novel polyamine conjugates interact with DNA in ways that can be exploited in non-viral gene therapy. *Biochem. Soc. Trans. 31*, 397−406. (b) Remy, J.-S., Abdallah, B., Zanta, M. A., Boussif, O., Behr, J.-P., and Demeneix, B. (1998) Gene transfer with lipospermines and polyethylenimines. *Adv. Drug. Delivery Rev. 30*, 85−95. (c) Geall, A. J., Eaton, M. A. W., Baker, T., Catterall, C., and Blagborough, I. S. (1999) The regiochemical distribution of positive charges along cholesterol polyamine carbamates plays significant roles in modulating DNA binding affinity and lipofection. *FEBS Lett. 459*, 337−342. (d) Ronsin, G., Perrin, C., Guédat, P., Kremer, A., Camilleri, P., and Kirby, A. J. (2001) Novel spermine-based cationic gemini sufactants for gene delivery. *Chem. Commun.* 2234−2235. (e) Geall, A. J., Al-Hadithi, D., and Blagborough, I. S. (2002) Efficient calf thymus DNA condensation upon binding with

novel bile acid polyamine amides. *Bioconjugate Chem. 13*, 481−490. (f) Boulanger, C., Di Giorgio, C., Gaucheron, J., and Vierling, P. (2004) Transfection with fluorinated lipoplexes based on new fluorinated cationic lipids and in the presence of a bile salt surfactant. *Bioconjugate Chem. 15*, 901−908. (g) Dewa, T., Ieda, Y., Morita, K., Wang, L., MacDonald, R. C., Iida, K., Yamashita, K., Oku, N., and Nango, M. (2004) Novel polyamine-dialkyl phosphate conjugates for gene carriers. Facile synthetic route via an unprecedented dialkyl phosphate. *Bioconjugate Chem. 15*, 824−830.

(17) Behr, J. P., Demeneix, B. A., Loeffler, J. P., and Perez-Mutul, J. (1989) Efficient gene transfer into mammalian primary endocrine-cells with lipopolyamine-coated DNA. *Proc. Natl. Acad. Sci. U.S.A. 86*, 6982−6986.

(18) (a) Lee, E. R., Marshall, J., Siegel, C. S., Jiang, C., Yew, N. S., Nichols, M. R., Nietupski, J. B., Ziegler, R. J., Lane, M., Wang, K. X., Scheule, R. K., Harris, D. J., Smith, A. E., and Cheng, S. H.; (1996) Detailed analysis of structures and formulations of cationic lipids for efficient gene transfer to the lung. *Hum. Gene Ther. 7*, 1701−1717. (b) Cockett, M. I. (1999) Technology evaluation: cystic fibrosis therapy, Genzyme. *Curr. Opin. Mol. Ther. 1*, 279−283.

(19) Byk, G., Dubertret, C., Escriou, V., Frederic, M., Jaslin, G., Rangara, R., Pitard, B., Crouzet, J., Wils, P., Schwartz, B., and Scherman, D.(1998) Synthesis, activity and structure−activity relationship studies of novel cationic lipids for DNA transfer. *J. Med. Chem. 41*, 224−235.

(20) (a) Tabor, C. W., and Tabor, H. (1984) Polyamines. *Annu. Rev. Biochem.* 740−790. (b) Vijayanathan, V., Thomas, T., Shirahata, A., and Thomas, T. J. (2001) DNA condensation by polyamines: A laser light scattering study of structural effects. *Biochemistry 40*, 13644−13651. (c) Vijayanathan, V., Lyall, J., Thomas, T., Shirahata, A., and Thomas, T. J. (2005) Ionic, structural, and temperature effects on DNA nanoparticles formed by natural and synthetic polyamines. *Biomacromolecules 6*, 1097−1103.

(21) (a) Korolev, N., Lyubartsev, A. P., Nordenskiöld, L., and Laaksonen, A. (2001) Spermine: An "invisible" component in the crystals of B-DNA. A grand canonical Monte Carlo and molecular dynamics simulation study. *J. Mol. Biol. 308*, 907−917. (b) Burak, Y., Ariel, G., and Andelman, D. (2004) Competition between condensation of monovalent and multivalent ions in DNA aggregation. *Curr. Opin. Colloid Interface Sci. 9*, 53−58.

(22) Kostiainen M. A., Hardy, J. G., and Smith, D. K. (2005) High-affinity multivalent DNA binding by using low-molecular-weight dendrons. *Angew. Chem., Int. Ed. 44*, 2556−2559.

(23) (a) Newkome, G. R., and Lin, X. (1991) Symmetrical, 4-directional, poly(ether amide) cascade polymers. *Macromolecules 24*, 1443−1444. (b) Newkome, G. R., Lin, X., and Weis, C. D. (1991) Polytryptophan terminated dendritic macromolecules. *Tetrahedron: Asymmetry 2*, 957−960. (c) Young, J. K., Baker, G. R., Newkome, G. R., Morris, K. F., and Johnson Jr., C. S. (1994) Smart cascade polymers − modular synthesis of 4-directional dendritic macromolecules with acidic, neutral or basic terminal groups and the effect of pH changes on their hydrodynamic radii. *Macromolecules 27*, 3464−3471. (d) Nierengarten, J.-F., Habicher, T., Kessinger, R., Cardullo, F., Diederich, F., Gramlich, V., Gisselbrecht, J.-P., Boudon, C., and Gross, M. (1997) Macrocyclization on the fullerene core: Direct regio- and diastereoselective multi-functionalization of [60]fullerene, and synthesis of fullerene-dendrimer derivatives. *Helv. Chim. Acta 80*, 2238−2276. (e) Cardona, C. M., Gawley, R. E., and Gawley, C. (2002) An improved synthesis of a trifurcated Newkome-type monomer and orthogonally protected two-generation dendrons. *J. Org. Chem. 67*, 1411−1413.

(24) (a) Azzam, T., Eliyahu, H., Makovitzki, A., Linial, M., and Domb, A. J. (2004) Hydrophobized dextran-spermine conjugate as potential vector for in vitro gene transfection. *J. Controlled Release 96*, 309−323. (b) Hosseinkhani, H., Azzam, T., Tabata, Y., and Domb, A. J. (2004) Dextran-spermine polycation: An efficient nonviral vector for in vitro and in vivo gene transfection. *Gene Ther. 11*, 194−203. (c) Eliyahu, H., Makovitzki, A., Azzam, T., Zlotkin, A., Joseph, A., Gazit, D., Barenholz, Y., and Domb, A. J. (2005) Novel dextran-spermine conjugates as transfecting agents: comparing water-soluble and micellar polymers. *Gene Ther. 12*, 494−503.

(25) Stevens, M. G., and Olsen, S. (1993) Comparative analysis of using MTT and XTT in colorimetric assays for quantitating bovine neutrophil bactericidal activity. *J. Immunol. Methods 157*, 225−231.

(26) (a) Dunlap, D. D., Maggi, A., Soria, M. R., and Monaco, L. (1997) Nanoscopic structure of DNA condensed for gene delivery. *Nucleic Acids Res. 25*, 3095−3101. (b) Liu, G., Molas, M., Grossmann, G. A., Pasumarthy, M., Perales, J. C., Cooper, M. J., and Hanson, R. W. (2001) Biological properties of poly-L-lysine -DNA complexes generated by cooperative binding of the polycation. *J. Biol. Chem. 276*, 34379−34387.

(27) (a) Felgner, J. H., Kumar, R., Sridhar, C. N., Wheeler, C. J., Tsai, Y. J., Border, R., Ramsey, P., Martin, M., and Felgner, P. L. (1994) Enhanced gene delivery and mechanism studies with a novel series of cationic lipid formulations. *J. Biol. Chem. 269*, 2550−2561. (b) Erbacher, P., Roche, A. C., Monsigny, M., and Midoux, P. (1996) Putative role of chloroquine in gene transfer into a human hepatoma cell line by DNA/lactosylated polylysine complex. *Exp. Cell. Res. 225*, 186−194. (c) Forrest, M. L., and Pack, D. W. (2002) On the kinetics of polyplex endocytic trafficking: Implications for gene delivery vector design. *Mol. Ther. 6*, 57−66.

(28) McGregor, C., Perrin, C., Monck, M., Camilleri, P., and Kirby, A. J. (2001) Rational approaches to the design of cationic gemini surfactants for gene delivery. *J. Am. Chem. Soc. 123*, 6215−6220.

BC050212R

N-Terminally PEGylated Human Interferon-β-1a with Improved Pharmacokinetic Properties and in Vivo Efficacy in a Melanoma Angiogenesis Model[§]

Darren P. Baker,*[,†,§] Edward Y. Lin,[†] KoChung Lin,[†] Maria Pellegrini,[†] Russell C. Petter,[†] Ling Ling Chen,[†] Robert M. Arduini,[†] Margot Brickelmaier,[†] Dingyi Wen,[†] Donna M. Hess,[†] Liqing Chen,[†] Donna Grant,[†] Adrian Whitty,[†] Alan Gill,[†] Daniel J. Lindner,[‡] and R. Blake Pepinsky[†]

BiogenIdec Inc., 14 Cambridge Center, Cambridge, Massachusetts 02142, and Taussig Cancer Center, Cleveland Clinic Foundation, Cleveland, Ohio 44195. Received August 4, 2005; Revised Manuscript Received October 14, 2005

PEGylation of IFN-α has been used successfully to improve the pharmacokinetic properties and efficacy of the drug. To prepare a PEGylated form of human interferon-β-1a (IFN-β-1a) suitable for testing in vivo, we have synthesized 20 kDa mPEG-O-2-methylpropionaldehyde and used it to modify the N-terminal α-amino group of the cytokine. The PEGylated protein retained ∼50% of the activity of the unmodified protein and had significantly improved pharmacokinetic properties following intravenous administration in rats. The clearance and volume of distribution at steady state were reduced ∼30-fold and ∼4-fold, respectively, resulting in a significant increase in systemic exposure as determined by the area under the curve. The elimination half-life of the PEGylated protein was ∼13-fold greater than for the unmodified protein. The unmodified and PEGylated proteins were tested for their ability to inhibit the formation of radially oriented blood vessels entering the periphery of human SK-MEL-1 melanoma tumors in athymic nude homozygous (*nu*/*nu*) mice. In a single dose comparison study, administration of 1×10^6 units of unmodified IFN-β-1a resulted in a 29% reduction in vessel number, while 1×10^6 units of PEGylated IFN-β-1a resulted in a 58% reduction. Both treatments resulted in statistically significant reductions in mean vessel number as compared to the vehicle (control)-treated mice, with the PEGylated IFN-β-1a-treated mice showing a statistically significantly greater reduction in mean vessel number as compared to the unmodified IFN-β-1a-treated mice. In a multiple versus single dose comparison study, daily administration of 1×10^6 units of unmodified IFN-β-1a for 9 days resulted in a 51% reduction in vessel number, while a single dose of 1×10^6 units of the PEGylated protein resulted in a 66% reduction. Both treatments resulted in statistically significant reductions in mean vessel number as compared to the vehicle-treated mice, with the PEGylated IFN-β-1a-treated mice showing a statistically significantly greater reduction in mean vessel number as compared to the unmodified IFN-β-1a-treated mice. Therefore, the improved pharmacokinetic properties of the modified protein translated into improved efficacy. Since unmodified IFN-β is used for the treatment of multiple sclerosis and hepatitis C virus infection, a PEGylated form of the protein such as 20 kDa mPEG-O-2-methylpropionaldehyde-modified IFN-β-1a may serve as a useful adjunct for the treatment of these diseases. In addition, the antiangiogenic effects of PEGylated IFN-β-1a may be harnessed for the treatment of certain cancers, either as a sole agent or in combination with other antitumor drugs.

INTRODUCTION

Interferons (IFNs)[1] are a family of cytokines that mediate antiviral, antiproliferative, and immunomodulatory effects in response to biological and chemical stimuli (*1*−*3*). Two types of IFN are recognized on the basis of their physical and biological properties: Type I IFNs, members of which include the IFN-α subtypes, IFN-β, IFN-τ, and IFN-ω, and Type II, the only member of which is IFN-γ. The Type I IFN's signal through a common cell surface receptor composed of the IFNAR1 and IFNAR2 chains (*4*−*7*). The intracellular portions of IFNAR1 and IFNAR2 associate with the Janus tyrosine kinases Tyk2 and JAK1, respectively (*8*−*11*), and, following ligand binding, the kinases phosphorylate each other and the receptor chains, thereby creating binding sites for STAT proteins (*12*, *13*). The STAT proteins are subsequently phosphorylated, dimerize, migrate to the nucleus, and drive the expression of IFN-stimulated genes (*14*).

Type I IFNs have been approved for the treatment of a number of diseases for which their antiviral, antiproliferative, and immunomodulatory activities underlie their mechanism of action. Recombinant IFN-α-2b (Intron-A, Schering-Plough) has been approved for the treatment of chronic hepatitis B and hepatitis C virus (HCV) infection, genital warts, AIDS-related Kaposi's sarcoma, follicular non-Hodgkin's lymphoma, malignant melanoma, and hairy cell leukemia, while recombinant IFN-α-2a (Roferon-A, Hoffman La−Roche) is approved for the treatment of HCV, hairy cell leukemia, and chronic phase Philadelphia chromosome-positive chronic myelogenous leukemia. In addition, IFN-α-2b has been shown to be effective for the treatment of giant cell angioblastoma, a destructive pediatric tumor (*15*), and both IFN-α-2b and IFN-α-2a have been used for the treatment of life-threatening pediatric hemangiomas (*16*, *17*). Recombinant forms of IFN-β-1a (Avonex, BiogenIdec; Rebif, Serono) and IFN-β-1b (Betaferon, Schering

§ This paper is dedicated to the memory of my friend, mentor, and colleague Professor Charles A. Fewson, OBE (Sept 8, 1937 to Aug 28, 2005), whose personal and intellectual contributions to the scientific community will be sorely missed.

* Corresponding author. e-mail: darren.baker@biogenidec.com; telephone: 617-679 2165; fax: 617-679 2304.

† BiogenIdec Inc.

‡ Taussig Cancer Center.

[1] Abbreviations. IFN, interferon; PEG, poly(ethylene glycol); mPEG, methoxy poly(ethylene glycol); PEGylated, poly(ethylene glycol)-modified; EMC, encephalomyocarditis; PBS, phosphate-buffered saline; AUC, area under the curve; C_{max}, maximal concentration; CL, systemic clearance; $t_{1/2}$, elimination half-life; V_{ss}, volume of distribution at steady state.

10.1021/bc050237q CCC: $33.50 © 2006 American Chemical Society
Published on Web 12/03/2005

AG) are approved for the treatment of multiple sclerosis, while nonrecombinant forms of IFN-β (e.g. Feron, Toray) are approved in Japan for the treatment of HCV.

As with other small protein drugs, Type I IFNs have relatively short circulating half-lives that may necessitate frequent parenteral administration to achieve efficacy. To reduce the dosing frequency, and to improve the pharmacokinetics and efficacy, PEGylated forms of type I IFN's have been developed (*18*−*20*). PEGylation of IFN-α-2b with a linear 12 kDa PEG (PEG-Intron, Schering-Plough) increased the half-life following subcutaneous administration from 4−7 to 30−40 h (*21*) and improved the sustained virological response (SVR) against HCV from 12 to ∼24% (*22*). When given in combination with the antiviral drug ribavirin, the SVR with PEG-Intron increased to 54% (*23*). Similarly, PEGylation of IFN-α-2a with a branched 40 kDa PEG (Pegasys, Hoffman La−Roche) increased the half-life following intravenous administration from 3−8 to 65 h (*24*) and improved the SVR from 19 to 39% in HCV patients (*25*), and from 8 to 30% in HCV patients with concomitant cirrhosis of the liver (*26*). When administered in combination with ribavirin, the SVR of PEGylated IFN-α-2a improved to 56% (*27*). In addition to a significant improvement in the SVR, the frequency of dosing for the PEGylated proteins was reduced from thrice weekly to only once per week, a factor that increases patient compliance and therefore the effectiveness of the overall treatment regimen. A similar reduction in dosing frequency was observed upon modification of recombinant granulocyte colony-stimulating factor with a linear 20 kDa PEG (Neulasta, Amgen), administered for the treatment of neutropenia in cancer patients undergoing chemotherapy (*28*).

While the PEGylation of IFN-α-2b and IFN-α-2a serves as a clear example of the benefits that can be achieved by administering a longer half-life molecule, it is perhaps surprising that a PEGylated form of IFN-β has not been tested in clinical trials of either multiple sclerosis or HCV, especially when considering that the unmodified proteins used to treat these diseases often require frequent dosing to achieve efficacy. For multiple sclerosis, two of the three approved IFN-β products are administered multiple times per week: IFN-β-1a (Rebif) is injected subcutaneously thrice weekly (*29*), while IFN-β-1b (Betaferon) is injected subcutaneously every other day (*30*). For HCV, efficacy of recombinant IFN-β in European patients has been established following thrice weekly subcutaneous administration (*31*), and following daily dosing for 6 days a week for twelve weeks by intravenous administration (*32*). In Japan, where nonrecombinant forms of IFN-β have been used widely for the treatment of HCV, the unmodified protein is also administered frequently, typically every day for 2 weeks followed by thrice weekly for the remainder of the treatment regimen, although twice-daily regimens have also been tested (*33*−*35*). Therefore, development of a PEGylated form of IFN-β may be useful for the treatment of diseases such as multiple sclerosis or HCV where some of the current therapies require frequent dosing. Moreover, the use of a PEGylated form of IFN-β for the treatment of HCV may, in addition to reducing the dosing frequency, also offer the potential of a better safety profile compared to PEGylated IFN-α-2b and IFN-α-2a. While many patients must reduce the dose of PEGylated IFN-α or stop treatment due to adverse reactions, data from clinical trials of IFN-β in multiple sclerosis and HCV indicate that treatment with this cytokine is associated with a good safety and tolerability profile (*36*).

With the aim of developing a PEGylated form of IFN-β-1a suitable for testing in preclinical studies and potentially in human clinical trials, we have synthesized 20 kDa mPEG-O-2-methylpropionaldehyde for targeting the N-terminal α-amino group of the protein. Since the N-terminus of human IFN-β-1a is not critical for activity (alanine scanning mutagenesis of the N-terminal region (*37*), and deletion of the N-terminal methionine (*38*) have no effect on the antiviral activity), it was likely that modification of the protein with 20 kDa mPEG-O-2-methylpropionaldehyde would result in a protein that retained significant activity and that had improved pharmacokinetic properties. Indeed, Pepinsky et al. (*39*) have shown that modification of the N-terminal α-amino group of IFN-β-1a with 20 kDa mPEG-propionaldehyde resulted in a protein that retained full in vitro antiviral activity, had improved pharmacokinetic properties in mice, rats, and rhesus monkeys, and was pharmacologically active in the latter species as judged by the induction of the IFN-responsive markers neopterin and β2-microglobulin. However, while this report described the effects of PEGylation on the pharmacokinetic and pharmacodynamic properties of the protein, the unmodified and PEGylated proteins were not tested in an animal model of disease. Therefore, it remained an open question as to whether the improved pharmacokinetic properties would translate into improved efficacy.

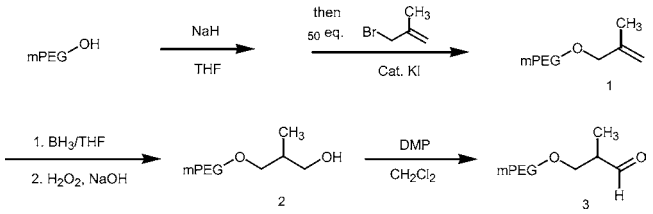

Figure 1. Schematic representation of the steps used in the synthesis of 20 kDa mPEG-O-2-methylpropionaldehyde.

Here we report on the synthesis and characterization of 20 kDa mPEG-O-2-methylpropionaldehyde, and the preparation and characterization of IFN-β-1a modified at the N-terminus with this PEG group. We further report on the pharmacokinetics of the unmodified and PEGylated proteins in rats, and the efficacy of the two proteins in a murine dermis model of angiogenesis inhibition. The improved efficacy of the PEGylated protein is shown to correlate with the improvement in its pharmacokinetic properties.

MATERIALS AND METHODS

Materials. SP-Sepharose, a Superose 6 HR 10/30 column, and ^{3}H-thymidine were obtained from GE Healthcare (Piscataway, NJ); 20 kDa mPEG-OH was from Sunbio (Anyang City, South Korea); recombinant human interferon-β-1a was from BiogenIdec (Cambridge, MA); sodium cyanoborohydride was from Sigma-Aldrich (St. Louis, MO); human serum albumin was from Instituto Grifols (Barcelona, Spain); endoproteinase Lys-C was from Wako Pure Chemical Industries (Osaka, Japan); sodium hydride (60% dispersion in mineral oil), 3-bromo-2-methylpropene, borane tetrahydrofuran complex (1 M in THF), and 30% hydrogen peroxide were from Aldrich (Milwaukee, WI); potassium iodide, sodium hydroxide, sodium bicarbonate, and sodium thiosulfate were from Fisher (Fair Lawn, NJ); and Dess−Martin periodinane was from Lancaster (Windham, NH).

Synthesis of 20 kDa mPEG-O-2-methylpropionaldehyde. The synthesis of 20 kDa mPEG-O-2-methylpropionaldehyde is given in Figure 1. Linear mPEG-OH with a molecular weight of 20000 Da (mPEG-OH 20 kDa; 2.0 g, 0.1 mmol) was treated with 60% NaH (32 mg, 0.8 mmol) in THF (35 mL). 3-Bromo-2-methylpropene (0.67 g, 5 mmol) and a catalytic amount of potassium iodide were added, and the mixture was heated to reflux for 17 h. The solvent was then removed under vacuum. CH_2Cl_2 (20 mL) was added to the residue, and the organic layer was separated and dried over anhydrous Na_2SO_4, and the volume was reduced to approximately 6 mL. The CH_2Cl_2 solution was added to ether (150 mL) dropwise. The resulting white precipitate was collected and dried under vacuum, yielding 1.8

g (~90% recovery) of compound **1**. ^{1}H NMR ($CDCl_3$, 400 MHz) and ^{1}H−^{13}C HSQC 2D NMR ($CDCl_3$, 400 MHz) showed ^{1}H δ 4.92 (s, 1H), 4.85 (s, 1H), 3.89 (s), 3.35 (s), 1.70 (s, 3H); ^{13}C δ 112, 76, 59, 20. To compound **1** (0.77 g, 0.04 mmol) in THF (7 mL) and CH_2Cl_2 (0.7 mL) at 0 °C was added BH_3·THF (1.0 M, 1.4 mL). The mixture was stirred in an ice bath for 1 h. NaOH (2 M, 1.0 mL) was added slowly, followed by 30% H_2O_2 (0.3 mL). The reaction was warmed to ambient temperature and stirred for 16 h. The above workup procedure was followed (CH_2Cl_2 extraction, followed by precipitation from ether and drying), to yield 0.60 g (~78% recovery) of compound **2** as a white solid. ^{1}H NMR ($CDCl_3$, 400 MHz), ^{1}H−^{1}H TOCSY 2D NMR ($CDCl_3$, 400 MHz), and ^{1}H−^{13}C HSQC 2D NMR ($CDCl_3$, 400 MHz) showed ^{1}H δ 3.35 (s), 2.01 (m, 1H), 0.84 (d, 3H); ^{13}C δ 59, 36, 13. Compound **2** (250 mg, 0.013 mmol) was dissolved in CH_2Cl_2 (2.5 mL) and Dess−Martin periodinane (DMP; 25 mg, 0.059 mmol) was added with stirring. The reaction was stirred for 30 min at ambient temperature. Saturated aqueous $NaHCO_3$ and $Na_2S_2O_3$ (2 mL each) were added, and the mixture was stirred at ambient temperature for 1 h. The above workup procedure was followed (CH_2Cl_2 extraction, followed by precipitation from ether and drying) to yield 194 mg (~77% recovery) of compound **3** (20 kDa mPEG-O-2-methylpropionaldehyde) as a white solid. ^{1}H NMR ($CDCl_3$, 400 MHz), ^{1}H−^{1}H TOCSY 2D NMR ($CDCl_3$, 400 MHz), and ^{1}H−^{13}C HSQC 2D NMR ($CDCl_3$, 400 MHz) showed ^{1}H δ 9.70 (s, 1H), 3.35, 2.63 (m), 1.09 (d, 3H); ^{13}C δ 59, 47, 11. The synthesis of 20 kDa mPEG-O-2-methylpropionaldehyde as described was repeated numerous times, up to a 20 g scale.

Preparation of 20 kDa mPEG-O-2-methylpropionaldehyde-modified IFN-β-1a. Recombinant human IFN-β-1a (5.6 mg at 1.1 mg/mL in 50 mM Na_2HPO_4 pH 6.0, 270 mM NaCl) was treated with 20 kDa mPEG-O-2-methylpropionaldehyde (5 mg/mL) in the presence of sodium cyanoborohydride (5 mM), in the dark for 19.25 h at ambient temperature. The reaction mixture was diluted with 4 volumes of 20 mM MES pH 5.0 and loaded under gravity onto a 4.5 mL (1 cm internal diameter × 5.7 cm) column of SP-Sepharose Fast Flow resin that had been equilibrated in 5 mM Na_2HPO_4 pH 5.5. The column was washed with 45 mL of 5 mM Na_2HPO_4 pH 5.5 and then bound protein eluted with 25 mM MES pH 6.4, 400 mM NaCl. Fractions containing protein were pooled and then concentrated with Centricon YM 3 concentrators (Millipore). The unmodified and PEGylated forms of IFN-β-1a were separated on a Superose 6 HR 10/30 column run at 0.4 mL/min in 5 mM Na_2HPO_4 pH 5.5, 150 mM NaCl as the mobile phase. Fractions were collected and analyzed by SDS−PAGE, and those containing only the singly modified protein were pooled. The PEGylated protein was filter-sterilized (0.2 μm), and the concentration of the protein determined as described below. The final yield of the PEGylated IFN-β-1a (excluding the mass of the attached PEG) was 27%. Sufficient protein was removed for analytical characterization, and the remainder was formulated at 100 μg/mL in 5 mM Na_2HPO_4 pH 5.5, 150 mM NaCl containing 45.6 mg/mL human serum albumin and stored at −70 °C.

Determination of Protein Concentration. The concentration of unmodified and PEGylated IFN-β-1a was determined by absorbance measurements at 280 nm using the predicted extinction coefficient of 29990 L mol^{-1} cm^{-1} based on the tryptophan, tyrosine, and cystine (disulfide) content (*40*). The same value for the extinction coefficient was used for the PEGylated protein as for the unmodified protein since the PEG group does not contribute to the absorbance at 280 nm (a 1 mg/mL solution of 20 kDa mPEG-O-2-methylpropionaldehyde was found to have an absorbance of 0.002 as compared to 1.50 for 1 mg/mL IFN-β-1a). Therefore, an identical absorbance at 280 nm equates to the same mass of IFN-β-1a irrespective of the presence of the attached PEG. When referring to the mass of the PEGylated protein, the contribution of the PEG moiety is not included.

Peptide Mapping. Peptides were generated by digestion of ~13 μg of unmodified or PEGylated IFN-β-1a with 20% (w/w) endoproteinase Lys-C in 100 μL of PBS pH 7.6, 1 mM EDTA, 5 mM DTT for 24 h at ambient temperature. 4 μL of 1 M DTT and 100 μL of 8 M urea were then added, and the digest was loaded onto a YMC (Milford, MA) C_{18} (1.0 mm internal diameter × 250 mm) reverse-phase HPLC column (AA12S052501WT). The column was developed with the following gradient at 0.07 mL/min where A = water, 0.03% TFA and B = acetonitrile, 0.024% TFA: 0−50% B in 50 min, 50−70% B in 10 min, 70% B in 10 min. Peptide peaks were detected on-line with a 2690/ZMD LC-MS system (Waters, Milford, MA). The digests were also loaded onto a Vydac (Hesperia, CA) C_4 (1.0 mm internal diameter × 250 mm) reverse-phase HPLC column (214TP51). The column was developed with the following gradient where A = water, 0.1% TFA and B = acetonitrile, 0.08% TFA: 0−63% B in 70 min, 63−80% B in 10 min. Peptide peaks were detected on-line with a Waters (Milford, MA) Model 996 photodiode array detector.

Determination of Antiviral Activity. The specific antiviral activity of IFN-β-1a was determined using a cytopathic effect (CPE) bioassay that measures the ability of the protein to protect human lung carcinoma A549 cells (grown at 37 °C/5% CO_2) challenged with encephalomyocarditis (EMC) virus. For the assay, 3 × 10^4 A549 cells in 100 μL of Dulbecco's modified eagles medium containing 10% fetal bovine serum, 2 mM L-glutamine, 100 U/mL penicillin, and 100 μg/mL streptomycin, were added to wells of 96-well microtiter plates and incubated for 5−6 h. Serial dilutions of duplicate IFN-β-1a standards and test samples were then added, and the cells were incubated for a further 24 h. The medium was removed, and EMC virus was added. The cells were incubated for 48 h, and 50 μL of 5 mg/mL 3-(4,5-dimethyl-2-thiazolyl)-2,5-diphenyl-2*H*-tetrazolium bromide (MTT) in PBS was then added. After a 1 h incubation, the medium was removed, the wells were washed with 100 μL of PBS, and the cells and dye were solubilized with 100 μL of 1.2 N HCl in 2-propanol. The plates were then read at 450 nm, and the data were analyzed using four-parameter curve fitting with Softmax Pro software (Molecular Devices, Sunnyvale, CA).

Determination of Antiproliferative Activity. The specific antiproliferative activity of IFN-β-1a was determined using a bioassay that measures the ability of the protein to inhibit the growth of Daudi human B cells (grown at 37 °C/5% CO_2). For the assay, 1 × 10^4 Daudi cells in 150 μL of RPMI-1640 medium containing 10% fetal bovine serum and 2 mM L-glutamine were added to wells of 96-well microtiter plates and incubated for 48 h with serial dilutions of quadruplet IFN-β-1a samples. ^{3}H-Thymidine (1 μCi in 50 μL medium/well) was added, the cells incubated for a further 16 h, and the cultures were harvested using a Tomtec (Hamden, CT) 96 Mach III harvester. Thymidine incorporation was measured using a Perkin-Elmer (Wellesley, MA) 1450 MicroBeta JET scintillation counter. The data were analyzed using four-parameter curve fitting with DeltaGraph software version 4.5 (SPSS Inc., Chicago, IL).

Determination of Pharmacokinetic Parameters. Pharmacokinetic parameters following intravenous administration of unmodified and PEGylated IFN-β-1a were determined using precannulated (jugular vein) female Lewis rats (weight 200−250 g) obtained from Charles River Laboratories (Research Triangle Park, Raleigh-Durham, NC). Three rats were used for the unmodified IFN-β-1a and three for the PEGylated protein. Animals were acclimated in the BiogenIdec animal facility prior to the experiment. Food was withheld overnight prior to beginning the study. Water was available ad libitum. Experimental procedures were carried out according to an approved

Institutional Animal Care and Use Committee (IACUC) protocol. Unmodified and PEGylated IFN-β-1a were formulated in 15 mg/mL human serum albumin in PBS, and a single dose of unmodified IFN-β-1a (80 μg/kg) or PEGylated IFN-β-1a (24 μg/kg) was administered. Blood samples (200 μL) were drawn at the following times: unmodified IFN-β-1a; 0, 0.083, 0.25, 0.5, 1.25, 3, and 5 h; PEGylated IFN-β-1a; 0, 0.083, 0.25, 0.5, 1.25, 3, 24, 48, and 72 h. To minimize blood volume depletion, each blood sample removed was replaced with an equivalent volume of sterile normal saline. Blood samples were allowed to clot for 60 min at ambient temperature and centrifuged, and serum was separated and stored at −70 °C. The amount of unmodified and PEGylated IFN-β-1a present in the serum samples was determined using the A549 cell/EMC virus CPE bioassay described above, using the unmodified or PEGylated protein as the standard, respectively. Pharmacokinetic parameters were calculated using WinNonLin software version 3 (Pharsight, Mountain View, CA) using noncompartmental analysis.

Determination of in Vivo Antiangiogenic Activity. Unmodified and PEGylated IFN-β-1a were tested for their ability to inhibit the formation of radially oriented blood vessels entering the periphery of human SK-MEL-1 melanoma tumors grown in athymic nude homozygous (*nu*/*nu*) mice. SK-MEL-1 cells (2×10^6) were inoculated on day 0 into the dermis in the flanks of the mid axillary line of 3-week-old *nu*/*nu* NCR mice. 24 h later (day 1), groups of four mice each received the following subcutaneous doses of human serum albumin solution (HSA, vehicle control), or HSA containing either unmodified or PEGylated IFN-β-1a: Group 1, 0.1 mL of 45.6 mg/mL HSA once on day 1 only; Group 2, 0.1 mL of 45.6 mg/mL HSA containing 1×10^6 units of unmodified IFN-β-1a once on day 1 only; and Group 3, 0.1 mL of 45.6 mg/mL HSA containing 1×10^6 units of PEGylated IFN-β-1a once on day 1 only. Mice were sacrificed on day 10 and the tumor inoculation site assessed for neovascularization, measured by an observer blinded as to the treatment (*41*). Every radially oriented vessel entering the periphery of the tumor was scored as a single vessel. In an independent study, groups of three mice each received the following subcutaneous doses of HSA, or HSA containing either unmodified or PEGylated IFN-β-1a: Group 1: 0.1 mL of 45.6 mg/mL HSA once on day 1 only; Group 2, 0.1 mL of 45.6 mg/mL HSA containing 1×10^6 units of PEGylated IFN-β-1a once on day 1 only; Group 3, 0.1 mL of 45.6 mg/mL HSA on days 1−9 inclusive; Group 4, 0.1 mL of 45.6 mg/mL HSA containing 1×10^6 units of unmodified IFN-β-1a on days 1−9 inclusive. Mice were sacrificed on day 10 and neovascularization of the tumors determined as described above. Experimental procedures were carried out according to an approved IACUC protocol. Statistical analysis of the data was carried out using GraphPad Prism software version 4 (GraphPad Software, San Diego, CA).

RESULTS

PEGylation of IFN-β-1a. IFN-β-1a was modified with 20 kDa mPEG-O-2-methylpropionaldehyde, and the pharmacokinetic and efficacy profiles of the unmodified and PEGylated proteins were compared. Reaction of IFN-β-1a with 20 kDa mPEG-O-2-methylpropionaldehyde resulted in the formation of predominantly singly modified protein, with lesser amounts of more highly modified forms present (data not shown). The unmodified and PEGylated forms were separated from one another by size exclusion chromatography. Figure 2, lane C shows that the singly modified protein was purified to homogeneity, with no unmodified or multiply modified forms detected. Incorporation of a single PEG resulted in an increase in the apparent M_r of the protein by reducing SDS−PAGE from ~25 kDa (Figure 2, lane B) to ~55 kDa (Figure 2, lane C). By size exclusion chromatography, the singly modified protein had an apparent M_r of 320000 Da. The ~10-fold increase in the apparent mass compared to the unmodified protein results from a large increase in the hydrodynamic volume of the PEGylated protein, a typical consequence of this type of modification.

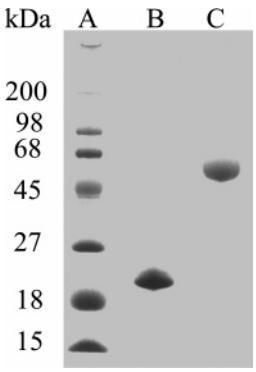

Figure 2. SDS−PAGE of unmodified and PEGylated human IFN-β-1a. Purified proteins (4 μg) were electrophoresed on a reducing 10−20% gradient gel and stained with Coomassie brilliant blue. Lane A, molecular weight markers; lane B, unmodified IFN-β-1a; lane C, PEGylated IFN-β-1a.

The specificity of the PEGylation reaction was determined by peptide mapping. Peptide maps of unmodified and PEGylated IFN-β-1a were generated with endoproteinase Lys-C (Figure 3). For the PEGylated protein, 93% of the PEG was attached to the N-terminal peptides consisting of residues 1−19 (MSYNLLGFLQRSSNFQCQK) and 2−19 (SYNLLGFLQRSSNFQCQK) as evident by their disappearance from the map (Figure 3, compare panels A and B). The presence of two N-terminal peptides stems from the fact that the preparation of IFN-β-1a used contained a small amount (11%) of a truncated species in which the N-terminal methionine was missing, and in which the α-amino group of the second residue, serine, was modified. The mapping data therefore show that the PEG is primarily attached to the N-terminal peptide(s). Furthermore, the observation that the peaks corresponding to the adjacent peptides (residues 20−30 and 20−33) do not decrease in size (Figure 3, compare panels A and B) suggests that the modification is at the N-terminal α-amino group rather than at the ϵ-amino group of Lys-19. Had Lys-19 been modified, endoproteinase Lys-C would not be expected to cleave the peptide bond between Lys-19 and Leu-20, and the amount of peptide 20−30 and 20−33 would have subsequently been reduced. However, while the PEGylated protein consists primarily of a species in which the N-terminal α-amino group is modified, the observation that some (~7%) of the N-terminal peptide corresponding to residues 1−19 remains (Figure 3, panel B) indicates that the preparation must also contain singly modified form(s) in which the PEG is attached at site(s) other than at the N-terminus. However, these are not readily assigned based on a comparison of the maps for unmodified and PEGylated protein, since they represent only a small fraction of the total population and the modification(s) may occur at more than one site.

To determine the effect of PEGylation on the specific antiviral activity of IFN-β-1a, the unmodified and PEGylated proteins were assayed in the A549 cell/EMC virus CPE bioassay. Figure 4A shows that incorporation of a single 20 kDa mPEG-O-2-methylpropionaldehyde moiety at the N-terminus of IFN-β-1a produces an approximately 2-fold loss of specific activity as compared to the unmodified protein. For the unmodified protein, the mean EC_{50} value was 5.7 ± 0.76 pg/mL ($n = 4$ replicates), while for the PEGylated protein, the mean EC_{50} value was 11.9 ± 0.85 pg/mL ($n = 4$ replicates). Therefore, the specific antiviral activity of the PEGylated IFN-β-1a is $\sim 1 \times 10^8$ units/mg. The unmodified and PEGylated proteins were also tested for their

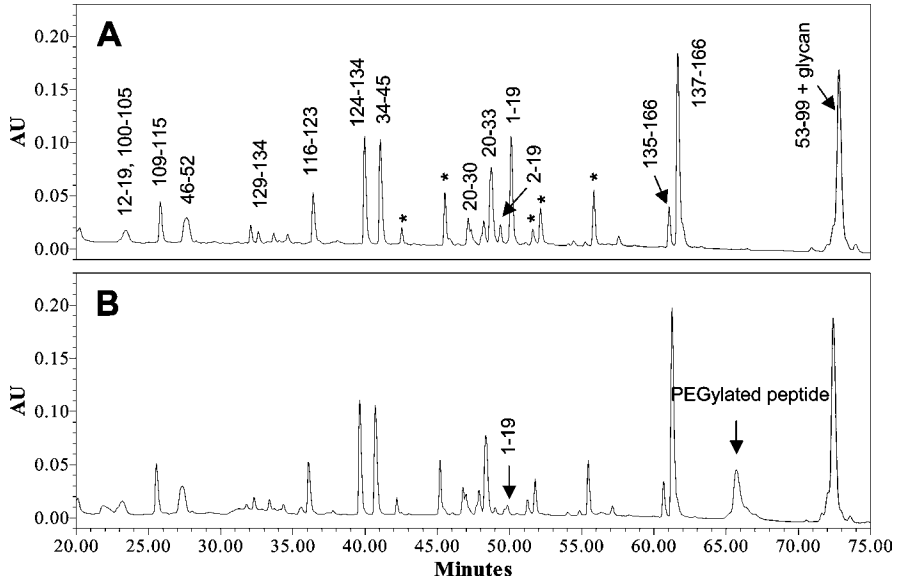

Figure 3. Endoproteinase Lys-C peptide maps of unmodified (A) and PEGylated (B) IFN-β-1a. Peptide peaks were detected on-line with a 2690/ZMD LC-MS system. Peptides are denoted by residue number and asterisks denote peptides from endoproteinase Lys-C generated by protease autodigestion.

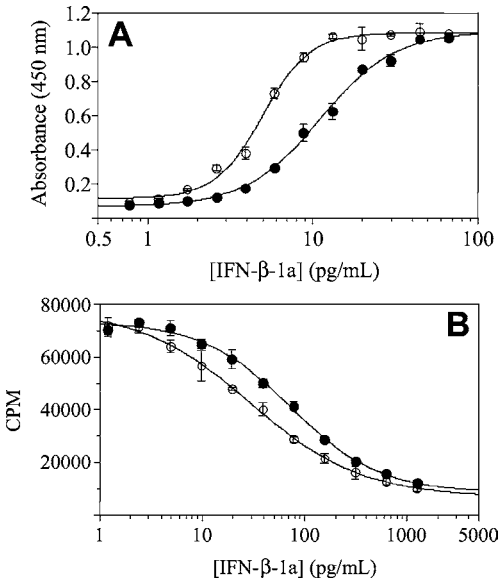

Figure 4. (A) Antiviral activity of unmodified and PEGylated IFN-β-1a assayed on human lung carcinoma A549 cells challenged with EMC virus. Assays were performed in duplicate and error bars show the spread between the determinations. The data were analyzed using four-parameter curve fitting. Unmodified IFN-β-1a (○), PEGylated IFN-β-1a (●). (B) Antiproliferative activity of unmodified and PEGylated IFN-β-1a assayed on Daudi human B cells. Assays were performed in quadruplet and error bars show the standard deviation about the mean. The data were analyzed using four-parameter curve fitting. Unmodified IFN-β-1a (○), PEGylated IFN-β-1a (●).

ability to inhibit the growth of Daudi human B cells. Figure 4B shows that the PEGylated protein was 2.4-fold less potent than the unmodified IFN-β-1a. For the unmodified protein, the IC_{50} value was 30 pg/mL, while for the PEGylated protein, the IC_{50} value was 73 pg/mL. Therefore, the PEGylated protein showed the same ∼2-fold loss of potency as compared to the unmodified protein in assays measuring antiviral and antiproliferative activities.

Pharmacokinetics of Unmodified and PEGylated IFN-β-1a. Pharmacokinetic parameters were determined for unmodified and PEGylated IFN-β-1a following intravenous administration in female Lewis rats. The mean blood serum curves for unmodified and PEGylated IFN-β-1a are shown in Figure 5 panels A and B, respectively. Systemic clearance, elimination half-life ($t_{1/2}$), and the volume of distribution at steady state (V_{ss}) were calculated and are shown in Table 1. Incorporation of 20 kDa mPEG-O-2-methylpropionaldehyde at the N-terminus of IFN-β-1a reduced the clearance by ∼30-fold and increased $t_{1/2}$ by ∼13-fold as compared to the unmodified protein (Table 1). In addition, the volume of distribution decreased ∼4-fold for the PEGylated protein, suggesting that the PEG moiety reduces the ability of the protein to distribute outside of the central vasculature. The maximal observed concentration (C_{max}) for the unmodified protein was ∼2-fold greater than for the PEGylated protein although this was not unexpected since the unmodified protein was dosed at 80 μg/kg as compared to 24 μg/kg for the PEGylated protein, i.e., ∼3-fold greater amount in terms of IFN-β-1a equivalents. The unmodified protein was dosed at a higher level to ensure that sufficient protein remained in circulation to be detected in the CPE bioassay and thus enable calculation of its pharmacokinetic parameters. The AUC for the PEGylated protein was ∼10-fold greater than for the unmodified protein, despite being dosed at a level ∼3-fold lower than the unmodified protein. Therefore, PEGylation of the N-terminus of IFN-β-1a with 20 kDa mPEG-O-2-methylpropionaldehyde results in a significant increase in the systemic exposure as compared to the unmodified protein.

In Vivo Efficacy of Unmodified and PEGylated IFN-β-1a. To determine whether the improved pharmacokinetic properties of the PEGylated IFN-β-1a translated into an improvement in efficacy, the unmodified and PEGylated proteins were tested for their ability to inhibit the formation of radially oriented blood vessels entering the periphery of human SK-MEL-1 melanoma tumors grown in athymic nude homozygous (*nu*/*nu*) mice. This murine dermis model, described by Bauer et al. (*42*), has been used previously to evaluate the antiangiogenic effects of unmodified and PEGylated IFN-α-2b and was therefore a useful system for comparing the efficacy of unmodified and PEGylated IFN-β-1a.

Two studies were performed to compare the efficacy of the unmodified and PEGylated proteins. In one study, groups of four mice carrying SK-MEL-1 melanoma tumors received either human serum albumin solution (HSA, vehicle control) once on day 1 only (Group 1), HSA containing 1×10^6 units of unmodified IFN-β-1a once on day 1 only (Group 2), or HSA containing 1×10^6 units of PEGylated IFN-β-1a once on day

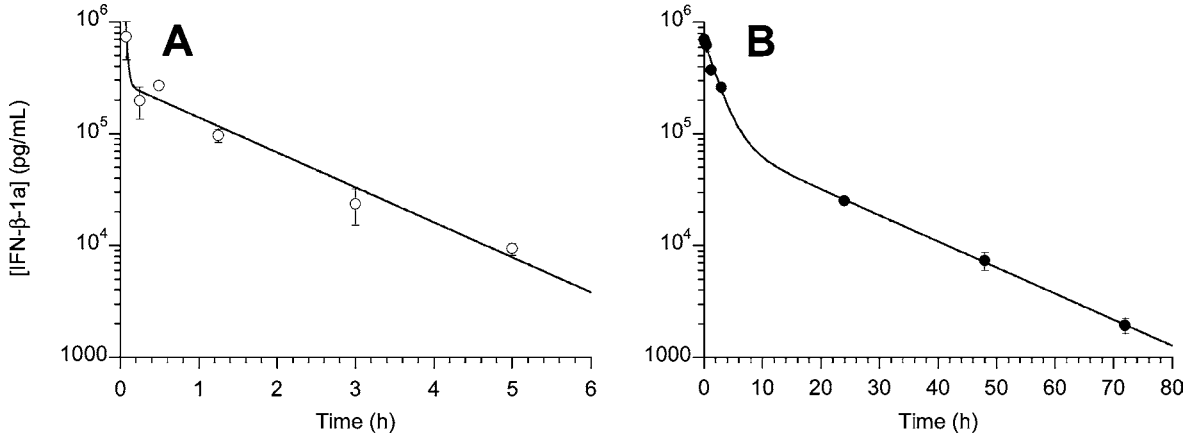

Figure 5. Pharmacokinetic profiles of unmodified and PEGylated IFN-β-1a in rats following intravenous administration. Female Lewis rats were injected with unmodified (A) or PEGylated (B) IFN-β-1a. Blood was collected at the time points indicated and assayed for serum levels of interferon by activity in the A549 cell/EMC virus CPE bioassay. Data points are means of values obtained from three rats. Pharmacokinetic parameters were calculated using noncompartmental analysis. For visual presentation, the data were fitted using a two-compartment model. Unmodified IFN-β-1a (○), PEGylated IFN-β-1a (●).

Table 1. Pharmacokinetic Parameters for Unmodified and PEGylated Human IFN-β-1a in Female Lewis Rats Following Intravenous Administration

protein	dose (μg/kg)	C_{max} (pg/mL)	AUC (pg/h/mL)	$t_{1/2}$ (h)	CL (mL/h/kg)	V_{ss} (mL/kg)
unmodified	80	1400000	510000	0.98	160	160
PEGylated	24	720000	4800000	13	5.0	39

1 only (Group 3) (Figure 6A). Since the PEGylated protein was shown to have a specific activity 2-fold lower than that of the unmodified protein (see above), the mice were administered with 5 μg of unmodified IFN-β-1a or 10 μg of PEGylated IFN-β-1a thus ensuring equal dosing on a unit (antiviral/antiproliferative activity) basis. As shown in Figure 6A, treatment of the mice on day 1 only with a single dose of 1×10^6 units of unmodified IFN-β-1a resulted in a mean vessel number of 36.0 ± 4.2 as compared to 50.8 ± 5.3 for the vehicle-treated mice (Figure 6A, compare Groups 2 and 1, respectively). By contrast, treatment with a single dose of 1×10^6 units of PEGylated IFN-β-1a resulted in a mean vessel number of 21.3 ± 3.9 (Figure 6A, compare Groups 3 and 1, respectively). Therefore, a single dose of the PEGylated protein resulted in a 58% reduction in vessel number as compared to a 29% reduction for the unmodified protein. Analysis of variance followed by a Newmann-Keuls multiple comparison test indicated that both treatments resulted in statistically significant reductions in mean vessel number as compared to the vehicle-treated mice ($p < 0.01$ for the unmodified IFN-β-1a-treated mice and $p < 0.001$ for the PEGylated IFN-β-1a-treated mice). Furthermore, the mean vessel number of the PEGylated IFN-β-1a-treated mice was statistically significantly different from that of the unmodified IFN-β-1a-treated mice ($p < 0.01$).

To determine whether the efficacy of the PEGylated IFN-β-1a could be matched by increasing the dose and frequency of the unmodified protein, an independent study was carried out in which groups of three mice carrying SK-MEL-1 melanoma tumors received either HSA once on day 1 only (Group 1), HSA containing 1×10^6 units of PEGylated IFN-β-1a once on day 1 only (Group 2), HSA daily on days 1−9 inclusive (Group 3), or HSA containing 1×10^6 units of unmodified IFN-β-1a daily on days 1−9 inclusive (Group 4) (Figure 6B). Results from Group 2 (single dose of PEGylated IFN-β-1a) were compared to Group 1 (single dose of vehicle control), while results from Group 4 (unmodified IFN-β-1a administered daily) were compared to Group 3 (vehicle control administered daily) to control for any effects resulting from the multiple dosing regimen. As shown in Figure 6B, treatment of the mice on day 1 only with a single dose of 1×10^6 units of PEGylated IFN-β-1a resulted in a mean vessel number of 17.3 ± 2.5 as compared to 51.0 ± 5.6 for the mice treated with vehicle control once on day 1 only (Figure 6B, compare Groups 2 and 1, respectively). For the multiply dosed mice, treatment with 1×10^6 units of unmodified IFN-β-1a daily resulted in a mean vessel number of 21.7 ± 4.0 as compared to 44.0 ± 4.6 for the mice treated daily with vehicle control (Figure 6B, compare Groups 4 and 3, respectively). Hence, a single dose of 1×10^6 units of the PEGylated protein resulted in a 66% reduction in vessel number compared to a 51% reduction following daily administration of 1×10^6 units of the unmodified protein. Analysis of the data using an unpaired Student's *t* test indicated that both treatments resulted in statistically significant reductions in mean vessel number as compared to the respective vehicle control ($p = 0.0032$ for the unmodified IFN-β-1a-treated mice, and $p = 0.0007$ for the PEGylated IFN-β-1a-treated mice). Further analysis was carried out to determine whether the difference in mean vessel number between the unmodified IFN-β-1a-treated mice and the PEGylated IFN-β-1a-treated mice was statistically significant. Mean vessel numbers for the test and the corresponding control group were ranked. Differences were calculated between each test and control value at the same rank level. The decrease in mean vessel number was 22.33 ± 0.33 for the unmodified IFN-β-1a-treated mice and 33.67 ± 1.86 for the PEGylated IFN-β-1a-treated mice. The mean decreases were then tested using an unpaired *t*-test that gave a *P* value of 0.0039, i.e., the resulting mean vessel number following a single dose of the PEGylated protein on day 1 only was significantly different from that when the unmodified protein was given on days 1−9 inclusive.

DISCUSSION

PEGylation of therapeutic proteins is an established method to improve pharmacokinetic properties, to reduce dosing frequency, and to potentially improve pharmacodynamic responses and clinical efficacy. The benefit of this technology is clearly seen in the case of IFN-α-2b and IFN-α-2a where dosing frequency was reduced and efficacy against HCV infection improved, following PEGylation (*22*, *23*, *25*−*27*). To prepare a PEGylated form of IFN-β-1a that could be tested and compared to the unmodified protein in preclinical studies and potentially in human clinical trials, we modified the protein at the N-terminal α-amino group with 20 kDa mPEG-O-2-methylpropionaldehyde.

N-Terminal PEGylation of IFN-β-1a with 20 kDa mPEG-O-2-methylpropionaldehyde significantly increased the systemic

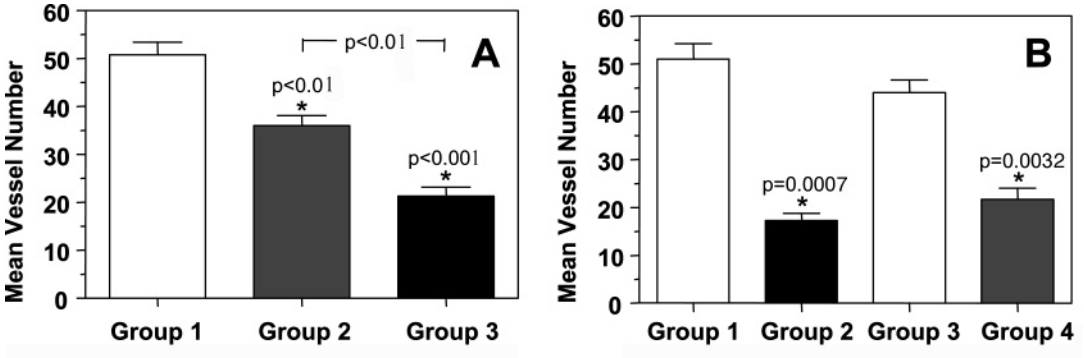

Figure 6. In vivo antiangiogenic activity of unmodified and PEGylated IFN-β-1a. The unmodified and PEGylated proteins were tested for their ability to inhibit the formation of radially oriented blood vessels entering the periphery of human SK-MEL-1 melanoma tumors grown in athymic nude homozygous (*nu*/*nu*) mice. Mice were injected with SK-MEL-1 cells (2×10^6) on day 0, followed by subcutaneous administration of either human serum albumin solution (HSA, vehicle control), HSA containing 1×10^6 units of unmodified IFN-β-1a, or HSA containing 1×10^6 units of PEGylated IFN-β-1a. For (A), groups of four mice received either HSA once on day 1 only (Group 1), HSA containing 1×10^6 units of unmodified IFN-β-1a once on day 1 only (Group 2), or HSA containing 1×10^6 units of PEGylated IFN-β-1a once on day 1 only (Group 3). For (B), groups of three mice received either HSA once on day 1 only (Group 1), HSA containing 1×10^6 units of PEGylated IFN-β-1a once on day 1 only (Group 2), HSA on days 1−9 inclusive (Group 3), or HSA containing 1×10^6 units of unmodified IFN-β-1a on days 1−9 inclusive (Group 4). Mice were sacrificed on day 10, and the tumor inoculation site was assessed for neovascularization, measured by an observer blinded as to the treatment. The mean vessel number ± the standard error of the mean is shown. Asterisks denote statistically significant differences between the unmodified or PEGylated IFN-β-1a-treated mice and the corresponding vehicle-treated mice.

exposure in rats following intravenous administration. The increase in $t_{1/2}$ and AUC for the PEGylated protein was ~13-fold and ~10-fold, respectively, compared to the unmodified protein, resulting from decreases in the clearance and volume of distribution at steady state (Table 1). While a direct side-by-side comparison of the pharmacokinetic parameters of 20 kDa mPEG-O-2-methylpropionaldehyde-modified IFN-β-1a and 20 kDa mPEG-propionaldehyde-modified IFN-β-1a was not carried out, a comparison of the $t_{1/2}$ values obtained for unmodified IFN-β-1a and the PEGylated forms in this and in the previously published study (*39*) indicates that they were comparable with respect to half-life. For the unmodified and 20 kDa mPEG-propionaldehyde-modified IFN-β-1a, the $t_{1/2}$ values were 1.47 and 10.13 h, respectively (*39*), while for the unmodified and 20 kDa mPEG-O-2-methylpropionaldehyde-modfied IFN-β-1a (this study), the $t_{1/2}$ values were 0.98 and 13 h, respectively (Table 1). While we did not determine the pharmacokinetic properties of 20 kDa mPEG-O-2-methylpropionaldehyde-modified IFN-β-1a following subcutaneous or intraperitoneal administration in rats, we anticipate that it will also show improved pharmacokinetic parameters compared to the unmodified protein since human IFN-β-1a and rat IFN-β modified at the N-terminus with 20 kDa mPEG-propionaldehyde both show improved pharmacokinetic parameters as compared to their respective unmodified forms following these routes of administration (*39*, *43*). Similar improvements in pharmacokinetic properties were observed for IFN-β-1a modified on Cys-17 with a 40 kDa branched PEG following subcutaneous administration to cynamologous monkeys (*44*).

The unmodified and 20 kDa mPEG-O-2-methylpropionaldehyde-modified IFN-β-1a were tested in a murine dermis model to determine whether the improved pharmacokinetics of the modified protein would translate into an improvement in efficacy. When a single dose of 1×10^6 units of unmodified IFN-β-1a was given once on day 1 only, the number of radially oriented blood vessels entering the periphery of the SK-MEL-1 tumors at day 10 was reduced 29% as compared to the vehicle control. By contrast, a single dose of 1×10^6 units of PEGylated IFN-β-1a given once on day 1 only resulted in a 58% reduction (Figure 6A). Both treatments resulted in statistically significant reductions in mean vessel number as compared to the vehicle-treated mice, with the PEGylated IFN-β-1a-treated mice showing a statistically significant reduction in mean vessel number as compared to the unmodified IFN-β-1a-treated mice. Therefore, the attached 20 kDa PEG moiety significantly improved the efficacy of the protein, indicating that the pharmacokinetic properties and efficacy are correlated. To address the question as to whether the efficacy of the unmodified protein could be improved to a level commensurate with that of the modified protein, a single dose of 1×10^6 units of PEGylated IFN-β-1a was administered once on day 1 only, and compared to administration of 1×10^6 units of unmodified IFN-β-1a given daily on days 1−9 inclusive. Treatment of the mice with a single dose of 1×10^6 units of PEGylated IFN-β-1a once on day 1 only resulted in a mean vessel number of 17.3 ± 2.5 as compared to 51.0 ± 5.6 for the mice treated with vehicle control once on day 1 only (66% reduction, Figure 6B). This result was very similar to that obtained for the same samples in the single dose comparison study, where a single dose of the PEGylated protein resulted in a mean vessel number of 21.3 ± 3.9 as compared to 50.8 ± 5.3 for the vehicle control (Figure 6A). For the multiply dosed mice, treatment with 1×10^6 units of unmodified IFN-β-1a daily on days 1−9 inclusive resulted in a mean vessel number of 21.7 ± 4.0 as compared to 44.0 ± 4.6 for the mice treated daily with vehicle control (51% reduction, Figure 6B). Both treatments resulted in statistically significant reductions in mean vessel number as compared to the respective vehicle-treated mice, with the PEGylated IFN-β-1a-treated mice showing a statistically significant reduction in mean vessel number as compared to the unmodified IFN-β-1a-treated mice. Therefore, even though the cumulative total dose of the unmodified protein was 9-fold greater than that of the PEGylated protein on a unit (activity) basis (4.5-fold greater on an IFN-β-1a mass basis), the PEGylated protein was still more efficacious than the unmodified protein. A similar study using the same murine dermis model was carried out to compare the efficacy of unmodified IFN-α-2b (Intron-A) and PEGylated IFN-α-2b (PEG-Intron) (*42*). In this study, mice received either 0, 1×10^3, 1×10^4, 1×10^5, 1×10^6, or 1×10^7 units of unmodified IFN-α-2b on days 1−10 inclusive, and the mean number of vessels compared to mice that received the same amount (units) of PEGylated IFN-α-2b (PEG-Intron) as a single dose. While at 1×10^3 units there was no effect with either protein, at 1×10^4 units and above there was a significant reduction in the vessel number as compared to the control-treated mice. However, there was no significant difference observed between mice receiving either a single dose of PEGylated IFN-α-2b or daily administration of the unmodified protein. Fol-

lowing a single dose of 1×10^6 units of PEGylated IFN-α-2b, the reduction in vessel number was ~70% (*42*), similar to the values obtained in this study for 1×10^6 units of PEGylated IFN-*β*-1a (58% and 66%, Figure 6).

PEGylation of IFN-*β*-1a at the N-terminus with 20 kDa mPEG-O-2-methylpropionaldehyde, in addition to improving pharmacokinetic properties and in vivo efficacy, also has the benefit of yielding a product with essentially a single site of modification; thereby simplifying product characterization. By contrast, PEGylated IFN-α-2b (PEG-Intron), which is modified with a linear 12 kDa PEG using a succinimidyl carbonate chemistry, is a mixture of 14 different monoPEGylated positional isomers in which the PEG chain is attached to either lysine, tyrosine, histidine, serine, or cysteine residues (*45*). Similarly, for PEGylated IFN-α-2a (Pegasys), modification with a branched 40 kDa PEG using an *N*-hydroxysuccinamide ester derivative results in a mixture of 6 different monoPEGylated positional isomers, all of which are attached to lysine residues (*46*). A consequence of using these nonspecific amine-coupling chemistries is that the product is a heterogeneous mixture that requires extensive analytical characterization following production to ensure batch-to-batch consistency. Furthermore, PEG chains can become attached at site(s) that interfere with the binding of the protein to the IFNAR1/IFNAR2 receptor. Indeed, many of the residues that are modified in these proteins have been shown by site-specific mutagenesis to be important for activity (*4*), and it is therefore not surprising that both PEGylated IFNs-α show a significant reduction in their in vitro antiviral activity as compared to their respective unmodified form. For PEG-Intron, the antiviral activity of the mixture is 28% of that of the unmodified protein and ranges from 6 to 37% for the individual species (*45*), while for Pegasys, the mixture has an antiviral activity of only 7% of the unmodified IFN-α-2a (*46*). The data for 20 kDa mPEG-O-2-methylpropionaldehyde-modified IFN-*β*-1a (50% retention of activity), and for 20 kDa mPEG-propionaldehyde-modified IFN-*β*-1a (*39*) and 20 kDa mPEG-propionaldehyde-modified rat IFN-*β* (*43*), both of which retain full in vitro antiviral activity, highlights the importance of modifying sites distal to receptor binding site(s) if retention of activity is a desired outcome. The N-terminus of IFN-*β*-1a therefore serves as an attractive site for modification since alanine scanning mutagenesis of the N-terminal region (*37*) and deletion of the N-terminal methionine (*38*) have no affect on activity, and analysis of the preliminary X-ray crystal structure of IFN-*β*-1a complexed with the extracellular portion of the human IFNAR2 chain shows that the N-terminus does not participate in the binding site (Ann Boriack-Sjodin, personal communication). In addition to IFN-*β*-1a, the N-terminus of IFN-α-2 also appears to be suitable for PEGylation. Using site-specific mutagenesis to replace glutamine at position 5 with a cysteine, Rosendahl et al. (*47*) have recently shown that the cysteine can be modified with linear 5 kDa, 10 kDa, or 20 kDa maleimide-PEGs, or with a branched 40 kDa maleimide PEG, resulting in the production of site-specific monoPEGylated proteins. The 5 kDa PEG-maleimide-modified protein retained ~50% of the antiproliferative activity of the unmodified wild type or Q5C mutant protein, while the activities of the 10 kDa, 20 kDa, and 40 kDa PEG-maleimide-modified proteins were within 3−4-fold of the unmodified wild type or Q5C mutant (*47*). As expected, the pharmacokinetic properties of the PEGylated proteins were superior to that of the unmodified protein. Following intravenous administration in rats, the $t_{1/2}$ value for the unmodified wild-type protein was 0.5 h, while for the 10 kDa, 20 kDa, and 40 kDa PEG-maleimide-modified proteins, the $t_{1/2}$ values were 22, 24, and 32 h, respectively (*47*). The superior retention of activity of the 40 kDa PEG-maleimide-modified IFN-α-2 (3−4-fold lower than that of the unmodified protein) as compared to Pegasys (14-fold lower) presumably reflects the fact that the N-terminal region of IFN-α-2, like that of IFN-*β*-1a, is not critical for receptor binding. Indeed, site-directed mutagenesis and modeling studies indicate that the N-terminus of the cytokine does not interact with the IFNAR2 chain, rather the binding interface between IFN-α-2 and IFNAR2 is formed by a primarily hydrophobic patch composed of several residues, the most N-terminal of which is leucine-26 (*48*−*50*).

PEGylation of the N-terminus of IFN-*β*-1a, with the retention of significant activity, is also desirable since a lower dose may be required to achieve efficacy as compared to the unmodified protein, or as compared to a protein that has lost substantial activity following modification. This not only affects factors such as the cost of making the drug, but may also play an important role in reducing immunogenicity and the formation of neutralizing antibodies. For IFN-*β*-1a, for example, administration of the two different products currently available for the treatment of multiple sclerosis results in the formation of different levels of neutralizing antibodies. In a side-by-side comparison of the efficacious dose of Rebif (Serono), given as a 44 *μ*g subcutaneous injection thrice weekly, and Avonex (BiogenIdec), given as a 30 *μ*g intramuscular injection once per week, 25% of the multiple sclerosis patients receiving Rebif were positive for neutralizing antibodies (defined as titers of ≥20 neutralizing units/mL), as compared to only 2% of patients receiving Avonex (*51*). Therefore, a higher dose given more frequently correlates with a higher incidence of neutralizing antibody formation. The ability to produce a PEGylated form of IFN-*β*-1a with high potency may enable a lower protein mass to be administered and possibly reduce the incidence and level of neutralizing antibodies. However, immunogenicity data from clinical trial(s) would be required to fully address this issue.

In summary, we have prepared a modified form of IFN-*β*-1a in which 20 kDa mPEG-O-2-methylpropionaldehyde is covalently attached to the N-terminal α-amino group of the protein. The modified protein retains ~50% of the in vitro antiviral and antiproliferative activity of the unmodified form, has improved pharmacokinetic properties in rats, and has improved efficacy with respect to its ability to inhibit the formation of tumor-induced blood vessels entering the periphery of human SK-MEL-1 melanoma tumors grown in athymic nude homozygous (*nu*/*nu*) mice. With the known efficacy of unmodified IFN-*β* in multiple sclerosis and HCV, this modified form of the protein may serve as a useful adjunct for the treatment of these diseases, not only in terms of potentially increasing efficacy but also by reducing dosing frequency, and thereby patient convenience and compliance. N-Terminally PEGylated IFN-*β*-1a may also be useful for the treatment of certain cancers, either as sole therapy or in combination with other drugs such as tamoxifen for example, that has been shown to have additive/synergistic antitumor effects when administered with IFN-*β* (*41*, *52*), or thalidomide, that has been shown to have synergistic antitumor effect when administered with IFN-α-2b (*42*).

LITERATURE CITED

(1) Sen, G., and Lengyel, P. (1992) The Interferon System: a Bird's Eye View of Its Biochemistry. *J. Biol. Chem. 267,* 5017−5020.
(2) Tyring, S. K. (1995) Interferons: Biochemistry and Mechanisms of Action. *Am. J. Obstet. Gynecol. 172*.
(3) Peters, M. (1996) Actions of Cytokines on the Immune Response and Viral Interactions: an Overview. *Hepatology 23,* 909−916.
(4) Uze, G., Lutfalla, G., and Mogensen, K. E. (1995) α and *β* Interferons and their Receptors and their Friends and Relations. *J. Interferon Cytokine Res. 15,* 3−26.
(5) Cohen, B., Novick, D., Barak, S., and Rubinstein, M. (1995) Ligand-induced Association of the Type I Interferon Receptor Components. *Mol. Cell. Biol. 15,* 4208−4214.

(6) Piehler, J., and Schreiber, G. (1999) Biophysical Analysis of the Interaction of Human Ifnar2 Expressed in *E.coli* with IFNα2. *J. Mol. Biol. 289*, 57−67.

(7) Arduini, R. M., Strauch, K. L., Runkel, L. A., Carlson, M. M., Hronowski, X., Foley, S. F., Young, C. N., Cheng, W., Hochman, P. S., and Baker, D. P. (1999) Characterization of a Soluble Ternary Complex Formed Between Human Interferon-β-1a and its Receptor Chains. *Protein Science 8*, 1867−1877.

(8) Velazquez, L., Fellous, M., Stark, G. R., and Pellegrini, S. (1992) A Protein Tyrosine Kinase in the Interferon α/β Signaling Pathway. *Cell 70*, 313−322.

(9) Colamonici, O. R., Uyttendaele, H., Domanski, P., Yan, H., and Krolewski, J. J. (1994) p135^{tyk2}, an Interferon-α-activated Tyrosine Kinase, is Physically Associated with an Interferon-α Receptor. *J. Biol. Chem. 269*, 3518−3522.

(10) Colamonici, O., Yan, H., Domanski, P., Handa, R., Smalley, D., Mullersman, J., Witte, M., Krishnan, K., and Krolewski, J. (1994) Direct Binding to and Tyrosine Phosphorylation of the α Subunit of the Type I Interferon Receptor by p135^{tyk2} Tyrosine Kinase. *Mol. Cell. Biol. 14*, 8133−8142.

(11) Novick, D., Cohen, B., and Rubinstein, M. (1994) The Human Interferon α/β Receptor: Characterization and Molecular Cloning. *Cell 77*, 391−400.

(12) Yang, C.-H., Shi, W., Basu, L., Murti, A., Constantinescu, S. N., Blatte, L., Croze, E., Mullersman, J. E., and Pfeffer, L. M. (1996) Direct Association of STAT3 with the IFNAR-1 Chain of the Human Type I Interferon Receptor. *J. Biol. Chem. 271*, 8057−8061.

(13) Li, X., Leung, S., Kerr, I. M., and Stark, G. R. (1997) Functional Subdomains of STAT2 Required for Preassociation with the Alpha Interferon Receptor and for Signaling. *Mol. Cell. Biol. 17*, 2048−2056.

(14) Darnell, J. E., Kerr, I. M., and Stark, G. R. (1994) Jak-STAT Pathways and Transcriptional Activation in Response to IFNs and Other Extracellular Signaling Proteins. *Science 264*, 1415−1421.

(15) Marler, J. J., Rubin, J. B., Trede, N. S., Connors, S., Grier, H., Upton, J., Mulliken, J. B., and Folkman, J. (2002) Successful Antiangiogenic Therapy of Giant Cell Angioblastoma with Interferon Alfa 2b: Report of 2 Cases. *Pediatrics 109*, E37.

(16) Orchard, P. J., Smith, C. M., Woods, W. G., Day, D. L., Dehner, L. P., and Shapiro, R. (1989) Treatment of Haemangioendotheliomas with Alpha Interferon. *Lancet 2*, 565−567.

(17) Ezekowitz, R. A. B., Mulliken, J. B., and Folkman, J. (1992) Interferon Alfa-2a Therapy for Life-Threatening Hemangiomas of Infancy. *N. Eng. J. Med. 326*, 1456−1463.

(18) Kozlowski, A., Charles, S. A., and Harris, J. M. (2001) Development of Pegylated Interferons for the Treatment of Chronic Hepatitis C. *Biodrugs 15*, 419−429.

(19) Baker, D. E. (2001) Pegylated Interferons. *Rev. Gastroenterol. Disord. 1*, 87−99.

(20) Harris, J. M., and Chess, R. B. (2003) Effect of Pegylation on Pharmaceuticals. *Nature Rev. 2*, 214−221.

(21) Glue, P., Fang, J. W. S., Rouzier-Panis, R., Raffanel, C., Sabo, R., Gupta, S. K., Salfi, M., Jacobs, S., and the Hepatitis C Intervention Therapy Group (2000) Pegylated Interferon-α2b: Pharmacokinetics, Pharmacodynamics, Safety, and Preliminary Efficacy Data. *Clin. Pharmacol. Ther. 68*, 556−567.

(22) Lindsay, K. L., Trepo, C., Heintges, T., Shiffman, M. L., Gordon, S. C., Hoefs, J. C., Schiff, E. R., Goodman, Z. D., Laughlin, M., Yao, R., Albrecht, J. K., for the Hepatitis Interventional Therapy Group (2001) A Randomized, Double-Blind Trial Comparing Pegylated Interferon Alfa-2b to Interferon Alfa-2b as Initial Treatment for Chronic Hepatitis C. *Hepatology 34*, 395−403.

(23) Manns, M. P., McHutchinson, J. G., Gordon, S. C., Rustgi, V. K., Shiffman, M. L., Reindollar, R., Goodman, Z. D., Koury, K., Ling, M.-H., Albrecht, J. K., and the International Hepatitis Interventional Therapy Group (2001) Peginterferon Alfa-2b Plus Ribavirin Compared with Interferon Alfa-2b Plus Ribavirin for the Initial Treatment of Chronic Hepatitis C: a Randomized Trial. *Lancet 358*, 958−965.

(24) Reddy, K. R., Modi, M. W., and Pedder, S. (2002) Use of Peginterferon alfa-2a (40 KD) (Pegasys) for the Treatment of Hepatitis C. *Adv. Drug Delivery Rev. 54*, 571−586.

(25) Zeuzem, S., Feinman, S. V., Rasenack, J., Heathcote, E. J., Lai, M.-Y., Gane, E., O'Grady, J., Reichen, J., Diago, M., Lin, A., Hoffman, J., and Brunda, M. J. (2000) Peginterferon Alfa-2a in Patients with Chronic Hepatitis C. *N. Eng. J. Med. 343*, 1666−1672.

(26) Heathcote, E. J., Shiffman, M. L., Cooksley, W. G. E., Dusheiko, G. M., Lee, S. S., Balart, L., Reindollar, R., Reddy, R. K., Wright, T. L., Lin, A., Hoffman, J., and de Pamphilis, J. (2000) Peginterferon Alfa-2a in Patients with Chronic Hepatitis C and Cirrhosis. *N. Eng. J. Med. 343*, 1673−1680.

(27) Fried, M. W., Shiffman, M. L., Reddy, R. K., Smith, C., Marinos, G., Goncales, F. L., Haussinger, D., Diago, M., Carosi, G., Dhumeaux, D., Craxi, A., Lin, A., Hoffman, J., and Yu, J. (2002) Peginterferon Alfa-2a Plus Ribavirin for Chronic Hepatitis C Virus Infection. *N. Eng. J. Med. 347*, 975−982.

(28) Crawford, J. (2002) Pegfilgrastim administered once per cycle reduces incidence of chemotherapy-induced neutropenia. *Drugs 62*, 89−98.

(29) Li, D. K. B., Paty, D. W., and the UBC MS/MRI Analysis Research Group and the PRISMS Study Group (1999) Magnetic Resonace Imaging Results of the PRISMS Trial: A Randomized, Double-Blind, Placebo-Controlled Study of Interferon-β1a in Relapsing-Remitting Multiple Sclerosis. *Ann. Neurol. 46*, 197−206.

(30) The IFNβ Multiple Sclerosis Study Group (1993) Interferon Beta-1b is Effective in Relapsing-Remitting Multiple Sclerosis. I. Clinical Results of a Multicenter, Randomized, Double-Blind, Placebo-Controlled Trial. *Neurology 43*, 655−661.

(31) Habersetzer, F., Boyer, N., Marcellin, P., Bailly, F., Ahmed, S. N., Alam, J. J., Benhamou, J. P., and Trepo, C. (2000) A Pilot Study of Recombinant Interferon Beta-1a for the Treatment of Chronic Hepatitis C. *Liver 20*, 437−441.

(32) Barbaro, G., Di Lorenzo, G., Soldini, M., Giancaspro, G., Pellicelli, A., Grisorio, B., and Barbarini, G. (1999) Intravenous Recombinant Interferon-Beta versus Interferon-Alpha-2b and Ribavirin in Combination for Short-Term Treatment of Chronic Hepatitis C Patients not Responding to Interferon-Alpha. *Scand. J. Gastroenterol. 34*, 928−933.

(33) Kakizaki, S., Tagaki, H., Yamada, T., Ichikawa, T., Abe, T., Sohara, N., Kosone, T., Kaneko, M., Takezawa, J., Takayama, H., Nagamine, T., and Mori, M. (1999) Evaluation of Twice-Daily Administration of Interferon-Beta for Chronic Hepatitis C. *J. Viral Hepatol. 6*, 315−319.

(34) Yoshioka, K., Yano, M., Hirofuji, H., Arao, M., Kusakabe, A., Sameshima, Y., Kuriki, J., Kurowaka, S., Murase, K., Ishikawa, T., and Kakumu, S. (2000) Randomized Controlled Trial of Twice-a-Day Administration of Natural Interferon Beta for Chronic Hepatitis C. *Hepatol. Res. 18*, 310−319.

(35) Kaito, M., Yasui-Kawamura, N., Iwasa, M., Kobayashi, Y., Nakagawa, N., Fujita, N., Ikoma, J., Gabazza, E. C., Watanabe, S., and Adachi, Y. (2003) Twice-a-Day Versus Once-a-Day Interferon-Beta Therapy in Chronic Hepatitis C. *Hepatogastroenterology 50*, 775−778.

(36) Festi, D., Sandri, L., Mazzella, G., Roda, E., Sacco, T., Staniscia, T., Capodisca, S., Vestito, A., and Colecchia, A. (2004) Safety of Interferon Beta Treatment for Chronic HCV Hepatitis. *World J. Gastroenterol. 10*, 12−16.

(37) Runkel, L. A., deDios, C., Karpusas, M., Betzenhauser, M., Muldowney, C., Zafari, M., Benjamin, C. D., Miller, S., Hochman, P. S., and Whitty, A. (2000) Systematic Mutational Mapping of Sites on Human Interferon-β-1a that are Important for Receptor Binding and Functional Activity. *Biochemistry 39*, 2538−2551.

(38) Runkel, L., Meier, W., Pepinsky, R. B., Karpusas, M., Whitty, A., Kimball, K., Brickelmaier, M., Muldowney, C., Jones, W., and Goelz, S. E. (1998) Structural and Functional Differences Between Glycosylated and Non-Glycosylated Forms of Human Interferon-β (IFN-β). *Pharm. Res. 15*, 641−649.

(39) Pepinsky, R. B., Lepage, D. J., Gill, A., Chakraborty, A., Vaidyanathan, S., Green, M., Baker, D. P., Whalley, E., Hochman, P. S., and Martin, P. (2001) Improved Pharmacokinetic Properties of a Polyethylene Glycol-Modified Form of Interferon-β-1a with Preserved *In Vitro* Bioactivity. *J. Pharmacol. Exp. Ther. 297*, 1059−1066.

(40) Gill, S. C., and von Hippel, P. H. (1989) Calculation of Protein Extinction Coefficients from Amino Acid Sequence Data. *Anal. Biochem. 182*, 319−326.

(41) Lindner, D. J., and Borden, E. C. (1997) Effects of Tamoxifen and Interferon-β or the Combination on Tumor-Induced Angiogenesis. *Int. J. Cancer 71*, 456−461.

(42) Bauer, J. A., Morrison, B. H., Grane, R. W., Jacobs, B. S., Borden, E. C., and Lindner, J. (2003) IFN-α2b and Thalidomide Synergistically Inhibit Tumor-Induced Angiogenesis. *J. Interferon Cytokine Res. 23*, 3−10.

(43) Arduini, R. M., Li, Z., Rapoza, A., Gronke, R., Hess, D. M., Wen, D., Miatkowski, K., Coots, C., Kaffashan, A., Viseux, N., Delaney, J., Domon, B., Young, C. N., Boynton, R., Chen, L. L., Chen, L., Betzenhauser, M., Miller, S., Gill, A., Pepinsky, R. B., Hochman, P. S., and Baker, D. P. (2004) Expression, Purification, and Characterization of Rat Interferon-*β*, and Preparation of an N−Terminally PEGylated Form with Improved Pharmacokinetic Parameters. *Protein Expression Purification 34*, 229−242.

(44) Mager, D. E., Neuteboom, B., and Jusko, W. J. (2005) Pharmacokinetics and Pharmacodynamics of PEGylated IFN-*β* 1a Following Subcutaneous Administration in Monkeys. *Pharm. Res. 22*, 58−61.

(45) Grace, M., Youngster, S., Gitlin, G., Sydor, W., Xie, L., Westreich, L., Jacobs, S., Brassard, D., Bausch, J., and Bordens, R. (2001) Structural and Biological Characterization of Pegylated Recombinant IFN-α2b. *J. Interferon Cytokine Res. 21*, 1103−1115.

(46) Bailon, P., Palleroni, A., Schaffer, C. A., Spence, C. L., Fung, W.-J., Porter, J. E., Ehrlich, G. K., Pan, W., Xu, Z.-X., Modi, M. W., Farid, A., Berthold, W., and Graves, M. (2001) Rational Design of a Potent, Long-Lasting Form of Interferon: A 40 kDa Branched Polyethylene Glycol-Conjugated Interferon α-2a for the Treatment of Hepatitis C. *Bioconjugate Chem. 12*, 195−202.

(47) Rosendahl, M. S., Doherty, D. H., Smith, D. J., Carlson, S. J., Chlipala, E. A., and Cox, G. N. (2005) A Long-Acting, Highly Potent Interferon α-2 Conjugate Created Using Site-Specific Mutagenesis. *Bioconjugate Chem. 16*, 200−207.

(48) Piehler, J., and Schreiber, G. (1999) Mutational and Structural Analysis of the Binding Interface Between Type I Interferons and their Receptor Ifnar2. *J. Mol. Biol. 294*, 223−237.

(49) Roisman, L. C., Piehler, J., Trosset, J.-Y., Scheraga, H. A., and Schreiber, G. (2001) Structure of the Interferon-Receptor Complex Determined by Distance Constraints from Double-Mutant and Flexible Docking. *Proc. Natl. Acad. Sci. U.S.A. 98*, 13231−13236.

(50) Chill, J. H., Quadt, S. R., Levy, R., Schreiber, G., and Anglister, J. (2003) The Human Type I Interferon Receptor: NMR Structure Reveals the Molecular Basis of Ligand Binding. *Structure 11*, 791−802.

(51) Panitch, H., Goodin, D. S., Francis, G., Chang, P., Coyle, P. K., O'Connor, P., Monaghan, E., Li, D. K. B., Weinshenker, B., for the EVIDENCE Study Group and the University of British Columbia MS/MRI Research Group (2002) Randomized, Comparative Study of Interferon *β*-1a Treatment Regimens in MS: The EVIDENCE Trial. *Neurology 59*, 1496−1506.

(52) Lindner, D. J., and Borden, E. C. (1997) Synergistic Antitumor Effects of a Combination of Interferon and Tamoxifen on Estrogen Receptor-Positive and Receptor-Negative Human Tumor Cell Lines In Vivo and In Vitro. *J. Interferon Cytokine Res. 17*, 681−693.

BC050237Q

Cellular Delivery of Polyheteroaromate−Peptide Nucleic Acid Conjugates Mediated by Cationic Lipids

Takehiko Shiraishi, Nadia Bendifallah, and Peter E. Nielsen*

Department of Medical Biochemistry and Genetics, The Panum Institute, University of Copenhagen, Blegdamsvej 3c, 2200 Copenhagen N, Denmark. Received August 11, 2005; Revised Manuscript Received November 8, 2005

In the search of facile and efficient methods for PNA cellular delivery, we have tested a series of PNA conjugates based on (hetero) aromatic, lipophilic compounds such as 9-aminoacridine, benzimidazoles, carbazole, anthraquinone, porphyrine, psoralen, pyrene, and phenyl-bis-benzimidazole ("Hoechst"). These chemically modified PNAs were delivered to cultured pLuc705HeLa cells mediated by cationic liposomes (LipofectAMINE or LiofectAMINE2000), and their nuclear delivery was inferred from induced luciferase activity as a consequence of pre-mRNA splicing correction by the antisense-PNA. PNAs modified with 9-aminoacridine, "Hoechst", or acetyl-"Hoechst" showed highest antisense activities (while unmodified PNA failed to show any significant antisense activity). In particular, bis-acridine-conjugated PNA showed nearly 60% splicing correction at 250 nM concentration in combination with LipofectAMINE2000. Interestingly, relative differences between the derivatives were observed when LipofectAMINE was used as compared to LipofectAMINE2000, but in general the latter yielded the higher antisense activity. The most active modifications of these PNA constructs were further tested for antisense down-regulation of luciferase in p53R cells in order to evaluate the cytoplasmic activity (uptake) of the PNAs. A dose-dependent down regulation of luciferase was demonstrated also in this system. The PNA conjugated to acetyl-Hoechst caused a reduction of luciferase activity to less than 40% of the control at a concentration of 1 μM. These results indicate that conjugation of (hetero) polyaromatic compounds to PNA can dramatically improve liposome-mediated cellular delivery both to cytoplasm as well as to the nucleus. However, no clear structure/activity relations are apparent from the present results, except that both 9-aminoacridine and "Hoechst" are also nucleic acid binding ligands.

INTRODUCTION

Peptide nucleic acids (PNA) (*1*) are potentially attractive candidates for discovery and development of gene therapeutic antisense and antigene drugs (*2*−*4*). However, rapid progress has been difficult because of a lack of facile and robust cellular delivery methods (*5*, *6*). Several methods have been devised, to improve the poor cellular uptake of the unmodified PNA. These methods involve conjugation of PNA to cell-penetrating peptides (*7*−*11*) (such as penetratin (*12*), transportan (*13*), oligo arginine (*14*), Tat-peptide (*15*), or a combination of these (*16*)) or the employment of cationic liposome carriers (*17*−*19*). In the former case, nontrivial synthesis of the conjugates is often encountered as well as relatively low efficacy of the conjugates due to endosomal entrapment (*11*). In the latter case, PNA modifications are required such as covalent (PNA-DNA chimera) (*20*) or noncovalent conjugation (PNA/DNA complexation by hybridization (*17*)) to DNA phosphodiester oligomers, or covalent conjugation to lipophilic compounds (*18*, *19*), all with the purpose of increasing the affinity of the PNAs for the cationic liposome carriers. Synthesis of PNA-DNA chimera requires tedious synthesis, and PNA/DNA hybrid transfection requires multistep transfection and careful optimization of the complementary DNA sequences for each PNA although this method is relatively efficient (*9*, *21*).

Conjugation of PNAs to fatty acids is straightforward and allows cationic liposome delivery of the conjugates (*18*, *19*), but unfortunately the conjugates have poor aqueous solubility and a high propensity for aggregation. However, we recently discovered that PNAs conjugated to the tricyclic, heteroaromatic DNA intercalator 9-aminoacridine can be effectively delivered to eucaryotic cells in culture by cationic lipids (*22*). We tentatively ascribed this effect of the acridine to its lipophilic character (of the nonprotonated form), combined with the reasonable aqueous solubility of the protonated form. These results would hold promise that other polycyclic heteroaromatic ligands could be identified that (more) effectively promote cationic lipid assisted PNA delivery.

To elucidate this possibility, we have synthesized eight new PNA conjugates with different lipophilic, polycyclic heteroaromatic ligands (including nucleic acid binding ligands) and tested these for lipid-mediated antisense activities both in HeLa pLuc 705 cells (splicing correction) and p53R cells (translational inhibition). These results show that simple modification of the PNAs with lipophilic compounds dramatically improved lipid-mediated delivery of the PNA both to cytoplasm as well as to the nucleus.

EXPERIMENTAL PROCEDURES

Synthesis of PNAs. The sequences and targets of the PNAs are listed in Table 1. PNA synthesis was carried out as reported previously (*23*). A variety of (hetero) polyaromatic ligands (Chart 1) obtained as carboxylic acid derivatives were covalently linked to PNA at the N-terminal on the solid support through a glycine, ethylene glycol linker (eg1, 8-amino-2,6-dioxaoctanoic acid) or 6-aminohexanoic acid (-aha-) via continuous synthesis (Table 1). All conjugates except those with benzimidazole and anthraquinone showed one major peak by reverse phase HPLC analysis of the raw product, and this was readily purified by HPLC and corresponded to the desired conjugates as characterized by MALDI-TOF mass spectrometry. The PNAs were lyophilized and stored at 4 °C until use, at which time they were dissolved in water and thereafter stored at −20 °C.

* Corresponding author. Tel: +45-35327762; fax: +45-35396042; e-mail: pen@imbg.ku.dk.

10.1021/bc050246z CCC: $33.50 © 2006 American Chemical Society
Published on Web 12/24/2005

Table 1. PNAs Used in This Study

target	PNA no.	sequence	mass found (calcd)	purity (%)[a]
splicing[b]	2389	H-CCTCTTACCTCAGTTACA-NH_2	4767 (4765)	95+
	2390	adamantyl-CCTCTTACCTCAGTTACA-NH_2	4941 (4942)	95+
	2391	Acr-eg1-CCTCTTACCTCAGTTACA-NH_2	5301 (5301)	98+
	2490	Acr-(Acr^{aeg})-eg1-CCTCTTACCTCAGTTACA-NH_2[c]	5593 (5591)	98+
	2846	porphyrin-aha-CCTCTTACCTCAGTTACA-NH_2	5518 (5519)	98+
	2847	pyrene-CCTCTTACCTCAGTTACA-NH_2	5034 (5036)	95+
	2848	Hoechst-aha-CCTCTTACCTCAGTTACA-NH_2	5243 (5243)	98+
	2849	Ac-Hoechst-aha-CCTCTTACCTCAGTTACA-NH_2	5288 (5286)	98+
	2850	carbazole-CCTCTTACCTCAGTTACA-NH_2	4987 (4987)	98+
	2851	psoralen-aha-CCTCTTACCTCAGTTACA-NH_2	5120 (5121)	95+
	2858	anthraquinone-aha-CCTCTTACCTCAGTTACA-NH_2	5113 (5113)	90+
	2861	benzimidazole-Lys(benzimidazole)-CCTCTTACCTCAGTTACA-NH_2	5239 (5238)	90+
	2862	Ac-Lys(benzimidazole)-CCTCTTACCTCAGTTACA-NH_2	5107 (5108)	90+
	2863	perimidine-aha-CCTCTTACCTCAGTTACA-NH_2	5136 (5137)	95+
	2870	Ac-CCTCTTACCTCAGTTACA-NH_2	4953 (4953)	98+
translation[d]	2840	Acr-eg1-CCT TTC TTTATG TTT-NH_2	4435 (4435)	98+
	2841	Acr-eg1-GCG TCT TCC ATG GTG-NH_2	4520 (4520)	98+
	2842	Acr-eg1-TGG TGG CTT TAC CAA-NH_2	4528 (4528)	95+
	2882	Hoechst-aha- GCG TCT TCC ATG GTG-NH_2	4564 (4563)	95+
	2883	Ac-Hoechst-aha- GCG TCT TCC ATG GTG-NH_2	4608 (4695)	95+

[a] 98+ corresponds to single HPLC peak; 95+ corresponds to single peak with slight foot. [b] Targeting aberrant splice site of luciferase pre-mRNA in HeLa pLuc705 cells. [c] Acr^{aeg} is a 9-aminoacridine monomer based on the aminoethylglycine PNA backbone (*27*). [d] Targeting translational initiation site of luciferase mRNA in p53R cells.

Chart 1. Chemical Structures of the Ligands Conjugated to PNA on the Solid Support[a]

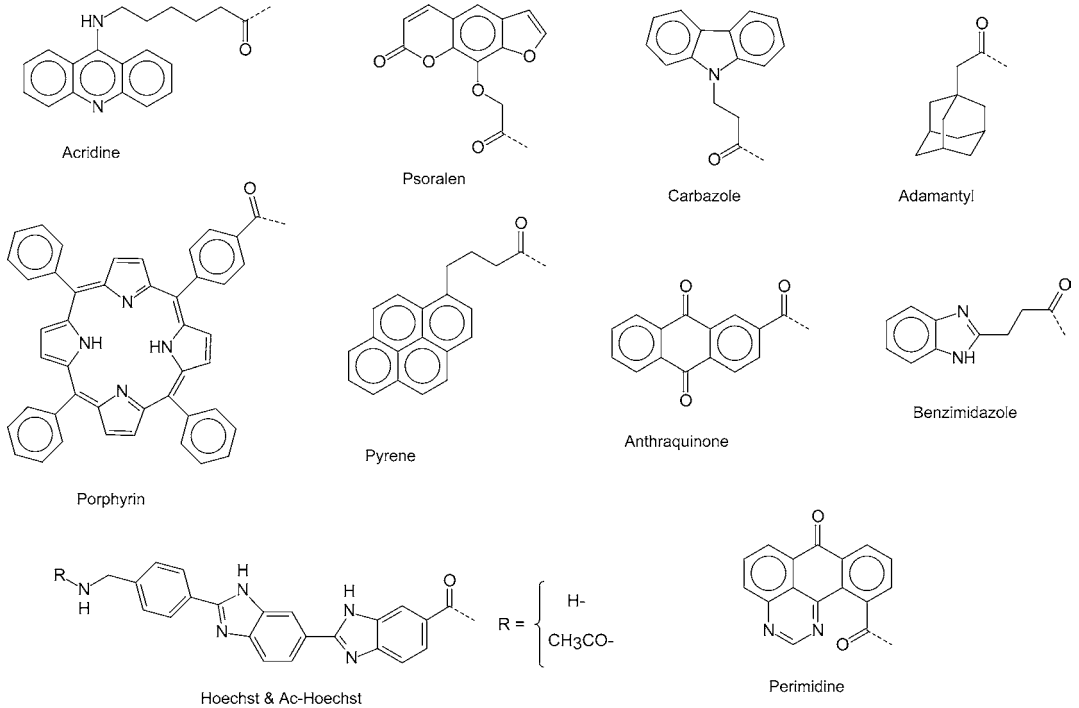

[a] The carboxylic acid derivatives of the ligands were obtained from commercial sources (Sigma-Aldrich: adamantly, anthraquinone, benzimidazole, carbazole, perimidine, pyrene; Porhyrin Systems, Germany: porphyrin) or synthesized as described (acridine (*27*); Hoecshst (*28*); psoralen (*29*)).

Cell Culture. HeLa pLuc705 cells and p53R cells were purchased from Gene Tools and ATCC, respectively. The cells were cultured in RPMI-1640 medium (Sigma) supplemented with 10% fetal bovine serum (FBS), 1.5% glutamax (Gibco), penicillin (100 U/mL), and streptomycin (100 μg/mL) at 37 °C in humidified air with 5% CO_2. For the transfection studies in 96-well plate format, cells were trypsinized and seeded (1.2×10^4 cells/well) 16−24 h before transfection. For the 24-well plate, 7.2×10^4 cells/well were used.

Polyheteroaromate−PNA Conjugate Transfection. Cells, seeded in 96-well plates the day before transfections, were treated with 100 μL/well of OPTI-MEM (Gibco) containing the PNA/lipid complex at the desired concentration for 4 h. The PNA−lipid complex was formed by incubating 10 μL of PNA solution (in water) with LipofectAMINE (LFA, Invitrogen) or LipofectAMINE2000 (LFA2K, Invitrogen) in 10 μL OPTI-MEM for 5 min at room temperature. Following addition of 80 μL of OPTI-MEM, this mixture was added to the cells. (Concentrations of LFA or LFA2K were 12 μL/ml or 8 μL/ml (final concentration), respectively, unless otherwise stated). After 4 h incubation, 100 μL/well of growth medium (RPMI-1640 containing 20% FBS and 1.5% glutamax) was added to the transfection mixture and incubated further for 24 h. For the transfection in 24-well plate format, 0.25 mL/well of OPTI-MEM and growth medium were used.

PNA/DNA Heteroduplex Transfection. Cells, seeded in 24-well plates the day before transfections, were treated with 250 μL/well of OPTI-MEM (Gibco) containing the PNA/DNA/

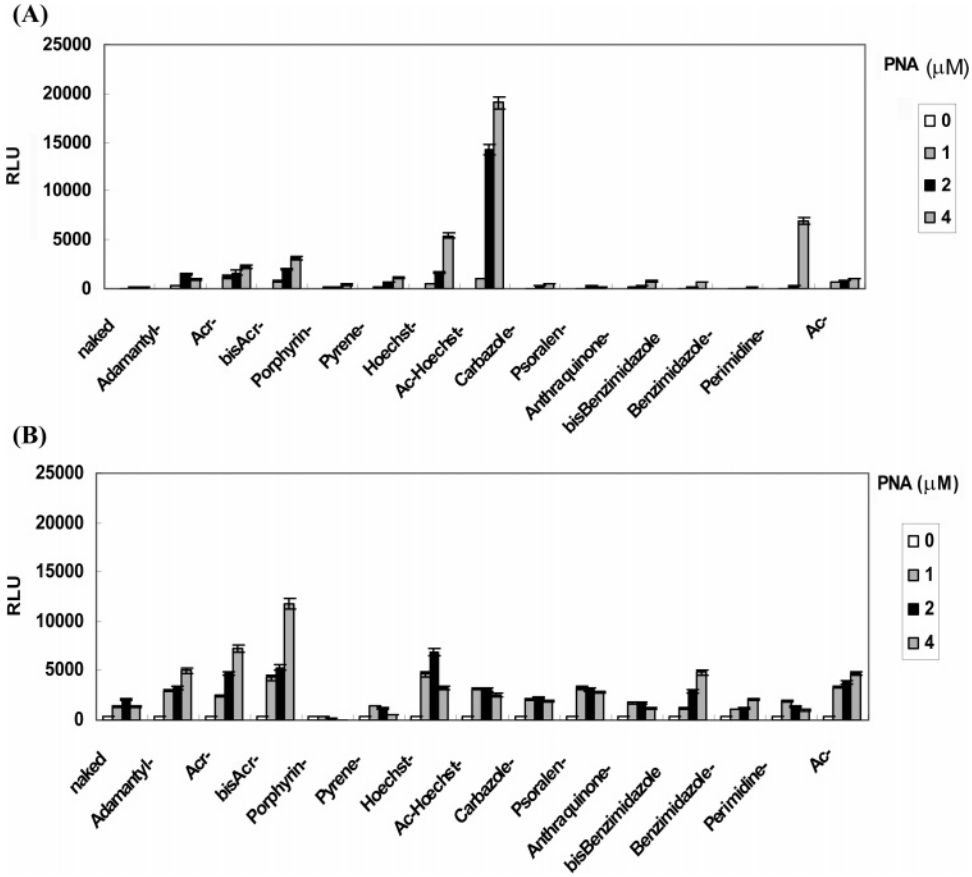

Figure 1. Screening of the PNAs conjugated with heteroaromatic compounds for the transfection in combination with cationic lipids. PNAs, targeting splicing correction, were listed in Table 1. PNAs were complexed with LipofectAMINE (LFA (A)) or LipofectAMINE2000 (LFA2K, (B)) and used for the transfection. HeLa pLuc705 cells were transfected with PNA/LFA or PNA LFA2K complex for 4 h in the absence of serum and incubated for an additional 24 h in the presence of serum. After PNA transfections, the cells were subjected to the luciferase assay with Bright-Glo assay (Promega). The values represent the mean ± SD of three experiments.

LFA2K complex at the desired concentration for 4 h. For the formation of PNA/DNA heteroduplex, PNA2389 was hybridized with DNA2389 (5′-AATATGTAACTGAGGTA-3′) as reported previously (*22*). The PNA/DNA heteroduplex was incubated with LFA2K in 50 μL of OPTI-MEM for 10 min and added to the cells after addition of 200 μL of OPTI-MEM. After 4 h transfection, 250 μL/well of growth medium (RPMI-1640 containing 20% FBS and 1.5% glutamax) was added to the transfection mixture and incubated further for 24 h.

Luciferase Assay. After PNA transfections, the cells were subjected to the luciferase analysis. Luciferase activity of the cells in 96-well plate format or 24-well plate format were measured by using Bright-Glo Luciferase assay system (Promega) or Luciferase Assay System (Promega), respectively, according to the manufacturer's instructions. Luminescent readings from 96-well plate formats (with background subtracted) are presented as relative light units (RLU). For the cells in 24-well plate formats, cell were lysed with Passive Lysis buffer (Promega) and subjected to the luciferase assay. Obtained RLU values were normalized by protein concentrations and are presented as RLU/mg protein. Protein concentrations were measured using BCA protein assay (Pierce) according to the manufacturer's instruction.

RT-PCR. Total RNA was extracted from the samples in Passive Lysis buffer using RNeasy Mini kit (Qiagen) according to the manufacturer's instruction. Three ng of total RNA was used for RT-PCR reaction (20 μL/reaction) by using OneStep RT-PCR kit (Qiagen). Primers for the RT-PCR were as follows: forward primer, 5′-TTGATATGTGGATTTCGAGTCGTC-3′; reverse primer, 5′-TGTCAAT-CAGAGTGCTTTTGGCG-3′. The RT-PCR program was as follows:{(55 °C, 35 min) × 1 cycle, (95 °C, 15 min) × 1 cycle, (94 °C, 0.5 min; 55 °C, 0.5 min; 72 °C, 0.5 min) × 26−28 cycles}. RT-PCR products were analyzed on 2% agarose gel with 1× TBE buffer and visualized by ethidium bromide staining. Gel images were captured by ImageMaster (Pharmacia Biotech) and analyzed by UN-SCAN-IT software (Silk Scientific Corporation).

RESULTS AND DISCUSSION

The PNA conjugates listed in Table 1 (splicing) were synthesized. These all contain the same PNA oligomer targeting the cryptic splice site within the luciferase gene in HeLa pLuc705 cells and previously shown to effectively correct missplicing of this modified luciferase gene and induce the production of normal luciferase protein (*22, 24*). Therefore, the antisense effect in this cellular system provides a very good measure of the cellular and nuclear uptake of the PNA conjugates. The PNAs were tested in combination with two types of cationic liposomes, LipofectAMINE (LFA) or LipofectAMINE 2000 (LFA2K) (Figure 1,parts A and B, respectively).

In this series of PNA conjugates, the PNA conjugated to the acetylated minor groove binder, "Ac-Hoechst" (Chart 1), showed the highest activity in combination with LFA (Figure 1A), being approximately 10 times more active than all other conjugates. As expected, unmodified PNA did not show any significant activities neither in the presence nor in the absence of cationic liposomes, but a few of the other new conjugates (apart from the already described adamantyl and acridine conjugates) were also active, in particular the Hoechst and the perimidine conjugates.

We also tested these PNAs in combination with a more recently introduced lipofection reagent, LFA2K (Figure 1B).

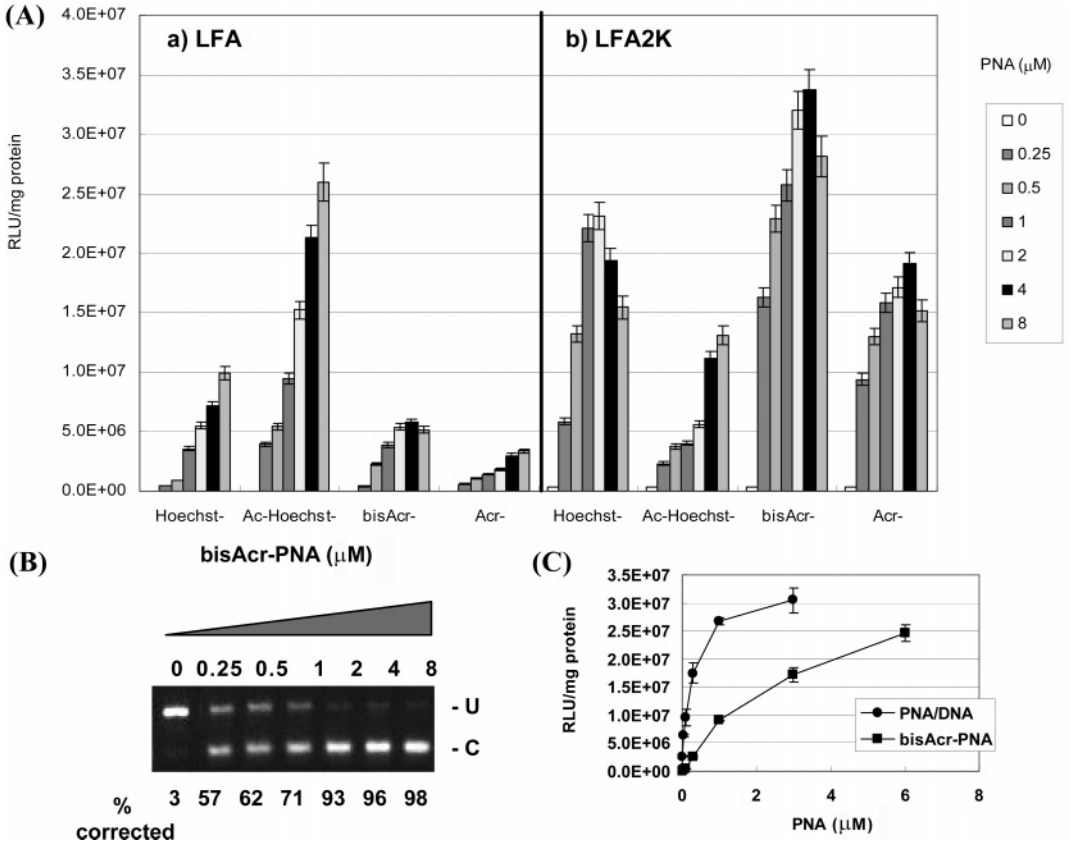

Figure 2. Transfection of the heteroaromate−PNAs (conjugated with Hoechst, acetyl-Hoechst (Ac-Hoechst), 9-aminoacridine (Acr), or bis-acridine (bisAcr)) or PNA/DNA heteroduplex in combination with LipofectAMINE (LFA) or LipofectAMINE2000 (LFA2K). (A) HeLa pLuc705 cells were transfected with Hoechst, Ac-Hoechst, Acr, and bisAcr−PNA in complex with LFA(a) or LFA2K (b) as mentioned in Figure 1. After 28 h transfection of the PNAs, cells were subjected to the luciferase analysis. Luciferase activities were measured using Luciferase Assay System (Promega) and normalized by protein concentration (shown as RLU/mg protein). The values represent the mean ± SD of three experiments. (B) RT-PCR analysis of the missplicing correction of luciferase pre-mRNAs by bisAcrPNA/LFA2k complex. Total RNA was extracted from the same samples in (A) and subjected to RT-PCR. U, fragments without mis-splicing correction (268 bp). C, fragments with mis-splicing correction (142 bp). The numbers under the figure indicate the relative amount (%) of the corrected form to the sum of corrected form and uncorrected form. (C) Comparison of cationic lipid mediated delivery between bisAcr−PNA and PNA/DNA heteroduplex. For the bisAcr−PNA transfection, PNA2490 was transfected to the cells in complex with LFA2K (8 μL/ml). For the PNA/DNA heteroduplex transfection, PNA2389 was hybridized with its complementary DNA (DNA2389) and transfected to the cells in complex with LFA2K (8 μL/mL). After 28 h transfection, cells were subjected to the luciferase analysis using Luciferase Assay System (Promega). Luciferase activity was normalized by protein concentration and shown as RLU/mg protein. The values represent the mean ± SD of three experiments.

Most of the PNA conjugates showed a higher effect than with LFA, and with this agent even unmodified and acetylated PNAs were somewhat active, but the best activity was observed with the acridine and in particular with a bis-acridine PNA conjugate. In contrast, Ac-Hoechst showed significantly lower activity than with LFA, while Hoechst PNA showed higher activity with LFA2K. These results clearly indicate the complexity of the lipid-mediated PNA delivery in terms of the combination of cationic liposome and auxiliary ligand. Thus, we decided to focus on the four seemingly most active PNA constructs (namely, Acr, bisAcr, Hoechst, and Ac-Hoechst) for further studies.

A more elaborate dose response experiment was performed with these four PNAs in combination with LFA and LFA2K (Figure 2A). These results confirm the results obtained from the initial screening (Figure 1) but provide a much more detailed picture of the activities. In particular, the superiority of the Ac-Hoechst conjugate in combination with LFA and the both relative and absolute superiority of the bis-acridine conjugate in combination with LFA2K is noteworthy. To further support that the increment of luciferase activity is indeed the result of splicing correction, we performed an RNA analysis by RT-PCR. Total RNA was extracted from the same samples as used for luciferase assay and subjected to RT-PCR analysis (Figure 2B). These results fully corroborate the enzyme activity data showing 57% splicing correction at 250 nM and essentially full correction at 2 μM.

However, it is important to realize that transfection experiments are not quantitatively reproducible from one set of experiments to the next due to differences in the exact state of the cell culture, subtle differences in the liposome preparation, etc. (Rasmussen, Nielsen, and Koppelhus et al., manuscript in preparation). Therefore, only results within the same experiment should be directly compared. In this context we performed a direct comparison of the antisense effect of the bis-acr−PNA conjugate delivered by LFA2K with that of the same unmodified PNA delivered by LFA2K as a sequence and length optimized DNA−PNA hybrid (Rasmussen, Nielsen, Koppelhus et al., manuscript in preparation). This experiment (Figure 2C) indicates that DNA mediated delivery is slightly (2−3-fold) more effective than "direct" delivery of the conjugate. Furthermore, the relative difference in efficacy most certainly will vary with cell type and gene target.

The antisense activity in the HeLa pLuc 705 cellular system only reflects the PNA concentrations in the nucleus although the size of the PNA molecules (<10 kDa) is considered sufficiently small not to hinder passage through the nuclear pores for efficient migration from the cytoplasm in to the nucleus. Indeed, it cannot be excluded that PNA oligomers and especially the conjugates with nucleic acid (DNA) binding ligands would

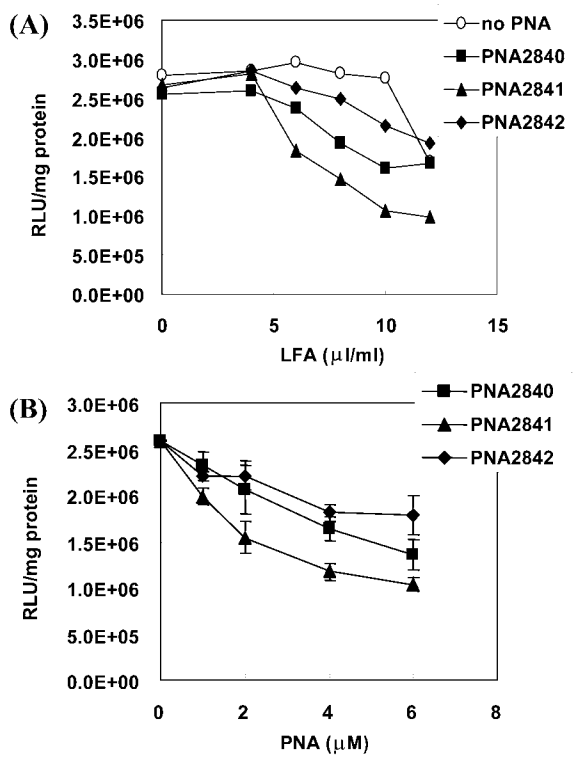

Figure 3. Screening of PNA sequences for the antisense down-regulation of luciferase in p53R cells. Three 9-aminoaridine-conjugated PNAs (15 mer), targeting three different position at the vicinity of start codon, were complexed with LipofectAMINE (LFA) and used for transfections. The p53R cells were transfected with PNA/LFA complex for 4 h and incubated for additional 24 h in the presence of serum. After 24 h, cells were subjected to the luciferase assay with luciferase assay (Promega). Luciferase activity was normalized by protein concentration and shown as RLU/mg protein. (A) Acr−PNA (2 μM) was complexed with the designated concentrations of LFA and used for transfections. Each data showed average of two independent experiments. (B) Different concentrations of Acr−PNAs were complexed with LFA (final concentration of 10 μL/ml) and used for transfections. The values represent the mean ± SD of three experiments

accumulate in the nucleus and thus possibly be depleted in the cytoplasm.

Therefore, to directly asses cytoplasmic delivery of the PNA conjugates by liposome-mediated transfection, we decided to test the transfection into p53R cells which are expressing normal luciferase. Initially, we tested three different PNA sequences (15 mer), targeting translation at three different locations at the vicinity of start codon, for the antisense down-regulation of luciferase in p53R cells. These PNAs (Table 1, 2840−2841) were modified by simple Acr derivatization because of the synthetic simplicity. For all PNAs (at 2 μM), an LFA-dose dependent decrease of luciferase activity was observed, while no such down-regulation was observed with LFA alone up to 10 μL/ml. However, a decrease in luciferase activity even for the control samples was seen at 12 μL/mL of LFA. This decrease is ascribed to a toxic effect of LFA itself. Based on this result, a dose−response experiment with the PNA complexed with LFA at 10 μL/mL was performed (Figure 3B). Among the three PNAs, PNA2841 showed the highest down-regulation at every concentration. With this PNA, the luciferase activity was decreased to 45% and 35% of the control at 4 μM and 6 μM PNA, respectively. Consequently, this PNA sequence (PNA2841) was selected for further studies, and we conjugated the PNA to Hoechst (PNA2882) or Ac-Hoechst (PNA2883). These three PNA conjugates (Acr−PNA, Hoechst−PNA, and Ac-Hoechst−PNA) were tested for their ability to down-regulate luciferase activity in p53R cells when delivered by LFA or LFA2K (Figure 4). In complex with LFA (Figure 4 A), Ac-Hoechst−PNA conjugate was the more active, whereas all three conjugates exhibited comparable activity when delivered with LFA2K (Figure 4B). It is noted that the absolute efficacy (corresponding to C_{50} values) of PNA-mediated gene silencing is considerable less in the p53R system as compared to the pluc705 system. We cannot at present provide the explanation for this difference as many factors may play a role: Two different molecular mechanisms that may exhibit different antisense sensitivities are involved, and these take place in two different cellular compartments (cytoplasm and nucleus). The sequence targets are unequally optimized, and the two cell types may respond differently to the (lipofection) delivery. However, the results unequivocally show that antisense targets in the cytoplasm as well as in the nucleus can be reached by the PNA conjugates via lipofection delivery.

CONCLUSION

The present results show that attachment of lipophilic poly (hetero) aromatic compounds to PNA can significantly improve cationic liposome-mediated cellular delivery of PNA oligomers uptake both to the cytoplasm as well as to the nucleus. It is also most likely that the activity of other uncharged antisense compounds such as the morpholino oligomers (*25*, *26*) should be improved through analogous conjugation. Although no clear structure/activity relationships are apparent from the present results, it is noteworthy that both 9-aminoacridine and "Hoechst"

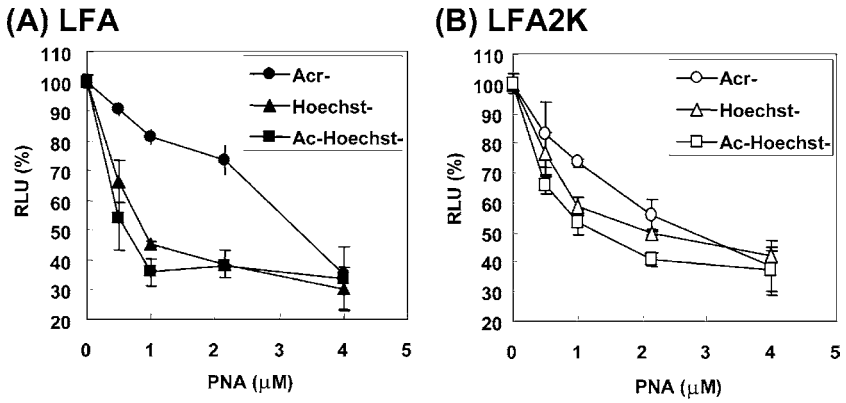

Figure 4. Comparison of antisense downregulation of PNAs conjugated with 9-aminoacridine (Acr−PNA), Hoechst (Hoechst−PNA), and acetyl Hoechst (Ac-Hoechst−PNA) in combination with LipofectAMINE (LFA) (A) or LipofecAMINE2000 (LFA2K) (B). PNA was complexed with LFA or LA2K and used for the transfections. p53R cells were transfected with PNA/LFA or PNA/LFA2K complex for 4 h and incubated for additional 24 h in the presence of serum. Luciferase activities were normalized by protein concentrations and showed as RLU/mg protein. The values represent the mean ± SD of three experiments.

which are the most active ligands in terms of uptake potentiation are also nucleic acid binding ligands. Furthermore, dsDNA targeted PNA oligomers conjugated to acridine or Hoechst have superior properties that can be exploited in the discovery of antigene agents (*30*, *31*). Therefore, these ligands may serve a dual role for PNA activity. In view of the number of alternative ligands that may be considered and possible combinations of these, it is likely that more potent conjugates may be discovered. The possibility of exploiting cleavable linkers could also be explored.

ACKNOWLEDGMENT

This study was supported by the Danish Cancer Society, Dansk Kræftforskningsfond, The Lundbeck Foundation (Senior research fellowship to T.S.), and the Danish Medical Research Council.

LITERATURE CITED

(1) Nielsen, P. E., Egholm, M., Berg, R. H., and Buchardt, O. (1991). Sequence-selective recognition of DNA by strand displacement with a thymine-substituted polyamide. *Science 254*, 1497−1500.

(2) Nielsen, P. E. (2000). Antisense peptide nucleic acids. *Curr. Opin. Mol. Ther. 2*, 282−287.

(3) Hyrup, B., and Nielsen, P. E. (1996). Peptide nucleic acids (PNA): synthesis, properties and potential applications. *Bioorg. Med. Chem. 4*, 5−23.

(4) Good, L., and Nielsen, P. E. (1997). Progress in developing PNA as a gene-targeted drug. *Antisense Nucleic Acid Drug Dev. 7*, 431−437.

(5) Bonham, M. A., Brown, S., Boyd, A. L., Brown, P. H., Bruckenstein, D. A., Hanvey, J. C., Thomson, S. A., Pipe, A., Hassman, F., Bisi, J. E. et al. (1995). An assessment of the antisense properties of RNase H-competent and steric-blocking oligomers. *Nucleic Acids Res. 23*, 1197−1203.

(6) Gray, G. D., Basu, S., and Wickstrom, E. (1997). Transformed and immortalized cellular uptake of oligodeoxynucleoside phosphorothioates, 3′-alkylamino oligodeoxynucleotides, 2′-O-methyl oligoribonucleotides, oligodeoxynucleoside methylphosphonates, and peptide nucleic acids. *Biochem. Pharmacol. 53*, 1465−1476.

(7) Aldrian-Herrada, G., Desarmenien, M. G., Orcel, H., Boissin-Agasse, L., Mery, J., Brugidou, J., and Rabie, A. (1998). A peptide nucleic acid (PNA) is more rapidly internalized in cultured neurons when coupled to a retro-inverso delivery peptide. The antisense activity depresses the target mRNA and protein in magnocellular oxytocin neurons. *Nucleic Acids Res. 26*, 4910−4916.

(8) Cutrona, G., Carpaneto, E. M., Ponzanelli, A., Ulivi, M., Millo, E., Scarfi, S., Roncella, S., Benatti, U., Boffa, L. C., and Ferrarini, M. (2003). Inhibition of the translocated c-myc in Burkitt's lymphoma by a PNA complementary to the E mu enhancer. *Cancer Res. 63*, 6144−6148.

(9) Kaihatsu, K., Huffman, K. E., and Corey, D. R. (2004). Intracellular uptake and inhibition of gene expression by PNAs and PNA-peptide conjugates. *Biochemistry 43*, 14340−14347.

(10) Pooga, M., Soomets, U., Hallbrink, M., Valkna, A., Saar, K., Rezaei, K., Kahl, U., Hao, J. X., Xu, X. J., Wiesenfeld-Hallin, Z., Hokfelt, T., Bartfai, T., and Langel, U. (1998). Cell penetrating PNA constructs regulate galanin receptor levels and modify pain transmission in vivo. *Nat. Biotechnol. 16*, 857−861.

(11) Koppelhus, U., Awasthi, S. K., Zachar, V., Holst, H. U., Ebbesen, P., and Nielsen, P. E. (2002). Cell-dependent differential cellular uptake of PNA, peptides, and PNA-peptide conjugates. *Antisense Nucleic Acid Drug Dev. 12*, 51−63.

(12) Derossi, D., Joliot, A. H., Chassaing, G., and Prochiantz, A. (1994). The third helix of the Antennapedia homeodomain translocates through biological membranes. *J. Biol. Chem. 269*, 10444−10450.

(13) Pooga, M., Hallbrink, M., Zorko, M., and Langel, U. (1998). Cell penetration by transportan. *FASEB J. 12*, 67−77.

(14) Mitchell, D. J., Kim, D. T., Steinman, L., Fathman, C. G., and Rothbard, J. B. (2000). Polyarginine enters cells more efficiently than other polycationic homopolymers. *J. Pept. Res. 56*, 318−325.

(15) Frankel, A. D., and Pabo, C. O. (1988). Cellular uptake of the tat protein from human immunodeficiency virus. *Cell 55*, 1189−1193.

(16) Braun, K., Peschke, P., Pipkorn, R., Lampel, S., Wachsmuth, M., Waldeck, W., Friedrich, E., and Debus, J. (2002). A biological transporter for the delivery of peptide nucleic acids (PNAs) to the nuclear compartment of living cells. *J. Mol. Biol. 318*, 237−243.

(17) Hamilton, S. E., Simmons, C. G., Kathiriya, I. S., and Corey, D. R. (1999). Cellular delivery of peptide nucleic acids and inhibition of human telomerase. *Chem. Biol. 6*, 343−351.

(18) Ljungstrom, T., Knudsen, H., and Nielsen, P. E. (1999). Cellular uptake of adamantyl conjugated peptide nucleic acids. *Bioconjugate Chem. 10*, 965−972.

(19) Mologni, L., Marchesi, E., Nielsen, P. E., and Gambacorti-Passerini, C. (2001). Inhibition of promyelocytic leukemia (PML)/retinoic acid receptor-alpha and PML expression in acute promyelocytic leukemia cells by anti-PML peptide nucleic acid. *Cancer Res. 61*, 5468−5473.

(20) Uhlmann, E. (1998). Peptide nucleic acids (PNA) and PNA-DNA chimeras: from high binding affinity towards biological function. *Biol. Chem. 379*, 1045−1052..

(21) Doyle, D. F., Braasch, D. A., Simmons, C. G., Janowski, B. A., and Corey, D. R. (2001). Inhibition of gene expression inside cells by peptide nucleic acids: effect of mRNA target sequence, mismatched bases, and PNA length. *Biochemistry 40*, 53−64.

(22) Shiraishi, T., and Nielsen, P. E. (2004). Down-regulation of MDM2 and activation of p53 in human cancer cells by antisense 9-aminoacridine-PNA (peptide nucleic acid) conjugates. *Nucleic Acids Res. 32*, 4893−4902.

(23) Christensen, L., Fitzpatrick, R., Gildea, B., Petersen, K. H., Hansen, H. F., Koch, T., Egholm, M., Buchardt, O., Nielsen, P. E., Coull, J., and et al. (1995). Solid-phase synthesis of peptide nucleic acids. *J. Pept. Sci. 1*, 175−183.

(24) Kang, S. H., Cho, M. J., and Kole, R. (1998). Up-regulation of luciferase gene expression with antisense oligonucleotides: implications and applications in functional assay development. *Biochemistry 37*, 6235−6239.

(25) Summerton, J., and Weller, D. (1997). Morpholino antisense oligomers: design, preparation, and properties. *Antisense Nucleic Acid Drug Dev. 7*, 187−195.

(26) Moulton, H. M., Nelson, M. H., Hatlevig, S. A., Reddy, M. T., and Iversen, P. L. (2004). Cellular uptake of antisense morpholino oligomers conjugated to arginine-rich peptides. *Bioconjugate. Chem. 15*, 290−299.

(27) Shiraishi, T., Hamzavi, R., and Nielsen, P. E. (2005). Targeted delivery of plasmid DNA into the nucleus of cells via Nuclear Localization Signal peptide conjugated to DNA intercalating bis- and tris-acridines. *Bioconjugate Chem. 16*, 112−116.

(28) Behrens, C., Harrit, N., and Nielsen, P. E. (2001). Synthesis of a Hoechst 32258 analogue amino acid building block for direct incorporation of a fluorescent, high-affinity DNA binding motif into peptides. *Bioconjugate Chem. 12*, 1021−1027.

(29) Okamoto, A., Tanabe, K., and Saito, I. (2001). Synthesis and properties of peptide nucleic acids containing a psoralen unit. *Org. Lett. 3*, 925−927.

(30) Bentin, T., and Nielsen, P. E. (2003) Superior duplex DNA strand invasion by acridine conjugated Peptide Nucleic Acids. *J. Am. Chem. Soc. 125*, 6378−6379.

(31) Nielsen, P. E., Frederiksen, K., and Behrens, C. (2005) Extended target sequence specificity of PNA-minor-groove binder conjugates. *Chembiochem 6*, 66−68.

BC050246Z

Synthesis and Evaluation of Glycosylated Octreotate Analogues Labeled with Radioiodine and ^{211}At via a Tin Precursor

G. Vaidyanathan,*,† D. J. Affleck,† M. Schottelius,‡ H. Wester,‡ H. S. Friedman,§ and M. R. Zalutsky†

Departments of Radiology and Neurooncology, Duke University Medical Center, Durham, North Carolina 27710 and Technical University of Munich, Munich, Germany. Received August 19, 2005; Revised Manuscript Received October 18, 2005

Carbohydration of N-terminus and substitution of a threonine for the threoninol residue at the C-terminus of Tyr^3-octreotide (TOC) has resulted in improved pharmacokinetics and tumor targeting of its radioiodinated derivatives. Yet, these peptides are very susceptible to in vivo deiodination due to the similarity of monoiodotyrosine (MIT) to thyroid hormone. The goal of this work was to develop octreotate analogues containing both a sugar moiety and a nontyrosine prosthetic group on which a radioiodine or ^{211}At can be introduced. Solid-phase synthesis and subsequent modifications delivered an iodo standard of the target peptide N^{α}-(1-deoxy-D-fructosyl)-N^{ϵ}-(3-iodobenzoyl)-Lys^0-octreotate (GIBLO) and the corresponding tin precursor N^{α}-(1-deoxy-D-fructosyl)-N^{ϵ}-[(3-tri-*n*-butylstannyl)benzoyl]-Lys^0-octreotate (GTBLO). GIBLO displaced [^{125}I]TOC from somatostatin receptor subtype 2 ($SSTR_2$)-positive AR42J rat pancreatic tumor cell membranes with an IC_{50} of 0.46 ± 0.05 nM suggesting that GIBLO retained affinity to $SSTR_2$. GTBLO was radiohalogenated to [^{131}I]GIBLO and N^{α}-(1-deoxy-D-fructosyl)-N^{ϵ}-(3-[^{211}At]astatobenzoyl)-Lys^0-octreotate ([^{211}At]GABLO) in 21.2 ± 4.9% and 46.8 ± 9.5% radiochemical yields, respectively. From a paired-label internalization assay using D341 Med medulloblastoma cells, the maximum specific internalized radioactivity from [^{131}I]GIBLO was 1.78 ± 0.8% of input dose compared to 9.67 ± 0.43% for N^{α}-(1-deoxy-D-fructosyl)-[^{125}I]iodo-Tyr^3-octreotate ([^{125}I]I-Gluc-TOCA). Over a 4 h period, the extent of internalization of [^{131}I]GIBLO and [^{211}At]GABLO was similar in this cell line. In D341 Med murine subcutaneous xenografts, the uptake of [^{125}I]I-Gluc-TOCA at 0.5, 1 and 4 h was 21.5 ± 4.0% ID/g, 18.8 ± 7.7% ID/g, and 0.9 ± 0.4% ID/g, respectively. In comparison, these values for [^{131}I]GIBLO were 6.9 ± 1.2% ID/g, 4.7 ± 1.4% ID/g, and 0.8 ± 0.5% ID/g. Both in vitro and in vivo catabolism studies did not suggest the severance of the lys^0 along with its appendages from the peptide. Taken together, although GIBLO maintained affinity to $SSTR_2$, its tumor uptake both in vitro and in vivo was substantially lower than that of I-Gluc-TOCA suggesting other factors such as net charge and overall geometry of the peptide may be important.

INTRODUCTION

The expression of high levels of somatostatin receptors (SSTR[1]) on a variety of tumors has provided the impetus for the development of radiolabeled octreotide derivatives, which target SSTR, and can be utilized for imaging and treating these cancers (*1*−*3*). Among the radionuclides investigated for these purposes are those of iodine, which have a range of physical characteristics suited for a variety of imaging (SPECT, PET) and therapy (*β*-particle, Auger electron) approaches. Direct radioiodination of peptides is achieved by substitution on constituent tyrosine residues; the absence of tyrosines in octreotide led to the development of Tyr^3-octreotide (TOC) (*4*). Although TOC can be readily labeled, it is not a useful radiopharmaceutical because it exhibits only marginal tumor targeting, due in part to the fact that it undergoes rapid deiodination.

A number of TOC structural modifications have been investigated with the goal of providing a labeled peptide with greater clinical potential. These include N-terminal sugar conjugation and Thr-for-Thr(ol) exchange (octreotide → octreotate), both of which have been shown to improve the intracellular retention of radioiodine in vitro as well as tumor-to-normal tissue ratios in mice bearing SSTR-expressing xenografts (*5*, *6*). Synergistic enhancements in tumor targeting were achieved when both tactics were combined, exemplified by the results obtained with N^{α}-(1-deoxy-D-fructosyl)-[^{131}I]I-Tyr^3-octreotate ([^{131}I]I-Gluc-TOCA). For example, 1 h after injection, tumor uptake of [^{131}I]I-Gluc-TOCA was about 5 times higher than that of coadministered [^{125}I]TOC (*7*).

An important consideration in peptide radiohalogenation is whether the procedure utilized for radioiodination can also be adapted for use with ^{211}At. Astatine-211 is a radiohalogen that emits α-particles, a type of radiation with many potential advantages for targeted radiotherapy, notably a higher cytotoxicity compared to *β*-particles (*8*). Furthermore, its half-life of 7.2 h is well matched to peptide pharmacokinetics. Even though peptides such as Gluc-TOCA offer many advantages compared with TOC, they still undergo radiohalogenation by direct substitution on Tyr^3. With radioiodine, this feature results in

* Correspondence to Ganesan Vaidyanathan, Ph.D., Research Professor, Department of Radiology, Duke University Medical Center, Durham, NC 27710. Phone: (919) 684-7811. Fax: (919) 684-7122. E-mail: ganesan.v@duke.edu.

† Department of Radiology, Duke University Medical Center.

‡ Technical University of Munich.

§ Department of Neurooncology, Duke University Medical Center.

[1] Abbreviations (uncommon) used: [^{211}At]GABLO, N^{α}-(1-deoxy-D-fructosyl)-N^{ϵ}-(3-[^{211}At]astatobenzoyl)-Lys^0-octreotate; Dde, 1-(4,4-dimethyl-2,6-dioxocyclohex-1-ylidene)ethyl; GIBLO, N^{α}-(1-deoxy-D-fructosyl)-N^{ϵ}-(3-iodobenzoyl)-Lys^0-octreotate; Gluc-Lys^0-Lys^5(Dde)-TOCA, N^{α}-(1-deoxy-D-fructosyl)-Lys^0-Lys^5(Dde)-TOCA; Gluc-TOCA, N^{α}-(1-deoxy-D-fructosyl)-Tyr^3-octreotate; GMIBO, *N*-(4-guanidinomethyl-3-iodobenzoyl)-Phe^1-octreotate; GTBLO, N^{α}-(1-deoxy-D-fructosyl)-N^{ϵ}-(3-tri-*n*-butylstannyl-benzoyl)-Lys^0-octreotate; I-Gluc-Lys^0-TOCA, N^{α}-(1-deoxy-D-fructosyl)-Lys^0-TOCA; I-Gluc-TOCA, N^{α}-(1-deoxy-D-fructosyl)-iodo-Tyr^3-octreotate; MIT, monoiodotyrosine or 3-iodotyrosine; SIB, *N*-succinimidyl 3-iodobenzoate; SSTR, somatostatin receptor; STB, *N*-succinimidyl 3-(tri-*n*-butyl)stannylbenzoate; TOC, Tyr^3-octreotide; TOCA, Tyr^3-octreotate.

10.1021/bc0502560 CCC: $33.50 © 2006 American Chemical Society
Published on Web 12/23/2005

Chart 1. Chemical Structures of Octreotide, I-Gluc-TOCA, I-Gluc-Lys^0-TOCA, and GIBLO

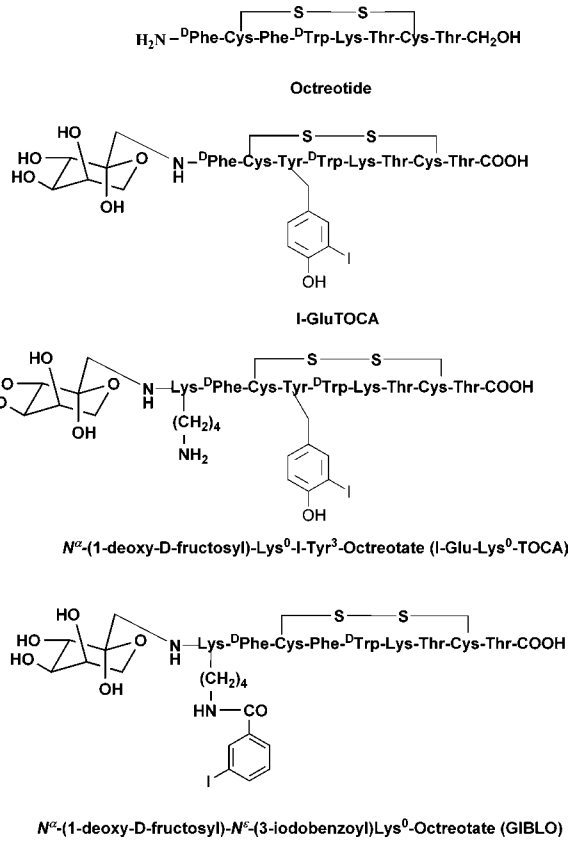

extensive deiodination in vivo, presumably due to recognition by endogenous deiodinases; with ^{211}At, the known instability of astatotyrosine even under in vitro conditions excludes direct radioastatination as a viable labeling strategy (*9*, *10*).

To circumvent these problems, we have developed derivatives of octreotide and octreotate in which the radiohalogen resides in a prosthetic group attached to the N-terminus of the peptide (*11*, *12*). Radioiodinated and ^{211}At-labeled peptides could be synthesized in reasonable yield and were shown to be resistant to dehalogenation. Moreover, the second generation peptide, *N*-(4-guanidinomethyl-3-iodobenzoyl)-Phe^1-octreotate (GMIBO) had a significantly higher intracellular accumulation in vitro compared with [^{125}I]I-Gluc-TOCA (*12*). Unfortunately, normal organ levels, particularly in the liver and kidney, of [^{131}I]GMIBO were several-fold higher than those of [^{125}I]I-Gluc-TOCA, consistent with previous results demonstrating the ameliorative effects of N-terminal sugar conjugation on normal tissue uptake.

The goal of this study was to investigate the strategy of synthesizing an SSTR-avid peptide combining the three structural elements noted above: N-terminal sugar conjugation, Thr-for-Thr(ol) exchange, and a prosthetic group carrying the radiohalogen. Glucose was selected as the sugar, and as the prosthetic group, the halobenzoyl template was utilized (Chart 1). Because two functional groups are needed to attach these two subunits, an extra lysine was introduced at the N-terminus of octreotate. The synthesis, radiohalogenation, and evaluation of the radiohalogenated peptides are described herein.

EXPERIMENTAL PROCEDURES

General. All chemicals were purchased from Sigma-Aldrich unless otherwise noted. Sodium [^{125}I]iodide and sodium [^{131}I]-iodide with specific activities of 2200 Ci/mmol and 1200 Ci/mmol, respectively, were obtained from Perkin-Elmer Life and Analytical Sciences (Boston, MA). The ^{211}At activity was produced on the Duke University Medical Center CS-30 cyclotron via the ^{209}Bi(α, 2n)^{211}At reaction by bombarding natural bismuth metal targets with 28 MeV α-particles (*13*), and the radioactivity was isolated from the target by dry distillation and extracted into chloroform. Unlabeled *N*-succinimidyl 3-iodobenzoate (SIB) as well as *N*-succinimidyl 3-(tri-*n*-butyl)stannylbenzoate (STB) were synthesized as reported (*14*). Octreotide (Sandostatin) was purchased as an aqueous solution (0.5 mg/mL) from the Duke University Medical Center Pharmacy (Durham, NC). TCP (trityl chloride polystyrene) resin was purchased from PepChem (Tubingen, Germany). Appropriately protected amino acids were obtained from Novabiochem (Bad Soden, Germany).

Solid-phase peptide syntheses were carried out manually using a flask shaker (St. Johns Associates, Inc., Beltsville, MD). Three HPLC systems were used. For radiochemistry, either of two Beckman systems (System Gold) was used. System 1 was equipped with a Model 126 programmable solvent module, a Model 168 diode array detector, and a Model 170 radioisotope detector, which was interfaced using a Model 406 analog interface module. System 2 was equipped with a Model 126 programmable solvent module, a Model 166 NM variable wavelength detector, a Model 170 radioisotope detector, and a Beckman System Gold remote interface module SS420X; data were acquired using 32 Karat software. For nonradioactive and preparative work, a Waters Model Delta 600 semi-prep system with a Model 600 controller and a Model 2487 dual wavelength absorbance detector were used; data were acquired using Millenium software. Waters XTerra C18 columns of dimensions 4.6 $\times$ 250 mm (5 μm) and 19 $\times$ 150 mm (7 μm) were used for analytical and semipreparative chromatography, respectively. Mass spectra were obtained on either a JEOL SX-102 high-resolution mass spectrometer (FAB), an Applied Biosystems Voyager DE Pro (MALDI), or an Agilent 1100 LC/MSD Trap SL (electrospray). Amino acid analysis was performed at the Protein Chemistry Lab, University of North Carolina (Chapel Hill, NC).

Peptide Syntheses. *Gluc-TOCA.* As reported previously (*7*), Tyr^3-octreotate, with its Lys^5, ϵ-amino function protected with a Dde group, was prepared by solid-phase synthesis. The peptide was cleaved from the resin and cyclized. The N-terminal amino group was glycosylated via a Maillard reaction and the Dde group was subsequently removed.

N$^\alpha$-(1-Deoxy-D-fructosyl)-N$^\epsilon$-(3-iodobenzoyl)-Lys^0-octreotate (GIBLO). The peptide sequence Boc-Lys(Fmoc)-DPhe-Cys-(Trt)-Phe-DTrp(Boc)-Lys(Dde)-Thr(tBu)-Cys(Trt) (Scheme 1) was assembled on resin-bound Thr(tBu) by manual solid-phase synthesis using the standard Fmoc protocol. The peptide was cleaved from the resin, cyclized, and glycosylated as reported previously for similar peptides (*2*, *5*, *6*). Then, the Fmoc protecting group on the Lys^0 side chain was removed using 20% piperidine in DMF and purified using preparative reversed-phase HPLC. To the above peptide (3.5−4 mg) in a 1 mL Reacti-vial was added a solution of SIB (5 mg) in 0.2 mL of 1% TEA in DMF. The homogeneous reaction mixture was left at room temperature under argon for 18 h. The progress of reaction was followed by analytical HPLC using the following gradient: 0.1% (w/v) TFA in water (solvent A) and 0.1% (w/v) TFA in acetonitrile (solvent B) at a flow rate of 1 mL/min, with %B increased from 30 to 60 over 30 min and then to 90 over another 10 min and then held at 90 for 5 min. The retention times of the starting peptide, SIB, and the SIB-modified peptide were 17.0, 26.8, and 24.9 min, respectively. The SIB modified peptide was precipitated by the addition of a large excess of ether, isolated by centrifugation, and washed several times with ether. MS (MALDI) *m*/*z*: Calcd for $C_{78}H_{101}IN_{12}O_{20}S_2$: 1717.7. Found: 1717.6 (M^+), 817.8, 556.5. The above peptide was taken

Scheme 1. Synthesis of GIBLO and Its Tin Precursor[a]

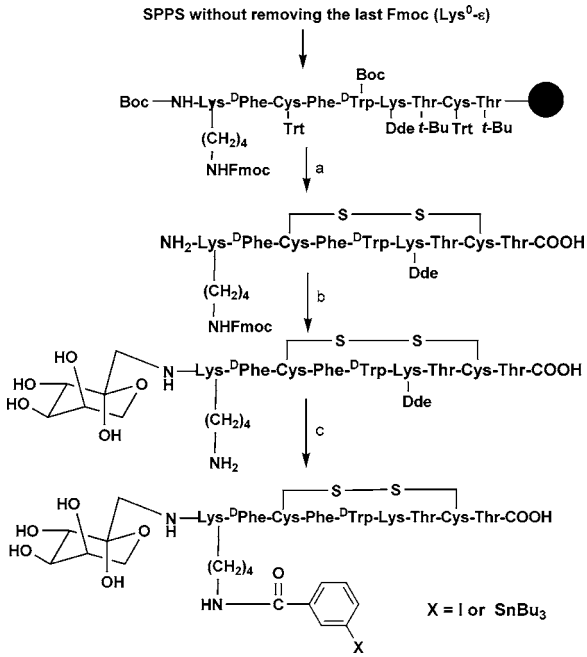

[a] Reagents and conditions: (a) i. 95:2.5:2.5 (v/v/v/) TFA:water: triisopropylsilane, ii. H_2O_2, THF, 0.05 M NH_4OAc; (b) i. D-glucose, HOAc/MeOH, ii. 20% piperidine in DMF; (c) i. *N*-succinimidyl 3-iodobenzoate or *N*-succinimidyl 3-(tri-n-butylstannyl)benzoate, DIEA/NMP, ii. 1:1 ethanolamine:EtOH.

up in 2.5 mL of ethanol, and 0.5 mL of ethanolamine was added. The reaction was determined to be complete in 1 h by HPLC (t_R = 16.9 min for the final product). The product was isolated by semipreparative HPLC using the same solvents and gradient described above but at a flow rate of 10 mL/min and using the semipreparative column. Solvents were evaporated from the HPLC fractions, and the peptide was redissolved in ethanol. The concentration of this solution was determined by amino acid analysis. MS (MALDI) *m*/*z*: Calcd for $C_{68}H_{89}IN_{12}O_{18}S_2$: 1553.5. Found: 1553.6 (M^+).

N^{α}-(1-Deoxy-D-fructosyl)-N^{ϵ}-(3-tri-n-butylstannyl-benzoyl)-Lys⁰-octreotate (GTBLO). This was prepared essentially as above but with STB as the acylation agent. The intermediate peptide with the Dde group had a retention time of 41.5 min (vs 49 min for STB) under the HPLC conditions used for GIBLO. MS (FAB^+) *m*/*z*: Calcd for $C_{90}H_{128}N_{12}O_{20}S_2{}^{120}Sn$: 1882.1. Found: cluster peaks around 1883.6 $(M + H)^+$. For the final step (removal Dde) a different gradient was used for both analytical and semipreparative chromatography. The solvents used were 0.2% HOAc in 30% methanol in water (A) and 0.2% HOAc in 90% MeOH in water (B). The %B was increased from 0 to 100 over 30 min and then run for another 10 min. The retention time of the product peptide under the analytical conditions was 29.5 min. MS (MALDI) *m*/z: Calcd for $C_{80}H_{116}N_{12}O_{18}S_2{}^{120}Sn$: 1717.9. Found: 1740 $(M + Na)^+$, 1717.5 (M^+).

N^{α}-(1-Deoxy-D-fructosyl)-Lys⁰(Dde)-TOCA (Gluc-Lys⁰-TOCA-Dde). This was synthesized as reported before (*15*, *16*).

N^{α}-(1-Deoxy-D-fructosyl)-N^{ϵ}-(3-iodobenzoyl)-lysine. This compound was synthesized for use as an HPLC standard. To a suspension of N^{α}-Boc-N^{ϵ}-(3-iodobenzoyl)lysine (*17*) (24 mg; 0.05 mmol) in 0.2 mL of methylene chloride in a Reacti-vial was added 0.2 mL of TFA, and the mixture was stirred at room temperature for 30 min. The solvents were evaporated using a stream of argon, and the residue was taken up in 0.5 mL of 5% acetic acid (v/v) in methanol. To the resultant solution was added 90 mg of α-D-glucose, and the capped vial was heated overnight at 60 °C. The reaction was followed by reversed-phase HPLC. For this, the analytical column was eluted at 1 mL/min with a gradient consisting of 0.1% TFA in each 90:10 water:acetonitrile (solvent A) and 10:90 water:acetonitrile (solvent B). The %B was held at 0 for 10 min, increased to 100 over the next 30 min, and held at 100 for another 5 min. Under these conditions, the starting material had a t_R of 25.1 min and the product, 24.3 min. Because HPLC analysis did not indicate much progress in the reaction, 107 mg of α-D-glucose in 1.3 mL of solvent was added and the heating continued for 2 days, after which only moderate progress was seen. Semipreparative HPLC using the same gradient as above at a flow rate of 10 mL/min yielded 0.6 mg of product: MS (ESI) *m*/*z*: 539.72 (MH^+); 561.52 $(M + Na)^+$ (100%); 583.02 $(M + 2Na - H)^+$.

Radiohalogenation. *[^{125}I]I-TOC and [^{125}I]I-Gluc-TOCA.* These were prepared as reported (*7*). Briefly, to a solution of sodium [^{125}I]iodide (1−2 mCi in 3 μL of 0.1 N NaOH) in a Reacti-vial was added 20 μL of 0.05 M phosphate buffer (pH 7.5) and a solution of 14 μg of Gluc-TOCA in 20 μL 0.05 M acetic acid. After vortexing this mixture, 0.16 μg of Chloramine-T in 20 μL of the above phosphate buffer was added. After a 1-min reaction at room temperature, the labeled peptide was isolated from the reaction mixture by reversed-phase HPLC.

[^{131}I]I-Gluc-Lys⁰-TOCA. Gluc-Lys⁰-Lys⁵(Dde)-TOCA was labeled with ^{131}I essentially as described above for [^{125}I]I-Gluc-TOCA. The reaction mixture was passed through an activated C-18 cartridge, which was further washed with 2 × 5 mL water, and the product was eluted with 0.25 mL portions of ethanol. The fractions containing the product were pooled and ethanol was evaporated. To the residual activity, 10 μL of a solution of hydrazine in DMF (2% v/v) was added. Ten minutes later, the reaction mixture was diluted with 25 μL of ethanol and injected onto a reversed-phase HPLC column. It was eluted with a linear gradient (10−40% B over a period of 30 min) consisting of solvents 0.1% TFA in water (A) and 0.1% TFA in acetonitrile (B) at a flow rate of 1 mL/min. The retention times of [^{131}I]I-Gluc-Lys⁰-TOCA and its Dde-protected precursor under these conditions were 26.1 and 36.2 min, respectively. The fractions containing the final labeled product were isolated and concentrated by solid-phase extraction as described above for the intermediate peptide.

[^{131}I]GIBLO and [^{211}At]GABLO. A solution of GTBLO (∼100 μg) in ethanol (50 μL) was transferred to a 1 mL Reacti-vial and the ethanol was evaporated with a gentle stream of argon. To this were added ^{131}I (0.5−2 mCi in 1−3 μl) and *N*-chlorosuccinimide (5 μg in 10 μL of HOAc), and the mixture was sonicated at room temperature for 2 min. The entire reaction mixture was injected into an analytical reversed-phase column. The column was eluted using the gradient described for the synthesis of unlabeled GIBLO (t_R = 17−18 min). The labeled peptide was isolated in 21.2 ± 4.9% radiochemical yields. For astatination, the ^{211}At activity in chloroform was first extracted into 1−2 μL of 0.1 N NaOH in a Reacti-vial, and the procedure described above for iodination was followed. [^{211}At]GABLO was obtained in about 46.8 ± 9.5% radiochemical yields. The HPLC fractions containing the labeled peptide were concentrated using a C18 solid-phase cartridge. A Waters tC18ENV Sep-pak cartridge was activated by elution with 5 mL each of water and ethanol. HPLC fractions were purged with an argon stream to remove most of the acetonitrile, diluted with water, and passed through the solid-phase cartridge. The cartridge was washed twice with 5 mL of water and then eluted with 0.25 mL portions of ethanol. The labeled peptide generally eluted in fractions 4−6. Ethanol was evaporated from the combined fractions, and the product was reconstituted in PBS containing 1% BSA.

Cells and Culture Conditions. The SSTR-expressing AR42J rat pancreatic tumor cell line (*18*) was obtained from American

Type Culture Collection (Manassas, VA) and grown in DMEM containing 2 mM glutamine, 10% FCS, and 5 g/L glucose. D341 Med is a human medulloblastoma cell line derived from a patient tumor biopsy (*19*) and grown in 10% FCS and zinc option medium. Cells were maintained in a humidified atmosphere (37 °C, 5% CO_2).

Receptor Binding Assay. The SSTR receptor binding affinity of GIBLO was determined by a competitive binding assay using AR42J membranes according to a literature protocol (*20*). About 50 μg of membranes was incubated in triplicate at 37 °C for 1 h with ~25 nCi of [^{125}I]TOC in the absence or presence of various concentrations of unlabeled GIBLO or octreotide. Radioactivity bound to the membranes in the presence of 50 nM unlabeled peptide was considered to be nonspecific binding. The IC_{50} values were calculated from the specific binding versus peptide concentration plots.

Internalization Assay. Three paired-label assays were performed following a previously reported protocol (*12*). D341 Med cells (5×10^5 per tube per mL) were incubated at 37 °C with (a) [^{125}I]I-Gluc-TOCA (5.1 fmol) and [^{131}I]GIBLO (31.0 fmol), (b) [^{131}I]GIBLO (19.4 fmol) and [^{211}At]GABLO (0.02 fmol), or (c) [^{125}I]I-Gluc-TOCA (13.8 fmol) and [^{131}I]I-GIu-Lys^0-TOCA (2.6 fmol) for 0.5, 1, 2, 3, and 4 h. At each time point, radioactivity in the cell culture supernatant, that bound to the cell surface, and that trapped inside the cells were determined. The percent of input dose that was internalized was plotted versus the time.

Tissue Distribution Experiments. Animal studies were performed under the guidelines established by the Duke University Institutional Animal Care and Use Committee. Athymic BALB/c-nu (SPF) mice weighing 20−25 g with subcutaneous D341 Med human medulloblastoma xenografts were utilized (*19*). The biodistribution studies were initiated when tumors were about 200−300 mm^3. Mice received 4 μCi of [^{125}I]I-Gluc-TOCA and 3 μCi of [^{131}I]GIBLO via the tail vein and groups of five animals were killed 0.5,1, 4, 16, and 24 h after injection. Mice were killed with an overdose of halothane, dissected and tissues of interest were isolated, weighed, and counted in a dual channel gamma counter. A paired Student's *t* test was used to determine the statistical significance of differences between the two peptides.

Paired-Label Catabolism [^{125}I]I-Gluc-TOCA and [^{131}I]-GIBLO. *In Vitro*. The internalization assay described above was repeated at 0.5 and 4 h with 10 μCi of each tracer. After washing off cell surface-bound radioactivity, the cells were lysed in 100 μL of 0.5% NP-40 in PBS. Reversed-phase HPLC of cell culture supernatant, cell lysate, and acid washes were performed along with intact peptide standards, 3-iodotyrosine, and N^{α}-(1-deoxy-D-fructosyl)-N^{ϵ}-(3-iodobenzoyl)-lysine. For this, a C-18 analytical column was eluted at 1 mL/min with a gradient consisting of solvents A, 0.1% TFA in water, and B, 0.1% TFA in acetonitrile. The percent B was held at 10 for 10 min and then increased to 90 over 30 min. Under these conditions, the retention times of I-Gluc-TOCA, GIBLO, 3-iodotyrosine, and N^{α}-(1-deoxy-D-fructosyl)-N^{ϵ}-(3-iodobenzoyl)-lysine were 25−26 min, 29−30 min, 18−19 min, and 25−26 min, respectively.

In Vivo. Two groups of three mice bearing the D-341 Med xenografts were injected with 10 μCi of each tracer. Necropsies were performed 0.5 and 1 h postinjection, and blood, urine, liver, kidney, and tumor were obtained. Serum was isolated from blood by centrifugation and urine was filtered through a Spin-X filter (Corning, New York, NY). Tissues were homogenized in 2 mL of 80:20 EtOH:HEPES (1.0 M, pH 7.0) with a hand-held homogenizer. The homogenates were centrifuged, and the pellets were extracted once more with one volume of the solvent.

Scheme 2. Synthesis of Gluc-Lys^0-Lys^5(Dde)-TOCA[a]

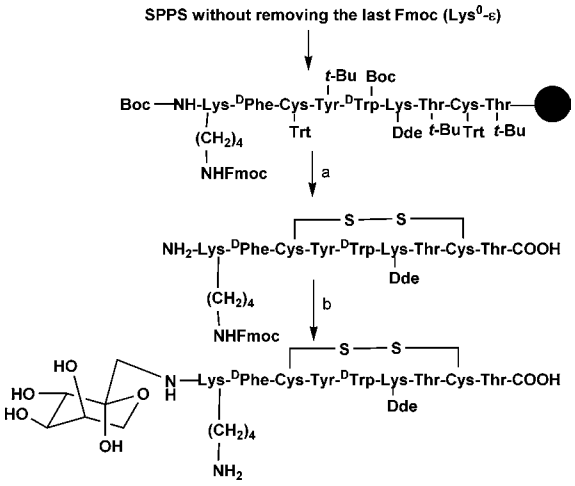

[a] Reagents and conditions: (a) i. 95:2.5:2.5 TFA:water:triisopropylsilane, ii. H_2O_2, THF, 0.05 M NH_4OAc; (b) i. D-glucose, HOAc/MeOH. ii. piperidine.

Aliquots of the combined supernatants were analyzed by HPLC as described above.

RESULTS AND DISCUSSION

The goal of this study was to synthesize an octreotate−glucose conjugate that also possessed a pendant group on which radioiodine or ^{211}At could be introduced in a stable fashion via a halodestannylation reaction in a single radiochemical step. To accomplish this, it was necessary to append an extra lysine at the N-terminus of octreotate. Because a tyrosine residue might compete with the tin precursor as a radioiodination site, octreotate was chosen as the peptide instead of TOCA. Unfortunately, a disadvantage of this approach is that the higher lipophilicity of octreotate compared with TOCA has been shown to yield less favorable pharmacokinetics (*21*, *22*).

Solid-phase peptide synthesis without the removal of the Fmoc group in the last step and subsequent cleavage from the resin delivered the N^{ϵ}-Fmoc-Lys^0-N^{ϵ}-Dde-Lys^5-octreotate (Scheme 1). A fructose unit was appended to the α amino group of Lys^0 of this peptide via a Maillard reaction with glucose and subsequent Amadori rearrangement (*23*). The Fmoc group on the ϵ-amino group of Lys^0 was removed, and the resultant peptide was treated with either *N*-succinimidyl 3-iodobenzoate (SIB) or *N*-succinimidyl 3-(tri-*n*-butylstannyl)benzoate (STB). Removal of the Dde group from the ϵ-amino group of Lys^5 of these peptides delivered the iodo standard of the target peptide (GIBLO; Chart 1) and its tin precursor, respectively. To investigate the effect of an extra lysine (Lys^0), Gluc-Lys^0-Lys^5(Dde)-TOCA was also synthesized (Scheme 2). The peptide was assembled on the resin as for the GIBLO synthesis except a Tyr^3 instead of a Phe^3 was used. The target peptide was obtained by glycosylation and subsequent removal of the Fmoc group (*15*, *16*).

Radioiodination of the tin precursor with *N*-chlorosuccinimide as the oxidant and acetic acid as the solvent gave [^{131}I]GIBLO in about 21.2 ± 4.9% radiochemical yield (n = 10) (Scheme 3). The radiochemical yield of [^{211}At]GABLO was 46.8 ± 9.5% (n = 5); the difference between radioiodination and astatination yields is statistically significant. These results are enigmatic as astatination of the same tin precursor generally gives somewhat lower yields than radioiodination, presumably due to steric hindrance caused by the larger atomic size of astatine. It should be noted, however, that a radioactive peak of similar size as the product but with slightly higher retention time was seen in the HPLC trace of the radioiodination reaction mixture; the

Scheme 3. Synthesis of [*I]GIBLO and [^{211}At]GABLO

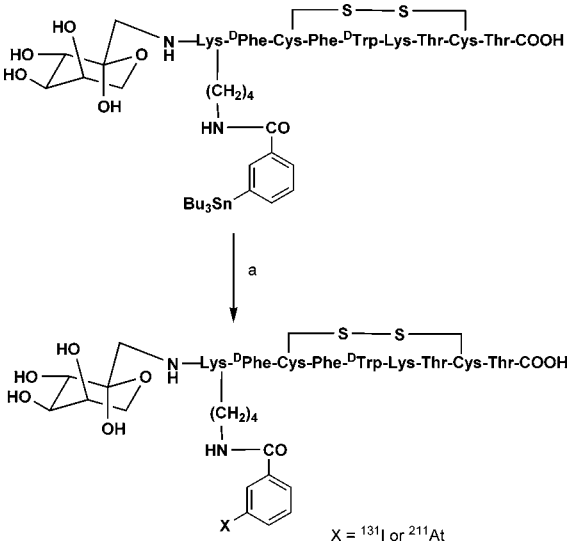

[a] Reagents and conditions: (a) ^{131}I or ^{211}At, NCS, HOAc.

Scheme 4. Radioiodination of Gluc-Lys^0-TOCA

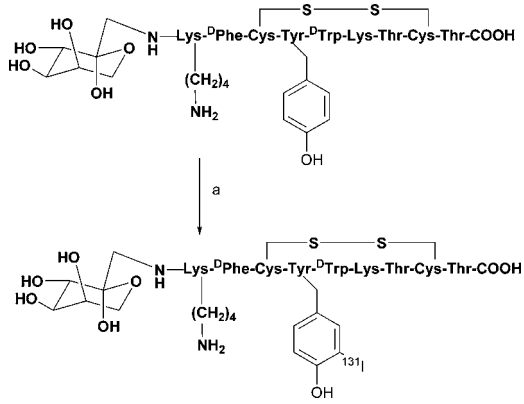

[a] Reagents and conditions: (a) ^{131}I, Chloramine-T, phosphate buffer.

intensity of this peak was considerably lower in the case of astatination. The radiochemical purity of the labeled peptides was >90% with no detectable coeluting UV peaks present.

[^{131}I]I-Gluc-Lys^0-TOCA also was synthesized to investigate the effect of an extra lysine at the N-terminus on peptide behavior. Although it should be possible to remove the Dde protecting group from Gluc-Lys^0-Lys^5(Dde)-TOCA and generate [^{131}I]I-Gluc-Lys^0-TOCA from the resultant peptide in a single radiochemical step, we opted to first label Gluc-Lys^0-Lys^5(Dde)-TOCA and then remove the Dde group (Scheme 4) simply because of the limited availability of Gluc-Lys^0-Lys^5(Dde)-TOCA. Only a few reactions could be attempted, and [^{131}I]I-Gluc-Lys^0-TOCA was obtained after two steps in 25% radiochemical yield and >95% radiochemical purity.

The affinity of GIBLO was measured indirectly by a competitive binding assay using AR42J rat pancreatic tumor membranes. The "gold standard" approach in the literature used to determine the binding affinity of octreotide derivatives to SSTR involves the use of $SSTR_2$-expressing AR42J membranes. The ability of GIBLO to displace [^{125}I]TOC bound to AR42J membranes was determined. For comparison, the ability of octreotide to displace this tracer was also measured in a parallel assay. As shown in Figure 1, both GIBLO and octreotide displaced AR42J membrane-bound [^{125}I]TOC in a concentration-dependent manner. The calculated IC_{50} values for GIBLO and octreotide were 0.46 ± 0.05 nM and 0.99 ± 0.13 nM, respectively, indicating that the novel peptide bound with high affinity to SSTR. An IC_{50} of 2.8 ± 0.4 nM was reported for

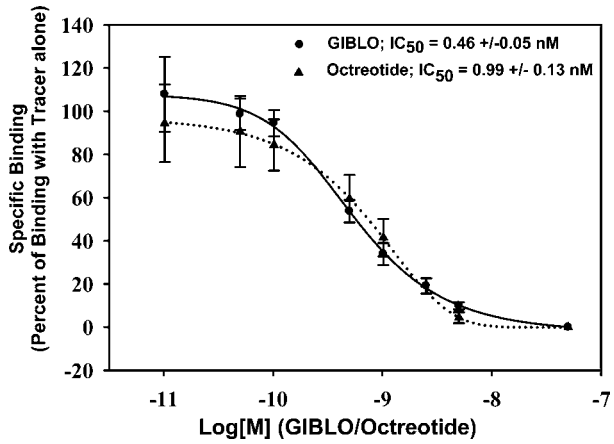

Figure 1. Competitive displacement of [^{125}I]TOC from sst_2-expressing AR42J rat pancreatic cell membranes by GIBLO (circles) and by octreotide (triangles). AR42J membranes were incubated with [^{125}I]-TOC and none or increasing concentrations of either octreotide or GIBLO. Specific binding, determined by subtracting the value at 50 nM concentration of the ligand from total binding, was plotted as a function of logarithm of ligand concentration.

Gluc-Lys^0-fluoropropionyl-TOCA, another peptide with a Lys^0 modification, to membranes from CHO cells transfected to express $SSTR_2$ (*15*, *16*). The IC_{50} values reported for other octreotide derivatives in displacing labeled analogues bound to AR42J rat pancreatic tumor membranes have been in the low nanomolar and sub-nanomolar range (see for example ref 21). Taken together, our results suggest that conjugation of an N-terminal sugar and a pendant prosthetic group for radiohalogenation to octreotate can be accomplished without compromising $SSTR_2$ binding affinity. Receptor binding affinity assay with D341 membranes was not performed, as we were not successful in the past in obtaining reproducible results using these membranes with other octreotate derivatives.

Because of our clinical interest in utilizing radiolabeled octreotide conjugates for the targeted radiotherapy of medulloblastoma, the internalization assays and the biodistribution study were performed with the D341 Med human medulloblastoma line. Previously we reported that, of the four radioiodinated octreotide analogues investigated, [^{125}I]I-Gluc-TOCA has the highest level of intracellularly trapped radioactivity, reaching 10−15% of added radioactivity after a 4 h incubation with D341 Med cells (*7*, *12*). Therefore, this peptide was selected as a positive control to evaluate the internalization of the carbohydrated peptides [^{131}I]GIBLO and [^{211}At]GABLO. As shown in Figure 2A, consistent with earlier results, about 10% of the input dose of [^{125}I]I-Gluc-TOCA was internalized at 4 h. Disappointingly however, the specific internalized radioactivity for [^{131}I]-GIBLO was considerably lower, <2% at 4 h. This degree of internalized counts is similar to that observed previously on this cell line for [^{125}I]TOC, the peptide lacking the N-terminal and C-terminal structural modifications previously shown to significantly increase internalization (*7*). The results presented in Figure 2B demonstrate that [^{211}At]GABLO behaved in fashion similar to [^{131}I]GIBLO, suggesting that substitution of ^{211}At for ^{131}I in this peptide had no significant effect on its uptake and internalization by D341 Med cells.

The subpar internalization of these novel labeled octreotate analogues could be due to multiple factors. The above results are not unprecedented; retention of SSTR affinity but with a substantial decrease in internalization has been observed for ^{99m}Tc-labeled TOCA derivatives with bulky lipophilic chelating groups on the Lys^0 side chain (Schottelius and Wester, unpublished results). Furthermore, while there are instances where the internalization is proportional to SSTR affinity (*24*), octreotide derivatives of similar affinities have demonstrated

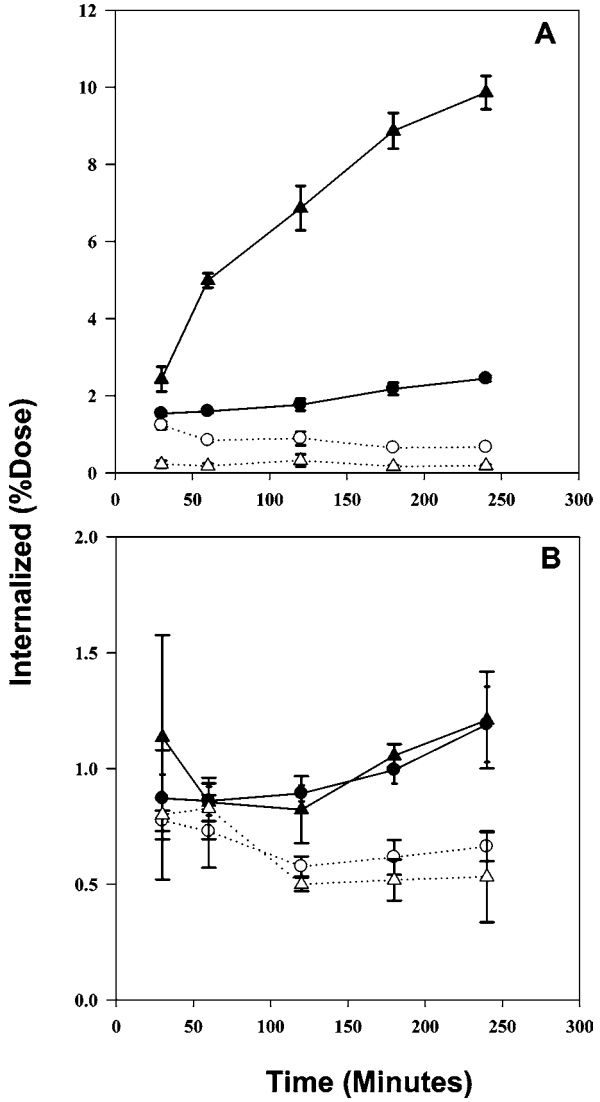

Figure 2. Time-dependent internalization of [^{125}I]I-Gluc-TOCA (triangle) and [^{131}I]GIBLO (circle) (A; upper panel) and of [^{131}I]GIBLO (circle) and [^{211}At]GABLO (triangle) (B; lower panel) by sst_2-expressing D341 human medulloblastoma cells in the presence (open symbols) and absence (closed symbols) of 1 μM octreotide. Percentage of radioactivity in the incubation medium that was trapped in the intracellular compartment as a function of time is shown.

different internalization efficiencies (*3*, *15*, *25*, *26*). The presence of bulky aromatic prosthetic groups may negatively influence the uptake and retention of these radiolabeled peptides in tumor cells (*15*). Net charge, geometry, and metabolism all also can play a role (*15*). In rats, ^{111}In-DTPA-octreotide is known to undergo metabolism with the cleavage of radiolabel-carrying N-terminus amino acids (*27*, *28*). If that were to happen with GIBLO and GABLO, the internalization results probably can be rationalized. A possible contributing factor is the higher lipophilicity of GIBLO compared to I-Gluc-TOCA not only because of the iodobenzoyl prosthetic group but also because of the presence of a Phe instead of Tyr at position 3 of the peptide backbone. The higher nonspecific binding of GIBLO seen in Figure 2A is consistent with this difference.

Another possibility is that the poor retention of radioiodine in the intracellular compartment was in some way related to the additional lysine residue added to the N-terminus of octreotate. To investigate this, we synthesized [^{131}I]I-GIu-Lys^0-TOCA and compared its internalization properties on D341 Med cells to that of [^{125}I]I-Gluc-TOCA, both labeled on their Tyr^3 residues. The absolute magnitude of internalization of [^{125}I]I-Gluc-TOCA was lower than that observed in the previous experiment (Figure 2A), perhaps due to some unknown difference in cell characteristics; however, this should not interfere with a direct comparison of two peptides in a paired-label format assay. As shown in Figure 3, receptor-mediated intracellular activity for [^{131}I]I-Gluc-Lys^0-TOCA was significantly lower than that of [^{125}I]I-Gluc-TOCA at all time points with the difference reaching about 3-fold at 4 h (Figure 3). In comparison, the receptor mediated intracellular activity for [^{131}I]GIBLO was about 4 times lower than that of coincubated [^{125}I]I-Gluc-TOCA at 4 h. It should be noted that a somewhat similar peptide, N^{α}-Gluc-N^{ϵ}-[^{18}F]fluoropropyl-lys^0-TOCA, has been synthesized but no internalization data were presented (*15*). However, specific targeting of an SSTR-expressing xenograft and delineation of tumor with high contrast in a carcinoid patient was possible with this ^{18}F-labeled peptide (*16*).

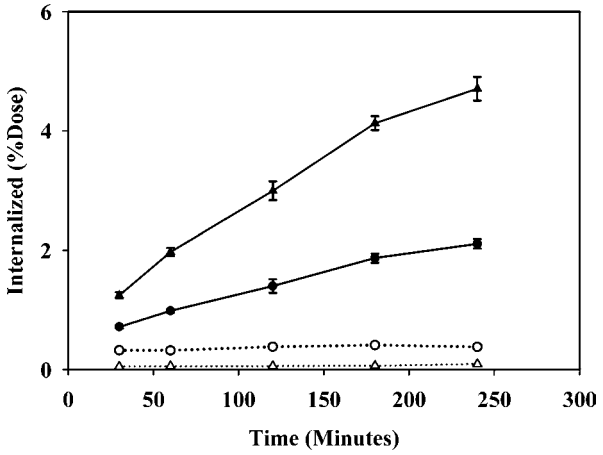

Figure 3. Time-dependent internalization of [^{125}I]I-Gluc-TOCA (triangle) and [^{131}I]I-GIu-Lys^0-TOCA (circle) by sst_2-expressing D341 human medulloblastoma cells in the presence (open symbols) and absence (closed symbols) of 1 μM octreotide. Percentage of radioactivity in the incubation medium that was trapped in the intracellular compartment as a function of time is shown.

We speculate that the amide bond between Lys^0 and D-Phe^1 may be susceptible to cleavage. In the case of [^{131}I]I-Gluc-Lys^0-TOCA, this would yield [^{131}I]I-TOCA, which, consistent with the current study, was shown to exhibit about 2.5 times lower internalized counts than [^{131}I]I-Gluc-TOCA (*7*). However, some additional feature must play a role in the case of GILBO, perhaps its lipophilicity or the size/geometry of the Lys^0-iodobenzoyl moiety. Appending a haloaryl moiety cannot be the sole cause because the internalization of *N*-(4-guanidinomethyl-3-iodobenzoyl)-Phe^1-octreotate (GMIBO) by D341 Med cells was 20−40% higher than that of [^{131}I]I-Gluc-TOCA (*12*). However, in this case, the prosthetic group was positively charged and was present on Phe^1 rather than Lys^0.

From the catabolism studies, for both peptides, the radioactivity HPLC profile of cell lysates, cell culture supernatants, and of surface-bound fractions at both time points was similar with the peak corresponding to intact peptide being the predominant species. For example, HPLC chromatograms of the cell lysate and cell culture supernatant obtained after the 4 h incubation period are shown in Figure 4A and 4B. No peak corresponding to [^{125}I]MIT (t_R = ~18 min) was seen. There was no evidence for the generation of N^{α}-(1-deoxy-D-fructosyl)-N^{ϵ}-(3-[^{131}I]iodobenzoyl)-lysine (t_R = 24−25 min), which would be the expected catabolite resulting from the cleavage of Lys^0 with its substituents from [^{131}I]GIBLO. This suggests that either cleavage of the peptide at Lys^0-Phe^1 did not occur, or was rapidly followed by further catabolism to unidentified labeled fragments. N^{ϵ}-(3-iodobenzoyl)-lysine (*17*), another potential catabolite, was also

Table 1. Paired-Label Tissue Distribution of [^{131}I]GIBLO and [^{125}I]I-Gluc-TOCA in Athymic Mice Bearing D341 Med Xenografts

	percent ID/g (mean ± SD; $n = 5$)					
	0.5 h		4 h		16 h	
tissue	[^{131}I]GIBLO	[^{125}I]I-Gluc-TOCA	[^{131}I]GIBLO	[^{125}I]I-Gluc-TOCA	[^{131}I]GIBLO	[^{125}I]I-Gluc-TOCA
liver	6.76 ± 0.74	2.37 ± 0.23	0.79 ± 0.20	0.55 ± 0.11	0.20 ± 0.02	0.20 ± 0.03[b]
spleen	1.22 ± 0.14	3.54 ± 1.03	0.37 ± 0.07	1.22 ± 0.21	0.20 ± 0.03	0.35 ± 0.11
lungs	3.85 ±0.45	14.13 ± 1.59	1.00 ± 0.27	3.25 ± 1.38	0.29 ± 0.05	0.61 ± 0.14
heart	1.07 ± 0.09	0.80 ± 0.07	0.18 ± 0.04	0.31 ± 0.08	0.06 ± 0.01	0.07 ± 0.01
kidneys	8.36 ± 0.60	4.70 ± 0.52	2.74 ± 0.62	0.77 ± 0.27	0.80 ± 0.10	0.15 ± 0.02
stomach	4.40 ± 1.56	17.56 ± 3.32	1.32 ± 0.39	5.84 ± 1.70	0.36 ± 0.28	0.84 ± 0.46
thyroid[a]	0.14 ± 0.02	0.10 ± 0.02	0.12 ± 0.04	0.34 ± 0.10	0.30 ± 0.06	1.26 ± 0.24
muscle	0.33 ± 0.11	0.27 ± 0.05[b]	0.08 ± 0.04	0.14 ± 0.06	0.02 ± 0.00	0.01 ± 0.00
sm. intestine	57.25 ± 3.10	17.06 ± 1.83	1.61 ± 0.61	2.65 ± 0.78	0.15 ± 0.04	0.29 ± 0.05
lg. intestine	0.76 ± 0.80	3.16 ± 0.76	32.19 ± 10.28	13.9 ± 3.35	0.89 ± 0.40	1.29 ± 0.28
blood	2.81 ± 0.41	1.06 ± 0.14	0.39 ± 0.08	0.32 ± 0.11[b]	0.10 ± 0.01	0.04 ± 0.01
tumor	6.91 ± 1.23	21.53 ± 4.01	0.81 ± 0.53	0.85 ± 0.42[b]	1.65 ± 0.97	1.17 ± 0.78[b]

[a] Percent ID/organ. [b] Difference between the two values were not statistically significant ($p > 0.05$).

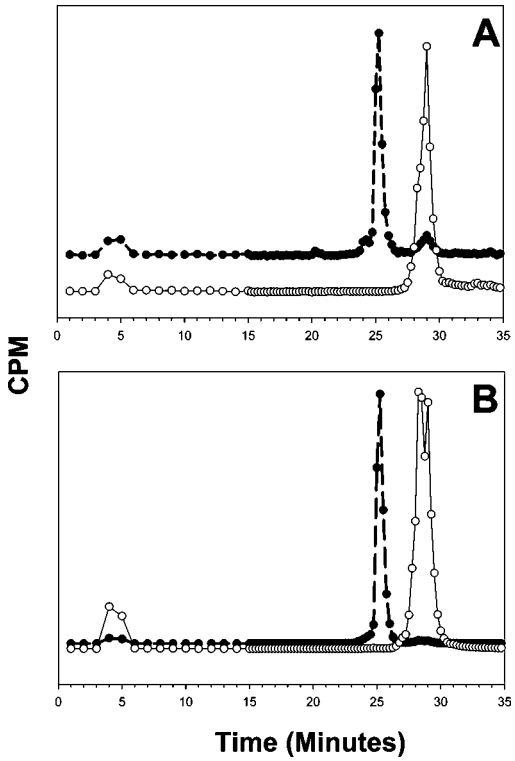

Figure 4. Paired-label in vitro catabolism: HPLC profiles of cell extracts (internalized) (A) and cell culture supernatants (B) at 4 h. A paired-label internalization assay was performed by incubating D341 Med cells with 10 μCi each of [^{125}I]Gluc-TOCA (filled circle) and [^{131}I]-GIBLO (open circle). Cell lysates (internalized), cell culture supernatants, and surface-bound fractions at 30 min and 4 h were analyzed by reversed-phase HPLC. Data shown are for cell lysates and cell culture supernatants at 4 h.

not present as this elutes at 21−22 min under the HPLC conditions used for the catabolism experiments.

We next evaluated the biodistribution of [^{131}I]GIBLO in comparison with [^{125}I]I-Gluc-TOCA in a paired-label format in athymic mice bearing subcutaneous D341 Med xenografts; data for selected time points are shown in Table 1. The tumor localization of [^{125}I]I-Gluc-TOCA was 2- to 3-fold higher than that of [^{131}I]GIBLO at early time points. For example, the tumor uptake of [^{125}I]I-Gluc-TOCA at 0.5 and 1 h was 21.5 ± 4.0% ID/g and 18.8 ± 7.7% ID/g compared to 6.9 ± 1.2% ID/g and 4.7 ± 1.4% ID/g, respectively for [^{131}I]GIBLO. The differences in uptake between the two tracers were statistically significant ($p < 0.05$). The tumor uptake of [^{125}I]I-Gluc-TOCA at these time points was consistent with that seen earlier in this xenograft model (*7*). Tumor levels of radioiodine for [^{131}I]GIBLO were higher than those for [^{125}I]I-Gluc-TOCA at 16 and 24 h; however, the difference was statistically significant only at 24 h (0.90 ± 0.20% ID/g versus 0.40 ± 0.07% ID/g).

Normal tissue radioiodine levels observed after administration of [^{131}I]GIBLO and [^{125}I]I-Gluc-TOCA are summarized in Table 1. As expected, the strategy of avoiding radioiodination of Tyr^3 resulted in significantly lower levels of radioiodine in the thyroid, consistent with a lower degree of deiodination. For example, 16 h after injection, the % injected dose in the thyroid for [^{131}I]GIBLO was more than 4 times lower than that for [^{125}I]I-Gluc-TOCA. The lower tumor uptake of [^{131}I]GIBLO at early time points might be due to its concomitantly higher uptake in liver, kidney and particularly, small intestine (Table 1). In contrast, uptake of [^{125}I]I-Gluc-TOCA was consistently higher in lungs and stomach, which are some of the tissues known to express somatostatin receptors (*7*). Alternatively, because of the proclivity of free iodide for the stomach, the higher accumulation of [^{125}I]I-Gluc-TOCA in this organ could reflect the greater degree of dehalogenation of this peptide.

HPLC analyses of tumor, kidney, liver, blood, and urine samples obtained 30 and 60 min after [^{125}I]I-Gluc-TOCA and [^{131}I]GIBLO injection were performed to determine the nature of the labeled species present in these tissues. In blood and urine, the majority of the radioactivity present at 30 and 60 min for both peptides eluted with a retention time corresponding to the intact peptide. In blood, 15 and 38% of the total ^{125}I activity eluted in the solvent front peak at 30 and 60 min, respectively; for ^{131}I, these values were 9 and 13%. In urine, about 3% of total ^{125}I activity was in the solvent front peak at both time points and for ^{131}I, 19% and 6% of total activity was in this peak at 30 and 60 min, respectively. In kidney and liver, very low levels of intact [^{125}I]I-Gluc-TOCA were seen at both time points; most of the radioactivity eluted at the solvent front. The HPLC profiles for [^{131}I]GIBLO catabolites indicated a distribution of ^{131}I in ratios of 3:1 and 2:1 for kidney and liver, respectively, between solvent front peak and intact peak. It is possible that the solvent front peak may reflect free iodide, and this is consistent with the fact that it accounts for a smaller fraction of the eluted activity for [^{131}I]GIBLO compared with [^{125}I]I-Gluc-TOCA. On the other hand, the radioactivity present in tumor for both peptides was predominantly in the solvent front peak (Figure 5) (~65−70% at both time points). Consistent with the results obtained in vitro with D341 Med medulloblastoma cells, peaks corresponding to [^{125}I]MIT and N^{α}-(1-deoxy-D-fructosyl)-N^{ϵ}-(3-[^{131}I]iodobenzoyl)-lysine were not seen in the HPLC profiles of any of the in vivo samples. Unfortunately, these catabolism results fail to offer a cogent explanation for the inferior tumor targeting properties of [^{131}I]GIBLO. Phe for Tyr substitution, addition of Lys^0, and the presence of bulky aromatic prosthetic group could have had a combined effect in

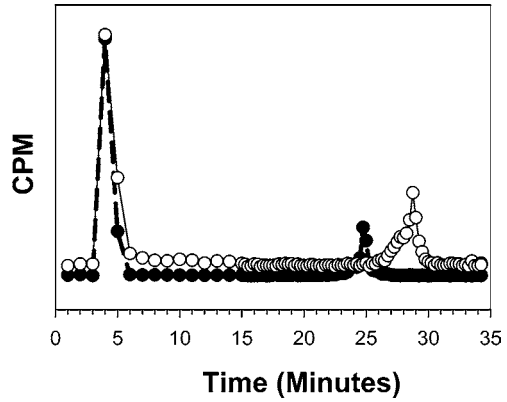

Figure 5. Paired-label in vivo catabolism: HPLC profile of tumor extracts in vivo at 60 min. Mice were injected with 10 μCi each of [^{125}I]Gluc-TOCA (filled circle) and [^{131}I]GIBLO (open circle). Necropsies were performed at 30 and 60 min postinjection. Tumor (and other tissues) was isolated and homogenized. The supernatant, after removal of cell debris, was analyzed by reversed-phase HPLC.

decreasing the extent of internalization and consequent decrease in tumor uptake.

In conclusion, we have developed methods for synthesizing octreotate derivatives with two prosthetic groups, one containing a carbohydrate unit and the other, a tin group-containing aryl moiety suitable for radiohalogenation. The new peptide conjugate, GIBLO, maintained high affinity for SSTR and exhibited lower levels of deiodination than I-Gluc-TOCA. Its internalization properties in vitro and tumor targeting in vivo, while inferior to that of I-Gluc-TOCA, were similar to those of I-TOC. Although the factors responsible for the less than ideal internalization and tumor targeting of GIBLO are not known at this time, it is clear that alternate approaches for maximizing the intracellular trapping of radiohalogen and concomitant improvement in pharmacokinetics are needed. Toward that goal, we are currently working on next-generation octreotate analogues that include hydrophilic, charged aryl tin precursors that can be labeled with either radioiodine nuclides or ^{211}At.

ACKNOWLEDGMENT

The authors want to thank Philip C. Welsh, Holly Legrand, and Kevin Alston for their excellent technical assistance. The work was supported by Grants CA91927, CA78417, CA42324, and CA93371 from the National Institutes of Health, as well as by a grant from the Pediatric Brain Tumor Foundation.

LITERATURE CITED

(1) Kwekkeboom, D. J., Mueller-Brand, J., Paganelli, G., Anthony, L. B., Pauwels, S., Kvols, L. K., O'Dorisio, T. M., Valkema, R., Bodei, L., Chinol, M., Maecke, H. R., and Krenning, E. P. (2005) Overview of results of peptide receptor radionuclide therapy with 3 radiolabeled somatostatin analogues. *J. Nucl. Med. 46 Suppl. 1,* 62S−66S.

(2) Schottelius, M., Rau, F., Reubi, J. C., Schwaiger, M., and Wester, H. J. (2005) Modulation of pharmacokinetics of radioiodinated sugar-conjugated somatostatin analogues by variation of peptide net charge and carbohydration chemistry. *Bioconjugate Chem. 16*, 429−437.

(3) Schottelius, M., Reubi, J. C., Eltschinger, V., Schwaiger, M., and Wester, H. J. (2005) N-terminal sugar conjugation and C-terminal Thr-for-Thr(ol) exchange in radioiodinated Tyr^3-octreotide: effect on cellular ligand trafficking in vitro and tumor accumulation in vivo. *J. Med. Chem. 48*, 2778−2789.

(4) Reubi, J. C. (1985) New specific radioligand for one subpopulation of brain somatostatin receptors. *Life Sci. 36*, 1829−1836.

(5) Wester, H. J., Schottelius, M., Scheidhauer, K., Reubi, J. C., Wolf, I., and Schwaiger, M. (2002) Comparison of radioiodinated TOC, TOCA and Mtr-TOCA: the effect of carbohydration on the pharmacokinetics. *Eur. J. Nucl. Med. Mol. Imaging 29*, 28−38.

(6) Schottelius, M., Wester, H. J., Reubi, J. C., Senekowitsch-Schmidtke, R., and Schwaiger, M. (2002) Improvement of pharmacokinetics of radioiodinated Tyr(3)-octreotide by conjugation with carbohydrates. *Bioconjugate Chem. 13*, 1021−1030.

(7) Vaidyanathan, G., Friedman, H. S., Affleck, D. J., Schottelius, M., Wester, H. J., and Zalutsky, M. R. (2003) Specific and high-level targeting of radiolabeled octreotide analogues to human medulloblastoma xenografts. *Clin. Cancer Res. 9*, 1868−1876.

(8) Zalutsky, M. R., and Vaidyanathan, G. (2000) Astatine-211-labeled radiotherapeutics: an emerging approach to targeted alpha-particle radiotherapy. *Curr. Pharm. Des. 6*, 1433−1455.

(9) Aaij, C., Tschroots, W., Lindner, L., and Feltkamp, T. E. (1975) The preparation of astatine labelled proteins. *Int. J. Appl. Radiat. Isot. 26*, 25−30.

(10) Vaughan, A. T., and Fremlin, J. H. (1978) The preparation of astatine labeled proteins using an electrophilic reaction. *Int. J. Nucl. Med. Biol. 5*, 229−230.

(11) Vaidyanathan, G., Affleck, D., Welsh, P., Srinivasan, A., Schmidt, M., and Zalutsky, M. R. (2000) Radioiodination and astatination of octreotide by conjugation labeling. *Nucl. Med. Biol. 27*, 329−337.

(12) Vaidyanathan, G., Boskovitz, A., Shankar, S., and Zalutsky, M. R. (2004) Radioiodine and ^{211}At-labeled guanidinomethyl halobenzoyl octreotate conjugates: potential peptide radiotherapeutics for somatostatin receptor-positive cancers. *Peptides 25*, 2087−2097.

(13) Larsen, R. H., Wieland, B. W., and Zalutsky, M. R. (1996) Evaluation of an internal cyclotron target for the production of ^{211}At via the ^{209}Bi (α,2n)^{211}At reaction. *Appl. Radiat. Isot. 47*, 135−143.

(14) Zalutsky, M. R., and Narula, A. S. (1987) A method for the radiohalogenation of proteins resulting in decreased thyroid uptake of radioiodine. *Int. J. Rad. Appl. Instrum. [A] 38*, 1051−1055.

(15) Schottelius, M., Poethko, T., Herz, M., Reubi, J. C., Kessler, H., Schwaiger, M., and Wester, H. J. (2004) First ^{18}F-labeled tracer suitable for routine clinical imaging of sst receptor-expressing tumors using positron emission tomography. *Clin. Cancer Res. 10*, 3593−3606.

(16) Wester, H. J., Schottelius, M., Scheidhauer, K., Meisetschlager, G., Herz, M., Rau, F. C., Reubi, J. C., and Schwaiger, M. (2003) PET imaging of somatostatin receptors: design, synthesis and preclinical evaluation of a novel ^{18}F-labeled, carbohydrated analogue of octreotide. *Eur. J. Nucl. Med. Mol. Imaging 30*, 117−122.

(17) Garg, P. K., Alston, K. L., and Zalutsky, M. R. (1995) Catabolism of radioiodinated murine monoclonal antibody F(ab′)$_2$ fragment labeled using N-succinimidyl 3-iodobenzoate and Iodogen methods. *Bioconjugate Chem. 6*, 493−501.

(18) De Jong, M., Bernard, B. F., De Bruin, E., Van Gameren, A., Bakker, W. H., Visser, T. J., Macke, H. R., and Krenning, E. P. (1998) Internalization of radiolabelled [DTPA^0]octreotide and [DOTA^0,Tyr^3]octreotide: peptides for somatostatin receptor-targeted scintigraphy and radionuclide therapy. *Nucl. Med. Commun. 19*, 283−288.

(19) Friedman, H. S., Burger, P. C., Bigner, S. H., Trojanowski, J. Q., Brodeur, G. M., He, X. M., Wikstrand, C. J., Kurtzberg, J., Berens, M. E., Halperin, E. C., and et al. (1988) Phenotypic and genotypic analysis of a human medulloblastoma cell line and transplantable xenograft (D341 Med) demonstrating amplification of c-myc. *Am. J. Pathol. 130*, 472−484.

(20) Froidevaux, S., Meier, M., Hausler, M., Macke, H., Beglinger, C., and Eberle, A. N. (1999) A microplate binding assay for the somatostatin type-2 receptor (SSTR2). *J. Recept. Signal Transduct. Res. 19*, 167−180.

(21) Lewis, J. S., Lewis, M. R., Srinivasan, A., Schmidt, M. A., Wang, J., and Anderson, C. J. (1999) Comparison of four ^{64}Cu-labeled somatostatin analogues in vitro and in a tumor-bearing rat model: evaluation of new derivatives for positron emission tomography imaging and targeted radiotherapy. *J. Med. Chem. 42*, 1341−1347.

(22) Lewis, J. S., Srinivasan, A., Schmidt, M. A., and Anderson, C. J. (1999) In vitro and in vivo evaluation of ^{64}Cu-TETA-Tyr^3-octreotate. A new somatostatin analogue with improved target tissue uptake. *Nucl. Med. Biol. 26*, 267−273.

(23) Albert, R., Marbach, P., Bauer, W., Briner, U., Fricker, G., Bruns, C., and Pless, J. (1993) SDZ CO 611: a highly potent glycated analog of somatostatin with improved oral activity. *Life Sci. 53*, 517−525.

(24) Ginj, M., Chen, J., Walter, M. A., Eltschinger, V., Reubi, J. C., and Maecke, H. R. (2005) Preclinical evaluation of new and highly potent analogues of octreotide for predictive imaging and targeted radiotherapy. *Clin. Cancer Res. 11*, 1136−1145.

(25) de Jong, M., Breeman, W. A., Bakker, W. H., Kooij, P. P., Bernard, B. F., Hofland, L. J., Visser, T. J., Srinivasan, A., Schmidt, M. A., Erion, J. L., Bugaj, J. E., Macke, H. R., and Krenning, E. P. (1998) Comparison of ^{111}In-labeled somatostatin analogues for tumor scintigraphy and radionuclide therapy. *Cancer Res. 58*, 437−441.

(26) Hofland, L. J., Breeman, W. A., Krenning, E. P., de Jong, M., Waaijers, M., van Koetsveld, P. M., Macke, H. R., and Lamberts, S. W. (1999) Internalization of [DOTA^{0,125}I-Tyr^{3}]octreotide by somatostatin receptor-positive cells in vitro and in vivo: implications for somatostatin receptor-targeted radio-guided surgery. *Proc. Assoc. Am. Physicians 111*, 63−69.

(27) Akizawa, H., Arano, Y., Uezono, T., Ono, M., Fujioka, Y., Uehara, T., Yokoyama, A., Akaji, K., Kiso, Y., Koizumi, M., and Saji, H. (1998) Renal metabolism of ^{111}In-DTPA-D-Phe^{1}-octreotide in vivo. *Bioconjugate Chem. 9*, 662−670.

(28) Bass, L. A., Lanahan, M. V., Duncan, J. R., Erion, J. L., Srinivasan, A., Schmidt, M. A., and Anderson, C. J. (1998) Identification of the soluble in vivo metabolites of indium-111-diethylenetriaminepentaacetic acid-D-Phe^{1}-octreotide. *Bioconjugate Chem. 9*, 192−200.

BC0502560

Use of the Sonogashira Coupling Reaction for the "Two-Step" Labeling of Phenylalanine Peptide Side Chains with Organometallic Compounds

Ulrich Hoffmanns and Nils Metzler-Nolte*

Institute of Pharmacy and Molecular Biotechnology, University of Heidelberg, Im Neuenheimer Feld 364, D-69120 Heidelberg, Germany. Received August 24, 2005; Revised Manuscript Received November 25, 2005

The Pd-catalyzed Sonogashira coupling of ferrocene alkyne derivatives as metal probes to iodophenylalanine containing peptides is described. 4-Iodophenylalanine was incorporated into dipeptides and the neuropeptide [Leu^5]-enkephalin (Enk) by solid phase peptide synthesis, thereby creating a functional group suitable for the Sonogashira coupling. The reaction with two different ferrocene alkynes resulted in the corresponding ferrocene-labeled derivatives, which were obtained in good yield and purity. All new compounds were comprehensively characterized, including elemental analysis, 1D and 2D NMR, EI-, FAB- or ESI-MS, IR and UV−vis spectroscopy, and electrochemistry of the ferrocene label. Unlike well-established conjugation methods for peptide side chains such as lysine and cystein, the phenyl group in Phe is not readily available for derivatization. This work presents a versatile procedure for the regioselective introduction of an organometallic label into biologically relevant peptides as exemplified for enkephalin.

INTRODUCTION

The search for mild and selective labeling of peptide side chains is an active field of research. In addition to the well-established methods using thiol (Cys), carboxylic acid (Asp and Glu), and amino (Lys) functional groups, the focus has shifted to other amino acids and their derivatives in recent years. One promising method for the formation of bioconjugates is the Sonogashira coupling (*1*, *2*). This Pd-catalyzed C−C cross coupling reaction uses alkynes and aromatic bromides, iodides, or triflates. It is compatible with many functional groups in biomolecules and can be performed under aerobic, aqueous conditions. It has been successfully applied to amino acids, peptides, and nucleic acid derivatives. In nucleic acid chemistry, iodouracil and bromoadenine are the preferred starting materials. Peptides were derivatized with compounds such as *p*-iodobenzoic acid or propargylamine to make them amendable to Sonogashira coupling reactions (*3*, *4*). The use of *p*-iodophenylalanine or *p*-ethynylphenylalanine as non-natural amino acids is an alternative starting point for this versatile derivatization method (*5*-*7*). In fact, *p*-ethynylphenylalanine, which is a potent inhibitor of tryptophan hydroxylase (*8*), is readily prepared from the *p*-iodoamino acid via Sonogashira coupling with silyl-protected ethyne (*9*).

Because it is a mild and chemically versatile derivatization method, the Sonogashira coupling seems particularly attractive for the introduction of organometallic compounds as labels. The area of bioorganometallic chemistry has recently attracted a lot of attention (*10*-*17*). Organometallic labels offer unique opportunities for detection of the conjugates, for instance by electrochemical methods (*18*−*20*), immunoassays (*21*−*23*), or infrared (*24*, *25*) or optical spectroscopy (*26*−*28*). The majority of compounds were prepared using ferrocene (dicyclopentadienyliron, Cp_2Fe) as the organometallic label. Ferrocene is chemically robust, and its chemistry is well explored, giving easy access to a variety of derivatives. In addition, its favorable electrochemical properties make it an ideal sensor in DNA detection devices (*15*, *18*, *19*, *29*) or electrochemical glucose sensor (*15*, *20*, *30*, *31*). Although a vast number of ferrocene derivatives of simple amino acids, proteins, sugars, and nucleic acids were prepared, there is a striking absence of ferrocene derivatives of small peptides (*15*). A few early attempts met with moderate success (*32*−*34*). The ferrocene peptides partly decomposed under the harsh conditions of the original Merrifield solid phase peptide synthesis (SPPS), in particular cleavage and side chain deprotection using concentrated HF. Some biological testing was performed, but the chemical characterization of those early ferrocene peptide conjugates is scarse (*33*, *35*, *36*). We have recently published the chemical synthesis of metallocene peptides and their cellular uptake and nuclear localization by fluorescence microscopy (*37*). Kraatz and co-workers published a series of papers on the use of ferrocenyl peptide derivatives in electrochemical sensors (*38*−*40*). Those compounds were invariably pepared by solution chemistry throughout. On the other hand, SPPS is the method of choice for the chemical synthesis of small to medium sized peptides. Obviously, much milder methods are required for a reliable labeling of peptides with ferrocene as an electrochemical marker.

In light of these early results, we set out to explore the use of Sonogashira coupling for the synthesis of ferrocene peptide derivatives. Phenylalanine was chosen as the site for derivatization, and we used Leu^5-enkephalin as the model peptide. Enkephalin (Enk, primary sequence H-Tyr-Gly-Gly-Phe-Xxx-OH) is a five amino acid neuropeptide which is a natural ligand for the opiate receptors (*41*−*43*). It is formed from proenkephalin and exists in two forms which differ in the C-terminal amino acid, namely [Met^5]-Enk (Xxx = Met) and [Leu^5]-Enk (Xxx = Leu) (*44*). The pentapeptides were detected in various human tissues but mainly in the brain and central nervous system. Upon binding to the opiate receptor, their function is primarily associated with pain sensation. [Leu^5]-Enk has been the most popular target peptide for the derivatization with organometallic markers. In those studies, the amino acid phenylalanine was replaced by the organometallic derivatives ferrocenylalanine (Fc-CH_2-$CH(NH_2)$-CO_2H) (*32*, *33*, *36*) or cymantrenylalanine ($((CO)_3MnC_5H_4$-CH_2-$CH(NH_2)$-CO_2H) (*45*). As noted above, the chemical synthesis of those peptides was not straightforward and partial decomposition was observed,

* Fax: (international) +49-6221-54 64 41. E-mail: nils.metzler-nolte@urz.uni-heidelberg.de.

10.1021/bc050259c CCC: $33.50 © 2006 American Chemical Society
Published on Web 12/23/2005

rendering the biological results questionable. We have recently reported two different organometallic Mo enkephalin derivatives (*46*, *47*). These compounds were obtained in high yield and purity using the Fmoc strategy and the HMBA linker, which can be cleaved with concentrated NH_3, thus replacing the harsh original Merrifield SPPS conditions.

In this paper, we describe the synthesis and full chemical characterization of several *p*-iodophenylalanine containing dipeptides and the preparation of *p*-iodophenylalanine enkephalin derivatives by SPPS. In addition, an enkephalin derivate with an *N*-terminal iodoarene is also described. All peptides were transformed into their ferrocene derivatives by Sonogashira coupling in solution under mild conditions using two different ferrocene alkynes.

EXPERIMENTAL PROCEDURES

All peptide synthesis reactions were carried out in ordinary glassware and solvents. Chemicals were obtained from Aldrich, Iris, or Novabiochem. DMF for peptide synthesis was obtained from Roth. Enantiomerically pure L-amino acids were used. The dipeptides Boc-Aa1-Aa2-OMe[1] were prepared according to standard peptide chemistry techniques from Boc-Aa1-OH and H-Aa2-OMe·HCl, employing isobutyl chloroformiate as the coupling reagent (*48*). The compounds *p*-iodophenylalanine (**1**) (*49*) and [Fe(Cp)(C_5H_4-CONH-CEt_2-CC-H)] (*4*) (**7**, H-DEPA-CO−Fc, Cp = η-C_5H_5) were synthesized according to the literature.

Elemental analyses were performed on a Foss Heraeus Vario EL Elementar Analysator in C,H,N mode. Infrared spectra were recorded on a Brucker Equinox55 FT-IR as KBr disks and/or in CH_2Cl_2 solution between NaCl windows. Frequencies ν are given in cm^{-1}. UV−vis spectra were measured on a Varian CARY 100 instrument in 1 cm quartz Suprasil cells thermostated at 20 °C. Absorption maxima (λ_{max}) and molar absorption coefficients (ϵ_{max}) are given in nm and M^{-1} cm^{-1}, respectively. Mass spectra were recorded on a Finnigan MAT 8200 instrument (EI, 70 eV) or on a Finnigan TSQ 700 mass spectrometer (ESI; solvent and detection mode are given in parentheses). Only characteristic fragments with possible composition are given in brackets. For fragments containing metals only the isotopomer with highest intensity was described. Cyclic voltammograms (CV) and square wave voltammograms (SWV) were recorded in CH_2Cl_2, with NBu_4PF_6 as supporting electrolyte, by using a Princeton Applied Research BES Potentiostat/Galvanostat. A three-electrode cell was employed with a glassy-carbon working electrode, a platinum wire auxiliary electrode, and a $Ag/AgNO_3$ reference electrode (0.01 M $AgNO_3$ in MeCN). For determination of the redox potentials, ferrocene was added as an internal standard. ^1H and ^{13}C NMR spectra were recorded on a Bruker AM 360 spectrometer (^1H at 360.14 MHz, ^{13}C at 90.56 MHz) and a Bruker AM 300 (^1H at 300.16 MHz, ^{13}C at 75.47 MHz). ^1H and ^{13}C NMR spectra were referenced to TMS, using the ^{13}C or residual proton signals of the deuterated solvents as internal standards ($CDCl_3 \equiv 7.24$ (^1H) and 77.0 (^{13}C); DMSO $\equiv 2.49$ (^1H) and 39.5 (^{13}C)). High performance liquid chromatography (HPLC) was performed on a customized Varian ProStar system on reverse-phase Dynamax Microsorb 60-8 C_{18} columns (analytical: C18 microsorb 60 Å, diameter 4.5 mm, 250 mm; preparative: C18 microsorb 60 Å, diameter 21.4 mm, 250 mm) with water and acetonitrile, both containing 0.1% TFA, as eluents using the linear gradient 5 to 95% acetonitrile for 35 min.

Preparation of 4-Iodophenylalanine Methyl Ester Hydrochloride 2. Thionyl chloride (100 mmol, 11.90 g) was added dropwise to 100 mL of CH_3OH cooled with an ice-bath followed by the addition of 40 mmol of 4-iodophenylalanin (**1**) (11.64 g). After stirring for 12 h, the solvent was removed at 40 °C under reduced pressure to obtain the crude product. The slightly green solid was dissolved in as little CH_3OH as possible, and the solution was poured into 350 mL of diethyl ether to precipitate a white solid. After filtration and washing with an additional aliquot of 200 mL of diethyl ether, the pure product was dried in vacuo. Yield: 10.63 g (78.0%). Anal. Calc for $C_{10}H_{13}ClINO_2$ (340.96 g/mol): C, 35.16; H, 3.48; N, 4.10. Found: C, 34.52; H, 3.89; N, 4.00. IR (KBr): ν 2838 (vs, br, ν_{CH}), 1738 (vs, ν_{COO}), 1245 (s, ν_{C-O}), 835 (m, δ_{CH}). MS (FAB, pos): *m*/*z* 306 [$M^+ - Cl$], 289 [$M^+ - Cl - CH_3$]. ^1H NMR (D_2O, 360 MHz): δ 7.80 (d, 2H, $J = 8.0$, H_{Ar}), 7.08 (d, 2H, $J = 8.0$, H_{Ar}), 4.43 (t, 1H, $J = 6.7$, $C_\alpha H$), 3.38 (s, 3H, CH_3), 3.26 (m, 2H, $C_{\beta,Phe}H$). ^{13}C NMR (D_2O, 90 MHz): δ 170.8 (COO), 139.2, 132.3 (C_{Ar}), 134.5 ($C_{Ar,q}$), 94.0 (C_{Ar-I}), 54.8 (C_α), 54.5 (CH_3), 36.2 (C_β)

Preparation of 4-Iodophenylalanine Dipeptides 3−6. To a stirred solution of 10 mmol of the Boc-protected amino acid in THF was added *N*-methylmorpholine (1.12 mL, 1.02 g, 10 mmol) followed by the addition of isobutyl chloroformiate (1.32 mL, 1.36 g, 10 mmol), resulting in precipitation of a white solid. In a second flask, 4-iodo-L-phenylalanine-methylester hydrochloride (**2**) (3.41 g, 10 mmol) was suspended in 50 mL of THF containing triethylamine (1.38 mL, 1.02 g, 10 mmol). Both suspensions were mixed and stirred for 60 min at room temperature. After removal of the white precipitates by filtration, the solvent was removed under reduced pressure and the residual oil was dissolved in 100 mL of $CHCl_3$. The solution was washed with H_2O (50 mL), and the aqueous solution was extracted with three 50 mL aliquots of $CHCl_3$. The combined $CHCl_3$ solutions were dried over Na_2SO_4. Evaporation of the solvent under reduced pressure yielded the dipeptides **3**−**6** as a white solid. The products could be recrystallized from THF/heptane.

Analytical Data for **3**. Anal. Calc for $C_{18}H_{25}IN_2O_5$ (476.08 g/mol): C, 45.39; H, 5.29; N, 5.88. Found: C, 44.89; H, 5.26; N, 5.81. IR (KBr): ν 3336 (s, ν_{NH}), 2981 (m, ν_{CH}), 1743 (s, ν_{COO}), 1664 (vs, ν_{CON}), 1522 (s, δ_{NH}). MS (FAB, pos): *m*/*z* 477 $[M + 1]^+$, 463 [$M^+ - CH_3$], 421 [$M^+ - C_4H_9$], 377 [M^+ − Boc]. ^1H NMR (DMSO-d_6, 360 MHz): δ 8.13 (d, 1H, $J =$ 7.5, NH_{Phe}), 7.61 (d, 2H, $J = 7.9$, H_{Ar}), 7.03 (d, 2H, $J = 7.5$, H_{Ar}), 6.85 (d, 1H, $J = 7.2$, NH_{Boc}), 4.47 (m, 1H, $C_{\alpha,Phe}H$), 3.95 (m, 1H, $C_{\alpha,Ala}H$), 3.60 (s, 3H, CH_3), 2.92 (m, 2H, $C_\beta H$), 1.37 (s, 9H, $CH_{3,Boc}$), 1.11 (d, 3H, $J = 6.4$, $CH_{3,Ala}$). ^{13}C NMR (DMSO-d_6, 90 MHz): δ 172.7, 171.4 (COO, CON), 154.7 (CO_{Boc}), 136.8 ($C_{Ar,q}$), 136.8, 131.5 (C_{Ar}), 92.3 (C_{Ar-I}), 77.9 ($C_{Boc,q}$), 52.8 ($C_{\alpha,Ala}$), 51.7 (CH_3), 49.4 ($C_{\alpha,Phe}$), 35.9 (C_β), 28.0 ($CH_{3,Boc}$), 17.9 ($CH_{3,Ala}$). UV−vis: 232 (15 440). Yield: 3.68 g (77%).

Analytical Data for **4**. Anal. Calc for $C_{21}H_{31}IN_2O_5$ (518.13 g/mol): C, 48.66; H, 6.03; N, 5.40. Found: C, 48.33; H, 6.01; N, 5.37. IR (KBr): ν 3338 (s, ν_{NH}), 2955 (m, ν_{CH}), 1747 (m, ν_{COO}), 1658 (vs, ν_{CON}), 1521 (s, δ_{NH}). MS (FAB, pos): *m*/*z* 519 $[M + 1]^+$, 463 [$M^+ - C_4H_9$], 417 [M^+ − Boc]. ^1H NMR (DMSO-d_6, 360 MHz): δ 8.12 (d, 1H, $J = 7.8$, NH_{Phe}), 7.61 (d, 2H, $J = 8.1$, H_{Ar}), 7.04 (d, 2H, $J = 8.1$, H_{Ar}), 6.80 (d, 1H, $J = 8.4$, NH_{Boc}), 4.50 (dd, 1H, $C_\alpha H_{Phe}$), 3.94 (dd, 1H, $C_\alpha H_{Ala}$), 3.61 (s, 3H, CH_3), 2.95 (m, 2H, $C_{\beta,Phe}H$), 1.51 (sep, 1H, $J =$ 6.6, $CH(CH_3)$), 1.38 (s, 9H, $CH_{3,Boc}$), 1.30 (m, 2H, $C_{\beta,Leu}H$), 0.84 (pseudo-t, 6H, $CH_{3,Leu}$). ^{13}C NMR (DMSO-d_6, 90 MHz): δ 172.5, 171.6 (COO, CON), 155.1 (CO_{Boc}), 136.9 ($C_{Ar,q}$),

[1] Abbreviations: Aaa, any amino acid; Boc, *tert*-butoxycarbonyl; Cp, η-(C_5H_5); CV, cyclic voltammogram; H-DEPA, diethylpropargylamine; DIPEA, *N*,*N*-diisopropylethylamine; Enk, [Leu]^5-enkephalin; Fc, ferrocenyl- ($CpFeC_5H_4$-); Fmoc, 9-fluorenylmethoxycarbonyl; HOBt, 1-hydroxybenzotriazole; I-BA, *p*-iodobenzoic acid; SWV, square wave voltammogram; TBTU, *O*-(benzotriazol-1-yl)-*N*,*N*,*N*′,*N*′-tetramethyluronium tetrafluoroborate; TIS, triisopropylsilane; TFA, trifluoroacetic acid.

136.9, 131.6 (C_{Ar}), 92.3 (C_{Ar-I}), 78.1 ($C_{Boc,q}$), 52.8 ($C_{\alpha,Ala,Phe}$), 51.9 (CH_3), 40.0 ($C_{\beta,Leu}$), 36.1 ($C_{\beta,Phe}$), 28.2 ($CH_{3,Boc}$), 24.1, 22.8 ($CH_{3,Leu}$), 21.7 ($C(CH_3)_2$). UV−vis: 231 (15151). Yield: 4.26 g (82%).

Analytical Data for **5**. Anal. Calc for $C_{24}H_{29}IN_2O_5$ (552.11 g/mol): C, 52.18; H, 5.29; N, 5.07. Found: C, 51.59; H, 5.36; N, 5.07. IR (KBr): ν 3337 (s, ν_{NH}), 2980 (m, ν_{CH}), 1739 (s, ν_{COO}), 1662 (vs, ν_{CON}), 1521 (s, δ_{NH}). MS (FAB, pos): *m/z* 553 $[M + 1]^+$, 497 $[M^+ - C_4H_9]$, 453 $[M^+ - Boc]$. ^{1}H NMR (DMSO-d_6, 360 MHz): δ 8.33 (d, 1H, $J = 7.6$, NH_{Phe}), 7.62 (d, 2H, $J = 7.5$, H_{Ar}), 7.22 (m, 5H, H_{Ar}), 7.05 (d, 2H, $J = 7.5$, H_{Ar}), 6.87 (d, 1H, $J = 8.6$, NH_{Boc}), 4.50 (dd, 1H, $J = 7.1$, 13.2, $C_{\alpha,Phe-I}H$), 4.17 (dd, 1H, $J = 7.2$, 13.4, $C_{\alpha,Phe}H$), 3.60 (s, 3H, CH_3), 2.97 (m, 2H, $C_{\beta,Phe-I}H$), 2.74 (m, 2H, $C_{\beta,Phe}H$), 1.29 (s, 9H, $CH_{3,Boc}$). ^{13}C NMR (DMSO-d_6, 90 MHz): δ 171.7, 171.5 (COO, CON), 155.0 (CO_{Boc}), 137.9, 136.8 ($C_{Ar,q}$), 136.9, 131.5, 129.0, 127.9, 126.1 (C_{Ar}), 92.4 (C_{Ar-I}), 78.0 ($C_{Boc,q}$), 55.5 ($C_{\alpha,Phe}$), 53.1 ($C_{\alpha,Phe-I}$), 51.8 (CH_3), 37.3 ($C_{\beta,Phe}$), 36.1 ($C_{\beta,Phe-I}$), 28.0 ($CH_{3,Boc}$). UV−vis: 231 (14153). Yield: 3.90 g (71%).

Analytical Data for **6**. Anal. Calc for $C_{24}H_{29}IN_2O_6$ (568.11 g/mol): C, 50.71; H, 5.14; N, 4.93. Found: C, 50.43; H, 5.17; N, 4.88. IR (KBr): ν 3306 (s, ν_{NH}), 2978 (m, ν_{CH}), 1709 (s, ν_{COO}), 1661 (vs, ν_{CON}), 1522 (s, δ_{NH}). MS (FAB, pos): *m/z* 569 $[M + 1]^+$, 513 $[M^+ - C_4H_9]$, 469 $[M^+ - Boc]$. ^{1}H NMR (DMSO-d_6, 360 MHz): δ 9.14 (s, OH_{Tyr}), 8.25 (d, 1H, $J = 7.7$, NH_{Phe}), 7.60 (d, 2H, $J = 8.0$, $H_{Ar,Phe}$), 7.03 (d, 2H, $J = 8.0$, $H_{Ar,Phe}$), 6.98 (d, 2H, $J = 8.2$, $H_{Ar,Tyr}$), 6.76 (d, 1H, $J = 8.6$, NH_{Boc}), 6.62 (d, 2H, $J = 8.1$, $H_{Ar,Tyr}$), 4.48 (dd, 1H, $J = 7.9$, 13.6, $C_{\alpha,Phe-I}H$), 4.06 (dd, 1H, $J = 7.6$, 13.2, $C_{\alpha,Phe}H$), 3.58 (s, 3H, CH_3), 2.94 (m, 2H, $C_{\beta,Phe-I}H$), 2.62 (m, 2H, $C_{\beta,Phe}H$), 1.29 (s, 9H, $CH_{3,Boc}$). ^{13}C NMR (DMSO-d_6, 90 MHz): δ 172.0, 171.6 (COO, CON), 155.6 ($C_{Ar}OH_{Tyr}$), 154.9 (CO_{Boc}), 136.7, 127.8 ($C_{Ar,q}$), 136.8, 131.5, 129.9, 114.7 (C_{Ar}), 92.4 (C_{Ar-I}), 77.9 ($C_{Boc,q}$), 55.7 ($C_{\alpha,Tyr}$), 52.9 ($C_{\alpha,Phe-I}$), 51.8 (CH_3), 36.5 ($C_{\beta,Tyr}$), 36.0 ($C_{\beta,Phe-I}$), 28.1 ($CH_{3,Boc}$). UV−vis: 229 (19492), 276 (1172). Yield: 5.24 g (92%).

Preparation of Ferrocenoyldiethylpropargyl Amide (H-DEPA-CO-Fc) (7). To a suspension of 2.3 g of ferrocenecarboxylic acid (10 mmol) in 50 mL of dried and degassed DCM was added under argon 1.78 g of thionyl chloride (15 mmol). The mixture was heated at reflux for 1 h. The clear and orange solution was allowed to cool, and the solvent was removed under reduced pressure, leaving a dark orange solid. The latter was dissolved in 50 mL of dried DCM and treated with 1.1 g of 1,1-diethylpropargylamine (10 mmol) and 1.01 g of NEt_3 (10 mmol). After 6 h of stirring at ambient temperature and removal of triethylamine hydrochloride by filtration through Celite, the solvent was removed by rotary evaporation. The remaining orange solid was dissolved in 50 mL of chloroform and washed three times with water. After drying over Na_2SO_4 and filtration, the solution was rotary evaporated to dryness. The crude product could be recrystallized from methanol. Anal. Calc for $C_{18}H_{21}FeNO$ (323.10 g/mol): C, 66.89; H, 6.55; N, 4.33. Found: C, 66.65; H, 6.60; N, 4.30. IR (KBr): ν 3300 (s, $\nu_{CC,alkyne}$), 3276 (s, ν_{NH}), 2972, 2877 (m, ν_{CH}), 1630 (vs, ν_{CON}), 1526 (s, δ_{NH}). MS (EI): *m/z* 323 (100%, M^+), 295 (12%, M^+ − ethyl), 267 (10%, M^+ − 2 ethyl), 213 (40%, Fc-CO^+), 185 (22%, Fc^+). ^{1}H NMR (DMSO-d_6, 360 MHz): δ 7.08 (s, NH), 4.89 (m, 2H, $CpH_{1,2}$), 4.33 (m, 2H, $CpH_{3,4}$), 4.18 (s, 5H, Cp), 3.19 (s, 1H, CH_{alkyne}), 2.01 (qd, 2H, $J = 7.3$, 14.5, $CH_{2,DEPA}$), 1.83 (qd, 2H, $J = 7.3$, 14.6, $CH_{2,DEPA}$), 0.95 (pseudo-t, 6H, $CH_{3,DEPA}$). ^{13}C NMR (DMSO-d_6, 90 MHz): δ 168.0 (CON), 85.9, 72.8 (C_{alkyne}), 76.6 ($C_{Cp,\ 1}$), 69.6 ($C_{Cp,2,5}$), 69.0 ($C_{Cp'}$), 68.2 ($C_{Cp,3,4}$), 55.1 ($C_{DEPA,q}$), 29.7 ($CH_{2,DEPA}$), 8.2 ($CH_{3,DEPA}$). UV−vis: 259 (3649), 304 (760), 444 (232). Yield: 2.89 g (89%).

Preparation of Ferrocenylated Dipeptides 8−11. 12 mL of dried THF and NEt_3 (1:1) was thoroughly degassed in a Schlenck tube. To this solution was added 1 mmol of the corresponding dipeptide **3**−**6** and 356 mg (1.1 mmol) of **7**. Then a mixture of 14 mg of $Pd(PPh_3)_2Cl_2$ (0.02 mmol, 2 mol %) and CuI (6 mg, 0.03 mmol, 3 mol %) was added as a catalyst. The mixture was stirred under argon until no more triethylamine hydroiodide precipitated (6h). After removal of the salts by filtration the solvents were removed under reduced pressure and the product was purified by column chromatography on silica using ethyl acetate/hexane (2:1).

Analytical Data for **8**. Anal. Calc for $C_{36}H_{45}FeN_3O_6$ (671.27 g/mol): C, 64.38; H, 6.75; N, 6.26. Found: C, 64.26; H, 6.64; N, 5.68. IR (KBr): ν 3321 (s, ν_{NH}), 2974 (m, ν_{CH}), 1743 (s, ν_{COO}), 1653 (vs, ν_{CON}), 1508 (s, δ_{NH}), 821 (m, δ_{CH}). MS (FAB, pos): *m/z* 671 $[M^+]$, 572 $[M^+ - Boc]$, 213 [Fc-CO]$^+$, 185 $[Fc]^+$. ^{1}H NMR ($CDCl_3$, 360 MHz): δ 7.36 (d, 2H, $J = 8.0$, H_{Ar}), 7.04 (d, 2H, $J = 8.0$, H_{Ar}), 6.67 (d, 1H, $J = 7.5$, NH_{Phe}), 5.74 (s, 1H, NH_{Fc}), 5.03 (d, 1H, $J = 5.6$, NH_{Boc}), 4.81 (m, 1H, $C_{\alpha,Phe}H$), 4.64 (m, 2H, $CpH_{1,2}$), 4.31 (m, 2H, $CpH_{3,4}$), 4.21 (s, 5H, CpH), 4.14 (m, 1H, $C_{\alpha,Ala}H$), 3.69 (s, 3H, CH_3), 3.09 (m, 2H, $C_{\beta,Phe}H$), 2.38 (qd, 2H, $J = 7.2$, 14.4, $CH_{2,DEPA}$), 1.91 (qd, 2H, $J = 7.3$, 14.5, $CH_{2,DEPA}$), 1.41 (s, 9H, $CH_{3,Boc}$), 1.30 (d, 3H, $J = 7.1$, $CH_{3,Ala}$), 1.09 (pseudo-t, 6H, $CH_{3,DEPA}$). ^{13}C NMR ($CDCl_3$, 90 MHz): δ 172.3, 171.4 (COO, CON), 169.0 (CO_{Fc}), 155.3 (CO_{Boc}), 136.2 ($C_{Ar,q}$), 131.9, 129.2 (C_{Ar}), 121.5 ($C_{Ar,alkyne}$), 91.1, 83.3 (C_{alkyne}), 80.0 ($C_{Boc,q}$), 76.8 ($C_{Cp,1}$), 70.2 ($C_{Cp,2,5}$), 69.6 ($C_{Cp'}$), 68.0 ($C_{Cp,3,4}$), 58.4 ($C_{DEPA,\ q}$), 53.0 ($C_{\alpha,Phe}$), 52.3 (CH_3), 50.0 ($C_{\alpha,Ala}$), 36.6 ($C_{\beta,Phe}$), 30.9 ($CH_{2,DEPA}$), 28.2 ($CH_{3,Boc}$), 18.1 ($CH_{3,Ala}$), 9.0 ($CH_{3,DEPA}$). UV−vis: 246 (24825), 256 (22152), 442 (236). Yield: 504 mg (74%).

Analytical Data for ***9***. Anal. Calc for $C_{39}H_{51}FeN_3O_6$ (713.31 g/mol): C, 65.63; H, 7.20; N, 5.89. Found: C, 65.53; H, 7.41; N, 5.50. IR (KBr): ν 3318 (s, ν_{NH}), 2964 (m, ν_{CH}), 1748 (s, ν_{COO}), 1662 (vs, ν_{CON}), 1507 (s, δ_{NH}), 822 (m, δ_{CH}). MS (FAB, pos): *m/z* 713 $[M]^+$, 614 $[M^+ - Boc]$, 213 [Fc-CO]$^+$, 185 $[Fc]^+$. ^{1}H NMR ($CDCl_3$, 360 MHz): δ 7.37 (d, 2H, $J = 8.0$, H_{Ar}), 7.06 (d, 2H, $J = 8.0$, H_{Ar}), 6.57 (d, 1H, $J = 7.7$, NH_{Phe}), 5.73 (s, 1H, NH_{Fc}), 4.83 (m, 1H, $C_{\alpha,Phe}H$), 4.65 (m, 2H, $CpH_{1,2}$), 4.32 (m, 2H, $CpH_{3,4}$), 4.23 (s, 5H, CpH), 4.18 (m, 1H, $C_{\alpha,Ala}H$), 3.71 (s, 3H, CH_3), 3.11 (m, 2H, $C_{\beta,Phe}H$), 2.40 (qd, 2H, $J = 7.3$, 14.5, $CH_{2,DEPA}$), 1.92 (qd, 2H, $J = 7.2$, 14.3, $CH_{2,DEPA}$), 1.43 (s, 9H, $CH_{3,Boc}$), 1.43 (m, 2H, $C_{\beta,Leu}H$), 1.10 (t, 6H, $J = 7.3$, $CH_{3,DEPA}$), 0.91 (t, 6H, $J = 6.0$, $CH_{3,Leu}$). ^{13}C NMR ($CDCl_3$, 90 MHz): δ 172.1, 171.4 (COO, CON), 169.0 (CO_{Fc}), 155.5 (CO_{Boc}), 136.2 ($C_{Ar,q}$), 131.9, 129.3 (C_{Ar}), 121.6 ($C_{Ar,alkyne}$), 91.2, 83.4 (C_{alkyne}), 80.1 ($C_{Boc,q}$), 76.9 ($C_{Cp,\ 1}$), 70.2 ($C_{Cp,2,5}$), 69.7 ($C_{Cp'}$), 68.1 ($C_{Cp,3,4}$), 58.6 ($C_{DEPA,\ q}$), 53.2 ($C_{\alpha,Leu}$), 53.1 ($C_{\alpha,Phe}$), 52.3 (CH_3), 41.1 ($C_{\beta,Leu}$), 37.7 ($C_{\beta,Phe}$), 31.0 ($CH_{2,DEPA}$), 28.2 ($CH_{3,Boc}$), 24.7 ($CH_{3,Leu}$), 22.8 ($CH(CH_3)_2$), 9.1 ($CH_{3,DEPA}$). UV−vis: 246 (28332), 255 (24239), 444 (249). Yield: 650 mg (91%).

Analytical Data for **10**. Anal. Calc for $C_{42}H_{49}FeN_3O_6$ (747.30 g/mol): C, 67.47; H, 6.61; N, 5.62. Found: C, 66.92; H, 6.42; N, 5.44. IR (KBr): ν 3316 (s, ν_{NH}), 2973 (m, ν_{CH}), 1744 (s, ν_{COO}), 1663 (vs, ν_{CON}), 1507 (s, δ_{NH}), 821 (m, δ_{CH}). MS (FAB, pos): *m/z* 747 $[M]^+$, 648 $[M^+ - Boc]$, 582 $[M^+ - Boc - Cp]$, 213 [Fc-CO]$^+$, 185 $[Fc]^+$. ^{1}H NMR ($CDCl_3$, 360 MHz): δ 7.33 (d, 2H, $J = 8.1$, $H_{Ar,Phe}$), 7.23 (m, 5H, H_{Ar}), 6.94 (d, 2H, $J = 7.9$, H_{Ar}), 6.35 (d, 1H, $J = 7.4$, NH_{Phe}), 5.73 (s, 1H, NH_{Fc}), 4.97 (m, 1H, NH_{Boc}), 4.77 (m, 1H, $C_{\alpha,Phe}H$), 4.65 (m, 2H, $CpH_{1,2}$), 4.33 (m, 2H, $CpH_{3,4}$), 4.24 (s, 5H, CpH), 4.18 (m, 1H, $C_{\alpha,Phe}H$), 3.66 (s, 3H, CH_3), 3.04 (m, 4H, $C_{\beta}H$), 2.41 (qd, 2H, $J = 7.2$, 14.4, $CH_{2,DEPA}$), 1.93 (qd, 2H, $J = 7.3$, 14.6, $CH_{2,DEPA}$), 1.40 (s, 9H, $CH_{3,Boc}$), 1.11 (pseudo-t, 6H, $CH_{3,DEPA}$). ^{13}C NMR ($CDCl_3$, 90 MHz): δ 171.0, 170.7 (COO, CON), 169.0 (CO_{Fc}), 155.2 (CO_{Boc}), 136.4, 136.0 ($C_{Ar,q}$), 131.9, 129.3, 129.1, 128.6, 126.9 (C_{Ar}), 121.6 ($C_{Ar,alkyne}$), 91.2, 83.3 (C_{alkyne}), 80.2 ($C_{Boc,q}$), 76.9 ($C_{Cp,1}$), 70.3 ($C_{Cp,2,5}$), 69.6 ($C_{Cp'}$), 68.0 ($C_{Cp,3,4}$), 58.5 ($C_{DEPA,q}$), 55.7 ($C_{\alpha,Phe}$), 53.1 ($C_{\alpha,Phe}$), 52.3 (CH_3), 38.1 ($C_{\beta,Phe}$),

37.7 ($C_{\beta,Phe}$), 31.0 ($CH_{2,DEPA}$), 28.2 ($CH_{3,Boc}$), 9.1 ($CH_{3,DEPA}$). UV−vis: 246 (27984), 256 (24511), 442 (276). Yield: 539 mg (72%).

Analytical Data for **11**. Anal. Calc for $C_{42}H_{49}FeN_3O_7$ (763.29 g/mol): C, 66.05; H, 6.47; N, 5.50. Found: C, 65.52; H, 6.79; N, 5.02. IR (KBr): ν 3337 (s, ν_{NH}), 2972 (m, ν_{CH}), 1740 (s, ν_{COO}), 1663 (vs, ν_{CON}), 1516 (s, δ_{NH}), 821 (m, δ_{CH}). MS (FAB): *m/z* 764 $[M + 1]^+$, 664 $[M^+ - Boc]$, 598 $[M^+ - Boc - Cp]$, 213 $[Fc\text{-}CO]^+$, 185 $[Fc]^+$. ^1H NMR ($CDCl_3$, 360 MHz): δ 8.63 (s, 1H, OH_{Tyr}), 7.32 (d, 2H, $J = 7.9$, $H_{Ar,Phe}$), 6.92 (d, 2H, $J = 7.9$, $H_{Ar,Phe}$), 6.81 (m, br, 4H, $H_{Ar,Tyr}$), 6.26 (d, 1H, $J = 8.1$, NH_{Phe}), 5.82 (s, 1H, NH_{Fc}), 4.97 (s, br, 1H, NH_{Boc}), 4.84 (dd, 1H, $J = 7.5$, 13.0, $C_{\alpha,Phe}H$), 4.70 (m, 2H, $CpH_{1,2}$), 4.35 (m, 2H, $CpH_{3,4}$), 4.31 (m, 1H, $C_{\alpha,Tyr}H$), 4.24 (s, 5H, CpH), 3.70 (s, 3H, CH_3), 3.13 (m, 2H, $C_{\beta,Phe}H$), 2.80 (m, 2H, $C_{\beta,Tyr}H$), 2.14 (m, 2H, $CH_{2,DEPA}$), 2.04 (m, 2H, $CH_{2,DEPA}$), 1.45 (s, 9H, $CH_{3,Boc}$), 1.11 (pseudo-t, 6H, $CH_{3,DEPA}$). ^{13}C NMR ($CDCl_3$, 90 MHz): δ 171.3, 171.2 (COO, CON), 170.2 (CO_{Fc}), 156.3 ($C_{Ar,Tyr}OH$), 155.2 (CO_{Boc}), 135.6, 126.4 ($C_{Ar,q}$), 131.8, 139.2, 128.9, 115.7 (C_{Ar}), 121.6 ($C_{Ar,alkyne}$), 90.7, 83.5 (C_{alkyne}), 80.2 ($C_{Boc,q}$), 76.7 ($C_{Cp,1}$), 70.7 ($C_{Cp,2,5}$), 69.7 ($C_{Cp'}$), 68.1 ($C_{Cp,3,4}$), 56.8 ($C_{DEPA,q}$), 55.3 ($C_{\alpha,Tyr}$), 52.7 ($C_{\alpha,Phe}$), 52.3 (CH_3), 37.6 ($C_{\beta,Phe}$), 36.7 ($C_{\beta,Tyr}$), 31.0 ($CH_{2,DEPA}$), 28.2 ($CH_{3,Boc}$), 8.7 ($CH_{3,DEPA}$). UV−vis: 246 (26010), 256 (22840), 442 (231). Yield: 581 mg (76%).

Preparation of Ethynylferrocene-Substituted Dipeptides 12−15. 12 mL of dried THF and NEt_3 (1:1) was thoroughly degassed in a Schlenck tube. To this solution was added 1 mmol of the corresponding dipeptide **3**−**6** and 231 mg (1.1 mmol) of ethynylferrocene. Then a mixture of 14 mg of $Pd(PPh_3)_2Cl_2$ (0.02 mmol, 2 mol %) and CuI (6 mg, 0.03 mmol, 3 mol %) was added as a catalyst. The mixture was stirred under argon until no more triethylamine hydroiodide precipitated (6 h). After removal of the salts by filtration, the solvents were removed under reduced pressure and the product was purified by column chromatography on silica using ethyl acetate/hexane (4:5).

Analytical Data for **12**. Anal. Calc for $C_{30}H_{34}FeN_2O_5$ (558.18 g/mol): C, 64.52; H, 6.14; N, 5.02. Found: C, 62.53; H, 6.24; N, 4.52. IR (KBr): ν 3315 (s, ν_{NH}), 2976 (m, ν_{CH}), 1710 (s, ν_{COO}), 1662 (vs, ν_{CON}), 1515 (s, δ_{NH}), 820 (m, δ_{CH}). MS (EI): *m/z* 558 (100%, $M^+ + 1$), 502 (21%, $M^+ - C_4H_9$), 484 (20%, $M^+ - OC_4H_9$), 458 (18%, $M^+ - Boc$), 299 (80%, Fc-alkynyl-Ph-CH_2^+). ^1H NMR ($CDCl_3$, 360 MHz): δ 7.32 (d, 2H, $J = 8.0$, H_{Ar}), 6.99 (d, 2H, $J = 8.0$, H_{Ar}), 6.55 (d, 1H, $J = 7.4$, NH_{Phe}), 4.90 (m, 1H, NH_{Boc}), 4.77 (dd, 1H, $J = 5.9$, 13.3, $C_{\alpha,Phe}H$), 4.41 (m, 2H, $CpH_{1,2}$), 4.20 (s, 2H, $CpH_{3,4}$), 4.16 (s, 5H, CpH), 4.09 (m, 1H, $C_{\alpha,Ala}H$), 3.64 (s, 3H, CH_3), 3.05 (m, 2H, $C_{\beta}H$), 1.38 (s, 9H, $CH_{3,Boc}$), 1.25 (d, 3H, $J = 7.0$, $CH_{3,Ala}$). ^{13}C NMR ($CDCl_3$, 90 MHz): δ 172.3, 171.5 (COO, CON), 155.3 (CO_{Boc}), 135.4 ($C_{Ar,q}$), 131.5, 129.2 (C_{Ar}), 122.7 ($C_{Ar,alkyne}$), 88.5, 85.3 (C_{alkyne}), 80.21 ($C_{Boc,q}$), 71.3 ($C_{Cp,2,5}$), 69.9 ($C_{Cp'}$), 68.7 ($C_{Cp,3,4}$), 65.1 ($C_{Cp,1}$), 53.0 ($C_{\alpha,Phe}$), 52.3 (CH_3), 50.1 ($C_{\alpha,Ala}$), 37.7 (C_{β}), 28.2 ($CH_{3,Boc}$), 18.1 ($CH_{3,Ala}$). UV−vis: 256 (18335), 300 (16305), 445 (563). Yield: 386 mg (70%).

Analytical Data for **13**. Anal. Calc for $C_{33}H_{40}FeN_2O_5$ (600.23 g/mol): C, 66.00; H, 6.71; N, 4.66. Found: C, 65.06; H, 6.63; N, 4.40. IR (KBr): ν 3303 (s, ν_{NH}), 2956 (m, ν_{CH}), 1709 (s, ν_{COO}), 1659 (vs, ν_{CON}), 1515 (s, δ_{NH}), 820 (m, δ_{CH}). MS (FAB, pos): *m/z* 600 $[M]^+$, 545 $[M^+ - C_4H_9]$, 501 $[M^+ - Boc]$, 299 [Fc-alkynyl-Ph-CH_2^+]. ^1H NMR ($CDCl_3$, 360 MHz): δ 7.32 (d, 2H, $J = 8.1$, H_{Ar}), 7.00 (d, 2H, $J = 8.0$, H_{Ar}), 6.59 (d, 1H, $J = 7.5$, NH_{Phe}), 4.86 (d, 1H, $J = 7.8$, NH_{Boc}), 4.77 (m, 1H, $C_{\alpha,Phe}H$), 4.41 (m, 2H, $CpH_{1,2}$), 4.23 (s, 2H, $CpH_{3,4}$), 4.19 (s, 5H, CpH), 4.16 (m, 1H, $C_{\alpha,Ala}H$), 3.63 (s, 3H, CH_3), 3.04 (m, 2H, $C_{\beta}H$), 1.56 (m, 1H, $CH(CH_3)$), 1.38 (s, 9H, $CH_{3,Boc}$), 0.85 (pseudo-t, 6H, $CH_{3,Leu}$). ^{13}C NMR ($CDCl_3$, 90 MHz): δ 172.2, 171.5 (COO, CON), 155.5 (CO_{Boc}), 135.4 ($C_{Ar,q}$), 131.4, 129.2 (C_{Ar}), 122.7 ($C_{Ar,alkyne}$), 88.4, 85.4 (C_{alkyne}), 79.9 ($C_{Boc,q}$), 71.3 ($C_{Cp,2,5}$), 69.9 ($C_{Cp'}$), 68.7 ($C_{Cp,3,4}$), 65.2 ($C_{Cp,1}$), 53.0 ($C_{\alpha,Phe}$), 52.9 ($C_{\alpha,Leu}$), 52.2 (CH_3), 41.1 ($C_{\beta,Leu}$), 37.7 ($C_{\beta,Phe}$), 28.2 ($CH_{3,Boc}$), 24.6 ($CH_{3,Leu}$), 22.8 ($CH(CH_3)_2$). UV−vis: 256 (17927), 301 (16026), 445 (582). Yield: 430 mg (72%).

Analytical Data for **14**. Anal. Calc for $C_{36}H_{38}FeN_2O_5$ (634.21 g/mol): C, 68.14; H, 6.04; N, 4.41. Found: C, 67.70; H, 6.12; N, 4.29. IR (KBr): ν 3308 (s, ν_{NH}), 2976 (m, ν_{CH}), 1696 (s, ν_{COO}), 1662 (vs, ν_{CON}), 1516 (s, δ_{NH}), 820 (m, δ_{CH}). MS (FAB, pos): *m/z* 634 $[M]^+$, 579 $[M^+ - C_4H_9]$, 535 $[M^+ - Boc]$, 299 [Fc-alkynyl-Ph-CH_2^+]. ^1H NMR ($CDCl_3$, 360 MHz): δ 7.35 (d, 2H, $J = 8.1$, H_{Ar}), 7.25 (m, 5H, $H_{Ar,\ Ph}$), 6.93 (d, 2H, $J = 8.1$, H_{Ar}), 6.35 (d, 1H, $J = 7.3$, NH_{Phe}), 4.97 (m, 1H, NH_{Boc}), 4.79 (m, 1H, $C_{\alpha,Phe}H$), 4.48 (m, 2H, $CpH_{1,2}$), 4.36 (m, 1H, $C_{\alpha,Phe}H$), 4.23 (s, 2H, $CpH_{3,4}$), 4.23 (s, 5H, CpH), 3.67 (s, 3H, CH_3), 3.05 (m, 4H, $C_{\beta}H$), 1.41 (s, 9H, $CH_{3,Boc}$). ^{13}C NMR ($CDCl_3$, 90 MHz): δ 171.1, 170.8 (COO, CON), 155.2 (CO_{Boc}), 136.4, 135.2 ($C_{Ar,q}$), 131.4, 129.3, 129.1, 128.7, 126.9 (C_{Ar}), 122.7 ($C_{Ar,alkyne}$), 88.5, 85.4 (C_{alkyne}), 80.2 ($C_{Boc,q}$), 71.3 ($C_{Cp,2,5}$), 69.9 ($C_{Cp'}$), 68.7 ($C_{Cp,3,4}$), 65.2 ($C_{Cp,1}$), 55.0 ($C_{\alpha,Phe}$), 53.1 ($C_{\alpha,Phe}$), 52.2 (CH_3), 38.1 ($C_{\beta,Phe}$), 37.8 ($C_{\beta,Phe}$), 28.2 ($CH_{3,Boc}$). UV−vis: 256 (18338), 301 (16234), 446 (586). Yield: 489 mg (77%).

Analytical Data for **15**. Anal. Calc for $C_{36}H_{38}FeN_2O_6$ (650.21 g/mol): C, 66.47; H, 5.89; N, 4.31. Found: C, 64.93; H, 5.92; N, 4.04. IR (KBr): ν 3334 (s, ν_{NH}), 2977 (m, ν_{CH}), 1739 (s, ν_{COO}), 1662 (vs, ν_{CON}), 1516 (s, δ_{NH}), 822 (m, δ_{CH}). MS (FAB, pos): *m/z* 650 $[M]^+$, 595 $[M^+ - C_4H_9 + H]$, 551 $[M^+ - Boc]$, 299 [Fc-alkynyl-Ph-CH_2^+]. ^1H NMR (DMSO-d_6, 360 MHz): δ 9.16 (s, 1H, OH_{Tyr}), 8.24 (d, 1H, $J = 7.7$, NH_{Phe}), 7.35 (d, 2H, $J = 7.9$, $H_{Ar,Phe}$), 7.20 (d, 2H, $J = 7.9$, $H_{Ar,Phe}$), 6.97 (d, 2H, $J = 8.1$, $H_{Ar,Tyr}$), 6.71 (d, 1H, $J = 8.6$, NH_{Boc}), 6.62 (d, 2H, $J = 8.1$, $H_{Ar,Tyr}$), 4.52 (m, 2H, $CpH_{1,2}$), 4.49 (m, 1H, $C_{\alpha,Tyr}H$), 4.29 (m, 2H, $CpH_{3,4}$), 4.23 (s, 5H, CpH), 4.07 (m, 1H, $C_{\alpha,Phe}H$), 3.58 (s, 3H, CH_3), 2.97 (m, 2H, $C_{\beta,Phe}H$), 2.65 (m, 2H, $C_{\beta,Tyr}H$), 1.29 (s, 9H, $CH_{3,Boc}$). ^{13}C NMR (DMSO-d_6, 90 MHz): δ 171.9, 171.6 (COO, CON), 155.7 ($C_{Ar,Tyr}OH$), 155.0 (CO_{Boc}), 137.1, 127.9 ($C_{Ar,q}$), 130.9, 130.0, 129.5, 114.7 (C_{Ar}), 121.2 ($C_{Ar,alkyne}$), 88.3, 85.3 (C_{alkyne}), 78.0 ($C_{Boc,q}$), 71.0 ($C_{Cp,2,5}$), 69.7 ($C_{Cp'}$), 68.9 ($C_{Cp,3,4}$), 64.4 ($C_{Cp,\ 1}$), 55.8 ($C_{\alpha,Tyr}$), 53.0 ($C_{\alpha,Phe}$), 51.8 (CH_3), 36.6 ($C_{\beta,Phe}$), 36.5 ($C_{\beta,Tyr}$), 28.1 ($CH_{3,Boc}$). UV−vis: 256 (18338), 301 (16234), 446 (586). Yield: 525 mg (81%).

Preparation of Ac-Enk-[Phe^4(I)]-OH 16. The synthesis was performed manually in a syringe equipped with a porous filter (10 mL, MultiSynTech) using Fmoc-protected Leu−Wang resin (400 mg, loading 0.63 mmol/g, Novabiochem), Fmoc-protected amino acid monomers, 4-iodophenylalanine **1**, and amine free DMF as solvent. The tyrosine side chain protecting group was *tert*-butyl. Synthesis cycle: (A) *deprotection* using two times about 3 mL of a 20% piperidin solution in DMF, first at 5 min and then at 10 min, without washing in between; (B) *washing* 5 times with about 6 mL of DMF; (C) *coupling* using a solution of activated amino acid for 30 min; and (D) *washing* 5 times with 3 mL. The coupling mixture contained the protected amino acid monomer (5-fold excess), TBTU (396.4 mg, 4.9-fold excess), and HOBt (192.9 mg, 5-fold excess) dissolved in DMF (5 mL);); then DIPEA (325.8 mg, 10-fold excess, activation period 2 min) was added. Work up: After the resin was successively rinsed with DMF and DCM and dried under reduced pressure (1 h, 10 mbar), final deprotection and cleavage from the resin was performed with a TFA mixture (TFA/H_2O/TIS = 95:2.5:2.5, 3 mL, 3 h). The suspension was filtered and the resin washed with TFA (2 × 1.5 mL). The combined TFA solutions were poured into cold ether (10 mL, −30 °C), and the suspension was centrifuged (8000 rpm, 6 min). After decanting the supernatant, the crude product was washed with

cold ether (2 × 10 mL), dissolved in water, filtered, and lyophilized, yielding a white solid.

Analytical Data for $C_{30}H_{38}IN_5O_8$ (723.18 g/mol). MS (FAB, pos): *m/z* 746 [M^+ + Na], 724 [M^+ + H], 593 [M^+ − H-Leu-OH], 320 [M^+ − H-Phe(I)-Leu-OH], 263 [M^+ − H-Gly-Phe-(I)-Leu-OH]. ^{1}H NMR (DMSO-d_6, 360 MHz): δ 12.58 (s, br, 1H, COOH), 9.15 (s, br, 1H, OH_{Tyr}), 8.27 (d, 1H, J = 8.1, NH_{Leu}), 8.22 (t, 1H, J = 5.4, NH_{Gly}), 8.06 (d, 1H, J = 8.0, NH_{Tyr}), 7.99 (d, 1H, J = 8.5, N_{I-Phe}, 7.93 (t, 1H, J = 5.5, NH_{Gly}), 7.60 (d, 2H, J = 8.1, $H_{Ar,I-Phe}$), 7.07 (d, 2H, J = 8.2, $H_{Ar,I-Phe}$), 7.02 (d, 2H, J = 8.3, $H_{Ar,Tyr}$), 6.63 (d, 2H, J = 8.3, $H_{Ar,Tyr}$), 4.54 (dt, 1H, J = 3.7, 9.0, $C_{\alpha,I-Phe}H$), 4.39 (dt, 1H, J = 4.8, 9.1, $C_{\alpha,Tyr}H$), 4.21 (m, 1H, $C_{\alpha,Leu}H$), 3.66 (m, 4H, $C_{\alpha,Gly}H$), 2.81 (m, 4H, $C_{\beta,Phe,Tyr}H$), 1.61 (m, 1H, $CH(CH_3)_2$), 1.54 (m, 2H, $C_{\beta,Leu}H$), 0.87 (m, 6H, $CH(CH_3)_2$). ^{13}C NMR (DMSO-d_6, 90 MHz): δ 173.7 (COO), 171.8, 170.7, 169.3 (CON), 168.9 (CON_{Ac}), 168.3 (CON), 155.6 ($C_{Ar,Tyr}OH$), 137.5 ($C_{Ar,q,I-Phe}$), 136.7 ($C_{Ar,I-Phe}$), 131.7 ($C_{Ar,q,Tyr}$), 129.8, 128.0, 114.8 (C_{Ar}), 92.1 ($C_{Ar,q,I-Phe}$), 54.4 ($C_{\alpha,I-Phe}$), 53.2 ($C_{\alpha,Tyr}$), 50.2 ($C_{\alpha,Leu}$), 42.0, 41.7 ($C_{\alpha,Gly}$), 37.0 ($C_{\beta,Phe}$), 36.5 ($C_{\beta,Tyr}$), 24.2 ($C_{\beta,Leu}$), 22.7 ($CH_{3,Leu}$), 22.4 ($CH_{3,Ac}$), 21.2 ($CH(CH_3)_2$). Yield: 144 mg (79%).

Preparation of I-PBA-Enk-OH (17). The synthesis was carried out in analogy to that of Ac-Enk-[Phe^4(I)]-OH (**16**). Instead of 4-iodophenylalanine, L-phenylalanine was used. In one additional last coupling reaction, *p*-iodobenzoic acid (I-BA) was coupled to the N-terminal tyrosine group.

Analytical Data for $C_{35}H_{40}IN_5O_8$ (785.19 g/mol). MS (FAB, pos): *m/z* 808 [M^+ + Na], 786 [M^+ + H], 655 [M^+ − H-Leu-OH], 508 [M^+ − H-Phe-Leu-OH], 451 [M^+ − H-Gly-Phe-Leu-OH]. ^{1}H NMR (DMSO-d_6, 360 MHz): δ 12.54 (s, br, 1H, COOH), 9.12 (s, br, 1H, OH_{Tyr}), 8.61 (d, 1H, J = 8.2, NH_{Tyr}), 8.31 (t, 1H, J = 5.5, NH_{Gly}), 8.26 (d, 1H, J = 7.9, NH_{Leu}), 8.04 (d, 1H, J = 8.4, NH_{Phe}), 7.96 (t, 1H, J = 5.5, NH_{Gly}), 7.82 (d, 2H, J = 8.4, $H_{Ar,I-Ph}$), 7.57 (d, 2H, J = 8.4, $H_{Ar,I-Ph}$), 7.25 (m, 5H, $H_{Ar,Phe}$), 7.09 (d, 2H, J = 8.3, $H_{Ar,Tyr}$), 6.61 (d, 2H, J = 8.4, $H_{Ar,Tyr}$), 4.59 (m, 2H, $C_{\alpha,Phe,Tyr}H$), 4.22 (dd, 1H, J = 8.4, 14.0, $C_{\alpha,Leu}H$), 3.63 (m, 4H, $C_{\alpha,Gly}H$), 2.85 (m, 4H, $C_{\beta,Phe,Tyr}H$), 1.64 (m, 1H, $CH(CH_3)_2$), 1.54 (m, 2H, $C_{\beta,Leu}H$), 0.87 (m, 6H, $CH(CH_3)_2$). ^{13}C NMR (DMSO-d_6, 90 MHz): δ 173.7 (COO), 171.6, 170.9, 168.8, 168.1 (CON), 165.6 (CON_{I-Ph}), 155.6 ($C_{Ar,Tyr}OH$), 137.6 ($C_{Ar,q,Phe}$), 136.9 ($C_{Ar,I-Ph}$), 133.4 ($C_{Ar,q,I-Ph}$), 129.9, 129.3, 129.1 (C_{Ar}), 128.3 ($C_{Ar,q,Tyr}$), 127.9, 126.1, 114.8 (C_{Ar}), 98.7 ($C_{Ar,q,I-Ph}$), 55.2 ($C_{\alpha,Phe}$), 52.7 ($C_{\alpha,Phe}$), 53.4 ($C_{\alpha,Tyr}$), 50.2 ($C_{\alpha,Leu}$), 42.0, 41.6 ($C_{\alpha,Gly}$), 37.5 ($C_{\beta,Phe}$), 36.1 ($C_{\beta,Tyr}$), 24.2 ($C_{\beta,Leu}$), 22.7 ($CH_{3,Leu}$), 21.2 ($CH(CH_3)_2$). Yield: 184 mg (93%).

Preparation of Ac-Enk-[Phe^4(DEPA-CO-Fc)]-OH (18). Ac-Enk[Phe^4(I)]-OH (**16**) (100 mg, 0.134 mmol) was dissolved in 8 mL of a well degassed mixture of DMF/NEt_3 (1:1) in a Schlenck tube. After complete dissolution, 1.1 equiv (47.6 mg, 0.147 mmol) of H-DEPA-Fc (**7**) was dissolved in the reaction mixture, followed by another 15 min of degassing. Then CuI (14 mg) and $Pd(PPh_3)_2Cl_2$ (28 mg) were added and the mixture was stirred for 12 h. The solution was filtered through a syringe filter (22 μm pore size), the solvent was evaporated *in vacuo*, and the residual oil was redissolved in acetonitrile. The compound was purified by preparative HPLC.

Analytical Data for $C_{48}H_{58}IN_6O_9$ (918.36 g/mol). MS (ESI, neg): *m/z* 917.4 [M − H]$^-$. MS (ESI, pos): *m/z* 919.4 [M + H]$^+$, 941.4 [M^+ + Na], 957.5 [M^+ + K]. ^{1}H NMR (DMSO-d_6, 400 MHz): δ 12.59 (s, br, 1H, COOH), 9.17 (s, 1H, OH_{Tyr}), 8.30 (d, 1H, J = 7.9, NH_{Leu}), 8.25 (t, 1H, J = 5.6, NH_{Gly}), 8.07 (d, 1H, J = 8.1, NH_{Tyr}), 8.02 (d, 1H, J = 8.7, NH_{Phe}), 7.94 (t, 1H, J = 5.5, NH_{Gly}), 7.58 (m, 2H, $H_{Ar,Phe}$), 7.25 (d, 2H, J = 5.8, $H_{Ar,Phe}$), 7.01 (d, 2H, J = 8.4, $H_{Ar,Tyr}$), 6.63 (d, 2H, J = 8.4, $H_{Ar,Tyr}$), 4.92 (m, 2H, $CpH_{1,4}$), 4.56 (dt, 1H, J = 3.8, 9.5, $C_{\alpha,Phe}H$), 4.38 (dt, 1H, J = 4.6, 9.4, $C_{\alpha,Tyr}H$), 4.33 (m, 2H, $CpH_{2,3}$), 4.19 (s, 5H, CpH), 4.16 (m, 1H, $C_{\alpha,Leu}H$), 3.63 (m, 4H, $C_{\alpha,Gly}H$), 2.82 (m, 4H, $C_{\beta,Phe,Tyr}H$), 2.10 (m, 2H, $CH_{2,DEPA}$), 1.90 (m, 2H, $CH_{2,DEPA}$), 1.76 (s, 3H, $CH_{3,\ acetyl}$), 1.62 (m, 1H, $CH(CH_3)_2$), 1.54 (m, 2H, $C_{\beta,Leu}H$), 1.01 (pseudo-t, 6H, $CH_{3,DEPA}$), 0.87 (m, 6H, $CH(CH_3)_2$). ^{13}C NMR (DMSO-d_6, 100 MHz): δ 173.6 (COO), 171.7, 170.7 (CON), 169.1 (CON_{Ac}), 168.6, 168.0, 167.9 (CON), 155.4 ($C_{Ar,Tyr}OH$), 137.7 ($C_{Ar,q,Phe}$), 130.6 ($C_{Ar,q,Tyr}$), 129.7, 129.1, 127.8, 120.6, 114.5 (C_{Ar}), 91.6, 82.0 (C_{alkyne}), 76.5 ($C_{Cp,1}$), 69.6 ($C_{Cp,2,5}$), 68.9 ($C_{Cp'}$), 68.1 ($C_{Cp,3,4}$), 55.6 ($C_{DEPA,q}$), 54.2 ($C_{\alpha,\ Phe}$), 53.0 ($C_{\alpha,Tyr}$), 50.0 ($C_{\alpha,Leu}$), 41.7, 41.3 ($C_{\alpha,Gly}$), 37.2 ($C_{\beta,Phe}$), 36.3 ($C_{\beta,Tyr}$), 29.9 ($CH_{2,DEPA}$), 24.0 ($C_{\beta,Leu}$), 22.5 ($CH_{3,Leu}$), 22.1 ($CH_{3,Ac}$), 21.0 ($CH(CH_3)_2$), 8.4 ($CH_{3,DEPA}$). UV−vis: 246 (25165), 257 (22570), 444 (272). Yield: 58.6 mg (47.6%).

Preparation of Fc-CO-DEPA-BA-Enk-OH (19). The synthesis was carried out in analogy to that of **18**. I-Ph-Enk-OH (**17**) (100 mg, 0.127 mmol) was used. The product was purified by preparative HPLC.

Analytical Data for $C_{53}H_{60}FeN_6O_9$ (980.38 g/mol). MS (ESI, neg): *m/z* 979.5 [M − H]$^-$. ^{1}H NMR (DMSO-d_6, 400 MHz): δ 12.58 (s, br, 1H, COOH), 9.16 (s, br, 1H, OH_{Tyr}), 8.64 (d, 1H, J = 8.1, NH_{Tyr}), 8.35 (t, 1H, J = 5.7, NH_{Gly}), 8.29 (d, 1H, J = 7.9, NH_{Leu}), 8.08 (d, 1H, J = 8.4, NH_{Phe}), 7.99 (t, 1H, J = 5.6, NH_{Gly}), 7.81 (d, 2H, J = 8.3, $H_{Ar,Ph}$), 7.48 (d, 2H, J = 8.3, $H_{Ar,Ph}$), 7.27 (m, 5H, $H_{Ar,Phe}$), 7.11 (d, 2H, J = 7.6, $H_{Ar,Tyr}$), 6.63 (d, 2H, J = 8.4, $H_{Ar,Tyr}$), 5.73 (s, 1H, NH_{Fc}), 4.95 (m, 2H, $CpH_{1,2}$), 4.62 (m, 2H, $C_{\alpha,Phe,Tyr}H$), 4.37 (m, 2H, $CpH_{3,4}$), 4.21 (s, 5H, CpH), 4.19 (m, 1H, $C_{\alpha,Leu}H$), 3.69 (m, 4H, $C_{\alpha,Gly}H$), 2.91 (m, 4H, $C_{\beta,Phe,Tyr}H$), 2.13 (m, 2H, $CH_{2,ethyl}$), 1.97 (m, 2H, $CH_{2,ethyl}$), 1.66 (m, 1H, $CH(CH_3)_2$), 1.55 (m, 2H, $C_{\beta,Leu}H$), 1.05 (t, 6H, $CH_{3,ethyl}$), 0.88 (m, 6H, $CH(CH_3)_2$). UV−vis: 269 (27210), 442 (329). Yield: 28.0 mg (22.5%).

RESULTS AND DISCUSSION

Synthesis of Dipeptides. The dipeptides **3**−**6** were synthesized from the N$^\alpha$-Boc-protected amino acids alanine, leucine, phenylalanine, and tyrosine with 4-iodophenylalanine methyl ester **(2)**. Activation of the Boc amino acids was achieved by isobutyl chloroformiate (Scheme 1). After filtration from salt precipitates, the dipeptide products were isolated in good yields (>75%) and could be comprehensively characterized. The spectroscopic data of the dipeptides **3**−**6** did not reveal any unexpected signals, and the reactions were straightforward. The elemental analyses confirm the correct chemical compositions. The FAB mass spectra show the calculated [M + 1]$^+$ peaks in all cases and also molecular fragments of the type ($M^+ - C_4H_9$) and (M^+ − Boc). The ^{1}H NMR spectrum shows the Boc amide proton between 6.76 and 6.87 ppm and the amide proton of 4-iodophenylalanine between 8.13 and 8.33 ppm. The aromatic protons of the 4-iodo-substituted phenyl ring resonate at 7.60 and 7.00 ppm, leaving a shift difference of 0.60 ppm between both signal groups. Since the *p*-iodophenylalanine is the location of attachment of the alkyne group, the chemical shift and shift difference of these signals are of interest for the monitoring of a successful reaction (Figure 1).

Sonogashira Coupling with Dipeptides. For the introduction of the ferrocene group into a iodophenyl-derivatized biomolecule via Sonogashira coupling, an alkyne group has to be present in the ferrocene molecule. This can be provided by derivatization of ferrocenecarboxylic acid. The synthesis of ferrocenoyl diethylpropargylamide (Fc-CO-DEPA-H) (**7**) using diethylpropargylamine has been described and was reproduced in this work. The X-ray single-crystal structure of **7** has also been reported (*4*). All dipeptides **3**−**6** were reacted with H-DEPA-CO-Fc (**7**) and also with commercially available ethynylferrocene **7a**, to explore the scope of the reaction. The reactions were carried out under argon and in degassed and thoroughly

Scheme 1. Sonogashira Coupling of *p*-Iodophenylalanine Dipeptides with Ferrocenyl Alkynes 7 and 7a

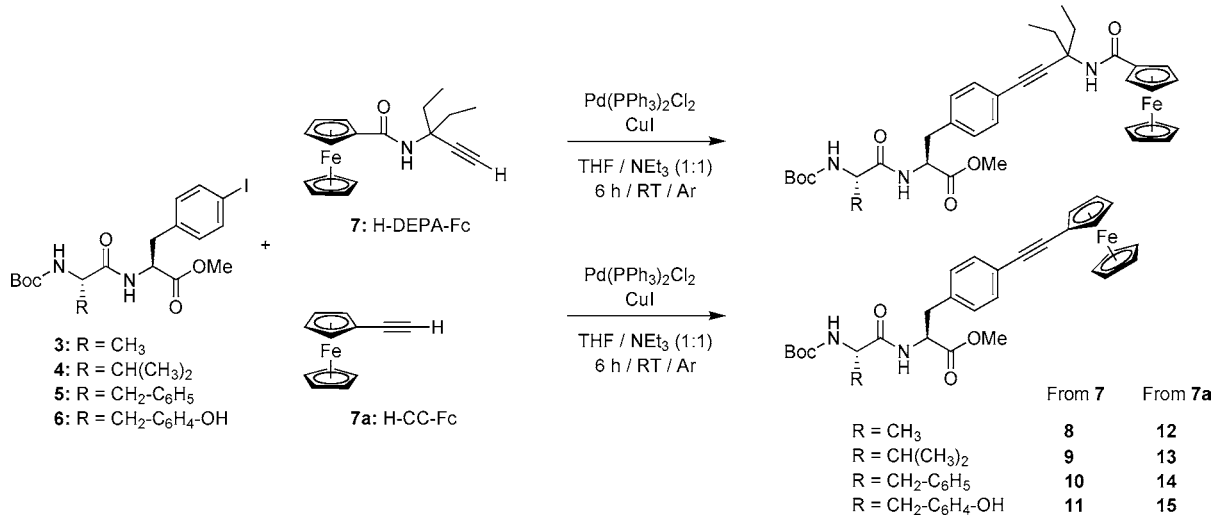

dried solvents. A mixture of $(Ph_3P)_2PdCl_2$ and CuI was used as the catalyst. After various attempts with different solvents and bases, a mixture of THF and NEt_3 in a ratio of 1:1 turned out to be most successful. Shortly after all reagents had been added, the clear solutions became cloudy and green ammonium salts precipitated, which indicated the proceeding reaction. After filtration from the precipitate, the solutions were purified by silica column chromatography, using mixtures of ethyl acetate and hexane. All products were isolated as orange powders, which readily dissolved in organic solvents such as CH_3CN, THF, DMF, DCM, EtOH, and CH_3OH but showed only moderate solubility in water. The purified DEPA-CO-Fc-labeled dipeptides **8**−**11** were submitted to elemental analysis, HPLC, NMR, and mass spectrometry, confirming the successful reaction. The FAB mass spectra show, in addition to the M^+ peaks, signals for $[M - Boc]^+$, $[M - Boc - Cp]^+$ and also fragments of $m/z = 213$ and 185, which can be assigned to $[Fc\text{-}CO]^+$ and $[Fc]^+$, respectively. Proton NMR signals for the Cp rings were observed at 4.64, 4.30, and 4.21 ppm in the usual 2−2−5 intensity pattern (*50*). The ^1H NMR spectrum also shows a singlet for the DEPA-CO-Fc amide proton at 5.74 ppm, which is the same for all four compounds. Protons of the para-substituted phenyl ring still show the typical two pseudodoublets of a AA′BB′ system. However, the signals have changed positions and show a much smaller shift difference compared to the case of the dipeptide starting material (Figure 1).

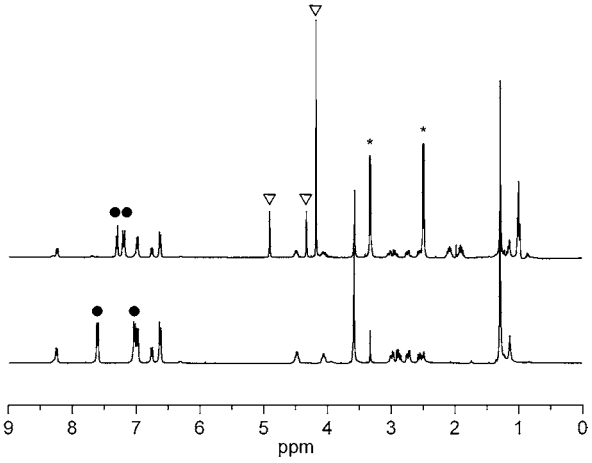

Figure 1. ^1H NMR overlay of Boc-Tyr-Phe(I)-OMe (**6**) and Sonogashira product Boc-Tyr-Phe(DEPA-CO−Fc)-OMe (**11**). Spectra were measured in DMSO-d_6 at 300.16 MHz; solvent and water signals are indicated by asterisk. Triangles indicate Cp signals; filled circles indicate *p*-substituted phenyl signals.

Enkephalin Derivatives. *Synthesis of Ac-Enk[Phe^4(I)]-OH (**16**).* Encouraged by the successful Sonogashira reaction using *p*-iodophenylalanine as a modified amino acid, the biologically relevant pentapeptide enkephalin (H-Tyr-Gly-Gly-Phe-Leu-OH) was modified accordingly. The compound Ac-Enk[Phe^4(I)]-OH (**16**) was synthesized by standard solid-phase peptide synthesis (Scheme 2). Fmoc-Phe-OH was replaced by the modified amino acid Fmoc-Phe(I)-OH, which had been synthesized from **1** using a standard Fmoc protection procedure. The synthesis was carried out on Wang resin, and the cleavage conditions comprised a mixture of 95% TFA, 2.5% H_2O, and 2.5% TIS and a duration of 3 h. The crude product (yield: 79%) was purified by preparative HPLC to give a white powder, which shows good solubility in both organic solvents and water. The FAB mass spectrum displays two product peaks for $m/z = 746$ $[M + Na]^+$ and 724 $[M + H]^+$ and a number of fragment signals which could be assigned to $[M\text{-(Leu-OH)}]^+$, $[M - \text{Phe(I)-Leu-OH}]^+$, and $[M - \text{Gly-Phe(I)-Leu-OH}]^+$, observable at $m/z = 593$, 320, and 263, respectively. All signals for [Leu]^5-enkephalin can be found in the proton NMR spectrum. In addition, two pseudo-doublets at 7.99 and 7.60 ppm are visible for the *p*-iodophenylalanine residue. The shift difference is 0.39 ppm smaller than the value of 0.57 ppm that was observed in the dipeptides. The assignment of all signals was supported by HH-COSY 2D NMR spectroscopy.

*Synthesis of I-BA-Enk-OH (**17**).* In some cases the target biomolecule may not offer a phenylalanine residue which can be replaced by the *p*-iodophenylalanine group. For such cases, the N-terminally modified enkephalin derivative I-BA-Enk-OH (**17**) was synthesized in order to explore an alternative route (I-BA: *p*-iodobenzoic acid). I-BA was introduced at the N-terminus of Enk as the last step in the SPPS. Cleavage of the product from the Wang resin was performed under standard conditions. After removal of the solvents and subsequent precipitation with diethyl ether, nearly pure **17** was obtained in 86% yield. The white powder was submitted to FAB mass spectrometry showing the correct peaks at $m/z = 808$ $[M + Na]^+$ and 786 $[M + H]^+$. Additional fragments were observed in analogy to **16**. The successful introduction of the *p*-iodophenyl residue at the N-terminal side of the peptide is confirmed by the corresponding ^1H NMR signals at 7.82 and 7.57 ppm. The ^{13}C NMR spectrum shows six carbonyl carbon resonances between 173.7 (*C*OOH) and 165.6 ppm (I-BA). In addition, all 12 aromatic carbon signals were detected between 155.6 ppm (Tyr) and the iodine bound carbon atom at 98.7 ppm. Similar to the case for compound **16**, the shielding effect of the iodine atom is responsible for the high-field shift and the cross-coupling

Scheme 2. Synthesis of Enkephalin Derivative 16 by SPPS and Sonogashira Coupling with H-DEPA-CO-Fc (7) To Yield the Organometallic Conjugate 18.

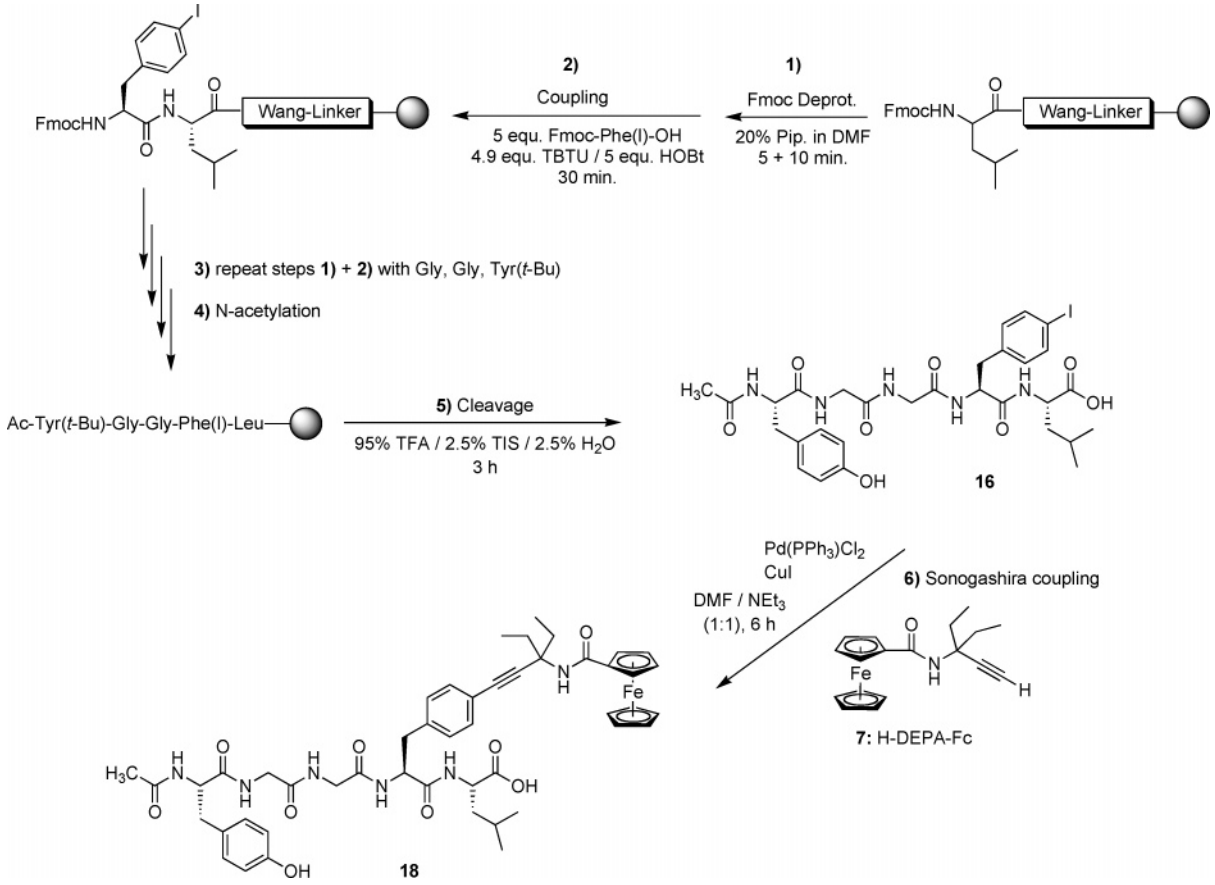

reaction is expected to make the signal move downfield by more than 30 ppm. Therefore, this signal is also indicative for a successful Sonogashira coupling.

Sonogashira Coupling with Enkephalins. *Synthesis of Ac-Enk-[Phe⁴(DEPA-CO-Fc)]-OH (**18**).* In contrast to the synthesis of the ferrocene dipeptides **3**−**6** and **8**−**11**, the side-chain-modified enkephalin derivative **16** was reacted in a mixture of DMF/NEt_3 (1:1) for solubility reasons (Scheme 2). The reaction was monitored by HPLC, and the synthesis was finished after 12 h, when no more peptide starting material could be detected. The solvents were removed on a vacuum pump, and the residual oil was redissolved in acetonitrile and purified by preparative HPLC. The light yellow powder was characterized by ESI (neg) mass spectrometry where the spectrum shows a peak for $[M-H]^-$ at $m/z = 917.4$. The ESI (pos) spectrum confirms this observation, showing three peaks at m/z 919.4 $[M + H]^+$, 941.4 $[M + Na]^+$, and 957.5 $[M + K]^+$. The successful coupling to the ferrocene label is also proven by the typical 2−2−5 Cp signal pattern in the ^1H NMR spectrum between 4 and 5 ppm. The cyclopentadienyl ^{13}C NMR signals were found between 76.5 and 68.2 ppm, also underlining the successful reaction. The carbon atom to which the iodine atom was connected has shifted from 92.1 ppm in **16** to 120.5 ppm in **18**, while the alkyne carbon atoms resonate at 91.7 and 82.0 ppm. The yellow color of the conjugate results from a characteristic absorbance at 444 nm for the ferrocenyl group in the UV−vis spectrum. The extinction coefficient $\epsilon = 272$ l mol^{-1} cm^{-1} corresponds well to all other DEPA-CO-Fc derivatives **3**−**6** and previous work. The ethynylferrocene dipeptides **8**−**11** have higher extinction coefficients between 535 and 585 l mol^{-1} cm^{-1}, albeit with the same absorbance maximum at 445 nm.

*Synthesis of Fc-CO-DEPA-BA-Enk-OH (**19**).* H-DEPA-CO-Fc (**7**) was coupled to the N-terminal I-BA-derivatized enkephalin **17** under the same reaction conditions as those for **18.** Again, the reaction progress was followed by analytical HPLC and the conversion was finished after 10 h. The solvents were removed, and the crude product was purified by preparative HPLC. However, the yield was significantly lower in comparison to that of **18**, and only a few milligrams of pure substance were obtained (Figure 2; Scheme 3). The peak at $m/z = 979.5$ (ESI, neg) can be assigned to the molecular $[M - H]^-$ anion. NMR signals similar to the ones observed for **18** confirm the constitution of **19** unambiguously. Also, the UV−vis experiment shows the ferrocene absorbance maximum at 442 nm, which is responsible for the yellow−orange color of all ferrocene containing bioconjugates.

Electrochemical Characterization. The characteristic electrochemical properties of the ferrocene moiety offer a very sensitive detection for such marked biomolecules using methods such as HPLC with electrochemical detection (HPLC-ECD), which range down to the picomolar scale. Therefore, cyclic voltammograms (CV) and square wave voltammograms (SWV) were recorded for all presented compounds (Table 1). Measurements were recorded in 5 mL of CH_3CN/H_2O (1:1), with $NaClO_4$ as the supporting electrolyte (0.1 M) and an analyte concentration of 1 mM. These electrochemical measurements revealed a one-electron, fully reversible behavior for the ferrocenyl group (Figure 3). For all DEPA-CO-Fc-modified peptides, half-wave potentials between 209.5 and 216 mV and peak separations between 80 and 87 mV were found. In comparison, the alkynylferrocene-labeled peptides show similar peak separations but a half-wave potential of around 160 mV.

DISCUSSION

The successful introduction of alkynylated Fc derivatives into dipeptides and different positions of a pentapeptide has been

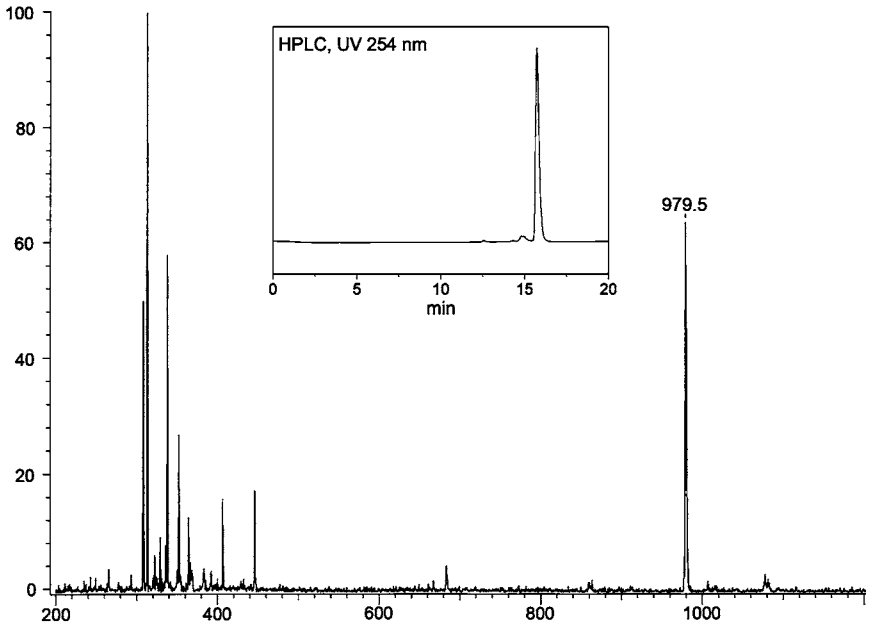

Figure 2. ESI (neg) mass spectrum and HPLC spectrum (RP-C18, 254 nm) of Fc-CO-DEPA-BA-Enk-OH (**19**).

Scheme 3. Synthesis of Enkephalin Derivative 17 by SPPS and Labeling with H-DEPA-CO-Fc (7) To Yield the N-Terminally Labeled Organometallic Conjugate 19

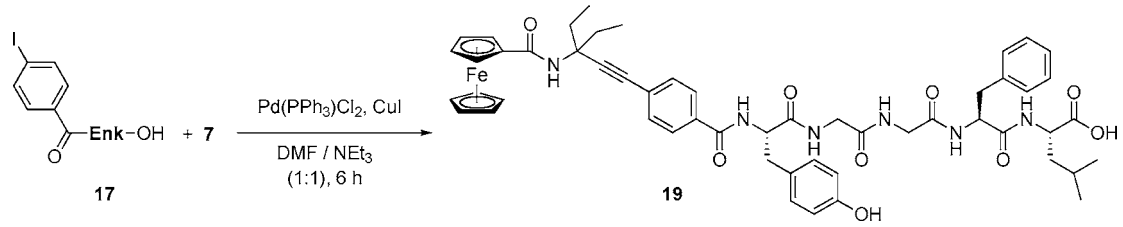

Table 1. Half-Wave Potentials ($E_{1/2}$) and Peak Separation Values (ΔE_{a-c}) of All Ferrocene Conjugates in This Paper

compound	no.	$E_{1/2}$ (mV)	ΔE_{a-c} (mV)
H-DEPA-CO-Fc	**7**	223.0	86
Boc-Ala-Phe(DEPA-CO-Fc)-OMe	**8**	213.0	82
Boc-Leu-Phe(DEPA-CO-Fc)-OMe	**9**	212.0	80
Boc-Phe-Phe(DEPA-CO-Fc)-OMe	**10**	211.5	87
Boc-Tyr-Phe(DEPA-CO-Fc)-OMe	**11**	209.5	85
Boc-Ala-Phe(CC-Fc)-OMe	**12**	163.0	142
Boc-Leu-Phe(CC-Fc)-OMe	**13**	169.0	98
Boc-Phe-Phe(CC-Fc)-OMe	**14**	152.0	73
Boc-Tyr-Phe(CC-Fc)-OMe	**15**	161.0	82
Ac-Enk[Phe^4(DEPA-CO-Fc)]-OH	**18**	210.0	80
Fc-CO-DEPA-BA-Enk-OH	**19**	216.0	80

presented. These results prove the Sonogashira coupling method to be of high value for the easy tethering of metal compounds to modified biomolecules. In this work, we have chosen phenylalanine as the site for modification, which is not easily achieved by other methods. Modification of the phenyl residue may of course alter the binding characteristics of the peptide enkephalin to the opiate receptor. Earlier work on organometallic enkephalin derivatives in which Phe is substituted by ferrocenylalanine ([Fer^4, Leu^5]-Enk) shows a reduced binding affinity (*32*, *33*). On the other hand, a bulky carboranylalanine derivative (Car), which was prepared as a structural probe for Enk ([Car^4, Leu^5]-Enk), shows a 3-fold increased affinity for the opiate receptor as shown in a naloxone displacement assay (*51*, *52*). These results show that there is at least some space in the opiate receptor to accommodate bulky substituents. An interesting Sonogashira method for the synthesis of ferrocene-labeled oligodeoxynucleotides had been presented by Grinstaff and co-workers (*53*). In their work, the Sonogashira coupling reaction was most successful when the oligodeoxynucleotide was still bound to the resin. However, no useful protocol for the regioselective labeling of small peptides was known. In our case, Sonogashira coupling on the resin usually gave a lesser yield of pure products. Therefore, binding of the marker molecule is performed under mild conditions in solution so that neither biomolecule nor labeling group decompose. This process should therefore be suitable for the labeling of more complicated and larger biomolecules. The "expansion of the genetic code" presented by Schultz and co-workers (*54*, *55*) may be an interface for that, since it provides the possibility to introduce unnatural amino acids such as 4-iodophenylalanine into a large number of proteins by recombinant methods (*56*). Such labeled

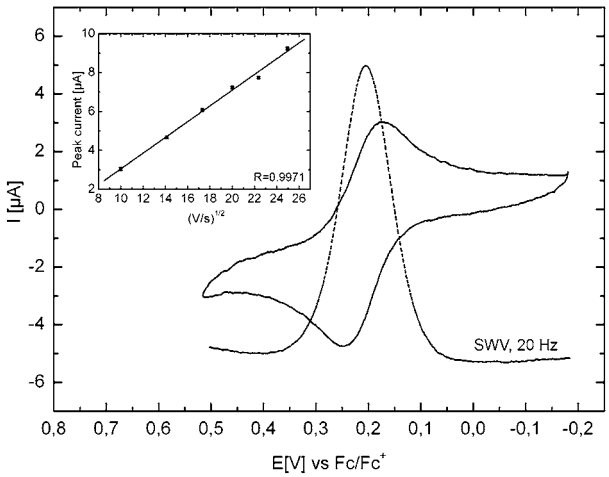

Figure 3. Cyclic and square wave voltammograms of Ac-Enk[Phe^4-(DEPA-CO-Fc)]-OH (**18**). The linearity of the inserted Randles−Sevcik plot indicates a reversible (Nernstian) behavior.

proteins could be purified by HPLC using the very favorable electrochemical properties of the ferrocene label for electrochemical detection, as shown herein.

ACKNOWLEDGMENT

This work was in part financially supported by the Deutsche Forschungsgemeinschaft (DFG) and the Fond der Chemischen Industrie. The authors are grateful to H. Rudy (MS), A. Seith (MS), T. Timmermann (NMR), and T. Coelho (NMR) for technical assistance. Experimental help and insightful discussions with Prof. T. J. J. Müller (Heidelberg) are gratefully appreciated.

LITERATURE CITED

(1) Hagihara, N., Takahashi, S., Kuroyama, Y., and Sonogashira, K. (1980) A Convenient Synthesis of Ethynylarenes and Diethynylarenes. *Synthesis*, 627−630.

(2) Sonogashira, K., Tohda, Y., and Hagihara, N. (1975) A convenient Synthesis of Acetylenes: Catalytic Substitutions of Acetylenic Hydrogen with Bromoalkenes, Iodoarenes and Bromopyridines. *Tetrahedron Lett. 50*, 4467−4470.

(3) Brosch, O., Weyhermüller, T., and Metzler-Nolte, N. (1999) Synthesis of Alkynyl Amino Acids and Peptides and their Palladium-catalyzed Coupling to Ferrocene. *Inorg. Chem. 38*, 5308−5313.

(4) Brosch, O., Weyhermüller, T., and Metzler-Nolte, N. (2000) A two-step Palladium-catalyzed Coupling Scheme for the Synthesis of Ferrocene-labeled Amino Acids. *Eur. J. Inorg. Chem.*, 323−330.

(5) Kayser, B., Altman, J., Nöth, H., Knizek, J., and Beck, W. (1998) Metal Complexes of Alkyne-Bridged α-Amino Acids. *Eur. J. Inorg. Chem.*, 1791−1798.

(6) Kayser, B., Altman, J., and Beck, W. (1999) Benzene-bridged hexaalkynylphenylalanines and first-generation dendrimers thereof. *Chem. Eur. J. 5*, 754−758.

(7) Dibowski, H., and Schmidtchen, F. P. (1998) Bioconjugation of Peptides by Palladium-Catalyzed C−C Cross-Coupling in Water. *Angew. Chem., Int. Ed. 37*, 476−478.

(8) Stokes, A. H., Xu, Y., Tamir, H., Gershon, M. D., Butkerait, P., Kayser, B., Altman, J., Beck, W., and Vrana, K. E. (1998) Para-ethynylphenylalanine (pEPA): A potent inhibitor of tryptophan hydroxylase. *J. Neurochem. 70*, S29.

(9) Kayser, B., Altman, J., and Beck, W. (1997) Alkyne Bridged α-Amino Acids by Palladium Mediated Coupling of Alkynes with *N-t*-Boc-4-iodo-phenylalanine Methyl Ester. *Tetrahedron 53*, 2475−2484.

(10) Ryabov, A. D. (1991) The Biochemical Reactions of Organometallics with Enzymes and Proteins. *Angew. Chem., Int. Ed. Engl. 30*, 931−941.

(11) Jaouen, G., Vessières, A., and Butler, I. S. (1993) Bioorganometallic Chemistry: A Future Direction for Transition Metal Organometallic Chemistry? *Acc. Chem. Res. 26*, 361−369.

(12) Severin, K., Bergs, R., and Beck, W. (1998) Bioorganometallic Chemistry−Transition Metal Complexes with α-Amino Acids and Peptides. *Angew. Chem., Int. Ed. 37*, 1634−1654.

(13) Metzler-Nolte, N. (2001) Labeling of Biomolecules for Medicinal Applications−Bioorganometallic Chemistry at Its Best. *Angew. Chem., Int. Ed. 40*, 1040−1044.

(14) Fish, R. H., and Jaouen, G. (2003) Bioorganometallic Chemistry: Structural Diversity of Organometallic Complexes with Bioligands and Molecular Recognition Studies of Several Supramolecular Hosts with Biomolecules, Alkali-Metal Ions, and Organometallic Pharmaceuticals. *Organometallics 22*, 2166.

(15) van Staveren, D. R., and Metzler-Nolte, N. (2004) Bioorganometallic Chemistry of Ferrocene. *Chem. Rev. 104*, 5931−5985.

(16) Waern, J. B., and Harding, M. M. (2004) Bioorganometallic chemistry of molybdocene dichloride. *J. Organomet. Chem. 689*, 4655−4668.

(17) Allardyce, C. S., Dorcier, A., Scolaro, C., and Dyson, P. J. (2005) Development of organometallic (organo-transition metal) pharmaceuticals. *Appl. Organomet. Chem. 19*, 1−10.

(18) Farkas, D. H. (2001) Bioelectronic DNA chips for the clinical laboratory. *Clin. Chem. 47*, 1871−1872.

(19) Zatsepin, T. S., Andreev, S. Y., Hianik, T., and Oretskaya, T. S. (2003) Ferrocene-containing nucleic acids. Synthesis and electrochemical properties. *Russ. Chem. Rev. 72*, 537−554.

(20) Wang, J. (2001) Glucose Biosensors: 40 Years of Advances and Challenges. *Electroanalysis 13*, 983−988.

(21) Cais, M., Dani, S., Eden, Y., Gandolfi, O., Horn, M., Isaacs, E. E., Josephy, Y., Saar, Y., Slovin, E., and Snarsky, L. (1977) Metalloimmunoassay. *Nature 270*, 535−536.

(22) Cais, M., Slovin, E., and Snarsky, L. (1978) Metalloimmunoassay II. Iron-Metallohaptens from Estrogen steroids. *J. Organomet. Chem. 160*, 223−230.

(23) Forrow, N. J., Foulds, N. C., Frew, J. E., and Law, J. T. (2004) Synthesis, Characterization, and Evaluation of Ferrocene-Theophylline Conjugates for Use in Electrochemical Enzyme Immunoassay. *Bioconjugate Chem. 15*, 137−144.

(24) Salmain, M., Vessières, A., Brossier, P., Butler, I. S., and Jaouen, G. (1992) Carbonylmetalloimmunoassay (CMIA) a new type of nonradioisotopic immunoassay. *J. Immunol. Methods 148*, 65−75.

(25) Vessières, A., Salmain, M., Brossier, P., and Jaouen, G. (1999) Carbonylmetallo immuno assay: a new application for Fourier transform infrared spectroscopy. *J. Pharm. Biomed. Anal. 21*, 625−633.

(26) Guillena, G., Rodriguez, G., Albrecht, M., and Van Koten, G. (2002) Covalently bonded platinum(II) complexes of a-amino acids and peptides as a potential tool for protein labeling. *Chem. Eur. J. 8*, 5368−5376.

(27) Guillena, G., Halkes, K. M., Rodriguez, G., Batema, G. D., van Koten, G., and Kamerling, J. P. (2003) Organoplatinum(II) Complexes as a Color Biomarker in Solid-Phase Peptide Chemistry and Screening. *Org. Lett. 5*, 2021−2024.

(28) Albrecht, M., and van Koten, G. (2001) Platinum group organometallics based on "pincer" complexes: sensors, switches, and catalysts. *Angew. Chem., Int. Ed. 40*, 3750−3781.

(29) Takenaka, S. (2001) Highly Sesitive Probe for Gene Analysis by Electrochemical Approach. *Bull. Chem. Soc. Jpn. 74*, 217−224.

(30) Degani, Y., and Heller, A. (1988) Direct Electrical Communication between Chemically Modified Enzymes and Metal Electrodes. 2. Methods for Bonding Electron-Transfer Relays to Glucose Oxidase and D-Amino-Acid Oxidase. *J. Am. Chem. Soc. 110*, 2615−2620.

(31) Schuhmann, W., Ohara, T. J., Schmidt, H.-L., and Heller, A. (1991) Electron Transfer between Glucose Oxidase and Electrodes via Redox Mediators Bound with Flexible Chains to the Enzyme Surface. *J. Am. Chem. Soc. 113*, 1394−1397.

(32) Cuignet, E., Sergheraert, C., Tartar, A., and Dautrevaux, M. (1980) *β*-Ferrocenylalanyl Peptides. I. Synthesis of [Fer^4, Leu^5] Enkephalin. *J. Organomet. Chem. 195*, 325−329.

(33) Cuignet, E., Dautrevaux, M., Sergheraert, C., Tartar, A., Attali, B., and Cros, J. (1982) Synthesis and biological activity of metallocene enkephalin analogs. *Eur. J. Med. Chem. 17*, 203−206.

(34) Maes, P., Ricouart, A., Escher, E., Tartar, A., and Sergheraert, C. (1988) Synthesis and biological Activity of new metallocenic Angiotensin II Analogs. *Collect. Czech. Chem. Commun. 53*, 2914−2919.

(35) Brunet, J. C., Cuignet, E., Dautrevaux, M., Demarly, A., Gras, H., Marcincal, P., Sergheraert, C., Tartar, A., Vanvoorde, J. C., and Vanpoucke, M. (1981) Use of Organometallic amino acids as a tool for studying interactions in Phenylalanine-containing Peptides. In *Peptides 1980. Proceedings of the Sixteenth European Peptide Symposium* (Brunfeldt, K., Ed.) pp 603−607, Scriptor: Copenhagen.

(36) Epton, R., Marr, G., Willmore, G. A., Hudson, D., Snell, P. H., and Snell, C. R. (1981) Synthesis and biological activity of (D-Fer, Leu5)- and (L-Fer4, Leu5)- enkephalins. *Int. J. Biol. Macromol. 3*, 395−396.

(37) Noor, F., Wüstholz, A., Kinscherf, R., and Metzler-Nolte, N. (2005) A cobaltocenium peptide bioconjugate shows enhanced cellular uptake and directed nuclear delivery. *Angew. Chem., Int. Ed. 44*, 2429−2432.

(38) Galka, M. M., and Kraatz, H.-B. (2002) Electron-Transfer Studies on Self-Assembled Monolayers of Helical Ferrocenoyl-Oligoproline-Cystamine Bound to Gold. *ChemPhysChem*, 356−359.

(39) Plumb, K., and Kraatz, H.-B. (2003) Interaction of a Ferrocenoyl-Modified Peptide with Papain: Toward Protein-Sensitive Electrochemical Probes. *Bioconjugate Chem. 14*, 601−606.

(40) Bediako-Amoa, I., Sutherland, T. C., Li, C.-Z., Silerova, R., and Kraatz, H.-B. (2004) Electrochemical and Surface Study of Ferrocenoyl Oligopeptides. *J. Phys. Chem. B 108*, 704−714.

(41) Hughes, J., Smith, T. W., Kosterlitz, H. W., Fothergill, L. A., Morgan, B. A., and Morris, H. R. (1975) Identification of two related pentapeptides from the brain with potent opiate agonist activity. *Nature 258*, 577−579.

(42) Clement-Jones, V., and Besser, G. M. (1984) Opiod Peptides in Humans and their Clinical Significance. In *The Peptides: Analysis, Synthesis, Biology* (Udenfried, S., and Meienhofer, J., Eds.) pp 323−389, Adademic Press: New York.

(43) Morley, J. S. (1980) Structure-Acitivity Relationships of Enkephalin-Like Peptides. *Annu. Rev. Pharmacol. Toxicol. 20*, 81−110.

(44) Griffin, J. F., Langs, D. A., Smith, G. D., Blundell, T. L., Tickle, I. J., and Bedarkar, S. (1986) The crystal structures of [Met5]-enkephalin and a third form of [Leu5]enkephalin: Observations of a novel pleated β-sheet. *Proc. Natl. Acad. Sci. U.S.A. 83*, 3272−3276.

(45) Ricouart, A., Maes, P., Battmann, T., Kerdelhue, B., Tartar, A., and Sergheraert, C. (1988) Photosubstitution of cymantrenylalanine as a tool in peptide chemistry. Synthesis and biological activity of new GnRH analogs. *Int. J. Pept. Protein Res. 32*, 56−63.

(46) van Staveren, D. R., and Metzler-Nolte, N. (2002) Labeling of [Leu^5]-Enkephalin with organometallic Mo complexes by solid-phase synthesis. *J. Chem. Soc., Chem. Commun.*, 1406−1407.

(47) Metzler-Nolte, N. (2002) Labeling of Peptides with Organometallics by SPPS. *Spec. Chem. Mag.*, 34−36.

(48) Meienhofer, J. (1979) *The Mixed Carbonic Anhydride Method of Peptide Synthesis*, Academic Press: London.

(49) Lei, H., Stoakes, M. S., Herath, K. P. B., Lee, J., and Schwabacher, A. W. (1994) Efficient synthesis of a Phosphinate Bis-Amino Acid and its Use in the Construction of Amphiphilic Peptides. *J. Org. Chem. 59*, 4206−4210.

(50) de Hatten, X., Weyhermüller, T., and Metzler-Nolte, N. (2004) Ferrocenoyl peptides with sulfur-containing side chains: Synthesis, solid state and solution structures. *J. Organomet. Chem. 689*, 4856−4867.

(51) Eberle, A., Leukart, O., Schiller, P., Fauchère, J.-L., and Schwyzer, R. (1977) Hormone-Receptor Interactions: [4-Carboranylalanine, 5-Leucine]-Enkephalin as a Structural Probe for the Opiate Receptor. *FEBS Lett. 82*, 325−328.

(52) Fauchère, J., Leukart, O., Eberle, A., and Schwyzer, R. (1979) The Synthesis of [4-Carboranylalanine, 5-Leucine]-Enkephalin. *Helv. Chim. Acta 62*, 1385−1395.

(53) Beilstein, A., and Grinstaff, M. W. (2001) Synthesis and characterization of ferrocene-labeled oligodeoxynucleotides. *J. Organomet. Chem. 637−639*, 398−406.

(54) Ellman, J. A., Mendel, D., Anthony-Cahill, S., Noren, C. J., and Schultz, P. G. (1991) Biosynthetic Methods for Introducing Unnatural Amino Acids Site-Specifically into Proteins. *Methods Enzymol. 202*, 301−336.

(55) Cornish, V. W., Benson, D. R., Altenbach, C. A., Hideg, K., Hubbell, W. L., and Schultz, P. G. (1994) Site-specific Incorporation of Biophysical Probes into Proteins. *Proc. Natl. Acad. Sci. U.S.A. 91*, 2910−2914.

(56) Xie, J., Wang, L., Wu, N., Brock, A., Spraggon, G., and Schultz, P. G. (2004) The site-specific incorporation of *p*-iodo-L-phenylalanine into proteins for structure determination. *Nature Biotechnol. 22*, 1297−1301.

BC050259C

PNA−Nitrogen Mustard Conjugates Are Effective Suppressors of HER-2/neu and Biological Tools for Recognition of PNA/DNA Interactions

Zhanna V. Zhilina,[†] Amy J. Ziemba,[†] Peter E. Nielsen,[‡] and Scot W. Ebbinghaus[†,*]

Arizona Cancer Center, University of Arizona, 1515 North Campbell, 85724, Tucson, Arizona, and Department of Medical Biochemistry and Genetics, The Panum Institute, University of Copenhagen, Blegdamsvej 3c, 2200 Copenhagen N, Denmark.
Received October 7, 2005

Peptide nucleic acids (PNAs) are promising tools for gene regulation. One of the challenges of using PNAs as gene regulators is the need to optimize the efficiency of interaction with critical sequences of DNA. To improve the efficiency of binding between PNAs and the HER-2/neu promoter, mono- and bis-pyrimidine-rich PNAs were conjugated to a nitrogen mustard at either the amino or carboxy terminus. Gel shift analysis demonstrated that conjugation to an alkylating agent slowed PNA binding and favored PNA:DNA:DNA triplex helix formation while preserving a high binding affinity. Sites of DNA alkylation were visualized by piperidine cleavage and showed PNA binding first by Hoogsteen bond formation with the target duplex to form a stable PNA:DNA:DNA triplex structure which is later converted to a PNA:DNA:PNA triple helix by strand invasion and Watson−Crick base pairing by a second PNA molecule. In this way, PNA-directed DNA alkylation was used to deduce the mode of PNA binding. Transient transfection experiments demonstrated that the PNA−nitrogen mustard conjugates suppressed HER-2/neu expression by up to 80%. In comparison with an unmodified mono-PNA or a bis-PNA, these results indicate that the covalent adducts stabilized PNA binding in cells and suggest that the conjugation of PNAs to nitrogen mustards is a robust strategy for developing antigene PNA oligonucleotides to prevent transcription.

INTRODUCTION

Antigene and antisense strategies with peptide nucleic acids (PNAs)[1] have attracted a great deal of attention in medicinal and biological chemistry (*1*−*5*). The ability of oligonucleotides to recognize specific DNA or RNA sequences affords a versatile approach to control gene expression, but native DNA or RNA oligomers are susceptible to endogenous nucleases and lack the membrane permeability necessary for many in vivo applications. As a result, there has been considerable interest in the development of synthetic structures that specifically recognize and bind selectively to DNA, possess increased resistance to nuclease digestion, and optimize membrane permeability (*6*−*8*). Peptide nucleic acids are DNA mimics in which the sugar−phosphate backbone has been substituted by *N*-(2-aminoethyl)glycine units; therefore, PNAs possess a neutral backbone, which provides a unique advantage for hybridization relative to DNA or RNA oligomers (*9*−*11*). PNAs can bind to complementary sequences by Watson−Crick base pairing, and are able to discriminate single base mismatches. Binding is characterized by high affinity and high rates of association, together giving PNAs the ability to disrupt double stranded DNA by forming a DNA−PNA strand-invasion complex. PNAs are not substrates for endogenous nucleases or proteases, suggesting that they will be highly active in vivo (*12*−*14*).

The inhibition of gene transcription by PNAs presents a series of technical challenges. One of them is the need to optimize the efficiency of DNA binding to critical sequences within gene promoters, which might be accomplished by modifying the PNA via terminal conjugation of a small molecule. Different chelating and intercalating agents were successfully conjugated to PNAs in order to enhance the duplex invasion potency of the PNAs and increase the stability of the PNA−DNA complex (*15*−*20*). However, there are no reports on PNA terminal modification with small molecules resulting in more effective downregulation of gene expression. We postulated that PNA conjugation to a DNA alkylating agent would significantly improve gene regulation by stabilizing PNA binding to a target sequence. In this report we present the synthesis of a PNA−alkylator conjugate, using a short, symmetric PNA and a nitrogen mustard as an alkylating agent.

The HER-2/neu oncogene is overexpressed in a number of human cancers, and its overexpression correlates with poor clinical outcome (*21*−*23*). The results of clinical studies with HER-2/neu-directed therapies demonstrate that preventing the expression or function of the HER-2/neu gene product can induce the regression of metastatic tumors that overexpresses HER-2/neu (*24*, *25*). The HER-2/neu oncogene is a good target for antigene oligonucleotide strategies because of the presence of polypurine tracts capable of triplex formation with triplex-forming oligonucloetides (TFOs) that can prevent in vitro transcription (*26*, *27*) and transcription factor binding (*28*), and reduce HER-2/neu mRNA levels in a breast cancer cell line (*29*). The HER-2/neu promoter was successfully used for evaluating triplex formation with TFO−alkylator or TFO−minor groove binder conjugates (*30*−*32*) and strand invasion complex formation with PNAs (*33*). The polypurine tract is located from −218 to −245 upstream of the first codon (+1) in a region of the HER-2/neu promoter (Figure 1) that serves as an alternate transcription initiator that can function independently of the TATA box (*34*).

Nitrogen mustard derivatives are widely used in chemotherapy (*35*−*37*). The biological activity of these agents is usually

* To whom correspondence should be addressed: E-mail: sebbinghaus@azcc.arizona.edu; phone (520) 626-3424; fax (520) 626-5462.

[†] University of Arizona.

[‡] University of Copenhagen.

[1] Abbreviations. PNA, peptide nucleic acid; TFO, triplex forming oligonucleotide, PAM, phenyl acetic acid mustard; Chl, chlorambucil.

10.1021/bc0502964 CCC: $33.50 © 2006 American Chemical Society
Published on Web 01/04/2006

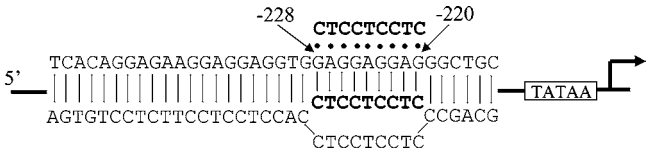

Figure 1. Schematic representation of the HER-2/neu promoter target sequence and two PNA molecules forming a strand invasion complex. The target sequence is a 9 bp purine/pyrimidine tract from −220 to −228 upstream of the first codon. Dots represent Hoogsteen hydrogen bonds and vertical lines represent Watson−Crick bonds.

mediated through alkylation at N-7 of guanine and subsequent DNA interstrand cross-linking (*38*−*40*). However, covalent binding can occur at multiple DNA sites, bringing nonspecific toxicity; moreover, the efficiency of the nitrogen mustards is limited because of deactivation by hydrolysis or due to reaction with nucleophilic molecules other than DNA. Nitrogen mustards have been conjugated to TFOs in order to direct highly specific DNA alkylation (*41*, *42*). Because PNAs are highly resistant to degradation by a variety of enzymes, we began investigating them as candidate antigene molecules for suppression of HER-2/neu expression. We initially postulated that PNA modification with an alkylating agent would not only stabilize the DNA/PNA complex but might also facilitate strand invasion by stabilizing Hoogsteen strand during the process of disrupting the duplex by a second PNA strand. Furthermore, PNA−alkylator conjugates can be used as tools to study the binding mechanism between DNA and PNA by positioning the alkylating moiety at different PNA ends and analyzing the sites of interaction with the target duplex.

In this report we describe the design and synthesis of novel bioconjugates of the nitrogen mustards (phenylacetic acid mustard (PAM) and chlorambucil (Chl)) to a PNA, demonstrate site-specific DNA alkylation with the target site in the HER-2/neu promoter, and show strong downregulation of HER-2/neu promoter activity in reporter gene assays.

EXPERIMENTAL PROCEDURES

Materials. Solvents and chemicals obtained from commercial sources were analytical grade or better and were used without further purification. Solvents for HPLC analysis were obtained as HPLC grade and were filtered (0.2 μM) prior to use. PNA VII (see Table 1 for sequence information) was synthesized according to published procedures (*43*, *44*). PNAs I, III, V, and IX were purchased from BioSynthesis, Inc. (Lewisville, TX) on a 2 μM scale and obtained on solid support prior to final deprotection for further modification. A small portion of the PNAs (about 1/10 of the provided PNAs on resin) was cleaved from the solid support before modification for analysis. PNAs were cleaved from the solid support by mixing the resin with 300 μL of cleavage cocktail (95% TFA, 5% *m*-cresol). The mixture was agitated for 90 min, filtered off, and precipitated with cold diethyl ether, followed by HPLC purification. All PNAs were 95% pure or greater by C18 HPLC. Pentafluorophenyl esters of phenylacetate mustard (PFP−PAM) and chlorambucil (PFP−Chl) were synthesized in our group as previously described (*45*).

Spectral Analysis. Matrix-assisted laser desorption/ionization-time-of-flight (MALDI-TOF) mass spectra were acquired using a Micromass (Manchester, UK) MALDI-LR TOF mass spectrometer and Applied Biosystems Voyager DE-STR (Framingham, MA), operating a 337 nm nitrogen laser. Samples were mixed with an equal volume of a saturated α-cyano solution in 50% acetonitrile/50% water containing 0.1% trifluoroacetic acid (TFA), and 1 μL was spotted on the target plate and allowed to air-dry prior to mass analysis. Mass spectra acquired using the Micromass mass spectrometer were collected in Reflection mode with a 15000 V source voltage using a 0.5 ns sample period. The reflection voltage was set to 2000 V. The detector was held at 1800 V and 5 laser shots at 3 Hz were combined per mass spectrum recorded. Mass spectra acquired using the Applied Biosystems MALDI-TOF mass spectrometer were collected in positive reflection mode with an acceleratory voltage of 20000 V. The grid voltage was set at 66% with an extraction delay time of 275 ns. 400 laser shots at 20 Hz were combined per mass spectrum recorded. All modified and unmodified PNAs were analyzed by reverse phase HPLC using a VYDAC C18 250 × 10 mm column with a gradient of 0 to 80% solvent B over 40 min. Solvent B was 0.1% TFA in acetonitrile (flow rate 4 mL/min), solvent A was 0.1% TFA in water. Detection was carried out by UV absorbance at 260 nm. Preparative HPLC purification was performed on Varian proStar system equipped with a photodiode array (PDA) detector.

Synthesis of PNA−Mustard Conjugates. *Mono-PNA−5′PAM Conjugate (PNA II).* The mono-PNA (I) was obtained on solid support with the free 5′ (N-terminal) amino group but all other side chain protecting groups in place and was incubated in 300 μL of dry dichloromethane (DCM) for 2 h, then the resin was filtered and washed with DCM (2 × 2 mL). PFP−PAM (2.5 mg, 6 μmol) was dissolved in 150 μL of DCM and mixed with 150 μL of dry dimethylformamide (DMF) and 50 μL of triethylamine (Et_3N). The resulting mixture was added to the resin and bubbled through with argon for 3 h. The resin was filtered, washed with DMF (2 × 2 mL), DCM (2 × 2 mL), and dried under vacuum for 2 h and then overnight in a desiccator. The resulting PNA−5′PAM conjugate was then cleaved from the resin by using 500 μL of TFA/*m*-cresol cleavage cocktail as described for unmodified PNAs, HPLC purified (t_R = 19.4 min) and lyophilized. MALDI-TOF MS analysis for PNA II ($C_{123}H_{170}Cl_2N_{48}O_{37}$): calculated 2982.9; found 2983.5.

Mono-PNA−3′Chl Conjugate (PNA IV). The mono-PNA (III) was obtained on the solid support with standard protecting groups on the 5′ terminus and side chains except for a lysine at the 3′ end that was protected with methoxytrityl (Mmt) for selective deprotection. PNA IV had a cysteine (S) at the C-terminus to separate the target lysine from the solid support and provide a potential site for additional conjugation. The resin was incubated and washed with DCM as described for PNA I.

Table 1. PNA Analysis by MALDI-TOF and HPLC[a]

name	description	sequence	$M_{calcd.}$	$M_{obsd.}$	t_R, min
I	mono-PNA	CTCCTCCTC-O-KK	2724.5	2725.3	14.8
II	PNA−5′PAM	PAM-CTCCTCCTC-O-KK	2982.9	2983.5	19.4
III	PNA−SH	CTCCTCCTC-O-KK-S	2848.7	2850.9	15.5
IV	PNA−3′Chl	CTCCTCCTC-O-KK(Chl)-S	3098.9	3100.6	17.2
V	bis-PNA(4K)	KK-TCCTCCTCC-OOO-CCTCCTCCT-KK	5577.69	5577.16	15.1
VI	bis-PNA(4K)−5′Chl	Chl-KK-TCCTCCTCC-OOO-CCTCCTCCT-KK	5847.9	5847.03	16.22
VII	bis-PNA(J)	KK-TCCTCCTCC-OOO-JJTJJTJJT-KSG	5609.7	5610.2	15.1
VIII	bis-PNA(J)−5′Chl	Chl-KK-TCCTCCTCC-OOO-JJTJJTJJT-KSG	5881.7	5882.4	18.64
IX	bis-PNA	TCCTCCTCC-OOO-K-CCTCCTCCT	5193.2	5193.9	18.2

[a] C, T, J = cytosine, thymine, and pseudoisocytosine PNA residues; O = linker; K, S, G = lysine, cysteine, and glycine amino acid residues; PAM = phenylacetic acid mustard; Chl = chlorambucil.

To remove the Mmt protecting group, the resin was treated with 3% TFA in DCM (2 × 200 μL for 10 min each) and washed with DCM and DMF (2 × 2 mL) between and after each treatment. PFP−Chl (2.6 mg, 6 μmol) was dissolved in 150 μL of DCM and mixed with 150 μL of DMF and 50 μL of Et_3N. The resulting mixture was added to the resin and bubbled through with argon for 3 h. The resin was filtered and washed with DMF (2 × 2 mL) and DCM (2 × 2 mL). The PNA was then deprotected with 200 μL of piperidine/DMF (1/4 v/v) for 30 min. The resin was filtered, washed with DMF (2 × 2 mL) and DCM (2 × 2 mL), dried under vacuum for 2 h, and left overnight in a desiccator. The resulting PNA−3′Chl conjugate (IV) was cleaved from the resin with TFA/*m*-cresol, HPLC purified (t_R = 17.2 min) and lyophilized as described above. MALDI-TOF MS analysis for PNA IV ($C_{127}H_{177}Cl_2N_{49}O_{38}S$): calculated 3098.9; found 3100.6.

Bis-PNA−5′Chl Conjugates (PNAs VI and VIII). The unmodified bis-PNAs (V and VII) were obtained on solid support with the free 5′ (N-terminal) amino group but all other side chain protecting groups in place. They were conjugated to Chl at the 5′ end as described above for PNA II, except that PFP−Chl (2.6 mg, 6 μmol for each PNA) was used in place of PFP−PAM. After synthesis, the conjugates were HPLC purified (PNA VI t_R = 16.22 min; PNA VIII t_R = 18.64 min) and lyophilized. MALDI-TOF MS analysis for PNA VI ($C_{241}H_{339}Cl_2N_{97}O_{74}$): calculated 5847.9; found 5947.03. MALDI-TOF MS analysis for VIII ($C_{240}H_{360}Cl_2N_{97}O_{75}S$): calculated 5881.7; found 5882.4.

Electrophoretic Mobility Shift Assay (EMSA) Analysis of DNA/PNA Interaction. PNAs were incubated with a 36-base pair HER-2/neu duplex target sequence end-labeled on the pyrimidine strand. Reaction mixtures including increasing concentrations of the PNA with 0.01 μM target duplex in $NaPO_4$ buffer (10 mM, pH 6.5) were incubated for 24 h. The complexes were separated on a 10% nondenaturing gel at room temperature with 1× TAE (pH 6.5) in both the gel and running buffer and visualized by autoradiography. The rate of PNA binding was analyzed by adding 0.1 μM PNAs and 36-base pair HER-2/neu duplex target sequence (0.01 μM) end-labeled on the purine strand and stopping the reactions by freezing the samples at −80 °C at various time points from 1 to 18 h. The products were then separated on nondenaturing gels and visualized by autoradiography.

Piperidine Cleavage. A 250 base pairs (bp) Pst/XmaI fragment of the pGL3/HNP410 plasmid containing a 410 bp HER-2/neu promoter in the pGL3 basic luciferase plasmid (Promega) was used to create an end-labeled template by Klenow filling. DNA/PNA complex formation was performed by incubating 0.02 μM of labeled promoter fragment with 2 concentrations of PNA−5′PAM and PNA−3′Chl (0.1 and 1.0 μM) for 2, 4, 8, and 18 h in a final volume of 10 μL of 10 mM $NaPO_4$ (pH 6.5) at 37 °C. Reactions without PNAs were performed to show nonspecific cleavage sites of the radiolabled template by piperidine. Piperidine cleavage reactions were separated on a 10% denaturing gel and subjected to autoradiography. Maxam−Gilbert G-reactions were performed to identify alkylated guanine residues, and these reactions were run alongside the piperidine cleavage lanes as indicated in Figures 4 and 5; however, images from different autoradiographs were combined into composite figures in these illustrations in order to optimize the intensity of the exposure between the piperidine cleavage lanes and the G-reactions.

Transient Transfection Analysis. HeLa cells were obtained from the American Type Culture Collection and cultured as recommended by the supplier. The pGL3/HNP410 plasmid (2 μg) containing the HER-2/neu promoter was incubated in 10mM $NaPO_4$ (pH 6.5) at 37 °C with 1 and 10 μM of PNAs for 18 h. Transfection mixtures included the pGL3/HNP410 plasmid (with or without PNAs), 20 ng of an internal control plasmid (pRL/SV40, Promega), and 2 μL of Lipofectamine 2000 (Invitrogen). HeLa cells were incubated with the transfection mixture, cell lysates were obtained at 24, 48, and 72 h, and dual luciferase assays (Promega) were performed. All experiments were repeated three times, normalized for transfection efficiency, and are presented as a percentage of luciferase activity from plasmid without PNA treatment.

RESULTS

Design of the PNA−PAM Conjugates. Our previous results on targeting a polypurine tract in the HER-2/neu promoter with TFOs demonstrated that unmodified TFOs easily dissociated from the target sequence when transfected into tumor cells, while TFOs modified with an alkylating agent prevented helicase activity and suppressed HER-2/neu driven luciferase activity in cells for up to 72 h (*31*). We postulated that PNAs similarly modified with an alkylating agent would improve the stability of the PNA/DNA complex and improve the PNAs ability to prevent HER-2/neu expression. To simplify synthesis and product analysis, we decided to start with short mono-PNAs, and designed a mono-PNA (I) to target the HER-2/neu polypurine tract from −220 to −228 (Figure 1). This PNA, CTCCTCCTC, has perfect mirror symmetry and was designed to be able to simultaneously bind to the target sequence by Hoogsteen bonding (triplex formation) in parallel to the purine rich strand and by Watson−Crick bonding (strand invasion) in antiparallel orientation to the purine strand. To increase PNA solubility and strand invasion, two lysine residues were added to the C-terminus of the PNAs through a single 8-amino-2,6-dioxaoctanoic acid (O) linker (Table 1).

To conjugate the N-terminus of PNA I to the drug, we used the α-amino group of the peptide backbone of the last nucleic base in the PNA I sequence. To modify the C-terminus, we used the ϵ-amino group of one of the lysines of PNA III. That ϵ-amino group was protected with an acid-labile monomethoxytrityl (Mmt) protecting group. Deprotection of the Mmt group can be done with mild acidic conditions (3% TFA in DCM) while keeping nucleic bases, the other lysine side chain, and the N-terminus protected to create PNA−drug conjugation only at C-terminus (*46*). PNA III was also designed with a cysteine residue at the C-terminus that separated the target lysine from the solid support for the conjugation reaction and could eventually be used as a site of further conjugation, for example with a carrier peptide. For these studies we selected two commonly used nitrogen mustards, phenyl acetic acid mustard (PAM) and chlorambucil (Chl). To demonstrate the feasibility of the conjugation between PNA and alkylating agent, we started with commercially available chlorambucil, which was easily modified with PFP for conjugation in one step (*45*). PAM has a longer hydrolysis half-life but is slightly less reactive compared to chlorambucil. In this way we could evaluate the ability of two reactive nitrogen mustards conjugated to the PNA to direct site-specific DNA alkylation and regulate gene expression.

Conjugation of the Nitrogen Mustards to PNAs. The conjugation of the nitrogen mustard to the PNAs was done manually on solid support using an acylation reaction with the active ester of the nitrogen mustard and a free amino group of the PNA. Pentafluorophenyl esters are widely used in reactions with free amino groups to give amide bonds, and we synthesized the pentafluorophenyl (PFP) ester of phenylactate mustard and chlorambucil according to previously published methods (*45*). A mixture of anhydrous solvents was used for the coupling, with DMF as a traditional solvent for coupling in peptide synthesis on solid support, DCM as a more suitable solvent for the highly lipophilic PFP−PAM, and an excess of anhydrous triethylamine as an activating agent. The anhydrous conditions

Scheme 1. Synthesis of PNA−5′PAM (II)

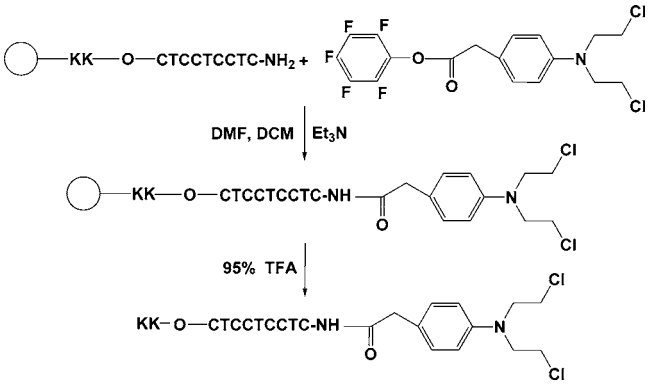

Scheme 2. Synthesis of PNA−3′Chl (IV)

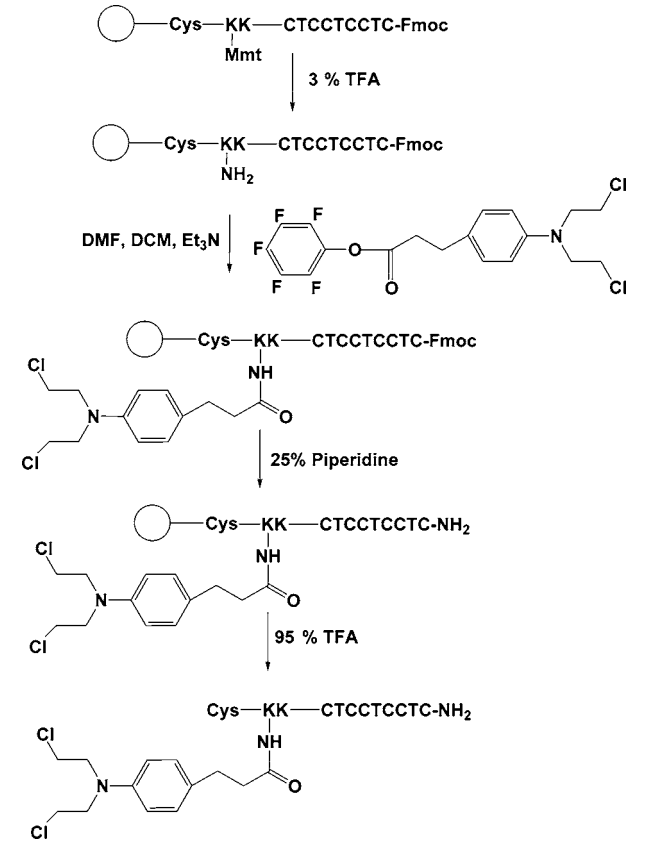

protect the nitrogen mustard from hydrolysis, and coupling requires only a small excess of PFP−PAM. PNA I on solid support had a free amino group at the N-terminus (Scheme 1) and was ready for conjugation unlike PNA III, which needed additional preparation for the coupling (Scheme 2). To put the drug molecule specifically on the C-terminus and avoid side reactions, we applied the strategy of selectively deprotecting a lysine bearing a labile protecting group, specifically an Mmt group on the ϵ-amine of the lysine at the C-terminus of PNA III. Mmt is a well-known acid-sensitive, trityl-type protecting group that can be removed with 3% TFA in DCM. The mild conditions allowed us to deprotect only the desired ϵ-amino group of the lysine at the C-terminus and proceed with coupling at this position. After the coupling reaction (3 h), the resin was dried and then cleaved using standard conditions. HPLC chromatograms (Figure 2) of the coupling reaction mixtures demonstrated the peak of unmodified PNA (t_R 14−15 min) and a smaller peak of conjugated product (t_R 17−19 min), the estimated yield was 20−40%, and prolonging the coupling reaction up to 18 h did not improve the yield. The conjugates

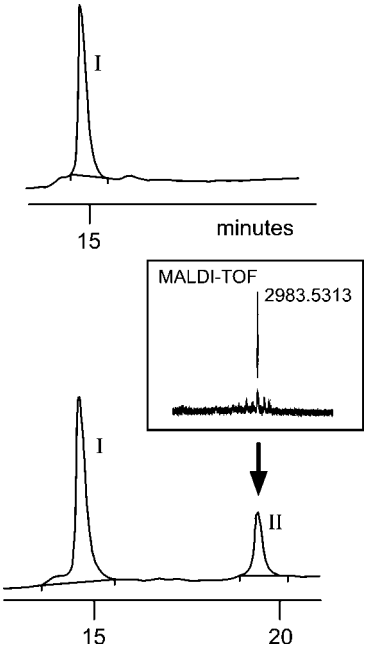

Figure 2. HPLC monitoring of the PNA−PAM conjugation reaction and MALDI-TOF spectra of conjugate II. The top chromatogram shows unconjugated mono-PNA (I), t_R= 14.8 min. The bottom chromatogram shows the reaction mixture with a new peak of the PNA−5′PAM conjugate (II), t_R= 19.4 min.

were characterized by mass spectral analysis, confirming the expected molecular weights (Table 1).

Analysis of PNA−Nitrogen Mustard Binding by EMSA. To evaluate the influence of the alkylating agent on the efficiency, mode, and rate of mono-PNA binding, PNA I (unmodified) was compared to PNA II (5′ PAM conjugate) by EMSA. The PNAs were incubated with a synthetic 36-mer duplex target sequence end-labeled on the pyrimidine strand in order to show displacement of the pyrimidine strand (Figure 3A). To monitor the rate of PNA binding, PNAs were incubated with the synthetic 36-mer duplex target end-labeled on the purine strand at a fixed concentration of the PNA, and reactions were stopped at various time points (Figure 3B). PNA I and PNA II showed similar affinities for the target duplex at pH 6.5, producing a transition of the target duplex to single stranded DNA and slow mobility complexes at 100 nM PNA concentrations, with complete disappearance of the duplex band at 1 μM (Figure 3A). PNAs and particularly covalently bound PNA−nitrogen mustard conjugates are not expected to dissociate from DNA in solution, so that equilibrium dissociation constants are not practical. C_{50} values (PNA concentration leading to 50% duplex DNA binding) can be used to estimate and compare the affinity of PNAs for duplex DNA under given experimental conditions, and C_{50} values for both PNA I and II would be $<$100 nM, slightly favoring PNA I, since this concentration leads to $>$50% DNA binding (shift in the duplex band to single stranded DNA and slow mobility PNA:DNA complexes at 100 nM PNA). Conjugation to a nitrogen mustard did not improve the pH dependent binding by the cytosine-rich PNA, and although binding was less efficient for both PNAs at pH 7.0, it was similar for PNA I and PNA II, again slightly favoring PNA I (not shown).

Interestingly, when the efficiency of PNA binding was evaluated over time, the presence of the nitrogen mustard on the PNA slowed binding to duplex DNA and appeared to favor binding by PNA$(DNA)_2$ triplex formation (Figure 3B). Both PNA I and II probably first bind by triplex formation with duplex DNA, forming PNA$(DNA)_2$ triplexes (seen as a shift in the duplex to a slower mobility complex at 100 nM PNA in

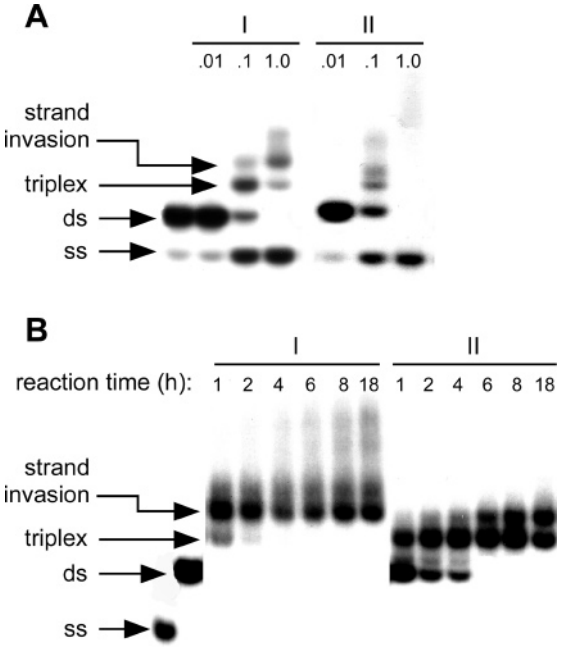

Figure 3. PNA binding to a synthetic duplex target sequence by EMSA. Representative native EMSAs comparing an unmodified mono-PNA (PNA I) to the same PNA conjugated to PAM at the 5′ terminus (PNA II). (A) Increasing concentrations of PNAs were mixed with duplex DNA radiolabeled on the pyrimidine strand for a fixed incubation time of 18 h at pH 6.5. (B) Fixed concentrations of the PNAs (100 nM) were mixed with duplex DNA radiolabeled on the purine strand for increasing incubation times at pH 6.5.

Figure 3A and 3B, accompanied by partial displacement of the pyrimidine strand in Figure 3A). Higher PNA concentrations (Figure 3A) or longer incubation times (Figure 3B) resulted in a further shift of the duplex to even slower mobility complexes (Figure 3A and 3B), accompanied by complete displacement of the pyrimidine DNA strand (Figure 3A), which is a characteristic of strand invasion and $(PNA)_2$DNA triplex formation with the binding of a second PNA molecule.

Piperidine Cleavage Analysis of Site-Directed DNA Alkylation by PNA−Nitrogen Mustard Conjugates. To determine the DNA alkylation sites and deduce the orientation of PNA−alkylator conjugate binding, piperidine cleavage was used. Sites of DNA alkylation can be visualized by converting these sites into single strand breaks with piperidine and heat as previously described (*30*). A 250 base pair promoter fragment was end-labeled on the purine-rich strand and incubated with 0.1 and 1 μM of 5′ and 3′ mono-PNA−alkylator conjugates (PNAs II and IV) over increasing amounts of time. The cleavage products were resolved on a sequencing gel and aligned with a G reaction to determine the alkylated bases.

PNA II (Figure 4A) demonstrated highly specific covalent adduct formation with G-229 with 0.1 μM of the conjugate, consistent with binding in a parallel orientation with Hoogsteen bonds to the duplex to direct the alkylation to the duplex/triplex junction. At higher concentrations and after prolonged incubation, alkylation of several additional guanines was observed, most prominently G-219, consistent with strand invasion and PNA binding in antiparallel orientation to the purine strand during the formation of a triplex invasion complex. Minor alkylation sites at G-241, G-238, and G-231 were also observed, probably due to binding of the PNA to less ideal binding sites in the highly repetitive HER-2/neu polypurine tract; for example, the PNA could bind to a single mismatch target sequence from −232 to −240, placing the alkylator at G-241 and G-231 at the junction of the duplex/triplex junction.

For PNA IV (Figure 4B), the major alkylation site is G-219, again consistent with the conjugate binding in parallel orientation to dsDNA through Hoogsteen bond formation. Minor alkylation at G-232 is most likely due to strand invasion and the influence of the spacing betweent the last PNA base and the alkylator moiety. In PNA IV the Chl is coupled to the ϵ-amino group of the second lysine residue and thus separated from the most 3′ PNA base by the 2,6-dioxaoctanoic acid linker, two amino acid residues, and the lysine side chain, resulting in a flexible, 18 atom linker between PNA and Chl. Alternately, the PNA could potentially bind (with less efficiency) to a single mismatch target sequence from −232 to −240, placing the chlorambucil in the proximity of G-232, but alkylation of a guanine in the PNA:DNA complex (G-232) would not be expected, since the N7 of this guanine would not be accessible to the Chl. Unconjugated PNAs did not demonstrate any cleavage sites (not shown). In both cases, the estimate of the alkylation efficiency at major sites was at least 80%. Figures 4C and 4D illustrate the deduced modes of binding and site-directed DNA alkylation by 5′ and 3′ PNA−alkylator conjugates, based on the major alkylation sites observed by piperidine cleavage.

We recently reported that a bis-PNA (PNA IX) composed of two linked 9-mers with $(TCC)_3$ sequences could target the HER-2/neu PPT at two adjacent $(GGA)_3$ or $(AGG)_3$ sequences (*33*). Because of the repetitive nature of the target sequence, this bis-PNA could bind in different orientations, depending on which of the PNA arms contributes to Hoogsteen binding versus Watson−Crick binding. If the N-terminal arm was the Hoogsteen strand, the bis-PNA would prefer to target 5′$(AGG)_3$ sequences with the linker oriented 3′ to the purine strand of the target sequence, whereas if the C-terminal arm was the Hoogsteen strand, the bis-PNA would prefer to target 5′$(GGA)_3$ sequences with the linker oriented 5′ to the purine strand (Figure 5A). We therefore synthesized bis-PNA−alkylator conjugates and probed for the orientation of bis-PNA binding by piperidine cleavage.

PNA V is a bis-PNA with linked $(TCC)_3$ arms, and PNA VII is an analogous bis-PNA with J-base substitutions in the C-terminal PNA arm [$(TCC)_3$-$(TJJ)_3$] to favor Hoogsteen binding by this arm of the bis-PNA at neutral pH. Compared to the PNA we previously studied (PNA IX), these PNAs were designed with additional lysine residues to enhance solubility and improve DNA binding. Both PNAs were conjugated to chlorambucil at their N-termini (PNAs VI and VIII). PNA V and VI could bind to adjacent $(AGG)_3$ sequences in the HER-2/neu PPT from −231 to −239 and from −219 to −227 if the N-terminal PNA arm serves as the Hoogsteen strand of the bis-PNA. Piperidine cleavage with PNA VI (Figure 5B) shows major alkylation products at G-228 and G-241, which is consistent with binding in this orientation, placing the alkylator at the guanines immediately adjacent (G-228) or near (G-241) the PNA/DNA junction (Figure 5D).

PNAs VII and VIII would prefer to bind to the $(GGA)_3$ sequence from −221 to −229, using the C-terminal PNA arm bearing J-base substitutions as the Hoogsteen strand of this bis-PNA. Piperidine cleavage with PNA VIII (Figure 5B) confirms this binding orientation with major alkylation products at G-218 and G-219, consistent with PNA binding to the HER-2/neu PPT from −221 to −229, placing the alkylator near the PNA/DNA junction (Figure 5C). An additional alkylation site at −231 is probably explained by PNA binding to an adjacent, single mismatch $(GGA)_3$ sequence from −233 to −241, placing the alkylator at G-231 near the PNA/DNA junction.

With TFO-nitrogen mustard conjugates, we and others have observed that guanine adducts form most efficiently with a guanine on the purine strand immediately adjacent to the triple helix (*30*, *31*, *47*). It is interesting to note that some of the PNA-

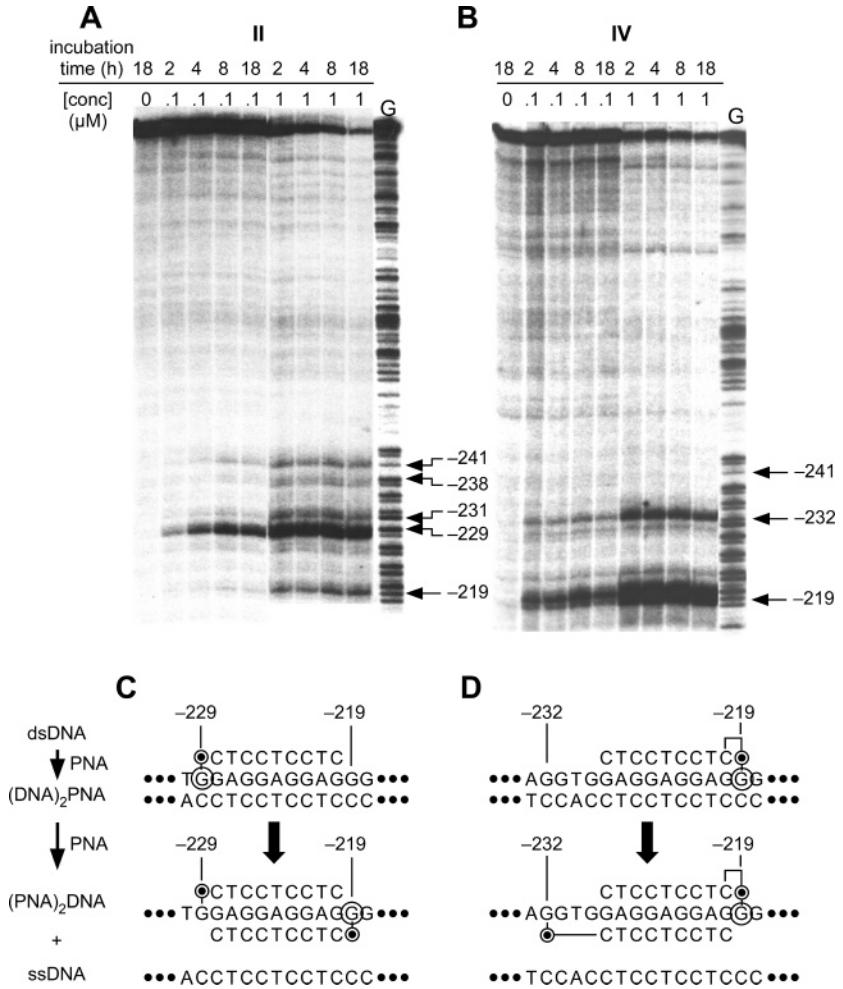

Figure 4. Representative piperidine cleavage gels demonstrating sites of alkylation for (A) the PNA−5′PAM conjugate (II) and (B) the PNA−3′Chl conjugate (IV). A ∼250 bp restriction fragment containing the HER-2/neu promoter was labeled on the 3′ end on the purine strand and incubated with 0.1−1 μM PNA for 2−18 h. Maxim-Gilbert G-reactions with the same template were used to identify the alkylation sites. Major alkylation sites are observed at G-229 for the 5′ alkylator conjugate (PNA II) and G-219 for the 3′ alkylator conjugate (PNA IV). Schematic representations of PNA−alkylator conjugate binding and covalent adduct formation deduced from piperidine cleavage analysis for PNA II (C) and PNA IV (D). The DNA:DNA:PNA triplex forms first and directs the nitrogen mustard to form a covalent adduct with the guanine adjacent to the triple helix, producing the major alkylation sites at G-229 for PNA II or G-219 for PNA IV. With either higher concentrations of the PNA−alkylators or prolonged incubation times, the PNA:DNA:PNA strand invasion complex is formed, producing the minor alkylation sites at G-219 for PNA II and G-232 for PNA IV. The linker in PNA IV allows the nitrogen mustard to reach G-232, 4 bp upstream of the strand invasion complex. Black circles represent the nitrogen mustards, and the guanines they bind are circled with open circles.

directed guanine adducts with PNAs IV, VI, and VIII are not immediately adjacent to the PNA/DNA junction. For example, it is surprising that PNA VIII does not form a guanine adduct with G-220, immediately adjacent to the PNA/DNA junction, but prefers G-218 and G-219. These findings are most likely explained by the spacing between the chlorambucil and the last PNA base, separated by two amino acid residues in PNA VI and VIII, and by the longer 18 atom linker in PNA IV. In contrast, the major and minor alkylation sites with PNA II, in which the PAM is conjugated to the α-amino group of the PNA base at the 5'terminus, occur immediately adjacent to the PNA binding site.

Inhibition of HER-2/neu Transcription. To determine whether conjugation with a nitrogen mustard can improve the antigene activity of a PNA, transient transfection analysis was performed using a HER-2/neu promoter-luciferase expression plasmid (pGL3/HNP410). In these experiments, PNAs were incubated with the plasmid prior to transfection, and the effect of PNA binding to the HER-2/neu promoter on HER-2/neu transcription was measured by luciferase activity (Figure 6). An indirect measurement of the stability of PNA binding in tumor cells is derived from the relative luciferase activity at various time points after transfection (Figure 6B). The specificity of PNA binding was also evaluated by treating a control luciferase expression plasmid containing the SV40 promoter (not shown). The mono- and bis-PNAs conjugated to nitrogen mustards were generally much more active than their unmodified counterparts in this assay, and two of the PNA−alkylator conjugates were capable of specifically suppressing HER-2/neu expression in HeLa cells by greater than 80%, depending on the concentration of PNA used to drive complete binding to the plasmid.

PNA II and PNA VIII demonstrated over 80% suppression of HER-2/neu transcription when the plasmid was incubated with 10 μM PNA and luciferase activity was analyzed at 24 h (Figure 6A). In comparison, the unmodified mono-PNA (I) had only a small effect on HER-2/neu transcription (13% suppression), and the unmodified bis-PNAs (PNAVII and IX) had a modest (40−55% suppression) impact on HER-2/neu transcription under these conditions. The high concentration of the PNAs (10 μM) was used to ensure rapid saturation of the PNA binding site(s) in the plasmid and thereby improve the efficiency of site-directed alkylation at the target sequence, since PNA binding must occur within the time frame of the hydrolysis half-life of the nitrogen mustards for alkylation to occur. Incubation of the SV40 control plasmid with this high concentration of the PNA−

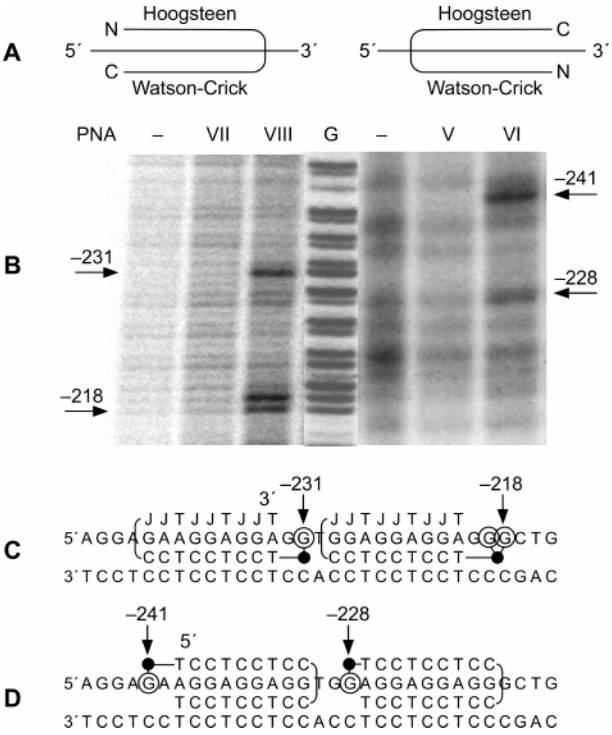

Figure 5. Representative piperidine cleavage gels demonstrating sites of alkylation for bis-PNA−5′Chl conjugate (VI) and bis-PNA(J)−5′Chl conjugate (VIII). (A) Possible orientations of bis-PNA binding to the purine strand of duplex DNA. (B) A ∼250 bp restriction fragment containing the HER-2/neu promoter was labeled on the 3′ end on the purine strand and incubated with 1 μM PNA for 18 h. Maxim−Gilbert G-reactions with the same template were used to identify the alkylation sites. Schematic representations of PNA−alkylator conjugate binding and covalent adduct formation deduced from piperidine cleavage analysis for PNA VIII (C) and PNA VI (D). Black circles represent the nitrogen mustards, and the guanines they bind are circled with open circles.

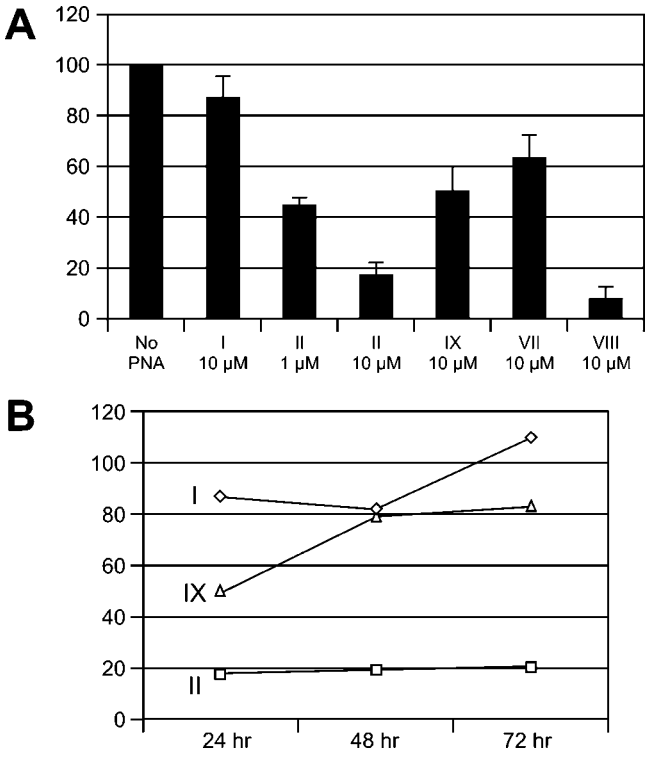

Figure 6. Transient transfection analysis of the HER-2/neu promoter-luciferase plasmid incubated with PNAs and transfected into HeLa cells. (A) Luciferase activity was analyzed with various PNAs at 24 h. (B) The stability of PNA binding and inhibition of HER-2/neu promoter activity was analyzed for up to 72 h with selected PNAs, when the plasmid was preincubated with the indicated PNA at 10 μM. The luciferase activity from cells transfected with untreated plasmid was defined as 100% promoter activity at each time point, and the effect of the PNAs on HER-2/neu transcription is presented as a percentage of full promoter activity.

alkylator conjugates also lead to a 15−20% decrease in SV40 driven luciferase activity, presumably due to some degree of nontarget binding by the PNA (not shown). Incubation of the HER-2/neu luciferase construct with a lower (1 μM) concentration of PNA II improved the specificity for the target sequence, but resulted in a lower level of suppression of HER-2/neu transcription, 55−60%, with minimal effect on the SV40 control plasmid. The effect of the mono-PNA−PAM conjugate (II) on HER-2/neu transcription at both concentrations remained stable for 72 h after transfection (Figure 6B). For comparison, we used the unmodified mono-PNA (I) as well as the unmodified bis-PNA (IX) from our recent studies (*33*), showing that the small effect observed with PNA I was not observed beyond 48 h and that the level of suppression by PNA IX decreased significantly at 72 h. Collectively, these data comparing unmodified PNAs with their nitrogen mustard conjugates demonstrate that the nitrogen mustard significantly improves the biological activity of the PNA and improves the stability of PNA binding within cells.

DISCUSSION

This is the first report of a PNA conjugated to a DNA alkylating agent. The PNA−alkylator conjugates directed the site-specific alkylation of the guanines adjacent to the bound PNA, stabilized the binding of the PNA in tumor cells, and markedly enhanced the ability of the PNA to suppress target gene transcription.

Intercalating agents have been shown to enhance helix invasion by homopyrimidine PNAs (*18*, *19*), but none have been shown to enhance the ability of a PNA to downregulate gene expression. In the present experiments, formation of helix invasion complexes with unmodified mono-PNA or bis-PNAs resulted in minimal to modest suppression of target gene transcription, while PNA binding stabilized by covalent adduct formation with a nitrogen mustard resulted in much higher inhibitory activity.

Nitrogen mustard conjugated to oligonucleotides have served as valuable probes for nucleic acid structure, for example in the Holliday junctions formed during DNA recombination events (*48*). The present PNA−alkylator conjugates also function as probes for studiyng the mechanism of PNA interaction with DNA. We took advantage of the ability of the nitrogen mustard to alkylate at a single site adjacent to the PNA binding site which could subsequently be converted to an easily detectable single strand scission by piperidine treatment. Visualizing the alkylation site allowed us to deduce not only the PNA binding site but also the orientation of PNA binding. The binding of a homopyrimidine PNA to dsDNA usually does not result in a conventional triplex with duplex DNA but rather in a triplex invasion complex as the thermodynamically most stable complex (*9*, *49*, *50*). However, as also demonstrated here, the formation of a traditional triple helix does indeed take place (at least for cytosine-rich PNAs) (*51*, *52*), and for the PNA−alkylator conjugates used in the present study, the conventional triplex is most probably responsible for their effect on gene transcription.

Oxidative cleavage or photocleavage by bis-PNAs conjugated to an anthraquinone DNA intercalator or to a metalloporphyrin metal chelator have previously been used to deduce the sites and modes of PNA binding (*17*, *19*). The present PNA−alkylator conjugates predominantly directed covalent adduct

formation to the duplex−triplex junction, similar to the sites of cleavage seen with the PNA−metalloporphyrin conjugate but in contrast to the PNA−anthraquinone conjugate, which caused the strongest cleavage sites within the displaced strand, perhaps because the single stranded loop is more prone to photooxidation. Our results are consistent with a mechanism in which the nitrogen mustard extends along the major groove and covalently binds to the exposed N7 of nearby guanines. It is well established that for PNA/DNA binding the antiparallel orientation is preferred for Watson−Crick duplex binding while the parallel orientation is preferred for Hoogsteen triplex binding (*52*). If triplex (invasion) PNA:DNA:PNA complexes are formed using only one type of PNA (mono-PNA), the overall parallel configuration is preferred (*52*). Concordingly, the mono-PNA−nitrogen mustard conjugate also prefers to bind in the parallel orientation. EMSAs with the PNA−PAM conjugate clearly demonstrate a discrete triplex band as well as additional bands of even lower mobility that are ascribed to helix invasion complexes, which are formed upon prolonged incubation or using higher PNA concentrations. We were able to differentiate triplex formation from strand invasion by monitoring the displacement of the pyrimidine strand.

The distance between the oligomer and the DNA interactive drug can significantly impact the reaction site and affinity of the conjugate. In the present work we did not systematically study linker length, but the piperidine cleavage experiments demonstrated that without a linker, PAM attached to the PNA N-terminus is able to effectively alkylate a guanine at the duplex/triplex junction. At the same time, the presence of a additional amino acid residues or a long 18 atom linker between the last PNA base and chlorambucil allows the nitrogen mustard to alkylate guanines a few base pairs away from the duplex/triplex junction, as demonstrated by a minor cleavage sites four base pairs away from the predicted PNA binding site for the PNA−3′chl conjugate.

In summary, we have demonstrated the facile synthesis of PNA−nitrogen mustard conjugates and their ability to suppress HER-2/neu transcription in a reporter plasmid model system. Such PNA−alkylator conjugates provide a new class of probes for sequence specific PNA−DNA interactions and warrant further study for gene targeting.

ACKNOWLEDGMENT

This work is supported by grants from the NIH (CA85306) and the Flinn Foundation (1580). Mass spectra were acquired in the AZCC/SWEHSC Proteomics Core, supported by grants from the NIH (ES06694 and CA023074).

LITERATURE CITED

(1) Milligan, J. F., Matteucci, M. D., and Martin, J. C. (1993) Current Concepts in Antisense Drug Design. *J. Med. Chem. 36*, 1923−1937.

(2) Crooke, S. T. (1992) Therapeutic Applications of Oligonucleotides. *Bio-Technology 10*, 882−886.

(3) Helene, C. (1991) Rational Design of Sequence-Specific Oncogene Inhibitors Based on Antisense and Antigen Oligonucleotides. *Eur. J. Cancer 27*, 1466−1471.

(4) Thuong, N. T., and Helene, C. (1993) Sequence-Specific Recognition and Modification of Double-Helical Dna by Oligonucleotides. *Angew. Chem., Int. Ed. Engl. 32*, 666−690.

(5) Uhlmann, E., and Peyman, A. (1990) Antisense Oligonucleotides − A New Therapeutic Principle. *Chem. Rev. 90*, 543−584.

(6) Gryaznov, S., and Chen, J. K. (1994) Oligodeoxyribonucleotide N3′-]P5′ Phosphoramidates − Synthesis and Hybridization Properties. *J. Am. Chem. Soc. 116*, 3143−3144.

(7) Demesmaeker, A., Waldner, A., Lebreton, J., Hoffmann, P., Fritsch, V., Wolf, R. M., and Freier, S. M. (1994) Amides As A New-Type of Backbone Modification in Oligonucleotides. *Angew. Chem., Int. Ed. Engl. 33*, 226−229.

(8) Jones, R. J., Lin, K. Y., Milligan, J. F., Wadwani, S., and Matteucci, M. D. (1993) Synthesis and Binding-Properties of Pyrimidine Oligodeoxynucleoside Analogues Containing Neutral Phosphodiester Replacements − the Formacetal and 3′-Thioformacetal Internucleoside Linkages. *J. Org. Chem. 58*, 2983−2991.

(9) Nielsen, P. E., Egholm, M., Berg, R. H., and Buchardt, O. (1991) Sequence-Selective Recognition of Dna by Strand Displacement with A Thymine-Substituted Polyamide. *Science 254*, 1497−1500.

(10) Kuhn, H., Demidov, V. V., Coull, J. M., Fiandaca, M. J., Gildea, B. D., and Frank-Kamenetskii, M. D. (2002) Hybridization of DNA and PNA molecular beacons to single-stranded and double-stranded DNA targets. *J. Am. Chem. Soc. 124*, 1097−1103.

(11) Liu, B., Han, Y., Corey, D. R., and Kodadek, T. (2002) Toward synthetic transcription activators: Recruitment of transcription factors to DNA by a PNA−peptide chimera. *J. Am. Chem. Soc. 124*, 1838−1839.

(12) Demidov, V. V., Potaman, V. N., Frankkamenetskii, M. D., Egholm, M., Buchard, O., Sonnichsen, S. H., and Nielsen, P. E. (1994) Stability of Peptide Nucleic-Acids in Human Serum and Cellular-Extracts. *Biochem. Pharmacol. 48*, 1310−1313.

(13) Borgatti, M., Romanelli, A., Saviano, M., Pedone, C., Lampronti, I., Breda, L., Nastruzzi, C., Bianchi, N., Mischiati, C., and Gambari, R. (2003) Resistance of decoy PNA-DNA chimeras to enzymatic degradation in cellular extracts and serum. *Oncol. Res. 13*, 279−287.

(14) McMahon, B. M., Mays, D., Lipsky, J., Stewart, J. A., Fauq, A., and Richelson, E. (2002) Pharmacokinetics and tissue distribution of a peptide nucleic acid after intravenous administration. *Antisense Nucleic Acid Drug Dev. 12*, 65−70.

(15) Okamoto, A., Tanabe, K., and Saito, I. (2001) Synthesis and properties of peptide nucleic acids containing a psoralen unit. *Org. Lett. 3*, 925−927.

(16) Mokhir, A. A., and Kraemer, R. (2003) Conjugates of PNA with naphthalene diimide derivatives having a broad range of DNA affinities. *Bioconjugate Chem. 14*, 877−883.

(17) Armitage, B., Koch, T., Frydenlund, H., Orum, H., Batz, H. G., and Schuster, G. B. (1997) Peptide nucleic acid-anthraquinone conjugates: strand invasion and photoinduced cleavage of duplex DNA. *Nucleic Acids Res. 25*, 4674−4678.

(18) Bentin, T., and Nielsen, P. E. (2003) Superior duplex DNA strand invasion by acridine conjugated peptide nucleic acids. *J. Am. Chem. Soc. 125*, 6378−6379.

(19) Bigey, P., Sonnichsen, S. H., Meunier, B., and Nielsen, P. E. (1997) DNA binding and cleavage by a cationic manganese porphyrin-peptide nucleic acid conjugate. *Bioconjugate Chem. 8*, 267−270.

(20) Ross, G. F., Smith, P. M., McGregor, A., Turnbull, D. M., and Lightowlers, R. N. (2003) Synthesis of trifunctional PNA−benzophenone derivatives for mitochondrial targeting, selective DNA binding, and photo-cross-linking. *Bioconjugate Chem. 14*, 962−966.

(21) Jardines, L., Fowble, B., Schultz, D., Mackie, J., Buzby, G., Torosian, M., Daly, J., Weiss, M., Orel, S., and Rosato, E. (1995) Factors associated with a positive reexcision after excisional biopsy for invasive breast cancer. *Surgery 118*, 803−809.

(22) Kern, J. A., Schwartz, D. A., Nordberg, J. E., Weiner, D. B., Greene, M. I., Torney, L., and Robinson, R. A. (1990) P185Neu Expression in Human Lung Adenocarcinomas Predicts Shortened Survival. *Cancer Res. 50*, 5184−5191.

(23) Yu, D., Wang, S. S., Dulski, K. M., Tsai, C. M., Nicolson, G. L., and Hung, M. C. (1994) c-erbB-2/neu overexpression enhances metastatic potential of human lung cancer cells by induction of metastasis-associated properties, *Cancer Res. 54*, 3260−3266.

(24) Agus, D. B., Bunn, P. A., Jr., Franklin, W., Garcia, M., and Ozols, R. F. (2000) HER-2/neu as a therapeutic target in nonsmall cell lung cancer, prostate cancer, and ovarian cancer. *Semin. Oncol. 27*, 53−63.

(25) Meric, F., Hung, M. C., Hortobagyi, G. N., and Hunt, K. K. (2002) HER2/neu in the management of invasive breast cancer. *J Am. Coll. Surg. 194*, 488−501.

(26) Ebbinghaus, S. W., Gee, J. E., Rodu, B., Mayfield, C. A., Sanders, G., and Miller, D. M. (1993) Triplex Formation Inhibits Her-2 Neu Transcription In-Vitro. *J. Clin. Invest. 92*, 2433−2439.

(27) Ebbinghaus, S. W., Fortinberry, H., and Gamper, H. B. (1999) Inhibition of transcription elongation in the HER-2/neu coding

sequence by triplex-directed covalent modification of the template strand. *Biochemistry 38*, 619−628.
(28) Noonberg, S. B., Scott, G. K., Hunt, C. A., Hogan, M. E., and Benz, C. C. (1994) Inhibition of Transcription Factor-Binding to the Her2 Promoter by Triplex-Forming Oligodeoxyribonucleotides. *Gene 149*, 123−126.
(29) Porumb, H., Gousset, H., Letellier, R., Salle, V., Briane, D., Vassy, J., AmorGueret, M., Israel, L., and Taillandier, E. (1996) Temporary ex vivo inhibition of the expression of the human oncogene HER2-(NEU) by a triple helix-forming oligonucleotide. *Cancer Res. 56*, 515−522.
(30) Ziemba, A., Derosier, L. C., Methvin, R., Song, C. Y., Clary, E., Kahn, W., Milesi, D., Gorn, V., Reed, M., and Ebbinghaus, S. (2001) Repair of triplex-directed DNA alkylation by nucleotide excision repair. *Nucleic Acids Res. 29*, 4257−4263.
(31) Ziemba, A. J., Reed, M. W., Raney, K. D., Byrd, A. B., and Ebbinghaus, S. W. (2003) A bis-alkylating triplex forming oligonucleotide inhibits intracellular reporter gene expression and prevents triplex unwinding due to helicase activity. *Biochemistry 42*, 5013−5024.
(32) Zhilina, Z. V., Ziemba, A. J., Trent, J. O., Reed, M. W., Gorn, V., Zhou, Q., Duan, W., Hurley, L., and Ebbinghaus, S. W. (2004) Synthesis and evaluation of a triplex-forming oligonucleotide-pyrrolobenzodiazepine conjugate. *Bioconjugate Chem. 15*, 1182−1192.
(33) Ziemba, A. J., Zhilina, Z. V., Krotova-Khan, Y., Stankova, L., and Ebbinghaus, S. W. (2005) Targeting and regulation of the HER-2/neu oncogene promoter with bis-peptide nucleic acids. *Oligonucleotides 15*, 36−50.
(34) Mizuguchi, G., Kaneiishii, C., Sawazaki, T., Horikoshi, M., Roeder, R. G., Yamamoto, T., and Ishii, S. (1994) Independent Control of Transcription Initiations from 2 Sites by An Initiator-Like Element and Tata Box in the Human C−Erbb-2 Promoter. *FEBS Lett. 348*, 80−88.
(35) Wendtner, C. M., Eichhorst, B. F., and Hallek, M. J. (2004) Advances in chemotherapy for chronic lymphocytic leukemia. *Semin. Hematol. 41*, 224−233.
(36) Panasci, L., Paiement, J. P., Christodoulopoulos, G., Belenkov, A., Malapetsa, A., and Aloyz, R. (2001) Chlorambucil drug resistance in chronic lymphocytic leukemia: the emerging role of DNA repair. *Clin. Cancer Res. 7*, 454−461.
(37) Pukhalsky, A. L., and Shmarina, G. V. (2001) Stimulatory and protective effects of alkylating agents applied in ultra-low concentrations. *Pharmacology 62*, 129−132.
(38) Povirk, L. F., and Shuker, D. E. (1994) DNA damage and mutagenesis induced by nitrogen mustards. *Mutat. Res. 318*, 205−226.
(39) Mattes, W. B., Hartley, J. A., and Kohn, K. W. (1986) DNA sequence selectivity of guanine-N7 alkylation by nitrogen mustards. *Nucleic Acids Res. 14*, 2971−2987.
(40) Kutyavin, I. V., Gamper, H. B., Gall, A. A., and Meyer, R. B. (1993) Efficient, Specific Interstrand Cross-Linking of Double-Stranded DNA by A Chlorambucil-Modified, Triplex-Forming Oligonucleotide. *J. Am. Chem. Soc. 115*, 9303−9304.
(41) Vlassov, V. V., Zarytova, V. F., Kutyavin, I. V., and Mamaev, S. V. (1988) Sequence-Specific Chemical Modification of A Hybrid Bacteriophage-M13 Single-Stranded-Dna by Alkylating Oligonucleotide Derivatives. *FEBS Lett. 231*, 352−354.
(42) Belousov, E. S., Afonina, I. A., Kutyavin, I. V., Gall, A. A., Reed, M. W., Gamper, H. B., Wydro, R. M., and Meyer, R. B. (1998) Triplex targeting of a native gene in permeabilized intact cells: covalent modification of the gene for the chemokine receptor CCR5. *Nucleic Acids Res. 26*, 1324−1328.
(43) Christensen, L., Fitzpatrick, R., Gildea, B., Petersen, K. H., Hansen, H. F., Koch, T., Egholm, M., Buchardt, O., Nielsen, P. E., Coull, J., and. (1995) Solid-phase synthesis of peptide nucleic acids. *J. Pept. Sci. 1*, 175−183.
(44) Dueholm, K. L., Egholm, M., Behrens, C., Christensen, L., Hansen, H. F., Vulpius, T., Petersen, K. H., Berg, R. H., Nielsen, P. E., and Buchardt, O. (1994) Synthesis of Peptide Nucleic-Acid Monomers Containing the 4 Natural Nucleobases − Thymine, Cytosine, Adenine, and Guanine and Their Oligomerization, *J. Org. Chem. 59*, 5767−5773.
(45) Reed, M. W., Lukhtanov, E. A., Gorn, V., Kutyavin, I., Gall, A., Wald, A., and Meyer, R. B. (1998) Synthesis and reactivity of aryl nitrogen mustard oligodeoxyribonucleotide conjugates. *Bioconjugate Chem. 9*, 64−71.
(46) Musumeci, D., Roviello, G. N., Valente, M., Sapio, R., Pedone, C., and Bucci, E. M. (2004) New synthesis of PNA-3′DNA linker monomers, useful building blocks to obtain PNA/DNA chimeras. *Biopolymers 76*, 535−542.
(47) Lampe, J. N., Kutyavin, I. V., Rhinehart, R., Reed, M. W., Meyer, R. B., and Gamper, H. B. (1997) Factors influencing the extent and selectivity of alkylation within triplexes by reactive G/A motif oligonucleotides. *Nucleic Acids Res. 25*, 4123−4131.
(48) Podyminogin, M. A., Meyer, R. B., and Gamper, H. B. (1995) Sequence-Specific Covalent Modification of Dna by Cross-Linking Oligonucleotides − Catalysis by Reca and Implication for the Mechanism of Synaptic Joint Formation. *Biochemistry 34*, 13098−13108.
(49) Egholm, M., Behrens, C., Christensen, L., Berg, R. H., Nielsen, P. E., and Buchardt, O. (1993) Peptide Nucleic-Acids Containing Adenine Or Guanine Recognize Thymine and Cytosine in Complementary-Dna Sequences, *J. Chem. Soc., Chem. Commun.* 800−801.
(50) Egholm, M., Nielsen, P. E., Buchardt, O., and Berg, R. H. (1992) Recognition of Guanine and Adenine in Dna by Cytosine and Thymine Containing Peptide Nucleic-Acids (PNA). *J. Am. Chem. Soc. 114*, 9677−9678.
(51) Wittung, P., Nielsen, P., and Norden, B. (1997) Extended DNA-recognition repertoire of peptide nucleic acid (PNA): PNA-dsDNA triplex formed with cytosine-rich homopyrimidine PNA. *Biochemistry 36*, 7973−7979.
(52) Egholm, M., Christensen, L., Dueholm, K. L., Buchardt, O., Coull, J., and Nielsen, P. E. (1995) Efficient Ph-Independent Sequence-Specific Dna-Binding by Pseudoisocytosine-Containing Bis-PNA. *Nucleic Acids Res. 23*, 217−222.

BC0502964

TECHNICAL NOTES

Novel and Efficient Preparation of Precursor $[^{188}Re(OH_2)_3(CO)_3]^+$ for the Labeling of Biomolecules

Sang Hyun Park,[†,*] Sepp Seifert,[‡] and Hans-Jurgen Pietzsch[‡]

Division of Radioisotope Production and Application, Korea Atomic Energy Research Institute, Daejeon, Republic of Korea, and Forschungszentrum Rossendorf, Institute for Bioinorganic and Radiopharmaceutical Chemistry, PF 510 119, D-01314 Dresden, Germany. Received June 30, 2005; Revised Manuscript Received September 8, 2005

A novel and efficient method for preparing ^{188}Re(I) tricarbonyl precursor $[^{188}Re(OH_2)_3(CO)_3]^+$ has been developed by reacting [^{188}Re]perrhenate with Schibli's kit in the presence of borohydride exchange resin (BER) as a reducing agent and an anion scavanger. The precursor was produced in more than 97% yield by reacting a solution of tetrahydroborate exchange resin (BER, 3 mg), borane−ammonia ($BH_3{\cdot}NH_3$, 3 mg), and potassium boranocarbonate ($K_2[H_3BCO_2]$, 3 mg) in 0.9% saline with a solution of sodium perrhenate ($Na^{188}ReO_4$) with up to 50 MBq and concentrated phosphoric acid (85%, 7 μL) at 60 °C for 15 min. HPLC and TLC revealed 0% unreacted [^{188}Re]-perrhenate ion and <3% of colloidal $^{188}ReO_2$. Since the precursor is produced with high radiochemical purity and labeling efficiency under the milder conditions than those required for the conventional reducing agents, the latter can be replaced.

INTRODUCTION

The ^{99m}Tc(I) and ^{188}Re(I) tricarbonyl precursors $[M(OH_2)_3(CO)_3]^+$ have been shown to be excellent starting materials for the synthesis of further ^{99m}Tc(I) and ^{188}Re(I) tricarbonyl complexes as well as radiolabeling of target specific biomolecules (*1*−*8*). Recently, a user-friendly kit formulation (IsoLink) was developed using potassium boranocarbonate, $K_2[BH_3CO_2]$, for preparation of the ^{99m}Tc precursor complex. This solid reagent serves both as a source of carbon monoxide and a reducing agent for technetium. It was also used by Schibli and co-workers for the preparation of the corresponding ^{188}Re precursor complex (*9*). [^{188}Re]Perrhenate eluate (1 mL) was reduced in neutral solution with 3 mg of $K_2[BH_3CO_2]$ and 5 mg of $BH_3{\cdot}NH_3$ by incubation at 60 °C for 15 min. The amount of reducing agents and acid (concentrated phosphoric acid) was carefully balanced not only to avoid fast hydrolysis of the boranes, but also to maintain a sufficient low pH to stabilize reduced rhenium intermediates. The preparations resulted in yields >85% of the desired precursor complex, remaining perrhenate (7±3%), colloidal $^{188}ReO_2$ (<5%), and a byproduct of unknown composition.

To overcome the moderate yields we used the recently described borohydride exchange resin (BER) as an additional reducing agent and an anion scavenger (*10*).

EXPERIMENTAL PROCEDURES

Unless otherwise stated, all chemicals were of reagent grade and used without further purification. Sodium perrhenate ($Na^{188}ReO_4$) was eluted from a $^{188}W/^{188}Re$ generator (Oak Ridge National Laboratories, Oak Ridge, TN) using 0.9% saline. For the separation of $[^{188}Re(OH_2)_3(CO)_3]^+$, HPLC analyses were performed on a Waters system equipped with a radiometric detector using a reversed phase XTerra RP_{18} 5 μm column (4.6 × 250 mm, Waters, Ireland). HPLC solvents consisted of methanol (solvent A) and 0.05 M TEAP (tetraethylammonium phosphate) buffer, pH 2.25, solvent B). HPLC gradient: 0−5 min: a linear gradient to 0% A/100% B from 100% A/0% B; 5−8 min: a linear gradient to 25% A/75% B from 0% A/100% B; 8−11 min: a linear gradient to 34% A/66% B from 25% A/75% B; 11−22 min: a linear gradient to 100% A/0% B from 34% A/66% B; 22−24 min: a linear gradient to 0% A/100% B from 100% A/0% B. The flow rate was 1 mL per min. For the separation of ^{188}Re(I) tricarbonyl histidine, HPLC analyses were performed on a Perkin Elmer system equipped with a radiometric detector (IsoScan LC gamma, Biostep, Germany) using a Hypersil ODS column (packing material 10 μm, 250 × 4 mm, Knauer, Berlin, Germany). HPLC solvents consisted of ethanol (solvent A) and 0.05 M TEAP (triethylammonium phosphate) buffer, pH 1.95 (solvent B). HPLC gradient: 0−10 min: a linear gradient to 100% A/0% B from 0% A/100% B; 10−20 min: 100% A; 20−25 min; a linear gradient to 0% A/100% B from 100% A/0% B. The flow rate was 1 mL per min. All solvents for the mobile phase were of HPLC grade and prefiltered with 0.2 μm pore size bottle filter. The instant thin-layer chromatography (ITLC) analyses were performed on a TLC analysis system equipped with a gamma-ray scanner (RITA TLC Analysis, Raytest, Germany). The thin-layer chromatography (TLC) system was performed using either silica gel plates ($60F_{254}$, Merck, Darmstadt, Germany) and 99% methanol/1% concentrated HCl as an evolving solvent or paper (Whatman No. 1) and 99.5% methanol/0.5% 6 M HCl as an evolving solvent.

Synthesis and Radiolabeling. *^{188}Re(I) Tricarbonyl Precursor (1) $[^{188}Re(OH_2)_3(CO)_3]^+$.* A 10 mL vial containing tetrahydroborate exchange resin (BER, 3 mg), borane−ammonia ($BH_3{\cdot}NH_3$, 3 mg), and potassium boranocarbonate ($K_2[H_3BCO_2]$, 3

* To whom correspondence should be addressed. Tel: 82-42-868-8514, Fax: 82-42-868-8448, e-mail: parksh@kaeri.re.kr.

† Korea Atomic Energy Research Institute.

‡ Forschungszentrum Rossendorf.

10.1021/bc050192t CCC: $33.50 © 2006 American Chemical Society
Published on Web 12/15/2005

Scheme 1. Synthesis of ^{188}Re(I) Tricarbonyl Precursor (1) and ^{188}Re(I) Tricarbonyl Histidine (2)

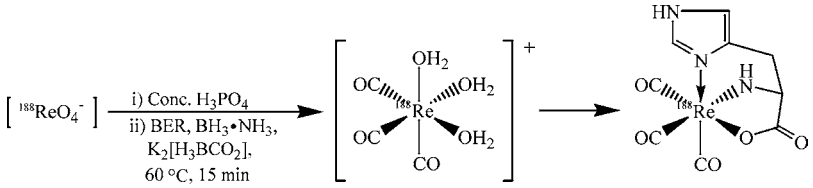

1 **2**

mg) were capped with a rubber stopper. A solution of 1 mL of sodium perrhenate ($Na^{188}ReO_4$) with up to 50 MBq and 7 μL of concentrated phosphoric acid (85%) was added into the vial by a 20 mL syringe and then heated to 60 °C in a boiling water bath for 15 min. Pressure from the evolving gas (about 10 mL) was balanced with the syringe. After cooling to room temperature, the neutral ^{188}Re(I) tricarbonyl precursor was obtained (Scheme 1). Yield: >97% determined by means of HPLC and TLC.

^{188}Re(I) Tricarbonyl Histidine (2). A 10 mL vial containing histidine (500 μL) was capped with a rubber stopper. A solution of 800 μL of $[^{188}Re(OH_2)_3(CO)_3]^+$ with up to 50 MBq was added into the vial by a 1 mL syringe. The reaction vial was sealed and heated to 75 °C for 30 min. After 30 min, the reaction mixture was cooled to room temperature (Scheme 1). Yield: >97% determined by means of HPLC and TLC.

Tetrahydroborate Exchange Resin (BER). The tetrahydroborate exchange resin (BER) as a reducing agent was prepared by the reported method. Chloride-form resin (Amberlite ion-exchange resin, 12.5 g) was slurry-packed with water into a 30-mL fritted glass funnel mounted on a filter flask. Then, an aqueous sodium tetrahydroborate solution (200 mL, 0.25 M) was slowly passed through the resin over a period of 30 min. The resulting resins were washed thoroughly with distilled water until free of excess and finally with ethanol. The tetrahydroborate-form anion-exchange resin was then partially air-dried by removing ethanol on the surface of the BER. This resin was analyzed for its tetrahydroborate content by hydrogen evolution upon an acidification with 0.08 M HCl, and the average capacity of BER was found to be 2.5 mequiv of tetrahydroborate ion per gram.

RESULTS

The HPLC chromatogram of ^{188}Re(I) tricarbonyl precursor **1** and $^{188}ReO_4^-$ showed that retention times of those species are 4.7 and 9.8 min, respectively. The retention time of the ^{188}Re(I) tricarbonyl precursor was compared to that of ^{99m}Tc(I) tricarbonyl precursor and they were found to be identical. The radiolabeling yield of ^{188}Re(I) tricarbonyl precursor in the reaction mixture was determined by the HPLC analysis and found to be 100%. The HPLC chromatogram of ^{188}Re(I) tricarbonyl precursor in the reaction mixture is shown in Figure 1. The complex is stable (>95%) for approximately 3 h. After this time, decomposition of the complex was observed. Paper electrophoresis investigations in aqueous solution confirmed the cationic charge of ^{188}Re(I) tricarbonyl precursor in a neutral solution. The assay for the formation of the ^{188}Re(I) tricarbonyl precursor, reduced hydrolyzed ^{188}Re, and [^{188}Re]perrhenate ion

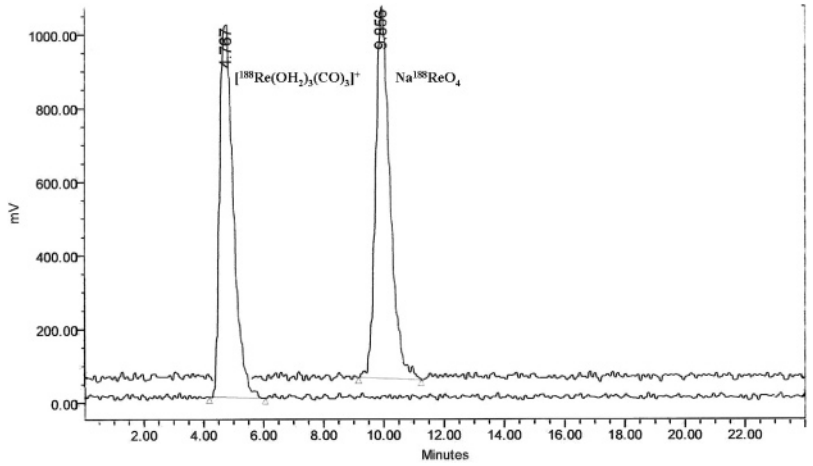

Figure 1. HPLC chromatograms of ^{188}Re(I) tricarbonyl precursor and $Na^{188}ReO_4$.

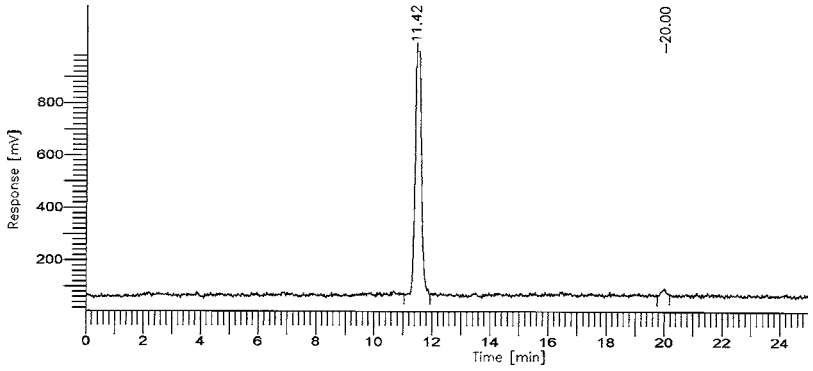

Figure 2. HPLC chromatogram of ^{188}Re(I) tricarbonyl histidine (**2**).

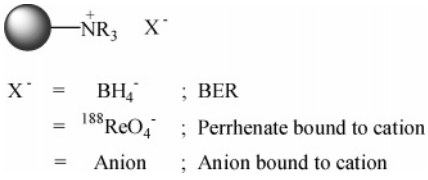

Figure 3. BER as a solid-phase reducing agent and an anion scavenger.

was achieved by investigating their positions using an instant thin-layer chromatography (ITLC). ^{188}Re(I) tricarbonyl precursor: >95% (R_f = 0.4); reduced hydrolyzed ^{188}Re: less than 3% (origin); [^{188}Re]perrhenate ion: 0% (R_f = 0.8). The HPLC chromatogram of ^{188}Re(I) tricarbonyl histidine showed that the retention time of the complex is 11.4 min. The radiolabeling yield of ^{188}Re(I) tricarbonyl histidine in the reaction mixture was determined by the HPLC analysis and found to be >97%. The HPLC chromatogram of ^{188}Re(I) tricarbonyl histidine (**2**) in the reaction mixture is shown in Figure 2. The retention time of the ^{188}Re(I) tricarbonyl histidine was compared to that of ^{99m}Tc(I) tricarbonyl histidine and they were found to be identical.

DISCUSSION

Tetrahydroborate exchange resin (BER) contains tetrahydroborate ion (BH_4^-) bound to the cation which is supported on polystyrene matrix, and the cation has a quaternary alkylammonium functionality used for adhering the tetrahydroborate ion or negatively charged species. BER is shown in Figure 3.

According to the present study, employing the borohydride exchange resin (BER) as a novel reducing agent and an anion scavenger, ^{188}Re(I) tricarbonyl precursor having high radiochemical purity and labeling efficiency can be prepared without nitrogen gas flushing and ice bath cooling compared to the conventional method (*9*). The BER is advantageous in terms of being stable over a wide range of pH (2−11) and applicable to biologically active molecules, as well as being easily removable through filtration when being administrated (*10*), thus providing the potential to economically and effectively produce ^{188}Re(I) tricarbonyl precursor without the formation of unreacted $^{188}ReO_4^-$, colloidal $^{188}ReO_2$, and negatively charged impurities by reinforcing the conventional reducing agent requiring very stringent condition for preparation.

ACKNOWLEDGMENT

This work was supported by the Nuclear R & D Program of the Korean Ministry of Science and Technology and the Technical Cooperation Program of the International Atomic Energy Agency. We would like to thank K. Landrock for her assistance in preparing HPLC, ITLC, and electrophoresis.

LITERATURE CITED

(1) Alberto, R., Schibli, R., Waibel, R., Abram, U., and Schubiger, A. (1999) Basic aqueous chemistry of $[M(OH_2)_3(CO)_3]^+$(M = Re, Tc) directed towards radiopharmaceutical application. *Coord. Chem. Rev.* 901−919.

(2) Pietzsch, H. J., Gupta, A., Reisgys, M., Drews, A., Seifert, S., Syhre, R., Spies, H., Alberto, R., Abram, U., Schubiger, P. A., and Johannsen, B. (2000) Chemical and biological characterization of technetium(I) and rhenium(I) tricarbonyl complexes with dithioether ligands serving as linkers for coupling the $Tc(CO)_3$ and $Re(CO)_3$ moieties to biologically active molecules. *Bioconjugate Chem. 11*, 414−424.

(3) Schibli, R., Bella, R., Alberto, R., Garcia-Garayoa, E., Ortner, K., Abram, U., and Schubiger, P. A. (2000) Influence of the denticity of ligand systems on the in vitro and in vivo behavior of ^{99m}Tc(I)-tricarbonyl complexes: a hint for the future functionalization of biomolecules. *Bioconjugate Chem. 11*, 345−351.

(4) Arterburn, J., Corona, C., Venkateswara, R., Carlson, K. E., and Katzenellenbogen, J. A. (2003) Synthesis of 17-α-substituted estradiol-pyridin-2-yl hydrazine conjugates as effective ligands for labeling with Alberto's complex *fac*-$[Re(OH_2)_3(CO)_3]^+$ in water. *J. Org. Chem. 68*, 7063−7070.

(5) Seifert, S., Kunstler, J. U., Gupta, A., Funke, H., Reich, T., Pietzsch, H. J., Alberto, R., and Johannsen, B. (2001) Reactivity of technetium-(I) thioether carbonyl complexes towards histidine-an EXAFS study in solution. *Inorg. Chim. Acta 322*, 79−86.

(6) Bayly, S. R., Fisher, C. L., Storr, T., Adam, M. J., and Orvig, C. (2004) Carbohydrate conjugates for molecular imaging and radiotherapy: ^{99m}Tc(I) and ^{188}Re(I) tricarbonyl complexes of *N*-(2′-hydroxybenzyl)-2-amino-2-deoxy-D-glucose. *Bioconjugate Chem. 15*, 923−926.

(7) Mundwiler, S., Kuendig, M., Ortner, K., and Alberto, R. (2004) A new [2+1] mixed ligand concept based on $[^{99m}Tc(OH_2)_3(CO)_3]^+$: a basic study. *Dalton Trans.* 1320−1328.

(8) Alberto, R., Schibli, R., Egli, A., and Schubiger, A. P. (1998) A novel organometallic aqua complex of technetium for the labeling of biomolecules: synthesis of $[^{99m}Tc(OH_2)_3(CO)_3]^+$ from $[^{99m}TcO_4]^-$ in aqueous solution and its reaction with a bifunctional ligand. *J. Am. Chem Soc. 120*, 7987−7988.

(9) Schibli, R., Schwarz, R., Alberto, R., Ortner, K., Schmalle, H., Dumas, C., Egli, A., and Schubiger, P. A. (2002) Steps toward high specific activity labeling of biomolecules for therapeutic application: preparation of precursor $[^{188}Re(OH_2)_3(CO)_3]^+$ and synthesis of tailor-made bifunctional ligand systems. *Bioconjugate Chem. 13*, 750−756.

(10) Park, S. H., Gwon, H. J., and Park, K. B. (2004) Synthesis and characterization of ^{99m}Tc-labeled biologically active molecules using borohydride exchange resin as a reducing agent for the preparation of radiopharmaceuticals. *J. Labelled Compd. Radiopharm. 47*, 683−697.

BC050192T

A Solid-Phase Labeling Strategy for the Preparation of Technetium and Rhenium Bifunctional Chelate Complexes and Associated Peptide Conjugates

R. William Riddoch, Paul Schaffer, and John F. Valliant*

Departments of Chemistry and Medical Physics and Applied Radiation Sciences, McMaster University, 1280 Main Street West, Hamilton, Ontario, Canada, L8S 4M1. Received July 21, 2005; Revised Manuscript Received October 21, 2005

A new solid-phase labeling strategy for the preparation of ^{99m}Tc and Re chelate complexes and associated peptide derivatives, was developed. Resin-bound monoamide monoamine (MAMA) chelates were prepared in such a manner that upon the addition of a suitable Re(V) and Tc(V) precursor the target metal complexes were selectively released from the resin. The desired products were isolated from unreacted ligand by a simple filtration/solid-phase extraction procedure. In addition to the preparation of a series of functionalized ligands, a peptide conjugate was constructed from one of the resin-bound chelates using a conventional automated peptide synthesizer. The yields of the Re chelate complexes were typically greater than 70%, while the maximum yield for reactions run at the tracer level using ^{99m}Tc was 50%. The reported approach has a number of attractive features, including the opportunity to prepare libraries of novel agents, the ability to isolate macroscopic amounts of Re complexes for use in in vitro screening studies and as well-characterized standards for tracer level work, and the ability to produce ^{99m}Tc complexes that are free of any unreacted starting material without having to employ preparative HPLC.

INTRODUCTION

Solid-phase labeling strategies (SPLS) are an attractive means of preparing radiotracers because they facilitate the process of separating the desired product from the excess starting materials used during standard labeling procedures (*1*). Removal of unlabeled ligands to give high effective specific activity formulations is particularly important in situations in which a precursor (i.e., unlabeled ligand) can compete with the tracer for the target receptor. It is also relevant to studies involving small animal positron emission tomography (PET) and single photon emission computed tomography (SPECT) scanners where minute amounts of unlabeled material can be toxic to the animal and/or have a significant impact on the distribution of a tracer (*2*). SPLS are easy to automate, which is important when high levels of activity are needed, and, although it has not been widely exploited, SPLS also engender the opportunity to incorporate modern drug discovery techniques, including combinatorial chemistry, into the radiopharmaceutical development process.

SPLS typically involve covalent attachment of a substrate to an insoluble support through a linker that is cleaved when the resin-bound material reacts with a particular radioisotope. For instance, Hunter and co-workers developed a convenient strategy for radio-iodinating aromatic rings by attaching benzoic acid and benzylamine derivatives to a solid support through a tin linker (*3*). In this way, iodinated compounds, including [^{131}I]-meta-iodobenzylguanidine (MIBG), were prepared in excellent yield, purity, and specific activity.

Similar strategies for labeling with ^{99m}Tc, the most widely used radionuclide in diagnostic medicine, have also been developed (*4*). Dunn-Dufault et al. showed that it was possible to label an N_3S chelate that was connected via the thiol residue (through a succinimidyl linker) to a variety of different supports (*5*). Although these systems afforded high (effective) specific activity formulations, radiochemical yields varied significantly (13−80%). Alternatively, the same chelate, derivatized with a peptide, was linked through a thiol group to a support consisting of gold particles (*6*). Upon labeling with ^{99m}Tc, the desired product was isolated in excellent radiochemical yield. More recently, Alberto et al. published a solid-phase labeling system for the technetium(I) tricarbonyl ($[Tc(CO)_3]^+$) core (*7*). In this approach, a derivative of diethylene triamine was attached to the solid support via the secondary amine. Upon the addition of $[^{99m}Tc(OH_2)_3(CO)_3]^+$, the technetium bound to the triamine ligand, and it was postulated that one of the displaced water molecules reacts with the carbon−nitrogen bond, thus freeing the coordination complex from the solid support.

Existing SPLS for technetium are often designed for incorporating ^{99m}Tc into compounds, but they have not been particularly effective at producing macroscopic quantities of Re or ^{99}Tc complexes which are needed for screening potential radiopharmaceuticals in vitro and as reference compounds for work done at the tracer level. Furthermore, there has been only limited investigation into the use of the supported synthons as platforms for preparing receptor targeted radiopharmaceuticals using automated solid-phase synthesis (*8*−*10*).

The objective of the work described herein was to develop a SPLS that could be used to prepare both Re and ^{99m}Tc complexes of functionalized chelates. The methodology was designed to enable the preparation of discrete compounds in useful quantities while also offering the opportunity to prepare libraries of peptide−chelate conjugates. Merrifield-type resins were selected as the support because an extensive collection of prefunctionalized derivatives are commercially available and the polystyrene-based resins are already widely used in automated peptide and organic synthesizers. The monoamide monoamine chelate (MAMA) (*11*, *12*) was chosen as one of many possible ligand systems because it forms neutral, stable, and well-defined complexes with both Tc(V) and Re(V), and it can be easily derivatized, regioselectively, with a wide range of different functional groups (*13*−*15*), which imparts a great deal of flexibility when designing libraries.

* To whom correspondence should be addressed: Tel: 905-525-9140 ext. 22840. FAX: 905-522-2509. E-mail: valliant@mcmaster.ca.

10.1021/bc050216w CCC: $33.50 © 2006 American Chemical Society
Published on Web 12/22/2005

EXPERIMENTAL PROCEDURES

Instrumentation. All peptides were prepared on an Advanced ChemTech 348 Ω Peptide synthesizer using a 40-well reaction block. Electrospray ionization (ESI) mass spectrometry experiments were performed on a Micromass Quattro Ultima instrument where samples were dissolved in 1:1 CH_3OH/ H_2O or 1:1 CH_3CN/H_2O mixtures. High-resolution MS was obtained using a Micromass Global Q-TOF Ultima instrument. FTIR spectra were acquired on a Bio-Rad FTS-40 FTIR spectrometer. NMR experiments were performed using Bruker Avance DRX-500, Avance AV-600 or AC-200 spectrometers. For a pair of geminal protons, A refers to the proton associated with the higher frequency signal, while B refers to the proton giving rise to the lower frequency resonance. For the Re complexes, α refers to ring protons that are endo relative to the Re−oxygen bond, while β refers to protons that are oriented exo.

Analytical HPLC studies for nonradioactive samples were performed using a Varian Pro Star model 230 solvent delivery system, 330 PDA detector fitted with a C-18 Microsorb column (4.6 × 250 mm, 300 Å-5 μm). The elution protocol for nonpeptide based compounds was a gradient of 25 to 40% CH_3CN (containing 0.1% TFA) over 15 min at a flow rate of 1.0 mL/min. All analytical HPLC experiments were monitored at λ = 254 and 214 nm. For peptides, a gradient range of 5 to 20% CH_3CN over 15 min was used. For labeling reactions with ^{99m}Tc, approximately 100 μL of sample was removed from a reaction mixture and diluted to 1 mL with distilled water. A total of 10 μL of this solution was injected onto a Nucleosil C-18 column (250 × 4.6 mm, 5 μm). The runs employed the same gradients used for the Re analogues.

Materials, Methods, and Characterization Data. Unless otherwise stated, all reagents and solvents were ACS grade or higher and used without further purification from commercial suppliers. Polystyrene-based *N*-α-9-fluorenylmethoxycarbonyl (Fmoc)-glycine loaded SASRIN resin (0.69 mmol g^{-1}, 1% divinylbenzene, 200−400 mesh) was obtained from Bachem Inc. Fmoc-protected amino acids were purchased from Novabiochem, Bachem Inc, and Advanced ChemTech Inc. Cysteamine 4-methoxytrityl resin was purchased from Novabiochem and TentaGel S Trt-OH resin from Advanced ChemTech. ^{99m}Tc was obtained by elution of a generator obtained from Bristol-Myers Squibb.

***S*-(((4-Methoxyphenyl)diphenyl)methyl)-2-aminoethanethiol.** To a solution of cysteamine hydrochloride (7.7 g, 68.1 mmol) in TFA (100 mL) was added *p*-anisylchlorodiphenylmethane (20 g, 64.8 mmol). After 3 h of stirring of the sample under an atmosphere of N_2, the TFA was removed under reduced pressure, and the resulting colorless oil was suspended in CH_2Cl_2 (200 mL) and extracted with 3 N NaOH (3 × 100 mL) (Note: the oil does not go into CH_2Cl_2 until the addition of NaOH). The organic layer was dried over sodium sulfate and evaporated under reduced pressure to yield a white solid (16.6 g, 70%). TLC R_f = 0.11 (3% MeOH/CH_2Cl_2); IR (NaCl disk, cm^{-1}): 3058, 3001, 2955, 2927, 2855; ^{1}H NMR (200 MHz, $CDCl_3$): δ7.27 (bm, 12 H, H-aryl), 6.77 (d, J = 8.8, 2H, H-aryl), 3.69 (s, 3H, OCH_3), 2.54 (t, J = 6.3, 2H, C**H$_2$**NH_2), 2.29 (t, J = 6.3, 2H, TrS**CH$_2$**), 1.12 (b s, 2H, NH_2); ^{13}C NMR (50 MHz, $CDCl_3$): δ158, 145, 137, 130, 129, 128, 126, 113, 66, 55, 41, 36; MS (ESI): *m*/*z* 273 [$(MeOTr)^+$], 350 [$(M + H)^+$].

***S*-Linked Resin-Bound MAMA Chelate (4).** Cysteamine-4-methoxytrityl resin (1.0 g, 0.31 mmol/g) was suspended in 10 mL of dry DMF in a fritted vessel and argon was bubbled through the suspension for 15 min. The solution was filtered, and fresh DMF (10 mL) containing NMM (375 μL, 3.41 mmol) was added. In a separate flask, bromoacetic acid (431 mg, 3.1 mmol), HOBT (1.0 g, 3.1 mmol), and HBTU (1.17 g, 3.1 mmol) were dissolved in DMF (4 mL), and the sample was stirred for 5 min at room temperature. This solution was added to the suspension containing the polymer and the mixture agitated for 3 h. After filtration of the sample and thoroughly washing the resin with CH_2Cl_2, DMF, MeOH, DMF, and CH_2Cl_2, a solution of NMM (1.25 g, 12.4 mmol) in DMF (10 mL) was added, and the suspension was agitated with a flow of argon for 15 min. Methoxytrityl-protected cysteamine (4.7 g, 13.5 mmol) was subsequently added, and the reaction was agitated for an additional 48 h. Filtration followed by thorough washing with CH_2Cl_2, DMF, MeOH, DMF, and CH_2Cl_2 yielded a yellow solid (1.12 g, 89%). IR (KBr, cm^{-1}): 2926, 2865, 2363, 2337, 1685.

ReO-MAMA (1). Compound **4** (100 mg) was allowed to swell in a solution (v/v/v) of 5% MeOH, 1% pyridine in DMF (5 mL) for 5 min prior to the addition of $[NBu_4][ReOCl_4]$ (19 mg, 0.031 mmol). The resulting green suspension was stirred at 85 °C for 16 h. The solution was then filtered, and the DMF was removed under reduced pressure (55 °C at 1 Torr). The product (10 mg, 85%), a reddish-brown solid, was isolated by silica gel column chromatography (5% MeOH/CH_2Cl_2). TLC R_f = 0.15 (10% MeOH/CH_2Cl_2); IR (NaCl disk, cm^{-1}): 1654, 966; ^{1}H NMR (600 MHz, CD_3OD): δ5.00 (m, $J_{4\beta,4\alpha}$ = −18.6, H-4β), 4.07 (m, H-4α), 4.03 (m, $J_{2\beta,2\alpha}$ = −12.0, $J_{1\beta,2\beta}$ = 6.0, $J_{1\alpha,2\beta}$ = 6.0, H-2β), 3.83 (m, $J_{6\beta,6\alpha}$ = −10.2, $J_{5\alpha,6\beta}$ = 6.6, H-6β), 3.44 (m, $J_{1\beta,2\alpha}$ = 7.2, $J_{1\beta,2\alpha}$ = 7.2, H-2α), 3.21 (m, H-5 β), 2.96 (m, H-1β), 2.89 (m, $J_{1\beta,1\alpha}$ = −11.4, H-1α), 2.84 (m, $J_{5\beta,6\alpha}$ = 6.6, $J_{5\alpha,6\alpha}$ = 12.6, H-6α), 2.70 (m, $J_{5\beta,5\alpha}$ = −10.8, H-5α); ^{13}C NMR (151 MHz, $CDCl_3$): δ 191.1, 70.0, 66.1, 39.9, 39.8, 38.6; HRMS (TOF-EI) calcd. for $C_6H_{11}N_2S_2O_2Re$: 393.9820. Found 393.9807.

Methyl [2-(*S*-4′-methoxytrityl)-thioethyl)amino]acetate (6). Compound **5** (2.0 g, 5.73 mmol), *N*-methylmorpholine (700 μL) and methylbromoacetate (493 μL, 5.16 mmol) were dissolved in CH_2Cl_2 (50 mL). Following stirring for 24 h under N_2, the solution was extracted with water three times (50 mL each) and dried over Na_2SO_4. Removal of the solvent by rotary evaporation followed by silica gel column chromatography (50% ethyl acetate/hexanes) yielded the product as a colorless oil (1.96 g, 90%). TLC R_f = 0.50 (5% MeOH/CH_2Cl_2); IR (NaCl disk, cm^{-1}): 3336, 3059, 1742; ^{1}H NMR (200 MHz, $CDCl_3$): δ 7.30 (m, 12H, H-aryl), 6.80 (d, J = 8.9 Hz, 2H, H-aryl), 3.79, (s, 3H, phenyl-OCH_3), 3.70 (S, 3H, (CO)-OCH_3), 3.30 (s, 2H, (CO)CH_2NH), 3.55 (t, J = 7.7 Hz, 2H, NHCH_2CH_2S), 3.36 (t, 2H, $NHCH_2CH_2$S), 1.97 (s, 1H, NH); ^{13}C NMR (50 MHz, $CDCl_3$): δ 171.5, 158.0, 145.0, 136.8, 130.7, 129.4, 127.8, 126.5, 113.1, 55.2, 51.8, 50.2, 47.9, 32.0; $ESMS^+$: *m*/*z* 273 [$(4\text{-MeOTr})^+$], 422 [$(M + H)^+$].

Methyl [2-(*S*-4′-methoxytrityl)-thioethyl)-*N*-benzyl-amino]-acetate (7). Compound **6** (410 mg, 0.973 mmol), NMM (1 mL), and benzyl bromide (1 mL, 8.36 mmol) were stirred in CH_2Cl_2 (75 mL) for 16 h. The solvent was removed under reduced pressure, and the product was purified by silica gel column chromatography (30% ethyl acetate/hexanes) yielding the product as a colorless oil (497 mg, 99%); TLC R_f = 0.90 (5% MeOH/CH_2Cl_2); IR (NaCl disk, cm^{-1}): 3059, 3030, 1742; ^{1}H NMR: (200 MHz, $CDCl_3$): δ7.30 (m, 17H, H-aryl), 6.80 (d, J = 8.9 Hz, 2H, H-aryl), 3.78, (s, 3H, phenyl-OCH_3), 3.65 (s, 2H, benzyl-CH_2), 3.63 (s, 3H, OCH_3), 3.18 (s, 2H, (CO)CH_2-NH), 2.66 (t, J = 7.7 Hz, 2H, NHCH_2CH_2S), 2.32 (t, 2H, $NHCH_2CH_2$S); ^{13}C NMR (50 MHz, $CDCl_3$): δ172.1, 158.2, 145.3, 130.8, 129.5, 128.9, 128.2, 127.8, 127.1, 126.5, 113.1, 111.7, 57.7, 55.2, 53.7, 53.0, 51.1, 30.4; MS (ESI): *m*/*z* 273 [$(4\text{-MeOTr})^+$], 512 [$(M + H)^+$].

Potassium [2-(*S*-4′-methoxytrityl)-thioethyl)-*N*-benzyl-amino]acetate (8). Compound **7** (497 mg, 0.973 mmol) was dissolved in diethyl ether (5 mL) and potassium trimethylsilanoate (156 mg, 1.22 mmol) was added and the suspension was stirred for 6 h. The resulting colorless precipitate was dissolved

in EtOAc and purified by silica gel column chromatography (3% MeOH/EtOAc then 10% MeOH/EtOAc) to give the product as a white foam (416 mg, 80%). TLC $R_f = 0.15$ (10% MeOH/CH_2Cl_2); IR (NaCl disk, cm^{-1}): 3351, 3059, 3031, 1654; ^1H NMR (200 MHz, $CDCl_3$): δ7.24 (m, 17H, H-aryl), 6.73 (d, $J = 8.9$ Hz, 2H, H-aryl), 3.77 (s, 3H, phenyl-OCH_3), 3.77 (s, 2H, benzyl-CH_2), 3.02 (s, 2H, $(CO)CH_2NH$), 2.45 (bs, 4H, SCH_2CH_2NH); ^{13}C NMR (50 MHz, $CDCl_3$): δ173.1, 158.0, 144.8, 136.6, 134.1, 130.6, 130.1, 129.4, 128.5, 127.8, 126.6, 113.1, 66.4, 57.4, 55.5, 55.1, 52.7; MS (ESI): *m*/*z* 497 $[(M)^-]$.

S-Linked Resin-Bound (*N*-Bn)-MAMA Chelate (9). Compound **8** (215 mg, 0.402 mmol), HOBt (540 mg, 4.02 mmol), and HBTU (1.52 g, 4.02 mmol) were dissolved in DMF (5 mL) and mixed using an orbital shaker for 5 min. At the same time, cysteamine-4-methoxytrityl resin (100 mg, 0.31 mmol/g) was swelled in a mixture of DMF (5 mL) and NMM (34 μL). The solution containing the carboxylic acid was then added to the resin, and the resulting mixture was shaken for 4 h. The resin was washed with DMF (2 × 20 mL, 10 min), MeOH (2 × 20 mL, 10 min), DMF (2 × 20 mL, 10 min), and CH_2Cl_2 (2 × 20 mL, 10 min).

ReO-MAMA-(*N*-Bn)(10). Compound **9** (200 mg) was allowed to swell in 5 mL of a solution of 5% MeOH and 1% pyridine in DMF (v/v/v). $[NBu_4][ReOCl_4]$ (37 mg, 0.063 mmol) was added, and the vial was heated at 85 °C for 16 h. The solvent was then removed, and the brownish red residue was dissolved in dichloromethane and purified by passing it through a short plug of silica (50:50 hexanes/EtOAc, then EtOAc) to give the product as a red solid (21 mg, 70%). TLC $R_f = 0.25$ (5% MeOH/CH_2Cl_2); IR (NaCl disk, cm^{-1}): 1654, 966; ^1H NMR (syn isomer, 600 MHz, $CDCl_3$): δ 7.72 (m, $J_{9,10} = 2.4$, $J_{10,11} = 2.4$, H-10), 7.49 (m, H-9, H-11), 5.11 (d, $J_{7A,7B} = -13.5$, H-7A), 5.00 (d, $J_{4\beta,4\alpha} = -16.2$, H-4$\beta$), 4.74 (m, $J_{5\alpha,7B} = 1.1$, H-7B), 4.44 (m, $J_{2\beta,2\alpha} = -12.4$, $J_{1\beta,2\beta} = 1.0$, $J_{1\alpha,2\beta} = 5.6$, H-2β), 4.12 (m, $J_{1\beta,1\alpha} = -11.3$, $J_{1\beta,2\beta} = 1.1$, $J_{1\beta,2\alpha} = 5.2$, H-1β), 3.82 (d, H-4α), 3.73 (m, $J_{6\beta,6\alpha} = -13.0$, $J_{5\beta,6\beta} = 3.8$, $J_{5\alpha,6\beta} = 13.0$, H-6$\beta$), 3.25 (m, H-1$\alpha$, H-2$\alpha$), 3.09 (m, $J_{5\beta,5\alpha} = -12.9$, $J_{5\beta,6\alpha} = 2.3$, H-5β), 2.91 (m, $J_{5\alpha,6\alpha} = 4.5$, H-6$\alpha$), 1.48 (m, H-5$\alpha$); ^{13}C NMR (syn isomer, 151 MHz, $CDCl_3$): δ 187.5, 132.3, 131.2, 129.4, 128.7, 65.4, 64.8, 62.7, 59.6, 46.9, 38.0. HRMS calcd. for $C_{13}H_{17}N_2S_2O_2Re$: 484.0289. Found 484.0274.

***S*-(Triphenylmethyl)-2-aminoethanethiol (11).** The method of O'Neil et al. was followed with minor modifications. To a solution of cysteamine hydrochloride (19.2 g, 170 mmol) in TFA (120 mL) was added triphenylmethanol (44.0 g, 169 mmol). After 3 h of stirring under an atmosphere of N_2, the TFA was removed under reduced pressure. The resulting white solid was suspended in CH_2Cl_2 (300 mL) and extracted with 3 N NaOH (4 × 150 mL) (Note: the solid does not go into CH_2Cl_2 until the addition of NaOH), H_2O (3 × 150 mL), $NaHCO_3$ (2 × 50 mL), and brine (2 × 50 mL). The organic layer was dried over sodium sulfate and evaporated under reduced pressure to yield the product (45 g, 85%) as a white solid. TLC $R_f = 0.12$ (3% MeOH/CH_2Cl_2); IR (NaCl disk, cm^{-1}): 3056, 3020; ^1H NMR (200 MHz, $CDCl_3$): δ7.27 (m, 15 H, H-aryl), 2.54 (t, $J = 6.3$, 2H, CH_2NH_2), 2.29 (t, $J = 6.3$, 2H, $TrSCH_2$), 1.12 (bs, 2H, NH_2); ^{13}C NMR (50 MHz, $CDCl_3$): δ158.1, 129.7, 127.8, 126.6, 125.6, 39.4, 34.4; MS (ESI): *m*/*z* 243 $[(Tr)^+]$, 320 $[(M+H)^+]$.

***S*-(Triphenylmethyl)-2-aminoethanethiol-*N*,*N*-diacetate-(13).** To a stirred solution of compound **11** (1.84 g, 5.77 mmol) in CH_2Cl_2 (20 mL) containing triethylamine (4.7 g, 46.16 mmol), bromo methyl acetate (7.1 g, 46.16 mmol) was added dropwise. The solution was stirred for 12 h under an atmosphere of nitrogen whereupon the solvent was concentrated in vacuo, and the resulting solution was loaded onto a column of silica (64 cm × 10 cm). The column was washed with hexanes (250 mL), 10% ethyl acetate/hexanes (250 mL), and 50% ethyl acetate/hexanes (250 mL). The solvent in the final fraction was evaporated, and the dimethyl ester (2.55 g) was dissolved in methanol (35 mL) and a solution of KOH (2.48 g, 44.2 mmol) in water (5 mL) was added. The resulting colorless solution was stirred for 12 h under argon. Upon removal of the solvent, the resulting semisolid was dissolved in water (75 mL), and the pH was adjusted to 2.0 by the dropwise addition of HCl which was accompanied by rapid stirring. The resulting precipitate (2.3 g, 92%) was isolated by filtration and washed with 10 mM HCl (3 × 10 mL). TLC $R_f = 0.05$ (10% MeOH/CH_2Cl_2); IR (NaCl disk, cm^{-1}): 3300, 3062, 3022, 1676; ^1H NMR (200 MHz, $CDCl_3$): δ7.21 (m, 15H, H-aryl), 3.70, (s, 4H, $CH_2(CO)$), 2.00 (m, 4H, S-CH_2CH_2NH); ^{13}C NMR (50 MHz, D_2O): δ171.5, 145.8, 130.74, 129.10, 128.06, 56.28, 55.58, 28.77, 28.72; MS (ESI): *m*/*z* 434 $[(M - H)^-]$.

***S*-Linked Resin-Bound (*N*-CH_2CO_2H)-MAMA Chelate (14).** Cysteamine-4-methoxytrityl-PS resin (100 mg, 0.31 mmol/g) was stirred with CH_2Cl_2 (2 × 10 mL, 10 min per wash) and DMF (2 × 10 mL, 10 min per wash), filtered, and then suspended for 5 min in DMF (5 mL) containing NMM (40 μL). Meanwhile, compound **13** (126 mg, 0.31 mmol), HBTU (117 mg, 0.31 mmol), and HOBT (42 mg, 0.31 mmol) were dissolved in DMF (1 mL) and mixed using an orbital shaker for 5 min. The solution containing the di-carboxylic acid was subsequently added to the amine and stirred by bubbling Ar through the mixture for 4 h at which time the resin was negative to the Kaiser test. The resin was washed with DMF (2 × 20 mL, 10 min per wash), CH_2Cl_2 (2 × 20 mL, 10 min per wash), and MeOH (2 × 20 mL, 10 min per wash) and then treated with a mixture of acetic anhydride in DMF (1:9 v/v) for 30 min. The solution was filtered, and the resin was washed with DMF (2 × 20 mL, 10 min per wash), CH_2Cl_2 (2 × 20 mL,10 min per wash), and MeOH (2 × 20 mL, 10 min per wash) and finally dried in vacuo. MS (ESI) (cleaved sample): *m*/*z* =251 $[(M - H)^-]$.

ReO-MAMA-(*N*-CH_2CO_2H) (15a). Compound **14** (100 mg) was washed with CH_2Cl_2 (2 × 10 mL, 10 min per wash) and DMF (2 × 10 mL, 10 min per wash) and then suspended in a 5 mL solution of 5% MeOH and 1% pyridine in DMF (v/v/v) containing $[NBu_4][ReOCl_4]$ (18.6 mg, 31.2 μmol). After the green suspension was heated to 85 °C in an oil bath for 16 h, the solution was filtered and concentrated in vacuo. The resulting red/brown solid was dissolved in 50/50 MeOH/CH_2Cl_2 and purified by passing it through a plug of silica (CH_2Cl_2, 50/50 MeOH/CH_2Cl_2). Concentration of the solvent by rotary evaporation gave the product as a red solid (10 mg, 70%). TLC $R_f = 0.25$ (5% MeOH/CH_2Cl_2); IR (NaCl disk, cm^{-1}): 1654, 966; ^1H NMR (600 MHz, CD_3OD): δ5.12 (d, $J_{4\beta,4\alpha} = -17.6$, H-4$\beta$), 4.65 (d, H-4$\alpha$), 4.47 (d, $J_{2\beta,2\alpha} = -12.8$, H-2$\beta$), 4.47 (d, $J_{7A,7B} = -16.6$, H-7β), 4.22 (m, $J_{5\alpha,7B} = 1.3$, H-7α), 4.12 (m, $J_{5\beta,5\alpha} = -12.3$, H-5$\beta$), 3.98 (m, $J_{1\beta,1\alpha} = -10.8$, $J_{1\beta,2\alpha} = 4.6$, H-1β), 3.42 (m, $J_{6\beta,6\alpha} = -13.3$, $J_{6\beta,5\beta} = 3.8$, $J_{6\beta,5\alpha} = 13.3$, H-6$\beta$), 3.11 (m, $J_{1\alpha,2\alpha} = 12.3$, H-2$\alpha$), 3.04 (m, $J_{1\alpha,2\beta} = 6.0$, H-1α), 2.88 (m, $J_{5\alpha,6\alpha} = 4.4$, H-6$\alpha$), 1.57 (m, H-5$\alpha$); ^{13}C NMR (151 MHz, CD_3OD): δ189.8, 170.1, 67.8, 64.4, 61.1, 58.6, 46.2, 38.2; HRMS (TOF-ESI) calcd. for $C_8H_{12}N_2S_2O_4Re$: 450.9793. Found 450.9797.

***S*-Linked Resin-Bound (*N*-$CH_2CONHCH_2CO_2Bn$)-MAMA Chelate (16).** Compound **14** (100 mg) was washed with CH_2Cl_2 (2 × 10 mL, 10 min per wash) and DMF (2 × 10 mL, 10 min per wash) and then suspended for 5 min in DMF (5 mL) containing HBTU (117 mg, 0.31 mmol) and HOBT (42 mg, 0.31 mmol). Meanwhile, O-Bn-glycine (62 mg, 0.31 mmol) and NMM (40 μL) were dissolved in DMF (1 mL), and the mixture was agitated for 5 min. The solution containing the amine was

added to the resin, and the mixture was stirred by bubbling Ar through the solution for 3 h at which time the resin was negative to the Kaiser test. The solution was filtered, and the resin was washed with DMF (2 × 20 mL, 10 min per wash), CH_2Cl_2 (2 × 20 mL, 10 min per wash), and MeOH (2 × 20 mL, 10 min per wash). MS(ESI) (cleaved sample): *m*/*z* 400 [$(M + H)^+$].

ReO-MAMA-(*N*-$CH_2CONHCH_2CO_2Bn$) (17). Compound **16** (100 mg) was washed with CH_2Cl_2 (2 × 10 mL, 10 min per wash) and DMF (2 × 10 mL, 10 min per wash) and then suspended in 5 mL of a solution of 5% MeOH and 1% pyridine in DMF (v/v/v) containing $[NBu_4][ReOCl_4]$ (19 mg, 31.2 μmol). After the green suspension was heated to 85 °C with an oil bath for 16 h, the resin was collected by filtration and the filtrate concentrated by rotary evaporation. The resulting red/brown solid was dissolved in CH_2Cl_2, washed with water, and then purified by passing it through a plug of silica (50/50 hexanes/EtOAc; 95/5 CH_2Cl_2/MeOH). Removal of the solvent by rotary evaporation gave the product as a red solid (12 mg, 68%). TLC $R_f = 0.25$ (5% MeOH/CH_2Cl_2); IR (NaCl disk, cm^{-1}): 1654, 966; ^1H NMR (600 MHz, $CDCl_3$): δ7.39 (m, H-aryl), 5.22 (d, $J = -10$, H-11A), 5.19 (d, H-11B), 4.92 (d, $J_{4\beta,4\alpha} = -17.4$, H-4$\beta$), 4.73 (d, H-4$\alpha$), 4.71 (d, $J_{7\beta,7\alpha} = -15.9$, H-7A), 4.65 (m, $J_{2\beta,2\alpha} = -10.4$, $J_{1\alpha,2\beta} = 4.1$, H-2β), 4.29 (d, H-7B), 4.16 (d, $J = -15$, H-9A), 4.12 (m, $J_{1\beta,1\alpha} = -10.6$, $J_{1\beta,2\alpha} = 4.6$, H-1β), 4.07 (d, H-9B), 3.86 (m, $J_{5\beta,5\alpha} = -12.3$, $J_{5\beta,6\beta} = 3.5$, H-5β), 3.39 (m, $J_{6\beta,6\alpha} = -13.7$, $J_{6\beta,5\alpha} = 13.6$, H-6$\beta$), 3.25 (m, $J_{1\alpha,2\alpha} = 12.3$, H-2$\alpha$), 3.18 (m, H-1$\alpha$), 2.86 (m, $J_{5\alpha,6\alpha} = 5.5$, H-6$\alpha$), 1.56 (m, H-5$\alpha$); MS(ESI): *m*/*z* 598 [$(M + H)^+$], 600 [$(M + H)^+$].

***S*-Linked Resin-Bound (*N*-$CH_2CONHCH_2CH_2NH_2$)-MAMA Chelate (18).** Compound **14** (100 mg) was washed CH_2Cl_2 (2 × 10 mL, 10 min per wash) and DMF (2 × 10 mL, 10 min per wash) and then suspended for 5 min in DMF (5 mL) containing HBTU (200 mg, 0.53 mmol) and HOBT (100 mg, 0.73 mmol). Ethylenediamine (2 mL) was then added to the resin, and the mixture was stirred by bubbling Ar through the solution for 3 h. The resin was collected by filtration and washed with DMF (2 × 20 mL, 10 min per wash), CH_2Cl_2 (2 × 20 mL, 10 min per wash), and MeOH (2 × 20 mL, 10 min per wash).

Resin-Bound MAMA−Peptide Conjugate (20). Compound **18** (150 mg) was added to two reaction wells, suspended in DMF (2 mL/well), and shaken at 900 rpm for 1 min. The wells were subsequently filtered, suspended in THF (2 mL/well), shaken at 900 rpm for 1 min, and drained for 90 s. The THF wash was repeated two more times. The DMF wash was then repeated a final two times to complete the general wash cycle. This procedure was used between every deprotection and coupling step. Fmoc deprotection was brought about through the addition of 20% v/v piperidine−DMF solution to the active vessels (2 mL/well) and shaking for 5 min at 900 rpm. Following filtration, the process was repeated, shaking for 10 min. The deprotected resin-bound amino acid was washed using the general wash procedure and subsequently coupled to the next Fmoc-protected amino acid using a standard HBTU coupling technique. Coupling reactions initially involved adding DMF (200 μL) to the active vessels followed by the addition of a 4-fold excess of the protected amino acid as a 0.5 M solution in DMF. Four equivalents of HBTU as a 0.5 M solution in DMF was then added followed by a 8-fold excess of DIPEA as 2.0 M solution in DMF. The reaction block was subsequently shaken for 80 min at 900 rpm. Following filtration, the resin was washed using the general washing procedure prior to the start of the next cycle.

Once the final amino acid had been added and the Fmoc group removed, a pause was introduced into the peptide program so that 10 equiv of the *n*-butyl isocyanate in DMF (0.5 M solution) could be added. The reaction block was then shaken at 900 rpm under nitrogen for 12 h. The reaction vessels were emptied, and the resins were washed using the general wash cycle. The cleavage cocktail, which consisted of 20% TFA and 2% TIS in DCM (v/v/v), was cooled to 0 °C and added to the resin. The mixture was allowed to warm to room temperature over 60 min and subsequently filtered into cold diethyl ether. The resulting heterogeneous solution was centrifuged at 3000 rpm and −5 °C for 10 min. MS (ESI): *m*/*z* 767 [$(M + H)^+$].

ReO-MAMA Peptide Conjugate (21a). Compound **20** (100 mg) was washed with CH_2Cl_2 (2 × 10 mL, 10 min per wash) and DMF (2 × 10 mL, 10 min per wash) and then suspended in 2 mL of a solution of 5% MeOH and 1% pyridine in DMF (v/v/v) containing $[NBu_4][ReOCl_4]$ (18.6 mg, 31.2 μmol). After the green suspension was heated to 85 °C in an oil bath for 16 h, the resin was collected by filtration and the filtrate was concentrated by rotary evaporation. The resulting red/brown solid was dissolved in a mixture of 10% MeOH in CH_2Cl_2 (v/v) and purified by passing the mixture through a plug of silica (CH_2Cl_2 then 50/50 MeOH/CH_2Cl_2). Concentration of the later fractions gave a red solid (14 mg, 47%). MS(ESI): *m*/*z* 966, 968 [$(M + H)^+$].

Tentagel-*S*-Tr-OH Resin MAMA−Peptide Conjugate. Tentagel-S-Trt-OH resin (1.0 g, 0.4 mmol/g) was suspended in a solution of 2-aminoethane thiol hydrochloride (1.0 g, 0.9 mmol) in TFA (10 mL). The solution was gently agitated with a stream of Ar, and after 2 h, the solution was filtered and the resin washed with CH_2Cl_2 (2 × 10 mL, 10 min per wash) and DMF (2 × 10 mL, 10 min per wash) and then suspended for 5 min in DMF (5 mL) containing DIP (40 μL). Meanwhile, compound **13** (1.26 g, 3.1 mmol), HBTU (1.17 g, 3.1 mmol), and HOBT (420 mg, 0.31 mmol) were dissolved in DMF (10 mL) and shaken for 5 min. The solution containing the di-carboxylic acid was then added to the resin-bound amine, and the mixture was stirred by bubbling Ar through the solution for 4 h at which time the resin was negative to the Kaiser test. The resin was collected by filtration, washed with DMF (2 × 20 mL, 10 min per wash), CH_2Cl_2 (2 × 20 mL, 10 min per wash), and MeOH (2 × 20 mL, 10 min per wash), and then treated with a solution of acetic anhydride−DMF (1:9 v/v). After 30 min, the resin was collected by filtration, washed with DMF (2 × 20 mL, 10 min per wash), CH_2Cl_2 (2 × 20 mL, 10 min per wash), and MeOH (2 × 20 mL, 10 min per wash), and finally dried in vacuo. MS(ESI) (cleaved sample): *m*/*z* 251 [$(M - H)^-$].

General Labeling Procedure. Na[$^{99m}TcO_4$] was eluted from a $^{99}Mo/^{99m}Tc$ generator using a solution of 0.9% saline. Transfer chelate-tin solutions were prepared by dissolving 12.5 g of the transfer chelate in 75 mL of nitrogen sparged water. Stannous chloride dihydrate (200 mg) was dissolved in 1 mL of 1 M HCl and added to the solution containing the transfer chelate. The pH of the resulting solution was adjusted to 7.2 using 1 N NaOH, and the volume was increased to 100 mL with nitrogen sparged water. Note that the solution must be used within 3 h of preparation to preserve the stannous chloride dihydrate.

The transfer chelate solution (0.1, 1 or 2 mL) was added to a serum vial containing the resin (25, 100, or 200 mg) and a stir-bar. The vial was crimp-sealed, and the headspace was replaced with nitrogen. Sodium pertechnetate was then added to each vial (2−15 mCi, 0.05−0.41 MBq), and the volume was adjusted to 2.5 mL with nitrogen sparged water. EtOH (250 μL) was then added, and the reaction mixture was allowed to proceed for 2.5−3 h. The reaction mixture was then heated to 80 °C in a Reacti-Therm heater-stirrer under a stream of N_2 to remove the residual ethanol, and the reaction mixture was subsequently cooled in an ice−water bath. The mixture was then loaded onto a C-18 Sep-Pak (Waters), which was washed

Scheme 1

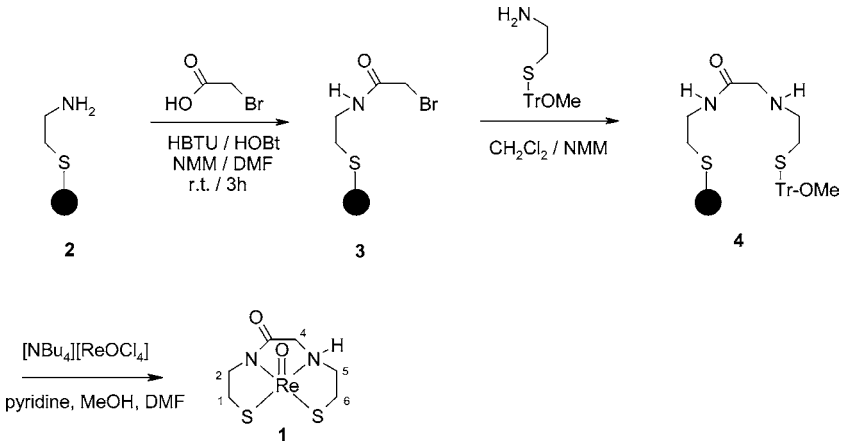

Table 1

solvent	reagents[a]	temp (°C)	yield (%)
CH_2Cl_2	[TBA][$ReOCl_4$]	25	7
DMF	[TBA][$ReOCl_4$]	25	9
DMF	[TBA][$ReOCl_4$]	85	40
DMF	[TBA][$ReOCl_4$], Et_3SiH	85	0
DMF	[TBA][$ReOCl_4$], 5% MeOH	85	47
DMF	[TBA][$ReOCl_4$], 1% pyridine	85	55
DMF	[TBA][$ReOCl_4$], 5% MeOH, 1% pyridine	85	85

[a] TBA = tetra-*n*-butylammonium.

two times with 10 mL of water, and then the product was eluted using 100% ethanol.

RESULTS AND DISCUSSION

From some preliminary solution-phase studies, we found that *S*-*p*-methoxytrityl (PMT) groups on the MAMA chelate were readily cleaved in the presence of $[TcOCl_4]^-$ and $[ReOCl_4]^-$. Consequently, the MAMA chelate was prepared on a solid support, in which one of the pendant thiol groups was linked to a polystyrene resin through a PMT group. Commercially available 2-aminoethanethiol loaded-4-MeOTr-polystyrene resin was placed into a reaction chamber of a solid-phase synthesis vessel and swelled in DMF. Following the solution phase approach, bromoacetyl bromide was added at −30 °C in the presence of triethylamine under a constant bubbling of Ar. Despite a number of attempts using a variety of conditions, the yields of **3** were unacceptably low. In turn, success was achieved when bromoacetic acid was coupled to the resin-bound amine using HBTU−HOBt (*16*) (Scheme 1). After 2 h under these coupling conditions, the Kaiser test (*17*) indicated the reaction had gone to completion. The desired chelant **4** was prepared by adding a large excess of the thiol-protected cysteamine to drive the reaction to completion. The progress of the reaction was followed by cleaving small amounts of the resin using 5% TFA in CH_2Cl_2 and analyzing the products by HPLC-MS. After 48 h, the major peak in the chromatogram corresponded to that of the MAMA chelate.

The optimal conditions for preparing the Re-MAMA complexes were identified by varying the choice of solvent, base, and reaction temperature (Table 1). In a typical experiment, the resin was swelled in a solvent or solvent mixture and $[NBu_4][ReOCl_4]$ was added, and the contents of the vial were agitated using a platform mixer (300 rpm). For reactions run at room temperature in the absence of base, the color of the resin changed to deep green within 3 h. This, in our experience, indicated the presence of a partially chelated intermediate. The greenish resin was analyzed by IR, and a strong absorbance at 909 cm^{-1} was observed, which is indicative of a Re═O stretch (*18*). When the reaction mixture was left shaking overnight in CH_2Cl_2 in the absence of base, the solution took on a light orange color, and small amount of a red solid was seen in the bottom of the reaction vial. The precipitate was in fact the target compound, which was established by comparing the characterization data of the isolated product with that obtained from an authentic standard prepared by following literature procedures (*12*). The yield of the metal complex improved substantially when the temperature of the reaction was increased to 85 °C and when the solvent was changed to a mixture of DMF and MeOH. Methanol was added to trap the cation that is formed upon liberation of the protecting group and release of the chelate from the resin. In contrast, the use of triethylsilane as a scavenger in place of methanol did not improve the yield. An additional increase in yield to 85% was achieved when a small amount of pyridine was added to the reaction. Pyridine prevented disproportionation of the M(V) chlorides at the higher reaction temperatures and likely facilitated deprotonation of the amide group on the chelate. From this reaction, the product was isolated through a plug of silica gel or a silica gel Sep-Pak, which was necessary to separate the cleaved protecting group from the target compound.

Direct functionalization of the amino group of **4** proved to be very difficult. The efficiency of the derivatization with a variety of reactive alkylating agents, including benzyl bromide and allyl bromide, was highly variable, and despite numerous attempts involving an array of reaction conditions, the yields of the desired products were not acceptable. To circumvent this issue, an alternate route was developed whereby a large portion of the chelate was synthesized in solution and then coupled to the resin in the final step using a robust amide bond forming reaction.

The initial target for the convergent approach was the *N*-benzyl MAMA derivative, which was previously prepared in solution by O'Neil et al. (*12*). The requisite precursor, compound **6**, was prepared in 90% yield by reacting methyl bromoacetate with *S*-(4-methoxytrityl)-2-aminoethane thiol (Scheme 2). Alkylation of **6** with benzyl bromide to give **7** occurred quantitatively in the presence of triethylamine. Conversion of the methyl ester to the acid was carried out by treating **7** with potassium trimethylsilanoate in ether (*19*). Over the course of 4 h, a thick white paste formed in the bottom of the reaction vessel, which was the potassium salt **8**. The product was collected by filtration and passed down a short column of silica to separate it from any excess potassium trimethylsilanoate. Compound **8** was subsequently coupled to the resin-bound amine using HBTU and HOBt. After 4 h, the resin gave a negative Kaiser test and was therefore filtered, washed rigorously, and dried under vacuum.

Scheme 2

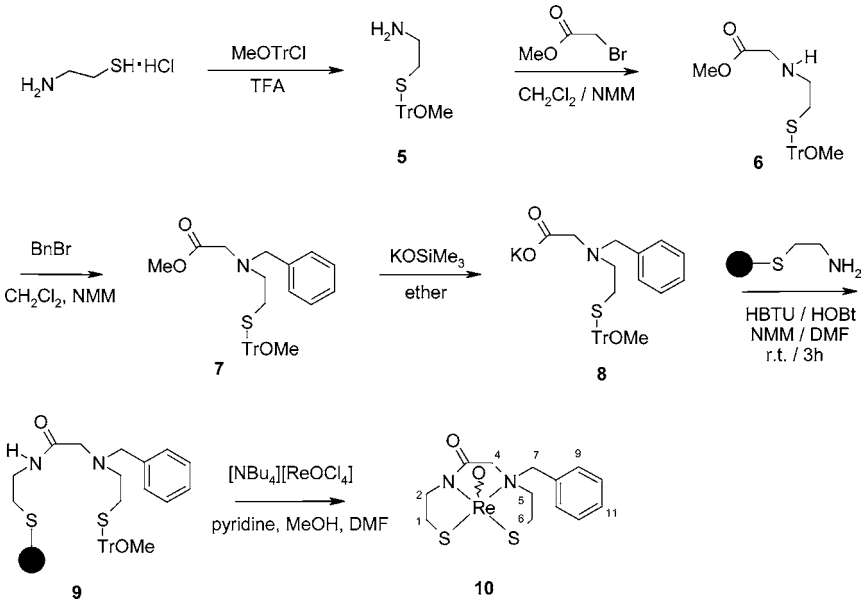

Scheme 3

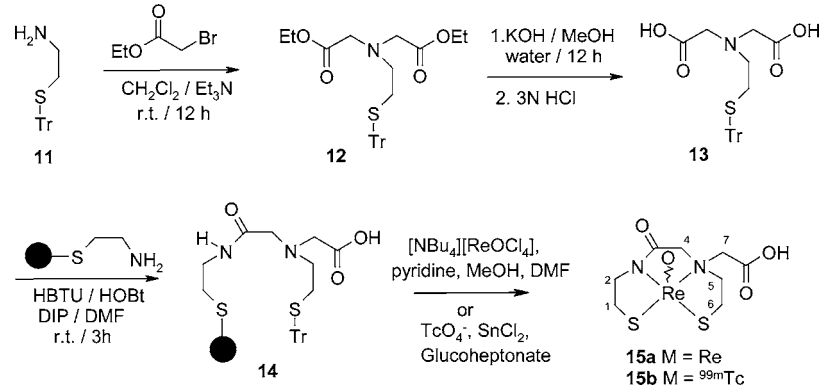

The complexation−cleavage reaction was run under the optimum conditions identified for the unsubstituted MAMA complex. The resin **9** (200 mg) was suspended in 5 mL of a solution containing MeOH (5%), pyridine (1%), and DMF. [TBA][$ReOCl_4$] was added and the vial was heated to 85 °C for 16 h. The Re complex **10** was isolated in 70% yield through a simple plug of silica. The spectroscopic data for the product were consistent with reported values. Interestingly, the ^{1}H NMR of the product showed that compound **10** was isolated as a mixture of syn and anti diastereomers in approximately a 12:1 ratio. In the case of compound **1** and all subsequent N-substituted ligands, only the syn isomers were observed in the ^{1}H NMR.

To introduce a functional group that can be used to link to amine groups, the resin-bound chelate **14** was prepared (Scheme 3). The synthesis involved first preparing the di-ester **12** by condensing 2 equiv of protected 2-aminoethanethiol with an excess of methylbromoacetate. Unfortunately, the reaction conditions required to prepare and isolate compound **12** necessitated the use of the trityl (Tr) protecting group in place of the PMT group. Compound **12** was converted to the diacid **13**, which was subsequently attached to the resin-bound amine via a HBTU−HOBt coupling procedure taking advantage of the inherently dilute nature of the resin to ensure monosubstitution. The resin-bound chelate was subsequently suspended in DMF containing 1% pyridine and 5% MeOH and treated with [NBu_4]-[$ReOCl_4$]. After 16 h, the dark orange solution was concentrated in vacuo yielding the desired product, as a red solid, in 70% yield.

The IR spectrum of **15a** showed a carbonyl stretch at 1654 cm^{-1} and the rhenium oxo stretch at 966 cm^{-1}. The splitting patterns present in the chelate portion of the ^{1}H NMR spectrum of **15a** are similar to those for compound **10**. The main difference was that the chemical shifts of the methylene protons in the chelate were for the most part shifted downfield relative to those in the benzyl derivative. The methylene protons for the pendent acid are diastereotopic and appear as a doublet (H-7A, 4.47 ppm) and a doublet of doublets (H-7B, 4.22 ppm), which in the latter case includes weak coupling to H-5α. The good yield of **15a** was achieved despite the fact that the trityl protecting group is much less reactive than the methoxy-trityl protecting group present in compound **9**.

Prior to automated solid-phase synthesis work, the reactivity of the pendent group was investigated by attempting to couple O-benzyl glycine, as a model amine, to the resin-bound chelate **14** (Scheme 4). The amine and *N*-methyl morpholine (NMM) in DMF was added to the carboxylic acid, which had been premixed with HOBt/HBTU, and the mixture was agitated using a flow of Ar for 3 h. After the sample was filtered and washed, the Re-O-benzyl glycine-MAMA complex **17** was prepared by reacting the O-benzyl glycine functionalized resin **16** with [TBA][$ReOCl_4$]. The product, a red solid, was again isolated through a plug of silica in 68% yield. The ease with which the acid can be derivatized affords the opportunity to attach a wide array of targeting agents, beyond simply peptides, to the resin-bound chelate.

Peptide Conjugation. The next goal was to develop a system that would be suitable for the preparation of peptide−MAMA

Scheme 4

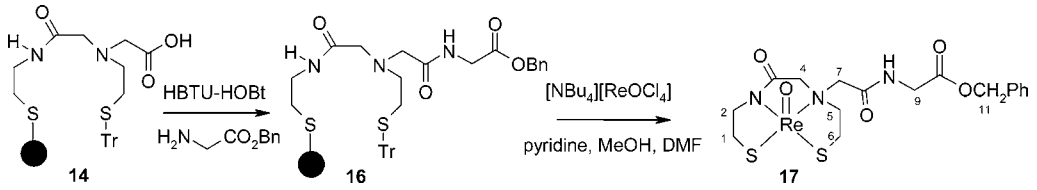

Scheme 5

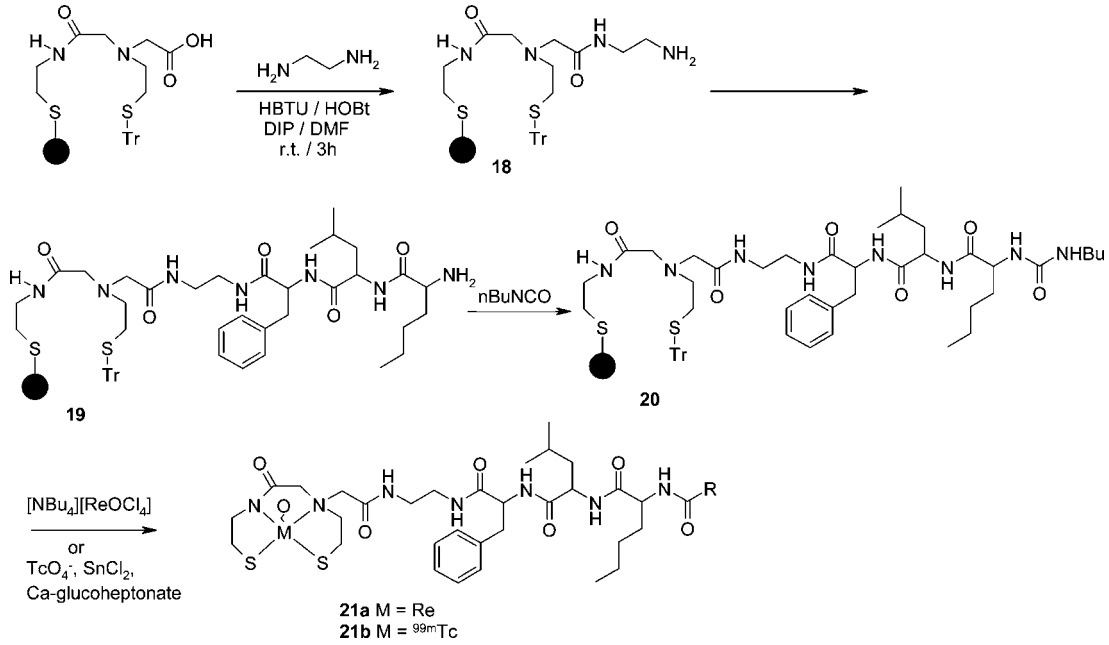

conjugates. Although it is conceivable to build peptides off the carboxylic acid funtionalized MAMA derivative, automated peptide synthesis is more often performed starting from a primary amine using Fmoc-protected amino acids. A primary amine functionalized MAMA chelate was prepared by coupling a diamine to the carboxylic acid of **14** (Scheme 5). An excess of ethylenediamine was added to the carboxylic acid functionalized resin **14** in the presence of HBTU and HOBt and the reaction was allowed to proceed for 3 h at room temperature. A small sample of resin was cleaved and analyzed by ESMS, which showed a peak corresponding to the product and no signs of unreacted acid.

Compound **18** was subsequently added to the reaction well of an Advanced Chemtech automated synthesizer and a model peptide was built up using a standard Fmoc/HBTU protection/coupling method. The target peptide was a *n*-butyl urea derivative of Phe-Leu-Nle, which is an antagonist for the formyl peptide receptor (FPR) (*20*). This ligand was of interest because radiolabeled compounds that are capable of binding selectively to the FPR on white blood cells can be used to image sites of infection and inflammation (*21*). The synthesis of the model peptide began by reacting a 4-fold excess of Fmoc-protected phenyl alanine with **18** using HBTU as the coupling agent. After the resin was washed and the Fmoc group removed using 20% piperidine in DMF, the next two amino acids, Fmoc-leucine and Fmoc-norleucine were added in an analogous manner. After deprotection of the terminal amine, conversion to the urea was carried out by adding a 10 fold excess of *n*-butyl isocyanate and shaking the mixture for 12 h. To ensure the desired conjugate had formed, a sample was cleaved from the support using a cocktail consisting of 20% TFA and 2% triisopropylsilane in DCM and the solution analyzed by LC-MS, which showed only the desired product. The peptide-functionalized resin was subsequently treated with [TBA][$ReOCl_4$] and after the green suspension was heated in an oil bath for 16 h, the resin was removed by filtration and the filtrate concentrated by rotary evaporation. The resulting red/brown solid was dissolved in a mixture of methanol and dichloromethane and purified by passing it through a plug of silica to remove the residual protecting group. The product, which showed a single peak in the HPLC, was isolated in 47% yield.

Radiolabeling. Initial attempts at labeling with ^{99m}Tc were performed using the carboxylic acid functionalized chelate **14**. The resin (100 mg) was suspended in saline, and a solution of stannous chloride dihydrate and calcium glucoheptonate was added. The latter compound, which was selected by screening a number of transfer chelates, was added to prevent premature reduction of TcO_4^- to $TcO_2 \cdot 2H_2O$. To the suspension, freshly eluted pertechnetate was subsequently added, and the mixture was analyzed by HPLC as a function of time. The desired product appeared after 6 h at room temperature; however, it took 16 h to reach a maximum yield of 40% with the other major product being TcO_4^-. The addition of EtOH as a cosolvent and heating did not increase the overall yield of **15b** or change the kinetics of the reaction. The long reaction time and suboptimal yield is likely a result of the poor compatibility of the polystyrene-based resin with water. Despite the low concentration of technetium in the reaction, it also appeared as though there were insufficient numbers of accessible reaction sites on the support to afford high yields of the desired product. In the absence of the complexation reaction, oxidation becomes a competing reaction pathway, which explains the appearance of TcO_4^-.

In an attempt to improve the yield and/or reduce the reaction time, the polystyrene support was substituted with a Tentagel resin. Tentagel-type resins are copolymers consisting of a low cross-linked polystyrene matrix on which poly(ethylene glycol) (PEG) is grafted. The presence of PEG enables the support to

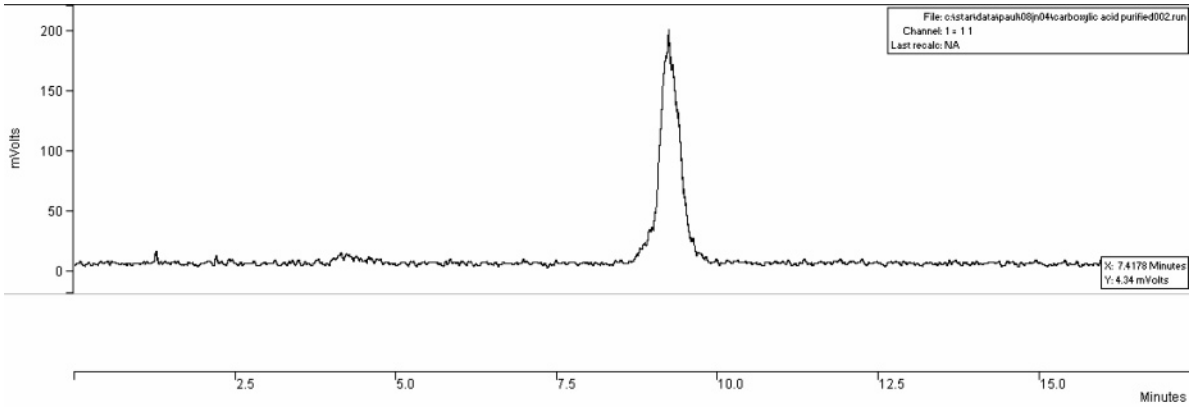

Figure 1. HPLC γ-radiochromatogram of **15b**.

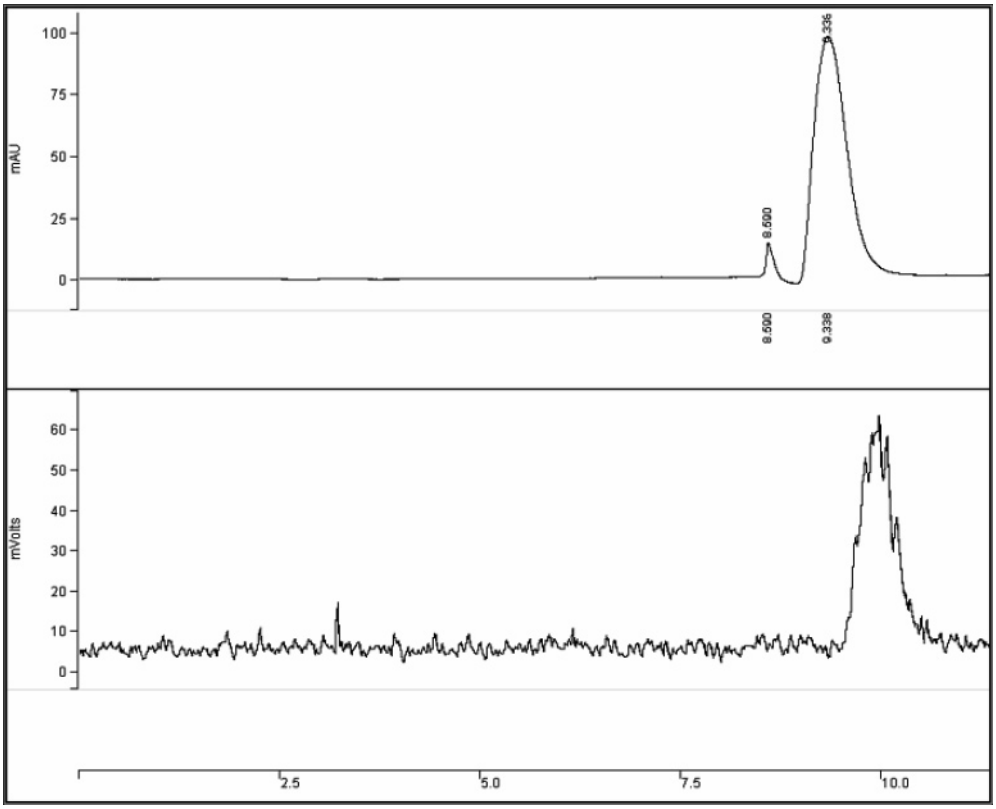

Figure 2. HPLC chromatograms of Re-peptide complex **21a** (UV, top) and ^{99m}Tc complex **21b** (γ). The difference in retention time corresponds to the separation of the detectors which are connected in series.

swell in polar solvents including water, a feature that was used successfully by Alberto et al. for the solid-phase synthesis of Tc(I) amine complexes (*7*). The one disadvantage of switching resins was that the commercially available form of the Tentagel resin has the trityl linker bound to the polymer via an electron with drawing carbonyl group. This could decrease the reactivity of the chelate derivative toward the complexation and cleavage reactions compared to the analogue bound to the methoxy-trityl substituted polystyrene resin.

After loading 2-aminoethane thiol was carried out, the carboxylic acid derivative was prepared on the Tentagel resin by coupling the resin-bound primary amine with the dicarboxylic acid **13** using HBTU, HOBt, and DIP following a similar methodology used to prepare the polystyrene analogue. After 3 h, a small amount of the resin was removed, filtered, washed, and tested for the presence of primary amines using the Kaiser test. No color (blue) developed even after extensively heating the resin, suggesting that the majority of the primary amine sites had reacted.

Radiolabeling of the TentaGel version of **14** was carried out using different amounts of resin in solutions containing varying amounts of calcium glucoheptonate and stannous chloride dihydrate. To prevent unwanted reoxidation, all reactions were performed in crimp-sealed vials in which the headspace gas was exchanged with nitrogen and all solvents were sparged with nitrogen. Reactions containing 2.5, 12.5, and 25 mg of the transfer chelator (and 100 mg of resin) were analyzed after 2 h by HPLC. There was three times the yield of the target when 12.5 mg of calcium glucoheptonate compared to the reaction with 2.5 mg of ligand, but no further increase in the amount of **15b** was observed when 25 mg was added to the reaction mixture. As a result, 12.5 mg of transfer chelate was used in all subsequent reactions.

Similar experiments were conducted to determine the optimal amount of resin. Reactions were carried out with 25, 100, or 200 mg of resin (10, 40, or 80 μmol of resin-bound substrate). Upon combining the resin with the calcium glucoheptonate−stannous chloride mixture and $^{99m}TcO_4^-$, the vials were heated

with stirring for 2 h. The radiochemical yield of the reaction with 200 mg of resin was 38%, while that for the 100 mg and 25 mg samples were 17 and 5%, respectively. The impact of changing the amount of resin on the radiochemical yield is somewhat surprising, given the large excess of reactive sites compared the amount of ^{99m}Tc even at the lowest amount of resin used. HPLC analysis of the reactions as a function of time revealed that after 2 h there was little change in radiochemical yield. At the time the yield reached a maximum there was still unreacted Tc-glucoheptonate present in solution, which suggests that even with the PEG modified resin, reactions were taking place only at a very small portion of the available reactive sites and that a kinetic barrier was limiting the overall yield.

To increase swelling as a means of improving accessibility to the chelate, a small amount of ethanol was added to the reaction immediately prior to heating. This resulted in a change in the appearance of the resin, which became an evenly distributed collection of beads as opposed to a congealed gellike mass. After 2 h of heating, HPLC indicated nearly 50% conversion versus 38% for the same reaction performed without EtOH present. Prior to purification, ethanol was removed by heating the reaction vial to 80 °C under a stream of nitrogen for 5 min. The reaction mixture was then loaded onto a C-18 Sep-Pak and washed two times with 10 mL of water. The activity that was eluted in these fractions corresponded to pertechnetate and Tc-glucoheptonate. Subsequent elution with 100% ethanol removed all of the remaining activity on the Sep-Pak where HPLC analysis (Figure 1) of the fraction showed a single peak whose retention time matched that for **15a**. The radiochemical purity of **15b** was 97%, which is greater than the radiochemical purity requirements for technetium kits and certainly acceptable for performing preclinical imaging studies.

The acid **14** attached to the Tentagel resin was subsequently derivatized with the model peptide in the same manner used to prepare **20**. Radiolabeling was conducted under the conditions developed for **14** using 555 MBq (15 mCi) of activity in saline containing 12.5 mg of glucoheptonate, 2 mg of $SnCl_2 \cdot 2H_2O$ and 250 μL of EtOH at pH 7.2. Purification was performed again using a simple solid-phase extraction on a C-18 cartridge where the product was isolated in 35% radiochemical yield with a radiochemical purity exceeding 99%. The peak in the γ-trace corresponded with the peak in the UV trace of the cold rhenium analogue (Figure 2). In the UV chromatogram of the HPLC trace, there was no evidence of unlabeled peptide.

The SPS labeling system described here is capable of producing Re-MAMA complexes in good yield and the corresponding ^{99m}Tc complexes in reasonable yield. The discrepancy between the two is likely associated with the fact that the Tc reactions are carried out at much lower concentrations and in a highly polar reaction medium using a hydrophilic starting material (Tc-gluconate complex). As part of the future work, the corresponding ^{186}Re and ^{188}Re complexes of the polymer bound ligands will be prepared, which will help validate our hypothesis in terms of the influences of the reaction medium and reagent concentrations. Despite the low yields of the ^{99m}Tc complexes, all products were isolated in high purity free from any unreacted starting material. The only impurities that had to be separated from the product were the cleaved protecting group and residual metal salts. This was accomplished by employing simple solid-phase extraction procedures, which can be easily automated. During the development of the solid-phase labeling system, a series of functionalized MAMA derivatives were prepared. Derivatives included both acid an amine functionalized resins. These compounds, which react efficiently with amines and carboxylic acids, respectively, can be used to prepare a wide range of other biomolecule conjugates and their corresponding Re and ^{99m}Tc complexes.

CONCLUSIONS

A convenient solid-phase synthesis methodology for the preparation of bifunctional Re and Tc chelate complexes was developed. The products, which can be prepared in parallel, can be isolated by a simple solid-phase extraction procedure that is easily automated. It was demonstrated that peptide conjugates of the functionalized resins can be prepared in high yield using traditional automated peptide synthesis protocols thereby creating the opportunity to prepare libraries of novel tracers. The yields of the products at tracer level were not quantitative, which is a barrier that will need to be overcome if this approach is to be used for the clinical production of radiotracers. This can be accomplished by screening different polymer supports and more reactive linkers. Notwithstanding, the ability to produce Re and high specific activity ^{99m}Tc complexes in parallel without the need to use HPLC along with the opportunity to prepare libraries of peptide−ligand conjugates using conventional automated peptide synthesis will render the reported method particularly useful for preclinical discovery work.

ACKNOWLEDGMENT

We would like to acknowledge the Ontario Research and Development Challenge Fund (ORDCF) and The National Sciences and Engineering Research Council (NSERC) of Canada for funding.

Supporting Information Available: HPLC and ^{1}H NMR spectra for the Re complexes. This material is available free of charge via the Internet at http://pubs.acs.org.

LITERATURE CITED

(1) Culbert, P. A, and Hunter, D. H. (1993) Polymer-supported radiopharmaceuticals: iodine-123- and iodine-131-labeled N-isopropyl-4-iodoamphetamine. *React. Polym. 19*, 247−253.

(2) Jagoda, E. M., Vaquero, J. J., Seidel, J., Green, M. V., and Eckelman, W. C. (2004) Experiment assessment of mass effects in the rat: implications for small animal PET imaging. *Nucl. Med. Biol. 31*, 771−779.

(3) Hunter, D. H., and Zhu, X. (1999) Polymer-supported radiopharmaceuticals: [^{131}I]MIBG and [^{123}I]MIBG. *J. Label. Compd. Radiopharm. 42*, 653−661.

(4) Bravo, J. A., Gibson, A., Loughran, K., and Bradley, M. (2001) Solid-phase synthesis of oxo(mercaptoacetylglycylglycylglycine)-rhenate(V). *Chem. Commun. 9*, 837−838.

(5) Dunn-Dufault, R., Pollak, A., Thornback, J. R., and Ballinger, J. R. (1999) Convenient preparation of no-carrier-added technetium-99m radiopharmaceuticals using solid-phase technology. *Bioconjugate Chem. 10*, 832−837.

(6) Pollak, A., Roe, D. G., Pollock, C. M., Lu, L. F. L., and Thornback, J. R. (1999) A convenient method of preparing high specific activity technetium complexes using thiol-containing chelators adsorbed on gold. *J. Am. Chem. Soc. 121*, 11593−11594.

(7) Mundwiler, S., Candreia, L., Haefliger, P., Ortner, K., and Alberto, R. (2004) Preparation of no-carrier-added technetium-99m complexes via metal-assisted cleavage from a solid phase. *Bioconjugate Chem. 15*, 195−202.

(8) Gariépy, J., Rémy, S., Zhang, X., Ballinger, J. R., Bolewska-Pedyczak, E., Rauth, M., and Bisland, S. K. (2002) A simple two-step approach for introducing a protected diaminedithiol chelator during solid-phase assembly of peptides. *Bioconjugate Chem. 13*, 679−684.

(9) Greenland, W. E. P., Howland, K., Hardy, J., Fogelman, I., and Blower, P. J. (2003) Solid-phase synthesis of peptide radiopharmaceuticals using Fmoc-N-ϵ-(Hynic-Boc)-lysine, a technetium-binding amino acid: application to Tc-99m-labeled salmon calcitonin. *J. Med. Chem. 46*, 1751−1757.

(10) Stephenson, K. A., Zubieta, J., Banerjee, S. R., Levadala, M. K., Taggart, L., Ryan, L.; McFarlane, N., Boreham, D. R.; Maresca, K.

P., Babich, J. W., and Valliant, J. F. (2004) A new strategy for the preparation of peptide-targeted radiopharmaceuticals based on an Fmoc-lysine-derived single amino acid chelate (SAAC). Automated solid-phase synthesis, nmr characterization, and in vitro screening of fMLF(SAAC)G and fMLF[(SAAC)-Re$(CO)_3)^+$]G. *Bioconjugate Chem. 15*, 128−136.

(11) Gustavson, L. M., Rao, T. N., Jones, D. S., Fritzberg, A. R., and Srinivasan, A. (1991) Synthesis of a new class of technetium chelating agents: N2S2 monoaminemonoamide (MAMA) ligands. *Tetrahedron Lett. 32*, 5485−5488.

(12) O'Neil, J. P., Wilson, S. R., and Katzenellenbogen, J. A. (1994) Preparation and structural characterization of monoamine-monoamide bis(thiol) oxo complexes of technetium(V) and rhenium(V). *Inorg. Chem. 33*, 319−323.

(13) Magata, Y., Kawaguchi, T., MisaUkon, N. Y., Uehara, T., Ogawa, K.; Arano, Y., Temma, T., Mukai, T., Tadamura, E., and Saji, H. (2004) A Tc-99m-labeled long chain fatty acid derivative for myocardial imaging. *Bioconjugate Chem. 15*, 389−393.

(14) Dezutter, N. A., Dom, R. J., de Groot, T. J., Bormans, G. M., and Verbruggen, A. M. (1999) 99mTc-MAMA-chrysamine G, a probe for beta-amyloid protein of Alzheimer's disease. *Eur. J. Nucl. Med. 26*, 1392−1399.

(15) Zhuang, Z.-P., Kung, M.-P., Hou, C., Ploessl, K., and Kung, H. F. (2005) Biphenyls labeled with technetium 99m for imaging β-amyloid plaques in the brain. *Nucl. Med. Biol. 32*, 171−184.

(16) Knorr, R., Trzeciak, A., Bannwarth, W., and Gillessen, D. (1989) New coupling reagents in peptide chemistry. *Tetrahedron Lett. 30*, 1927−1930.

(17) Kaiser, E., Colescott, R. L., Bossinger, C. D., and Cook, P. I. (1970) Color test for detection of free terminal amino groups in the solid-phase synthesis of peptides. *Anal. Biochem. 34*, 595−598.

(18) Pikl, R., Weber, K., Sundermeyer, J., Herrmann, W. A. and Kiefer, W. (1997) Vibrational study on rhenium oxo complexes: normal coordinate analysis of H_3C-ReO_3 and [L-ReO_3]$^+$ {L = $Ph_3P{=}C{=}PPh_3$}. *Vib. Spectrosc. 14*, 299−302.

(19) Laganis, E. D., and Chenard, B. L. (1984) Metal silanolates: organic soluble equivalents for atomic oxygen ion (O-2). *Tetrahedron Lett. 25*, 5831−5834.

(20) Higgins III, J. D., Bridger, G. J., Derian, C. K., Beblavy, M. J., Hernandez, P. E., Gaul, F. E., Abrams, M. J., Pike, M. C., and Soloman, H. F. (1996) N-terminus urea-substituted chemotactic peptides: new potent agonists and antagonists toward the neutrophil fMLF receptor. *J. Med. Chem. 39*, 1013−1015.

(21) Babich, J. W., Graham, W., Barrow, S. A., Dragotakes, S. C., Tompkins, R. G., Rubin, R. H., and Fischman, A. J. (1993) Technetium-99m-labeled chemotactic peptides: comparison with indium-111-labeled white blood cells for localizing acute bacterial infection in the rabbit. *J. Nucl. Med. 34*, 2176−2181.

BC050216W

Encapsulation of Myoglobin with a Mesoporous Silicate Results in New Capabilities

Tetsuji Itoh,*,† Ryo Ishii,† Takeo Ebina,† Takaaki Hanaoka,† Yoshiaki Fukushima,‡ and Fujio Mizukami†

National Institute of Advanced Industrial Science and Technology (AIST), Nigatake 4-2-1, Miyagino-ku, Sendai, 983-8551, Japan, and Toyota Central R & D Labs. Inc., Yokomichi, Nagakute, Aichi 480-1192, Japan. Received August 5, 2005; Revised Manuscript Received October 4, 2005

A metmyoglobin (Fe^{3+}), an oxidized form of myoglobin (Fe^{2+}), was confined in nanospaces of about 4 nm in diameter in mesoporous silica (FSM; folded-sheet mesoporous material), forming a metmyoglobin (Fe^{3+})−FSM nanoconjugate. The spectral characteristics of metmyoglobin (Fe^{3+})− and myoglobin (Fe^{2+})−FSM show an absorption curve quite similar to that of native metmyoglobin, indicating that myoglobin retains its higher-order structure in the pores of FSM. The metmyoglobin (Fe^{3+})−FSM conjugate had not only a peroxidase-like activity in the presence of hydrogen peroxide (a hydrogen acceptor) and 2,2-azino-bis(3-ethylbenzothiazoline)-6-sulfomic acid (ABTS) or guaiacol (a hydrogen donor) but also an advanced molecular recognition ability enabling it to distinguish between ABTS and guaiacol. Furthermore, the metmyoglobin (Fe^{3+})−FSM showed the peroxidase-like activity even in an organic media using benzoyl peroxide as the hydrogen acceptor and leucocrystal violet as the hydrogen donor. The simple immobilization of metmyoglobin (Fe^{3+}) into FSM results in enhanced catalytic activity in organic media compared to that of native metmyoglobin (Fe^{3+}).

INTRODUCTION

For vital biological functions to occur, it is necessary that the components of which the organs consist are arranged on a nanoscale and assume highly ordered or, in other words, particular higher-order structures. In the biomimetic systems developed recently, different nanoparts, for instance, heme for the selective adsorption−desorption of O_2, CO, or NO (*1*, *2*), have been recognized and employed. However, we lack the means to organize nanoparts such as proteins, which, in the case of natural hemoglobin or myoglobin, is essential for their activation and enhancement. Myoglobin (Fe^{2+}), which is a constituent of muscle that binds oxygen reversibly, is a single polypeptide (153 amino acids) protein (globin protein) of 18000 Da with one protoheme prosthetic group (*3*, *4*). Its oxygenated form is called oxymyoglobin, MbO_2, while it is known as carboxymyoglobin, MbCO, when the oxygen is displaced by carbon monoxide. The myoglobin (Fe^{2+}) molecule has a compact spheroidal structure of 2.8 by 3.2 by 4.5 nm (*5*). Intercooperation between the heme and globin protein is likely to be important for it to achieve its functions. On the other hand, when the iron in myoglobin is oxidized from the ferrous (Fe^{2+}) to the ferric (Fe^{3+}), the compound is called metmyoglobin (Fe^{3+}) and assumes a catalytic ability instead of losing its oxygen-binding capability, as well as a peroxidase-like activity in aqueous solution, as has been reported so far (*6*−*8*).

Much attention has been devoted to mesoporous materials such as MCM (mobile crystalline material) (*9*) and FSM (folded-sheet mesoporous material) (*10*) having honeycomb (hexagonal) structures with ordered cylindrical channels of 2−10 nm in diameter, larger than the microporous cavities of conventional zeolites (0.6−1.2 nm). Enzymes, horseradish peroxidase (*11*, *12*), cytochrome *c* (*13*, *14*), or lysozyme (*15*), have been introduced into mesoporous silica materials. We have also reported the incorporation of a large amount of chlorophyll *a* molecules into a FSM (*16*−*18*). The incorporation seems to increase the stability of the incorporated molecules, and such host−guest reactions should be useful for the arrangement and accumulation of the molecules and enzymes.

The present paper deals with the preparation and characterization of FSM conjugated with myoglobin and the catalytic activity and chemical stability of myoglobin encaged in the nanopores.

EXPERIMENTAL SECTION

General. Myoglobin from horse heart, 2,2-azino-bis(3-ethylbenzothiazoline)-6-sulfomic acid (ABTS), and *o*-methoxyphenol (guaiacol) were purchased from Wako Pure Chemical Industries, Ltd (Osaka, Japan). Docosyltrimethylammonium chloride [$C_{22}H_{45}N(CH_3)_3Cl$] was kindly donated by Lion Corporation (Tokyo, Japan). Kanemite (layered polysilicate) was kindly donated by Tokuyama Siltech Co., Ltd (Yamaguchi, Japan). Leucocrystal violet was obtained from Tokyo Kasei Co., Ltd. (Tokyo, Japan). Benzoyl peroxide was obtained from Nacalai Tesque, Inc. (Osaka, Japan). Mesoporous materials, FSM-16 and -22 materials, 2.7 and 4 nm in pore diameter, respectively, were prepared from kanemite (layered polysilicate) using alkyltrimethylammonium [$C_nH_{2n+1}N^+(CH_3)_3$] with different alkyl-chain lengths (n = 16 and 22), according to the method reported by Inagaki et al. (*10*). Other reagents were of analytical grade.

Characterization. Absorption spectra were measured with a Shimadzu (Kyoto, Japan) spectrophotometer, MPS-2400. Nitrogen adsorption isotherms were measured at 77 K on automatic gas adsorption apparatus, a Belsorp 28SA (BEL Japan, Inc. (Osaka, Japan). Specific surface areas were calculated by the BET method using adsorption data ranging from P/P_0 = 0.05 to 0.30, and the pore size distributions were determined by analyzing the adsorption branch by the BJH method (*19*).

Preparation of Metmyoglobin (Fe^{3+})−FSM. A metmyoglobin (Fe^{3+})−FSM conjugate was prepared as follows. To 5.0

* Corresponding author. Phone: (+81)22-237-3097, FAX: (+81)-22-237-5226, E-mail: t-itoh@ni.aist.go.jp.

† National Institute of Advanced Industrial Science and Technology (AIST).

‡ Toyota Central R & D Labs. Inc.

10.1021/bc050238i CCC: $33.50 © 2006 American Chemical Society
Published on Web 12/20/2005

mL of metmyoglobin (Fe^{3+}) obtained by the oxidation of myoglobin (Fe^{2+}) (0−30 mg) dissolved in phosphate buffer (pH 6.9) was added 100 mg of FSM-16 or FSM-22. The suspension was then shaken for 10 h at 25 °C to establish an adsorption equilibrium. The metmyoglobin (Fe^{3+})−FSM conjugate was collected by centrifugation. The amount of metmyoglobin (Fe^{3+}) adsorbed into the pores of the FSMs was spectrophotometrically determined by measuring the absorbance of the supernatant obtained after centrifugation at 420 nm, which is characteristic of the absorption band of metmyoglobin (Fe^{3+}).

Reaction of Carbon Monoxide and Myoglobin (Fe^{2+})−FSM. The metmyoglobin (Fe^{3+})−FSM conjugate (2.57 mg/mL: 0.57 mg as metmyoglobin) was reduced by the addition of sodium dithionite (10 mg) in water (10 mL), to yield a myoglobin (Fe^{2+})−FSM conjugate. Carbon monoxide was reacted with myoglobin (Fe^{2+})−FSM by bubbling CO gas in the aqueous solution containing the conjugate, after which the UV−visible spectra of 3 mL portions (3 mL: 0.077 mg/mL: 0.017 as metmyoglobin) of the solution were taken with a Shimadzu (Kyoto, Japan) spectrophotometer, MPS-2400.

Peroxidase-Like Activity of Metmyoglobin−FSM in Aqueous Solution. The experiments were conducted by measuring the peroxidase-like activity of the metmyoglobin−FSM using guaiacol and 2,2-azino-bis(3-methylbenzthiazoline)-6-sulfomic acid (ABTS), respectively, as the substrates. When the substrate was guaiacol (0.18 mmol), the metmyoglobin−FSM (0.95 mg: 0.21 mg as metmyoglobin) or metmyoglobin (0.2 mg) was suspended in 3 mL of phosphate buffer (pH 6.9) containing hydrogen peroxide (0.1%). In the case of ABTS acid (2.9 μmol), the metmyoglobin−FSM (0.0476 mg: 0.0093 mg as metmyoglobin) or metmyoglobin (0.009 mg) was suspended in 3 mL of phosphate buffer (pH 6.9) containing hydrogen peroxide (0.02%). The peroxidase activity of metmyoglobin (Fe^{3+})−FSM in the aqueous solution was spectrophotometrically determined by measuring the amount of oxidized guaiacol and ABTS using the respective molar extinction coefficients of $\epsilon_{at\ 435\ nm} = 2.55 \times 10^4\ M^{-1}\ cm^{-1}$ (*20*) and $\epsilon_{at\ 410\ nm} = 3.6 \times 10^4\ M^{-1}\ cm^{-1}$ (*21*).

Measurement of Peroxidase-Like Activity of Metmyoglobin−FSM in Toluene. The peroxidase activity of metmyoglobin (Fe^{3+})−FSM was tested by the modified method of Ajima et al. (*22*). The experiment was conducted in 3 mL of toluene, using metmyoglobin (Fe^{3+})−FSM (2 mg/mL: 0.4 mg as metmyoglobin) and metmyoglobin (Fe^{3+})(0.4 mg/mL). Benzoyl peroxide (0.28 mM) and leucocrystal violet (8 mM) were employed as a hydrogen acceptor and donor, respectively. The reaction was carried out for 200 s at 25 °C. The peroxidase activity of metmyoglobin(Fe^{3+})−FSM in the organic solvent was spectrophotometrically determined by measuring the amount of oxidized crystal violet using the molar extinction coefficient of $\epsilon_{at\ 604\ nm} = 1.2 \times 10^5\ M^{-1}\ cm^{-1}$ (*22*).

RESULTS AND DISCUSSION

Adsorption of Metmyoglobin (Fe^{3+}) into the Pores of FSMs. The adsorption amounts of metmyoglobin (Fe^{3+}) onto FSM-16 and -22 powder in phosphate buffer (pH 6.9) were spectrophotometically measured with respect to the equilibrium concentration of metmyoglobin (Fe^{3+}) (Figure 1). The adsorptions of metmyoglobin (Fe^{3+}) onto the FSM-16 and -22 of 2.7 and 4.0 nm in pore diameter, respectively, are shown by A and B, respectively. When the pores are large, the adsorption proceeds efficiently with an increase in the equilibrium concentration of metmyoglobin (Fe^{3+}) and reaches a constant level at 1.2 mg/mL (curve B). In this case, 24 mg of the 30 mg of metmyoglobin (Fe^{3+}) was adsorbed onto FSM (100 mg) in phosphate buffer (pH 6.9). On the other hand, the amount of metmyoglobin (Fe^{3+}) adsorbed onto FSM-16, the pore size of

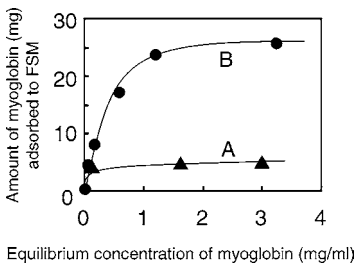

Figure 1. The adsorption of metmyoglobin (Fe^{3+}) onto FSM-16 (curve A) and FSM-22 (curve B) in phosphate buffer (pH 6.9), spectrophotometrically measured with respect to the equilibrium concentrations of metmyoglobin (Fe^{3+}) and metmyoglobin (Fe^{3+})−FSM.

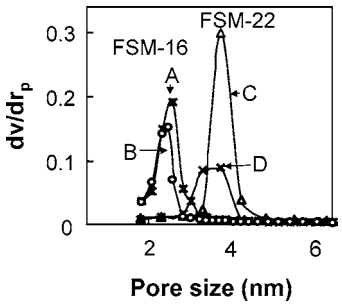

Figure 2. Pore size distributions obtained from the adsorption branch by the BJH method. Curves A, B, C, and D correspond to FSM-16, metmyoglobin-(Fe^{3+})−FSM-16, FSM-22, and metmyoglobin (Fe^{3+})−FSM-22, respectively.

which is smaller than that of FSM-22, was only slight (curve A). This difference in the adsorption behavior of metmyoglobin (Fe^{3+}) between FSM-16 and FSM-22 suggests that metmyoglobin (Fe^{3+}) is absorbed more easily into the pores than onto the outer surfaces. The corresponding pore size distributions of FSM-16 and -22 before and after metmyoglobin (Fe^{3+}) loading are shown in Figure 2. The pore volume of FSM-16 was little changed before (curve A) and after (curve B) metmyoglobin (Fe^{3+}) loading. The pore volume of FSM-22 dramatically decreased after the immobilization treatment (compare C and D). From the results, it can be seen that metmyoglobin (Fe^{3+}) molecules do not occupy the mesopore spaces of FSM-16 but exist on the outer surfaces of the particles, where as FSM-22, on the other hand, absorbs metmyoglobin (Fe^{3+}) molecules into the pores. This would further indicate that in the case of FSM, the pores of which are large enough to accommodate metmyoglobin (Fe^{3+}) or protein, such protein tends to be much more easily immobilized in the pores rather than on the outer surface, because the molecular size of metmyoglobin (Fe^{3+}) (2.8 by 3.2 by 4.5 nm) lies between the pore sizes of FSM-16 and -22, and the amount of metmyoglobin (Fe^{3+}) adsorbed onto FSM-16 was only slight.

The nitrogen adsorption isotherm of metmyoglobin (Fe^{3+}) was examined for FSM-22 (Figure 3a). With an increasing amount of metmyoglobin (Fe^{3+}) (0, 4.3, 9.2, 17, and 24 mg) confined into the pores of FSM-22 (100 mg), the amount of nitrogen adsorbed onto the metmyoglobin (Fe^{3+})−FSM decreased, as shown by curves A, B, C, D, and E, respectively. A steep increase in nitrogen uptake at the relative pressure of 0.4 for FSM is probably due to capillary condensation (curve A). On the other hand, the nitrogen uptakes by the metmyoglobin (Fe^{3+})−FSM (curves B−E) were lower than that of FSM. In the case of curve E, the pore volume of metmyoglobin (Fe^{3+})−FSM was only ca. 46% that of FSM-22. In line with the BET surface areas and pore volumes of FSM (Table 1), the pore peaks (Figure 3b) decreased with an increase in the amount of metmyoglobin (Fe^{3+}) adsorbed into the pores of FSM (Table 1). These results indicate that the pores of FSM were occupied

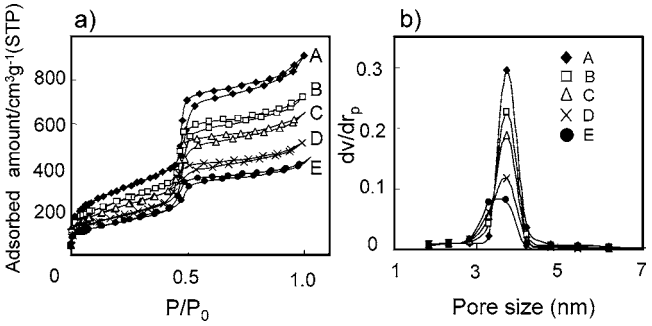

Figure 3. Changes in nitrogen adsorption isotherms of metmyoglobin (Fe^{3+})−FSM conjugates (a) and the corresponding pore size distributions obtained from the adsorption branch by the BJH method (b). Curves A, B, C, D, and E indicate the amounts of metmyoglobin (Fe^{3+}) adsorbed to the pores of FSM (100 mg), 0, 4.3, 9.2, 17.0, and 24.0 mg, respectively.

Table 1. Physicochemical Properties of the Myoglobin−FSM Conjugate

myoglobin adsorbed (mg/100 mg FSM)	pore volume ($cm^3\ g^{-1}$)	specific surface area ($m^2\ g^{-1}$)
0	1.39	1110
4.3	1.11	886
9.2	0.99	856
17.0	0.78	722
24.0	0.64	561

by metmyoglobin (Fe^{3+}) and support the opinion expressed in the preceding paragraph.

Reaction of Myoglobin (Fe^{2+})−FSM with Carbon Monoxide. The absorption spectrum of the myoglobin (Fe^{2+})−FSM conjugate in water, shown in Figure 4 (curve B), differs considerably from that of the metmyoglobin (Fe^{3+})−FSM conjugate (curve A). Upon reducing the conjugate with dithionate, the metmyoglobin (Fe^{3+})−FSM spectrum (curve A in Figure 4) changed remarkably, the Soret shifting from 420 to 431 nm and a sharp single peak appearing in the visible region at 557 nm (curve B in Figure 4). The single adsorption band (λ_{max} = 557 nm) in the α, β region compared favorably with the wavelengths of deoxymyoglobin (*23*). The addition of carbon monoxide to the myoglobin (Fe^{2+})−FSM conjugate caused the formation of a CO-myoglobin−FSM having absorption maxima at 567, 539, and 420 nm (Figure 4: curve C). The spectrum has two clearly split peaks (α- and β-bands) in the visible region and a Soret peak. It is well-known that deoxymyoglobin changes easily into carboxymyoglobin in the presence of carbon monoxide with a spectral change. Thus, the change of spectrum from B to C, that is, the band shift from 557 and 433 nm to 567, 539 and 420 nm, respectively, corresponds to the change of myoglobin (Fe^{2+})−FSM to CO-myoglobin (Fe^{2+})−FSM. In addition, CO-myoglobin (Fe^{2+})−FSM shows an absorption curve quite similar to that of CO-heme coupled with native myoglobin (*23*). From the results above, it is deduced that myoglobin retains its higher-order structure in the pores of FSM.

Peroxidase-Like Activity of Metmyoglobin (Fe^{3+})−FSM. Figures 5a and 5b show the peroxidase-like activity of the metmyoglobin (Fe^{3+})−FSM conjugate against incubation time in the reactions using hydrogen peroxide (a hydrogen acceptor) and guaiacol (*23*) or ABTS (*25*) (hydrogen donors) in aqueous solution (Scheme 1). When guaiacol was the hydrogen donor, the metmyoglobin (Fe^{3+})−FSM conjugate (Figure 5a, curve A) showed activity similar to that of the native form (Figure 5a, curve B). The reaction rate with the metmyoglobin (Fe^{3+})−FSM and the native form were 1.59×10^{-6} and 1.26×10^{-6} M/min, respectively. In the absence of myoglobin−FSM in the reaction systems, no oxidation of organic substrate occurs (date not shown). This clearly indicates that the metmyoglobin does not lose its activity by encapsulation into the pores of FSM and probably maintains its nominal higher-order structure. However, when ABTS was the hydrogen donor, the amount of oxidized hydrogen donor increased with time for both the metmyoglobin (Fe^{3+})−FSM and the native form (Figure 5b, curve B), but oxidation did proceed slightly with metmyoglobin (Fe^{3+})−FSM (Figure 5b, curve A). The reaction rate with the metmyoglobin (Fe^{3+})−FSM and the native form were 0.9×10^{-6} and 3.8×10^{-6} M/min, respectively. Generally, in a process catalyzed by an enzyme, the reaction proceeds with the enzyme first recognizing the substrate and/or reactant to form

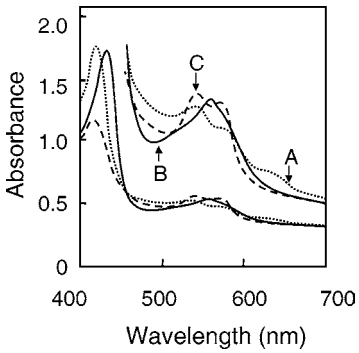

Figure 4. Absorption spectra of metmyoglobin (Fe^{3+})−FSM (curve A), deoxymyoglobin (Fe^{2+})−FSM (curve B), and CO−myoglobin (Fe^{2+})−FSM (curve C) in phosphate buffer (pH 6.9). Curve B in the spectrum of deoxymyoglobin (Fe^{2+})−FSM in phosphate buffer (pH 6.9) was obtained by adding dithionite to metmyoglobin (Fe^{3+})−FSM. The concentration of metmyoglobin (Fe^{3+})−FSM was 0.077 mg/mL (0.017 as metmyoglobin). The peak positions of the α, β, and Soret bands for metmyoglobin (Fe^{3+})−FSM change from 640, 538, and 420 nm to 557 and 432 nm, respectively. Curve C is the spectrum of CO−myoglobin (Fe^{2+})−FSM obtained by adding carbonmonoxide,CO, to deoxymyoglobin (Fe^{2+})−FSM. The peak positions of the α, β and Soret bands for deoxymyoglobin (Fe^{2+})−FSM change from 557 and 432 nm to 567, 539, and 420 nm, respectively.

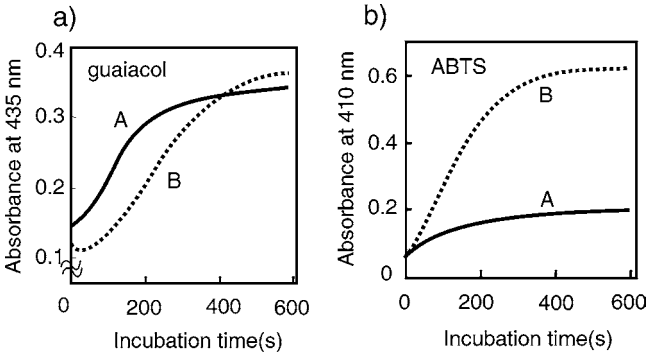

Figure 5. The peroxidase-like activity spectrophotometrically determined by measuring the absorbance at 435 and 410 nm for the respective oxidations of guaiacol (a) and 2,2-azino- bis(3-methylbenthzthiaoline)-6-sulfomic acid (ABTS) (b). (a) Oxidation of guaiacol (0.18 mmol) with hydrogen peroxide (0.1%) in 3 mL of phosphate buffer (pH 6.9) catalyzed by metmyoglobin−FSM (0.95 mg: 0.21 mg as metmyoglobin) (curve A) or metmyoglobin (0.2 mg) (curve B). (b) Oxidation of ABTS (2.9 μmol) with hydrogen peroxide (0.02%) in 3 mL of phosphate buffer (pH 6.9) catalyzed by myoglobin−FSM (0.0476 mg: 0.0093 mg as metmyoglobin) (curve A) or metmyoglobin (0.009 mg) (curve B).

Scheme 1

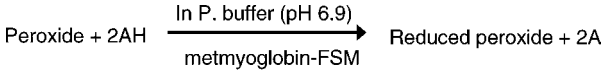

Peroxide: H_2O_2 AH: guaiacol or ABTS

guaiacol : o-methoxyphenol
ABTS: 2,2-azino-bis(3-methylbenzthiazoline)-6-sulfomic

Scheme 2

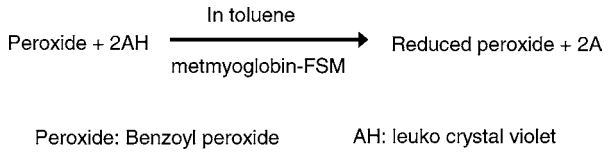

a certain activation complex with them. Thus, the difference between the activities of metmyoglobin (Fe^{3+})−FSM conjugate for guaiacol and ABTS indicates that the metmyoglobin could not form such an activation complex with ABTS but could with guaiacol. In other words, it can be said that by the encapsulation, the metmyoglobin obtained an advanced molecular recognition ability that can distinguish between ABTS and guaiacol. Although it is not completely clear how the new ability comes about at present, it may be due to the limited flexibility in the higher-order structure of metmyoglobin and the selective adsorption properties (*16*−*18*) of metmyoglobin−FSM caused by the encapsulation.

Peroxidase-Like Activity of Metmyoglobin (Fe^{3+})−FSM in Toluene. The finding shown above suggested that we examine the action of metmyoglobin (Fe^{3+})−FSM conjugate in an organic solvent. Thus, the catalysis of metmyoglobin (Fe^{3+})−FSM was investigated for the oxidation of leucocrystal violet (*26*) (AH) with benzoyl peroxide in toluene as shown below (Scheme 2). The absorption spectrum of metmyoglobin (Fe^{3+})−FSM in toluene is shown as a solid line in Figure 6 and shows a sharp Soret band at 410 nm. The absorption spectrum of metmyoglobin (Fe^{3+}), the dashed line in Figure 6, shows a broad Soret band at approximate 420 nm, clearly indicating an agglutinated form of metmyoglobin (Fe^{3+}). From the results obtained above, it can be seen that metmyoglobin (Fe^{3+}) (native) is easily deactivated in the organic media, but the metmyoglobin (Fe^{3+}) encaged in the pore of FSM is not denatured. Figure 7 shows the oxidation of leucocrystal violet (AH) with benzoyl peroxide catalyzed by metmyoglobin−FSM in toluene. The peroxidase activities of metmyoglobin (Fe^{3+})−FSM and metmyoglobin (Fe^{3+}) against incubation time correspond to curves A and B, respectively. The activity of the metmyoglobin (Fe^{3+})−FSM increased with time, while the native form showed almost no activity. On the basis of the above results, we can point out the following. Although the aggregation of metmyoglobin is accelerated in toluene, it can be prevented by encapsulation with FSM. Another role of encapsulation is to retain metmyoglobin (Fe^{3+}) in its active form or, in other words, at the nominal higher-order structure, as can be seen from the high activity of metmyoglobin(Fe^{3+})−FSM for the reaction mentioned above. As for the reasons why the metmyoglobin (Fe^{3+}) encaged in FSM retains the nominal higher-order structure and acts as a catalyst even in toluene, various factors can be considered. First of all, if the pores of FSM are highly hydrophobic, they can expel toluene molecules. If so, toluene

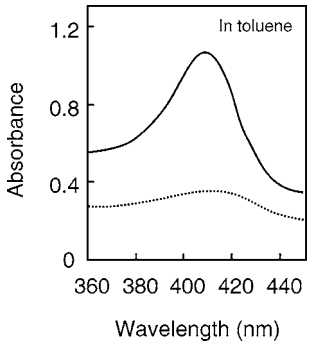

Figure 6. Absorption spectra of metmyoglobin (dashed line) and metmyoglobin−FSM (solid line) in toluene.

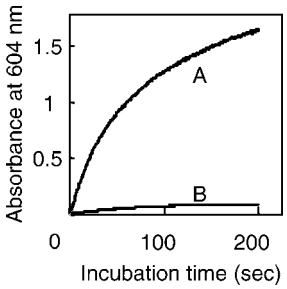

Figure 7. Oxidation of crystal violet with benzoyl peroxide catalyzed by metmyoglobin−FSM (curve A) and metmyoglobin (curve B) in toluene. Benzoyl peroxide (0.28 mM) and leucocrystal violet (8 mM) were used as a hydrogen acceptor and donor, respectively, in 3 mL of toluene. The reaction was carried out for 200 s at 25 °C. Curve A: metmyoglobin (Fe^{3+})−FSM (2 mg/mL: 0.4 mg as metmyoglobin). Curve B: metmyoglobin (Fe^{3+})(0.4 mg/mL). The reaction system is the same as that of curve A.

cannot do any damage to the metmyoglobin (Fe^{3+}). Thus, the adsorption isotherm of toluene into metmyoglobin (Fe^{3+})−FSM (20 mg of metmyoglobin /100 mg of FSM) was measured for the purpose of examining whether toluene molecules could enter into the pore cavity. The pore volume of metmyoglobin (Fe^{3+})−FSM calculated on the basis of the toluene adsorption isotherm was the same as that obtained from the corresponding nitrogen adsorption isotherm. Accordingly toluene molecules can enter the pore cavity of metmyoglobin (Fe^{3+})−FSM, yet they do not deactivate the metmyoglobin (Fe^{3+}). This may be due to the limited flexibility of metmyoglobin (Fe^{3+}) in the pores of FSM. Note that Wang et al. (*27*) have found that hemoglobin immobilized between titanate layers does not lose its activity in organic solvents; they postulate that water between the layers plays an important role in retaining the activity of the enzyme in its higher-order structure. Furthermore, the interlayer water is presumed to prevent organic solvents from taking water molecules which the enzyme originally possesses, resulting in retention of the activity and higher-order structure though the interaction between the interlayer water and the enzyme-bound water molecules. A similar mechanism may be considered relevant in this work.

In conclusion, the encapsulation of myoglobin into the silicate mesoporous increases not only the molecular recognition ability of myoglobin but also the resistance to organic solvents, or surroundings. Thus, the encapsulation of enzymes with mesoporous materials is quite useful for establishing new functions and will have wide application to different chemical processes.

LITERATURE CITED

(1) Wang, J. H. (1970) Synthetic biochemical models. *Acc. Chem. Res. 3*, 90−97.

(2) Wang, J. H. (1958) Hemoglobin studies. II. a synthetic material with hemoglobin-like property. *J. Am. Chem. Soc. 80*, 3168−3169.

(3) Perutz, M. F. (1969) Symbols, signs, and abbreviation. *Proc. R. Soc. (B) 173*, 113−140.

(4) Perutz, M. F. (1964) The hemoglobin molecule. *Sci. Am. 211*, 64−76.

(5) Pum, D., Sara, M., and Sleytr, U. B. (1989) Structure, surfsace-charge, and self-assembly of the s-layer lattice from bacillus-coagulans E38-66. *J. Bacteriol. 171*, 5296−5303.

(6) Nakamura, Y., Samejima, T., Kurihara, K., Tojo, M., and Shibata, K. (1960) Proxidase activity of hemoproteins II. metmyoglobin and cytochrome *c*. *J. Biochem. 48*, 862−868.

(7) Inada, Y., Kurozumi, T., and Shibata, K. (1961) Peroxidase activity of hemoproteins. I. Generation of activity by acid or alkali denaturation of methemoglobin and catalase. *Arch. Biochem. Biophys. 93*, 30−36.

(8) Tojo, M., Nakamura, Y., Kurihara, K., Samejima, T., Hachimori, Y., and Shibata, K. (1962) Peroxidase activity of hemoproteins. IV. Hematin complexes as model enzymes of peroxidase. *Arch. Biochem. Biophys. 99*, 222−240

(9) Kresge, C. T., Leonowicz, M. E., Roth, W. J., Vartuli, J. C., and Beck, J. S. (1992) Ordered mesoporous molecular sieves synthesized by a liquid-crystal template mechanism. *Nature 395*, 710.

(10) Inagaki, S., Fukushima, Y., and Kuroda, K. (1993) Synthesis of highly ordered mesoporous materials from a layered polysilicate. *J. Chem. Soc., Chem. Commun.* 680−682.

(11) Takahashi, H., Li, B., Sasaki, T., Miyazaki, C., Kajino. T., and Inagaki, S. (2000) Catalytic activity in organic solvents and stability of immobilized enzymes depend on the pore size and surface characteristics of mesoporous silica. *Chem. Mater. 12*, 3301−3305

(12) Deere, J., Magner, E., Wall, J. G., and Hodnett, B. K. (2003) Adsorption and activity of proteins onto mesoporous silica. *Catal. Lett. 85*, 19−23.

(13) Deere, J., Magner, E., Wall, J. G., and Hodnett, B. K. (2001) Adsorption and activity of cytochrome *c* on mesoporous silicates**.** *Chem. Commun. 5*, 465−466.

(14) Vinu, A., Murugesan, V., Tangermann, O., and Hartmann, M. (2004) Adsorption of cytochrome *c* on mesoporous molecular sieves: Influence of pH, pore diameter, and aluminum incorporation. *Chem. Mater*. *16*, 3056−3065.

(15) Fan, J., Lei, J., Wang, L., Yu, C., Tu, B., and Zhao, D. (2003) Rapid and high-capacity immobilization of enzymes based on mesoporous silicas with controlled morphologies. *Chem. Commun*. *17*, 2140−2141.

(16) Itoh, T., Yano, K., Inada, Y., and Fukushima, Y. (2002) Photostabilized Chlorophyll *a* in Mesoporous. Adsorption properties of chlorophyll *a* and photoreduction activity. *J. Am. Chem. Soc*. *124*, 13437−13441.

(17) Itoh, T., Yano, K., Inada, Y., and Fukushima, Y. (2002) Stabilizetion of chlorophyll *a* in mesoporous silica and its pore size dependence. *J. Mater. Chem*. *12*, 3275−3277.

(18) Itoh, T., Yano, K., Inada, Y., Kajino, T., Itoh, S., Shibata, Y., Mino, H., Miyamoto, R., Inada, Y., Iwai, S., and Fukushima, Y. (2004) Nanoscale organization of chlorophyll *a* in mesoporous silica: efficient energy transfer and stabilized charge separation as in natural photosynthesis. *J. Phys. Chem. B. 108*, 13683−13687.

(19) Barret, E. P., Joyner, L. G., and Halenda, P. P. (1951) The determination of pore volume and area distributions in porous substance. Computation from nitrogen isotherms. *J. Am. Chem. Soc. 73*, 373−380.

(20) Bergmeyer, H. U. (1974) *Methods of Enzymatic Analysis*, 2nd ed., pp 494−495, Academic Press, New York.

(21) Bédouet, L., Adenier, H., Pulven, S., Bedel-Cloutour, C., and Thomas, D. (2004) Recovery of the oxidative activity of caged bovine haemoglobin after UV photolysis. *Biochem. Biophys. Res. Commun. 320*, 939−944.

(22) Ajima, A., Cao, S. G., Takahashi, K., Matsushima, A., Saito, Y., and Inada, Y. (1987) An attempt to determine lipid peroxidase with polyethylene gliycol-modified hemin. *Biotechnol. Appl. Biochem. 9*, 53−57.

(23) Mahler, H. R., and Corde E. H. (1969) *Biological Chemistry*, pp 583−589, Harper & Row, London.

(24) Doerge, D. R., Divi, R. L., and Churchwell M. I. (1997) Identification of the colored guaiacol oxidation product produced by peroxidases. *Anal. Biochem. 250*, 10−17.

(25) Wolfenden B. S., and Willson R. L. (1982) Radical-cations as reference chromogens in kinetic-studies of one-electron transfer-reactions − pulse-radiolysis studies of 2,2′-azinobis(3-ethylbenzothiazoline- 6-sulfomate). *J. Chem. Soc., Perkin Trans. 2*. 805−812

(26) Safarikova, M., and Safarik, I. (2002) Magnetic solid-phase extraction of target analytes from large volumes of urine. *Eur. Cells Mater. 3*, 192−195

(27) Wang, Q., Gao, Q., and Shi, J. (2004) Enhanced catalytic activity of hemoglobin in organic solvents by layered titanate immobilization. *J. Am. Chem. Soc. 126*, 14346−14347.

BC050238I

Comparative Evaluation of Target-Specific GFP Gene Silencing Efficiencies for Antisense ODN, Synthetic siRNA, and siRNA Plasmid Complexed with PEI−PEG−FOL Conjugate

Sun Hwa Kim,[†] Hyejung Mok,[†] Ji Hoon Jeong,[‡] Sung Wan Kim,[‡] and Tae Gwan Park*,[†]

Department of Biological Sciences, Korea Advanced Institute of Science and Technology, Daejeon 305-701, South Korea, and Center for Controlled Chemical Delivery (CCCD)/Department of Pharmaceutics and Pharmaceutical Chemistry, University of Utah, Salt Lake City, Utah 84112. Received October 4, 2005; Revised Manuscript Received November 1, 2005

Cell specific gene silencing effects of antisense oligodeoxynucleotide (AS-ODN), synthetic small interfering RNA (siRNA-S), and siRNA expressing plasmid (siRNA-P) were comparatively evaluated. Poly(ethylenimine) (PEI) and PEI−*graft*-poly(ethylene glycol)−folate (PEI−PEG−FOL) conjugate were used to form nanosized polyelectrolyte complexes with the above three nucleic acids coding for inhibition of green fluorescent protein (GFP) expression. The three nucleic acid complexes formulated with either PEI or PEI−PEG−FOL had comparable sizes and surface ζ potential values. Among the three inhibitory nucleic acids, siRNA-S, when complexed with PEI−PEG−FOL, exhibited the most dose-effective and fastest gene silencing effect for FOL receptor overexpressing KB cells, because the siRNA-S could be directly delivered, via FOL receptor-mediated endocytosis, into the cytoplasm compartment where the degradation processing of target GFP mRNA occurred in a sequence-specific manner.

INTRODUCTION

Posttranscriptional gene silencing approaches, using various nucleic acid based molecules such as antisense oligodeoxynucleotides (AS-ODNs), ribozymes, and small interfering RNAs (siRNAs), have drawn much attention because of their potential therapeutic impact on treating various genetic disorder and infectious diseases including cancer. For the last two decades, AS-ODNs and ribozymes have been popularly used to knock down expression of specific genes. Quite recently, siRNA, which inhibits specific genes by double-stranded RNA molecules having 21−23 nucleotides, has emerged as a more powerful therapeutic genetic agent (*1*−*3*). Both AS-ODN and siRNA similarly inhibit posttranscriptional process of a target mRNA in a sequence-specific manner, but their action mechanisms in a cellular and molecular basis are vastly different. Although both of them exhibit considerable gene inhibition effects in vitro, their transfection efficiencies still remain in a relatively low level mainly due to poor intracellular uptake and severe enzymatic degradations in serum conditions (*4*, *5*). To promote their gene inhibition effect, a wide range of cationic polymers and lipids have been employed to form nanoparticulate polyelectrolyte complexes with negatively charged AS-ODN and siRNA (*6*−*8*). The formation of nanosized complexes enhances the extent of intracellular uptake, increases stability against nucleases, and additionally confers cell specificity when conjugating a targeting moiety to the complexes.

Among the nonviral carriers, PEI has been popularly used for delivering plasmid DNA and AS-ODN for its superior transfection efficiency. A variety of chemically modified PEI derivatives such as PEGylated PEI and cross-linked PEI were also used to reduce its inherent cytotoxic problem and to enhance colloidal stability against aggregation under serum conditions (*9*−*11*). In our previous works, PEI was grafted with PEG chains having a folate (FOL) moiety at its distal end to produce PEI−PEG−FOL conjugate (*12*). When the conjugate was complexed with plasmid DNA to form nanosized polyelectrolyte particles, greatly increased specific cellular uptake to FOL receptor overexpressing cancer cells was observed with concomitantly improved colloidal stability, compared to unmodified PEI. As a result, gene transfection efficiency with PEI−PEG−FOL was enhanced to a greater extent than that with unmodified PEI for FOL receptor overexpressing cells. This was attributed to folate receptor mediated endocytosis.

It is of great interest to compare gene silencing efficiencies between AS-ODN and siRNA, using PEI−PEG−FOL conjugate as a cell-specific gene carrier, since their modes of action are fundamentally different. Herein we report comparative gene silencing effects of three types of nucleic acid based molecules coding for inhibiting green fluorescent protein (GFP) expression. AS-ODN, synthetic siRNA (siRNA-S), and siRNA plasmid (siRNA-P) were used to form polyelectrolyte complexes with PEI or PEI−PEG−FOL. The complexes were characterized in terms of diameter and surface charge value. Their gene inhibition extents of an exogenous GFP gene expressed in KB cells were quantitatively evaluated in terms of dose and incubation time.

EXPERIMENTAL PROCEDURES

1. Materials. Folate (FOL) was purchased from Sigma Chemical Co. (St. Louis, MO). Poly(ethylenimine) (branched PEI, MW 25 000) was obtained from Aldrich (Milwaukee, WI). Poly(ethylene glycol) ($COOH-PEG-NH_2$, MW 3400) was supplied by Nektar (Huntsville, AL). Dulbecco's phosphate buffered saline (PBS), fetal bovine serum (FBS), and Roswell Park Memorial Institute 1640 medium (RPMI 1640 w/o folate) were purchased from Gibco BRL (Grand Island, NY). A pEGFP-C1 vector was obtained from BD Bioscience Clontech (Palo Alto, CA). All other chemicals and reagents were of analytical grade.

2. Antisense ODN, Synthetic siRNA, and siRNA Plasmid. Antisense ODN, synthetic siRNA, and plasmid siRNA targeted

* Corresponding author. Tel: +82-42-869-2621. Fax: +82-42-869-2610. E-mail address: tgpark@kaist.ac.kr.

[†] Korea Advanced Institute of Science and Technology.

[‡] University of Utah.

10.1021/bc050289f CCC: $33.50 © 2006 American Chemical Society
Published on Web 12/30/2005

Table 1. GFP Target Sequences for Antisense ODN, Synthetic siRNA, and siRNA Plasmid

nucleic acid type	sequence
antisense ODN	GAGCTGCACGCTGCCGTC (18-mer)
synthetic siRNA	
sense	AACUUCAGGGUCAGCUUGC (19-mer)
antisense	GCAAGCUGACCCUGAAGUU (19-mer)
siRNA plasmid	
forward	GATCCCCGCAAGCTGACCCTGAAGTTCTTCAAGAG-AGAACTTCAGGGTCAGCTTGCTTTTTGGAAA
reverse	AGCTTTTCCAAAAAGCAAGCTGACCCTGAAGTTCTC-TCTTGAAGAACTTCAGGGTCAGCTTGCGGG

to the GFP gene were designed as shown in Table 1. HPLC-purified phosphorothioated antisense ODN was purchased from Bioneer (Daejeon, South Korea). Synthetic siRNA (antisense and sense strands) was obtained from Invitrogen (Carlsbad, CA). siRNA plasmid (pSUPER-siGFP), producing anti-GFP siRNA hairpin transcript in the cells, was constructed by using pSUPER-RNAi vector system (Oligoengine, Seattle, WA) and forward and reverse oligonucleotides (*1*). Forward and reverse oligonucleotides for cloning the pSUPER-siGFP were synthesized and purified by Bioneer (Daejeon, South Korea).

3. Preparation of PEI−PEG−FOL Conjugate. A cancer target ligand, folate, was introduced into the highly branched cationic polymer, PEI, to prepare a target-specific gene delivery vector. The PEI−PEG−FOL conjugate was synthesized according to the previous method (*10*, *12*). The stoichiometric conjugation molar ratio between PEI and PEG−FOL was 1:4.46 as determined by ^{1}H NMR spectra. The calculated molecular weight of the resulting conjugate was about MW 42824.

4. Preparation and Characterization of Polyelectrolyte Complexes between PEI−PEG−FOL Conjugate and Various Nucleic Acids. Anionic nucleic acids and cationic polymeric conjugates produced self-assembled polyelectrolyte complexes in an aqueous phase due to their electrical interactions. AS-ODN, siRNA-S, and siRNA-P were separately complexed with unmodified PEI and PEI−PEG−FOL conjugate under various conditions. Three types of the nucleic acids (4 μg) dissolved in 200 μL of phosphate buffered saline (PBS, pH 7.2) were respectively mixed with 10.6 μg of PEI−PEG−FOL (nitrogen/phosphate ratio = 16) in 300 μL of PBS solution. The mixtures were incubated for 20 min at room temperature and diluted 5-fold into PBS solution. To determine the hydrodynamic diameter and ζ potential of the PEI−PEG−FOL (or PEI)/nucleic acid complexes, the resulting complex solutions were analyzed by a dynamic light scattering instrument (Zeta-Plus, Brookhaven, NY).

5. Cell Culture and Transfection. KB cells (human epidermal carcinoma, Korean Cell Line Bank, Seoul, South Korea), were cultured in RPMI 1640 w/o folate medium supplemented with 10% FBS (the only source of folate) at 37 °C in a humidified atmosphere of 5% of CO_2. For gene silencing experiments, the nucleic acid complexes were cotransfected to KB cells along with the GFP plasmid according to the previously published method with minor modifications (*13*). Briefly, the cells were transfected with 2 μg of pEGFP-C1 vector using Lipofectamine 2000 reagent (2 mg/mL, Invitrogen, Carlsbad, CA) in 1 mL of RPMI1640 without folate containing 10% FBS for 3 h at 37 °C. The three nucleic acids were simultaneously cotransfected using 2 μg of AS-ODN, 0.5 μg of siRNA-S, or 2 μg of siRNA-P condensed with PEI or PEI−PEG−FOL conjugates at various nitrogen/phosphate (N/P) ratios from 0 to 24. To determine a dose dependence of the nucleic acids on the inhibition of the target gene expression, cells were transfected with the complexes prepared at an N/P ratio of 16. The concentrations of the nucleic acids were as follows. AS-ODN and siRNA-P: 0.0, 0.1, 0.5, 1.0, 2.0, and 4.0 μg. siRNA-S: 0.00, 0.05, 0.10, 0.25, 0.50, and 1.00 μg. After replacing the transfection medium with 1 mL of serum containing medium, the transfected cells were incubated for a further 24 h and harvested by treatment of a cell lysis buffer solution (CelLytic M cell lysis reagent, Sigma-Aldrich, St. Louis, MO). For a time dependent GFP expression trend, PEI−PEG−FOL complexes were prepared with AS-ODN (2 μg), siRNA-S (0.5 μg), and siRNA-P (2 μg) at an N/P ratio of 16 and incubated for different time intervals after transfection. The level of GFP fluorescence was determined using a spectrofluorophotometer (SLM-AMINCO 8100, SLM Instruments Inc., Rochester, NY) with an excitation and emission wavelength at 488 and 507 nm, respectively. All values were normalized by cellular protein content, as determined by Micro-BCA protein assay (Pierce, Rockford, IL). The relative GFP expression level was then calculated as a relative percentage of GFP gene expression for the pEGFP-C1 transfected KB cells (negative control) compared to those cotransfected with nucleic acid complexes (AS-ODN, siRNA-S, or siRNA-P) [% GFP expression = (GFP intensity in sample/GFP intensity in negative control) × 100].

RESULTS AND DISCUSSION

Table 1 shows nucleotide sequences of anti-GFP AS-ODN, siRNA-S, and siRNA-P. Both siRNA-S and siRNA-P have the same target site in an mRNA sequence of GFP, but AS-ODN has a different one. For siRNA-P construction, forward and reverse ODN oligomers were cloned with a pSUPER-RNAi vector system as reported in our previous study (*12*). The three anti-GFP nucleic acid molecules, AS-ODN, siRNA-S, and siRNA-P, were complexed with PEI or PEI−PEG−FOL at an N/P ratio of 16. As listed in Table 2, the complexes of PEI−PEG−FOL with AS-ODN, siRNA-S, and siRNA-P were 94.4 ± 20.0, 120 ± 34.5, and 108.5 ± 19.0 nm in diameter with positive surface charge values of 1.0 ± 0.5, 2.5 ± 0.9, and 1.3 ± 0.7 mV, respectively. The complexes with PEI had slightly larger particle sizes with greater surface charge values than those with PEI−PEG−FOL, which was likely due to a charge shielding effect by PEGylation (*14*). At a fixed N/P ratio, the PEI and PEI−PEG−FOL complexes respectively showed comparable sizes and surface charge values regardless of nucleic acid molecules.

Target-specific GFP silencing activities of the three complexes were comparatively determined with folate receptor overexpressing KB cells. Anti-GFP nucleic acids (AS-ODN, siRNA-S, and siRNA-P) were complexed with PEI or PEI−PEG−FOL at different N/P ratios, and the resultant complexes were cotransfected with Lipofectamine/GFP plasmid (pEGFP-C1 vector) complexes. GFP gene silencing efficiencies of the complexes are shown in Figure 1. With increasing the N/P ratio, PEI−PEG−FOL complexes exhibited greater suppression of GFP expression than PEI complexes for the three nucleic acids. At an N/P ratio of 16, PEI−PEG−FOL complexes with AS-ODN, siRNA-S, and siRNA-P showed 68.9 ± 8.0%, 75.0 ± 15.3%, and 59.2 ± 3.4% inhibition of GFP expression,

Table 2. Particle Characterization of Antisense ODN, Synthetic siRNA, and siRNA Plasmid Condensed with PEI or PEI−PEG−FOL Conjugate

	PEI			PEI−PEG−FOL		
condensation agent	antisense ODN	synthetic siRNA	siRNA plasmid	antisense ODN	synthetic siRNA	siRNA plasmid
particle size (nm)	115.2 ± 15.3	164.2 ± 22.8	156.6 ± 26.3	94.4 ± 20.0	120 ± 34.5	108.5 ± 19.0
ζ potential (mV)	8.8 ± 1.3	10.3 ± 1.9	8.2 ± 2.0	1.0 ± 0.5	2.5 ± 0.9	1.3 ± 0.7

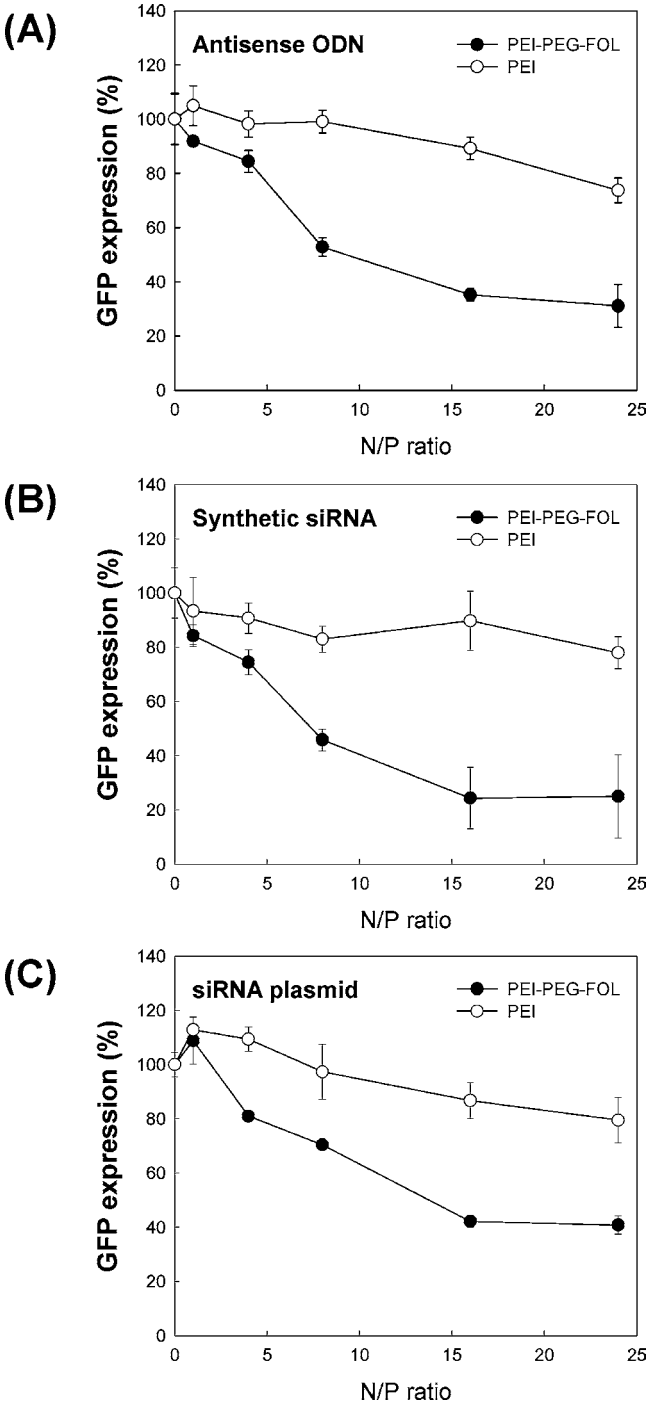

Figure 1. Cancer cell targeted GFP gene silencing effect of (A) antisense ODN, (B) synthetic siRNA, and (C) siRNA plasmid complexes with PEI (open circles) and PEI−PEG−FOL (filled circles) as a function of N/P ratio from 0 to 24 for KB cells.

respectively, while PEI complexes showed an inhibition degree of 26.3 ± 4.6%, 22.1 ± 5.9%, and 20.5 ± 8.4%, in the same order. These results evidently indicate that the PEI−PEG−FOL complexes were far more effective in GFP silencing than the PEI complexes due to their enhanced extents of cellular uptake (*12*). For the three PEI−PEG−FOL complexes, folate receptor mediated endocytosis certainly played a key role in facilitating them to transport within cells, resulting in effectively knocking down the expression of GFP gene. Since the gene transfection experiments were performed in the medium containing 10% serum, the gene silencing efficiencies of the PEI complexes were relatively lower compared to those of the PEI−PEG−FOL complexes. The enhanced gene silencing effects of the PEI−PEG−FOL complexes could be additionally attributed to the presence of a PEG protective layer on the surface, preventing nonspecific adsorption of serum proteins and minimizing interparticular aggregation (*15*). It should be noted that, in our previous study, anti-GFP siRNA-P complexed with PEI−PEG−FOL inhibited GFP expression up to 89.5% for the KB cells that were pretransfected with GFP plasmid (*12*). In that study, the KB cells were pretransfected with GFP plasmid, and only GFP-positive cells were sorted for the transfection experiment. The reduced inhibition extent (59.2%) of GFP expression observed in the current study was likely caused by the fact that the KB cells were cotransfected with GFP plasmid and anti-GFP siRNA. The mixed population of GFP-positive and GFP-negative KB cells might result in the reduced extent of gene inhibition by siRNA.

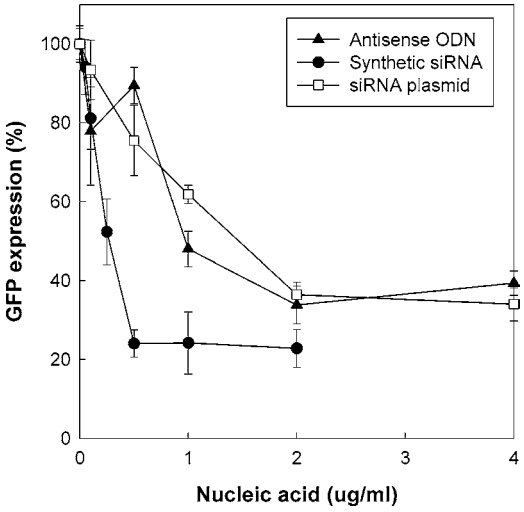

Figure 2. Comparative GFP gene suppression of antisense ODN (filled triangles), synthetic siRNA (filled circles), and siRNA plasmid (open squares) as a function of nucleic acid concentration. Antisense ODN and siRNA plasmid: 0.0−4.0 μg. Synthetic siRNA: 0.0−1.0 μg. Nucleic acids were complexed with PEI−PEG−FOL at an N/P ratio of 16.

Among the three nucleic acids, siRNA-S showed the most pronounced gene silencing effect. Although AS-ODN and siRNA-S have different GFP mRNA target sites, they must be delivered in the cytoplasm and inhibited translation of their respective target GFP mRNA sequences. siRNA-S exhibited a more effective gene inhibition effect than AS-ODN, which might be due to its greater specific gene suppression mechanism (*16*). It is also noted that siRNA-S showed greater gene silencing effects than siRNA-P with increasing N/P ratios. This was mostly likely caused by different intracellular gene trafficking and processing mechanisms between the two nucleic acids. siRNA-P must be located and transcribed in the nucleus prior to releasing several copies of siRNA transcripts to the cytoplasm. Thus it is reasonable to say that siRNA-S directly delivered in the cytoplasm exhibited more effective silencing of GFP expression compared to siRNA-P.

Dose-dependent anti-GFP activities of the three nucleic acids complexed with PEI−PEG−FOL (N/P ratio =16) are shown in Figure 2. With increasing the nucleic acid amount used in the transfection experiments, the three complexes inhibited GFP expression to a greater extent. However, siRNA-S complexes demonstrated the most powerful gene silencing effect. Nearly 76.0 ± 3.4% of GFP inhibition could be obtained at a dose of 0.5 μg/mL for siRNA-S, whereas 66.2 ± 4.8% and 63.5 ± 3.2% of GFP inhibition were attained at a dose of 2 μg/mL for AS-ODN and siRNA-P, respectively. These results reveal that target-specific gene silencing could be achieved by using much smaller amount of siRNA-S than AS-ODN and siRNA-P. This can be

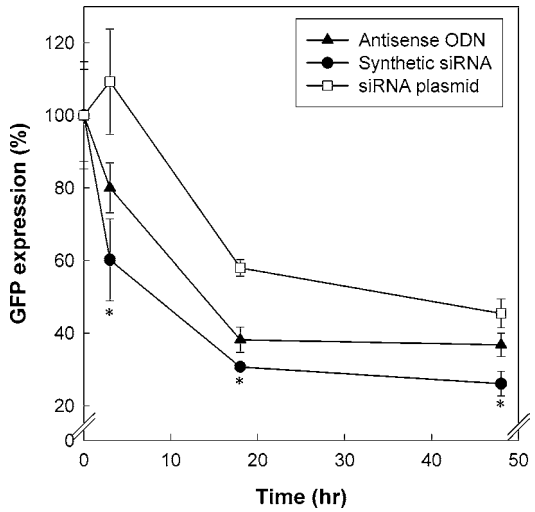

Figure 3. Time dependent inhibition of GFP gene expression by using antisense ODN (filled triangles), synthetic siRNA (filled circles), and siRNA plasmid (open squares). Nucleic acids were complexed with PEI−PEG−FOL at an N/P ratio of 16. Each dot represents the mean ± SD from three replicate experiments; (*) $P < 0.05$ versus AS-ODN (Student's *t*-test).

attributed to the inherently specific and unique gene inhibition mode of siRNA-S, as described in the literature (*16*). Figure 3 shows GFP gene suppression profiles of the three nucleic acid complexes (N/P ratio = 16; nucleic acid amount: 2.0 μg of AS-ODN, 0.5 μg of siRNA-S, and 2.0 μg of siRNA-P) as a function of time. siRNA-S and AS-ODN complexes inhibited GFP expression more rapidly than siRNA-P complexes. The siRNA-P complexes had a lag period before exerting its GFP gene silencing effect, presumably because they underwent a series of subcellular trafficking events, which hampers the production and localization of siRNA transcripts in the cytoplasm (*17*). Hence siRNA-P complexes exhibited more delayed gene silencing effect than siRNA-S and AS-ODN complexes.

In conclusion, three anti-GFP nucleic acids (AS-ODN, siRNA-S, and siRNA-P) were complexed with PEI−PEG−FOL conjugate and transfected to FOL receptor overexpressing cells to compare their FOL receptor-specific gene silencing efficiencies. All three complexes exhibited cancer cell specific gene inhibition behaviors, but siRNA-S was the most effective in gene silencing.

ACKNOWLEDGMENT

This work was supported by a grant (M10414030002-05N1403-00210) from the Ministry of Science and Technology, Republic of Korea.

LITERATURE CITED

(1) Jeong, J. H., Kim, S. W., and Park, T. G. (2003) A new antisense oligonucleotide delivery system based on self-assembled ODN-PEG hybrid conjugate micelles. *J. Controlled Release 93*, 183−191.

(2) Jeong, J. H., Kim, S. W., and Park, T. G. (2003) Novel intracellular delivery system of antisense oligonucleotide by self-assembled hybrid micelles composed of DNA/PEG conjugate and cationic fusogenic peptide. *Bioconjugate Chem. 14*, 473−479.

(3) Michael, T. M., and Phillip, A. S. (2002) Gene silencing in mammals by small interfering RNAs. *Nat. Rev. Genet. 3*, 737−747.

(4) Raymond, M. S., Aslam, A., Jun, X., Qin, Z., Qingquan, T., Gert, S., Grietje, M., Patrick, Y. L., Puthuppatampil, V. S., and Martin, C. W. (2004) Cancer siRNA therapy by tumor selective delivery with ligand-targeted sterically stabilized nanoparticle. *Nucleic Acids Res. 32*, e149.

(5) Thazha, P. P., Charles, R. A., Prasad, D., Timothy, A. V., Namir, S., Russell, J., Brenda, F. B., Eric, E. S., Rechard, H. G., and Balkrishen, B. (2005) Positional effect of chemical modifications on short interference RNA activity in mammalian cells. *J. Med. Chem. 48*, 4247−4253.

(6) Oishi, M., Nagsaki, Y., Itaka, K., Nishiyama, N., and Kataoka, K. (2005) Lactosylated poly(ethylene glycol)-siRNA conjugate through acid-labile β-thiopropionate linkage to construct pH-sensitive polyion complex micelles achieving enhanced gene silencing in hepatoma cells. *J. Am. Chem. Soc. 127*, 1624−1625.

(7) Wilson, A., Zhou, W., Champion, H. C., Alber, S., Tang, Z. L., Kennel, S., Watkins, S., Huang, L., Pitt, B., and Li, S. (2005) Targeted delivery of oligodeoxynucleotides to mouse lung endothelial cells in vitro and in vivo. *Mol. Ther. 12*, 510−518.

(8) Jeong, J. H., Kim, S. H., Kim, S. W., and Park, T. G. (2005) Polyelectrolyte complex micelles composed of c-raf anti-sense oligodeoxynucleotide-poly(ethylene glycol) conjugate and poly(ethylenimine): Effect of systemic administration on tumor growth. *Bioconjugate Chem. 16*, 1034−1037.

(9) Merdan, T., Kunath, K., Petersen, H., Bakowsky, U., Voigt, K. H., Kopecek, J., and Kissel, T. (2005) PEGylation of poly(ethylenimine) affects stability of complexes with plasmid DNA under in vivo condition in a dose dependent manner after intravenous injection into mice. *Bioconjugate Chem. 16*, 785−792.

(10) Cho, K. C., Jeong, J. H., Chung, H. J., Joe, C. O., Kim, S. W., and Park, T. G. (2005) Folate receptor-mediated intracellular delivery of recombinant caspase-3 for inducing apoptosis. *J. Controlled Release 108*, 121−131.

(11) Kim, W. J., Yockman, J. W., Lee, M. H., Jeong, J. H., Kim, Y. H., and Kim, S. W. (2005) Soluble Flt-1 gene delivery using PEI-g-PEG-RGD conjugate for anti-angiogenesis. *J. Controlled Release 106*, 224−234.

(12) Kim, S. H., Jeong, J. H., Cho, K. C., Kim, S. W., and Park, T. G. (2005) Target-specific gene silencing by siRNA plasmid DNA complexed with folate-modified poly(ethylenimine). *J. Controlled Release 104*, 223−232.

(13) Takuro, H., Nobuhiko, Y., Fuminori, S., Tomoki, S., and Masaaki, H. (2004) Evaluation of RNA interference in developing porcine granulose cells using fluorescence reporter genes. *J. Reprod. Dev. 50*, 599−603.

(14) Verbaan, F. J., Oussoren, C., Snel, C. J., Crommelin, D. J., Hennink, W. E., and Storm, G. (2004) Steric stabilization of poly(2-(dimethylamino)ethylmethacrylate)-based polyplexes mediates prolonged circulation and tumor targeting in mice. *J. Gene Med. 6*, 64−75.

(15) Tang, G. P., Zeng, J. M., Gao, S. J., Maa, Y. X., Shi, L., Li, Y., Too, H.-P., and Wang, S. (2003) Polyethylene glycol modified polyethylenimine for improved CNS gene transfer: effects of PEGylation extent. *Biomaterials 24*, 2351−2362.

(16) Ryther, R. C., Flynt, A. S., Phillips, J. A., III, and Patton, J. G. (2005) siRNA therapeutics: big potential from small RNAs. *Gene Ther. 12*, 5−11.

(17) Christopher, W. A., Guilin, T., and Asher, Z. (2003) Vector systems for the delivery of small interfering RNAs: Managing the RISC. *ChemBioChem 4*, 1129−1136.

BC050289F

Microstructured Liposome Array

Barnabé Chaize,[†] Michel Nguyen,[‡] Tristan Ruysschaert,[†] Véronique le Berre,[§] Emmanuelle Trévisiol,[§] Anne-Marie Caminade,[‡] Jean Pierre Majoral,[‡] Geneviève Pratviel,[‡] Bernard Meunier,[‡] Mathias Winterhalter,[†,||] and Didier Fournier*[,†]

Institut de Pharmacologie et de Biologie Structurale, 205, route de Narbonne 31077 Toulouse Cedex, France, Laboratoire de Chimie de Coordination, 205, route de Narbonne 31077 Toulouse Cedex 4, France, Biochips Platforms of Genopole Toulouse Midi-Pyrénées, UMR-CNRS 5504, UMR-INRA 792, Toulouse, France, and International University Bremen, P.O. Box 750 561, 28725 Bremen, Germany. Received September 9, 2005; Revised Manuscript Received November 24, 2005

Conversion of a DNA chip to a nanocapsule array was performed by grafting on a liposome an oligonucleotide complementary to an oligonucleotide bound to the array. Each liposome may be loaded by a soluble molecule or may present a hydrophobic or amphiphilic molecule inserted in its wall. To detect liposomes on the chip, we used fluorescent dyes encapsulated in the liposome internal volume or fluorescent lipids. We observed that an oligonucleotide-grafted liposome containing a defined dye specifically accumulated on the area where its complementary oligonucleotide had been spotted on the array. The virtually unlimited amount of addresses allows the specific binding of large amounts of liposomes in one single batch.

INTRODUCTION

DNA microarrays or DNA chips allow us to analyze the expression of hundreds of genes in a single experiment (*1*). The technique consists of immobilizing a specific single stranded DNA sequence on a solid support using an automated spotting device. The obtained microstructured array is incubated with single stranded cDNA fragments obtained from RNA extracted from cells that are investigated. Complementary DNA fragments present in the solution will hybridize with the DNA linked to the array. Crossed correlation analysis of the hybridized DNA allows the discovery and the understanding of gene expression and metabolic pathway activation in organisms (*2*). This technology stimulated the development of other chips such as protein chips as diagnostic tools or as biosensors utilizing immobilized enzymes, antibodies, or membrane proteins (*3*, *4*). However, protein structures are fragile. Immobilization with a harsh chemical treatment often leads to an uncontrolled decrease in activity and limits the use of this technology.

The aim of this paper consists of using the nowadays well-established DNA microarray technology to allow immobilization of nanocontainers on the chip. Since proteins may be encapsulated in these containers in their native states, they remain in an ideal environment and resist protein denaturation due to dilution and to digestion by proteases (*5*, *6*). Hydrophobic or amphiphilic molecules such as membrane proteins may be inserted in the nanocapsule wall. Thus, conversion of a DNA chip to a nanocontainer chip may result in the conversion of a DNA chip to a protein chip (Figure 1).

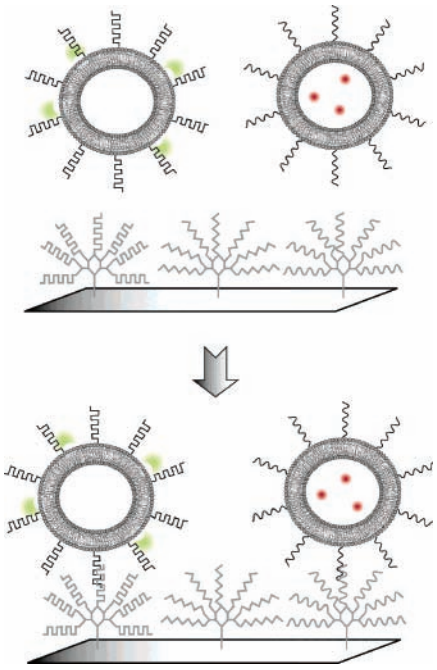

Figure 1. Specific liposome attachment on the array via oligonucleotide hybridization. The specificity of the binding is guaranteed by the sequence dependent hybridization between the liposome grafted one and the one bound on the array.

EXPERIMENTAL PROCEDURES

Liposomes were prepared by hydration of a lipid film followed by freeze−thaw cycles and extrusion. 100 μL of 100 mM eggPC lipids (Lipoid, Ludwigshafen, Germany) in $CHCl_3$ and 10 μL of 84 μM lipids DSPE-PEG(2000) Maleimide lipids (Avanti Polar Lipids, Alabaster, AL) in $CHCl_3$ were driedin a 15 mL glass tube under N_2 and then dried in a vacuum for 3 h.

To identify liposomes on the array, we used a fluorescent probe. A lipid grafted rhodamine was used as dye for labeling the liposome membrane. We used 3 μL of 0.8 mM Rhod-PE lipids (Avanti Polar Lipids, Alabaster, AL) in $CHCl_3$ in the formulation of the lipid film. As a soluble probe, we encapsulated the water-soluble fluorescent dye Cy5. The encapsulation was performed by freeze−thaw cycles in a buffer solution containing the probe to encapsulate (*6*, *7*). 100 μL of 4.4 mM Cy5 fluorescent dye (Molecular Probes, Eugene, OR) in 2xSSPE (20 mM sodium phosphate buffer pH 7.4, 300 mM NaCl, 2 mM EDTA) was added and firmly vortexed to peel off and

* Corresponding author.
[†] Institut de Pharmacologie et de Biologie Structurale.
[‡] Laboratoire de Chimie de Coordination.
[§] Biochips Platforms of Genopole Toulouse Midi-Pyrénées.
[||] International University Bremen.

10.1021/bc050273p CCC: $33.50 © 2006 American Chemical Society
Published on Web 12/27/2005

Dendrimer

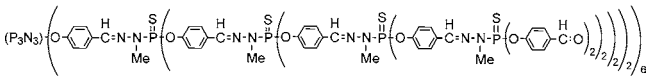

Oligonucleotides

A′: 5′-TGCGACTCGGTCATGCCATACGATTTT-SH-3′
B′: 5′-ATGCATTTCCTAAGTCCGGCAGGCTTT-SH-3′
A : 5′-ATCGTATGGCATGACCGAGTCGCATTT-NH2-3′
B : 5′-GCCTGCCGGACTTAGGAAATGCATTTT-NH2-3′
C : 5′-TAGACTAGTCGGATAGGCCCATGCTTT-NH2-3′.

Figure 2. Structures of dendrimer and oligonucleotides used.

dissolve the dried lipid film. The liposome suspension was frozen and thawed 30 times successively dipping the glass tube in liquid N_2 and a 37 °C water bath. Then the volume of the solution was increased to 10 mL with 2xSSPE, and the solution was extruded through a 200 μm membrane filter (Schleicher & Schuell, Dassel, Germany) to calibrate the liposomes. At last, nonencapsulated probe was removed by gel filtration using a desalting column previously equilibrated with 2xSSPE (PD10, Amersham Biosciences, Uppsala, Sweden).

To perform anchoring of oligonucleotides on the liposome surface, maleimide functionalized lipids were added in the lipid composition of the liposome membrane (1/100). The maleimide chemical function exhibited outside the liposome reacted with thiol chemical functions present at the 3′ end of the 27-base oligonucleotides A′ and B′ (Figure 2). The anchoring reaction occurred after 1 h at room temperature in 2xSSPE (1/1, thiol/maleimide group). The maleimide grafted lipids that had not reacted thus far with the oligonucleotides were inactivated with an excess of cystein. 10 μL of 2 mM *N*-acetylcystein (Sigma, St. Louis, MO) in H_2O was added to the liposome suspension, and the resulting mixture was incubated under agitation for 1 h.

As DNA chips, we used dendrislides, which showed better sensitivity than classical slides; they were prepared as described (*10, 11*). Briefly, microscope glass slides were cleaned with an alcoholic solution of NaOH (2.5 M in alcohol/water: 3/2, v/v), rinsed with water, and silanized with (3-aminopropyl)triethoxysilane. The silanized glass slides were activated by KOH, then rinsed by water, and incubated in a solution containing the generation 4 of a phosphorus dendrimer harboring aldehyde functions at its surface (Figure 2) (58 μM) in tetrahydrofuran. The slides were then washed with tetrahydrofuran and with ethanol. Then 27-base oligonucleotides modified with an amine function at their 3′ extremities were spotted onto this dendrimer surface and reacted with their aldehyde functions. Oligonucleotides A, B, and C (Figure 2) were spotted on the support as for standard DNA chips, A and B were complementary to oligonucleotides grafted to the lipid containers, and C was used as control. An automated spotting device (Chip Writer Pro from Bio-Rad) allowed attaching 200 fmol of oligonucleotides on the support in a 150 μm diameter spot. The imines function formed between probes and dendrimers, aminosilane and dendrimer, as well as the unreacted aldehyde were reduced by immersion of the slides into an aqueous solution containing $NaBH_4$ at 3.5 mg/mL, then washing with water during 5 min (3 times), and then drying under a stream of N_2 or by centrifugation (800 rpm, 8 min).

To bind liposomes on the slides, we took advantage of the complementarity between oligonucleotides grafted on liposomes and oligonucleotides spotted on the dendrislide. Liposome solutions were incubated overnight on the spotted coated glass slides. 1 mL of the liposome suspension (10 μM eggPC) was added to 9 mL of 2xSSPE and overnight incubated at 37 °C with the slide in a Petri dish. Following two washings with the same buffer, the reading of the fluorescence on the array was performed with a laser scanner (GenePix 4000A from Axon Inc.) at 532 and 635 nm, at appropriate sensitivity levels of the photomultiplier.

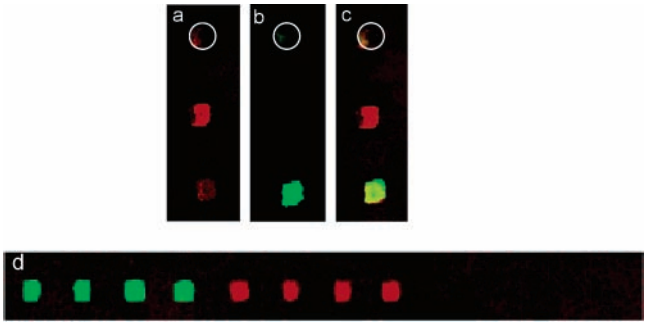

Figure 3. Fluorescence image of bound liposomes on a DNA chip. To demonstrate the selectivity of the process, two examples treated in a slightly different manner are shown. The first slide (parts 3a−c) was functionalized with three different oligonucleotide spots: the upper one contains a random sequence, the middle one the complement to the red labeled (Cy5 at 635 nm) liposomes, and the bottom one the complementary nucleotides for the green labeled (rhodamine labeled lipids at 532 nm) liposomes. Clearly outside the oligonucleotide spots, binding of labeled vesicles was negligible. (a) Visualization by excitation at 635 nm of the red liposomes alone revealed an intensive red spot in the middle but also two less intense but still clear spots. (b) The same slide but with exciting (at 532 nm) of only the green color. Here, in addition to the expected main spot at the bottom, a small background is visible for the random sequence. (c) Overlay of both colors. (d) Increasing washing time improved the selectivity. We spotted on the left side oligonucleotides for green liposomes and in the middle four corresponding to the red liposomes; in the four spots with random sequence no color is revealed.

RESULTS AND DISCUSSION

Liposomes containing Rhod-PE lipids were grafted with oligonucleotide A, and liposomes grafted with oligonucleotide B were loaded with fluorescent dye Cy5. Both liposome solutions were mixed and laid down a glass slide spotted with three oligonucleotides, A complementary to A′, B complementary to B′, and C a noncomplementary oligonucleotide. Following hybridization and extensive washing, reading of the fluorescence on the chip revealed colored spots corresponding to the two fluorescent dyes used; hybridization created a well-localized predefined liposome array (Figure 3). The red spots correspond to an accumulation of liposomes containing the soluble Cy5 dyes detected with an excitation at 635 nm. The green spots correspond to an accumulation of liposomes having the membrane cross-linked rhodamine dye, which were detected with an excitation at 532 nm. Each dye corresponds to a liposome preparation with a specific oligonucleotide grafted on the external surface of the lipid membrane. Each kind of liposome binds to the spots corresponding to the complementary oligonucleotide on the chip. Typically the signal detected over each spot was 4 times higher than the background for the red spots and 6 times higher than the background for the green spots. The digital combination of the images obtained by exciting at 635 and 532 nm gives a full vision of the localization of each kind of liposomes on the chip.

This experiment confirms that oligonucleotide hybridization may be used to tether a liposome on a surface (*8, 9*). We show here that, using a DNA chip and the specificity of hybridization, it is possible to immobilize liposomes at specific positions. Each liposome may contain a specific molecule and potentially protein; this allows a general conversion of a DNA chip into another chip such as a protein chip. On the basis of our previous work, the encapsulation procedure can be generalized for a wide range of water-soluble proteins. Encapsulation provides a controlled local environment for the protein and may avoid the

spreading of enzymatic products into the solution by trapping in the container when the product is charged (*5*). In addition, this method should be useful for membrane bound proteins (receptors, channels) which need to be in a lipid environment to keep their conformation and activity. The use of liposomes appears to be an alternative to the microspotting of lipidic membranes on γ-aminopropylsilane coated slides (*4*). An advantage of using nanocontainers is the possibility to substitute liposomes by polymersomes, which are usually more stable. Furthermore, this process allows their specific binding in a single step because of the high specificity of the oligonucleotide hybridization.

Oligonucleotide-grafted liposomes are very exciting building blocks to create networks and other superstructures. DNA provides a virtual addressing without limits. Earlier systems used competitive binding of oligonucleotide to DNA covered liposomes to probe for the presence of specific DNA fragments. However, the liposomes serve only as an amplifier due to their size (*12*). Others created a larger network, and cross-linking was observed via turbidity measurements. Here the presented system is different. The liposomes appear to be excellent carriers for molecules to design a new kind of chip. The use of oligonucleotides as a means of anchoring shows a very high specificity and simplifies the localization of molecules on the array. Then molecules can be directed to their assigned place on the array in a single incubation step. However, the possibility to detect chemical enzymatic reactions is still limited by the finding of a unique reaction substrate for all the spotted proteins, and a system to avoid the spreading of the detectable product on the surface of the array. Here again the use of containers could be an advantage to maintain proteins in a specific reaction environment and to trap the enzymatic reaction products.

ACKNOWLEDGMENT

This work was supported by the CNRS program "Proteomique et génie des protéines" and by the ACI nanosciences−nanotechnologies NN082.

LITERATURE CITED

(1) Chittur, S. V. (2004) DNA microarrays: tools for the 21st Century. *Comb. Chem. High Throughput Screen 7*, 531−7.

(2) Aittokallio, T., Kurki, M., Nevalainen, O., Nikula, T., West, A., and Lahesmaa, R. (2003) Computational strategies for analyzing data in gene expression microarray experiments. *J. Bioinform. Comput. Biol. 1*, 541−86.

(3) Predki, P. F. (2004) Functional protein microarrays: ripe for discovery. *Curr. Opin. Chem. Biol. 8*, 8−13.

(4) Fang, Y., Frutos, A. G., and Lahiri, J., (2002) Membrane protein microarrays. *J. Am. Chem. Soc. 124*, 2394−5.

(5) Chaize, B., and Fournier, D. (2004) Sorting out molecules reacting with acetylcholinesterase by enzyme encapsulation in liposome. *Biosens. Bioelectron. 20*, 628−32.

(6) Colletier, J. P., Chaize, B., Winterhalter, M., and Fournier, D. (2002) Protein encapsulation in liposomes: efficiency depends on interactions between protein and phospholipid bilayer. *BMC Biotechnol. 2*, 9.

(7) Chaize, B., Winterhalter, M., and Fournier, D. (2003) Encapsulation of acetylcholinesterase in preformed liposomes. *Biotechniques 34*, 1158−60, 1162.

(8) Yoshina-Ishii, C., and Boxer, S. G. (2003) Arrays of mobile tethered vesicles on supported lipid bilayers. *J. Am. Chem. Soc. 125*, 3696−7.

(9) Yoshina-Ishii, C., Miller, G. P., Kraft, M. L., Kool, E. T., and Boxer, S. G. (2005) General method for modification of liposomes for encoded assembly on supported bilayers. *J. Am. Chem. Soc. 127*, 1356−7.

(10) Le Berre, V., Trevisiol, E., Dagkessamanskaia, A., Sokol, S., Caminade, A. M., Majoral, J. P., Meunier, B., and Francois, J. (2003) Dendrimeric coating of glass slides for sensitive DNA microarrays analysis. *Nucleic Acids Res. 31*, e88.

(11) Trévisiol, E., Leberre-Anton, V., Leclaire, J., Pratviel, G., Caminade, A.-M., Majoral, J.-P., François, J.-P., and Meunier, B. (2003) Dendrislides, dendrichips: a simple chemical functionalization of glass slides with phosphorus dendrimers as an effective means for the preparation of biochips. *New J. Chem. 27*, 1713−1719.

(12) Baeumner, A. J., Cohen, R. N., Miksic, V., and Min, J. (2003) RNA biosensor for the rapid detection of viable Escherichia coli in drinking water. *Biosens. Bioelectron. 18*, 405−13.

BC050273P

Synthesis of Acid-Cleavable Light Isotope-Coded Affinity Tags (ICAT-*L*) for Potential Use in Proteomic Expression Profiling Analysis

Abdul H. Fauq,*,§ Rajashaker Kache,§ Murad A. Khan,§ and Irving E. Vega†

Chemistry Core Facility, Mayo Clinic Jacksonville, 4500 San Pablo Road, Jacksonville, Florida 32224, and Department of Neuroscience, Mayo Clinic Jacksonville, 4500 San Pablo Road, Jacksonville, Florida 32224. Received October 14, 2005; Revised Manuscript Received December 2, 2005

A convenient synthesis of some homologous light isotope-coded affinity tags (ICAT-*L*) containing an acid-labile moiety between the affinity component biotin and an electrophilic polar linker is described. These light ICAT reagents give smooth mass spectral signals in tandem mass spectrometry (MS/MS) analyses of some commercially available cysteine-containing peptides. However, these ICAT molecules are designed for use in identification and relative quantification of whole or partially purified cellular and tissue proteomes. Since the biotin moiety can be readily cleaved off the reagent after mass tagging, undesired residual fragmentation patterns caused by biotin of derived peptides, as normally observed using biotin-containing ICAT reagents, are effectively eliminated. This strategy should enhance peptide sequence coverage significantly which, in turn, should result in improving the quality of data obtained during data-dependent peptide mass and tandem mass spectral analysis of whole proteomes.

INTRODUCTION

The past decade has seen decoding of complete genomes of several lower and higher organisms. Many of these breakthrough discoveries have resulted in identification of novel proteins as drug targets. Recently, novel and high-throughput methodologies for protein identification and quantification have been uncovered using new and improved mass spectrometry techniques (*1*−*3*). Mass spectrometers are now routinely used in many labs to efficiently identify and quantify known proteins in complex proteomes of cell cultures and tissues (*4*, *5*). The absolute as well as relative quantification of proteins in complex biological mixtures is carried out by using several traditional separation techniques including 2D gel electrophoresis (*6*, *7*), high-performance liquid chromatography (HPLC) on reverse phase, and ion-exchange stationary phases (*8*). Recently, the use of computer-assisted mass spectrometry (MS) and tandem mass spectrometry (MS/MS) in electrospray (ES) modes has revolutionized the qualitative and quantitative analysis of whole proteomes (*9*). This technology has yielded high-value information about the nature and quantity, as well as function, of many proteins even in their complex association environments.

A number of methods for relative quantification of proteins have been described in the literature, including staining of proteins separated by two-dimensional polyacrylamide gel electrophoresis (2D-PAGE) and their quantitation by fluorescence intensity measurement (*6*, *7*) and heavy-isotope-coded affinity tags (ICAT) (*10*−*14*). The latter technique has several advantages over the gel-based protein quantifications in terms of convenience, reduction in process time, accuracy, and throughput. Both solid-phase and solution-phase ICATs are known (*15*). Recently, a visible ICAT has also been reported (*16*). A prototypical solution-phase ICAT molecule has three parts in its molecular structural framework, namely, a peptide enrichment moiety that can greatly simplify analysis of complex mixtures of protein hydrolyzates, a heavy isotope carrier label, and an alkylator moiety that specifically labels reactive amino acids such as cysteine (Figure 1a). The peptide enrichment moiety is usually a biotin that can selectively serve to enrich exclusively ICAT-linked peptides based on its specific affinity for avidin employed as a coating on beads or other solid phases. The linker could be a C-13-labeled polyalanine peptide or a diamine with mono- or diethylene ether backbone. The alkylator moiety can be either a cysteine-reactive iodoacetamide or a maleimide that can react with the thiol group of cysteine by S_N2-displacement or 1,4-addition, respectively.

An ICAT can also be obtained with a reactive thiol group at one terminal that serves as a Michael donor for dephosphorylated proteins containing dehydroserine and dehydrothreonine residues, which, in turn, are obtained by base-catalyzed β-elimination of phosphoproteins (*17*, *18*). The latter is an important constituent of posttranslational modifications of proteins involved in important biological phenomena such as signal transduction and enzyme or receptor activation.

Reported herein is the synthesis of some novel light versions of homologous acid-cleavable ICAT reagents. Our preliminary results show that these versions furnish expected MS/MS spectral patterns when certain peptides are derivatized with any of the synthesized homologues of ICAT-*L*.

EXPERIMENTAL PROCEDURES

Materials and Instrumentation. The column chromatographic separations were performed with J. T. Baker Silica gel (230−400 mesh). THF and diethyl ether were distilled from sodium/benzophenone ketyl. Anhydrous DMF was purchased from Aldrich Chemicals.

Methylene chloride was distilled over CaH_2 or P_2O_5. Acetonitrile was reagent grade from E. M. SCIENCE and was used without further purification. Ethyl acetate and hexane were used as received. The purity of all reported compounds was shown to be >95% by TLC and high-field ^{1}H NMR (Brüker Avance-300 at 300 MHz frequency). The ^{1}H NMR chemical shifts are reported in δ ppm units downfield from the tetramethylsilane standard set at $\delta = 0$. IR spectra were measured with an Avatar 370 FT-IR instrument from ThermoNicolet. Mass spectral analyses were performed with Micromass Platform II with a

* Corresponding author. E-mail: Fauq.abdul@mayo.edu. Phone: 904-953-8034. Fax: 904-953-7117.

§ Chemistry Core Facility.

† Department of Neuroscience.

10.1021/bc0503059 CCC: $33.50 © 2006 American Chemical Society
Published on Web 12/30/2005

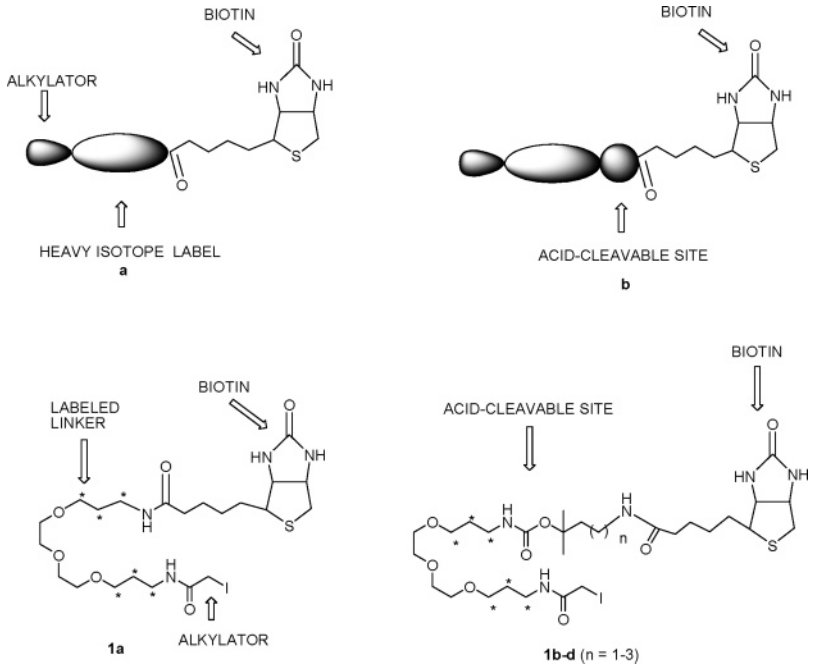

Figure 1. Schematic of two variants of ICAT reagents.

single quadrupole electrospray ionizer and MassLynx software, and the samples were infused in a 1:1 MeOH/$CHCl_3$ mixture containing 0.1 mM NH_4OAc.

Esterification of Bromoesters. 3-Bromopropanoic acid (30 g, 0.19 mol) was dissolved in dry MeOH (100 mL) and cooled to 0 °C. Through this, dry HCl gas was passed for 10−15 min, and the mixture was kept overnight at room temperature. Methanol was removed under reduced pressure, aq $NaHCO_3$ solution was added, and the compound was extracted with ether (×2). The combined ethereal layers were washed with water and brine, dried over anhydrous Na_2SO_4, and concentrated. The crude esters were used directly for the next reaction. Yield 14.0 g (43%). ^{1}H NMR ($CDCl_3$) 3.73 (s, 3H), 3.58 (t, 2H, J = 6.8 Hz), 2.93 (t, 2H, J = 6.8 Hz). The corresponding methyl esters from 4-bromobutanoic acid and 5-bromopentanoic acid were prepared and characterized in a similar fashion. Methyl 4-bromobutanoate: Yield 4.0 g (72%). ^{1}H NMR ($CDCl_3$) 3.69 (s, 3H), 3.47 (t, 2H, J = 6.8 Hz), 2.51 (t, 2H, J = 7.4 Hz), 2.18 (m, 2H). Methyl 5-bromopentanoate: Yield 85%. ^{1}H NMR ($CDCl_3$) 3.41 (t, 2H, J = 6.6 Hz), 2.35 (t, 2H, J = 7.5 Hz), 1.95−1.74 (m, 4H).

Reduction of Bromoesters to Tertiary Alcohols. The 3-bromopropanoic acid methyl ester (14 g, 0.083 mole) was taken up in dry ether (100 mL) under nitrogen and cooled to −20 °C. To this, CH_3MgBr (83 mL of 3.0 M solution in diethyl ether, 0.25 mol) was added in a dropwise fashion, and the resulting mixture stirred for 0.5 h. Reaction mixture was quenched by slow addition of cold aq NH_4Cl. The resulting suspension was extracted with diethyl ether (×2). The combined ethereal extracts were washed with water, dried over anhydrous Na_2SO_4, and concentrated and the product, 4-bromo-2-methyl-2-butanol, obtained as a colorless oil was used without purification for the next reaction. Yield 10.0 g (71%). ^{1}H NMR ($CDCl_3$) 3.43 (t, 2H, J = 8.3 Hz), 2.02 (t, 2H, J = 8.6 Hz), 1.19 (s, 6H). MS 149 (M − 17), 167 (M^+ + 1). IR: 3374, 2967, 1728, 1671, 1377, 1206, 1093, 922, 649 cm^{-1}. The corresponding tertiary alcohols from 4-bromobutanoic and 5-bromopentanoic acid methyl ester were prepared in a similar fashion. 5-Bromo-2-methyl-2-pentanol: Yield 82%. ^{1}H NMR ($CDCl_3$) 3.44 (t, 2H J = 6.8 Hz), 1.91−2.03 (m, 2H), 1.64−1.56 (m, 2H), 1.24 (s, 6H). 6-Bromo-2-methyl-2-hexanol: Yield 78%. ^{1}H NMR ($CDCl_3$) 3.43 (t, 2H, J = 6.8 Hz), 1.94−1.81 (m, 2H), 1.59−1.47 (m, 4H), 1.23 (s, 6H).

Azido Alcohols 10a−c. The 4-bromo-2-methyl-2-butanol (18.0 g, 0.107 mol) was dissolved in dry DMF (100 mL) under nitrogen. Sodium azide (42.0 g, 0.646 mol) was added, and the suspension was stirred at 90 °C for 16 h. The reaction mixture was diluted with excess ether, washed thoroughly with water and brine, and dried over anhydrous Na_2SO_4. Concentration under reduced pressure followed by purification by vacuum distillation produced the azide **10** as a colorless oil. Yield 5.44 g (39%). NMR ($CDCl_3$) 3.46 (t, 2H, J = 7.3 Hz), 1.77 (t, 2H, J = 7.4 Hz), 1.26 (s, 6 Hz). IR 3405, 2966, 2089, 1660, 1376, 1252, 1211, 1154 cm^{-1}. The homologous tertiary azido alcohols 5-azido-2-methyl-2-pentanol and 6-azido-2-methyl-2-hexanol were prepared as above. 5-Azido-2-methyl-2-pentanol **10b**: Yield 72%. ^{1}H NMR ($CDCl_3$) 3.30 (t, 2H, J = 6.3 Hz), 1.75−1.65 (m, 2H), 1.56−1.50 (m, 2H), 1.24 (s, 6H). MS 161.2 (M + NH^{4+}), 143.99 (M + 1). IR 3395, 2972, 2084, 1671, 1475, 1371, 1268, 1150, 917, 669 cm^{-1}. 6-Azido-2-methyl-2-hexanol **10c**: Yield 70%. ^{1}H NMR ($CDCl_3$) 3.29 (t, 2H, J = 6.8 Hz), 1.66−1.57 (m, 2H), 1.48−1.43 (m, 4H), 1.22 (s, 6H). IR 3385, 2966, 2939, 2089, 1465, 1374, 1266, 1137, 890 cm^{-1}.

Preparation of Chlorocarbonates 8a−c. The 4-azido-2-methyl-2-butanol (5.0 g, 38.7 mmol) and 1-chloroethyl chloroformate (6.10 g, 42.6 mmol) were dissolved in dry CH_2Cl_2 (12 mL) and cooled to 0 °C under nitrogen. Dry pyridine (3.68 g, 46.5 mmol) was added dropwise, and the reaction mixture was allowed to stir at room temperature for 15−16 h, at which point 0.5 M dil HCl was added and the reaction mixture was extracted with CH_2Cl_2 (×2). The CH_2Cl_2 washings were dried over anhydrous Na_2SO_4, filtered, and concentrated. The residue was purified by silica gel column chromatography (EtOAc/hexane as eluent) to furnish **8a** as a colorless oil. Yield 8.59 g (93%). ^{1}H NMR 6.35 ($CDCl_3$) (q, 1H, J = 5.8 Hz), 3.40 (t, 2H, J = 7.5 Hz), 2.19−2.01 (m, 2H), 1.81 (d, 3H, J = 5.8 Hz), 1.55 (s, 3H), 1.54 (s, 3H). MS 253/255 (M^+ + NH_4^+), 258/260 (M + Na^+). IR: 2092, 1754, 1258, 1094, 663 cm^{-1}. The homologous chloroformates **8b**,**c** were prepared in similar yields. Chlorocarbonate from the azidoalcohol **8b**. Yield 68%. ^{1}H NMR ($CDCl_3$) 6.38 (q, 1H), 3.30 (m, 2H), 1.91−183 (m, 2H), 1.81 (d, 3H, J = 5.9 Hz), 1.52 (s, 3H), 1.50 (s, 3H). Chlorocarbonate

from the azidoalochol **8c**. Yield 88%. ^{1}H NMR ($CDCl_3$) 6.38 (q, 1H), 3.29 (t, 2H, J = 7.1 Hz), 1.91−1.73 (m, 5H), 1.68−1.54 (m, 2H), 1.50 (s, 3H), 1.49 (s, 3H), 1.47−1.35 (m, 2H).

Coupling of Carbonates 8a−c with Diamine 4—Synthesis of Azidoamines 13a−c. Diamine **4** (2.80 g, 12.0 mmol) was dissolved in dry DMF (10 mL) under nitrogen at room temperature. The chlorocarbonate **8a** (3.0 g, 12.0 mmol) was dissolved separately in 20 mL of dry DMF under nitrogen and was added via a syringe pump to the reaction mixture over a period of 1 h. The clear reaction mixture was left stirring overnight. After completion of the reaction (TLC monitoring), the DMF was removed under reduced pressure. Water (50 mL) was added, and after the reaction mixture was stirred for 5 min (to decompose any unreacted carbonates), the reaction mixture was concentrated under rotary evaporation, and the residual moisture was removed by rigorous lyophilization. The residue was purified using column chromatography to give pure azidoamine **13a**. Yield 3.18 g (71%). ^{1}H NMR (D_2O) 3.70−3.66 (m, 10H), 3.58 (t, 2H, J = 6.5 Hz), 3.44 (t, 2H, 7.1 Hz), 3.18−3.09 (m, 4H), 2.09 (t, 2H, J = 7.2 Hz), 2.0−1.92 (m, 2H), 1.81−1.73 (m, 2H), 1.46 (s, 6H). MS 376 ($M^+ + 1$). The homologous compounds **13b**,**c** were prepared from appropriate starting materials in the same manner. Azidoamine **13b:** Yield 34%. ^{1}H NMR (D_2O) 3.70−3.65 (m, 10H), 3.58 (t, 2H, J = 6.3 Hz), 3.34 (t, 2H, J = 6.4 Hz), 3.17−3.09 (m, 4H), 1.96 (m, 2H), 1.86−1.62 (m, 6H), 1.43 (s, 6H). MS 390.3 (M + 1). IR 3348, 2939, 2869, 2090, 1703, 1525, 1364, 1262, 1111, 1127 cm^{-1}; Azidoamine **13c**: Yield 28%. ^{1}H NMR (D_2O) 3.73−3.62 (m, 8H), 3.58 (t, 2H J = 6.03 and 12.24 Hz), 3.38−3.31 (m, 4H), 1.96 (quintet, 2H, J = 6.03 and 6.96 Hz), 1.84−1.70 (m, 6H), 1.61 (quintet, 2H), 1.42 (s, 6H). MS 404.4 (M + 1), 426 (M + Na^+). IR 3364, 2924, 2859, 2090, 1697, 1504, 1251, 1106 cm^{-1}.

TEOC Protection of the Azidoamines 13a−c. Azidoamine **13a** (0.795 g, 2.1 mmol) was dissolved in dioxane/water (3:1 v/v) at room temperature. Solid $NaHCO_3$ (0.356 g, 4.2 mmols) was added. After the mixture was stirred for 2−3 min at room temperature, TEOC−succinimide (0.824 g, 3.2 mmol) was added portion-wise, and the stirring was continued for 12 h. The reaction mixture was diluted with ethyl acetate and filtered. The volatiles were removed by rotary evaporation, and the residue was chromatographed using EtOAc/hexane as eluent to give the TEOC-protected product **14a** as a colorless oil. Yield 0.67 g (60%). ^{1}H NMR ($CDCl_3$) 5.03−5.26 (m, 2H, 2NH), 4.09 (t, 2H, J = 8.0 Hz), 3.63−3.49 (m, 14H), 3.34−3.17 (m, 6H), 2.03 (t, 2H, 7.5 Hz), 1.81−1.71 (m, 4H), 1.43 (s, 6H), 0.93 (t, 2H, J = 8.3 Hz), 0.31 (s, 9H). MS 542 (M + Na^+). IR 3329, 2956, 2862, 2092, 1689, 1526, 1258 cm^{-1}. The homologous amines were protected to give **14b**,**c**. TEOC-protected **13b**: Yield 62.5%. ^{1}H NMR ($CDCl_3$) 5.24 (br s, NH), 5.09 (br s, NH), 4.09 (t, 2H, J = 8.3 Hz), 3.64−3.46 (m, 12H), 3.28−3.11 (m, 6H), 1.84−1.53 (m, 8H), 1.39 (s, 6H), 0.92 (t, 2H, J = 6.7 Hz), 0.30 (s, 9H). MS 556 (M+Na^+). IR 3351, 2952, 2867, 2093, 1694, 1514, 1245, 1125 cm^{-1}; TEOC−Protected **13c:** Yield 73%. ^{1}H NMR ($CDCl_3$) 5.11 (br s, NH, 1H), 4.94 (br s, 1H, NH), 4.10 (t, 2H, J = 7.4 Hz), 3.70−3.42 (m, 12H), 3.31−3.09 (m, 6H), 1.81−1.65 (m, 5H), 1.63−1.48 (m, 5H), 1.37 (s, 6H), 0.93 (t, 2H, J = 8.5 Hz), 0.29 (s, 9H). MS 548.5 (M+1), 570.7 (M+Na^+). IR 3337, 2948, 2852, 2084, 1691, 1528, 1249, 1134, 834 cm^{-1}.

Reduction of TEOC-azides 14a−c to TEOC-amines. The TEOC-protected azide **14a** (0.67 g, 1.3 mmols) was hydrogenated in ethyl acetate at a pressure of 1 atm of hydrogen gas in the presence of 10% Pd/C (0.150 g) for 12 h. The reaction mixture was filtered over Celite and concentrated. The residue was purified over silica gel using 10% MeOH in DCM to give monoprotected amines **15a** as an oil. Yield 0.122 g (19%). ^{1}H NMR ($CDCl_3$) 5.32 (br s, 1H, NH), 5.23 (br s, 1H, NH), 4.09 (t, 2H), 3.49−3.66 (m, 14H), 3.17−3.23 (m, 6H), 3.02 (br s, 2H), 2.95 (distorted t, 2H), 1.94−1.96 (distorted t, 2H), 1.73 (q, 4H), 1.42 (s, 6H), 0.93 (t, 2H, J = 8.2 Hz), 0.32 (s, 9H). MS 494.3 (M+1), 516.2 (M+Na^+). IR 3341, 2950, 2874, 1707, 1538, 1252, 1124 cm^{-1}. The homologous amines from the azides **14b−c** were prepared in a similar manner. TEOC protected **14b**: Yield 34%. ^{1}H NMR ($CDCl_3$) 5.24 (br s, 1H, NH), 5.00 (br s, 1H, NH), 4.09 (t, 2H, 17.1, 8.1 Hz), 3.65−3.44 (m, 12H), 3.30−3.07 (m, 4H), 2.65 (t, 2H, 14.1, 7.0 Hz), 1.80−1.64 (m, 6H), 1.58−1.42 (m, 2H), 1.38 (s, 6H), 0.93 (t, 2H, J = 8.1 Hz), 0.32 (s, 9H). MS 508 (M+1), 530 (M+Na^+). IR 3338, 2946, 2858, 1692, 1526, 1397, 1242, 1113, 1041, 855 cm^{-1}. TEOC protected **14c**: Yield 41%. ^{1}H NMR ($CDCl_3$) 5.17 (br s, 1H, NH), 4.96 (br s, 1H, NH), 4.10 (t, 2H, J = 14.3, 7.1 Hz), 3.64−3.45 (m, 12H), 3.31−3.04 (m, 4H), 2.66 (t, 2H, J = 7.0 Hz), 1.81−1.64 (m, 6H), 1.63−1.50 (m, 4H), 1.37 (s, 6H), 0.92 (t, 2H, J = 9.0 Hz), 0.29 (s, 9H)

Coupling of the TEOC-amines with Biotin To Give Compounds 15a−c. The amine obtained by reduction of the azide **14a** (1.0 g, 2.0 mmol) was dissolved in dry DMF (15 mL) under nitrogen at room temperature. Triethylamine (0.41 mL, 3.0 mmol) was added and the mixture was stirred for 5 min. Then, a solution of biotin succinimide (0.760 g, 2.23 mmol) in dry DMF (3 mL) was slowly added via cannula at room temperature and the resulting mixture was left stirred overnight. The DMF was removed by rotary evaporation at reduced pressure and the residue thus obtained was purified by column chromatography. Yield 0.63 g (43%). ^{1}H NMR ($CDCl_3$) 6.30 (br s, 1H, NH), 6.27 (br s, 1H, NH), 5.52 (br s, 1H, NH), 5.12−5.53 (m, 2H, 2NH), 4.47 (t, 2H, J = 7.0 Hz), 4.29 (t, 2H, J = 4.1 Hz), 4.09 (t, 2H, J = 7.9 Hz), 3.49−3.61 (m, 12H), 3.17−3.29 (m, 7H), 2.88 (dd, 1H, J = 12.5, 5 Hz), 2.71 (d, 1H, J = 12.5 Hz), 2.15 (t, 2H, 7.2 Hz), 1.97 (distorted t, 2H), 1.59−1.80 (m, 10H), 1.40 (s, 6H), 0.93 (t, 2H, 8.5 Hz), 0.30 (s, 9H). MS 720 ($M^+ + 1$), 742 (M + Na^+). The homologous biotinylated compounds **15b**,**c** were prepared in a similar manner. Compound **15b:** Yield 55%. ^{1}H NMR ($CDCl_3$) 6.05 (br s, NH), 5.66 (br s, NH), 5.20 (br s, 2H, 2NH), 5.03 (br s, NH), 4.53−4.46 (m, 1H), 4.34−4.26 (m, 1H), 4.14−4.03 (m, 2H), 3.65−3.45 (m, 12H), 3.29−3.06 (m, 7H), 2.89 (dd, 1H, J = 12.8, 5.0 Hz), 2.72 (s, 1H), 2.68 (2, 1H), 2.22−2.11 (m, 2H), 1.81 −1.55 (m, 14H), 1.36 (s, 6H), 0.93 (t, 2H, J = 17.1, 8.64 Hz), 0.29 (s, 9H). MS 735 (M + 1), 757 (M + Na^+). Compound **15c:** Yield 43%. ^{1}H NMR ($CDCl_3$) 6.50 (br s, NH, 1H), 6.32 (br s, NH, 1H), 5.79 (br s, NH, 2H), 5.21 (br, NH, 1H), 4.53−4.43 (m, 1H), 4.33−4.22 (m, 1H), 4.09 (t, 2H, J = 8.31, 17.16 Hz), 3.66−3.45 (m, 12H), 3.32−3.03 (m, 7H), 2.87 (dd, 1H, 5.69, 7.32 Hz), 2.70 (m, 1H), 2.16 (t, 2H, 7.92 Hz), 1.83−1.54 (m, 10H), 1.52−1.22 (m, 6H), 1.08−0.84 (m, 2H), 0.31 (s, 9H). MS 749 (M+1), 766 (M + NH_4^+), 771 (M + Na^+). IR 3328, 2946, 2858, 1692, 1542, 1454, 1253, 1237, 1124, 855, 848, 829, 690 cm^{-1}.

Synthesis of ICAT Reagents 1b−d from the Amines 15a−c. The TEOC-protected biotinylated compound **15a** (112 mg, 0.16 mmol) was dissolved in dry DMSO (2 mL). After adding a solution of tetrabutylammonium fluoride (1 M in THF, 0.186 mmol, 186 μL) under nitrogen, the mixture was heated at 45 °C for 16 h. The volatiles were evaporated under high vacuum to leave a deprotected amine as a gummy residue. To a solution of the crude amine in DMF (2 mL) was added solid iodoacetic anhydride **5** (0.92 g, 2.61 mmol) and diisopropylethylamine (0.77 mL, 4.35 mmol). The resulting mixture was stirred 3 h. Solvent was removed under reduced pressure, and the product was purified to homogeneity by HPLC on a RP Vydac column (2.2 cm × 25 cm, 18 μm) using a gradient of 10% acetonitrile/water to 100% acetonitrile in 60 min, R_f 8 mL/min; R_t 23 min. The ICAT **1b** was obtained as a colorless oil. ^{1}H NMR (DMSO-

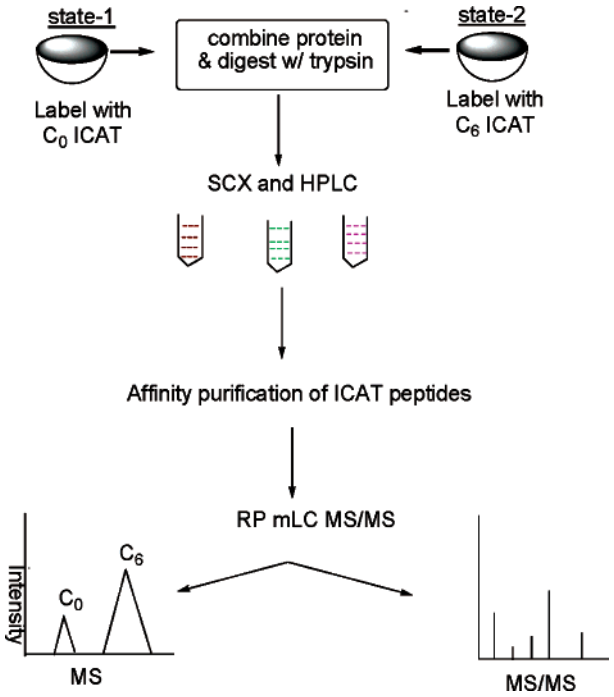

Figure 2. Protocol for coupling ICAT reagents.

d_6) 7.72 (br t, 1H, NH), 6.81 (br t, NH), 6.42 (br s, NH), 6.36 (s, NH), 4.91 (br t, 1H, NH), 4.30 (m, 1H), 4.12 (m, 1H), 3.60−3.47 (m, 12H), 3.19−2.91 (m, 9H), 2.82 (dd, 1H, J = 12.5, 6.0 Hz), 2.57 (d, 1H, J = 12.5 Hz), 2.03 (t, 2H, J = 7.2 Hz), 1.84 (distorted t, 2H), 1.63−1.46 (m, 10H), 1.36 (s, 6H). MS 744.8 (M + 1), 766.8 (M + Na^+). The acid-labile ICAT reagents **1c**,**d** were obtained in a similar fashion from appropriate amines **15b**,**c.** Spectral data for **1c:** ^{1}H NMR (DMSO-d_6) 8.21 (br t, 1H, NH), 7.76 (br t, NH), 6.75 (br s, NH), 6.41 (s, NH), 6.35 (br t, 1H, NH), 4.31 (m, 1H), 4.12 (m, 1H), 3.52−3.42 (m, 12H), 3.18−2.90 (m, 9H), 2.80 (dd, 1H, J = 12.5, 6.0 Hz), 2.55 (d, 1H, J = 12.5 Hz), 2.05 (t, 2H, J = 7.2 Hz), 1.68−1.5 (m, 12H), 1.31 (s, 6H). MS 758.8 (M + 1), 770.8 (M + Na^+). Spectral data for **1d:** ^{1}H NMR (DMSO-d_6) 8.22 (br t, 1H, NH), 7.79 (br t, NH), 6.75 (br s, NH), 6.42 (s, NH), 6.36 (br t, 1H, NH), 4.31 (m, 1H), 4.15 (m, 1H), 3.60−3.45 (m, 12H), 3.20−2.90 (m, 9H), 2.83 (dd, 1H, J = 12.5, 6.0 Hz), 2.58 (d, 1H, J = 12.5 Hz), 2.05 (t, 2H, J = 7.2 Hz), 1.63−1.46 (m, 14H), 1.33 (s, 6H). MS 772.8 (M + 1), 794.8 (M + Na^+).

RESULTS AND DISCUSSION

Unfortunately, the three-component ICAT system has some serious disadvantages. The biotin moiety, while crucial for tagged peptide enrichment and simplification, has been found to complicate the MS/MS analysis through undesired fragmentation paths. These superfluous fragmentations patterns yield significantly low sequence coverage of peptides resulting in unsatisfactory protein profiles of relatively complex biological milieu. It is therefore desirable that the biotin moiety is removed after the enrichment step and before the online chromatographic and MS/MS analysis routine. Recently, an acid-cleavable version has been made commercially available that has been used to analyze peptides without biotin (*15*, *18*−*23*). However, its detailed molecular structure has not been disclosed. We now report herein a series of novel four-component ICAT reagents that possess an acid-labile carbamate moiety inserted between the linker and biotin moieties (Figure 1, **1b**−**d**). This structural modification allows removal of biotin before MS and MS/MS analysis and is expected to significantly facilitate the sequence coverage of complex peptide mixtures. Higher sequence coverage of peptides is crucial to any extensive protein expression profiling protocol.

A general scheme for profiling protein concentration changes in two biological systems or cell states under study is given in Figure 2. Briefly, the proteins from the two cell or tissue states are separately extracted after homogenization. The extracts are reduced with a thiophilic reagent to convert disulfide bonds to thiols. One extract is labeled with the light form of the ICAT (ICAT-*L*), while the other is labeled with the heavy isotope form (ICAT-H) in otherwise identical conditions. The two extracts are then mixed together, and the mixture is proteolyzed with trypsin or some other proteolytic enzyme. The resulting peptide

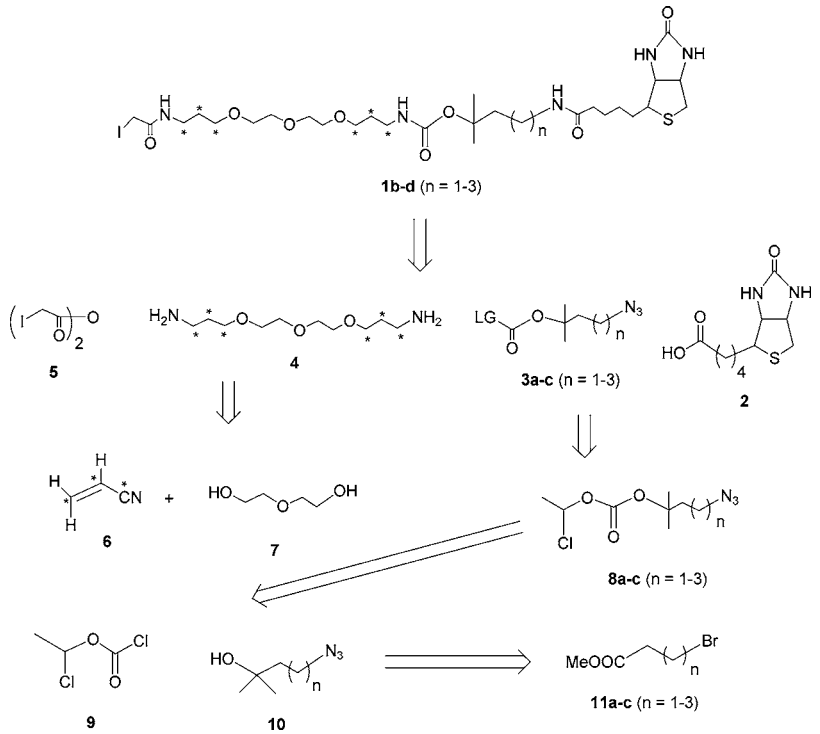

Figure 3. Retrosynthetic analysis of the reported ICAT reagents.

Scheme 1. Synthesis of the Acid-Cleavable Carbamate Moiety

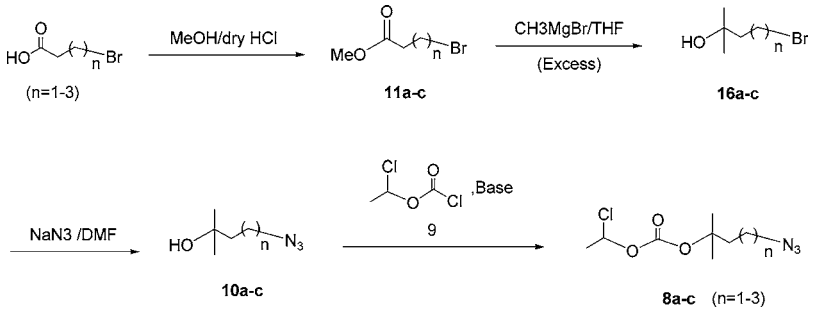

Scheme 2. Synthesis of the Acid-Cleavable ICAT Reagents

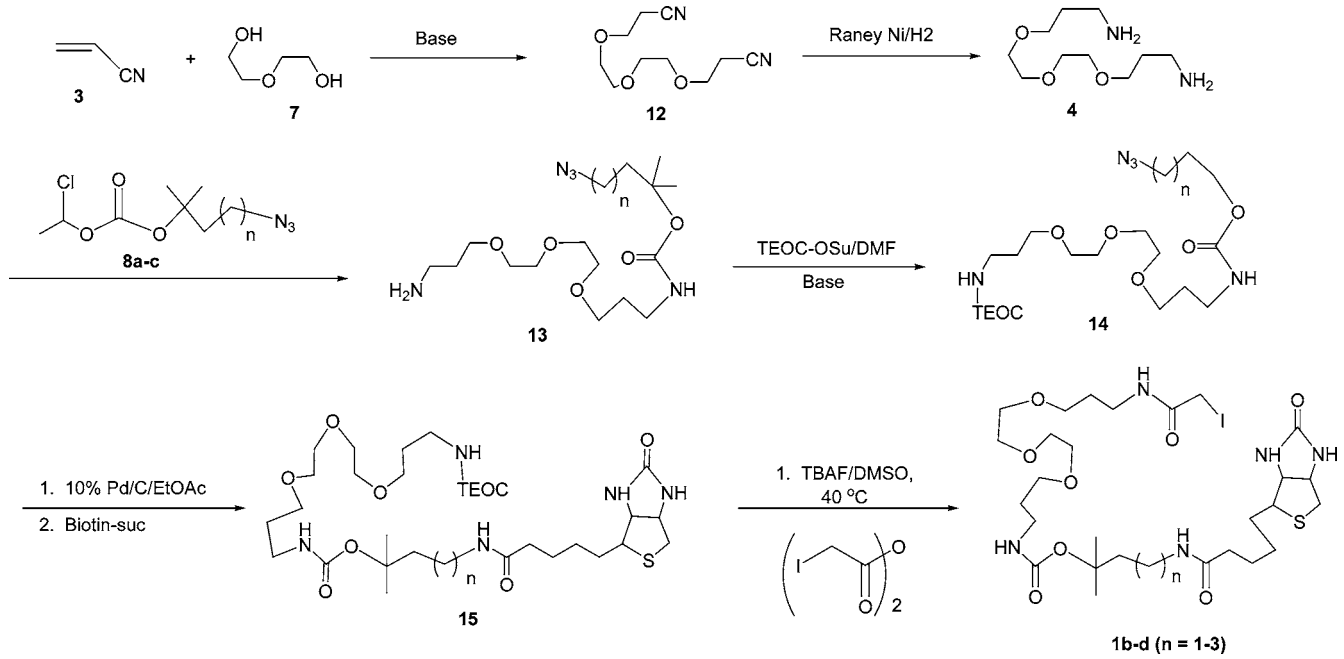

hydrolyzate is enriched on an avidin column to concentrate only cysteine-modified ICAT-labeled peptides, which are then lyophilized, redissloved in buffers, and exposed to TFA-catalyzed acidolytic cleavage to remove the biotin moiety. The debiotinylated peptides are finally separated online by ion-exchange and RP-HPLC and analyzed on an ESI-based mass spectrometer.

The retrosynthetic analysis for the synthesis of the novel four-component, acid-labile ICAT reagents (Figure 1, **1b**−**d**) is presented in Figure 3. The diamine **4** required an orthogonal protection so that one end could be iodoacetylated while the other could be manipulated to introduce the acid cleavable and biotin moieties. The acid cleavable moiety, while requiring an electrophilic locus, also necessitated the presence of a terminally protected primary amino group for the attachment of the biotin. To this end, we envisaged synthesizing fragments **8a**−**c** (n = 1−3), which have an azido function as a protected form of an amino group, as well as a reactive electrophilic terminal for installation of an acid labile insert. This fragment is accessible through the commercially available acid chlorocarbonate **9** and azido alcohols **10** which, in turn, can be readily prepared from bromoesters **11**. The object of having two to four methylene groups between the amide nitrogen and a tertiary carbon atom was to assess limits of stability of the final ICAT molecules as well as flexibility of their solubility profiles in buffered solvents used during the ICAT-mediated analysis of protein mixtures.

In the synthetic direction (Schemes 1 and 2), the required carbonate fragments **8a**−**c** for coupling to the known diamine **4** were synthesized as outlined in Scheme 1. The bromoesters **11** containing two to four methylene group spacers were prepared by Fischer esterification of the corresponding carboxylic acids and were treated with methyl Grignard to yield tertiary alcohols. The azide displacement of the bromine in DMF yielded azido alcohols **10**. Several leaving groups of variants of chloroformate **9** were examined, such as, phenyl chloroformate (*24*), 2,2,2-trichloroethyl chloroformate (*25*), and 4-nitrophenyl chloroformate (*26*). These reagents have been reported for acylation of tertiary alcohols to give carbonates that could be carbamoylated with common amino acids. All of these reagents worked well for carbonate formation with the azides **10** to give analogues of **8a**−**c**. However, none of these carbonates gave acceptable yields of coupled products **13** (Scheme 2) when selective monocarbamoylation of the diamine **4** was attempted. Success was finally realized when the commercially available 1-chloroethyl chloroformate (*27*) was reacted with the tertiary azido alcohols **10** to give 1-chloroethyl carbonates **8a**−**c** (Scheme 2) that were then reacted with a slight excess of the diamine **4** to give the carbamates **13a**−**c**.

The synthesis of the diamine component **4** was completed following a literature procedure (Scheme 2) (*28*, *29*). Thus, two molar equivalents of diethylene glycol **7** were added in a 1,4-addtion reaction to acrylonitrile. The biscyanide thus obtained was reduced directly to the diamine **4**, which was then acylated with the carbonate reagents **8a**−**c** to give monocarbamoylated products **13a**−**c**. This fragment provides a locus for the acid-cleavable site in the middle of the molecule as well as a scaffold for holding the terminal biotin and iodoacetamide moieties. While the right-hand azido terminus of **13a**−**c** served as masked primary amino group, the left-hand was protected as a trimeth-

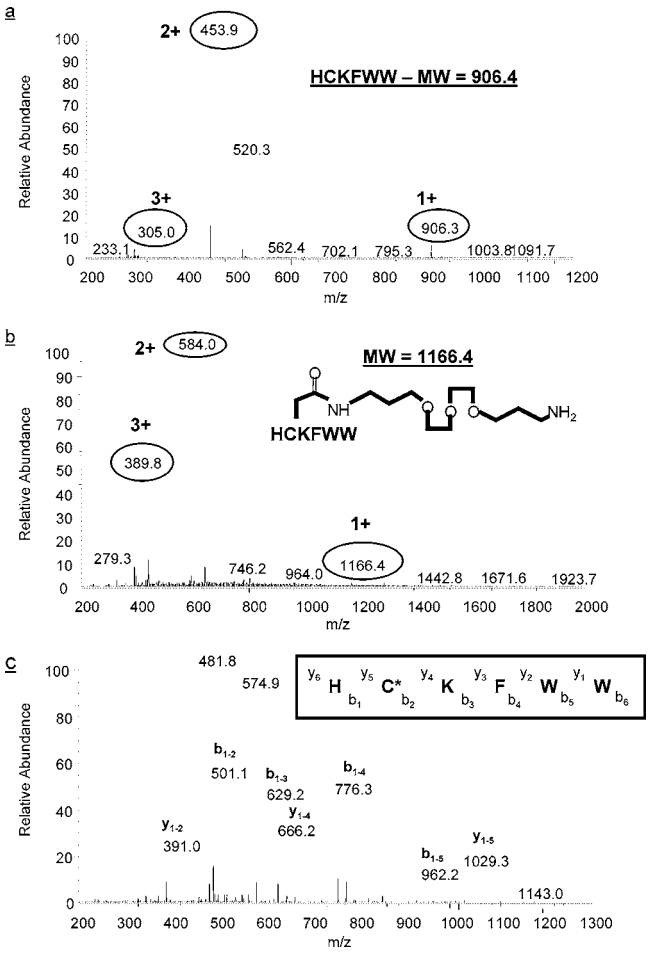

Figure 4. Peptide HCKFWW ICAT labeled after acidic cleavage.

ylsilylethoxycarbonyl (TEOC) group. This differential protection allowed reduction of the azide (10% Pd−C/H_2) function to a free amine that was readily linked to the biotin moiety under standard conditions for amide formation (biotin succinimide ester/DMF) to give compounds **15a**−**c**. The removal of the TEOC group required heating **15a**−**c** in dimethylsulfoxide at 40 °C. The crude **15a**−**c** obtained were immediately acylated with iodoacetic anhydride in DMF. The final ICAT reagents were purified by HPLC.

Since synthesis of a d_8- and C_6-labeled diamine **4** has been reported in the literature, the d_8- and C_6-labeled versions of the ICAT reagents **1b**−**d** (Figure 3) can be easily synthesized. However, before embarking on their preparation, it was deemed prudent to establish the utility of the "light" reagents in preliminary experiments.

To assess the utility of these unlabeled ICAT reagents, some commercially available cysteine-containing peptides were labeled with "light" ICAT molecules under standard buffer conditions and acidolyzed before infusion into the Finnigan Deca XP-Plus (ESI probe) for MS and tandem MS analysis. These tagged peptides gave satisfactory parent masses, as well as MS/MS peak patterns. A peptide HCKFWW was used as a model to measure the conjugation efficiency of the synthesized ICAT reagent. Figure 4a shows mass spectrometric analysis of the unmodified peptide used in one of these experiments. A distinct peak at 906.3 *m*/*z* was detected in the full mass spectrum. This peak corresponds to the monoisotopic mass of the unmodified peptide (906.4). The most abundant peak in the mass spectrum (453.9 *m*/*z*), however, corresponded to the doubly charged unmodified peptide. The double charge is due to the presence of a positively charged lysine in the peptide in addition to the peptide's amino terminus. A mass shift was detected after conjugation of the ICAT reagent to the peptide and acid treatment (Figure 4b). The mass spectrum of the modified peptide showed a peak at 1166.4. This peak corresponds to the monoisotopic mass of the peptide plus the acid-cleaved ICAT fragment (906.4 + 260 = 1166.4). As expected, the doubly charged ion was the most abundant in the mass spectrum (584.0 *m*/*z*). To confirm that the ICAT reagent was conjugated to a cysteine residue in the peptide sequence, the most abundant ion was subjected to collision-induced dissociation (CID). The b and y ions corresponding to the sequence of the modified peptides were detected in the MS/MS spectrum (Figure 4c). Importantly, the detection of the b1−2 and y1−5 product ions demonstrated that the acid-cleaved ICAT fragment was conjugated to the cysteine residue (Figure 4c). Therefore, these results demonstrated that the synthesized ICAT reagent can be conjugated to a thiol group of cysteine residues in the context of a peptide sequence as well as cleaved efficiently under acidic (TFA) conditions. Furthermore, the peak pattern of the MS/MS spectra did not indicate any significant undesired fragmentation that could possibly originate from the polyether linker.

The heavy isotope labeled analogues, such as d_8- or C_6, can be readily synthesized using commercially available acrylonitrile-d_3/diethylene glycol-d_2 for acid-cleavable ICAT-d_8, or acrylonitrile-$^{13}C_3$ for ICAT-$^{13}C_6$ synthesis employing protocols detailed in this report. These reagents will then be evaluated for their intended use in more complex proteomic analyses.

In summary, a practical synthesis of novel light isotope versions of acid-cleavable isotope-coded-affinity tags (ICAT-L) has been accomplished in overall reasonable yield. These ICAT reagents should avoid complications of MS/MS analysis of tagged peptide fragments introduced by the biotin moiety because the biotin, after isolation of tagged peptides, can be cleanly cleaved off by acid hydrolysis. Additionally, these light reagents can be readily converted to acid-cleavable PhIAT reagents in one step by reacting them with undeuterated and deuterated ethanedithiol. Some noncleavable PhIAT reagents for analysis of serine- and threonine-specific phosphoproteins have been reported (*30*). Studies are ongoing regarding the preparation of PhIAT and synthesis of heavy acid-cleavable ICAT versions (ICAT-H) leading to application of these reagents to more complex analyses of protein mixtures.

ACKNOWLEDGMENT

This work was supported by internal institutional funding for the Chemistry Core Facility, Mayo Clinic Jacksonville, Jacksonville, FL, and by NIH/NINDS Grant F32NSOY7930.

LITERATURE CITED

(1) Blackstock, W. P., and Weir, M. P. (1999) Proteomics: quantitative and physical mapping of cellular proteins. *Trends Biotechnol. 17*, 121−127.

(2) Gabor Miklos, G. L., and Maleszka, R. (2001) Integrating molecular medicine with functional proteomics: Realities and expectations. *Proteomics 1*, 30−41.

(3) Witzmann, F. A., and Li, J. (2002) Cutting-Edge Technology: II. Proteomics: core technologies and applications in physiology. *Am. J. Physiol. Gastrointest. Liver Physiol. 282*, G735−G741.

(4) Aebersold, R., and Goodlett, D. R. (2001) Mass Spectrometry in Proteomics. *Chem. Rev. 101*, 269−296.

(5) Han, D. K., Eng, J., Zhou, H., and Aebersold, R. (2001) Quantitative profiling of differentiation-induced microsomal proteins using isotope-coded affinity tags and mass spectrometry. *Nat. Biotechnol. 19*, 946−951.

(6) Rabilloud, T. (2002) Two-dimensional gel electrophoresis in proteomics: Old, old fashioned, but it still climbs up the mountains. *Proteomics 2*, 3−10.

(7) Lilley, K. S., Razzaq, A., and Dupree, P. (2002) Two-dimensional gel electrophoresis: recent advances in sample preparation, detection and quantitation. *Curr. Opin. Chem. Biol. 6*, 46−50 and references therein.

(8) Yang, H., Yan, W., and Aebersold, R. (2004) Chemical probes and tandem mass spectrometry: a strategy for the quantitative analysis of proteomes and subproteomes. *Curr. Opin. Chem. Biol. 8*, 66−75.

(9) Aebersold, R., and Mann, M. (2003) Mass spectrometry-based proteomics. *Nature 422*, 198−207.

(10) Gygi, S. P., Rist. B., Gerber, S. A., Turecek, F., Gelb, M. H., and Aebersold, R. (1999) Quantitative analysis of complex protein mixtures using isotope-coded affinity. *Nat. Biotechnol. 17*, 994−999.

(11) Gygi, S. P., and Aebersold, R. (2000) Mass spectrometry and proteomics. *Curr. Opin. Chem. Biol. 4*, 489−494.

(12) Mo, W., and Karger, B. L. (2002) Analytical aspects of mass spectrometry and proteomics. *Curr. Opin. Chem. Biol. 6*, 666−675.

(13) Turecek, F. (2002) Mass spectrometry in coupling with affinity capture-release and isotope-coded affinity tags for quantitative protein analysis. *J. Mass Spectrom. 37*, 1−14.

(14) Shen, M., Guo, L., Wallace, A., Fitzner, J., Eisenman, J., Jacobson, E., and Johnson, R. S. (2003) Isolation and Isotope Labeling of Cysteine- and Methionine-containing Tryptic Peptides: Application to the Study of Cell Surface Proteolysis. *Mol. Cell. Proteomics 2*, 315−324.

(15) Qiu, Y., Sousa, E. A., Hewick, R. M., and Wang, J. H. (2002) Acid-Labile Isotope-Coded Extractants: A Class of Reagents for Quantitative Mass Spectrometric Analysis of Complex Protein Mixtures. *Anal. Chem. 74*, 4969−4979.

(16) Bottari, P., Aebersold, R., Turecek, F., and Gelb, M. H. (2004) Design and Synthesis of Visible Isotope-Coded Affinity Tags for the Absolute Quantification of Specific Proteins in Complex Mixtures. *Bioconjugate Chem. 15*, 380−388.

(17) Vosseller, K., Hansen, K. C., Chalkley, R. J., Trinidad, J. C., Wells, L., Hart, G. W., and Burlingame, A. L. (2005) Quantitative analysis of both protein expression and serine/threonine posttranslational modifications through stable isotope labeling with dithiothreitol. *Proteomics 5*, 388−398.

(18) Meyer, H. E., Hoffmann-Rosorske, E., Korte, H., and Heilmeyer, L. M. G., Jr. (1986) Sequence analysis of phosphoserine-containing peptides: Modification for picomolar sensitivity. *FEBS Lett. 204*, 61−66.

(19) A form of a cleavable ICAT is available from Applied Biosystems, Framingham, MA, but its structure has not been published. For some examples of its use in proteomics, see refs 20−23.

(20) Yu, L.-R., Conrads, T. P., Uo, T., Isaaq, H. J., Morrison, R. S., and Veenstra, T. D. (2004) Evaluation of the Acid-Cleavable Isotope-Coded Affinity Tag Reagents: Application to Camptothecin-Treated Cortical Neurons. *J. Proteome Res. 3*, 469−477.

(21) Molloy, M. P., Donohoe, S., Brzezinski, E. E., Kilby, G. W., Stevenson, T. I., Baker, J. D., Goodlett, D. R., and Gage, D. A. (2005) Large-scale evaluation of quantitative reproducibility and proteome coverage using acid cleavable isotope coded affinity tag mass spectrometry for proteomic profiling. *Proteomics 5*, 1204−1208.

(22) Yi, E. C., Li, X.-J., Cooke, K., Lee, H., Raught, B., Page, A., Aneliunas, V., Hieter, P., Goodlett, D. R., and Aebersold, R. (2005) Increased quantitative proteome coverage with 13C/12C-based, acid-cleavable isotope-coded affinity tag reagent and modified data acquisition scheme. *Proteomics 5*, 380−387.

(23) Hansen, K. C., Schimitt-Ulms, G., Chalkley, R. J., Hirsch, H., Baldwin, M. A., and Burlingame, A. L. (2003) Mass Spectrometric Analysis of Protein Mixtures at Low Levels Using Cleavable 13C−Isotope-coded Affinity Tag and Multidimensional Chromatography. *Mol. Cell. Proteomics 2*, 299−314.

(24) Miyazawa S., Okano, K., Shimomura, N., Clark, R. S., Kawahara, T., Asano, O., Yoshimura, H., Miyamoto, M., Sakuma, Y., Muramoto, K., et al. (1991) Structure−activity studies on triazolothienodiazepine derivatives as platelet-activating factor antagonists. *Chem. Pharm. Bull. 39*, 3215−3220.

(25) Appendino G., Gariboldi P. L., Gabetta B., Pace R., Bombardelli E., and Viterbo D. (1992) 14b-Hydroxy-10-Deacetylbaccatin Ill, a New Taxane from Himalayan Yew Taxus wallichiana Zucc. *J. Chem. Soc., Perkin Trans. 1*, 2925−2929.

(26) Konakahara, T., Ozaki, T., Sato, K., and Gold, B. (1993) A Convenient method for the Synthesis of Activated *N*-Methylcarbamates. *Synthesis* 103−106.

(27) For an application of 1-chloroethylchloroformate for ester synthesis, see: Dang, A. V., Olofson, R. A., Wolf, P. R., Piteau, M. D., and Senet, J.-P. G. (1990) A simple conversion of 1-chloroethyl carbonates to fluoroformates: value in the preparation. *J. Org. Chem. 55*, 1847−1851.

(28) Gerber, S. A., Scott, C. R., Turecek, F., and Gelb, M. H. (1999) Analysis of Rates of Multiple Enzymes in Cell Lysates by Electrospray Ionization Mass Spectrometry. *J. Am. Chem. Soc. 121*, 1102−1103.

(29) For an improved synthesis of the diamine **4**, see: Zhang, A., Edwards, P. J., Roeske, R. W., and Guo, L. (2005) Synthesis and Self-Alkylation of Isotope-Coded Affinity Tag Reagents. *Bioconjugate Chem. 16*, 458−464.

(30) Goshe, M. B., Conrads, T. P., Panisko, E. A., Angell, N. H., Veenstra, T. D., and Smith, R. D. (2001) Phosphoprotein Isotope-Coded Affinity Tag Approach for Isolating and Quantitating Phosphopeptides in Proteome-Wide Analyses. *Anal. Chem. 73*, 2578−2586.

BC0503059

MARCH/APRIL 2006
Volume 17, Number 2

© *Copyright 2006 by the American Chemical Society*

Bioconjugate Chemistry

COMMUNICATIONS

Fluorescence Probe with a pH-Sensitive Trigger

Amit K. Galande, Ralph Weissleder, and Ching-Hsuan Tung*

Center for Molecular Imaging Research, Massachusetts General Hospital, Harvard Medical School, Charlestown, Massachusetts 02129. Received November 17, 2005; Revised Manuscript Received February 7, 2006

Acid-catalyzed hydrolysis was used as the mechanism to design a new type of environmentally sensitive fluorescence probe. A mild and selective periodate oxidation of the 2-amino alcohol of serine in the presence of a disulfide bond was developed to prepare dialdehyde peptides. Two identical fluorochrome hydrazide derivatives were then linked to the dialdehyde peptide forming an acid-labile hydrazone linkage. This self-quenched probe is weakly fluorescent at a physiological pH of 7.4 but shows more than 3-fold fluorescence enhancement at pH 4.5.

Molecular probes for imaging applications are often designed using fluorescence resonance energy transfer (FRET)-related mechanisms to reduce background (*1*). FRET-based probes typically incorporate a pair of two different dye molecules, a fluorescent donor, and a fluorescent acceptor or a fluorochrome and a nonfluorescent quencher. Recently, self-quenched fluorescent probes consisting of multiple copies of the same fluorescent dye molecule have also been developed for molecular imaging (*2*, *3*). Biological processes such as conformational changes of protein, receptor binding of ligands, and catalytic function of proteases have been exploited as molecular targets for various fluorescence emission probes (*4*−*8*). In addition, activity-based probes have also been developed for different enzyme classes (*9*, *10*). In this report, a new approach involving acid-catalyzed hydrolysis as the mechanism of fluorescence activation is demonstrated.

CY5G2, an aminopeptidase N (APN)-targeted fluorescence probe (Scheme 1), was constructed using an acid-sensitive hydrazone linkage. CY5G2 has been designed in such a way that it stays weakly fluorescent at the extracellular pH of 7.4 and becomes strongly fluorescent at the intracellular lysosomal pH of 4.5. CY5G2 incorporates a disulfide-constrained NGR (Asn-Gly-Arg) motif, which is a ligand for the APN receptor and is likely to facilitate entry of the probe into endosome and then into acidic lysosome (*8*, *11*, *12*). Here we report design and synthesis of CY5G2 along with its evaluation under physiologically relevant pH environments.

The probe was constructed on a flexible polyglycine backbone. The N-terminus of the peptide was extended to incorporate the disulfide-bridged NGR motif, while toward the C-terminus two molecules of Cy5 were conjugated via an acid-sensitive hydrazone linkage. Cy5 dyes were chosen because of their far-red fluorescence emission (670 nm). Fluorescence in the far-red to near-infrared region (650−900 nm) has been found to be most suitable for in vivo optical imaging (*13*). The two Cy5 dyes on CY5G2 are separated from the disulfide-constrained NGR motif by two glycine residues. Another short spacer (<10 Å) of two glycine residues separates the two Cy5 molecules from each other. Considering the close proximity of the dye molecules to each other and the narrow Stoke's shift of Cy5 (18 nm), the dyes are likely to be self-quenched due to a combination of static quenching and FRET mechanisms (*14*).

* To whom correspondence should be addressed: Ching H. Tung, Center for Molecular Imaging Research, Massachusetts General Hospital. 149 13th St., Rm. 5410, Charlestown, MA 02129. Tel: 617 726-5779, Fax: 617 726-5708 E-mail: tung@helix.mgh.harvard.edu.

10.1021/bc050330e CCC: $33.50 © 2006 American Chemical Society
Published on Web 02/18/2006

Scheme 1. Synthesis of CY5G2

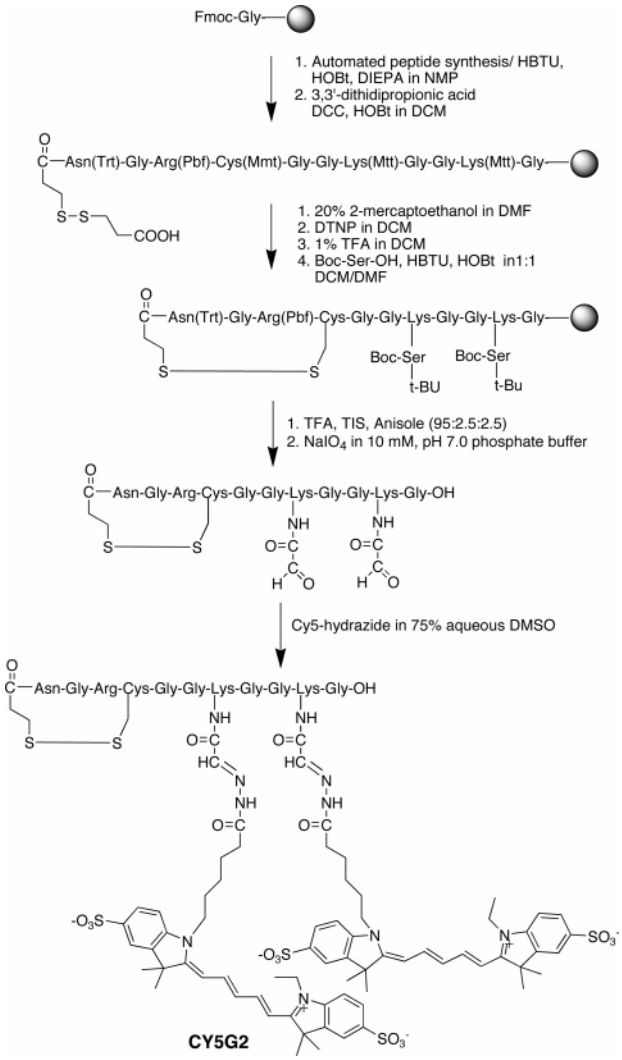

The fluorescence quenching of CY5G2 is possible only when the hydrazone linkages are intact. In an acidic environment, however, hydrolysis of the hydrazone linkages would release the fluorochromes from the peptide backbone. This would eliminate distance-dependent quenching of the fluorochromes and show enhancement in the Cy5 fluorescence emission.

CY5G2 was synthesized by a combination of solid-phase and solution-phase reactions. The synthesis was started with Fmoc-Gly-Wang resin (0.66 mmol/g), on which the peptide chain was extended using an automated peptide synthesizer as shown in Scheme 1. To the N-terminus of the peptide, 3,3′-dithiodipropionic acid was manually incorporated using *N*,*N*′-dicyclohexycarbodiimide/1-hydroxybenzotriazole (DCC/HOBt) as coupling agents. This was followed by the construction of an intramolecular disulfide bridge on the solid support utilizing 2,2′-dithiobis(5-nitropyridine) (DTNP) as previously developed (*15*, *16*). Treatment of the resin with 1% trifluoroacetic acid (TFA) also selectively deprotected the methyltrityl (Mtt) groups of the lysine residues. Thereafter, side chain amines of these lysine residues were neutralized by washing the resin twice with 5% *N*,*N*′-diisopropylethylamine (DIPEA) in *N*,*N*′-dimethylformamide (DMF), and then Boc-Ser(t-But)-OH was coupled. The peptide was cleaved from the solid support under strong acidic conditions (Scheme 1). Then the crude peptide was purified using reversed phase-high-pressure liquid chromatography (RP-HPLC) and lyophilized to obtain the diserine peptide as white powder. The overall yield (by weight) of the purified diserine peptide based on the initial resin substitution was 50% (see Supporting Information for the product characterization).

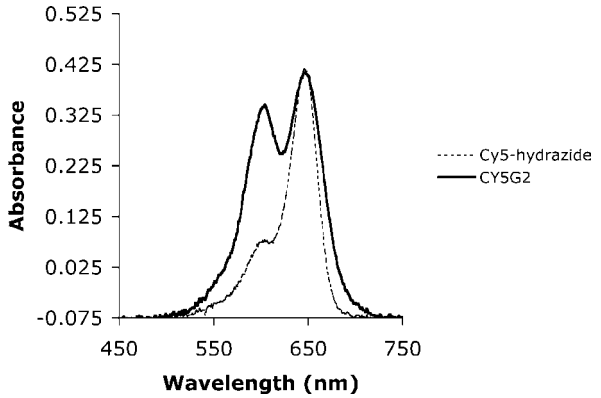

Figure 1. Absorption spectra of CY5G2 and Cy5-hydrazide.

Purified diserine peptide was converted into the dialdehyde peptide under mild oxidizing conditions of sodium periodate ($NaIO_4$) (Scheme 1). Transformation of an N-terminal seryl peptide into an N-terminal glyoxylyl peptide by periodate oxidation is a well-known reaction (*17*). Periodate oxidation of 2-amino alcohols, such as N-terminal serine, is reported to be about 1000-fold faster as compared to the oxidation of 1,2-diols under similar conditions (*17*). Hence instead of incorporating serine into the peptide chain, serine residues were conjugated to the side chain of the lysine residues, thus making the 2-amino alcohol moiety of serine available for the oxidation reaction. However, even under mild reaction conditions, $NaIO_4$ is known to oxidize residues such as the side chain thiol of cysteine and the thioether of the methionine side chain (*17*). A few disulfide proteins containing N-terminal serine have been treated with periodate (*18*), but no systematic efforts have been carried out to explore the selectivity of periodate treatment in the presence of a disulfide bond, in which the sulfur atoms are likely to get oxidized to sulfoxides. A variety of reaction conditions were attempted by changing reaction time and the amount of $NaIO_4$, and a protocol was established to selectively oxidize the 2-amino alcohol of serine in the presence of a disulfide bond. Longer reaction times or higher than 2.5 equiv of $NaIO_4$ showed oxidation of either one or both sulfur atoms of a disulfide as indicated by matrix-assisted laser desorption ionization-time-of-flight mass spectrometry (MALDI-TOF-MS) analysis.

Hydrazide-functionalized dye (Cy5-hydrazide) was conjugated to the purified dialdehyde peptide to obtain CY5G2. Peptide aldehydes are susceptible to the nucleophilic attack from the primary amine of the peptide N-terminus yielding undesired intermolecular imine linkages. By substituting N-terminal cysteine with mercaptopropionic acid in the construction of the disulfide bridge, we eliminated such possible side reactions. Following the conjugation of Cy5-hydrazide, CY5G2 was purified on the RP-HPLC to remove excess Cy5-hydrazide. Following lyophilization, CY5G2 was obtained as a blue powder in 35% yield (see Supporting Information for the product characterization).

Absorption spectrum of CY5G2 was compared with that of free Cy5-hydrazide dye (Figure 1). Concentrations of Cy5-hydrazide and CY5G2 were adjusted to 0.4 optical density (OD) based on the absorption peak at 647 nm (Figure 1). CY5G2 showed an additional peak that is blue-shifted by about 40 nm. This peak indicates aggregation of the two Cy5 molecules attached to the peptide backbone to form an H-type dimeric complex. H-type aggregates tend to quench the fluorescence of cyanine dyes because of static quenching (*19*). Hence, CY5G2 is likely to have weak fluorescence emission from the dyes. Fluorescence measurements revealed about 75% quenching of

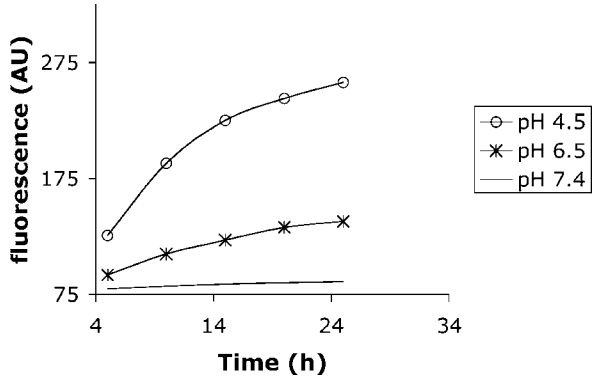

Figure 2. pH-Dependent fluorescence activation profile of CY5G2.

the fluorescence emission of CY5G2 as compared to that of Cy5-hydrazide of an equimolar (1.6 μM) concentration.

Next, fluorescence measurements were carried out to examine if the fluorescence emission of CY5G2 could be enhanced under acidic environment following hydrolytic cleavage of the hydrazone linkages. Accordingly, CY5G2 was incubated with buffer solutions of pH 4.5 (lysosomal compartment), pH 6.5 (tumor interstitial environment), and pH 7.4 (extracellular environment) at 37 °C. Figure 2 shows kinetic profiles of fluorescence activation of CY5G2 at different pH values. The fluorescence emission essentially remains unchanged at pH 7.4. Under mildly acidic conditions (pH 6.5), CY5G2 showed a slight increase in fluorescence emission, and under lysosomal acidic environment (pH 4.5) CY5G2 showed a three-fold increase in fluorescence after 24 h. Absorption spectra of CY5G2 recorded following 24 h incubation under pH 4.5 showed more than 80% elimination of the blue-shifted aggregation peak, indicating hydrolysis of hydrazone linkages and subsequent release of the fluorochromes from the peptide backbone.

Previously, we reported several examples of protease-sensitive NIR probes, which remain nonfluorescent or weakly fluorescent under normal physiological conditions and fluoresce brightly when cleaved by certain proteases overexpressed in the tumor environment (*20*). These enzyme-activatable fluorescent probes have been widely used for in vivo molecular imaging and involve cleavage of amide bonds of peptide substrates by the proteases to release fluorochromes. In this study, an environmentally sensitive probe was designed based on a completely different mechanism. CY5G2 demonstrates utility of the pH-sensitive hydrazone linkage for making activatable fluorescent probes. Because APN is overexpressed in tumor vasculature, CY5G2 has potential applications in monitoring tumor angiogenesis and probing the acidic environment of the tumor interstitium (*21*, *22*). It also provides a tool for in vivo imaging of pharmacokinetics of hydrazone-linked prodrugs (*23*−*25*).

ACKNOWLEDGMENT

This research was supported in part by NIH P50-CA86355, RO1 CA99385, and R21 CA114149.

Supporting Information Available: MALDI-TOF mass spectrograms and RP-HPLC chromatograms of CY5G2 and the peptide intermediates along with detailed experimental procedures. This material is available free of charge via the Internet at http://pubs.acs.org.

LITERATURE CITED

(1) Selvin P. R. (2000) The renaissance of fluorescence resonance energy transfer *Nat. Struct. Biol. 7*, 730−734.
(2) Weissleder, R., Tung, C. H., Mahmood, U., and Bogdanov, A., Jr. (1999) In vivo imaging of tumors with protease-activated near-infrared fluorescent probes. *Nat. Biotechnol. 17*, 375−378.
(3) Bremer, C., Tung, C. H., and Weissleder, R. (2001) In vivo molecular target assessment of matrix metalloproteinase inhibition. *Nat. Med. 7*, 743−748.
(4) Zhang, J., Campbell, R. E., Ting, A. Y., and Tsien, R. Y. (2002) Creating new fluorescent probes for cell biology. *Nat. Rev. Mol. Cell Biol. 3*, 906−918.
(5) Becker, A., Hessenius, C., Licha, K., Ebert, B., Sukowski, U., Semmler, W., Wiedenmann, B., and Grotzinger, C. (2001) Receptor-targeted optical imaging of tumors with near-infrared fluorescent ligands. *Nat. Biotechnol. 19*, 327−331.
(6) Tung, C. H., Quinti, L., Jaffer, F. A., and Weissleder, R. (2004) A branched fluorescent peptide probe for imaging of activated platelets. *Mol. Phram. 2*, 92−95.
(7) Tung, C. H., Bredow, S., Mahmood, U., and Weissleder, R. (1999) Preparation of a cathepsin-D sensitive near-infrared fluorescent probe for imaging. *Bioconjugate Chem. 10*, 892−896.
(8) Zhang, Z., Harada, H., Tanabe, K., Hatta, H., Hiraoka, M. and Nishimoto, S. (2005) Aminopeptidase N/CD13 targeting fluorescent probes: Synthesis and application to tumor cell imaging. *Peptides 26*, 2182−2187.
(9) Law, B., Weissleder, R., and Tung, C. H. (2005) Mechanism-based fluorescent reporter for protein kinase A detection. *ChemBioChem 6*, 1361−1367.
(10) Kato, D., Boatright, K. M., Berger, A. C., Nazif, T., Blum, G., Ryan, C., chehade, K. A. H., Salvesen, G. S., and Bogyo, M. (2005) Activity-based probes that target diverse cysteine protease families. *Nat. Chem. Biol. 1*, 33−38.
(11) Arap, W., Pasquilini, R., and Ruoslahti, E. (1998) Cancer treatment by targeted drug delivery to tumor vasculature in a mouse model. *Science 279*, 377−380
(12) Ellerby, H. M., Arap, W., Ellerby, L. M., Kain, R., Andrusiak, R., Rio, G. L., Krajewski, S., Lombardo, C. R., Rao, R., Ruoslahti, E., Bredesen, D. E., and Pasquilini, R. (1999) Anti-cancer activity of targeted pro-apoptotic peptides. *Nat. Med. 5*, 1032−1038.
(13) Weissleder, R., and Ntziachristos, V. (2003) Shedding light onto live molecular targets *Nat. Med. 9*, 123−128.
(14) Johansson, M. K., and Cook, R. M. (2003) Intramolecular dimers: A new design strategy for fluorescence-quenched probes. *Chem. Eur. J. 9*, 3466−3471.
(15) Galande, A. K., Weissleder, R., and Tung C. H. (2005) An effective method of on-resin disulfide bond formation in peptides. *J. Comb. Chem. 7*, 174−177.
(16) Galande, A. K., and Spatola, A. F. (2003) Solid-phase synthesis of disulfide heterodimers of peptides. *Org. Lett. 5*, 3431−3434.
(17) Geoghegan K. F., and Stroh, J. G. (1992) Site-directed conjugation of nonpeptide groups to peptides and proteins via periodate oxidation of a 2-amino alcohol. Application to modification at N-terminal serine. *Bioconjugate. Chem. 3*, 138−146.
(18) Offord, R. E., Gaertner, H. F., Wells, T. N. C., Proudfoot, A. E. I. (1997) Synthesis and evaluation of fluorescent chemokines labeled at the amino terminal. *Methods Enzymol. 287*, 348−369.
(19) Packard, B. Z., Toptygin, D. D., Komoriya, A., and Brand L. (1997) Design of profluorescent protease substrates guided by exciton theory. *Methods Enzymol. 278*, 15−23.
(20) Tung, C. H. (2004) Fluorescent peptide probes for in vivo diagnostic imaging. *Biopolymers 76*, 391−403.
(21) Curnis, F., Arrigoni, G., Sacchi, A., Fischetti, L., Arap, W., Pasquilini, R., and Corti, A. (2002) Differential binding of drugs containing the NGR motif to CD13 isoforms in tumor vessels, epithelia, and myeloid cells. *Cancer Res. 62*, 867−874.
(22) Gerweck, L. E., and Seetharaman, K. (1996) Cellular pH gradient in tumor versus normal tissue: Potential exploitation for the treatment of cancer. *Cancer Res. 56*, 1194−1198.
(23) Zhang, Z., Hatta, H., Tanabe, K., and Nishimoto, S. (2005) A new class of 5-fluoro-2′-deoxyuridine prodrugs conjugated with a tumor-homing cyclic peptide CNGRC by ester linkers: Synthesis, reactivity, and tumor-cell-selective cytotoxicity. *Pharm. Res. 22*, 381−389.
(24) Hensbergen, Y. V., Broxterman, H. J., Elderkamp, Y. W., Lankelma, J., Beers, J. C. C., Heijn, M., Boven, E., Hoekman, K., and Pinedo, H. M. (2002) A doxorubicin-CNGRC-peptide conjugate with prodrug properties. *Biochem. Pharmacol. 63*, 897−908.
(25) Rudin, M., and Weissleder, R. (2003) Molecular imaging in drug discovery and development. *Nat. Rev. Drug Discovery 2*, 123−131.

BC050330E

Supporting Information

Fluorescence probe with a pH-sensitive trigger

Amit K. Galande, Ralph Weissleder, and Ching-Hsuan Tung*

Center for Molecular Imaging Research, Massachusetts General Hospital, Harvard Medical School, Charlestown, Massachusetts 02129

Experimental Procedures

Automated peptide synthesis: Peptide synthesis was performed on an automated peptide synthesizer (ABI 433A, Applied Biosystems, Foster City, CA) employing the traditional Fmoc methodology using FastMoc 0.1 MonPrevPk protocol. Synthesis was started with Fmoc-Gly-wang resin (150 mg, ~0.1 mmol). All amino acids (10 equiv) were attached to the resin by stepwise elongation with HOBt (10 equiv), HBTU (10 equiv), and N,N-diisopropylethylethylamine (DIPEA, 20 equiv) as coupling reagents in the presence of N-methylpyrrolidone (NMP; 15 mL). The Fmoc protecting groups were removed by 20 % (v/v) of piperidine in NMP (15 mL).

Coupling of 3,3'-dithiodipropionic acid: 3,3'Dithiodipropionic acid (0.5 mmol) and HOBt (0.5 mmol) were dissolved in 4 mL 9:1 DCM/DMF. The solution was added to the resin (0.1 mmol, 0.66 mmol/g) and shaken for 10 min. To the resin suspension, solution of DCC in DCM (0.5 mmol in 0.1 mL) was added and the suspension was shaken for 3 h.

Coupling of Boc-Ser-OH: Boc-Ser-OH was purchased (EMD Biosciences, San Diego, CA) as its dicyclohexylamine (DCHA) salt. Free Boc-Ser-OH was generated by dissolving 1 mmol of Boc-Ser-OH.DCHA in 1.5 mL DCM and extracting this solution (3 × 3mL) with ice-cold aqueous solution (0.3 M) of $KHSO_4$. Following extraction and solvent evaporation, 1 mmol of Boc-Ser-OH, HBTU and HOBt were dissolved in 3 mL of 1:1 DMF/DCM followed by the addition of 2 mmol of DIPEA. The solution was then immediately added to the resin (0.1 mmol) without any preactivation to avoid possible racemization. Four hours later, the ninhydrin test confirmed quantitative coupling.

Periodate oxidation of the diserine peptide: Purified peptide (4.8 mg, 3.84 μmol) was dissolved in 75 μL of 10 mM phosphate buffer (pH 7.0). If required, pH of the solution was further adjusted using 0.1 N NaOH. To this, 120 μL of 140 mM $NaIO_4$ solution (2.2 equivalents) in 10 mM phosphate buffer (pH 7.0) was added. The solution was sonicated for 10 sec and further incubated for 17 min. The reaction mixture was then injected into the preparative RP-HPLC column and the fraction corresponding to the aldehyde peptide was collected.

Coupling of oxidized peptide: The aldehyde Peptide (0.4-0.5 mg, ~ 0.37 μmol) was dissolved in 50 μL of 10 mM phosphate buffer solution of pH 7.0; and 0.7 mg of the Cy5-hydrazide (0.89 μmol, 1.2 equivalents, purchased from Amersham Biosciences NJ, USA) was dissolved in 100 μL of DMSO. The dye solution was mixed with the peptide solution and incubated for 16 h. The reaction mixture was then passed through RP-HPLC (buffer A: 0.004% TFA in water, buffer B: 0.004% TFA in acetonitrile, C18 analytical column, Vydac, 218TP54, flow rate 1 ml/min. 100% buffer A to 100% buffer B in 50 min) and the fraction corresponding to CY5G2 (retention time 23.56 min) was collected.

Fluorescence measurement: All the fluorescence measurements were performed in a 96-well assay plate 3603 (Corning Inc. NY USA). Fluorescence measurements were obtained in a fully modular monochromator-based microplate detection system (Safire^2, Tecan, San Jose, CA). Excitation and emission were set at 640 nm and 665 nm, respectively, with the bandwidth of 10 nm and the gain value of 40. Fluorescence emission was monitored at 37^0C.

Compound: CY5G2

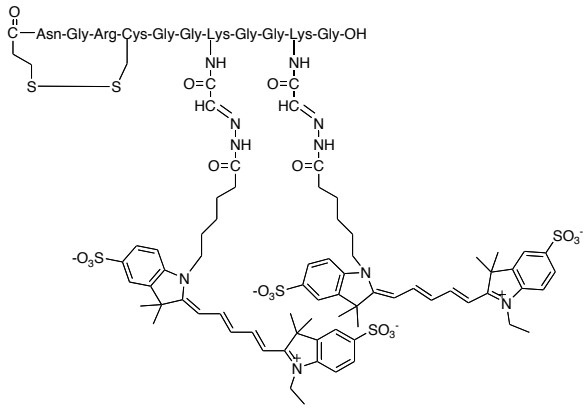

MALDI-TOF mass spectrogram:

MASS EXPECTED: 2488.91
MASS FOUND: 2488.66

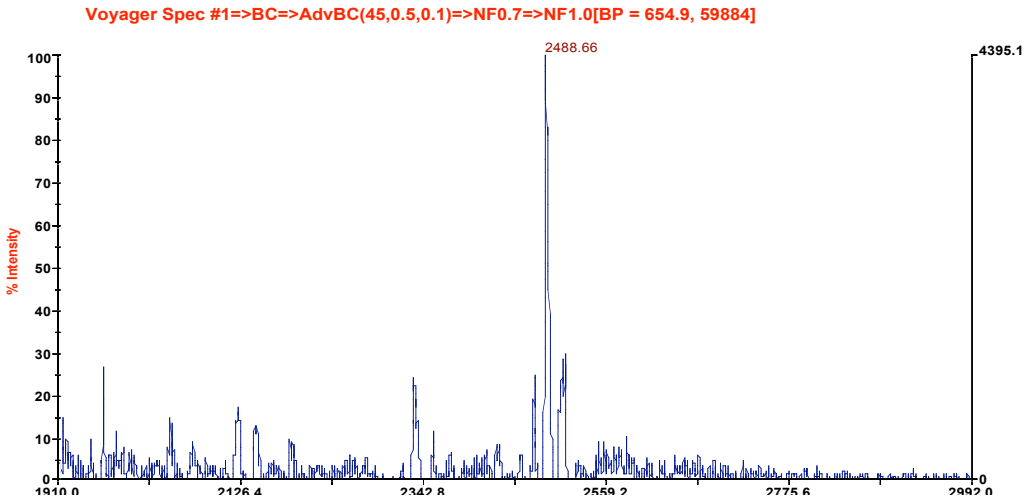

MALDI-TOF conditions: Instrument: Voyager-DE PRO (PerSeptive Biosystems), Instrument mode: Negative, VOLTAGES: Accelerating: 20000, Grid: 95, Guide Wire: 0.05, Delay Time: 100 nsec.
NOTE: Partial cleavage of the hydrazone linkage was observed under MALDI conditions (alpha-cyano-4-hydroxycinnamic acid as a matrix and 0.1% trifuoroacetic acid in 50% acetonitrile) homogeneity and purity of CY5G2 was confirmed using RP-HPLC (see below)

RP-HPLC Chromatogram

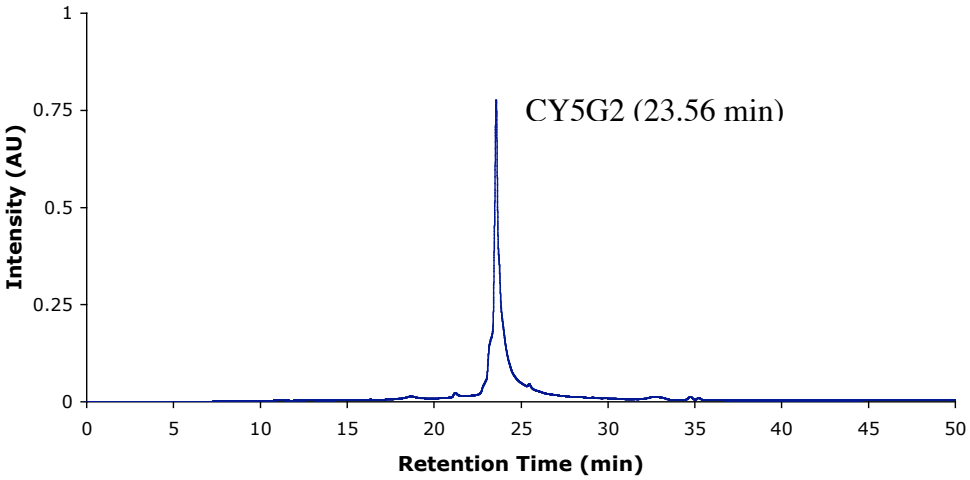

RP-HPLC conditions: Solvent A: 0.004% TFA in water, Solvent B: 0.004% TFA in acetonitrile, C18 analytical column,Vydac, 218TP54, flow rate 1 ml/min. 100% solvent A to 100% solvent B in 50 min.

Under the above-mentioned HPLC conditions, the hydrazide functionalized dye (Cy5-hydrazide) showed retention time of 20.87 min.

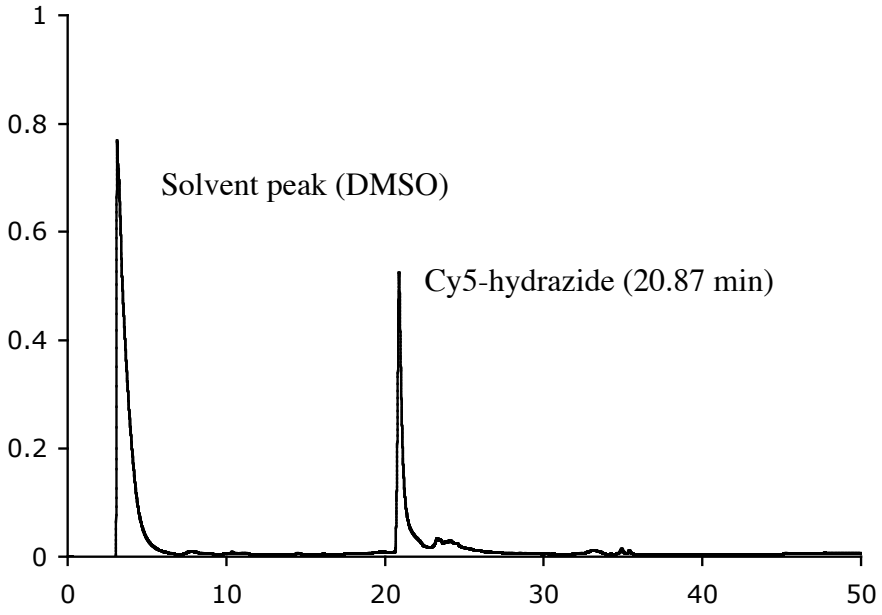

Compound: Diserine peptide

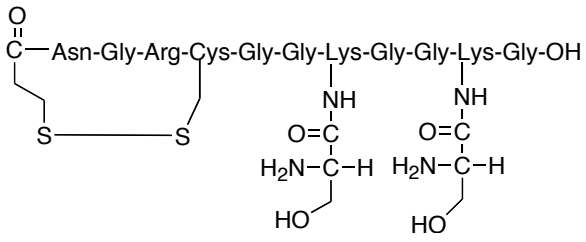

MALDI-TOF mass spectrogram

MASS EXPECTED: 1250.53
MASS FOUND: 1249.00

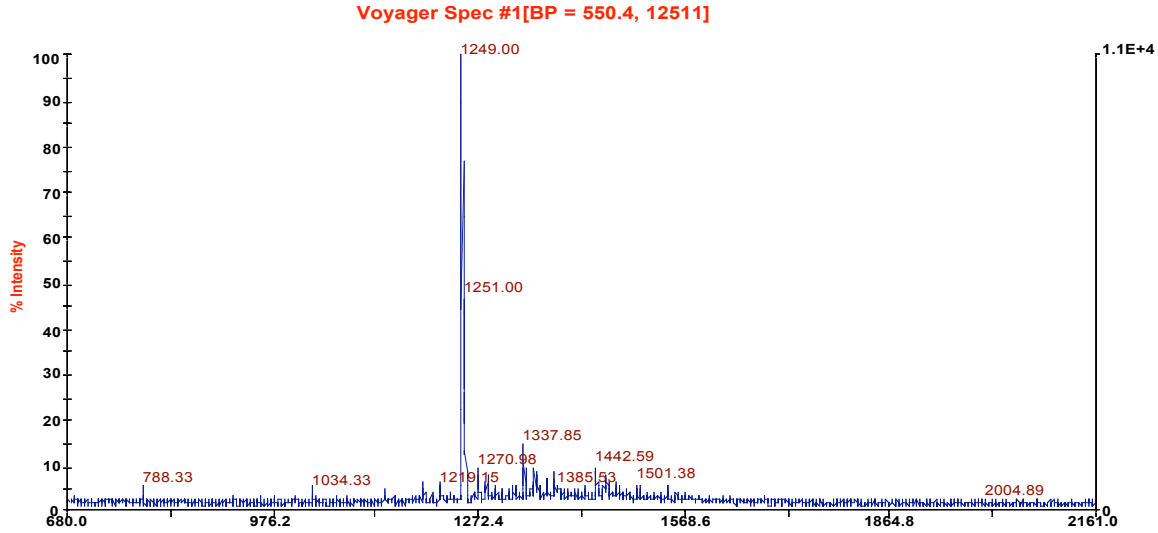

RP-HPLC Chromatogram

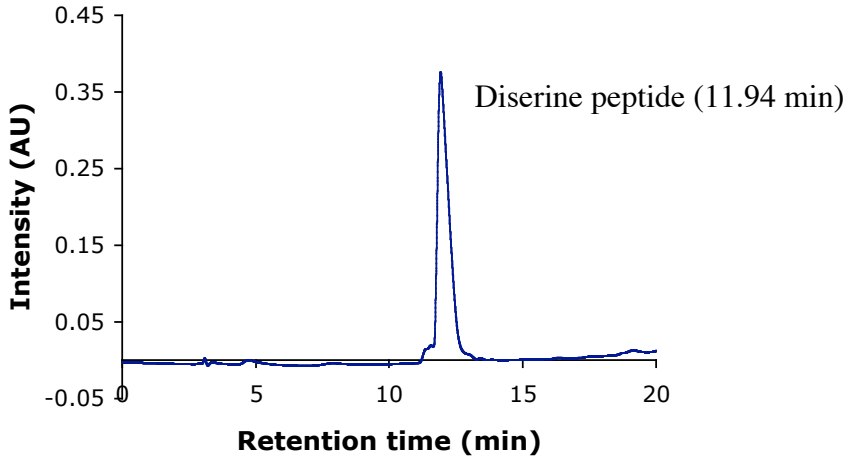

RP-HPLC conditions: Solvent A: 0.1% TFA in water, solvent B: 0.1% TFA in acetonitrile, C18 analytical column,Vydac, 218TP54, flow rate 1 ml/min. 100% solvent A to 100% solvent B in 50 min.

A General Approach for Antibody Purification Utilizing [Protein A-Catechol:Fe^{3+}] Macro-Complexes

Guy Patchornik[†,*] and Amnon Albeck[§]

Affisink Biotechnology Ltd, 11 Hamaccabee St. Kiryat-Ono 55572, Israel, and The Julius Spokojny Bioorganic Chemistry Laboratory, Department of Chemistry, Bar-Ilan University, Ramat-Gan 52900, Israel. Received December 23, 2005; Revised Manuscript Received January 27, 2006

A general platform for antibody purification utilizing free nonimmobilized Protein A modified with the strong metal chelator catechol (ProA-CAT) and Fe^{3+} ions is presented. The mechanism of purification requires formation and precipitation of macro-complexes composed of [ProA-CAT:IgG:Fe^{3+}]. Target IgGs are eluted directly from the precipitates (i.e. pellets) at pH 3 in high yields (71−80%) and high purity (>95%), without dissociating the [ProA-CAT:Fe^{3+}] insoluble macro-complex.

Highly purified antibody preparations represent a major scientific and industrial need. In a previous study (*1*) we presented a novel purification approach (affinity-sinking, AS[1]), utilizing free nonimmobilized desthiobiotinylated ligands (e.g., Protein A; Concanavalin A) and free avidin. The nonimmobilized state of the ligand circumvents the need for immobilizing ligands to polymeric supports; hence, polymers are excluded from the process and purification is accomplished without chromatographic columns. This study further demonstrates the implementation of AS on a novel, more challenging platform, the metal:chelator platform. Therefore, Protein A, a 42 kDa factor produced by several stains of *Staphylococcus aureus* which binds specifically to the Fc region of different classes of immunoglobulins (*2*), was covalently modified according to ref 3 with a synthesized active ester derivative of the strong metal chelator catechol, catechol-NHS (Figure 1; see synthesis in Supporting Information) (*4*). The modified Protein A (ProA-CAT) serves as the nonimmobilized ligand and is used for purification of rabbit and bovine IgGs from *E. coli* cell lysate.

The mechanism of purification according to AS requires three successive steps:

1. Incubation of the modified ligand (ProA-CAT) with the target IgG to initiate specific binding and formation of the [ProA-CAT:IgG] soluble complex (Figure 2A).

2. Precipitation of the [ProA-CAT:IgG] complex upon addition of Fe^{3+} ions which generate insoluble macro-complexes composed of [ProA-CAT:IgG:Fe^{3+}], whereas impurities are left in the supernatant and are discarded by centrifugation (Figure 2B).

3. Elution of the IgG from the [ProA-CAT:IgG:Fe^{3+}] insoluble macro-complex (i.e. pellet) under conditions which essentially do not dissociate the [ProA-CAT:Fe^{3+}] macro-complex, thus leading to a simple and fast recovery of the target IgG (Figure 2C).

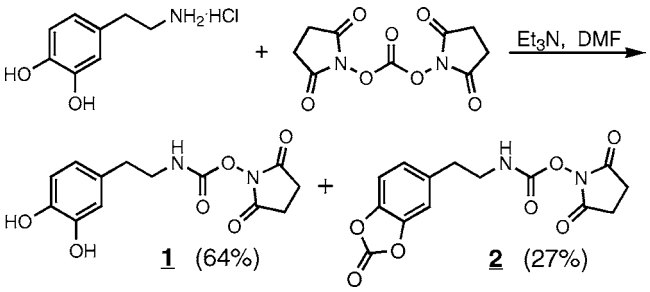

Figure 1. Synthesis of the catechol-NHS derivative **1** used to modify Protein A.

In a typical experiment, 0.46 mg/mL of ProA-CAT was added to *E. coli* cell lysate (first dialyzed to remove possible iron chelators) containing 0.5 mg/mL rabbit IgG, 10 mM NaPi, 400 mM NaCl at pH 7. After 3−5 min of incubation at 4 °C, 3 mM Fe^{3+} ions were added to initiate precipitation of the [ProA-CAT:IgG] soluble complex (Figure 2B). The short incubation time (3−5 min) reflects the advantage of binding in homogeneous solutions rather than heterogeneous solutions in affinity chromatography. To suppress nonspecific interactions between the generated macro-complexes and impurities possessing weak chelating amino acid residues (e.g., His, Cys), 200 mM imidazole was added as well. After a short spin at 14 000 rpm, the supernatant was analyzed and found to contain primarily impurities whereas ProA-CAT and the IgG were absent (Figure 3A, lane 7). The pellet (containing the complexed IgG) was then washed once with 100 μL of fresh buffer containing 20 mM NaPi pH 7, to remove traces of impurities.

Rabbit IgG was eluted from the washed pellet by resuspending it for 3−5 min at 4 °C in 0.4 M Gly and 0.3 M His at pH 3. After a short spin (20 s) at 14 000 rpm, the supernatant was removed, neutralized, and found to contain the target IgG. The average recovery yield was 80% with purity greater than 95% by densitometry (Figure 3A, lane 6). Similar results (yield: 71%; purity >95%) were obtained with bovine IgG, thus demonstrating the applicability of the approach to targets possessing lower affinity toward Protein A (data not shown).

* Corresponding author. E-mail: guy@affisink.com, Tel: 972-8-9302575, Fax: 972-8-9302565.

† Affisink Biotechnology Ltd.

§ Bar-Ilan University.

[1] Abbreviations: AC, affinity chromatography; AS, affinity sinking; Cys, cysteine; desferal, deferoxamine mesylate; EDTA, ethylenediamine tetraacetic acid; Gly, glycine; His, histidine; HPLC, high-pressure liquid chromatography; IgG, immunoglobulin G; ProA-CAT, the modified Protein A catechol derivative.

10.1021/bc050361+ CCC: $33.50 © 2006 American Chemical Society
Published on Web 02/21/2006

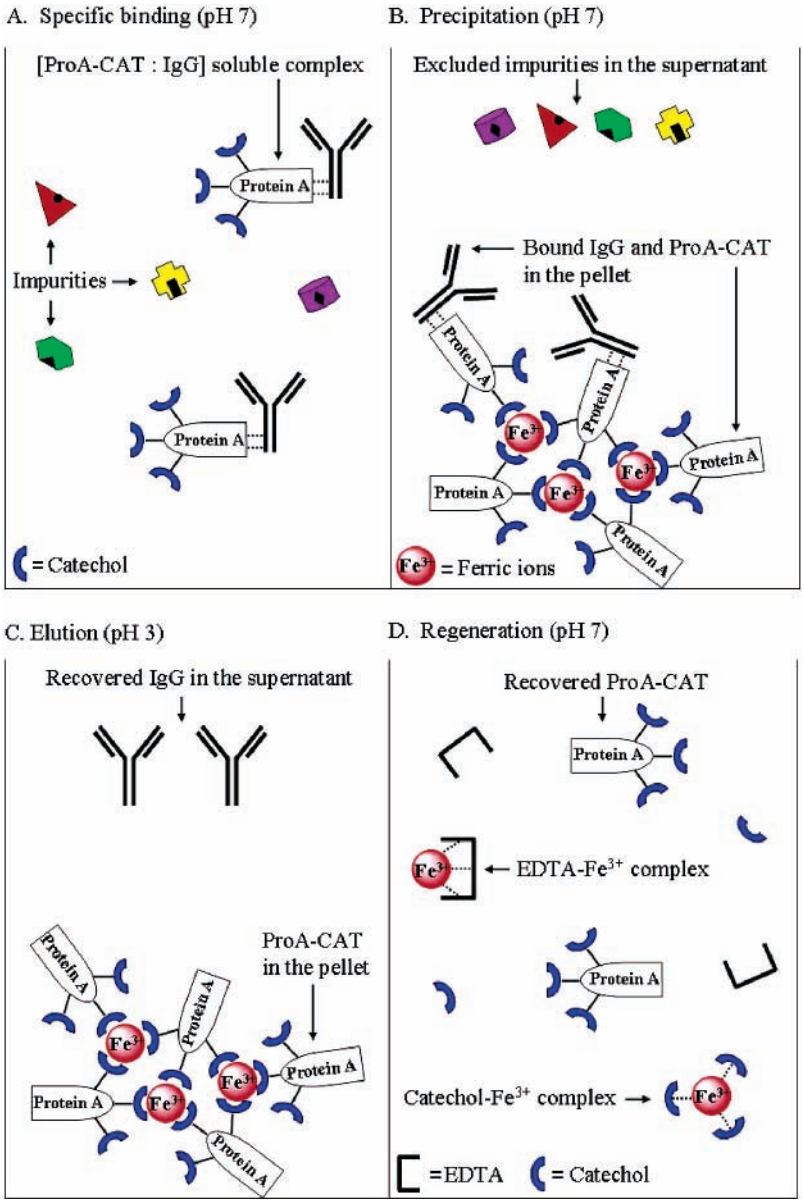

Figure 2. Illustration of antibody purification utilizing a modified Protein A (ProA-CAT) and Fe^{3+} ions. A. Specific binding of ProA-CAT to the target IgG leads to the formation of the [ProA-CAT:target IgG] soluble complex. B. Precipitation of the latter upon addition of Fe^{3+} ions, which generate insoluble macro-complexes containing the target IgG. Impurities, left in the supernatant are discarded by centrifugation. C. Target IgG is eluted under acidic conditions without dissociating the [ProA-CAT:Fe^{3+}] macro-complex, kept insoluble in the pellet. D. Regeneration of ProA-CAT in the presence of strong metal chelators which compete for the complexed Fe^{3+} ions thereby dissociating the macro-complex (i.e., pellet). The complexed Fe^{3+} ions and free chelators are excluded by dialysis while the free ProA-CAT can be reused.

Catechol was chosen as the preferred chelator since it (a) exhibits high affinity toward diverse transition metals (*5*, *6*), thus enabling utilization of a variety of transition metals, (b) requires three independent catechol moieties to chelate a single Fe^{3+} ion, thereby increasing the possibility of interconnecting adjacent [ProA-CAT:IgG] soluble complexes, and (c) was expected to retain its chelating ability even at acidic conditions (pH 3) due to the absence of basic atoms (e.g. nitrogen) required for complex formation. A nitrogen atom (if existed) would be protonated at low pH and presumably not be available for chelating Fe^{3+} ions.

ProA-CAT was regenerated without any chromatographic process at neutral pH in the presence of strong metal chelators such as EDTA and catechol. It was assumed that these chelators will compete with the ProA-CAT on the complexed Fe^{3+} ions, thereby leading to dissolution of the [ProA-CAT:Fe^{3+}] macro-complex (Figure 2D). Indeed, a short incubation (5 min) at 4 °C in the presence of 50 mM NaPi pH 7, 100 mM EDTA, 50 mM catechol, and 10% ethylene glycol led to quantitative dissolution of the pellet and regeneration of the ProA-CAT in 75−85% yield (data not shown). The recovery yield may increase in the presence of low concentration of a detergent such as SDS. Free and complexed chelators together with all other reagents could then be dialyzed, enabling the reuse of ProA-CAT.

Several independent results imply that Fe^{3+} ions function as the interconnecting entity: (a) Precipitation of the [ProA-CAT: IgG] complex was abolished in the presence of strong chelators (e.g., EDTA, catechol) as well as in the presence of a specific Fe^{3+} chelator: desferal (*7*, *8*). (b) Other transition metals (e.g., Cu^{2+}, Zn^{2+}, Mg^{2+}, Ni^{2+}) possessing lower affinity toward catechol (*5*, *6*) did not lead to substantial precipitation under identical precipitating conditions. (c) Regeneration of ProA-CAT at physiological pH was accomplished only in the presence of strong metal chelators.

Generally, greater volumes of buffer are required to remove

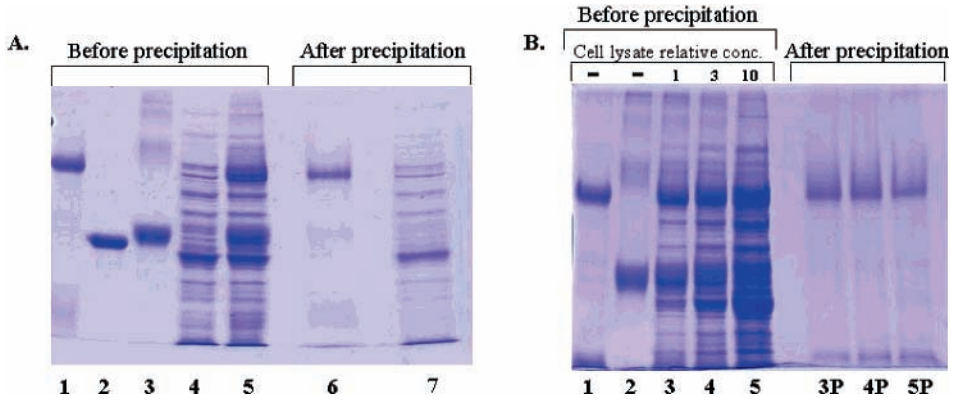

Figure 3. A. Purification of rabbit IgG from *E. coli* cell lysate utilizing ProA-CAT and Fe^{3+} ions. Lane 1 rabbit IgG; lane 2 native protein A; lane 3 ProA-CAT; lane 4 *E. coli* cell lysate; lane 5 rabbit IgG, ProA-CAT and *E. coli* cell lysate; lane 6 recovered rabbit IgG after elution at pH 3; lane 7 content of supernatant after addition of Fe^{3+} ions to the mixture shown in lane 5. B. The effect of increased background contamination on the purity of the recovered IgG. Lane 1 rabbit IgG; lane 2 ProA-CAT; lanes 3−5 constant concentration of rabbit IgG and ProA-CAT in the presence of increased *E. coli* cell lysate concentrations; lanes 3P−5P recovered IgG from pellets generated in lanes 3−5, respectively.

impurities that adsorb nonspecifically to polymeric matrixes in chromatographic columns as the contamination increases. Since no polymeric matrixes exist in AS, we postulated that an increase in the background contamination should not affect the purity of the recovered IgG. To demonstrate such a phenomenon, constant concentration of rabbit IgG and ProA-CAT were added into increasing concentrations of *E. coli* cell lysate (Figure 3B, lanes 3−5) and all generated pellets were washed only once with a minute volume (100 μL) of buffer regardless their contamination background. Though the recovery yield of the IgG decreased with increased contamination background (from ∼80% to ∼70−75%), the purity (>95%) was similar (Figure 3B, lanes 3P−5P), thus supporting our assumption and emphasizing the advantage of a purification approach lacking a polymeric component.

The following are points of emphasis: (a) Ligands other than Protein A may be utilized similarly (e.g. Protein G and L, lectins). (b) The simple (no HPLC) and fast purification process would be advantageous to targets that tend to aggregate or denature rapidly. (c) The purification process can be easily up scaled by the addition of higher concentrations of the modified ligand (being a reagent), whereas affinity columns are limited by the concentration of the immobilized ligand. Moreover, efficient capture of low abundance targets is expected due to the possibility of increasing the modified ligand concentration without significantly diluting the sample, thereby increasing the rate of complex formation (i.e. rate = k[free ligand][target]). (d) Targets are not diluted within the process (unlike column chromatography) and are eluted into small volumes of elution buffer, resulting in concentrated preparations which may be used for other applications such as crystallization. (e) The core macrocomplex [ProA-CAT:IgG:Fe^{3+}] can be further utilized for isolation of targets other than antibodies. For example, positive (or negative) cell selection can be performed by incubating a cell suspension with a mAb targeted at a specific epitope on the target cell, followed by the addition of ProA-CAT and Fe^{3+} ions. Immunoprecipitation and virus depletion can be performed accordingly.

In conclusion, the metal:chelator platform, together with the previously described desthiobiotin:avidin platform (*1*), represents two distinct practical alternatives with characteristic advantages to known purification methodologies utilizing immobilized ligands.

Supporting Information Available: Synthetic procedure and spectroscopic characterization of compounds **1** and **2**. This material is available free of charge via the Internet at http://pubs.acs.org/BC.

LITERATURE CITED

(1) Patchornik, G., and Albeck, A. (2005) Free nonimmobilized ligands as a tool for purification of proteins. *Bioconjugate Chem. 16*, 1310−1315.

(2) Nilsson, J., Ståhl, S., Lundeberg, J., Uhlén, M., and Nygren, P. (1997) Affinity Fusion Strategies for Detection, Purification and Immobilization of Recombinant Proteins. *Protein Expr. Purif. 11*, 1−16.

(3) Bayer, E. D., Wilchek, M., and Skutelsky, E. (1976) Affinity cytochemistry: the localization of lectin and antibody receptors on erythrocytes via the avidin−biotin complex. *FEBS Lett. 68*, 240−244.

(4) Morpurgo, M., Bayer, E. A., and Wilchek, M. (1999) N-hydroxysuccinimide carbonates and carbamates are useful reactive reagents for coupling ligands to lysines on proteins. *J. Biochem. Biophys. Methods 38*, 17−28.

(5) Martell, A. E., and Smith, R. M. (1974) *Critical Stability Constants*, Volume 3, pp 303−304, Plenum Press, New York.

(6) Binding affinities, expressed as logK values at 25 °C and ionic strength 1.0, of catechol with Cu^{2+}, Ni^{2+}, Co^{2+}, Fe^{2+}, Mn^{2+}, Fe^{3+} are 13.62, 8.77, 8.32, 7.95, 7.47, 43.8, respectively.

(7) Martell, A. E., and Smith, R. M. (1974) *Critical Stability Constants*, Volume 3, pp 200−202, Plenum Press, New York.

(8) Binding affinities, expressed as log K values at 25 °C and ionic strength 0.1, of desferal with Cu^{2+}, Ni^{2+}, Co^{2+}, Fe^{2+}, Zn^{2+}, Fe^{3+} are 14.12, 10.90, 10.31, 7.20, 10.07, 30.60, respectively.

BC050361+

Supporting Information

Synthesis of catechol-NHS

[2-(3,4-Dihydroxy-phenyl)-ethyl]-carbamic acid 2,5-dioxo-pyrrolidin-1-yl ester (catechol-NHS; **1**) was prepared according to the procedure of Wilchek and coworkers (*1*). A solution of dopamine hydrochloride (190 mg, 1 mmol) in DMF (2 mL) was added dropwise over 30 min to a solution of disuccinimidyl carbonate (512 mg, 2 mmol) in DMF (15 mL), followed by slow addition of triethylamine (277 μL, 2 mmol) while stirring. After 60 min, the solvent was partially evaporated (to 5 mL), 1N HCl (30 mL) was added, and the solution was extracted with EtOAc (30 mL). Evaporation of the organic phase to dryness and crystallization from EtOAc afforded a crystalline carbonated side product, [2-(2-Oxo-benzo[1,3]dioxol-5-yl)-ethyl]-carbamic acid 2,5-dioxo-pyrrolidin-1-yl ester (**2**) (27% yield) and the clean product **1** (64% yield) in the solution.

1: ^{1}H NMR (DMSO-d_6) δ 2.59 (t, J = 6.2 Hz, 2H, $PhCH_2$), 2.76 (s, 4H, CH_2CH_2), 3.19 (Q, J = 6.2 Hz, 2H, CH_2N), 6.45 (d, J = 7.8 Hz, 1H, Ph), 6.59 (s, 1H, Ph), 6.64 (d, J = 7.8 Hz, 1H, Ph), 8.33 (bt, 1H, NH). ^{13}C NMR (DMSO-d_6) δ 25.5 (CH_2CH_2), 34.5 (CH_2Ph), 42.8 (CH_2N), 115.5, 115.9, 119.2, 129.3, 143.6, 145.1 (Ph), 151.7 (NCO_2), 171.2 (CON). MS *m/z* 333 (MK^+, 100), 317 (MNa^+, 59), 295 (MH^+, 6), 238 (92). TLC (E. Merck 0.2 mm pre-coated silica 60 plates) Rf (EtOAc) 0.24.

2: ^{1}H NMR (DMSO-d_6) δ 2.76 (s, 4H, CH_2CH_2), 2.85 (t, J = 7.2 Hz, 2H, $PhCH_2$), 3.32 (td, J = 7.2, 5.7 Hz, 2H, CH_2N), 7.15 (dd, J = 8.2, 1.8 Hz, 1H, Ph), 7.35 (d, J = 1.8 Hz, 1H. Ph), 7.36 (d, J = 8.2, 1H, Ph), 8.35 (t, J = 5.7, 1H, NH). ^{13}C NMR (DMSO-d_6) δ 25.3 (CH_2CH_2), 34.5 (CH_2Ph), 42.5 (CH_2N), 110.0, 110.7, 125.0, 136.0, 141.5, 143.0

(Ph), 151.0 (CO_3), 151.7 (NCO_2), 170.5 (CON). MS *m/z* 359 (MK^+, 37), 321 (MH^+, 100), 306 (64) 254 (59), 253 (97), 243 (64), 238 (76), 234 (62).

(1) Morpurgo, M., Bayer, E.A., and Wilchek, M. (1999) N-hydroxysuccinimide carbonates and carbamates are useful reactive reagents for coupling ligands to lysines on proteins. *J. Biochem. Biophys. Methods 38,* 17-28.

Synthesis and in Vitro Evaluation of Biotinylated RG108: A High Affinity Compound for Studying Binding Interactions with Human DNA Methyltransferases

Esther Schirrmacher,[†] Carmen Beck,[‡] Bodo Brueckner,[†] Frank Schmitges,[†] Pawel Siedlecki,[§] Peter Bartenstein,[#] Frank Lyko,[†] and Ralf Schirrmacher[#,*]

Division of Epigenetics, Deutsches Krebsforschungszentrum, Im Neuenheimer Feld 580, 69120 Heidelberg, Germany, Division of Nuclear Medicine, University of Heidelberg, Im Neuenheimer Feld 400, 69120 Heidelberg, Institute of Biochemistry and Biophysics, Polish Academy of Science, Pawinskiego 5a, 02-106 Warsaw, Poland, and Department of Nuclear Medicine, Johannes Gutenberg University Mainz, Langenbeckstrasse 1, 55131 Mainz, Germany. Received October 11, 2005; Revised Manuscript Received January 3, 2006

Small-molecule inhibitors of DNA methyltransferases such as RG108 represent promising candidates for cancer drug development. We report the synthesis and in vitro analysis of a biotinylated RG108 conjugate, 2-(1,3-dioxo-1,3-dihydro-isoindol-2-yl)-3-(5-{3-[5-(2-oxo-hexahydro-thieno[3,4-*d*]imidazol-4-yl)pentanoylamino]-propoxy}-1*H*-indol-3-yl)propionic acid (bio-RG108), for the evaluation of interactions with DNA methyltransferase enzymes. The structural design of the chemically modified inhibitor was aided by molecular modeling, which suggested the possibility for extensive chemical modifications at the 5-position of the tryptophan moiety in RG108. The inhibitory activity of the corresponding derivative was confirmed in a cell-free biochemical assay, where bio-RG108 showed an undiminished inhibition of DNA methyltransferase activity (IC_{50} = 40 nM). Bio-RG108 therefore represents a suitable bioconjugate for the elucidation of inhibitory mechanisms and for the affinity purification of RG108-associated proteins.

INTRODUCTION

The elucidation of protein interactions is a fundamental aspect in our understanding of biological processes. One approach to discover the identity of interacting proteins is the use of chemical cross-linking, a method capable of irreversibly capturing proteins by covalently fixing a biotin affinity handle to the compound interacting with the protein. The binding of biotin to (strept)-avidin has therefore found widespread application in life sciences, which is primarily due to its extraordinarily strong noncovalent interaction (*1*−*5*) with a binding constant of 1.3×10^{-15} M. Bioanalytical applications derived from biotin/(strept)avidin interaction have been used in enzymatic reactions, radiolabeling techniques, and fluorescence assays (*6*−*8*).

DNA methyltransferases catalyze the covalent addition of methyl groups to the carbon-5 position of cytosine residues in the context of genomic DNA (*9*). The resulting DNA methylation patterns play an important role in the regulation of gene expression and local hypermethylation has been frequently found to be associated with gene silencing (*10*). One of the most prominent examples for this phenomenon is the hypermethylation of tumor suppressor genes during tumorigenesis (*11*), which has established DNA methyltransferases as promising targets for oncology drug development (*12*).

The first DNA methyltransferase inhibitor 5-azacytidine has been synthesized 40 years ago (*13*), has shown clinical effectiveness in phase III trials (*14*), and has recently gained Food and Drug Administration approval as an anticancer drug. 5-Azacytidine and related compounds inhibit DNA methyltransferases by covalent enzyme trapping, which has been associated with their significant toxicity (*15*). This characteristic has complicated the clinical application of azanucleoside inhibitors and invigorated the search for novel compounds. More recent analyses have also suggested that noncovalent "active site blockers" of DNA methyltransferases might be characterized by higher specificity and less toxicity (*16*). This is exemplified by the molecular characteristics of RG108, the first rationally designed small-molecule inhibitor of DNA methyltransferases (*17*). More specifically, RG108 has been shown to be well-tolerated by human cancer cell lines and to inhibit DNA methyltransferases in a noncovalent manner (*17*). However, the molecular interactions between RG108 and the various DNA methyltransferases (and their associated factors) could not be demonstrated so far. A biotin-conjugated derivative of RG108 displaying the same binding characteristics as the original nonconjugated molecule could provide an opportunity to study the interactions between RG108 and its cellular targets in great detail. In addition, such a bioconjugate could also represent a valuable tool for the biochemical purification of DNA methyltransferase-associated protein factors.

EXPERIMENTAL SECTION

Chemicals and Reagents. Biotin, HBTU, and biotin nitrophenyl ester were purchased from Novabiochem (Merck). 5-Hydroxy-DL-tryptophan, 4-nitrobenzylbromide, triphenylphosphine, *tert*-butyl-3-hydroxypropyl carbamate, diethyl azodicarboxylate, 3-hydroxypropylcarbamic acid allyl ester, tetrakis(triphenylphosphine)palladium(0), 3-aminopropanol, 1,3-dimethoxybenzene, 5,5-dimethyl-1,3-cyclohexadione, and tetraeth-

* To whom correspondence should be addressed. Tel: +496131176736; fax: +496131172386; E-mail: schirrmacher@nuklear.klinik.uni-mainz.de.

[†] Deutsches Krebsforschungszentrum.

[‡] University of Heidelberg.

[§] Polish Academy of Science.

[#] Johannes Gutenberg University Mainz.

10.1021/bc050300b CCC: $33.50 © 2006 American Chemical Society
Published on Web 02/11/2006

ylammonium fluoride from Aldrich were used as received. Cesium carbonate was purchased from Alfa Aesar. *N*-Ethyldiisopropylamine, acetonitrile, DMF, methylene chloride, methanol, ethanol, ethyl acetate, cyclohexane, *n*-hexane, toluene, and chloroform were obtained from Merck and were used without further purification.

Instruments. ^{1}H NMR and ^{13}C NMR were recorded on a 400-MHz FT-NMR spectrometer (DRX 400, Bruker Analytik GmbH). FD-mass spectra and ESI mass spectra were obtained using a MAT90-spectrometer (Finnigan) and Navigator (ThermoQuest), respectively.

3-(5-Hydroxy-1*H*-indol-3-yl)-2-(1,3-dioxoisoindolin-2-yl)-propanoic Acid (2). 5-Hydroxy-DL-tryptophan (1) (440.4 mg, 2 mmol) and sodium carbonate (1.38 g, 10 mmol) were dissolved in water (15 mL). Phthalic acid mono succinimidyl ester (554 mg, 2 mmol) dissolved in acetonitrile (25 mL) was added, and the reaction mixture was stirred for 4 h until thin-layer chromatography showed the absence of starting material. The mixture was diluted with ethyl acetate (100 mL), and 1 N hydrochloric acid was added until pH reached 2. The organic phase was separated and washed twice with 1 N hydrochloric acid (50 mL) and water, respectively (50 mL). The organic phase was dried over sodium sulfate and evaporated to yield 660 mg (95%) of compound **2**. ^{1}H NMR: 13.10 (s_{br}, 1H); 10.42 (s, 1H); 8.56 (s, 1H); 7.82 (s, 4H); 7.15 (d, 1H, J = 8.85); 6.84 (d, 1H, J = 2.04 Hz); 6.79 (d, 1H, J = 2.04 Hz); 6.52 (dd, 1H, J = 2.04 Hz, J = 8.52 Hz); 5.1 (m, 1H); 3.5 (m, 2H). ^{13}C NMR: 171.25; 167.82; 150.52; 135.12; 131.56; 130.97; 128.17; 124.01; 123.85; 112.05; 111.75; 109.20; 102.04; 52.98; 24.53. FD mass spectroscopy: 350.2 ([M]$^+$, 100%). Elem. Anal. (%) calcd: C (65.14), H (4.03), N (8.06). Found: C (65.38), H (4.17), N (7.98).

4-Nitrobenzyl 3-(5-Hydroxy-1*H*-indol-3-yl)-2-(1,3-dioxoisoindolin-2-yl)propanoate (3). 2 (0.5 g, 1.4 mmol) was dissolved in ethanol (6.9 mL) and water (0.69 mL). Cesium carbonate solution (20%, 0.95 mL) was added, the mixture was stirred for 5 min at room temperature, and the solvents were removed in vacuo. For azeotropic drying, ethanol (3 mL) was added and the solvent again removed in vacuo. The dry residue was dissolved in dimethylformamide (6.9 mL), and 4-nitrobenzyl bromide (400 mg, 1.8 mmol) was added. The reaction mixture was stirred for 6 h. After filtration, the solvent was removed and the residue was purified via column chromatography (ethyl acetate/cyclohexane 50:50) to obtain 415 mg (60%) of **3**. ^{1}H NMR (DMSO-d_6): 10.5 (s, 1H); 8.5 (s, 1H); 8.2 (d, 2H, J = 8.86 Hz); 7.8 (s, 4H); 7.6 (d, 2H, J = 8.86 Hz); 7.1 (d, 1H, J = 8.52 Hz); 6.9 (d, 1H, J = 2.38 Hz); 6.8 (d, 1H, J = 2.38 Hz); 6.5 (dd, 1H, J = 2.04 Hz, J = 8.52 Hz); 5.4 (s, 2H); 5.3 (m, 1H); 3.5 (m, 2H). ^{13}C NMR (DMSO-d_6): 168.98;167.31; 150.63; 147.40; 143.72; 135.21; 131.02; 130.84; 128.74; 127.89; 124.25; 123.76; 112.02; 111.71; 108.76; 108.36; 102.19; 65.83; 52.67; 39.79; 39.58; 24.53; 24.41; 23.88. FD mass spectroscopy: 485.1 ([M]$^+$, 100%). Elem. anal.(%) calcd: C (64.33), H (3.95), N (8.66). Found: C (64.25), H (4.00), N (8.56).

3-[5-(3-*tert*-Butoxycarbonylaminopropoxy)-1*H*-indol-3-yl]-2-(1,3-dioxoisoindolin-2-yl)propionic Acid 4-Nitrobenzyl Ester (5). 3 (300 mg, 0.62 mmol) was dissolved in methylene chloride (10.8 mL), and triphenylphosphine (0.243 g, 0.93 mmol) and *tert*-butyl-3-hydroxypropylcarbamate (0.215 g, 1.2 mmol) were added. A solution of diethyl azodicarboxylate (0.145 mL) in methylene chloride (4 mL) was added dropwise over a period of 1h. The reaction mixture was stirred for 2 h at room temperature. After evaporation of the solvent under reduced pressure and workup with column chromatography (ethyl acetate/*n*-hexane 3.5:4), 258 mg (65%) of **5** was obtained. ^{1}H NMR (DMSO-d_6): 10.5 (s, 1H); 8.2 (d, 2H, J = 8.51 Hz); 7.82 (s, 4H); 7.6 (d, 2H, J = 8.51 Hz); 7.15 (d, 2H, J = 8.85 Hz); 7.05 (d, 1H, J = 2.04 Hz); 6.95 (d, 1H, J = 2.04); 6.87 (m, 1H); 6.63 (dd, 1H, J = 2.04 Hz, J = 8.85 Hz); 5.37 (s, 2H); 5.35 (t, 1H, J = 5.45); 3.8 (m, 2H), 3.48 (m, 2H); 3.15 (m, 2H); 1.8 (m, 2H); 1.4 (s, 9H). ^{13}C NMR (DMSO-d_6): 168.96; 167.25; 155.91; 152.54; 147.39; 143.66; 135.20; 131.46; 131.01; 128.66; 127.51; 124.61; 123.76; 112.26; 111.90; 109.09; 101.18; 65.77; 58.78; 52.70; 37.45; 33.02; 29.72; 28.52; 24.52. FD mass spectroscopy: 642.0 ([M]$^+$, 100%). Elem. anal. (%) calcd: C (63.54), H (5.33), N (8.72). Found: C (63.52), H (5.22), N (8.78).

3-[5-(3-Alloxycarbonylaminopropoxy)-1*H*-indol-3-yl]-2-(1,3-dioxoisoindolin-2-yl)propionic Acid 4-Nitrobenzyl Ester (6). 3 (300 mg, 0.62 mmol) was dissolved in methylene chloride (10.8 mL), and triphenylphosphine (0.243 g, 0.93 mmol) and 3-hydroxypropylcarbamic acid allyl ester (0.191 g, 1.2 mmol) were added. A solution of diethyl azodicarboxylate (0.145 mL) in methylene chloride (4 mL) was added dropwise over a period of 1 h. The reaction mixture was stirred for 2 h at room temperature. After evaporation of the solvent under reduced pressure and workup with column chromatography (ethyl acetate/*n*-hexane 3.5:4), 250 mg (65%) of **6** was obtained. ^{1}H NMR (DMSO-d_6): 10.60 (s, 1H); 8.98 (s, 1H); 8.20 (d, 2H, J = 8.85 Hz); 7.82 (s, 4H); 7.60 (d, 2H, J = 8.85 Hz); 7.13 (d, 2H, J = 8.85 Hz); 7.02 (d, 1H, J = 2.38 Hz); 6.97 (d, 1H, J = 2.38 Hz); 6.63 (dd, 1H, J = 2.04 Hz, J = 8.51 Hz); 5.85−5.96 (m, 1H); 5.38 (s, 2H); 5.35 (t, 1H, J = 5.45 Hz); 5.25−5.30 (m, 1H); 5.15−5.18 (m, 1H); 4.48 (d, 2H, J = 5.45 Hz); 3.76−3.90 (m, 2H); 3.49−3.6 (m, 2H); 3.13−3.18 (m, 2H); 1.80−1.86 (m, 2H). ^{13}C NMR (DMSO-d_6): 168.97; 167.26; 156.82; 156.24; 152.50; 147.39; 143.66; 135.21; 134.11; 131.48; 131.01; 128.66; 127.52; 123.70; 117.14; 112.26; 111.91; 109.11; 101.24; 65.77; 64.45; 60.71; 52.72; 37.79; 29.63; 24.51. FD mass spectroscopy: 626.2 ([M]$^+$, 100%). Elem. anal. (%) calcd: C (63.25), H (4.83), N (8.94). Found: C (63.28), H (4.85), N (8.92).

2-(1,3-Dioxoisoindolin-2-yl)-3-(5-{3-[5-(2-oxohexahydrothieno[3,4-*d*]imidazol-4-yl)pentanoylamino]propoxy}-1*H*-indol-3-yl)propionic Acid 4-Nitrobenzyl Ester (7) (via Boc-deprotection). 5 (1 g, 1.5 mmol) was dissolved in trifluoroacetic acid (40 mL) containing 1,3-dimethoxybenzene (0.55 mL). After stirring for 30 min, the trifluoroacetic acid was removed under reduced pressure. Last traces were coevaporated with 2 mL of toluene. The residue was dissolved in 10 mL of dimethylformamide, and 548 mg (1.5 mmol) biotin nitrophenyl ester was added. After stirring for 10 h, the solvent was removed under vacuum and the residue was purified via column chromatography (chloroform/methanol 9:1) to yield 179 mg (15%) of **7**.

2-(1,3-Dioxoisoindolin-2-yl)-3-(5-{3-[5-(2-oxohexahydrothieno[3,4-*d*]imidazol-4-yl)pentanoylamino]propoxy}-1*H*-indol-3-yl)propionic Acid 4-Nitrobenzyl Ester (7) (via Alloc-deprotection). 6 (430 mg, 0.68 mmol) was dissolved in tetrahydrofuran (5.3 mL) under argon atmosphere. Tetrakis-(triphenylphosphine)palladium(0) (77 mg, 0.066 mmol) and 5,5-dimethyl-1,3-cyclohexadione (0.71 g, 5 mmol) were added, and the reaction mixture was stirred for 30 min at room temperature. The solvent was removed under reduced pressure, and the residue was extracted with diethyl ether (40 mL). The slurry was filtrated and extracted four times with 20 mL of 0.5 N hydrochloric acid. The aqueous phase was adjusted to pH 10 with sodium carbonate and extracted with ethyl acetate (4 × 50 mL). After removal of the solvent, the residue was dissolved in dimethylformamide (5 mL) and biotin nitrophenyl ester (274 mg, 0.75 mmol) was added. After stirring for 10 h, the solvent was removed under vacuum and the residue was purified via column chromatography (chloroform/methanol 9:1) to yield 158 mg (30%) of compound **7**. ^{1}H NMR (DMSO-d_6): 10.60 (s, 1H); 8.21 (d, 2H, J = 8.85 Hz); 7.83 (s, 4H); 7.60 (d, 2H, J = 8.85

Hz); 7.13 (d, 1H; J = 8.85 Hz); 7.01 (d, 1H, J = 2.38 Hz); 6.95 (d, 1H, J = 2.38 Hz); 6.63 (dd, 1H, J = 2.38 Hz, J = 8.51 Hz); 6.61 (s, 1H); 6.34 (s, 1H); 5.38 (s, 2H); 5.35 (t, 1H, J = 5.10 Hz); 4.30−4.25 (m, 1H); 4.11−4.08 (m, 1H); 3.92−3.76 (m, 2H); 3.61−3.48 (m, 2H); 3.22−3.17 (m, 2H); 3.09−3.04 (m, 1H); 2.81−2.76 (m, 1H); 2.56 (d, 1H, J = 12.60 Hz); 2.10−2.06 (m, 2H); 1.84−1.78 (m, 2H); 1.58−1.41 (m, 4H); 1.36−1.23 (m, 2H). ^{13}C NMR (DMSO-d_6): 172.27; 168.97; 167.26; 162.94; 155.65; 152.49; 147.39; 145.25; 143.66; 135.23; 131.47; 131.01; 128.66; 127.54; 125.53; 123.78; 123.46; 112.26; 111.86; 109.08; 101.30; 65.96; 65.77; 61.28; 59.43; 55.67; 52.69; 35.93; 35.49; 33.45; 29.44; 28.48; 28.29; 25.58; 24.48. FD mass spectroscopy: 768.5 ([M]+, 100%). Elem. anal. (%) calcd: C (60.93), H (5.24), N (10.93). Found: C (61.10), H (5.11), N (11.61). The purity of compound **7** was additionally confirmed by HPLC: column: LiChrosorb RP select B 250 × 4 mm, solvent: 0 min: 70/30 water/acetonitrile; 30 min: 100% acetonitrile (flow: 0.7 mL/min, t_R (**7**): 18.1 min)

2-(1,3-Dioxoisoindolin-2-yl)-3-(5-{3-[5-(2-oxohexahydrothieno[3,4-*d*]imidazol-4-yl)pentanoylamino]propoxy}-1*H*-indol-3-yl)propionic Acid (8) (bio-RG108). **7** (65 mg, 0.084 mmol) was dissolved in dimethylformamide (2.3 mL). Tetraethylammonium fluoride (31.5 mg, 0.21 mmol) was added, and the reaction mixture was stirred for 30 min. The solvent was removed under vacuum, and the residue was taken up in ethyl acetate (3 mL) and washed with water (twice with 1.5 mL). The solvent was removed under reduced pressure, and 10 mL of a mixture of acetonitrile/diethyl ether (50:50) was added. The slurry was ultrasonicated for 5 min, and the resulting precipitate was filtered and washed with diethyl ether. The precipitate was dissolved in ethanol (2 mL), and 5 mL water was added. The resulting mixture was lyophilized overnight to yield compound 37 mg (70%) of compound **8**. ^{1}H NMR (DMSO-d_6): 10.56 (s, 1H); 7.86 (t, 1H, J = 6.80 Hz); 7.82 (s, 4H); 7.12 (d, 1H, J = 8.85 Hz); 6.98 (d, 1H, J = 2.38 Hz); 6.92 (d, 1H, J = 2.38 Hz); 6.65 (dd, 1H, J = 8.85 Hz, J = 2.04 Hz); 6.41 (s, 1H); 6.34 (s, 1H); 5.08 (t, 1H, J = 8.50 Hz); 4.26−4.33 (m, 1H); 3.74−3.92 (m, 2H); 3.5 (d, 2H, J = 6.8 Hz); 3.14−3.23 (m, 2H); 2.83−2.95 (m, 1H); 2.75−2.82 (m, 1H); 2.54 (d, 1H, J = 12.60 Hz); 2.04−2.13 (m, 2H); 1.17−1.27 (m, 2H); 1.26−1.66 (m, 6H). ^{13}C NMR: 172.27; 170.62; 167.45; 162.95; 161.46; 152.47; 135.10; 131.46; 131.16; 130.97; 127.53; 124.01; 123.58; 112.26; 109.75; 101.10; 70.20; 65.93; 61.28; 59.44; 56.05; 55.07; 52.89; 35,91; 35.49; 29.43; 28.30; 25.58; 24.38. ESI mass spectroscopy: 656.2 ([M + Na]$^+$, 100%). The purity of compound 8 was confirmed using two independent HPLC methods: First method: column: LiChrosorb RP select B 250 × 4 mm; solvent: 0 min: 100% water; 30 min: 100% acetonitrile; flow: 0.7 mL/min; t_R (8): 20.1 min, Second method: column: LiChrosorb RP select B 250 × 4 mm; solvent: 50:50 methanol/water; flow: 0.5 mL/min; t_R (8): 7.5 min

5-(Hexahydro-2-oxo-1*H*-thieno[3,4-*d*]imidazol-4-yl)-*N*-(3-hydroxypropyl)pentamide (9). Biotin (1 g, 4.09 mmol) and HBTU (1.36 g, 3.6 mmol) were suspended in DMF (50 mL), and DIPEA (0.70 g, 5.4 mmol) was added with stirring. The clear solution was transferred into a dropping funnel and added dropwise to a solution of 3-aminopropanol (0.52 g, 7 mmol) in DMF (75 mL). The solvent was removed in vacuo, and the crude product was dissolved in a minimum amount of methanol (4−7 mL). Diethyl ether (20 mL) was added, and the solution was kept at −20 °C for 12 h. The white crystalline precipitate was filtered by suction and washed with cold diethyl ether to yield 1.1 g (89%) of the product. ^{1}H NMR (DMSO-d_6): 7.73 (t, 1H, J = 5.45 Hz); 6.43 (s, 1H); 6.36 (s, 1H); 4.40 (s_{br}, 1H); 4.31 (dd, 1H, J = 5.10 Hz, J = 7.49 Hz); 4.12 (dt, 1H, J = 1.70 Hz, J = 6.13 Hz); 3.38 (t, 2H, J = 6.13 Hz); 3.03−3.13 (m, 3H); 2.80 (dd, 1H, J = 5.10 Hz, J = 12.60 Hz); 2.57 (d, 1H, J = 12.60 Hz); 2.04 (t, 1H, J = 7.49 Hz); 1.40−1.57 (m, 6H); 1.20−1.36 (m, 2H). ^{13}C NMR (DMSO-d_6): 172.28; 162.99; 61.30; 59.46; 58.67; 55.66; 35.86; 35.45; 32.74; 28.46; 28.27; 25.57. FD mass spectroscopy: 302.2 ([M + H]$^+$, 100%). Elem. anal. (%) calcd: C (51.80); H (7.69); N (13.94). Found: C (52.11); H (7.56); N (14.61)

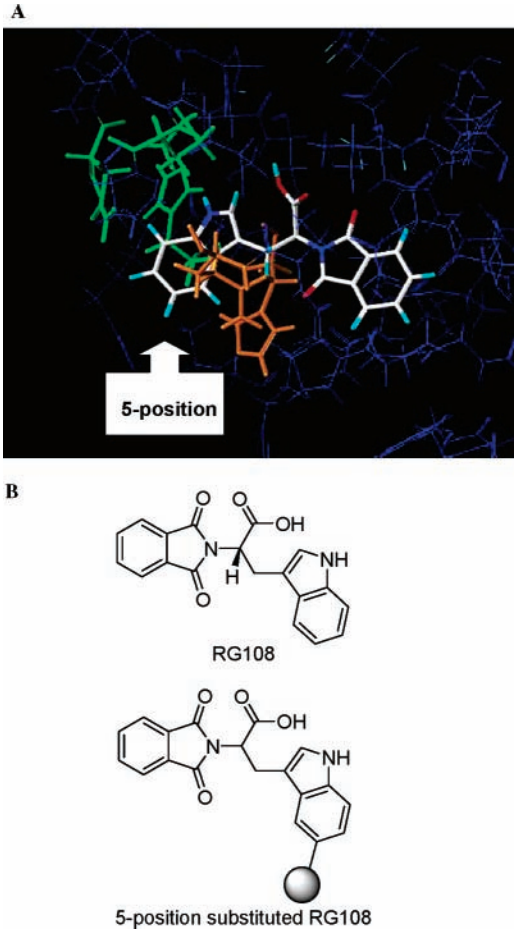

Figure 1. Molecular modeling and structure of 5-substituted RG108. A, RG108 docked into the active site of human DNMT1. Green and orange amino acids form the entry site to the catalytic pocket. The 5-position of the tryptophan moiety (arrow) appeared to protrude from the catalytic pocket and was therefore considered to be particularly amenable to functionally neutral chemical modification. B, chemical structure of original RG108 and 5-substituted RG108.

In Vitro Methylation Assay. A 798 bp promoter fragment (−423/+375 relative to the initiation codon) from the human p16^{Ink4a} gene was used as unmethylated substrate DNA. Four hundred nanograms of substrate DNA, 2 units of M.SssI methylase (New England Biolabs, Frankfurt, Germany), and the cofactor *S*-adenosyl-L-methionine (final concentration: 80 μM; New England Biolabs) were added to a final reaction volume of 50 μL. Test compounds were added to final concentrations of 10, 30, 100, 300, and 500 μM, and the reactions were incubated for 2 h at 37 °C. After incubation the reactions were purified using the QIAquick PCR Purification kit (Qiagen, Hilden, Germany). Three hundred nanograms of purified DNA was digested for 3 h at 60 °C with 30 units of *Bst*UI (New England Biolabs) and analyzed on 3% Tris-borate EDTA agarose gels.

RESULTS AND DISCUSSION

Previous results have strongly suggested that RG108 binds deep in the active site of DNA methyltransferases (*16*), which rendered the identification of chemically modifyable positions

Scheme 1

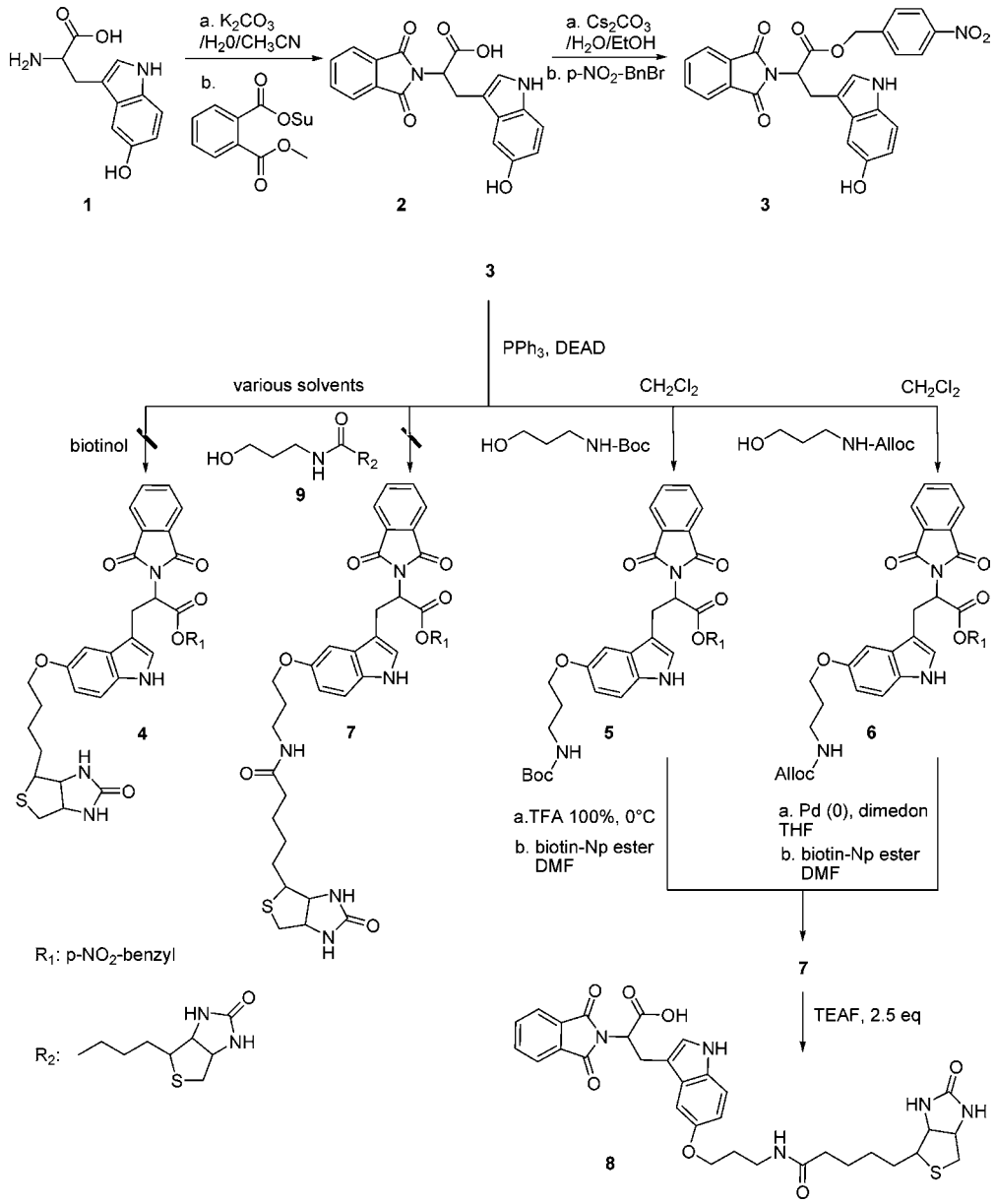

critically important. We therefore used molecular modeling and a previously established three-dimensional model of the human DNMT1 catalytic domain (*18*) for an analysis of the molecular interactions between RG108 and the DNA methyltransferase active site. Docking of RG108 revealed that the 5-position of the tryptophan moiety protruded from the active site pocket, suggesting that modifications at this position were unlikely to interfere with the various interactions between enzyme and inhibitor (Figure 1). This analysis also indicated that more extensive modifications could be accommodated by the addition of an aminoalkyl spacer (data not shown). Last, the synthesis of 5-substituted RG108 derivatives also appeared favorable in light of the fact that 5-hydroxytryptophan could be used as a convenient starting point for chemical syntheses which are amenable to various chemical alterations, such as Mitsunobu coupling of alcohols.

Biotinylated RG108 (bio-RG108) was synthesized starting from racemic 5-hydroxy-DL-tryptophan **1** (Scheme 1) which was phthaloylated using methyl 2-[(succinimido)oxycarbonyl]benzoate (*19*) to yield 5-hydroxy-RG108 (**2**) in almost quantitative yields. Racemic mixtures of RG108 have previously been shown to be effective in various assays (*16*), and therefore racemic compound **1** was used. The phthaloylation of **1** was slightly modified because the original procedure for the synthesis of RG108 (*17*) gave yields of 50−60% only. Potassium carbonate was used instead of sodium carbonate for the deprotonation of **1** and 1 N HCl instead of 2 N HCl for the final workup yielding **2** in high yields and high chemical purity, making further purification unnecessary. For further derivatization of **2** at the 5-position of tryptophan, it is essential to protect the carboxy moiety by esterification. Lescrinier et al. reported the successful synthesis of N-Treoc-protected 5-hydroxytryptophan *p*-nitrobenzyl ester for incorporation of 5-hydroxytryptophan in oligopeptides via conversion of the carboxylic acid into its cesium salt by titration to pH 7 with Cs_2CO_3 (*20*). This method was applied to the phthaloylated amino acid **2**, and the resulting Cs-salt was subsequently reacted with *p*-NO_2-benzyl bromide in DMF giving compound **3** in 65% yield after column chromatography.

Our first attempt to conjugate biotin to **3** was via Mitsunobu coupling of biotinol, which was obtained by reduction of biotin-SU ester with $NaBH_4$ (*21*). Unfortunately, the coupling reaction was unsuccessful due to the limited solubility of biotinol in solvents commonly applied in Mitsunobu reactions (CH_2Cl_2, $CHCl_3$, THF, benzene, ethyl acetate) and even in DMF or

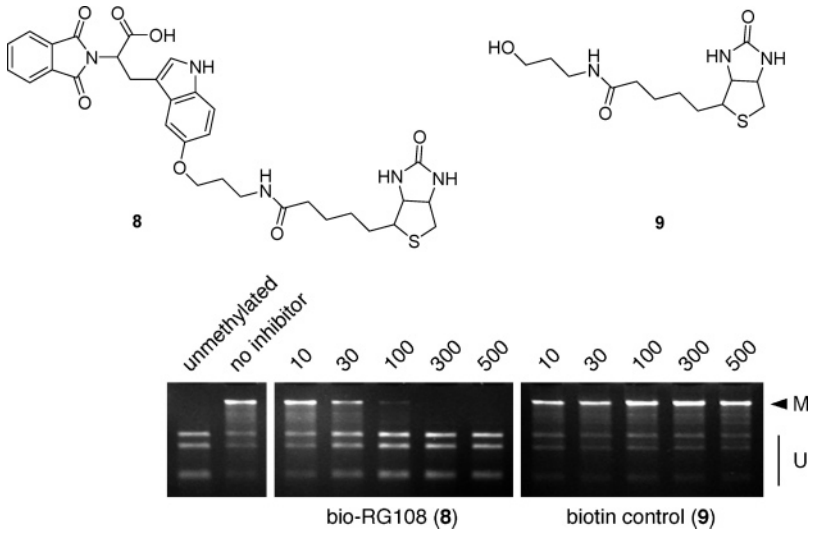

Figure 2. Inhibition of purified recombinant DNA methyltransferase activity by bio-RG108. Incubation of an unmethylated DNA fragment with purified SssI methylase results in the generation of a methylated fragment (M) that is protected against restriction cleavage by BstUI. Inhibition of DNMT activity generates unmethylated (U) fragments that are products of BstUI restriction. Numbers indicate inhibitor concentrations (in μM). An biotin derivative lacking the RG108 moiety (**9**) was analyzed in control experiments and did not show any detectable inhibitory activity.

HMPA. One further attempt with N-biotinylated 3-aminopropan-1-ol **9** was also found to be unsuitable, but N-Boc- and N-Alloc-protected 3-aminopropan-1-ol in CH_2Cl_2 could be coupled in moderate yields of 55−60% to yield compounds **5** and **6**. The deprotection of **5** with TFA at 0 °C and the subsequent workup to isolate the primary amine was unsuccessful due to decomposition on silica gel. We therefore decided to use the crude amine for direct reaction with commercially available biotin-Np ester in DMF and were able to isolate *p*-NO_2-benzyl ester protected **7** in 15% yield. Because of these unsatisfying results, we synthesized the Alloc-protected compound **6** which was deprotected with Pd(0) and dimedon in THF. The instability of the amine upon contact with silica gel was confirmed, and so the crude amine was further reacted with biotin-Np ester to yield *p*-NO_2-benzyl ester protected **7** in 30% yield. Despite the presence of acidic dimedon, the main product (65%) was an enamine built from excess dimedon and the primary amine. To obtain the final bio-RG108 **8**, the *p*-NO_2-benzyl ester was deprotected with 2.5 equiv of tetraethylammonium fluoride (TEAF) in DMF in 70% yield. The yields dramatically decreased when using more than 2.5 equiv which was proved by HPLC monitoring of the crude reaction mixture using 2−10 equiv of TEAF. Starting from commercially available 5-hydroxytryptophan and biotin nitrophenyl ester, final compound bio-RG108 could be synthesized in an overall chemical yield of 4% (via compound **5**) or 8% (via compound **6**). The purity of all compounds was determined by ^{1}H and ^{13}C NMR, mass spectroscopy, elemental analysis, and/or HPLC.

Due to the major structural alterations, we needed to analyze the inhibitory activity of bio-RG108 **8**. To this end, we used a cell-free in vitro assay with purified recombinant CpG methylase (*17*). The results showed that bio-RG108 was able to efficiently inhibit DNA methylation (Figure 2). After normalization to 1 nM enzyme concentration, the IC_{50} concentration of bio-RG108 was determined to be 40 nM. This is similar to the IC_{50} concentration of unmodified RG108 (115 nM, cf. ref 17) with the improved potency likely due to the better solubility of bio-RG108. Importantly, no inhibitory effect could be observed for a biotin derivative that lacks the RG108 moiety (Figure 2, biotin control), which further confirmed the specificity of bio-RG108.

In conclusion, we prepared a biotinylated derivative of the novel mechanism-independent DNA methyltransferase inhibitor RG108 for the evaluation of binding interactions using a biotin/(strept)avidin binding assay. Despite major derivatization, the novel compound bio-RG108 exhibited a high inhibitory activity with purified recombinant DNA methyltransferase, thus confirming the results from our molecular modeling approach. Bio-RG108 therefore represents a valuable probe for the selective immobilization of human DNA methyltransferases and further investigation of proteins interacting with RG108. Additionally, proving the 5-position of RG108 to be most suitable for chemical alterations provides an opportunity to synthesize various bioconjugates such as carbohydrate and peptide conjugates for specific tumor-targeting. A great variety of suitable linkers, e.g. hydroxyalkylcarboxylic acid esters, N-protected aminoalkyl alcohols, etc., can be conveniently attached to the 5-position of 5-hydroxy-RG108, applying mild Mitsunobu conditions and used for further derivatization.

ACKNOWLEDGMENT

The authors would like to thank B. Mathiasch, N. Haunold, and A. Vierengel for the recording of NMR and mass spectra. This work was supported by a grant from Cancer Research Technologies (to F.L).

LITERATURE CITED

(1) Wilchek, M., and Bayer, E. A. (1990) *Methods of Enzymology*, Vol. 184, Academic Press, San Diego.

(2) Weizmann, Y., Patolsky, F., Katz, E., and Willner, I. (2003) Amplified DNA Sensing and Immunosensing by the Rotation of Functional Sensing and Immunosensing by Rotation of Functional Magnetic Particles. *J. Am. Chem. Soc. 125*, 452−3454.

(3) Rivera, V. R., Merrill, G. A., White, J. A., and Poli, M. A. (2003) An Enzymatic Electrochemiluminescence Assay for the Lethal Factor of Anthrax. *Anal. Biochem. 321*, 125−130.

(4) Richter, J., Adler, M., and Niemeyer, C. M. (2003) Monte Carlo Simulation of the Assembly of bis-Biotinylated DNA and Streptavidin. *ChemPhysChem. 4*, 79−83.

(5) Caswell, K. K., Wilson, J. N., Bunz, U. H. F., and Murphy, C. J. (2003) Preferential End-to-End Assembly of Gold Nanorods by Biotin−Streptavidin connectors. *J. Am. Chem. Soc. 125*, 13914−13915.

(6) Hermanson, G. T. (1996) *Bioconjugate Techniques*, Academic Press, San Diego.

(7) Schetters, H. (1999) Avidin and Streptavidin in Clinical Diagnostics. *Biomol. Eng. 16*, 73−78.

(8) Hadour, N. N., Gondran, C., and Cosnier, S. (2004) A New Biotinylated tris Bipyridyl Iron (II) Complex as Redox Biotin-Bridge

for the Construction of Supramolecular Biosensing Architectures. *Chem. Commun*. *3*, 324−325.
(9) Goll, M. G., and Bestor, T. H. (2005) Eukaryotic Cytosine Methyltransferases. *Annu. Rev. Biochem. 74*, 481−514.
(10) Bird, A. (2002) DNA methylation patterns and epigenetic memory. *Genes Dev. 16*, 6−21.
(11) Jones, P. A., and Baylin, S. B. (2002) The fundamental role of epigenetic events in cancer. *Nat. Rev. Genet*. *3*, 415−428.
(12) Lyko, F., and Brown, R. (2005) DNA methyltransferase inhibitors and the development of epigenetic cancer therapies. *J. Natl. Cancer Inst*. *97*, 1498−1506.
(13) Sorm, F., Piskala, A., Cihak, A., and Vesely, J. (1964) 5-Azacytidine, a new, highly effective cancerostatic. *Experientia 20*, 202−203.
(14) Silvermann, L. R., Deamos, E. P., and Peterson, B. L. et al. (2002) Randomized controlled trial of azacitidine in patients with the myelodysplastic syndrome: a study of the cancer and leukemia group B. *J. Clin. Oncol*. *20*, 2429−2440.
(15) Juttermann, R., Li, E., and Jaenisccb, R. (1994) Toxicity of 5-aza-2′-deoxycytidine to mammalian cells is mediated primarily by covalent trapping of DNA methyltransferase rather than DNA demethylation. *Proc. Natl. Acad. Sci. U.S.A. 91*, 11797−11801.
(16) Siedlecki, P., Boy, R. G., Musch, T., Brueckner, B., Suhai, S., Lyko, F., and Zielenkiewicz, P. (2006) Discovery of two novel small-molecule inhibitors of DNA methylation. *J. Med. Chem*. *49*, 678−683.
(17) Brueckner, B., Garcia-Boy, R., Siedlecki, P., Musch, T., Kliem, H. C., Zielenkiewicz, P., Suhai, S, Wiessler, M., and Lyko, F. (2005) Epigenetic reactivation of tumor suppressor genes by a novel small-molecule inhibitor of human DNA methyltransferases. *Cancer Res*. *65*, 6305−6311.
(18) Siedlecki, P., Garcia Boy, R., Comagic, S., Schirrmacher, R., Wiessler, M., Zielenkiewicz, P., Suhai, S., and Lyko, F. (2003) Establishment and functional validation of a structural homology model for human DNA methyltransferase 1. *Biochem. Biophys. Res. Commun. 306*, 558−563.
(19) Casimir, J. R., Guichard, G., and Briand, J. P. (2002) Methyl 2-((succinimidooxy)carbonyl)benzoate (MSB): a new, efficient reagent for N-phthaloylation of amino acid and peptide derivatives. *J. Org. Chem*. *67*, 3764−3768.
(20) Lescrinier, T., Busson, R., Rozenski, J., Janssen, G., Van Aerschot, A., and Herdewijn, P. (1996) Incorporation of 5-Hydroxytryptophan in Oligopeptides. *Tetrahedron 52*, 6965−6972.
(21) Islam, I., Ng, K., Chong, K. T., McQuade, T. J., Hui, J. O., Wilkinson, K. F., Rush, B. D., Ruwart, M. J., Borchardt, R. T., and Fisher, J. F. (1994) Evaluation of a Vitamin-Cloaking Strategy for Oligopeptide Therapeutics: Biotinylated HIV-1 Protease Inhibitors. *J. Med. Chem*. *37*, 293−304.

BC050300B

ARTICLES

Amphiphilic Conjugates of Human Brain Natriuretic Peptide Designed for Oral Delivery: In Vitro Activity Screening

Mark A. Miller,† Navdeep B. Malkar,† Diana Severynse-Stevens, Kevin G. Yarbrough, Mark J. Bednarcik, Robert E. Dugdell, Monica E. Puskas, Radha Krishnan, and Kenneth D. James*

Nobex Corporation, 617 Davis Drive, Suite 100, Durham, North Carolina 27713. Received March 31, 2005; Revised Manuscript Received January 20, 2006

Congestive heart failure (CHF) is a complex syndrome involving altered neurohormonal levels and impaired cardiac and renal function. In recent years, intravenous administration of exogenous human brain-type natriuretic peptide (hBNP) has become an important therapy in treating patients with acutely decompensated CHF. However, reports during the past year suggest that hBNP could play a prominent role in the chronic treatment of CHF patients as well. We are currently developing conjugates of hBNP suitable for oral delivery to provide a patient-friendly treatment option for chronic heart failure patients. In this report, we present in vitro activity results obtained from hBNP conjugates featuring a variety of rationally designed amphiphilic oligomers. Mapping studies revealed that the hydrophobic/hydrophilic balance of the oligomer impacted the regioselectivity of conjugation. Additionally, the regiochemistry and extent of conjugation had a significant impact on activity. Many monoconjugates retained activity comparable to native peptide and are currently under evaluation in subsequent in vivo screens.

INTRODUCTION

Cardiovascular diseases constitute the leading cause of death in the United States regardless of gender or ethnicity. Of these diseases, congestive heart failure (CHF) is the only one that is increasing in prevalence (*1*, *2*). Hospital expenses for the treatment of CHF are more than double those for all forms of cancer combined (*3*). Approximately 78% of CHF patients are being hospitalized at least twice per year, accounting for nearly 6 million hospital days in the United States alone (*4*). Despite the prevalence of this disease, there is still no curative therapeutic approach (*5*). Multiple hospitalizations and inadequate therapeutics define the current situation faced by those who suffer from CHF.

In August 2001, recombinant hBNP (human brain-type natriuretic peptide; Scios, Inc.) was approved by the FDA for the treatment of patients with acutely decompensated CHF with dyspnea at rest or with minimal activity. Although the current use of hBNP is limited to acute intravenous infusion, recent studies in patients with moderate to severe heart failure indicate that hBNP could play an important role as a chronically administered therapeutic (*6*−*8*). BNP is one of a family of peptides that are involved in cardiovascular, renal, and endocrine homeostasis (*9*). It has natriuretic, diuretic, vasorelaxant, lusitropic, anti-aldosterone, and anti-fibrotic properties (*10*). It was discovered in 1988 (*11*), almost a decade after the discovery of atrial natriuretic peptide (ANP). First isolated from porcine brain, it is known for its activity at receptors in cardiac, renal, vascular smooth muscle, and endothelial cells. BNP binds to the natriuretic peptide receptor A (NPR-A), a membrane-bound protein on the cell surface. The binding event triggers the synthesis of cGMP in the cytosol by guanylate cyclase. It is through this secondary messenger that BNP mediates its physiological effects.

Our objective has been to generate an amphiphilic conjugate of hBNP that would be suitable for oral administration and the chronic treatment of CHF as part of an outpatient or home-based therapy. The amphiphilic oligomers that were used are composed of both hydrophilic and hydrophobic moieties. The hydrophilic portion is composed of poly(ethylene glycol) (PEG), the attachment of which has been demonstrated to increase circulating half-life and reduce immunogenicity (*12*−*14*). The hydrophobic portion is composed of an alkyl group and is intended to provide amphiphilic balance, a feature that is an essential characteristic of oral drugs (*15*). While the conjugation of amphiphilic oligomers can be an important tool to improve the pharmacokinetics and pharmacodynamics of a drug, it is important that the agonist activity of the resultant conjugate is not severely compromised. In this report we describe the impact of various oligomers and the site of conjugation to hBNP on the in vitro production of cGMP by human aortic endothelial cells (HAEC). The lead conjugates from this activity screen are currently being tested in healthy dogs after oral administration. Preliminary results from these studies have recently been published (*16*).

EXPERIMENTAL PROCEDURES

General. Unless otherwise mentioned, all reagents were purchased from Aldrich (Milwaukee, WI). PEGs and MPEGs were purchased from TCI America (Portland, OR). Lysyl endopeptidase was purchased from Wako BioProducts (Richmond, VA). HPLC columns were purchased from Phenomenex

* Corresponding author. Kenneth D. James, 617 Davis Drive, Suite 100, Durham, NC 27713. Phone: (919) 474-0507. Fax (919) 474-9407. E-mail: kjames@nobexcorp.com.

† Equal contributions to this work.

10.1021/bc0501000 CCC: $33.50 © 2006 American Chemical Society
Published on Web 02/24/2006

(Torrance, CA). ELISA kits were purchased from Molecular Devices (Sunnyvale, CA). Primary human aortic endothelial cells (HAEC) were purchased from Cambrex (Clonetics; East Rutherford, NJ). Chemical shifts are reported in reference to TMS internal standard.

General Procedure for Conjugation of Amphiphilic Oligomers to hBNP. *Method 1: Preparation of Monoconjugates.* hBNP (1 equiv) was dissolved in DMSO (1 mL/35 mg of hBNP). The activated oligomer (1.1 equiv) was dissolved in a minimal amount of THF and added to the solution. The progress of the reaction was monitored by HPLC: 50 μL aliquots were diluted in 500 μL of H_2O containing 0.1% TFA. Reactions were typically complete within 45 min.

Method 2: Preparation of Di-, Tri-, and Tetraconjugates. hBNP (1 equiv) was dissolved in DMSO (1 mL/35 mg of hBNP). Triethylamine (120 equiv) was added. After 5 min, the activated oligomer (2.2 equiv for diconjugate, 4 equiv for triconjugate, 5 equiv for tetraconjugate) was dissolved in a minimal amount of THF and added to the solution. The progress of the reaction was monitored by HPLC: 50 μL aliquots were diluted in 500 μL of H_2O containing 0.1% TFA. Reactions were typically complete within 45 min.

General Procedure for Purification of hBNP Conjugates. The conjugates prepared by Methods 1 and 2 were isolated using reversed-phase HPLC (C18, 1.0 cm. i.d. × 25 cm length). A single gradient system was sufficient for purification of most of the conjugates (A: H_2O with 0.1% TFA; B: acetonitrile with 0.1% TFA; %B: 25−75 over 120 min). Each conjugate was obtained as a white powder after rotary evaporation and lyophilization.

Activation of Oligomers. Method 1. The acid (1.0 equiv) and *N*-hydroxysuccinimide (1.1 equiv) were dissolved in dry CH_2Cl_2 (0.2 M with respect to acid). Ethyl dimethylaminopropyl carbodiimide hydrochloride (EDC, 1.0 equiv) was added. After being stirred at room-temperature overnight, the reaction mixture was diluted with CH_2Cl_2 and was washed with water (2×). The organic layer was dried ($MgSO_4$) and concentrated to a constant weight. The products were typically colorless oils.

Activation of Oligomers. Method 2. The alkyl-PEG (1.0 equiv) was dissolved in acetonitrile (0.1−0.2 M with respect to alkyl-PEG). After the addition of disuccinimidyl carbonate (DSC, 1.5 equiv), triethylamine (1.5 equiv) was added dropwise over the course of 10 min. After being stirred overnight at room temperature, the crude reaction mixture was concentrated, dissolved in sat. $NaHCO_3$, and extracted with ethyl acetate (2×). The organic layer was dried ($MgSO_4$) and concentrated. Purification by silica gel chromatography (EtOAc/MeOH, 10:1) afforded the activated products.

Activation of Oligomers. Method 3. The alkyl-PEG (1.0 equiv) dissolved in toluene was added dropwise to a stirring 20% phosgene solution in toluene at −10 °C (0.2 M with respect to alkyl-PEG). After 30 min, the reaction mixture was allowed to warm to room-temperature overnight. Phosgene and toluene were removed by vacuum distillation. The crude acid chloride was dissolved in CH_2Cl_2 (0.4 M with respect to acid chloride), and *N*-hydroxysuccinimide (1.1 equiv) was added. Triethylamine (1.1 equiv) was added dropwise over the course of 10 min. After being stirred overnight at room temperature, the crude reaction mixture was concentrated, dissolved in sat. $NaHCO_3$ (20 mL), and extracted with ethyl acetate (2×). The organic layer was dried ($MgSO_4$) and concentrated. Purification by silica gel chromatography (EtOAc) afforded the activated product.

$MPEG_7C_{16}$ Succinimidyl Ester (4). To a solution of the acid **21** (15.3 g, 45 mmol) in ethanol (300 mL) was added H_2SO_4 (1.5 mL, 31.25 mmol). After being stirred for 48 h, the crude reaction mixture was diluted with water and extracted with CH_2Cl_2 (2 × 300 mL). The organic layer was washed with H_2O (2 × 300 mL) and sat. $NaHCO_3$ (2 × 300 mL). The organic layer was then dried ($MgSO_4$) and evaporated to dryness to afford an off-white solid (16.03 g, 98%): MS (ESI+) 364 (M + 1).

To a solution of heptaethylene glycol monomethyl ether (8.51 g, 25 mmol) in THF (250 mL) was added potassium *tert*-butoxide (3.1 g, 27.5 mmol) in small portions over 30 min. The reaction mixture was then stirred for an additional 1 h. The ester (10 g, 27.5 mol in 90 mL THF) was added dropwise over 30 min, and the reaction mixture was stirred overnight. The crude reaction mixture was filtered through Celite and concentrated. The crude oil was purified by silica gel chromatography (2−5% MeOH in $CHCl_3$) to yield **24** as a clear yellow oil (2.48 g, 16%): MS (ESI+) 623 (M + 1), 645 (M + Na^+).

To a solution of the ester **24** (2.22 g, 3.56 mmol) in alcohol (1:1 MeOH:EtOH, 50 mL) was added 1 N NaOH (50.0 mL). After being stirred for 24 h, the reaction mixture was concentrated, acidified to pH 2 with 1 M HCl, saturated with NaCl, and extracted with CH_2Cl_2 (3 × 75 mL). The organic layers were combined, washed with sat. NaCl, dried ($MgSO_4$), and concentrated. Purification of the crude solid by silica gel chromatography (ethyl acetate) provided the amphiphilic acid as a white powder (858 mg, 40%): MS (ESI+) 617 (M + Na^+).

The acid (324 mg, 544 mmol) was activated according to Activation Method 1. The product **4** was obtained as a clear oil (290 mg, 77%): ^{1}H NMR (400 MHz, $CDCl_3$, δ): 1.27 (m, 18H), 1.40 (m, 2H), 1.58 (m, 2H), 1.73 (m, 4H), 2.60 (t, 2H), 2.84 (m, 4H), 3.38 (s, 3H), 3.45 (t, 2H), 3.56 (m, 6H), 3.62 (m, 22H); MS (ESI+) 714 (M + Na^+).

$MPEG_3C_3$ Succinimidyl Ester (1). Methyl triethylene glycol (3.84 g, 23.4 mmol) and *tert*-butyl acrylate (1.71 mL, 11.7 mmol) were dissolved in dry THF (10 mL). Sodium metal (27 mg, 0.117 mmol) was added to the solution. After being stirred for 4 h at room temperature, the reaction mixture was quenched by the addition of 1 M HCl (30 mL). The quenched reaction mixture was then extracted with CH_2Cl_2 (1 × 100 mL, 1 × 50 mL). The organic layer was dried ($MgSO_4$) and concentrated. After purification by silica gel chromatography (ethyl acetate), the product was obtained as an oil (2.94 g, 86%): MS (ESI+) 315 (M + Na^+).

The *tert*-butyl ester **25** (1.00 g, 3.42 mmol) was deprotected by stirring at room temperature in trifluoroacetic acid (5.0 mL). The contents were then concentrated to a constant weight (0.708 g, 88%): MS (ESI+) 236 (M^+), 239 (M + Na^+).

The acid (0.705 g, 2.99 mmol) was activated according to Activation Method 1. The product **1** was an oil (0.848 g, 85%): ^{1}H NMR (400 MHz, $CDCl_3$, δ): 2.81 (m, 4H), 2.87 (t, 2H), 3.35 (s, 3H), 3.52 (m, 2H), 3.61 (m, 10H), 3.82 (t, 2H); MS (ESI+) 356 (M + Na^+).

C_6PEG_7 Succinimidyl Carbonate (5). Triethylene glycol (30 g, 0.2 mol) was dissolved in 8 mL of 100% NaOH and stirred for 10 min. Benzyl chloride (7.8 g, 61.6 mmol) was added, and the reaction was stirred at reflux overnight. The reaction mixture was diluted with sat. NaCl (500 mL) and extracted with CH_2Cl_2 (2 × 400 mL). Organic layers were combined, washed sat. NaCl (800 mL), dried ($MgSO_4$), and evaporated to dryness. Silica gel chromatography (ethyl acetate) provided the protected PEG_3 as a yellowish oil (9.84 g, 66%): MS (FAB+) 241 (M + 1).

Triethylamine (7.1 mL, 0.054 mol) was added to a solution of benzyl PEG_3 (9.84 g, 0.041 mol) in CH_2Cl_2 (50 mL). The solution was cooled to 0 °C, and methanesulfonyl chloride (3.9 mL, 0.049 mol), dissolved in CH_2Cl_2 (10 mL), was added via addition funnel. The reaction was stirred for 0.5 h at 0 °C and then 4 h at room temperature. The reaction mixture was filtered through Celite and diluted with CH_2Cl_2 (150 mL). The filtrate was then washed with H_2O (200 mL), sat. $NaHCO_3$ (200 mL), and H_2O (200 mL). The organic layer was dried ($MgSO_4$) and

concentrated to a constant weight, affording the mesylate as a yellowish oil (10.85 g, 83%): MS (FAB+) 319 (M + 1).

NaH (0.45 g, 0.019 mol) was added portionwise over 0.5 h to a solution of tetraethylene glycol (7.32 g, 0.038 mol) in tetrahydrofuran (140 mL). The mixture was stirred for 1 h. Then the benzyl PEG_3 mesylate (6.0 g, 0.019 mol), dissolved in tetrahydrofuran (20 mL), was added dropwise via addition funnel. After being stirred overnight at room temperature, the reaction mixture was filtered through Celite and evaporated to dryness. The resultant oil was dissolved in CH_2Cl_2 (150 mL) and washed with H_2O (150 mL), sat. $NaHCO_3$ (150 mL), and H_2O (150 mL). The organic layer was dried ($MgSO_4$) and concentrated. Silica gel chromatography (ethyl acetate/methanol, 10:1) afforded benzyl PEG_7 (**26**) as a clear oil (3.83 g, 49%): MS (FAB+) 417 (M + 1).

To a solution of **26** (5.45 g, 0.013 mol) in tetrahydrofuran (160 mL) was added potassium *tert*-butoxide (1.6 g, 0.014 mol), and the reaction mixture was stirred for 1 h. Then hexylmethanesulfonate (2.59 g, 0.014 mol), dissolved in tetrahydrofuran (20 mL), was added via addition funnel, and the reaction was stirred overnight at room temperature. The reaction mixture was filtered through Celite and concentrated. The resultant oil was dissolved in ethyl acetate (150 mL), washed with H_2O (2 × 150 mL), dried ($MgSO_4$), and concentrated. Silica gel chromatography (ethyl acetate) afforded the protected alkyl PEG_7 (**27**) as a clear oil (2.40 g, 36%): MS (FAB+) 501 (M + 1).

To a solution of **27** (2.40 g, 4.8 mmol) in ethyl acetate (16 mL) was added palladium on activated carbon (1 g, 10wt % on carbon). The reaction vessel was stirred under H_2 atmosphere overnight at room temperature. The reaction mixture was then filtered through Celite and concentrated to afford the alkyl-PEG_7-OH as a clear oil (1.61 g, 82%): MS (FAB+) 411 (M + 1).

The alkyl-PEG_7OH (1.60 g, 3.9 mmol) was activated according to Activation Method 3. The product was a clear oil (1.06 g, 53%): ^{1}H NMR (400 MHz, $CDCl_3$, δ): 0.88 (m, 3H), 1.29 (m, 4H), 1.58 (m, 2H), 2.84 (m, 4H), 3.45 (t, 2H), 3.58 (m, 2H), 3.65 (m, 22H), 3.79 (m, 2H), 4.47 (m, 2H); MS (FAB+) 552 (M + 1).

(Branched $MPEG_4$) Urethanyl C_6 Succinimidyl Ester (11). Tetraethylene glycol monomethyl ether (14.0 g, 67 mmol) was dissolved in tetrahydrofuran (90 mL). NaH (1.77 g, 74 mmol) was added portionwise, and the reaction was stirred for 2 h. Then epichlorohydrin (26.3 mL, 0.34 mol) was added dropwise and the reaction was stirred at room temperature for 48 h. The crude reaction mixture was filtered through Celite and washed CH_2Cl_2 (250 mL). The filtrate was washed H_2O (2 × 250 mL), dried ($MgSO_4$), and evaporated to dryness. Column chromatography (silica, ethyl acetate) afforded **28** a clear oil (10.15 g, 57%): MS (ESI+) 287 (M + Na^+).

Tetraethylene glycol monomethyl ether (7.96 g, 0.038 mol) and **28** (10.1 g, 0.038 mol) were dissolved in CH_2Cl_2 (100 mL). $BF_3{\cdot}OEt_2$ (0.48 mL, 0.0038 mol) was added and the reaction mixture was stirred overnight at room temperature. The crude mix was diluted with CH_2Cl_2 (200 mL), washed with sat. $NaHCO_3$ (300 mL) and H_2O (300 mL), dried ($MgSO_4$), and evaporated to dryness. Column chromatography (silica, ethyl acetate/MeOH, 10:1) afforded **29** a clear oil (4.5 g, 25%): MS (ESI+) 495 (M + Na^+).

4-Nitrochloroformate (2.87 g, 14.3 mmol) and **29** (4.5 g, 9.5 mmol) were dissolved in CH_2Cl_2 (45 mL). After the reaction mixture was stirred for 10 min, TEA (2.1 mL, 15 mmol) was added and reaction stirred overnight at room temperature. The crude mix was diluted with CH_2Cl_2 (130 mL), washed with 1M HCl (175 mL) and H_2O (175 mL), dried ($MgSO_4$), and evaporated to dryness. Column chromatography (silica, ethyl acetate/MeOH, 15:1) afforded **30** a yellowish oil (2.38 g, 40%): MS (ESI+) 660 (M + Na^+).

6-Aminocaproic acid (0.126 g, 0.96 mmol) and K_2CO_3 (0.221 g, 1.6 mmol) were dissolved in H_2O (DI, 5 mL). Then **30** (0.5 g, 0.8 mmol) was dissolved in THF (0.7 mL) and added dropwise. After being stirred overnight at room temperature, the reaction mixture was diluted with H_2O (20 mL), acidified to pH ~ 1 with HCl, and extracted with CH_2Cl_2 (2 × 25 mL). The organic layers were combined, dried ($MgSO_4$), and evaporated to dryness. Column chromatograpy (silica, $CHCl_3$/MeOH, 15:1) afforded **31** a clear oil (0.428 g, 85%): MS (ESI+) 652 (M + Na^+).

The acid was activated using Method 1:**31** (0.40 g, 0.64 mmol), *N*-hydroxysuccinimide (0.088 g, 0.77 mmol), EDC (0.160 g, 0.83 mmol), and CH_2Cl_2 (5 mL). Column chromatography (silica, ethyl acetate/MeOH, 10:1) afforded **11** a clear oil (0.320 g, 69%): ^{1}H NMR (400 MHz, $CDCl_3$, δ): 1.45 (m, 2H), 1.53 (m, 2H), 1.77 (m, 2H), 1.87 (br s, 1H), 2.62 (t, 2H), 2.84 (m, 4H), 3.16 (m, 2H), 3.38 (s, 6H), 3.55 (m, 6H), 3.65 (m, 38H), 5.01 (m, 1H); MS (ESI+) 749 (M + Na^+).

Peptide Mapping. Either native hBNP or a conjugate (1.0 mg) and lysyl endopeptidase (2.0 ng) were incubated in 1.0 mL Tris buffer (0.1 M, pH 9) at 30 °C for 1 h. Reactions were quenched by the addition of 50% acetic acid (50 μL) to bring the solutions to pH ≈ 4. As a negative control, hBNP was also incubated at 30 °C without addition of the lysyl endopeptidase. All hBNP and conjugate solutions were analyzed by HPLC prior to incubation to determine purity and concentration. The incubated samples were analyzed by HPLC to reveal the fragment profile. Sites of conjugation were determined after subsequent isolation and mass spectral analyses of the peptide fragments.

cGMP Assay. Primary human aortic endothelial cells (HAEC) were thawed and placed in a T75 flask prior to use in an experiment. Cells were grown for 2 days until they reached 70−80% confluence and were then plated into 12-well plates at 2.5 × 10^4 cells/well. The next day the media was removed, and cells were preincubated for 10 min at 37 °C with 0.5 mM IBMX to inhibit phosphodiesterases. Conjugates to be screened were added to the cells for an additional 60 min at 37 °C. Incubation was stopped by lysing cells using Cell Lysis Solution (Molecular Devices; Sunnyvale, CA). The released intracellular cGMP was then acetylated using a 2:1 mixture of triethylamine to acetic anhydride. Acetylation of the cGMP lysate was found to increase the sensitivity of this assay 5-fold. Acetylated cGMP was then measured using an ELISA-based system (CatchPoint-cyclic GMP Fluorescent Assay Kit), which quantitates cGMP via a competitive immunoassay in 96-well format. Lysates were added to the coated microplate followed by the addition of an anti-cGMP antibody and a horseradish peroxidase (HRP)-cGMP conjugate. Plates were incubated for 2 h at room temperature, followed by four washes. A substrate solution was added and the fluorescent intensity of each well was quantitated. The fluorescent signal intensity decreased with increasing levels of cGMP. Native hBNP was tested in each experiment as a positive control. Statistical analyses were performed with SigmaStat using a one-way ANOVA and a post-hoc Dunnett's test with significance set at $p < 0.05$.

RESULTS AND DISCUSSION

Sites of Conjugation. The hormone hBNP is expressed as the inactive prepro-peptide (*17*−*19*), which is cleaved after translation by the enzyme Corin (*20*) to the mature peptide shown in Figure 1. It has four prominent sites for conjugation: Ser1, Lys3, Lys14, and Lys27. Because binding to the NPR-A is believed to occur mostly in the loop region, we expected that activity would likely be compromised upon conjugation to Lys14 and perhaps Lys27. Thus, we anticipated that mono- or

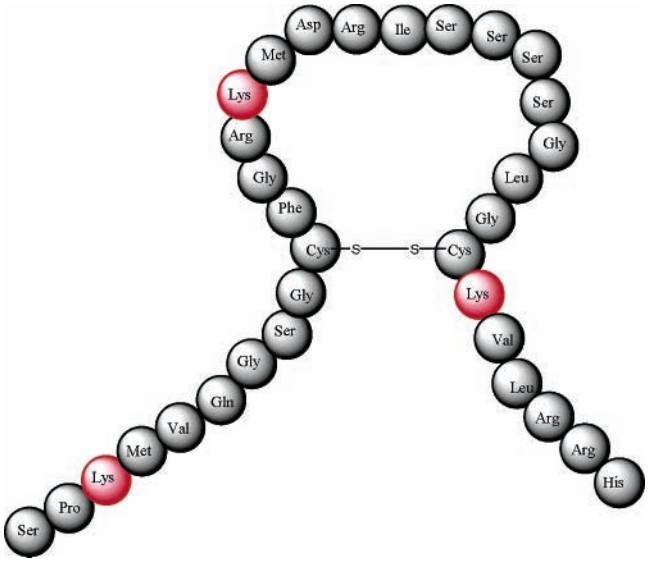

Figure 1. Primary structure of mature hBNP. It is a 32-amino acid peptide with a loop region composed of 17 residues, which is the characteristic loop size for the various natriuretic peptides. hBNP has four sites suitable for conjugation with these oligomers: the free N-terminus and three lysine residues (shown in red).

diconjugates composed only of Ser1 and Lys3 conjugates would have little adverse effect on activity, whereas mono-, di-, or triconjugates involving one or both of the Lys14 and Lys27 positions may reduce or eliminate activity. However, the verity of these assumptions and the extent of impact of conjugation at these sites had not yet been demonstrated.

Conjugation reactions performed in aqueous phosphate buffer (10 mM; pH 7.4 and 9.5) led to undesirable mixtures of products with little indication of selectivity. In contrast, reactions performed in polar organic solvents (DMSO and DMF) resulted in much cleaner product profiles. The sites of attachment of the oligomers were determined by peptide mapping studies using lysyl endopeptidase, followed by analyses of the fragments by HPLC and mass spectrometry. Characteristic results from these studies are presented in Table 1. The six potential fragments are listed in the table in addition to the intact hBNP or conjugate. The presence of specific fragments were verified by retention time (R_f) and molecular weight. Because the conjugated lysines are resistant to lysyl endopeptidase, the presence of particular fragments indicates the lysine residues that were not conjugated. Conversely, the absence of fragments indicates conjugation at a specific site. These indications are verified by the molecular weights of the fragments. Predictably, unconjugated hBNP was fragmented into the peptides expected from cleavage at each of the three lysine residues. Cleavage at Lys14 (for native hBNP or a conjugate) results in the peptide fragments that remain covalently attached through the disulfide linkage rather than through a peptide bond. The tri- and tetraconjugates were completely resistant to proteolysis with lysyl endopeptidase, resulting in no fragmentation.

The site preference for attachment of the oligomers in either DMSO or DMF followed the trend Lys3 > Lys14 > Lys27 ≫ Ser1 (Figure 2a). Conditions could be adjusted so that the Lys3 monoconjugate was the major product. Diconjugates tended to form only transiently. Rather than accumulating, the diconjugates were excellent substrates for conjugation and rapidly proceeded to the triconjugate, a phenomenon we have occasionally observed with other peptides. The N-terminus was so unreactive that the triconjugate could be obtained as the exclusive product. Nonetheless, the tetraconjugate could be formed by the addition of excess oligomer and extension of reaction times. The stated trend held true for the majority, but not all, of the oligomers that were tested. Oligomers that were very nonpolar overall or that consisted of a nonpolar moiety distal from the site of conjugation resulted in a different trend: Lys14 > Lys3 > Lys27 ≫ Ser1 (Figure 2b). Because other reaction conditions were unchanged, presumably the switch in selectivity is due to nonpolar interactions bringing the active ester of the hydrophobic oligomers proximal to the lysine of the loop region.

Oligomer Design. The objective through these conjugations is to maximize the benefits imparted to the peptide while minimizing perturbation and adverse effects on activity. The effects of the site and extent of conjugation on activity were first addressed using oligomer **2**, a linear oligomer of moderate length and balanced amphiphilicity that has been used effectively with insulin (*21*−*23*). Reactions with this oligomer led to the generation of the mono-, di-, tri-, and tetraconjugates. Oligomer **2** is representative of the Class I (nonhydrolyzable) oligomers, which are designed to remain intact from dosing to target. A series of linear and branched non-hydrolyzable oligomers are shown in Figure 3.

Because the tri- and tetraconjugates using **2** were virtually inactive, we did not know whether the higher conjugates were forbidden or if smaller oligomers would enable the higher conjugates to retain partial activity. To address this question, a series of micropegylated conjugates, which utilize Class II oligomers, were designed. These oligomers retain the amphiphilic properties of the Class I oligomers initially, but are intended to shed the hydrophobic portion before they reach the receptor (Figure 4). To mimic the activity of micropegylated conjugates after hydrolysis in vivo, a series of higher conjugates were prepared using oligomers of minimal size, ranging from one to three PEG units. Figure 5 illustrates the Class II oligomers that were used to make the various micropegylated conjugates. Also depicted are the corresponding oligomers that were intended to model the Class II oligomers after hydrolysis. We do note that the model oligomers end with a methoxy group rather than a hydroxy group. Nevertheless, both the Class II oligomers posthydrolysis and the model oligomers remove the charge of the lysines and contain the same number of ethylene

Table 1. Mapping Results from the Incubation of hBNP or hBNP Conjugates with Lysyl Endopeptidase[a]

	compound				
fragment present? (R_f/MW)	hBNP	**C1**	**C2**	**C3**	**C8**
1−3	4.2/330	−	−	−	−
28−32	8.4/680	8.4/680	−	−	8.4/680
4−14 + 15−27[b]	13.7/2508	−	−	−	−
1−14 + 15−27 + oligomer[b]	−	16.4/3257	−	−	−
4−14 + 15−32 + oligomer[b]	−	−	−	−	−
1−27 + 2x oligomer	−	−	−	−	18.5/3675
intact BNP or conjugate	15.4/3464	17.2/3901	18.6/4775	19.3/5212	18.2/4355

[a] Each of the conjugates depicted was made using oligomer 2. If a fragment was present after incubation, its retention time and molecular weight are listed. The corresponding values for the parent compound are provided for comparison. [b] The backbone was cleaved at Lys14, but the fragments are linked by a disulfide bond.

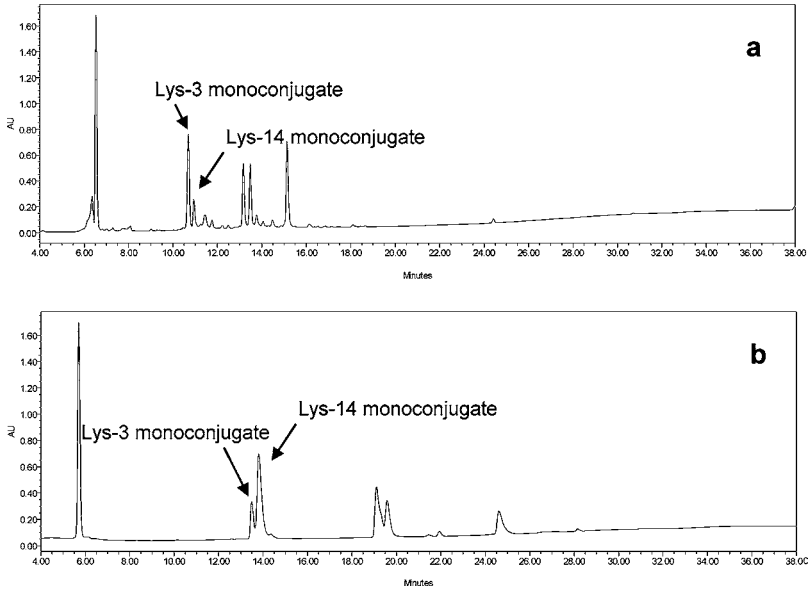

Figure 2. Chromatograms illustrating differing selectivity based on the amphiphilic balance of the oligomer. Detection was set at 220 nm. a. Hydrophilic oligomers react first at Lys3. b. Hydrophobic oligomers react preferentially at Lys14.

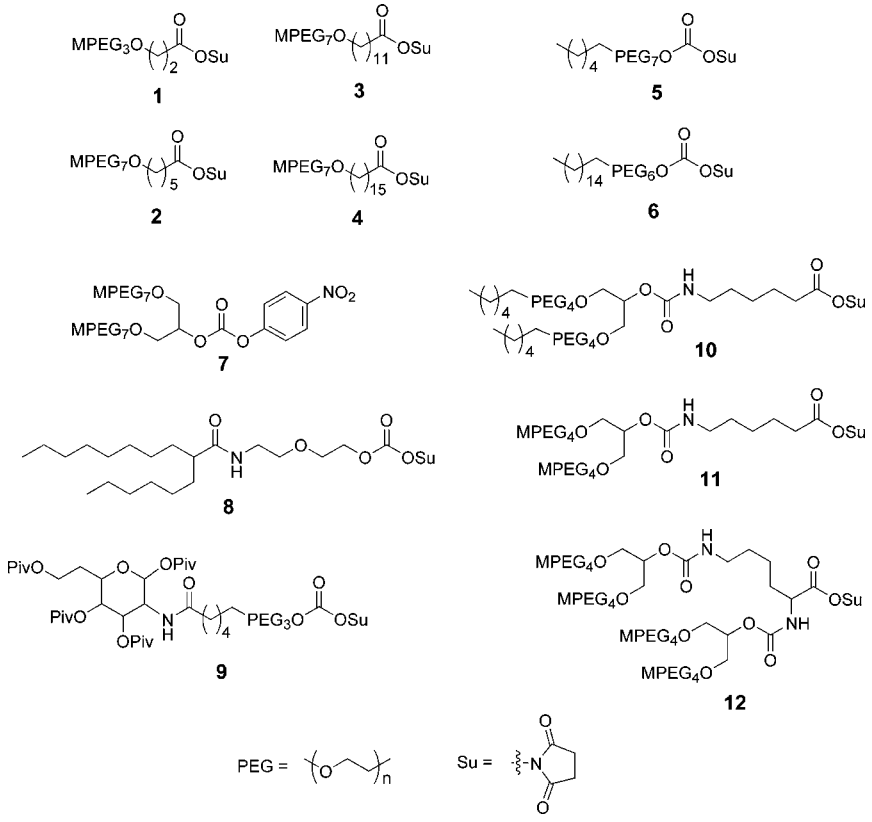

Figure 3. Linear and branched Class 1 oligomers.

glycol units. We therefore regarded them as acceptable models at this stage in screening.

Both the tri- and tetraconjugates were inactive even with the smallest of oligomers, prompting a focus on Lys3 monoconjugates. Even larger Class I oligomers attached at Lys3 resulted in active conjugates; therefore, Class II oligomers offered no advantage for this peptide.

Syntheses of Oligomers. The linear Class 1 oligomers were mostly prepared by similar methods, varying only according to the orientation of the polyetheylene glycol (PEG) and alkyl moieties (Scheme 1 A−C). For oligomers featuring the alkyl moiety inside, the substituted alkanoic acid was first esterified. The monomethoxy PEG (MPEG) was then attached. Depending on availability, either the terminal bromide or hydroxyl (activated as the mesylate) was used. Ester hydrolysis and activation as the succinimidyl ester led to the desired oligomers. The one exception to this group is the oligomer **1**. In this case, the MPEG moiety was coupled to *tert*-butyl acrylate in the presence of sodium catalyst. After deprotection of **25** in neat TFA, the oligomer was activated as previously described.

The oligomers featuring the PEG moiety inside were made by different means. Briefly, the PEG diol was singly protected

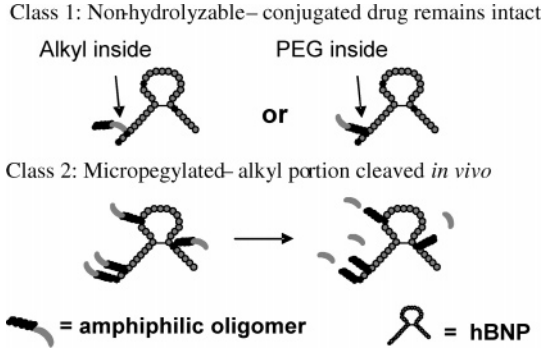

Figure 4. Different categories of oligomers used in the study. Class 1 oligomers had either the PEG or the alkyl moiety proximal to the peptide. Class 2 oligomers all featured the PEG portion proximal to the peptide.

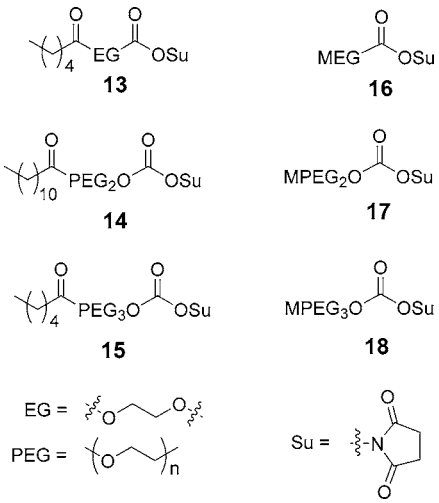

Figure 5. Class 2 oligomers and their corresponding model oligomers.

with a benzyl group. After coupling to an alkyl mesylate, the benzyl group was removed by hydrogenolysis. Subsequent activation afforded the desired succinimidyl carbonate.

The Class 2 oligomers were prepared in like manner. The benzyl PEG was first coupled with the appropriate alkanoic acid chloride. Hydrogenolysis followed by activation with disuccinimidyl carbonate completed the syntheses.

Many of the Class 1 oligomers featuring branched PEGs utilized glycerol as the source of branching. Rather than starting with a poor nucleophile like glycerol itself or a protected glycerol, we found it advantageous to use a good electrophile such as epichlorohydrin (Scheme 2). Our initial attempts to go directly from epichlorohydrin to the branched PEG required reflux conditions and led to undesirable product mixtures. In the stepwise approach, the first epoxide opening proceeded smoothly, but the second epoxide opening using catalytic NaH and refluxing conditions produced low yields and likewise resulted in a mixture of products. However, better yields and cleaner product distributions were attained at ambient temperatures when a Lewis acid catalyst was used for the second epoxide opening. This method worked well with short PEGs, but yields dropped with increasing PEG length.

Activation of the secondary alcohol was accomplished with *p*-nitrophenyl chloroformate, a reagent that proved more suitable than either phosgene or *N*,*N*′-disuccinimidyl carbonate. At this stage, the oligomer could either be conjugated to the peptide directly or be attached to a spacer, such as an ϵ-amino acid. Addition of the amino acid in an aqueous or aqueous/ethanol solution of potassium carbonate afforded the carbamate in good yield. Activation as the succinimidyl ester resulted in the branched amphiphilic oligomer, which could be conjugated to peptides.

In Vitro Activity. To evaluate the activity of each conjugate at the natriuretic peptide receptor A (NPR-A), conjugates were screened using a human aortic endothelial cell (HAEC) system. HAEC cultures contain normal primary aortic endothelial cells and when exposed to hBNP, produce cGMP in a dose-dependent manner. The activity of each of the conjugates was measured by assay of the extracellular levels of cGMP. The impact of the site and the extent of conjugation is well demonstrated by the various conjugates that were made with oligomer **2** (Figure 6). Conjugate **C1** (a Lys3 monoconjugate) retained good activity and potency in comparison to the unconjugated peptide. By contrast, **C7** (a Lys14 monoconjugate) exhibited a partial loss of both activity and potency. When both the Lys14 and Lys 27 positions were conjugated (**C2** and **C3**), the compounds did not induce cGMP production above background levels.

The results for conjugates utilizing Class 1 and Class 2 oligomers are listed in Table 2. In general, the Lys3 monoconjugates consistently performed well in the assay in terms of both potency and activity. The two exceptions were **C18** and **C21**. These conjugates share the trait of having a branched oligomer with hydrophobic portions distal from the site of attachment. It is possible that such oligomers induced a conformational change or aggregation that made them weaker agonists, but this question was not investigated. With those exceptions, oligomers of great variety of structure and size were conjugated to Lys3 while retaining activity comparable to the unconjugated peptide.

Scheme 1. Routes for Preparation of Linear Oligomers[a]

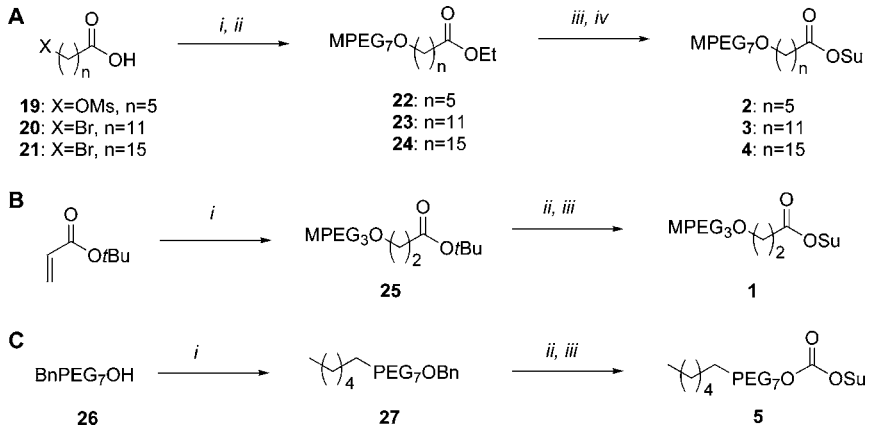

[a] A. (i) EtOH, H_2SO_4, 98%; (ii) MPEG$_n$OH, KO*t*Bu, THF, 4 h, 16%; (iii) 1 N NaOH, 40%; (iv) Method 1, 77%. B. (i) MPEG$_3$OH, Na^0, THF, 4 h, 86%; (ii) TFA Neat, 88%; (iii) Method 1, 85%. C. (i) Hexylmethanesulfonate, KO*t*Bu, THF, 36%; (ii) H_2, Pd/C, 82%; (iii) Method 3, 53%.

Scheme 2 [a]

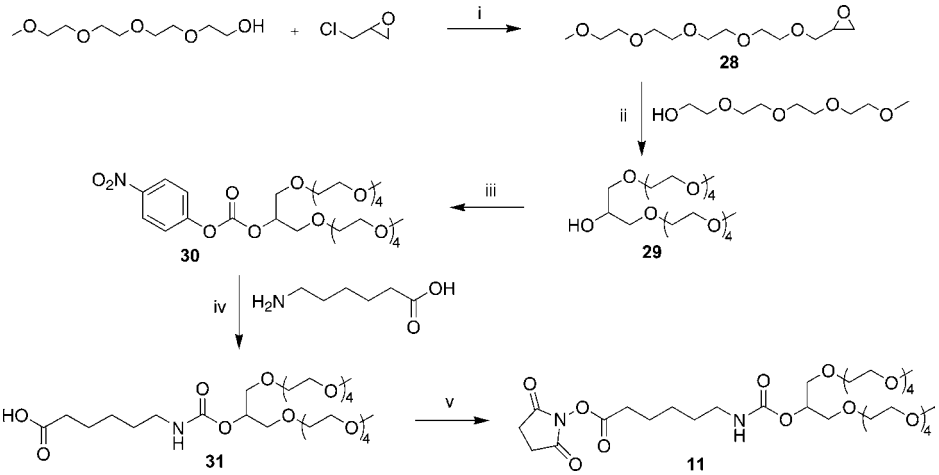

[a] (i) NaH, THF, 57%, (ii) $BF_3{\cdot}OEt_2$, CH_2Cl_2, 25%, (iii) 4-nitrophenyl chloroformate, TEA, CH_2Cl_2, 40%, (iv) K_2CO_3, H_2O, 85%, (v) *N*-hydroxysuccinimide, EDC, CH_2Cl_2, 69%.

Table 2. In Vitro Activity Results of Various Conjugates of hBNP[a]

compound	oligomer	position of conjugation	calculated mass	observed mass	average $EC_{50} \pm$ SD (nM)	average $E_{max} \pm$ SD
hBNP	–	–	3464	3465	235 ± 110	100.0 ± 0.0
C1	**2**	3	3900	3901	444 ± 30	101.0 ± 6.8
C2	**2**	3, 14, 27	4772	4775	>10000	<20.0
C3	**2**	1, 3, 14, 27	5208	5211	>10000	<20.0
C4	**14**	3, 14, 27	4406	4404	>10000	<20.0
C5	**14**	1, 3, 14, 27	4720	4722	>10000	<20.0
C6	**15**	1, 3, 14, 27	4560	4563	>10000	<20.0
C7	**2**	14	3900	3901	1110 ± 330	71.2 ± 21.2
C8	**2**	3, 14	4336	4360	1710 ± 250	60.8 ± 19.2
C9	**18**	1, 3, 14, 27	4224	4224	>10000	<20.0
C10	**17**	3, 14, 27	3902	3904	>10000	26.5 ± 7.4
C11	**17**	1, 3, 14, 27	4048	4049	>10000	<20.0
C12	**16**	1, 3, 14, 27	3872	3873	>10000	24.6 ± 6.5
C13	**13**	1, 3, 14, 27	4208	4209	>10000	<20.0
C14	**11**	3	4075	4075	369 ± 220	91.8 ± 1.9
C15	**5**	3	3900	3900	281 ± 81	75.7 ± 9.2
C16	**3**	3	3984	3985	321 ± 180	106.2 ± 42.7
C17	**3**	3, 14	4504	4505	>10000	43.5 ± 3.0
C18	**10**	3	4215	4216	>10000	28.3 ± 2.4
C19	**10**	14	4215	4216	>10000	34.0 ± 13.3
C20	**6**	14	3996	3997	126 ± 47	53.6 ± 5.6
C21	**8**	3	3833	3834	358 ± 180	30.5 ± 6.9
C22	**8**	1	3833	3834	146 ± 95	37.9 ± 12.2
C23	**9**	3/14	4295	4296	245 ± 120	60.5 ± 23.6
C24	**4**	3/14	4040	4040	815 ± 550	40.2 ± 6.6
C25	**7**	3	4227	NA	171 ± 52	94.4 ± 22.9
C26	**12**	3	4590	NA	556 ± 240	106.2 ± 16.6
C27	**6**	3/14	3996	3997	212 ± 10	60.1 ± 7.4
C28	**1**	3	3682	NA	265 ± 74	99.0 ± 3.6

[a] The position of conjugation lists the residue numbers to which the particular oligomer was attached. Thus, diconjugates, triconjugates, and tetraconjugates have 2, 3, and 4 numbers, respectively. For C23, C24, and C27, the Lys3 and Lys14 conjugates coeluted during purification. These samples were evaluated as the mixtures of monoconjugates.

For the Class 2 oligomers, the conjugates were tested with and without the alkyl chain attached. It is clearly evident that tri- and tetraconjugates retain virtually none of the activity of the native peptide, even when the smallest oligomers are used. No accurate EC_{50} values could be calculated for these conjugates in the concentration range tested, but the EC_{50} values were greater than 10 000 nM. It was not expected that any of these conjugates would exhibit greater activity or potency than did the native peptide. Rather, we sought conjugates that would have minimal or no adverse effects on activity.

In Vivo Activity after Oral Dosing. Bioactivity studies in healthy dogs are ongoing. In these studies, the effects of acute oral dosing of the hBNP conjugates are being assessed by measuring mean arterial pressure (MAP) and systemic levels of cGMP. To provide indication whether the biochemical and hemodynamic effects are attributable to the exogenous hBNP conjugates or if they could be due to changing levels of natural canine hormones, systemic levels of hBNP conjugate, canine ANP, and canine BNP are being evaluated. Results from the oral dosing of conjugate **C14** have recently been reported (*16*). In this preliminary work, an acute oral dose of **C14** led to a statistically significant increase of cGMP and a statistically significant decrease of MAP. Neither of these parameters differed from baseline levels after an acute oral dose of either placebo or unconjugated hBNP was dosed to healthy dogs. Levels of endogenous canine natriuretic peptides were unchanged in each dosing group. Thus, after oral administration, only the conjugated hBNP led to the biochemical and hemodynamic effects expected from increased levels of a natriuretic peptide.

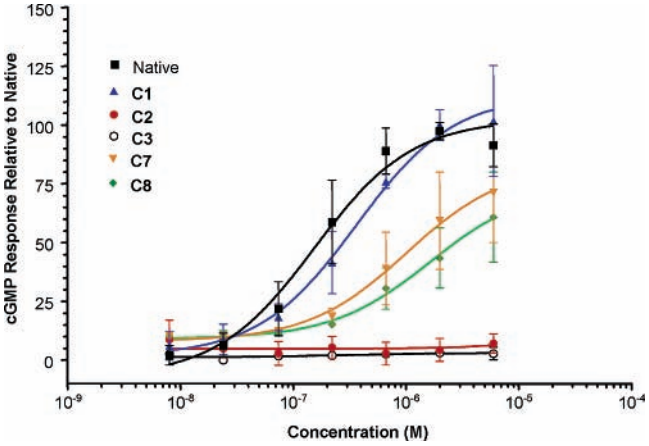

Figure 6. Activity curves depicting cGMP production from HAEC after exposure to conjugates utilizing oligomer **2**. The conjugates differ in site and/or extent of conjugation.

CONCLUSIONS

The cardiac hormone hBNP is a suitable substrate for conjugation technologies. By using the primary amines as sites for conjugation, various monoconjugates, one triconjugate, or one tetraconjugate could be readily obtained depending on the conditions for conjugation. Diconjugates were obtained only as minor products. The amphiphilic balance and the structure of the oligomer had some influence in the regioselectivity of conjugation. The cGMP assay in the HAEC line served as a good in vitro activity screen in our work toward a conjugated hBNP intended for oral administration. Of the oligomers used in this study, conjugation at one of the sites of the loop region (Lys14 or Lys27) resulted in partial agonists. Conjugation at both sites resulted in complete loss of agonist activity, even with the shortest of oligomers. However, conjugation at Lys3 generally resulted in conjugates displaying activity comparable to the native peptide. Some of the active hBNP conjugates are currently being evaluated in vivo and exhibit bioactivity after acute oral administration.

ACKNOWLEDGMENT

The authors thank Dr. John C. Burnett, Jr. and Dr. Alessandro Cataliotti of the Mayo Clinic for many helpful discussions. This work was supported by NIH grant 1 R43 HL74529-01 (K.D.J.).

LITERATURE CITED

(1) Massie, B. M., and Shah, N. B. (1997) Evolving trends in the epidemiologic factors of heart failure: rationale for preventive strategies and comprehensive disease management. *Am. Heart J. 133*, 703−712.

(2) Packer, M., and Cohn, H. M. (1999) Consensus recommendations for the management of chronic heart failure. On behalf of the membership of the advisory council to improve outcomes nationwide in heart failure. *Am. J. Cardiol. 83*, 1A-38A.

(3) O'Connell, J. B., and Bristow, M. R. (1994) Economic impact of heart failure in the United States: time for a different approach. *J. Heart Lung Transplant 13*, S107−112.

(4) Wald, J. D., Boylan, J., and Matthews, F. T. (2003). *Cardiology Update: 2003* (Edwards, A. G., Ed.) A. G. Edwards and Sons, St. Louis, MO.

(5) Knebel, F., and Baumann, G. (2003) Heart failure: state-of-the-art treatment and new therapeutic options. *Clin. Nephrol. 60 Suppl 1*, S59−66.

(6) Chen, H. H., Redfield, M. M., Nordstrom, L. J., Horton, D. P., and Burnett, J. C., Jr. (2004) Subcutaneous administration of the cardiac hormone BNP in symptomatic human heart failure. *J. Card. Failure 10*, 115−119.

(7) Yancy, C. W., Saltzberg, M. T., Berkowitz, R. L., Bertolet, B., Vijayaraghavan, K., Burnham, K., Oren, R. M., Walker, K., Horton, D. P., and Silver, M. A. (2004) Safety and feasibility of using serial infusions of nesiritide for heart failure in an outpatient setting (from the FUSION I trial). *Am. J. Cardiol. 94*, 595−601.

(8) James, K. D., Cataliotti, A., Schirger, J. A., Plonka, S., and Burnett, Jr., J. C. (2005) Congestive heart failure: pharmacological agents and the potential of B-type natriuretic peptide. *Curr. Med. Chem. 12*, 1439−1447.

(9) Chen, H. H., and Burnett, J. C. (2000) Natriuretic peptides in the pathophysiology of congestive heart failure. *Curr. Cardiol. Rep. 2*, 198−205.

(10) Levin, E. R., Gardner, D. G., and Samson, W. K. (1998) Natriuretic peptides. *N. Engl. J. Med. 339*, 321−328.

(11) Sudoh, T., Kangawa, K., Minamino, N., and Matsuo, H. (1988) A new natriuretic peptide in porcine brain. *Nature 332*, 78−81.

(12) Abuchowski, A., van Es, T., Palczuk, N. C., and Davis, F. F. (1977) Alteration of immunological properties of bovine serum albumin by covalent attachment of polyethylene glycol. *J. Biol. Chem. 252*, 3578−3581.

(13) Abuchowski, A., McCoy, J. R., Palczuk, N. C., van Es, T., and Davis, F. F. (1977) Effect of covalent attachment of polyethylene glycol on immunogenicity and circulating life of bovine liver catalase. *J. Biol. Chem. 252*, 3582−3586.

(14) Veronese, F. M. (2001) Peptide and protein PEGylation: a review of problems and solutions. *Biomaterials 22*, 405−417.

(15) Leeson, P. D., and Davis, A. M. (2004) Time-related differences in the physical property profiles of oral drugs. *J. Med. Chem. 47*, 6338−6348.

(16) Cataliotti, A., Schirger, J. A., Martin, F. L., Chen, H. H., McKie, P. M., Boerrigter, G., Costello-Boerrigter, L. C., Harty, G., Heublein, D. M., Sandberg, S. M., James, K. D., Miller, M. M., Malkar, N. B., Polowy, K., and Burnett, Jr., J. C. (2005) Oral human brain natriuretic peptide activates cyclic guanosine 3′, 5′-monophosphate and decreases mean arterial pressure in normal dogs. *Circulation 112*, 836−840.

(17) Saito, Y., Nakao, K., Itoh, H., Yamada, T., Mukoyama, M., Arai, H., Hosoda, K., Shirakami, G., Suga, S., Minamino, N., and et al. (1989) Brain natriuretic peptide is a novel cardiac hormone. *Biochem. Biophys. Res. Commun. 158*, 360−368.

(18) Kambayashi, Y., Nakao, K., Mukoyama, M., Saito, Y., Ogawa, Y., Shiono, S., Inouye, K., Yoshida, N., and Imura, H. (1990) Isolation and sequence determination of human brain natriuretic peptide in human atrium. *FEBS Lett. 259*, 341−345.

(19) Mukoyama, M., Nakao, K., Hosoda, K., Suga, S., Saito, Y., Ogawa, Y., Shirakami, G., Jougasaki, M., Obata, K., Yasue, H., and et al. (1991) Brain natriuretic peptide as a novel cardiac hormone in humans. Evidence for an exquisite dual natriuretic peptide system, atrial natriuretic peptide and brain natriuretic peptide. *J. Clin. Invest. 87*, 1402−1412.

(20) Yan, W., Wu, F., Morser, J., and Wu, Q. (2000) Corin, a transmembrane cardiac serine protease, acts as a pro-atrial natriuretic peptide-converting enzyme. *Proc. Natl. Acad. Sci. U. S. A. 97*, 8525−8529.

(21) Clement, S., Still, J. G., Kosutic, G., and McAllister, R. G. (2002) Oral insulin product hexyl-insulin monoconjugate 2 (HIM2) in type 1 diabetes mellitus: the glucose stabilization effects of HIM2. *Diabetes Technol. Ther. 4*, 459−466.

(22) Kipnes, M., Dandona, P., Tripathy, D., Still, J. G., and Kosutic, G. (2003) Control of postprandial plasma glucose by an oral insulin product (HIM2) in patients with type 2 diabetes. *Diabetes Care 26*, 421−426.

(23) Clement, S., Dandona, P., Still, J. G., and Kosutic, G. (2004) Oral modified insulin (HIM2) in patients with type 1 diabetes mellitus: results from a phase I/II clinical trial. *Metabolism 53*, 54−58.

BC0501000

Activity of Dendrimer−Methotrexate Conjugates on Methotrexate-Sensitive and -Resistant Cell Lines

Sezen Gurdag,[†] Jayant Khandare,[†,⊥] Sarah Stapels,[‡] Larry H. Matherly,[‡,§,#] and Rangaramanujam M. Kannan*[,†,#]

Department of Chemical Engineering and Material Science, and Biomedical Engineering, Wayne State University, Detroit, Michigan 48202, and Cancer Biology Graduate Program, Department of Pharmacology, and Developmental Therapeutics Program, Barbara Ann Karmanos Cancer Institute, Wayne State University School of Medicine, Detroit, Michigan 48201. Received June 27, 2005; Revised Manuscript Received January 25, 2006

Dendritic nanostructures can play a key role in drug delivery, due to the high density and variety of surface functional groups that can facilitate and modulate the delivery process. We have investigated the effect of dendrimer end-functionality on the activity of polyamido amine (PAMAM) dendrimer−methotrexate (MTX) conjugates in MTX-sensitive and MTX-resistant human acute lymphoblastoid leukemia (CCRF-CEM) and Chinese hamster ovary (CHO) cell lines. Two amide-bonded PAMAM dendrimer−MTX conjugates were prepared using a dicyclohexylcarbodiimide (DCC) coupling reaction: one between a carboxylic acid-terminated G2.5 dendrimer and the amine groups of the MTX (conjugate A) and another between an amine-terminated G3 dendrimer and the carboxylic acid group of the MTX (conjugate B). Our studies suggest that conjugate A showed an increased drug activity compared to an equimolar amount of free MTX toward both sensitive and resistant cell lines, whereas conjugate B did not show significant activity on any of the cell lines. Despite substantially impaired MTX transport by MTX-resistant CEM/MTX and RII cells, conjugate A showed sensitivity increases of approximately 8- and 24-fold (based on IC_{50} values), respectively, compared to free MTX. Co-incubation of the cells with adenosine and thymidine along with either conjugate A or MTX resulted in almost complete protection, suggesting that the conjugate achieves its effect on dihyrofolate reductase (DHFR) enzyme through the same mechanism as that of MTX. The differences in cytotoxicity of these amide-bonded conjugates may be indicative of differences in the intracellular drug release from the cationic dendrimer (conjugate B) versus the anionic dendrimer (conjugate A), perhaps due to the differences in lysosomal residence times dictated by the surface functionality. These findings demonstrate the feasibility of using dendrimers as drug delivery vehicles for achieving higher therapeutic effects in chemotherapy, especially in drug-resistant cells.

INTRODUCTION

Polymers have been used as drug carriers due to their ability to release drugs in a controlled manner, prolong circulation times, and increase drug solubility. They have also demonstrated an affinity for preferential accumulation in tumor tissues as a result of enhanced permeability and retention (EPR) effect (*1*−*3*). For cancer therapy, it is desirable to achieve increased efficacy of drugs, enhanced cellular entry, and reduced side effects. To this end, several polymer-based drug delivery methods are being investigated in which the drug is encapsulated, complexed, or conjugated to polymers. Uptake of doxorubicin-PEG-coated liposomes with folate moieties by oral carcinoma KB cells was investigated and found to be 45 times higher than that of nontargeted liposomes (*4*). Several linear polymer−cancer drug conjugates have shown superior in vivo activities compared to those of the free drugs (*5*). The therapeutic effect of adriamycin coupled to *N*-(2-hydroxypropyl) methacrylamide copolymer in rat and mouse models was greater than that of free drug. It was observed that the half-life of the polymer−adriamcyin conjugate was 15 times higher compared to unconjugated drug (*6*). However, the in vitro activities of polymer−drug conjugates have mostly been lower than those of free drugs.

Recently, hyperbranched polymers and dendrimers have found a vast number of applications in delivering drugs and genetic materials into cells (*7*−*16*). Compared to conventional polymers, dendrimers have structural and functional advantages emanating from the multiplicity and additivity effects that can be achieved by manipulating the densely packed end groups. It is possible to encapsulate, complex, or conjugate several molecules onto one dendrimer molecule. At the same time, different entities can be easily attached to these end groups at once to target, treat, and signal. Cancer is one of the applications for these unique nanostructures. Typically, significant amounts of chemotherapeutic agents are lost in the circulation prior to cellular uptake of the drug by tumor cells. Moreover, cellular entry of chemotherapeutic drugs is often the limiting factor for their therapeutic effectiveness. To achieve improved therapeutic effects in the treatment of cancer, it is essential to increase tumor uptake of chemotherapeutic drugs by employing drug delivery vehicles. This study explores the use of dendritic polymers for this purpose.

Conjugation of methotrexate (MTX) and folic acid to hydrazide-terminated dendrimers revealed that MTX and folic acid can be coupled to the dendrimer with conjugation ratios of 4.7 and 12.6, respectively (*17*). In another study, a fifth generation PAMAM dendrimer was used for the synthesis of

* Department of Chemical Engineering and Material Science, Wayne State University, 5050 Anthony Wayne Drive, Detroit, MI-48202. Phone: 313-577-3879. Fax: 313-577-3810. E-mail: rkannan@chem1.eng.wayne.edu.

[†] Department of Chemical Engineering and Material Science, and Biomedical Engineering.

[‡] Cancer Biology Graduate Program.

[§] Department of Pharmacology.

[#] Developmental Therapeutics Program.

[⊥] Present address: Department of Pharmacy, Rutgers State University of New Jersey.

10.1021/bc0501855 CCC: $33.50 © 2006 American Chemical Society
Published on Web 02/28/2006

nanodevices containing an anticancer drug (MTX), an imaging agent (fluorescein isothiocyanate, FITC), and folic acid (FA) as the targeting agent. The FA-containing conjugate possessing an ester bond between MTX and the dendrimer showed 5 times more cytotoxicity compared to free MTX against the KB cell line overexpressing the folate receptors. Furthermore, an untargeted analogue of this conjugate did not produce any cell growth inhibition in the same cell line (*16*). However, a MTX−dendrimer conjugate with an amide bond showed less activity than free MTX (*18*). In PEGylated PAMAM dendrimers, drug encapsulation efficiency depended on the dendrimer generation number, and the molecular weight of the grafted PEG units. Twenty-six molecules of MTX were encapsulated in the generation-4 PAMAM dendrimer with 63−65 PEG grafts of 2000 as the molecular weight. Since not only dendrimers but also cationic macromolecules can cause cell lysis as a result of destabilization of the cellular membrane, many researchers seek to manipulate the surface charge of these structures. In this respect, drug loading capacity, drug release, and the hemolytic effect of the PEGylated generation-4 PAMAM dendrimer were investigated by encapsulating 5-FU. PEGylation improved the drug loading while reducing the drug release and hemolytic effect (*19*).

The use of either conjugation or encapsulation approaches can change the cellular transport characteristics, pharmacodynamics, and pharmacokinetics of the parent drug, resulting in increased or decreased cytotoxicity, along with altered in vivo distribution. Polyester dendrimer−doxorubicin conjugates showed very slow drug release at neutral pH. On the other hand, a decrease in pH from 7.4 down to 4−6 facilitated drug release from the conjugate due to the pH-labile characteristics of the hydrazone bond. Although the conjugate hampered the cytotoxicity of the drug by 80−98%, it did not demonstrate significant accumulation in vital organs such as liver, heart, and lungs (*20*). PAMAM dendrimer−cisplatin conjugates formed using amide bonds showed 100 times less cytotoxicity against human lymphoblastoid leukemia cell line CCRF-CEM (*21*). In some cases, the drug may not need to be released from the conjugate to inhibit cell growth. Conjugation of MTX to PEG yielded conjugates, which were able to inhibit the activity of its target enzyme dihydrofolate reductase (DHFR) enzyme, even in the conjugated form, in cell-free activity assays. Yet, they were appreciably less active compared to free MTX (*22*).

MTX belongs to the class of antimetabolites. Understanding the mechanism of MTX action can help gain insights into the mode of action of dendrimer−MTX conjugates by employing correct tools. As an antifolate, MTX exerts profound effects on the distribution of intracellular reduced folates that act as cofactors for many of the enzymatic reactions leading to nucleotide biosynthesis. Thus, treatment of tumor cells with MTX inhibits purine and thymidylate biosynthesis, resulting in the inhibition of DNA replication (*23*, *24*). The transformation of MTX to its polyglutamate derivatives, driven by folylpolyglutamate synthase (FPGS), prolongs the retention time of the drug inside the cells (*23*).

Entry of MTX into mammalian cells is significantly restricted because of the charged character of the -COOH groups at physiological pH. Therefore, the contribution of diffusion to net MTX accumulation is nominal. The main uptake route for MTX into mammalian cells is carrier-mediated by the reduced folate carrier (RFC), where the driving force is provided by anion exchange gradients acting as exchange substrates (*25*). However, despite the high affinity of the carrier to MTX, cellular uptake of dianionic MTX by RFC is limited due to the capacity of the transport system and the negative charge of the cells. Moreover, loss of RFC function is a common mode of MTX resistance (*24*, *26*). MTX is highly cytotoxic against not only neoplastic cells but also rapidly replicating healthy cells such as bone-marrow cells. It causes bone-marrow depression, as well as disturbance and inflammation in the gastrointestinal tract, which is serious at high doses (*23*). Thus, to decrease the cytotoxicity of MTX to susceptible normal cells, it is crucial to modify the administered drug dose and schedule and the use of rescue or protection agents such as leucovorin ((6*R*,*S*) 5-formyltetrahydrofolate; 5-CHO-THF) or nucleosides. Additions such as adenosine, thymidine, and hypoxantine are exploited to rescue the cells in a noncompetitive manner (*24*, *27*, *28*). In contrast, leucovorin rescue shows a competitive relationship with MTX due to effects on membrane transport, polyglutamylation, and enzyme binding (*24*, *26*−*28*).

Recently, we have shown that complexes and conjugates of dendrimers with different drugs can be prepared with high drug payloads. The conjugates demonstrated rapid cellular entry and therapeutic activity in A549 human lung carcinoma cells (*10*−*13*). In this study, we report the carbodiimide-mediated conjugation of MTX to PAMAM-G2.5-COOH and PAMAM-G3-NH_2 dendrimers, employing either -NH_2 or -COOH groups of MTX. We investigated the importance of the functional groups involved in the conjugation and the surface charge of the overall conjugate on the cytotoxic activity of the conjugates toward both MTX-sensitive and MTX-resistant cell lines characterized by a nearly complete loss of RFC function. To understand the mechanism of action of conjugated MTX, cellular rescue was performed by co-incubating with adenosine and thymidine nucleosides.

EXPERIMENTAL PROCEDURES

Materials. MTX and leucovorin were obtained from National Cancer Institute (Drug Synthesis and Chemistry Branch, Developmental Therapeutics Program, Division of Cancer Treatment and Diagnosis). Polyamidoamine (PAMAM) dendrimers (generation 2.5 with -COOH end groups and generation 3 with -NH_2 end groups) were purchased from Aldrich Chemical Co. (some physical properties of these polymers as well as those of MTX can be found in Table 1). Other reagents were obtained from assorted vendors in the highest quality available and include *N*,*N*-dicyclohexyl carbodiimide (DCC, Fluka), RPMI 1640 culture medium (Invitrogen), penicillin and streptomycin (Invitrogen), dialyzed fetal bovine serum (Invitrogen), CellTiter Blue cell viability kit (Invitrogen), α-MEM culture medium (Mediatech), Hank's balanced salt solution (Sigma), Dulbecco's phosphate buffered saline (PBS) (Sigma), nucleosides (Sigma), iron supplemented defined bovine calf serum (HyClone), dihydrofolate reductase (DHFR) (Sigma), dihydrofolic acid (DHF) (Sigma), and β-nicotinamide adenosine dinucleotide phosphate, reduced form (β-NADPH) (Sigma). All the solvents used were purchased from Fisher Scientific except HPLC-grade dimethyl sulfoxide (OmniSolv methylsulfoxide) (VWR).

Synthesis of MTX−PAMAM Dendrimer Conjugates. *Scheme for Conjugate A. Conjugation of MTX to PAMAM-G2.5-COOH*. MTX and molar end group equivalent of PAMAM-G2.5-COOH were dissolved in 10 mL of anhydrous DMSO, followed by the addition of a molar equivalent amount of DCC. The reaction mixture was stirred continuously for 72 h at room temperature in the dark. After 72 h, it was filtered to remove dicyclohexyl urea (DCU), and the filtrate was dialyzed against an excess amount of DMSO using membrane (MW cutoff = 3500 Da) for 24 h to remove free MTX and unreacted DCC. The filtrate was vacuum-dried at room temperature to obtain MTX−dendrimer conjugate. The conjugate was formed as a result of the generation of an amide bond between -COOH groups of the dendrimer and -NH_2 group of MTX. This conjugate (conjugate A) was characterized using a Varian 400 MHz spectrometer to estimate the conjugation ratio between

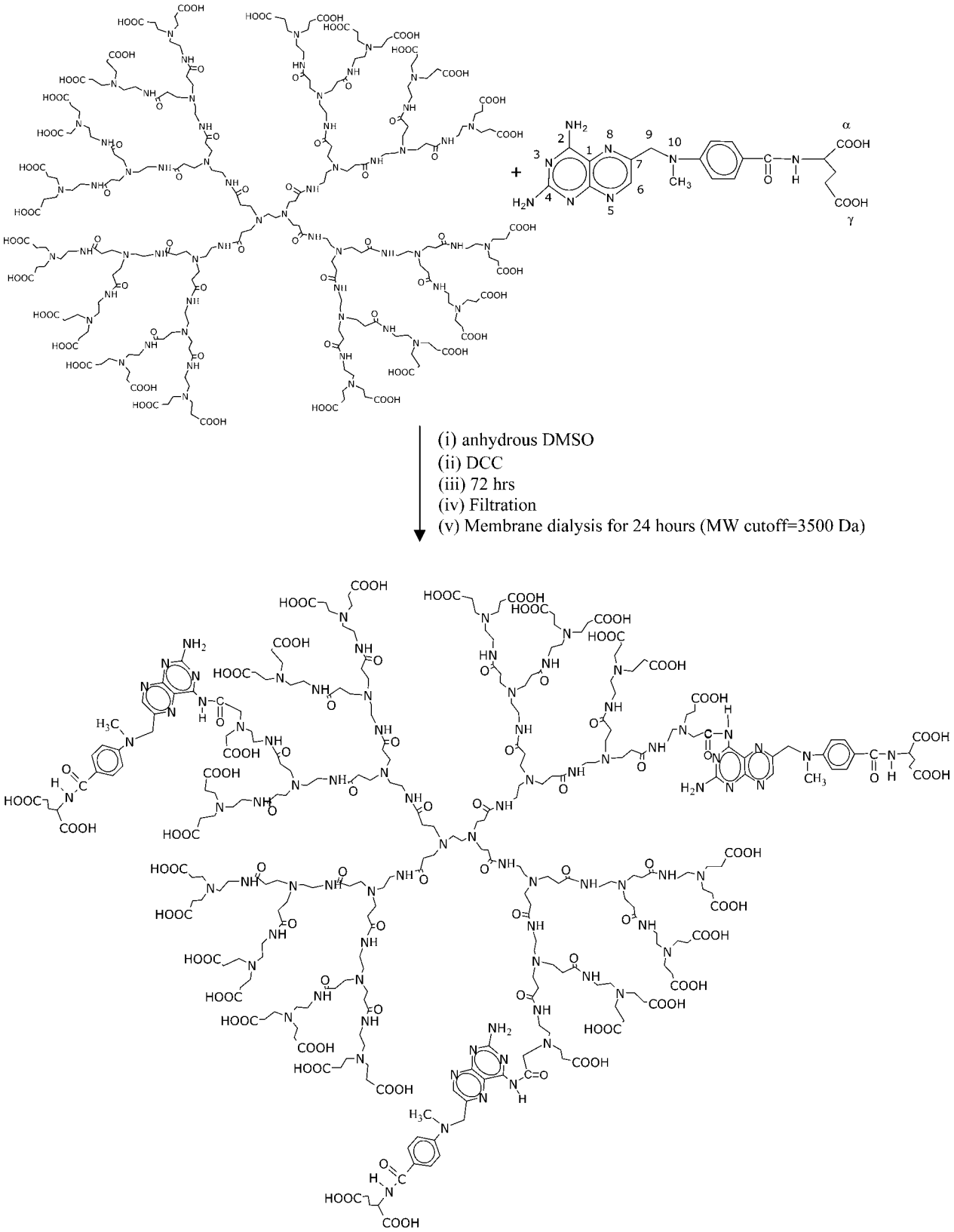

Figure 1. Synthesis scheme for PAMAM-G2.5-COOH-MTX conjugate (designated as conjugate A). (A similar procedure was used to synthesize conjugate B.)

MTX and the dendrimer. Figure 1 summarizes the synthesis scheme followed. ^{1}H NMR spectrum for the conjugate (Supplemental Figure A, Supporting Information) (400 MHz, DMSO-d_6): δ (ppm) 2.31−3.57 (m, 356 H, CH protons of PAMAM, overlapping with 9 H aliphatic singlets of MTX), 6.53 (s, 2 H, aromatic NH_2 of MTX), 6.82 (d, 2 H, aromatic CH of MTX), 7.67 (s, 2 H, aromatic NH_2 of MTX), 7.91 (d, 2 H, aromatic CH of MTX), 4.76 (s, 2 H, CH_2 of MTX), 8.5 (s, 1 H, aromatic CH of MTX).

Scheme for Conjugate B. Conjugation of MTX to PAMAM-G3-NH$_2$. MTX and molar end group equivalent of PAMAM-G3-NH_2 (60 mg, 8.68 μmol, based on 32 end functional groups) were dissolved in 10 mL of DMSO, followed by the addition of a molar equivalent of DCC (57.4 mg, 278 μmol). The reaction

Table 1. Properties of PAMAM Dendrimers and MTX

	av mol wt (g/mol)	generation	end functionality	no. of end groups	conjugation ratio (MTX/polymer)	(%) payload
PAMAM-G2.5 dendrimer	6267[a]	2.5	COOH	32	0.40	2.8
PAMAM-G3 dendrimer	6909[a]	3	NH_2	32	4.4	22.4
MTX	454.45	N/A	COOH, NH_2	4	N/A	N/A

[a] Data supplied by Aldrich.

conditions and the purification steps were similar to those mentioned above. Conjugate B was formed as a result of amide bond formation between the -NH_2 groups of the dendrimer and the -COOH group of MTX. ^{1}H NMR spectrum for the conjugate (Supplemental Figure B, Supporting Information) (400 MHz, DMSO-d_6): δ (ppm) 2.18−3.46 (m, 484 H, CH protons of PAMAM, overlapping with 9 H aliphatic singlets of MTX), 6.77 (d, 2 H, aromatic CH of MTX), 7.54 (s, 2 H, aromatic NH_2 of MTX), 7.70 (d, 2H, aromatic CH of MTX), 7.95 (s, 2H, aromatic NH_2 of MTX), 4.76 (s, 2 H, CH_2 of MTX), 8.51 (s, 1 H, aromatic CH of MTX), 4.30 (s, 1 H, aliphatic CH of MTX).

The drug payload in the conjugate was estimated using the proton integration method, by taking the characteristic peaks of MTX and the PAMAM dendrimer into account, as explained elsewhere (*29*−*33*). We estimated the payload of MTX in Conjugates A and B to be 0.4 and 4.4, respectively (Table 1). It is possible that the product might contain unreacted dendrimer along with the successfully conjugated portion. Considering the fact that both of the conjugates have less than five MTX molecules per dendrimer, the separation of reacted and unreacted dendrimer is difficult, due to the restrictions related to mainly molecular weight and altered physicochemical characteristics of the dendrimer upon conjugation. However, extensive dialysis and lack of MTX release from the conjugate suggest that encapsulated MTX should be minimal (as discussed later).

Also, dendrimers and the conjugates were characterized by gel permeation chromatography coupled with Shimadzu LC-10ADVP liquid chromatography equipped with a CTO-10ASVP Shimadzu column oven and MesoPore 300 × 7.5 mm column (Polymer Laboratories) using HPLC-grade DMSO as the eluent at a flow rate of 0.5 mL/min at 35 °C.

MALDI-TOF mass spectrometry was also performed using a Bruker Daltonics Ultraflex matrix-assisted laser desorption/ionization mass spectrometer with time-of-flight mass analyzer (MALDI-TOF) (linear operation mode) for further characterization of the conjugates. For the amine-terminated cationic PAMAM dendrimer, MALDI-TOF proved to be a useful technique showing a strong peak corresponding to 6909 Da as the suggested theoretical molecular weight for this compound. MALDI-TOF analysis of a new batch of conjugate B (prepared using the same procedure, resulting in a slightly higher drug payload) agreed well with the results obtained from ^{1}H NMR (data not shown). This suggests that the ^{1}H NMR and GPC characterization provide a reasonable estimate of the drug payload in the present conjugates.

Cell Cultures. The human lymphoblastoid leukemia wild-type CCRF-CEM cell line and its MTX-resistant counterpart (CEM/MTX) were maintained in RPMI 1640, with iron supplemented fetal calf serum (Hyclone), glutamine (2 mM), penicillin (100 U/mL), and streptomycin (100 μg/mL) at 37 °C in 5% CO_2 atmosphere (*35*−*37*). CEM/MTX cells were supplemented with 500 nM MTX. In additional experiments, Chinese hamster ovary (CHO) cells were used including MTX-resistant MTXRIIOua^{R}2-4 (RII) and RII cells transfected with the human RFC (designated PC43/10) (*38*). CHO cells were grown in α-MEM including serum as previously described (*38*).

In Vitro Cytotoxicity Studies. In vitro cytotoxicity for the CCRF-CEM human leukemic cells (both MTX-sensitive and MTX-resistant), treated either with free MTX or with dendrimer-conjugated MTX, was assessed by direct counting using a hemacytometer. Cells were seeded in 24-well plates at 1.5 × 10^5/2 mL/well in complete RPMI media including 10% dialyzed fetal bovine serum and incubated over 96 h with serial dilutions of either free MTX or conjugated MTX. All experiments were done at least in duplicate.

For CHO cells, a fluorimetric assay was used for measuring drug sensitivities. Cells were plated in duplicate at 4000 cells/200μL/well in a 96-well culture plate in complete RPMI 1640 medium containing dialyzed serum and serial dilutions of MTX or conjugated MTX. Cells were grown for 4 days, and cell viabilities were determined with the CellTiter Blue assay kit. Incubations with the assay reagent were for 4 h, after which the number of viable cells in each well was determined by measuring the fluorescence at 560 nm (excitation) and 590 nm (emission) on a fluorescent multiplate reader. Experiments were performed three times. Cell viability is expressed as the percentage of that obtained for untreated control cells in parallel. For some experiments, cells were treated with free MTX or conjugated MTX along with nucleoside protection agents (60 μM adenosine and 10 μM thymidine), to confirm the antifolate activities of the drugs.

In all the experiments, amounts of conjugated MTX in the MTX−dendrimer conjugates were determined from the conjugation ratios estimated by ^{1}H NMR. The concentrations of conjugates in the incubations were adjusted to maintain equivalent molar amounts of MTX to that for the free MTX treatments.

DHFR Inhibition Assay. The effect of either free MTX or conjugated MTX on the target enzyme, DHFR, was measured in a microplate type of assay where oxidation of NADPH to $NAPD^+$ was followed at 340 nm. Assay mixture contained 0.05 M Tris buffer (pH of 7.5). 20 μL of test compound dissolved in 10 nM PBS to achieve final concentrations of 0−100 nM (or only the solvent for the control well), was added to a reaction mixture of 0.003 units of human recombinant DHFR enzyme expressed in E.Coli and 87 μM NADPH. Reaction mixture was allowed to stand for 5 min at room temperature, which was followed by the addition of 153 μM DHF completing the final volume to 300 μL. The change in the absorbance was measured using kinetic mode with a reading interval of 20 s for the duration of 20 min. Blank reaction rate was determined by processing the absorbance from 2 to 18 min. Comparison of the linear decrease in the same time period in the test wells with the blank well gave the DHFR inhibition activity of the test samples. Results were given as percent inhibition of the enzymatic activity in comparison to the control.

RESULTS

Synthesis and Characterization of Conjugates. MTX contains both α- and γ-COOH groups in the glutamate moiety, as well as -NH_2 groups at the second and fourth positions in the 2,4-diamino-6-pteridinyl group as shown in Figure 1. MTX was successfully conjugated to PAMAM-G2.5-COOH and PAMAM-G3-NH_2 dendrimers using DCC as a coupling agent using a one-pot reaction synthesis scheme. In the past, MTX has been conjugated with -NH_2 terminal dendrimers specifically using -COOH groups. Even though one might argue that in DCC coupling reactions two carboxylic acids can come together to

form acid anhydride as shown over long-chain fatty acids, this formation is highly unlikely in the presence of competitive reactants. Eventually, an amide-bonded conjugate of the dendrimer and the drug is likely (*39*). However, it has been reported that the presence of free -COOH groups, especially at the α-position, is critical for its cytotoxic activity in the conjugated form (*29*, *34*, *40*). Therefore, we decided that it was worthwhile to utilize the -NH_2 group in the pteridine of MTX for conjugation with -COOH terminal groups on the dendrimer, leaving the -COOH groups on MTX free.

The difference in the conjugation ratios of MTX to the dendrimers could be explained by the differences in the reactivities of the -COOH and -NH_2 groups of MTX toward the -NH_2 and -COOH functional groups of each dendrimer, respectively. Also, there are two -COOH groups on MTX readily available for the interaction with amines, which may improve the probability of reaction for conjugate B. As a result, the amine-terminated dendrimer when the -COOH group on MTX was used as the linkage site had higher drug loading. The COOH-terminated dendrimer had lower MTX loading due to lesser reactivity of sterically more stabilized -NH_2 in the 2,4-diamino-6-pteridinyl group of MTX with the dendrimer surface functional groups.

The MTX payload in conjugate B is comparable to that obtained in the literature (*17*, *18*). Even though we did not confirm which of the two -COOH groups in the glutamate moiety of MTX interacts with NH_2 groups of the dendrimer, it is most likely the carboxyl group at the γ-position, since Kono et al. showed that the conjugation of folic acid to hydrazide-terminated dendrimers could occur through its γ-COOH group, which is more reactive toward the amino groups in carbodiimide coupling reactions (*17*). Additionally, conjugation of MTX to human serum albumin occurred mainly through the involvement of the γ-COOH group of MTX (*41*). For conjugate A, it is not clear whether the -NH_2 at the second or the fourth position in the pteridinyl group is used for conjugation, even though the amine group at the fourth position is expected to be involved in the coupling reaction to a higher extent due to lesser sterical crowding. In addition, the feasibility of removing unreacted or encapsulated MTX from end product by dialysis, as well as the stability of the conjugate in DMSO was validated using conjugate B. A known amount of conjugate B dissolved in DMSO was placed in a dialysis membrane with a molecular cutoff size of 1000 Da where the outside phase contained only DMSO. Chromatographic analysis of the samples passing to the outside of the membrane collected over a period of 24 h indicated that a negligible fraction of drug from the conjugate was released from the dialysis bag. This suggests that conjugate is stable, and free MTX in the conjugate was minimal after purification.

Further characterization of the pure dendrimers and the conjugates has been done using gel permeation chromatography (GPC). The elution profiles of cationic PAMAM G3 dendrimer and the corresponding conjugate, measured using the light scattering detector, are displayed in Figure 2. Peak elution volume of the pure dendrimer was observed at 8.32 mL, while it was 8.1 mL for conjugate B. The monomodal nature, and a clear shift toward lower elution volume (and shorter elution times) for the conjugate, suggest the formation of a larger molecular weight object, which is monodisperse. The absence of a peak at 12 mL (peak elution volume for free MTX) for the conjugate is suggestive of the absence of unconjugated MTX in the conjugate (not shown). Conjugate A did not yield an appreciable shift in the elution profiles since it has only 0.4 MTX molecules attached to the dendrimer. Therefore, analysis method is insensitive to such small molecular weight change in the analyte. In these reactions, we expect dimers of MTX to

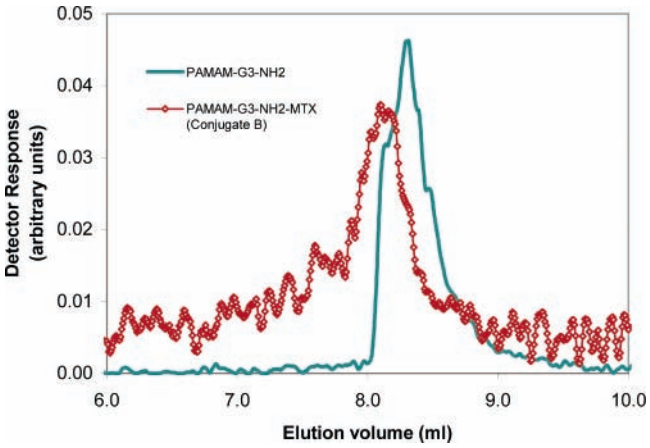

Figure 2. LC-GPC elution profiles of cationic third generation PAMAM dendrimer and the corresponding conjugate with MTX, conjugate B.

be dialyzed out during purification, as evidenced by the lack of additional peaks in GPC near the MTX peak. To improve the yield, we have started pursuing amine/carboxyl group protection approaches to enhance and optimize the conjugation scheme. For this, protection of either carboxyl or amine group of MTX is done by using ethyltrifluoroacetic acid (ETFA) or di-*tert*-butyl dicarbonate (N-boc), respectively.

In Vitro Evaluation of MTX, Dendrimers, and MTX−Dendrimer Conjugates. In vitro growth inhibition activities of free MTX, dendrimers, conjugate A, and conjugate B were investigated initially with the CCRF-CEM and CEM/MTX lymphoblastic leukemia cell lines. Following these initial studies, MTX-resistant and -sensitive CHO cells (designated RII and PC43/10) were studied using a fluorescence-based cell viability assay. Both CEM/MTX and RII cells are characterized by a nearly complete loss of RFC-mediated MTX uptake (*35*−*38*). Whereas a range of MTX and MTX-conjugate concentrations were used for these experiments, the molar equivalents of MTX added to cells were the same regardless of whether the conjugated or free drug forms were used.

In Vitro Cytotoxicity of MTX, PAMAM Dendrimers, and Dendrimer−MTX Conjugates. *In Vitro Cytotoxicities of PAMAM Dendrimers.* The CCRF-CEM and CEM/MTX human lymphoblastic leukemia cell lines (T-ALL) were treated with pure dendrimers (0−6667 nM for PAMAM-G2.5-COOH and 0−1112 nM for PAMAM-G3-NH_2), and growth was assayed as described earlier. These polymer concentrations correspond to the amounts of dendrimer that would be present in the MTX conjugates used for the cytotoxicity experiments.

Neither of the dendrimers showed significant cell toxicity over a wide range of concentrations (not shown). For the PAMAM-G2.5-COOH dendrimer, even at 6667 nM (0.042 mg/mL), more than 90% of the CEM/MTX cells were viable. Similarly, Malik et al. observed that the PAMAM-G2.5-COOH dendrimer did not exhibit any significant toxicity against B16F10 melanoma cells at 2 mg/mL, a much higher concentration than those used in our experiments. They also reported an IC_{50} for PAMAM-G3-NH_2 toward B16F10 cells of 0.05 mg/mL (*42*). The highest concentration used in our studies was only 1112 nM (0.0077 mg/mL). Cell viability of CEM/MTX cells treated with this concentration approached 100% (not shown).

In Vitro Cytotoxicities of Free MTX and Dendrimer−MTX Conjugates. The in vitro activities of MTX and both the conjugates were tested in terms of growth inhibition of human leukemia and hamster ovary cell lines. Figure 3a shows the responses of CCRF-CEM and CEM/MTX cell lines to both free MTX and conjugate A. The IC_{50} values for free MTX in the MTX-sensitive and -resistant (CEM/MTX) cell lines were

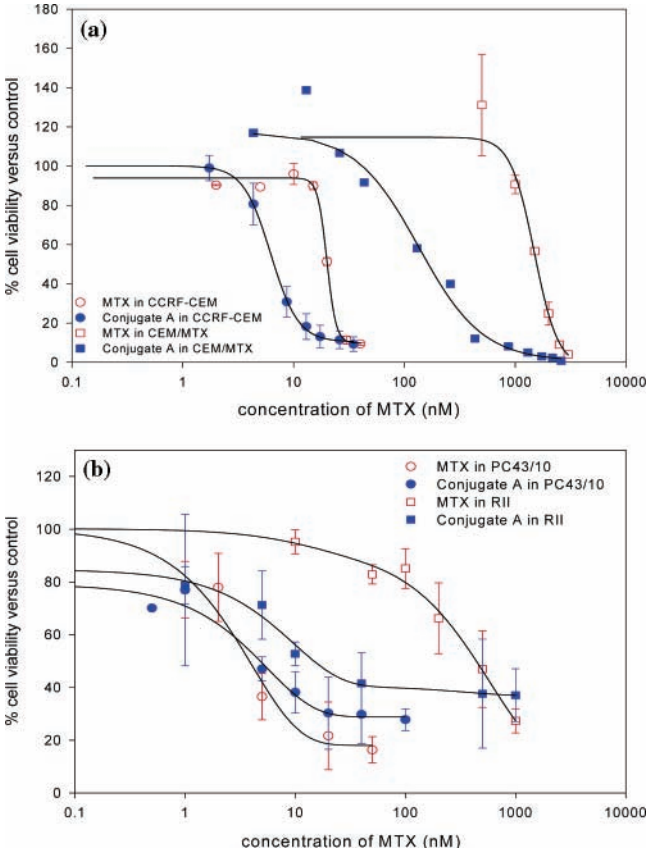

Figure 3. (a) Comparative growth inhibition profiles of free MTX and conjugate A in CCRF-CEM and CEM/MTX cell lines. (b) Comparative growth inhibition profiles of free MTX and conjugate A in RII and PC43/10 cell lines.

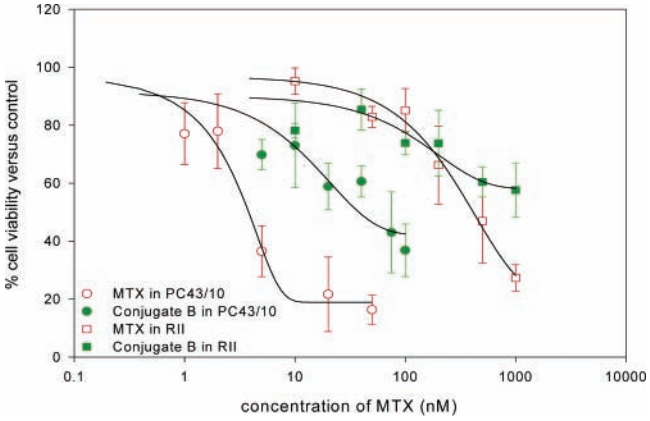

Figure 4. Comparative growth inhibition profiles of free MTX and conjugate B in RII and PC43/10 cell lines.

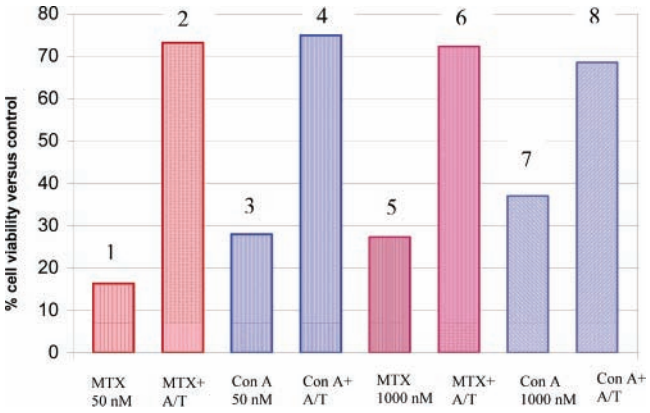

Figure 5. Comparative growth inhibition profiles of free MTX and conjugate A with and without rescue agents (60 μM adenosine + 10 μM thymidine) in RII and PC43/10 cell lines. Bars 1−4: PC43/10 cells; bars 5−8: RII cells.

approximately 20 and 1575 nM, respectively, comparable to the values reported in literature (*22*, *29*, *34*−*37*, *40*). By comparison,
the IC_{50} values for conjugate A (listed in MTX equivalents) in the CCRF-CEM and CEM/MTX cell lines were 6.8 and 206 nM, respectively. Thus, conjugate A is approximately 3-fold more potent than free MTX toward the MTX-sensitive CCRF-CEM cells and approximately 8-fold more potent toward the resistant CEM/MTX cell line.

With the CHO cells, similar in vitro growth inhibition profiles for free MTX and conjugate A were seen (Figure 3b). The MTX-sensitive CHO cells (PC43/10) expressing high levels of human RFC, showed an IC_{50} for free MTX of approximately 4 nM, similar to an earlier report (*38*). Likewise, the IC_{50} for the MTX transport impaired RII cells (420 nM) was only slightly different from the value previously reported by Wong et al. (*38*). Importantly, for conjugate A, an IC_{50} of 5 nM was measured in PC43/10 cells, whereas a value of 17 nM was recorded in the MTX-resistant CHO cell line, an increase of 24-fold over unconjugated MTX.

The conjugate of MTX with PAMAM-G3-NH_2 dendrimer (conjugate B) was also evaluated in terms of growth inhibition activity. For both the CCRF-CEM and CHO cell lines, sensitivity to conjugate B was significantly reduced compared to either MTX or conjugate A. Representative results are shown in Figure 4 for the CHO sublines. For PC43/10 cells, the IC_{50} was increased from that for MTX by about a factor of 10. In RII cells, 65% of maximal growth was seen in the presence of 1000 nM of conjugate B. Similar results were seen in the CCRF-CEM sublines (not shown).

Altogether, these data demonstrate that conjugation of MTX through an -NH_2 group on the pteridine ring in conjugate A results in a more potent growth inhibition than either free MTX or the conjugate formed between the -COOH group on MTX and the -NH_2 on the dendrimer (conjugate B). This was true in both the MTX-sensitive and MTX-resistant cells. Notably, conjugate A was able to significantly circumvent the loss of RFC function in both transport-impaired cell lines.

Long-term incubation of the cells (96 h) ensured the arrest of the cells mainly in S-phase as it is highly cell cycle-dependent. Capture of the cell in this phase prevents DNA synthesis, which will lead to the death of the cells when they are most susceptible to the drug. At the same time, MTX may also interfere with protein synthesis in G_1 phase especially at high concentrations as a result of prevention of amino acid interconversions. Thus, the cells that escaped from cytotoxic activity of the drug during S-phase will succumb due to deprived protein synthesis for a long period of time (*43*). In addition, a 4-day incubation period was found to be the best for the cell model in this experimental system in terms of the cellular viability difference between the control and the treatment wells.

To further investigate the possible mechanism responsible for the growth inhibitory effects of conjugate A, we cultured the CHO cells with the drug (either free drug or in conjugated form) in the presence of a combination of 60 μM adenosine and 10 μM thymidine. Previous studies have shown that individual nucleosides only partially circumvent the cytotoxic effects of DHFR inhibitors such as MTX, while a source of purines and thymidine can significantly rescue cells from antifolate activity of MTX (*27*, *28*). Figure 5 compares the cytotoxic effects of MTX and conjugate A toward PC43/10 and RII cells in the absence and in the presence of nucleosides. As expected, significant protection was seen at 50 nM free MTX

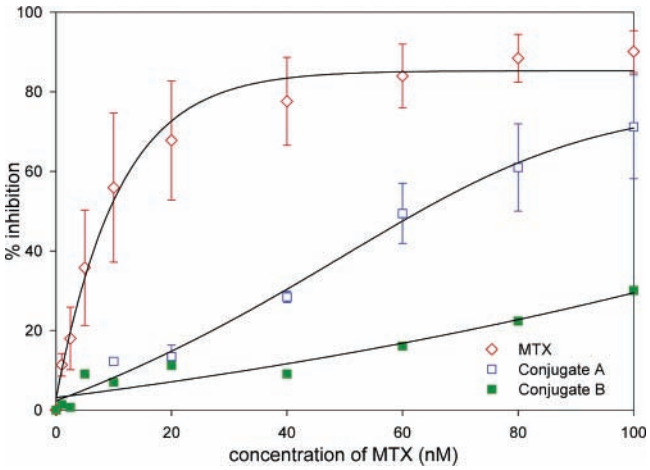

Figure 6. Comparative inhibition pattern of MTX and the conjugates against enzymatic activity of DHFR.

or conjugate A for the sensitive cells, and at 1000 nM MTX or conjugate A for the RII cells.

From these results, it can be concluded that mechanism of action (over 96 h) for the conjugated drug is most likely the same as that for free MTX, namely, via inhibition of DHFR. However, when the cells were supplied with nucleosides, this circumvents the effects on cell growth by bypassing the requirement for reduced folates for the synthesis of necessary nucleotides for de novo synthesis of DNA. In other experiments, 60 μM adenosine and 10 μM thymidine were ineffective in completely rescuing the MTX-sensitive PC43/10 cells from the growth inhibitory effects of conjugate B. The reasons for this response are currently under investigation.

DHFR Inhibition Activities of MTX and the Conjugates. The enzyme inhibition activities of free MTX and the conjugated MTX were evaluated in a cell-free assay (Figure 6). As can be seen from the figure, all three forms of the drug showed concentration-dependent inhibitory activity against the target enzyme. Free MTX showed an IC_{50} value of 7 nM, which agrees with the literature (*29*, *44*, *45*). Conjugate A showed an IC_{50} value of 65 nM, while even at the highest concentration of 100 nM conjugate B was able to circumvent only 30% of the enzyme activity. What is more interesting is that conjugate A inhibited more of the enzyme activity than conjugate B. If MTX were to show inhibitory activity in the conjugated form, one would expect conjugate B more active in a cell-free assay such as this since during the synthesis the enzyme-binding site, which is suggested as NH_2 at the fourth position in the pteridine ring, is left free for the interaction with the target in conjugate B (*46*, *47*). However, in conjugate A this site was occupied by the dendrimer. Therefore, in intact form it is highly unlikely for MTX in conjugate A to get into contact with the binding site in the enzyme and show even higher response than conjugate B. The reason for this difference is under investigation. Most importantly, the activity of the intact conjugates is significantly lower than those of free MTX. Therefore, the improved activity of Conjugate A is not likely because it is intact inside cells.

DISCUSSION

MTX has been coupled to many natural and synthetic carriers mainly in carbodiimide-mediated reactions, resulting in either amide or ester bond formation. Conjugation may inhibit its inherent cytotoxic activity, depending on the nature of the resultant bond as well as the inherent characteristics of the carrier. In our study, we compared two amide-bonded conjugates, where dendrimers with different surface groups were conjugated to distinct functional groups on the drug. Surprisingly, despite the relatively lower drug content of conjugate A (the amide-bonded conjugate between the anionic dendrimer [PAMAM-G2.5-COOH] and the -NH_2 group of MTX), it showed substantially higher cytotoxicity, up to 24 times higher than free drug, in MTX-resistant cells. On the other hand, for the amide-bonded conjugate between the cationic dendrimer (PAMAM-G3-NH_2) and the -COOH group of MTX (conjugate B) cytotoxicity was demonstrably reduced.

The improved cytotoxicity of amide-bonded conjugate A reported here is somewhat unique. Quintana et al. reported that a folic acid targeted MTX conjugate with fifth generation PAMAM dendrimers having an amide bond required approximately 2 times higher drug concentration, while the conjugate having an ester bond was able to reduce the IC_{50} value by 5-fold (*18*). Furthermore, a nontargeted analogue of this conjugate failed to demonstrate any cytotoxic activity on the same cell line. The amide-bonded conjugate of cisplatin with anionic 3.5 generation PAMAM dendrimer was significantly less active than free drug under in vitro conditions (*21*).

The higher growth inhibition activity of conjugate A can be envisaged to be related to three different aspects: (a) cellular uptake, (b) DHFR inhibition mechanisms, and (c) intracellular drug release from the conjugates. The higher antimetabolite activity of the conjugate A toward both of the MTX-resistant cell lines implies that conjugated MTX can be internalized in higher quantities than free MTX in this model. While only a small fraction, less than 5%, of the total amount of extracellular MTX is typically taken up under the normal conditions over several hours (*24*, *25*), a large fraction of dendrimer has been reported to enter A549 cells in as little as 1 h, most likely by fluid phase endocytosis, an internalization route for macromolecules (*10*−*12*). This is in accordance with the literature demonstrating the presence of an efficient uptake mechanism used by various generations of anionic and cationic PAMAM dendrimers in everted rat intestinal system (*15*). Also, recently Pillai et al. studied the different endocytotic pathways used by anionic and cationic PAMAM dendrimers, which are in question here (*48*). It has been shown that while anionic dendrimers appear to be primarily using caveolae-mediated endocytosis, cationic analogues are mostly internalized by clathrin-mediated fluid phase endocytosis. Still both of the dendrimers are taken up efficiently by the cells. Since CEM/MTX and RII cells are severely transport impaired due to loss of RFC (*36*−*38*), such a mechanism involving conjugated MTX could lead to a greater net uptake of MTX, resulting in a disproportionate level of cytotoxicity compared to MTX-sensitive cells. It does appear that dendrimers are effective in facilitating uptake of MTX inside the cells, as is evident from the significantly improved cytotoxicity of conjugate A in the resistant cell lines. In fact, the lack of toxicity of conjugate B is most likely not due to the lack of conjugate uptake but rather due to the surface charge of the dendrimer, which will be discussed later.

It is also likely for the drug to be active in the conjugated form. To evaluate the validity of this hypothesis, we determined DHFR enzyme inhibition activities in cell-free multiplate enzyme binding assays. Our preliminary results suggest that free MTX had an IC_{50} of approximately 7 nM, being the most active form of the drug. On the other hand, conjugates inhibited enzymatic activity to a much lesser extent. If the improved activity of conjugate A is because the conjugated drug is more active, we would expect a lower IC_{50} for the conjugate. Yet, it is a factor of 9 higher. Accordingly, we hypothesize that free MTX is most likely released from conjugate A within cells prior to the enzyme binding to achieve higher growth inhibition compared to the free drug as shown in Figure 3a,b.

In addition, in this current study, we addressed the mechanism of action of the conjugated MTX by employing salvage pathways where adenosine and thymidine nucleosides were used

as purine and prymidine base sources, respectively. For both free MTX and conjugated MTX, cell viabilities were close to 70% or higher in the presence of the nucleosides. This suggests that conjugated MTX in conjugate A still relies on the inhibition of DHFR as its primary target resulting in downstream effects on tetrahydrofolate-dependent reactions leading to synthesis of purines and thymidylate. However, the low level cytotoxicity seen with conjugate B in PC43/10 cells was incompletely reversed by adenosine and thymidine, suggesting a non-DHFR-mediated effect for this conjugate.

The third aspect of intracellular drug release could play a key role. Although we did not investigate the in vitro release of the drug from the conjugates in the absence of cells, we expect them to be stable in the culture media until internalization. Previous work suggested that linear polymer−drug conjugates with ester bonds typically release the drug very fast, up to 80% within in 1 h, showing an increasing amount of the released drug with a decrease in pH from 7.4 to 5.5 (*5*). However, amide-bonded conjugates either do not release the drug at all, or release very small quantities, less than 10%, over a period of 72 h (*5*). Our preliminary drug release studies in DMSO (using a dialysis membrane with 1000 MW cutoff size) showed no spontaneous drug release. This is also supported by the results of Malik et al. on the release profile of generation 3.5 PAMAM dendrimer conjugated cisplatin possessing a similar amide bond. In this study, less than 1% of the conjugated cisplatin was released in two different cell free media with pH of 7.4 and 5.5 (PBS and citrate buffer, respectively), even after incubation times as long as 74 h (*20*).

Since both conjugates are amide-bonded and are likely transported effectively into cells, differences in lysosomal residence times could be responsible for higher or lower activities of the conjugates, as lysosomal enzymes may play a crucial role in the release of free MTX from the conjugates. Preliminary studies involving FITC-labeled anionic and cationic PAMAM dendrimers gave evidence for the differences in the residence times of the dendrimers. The cells treated with 2.5 generation anionic dendrimer showed higher fluorescence intensity in the lysosomal compartments due to Lysotracker Red dye compared to those treated with cationic dendrimer. It can be explained by the displacement of small basic molecules by the macromolecules with highly cationic charge (*49*−*51*). An increase in the lysosomal pH and disruption of lysosomal membrane together called the lysosomotropic effect would be responsible for shorter lysosomal residence time as a result of a H^+ pump process leading to insufficient drug release from conjugate B. On the other hand, conjugate A involving anionic dendrimer may have a better chance to stay in the lysosomes to better interact with proteases, which would lead to higher amounts of released drug. Experiments are underway to address this question, using our dendrimers and confocal microscopy to assess colocalization of the conjugates and a lysosomal marker (Lysotracker Red DND-99) (*49*, *50*).

CONCLUSIONS

DCC conjugation of MTX to anionic and cationic dendrimers, through the formation of an amide bond, yielded conjugates of different characteristics in terms of both drug loading and cytotoxicity. Conjugate A showed significantly improved cytotoxicity in resistant cells (CEM/MTX and RII) compared to free MTX, whereas conjugate B showed relatively little cytotoxicity. The significantly improved activity (up to 24-fold improvement in the IC_{50} values) of the anionic dendrimer−MTX conjugate, even in the resistant cells, is unique. The differences in the activities of the anionic and cationic conjugates is hypothesized to result from the distinct intracellular release profiles of the drug from the conjugates, due the ionic nature of the dendrimer surface. While the present results suggest an augmentation of conjugate A independent of RFC status, for tumor cells that express the folate receptor (e.g., ovarian, cervical, and choriocarcinomas), use of targeting agents such as folic acid may further selectively enhance the level of internalized MTX due to specific accumulation of the nanodevice in tumor versus normal tissues.

Supporting Information Available: ^{1}H NMR spectrum of conjugates A and B in DMSO. This material is available free of charge via the Internet at http://pubs.acs.org.

LITERATURE CITED

(1) Duncan, R. (1999) Polymer conjugates for tumour targeting and intracytoplasmic delivery. The EPR effect as a common gateway? *Pharm. Sci. Technol. Today 2*, 441−449.

(2) Kopecek, J., Kopeckova, P., Minko, T., and Lu, Z. (2000) HPMA copolymer-anticancer drug conjugates: design, activity, and mechanism of action. *Eur. J. Pharm. Biopharm.* 50, 61−81.

(3) Kopecek, J., Kopeckova, P., Minko, T., Lu, Z. R., and Peterson, C. M. (2001) Water-soluble polymers in tumor targeted delivery. *J. Controlled Release 74*, 147−158.

(4) Lee, R. J., and Low, P. S. (1995) Folate-mediated tumor cell targeting of liposome-entrapped doxorubicin in vitro. *Biochim. Biophys. Acta 1233*, 134−144.

(5) Gianasi, E., Wasil, M., Evagorou, E. G., Keddle, A., Wilson, G., and Duncan, R. (1999) HPMA copolymer platinates as novel antitumour agents: in vitro properties, pharmacokinetics and antitumour activity in vivo. *Eur. J. Cancer 35*, 994−1002.

(6) Kopecek, J. (1990). The potential of water-soluble polymeric carriers in targeted and site-specific drug delivery. *J. Controlled Release 11*, 279−290.

(7) Cloninger, M. J. (2002) Biological applications of dendrimers. *Curr. Opin. Chem. Biol. 6*, 742−748.

(8) Frey, H., and Haag, R. (2002) Dendritic polyglycerol: a new versatile biocompatible-material. *J. Biotechnol. 90*, 257−267.

(9) Godbey, W. T., Wu, K. K., and Mikos, A. G. (1999) Poly(ethylenimine) and its role in gene delivery. *J. Controlled Release 60*, 149−160.

(10) Kannan, S., Kolhe, P., Raykova, V., Glibatec, M., Kannan, R. M., Lieh-Lai, M., and Bassett, D. (2004) Dynamics of cellular entry and drug delivery by dendritic polymers into human lung epithelial carcinoma cells. *J. Biomater. Sci. Polym. Ed. 15*, 311−330.

(11) Khandare, J., Kolhe, P., Pillai, O., Kannan, S., Lieh-Lai, M., and Kannan, R. M. (2005) Synthesis, cellular transport, and activity of polyamidoamine dendrimer-methylprednisolone conjugates. *Bioconjugate Chem. 16*, 330−337.

(12) Kolhe, P., Misra, E., Kannan, R. M., Kannan, S., and Lieh-Lai, M. (2003) Drug complexation, in vitro release and cellular entry of dendrimers and hyperbranched polymers. *Int. J. Pharm. 259*, 143−160.

(13) Kolhe, P., Khandare, J., Pillai, O., Kannan, S., Lieh-Lai, M., and Kannan, R. M. (2004) Hyperbranched polymer-drug conjugates with high drug payload for enhanced cellular delivery. *Pharm. Res. 21*, 2185−2195.

(14) Ooya, T., Lee, J., and Park, K. (2003) Effects of ethylene glycol-based graft, star-shaped, and dendritic polymers on solubilization and controlled release of paclitaxel. *J. Control. Release 93*, 121−127.

(15) Wiwattanapatapee, R., Carreno-Gomez, B., Malik, N., and Duncan, R. (2000) Anionic PAMAM dendrimers rapidly cross adult rat intestine in vitro: a potential oral delivery system? *Pharm. Res. 17*, 991−998.

(16) Thomas TP, Majoros IJ, Kotlyar A, Kukowska-Latallo JF, Bielinska A, Myc A, (2005) Targeting and inhibition of cell growth by an engineered dendritic nanodevice. *J. Med. Chem. 48*, 3729−3735.

(17) Kono, K., Liu, M., and Frechet, J. M. (1999) Design of dendritic macromolecules containing folate or methotrexate residues. *Bioconjugate Chem. 10*, 1115−1121.

(18) Quintana, A., Raczka, E., Piehler, L., Lee, I., Myc, A., Majoros, I., Patri, A. K., Thomas, T., Mule, J., and Baker, J. R., Jr. (2002)

Design and function of a dendrimer-based therapeutic nanodevice targeted to tumor cells through the folate receptor. *Pharm. Res. 19*, 1310−1316.
(19) Bhadra, D., Bhadra, S., Jain, S., and Jain, N. K. (2003) A PEGylated dendritic nanoparticulate carrier of fluorouracil. *Int. J. Pharm. 257*, 111−124.
(20) Padilla De Jesus, O. L., Ihre, H. R., Gagne, L., Frechet, J. M., and Szoka, F. C. Jr. (2002) Polyester dendritic systems for drug delivery applications: in vitro and in vivo evaluation. *Bioconjugate Chem. 13*, 453−461.
(21) Malik, N., and Duncan, R. (2003) Dendritic-platinate drug delivery systems. U.S. Patent 6585956, July 1.
(22) Riebeseel, K., Biedermann, E., Loser, R., Breiter, N., Hanselmann, R., Mulhaupt, R., Unger, C., and Kratz, F. (2002) Poly(ethylene glycol) conjugates of methotrexate varying in their molecular weight from MW 750 to MW 40000: synthesis, characterization, and structure−activity relationships in vitro and in vivo. *Bioconjugate Chem. 13*, 773−785.
(23) Chu, E., and Allegra, C. J. *Antifolates in Cancer Chemotherapy and Biotherapy* (Chabner, B. A., and Longo, D. L., Eds.) pp 109−248, Lippincott-Raven, Philadelphia.
(24) Goldman, I. D.; Matherly, L. H. (1985) The cellular pharmacology of methotrexate. *Pharmacol. Ther. 28*, 77−102.
(25) Matherly, L. H.; Goldman, I. D. (2003) Membrane transport of folates. *Vitam. Horm. 66*, 405−457.
(26) Zhao, R.; Goldman, I. D. (2003) Resistance to antifolates. *Oncogene 22*, 7431−7457.
(27) Rosenblatt, D. S., Whitehead, V. M., Matiaszuk, N. V., Pottier, A., Vuchich, M. J., and Beaulieu, D. (1982) Differential effects of folinic acid and glycine, adenosine, and thymidine as rescue agents in methotrexate-treated human cells in relation to the accumulation of methotrexate polyglutamates. *Mol. Pharmacol. 21*, 718−722.
(28) Pinedo, H. M., Zaharko, D. S., Bull, J. M., and Chabner, B. A. (1976) The reversal of methotrexate cytotoxicity to mouse bone marrow cells by leucovorin and nucleosides. *Cancer Res. 36*, 4418−4424.
(29) Pignatello, R., Guccione, S., Forte, S., Di, G. C., Sorrenti, V., Vicari, L., Uccello, B. G., Balzano, F., and Puglisi, G. (2004) Lipophilic conjugates of methotrexate with short-chain alkylamino acids as DHFR inhibitors. Synthesis, biological evaluation, and molecular modeling. *Bioorg. Med. Chem. 12*, 2951−2964.
(30) Kang, H., Kim, J. D., Han, S. H., and Chang, I. S. (2002) Self-aggregates of poly(2-hydroxyethyl aspartamide) copolymers loaded with methotrexate by physical and chemical entrapments. *J. Controlled Release 81*, 135−144.
(31) Wiwattanapatapee, R., Lomlim, L., and Saramunee, K. (2003) Dendrimers conjugates for colonic delivery of 5-aminosalicylic acid. *J. Controlled Release 88*, 1−9.
(32) Choi Y., Thomas, T., Kotlyar, A, Islam, M. T., and Baker, J. R., Jr. (2005) Synthesis and functional evaluation of DNA-assembled polyamidoamine dendrimer clusters for cancer cell-specific targeting. *Chem. Biol. 12*, 35−43.
(33) Zhuo, R. X., Du, B., and Lu, Z. R. (1999) In vitro release of 5-fluorouracil with cyclic core dendritic polymer. *J. Controlled Release 57*, 249−257.
(34) Warlick, C. A., Sweeney, C. L., and McIvor, R. S. (2000) Maintenance of differential methotrexate toxicity between cells expressing drug-resistant and wild-type dihydrofolate reductase activities in the presence of nucleosides through nucleoside transport inhibition. *Biochem. Pharmacol. 59*, 141−151.
(35) Matherly, L. H., Angeles, S. M., and McGuire, J. J. (1993) Determinants of the disparate antitumor activities of (6*R*)-5,10-dideaza-5,6,7,8-tetrahydrofolate and methotrexate toward human lymphoblastic leukemia cells, characterized by severely impaired antifolate membrane transport. *Biochem. Pharmacol. 46*, 2185−2195.
(36) Rosowsky, A., Lazarus, H., Yuan, G. C., Beltz, W. R., Mangini, L., Abelson, H. T., Modest, E. J., and Frei, E. (1980) III. Effects of methotrexate esters and other lipophilic antifolates on methotrexate-resistant human leukemic lymphoblasts. *Biochem. Pharmacol. 29*, 648−652.
(37) Wong, C., Zhang, L., Witt, T. L., Proefke, S. A., Bhushan, A., and Matherly, L. H. (1999) Impaired methotrexate transport in methotrexate resistant CCRF-CEM cells involves early translation termination and increased turnover of a mutant reduced folate carrier. *J. Biol. Chem. 274*, 10388−10394.
(38) Wong, S. C., Proefke, S. A., Bhushan, A., and Matherly, L. H. (1995) Isolation of human cDNAs that restore methotrexate sensitivity and reduced folate carrier activity in methotrexate transport-defective Chinese hamster ovary cells. *J. Biol. Chem. 270*, 17468−17475.
(39) Selinger, Z., and Lapidot, Y. (1966) Synthesis of fatty acid anhydrides by reaction with dicyclocarbodiimide. *J. Lipid Res. 7*, 174−175.
(40) Pignatello, R., Spampinato, G., Sorrenti, V., Di, G. C., Vicari, L., McGuire, J. J., Russell, C. A., Puglisi, G., and Toth, I. (2000) Lipophilic methotrexate conjugates with antitumor activity. *Eur. J. Pharm. Sci. 10*, 237−245.
(41) Wosikowski, K., Biedermann, E., Rattel, B., Breiter, N., Jank, P., Loser, R., et al. (2003) In vitro and in vivo antitumor activity of methotrexate conjugated to human serum albumin in human cancer cells. *Clin. Cancer Res. 9*, 1917−1926.
(42) Malik, N., Wiwattanapatapee, R., Klopsch, R., Lorenz, K., Frey, H., Weener, J. W., Meijer, E. W., Paulus, W., and Duncan, R. (2000) Dendrimers: relationship between structure and biocompatibility in vitro, and preliminary studies on the biodistribution of 125I-labeled polyamidoamine dendrimers in vivo. *J. Controlled Release 65*, 133−148.
(43) Jurgens, H., and Gobel, U. (1986) Pharmacology, toxicology and drug interactions of methotrexate. *Rheumatology 9*, 6−19.
(44) Liang, M., and Kovacs, J. A. (2000) Expression and characterization of recombinant human-derived *Pneumocystis carinii* dihydrofolate reductase. *Antimicrob. Agents Chemother. 44*, 3092−3096.
(45) Widemann, B. C., Balis, F. M., and Adamson, P. C. (1999) Dihydrofolate reductase enzyme inhibition assay for plasma methotrexate determination using a 96-well microplate reader. *Clin. Chem. 45*, 223−228.
(46) Cannon, W. R., Garrison, B. J., and, S. J. Benkovic. (1997) Consideration of the pH-dependent inhibition of dihydrofolate reductase by methotrexate. *J. Mol. Biol. 271*, 656−668.
(47) Verkhivker, G. M., Rejto, P. A., Bouzida, D., Arthurs, S., Colson, A. B., Freer, S. T., Gehlhaar, D. K., Larson, V., Luty, B. A., Marrone, T., and Rose, P. W. (1999) Towards understanding the mechanisms of molecular recognition by computer simulations of ligand-protein interactions. *J. Mol. Recognit. 12*, 371−389.
(48) Perumal, O. P, Kannan, R. M., and Kannan, S. (2005) Surface charge influences cellular trafficking mechanisms of dendritic nanomaterials, submitted to *Pharm. Res.*
(49) Panyam, J., Zhou, W. Z., Prabha, S., Sahoo, S. K., and Labhasetwar, V. (2002) Rapid endo-lysosomal escape of poly(DL-lactide-*co*-glycolide) nanoparticles: implications for drug and gene delivery. *FASEB J. 16*, 1217−1226.
(50) Lemieux, B., Percival, M. D., and Falgueyret, J. P. (2004) Quantitation of the lysosomotropic character of cationic amphiphilic drugs using the fluorescent basic amine Red DND-99, *Anal. Biochem. 327*, 247−251.
(51) Ohkuma, S., and Poole, B. (1978) Fluorescence probe measurement of the intralysosomal pH in living cells and the perturbation of pH by various agents. *Proc. Natl. Acad. Sci. U.S.A. 75*, 3327−3331.

BC0501855

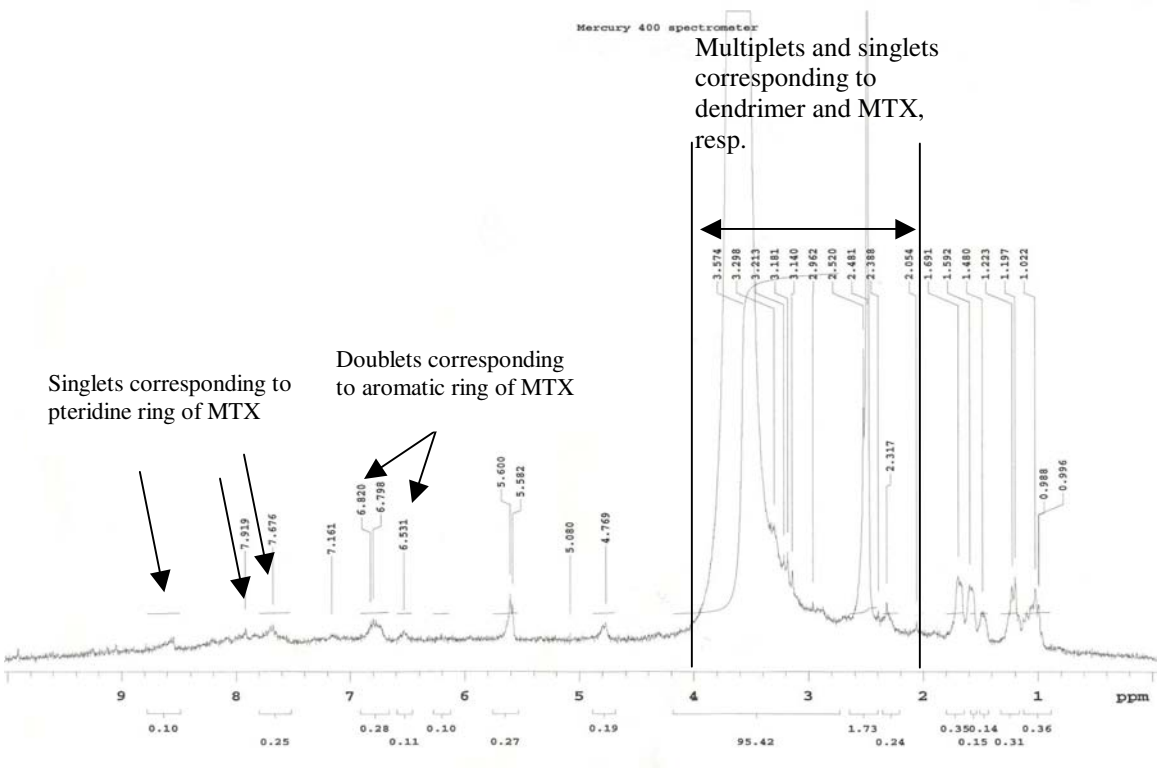

Supplemental Figure A. ^{1}H NMR spectrum of Conjugate A in DMSO.

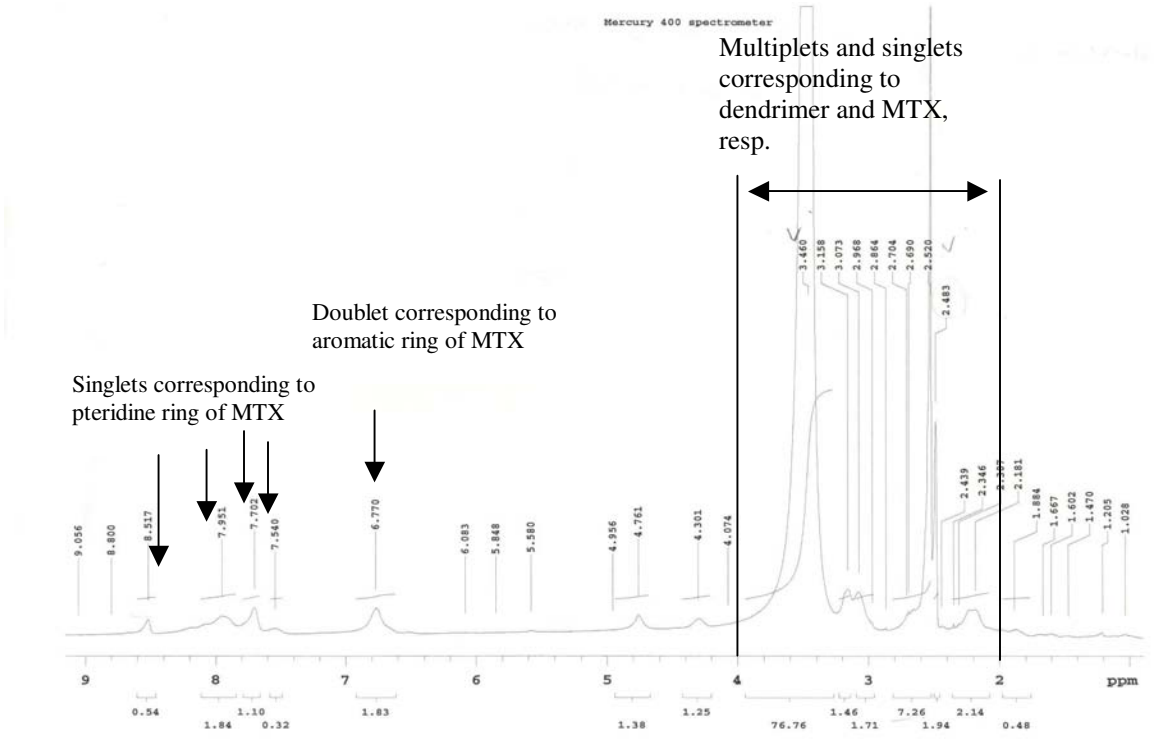

Supplemental Figure B. ^{1}H NMR spectrum of Conjugate B in DMSO

Functionalization and Cellular Uptake of Boron Carbide Nanoparticles. The First Step toward T Cell-Guided Boron Neutron Capture Therapy

M. W. Mortensen,[§] O. Björkdahl,[†] P. G. Sørensen,[†] T. Hansen,[†] M. R. Jensen,[†] H. J. G. Gundersen,[‡] and T. Bjørnholm[§,*]

Nano-Science Center, University of Copenhagen, Universitetsparken 5, DK-2100 Copenhagen, Denmark, T-Cellic A/S, Agern Allé 7, DK-2970 Hørsholm, Denmark, and Stereological Research Laboratory, University of Aarhus, DK-8000 Aarhus, Denmark. Received July 14, 2005; Revised Manuscript Received December 22, 2005

In this paper we present surface modification strategies of boron carbide nanoparticles, which allow for bioconjugation of the transacting transcriptional activator (TAT) peptide and fluorescent dyes. Coated nanoparticles can be translocated into murine EL4 thymoma cells and B16 F10 maligant melanoma cells in amounts as high as 0.3 wt. % and 1 wt. %, respectively. Neutron irradiation of a test system consisting of untreated B16 cells mixed with B16 cells loaded with boron carbide nanoparticles were found to inhibit the proliferative capacity of untreated cells, showing that cells loaded with boron-containing nanoparticles can hinder the growth of neighboring cells upon neutron irradiation. This could provide the first step toward a T cell-guided boron neutron capture therapy.

INTRODUCTION

Boron neutron capture therapy (BNCT) relies critically on methods that can provide a significant ^{10}B contrast between malignant and normal tissue and an absolute ^{10}B concentration in malignant tissue above the therapeutic limit. Following delivery of a boron compound to the tumor, thermal neutrons are used to initiate a nuclear reaction in ^{10}B. In this reaction the main therapeutic effect is obtained by the emitted alpha particle which causes damage to the tissue within 10 μm from the site of the neutron capture. To reduce the damage to normal tissue, specific delivery of ^{10}B to the tumor site is needed. Traditionally, a molecular boron-containing compound, such as boronphenylalanine (BPA), is infused into the patient, resulting in a tumor-to-normal tissue ratio between 3:1 and 4:1 (*1*, *2*). The minimum boron concentration needed in tumor, to obtain a therapeutic effect, is 20−30 μg/g (*3*−*5*). The therapeutic effectiveness of this system is yet to be proven in clinical trials (*6*). The therapeutic efficiency could be improved by optimizing the delivery of boron compounds to the tumor tissue thereby increasing (1) the boron concentration in tumor tissue and (2) the boron contrast between tumor tissue and normal tissue (*7*).

As an alternative to intravenous infusion we suggest the use of boron carbide nanoparticles as a new carrier of ^{10}B (*8*) in conjunction with adoptive immunotherapy, where tumor specific T cells migrate to the tumor site (*9*−*11*). T cell-guided cancer therapy is based on using a patients own immune system to carry a cytotoxic compound to the tumor site (*12*). By loading T cells with boron-containing nanoparticles and re-injecting the loaded T cells into the patient, the boron would be selectively delivered to the tumor by T cells, thereby achieving a high local boron concentration.

A prerequisite in T cell-guided BNCT is thus to initially load a high amount of boron into the T cells. The experimental strategy of the present work has been to achieve this by loading T cells with solid boron-containing nanoparticles.

In traditional drug delivery systems where a molecule is to be internalized into cells, the drug is typically incapsulated into micelles/vesicles or polymeric structures (*13*). Several similar types of coatings have been used to encapsulate nanoparticles: Iron oxide nanoparticles have been coated with lipids (*14*, *15*) or dextran (*16*−*18*), CdSe−ZnS nanoparticles have been coated with peptide derivatives (*19*) and poly(D,L-lactic-*co*-glycolic acid) nanoparticles have been coated with di-*block*-copolymers (*20*).

Furthermore, the attachment of short cationic peptide sequences from the transacting transcriptional activator (TAT) protein derived from human immunodeficiency virus (HIV) have been shown to improve cellular uptake of nanoparticles and liposomes (*21*−*23*).

In this paper we describe various coating strategies based on both covalent binding to the particle surface and association by hydrophobic interaction, which enable labeling of boron carbide nanoparticles with fluorescent dyes and peptides. Details concerning the preparation and characterization of the boron carbide core is described in a recent publication (*24*). Cellular uptake of coated boron carbide nanoparticles were tested using two different cell lines, murine EL4 thymoma cells and B16 F10 melanoma cells. In addition, a test system consisting of particle-loaded and unloaded B16 F10 melanoma cells were used to evaluate the effects of neutron irradiation.

EXPERIMENTAL PROCEDURES

Reagents. Water was Millipore grade and 0.2 μm filtered. Octadecyltrichlorsilane (+90% 10,481-7), sodium hydride (60% in mineral oil, 45,291-2), 1,10-diaminodecane (97%, D1,420-4), polyoxyethylene lauryl ether (Brij30, P4391), sodium hydroxide (R06203), epichlorohydrin (24,069−9), 4-(*N*-maleimidomethyl)cyclohexane-1-carboxylic acid *N*-hydroxysuccinimide (SMCC, M5525), RPMI-1640 × 10 (cat no R1145), HEPES buffer (HO887), L-glutamine (G7513), penicillin/streptomycin (P0781), and sodium bicarbonate (S5761) were purchased from Sigma-Aldrich. Boron carbide (043002) with natural abundance of ^{10}B was purchased from Alfa Aesar and ^{10}B (>96 at. %, B0008-046)-enriched boron carbide was purchased from Eagle Picher Technologies. Dichloromethane,

* Corresponding author. Tel.: +45 353 21835. Fax.: +45 353 20406. E-mail: tb@nano.ku.dk.
[§] University of Copenhagen.
[†] T-Cellic A/S.
[‡] University of Aarhus.

10.1021/bc050206v CCC: $33.50 © 2006 American Chemical Society
Published on Web 02/17/2006

Table 1. Functionalization Strategy[a]

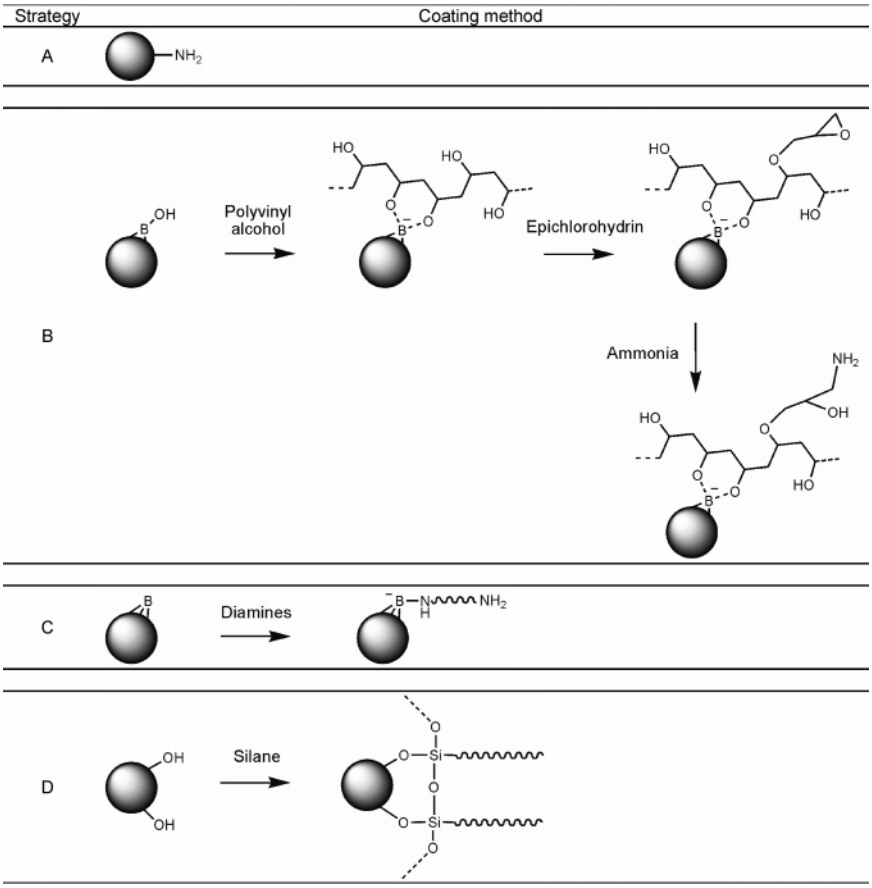

[a] Strategies A−C rely on the introduction of a chemically reactive amino group on the particle surface which could be used as a handle for covalent bioconjugation of dyes and peptides. Strategy A, utilize native surface amino groups. Strategy B, utilize a cross-linked and aminated poly(vinyl alcohol) coating. Strategy C, utilize a 1,10-diaminodecane coating. Strategy D, rely on the introduction of hydrocarbon chains on the particle surface using octadecyltrichlorosilane. Hydrophobic particles could be used as a template for association of amphiphilic molecules by hydrophobic interactions.

chloroform, methanol, toluene, acetonitrile, and dimethylformamide were HPLC grade purchased from LabScan-Analytical Sciences. Ammonia (25% aq) was purchased from Bie & Berntsen. Poly(vinyl alcohol) (PVA, MW 49000, 81383) and dodecyltrimethylammonium chloride (DDTMAC, 44242) were purchased from Fluka. Triethylamine (99%) was purchased from Acros Organics. Sodium Sulfate (1.06649.1000) was purchased from Merck. Two peptides, H-GRKKRRQRRRGY(K-FITC)C-NH_2 (HS-TAT-FITC) and C_{16}-GSGSGRKKRRQRRRGYK(C-FITC)-OH (C_{16}-TAT-FITC) where FITC is fluorescein isothiocyanate were synthesized by Shafer-Nielsen A/S. Rhodamin B sulfonyl chloride (Lissamine, L-20) was purchased from Molecular Probes. 2-Mercaptoethanol (31350−010) was purchased from Invitrogen and fetal calf serum (A15−043) was purchased from PAA Laboratories, GmbH. Cell separation media (CL5031) were purchased from Cedarlane. Sepharose CL4B was purchased from Amersham.

Preparation of Boron Carbide Nanoparticles. Commercially available boron carbide was processed by ball milling in an air, nitrogen, or argon atmosphere in order to reduce the particle size. Details on the preparation of boron carbide nanoparticles with respect to particle size and other physiochemical properties of ball milled boron carbide can be found in ref 24. All coating development studies were conducted on boron carbide with natural abundance of ^{10}B, whereas studies involving irradiation were conducted on enriched boron carbide.

Coating of Nanoparticles. The different strategies (A to D), described below, are summarized in Table 1.

Strategy A. Lissamine (1 mL, 6.45 mg/mL) and triethylamine (0.4 mL) were added to a suspension of boron carbide nanoparticles (40 mg, milled in nitrogen) in DMF (2 mL). The reaction mixture was stirred at RT overnight. The particles were pelleted by centrifugation (Eppendorf miniSpin+, 6 krpm, 5 min), and the supernatant was discarded. The pellet was resuspended in DMF and centrifuged again. The washing procedure was repeated a total of 5 times (×1 with DMF and ×4 with water). The particles were resuspended in water.

Strategy B. Poly(vinyl alcohol) (1.25 g) was dissolved in water (50 mL) by magnetic stirring for 1 h at 70−85 °C. Boron carbide nanoparticles (100 mg, argon milled) were suspended in an aqueous solution of NaOH (10 mL, 0.1 M) and added dropwise to the PVA solution. The suspension was stirred overnight at 70 °C. The suspension was allowed to cool to RT, the particles were pelleted by centrifugation (Eppendorf miniSpin+, 14.5 krpm, 90 s), and the supernatant was discarded. The pellet was resuspended in 0.1 M NaOH and centrifuged again. The washed product was resuspended in 0.1 M NaOH (5 mL). Epichlorohydrin (5 mL) and 2 M NaOH (0.25 mL) was added, and the suspension was stirred at least 4 h. The product was isolated by centrifugation (as described above) and resuspended in water (5 mL). Ammonia (25%) (10 mL) was added to the suspension, and the mixture was stirred at least overnight. The product was purified by successive centrifugation and washing (as described above) with water a total of three times and dried using nitrogen flow. The product (9.96 mg) was suspended in DMF (0.8 mL) whereupon triethylamine (10 μl), lissamine (0.1 mL, 23.9 mg/mL in DMF), and SMCC (0.1 mL, 12.6 mg/mL in DMF) were added. After 1 h the product was purified by successive centrifugation and washing (as described above) a total of four times (×3 DMF and ×1 HEPES

(10 mM)). The pellet was resuspended in HEPES (1 mL, 10 mM) and mixed with the peptide solution HS-TAT-FITC (1 mL, 40 μg/mL in HEPES). The suspension was allowed to incubate overnight, and the product was purified by successive centrifugation and washing with water (as described above) a total of four times. The particles were resuspended in water.

Strategy C. 1,10-Diaminodecane (2.1 g) was added to a suspension of boron carbide nanoparticles (400 mg, argon milled) in dry toluene (75 mL). Sodium hydride (0.6 g, 60% in mineral oil) was added in portions under nitrogen. The reaction mixture was stirred at RT for 30 min, whereupon the reaction mixture was heated to gentle reflux for 72 h. The heating was removed, and the reaction mixture was quenched with water. The hydrophobic product was pelleted by centrifugation, and the supernatant was discarded. The pellet was resuspended in water and centrifuged again. The washing procedure was repeated a total of four times ($\times$1 with water and $\times$3 with methanol). The washed product was dried with nitrogen flow. The product (107 mg) was suspended in acetonitrile (4 mL) by ultrasonication (Misonix Probe Sonicator, pulse time 9 $\times$ 1 s., 6 W) whereupon Lissamine (0.25 mg), SMCC (1.25 mg), and triethylamine (0.2 mL) were added. The suspension was stirred for 24 h at RT in a nitrogen atmosphere. The product was purified by successive centrifugation and washing (as described above) a total of eight times ($\times$3 with water and $\times$5 with acetonitrile) and resuspended in acetonitrile (3 mL). HS-TAT-FITC (0.5 mg) in acetonitrile (1 mL) was added to the suspension, and the reaction mixture was stirred for 24 h. The product was purified by successive centrifugation and washing (as described above) a total of four times ($\times$2 with water and $\times$2 with acetonitrile). The product was ultrasonicated (Misonix Probe Sonicator, 3 s, 6 W) in a suspension of Brij30 (4 mL, 1 mM) and stirred for 24 h. The product was purified by successive centrifugation and washing with water (as described above) a total of four times. The particles were resuspended in water.

Strategy D. Boron carbide nanoparticles (300 mg, air milled) were suspended in methylene chloride (18 mL) using ultrasonication (Misonix Probe Sonicator, pulse time 3 $\times$ 10 s, 0.5 W). Octadecyltrichlorsilane (2 mL) was added to the suspension and stirred at RT overnight. The particles were pelleted by centrifugation (Eppendorf miniSpin+, 14.5 krpm, 5 min), and the supernatant was discarded. The product was resuspended in methylene chloride and centrifuged again. The washing procedure was repeated a total of three times. The product was dried using nitrogen flow. Twenty milligrams of the hydrophobic powder was resuspended by ultrasonication (Misonix Probe Sonicator, pulse time 3 $\times$ 1 s, 0.5 W) in a 995:5 molar mixture of DDTMAC (2.6 mL, 12.42 mg/mL) and C_{16}-TAT-FITC (0.5 mL, 3.44 mg/mL) and stirred at RT overnight. The total detergent solution was $\sim$40 mM. The particle suspension (100 μL) was mixed with a solution of Na_2SO_4 (100 μL, 1 M) and applied on a gel filtration column equilibrated in water (Sepharose CL4B, width 1 cm, height 5 cm, 1 mL fractions were collected). The fractions (3 and 4) containing particles were pooled.

Fluorescence and Dark Field Microscopy of Nanoparticles. A Zeiss axiotech microscope was equipped with a dark field system in order to identify light scattering objects and a fluorescence system in order to identify the fluorophores (filter for FITC: Set 41017, exciter: HQ470/40, emitter: HQ525/50. Filters for rhodamine B: set 41004, exciter: HQ560/55, emitter: HQ645/75. Chroma Technology Corp.).

Loading of Cells with Boron Carbide Nanoparticles. Suspensions (1 mg/mL) of functionalized nanoparticles (prepared using strategy C) were mixed with a 10 x cell culture media master mix. After the addition of cell culture master mix, each milliliter of colloid contained 100 μL of RPMI-1640 x 10, 10 μL of 1 M HEPES buffer, 10 mL of 200 mM L-glutamine, 10 μL of penicillin/streptomycin, 50 μL of 40 mg/mL sodium bicarbonate, 1 μL of 50 mM 2-mercaptoethanol, and 100 μL of fetal calf serum.

This particle suspension was incubated for 1 h at RT to let large particles/aggregates sediment to the bottom of the tube (Since particles prepared according to strategy C were hydrophobic, some aggregates could not be solubilized by Brij30. The simplest way of removing these aggregates was by sedimentation for 1 h). The murine EL4 thymoma cell line (ATCC) was used in exponential growth. The particle colloid (leaving the sedimented aggregates) was finally mixed with the cells resulting in a cell concentration of 1 $\times$ 10^6 cells/mL. The cell/nanoparticle mix was incubated at 37 °C for 4 or 17 h. To remove non-cell-associated particles from the cell suspension lympholyte separation was performed. The samples were centrifuged (10 min at 1300 rpm), and the supernatant was discarded. Cells were washed $\times$2 in Hanks Balanced Salt Solution (HBSS). The cell concentration was adjusted to approximately 5 $\times$ 10^6 cells per mL in HBSS. Lympholyte cell separation media (3 mL) was carefully deposited in a 10 mL centrifugation tube, taking care not to leave droplets of lympholyte on the sides of the tube (in order not to mix the phases in the density gradient). Thereafter, 3 mL of the cell suspension was layered on top of the lympholyte solution using a pipet, taking care to cause as little mixing as possible between the two solutions. The tube was centrifuged for 20 min at 2100 rpm (approximately 1000 g) at RT, no brake. Following centrifugation, the interphase, containing the cells, was carefully collected and transferred to a 50 mL tube containing 25 mL of complete RPMI media. Cells were centrifuged for 10 min at 1200 rpm, the supernatant was discarded, and the wash step was repeated once. Negative control samples, where no particles were added but otherwise handled identically to particle-loaded cells, were referred to as mock-loaded cells.

Fluorescence Microscopy Analysis of Cells. Cells, prepared as described above, and cells without nanoparticles were resuspended in an appropriate volume of growth media and investigated using a Nikon eclipse 80*i* fluorescence microscope (filters: B-2E/C (FITC): ex 465−495, dm 505, ba 515−555, and G-2E/C (TRITC): ex 540/25, dm 565, ba 605/55).

Quantitative Determination of Cell-Associated Boron after Cellular Loading. The boron content of cells loaded with boron carbide nanoparticles (see above) and cell samples without nanoparticles (typically (0.5−2) $\times$ 10^6 cells/sample) was analyzed by Nuclear Research and Consultancy Group (NRG), Petten, The Netherlands, using inductively coupled plasma atomic emission spectroscopy (ICP-AES). The ICP-AES method was verified using boron carbide control samples with a known boron concentration 7.9 $\times$ 10^{-1} μg/g and 7.9 μg/g. The measured boron content in these samples was 8.1 $\times$ 10^{-1} μg/g and 7.9 μg/g, respectively.

Cellular Survival after Irradiation. B16 F10 melanoma cells (ATCC) were loaded with the functionalized nanoparticles followed by lympholyte separation in order to separate free nanoparticles from boron-loaded cells, as described above. The loaded cells were then irradiated at LFR Unit, Institute for Energy in Petten, The Netherlands. All irradiation experiments were done using a thermal neutron flux of 1.26 $\times$ 10^9 $cm^{-2}s^{-1}$, a γ dose rate of 0.02717 Gy min^{-1}, and a fast neutron dose rate of 0.00650 Gy min^{-1}. The cells were either left unirradiated or were irradiated for 5 or 10 min. Furthermore, the boron nanoparticle-loaded cells were either irradiated themselves or mixed with untreated B16 melanoma cells (1:2 ratio) before irradiation. After irradiation, the cells were pelleted by cen-

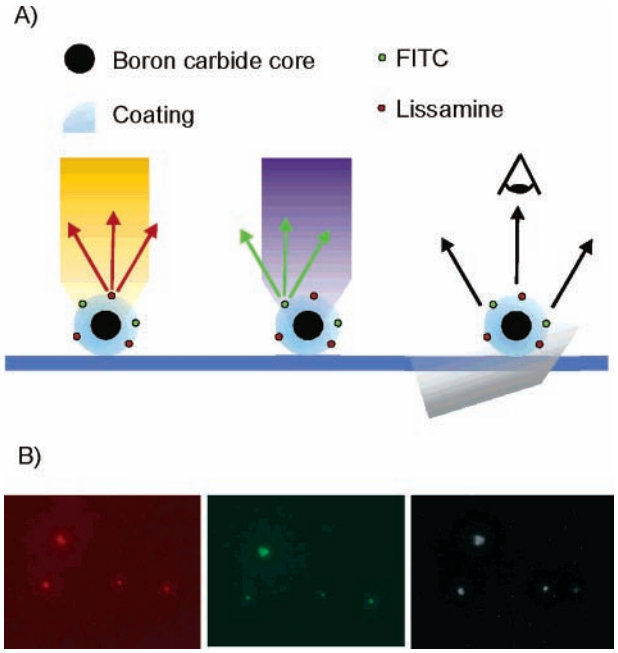

Figure 1. Combined dark field and fluorescence microscopy. (A) Generalized components of nanoparticle and an illustration of fluorescence excitation (left and center) and dark field illumination (right). (B) As recorded images of functionalized boron carbide nanoparticles, rhodamine filter (left), fluorescein filter (center), and dark field (right).

trifugation, the medium was changed, and the cells were resuspended in fresh complete cell culture medium.

The survival of cells after irradiation was determined by following the proliferative capacity of the cells. In brief, 2 (or 2.5) $\times$ 10^4 cells/well were plated in the top wells of 96-well plates, and 2-fold dilutions were performed, leaving the final row without cells. Total volume in wells was 200 μL. The cells were incubated for 48 h at 37 °C, and during the last 6 h, the cells were pulsed with 1 μCi ^{3}H-thymidine/well. The cells were harvested using a semiautomated sample harvester, and the ^{3}H-thymidine incorporation was measured in a β-scintillation counter.

RESULTS AND DISCUSSION

Dark Field and Fluorescent Microscopy of Nanoparticles. An optical setup based on dark field microscopy was used to investigate the light scattering properties of boron carbide nanoparticles, (see Figure 1A). Boron carbide nanoparticles were found to be strong scattering objects when subjected to a standard 50 W halogen lamp. This method could therefore be used to monitor the position of a single boron carbide nanoparticle. To monitor the fluorescent labels, a fluorescence setup was installed with appropriate filters for monitoring fluorescein (FITC) and rhodamin B (Lissamine). By simply switching between the dark field light source and the fluorescence excitation source, fluorescence was seen to be correlated with scattering intensity (see Figure 1B). This method was used to evaluate if a fluorescent dye was associated with a nanoparticle.

Surface Functionalization. To achieve covalent bioconjugation to the particle surface, a chemically reactive group needs to be present on the particle surface. This functionality could either be a native chemical group on the surface of the particle or be introduced by first coating the particles with another species containing the desired functionality. The strategies suggested here (Table 1A−C) focus on the introduction of chemically reactive amino groups which could be used for covalent bioconjugation of dyes or peptides.

The amino reactive fluorophore, Rhodamine B sulfonyl chloride (lissamine), was used to covalently label the nanoparticles with a fluorescent dye and the bifunctional linker 4-(*N*-maleimidomethyl)cyclohexane-1-carboxylic acid *N*-hydroxysuccinimide (SMCC) was used to couple a cysteine-containing peptide sequence (HS-TAT-FITC, the peptide sequence was labeled with a FITC fluorophore) to a surface-bound amino group.

Strategy A (Table 1 A) was based on covalent coupling to the uncoated boron carbide surface, since nanoparticles prepared by ball milling in an nitrogen-containing environment (*24*) were tested positive for ninhydrin, i.e., an indication of surface bound amino groups. (The formation of amino groups was most likely related to high chemical reactivity of newly exposed surface atoms in boron carbide during the milling process). Boron carbide nanoparticles could however not be labeled with lissamine, leading to the conclusion that the amino groups on the surface had too low reactivity for covalent bonding.

Strategy B (Table 1 B) was based on poly(vinyl alcohol) (PVA) as a coating material due to the fact that diol-containing species are known to form complexes with boric acid/borate ions in solution (*25*); hence, boric acid/borate surface groups could form similar complexes. The particles were first coated with PVA, and the adjunct polymer hydroxy groups were cross-linked using epichlorohydrin. Amino groups were finally introduced in the polymer by treating unreacted epoxy groups with ammonia according to Wunderbaldinger et al. (*26*). The polymer-coated nanoparticles were successfully labeled with Lissamine. Furthermore, the HS-TAT-FITC peptide was accordingly coupled to the aminated polymer surface using SMCC.

Strategy C (Table 1C) was based on 1,10-diaminodecane as a coating material. The mechanism of the covalent bond formation between deprotonated 1,10-diaminodecane and the boron surface was believed to be based on the reaction between a Lewis acid and a Lewis base. Boron, being electron deficient, will tend to acquire an electron pair from an electron donor such as 1,10-diaminodecane. The diamine-coated particles were successfully labeled with Lissamine and HS-TAT-FITC using the SMCC cross-linker. The water solubility of these particles was regulated using an amphiphilic polyoxyethylene lauryl ether (Brij30) solution.

Association of amphiphilic molecules using hydrophobic interactions were also investigated, as an alternative to covalent bioconjugation. This strategy was based on introducing hydrocarbon chains on the surface making the particles hydrophobic (Table 1D). By mixing hydrophobic particles with amphiphilic molecules in an aqueous solution, the amphiphilic molecules (such as the TAT peptide derivatized with a hydrocarbon tail C_{16}-TAT-FITC) could be expected to associate with the hydrophobic particle surface, due to hydrophobic interactions.

Strategy D (Table 1D) was based on octadecyltrichlorosilane as a coating material. The binding mechanism between octadecyltrichlorosilane (OTS) and the boron surface is believed to be silylation whereby a chlorosilane group Si−Cl reacts with a surface hydroxy group. In addition, hydration of Si−Cl to Si−OH and subsequent condensation reactions between silanol groups will result in the formation of a Si−O−Si network on the particle surface. By adding the hydrophobic particles to a solution of amphiphiles, the particles were solubilized in a mixture of dodecyltrimethylammonium chloride (DDTMAC) and C_{16}-TAT-FITC, thereby associating the TAT peptide sequence with the particles by hydrophobic interaction.

Covalent coupling of fluorescent dyes and peptides (strategies B and C) were preferred for cellular uptake experiments since the fluorescence intensity could then directly be interpreted as particle uptake, hence eliminating the risk of false positives due to desorption of fluorescent species which had not been covalently bonded to the particle surface. On the basis of initial uptake experiments the 1,10-diaminodecane-coated boron car-

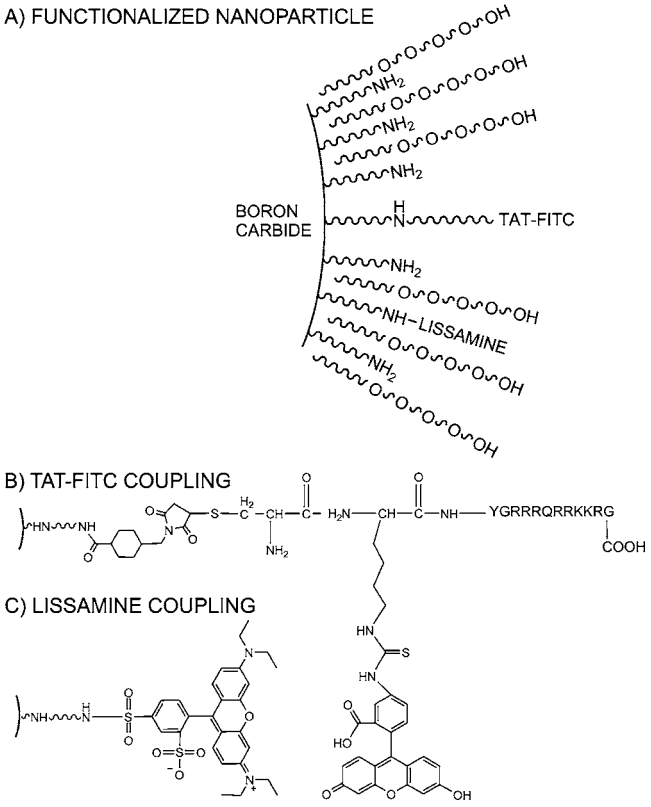

Figure 2. Sketch of functionalized boron carbide nanoparticle, according to strategy C, used for cellular uptake experiments. (A) The overall surface coating including Brij30 amphiphiles, (B) the specific HS-TAT-FITC coupling, and (C) the specific Lissamine coupling.

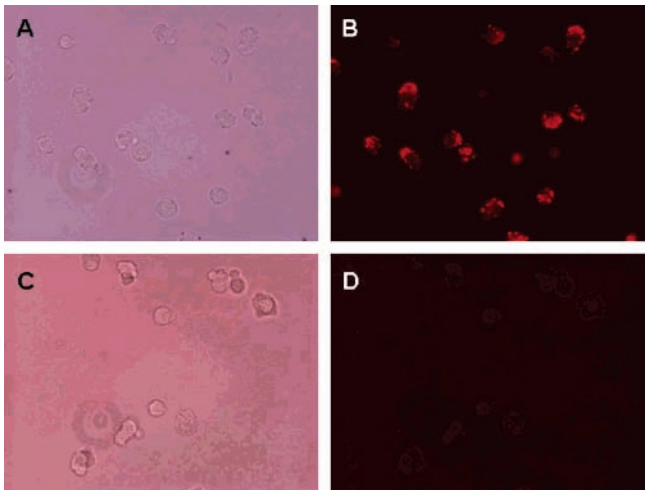

Figure 3. Bright field and fluorescence microscopy of EL4 T cells loaded with nanoparticles (a and b) and cells alone (c and d).

bide nanoparticle (Table 1 C) showed the best cellular uptake compared to the PVA-coated particles. A detailed sketch of the fully functionalized nanoparticle used for cellular uptake experiments is shown in Figure 2. Fully functionalized nanoparticles were inspected by fluorescence microscopy, just after completion of the synthesis and again just before cellular loading, to verify the stability of the conjugated species.

Cellular Loading with Boron-Containing Nanoparticles As Determined by Fluorescence Microscopy and Inductively Coupled Plasma Atomic Emission Spectroscopy. Analysis of cells by fluorescence microscopy following particle-loading revealed a significant fluorescent labeling of the cells. As seen in Figure 3B, cellular loading of EL4 T cells with the nanoparticles (particle-loading overnight), followed by lympholyte separation, resulted in a profound cell-associated lissamine signal, indicating particle-loading of the cells. Mock-loaded (handling of cells identical to particle-loaded cells, but without particles) cells did not result in any lissamine signal (Figure 3D). Figures 3A and 3C show the corresponding particle-loaded (A) and mock-loaded (C) cells using bright field instead of fluorescence microscopy.

Although fluorescence microscopy is an illustrative way of showing particle-loading of cells, it is a qualitative method of analysis and an indirect way of showing the presence of cell-associated boron. To formally prove the presence of cell-associated boron, the cell samples were further analyzed by ICP-AES to determine the boron content (Table 2). These analysis showed that the particle-loaded EL4 cell samples contained approximately 2.7−2.8 μg/g boron (correspond to approximately 0.8−1.8 pg/cell), whereas the concentration of boron in the mock-loaded cell samples was 0.024−0.085 μg/g (Table 2 column 4). Comparing to EL4 cells, the boron uptake in B16 melanoma cells was much higher (5−40 pg/cell). The boron uptake per cell (pg/cell) was calculated using the mass of the sample, the boron concentration of the sample determined by ICP-AES, and the number of cells in each sample. To make sure that the lympholyte separation did work properly, i.e., that free boron nanoparticles were not situated in the interphase where the cells are collected after the centrifugation, a control sample with particles only (no cells) was included in the experiment and went through the complete experimental procedure (Table 2, column 5). The boron concentration of these control samples was under the detection limit of 0.07 μg/g, strongly indicating that the measured boron after cellular loading is cell-associated. The highest boron content obtained in EL4 cells was thus ∼0.3 wt % and ∼1 wt % for B16 cells.

The Effect of Irradiation of Boron Nanoparticle-Loaded Cells. As a first step of evaluating our nanoparticles as an agent for BNCT, murine B16 melanoma cells were loaded with the nanoparticles and subsequently irradiated for either 5 or 10 min or left unirradiated. Two experimental setups were tested: (1) irradiation of particle-loaded B16 cells alone and (2) irradiation of a mixture of particle-loaded B16 cells and untreated B16 cells. Following irradiation, the proliferative capacity (viability) of the cells was analyzed by measuring ^{3}H-thymidine incorporation. The first approach, irradiating boron-loaded cells only, would simply tell us whether we induced cell death following irradiation of particle-containing cells. The latter approach would provide us with the information whether irradiation of nanoparticle-containing cells may induce cell death of unloaded cells that are situated in close vicinity to nanoparticle-containing cells.

Figure 4A shows the proliferative capacity after irradiation of particle-loaded B16 cells (∼5 pg/cell) compared to unloaded cells. As seen in the figure, the proliferation of particle-loaded cells is significantly inhibited after irradiation whereas particle-loading per se (no irradiation) does not seem to inhibit the proliferation significantly. Furthermore, no proliferative inhibition is observed following irradiation of mock-loaded or untreated B16 cells, strongly indicating that the proliferative inhibition of particle-loaded B16 cells is the effect of α-particles generated from ^{10}B during irradiation.

Moreover, irradiation of a mixture of particle-loaded (∼40 pg/cell) and untreated B16 cells (cell ratio 1:2) showed that also unloaded cells situated in close vicinity to particle-loaded cells where affected and a significant proliferative inhibition of these cells was observed (Figure 4B, right). As expected, irradiation of a mixture of mock-loaded and untreated B16 cells did not significantly affect the proliferative capacity (Figure 4B, left).

In conclusion, by introducing chemically reactive amino groups using coating strategies B and C, translocation peptides and fluorescent dyes were covalently coupled to the boron

Table 2. Cellular Uptake of Boron Carbide Nanoparticles Prepared Using Method C[a]

		boron concentration in sample measured by ICP-AES [μg/g]			boron content per cell [pg/cell]	boron concentration in cells [wt %]
cell type	incubation time	particle loaded	mock loaded	lympholyte interface	particle loaded	particle loaded
EL4	4 h	2.7	0.085	0.022	1.8	0.34
EL4	o.n.[b]	2.8	0.024	0.051	0.8	0.15
B16	o.n.	5	0.075	-	5	0.12
B16	o.n.	15	0.085	-	40	0.95

[a] Boron uptake in EL4 T cells and B16 melanoma cells using boron carbide nanoparticle-coated using Strategy C. The boron concentration, measured by ICP-AES, in each sample (particle-loaded, mock-loaded and Lympholyte interphase) is listed in columns 3, 4, and 5. The boron content in particle-loaded cells (column 6) were calculated using the boron concentration determined by ICP-AES of a sample with known mass and the number of cells in each sample. The boron concentration in a particle-loaded cell was estimated by calculating the mass of a cell using the size (diameter of EL4 $\sim$ 10 μm, diameter of B16 $\sim$ 20 μm) and density ($\sim$1 g/cm^3) of a cell (See column 7). [b] o.n.: overnight.

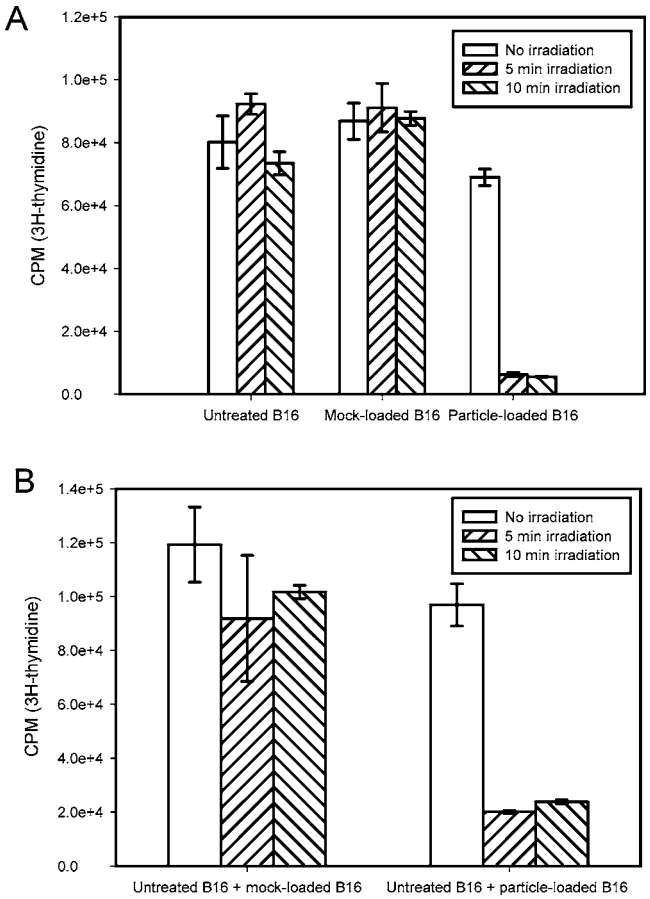

Figure 4. Irradiation of B16 melanoma cells. (A) The proliferative capacity of untreated B16, mock-loaded B16, and particle-loaded B16 cells evaluated by thymidine uptake. (B) The proliferative capacity of untreated cells mixed with mock-loaded B16 cells and untreated cells mixed with particle-loaded B16 cells evaluated by thymidine uptake. Error bars represent standard deviations (SD) on a triplicate analysis ($N = 3$).

carbide surface. As an alternative to covalent binding, association by hydrophobic interactions were also found to be a feasible method to associate amphiphilic molecules with hydrophobic particles (strategy D). Boron carbide particles modified according to strategy C resulted in a cellular boron loading of 0.3 wt % in EL4 cells and 1 wt % in B16 cells. The proliferative capacity of particle-loaded B16 cells was significantly inhibited upon neutron irradiation. More importantly the proliferative capacity of untreated cells in close proximity to particle-loaded cells was also significantly inhibited. The prerequisites for T cell-guided BNCT were initial high loading of T cells with ^{10}B (as demonstrated here using EL4 cells) and the effective killing of neighboring unloaded cells (as demonstrated here using B16 melanoma cells). Both of these goals were achieved using derivatized boron carbide nanoparticles and therefore conceptionally prove that these particles may be used for T cell-guided BNCT.

ACKNOWLEDGMENT

We would like to acknowledge A. B. Petersen for fruitful discussions concerning organic synthesis and R. Huiskamp (Nuclear Research and Consultancy Group (NRG), Petten, The Netherlands) for fruitful discussions concerning BNCT.

LITERATURE CITED

(1) Barth, R. F., Soloway, A. H., Goodman, J. H., Gahbauer, R. A., Gupta, N., Blue, T. E., Yang, W., and Tjarks, W. (1999) Boron Neutron Capture Therapy of Brain Tumors: An Emerging Therapeutic Modality. *Neurosurgery 44*, 433−451.

(2) Coderre, J. A., Chanana, A. D., Joel, D. D., Elowitz, E. H., Micca, P. L., Nawrocky, M. M., Chadha, M., Gebbers, J.-O., Shady, M., Peress, N. S., and Slatkin, D. N. (1998) Biodistribution of Boronphenylalanine in Patients with Glioblastoma Multiforme: Boron Concentration Correlates with Tumor Cellularity. *Radiat. Res. 149*, 163−170.

(3) Barth, R. F., and Soloway, A. H. (1992) Boron Neutron Capture Therapy for Cancer − Realities and Prospects. *Cancer 70*, 2995−3007.

(4) Javid, M., Brownell, G. L., and Sweet, W. H. (1952) The possible use of neutron-capturing isotopes such as Boron^{10} in the treatment of neoplasms. II. Computation of the radiation energies and estimates of the effects in normal and neoplastic brain. *J. Clin. Invest. 31*, 604−610.

(5) Tolpin, E. I., Wellum, F. C., Dohan, F. C. jr., Kornblith, P. L., and Zamenhof, R. G. (1975) Boron Neutron Capture Therapy of Cerebral Gliomas. *Oncology 32*, 223−246.

(6) Barth, R. F. (2003) A critical assessment of boron neutron capture therapy: an overview. *J. Neurooncol. 62*, 1−5.

(7) Coderre, J. A. and Morris, G. M. (1999) The radiation biology of Boron Neutron Capture Therapy. *Radiat. Res. 151*, 1−18.

(8) Mortensen, M. W., Sørensen, P. G., Jørgensen, J. T., Gundersen, H. J. G., Bjørnholm, T., Hansen, T., Petersen, A. B., Björkdahl, O. (2004) Boron containing nanoparticles. PCT/EP2005/002040.

(9) Kircher, M. F., Allport, J. R., Graves, E. E., Love, V., Josephson, L., Lichtman, A. H., and Weissleder, R. (2003) In vivo high-resolution three-dimensional imaging of antigen-specific cytotoxic T-Lymphocytes trafficking to tumors. *Cancer Res. 63*, 6838−6846.

(10) Gundersen, H. J., Hansen, S. B., Gjedde, A., Stødkilde-Jørgensen, H., Marqversen, J., Agger, R., Andersen, T. E., Fleischer, C. C., Petersen, M. S., Hokland, M., Hulgaard, E., Jørgensen, J. T., and Skands, U. (2004) A methodology for quantifying and visualising cell homing/accumulation by combined positron tomography and magnetic resonance imaging. *Proc. SPIE Med. Imaging* 2004 5, 361−370.

(11) Yee, C., Thompson, J. A., Byrd, D., Riddell, S. R., Roche, P., Celis, E., and Greenberg, P. D. (2002) Adoptive T cell therapy using antigen-specific CD8$^+$ T cell clones for the treatment of patients with metastatic melanoma: In vivo persistence, migration, and antitumor effect of transferred T cells. *Proc. Natl. Acad. Sci. U.S.A. 99*, 16168−16173.

(12) Gundersen, H. J. G., Zeuthen, J. and Nielsen, S. J. (2000) Detection of immunological memory T cell conjugates for pathology imaging and therapy. WO 01/70938 A1.
(13) Mainardes, R. M., and Silva, L. P. (2004) Drug Delivery Systems: Past, Present, and Future. *Curr. Drug Targets 5*, 449−455.
(14) Le, B., Shinkai, M., Kitade, T., Honda, H., Yoshida, J., Wakabayashi, T., and Kobayashi, T. (2001) Preparation of Tumor-Specific Magnetoliposomes and Their Application for Hyperthermia. *J. Chem. Eng. Jpn. 34*, 66−72.
(15) Ito, A., Kuga, Y., Honda, H., Kikkawa, H., Horiuchi, A., Watanabe, Y., and Kobayashi, T. (2004) Magnetic nanoparticle-loaded anti-HER2 immunoliposomes for combination of antibody therapy with hyperthermia. *Cancer Lett. 212*, 167−175.
(16) Cox, J. S. G., Kennedy, G. R., King, J., Marshall, P. R., and Rutherford, D. (1971) Structure of an iron-dextran complex. *J. Pharm. Pharmacol.* 24, 513−517.
(17) Molday, R. S., and Mackenzie, D. (1982) Immunospecific ferromagnetic iron-dextran reagents for the labeling and magnetic separation of cells. *J. Immunol. Methods 52*, 353−367.
(18) Shen, T., Weissleder, R., Papisov, M., Bogdanov, A., and Brady, T. J. (1993) Monocrystalline Iron Oxide Nanocompounds (MION): Physicochemical Properties. *Magnet. Reson. Med. 29*, 599−604.
(19) Pinaud, F., King, D., Moore, H.-P., and Weiss, S. (2004) Bioactivation and cell Targeting of semiconductor CdSe/ZnS Nanocrystals with Phytochelatin-Related Peptides. *J. Am. Chem. Soc. 126*, 6115−6123.
(20) Kim, S. H, Jeong, J. H., Chun, K. W., and Park, T. G. (2005) Target-Specific cellular uptake of PLGA nanoparticles coated with poly(L-lysine)-poly(ethylene glycol)-folate conjugate. *Langmuir 21*, 8852−8857.
(21) Lewin, M., Carlesso, N., Tung, C.-H., Tang, X.-W., Cory, D., Scadden, D. T., and Weissleder, R. (2000) Tat peptide-derivatized magnetic nanoparticles allow in vivo tracking and recovery of progenitor cells. *Nature Biotechnol. 18*, 410−414.
(22) Levchenko, T. S., Rammohan, R., Volodina, N., and Torchilin, V. P. (2003) TAT peptide-mediated intracellular delivery of liposomes. *Methods. Enzymol. 372*, 339−349.
(23) MacKay, J. A., and Szoka, F. C. Jr. (2003) HIV TAT Protein Transduction Domain Mediated Cell Binding and Intracellular Delivery. *J. Dispersion Sci. Technol. 24*, 465−273.
(24) Mortensen, M. W., Sørensen, P. G., Björkdahl, O., Jensen, M. R., Gundersen, H. J. G., and Bjørnholm, T. (2006) Preparation and Characterisation of Boron Carbide Nanoparticles for use as a Novel Agent in T cell Guided Boron Neutron Capture Therapy. *App. Radiat. Isot. 64*, 315−324.
(25) Wang, H.-H., Shyr, T.-W., and Hu, M.-S. (1999) The elastic property of poly(vinyl alcohol) gel with boric acid as a cross-linking agent. *J. Appl. Polym. Sci. 74*, 3046−3052.
(26) Wunderbaldinger, P., Josephson, L., and Weissleder, R. (2002) Tat peptide directs enhanced clearance and hepatic permeability of magnetic nanoparticles. *Bioconjugate Chem. 13*, 264−268.

BC050206V

Paclitaxel-Loaded Poly(γ-glutamic acid)-poly(lactide) Nanoparticles as a Targeted Drug Delivery System against Cultured HepG2 Cells

Hsiang-Fa Liang,[†] Sung-Ching Chen,[†] Mei-Chin Chen,[†] Po-Wei Lee,[†] Chiung-Tong Chen,[‡] and Hsing-Wen Sung*[,†]

Department of Chemical Engineering, National Tsing Hua University, Hsinchu, Taiwan, R.O.C., and Division of Biotechnology and Pharmaceutical Research, National Health Research Institutes, Taipei, Taiwan, R.O.C.. Received July 19, 2005; Revised Manuscript Received December 20, 2005

The study was to develop paclitaxel-loaded formulations using a novel type of self-assembled nanoparticles that was composed of block copolymers synthesized from poly(γ-glutamic acid) and poly(lactide) via a simple coupling reaction. The nanoparticles (the NPs) were prepared with various feed weight ratios of paclitaxel to block copolymer (the P/BC ratio). The morphology of all prepared nanoparticles was spherical and the surfaces were smooth. Increasing the P/BC ratio significantly increased the drug loading content of the prepared nanoparticles, but remarkably reduced the drug loading efficiency. The release rate of paclitaxel from the NPs decreased significantly as the P/BC ratio increased. For the potential of targeting liver cancer cells, galactosamine was further conjugated on the prepared nanoparticles (the Gal-NPs) as a targeting moiety. It was found that the activity in inhibiting the growth of HepG2 cells (a liver cancer cell line) by the Gal-NPs was comparable to that of a clinically available paclitaxel formulation, while the NPs displayed a significantly less activity. This may be attributed to the fact that the Gal-NPs had a specific interaction with HepG2 cells via ligand−receptor recognition. Cells treated with distinct paclitaxel formulations resulted in arrest in the G2/M phase. The arrest of cells in the G2/M phase was highly suggestive of interference by paclitaxel with spindle formation and was consistent with the morphological findings presented herein. In conclusion, the active targeting nature of the Gal-NPs prepared in the study may be used as a potential drug delivery system for the targeted delivery to liver cancers.

INTRODUCTION

The toxicity of anticancer drugs to normal tissues limits the development of chemotherapeutic agents for the treatment of cancers. Various drug carriers have been investigated to reduce the toxicity and increase the therapeutic efficacy of anticancer drugs (*1*−*4*). The pharmaceutical applications of self-assembled nanoparticles have recently attracted considerable attention (*5*). The self-assembled nanoparticles, composed of amphiphilic block copolymers, have a hydrophobic inner core and a hydrophilic outer shell.

In our previous study, poly(γ-glutamic acid) (γ-PGA) and poly(lactide) (PLA) were used to synthesize amphiphilic block copolymers via a simple coupling reaction to prepare a novel type of self-assembled nanoparticles (*6*). γ-PGA, a natural compound, is produced as capsular substance or as slime by members of the genus *Bacillus* (*7*). It is uniquely composed of naturally occurring L-glutamic acids linked by amide bonds. It is known that γ-PGA is water-soluble, biodegradable, nontoxic (*7*), and relatively nonimmunogenic (*8*). In our previous stability study, no aggregation or precipitation of the nanoparticles was observed during storage for up to 1 month, since it was prevented by the electrostatic repulsion between the negatively charged nanoparticles (*6*).

The aim of this study was to develop paclitaxel-loaded formulations using the aforementioned nanoparticles that were composed of amphiphilic γ-PGA-PLA block copolymers. Galactosamine was further conjugated on the prepared nanoparticles as a targeting moiety to develop the potential of targeting liver cancer cells. The unique structure of paclitaxel enables it readily to enter mammalian cells and preferentially bind to tubulin in polymerized microtubules (*9*). This stabilizes microtubules and greatly interferes with microtubular reorganization necessary, among other processed, for spindle formation and cell division (*10*). Therefore, the exposure of susceptible cells to paclitaxel has been shown to arrest the G2/M phase initially and finally cause cell death through apoptosis (*11*).

However, the hydrophobicity of paclitaxel raises great difficulties in the preparation of formulations. Many research groups and pharmaceutical companies have endeavored to develop better and improved paclitaxel formulations that are suitable for different applications (*12*). Even though paclitaxel is mainly prescribed to treat breast and ovarian cancers, it is known that various cancer cells including hepatoma cells can be killed effectively by this drug (*13*, *14*).

In this study, the effects of the feeding ratio of drug to copolymer on the distribution of particle sizes, the zeta potential, the drug loading content, and the drug loading efficiency of the prepared nanoparticles and their in vitro release profiles were evaluated. The morphology of the prepared nanoparticles was examined by the transmission electron microscopy (TEM) and the atomic force microscopy (AFM). Additionally, the cytotoxicity of the prepared nanoparticles with or without galactosamine conjugated on HepG2 cells (a liver cancer cell line) was compared to that of a clinically available paclitaxel formulation in vitro. The effect of the prepared nanoparticles on the cellular microtubules and the restriction of HepG2 cells in specific cell cycle stages was investigated using a confocal laser scanning microscope (CLSM) and a flow cytometer.

EXPERIMENTAL SECTION

Materials. Paclitaxel powder (purity > 99%) and clinical commercial paclitaxel [Phyxol, contained 6 mg paclitaxel, 527 mg Cremaphor EL and 47.7% (v/v) alcohol per milliliter] were

* To whom correspondence should be addressed. Tel:886-3-574-2504, Fax:886-3-572-6832, E-mail: hwsung@che.nthu.edu.tw.

[†] National Tsing Hua University.

[‡] National Health Research Institutes.

10.1021/bc0502107 CCC: $33.50 © 2006 American Chemical Society
Published on Web 02/18/2006

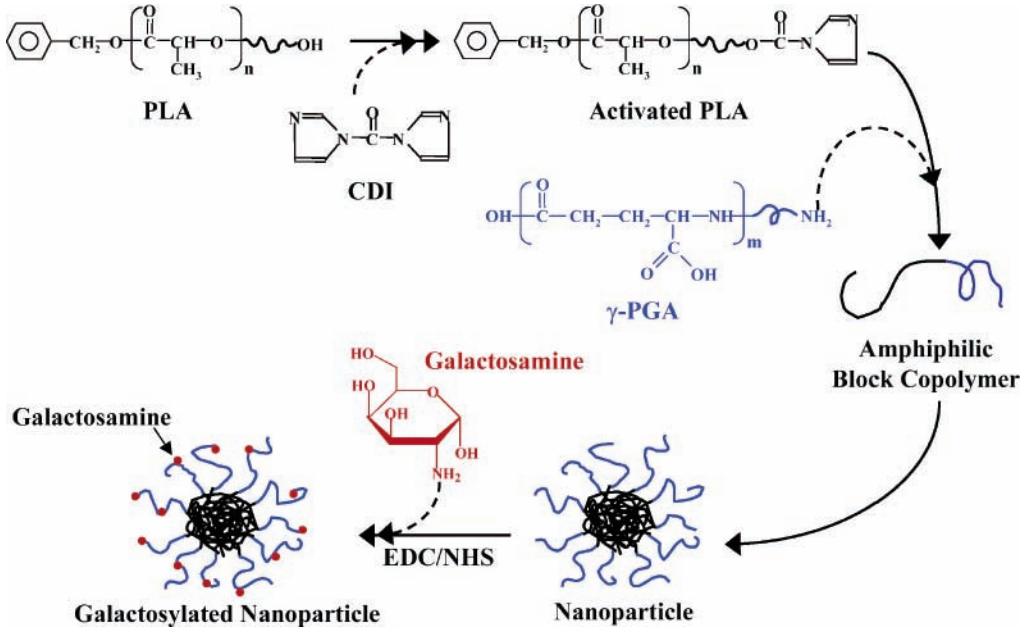

Figure 1. Schematic illustrations of synthesis of γ-PGA-PLA block copolymers and formation of self-assembled nanoparticles with conjugated galactosamine.

obtained from Sinphar Pharmaceutical Co., Ltd. (Taipei, Taiwan). PLA [poly(L-lactide), M_n: 10 kDa, with a polydispersity of 1.1 determined by the GPC analysis] was kindly supplied by the Biomedical Engineering Center, Industrial Technology Research Institute (Hsinchu, Taiwan). Dimethyl sulfoxide (DMSO < 0.01% water), *N*,*N*′-carbonyldiimidazole (CDI, 98%), and dichloromethane were acquired from Fluka (Buchs, Switzerland). L-Glutamic acid (purity > 99%), *N*-(3-dimethylaminopropyl)-*N*′-ethylcarbodiimide (EDC), *N*-hydroxysuccinimide (NHS), galactosamine, and sodium cholate were purchased from Sigma (St. Louis, MO). 4-(Dimethylamino)pyridine (DMAP) and 1,4-dioxane were obtained from ACROS (Janssen Pharmaceuticalaan, Belgium). All other used chemicals were reagent grade.

Production of γ-PGA. γ-PGA (Figure 1) was produced by *Bacillus licheniformis* (ATCC 9945, Bioresources Collection and Research Center, Hsinchu, Taiwan) and purified as per a method reported by Yoon et al. with slight modifications (*15*). Details of the methodology were reported in our previous publication (*6*).

Hydrolysis of γ-PGA. The average molecular weight (M_n) of the purified γ-PGA obtained via the previous fermentation procedure was about 320 kDa. The purified γ-PGA was then hydrolyzed in a tightly sealed steel container at 150 °C for specified durations (*16*). The average molecular weight along with the polydispersity of the hydrolyzed γ-PGA were determined using a gel permeation chromatography (GPC) system equipped with a series of PL aquagel-OH columns (one Guard 8 μm, 50 × 7.5 mm and two MIXED 8 μm, 300 × 7.5 mm, PL Laboratories, UK) and a refractive index (RI) detector (RI2000-F, SFD, Torrance, CA). Poly(ethylene glycol) (molecular weights of 106−22000 g/mol) and poly(ethylene oxide) (with molecular weights of 20000−1000000 g/mol) standards of narrow polydispersity (PL Laboratories, UK) were used to construct a calibration curve. The mobile phase contained 0.01 M NaH_2PO_4 and 0.2 M $NaNO_3$ and was brought to a pH of 7.0. The flow rate of the mobile phase was 1.0 mL/min, and the columns and the RI detector cell were maintained at 30 °C.

Synthesis of γ-PGA-PLA Block Copolymers. Block copolymers composed of γ-PGA and PLA were synthesized using CDI to activate the terminal hydroxyl group of PLA (*17*). CDI (82 mg) was dissolved in 1,4-dioxane (20 mL) in a nitrogen atmosphere and PLA (0.1 g) was subsequently added to the solution. The clear solution was stirred at 37 °C for 2 h. Afterward, the solution was dialyzed extensively against deionized water at 4 °C. Finally, the activated PLA was obtained via centrifugation.

The acidified form of the hydrolyzed γ-PGA (10 mg, M_n ~4 kDa, PDI = 1.3) was dissolved in DMSO (5 mL) in a dry, stoppered 20 mL round-bottomed flask in a nitrogen atmosphere. After DMAP (3 mg) was dissolved, a calculated amount of activated PLA (25 mg) was added. The solution was stirred at room temperature for 3 days, after which the reaction was stopped by adding 0.1 mL of concentrated HCl to neutralize DMAP and imidazole. The reaction mixture was transferred to a dialysis tube (MWCO: 6000−8000), followed by dialysis for 2 days against deionized water for several times at 4°C to remove the un-conjugated γ-PGA. Additionally, the un-conjugated PLA was separated due to its self-precipitation. Finally, the product was lyophilized and stored at −20 °C until used. The molecular weight distribution of the synthesized block copolymers was determined using a GPC system equipped with a Jordi Gel DVB Mixed Bed column (250 × 10 mm, Jordi Associates, Inc., MA) and an RI detector. Tetrahydrofuran (THF) was used as an elution solvent (1 mL/min) and polystyrene standards for column calibration.

Preparation of the Paclitaxel-loaded Nanoparticles. The paclitaxel-loaded nanoparticles were produced using an emulsion/solvent evaporation technique (*18*). Briefly, 10 mg of block copolymers were dissolved in 1 mL of methylene chloride, and paclitaxel was subsequently added with various feed weight ratios to block copolymer [paclitaxel/copolymer (P/BC) = 0.5/10, 1/10, 2/10, and 3/10]. The solution was then stirred for 2 h at room temperature and emulsified in 50 mL of a 0.1 wt % sodium cholate solution using a sonicator (VCX-750, Sonics & Materials Inc., Newtown, CT; cycles were of 1 s sonication followed by a 1 s pause, over a total period of 20 min). Afterward, the solvent was evaporated in a vacuum oven at 37 °C for 1 h. The resulting suspension was filtered through a 0.8 μm membrane filter (Whatman) and then centrifuged for 60 min at 18000 rpm at 4 °C. The supernatant was subsequently discarded and the pellet was resuspended in 10 mL of phosphate-buffered saline (PBS, pH 7.4, Sigma). The size distribution and

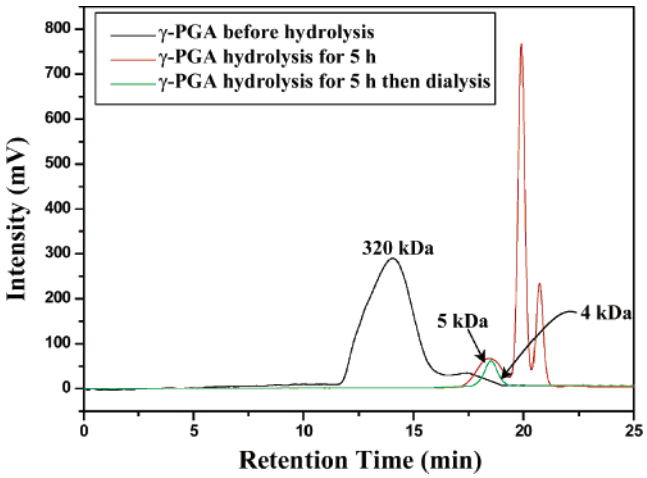

Figure 2. Chromatograms of purified γ-PGA obtained by fermentation (γ-PGA before hydrolysis), obtained γ-PGA after 5 h of hydrolysis at 150 °C (γ-PGA hydrolysis for 5h), and hydrolyzed γ-PGA after dialysis twice against deionized water (γ-PGA hydrolysis for 5 h then dialysis).

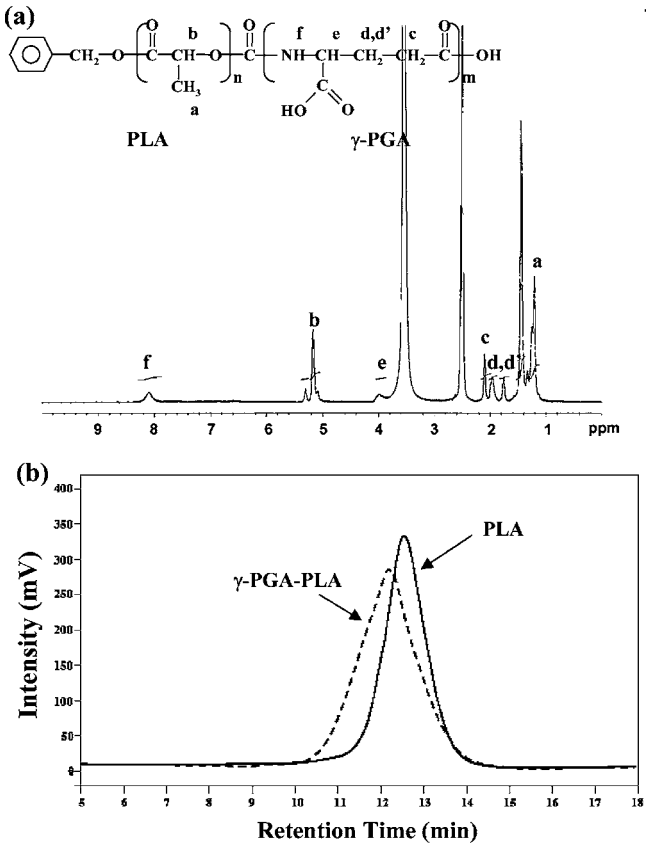

Figure 3. (a) ^{1}H NMR spectrum of synthesized γ-PGA-PLA block copolymer. (b) GPC chromatograms of PLA (solid curve) and the synthesized γ-PGA-PLA block copolymer (dotted curve).

zeta potential of the prepared nanoparticles were measured using a Zetasizer (3000HS, Malvern Instruments Ltd., Worcestershire, UK).

TEM and AFM were used to observe the morphology of the paclitaxel-loaded nanoparticles. The TEM sample was prepared by placing a drop of the paclitaxel-loaded nanoparticle solution onto a 400 mesh copper grid coated with carbon. About 2 min after deposition, a filter paper was tapped to the grid to remove surface water and negatively stained using a 2% (by w/v) phosphortungsten acid (PTA) solution. The AFM sample was prepared by placing a drop of the paclitaxel-loaded nanoparticle solution on a glass slide and then drying it in a vacuum.

Table 1. Particle Size, Zeta Potential, and Drug Loading Content (LC) and Loading Efficiency (LE) of Nanoparticles Prepared with Various Feed Weight Ratios of Paclitaxel to Block Copolymer (the P/BC ratio)

P/BC ratio ($n = 4$)	particle size (nm)	zeta potential (mV)	LC (%)	LE (%)
0/10	115.4 ± 4.2	−21.4 ± 2.3	–	–
0.5/10	125.9 ± 5.5	−22.5 ± 3.2	3.7 ± 0.1	76.5 ± 2.4
1/10	128.8 ± 3.4	−19.6 ± 1.8	5.1 ± 0.2	53.7 ± 1.7
2/10	144.4 ± 2.6	−20.3 ± 2.7	5.8 ± 0.2	30.8 ± 2.3
3/10	263.2 ± 6.8	−19.2 ± 2.2	6.1 ± 0.2	21.7 ± 4.2

Loading Content and Loading Efficiency of the Paclitaxel-Loaded Nanoparticles. The drug loading content and the loading efficiency of the nanoparticles were determined using a high-performance liquid chromatography (HPLC) system equipped with a C_{18} analytic column (4.6 × 250 mm, particle size 5 μm, ThermoQuest, BDS, Runcorn, UK) (*19*). Two milligrams of the freeze-dried paclitaxel-loaded nanoparticles were dissolved in 1 mL dichloromethane with vigorous vortexing. This solution was dried by evaporating dichloromethane in a vacuum. It then was dissolved in a mixture of 50/50 (v/v) ethanol and deionized water to perform the HPLC analysis. The flow rate of the mobile phase (60% acetonitrile and 40% deionized water by v/v), delivered by an HPLC pump (TCP, P-100, Riviera Beach, FL), was 1 mL/min at 30 °C. The injection volume was 40 μL, and paclitaxel eluted from the column was monitored with an UV detector (Jasco 875-UV, Tokyo, Japan) at 227 nm. The drug loading content and the loading efficiency of the nanoparticles were calculated using the following equations (*20*).

$$\text{loading content (\%)} = \frac{\text{weight of paclitaxel in the nanoparticles}}{\text{weight of the nanoparticles}} \times 100\%$$

$$\text{loading efficiency (\%)} = \frac{\text{weight of paclitaxel in the nanoparticles}}{\text{weight of the feeding paclitaxel}} \times 100\%$$

Release of Paclitaxel from the Loaded Nanoparticles. The release profiles of paclitaxel from the prepared nanoparticles in PBS at 37 °C were investigated (*19*). The freeze-dried paclitaxel-loaded nanoparticles were weighed and resuspended in a centrifuge tube containing 20 mL of PBS. The tube was placed in a shaker water bath at 37 °C. At particular time intervals, the tube was removed and centrifuged. The supernatant was poured out, freeze-dried, and then dissolved in a mixture of 50/50 (v/v) ethanol and deionized water to conduct HPLC analysis. The pellet was resuspended in 20 mL of fresh PBS to make continuous release measurements. The paclitaxel released at each time point was calculated using a calibration curve (*19*).

Conjugation of Galactosamine to the Paclitaxel-Loaded Nanoparticles. Galactosamine was conjugated to the paclitaxel-loaded nanoparticles via an amide link by EDC in the presence of NHS (*21*, *22*). The conditions in our previous study, under which galactosamine was conjugated on nanoparticles that had the most nanoparticles internalized in HepG2 cells, were used herein (*6*). The obtained galactosylated nanoparticles were separated from unreacted molecules via ultrafiltration and then lyophilized. The content of galactosamine conjugated on the nanoparticles was determined by the Morgan Elson assay (*23*).

Viability of HepG2 Cells Treated with Distinct Paclitaxel Formulations. The cytotoxicity of the paclitaxel-loaded nanoparticles with or without galactosamine conjugated was evaluated in vitro by the MTT assay, using a clinically available paclitaxel formulation (Phyxol, Sinphar Pharmaceutical) as a control (*24*). The assay is based on mitochondrial dehydrogenase

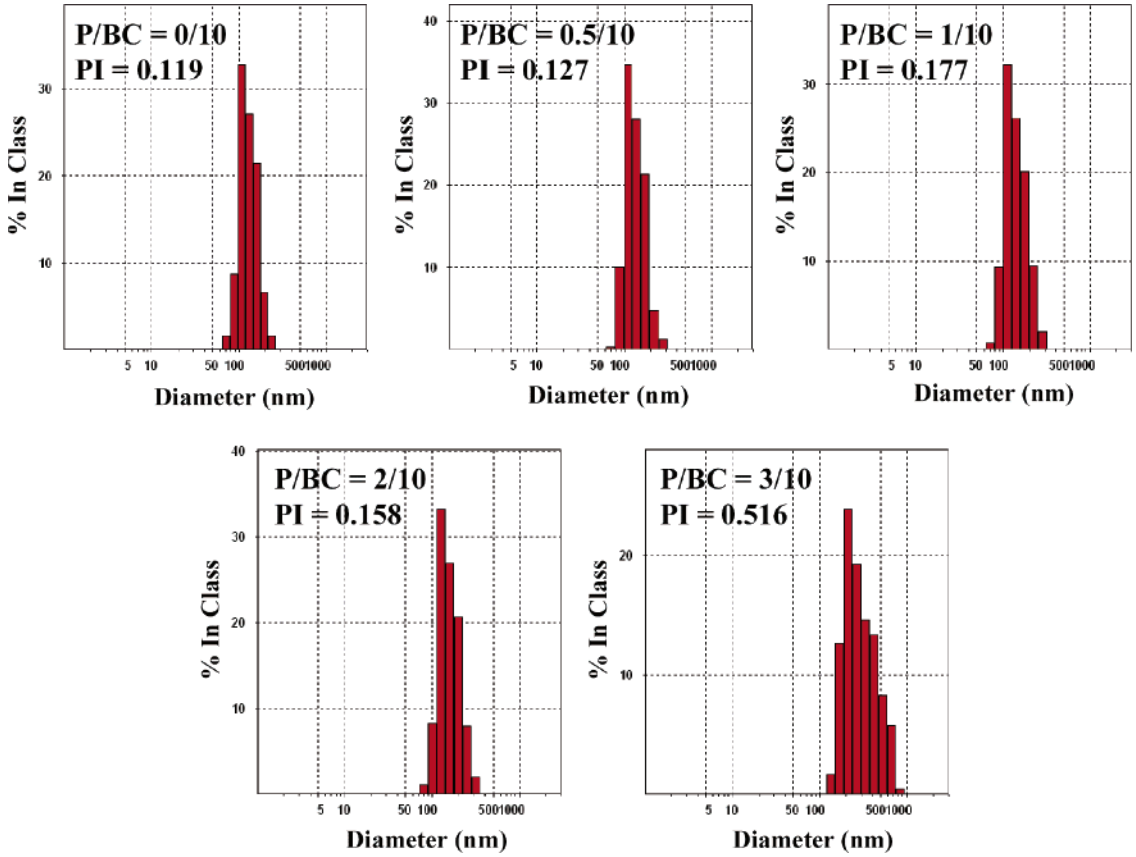

Figure 4. Size distributions of nanoparticles prepared with various feed weight ratios of paclitaxel to block copolymer (P/BC ratios). PI: polydispersity index of size distribution of prepared nanoparticles.

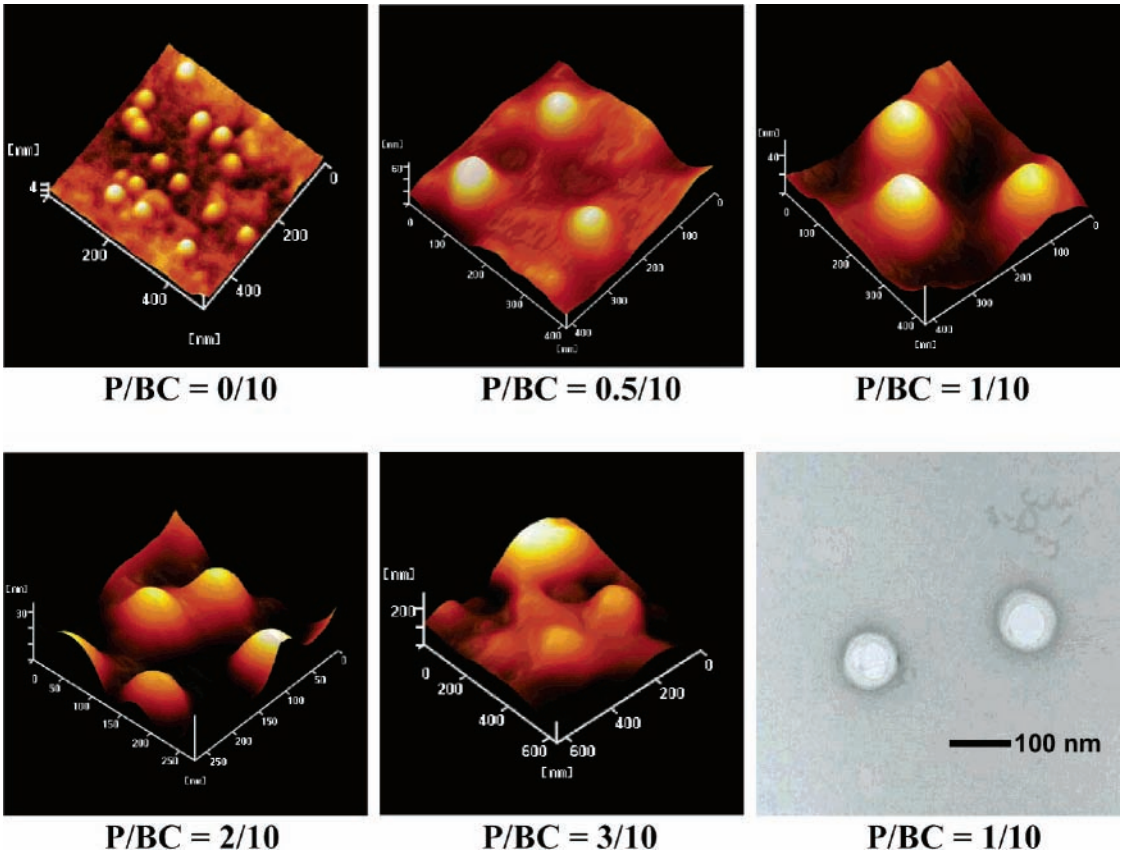

Figure 5. Morphology of nanoparticles prepared with various feed weight ratios of paclitaxel to block copolymer (P/BC ratios) obtained by AFM and TEM.

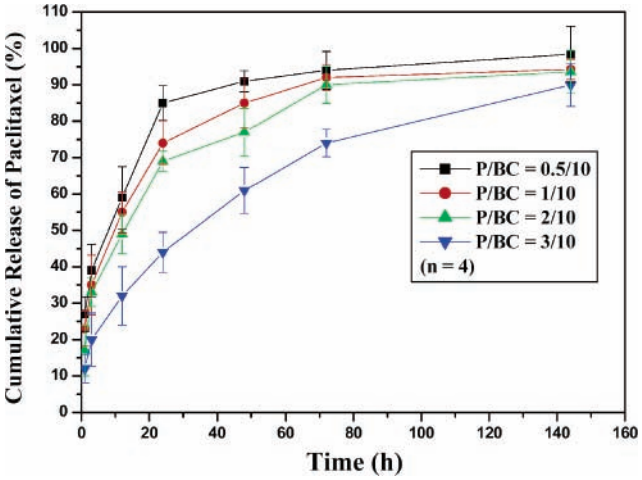

Figure 6. Release profiles of paclitaxel from nanoparticles prepared with various feed weight ratios of paclitaxel to block copolymer (P/BC ratios).

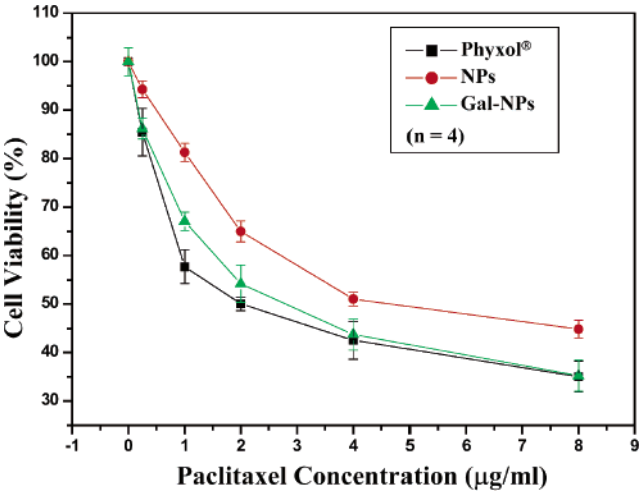

Figure 7. Viability of HepG2 cells treated with distinct paclitaxel formulations at various paclitaxel concentrations for 3 days. Phyxol: cells treated with a clinically available paclitaxel formulation (Sinphar Pharmaceutical); NPs: cells treated with paclitaxel-loaded nanoparticles without conjugated galactosamine; and Gal-NPs: cells treated with paclitaxel-loaded nanoparticles with conjugated galactosamine.

cell activity as an indicator of cell viability. Briefly, MTT [3-(4,5-dimethyl-thiazol-yl)-2,5-diphenyltetrazolium bromide, Sigma] was dissolved in PBS to a concentration of 5 mg/mL as a stock MTT solution and filtered for sterilization. An amount of 5×10^4 HepG2 cells/well was seeded in 24-well plates and allowed to adhere overnight. The growth medium was replaced with a fresh medium that contained various concentrations (0.25−8 μg/mL) of the following paclitaxel formulations: Phyxol, nanoparticles without conjugated galactosamine (NPs), and nanoparticles with conjugated galactosamine (Gal-NPs).

The cells were then incubated for 3 days and washed twice in 1 mL of PBS. Subsequently, the cells were incubated in a growth medium that contained 1 mg/mL MTT agent for an additional 4 h at 37 °C; 500 μL of DMSO was added to each well to ensure that the formazan crystals dissolved. Finally, the optical density readings were taken using a multiwell scanning spectrophotometer (MRX Microplate Reader, Dynatech Laboratories Inc., Chantilly, VA) at a wavelength of 570 nm.

Immunofluorescence Analysis of HepG2 Cells Treated with Distinct Paclitaxel Formulations. HepG2 cells were grown on glass coverslips and then treated with distinct paclitaxel formulations with a final paclitaxel concentration of 8 μg/mL. After incubation for 3 days, the cells were fixed with 3.7% formaldehyde in PBS for 10 min at room temperature and then permeabilized in 0.1% Triton X-100 in PBS that contained 1% bovine serum albumin (PBS−BSA) and RNase 100 μg/mL. After they had been washed three times with PBS−BSA, the cells were treated with Oregon Green 514 palloidin (1:100 v/v, Molecular Probes) in PBS−BSA for 20 min. The cells were then incubated for 60 min with anti-bovine α-tubulin mouse mAb (1 μg/mL, Molecular Probes) in PBS−BSA. The Alexa Fluor 633-conjugated goat anti-mouse IgG antibody (2 μg/mL, Molecular Probes) was added, and the cells were incubated for another 60 min. They were then rinsed three times with PBS−BSA and treated with 100 nM propidium iodide (PI, Sigma) for 5 min.

Before the samples were mounted for CLSM examinations, they were again washed with PBS and deionized water. Oregon Green 514 palloidin, PI, or Alexa Fluor 633 stainings were visualized with excitations at 488, 543, and 633 nm, respectively, using an inverted CLSM (TCS SL, Leica, Germany). Images were imposed using LCS Lite software (version 2.0).

Altered Cycling States of HepG2 Cells Treated with Distinct Paclitaxel Formulations. To demonstrate whether paclitaxel released from the prepared NPs or the Gal-NPs could restrict HepG2 cells in specific cell cycle stages, flow cytrometric studies were performed. HepG2 cells treated with distinct paclitaxel formulations with a final paclitaxel concentration of 1 μg/mL for 3 days were pelleted at 1500 rpm for 5 min and then resuspended in PBS (*25*). Methanol (100%) precooled to −20 °C for 15 min was then added to the cell suspension, which was then centrifuged at 1500 rpm for 5 min. The supernatant was discarded, and the cell pellet was rehydrated with PBS. The pellet was stained with DNA staining solution (10 μg/mL PI and 1 mg/mL RNase A) for 45 min. The DNA content of each cell was measured using a Becton Dickinson FACSCalibur flow cytometer (San Jose, CA).

Statistical Analysis. Statistical analysis was performed to determine differences between the measured properties of groups. One-way analysis of variance was performed, and confidence intervals were determined using a statistical program (Statistical Analysis System, Version 6.08, SAS Institute Inc., Cary, NC). All data are presented as a mean value with its standard deviation indicated (mean ± SD).

RESULTS AND DISCUSSION

Production of γ-PGA. In the ^{1}H NMR spectrum of the purified γ-PGA produced by fermentation, the five main signals at 1.73, 1.94, 2.19, 4.14, and 8.15 ppm represented the protons of β-CH_2, γ-CH_2, α-CH, and amide, respectively. Additionally, the fermented product after purification showed no macromolecular impurity, according to the ^{1}H NMR analysis, suggesting that the obtained white γ-PGA powder was highly pure.

Hydrolysis of γ-PGA. Low-molecular-weight γ-PGA was produced by hydrolyzing purified γ-PGA obtained from fermentation at 150 °C for distinct durations. Solutions of purified γ-PGA obtained by fermentation and hydrolyzed γ-PGA were analyzed by a GPC system. Figure 2 shows that the purified γ-PGA obtained by fermentation had a high average molecular weight (M_n ~320 kDa) with a polydispersity of about 1.8. When γ-PGA was hydrolyzed at 150 °C for 5 h, its average molecular weight of γ-PGA was reduced to about 5 kDa. To reduce the polydispersity of the hydrolyzed γ-PGA, the hydrolyzed γ-PGA (~5 kDa) was further dialyzed twice (using a membrane with MWCO: 3500 and a membrane with MWCO: 6000−8000) against deionized water. Thus, the obtained γ-PGA had an average molecular weight of about 4 kDa with a polydispersity of 1.3 (Figure 2). This specific γ-PGA was used subsequently, together with PLA, to synthesize block copolymers to prepare the nanoparticles.

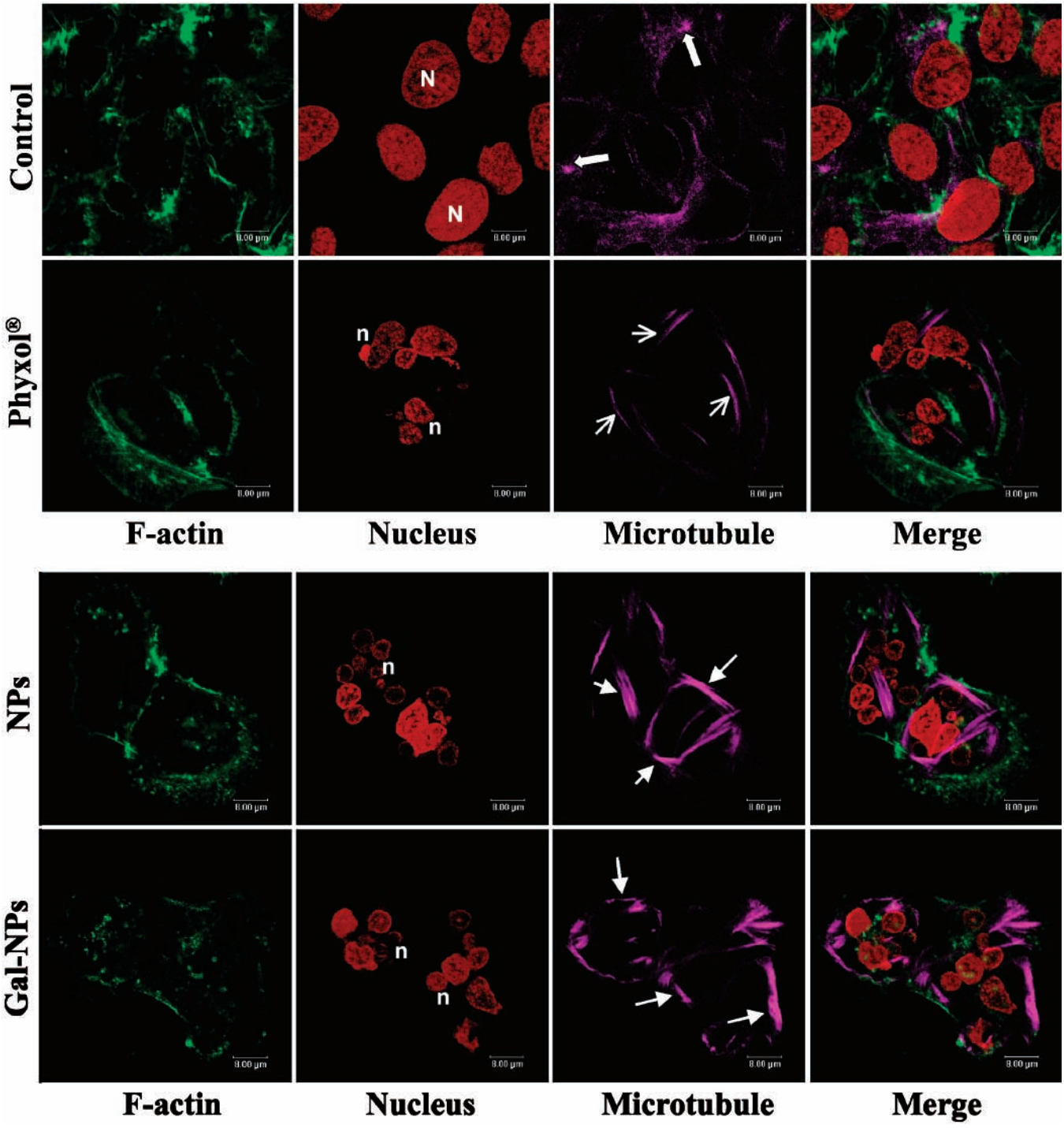

Figure 8. CLSM images of HepG2 cells treated with distinct paclitaxel formulations for 3 days. Control: untreated cells; Phyxol: cells treated with a clinically available paclitaxel formulation (Sinphar Pharmaceutical); NPs: cells treated with paclitaxel-loaded nanoparticles without conjugated galactosamine; and Gal-NPs: cells treated with paclitaxel-loaded nanoparticles with conjugated galactosamine. N: normal nuclei; n: micronuclear formation; bold arrow right: centrosomes; and →: condensation of cytoplasmic microtubules.

Synthesis of γ-PGA-PLA Block Copolymers. Figure 3a and 3b show the ^{1}H NMR spectrum and the GPC chromatogram of the synthesized γ-PGA-PLA block copolymers, respectively. In the ^{1}H NMR spectrum (Figure 3a), the chemical shifts at 1.42 and 5.20 ppm corresponded to the protons of the methyl group (CH_3) and methine (CH) on PLA, respectively, while the main chemical shifts exhibited by γ-PGA, described above, were also detected. The GPC chromatograms (Figure 3b) indicated that the molecular weight of γ-PGA-PLA slightly exceeded that of PLA. The aforementioned results indicated that γ-PGA was successfully conjugated to PLA by CDI.

Particle Size and Morphology of Paclitaxel-Loaded Nanoparticles. The distribution of sizes and the zeta potential of the prepared nanoparticles may importantly determine their fates after administration (*19*). As shown in Table 1, the particle sizes of the prepared nanoparticles increased significantly with the P/BC ratio. Dynamic light scattering measurements further demonstrated that all of the prepared nanoparticles had a narrow size distribution, with the exception of those prepared with a P/BC ratio of 3/10 (Figure 4). AFM and TEM showed that the morphologies of all of the prepared nanoparticles were spherical, and their surfaces were smooth (Figure 5).

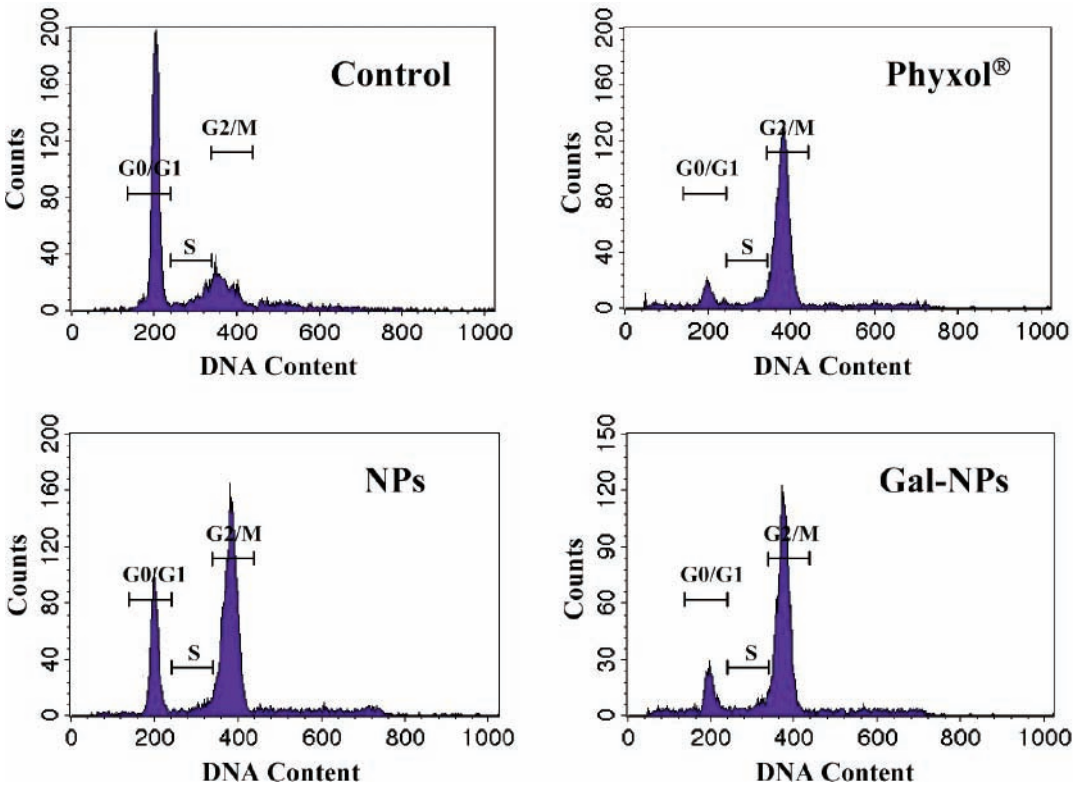

Figure 9. Analysis, using a flow cytometer, of DNA content in cell cycle of HepG2 cells treated with distinct paclitaxel formulations for 3 days. Control: untreated cells; Phyxol: cells treated with a clinically available paclitaxel formulation (Sinphar Pharmaceutical); NPs: cells treated with paclitaxel-loaded nanoparticles without conjugated galactosamine; and Gal-NPs: cells treated with paclitaxel-loaded nanoparticles with conjugated galactosamine.

Hashida et al. reported that the majority of the diameter of the fenestrate of the liver sinusoid is usually smaller than 200 nm (*26*). Thus, large particles hardly reach the parenchymal cells of the liver. Additionally, drug carriers with diameters of larger than 200 nm are readily scavenged nonspecifically by monocytes and the reticuloendothelial system (*27*). It was reported that smaller particles tended to accumulate at the tumor sites because of the EPR (enhanced permeability and retention) effect (*28*); greater internalization was also observed (*1*).

It was found that the prepared paclitaxel-loaded nanoparticles had a negative surface charge with a zeta potential of about −20 mV (Table 1), because of the carboxyl (COO) groups on the hydrophilic γ-PGA shell. This may affect the cellular uptake of the prepared nanoparticles due to electrostatic repulsion forces between the nanoparticles and the rather negatively charged surface of cells (*1*). However, Wakebayashi et al. suggested that the introduction of a specific ligand onto the nanoparticles may enhance their cellular uptake by receptor-mediated endocytosis (*29*). Additionally, positively charged carriers are reported to be able to induce a nonspecific interaction with unintended target tissues, particularly under in vivo conditions after administration (*29, 30*).

Loading Content and Loading Efficiency of Paclitaxel-Loaded Nanoparticles. Paclitaxel is highly hydrophobic and has a solubility of approximately 1 μg/mL in aqueous solution at pH 7.4 (*31*). Thus, in the drug loading process, the incorporation of paclitaxel in the nanoparticles competed with the precipitation of paclitaxel in aqueous solution (*31*). As the P/BC ratio increased, the incorporation of paclitaxel in the nanoparticles (the drug loading content) appeared to be increased, while the precipitation of paclitaxel in aqueous solution was more pronounced and thus significantly reduced the drug loading efficiency (Table 1, $p < 0.05$).

Release of Paclitaxel from Loaded Nanoparticles. As shown in Figure 6, paclitaxel was continuously released from nanoparticles prepared with distinct P/BC ratios. All samples released a burst of paclitaxel in the initial stage. An amount of 10−25% of the encapsulated drug was released in the first hour. This may be due to some of the drugs were deposited near the γ-PGA shell of the prepared nanoparticles.

As the P/BC ratio increased, the rate of release of paclitaxel from the prepared nanoparticles decreased significantly. It was reported that a hydrophobic drug encapsulated within nanoparticles partially crystallized at a higher drug loading content, while it formed a molecular dispersion at a lower drug loading content (*32*). The crystallized drug in the hydrophobic core of the nanoparticles is expected to dissolve more gradually and to diffuse to their outer aqueous phase more slowly than the drug in the form of a molecular dispersion (*2*). Additionally, the encapsulated drug took longer to diffuse through the polymer matrix to the aqueous medium when the nanoparticles were larger (i.e., as the P/BC ratio increased, as in Table 1) (*32*).

Conjugation of Galactosamine to Paclitaxel-Loaded Nanoparticles. As discussed above, the drug loading content of the prepared nanoparticles increased significantly with the P/BC ratio, while their drug loading efficiency decreased remarkably (Table 1). To obtain a comparatively high drug loading content with a high loading efficiency (Table 1), nanoparticles prepared with a P/BC ratio of 1/10 (the NPs) were used in the rest of this study. For the potential of targeting liver cancer cells, galactosamine was conjugated to the paclitaxel-loaded nanoparticles (the Gal-NPs). As determined by the Morgan Elson assay, the amount of galactosamine conjugated on the Gal-NPs was 66.2 ± 2.4 nmol/mg nanoparticles (or $4.0 \pm 0.1 \times 10^{16}$ galactosamine moieties per mg of the targeted nanoparticles, $n = 4$). The particle size of the Gal-NPs (127.5 ± 2.5 nm) was comparable to that of the NPs (128.8 ± 3.4 nm, $p > 0.05$). However, the zeta potential of the former (−10.6 ± 2.0 mV) was significantly lower than that of the latter (−19.6 ± 1.8 mV, $p < 0.05$), because galactosamine was conjugated to the

carboxyl (COO) groups on γ-PGA, reducing the negative surface charge of the Gal-NPs.

Viability of HepG2 Cells Treated with Distinct Paclitaxel Formulations. Figure 7 shows the viability of HepG2 cells treated with the paclitaxel formulations investigated herein. The inhibition of the growth of cells by the Gal-NPs was comparable to that of a clinically available paclitaxel formulation (Phyxol, $p > 0.05$); the NPs exhibited significantly less inhibitory activity ($p < 0.05$).

Hepatoma cells are known to recognize galactose- and *N*-acetylgalactosamine-terminated glycoproteins via the asialoglycoprotein (ASGP) receptors located on their surfaces (*33*). It was found in our previous study that during incubation with rhodamine-123-containing nanoparticles without conjugated galactosamine, little fluorescence was observed on the images of HepG2 cells taken by the CLSM (*6*). This indicated that without galactosamine only a small proportion of the nanoparticles could be internalized in the cells, because of the electrostatic repulsion forces between the nanoparticles and the cells as mentioned earlier. Hence, the NPs prepared herein released paclitaxel mainly outside the cells (in the culture medium). The released paclitaxel then diffused into the HepG2 cells, inhibiting the growth of the cells. Accordingly, under in vivo conditions after administration, the normal tissues may be nonselectively exposed to paclitaxel released from the NPs in the blood stream, potentially causing unwanted toxic side effects.

In contrast, with increasing the galactosamine content conjugated on the rhodamine-123-containing nanoparticles, the intensity of fluorescence observed in HepG2 cells increased significantly at 30 min after incubation (*6*). This indicated that the galactosylated nanoparticles interacted in a specified manner with HepG2 cells via ligand−receptor (ASGP) recognition. Therefore, the Gal-NPs prepared in this study were first internalized into HepG2 cells via the ASGP receptors, and then the encapsulated paclitaxel was released inside the cytoplasm, inhibiting the growth of the cells. Thus, the active targeting nature of the Gal-NPs may lead to high selectivity to the hepatic tumor and enhance their cellular uptake, with a consequent decrease in systemic toxicity.

Figure 8 shows CLSM images of HepG2 cells treated with Phyxol, the NPs, or the Gal-NPs. The untreated HepG2 cells (control) demonstrated normal nuclei, centrosomes, and microtubule networks. In contrast, HepG2 cells that had been exposed to Phyxol, NPs, or Gal-NPs exhibited significantly disrupted polar spindles of cells and the characteristic condensation of cytoplasmic microtubules. Additionally, improper mitotic spindle assembly caused micronuclear formation.

Figure 9 shows that HepG2 cells that had been treated with distinct paclitaxel formulations arrested the G2/M phase. The arrest of the growth of cells in the G2/M phase strongly suggested interference by paclitaxel with spindle formation and was consistent with the morphological findings presented in Figure 8. As compared to the untreated cells (control), the sharp peak observed in the G0/G1 phase was markedly attenuated and was instead mostly in the G2/M phase for the cells treated with Phyxol or the Gal-NPs. In contrast, for those cells treated with the NPs, this observation was less significant ($p < 0.05$). This finding again may be owing to that without galactosamine, only a small proportion of the nanoparticles (the NPs) could be internalized in the cells. Therefore, the NPs released paclitaxel mainly outside the HepG2 cells.

CONCLUSIONS

In conclusion, the aforementioned results indicated that the paclitaxel-loaded nanoparticles with conjugated galactosamine prepared herein may be internalized into HepG2 cells via receptor-mediated endocytosis, inhibiting the growth of cells. Therefore, the prepared nanoparticles may be used as a potential targeted drug delivery system to fight liver cancers.

ACKNOWLEDGMENT

The authors would like to thank the National Science Council of the Republic of China, Taiwan (Contract No. NSC 93-2213-B-007-051), and the National Health Research Institutes of the Republic of China, Taiwan (Contract No. NHRI-EX93-9221EI), for financially supporting this research.

LITERATURE CITED

(1) Li, C. (2002) Poly(L-glutamic acid)-anticancer drug conjugates. *Adv. Drug Delivery Rev. 54*, 695−713.

(2) Na, K., Park, K. H., Kim, S. W., and Bae, Y. H. (2000) Self-assembled hydrogel nanoparticles from curdlan derivatives: Characterization, anti-cancer drug release and interaction with a hepatoma cell line (HepG2). *J. Controlled Release 69*, 225−236.

(3) Saul, J. M., Annapragada, A., Natarajan, J. V., and Bellamkonda, R. V. (2003) Controlled targeting of liposomal doxorubicin via the folate receptor in vitro. *J. Controlled Release 92*, 49−67.

(4) Liang, H. C., Chang, W. H., Lin, K. J., and Sung, H. W. (2003) Genipin-crosslinked gelatin microspheres as a drug carrier for intramuscular administration: In vitro and in vivo studies. *J. Biomed. Mater. Res. 65A*, 271−282.

(5) Na, K., Lee, T. B., Park, K. G., Shin, E. K., Lee, Y. B., and Choi, H. K. (2003) Self-assembled nanoparticles of hydrophobically modified polysaccharide bearing vitamin H as a targeted anti-cancer drug delivery system. *Eur. J. Pharm. Sci. 18*, 165−173.

(6) Liang, H. F., Yang, T. F., Huang, C. T., Chen, M. C., and Sung, H. W. (2005) Preparation of nanoparticles composed of poly(γ-glutamic acid)-poly(lactide) block copolymers and evaluation of their uptake by HepG2 cells. *J. Controlled Release 105*, 213−225.

(7) Richard, A., and Margaritis, A. (2001) Poly(glutamic acid) for biomedical applications. *Crit. Rev. Biotechnol. 21*, 219−232.

(8) Prodhomme, E. J. F., Tutt, A. L., Glennie, M. J., and Bugg, T. D. H. (2003) Multivalent conjugates of poly-γ-D-glutamic acid from Bacillus Licheniformis with antibody F(ab′) and glycopeptide ligands. *Bioconjugate Chem. 14*, 1148−1155.

(9) Rao, S., Orr, G. A., Chaudhary, A. G., Kingston, D. G., and Horwitz, S. B. (1995) Characterization of Taxol binding site on the microtubule, 2-(M-Azidobenzoyl) Taxol photolabels a peptide (amino acids 217−231) of beta-tubulin. *J. Biol. Chem. 270*, 20235−20238.

(10) Gagandeep, S., Novikoff, P. M., Ott, M., and Gupta, S. (1999) Paclitaxel shows cytotoxic activity in human Hepatocellular carcinoma cell lines. *Cancer Lett. 136*, 109−118.

(11) Jordan, M. A., Wendell, K., Gardiner, S., Derry, W. B., Copp, H., and Wilson, L. (1996) Mitotic block induced in HeLa cells by low concentrations of paclitaxel results in abnormal mitotic exit and apoptotic cell death. *Cancer Res. 56*, 816−825.

(12) Lee, I. H., Park, Y. T., Roh, K., Chung, H., Kwon, I. C., and Jeong, S. Y. (2005) Stable paclitaxel formulations in oily contrast medium. *J. Controlled Release 102*, 415−425.

(13) Lin, H. L., Liu, T. Y., Chau, G. Y., Lui, W. Y., and Chi, C. W. (2000) Comparison of 2-methoxyestradiol-induced, docetaxel-induced, and paclitaxel-induced apoptosis in hepatoma cells and its correlation with reactive oxygen species. *Cancer 89*, 983−994.

(14) Kang, T. H., Pae, H. O., Yoo, J. C., Kim, N. Y., Kim, Y. C., Ko, G. I., and Chung, H. T. (2000) Antiproliferative effect of alkaloids from *Sedum sarmentosum* on murine and human hepatoma cell line. *J. Ethnopharmacol. 70*, 177−182.

(15) Yoon, S. H., Do, J. H., Lee, S. Y., and Chang, H. N. (2000) Production of poly-γ-glutamic acid by fed-batch culture of *Bacillus licheniformis*. *Biotechnol. Lett. 22*, 585−588.

(16) Troy, F. A. (1973) Chemistry and biosynthesis of the poly(γ-D-glutamyl) capsule in *Bacillus* licheniformis II. Characterization and structural properties of the enzymatically synthesized polymer. *J. Biol. Chem. 248*, 316−324.

(17) Van Dijk-Wolthuis, W. N. E., Tsang, S. K. Y., Kettenes-van den Bosch, J. J., and Hennink, W. E. (1997) A new class of polymerizable dextrans with hydrolysable groups: Hydroxyethyl methacrylated

dextran with and without oligolactate spacer. *Polymer 38*, 6235−6242.
(18) Gref, R., Luck, M., Quellec, P., Marchand, M., Dellacherie, E., Harnisch, S., Blunk, T., and Muller, R. H. (2000) "Stealth" corona-core nanoparticles surface modified by polyethylene glycol (PEG): Influences of the corona (PEG chain length and surface density) and of the core composition on phagocytic uptake and plasma protein adsorption. *Colloid. Surface. B18*, 301−313.
(19) Dong, Y., and Feng, S. S. (2004) Methoxy poly(ethylene glycol)-poly(lactide) (MPEG-PLA) nanoparticles for controlled delivery of anticancer drugs. *Biomaterials 25*, 2843−2849.
(20) Zhang, L., Hu, Y., Jiang, X., Yang, C., Lu, W., and Yang, Y. H. (2004) Camptothecin derivative-loaded poly(caprolactone-co-lactide)-b-PEG-b- poly(caprolactone-co-lactide) nanoparticles and their biodistribution in mice. *J. Controlled Release 96*, 135−148.
(21) Sung, H. W., Chang, W. H., Ma, C. Y., and Lee, M. H. (2003) Crosslinking of biological tissues using genipin and/or carbodiimide. *J. Biomed. Mater. Res. 64A*, 427−438.
(22) Liang, H. C., Chang, W. H., Liang, H. F., Lee, M. H., and Sung, H. W. (2004) Crosslinking structures of gelatin hydrogels crosslinked with genipin or a water-soluble carbodiimide. *J. Appl. Polym. Sci. 91*, 4017−4026.
(23) David, A., Kopeckova, P., Rubinstein, A., and Kopeccek, J. (2001) Enhanced biorecognition and internalization of HPMA copolymers containing multi- or multivalent carbohydrate side-chains by human hepatocarcinoma cells. *Bioconjugate Chem. 12*, 890−899.
(24) Chen, C. N., Sung, H. W., Liang, H. F., and Chang, W. H. (2002) Feasibility study using a natural compound (reuterin) produced by *Lactobacillus reuterin* in sterilizing and crosslinking biological tissues. *J. Biomed. Mater. Res. 61*, 360−369.
(25) Saito, T., Dojima, T., Toriyama, M., Park, E. Y. (2002) The effect of cell cycle on GFPuv gene expression in the baculovirus expression system. *J. Biotechnol. 93*, 121−129.
(26) Hashida, M., Takemura, S., Nishikawa, M., and Takakura, Y. (1998) Targeted delivery of plasmid DNA complexed with galactosylated poly(L-lysine). *J. Controlled Release 53*, 301−310.
(27) Litzinger, D. C., Buiting, A. M. J., Rooijen, N., and Huang, L. (1994) Effect of liposome size on the circulation time and intraorgan distribution of amphipathic poly(ethylene glycol)-containing liposomes. *Biochim. Biophys. Acta 1190*, 99−107.
(28) Maeda, H., and Matsumura, Y. (1989) Tumoritropic and lymphotropic principles of macromolecular drugs. *Crit. Rev. Ther. Drug Carrier Syst. 6*, 193-210.
(29) Wakebayashi, D., Nishiyama, N., Yamasaki, Y., Itaka, K., Kanayama, N., Harada, A., Nagasaki, Y., and Kataoka, K. (2004) Lactose-conjugated polyion complex micelles incorporating plasmid DNA as a targetable gene vector system: their preparation and gene transfecting efficiency against cultured HepG2 cells. *J. Controlled Release 95*, 653−664.
(30) Ward, C. M., Read, M. L., and Seymour, L. W. (2001) Systemic circulation of poly(L-lysine)/DNA vectors is influenced by polycation molecular weight and type of DNA: differential circulation in mice and rats and the implications for human gene delivery. *Blood 97*, 2221−2229.
(31) Lee, S. C., Kim, C., Kwon, I. C., Chung, H., and Jeong, S. Y. (2003) Polymeric micelles of poly(2-ethyl-2-oxazoline)-block-poly-(ϵ-caprolactone) copolymer as a carrier for paclitaxel. *J. Controlled Release 89*, 437−446.
(32) Gref, R., Minamitake, Y., Peracchia, M. T., Trubetskoy, V., Torchilin, V., and Langer, R. (1994) Biodegradable long-circulating polymeric nanospheres. *Science 263*, 1600−1603.
(33) Han, J. H., Oh, Y. K., Kim, D. S., and Kim, C. K. (1999) Enhanced hepatocyte uptake and liver targeting of methotrexate using galactosylated albumin as a carrier. *Int. J. Pharm. 188*, 39−47.

BC0502107

NMR and Crystallographic Characterization of Adventitious Borate Binding by Trypsin

Thomas R. Transue, Scott A. Gabel, and Robert E. London*

National Institute of Environmental Health Sciences, Laboratory of Structural Biology, Box 12233, Research Triangle Park, North Carolina 27709. Received July 25, 2005; Revised Manuscript Received November 23, 2005

Recent ^{11}B NMR studies of the formation of ternary complexes of trypsin, borate, and S1-binding alcohols revealed evidence for an additional binding interaction external to the enzyme active site. We have explored this binding interaction as a prototypical interaction of borate and boronate ligands with residues on the protein surface. NMR studies of trypsin in which the active site is blocked with leupeptin or with the irreversible inhibitor 4-(2-aminoethyl) benzenesulfonyl fluoride hydrochloride (AEBSF) indicate the existence of a low-affinity borate binding site with an apparent dissociation constant of 97 mM, measured at pH 8.0. Observation of a field-dependent dynamic frequency shift of the ^{11}B resonance indicates that it corresponds to a complex for which $\omega\tau \gg 1$. The 0.12 ppm shift difference of the borate resonances measured at 11.75 and 7.05 T, corresponds to a quadrupole coupling constant of 260 kHz. A much larger 2.0 ppm shift is observed in the ^{11}B NMR spectra of trypsin complexed with benzene boronic acid (BBA), leading to a calculated quadrupole coupling constant of 1.1 MHz for this complex. Crystallographic studies identify the second borate binding site as a serine-rich region on the surface of the molecule. Specifically, a complex obtained at pH 10.6 shows a borate ion covalently bonded to the hydroxyl oxygen atoms of Ser164 and Ser167, with additional stabilization coming from two hydrogen-bonding interactions. A similar structure, although with low occupancy (30%), is observed for a trypsin−BBA complex. In this case, the BBA is also observed in the active site, covalently bound in two different conformations to both His57 Nϵ and Ser195 Oγ. An analysis of pairwise hydroxyl oxygen distances was able to predict the secondary borate binding site in porcine trypsin, and this approach is potentially useful for prediction of borate binding sites on the surfaces of other proteins. However, the distances between the Ser164/Ser167 Oγ atoms in all of the reported trypsin crystal structures is significantly greater than the Oγ distances of 2.2 and 1.9 Å observed in the trypsin complexes with borate and BBA, respectively. Thus, the ability of the hydroxyl oxygens to adopt a sufficiently close orientation to allow bidentate ligation is a critical limit on the borate binding affinity of surface-accessible serine/threonine/tyrosine residues.

INTRODUCTION

Analysis of the human genome is expected to expand the number of potential protein drug targets by an order of magnitude (*1*). In contrast with enzymatic targets for which activity-based assays are generally straightforward, it can be anticipated that in many cases drug development will target the interruption of protein−protein interactions involved in signal transduction processes. Target sites on protein surfaces are not typically characterized by the recessed cleft topology of most enzyme active sites and thus exhibit a reduced tendency to trap small molecules that can serve as lead compounds for ligand development. This analysis is supported by recent NMR screening studies, which indicate that the ability of small molecules to bind noncovalently to proteins is strongly dependent on local topology, being largely determined by the existence of pockets with optimal volume, compactness, and surface roughness (*2*).

Boric acid forms complexes with sugars and other small molecules containing hydroxyl, carboxyl, or ring nitrogen functionalities (*3*−*7*). The presence of these groups on proteins suggests that analogous protein complexes should exist. Consistent with this expectation, binding interactions between borate and cytochrome *c* have been detected by NMR spectroscopy (*8*, *9*). Noncovalently associated boric acid (*10*; pdb code 1B33) and borate (*11*; pdb code 1A95) occasionally have been observed in protein crystal structures; however, we are not aware of previous reports of covalent complexes involving borate and the residues on protein surfaces. Of course, the binding of boronate inhibitors to the active site of serine proteases has been studied extensively (*12*−*23* and references therein). Recent ^{11}B NMR studies of ternary complexes formed from trypsin, borate, and S1-binding alcohols revealed the existence of an additional borate binding site(s) of unknown location and composition (*24*, *25*). The ^{11}B NMR characteristics of this additional borate resonance are consistent with a polydentate, tetrahedral borate species that is in slow exchange with uncomplexed borate.

The present studies were undertaken to further clarify whether this resonance corresponds to a secondary binding site on the trypsin or to a contaminant, to characterize the binding affinity and structure of the adduct formed, to identify the boron ligands involved in the complex, and to evaluate whether structurally related boronate molecules might also interact with the putative secondary binding site. It was further postulated that if borate does bind to a secondary binding site on the surface of trypsin, then this type of binding interaction is unlikely to be unique. The specificity of such interactions might lead to a different type of ligand selectivity than that which can be achieved based on a combination of noncovalent hydrophobic and electrostatic interactions.

EXPERIMENTAL PROCEDURES

Crystallography. Type IX porcine pancreatic trypsin (Sigma, St. Louis, MO) was crystallized in the presence of 100 mM guanidino-3-propanol (G3P)[1] as described previously (*25*). For complexes containing borate bound at the second site, a crystal

10.1021/bc0502210 Not subject to U.S. Copyright. Published 2006 by American Chemical Society
Published on Web 02/23/2006

Table 1. Crystallographic Data Summary

	Crystallographic Data Statistics	
data set	borate complex	BBA complex
pH	10.6	10.5
soaked with	200 mM borate, 50 mM G3P, 5 mM $CaCl_2$	1 M BBA
cryoprotectant	90% saturating $MgSO_4$	1 M CAPS buffer
unit cell	$a = 76.30$, $b = 53.45$, $c = 46.47$ Å	$a = 76.85$, $b = 53.70$, $c = 46.71$ Å
	$\alpha = \beta = \gamma = 90°$	$\alpha = \beta = \gamma = 90°$
space group	$P2_12_12_1$	$P2_12_12_1$
resolution (Å)	1.25	1.5
no. of observations	581 590	317 430
unique reflns	47 257	31 465
R_{sym} (%) (last shell)	8.2 (31.0)	8.7 (44.6)
$I/(\sigma I)$ (last shell)	28.1 (4.7)	17.2 (2.1)
mosaicity (deg)	0.41−0.75 (avg = 0.58)	0.5
completeness (%) (last shell)	88.6 (70.5)	99.4 (96.0)
redundancy	12.3	5.5
	Refinement Statistics	
R_{cryst} (%)[a]	13.8	16.8
R_{free} (%)[b]	15.2	18.9
no. of waters	413	325
mean B value (Å) (protein only)	13.2 (10.9)	18.8 (16.4)
	rms Deviation from Target Values	
bond length (Å)	0.011	0.008
bond angle (deg)	2.14	2.02
	Ramachandran Statistics	
residues in favored (98%) regions (%)	97.7	98.6
residues in allowed (>99.8%) regions (%)	100.0	100.0

[a] R-factor $= \sum||F_o| - |F_c||/\sum|F_o|$ calculated from working data set. [b] Free R is calculated from 5% of data randomly chosen to be excluded in refinement.

was transferred in four 1 min steps to a final solution containing 90% saturated $MgSO_4$ (acting as a cryoprotectant), 200 mM borate, pH 10.6, 50 mM G3P, and 5 mM $CaCl_2$. The solutions for each step contained ratios of mother liquor to final solution of 50:50, 10:90, 0:100, and 0:100. The crystal was then flash frozen in liquid nitrogen and mounted for data collection. For benzene boronic acid (BBA), a crystal was transferred via several dilutions with mother liquor to a final solution containing 1 M CAPS buffer pH 10.5 (acting as a buffer and cryoprotectant) and 1 M BBA. The crystal was then frozen in liquid nitrogen and mounted for data collection.

Data were collected as described previously (*25*) using a Rigaku rotating anode generator and an R-AXIS IV detector (Molecular Structure Corporation). Data were reduced using DENZO and SCALEPACK (HKL Research) (*26*). All models were refined using a maximum likelihood target against all intensities using CNS (*27*). Force parameters were taken from the AMBER force field (*28*). The relative occupancy of alternate models (including alternate side chain conformations and alternately occupied borate or BBA binding sites) was iteratively estimated by minimizing difference electron density and by comparing the refined *B*-factors looking for a minimal difference. Water molecule occupancies were refined and then examined manually to avoid very low occupancies or very high *B* factors. For the borate crystal, a complete data set to 1.25 Å resolution was collected. The BBA complex crystal produced a data set complete to 1.5 Å. Data collection statistics as well as refinement statistics are provided in Table 1. Crystal structures showing the complex of trypsin with borate and with BBA have been deposited in the protein data bank with accession numbers 2A31 and 2A32, respectively.

[1] Abbreviations: 4AB, 4-amino-1-butanol; AEBSF, 4-(2-aminoethyl) benzenesulfonyl fluoride hydrochloride; AEBS−trypsin, AEBSF-modified trypsin; BBA, benzene boronic acid (sometimes referred to as phenylboronic acid); CAPS, *N*-cyclohexyl-3-aminopropanesulfonic acid; G3P, guanidino-3-propanol.

NMR Spectroscopy. ^{11}B NMR spectra were obtained on a Varian INOVA 500 NMR spectrometer operating at 160.6 MHz for boron or on a Varian Gemini 300 NMR spectrometer operating at 96.3 MHz. In both cases, the ^{11}B measurements were performed using quartz NMR tubes (Wilmad, Buena, NJ) and 5 mm variable-temperature broadband probes that had been modified to reduce the ^{11}B background signal. The probe used for the ^{11}B studies on the Gemini 300 was modified by JS Reasearch (Quincy, MA), and the probe used for the ^{11}B studies on the INOVA 500 was modified by Alex Funk. For the line width analysis and for determination of the apparent dissociation constant of the trypsin−borate complex involving the second binding site, the trypsin was pretreated with 5 mM 4-(2-aminoethyl) benzenesulfonyl fluoride hydrochloride (AEBSF) for 1 h at 4 °C to irreversibly block binding at the active site. We have referred to trypsin modified in this way as AEBS−trypsin. Additionally, 3 mM leupeptin (Bachem, King of Prussia, PA) was added to the sample to competitively bind to any unmodified active sites. Typical INOVA 500 spectral parameters were as follows: sweep width, 16 kHz; acquisition time, 1.0 s; transients, 2000. Gemini 300 spectral parameters were as follows: sweep width, 10 kHz; acquisition time, 0.6 s; transients, 44 400. ^{11}B shifts are referenced to external boric acid at pH 4.0. Since the boric acid/borate concentrations in most of the studies were relatively high, the spectra shown correspond to an expanded region around the bound borate species and do not include the resonance of the uncomplexed boric acid/borate. In most cases, the curved baseline resulting from the large boric acid/borate resonance was corrected using the polynomical fit of the Varian VNMR software.

Software. We developed a simple PERL script to check for neighboring hydroxyl oxygen atoms in any given PDB file. The script searches for serine, threonine, and tyrosine residues, records the coordinates of the hydroxyl oxygen atoms, and then computes pairwise distances. The residues, atoms, and distance

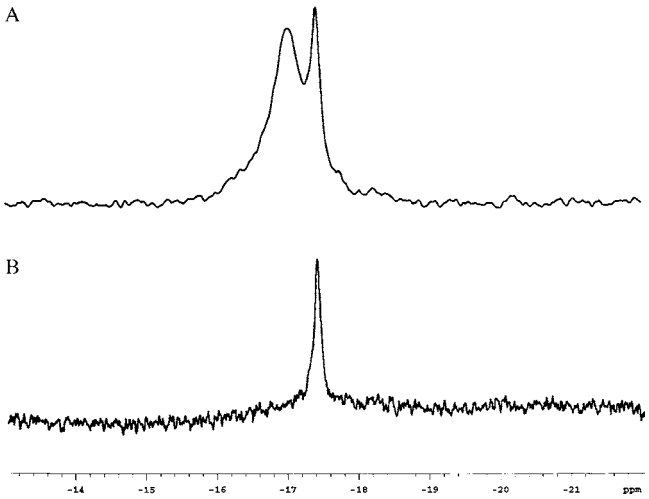

Figure 1. Effect of the leupeptin inhibitor on the binding of borate: (A) ^{11}B NMR spectrum of 2 mM trypsin, 50 mM borate, and 10 mM 4-aminobutanol in 50 mM HEPES, pH 8.0; (B) ^{11}B NMR spectrum of the sample shown in panel A with the addition of 3 mM leupeptin. ^{11}B spectra were obtained at 160.6 MHz on a Varian INOVA 500 at 25 °C.

for any pair closer than a defined distance (set to 6.0 Å in this case) are tabulated.

RESULTS

NMR Studies of the Trypsin−Borate Complex. Recent NMR studies of trypsin−borate complexes yielded evidence for additional borate binding interactions extending beyond the active site of the enzyme (*24*, *25*). For example, ^{11}B NMR studies reveal a resonance that can be assigned to a ternary trypsin−borate−4-aminobutanol (4AB) complex that forms at the active site in the presence of 5 mM borate. However, further increases in the borate concentration resulted in increased intensity of this resonance, which in some cases exhibited a structure indicating that it was composed of more than one component peak (Figure 1A). The presence of an additional binding site was confirmed by the addition of leupeptin, an inhibitor expected to compete with the active site borate−4AB complex (Figure 1B). Since borate binds to a large number of small molecule ligands that might be present in the enzyme preparation, for example, glycerol, citrate, tris buffer, etc., it was initially unclear whether this additional resonance resulted from an interaction with trypsin or with small molecule contaminants. However, ^{1}H NMR studies of the trypsin−borate complex failed to provide evidence of significant small molecule contaminants. Additional dialysis of the trypsin against buffer using a Slide-A-Lyzer also failed to eliminate the additional borate signal. Since protein surfaces contain the same functional groups present in many small borate ligands, it was hypothesized that low-affinity borate binding sites might be a general characteristic of protein surfaces. NMR evidence for the existence of such sites in cytochrome *c* has previously been reported (*8*, *9*). Exploration of the surface of the trypsin molecule immediately revealed a serine-rich region on the surface including residues Ser164, Ser166, Ser167, Ser170, and Ser171 as a potential borate binding site.

To obtain a more quantitative estimate of the binding affinity, the trypsin was treated with AEBSF, an irreversible, active-site-directed inhibitor of the enzyme, to eliminate this binding interaction. Boron-11 NMR studies were then performed on a sample containing 2 mM AEBS−trypsin, 2 mM lactate, and 50 mM HEPES buffer, pH 8.0. The sample also contained 3 mM leupeptin to further suppress any borate complex formation with unreacted trypsin. Lactate, which forms a binary lactate−borate complex (*3*), was used as an internal standard. As can be seen from Figure 2, the ^{11}B NMR spectrum shows the progressive formation of the borate−lactate and (AEBS−trypsin)−borate complexes, where the latter must arise from borate binding to a second site since the active site has been blocked. An additional resonance at $\delta = -19.5$ ppm apparent at higher borate concentrations, is assigned to the borate component of pentaborate, based on the shift data reported by Coddington and Taylor (*4*). Conceivably, the pentaborate or other polyborate species present at high borate concentrations could also bind to trypsin.

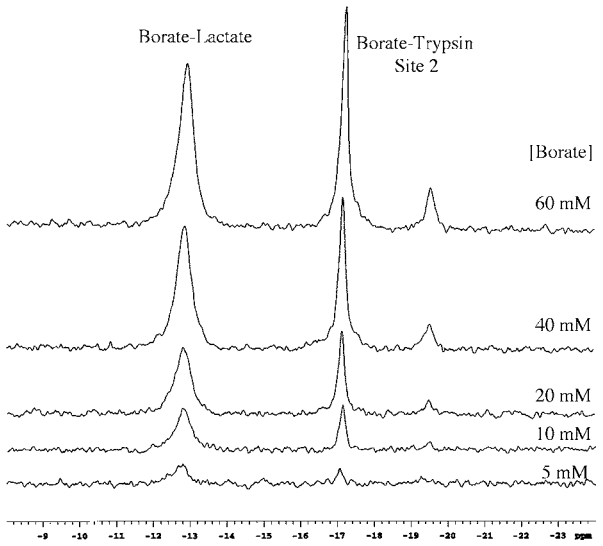

Figure 2. Borate titration of trypsin. ^{11}B NMR spectra of a sample containing 2.0 mM lactate, 2.0 mM AEBS−trypsin, 3 mM leupeptin, and 50 mM HEPES, pH 8.0, as a function of borate concentration. The identity of the upfield resonance at $\delta = -19.5$ ppm, which becomes apparent at high borate concentration, is tentatively assigned to pentaborate (*4*). ^{11}B spectra were obtained at 160.6 MHz on a Varian INOVA 500 at 22 °C.

Based on the data of Pizer and Selzer (*3*), the lactate−borate complex has an apparent K_D value of 128 mM at pH 8. To analyze the data of Figure 2, we also need to account for the fact that we are presumably only observing the central $^1/_2 \leftrightarrow -^1/_2$ transition for the borate−trypsin complex, corresponding to a fractional peak intensity given by (*29*)

$$I_{1/2,-1/2} = \frac{3}{2}\left(\frac{2s+1}{2s(2s+2)}\right) = 0.4 \quad \text{for} \quad ^{11}\text{B} \qquad (1)$$

where $I_{1/2,-1/2}$ is the fractional intensity of the central transition for a quadrupolar nucleus with half-integral spin value s with the latter equality corresponding to ^{11}B for which $s = {}^3/_2$. Analysis of the data shown in Figure 2 gave a value of $K_D =$ 97 mM for the (AEBS−trypsin)−borate complex. This interaction is similar to the inhibition constant of 80 mM measured previously for borate inhibition of trypsin (*24*). For reference, the apparent K_I for the inhibition of trypsin by borate is lowered to 18 mM in the presence of saturating 4-aminobutanol, which binds cooperatively (*24*).

Crystal Structure of the Borate Complex. Previous crystallographic studies have verified the formation of ternary and quaternary trypsin−borate−alcohol complexes that form in the active site (*25*, *30*), confirming the results of earlier NMR studies (*24*). As discussed previously, the nature of these complexes is also apparently influenced by crystal packing effects (*25*, *30*). No additional borate binding interactions were observed in crystallographic studies performed at pH 8.0 (e.g., Figure 3a). To obtain more specific insight into the second borate binding site on trypsin, a crystal containing a trypsin−G3P complex

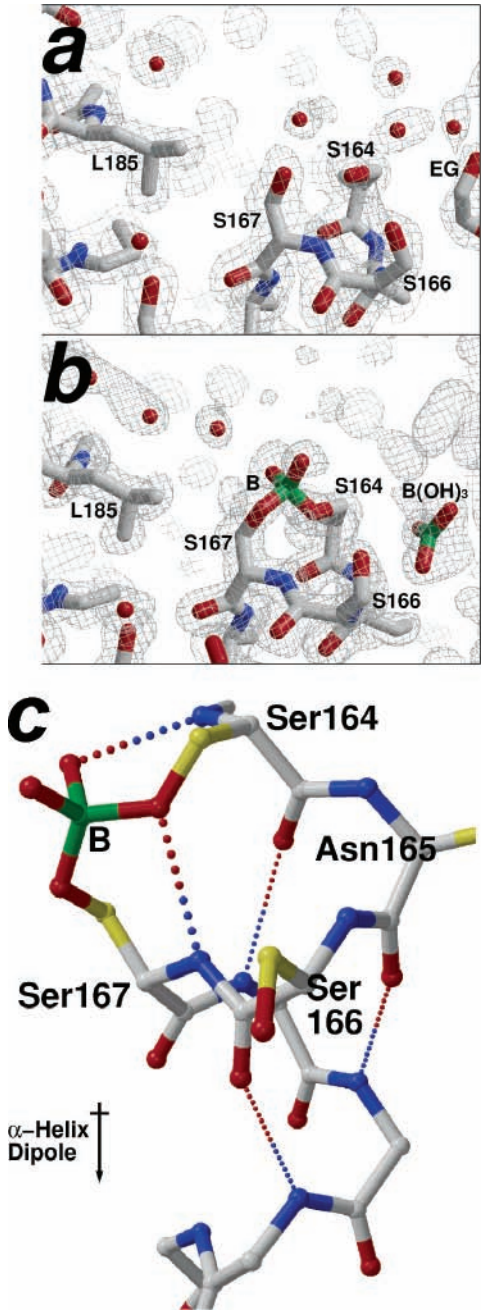

Figure 3. Crystallographic structure of the second borate binding site in trypsin: (a) X-ray structure of a serine-rich region of the trypsin surface obtained at pH 8.0 in the presence of 200 mM borate. PDB code: 1S6F; (b) structure of the same region of the protein crystallized at pH 10.6 in the presence of 200 mM borate, showing a borate ion covalently bound to the hydroxyl oxygens of Ser164 and Ser167; (c) covalent and hydrogen bonding interactions of borate bound at site 2. For clarity, the boron is indicated in green and the β-carbons in yellow. The two hydrogen bonding interactions involving the borate anion are indicated by large dotted lines. Small dotted lines indicate hydrogen bonds characteristic of α-helical secondary structure.

was soaked in a solution containing 200 mM borate at pH 10.6, and the resulting complex was analyzed by X-ray crystallography (Table 1). In this crystal form, a lattice contact inhibits ternary complex formation at the active site (*25*, *30*). However, the structure reveals a non-active-site bidentate borate complex with an occupancy of 50% formed from the Ser164 and Ser167 hydroxyl groups (Figure 3b). In addition to the covalent interactions with Ser164 and Ser167 hydroxyl oxygens, the complex is stabilized by a pair of hydrogen bonds (Figure 3c): the amide nitrogen of Ser164 is within hydrogen bonding range (2.8 Å) of one of the borate hydroxyl oxygens, and the amide nitrogen of Ser167 is within hydrogen bonding range (2.9 Å) of the covalently linked Ser164 Oγ. Electron density of the five electron boron atom is visible and continuous with that of the two serine oxygens, which are 2.2 Å apart. In the uncomplexed model representing the other 50% occupancy, the two serine hydroxyl oxygens are separated by 2.6 Å, and a water molecule is present at one of the sites occupied by a borate hydroxyl in the structure of the complex. At 1.25 Å resolution, the unbiased electron density ($F_o - F_c$ before modeling borate), as well as the final $2F_o - F_c$ density, unambiguously identifies this site as forming two covalent linkages to borate.

Crystal Structure of the Benzene Boronic Acid−Trypsin Complex. To further explore the borate binding site on the surface of trypsin that was identified by NMR and X-ray crystallography, we soaked the trypsin crystals in solutions containing a series of boronate ligands. In general, site 2 was found to be a relatively poor boronate binding site, presumably as a result of the lack of other useful interacting groups well positioned to stabilize the boronate complexes and, in the crystalline state, the potential limiting effects of crystal packing interactions. A complex of the enzyme with benzene boronic acid (BBA) bound to both the active and secondary sites was obtained at high pH using high BBA concentrations (Table 1). In this structure, BBA binds to the active site in either of two conformations, both of which involve bidentate covalent ligation to the His57 Nϵ and the Ser195 Oγ (Figure 4a). In one of the conformations, BBA(2), the phenyl ring extends into the S1 pocket and makes contact with the Cα and Cβ of Gln192, while in the second, BBA(1), it extends away from the pocket toward Phe41 and the Cys42−Cys58 disulfide bond. In this binding mode, the orientation of the BBA phenyl ring more closely approximates the P1′ residue (after the cleavage site) and the interactions are with trypsin residues in the S1′ subsite (e.g., see ref *31*). Binding to both the His Nϵ2 and the Ser Oγ has also been observed in some boronate complexes of γ-chymotrypsin (*19*).

The BBA is also bound to the second borate-binding site identified above in studies with borate, but with a 30% occupancy (Figure 4b). As with the borate complex (Figure 3b,c), the BBA molecule forms two covalent bonds with the serine hydroxyl groups, and two of the boron-bound oxygen atoms are within H-bonding distance of Ser164 NH (2.9 Å) and Ser167 NH (3.0 Å). The phenyl ring extends away from the surface of the protein so that the hydrogen bond from the Ser164 amide nitrogen to the only free hydroxyl is the same as that seen in the borate complex. Electron density does not support the alternate orientation of the phenyl ring, presumably because this would result in an amide nitrogen to aromatic carbon clash. There was apparently some borate present in the BBA sample used, because borate was alternately observed in site 2, also with 30% occupancy (i.e., the phenyl ring has lower occupancy than the other three heavy atoms). The remaining 40% appears to contain unbound serine 164 and 167, rotated slightly to place the Oγ atoms about 2.8 Å apart. The observation of equal populations of trypsin-complexed BBA and borate in this study was somewhat surprising, since the borate was present only as a contaminant. Based on a measurement of the resonance intensities in the ^{11}B NMR spectrum of the BBA, the borate contamination is ∼3%. BBA generally is expected to form tighter complexes due to the higher affinity for hydroxyl groups reflected in the lower p*K* value. An examination of lattice contacts suggests that unfavorable crystal packing effects may destabilize the trypsin−BBA complex. Specifically, the phenyl ring of the BBA comes in close proximity with the Ser61 and Arg62 residues of a symmetry-related molecule, which may exert a destabilizing effect. Alternatively, favorable interactions

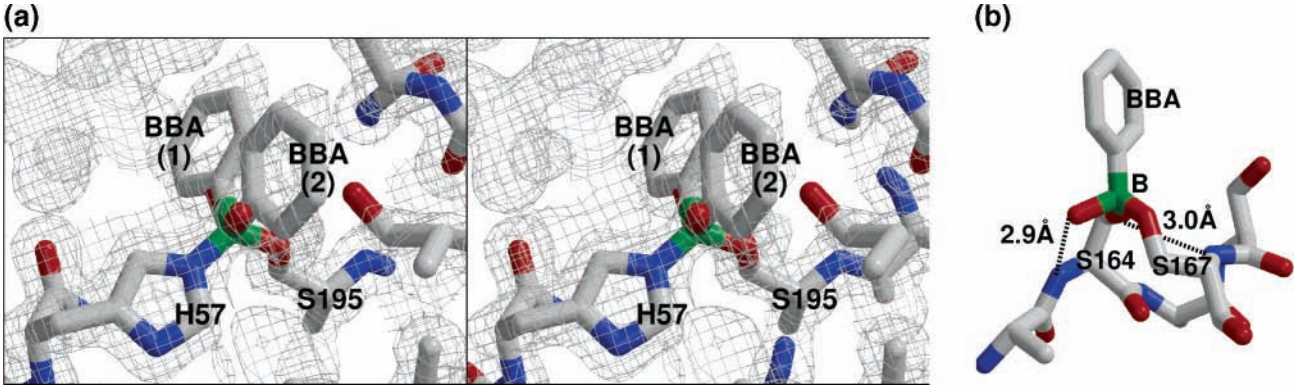

Figure 4. Crystal structure of the benzene boronic acid−trypsin complex: (a) Wall-eyed stereoview of the active site of the enzyme showing two similarly populated orientations of bound BBA; (b) interaction of BBA with the second borate bonding site formed from serine residues 164 and 167.

of borate with both of these residues might act to stabilize the borate complex. Of course, such interactions would not be present in solution. The Ser164/Ser167 Oγ−Oγ distances of 1.9 Å and 2.2 Å in the BBA and borate complexes, respectively, are significantly shorter than the distances observed for uncomplexed trypsin (see below). The need to force the Oγ nuclei together to achieve binding is thus probably an important constraint on the surface binding interactions observed here.

Analysis of Dynamic Frequency Shifts. To further characterize the borate/boronate binding interactions with trypsin, we performed field-dependent ^{11}B NMR studies on the complexes. In the slow tumbling limit, which characterizes the trypsin−borate complexes under study here, quadrupolar nuclei with half-integral spin, such as ^{11}B, exhibit unusual relaxation and shift characteristics, which can be useful for understanding the nature of the complex. In this limit, the $J(0)$ spectral density term, which typically makes the dominant contribution to transverse relaxation behavior in the slow tumbling limit, does not contribute to the relaxation of the central $^1/_2 \leftrightarrow -^1/_2$ transition, resulting in a relatively narrow signal, while the remaining transitions are very broad and generally unobserved (*29*, *32*−*34*).

The central transition for the ^{11}B in this slow tumbling limit is subject to a second-order dynamic frequency shift given by (*34*)

$$\delta = \frac{8s(s+1)-6}{s^2(2s-1)^2}\left(L^{Q}(\omega) - L^{Q}(2\omega)\right) \qquad (2)$$

where

$$L^{Q}(\omega) = \frac{3\chi^2}{160}\left(\frac{\omega\tau^2}{1+\omega^2\tau^2}\right) \qquad (3)$$

where χ, the quadrupolar coupling constant, is equal to $e^2Qq/(h/(2\pi))$, and τ is the isotropic rotational correlation time. In the limit $\omega\tau \gg 1$, we then obtain

$$\delta \approx \frac{4s(s+1)-3}{s^2(2s-1)^2}\left(\frac{3\chi^2}{160}\right)\left(\frac{1}{\omega}\right) \approx \frac{\chi^2}{40\omega} \quad \text{for} \quad s=\frac{3}{2} \qquad (4)$$

This can be expressed in ppm as (*35*)

$$\delta_{\text{ppm}} \approx \frac{-2.5\times10^4\chi^2}{\omega^2} = \frac{-2.5\times10^4}{\nu_0^2}\left(\frac{e^2Qq}{h}\right)^2 \qquad (5)$$

where we have introduced the negative sign indicating an upfield shift. The second equality above is useful if the quadrupole coupling constant is expressed in hertz rather than radians per second.

Boron-11 NMR spectra for solutions containing 2 mM trypsin, 6 mM lactate, 250 mM 4AB, and 50 mM borate in 50 mM HEPES, pH 8.0, were obtained at both 7 and 11.75 T to evaluate the relaxation behavior of the ^{11}B nucleus (Figure 5). The lactate standard was included to obtain a signal from a small molecule complex, which would not be subject to slow tumbling and should exhibit negligible dynamic frequency shifts. The ^{11}B NMR spectra show, in addition to the free boric acid resonance, a resonance corresponding to the lactate−borate complex at −13.0 ppm and two poorly resolved peaks at −17.1 ppm, which we assign to the ternary trypsin−4AB−borate complex at the active site and to the binary trypsin−borate complex that involves complex formation with Ser164 and Ser167 discussed above (Figure 3). We note that the resolution of the two component peaks in this study is somewhat poorer than that in Figure 1, apparently due to a small drop in pH of the sample, as well as to the higher 4AB concentration used. Although the field-dependent shift difference is small, using the borate−lactate complex as a reference, both of the components of the trypsin−borate complex shift downfield by 0.12 ppm at the higher magnetic field strength. Inserting the observed shift difference of 0.12 ppm into eq 5 and taking the ratio at the two fields gives

$$\frac{\delta_{500}}{\delta_{300}} = \frac{\delta_{500}}{\delta_{500}+0.12} = \left(\frac{300}{500}\right)^2 = 0.36 \qquad (6)$$

where we have assumed that χ is field-independent, giving for the dynamic frequency shift at 500 MHz, $\delta_{500} = 0.0675$ ppm. Based on this value, solution of eq 5 then gives $\chi = 264$ kHz. This small value is similar to typical values for deuterium and reflects the relative symmetry of the boron electronic structure in the bound borate.

To further probe these effects, similar field-dependent ^{11}B NMR studies were performed on a sample containing 2 mM trypsin, 6 mM lactate, 50 mM BBA, and 250 mM 4AB in 50 mM HEPES, pH 7.0. The lower pH was used in this case to provide better separation between the resonances of the free benzene boronic acid and the complexes, since this compound has a lower pK (8.72) than boric acid (8.98) (*36*). In contrast with the results for the borate complexes, the trypsin−BBA peaks, which cannot be individually resolved in this case,

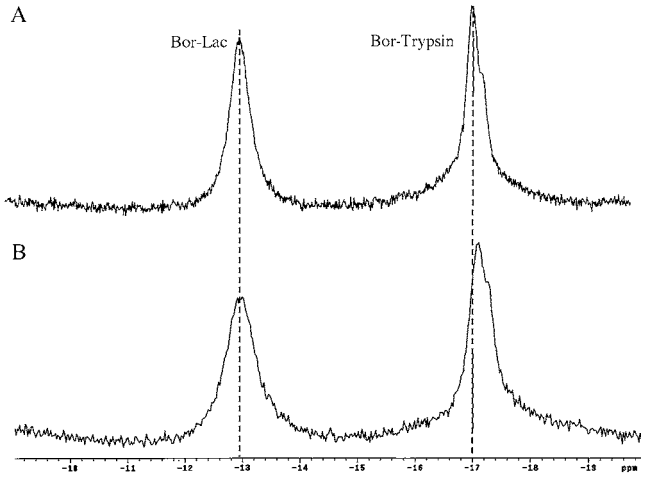

Figure 5. Frequency dependence of the ^{11}B NMR spectra of a trypsin−borate complex: (A) spectrum obtained at 7 T (^{11}B frequency = 96.326 MHz); (B) spectrum obtained at 11.75 T (^{11}B frequency 160.606 MHz). The sample contained 2.0 mM trypsin, 6.0 mM lactate, 50 mM borate, and 250 mM 4-aminobutanol in 50 mM HEPES, pH 8.0, buffer. Spectra were run at 25 °C.

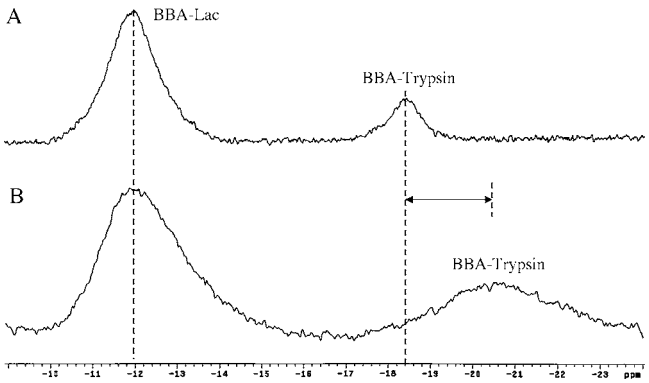

Figure 6. ^{11}B NMR spectra of a sample containing 6.0 mM lactate, 2.0 mM trypsin, 250 mM 4-aminobutanol, and 50 mM BBA in 50 mM HEPES, pH 7.0, buffer: (A) spectrum obtained at 7 T (^{11}B frequency = 96.326 MHz; (B) spectrum obtained at 11.75 T (^{11}B frequency 160.606 MHz). Spectra were run at 25 °C. There is an apparent dynamic frequency shift of 2.0 ppm.

experience a significantly greater upfield shift at the lower field (Figure 6). On the basis of the observed shift difference of 2.0 ppm and using eq 5, we have

$$\frac{\delta_{500}}{\delta_{300}} = \frac{\delta_{500}}{\delta_{500} + 2.0} = \left(\frac{300}{500}\right)^2 = 0.36 \qquad (7)$$

giving for the dynamic frequency shift at 500 MHz, $\delta_{500} = 1.125$ ppm. Insertion of this value into eq 5 gives $\chi = 1.08$ MHz for the quadrupole coupling constant of ^{11}B in the benzene boronate complex with trypsin. This value is similar to the 0.87 MHz determined from spin lattice relaxation measurements of BBA in the presence of chymotrypsin (*13*). Of course, as noted above, this value actually corresponds to a mixture of species. However, it is presumably dominated by the local environment of the boron and hence not strongly dependent on the detailed differences of the various component complexes. We note that if there were other small molecule complexes present in this system besides the borate−lactate complex that was specifically introduced, the field-dependent data should allow resolution of these species. The absence of additional resonances, particularly at the lower field, is consistent with our previous conclusion that the additional binding interaction observed in our previous studies (*24*, *25*) arose from binding to the second Ser164/Ser167

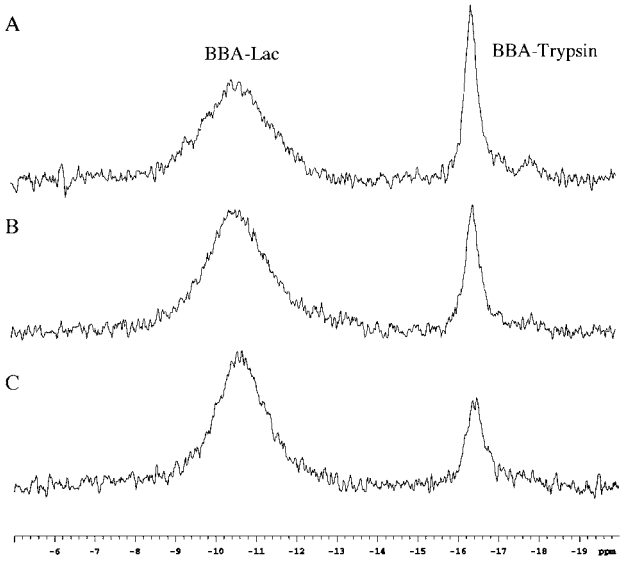

Figure 7. Temperature dependence of the ^{11}B NMR spectrum of the BBA−trypsin complex. To eliminate the contributions from BBA bound to the active site, the trypsin was treated with AEBSF, as described in the methods section. The sample contained 2 mM AEBS-trypsin, 2 mM lactate, and 50 mM benzene boronic acid in 50 mM HEPES, pH 8.0. ^{11}B NMR spectra were obtained at (A) 5, (B) 15, and (C) 25 °C.

binding site, rather than from binding to a small molecule contaminant.

To obtain further insight into this relaxation behavior, analogous studies were performed on benzene boronic acid in the presence of another serine protease, subtilisin Carlsberg. Benzene boronic acid (*13*) and its 4-fluoro analogue (*37*) have been shown to bind to this protease. Interestingly, the measured dynamic frequency shift was found to be 2.0 ppm, essentially identical to the result for trypsin with its multiple binding sites (data not shown). This result is consistent with eq 5, which indicates that the only significant parameter in predicting this shift under the slow tumbling approximation is the quadrupole coupling constant, which is presumably very similar for the benzene boronate, whether it is complexed with trypsin or subtilisin Carlsberg.

Line Width Effects in the BBA Complex. Temperature-dependent ^{11}B NMR spectra of the (AEBSF-treated trypsin)−BBA complex are shown in Figure 7. As in the above study, the sample also contained lactate (2 mM) to provide a reference borate complex. When the same set of approximations is used to analyze the relaxation behavior of the central component of the ^{11}B resonance, the line width of the central transition is given by (*29*, *34*)

$$\Delta\nu_{1/2} = \frac{1}{\pi T_2} = \frac{2s+3}{\pi s^2(2s-1)}\{2J_1^Q(\omega) + [(s+{}^3/_2)(s-{}^1/_2) - 1](J_2^Q(2\omega)\} \qquad (8)$$

where

$$J^Q(\omega) = \frac{3\chi^2}{160}\left(\frac{\tau}{1+\omega^2\tau^2}\right) \qquad (9)$$

where χ is the quadrupole coupling constant, $e^2Qq/(h/(2\pi))$, nucleus S has spin s and Larmor frequency ω, τ is the rotational correlation time, and isotropic motion is assumed. In

the limit $\omega\tau \gg 1$, we obtain

$$\Delta\nu_{1/2} = \frac{1}{\pi T_2} \approx \left(\frac{2(2s+3)}{\pi s^2(2s-1)}\right)\left(1 + \frac{1}{8}((s+{}^3/_2)(s-{}^1/_2)-1)\right)\frac{3\chi^2}{160}\frac{1}{\omega^2\tau} = \frac{\chi^2}{16\pi}\frac{1}{\omega^2\tau} = \frac{1}{16\pi}\left(\frac{e^2Qq}{h}\right)^2\frac{1}{\nu_0{}^2\tau} \quad \text{for} \quad s = \frac{3}{2} \quad (10)$$

where the second equality converts the quadrupole coupling constant to units of hertz.

This inverse dependence on τ contrasts with the line width predictions based on other relaxation mechanisms such as the dipolar interaction and chemical shift anisotropy, which predict $\Delta\nu_{1/2} \approx J(0) \approx \tau$. However, chemical exchange between uncomplexed and variously complexed forms of the borate ion also can make significant contributions to the line width. ^{11}B line widths measured for BBA complexed with AEBSF-treated trypsin to eliminate the contribution of BBA bound to the active site were measured at 5, 15, and 25 °C and yielded values of 51.5, 62.9, and 82.4 Hz, respectively.

We have compared this temperature dependence with the behavior predicted from an isotropic tumbling model:

$$\tau = \frac{4}{3}\pi r^3\frac{\eta}{kT} \quad (11)$$

where η is the viscosity of the solution. Using a table of water viscosity from the *Handbook of Chemistry and Physics* (*38*), the ratio of correlation times at the 5, 15, and 25 °C is calculated to be 1.0:0.74:0.55, so that based on eq 10 above, the ratios of the line widths at the three temperatures are predicted to be 1:1.35:1.82. The three experimental line widths given above have the ratio 1:1.22:1.60, in reasonable agreement with the prediction. Using eq 10, the rotational correlation times calculated from the line width of the central component of the ^{11}B signal at 5, 15, and 25 °C are 1.74×10^{-8}, 1.44×10^{-8}, and 1.10×10^{-8} s, respectively. These values are reasonable for a protein the size of trypsin (MW = 23 281).

Prediction of Adventitious Borate Binding Sites. Studies of model borate complexes indicate that borate readily interacts with hydroxyl, carboxyl, ring nitrogen, and occasionally amino groups. Typically, multidentate chelation is sufficient to give rise to slowly exchanging ^{11}B resonances, although at sufficiently high fields and low temperatures, even monodentate interactions can sometimes produce resolved resonances. Despite the ubiquitous occurrence of these potential ligands in proteins, the present NMR and crystallographic studies detected only one nonspecific binding site at borate concentrations under 100 mM involving a pair of serine hydroxyl groups. Since the multidentate complexes formed with hydroxyl ions are usually sufficiently stable to allow the observation of ^{11}B resonances that are in slow exchange (e.g., ref *4*), these are generally the easiest to observe. Based on the hypothesis that multidentate interactions with hydroxyl ligands provide the most prevalent basis for nonspecific borate binding, a calculation of the hydroxyl distances should provide a crude predictive tool for potential borate binding sites. Results of this analysis are summarized in Table 2. The closest pairing of hydroxyl groups occurs for the hydrogen-bonded S190 and Y228 residues that are buried in the interior of the protein and hence not accessible for binding. The S164−S167 site identified in the present study corresponded to the second shortest hydroxyl−hydroxyl distance, supporting the conclusion that this is a valid approach for predicting adventitious borate binding. Based on the results summarized in Table 2, we examined a sample containing bovine trypsin plus 50 mM borate under conditions similar to those of Figure 1 and observed a borate resonance with a shift similar to that of the bound borate in the procine trypsin−borate complex (spectrum not shown). Thus, it is likely that a similar complex forms with bovine trypsin.

Table 2. Hydroxyl Oxygen Distances in Crystal Structures

residue 1	residue 2	distances[a] min (mean)	distances[b] min (mean)
S190	Y228	2.74 (2.77)	2.70 (2.83)
S164	S167	2.80 (3.42)	2.92 (3.26)
S164	S166	3.03 (4.43)	3.36 (3.65)
S37	Y39		3.20 (3.43)
T144	S150	3.32 (3.69)	3.97 (4.06)
S146	S147	4.19 (5.19)	3.50 (4.78)
S214	T229	3.81 (3.98)	3.78 (3.86)
T125	S127		4.00 (4.23)
S109	S110	4.14 (4.78)	
S130	T134		4.18 (4.82)
S166	S170	4.28 (5.81)	4.90 (6.18)
S170	S171	4.40 (5.20)	
S149	Y151	4.44 (5.88)	4.75 (5.66)
S166	S167	4.45 (5.05)	5.18 (5.39)
Y172	S217		4.56 (5.15)
Y94	S96		4.81 (4.93)
Y29	S139	4.89 (4.94)	5.00 (5.05)
Y59	S61	4.89 (5.80)	5.01 (5.22)
T177	S178		4.96 (5.21)

[a] For porcine trypsin crystal structures 1S83, 1FNI, 1MCT, 1QQU, and 1AVW. [b] For bovine trypsin crystal structures 1HJ9, 1UTN, 1J8A, 1O3D, and 5PTP.

The Ser164−Ser167 Oγ−Oγ distance was determined to be 2.2 Å in the borate complex and 1.9 Å in the BBA complex. In contrast, the Ser164/Ser167 Oγ−Oγ distances in the crystal structures of uncomplexed trypsin are significantly longer so that a conformational change must occur upon borate/boronate complex formation. Depending on the protein, this geometric constraint may not be achievable. A survey of a series of proteins currently under study in our lab in the presence of 50 mM borate generally did not show a significant ^{11}B resonance corresponding to bound borate. The protein ubiquitin provides a good example of a protein containing a pair of hydroxyl groups, corresponding to Thr7 and Thr9, which appear to provide a potential borate binding site. Analysis of three high-resolution structures, 1UBQ, 1UBI, and 1D3Z, gave a mean Oγ−Oγ distance of 3.18 Å for Thr7/Thr9, shorter than the mean Oγ−Oγ distance for Ser64/Ser167 in trypsin, but at 50 mM borate, no bound resonance was observed. Analogous to the trypsin structure, the Oγ of Thr7 appears to be H-bonded to the Thr9 NH, orienting the side chain toward the Thr7 Oγ. In this case, variation of the χ1 angles for both threonine residues to achieve closest approach of the Oγ atoms reduces the Oγ−Oγ distance to ~2.6−2.7 Å, substantially greater than the distance of 2.2 Å for Ser164−Ser167 in the trypsin−borate complex, and achieving the 2.6 Å separation leads to significant steric conflict. Hence, the inability to reach sufficient proximity for bidentate ligation may be a limiting factor for borate complexation with Thr7/Thr9 in ubiquitin.

CONCLUSIONS

The complexes formed by boronate ligands with serine proteases and mechanistically related enzymes have been characterized extensively by X-ray crystallography, NMR spectroscopy, and other physical methods (*12*−*23*). These complexes generally contain a covalent bond between the active site serine Oγ and the boron to form a boronate structure believed to mimic the transition state, although binding to the active site histidine imidazole Nϵ2 has also been observed (*15*, *16*, *19*). Structurally analogous ternary and quaternary complexes involving serine proteases, borate, and alcohols also have been

observed recently (*24*, *25*, *30*). Recent ^{11}B NMR studies of trypsin complexes also provided evidence that at higher concentrations, an additional interaction between borate and trypsin was occurring (*24*, *25*). The studies described here were undertaken to more fully characterize this adventitious binding with a view toward exploitation of such interactions for the more general development of surface-directed protein ligands.

In the present studies, we have determined that the secondary trypsin−borate binding site involves covalent binding to the hydroxyl groups of Ser164 and Ser167, with additional stabilization resulting from a pair of hydrogen bonding interactions. An apparent borate dissociation constant of 97 mM at pH 8.0 was determined for this site, which can also be occupied by benzene boronic acid. Since the interaction does not involve residues of the serine protease active site, it is likely that this type of binding interaction is not unique. An upfield borate resonance with characteristics similar to the bound borate was also observed in a sample of bovine trypsin. Interesingly, the K_D value of 97 mM is similar to the K_I value for borate for the active site of trypsin (*24*) and other serine proteases (*39*). In contrast with the surface binding site, active site binding is typically monodentate (however, note Figure 4a) and is characterized by much higher k_{on} and k_{off} rates, so no separate ^{11}B resonance can be observed. In the presence of alcohols that form a ternary complex, a bidentate borate interaction with the enzyme and the alcohol creates a more stable complex so that a separate ^{11}B resonance does become observable (*24*, *25*).

It was initially anticipated that if borate binding to a second site located on the protein surface was occurring, then it would be possible to identify a boronate compound with greater affinity for this site due to the contribution of additional interactions with the substituent on the boron. However, none of the boronate compounds studied showed evidence of significantly enhanced affinity. One explanation for this observation is the significantly shorter Oγ−Oγ distance between the ligating Ser164/Ser167 hydroxyl oxygens observed in the BBA compared with the borate complex. Since these Oγ−Oγ distances are both substantially shorter than the values observed in the absence of borate/BBA (Table 2), it appears that in both cases the site must adjust for bidentate ligation, and the adjustment must be greater in the case of BBA. A second explanation suggested by the structure of the trypsin−BBA complex is that the phenyl ring of the BBA is approximately normal to the protein surface, precluding any additional interaction with the protein. Since serine residues contribute two of the oxygen ligands and a third hydroxyl group is hydrogen bonded to the Ser164 NH group, the carbon substituent of the boronate is forced to point away from the surface of the protein, so additional interactions of the boronate ligand with the protein in site 2 are essentially eliminated. In this orientation, unfavorable lattice contact may further destabilize the BBA complex, stabilize the borate complex, or both.

The results of the present study pose an interesting question: what properties of binding site 2 confer the borate binding affinity, and how unique is this type of interaction? Studies of small molecule complexes reveal that optimal positioning of boron ligands is essential for obtaining high binding affinity. For example, a study of the borate complexes formed by a series of pentoses demonstrated that borate complexes are formed exclusively with the *cis*-hydroxyl groups of the furanose and not the pyranose forms of the sugars (*40*). To form a borate binding site on the protein surface with reasonable affinity, it appears critical to have at least two boron ligands that are positioned to allow bidentate ligation. Hydroxyl groups that are not well positioned or that are highly dynamic and rapidly sample many different conformational states will not be optimal for borate binding. From this perspective, we note that the assigned hydrogen bonding interaction between Ser164 Oγ and the Ser167 NH group that characterizes the trypsin complexes with both borate and BBA appears to be present in a majority of the uncomplexed structures as well. This interaction probably contributes to borate binding by orienting the Ser164 side chain toward Ser167. Alternatively, in trypsin crystals with no borate bound to the second site, the side chain of Ser167 typically adopts multiple conformations, some oriented so that the OγH is within H-bonding range of the Ser167 carbonyl oxygen and some oriented with OγH within H-bonding distance of the Ser164 side chain. These results are consistent with a moderate affinity borate binding site and further suggest that a higher affinity borate binding site characterized by more optimally positioned and more conformationally constrained hydroxyl groups could, in principle, exist in other proteins. Most critically, the pair of Oγ ligands contributed by serine, threonine, or tyrosine must be able to move close enough to form a bidentate complex.

Additional stabilization of the trypsin complexes with both borate and BBA results from a hydrogen bond between one of the borate hydroxyl oxygens and the Ser164 NH (Figures 3 and 4b). Since this NH group is on the same residue involved in borate chelation, it is possible that this type of interaction could be a typical feature of other surface binding sites. A positively charged residue, functionally analogous to the oxyanion hole in the active site of a serine protease (*41*), could also provide additional stability. There appears to be no well-positioned cationic residue that could further stabilize the bound borate at site 2 of trypsin; however, proximity to the N-terminus of the α-helix with its associated dipole moment may make the Ser164/Ser167 binding site more favorable for anionic species.

Since the secondary borate binding site on the surface of trypsin identified in this study does not involve catalytic residues, it is unlikely that this type of binding interaction is unique to trypsin. Potentially, this type of borate binding interaction could form the basis for the development of boronate ligands that target the protein surface. A simple calculation of pairwise hydroxyl oxygen distances provides a rough predictive tool of potential borate binding sites, particularly if inaccessible sites are excluded. However, as illustrated by the lack of significant binding to ubiquitin, it must be possible to easily reorient the hydroxyl oxygens to within ∼2.5 Å, or perhaps slightly longer distances in some cases, without significantly perturbing the local protein structure to form a bidentate complex. The present results also illustrate the potential of dynamic frequency shifts of boronate ligands to distinguish ligands on the basis of rotational correlation times and hence molecular weight. This is a significant issue for borate and boronate compounds due to potential binding interactions with many small molecules. Additionally, this analysis provides a useful approach for the determination of quadrupole coupling constants and for obtaining dynamic information related to the protein−borate/boronate complex.

ACKNOWLEDGMENT

The authors are grateful to Dr. Lawrence Werbelow and Dr. Eugene DeRose for suggestions and helpful discussions. This research was supported by the Intramural Research Program of the NIH, and NIEHS.

LITERATURE CITED

(1) Drews, J. (1998) *In search of tomorrow's medicines*, Springer, New York.

(2) Hajduk, P. J., Huth, J. R., and Fesik, S. W. (2005) Druggability indices for protein targets derived from NMR-based screening data. *J. Med. Chem. 48*, 2518−2525.

(3) Pizer, R., and Selzer, R. (1984) The boric acid/lactic acid system. Equilibria and reaction mechanism. *Inorg. Chem. 23*, 3023−3026.
(4) Coddington, J. M., and Taylor, M. J. (1989) High field ^{11}B and ^{13}C NMR investigations of aqueous borate solutions and borate-diol complexes. *J. Coord. Chem. 20*, 27−38.
(5) Vandenberg, R., Peters, J. A., and van Bekkum, H. (1994) The structure and (local) stability constants of borate esters of monosaccharides and disaccharides as studied by B-11 and C-13 NMR spectroscopy. *Carbohydr. Res. 253*, 1−12.
(6) van Haveren, J., Peters, J. A., Batelaan, J. G., Kieboom, A. P. G., and van Bekkum, H. (1989) pH-dependence of the stability of boric-acid and borate esters of amino-acids and amino diols in aqueous medium as studied by B-11 and H-1 NMR spectroscopy. *Recl. Trav. Chim. Pays-Bas 108*, 179−184.
(7) London, R. E., and Gabel, S. A. (1994) ^{19}F NMR studies of fluorobenzene boronic acids. 1. Interaction kinetics with biologically significant ligands. *J. Am. Chem. Soc. 116*, 2562−2569.
(8) Taler, G., Schejter, A., and Navon, G. (1998) H-1 and B-11 NMR evidence for specific binding of borate ion to cytochrome *c*. *Inorg. Chim. Acta 273*, 388−392.
(9) Taler, G., Eliav, U., and Navon, G. (1999) Detection and characterization of boric acid and borate ion binding to cytochrome *c* using multiple quantum filtered NMR. *J. Magn. Reson. 141*, 228−238.
(10) Reuter, W., Wiegand, G., Huber, R., and Than, M. E. (1999) Structural analysis at 2.2 Å of orthorhombic crystals presents the asymmetry of the allophycocyanin-linker complex, AP•$L_C^{7.8}$, from phycobilisomes of Mastigocladus laminosus. *Proc. Natl. Acad. Sci. U.S.A. 96*, 1363−1368.
(11) Vos, S., Parry, R. J., Burns, M. R., De Jersey, J., and Martin, J. L. (1998) Structures of Free and Complexed Forms of Escherichia Coli Xanthine-Guanine Phosphoribosyltransferase. *J. Mol. Biol. 282*, 875−889.
(12) Tulinsky, A., and Blevins, R. A. (1987) Structure of a tetrahedral transition state complex of alpha-chymotrypsin dimer at 1.8-Å resolution. *J. Biol. Chem. 262*, 7737−7743.
(13) Adebodun, F., and Jordan, F. (1988) ^{11}B nuclear magnetic resonance studies of the sstructure of the transition-state analogue phenylboronic acid bound to chymotrypsin. *J. Am. Chem. Soc. 110*, 309−310.
(14) Baldwin, J. E., Claridge, T. D. W., Derome, A. E., Schofield, C. J., and Smith, B. D. (1991) ^{11}B NMR studies of an aryl boronic acid bound to chymotrypsin and subtilisin. *Bioorg. Med. Chem. Lett. 1*, 9−12.
(15) Tsilikounas, E., Kettner, C. A., and Bachovchin, W. W. (1993) Boron-11 NMR spectroscopy of peptide boronic acid inhibitor complexes of α-lytic protease − direct evidence for tetrahedral boron in both boron−histidine and boron−serine adduct complexes. *Biochemistry 32*, 12651−12655.
(16) Tsilikounas, E., Kettner, C. A., and Bachovchin, W. W. (1992) Identification of serine and histidine adducts in complexes of trypsin and trypsinogen with peptide and nonpeptide boronic acid inhibitors by H-1 NMR spectroscopy. *Biochemistry 31*, 12839−12846.
(17) Bone, R., Fujishige, A., Kettner, C. A., and Agard, D. A. (1991) Structural basis for broad specificity in alpha-lytic protease mutants. *Biochemistry 30*, 10388−10398.
(18) Bone, R., Frank, D., Kettner, C. A., and Agard, D. A. (1989) Structural analysis of specificity: alpha-lytic protease complexes with analogues of reaction intermediates. *Biochemistry 28*, 7600−7609.
(19) Stoll, V. S., Eger, B. T., Hynes, R. C., Martichonok, V., Jones, J. B., and Pai, E. F. (1998) Differences in binding modes of enantiomers of 1-acetamido boronic acid based protease inhibitors: crystal structures of gamma-chymotrypsin and subtilisin Carlsberg complexes. *Biochemistry 37*, 451−462.
(20) Holyoak, T., Wilson, M. A., Fenn, T. D., Kettner, C. A., Petsko, G. A., Fuller, R. S., and Ringe, D. (2003) 2.4 Å Resolution Crystal Structure of the Prototypical Hormone-Processing Protease Kex2 in Complex with an Ala-Lys-Arg Boronic Acid Inhibitor. *Biochemistry 42*, 6709−6718.
(21) Wang, X., Minasov, G., Blazquez, J., Caselli, E., Prati, F., and Shoichet, B. K. (2003) Recognition and Resistance in Tem β-Lactamase *Biochemistry 42*, 8434−8444.
(22) Chen, Y., Shoichet, B., and Bonnet, R. (2005) Structure, Function, and Inhibition Along the Reaction Coordinate of Ctx-M β-Lactamases. *J. Am. Chem. Soc. 127*, 5423−5434.
(23) Nicola, G., Peddi, S., Stefanova, M., Nicholas, R. A., Gutheil, W. G., and Davies, C. (2005) Crystal Structure of *Escherichia coli* Penicillin-Binding Protein 5 Bound to a Tripeptide Boronic Acid Inhibitor: A Role for Ser-110 in Deacylation. *Biochemistry 44*, 8207−8217.
(24) London, R. E., and Gabel, S. A. (2002) Formation of a trypsin−borate−4-aminobutanol ternary complex. *Biochemistry 41*, 5963−5967.
(25) Transue, T. R., Krahn, J. M., Gabel, S. A., DeRose, E. F., and London, R. E. (2004) X-ray and NMR characterization of covalent complexes of trypsin, borate and alcohols. *Biochemistry 43*, 2829−2839.
(26) Otwinowski, Z., and Minor, W. (1997) Processing of X-ray diffraction data collected in oscillation mode. *Methods Enzymol. 276*, 307−326.
(27) Brunger, A. T., Adams, P. D., Clore, G. M., Delano, W. L., Gros, P., Grosse-Kunsteleve, R. W., Jiang, J.-S., Kuszewski, J., Nilges, N., Pannu, N. S., Read, R. J., Rice, L. M., Simonson, T., and Warren, G. L. (1998). Crystallography and NMR System (CNS): A New Software System for Macromolecular Structure Determination. *Acta Crystallogr. D54*, 905−921.
(28) Cornell, W. D., Cieplak, P., Bayly, C. I., Gould, I. R., Merz, K. M., Ferguson, D. M., Spellmeyer, D. C., Fox, T., Caldwell, J. W., and Kollman, P. A. (1995) A second generation force field for the simulation of proteins, nucleic acids, and organic molecules. *J. Am. Chem. Soc. 117*, 5179−5197.
(29) Werbelow, L. G., and Pouzard, G. (1981) Quadrupolar relaxation − the multiquantum coherences. *J. Phys. Chem. 85*, 3887−3891.
(30) Babine, R. E., Rynkiewicz, M. J., Jin, L., and Abdel-Meguid, S. S. (2004) Towards and Experimental de Novo design protocol. The use of protein crystallography to deconvolute dynamic combinatorial processes. *Lett. Drug Des. Discovery 1*, 35−44.
(31) Sheidig, A. J., Hynes, T. R., Pelletier, L. A., Wells, J. A., and Kossiakoff, A. A. (1997) Crystal structures of bovine chymotrypsin and trypsin complexed to the inhibitor domain of Alzheimer's amyloid β-protein precursor (APPI) and basic pancreatic trypsin inhibitor (BPTI): Engineering of inhibitors with altered specifities. *Protein Sci. 6*, 1806−1824.
(32) Werbelow, L. G. (1979) NMR Dynamic frequency shifts and the quadrupolar interaction. *J. Chem. Phys. 70*, 5381−5383.
(33) Werbelow, L. G., and Marshall, A. G. (1981) The NMR of spin 3/2 nuclei − The effect of second-order dynamic frequency shifts. *J. Magn. Reson. 43*, 443−448.
(34) Werbelow, L. G. (1995) in *Encyclopedia of Nuclear Magnetic Resonance* (Grant, D. M., Ed.) Vol. 6, pp 4092−4102, John Wiley & Sons, New York.
(35) Aramini, J., and Vogel, H. J. (1998) Quadrupolar metal ion NMR studies of metalloproteins. *Biochim. Biol. Cell. 76*, 210−222.
(36) Babcock, L., and Pizer, R. (1980) Dynamics of boron acid complexation reactions. Formation of 1:1 boron acid−ligand complexes. *Inorg. Chem. 19*, 56−61.
(37) London, R. E., and Gabel, S. A. (1994) Fluorine-19 NMR studies of fluorobenzenboronic acids. 2. Kinetic characterization of the interaction with subtilisin Carlsberg and model ligands. *J. Am. Chem. Soc. 116*, 2570−2575.
(38) Viscosity data taken from: Weast, Robert C., Ed. (1995) *CRC Handbook of Chemistry & Physics*, 56th ed., p F-49, CRC Press, Cleveland, OH.
(39) Antonov, V. K., Ivanina, TY. V., Berezin, I. V, and Martinek, K. (1968) Bifunctional reversible inhibitors of proteolytic enzymes. Interaction between alpha-chymotrypsin and hexylboron acid. *Dokl. Acad. Nauk. SSSR 183*, 1435−1438.
(40) Chapelle, S., and Verchere, J.-F. (1988) A ^{11}B and ^{13}C NMR determination of the structures of borate complexes of pentoses and related sugars. *Tetrahedron 44*, 4469−4482.
(41) Menard, R., and Storer, A. C. (1992) Oxyanion hole interactions in serine and cysteine proteases. *Biol. Chem. Hoppe-Seyler 373*, 393−400.

BC0502210

Lactosylated Chitosan for DNA Delivery into Hepatocytes: The Effect of Lactosylation on the Physicochemical Properties and Intracellular Trafficking of pDNA/Chitosan Complexes

Mayu Hashimoto,[†] Minoru Morimoto,[‡] Hiroyuki Saimoto,[‡] Yoshihiro Shigemasa,[‡] and Toshinori Sato[†,*]

Faculty of Science and Technology, Keio University, 3-14-1 Hiyoshi, Yokohama, 223-8522, Japan and Faculty of Engineering, Tottori University, 4-101 Koyama-Minami, Tottori 680-8552, Japan. Received July 28, 2005; Revised Manuscript Received December 15, 2005

Chitosan is a useful nonviral vector for gene delivery. To make a pDNA/chitosan complex specific to hepatocytes, lactose-modified chitosan (lac-chitosan) was synthesized. When the percentage of lactose residues substituted was 8%, lac-chitosan showed excellent DNA-binding ability, good protection of DNA from nuclease, and the suppression of self-aggregation and serum-induced aggregation. Although the cellular uptake efficiency of the pDNA/lac-chitosan complex was almost the same as that of the pDNA/chitosan complex, the cell transfection efficiency of the former was greater for HepG2 cells having asialoglycoprotein receptors. Inhibitor of endocytosis such as bafilomycin A_1 and nocodazole significantly reduced the transfection efficiency of the pDNA/lac-chitosan complex. Observations with a confocal laser scanning microscope indicated that the pDNA/lac-chitosan complexes traversed endocytic compartments more rapidly than the pDNA/chitosan complex. Furthermore, the pDNA/lac-chitosan complexes were delivered to the late endosome and have the advantage of delivering DNA to the perinuclear region.

INTRODUCTION

A number of nonviral vectors have been developed because of current interest in gene therapy. Cationic lipids and polymers have been widely employed as nonviral DNA carriers. Although the usage of cationic liposomes can bring about the strong expression of an exogeneous gene (plasmid DNA, pDNA), complexes of DNA/cationic liposome are unstable in vivo (*1*). Cationic polymers, such as poly(ethylene)imine (PEI), chitosan, and poly-L-lysine (PLL), have been also used frequently (*2*). Although PEI achieved the high-level expression of a transgene in vitro and in vivo, it was not biodegradable and showed cytotoxicity (*3*).

Chitosan is a naturally occurring polysaccharide consisting of D-glucosamine and *N*-acetyl-D-glucosamine linked by a β-(1→4) glycosidic bond and has the potential to condense anionic DNA into a compact structure through electrostatic interaction. DNA/chitosan complexes have shown high transfection efficiency in several cell lines (*4*−*10*). Chitosan plays an important role in the protection of DNA from nucleases, escape from the endosome, and nuclear transport of DNA as well as other cationic polymers (*11*, *12*). Moreover, chitosan is biodegradable and nontoxic compared to other synthetic polymers (*13*). However, an increase in transfection efficiency and target-specific delivery is required for the practical use of chitosan as a nonviral vector.

Receptor-mediated gene delivery is a promising way to achieve target-specificity. Various nonviral vectors conjugated with antibody, asialoglycoprotein, epidermal growth factor (EGF), glycosides, and transferrin as cell-recognition devices have been investigated (*14*). Notably, the transfer of genes to hepatocytes via the asialoglycoprotein receptor (ASGP-R) has been accomplished using a galactosylated polymer (*15*−*17*).

Gene carriers such as PEI and PLL have been modified with galactose or lactose to obtain specificity for hepatocytes or hepatoma, and the optimal degree of substitution of galactose residues was 40% (*17*) and 5% (*18*), respectively. Although galactosylated chitosan has been also examined (*19*−*21*), the influence of the extent of the substitution of galactose has not been investigated yet. The recognition of carbohydrates often depends on sugar density and is strengthened by the multivalent effect. However, the modification of amino groups in chitosan would decrease the charge density of chitosan and the DNA-binding strength (*18*). Thus, efficient cell transfection by receptor-mediated gene delivery would be accomplished by a balance between DNA condensation and carbohydrate recognition. Moreover, although the contribution of sugar residues to receptor-mediated cellular interaction has been well investigated, their effect on the intracellular trafficking of DNA complexes has not.

Here we employed lactosylated chitosan to obtain more information about the effect of the lactosylation of chitosan on the formation of DNA complexes and intracellular trafficking. First, the physicochemical characterization of pDNA/lac-chitosan complexes was carried out. Then, the cellular uptake and transfection efficiency were evaluated in vitro. Notably, the intracellular trafficking of DNA complexes was investigated by examining of subcellular distribution with a confocal laser scanning microscope and by evaluating the effect of endocytosis inhibitors on the cell transfection.

MATERIALS AND METHODS

Preparation of Lac-chitosan. Chitosan (the average molecular weight of 53 kDa, the degree of deacetylation was 93%) was obtained from Koyo Chemical Co. Ltd. Lactosylated chitosan (lac-chitosan) was synthesized according to the literature (Scheme 1) (*22*). Briefly, chitosan dissolved in 1% aqueous acetic acid was coupled with lactonolactone by reductive alkylation in the presence of sodium cyanoborohydride. The degree of substitution (DS) was calculated to be 8% and 33%

* To whom correspondence should be addressed. Tel.: +81-45-566-1771. Fax: +81-45-566-1447. E-mail: sato@bio.keio.ac.jp.

[†] Keio University.

[‡] Tottori University.

10.1021/bc050228h CCC: $33.50 © 2006 American Chemical Society
Published on Web 02/16/2006

Scheme 1. Synthesis of Lac-chitosan

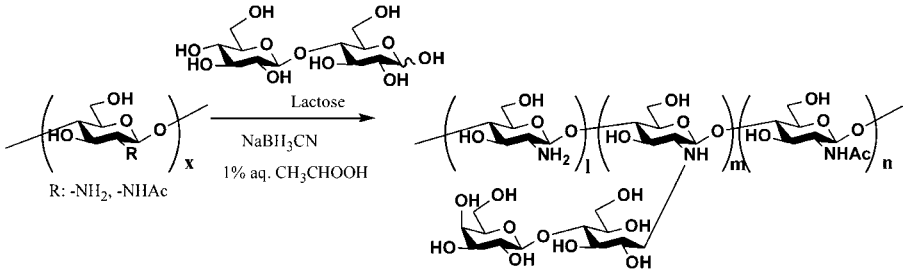

from elementary analysis. Calcd for 8% lac-chitosan ([$(C_8H_{13}NO_5)_{0.03}$ $(C_6H_{11}NO_4)_{0.89}$ $(C_{18}H_{32}NO_4)_{0.08}$] 1.1 H_2O): C, 40.62; H, 7.06; N, 6.67. Found: C, 40.49; H, 7.387; N, 6.585. Calcd for 33% lac-chitosan ([$(C_8H_{13}NO_5)_{0.03}$ $(C_6H_{11}NO_4)_{0.64}$ $(C_{18}H_{32}NO_4)_{0.33}$] 1.2 H_2O): C, 41.39; H, 6.35; N, 4.78. Found: C, 41.27; H, 7.379; N, 4.522.

Preparation of FITC-Labeled Chitosan. Chitosan and lac-chitosan were labeled with fluorescein isothiocyanate (FITC) as described previously (*23*). Briefly, chitosan or lac-chitosan (5 mg) was dissolved in water under acidic conditions caused by the addition of 1 N HCl, and thereafter the pH was adjusted to 6.5 with 1 N NaOH. FITC (0.1 mg, Dojindo) was added to the solution, and the mixture was stirred at room temperature for 24 h. The products were dialyzed in water using dialysis tubing and lyophilized. The amount of FITC in FITC-labeled chitosan was determined spectrophotometrically by visible absorption at 490 nm with reference to FITC. The average number of FITC residues was determined to be 1 per 100 monosaccharides.

Plasmid DNA. Plasmid DNA (pDNA), pGL3-Luc, encoding luciferase (Promega, Madison, WI) was amplified in *E. coli* DH5 α and isolated with a Qiagen Endotoxin-free Plasmid Giga Kit (Quiagen Inc., Chatsworth, CA) according to the instruction manual provided. pGL-3Luc was labeled with YOYO-1 (Molecular Probes Inc., Eugene, OR) (*24*). Briefly, 10 μL of pGL-3Luc (1 mg/mL) was mixed with 10 μL of 10 μM YOYO-1 and incubated at room temperature for 1 h in the dark.

Preparation of pDNA/Chitosan Complexes. pDNA/chitosan complexes were prepared as the method previously reported (*10*). The pDNA solution (0.1 mg/mL in water) was mixed with a given amount of chitosan solution (0.3 mg/mL) in PBS(−) adjusted to pH 6.5. The mixture of pDNA and chitosan was incubated at room temperature for 15 min. The YOYO-1-labeled pDNA described above was used for the evaluation of cellular uptake. The ratio of the plasmid's phosphate anion to chitosan's amino groups (N/P) was 5.

Atomic Force Microscopy (AFM). An aliquot of pDNA complexes (N/P = 5, [DNA] = 0.01 mg/mL) was dropped on freshly cleaved mica (1 cm × 1 cm). The excess liquid was removed by washing twice with 100 μL of deionized water, and the surface of the mica was dried with N_2 gas. AFM observation was carried out with a SPI-3700 system (SEIKO Instruments Inc., Japan).

Measurement of Zeta Potential and Particle Size. The concentration of pDNA was adjusted to 1.5 μg/mL by diluting with 20 mM HEPES buffer (pH 6.5). Zeta potentials of pDNA complexes were measured with a ZeeCom (Microtec Co. Ltd., Japan) at 25 °C. An average value for the zeta potential was calculated with the data from 40 particles tracked. Particle sizes were determined by dynamic light scattering (DLS) using a Laser Particle Size analyzer (HPPC, Malvern Instruments Co. Ltd.) at 25 °C.

DNase I Digestion Assay. The digestion of free pDNA (1 μg) and pDNA complexes by DNaseI (0.1 U, Takara, Japan) was assayed in 100 μL of 50 mM Tris-HCl buffer containing 10 mM $MgCl_2$, 100 mM NaCl, and 1 mM dithiotheretiol at 37 °C for 30 min. First, 4 μL of 0.5 M EDTA was added to all samples to inactivate DNase I. Subsequently, the pDNA complexes were mixed with 0.25 U/mL chitosanase (Seikagaku Kogyo Co., Ltd., Japan) at 42 °C and incubated for 4 h to release DNA from the chitosan completely. DNA was developed on 1% agarose gel and stained with ethidium bromide.

Lectin-Induced Aggregation. The pDNA complexes were incubated with 0.5 mg/mL *Ricinuns communis* agglutinin (RCA_{120}, Seikagaku Kogyo Co., Ltd.) in 100 μL of 10 mM HEPES buffer (pH6.5) at a final DNA concentration of 20 μg/mL. The turbidity at 350 nm was monitored with a UV−visible spectrophotometer (Ultrospec 300, Amersham Pharmacia).

BSA-Induced Aggregation. The pDNA complexes were incubated in the presence of bovine serum albumin (BSA, Sigma Co., Ltd.) for 1 h and 24 h at a final DNA concentration of 20 μg/mL. The concentration of BSA was 0.1, 0.2, 0.3, 0.4, 0.5, 1, and 2 mg/mL. The changes in turbidity at 350 nm upon the addition of BSA were monitored with a UV−visible spectrophotometer.

Cell Culture. COS7 cells and HepG2 cells were obtained from the Japanese Collection of Research Bioresources and RIKEN Cell Bank, respectively. COS7 cells were maintained in Dulbecco's Minimum Essential Medium (DMEM, Gibco BRL) containing 10% fetal bovine serum (FBS, JRH Biosciences Inc.), 100 U/mL penicillin, and 100 μg/mL streptomycin. HepG2 cells were maintained in Minimum Essential Medium (MEM, Nissui Pharm. Co., Ltd., Japan) containing 10% FBS and 10 mM nonessential amino acid (NEAA, Gibco BRL). Both cell lines were maintained at 37 °C in a 5% CO_2 humidified atmosphere.

Flow Cytofluorometry. COS7 and HepG2 cells were seeded at 2×10^5 cells/well in six-well plates 24 h prior to transfection. The pDNA complexes containing 5 μg of YOYO-1-labeled DNA were incubated with the cells in DMEM or MEM containing 10% FBS adjusted to pH 6.5 for 30 min. Then, the cells were washed twice with cold PBS (−) and harvested by trypsinization. To quench the extracellular fluorescence, the cell suspension was mixed with 50 μL of a 0.4% trypan blue (TB) solution in PBS (−). After 2 min, the cells were washed twice with cold PBS (−). The fluorescence intensity of the cells was measured with a flow cytofluorometer (Altra, Beckman Coulter) equipped with an argon ion laser. The experiments were carried out in triplicate.

Luciferase Assay. COS7 and HepG2 cells were seeded at 1×10^5 cells/well in 24-well plates 24 h prior to transfection. The pDNA complexes containing 2.5 μg of pDNA were incubated with cells in DMEM or MEM (pH 6.5) containing 10% FBS at 37 °C under a 5% CO_2 humidified atmosphere for 4 h. Then, the medium was replaced with fresh complete medium, and the cells were further incubated for 20 h before assays. Transfection with Lipofectin (Gibco BRL) was carried out according to the instruction manual. The transfected cells were washed three times with PBS (−) and lysed with the cell lysate buffer (Promega). Luciferase gene expression was measured using a Luciferase assay kit (Promega). The protein concentrations were determined with a DC protein assay kit

Table 1. Size of pDNA/Chitosan and pDNA/Lac-chitosan Complexes

	pDNA/chitosan complex		pDNA/8% lac-chitosan complex		pDNA/33% lac-chitosan complex	
N/P ratio	cumulant diameter (nm)	poly-dispersity index[a]	cumulant diameter (nm)	poly-dispersity index[a]	cumulant diameter (nm)	poly-dispersity index[a]
1	2221	0.283	1712	0.127	1322	0.207
3	1795	0.295	144	0.083	168	0.072
5	392	0.249	138	0.109	137	0.126
10	136	0.123	157	0.119	138	0.130

[a] Polydispersity index: [D(v, 90)-D(v, 10)]/D(v, 50), where D(v, 90), D(v, 50) and D(v, 10) are the equivalent volume diameters at 90, 50, and 10% cumulative volume, respectively.

(BIO-RAD, Hercules, CA). The relative light units (RLU) were measured with a luminometer and were corrected with the protein concentration.

For competition assay, HepG2 cells were preincubated with asialofetuin (4 mg/mL) for 15 min before the addition of pDNA complexes. Then, the cells were incubated with pDNA complexes for 4 h, and the luciferase activity was determined as described above.

The influence of endocytosis inhibitors on the transfection efficiency of pDNA/chitosan complexes was examined as follows. COS7 and HepG2 cells were preincubated for 30 min with 200 nM bafilomycin A_1 (Wako Pure Chem.) at 37 °C or 33 μM nocodazole (ICN Biomed. Inc.) at 4 °C. Then, the cells were incubated with pDNA complexes for 4 h and the luciferase activity was determined as described above.

Confocal Laser Scanning Microscopy. The subcellular distribution of pDNA/FITC-labeled chitosan complexes was observed with a confocal laser scanning microscope. Cells were seeded at 2×10^5 cells/well in glass-bottom dishes (ϕ35 mm, IWAKI) and incubated with pDNA/chitosan complexes for 15, 30, and 60 min. Renewal of the medium followed by washing with PBS (−). Cell fluorescence was analyzed with a confocal laser-scanning microscope (TCS−NT, Leica) equipped with a heating stage (Temp-Control 37−2, Leica) and a Kr/Ar laser.

RESULTS AND DISCUSSION

Formation of pDNA/Lac-chitosan Complexes. The DNA complexes were prepared by simple-mixing of the lac-chitosan and pDNA solutions in PBS (−) of pH 6.5. At N/P ≥ 3, the formation of pDNA/lac-chitosan complexes was confirmed by a gel retardation assay. The size of the complexes was determined by DLS as shown in Table 1. At N/P = 1, all complexes prepared in this study were more than 1 μm in size because the condensation of pDNA with chitosan or lac-chitosan was incomplete. At N/P ≥ 3, the pDNA/lac-chitosan complexes were particles with diameters of 140−170 nm with a relatively narrow distribution. At N/P = 3 and 5, the pDNA/lac-chitosan complexes were much smaller than the pDNA/chitosan complexes. The carbohydrate residues on the pDNA complexes are considered to contribute to the suppression of self-aggregation. Bettinger et al. reported the suppression of aggregation as an effect of glycosylation to pDNA/PEI complexes (*16*). Although PEI requires a tetrasaccharide with 5%DS to prevent self-aggregation, a disaccharide with 8%DS was enough to form stable pDNA/chitosan complexes.

Previously, we have shown that the optimum N/P ratio of pDNA/chitosan complex was 5 for cell transfection (*10*). When the N/P ratio was varied from 1 through 10, we found that both the pDNA/8% lac-chitosan complex and the pDNA/33% lac-chitosan complex had the highest transfection efficiency at N/P = 5. Therefore, the subsequent experiments were carried out at N/P = 5.

Table 2 shows the zeta potentials of the two pDNA/lac-chitosan complexes and the pDNA/chitosan complex at N/P = 5. The zeta potentials of the complexes were around 40−44 mV, with no significant difference among the three kinds of complexes.

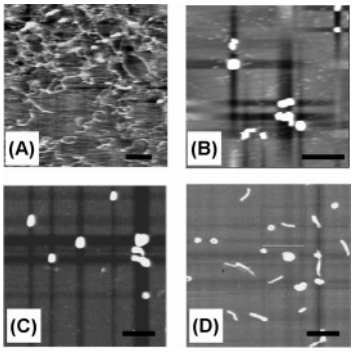

Figure 1. AFM images of pDNA complexes. (A) pDNA (pGL3-Luc), (B) pDNA/chitosan complex (N/P = 5), (C) pDNA/8% lac-chitosan complex (N/P = 5), (D) pDNA/33% lac-chitosan complex (N/P = 5). Scale bars represent 400 nm.

Table 2. ξ Potential of pDNA/Chitosan and pDNA/Lac-chitosan Complexes (N/P = 5)

complex	ξ potential (mV)
pDNA/chitosan	43.4 ± 7.0
pDNA/8% lac-chitosan	43.2 ± 5.8
pDNA/33% lac-chitosan	40.9 ± 8.1

AFM images revealed a difference in the morphology of the pDNA/8% lac-chitosan and the pDNA/33% lac-chitosan complexes (Figure 1), although the two complexes have almost the same particle size and zeta potential. The pDNA/8% lac-chitosan complex was spherical or short rodlike in structure similar to the pDNA/chitosan complex (Figure 1, parts B and C), while many of the pDNA/33% lac-chitosan complexes were long rod- and toroidlike (Figure 1D). The structure of several kinds of DNA complexes has been observed with AFM, TEM, or SEM. The spherical structure was observed in the pDNA/PEI complex (*12*). The short rod- and toroidlike structures were found in pDNA complexed with polycations such as poly(amidoamine)s (*25*), polylysine (*26*), and protamine (*27*). The short chain PLL of 4 kDa did not fully condense the pDNA and formed a long rodlike structure with the pDNA (*26*), similar in morphology to the pDNA/33% lac-chitosan complex. The conjugation of a large number of lactose residues to chitosan would result in steric hindrance and weaken the electrostatic interaction between the phosphate groups of DNA and amino groups of chitosan. Therefore, the degree of substitution of lactose residues in chitosan has to be controlled to retain the ability to bind with pDNA through electrostatic interaction.

Stability of pDNA/Lac-chitosan Complexes. The solubility in water and structural stability of pDNA/polycation complexes are often insufficient for practical use. Notably, cationic complexes bound with serum albumin and formed aggregates (*28*). The aggregation of pDNA complexes would induce a rapid clearance from plasma and be a disadvantage for nonviral gene delivery. Thus, the stability of the pDNA complexes in the

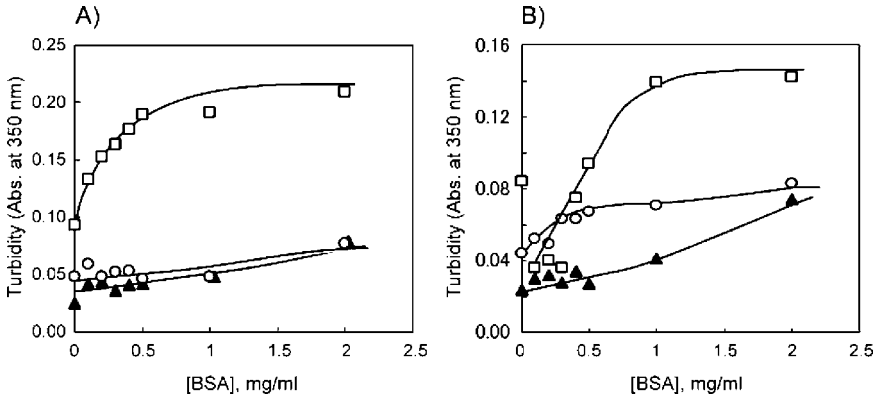

Figure 2. Turbidity of pDNA complexes at 1 h (A) and 24 h (B) after incubation with BSA. [pDNA] = 100 μg/mL. The pDNA complexes were formed at N/P = 5. □: pDNA/chitosan complex, ▲: pDNA/8%lac-chitosan complex, ○: pDNA/33%lac-chitosan complex.

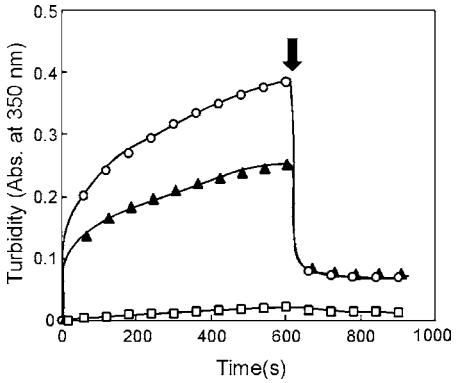

Figure 3. Time courses of turbidity changes of pDNA complexes at 350 nm after the addition of RCA_{120}. [pDNA] = 25 μg/mL, [RCA_{120}] = 0.5 mM. Lactose (final concentration 10 mM) was added at the time marked by the arrow. □: pDNA/chitosan complex, ▲: pDNA/8%lac-chitosan complex, ○: pDNA/33%lac-chitosan complex.

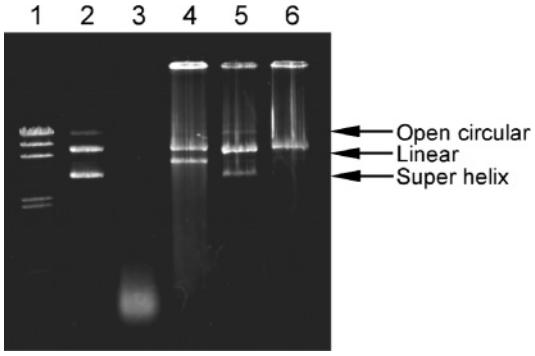

Figure 4. DNase I digestion assay of pDNA complexes. Naked pDNA and pDNA complexes were treated with 0.1 U of DNaseI and subsequently treated with chitosanase. Samples were subjected to 1% agarose gel electrophoresis. The samples were as follows, lane 1: λ-HindIII, lane 2: naked pDNA, lane 3: naked pDNA treated with DNase I, lane 4: pDNA/chitosan complex treated with DNase I and chitosanase, lane 5: pDNA/8% lac-chitosan complex treated with DNase I and chitosanase, lane 6: pDNA/33% lac-chitosan complex treated with DNase I and chitosanase.

presence of BSA was examined as a simple model. As shown in Figure 2, the pDNA/8% lac-chitosan complex and pDNA/33% lac-chitosan complex were very stable at 2 mg/mL of BSA, whereas the pDNA/chitosan complex showed a significant increase in turbidity. Even after incubation for 24 h with BSA, pDNA/lac-chitosan complexes were more stable than pDNA/chitosan complex (Figure 2B). AFM observation also supported the stability of pDNA/lac-chitosan complexes. The pDNA/lac-chitosan complex of 150 nm was observed after 1 h of incubation with BSA, although pDNA/chitosan complexes became large aggregates with a size of more than 1 μm (data not shown). Although the zeta-potential of the pDNA/lac-chitosan complexes was positive, BSA-induced aggregation was remarkably suppressed. This means that the modification of hydrophilic lactose residues to chitosan contributes to the stability of the pDNA complexes in the presence of serum.

Lectin-Induced Agglutination of pDNA/Lac-chitosan Complexes. The recognition of the pDNA/lac-chitosan complexes was determined by agglutination induced by galactose-binding RCA_{120}. With the addition of RCA_{120}, the turbidity of the pDNA/lac-chitosan complexes increased significantly, while the pDNA/chitosan complex showed no change of turbidity (Figure 3). Recognition of the pDNA/lac-chitosan complexes depended on the degree of substitution of lactose residues in chitosan. The change in turbidity of the pDNA/33% lac-chitosan complex was two times that of the pDNA/8% lac-chitosan complex. The agglutination of the pDNA/lac-chitosan complexes was reversed by adding of 10 mM lactose. These results indicated that the lactose moieties of pDNA complexes were specifically recognized by the sugar-binding protein. Murata et al. have reported that pDNA complexes with *N*,*N*,*N*-trimethylchitosan having 5 or 20% galactose residues were aggregated by APA lectin (*15*).

Resistance to DNase I Digestion. It is known that the condensation of pDNA by chitosan resulted in the protection of DNA from hydrolysis (*11*, *12*, *29*). Here, the resistance of pDNA/lac-chitosan complexes to DNA hydrolysis by DNase I was examined. Though naked pDNA was digested completely by the incubation with 0.1 U of DNase I for 30 min (Figure 4 lane 3), pDNA complexed with 8% lac-chitosan and 33% lac-chitosan showed resistance to DNase I (Figure 5 lane 5 and 6). After the treatment with DNase I, pDNA complexed with 8% lac-chitosan showed a supercoiled or linear structure, while pDNA complexed with 33% lac-chiotsan had only a linear structure. The pDNA complexed with conventional chitosan had a linear structure or unidentified structure between in linear and supercoiled (Figure 4, lane 4). Gebhart et al. detected a similar band between a linear and supercoiled structure for pDNA/pluronic-PEI complex digested with DNase I (*30*). They concluded that the unidentifiable structure is a stable secondary structure of pDNA.

The DNA digestion assay suggested that 33% lac-chitosan feebly formed a complex with DNA compared to chitosan and 8% lac-chitosan. As shown in Figure 1, AFM indicated that the pDNA was not sufficiently compacted by 33% lac-chitsoan because the morphology of pDNA/33% lac-chitosan complexes was not spherical. Thus, the results of the DNA digestion assay were well consistent with the AFM observation.

Through the physicochemical characterization, it was demonstrated that the lactosylation of chitosan suppressed the nonspecific interaction of the DNA/chitosan complex with BSA and increased the stability of the complex, in a manner

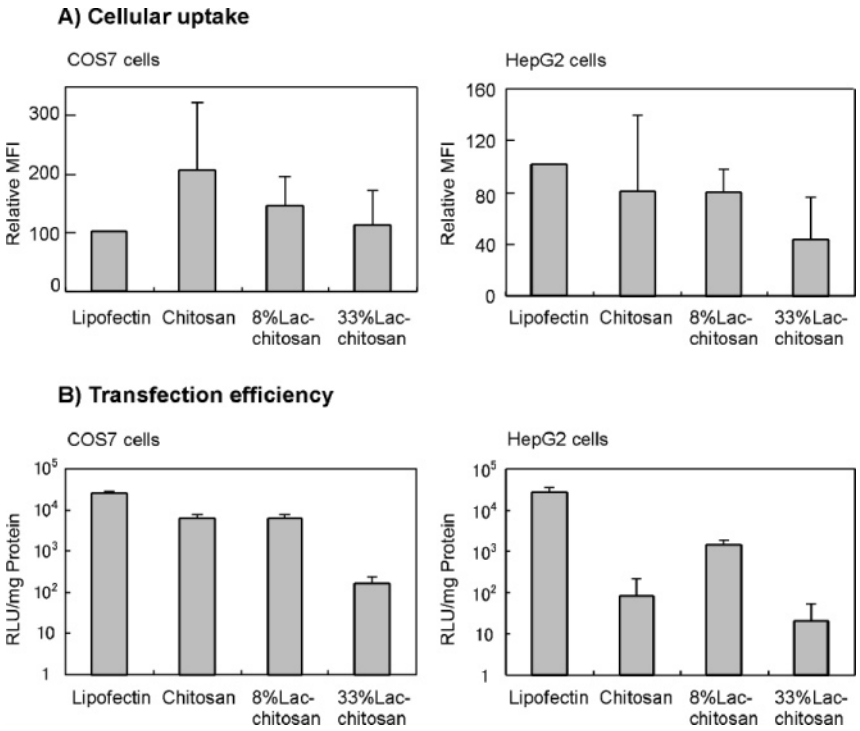

Figure 5. Cellular uptake and transfection efficiency of pDNA complexes for COS7 and HepG2 cells. (A) COS7 and HepG2 cells were incubated for 30 min with YOYO-1-labeled pDNA/chitosan complexes. After a subsequent washing and trypsinization, the mean fluorescence intensity (MFI) was analyzed with a flow cytofluorometer. MFI of pDNA/Lipofectin complex was normalized to 100. [pDNA] = 5 μg/mL, N/P = 5. (B) The cells were incubated for 4 h with the pDNA complexes. After the subsequent culture, the cells were lysed and the luciferae activities were measured. [pDNA] = 5 μg/mL. All pDNA complexes were prepared at N/P = 5.

independent of the substitution of lactose residues. The recognition of pDNA complexes depended on the degree of substitution of lactose residues, with 33% lac-chitosan being superior to 8% lac-chitosan. However, the condensation of pDNA governing enzymatic stability was sufficiently induced by 8% lac-chitosan but not by 33% lac-chitosan.

Cellular Uptake and Transfection with pDNA/Lac-chitosan Complexes. The cellular uptake and the cell transfection efficiency of pDNA complexes were investigated with HepG2 cells having asialoglycoprotein receptors, and COS7 cells as a control. To evaluate cellular uptake efficiency, pDNA was labeled with YOYO-1. The fluorescence of the complexes adsorbed on the cell surface was quenched by the addition of trypan blue to estimate the amount of pDNA internalized by cells (*31*). As shown in Figure 5A, there was no significant difference in mean fluorescence intensity (MFI) among pDNA/chitosan, pDNA/8% lac-chitosan, and pDNA/33% lac-chitosan complexes for both HepG2 cells and COS7 cells.

Figure 5B shows the transfection efficiency of pDNA/chitosan, pDNA/lac-chitosan complexes, and lipoplex for COS7 cells and HepG2 cells. For COS7 cells, the pDNA/8% lac-chitosan complex showed almost the same transfection efficiency as the pDNA/chitosan complex, whereas the transfection efficiency of the pDNA/33% lac-chitosan complex was 2 orders of magnitude lower. Since the pDNA/33% lac-chitosan complexes were easily hydrolyzed by DNase I as shown in Figure 4. They would be degraded by nuclease in the lysosome or cytosol after cellular uptake. Therefore, it was considered that the pDNA/33% lac-chitosan complex showed poor transfection despite being incorporated into cells as well as the pDNA/8% lac-chitosan complex.

Erbacher et al. examined the transfection of lac-chitosan, in which 3.3, 10, and 20% of lactose residues were substituted. However, the pDNA/lac-chitosan complex showed significantly less tranfection efficiency than the pDNA/chitosan complex for HeLa cells (*4*). The pDNA/chitosan complexes observed by TEM were donut-, rod-, or pretzellike in shape. These results suggest the interaction of pDNA with their lac-chitosan was relatively weak and the formation of the pDNA/chitosan complex was incomplete. Although they did not focus on the pH of the buffer used for the preparation of DNA complexes, we prepared the pDNA complex at pH 6.5 to protonate the amino groups of chitosan. Through the physicochemical characterization in our present study, it was demonstrated that 8% lac-chitosan had the potential to condense pDNA, although 33% lac-chitosan was too low in charge density to form complete complexes. The formation of incomplete complexes brought about a decrease in transgene expression even if they were well taken up into the cells.

For HepG2 cells, the transfection efficiency of pDNA/8% lac-chitosan complex was 16 times higher than that of pDNA/chitosan complex, although the cellular uptake efficiency showed no significant difference with the pDNA/chitosan complex. The low transfection efficiency of pDNA/33% lac-chitosan complexes seems to be caused by the instability in HepG2 cells as well as COS7 cells.

To confirm that cell transfection of pDNA/lac-chitosan complexes was mediated by asialoglycoprotein receptor, the competition assay was carried out using asialofetuin. The transfection efficiency of pDNA/chitosan complex was little affected by the addition of asialofatuin. On the other hand, those of the pDNA/8% lac-chitosan and the pDNA/33% lac-chitosan complexes were decreased by the addition of asialofetuin. These results suggested the pDNA/lac-chitosan complexes were internalized via asialoglycoprotein receptor.

The cationic pDNA/chitosan complexes would adsorb to the cell surface through electrostatic interaction and be internalized by endocytosis (*32*). On the other hand, the pDNA/8% lac-chitosan complex would bind to the asialoglycoprotein receptor. Therefore, it is suggested that both pDNA/chitosan and pDNA/lac-chitosan complexes brought about gene expression by different cellular uptake mechanisms and intracellular traffick-

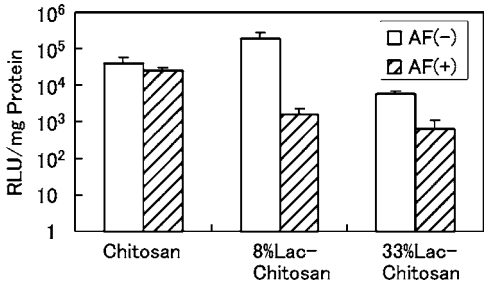

Figure 6. Competition assay of pDNA/lac-chitosan complexes by adding asialofetuin for HepG2 cells. 2 mg/well asialofetuin was added at 15 min before addition of pDNA complexes. The cells were incubated for 4 h with the pDNA complexes. After the subsequent culture, the cells were lysed and the luciferae activities were measured. [pDNA] = 5 μg/mL. All pDNA complexes were prepared at N/P = 5.

ing. It is reported that receptor-mediated and nonspecific endocytosis employs a different intracellular trafficking in hepatocytes (*33*). The rate of cellular uptake and degradation of asialo-orsomucoid, which was taken up via receptor-mediated endocytosis, and bovine serum albumin, which was taken up via pinocytosys, was affected by several endocytosis inhibitors independently. Thus, we assumed that the difference in intracellular trafficking between pDNA/chitosan and pDNA/lac-chitosan complexes resulted in the difference between the efficiency of cellular uptake and gene expression. Fajac et al. found a similar diferrence in gene transfer for airway epithelial cells, which have the mannose receptor, using sugar-modified PEI (*34*). Although the cellular uptake efficiencies of pDNA/Man-PEI, pDNA/Lac-PEI, and pDNA/PEI complexes complex were almost the same, pDNA/Lac-PEI complexes showed the highest transfection efficiency. However, the mechanism of gene transfer with pDNA/sugar-PEI complexes has not been clarified yet.

Subcellular Localization of the pDNA Complexes. The subcellular localization of pDNA complexes in HepG2 cells was observed with a confocal laser scanning microscope (Figure 7). The pDNA/chitosan complex was detected as large aggregates on the cell surface at 15 min, while the pDNA/8% lac-chitosan complex was distributed as small spot-like fluorescence on the cell surface and inside of cells at 5 min (Figure 7, parts A and D). Interestingly, the pDNA/8% lac-chitosan complexes were detected around the nucleus at 15 min (Figure 7, parts E and F). The localization of the pDNA/33% lac-chitosan complex was almost the same as that of the pDNA/8% lac-chitosan complex. Despite the large difference in cell transfection efficiency between the two pDNA/lac-chitosan complexes, their subcellular localization was almost the same. However, since pDNA/33% lac-chitosan complexes were easily hydrolyzed by DNase I, pDNA might be partly hydrolyzed by lysosome enzyme. In contrast, pDNA/chitosan complexes took over 4 h to concentrate around the nucleus (Figure 7, parts B and C). Godbey et al. have also observed that the pDNA/PEI complexes took over 4 h to be taken up into cells (*35*).

The pDNA/lac-chitosan complex also showed rapid intracellular trafficking in COS7 cells. Therefore, it is suggested that the lactose residue of pDNA/chitosan complexes contributed to the rapid intracellular delivery to the area around the nucleus for the two cell lines employed in this study. Next, we further investigated the cell transfection using endocytosis inhibitors, to know the correlation between their intracellular delivery and cell transfection.

Mechanism of Intracellular Trafficking of pDNA/Lac-chitosan. For a nonviral DNA delivery system, the escape of DNA complexes from the endosome is one of the most important processes for gene expression. The escape of pDNA/chitosan complexes from the endosome has been explained by

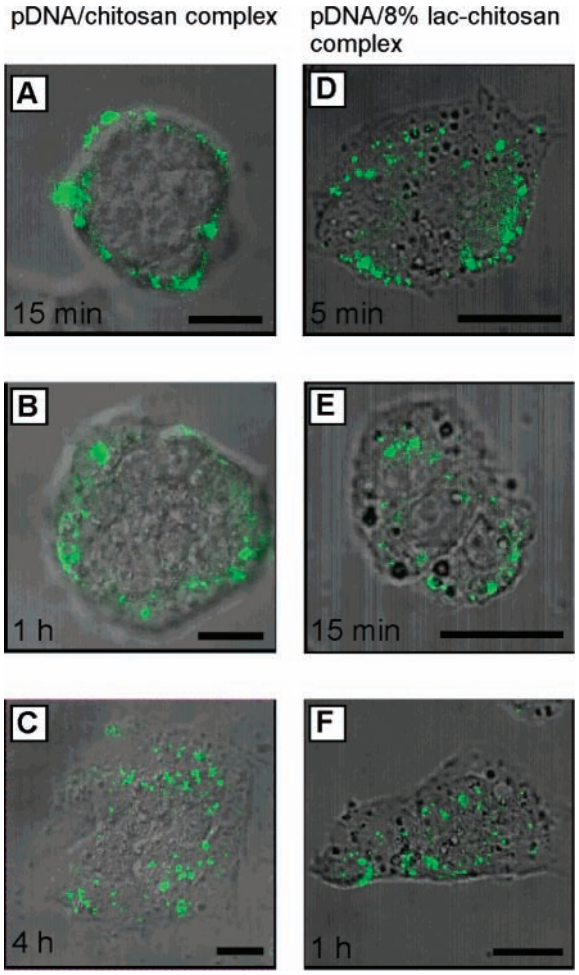

Figure 7. Time course of the subcellular localization of the pDNA/chitosan complex and pDNA/8% lac-chitosan complex in HepG2 cells. The cells were incubated with pDNA/FITC-labeled chitosan complex (A, B, C) and pDNA/FITC-labeled 8% lac-chitosan complex (D, E, F). Postaddition times were, (D) 5 min, (A, E) 15 min, (B, F) 1 h, and (C) 4 h. Scale bars represent 20 μm.

(1) a buffering effect (*11*), (2) membrane perturbation (*36*, *37*), and (3) water influx and swelling of the endosome caused by increasing osmolarity with chitosan degradation (*12*). In the present study, for a better understanding of the intracellular trafficking of the pDNA/lac-chitosan complexes, we examined the effect of the endocytosis inhibitors on the transfection efficiency in COS7 and HepG2 cells.

As shown in Figure 8A, Bafilomycin A_1, a proton pump inhibitor (*38*), greatly depressed the luciferase activity of both pDNA/chitosan and pDNA/lac-chitosan complexes. We also examined the effect of monensin, which is an inhibitor of endosomal acidification. Monensin also significantly decreased the gene expression of the pDNA/chitosan and pDNA/8% lac-chitosan complexes (data not shown). In a previous study, it has been implied that the influx of protons into the endosome is the mechanism by which pDNA/chitosan complexes escape from the endosome (*10*). In the present study, it is suggested that the pDNA/lac-chitosan complex also escapes from the endosome by the same mechanism as the pDNA/chitosan complex.

Nocodazole blocks transport from the early to late endosomes, resulting in an accumulation of cargo in the endosome compartment (*39*). Nocodazole increased the transfection efficiency of the pDNA/chitosan complex by 2−3-fold (Figure 8B). Since the pDNA/chitosan complexes were not transported to the late endosome and accumulated in the early endosome by nocodazole, they could escape the degradation in the late endosome.

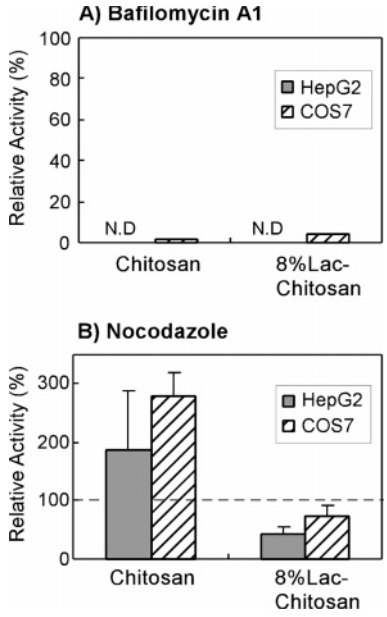

Figure 8. Effect of endocytosis inhibitors on transfection efficiency of the pDNA/chitosan and pDNA/8%lac-chitosan complexes for HepG2 cells. Prior to the incubation with pDNA complexes, HepG2 and COS7 cells were incubated for 30 min with 200 nM bafilomycin A_1 at 37 °C and 33 μM nocodazole at 4 °C. N.D. = not detected.

These results suggested that the pDNA/chitosan complex brought about high gene expression via release from the early endosome. Therefore, the localization of the pDNA/chitosan complexes in the late endosome around the nucleus might be disadvantageous for gene expression. In contrast, the transfection efficiency of pDNA/lac-chitosan complexes was not enhanced by nocodazole for COS 7 cells and was decreased to 60% of the control ($p < 0.05$) for HepG2 cells. These results infer that the entrapment of pDNA/8% lac-chitosan complexes in early endosome resulted in the obstruction of the release from the endosome and the transfer into the nucleus.

Chitosan is known to uniquely disturb the cell membrane (*36*, *37*), while lactosylation of chitosan would weaken the perturbation of the endosomal membrane. A further decrease of pH may be required for the pDNA/lac-chitosan complexes to escape from the endosome compartment. Although the transport of pDNA complexes to the late endosome/lysosome would raise the risk of the hydrolysis of DNA, the pDNA/8% lac-chitosan complex showed high transfection efficiency for HepG2 cells. This result suggested that the release of pDNA/8% lac-chitosan complexes from the late endosome is advantageous for the delivery of DNA to the perinuclear region. Some viruses, such as Semliki Forest virus and influenza virus, are known to escape specifically from the late endosome in the endocytosis pathway in order to gain access to the nucleus (*40*).

Ishii et al. has proposed the mechanism of cell transfection with pDNA/chitosan complexes (*11*). The pDNA/chitosan complexes were endocytosed and possibly released from the endosome due to swelling of the pDNA/chitosan complexes. Thereafter, the pDNA/chitosan complexes were accumulated in the nucleus. On the basis of the previous investigation, we considered the two possibilities to explain the high transfection efficiency of pDNA/lac-chitosan complex in HepG2 cells. One of the possibilities is that the endocytosis pathway of the pDNA/lac-chitosan complexes was distinct from that of the pDNA/chitosan complex and escaped from lysosome fusion. It has been reported that there is an endocytosis pathway in which the cargo such as the intracellular pathogen, mycobacteria, can escape delivery to and digestion in the lysosome (*41*). Thus, pDNA complexed with 8% lac-chitosan may escape from DNA digestion and efficiently transfer to the cytosol and nucleus. Another possibility is that the specific pathway from the late endosome to the nucleus may be ready for lactose-bearing nonviral delivery. Sugar-dependent nuclear import of a glycosylated protein has been reported (*42*). Although the size of pDNA complex is much larger than that of protein, the carbohydrate recognition may contribute to help nuclear import of the pDNA/lac-chitosan complexes.

Further experiments are needed to conclude the effect of lactosylation of pDNA/chitosan complexes on endocytosis pathway and nuclear transport. However, in this study, we investigated the intracellular trafficking of the pDNA/lac-chitosan complexes and found that the delivery of a sugar-modified DNA complex to late endosome was advantageous to gene expression.

SUMMARY

We investigated the effect of the lactosylation of chitosan on the formation of the DNA complex, cell transfection, and transfection mechanism. The lactosylation of chitosan increased the physicochemical stability of the pDNA complex and suppressed the BSA-induced aggregation. The pDNA/8% lac-chitosan complex showed high transfection efficiency for hepatocytes and the accumulation of DNA complexes in the late endosome/lysosome. The release from the late endosome may bring about the transfer into the perinuclear region. To our knowledge, this is the first finding on the effect of lactose on the intracellular delivery relating to gene expression. Finally, we concluded that the use of carbohydrates in gene delivery systems would widely contribute to the physicochemical properties, cellular interaction, intracellular delivery, and gene expression.

ACKNOWLEDGMENT

This work was partly supported by the Special Coordination of Funds for Promoting Science and Technology from the Ministry of Education, Culture, Sports, Science and Technology, the Japanese Government.

LITERATURE CITED

(1) Gao, X., and Huang, L. (1995) Cationic liposome-mediated gene transfer. *Gene Ther. 2*, 710−722.
(2) Kabanov, A. V., and Kabanov, V. A. (1995) DNA complexes with polycations for the delivery of genetic materials into cells. *Bioconjugate Chem. 6*, 7−20.
(3) Moghimi, S. M., Symond, P., Murray, J. C., Hunter, A. C., Debska, G., and Szewczyk, A. (2005) A Two-Stage Poly (ethylenimine)-Mediated Cytotoxicity: Implications for Gene Transfer/Therapy. *Mol. Ther. 11*, 990−995.
(4) Erbacher, P., Zou, S., Bettinger, T., Steffan, A. M., and Remy, J. S. (1998) Chitosan-based vector/DNA complexes for gene delivery: biophysical characteristics and transfection ability. *Pharm. Res. 15*, 1332−1339.
(5) Mumper, R. J., Wang, J., Claspell, J. M., and Rolland, A. P. (1995) Novel polymeric condensing carriers for gene delivery. *Proc Intern. Symp. Controlled Release Bioact. Mater. 20*, 178−179.
(6) Sato, T., Shirakawa, N., Nishi, H., and Okahata, Y. (1996) Formation of A DNA/polygalactosamine Complex and Its Interaction with Cells. *Chem. Lett.* 725−726.
(7) Thanou, M., Florea, B. I., Geldof, M., Junginger, H. E., and Borchard, G. (2002) Quaternized chitosan oligomers as novel gene delivery vectors in epithelial cell lines. *Biomaterials 23*, 153−159.
(8) Corsi, K., Chellat, F., Yahia, L., and Fernandes, J. C. (2003) Mesenchymal stem cells, MG63 and HEK293 transfection using chitosan-DNA nanoparticles. *Biomaterials 24*, 1255−1264.
(9) MacLaughlin, F. C., Mumper, R. J., Wang, J., Tagliaferri, J. M., Gill, I., Hinchcliffe, M., and Rolland, A. P. (1998) Chitosan and depolymerized chitosan oligomers as condensing carriers for *in vivo* plasmid delivery. *J. Controlled Release 56*, 259−272.

(10) Sato, T., Ishii, T., and Okahata, Y. (2001) *In vitro* gene delivery mediated by chitosan. Effect of pH, serum and molecular mass of chitosan on the transfection efficiency. *Biomaterials 22*, 2075−2080.
(11) Ishii, T., Okahata, Y., and Sato, T. (2001) Mechanism of cell transfection with plasmid/chitosan complexes. *Biochim. Biophys. Acta 1514*, 51−64.
(12) Köping-Höggård, M., Tubulekas, I., Guan, H., Edwards, K., Nilsson, M., Vårum, K. M., and Artursson, P. (2001) Chitosan as a nonviral gene delivery system: Structure−property relationships and characteristics compared with polyethylenimine *in vitro* and after lung administration *in vivo*. *Gene Ther. 8*, 1108−1121.
(13) Hirano, S., Seino, H., Akiyama, Y., and Nonaka, I. (1988) Biocompability of chitosan by oral and intravenous administration. *Polym. Eng. Sci.* 897−901.
(14) Varga, C. M., Wickham, T. J., and Lauffenburger, D. A. (2000) Receptor-Mediated Targeting of Gene Delivery Vector: Insights from Molecular Mechanisms for Improved Vehicle Design. *Biotechnol. Bioeng. 70*, 593−605.
(15) Murata, J., Ohya, Y., and Ouchi, T. (1996) Possibility of application of quaternary chitosan having pendant galactose residues as gene delivery tool. *Carbohydrate Polym. 29*, 69−74.
(16) Bettinger, T., Remy, J. S., and Erbacher, P. (1999) Size Reduction of Galactosylated PEI/DNA complexes Improves Lectin-Mediated Gene Transfer into Hepatocytes. *Bioconjugate Chem. 10*, 558−561.
(17) Gao, S., Chen, J., Xu, X., Ding, Z., Yang, Y. H., Hua, Z., and Zhang, J. (2003) Galactosylated low molecular weight chitosan as DNA carrier for hepatocyte-targeting. *Int. J. Pharm. 255*, 57−68.
(18) Zanta, M. A., Boussif, O., Adib, A., and Behr, J. P. (1997) In vitro gene delivery to hepatocytes with galactosylated polyethylenimine. *Bioconjugate Chem. 8*, 839−844.
(19) Park, I. K., Kim, T. H., Kim, S. I., Park, Y. H., Kim, W. J., Akaike, T., and Cho, C. S. (2003) Visualization of transfection of hepatocytes by galactosylated chitosan-graft-poly (ethylene glycol)/DNA complexes by confocal laser scanning microscopy. *Int. J. Pharm. 257*, 103−110.
(20) Kim, T. H., Park, I. K., Nah, J. W., Choi, Y. J., and Cho, C. S. (2004) Galactosylated chitosan/DNA nanoparticles prepared using water-soluble chitosan as a gene carrier. *Biomaterials 25*, 3783−3792.
(21) Erbachrer, P., Roche, A. C., Monsigny, M., and Midoux, P. (1995) Glycosylated polylysine/DNA complexes: gene transfer efficiency in relation with the size and the sugar substitution level of glycosylated polylysines and with the plamisd size. *Bioconjugate Chem. 6*, 401−410.
(22) Mansur, Y., and Hall, L. D. (1984) Some Chemical and Analytical Aspect of Polysacchride Modification. 3. Formation of Branched-Chain, Soluble Chitosan Derivatives. *Macromolecules 17*, 272−281.
(23) Onishi, H., and Machida, Y. (1999) Biodegradation and distribution of water-soluble chitosan in mice. *Biomaterials 20*, 175−182.
(24) Ogris, M., Wagner, E., and Steinlein, P. (2000) A versatile assay to study cellular uptake of gene transfer complexes by flow cytometry, *Biochim. Biophys. Acta 1474*, 237−243.
(25) Martin, A. L, Davies, M. C., Rackstraw, B. J., Roberts, C. J., Stolnik, S., Tendler, S. J. B., and Williams, P. M. (2000) Observation of DNA-polymer condensate formation in real time at a molecular level. *FEBS Lett. 480*, 106−112.
(26) Golan, R., Pietrasanta, L. I., Hsieh, W., and Hansma, H. G. (1999) DNA Toroids: stages in condensation. *Biochemistry 38*, 14069−14076.
(27) Allen, M. J., Bradbury, E. M., and Balhorn, R. (1997) AFM analysis of DNA-protamine complexes bound to mica. *Nucleic Acids Res. 25*, 2221−2226.
(28) Dash, P. R., Read, M. L., Barrett, L. B., Wolfert, M. A., and Seymour, L. W. (1999) Factors affecting blood clearance and in vivo distribution of polyelectrolyte complexes for gene delivery. *Gene Ther. 6*, 643−650.
(29) Mao, H.-Q., Roy, K., Troung-Le, V.-L., Janes, K. A., Lin, K. Y., Wang, Y., August, J. T., and Leong, K. W. (2001) Chitosan-DNA nanoparticles as gene carriers: synthesis, characterization and transfectopm effocoency.*J. Controlled Release 70*, 399−421.
(30) Gebhart, C. L., Sriadibhatla, S., Vinogradov, S., Lemieux, P., Alakhov, V., and Kabanov, A. V. (2002) Design and Formulation of Polyplexes Based on Pluronic-Polyethyleneimine Conjugates for Gene Transfer. *Bioconjugate Chem. 13*, 937−944.
(31) Sahlin, S., Hed, J., and Rundquist, I. (1983) Differentiation between Attached and Ingested immune Complexes by a Fluorescence Quenching Cytofluorometric Assay. *J. Immunol. Methods. 60*, 115−124.
(32) Mislick, K. A., and Baldeschwieler, J. D. (1996) Evidence for the role of proteoglycans in cation-mediated gene transfer. *Proc. Natl. Acad. Sci. U.S.A. 93*, 12349−12354.
(33) Stromhaug, P. E., Berg, T. O., Gjoen, T., and Seglen, P. O. (1997) Differences between fluid-phase endocytosis (pinocytosis) and receptor mediated endocytosis in isolated rat hepatocytes. *Eur. J. Cell Biol. 73*, 28−39.
(34) Fajac, I., Thevenot, G., Bedouet, L., Danel, C., Merten, M., Figarella, C., Dall′Ava-Santucci, J., Monisigny, M., and Briand, P. (2003) Uptake of plasmid/glycosylated polymer complexes and gene transfer efficiency in differentiated airway epithelial cells. *J. Gene Med. 5*, 38−48.
(35) Godbey, W. T., Wu, K. K., and Mikos, A. G. (1999) Tracking the intracellular path of poly(ethylenimine)/DNA complexes for gene delivery. *Proc. Natl. Acad. Sci. U.S.A. 96*, 5177−5181.
(36) Chan, V., Mao, H.-Q., Leong, K. W. (2001) Chitosan-Induced Perturbation of Dipalmitoyl-*sn*-glycero-3-phosphocholine Membrane Bilayer. *Langmuir 17*, 3749−3756.
(37) Fang, N., Chan, V., Mao, H.-Q., and Leong, K. W. (2001) Interactions of Phospholipid Bilayer with Chitosan: Effect of Molecular Weight and pH. *Biomacromolecules 2*, 1161−1168.
(38) Yoshimori, T., Yamamoto, A., Moriyama, Y., Futai, M., and Tashiro, Y. (1991) Bafilomycin A1, a specific inhibitor of vacuolar-type H(+)-ATPase, inhibits acidification and protein degradation in lysosomes of cultured cells. *J. Biol. Chem. 266*, 17707−17712.
(39) Bayer, N., Schober, D., Prchla, E., Murphy RF., Blaas, D., and Fuchs, R. (1998) Effect of Bafilomycin A1 and Nocodazole on Endocytic Transport in HeLa cells: Impilications for Viral Uncoating and Infection. *J. Virol. 72*, 9645−9655.
(40) Smith, A. E., and Helenius, A. (2004) How Virus Enter Animal Cells. *Science 304*, 237−243.
(41) Gatfield, J., and Pieters, J. (2000) Essential Role for Cholesterol in Entry of Mycobacteria into Macrophages. *Science 288*, 1647−1650.
(42) Rondanino, C., Bousser, M. T., Monsigny, M., and Roche, A. C. (2003) Sugar-dependent nuclear import of glycosylated protein in living cells. *Glycobiology 13*, 509−519.

BC050228H

Polycefin, a New Prototype of a Multifunctional Nanoconjugate Based on Poly(β-L-malic acid) for Drug Delivery

Bong-Seop Lee,[†,‡,||] Manabu Fujita,[†,||] Natalya M. Khazenzon,[†] Kolja A. Wawrowsky,[†] Sebastian Wachsmann-Hogiu,[§] Daniel L. Farkas,[§] Keith L. Black,[†,⊥] Julia Y. Ljubimova,[†,⊥] and Eggehard Holler*[,‡,⊥]

Institut für Biophysik und physikalische Biochemie der Universität Regensburg, Germany, Maxine Dunitz Neurosurgical Institute, Cedars-Sinai Medical Center, Los Angeles, California 90048, Department of Surgery, Cedars-Sinai Medical Center, Los Angeles, California, and Arrogene, Inc., Tarzana, California 91356. Received August 11, 2005; Revised Manuscript Received December 5, 2005

A new prototype of nanoconjugate, Polycefin, was synthesized for targeted delivery of antisense oligonucleotides and monoclonal antibodies to brain tumors. The macromolecular carrier contains: 1. biodegradable, nonimmunogenic, nontoxic β-poly(L-malic acid) of microbial origin; 2. Morpholino antisense oligonucleotides targeting laminin α4 and β1 chains of laminin-8, which is specifically overexpressed in glial brain tumors; 3. monoclonal anti-transferrin receptor antibody for specific tissue targeting; 4. oligonucleotide releasing disulfide units; 5. L-valine containing, pH-sensitive membrane disrupting unit(s), 6. protective poly(ethylene glycol); 7. a fluorescent dye (optional). Highly purified modules were conjugated directly with *N*-hydroxysuccinimidyl ester-activated β-poly(L-malic acid) at pendant carboxyl groups or at thiol containing spacers via thioether and disulfide bonds. Products were chemically validated by physical, chemical, and functional tests. In vitro experiments using two human glioma cell lines U87MG and T98G demonstrated that Polycefin was delivered into the tumor cells by a receptor-mediated endocytosis mechanism and was able to inhibit the synthesis of laminin-8 α4 and β1 chains at the same time. Inhibition of laminin-8 expression was in agreement with the designed endosomal membrane disruption and drug releasing activity. In vivo imaging showed the accumulation of intravenously injected Polycefin in brain tumor tissue via the antibody-targeted transferrin receptor-mediated endosomal pathway in addition to a less efficient mechanism known for high molecular mass biopolymers as enhanced permeability and retention effect. Polycefin was nontoxic to normal and tumor astrocytes in a wide range of concentrations, accumulated in brain tumor, and could be used for specific targeting of several biomarkers simultaneously.

INTRODUCTION

Targeted delivery of drugs reduces systemic toxicity and increases the drug concentration at the tumor site. It can be achieved by specific multicomponent nanoscale devices such as liposomes, particles, and nanoconjugates (*1*−*3*). High-molecular-mass nanoconjugates based on water-soluble macromolecules offer several advantages over direct delivery of drugs: 1. Delivery of both lipophilic and hydrophilic drugs, in particular, of antisense oligonucleotides, through biological barriers such as the blood−brain barrier (*4*, *5*); 2. Delivery of a multitude of different drugs by each single carrier molecule allowing synergism in recipient cells (*6*, *7*); 3. Targeting of a drug delivery device to tumors with minimal damage to healthy tissue; 4. Targeting to tumor cells due to an enhanced permeability and retention (EPR)[1] effect (*8*−*12*); 5. Targeting by receptor-mediated binding to surfaces of recipient cells and endosomal uptake into these cells (*13*−*16*); 6. Provision of an activity for disruption of endosomal membranes and for the release of the drug carrier system into the cytoplasm (*17*−*22*); 7. A cleavable linkage for the release of the drug from the carrier system (*23*−*26*); 8. A prolonged circulation through protection by PEG against degradation activities (*27*−*30*); and 9. Attachment of a fluorescent reporter for the localization of the carrier system. Available drug delivery systems either do not comply with a complete set of these demands or they have several of these properties but suffer from nonbiodegradability, immunogenicity and toxicity. We designed and synthesized a prototype nanoconjugate intended to fulfill the above criteria and to be used as a future anticancer drug delivery system to brain tumors.

Ideally, a nanoconjugate contains a central scaffold with numerous pendant chemical groups allowing for covalently attaching modules with the above functions. These can be designed to vary in the kind and number of prodrug(s), targeting specificity, and drug releasing activity (endosomal or cytoplasmic). Of the highly developed nanoconjugate delivery systems, scaffolds frequently represent copolymers of substituted acrylic acid, notably *N*-(2-hydroxypropyl)methacrylamide (HPMA) copolymer (*31*−*35*). This kind of scaffold, however, suffers from resistance to biodegradation.

* Corresponding author. E-mail: eggehard.holler@biologie.uni-regensburg.de. Phone +49 941 943 3030. Fax +49 941 943 2813.

† Maxine Dunitz Neurosurgical Institute, Cedars-Sinai Medical Center.

‡ Institut für Biophysik und physikalische Biochemie der Universität Regensburg.

§ Department of Surgery, Cedars-Sinai Medical Center.

⊥ Arrogene, Inc.

|| Two authors contributed equally for this paper.

[1] Abbreviations: EPR, enhanced permeability and retention; HPMA, *N*-(2-hydroxypropyl)methacrylamide; PMLA, β-poly(L-malic acid); MORPH-AON, morpholino antisense oligonucleotide; BTB, blood−tumor barrier; PBS, phosphate-buffered saline; PDP, 3-(2-pyridyldithio)-propionate; MTS, [3-(4,5-dimethylthiazol-2-yl)-5-(3-carboxymethoxyphenyl)-2-(4-sulfophenyl)-2*H*-tetrazolium, inner salt]; RBC, red blood cell; SEC-HPLC, size exclusion-HPLC; DTT, dithiothreitol; 2-MEA, 2-mercaptoethylamine; NHS, *N*-hydroxysuccinimide; RP-HPLC, reversed phase-HPLC; TNBS, trinitrofluorobenzene; DCC, dicyclohexylcarbodiimide; SPDP, *N*-succinimidyl-3-(2-pyridyldithio)propinate; Polycefin(-mAb), Polycefin devoid of mAb.

10.1021/bc0502457 CCC: $33.50 © 2006 American Chemical Society
Published on Web 01/19/2006

We report here on the chemical synthesis of a new nanoconjugate prototype of drug delivery system, by sequential conjugation of functional modules to a nontoxic, nonimmunogenic, biogenic scaffold, β-poly(L-malic acid) (PMLA) (*36*). This polymer has been highly purified from the myxomycete *Physarum polycephalum*. PMLA resembles HPMA in carrying abundant carboxyl groups, but as a polyester of L-malic acid, it is completely biodegraded to carbon dioxide and water. On the basis of established synthetic methods, we succeeded to chemically conjugate functional modules to the pendant carboxyl groups in a controlled, newly developed manner to form novel nanoscale structures. Specifically, these modules were: 1. The drugs: Morpholino antisense oligonucleotide (MORPH-AON) to laminin α4 and MORPH-AON to laminin β1 chains, 2. The targeting molecule: transferrin receptor monoclonal antibody (mAb OX-26 for rat and mAb R17217 for mouse), 3. The drug releasing module: disulfide bridges between the MORPH-AON and the scaffold (*26*), 4. The endosome escaping module: hydrophobic stretches of valine or leucine ethyl ester-conjugated scaffold (*17*−*22*), 5. The degradation protecting module: PEG (*27*−*30*), 6. The optional reporter module: Fluorescein or Alexa Fluor 680.

MORPH-AONs were designed to inhibit the synthesis of α4 and β1 chains of laminin-8, which is overexpressed in vessel walls of highly vascular glial tumors, breast cancer and their metastases (*37*, *38*). This inhibition has been shown to reduce invasion of human gliomas in vitro (*39*). MORPH-AONs, unlike other oligonucleotides, are resistant against nucleolytic degradation and are highly specific at low concentrations (*40*). Transferrin receptor antibody was chosen to target the delivery device beyond the blood−tumor barrier (BTB) in brain to the glioma target cells by promoting receptor binding and endosomal uptake (*41*−*45*). Targeting to tumor was reinforced by the EPR effect (*8*−*12*). The delivery system is based on a biologically produced scaffold and has a complex modular structure.

EXPERIMENTAL PROCEDURES

Reagents Used. Morpholino-3'-NH_2 antisense oligonucleotides AGC-TCA-AAG-CCA-TTT-CTC-CGC-TGA-C to laminin α4 (MORPH-AON-1) and CTA-GCA-ACT-GGA-GAA-GCC-CCA-TGC−C to laminin β1 (MORPH-AON-2) (*38*, *39*) chains were custom-made by Gene Tools (Philomath, OR). Mouse anti-rat mAb (clone OX-26, IgG_{2a},κ, 1 mg/mL in PBS; cross-reacting with human as shown in this work) and rat anti-mouse mAb (clone R17217, IgG_{2a},κ, 1 mg/mL in PBS) to transferrin receptor (CD71) were obtained from Chemicon International (Temecula, CA). β-Poly(L-malic acid) (PMLA) (**1**), a natural polymer of molecular mass $M_w = 50000$ (polydispersity $M_w/M_n = 1.3$) from the culture broth of *Physarum polycephalum*, was highly purified (*36*) and size-fractionated on Sephadex G25. The lyophilized polyacid was devoid of material absorbing at 260 and 280 nm wavelengths. If not mentioned otherwise, molar quantities refer to total malyl residues. Chromatographically pure $mPEG_{5000}$-amine and maleimide-PEG_{3400}-maleimide were obtained from Nektar Therapeutics (San Carlos, CA). 3-(2-Pyridyldithio)-propionate (PDP) was synthesized as described (*46*). Fluorescein-5-maleimide was obtained from Molecular Probes (Leiden, The Netherlands) and Alexa Fluor 680 C_2-maleimide from Molecular Probes-Invitrogen (Karlsruhe, Germany). Endosomal marker FM 4-64 was purchased from Molecular Probes. All other chemicals of highest purity were bought from Merck (Darmstadt, Germany), Sigma-Aldrich (Munich, Germany), and Pierce (Rockford, IL). Glioma cell lines U87MG and T98G were from American Type Culture Collection (Manassas, VA), and normal human embryonic astrocyte cell line HAST040 was obtained from Clonexpress (Gaithersburg, MD).

Cell Lines and Culture Conditions. Two types of human GBM cell lines (T98G and U87MG) were used. Cells were cultured in Eagle's MEM with 10% fetal calf serum, L-glutamine, sodium bicarbonate, nonessential amino acids, antibiotics, and sodium pyruvate. Normal embryonic brain astrocyte cell line HAST040 (Clonexpress) was also used in toxicity assays.

Cell Viability Assay. To measure cell viability, cells were quantified using the CellTiter 96 AQueous One Solution Cell Proliferation Assay kit (Promega Mannheim, Germany) designed for the determination of the number of viable cells with MTS reagent [3-(4,5-dimethylthiazol-2-yl)-5-(3-carboxymethoxyphenyl)-2-(4-sulfophenyl)-2*H*-tetrazolium, inner salt]. Protocols supplied by the company were exactly followed. A_{490} was recorded on a Spectra Max Plus 384 ELISA reader (IBB, Atlanta, GA). Concentration of Polycefin equal to 1.4 μM corresponds to the concentration of MORPH-AONs of 2.5 mg/kg. It is the working concentration recommended for antisense nucleotides to block mRNA synthesis in vitro and in vivo (*47*).

In Vivo Fluorescence Imaging. Xenogen IVIS 200 imaging system (Xenogen, Alameda, CA) was used on whole body and isolated organs of glioma-bearing mice 6−72 h following Polycefin injection and after PBS organ/body perfusion to remove the fluorescent drug from circulation. For imaging experiments on mice, Polycefin with attached L-leucine ethyl ester instead of L-valine, with rat mAb R17217 to mouse transferrin receptor and Alexa Fluor 680 dye. The excitation wavelength for the dye was 660 nm. Images were acquired and analyzed at 3.9 cm (organs) or 13 cm (whole mouse) field of view using Living Image Software 2.50. In preliminary experiments, a proprietary MISTI imaging system equipped with 20 nm bandwidth interference filter (ChromaTech) and emission wavelength 700 nm was used. Both imaging systems produced similar results.

Animals. All surgical and nonsurgical procedures were performed in full accordance with IACUC protocol 001462, obtained in May 2005 at Cedars-Sinai Medical Center and with the tenets of the Declaration of Helsinki.

Nude Mice [Tac:Cr:(MCr)-*Foxn*^{nu} mice], after intraperitoneal anesthesia by ketamine 75 mg/kg and medetomidine 1.0 mg/kg, were used. A 10 mm middle line skin incision was made on mouse's skull. A hole in the skull 2 mm laterally and 1 mm rostrally from the Bregma (sagittal and transverse lines crossing point) was made using a dental drill by aseptic technique. Mice underwent stereotactic intracranial injection of 5×10^4 U87MG human glioma cells to the right basal ganglia field using a 2 μL Hamilton syringe over a period of 1 min.

On day 21 after tumor implantation, the mice underwent the intravenous injection of Polycefin at the concentration of 5 mg/kg (*47*) dissolved in PBS via the tail vein using a 30-gauge needle 1 mL syringe, at a rate of 100 μL within 5 s.

Confocal Microscopy. A TCS SP spectral scanner (Leica Microsystems, Mannheim, Germany) was used for confocal microscopy. Image stacks of 160 by 160 μm in size and 7.5 μm in depth of live U87MG glioma cells were acquired with a Leica PlanApo 63/1.2 NA lens. Live cells were placed in an Attofluor incubation chamber (Molecular Probes). A temperature of 37 °C was maintained by a separate lens and chamber heating system. The fluorescein derivatives of Polycefin with (**8**) or without (**18**) conjugated transferrin receptor mAb OX-26 were added to cells in serum-free medium at a concentration of 1.4 μM MORPH-AON. Simultaneously with Polycefin, cells received 5 μg/mL (as per the manufacturer's instructions) of lipophilic styryl red fluorescent dye FM 4-64 (Molecular Probes) to visualize endosomes.

Hemolytic Assay. To assess membrane-disrupting activities, hemolytic properties of Polycefin and other conjugates were

measured by the red blood cell (RBC) hemolysis assay (*21*) for 2 nmol of conjugate per 10^8 RBCs after incubation at 37 °C (1 h) in 1.5 mL of 100 mM sodium phosphate buffer at several given pHs. Percent hemolysis $(A - A_o)/(A_{tot} - A_o)$ as averaged over three independent measurements and calculated from A_{541} (= A) of the clear supernatant after pelletting. A_o refers to spontaneous and A_{tot} to complete hemolysis in distilled water.

Western Blot Analysis. Reducing SDS−PAGE (with 20 mM DTT) on 10% polyacrylamide gels (samples boiled for 5 min in 5% SDS) and routine Western blotting were carried out as published (*39*).

Polycefin (**8**) at a concentration of 1.4 μM MORPH-AON (*38*) was added to the medium of human glioma U87MG and T98G cultures on day 1 and 4 in culture media. For the detection of laminins, serum-free conditioned medium was sampled at day 6 from culture supernatants above equal numbers of cells that has been cultured for the same period of time. Samples were concentrated 10-fold by filtering through Centriplus filtration devices (Millipore, Bedford, MA) and proteins were separated using Tris-acetate 3−8% gradient SDS−PAGE (Invitrogen) under reducing conditions. Lysates of human glioma T98G, known to express laminin-8 (*48*), were used as a positive control. The gels were blotted onto nitrocellulose membrane (Invitrogen). The membranes were probed with mAbs followed by chemiluminescent detection using the Immune-Star kit with alkaline phosphatase-conjugated secondary antibodies (Bio-Rad Hercules, CA). Antibodies were used to laminin α4 [mAb 8B12 (*48*)] and β1 chains (mAb LT3). Antibody to human fibronectin 8th type III repeat [mAb 568 (*39*)] was used to control for equal loading of gel lanes.

Densitometric Analysis. The intensities of the bands of interest after Western blot analysis were determined using the AlphaImager 2000 densitometer (Alpha Innotech, Inc., San Leandro, CA) and expressed relative to the fibronectin band intensities for the same specimens. Background was subtracted from each reading before determining the intensity ratios.

Test of the Morpholino Oligonucleotides Releasing Module of Polycefin. To demonstrate the activity of the oligonucleotide releasing module, Polycefin (0.25 mM bound MORPH-AONs) was incubated with 3 mM GSH (γ-L-glutamyl-L-cysteinylglycine) in 50 mM phosphate buffer pH 7.4 at 37 °C. Samples at various times were stopped with 20 mM *N*-ethylmaleimide, and the liberated reduced oligonucleotide was detected as the *N*-ethylmaleimidyl derivative by SEC−HPLC, A_{260}. 100% release was measured in the presence of 50 mM dithiothreitol (DTT) (60 min, 37 °C).

Analytical Chemical Methods. Thiol residues of conjugates were assayed by the method of Ellman after removal of free 2-MEA by diafiltration (5 kDa cutoff). Amounts of maleimido groups were quantified by their reaction with a given amount of 2-MEA. During the preparation of PMLA conjugates, the substitution of *N*-hydroxysuccinimidyl (NHS) residues was followed by RP-HPLC analysis of the reaction mixtures. Amino acids were quantified by RP-HPLC after hydrolysis of conjugates in 6 M HCl at 100 °C and colorimetry with trinitrofluorobenzene (TNBS) following standard protocols.

Instrumentation. ^{1}H NMR spectra were recorded on a Bruker Model DMX-500 Fourier transform spectrometer with MTS as internal standard. Chromatography was performed on a Merck-Hitachi (Ghent, Belgium) analytical LaChrom D-7000 HPLC-UV and fluorescence detector system with either Macherey & Nagel (Düren, Germany) C_{18}-Nucleosil reversed phase RP (250/4 mm) or size exclusion Bio-Sil SEC 250-5 (5 μm, 300/7.8 mm) columns. Molecular mass markers were polystyrene sulfonates from Machery-Nagel and proteins from Sigma-Aldrich. Merck precoated silica gel 60 F_{254} aluminum sheets were used in thin-layer chromatography with *n*-butanol, water, and acetic acid (4:2:1 by volume) as solvent.

Synthesis of Polycefin. Synthesis of Intermediates and Conjugates. Polycefin, fluorescent dye-Polycefin, and other conjugates have been synthesized from the following intermediates (Scheme 1):

PMLA-N-hydroxysuccinimidyl Ester (PMLA-NHS) (2). A mixture of anhydrous 10 mmol PMLA (**1**), *N*-hydroxysuccinimide (NHS), and dicyclohexylcarbodiimide (DCC) (15 mmol) in DMF was incubated at room temperature. Dicyclohexylurea was exhaustively removed and product precipitated with ethyl acetate (P1), diethyl ether (P2), and *n*-hexane (P3) in this order. Products P1−P3 were dissolved in DMF, purified over Sephadex LH 20, and then stored as precipitates at −20 °C. PMLA-NHS ester was assayed by exhaustive reaction with *n*-butylamine and analysis of free NHS by RP-HPLC [aqueous 0.1% (v/v) TFA] recording A_{260} with reference to NHS standards. Contents were 35, 59, and 85% for P1, P2, and P3 (percentage refers to total PMLA-malyl residues). For the synthesis of Polycefin, P3 was used. Its overall yield was 50−60% with regard to input PMLA. ^{1}H NMR spectra of PMLA-NHS ester in $(CD_3)_2SO$ indicated chemical shifts at 2.8 ppm (singulet, 4H, N−CO−CH_2), 3.35 ppm (doublet, the methylene protons of the polyester backbone), and 5.85 ppm (triplet, the methine protons of the polyester backbone).

*(2-Pyridyldithio)propionyl Morpholino Antisense Oligonucleotides (PDP−MORPH-AONs) (conjugates **6**-α4 and **6**-β1 in Scheme 1).* Morpholino-3'-NH_2 oligonucleotide was coupled in 10% aqueous DMF with *N*-succinimidyl-3-(2-pyridyldithio)-propionate (SPDP) (2-fold excess, 20 °C). After passage over a Sephadex G-25 microspin column in 0.1 M sodium phosphate buffer (pH 6.5), 0.15 M NaCl, and 10 mM EDTA (Buffer A), the product was pure by TLC. The PDP-content was assayed by RP-HPLC after reaction with dithiothreitol (DTT). 2-Thiopyridone was detected at 341 nm wavelength and its concentration measured against reduced 2-aldrithiol as a standard. Yields were >80%.

*mAb OX-26-(S-succinimidyl-PEG_{3400}-maleimide)$_3$ (conjugate **4** in Scheme 1).* MAb OX-26 (20−30 nmol) or mAb R17217 was reduced in the presence of 53 μmol of solid 2-MEA hydrochloride in Buffer A (90 min at 37 °C). The product was washed over Sigma Ultrafree-CL microcentrifuge filters (30 kDa cutoff) to remove free 2-MEA (tests with Ellman's reagent). Free sulfhydryls were reacted with a 50-fold excess of maleimide-PEG_{3400}-maleimide over antibody, and excess reagent was removed by diafiltration (50 kDa cutoff). Purity was controlled by SEC−HPLC. Positions were 7.20−7.26 min for conjugate **4** and 13.4−13.7 min for maleimide-PEG_{3400}-maleimide. Of the thiol groups, 3.1−3.5 were detected in reduced antibody, and of the maleimido groups, 2.7−3.0 were detected in conjugate **4**, suggesting the formula mAb OX-26-(*S*-succinimidyl-PEG_{3400}-maleimide)$_3$ in Scheme 1.

*PMLA/$mPEG_{5000}$-NH_2 (5%)/2- MEA (10%)/valine (49%) (conjugate **3** in Scheme 1) and Other Conjugates.* The symbol "/" refers to conjugation of the indicated moiety with PMLA. PMLA-NHS esters dissolved in DMF were conjugated with $mPEG_{5000}$-NH_2, 2-MEA, and L-valine (or gylcine and L-alanine) by amide formation in this order. Specifically, PMLA-NHS P3 (1 mmol) was conjugated with 50 μmol $mPEG_{5000}$-NH_2 at 5% of the malyl residues (100% = all malyl groups in the preparation), followed by conjugation with 100 μmol of 2-MEA at 10% of the malyl residues. Completeness of each reaction was assayed by TLC and tested with ninhydrin. No precipitates were observed that could have affected stoichiometries. Finally, 1 mmol of L-valine (or glycine, L-alanine) was conjugated in DMF/PBS (a mixture of equal volumes) for 1 h at 20 °C. Again, no precipitate was observed. The product was transferred to

Scheme 1. Summary of the Synthesis of Dye-Polycefin (7)[a]

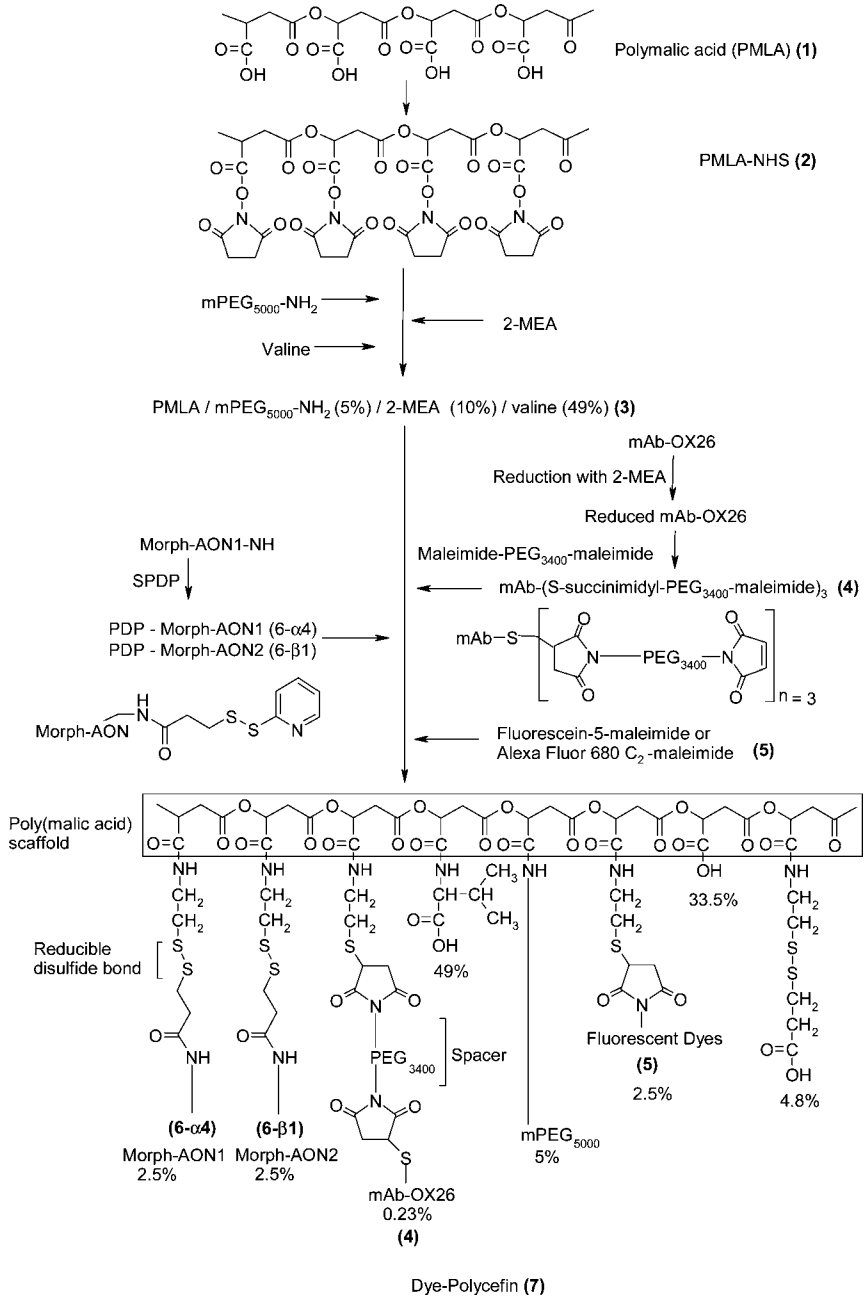

[a] Intermediates of the synthesis and of various modules are abbreviated by underlined numbers. Percent values refer to the number of malyl moieties of PMLA that are conjugated with a given module (100% = total malyl content). Polycefin (**8**) was synthesized with the omission of the fluorescent dye **5**. The distribution of conjugates along the scaffold is assumed to be random. Abbreviations are: PMLA, β-poly(L-malic acid); PMLA-NHS, *N*-hydroxysuccinimidyl ester at pending carboxyl groups of PMLA; $mPEG_{5000}$, methoxy poly(ethylene glycol) (5000 Da); 2-MEA, 2-mercaptoethylamine; mAb OX-26, mouse monoclonal antibody to rat transferrin receptor; maleimide-PEG_{3400}-maleimide, a bifunctional maleimide derivative of PEG (3400 Da); MORPH-AON-1, morpholino antisense oligonucleotide to laminin α4 chain; MORPH-AON-2, morpholino antisense oligonucleotide to laminin β1 chain.

Buffer A by solvent evaporation/complete resolubilization containing 0.5 mM DTT and purified over Sephadex G25 column. Lyophilized fractions were used in the synthesis of Polycefin. The composition of conjugate **3** was PMLA, $mPEG_{5000}$ (5%), 2-MEA (10%), and L-valine (49%). Each of the reactions was completed except for the amino acids, which were assayed after conjugation, validating the given composition. To measure effects of various conjugated groups (for instance on membrane stability by the hemolysis assay), additional conjugates were synthesized: **9** PMLA/$mPEG_{5000}$ (5%)/2-MEA (5%), **10** PMLA/$mPEG_{5000}$ (10%)/2-MEA (5%), **11** PMLA/$mPEG_{5000}$ (15%)/2-MEA (5%), **12** PMLA/$mPEG_{5000}$ (5%)/2-MEA (5%)/glycine (63%), **13** PMLA/$mPEG_{5000}$ (5%)/2-MEA (5%)/L-alanine (56%), **14** PMLA/$mPEG_{5000}$ (5%)/2-MEA (5%)/L-valine (55%), **15** PMLA/$mPEG_{5000}$-NH_2 (5%)/2-MEA (10%)/valine (15%), **16** PMLA/$mPEG_{5000}$-NH_2 (5%)/2-MEA (10%)/valine (34%), **17** PMLA/$mPEG_{5000}$-NH_2 (5%)/2-MEA (10%)/valine (55%), **18** PMLA/$mPEG_{5000}$-NH_2 (5%)/2-MEA (10%)/valine (50%)/(2-pyridyldithio)propionyl-morpholino AON to laminin α4 chain (2.5%)/(2-pyridyldithio)propionyl-morpholino AON to laminin β1 chain (2.5%)/3-(2-pyridyldithio)propionate, **19** PMLA/$mPEG_{5000}$-NH_2 (5%)/2-MEA (10%)/valine (50%)/mAB-(*S*-succinimidyl-PEG_{3400}-maleimide)$_3$ (0.23%)/3-(2-pyridyldithio)-propionate, **20** Polycefin variant with leucine ethyl ester instead of valine, with mAb R17217 to mouse, and with Alexa Fluor

680, **21** as for **20**, but without mAb. Free sulfhydryl groups were blocked with 3-(2-pyridyldithio)propionate (PDP).

*Synthesis of Dye-Polycefin (**7** in Scheme 1) and Polycefin (**8**).* Freshly prepared mAb OX-26-(*S*-succinyl-PEG_{3400}-maleimide)$_3$ (conjugate **4**) was added dropwise to conjugate **3** dissolved in Buffer A at 4 °C. Free thiol groups (conjugate **3**) were in 50-fold excess over maleimido groups (conjugate **4**). Next, 2.5 μmol of fluorescein-5-maleimide or Alexa Fluor 680 C_2-maleimide (compounds **5**), 5 μmol of PDP−Morph-AON1 (**6**-α4), and 5 μmol of PDP−Morph-AON2 (**6**-β1) were coupled overnight to the growing conjugate. To obtain Polycefin (**8**), the conjugation with **5** was omitted. Completeness of the reactions was indicated by a single peak after SEC−HPLC. Unreacted free sulfhydryl groups were blocked with 3-(2-pyridyldithio)propionate (PDP). The obtained conjugates **7** and **8** were purified by diafiltration (100 kDa cutoff) and lyophilized. The absolute yields were 75−80% with reference to conjugate **3** (100%), and the overall yield with reference to PMLA (**1**) input was 25%. For cell delivery and membrane disruption studies, conjugates resembling Polycefin, **18** either without mAb OX-26 or **19** without the oligonucleotides, and for imaging experiments, Polycefin variants **20** and **21**, were synthesized and purified by analogous methods.

RESULTS

Synthesis of Polycefin. The nanoscale synthesis of Polycefin outlined in Scheme 1 and described under Experimental Procedures afforded the highly controlled chemical coupling of macromolecular groups (modules) with the polymeric PMLA scaffold. In the beginning, the scaffold carboxyl groups were activated by forming *N*-hydroxysuccinimidyl esters of the polymer (PMLA-NHS) that were then substituted by PEG_{5000}-NH_2, 2-mercaptoethylamine (2-MEA), and L-valine in forming amide bonds with the carboxylates. The reactions were sequential without purification of intermediates. Products were validated by demonstrating complete consumption of the substituting amines and correlation with the released amount of NHS. Only the coupling of amino acids caused a small fraction of spontaneous hydrolysis of PMLA-NHS. The stoichiometry for valine and the other amino acids was derived from quantitative amino acid analysis. The multiple conjugate thus obtained (conjugate **3** in Scheme 1) contained 33−35% free carboxylates.

Probing PMLA and PMLA-NHS by SEC−HPLC indicated a dramatic change in conformation by the esterification from a probably extended to a compact structure in aqueous solution. The consequently decreased solubility in water was improved by conjugation of PEG_{5000}, which also should confer stability in body fluids (*27*−*30*). Only after conjugation of PEG, the pending thiol groups of conjugate **3** became accessible to the reactions with mAb OX-26 (or mAb R17217) and MORPH-AONs.

The reactions with mAb OX-26 or mAb R17217and MORPH-AONs required mild conditions in order to avoid irreversible denaturation. The conjugation of mAb involved at first a reduction of disulfide bridges resulting in the formation of 3 thiol residues per antibody and reaction with excessive maleimide-PEG_{3400}-maleimide forming the conjugate **4** (Scheme 1). The free unreacted maleimido groups were reserved to substitute at thiols of scaffold-bound 2-MEA (in conjugate **3**) forming thioether conjugates. SEC−HPLC and nonreducing SDS−PAGE prior to this conjugation indicated molecular masses of 150 kDa for both the reduced mAb and PEG-mAb, consistent with single mAb conjugates of maleimide-PEG_{3400}-maleimide (results not shown).

The cleavage site for the release of the MORPH-AONs from the carrier was constructed as an interspacing disulfide group between MORPH-AON and 2-MEA on the scaffold. This allowed the reductive cleavage by glutathione in the target cell cytoplasm. The disulfide was introduced by the disulfide exchange reaction of 2-MEA-thiol groups, bound to the scaffold, with PDP-MORPH-AONs (conjugates **6** in Scheme 1).

Polycefin and dye-Polycefin were assembled by the consecutive chemical coupling of the scaffold conjugate **3** with modules **4**, **5**, and **6** (Scheme 1). Their controlled synthesis together with their chromatographic and chemical characterization validated their structural composition, chemical functionality, and purity. At a 50-fold molar excess of thiol residues in conjugate **3** over conjugate **4**, the reaction with mAb was quantitative implicating an average of one molecule of antibody bound per molecule of scaffold. The covalent attachment of MORPH-AONs (conjugates **6**) was quantitative as verified by SEC−HPLC of educts and products.

Properties of Polycefin. The structure of dye-Polycefin is shown in Scheme 1 (in Polycefin, the dye module **5** is substituted by 3-thiopropionic acid). PMLA constitutes a scaffold that can bind a deliberate number of functional modules allowing versatile tissue-specific drug vehicles. The modules are statistically distributed over the scaffold at the abundances given in Scheme 1 in percentages of total malyl residues. The homogeneity of the scaffold-forming PMLA is characterized by its natural polydispersity. On the basis of a M_w of 50000 (corresponding to approximately 500 malyl residues), Polycefin molecules contain on average 1 molecule of mAb (targeting module), 11 molecules of conjugate **6**-α4, 11 molecules of conjugate **6**-β1, 22 molecules of $mPEG_{5000}$ (protecting module), 210−220 molecules of L-valine (membrane disrupting module), and 140−150 pending carboxylate residues. The composition accounted for a molecular mass of approximately 550000. The stoichiometry of 1:20−1:26 mAb relative to oligonucleotides was validated by disulfide reduction of Polycefin, separation of free protein and MORPH-AON by SEC−HPLC, and assessment of the amounts of MORPH-AON and protein on the basis of standardized A_{260} and the results of protein measurements. Freeze-dried Polycefin was colorless, nonhygroscopic, odorless, and stable at room temperature. The material was highly soluble in PBS and then stable for several days to weeks at 4 °C or at least 24 h at 37 °C. Polycefin had an UV-absorbance spectrum with a maximum at wavelengths <220 nm and a broad shoulder at 250−285 nm. The spectrum is indicative of carboxyl esters, carboxyamides, carboxylate, oligonucleotides, and protein. Dye-Polycefin showed also the absorbance and the fluorescence of the conjugated dye.

Analysis of Polycefin by Nonreducing SDS−PAGE. Sodium dodecyl sulfate polyacrylamide gel electrophoresis (SDS−PAGE) of Fluorescein-Polycefin was performed to identify the number of mAb molecules (shown is the result with mAb OX-26) conjugated with the PMLA scaffold (Figure 1). A single band of conjugated mAb of approximately 150 kDa was revealed under nonreducing conditions. Bands of higher molecular masses were not observed excluding the possibility of multiplets of conjugated IgG's.

To visualize which of the IgGchains were conjugated to the scaffold, samples were examined by SDS−PAGE under reducing conditions, and results were compared with those for unsubstituted mAb OX-26. Western blots, Fluorescein-dependent fluorescence, and protein staining (Coomassie Brilliant Blue) revealed bands of variable intensities in the range of 50 kDa and 62 kDa that referred to the intact H-chain and a main proteolytic fragment of mAb OX-26 (lanes R1 and R5) and Fluorescein-Polycefin (lanes R2−R4). L-Chains (25 kDa) were only protein stained (R4 and R5). The results indicated that PMLA was exclusively conjugated with the H-chain. It should be mentioned that the molecular mass scale by the polypeptide markers is not valid for Fluorescein-Polycefin, because the

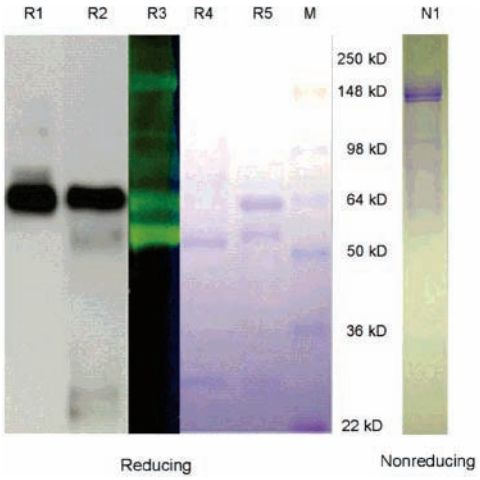

Figure 1. SDS−PAGE of mAb OX-26 and Fluorescein-Polycefin to demonstrate the conjugation of PMLA with the H-chain of the antibody, and the absence of multiple cross-linking of antibody. Lane N1, Fluorescein-Polycefin. Electrophoresis under nonreducing condition (DTT absent) showing the integral mAb after staining with Coomassie Brilliant Blue. Only the monomeric (150 kDa) but no multiple cross-linked mAbs (>150 kDa) are seen. Lanes R1−R5 and M, electrophoresis under reducing conditions (20 mM DTT) favoring dissociation into H- and L-chains. Detection of mAb OX-26 and its H-chains by Western blotting in lanes R1 and by Coomassie Brilliant Blue staining in lane R5. Detection by Western blotting in lane R2, by Fluorescein-specific fluorescence in lane R3, and by Coomassie Brilliant Blue in R4. Lane M, molecular mass markers. Bands in positions 150−165 kDa (R1−R5) refer to H-chain or a large fragment after a limited proteolytic nicking of the samples. Bands of approximately 25 kDa (R4 and R5) refer to L-chain. Fluorescence of the H-chain (fragment) in lane R3 indicates that this chain is conjugated with the scaffold.

PMLA scaffold, unlike polypeptides, has little or no affinity for SDS and does not measurably affect mobility retardation.

Morpholino Oligonucleotide Release from Polycefin. To test for the function of the MORPH-AON releasing module, Polycefin was incubated with glutathione at a concentration of 3 mM typical for cytoplasm. The time dependence of the observed disulfide exchange was biphasic, indicating the release of 50% MORPH-AONs after 30 min and 70% after 60 min. The release was completed after 4 h. Mixed disulfide between MORPH-AON and glutathione was an intermediate of the exchange reaction and amounted to 30% of total free and conjugated MORPH-AONs after 10 s, 50% after 30 min, 20% after 1 h, 12% after 3 h. The results are in agreement with Polycefin structure and suggest free MORPH-AONs shortly after entry into the cytoplasm.

Membrane Disruption. The membrane disrupting feature of Polycefin was tested by the hemolytic assay typically used elsewhere for measuring this kind of effects on biological membranes (*21*). Experiments were performed in the pH range 5−6 typically found in endosomes maturating to lysosomes. Figure 2a shows stimulation of cell rupture by Polycefin. The contribution by mAb OX-26 (comparison of conjugates **3** and **19**) was negligible, whereas the MORPH-AONs indicated a membrane stabilizing effect (comparison of conjugates **3** and **18**). Protection module $mPEG_{5000}$-NH_2 (5−15%) (comparison of conjugates **9**−**11**) also strongly stabilized red blood cells (Figure 2b), whereas 2-MEA residues alone had no effect (results not shown). Comparison of the amino acids glycine (63%), L-alanine (56%), and L-valine (55%) (conjugates **12**−**14**) in Figure 1c revealed amino acid side chain dependent rupture that increased according to hydrophobicity. The disrupting effect of L-valine increased as a function of scaffold loading (Figure 1d, conjugates **15**−**17**). The pH-dependence is in agreement with charge neutralization by protonation of carboxylates of PMLA and amino acid residues.

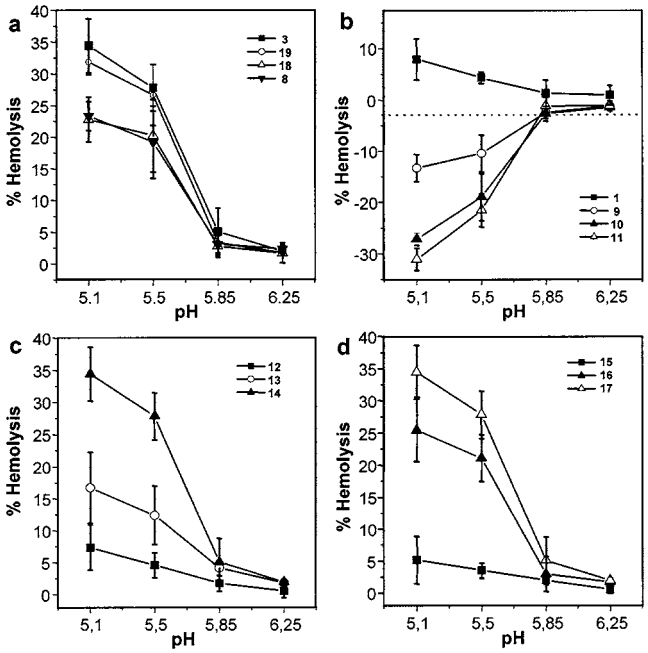

Figure 2. Comparison of the membrane disrupting activities of the Polycefin constituents measured by the hemolysis assay. Concentrations of tested conjugates were adjusted to 1.5×10^7 molecules per red blood cell. For referring numbers to conjugate compositions see Scheme 1 and text. Panel a, effects of the antibody and the oligonucleotides. **8**, Polycefin; **3**, Polycefin without antibody and oligonucleotides, **18**, Polycefin without antibody; **19**, Polycefin without oligonucleotides. Panel b, effect of $mPEG_{5000}$ at different loads. Unsubstituted PMLA **1** and 5% (**9**), 10% (**10**) or 15% (**11**) $mPEG_{5000}$. Panel c, effect of the hydrophobicity of the amino acid side chain. Glycine (**12**), L-alanine (**13**), or L-valine (**14**). Panel d, effect of different loads of valine. 13% (**15**), 34% (**16**), 55% (**17**) L-valine.

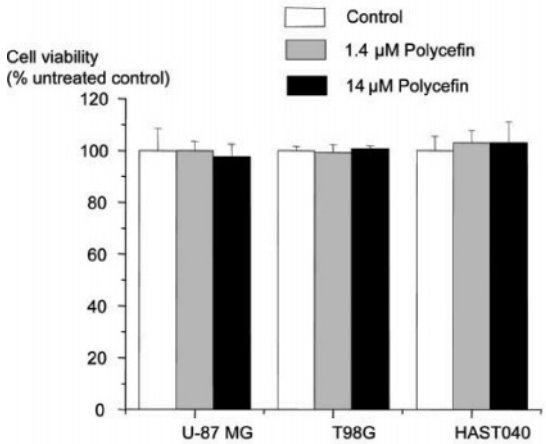

Figure 3. Cell viability of normal (HAST040) and malignant (U87MG and T98G) astrocyte cell culture after 48 h of Polycefin incubation. Different concentrations of Polycefin (1.4 μM and 14 μM) did not change the cell viability ($p > 0.05$) after 24 h (not shown) and 48 h treatment. 100% refers to conditions without treatment (control). Cell viability was measured twice in triplicates.

Polycefin Does Not Change Cell Viability. To evaluate the cytotoxicity, we have measured cell viability after treatment with Polycefin. The relative numbers of viable cells were measured in cultures of two human gliomas, U87MG and M059K, and normal human astrocytes, HAST 040. The numbers of treated cells were compared with those of replicate cultures without treatment (taken as 100%). Cell viability for each cell line in two separate experiments was higher than 90% (Figure 3). Untreated controls and treated cultures did not differ significantly from each other ($p > 0.05$). Based on these data we

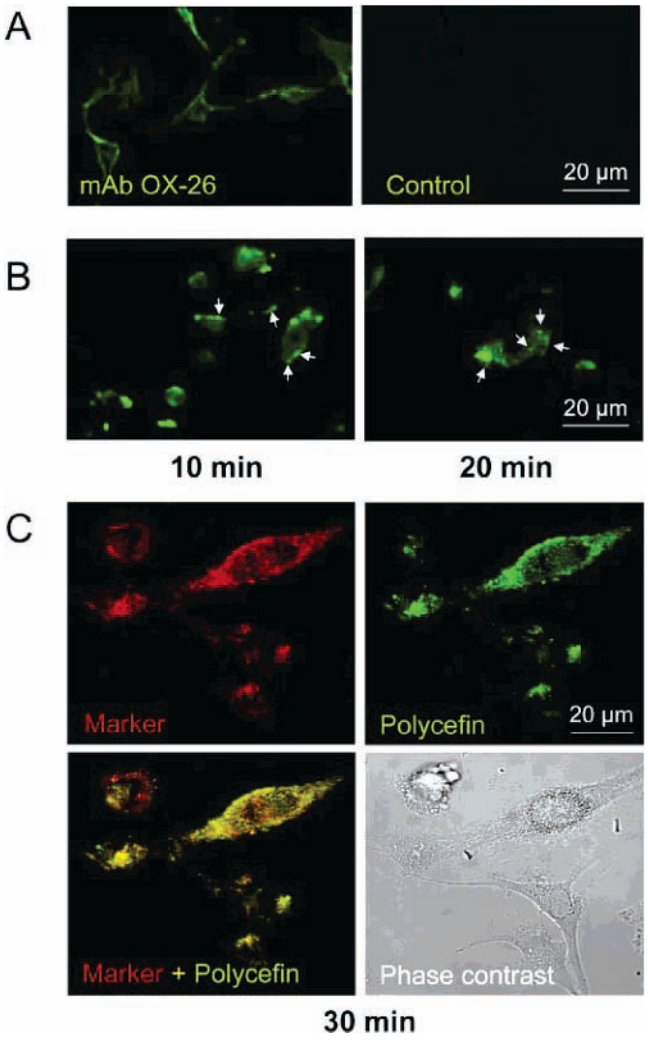

Figure 4. Drug delivery into cultured human glioma U87MG cells. A. U87MG glioma cells display surface staining with OX-26 antibody by indirect immunofluorescence demonstrating cross-reactivity with human antigen (left). Omission of primary antibody abolished staining (negative control, right). B. Left, 10 min of U87MG treatment with Fluorescein-labeled Polycefin. The location of Polycefin is indicated by green fluorescence near the cell membrane (arrows), and early endosomes are beginning to form. Right, endosomal formation after 20 min treatment with Polycefin. Maturing endosomes are visible inside the cells (arrows). C. Co-distribution of endosomal marker FM 4-64 (marker) with Fluorescein-Polycefin (30 min) in cultured U87MG cells 30 min after treatment. FM 4-64 stains endosomes (red color), and Polycefin is found in the same place (green color). Co-localization is revealed as yellow color (lower left). Confocal microscopy.

concluded that Polycefin at concentration 1.4 and 14 μM did not exert toxic effects on these cell lines.

In Vitro Studies of Polycefin Cell Delivery. In the in vitro studies with human U87MG and T98G glioblastoma cell lines, we have employed Polycefin (**8**) and its variant (**18**), Polycefin without mAb to transferrin receptor [Polycefin(-mAb)], both of them Fluorescein labeled.

We first established that anti-rat mAb OX-26 conjugated to Polycefin for subsequent intracranial glioma treatment in rats did cross-react with human transferrin receptor (Figure 4A). This Polycefin was further used to examine its internalization mechanism in U87MG glioma cultures. After treatment with Fluorescein-labeled Polycefin (**7**), fluorescence was localized near the cell membrane and in early endosomes after 10 min and inside the cells after 20 min after addition of the drug (Figure 4B). When U87MG were co-stained with fluorescent endosomal marker FM 4-64 (visualized with rhodamine filter),

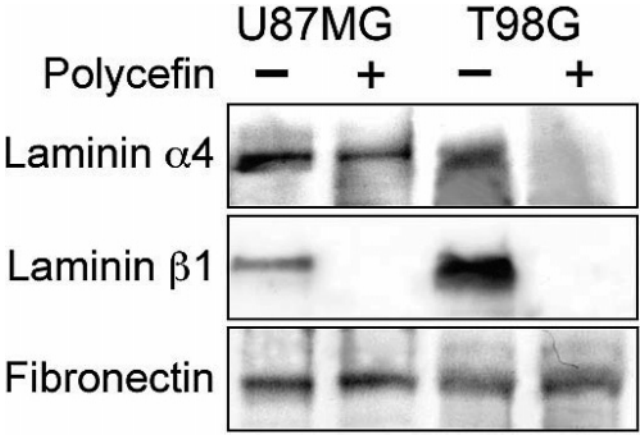

Figure 5. In vitro targeting and inhibition of laminin chain synthesis by Polycefin. Western blot analysis of laminin chain secretion into medium with or without Polycefin treatment. Conditioned media of both glioma cell lines, U87MG and T98G, contain α4 and β1 chains of laminin-8. Polycefin markedly inhibited secretion of both laminin chains, especially of β1 chain. Gel loading was normalized by the content of secreted fibronectin.

Table 1. Densitometric Evaluation of Western Blot Signal Intensities for Selected Proteins in Glioma-Conditioned Media with and without Polycefin Treatment[a]

	U87MG glioma cell line			T98G glioma cell line		
protein	control	treated	OD ratio	control	treated	OD ratio
laminin α4	924	301	0.33	675.5	0	0
laminin β1	187	0	0	2387.9	0	0
fibronectin	1014	1166	1.15	720.4	754.4	1.05

[a] Control, without Polycefin; Treated, with Polycefin; OD, optical density; OD ratio, treated/control

the staining for both Fluorescein-Polycefin (**7**) and FM 4-64 was co-localized after 30 min, indicated by the yellow color after superposition of red and green (Figure 4C). If cells were pretreated for 10 min with mAb OX-26 in order to block the cell surface transferrin receptor and then incubated with Polycefin, the drug was not internalized, and fluorescence was not seen inside the cells (result not shown). These experiments suggested that Polycefin delivery into the cells occurred by the mechanism of transferrin receptor-mediated endocytosis.

Fluorescein-labeled Polycefin(-mAb) (**18**) administered at the same concentration also passed through the cell membrane but was detected only 1 h after the first appearance inside the cells of Fluorescein-labeled Polycefin (**7**), about the time when free Fluorescein itself appeared, administered at the same concentration (data not shown). At this time, the fluorescence intensity of Fluorescein-Polycefin (**7**) inside the cells was markedly higher than in the controls. It was concluded that the mechanisms underlying cell penetration of Polycefin(-mAb) (**18**) and free Fluorescein were not receptor-mediated endocytosis.

To show that Polycefin was internalized into tumor cells via transferrin receptor mediated endocytosis followed by its escape through membrane disruption, the inhibition of laminin-8 chain synthesis in vitro was studied. Polycefin efficiently blocked secretion of laminin α4 and β1 chains in the culture medium of glioma cells as shown by semiquantitative Western blot analysis of conditioned culture media sampled after 6 days of culture (secreted human fibronectin served as gel loading control) as shown in Figure 5 and Table 1. In cultures treated with Polycefin (**8**) the expression of both chains was either significantly reduced (α4) or completely abolished (β1). The relative contents of both chains in U87MG and T98G glioma-conditioned medium before and after treatment were further analyzed semiquantitatively after densitometry with secreted human fibronectin as reference. Laminin α4 chain secretion was

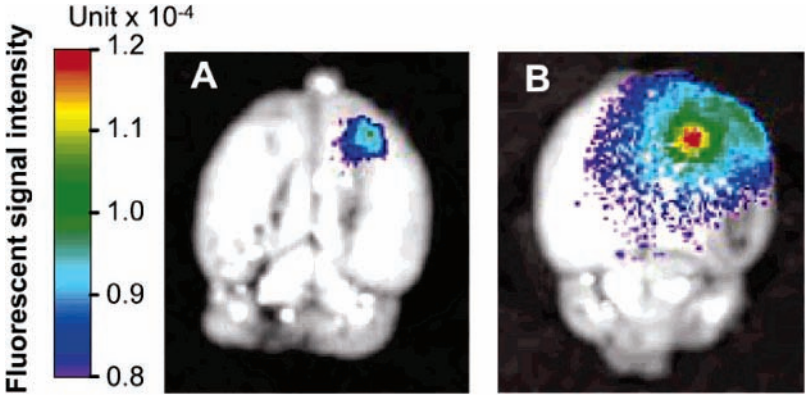

Figure 6. Xenogen IVIS 200 imaging of Polycefin in brain glioma. Polycefin variants **20** and Polycefin(-mAb) **21** are fluorescence labeled with Alexa Fluor 680, and the valine residue (Scheme 1) is replaced by L-leucine ethyl ester. Without targeting antibody, the drug still accumulates in tumor 72 h after intravenous injection (A). Complete Polycefin with mouse targeting antibody shows significantly higher tumor retention by both amount and area (B). Imaging was carried out after flushing perfused brains with sodium-buffered saline.

reduced in U87MG cells by 67% and was completely abolished in T98G cells after treatment, whereas β1 chain secretion was totally blocked in both cell lines (Table 1).

The results show that Polycefin was readily internalized by glioma cells via the transferrin receptor-mediated endocytosis mechanism, and that AON conjugated to the drug efficiently inhibited target protein expression in vitro.

Selective Accumulation of Polycefin in Tumor. To confirm that Polycefin was selectively accumulated in brain tumor, we have carried out intravenous injections into human brain tumor-bearing nude mice and monitored its distribution. In these experiments, we used Alexa-680-conjugated Polycefin variant **20** in comparison to Polycefin(-mAb) **21**. The replacement of Fluorescein by Alexa Fluor 680 was necessary, because Fluorescein-Polycefin had shown only a weak signal in preliminary imaging experiments at the border of detection and a high background in vivo. The new dye Alexa-680 has higher stability and gives stronger fluorescence intensity. Xenogen IVIS 200 imaging system was used to detect the drug distribution in whole body (not shown) and isolated mouse organs 5 min−72 h after injection. Repeated experiments have been conducted, giving qualitatively the same results as shown in typical images of whole brain in Figure 6. After 6 h, the drug signal was detected only in brain tumor and kidneys and was observed there during the whole examination time period up to 72 h. As shown in Figure 6A, 72 h after PBS perfusion Alexa-680-Polycefin-(-mAb) accumulated in tumor to some extent. However, a stronger signal was observed when Polycefin was conjugated with anti-transferrin receptor mAb (Figure 6B). Because this mAb may have also cross-reacted with human, it may have targeted the drug both to endothelial cells in the tumor and to tumor cells. Free dye administered in the same way was eliminated from the body in 1 h and did not accumulate in any organ (data not shown). In contrast, the accumulated drug could not be removed by flushing of the brain after perfusion. Polycefin(-mAb) may accumulate in tumors by EPR effect that has been reported for other high-molecular-mass drugs (*49*−*51*). The presence of the targeting anti-transferrin antibody resulted in a pronounced accumulation of the fluorescent label in the tumor to a far greater extent than seen for the antibody-free Polycefin variant. This demonstrated the importance of the receptor-mediated uptake mechanism. The results of the in vivo imaging experiment showed that Polycefin crossed BTB and accumulated in the brain tumor.

DISCUSSION

An ideal prototype of carrier system allows targeting of tumor tissue with the simultaneous delivery of more than a single kind of drugs at high site-directed concentrations. We have succeeded in synthesizing such a delivery system with a hitherto unprecedented variety of functionality. Our prototype complements commonly used HPMA copolymer in offering a biodegradable, nontoxic, and nonimmunogenic scaffold from a biological source, opening a new avenue for drug delivery without the danger of undegradable deposits and/or adverse reactions in the treated organism. This drug may be used for treating an individual patient's pathologic condition and for targeting multiple specific biomarkers in tissues and organs.

Our drug carrier composed of a multitude of low- and high-molecular-mass modules is a challenge for nanoscale synthesis. The strategy was based on the following rational: 1. Chemical activation of the PMLA scaffold at pendant carboxyl groups by virtue of the NHS-ester; 2. Exhaustive substitution of the highly reactive NHS-ester by formation of stable amide bonds with both the robust modules and with 2-mercaptoethylamine (2-MEA); 3. The coupling of the now scaffold-harbored thiols with the delicate, strictly water soluble modules such as proteins and nucleic acids; 4. High reaction yields and predictable stoichiometries; 5. Avoidance of side reactions/degradation of labile modules by employing mild reaction conditions; and 6. Simple and efficient purification of intermediates and end products.

Polymalic acid met the challenge as an optimal scaffold by several criteria: biological origin, highest optical and chemical purity, abundant pendant carboxyl groups for the attachment of a variety of residues, absence of rotational restriction around the polymer covalent bonds to achieve a minimum of molecular crowding, high solubility of the salt form in water, high solubility of the acid form in acetone, DMF, DMSO, and *N*-methylpyrrolidone. The biodegradability of PMLA and of its modules and the absence of toxicity of the nanoconjugate building blocks proved Polycefin to be nontoxic in the cell viability assay.

The composition and average structure of Polycefin in Scheme 1 as a conjugate with functional groups (modules) is in accord with chemical analysis and with the UV/vis/fluorescence spectra. Reducing SDS−PAGE revealed that the PMLA scaffold was conjugated with a single mAb at H-chains. Features in Scheme 1 are corroborated by the results of disulfide cleavage and membrane disruption assays. A release of the oligonucleotides by disulfide exchange in the presence of glutathione verified both the chemical presence of the prodrug in Polycefin and the function of the releasing module. The membrane disrupting module was demonstrated by the effect of Polycefin and especially by the amino acid substitutions on the lysis of red blood cells, showing the importance of the

hydrophobic valine side chains and of the carboxylate charge neutralization. Although the hemolysis assay did not represent an authentic test for endosomal membranes, the results qualitatively revealed the membrane stabilizing/destabilizing effects of PEG, MORPH-AONs, and amino acid conjugates.

The idea underlying the mechanisms that we have built into the structure of Polycefin was to cross BTB, enter glial tumor cells by the transferrin receptor-mediated endocytosis, and subsequently get released from endosomes by membrane destabilization. These features were successfully validated by the results of confocal microscopy and Western blotting, showing the cellular uptake of Polycefin via endosomes, the successful escape from endosomes, and the targeting of laminin chain coding antisense oligonucleotides to cytoplasm/nuclei, where they inhibited laminin protein synthesis. The mechanism of drug internalization was investigated in cultured U87MG glioma cells. It was shown that Polycefin-conjugated OX-26 anti-transferrin receptor mAb cross-reacted with human cells. This result was important for our xenogenic in vivo models to deliver the drug into both rat endothelial and human glioma cells. For mouse in vivo experiments we used Polycefin with anti-mouse/human transferrin receptor mAb. Thus, we prepared and tested Polycefin for future in vivo treatment and characterized its property for two independent species, rat and mouse, using anti-transferrin receptor mAb's recognizing these two species and cross-reacting with human for delivery into human tumors.

The function of antibody to transferrin receptor in targeting BTB and glioma cells was confirmed by the in vivo imaging experiments together with the confocal microscopic investigation of glioma cultures. These data demonstrate a substantial enhancement through antibody targeting in comparison to EPR effect-driven (*3*, *35*) macromolecule accumulation in the implanted brain tumor.

Previously described nanoconjugate drug delivery systems, such as poly(acrylic acid) based derivatives (*35*), contain in most cases a single lipophilic prodrug to be released by endosomal cleavage of a tetrapeptide unit, occasionally a tissue-targeting molecule, and in some cases an endosomal membrane disrupting module, but a complex multifunctional structure such as that of Polycefin and delivering simultaneously two kinds of antisense oligonucleotides has not been reported. The delivery by a single carrier molecule of multiple drugs has the effect to enhance the simultaneous (synergistic) action of drugs as compared to the delivery of mixtures of single drugs. This principle has been borne out for MORPH-AON-1 and MORPH-AON-2 in Polycefin. The synthesis of Polycefin as a prototype drug delivery device allows the development of carriers with variant conjugates of several drugs and functional modules per single carrier molecule. The drug as a high-molecular-mass chemical compound owns the basic EPR-mediated selective accumulation in tumors together with the enhanced accumulation by antibody targeting. In principle, using Polycefin as a prototype of multifunctional targeting system, it would be possible to achieve in the future an individual treatment of different human pathological conditions, based on molecular targets. These possibilities open interesting new therapeutic avenues.

ACKNOWLEDGMENT

The authors are indebted to Prof. Kiyotoshi Sekiguchi (Institute for Protein Research, Osaka University, Osaka, Japan) for kindly donating antibodies to laminin α4 chain. We thank Dr. John Young, Director of the Department of Comparative Medicine, Cedars-Sinai Medical Center, for invaluable help with IACUC protocols and animal work. The authors express their gratitude to Prof. Alexander V. Ljubimov for assisting in the preparation of the manuscript.

Note Added after ASAP Publication. In the version of the manuscript posted January 19, 2006, corrections were made to text in the first paragraph of Experimental Procedures and the last paragraph of Results. The corrected version of the manuscript was posted January 25, 2006.

LITERATURE CITED

(1) Moghimi, S. M., Hunter, A. C., and Murray, J. C. (2001) Long-circulating and target-specific nanoparticles: theory to practice. *Pharmacol. Rev. 53*, 283−318.

(2) Christie, R. J., and Grainger, D. W. (2003) Design strategies to improve soluble macromolecular delivery constructs. *Adv. Drug Delivery Rev. 55*, 421−437.

(3) Duncan, R. (2003) The dawning era of polymer therapeutics. *Nat Rev. 2*, 347−360.

(4) Zhang, Y., Zhu, C., and Pardridge, W. M. (2002) Antisense gene therapy of brain cancer with an artificial virus gene delivery system. *Mol. Ther. 6*, 67−72.

(5) Vinogradov, S. V., Batrakova, E. V., and Kabanov, A. V. (2004). Nanogels for oligonucleotide delivery to the brain. *Bioconjugate Chem. 15*, 50−60.

(6) Mineura, K., and Kowada, M. (1996) Enhancement of 5-fluorouracil cytotoxicity by cisplatin in brain tumor cell lines. *Cell Biol. Int. 20*, 355−357.

(7) Mologni, L., leCoutre, P., Nielsen, P. E., and Gambacorti-Passerini, C. (1998) Additive antisense effects of different PNAs on the in vitro translation of the PML/RARα gene. *Nucleic Acids Res. 26*, 1934−1938.

(8) Matsumura, Y., and Maeda, H. (1986) A new concept for macromolecular therapeutics in cancer chemotherapy: mechanism of tumoritropic accumulation of proteins and the antitumor agent SMANCS. *Cancer Res. 46*, 6387−6392.

(9) Muggia, F. M. (1999) Doxorubicin-polymer conjugates: further demonstration of the concept of enhanced permeability and retention. *Clin. Cancer Res. 5*, 7−8.

(10) Maeda, H. (2001) SMANCS and polymer-conjugated macromolecular drugs: advantages in cancer chemotherapy. *Adv. Drug Delivery Rev. 46*, 169−185.

(11) Maeda, H., Seymour, L. W., and Miyamoto, Y. (1992) Conjugates of anticancer agents and polymers: advantages of macromolecular therapeutics in vivo. *Bioconjugate Chem. 3*, 351−362.

(12) Seymour, L. W., Miyamoto, Y., Maeda, H., Brereton, M., Strohalm, J., Ulbrich, K., and Ducan, R. (1995) Influence of molecular weight on passive tumour accumulation of a soluble macromolecular drug carrier. *Eur. J. Cancer 31A*, 766−770.

(13) Pardridge, W. M. (1999) Vector-mediated drug delivery to the brain. *Adv. Drug Delivery Rev. 36*, 299−321.

(14) Qian, Z. M., Li, H., Sun, H., and Ho, K. (2002) Targeted drug delivery via the transferrin receptor-mediated endocytosis pathway. *Pharmacol. Rev. 54*, 561−587.

(15) Baselga, J. (2001) The EGFR as a target for anticancer therapy − focus on cetuximab. *Eur. J. Cancer 37*, S16−S22.

(16) Leamon, C. P., and Reddy, J. A. (2004) Folate-targeted chemotherapy. *Adv. Drug Delivery Rev. 56*, 1127−1141.

(17) Turk, M. J., Reddy, J. A., Chmielewski, J. A., and Low, P. S. (2002) Characterization of a novel pH-sensitive peptide that enhances drug release from folate-targeted liposomes at endosomal pHs. *Biochim. Biophys. Acta 1559*, 56−68.

(18) Rozema, D. B., Ekena, K., Lewis, D. L., Loomis, A. G., and Wolff, J. A. (2003) Endosomolysis by masking of a membrane-active agent (EMMA) for cytoplasmic release of macromolecules. *Bioconjugate Chem. 14*, 51−57.

(19) Philippova, O. E., Hourdet, D., Audebert, R., and Khokhlov, A. R. (1997) pH-responsive gels of hydrophobically modified poly(acrylic acid). *Macromolecules 30*, 8278−8285.

(20) Murthy, N., Robichaud, J. R., Tirrell, D. A., Stayton, P. S., and Hoffman, A. S. (1999) The design and synthesis of polymers for eukaryotic membrane disruption. *J. Controlled Release 61*, 137−143.

(21) Lackey, C. A., Murthy, N., Press, O. W., Tirrell, D. A., Hoffman, A. S., and Stayton, P. S. (1999) Hemolytic activity of pH-responsive polymer-streptavidin bioconjugates. *Bioconjugate Chem. 10*, 401−405.

(22) Cheung, C. Y., Murthy, N., Stayton, P. S., and Hoffman, A. S. (2001) A pH-sensitive polymer that enhances cationic lipid-mediated gene transfer. *Bioconjugate Chem. 12*, 906−910.
(23) Murthy, N., Xu, M., Schuck, S., Kunisawa, J., Shastri, N., and Frechet, J. M. (2003) A macromolecular delivery vehicle for protein-based vaccines: acid-degradable protein-loaded microgels. *Proc. Natl. Acad. Sci. 100*, 4995−5000.
(24) Friedrich, B., Jung, K., Lein, M., Türk, I., Rudolph, B., Hampel, G., Schnorr, D., and Loening, S. A. (1999) Cathepsins B, H, L and cysteine protease inhibitors in malignant prostate cell lines, primary cultured prostatic cells and prostatic tissue. *Eur. J. Cancer 35*, 138−144.
(25) Rodrigues, P. C. A., Scheuermann, K., Stockmar, C., Maier, G., Fiebig, H. H., Unger, C., Mülhaupt, R., and Kratza, F. (2003) Synthesis and in vitro efficacy of acid-sensitive poly(ethylene glycol) paclitaxel conjugates. *Bioorg. Med. Chem. Lett. 13*, 355−360.
(26) Saito, G., Swanson, J. A., and Lee, K. D. (2003) Drug delivery strategy utilizing conjugation via reversible disulfide linkages: role and site of cellular reducing activities. *Adv. Drug Delivery Rev. 55*, 199−215.
(27) Greenwald, R. B., Choe, Y. H., McGuire, J., and Conover, C. D. (2003) Effective drug delivery by PEGylated drug conjugates. *Adv. Drug Delivery Rev. 55*, 217−250.
(28) Otsuka, H., Nagasaki, Y., and Kataoka, K. (2003) PEGylated nanoparticles for biological and pharmaceutical applications. *Adv. Drug Delivery Rev. 55*, 403−419.
(29) Arpicco, S., Dosio, F., Bolognesi, A., Lubelli, C., Brusa, P., Stells, B., Ceruti, M., and Cattel, L. (2002) Novel Poly(ethylene glycol) derivatives for preparation of ribosome-inactivating protein conjugates. *Bioconjugate Chem. 13*, 757−765.
(30) Maruyama, K., Takahashi, N., Toshiaki, T., Nagaike, K., and Iwatsuru, M. (1997) Immunoliposomes bearing poly(ethylene glycol)-coupled Fab' fragment show prolonged circulation time and high extravasation into targeted solid tumors in vivo. *FEBS Lett. 413*, 177−180.
(31) Kopecek, J., Kopecková, P., Minko, T., and Lu, Z. (2000) HPMA copolymer-anticancer drug conjugates: design, activity, and mechanism of action. *Eur. J. Pharm. Biopharm. 50*, 61−81.
(32) Lu, Z. R., Shiah, J. G., Sakuma, S., Kopecková, P., and Kopecek, J. (2002) Design of novel bioconjugates for targeted drug delivery. *J. Controlled Release 78*, 165−173.
(33) David, A., Kopecková, P., Minko, T., Rubinstein, A., and Kopecek, J. (2004) Design of a multivalent galactoside ligand for selective targeting of HPMA copolymer-doxorubicin conjugates to human colon cancer cells. *Eur. J. Cancer 40*, 148−157.
(34) Ulbrich, K., and Subr, V. (2004) Polymeric anticancer drugs with pH-controlled activation. *Adv. Drug Delivery Rev. 56*, 1023−1050.
(35) Satchi-Fainaro, R., Puder, M., Davies, J. W., Tran, H. T., Samson, D. A., Greene, A. K., Corfas, G., and Folkman, J. (2004) Targeting angiogenesis with a conjugate of HPMA copolymer and TNP-470. *Nat. Med. 10*, 255−261.
(36) Lee, B. S., Vert, M., and Holler, E. (2002) Water-soluble aliphatic polyesters: poly(malic acid)s. *Biopolymers. Volume 3a: Polyesters I* (Doi Y., and Steinbuechel A., Eds.) pp 75−103, Chapter 3, Wiley-VCH, New York.
(37) Ljubimova, J. Y., Lakhter, A. J., Loksh, A., Yong, W. H., Riedinger; M. S., Miner, J. H., Sorokin, L. M., Ljubimov, A. V., and Black, K. L. (2001) Overexpression of α4 chain-containing laminins in human glial tumors identified by gene microarray analysis. *Cancer Res. 61*, 5601−5610.
(38) Fujita, M., Khazenzon, N. M., Bose, S., Sekiguchi, K., Sasaki, T., Carter, W. G., Ljubimov, A. V., Black, K. L., and Ljubimova, J. Y. (2005) Overexpression of β1 chain-containing laminins in capillary basement membranes of human breast cancer and its metastases. *Breast Cancer Res. 7*, 411−421.
(39) Khazenzon, N. M., Ljubimov, A. V., Lakhter, A. J., Fujita, M., Fujiwara, H., Sekiguchi, K., Sorokin, L. M., Petäjäemi, N., Virtanen, I., Black, K. L., and Ljubimova, J. Y. (2003) Antisense inhibition of laminin-8 expression reduces invasion of human gliomas in vitro. *Mol. Cancer Ther. 2*, 985−994.
(40) Summerton, J., and Weller, D. (1997) Morpholino antisense oligomers: Design, preparation and properties. *Antisense Nucleic Acid Drug Dev. 7*, 187−195.
(41) Jefferies, W. A., Brandon, M. R., Williams, A. F., and Hunt, V. (1985) Analysis of lymphopoietic stem cells with a monoclonal antibody to the rat transferrin receptor. *Immunology 54*, 333.
(42) Skarlatos, S., Yoshikawa, T., and Pardridge, W. M. (1995) Transport of ^{125}I-transferrin through the rat blood-brain barrier, *Brain Res. 683*, 164−171.
(43) Thorstensen, K., and Romslo, I. (1993) The transferrin receptor: its diagnostic value and its potential as therapeutic target. *Scand. J. Clin. Lab Invest. 53*, 113−120.
(44) Singh, M. (1999) Transferrin as a targeting ligand for liposomes and anticancer drugs. *Curr. Pharm. Des. 5*, 443−451.
(45) Broadwell, R. D., Baker-Cairns, B. J., Frieden, P. M., Oliver, C., and Villegas, J. C. (1996) Transcytosis of protein through the mammalian cerebral epithelium and endothelium III. Receptor-mediated transcytosis through the blood-brain barrier of blood-borne transferrin and antibody against the transferrin receptor. *Exp. Neurol. 142*, 47−65.
(46) Carlsson, J., Drevin, H., and Axen, R. (1978) Protein thiolation and reversible protein−protein conjugation. *Biochem. J. 173*, 723−737.
(47) Arora, V., Knapp, D. C., Smith, B. L., Stadtfield, M. L., Stein, D. A., Reddy, M. T., Weller, D. D., and Iversen, P. L. (2000) c-Myc antisense limits rat liver regeneration and indicates role for c-myc in regulating cytochrome P-450 3A activity. *J. Pharmacol. Exp. Ther. 292*, 921−928.
(48) Fujiwara, H., Kikkawa, Y., Sanzen, N., and Sekiguchi, K. (2001) Purification and characterization of human laminin-8. Laminin-8 stimulates cell adhesion and migration through $\alpha_3\beta_1$ and $\alpha_6\beta_1$ integrins. *J. Biol. Chem. 276*, 17550−17558.
(49) Duncan, R. (2003) The dawning era of polymer therapeutics. *Nat. Rev. Drug. Discovery 2*, 347−360.
(50) Nori, A., and Kopecek, J. (2005) Intracellular targeting of polymer-bound drugs for cancer chemotherapy. *Adv. Drug Delivery Rev. 57*, 609−636.
(51) Duncan, R., Vicent, M. J., Greco, F., and Nicholson, R. I. (2005) Polymer-drug conjugates: towards a novel approach for the treatment of endrocine-related cancer. *Endocr. Relat. Cancer* 12 Suppl. 1, S189−199.

BC0502457

DNA Transfer into Human Lung Cells Is Improved with Tat−RGD Peptide by Caveoli-Mediated Endocytosis

Aparna Renigunta,[‡] Gabriela Krasteva,[§] Peter König,[§] Frank Rose,[‡] Walter Klepetko,[||] Friedrich Grimminger,[‡] Werner Seeger,[‡] and Jörg Hänze*[,‡]

University of Giessen Lung Center (UGLC), Medical Clinic II, Biochemistry, Friedrichstrasse 24, D-35392 Giessen, Germany, Institute for Anatomy and Cell Biology, Aulweg 123, Justus-Liebig University, D-35392 Giessen, Germany, and Cardiothoracic Surgery, University Hospital, Währinger Grütel 18-20, 1220 Vienna, Austria. Received August 25, 2005; Revised Manuscript Received January 2, 2006

Cell lines and primary cells exhibit varying degrees of resistance to DNA transfection strategies. In this study, we employed the synthetic peptide Tat−RGD (TR), composed of the HIV-1 derived translocation peptide Tat fused to the integrin binding RGD motif, as a tool for improving DNA transfer into pulmonary cells. Binding experiments between DNA and TR and cytotoxicity measurements of TR treated cells were undertaken to optimize DNA and TR concentrations for transfection. Addition of a complex of TR and DNA (TRD) to A549 cells yielded significant transgene expression. When TRD was combined with Lipofectamine (TRDL), the expression was increased by 5-fold over Lipofectamine (DL) and by ∼30-fold over TRD-mediated transfections. Also, in primary smooth muscle cells (SMC) and fibroblasts (FB) derived from pulmonary arteries, an increase in TRDL-mediated transfection efficiency was observed by a factor of ∼2 and ∼3 over that of DL. Laser scanning confocal microscopy for visualizing TR-dependent DNA uptake demonstrated that the internalization of TRDL complexes is linked to caveoli in the plasma membrane. Interfering with caveoli formation by methyl-*b*-cyclo-dextrin drastically decreased the transfection efficiency by TR. In conclusion, the Tat−RGD peptide mediates efficient gene delivery in human pulmonary cells, in particular when combined with a standard cationic lipid based transfection reagent. The enhancement of DNA uptake by Tat−RGD is suggested to be mediated by caveoli-dependent endocytosis.

INTRODUCTION

Nonviral strategies for gene transfer into eukaryotic cells include various chemical and physical approaches. The potencies of these diverse techniques differ in a cell-specific manner. Human primary cells are particularly resistant to established transfection techniques. Recently, methods have been developed for the delivery of exogenous proteins into living cells with the help of membrane-permeable carrier peptides. By genetically (*1*) or chemically (*2*) hybridizing these carrier peptides, efficient intracellular delivery of various oligopeptides and proteins was achieved (*3*). Among these proteins, the HIV-1 derived Tat protein (*4*), *Drosophila* Antennapedia protein (*5*), herpes simplex virus type-1 VP22 transcription factor (*6*), and various RNA and DNA binding proteins and polyarginines were described (*7*).

Tat is a transcriptional activator that binds to a short nascent stem−bulge−loop leader RNA for its transactivation. The best studied region of Tat resides in amino acids 49−72 (domain 4), which contains an arginine-rich basic motif. This motif confers Tat binding to RNA and is important for nuclear localization and uptake of Tat by cells (*8*). Part of this domain can be folded into an α-helix structure with amphipathic characteristics. Such helical structures have been considered as key determinants for the uptake of several enveloped viruses by fusion or endocytosis (*9*). Coupling of a Tat-derived peptide to several proteins allowed their functional internalization into several cell lines or tissues (*10*).

Integrins are a family of about 20 heterodimeric membrane proteins that bind to extracellular matrix proteins or membrane proteins of adjacent cells and play an important role in organ structuring and cell−cell communication. Integrin receptors are exploited by a diverse range of pathogens including bacteria and viruses for cell binding and entry. On this basis, it was proposed that integrin targeting may also be an optional pathway for the uptake of synthetic gene delivery vehicles (*11*). This is further buttressed by a study performed on adenovirus type 41 lacking an RGD alpha (v)-integrin binding motif on the penton base, undergoing a delayed uptake in A549 cells (*12*).

The objective of this study was to employ a peptide conjugate composed of a Tat motif and an RGD motif for improvement of DNA transfection in human pulmonary cells. To this end, we synthesized the fusion protein Tat−RGD (TR) consisting of a 21 amino acid sequence derived from Tat and a 10 amino acid sequence representing the RGD motif. We employed this peptide to enhance DNA transfection in the human lung A549 cell line and in human primary pulmonary artery cells. Significant improvement of transfection efficiency was noted, which was found to be linked to caveoli-dependent membrane internalization.

EXPERIMENTAL PROCEDURES

Peptide Synthesis. The biotinylated Tat−RGD (TR) peptide consisting of the truncated Tat domain at the N-terminus and the domain with an RGD motif at the C-terminus had the following sequence: (biotin-GMLGISYGRKKRRQRRRPPQT GGCRGDMFGC). This peptide was synthesized (Peptide Synthesizer 432A, Applied Biosystems, Fmoc-chemistry) and labeled at the N-terminus with biotin. After deprotection, it was purified by HPLC. The two cysteine residues were oxidized by air oxygen and a second HPLC purification was performed.

* Corresponding author. Phone: + 49-641-9942425. Fax: +49-641-9942429. E-mail: joerg.haenze@uglc.de.

[‡] Justus-Liebig University Giessen, Medical Clinic.

[§] Justus-Liebig University Giessen, Institute for Anatomy and Cell Biology.

[||] Cardiothoracic Surgery, University Hospital Vienna.

10.1021/bc050263o CCC: $33.50 © 2006 American Chemical Society
Published on Web 02/23/2006

TR−DNA Binding. Different amounts of the biotinylated TR were incubated with plasmid DNA in phosphate-buffered saline (PBS). Free TR and TR bound with DNA was separated by gel chromatography (Sephadex G-100 column). Positive column fractions were quantified by colorimetric detection employing peroxidase-labeled streptavidin.

Particle Size Measurement. For particle size measurement, 1 μg of DNA was mixed with different concentrations of TR in a final volume of 75 μL with Hank's balanced salt solution (HBSS) and incubated for 15 min to obtain the TRD mixtures. TRDL complexes were obtained by adding 2 μL of lipofectamine to these TRD mixtures and incubating for 15 min at room temperature. The mixtures were then measured for particle size using a zeta sizer.

Cell Culture. Culturing of human epithelial lung cell line A549 was performed according to the protocol given by the American Type Culture Collection. Human cell preparations were established from excess lung tissue originating from human donor lungs employed for transplantation. This protocol was approved by the Justus-Liebig University Ethics committee. Cells were isolated by careful dissection of parenchymal connective tissue as described. Primary adventitial fibroblasts (FB) and smooth muscle cells (SMC) from the pulmonary artery were isolated and cultured as described (*13*).

Cytotoxicity Assay. The cytotoxicity measurement was performed with the CytoTox-ONE homogeneous membrane integrity assay (Promega, Mannheim, Germany) based on the release of lactate dehydrogenase. Cells (5×10^4 per well) were plated in a 96-well plate. The cells were incubated with test compounds TRD or TRDL for 4 h at 37 °C. Then, Cyto-Tox reagent was added, and further experimental procedure was performed following the company's prescribed protocol.

Transfections. Transfection by Lipofectamin 2000 (Invitrogen, Carlsbad, CA) was performed as follows: 2.5×10^4 cells were plated per well in a 96-well plate. The cells were 80−85% confluent for transfection on the following day. In each well, 0.2 μg of DNA was diluted in 25 μL of Opti-MEM (Invitrogen, Carlsbad, CA). Lipofectamine 2000 (0.5 μL/well) was diluted in 25 μL of Opti-MEM and incubated for 5 min at room temperature. The diluted DNA was slowly added to the diluted Lipofectamine, and they were mixed and incubated for 15 min at room temperature to facilitate the formation of DNA−Lipofectamine (DL) complexes. The DL complexes were added to the cells and incubated at 37 °C. After 4 h, the medium was replaced with culture medium.

Transfection by TRD and TRDL was performed as follows: the cells were plated in a 96-well plate as described above. DNA (0.2 μg) was mixed with 2.5 μg/well or 0.8 μg/well of TR for cell line and primary cells, respectively, and the volume was made up to 25 μL with HBSS. The TRD mixture was vortexed and incubated at room temperature for 15 min. The resulting mixture was directly used for TRD-mediated transfection. For preparation of TRDL complexes, 0.5 μL/well of Lipofectamine was added to the TRD mixture and incubated at room temperature for 15 min. The TRD or TRDL mixtures were added to the cells and incubated at 37 °C. After 4 h, the medium was replaced, and cells were further cultured under standard conditions. Dependent on the experiment, TRD, TRDL, and DL transfections were performed in well plates of different diameters. The transfection mixtures were scaled in proportion to different well areas.

Reporter Assays. As reporter plamids, we used the pEGFP-N2 plasmid (BD Bioscience Clontech, Mountainview, CA) for expression of green fluorescent protein (GFP) or the pGL3 plasmid (Promega, Mannheim, Germany) for expression of firefly luciferase. After overnight incubation at 37 °C in 5% CO_2, the cells were either observed under a fluorescent microscope for GFP detection or subjected to luciferase assay (Luciferase detection assay, Promega). The cells were lysed with passive lysis buffer (Promega, Mannheim, Germany), and luciferase activity was measured by a luminometer (Spectrafluor Plus, TECAN, Crilsheim, Germany).

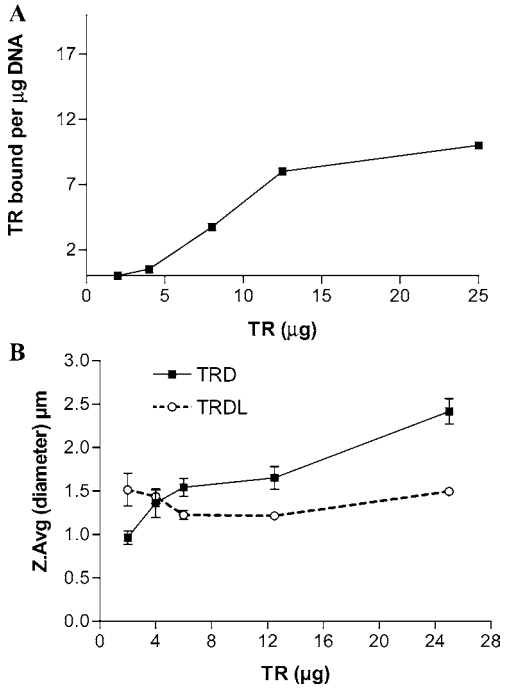

Figure 1. (A) Binding curve of TR and DNA. The *x*-coordinate shows the input amount of TR, the *y*-coordinate shows the amount of TR bound to 1 μg of DNA. (B) Measurement of particle sizes of different amounts of TR added to DNA (TRD) or different amounts of TR added to DNA complexed with Lipofectamine (TRDL). Z.Avg represents the average particle size (mean, SEM, $n = 3$).

Synthesis of DNA Fragment. DNA fragments of 400 bp were amplified from the pGL3 plasmid using the following primers (Metabion, Germany): forward 5′-ATG GAA AGT CCC TAT TGG CGT-3′ and reverse 5′-CTG TCC CCA GTG CAA GTG CA-3′. For generation of the fluorescent-labeled DNA fragment, the forward primer was labeled with fluorescein (FAM, Applied Biosystems, Weiterstadt, Germany). The PCR product was run in a regular agarose gel, and the 400 bp fragment was gel-eluted using the QIAEX II gel extraction kit (Qiagen, Hilden, Germany).

Cell-Adhesion Assay. A 48-well tissue culture plate was coated with fibronectin (20 μg/mL). After overnight incubation at 4 °C, the wells were washed twice with cold PBS. Bovine serum albumin (BSA, 1%) was added to the wells and incubated for 1 h to block the uncoated sites. The wells were washed twice with cold PBS. For the cell adhesion assay, confluent cultures of A549 cells were trypsinized, washed, and resuspended in medium containing specified concentrations of XJ735 (Sigma-Aldrich, Taufkirchen, Germany). Suspensions (200 μL) containing 0.5×10^5 cells/well were plated on the fibronectin-coated wells. Cell adhesion was allowed to occur for 2 h at 37 °C. Then, wells were washed once with PBS, trypsinized, and resuspended in culture medium. Ten microliters of this cell suspension was used for cell counting.

Confocal Imaging. *Tat−RGD and Caveolin-1 Colocalization.* A549 cells (0.5×10^5 cells/well) were plated in 8-well Permanox chamber slides (Lab-Tek, Naperville, IL) precoated with 300 μL of fibronectin (20 μg/mL). After overnight culturing, A549 cells were transfected with a 400 bp DNA fragment (CMV) employing the TRDL vector system. The cells were fixed at different time points for 2 h at room temperature with PFA (1 mL of 4% paraformaldehyde, 0.4 mL of 10× PBS,

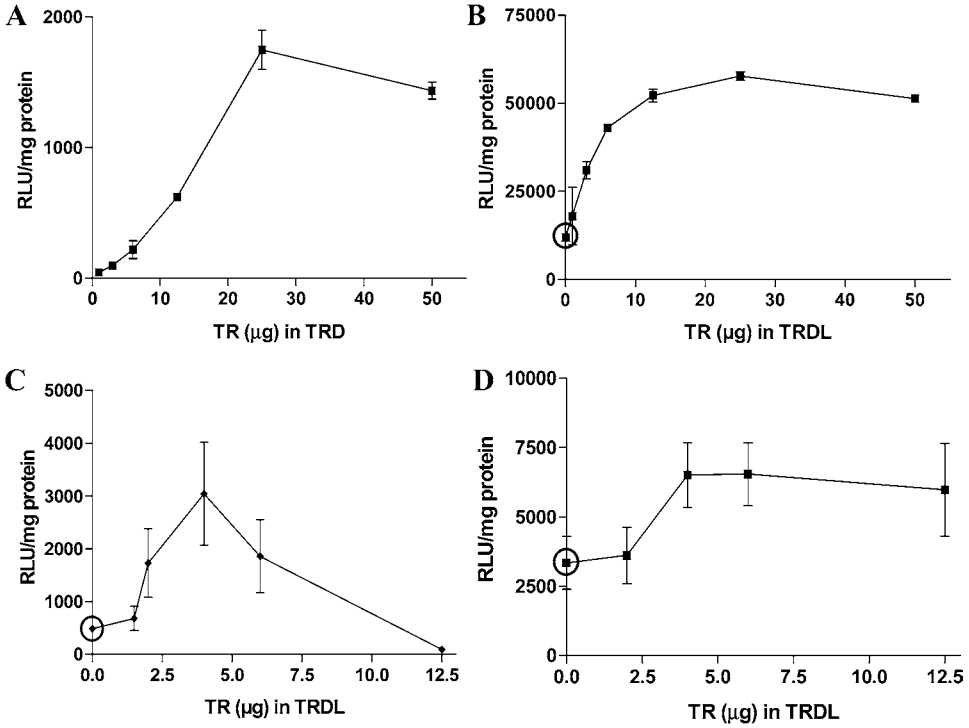

Figure 2. Analysis of luciferase reporter gene expression (RLU = relative light units) after transfection of cells with different amounts of TR: (A) A549 cells were transfected with different amounts TR added to 1 μg of DNA; (B) A549 cells were transfected with different amounts of TR added to 1 μg of DNA complexed with lipofectamine; (C) FB were transfected with different amounts of TR added to DNA complexed with lipofectamin; (D) SMC were transfected with different amounts of TR added to DNA complexed with lipofectamine (mean, SEM, $n > 2$). Note that transfections with DL alone correspond to 0 μg of TR (*x*-axis) and are circled.

and 2.6 mL of H_2O). The cells were washed three times with 1× PBS, and unspecific binding of the primary antibody was blocked for 1 h with 5% BSA and 5% normal goat serum in 1× PBS. Following this, the cells were washed and incubated overnight in a humid chamber with polyclonal rabbit anti-caveolin-1 primary antibody (1:400) (Santa Cruz, Santa Cruz, CA). The cells were washed and incubated for 1 h with Cy5-conjugated donkey anti-rabbit IgG secondary antibody (1:200) (Dianova, Hamburg, Germany). Then, the cells were washed and incubated for 1 h with Cy3-conjugated streptavidin (1:5000) (Dianova, Hamburg, Germany) for labeling biotin−Tat−RGD. The slides were mounted with a coverslip and analyzed by laser-scanning confocal fluorescence microscopy for TR and caveolin-1 colocalization.

Cellular Internalization of Tat−RGD. The cells were cultured, transfected, and fixed as mentioned above. Blocking and permeabilization was performed with 10% horse serum, 0.5% Tween 20, and 0.1% BSA in 1× PBS for 1 h. Permeabilization ensures that the secondary reagent (Cy3-conjugated streptavidin) enters the cells and labels the biotin−Tat−RGD, which can be analyzed by confocal microscopy for the cellular internalization of TR.

Intracellular Localization of DNA. Cells (A549 or SMC) were transfected with a FAM-labeled DNA fragment (FAM-CMV) employing that TRDL vector system and fixed at different time points with PFA. The cells were washed and blocked with 5% BSA and 5% normal goat serum in 1× PBS for 1 h. Following this, the cells were washed and incubated overnight in a humid chamber with polyclonal rabbit anti-caveolin-1 primary antibody (1:400) (Santa Cruz, Santa Cruz, CA). Then, the cells were washed and incubated for 1 h with Cy3-conjugated donkey anti-rabbit IgG secondary antibody (1:400) (Dianova, Hamburg, Germany). Afterward, the cells were incubated sequentially for 10 min with WGA-633 membrane dye (wheat germ agglutinin Alexa Fluor 663-conjugated, Molecular Probes, W-21404, 1:100) and TO-PRO-3 nuclear stain (Molecular Probes, 1:800). The cells were mounted with a coverslip and analyzed by laser-scanning confocal fluorescence microscopy for the intracellular localization of FAM-labeled DNA.

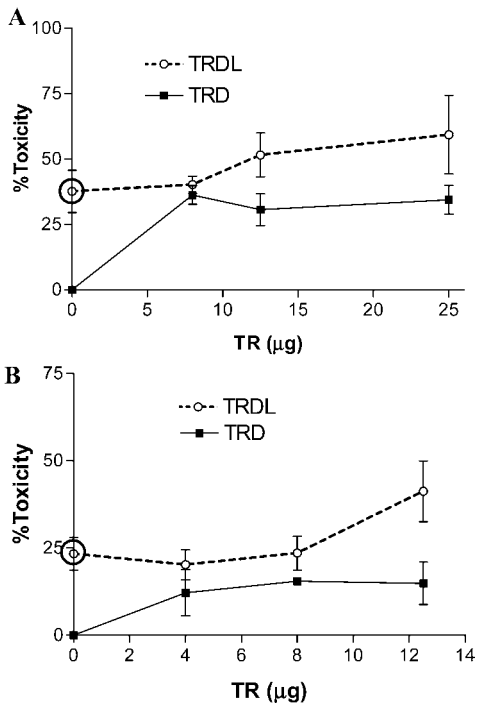

Figure 3. Measurement of cytotoxicity in (A) A549 cells and (B) FB treated with different concentrations of TR in the presence of a given amount (1 μg) of DNA (TRD) or of DNA and Lipofectamine (TRDL) (mean, SEM, $n = 3$). Note that cytotoxicities of cells transfected with DL alone correspond to 0 μg of TR (*x*-axis) and are circled.

The following laser lines were employed to detect the corresponding flurophores: FAM was detected using the 488

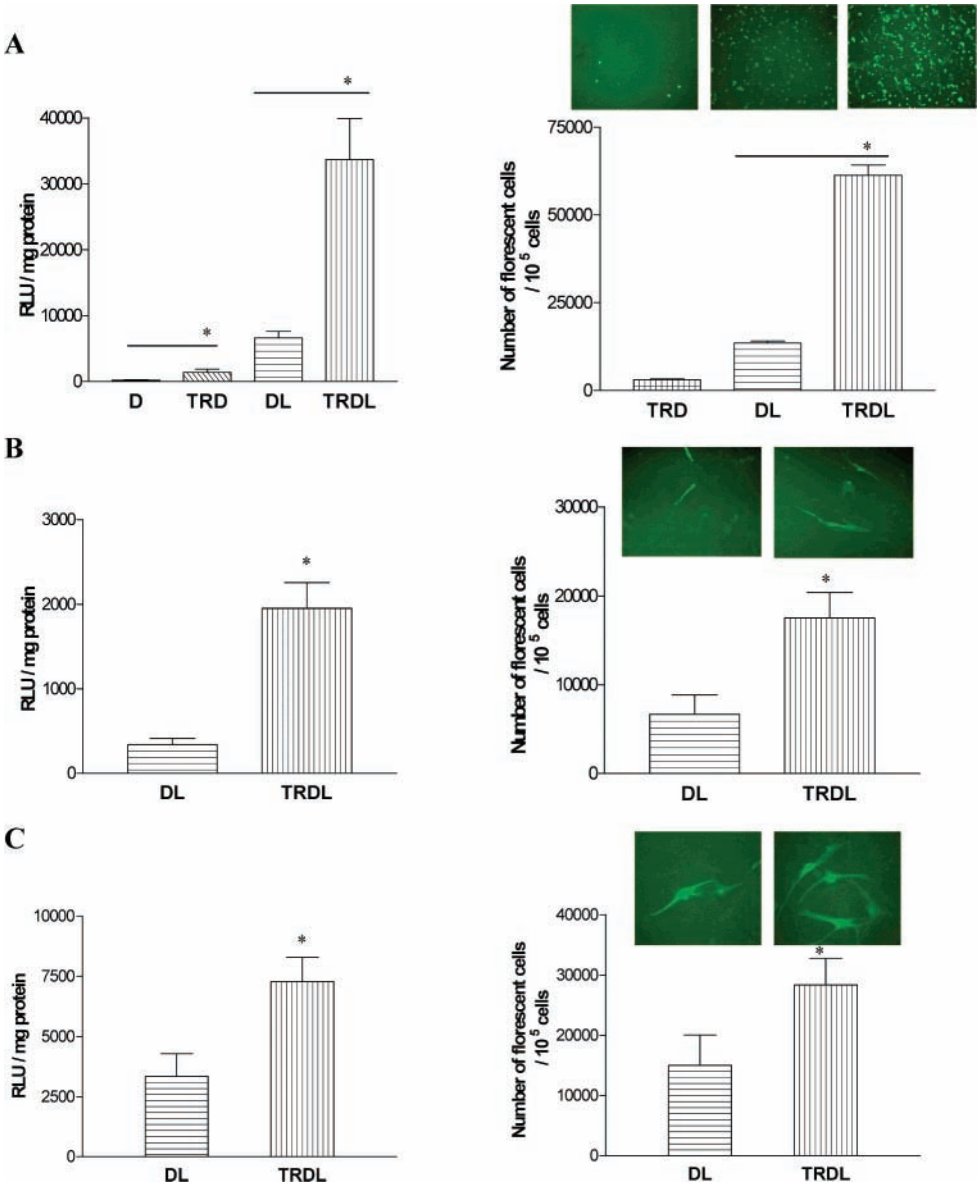

Figure 4. Summary of transgene expression levels employing different mixtures of TRD, DL, and TRDL as measured by luciferase reporter gene expression in the case of pGL3 transfection (RLU = relative light units; left, $n = 10$) or by counting the number of fluorescent cells in the case of pEGFP-N2 transfection (right, $n = 4$) in A549 (A), FB (B), and SMC (C) cells (mean, SEM, $*$ indicates $p < 0.05$, Man Whitney test).

nm laser line, Cy-3 was detected using the 543 nm laser line, and Cy-5, WGA-633, and TO-PRO-3 were detected using the 633 nm laser line, all with appropriate detection bandwidths for each fluorophore. Sequential scanning was performed to prevent bleed through into adjacent detection channels.

Gene Scan Analysis. Transfected FAM-labeled DNA fragments were recovered from cells by an extraction procedure with a PCR column purification kit (Qiagen, Hilden, Germany). The recovered samples were analyzed for their integrity (size) and quantity by capillary electrophoresis and a fluorescent detection unit (ABI Prism 310 genetic analyzer, Applied Biosystems, Weiterstadt, Germany).

RESULTS

The synthetic peptide Tat−RGD (TR) was employed for DNA transfection into different lung cells. Initially, we performed binding experiments between DNA and TR to determine an appropriate concentration ratio (Figure 1A). Binding saturated at approximately 10 μg of TR per microgram of DNA. Since the particle size is important for cellular internalization, also size measurements of TR complexed with DNA (TRD) or TR complexed with both DNA and Lipofectamine (TRDL) were performed (Figure 1B). The comparison of particle sizes of different ratios of TR and DNA is given in the presence and absence of Lipofectamine. Addition of Lipofectamine to TRD resulted in compaction of the particles, thus aiding internalization.

We next studied the effect of different TR amounts per microgram of DNA on transfection efficiency employing the luciferase reporter gene. In the case of A549 cells, we observed significant transfection efficiencies with TRD vectors (Figure 2A). Expression levels were observed to be substantially higher in the case of TRDL obtained by addition of Lipofectamine to TRD (Figure 2B).

In primary pulmonary artery cells, such as adventitial fibroblasts (FB) and smooth muscle cells (SMC), TR alone was not sufficient for DNA transfection. However, TRDL vectors significantly improved the luciferase expression levels over those of Lipofectamine standards (Figure 2C,D).

To derive an optimal TR concentration for transfection with minimally compromised cell viability, we assessed the cytotoxicitiy associated with different concentrations of TRD and

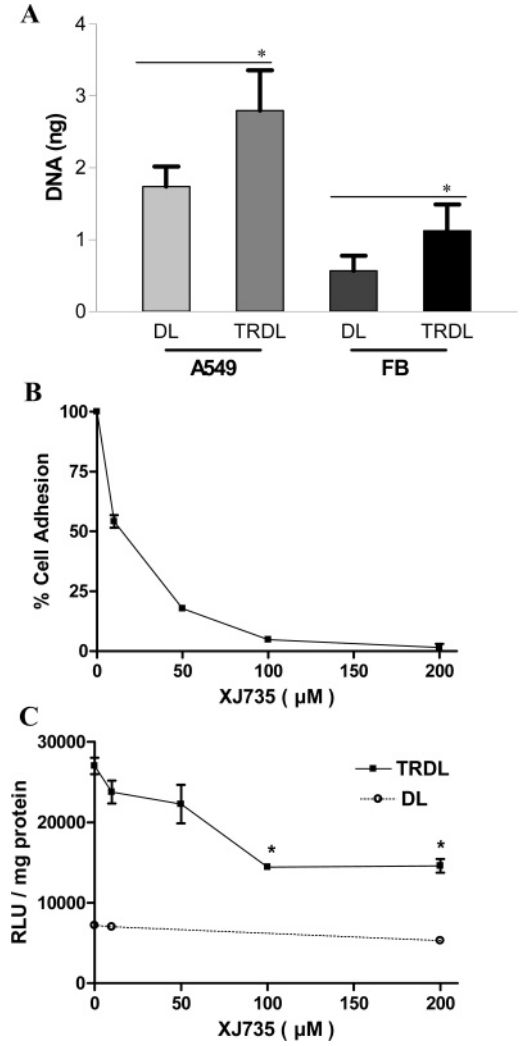

Figure 5. (A) Measurement by capillary gel electrophoresis of FAM-labeled DNA fragments recovered from transfected cells. A549 or FB cells were transfected by either DL or TRDL mixture. In cells containing TR in the transfection mixture, the cellular DNA recovery is increased over the non-TR-containing mixture, reflecting a higher DNA uptake in these cells (mean, SEM, $n = 3$, $*$ indicates $p < 0.05$, Man Whitney test). (B) Effect of XJ735 treatment on adhesion of A549 cells to fibronectin-coated plates. (C) Effect of XJ735 on transfection efficiency mediated by TRDL and DL. Cells were transfected with TRDL vectors in the presence of different concentrations of XJ735, and the luciferase reporter gene expression (RLU) was measured (mean, SEM, $n = 4$, $*$ indicates $p < 0.05$, Man Whitney test).

TRDL vectors on the A549 cell line and FB primary cells (Figure 3). Increasing amounts of TR enhanced the toxicity. Also, the toxicity was enhanced by the addition of Lipofectamine as observed when TRDL was delivered into the cells. Considering the curves of Figures 2 and 3, we estimated the optimal concentrations of TR (per microgram of DNA) to be employed in all further analysis using TRDL vectors as 12.5 μg for A549 and 4 μg for FB and SMC. The analysis of DNA transfection by TRD, DL, and TRDL is shown in comparison by measuring the reporter gene luciferase expression in cellular lysate or by counting the GFP positive cells by fluorescence microscopy (Figure 4). The improvement of transfection by addition of TR is demonstrated for A549 cells, as well as for primary FB and SMC cells. For characterization of the facilitated gene transfer, the cellular uptake of fluorescent FAM−DNA fragments was studied in A549 cells and FB transfected with either DL or TRDL (Figure 5A). These data showed that TRDL significantly enhanced cellular DNA uptake over that of the DL vector system and that the effect is more pronounced in A549 cells than in FB.

To analyze the significance of the RGD component of Tat−RGD for enhancing the affinity toward cells and thus relevance for improving the transfection efficiency, we treated A549 cells with different concentrations of XJ735, an antagonist of RGD (Figure 5B). At first, we confirmed that XJ735 could block the adhesion of A549 cells to fibronectin-coated culture dishes. Thus the expression of RGD binding integrins on the cell surface and their interaction with XJ735 were confirmed. Second, we performed transfection studies with TRDL and DL in the presence of different amounts of XJ375 and quantified it by luciferase reporter gene assay (Figure 5C). In the case of TRDL, we observed a decrease of ∼40% of luciferase expression, whereas in the case of DL no significant reduction was observed.

To explore whether the mode of internalization exploited by the TRDL vector system is linked with caveoli-mediated endocytosis, we performed laser scanning fluorescent confocal microscopic analysis by immunostaining the cells for caveolin-1 (blue) and TR (red). The cells were not permeabilized to detect only the TR localized at the membrane. In these experiments, we found a significant colocalization between caveolin and TR (pink color). The fluorescent signal of TR was visualized at different time points during transfection (Figure 6A, images a−c). The signal was initially localized on the cell membrane with subsequent time-dependent clearance of the signal from the cell membrane.

To show the time-dependent cellular internalization of TR, the cells were permeabilized and then stained with streptavidin−Cy3 (red) for intracellular tracking of TR. We observed a strong Cy3 signal at the cell periphery at 2 h, which gradually moved into the cell cytoplasm after longer incubation, resulting in a strong cytoplasmic signal after 15 h (Figure 6A, images d−f).

To examine whether DNA internalization corresponded with that of TR, the cells were transfected with a 400 bp FAM-labeled DNA fragment using the TRDL vector system, and the transfection process was examined by visualizing the uptake of FAM-labeled DNA into the cells at different time points (Figure 6B, images a−c). We employed Cy3-tagged secondary antibody for caveolin-1 in these experiments and labeled the cytoplasmic and nuclear compartments of the cell with WGA-633 and TO-PRO-3 for the membrane and nucleus, respectively. We observed a strong correlation in time between the cellular internalization of DNA and that of TR.

To demonstrate further that internalization of TRDL complexes exploits the caveolar endocytic system, we tested the effect of methyl-β-cyclodextrin (MBC), a drug that specifically disrupts the formation of caveoli without interfering with other modes of endocytosis (*14*). Cells were pretreated with 1% MBC for 30 min and transfected with TRDL complexes. MBC drastically decreased the transfection efficiency with the TRDL vector system, while that of DL remained unaffected (Figure 7), suggesting the role of caveoli in the cellular internalization of TRDL complexes.

For studying whether differences of TRDL transfection efficiencies depend on the expression of caveolin-1, we compared the expression of caveolin-1 in A549 cells and SMC cells (Figure 8). A549 cells revealed a significantly stronger caveolin-1 staining than SMC. In this experiment, we also detected that internalized FAM−DNA exhibited a much stronger signal in A549 cells than in SMC, suggesting that differences in caveolin-1 expression are a likely reason for the lower transfection efficiency observed in SMC as compared to that of A549 cells.

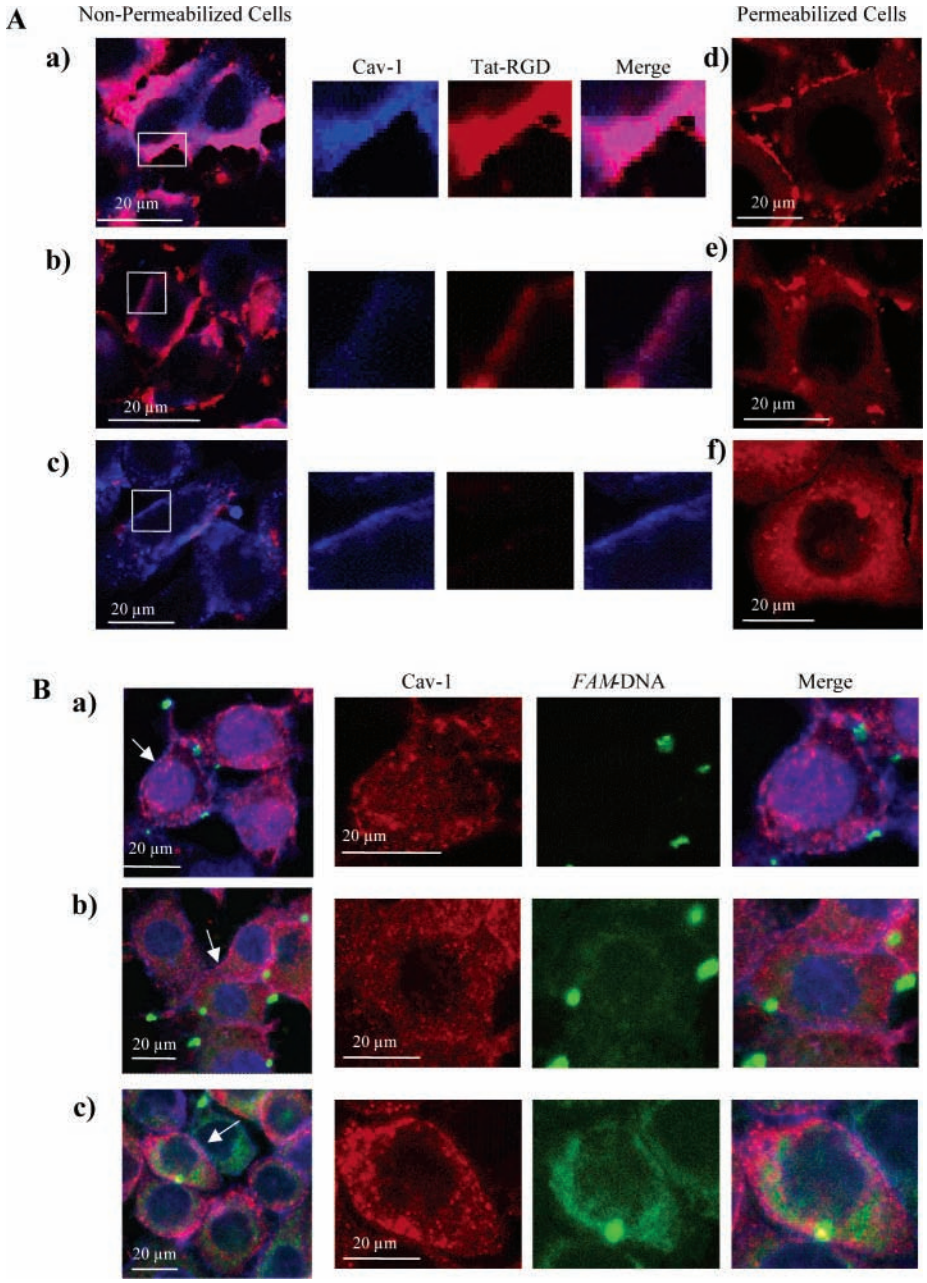

Figure 6. (A) Tat−RGD colocalization with caveolin-1 and its cellular internalization. A549 cells were transfected with a 400 bp DNA fragment using the TRDL vector system and fixed at 2 (a), 4 (b), and 15 h (c) time points, and without prior permeabilization immunostained for caveolin-1 (blue) and TR (red). We observed colocalization (merge) of TR with caveolin-1 (pink) and a time-dependent clearance of TR from the cell membrane. When cells were permeabilized and stained with streptavidin−Cy3 for biotin−TR, we observed a time-dependent internalization of TR (red) in the cytoplasmic compartment of the cells [2 (d), 4 (e), and 15 h (f)]. (B) TR-mediated DNA internalization in cellular compartments. A549 cells were transfected with a 400 bp FAM-labeled DNA fragment (400 bp, FAM) using the TRDL vector system, fixed at 2 (a), 4 (b), and 15 h (c) time points, and immunostained for caveolin-1 (red). To distinguish the cellular compartments, the cells were stained with WGA-633 and TO-PRO-3 for cell membrane and nucleus, respectively. We observed a time-dependent cellular internalization of FAM-labeled DNA, which corresponded with the internalization patterns of TR in permeabilized cells.

DISCUSSION

In this study, we have analyzed the potency and mode of transfection of pulmonary cells employing the peptide conjugate Tat−RGD (TR). HIV-1 derived Tat protein has been described to promote the delivery of proteins or nucleic acids (*1*, *2*, *4*, *8*). Here, we utilized a truncated 21-mer Tat peptide corresponding to the region between amino acid residues 43 and 60 consisting of a critical basic amino acid stretch (RKKRRQRRR) with six arginines. This domain is supposed to be involved in membrane translocation and in nuclear targeting. Particularly, it forms an amphipathic α-helical structure, which is involved in endocytosis (*9*). This Tat peptide was conjugated with a peptide sequence displaying an RGD motif containing one more arginine residue, which may further facilitate DNA binding and cellular uptake (*7*). Particularly, the RGD peptide motif has high affinity toward integrin receptors (α$V\beta3$, α$5\beta1$) expressed on cell surfaces and therefore may improve DNA binding to cells. Previous studies have proposed the role of integrin targeting as an efficient pathway for the uptake of synthetic gene delivery vehicles (*11*). Also, this motif has been described to mediate adenovirus uptake (*12*).

Since this peptide was labeled with biotin, we could perform binding studies between DNA and TR. Binding experiments demonstrated affinity between TR and DNA (TRD), which is most likely based on interaction between positively charged arginines of Tat and the DNA phosphate backbone. The data

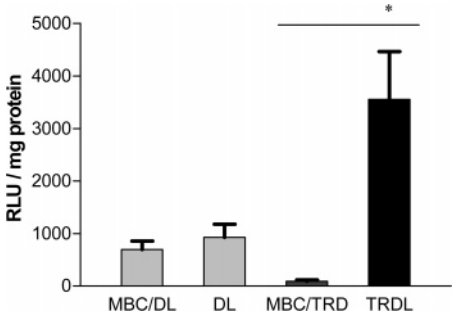

Figure 7. Effect of MBC pretreatment on TRDL uptake in A549 cells. A549 Cells were pretreated with 1% MBC for 30 min and transfected with TRDL and DL vector systems, and the luciferase reporter gene expression was measured. Cells untreated with MBC were taken as controls for both TRDL and DL transfection (mean, SEM, $n = 7$, $*$ indicates $p < 0.05$, Man Whitney test).

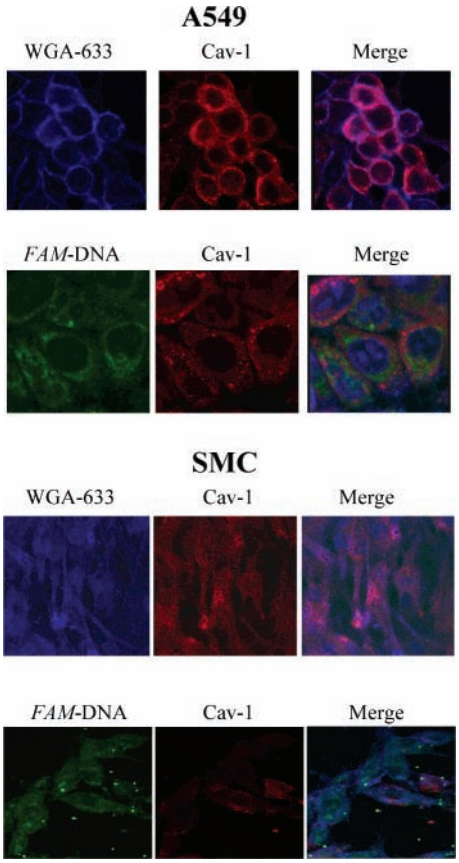

Figure 8. A549 cell line and SMC were transfected with FAM−DNA (green) employing the TRDL vector system and stained with WGA-633 (blue), TO-PRO-3 (blue), and anti-caveolin (red) for cell membrane, nucleus, and caveoli, respectively. We observed that the caveolin-1 staining at the cell membrane was strong in A549 cells and relatively weak in SMC cells (top rows). In accordance with our hypothesis that TRDL vector systems exploit caveoli-mediated internalization, we observed that FAM−DNA localization in the cellular and nuclear compartments was strong in A549 cells and relatively weak in SMC cells (bottom rows).

from these experiments suggested the most suitable concentration ratio of DNA and Tat−RGD.

Particle size measurements revealed lowering of the size of the TRD complexes upon Lipofectamine addition, which is an important feature for successful internalization of these complexes. Further, since the utility of such complexes is limited by their toxicity, we performed cytotoxicity assays to derive the optimal concentrations of TR for gene transfer in pulmonary cells.

TR was successfully applied for the improvement of DNA delivery into human pulmonary cell lines and primary cells. Addition of a complex of TR and DNA already yielded significant transgene expression levels in A549 cells. However, when TR was combined with Lipofectamine, the expression was increased 5-fold over Lipofectamine alone and ∼30-fold over TRD alone. This effect was also observed in primary SMC and FB from pulmonary artery, where transfection efficiencies were enhanced by a factor of ∼2 and ∼3, respectively, over Lipofectamine alone.

To check the role of RGD in Tat−RGD (TRDL)-mediated transfection, cells were treated with the cyclic RGD mimetic compound XJ735 (*14*). This compound is an antagonist of RGD binding to $\alpha V\beta 3$ integrins. XJ735 strongly affected the cell adhesion of A549 cells, thus revealing its interaction with A549 cells. Furthermore, treatment of cells with XJ735 caused a significant decrease in TRDL-mediated transfection efficiency. However, XJ735 had no effect on Lipofectamine-mediated transfection efficiency, which is suggested to be independent of cell surface integrins. These findings indicate the impact of the RGD motif for the cellular internalization process of Tat−RGD likely by enhancing its affinity toward the cell surface.

Biotinylation of TR allowed the monitoring of its cellular uptake. One possible mechanism to enter cells represents caveoli-dependent endocytosis. This pathway has been described for several nonenveloped viruses, some bacterial toxins, membrane constituents, and ligands (*15*). Caveoli are invaginated plasma membrane domains characterized by the presence of the integral membrane protein caveolin-1. They are also involved in many endogenous cellular processes such as cholesterol homeostasis, glycosphingolipid transport, and glycosyl-phosphatidyl-inositol anchored protein recycling (*16*). There is also evidence that HIV-1 Tat (*10*) and HIV-1 virus itself (*17*) can use caveoli for transcytosis across the endothelium. Interestingly, type 1 pneumocytes abundantly express caveolin-1 and have high numbers of caveoli. We investigated whether TRDL internalization follows a caveoli-mediated pathway. Our confocal microscopic analysis revealed colocalization of Tat−RGD and caveolin-1 in A549 cells transfected with TRDL vector systems. We also observed a time-dependent clearance of TR from the cell membrane. The cells were permeabilized to observe the cellular internalization of TR. At 2 h incubation, the TR signal was confined to the cell membrane, after 4 h, we observed moderate amounts of signal in the cytoplasm, and after 15 h incubation, we observed the maximum signal in the cytoplasm. Corresponding time-dependent internalization of FAM-labeled DNA was also observed. Thus, TR containing vectors are internalized through a slow internalization process similar to that observed with full length Tat (*10*). This slow movement is incompatible with the fast dynamics described for constitutive endocytic trafficking of clathrin-coated pits and vesicles (*18*). Slow dynamics associated with the endocytic pathway was recently demonstrated to involve a nonconstitutive and highly stable caveolin-1 positive endocytic pathway in transfected HeLa cells (*19*). Additional evidence for this mechanism and its dynamics can be found elsewhere (*20*).

To further demonstrate that TRDL complexes undergo caveoli-mediated internalization, disruption of the caveoli was performed employing the inhibitor methyl-β-cyclodextrin. This drug has been described to affect caveoli-mediated but not clathrin-mediated endocytosis (*21*, *22*). Treatment of cells with methyl-β-cyclodextrin drastically decreased the transfection efficiency of Tat−RGD. Interestingly, primary SMC, which showed less TR-dependent transfection efficiency, also revealed reduced levels of calveolin-1 expression when compared to A549 cells in immune cytochemical analysis. Therefore we

suggest a strong correlation between TR-mediated DNA internalization and the expression pattern of caveolins in these cell types.

In conclusion, the present work indicates that the Tat−RGD peptide mediates efficient gene delivery in human pulmonary cells. In particular, the combination of Tat−RGD with a standard cationic lipid based transfection reagent resulted in enhanced gene transfer. The improved DNA uptake by Tat−RGD appears to be mediated by caveoli-dependent endocytosis. Thus, Tat−RGD offers improved DNA uptake in lung cells and may also be considered for gene delivery in other transfection-resistant cell types.

ACKNOWLEDGMENT

We thank Dr. Michael Krause (Institute for Molecular Biology and Tumor Research, Microchemistry, Philipps-University, Marburg, Germany) for synthesis of the Tat−RGD fusion peptide. We thank C. Packhauser for helping with particle size measurements. We thank Prof. T. Kissel (Department of Pharmaceutics and Biopharmacy, Marburg, Germany) for useful discussions. We also thank Annette Tschuschner for technical support. This work was supported by the Deutsche Forschungsgemeinschaft: Sonderforschungsbereich SFB 547, project B9, and the Graduate Seminar (GK534) "Biological Fundamentals of Vascular Medicine" sponsoring A. Renigunta.

LITERATURE CITED

(1) Schwarze, S. R., Ho, A., Vocero-Akbani, A., and Dowdy, S. F. (1999) In vivo protein transduction: delivery of a biologically active protein into the mouse. *Science 285*, 1569−72.

(2) Fawell, S., Seery, J., Daikh, Y., Moore, C., Chen, L. L., Pepinsky, B., and Barsoum, J. (1994) Tat-mediated delivery of heterologous proteins into cells. *Proc. Natl. Acad. Sci. U.S.A. 91*, 664−8.

(3) Rudolph, C., Plank, C., Lausier, J., Schillinger, U., Muller, R. H., and Rosenecker, J. (2003) Oligomers of the arginine-rich motif of the HIV-1 TAT protein are capable of transferring plasmid DNA into cells. *J. Biol. Chem. 278*, 11411−8.

(4) Frankel, A. D., and Pabo, C. O. (1988) Cellular uptake of the tat protein from human immunodeficiency virus. *Cell 55*, 1189−93.

(5) Joliot, A., Pernelle, C., Deagostini-Bazin, H., and Prochiantz, A. (1991) Antennapedia homeobox peptide regulates neural morphogenesis. *Proc. Natl. Acad. Sci. U.S.A. 88*, 1864−8.

(6) Elliott, G., and O'Hare, P. (1999) Intercellular trafficking of VP22-GFP fusion proteins. *Gene Ther. 6*, 149−51.

(7) Futaki, S., Suzuki, T., Ohashi, W., Yagami, T., Tanaka, S., Ueda, K., and Sugiura, Y. (2001) Arginine-rich peptides. An abundant source of membrane-permeable peptides having potential as carriers for intracellular protein delivery. *J. Biol. Chem. 276*, 5836−40.

(8) Jeang, K. T., Xiao, H., and Rich, E. A. (1999) Multifaceted activities of the HIV-1 transactivator of transcription, Tat. *J. Biol. Chem. 274*, 28837−40.

(9) Vives, E., Brodin, P., and Lebleu, B. (1997) A truncated HIV-1 Tat protein basic domain rapidly translocates through the plasma membrane and accumulates in the cell nucleus. *J. Biol. Chem. 272*, 16010−7.

(10) Ferrari, A., Pellegrini, V., Arcangeli, C., Fittipaldi, A., Giacca, M., and Beltram, F. (2003) Caveolae-mediated internalization of extracellular HIV-1 tat fusion proteins visualized in real time. *Mol. Ther. 8*, 284−94.

(11) Uduehi, A., Mailhos, C., Truman, H., Thrasher, A. J., Kinnon, C., and Hart, S. L. (2003) Enhancement of integrin-mediated transfection of haematopoietic cells with a synthetic vector system. *Biotechnol. Appl. Biochem. 38*, 201−9.

(12) Albinsson, B., and Kidd, A. H. (1999) Adenovirus type 41 lacks an RGD alpha(v)-integrin binding motif on the penton base and undergoes delayed uptake in A549 cells. *Virus Res. 64*, 125−36.

(13) Rose, F., Grimminger, F., Appel, J., Heller, M., Pies, V., Weissmann, N., Fink, L., Schmidt, S., Krick, S., Camenisch, G., Gassmann, M., Seeger, W., and Hänze, J. (2002) Hypoxic pulmonary artery fibroblasts trigger proliferation of vascular smooth muscle cells: role of hypoxia-inducible transcription factors. *FASEB J. 16*, 1660−1.

(14) Hein, T. W., Platts, S. H., Waitkus-Edwaers, K. R., Kuo, L., Mousa, S. A., and Meininger, G. A. (2001) Intrgrin-binding peptides containing RGD produce coronary arteriolar dilation via cyclooxygenase activation. *Am. J. Physiol. Heart Circ. Physiol. 281* (6), H2378−84.

(15) Pelkmans, L., Kartenbeck, J., and Helenius, A. (2001) Caveolar endocytosis of simian virus 40 reveals a new two-step vesicular-transport pathway to the ER. *Nat. Cell Biol. 3*, 473−83.

(16) Ikonen, E., and Parton, R. G. (2000) Caveolins and cellular cholesterol balance. *Traffic 1*, 212−7.

(17) Campbell, S. M., Crowe, S. M., and Mak, J. (2001) Lipid rafts and HIV-1: from viral entry to assembly of progeny virions. *J. Clin. Virol. 22*, 217−27.

(18) Wacker, I., Kaether, C., Kromer, A., Migala, A., Almers, W., and Gerdes, H. H. (1997) Microtubule-dependent transport of secretory vesicles visualized in real time with a GFP-tagged secretory protein. *J. Cell. Sci. 110* (Part 13), 1453−63.

(19) Thomsen, P., Roepstorff, K., Stahlhut, M., and van Deurs, B. (2002) Caveolae are highly immobile plasma membrane microdomains, which are not involved in constitutive endocytic trafficking. *Mol. Biol. Cell 13*, 238−50.

(20) Fittipaldi, A., Ferrari, A., Zoppe, M., Arcangeli, C., Pellegrini, V., Beltram, F., and Giacca, M. (2003) Cell membrane lipid rafts mediate caveolar endocytosis of HIV-1 Tat fusion proteins. *J. Biol. Chem. 278*, 34141−9.

(21) Sieczkarski, S. B., and Whittaker, G. R. (2002) Dissecting virus entry via endocytosis. *J. Gen. Virol. 83*, 1535−45.

(22) Hansen, G. H., Pedersen, J., Niels-Christiansen, L. L., Immerdal, L., and Danielsen, E. M. (2003) Deep-apical tubules: dynamic lipid-raft microdomains in the brush-border region of enterocytes. *Biochem. J. 373*, 125−32.

BC050263O

Synthesis and Screening of a Random Dimeric Peptide Library Using the One-Bead−One-Dimer Combinatorial Approach

Saurabh Aggarwal,[†] James L. Harden,[†] and Samuel R. Denmeade[†,§,*]

Department of Chemical and Biomolecular Engineering, The Johns Hopkins University Whiting School of Engineering, and The Sidney Kimmel Comprehensive Cancer Center, The Johns Hopkins University School of Medicine (SRD), Baltimore, Maryland 21231. Received September 1, 2005; Revised Manuscript Received October 24, 2005

Large combinatorial libraries of random peptides have been used for a variety of applications that include analysis of protein−protein interactions, epitope mapping, and drug targeting. The major obstacle in screening these libraries is the loss of specific but low affinity binding peptides during washing steps. Loss of these specific binders often results in isolation of peptides that bind nonspecifically to components used in the selection process. Previously, it has been demonstrated that dimerizing or multimerizing a peptide can remarkably improve its binding kinetics by 10- to 1000-fold due to an avidity effect. To take advantage of this observation, we constructed a random library of 12 amino acid dimeric peptides on polyethylene glycol acrylamide (PEGA) beads by modifying the 'one-bead−one-compound' approach. The chemical synthesis of 100 000 peptides as dimers can be problematic due to steric and aggregation effects and the presence of many peptide sequences that are difficult to synthesize. We have designed a method, described in detail here, to minimize the problems inherent in the synthesis of a dimeric library by modifying the existing 'split and pool' synthetic method. Using this approach the dimeric library was used to isolate a series of peptides that bound selectively to epithelial cancer cells. One peptide with the amino acid sequence QMARIPKRLARH bound as a dimer to prostate cancer cells spiked into the blood but did not bind to circulating hematopoeitic cells. The monomeric form of this peptide, however, did not bind well to the same LNCaP cell line. These data demonstrate that "hits" obtained from such a 'one-bead−one-dimer' library can be used directly for the final application or used as leads for construction of second generation libraries.

INTRODUCTION

Peptides are versatile small molecules that are increasingly being used alone or as part of bioconjugates in the therapy of a variety of human diseases, including cancer, diabetes, and osteoporosis. For example, peptide analogues of the luteinizing hormone-releasing hormone (LHRH) are the mainstay of treatment for metastatic prostate cancer. Peptides derived from fragments of human proteins such as the Arg-Gly-Asp (RGD)-based motifs from extracellular matrix (ECM)(*1*), endostatin from collagen, and angiostatin from plasminogen have been tested as anticancer therapies (*2*−*4*). Targeted peptides holds special promise for cancer, because many of the antibody-based targeted drugs have been shown to have difficulty permeating into tumors (*5*, *6*). Because of their size, small peptides can be more effective in delivering a therapeutic dose deep into tumors. On this basis, peptide-cytotoxin conjugates are under development that selectively target proteases and receptors within sites of cancer (*7*−*9*). Peptides are also under study as targeted imaging agents (*10*). As an additional application, our laboratory is interested in using peptides to develop indwelling probes or ex vivo blood filtration systems that can continuously extract circulating cancer cells from blood over an appropriate diagnostic period (*11*). As an alternative approach to antibody-based cell binding, we are instead identifying small peptides that bind selectively to epithelial cells. Small peptides of 12 amino acids are easily synthesized and are not highly immunogenic. Compared to antibodies, these peptides are relatively inexpensive, stable, and easily coupled to a probe surface.

Previously it has been demonstrated that dimerizing or multimerizing a peptide ligand can improve its binding kinetics 10−1000-fold due to an avidity effect (*12*−*15*). On this basis, using the one-bead one-peptide approach we synthesized a random dimeric peptide library using a C-terminal lysine residue as a branch point on poly(ethylene glycol) acrylamide (PEGA) beads (*11*). The production of a cell-binding surface coated with peptide ligand requires that the surface of the probe be relatively inert and not adsorb proteins and/or cells nonspecifically. Therefore, for this application, poly(ethylene glycol) (*16*) was selected as the screening surface because it has been demonstrated to be one of the most effective biomaterials for coating surfaces to prevent nonspecific adsorption (*17*−*19*). In this case, the synthesis of peptides on PEGA beads, which have a PEG outer surface, mimics potential catheter surface conditions from the outset in the selection of cell-binding peptides. In this previous study, no cell binding was observed on PEGA beads when peptides were synthesized as monomers (*11*). In contrast, screening of a dimeric peptide library containing approximately 100 000 peptides yielded a series of peptide ligands that bound selectively to human cancer cells in the blood, but did not bind to circulating leukocytes (*11*).

The synthesis and screening of a novel dimeric library, to our knowledge, has not been described previously. The use of such a dimeric library in screening strategies enhances the isolation of cell and/or protein specific ligands for applications such as drug targeting, imaging, and biosensors. The goal of this current study is to provide a detailed description of the methods used to synthesize, screen, and sequence a large combinatorial dimeric peptide library with the intent that this would allow for more widespread application in the future of the 'one-bead−one-compound' combinatorial approach in the selection of peptide binding ligands.

* To whom all correspondence should be sent: Bunting Blaustein Cancer Research Building, 1650 Orleans St., Baltimore, MD 21231. Phone: 410.502.3941. Fax: 410.614.9397. E-mail: denmesa@jhmi.edu.

[†] The Johns Hopkins University Whiting School of Engineering.

[§] The Johns Hopkins University School of Medicine.

10.1021/bc0502659 CCC: $33.50 © 2006 American Chemical Society
Published on Web 02/08/2006

EXPERIMENTAL PROCEDURES

Materials. Poly(ethylene glycol) amide (PEGA) beads were from Polymer Labs (Amherst, MA). Fmoc-blocked amino acids, 1-hydroxybenzotriazole (HOBT), and 1,3-diisopropylcarbodiimide (DIC) were purchased from Advanced ChemTech, (Louisville, KY). *N*,*N*-Diisopropylethylamine (DIEPA), *N*-methyl-2-pyrrolidinone (NMP), dimethylformamide (DMF), and methylene chloride (DCM) were from Sigma. The human prostate cancer cell line LNCaP was obtained from ATCC (Manassas, VA). Cell Tracker Green and Orange were from Invitrogen (Rockville, MD). Unless otherwise specified, all other reagents were from Sigma (St. Louis, MO).

Synthesis of AG-73 Peptide on PEGA Beads. Heparin binding peptide sequence from laminin AG73 (RKRLQVQLSIRT)(*20*) was synthesized on Fmoc-Gly-loaded PEGA beads using an automated peptide synthesizer (PS-3, Rainin, Tucson, AZ). Dimeric peptides were synthesized by precoupling Fmoc-Lys(Fmoc)-OH to Gly-PEGA followed by solid-phase synthesis of the remaining peptide.

Preparation of PEGA Beads and Fmoc Amino Acids. PEGA beads with lower substitution level of 0.2 mmol/g were used to avoid any aggregation effect from higher loading. Five grams of PEGA beads [supplied beads are 10.7% w/w (i.e. 5 *g* = 46.7 g of suspension)] were washed with DMF. For the first overnight coupling, 1.5 mmol of Fmoc-Lys(Fmoc)-OH (0.88 g), 1.5 mmol of HOBT (0.208 g), and 1.69 mmoles of DIC (261 μL), and 6 mL of 10% DEIPA were added to 10 mL of DMF and activated for 30 min. Activated complex was added to the beads and allowed to react overnight at room temperature. Completion of coupling was verified by Kaiser test with a small subset of beads (*21*). Repeated couplings with 2-fold molar excess of the above-mentioned reagents were performed. The second coupling was done for 2 h at room temperature. Completion of coupling was again verified by Kaiser test. Beads were washed 5−6 times with DCM and DMF and stored at 4 °C in DMF until later use.

Fmoc was removed from preloaded Lys in the presence of 20% piperidine in NMP. Deprotection was repeated four times for 5 min each. After extensive washing, beads were split into 19 pools for coupling of all natural amino acids with the exception of cysteine. Pools were divided to have 50 μmol of total peptide in each reaction vessel. A combinatorial peptide synthesis platform from Advanced ChemTech was used for the split and pool couplings. This apparatus is designed specifically to generate split and mix peptide libraries. The library was always pooled in a polypropylene vessel.

Concentrated stock solutions of all 19 Fmoc amino acids with HOBT were prepared and stored at −20 °C. Fmoc amino acids (0.5 M) with HOBT (0.49 M) stocks were prepared in DMF (except for Fmoc-phenylalanine which was prepared in NMP).

Coupling of Fmoc Amino Acids To Generate 12-mer Library. Double coupling was done for all Fmoc amino acids. For the first coupling, 4× molar excess i.e., 200 μmol of Fmoc amino acid, and HOBT (400 μL of 0.5 M stock) and 50 μL of DIC were allowed to react for 45 min at room temp and then added to 19 reaction vessels. Beads were mixed for 1 min with the activated fmoc amino acids. DIEPA (0.5 mL of 10% solution) was added, and the reaction was allowed to continue for 2−4 h. After this coupling, the beads were washed extensively with NMP. Coupling was repeated for 30 min with 2× molar excess of the activated Fmoc amino acids. Beads were again washed with DMF. A final wash was done with methanol. A small number of beads from all 19 vessels were taken for the Kaiser test. Deprotection was done twice with 20% piperidine in NMP for 30 min each. Beads were washed extensively and later pooled into a beaker with methanol. Beads were stored at −20 °C till later use.

Before the removal of the final N-terminal Fmoc, the library was acetylated with a 1:3 dilution of acetic anhydride in 10% DIEPA in NMP. Acetylation was done for 30 min. Completion of reaction was confirmed by the Kaiser test. The final Fmoc was removed as mentioned above. After 8−9× volume wash with NMP and DCM the library was stored at −20 °C till later use.

The library was washed with methanol and partially dried under an aspiration setup. Beads were suspended in 20 mL of Reagent K (TFA:H_2O:thioanisole:ethanedithiol:phenol 85:5:5:2.5:2.5). This Reagent K solution was aspirated after 10 min, and the beads were suspended in another 20 mL. Deprotection was done for 3 h with gentle shaking. Beads were washed 10 times with NMP and DCM and finally stored in methanol at −20 °C.

Dimeric Library Screening for Cell Binding. An amount of 100 000 beads suspended in methanol were washed three times with water. Beads were washed and equilibrated in PBS and finally suspended in RPMI 1640 Media containing 10% fetal calf serum (Invitrogen, Rockville, MD). Beads were incubated with 10% serum containing media for 1 h at room temperature. LNCaP cells were removed from culture flasks with trypsin/EDTA, washed and re-suspended in RPMI 1640. Cells were incubated with Cell Tracker orange (10 μM for 30 min at 37 °C). To remove excess dye, cells were pelleted and resuspended in 10% serum containing media at a final density of 5 million cells/ml. The cell suspension was mixed with the beads and incubated at 37 °C with gentle shaking for 30−40 min. Beads were gently washed with Hanks Balanced Salt Solution (HBSS) and fixed for visualization with 80% Methanol in dH_2O. After fixation, the bead pool was evaluated under a fluorescent microscope equipped with the appropriate filter set for either FITC or rhodamine.

Isolation and Preparation of Beads for Sequencing. Single positive beads containing fluorescently tagged cells were identified using a fluorescent microscope under 2.5× objective magnification and removed manually with a 200 μL pipetter using pipet tips in which the last third of the tip had been removed with a razor blade. Selected beads were washed with water and stripped of cells with excess 8 M urea or 6 M guanidine HCl for 24−48 h with intense shaking. Urea or guanidine HCl was removed by 4−5 washes with water. A dissecting microscope was used to confirm that the beads were not lost during washing. Single beads suspended in water were sent for sequencing to University of Arizona Peptide Sequencing Core.

Sequencing of Single Beads with Edman Degradation. Peptide sequencing was completed by Wallace Clark at the University of Arizona using an Applied Biosystem 477A Protein/Peptide sequencer (Edman chemistry) interfaced with a 120A HPLC (C-18 PTH column, reverse-phase chromatography) analyzer to determine phenylthiohydantoin (PTH) amino acids. One sample bead was analyzed per sequence by placing onto a glass fiber filter, which was then assembled within a quartz cylinder and sequenced.

RESULTS

Dimerization Enhances Cell Binding. AG-73 (RKRLQVQLSIRT) is a heparin-binding peptide sequence derived from laminin that has previously been demonstrated to support cell attachment. The AG-73 peptide was synthesized on the PEGA beads as both a monomer and a dimer. Both types of beads were blocked with 10% serum containing media and then incubated with Cell Tracker Green labeled LNCaP cells and compared for the degree of cell binding. After 30 min incubation, excess cells were washed, and beads were fixed and visualized under a fluorescence microscope. No cells bound to

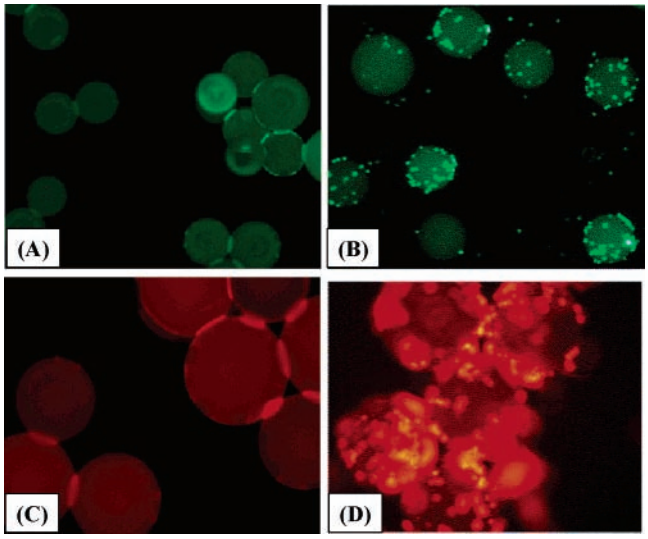

Figure 1. LNCaP cell binding to monomeric and dimeric peptides on PEGA beads. (a) Binding of Cell Tracker Green loaded cells to monomeric AG-73 (10× objective); (b) binding to dimeric AG-73 (10× objective); (c) binding of Cell Tracker Orange labeled cells to monomeric QMARIPKRLARH (20× objective); (d) dimeric QMARIP-KRLARH peptide (20× objective).

monomeric AG-73-containing beads, (Figure 1a). In contrast, LNCaP cells bound readily to the dimeric form of AG-73 (Figure 1b). These results support previous findings that dimeric peptides have enhanced cell binding capabilities due to an avidity effect.

Substitution Level of PEGA Beads with Fmoc-Lys (Fmoc)-OH Affects Synthesis. While these results with the AG-73 peptide demonstrated the superior binding characteristics of the dimeric compared to the monomeric peptide, the AG-73 peptide was initially selected solely for its ability to bind to a target antigen. Our goal in these studies was to identify peptides that can bind selectively to circulating epithelial cancer cells while not binding to highly abundant circulating leukocytes. Therefore, we opted to use the combinatorial-based peptide library approach to identify peptides meeting these two characteristics. As proof of concept, a strategy was developed to synthesize a library of dimeric peptides in which each "arm" of the peptide consisted of 12 positions of randomized to one of 19 amino acids (i.e. cysteine omitted) connected by a lysine linker. On this basis a library of $\sim 10^5$ peptides out of a total of 19^{12} (i.e. 2.2×10^{15}) possible members was generated and screened for selective epithelial cancer cell binding.

The steps used to synthesize this dimeric library are outlined in Figure 2. The synthesis of dimeric library of 12-mer peptides can be limiting for a fraction of a library because of steric hindrance of bulky side functional groups and bulky protection agents. Standard substitution levels of 0.4−0.5 mmol/g used in synthesis of a test dimeric peptides (e.g. Wang resin) markedly decreased peptide yield, Figure 3a. To minimize such a steric effect, PEGA beads with a lower substitution level of 0.2 mmol/ml were utilized. To produce a branched peptide, Fmoc-Lys-Fmoc-OH was coupled to the low substitution PEGA. Coupling was confirmed to be positive by a Kaiser test before proceeding with synthesis of the library using the two amino groups of deprotected lysine. The use of the lower substitution PEGA beads enhanced the yield of the test peptide and minimized incomplete coupling observed with the higher substitution PEGA, Figure 3b.

Quality Control of Library Synthesis with the Kaiser Test. The large scale manual nature of this procedure makes the syntheses liable to error, and hence it proved critical to check all 19 reaction vessels for completion of coupling (*21*). Although the Kaiser test is a qualitative test and will not be able to detect rare and partial incomplete couplings, it was, in general useful to rapidly confirm overall coupling efficiency. Subsequent coupling of amino acids were done twice and were checked for completion by the Kaiser test. In some cases, the couplings were repeated till a negative Kaiser test was confirmed.

Final Capping of Library before Removal of Terminal Fmoc. The sequencing of individual selected beads using Edman degradation depends on the completion of coupling after each round. In such a combinatorial synthesis of a large number of peptides there are some peptide sequences that contain difficult coupling steps that can lead to some percentage of partially synthesized peptide on an individual bead. These incomplete peptides can complicate interpretation of sequencing results and can make it difficult to determine the full sequence of the actual peptide, Figure 4a. Acetylating the amino terminal amine of any incomplete peptides using acetic anhydride can help to resolve this problem. For best results the capping should be done after each coupling. However, we determined that capping the terminal amine was sufficient and gave enough signal upon sequencing to identify the peptide sequence, Figure 4b. Capping was accomplished by acetylating the library with 1: 3 dilution of acetic anhydride in 10% DIEPA in NMP for 30 min prior to the removal of final N-terminal Fmoc of the full length peptide.

Screening the Library for Binding to Cells. The dimeric library on low substitution PEGA beads was blocked and incubated with LNCaP prostate cancer cells preloaded with Cell Tracker Orange. Cell Tracker Orange was used instead of the Cell Tracker Green used to screen the AG-73 peptide because the Orange dye provided better signal-to-noise and markedly less autofluorescence. This made the few positive beads in a field of thousands of negative beads easier to rapidly visualize and select. An amount of 100 000 beads was screened and, of these, approximately 100 cell-coated beads (i.e. "hits") were observed. The remaining 99.9% of the beads were totally negative for cell binding. The 100 positive beads were difficult to grade because each of them was highly coated with cells. Without a bead sorter these beads were picked manually based on the relative number of bound cells under a fluorescence microscope. On this basis, 10 beads were picked and subsequently sequenced by Edman degradation. The amount of peptide that can be obtained from a single PEGA bead with 0.2 mmol/mL substitution on average is ~40 pmol. This limits the number of analytical techniques which can be used for determining the sequence.

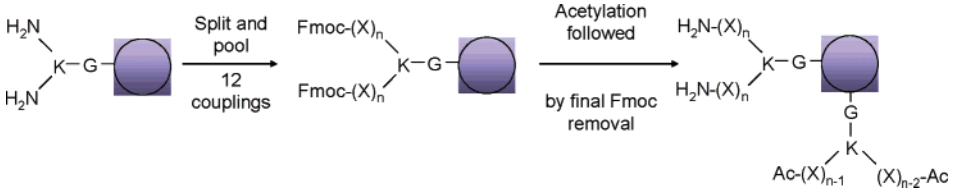

Figure 2. Schematic representation of random peptide library synthesized by 'split and mix' method where each bead contains multiple copies of a unique 12 amino acid peptide. One of 19 defined amino acids (i.e. cystein omitted) was added during each step of synthesis followed by mixing and then splitting into 19 separate flasks prior to addition of next set of defined amino acids. The scheme illustrates the utility of capping incompletely synthesized peptides with acetic anhydride prior to the removal of the final Fmoc protecting group on the N-terminal amine.

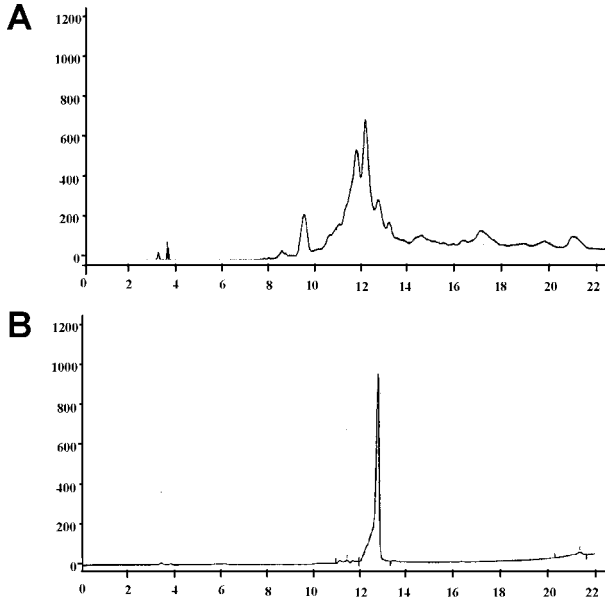

Figure 3. Reversed phase HPLC C_{18} chromatograms of dimeric peptide $(QMARIPKRLARH)_2KG$ synthesized on glycine Wang resin. (a) 0.4 mmol/g substitution level yields broad multiple peaks indicating mixture of peptides (b) 0.2 mmole/g substitution level yields narrow discrete peak consistent with high yield of single peptide.

Selected peptide sequences were synthesized again as either a monomer or a dimer on PEGA beads and rescreened for binding to different cell lines. LNCaP cells did not bind to resynthesized monomeric peptide beads to any significant degree, Figure 1c. In contrast, all of the dimeric versions of the peptides selected from the screen bound the LNCaP cells, Figure 1d. Additional analysis demonstrated that a subset of these selected peptide sequences bound only malignant epithelial cancer cells but not leukocytes.

DISCUSSION

Peptides that bind selectively to a specific cell type or protein have been identified from large combinatorial libraries of peptides. Such libraries can be either biologically synthesized as phage display libraries ($\sim 10^9$ different peptides) (*22*) or they can be chemically synthesized as the 'one-bead−one-peptide' libraries ($\sim 10^5-10^6$ different peptides) (*23*). Phage display libraries are widely used and have been employed to successfully isolate peptide ligands that bind to purified protein targets such as erythropoietin (EPO)(*12*), thrombopoetin (TPO) (*15*), and fibroblast growth factor (FGF) (*24*). However, the selection of cell-binding peptides from phage display libraries screened on whole cells has been problematic (*25*, *26*). A phage display library has the limitation of displaying only five copies of monomeric peptides on the pIII coat protein per individual phage. Initial screens of phage libraries typically yield peptides with low binding affinities and rapid off rates (on the order of few minutes). The fast dissociation of these low-affinity, but cell-type specific, binding peptides often results in isolation of more nonspecific than specific ones binding phage (*26*). To address the problem of low affinities, Zwick et al. (*27*) developed a method to make a phage display library of homodimeric peptides. However, as described by Zwick et al., the construction of this homodimeric phage library was complicated and would not be applicable for widespread use.

Synthetic peptide libraries have a number of unique attributes when compared to phage libraries. Such libraries allow for the incorporation of D-amino acids as well as unnatural amino acids which is not possible using phage display. In contrast to phage libraries, thousands to millions of copies of a unique peptide sequence can be displayed on the surface of a synthetic bead.

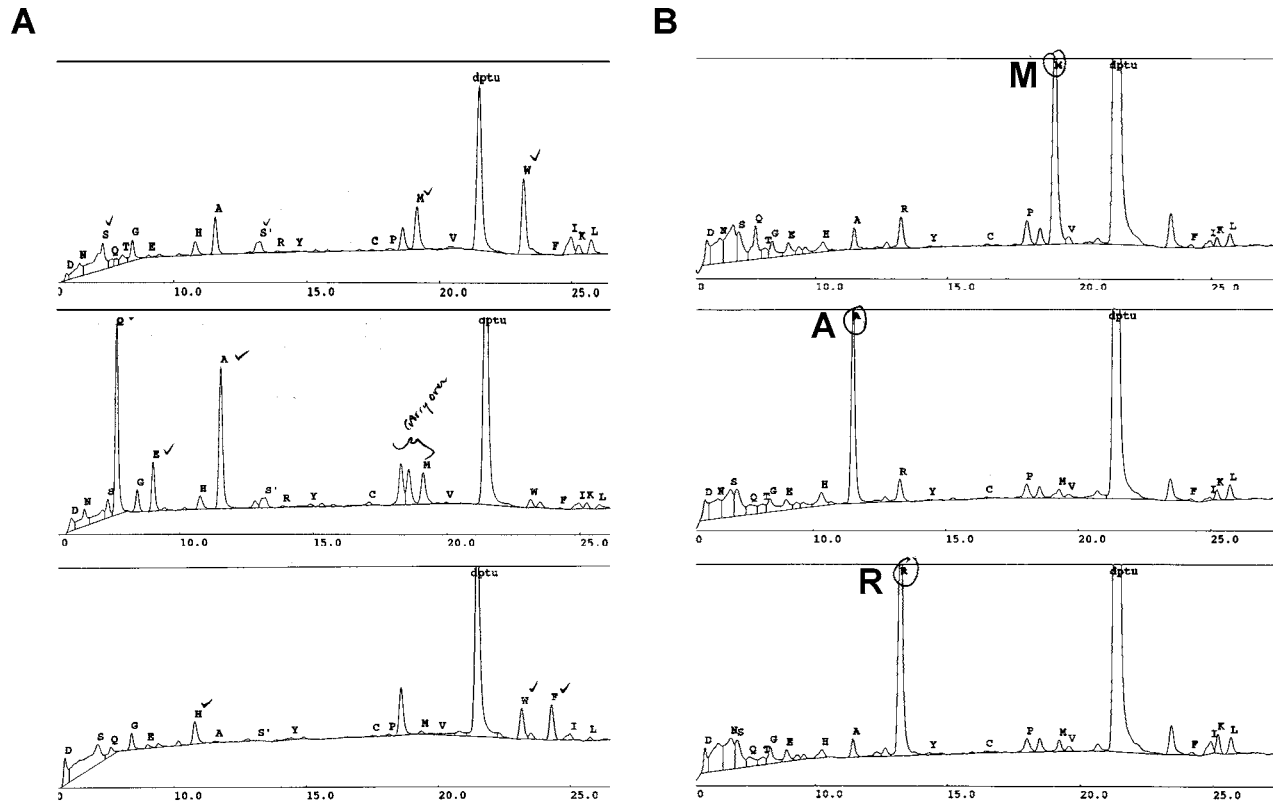

Figure 4. Sample chromatograms for three positions of Edman sequencing of a dimeric peptide on 0.2 mmol/g PEGA beads following (a) synthesis without final capping and (b) synthesis with a final capping. Without capping, sequencing reveals multiple amino acid peaks for each position, whereas with capping, distinct single peaks are observed.

Thus, bead-based libraries seem particularly suited for cell capture applications because the beads can provide multiple binding sites across the cell surface. However, since the first report describing this combinatorial method in 1991, there have been few reports on the use of such libraries for selection of cell binding ligands. The technical expertise and sophistication required in implementing the protocol for synthesis and screening such libraries, particularly those with cyclic peptides, appears to have limited the application of this screening method to only a few laboratories. In addition, like phage display, screening of bead-based libraries often yields low affinity peptides or nonspecific binders. Proteins for which peptides are not the natural ligands typically display low affinity interactions (*28*), and this leads to fast dissociation kinetics with k_{off} of the order of few minutes (*26*). Many of these specific but low affinity binders are lost during multiple washing steps involved in the screening process.

A number of studies have now demonstrated that dimerizing or multimerizing a peptide ligand can improve its binding kinetics due to an avidity effect. For example, Wrighton et al. had demonstrated that affinity for peptides binding to the erythropoietin receptor could be increased 100-fold when peptides were synthesized in a dimeric form (*12*). Previously a dimeric version of an RGD integrin-binding peptide was shown to have enhanced binding characteristics and nanomolar affinity. Dimeric RGD peptide has also been used by many groups for targeting drugs and for imaging applications (*29*). Previously, Terskikh et al. demonstrated that the affinity of a peptide isolated from phage display screening could be increased 200 000-fold by making a pentamer (i.e. "peptabody") using the pentamerization domain of a cartilage oligomeric protein (*13*). In our own studies we have demonstrated that incubation of biotinylated peptides with avidin forms a tetrameric species with enhanced binding characteristics compared to monomeric peptide (*11*).

To demonstrate the utility of screening a dimeric peptide library, a strategy was developed to synthesize a library of dimeric peptides in which each "arm" of the peptide consisted of 12 positions of randomized to one of 19 amino acids (i.e. cysteine omitted) connected by a lysine linker. On this basis a library of $\sim 10^5$ peptides out of a total of 19^{12} (i.e. 2.2×10^{15}) possible members was generated and screened for selective epithelial cancer cell binding. This library represents only a small fraction of potential peptide sequences. However, the use of the dimeric library can increase the chance of obtaining "hits" in the first round of screening. These "hits" can then later be optimized by synthesizing a second random library in which different positions in the original dimeric "hit" can be modified to evaluate the effect of modification on overall binding. This second round of synthesis and screening, based on the QMARIPKRLARH peptide, is currently underway in our laboratory

The solid-phase "split and mix" method used to synthesize this dimeric library was similar in many ways to previously published methods for synthesizing monomeric libraries. However, to optimize both the synthesis and identification of individual dimeric peptides in the library, a few modifications were made to the standard methodologies. First, synthesis of a test dimeric peptide $(QMARIPKRLARH)_2KG$ on standard substitution resins (0.4−0.5 mmol/g) yielded a mixture of peptides on an individual bead. This incomplete coupling of amino acids was due, most likely, to intermolecular steric hindrance of bulky side functional groups and bulky protection agents. Synthesis of the test peptide on resin with a lower substitution level of 0.2 mmol/g minimized such steric effects and resulted in higher yields of the dimeric test peptide. Additionally, with the use of lower substitution resin in the production of the dimeric library, the majority (i.e. >90%) of the selected beads from the screen yielded a complete 12 amino acid peptide sequence. However, even with this lower substitution resin, some of the selected dimeric peptides were difficult to resynthesize in large quantities in high yield again due to sequence-dependent intramolecular steric hindrance.

A second important modification to the standard screening methodology was the use of capping by acetylation of the amino terminus of incompletely synthesized peptides. This capping step is not always performed in the standard synthesis of monomeric libraries. In this case, however, the more complex nature of the dimeric peptide results in a higher percentage of incomplete couplings on an individual resin bead. Capping of incomplete peptides before removal of the final Fmoc group proved critical to the elucidation of the peptide sequence. Without capping, mixtures of amino acids were frequently observed after each round of Edman degradation.

In this study we provide further evidence demonstrating enhanced binding characteristics of dimeric peptides compared to monomers. However, unlike other reports in which the monomeric peptide sequence was first selected from a random pool and then dimerized, in this study we have directly screened a random dimeric peptide library. The use of this dimeric library improves chances of selecting binding peptides that might otherwise not been identified from a monomeric library screen. In fact, in each case, the monomeric version of the dimeric peptide selected in this screen did not bind to cells to any significant degree. Studies are underway in our laboratory to identify the cognate protein receptor for the $QMARIPKRLARH)_2KG$ peptide. The fact that the dimeric peptide binds better than the monomeric version suggests that the cognate receptor itself may be a dimeric protein. In this regard, Wrighton et al. synthesized a dimeric version of a 20 amino acid peptide using a single lysine as a branch point and demonstrated that this dimeric peptide had 100-fold increased affinity for the erythropoietin receptor compared to the monomeric peptide. The authors of this study concluded that the proposed mechanism of increased potency of the dimer over the monomer was that the dimeric peptide was able to span the cleft and interact with both molecules of the EPOR extracellular domain. This conclusion was based on the structure of a cocrystal of the EPOR binding peptide and the extracellular domain of the EPOR in which a noncovalent peptide dimer is seen spanning the cleft between two molecules of the EPOR extracellular domain (*30*).

On the basis of these results, therefore, we conclude that synthetic dimeric peptide libraries should be considered in the future for a variety of screening applications. We hope that the detailed methodologies described here can serve as a reference to aid other investigators interested in using this powerful combinatorial approach in peptide screening applications.

ACKNOWLEDGMENT

The authors acknowledge Jacqueline Robinson for excellent assistance in the preparation of the manuscript. They also acknowledge Mr. Wallace Clark from the University of Arizona Peptide Sequencing Facility for expertise in sequencing peptides. This work was supported by funding from Alexander and Margaret Stewart Trust to S.R.D. and partial support from the NASA Human Exploration and Development of Space program NAG 9-1345 to J.L.H.

LITERATURE CITED

(1) Aumailley, M., Gurrath, M., Muller, G., Calvete, J., Timpl, R., and Kessler, H. (1991) Arg-Gly-Asp constrained within cyclic pentapeptides. Strong and selective inhibitors of cell adhesion to vitronectin and laminin fragment P1. *FEBS Lett. 291*, 50−4.

(2) O'Reilly, M. S., Boehm, T., Shing, Y., Fukai, N., Vasios, G., Lane, W. S., Flynn, E., Birkhead, J. R., Olsen, B. R., and Folkman, J. (1997) Endostatin: an endogenous inhibitor of angiogenesis and tumor growth. *Cell 88*, 277−85.
(3) Folkman, J. (1996) Fighting cancer by attacking its blood supply. *Sci. Am. 275*, 150−4.
(4) Mendoza, F. J., Espino, P. S., Cann, K. L., Bristow, N., McCrea, K., and Los, M. (2005) Antitumor chemotherapy utilizing peptide-based approaches−apoptotic pathways, kinases, and proteasome as targets. *Arch. Immunol. Ther Exp (Warsz) 53*, 47−60.
(5) Christiansen, J., and Rajasekaran, A. K. (2004) Biological impediments to monoclonal antibody-based cancer immunotherapy. *Mol. Cancer Ther. 3*, 1493−501.
(6) Aina, O. H., Sroka, T. C., Chen, M. L., and Lam, K. S. (2002) Therapeutic cancer targeting peptides. *Biopolymers 66*, 184−99.
(7) Denmeade, S. R., Nagy, A., Gao, J., Lilja, H., Schally, A. V., and Isaacs, J. T. (1998) Enzymatic activation of a doxorubicin-peptide prodrug by prostate-specific antigen. *Cancer Res. 58*, 2537−40.
(8) Denmeade, S. R., Jakobsen, C. M., Janssen, S., Khan, S. R., Garrett, E. S., Lilja, H., Christensen, S. B., and Isaacs, J. T. (2003) Prostate-specific antigen-activated thapsigargin prodrug as targeted therapy for prostate cancer. *J. Natl. Cancer Inst. 95*, 990−1000.
(9) Schally, A. V., and Nagy, A. (2003) New approaches to treatment of various cancers based on cytotoxic analogues of LHRH, somatostatin and bombesin. *Life Sci. 72*, 2305−20.
(10) Chen, X., Conti, P. S., and Moats, R. A. (2004) In vivo near-infrared fluorescence imaging of integrin alphavbeta3 in brain tumor xenografts. *Cancer Res. 64*, 8009−14.
(11) Aggarwal, S., Janssen, S., Wadkins, R. M., Harden, J. L., and Denmeade, S. R. (2005) A combinatorial approach to the selective capture of circulating malignant epithelial cells by peptide ligands. *Biomaterials 26*, 6077−86.
(12) Wrighton, N. C., Farrell, F. X., Chang, R., Kashyap, A. K., Barbone, F. P., Mulcahy, L. S., Johnson, D. L., Barrett, R. W., Jolliffe, L. K., and Dower, W. J. (1996) Small peptides as potent mimetics of the protein hormone erythropoietin. *Science 273*, 458−64.
(13) Terskikh, A. V., Le Doussal, J. M., Crameri, R., Fisch, I., Mach, J. P., and Kajava, A. V. (1997) "Peptabody": a new type of high avidity binding protein. *Proc. Natl. Acad. Sci. U.S.A. 94*, 1663−8.
(14) Janssen, M., Oyen, W. J., Massuger, L. F., Frielink, C., Dijkgraaf, I., Edwards, D. S., Radjopadhye, M., Corstens, F. H., and Boerman, O. C. (2002) Comparison of a monomeric and dimeric radiolabeled RGD-peptide for tumor targeting. *Cancer Biother. Radiopharm. 17*, 641−6.
(15) Cwirla, S. E., Balasubramanian, P., Duffin, D. J., Wagstrom, C. R., Gates, C. M., Singer, S. C., Davis, A. M., Tansik, R. L., Mattheakis, L. C., Boytos, C. M., Schatz, P. J., Baccanari, D. P., Wrighton, N. C., Barrett, R. W., and Dower, W. J. (1997) Peptide agonist of the thrombopoietin receptor as potent as the natural cytokine. *Science 276*, 1696−9.
(16) Pegram, M. D., Pietras, R., Bajamonde, A., Klein, P., and Fyfe, G. (2005) Targeted therapy: wave of the future. *J. Clin. Oncol. 23*, 1776−81.
(17) Harris, J. M., and Chess, R. B. (2003) Effect of pegylation on pharmaceuticals. *Nat. Rev. Drug Discovery 2*, 214−21.
(18) Ratner, B. D., and Bryant, S. J. (2004) Biomaterials: where we have been and where we are going. *Annu. Rev. Biomed. Eng. 6*, 41−75.
(19) Bures, P., Huang, Y., Oral, E., and Peppas, N. A. (2001) Surface modifications and molecular imprinting of polymers in medical and pharmaceutical applications. *J Controlled Release 72*, 25−33.
(20) Nomizu, M., Kim, W. H., Yamamura, K., Utani, A., Song, S. Y., Otaka, A., Roller, P. P., Kleinman, H. K., and Yamada, Y. (1995) Identification of cell binding sites in the laminin alpha 1 chain carboxyl-terminal globular domain by systematic screening of synthetic peptides. *J. Biol. Chem. 270*, 20583−90.
(21) Kaiser, E., Colescott, R. L., Bossinger, C. D., and Cook, P. I. (1970) Color test for detection of free terminal amino groups in the solid-phase synthesis of peptides. *Anal.Biochem. 34*, 595−8.
(22) Smith, G. P., and Petrenko, V. A. (1997) Phage Display. *Chem Rev 97*, 391−410.
(23) Lam, K. S., Salmon, S. E., Hersh, E. M., Hruby, V. J., Kazmierski, W. M., and Knapp, R. J. (1991) A new type of synthetic peptide library for identifying ligand-binding activity. *Nature 354*, 82−4.
(24) Ballinger, M. D., Shyamala, V., Forrest, L. D., Deuter-Reinhard, M., Doyle, L. V., Wang, J. X., Panganiban-Lustan, L., Stratton, J. R., Apell, G., Winter, J. A., Doyle, M. V., Rosenberg, S., and Kavanaugh, W. M. (1999) Semirational design of a potent, artificial agonist of fibroblast growth factor receptors. *Nat. Biotechnol. 17*, 1199−204.
(25) Mori, T. (2004) Cancer-specific ligands identified from screening of peptide-display libraries. *Curr. Pharm. Des. 10*, 2335−43.
(26) Giordano, R. J., Cardo-Vila, M., Lahdenranta, J., Pasqualini, R., and Arap, W. (2001) Biopanning and rapid analysis of selective interactive ligands. *Nat. Med. 7*, 1249−53.
(27) Zwick, M. B., Shen, J., and Scott, J. K. (2000) Homodimeric peptides displayed by the major coat protein of filamentous phage. *J. Mol. Biol. 300*, 307−20.
(28) Menendez, A., and Scott, J. K. (2005) The nature of target-unrelated peptides recovered in the screening of phage-displayed random peptide libraries with antibodies. *Anal.Biochem 336*, 145−57.
(29) Chen, X., Sievers, E., Hou, Y., Park, R., Tohme, M., Bart, R., Bremner, R., Bading, J. R., and Conti, P. S. (2005) Integrin alpha v beta 3-targeted imaging of lung cancer. *Neoplasia 7*, 271−9.
(30) Livnah O, Stura EA, Johnson DL, Middleton SA, Mulcahy LS, Wrighton NC, Dower WJ, Jolliffe LK, Wilson IA. (1996) Functional mimicry of a protein hormone by a peptide agonist: the EPO receptor complex at 2.8 A. *Science 273*, 464−71.

BC0502659

Linear and Branched Bicin Linkers for Releasable PEGylation of Macromolecules: Controlled Release in Vivo and in Vitro from Mono- and Multi-PEGylated Proteins

Hong Zhao, Karen Yang, Anthony Martinez, Amartya Basu, Ramesh Chintala, Hsien-Ching Liu, Ahsen Janjua, Maoliang Wang, and David Filpula*

Enzon Pharmaceuticals, Inc., 20 Kingsbridge Road, Piscataway, New Jersey 08854. Received September 6, 2005; Revised Manuscript Received January 12, 2006

The utility of PEGylation for improving therapeutic protein pharmacology would be substantially expanded if the authentic protein drugs could be regenerated in vivo. Diminution of kinetic constants of both enzymes and protein ligands are commonly encountered following permanent bioconjugation with poly(ethylene glycol) polymers. In further development of releasable linker technology, we investigated an amino PEG anchimeric prodrug system, based on either the linear or branched bicin3 (BCN3) linkage, one promising representative of several aliphatic ester structures synthesized from N-modifed bis-2-hydroxyethylglycinamide (bicin). Protein models included an enzyme, lysozyme, and a receptor ligand, interferon-beta-1b, for preparation of linear or branched mono- and multi-PEGylated conjugates as inactive PEG-BCN3 prodrugs. The kinetics of protein release, both in plasma (in vitro) and in mice (in vivo), correlated with the number of PEG attachments, and the plasma half-lives of PEG release spanned a duration of hours to days within the therapeutically relevant window. Capillary electrophoresis, SDS−PAGE, mass determination, and enzymatic and antiviral activity determinations demonstrated regeneration of equivalent native proteins from the inactive PEG-BCN3 conjugates. Pharmacokinetic analysis of the PEGylated interferon-beta-1b administered subcutaneously in mice demonstrated an over 20-fold expansion of the area under the curve exposure of bioactive protein when compared to native protein.

INTRODUCTION

Bioconjugation of proteins with poly(ethylene glycol) (PEG[1]) via permanent linkages, the locus classicus of PEGylation science, is a mature technology employed in at least six PEGylated protein therapeutics which are now on the market (*1*, *2*). A rapid clearance of proteins following parenteral administration may transpire from renal filtration, antibody or cellular recognition, or physical degradation. PEG attachments to proteins have significant benefits in prolonging the in vivo activity of proteins (*3*−*6*). A recent trend in PEGylation technology attempts to optimally design the composite bioconjugate using both protein engineering and improved chemical linkages (*7*−*10*). Site-specific attachments of PEG polymer strands may afford better retention of bioactivity, while abridging the heterogeneity of the conjugate compounds. However, even well designed bioconjugates may exhibit imperfect pharmacological properties, owing to an altered structure or function of the bioconjugate when compared to the native protein molecule, which itself may have intrinsic deficiencies when examined in therapeutic applications. Therefore, recent research has examined the potential development of releasable PEGylation, wherein covalent attachments of strands of PEG polymers are shed via a controlled release mechanism derived from a degradable linkage at the attachment site on the protein surface (*11*−*19*). Releasable PEGylation may offer the greatest benefits to small molecules which are inactivated by the bulky PEG partner. Examples are peptides, oligonucleotides, and analogues of protein domains. In addition, protein therapeutics, such as toxins and signal transduction domains, requiring intracellular entry and processing might also employ a releasable PEG format. Releasable PEGs provide the option of extensive surface modification of highly immunogenic or antigenic proteins with gradual release of the active compound. Finally, it will be instructional to examine the side-by-side in vivo efficacy performance of cytokine or growth factor therapeutics that already demonstrated superior performance as nonreleasable PEGylated derivatives. Two attractive features of rPEGylation that might justify this reinvestigation are (1) the potential for improved manufacturing yields by extensive rPEGylation of the therapeutic, which allows nearly complete product recovery, and (2) the capacity of rPEGylated therapeutics to release the authentic and fully active drug.

One prodrug strategy for releasable PEGylation employs the rapid hydrolysis of bis-*N*-2-hydroxyethylglycinamide (bicin) whereby an anchimeric assisted hydrolysis facilitates the release of amine-conjugated molecules (*20*). This is a promising linker design that is wholly aliphatic and compatible with amino group derivatization, a common linkage site for protein conjugation. By the use of α-substituents on the ester moiety between the bicin group and the PEG polymer, the half-life of the prodrugs can be adjusted for various applications. However, this PEG−protein conjugate (*20*, Scheme 1) is a double prodrug, and the stepwise release of PEG from the branched PEG leads initially to a monosubstituted linear PEGylated species. The branched PEG design, featuring more PEG mass per attachment, may be preferable for optimal protection of some therapeutics; however, the two-step releasing mechanism (Scheme 2) may result in excessively complex pharmacokinetic parameters for the released protein. Therefore it is desirable to design a bis-*N*-2-

* To whom correspondence should be addressed. Phone: (732) 980-4941, Fax: 732-885-2950, E-mail: david.filpula@enzon.com.

[1] Abbreviations: PEG, poly(ethylene glycol); BCN3, bicin3; MW, molecular weight; interferon-beta-1b, IFN-β-1b; rU-PEG, releasable branched (umbrella) linker with two attached PEG polymers; U, branched (umbrella) linker with two attached PEG polymers; rPEGylation, releasable PEGylation; CE, capillary electrophoresis; SC, succinimidyl carbonate; SPA, succinimidyl propionate.

10.1021/bc050270c CCC: $33.50 © 2006 American Chemical Society
Published on Web 02/17/2006

Scheme 1

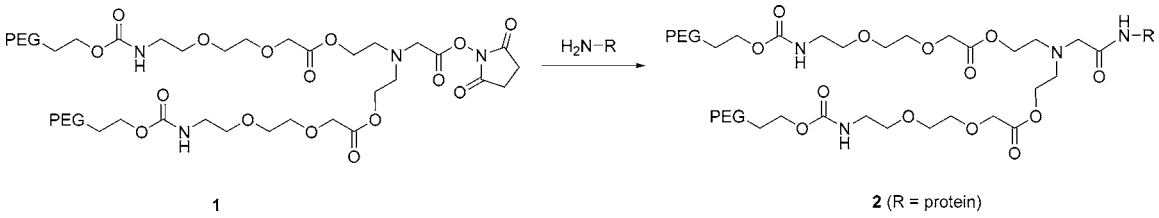

1 **2** (R = protein)

Scheme 2

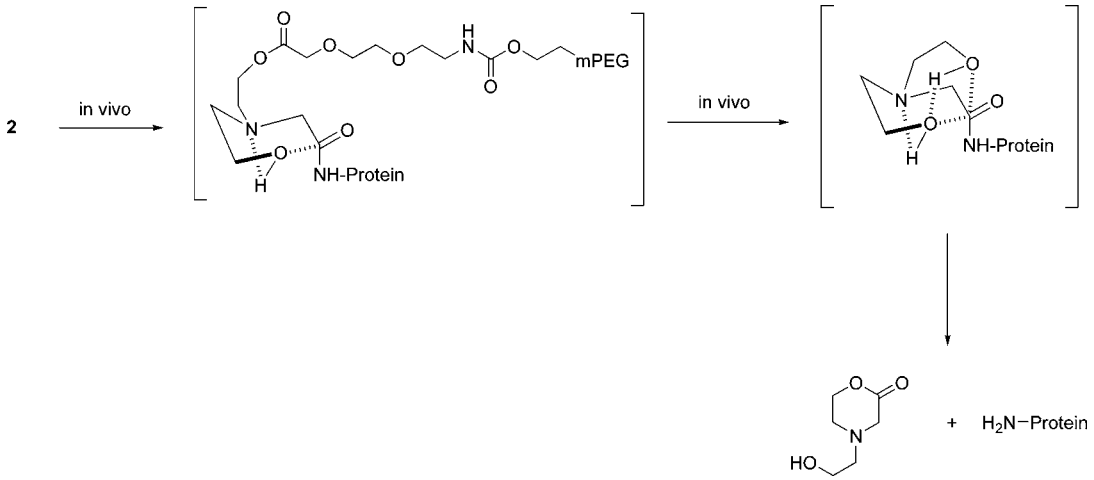

hydroxyethylglycinamide-based system with a simpler, or one-step, releasing mechanism of the PEG. This report will focus, in part, on the design of such a system and the application of the releasable PEG linker, bicin3 (BCN3), to protein conjugation. BCN3 is so designated as the third of several BCN derivatives which we have synthesized. We also report further investigations on the in vivo performance of the branched BCN3 design.

As model proteins, we chose to investigate both an enzyme and a receptor-binding ligand. Lysozyme is one of the most thoroughly investigated enzymes and is also an important constituent of the innate immunity versus infection. Development of improved antimicrobial enzymes may ultimately be important as existing antibiotics are challenged by resistant organisms (*21*). Lysozyme lyses Gram-positive bacteria by hydrolyzing a 1−4 β-glycosidic linkage of the *N*-acetylmuramic: *N*-acetylglucosamine cell wall polymer. As an illustration of the sensitivity of the enzyme active site to steric disruption, this reaction may be inhibited by ester-linked *O*-acetyl C6 substitutions on *N*-acetylmuramic acid and by teichoic acid side chains; the enzyme action may also be inhibited by binding and neutralizing immunoglobulins (*22*). In this connection, we find a single attachment of 12 kDa PEG to one of the seven primary amines of lysozyme provides nearly complete inhibition of bacteriolytic activity. Complete release of enzymes from the experimental BCN3 mono- and multi-PEGylated conjugates may be measured by the regeneration of enzymatic activity.

The second model investigates BCN3 PEGylated human interferon beta-1b (IFN-β-1b). The receptor signaling events mediated by IFN-β-1b are partially understood and the protection of cells from viral infection may be measured by bioassays based on reduction of the cytopathic effect (*23*, *24*). IFN-β-1b is a first-line therapy for relapsing-remitting multiple sclerosis. As demonstrated for many cytokines, interferons may be further engineered to improve their circulating half-life and drug exposure, while sometimes reducing immunogenicity (*4*, *5*, *25*). In particular, IFN-β-1b is a very hydrophobic protein presenting formulation challenges (*26*, *27*). IFN-β-1b clears rapidly following subcutaneous administration and has demonstrated substantial immunogenicity, including generation of neutralizing antibodies (*28*). Mono-PEGylation of interferons has proven to be productive, but PEGylation of interferons with multiple permanent attachments generally results in an inactivated protein (*4*, *9*, D. Filpula, unpublished results). We focused the current studies on releasable 24 kDa PEG-BCN3 and 40 kDa PEG-BCN3 conjugates with a defined multiple PEG number. Our investigations of the comparative pharmacokinetics of native IFN-β-1b and BCN3−PEGylated IFN-β-1b compounds demonstrate a new paradigm for interferon therapy through controlled release.

EXPERIMENTAL PROCEDURES

Materials. Chicken egg white lysozyme (EC 3.2.1.17), lysozyme substrate bacteria (*Micrococcus lysodeikticus*), and PBS (10 mM phosphate, pH 7.4, 138 mM NaCl, 2.7 mM KCl) were purchased from Sigma Inc. (St. Louis, MO). Hiload Superdex 200 was supplied by Amersham BioSciences (now GE Healthcare, Piscataway, NJ) and Poros HS was supplied by Applied Biosystems (Foster City, CA). Pre-cast 4−20% Tris-glycine SDS electrophoresis gels and the gel running buffer were obtained from Invitrogen (Carlsbad, CA). Recombinant human interferon-beta-1b (30 MIU/mg) was supplied by Enzon, Inc. Encephalomyocarditis virus (EMCV; VR-129B) and Vero cells (CCL-81) were from ATCC. SC-PEG-12 kDa and SPA-PEG-20 kDa were obtained from Enzon Pharmaceuticals and Nektar Therapeutics, respectively.

Chemistry. All reactions were run under an atmosphere of dry nitrogen or argon. Commercial reagents were used without further purification. All PEG compounds were dried under vacuum or by azeotropic distillation from toluene prior to use. NMR spectra were obtained using a Varian Mercury 300 NMR spectrometer and deuterated chloroform as the solvent unless otherwise specified. Chemical shifts (δ) are reported in parts per million (ppm) downfield from tetramethylsilane (TMS). Mass spectral analysis was performed by the W.M Keck Foundation Biotechnology Resource Laboratory, Yale University, New Haven, CT.

Scheme 3

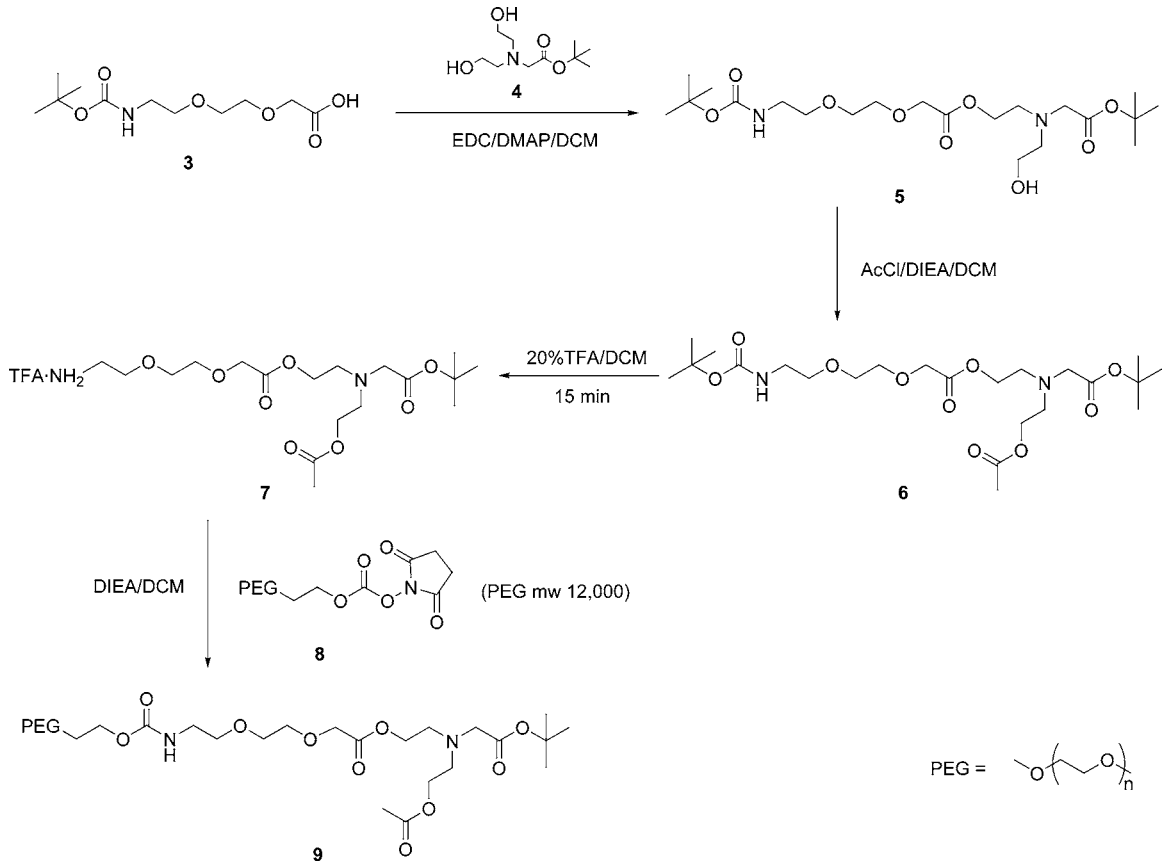

Prior to synthesis of the linear PEG BCN linker, monofunctional bis-*N*-hydroxyethylglycine derivative **5** had to be prepared first (Scheme 3). To do so, protected acid **3** was reacted with equal moles of the *tert*-butyl ester of bicin **4**, and after the acid wash, pure **5** was obtained without any further purification. The free hydroxyl group of **5** was then capped by an acetyl group to give **6**. Subsequently, the BOC-glycine ester, compound **6**, was deblocked using mild conditions (20% TFA for 15 min) to give the amine salt **7** without altering the *tert*-butyl ester. Condensation of **7** with mPEG-succinimidyl carbonate (**8**, SC-PEG, mw 12000 used as an example; ref 29) produced the linear PEG-BCN3 derivative **9**, which was hydrolyzed using more concentrated TFA (33%) in DCM for a 15 h period, producing the linear PEG acid **10** (Scheme 4). Activation of **10** by EDC/NHS produced the NHS activated ester, **11**.

Compound 5. A solution of **3** (2.3 g, 8.7 mmol), **4** (1.9 g, 8.8 mmol), and DMAP (1.6 g, 12.9 mmol) in 30 mL of dry methylene chloride was cooled to 0 °C in an ice bath, followed by addition of EDC hydrochloride (2.3 g, 12.0 mmol). This mixture was allowed to warm to room-temperature overnight, followed by washing with 0.1 N HCl. The organic layer was dried over anhydrous sodium sulfate and filtered and the solvent removed from the filtrate by rotovaporation to yield **5** (3.6 g, 7.8 mmol, 90%). ^{13}C NMR (75.4 MHz, $CDCl_3$) δ 170.04, 169.86, 155.54, 80.87, 78.66, 70.49, 69.95, 68.14, 62.71, 55.85, 52.59, 40.02, 28.15, 27.91. ^{1}H NMR (300 MHz, $CDCl_3$) δ: 1.44 (9H, s), 1.51 (9H, s), 3.24−3.36 (2H, m), 3.54 (2H, t), 3.57−3.69 (4H, m), 3.69−3.78 (2H, m), 3.79−3.90 (2H, br s), 4.00−4.10 (2H, br s) 4.13−4.23 (2H, br s), 4.27 (2H, s), 4.64−4.74 (2H, br s), 5.19 (1H, br s), 5.34 (1H, s). TOF MS (ES^+) calculated for $C_{21}H_{41}O_9N_2$ $(M + H)^+$ 465.56, found 465.42.

Compound 6. To a solution of **5** (1.8 g, 3.9 mmol) in 35 mL of dry methylene chloride was added acetyl chloride (0.49 g, 6.2 mmol), followed by diisopropylethylamine (1.82 g, 14 mmol). This mixture was stirred for 10 min at room temperature, at which time no starting material was detected by TLC. This mixture was washed with saturated sodium bicarbonate, dried over anhydrous sodium sulfate, and filtered, and the solvent was removed from the filtrate by rotovaporation to yield 1.6 g of crude product. This material was purified by column chromatography on silica gel and eluted with 2.5% acetonitrile in ethyl acetate to yield **6** (0.69 g, 1.4 mmol, 35%). ^{13}C NMR (75.4 MHz, $CDCl_3$) δ 170.60, 170.27, 170.02, 155.68, 80.99, 78.88, 70.68, 70.13, 70.10, 68.34, 62.93, 62.74, 56.11, 52.81, 52.76, 40.21, 28.29, 28.08, 20.88. ^{1}H NMR (300 MHz, $CDCl_3$) δ: 1.42−1.52 (18H, m), 2.04−2.10 (3H, m), 2.94−3.06 (4H, m), 3.28−3.42 (4H, m), 3.52−3.62 (2H, m), 3.63−3.70 (2H, m), 3.70−3.77 (2H, m), 4.08−4.28 (6H, m), 5.11 (1H, s). HRMS calculated for $C_{23}H_{43}O_{10}N_2$ $(M + H)^+$ 507.2912, found 507.2895.

Compound 9. A 0.15 g (0.3 mmol) sample of **6** was stirred for 15 min in a solution of 20 mL of methylene chloride and 5 mL of TFA, followed by removal of the solvents by rotovaporation to generate **7**, which was combined with 5 mL of dry methylene chloride, followed by addition of DIEA until the pH was above 8.0. This solution of **7** was added to a solution of 3.0 g (0.15 mmol) of **8** in 45 mL of dry methylene chloride and stirred overnight at room temperature. At this time, the solvent was partially removed by rotovaporation, and the product was precipitated with ether, and collected and washed with ether. This crude product was recrystallized from 12% DMF/IPA to yield **9** (2.8 g, 93% yield). ^{13}C NMR (75.4 MHz, $CDCl_3$) δ 170.31, 170.02, 169.74, 155.91, 80.72, 72.94−68.13(PEG), 63.51, 62.73, 62.52, 58.65, 55.92, 52.62, 40.44, 27.90, 20.69.

Compound 10. A solution of **9** (4.1 g, 0.13 mmol) in 50 mL of DCM and 25 mL of TFA was stirred for 15 h at room temperature, followed by partial removal of the solvent by rotovaporation, and precipitation of the product with ether. The solid was collected by filtration and washed several times with ether and dried to yield **10** (4.0 g, 98%) of product. ^{13}C NMR

Scheme 4

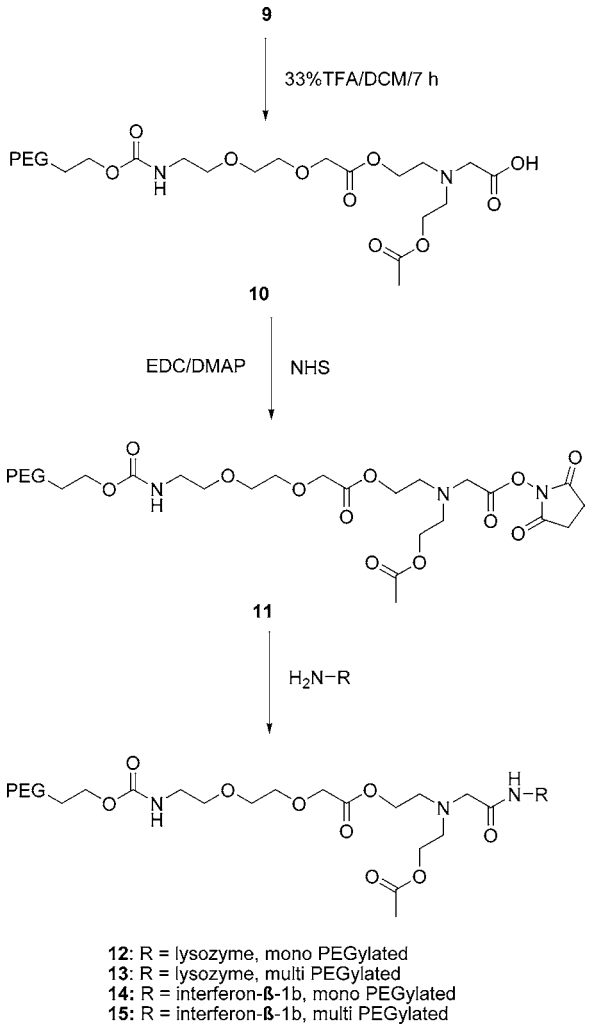

(75.4 MHz, $CDCl_3$) δ 171.19, 170.26, 169.73, 72.99−68.16 (PEG), 63.52, 62.35, 64.98, 58.67, 55.86, 53.13, 53.02, 40.46, 20.62.

Compound 11. A solution of **10** (3.9 g, 0.13 mmol), 0.059 g (0.51 mmol) of NHS, 0.2 mL (1.1 mmol) of DIEA, and 0.0015 g (0.012 mmol) of DMAP was combined with 30 mL of dry methylene chloride and cooled to 0 °C, followed by the addition of 0.2 g (1.03 mmol), of EDC hydrochloride. This mixture was allowed to warm to room temperature overnight. At this time, the solvent was partially removed by rotovaporation, and the product precipitated with ether, collected, and washed with ether. This crude product was recrystallized from 12% DMF/IPA to yield **11** (3.72 g, 95% yield). ^{13}C NMR (75.4 MHz, $CDCl_3$) δ 170.34, 169.80, 168.52, 165.83, 155.96, 71.58−68.16 (PEG), 63.57, 62.64, 62.35, 58.70, 52.73, 52.53, 52.46, 40.49, 25.32, 20.66. Compound **11** was used in the preparation of mono-PEGylated or multi-PEGylated lysozyme and IFN-β-1b compounds (**12**, **13**, **14**, and **15**).

HPLC Methods. The reaction mixtures and the purity of intermediates and final products were monitored by a Beckman Coulter System Gold HPLC instrument employing a ZOBAX 300 SB C-8 reversed phase column (150 × 4.6 mm) or a Phenomenex Jupiter 300A C18 reversed phase column (150 × 4.6 mm) with a multiwavelength UV detector, using a gradient of 30−90% of acetonitrile in 0.5% trifluoroacetic acid (TFA) at a flow rate of 1 mL/min for 30 min.

Determination of Hydrolysis Rate and Reaction Rate. The hydrolysis of PEG compounds in 0.1 M sodium phosphate, pH 7.8, 23 °C was conducted on a Cary 50 Bio UV-Visible Spectrophotometer. The PEG compound concentration was 2×10^{-4} M based on polymer mass (1 mg/mL for 5 kDa, 2.4 mg/mL for 12 kDa, 4.8 mg/mL for 24 kDa, and 6 mg/mL for 30 kDa). The hydrolysis was monitored at 260 nm for the production of *N*-hydroxysuccinimide (NHS). The extinction coefficient of NHS in 0.1 M sodium phosphate, pH 7.8, 23 °C was 7.5×10^3 L·mol^{-1}·cm^{-1} ($R^2 = 0.999$). The hydrolysis rate was calculated with Cary WinUV software using a first-order kinetics model. The reaction of PEG linkers with glycine was conducted by adding glycine to a PEG linker solution at a 1:1 molar ratio. The reaction was monitored at 260 nm. The difference in kinetic constants between hydrolysis alone, and hydrolysis plus reaction with glycine, was determined for the corrected reaction rates.

Kinetic Studies in Rat Plasma. The PEG-BCN3 derivative, 15 mg, was dissolved in 1000 μL of a mixture of MeCN and MeOH (1:1, v/v). The solution (100 μL) was transferred to each vial (eight vials total, StepVial System II). Solvent was removed under reduced pressure, and 100 μL of rat plasma was added to each vial. The vial was sealed and vortexed for 1 min after which time the vial was incubated at 37 °C for 0, 0.5, 1, 2, 4, 6, and 20 h, respectively. To each vial was again added 400 μL of MeCN and MeOH (1:1, v/v) and the vial vortexed for 1 min. The mixture was filtered through a 0.45 micron filter membrane, and 50 μL of the filtrate was injected directly into the HPLC system.

Enzyme Activity Assay. In a typical lysozyme activity assay, 0.2 mL of 0.02% (w/v) *M. lysodeikticus* was added to 0.12−2.0 μg of lysozyme in 50 μL of 66 mM potassium phosphate, pH 6.2 containing 0.01% BSA, on a 96-well titer plate. The absorbance at 450 nm was followed for 5 min on a SpectraMax 190 instrument (Molecular Devices). The rate of decrease in absorbance was used as a measure of enzyme activity. One unit of enzyme activity produces a change of 0.001 absorbance units/min at 25 °C. Free PEG or rat plasma had no effect on this assay.

Preparation of Mono-PEGylated-Lysozyme Conjugates. With fast stirring, the activated PEG linker powder (compound **11**), at a reaction molar ratio of 1.75:1 (PEG:lysozyme), was added to a lysozyme solution of 5 mg/mL in 50 mM phosphate buffer, pH 7.6. After 60 min at 25 °C, the reaction mixture was diluted 5-fold with 20 mM sodium phosphate, pH 5.1, to a conductivity lower than 2 mS, and mono-PEGylated PEG-lysozyme was purified on a cation exchange column (Poros, HS) using a solvent system of 20 mM sodium phosphate at pH 5.1 and a NaCl gradient. The peak of mono PEG-lysozyme was collected, dialyzed against 140 mM NaCl, and concentrated using an ultrafree centrifugal filter device with a 10 kDa NMWL membrane (Millipore Corp., Bedford, MA). The compositions of mono PEG-lysozyme crude conjugate preparations (compound **12**) were also determined from the peak areas of the chromatograms from HS chromatography. The overall yields of with different PEG linkers are 12kDa SC-PEG-lysozyme (83% conjugation yield with 100% mono-PEG-lysozyme), 12 kDa PEG-BCN3-lysozyme (73% conjugation yield; 74% mono-PEG-lysozyme and 26% di-PEG-lysozyme), and 20 kDa PEG-BCN3-lysozyme (74% conjugation yield; 65% mono-PEG-lysozyme and 35% di-PEG-lysozyme).

Preparation of Multi-PEGylated-Lysozyme Conjugates. With fast stirring, the activated PEG linker powder (compound **11**) at a reaction molar ratio of 20:1 (PEG:lysozyme) was added to a lysozyme solution of 5 mg/mL in 0.1 M phosphate buffer, pH 7.6. After 60 min at 25 °C, the reaction was stopped by adding a 5-fold volume of 140 mM NaCl, 20 mM sodium phosphate, pH 6.0, filtered through a 0.2 μm membrane, and separated on a Hiload Superdex 200 column which was equilibrated with 20 mM sodium phosphate, pH 6.0, 140 mM

NaCl. The fractions of the desired peak were pooled, dialyzed against 140 mM NaCl, and concentrated using an ultrafree centrifugal filter device with a 30 kDa NMWL membrane (Millipore Corp., Bedford, MA). The final conjugate contained 3−4 PEG attachments per lysozyme molecule for 20 kDa PEG-BCN3-lysozyme conjugates and 4−5 PEG attachments for 12 kDa PEG-BCN3-lysozyme conjugates, as estimated on SDS−PAGE and SEC analysis. The overall yields of all the multi-PEGylated lysozyme conjugates using either 12 kDa SC-PEG, 12 kDa PEG-BCN3, or 20 kDa PEG-BCN3 linker were about 85%.

rPEGylation of IFN-β-1b. IFN-β-1b (0.28 mg/mL; 50 mL) in 50 mM HEPES, 0.1% zwittergent 3−14, pH 7.8, was conjugated with either of two rU-PEG-BCN3 polymers with PEG mass of 24 kDa and 40 kDa, respectively. A 30-fold molar excess of the PEG-BCN3 activated polymer was added slowly into the IFN-β-1b solution over a period of 1 min with stirring and continued at 25 °C for 2 h. The reaction was quenched by lowering the pH to 3−4 with dilute acetic acid and then diluted with water to lower the conductivity to 1 mS. Poros 50 HS (8 mL column volume) was equilibrated with buffer containing 20 mM sodium acetate, pH 4.75. The dilute reaction mixture was loaded onto the equilibrated column at 7 mL/min. The column was chased to baseline and washed with five column volumes of equilibration buffer to remove zwittergent and unreacted PEGs. The bound PEGylated IFN-β-1b conjugate was eluted from the column using a linear gradient of elution buffer (1 M NaCl in equilibration buffer) of 200 mL over 40 min at a 5 mL/min flow rate and peak fractions were collected based on SDS−PAGE analysis of fractions. The fractions were dialyzed using a 25 kDa-MW-cutoff membrane against 5% mannitol, 3 mM acetic acid, pH 3.7 at 4 °C overnight with two changes of buffer. The PEGylated IFN-β-1b conjugate solution was concentrated using a 10 kDa Amicon filtration system and sterile filtered to a final concentration of 0.2−0.5 mg protein/mL. The number of PEG attachments per protein was determined independently by SDS−PAGE and gel filtration.

PEGylation of IFN-β-1b with SC or SPA Linkers. IFN-β-1b (0.8 mg/mL; 5 mL) in 100 mM sodium phosphate, 0.05% Zwittergent 3−14, 2 mM EDTA, pH 7.8, was conjugated with activated PEG polymers with PEG mass of 12 kDa or 20 kDa. PEG-SC or PEG-SPA compounds were dissolved in 0.1 mM acetic acid. With fast stirring without generating foam, the PEG solution was added at 0.5−1.0 g/min to a final 10-fold molar excess over protein. The reaction was conducted at 25 °C for 60 min, quenched by adding glycine to a final molar ratio of 50:1 (glycine:PEG) and filtered through a 0.2 μm membrane before the column purification.

Purification of PEG-IFN-β-1b. The PEGylation reaction (5 mL; 0.8 mg protein/mL) was purified by Superdex 200 High Load chromatography with a 10 mM sodium phosphate, pH 7.3, 0.05% Zwittergent running buffer at a flow rate of 2 mL/min. In the second step, 8 mL of peak fractions were loaded onto an HS-50 column with 10 mM sodium phosphate, pH 7.3, 5% mannitol running buffer. The PEG-IFN-β-1b was eluted with 1 M NaCl in equilibration buffer at 2 mL/min and 2 mL/fraction over a period of 40 min. Fractions identified on SDS−PAGE were combined and the pH of the sample was immediately adjusted to 3.7 with HAc. It was then dialyzed using a 30 kDa-MW-cutoff membrane against 5% mannitol, 3 mM HAc, pH 3.7 at 4 °C for 12 h. The fractions were diafiltered on Amicon membranes to a final concentration of 0.5−1 mg/mL in 3 mM HAc, pH 3.7, 5% mannitol.

Determination of Release of Lysozyme from PEG-Lysozyme Conjugates. Under the conjugation reaction conditions for these experimental procedures, lysozyme enzymatic activity was virtually eliminated after the attachment with only one PEG strand. The release of the lysozyme from the conjugate was determined by regeneration of the lysozyme activity under various release conditions and confirmed on SDS polyacrylamide gel electrophoresis. For most experiments, lysozyme conjugates (0.5 mg/mL) were incubated in 0.1 M borate buffer, pH 9.2, 37 °C for 16 h. The activity was compared with the activity of native lysozyme stored in 140 mM NaCl at 4°C.

Analytical Characterization of Lysozyme, IFN-β-1b, and PEG-Protein Conjugates. Protein concentrations were determined by measuring the UV absorbance at 280 nm, using a determined IFN-β-1b extinction coefficient of 1.5 mL/mg/cm. The concentration was also confirmed by the bicinchoninic acid assay (BCA), obtained as a Micro BCA Protein Assay Reagent kit from Pierce Biotechnology using lysozyme or BSA as standards. Mass values of IFN-β-1b and lysozyme were determined by matrix-assisted laser desorption/ionization time-of-flight mass spectrometry (MALDI-TOF-MS) (Bruker Daltronics OmniFlex NT) using an internal standard with a similar molecular weight. Apparent molecular weights (Stoke radius) of the compounds were estimated using Superdex 200 HR 10/30 gel filtration column chromatography (Amersham Bio-Sciences) in 100 mM sodium phosphate, pH 6.8, at 24 °C with BioRad (Hercules, CA) molecular weight standards or PEG−protein molecular mass standards (Enzon).

Capillary Electrophoresis (CE). CE was performed on a P/ACE MDQ capillary electrophoresis system (Beckman, Fullerton, CA) equipped with a fused silica capillary (inner diameter 75 μm; 50 cm effective length, 57 cm total length). The parameters of PDA were set at 214, 220, and 280 nm and separation was conducted at +30 kV. The sample running buffer was composed of 25 mM sodium phosphate, pH 2.7, 0.1 mg/mL PEG. The capillary temperature was maintained at 23 °C by the thermostated coolant from Beckman. Between each run, the capillary was regenerated with 1 N HCl (5 min), H_2O (2 min), 0.1 N NaOH (10 min), H_2O (2 min), and then 25 mM sodium phosphate, pH 2.7, 0.1 mg/mL PEG (20 min) at 20 psi.

Antiviral Assays of IFN-β-1b. Specific antiviral activity from the cytopathic effect of IFN-β-1b was assayed by published methods (*24*) using Vero cells and EMCV virus, which were cultivated as recommended by the ATCC supplier. Vero cells were distributed on 96-microtiter plates (20000 cells/well) in 0.05 mL of culture medium. Serial dilutions of 0.05 mL of the IFN-β samples were incubated at 37 °C, 5% CO_2, for 24 h. EMCV (200 pfu/20 μL) were added to each well at 25 °C for 30 min; then incubated at 37 °C for 24 h. After the addition of 20 μL of 10 mg/mL 3-(4,5-dimethyl-2-thiazoyl)-2,5-diphenyl-2*H*-tetrazolium bromide (MTT; Promega, Madison, WI) dye solution to each well, incubation was continued for 4 h, 100 μL of stop solution (1.2 N HCl in 2-propanol) was added to each well, and the plate was read at 570 nm in a 96-well plate reader (Molecular Devices, Sunnyvale, CA) to determine EC_{50} values, as analyzed with Softmax Pro software. Native IFN-β-1b, PEGylated IFN-β-1b, and released PEG-IFN-β-1b were analyzed in triplicate on each plate. Conversion of antiviral activity units to protein mass was attained using the specific activity of the parent compounds (native IFN-β-1b or PEG-IFN-β-1b).

Pharmacokinetic Analysis of PEG-IFN-β-1b. C57BL/6 mice (7−8 week, female) were supplied by Sprague Dawley Harlan (Madison, WI). Mice (5/group) were injected subcutaneously intrascapular, with 100 μL per mouse (0.2 mg/kg) of IFN-β-1b, or its PEGylated conjugates. Following sedation with 0.09% avertin, sampling of blood was undertaken into vials containing EDTA. At 2, 15, 30, and 60 min, the mice were bled 100 μL, and at 4, 24, 48, 72, and 96 h, the mice were terminally bled by cardiac puncture. The plasma was collected following centrifugation of the blood at 5000 rpm at 4 °C for

Scheme 5

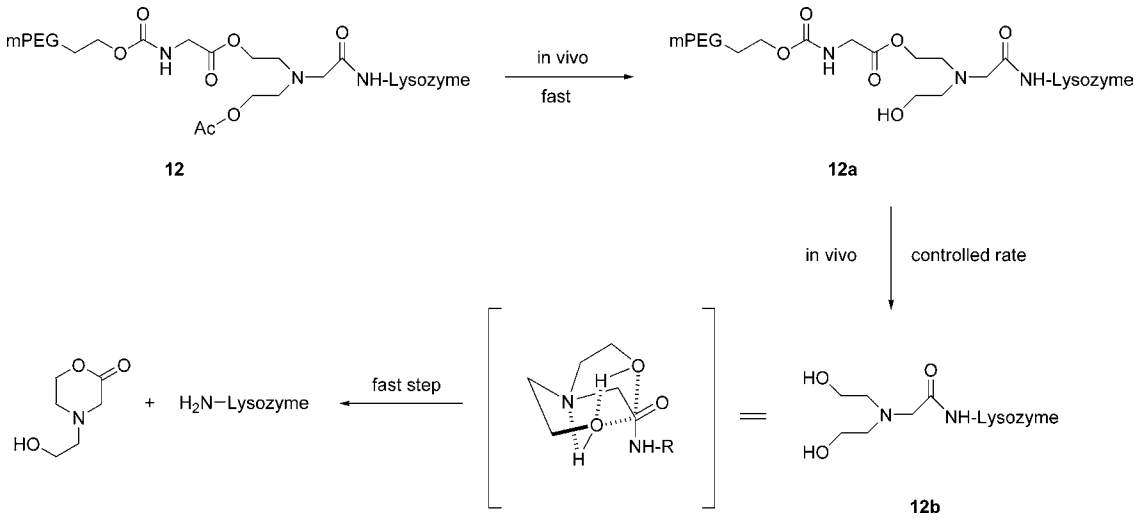

Table 1. Composition and Analysis of Protein Conjugates

compound	protein	linker[a]	linkage[b]	PEG unit mass (kDa)[c]	PEG no.[d]	PEG total mass (kDa)	analytics[e]
16.	lysozyme	SC	P	12	1	12	EA, CE, PAGE
17.	lysozyme	SC	P	12	4−5	48−60	EA, CE, PAGE
18.	lysozyme	BCN3	R	12	1	12	EA, CE, PAGE
19.	lysozyme	BCN3	R	12	4−5	48−60	EA, CE, PAGE
20.	lysozyme	BCN3	R	12	2	24	EA, CE, PAGE
21.	lysozyme	BCN3	R	20	1	20	EA, CE, PAGE
22.	lysozyme	BCN3	R	20	3−4	60−80	EA, CE, PAGE
23.	lysozyme	rU-BCN3	R	24 (12 × 2)	1	24	EA, CE, PAGE
24.	lysozyme	rU-BCN3	R	24 (12 × 2)	2−3	48−72	EA, CE, PAGE
25.	IFN-β-1b	rU-BCN3	R	24 (12 × 2)	3	72	BA, PAGE, SEC, MS
26.	IFN-β-1b	rU-BCN3	R	40 (20 × 2)	2	80	BA, PAGE, SEC, MS
27.	IFN-β-1b	SPA	P	20	2	40	BA, PAGE, SEC, MS

[a] Linkers are either permanent (SC; SPA), linear releasable (BCN3), or branched releasable (rU-BCN3). [b] P, permanent linkage; R, releasable linkage. [c] Mass of PEG polymer strand used in linear or branched configuration. [d] Number of attachments of PEG linker on protein. [e] Number of PEG attachments measured by EA, enzymatic activity; CE, capillary electrophoresis; PAGE, reducing SDS−PAGE; BA, antiviral bioactivity; SEC, size exclusion chromatography; MS, MALDI-TOF mass spectrometry.

5 min and immediately frozen on dry ice. The concentrations of the compounds were analyzed by both antiviral activity and by ELISA. The data were modeled using WinNonlin software (WinNonlin Pharsight, Mountain View, CA) to determine pharmacokinetic parameters.

RESULTS AND DISCUSSION

Design of the BCN3 Linker and Nomenclature. Releasable PEGylation was investigated using designed BCN3 linkers with either one PEG per linker (linear design) or two PEGs per linker (branched design). In this investigation, we have modified and further examined the previous branched (rU-PEG; releasable umbrella PEG) design (*20*) and, most significantly, designed new linear bicin linkers, which are more easily synthesized and less complex in the chemical pathway of protein release (Scheme 5). The linear PEG BCN3 linkers were investigated with PEG polymers of different molecular weights, and with differing numbers of PEG attachments, in conjugates with model proteins, lysozyme, and IFN-β-1b. Our present investigation focuses on the performance of both types of PEG BCN3 linkers, i.e., linear PEG BCN3 and rU-PEG BCN3. In this nomenclature, compounds designated "linear PEG-BCN3" employ one polymer per linker, whereas compounds designated "rU-PEG-BCN3" contain two polymers per linker. The terms "mono-PEGylated" and "multi-PEGylated" identify bioconjugates consisting of either one, or multiple, PEG attachment sites per protein, respectively. All protein conjugate compounds are identified by number in Table 1.

Due to difficulties in purification of the rU-PEG BCN3 polymer (separating the two stranded PEG from the single stranded PEG), there are detectable amounts of linear PEG BCN3 in the final rU-PEG-BCN3 compound. As a result, in the protein conjugation mixture, there was a minor impurity of linear PEG-BCN3-protein and the impurity profile would become more complex when multisite PEGylation was employed. On the other hand, we expected that if a linear PEG-BCN3 linker were used as the only activated PEG species, the protein conjugation mixture would be much more homogeneous. As shown in the Scheme 5, the acetyl group of compound **12** is predicted to quickly release in vivo to produce compound **12a**. The cleavage of PEG from the conjugate is the rate-determining step and can be controlled by using different linker side-chains between the PEG and the bicin moiety. After the intermediate **12b** is formed, it will quickly fold into the "double" assisting conformation and the coordination of two hydroxyl groups facilitates the breakdown of the amide bond to release intact protein. When a different acid than **3** is used in the synthesis, linear PEG BCN linkers with different hydrolysis rates may also be constructed. The current study focused on the application of the specific BCN3 linker design (compounds **1** and **11**) for controlled release of protein from PEG conjugates.

Preparation of Linear PEG-BCN3-Lysozyme. Mono-PEGylated linear 12 kDa or 20 kDa PEG-BCN3-lysozyme compounds (**18**, **21**) were prepared and purified by cation exchange chromatography to separate di- or multi-PEGylated conjugates. The PEG-BCN3-lysozyme conjugates were analyzed by SDS−PAGE and size exclusion chromatography. A representative 4−20% SDS−PAGE analysis of a purified linear 12 kDa PEG-BCN3-lysozyme conjugate is shown in Figure 1A.

Table 2. Lysozyme Activity (%) after 16 h Release in Vitro from Linear PEG-BCN3-Lysozyme Conjugates

		mono-PEGylated-lysozyme			multi-PEGylated-lysozyme		
	lysozyme	SC-12k	BCN3-12k	BCN3-20k	SC-12k	BCN3-12k	BCN3-20k
compound no.		16	18	21	17	19	22
untreated	100	2.3	2.8	1.4	1.5	1.5	1.1
control (140 mM NaCl in H_2O)	100	2.3	34.0	54.7	2.3	0.9	3.4
hydrolysis (0.1 M borate, pH 9.2)	93.8	9.6	97.4	101.6	2.3	95.8	99.7

Reversibility of Linear PEG-BCN3-Lysozyme Linkage. Linear PEG-BCN3-lysozyme conjugates (0.5 mg/mL) were incubated in 0.1 M borate buffer, pH 9.2, 37 °C for 16 h. An aliquot was withdrawn and lysozyme activity was analyzed. The activity was compared with the activity of native or PEGylated lysozyme stored in 140 mM NaCl at 4 °C. The results indicate that lysozyme activity of linear PEG-BCN3-lysozyme was fully recoverable after the 16 h high-pH incubation in vitro. When lysozyme was permanently PEGylated with one or more SC-PEG polymers, the lysozyme activity from such conjugates was not restored during the entire incubation period. The analysis of enzyme activity of BCN3-PEG conjugates following protein release at high-pH in vitro is shown in Table 2.

Lysozyme has seven amine groups: six ϵ-amine groups of lysine and one α-amine of the N-terminal amino acid. When lysozyme was treated with maleic anhydride at 1:1.5 molar ratio, thereby mimicking the PEGylation stoichiometry, the activity of lysozyme was reduced by 60% (data not shown), demonstrating that attachment of a small molecule such as maleic anhydride to an amine group of lysozyme could also inhibit enzyme activity. The full recovery of lysozyme activity in the linear PEG-BCN3-lysozyme conjugates implies a complete release of lysozyme from both the PEG and the linker under the conditions described.

Capillary Electrophoresis Analysis of Protein Release from BCN3-PEG. The complete release of lysozyme was also confirmed by CE analysis. The linear 12 kDa PEG BCN3-lysozyme conjugate (**18**) was incubated in 5 mM sodium borate buffer, pH 9.5, 37 °C for 24 h, after which one-tenth sample volume of 250 mM sodium phosphate, 1 mg/mL 12 kDa PEG was added. CE was conducted as described in Experimental Procedures. The electropherograms of lysozyme and linear 12 kDa PEG-BCN3-lysozyme (**18**) before and after hydrolysis are shown in Figure 2. Linear 12 kDa PEG-BCN3-lysozyme, after lysozyme release, exhibited an identical electropherogram compared to native lysozyme ($t = 6.65-6.82$) indicating a full release of lysozyme from both PEG and PEG linker. The PEG conjugate migrated as a broad peak ($t = 22.55$) with a detected trace of native lysozyme. The 24 kDa rU-PEG-BCN3-lysozyme (**23**) also demonstrated complete release of enzyme under identical in vitro release conditions when analyzed by SDS−PAGE (Figure 1B).

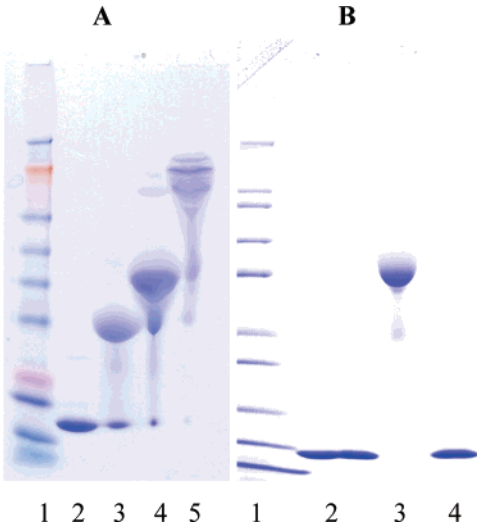

Figure 1. SDS−PAGE analysis of BCN3 PEGylated lysozyme formulations. Coomassie blue stained proteins and conjugates were analyzed by 4−20% SDS−PAGE. (A) Lane 1: molecular weight standards (250, 148, 98, 64, 50, 36, 22, 16, 6, and 4 kDa); Lane 2: native lysozyme; Lane 3: mono-PEGylated linear 12 kDa PEG-BCN3-lysozyme (**18**); Lane 4: di-PEGylated linear 12 kDa PEG-BCN3-lysozyme (**20**); Lane 5: multi-PEGylated linear 12 kDa PEG-BCN3-lysozyme (**19**). (B) Lane 1: molecular weight standards (200, 116, 97, 66, 55, 36, 31, 22, 14, 6, and 4 kDa); Lane 2: native lysozyme; Lane 3: 24 kDa rU-PEG-BCN3-lysozyme (**23**) before release at high pH; Lane 4: 24 kDa rU-PEG-BCN3-rU-lysozyme (**23**) after release at high pH.

Table 3. Hydrolysis Rate of PEG-NHS at pH 7.8, 23 °C

NHS linker	PEG, kDa	k (min^{-1})	$t_{1/2}$ (min)
SC (**8**)	12	0.0325 ± 0.0080	22.24 ± 5.64
linear BCN3 (**11**)	5	0.0470 ± 0.0005	14.76 ± 0.02
linear BCN3 (**11**)	12	0.0406 ± 0.0004	17.09 ± 0.17
linear BCN3 (**11**)	30	0.0553 ± 0.0013	12.54 ± 0.29
BCN3-rU (**1**)	24	0.0423 ± 0.0003	16.38 ± 0.12

Hydrolysis of PEG-BCN3 Linker and Reaction with Glycine. We investigated the intrinsic aqueous stability of the activated linear PEG-BCN3 polymer as its NHS ester to determine its suitability as a functional reagent. The hydrolysis rates were investigated for SC-PEG (**8**), linear PEG-BCN3 (**11**), and rU-PEG-BCN3 (**1**) linkers by determination of NHS elimination by UV spectroscopy. The results demonstrated that the hydrolysis rate of linear PEG-BCN3 was faster than SC and similar to rU-PEG-BCN3 (Table 3). Since both linear PEG-BCN3 and rU-PEG-BCN3 contain the same linking moiety but a different number of PEG chains, similar hydrolysis rates were expected. The reaction with glycine at an equal molar ratio of all the linkers was faster than the buffer hydrolysis rate. Based

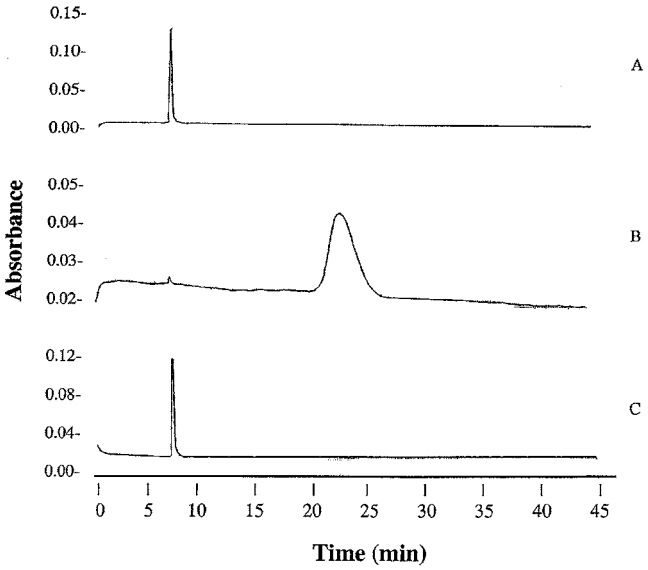

Figure 2. CE electropherograms of lysozyme and linear 12 kDa PEG-BCN3-lysozyme (**18**) before and after lysozyme release. (A) Native lysozyme. (B) Linear 12 kDa PEG-BCN3-lysozyme before release at high pH. (C) Linear 12 kDa PEG-BCN3-lysozyme (**18**) after release at high pH.

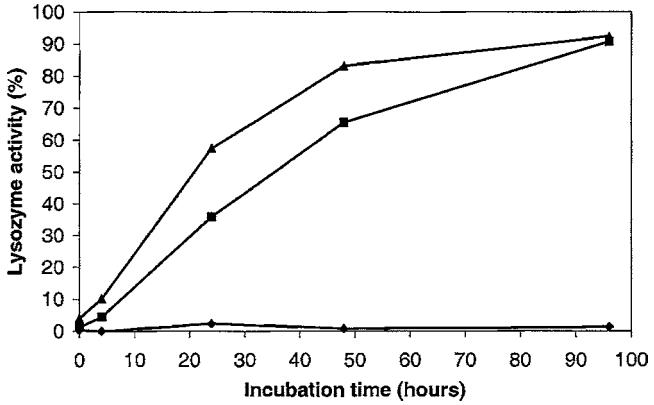

Figure 3. Release profile in vitro of lysozyme from multi-PEGylated linear BCN3-lysozyme conjugates incubated in rat plasma. Enzymatic activity (% recovered) of linear 12 kDa PEG-BCN3 (**19**) (■) and linear 20 kDa PEG-BCN3 (**22**) (▲) conjugates are compared with the linear 12 kDa PEG-SC permanent linker derivative (**17**) (◆).

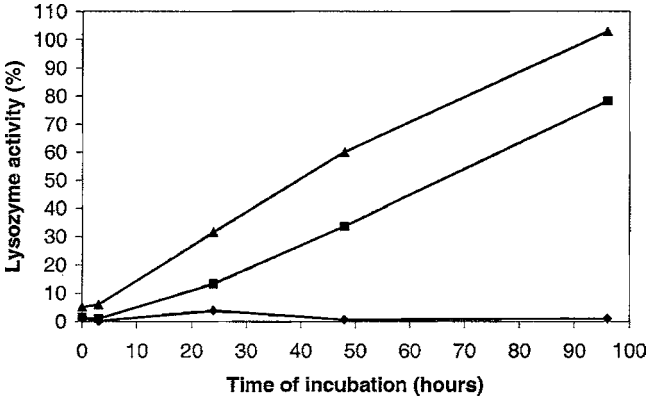

Figure 4. Release profile in vitro of lysozyme from multi-PEGylated linear BCN3-lysozyme conjugates incubated in PBS, pH 7.4. Enzymatic activity (% recovered) of linear BCN3-12k (**19**) (■) and linear BCN3-20k (**22**) (▲) conjugates are compared with the SC-12k permanent linker derivative (**17**) (◆).

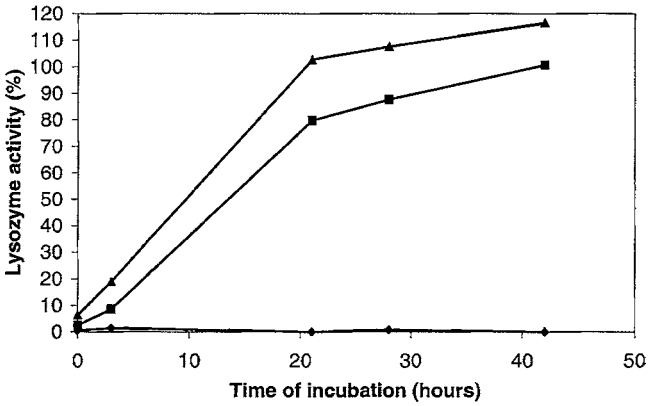

Figure 5. Release profile in vitro of lysozyme from multi-PEGylated linear BCN3-lysozyme conjugates incubated at pH 8.5. Enzymatic activity (% recovered) of linear 12 kDa PEG-BCN3 (**19**) (■) and linear 20 kDa PEG-BCN3 (**22**) (▲) conjugates are compared with the linear 12 kDa PEG-SC permanent linker derivative (**17**) (◆).

on first-order kinetics for the initial rate, the reaction rate with glycine was about 2−3-fold faster than that of buffer hydrolysis rates (data not shown). These studies demonstrate that the BCN3 compounds display the necessary stability to be used as practical reagents.

Release Rate of Lysozyme from Multi-PEGylated Linear BCN3 Conjugates in Rat Plasma. Multi-PEGylated-lysozyme conjugates (0.15 mg/mL) were incubated in rat plasma at 37 °C under nitrogen. At the times indicated in Figure 3, an aliquot was withdrawn, acidified with 0.2 M sodium phosphate, pH 5.0 to pH 6.5, and stored at −20 °C until enzyme analysis. The half-lives of protein release were estimated from the graph of incubation time versus activity as described in Experimental Procedures. The purified multi-PEGylated lysozyme conjugates have three to four PEG strands per lysozyme for linear 20 kDa PEG-BCN3 compounds (**22**), and four to five PEG polymer strands per lysozyme for the linear 12 kDa PEG-BCN3 compounds (**19**). As shown in Figure 3, a slightly higher release rate from multi-PEGylated lysozyme for the linear 20 kDa PEG-BCN3-lysozyme (total PEG mass ∼ 70 kDa) was observed compared to the linear 12 kDa PEG-BCN3-lysozyme (total PEG mass ∼ 55 kDa) of 21 h vs 35 h, respectively. This phenomenon might correspond to the higher number of PEG linker attachments, and greater steric hindrance, in the latter compound. No detectable protein release was observed for the permanently PEGylated lysozyme conjugate using SC-PEG (**17**). The similar release profiles of PEG-BCN3-lysozyme conjugates of differing mass suggest that the release rates are primarily dependent on characteristics of the PEG linker, rather than PEG size.

Influence of pH on Release Rate of Lysozyme from Linear PEG-BCN3-Lysozyme Conjugates. Multi-PEGylated linear PEG-BCN3-lysozyme (0.15 mg/mL) was incubated in phosphate buffered saline (PBS), pH 7.4, 37 °C, or in 50 mM Tris, pH 8.5, 37 °C, under nitrogen. At the times indicated in Figure 4 and Figure 5, respectively, an aliquot was withdrawn, acidified with 0.2 M sodium phosphate, pH 5.0 to pH 6.5, and stored at −20 °C until enzyme analysis. The half-lives of protein release were estimated from the graph of time of incubation versus activity. A control experiment demonstrated that native lysozyme retained full activity after a two-day incubation in 50 mM Tris, pH 8.5, at 37 °C. Compared to the release rate in rat plasma and PBS (pH 7.4−7.6), the faster release rate at pH 8.5 suggests a simple hydrolytic reaction enabling the release of lysozyme from the PEG-lysozyme conjugates. Both multi-PEGylated 12 kDa PEG-BCN3-lysozyme (**19**) (t = 18 h) and multi-PEGylated 20 kDa PEG-BCN3-lysozyme (**22**) (t = 12 h) showed similar release profiles in Figure 5, while the permanent conjugate made from SC-PEG exhibited no detectable release after the 5 day incubation. The relatively higher release rates in plasma compared to PBS could be influenced by a slight pH difference in plasma (pH 7.6 versus 7.4) or involve additional unidentified nucleophiles in plasma. We do not have evidence of enzyme involvement in the release of lysozyme from the conjugates in rat plasma, although the participation of hydrolytic enzymes in this pathway is possible.

Comparison of rU-PEG-BCN3-Lysozyme and Linear PEG-BCN3-Lysozyme Conjugates. Table 4 summarizes the properties of the rU and linear BCN3 designs and illustrates the benefits of both categories of linkers. The mono-PEGylated conjugates and multi-PEGylated conjugates display release parameters that span a range of hours to days, as would be required for therapeutic applications. The stability of linear PEG-BCN3-lysozyme conjugates (0.3 mg/mL) in PBS, pH 7.4, at different temperatures such as 4 °C, 25 °C, and 37 °C were monitored by analyzing lysozyme activity. The results demonstrated that the stability of linear PEG-BCN3-lysozyme conjugates was temperature dependent, with diminished stability at elevated temperatures. No detectable protein release was observed in multi-PEGylated BCN3-PEG-lysozyme compounds at 4 °C after the five-day incubation.

The release of lysozyme from linear PEG-BCN3-lysozyme conjugates corresponds to the second strand of PEG release from rU-PEG-BCN3-lysozyme conjugates. From our prior results (*20*), it was predicted from considerations of steric hindrance that the second strand PEG liberation from rU-PEG-BCN3-lysozyme would be much faster than the first strand release.

Table 4. Comparison of Release Rates of Branched and Linear BCN3-Lysozyme PEG Conjugates[a]

conjugate	PBS, 37 °C	PBS, 25 °C	PBS, 4 °C	plasma, 37 °C	pH 8.5, 37 °C
		Mono-PEGylated Compounds			
linear 12kDa BCN3-lysozyme (**18**)	4	75	>120	5	N.D.[b]
linear 20kDa BCN3-lysozyme (**21**)	7	37	>120	4	N.D.
rU 24kDa BCN3-lysozyme (**23**)	33	101	>168	14	3.2
mono PEG-lysozyme (12 kDa SC-PEG)[c] (**16**)	N.R.[d]	N.R.	N.R.	N.R.	N.R.
		Multi-PEGylated Compounds			
multi linear BCN3-12kDa-lysozyme (**19**)	65	>96	N.R.	35	18
multi linear BCN3-20kDa-lysozyme (**22**)	40	>96	N.R.	21	12
multi BCN3-rU-24kDa-lysozyme (**24**)	84	>168	N.R.	29	16
multi PEG-lysozyme (12 kDa SC-PEG) (**17**)	N.R.	N.R.	N.R.	N.R.	N.R.

[a] Half-life of protein release (h). [b] N.D. indicates the release was too rapid to determine half-life. [c] SC-PEG forms permanent carbamate linkage. [d] N.R. indicates no release after 96-h incubation.

Table 5. Pharmacokinetic Parameters of IFN-β-1b and PEG-IFN-β-1b Compounds in Mice[a]

compound[b]	route	dose (mg/kg)	AUC (h/ng/mL)	AUC (h/U/mL)	K_HL $t_{1/2}$ (h)	T_{max} (h)	C_{max} (ng/mL)
IFN-β-1b	sc	0.2	226	6780	1.29	1.38	21
BCN3-24k (**25**)	sc	0.2	11248	89984	1.87	4.31	961
BCN3-40k (**26**)	sc	0.2	74792	149584	5.07	9.27	2967
SPA-20k (**27**)	sc	0.2	32610	195660	8.93	12.9	930

[a] sc, subcutaneous; AUC, area under the curve; K_HL, biological half-life; T_{max}, time of maximal concentration; C_{max}, maximal concentration. [b] BCN3-rU-24k-PEG compound has three conjugated 24 kDa U-PEGs per IFN-β-1b; BCN3-rU-40k-PEG compound has two conjugated 40 kDa U-PEGs per IFN-β-1b; SPA-20k-PEG compound has two conjugated linear 20 kDa PEGs per IFN-β-1b.

The results in Table 4 demonstrate that mono-PEGylated linear PEG-BCN3-lysozyme conjugates **18** and **21** ($t = 4$ h when PEG mw is 12 kDa; $t = 7$ h when PEG mw is 20 kDa) indeed showed a statistically significant faster release rate of native lysozyme than that of **23**, the mono-PEGylated 24 kDa rU-PEG-BCN3-lysozyme ($t = 33$ h). We propose that steric hindrance in the rU-PEG design contributes to the slower releasing rates.

The results also show that the release rates of native lysozyme from the multi-PEGylated compounds are slower than from the mono-PEGylated compounds. Possibly, the influence of additional neighboring polymers on the protein surface, with respect to steric effects, is already near maximal at a PEG number of about three polymer strands per protein. There are two to three attachments of U-PEG per lysozyme for 24 kDa rU-PEG-BCN3-lysozyme (**24**), four to five PEG for linear 12 kDa PEG-BCN3-lysozyme (**19**), and three to four PEG for linear 20 kDa PEG-BCN3-lysozyme (**22**).

PEGylation of IFN-β-1b Using rU-PEG-BCN3 Linker. To extend our characterization of the utility of releasable rU-PEG-BCN designs in vivo, we investigated multi-PEGylated derivatives of human IFN-β-1b. Two bioconjugates, 24 kDa rU-PEG-BCN3-IFN-β-1b (**25**) (three U-PEG attachments per protein) and 40 kDa rU-PEG-BCN3-IFN-β-1b (**26**) (two U-PEG attachments per protein), were prepared with a one-step HS cation exchange chromatography as described in Experimental Procedures. We chose these particular experimental compounds for initial examination because they exhibit a comparable total PEG mass (72 kDa and 80 kDa). The compositions of the conjugates were confirmed by molecular mass determinations on SEC, SDS−PAGE, and MALDI-TOF. The increased mass of the di-PEGylated 40 kDa rU-PEG-BCN3 bioconjugate (~108 kDa) and the triple-PEGylated 24 kDa U-PEG bioconjugate (~91 kDa), when compared to the native IFN-β-1b protein (19876 Da), resulted in a marked increase in Stokes radius and apparent molecular size (>1000 kDa) for both bioconjugates due to the hydrophilicity and flexibility of the PEG polymers. The PEGylated IFN-β-1b compounds were stable when stored for a week at 4 °C as described in Experimental Procedures; an additional positive attribute for these multi-PEGylated proteins may prove to be an amelioration of the propensity of IFN-β toward self-aggregation.

Bioassays which measured antiviral activity of IFN-β-1b in cell culture demonstrated the expected specific activity of native IFN-β-1b (30 MIU/mg), and a diminished specific activity for the 40 kDa rU-PEG-BCN3-IFN-β-1b (compound **26**; 2 MIU/mg) and the 24 kDa rU-PEG-BCN3-IFN-β-1b (compound **25**; 8 MIU/mg) compounds. However, it is expected that protein release occurs during the cell incubation in the bioassay for the releasable compounds. Therefore, each analyzed sample was measured with internal controls for both the unmodified and permanently or releasably PEGylated protein. Since the PEG strands are continuously releasing in both in vitro and in vivo environments, it is not possible to obtain a complete image of these molecules without the use of radioisotope tracers and/or real time mass spectrometric analysis. In the current pilot investigation, an initial comparative analysis was performed with inclusion of a permanently PEGylated analogue. We observed that an IFN-β-1b permanently conjugated with three attachments of 20 kDa PEG or two attachments of 40 kDa demonstrated virtually undetectable bioactivity with in vitro assays (data not shown). Therefore, as the closest comparative, yet, active molecule, we prepared a conjugate of IFN-β-1b with two 20 kDa PEG polymers, randomly attached via an SPA linker (compound **27**; 6 MIU/mg). This conjugate also demonstrated similar characteristics to a conjugate with a single permanent 40 kDa branched PEG (data not shown).

Pharmacokinetics of IFN-β-1b and PEG-BCN3-IFN-β-1b in Mice. Pharmacokinetic (PK) parameters of the IFN-β-1b, PEG-SPA conjugate, and the PEG-BCN3 conjugates were determined following subcutaneous administration in mice of 0.2 mg/kg of protein (Table 5). Plasma samples in EDTA were stored in dry ice before analysis. The antiviral bioactivity assay was employed for measurement of active compounds in the collected plasma samples, as described in Experimental Procedures. Protein quantities of IFN-β-1b in these samples were derived from the determined specific activity of the parent bioconjugates. An ELISA assay which measured total compound concentrations was also developed for analysis of the PK parameters. While these immunoassay and bioactivity data were in agreement in ranking the PK profiles for the bioconjugates, the sensitivity of the ELISA format did not permit detection of the non-PEGylated IFN-β-1b in the PK analysis due to its rapid elimination (data not shown). Subcutaneous administration of the 24 kDa rU-PEG-BCN3-IFN-β-1b (**25**) and 40 kDa rU-PEG-BCN3-IFN-β-1b (**26**) compounds resulted in a 50-fold and 330-fold increase, respectively, in area under the curve (AUC; h·

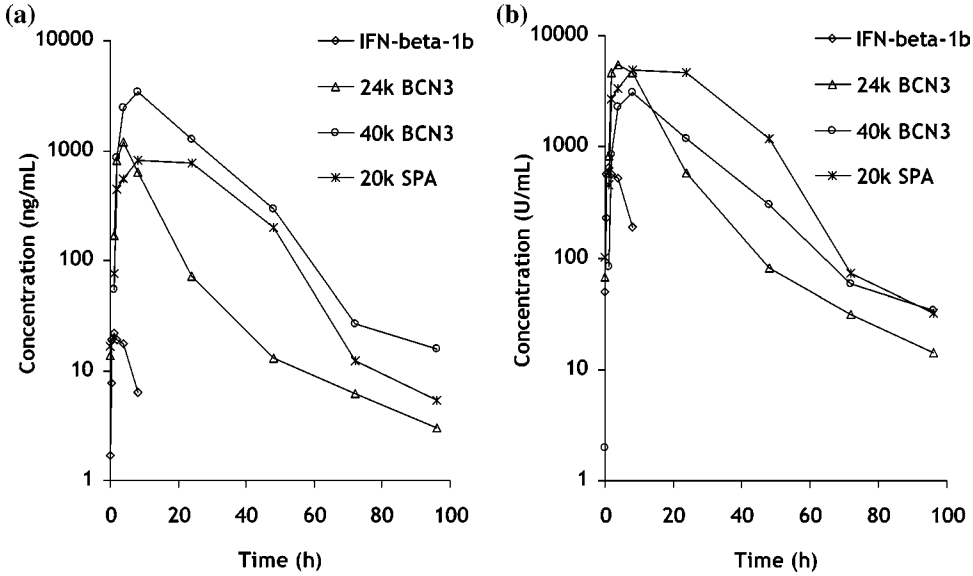

Figure 6. Pharmacokinetics of IFN-β-1b and BCN3 multi-PEGylated IFN-β-1b in mice. Subcutaneous administration of 0.2 mg of IFN-β-1b protein/kg for IFN-beta-1b (◇), 24 kDa rU-PEG-BCN3 multi-PEGylated IFN-β-1b (**25**) (△), 40 kDa rU-PEG-BCN3 multi-PEGylated IFN-β-1b (**26**) (○); and 20 kDa linear PEG-SPA multi-PEGylated IFN-β-1b (**27**) (×); mean of three mice per group. (A) The PK profiles are shown with ng protein/mL. (B) The PK profiles are shown with U/mL. The IFN-β-1b conjugates have either two (40 kDa rU-PEG-BCN3); two (20 kDa linear PEG-SPA); or three (24 kDa rU-PEG-BCN3) attached polymers per IFN-β-1b.

ng/mL) for each protein conjugate compared with native interferon (Figure 6A). As shown in Figure 6B, the extensions of AUC for the BCN3 derivatives relative to native protein or the permanent conjugate, when determined in units of antiviral activity by bioassay, are less pronounced due to the diminished in vitro activity of the releasable conjugates.

The expansive prolongation of pharmacological exposure for BCN3 bioconjugates addresses a limitation of native interferons as therapeutics due to their rapid systemic elimination, and the observed systemic exposure of the BCN3 released IFN-β activity over a period of hours to days is within a therapeutically useful range. While the investigated conjugates were chosen to exhibit an intermediate degree of PEGylation (two to three attachments per interferon), one can expect that purified conjugates containing BCN3 attachments ranging from only one, up to twelve amine-directed sites per interferon, could be similarly produced and that the controlled release of the native interferon could be designed to span an even larger pharmacokinetic profile. As shown in Table 5, a markedly increased maximal concentration and total exposure may be achieved with the BCN3 bioconjugates, and this correlates with a diminished clearance of both PEG-BCN3-IFN-β-1b compounds compared to unmodified IFN-β-1b. Although the pharmacological profile of the optimal permanent PEG conjugate showed similar benefits, the data support further investigation of rPEGylated interferons that examine the key in vivo performance parameters corresponding to efficacy or pharmacodynamic biomarkers. Indeed, we expect that therapeutics utilizing releasable PEG polymers can only be fully understood by monitoring in vivo biological effects.

CONCLUSIONS

We describe the synthesis and in vitro and ex vivo performance of a new releasable linker, i.e., the linear PEG-BCN3 linker, designed for the controlled release of proteins and other macromolecules from their PEG conjugates. The design of the linear PEG-BCN3 linker was accomplished by selective esterification of the hydroxyl group of bis-*N*-2-hydroxyethylglycinamide derivative followed by a temporary capping of the second hydroxyl group with the acetyl function, which can be quickly removed by in vivo hydrolysis. The conjugation of the linear PEG-BCN3 linker with proteins proceeded similarly to the branched rU-PEG-BCN3 linker in both the mono-PEGylation and multi-PEGylation approaches. The rate of protein release from the linear PEG conjugates in general was faster than with the rU-PEG counterparts. This phenomenon could be due to reduced hindrance of the linear PEG conjugates toward esterase or nonenzymatic hydrolysis of the PEG conjugates. Steric hindrance within the linker structure has frequently played an important role in the release kinetics of proteins from their PEG conjugates.

The PEG-BCN3 linker displays suitable characteristics for applications in formulation of therapeutic proteins. Our results support the performance of both types of PEG-BCN3 linkers in regeneration of physically and functionally equivalent native proteins from their PEG-conjugates in a therapeutically relevant period of hours to days. Although attachment of permanent PEG polymers will continue to offer benefits to clinical protein candidates, it will be instructive to determine whether those protein therapeutics which exhibit significant activity losses following conjugation might demonstrate superior effects with releasable PEGylation. The ability to apply PEGylation in a controlled release fashion opens new opportunities to capture the inherit benefits of PEGylation. New clinical uses and routes of administration may be facilitated by the tailored pharmacokinetics employing releasable PEG linkers that can gradually deliver the sequestered authentic drug compounds. The two model compounds in our investigations illustrate these possibilities. Enzyme therapeutics, such as lysozyme, may be inactivated by permanent PEGylation due to the requirement for extended substrate interactions with an expansive and intricate active site cleft. Unlike many conventional PEG modified cytokines and growth factors, rPEGylated interferons may reacquire full bioactivity in vivo following programmed release. Since an interferon's biodistribution, potency, bioavailability, immunogenicity, antigenicity, and other pharmacological properties may be improved by diverse formulation approaches, it will be particularly interesting to further explore the in vivo consequences of rPEGylated interferon compounds. The benefits in avoidance of early systemic clearance mechanisms and the designed deposition of released native protein therapeutics offer a new avenue to the application of PEGylation science.

ACKNOWLEDGMENT

We thank Sam Liu and Magda Mendez for preparation of IFN-β-1b. We are grateful to Mary Mehlig and Cliff Longley for performance of animal studies and pharmacokinetic data analysis. We also thank Jack Lipman for a critical review of the manuscript and Carol Aitken for clerical assistance.

LITERATURE CITED

(1) Harris, J. M., and Chess, R. B. (2003) Effect of PEGylation on pharmaceuticals. *Nat. Rev. Drug Discovery 2*, 214−221.

(2) Frokjaer, S., and Otzen, D. E. (2005) Protein drug stability: a formulation challenge. *Nat. Rev. Drug Discovery 4*, 298−306.

(3) Greenwald, R. B. (2001) PEG drugs: an overview. *J. Controlled Release 74*, 159−171.

(4) Bailon, P., Palleroni, A., Schaffer, C. A., Spence, C. L., Fung, W. J., Porter, J. E., Ehrlich, G. K., Pan, W., Xu, Z. X., Modi, M. W., Farid, A., Berthold, W., and Graves, M. (2001) Rational design of a potent, long-lasting form of interferon: a 40 kDa branched poly(ethylene glycol)-conjugated interferon α-2a for the treatment of hepatitis C. *Bioconjugate Chem. 12*, 195−202.

(5) Grace, M., Youngster, S., Gitlin, G., Sydor, W., Xie, L., Westreich, L., Jacobs, S., Brassard, D., Bausch, J., and Bordens, R. (2001) Structural and biologic characterization of pegylated recombinant IFN-α2b. *J. Interferon Cytokine Res. 21*, 1103−1115.

(6) Lee, L. S., Conover, C., Shi, C., Whitlow, M., and Filpula, D. (1999) Prolonged circulating lives of single-chain Fv proteins conjugated with poly(ethylene glycol): a comparison of conjugation chemistries and compounds. *Bioconjugate Chem. 10*, 973−981.

(7) Yang, K., Basu, A., Wang, M., Chintala, R., Hsieh, M.-C., Liu, S., Hua, J., Zhang, Z., Zhou, J., Li, M., Phyu, H., Petti, G., Mendez, M., Janjua, H., Peng, P., Longley, C., Borowski, V., Mehlig, M., and Filpula, D. (2003) Tailoring structure−function and pharmacokinetic properties of single-chain Fv proteins by site-specific PEGylation. *Protein Eng. 16*, 761−770.

(8) Rosendahl, M. S., Doherty, D. H., Smith, D. J., Carlson, S. J., Chlipala, E. A., and Cox, G. N. (2005) A long-acting, highly potent interferon α-2 conjugate created using site-specific PEGylation. *Bioconjugate Chem. 16*, 200−207.

(9) Pepinsky, R. B., Lepage, D. J., Gill, A., Chakraborty, A., Vaidyanathan, S., Green, M., Baker, D. P., Whalley, E., Hochman, P. S., and Martin, P. (2001) Improved pharmacokinetic properties of a polyethylene glycol-modified form of interferon-β-1a with preserved in vitro bioactivity. *J. Pharmacol. Exp. Ther. 297*, 1059−1066.

(10) Tsunoda, S., Ishikawa, T., Yamamoto, Y., Kamada, H., Koizumi, K., Matsui, J., Tsutsumi, Y., Hirano, T., and Mayumi, T. (1999) Enhanced antitumor potency of polyethylene glycolylated tumor necrosis factor-α: a novel polymer-conjugation technique with a reversible amino-protective reagent. *J. Pharmacol. Exp. Ther. 290*, 368−372.

(11) Roberts, M. J., and Harris, J. M. (1998) Attachment of degradable poly(ethylene glycol) to proteins has the potential to increase therapeutic efficacy. *J. Pharm.. Sci. 87*, 1440−1445.

(12) Lee, S., Greenwald, R. B., McGuire, J., Yang, K., and Shi, C. (2001) Drug delivery systems employing 1,6-elimination: releasable poly(ethylene glycol) conjugates of proteins. *Bioconjugate Chem. 12*, 163−169.

(13) Greenwald, R. B., Pendri, A., Conover, C. D., Zhao, H., Choe, Y. H., Martinez, A., Shum, K., and Guan, S. (1999) Drug delivery systems employing 1,4- or 1,6-elimination: poly(ethylene glycol) prodrugs of amine-containing compounds. *J. Med. Chem. 42*, 3657−3667.

(14) Greenwald, R. B., Choe, Y. H., Conover, C. D., Shum, K., Wu, D., and Royzen, M. (2000) Drug delivery systems based on trimethyl lock lactonization: poly(ethylene glycol) prodrugs of amine-containing compounds. *J. Med. Chem. 43*, 475−487.

(15) Greenwald, R. B., Yang, K., Zhao, H., Conover, C. D., Lee, S., and Filpula, D. (2003) Controlled release of proteins from their poly(ethylene glycol) conjugates: drug delivery systems employing 1,6-elimination. *Bioconjugate Chem. 14*, 395−403.

(16) Greenwald, R. B., Choe, Y. H., McGuire, J., and Conover, C. D. (2003) Effective drug delivery by PEGylated drug conjugates. *Adv. Drug Delivery Rev. 55*, 217−250.

(17) Zalipsky, S., Qazen, M., Walker, J. A., II, Mullah, N., Quinn, Y. P., and Huang, S. K. (1999) New detachable poly(ethylene glycol) conjugates: cysteine-cleavable lipopolymers regenerating natural phospholipid, diacyl phosphatidylethanolamine. *Bioconjugate Chem. 10*, 703−707.

(18) Tsubery, H., Mironchik, M., Fridkin, M., and Shechter, Y. (2004) Prolonging the action of protein and peptide drugs by a novel approach of reversible polyethylene glycol modification. *J. Biol. Chem. 279*, 38118−38124.

(19) Peleg-Shulman, T., Tsubery, H., Mironchik, M., Fridkin, M., Schreiber, G., and Shechter, Y. (2004) Reversible PEGylation: a novel technology to release native interferon α2 over a prolonged time period. *J. Med. Chem. 47*, 4897−4904.

(20) Greenwald, R. B., Zhao, H., Yang, K., Reddy, P., and Martinez, A. (2004) A new aliphatic amino prodrug system for the delivery of small molecules and proteins utilizing novel PEG derivatives. *J. Med. Chem. 47*, 726−734.

(21) Walsh, S., Shah, A., and Mond, J. (2003) Improved pharmacokinetics and reduced antibody reactivity of lysostaphin conjugated to polyethylene glycol. *Antimicrob. Agents Chemother. 47*, 554−558.

(22) Padlan, E. A. (1994) Antibody−antigen complexes. In *Molecular Biology Intelligence Unit:* Antibody−Antigen Complexes, pp 31−42, R. G. Landes, Austin, TX.

(23) David, M. (2002) Signal transduction by Type I interferons. *BioTechniques 33*, S58−S65.

(24) Rubinstein, S., Familletti, P. C., and Pestka, S. (1981) Convenient assay for interferons. *J. Virol. 37*, 755−758.

(25) Foser, S., Schacher, A., Weyer, K. A., Brugger, D., Dietel, E., Marti, S., and Schreitmuller, T. (2003) Isolation, structural characterization, and antiviral activity of positional isomers of monopegylated interferon α-2a (PEGASYS). *Protein Expr. Purif. 30*, 78−87.

(26) Russell-Harde, D., Knauf, M., and Croze, E. (1995) The use of zwittergent 3−14 in the purification of recombinant human interferon-β ser^{17} (Betaseron). *J. Interferon Cytokine Res. 15*, 31−37.

(27) Karpusas, M., Nolte, M., Benton, C. B., Meier, W., Lipscomb, W. N., and Goelz, S. (1997) The crystal structure of human interferon β at 2.2-Å resolution. *Proc. Natl. Acad. Sci. USA 94*, 11813−11818.

(28) Bertolotto, A., Gilli, F., Sala, A., Capobianco, M., Malucchi, S., Milano, E., Melis, F., Marnetto, F., Lindberg, R. L. P., Bottero, R., Di Sapio, A., and Giordana, M. T. (2003) Persistent neutralizing antibodies abolish the interferon β bioavailability in MS patients. *Neurology 60*, 634−639.

(29) Miron, T., and Wilchek, M. (1993) A simplified method for the preparation of succinimidyl carbonate poly(ethylene glycol) for coupling to proteins. *Bioconjugate Chem. 4*, 568−569.

BC050270C

Orientation and Affinity of HIV-1 Tat Fragments in Tat−TAR Complex Determined by Fluorescence Resonance Energy Transfer

Hong Cao,[§] Natarajan Tamilarasu,[§,†] and Tariq M. Rana*

Department of Biochemistry and Molecular Pharmacology, University of Massachusetts Medical School, Worcester, Massachusetts 01605. Received September 15, 2005; Revised Manuscript Received January 2, 2006

The human immunodeficiency virus (HIV-1) encodes a transcriptional activator protein, Tat, which is expressed early in the viral life cycle and is essential for viral gene expression, replication, and pathogenesis. Tat interacts with the transactivation responsive region (TAR) RNA, a 59-base stem-loop structure located at the 5′-end of all HIV mRNAs. Tat-derived peptides that contain the basic arginine-rich region of Tat are able to form in vitro complexes with TAR RNA, and these peptides provide a well-characterized system for understanding the mechanism of RNA−protein recognition. It is not known how RNA-binding Tat peptides are folded or docked in the Tat−TAR complex, and to what extent structural reorganization occurs upon TAR binding. To address these questions, we developed a fluorescence resonance energy transfer (FRET) system to analyze the interactions between TAR RNA and a Tat protein fragment (aa 38−72) uniquely labeled with donor and acceptor dye molecules, respectively. Using this FRET assay, we determined the binding affinity of Tat (47−58) and Tat (38−72) for TAR RNA under physiological conditions. We also delineated the distance between the N- and C-terminus of Tat (38−72) and the distance between the two termini and the 5′ end of TAR when Tat (38−72) is bound to TAR. Our results suggest that the N- and C-termini of Tat (38−72) are close to each other when the peptide is folded and that the peptide does not go through a large structural change upon TAR binding.

INTRODUCTION

RNA-protein interactions are vital for many regulatory processes, including gene regulation during which proteins specifically interact with binding sites found within RNA transcripts. Human immunodeficiency virus (HIV-1) encodes transcriptional activator protein, Tat, which binds RNA to regulate transcription. Tat is expressed early in the viral life cycle and is essential for viral gene expression, replication, and pathogenesis (reviewed in refs 1−3). Tat enhances the processivity of RNA polymerase II (RNA Pol II) elongation complexes that initiate transcription in the HIV-1 long terminal repeat (LTR) region. To accomplish this, Tat binds the TAR (*trans*-activation responsive) RNA element, a 59-base stem-loop structure located at the 5′ end of all nascent HIV-1 transcripts (*4*). This Tat−TAR interaction results in the recruitment of positive transcription elongation factors that increase the processivity of RNA Pol II.

TAR RNA was originally localized to nucleotides +1 to +80 within the viral long terminal repeat (LTR). Subsequent deletion studies have established that the region from +19 to +42 incorporates the minimal domain that is both necessary and sufficient for Tat responsiveness in vivo (reviewed in ref 4). TAR RNA contains a six-nucleotide loop and a three-nucleotide pyrimidine bulge which separates two helical stem regions (Figure 1). Due to difficulties in Tat purification, small Tat peptides that specifically bind TAR RNA with high affinity have been used in Tat−TAR studies (*5*−*12*). Since Tat-derived peptides containing the basic arginine-rich region of Tat (aa 48−57) are able to form in vitro complexes with TAR RNA (*5*−*12*), these peptides provide a well-characterized system for understanding principles of RNA−protein recognition.

Although Tat peptide−TAR-binding affinities have been well studied by electrophoretic mobility shift assays (*5*−*8*, *12*−*16*), there is little known about Tat peptide−TAR affinities in solution under physiological conditions. RNA molecules can fold into extensive structures containing regions of double-stranded duplexes, hairpins, internal loops, bulged bases, and pseudoknotted structures (*17*). Due to the complexity of RNA structure, the rules governing sequence-specific RNA−protein recognition are not well understood, which makes it difficult to design ligands for sequence-specific RNA recognition. Recent structural and biochemical studies have provided insight into TAR RNA folding in the absence and presence of various ligands and Tat peptides (reviewed in ref 4). NMR studies showed that TAR RNA undergoes structural changes upon L-argininamide and Tat peptide binding (*13*, *18*, *19*). However, it is not known how RNA-binding Tat peptides are folded or docked in the Tat−TAR complex, and to what extent structural reorganization occurs upon TAR binding.

To dissect the Tat−TAR interaction under physiological conditions, we used a fluorescence resonance energy transfer (FRET) assay to determine RNA−peptide binding affinities and the peptide orientation in RNA−protein complexes. We found that the N- and C-termini of Tat (38−72) are close to each other when the peptide is folded and that the peptide does not go through a large structural change upon TAR binding. These findings suggest that the architecture of TAR RNA bulge is the key element that defines intramolecular interactions and structural reorganization essential for Tat peptide−TAR interactions.

* To whom correspondence should be addressed: Tariq M. Rana, Department of Biochemistry and Molecular Pharmacology, University of Massachusetts Medical School, 364 Plantation St., Worcester, MA 01605. Phone: 508-856-6216. Fax: 508-856-6696. E-mail: tariq.rana@umassmed.edu.

§ These authors contributed equally to the work.

† Present address: PTC Therapeutics Inc., 100 Corporate Court, South Plainfield, NJ 07080-2449.

10.1021/bc050277u CCC: $33.50 © 2006 American Chemical Society
Published on Web 02/11/2006

A

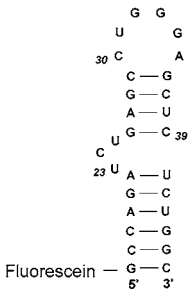

B

Tat(38-72)	FTTKALGISYGRKKRRQRRRPPQGSQTHQVSLSKQ
Rh-Tat(47-58)	N^{α}–Rhodamine-Tat(47-58)
Fl-Tat(47-58)	N^{α}–Fluorescein-Tat(47-58)
Rh-Tat(38-72)	N^{α}–Rhodamine-Tat(38-72)
Tat(38-72)C-Rh	Tat(38-72)Cys-Rhodamine
Fl-Tat(38-72)C-Rh	N^{α}–Fluorescein-Tat(38-72)Cys-Rhodamine

Figure 1. (A) Secondary structure of TAR RNA used in this study. TAR RNA spans the minimal sequences that are required for Tat responsiveness in vivo and for in vitro binding of Tat-derived peptides (*25*). TAR RNA (1 μmole) was chemically synthesized on a CPG 500 support. After deprotection, RNA was purified and characterized as described previously (*26*). (B) Sequence of Tat (38−72) peptide and four dye-labeled Tat peptides indicating the positions of modification. Tat-derived peptides were synthesized by using FastMoc chemistry on an automated 431 ABI peptide synthesizer. Rhodamine or fluorescein attachment at the amino terminal position was accomplished on the solid support using carboxyl derivatives of the dyes and peptide coupling reagent (Schemes I, II, and III). For carboxyl terminal labeling, a Cys residue was added at position 73, which was postsynthetically modified with tetramethylrhodamine-5-iodoacetamide. All dye-Tat conjugates were purified by reverse phase HPLC and characterized by mass spectrometry. The relative dissociation constants for dye-peptides were determined and compared with those of wild-type peptide as described previously (*8*, *27*). Tat peptide modifications did not significantly alter the structure of Tat (38−72), preserving the TAR-binding affinities of the peptide (data not shown).

MATERIALS AND METHODS

Synthesis of Tat (38−72). Tat-derived peptide (amino acids 38−72) was synthesized on HMP[1] resin (Novabiochem) (0.1 mmol) on an Applied Biosystems 431A peptide synthesizer using standard FastMoc protocols. Cleavage and deprotection of the peptide were carried out in reagent K. After cleavage and deprotection, the peptide was purified by HPLC on a Zorbax SB-C8 reverse phase column. The mass of the peptide was confirmed by MALDI mass spectrometry. Calculated mass for tat (38−72), 4083.70 [M + H]; found 4083.55.

Synthesis of N-Terminal-rhodamine Tat (38−72) on Solid Support. An amount of 1.0 μmol of the HMP resin containing the peptide N^{α}-free Tat (38−72) was coupled with 5-carboxy tetramethyl rhodamine (4.3 mg) using HBTU/HOBT (0.45 M in DMF, 22.0 μL) and DIEA (4.0 μL) in NMP (500 μL) for 5 h at room temperature (Scheme 1). All Fmoc-amino acids, piperidine, 4-(dimethylamino)pyridine, dichloromethane, *N*,*N*-dimethylforamide, 1-hydroxybenzotriazole (HOBT), 2-(1*H*-benzotriazol-1-yl)-1,1,3,3-tetramethyluronium hexafluorophosphate (HBTU), diisopropylethylamine (DIEA), and HMP-linked polystyrene resin were obtained from Bachem, CA. Trifluoroacetic acid, 1,2-ethanedithiol, phenol, and thioanisole were from

Scheme 1. Synthesis of N-Terminal-rhodamine Tat(38−72)

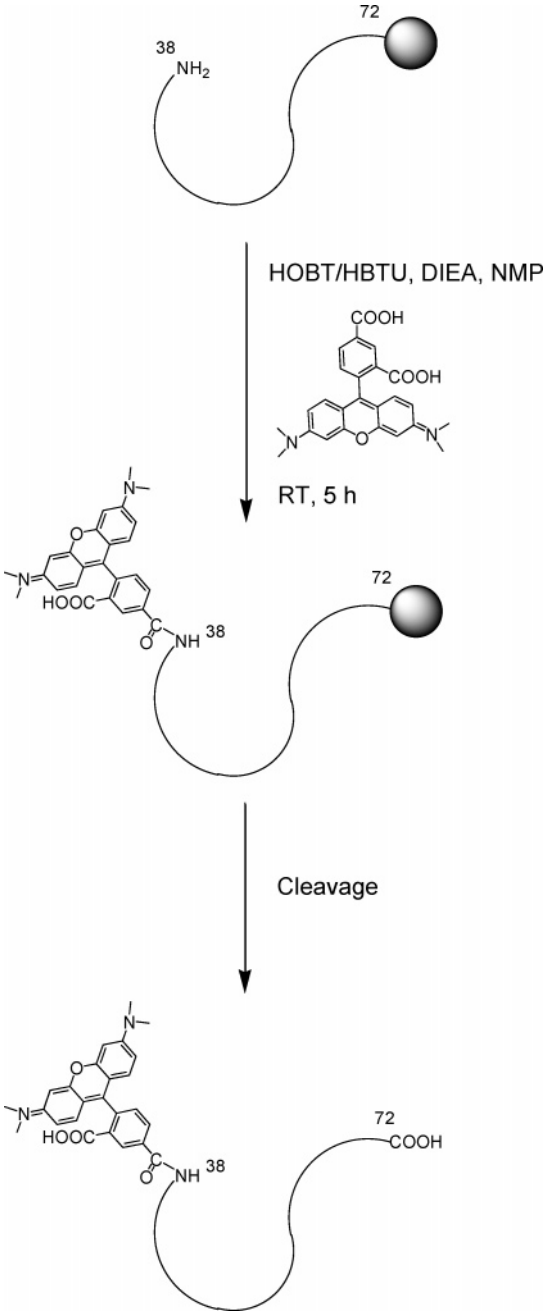

Sigma. Cleavage and deprotection of the peptide was carried out in 2 mL of Reagent K for 6 h at room temperature. Reagent K contained 1.75 mL of TFA, 100 μL of thioanisole, 100 μL of water, and 50 μL of ethanedithiol. The resin was thoroughly washed with NMP followed by dichloromethane and dried. After cleavage and deprotection, the peptide was purified by HPLC on a Zorbax SB-C8 reverse phase column. The mass of the peptide was confirmed by MALDI mass spectrometry. Calculated mass for N-terminal-rhodamine tat (38−72), 4496.16 [M + H]; found 4493.14.

Synthesis of Tat (38−72) Cys-73. Tat-derived peptide (amino acids 38−72) Cys-73 was synthesized on SASRIN resin (BACHEM) (0.1 mmol) on an Applied Biosystems 431A peptide synthesizer using standard FastMoc protocols. Cleavage and deprotection of the peptide were carried out in reagent K. After cleavage and deprotection the peptide was purified by HPLC on a Zorbax SB-C8 reverse phase column. The mass of the peptide was confirmed by MALDI mass spectrometry.

[1] Abbreviations: HMP, 4-hydroxymethylphenoxy, TCEP, tris(2-carboxyethyl)phosphine, NMP, *N*-methylpyrrolidone, DMSO, dimethyl sulfoxide.

Scheme 2. Synthesis of C-Terminal-rhodamine Tat(38−72) Cys-73

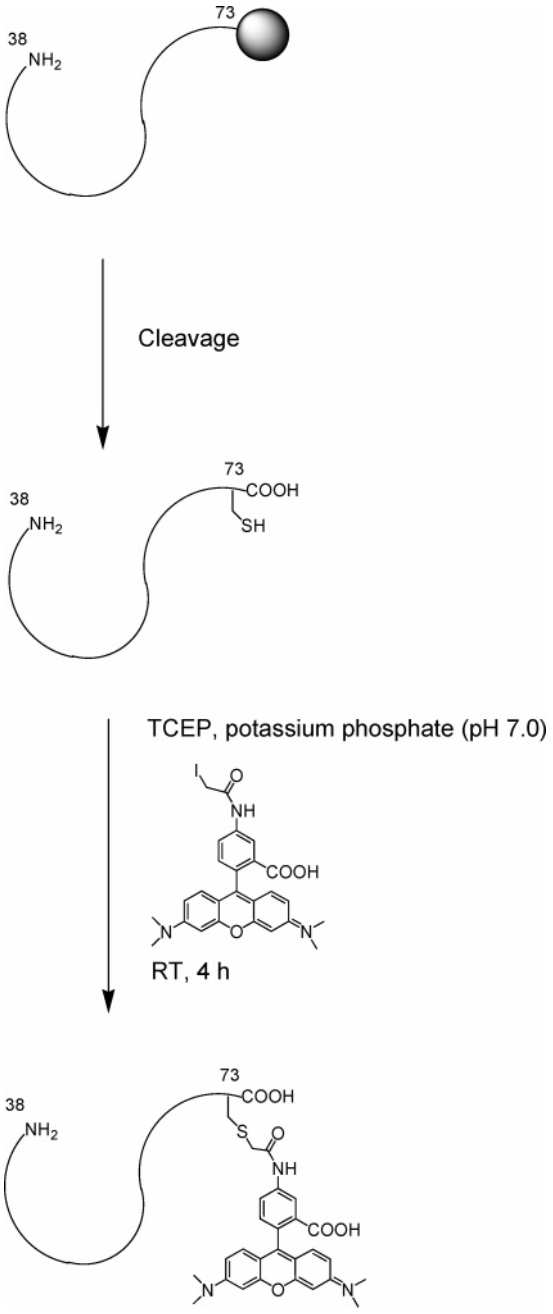

Calculated mass for tat (38−72) Cys-73, 4186.83 [M + H]; found 4185.20.

Synthesis of C-Terminal-rhodamine Tat (38−72) Cys-73. Tat (38−72) Cys-73 (1.0 mM, 500 μL) in potassium phosphate buffer (pH 7.0) containing TCEP (20.0 mM, 50.0 μL) was added to a freshly prepared solution of tetramethylrhoadamine-5-iodoacetamide·2HI (15.0 mM, 100 μL) in DMSO (Scheme 2). The reaction was incubated at room temperature for 4 h and purified by gel filtration (Sephadex G-25, eluent 0.1% TFA/water) followed by reverse phase HPLC (Zorbax SB-C8 reverse phase column). Calculated mass for C-terminal-rhodamine Tat (38−72) Cys-73, 4629.00 [M + H]; found 4631.54.

Synthesis of N-Terminal-fluorescein Tat (38−72) Cys-73. An amount of 2.0 μmol of the resin containing N^{α}-free Tat (38−72) Cys-73 was coupled with 5-carboxyfluorescein (7.5 mg) using HBTU/HOBT (0.45 M in DMF, 44.0 μL) and DIEA (8.0 μL) in NMP (500 μL) for 3 h at room temperature. The resin was thoroughly washed with NMP followed by dichloromethane and dried. Cleavage and deprotection of the peptide were carried out in reagent K (1.0 mL, 5 h, room temperature). After cleavage and deprotection, the peptide was purified by HPLC on a Zorbax SB-C8 reverse phase column. The mass of the peptide was confirmed by MALDI mass spectrometry. Calculated mass for N-terminal-fluorescein Tat (38−72) Cys-73, 4544.9 [M + H]; found 4548.4.

Synthesis of N-Terminal-fluorescein C-Terminal-rhodamine Tat (38−72) Cys-73. N-Terminal-fluorescein Tat (38−72) Cys-73 peptide (38.0 μM, 146.0 μL) in potassium phosphate buffer (pH 7.0) containing TCEP (20.0 mM, 20.0 μL) was added to a freshly prepared solution of tetramethylrhoadamine-5-iodoacetamide·2HI (2.2 mM, 50.0 μL) in DMSO. The reaction was incubated at room temperature for 4 h and purified by gel filtration followed by reverse phase HPLC (Zorbax SB-C8 reverse phase column). Calculated mass for N-terminal-fluorescein C-terminal-rhodamine Tat (38−72) Cys-73, 4987.06 [M + H]; found 4986.46.

Preparation of Dye-Labeled-TAR RNA. RNAs were prepared by chemical and enzymatic methods. Modified TAR RNA was synthesized on an Applied Biosystems Model 392 DNA/RNA synthesizer using 2-cyanoethyl phosphoramite chemistry (Figure 1). All monomers of 2-cyanoethyl phosphoramite were obtained from Glen Research (Sterling, VA). Cleavage and deprotection of dye-labeled RNA was carried out in methanolic ammonia (1 mL) for 16 h at room temperature. After cleavage from the resin, the methanolic supernatant was transferred to an Eppendorff tube and dried under a stream of nitrogen. The green pellet was desilylated in 50% triethylamine trihydrofluoride in dimethyl sulfoxide (0.5 mL) for 16 h at room temperature. The crude red dye-labeled RNA was precipitated by adding 2-propanol (1 mL) at −78 °C for 1 h. The desired RNA was purified on 20% acrylamide−8 M urea denaturing gels.

Measurement of FRET and RNA−Protein Binding Affinities. Fluorescence resonance energy transfer (FRET) from fluorescein to rhodamine was measured on a PTI (Photon Technology International) fluorescence spectrophotometer. The fluorescein-labeled TAR RNA (Fl-TAR) was excited at 490 nm. The emission spectrum was recorded from 500 to 650 nm for each scan. The slits were set 4 nm for both excitation and emission lights. All experiments were carried out in Tris-HCl buffer, pH 7.4, at room temperature.

The initial concentration of Fl-TAR was 10 nM for all experiments. Each addition of rhodamine-labeled Tat (Rh-Tat or Tat-Rh) to the Fl-TAR was followed by a 2 min equilibration before the fluorescence spectrum was recorded. The stock concentration of Rh-Tat (or Tat-Rh) for titration was 2 μM (determined at 555 nm using a molar extinction coefficient (ϵ) of 9.5×10^4 M^{-1} cm^{-1}). The fluorescence intensities were subtracted from background of buffer.

The energy transfer efficiency (E) from donor to acceptor was calculated from the decrease of donor fluorescence intensity at 514 nm according to eq 1.

$$E = \left(1 - \frac{I_{DA}}{I_D}\right) \quad (1)$$

where I_{DA} and I_D are the donor fluorescence intensities in the presence and absence of an acceptor, respectively. The distance (R) between donor and acceptor was calculated according to eq 2.

$$R = R_0(E^{-1} - 1)^{1/6} \quad (2)$$

where $R_0 = 47.6$ Å for the fluorescein−rhodamine pair (*21*). The dissociation constant (K_D) of Tat and TAR RNA complex

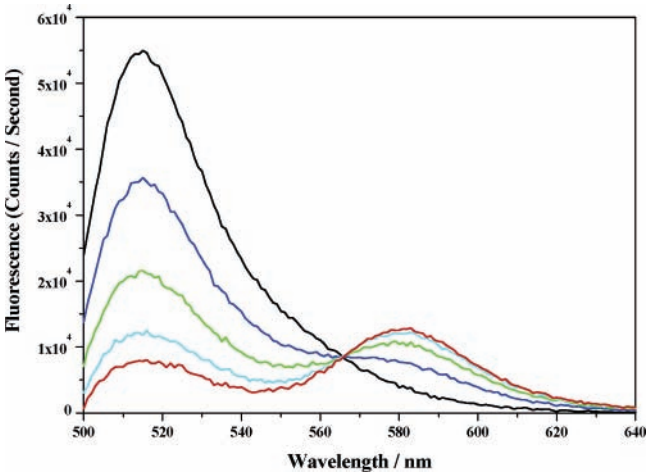

Figure 2. Fluorescence spectra of 10 nM Fl-TAR with (1) 0 nM (black), (2) 3.33 nM (blue), (3) 6.64 nM (green), (4) 9.95 nM (cyan), and (5) 13.25 nM (red) of Rh-Tat(47−58) after excitation at 490 nm.

was determined by using Grafit program (Erithcus software Ltd, version 5) to fit the experimental data. The equation for the fitting was as follows.

$$y = \frac{-(K_D + x + \mathrm{Cap}) + \sqrt{(K_D + x + \mathrm{Cap})^2 - 4x\mathrm{Cap}}}{2} \quad (3)$$

where y is the relative fluorescence intensity of the donor and x is the total ligand (Tat) concentration that is used. Cap is moles of bound ligand.

RESULTS AND DISCUSSION

Determination of Tat (47−58)−TAR RNA Binding Affinity Using FRET. To determine the binding affinities of Tat fragments with TAR RNA under physiological conditions, we developed a fluorescence resonance energy transfer (FRET) system containing TAR RNA and a Tat protein fragment uniquely labeled with donor and acceptor dye molecules, respectively (Figure 1). FRET, in which a fluorescent donor molecule transfers energy via a nonradiative dipole−dipole interaction to an acceptor molecule (which is usually also a fluorescent molecule) is a standard spectroscopic technique for measuring distances in the 10−70 Å range (*20*). The donor's lifetime and quantum yield are reduced upon energy transfer, and the acceptor fluorescence is increased, or sensitized. Quantification of the efficiency of energy transfer allows determination of the distance between the two fluorophores.

The TAR RNA binding region corresponds to amino acids 48−57 of Tat, which has six arginines and two lysines and preferentially binds to the bulge region of TAR. To quantitatively determine Tat−TAR binding affinity using FRET, fluorescein-labeled TAR RNA (Fl-TAR) and rhodamine-labeled Tat (47−58) (Rh-Tat (47−58)) were chemically synthesized as described in Materials and Methods and shown in Figure 1. Gel-shift experiments using equimolar amounts of Tat peptides (modified or unmodified) caused similar mobility shifts in radiolabeled TAR RNA, indicating that neither modification affected the functional properties of Tat or TAR (ref *21*; data not shown). Fluorescein and rhodamine were used because they are a well-characterized fluorescence energy transfer pair with high fluorescence quantum yields and the fluorescein emission and rhodamine absorption spectra overlap significantly.

We measured the fluorescence spectra of F-TAR in the absence and presence of the Rh-Tat (47−58) by exciting at 490 nm (Figure 2). The spectrum of Fl-TAR alone was characterized

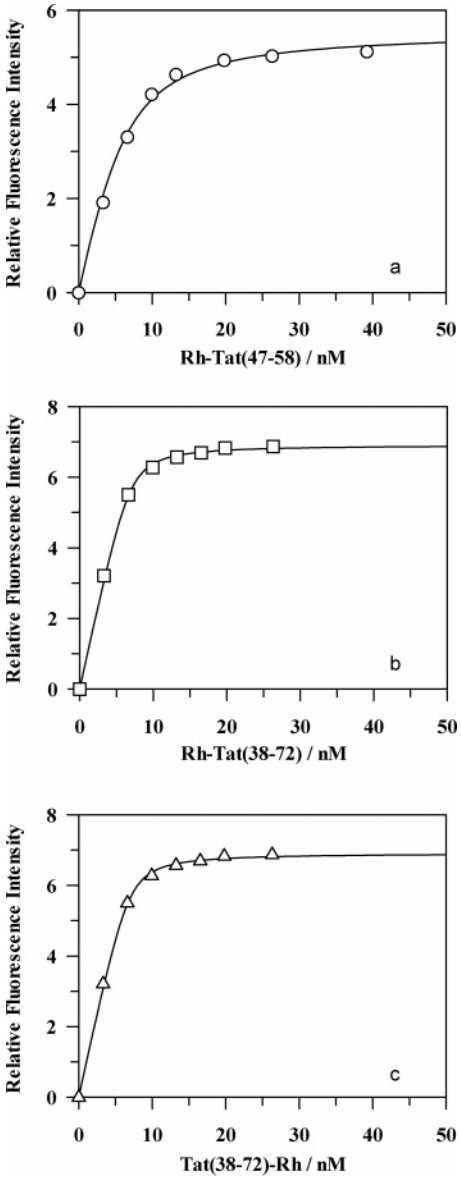

Figure 3. Relative fluorescence intensity (514 nm) of 10 nM Fl-TAR as a function of the concentrations of (a) Rh-Tat (47−58); (b) Rh-Tat (38−72); (c) Tat (38−72)-Rh. The solid lines represent the best fitting of the data by nonlinear regression to eq 3.

by an emission maximum at 514 nm, precisely the wavelength position expected for fluorescein; no emission was recorded at 575 nm. Addition of unlabeled Tat (47−58) caused no change in the intensity of emission (data not shown). Addition of Rh-Tat (47−58), however, resulted in a significant decrease in the intensity of the fluorescein emission at 514 nm and a small increase in rhodamine emission at 575 nm. As predicted, Rh-Tat (47−58) binding to Fl-TAR decreased the distance between the two dyes to within range of Förster distance (R_0) (*20*), which allowed for energy transfer from fluorescein to rhodamine. It is unlikely that the fluorescence intensity of fluorescein was quenched by intramolecular collisions since quenching was only observed in the presence of Rh-Tat (47−58) and not unlabeled Tat (47−58) and because the concentrations for both samples were very low (low nanomolar range).

Figure 3a is a typical titration curve for the binding of Rh-Tat (47−58) to Fl-TAR. While the addition of Rh-Tat (47−58) resulted in a rapid increase in the relative fluorescence intensity, which is the difference between the donor only intensity and the donor intensity in the presence of the acceptor, the same amount of buffer solution did not have any effect on

Table 1. Binding Dissociation Constant, Energy Transfer Efficiency, and Distance between Two Dyes upon Tat and TAR RNA Binding

Tat	K_D (nM)	E (%)	R (Å)
Rh-Tat(47−58)	2.1 ± 0.2	94.4 ± 0.4	29.7
Rh-Tat(38−72)	1.0 ± 0.1	91.2 ± 0.5	32.2
Tat(38−72)C-Rh	0.31 ± 0.04	89.5 ± 0.4	33.3

the fluorescence intensity of Fl-TAR. These results indicated that the enhanced relative fluorescence intensity was a result of specific binding. The data of relative fluorescence intensity as a function of Rh-Tat (47−58) concentration was fitted to eq 3 and a dissociation constant K_D of 2.1 ± 0.2 nM was obtained (Table 1). This K_D value confirmed the formation of a high affinity Tat−TAR complex. We had previously measured a K_D of 0.78 ± 0.05 μM for the formation of the Tat−TAR complex using direct and competition electrophoretic mobility assays (*18*). Since a higher concentration of labeled Tat or TAR is required to detect a gel shift, the K_D value is always underestimated when calculated from gel shift assays. Our fluorescence-based assays were more sensitive than gel shift assays and were performed in an environment that more closely resembles physiological conditions. Therefore, these results demonstrate that we have established a quantitative FRET method to determine RNA−protein binding affinities under physiological conditions.

According to eq 1, energy transfer efficiency (E) can be measured experimentally by calculating the ratio of Fl-TAR intensity in the absence and presence of Rh-Tat (47−58). An efficiency of 94% was obtained from this experiment. Furthermore, a distance of 30 Å between the two dyes was calculated from eq 2 (Table 1). This calculated distance is based on the assumption that both the donor and acceptor have high rotational mobility (*27*) and is supported by the low anisotropy values in our system. The anisotropy are 0.08 and 0.09 for Fl-TAR and Rh-Tat(47−58), respectively. Since the error of energy transfer efficiency is ∼0.4%, this error should not significantly affect the estimated distance between the donor and acceptor.

Binding Affinity of Tat (38−72) to TAR RNA. To address whether additional amino acids from other region outside the basic region of Tat increase its RNA binding affinity, we used FRET to measure the binding affinity of TAR for Tat (38−72), which is composed of core, basic, and glutamine-rich functional regions of Tat. Rhodamine was used to label the N-terminus and C-terminus of Tat (38−72) (Rh-Tat (38−72) and Tat (38−72)-Rh, respectively). The change in fluorescence intensity upon Fl-TAR binding to Rh-Tat (38−72) and Tat (38−72)-Rh are presented in Figure 3b and 3c. A K_D of 1.0 ± 0.1 nM and 0.31 ± 0.04 nM was obtained for Rh-Tat (38−72) and for Tat (38−72)-Rh, respectively (Table 1).

Several control experiments support these findings and demonstrate the specificity of Tat−TAR interactions. First, unmodified Tat (38−72) had no effect on the emission spectrum of Fl-TAR. Second, in the presence of a Tat peptide that does not contain TAR-interacting sequences, quenching of Fl-TAR RNA was not observed. FRET was also not observed when Fl-TAR was incubated with free rhodamine dye. Finally, wild type unlabeled TAR RNA successfully competed with the labeled TAR RNA bound to Tat (38−72) (data not shown), indicating that Fl-TAR RNA and Tat (38−72)-Rh exhibit FRET because they specifically interact. Further by measuring anisotropy changes in Fl-TAR using unlabeled peptides, we obtained K_D values for Tat−TAR that were identical to the values shown in Table 1 (unpublished results).

When comparing the binding affinity of the three different rhodamine-labeled Tat fragments, the TAR−Tat binding affinity ordered from highest to lowest is Tat (38−72)-Rh > Rh-Tat (38−72) > Rh-Tat (48−57). The higher binding affinity of Tat (38−72) as compared to Tat (48−57) is consistent with previous studies that showed that the core region plays an important role in Tat function (*7*, *11*, *12*). Amino acids from the core region make additional contacts with TAR RNA and stabilize the structure of the TAR−Tat complex to enhance the affinity and specificity of Tat for TAR.

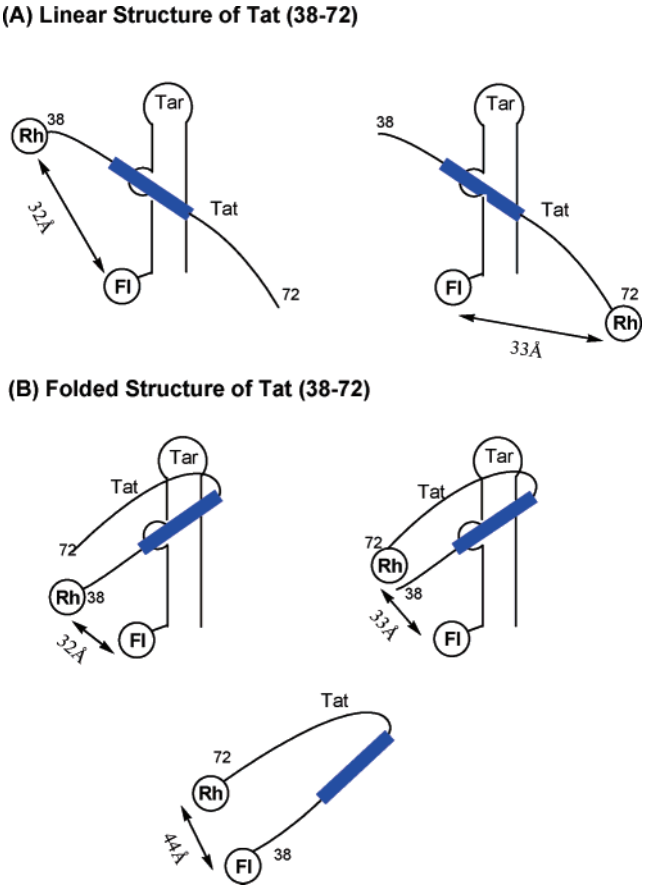

Figure 4. Models for Tat−TAR interactions: (A) linear structure of Tat (38−72), and (B) folded structure of Tat (38−72). RNA-binding region of Tat is highlighted in blue. See text for details.

It is worth noting that the K_D value of TAR−Tat (38−72)-Rh is 3-fold greater than TAR−Rh-Tat (38−72). The only difference between the two Tat conjugates is the position of the rhodamine label. The rhodamine moiety of Tat (38−72)-Rh is relatively far from the basic binding region of Tat (15 aa) and should not influence the binding affinity significantly. However, the N-terminal rhodamine of Rh-Tat (38−72) was conjugated to Tat residue 38, which is near the RNA binding region (within 10 aa) and associated with the core region that significantly contributes to binding. Rhodamine is 12.1 Å (end-to-end distance, according to the structure at a minimum energy), which is equivalent to two amino acid residues (for example, 6.6 Å for lysine and 5.8 Å for arginine). Therefore, it is possible that the relatively bigger rhodamine molecule at the N-terminus of Tat (38−72) weakened hydrogen bonding or diminished van der Waals interaction normally formed between TAR RNA and the core or basic region of Tat (38−72), accounting for the lower binding affinity we observed.

Tat (38−72) Binds TAR in a Folded Conformation. We next used our FRET system and Tat (38−72) labeled with rhodamine at different terminals to determine the conformation of rhodamine-labeled Tat (38−72) when it is bound to RNA. FRET allowed us to estimate the distance between fluorescein and rhodamine when rhodamine-labeled Tat (38−72) was bound to Fl-TAR RNA, which were 32 Å Rh-Tat (38−72) and 33 Å

Scheme 3. Synthesis of N-Terminal-fluorescein and C-Terminal-rhodamine Tat(38−72) Cys-73

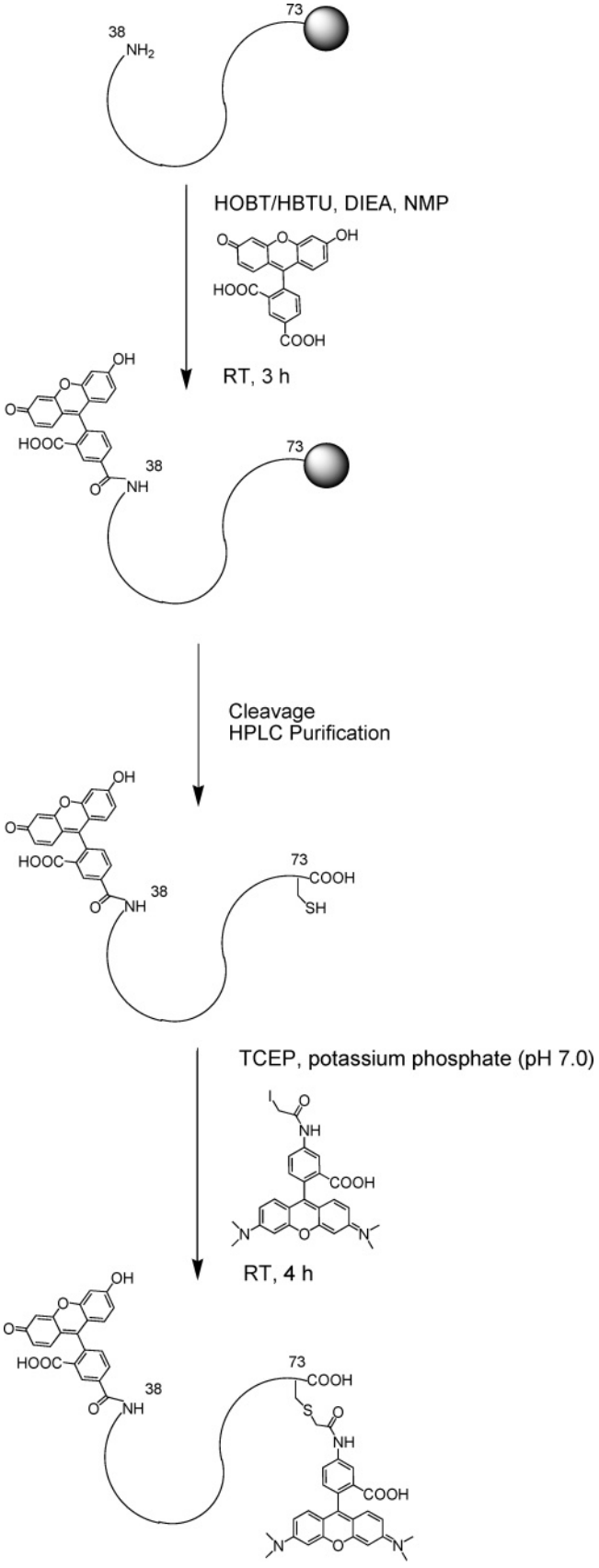

for Tat (38−72)-Rh, respectively (Table 1). Although the binding affinities for Rh-Tat (38−72) and Tat (38−72)-Rh are quite different, the distance between the fluorophores was about the same. To begin to establish the conformation of Tat (38−72) associated with RNA, we first visualized the conformation of Tat (38−72) when bound to RNA if Tat (38−72) had a linear structure (see Figure 4a). In this scenario, the basic region of Tat binds TAR RNA, resulting in the farthest possible distance between its N- and C-termini, but in relation to the fluorescein label at the 5′-end of TAR, the distance between either terminus and fluorescein is the same. On the other hand, if we assume the amino acid sequence of Tat is flexible and amenable to folding (see Figure 4 b), the C-terminus of Tat (38−72) would fold toward the N-terminus bringing them close in proximity. However, in this folded conformation, the distance from either termini to the fluorescein label would still be about the same as when they were farthest apart.

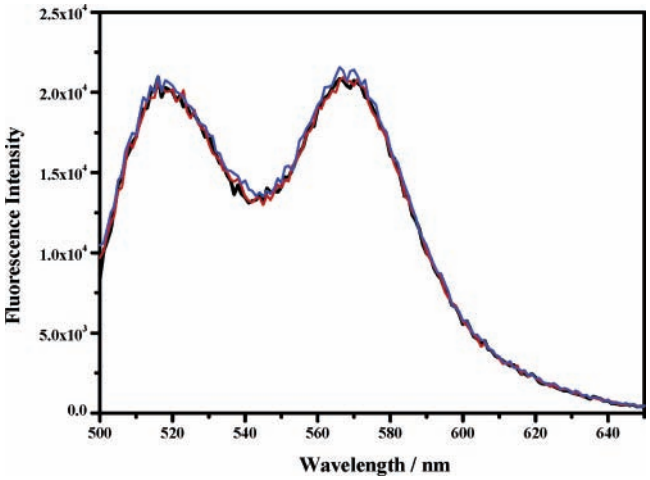

Figure 5. Fluorescence spectra of 10 nM Fl-Tat (38−72)-Rh with 0 nM (black line); 3.33 nM (red line); 558 nM (blue line) wild-type unlabeled TAR RNA after excitation at 490 nm.

To distinguish whether either of our models is correct, we labeled Tat (38−72) with fluorescein on its N-terminus and rhodamine on its C-terminus (Figure 1 and Scheme 3; (Fl-Tat (38−72)-Rh)). Under the same experimental conditions used to measure FRET above, the fluorescence emission spectrum of Fl-Tat (38−72)-Rh after excitation at 490 nm was recorded. The spectrum of Fl-Tat (38−72)-Rh (10 nM) shows two emission bands at 514 and 575 nm (Figure 5), which belong to fluorescein and rhodamine, respectively. To measure FRET, we compared the rhodamine emission detected after direct excitation to the rhodamine emission detected after excitation via fluorescein. The emission of Tat (38−72)-Rh at 575 nm seen after excitation at 490 nm was 50% of the intensity of Fl-Tat (38−72)-Rh at 575 nm. This difference reflected the intramolecular energy transfer from fluorescein to rhodamine in Fl-Tat (38−72)-Rh.

We next synthesized fluorescein-labeled Tat (47−58) (Fl-Tat (47−58)) (Figure 1B) to determine the efficiency of intramolecular energy transfer for Fl-Tat (38−72)-Rh. The fluorescence intensity of Fl-Tat (47−58) (10 nM) at 514 nm after excitation at 490 nm was about 3-fold greater than Fl-Tat (38−72)-Rh under exactly the same conditions. From this measurement, we were able to calculate an intramolecular energy transfer efficiency, E, of 60% for Fl-Tat(38−72)-Rh. The distance R between the N-terminal fluorescein and C-terminal rhodamine of Fl-Tat (38−72)-Rh is 44 Å (Figure 4b). These results suggest that Tat (38−72) has a folded structure and is not in a linear conformation because FRET can only be observed if the two termini are close enough in proximity for energy transfer. According to Förster theory, when R is greater than R_0, the energy transfer efficiency decreases steeply since E is inversely proportional to the sixth power of R. The Förster distance depends on the donor−acceptor dye pair which was

fluorescein−rhodamine in our experiments. If Tat (38−72) was linear, the distance between the two termini should be much longer than R_0 and would not allow for the energy transfer we observed for Fl-Tat (38−72)-Rh. Titration of Fl-Tat (38−72)-Rh with up to ∼560 nM of wild-type TAR RNA did not alter the emission spectra observed with Fl-Tat (38−72)-Rh alone (Figure 5), suggesting that the distance between the N- and C-terminus is maintained before and after RNA binding. This observation indicates that Tat (38−72) was in a folded conformation regardless of whether it was bound to TAR RNA. This finding is consistent with the structure of the bovine immunodeficiency virus (BIV) Tat−TAR complex determined previously by NMR (*22*, *23*). These studies showed that the RNA-binding region of Tat adopts a β-turn conformation rather than a linear conformation. Computer modeling of HIV-1 Tat−TAR complexes (*24*) also suggested that HIV-1 Tat(46−58) forms a hairpin loop when complexed with TAR that is strikingly similar to the hairpin formed by the structure of BIV Tat protein.

Combining all of the distances derived from our FRET analysis, we can visualize the distance between the two termini of Tat (38−72) and the distance from each terminal end to the 5′-end of TAR RNA. These results suggested the possible orientation of Tat peptide in the Tat−TAR complex where the amino and carboxyl termini of Tat (38−72) are close to each other but they are arranged in three-dimensional space at equal distance from the 5′-end of TAR RNA (Figure 4). Collectively, this study demonstrates that the N- and C-termini of Tat (38−72) are in close proximity to each other when the peptide is folded and that the peptide does not go through a large structural change upon TAR binding.

ACKNOWLEDGMENT

This work was supported in part by NIH grants AI 41404 and AI43198.

LITERATURE CITED

(1) Cullen, B. R. (1998) HIV-1 auxiliary proteins: making connections in a dying cell. *Cell 93*, 685−92.
(2) Karn, J. (1999) Tackling Tat. *J. Mol. Biol. 293*, 235−254.
(3) Taube, R., Fujinaga, K., Wimmer, J., Barboric, M., and Peterlin, B. M. (1999) Tat transactivation: a model for the regulation of eukaryotic transcriptional elongation. *Virology 264*, 245−253.
(4) Rana, T. M., and Jeang, K. T. (1999) Biochemical and functional interactions between HIV-1 Tat protein and TAR RNA. *Arch Biochem. Biophys. 365*, 175−185.
(5) Calnan, B. J., Biancalana, S., Hudson, D., and Frankel, A. D. (1991) Analysis of arginine-rich peptides from the HIV Tat protein reveals unusual features of RNA-protein recognition. *Genes Dev. 5*, 201−10.
(6) Calnan, B. J., Tidor, B., Biancalana, S., Hudson, D., and Frankel, A. D. (1991) Arginine-mediated RNA recognition: the arginine fork. *Science 252*, 1167−71.
(7) Churcher, M. J., Lamont, C., Hamy, F., Dingwall, C., Green, S. M., Lowe, A. D., Butler, J. G., Gait, M. J., and Karn, J. (1993) High affinity binding of TAR RNA by the human immunodeficiency virus type-1 tat protein requires base-pairs in the RNA stem and amino acid residues flanking the basic region. *J. Mol. Biol. 230*, 90−110.
(8) Huq, I., and Rana, T. M. (1997) Probing the proximity of the core domain of an HIV-1 Tat fragment in a Tat−TAR complex by affinity cleaving. *Biochemistry 36*, 12592−9.
(9) Wang, Z., Huq, I., and Rana, T. M. (1999) Proximity of a Tat peptide to the HIV-1 TAR RNA loop region determined by site-specific photocross-linking. *Bioconjugate Chem. 10*, 512−9.
(10) Wang, Z., and Rana, T. M. (1998) RNA−protein interactions in the Tat-trans-activation response element complex determined by site-specific photocross-linking. *Biochemistry 37*, 4235−4243.
(11) Wang, Z., Shah, K., and Rana, T. M. (2001) Probing Tat peptide−TAR RNA interactions by psoralen photocross-linking. *Biochemistry 40*, 6458−64.
(12) Wang, Z., Wang, X., and Rana, T. M. (1996) Protein orientation in the Tat-TAR complex determined by psoralen photocross-linking. *J. Biol. Chem. 271*, 16995−8.
(13) Long, K. S., and Crothers, D. M. (1995) Interaction of human immunodeficiency virus type 1 Tat-derived peptides with TAR RNA. *Biochemistry 34*, 8885−95.
(14) Long, K. S., and Crothers, D. M. (1999) Characterization of the solution conformations of unbound and Tat peptide-bound forms of HIV-1 TAR RNA. *Biochemistry 38*, 10059−69.
(15) Weeks, K. M., Ampe, C., Schultz, S. C., Steitz, T. A., and Crothers, D. M. (1990) Fragments of the HIV-1 Tat protein specifically bind TAR RNA. *Science 249*, 1281−5.
(16) Weeks, K. M., and Crothers, D. M. (1991) RNA recognition by Tat-derived peptides: interaction in the major groove? *Cell 66*, 577−588.
(17) Tinoco, I., Jr. (2002) Physical chemistry of nucleic acids. *Annu. Rev. Phys. Chem. 53*, 1−15.
(18) Puglisi, J. D., Tan, R., Calnan, B. J., Frankel, A. D., and Williamson, J. R. (1992) Conformation of the TAR RNA-arginine complex by NMR spectroscopy. *Science 257*, 76−80.
(19) Aboul-ela, F., Karn, J., and Varani, G. (1995) The structure of the human immunodeficiency virus type-1 TAR RNA reveals principles of RNA recognition by Tat protein. *J. Mol. Biol. 253*, 313−32.
(20) Lakowicz, J. R. (1999) *Principles of fluorescence spectroscopy*, 2nd ed., Kluwer Academic/Plenum, New York.
(21) Zhang, J., Tamilarasu, N., Hwang, S., Garber, M. E., Huq, I., Jones, K. A., and Rana, T. M. (2000) HIV-1 TAR RNA enhances the interaction between tat and cyclin T1. *J. Biol. Chem. 275*, 34314−34319.
(22) Puglisi, J. D., Chen, L., Blanchard, S., and Frankel, A. D. (1995) Solution structure of a bovine immunodeficiency virus Tat-TAR peptide-RNA complex. *Science 270*, 1200−3.
(23) Ye, X., Kumar, R. A., and Patel, D. J. (1995) Molecular recognition in the bovine immunodeficiency virus Tat peptide-TAR RNA complex. *Chem. Biol. 2*, 827−40.
(24) Seewald, M. J., Metzger, A. U., Willbold, D., Rosch, P., and Sticht, H. (1998) Structural model of the HIV-1 Tat(46−58)-TAR complex. *J. Biomol. Struct. Dyn. 16*, 683−92.
(25) Cordingley, M. G., LaFemina, R. L., Callahan, P. L., Condra, J. H., Sardana, V. V., Graham, D. J., Nguyen, T. M., LeGrow, K., Gotlib, L., Schlabach, A. J., and et al. (1990) Sequence-specific interaction of Tat protein and Tat peptides with the transactivation-responsive sequence element of human immunodeficiency virus type 1 in vitro. *Proc. Natl. Acad. Sci. U.S.A. 87*, 8985−9.
(26) Shah, K., Neenhold, H., Wang, Z., and Rana, T. M. (1996) Incorporation of an artificial protease and nuclease at the HIV-1 Tat binding site of trans-activation responsive RNA. *Bioconjugate Chem. 7*, 283−9.
(27) Huq, I., Wang, X., and Rana, T. M. (1997) Specific recognition of HIV-1 TAR RNA by a D-Tat peptide. *Nat. Struct. Biol. 4*, 881−2.

BC050277U

Diazo Coupling Method for Covalent Attachment of Proteins to Solid Substrates

Yang Wu,[†] Tione Buranda,[‡] Robert L. Metzenberg,[§] Larry A. Sklar,[‡] and Gabriel P. Lopez*[,†]

Department of Chemical and Nuclear Engineering, University of New Mexico, Albuquerque, New Mexico 87131, Department of Pathology and Cancer Research Facility, University of New Mexico Health Sciences Center, Albuquerque, New Mexico 87131, and Department of Biological Sciences, Stanford University, Stanford, California 94305. Received September 16, 2005; Revised Manuscript Received February 6, 2006

We describe a process for covalently linking proteins to glass microscope slides and microbeads in a manner that optimizes the reactivity of the immobilized proteins and that is suitable for high-throughput microarray and flow cytometry analysis. The method involves the diazo coupling of proteins onto activated self-assembled monolayers formed from *p*-aminophenyl trimethoxysilane. Proteins immobilized by this method maintained bioactivity and produced enhanced levels of protein−protein interaction, low background fluorescence, and high selectivity. The binding of immobilized proteins to their specific binding partner was analyzed quantitatively and successfully correlated with solution concentrations. Diazotized surfaces bound more efficiently to proteins containing a hexahistidine tag than those without a his-tag. Moreover, significantly higher reactivity of the immobilized his-tagged proteins was observed on diazotized surfaces than on amine-terminated surfaces. Results suggest that his-tagged proteins are immobilized by reaction of the his-tag with the diazotized surface, thus offering the possibility for preferential orientation of covalently bound proteins.

INTRODUCTION

Understanding of the functions, modification and regulation of proteins will continue to improve our knowledge of complex biological systems (*1*−*4*). Because each biological system can include thousands of different proteins, the ability to simultaneously analyze proteins by a cost-effective and reproducible methodology has become extremely attractive (*5*). Protein arrays that provide high-throughput, quantitative measurement of receptor−ligand complexation are finding applications broadly in proteomics (*6*, *7*), drug development (*8*, *9*), and diagnostics (*10*, *11*). Two popular array formats, planar substrates used in high-throughput microarray technology (*12*−*15*), and microparticle-based assays that can be used for high-throughput flow cytometry (*16*−*18*), have been developed for these applications. Both type of arrays are fabricated by immobilizing receptor proteins onto a solid substrate. The reactivity of the receptor proteins, which can directly affect the sensitivity and specificity of the array, is largely dependent on the immobilization chemistry (*1*, *19*).

There are several substrates commonly used in the fabrication of protein arrays. These include aldehyde-containing silane surfaces (i.e. SuperAldehyde substrate from TeleChem, International Inc.) that react with primary amines on the proteins, amine-terminated surfaces (i.e. GAPS-coated slides from Corning) that carry a positive charge at a neutral pH and will form ionic bonds with negatively charged amino acid residues, Ni-coated surfaces that will specifically bind proteins engineered with histidine tags (*4*, *6*, *20*), BSA-*N*-hydroxysuccinimide modified substrates (*3*, *12*), and glyoxylyl-modified surfaces (*13*). A detailed comparison of several methods for protein immobilization is found in Seong's work (*21*). However, because proteins have a heterogeneous structure, and are very likely to denature or lose activity after immobilization, the search for a suitable solid support for protein arrays remains active (*1*, *22*). The optimization of the orientation and stability of immobilized receptor proteins, which will likely affect binding efficiency and specificity of the immobilized proteins, is one of the issues that remains to be addressed.

We describe a chemical process for covalently linking proteins onto ordinary microscope slides and glass microbeads in a manner that preserves their activity. We have previously used diazo coupling chemistry to covalently immobilize nucleic acids to activated self-assembled monolayers (SAMs)[1] formed from *p*-aminophenyl trimethoxysilane (ATMS) in the manufacture of DNA microarrays(*23*). Our goal in this study is to extend the application of this method to covalently couple proteins to glass substrata. Although the application of diazo coupling reaction for biomolecular immobilization can be traced back to the late 1970s when Stark et al. coupled single-standed DNA on diazotized Whatman paper (*23*), and has been extended to coupling proteins with cellulose (to be used in affinity chromatography) (*24*) as well as polymer supports (*25*), in-depth, quantitative analysis of immobilized proteins over glass substrata has not been performed. To this end, we have characterized the binding efficiency of the substrata and the binding specificity and reactivity of the immobilized proteins. Moreover, because randomly oriented proteins may exhibit severely reduced reactivity, the possibility of directed orientation of the immobilized proteins on the surfaces is also studied. To achieve preferential orientation, hexahistidine-tagged (his-tagged) proteins were used because (a) histidine is one of two common

* To whom correspondence should be addressed. Tel: (505) 277-4939; Fax: (505) 277-5433; E-mail: gplopez@unm.edu.

[†] Department of Chemical and Nuclear Engineering, University of New Mexico.

[‡] Department of Pathology and Cancer Research Facility, University of New Mexico Health Sciences Center.

[§] Stanford University.

[1] Abbreviations: ATMS, *p*-aminophenyl trimethoxysilane; GFP, green fluorescent protein; His_6GFP, hexahistidine-tagged wild-type GFP; HRP, horseradish peroxidase; HisProbe-HRP, HisProbe horserasish peroxidase; FITC, fluorescein-5-isothiocyanate; FITC-antiHRP, FITC-conjugated affinity purified anti-horseradish peroxidase; SAMs, self-assembled monolayers; EtOH, ethanol; MeOH, methanol; BSA, bovine serum albumin; SSC, sodium citrate buffer (0.3 M sodium citrate/3 M sodium chloride); SDS, sodium dodecyl sulfate; FLAG peptide, Asp-Tyr-Lys-Asp-Asp-Asp-Asp-Lys.

10.1021/bc050278m CCC: $33.50 © 2006 American Chemical Society
Published on Web 02/24/2006

amino acids that can be covalently coupled with diazotized surfaces (*25*, *26*), (b) the attachment of a hexahistidine tag is commonly used in the production of recombinant proteins, and (c) currently there are many commercially available his-tagged proteins (*27*−*29*). Our data suggest that the process described results in preferential reaction of the his-tags on proteins with surface diazonium groups, thus enabling covalent immobilization of oriented protein layers.

EXPERIMENTAL PROCEDURES

Materials. *p*-Aminophenyl trimethoxysilane (ATMS) (90%; Gelest Inc., PA), sodium nitrite (Sigma, St. Louis, MO), sodium acetate (Sigma), ethanol (EtOH, absolute; Aaper Alcohols and Chemical Company, KY), glycine (Aldrich, WI), 20× SSC (0.3M sodium citrate/3M sodium chloride, Sigma), and SDS (sodium dodecyl sulfate, Sigma) were used as obtained. Glass beads (4.9 μm diameter) were obtained from Duke Scientific Corp. (Palo Alto, CA). Hexahistidine-tagged wild-type green fluorescent protein (His_6GFP, $\lambda_{ex} \approx 395$ nm) and HisProbe horseradish peroxidase (HisProbe-HRP) were obtained from Pierce Biotechnology Inc. (Rockford, IL) and used without further purification. FITC-conjugated, affinity-purified anti-horseradish peroxidase (FITC-antiHRP) was obtained from Jackson ImmunoResearch Laboratories, Inc. (West Grove, PA). M1 anti-FLAG antibody and FITC-FLAG (FITC-DYKDDDDK) were obtained from Sigma. Unless otherwise indicated, all antibodies are monoclonal to ensure high binding specificity. All other biological reagents were obtained from Molecular Probes Inc. (Eugene, OR) and used without further purification unless specified. Protein solutions were made in Tris buffer (100 mM Tris, 150 mM NaCl, pH 7.4 to 8.0, all from Sigma) or Tris-BSA buffer (Tris buffer containing 0.1% bovine serum albumin (BSA), pH 7.5).

Cleaning of Substrata. The covalent attachment of organosilanes to glass surfaces is partially dependent on the number of hydroxyl groups exposed on the substrate (*30*). There are several commonly used methods for cleaning silica substrata, including washes with acid or base solutions (e.g. concentrated HCl (*31*), NH_4OH/H_2O_2(*32*), piranha(*31*, *33*−*36*)), and UV/ozone treatment (*37*−*39*). Eight different chemical cleaning methods for glass were compared by Cras et al. (*30*), who found that 30 min incubation in 1:1 MeOH:HCl followed by an additional 30 min incubation in concentrated H_2SO_4 yielded the highest concentration of surface OH groups after treatment and provided the best surface for subsequent silanization without the requirement of heating or other extreme procedures. This method was chosen as our treatment procedure.

Formation of Silane Layers. After the cleaning procedure, glass slides were rinsed with deionized water (dH_2O) and EtOH, dried in a stream of N_2, and immersed into 3 mM ATMS in toluene for 3 h. ATMS-functionalized glass slides were then rinsed exhaustively in EtOH and dH_2O, dried in a stream of N_2, and stored in an airtight container at 4 °C until further use. After the cleaning procedure, glass beads were rinsed with dH_2O and EtOH, centrifuged briefly at 135 000*g* to remove the rinse solutions, and then incubated with 3mM ATMS in toluene for 3 h with mild vortexing. ATMS-coated glass beads were then washed with EtOH and dH_2O, recentrifuged, and used within 24 h.

Diazotization of ATMS-Functionalized Surfaces. Before reacting with biomolecules, ATMS-coated surfaces were converted to the diazobenzyl form by treatment with a solution containing 40 mL of water, 80 mL of 400 mM HCl, and 3.2 mL of freshly prepared solution of $NaNO_2$ (200 mM) for 30 min at 4 °C (*40*). The diazotized surfaces were then washed three times, each for 3 min, with ice-cold sodium acetate buffer (50 mM, pH 4.7) followed by washing with ice-cold deionized water and then EtOH two times each (5 min washes). The diazotized glass slides were air-dried and gently blotted with Kimwipes (Kimberly-Clark, GA) and kept at 4 °C. Diazotized glass beads were also maintained at 4 °C after discarding the wash solution. Diazotized glass slides or glass beads were used immediately for protein immobilization. Uibel and Harris have carried out quantitative studies of this diazo coupling reaction on porous silica gel, and concluded that a surface coverage of 0.36 μmol/m^2 of amine group resulted in approximately 80% diazotization (*41*−*44*). We estimate a surface coverage of $\approx 2 \times 10^7$ amines per 4.9 μm diameter bead prior to diazotization (*43*, *44*). Assuming an 80% rate of diazotization, we expect at least 1×10^7 diazonium salts per bead to be formed.

Formation of Protein Microarrays. Aliquots (10 μL) of different types and concentrations of sample proteins were loaded into a 96-well microtiter plate prior to each set of experiments. These proteins were transferred onto the diazotized microscope slides using a microarrayer (Packard Bioscience, Meriden CT) at room temperature and > 40% humidity. This array-printing process was computer driven, and took ~ 15min/slide when employing four printing pins. Printed slides were then transferred from the microarrayer to a humid chamber and incubated for 1−4 h at room temperature before use. Printed glass slides were blocked with 1% BSA in Tris (pH 7.5) for 1−2 h and incubated with up to 1 μM solution of complementary antigens or antibodies under a glass coverslip in a humid chamber at room temperature for 2 h, followed by sequential washes in 1 × SSC + 0.1% SDS, 0.1 × SSC + 0.1% SDS, 0.1 × SSC, and dH_2O.

Protein-Bearing Microbeads. Suspensions containing ~100 000 ATMS-functionalized glass microbeads in 400 μL aliquots of pH 8.0 Tris buffer were reacted with nM to 3 μM protein (streptavidin, M1 anti-FLAG antibody, or His_6GFP) for 1 h at room temperature under mild vortexing. The samples were then rinsed with deionized water and resuspended in Tris buffer. The respective site densities of streptavidin, M1 anti-FLAG antibody, and His_6GFP were analyzed on the basis of their binding to fluorescent ligands. It is worth noting that the wild-type His_6GFP obtained from Pierce has an excitation wavelength maximum of 395 nm, which is not suitable for routine flow cytometric detection. Thus a fluorescently labeled anti-GFP was employed to detect the presence of His_6GFP. The experimental procedures used have been described elsewhere (*45*). The binding characteristics of protein-coated beads to fluorescein biotin (streptavidin beads), FITC-FLAG peptides (M1 beads), and Alexa488-antiGFP were generally determined by incubation of 40 000 protein-coated beads in 400 μL of fluorescently labeled ligand solutions (10^{-9} to 10^{-6} M) for 1−2 h, unless otherwise specified. Protein-bearing beads were exposed to 1% BSA in Tris buffer for 1 h before ligand incubation in order to reduce nonspecific binding. Measurements of fluorescence associated with samples blocked with large excesses of nonfluorescent ligands (>5-fold) before exposure to fluorescently labeled ligands were preformed in parallel to estimate nonspecific binding. We determined the amount of specific binding by subtracting signals of blocked samples from unblocked samples and then quantified the fluorescence intensity (488 nm excitation) by comparison to calibrated fluorescent beads (*45*, *46*). For diazotized substrates, nonspecific binding was less then 30% of total binding in all experiments.

Data Collection and Analysis. Protein microarrays were visualized with a confocal laser scanner, GenePix 4000B from Axon Instruments, Inc., and data were processed using the associated image-processing software (GenePix 3.0) (*40*). The surface density of immobilized proteins on beads was determined by centrifugation assays and flow cytometry (*45*, *46*). The flow cytometric analysis used a Becton-Dickinson FACScan

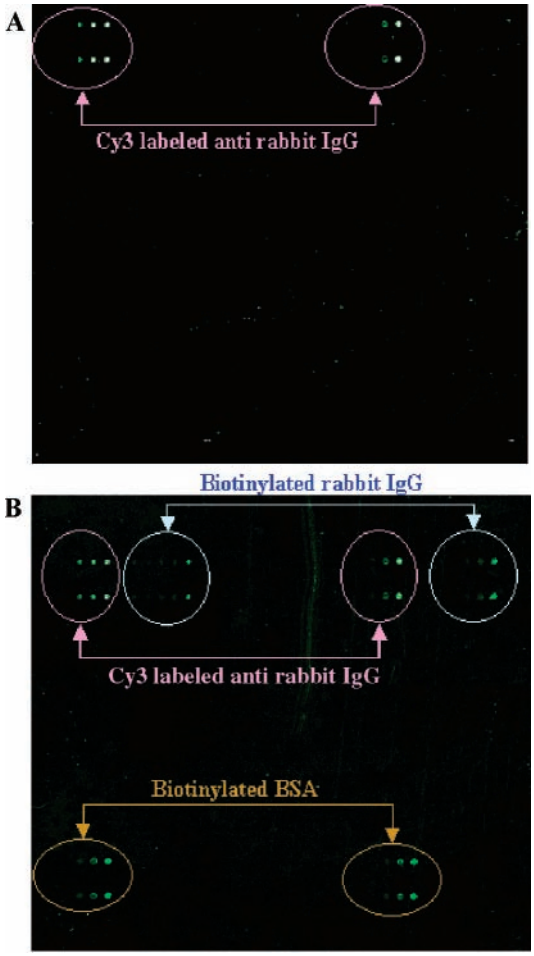

Figure 1. A protein microarray formed on an ATMS/diazotized glass slide. Spot sizes are about 100 μm in diameter. A. Scanned image before FITC-streptavidin incubation. Different proteins were arrayed onto the slide in duplicates of five different concentrations: Cy3-labeled anti mIgG (0.06, 0.6, 6, 60, 600 pM), biotinylated rIgG (0.06, 0.6, 6, 60, 600 pM), and biotinylated BSA (0.3, 3, 30, 300, 3000 pM). B. Scanned image of the same protein microarray after incubation with FITC-streptavidin.

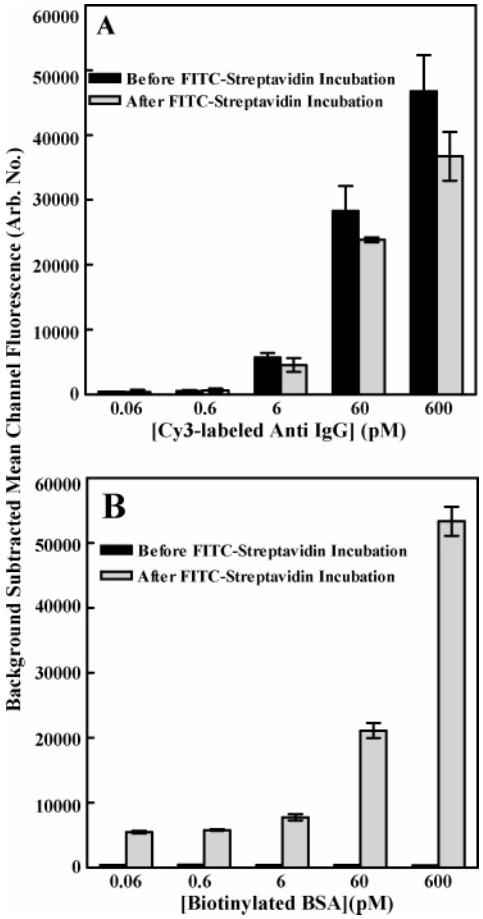

Figure 2. Quantitative intensity analysis of protein microarrays imaged in Figure 1 before and after incubation with FITC-streptavidin. A. Intensity of Cy3-labeled anti mIgG spots (λ_{em} = 530 nm). B. Intensity of biotinylated BSA spots. The microarrays were prepared by spotting the proteins at the concentrations indicated.

flow cytometer (Sunnyvale, CA) interfaced to a Power PC Macintosh running CellQuest software package. The FACScan is equipped with a 15 mW air-cooled argon ion laser. It has been shown elsewhere (*46*) that the mean of the histogram is the quantity relevant to binding capacity. The average fluorescence of a single bead is converted to the number of fluorophores per bead on the basis of flow cytometric calibration beads (*46*). Data were subsequently analyzed using Microsoft Excel or GraphPad Prism software (GraphPad Software, Inc. San Diego, CA).

RESULTS AND DISCUSSION

Protein Microarrays. In a previous report, we demonstrated that the ATMS-based diazo coupling method can produce reusable DNA microarrays that provide uniform DNA spots with high spot intensity (*40*). These microarrays have been used to successfully quantify differential gene expression in different RNA libraries (Dolan P. L., Nelson M. A., unpublished data). Similar experimental procedures were used as a starting point for the fabrication of protein microarrays. Scanned images and quantitative analyses of protein microarrays are presented in Figure 1 and Figures 2 and 3, respectively.

Figure 1 shows the scanned images of a typical protein microarray before (Figure 1A) and after 2 h incubation of 1 μM FITC-labeled streptavidin in Tris−BSA (Figure 1B). Three different proteins, including a fluorescently labeled "control protein", Cy3-anti mouse IgG (Cy3-anti mIgG), and two biotinylated proteins, biotinylated BSA and biotinylated rabbit IgG (rIgG), that bind specifically to FITC-labeled streptavidin, were arrayed on diazotized glass microscope slides at five different concentrations, each in duplicates. The scanned images in Figure 1 show that (1) signals representing the control protein, i.e., Cy3-anti mIgG, appear clearly on both images with similar spot intensity, (2) signals from biotinylated areas are visible only after the incubation in FITC-labeled streptavidin, and (3) the signal intensity of all three types of proteins reflect protein concentration in the spotted samples. Results of spot intensity analysis are shown in Figure 2.

Figure 2A shows the background-subtracted mean spot intensity of Cy3-anti mIgG before and after incubation with FITC-streptavidin. Although some signal decrease is observed (likely due to photobleaching occurring during scanning), neither the mean spot intensity nor the proportional relationship between different concentrations of the immobilized control protein is significantly influenced by the incubation of FITC-streptavidin. In contrast, spot intensities of biotinylated BSA shown in Figure 2B increase dramatically after incubation with FITC-streptavidin, which binds specifically with the biotinylated protein. The spot intensity after FITC-streptavidin incubation reflects the concentration of biotinylated BSA in the spotted samples. Similar results were obtained on the spots of biotinylated rIgG (data not shown). These observations indicate the possibility of applying the diazo coupling method to produce protein microarrays for quantitative analysis.

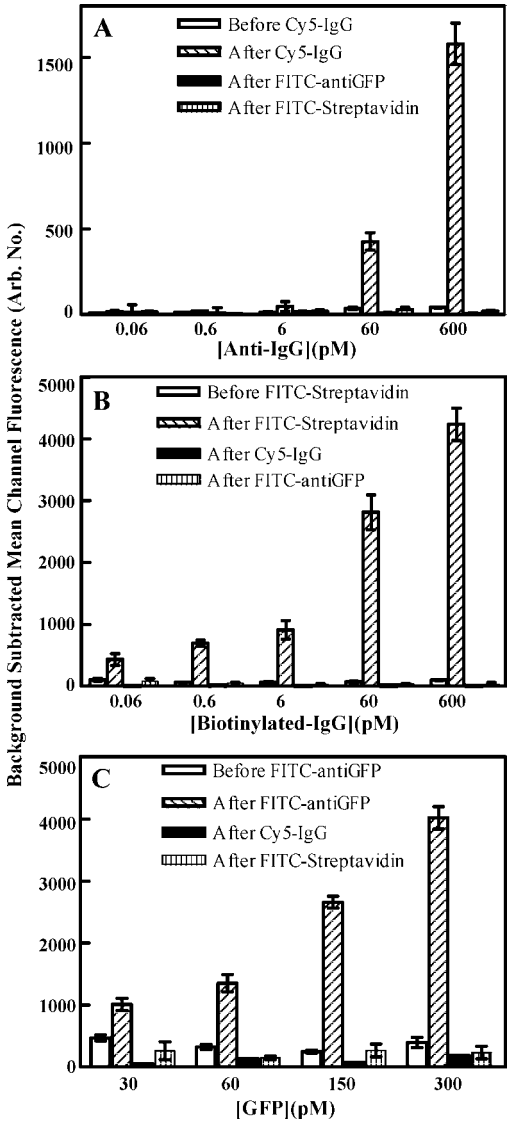

Figure 3. Responses of different proteins arrayed on diazotized surface to their specific binding partner. The microarrays were prepared by spotting the proteins at the concentrations indicated. Intensity of anti-mIgG spots (A), biotinylated rIgG spots (B), and His_6GFP spots (C) before and after the incubation of 1 μM Cy5-mIgG, FITC-streptavidin, or FITC-antiGFP.

An important criterion for the success of covalent protein immobilization strategies is the preservation of bioactivity of immobilized proteins, i.e., their ability to recognize specific binding partners. We demonstrated binding specificity of proteins immobilized on diazotized substrates by first forming microarrays consisted of five different concentrations of three different types of proteins, an antibody (anti-mIgG), an antigen (GFP), and a conjugated protein (biotinylated rIgG). The printed slides were then incubated with Cy5-labeled mIgG, FITC-labeled antiGFP, or FITC-labeled streptavidin at room temperature for 1 h, to compare the reactivity of the arrayed proteins. Intensity analysis results in Figure 3 show all three immobilized proteins bound specifically to their binding partners, and the signal intensities are proportional to the protein concentration in spotted samples. These observations indicate that protein microarrays formed on the ATMS-based diazonium surfaces maintain relatively high binding specificity, and that it is also possible to obtain quantitative data using this protein immobilization method.

Protein-Bearing Micro Particle Assays. Among the 20 common amino acids, only four contain an aromatic ring, and

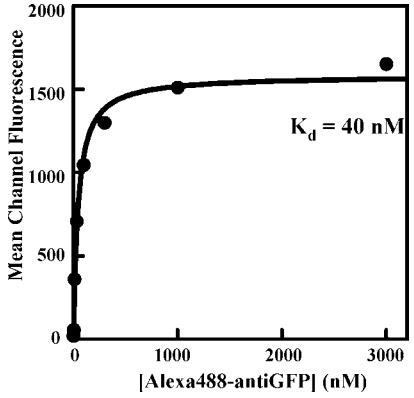

Figure 4. Equilibrium binding curve of Alexa488-antiGFP binding to His_6GFP. Samples for binding curve analysis were prepared by incubating diazotized beads in 400 μL of 200 nM His_6GFP for 1 h at room temperature under mild vortexing, and then the beads were reacted with nM to μM range of Alexa488-antiGFP for 1 h.

of these, only histidine and tyrosine readily bind covalently to diazonium salts (*25*, *26*). Our expectation is that the rapid reaction between the diazonium group and tyrosine or histidine residues in proteins is the basis for the immobilization described here. Polyhistidine tags that consist of five or six contiguous histidine residues, attached to either the N or the C terminus of the protein and exposed at protein surfaces, are widely employed in the purification of recombinant proteins (*28*, *47*). Therefore, we compared the reactivity of diazotized surfaces with proteins bearing and lacking histidine tags.

We investigated the binding of His_6GFP, streptavidin, and M1 anti-FLAG antibody to diazotized glass microbeads (4.9 μm in diameter) and performed quantitative analysis by flow cytometry. We used fluorescein biotin to measure the surface concentration of streptavidin (MW $\sim$ 66 kDa; $K_d = 10^{-13}$ M (*46*, *48*)), FITC-FLAG to detect M1 anti-FLAG antibody (MW $\sim$ 150 kDa; $K_d \sim 8$ nM (*45*)), and Alexa488-antiGFP to detect His_6GFP (MW $\sim$ 27 kDa). High concentrations of fluorescently labeled ligands (at least 10 times higher than K_d) were used in order to ensure characterization of the amount of proteins bound to the diazotized surface at saturation. To determine the affinity of Alexa488-antiGFP to His_6GFP bound to the diazotized bead surface, a binding curve (Figure 4) was measured. A one-site binding hyperbola was used to analyze the experimental data in Prism software, and the best-fit values gave the equilibrium dissociation constant, K_d, after background subtraction, as $\sim$40 nM (Figure 4). On the basis of this result, 400 nM antiGFP (i.e., $10 \times K_d$ of the antiGFP/GFP reaction) was chosen for the characterization of the reaction of His_6GFP with the diazo beads, while 100 nM of FITC-FLAG and 200 nM of fluorescein biotin were chosen to characterize the reaction of M1 and streptavidin, respectively, with the diazotized beads.

Figure 5 compares the binding efficiency of His_6GFP (Figure 5A), streptavidin, and M1 anti-FLAG antibody (Figure 5B). These data indicate that each of the tested proteins was immobilized to the diazotized surface consistently, and that the diazotized surface showed especially high binding of the his-tagged protein. To ascertain whether this is due to high binding reactivity of diazotized surfaces for his-tagged proteins or to the size of the immobilized proteins, the maximum possible protein coverage over diazotized microbead surfaces was estimated. As described in the Experimental Procedures, approximately 1×10^7 active sites/bead are expected after diazotization; however, the degree of protein binding may also depend on characteristics of the protein molecule, e.g., tertiary structures. GFP is an 11-stranded β-barrel threaded by an α-helix running through the axis of the cylinder (*49*). These cylinders have a diameter of about 30 Å and a length of 40 Å (*50*). The

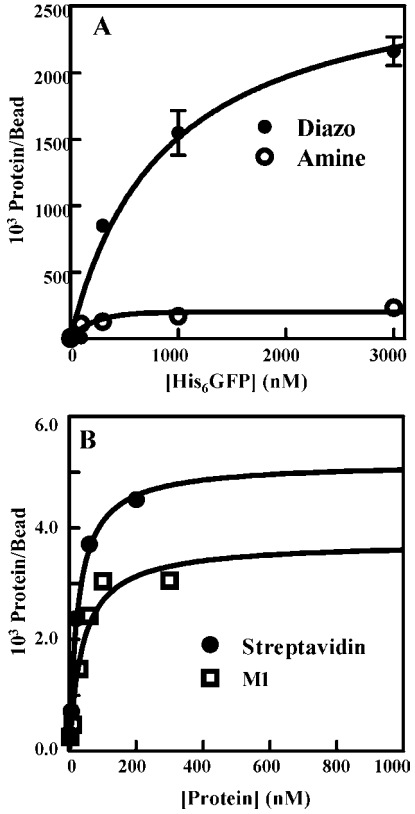

Figure 5. Comparison of diazo coupling reaction for proteins with and without histidine tag. A. Comparison of binding efficiency of His_6GFP with diazotized and amine terminated surface. B. Binding efficiency of proteins without a histidine tag (streptavidin, and M1 anti-FLAG antibody) with diazotized surfaces.

minimum surface coverage for a single GFP molecule is thus ~780 Å^2. Because the surface area of a 4.9 μm diameter bead is ~7.5 × 10^9 Å^2, the maximum number of His_6GFP molecules that can be attached to a 4.9 μm bead is ~1 × 10^7. On the basis of a similar estimation, there should be a maximum of about 4 million streptavidin molecules [dimension ~ 40 Å × 50 Å × 50 Å] (*51*, *52*) and 0.4 million M1 molecules [~15 nm in diameter] that can be packed onto a single 4.9 μm bead.

Results in Figure 5 show that when incubated in 300 nM protein solution, approximately 900 000 His_6GFP molecules per bead were detected, while less than 5000 protein/bead (or less than 0.5% of the bound His_6GFP) were detected for both non-his-tagged proteins (streptavidin and M1 anti-FLAG antibody). Moreover, as illustrated in the Figure, detectable His_6GFP molecules/bead increased to approximately 2.2 million (when the His_6GFP concentration in solution was 3 μM), which is about 20% of the estimated maximum His_6GFP binding sites/bead. Geometrically, the maximum number of His_6GFP that can pack on a single glass bead should only be about twice that of streptavidin and twenty times more than that of M1 anti-FLAG antibody. Thus, these results indicate that the his-tagged proteins are substantially more reactive with the diazotized surface than non-his-tagged proteins.

The identification of an immobilization chemistry that can preserve the reactivity of the bound proteins has always been a challenge for high-throughput protein analysis (*21*, *53*). Reactivity of the surface bound proteins can be a function of the structure, orientation, and packing of the protein. We compared the reactivity of his-tagged proteins for activated diazotized surfaces with their reactivity to unactivated primary amine-terminated surfaces. Figure 5A presents the amount of reactive His_6GFP bound to diazotized and unactivated SAMs formed from ATMS as detected by the binding of Alexa488-antiGFP.

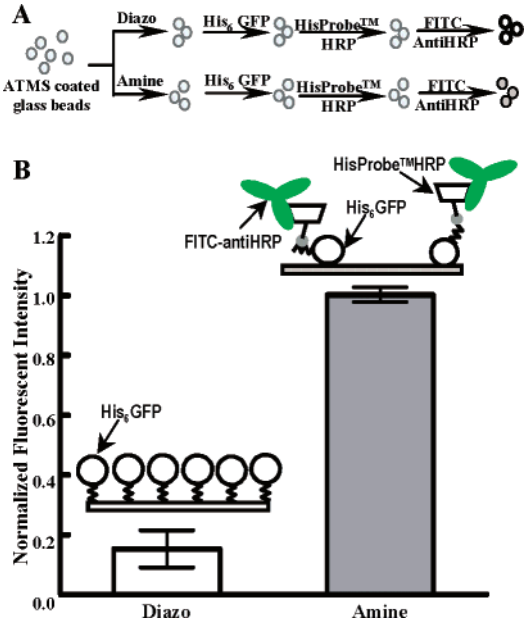

Figure 6. A. Experimental design for studying the reactivity of his-tagged protein immobilized on diazotized surfaces. B. Results of experiments in part A detected by flow cytometry. Diazo: represents response of immobilized His_6GFP on diazotized beads coupled to HisProbe-HRP detected by FITC-antiHRP. Amine: response of immobilized His_6GFP on primary amine-terminated beads coupled to HisProbe HRP detected by FITC-antiHRP. Inserts schematically depict possible protein orientations on each surface.

The amount of reactive his-tagged protein measured on the diazotized surface is considerably higher than that observed on the amine surface, reaching a maximum of 1000% higher at a solution concentration of 3 μM of His_6GFP. Similar experiments with proteins without a his-tag did not show any significant difference between diazotized surfaces and amine-terminated surfaces. These observations indicate that when compared to amine surfaces, the diazo-coupling method can result in much higher levels of adsorbed his-tagged proteins.

Because the ligand binding site(s) over a protein surface is generally asymmetric, the geometric orientation of the immobilized protein may determine whether it retains its binding activity (*22*, *54*). Figure 5A indicates that the coupling reaction of His_6GFP with diazotized beads yields a much greater surface density of the reporter Alexa488-antiGFP antibodies than the primary amine (i.e. unactivated ATMS) surfaces. The reporter antibody (Alexa488-antiGFP) can be considered as an indirect measure of surface His_6GFP coverage. However, it is not possible to definitively distinguish whether the higher surface coverage of the reporter antibody at diazotized surface is due to improved coupling efficiency to His_6GFP molecules, or to proper orientation of GFP that allows optimum antibody capture, or both. To assess whether the results shown in Figure 5 were related to the geometric orientation of the immobilized his-tagged proteins, we further investigated the diazo coupling method as a means of covalent immobilization of oriented proteins on surfaces. An assay specifically targeting surface-accessible his tags using HisProbe-HRP was employed to explore this issue.

HisProbe-HRP is a Ni^{2+} activated HRP derivative, that can be used to detect surface-exposed his-tags (http://www.piercenet.com/). Figure 6A shows a typical experimental scheme that was followed. The results are shown in Figure 6B. The results indicate that a higher amount of HisProbe-HRP is bound to GFP treated primary amine surfaces than to GFP-treated diazotized SAMs. Because HisProbe-HRP is only able to bind to surface-exposed histidine residues, this indicates that

few his-tags are available for binding on the GFP-treated diazotized SAMs. Taken together with the data presented in Figure 5A, these results suggest that high levels of His_6GFP were bound to the diazotized SAMs, and that a large percentage of the immobilized His_6GFP was bound in an oriented fashion on these surfaces (see inserts of Figure 6B). These proteins were likely coupled to the diazotized surfaces via a covalent linkage to the his-tags. The results further suggest that amine-terminated surfaces do not react as efficiently with his-tagged proteins as diazotized surfaces, and that they may react nonspecifically with other negatively charged amino acid residues scattered on the protein surface, as discussed previously (*21*), to result in a nonpreferential orientation of the adsorbed His_6GFP molecules.

SUMMARY

A diazo coupling method was used to covalently immobilize proteins onto solid substrates. When compared with commonly used microarray supports, e.g., amine-terminated surfaces, the diazotized surfaces provide low background fluorescence and high signal/noise ratio. Proteins containing a hexahistidine tag exhibited over 10× higher reactivity compared to non-his-tagged proteins. Results indicate that immobilized his-tagged proteins are likely coupled to diazotized surfaces through the histidine tag, which allows for preferential orientation of the immobilized proteins and thereby can be used to optimize the reactivity of the protein to interact with specific binding partners. Because of the wide availability of his-tagged proteins, the described surface immobilization described herein may be useful in the fabrication of protein arrays and protein-coated microbeads for high throughput analyses.

ACKNOWLEDGMENT

This project was funded by the National Science Foundation (Grant CTS-0332315), the National Institutes of Health (Grant GM60799/EB00264), and the Department of Energy through the US/Mexico Materials Corridor Initiative.

LITERATURE CITED

(1) Kusnezow, W., and Hoheisel, J. (2003) Solid supports for microarray immunoassays. *J. Mol. Recognit. 16*, 165−176.

(2) Beier, M., and Hoheisel, J. (1999) Versatile derivatisation of solid support media for covalent bonding on DNA-microchips. *Nucleic Acids Res. 27*, 1970−1977.

(3) MacBeath, G., Koehler, A., and Schreiber, S. (1999) Printing small molecules as microarrays and detecting protein−ligand interactions en masse. *J. Am. Chem. Soc. 121*, 7967−7968.

(4) Zhu, H., Bilgin, M., Bangham, R., Hall, D., Casamayor, A., *et al.* (2001) Global analysis of protein activities using proteome chips. *Science 293*, 2101−2105.

(5) Huang, J., Mehrens, D., Wiese, R., Lee, S., Tam, S., *et al.* (2001) High-throughput genomic and proteomic analysis using microarray technology. *Clin. Chem. 47*, 1912−1916.

(6) MacBeath, G. (2001) Proteomics comes to the surface − Microarrays of purified proteins, representing most of the yeast genome, prove useful for studying protein function on a genome-wide scale. *Nat. Biotechnol. 19*, 828−829.

(7) MacBeath, G. (2002) Protein microarrays and proteomics. *Nature Genet. 32*, 526−532.

(8) Zhu, H., Bilgin, M., and Snyder, M. (2003) Proteomics. *Annu. Rev. Biochem. 72*, 783−812.

(9) Lee, Y., Kang, D. K., Chang, S. I., Han, M. H., and Kang, I. C. (2004) High-throughput screening of novel peptide inhibitors of an integrin receptor from the hexapeptide library by using a protein microarray chip. *J. Biomol. Screening 9*, 687−694.

(10) Nishizuka, S., Chen, S. T., Gwadry, F. G., Alexander, J., Major, S. M., et al. (2003) Diagnostic markers that distinguish colon and ovarian adenocarcinomas: identification by genomic, proteomic, and tissue array profiling. *Cancer Res. 63*, 5243−5250.

(11) Yuk, C. S., Lee, H. K., Kim, H. T., Choi, Y. K., Lee, B. C., *et al.* (2004) Development and evaluation of a protein microarray chip for diagnosis of hepatitis C virus. *Biotechnol. Lett. 26*, 1563−1568.

(12) MacBeath, G., and Schreiber, S. (2000) Printing proteins as microarrays for high-throughput function determination. *Science 289*, 1760−1763.

(13) Falsey, J., Renil, M., Park, S., Li, S., and Lam, K. (2001) Peptide and small molecule microarray for high throughput cell adhesion and functional assays. *Bioconjugate Chem. 12*, 346−353.

(14) Templin, M., Stoll, D., Schrenk, M., Traub, P., Vohringer, C., *et al.* (2002) Protein microarray technology. *Drug Discovery Today 7*, 815−822.

(15) Zhu, H., and Snyder, M. (2003) Protein chip technology. *Curr. Opin. Chem. Biol. 7*, 55−63.

(16) Taylor, J. D., Briley, D., Nguyen, Q., Long, K., Iannone, M. A., *et al.* (2001) Flow cytometric platform for high-throughput single nucleotide polymorphism analysis. *Biotechniques 30*, 661−669.

(17) Nolan, J., and Sklar, L. (2002) Suspension array technology: evolution of the flat-array paradigm. *Trends Biotechnol. 20*, 9−12.

(18) Carson, R. T., and Vignali, D. A. A. (1999) Simultaneous quantitation of 15 cytokines using a multiplexed flow cytometric assay. *J. Immunol. Methods 227*, 41−52.

(19) Hlady, V., and Buijs, J. (1996) Protein adsorption on solid surfaces. *Curr. Opin. Biotechnol. 7*, 72−77.

(20) Johnson, D., and Martin, L. (2005) Controlling protein orientation at interfaces using histidine tags: an alternative to Ni/NTA. *J. Am. Chem. Soc. 127*, 2018−2019.

(21) Seong, S. (2002) Microimmunoassay using a protein chip: Optimizing conditions for protein immobilization. *Clin. Diagnost. Lab. Immunol. 9*, 927−930.

(22) Vijayendran, R. A., and Leckband, D. E. (2001) A quantitative assessment of heterogeneity for surface-immobilized proteins. *Anal. Chem. 73*, 471−480.

(23) Alwine, J., Kemp, D., and Stark, G. (1977) Method for detection of specific RNAs in agarose gels by transfer to diazobenzyloxymethyl-paper and hybridization with DNA probes. *Proc. Natl. Acad. Sci. U.S.A. 74*, 5350−5354.

(24) Dean, P. D. G., Johnson, W. S., and Middle, F. A. (1985) *Affinity Chromatography: A Practical Approach*, pp 215, IRL Press, Washington, DC.

(25) Curreli, N., Oliva, S., Rescigno, A., Rinaldi, A., Sollai, F., *et al.* (1997) Novel diazonium-functionalized support for immobilization experiments. *J. Appl. Polym. Sci. 66*, 1433−1438.

(26) Hermanson, G. (1996) *Bioconjugated Techniques*, Academic Press, New York.

(27) Wegner, G., Lee, N., Marriott, G., and Corn, R. (2003) Fabrication of histidine-tagged fusion protein arrays for surface plasmon resonance imaging studies of protein−protein and protein−DNA interactions. *Anal. Chem. 75*, 4740−4746.

(28) Mason, A., He, Q., Halbrooks, P., Everse, S., Gumerov, D., *et al.* (2002) Differential effect of a His tag at the N- and C-termini: Functional studies with recombinant human serum transferrin. *Biochemistry 41*, 9448−9454.

(29) Botting, C., and Randall, R. (1995) Reporter enzyme-nitrilotriacetic acid-nickel conjugates − reagents for detecting histidine-tagged proteins. *Biotechniques 19*, 362−363.

(30) Cras, J., Rowe-Taitt, C., Nivens, D., and Ligler, F. (1999) Comparison of chemical cleaning methods of glass in preparation for silanization. *Biosens. Bioelectron. 14*, 683−688.

(31) Giesbers, M., Kleijn, J., and Stuart, M. (2002) Interactions between acid- and base-functionalized surfaces. *J. Colloid Interface Sci. 252*, 138−148.

(32) Petri, D., Wenz, G., Schunk, P., and Schimmel, T. (1999) An improved method for the assembly of amino-terminated monolayers on SiO2 and the vapor deposition of gold layers. *Langmuir 15*, 4520−4523.

(33) Sekar, M., Hampton, P., Buranda, T., and Lopez, G. P. (1999) Multifunctional monolayer assemblies for reversible direct fluorescence transduction of protein−ligand interactions at surfaces. *J. Am. Chem.* Soc. *121*, 5135−5141.

(34) Fadeev, A., and McCarthy, T. (1998) Surface modification of poly(ethylene terephthalate) to prepare surfaces with silica-like reactivity. *Langmuir 14*, 5586−5593.

(35) Fadeev, A., and McCarthy, T. (1999) Trialkylsilane monolayers covalently attached to silicon surfaces: Wettability studies indicating that molecular topography contributes to contact angle hysteresis. *Langmuir 15*, 3759−3766.
(36) Sekar, M., Hampton, P., Buranda, T., and Lopez, G. P. (1999) Multifunctional monolayer assemblies for reversible direct fluorescence transduction of protein−ligand interactions at surfaces. *J. Am. Chem.* Soc. *121*, 5135−5141.
(37) VigneMaeder, F., and Sautet, P. (1997) Theoretical study of hydroxylated and dehydroxylated surfaces of a cristobalite model of silica. *J. Phys. Chem. B 101*, 8197−8203.
(38) Brunner, H., Vallant, T., Mayer, U., Hoffmann, H., Basnar, B., *et al.* (1999) Substrate effects on the formation of alkylsiloxane monolayers. *Langmuir 15*, 1899−1901.
(39) Hozumi, A., Yokogawa, Y., Kameyama, T., Sugimura, H., Hayashi, K., *et al.* (2001) Amino-terminated self-assembled monolayer on a SiO2 surface formed by chemical vapor deposition. *J. Vac. Sci. Technol. A 19*, 1812−1816.
(40) Dolan, P. L., Wu, Y., Ista, L. K., Metzenberg, R. L., Nelson, M. A., *et al.* (2001) Robust and efficient synthetic method for forming DNA microarrays. *Nucleic Acids Res. 29*, U37−U44.
(41) Uibel, R., and Harris, J. (2000) Fiber-optic Raman spectroscopy for in situ monitoring of metal-ion complexation by ligands immobilized onto silica gel. *Appl. Spectrosc. 54*, 1868−1875.
(42) Uibel, R., and Harris, J. (2002) In situ Raman spectroscopy studies of metal ion complexation by 8-hydroxyquinoline covalently bound to silica surfaces. *Anal. Chem. 74*, 5112−5120.
(43) Marshall, M., and Mottola, H. (1983) Synthesis of silica-immobilized 8-quinolinol with (aminophenyl)trimethoxysilane. *Anal. Chem. 55*, 2089−2093.
(44) Marshall, M., and Mottola, H. (1985) Silane isomer effect on the capacity of silica-immobilized 8-quinolinol. *Anal. Chem. 57*, 375.
(45) Buranda, T., Lopez, G. P., Simons, P. C., Pastuszyn, A., and Sklar, L. A. (2001) Detection of epitope-tagged proteins in flow cytometry: Fluorescence resonance energy transfer-based assays on beads with femtomole resolution. *Anal. Biochem. 298*, 151−162.
(46) Buranda, T., Jones, G. M., Nolan, J. P., Keij, J., Lopez, G. P., *et al.* (1999) Ligand receptor dynamics at streptavidin-coated particle surfaces: A flow cytometric and spectrofluorimetric study. *J. Phys.* Chem. B *103*, 3399−3410.
(47) Suemori, A., Ozawa, M., and Iwakura, M. (2001) Engineering of histidine tail in the N-terminal region of p-hydroxybenzoate hydroxylase from Pseudomonas fluorescens. *Biotechnol. Lett. 23*, 489−495.
(48) Chilkoti, A., and Stayton, P. (1995) Molecular-origins of the slow streptavidin−biotin dissociation kinetics. *J. Am. Chem. Soc. 117*, 10622−10628.
(49) Tsien, R. Y. (1998) The Green Fluorescent Protein. *Annu. Rev. Biochem. 67*, 509−544.
(50) Yang, F., Moss, Larry G., and Phillips, Geroge N. Jr. (1996) The Molecular Structure of Green Fluorescent Protein. *Nat. Biotechnol. 14*, 1246−1251.
(51) Bayer, E. A., Benhur, H., and Wilchek, M. (1990) Isolation and properties of streptavidin. *Methods Enzymol. 184*, 80−89.
(52) Green, N. (1990) Avidin and streptavidin. *Methods Enzymol. 184*, 51−67.
(53) Kusnezow, W., and Hoheisel, J. D. (2003) Solid supports for microarray immunoassays. *J. Mol. Recognit. 16*, 165−176.
(54) Wood, L. L. C., S.; Edmiston, P. L.; and Saavedra, S. S. (1997) Molecular orientation distributions in protein films. 2. Site-directed immobilization of yeast cytochrome *c* on thiol-capped, self-assembled monolayers. *J. Am. Chem. Soc. 119*, 571−576.

BC050278M

Selection of Streptavidin Binders from a DNA-Encoded Chemical Library

Christoph E. Dumelin,§ Jörg Scheuermann,§ Samu Melkko, and Dario Neri*

Institute of Pharmaceutical Sciences, Department of Chemistry and Applied Biosciences, ETH Zürich, Wolfgang-Pauli-Strasse 10, CH-8093 Zurich, Switzerland. Received September 21, 2005; Revised Manuscript Received January 26, 2006

DNA-encoded libraries of small organic molecules facilitate the construction of large, encoded self-assembling chemical libraries for the identification of high-affinity binders to protein targets. We have constructed a library of 477 chemical compounds, coupled to 48mer-oligonucleotides, each containing a unique six-base sequence serving as "bar-code" for the identification of the chemical moiety. The functionality of the library was confirmed by selection and amplification of both high- and low-affinity binding molecules specific to streptavidin.

INTRODUCTION

The isolation of molecules capable of high-affinity and specific binding to a biological target is a central problem in chemistry, biology, and pharmaceutical sciences. The construction of libraries of compounds which carry a unique DNA sequence as a "bar-code" for each library member promises to facilitate the identification of binding molecules and to speed-up and miniaturize screening procedures. In principle, very large libraries of compounds can be panned with the target protein of interest immobilized on a suitable support, followed by the identification of the preferentially enriched compounds by procedures which may involve PCR[1] amplification of the DNA codes, sequencing, and/or hybridization to a DNA microarray (*1*−*4*).

Our group has recently developed a novel technology for the construction of large encoded self-assembling chemical (ESAC) libraries (*4*). The self-assembly of DNA oligonucleotides carrying individual chemical compounds at their extremity enables the facile generation of large chemical libraries from smaller sublibraries. Chemical groups which display a synergistic chelate binding mode to the target protein of interest can be identified from an ESAC library. The corresponding bidentate ligands can display a binding affinity which is dramatically higher compared to the individual chemical moieties (*4*).

Encouraged by the first ESAC affinity-maturation selections for binders to human serum albumin and bovine carbonic anhydrase (*4*), we have now constructed a large library containing 477 compounds [with molecular weights ranging between 100 and 500 Da], covalently coupled to a primary amino group at the 5′ extremity of 477 individual oligonucleotides of general structure 5′-$NH_2(CH_2)_6PO_4$-GGA GCT TCT GAA TTC TGT GTG CTG XXX XXX CGA GTC CCA TGG CGC AGC-3′ (where XXX XXX denotes different unique combinations of six bases for the individual compounds, with three/six bases being G or C). The performance of this large library in the selection, read-out, and identification procedure was analyzed in a screening against streptavidin. Thereby one high- and two low-affinity binding molecules to streptavidin were identified.

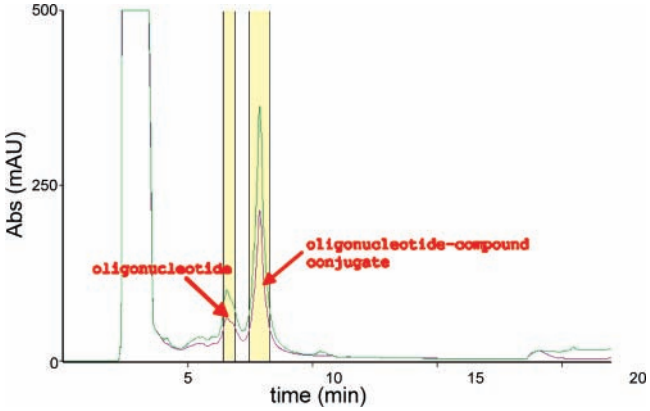

Figure 1. HPLC purification of the oligonucleotide−compound conjugate **337**. The green chromatogram indicates the absorption at 260 nm, the purple chromatogram at 280 nm. The peaks highlighted in yellow indicate the collected fractions.

EXPERIMENTAL PROCEDURES

Preparation of Oligonucleotide−Compound Conjugates. The coupling of compounds to DNA was accomplished by formation of either an amide or a thiourea. The oligonucleotide carrying a primary amino group (IBA) was coupled to carboxylic acids, acyl chlorides, cyclic anhydrides, or isothiocyanates. Some of the carboxylic acids further contained an Fmoc-protected amino group. Scheme 1 shows the different classes of compounds present in the library and the resulting oligonucleotide−compound conjugates. For acyl chlorides, 200 μL of a 25 μM solution of oligonucleotide in 100 mM $NaHCO_3$, pH 9, was added to 200 μL of a 4 mM solution of acyl chloride in MeCN. In the case of isothiocyanates, 100 μL of a 50 μM solution of oligonucleotide in 100 mM $KHPO_4$, pH 7.1, was added to 200 μL of a 2.6 mM solution of isothiocyanate in DMSO. For cyclic anhydrides, 100 μL of a 50 μM solution of oligonucleotide in 100 mM $KHPO_4$, pH 7.1, was added to 200 μL of a 2.6 mM solution of anhydride in DMSO. To activate the carboxylic acids, 22 μL of a solution containing 45 mM EDC and 180 mM sulfo-NHS in 15% H_2O/85% DMSO was added to 230 μL of a 5.5 mM solution of the carboxylic acid in DMSO. After 30 min at 30 °C, 60 μL of a solution of 83 μM oligonucleotide in 420 mM TEA/HCl, pH 10, was added. All reactions were

* Corresponding author. E-mail: neri@pharma.ethz.ch. Fax: +41 633 13 58. Tel: + 41 633 74 01.

§ These authors contributed equally to this work.

[1] Abbreviations: DMSO, dimethyl sulfoxide; EDC, 1-ethyl-3-[3-(dimethylamino)propyl]carbodiimide; ESAC library, encoded self-assembling chemical library; Fmoc, 9-fluorenylmethyloxycarbonyl; HFIP, hexafluoro-2-propanol; PBS, phosphate-buffered saline; PCR, polymerase chain reaction; TEA, triethylamine; TEAA, triethylammonium acetate; TBE, Tris-borate-EDTA; SSC, sodium chloride-sodium citrate; sulfo-NHS, hydroxy-2,5-dioxopyrrolidine-3-sulfonic acid.

10.1021/bc050282y CCC: $33.50 © 2006 American Chemical Society
Published on Web 02/18/2006

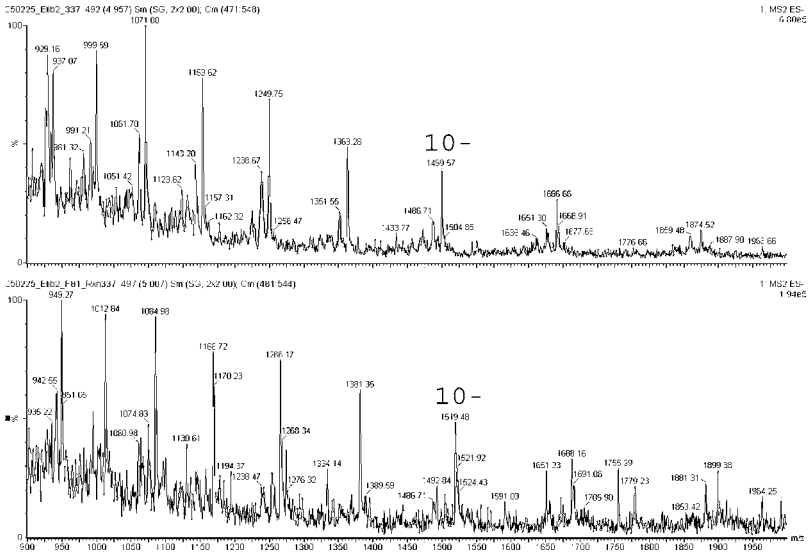

Figure 2. Mass spectra of the unconjugated oligonucleotide of **337** (above) and the purified oligonucleotide−compound conjugate **337** (below). The peaks of the tenfold negatively charged molecules are indicated.

Scheme 1. Functional Groups Used for the Coupling of Different Compound Classes to Amino-Tagged 48mer Oligonucleotides

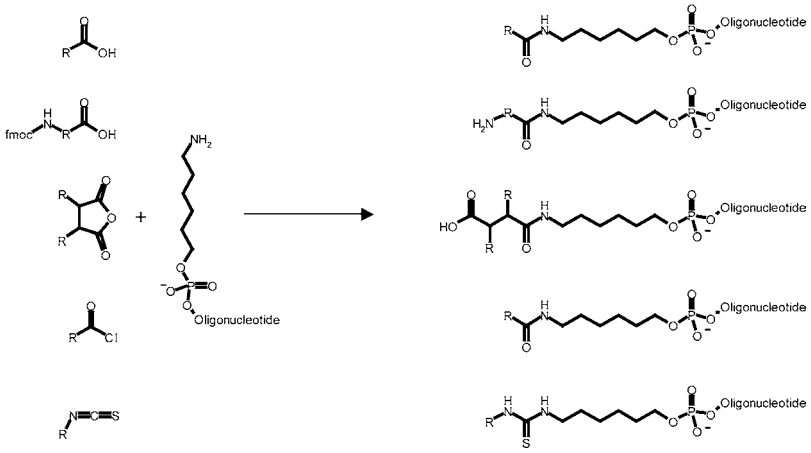

stirred for 12 h at 30 °C. The reactions were quenched by adding 20 μL of 500 mM Tris/HCl, pH 8, and stirred for an additional 1 h at 30 °C. In the case of Fmoc-protected compounds, the quenching and removal of the Fmoc group was performed by addition of 5 μL of 1 M Tris and 5 μL of triethylamine and stirring for 1 h at 30 °C.

Purification of Oligonucleotide−Compound Conjugates. Prior to HPLC purification, 400 μL of 100 mM TEAA, pH 7, was added to the reaction mixture. In the case of the Fmoc samples, 20 μL of 1 M HCl was additionally added. Purifications were performed by HPLC on an XTerra Prep RP_{18} column (5 μM, 10 × 150 mm) using a linear gradient from 10 to 40% MeCN in 100mM TEAA. The HPLC purification chromatogram of the oligonucleotide−compound conjugate **337** is given as an example in Figure 1. Fractions absorbing at 260 nm were collected, and those with an absorption ratio 260 nm/280 nm of 1.8:1 were dried under vacuum.

LC-ESI-MS. The desired samples were redissolved in 100 μL of H_2O. An amount of 5 μL was analyzed by LC-ESI-MS on an XTerra RP_{18} column (5 μM, 4.6 × 20 mm) using a linear gradient from 0 to 50% MeOH over 1 min in 400 mM HFIP/5 mM TEA. The mass spectrum was measured from 900 to 2000 *m*/*z* by a Waters Quattro Micro instrument. The mass spectra of oligonucleotide **337** before and after conjugation are given as an example in Figure 2. The samples containing the oligonucleotide−compound conjugates of the expected size were pooled and precipitated by adding 10% v/v of 3 M NaAc, pH 4.7, and 250% v/v of EtOH. The pellets were collected by centrifugation and washed by addition of ice cold 85% EtOH, followed by drying under vacuum. The oligonucleotide−compound conjugates were then redissolved in 100 μL of H_2O, and the OD_{260} was determined by a ND-1000 (Nanodrop).

Screening Procedure. All library members were pooled to a final total oligonucleotide−compound conjugate concentration of 900 nM (1.8 nM for each individual oligonucleotide−compound conjugate). The library was dimerized by heterodu-

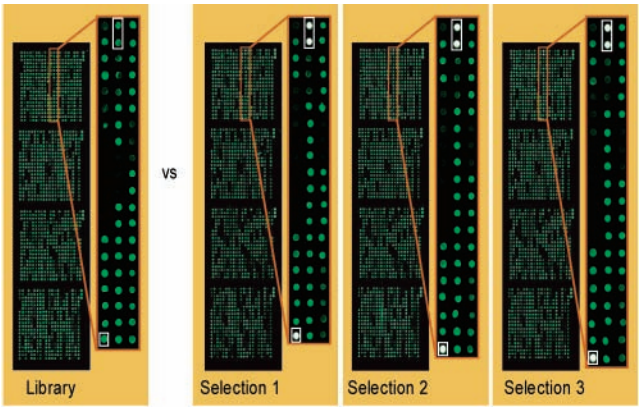

Figure 3. Microarray readout of the PCR amplification of the library before selection and after selection (in triplicate). The inset highlights the enhancement of the signal from compound **337** (spotted in triplicate).

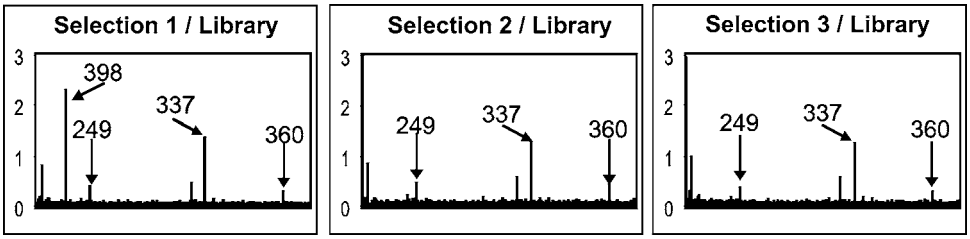

Figure 4. Ratios of the fluorescence signal after and before the selections. The signals of compounds **249**, **337**, and **360** are highlighted. Compounds are sorted on the *x*-axis according to increasing signal intensities on the library slide. Approximately 20 compounds in the left part of the graph show larger signal variability due to their low fluorescence signal. The enrichment of **398** is an artifact.

plex formation with an unmodified pairing oligonucleotide at a concentration of 100 nM. The resulting DNA duplex was diluted 1:10 in PBS, and 100 μL was added to 50 μL of streptavidin-sepharose slurry (GE Healthcare) preincubated with PBS, 0.3 mg/mL herring sperm DNA. After incubation for 1 h at 25 °C, the mixture was transferred to a SpinX column (Corning Incorporated), the supernatant removed, and the resin washed 3× with 300 μL of 1 mM $MgCl_2$, 0.1% Tween 20 in PBS. The resin was resuspended in 100 μL of H_2O.

Identification of Binding Molecules. The codes of the oligonucleotide−compound conjugates were amplified before and after selection by PCR (50 μL, 25 cycles of 1 min at 94 °C, 1 min at 55 °C, 40 s at 72 °C) of either 5 μL of the resuspended resin or 5 μL of 100 fM DNA duplex library using primers AB_fo_short (GGA GCT TCT GAA TTC TGT GTG CTG) and Elib2_ba (GCT GCG CCA TGG GAC TCG). The product was purified and subsequently linearly amplified by PCR (see above) using 5′-Cy3-labeled Elib2_ba as primer. The product was precipitated in EtOH as described above and redissolved in 120 μL of hybridization buffer (4 × SSC, 50 mM HEPES, 0.2% SDS, pH 7) and incubated with microarray glass slides (displaying 19mers with the structure 5′-TGTGCT-GXXXXXXCGAGTC-3′ in triplicate) in a Tecan HS 400 hybridization instrument for 4 h at 44 °C followed by successive washing steps with 2 × SSC/0.2% (w/v) SDS, 0.2 × SSC/0.2% (w/v) SDS, and 0.2 × SSC. After hybridization, microarrays were analyzed by using a Genepix professional 4200A scanner (λ_{ex} = 532 nm, 100% laser power, photomultiplier 300). Spot intensities were quantified and evaluated using Genespotter (v2.4.3). After background subtraction, the mean value was used as spot signal intensity (average of three spots).

Affinity Measurements. The enriched compounds **249**, **337**, and **360** were coupled to bovine serum albumin following the same procedure as for the oligonucleotides, except that the protein was added as 750 μL of a solution of 6.7 μM bovine serum albumin in 33 mM TEA/HCl, pH 10. After purification on a PD-10 column (GE Healthcare), 20 μL of the eluted protein (2.7 μM) was injected onto a streptavidin-coated BIAcore chip.

Fluorescein isothiocyanate was conjugated to ethylenediamine in DMSO. The fluorescein−ethylenediamine conjugate was coupled to compounds **249** and **360** following the same procedure as for oligonucleotides. Fluorescein−compound conjugates (500 nM) and fluorescein as negative control were incubated with increasing amounts of streptavidin in PBS, 5% DMSO, for 1 h at 25 °C. The biotin competition was performed by incubating 500 nM fluorescein−compound conjugates with 200 μM streptavidin either with or without 250 μM biotin in PBS, 5% DMSO, for 1 h. The fluorescence polarization was determined by excitation at 485 nm and measurement at 535 nm (TECAN Polarion).

The oligonucleotide−compound conjugate **337** was hybridized to a pairing 24mer carrying a Cy3 label at the 3′ end. The resulting duplex (13 nM) was incubated with increasing concentrations of streptavidin in 150 mM Tris/HCl, 10 mM $MgCl_2$, pH 8.9, for 1 h and analyzed on a 20% TBE polyacrylamide gel.

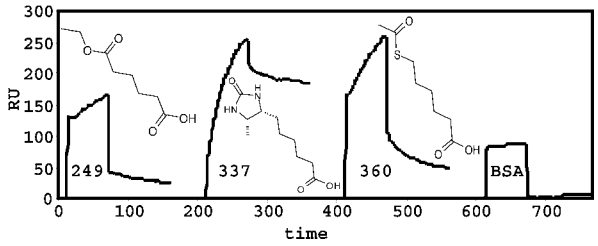

Figure 5. BIAcore measurements of **249**, **337**, and **360** coupled to BSA and BSA alone on streptavidin chips together with the structures of the binding compounds.

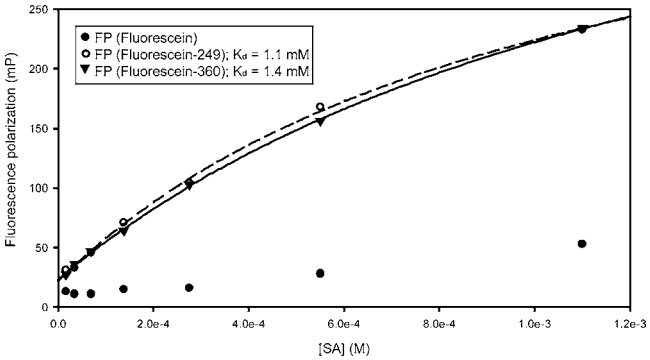

Figure 6. Fluorescence polarization of fluorescein and of fluorescein conjugated to either compound **249** or **360** titrated with increasing amounts of streptavidin. The fitting for the fluorescein−compound **249** conjugate (dashed line) and the fluorescein−compound **360** conjugate (solid line) is indicated.

Isothermal titration calorimetry measurements were performed using a VP-ITC instrument (Microcal). Streptavidin (1 μM) in PBS was titrated with a 10 μM solution of compound **337** in PBS at 30 °C (after an initial dummy injection of 1 μL, 29 injections of 10 μL each were performed). The resulting titration curves were then processed and fitted with the Origin 7 software (Microcal).

Quantitative Model Selection Experiments. A 24mer oligonucleotide with a complementary sequence to the hybridization domain of the library oligonucleotides was radioactively labeled at the 5′ terminus using γ^{33}P-ATP (GE Healthcare) and T4 polynucleotide kinase (USB). In three separate tubes the radiolabeled oligonucleotide was hybridized either with the oligonucleotide−compound conjugate **337**, the oligonucleotide-compound conjugate **360**, or an unconjugated oligonucleotide as negative control at an oligonucleotide concentration of 100 nM each. Aliquots of these oligonucleotide duplex pairs were incubated with streptavidin-sepharose slurry (with different coating densities of streptavidin) or with unconjugated sepharose in PBS. After 2 h of incubation, repeated rounds of washing were performed with PBS, and the remaining beads as well as aliquots of the input, flow-through, and all washing fractions were subjected to ^{33}P radioactivity counting with a Beckman LS 6500 scintillation counter. Streptavidin was conjugated to sepharose beads as follows: Different concentrations of strepta-

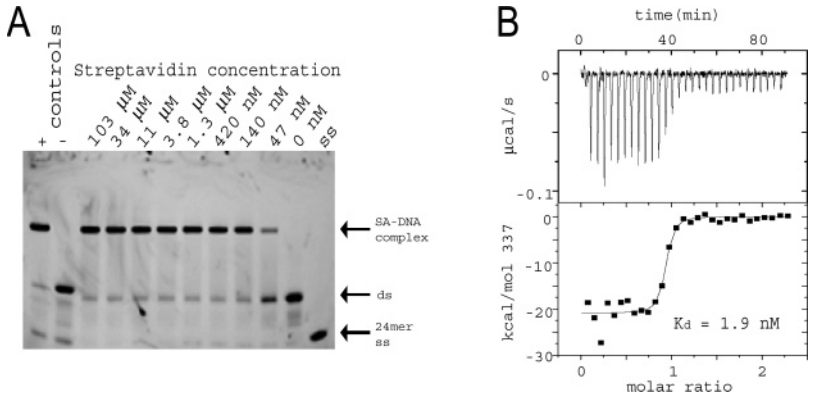

Figure 7. (A) Affinity of the oligonucleotide−compound conjugate **337** paired with a 24mer carrying no modification measured in an electromobility shift assay. (B) Isothermal titration calorimetry profile of compound **337**.

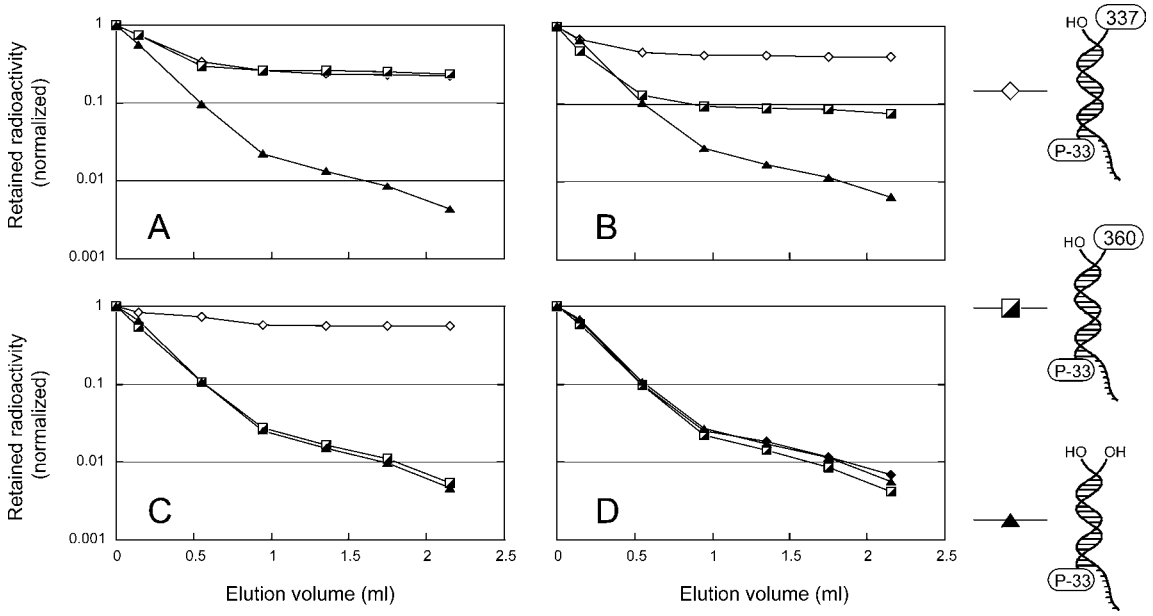

Figure 8. Recovery profiles of the oligonucleotide−compound conjugates **337** and **360** and an unconjugated control oligonucleotide hybridized with ^{33}P-labeled oligonucleotide in selection experiments to streptavidin. Experiments were performed with sepharose beads conjugated to streptavidin at 1 mg/mL (A), 0.2 mg/mL (B), and 8 μg/mL (C) and with unconjugated sepharose (D). The remaining radioactivity was normalized to the input value and plotted as function of the elution volume by adding up the fractions of radioactivity measured in the different washing steps in the selection procedure.

vidin (end concentration 1 mg/mL, 0.2 mg/mL, 8 μg/mL) (Biospa) were incubated overnight at 4 °C with 150 mg of CNBr-sepharose beads (GE Healthcare) in a total volume of 900 μL in coupling buffer (0.1 mM $NaCO_3$, 0.5 mM NaCl, pH 9). Excess reactive groups on the beads were quenched using 100 mM Tris/HCl, pH 8.9, and the beads were washed repeatedly with alternating buffers (0.1 M sodium acetate, 0.5 M NaCl, pH 4, and 0.1 M Tris/HCl, 0.5 M NaCl, pH 8) using SpinX columns (Corning Incorporated).

RESULTS

To test the functionality of the library and the reliability of the selection and read-out procedure, we hybridized an equimolar mixture of the 477 oligonucleotide derivatives with a single 24-mer oligonucleotide, complementary to the conserved DNA sequence at the 5′ extremity of the library members. The resulting library of compounds was biopanned onto streptavidin-sepharose in three independent selection procedures. The library was PCR-amplified before and after selection with a fluorescently labeled oligonucleotide primer, thus allowing a microarray read-out of the codes of those compounds which had been preferentially enriched during the selections (*4*). Figure 3 shows a fluorescence imaging of the microarray decoding of the 477 member library before and after the three independent streptavidin selections. Each library compound was represented by one oligonucleotide, spotted in triplicate onto the microarray. Some compounds (see insets) appear to be preferentially enriched as a result of the biopanning. Figure 4 shows a plot of the ratios of the fluorescence intensities before and after selection. In all three panning procedures, compound **337** among others appears to be preferentially enriched compared to the background of nonbinding compounds. Interestingly, compound **337** turned out to be D-desthiobiotin, a known binder to streptavidin (*5*, *6*).

The binding of **337** to streptavidin could be confirmed by real-time interaction analysis on a BIAcore instrument, following conjugation of **337** to bovine serum albumin (BSA). The binding of compounds **249** (adipic acid monoethyl ester) and **360** (6-acetylthiohexanoic acid) could also be verified by BIAcore analysis using multivalent conjugates to BSA (Figure 5).

For the precise determination of the binding affinities of compounds **249** and **360** in solution, these molecules were conjugated to fluorescein. Fitting of the increase in fluorescence polarization of the fluorescein−compound conjugates when titrating with streptavidin gave rise to binding constants of K_d = 1.1 mM for the **249** conjugate and K_d = 1.4 mM for the **360**

conjugate (Figure 6). Adding biotin as competitor diminished the fluorescence polarization induced by the streptavidin binding indicating that both compounds bind to the same pocket (data not shown).

A band-shift analysis of the **337**−oligonucleotide conjugate exhibited an apparent dissociation constant for streptavidin of $K_d = 47$ nM (Figure 7A). Isothermal titration of streptavidin with the carboxylic acid of **337** gave rise to a $K_d = 1.9$ nM (Figure 7B).

To determine whether the selection procedure allowed for distinction of high- and low affinity binding molecules the recovery of ^{33}P-labeled oligonucleotide−compound conjugates of **337** and **360** throughout a panning experiment under different conditions was monitored. This revealed that the recovery of **360** rapidly decreased when reducing the amount of streptavidin present on the beads whereas the recovery of **337** was not affected (Figure 8).

DISCUSSION

The results presented in this study show that binders with dissociation constants ranging from nanomolar to millimolar for a target antigen can rapidly be identified out of a large DNA-encoded library, containing 477 compounds. Varying the surface density of target protein in the panning experiment enables the discrimination between high- and low-affinity binding molecules. The decoding procedure, featuring an asymmetric PCR amplification and microarray hybridization, appears to be a convenient methodology for identifying compounds which are preferentially enriched. Furthermore, the oligonucleotide derivatives (corresponding to the individual library members) are immediately available for the confirmation of binding specificity and for the determination of the affinity constant of the compounds to the respective target protein.

The availability of the large DNA-encoded chemical library promises to be particularly useful for the rapid affinity maturation of low affinity binders (mM to μM) to a number of different proteins, by the formation of suitable bidentate derivatives (*4*), or for the de novo identification of synergistic binding pairs from two ESAC sublibraries. ESAC libraries can be synthesized with a stringent quality control of each individual library member and can be used at subnanomolar concentrations in selection experiments, thus allowing thousands of selections using different antigens and/or different experimental conditions.

ACKNOWLEDGMENT

The authors acknowledge a financial contribution from the ETH Zürich (CLE' INIT), the Bundesamt für Bildung und Wissenschaft (BBW) for the EU Project STROMA, and from Philogen. C.E.D. is the recipient of a bursary from the Roche Research Foundation. The experimental support of Dr. Jens Sobek and Dr. Ralph Schlapbach (Functional Genomics Center Zurich) for microarray decoding and of Ms. Madalina Jaggi for the quality controls of the library is gratefully acknowledged.

LITERATURE CITED

(1) Brenner, S., and Lerner, R. A. (1992) Encoded combinatorial chemistry. *Proc. Natl. Acad. Sci. U. S. A. 89*, 5381−3.

(2) Gartner, Z. J., Tse, B. N., Grubina, R., Doyon, J. B., Snyder, T. M., and Liu, D. R. (2004) DNA-templated organic synthesis and selection of a library of macrocycles. *Science 305*, 1601−5.

(3) Halpin, D. R., and Harbury, P. B. (2004) DNA display II. Genetic manipulation of combinatorial chemistry libraries for small-molecule evolution. *PLoS Biol. 2*, E174.

(4) Melkko, S., Scheuermann, J., Dumelin, C. E., and Neri, D. (2004) Encoded self-assembling chemical libraries. *Nat. Biotechnol. 22*, 568−74

(5) Torreggiani, A., and Fini, G. (1998) The binding of biotin analogues by streptavidin: A Raman spectroscopic study. *Biospectroscopy 4*, 197−208

(6) Hirsch, J. D., Eslamizar, L., Filanoski, B. J., Malekzadeh, N., Haugland, R. P., Beechem J. M., and Haugland, R. P. (2002) Easily reversible desthiobiotin binding to streptavidin, avidin, and other biotin-binding proteins: uses for protein labeling, detection, and isolation. *Anal. Biochem. 308*, 343−57.

BC050282Y

A Structured Chitosan-Based Platform for Biomolecule Attachment to Solid Surfaces: Application to DNA Microarray Preparation

Clarissa Consolandi,[†,*] Marco Severgnini,[†] Bianca Castiglioni,[§] Roberta Bordoni,[†] Andrea Frosini,[‡] Cristina Battaglia,[‡] Luigi Rossi Bernardi,[‡] and Gianluca De Bellis[†]

Istituto di Tecnologie Biomediche, Consiglio Nazionale delle Ricerche, LITA, via F.lli Cervi, 93 20090 Segrate (MI) Italy, Istituto di Biologia e Biotecnologia Agraria, Consiglio Nazionale delle Ricerche, and Dipartimento di Scienze e Tecnologie Biomediche, Universita' degli Studi di Milano, Milan, Italy. Received September 26, 2005; Revised Manuscript Received January 16, 2006

A structured chemical platform based on chitosan, an amine-rich polysaccharide, is presented as an alternative chemistry to functionalize solid support (in this case, glass slides) for grafting biomolecules. This approach has been adopted for generating arrays using amino-modified oligonucleotides with two different lengths (25-mer and 70-mer) for different purposes. Results using these chitosan-activated surfaces indicate high oligonucleotide loading capacity, good availability to hybridization against targets, and effectiveness in enzyme-mediated single nucleotide polymorphism (SNP) detection procedures by DNA polymerase and DNA ligase enzymes with low background. Universal arrays have been prepared and extensively used with excellent results in different applications. The chitosan-treated surfaces were also evaluated for their performance in a gene expression experiment.

INTRODUCTION

Chemical binding of biomolecules to solid surfaces is a key step in a very large set of applications. Among many others, the generation of arrays of biomolecules is a relevant field where proper chemical platforms are needed. Microarrays consisting of oligonucleotides, polynucleotides, peptide nucleic acids, peptides, proteins, and other molecules are becoming a valuable tool in modern molecular biology (*1*), opening a way for large-scale screening of mutations and studies of gene polymorphisms, gene expression analysis, and functional biology. The most relevant example of the application of arrays is their use for massive DNA analyses in parallel using oligonucleotides or polynucleotides as molecular probes. Oligonucleotide microarrays can be mass produced by photolithographic techniques in situ (*2*), but many users prefer homemade microarrays prepared by the spotting of modified oligonucleotides (*3*). This widely adopted option requires direct attachment of presynthesized oligonucleotides to an activated surface. This approach permits a very quick set up of new microarrays and their upgrading, incorporating new genetic information.

A key step in this approach is the preparation of surfaces modified with appropriate functional groups allowing for the attachment of oligonucleotides to the solid support. Many different approaches have been proposed including those compatible with 5′-thiolated oligonucleotides (*4*), although in general amino-modified oligonucleotides are preferred. Gel pads have been proposed (*5*) as well as the use of branched linkers (*6*). Similarly, chemically preactivated microscope slides have been commercially proposed offering 3D reactive structures (*7*).

We started exploring the potentials and pitfalls of a structured approach to the preparation of coated surfaces aimed especially at the microarray preparation. This approach requires proper functionalization of the glass surface with silanes chosen according to the functional moiety to be reacted, the scaffold creation using a polymer (either natural or synthetic), and finally the activation of the resulting surface using proper moieties. We presented our results using poly-L-lysine and acrylamide/acrylic acid copolymer as scaffolds for oligonucleotide microarray preparation (*8*). These two polymers are well-known in the field and have been already used. Here we present our results using chitosan, an amine-rich polysaccharide derived by partial deacetylation of chitin (*9*). Its deprotonated amino groups can react with a variety of electrophiles. As a result, various chemistries can be exploited to cross-link chitosan and to graft substituents onto this polymer (*10*−*14*).

We prepared three chemical supports using chitosan with three different molecular weights (120 kDa, 400 kDa, 650 kDa), each of these with or without KCl. In all these cases, the polymer is covalently bound to glass slides activated with 3-glycidoxypropyltrimethoxysilane (GOPS) as a scaffold for generating arrays. Polymer-coated slides have been activated with 1,4-phenylene diisothiocyanate (PDITC) for generating arrays with presynthesized oligonucleotides bearing amino groups.

Results obtained using this coupling platform show simple preparation of the surface, high oligonucleotide loading capacity, good binding efficiency, remarkably uniform performance over the entire surface, and no particular care required for their storage. We also demonstrate that the attachment of amino-modified oligonucleotides consistently yields arrays of readily accessible probes with different lengths (25-mer and 70-mer) to hybridization. Mutation detection by enzyme (ligase or polymerase)-mediated approaches has been successfully performed with low background. In combination with a universal array prepared using this platform, a PCR-ligation detection reaction approach was used for the single nucleotide polymorphism (SNP) detection in different fields with excellent specific-

* To whom correspondence should be addressed. Telephone: +39 0226422724/5. Telefax: +39 0226422770. E-mail: clarissa.consolandi@itb.cnr.it.

† Istituto di Tecnologie Biomediche, Consiglio Nazionale delle Ricerche.

§ Istituto di Biologia e Biotecnologia Agraria, Consiglio Nazionale delle Ricerche.

‡ Universita' degli Studi di Milano.

10.1021/bc050285a CCC: $33.50 © 2006 American Chemical Society
Published on Web 02/22/2006

Table 1. Oligonucleotide Sequences Used in the Experiments as Probes and Templates

name	sequence[a]	5′-modification	3′-modification
	a. Oligonucleotides Used in All Experiments for Hybridization Efficiency and Surface Loading		
25-mer	5′-AAAAAAAAAATACCGGCGGCAGCACCAGCGGTAAC-3′	NH2	Cy3
70-mer	5′-AAAAAAAAAGAGAAGGATTATGAGGAGGTTGGTG TGGATTCTGTTGAAGGAGAGGGTGAGGAAGAAGGAGAGGAATAC-3′	NH2	Cy3
25-mer-compl	5′-GTTACCGCTGGTGCTGCCGCCGGTA-3′	Cy5	none
70-mer-compl	5′-GTATTCCTCTCCTTCTTCCTCACCCTCTCCTTCA ACAGAATCCACACCAACCTCCTCATAATCCTTCTCT-3′	Cy5	none
	b. Oligonucleotides Used as Probes and Template in the Minisequencing Experiment		
1450-1 ATTINO1	5′-TTGTACACACCGCCCGTCACGT-3′	NH_2	none
1450-1 ATTINO2	5′-TTGTACACACCGCCCGTCACGTC-3′	NH_2	none
1450-1 ATTINO3	5′-TTGTACACACCGCCCGTCACG-3′	NH_2	none
1336 PSEUDO	5′-CTAATCCCAIAAAACCGATCGT-3′	NH_2	none
Actinomycetes 16S RNA template	(5′-GGTGTTTCCGACTTTCC**TGA**CGTGACGGGCGGTGTGTACAA-3′)	none	none

[a] Bases printed in bold and underlined are targeted by the ATTINO probes in the minisequencing reaction.

ity and high sensitivity. Finally, a large microarray for the detection of RNA expression levels has been prepared.

EXPERIMENTAL PROCEDURES

All chemicals and solvents were purchased from Sigma-Aldrich (Milan, Italy) and, unless otherwise stated, used without further purification. Precleaned nonderivatized microscope slides (25 × 75 × 1 mm) were used (Sigma-Aldrich). Oligonucleotides were purchased from Thermo Hybaid (Ulm, Germany). They were HPLC purified and checked by MALDI-MS.

Cleaning and Silanization of Microscope Slides. Glass slides were cleaned by soaking in 1 M NaOH for 2 h on a shaker followed by rinsing with distilled water, immersed in 1 N HCl solution overnight on a shaker, and then rinsed again in distilled water. Slides were immersed in 96% ethanol for 10 min and then washed three times with distilled water. Slides were immersed in acetone for 10 min, removed, and dried. Then they were treated with 1% (v/v) GOPS (3-glycidoxypropylsilane) in 95% ethanol for 1 h. Excess silane was removed by dipping the slides in 95% ethanol for 1 min. Finally they were dried at 150 °C for 20 min.

Polymeric Coating Synthesis and Surface Activation. The polymer solution was prepared by dissolving 10 g of chitosan (120, 400, or 650 kDa) in a liter of HCl 50 mM. Each different polymer solution was prepared with or without KCl (0.5 M) in order to have six different coatings. The solutions were heated at 70 °C, stirred for 1 h, and then filtered. Treated slides were left in a water solution containing 10% PBS and 10% polymer (0.1% w/v) for 1 h on a shaker. The slides were washed five times with distilled water, centrifuged at 800 rpm for 3 min. and dried for 10 min at 45 °C.

The slides were then activated by immersion into a 0.2% solution of 1,4-phenylene diisothiocyanate in 90% *N*,*N*-dimethylformamide and 10% pyridine. The activation reaction was carried out at room temperature for 2 h. After being washed with methanol and acetone (2 min each), the activated slides were dried and stored, until used, in a dark closed box under vacuum.

Oligonucleotide Immobilization. Amino-modified oligonucleotides were diluted in printing buffer (150 mM sodium phosphate, pH 8.5) and spotted onto the treated slides. The spotting was performed using a contact system (MicroGrid II Compact, Biorobotics, UK).

The covalent attachment to activated supports and the deactivation process were performed according to the following protocol: (a) The printed slides were placed in a saturated NaCl humidification chamber. (b) After overnight incubation at RT, the deactivation step was carried out by treatment with a solution consisting of 50 mM ethanolamine, 0.1 M Tris (pH 9), and 0.1% SDS at 50 °C for 15 min. (c) After being rinsed twice with distilled water, the modified surfaces were immersed into a 4X SSC/0.1% SDS solution (prewarmed to 50 °C) for 15 min on a shaker. (d) Finally, printed surfaces were washed twice with distilled water and spun at 800 rpm for 3 min.

We chose to use two different deposition schemes to test the loading and the binding capacity of our surfaces.

(a) Coupling Efficiency (loading capacity). The loading capacity of the six chemically modified surfaces was tested by spotting at 10 different final concentrations (0.1−50 μM) of two oligonucleotides with two different lengths (25-mer and 70-mer) (Table 1a) bearing a 5′-amino modification and a 3′-Cy3 fluorescent label. Each slide contains eight identical subarrays in a 2 × 4 conformation: the spots are arranged in a 16 × 13 matrix. Each concentration was replicated four times (*15*).

(b) Binding Capacity. The activated surfaces were tested in hybridization experiments. These were performed using two 5′-Cy5-labeled oligonucleotides with a sequence complementary to the 25-mer and 70-mer covalently attached amino-modified oligonucleotides (Table 1a), respectively.

The two different oligonucleotides were spotted at a final concentration of 50 μM in a 150 mM sodium phosphate buffer (ph 8.5) onto the six different surfaces, using the attachment protocol described above. The deposition scheme has the usual structure of eight identical subarrays in a 2 × 4 conformation. Each oligonucleotide was replicated 64 times in each subarray.

An amount of 65 μL of hybridization solution consisting of the Cy5-labeled oligonucleotides (0.1−1 μM), 5X SSC, 0.1% SDS, and 0.1 mg/mL denatured salmon sperm DNA was used to perform hybridization in a homemade multiple sample chamber (eight-well chamber), using Press-To-Seal silicone isolators (Schleicher & Schuell, Germany). The hybridization solution was heated in a boiling water bath for 2 min and then cooled in ice before the application onto the array. Hybridization experiments were carried out at 65 °C for 1.5 h. After incubation, slides underwent four washing steps at 65 °C by using 1X SSC/0.1% SDS for 15 min in a oven. Finally, hybridized oligo-arrays were spun at 800 rpm for 3 min.

Ligation Detection Reaction and a Universal Array Format. We chose to use chitosan with medium molecular weight to prepare universal arrays. Solutions of 5′-amino-modified oligonucleotides with a 5′-polyA tail, called zip-codes, were transferred into a 384-well microtiter plate in a volume of 30 μL and spotted at a final concentration of 50 μM in 150 mM sodium phosphate buffer (pH 8.5) onto the surface using the attachment protocol described above.

The oligonucleotides were applied onto the slides by contact printing using the MicroGrid II Compact arrayer. Each microscope slide contains eight identical subarrays, represented as a universal array whose layout (*15*) consisted of zip-codes

printed in quadruplicate distributed within the printing area; two zip-codes, namely 63 and 66, were associated to a ligation control and a hybridization control, respectively (*15*); as a negative control (blank), printing buffer was used. Each universal array was a subarray consisting of 208 spots of 13 rows × 16 columns.

As described in detail in Consolandi et al. (*15*), two discriminating probes (allele-specific probes designed to have their 3′-position placed just over the polymorphic site) labeled with two distinct fluorocromes (cyanine 3 and cyanine 5) and a common probe were selected for each SNP. Common probes were designed with a complementary zip-code sequence affixed to their 3′-end to unify the kinetics of the hybridization. Each zip-code sequence has a unique specific array location. The LDR mixture contained 81 oligonucleotides (27 common probes and 54 discriminating oligos), designed to identify 27 polymorphic sites in the HLA-A gene. As target, we used a heterozygous sample (A*0201/030101). The LDR mixture was cycled for 30 rounds of 94 °C for 30 s and 65 °C for 4 min in a thermal cycler (GeneAmp, PCR System 9700, Applied Biosystem, Foster City, CA) and then diluted to prepare the hybridization mixture. The mixture, after heating to 94 °C for 2 min and chilling on ice, was applied onto the subarray under a homemade multiple sample chamber (eight-well chamber), using Press-To-Seal silicone isolators (Schleicher & Schuell, Germany). Hybridization was carried out in the dark at 65 °C for 1.5 h, in a temperature-controlled system (Shack′n′Stack, Hybaid, England). After removal of the chamber, the slide was washed for 15 min in a prewarmed (65 °C) solution of 1X SSC/0.1% SDS with gentle shaking (Shack'n'Stack, Hybaid, England). Finally, the slide was spun at 800 rpm for 3 min.

Solid-Phase Minisequencing Reaction Using a Synthetic Template. In the minisequencing technique (*16*), a primer extension reaction is performed, starting from a specifc primer that is designed to anneal directly adjacent to the mutation site, by the incorporation of a single fluorescent dideoxynucleotide (ddNTP) which is complementary to the variant base in the template. Each ddNTP is labeled with a different fluorophore with distinct spectral emission, thus allowing the identification of the incorporated base.

The minisequencing reaction was performed onto an oligo-array, prepared by spotting of four oligonucleotides designed on the *Actinomyces* 16S ribosomal RNA sequence, according to Busti et al. (*17*). Three oligonucleotides (1450-1 ATTINO1, 1450-1 ATTINO2, 1450-1 ATTINO3) were designed in order to anneal directly adjacent to three consecutive bases while another oligonucleotide represents the negative control (1336 PSEUDO) (Table 1b). Each oligonucleotide was spotted 10 times in a row. We used a synthetic template as a sample at 1 μM final concentration and a labeled-ddNTPs mix (Tamra-ddCTP, Cy5-ddUTP, R110-ddGTP, TexasRed-ddATP) at 0.1 μM final concentration. The reaction buffer consisted of 26 mM Tris-HCl pH 9.5, 6.5 mM $MgCl_2$, and 0.2% Triton X-100 buffer with 0.25 U/μL Dynazime DNA polymerase (Finnzymes OY, Helsinki, Finland). The mixture, after heating to 94 °C for 2 min and chilling on ice, was applied onto the array under the homemade multiple sample chamber described above. The reaction was carried out in the dark at 55 °C for 1 h, in a temperature-controlled system (Shack'n'Stack, Hybaid, UK). After removal of the chamber, the slide was washed for 5 min in MilliQ-filtered water with gentle shaking (Shack'n'Stack, Hybaid, England). Finally, the slide was spun at 800 rpm for 3 min.

Detection of RNA Expression Levels. Finally, the performance of the chitosan treated surface was evaluated in a gene expression experiment. A set of 5376 probes, comprising 4998 peach genes (Operon Technologies, Alameda, CA), 188 randomly generated controls, 30 human spike-in controls, 15 hybridization controls, and 145 Blanks negative controls, were deposited by a MicroGrid II Compact arrayer, equipped with 4 Apogent Discoveries Microspot 10K pins. Oligonucleotides were resuspended in 384-well plates in a sodium phosphate buffer, to reach a final concentration of 15 pmol/μL oligonucleotide in each well. All probes were 5′-amino-modified 70-mers. Each probe was spotted in duplicate.

Slides were processed according to the protocol described in the Oligonucleotide Immobilization section. We evaluated the quality of the slides by using both a 9-mer complementary oligonucleotide and two aliquots of peach RNA, labeled with two different fluorochromes in a self-to-self-experiment.

The 9-mer hybridization solution was prepared as follows: 7.5 pmol/mL 5′-Cy3-labeled 9-mer, 5X SSC, 0.1% SDS, and 0.1 mg/mL salmon sperm DNA. The hybridization was performed at 16 °C for 8 h in a GenTac HybStation (Genomic Solutions, Perkin-Elmer Life Sciences, Boston, MA); then the slides were washed with a 2X SSC, 0.1% SDS solution for 5 min at 16 °C.

Target cDNAs, labeled with Cy3 and Cy5, were independently generated according to the SuperScript Indirect cDNA Labeling System (Invitrogen, Life Technologies, Paislay, UK). A 20 μg amount of RNA was used in each reaction. The resultant cDNA targets labeled with Cy3 and Cy5 were then purified using a PCR purification kit (Invitrogen, Life Technologies, Paislay, UK), as described by the manufacturer, and mixed together just before hybridization.

The hybridization solution for the self-to self-experiment was the same as that used in the experiment with the 9-mer oligonucleotide. Hybridization was performed in the hybridization station for 8 h at 42 °C. The slides were washed with a preheated solution that contained 2X SSC, 0.1% SDS for 5 min at 42 °C and then with SSC 0.2% for 5 min.

Signal Detection. Fluorescent signals were acquired at 5 μm resolution using a ScanArray 4000 laser scanning system (Perkin-Elmer Life Sciences, Boston, MA). The Green laser was used for CY3 dye (λ_{ex} 543 nm/λ_{em} 570 nm), Tamra dye (λ_{ex} 552 nm/λ_{em} 575 nm), the Red laser for CY5 dye (λ_{ex} 633 nm/λ_{em} 670 nm), the Yellow laser for Texas Red (λ_{ex} 593 nm/λ_{em} 612 nm), and finally the Blue laser for Rhodamine 110 (R110) (λ_{ex} 505 nm/λ_{em} 530 nm). Both the laser and photomultiplier tube (PMT) power were set in order to have no saturated signals in any case.

Data Analysis. To quantitate the fluorescent intensity of spots, we used the QuantArray Quantitative Microarray Analysis software (Perkin-Elmer Life Sciences, Boston, MA). The quantitation method we chose was the "fixed circle" method. Spot intensities were calculated using the mean intensity option. Data analysis of each experiment was performed by the following calculations: local background was subtracted from the intensity of each spot; fluorescent intensities (IF) of the replicates spots were averaged and the coefficient of variation was calculated.

RESULTS AND DISCUSSION

Since the advent of microarray technology, several chemistries have been proposed for oligonucleotide attachment to glass surfaces (*16*, *18*). We have tested many of the simplest strategies to attach amino-modified oligonucleotides. Our experience indicates that such chemistries are not suited for oligonucleotide microarray preparation aimed at polymorphism or mutation detection. More complex strategies have been proposed, including those that incorporate polyfunctional linkers such as polyacrylamide gel pads (*5*), branched chains (*3*), and poly(acrylic acid-*co*-acrylamide) copolymers generated in situ (*18*). Such approaches overcome some difficulties arising from poor

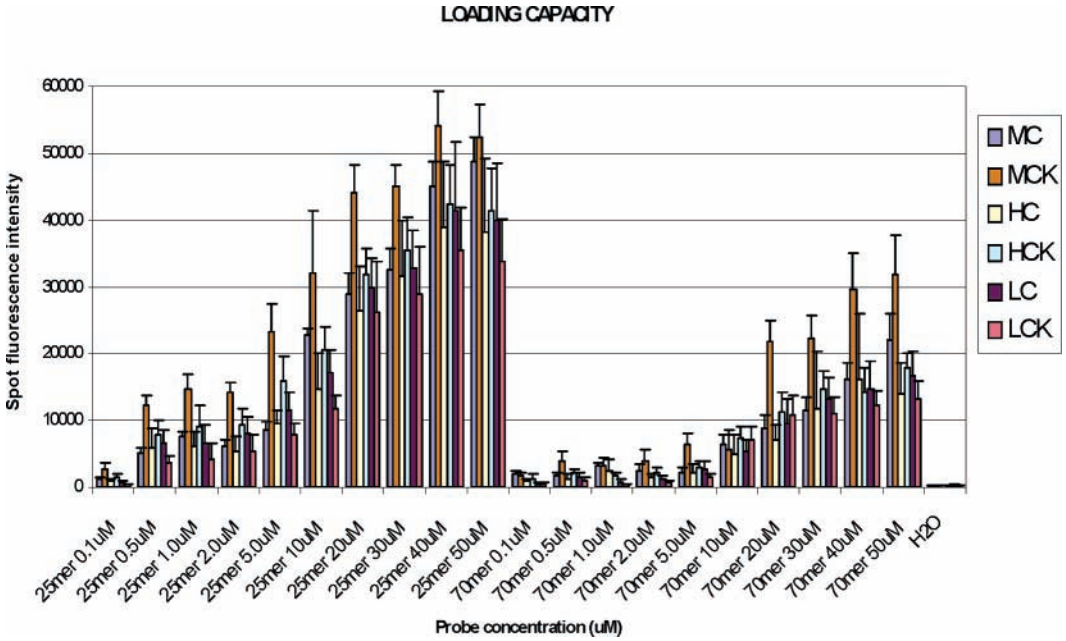

Figure 1. Array loading capacity. GOPS-chitosan-modified surfaces were spotted by using increasing concentrations from 0.1 to 50 μM of two oligonucleotides with two different lengths (25-mer and 70-mer) bearing a 5′-amino modification and a 3′-Cy3 fluorescent label. The graph shows the relationship between the oligonucleotide concentration and the surface-loading capacity measured as spot fluorescence intensity for the six modified surfaces (MC = medium chitosan, MCK = medium chitosan plus KCl, HC = high chitosan, HCK = high chitosan plus KCl, LC = low chitosan, LCK = Low chitosan plus KCl. Low corresponds to 120 kDa as molecular weight, medium corresponds to 400 kDa, and high corresponds to 650 kDa).

loading capacity of the (two-dimensional) glass surface, thanks to the three-dimensional structure of the swollen polymers. Following such an approach, we recently started experimenting with a three stage-process for preparing such surfaces involving (a) the functionalization of the glass surface, (b) attachment of a natural or synthetic polymer creating the scaffold, and (c) proper polymer scaffold activation against moieties to be targeted on the probes. Following our preliminary studies (*8*) using poly-L-lysine and acrylamide/acrylic acid copolymer, we selected chitosan, a polycation, to create a chemical platform suitable for biomolecules attachment to solid surfaces.

Our approach involves the creation of a polymeric layer covalently bound to the surface and activated with phenyldiisothiocyanate (PDITC). This allows the attachment of amine-bearing molecules. We analyzed the performance of these chemical platforms in order to characterize their behavior and ascertain their potential in oligonucleotide microarray preparation. All the sequences of the oligonucleotides used in the applications are reported in Table 1 (parts a and b).

Efficiency and Specificity of Oligonucleotide Covalent Attachment: Array-Loading Capacity. The chitosan-modified surfaces were analyzed before oligonucleotide spotting by laser scanning at 543 nm (suitable for cyanine 3 dye excitation) and at 633 nm (suitable for cyanine dye excitation) to determine their overall fluorescent background, which was found in all cases to be very low at both wavelengths (data not shown).

For DNA microarray fabrication, a pin contact arrayer was used. We tested a contact pin spotter (MicroGrid II Compact, Biorobotics, UK), demonstrating the mechanical stability of the polymeric coatings we propose (data not shown).

We employed 5′-amino, 3′-Cy3-modified 25-mer and 70-mer oligonucleotides to investigate the influence of the six different coating solutions on the surface-loading capacity. To explore this issue, we analyzed our six derivatized surfaces by spotting the doubly modified oligonucleotides at different concentrations (ranging from 0.1 μM to 50 μM in 10 different concentrations) arranged in a 16 $\times$ 13 matrix. The corresponding signals were quantitated using QuantArray Quantitative Microarray Analysis software. Sixty-four spots (two slides, eight subarray, four replicates) for each concentration were used to calculate mean and standard deviation.

The results, shown in Figure 1, illustrate the relationship between the oligonucleotide concentration and the surface-loading capacity measured as spot fluorescence intensity collected at 543 nm for the six modified surfaces. The loading capacity increases with increasing of the concentration of the spotted oligonucleotides in the both cases (25−70-mer). The 25-mer oligonucleotide shows a loading capacity higher than that of the 70-mer one. The surface prepared using the medium molecular weight chitosan with KCl shows the best spot fluorescence intensity (Figure 1), but the use of the same polymer without KCl gives a support with the best CV range (5% < CV < 17%), thus becoming the most reliable surface. The worst spot fluorescence intensity and the worst CV range are found for the surface prepared using the low molecular weight chitosan with KCl.

Efficiency of Hybridization to Immobilized Oligonucleotides. A set of experiments was performed to evaluate the fluorescence signal produced in an oligo-oligo hybridization model experiment by determining the relationship between the loaded oligonucleotide concentration and the hybridization efficiency. This test is of great importance, as the major concern in oligonucleotide arrays preparation is the accessibility of the probe for hybridization, as well as the specificity obtained in the interaction. DNA microarrays described above were hybridized with two Cy5-labeled oligonucleotides complementary to the 25-mer and 70-mer spotted sequences using a range of oligonucleotide concentration from 0.1 to 1 μM. Figure 2a,b depicts the relationship between the loaded oligonucleotide concentration and the hybridization signal intensity for the both oligonucleotides.

As shown in Figure 1, the loading capacity and availability to hybridization are good (Figure 2a,b). Above a probe concentration threshold, loading and availability remain nearly constant (tested at either 1 or 10 μM template concentration). This can be explained assuming that these chemistries yield

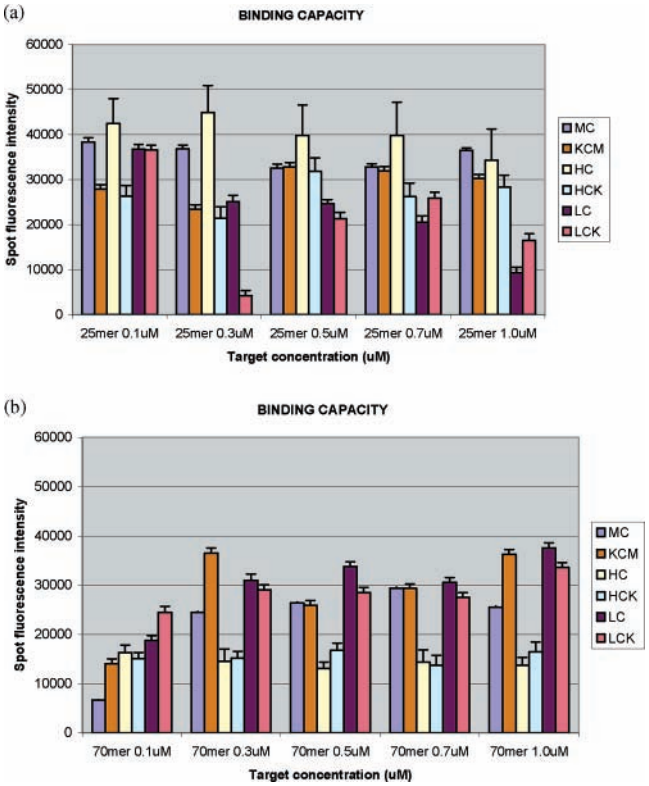

Figure 2. Binding capacity. Printed slides with 10 different concentrations of covalently attached oligonucleotides were hybridized with five different concentrations (0.1−1 μM) of Cy5-labeled oligonucleotide complementary to the spotted ones. The graph depicts the relationship between the loaded oligonucleotide concentration and the hybridization signal intensity for the both oligonucleotides (a, b). (MC = medium chitosan, MCK = medium chitosan plus KCl, HC = high chitosan, HCK = high chitosan plus KCl, LC = low chitosan, LCK = low chitosan plus KCl. Low corresponds to 120 kDa as molecular weight, medium corresponds to 400 kDa, and high corresponds to 650 kDa).

surfaces with fairly well-spaced reactive groups that avoid excessive crowding of probes that could negatively affect the microarray performance.

Applications. *Efficiency of Ligation Detection Reaction Combined to a Universal Array.* To explore the potential of the new surfaces, a ligation detection reaction (LDR) combined to a Universal Array (UA) platform has been optimized to analyze single nucleotide polymorphisms distributed within exons 2 and 3 of the HLA-A gene. The assay involves the amplification by PCR of the HLA-A genomic region (1900 bp), a multiplex LDR carried out to type twenty-seven HLA polymorphic sites followed by the capture of ligated products through hybridization onto a universal array. According to Consolandi et al. (*15*), a polymorphic site is typed by using two discriminating oligonucleotides labeled at their 5′-end with two fluorophores. Figure 3 shows the scanner analysis of the ligation detection reaction/universal array experiments obtained using a heterozygous sample (A*0201/030101). HLA genotyping by PCR/LDR/UA is in perfect agreement with typing obtained by direct sequencing. Our results clearly demonstrate that our treated surfaces are suitable to support hybridization reactions of complex targets, showing good specificity and efficiency. Good spot quality facilitates the subsequent evaluation of array data and has immediate effects on the reliability of the results.

Enzymatic Reaction: Efficiency of Minisequencing Reaction onto the Surface. Our slides were also tested for their performance as supports for in-situ enzymatic reactions. In respect to the experiment described above, in which the enzymatic reaction was performed in liquid phase, we carried out the minisequencing reaction directly on the surface. The concept of the minisequencing assay is to anneal a detection primer to the nucleic acid sequence immediately 3′ of the nucleotide position to be analyzed and to extend this primer with a single labeled dideoxynucleotide using a DNA polymerase.

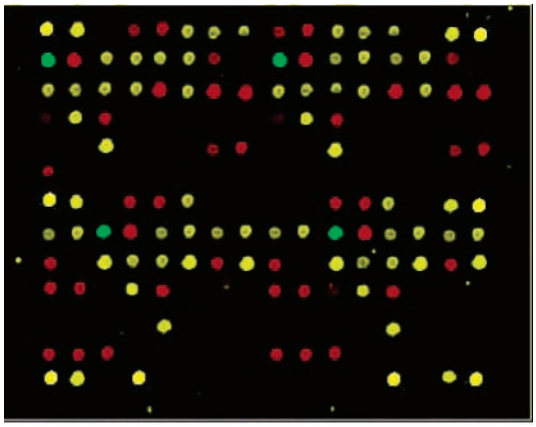

Figure 3. Scanner analysis of ligation detection reaction/universal array experiment. Fluorescent laser scanning of a heterozygous (A*0201/030101) sample analysis by using PCR/LDR/UA approach. This composite image is realized by overimposing Cy3 fluorescent signals (green palette) and Cy5 fluorescent signals (red palette). Yellow spots are the combination of Cy3 and Cy5 dyes.

To test this enzymatic procedure, we chose the *Actinomyces* 16S ribosomal RNA gene as reference sequence to design our synthetic template (see Experimental Procedures section) and probes (Table 1, part b). Three out of the four oligonucleotides (1450-1 ATTINO1, 1450-1 ATTINO2, 1450-1 ATTINO3) were designed in order to anneal directly adjacent to the targeted site. The 1336 PSEUDO oligonucleotide represent a negative control. The oligo-array contains the four oligonucleotides, acting as primers in the minisequencing reaction, each spotted 10 times in a row. During the reaction, the DNA polymerase carried out the incorporation of the fluorescent dideoxynucleotide (ddNTP), which is complementary to the targeted base in the template DNA. The extended probes, covalently bound to the solid support, can be detected thanks to the incorporation of fluorescent dyes. Figure 4 shows the fluorescent signals obtained using the four filters for the detection of the fluorescent signal due to the incorporation of the ddNTPs labeled with Tamra, Cy5, Rhodamine110, and Texas Red dyes. As expected, a fluorescent signal of the proper wavelength is detected identifying the targeted base on the template. No signal is detected from the negative control. This result suggests that our surfaces allow primer extension in-situ.

Detection of RNA Expression Levels. In the 9-mer hybridization, 99.1% of the 4998 "discovery" genes was present with at least one replicate per array. The randomly generated sequences and the spike-in controls were all present with at least one replicate per slide, whereas 98.5% of the hybridization controls performed as expected; at the same time 93.5% of the blank spots were not found by the quantitation software.

In the self-to-self-hybridization, instead, we found that 3238 "discovery" probes (65%) were found as present by the quantitation software. The background subtracted intensities for the two channels were then drawn as a scatter plot against each other, to represent levels of up or down regulation. As the samples were aliquots of the same starting RNA, we expected no change or a very little number of transcripts to be differentially expressed. Given a threshold of 2-fold change as the limit of differential expression, only 131 out of the 3238 "discovery" genes were obtained. This means that about 96% of the transcripts were not recognized as differentially expressed. Pearson's correlation coefficient between the two channels was

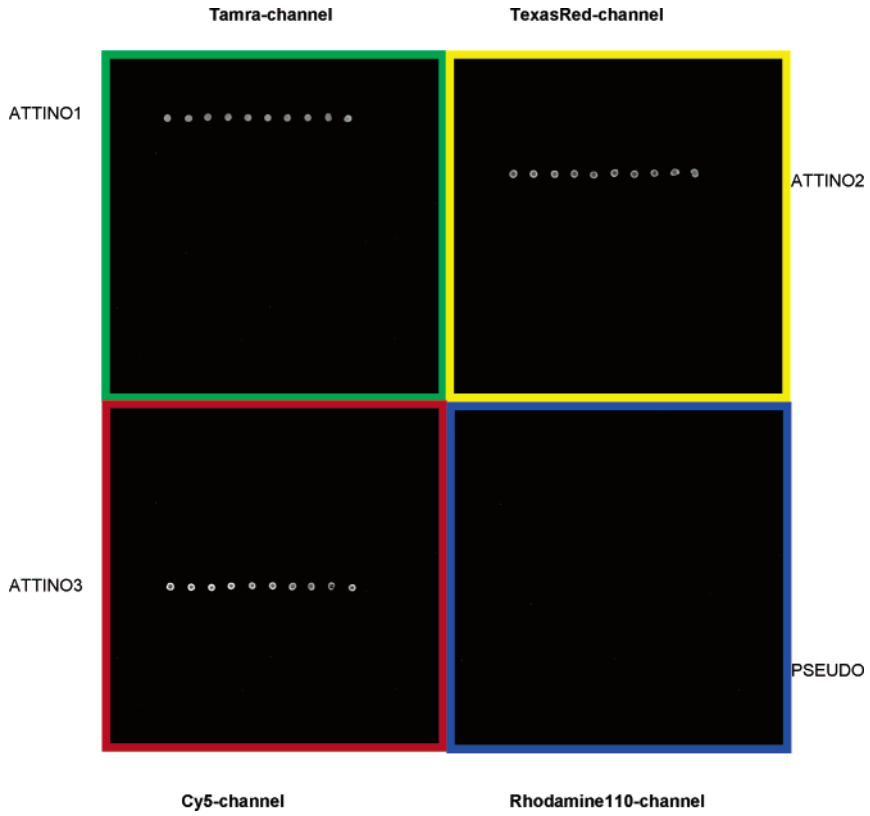

Figure 4. Scanner analysis of the minisequencing experiment. An oligo-array, prepared by spotting of four oligonucleotides (Table 1b) designed on the Actynomices 16S rRNA sequence, is scanned by using the four filters for the detection of the fluorescent signal due to the incorporation of the ddNTPs labeled with Tamra, Cy5, Rhodamine110, and Texas Red dyes. The green frame includes the fluorescent image scanned by Tamra filter, showing a C extension for 1450-1 ATTINO1 as expected. The yellow frame includes the image scanned by Texas Red filter, showing an A extension for 1450-1 ATTINO2 as expected. The red frame includes the image scanned by using Cy5 filter, showing a T extension for 1450-1 ATTINO3 as expected. No extension is detected in the blue frame (Rhodamine 110 filter). The fluorescent signals are visible only for the three oligonucleotides specific for the 16S rRNA sequence. In the fourth case (1336 PSEUDO sequence not specific for the template used), no signal is detected.

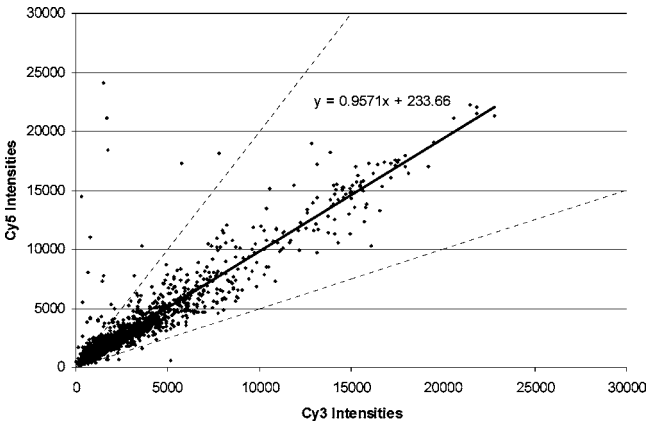

Figure 5. Scatter plot of intensities in the gene expression self-to-self-experiment. Values for each channel are plotted one against each other in black dots. The solid line is the linear regression curve, whose equation is also reported on the plot. The dotted lines represent the 2-fold change thresholds for differential expression.

0.937, indicating a very high reproducibility of the sample preparation procedure, whereas the slope of the linear regression curve was found to be 0.957, indicating that the two fluorophores were well balanced and there was no need for normalization or correction of the data (Figure 5).

We have reported here a robust chemical method for covalent immobilization of amino-modified oligonucleotides with two different lengths (25-mer and 70-mer) on glass surfaces based on polymeric coating. The DNA microarrays we prepared show good performance in terms of coupling specificity, and loading and binding capacity. As demonstrated by the discrimination of SNPs, oligonucleotides attached to our surfaces reveal highly specific hybridization properties and the accessibility to polymerase for enzyme-mediated reactions. Also labeled cDNAs react with the oligonucleotide probes attached to the functionalized surfaces, indicating an excellent availability to hybridization.

ACKNOWLEDGMENT

We gratefully acknowledge the financial support from CNR target project FIRB "Biochip", RBNE01TZZ8_001, FIRB "MICRAM", RBNE01ZB7A and FIRB 2003, RBLA03ER38_004.

LITERATURE CITED

(1) Ramsay, G. (1998) DNA chips: state-of-the art. *Nature Biotechnol. 16,* 40−44.

(2) Lipshutz, R. J., Fodor, S. P. A., Gingeras, R. T., and Lockart, D. J. (1999) High-density synthetic oligonucleotide arrays. *Nature Genet. 21,* 20−24.

(3) Beier, M. and Hoheisel, J. D. (1999) Versatile derivatisation of solid support media for covalent bonding on DNA-microchips. *Nucleic Acids Res. 27,* 1970−1977.

(4) Rogers, Y. H., Jiang-Baucom, P., Huang, Z. J., Bogdanov, V., Anderson, S., and Boyce-Jacino, M. T. (1999) Immobilization of oligonucleotides onto a glass support via disulfide bonds: A method for preparation of DNA microarrays. *Anal. Biochem. 266,* 23−30.

(5) Proudnikov, D., Timofeev, E., and Mirzabekov, A. (1998) Immobilization of DNA in polyacrylamide gel for the manufacture of DNA and DNA-oligonucleotide microchips. *Anal. Biochem. 259,* 34−41.

(6) Benters, R., Niemeyer, C. M., Drutschmann, D., Blohm, D., and Wohrle, D. (2002) DNA microarrays with PAMAM dendritic linker systems. *Nucleic Acids Res 15*, 30(2), e10.
(7) Ramakrishnan, R. et al. (2002) An assessment of Motorola CodeLink microarray performance for gene expression profiling applications. *Nucleic Acids Res. 30*(7), e30.
(8) Consolandi, C., Castiglioni, B., Bordoni, R., Busti, E., Battaglia, C., Rossi Bernardi, L., and De Bellis, G. (2002) Two efficient polymeric platforms for oligonucleotide microarray preparation. *Nucleosides, Nucleotides Nucleic Acids 21* (8, 9), 561−580.
(9) Hudson, S. M. and Smith, C. (1998) In *Biopolymers from Renewable Resources* (Kaplan, D. L., Ed) pp 96−118, Springer, Berlin.
(10) Hirano, S., Ohe, Y., and Ono, H. (1976) Selective N-acylation of chitosan. *Carbohydr. Res. 47*, 315−320.
(11) Yalpani, M. and Hall, L. D. (1984) Some chemical and analytical aspects of polysaccharide modifications. III. Formation of branched-chain, soluble chitosan derivatives. *Macromolecules 17*, 272−281.
(12) Gruber, J. V., Rutar, V., Bandekar, J., and Konish, P. N. (1995) Synthesis of N-[(3′-Hydroxy-2′,3′-dicarboxy)-ethyl]chitosan: A New, Water-Soluble Chitosan Derivative. *Macromolecules 28*, 8865−8867.
(13) Xu, J., McCarthy, S. P., Gross, R. A., and Kaplan, D. L. (1996) Chitosan Film Acylation and Effects on Biodegradability. *Macromolecules 29*, 3436−3440.
(14) Kurita, K., Ikeda, H., Yoshida, Y., Shimojoh, M., and Harata, M. (2002) Chemoselective Protection of the Amino Groups of Chitosan by Controlled Phthaloylation: Facile Preparation of a Precursor Useful for Chemical Modifications. *Biomacromolecules 3*, 1−4.
(15) Consolandi, C., Frosini, A., Pera, C., Ferrara, G. B., Bordoni, R., Castiglioni, B., Rizzi, E., Mezzelani, A., Rossi Bernardi, L., De Bellis, G., and Battaglia, C. (2004) Polymorphism analysis within the HLA-A locus by universal oligonucleotide array. *Hum. Mut. 24* (5), 428−34.
(16) Lindross, K., Liljiendahl, U., Raitio, M., and Syvanen, A. C. (2001) Minisequencing on oligonucleotide microarrays: comparison of immobilization chemistries. *Nucleic Acids Res. 29*, e69.
(17) Busti, E., Bordoni, R., Castiglioni, B., Monciardini, P., Sosio, M., Donadio, S., Consolandi**,** C., Rossi Bernardi, L., Battaglia, C., and De Bellis, G. (2002) Bacterial discrimination by means of a universal array approach mediated by LDR (ligase detection reaction). *BMC Microbiol. 2*, 27.
(18) Rehman, F. N., Audeh, M., Abrams, E. S., Hammond, P. W., Kennedy, M., and Boles, T. C. (1999) Immobilization of acrylamide-modified oligonucleotides by co-polymerization. *Nucleic Acids Research 27* (2), 649−655.

BC050285A

Interaction of C_{60}-Fullerene and Carboxyfullerene with Proteins: Docking and Binding Site Alignment

Hadar Benyamini,*,†,§ Alexandra Shulman-Peleg,‡ Haim J. Wolfson,‡ Bogdan Belgorodsky,§ Ludmila Fadeev,§ and Michael Gozin*,§

Bioinformatics Unit, George S. Wise Faculty of Life Sciences, Tel Aviv University, Tel Aviv 69978, Israel, School of Computer Science, Beverly and Raymond Sackler Faculty of Exact Sciences, Tel Aviv University, Tel Aviv 69978, Israel, and School of Chemistry, Beverly and Raymond Sackler Faculty of Exact Sciences, Tel Aviv University, Tel Aviv 69978, Israel. Received October 10, 2005; Revised Manuscript Received January 8, 2006

The unique properties of fullerenes have raised the interest of using them for biomedical applications. Within this framework, the interactions of fullerenes with proteins have been an exciting research target, yet little is known about how native proteins can bind fullerenes, and what is the nature of these interactions. Moreover, though some proteins have been shown to interact with fullerenes, up to date, no crystal structure of such complexes was obtained. Here we report docking studies aimed at examining the interactions of fullerene in two forms (C_{60} nonsubstituted fullerene and carboxyfullerene) with four proteins that are known to bind fullerene derivatives: HIV protease, fullerene-specific antibody, human serum albumin, and bovine serum albumin. Our work provides docking models with detailed binding pockets information, which closely match available experimental data. We further compare the predicted binding sites using a novel multiple binding site alignment method. A high similarity between the physicochemical properties and surface geometry was found for fullerene's binding sites of HIV protease and the human and bovine serum albumins.

INTRODUCTION

Since the discovery of fullerenes (*1*, *2*), these molecules and their derivatives (*3*) have been extensively explored for biomedical applications. Examples of fullerene bioactivity includes antibacterial activity (*3*), neuroprotection (*4*, *5*), DNA cleavage (*6*), apoptosis (*7*), ion channel inhibition (*8*), and amyloid formation inhibition (*9*). Enzyme inhibition by fullerene-based compounds was found for nitric oxide synthases (*10*) and glutathione reductase (*11*). Antiviral activity of fullerenes was demonstrated in the inhibition of the HIV protease, initially by modeling and subsequently by in vitro studies (*12*−*15*). Namely, the prediction that fullerene derivatives can potentially fit into the catalytic cavity of HIV protease was supported by binding and inhibition experiments. Interactions of fullerenes with some other proteins were also documented, including a fullerene-specific antibody (*16*, *17*), human serum albumin (HSA), and bovine serum albumin (BSA) (*18*−*20*). However, in all cases, the reported information provides only partial data regarding structures of these fullerene−protein complexes. We have recently reported the preparation, characterization, and a docking model of a stable complex of HSA with a C3-isomer of carboxyfullerene (CF) (*18*). The agreement of the docking predictions with the experimental results has encouraged us to generate docking models of fullerenes with additional proteins. Characterizing protein binding sites of fullerenes is an important step toward better understanding of mechanisms by which various enzymes and receptors are interacting with fullerenes.

Here, using leading computational tools for protein structure analysis, we first provide docking models for the interactions of C_{60} nonsubstituted fullerene (NS-C_{60}) and CF with four selected proteins: HSA, BSA, HIV protease, and the fullerene-specific antibody. Our models, obtained using the PatchDock algorithm (*21*−*23*), are consistent with previously reported experimental results and hence are highly reliable. The predicted binding sites were further compared using a novel method for multiple binding site alignment, MultiBind (*24*, *25*), which revealed a significant similarity between fullerene's binding sites of HSA, BSA, and HIV-protease.

METHODS

Protein Structures. For docking studies we used the following structures: (i) HSA. We used the structure of free HSA (PDB: 1ao6, (*26*)). (ii) BSA. Using the Swiss-model server (*27*), the HSA structure was used as a template in order to build a structural model for the BSA protein. The pairwise sequence alignment has only one gap over all the 578 residues of the BSA sequence, with 75% identity and 87% similarity shared between the human and bovine sequences (Figure 1). Thus, our model for BSA is reliable and is likely to resemble the native three-dimensional structure. (iii) HIV-protease. We used the structure of PDB: 1aid (*28*). (iv) Fullerene specific antibody. We used the structure of PDB: 1emt (*16*).

Docking. Docking models were obtained using the PatchDock algorithm (*21*). PatchDock takes as input two molecules and computes three-dimensional transformations of one of the molecules with respect to the other with the goal of maximizing surface shape complementarity while minimizing the number of steric clashes. Complexes may be of the types: protein−protein, protein−small molecule, antibody−antigen, or protein−nucleic acid. The program was tested and shown to successfully predict protein interactions for many examples (*21*, *22*, *29*, *30*). Given two molecules, PatchDock first divides their surfaces into patches according to the surface shape (concave, convex, or flat).

* To whom correspondence should be addressed. Hadar Benyamini, current address: Department of Organic Chemistry, The Hebrew University of Jerusalem, Givat Ram, Jerusalem 91904, Israel. Tel. +972-2-6584854, Fax. +972-2-6585345, E-mail: hadar@chem.ch.huji.ac.il. Michael Gozin: Tel. +972-3-6405878, Fax. +972-3-6405879; E-mail: cogozin@mgchem.tau.ac.il.

† Bioinformatics Unit.

‡ School of Computer Science.

§ School of Chemistry.

10.1021/bc050299g CCC: $33.50 © 2006 American Chemical Society
Published on Web 02/22/2006

```
Identities = 438/578 (75%), Positives = 509/578 (87%), Gaps = 1/578 (0%)

HSA:   1   SEVAHRFKDLGEENFKALVLIAFAQYLQQCPFEDHVKLVNEVTEFAKTCVADESAENCDK  60
           SE+AHRFKDLGEE+FK LVLIAF+QYLQQCPF++HVKLVNE+TEFAKTCVADES   C+K
BSA:  29   SEIAHRFKDLGEEHFKGLVLIAFSQYLQQCPFDEHVKLVNELTEFAKTCVADESHAGCEK  88

HSA:  61   SLHTLFGDKLCTVATLRETYGEMADCCAKQEPERNECFLQHKDDNPNLPRLVRPEVDVMC  120
           SLHTLFGD+LC VA+LRETYG+MADCC KQEPERNECFL HKDD+P+LP+L +P+ + +C
BSA:  89   SLHTLFGDELCKVASLRETYGDMADCCEKQEPERNECFLSHKDDSPDLPKL-KPDPNTLC  147

HSA:  121  TAFHDNEETFLKKYLYEIARRHPYFYAPELLFFAKRYKAAFTECCQAADKAACLLPKLDE  180
             F  +E+ F  KYLYEIARRHPYFYAPELL++A +Y   F ECCQA DK ACLLPK++
BSA:  148  DEFKADEKKFWGKYLYEIARRHPYFYAPELLYYANKYNGVFQECCQAEDKGACLLPKIET  207

HSA:  181  LRDEGKASSAKQRLKCASLQKFGERAFKAWAVARLSQRFPKAEFAEVSKLVTDLTKVHTE  240
           +R++  ASSA+QRL+CAS+QKFGERA KAW+VARLSQ+FPKAEF EV+KLVTDLTKVH E
BSA:  208  MREKVLASSARQRLRCASIQKFGERALKAWSVARLSQKFPKAEFVEVTKLVTDLTKVHKE  267

HSA:  241  CCHGDLLECADDRADLAKYICENQDSISSKLKECCEKPLLEKSHCIAEVENDEMPADLPS  300
           CCHGDLLECADDRADLAKYIC+NQD+ISSKLKECC+KPLLEKSHCIAEVE D +P +LP
BSA:  268  CCHGDLLECADDRADLAKYICDNQDTISSKLKECCDKPLLEKSHCIAEVEKDAIPENLPP  327

HSA:  301  LAADFVESKDVCKNYAEAKDVFLGMFLYEYARRHPDYSVVLLLRLAKTYETTLEKCCAAA  360
           L ADF E KDVCKNY EAKD FLG FLYEY+RRHP+Y+V +LLRLAK YE TLE+CCA
BSA:  328  LTADFAEDKDVCKNYQEAKDAFLGSFLYEYSRRHPEYAVSVLLRLAKEYEATLEECCAKD  387

HSA:  361  DPHECYAKVFDEFKPLVEEPQNLIKQNCELFEQLGEYKFQNALLVRYTKKVPQVSTPTLV  420
           DPH CY+ VFD+ K LV+EPQNLIKQNC+ FE+LGEY FQNAL+VRYT+KVPQVSTPTLV
BSA:  388  DPHACYSTVFDKLKHLVDEPQNLIKQNCDQFEKLGEYGFQNALIVRYTRKVPQVSTPTLV  447

HSA:  421  EVSRNLGKVGSKCCKHPEAKRMPCAEDYLSVVLNQLCVLHEKTPVSDRVTKCCTESLVNR  480
           EVSR+LGKVG++CC  PE++RMPC EDYLS++LN+LCVLHEKTPVS++VTKCCTESLVNR
BSA:  448  EVSRSLGKVGTRCCTKPESERMPCTEDYLSLILNRLCVLHEKTPVSEKVTKCCTESLVNR  507

HSA:  481  RPCFSALEVDETYVPKEFNAETFTFHADICTLSEKERQIKKQTALVELVKHKPKATKEQL  540
           RPCFSAL  DETYVPK F+ + FTFHADICTL + E+QIKKQTALVEL+KHKPKAT+EQL
BSA:  508  RPCFSALTPDETYVPKAFDEKLFTFHADICTLPDTEKQIKKQTALVELLKHKPKATEEQL  567

HSA:  541  KAVMDDFAAFVEKCCKADDKETCFAEEGKKLVAASQAA 578
           K VM++F AFV+KCC ADDKE CFA EG KLV ++Q A
BSA:  568  KTVMENFVAFVDKCCAADDKEACFAVEGPKLVVSTQTA 605
```

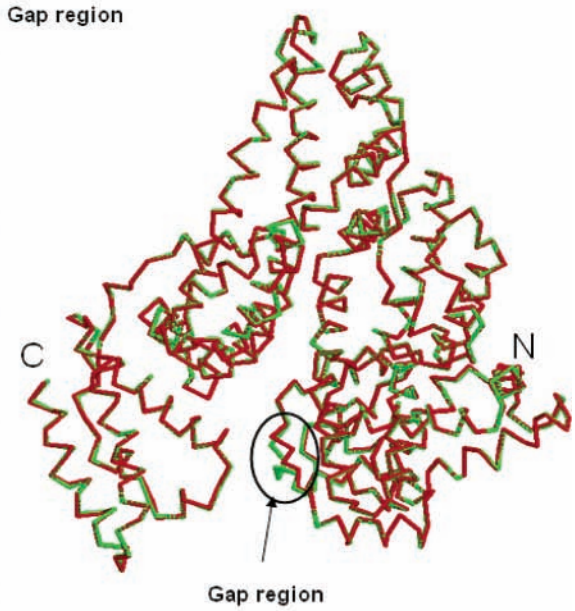

Figure 1. Sequence and structure alignment of human and bovine serum albumins. Left: sequence alignment. In the middle line of each three lines, identical residues are detailed; "+" stands for similar residues. Right: Structure alignment of HSA (PDB: 1ao6) with the model for BSA, built using the Swiss-model server (*27*). Structure alignment was performed using the C-α match program (http://bioinfo3d.cs.tau.ac.il). The gap region is marked in both alignments. Bovine serum albumin has one less amino acid residue, lacking a corresponding residue to Val112, using PDB: 1ao6 (HSA) numbering.

Then, it applies the Geometric Hashing algorithm to match concave patches with convex patches and flat patches with flat patches and generates a set of candidate transformations. Each candidate transformation is further evaluated by a set of scoring functions that estimate both the shape complementarity and the atomic desolvation energy (*31*) of the obtained complex. Finally, redundant solutions are discarded by the application of an RMSD (root-mean-square deviation) clustering. PatchDock is highly efficient, since it utilizes advanced data structures and spatial pattern detection techniques which are based on matching of local patches. The local shape information is then extended and integrated to achieve global solutions. The algorithm implicitly addresses surface flexibility by allowing minor penetrations.

Binding Sites Alignment. The alignment of the predicted binding sites of the modeled complexes was performed using the MultiBind algorithm (*24*, *25*). MultiBind considers protein binding sites represented by a set of three-dimensional points with assigned physicochemical and geometrical properties important for protein−ligand interactions. It performs multiple alignment of binding sites and allows recognition of the structurally conserved physicochemical and geometrical patterns that may be responsible for the binding and biological effect. The goal of MultiBind is to find a set of transformations that will superimpose the binding sites in a manner that will maximize the physicochemical score of the matched properties. Five physicochemical properties are considered: hydrophobic aliphatic, aromatic, hydrogen bond donors, hydrogen bond acceptors, and mixed donor/acceptors. The scoring function compares the similarity of the attributes, which are more important for the specific property. The molecules representation is based on the model of Schmitt et al. (*32*). According to this model, each amino acid is represented by a set of three-dimensional points in space, denoted as pseudocenters. Each pseudocenter represents one of the five considered properties. The pseudocenters are extracted from the side-chains, as well as from the protein backbone. For example, the side chain of arginine is represented by three donors (nitrogen atoms) and an aliphatic pseudocenter (located at the center of mass of its three carbons), while the side-chain of phenylalanine is represented by an aromatic pseudocenter, located at the center of its ring.

The MultiBind algorithm has three major computational steps. The first one is a generation of three-dimensional transformations that would align the binding sites. The second step is a search for a combination of three-dimensional transformations that would give the highest scoring common three-dimensional pattern of physicochemical properties. The final step is a computation of matching between points under multiple transformations. The MultiBind algorithm was applied to some well studied biological examples such as estradiol, ATP/ANP, and transition state analogues binding sites, providing results which agree with the available biological data (*24*, *25*).

Evaluation of Common Binding Patterns. To calculate the frequency of random occurrence of structural patterns recognized by MultiBind, we searched their occurrence on the complete surfaces of proteins in the nonredundant PDB representation by the ASTRAL dataset (*33*, *34*) (release 1.65, less than 40% sequence identity). The searched structural pattern was represented by the pseudocenters of the first molecule (in the alignment input order). Each pattern that was recognized on the surface of some protein was scored by the above-described physicochemical scoring function of MultiBind. The frequency of occurrence was calculated as the ratio between the number of times that a pattern with a score higher than a reference score was observed, relative to the total number of searched proteins.

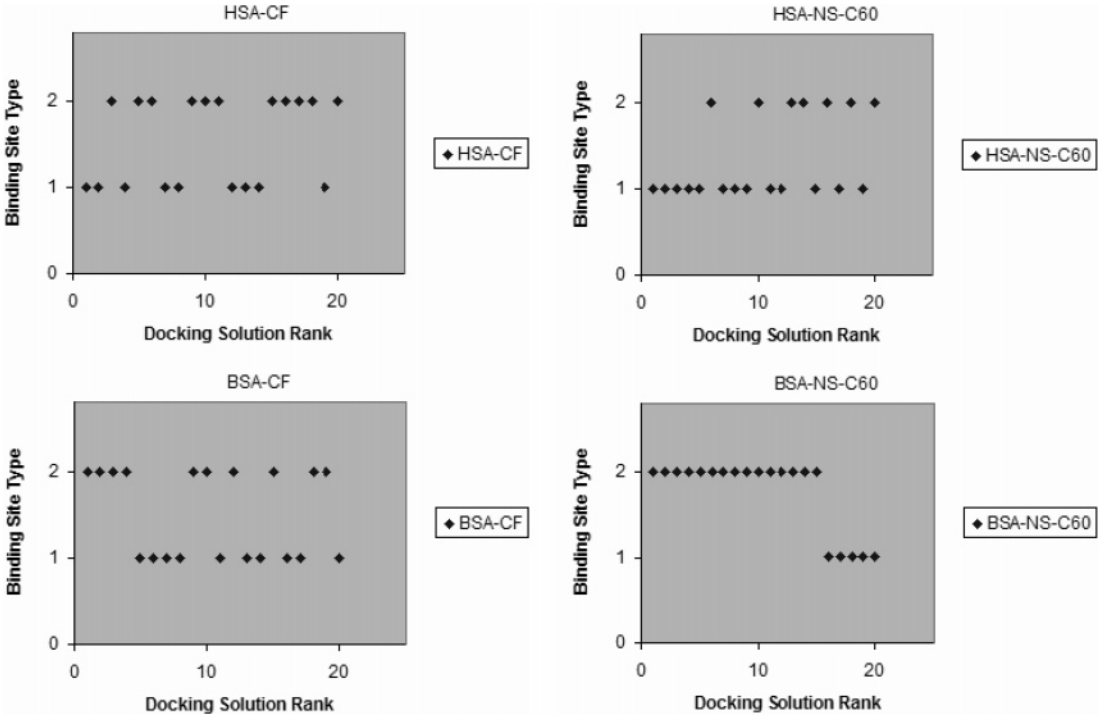

Figure 2. Distribution of the two fullerene binding sites on HSA and BSA among the top 20 ranking solutions. *X* axis: Rank of docking solution, from 0 to 20. The ranking of docking solutions is determined by their score, which optimizes geometric complementarity. *Y* axis: Type of binding site on human or bovine serum albumin. Note, that this axis has no numerical value and numbers 1 and 2 stand for the different binding sites (Figures 3 and 4 for type 1 and type 2 binding sites, respectively). The upper and lower graphs depict the distribution of HSA and BSA binding sites, respectively. The left and right graphs depict the sites distribution for carboxy- and nonsubstituted fullerene, respectively. For example, the top two ranked docking solutions for the binding of HSA to carboxyfullerene (up, left) are on the binding site type 1.

The reference score is defined to be the score of the outlier, i.e., lowest score of the most different binding site that participated in the pattern construction with MultiBind. The obtained ratio represents the estimation of the chances for a random occurrence of the recognized pattern. Using the score of the outlier as a reference score provides the highest possible ratio and the worst case estimation of the most frequent pattern.

RESULTS AND DISCUSSION

1. Docking Models of Nonsubstituted C_{60} Fullerene and Carboxyfullerene with Four Proteins. We docked nonsubstituted C_{60} fullerene (NS-C_{60}) and carboxyfullerene (CF) to four biomolecules: human serum albumin (HSA), bovine serum albumin (BSA), HIV protease (HIVP), and a fullerene-specific antibody. For three of the examined proteins, previously published data exists regarding fullerene binding sites: HIVP (*12*, *15*, *35*), fullerene-specific antibody (*16*, *17*), and HSA (*18*). PatchDock successfully detected surface pockets that are in agreement with previously suggested binding sites. In all the reported docking models, no a priori information was used as an input for the PatchDock algorithm, i.e., the surface pockets on the receptor molecules were detected fully automatically. Being able to reconstruct known fullerene binding sites makes PatchDock a reliable tool for prediction of fullerene binding sites in other proteins.

Docking of Fullerenes to HSA and BSA. The binding of HSA and BSA to fullerenes was observed experimentally (*18*−*20*). The location of CF binding site in HSA was suggested to be adjacent to the Trp214 residue, based on time-resolved FRET measurements (*18*). The results of our docking studies suggest that both proteins are capable of fullerene binding by two distinctive binding sites, located on the opposite faces of the albumin molecules and for clarity termed binding sites "type 1" and "type 2". For each of these proteins and for both ligands (NS-C_{60} and CF), the 20 top scored docking solutions were found to be distributed over these two sites (Figure 2). In HSA, the type 1 binding site docking solution positions the fullerene molecule in a short distance from Trp214 residue (Figure 3). In general, this binding pocket was found to be almost identical for both albumins and for HSA can be marked by Trp214, His288, and His440 residues (the complete list of residues in radius of 6 Å from the fullerene ligand is detailed in the Supporting Information). The type 2 binding site places the fullerene ligand in a pocket on the opposite face of the albumin molecules (Figure 4). In HSA, this binding pocket can be marked by residues Lys190, Glu425, and Arg428 (the complete list of residues in radius of 6 Å from the fullerene ligand is detailed in the Supporting Information). Figure 2 presents the distribution of the type 1 and type 2 binding sites among the top 20 docking solutions. As can be seen in the figure, although both type 1 and type 2 binding sites appear in the top 20 ranking docking solutions for HSA and BSA, HSA protein displayed preferential binding of fullerene toward type 1 site, while the BSA protein displayed preferential binding toward type 2 site (Figure 2). The correlation between binding preferences and clustering of docking solutions was recently discussed (*36*). We estimate that these differences can be mostly attributed to the fact that type 2 binding site of BSA lacks an amino acid corresponding to the Val112 residue, which is present in type 2 binding site of HSA. This difference appears to make the type 2 site of BSA more compatible and less sterically crowded for accommodation of fullerene, in comparison to the similar site in HSA.

Comparison between Binding of Fullerenes and Other Known HSA Ligands. The Protein Data Bank (*37*) currently holds 22 complexes of HSA with 14 different ligands, uniquely located at multiple various binding sites. Although, due to the substantial differences in ligands shapes, fullerene binding sites of types 1 and 2 are not identical to pockets of other known serum albumin ligands, these sites share many common amino

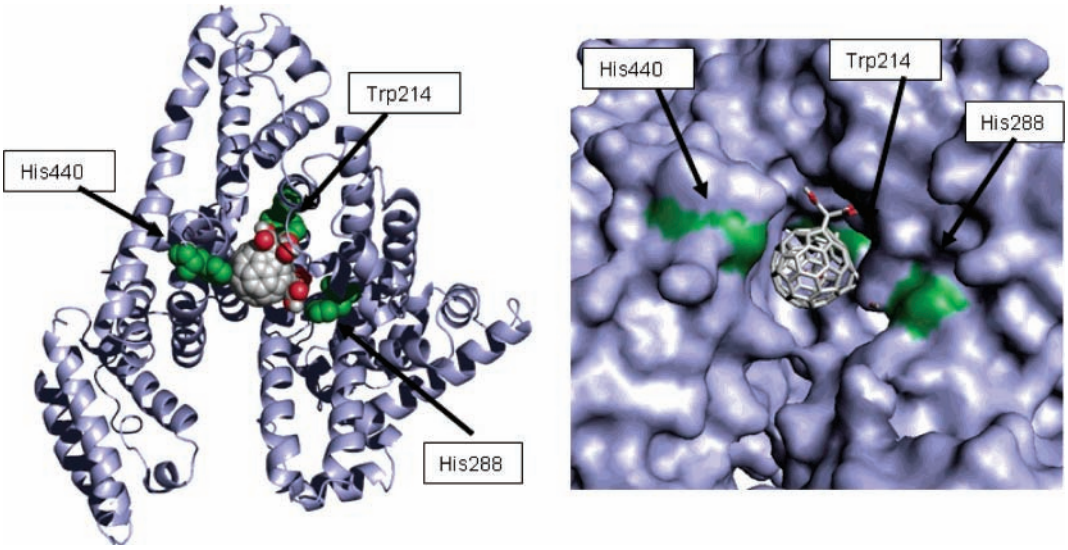

Figure 3. Predicted binding site (type 1) for carboxyfullerene on human serum albumin. Left: carboxyfullerene is represented in a spacefill model. HSA is represented in cartoon, except for His288, Trp214, and His440 which are represented in spacefill and colored green. Right: Fullerene is represented in sticks. HSA is represented by its surface and colored light blue except for His288, Trp214, and His440 which are colored green. This Figure, as well as Figures 4, 5, and 6 were prepared using PyMOL (*44*).

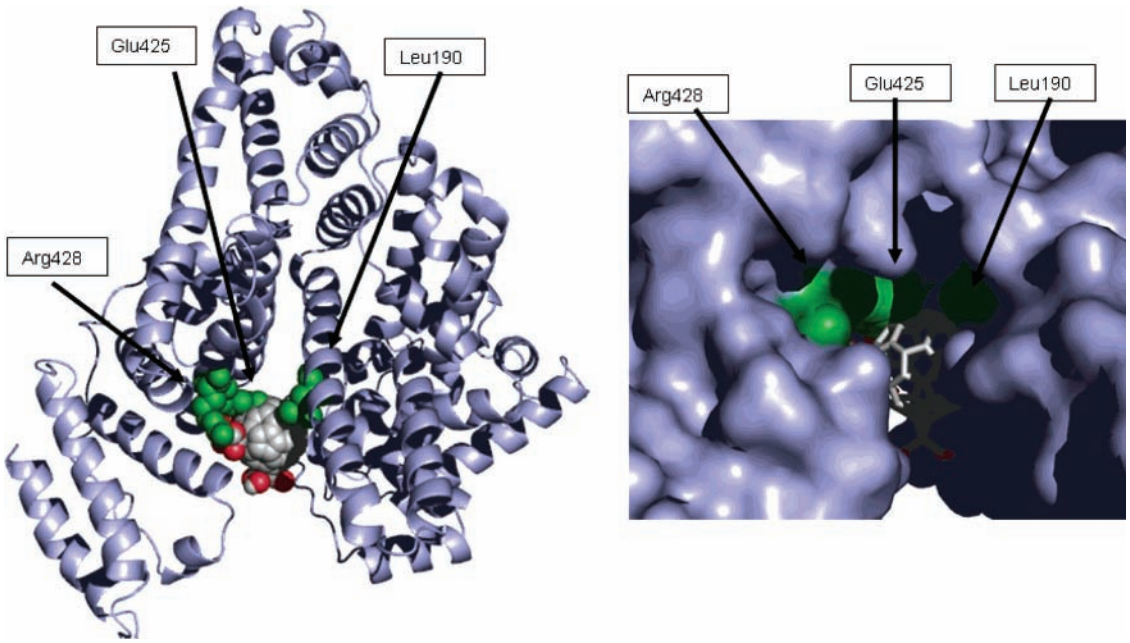

Figure 4. Predicted binding site (type 2) for carboxyfullerene on bovine serum albumin. Leu190, Glu425 and Arg428 are marked. Coloring and representation are the same as in Figure 3.

acid residues with other reported binding pockets of HSA. For example, the predicted type 1 binding site of fullerene consists of residues that participate in binding of the following ligands: tribenzoic acid (PDB: 1bke); 2-bromo-2-chloro-1,1,1-trifluoroethane (PDB: 1e7c); decanoic acid (PDB: 1e7e); lauric acid (PDB: 1e7f); myristic acid (PDB: 1e7g, 1hk4, 1hk5, 1o9x); palmitic acid (PDB: 1e7h); stearic acid (PDB: 1e7i); oleic acid (PDB: 1gni); arachidonic acid (PDB: 1gnj); *R*-wafarin (PDB: 1h9z); *S*-wafarin (PDB: 1HSA-2); 3,5,3′,5′-tetraiodo-L-thyronine (PDB: 1hk1, 1hk2, 1hk3); citric acid (PDB: 1tf0). The predicted type 2 binding site of fullerene consists of residues that participate in binding of the following ligands: tribenzoic acid (PDB: 1bke); myristic acid (PDB: 1bke, 1e7c, 1e7g, 1h9z, 1HSA-2, 1hk4,1hk5); 2-bromo-2-chloro-1,1,1-trifluoroethane (PDB: 1e7c); decanoic acid (PDB: 1e7e); lauric acid (PDB: 1e7f); palmitic acid (PDB: 1e7h); stearic acid (PDB: 1e7i); oleic acid (PDB: 1gni); arachidonic acid (PDB: 1gnj); 3,5,3′,5′-tetraiodo-L-thyronine (PDB: 1hk4, 1hk5); Fe-containing protoporphyrin IX (PDB: 1o9x, 1n5u).

Figure 1 in the Supporting Information displays side-by-side the docking model of HSA-CF complex aligned with the structure of the HSA complex with citric and decanoic acids (PDB: 1tf0, (*38*)). Coloring the fullerene's type 1 site residues on both the HSA-CF docking model and on the crystal structure of HSA complex with citric acid clearly demonstrates the similar residues that participate in the binding of both ligands.

Docking of Fullerenes to HIV Protease. The binding of fullerene to HIV protease (HIVP) was first demonstrated by Friedman and co-workers (*12*, *15*). Docking of fullerene to HIVP (PDB: 1aid, (*28*)), by using PatchDock, suggests the same binding pocket for NS-C_{60} and CF ligands (Figure 5). This cylindrically shaped, symmetric binding pocket can be marked by residues Asp25, Asp25′, Ile50, and Ile50′ (i.e. residues 25 and 50 on chains A and B; the complete list of residues is

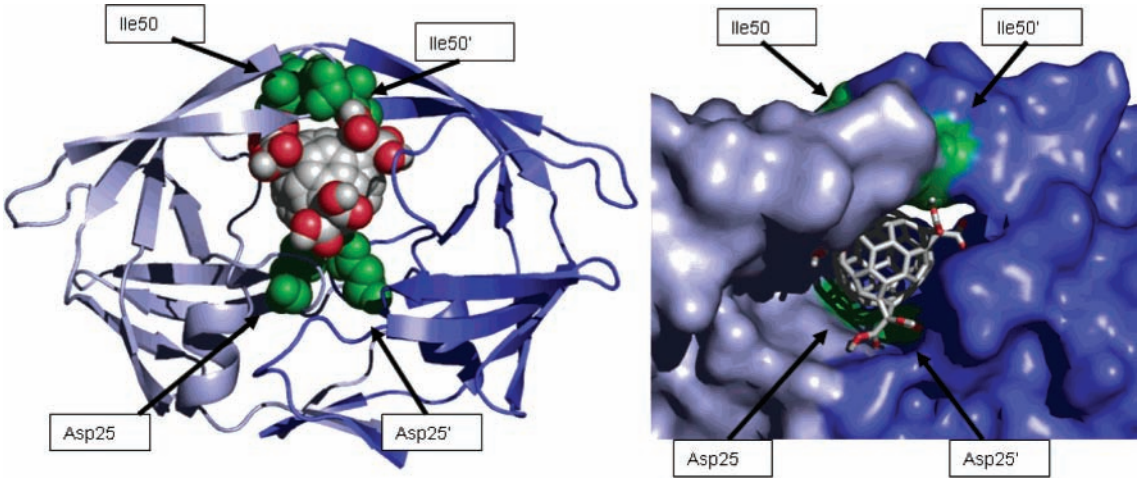

Figure 5. Predicted binding site for carboxyfullerene on HIV protease. Residues Asp25, Asp25′, Ile50, and Ile50′ are marked. Coloring and representation are the same as in Figure 3.

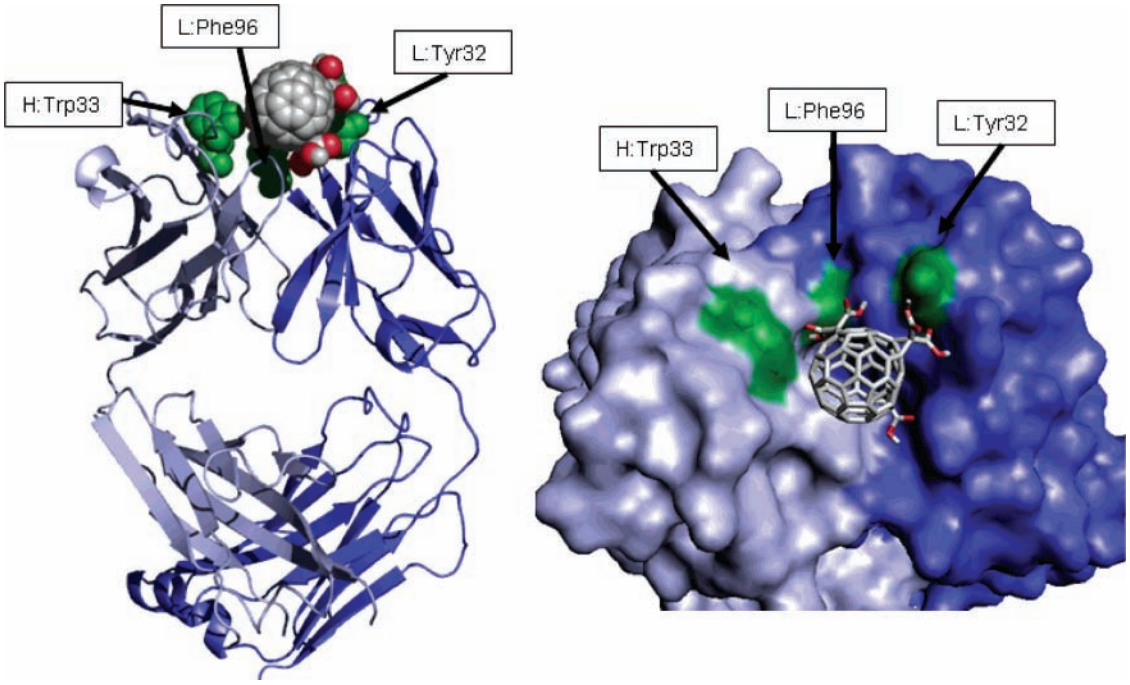

Figure 6. Predicted binding site for carboxyfullerene on a fullerene specific antibody. L chain residues Tyr32 and Phe96, as well as chain H residue Trp33 are marked. Coloring and representation are the same as in Figure 3.

detailed in the Supporting Information), which were reported to participate in various ligands binding and, in particular, in fullerene binding by HIVP (*39*).

Docking of Fullerene to a Fullerene-Specific Antibody. Erlanger and co-workers have prepared a monoclonal fullerene-specific antibody and determined its structure by X-ray crystallography (*16*, *17*). The suggested fullerene binding site was further subjected to molecular dynamics calculations (*40*), supporting the involvement of chain L residues Asn34, Leu46, Tyr49, Gln89, Tyr91, and Phe96, along with chain H residues Trp33, Trp47, Arg50, Tyr52, Ala97, and Ala101. In this work, by using the PatchDock algorithm with a set of parameters designed for antibody−antigen interactions prediction, we found the same pocket as the most likely site for fullerene binding by this antibody molecule (PDB: 1emt, (*16*)). Figure 6 displays the predicted binding site for fullerene on the fullerene-specific antibody. This binding pocket can be marked by chain L residues Tyr32 and Phe96, as well as chain H residue Trp33 (the complete list of residues is detailed in the Supporting Information).

2. Binding Sites Alignment and Analysis. After obtaining the docking models, our goal was to compare between the predicted binding sites and recognize the common features that may be related to the binding of fullerenes. Thus, we analyzed the similarities between the fullerene binding sites of HSA type 1, HSA type 2, HIVP, and the fullerene-specific antibody. The predicted binding sites of BSA were excluded from the multiple binding sites alignments, mainly due to these sites close resemblance to the corresponding HSA type 1 and type 2 sites. In addition, besides the inherent deviation of a docking model from the bound complex, additional deviations could exist due to the structure model building of BSA.

The four compared binding sites have different overall sequences and tertiary structures. Specifically, the sequence identity between the HIVP and HSA proteins is only 8% and between HSA and the fullerene-specific antibody is 15%. Obviously, HSA, HIVP, and the fullerene-specific antibody are also structurally nonrelated. Due to the above-mentioned differences, the proteins in our study cannot be aligned by standard alignment methods, that assume similarity of either sequence

Table 1. Details of the Common Pattern Calculated between the Three Most Similar Fullerene Binding Sites

HSA, type 2			HSA, type 1			HIV-protease		
residue number	residue type	feature[a]	residue number	residue type	feature	residue number[b]	residue type	feature[a]
111	Asn	Pii	292	Glu	Pii	49 (A)	Gly	Pii
111	Asn	acceptor	292	Glu	acceptor	49 (A)	Gly	acceptor
112	Lys	donor	293	Val	donor	49 (A)	Gly	donor
112	Lys	Pii	293	Val	Pii	48 (A)	Gly	Pii
112	Lys	acceptor	293	Val	acceptor	48 (A)	Gly	acceptor
114	Arg	donor	294	Glu	donor	48 (A)	Gly	donor
221	Pro	Pii	447	Pro	Pii	27 (A)	Gly	Pii
221	Pro	acceptor	447	Pro	acceptor	27 (A)	Gly	acceptor
422	Thr	mixed donor−acceptor	448	Cys	acceptor	25 (B)	Asp	acceptor
425	Glu	acceptor	451	Asp	acceptor	25 (A)	Asp	acceptor

[a] The common features detected by Multibind contain either Pii (aromatic) interactions, hydrogen bond donor or acceptor, or mixed donor−acceptor (can use as both). [b] The chain ID is in parentheses.

or backbone patterns (*41*−*43*). Thus, to compare between the predicted binding sites of the modeled complexes, we used a recently developed method, MultiBind (*24*, *25*), which performs a multiple structure alignment between protein binding sites, in the absence of overall sequence, fold, or binding partner similarity. The MultiBind method recognizes the common spatial arrangements of physicochemical properties shared by the compared binding sites. This method is suitable for the comparison of the diverse studied proteins due to the utilized physicochemical representation of the protein molecules, where each amino acid is represented by a set of three-dimensional points in space, denoted as pseudocenters (see Methods for details (*32*)). Additionally, MultiBind does not consider the location of the binding partners, and therefore it is most appropriate for comparison of docking models, which provide only an approximate representation of the bound complex.

Here, we describe the patterns of pseudocenters which were recognized as shared by the compared binding sites. The predicted binding sites of the modeled protein−fullerene complexes were compared with both NS-C_{60} and CF ligands. We analyzed the results of the alignments between a set of all four binding sites in addition to its different subsets (two and three binding sites). Then, we evaluated the quality and the significance of the resulted patterns recognized by MultiBind by calculating their frequency of occurrence on the surfaces of complete proteins in the nonredundant PDB representation by the ASTRAL dataset (*33*, *34*). The ratio of the number of observed patterns, relative to the size of the searched dataset, provides an estimation regarding the probability of observing such a pattern by chance, on a randomly selected protein. The lower the frequency of occurrence, the more significant and rare is the pattern. Additional details regarding the exact calculations are provided in Methods.

Multiple Alignments between Four Binding Sites (HSA type 1, HSA type 2, HIVP, and the fullerene-specific antibody). Multiple alignment between the four predicted binding sites of NS-C_{60} recognized a pattern of seven physicochemical properties. The pattern contained one aromatic property, one hydrogen bond donor, and five hydrogen bond acceptors. Although the NS-C_{60} ligands were not taken into account during any of MultiBind computational steps, transformations calculated by MultiBind for the binding sites superimpose the NS-C_{60} molecules to similar locations in space, supporting the correctness of the alignment. However, when the recognized pattern was searched in the proteins of the ASTRAL dataset, it was found in 36% of the cases. This suggests that the detected pattern is not likely to be specific enough to distinguish between proteins that can bind NS-C_{60} and those that cannot.

The application of MultiBind to the four predicted binding sites of CF recognized a pattern of six physicochemical properties. The pattern consisted of three aromatic pseudocenters and three hydrogen bond acceptors. Two properties, one acceptor and one aromatic, were created by backbone atoms in all of the compared binding sites. The frequency of occurrence of this pattern in the ASTRAL dataset was 37%, which is also too high to be statistically significant.

Multiple Alignments between Three Binding Sites. The alignment between all four binding sites has shown that the binding site of the fullerene-specific antibody was the most different from all the rest, since it received the lowest score in the alignment. The inclusion of the antibody in the multiple alignment significantly reduced the size, the score, and the statistical significance of the common pattern. Therefore, in the alignments below, we removed this binding site from the aligned ensemble and compared only between the three binding sites of HSA type 1, HSA type 2, and HIVP. It must be noted that since the sequence and the fold of HIVP is very different from those of HSA, these three binding sites cannot be compared by standard sequence and structural alignment methods. The binding sites of HSA type 1 and HSA type 2 are also very different. They are located at opposite faces of HSA and are created by different noncontiguous sequences of HSA.

Three NS-C_{60} Binding Sites. Comparison between the three predicted binding sites of NS-C_{60} revealed an interesting pattern of 10 common physicochemical properties. Table 1 presents the details of the recognized pattern. Figure 7 presents the spatial arrangement of the recognized features and the superimposition between the proteins and the fullerene ligands, according to the transformations suggested by MultiBind. The recognized pattern contained three aromatic properties, two donors, and five hydrogen acceptors. The frequency of occurrence of this pattern was 1%, which shows its relative rarity.

Three CF Binding Sites. Interestingly, the pattern recognized by the alignment of the three CF binding sites was almost the same as the pattern recognized by the alignment of the three NS-C_{60} binding sites. This pattern contained 10 features with exactly the same properties. The contribution of the backbone and side-chain atoms has also remained the same. The slight differences in the exact alignment correspondence details may be explained by the different boundaries of the binding sites and by the approximation algorithms of the MultiBind method (see Methods). In general, we can summarize that the same binding pattern was recognized for the predicted binding sites of both NS-C_{60} and CF.

Pairwise Alignments. To evaluate the similarity between the compared binding sites, we also performed all-against-all pairwise surface alignments (Table 2). Naturally, the patterns detected between pairs of binding sites contained more features than the patterns common to larger sets (three or four binding sites). The frequency of occurrence of the recognized pairwise patterns in the ASTRAL dataset was very low and ranged from 0 to 1.4%. The size of the pairwise patterns ranged from 11 to 20 (mean = 17) properties for the predicted NS-C_{60} binding

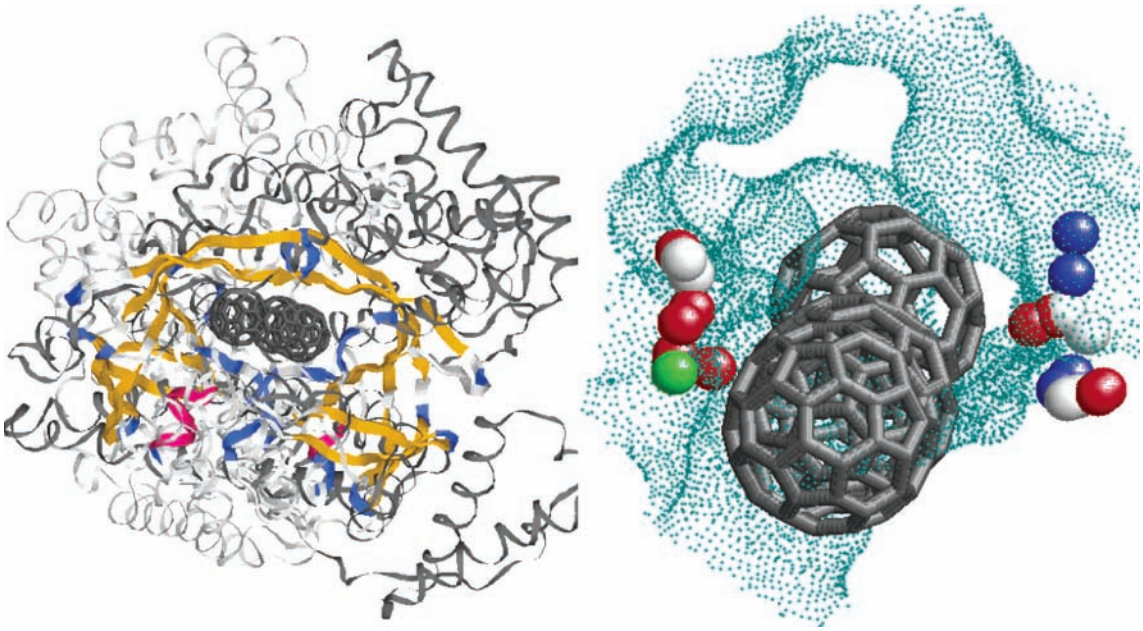

Figure 7. Surface alignment between the predicted binding sites of human serum albumin (types 1 and 2) and HIV protease. Left: the structures of human serum albumin (HSA) and HIV protease (HIVP) are represented by cartoons. HSA- type 1 is colored gray, HSA- type 2 is colored light gray and HIVP is colored according to secondary structure (β-strands are colored yellow and α-helices are colored pink). Fullerenes are represented as sticks and colored gray. The ligand molecules are presented for verification purpose only and are not a part of the input to MultiBind. Right: close-up on the aligned binding sites. Matched pseudocenters are represented by balls. Hydrogen bond donors are blue, acceptors are red, donors/acceptors are green, and aromatic is white. The surface of human serum albumin (type 2 binding site) is represented in dots and colored cyan. The figure was prepared using RasMol.

Table 2. Summary of Pairwise Alignments of Fullerene Binding Sites

compared proteins[a]	no. detected features	score	solution rank
Ligand: Nonsubstituted [C_{60}] Fullerene			
HSA-1, HSA-2	20	521.1	1
HIVP, HSA-2	19	489	1
HSA-1, HIVP	19	426.4	1
HSA-2, C_{60}Ab	16	337.0	1
HSA-1, C_{60}Ab	17	291.9	1
HIVP, C_{60}Ab	11	238.4	1
Ligand: Carboxyfullerene			
HIVP, HSA-2	21	454.3	1
HSA-1, HSA-2	20	446.7	1
HSA-1, HIVP	19	442.7	1
HSA-2, C_{60}Ab	15	318.4	1
HSA-1, C_{60}Ab	12	291.1	1
HIVP, C_{60}Ab	14	255.8	1

[a] HSA-1 = human serum albumin, type 1. HSA-2 = human serum albumin, type 2. HIVP = HIV protease. C_{60}Ab = fullerene specific antibody (*16, 17*). The columns containing the number of detected features, the score, and the solution rank are the output of the MultiBind algorithm.

sites and from 14 to 21 (mean = 18) for the CF binding sites. In both cases the alignments that involved the fullerene-specific antibody recognized smaller patterns, with lower score and with higher frequency of random occurrence than in the rest of the cases. Figure 2 in the Supporting Information presents the similarity relationships between the compared binding sites, according to the score of MultiBind, plotted using the statistical toolbox of the Matlab program. The two binding sites that were recognized to be most similar to each other are those of HSA type 1 and HSA type 2. As can be seen in this figure, the binding site of the fullerene-specific antibody was indeed the most different from all the rest.

Summary and Discussion of the Alignment Results. We have observed that patterns common to all the four binding sites are not specific enough and are not likely to represent the features essential for the binding of fullerenes. This can be explained by several factors. First, as shown by the pairwise comparisons, the binding site of the fullerene-specific antibody is very different from all the rest. Second, in all of the cases the binding sites were actually extracted from unbound complexes (i.e. the molecules are given in their structures that were determined separately). Both the docking and the alignment algorithms are rigid and address protein flexibility only implicitly through a set of thresholds that allow certain variability in locations. In practice, both the side-chains and the protein backbone can undergo conformational changes upon ligand binding. The alignment results suggest that either the fullerene binding sites are different on different proteins, or that the fullerene binding sites undergo more significant conformational changes.

A more interesting and significant pattern of shared physicochemical properties was recognized between the three binding sites of HSA type 1, HSA type 2, and HIVP. From the computational standpoint, the high similarity of the patterns recognized for the binding sites of NS-C_{60} and CF is encouraging and shows consistency of the docking and alignment methods. However, from the biological standpoint, we would have expected these patterns to be different. Specifically, NS-C_{60} is a hydrophobic ligand and we would expect the pattern that characterizes its binding to be more hydrophobic. On the other hand, the CF ligand has chargeable groups, and we would expect its binding pattern to be less hydrophobic. The same pattern obtained for NS-C_{60} and CF cases could be explained by the fact that we have used the same unbound protein structures to construct the docking models with both ligands.

The observation that most of the properties that constitute the recognized pattern are contributed by backbone atoms suggests the differences in side-chain orientations and conformations. In reality the side-chains of the considered binding sites may rearrange and undergo conformational changes to accommodate each of the considered ligands in a slightly different manner. However, only solving the structures with these ligands will provide an exact answer to this puzzle.

CONCLUSIONS

Here we have employed a computational approach in order to address the subject of fullerene interactions with proteins. We suggested docking models consistent with available experimental data for the interactions of fullerenes with four proteins. We further compared between the surface spatial and physicochemical properties of the suggested binding sites. A similarity was found between the (human and bovine) serum albumins and the HIV-protease binding sites, while the binding site of the fullerene-specific antibody was found to be different from the others.

ACKNOWLEDGMENT

We would like to thank Dina Schneidman-Duhovny for software support and critical reading of this manuscript. We would like to thank Maxim Shatsky for useful suggestions. This work was supported by the Israel Science Foundation.

Supporting Information Available: Detailed lists of amino acids that are within 6 Å distance from the docked ligand for each of the predicted binding sites. Two figures that depict (i) the similarity of the predicted binding site of carboxy-fullerene on HSA to binding sites of other known ligands, demonstrated for the case of citric acid (Figure S1) and (ii) similarity relationships between the four predicted binding sites of HSA-type 1, HSA-type 2, HIVP and a fullerene-specific antibody (Figure S2). This material is available free of charge via the Internet at http://pubs.acs.org.

LITERATURE CITED

(1) Kratschmer, W., Lamb, L. D., Fostiropoulos, K., and Huffman, D. R. (1990) Solid C60: a new form of carbon. *Nature 347*, 354−358.

(2) Kroto, H. W., Heath, J. R., O'Brien, S. C., Curl, R. F., and Smalley, R. E. (1985) C_{60}: Buckminsterfullerene. *Nature 318*, 162.

(3) Bosi, S., Da Ros, T., Spalluto, G., and Prato, M. (2003) Fullerene derivatives: an attractive tool for biological applications. *Eur. J. Med. Chem. 38*, 913−923.

(4) Dugan, L. L., Turetsky, D. M., Du, C., Lobner, D., Wheeler, M., Almli, C. R., Shen, C. K., Luh, T. Y., Choi, D. W., and Lin, T. S. (1997) Carboxyfullerenes as neuroprotective agents. *Proc. Natl. Acad. Sci. U. S. A. 94*, 9434−9439.

(5) Jin, H., Chen, W. Q., Tang, X. W., Chiang, L. Y., Yang, C. Y., Schloss, J. V., and Wu, J. Y. (2000) Polyhydroxylated C(60), fullerenols, as glutamate receptor antagonists and neuroprotective agents. *J. Neurosci. Res. 62*, 600−607.

(6) Tokuyama, H., Yamago, S., Nakamura, E., Shiraki, T., and Sugiura, Y. (1993) Photoinduced biochemical activity of fullerene carboxylic acid. *J. Am. Chem. Soc. 115*, 7918−7919.

(7) Huang, Y. L., Shen, C. K., Luh, T. Y., Yang, H. C., Hwang, K. C., and Chou, C. K. (1998) Blockage of apoptotic signaling of transforming growth factor-beta in human hepatoma cells by carboxyfullerene. *Eur. J. Biochem. 254*, 38−43.

(8) Park, K. H., Chhowalla, M., Iqbal, Z., and Sesti, F. (2003) Single-walled Carbon Nanotubes Are a New Class of Ion Channel Blockers. *J. Biol. Chem. 278*, 50212−50216.

(9) Kim, J. E., and Lee, M. (2003) Fullerene inhibits beta-amyloid peptide aggregation. *Biochem. Biophys. Res. Commun. 303*, 576−579.

(10) Wolff, D. J., Barbieri, C. M., Richardson, C. F., Schuster, D. I., and Wilson, S. R. (2002) Trisamine C(60)-fullerene adducts inhibit neuronal nitric oxide synthase by acting as highly potent calmodulin antagonists. *Arch. Biochem. Biophys. 399*, 130−141.

(11) Mashino, T., Okuda, K., Hirota, T., Hirobe, M., Nagano, T., and Mochizuki, M. (2001) Inhibitory effect of fullerene derivatives on glutathione reductase. *Fullerene Sci. Technol. 9*, 191−196.

(12) Friedman, S. H., DeCamp, D. L., Sijbesma, R., Srdanov, G., Wudl, F., and Kenyon, G. L. (1993) Inhibition of the HIV-1 protease by fullerene derivatives: Model building studies and experimental verification. *J. Am. Chem. Soc. 115*, 6506−6509.

(13) Marcorin, G. L., Da Ros, T., Castellano, S., Stefancich, G., Bonin, I., Miertus, S., and Prato, M. (2000) Design and synthesis of novel [60]fullerene derivatives as potential HIV aspartic protease inhibitors. *Org. Lett. 2*, 3955−3958.

(14) Schuster, D. I., Wilson, S. R., and Schinazi, R. F. (1996) Anti-human immunodeficiency virus activity and cytotoxicity of derivatized buckminsterfullerenes. *Bioorg. Med. Chem. Lett. 6*, 1253−1256.

(15) Sijbesma, R., Srdanov, G., Wudl, F., Castoro, J. A., Friedman, S. H., DeCamp, D. L., and Kenyon, G. L. (1993) Synthesis of a fullerene derivative for the inhibition of HIV enzymes. *J. Am. Chem. Soc. 115*, 6510−6512.

(16) Braden, B. C., Goldbaum, F. A., Chen, B. X., Kirschner, A. N., Wilson, S. R., and Erlanger, B. F. (2000) X-ray crystal structure of an anti-Buckminsterfullerene antibody fab fragment: biomolecular recognition of C(60). *Proc. Natl. Acad. Sci. U. S. A. 97*, 12193−12197.

(17) Chen, B. X., Wilson, S. R., Das, M., Coughlin, D. J., and Erlanger, B. F. (1998) Antigenicity of fullerenes: antibodies specific for fullerenes and their characteristics. *Proc. Natl. Acad. Sci. U. S. A. 95*, 10809−10813.

(18) Belgorodsky, B., Fadeev, L., Ittah, V., Benyamini, H., Zelner, S., Huppert, D., Kotlyar, A. B., and Gozin, M. (2005) Formation and characterization of stable human serum albumin-tris-malonic acid [C60]fullerene complex. *Bioconjugate Chem. 16*, 1058−1062.

(19) Rozhkov, S. P., Goryunov, A. S., Sukhanova, G. A., Borisova, A. G., Rozhkova, N. N., and Andrievsky, G. V. (2003) Protein interaction with hydrated C60 fullerene in aqueous solutions. *Biochem. Biophys. Res. Commun. 303*, 562−566.

(20) Bingshe, X., Xuguang, L., Xiaoqin, Y., Jinli, Q., and Weijun, J. (2001) *Mater. Res. Soc. Symp.* W7.4.1−W7.4.5.

(21) Duhovny, D., Nussinov, R., and Wolfson, H. J. (2002) *Workshop on Algorithms in Bioinformatics* (Guigo, R., and Gusfield, D., Eds.) vol. 2452, pp 185−200, LNCS, Rome, Italy.

(22) Schneidman-Duhovny, D., Inbar, Y., Polak, V., Shatsky, M., Halperin, I., Benyamini, H., Barzilai, A., Dror, O., Haspel, N., Nussinov, R., and Wolfson, H. J. (2003) Taking geometry to its edge: fast unbound rigid (and hinge-bent) docking. *Proteins 52*, 107−112.

(23) Schneidman-Duhovny, D., Inbar, Y., Nussinov, R., and Wolfson, H. J. (2005) PatchDock and SymmDock: servers for rigid and symmetric docking. *Nucleic Acids Res 33*, W363−367. http://bioinfo3d.cs.tau.ac.il/PatchDock.

(24) Shatsky, M., Shulman-Peleg, A., Nussinov, R., and Wolfson, H. J. (2005) *RECOMB 2005* (Miyano, S., Ed.) vol. 35000, pp 440−455, LNCS, Cambridge MA. http://bioinfo3d.cs.tau.ac.il/MultiBind.

(25) Shatsky, M., Shulman-Peleg, A., Nussinov, R., and Wolfson, H. J. (2006) The multiple common point set problem and its application to molecule binding pattern detection. *J. Comput. Biol.*, in press.

(26) Sugio, S., Kashima, A., Mochizuki, S., Noda, M., and Kobayashi, K. (1999) Crystal structure of human serum albumin at 2.5 A resolution. *Protein Eng 12*, 439−446.

(27) Schwede, T., Kopp, J., Guex, N., and Peitsch, M. C. (2003) SWISS-MODEL: An automated protein homology-modeling server. *Nucleic Acids Res. 31*, 3381−3385.

(28) Rutenber, E., Fauman, E. B., Keenan, R. J., Fong, S., Furth, P. S., Ortiz de Montellano, P. R., Meng, E., Kuntz, I. D., DeCamp, D. L., Salto, R., and et al. (1993) Structure of a non-peptide inhibitor complexed with HIV-1 protease. Developing a cycle of structure-based drug design. *J. Biol. Chem. 268*, 15343−15346.

(29) Inbar, Y., Schneidman-Duhovny, D., Halperin, I., Oron, A., Nussinov, R., and Wolfson, H. J. (2005) Approaching the CAPRI challenge with an efficient geometry-based docking. *Proteins 60*, 217−223.

(30) Gidalevitz, T., Biswas, C., Ding, H., Schneidman-Duhovny, D., Wolfson, H. J., Stevens, F., Radford, S., and Argon, Y. (2004) Identification of the N-terminal peptide binding site of glucose-regulated protein 94. *J. Biol. Chem. 279*, 16543−16552.

(31) Zhang, C., Vasmatzis, G., Cornette, J. L., and DeLisi, C. (1997) Determination of atomic desolvation energies from the structures of crystallized proteins. *J. Mol. Biol. 267*, 707−726.

(32) Schmitt, S., Kuhn, D., and Klebe, G. (2002) A new method to detect related function among proteins independent of sequence and fold homology. *J. Mol. Biol. 323*, 387−406.

(33) Brenner, S. E., Koehl, P., and Levitt, M. (2000) The ASTRAL compendium for protein structure and sequence analysis. *Nucleic Acids Res. 28*, 254−256.
(34) Chandonia, J. M., Hon, G., Walker, N. S., Lo Conte, L., Koehl, P., Levitt, M., and Brenner, S. E. (2004) The ASTRAL Compendium in 2004. *Nucleic Acids Res. 32*, D189−192.
(35) Friedman, S. H., Ganapathi, P. S., Rubin, Y., and Kenyon, G. L. (1998) Optimizing the binding of fullerene inhibitors of the HIV-1 protease through predicted increases in hydrophobic desolvation. *J. Med. Chem. 41*, 2424−2429.
(36) Kozakov, D., Clodfelter, K. H., Vajda, S., and Camacho, C. J. (2005) Optimal clustering for detecting near-native conformations in protein docking. *Biophys. J. 89*, 867−875.
(37) Berman, H. M., Westbrook, J., Feng, Z., Gilliland, G., Bhat, T. N., Weissig, H., Shindyalov, I. N., and Bourne, P. E. (2000) The Protein Data Bank. *Nucleic Acids Res. 28*, 235−242.
(38) Lejon, S., Frick, I. M., Bjorck, L., Wikstrom, M., and Svensson, S. (2004) Crystal structure and biological implications of a bacterial albumin binding module in complex with human serum albumin. *J. Biol. Chem. 279*, 42924−42928.
(39) Lebon, F., and Ledecq, M. (2000) Approaches to the design of effective HIV-1 protease inhibitors. *Curr. Med. Chem. 7*, 455−477.
(40) Noon, W. H., Kong, Y., and Ma, J. (2002) Molecular dynamics analysis of a buckyball-antibody complex. *Proc. Natl. Acad. Sci. U. S. A. 99 Suppl 2*, 6466−6470.
(41) Holm, L., and Sander, C. (1995) Dali: a network tool for protein structure comparison. *Trends Biochem. Sci. 20*, 478−480.
(42) Shatsky, M., Nussinov, R., and Wolfson, H. J. (2004) A method for simultaneous alignment of multiple protein structures. *Proteins 56*, 143−156.
(43) Thompson, J. D., Higgins, D. G., and Gibson, T. J. (1994) CLUSTAL W: improving the sensitivity of progressive multiple sequence alignment through sequence weighting, position-specific gap penalties and weight matrix choice. *Nucleic Acids Res. 22*, 4673−4680.
(44) Delano, W. L. (2002) The PyMOL Molecular Graphics System. DeLano Scientific LLC, San Carlos, CA. http://www.pymol.org.

BC050299G

Detailed below are the lists of residues that comprise the detected binding sites that are within 6Å distance from the docked ligand.

Residues participating in the NS-C_{60} pocket of type 1 on HSA are: Ala191, Ser192, Lys195, Gln196, Leu198, Lys199, Trp214, Arg218, Arg222, Ala291, Glu292, Val293, Val343, Lys436, Cys437, Pro447, Cys448, Ala449, Asp451, Tyr452, Leu453 and Val455.

Residues participating in the CF pocket of type 1 HSA are: Glu153, Glu188, Ala191, Ser192, Ala194, Lys195, Gln196, Leu198, Lys199, Trp214, Arg218, Gln221, Arg222, His288, Cys289, Ile290, Ala291, Glu292, Val293, Glu294, Asn295, Pro339, Val343, Lys436, Cys437, His440, Lys444, Pro447, Cys448, Ala449, Asp451, Tyr452 and Val455.

Residues participating in the NS-C_{60} pocket of type 2 on HSA are: Asp108, Asn109, Pro110, Asn111, Leu112, Pro113, Arg114, Leu115, Glu141, Arg145, His146, Arg186, Lys190, Pro421, Glu425, Gln459 and Leu463.

Residues participating in the CF pocket of type 2 on HSA are: Asp108, Asn109, Pro110, Asn111, Leu112, Pro113, Arg114, Leu115, Val116, Glu141, Ile142, Arg145, His146, Pro147, Arg186, Lys190, Ser193, Ala194, Pro421, Thr422, Val424, Glu425, Val426, Arg428, Asn429, Lys432, Gln459, Leu463, Lys519, Glu520 and Ile523.

Residues participating in the HIV binding site for NS-C_{60} (Chain A:) Leu23, Asp25, Gly27, Ala28, Asp29, Asp30, Val32, Ile47, Gly48, Gly49, Ile50, Thr80, Pro81, Val82, Ile84, (Chain B:) Arg8, Leu23, Asp25, Gly27, Ala28, Gly48, Gly49, Ile50, Thr80, Pro81, Val82 and Ile84.

Residues participating in the HIV binding site for CF (chain A:) Arg8, Leu23, Asp25, Gly27, Ala28, Asp29, Asp30, Val32, Ile47, Gly48, Gly49, Ile50, Ile54, Pro79, Thr80, Pro81, Val82, Asn83, Ile84.

(Chain B:) Leu23, Asp25, Thr26, Gly27, Ala28, Asp29, Ile47, Gly48, Gly49, Ile50, Gly51, Gly52, Phe53, Ile54, Pro81, Val82 and Ile84.

Residues participating in the fullerene specific antibody binding site for NS-C_{60} (chain L) Tyr32, Asn34, Tyr49, Tyr50, Tyr91, And Phe96; (chain H)Ser32, Trp33, Arg50, Thr98, Ser99, Ser100 and Ala104.

Residues participating in the fullerene specific antibody binding site for CF (chain L) Ser30, Asn31, Tyr32, Leu33, Asn34, Tyr36, Leu46, Tyr49, Tyr50, Ser53, Arg55, Gln89, Tyr91, Ser92, Arg93, Leu94 and Phe96; (chain H) Ser31, Ser32, Trp33, Asn35, Arg50, Thr98, Ser99, Ser100 and Ala104.

FIGURE CAPTIONS FOR SUPPORTING INFORMATION

Supplementary Figure 1. Predicted binding site for carboxy-fullererene on HSA occupying the known binding site for cytric acid. In all the four sub-figures, predicted binding site residues are colored green. Left: NS-C_{60} in its predicted binding site on free HSA (PDB: 1ao6). Right: the crystal structure of HSA complexed with cytric acid and decanoic acid (PDB: 1tf0). The lower figures provide a closer look on the surface of the binding sites.

Supplementary Figure 2. Similarity relationships between the four binding sites of HSA-type 1, HSA-type 2, HIVP and a fullerene-specific antibody. The dendrogram was constructed according to the score of MultiBind plotted using the statistical toolbox of Matlab. The similarity relationships are the same for both non-substituted fullerene and carboxyfullerene binding sites.

Supporting Figure 1.

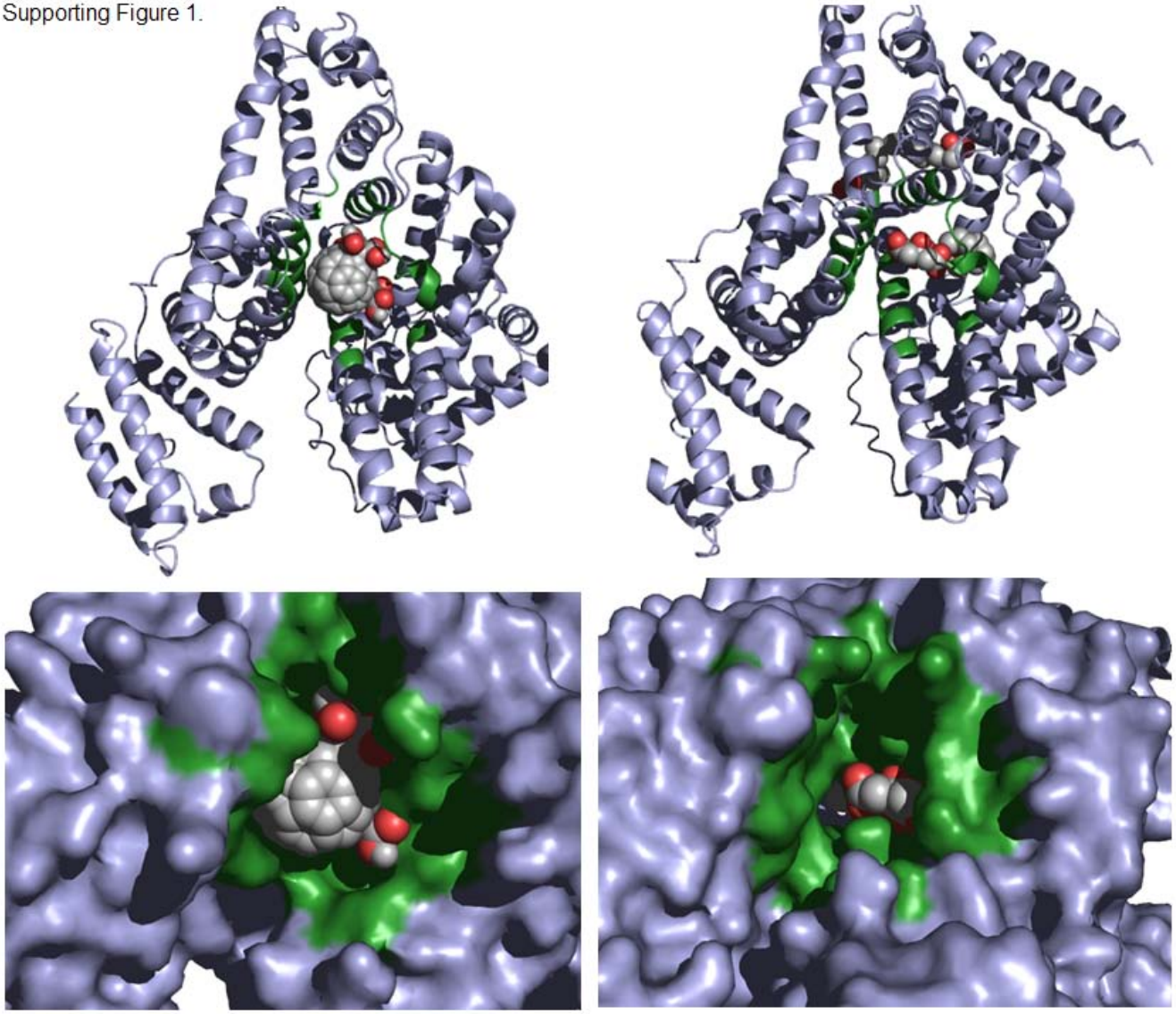

Supporting Figure 2.

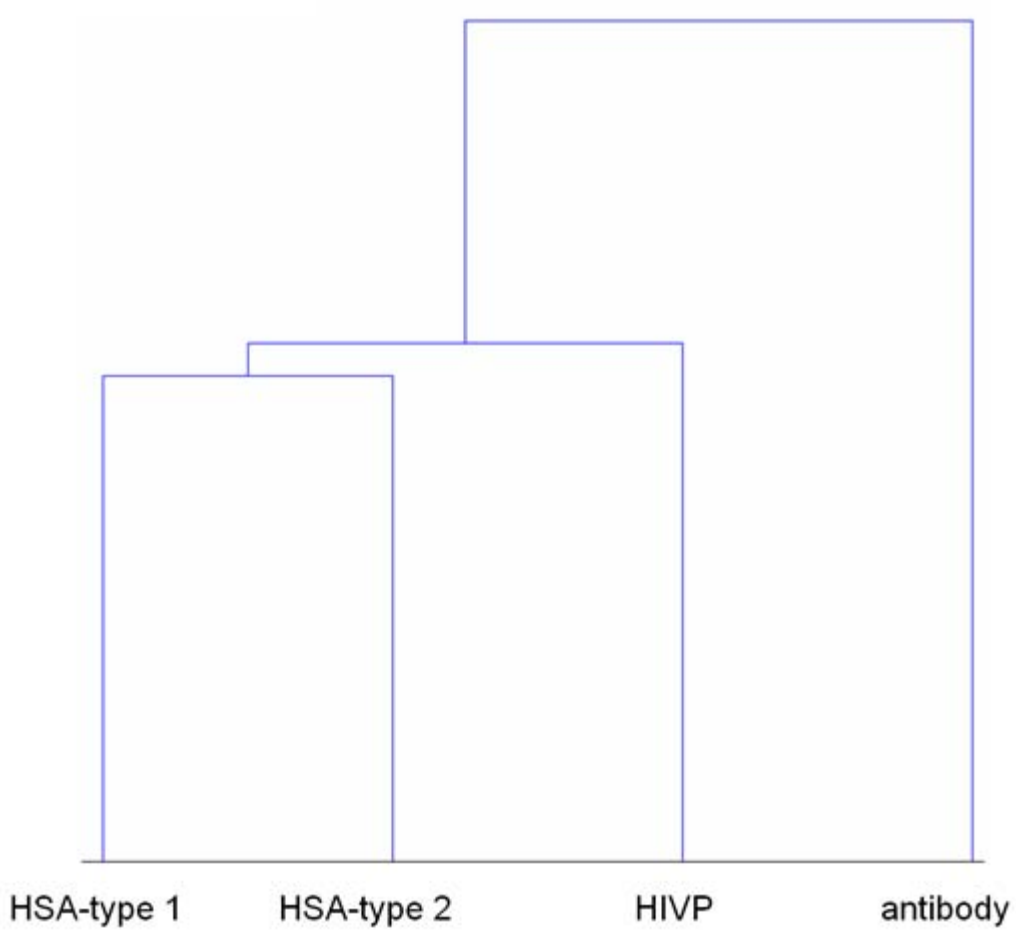

Synthesis of Thiol-Reactive, Long-Wavelength Fluorescent Phenoxazine Derivatives for Biosensor Applications

Douglas B. Sherman, J. Bruce Pitner, Arounaguiry Ambroise, and K. Joseph Thomas*

BD Technologies, 21 Davis Drive, Research Triangle Park, North Carolina 27709. Received October 24, 2005; Revised Manuscript Received January 10, 2006

Two environmentally sensitive, long-wavelength fluorescent phenoxazine derivatives, INR and IANR, were synthesized with linkers for conjugation to the thiol group of cysteine in binding proteins. The linkers were designed based on the attachment sites at two different positions on the phenoxazine, which were chosen in order to study the orientation of the dye with respect to the binding protein. Conjugation of the dyes to the S337C maltose binding protein (MBP) mutant provided conjugates of these dyes that are capable of detecting maltose with different sensitivities. The dye INR gave a 3-fold (+200%) change in fluorescence intensity upon maltose binding when conjugated to S337C MBP with a binding constant (K_d) of 435 μM. The fluorescence change for IANR was only 20% and the K_d was 1.4 mM. Conformational analysis of the dyes by molecular modeling suggested that the linker in IANR imparted greater conformational freedom to the dye, resulting in little change in environment between the open and the closed-form conformations. The linker in INR, on the other hand, showed restricted motion, which placed the dye in different environments in the open and closed forms of the protein. Thus, design and placement of the linker play a critical role in the performance of these dyes as environmentally sensitive probes.

INTRODUCTION

Long-wavelength fluorescent dyes that are thiol-reactive and environmentally sensitive can play an important role in biosensor chemistry (*1*, *2*). Particularly, when dealing with biological interferences during the in vivo measurement of metabolites such as glucose or lactate, dyes that fluoresce above 600 nm are preferred since tissue and serum fluorescence are minimal, and background scattering is limited to its lowest value in the long-wavelength window (*3*, *4*). This allows the measurement of fluorescence signal from a sensor dye with greater accuracy, and therefore the long-wavelength region is superior to visible spectral regions for fluorescence-based diagnostic applications. Although there are several dyes known to emit in the long-wavelength region (*5*−*7*), to our knowledge none are commercially available that are both environmentally sensitive and have a linker for specific conjugation to an engineered cysteine on a binding protein.

Binding proteins offer an alternative approach for sensing a variety of analytes such as maltose, glucose, lactate, and other metabolites (*8*−*11*). In contrast to enzymatic sensors, fluorophore-labeled binding proteins require no cofactors and produce no enzymatic byproducts, a source of potential biosensor degradation during longer implant times. Binding proteins can be specific to molecules of biological interest and can reversibly bind these ligands, properties that are desirable for constructing continuous biosensors. The most important property of these receptors is they all share a substantial conformational change upon ligand binding, typically a hinge-type motion centered around the ligand binding site that brings two protein domains toward each other. To take advantage of these receptor properties, the binding protein must be coupled to a reporter moiety that can reliably provide a quantitative signal corresponding to the concentration of the desired ligand.

A reliable approach for protein biosensor design is to place an environmentally sensitive fluorescent dye near the binding pocket (*12*). The fluorescence properties of such dyes can be correlated to changes in microenvironment associated with the binding of analytes to protein. Keeping this in mind, we have developed two long-wavelength fluorescent dyes suitable for bioconjugation that possess significant sensitivity to their microenvironment and emit in the 600−700 nm region. The two dyes are derivatives of Nile Red, a phenoxazine that is known to possess a very high environmental sensitivity. Various research groups have used Nile Red for probing the polarity of organic and micro-heterogeneous media. The absorption and emission maxima are in the range of 550 and 600 nm, respectively, with emission maxima shifting to as much as 650 nm when the dye interacts with the hydrophobic surface of tubulin, for example (*13*−*15*).

Although Nile Red derivatives have been reported that are amine-reactive (*16*−*18*), these would likely have little or no site-specificity when conjugated to proteins such as MBP that contain numerous lysines. A thiol-reactive moiety would provide site-specificity for protein attachment through a native or an engineered cysteine (*11*). The mutant S337C provides a cysteine location in MBP that has been previously shown to provide a significant signal with the environmentally sensitive visible fluorophore IANBD (*N*-[2-(iodoacetoxy)ethyl]-*N*-methylamino-7-nitrobenz-2-oxa-1,3-diazole) (*8*, *9*). One of our further objectives was to identify the optimal location on the phenoxazine dye for introducing a thiol-reactive linker. In the first design, the linker was placed on the dialkylamino group, and in the second, the linker was placed on the aromatic chromophore (Schemes 1 and 2). Herein we report the performance of these dyes for maltose detection on S337C MBP and examine the differences with respect to linker design and placement of the dyes.

EXPERIMENTAL PROCEDURES

Materials. The starting materials for the syntheses were either purchased from Sigma-Aldrich or from another commercial vendor as indicated. S337C MBP was produced by methods

* Corresponding author. Telephone: (919) 597-6617. Fax: (919) 597-6402. E-mail: joseph_thomas@bd.com.

10.1021/bc050309d CCC: $33.50 © 2006 American Chemical Society
Published on Web 02/21/2006

Scheme 1. Synthesis of INR (1)

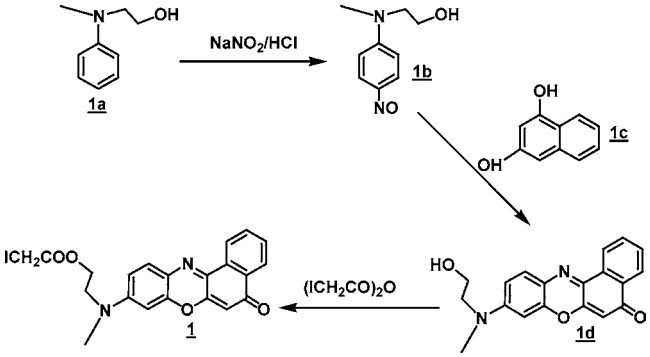

Scheme 2. Synthesis of IANR (2)

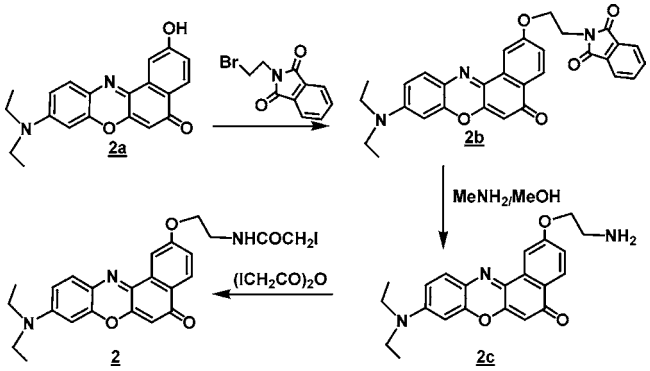

described by Gilardi et al. (*8*). Absorption spectra were recorded on a Cary 50 Bio UV−Vis spectrophotometer, and fluorescence measurements were taken on a PTI QM-4/2003 SE spectrofluorimeter. The NMR spectra were obtained on either a Varian Mercury 400 MHz or on a Bruker (400 MHz) AMX 400 spectrometer. Mass spectra were recorded on a Finnigan-MAT 212 (FAB) or on a Sciex 150 Electrospray spectrometer.

Synthesis of INR (1). *Intermediate **1b***: *N*-Phenyl-*N*-methylethanolamine **1a** (50 mmol) was suspended in concentrated HCl (28 mL) and was cooled to 5 °C. To this solution was added dropwise a sodium nitrite solution (6.67 g in 10 mL water) over a period of 40 min. After the addition, the reaction was kept stirring for 2 h more. The product was then filtered, washed with 0.5 M HCl, and dried in vacuo to give the nitroso compound **1b** (yield 40%). ^{1}H NMR (D_2O) δ ppm: 3.59 (s, CH_3, 3H); 3.90 (t, CH_2, 2H); 4.05 (t, CH_2, 2H); 7.22−7.30 (m, aromatic, 2H); 7.50 (d, aromatic, 1H); 7.77 (d, aromatic, 1H). ^{13}C NMR (D_2O) δ ppm: 42.44, 57.92, 58.72, 120.29, 122.52, 125.93, 140.56, 149.93, 163.21. Mol wt calculated for $C_9H_{12}N_2O_2$ is 180 (M^+), found 181 (M + 1) (FAB).

*Intermediate **1d***: 1,3-Dihydroxynaphthalene **1c** (5 mmol) was suspended in ethanol (25 mL) and was brought to reflux while stirring. To the refluxing solution was added intermediate **1b** (5 mmol) in fractions over a period of 45 min. After the addition, the reaction mixture was maintained at reflux for 4 h more and then cooled. The solvent was evaporated, and the product dye **1d** was purified by flash column chromatography over silica gel using methanol and chloroform (1:9) as eluent (yield 50%). ^{1}H NMR ($CDCl_3$) δ ppm: 2.98 (s, 3H); 3.48 (t, 2H); 3.83 (t, 2H); 6.20 (s, 1H); 6.77 (d, 1H); 7.10 (d, 1H); 7.45 (s, 1H); 7.60−7.75 (m, 2H); 7.72 (m, 1H); 8.08 (m, 1H). ^{13}C NMR ($CDCl_3$) δ ppm: 39.2, 55.6, 60.3, 102.2, 110.2, 113.6, 124.7, 126.3, 126.6, 126.8, 130.6, 132.3, 133.7, 135.1, 145.8, 148.2, 152.4, 182.5, 183.8. Mol wt calculated for $C_{19}H_{16}N_2O_3$ is 320 (M^+), found 321 (M + 1) (FAB).

*Compound **1** (INR)*: The intermediate dye **1d** was dissolved in anhydrous acetonitrile (10 mL), and *p*-(dimethylamino)-pyridine (3 mg) was added, followed by iodoacetic anhydride (250 mg). The reaction was stirred for 2 h. The product **1** was separated by evaporation of the solvent and then purified by repeated precipitation from methylene chloride and hexane (yield 25%). ^{1}H NMR ($CDCl_3$) δ ppm: 3.14 (s, 3H); 3.66 (s, 2H); 3.74 (t, 2H); 4.38 (t, 2H); 6.40 (s, 1H, ArH); 6.54 (d, 1H, ArH); 6.72 (d, 1H, ArH); 7.64−7.75 (m, 3H, ArH); 8.29 (d, 1H, ArH); 8.65 (d, 1H, ArH). ^{13}C NMR ($CDCl_3$) δ ppm: −6.1, 39.6, 50.9, 63.0, 97.5, 106.4, 110.1, 124.1, 125.6, 126.0, 130.6, 131.2, 131.7, 131.98, 132.0, 141.5, 146.5, 151.8, 152.2, 169.0, 184.1. Exact Mass Calculated for $C_{21}H_{17}IN_2O_4$ is 489.0317, found 489.0317 (HRMS).

Synthesis of IANR (2). *Intermediate **2b***: 9-Diethylamino-2-hydroxy-5*H*-benz[*a*]phenoxazin-5-one **2a** (50 mg, 0.15 mmol), *N*-bromoethylphthalimide (50 mg, 0.20 mmol), and potassium carbonate (60 mg, 0.09 mmol) were combined in DMF (15 mL) under argon with stirring. The reaction proceeded at reflux for 4.5 h. Additional bromoethylphthalimide (25 mg) was added at 4.5 h and at 6.5 h (15 mg). The temperature was lowered to 115 °C, and the reaction proceeded overnight. DMF was removed in vacuo, and the residue was dried in vacuo. Column chromatography over silica gel (2% MeOH/CH_2Cl_2 as mobile phase) afforded the product **2b** in 85% yield. ^{1}H NMR ($CDCl_3$) δ ppm: 1.22 (t, 6H); 3.40 (q, 4H); 4.19 (t, 2H); 4.40 (t, 2H); 6.23 (s, 1H); 6.36 (d, 1H); 6.59 (dd, 1H); 7.09 (d, 1H); 7.52 (d, 1H); 7.70 (m, 2H); 7.84 (m, 2H); 7.96 (d, 1H); 8.13 (d, 1H). ^{13}C NMR ($CDCl_3$) δ ppm: 12.8, 37.5, 45.2, 65.3, 96.3, 105.2, 106.5, 109.8, 118.6, 123.5, 124.9, 126.0, 127.9, 131.3, 132.1, 134.2, 139.6, 146.8, 150.7, 152.2, 161.0, 162.8, 168.4, 183.3. Mol wt calculated for $C_{30}H_{25}N_3O_5$ is 507, found 508 (MH^+) (FAB-MS).

*Intermediate **2c***: Intermediate **2b** (30 mg, 0.06 mmol) was dissolved in anhydrous MeOH (8 mL) and was kept under an atmosphere of argon. Next, methylamine (2 M in MeOH, 4 mL, 8 mmol) was added. The reaction was allowed to proceed for 5 min at RT and 2.5 h at reflux. Flash chromatography was performed over silica gel using 10% MeOH/CH_2Cl_2 as the mobile phase to remove fast moving impurities and then with 30% MeOH/CH_2Cl_2 to elute the product **2c**. Solvent was removed on a rotary evaporator, and the residue was dried in vacuo (70% yield). ^{1}H NMR ($CDCl_3$) δ ppm: 1.25 (t, 6H); 3.17 (t, 2H); 3.45 (q, 4H); 4.20 (t, 2H); 6.27 (s, 1H); 6.43 (d, 1H); 6.63 (dd, 1H); 7.15 (m, 1H); 7.56 (d, 1H); 8.02 (m, 1H); 8.18 (d, 1H). ^{13}C NMR ($CDCl_3$) δ ppm: 12.8, 41.6, 45.3, 63.9, 96.4, 105.4, 106.6, 109.9, 118.4, 124.9, 125.9, 127.4, 128.0, 131.3, 134.3, 147.1, 151.0, 152.3, 161.7, 183.5. Mol wt calculated for $C_{22}H_{23}N_3O_3$ is 377, found 378 (MH^+) (FAB-MS).

*Compound **2** (IANR)*: Intermediate **2c** (11 mg, 0.03 mmol) was dissolved in CH_2Cl_2 (5 mL). Iodoacetic anhydride (21 mg, 0.06 mmol) was then added and allowed to react for 40 min. An additional 25 mL of CH_2Cl_2 was added, and the reaction mixture was transferred to a separation funnel. The organic phase was washed with 10% Na_2CO_3 (10 mL each) twice, dried over anhydrous $MgSO_4$, and filtered. After the solvent was removed on a rotary evaporator, the final product **2** was dried under vacuum and precipitated from CH_2Cl_2/hexane (yield 87%). ^{1}H NMR ($CDCl_3$) δ ppm: 1.17 (t, 6H); 3.35 (q, 4H); 3.69 (t, 2H); 3.78 (s, 2H); 4.14 (t, 2H); 6.12 (s, 1H); 6.27 (s, 1H); 6.48 (dd, 1H); 6.91 (d, 1H); 7.34 (d, 1H); 7.74 (s, 1H); 7.95 (s, 1H). ^{13}C NMR ($CDCl_3$) δ ppm: 12.9, 29.9, 40.1, 45.3, 66.9, 96.3, 105.2, 106.7, 109.8, 118.0, 124.9, 125.9, 127.8, 131.3, 134.1, 139.4, 147.0, 151.0, 152.2, 161.1, 168.1, 183.3. Exact mass calculated for $C_{24}H_{24}IN_3O_4$ is 546.0889, found 546.0889 (HRMS).

Quantum Yield Measurements. Relative fluorescence quantum yields were determined using optically dilute solutions with rhodamine 101 in ethanol (quantum yield 1.0) (*19*). Typically, the absorption was matched to 0.05 at the excitation wavelength

Table 1. Absorption and Fluorescence Properties of INR and IANR in Different Solvents

	INR (**1**)[a]			IANR (**2**)[b]		
solvent	abs. max[c] (nm)	fl. max[d] (nm)	quantum yield[e]	abs. max[c] (nm)	fl. max[d] (nm)	quantum yield[e]
toluene	500	556	1.00	526	568	0.97
ethyl acetate	506	585	0.84	523	590	0.96
$CHCl_3$	512	577	0.78	540	592	0.82
CH_2Cl_2	515	585	0.78	539	603	0.83
acetone	516	600	0.66	533	609	0.63
acetonitrile	517	605	0.53	536	615	0.59
DMF	528	615	0.42	541	618	0.43
2-propanol	529	617	0.39	543	622	0.46
ethanol	532	623	0.33	546	628	0.33
methanol	534	627	0.25	553	632	0.25

[a] Extinction coefficient 14 000 M^{-1} cm^{-1}. [b] Extinction coefficient 29 000 M^{-1} cm^{-1}. [c] Absorption maximum. [d] Fluorescence maximum. [e] Quantum yield was measured using rhodamine 101 in ethanol as the reference.

and adjustments were made for minor changes in absorption at the excitation wavelength in fluorescence quantum yield measurements. Spectroscopic grade solvents were used for fluorescence measurements.

Bioconjugation of INR and IANR to MBP. Dyes were conjugated to the binding proteins in the following manner. To S337C MBP (4 nmol) in PBS (200 μL) was added dithiothreitol (8 nmol), and the reaction proceeded for 30 min at room temperature. INR or IANR were prepared as stock solutions (approximately 1 mg in 100 μL DMSO). An aliquot containing 40 nmol of the dye was added to the protein solution and was stirred for 4 h at room temperature in the dark. The reaction mixture was then passed through a NAP-5 size exclusion column (Amersham-Pharmacia, Uppsula, Sweden), with the product eluting in the second (0.5 mL) fraction. The percent change in fluorescence intensity was measured on a PTI fluorimeter using 1 μM protein with either 0 or 100 mM maltose.

Determination of Binding Constants. A 0.1 μM solution of S337C MBP/dye conjugate was titrated on the fluorimeter against maltose concentrations from 0 to 100 mM. The binding constant (K_d) was calculated using relationships shown below that were derived from similar calculations by Pisarchik and Thompson (*20*).

$$F = F_{inf} + \frac{F_0 - F_{inf}}{1 + x/K_d}$$

where F is fluorescence, F_{inf} and F_0 are fluorescence at infinity and at the initial value, and K_d is the binding constant. The free concentration of maltose ($[Mal]_{free}$) is denoted by x and is determined by the relationship:

$$[Mal]_{free} = \frac{[Mal]_{tot} - [Prot]_{tot} - K_d + \sqrt{([Mal]_{tot} - [Prot]_{tot} - K_d)^2 + 4 \times [Mal]_{tot} \times K_d}}{2}$$

where $[Mal]_{tot}$ and $[Pro]_{tot}$ are total maltose and protein concentrations, respectively. If $[Mal]_{tot} \gg K_d$ and $[Mal]_{tot} \gg [Pro]_{tot}$, then the equations simplify to the following form:

$$F = F_0 + [(F_{const} \times x)/(1 + x/K_d)]$$

where $F_{const} = (F_{inf} - F_0)/K_d$.

Molecular Modeling. Models of INR and IANR were constructed in Sybyl (Tripos, St. Louis, MO). X-ray crystal structures of MBP in the open (1OMP.pdb) and closed (1ANF.pdb) forms were obtained from the Protein Data Bank (*21*). After residue S337 was modified to Cys, the dyes were attached to form the models of the bioconjugates. Genetic algorithm (GA) conformational searches were then performed using the method provided in Sybyl. For INR, the eight bonds between the Cys alpha-carbon and the dialkylamino nitrogen were defined as rotatable. In the IANR linker, the amide bond was fixed in the trans conformation, and the bond between the aryl oxygen and the aromatic ring was defined as rotatable, which also produced a total of eight rotatable bonds. Default settings in the GA search were employed, except the duplicate window was set to 10. The results of the search were up to 20 conformers within a 20 kcal/mol energy window.

RESULTS

Synthesis. Nile Red derivative INR (**1**) was synthesized according to Scheme 1. Briefly, intermediate **1b** was synthesized by reacting *N*-phenyl-*N*-methylethanolamine **1a** with sodium nitrite at 5 °C in the presence of concentrated HCl, and the resulting product was dried to give **1b**. The parent dye **1d** was prepared by the cyclization reaction of **1b** with 1,3-dihydroxynaphthalene (**1c**) at reflux in ethanol followed by purification. Reaction of **1d** with iodoacetic anhydride in the presence of (dimethylamino)pyridine afforded the thiol-reactive product INR (**1**).

The synthesis of derivative IANR (**2**) was carried out in three steps according to Scheme 2. Starting material 9-diethylamino-2-hydroxy-5*H*-benz[*a*]phenoxazin-5-one **2a** was reacted with *N*-bromoethylphthalimide in DMF in the presence of potassium carbonate to produce the intermediate **2b**. Intermediate **2c** was then prepared by the deprotection of the amine in **2b** with methylamine at refluxing temperatures in methanol. The final thiol-reactive compound IANR (**2**) was synthesized by reaction of the amine derivative **2c** with iodoacetic anhydride.

Absorption and Fluorescence Properties. The sensitivity of INR and IANR toward surrounding microenvironment was tested by studying their spectral properties in solvents of varying dielectric constants. Table 1 summarizes the absorption, emission, and quantum yield of these dyes in a range of polar and nonpolar solvents. The absorption and emission spectra of INR and IANR showed a bathochromic shift with increase in polarity of the medium. For example, the absorption maximum of INR shifted from 500 nm in toluene to 534 nm in methanol, and the fluorescence emission maximum shifted from 556 to 627 nm. IANR gave the same trends, although the absorption maximum shifted 27 nm from toluene to methanol versus 34 nm for INR. The shift in fluorescence maximum was 71 nm for INR and 64 nm for IANR. When conjugated to S337C MBP (not shown in Table 1), the absorption maxima of the dyes in PBS shifted to 580 nm for INR and 550 nm for IANR. Likewise, the fluorescence emission maxima shifted significantly to 640 nm for INR and 653 nm for IANR, placing the emission maxima in the desired long-wavelength range.

In a nonpolar solvent such as toluene, the quantum yield of fluorescence was found to be 1.0 for INR and 0.97 for IANR. High fluorescence quantum yields were also observed in solvents such as chloroform and methylene chloride. With increasing solvent polarity the quantum yield decreases significantly. For

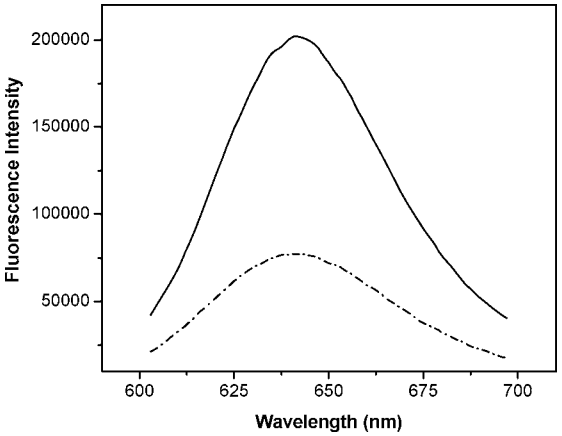

Figure 1. Fluorescence intensity change of S337C-INR MBP between 0 (dotted line) and 100 mM (solid line) maltose.

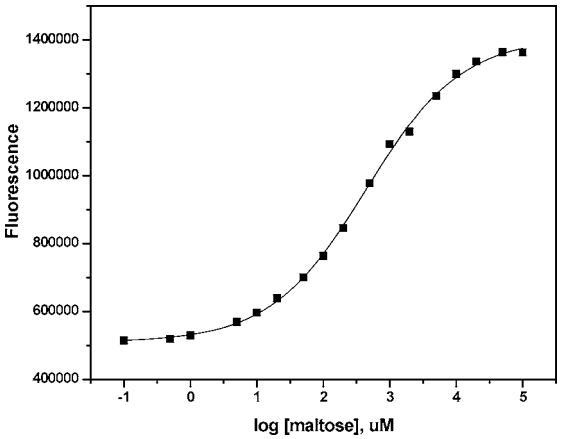

Figure 2. Plot for the determination of binding constant (K_d) for S337C-INR MBP conjugate.

example, in a moderately polar solvent such as acetonitrile, the quantum yield observed for INR was 0.53, and for IANR it was 0.59. In protic polar solvents the quantum yield was further reduced; in methanol the quantum yield for both INR and IANR was observed as 0.25. This is a 4-fold decrease in quantum yield as compared to toluene.

Bioconjugate Performance. Figure 1 shows the fluorescence spectrum of the conjugate S337C-INR MBP in PBS. Upon maltose binding by the protein, the fluorescence intensity underwent a 3-fold enhancement (+200%), whereas S337C-IANR MBP gave only a 20% change in fluorescence intensity. The binding curve for S337C-INR MBP is shown in Figure 2, and the binding constant (K_d) was calculated as described in Experimental Section. The K_d calculated for the S337C-INR MBP conjugate was 435 μM, and the K_d for S337C-IANR MBP was 1.4 mM. These values are higher than the K_d of 62 μM reported for S337C MBP conjugated with IANBD ester (*9*) and are 100 to 400 times higher than the K_d (3.5 μM) of wild-type MBP (*22*).

Molecular Modeling Analysis. Models of the dyes attached to S337C MBP in the open and closed form protein conformations were prepared, and GA conformational searches were performed as described in Experimental Procedures. Representative conformers are illustrated in Figure 3 for the open (left) and closed (right) forms of the protein. S337C-IANR MBP returned 20 conformers that formed five families in the open form as illustrated by representative structures in Figure 3a. All 20 conformers were within 5 kcal/mol of each other and were distributed in the cleft between the domains or near the surface of one of the domains. In the closed form, the conformational search of S337C-IANR MBP returned four families (Figure 3b). S337C-INR MBP, on the other hand, returned 20 conformers in the open form that were within 2 kcal/mol of each other and that formed a single family, as shown in Figure 3c. The search on S337C-INR MBP also returned a single family of 20 conformers (Figure 3d). Here the dye was parallel to the surface of the upper domain in the protein.

DISCUSSION

INR and IANR were synthesized in three steps as outlined in Schemes 1 and 2. Both dyes displayed absorption, emission, and quantum yield properties that demonstrated the environmental sensitivity required in order for these dyes to function as a reporter for binding protein-based reagentless biosensors. As the polarity of the solvent increased, INR and IANR displayed bathochromic shifts in absorption (up to 34 nm) and emission (up to 71 nm) wavelengths. Although both structures were based on the same chromophore, the absorption and emission maxima of INR were blue shifted compared to IANR in any given solvent. In the case of INR, placement of the linker at the dialkylamino group may be affecting the degree of charge transfer, which would in turn lead to a blue shift for INR with respect to IANR. The presence of the linker at the dialkylamino group may also be the reason that the molar extinction coefficient of INR (14 000 M^{-1} cm^{-1}) is lower than that of IANR (29 000 $M^{-1}cm^{-1}$).

Previous reports in the literature described similar trends for the parent dye Nile Red, which were explained as arising from a twisted intramolecular charge transfer (TICT) (*23*−*25*). TICT can occur upon excitation when an electron donor group in a molecule transfers an electron to an acceptor group in the molecule with a concomitant 90° rotation of the bond between the donor and acceptor (*26*−*28*). In Nile Red, the diethylamino group would serve as the donor, the ketone moiety would serve as the acceptor, and the single bond between the diethylamino group and the phenoxazine ring would rotate.

Later reports of experimental and theoretical calculations (*29*, *30*) on Nile Red suggested that the solvatochromic properties could be adequately explained based on the change in the dipole moment of the dye between the ground and excited state (*31*), which has been calculated to be in the range of 5.5 to 7.4D (*23*, *24*, *29*). Thus, the excited dye molecule could be better stabilized in a polar medium such as methanol or DMF as compared to a nonpolar medium such as toluene. This stabilization leads to lower free energy of the excited state, whereas the ground state remains relatively unaffected from nonpolar to polar medium. The decrease in the free energy of the excited state leads to the reduction in the separation between the S_0-S_1 state, and thereby a shift toward higher wavelength (bathochromic shift) is observed.

The quantum yield of both dyes showed a 4-fold decrease from toluene to methanol. The decrease in quantum yield of fluorescence between hydrophobic and polar solvent environments may also be explained based on changes in the dipole moment of the dyes. In nonpolar solvents, electrostatic interactions are limited with the solvent molecules, which would significantly arrest the nonradiative decay pathways. In toluene, all the nonradiative decay pathways for INR are eliminated, leading to an absolute quantum yield of fluorescence. However, in polar solvents such as methanol, strong electrostatic interactions exist between the dye and solvent molecules, leading to radiationless vibronic relaxations and thereby a significant decrease in fluorescence intensity.

INR and IANR displayed considerably different fluorescence responses when conjugated to S337C MBP for detection of maltose. The INR conjugate gave a +200% fluorescence change with a K_d of 435 μM, whereas IANR gave only a +20% fluorescence change with a K_d of 1.4 mM. These results

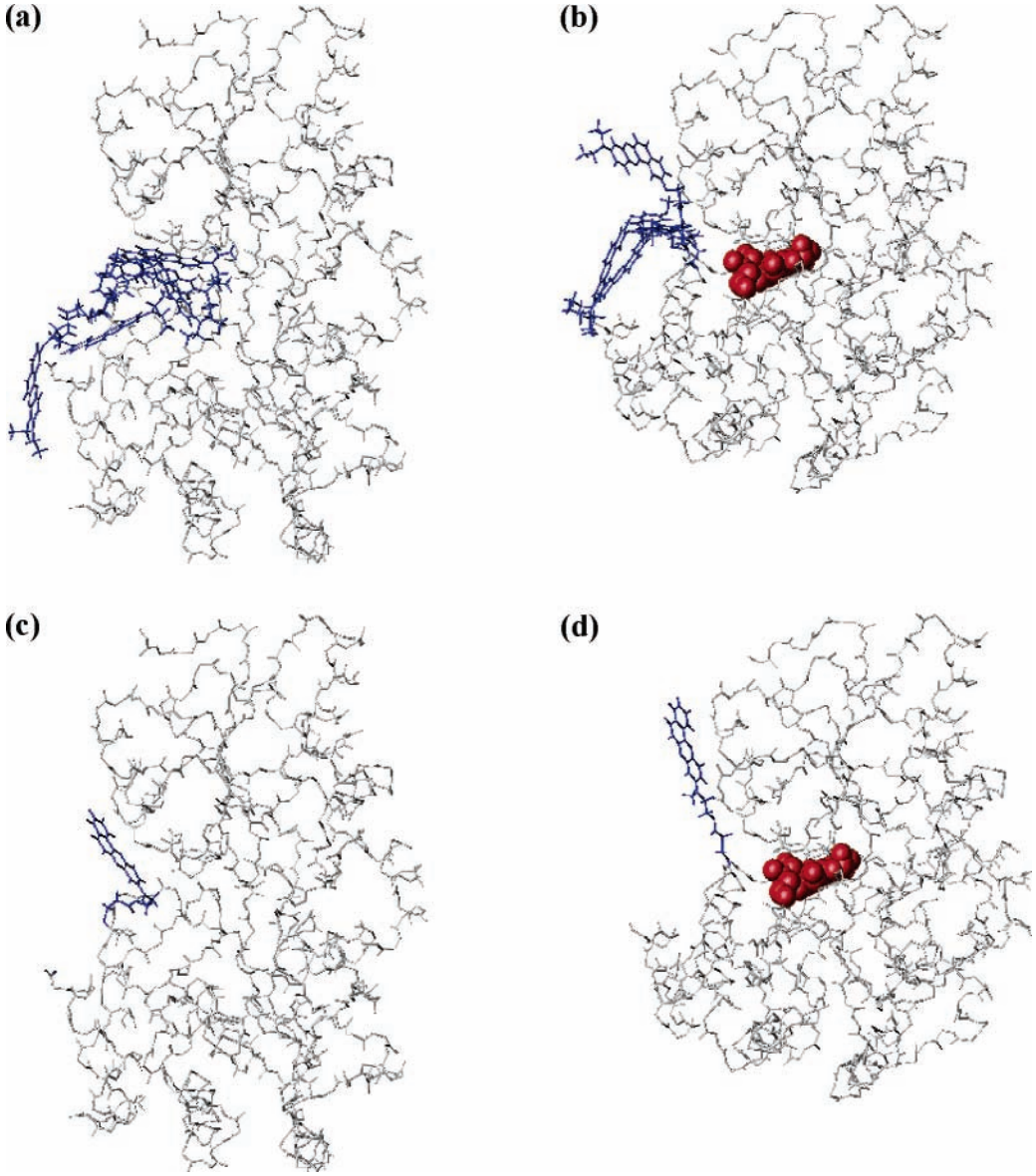

Figure 3. Results of genetic algorithm conformational searches for IANR (a and b) and INR (c and d) at S337C MBP in the open (left) and closed (right) conformations. Dye structures are in blue and maltose is in red.

suggested that the position and nature of the linker on the dye may have a profound effect on the sensor performance when these dyes are used to construct fluorescent sensors for maltose. Such behavior was previously reported for studies of phosphate binding protein (PBP), in which the coumarin dye *N*-[2-(1-maleimidyl)ethyl]-(diethylamino)coumarin-3-carboxamide (MDCC) gave a +405% fluorescence change when conjugated to mutant A197C of PBP (*32*). Replacement of the ethyl group between the coumarin carboxamide and the maleimide group with *n*-propyl (MPrCC) or a *p*-phenyl group (MPhCC) changed the binding activity to −4% and −22%, respectively. Retention of the ethyl group but replacement of the maleimide group with an iodoacetamide group resulted in no change in fluorescence (*33*). In the current study, the linker of INR contains a flexible ester compared to the more rigid amide in the linker of IANR. On the other hand, the INR linker is connected to the ring system of the dye through a dialkylamino group that donates electrons to the aromatic ring system as mentioned above, whereas the IANR linker is attached through an aryl ether bond that may allow greater freedom of rotation near the chromophore.

To evaluate the effect of the linker on dye orientation with respect to the S337 C MBP protein, molecular modeling studies were performed. The conformational analysis studies by molecular modeling suggested that IANR appeared to be much more flexible in the bound and unbound states than INR. The added flexibility in the linker may prevent IANR from experiencing a large change in environment between the bound and unbound states. INR, on the other hand, appeared locked into two conformations of distinctly different environments in the bound and unbound states, which would agree with the larger change in fluorescence that was observed for this dye, especially if the dye interacts more with polar residues on the surface of the protein in one conformation over the other (*34*). Furthermore, IANR was located more deeply and in parallel with the cleft between the two domains of the open form model than INR. It is possible that placement of the dye in this position may help to stabilize the open form of the protein relative to the closed form (*35*), which in turn would account for the weaker binding affinity for the IANR conjugate relative to the INR conjugate.

In conclusion, we have synthesized two long-wavelength fluorescent thiol-reactive derivatives of Nile red for biosensor applications. The thiol reactive pendants were placed at two different locations on the dye in order to understand the effect of linker position on the fluorescence response of the dyes, especially when conjugated to binding proteins. The high environmental sensitivity of these dyes was demonstrated by

measuring their spectral properties in solvents of varying dielectric constants. Bioconjugation of these dyes to maltose binding protein S337C MBP showed fluorescence changes of up to 200% upon binding of maltose for INR but only 20% for IANR. To a first approximation, the binding event places INR in an environment with relatively fewer interactions with the solvent water molecules, while IANR experiences less of an environmental change. Furthermore, we have observed that the attachment position of the linker to the dye and the flexibility of the linker play a key role in sensor performance, which was supported qualitatively by modeling studies. Placing the dye such that the charge transfer center would be closer to the protein surface may also explain the higher fluorescence performance for the biosensor. We believe that these dyes can be employed with binding proteins for other ligands, which can lead to the development of binding protein-based metabolite sensors that can be used with relatively low interference from the biological media when measured in vivo.

ACKNOWLEDGMENT

This work is supported in part by a grant from the Technologies for Metabolic Monitoring (TMM) program, contract number W81XWH-04-1-0076. The authors thank Dr. A. E. G. (Tony) Cass (Imperial College) for providing clones of S337C MBP as well as Colleen Nycz and David Wright of BD Technologies for assistance with protein production.

LITERATURE CITED

(1) Buschmann, V., Weston, K. D., and Sauer, M. (2003) Spectroscopic study and evaluation of red-absorbing fluorescent dyes. *Bioconjugate Chem. 14*, 195−204.

(2) Oswald, B., Patsenker, L., Duschl, J., Szmacinski, H., Wolfbeis, O. S., and Terpetschnig, E. (1999) Synthesis, spectral properties, and detection limits of reactive squaraine dyes, a new class of diode laser compatible fluorescent protein labels. *Bioconjugate Chem. 10*, 925−931.

(3) Hammer, R. P., Owens, C. V., Hwang, S.-H., Sayes, C. M., and Soper, S. A. (2002) Asymmetrical, water-soluble phthalocyanine dyes for covalent labeling of oligonucleotides. *Bioconjugate Chem. 13*, 1244−1252.

(4) Sophianopoulos, A. J., Lipowski, J., Narayanan, N., and Patonay, G. (1997) Association of near-infrared dyes with bovine serum albumin. *Appl. Spectrosc. 51*, 1511−1515.

(5) Fabian, J., Nakazumi, H., and Matsuoka, M. (1992) Near-infrared absorbing dyes. *Chem. Rev. 92*, 1197−1226.

(6) Daehne, S., Resch-Genger, U., and Wolfbeis, O. S. (Eds). (1998) *Near-infrared dyes for high technology applications (Nato Science Partnership Sub-series 3)*, Kluwer Academic Publishers, Boston.

(7) Cohen, B. E., Pralle, A., Yao, X., Swaminath, G., Gandhi, C. S., Jan, Y. N., Kobilka, B. K., Isacoff, E. Y., and Jan, L. Y. (2005) A fluorescent probe designed for studying protein conformational change. *Proc. Natl. Acad. Sci. U.S.A. 102*, 965−970.

(8) Gilardi, G., Zhou, L. Q., Hibbert, L., and Cass, A. E. G. (1994) Engineering the maltose binding protein for reagentless fluorescence sensing. *Anal. Chem. 66*, 3840−3847.

(9) Gilardi, G., Mei, G., Rosato, N., Agro, A. F., and Cass, A. E. G. (1997) Spectroscopic properties of an engineered maltose binding protein. *Protein Eng. 10*, 479−486.

(10) Marvin, J. S., Corcoran, E. E., Hattangadi, N. A., Zhang, J. V., Gere, S. A., and Hellinga, H. W. (1997) The rational design of allosteric interactions in a monomeric protein and its applications to the construction of biosensors. *Proc. Natl. Acad. Sci. U.S.A. 94*, 4366−4371.

(11) de Lorimier, R. M., Smith, J. J., Dwyer, M. A., Looger, L. L., Sali, K. M., Paavola, C. D., Rizk, S. S., Sadigov, S., Conrad, D. W., Loew, L., and Hellinga, H. W. (2002) Construction of a fluorescent biosensor family. *Protein Sci. 11*, 2655−2675.

(12) Dwyer, M. A., and Hellinga H. W. (2004) Periplasmic binding proteins: A versatile superfamily for protein engineering. *Curr. Opin. Struct. Biol. 14*, 495−504.

(13) Greenspan, P., Mayer, E. P., and Fowler, S. D. (1985) Nile red: A selective fluorescent stain for intracellular lipid droplets. *J. Cell Biol. 100*, 965−973.

(14) Sackett, D. L., and Wolff, J. (1987) Nile red as a polarity-sensitive fluorescent probe of hydrophobic protein surfaces. *Anal. Biochem. 167*, 228−234.

(15) Sackett, D. L., Knutson, J. R., and Wolff, J. (1990) Hydrophobic surfaces of tubulin probed by time-resolved and steady-state fluorescence of nile red. *J. Biol. Chem. 265*, 14899−14906.

(16) Briggs, M. S. J., Bruce, I., Miller, J. N., Moody, C. J., Simmonds, A. C., and Swann, E. (1997) Synthesis of functionalised fluorescent dyes and their coupling to amines and amino acids. *J. Chem. Soc., Perkin Trans. 1* 1051−1058.

(17) Long, J., Wang, Y., Matsuura, T., and Meng, J. (1999) Synthesis and fluorescence properties of novel benzo[*a*]phenoxazin-5-one derivatives. *J. Heterocycl. Chem. 36*, 895−899.

(18) Long, J., Wang, Y. M., and Meng. J. B. Synthesis of new near-infrared fluorescent dyes. (1999) *Chin. Chem. Lett. 10*, 659−660.

(19) Karstens, T., and Kobs, K. (1980) Rhodamine B and rhodamine 101 as reference substances for fluorescence quantum yield measurements. *J. Phys. Chem. 84*, 1871−1872.

(20) Pisarchick, M. L., and Thompson, N. L. (1990) Binding of a monoclonal antibody and its Fab fragment to supported phospholipid monolayers measured by total internal reflection fluorescence microscopy. *Biophys. J. 58*, 1235−1249.

(21) Berman, H. M., Westbrook, J., Feng, Z., Gilliland, G., Bhat, T. N., Weissig, H., Shindyalov, I. N., and Bourne, P. E. (2000) The protein data bank. *Nucleic Acids Res. 28*, 235−242.

(22) Sharff, A. J., Rodseth, L. E., and Quiocho, F. A. (1993) Refined 1.8-Å structure reveals the mode of binding of β-cyclodextrin to the maltodextrin binding protein. *Biochemistry 32*, 10553−10559.

(23) Sarkar, N., Das, K., Nath, D. N., and Bhattacharyya, K. (1994) Twisted charge-transfer process of nile red in homogeneous solution and in faujasite zeolite. *Langmuir 10*, 326−329.

(24) Dutta, A. K., Kamada, K., and Ohta, K. (1996) Spectroscopic studies of nile red in organic solvents and polymers. *J. Photochem. Photobiol. A: Chem. 93*, 57−64.

(25) Dutta, A. K., Kamada, K., and Ohta, K. (1996) Langmuir-Blodgett films of nile red: a steady-state and time-resolved fluorescence study. *Chem. Phys. Lett. 258*, 369−375.

(26) Lakowicz, J. R. (1999) *Principles of Fluorescence Spectroscopy*, 2nd ed., pp 185−210, Kluwer Academic/Plenum Publishers, New York.

(27) Grabowski, Z. R., Rotkiewicz, K., and Rettig, W. (2003) Structural changes accompanying intramolecular electron transfer: Focus on twisted intramolecular charge-transfer states and structures. *Chem. Rev. 103*, 3899−4031.

(28) Rettig, W., and Maus, M. (2000) Conformational changes accompanying intramolecular excited-state electron transfer. *Conformational Analysis of Molecules in Excited States* (Waluk, J., Ed.) pp 1−55, Wiley-VCH, New York.

(29) Golini, C. M., Williams, B. W., and Foresman, J. B. (1998) Further solvatochromatic, thermochromic, and theoretical studies on nile red. *J. Fluorescence 8*, 395−404.

(30) Dias, L. C. D., Jr., Custodio, R., and Pessine, F. B. T. (1999) Theoretical studies of nile red by ab initio and semiempirical methods. *Chem. Phys. Lett. 302*, 505−510.

(31) Reichardt, C. (2003) *Solvents and Solvent Effects in Organic Chemistry*, 3rd ed., Wiley−VCH Verlag GmbH & Co. KGaA, Weinheim, Germany.

(32) Brune, M., Hunter, J. L., Corrie, J. E. T., and Webb, M. R. (1994) Direct, real-time measurement of rapid inorganic phosphate release using a novel fluorescent probe and its application to actomyosin subfragment 1 ATPase. *Biochemistry 33*, 8262−8271.

(33) Corrie, J. E. T. (1994) Thiol-reactive fluorescent probes for protein labeling. *J. Chem. Soc., Perkin Trans. 1* 2975−2982.

(34) Dattelbaum, J. D., Looger, L. L., Benson, D. E., Sali, K. M., Thompson, R. B., and Hellinga, H. W. (2005) Analysis of allosteric signal transduction mechanisms in an engineered fluorescent maltose biosensor. *Protein Sci. 14*, 284−291.

(35) Marvin, J. S., and Hellinga, H. W. (2001) Manipulation of ligand binding affinity by exploitation of conformational coupling. *Nature Struct. Biol. 8*, 795−798.

BC050309D

Poly(ethylene glycol)-Conjugated Human Serum Albumin Including Iron Porphyrins: Surface Modification Improves the O_2-Transporting Ability

Yubin Huang,[†] Teruyuki Komatsu,[†,*] Rong-Min Wang,[†,‡] Akito Nakagawa,[†] and Eishun Tsuchida[†,*]

Advanced Research Institute for Science and Engineering, Waseda University, 3-4-1 Okubo, Shinjuku-ku, Tokyo 169-8555 Japan, and Key Laboratory of Polymer Materials of Gansu Province, Institute of Polymer, Northwest Normal University, Lanzhou 730070, China. Received November 3, 2005; Revised Manuscript Received February 10, 2006

Artificial O_2-carrying hemoprotein composed of human serum albumin including tetrakis(*o*-amidophenyl)-porphinatoiron(II) (Fe4P or Fe3P) [HSA−FeXP] has been modified by maleimide- or succinimide-terminated poly(ethylene glycol) (PEG), and the formed PEG bioconjugates have been physicochemically characterized. 2-Iminothiolane (IMT) reacted with the amino groups of Lys to create active thiol groups, which bind to α-maleimide-*ω*-methoxy PEG [Mw: 2-kDa (PEG_{M2}), 5-kDa (PEG_{M5})]. On the other hand, α-succinimidyl-*ω*-methoxy PEG [Mw: 2-kDa (PEG_{S2}), 5-kDa (PEG_{S5})] directly binds to Lys residues. MALDI-TOF MS of the PEG-conjugated HSA−FeXP showed distinct molecular ion peaks, which provide an accurate number of the PEG chains. In the case of PEG_{MY}(HSA−FeXP), the spectroscopic assay of the thiol groups also provided the mean of the binding numbers of the polymers, and the degree of the modification was controlled by the ratio of [IMT]/[HSA]. The viscosity and colloid osmotic pressures of the 2-kDa PEG conjugates (phosphate-buffered saline solution, [HSA] = 5 g dL^{-1}) were almost the same as that of the nonmodified one, whereas the 5-kDa PEG binding increased the rheological parameters. The presence of flexible polymers on the HSA surface retarded the association reaction of O_2 to FeXP and stabilized the oxygenated complex. Furthermore, PEG_{MY}(HSA−FeXP) exhibited a long circulation lifetime of FeXP in rats (13−16 h). On the basis of these results, it can be concluded that the surface modification of HSA−FeXP by PEG has improved its comprehensive O_2-transporting ability. In particular the PEG_{MY}(HSA−FeXP) solution could be a promising material for entirely synthetic O_2-carrying plasma expander as a red cell substitute.

INTRODUCTION

Poly(ethylene glycol) (PEG) is commonly used for the surface modification of peptides, proteins, enzymes, and liposome to confer several potential beneficial effects: not only a longer plasma half-life and nonimmunogenicity but also a solubility in organic solvents and extreme thermostability (*1*−*4*). To develop an artificial O_2 carrier, substantial efforts have been directed to the preparation of PEG-conjugated hemoglobin (Hb) over the past decades (*5*−*8*), and the optimized PEG−Hbs are currently being tested in clinical trials. Human serum albumin (HSA) is a versatile protein, which is found in our blood plasma at a high concentration (4−5 g dL^{-1}) (*9*). We have reported that HSA including tetrakis(*o*-amidophenyl)porphinatoiron(II) (Fe3P or Fe4P, Chart 1) [HSA−FeXP] can reversibly bind and release O_2 under physiological condition (pH 7.4, 37 °C) in a fashion similar to Hb (*10*). The administration of this synthetic O_2 carrier into anesthetized rats has proved its safety and O_2-transporting efficacy (*11*). Nevertheless, there is only one defect in that the FeXP molecule easily dissociates from HSA when infused into animals. This is due to the fact that FeXP is noncovalently bound to the hydrophobic cavity of albumin with binding constants (*K*) of 10^4−10^6 (M^{-1}). Natural heme, namely protoporphinatoiron IX, is also incorporated into HSA and shows a 10^2−10^4-fold higher *K* compared to FeXP (*12*); however, it is released from HSA during blood circulation with a half-life of 2.5−3.6 h (*13*, *14*). Under these circumstances,

Chart 1. Structures of O_2-Adduct Complexes of Tetrakis-(*o*-amidophenyl)porphinatoiron(II)

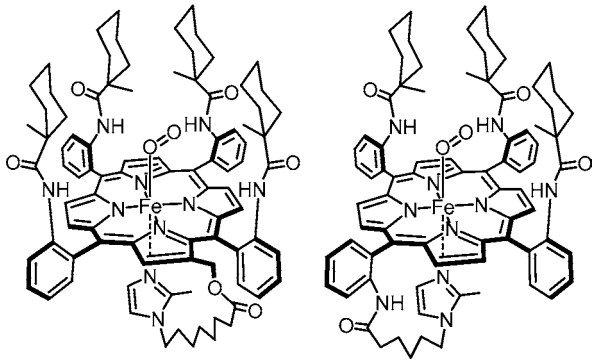

we postulated that the surface modification of HSA−FeXP by PEG could help to prolong the circulation life of FeXP and thereby retain its O_2-transporting ability for a long period. Although HSA is a very common plasma protein, its PEG conjugation chemistry has not yet been studied in detail. It is known that a huge variety of drugs are incorporated into specific sites of HSA (*9*). The PEG modification should prevent the rapid release of these drugs from the HSA scaffold and contribute to raising their potential therapeutic efficacies.

In the present study, we have systematically prepared several PEG-conjugated HSA−FeXPs and characterized their physicochemical properties. The surface modification by PEG affects the viscosity and colloid osmotic pressure of the solution, O_2-binding behavior of the parent HSA−FeXP, and circulatory lifetime of FeXP. The PEG-conjugated HSA−FeXP could be

* Corresponding authors: (E.T.) Tel: +81-3-5286-3120, Fax: +81-3-3205-4740, E-mail: eishun@waseda.jp. (T.K.) E-mail: teruyuki@waseda.jp; eishun@waseda.jp.

[†] Waseda University.

[‡] Northwest Normal University.

10.1021/bc050315+ CCC: $33.50 © 2006 American Chemical Society
Published on Web 02/22/2006

of extreme medical importance as a red cell substitute or O_2-therapeutic reagent.

EXPERIMENTAL PROCEDURES

Materials and Apparatus. All reagents were purchased from commercial sources as special grades and used without further purification. 2-Iminothiolane hydrochloride (IMT) was purchased from Wako Pure Chemical Industries, Ltd. (Osaka, Japan). α-[3-(3-Maleimido-1-oxopropyl)amino]propyl-ω-methoxy PEG [averaged Mw: 2333 (Sunbright ME-020MA, PEG_{M2}), averaged Mw: 5207 (Sunbright MEMAL-50H, PEG_{M5})] and α-succinimidyloxyglutaryl-ω-methoxy PEG [averaged Mw: 2325 (Sunbright MEGC-20HS, PEG_{S2}), averaged Mw: 5261 (Sunbright MEGC-50HS, PEG_{S5})] were purchased from NOF Corp. (Tokyo, Japan). 2-{8-(2-Methylimidazolyl-1-yl)-octanoyloxymethyl}-5,10,15,20-tetrakis{α,α,α,α-*o*-(1-methylcyclohexanamido)phenyl}porphinatoiron(III) chloride (Fe4P) and 5,10,15-tris{α,α,α-*o*-(1-methylcyclohexanamido)-phenyl}-20-mono-[β-*o*-{6-(2-methylimidazolyl) hexanamido}-phenyl]porphinatoiron(III) chloride (Fe3P) were synthesized using previously reported procedures (*10d,e*). Recombinant HSA was provided by the NIPRO Corp. (Osaka, Japan). The UV−vis absorption spectra were recorded using an Agilent 8453 UV−visible spectrophotometer fitted with an Agilent 89090A temperature control unit. The water was deionized using Millipore Elix and Simpli Lab-UV.

Preparation of PEG-Conjugated HSA−FeXP. The HSA−FeXP solutions ($X = 3$, 4, [HSA]: 5 g dL^{-1}, [FeXP]/[HSA]= 4 (mol/mol), pH 7.4) were prepared as described elsewhere (*10b,d*).

PEG_{MY}(HSA−FeXP): The modification of HSA−FeXP by α-maleimide-ω-methoxy PEG_{M2} was, for instance, carried out as follows. IMT (72 mg, 0.54 mmol) was slowly added to the HSA−FeXP solution (48 mL, [HSA]: 5 g dL^{-1}, [Fe4P] = 3 mM, pH 7.4) ([IMT]/[HSA] = 15/1, mol/mol) and gently stirred at room temperature in the dark. After 3 h, PEG_{M2} (1.44 g, [PEG_{M2}]/[HSA]:20/1, mol/mol) was added to the mixture, which was continually stirred for another 2 h. The resultant solution was ultrafiltered and washed by at least a 600 mL of phosphate-buffered saline (PBS) solution (pH 7.4) to remove any unreacted IMT and PEG_{M2} using the ADVANTEC UHP-76K holder with a Q0500 076E membrane (cutoff Mw: 50 kDa). The volume was finally condensed to 48 mL and sterilized by a DISMIC 0.45 μm filter, producing the PEG_{M2}(HSA−FeXP) solution. The FeXP concentration was determined by the assay of the iron ion by inductively coupled plasma (ICP) spectrometry using a Seiko Instruments SPS 7000A Spectrometer. The HSA concentration was calculated from the intensity of the circular dichroism spectrum at 208 nm, because the molar ellipticity of HSA (1.9×10^4 deg cm^2 $dmol^{-1}$) was unaltered after the PEG conjugation. Circular dichroism (CD) spectra were obtained using a JASCO J-725 spectropolarimeter. The concentration of the HSA sample was 0.15 μM in PBS, and quartz cuvettes with a 10-mm thickness were used for the measurements over the range of 195−250 nm. The PEG_{M2}(HSA−Fe3P) and PEG_{M5}-(HSA−Fe4P) solutions were also prepared by the same procedure. The product was sealed in a glass bottle under CO pressure and stored at 4 °C.

PEG_{SY}(HSA−Fe4P): The surface modification of HSA−Fe4P by α-succinimidyl-ω-methoxy PEG_{S2} was carried out as follows. PEG_{S2} (0.72 g, 0.36 mmol) was directly added to the HSA−Fe4P solution ([HSA]: 5 g dL^{-1}, [Fe4P] = 3 mM, pH 7.4) ([PEG_{S2}]/[HSA]:10/1, mol/mol), and the mixture was stirred at room temperature for 2 h. The resultant solution was ultrafiltered, condensed (48 mL), and sterilized as described above, producing the PEG_{S2}(HSA−Fe4P) solution. Using PEG_{S5} instead of PEG_{S2}, PEG_{S5}(HSA− Fe4P) was obtained. The Fe4P and HSA concentrations were determined by the same procedures for PEG_{MY}(HSA−FeXP).

Matrix-Associated Laser Desorption Ionization Time-of-Flight Mass Spectra (MALDI-TOF MS). The MALDI-TOF MS were obtained using a Shimadzu/Kratos AXIMA-CFR S/W Version 2, which was calibrated by BSA (Sigma A-0281) and HSA (Sigma A-3782). The specimens were prepared by mixing the aqueous sample solution (10 μM, 1 μL) and matrix (10 mg mL^{-1} sinapinic acid in 40% aqueous CH_3CN, 1 μL) on the measuring plate and air-drying.

Determination of Mean of PEG_{MY} Chains per Protein by Assay of Thiol Groups. The active thiol groups on the protein surface can be assayed by the disulfide exchange reaction with 2,2′-dithiopyridine (2,2′-DTP) to produce 2-thiopyridinone (2-TP) with an absorption at 343 nm (molar absorption coefficient (ϵ_{343}): 8.1×10^3 M^{-1} cm^{-1}) (*15*). Quantitative spectroscopic measurements conveniently provide the thiol concentration. The parent HSA−FeXP showed a small absorption band in this range, which should be subtracted from the spectrum after the disulfide exchange reaction. The difference in the thiol groups per HSA−FeXP before and after the PEG_{MY} modification corresponds to the mean of the PEG_{MY} chains on the protein surface.

Solution Properties. The viscosity and density of the PEG-conjugated HSA−FeXP solution (PBS, pH 7.4) were obtained using an Anton Paar DSC 300 capillary viscometer at 37 °C. The colloid osmotic pressures of the solutions (PBS, pH 7.4) were measured by a WESCOR 4420 Colloid Osmometer at 25 °C. A membrane filter with a 30 kDa cutoff was used.

O_2-Binding Parameters. O_2-binding to PEG-conjugated HSA−FeXP was expressed by eq 1,

$$\text{PEG(HSA}-\text{FeXP)} + \text{O}_2 \underset{k_{off}}{\overset{k_{on}}{\rightleftharpoons}} \text{PEG(HSA}-\text{FeXPO}_2\text{)} \quad (1)$$

where $K = k_{on}/k_{off}$. The O_2-binding affinity (gaseous pressure at half O_2 binding for FeXP, $P_{1/2} = 1/K$) was determined by spectral changes at various partial pressures of O_2/N_2 as previously reported (*10b,d*). The FeXP concentrations of 10−20 μM were normally used for the UV−vis absorption spectroscopy. The spectra were recorded within the range of 350−700 nm. The half-lifetime of the O_2-adduct complex was determined by the time dependence of the absorption intensity at 550 nm (O_2-adduct species). The association and dissociation rate constants for O_2 (k_{on}, k_{off}) were measured by a competitive rebinding technique using a Unisoku TSP-1000WK laser flash photolysis as reported in a previous paper (*16*).

Circulation Lifetime in Vivo. The animal investigations were carried out using twenty male Wistar rats (297 ± 29 g). All animal handling and care were in accordance with the NIH guidelines. The protocol details were approved by the Animal Care and Use Committee of Keio University. The PEG-conjugated HSA−FeXP solution (20% volume of the circulatory blood) was intravenously injected into rats from the tail vein (1 mL/min) under an inhalation anesthesia with diethyl ether ($n = 4$ each). Blood was taken from the tail vein at 3, 30 min, 1, 2, 4, 8, 16 h, 1, 2, 3 days (10 time points) after the infusion and then centrifuged to isolate the serum, which was colored brown by the presence of the sample. The animals were sacrificed after the experiments by hemorrhage. The FeXP concentration was measured by an iron ion assay using ICP spectrometry as described above.

RESULTS AND DISCUSSION

Synthesis of PEG-Conjugated HSA−FeXP. The HSA−FeXP molecules were conjugated with PEG having a terminal reactive chain-end, maleimide-PEG or succinimide-PEG, at

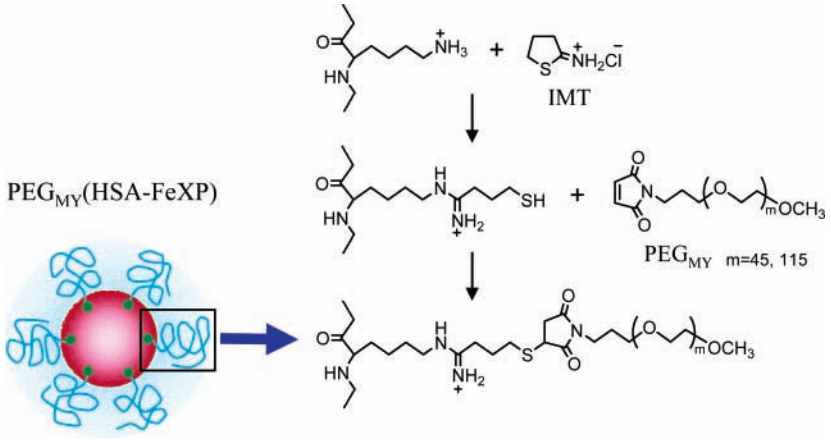

Figure 1. Two-step reaction schemes of IMT and maleimide-PEG (PEG$_{MY}$) with HSA−FeXP.

ambient temperature. Thiolation regent, IMT, quantitatively reacted with the amino groups of Lys to create active thiol groups, which bind to the α-maleimide-ω-methoxy PEG (PEG$_{M2}$ or PEG$_{M5}$) (Figure 1). The two-step reaction is reproducible and did not form any toxic side-product. On the other hand, the α-succinimidyl-ω-methoxy PEG (PEG$_{S2}$ or PEG$_{S5}$) directly binds to the amino groups of Lys. The gel permeation chromatogram (Sephacryl 200HR) of the well-washed PEG conjugate exhibited a single band, so that we did not need any further chromatographic purification.

The MALDI-TOF MS of PEG$_{M5}$(HSA−Fe4P), as prepared under the condition of [IMT]/[HSA−Fe4P] = 15/1 (mol/mol), showed five distinct ion peaks at 85, 90, 95, 101, and 106 kDa (Figure 2a). No unreacted HSA−FeXP was observed at all. The difference in each mass was 5.25 kDa, which implies that HSA−Fe4P is covalently bound to PEG$_{M5}$ and the individual peaks are attributed to PEG$_{M5}$(HSA−Fe4P) having a different number of PEG chains. Here, we have to be cautious whether these mass values involve a molecular weight of Fe4P, because our previous MALDI-TOF MS experiments of HSA−Fe4P demonstrated a single peak of HSA (Mw: 66.5 kDa); the incorporated Fe4P dissociated from the albumin during the ionization process (*10a*). In this study, we found that the mean of the surface PEG chains on HSA−FeXP is conveniently determined by a spectroscopic assay of the HSA scaffold and thiol groups. In general, the concentration of HSA is measured by the absorption at 280 nm or bromcresol green method (*17*), but they are probably obstructed by the surface modification. We then employed a CD measurement to determine the HSA concentration. The comparison of the CD spectra of HSA and PEG−HSA solutions revealed that the molecular ellipcity of albumin ($\epsilon_{208} = 1.9 \times 10^4$ deg cm^2 dmol^{-1}) is unaltered even after the PEG binding. Moreover, the presence of FeXP does not disturb the CD in the range of 190−250 nm. Therefore, the HSA concentration of PEG modified HSA−FeXP was quantitatively determined by its CD intensity at 208 nm. On the other hand, the active thiol groups on proteins are generally assayed by a disulfide exchange reaction with 2,2′-DTP (*15*). The combination of these two methodologies allows us to estimate the number of thiols on HSA−FeXP. The mean of the thiol groups was 6.7 per protein after the thiolation by IMT ([IMT]/[HSA−Fe4P] = 15 mol/mol) and decreased to 0.6 after the reaction with 20-fold excess moles of PEG$_{M5}$ (Table 1). These results suggested that the mean of 6.1 reactive thiols was conjugated with PEG$_{M5}$. The averaged molecular weight of this PEG$_{M5}$(HSA−FeXP) calculated from the intensity of the MS peak was 95 kDa. If one subtracts the total mass of the six PEG$_{M5}$ chains (5 kDa × 6 = 30 kDa) from 95 kDa, the difference of 65 kDa equals that

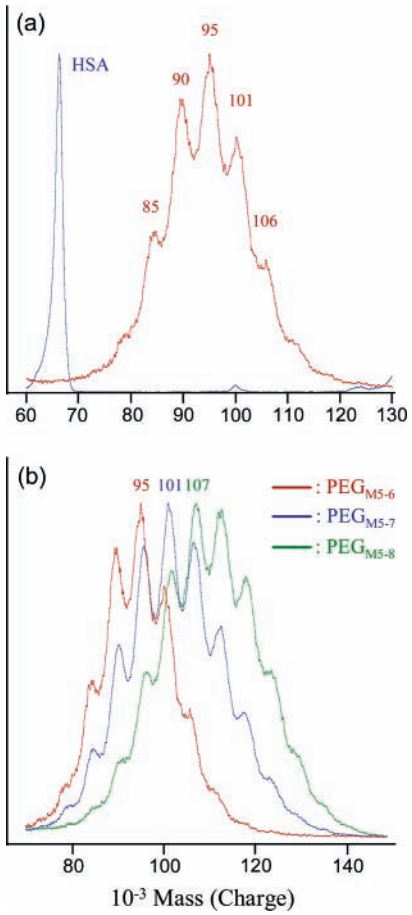

Figure 2. MALDI-TOF MS of (a) HSA and PEG$_{M5-6}$(HSA−Fe4P) and (b) PEG$_{M5}$(HSA−Fe4P) prepared in different [IMT]/[HSA−Fe4P] ratios of 15 (red), 20 (blue), and 30 (green) (mol/mol).

of HSA without Fe4P. Therefore, we concluded that all the mass ion peaks observed in the MALDI-TOF MS did not include the molecular weight of FeXP.

The number of the meleimide-PEG$_{M5}$ chains on HSA−Fe4P were modulated by the mixing ratio of [IMT]/[HSA−Fe4P] (mol/mol). The maximum peak of PEG$_{M5}$(HSA−Fe4P) in the MALDI-TOF MS significantly shifted to the higher molecular region (95 → 101 → 107 kDa) by increasing the IMT (Figure 2b). It is quite remarkable that the distributions of the entire spectral pattern were always identical. The averaged binding number of the PEG$_{M5}$ chains per HSA estimated from the intensity of the mass peak was consistent with the number determined from the assay of the thiol groups (Table 1).

Table 1. The Mean of Thiol Groups per HSA−Fe4P Molecule and Binding Number of the PEG Chains

PEG	[IMT]/[HSA−Fe4P] mol/mol	thiol groups per HSA after IMT addition (A)	thiol groups per HSA after PEG binding (B)	decreased thiol groups (B − A)[a]	averaged PEG number from MS
PEG_{M2}	10	5.6	0.5	5.1	4.6
	15	6.6	0.9	5.7	5.7
	20	8.3	1.1	7.2	6.6
PEG_{M5}	15	6.7	0.6	6.1	5.9
	20	8.0	0.9	7.1	7.2
	30	9.3	1.1	8.2	8.3

[a] This number corresponds to the binding numbers of PEG_{MY} on the protein surface.

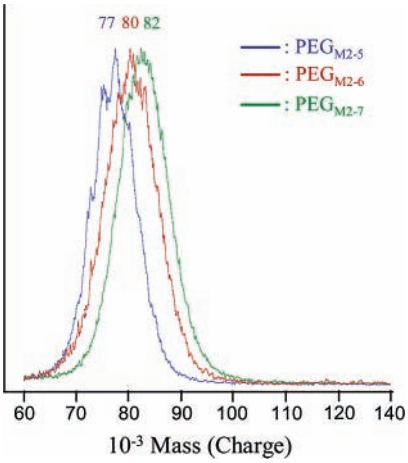

Figure 3. MALDI-TOF MS of PEG_{M2}(HSA−Fe4P) prepared in different [IMT]/[HSA−Fe4P] ratios of 10 (blue), 15 (red), and 20 (green) (mol/mol).

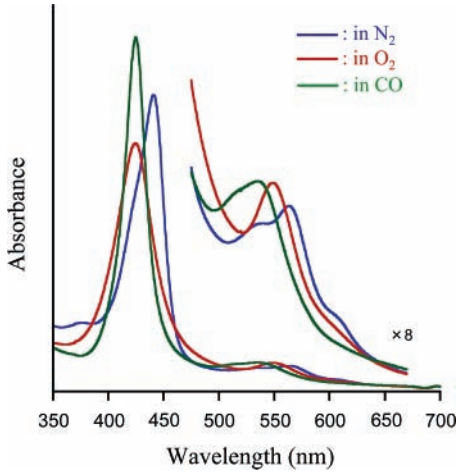

Figure 4. UV-vis absorption spectral change of PEG_{M2-6}(HSA−Fe4P) in PBS solution (pH 7.4).

Table 2. Solution Properties of PEG-Conjugated HSA−FeXP Solutions at 37 °C (pH 7.4, [FeXP] = 3 mM)

PEG	density (g/cm^3)	viscosity (cP)	COP (mmHg)
PEG_{M2-5}(HSA−Fe4P)	1.01	1.08	22
PEG_{M2-6}(HSA−Fe4P)	1.01	1.14	27
PEG_{M2-7}(HSA−Fe4P)	1.01	1.17	28
PEG_{M2-6}(HSA−Fe3P)	1.01	1.14	26
PEG_{M5-6}(HSA−Fe4P)	1.01	2.34	65
PEG_{S2-6}(HSA−Fe4P)	1.01	1.14	22
PEG_{S5-6}(HSA−Fe4P)	1.01	2.30	45
HSA−Fe4P	1.01	1.05	21
HSA	1.01	1.00	21

On the contrary, PEG_{M2}(HSA−Fe4P) demonstrated only one broad peak, because the difference in each mass is relatively close compared to the PEG_{M5} conjugate. The peak maxima of PEG_{M2}(HSA−Fe4P) also shifted to the higher region, dependent on the [IMT]/[HSA−Fe4P] ratio (Figure 3, Table 1).

The succinimide-PEG modified HSA−Fe4P showed the same MALDI-TOF MS patterns as PEG_{MY}(HSA−Fe4P) (data not shown). The number of 5-kDa PEG_{S5} chains per protein increased from 4 → 5 → 6 by elevating the ratio of [PEG_{S5}]/[HSA−Fe4P] (mol/mol): 10 → 20 → 30, respectively. However, the introduced 2-kDa PEG_{S2} number was always 6 in the range of [PEG_{S2}]/[HSA−Fe4P] 10−20. The stoichiometry of the PEG_{S2} binding could not be controlled. This is probably due to the hydrolysis of the succinimidyl end group in aqueous media. The concentration assays of [HSA] by CD and [FeXP] by ICP measurements showed that the initial FeXP/HSA ratio, 4/1 (mol/mol), were constant after the PEG conjugation.

Solution Properties. The viscosity and colloid osmotic pressure (COP) of the 2-kDa PEG-conjugates, PEG_{M2}(HSA−FeXP) and PEG_{S2}(HSA−Fe4P) (PBS solution, [HSA] = 5 g dL^{-1}, pH 7.4), were almost the same as those of the nonmodified HSA−FeXP independent of the number of the PEG chains (Table 2). In contrast, the 5-kDa PEG-conjugate solutions, PEG_{M5}(HSA−FeXP) and PEG_{S5}(HSA−Fe4P), showed a high viscosity (2.30−2.34, at a shear rate of 230 s^{-1}) and hyperoncotic property (45−65 mmHg) in comparison to those of HSA−Fe4P and HSA. From the viewpoint of the design of a blood alternative, it has to achieve a COP similar to that of human blood. However, to increase the effectiveness as a plasma expander, the COP should be higher than the physiological level (*18*). Similar approaches have been utilized for hypertonic saline−dextran formulations.

On the other hand, maintenance of the viscosity has recently been proposed as an important mechanism to preserve shear forces in the microcirculation which prevents loss of the functional capillary density (*19*). The latest PEG-Hb product has been designed to approach that of human whole blood (*7*). Anyway, the COP and viscosity of our PEG-conjugated HSA−FeXP can be adjustable to some extent based on the length of the PEG chains (2-kDa, 5-kDa) on the molecular surface.

O_2-Binding Properties. The UV−vis absorption spectrum of the PEG_{M2}(HSA−Fe4P) solution under an N_2 atmosphere showed λ_{max} at 441, 537, 563 nm (Figure 4), which indicates the formation of the ferrous five-N-coordinate high-spin complex of Fe4P with an intramolecular coordinated 2-methylimidazolyl-group (*10b,c, 20*). The other amino acid residue of HSA did not bind to the sixth-coordinate position of the central ferrous ion. Upon flowing O_2 gas through this solution, the spectral pattern shifted to that of the well-defined O_2-adduct complex of the tetrakis(phenyl)porphinatoiron(II) derivatives (λ_{max}: 424, 550 nm) (*10b,c, 20*). This oxygenation was reversibly observed, dependent on the O_2-partial pressure. After exposure of this solution to CO, PEG_{M2}(HSA−Fe4P) produced a very stable CO-adduct complex (λ_{max}: 425, 535 nm). The all maleimide- and succinimide-PEG-conjugated HSA−FeXP solutions showed similar UV−vis absorption spectra under N_2, O_2, and CO atmospheres. These spectral changes were completely the same as that observed in the nonmodified HSA−Fe4P.

Table 3. O_2-Binding Parameters of PEG-Conjugated HSA−FeXP Solution at 25 °C (pH 7.4)

system	k_{on} ($\mu M^{-1} s^{-1}$) fast	k_{on} slow	k_{off} (ms^{-1}) fast	k_{off} slow	$P_{1/2}$ (Torr)	$\tau_{1/2}$ (h) at 37 °C
PEG_{M2-5}(HSA−Fe4P)	11	5.8	0.16	0.08	38 (11)	13
PEG_{M2-6}(HSA−Fe4P)	12	4.6	0.17	0.07	32 (11)	12
PEG_{M2-7}(HSA−Fe4P)	9.3	4.7	0.16	0.08	35 (13)	12
PEG_{M2-6}(HSA−Fe3P)	15	4.2	0.52	0.14	41 (26)	8
PEG_{M5-6}(HSA−Fe4P)	12	6.2	0.17	0.09	31 (11)	16
PEG_{S2-6}(HSA−Fe4P)	10	4.3	0.14	0.06	36 (11)	13
PEG_{S5-6}(HSA−Fe4P)	12	5.5	0.25	0.11	32 (16)	18
HSA−Fe4P	31	7.3	0.53	0.13	34 (13)	9
HSA−Fe3P	29	4.4	1.1	0.16	45 (22)	4

The time course of the absorption decay after laser flash photolysis determined the association rate constants of the O_2binding to the PEG-conjugated HSA−FeXP (k_{on}). We have previously reported that the O_2-binding reaction to HSA−FeXP was significantly affected by the microenvironment around FeXP in the protein (e.g., steric hindrance of the amino acid residue and difference in polarity) (*10c*−*e*). As a result, the binding process of O_2 was observed as the sum of the two single-exponentials, giving fast and slow association rate constants [k_{on}-(fast) and k_{on}(slow)]. This unique property of HSA−FeXP has been unaltered after the surface modification by PEG, and all kinetics accompanying the O_2 recombinations consisted of two phases (Table 3). Interestingly, their k_{on}(fast) values were 1.9−3.3-fold lower than those of the corresponding HSA−FeXP, independent of the molecular weight (2-kDa or 5-kDa) and the linkage structure of the PEG. The differences observed in the slow phase were smaller. It may be considered that the presence of flexible polymers on the protein surface retarded the diffusion of the O_2 molecule.

The O_2-binding affinities ($P_{1/2} = K(O_2)^{-1}$) of the PEG-modified HSA−FeXP series were determined by measuring the UV−vis absorption spectral changes by O_2/N_2 titration (Table 3). All the PEG conjugates showed almost the same $P_{1/2}$ values relative to that of the original HSA−FeXP, indicating that the O_2-binding equilibria were not influenced by the presence of PEGs. In contrast, the surface modification by PEG delayed the proton-driven oxidation of the $FeXPO_2$ species and prolonged the half-lifetime of the O_2-adduct complex [$\tau_{1/2}(O_2)$]. The PEG_{M5-6}(HSA−Fe4P)O_2 complex showed the longest $\tau_{1/2}(O_2)$ of 16 h at 37 °C, which is greater than those of HSA−Fe4P and natural hemoprotein, myoglobin ($\tau_{1/2}(O_2)$: 12 h at pH 7, 35 °C) (*21*). Basic polymer PEG conjugation might change the local proton concentration of the HSA interior compared to the outer aqueous solution. Actually, it was shown that the surface PEG modification of hemoproteins has modulated the redox behavior of the active heme site (*1*, *2*, *22*).

Circulation Lifetime in Bloodstream of Rats. The circulation persistence of FeXP in the bloodstream after the administration of PEG_{MY-6}(HSA−FeXP) or PEG_{SY-6}(HSA−Fe4P) solution in rats is shown in Figure 5. The concentration decays of the PEG_{MY}(HSA−FeXP) series showed single exponentials, and the half-lifetimes ($\tau_{1/2}$) were 12.9−15.8 h, independent of the molecular weight of the polymers and FeXP structures. These values are much longer than those of the corresponding nonmodified HSA−FeXP (0.6−3.2 h) (*23*). The surface modification by PEG significantly prevented the rapid clearance of the incorporated FeXP and contributed to increasing the O_2-transporting efficacy.

On the contrary, the PEG_{SY}(HSA−Fe4P) series showed biphasic kinetics and a $\tau_{1/2}$ value of 1.5−2.1 h. We have postulated two reasons for this short circulation lifetime. The first reason is the charges of the Lys residues. The maleimide-PEG connects to Lys through the ring-opened IMT, which maintains the positive charge of Lys; therefore, PEG_{MY}(HSA−FeXP) could preserve the total electrostatic potential of albumin. In contrast, the succinimide-PEG directly binds to the amino group of Lys to form the amide bond, thereby reducing the positive charge and alters the surface electrostatic potential. This changing of the molecular charge may influence the rapid clearance of the incorporated FeXP.

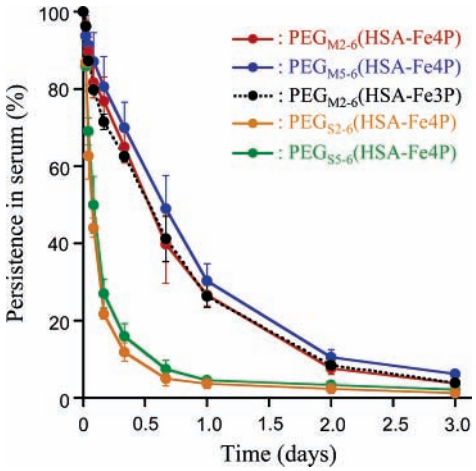

Figure 5. Persistence of FeXP in serum after administration of PEG-conjugated HSA−FeXP into Wistar rats. All values are mean ± SD (n = 4).

The second probability is the binding sites of the PEG chains. As shown in Table 1, the difference in the thiol number per protein before and after the reaction with maleimide-PEG was 0.5−1.1. This means that the binding position of PEG_{MY} is governed by the reaction place of IMT, which is small enough to statistically attach 59 Lys in HSA. Thus, the molecular surface of HSA−FeXP is uniformly covered by PEG_{MY}. On the other hand, the attaching sites of succinimide-PEG are presumably heterogeneous, because PEG_{SY} could only bind the accessible amino group of Lys due to the bulkiness of the long polymer. The incorporated Fe4P molecules might be more easily released from the PEG_{SY}-modified HSA in the circulatory system.

CONCLUSIONS

The surface modification of the albumin-based synthetic hemoprotein, HSA−FeXP, by PEG (Mw 2-kDa or 5-kDa) has improved its comprehensive O_2-transporting ability. The PEG conjugation decreased the O_2-association rate constant but retarded the irreversible oxidation of the central ferrous ion, thereby increasing the stability of the O_2-adduct complex. The 5-kDa PEG conjugation increased the viscosity and COP; however, the 2-kDa PEG conjugation did not change these rheological parameters. The linkage form of the PEG chain dramatically affects the circulation persistence of FeXP. In particular, the maleimide-PEG_{MY} conjugates showed a 6−8-fold longer lifetime compared to the succinimide-PEG_{SY} analogues. This is not dependent on the molecular weight of the polymer chains. In summary, the PEG_{MY}(HSA−FeXP) solution is the most promising candidate as an entirely synthetic O_2-carrying plasma expander for a red cell substitute.

Furthermore, we have recently found that water evaporation of the PEG_{MY}(HSA−FeXP) solution produced a red-colored thin film. Its UV−vis absorption spectrum reversibly changed from the deoxy state under an N_2 atmosphere to the oxy state by exposure to O_2 gas. This PEG_{MY}(HSA−FeXP) film was redissolved in nonaqeuous organic solvents, ethanol, chloroform, etc., and the reversible O_2 binding was again observed. The detailed study of the oxygenations of PEG_{MY}(HSA−FeXP) in a cast film and organic solvent are now underway.

ACKNOWLEDGMENT

This work was partially supported by a Grant-in-Aid for Scientific Research (No. 16350093) from JSPS, a Grant-in-Aid for Exploratory Research (No. 16655049) from MEXT Japan, and Health Science Research Grants (Regulatory Science) from MHLW Japan. Prof. Koichi Kobayashi, Dr. Hirohisa Horinouchi (Keio University), and Mr. Hisashi Yamamoto (NIPRO Corp.) are greatly appreciated for their cooperation with the animal experiments.

LITERATURE CITED

(1) (a) Harris, J. M., Ed. (1992) *Poly(ethylene glycol) Chemistry: Biotechnical and Biomedical Applications*, Plenum Press, New York; (b) Veronese, F. M., Harris, J. M. (2002) Introduction and overview of peptide and protein PEGylation. *Adv. Drug Delivery Rev. 54*, 453−456. (c) Roberts, M. J., Bentley, M. D., Harris, J. M. (2002) Chemistry for peptide and protein PEGylation. *Adv. Drug Delivery Rev. 54*, 459−476.

(2) Veronese, F. M. (2001) Peptide and protein PEGylation: a review of problems and solutions. *Biomaterials 22*, 405−417.

(3) Nucci, M. L., Shorr, R., and Abuchowski, A. (1991) The therapeutic value of poly(ethylene glycol) modified proteins. *Adv. Drug Delivery Rev. 6*, 133−151.

(4) Kawahara, N. Y., and Ohno, H. (1997) Induced thermostability of poly(ethylene oxide)-modified hemoglobin in glycols. *Bioconjugate Chem. 8*, 643−648.

(5) Yabuki, A., Yamaji, K., Ohki, H., and Iwashita, Y. (1990) Characterization of a pyridoxalated hemoglobin-polyoxyethylene conjugate as a physiologic oxygen carrier. *Transfusion 30*, 516−520.

(6) Talarico, T. L., Guise, K. J., and Stacey, C. J. (2000) Chemical characterization of pyridoxalated hemoglobin polyoxyethylene conjugate. *Biochim. Biophys. Acta 1476*, 53−65.

(7) Vandegriff, K. M., Malavalli, A., Wooldbridge, J., Lohman, J., and Winslow, R. M. (2003) MP4, a new nonvasoactive PEG-Hb conjugate. *Transfusion 43*, 509−516.

(8) Manjula, B. M., Tsai, A., Upadhya, R., Perumalsamy, K., Smith, P. K., Malavalli, A., Vandegriff, K., Winslow, R. M., Intaglietta, M., Prabhakaran, M., Friedman, J. M., and Acharya, A. S. (2003) Site-specific PEGylation of hemoglobin at Cys-93(β): correlation between the colligative properties of the PEGylated protein and the length of the conjugated PEG chain. *Bioconjugate Chem. 14*, 464−472.

(9) Peters, T. (1996) *All about Albumin: Biochemistry, Genetics and Medical Applications*, Academic Press, San Diego.

(10) (a) Komatsu, T., Hamamatsu, K., Wu, J., and Tsuchida, E. (1999) Physicochemical properties and O_2-coordination structure of human serum albumin incorporating tetrakis-(*o*-pivalamido)phenylporphyrinatoiron(II) derivatives. *Bioconjugate Chem. 10*, 82−86. (b) Tsuchida, E., Komatsu, T., Matsukawa, Y., Hamamastu, K., and Wu, J. (1999) Human serum albumin incorporating tetrakis(*o*-pivalamido)phenylporphinatoiron(II) derivative as a totally synthetic O_2-carrying hemoprotein. *Bioconjugate Chem. 10*, 797−802. (c) Komatsu, T., Matsukawa, Y., and Tsuchida, E. (2000) Kinetics of CO and O_2 binding to human serum albumin-heme hybrid. *Bioconjugate Chem. 11*, 772−776. (d) Komatsu, T., Matsukawa, and Y., Tsuchida E. (2002) Effect of heme structure on O_2-binding properties of human serum albumin-heme hybrids: Intramolecular histidine coordination provides a stable O_2-adduct complex. *Bioconjugate Chem. 13*, 397−402. (e) Nakagawa, A., Komatsu, T., Iizuka, M., and Tsuchida, E. (2006) Human serum albumin hybrid incorporating tailed porphyrinatoiron(II) in $\alpha,\alpha,\alpha,\beta$-conformer as an O_2 binding site. *Bioconjugate Chem. 17*, 146−151.

(11) (a) Komatsu, T., Huang, Y., Yamamoto, H., Horinouchi, H., Kobayashi. K., and Tsuchida, E. (2004) Exchange transfusion with synthetic oxygen-carrying plasma protein "albumin-heme" into an acute anemia rat model after seventy-percent hemodilution. *J. Biomed. Mater. Res. 71A*, 644−651. (b) Huang, Y., Komatsu, T., Yamamoto, H., Horinouchi, H., Kobayashi. K., and Tsuchida, E. (2004) Exchange transfusion with entirely synthetic red-cell substitute albumin-heme into rats: physiological responses and blood biochemical tests. *J. Biomed. Mater. Res. 71A*, 63−69.

(12) Adams, P. A., and Berman, M. C. (1980) Kinetics and mechanism of the interaction between human serum albumin and monomeric hemin. *Biochem. J. 191*, 95−102.

(13) Russo, S. M., Pepe, J. A., Donohue, S., Cable, E. E., Lambrecht, R. W., and Bonkovsky, H. L. (1995) Tissue distribution of zinc-mesoporphyrin in rats: relationship to inhibition of heme oxygenase. *J. Pharmacol. Exp. Ther. 272*, 766−774.

(14) Komatsu, T., Huang, Y., and Tsuchida, E. (2005) paper in preparation.

(15) Pedersen, A. O., and Jacobsen, J. (1980) Reactivity of the thiol group in human and bovine albumin at pH 3−9, as measured by exchange with 2,2′-dithiodipyridine. *Eur. J. Biochem. 106*, 291−295.

(16) Komatsu, T., Ohmichi, N., Nakagawa, A., Zunszain, P. A., Curry, S., and Tschida, E. (2005) O_2 and CO binding properties of artificial hemoproteins formed by complexing iron protoporphyrin IX with human serum albumin mutants. *J. Am. Chem. Soc. 127*, 15933−15942.

(17) Doumas, B. T., Watson, W. A., and Biggs, H. G. (1971) Albumin standards and measurement of serum albumin with bromcresol green. *Clin. Chim. Acta 31*, 87−96.

(18) Vandegriff, K. D., McCarthy, M., Rohlfs, R., and Winslow, R. M. (1997) Colloid osmotic properties of modified hemoglobins: chemically cross-linked versus polyethylene glycol surface-conjugated. *Biophys. J. 69*, 23−30.

(19) Tsai, A. G., Friesenecker, B., and McCarthy, M. (1998) Plasma viscosity regulates capillary perfusion during extreme hemodilution in hamster skinfold model. *Am. J. Physiol. 275*, H2170−80.

(20) Tsuchida, E., Komatsu, T., Kumamoto, S., Ando, K., and Nishide, H. (1995) Synthesis and O_2−Binding properties of tetraphenylporphyrinatoiron(II) derivatives bearing a proximal imidazole covalently bound at the β-pyrrolic position. *J. Chem. Soc., Perkin Trans. 2* 747−753.

(21) Sugawara, Y., Shikama, K. (1980) Autoxidation of native oxymyoglobin. *Eur. J. Biochem. 110*, 241−246.

(22) Ohno, H. and Tsukuda, T (1992) Electron-transfer reaction of polyethylene oxide-modified myoglobin in polyethylene oxide oligomera. *J. Electroanal. Chem. 341*, 137−149.

(23) Tsuchida, E., T. Komatsu, T., Hamamatsu, K., Matsukawa, Y., Tajima, A.; Yoshizu, A., Izumi, Y., and Kobayashi, K. (2000) Exchange transfusion of albumin-heme as an artificial O_2-infusion into anesthetized rats: physiological responses, O_2-delivery and reduction of the oxidized hemin sites by red blood cells. *Bioconjugate Chem. 11*, 46−50.

BC050315+

Epidermal Growth Factor-Conjugated Poly(ethylene glycol)-*block*-Poly(*δ*-valerolactone) Copolymer Micelles for Targeted Delivery of Chemotherapeutics

Faquan Zeng,[†] Helen Lee,[†] and Christine Allen*[,†,‡]

Departments of Pharmaceutical Sciences and Chemistry, University of Toronto, 19 Russell St., Toronto, Ontario, Canada M5S 2S2. Received December 8, 2005

Epidermal growth factor (EGF)-conjugated copolymer micelles were prepared from a mixture of diblock copolymers of methoxy poly(ethylene glycol)-*block*-poly(*δ*-valerolactone) (MePEG-*b*-PVL) and EGF-PEG-*b*-PVL for targeted delivery to EGF receptor (EGFR)-overexpressing cancers. The block copolymers and functionalized block copolymers were synthesized using PEG as the macroinitiator and HCl−diethyl ether as the catalyst. The MePEG-*b*-PVL and the carboxyl-terminated PEG-*b*-PVL (HOOC-PEG-*b*-PVL) copolymers were found to have molecular weights of 5940 and 5900, respectively, as determined by gel permeation chromatography (GPC) analyses. The HOOC-PEG-*b*-PVL copolymers were then activated by *N*-hydroxysuccinimide and subsequently reacted with EGF to form the EGF-PEG-*b*-PVL copolymers. The efficiency for the conjugation of EGF to the copolymer was found to be 60.9%. A hydrophobic fluorescent probe, CM-DiI, was loaded into both the nontargeted MePEG-*b*-PVL micelles and the targeted EGF-conjugated PEG-*b*-PVL micelles. The effective mean diameters of the CMDiI-loaded nontargeted and the CMDiI-loaded targeted micelles were found to be 32 ± 1 nm and 45 ± 2 nm, respectively, as determined by dynamic light scattering (DLS). The zeta potentials for the nontargeted micelles (no CM-DiI-loaded), CM-DiI-loaded nontargeted micelles, and CM-DiI-loaded targeted micelles were found to be −6.5, −8.7, and − 13.5 mV, respectively. Evaluation of the in vitro release of CM-DiI from the MePEG-*b*-PVL micelles in phosphate buffer saline (0.01 M, pH = 7.4) containing 10% (v/v) fetal bovine serum at 37 °C revealed that approximately 20% of the probe was released within the first 2 h. Confocal laser scanning microscopy (CLSM) analysis revealed that the targeted micelles containing CM-DiI accumulated intracellularly in EGFR-overexpressing MDA-MB-468 breast cancer cells following a 2 h incubation period, while no detectable cell uptake was observed for the nontargeted micelles. Results obtained from the confocal images were confirmed in an independent study by measuring the intracellular CM-DiI fluorescence in cell lysate. In addition, the presence of free EGF was found to decrease the extent of uptake of the targeted micelles. Nuclear staining of the cells with Hoechst 33258 indicated that the targeted micelles mainly localized in the perinuclear region and some of the micelles were localized in the nucleus. These results demonstrate that the EGF-conjugated copolymer micelles developed in this study have potential as vehicles for targeting hydrophobic drugs to EGFR-overexpressing cancers.

INTRODUCTION

In recent years, active targeting of colloidal drug carriers has gained increasing interest in the field of drug delivery. The enhanced therapeutic efficacy of anticancer drugs delivered in conventional colloidal carriers has mainly been attributed to increased tumor accumulation due to the enhanced permeation and retention (EPR) effect, also known as passive targeting. Active targeting of a delivery system should result in higher intracellular drug concentrations and therefore a further improvement in drug safety and efficacy. Indeed, the cell-type specificity introduced by these actively targeted drug carriers through ligand-conjugation has been shown to result in enhanced therapeutic efficacy and reduced systemic toxicity in several studies (*1*−*5*).

To date, active targeting of drug delivery vehicles as a strategy to improve tumor therapy has been most extensively pursued with long circulating liposomes (*5*−*7*). A wide variety of moieties, such as monoclonal antibodies (mAbs) (*2*, *5*, *7*−*9*) and growth factors (*6*, *10*, *11*), have been conjugated to the liposome surface as a means to achieve active targeting. Ishida et al. reported both increased in vitro cytotoxicity and in vivo therapeutic efficacy for doxorubicin formulated in mAb-conjugated liposomes that target CD19, an antigen expressed on B-lymphoma cells (*9*). Other examples of targeted systems include the anti-HER2-liposomes (*2*) and the F(ab′)$_2$/GAH-liposomes (*5*) for treatment of breast and gastrointestinal cancers, respectively. A few actively targeted liposome formulations are entering and have already entered clinical trial development (*7*, *12*). Therefore, much success has been realized with active targeting of liposome-based systems; however, this technology is most suitable for delivery of hydrophilic drugs or molecules that are susceptible to active loading techniques (*13*).

The hydrophobic nature of many anticancer drugs has directed researchers toward the design and development of other delivery strategies including polymeric nanoparticles (*14*, *15*), lipid micelles (*4*, *16*, *17*), and block copolymer micelles (*18*, *19*). Amphiphilic diblock copolymers with PEG as the hydrophilic block and a poly(ester) (*18*, *20*−*22*), poly(amino acid) (*23*−*26*), or poly(ether) (*27*−*29*) as the hydrophobic block have been explored extensively for applications in drug delivery. In an aqueous medium, these copolymers self-assemble to form micelles that consist of a hydrophobic core surrounded by a hydrophilic shell. The hydrophobic core may serve as a nanoreservoir for loading hydrophobic drugs, while the hydrophilic shell provides a protective coating between the core and

* To whom all correspondence should be addressed. Phone: (416) 946-8594. Fax: (416) 978-8511. E-mail: cj.allen@utoronto.ca.

[†] Department of Pharmaceutical Sciences.

[‡] Department of Chemistry.

10.1021/bc050350g CCC: $33.50 © 2006 American Chemical Society
Published on Web 01/12/2006

the external medium. Drug formulations based on block copolymer micelles have entered clinical trial development, and others have shown promise in preclinical evaluation (*30*−*32*).

To this point, few studies have focused on the preparation and characterization of actively targeted systems formed from micelles. One of the earliest reports on active targeting of a micelle system was put forth by Kabanov's group and included α_2-glycoprotein-conjugated Pluronic micelles. The α_2-glycoprotein-micelles were shown to have increased brain tissue localization and decreased clearance by the lung, when compared to nontargeted micelles (*33*, *34*). Recently, Yoo and Park also prepared folate-conjugated PEG-*b*-poly(lactide-*co*-glycolide) micelles loaded with doxorubicin for active targeting to folate receptor-overexpressing cancers such as epidermal carcinoma. Their experimental results revealed that both the in vitro IC_{50} and the in vivo tumor volume were reduced when treating the folate receptor-overexpressing cancers with doxorubicin formulated in these micelles (*3*). Also, Torchilin's group has demonstrated that lipid immuno-micelles, with the monoclonal antibody 2C5 attached to the surface, actively target Lewis lung tumors in nude mice (*4*, *35*).

At present, our group is focused on developing a diblock copolymer micelle system conjugated with epidermal growth factor (EGF) for active targeting to EGF receptor (EGFR)-overexpressing cancers. It is established that the EGF receptor is overexpressed in various human cancers such as lung, prostate, and breast (*36*). Therefore, several cancer treatments are being developed with the aim of targeting EGFR (*2*, *11*, *37*). For example, the radiopharmaceutical ^{111}In-DTPA-hEGF for treatment of EGFR-overexpressing breast cancer developed by Reilly's group is now in phase I clinical trial development (*38*, *39*). Several EGF-conjugated liposome-based formulations have also been designed (*6*, *10*, *11*, *40*). For example, Gedda's group has investigated the use of an EGF-conjugated liposome to overcome problems such as the low degree of specificity and the insufficient intracellular agent concentrations that are typically associated with boron capture neutron therapy (*6*, *10*, *11*). However, to date the utilization of EGF as a targeting moiety for a block copolymer micelle system has not been reported.

In an attempt to design and develop a novel, cancer cell specific delivery system we have synthesized a new telechelic diblock copolymer, carboxyl-terminated poly(ethylene glycol)-*b*-poly(δ-valerolactone) (HOOC-PEG-*b*-PVL) and conjugated EGF to the PEG terminus of the copolymer. GPC and ^{1}H NMR were used to confirm that the macroinitiator was consumed and the copolymer molecular weight and composition were as predicted. The successful conjugation of EGF to the copolymer was verified using an established in vitro assay. The critical micelle concentration (CMC) of the MePEG-*b*-PVL copolymer was measured using a traditional fluorescence-based method. The CellTracker fluorescent probe, CM-DiI, was physically entrapped within both the nontargeted and targeted micelles. CM-DiI-loaded nontargeted MePEG-*b*-PVL micelles and CM-DiI-loaded targeted EGF-conjugated micelles were prepared and characterized in terms of size, size distribution, and zeta potential. Cellular uptake of the nontargeted and targeted CM-DiI-loaded micelles was evaluated quantitatively using a fluorescence-based method and also monitored using confocal laser scanning microscopy (CLSM) in EGFR-overexpressing MDA-MB-468 breast cancer cells. Overall, these studies demonstrate the cell-type specific active targeting of nanosized copolymer micelles to EGFR-overexpressing breast cancer cells via receptor−ligand mediated internalization.

EXPERIMENTAL SECTION

Materials. MePEG (M_n= 2 000, M_w/M_n= 1.06 as determined by SEC) from Sigma-Aldrich and α-carboxyl-ω-hydroxyl-terminated PEG from Polymer Source Inc. (M_n = 2 000, M_w/M_n = 1.16) were dried twice by azeodistillation of toluene. Hydrogen chloride (1 M in diethyl ether, HCl−ether), 1,6-diphenyl-1,3,5-hexatriene (DPH), *N*-hydroxysuccinimide (NHS), and dicyclohexylcarbodiimide (DCC) were purchased from Sigma-Aldrich (Oakville, Ontario). Fluorescent probes including CellTracker CM-DiI, fluorescein phalloidin, and Hoechst 33258 were purchased from Molecular Probes Inc. (Eugene, OR). Toluene and δ-valerolactone (VL) were dried under calcium hydride and distilled prior to use. Other solvents such as hexane, ethyl ether, chloroform, acetone, and *N*,*N*-dimethylformamide were used as received.

Scheme 1. Scheme for Synthesis of HOOC-PEG-*b*-PVL, NHS-Activated PEG-*b*-PVL, and EGF−PEG-*b*-PVL Copolymers

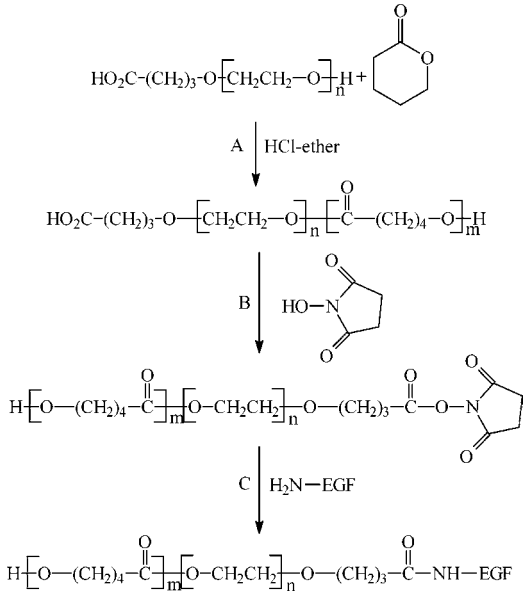

Synthesis of MePEG-*b*-PVL. The block copolymer was synthesized using a metal-free cationic method (*41*). A typical procedure was carried out as follows: In a flame dried flask, 5 g of monomethoxy-terminated poly(ethylene glycol) (2.5 mmol, M_n = 2 000, M_w/M_n = 1.06) was added and dried twice by toluene azeodistillation. An amount of 50 mL of dichloromethane (dried by calcium hydride) and 5 g of VL (50 mmol, dried and distilled over calcium hydride) were then added to the flask. 7.5 mL (1 M, 7.5 mmol) of the catalyst, hydrogen chloride in ether, was added to the mixture at 0 °C, and the reaction was maintained for 3 h at this temperature. The reaction was terminated by the addition of 0.5 mL of triethylamine, and the reaction mixture was then filtered. The copolymer was collected by precipitation in ether. The molecular weight of the PVL block was calculated from ^{1}H NMR and the known molecular weight of the MePEG precursor. ^{1}H NMR assignments were: 3.60 ppm for the MePEG unit (4H, b, OCH_2CH_2), signals for the PVL block appeared at 1.68 ppm (4H, m, $COCH_2CH_2CH_2CH_2O$), 2.35 ppm (2H, m, $COCH_2CH_2CH_2$-CH_2O), and 4.08 ppm (2H, m, $COCH_2CH_2CH_2CH_2O$).

Synthesis of α-Carboxy-ω-hydroxy-Terminated PEG-*b*-PVL (HOOC−PEG-*b*-PVL). Carboxyl-terminated PEG-*b*-PVL was synthesized using a similar method as that outlined for the synthesis of MePEG-*b*-PVL. The synthetic scheme is shown in Scheme 1A, and the detailed assignment for the ^{1}H NMR spectrum has been provided in the Results section.

Synthesis of NHS Activated PEG-*b*-PVL (NHS−PEG-*b*-PVL). To a round-bottom flask equipped with a magnetic stir bar and a rubber septum, attached to a nitrogen line and a bubbler, 0.5 g of α-carboxy-ω-hydroxy-terminated-PEG-*b*-PVL (0.128 mmol), 0.0396 g of *N*,*N*′-dicyclohexylcarbodiimide (1.5×

excess, 0.192 mmol), 0.0221 g of *N*-hydroxysuccinimide (1.5× excess, 0.192 mmol), and 5 mL of dichloromethane were added. The reaction was maintained for 24 h at room temperature. The reaction mixture was then filtered, concentrated under reduced pressure, and precipitated in cold diethyl ether. The yield was found to be 0.38 g (i.e. 76%).

Synthesis of EGF-Conjugated PEG-*b*-PVL (EGF−PEG-*b*-PVL). 5 mg of NHS-PEG-*b*-PVL ($M_{n,NMR}$ = 4569, M_w/M_n=1.32) was added to a solution of 100 μg of EGF in 0.6 mL PBS (pH = 7.4, equiv. 166 μg/mL). Following 4 h, an additional 5 mg of NHS-PEG-*b*-PVL was added to the reaction mixture. The reaction was then maintained for 24 h at room temperature. Following this period the reaction mixture was dialyzed against water using cellulose ester membrane with a molecular weight cut-off of 8000 (Spectrum Laboratories Inc.; Rancho Dominguez, CA) for 48 h in order to remove the uncoupled EGF (*42*). The EGF-conjugation efficiency was measured using the Micro BCA Protein Assay (Pierce Inc.; Rockford, IL) (*42*).

Characterization of Block Copolymers. ^{1}H NMR spectra were obtained on a Gemini 200 spectrometer (200 MHz for ^{1}H) in $CDCl_3$ solvent. Chemical shifts were reported in ppm with $CHCl_3$ as the internal standard. GPC measurements were carried out at room temperature using a Waters 590 liquid chromatography system equipped with three Waters Styragel HR 4E columns and a 410 differential refractometer detector. THF with 1% triethylamine was used as the solvent at a flow rate of 1.0 mL/min at 40 °C. Narrow polystyrene standards (Polysciences Inc.; Warrington, PA) were used to generate a calibration curve. The data obtained were recorded and manipulated using the Windows-based Millenium 2.0 software package (Waters Inc.; Milford, MA).

Measurement of Critical Micelle Concentration. The CMC of the MePEG-*b*-PVL copolymer was determined using an established fluorescence-based method (*43*). The copolymer studied had a total molecular weight of 4040 g/mol and block lengths of 2000-*b*-2020 (i.e. *x*-*b*-*y*, where *x* denotes the molecular weight of MePEG and *y* the molecular weight for PVL) as determined by ^{1}H NMR. In short, a specific aliquot of MePEG-*b*-PVL dissolved in chloroform was added to glass vials such that the concentration of copolymer ranged from 0.1 to 200 mg/L. An aliquot of a DPH stock solution was then added to each vial such that the concentration of DPH was maintained at 1 mg/L in each solution. The solutions were vigorously stirred for 4 h and then thoroughly dried under nitrogen. The dried vials were heated to 60 °C, and 1 mL of double distilled water was added into each vial. The solutions were equilibrated with stirring overnight at room temperature, and the fluorescence emission was measured at 430 nm (λ_{ex} = 350 nm) using a Spectra GeminiXS dual-scanning microplate spectrofluorometer (Molecular devices; Sunnyvale, CA).

Preparation of CM-DiI-Loaded Copolymer Micelles. 10 μg of CM-DiI and 5 mg of MePEG-*b*-PVL were codissolved in DMF. After stirring for 4 h, the DMF was removed under nitrogen. The dried CM-DiI-copolymer film was then heated to 60 °C and hydrated with 1 mL of PBS (0.01 M, pH = 7.4). For preparation of the targeted micelles, 0.25 mg of the EGF-PEG-*b*-PVL copolymer dissolved in filtered deionized water was added to the preformed nontargeted MePEG-*b*-PVL micelles. The mixture was stirred at 60 °C for 1 h and then overnight at room temperature (*10*).

Size and Size Distribution of Micelles (+/− EGF). The hydrodynamic diameters of micelles were determined by dynamic light scattering (DLS) at an angle of 90° and a temperature of 25 °C (90Plus Particle Size Analyzer; Brookhaven Instruments Corporation; Holtsville, NY). The sample solutions were diluted in distilled water and filtered prior to analysis (0.22 μm Millipore filter). The copolymer concentrations of the analyzed sample solutions were approximately 1 mg/mL. BIC Particle Sizing software was employed to determine the effective mean diameters of the targeted and nontargeted copolymer micelles (+/− EGF) using cumulant analysis. The software also determines the size distribution by multimodal size distribution analysis in which the data are fitted using the non-negatively constrained least squares (NNLS) algorithm.

Zeta Potential of Micelles. The zeta potentials of nontargeted, CM-DiI-loaded nontargeted and CMDiI-loaded targeted micelles were measured using a Zetasizer 3000HSA (Malvern Instruments). Micelle solutions were prepared as described above and were diluted 40 times in double-distilled water. The zeta potential measurements were analyzed using the Photon Correlation Spectroscopy software (version 1.6.1).

In Vitro Release of CM-DiI-Loaded MePEG-*b*-PVL Micelles. The release kinetics of the CM-DiI-loaded micelles was investigated using the dialysis method (*44*). Briefly, a micelle solution was placed in Spectra/Por 7 dialysis membrane with a molecular weight cut-off of 10 000 and dialyzed against an excess amount of PBS containing 10% (v/v) fetal bovine serum (FBS) at 37 °C. A 50 μL aliquot of the micelle sample was removed from the dialysis membrane at designated time points. A calibration curve for CM-DiI was obtained (i.e. linear range from 0.01 to 1.00 μg/mL), and the fluorescence intensity of the collected samples was measured (Fluoro Max-3, Jobin Yvon Inc.).

Cell Culture. EGFR-overexpressing breast cancer cells (MDA-MB-468) were kindly donated by Dr. R. M. Reilly (University of Toronto). The MDA-MB-468 cells were maintained in Dulbecco's Modified Eagle Medium (DMEM). The DMEM was supplemented with 10% (v/v) heat-inactivated FBS and 1% (v/v) penicillin−streptomycin (100 U/mL penicillin G and 100 μg/mL streptomycin). Cells were allowed to grow in a monolayer in a tissue culture flask incubated at 37 °C in 5% CO_2 atmosphere and 90% relative humidity.

Quantitative Evaluation of Cell Uptake. MDA-MB-468 cells were seeded onto 24-well plates at a density of 80 000 cells/well and then incubated for 24 h prior to treatment. As a negative control, cells were incubated with only DMEM. Targeted micelles (+ EGF) or nontargeted MePEG-*b*-PVL micelles (− EGF) were diluted in prewarmed DMEM to achieve a final CM-DiI concentration of 4 μM. For positive controls, free CM-DiI in sterile DMSO was diluted to a final CM-DiI concentration of 4 μM or 0.88 μM (i.e. equivalent to the 22% of the total CM-DiI loaded that is anticipated to be released from micelles during the 2 h incubation; refer to Results section). The cells were incubated with the treatments for 2 h at 37 °C. For competitive binding, the cells were preincubated with 1.7 μg/well of free EGF for 30 min at 37 °C prior to the addition of targeted micelles. The cells were washed with warm PBS three times to remove unbound micelles or free CM-DiI and trypsinized for fluorescence and cell viability measurements. To quantify CM-DiI fluorescence the cells were lysed with lysis buffer (2% Triton X-100 in PBS) and the fluorescence intensity was measured at λ_{ex} = 553 nm and λ_{em} = 570 nm (Fluoro Max-3, Jobin Yvon Inc.). Cell uptake was expressed as relative fluorescence normalized to the number of cells in each well as determined using the MTT assay described below.

Cell Fixation for Confocal Microscopy. MDA-MB-468 cells were seeded onto two-well Lab-Tek II Chamber Slide System (Nalge Nunc International; Naperville, IL) at a cell density of 300 000 cells/well. The cells were then incubated for 24 h to allow for adhesion prior to the cell uptake studies. The cells were treated with CM-DiI-loaded nontargeted or targeted micelles as described above. Following the incubation period the cells were washed with warm PBS three times in order to remove the unbound micelles. For fixation of the cells, 3.7%

Table 1. Summary of the Characteristics of the Block Copolymers

sample	$M_{n,GPC}$	$M_{n,PEG}$	$M_{n,PVL}$[a]	M_w/M_n	CMC (mg/L)
MePEG-*b*-PVL	5940	2000	2020	113	23.3
HOOC-PEG-*b*-PVL	5900	2000	1890	1.32	n.d.

[a] Molecular weight determined by ^{1}H NMR. $M_{n,PEG} + M_{n,PVL} = M_{n,NMR}$.

formaldehyde (Sigma-Aldrich; Oakville, Ontario) in PBS was added and the cells were incubated at room temperature for 10 min. The cells were then once again washed with warm PBS three times. Finally, the chambers were removed; the specimen was mounted with ProLong Gold anti-fade reagent (Molecular Probes Inc.; Eugene, OR) and a coverglass was added for confocal microscopy imaging.

Cytoplasmic and Nuclear Staining. Following cell fixation with 3.7% formaldehyde, 0.1% Triton X-100 (Sigma-Aldrich; Oakville, Ontario) in PBS was added and the cells were incubated at room temperature for 5 min for membrane permeabilization. The cells were then washed three times with warm PBS and incubated with fluorescein phalloidin in PBS (165 nM) at room temperature for 20 min to allow for cytoplasmic staining. Prior to proceeding to nuclear staining, the cells were washed with warm PBS three times to remove excess fluorescein phalloidin. An aliquot of Hoechst 33258 in water (5 μg/mL) was then added, and the cells were incubated for 5 min at room temperature. Excess Hoechst solution was removed by washing the cells with warm PBS three times, and the slides were then processed for mounting.

Confocal Laser Scanning Microscopy. Confocal fluorescence imaging was performed on an inverted microscope (Zeiss LSM510 META NLO) that is equipped with both confocal and two-photon scanning systems. CM-DiI (λ_{ex} = 553 nm; λ_{em} = 570 nm) and fluorescein phalloidin (λ_{ex} = 496 nm; λ_{em} = 516 nm) were excited by HeNe (543 nm) and argon (488 nm) lasers, respectively. Hoechst 33258 (λ_{ex} = 350 nm; λ_{em} = 452 nm) was excited by the tunable two-photon Chameleon laser at 750 nm. All images were acquired with a C-Apo 63×/1.4 oil lens. During the acquisition of all images, microscope settings including detector gain, amplification offset, amplification gain, and laser power were kept constant in order to allow for a comparison of the cell uptake of targeted and nontargeted micelles.

Cell Proliferation Studies. MDA-MB-468 cells were seeded onto 96-well plates at a density of 5000 cells/well and were incubated for 24 h prior to treatment. Free EGF, nontargeted micelles (MePEG-*b*-PVL) and targeted micelles (EGF-PEG-*b*-PVL) were diluted in DMEM such that the EGF and copolymer concentrations were identical to those employed during treatment with the targeted micelles. The cells were treated in triplicate and were incubated for 48 h prior to the assessment of cell viability. Cell viability was determined using the MTT assay as outlined in detail elsewhere (*45*). Briefly, 10 μL of 5 mg/mL of thiazolyl blue tetrazolium bromide solution was added to each well. Following a 4 h incubation period, the cells were lysed and cell viability was measured by optical absorbance at 570 nm using a SpectraMax plus microplate reader (Molecular Devices, Sunnyvale, CA). Cell viability was expressed relative to that of untreated cells which was assumed to have 100% viability.

RESULTS

Synthesis and Characterization of MePEG-*b*-PVL Copolymers. As shown in Table 1, the molecular weight of the MePEG-*b*-PVL copolymer was found to be 4020 and 5940 as determined by ^{1}H NMR and GPC analysis, respectively. The discrepancy between the values obtained for the molecular weight of the copolymer from ^{1}H NMR and GPC analyses may be attributed to the difference between the hydrodynamic volumes of the block copolymers and the polystyrene standards. The polydispersity of the copolymer was found to be M_w/M_n = 1.13 as determined by GPC analysis. The CMC of the MePEG-*b*-PVL copolymer (Table 1, Sample MePEG-*b*-PVL) was found to be 23.3 mg/L as determined by a fluorescence-based method using DPH as the probe.

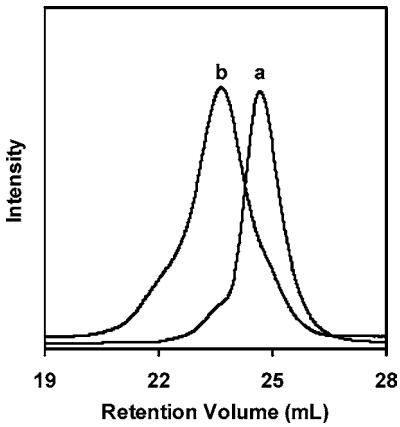

Figure 1. GPC traces for: (a) HOOC-PEG, M_n = 2000, M_w/M_n = 1.16; (b) HOOC-PEG-*b*-PVL, $M_{n,GPC}$ = 5900, M_w/M_n = 1.32 from crude product (Table 1, sample HOOC-PEG-*b*-PVL).

Synthesis and Characterization of the Carboxyl-Terminated PEG-*b*-PVL Copolymers (HOOC-PEG-*b*-PVL). Scheme 1A outlines the method employed for the synthesis of HOOC-PEG-*b*-PVL. The α-carboxyl-ω-hydroxyl PEG (HOOC-PEG) was selected as the macroinitiator and hydrogen chloride as the catalyst. The heterofunctional PEG was found to be able to initiate VL polymerization in dichloromethane at 0 °C and resulted in a copolymer having the predicted molecular weight and a slightly broad molecular weight distribution (M_w/M_n = 1.32) as revealed by GPC analysis. Figure 1 compares the GPC chromatograms of the HOOC-PEG macroinitiator (M_n = 2000, M_w/M_n = 1.16) and the HOOC-PEG-*b*-PVL diblock copolymer from the crude product. The GPC trace demonstrates that the peak corresponding to the macroinitiator is shifted to a higher molecular weight, which indicates the successful synthesis of the telechelic copolymer (HOOC-PEG-*b*-PVL). Figure 2a includes the ^{1}H NMR spectrum and the complete peak assignments for the diblock HOOC-PEG-*b*-PVL copolymer. ^{1}H NMR assignments are as follows: the signal *c* at 3.60 ppm corresponds to MePEG (4H, b, O*CH*$_2$CH$_2$), signals for PVL appeared at 1.68 ppm (4H, m, COCH$_2$*CH*$_2$CH$_2$CH$_2$O), 2.35 ppm (2H, m, CO*CH*$_2$CH$_2$CH$_2$CH$_2$O), and 4.08 ppm (2H, m, COCH$_2$CH$_2$-CH$_2$*CH*$_2$O). The molecular weight of the PVL block was calculated from the overall composition obtained from ^{1}H NMR (Figure 2a) and the known molecular weight of the HOOC-PEG macroinitiator.

Synthesis and Characterization of NHS-Activated PEG-*b*-PVL and EGF Conjugated PEG-*b*-PVL. In the second step, the carboxyl-terminated block copolymer was activated by reaction with NHS as shown in Scheme 1B. The chemical structure was confirmed by ^{1}H NMR (Figure 2b), and the coupling efficiency was found to be 92%. This further confirmed the successful synthesis of the carboxyl-functionalized block copolymer with functionality above 90%. The signal *c* at 2.82 ppm (4H, b, CO*CH*$_2$CH$_2$CO) was assigned to the protons of the NHS unit, which indicates the addition of NHS to the PEG terminus. The other assignments for the ^{1}H NMR spectrum are as follows: signal *a* at 1.67 ppm (4H, b, COCH$_2$*CH*$_2$CH$_2$CH$_2$O), signal *b* at 2.36 ppm (2H, b, CO*CH*$_2$CH$_2$CH$_2$CH$_2$O), signal *d* at 3.64 ppm (4H, b, O*CH*$_2$CH$_2$O), and signal *e* at 4.08 ppm (2H, b, COCH$_2$CH$_2$CH$_2$*CH*$_2$O).

Finally, the NHS-activated block copolymer was reacted with EGF in PBS (pH = 7.4) (Scheme 1, Step C). The uncoupled

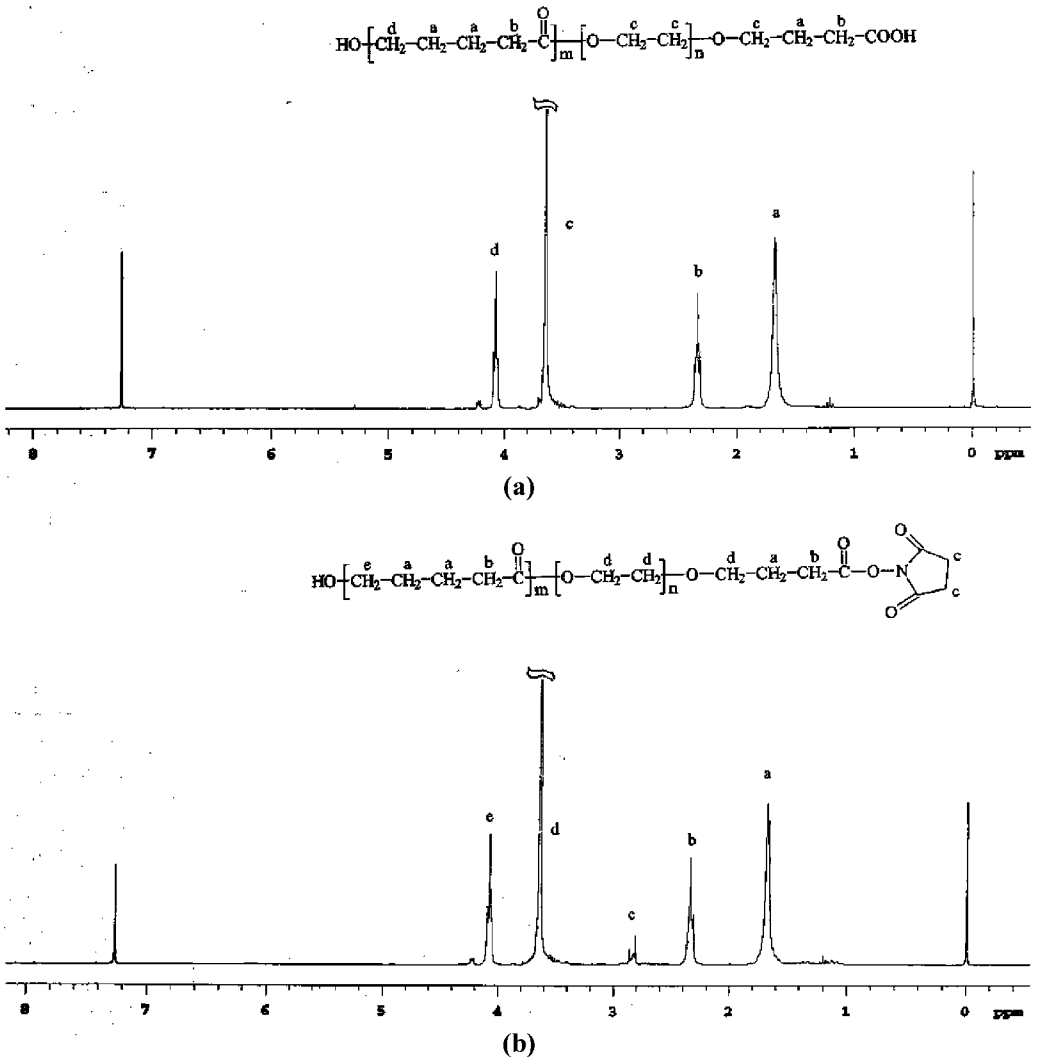

Figure 2. ^{1}H NMR spectra of HOOC-PEG-*b*-PVL and NHS-PEG-*b*-PVL copolymers: (a) HOOC-PEG-*b*-PVL, $M_{n,GPC} = 5900$, $M_w/M_n = 1.32$ (Table 1, sample HOOC-PEG-*b*-PVL); (b) NHS-PEG-*b*-PVL copolymer.

EGF was removed by dialysis, and the final product was recovered by lyophilization. The amount of EGF conjugated to the copolymer was quantified using the Micro BCA assay. It was found that 101.7 μg of EGF was conjugated per 10 mg of copolymer, which corresponds to a conjugation efficiency of 60.9%.

Size, Size Distribution, and Zeta Potential of Copolymer Micelles (+/− EGF). The effective mean diameters of the CM-DiI-loaded nontargeted MePEG-*b*-PVL micelles (− EGF) and targeted micelles (+ EGF) were found to be approximately 32 ± 1 nm and 45 ± 2 nm, respectively. Both micelle solutions (+/− EGF) were found to have a monomodal size distribution. The zeta potentials for the nontargeted MePEG-*b*-PVL micelles (no CM-DiI), the CMDiI-loaded nontargeted micelles and the CM-DiI-loaded targeted micelles were found to be − 6.5, − 8.7, and − 13.5 mV, respectively.

In Vitro Release of CM-DiI-Loaded MePEG-*b*-PVL Micelles. An evaluation of in vitro release was carried out in 0.01 M PBS (pH = 7.4) containing 10% fetal bovine serum (FBS) at 37 °C in order to mimic the conditions employed for the cell uptake studies. Figure 3 includes the 24-h release profile for CM-DiI from the MePEG-*b*-PVL micelles. Approximately 20% of the CM-DiI was released within the first 2 h of incubation, and 90% of the total probe was released over the entire 24 h incubation period.

Cell Uptake of Targeted Micelles (+ EGF) and Nontargeted Micelles (− EGF). Figure 4 illustrates the uptake profile

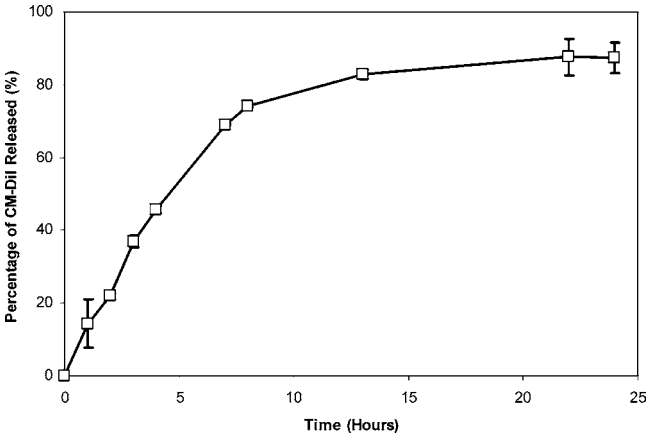

Figure 3. In vitro release of CM-DiI from MePEG-*b*-PVL micelles in PBS (0.01 M, pH = 7.4) at 37 °C.

of CM-DiI-loaded micelles in MDA-MB-468 cells as determined by fluorescence measurements. Untreated cells were found to have minimal autofluorescence, and the fluorescence was negligible when compared to treated cells. The amount of CM-DiI fluorescence detected in cells that were treated with targeted micelles (+ EGF) greatly exceeded that of cells treated with nontargeted micelles (- EGF). Similar results were observed with confocal microscopy. Figure 5a and 5d are fluorescence

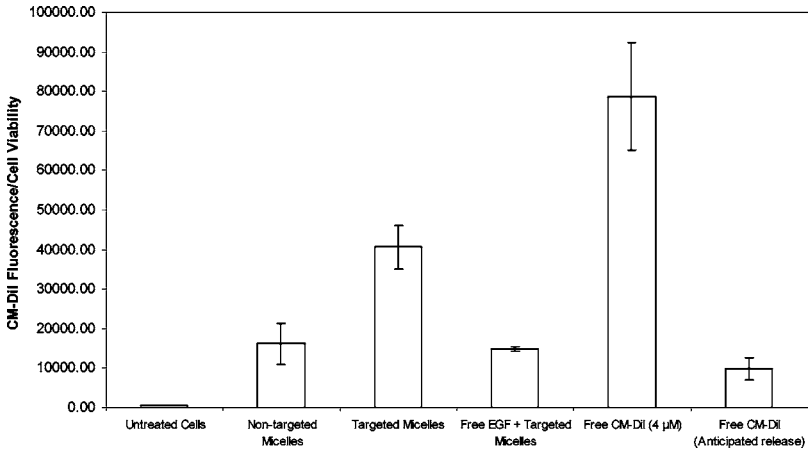

Figure 4. CM-DiI fluorescence of cell lysate measured from cells treated with cell culture medium (untreated group as negative control), CM-DiI-loaded nontargeted micelles, CM-DiI-loaded targeted micelles, free EGF with CM-DiI-loaded targeted micelles, 4 μM of free CM-DiI (equivalent to 100% loading in micelles as positive control), and 0.88 μM of free CM-DiI (fraction of anticipated release from micelles). Cell uptake was expressed in terms of the relative fluorescence intensity normalized to cell viability for each well.

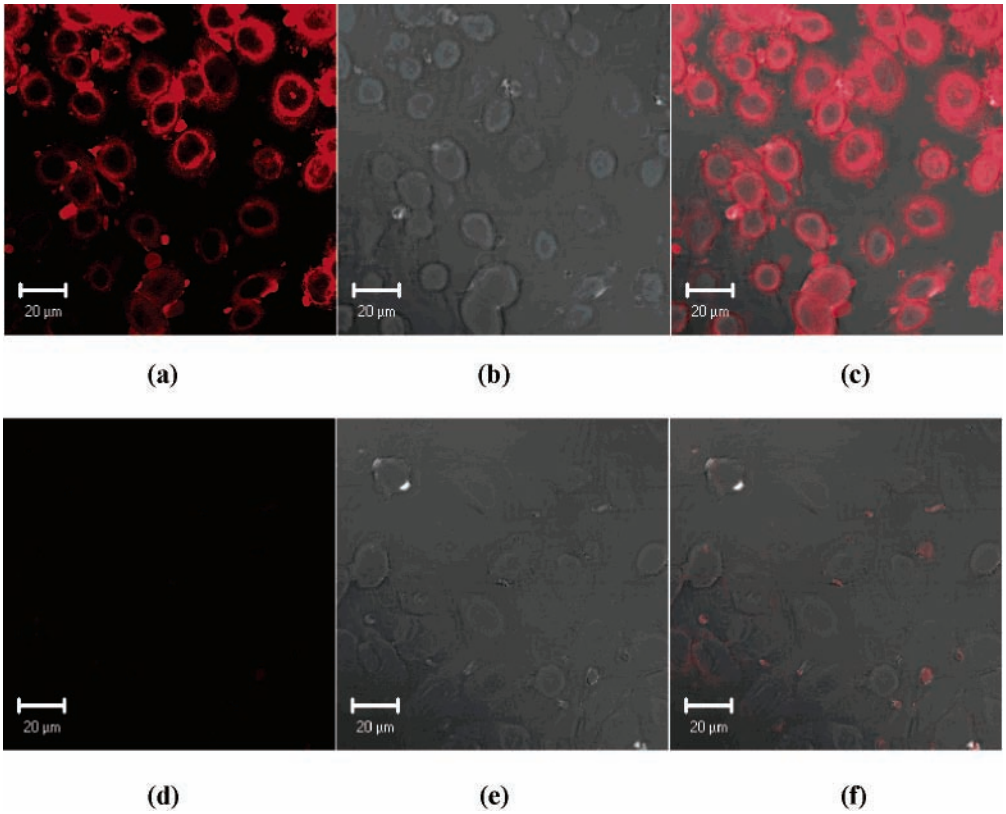

Figure 5. Images of EGFR-overexpressing (i.e. MDA-MB-468) cells that have been incubated with targeted PEG-*b*-PVL micelles (+ EGF) (a−c) or nontargeted MePEG-*b*-PVL micelles (− EGF) (d−f) for 2 h at 37 °C. Panels a and d include confocal images visualized using the fluorescence channel for CM-DiI. Panels b and e include the light microscopy images visualized using transmitted light (b is the same field as in a, e is the same field as in d). Panel c is a superimposition of panels a and b, while panel f is a superimposition of panels d and e. All microscope settings were held constant for imaging.

confocal images of cells that have been incubated with targeted micelles (+ EGF) and nontargeted micelles (− EGF), respectively. For the incubation of the cells with the nontargeted micelles, there appeared to be no accumulation of CM-DiI following the 2-h incubation period. In comparison, significant accumulation of CM-DiI was observed when the MDA-MB-468 cells were incubated with the targeted micelles. In addition, the results included in Figure 4 also demonstrate that preincubation of the cells with free EGF decreased the uptake of the targeted micelles due to competitive binding. These results suggest that the targeted micelles with EGF conjugated to the surface are selectively internalized into the EGFR-overexpressing MDA-MB-468 cells. Figure 5c includes an overlay of the confocal (Figure 5a) and transmitted light images (Figure 5b) and reveals that the CM-DiI fluorescence is concentrated around the nucleus with lower intensity fluorescence distributed throughout the cytoplasm. Furthermore, as shown in Figures 5a and 5c, there seems to be a small degree of nuclear localization of CM-DiI in the cells.

Localization of Targeted Micelles (+ EGF). Cytoplasmic (i.e. with fluorescein phalloidin) and nuclear staining (i.e. with Hoechst 33258) were performed in order to further investigate

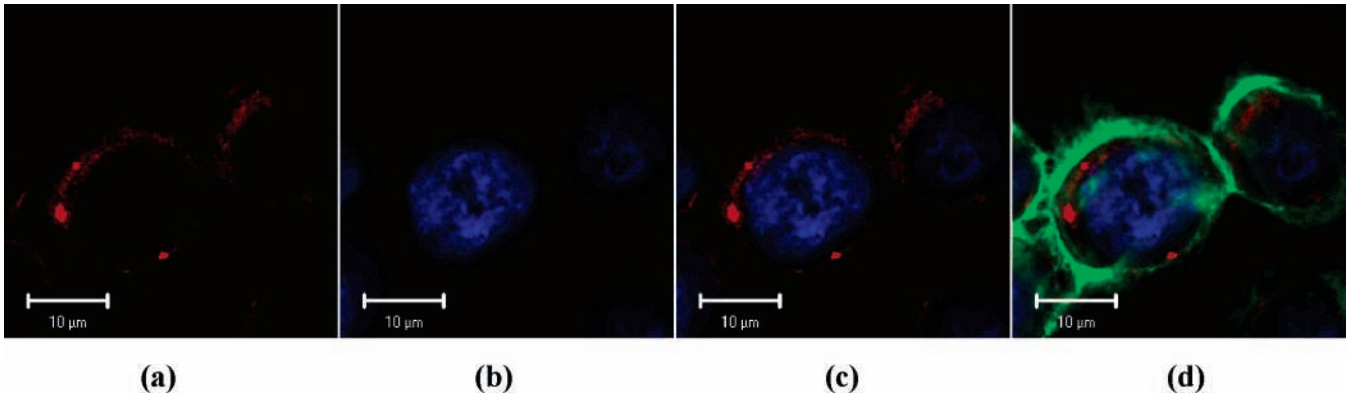

Figure 6. Confocal microscopy images of EGF-conjugated (targeted) micelles (red signal) in two representative cells. The cells were permeabilized with Triton X-100 and stained with both fluorescein phalloidin (green signal) and Hoechst 33258 (blue signal). (a) Visualized using the fluorescence channel for CM-DiI (targeted micelles). (b) Visualized using the fluorescence channel for Hoechst 33258 (i.e. nuclear stain). (c) A superimposition of panels a and b. (d) Same as panel c with additional superimposition of the image obtained using the fluorescence channel for fluorescein phalloidin (i.e. cytoplasmic stain).

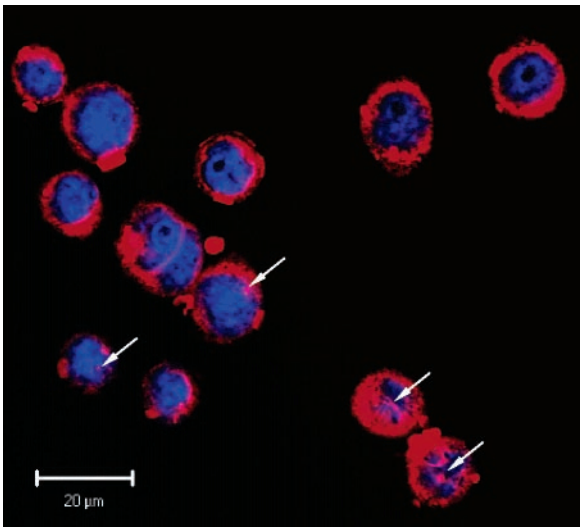

Figure 7. Confocal microscopy images of EGF-conjugated (targeted) micelles (red signal). The cells were nuclear stained (blue signal) with Hoechst 33258 without cell membrane permeabilization with Triton X-100. The white arrows indicate colocalization of the targeted micelles in the nucleus.

whether the EGFR-targeted micelles were indeed localizing at the nucleus. Figure 6 includes a series of images of two representative cells that had been incubated with EGFR-targeted micelles for 2 h prior to cytoplasmic (green signal in Figure 6d) and nuclear staining (blue signal in Figure 6b−d). Figure 6c provides a clear indication that the CM-DiI is mainly distributed in the perinuclear region. However, the CM-DiI intensity was much lower than that obtained in Figure 5a although the microscope settings were held constant. It was therefore hypothesized that some of the CM-DiI was washed away due to the addition of Triton X-100 which had been used to permeabilize the cell membrane. Permeabilization of the cell membrane is necessary for cytoplasmic staining with fluorescein phalloidin.

To confirm that the decrease in fluorescence intensity that was observed in Figure 6 could be attributed to membrane permeabilization during sample preparation, the cells were fixed and stained with Hoechst 33258 without incubating with Triton X-100. As illustrated in Figure 7, the intracellular signal for CM-DiI in cells that had not been incubated with Triton X-100 was much more intense than that in Figure 6 and similar to that in Figure 5a (i.e. cells not incubated with Triton X-100). Furthermore, once again the CM-DiI was found to be localized mostly in the perinuclear region with a small amount scattered throughout the cytoplasm. Also, some nuclear localization of CM-DiI was detected as indicated with white arrows in Figure 7.

Cell Proliferation Studies. EGF is an endogenous molecule that stimulates growth of cells (*46*, *47*). As a targeting moiety for drug carriers to treat EGFR-overexpressed cancers, EGF must not stimulate growth of tumor cells. The viability of MDA-MB-468 cells following treatment with free EGF, nontargeted micelles (MePEG-*b*-PVL) and targeted micelles (EGF-PEG-*b*-PVL) was found to be 55 ± 7%, 81 ± 7%, and 56 ± 6%, respectively. Therefore, the EGF-conjugated copolymers exert similar cell growth inhibition as that of free EGF at the same EGF concentration. This agrees with the results reported by Chen et al. which demonstrated that EGF inhibits cell growth at high concentrations (IC50 ∼ 500 pM in MDA-MB-468 cells) (*48*).

DISCUSSION

EGF, also known as urogastrone, is one of the proteins in the EGF family that exhibits binding affinity toward the EGF family of cell surface tyrosine kinase receptors (*36*). EGF is a 53-amino acid peptide with a molecular weight of 6 kDa and is generated by proteolytic cleavage of precursor proteins such as Neu and tissue plasminogen activator (*49*). Like other proteins, the binding affinity of EGF to its receptor is extremely sensitive to its conformation (*49*). To preserve the conformation of EGF, which is necessary for active targeting, the EGF-copolymer coupling reaction was carried out in the absence of any organic solvents.

The block copolymerization of VL was conducted following a reported procedure using MePEG as the macroinitiator and HCl as the catalyst in dichloromethane (*41*). The HOOC-PEG-*b*-PVL copolymer was then synthesized which allows the carboxyl terminus to serve as the EGF-conjugation site. To our knowledge, there has been no previous report of the synthesis of HOOC-PEG-*b*-PVL. To allow for coupling of EGF to the carboxyl terminus of HOOC-PEG-*b*-PVL, the copolymers were activated with NHS. The NHS-PEG-*b*-PVL copolymer was conjugated via an amide bond to the N-terminal end of EGF. This amide linkage is similar to that used by Lee et al. for conjugation of PEG to EGF and was found to be stable in the circulation in vivo (*42*). Many other studies have also reported on the conjugation of ligands, such as folate and transferrin, to PEG through an amide bond (*50*−*52*). The N-terminal conjugation site on EGF is located at a distance from the amino acid residues that are known to be responsible for binding to EGFR. Previous studies had demonstrated that the binding affinity of EGF for EGFR is not affected by conjugation of molecules to

this specific site on the peptide (*42*, *53*). The efficiency for coupling EGF to the PEG-*b*-PVL copolymer was found to be approximately 60%. This value appears reasonable when compared to that reported by other groups for the coupling of moieties to materials. For example, Kullberg et al. reported that the efficiency for conjugating EGF to maleimide-PEG-DSPE was 30% (*10*). Also recently, Mamot et al. reported that the efficiency for coupling C225-Fab′ to Mal-PEG-DSPE was 30−50% and that for coupling scFv C10 to Mal-PEG-DSPE was 50−80% (*8*).

The CMC of the copolymer was measured in order to evaluate the thermodynamic stability of the MePEG-*b*-PVL micelles. The CMC for the MePEG-*b*-PVL (i.e. 2000-*b*-2020) copolymer was found to be 23.3 mg/L which is slightly higher than that reported for a MePEG-*b*-poly(ϵ-caprolactone) copolymer of similar molecular weight (*54*). The lower CMC for the PCL-based copolymer is due to the more hydrophobic nature of poly(ϵ-caprolactone) when compared to PVL (*20*). Nevertheless, the CMC value obtained for MePEG-*b*-PVL is well below the typical range of concentrations of copolymer that would be anticipated following intraveneous administration of a drug formulated in block copolymer micelles (*30*). In this way, the MePEG-*b*-PVL micelles would be expected to be thermodynamically stable as drug carriers in vivo (*54*).

As mentioned previously, to achieve effective active targeting with EGF-conjugated micelles, the denaturation of the protein has to be avoided in order to preserve the conformation of the EGF binding domain. Therefore, the transfer method was employed to prepare the targeted CM-DiI-loaded micelles. For this method, the EGF-conjugated copolymers were added to the preformed MePEG-*b*-PVL micelles containing CM-DiI and allowed to incubate in order for the EGF-conjugated copolymer to become incorporated into the micelles. The transfer method has been established and commonly used in the preparation of other targeted delivery systems such as liposomes (*6*, *8*, *10*, *40*). For example, Kullberg et al. found that the optimal conditions for the insertion of EGF-conjugated lipids into preformed liposomes (i.e. DSPC/Chol/DSPE-PEG 60/35/5 mol %) is a 1-h incubuation at 60 °C. In their studies, it was also demonstrated that a 24-h incubation of EGF at 60 °C does not result in a significant loss in biological activity for the peptide and only causes a slight decrease in the EGF-substrate binding affinity (*10*). The incubation at an elevated temperature was required in order to increase the fluidity of the lipid bilayer as a means to promote lipid exchange and insertion. The MePEG-*b*-PVL copolymers employed in this study have a melting temperature (T_m) of approximately 46 °C as revealed by differential scanning calorimetry analysis (data not shown). Therefore, the EGF-PEG-*b*-PVL copolymers and the preformed micelles were incubated at a temperature above the T_m of the copolymer (i.e. 60 °C) in order to increase the fluidity of the micelle and maximize the efficiency of copolymer insertion. To ensure complete transfer of the conjugated copolymer, the micelle solution was left to equilibrate with constant stirring overnight at room temperature. It was estimated that once the micelle solution had come to equilibrium each micelle would include approximately five EGF molecules on its surface, assuming that the micelle has an aggregation number (i.e. number of copolymer molecules per micelle) of 250.

The incorporation of EGF-PEG-*b*-PVL copolymers into the MePEG-*b*-PVL micelles was further confirmed by the sizing results. DLS measurements indicated that the targeted micelles with EGF molecules at the surface have a slightly larger effective mean diameter (i.e. $D = 45$ nm) than the nontargeted micelles (i.e. $D = 32$ nm). Knowing that the molecular weight of EGF is approximately 6 kDa, it may be estimated that EGF has a hydrodynamic diameter of approximately 4 nm according to the Stokes−Einstein equation (*53*). Therefore, if it is assumed that the EGF molecules are equally distributed on the surface of the micelles, then the presence of EGF would be predicted to increase the size of the MePEG-*b*-PVL micelles by approximately 8 nm. In this way, the diameter of the targeted micelles would be expected to be 40 nm; which is in rough agreement with the measured value for the size of the micelles (i.e. $D = 45$ nm). Moreover, the in vitro studies in the EGFR-overexpressing cells, MDA-MB-468, clearly demonstrate an increase in cellular internalization of the targeted micelles, in comparison to the nontargeted micelles, which also confirms the successful transfer of the EGF-conjugated copolymer to the micelles. Although the insertion of the EGF-conjugated copolymer increased the effective diameter of the micelles by 13 nm, the diameter of the particles is still in the appropriate size range for consideration for in vivo applications. Particles with diameters of 200 nm or more are known to be cleared rapidly by the cells of the reticuloendothelial system and extravasation of particles of this size into tumor vasculature has been shown to be impeded (*4*, *55*).

The CM-DiI-loaded nontargeted and targeted micelles were found to have a slightly negative surface charge with zeta potentials of −8.7 and −13.5 mV, respectively. Comparison of the zeta potentials for the blank nontargeted micelles (i.e. −6.5 mV) and the CM-DiI-loaded nontargeted micelles (i.e. −8.7 mV) revealed that the incorporation of the fluorescent probe had a negligible effect on micelle surface charge. The slightly more negative surface charge for the targeted micelles may be due to the presence of negatively charged carboxyl end groups on PEG-*b*-PVL copolymers that did not react with EGF. This slight difference between the surface charge for the nontargeted and targeted micelles is unlikely to give rise to any significant difference between the potential for the nontargeted and targeted micelles to engage in cell interactions or undergo cellular uptake. Indeed, the negative surface charge for the micelles may result in electrostatic repulsions between the micelles and cells owing to the net negative charge of the cell surface (*56*, *57*).

The in vitro release of the fluorescent probe, CM-DiI, from the micelles was evaluated in order to confirm that it could be effectively used to follow the in vitro fate of the micelles over the 2-h incubation period. As shown in Figure 3, the in vitro release profile for the probe from the micelles is biphasic with a burst release phase for the first 8 h of the incubation period followed by a sustained release phase over the remainder of the 24 h period. The burst release phase of the profile may be attributed to the pool of drug that resides at the core−shell interface, as well as possible protein−probe interaction (release medium contains 10% FBS), while the drug that is solubilized in the hydrophobic core results in the sustained release phase. A similar biphasic profile was also obtained for the release of CM-DiI from PCL-*b*-PEO micelles as reported by Lim Soo et al. (*58*). Importantly, only 20% of the total probe loaded into the micelles is released over the initial 2-h incubation period (i.e. the period employed for the cell uptake studies). In this way, it is shown that the majority of the probe remains within the MePEG-*b*-PVL micelles over the incubation period employed for the in vitro cell studies. Figure 5d includes a confocal image of cells incubated with the nontargeted micelles, and as shown there is no measurable intracellular fluorescence. In this way, the free CM-DiI (i.e. fraction released from the nontargeted micelles) does not result in a detectable fluorescence signal within the cells. This has also been confirmed by quantification of the level of CM-DiI fluorescence in cells following incubation with this particular concentration of free CM-DiI (i.e. equivalent to the anticipated fraction released from the micelles within 2 h). The cells incubated with this concentration of CM-DiI were

found to have less fluorescence than cells incubated with the nontargeted micelles (Figure 4). Furthermore, the decrease in the extent of uptake of the EGF-conjugated micelles in the presence of excess free EGF suggests that the internalization of the targeted micelles was mediated via the EGF receptors. Therefore, the stronger fluorescence for CM-DiI that is observed in Figures 5a, 6, and 7 may be attributed to the specific cell uptake of the targeted micelles via EGF receptor−ligand-mediated internalization.

It has been reported that upon binding of EGF to the binding domain of cell surface EGFR, dimerization and clustering of the EGF-EGFR complex occurs rapidly at the cell surface. The EGF-EGFR complexes are then reported to be internalized into the cell (*59*, *60*). This receptor−ligand-mediated internalization has been shown to effectively allow for delivery of radiopharmaceuticals and liposome encapsulated agents into EGFR-overexpressing cells (*6*, *38*). Furthermore, Mamot et al. have developed liposomes conjugated with the monoclonal antibody fragment C225 for active targeting to EGFR-overexpressing MDA-MB-468 cells. The cell uptake profile obtained by Mamot et al. was similar to that obtained in these studies in that no cell uptake was observed for the nontargeted liposomes following a 2-h incubation with the MDA-MB-468 cells, while significant cytoplasmic accumulation of the C255-immunoliposomes was observed following the same incubation period (*8*). Several other studies have obtained similar cell uptake profiles for targeted and nontargeted delivery systems as reported elsewhere (*4*, *17*, *42*, *61*).

A few groups have demonstrated that the cell surface EGFR is able to translocate into the nucleus via a specific endocytotic pathway following stimulation of the cells with EGF (*38*, *62*, *63*). Torrisi et al. demonstrated that following saturated EGF binding, the cell surface EGFR redistributed into the cytoplasm and then the perinuclear region following 10 and 30 min incubation at 37 °C, respectively (*63*). A similar distribution for the fluorescence, which is attributed to the targeted micelles containing CM-DiI, is observed in Figures 6 and 7 where the signal is mostly localized in the perinuclear region following the 2-h incubation period. This observation further supports that the targeted micelles are internalized through a specific endocytotic pathway that is mediated by the binding of the EGF-conjugated micelles to cell surface EGFR on the MDA-MB-468 cells. Also, Wang et al. demonstrated that 16% of the ^{111}In-DTPA-HAS-hEGF radiopharmaceutical incubated with MDA-MB-468 cells was imported into the nucleus as measured by subcellular fractionation studies (*38*). In the present study, a small portion of the targeted micelles containing CM-DiI was also observed in the nucleus of the cells as shown in Figures 5c and 7. The nuclear localization of EGFR may be of particular significance when delivery is required for therapeutic agents whose site of action is intranuclear. Therefore, the EGFR-targeted delivery system developed in this study may not only serve to increase the overall intracellular accumulation of an encapsulated agent but may also facilitate the delivery of agents to the perinuclear or nuclear regions of the cell.

CONCLUSION

The carboxyl-terminated diblock copolymer of PEG-*b*-PVL was synthesized using a metal-free cationic polymerization method. EGF was then successfully conjugated to the PEG-*b*-PVL copolymer as a targeting moiety for the nanosized micelles. Targeted micelles prepared from the EGF-conjugated PEG-*b*-PVL copolymers were found to be internalized by the EGFR-overexpressing MDA-MB-468 breast cancer cells via receptor−ligand mediated endocytosis. By contrast there was no intracellular accumulation of the nontargeted MePEG-*b*-PVL micelles (− EGF) into cells over the period of time examined. Interestingly, the EGF-conjugated copolymer micelles were found to localize in the perinuclear region as well as the nucleus. These results suggest that the EGF-conjugated copolymer micelles developed in this study may serve as vehicles for targeting hydrophobic anticancer agents to EGFR-overexpressing cells.

ACKNOWLEDGMENT

C. Allen is grateful to Rx&D and Canadian Institutes of Health Research (CIHR) for a career award. The authors would also like to thank Dr. R. M. Reilly for kindly donating the MDA-MB-468 breast cancer cells, Dr. J. P. Uetrecht for use of the fluorescence microplate reader, Dr. Y. L. Cheng for use of the Particle Size Analyzer, and Mike Dunne for experimental assistance.

LITERATURE CITED

(1) Vega, J., Ke, S., Fan, Z., Wallace, S., Charsangavej, C., and Li, C. (2003) Targeting doxorubicin to epidermal growth factor receptors by site-specific conjugation of C225 to poly(L-glutamic acid) through a polyethylene glycol spacer. *Pharm. Res. 20*, 826−832.

(2) Park, J. W., Hong, K., Kirpotin, D. B., Colbern, G., Shalaby, R., Baselga, J., Shao, Y., Nielsen, U. B., Marks, J. D., Moore, D., Papahadjopoulos, D., and Benz, C. C. (2002) Anti-HER2 immunoliposomes: enhanced efficacy attributable to targeted delivery. *Clin. Cancer Res. 8*, 1172−1181.

(3) Yoo, H. S., and Park, T. G. (2004) Folate receptor targeted biodegradable polymeric doxorubicin micelles. *J. Controlled Release 96*, 273−283.

(4) Torchilin, V. P., Lukyanov, A. N., Gao, Z. G., and Papahadjopoulos-Sternberg, B. (2003) Immunomicelles: Targeted pharmaceutical carriers for poorly soluble drugs. *Proc. Natl. Acad. Sci. U.S.A. 100*, 6039−6044.

(5) Hosokawa, S., Tagawa, T., Niki, H., Hirakawa, Y., Nohga, K., and Nagaike, K. (2003) Efficacy of immunoliposomes on cancer models in a cell-surface-antigen-density-dependent manner. *Br. J. Cancer 89*, 1545−1551.

(6) Kullberg, E. B., Nestor, M., and Gedda, L. (2003) Tumor-cell targeted epidermal growth factor liposomes loaded with boronated acridine: Uptake and processing. *Pharm. Res. 20*, 229−236.

(7) Hamaguchi, T., Matsumura, Y., Nakanishi, Y., Muro, K., Yamada, Y., Shimada, Y., Shirao, K., Niki, H., Hosokawa, S., Tagawa, T., and Kakizoe, T. (2004) Antitumor effect of MCC-465, pegylated liposomal doxorubicin tagged with newly developed monoclonal antibody GAH, in colorectal cancer xenografts. *Cancer Sci. 95*, 608−613.

(8) Mamot, C., Drummond, D. C., Greiser, U., Hong, K., Kirpotin, D. B., Marks, J. D., and Park, J. W. (2003) Epidermal growth factor receptor (EGFR)-targeted immunoliposomes mediate specific and efficient drug delivery to EGFR- and EGFRvIII-overexpressing tumor cells. *Cancer Res. 63*, 3154−3161.

(9) Ishida, T., Kirchmeier, M. J., Moase, E. H., Zalipsky, S., and Allen, T. M. (2001) Targeted delivery and triggered release of liposomal doxorubicin enhances cytotoxicity against human B lymphoma cells. *Biochim. Biophys. Acta 1515*, 144−158.

(10) Kullberg, E. B., Bergstrand, N., Carlsson, J., Edwards, K., Johnsson, M., Sjoberg, S., and Gedda, L. (2002) Development of EGF-conjugated liposomes for targeted delivery of boronated DNA-binding agents. *Bioconjugate Chem. 13*, 737−743.

(11) Carlsson, J., Kullberg, E. B., Capala, J., Sjoberg, S., Edwards, K., and Gedda, L. (2003) Ligand liposomes and boron neutron capture therapy. *J. Neuro-Oncol. 62*, 47−59.

(12) Marcucci, F., and Lefoulon, F. (2004) Active targeting with particulate drug carriers in tumor therapy: fundamentals and recent progress. *Drug Discovery Today 9*, 219−228.

(13) Drummond, D. C., Meyer, O., Hong, K. L., Kirpotin, D. B., and Papahadjopoulos, D. (1999) Optimizing liposomes for delivery of chemotherapeutic agents to solid tumors. *Pharmacol. Rev. 51*, 691−743.

(14) Potineni, A., Lynn, D. M., Langer, R., and Amiji, M. M. (2003) Poly(ethylene oxide)-modified poly(beta-amino ester) nanoparticles

as a pH-sensitive biodegradable system for paclitaxel delivery. *J. Controlled Release 86*, 223−234.
(15) Williams, J., Lansdown, R., Sweitzer, R., Romanowski, M., LaBell, R., Ramaswami, R., and Unger, E. (2003) Nanoparticle drug delivery system for intravenous delivery of topoisomerase inhibitors. *J. Controlled Release 91*, 167−172.
(16) Torchilin, V. P. (2004) Targeted polymeric micelles for delivery of poorly soluble drugs. *Cell. Mol. Life Sci. 61*, 2549−2559.
(17) Torchilin, V. P. (2005) Fluorescence microscopy to follow the targeting of liposomes and micelles to cells and their intracellular fate. *Adv. Drug Delivery Rev. 57*, 95−109.
(18) Liggins, R. T., and Burt, H. M. (2002) Polyether-polyester diblock copolymers for the preparation of paclitaxel loaded polymeric micelle formulations. *Adv. Drug Delivery Rev. 54*, 191−202.
(19) Yokoyama, M., Opanasopit, P., Okano, T., Kawano, K., and Maitani, Y. (2004) Polymer design and incorporation methods for polymeric micelle carrier system containing water-insoluble anticancer agent camptothecin. *J. Drug Target. 12*, 373−384.
(20) Allen, C., Yu, Y., Maysinger, D., and Eisenberg, A. (1998) Polycaprolactone-*b*-poly(ethylene Oxide) Block Copolymer Micelles as a Novel Drug Delivery Vehicle for Neurotrophic Agents FK506 and L-685,818. *Bioconjugate Chem. 9*, 564−572.
(21) Burt, H. M., Zhang, X. C., Toleikis, P., Embree, L., and Hunter, W. L. (1999) Development of copolymers of poly(D,L-lactide) and methoxypoly(ethylene glycol) as micellar carriers of paclitaxel. *Colloid Surface B 16*, 161−171.
(22) Allen, C., Han, J. N., Yu, Y. S., Maysinger, D., and Eisenberg, A. (2000) Polycaprolactone-*b*-poly(ethylene oxide) copolymer micelles as a delivery vehicle for dihydrotestosterone. *J. Controlled Release 63*, 275−286.
(23) Kataoka, K., Matsumoto, T., Yokoyama, M., Okano, T., Sakurai, Y., Fukushima, S., Okamoto, K., and Kwon, G. S. (2000) Doxorubicin-loaded poly(ethylene glycol)-poly(beta-benzyl-l-aspartate) copolymer micelles: their pharmaceutical characteristics and biological significance. *J. Controlled Release 64*, 143−153.
(24) Kwon, G. S., and Kataoka, K. (1995) Block-Copolymer Micelles as Long-Circulating Drug Vehicles. *Adv. Drug Delivery Rev. 16*, 295−309.
(25) Yokoyama, M., Miyauchi, M., Yamada, N., Okano, T., Sakurai, Y., Kataoka, K., and Inoue, S. (1990) Polymer Micelles as Novel Drug Carrier − Adriamycin-Conjugated Poly(Ethylene Glycol) Poly(Aspartic Acid) Block Copolymer. *J. Controlled Release 11*, 269−278.
(26) La, S. B., Okano, T., and Kataoka, K. (1996) Preparation and Characterization of the Micelle-Forming Polymeric Drug Indomethacin-Incorporated Poly(ethylene oxide)-Poly(b-benzyl L-aspartate) Block Copolymer Micelles. *J. Pharm. Sci. 85*, 85−90.
(27) Kabanov, A. V., Batrakova, E. V., and Alakhov, V. Y. (2002) Pluronic (R) block copolymers as novel polymer therapeutics for drug and gene delivery. *J. Controlled Release 82*, 189−212.
(28) Oh, K. T., Bronich, T. K., and Kabanov, A. V. (2004) Micellar formulations for drug delivery based on mixtures of hydrophobic and hydrophilic Pluronic((R)) block copolymers. *J. Controlled Release 94*, 411−422.
(29) Batrakova, E. V., Li, S., Miller, D. W., and Kabanov, A. V. (1999) Pluronic P85 increases permeability of a broad spectrum of drugs in polarized BBMEC and Caco-2 cell monolayers. *Pharm. Res. 16*, 1366−1372.
(30) Kim, T. Y., Kim, D. W., Chung, J. Y., Shin, S. G., Kim, S. C., Heo, D. S., Kim, N. K., and Bang, Y. J. (2004) Phase I and pharmacokinetic study of Genexol-PM, a cremophor-free, polymeric micelle-formulated paclitaxel, in patients with advanced malignancies. *Clin. Cancer Res. 10*, 3708−3716.
(31) Matsumura, Y., Hamaguchi, T., Ura, T., Muro, K., Yamada, Y., Shimada, Y., Shirao, K., Okusaka, T., Ueno, H., Ikeda, M., and Watanabe, N. (2004) Phase I clinical trial and pharmacokinetic evaluation of NK911, a micelle-encapsulated doxorubicin. *Br. J. Cancer 91*, 1775−1781.
(32) Alakhov, V., Klinski, E., Li, S. M., Pietrzynski, G., Venne, A., Batrakova, E., Bronitch, T., and Kabanov, A. (1999) Block copolymer-based formulation of doxorubicin. From cell screen to clinical trials. *Colloid Surface B 16*, 113−134.
(33) Kabanov, A. V., and Batrakova, E. V. (2004) New technologies for drug delivery across the blood brain barrier. *Curr. Pharm. Des. 10*, 1355−1363.
(34) Kabanov, A. V., Batrakova, E. V., Meliknubarov, N. S., Fedoseev, N. A., Dorodnich, T. Y., Alakhov, V. Y., Chekhonin, V. P., Nazarova, I. R., and Kabanov, V. A. (1992) A New Class of Drug Carriers − Micelles of Poly(Oxyethylene)-Poly(Oxypropylene) Block Copolymers as Microcontainers for Drug Targeting from Blood in Brain. *J. Controlled Release 22*, 141−157.
(35) Gao, Z., Lukyanov, A. N., Chakilam, A. R., and Torchilin, V. P. (2003) PEG-PE/phosphatidylcholine mixed immunomicelles specifically deliver encapsulated taxol to tumor cells of different origin and promote their efficient killing. *J. Drug Target. 11*, 87−92.
(36) Salomon, D. S., Brandt, R., Ciardiello, F., and Normanno, N. (1995) Epidermal growth factor-related peptides and their receptors in human malignancies. *Crit. Rev. Oncol. Hematol. 19*, 183−232.
(37) Mendelsohn, J., and Baselga, J. (2000) The EGF receptor family as targets for cancer therapy. *Oncogene 19*, 6550−6565.
(38) Wang, J., Chen, P., Su, Z. F., Vallis, K., Sandhu, J., Cameron, R., Hendler, A., and Reilly, R. M. (2001) Amplified delivery of indium-111 to EGFR-positive human breast cancer cells. *Nucl. Med. Biol. 28*, 895−902.
(39) Chen, P., Cameron, R., Wang, J., Vallis, K. A., and Reilly, R. M. (2003) Antitumor effects and normal tissue toxicity of In-111-labeled epidermal growth factor administered to athymic mice bearing epidermal growth factor receptor-positive human breast cancer xenografts. *J. Nucl. Med. 44*, 1469−1478.
(40) Kullberg, E. B., Carlsson, J., Edwards, K., Capala, J., Sjoberg, S., and Gedda, L. (2003) Introductory experiments on ligand liposomes as delivery agents for boron neutron capture therapy. *Int. J. Oncol. 23*, 461−467.
(41) Lou, X. D., Detrembleur, C., and Jerome, R. (2002) Living cationic polymerization of delta-valerolactone and synthesis of high molecular weight homopolymer and asymmetric telechelic and block copolymer. *Macromolecules 35*, 1190−1195.
(42) Lee, H., Jang, I. H., Ryu, S. H., and Park, T. G. (2003) N-terminal site-specific mono-PEGylation of epidermal growth factor. *Pharm. Res. 20*, 818−825.
(43) Zhang, X. C., Jackson, J. K., and Burt, H. M. (1996) Determination of surfactant critical micelle concentration by a novel fluorescence depolarization technique. *J. Biochem. Biophys. Methods 31*, 145−150.
(44) Liu, J. B., Xiao, Y. H., and Allen, C. (2004) Polymer-drug compatibility: A guide to the development of delivery systems for the anticancer agent, Ellipticine. *J. Pharm. Sci. 93*, 132−143.
(45) Lee, H., Zeng, F., Dunne, M., and Allen, C. (2005) Methoxy poly(ethylene glycol)-*block*-poly(delta-valerolactone) copolymer micelles for formulation of hydrophobic drugs. *Biomacromolecules 6*, 3119−3128.
(46) Schaerli, P., and Jaggi, R. (1998) EGF-induced programmed cell death of human mammary carcinoma MDA-MB-468 cells is preceded by activation of AP-1. *Cell. Mol. Life Sci. 54*, 129−138.
(47) Kawamoto, T., Mendelsohn, J., Le, A., Sato, G. H., Lazar, C. S., and Gill, G. N. (1984) Relation of Epidermal Growth-Factor Receptor Concentration to Growth of Human Epidermoid Carcinoma A431 Cells. *J. Biol. Chem. 259*, 7761−7766.
(48) Chen, P., Mrkobrada, M., Vallis, K. A., Cameron, R., Sandhu, J., Hendler, A., and Reilly, R. M. (2002) Comparative antiproliferative effects of (111)In-DTPA-hEGF, chemotherapeutic agents and gamma-radiation on EGFR-positive breast cancer cells. *Nucl. Med. Biol. 29*, 693−699.
(49) Lodish, H. F. (2000) *Molecular cell biology*, 4th ed., Freeman, New York, NY.
(50) Nobs, L., Buchegger, F., Gurny, R., and Allemann, E. (2004) Current methods for attaching targeting ligands to liposomes and nanoparticles. *J. Pharm. Sci. 93*, 1980−1992.
(51) Stella, B., Arpicco, S., Peracchia, M. T., Desmaele, D., Hoebeke, J., Renoir, M., D'Angelo, J., Cattel, L., and Couvreur, P. (2000) Design of folic acid-conjugated nanoparticles for drug targeting. *J. Pharm. Sci. 89*, 1452−1464.
(52) Torchilin, V. P. (2005) Recent advances with liposomes as pharmaceutical carriers. *Nat. Rev. Drug Discovery 4*, 145−160.
(53) Thorne, R. G., Hrabetova, S., and Nicholson, C. (2004) Diffusion of epidermal growth factor in rat brain extracellular space measured by integrative optical imaging. *J. Neurophysiol. 92*, 3471−3481.
(54) Allen, C., Maysinger, D., and Eisenberg, A. (1999) Nano-engineering block copolymer aggregates for drug delivery. *Colloid Surface B 16*, 3−27.

(55) Moghimi, S. M., Hunter, A. C., and Murray, J. C. (2001) Long-circulating and target-specific nanoparticles: Theory to practice. *Pharmacol. Rev. 53*, 283−318.
(56) Liang, H. F., Yang, T. F., Huang, C. T., Chen, M. C., and Sung, H. W. (2005) Preparation of nanoparticles composed of poly(gamma-glutamic acid)-poly(lactide) block copolymers and evaluation of their uptake by HepG2 cells. *J. Controlled Release 105*, 213−225.
(57) Li, C. (2002) Poly(L-glutamic acid) − anticancer drug conjugates. *Adv. Drug Delivery Rev. 54*, 695−713.
(58) Lim Soo, P., Luo, L., Maysinger, D., and Eisenberg, A. (2002) Incorporation and Release of Hydrophobic Probes in Biocompatible Polycaprolactone-*block*-poly(ethylene oxide) Micelles: Implications for Drug Delivery. *Langmuir 18*, 9996−10004.
(59) Wang, Z. X., Zhang, L. F., Yeung, T. K., and Chen, X. M. (1999) Endocytosis deficiency of epidermal growth factor (EGF) receptor-ErbB2 heterodimers in response to EGF stimulation. *Mol. Biol. Cell. 10*, 1621−1636.
(60) Wang, Y., Pennock, S., Chen, X. M., and Wang, Z. X. (2002) Endosomal signaling of epidermal growth factor receptor stimulates signal transduction pathways leading to cell survival. *Mol. Cell Biol. 22*, 7279−7290.
(61) Farokhzad, O. C., Jon, S. Y., Khadelmhosseini, A., Tran, T. N. T., LaVan, D. A., and Langer, R. (2004) Nanopartide-aptamer bioconjugates: A new approach for targeting prostate cancer cells. *Cancer Res. 64*, 7668−7672.
(62) Lin, S. Y., Makino, K., Xia, W. Y., Matin, A., Wen, Y., Kwong, K. Y., Bourguignon, L., and Hung, M. C. (2001) Nuclear localization of EGF receptor and its potential new role as a transcription factor. *Nat. Cell Biol. 3*, 802−808.
(63) Torrisi, M. R., Lotti, L. V., Belleudi, F., Gradini, R., Salcini, A. E., Confalonieri, S., Pelicci, P. G., and Di Fiore, P. P. (1999) Eps15 is recruited to the plasma membrane upon epidermal growth factor receptor activation and localizes to components of the endocytic pathway during receptor internalization. *Mol. Biol. Cell 10*, 417−434.

BC050350G

Characterization of a CC49-Based Single-Chain Fragment−β-Lactamase Fusion Protein for Antibody-Directed Enzyme Prodrug Therapy (ADEPT)

Ralph F. Alderson,[†] Brian E. Toki,[§] Martin Roberge,[†] Wei Geng,[†] Joshua Basler,[†] Regina Chin,[†] Amy Liu,[†] Roanna Ueda,[†] Douglas Hodges,[†] Enrique Escandon,[†] Tianling Chen,[†] Tessi Kanavarioti,[†] Lilia Babé,[†] Peter D. Senter,[§] Judith A. Fox,[†] and Volker Schellenberger*[,†]

Genencor International, a Danisco company, 925 Page Mill Road, Palo Alto, California 94304, and Seattle Genetics, Inc., 21823 30th Dr. S. E., Bothell, Washington 98021. Received December 12, 2005; Revised Manuscript Received February 7, 2006

CC49 is a clinically validated antibody with specificity for TAG-72, a carbohydrate epitope that is overexpressed and exposed on the cell surface in a large fraction of solid malignancies. We constructed a single-chain fragment (scFv) based on CC49 and fused it to β-lactamase (BLA). Following optimization of the scFv domain by combinatorial consensus mutagenesis (CCM) for increased expression and stability, we characterized the protein variant for binding, in vivo pharmacokinetics (PK), and antitumor efficacy. The fusion protein TAB2.5 possessed a similar binding specificity relative to the parent antibody CC49. TAB2.5 also showed prolonged retention ($T_{1/2}$ = 36.9 h) in tumor-bearing mice with tumor/plasma ratios of up to 1000. Preliminary evaluation of TAB2.5, in combination with a novel prodrug, GC-Mel, resulted in significant efficacy in a colorectal xenograft tumor model and supports the utility of the protein as an agent for tumor-selective prodrug activation.

INTRODUCTION

Most chemotherapeutic drugs act against rapidly proliferating cells, which gives them limited selectivity for tumor tissues. Consequently, the effectiveness of these drugs is limited by their narrow therapeutic indices. In contrast, antibodies directed against tumor-specific antigens can bind to tumor tissues with high selectivity, which makes them suitable tools for the tumor-targeted delivery of drugs or radionuclides (*1*−*3*). One antibody-based approach for drug delivery is the direct conjugation of active drug molecules to a tumor-specific antibody (*4*). To be effective, this approach requires that the conjugate reach the great majority of tumor cells. However, penetration of antibodies into solid tumor tissue can be hindered by diffusion, thus limiting the efficacy of antibody−drug conjugates in the treatment of solid malignancies. An alterative method of using antibodies for tumor drug delivery is antibody-directed tumor prodrug therapy (ADEPT) (*5*−*7*). ADEPT is a two-step approach to cancer therapy. The first step involves the administration of an antibody−enzyme conjugate or fusion protein that specifically binds to tumor tissue. Subsequently, a small molecule prodrug is injected that is enzymatically activated at the tumor site by the tumor-bound fusion protein. As a result, small amounts of fusion protein at the tumor site can liberate large quantities of drug that can then further diffuse through tumor tissue. The abilities to deliver large quantities of drug, to achieve deep tissue penetration and to attain very high tumor/plasma ratios of drug exposure make ADEPT a very attractive strategy for the treatment of solid malignancies.

Recently, we described the construction of a fusion protein between β-lactamase (BLA) and a single-chain fragment (scFv) based on antibody CC49 (*8*). The fusion protein was optimized for high-level soluble production in *Escherichia coli* and good protease stability using combinatorial consensus mutagenesis. The resulting fusion protein, TAB2.5, should combine the proven tumor specificity of antibody CC49 (*9*) with the high catalytic activity of β-lactamase (BLA). CC49 is a second-generation murine antibody with specificity for the carbohydrate epitope TAG-72 (*9*). This epitope is highly expressed in the majority of solid malignancies (*10*, *11*), while its expression in normal tissues is relatively low (*12*). CC49 has been tested in various formats in clinical studies where significant tumor binding was observed (*13*−*15*). Single-chain fragments based on CC49 have been described in the past but they showed a relatively low level of expression and a tendency to form aggregates (*16*−*18*). BLA is a very versatile enzyme in its use for ADEPT. It has been shown that BLA can activate prodrugs derived from a variety of common cancer drugs such as vinblastin (*19*), paclitaxel (*20*, *21*), doxorubicin (*22*), and melphalan (*23*). Recently, we described the construction of a BLA variant with reduced immunogenicity (*24*) that should further enhance the therapeutic utility of this enzyme.

This report demonstrates that the engineered fusion protein TAB2.5 has a specificity that closely mimics the specificity of its parent antibody CC49. TAB2.5 shows very good tumor retention in mice bearing LS174T human colorectal tumor cells. In addition, very high tumor/plasma ratios of BLA activities were observed. Furthermore, we describe the synthesis of a novel prodrug, GC-Mel, that has good solubility and releases melphalan after BLA cleavage. Initial evidence of efficacy of the fusion protein TAB2.5 in combination with GC-Mel is reported.

EXPERIMENTAL PROCEDURES

Synthesis of Glutaryl Cephalosporin Bis-diphenylmethyl Ester (4). NaOH (20%, 13 mL, 80 mmol, 2.2 equiv) was added to a suspension of 7-aminocephalosporanic acid (7-ACA) **3** in water (75 mL) giving a dark brown solution. The deacetylation was complete in 30 min as measured by HPLC (0.05% aqueous formic acid−MeCN gradient). Glutaric anhydride (4.7 g, 40 mmol, 1.1 equiv) was added all at once as a solid, and the contents were stirred for 1.5 h. The reaction was diluted with THF (250 mL) and adjusted to pH 4 with concentrated HCl. Freshly prepared diphenyldiazomethane (*25*) in THF was added via a pipet while being monitored by HPLC (5 mM aqueous

* Corresponding author. Mailing address: Amunix Inc., 1455 Adams Dr., #1120, Menlo Park, CA 94025. E-mail: vschellenberger@amunix.com. Phone: 650-575-1440.

[†] Genencor International.

[§] Seattle Genetics, Inc.

10.1021/bc0503521 CCC: $33.50 © 2006 American Chemical Society
Published on Web 02/23/2006

phosphate (pH 7)−MeCN gradient). More diphenyldiazomethane was added as the purple color faded from the reaction mixture. Loss of the starting material occurred after about 1−2 h. However, formation of the second diphenylmethyl (DPM) ester was somewhat sluggish. HCl (1 M) was added to maintain a pH of 4.0−4.5 in the reaction mixture. After 30 h, the reaction was transferred to a separatory funnel and extracted with EtOAc (1 × 800 mL, 1 × 250 mL). The combined organics were dried, filtered, and evaporated to form an oil with a white precipitate (benzophenone azine). Addition of EtOAc and cooling caused further precipitation. After filtration, the filtrate was concentrated, taken up in DMSO, and purified by reversed-phase HPLC (C_{18} column, water−MeCN gradient). The fractions were analyzed by TLC (100% EtOAc) or HPLC. All fractions containing the product were pooled and concentrated to a yellow solid that was stored at 0 °C. The overall yield for the product was 7.31 g (30%). R_f 0.45 (100% EtOAc); ES-MS *m*/*z* 699 $[M + Na]^+$; UV λ_{max} 220, 260 nm. ^{1}H NMR (DMSO-d_6) δ 8.88 (1 H, d, J = 8.0 Hz, 7-NH), 7.23−7.52 (20 H, m, Ar−H), 6.88 (1 H, s, benzhydryl-CH), 6.77 (1 H, s, benzhydryl-CH), 5.68 (1 H, dd, $J_{NH,7}$ = 8.0 Hz, $J_{6,7}$ = 4.4 Hz, H-7), 5.16 (1 H, bt, J = 5.2 Hz, OH), 5.10 (1 H, d, $J_{6,7}$ = 4.8 Hz, H-6), 4.15−4.23 (1 H, m, CH_2OH), 3.62 (1 H, d, $J_{A,B}$ = 18 Hz, H-2_A), 3.54 (1 H, d, $J_{A,B}$ = 18 Hz, H-2_B), 2.46 (2 H, t, J = 7.6 Hz, glutaryl-CH_2), 2.23 (2 H, t, J = 7.6 Hz, glutaryl-CH_2), 1.79 (2 H, p, J = 7.2 Hz, glutaryl-CH_2).

Synthesis of Activated Glutaryl Cephalosporin (5). The cephalosporin intermediate **4** (3.9 g, 5.76 mmol) was dissolved in methylene chloride (50 mL) followed by the sequential addition of 1,2,2,2-tetrachloroethylchloroformate (0.90 mL, 5.76 mmol) and pyridine (0.52 mL, 6.34 mmol, 1.1 equiv). Reaction was complete in 1 h as measured by HPLC. Following completion of the reaction, ice (100 g) and 1 M HCl (10 mL) were added, and the contents were stirred for 2 min. The mixture was transferred to a separatory funnel that contained 100 mL of CH_2Cl_2, and the layers were separated. The organic layer was further washed with water and brine. Drying of the organic phase with $MgSO_4$, followed by filtration and partial solvent removal in vacuo down to about 100 mL, led to the formation of a yellow solution that was used in the next step without further purification. R_f 0.72 (1:1 hexanes−EtOAc); UV λ_{max} 260 nm.

The above mixture was cooled to 0 °C and treated with excess MCPBA (1.81 g, 8.02 mmol, 1.4 equiv). Reaction was completed in 20 min as measured by HPLC. $NaHSO_3$ (10%, 15 mL) followed by 0.1 N $NaHCO_3$ (100 mL) was added, and the contents were transferred to a separatory funnel containing chloroform (ca. 50 mL). The aqueous layer was discarded, and the organic phase was further washed with 0.1 N $NaHCO_3$, water, and brine. The organic layer was dried and filtered, and the solvent was removed to give a tan foam. The product was used in the next step without further purification. Overall yield of the product was 4.75 g (91% overall). R_f 0.30 (1:1 hexanes−EtOAc); ES-MS *m*/*z* 923.00 $[M + Na]^+$; UV λ_{max} 260 nm. ^{1}H NMR ($CDCl_3$) δ 7.27−7.48 (20 H, m, Ar-H), 6.95 (1 H, s, benzhydryl-CH), 6.89 (1 H, s, benzhydryl-CH), 6.64 (1 H, s, CHCl), 6.60 (1 H, d, J = 10.0 Hz, 7-NH), 6.13 (1 H, dd, $J_{NH,7}$ = 10.0 Hz, $J_{6,7}$ = 4.8 Hz, H-7), 5.64 (1 H, dd, $J_{A,B}$ = 14 Hz, $J_{CH,A}$ = 5.6 Hz, H-2_A), 4.91 (1 H, dd, $J_{A,B}$ = 14 Hz, $J_{CH,A}$ = 5.6 Hz, H-2_B), 4.46−4.50 (1 H, m, H-6), 3.80 (1 H, d, $J_{A,B}$ = 18.8 Hz, $CH_{2A}OCOO$), 3.22 (1 H, d, $J_{A,B}$ = 19.6 Hz, CH_{2B}-OCOO), 2.52 (2 H, t, J = 7.6 Hz, glutaryl-CH_2), 2.31 (2 H, t, J = 6.8 Hz, glutaryl-CH_2), 2.02 (2 H, p, J = 7.2 Hz, glutaryl-CH_2).

Synthesis of Glutaryl C-Mel (1) (Figure 1A,B). A solution of melphalan (0.31 g, 0.97 mmol) in a mixture of 0.5 N $NaHCO_3$ (5.1 mL, 2.53 mmol, 2.6 equiv), water (5 mL), and THF (10 mL) was added to a solution of activated cephalosporin **5** in THF (25 mL). The solution was stirred at ambient temperature for 30 min, and the reaction was found to be complete by HPLC analysis. Ice (ca. 10 g) and 1 N HCl (5 mL) were added to this mixture, and it was extracted with EtOAc (2 × 30 mL). The combined organic phases were washed with brine and dried. Filtration, followed by solvent removal, led to the formation of a yellow film that was dissolved in CH_2Cl_2 (100 mL) and treated with anisole (5 mL) and TFA (5 mL) for 1 h. Concentration of the reaction led to a dark oil that was precipitated with ether (ca. 150 mL). The product was filtered to give a tan solid that was further purified by reverse-phase HPLC (C_{18} column, 0.1% aqueous TFA−MeCN gradient). The desired fractions were pooled, frozen, and lyophilized to give a fluffy off-white powder. A total of 0.36 g (54%) of product was obtained. ES-MS *m*/*z* 690.93 $[M + H]^+$; UV λ_{max} 260, 300 nm. ^{1}H NMR (DMSO-d_6) δ 8.22 (1 H, d, $J_{NH,7}$ = 8.0 Hz, mel-NH), 7.65 (1 H, d, J = 8.0 Hz, 7-NH), 7.06 (2 H, d, J = 8.8 Hz, mel-Ar−CH ×2), 6.63 (2 H, d, J = 8.8 Hz, mel-Ar−CH ×2), 5.75 (1 H, dd, $J_{NH,7}$ = 8.0 Hz, $J_{6,7}$ = 4.8 Hz, H-7), 5.04 (1 H, d, $J_{A,B}$ = 13.6 Hz, $CH_{2A}OCONH$), 4.81 (1 H, d, $J_{6,7}$ = 3.6 Hz, H-6), 4.54 (1 H, d, $J_{A,B}$ = 13.2 Hz, $CH_{2B}OCONH$), 3.99−4.07 (1 H, m, mel-CH), 3.30−3.75 (10 H, m, H-2_A, H-2_B, NCH_2CH_2Cl ×2), 2.85−2.92 (1 H, m, mel-CH_{2A}), 2.64−2.73 (1 H, m, mel-CH_{2B}), 2.17−2.32 (4 H, m, glutaryl-CH_2 ×2) 1.70 (2 H, p, J = 7.2 Hz, glutaryl-CH_2).

Production and purification of TAB2.5. The production and purification of TAB2.5 is described elsewhere. In brief, *E. coli* cells carrying the production plasmid were cultured for 48 h at 30 °C. Cells were harvested by centrifugation and lysed, and soluble TAB2.5 was purified by affinity chromatography on phenylboronic acid agarose (Sigma, St. Louis, MI). Monomeric TAB2.5 was isolated by size-exclusion chromatography on Superdex 75 (Amersham, Piscataway, NJ) as shown in Figure 2. Peaks were assigned by electrospray mass spectrometry. The purified protein retained its monomeric state even after several months of storage at 4 °C or at −80 °C. As an additional step, material used for in vivo studies was passed through a 10 mL detoxi-gel column (Pierce, Rockford, IL) for endotoxin removal to achieve less than 5 EU/mg protein endotoxin level.

In Vivo Tumor Model Efficacy Studies. Female athymic nude mice (Charles River, approximately 21 g body weight, 4−6 weeks of age) were allowed to acclimate to the Genencor animal facility for at least 4 days prior to treatment. All animal-related procedures were in compliance with the Animal Welfare Act Regulations (9CFR 3). The LS174T cell line was obtained from ATCC (Manassas, VA). The cells were maintained in RPMI 1640 (Mediatech, Herdon, VA) supplemented with 15% (v/v) fetal bovine serum (Hyclone, Logan, UT), 0.5% (v/v) penicillin (10 000 IU), and streptomycin sulfate (10 mg/mL) and incubated in a 5% CO_2/95% humidity atmosphere at 37 °C. The adherent cells were dissociated and passaged as per supplier's instructions. For tumor implantations, the cells were harvested in log phase, washed once with PBS, and resuspended in Ham's F12 culture media (Mediatech, Herdon, VA) at a density of 4 × 10^7 cells/mL. The tumor cells were injected subcutaneously in 100 μL of fluid consisting of 50 μL of Ham's F12 containing 2 × 10^6 cells and 50 μL of Matrigel (BD Biosciences, San Diego, CA). Every 3−4 days, body weights were recorded, and the tumors were measured on two axes with calipers. Tumor volumes were calculated according to the following formula: tumor volume = long axis × (short axis)^2 × 0.4. TAB2.5 was diluted in a sterile saline solution, where necessary, for injection. The prodrug was reconstituted in 8% PEG 400, 2% dimethyl acetamide, 5% captisol (Cydex, Lenexa, KS), and 0.1 M NaCl containing 2.75 equiv of Tris buffer to neutralize its acidic groups.

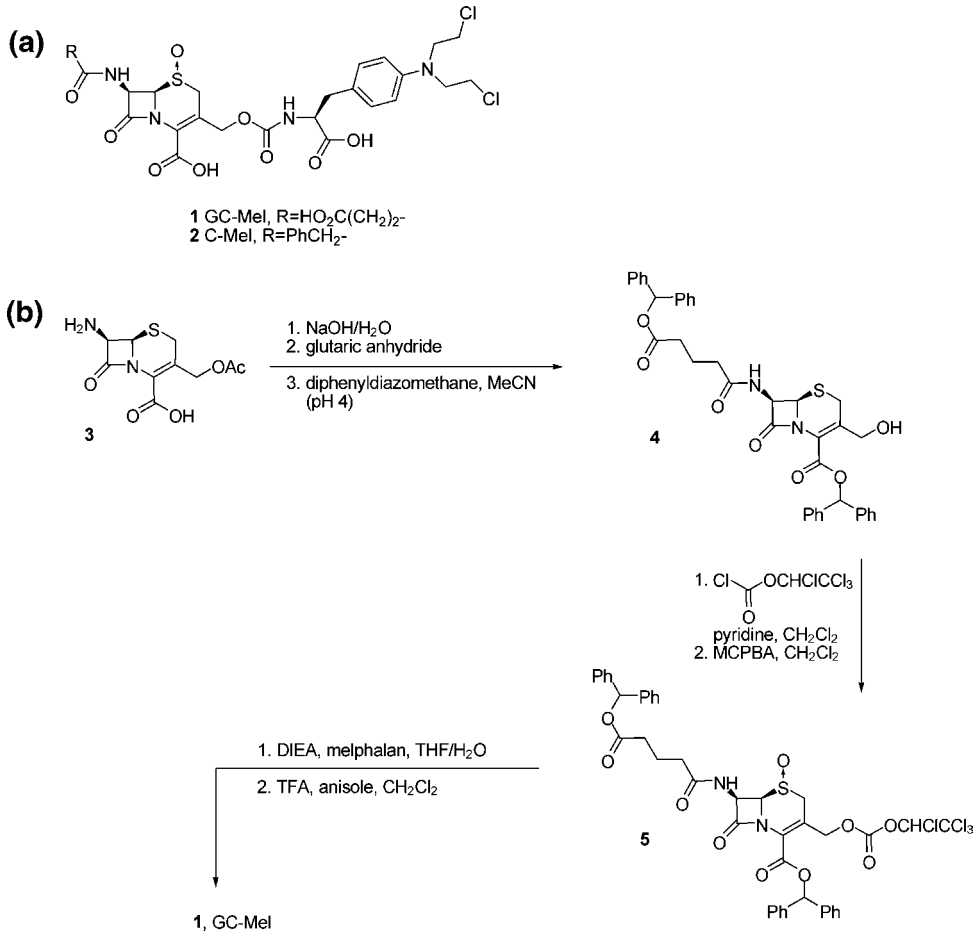

Figure 1. (A) Structure of GC-Mel, **1**, and C-Mel, **2**, and (B) schematic representation of the synthesis of GC-Mel, **1**, and the intermediates formed in the synthesis.

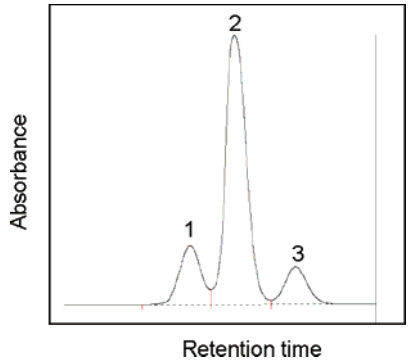

Figure 2. Size-exclusion chromatography of TAB2.5. Peak 1 (57.7min), dimer of TAB2.5; peak 2 (65.8 min), monomer fraction of TAB2.5; peak 3 (77.0 min), free BLA.

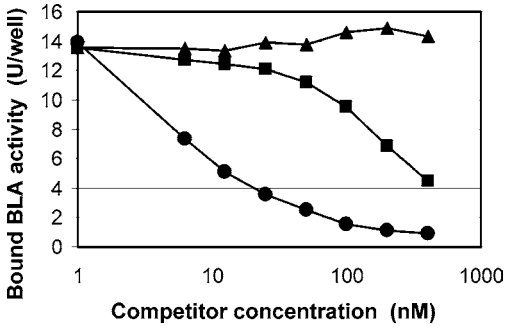

Figure 3. Target binding of TAB2.5 is effectively competed by CC49 or BSM. TAB2.5 binding to plate bound tumor lysate was measured in the presence of CC49 (●), BSM (■), or BSA (▲) as a negative control.

Binding of TAB2.5 to Tumor Lysate. LS174T xenograft tumor samples were homogenized in T-PER lysis solution (Pierce Inc., Rockford, IL) containing a protease inhibitor cocktail (Halt, Pierce, Rockford, IL) on ice. Insoluble material was removed by centrifugation, and the protein concentration of supernatant was measured using the BCA assay (Pierce, Rockford, IL). A microtiter plate was coated with 50 μL of 200 μg/mL LS174T tumor lysate in PBS by drying overnight at 4 °C. The plate was blocked with 300 μL/well of 2.5% BSA in PBS for 1 h at room temperature. A solution of 90 nM TAB2.5 was mixed with increasing concentrations of competitor CC49, bovine submaxillary mucin (BSM, Sigma, St. Louis, MO), or BSA in equal volume, and 100 μL of the mixture was added into each tumor lysate-coated well. The plate was incubated at room temperature for 2 h and washed four times with PBS−Tes (PBST) buffer, and bound BLA activity was measured by adding 100 μL of nitrocefin (Oxoid, Lenexa, AZ) in PBS containing 0.125% octylglucopyranoside.

Histochemistry. Formalin-fixed sections (colon tumor microarrays (Accumax, Isu Abixis Co., LTD, Seoul, South Korea) and LS174T solid tumor xenograft) were deparaffinized, rehydrated, and subjected to a heat-based antigen retrieval procedure (30 min incubation in a 1 mM EDTA, pH 8.0, solution at 90 °C). Sections were then rinsed with TBS and incubated in peroxidase blocking solution (DAKO, Carpinteria, CA), followed by a solution of 1% normal goat serum. Samples were then incubated with TAB2.5 or CC49 at 2.0 and 0.2 mg/mL, respectively, for 30 min in PBS containing 1% normal goat serum. TAB2.5-containing sections were then incubated with a rabbit polyclonal anti-BLA antibody for 30 min, while CC49-

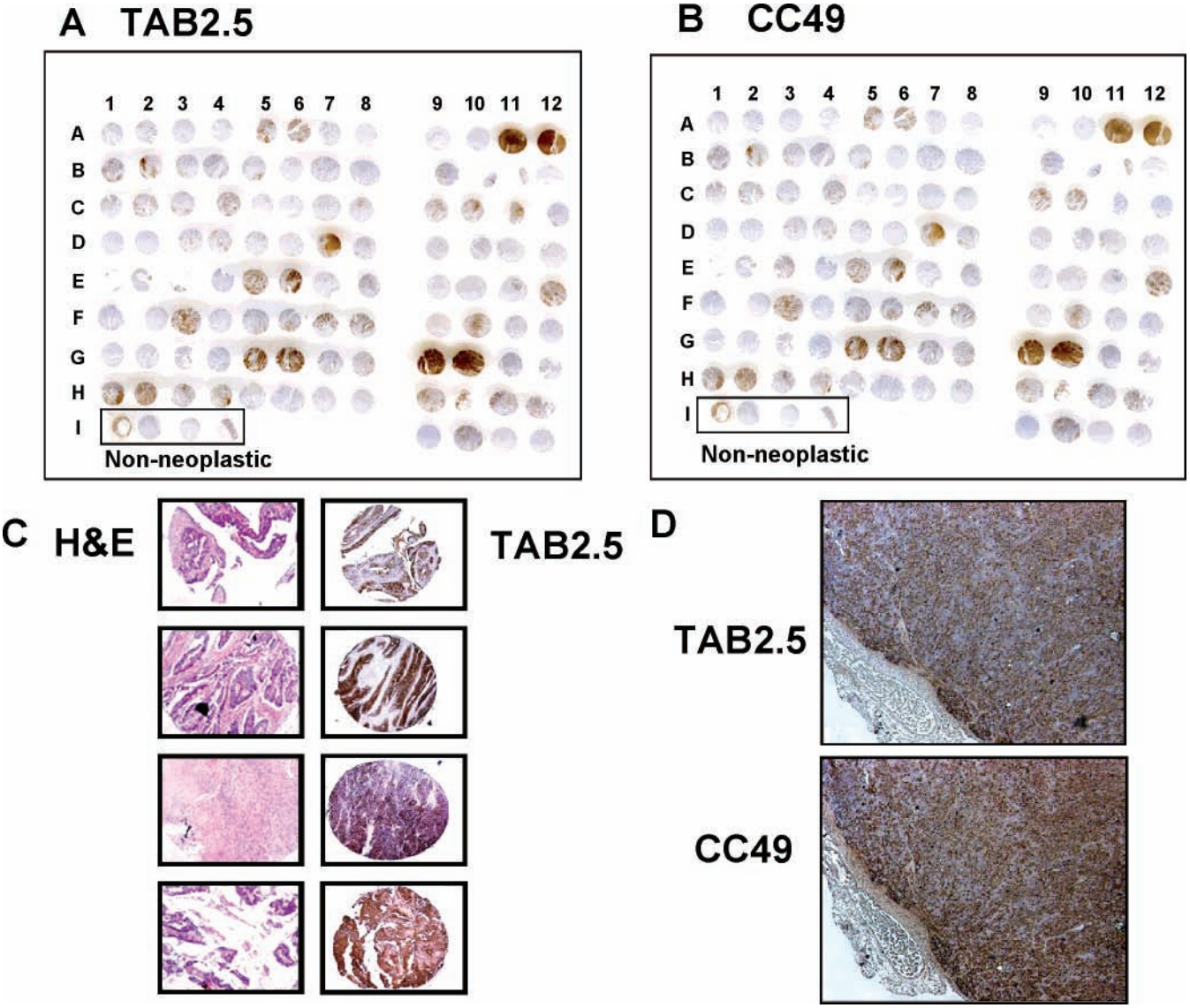

Figure 4. Immunohistochemical localization of TAG-72 in sections from human colorectal and LS174T xenograft tumors. Microarrays containing duplicate sections from 50 primary colorectal tumors and two nonneoplastic tissue samples were stained with TAB2.5 (A) or CC49 (B). In panel C, sections A6, G5, A11, and G9 (from panel A) are shown enlarged and stained with hematoxylin and eosin (H&E). In panel D, LS174T tumors were grown in vivo in athymic nude mice for 2 weeks prior to isolation and fixation.

containing sections were incubated with goat anti-mouse−HRP (DAKO, Mouse Envision+ System-HRP). The sections that were treated with TAB2.5 were rinsed and incubated with anti-rabbit−HRP antibody (DAKO, Rabbit Envision+ System-HRP) for 30 min. Finally, the TAB2.5- and the CC49-treated sections were rinsed and incubated with peroxidase substrate (DAB, DAKO) for color development and counterstained with hematoxylin.

In Vivo Pharmacokinetics and Tumor Retention. The pharmacokinetic studies were conducted with athymic animals bearing 100−200 mm^3 LS174T subcutaneous tumors. The animals were injected intravenously with 100 μL of TAB2.5 (1 or 5 mg/kg) or MUB3.4 (5 mg/kg) (a control construct with specificity for MUC1) diluted in PBS. Blood samples were drawn via tail vein bleeds at 0.033, 0.083, 0.25, 0.5, 1, 2, 4, 8, 12, 24, 48, 72, and 96 h. Solid tumors were collected, frozen, and maintained at −80 °C until use. Two milliliters of ice-cooled lysis buffer (PBS with 15 μg/mL Aprotinin) was added per gram of wet tissue that was weighed semifrozen, and the tissue was homogenized with a Polytron PT1200 homogenizer (Polytron Kinematica, Switzerland). Homogenate (75 μL) was combined with an equal volume of B-Per (Pierce) and shaken vigorously for 10 min at room temperature. Samples were then centrifuged for 10 min at 4 °C. The resulting supernatants (20 μL) were collected and assayed for BLA activity. Blood samples (0.6 mL) were collected in EDTA anticoagulant, placed on ice, and centrifuged at 5 °C within 30 min to harvest plasma. The resulting plasma samples were transferred into polypropylene tubes and stored at −70 ± 10 °C until analysis. BLA concentrations in plasma and tissue samples were measured using a capture assay as follows. Microtiter high binding capacity plates (Costar Co., Cambridge, U.K.) were coated with 5 μg/mL chicken polyclonal anti-BLA antibody (ProSci Inc., Poway, CA) in PBS and then blocked with casein blocker buffer (Pierce, Rockford, IL) at room temperature (RT) for 2 h. Plasma samples (20 μL) or negative controls were added to each well, followed by the addition of 80 μL/well of casein blocker buffer, and incubated for 2 h at RT. Samples were diluted as needed using negative control plasma or tissue lysate as reference. The plates were then washed, and 200 μL/well of nitrocefin substrate solution (100 μg/mL) in PBS containing 0.125% of *n*-octyl-β-D-glucopyranoside (Sigma, St. Louis, MO) was added to each well. The plates were read as a kinetic assay at 490 nm for 15 min at 25 °C. The limit of detection under these conditions was

5 ng/mL. The calculated concentration of TAB2.5 was determined by linear regression using a standard curve within the linear range of the concentration−response curve.

RESULTS

Synthesis of the Prodrug GC-Mel. Previous studies using prodrugs of doxorubicin and phenylenediamine mustard have demonstrated that anionic side chains of the 7-amino group of the cephem core decrease in vitro prodrug cytotoxic activity (*22*, *23*). The prodrugs are also more soluble, easier to formulate, and less toxic in vivo. In this study, we applied similar modifications to C-Mel (*2*), which was previously shown to be a highly active molecule when administered in animals that were pretreated with a scFv−BLA fusion protein (*23*). A more water-soluble form of **2** was expected to be less toxic and easier to administer (Figure 1A).

The synthesis of GC-Mel (*1*) is shown in Figure 1B. Briefly, 7-aminocephalosporanic acid (*3*) was converted to **4** in three steps involving saponification, acetylation with glutaric anhydride, and esterifications with diphenyldiazomethane. The resulting alcohol (intermediate **4**) was converted to the activated carbonate, followed by sulfide oxidation to give the key intermediate **5**. Melphalan was then added, followed by deprotection of the esters with trifluoroacetic acid, to provide GC-Mel, **1**. The aqueous solubility of GC-Mel was four times greater than that of C-Mel (data not shown).

Binding Properties of TAB2.5. Recently, we described the construction of a fusion protein between BLA and a scFv fragment based on antibody CC49. The fusion protein was optimized for high-level soluble production in *E. coli* and good protease stability using combinatorial consensus mutagenesis (*8*). Monomeric TAB2.5 was isolated as described in the Experimental Procedures (Figure 2). The binding specificity of TAB2.5 was validated in competition assays as shown in Figure 3. The data demonstrate that parent antibody CC49 or soluble target BSM effectively compete the binding of TAB2.5 to tumor lysate indicating that TAB2.5 and CC49 bind to the same epitope.

To further establish the relative equivalency of TAB2.5 and CC49 in terms of antigen detection, the binding to TAG-72 in primary colorectal tumor biopsies was determined by immunohistochemistry (Figure 4A,B). The molecules were compared at concentrations that resulted in comparable staining intensities. Very similar staining patterns were observed for TAB2.5 and CC49, which is evidence for the very similar binding specificity of both molecules. Consistent with previous reports, the expression of TAG-72 was heterogeneous within the tumor sections, although, in most cases the antigen was dispersed throughout the entire section. The majority of the sections that were strongly immunopositive were graded G2 or G3. Selected tumor sections at higher magnification are shown in Figure 4C, along with a corresponding section from the same tumor stained with hematoxylin and eosin. The colorectal cell line LS174T has previously been observed to express TAG-72 in vitro as well as in vivo (*26*). The presence of TAG-72 in LS174T tumors after 2 weeks of growth in vivo was confirmed using CC49 antibody and TAB2.5 fusion protein as shown in Figure 4D. Consistent with the expression pattern observed in the primary tumor tissue, the distribution of TAG-72 was heterogeneous in LS174T tumors, although the protein did appear dispersed throughout the tumor mass. No binding of TAB2.5 was observed for a variety of normal tissues (thyroid, lung, liver, ovary, uterus, stomach; data not shown).

In Vivo Pharmacokinetic Characteristics of TAB2.5. The plasma and tumor pharmacokinetics of TAB2.5 and MUB3.4, a nonbinding BLA fusion protein control, were compared in LS174T tumor-bearing animals (Figure 5A,B, respectively). The

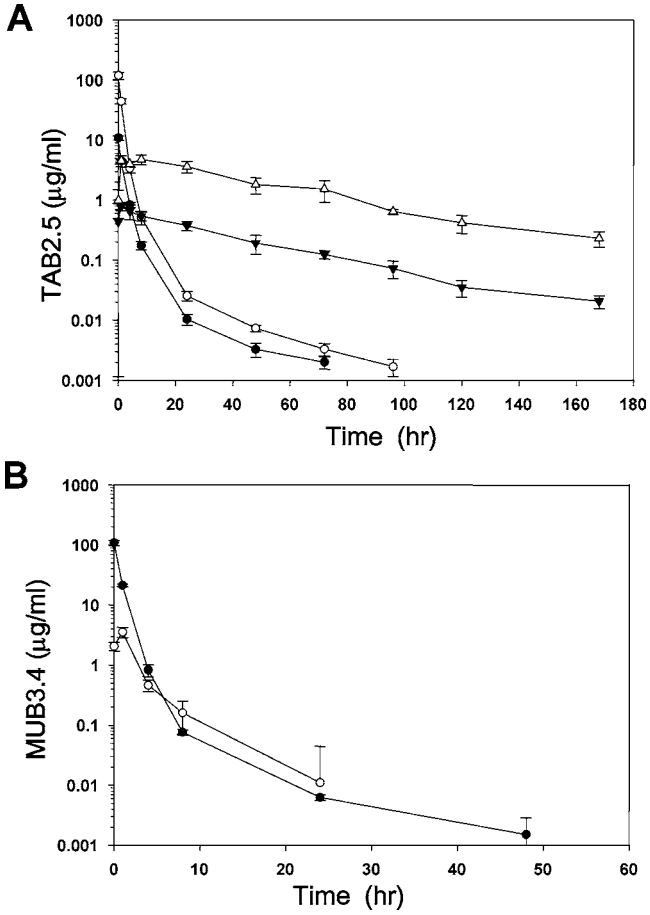

Figure 5. Pharmacokinetics of TAB2.5 and MUB3.4 in nude mice bearing human colorectal LS174T xenografts. The animals were administered TAB2.5 (A) iv at 1 (plasma, ●; tumor, ▼) and 5 mg/kg (plasma, ○; tumor, △) and MUB3.4 (B) at 5 mg/kg (plasma, ●; tumor, ○). Plasma and tumor samples ($n = 3$ per time point) were collected at various times up to 170 h. The concentrations of TAB2.5 and MUB3.4 were determined by comparing the level of BLA activity in the samples to the level of enzymatic activity in purified preparations.

pharmacokinetic data were analyzed using a compartmental model. The plasma distribution of both fusion proteins was multiphasic with the volume of distribution being comparable to the plasma volume. TAB2.5 when dosed iv at 1 or 5 mg/kg had an $\alpha T_{1/2}$ and a $\beta T_{1/2}$ in plasma of 1.3 and 1.0 and 20.0 and 18.4 h, respectively. While in the tumors, the $T_{1/2}$ at the two doses was 36.9 and 49.5 h, respectively. The total body clearance was 0.017 and 0.011 mL/min at 1 and 5 mg/kg, respectively. In contrast, when dosed iv at 1 mg/kg, MUB3.4 had an $\alpha T_{1/2}$ and a $\beta T_{1/2}$ in plasma of 0.56 and 7.3 h, respectively. While in the tumors, the $T_{1/2}$ for MUB3.4 was 5.0 h. The ratio of the $T_{1/2}$ values for the tumor elimination of TAB2.5 versus MUB3.4 was 5.0 demonstrating that TAB2.5 is specifically retained in the LS174T tumors for a substantial period of time, thus potentially allowing for sufficient systemic clearance to occur to provide for selective tumor targeting with the prodrug.

Efficacy of TAB2.5 during ADEPT Treatment. The efficacy of TAB2.5 was studied in combination with the prodrug GC-Mel. TAB2.5 was administered to female athymic nude mice on day 9 when tumor size reached 150−200 mm^3. Following an interval of 72 h to allow for the systemic clearance of unbound TAB2.5, the prodrug GC-Mel was administered at doses of 75, 150, 300, or 450 mg/kg. The subcutaneous tumors in the vehicle-treated control group grew rapidly, and the growth curves did not plateau over the course of the experiment (Figure 6A). Furthermore, no spontaneous tumor regression was noted in this tumor model. By day 19, the tumor volume in the control

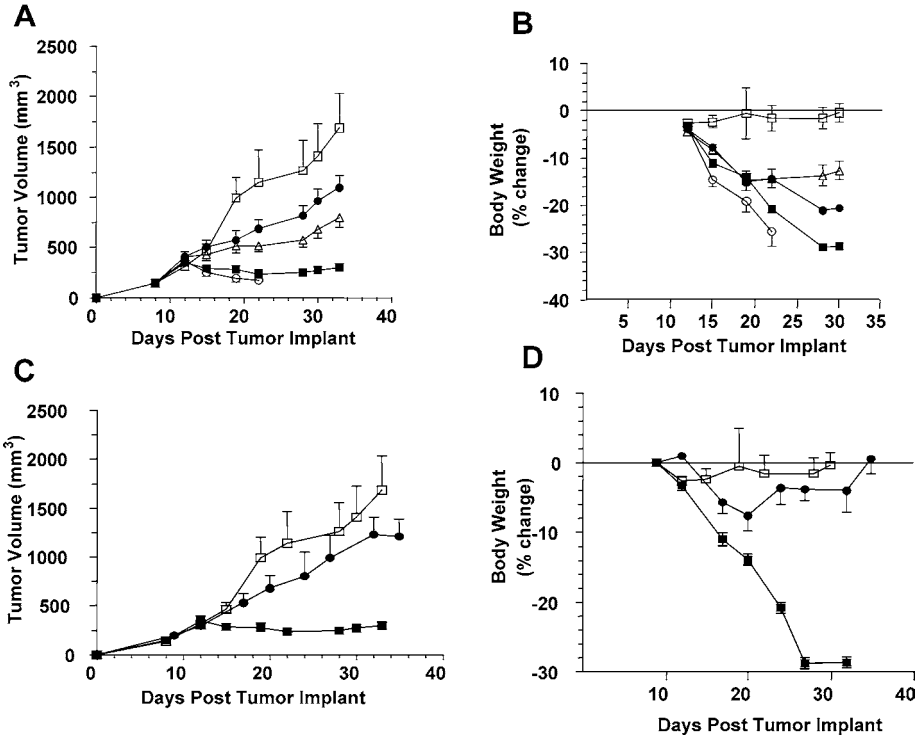

Figure 6. Antitumor activity of TAB2.5 and GC-Mel in nude mice bearing LS174T xenografts. In panel A, 8 days postinjection of the LS174T cells, the tumors were measured, and the animals were randomized into various control and treatment groups ($n = 10$/group). Seventy-two hours after the injection of TAB2.5 (1 mg/kg), the animals were administered control vehicle (□) or GC-Mel at 75 (●), 150 (△), 300 (■), and 450 mg/kg (○). Tumor growth was monitored every 3−4 days. Panel B shows the effect of the various treatments on body weight. The animals were weighed every 3−4 days, and the change in the body weight is expressed as a percentage of the animal's starting weight. Panel C shows tumor volumes from animals administered vehicle (control, □), GC-Mel (300 mg/kg, ●), or TAB2.5 (1 mg/kg) and then after 72 h GC-Mel (300 mg/kg, ■). Panel D shows body weights from the animals in the groups described in panel C.

group had increased by 7-fold to 990 ± 210 mm^3 and subsequently by 12-fold to 1700 ± 340 mm^3 by the end of the experiment on day 33. In contrast, a dose-dependent inhibition in tumor growth was observed in the groups that received GC-Mel. Doses of 75 and 150 mg/kg slowed the growth of the tumors, so by day 33 the average tumor volumes in these two treatment groups were 1100 ± 120 and 790 ± 96 mm^3 ($p = 0.033$, compared to control group), respectively. Treatment with 300 mg/kg GC-Mel resulted in a slow reduction in the volume of the tumors that reached a nadir by day 22. By day 33, no significant regrowth of the tumors was noted, and the average volume of tumors in the group was 300 ± 40 mm^3 ($p = 0.0018$, compared to control group).

As a measure of peripheral toxicity, the body weight of the animals was monitored regularly following treatment. All of the animals in the groups receiving GC-Mel lost a significant amount of body weight as shown in Figure 6B. By day 19, the groups that received the prodrug at a dose of 75, 150, or 300 mg/kg had lost 15.1%, 14.8%, and 14.0% of their starting body weight, respectively. The body weights of all animals in these groups were stabilized eventually by day 28. However, by the end of the experiment, they had not started to gain weight. The group that were dosed with 450 mg/kg GC-Mel lost more than 30% of their body weight by day 22 and had to be sacrificed.

To confirm that the release of free melphalan that was affecting tumor growth was associated with the β-lactamase activity retained in the tumor, GC-Mel was administered at the 300 mg/kg dose level to LS174T tumored animals in the absence of TAB2.5. GC-Mel alone or the melphalan formed from the spontaneous breakdown of GC-Mel had a minimal effect on the growth of the LS174T tumors (Figure 6C). On day 20, the average volume of the tumors in the group that received 300 mg/kg GC-Mel was not significantly different from the volume of the tumors in the control group. In regards to the peripheral toxicity, the 300 mg/kg treated group lost body weight with the nadir being reached within 1 week of the dosing of the animals (Figure 6D). In contrast to the response observed following the administration of the combination of TAB2.5 and GC-Mel, the extent of the weight reduction was less and the rate of recovery was faster. Thus, this data suggests that a portion of the peripheral toxicity observed following the administration of TAB2.5 and GC-Mel was due to the spontaneous release of melphalan, as well as to the free melphalan (0.3%) present in the prodrug preparation and in part to the leak back of melphalan from the tumor following the enzymatic cleavage by the β-lactamase.

To evaluate the sensitivity of the LS174T model to chemotherapy, we examined the efficacy of systemically delivered agents melphalan (single dose, iv), irinotecan (3 weekly doses, iv), and doxorubicin (3 weekly doses, ip). All three drugs led to only minor delays in tumor outgrowth as shown in Figure 7, even at concentrations that caused significant weight loss of the animals.

DISCUSSION

Several ADEPT systems have shown promising in vivo efficacy in a number of tumor models (*6*). There is clear evidence that ADEPT can deliver commonly used cancer drugs reaching high concentrations and targeting the tumor tissue with high selectivity. TAG-72 is a particularly attractive target because it is overexpressed in a large fraction of solid malignancies (*10*, *27*, *28*). Its expression in normal adult tissues is very low and is limited to a few immunoprivileged areas (*12*). CC49 is the best-characterized antibody against TAG-72. CC49 was tested in multiple clinical studies where it showed very high tumor selectivity (*13*, *14*, *29*). In addition, an ^{123}I-labeled scFv based on CC49 has been visualized in primary tumors and

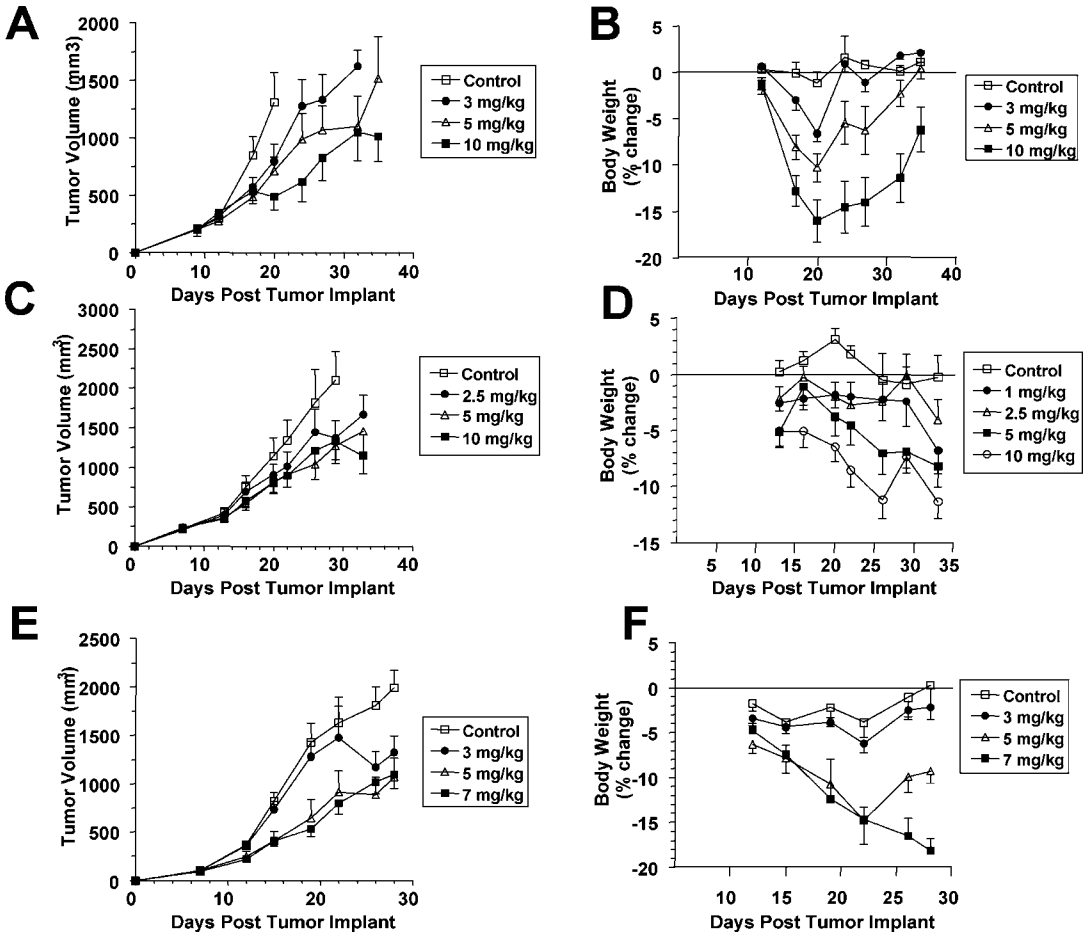

Figure 7. Antitumor activity of melphalan (A, B), irinotecan (C, D), and doxorubicin (E, F) in nude mice bearing LS174T xenografts. Animals were dosed iv with melphalan ($n = 10$/group) once on day 12, and the effect of the drug on tumor growth (A) and body weight (B) was monitored every 3−4 days. Animals were dosed iv with irinotecan ($n = 10$/group) weekly for 3 weeks, and the effect of the drug on tumor growth (C) and body weight (D) was monitored every 3−4 days. Animals were dosed ip ($n = 10$/group) weekly with doxorubicin for 3 weeks, and the effect of the drug on tumor growth (E) and body weight (F) was monitored every 3−4 days.

metastases of five colorectal cancer patients (*30*). Given the clinical validation of CC49, it was of critical importance that the fusion protein TAB2.5 retains the exact specificity of its parent antibody. Figure 3 shows that CC49 and TAB2.5 compete for the same epitope, and Figure 4 demonstrates that both proteins have extremely similar specificity. Thus, none of the mutations that were introduced to improve expression and stability of TAB2.5 appear to have impacted its target binding specificity.

TAB2.5 is very stable and shows excellent tumor retention in vivo as shown in Figure 5. Significant BLA activity can still be detected in tumor tissue approximately 1 week postinjection. If one considers tumor growth during the experiment, then the majority of the BLA activity that was bound in the tumor during the first 2 h after injection could still be found in the tumor after 1 week. This opens the opportunity to administer multiple prodrug injections after a single administration of TAB2.5. However, the growth of LS174T tumors is too aggressive to explore this option, and slower growing tumors will need to be studied.

Another important feature of TAB2.5 is its rapid clearance from the circulation. This is important for ADEPT treatment, because systemic BLA activity would lead to nonspecific prodrug activation. Previously described antibody−enzyme conjugates based on dimeric carboxypeptidase G2 showed slower plasma elimination and clearing antibodies (*31*) or mannosylation (*32*) had to be utilized to remove excess conjugate from the circulation. In contrast, the long tumor retention of TAB2.5 in combination with its rapid plasma elimination resulted in very high tumor/normal ratios of up to 1000 without any additional means of fusion protein clearance. Careful dose optimization will be required to translate this large tumor/plasma ratio of TAB2.5 into a large tumor/plasma ratio of drug exposure during ADEPT.

The novel prodrug GC-Mel was prepared to increase the solubility of C-Mel, which was previously reported to be very efficacious in ADEPT (*23*). Melphalan is an attractive choice for ADEPT due to its steep dose response (*33*), which makes it useful as an agent for high dose chemotherapy (*34*). Melphalan is an amino acid analogue that is actively transported into tumor cells (*35*, *36*). Thus, tumor cells actively take up free melphalan once it has been cleaved from the cephalosporin portion by BLA. This should help in reducing leakage of free active drug from tumor tissue during ADEPT.

The data in Figure 6 provide evidence for the efficacy of TAB2.5 in ADEPT, although the current dosing regimen led to significant toxicity. It is important to note that the LS174T model is extremely difficult to treat. Minimal efficacy was observed for systemic melphalan and doxorubicin, as well as irinotecan, which is the standard of care for colorectal cancer patients. The level of chemoresistance observed in the LS174T model described here is in agreement with literature reports, where irinotecan was found to have low activity (*37*). The further evaluation of TAB2.5 may require a tumor model with a slower in vivo growth profile, which would better reflect the growth rate in patients. Such a model will allow evaluation of longer intervals between the administration of TAB2.5 and GC-Mel to reduce systemic toxicity and allow administration of multiple

prodrug doses per protein dose. The careful optimization of dosing parameters such as dose of fusion protein and prodrug, as well as time interval between administrations of each component, should allow a further reduction of systemic toxicity while maintaining efficacy. The extremely favorable pharmacokinetic (PK) properties of TAB2.5 in tumor-bearing mice suggest that there is a wide window between tumor and systemic levels of BLA that can be exploited for ADEPT.

Based on the results from the PK studies, a 72 h time interval between the administration of TAB2.5 (1 mg/kg) and the prodrug was selected for the initial in vivo efficacy study. Using these conditions, a potent dose-dependent inhibition of the growth of the LS174T tumors was observed with the response appearing to saturate at 300 mg/kg. Treatment with 75 mg/kg of the prodrug resulted in a nearly equivalent response to that observed following the systemic administration of 10 mg/kg of melphalan. However, dosing with 300 or 450 mg/kg induced a pronounced loss of weight that did not show signs of recovery during the course of the experiment. Experiments conducted with the prodrug alone demonstrated that a portion of the weight loss was due to the spontaneous release of melphalan following the iv administration. However, the extent of the weight loss was much greater and no recovery was apparent in the animals that received the combination of TAB2.5 and GC-Mel suggesting that there may have been some "leak back" of melphalan from the tumor or a low-level of residual systemic TAB2.5. Regardless, using a lower initial dose of TAB2.5 or a longer time interval between the administration of the TAB2.5 and GC-Mel should allow reduction of the extent of the peripheral toxicity. Indeed this concept has been demonstrated to work with another targeting agent (Chen et al., manuscript in preparation). The advantage of using the ADEPT approach is clearly demonstrated when the extent of the inhibition of tumor growth achieved with TAB2.5 and GC-Mel, Figure 6, is compared to that observed with other chemotherapeutic agents that are currently being used in the clinic for treating colorectal cancer, for example, irinotecan, Figure 7. The latter uniformly produced only a weak cytostatic effect and a comparable amount of weight loss in the LS174T xenograft model.

In summary, we have described a novel fusion protein, TAB2.5, based on antibody CC49 that closely mimics the clinically validated specificity of CC49 and can be used in ADEPT. The prodrug GC-Mel shows good solubility and liberates melphalan upon exposure to TAB2.5. Further dose optimization will be required to fully evaluate the potential of both compounds for ADEPT. The clinical application of TAB2.5 will benefit from the removal of T cell epitopes from BLA that has been described recently (*24*).

LITERATURE CITED

(1) Kreitman, R. J. (1999) Immunotoxins in cancer therapy. *Curr. Opin. Immunol. 11*, 570−578.

(2) Trail, P. A., and Bianchi, A. B. (1999) Monoclonal antibody drug conjugates in the treatment of cancer. *Curr. Opin. Immunol. 11*, 584−588.

(3) DeNardo, S. J., Kroger, L. A., and DeNardo, G. L. (1999) A new era for radiolabeled antibodies in cancer? *Curr. Opin. Immunol. 11*, 563−569.

(4) Wu, A. M., and Senter, P. D. (2005) Arming antibodies: prospects and challenges for immunoconjugates. *Nat. Biotechnol. 23*, 1137−1146.

(5) Bagshawe, K. D., Sharma, S. K., and Begent, R. H. (2004) Antibody-directed enzyme prodrug therapy (ADEPT) for cancer. *Expert Opin. Biol. Ther. 4*, 1777−1789.

(6) Senter, P. D., and Springer, C. J. (2001) Selective activation of anticancer prodrugs by monoclonal antibody- enzyme conjugates. *Adv. Drug Delivery Rev. 53*, 247−264.

(7) Syrigos, K. N., and Epenetos, A. A. (1999) Antibody directed enzyme prodrug therapy (ADEPT): a review of the experimental and clinical considerations. *Anticancer Res. 19*, 605−613.

(8) Roberge, M., Estabrook, M., Basler, J., Chin, R., Gualfetti, P., Liu, A., Wong, S. B., Rashid, M. H., Graycar, T., Babe, L., and Schellenberger, V. (2006) Construction and optimization of a CC49−Based scFv-{beta}-lactamase fusion protein for ADEPT. *Protein Eng., Des. Sel.*, in press.

(9) Muraro, R., Kuroki, M., Wunderlich, D., Poole, D. J., Colcher, D., Thor, A., Greiner, J. W., Simpson, J. F., Molinolo, A., Noguchi, P., and Schlom, J. (1988) Generation and characterization of B72.3 s generation monoclonal antibodies reactive with the tumor-associated glycoprotein 72 antigen. *Cancer Res. 48*, 4588−4596.

(10) Galietta, A., Pizzi, C., Pettinato, G., Limite, G., Sgambato, A., Lamberti, M., Muraro, R., Formisano, C., Pensabene, M., Bianco, A. R., Mariani-Costantini, R., and Contegiacomo, A. (2002) Differential TAG-72 epitope expression in breast cancer and lymph node metastases: a marker of a more aggressive phenotype. *Oncol. Rep. 9*, 135−140.

(11) Victorzon, M., Nordling, S., Nilsson, O., Roberts, P. J., and Haglund, C. (1996) Sialyl Tn antigen is an independent predictor of outcome in patients with gastric cancer. *Int. J. Cancer 65*, 295−300.

(12) Cao, Y., Stosiek, P., Springer, G. F., and Karsten, U. (1996) Thomsen-Friedenreich-related carbohydrate antigens in normal adult human tissues: a systematic and comparative study. *Histochem. Cell Biol. 106*, 197−207.

(13) Meredith, R., Shen, S., Macey, D., Khazaeli, M. B., Carey, D., Robert, F., and LoBuglio, A. (2003) Comparison of biodistribution, dosimetry, and outcome from clinical trials of radionuclide-CC49 antibody therapy. *Cancer Biother. Radiopharm. 18*, 393−404.

(14) Murray, J. L., Macey, D. J., Kasi, L. P., Rieger, P., Cunningham, J., Bhadkamkar, V., Zhang, H. Z., Schlom, J., Rosenblum, M. G., and Podoloff, D. A. (1994) Phase II radioimmunotherapy trial with 131I−CC49 in colorectal cancer. *Cancer 73*, 1057−1066.

(15) McIntosh, D. G., Colcher, D., Seemayer, T., and Smith, M. L. (1997) The intraoperative detection of ovarian adenocarcinoma using radiolabeled CC49 monoclonal antibody and a hand-held gamma-detecting probe. *Cancer Biother. Radiopharm. 12*, 287−294.

(16) Milenic, D. E., Yokota, T., Filpula, D. R., Finkelman, M. A., Dodd, S. W., Wood, J. F., Whitlow, M., Snoy, P., and Schlom, J. (1991) Construction, binding properties, metabolism, and tumor targeting of a single-chain Fv derived from the pancarcinoma monoclonal antibody CC49. *Cancer Res. 51*, 6363−6371.

(17) Sawyer, J. R., Schlom, J., and Kashmiri, S. V. (1994) The effects of induction conditions on production of a soluble anti-tumor sFv in *Escherichia coli*. *Protein Eng. 7*, 1401−406.

(18) Pavlinkova, G., Beresford, G. W., Booth, B. J., Batra, S. K., and Colcher, D. (1999) Pharmacokinetics and biodistribution of engineered single-chain antibody constructs of MAb CC49 in colon carcinoma xenografts. *J. Nucl. Med. 40*, 1536−1546.

(19) Meyer, D. L., Jungheim, L. N., Law, K. L., Mikolajczyk, S. D., Shepherd, T. A., Mackensen, D. G., Briggs, S. L., and Starling, J. J. (1993) Site-specific prodrug activation by antibody-beta-lactamase conjugates: regression and long-term growth inhibition of human colon carcinoma xenograft models. *Cancer Res. 53*, 3956−3963.

(20) Rodrigues, M. L., Carter, P., Wirth, C., Mullins, S., Lee, A., and Blackburn, B. K. (1995) Synthesis and beta-lactamase-mediated activation of a cephalosporin-taxol prodrug. *Chem. Biol. 2*, 223−227.

(21) Vrudhula, V. M., Kerr, D. E., Siemers, N. O., Dubowchik, G. M., and Senter, P. D. (2003) Cephalosporin prodrugs of paclitaxel for immunologically specific activation by L-49-sFv-beta-Lactamase fusion protein. *Bioorg. Med. Chem. Lett. 13*, 539−542.

(22) Vrudhula, V. M., Svensson, H. P., and Senter, P. D. (1995) Cephalosporin derivatives of doxorubicin as prodrugs for activation by monoclonal antibody−β-lactamase conjugates. *J. Med. Chem. 38*, 1380−1385.

(23) Kerr, D. E., Li, Z., Siemers, N. O., Senter, P. D., and Vrudhula, V. M. (1998) Development and activities of a new melphalan prodrug designed for tumor-selective activation. *Bioconjugate Chem. 9*, 255−259.

(24) Harding, F. A., Liu, A. D., Stickler, M., Razo, O. J. Chin, R., Faravashi, N., Viola, W., Graycar, T., Yeung, V. P., Aehle, W., Meijer, D., Wong, S., Rashid, M. H., Valdes, A. M., and Schellen-

berger, V. (2005) A beta lactamase with reduced immunogenicity for the targeted delivery of chemotherapeutics using ADEPT. *Mol. Cancer Ther. 4*, 1791−1800.

(25) Murray, R., and Morgan, M. (1991) Electronic effects in the reaction of carbonyl oxides with aldehydes. *J. Org. Chem. 56*, 684−687.

(26) Horan Hand, H. P., Colcher, D., Salomon, D., Ridge, J., Noguchi, P., and Schlom, J. (1985) Influence of spatial configuration of carcinoma cell populations on the expression of a tumor-associated glycoprotein. *Cancer Res. 45*, 833−840.

(27) Bertoglio, S., Percivale, P., Schenone, F., Peressini, A., Murolo, C., and Badellino, F. (1998) Role of tumor-associated antigen expression in radioimmunoguided surgery for colorectal and breast cancer. *Semin. Surg. Oncol. 15*, 249−253.

(28) Brenner, P. C., Rettig, W. J., Sanz-Moncasi, M. P., Reuter, V., Aprikian, A., Old, L. J., Fair, W. R., and Garin-Chesa, P. (1995) TAG-72 expression in primary, metastatic and hormonally treated prostate cancer as defined by monoclonal antibody CC49. *J. Urol. 153*, 1575−1579.

(29) Nag, S., Martinez-Monge, R., Nieroda, C., and Martin, E., Jr. (1999) Radioimmunoguided-intraoperative radiation therapy in colorectal carcinoma: a new technique to precisely define the clinical target volume. *Int. J. Radiat. Oncol. Biol. Phys. 44*, 133−137.

(30) Larson, S. M., El-Shirbiny, A. M., Divgi, C. R., Sgouros, G., Finn, R. D., Tschmelitsch, J., Picon, A., Whitlow, M., Schlom, J., Zhang, J., and Cohen, A. M. (1997) Single chain antigen binding protein (sFv CC49): first human studies in colorectal carcinoma metastatic to liver. *Cancer 80*, 2458−2468.

(31) Sharma, S. K., Bagshawe, K. D., Burke, P. J., Boden, J. A., Rogers, G. T., Springer, C. J., Melton, R. G., and Sherwood, R. F. (1994) Galactosylated antibodies and antibody-enzyme conjugates in antibody-directed enzyme prodrug therapy. *Cancer 73*, 1114−1120.

(32) Medzihradszky, K. F., Spencer, D. I., Sharma, S. K., Bhatia, J., Pedley, R. B., Read, D. A., Begent, R. H., and Chester, K. A. (2004) Glycoforms obtained by expression in *Pichia pastoris* improve cancer targeting potential of a recombinant antibody-enzyme fusion protein. *Glycobiology 14*, 27−37.

(33) Frei, E., Teicher, B. A., Holden, S. A., Cathcart, K. N., and Wang, Y. Y. (1988) Preclinical studies and clinical correlation of the effect of alkylating dose. *Cancer Res. 48*, 6417−6423.

(34) Porrata, L. F., and Adjei, A. A. (2001) The pharmacologic basis of high dose chemotherapy with haematopoietic stem cell support for solid tumours. *Br. J. Cancer 85*, 484−489.

(35) Goldenberg, G. J., Lee, M., Lam, H. Y., and Begleiter, A. (1977) Evidence for carrier-mediated transport of melphalan by L5178Y lymphoblasts in vitro. *Cancer Res. 37*, 755−760.

(36) Goldenberg, G. J., and Begleiter, A. (1980) Membrane transport of alkylating agents. *Pharmacol. Ther. 8*, 237−274.

(37) Prijovich, Z. M., Chen, B. M., Leu, Y. L., Chern, J. W., and Roffler, S. R. (2002) Anti-tumour activity and toxicity of the new prodrug 9-aminocamptothecin glucuronide (9ACG) in mice. *Br. J. Cancer. 86*, 1634−1638.

BC0503521

From Symmetrical to Asymmetrical Nitrido Phosphino-thiol Complexes: A New Class of Neutral Mixed-Ligand ^{99m}Tc Compounds as Potential Brain Imaging Agents

Cristina Bolzati,*,‡ Elisa Benini,† Mario Cavazza-Ceccato,§ Emiliano Cazzola,† Erica Malagò,‡ Stefania Agostini,§ Francesco Tisato,‡ Fiorenzo Refosco,‡ and Giuliano Bandoli§

ICIS − CNR, Corso Stati Uniti, 4, 35127 Padova, Italy, Laboratory of Nuclear Medicine, Department of Clinical & Experimental Medicine, University of Ferrara, Via Borsari, 46, 44100 Ferrara, Italy, and Department of Pharmaceutical Sciences, University of Padova, Via Marzolo, 5, 35131 Padova, Italy. Received December 20, 2005

A general procedure is presented for the preparation of a new class of nitrido asymmetrical Tc-99m complexes containing two different bidentate ligands bound to the same $[Tc(N)]^{2+}$ core that could be used to design either essential or target specific imaging agents. This procedure is based on the chemical properties of a new monosubstituted $[Tc(N)(R_2PS)Cl(PPh_3)]$ species composed of a Tc≡N multiple bond and an ancillary phosphine thiol ligand (R_2PSH). This intermediate readily reacts with bidentate mononegative ligands (S^Y) containing soft π-donor coordinating atoms to give neutral pentacoordinate asymmetrical complexes of the type $[Tc(N)(R_2PS)(S^Y)]$. The ability of several bidentate ligands containing different combination of heteroatoms (S, N, O) to form complexes with the $[Tc(N)(R_2PS)]^+$ building block was investigated. It was found that mononegative dithiocarbamate (DTC) or cysteine carboxyl derivate ligands promptly react with the monosubstituted species to form the final mixed compound in high yield. Preliminary biodistribution data in rats of some representative $[Tc(N)(R_2PS)(DTC)]$ compounds revealed an interesting initial brain uptake (in the range 0.20 ± 0.01% ID/g and 0.91 ± 0.06% ID/g), indicating their ability to cross in and out of the intact BBB. In these complexes the dithiocarbamate, or more generally the bidentate ligand (S^Y), can be designed to carry a functional group or a bioactive molecule, which could be involved in a trapping mechanism to increase brain retention for longer time intervals. These results could be conveniently utilized to devise a new procedure for the production of a novel class of brain perfusion and/or brain receptor imaging agents.

INTRODUCTION

Over the past few years, several ^{99m}Tc-based radiopharmaceuticals have been approved by the FDA for determining organ functions or assessing disease status by imaging methods. Despite this, the development of new ^{99m}Tc-based brain perfusion or brain receptor imaging agents, which can play an important role in the diagnosis of various cerebrovascular, neurological, and neuropsychiatric disorders, remains a subject of great interest in the radiopharmaceutical field.

At present, Tc-99m-based radiopharmaceuticals used in the clinic for the assessment of brain perfusion are [^{99m}Tc]-HMPAO and [^{99m}Tc]-ECD, whereas [^{99m}Tc]-TRODAT-1 represents the first successful reported example of a Tc-based tracer for brain receptor imaging. Since these radiopharmaceuticals are far from ideal, the efforts to find more efficient Tc-99m brain perfusion and new CNS receptor imaging agents continue.

Generally, these agents must possess certain basic characteristics in order to cross the intact blood−brain barrier (BBB). They must be stable in vitro and in vivo, neutral in charge, lipophilic in character (Log *P* octanol/water in the range 1.0−2.5), and a molecular weight lower than 600 Da. Moreover, after crossing the BBB, a potential Tc-99m perfusion imaging agent must be retained in the tissue for a sufficient amount of time to allow SPECT imaging, via a trapping mechanism which typically involves enzymatic or chemical conversion into a more hydrophilic compound that prevents the agent from recrossing the BBB in the opposite direction. In addition, a potential Tc-99m receptor imaging agent must have the appropriate molecular shape to fit correctly with the target receptor site (IC_{50} value <10 nM) in order to localize selectively and specifically into the target receptor (*1*−*3*).

Recently a new strategy called 'metal-fragment' approach has been proposed to design receptor-specific Tc-99m tracers. This method is based on the reactivity of certain types of substitution labile technetium complexes toward ligands having a specific set of coordinating atoms (*4*). In these complexes some coordination positions are occupied by a chelating ligand (i.e. PXP hetero-diphosphine in $[Tc(N)(PXP)]^{2+}$ moieties) or by a set of ligands (i.e. CO groups in the $[Tc(CO)_3]^+$ moiety) which are strongly bound to the metal center defining a stable molecular building block. The remaining coordination positions are saturated by labile ligands (i.e. Cl, H_2O) that can selectively be replaced by other ligands carrying specific sets of coordinating atoms. Hence, the reaction between the precursor complex and the incoming ligand proves to be highly selective and produces a stable final hetero-complex in high yield. In this context, a target specific agent could be prepared as an asymmetrical complex containing two different coordinating systems, one which stabilizes the metal ion and the other designed to carry the bioactive molecule (*5*−*9*).

Recently we have reported a class of asymmetrical nitrido complexes characterized by the presence of two polidentate ligands bound to the same $[Tc(N)]^{2+}$ core. These mixed-ligand compounds are prepared by reacting the $[Tc(N)Cl_2(PNP)]$ precursor (where PNP is a diphosphine with a tertiary amine

* Author for correspondence. Phone +39 049 8275352. Fax +39 049 8275366. E-mail: bolzati@icis.cnr.it.
‡ ICIS − CNR.
† University of Ferrara.
§ Department of Pharmaceutical Sciences.

10.1021/bc050358q CCC: $33.50 © 2006 American Chemical Society
Published on Web 02/21/2006

incorporated in the chain) with bidentate ligands carrying π-donors as coordinating atoms (*10, 11*). The application of this approach has led to the production of a new class of cationic *pseudo*-octahedral compounds $[^{99m}Tc(N)(DTC)(PNP)]^+$ (DTC is a dithiocarbamate ligand), showing high myocardial uptake which are currently under investigation as potential myocardial imaging agent (*12*−*14*).

The use of the same $[Tc(N)(PNP)]^{2+}$ molecular fragment, where PNP was the bis(dimethylphosphinoethyl)methylamine (PNP4) in conjunction with dinegative mercaptoacetate $[O^-,S^-]$ or dithiol $[S^-,S^-]$ ligands (H_2L), generates a neutral [Tc(N)-(L)(PNP4)] species designed, in principle, for brain imaging (*15*). Despite the correct physicochemical properties of these agents (neutral charge, lipophilicity, and molecular weight), biodistribution data showed negligible brain uptake. This adverse behavior may be attributed either to in vivo structural alterations of the neutral native complex (e.g. protonation of the PNP amine function) into charged or polar adducts incapable of crossing the BBB or to the more crowded *pseudo*-octahedral arrangement of these complexes (*16*, *17*) compared with the pentacoordinated structures exhibited by [^{99m}Tc]-HMPAO and [^{99m}Tc]-ECD brain agents.

On the basis of these considerations, we proposed decreasing the complex coordination number by removing the tertiary amino nitrogen from the diphosphine framework. However, diphosphine ligands (P^P) incorporating only methylene units in the bridging chain did not promote the formation of mixed [Tc(N)(S^S)(P^P)] complexes when reacted with dithiol ligands (*18*). On the other hands, an identical P_2S_2 donor set, but with a different connection between P and S atoms, gave another series of stable, neutral pentacoordinated complexes of the type $[Tc(N)(R_2PS)_2]$, where R_2PS is a phosphino-thiol ligand (*19*). Biodistribution studies of this class of complexes have shown transient myocardial uptakes (*20*). One tracer of this series, incorporating the 2-dimethylphosphino propanethiolate ligand, has shown the additional ability to penetrate the intact BBB.

According to these preliminary results, we decided to further investigate the biological behavior of a further number of disubstituted $[Tc(N)(R_2PS)_2]$ complexes containing alkyl phosphino-thiolate ligands as potential brain perfusion imaging agents. In addition, aiming at the introduction of a bioactive molecule into a nitrido Tc-complex, we have devised a general procedure for the preparation of a new class of pentacoordinate neutral species of the type [Tc(N)(P^S)(S^Y)] where P^S is an ancillary ligand which stabilizes the $[Tc(N)]^{2+}$ core and S^Y is a bifunctional chelating agent (BFCa).

The opportunity of designing mixed ligand complexes of the type [^{99m}Tc(N)(P^S)(S^Y)] has been made possible by recent studies carried out at macroscopic level with the long-lived Tc-99g (*21*). The use of encumbering substituents at the P donor in phosphino thiol ligands led to the isolation of the monosubstituted compound $[^{99g}Tc(N)(R_2PS)Cl(PPh_3)]$ (R = cyclohexyl). This intermediate reacted with bidentate mononegative ligands (S^Y) to produce quantitatively neutral pentacoordinate asymmetrical complexes of the type $[Tc(N)(R_2PS)(S^Y)]$ (*22*).

In this study we report the synthesis and characterization of pentacoordinate $[^{99m}Tc(N)(R_2PS)_2]$ complexes and of a new class of pentacoordinate $[^{99m}Tc(N)(R_2PS)(S^Y)]$ mixed complexes. Alkylphosphino thiols and HS^Y ligands utilized in the studies are outlined in Figures 1 and 2. In vitro stability and tranchelation toward an excess of GSH and Cys of all synthesized symmetrical and asymmetrical compounds were evaluated. Tissue distribution data in rats of all $[^{99m}Tc(N)(R_2PS)_2]$ complexes and of some representative $[Tc(N)(R_2PS)(S^S)]$ compounds are also studied.

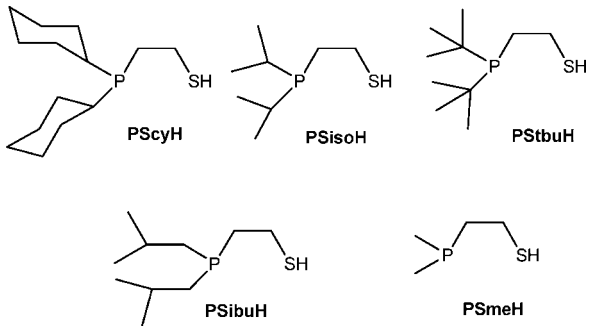

Figure 1. Phosphino thiol ligands (R_2PSH) utilized in this study.

EXPERIMENTAL SECTION

Materials. All chemicals and reagents were purchased from Aldrich Chemicals. The solvents were reagent grade and used without further purification. Due to the tendency of the phosphino-thiol ligand to oxidize, all the solvents were previously degassed to remove dissolved dioxygen traces and reactions were carried out under an inert atmosphere of dry dinitrogen. Technetium-99m as $Na^{99m}TcO_4$ was eluted from a $^{99}Mo/^{99m}Tc$ generator provided by Nicomed Amersham-Sorin (Saluggia, Italy). Disubstituted $[^{99g/99m}Tc(N)(PScy)_2]$ and monosubstituted $[^{99g}Tc(N)(PScy)Cl(PPh_3)]$ compounds were prepared as previously described (*19*−*21*). The phosphine thiol ligands used in these studies were purchased from Argus Chemicals (Prato, Italy). Dithiocarbazate (Dtcz) dithiocarbamate (DTC4), dithiophosphinate (PSS1, 2), dithiocarboxylate (DTCOX1, 2) ligands, as sodium salts, were synthesized according to the literature method (*23*−*26*). Dithiocarbammate (DTC1, 2, 3), cysteamine (SN), L-cysteine ethyl ester (SN-Cys), and the remaining bidentate ligands, tertiary phosphine (PPh_3, triphenylphosphine; TPPS (tris(3-sulfonatophenyl)phosphine)) and SDH (succinic dihydrazide), were purchased from Sigma Aldrich (Milan, Italy). PCN [tris(2-cyanoethyl)phosphine] and $P(CH_2OH)_3$ [tris(hydroxymethyl)phophine] were purchased from Sterm Chemicals, Inc. (Bischheim, France). Hydroxypropyl-beta-cyclodextrin (β-HPC) was purchased from Acros (Morris Plains, NJ). Sep-Pak RP-C18 and Oasis HLB extraction cartridges were purchased from Waters Corporation (Milford, MA).

Analysis. Radiochemical purity (RCP) and stability of the radioactive compounds were evaluated by thin-layer chromatography (TLC) carried out on SiO_2 F_{254S} or C18 F_{254S} (Merck) and high performance liquid chromatography (HPLC). Radioactivity on TLC plates were detected and measured using a Cyclone Instrument equipped with phosphorus imaging screen and OptiQuant image analysis software (Packard, Meridian, CT). HPLC was performed on a Beckman System Gold Instrument equipped with a programmable solvent system Model 126, a scanning detector Model 166 and a radioisotope detector Model B-FC-3200 Bioscan.

The chromatographic conditions used in TLC and HPLC analyses, together with the RCYs (radiochemical yields) and the chromatography results, are reported in Table 1.

To determine the chemical nature of the Tc-99m complexes, comparison by HPLC with the well characterized Tc-99g analogues was pursued applying parallel photometric and radiometric detection. Thus, after co-injection of appropriate Tc-99m/Tc-99g couples, identical retention times were observed (Figure 3).

Synthesis of Disubstituted Symmetrical ^{99m}Tc Complexes: $[^{99m}Tc(N)(R_2PS)_2]$ (R= CH_3, $CH(CH_3)_2$, $CH_2CH(CH_3)_2$, $C(CH_3)_3$). *Method 1:* 0.25 mL of saline containing $^{99m}TcO_4^-$ (activity ranging from 1.0 Mbq to 1.0 Gbq) was added to a vial containing 1 mg of Dtcz, or alternatively 5 mg of SDH,

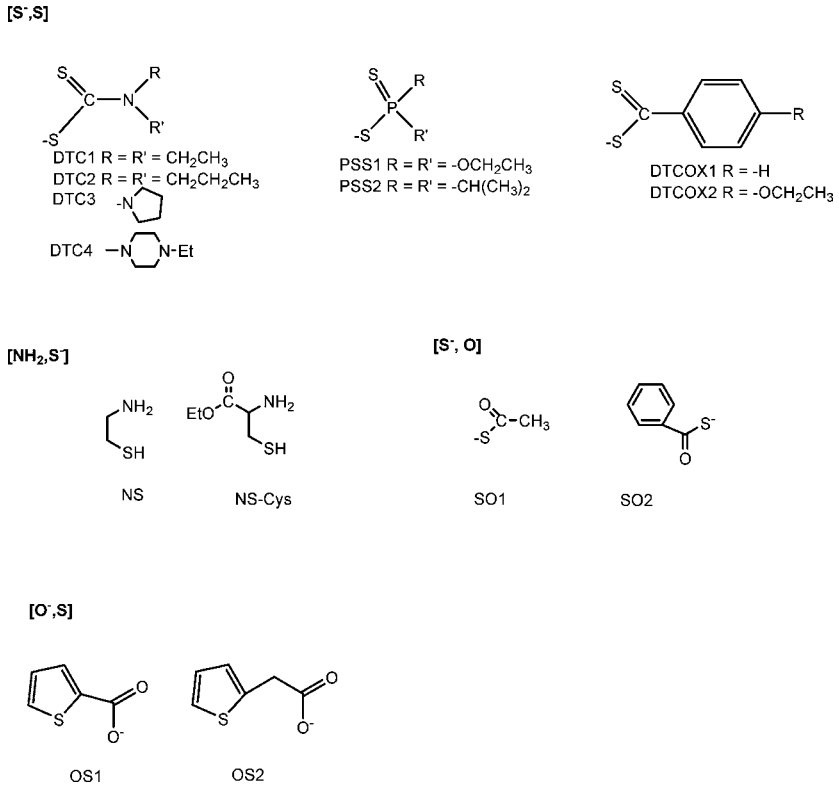

Figure 2. Bifunctional ligands (S^Y) utilized in this study.

0.1 mg of $SnCl_2$ suspended in 0.1 mL of saline, and 1.0 mL of EtOH. The resulting solution was kept at room temperature for 30 min, at which point 0.2 mL of an alcoholic solution containing 0.25−1 mg of the selected phosphino-thiol ligand followed by 0.1 mL of HCO_3^-/CO_3^{--} buffer (0.5 M) was added. The resulting solution was heated at 100 °C for 30 min.

Method 2: 0.25 mL of saline containing $[^{99m}TcO_4]^-$ (activity ranging from 1.0 Mbq to 1.0 Gbq) was added to a vial containing 5 mg of SDH, 3 mg of PPh_3, 0.1 mL of HCl (1 M), and 1.5 mL of EtOH. The resulting solution was heated at 100 °C for 15 min. After cooling, 0.2 mL of an alcoholic solution containing 0.25−1 mg of the selected R_2PSH ligand was added. Then, the pH was raised to 8 by adding 0.250 mL of HCO_3^-/CO_3^{--} buffer (0.5 M) and the resulting solution was incubated at room temperature for 1 h. RCP for the complexes, evaluated by TLC and HPLC, was reported in Table 1.

Method 3: 0.25 mL of saline containing $^{99m}TcO_4^-$ (activity ranging from 1.0 Mbq to 1.0 Gbq) was added to a vial containing 1 mg of Dtcz, 0.1 mL of HCl (1 M), 1.5 mL of EtOH, and 2 mg of the appropriate phosphino-thiol ligand. The resulting solution was heated at 100 °C for 15 min.

Purifications. The final disubstituted $[^{99m}Tc(N)(R_2PS)_2]$ compounds were purified from cold ligands, by Sep-Pak RP-C18. The preparation was diluted with water (8 mL) and loaded onto the cartridge previously activated with 95% ethanol (5 mL) and water (5 mL). The cartridge was rinsed with water (20 mL) followed by EtOH 30% (1 mL). $[^{99m}Tc(N)(PSme)_2]$ was eluted using 1 mL of EtOH 60% (1 × 0.25 mL, 1 × 0.75 mL). The other $[^{99m}Tc(N)(R_2PS)_2]$ complexes were eluted using 1 mL of EtOH 100% (1 × 0.25 mL, 1 × 0.75 mL). In all cases, the activity was collected in the second fraction.

$[^{99m}Tc(N)(S^Y)_2]$ (S^Y = DTC, PSS, DTCOX, etc.). The disubstituted symmetrical complexes were synthesized following the literature procedure (*24*−*26*).

Synthesis of Asymmetrical ^{99m}Tc Complexes: $[^{99m}Tc(N)(R_2PS)Cl(PPh_3)]$ (R= CH_3, $CH(CH_3)_2$, $CH_2CH(CH_3)_2$, C_6H_{11}, $C(CH_3)_3$). *Method a:* 0.25 mL of saline containing $^{99m}TcO_4^-$ (activity ranging from 1.0 Mbq to 1.0 Gbq) was added to a vial containing 5 mg of SDH, 3 mg of PPh_3, 0.1 mL of HCl (1 M), and 1.5 mL of EtOH. The resulting solution was heated at 100 °C for 15 min. After cooling, 0.2 mL of an alcoholic solution containing $\sim 10^{-4}$ mmol (0.025−0.050 mg) of the selected phosphino-thiol ligand was added. The resulting solution was incubated at room temperature for 1 h.

TLC and HPLC analysis revealed a mixture of different products. In all cases, when the reactions were carried out at 100 °C or at RT but in basic media, a conversion of the intermediate compounds into the corresponding disubstituted symmetrical complexes was observed.

Method b: 0.25 mL of saline containing $^{99m}TcO_4^-$ (activity ranging from 1.0 Mbq to 1.0 Gbq) was added to a vial containing 5 mg of SDH, 3 mg of PPh_3, 0.1 mL of HCl (1 M), 1.5 of EtOH, and 0.2 mL of an alcoholic solution containing $\sim 10^{-4}$ mmol of phosphino-thiol ligand. The resulting solution was heated at 50 °C for 15 min. The mixture revealed the same chromatographic profiles as those obtained by method a.

$[^{99m}Tc(N)(R_2PS)(S^Y)]$. This preparation implies the preliminary formation of the precursor complex $[^{99m}Tc(N)(R_2PS)Cl(PPh_3)]$ followed by its conversion into the final asymmetrical compound by reaction with 0.2 mL of water solution containing 1−0.025 mg of the appropriate bidentate ligand (S^Y), at room temperature. RCY, which evaluated by TLC and HPLC chromatography, was reported in Table 1 for each compound. TLC and HPLC characterizations of $[^{99m}Tc(N)(R_2PS)(NS\text{-}Cys)]$ showed the presence of two separate radioactive spots, which resulted from the formation of two distinct isomeric forms of the complex.

Purifications. The final mixed compounds were purified by HPLC. The desired fraction was diluted with water (8 mL) and loaded onto a Sep-Pak RP-C18 previously activated with 95% ethanol (5 mL) and water (5 mL). The cartridge was rinsed with water, and the Tc-99m species was eluted using 1 mL of EtOH (1 × 0.40 mL, 1 × 0.60 mL). The second fraction containing all the activity was diluted with saline to obtain an aqueous

Table 1. HPLC and TLC Data

complexes	HPLC, t_R (min) ^{99g}Tc	HPLC, t_R (min) ^{99m}Tc	TLC, R_f	log k_0'	mw	% RCY
[Tc(N)(PScy)$_2$]	35.20[a];	35.5[a]	0.2[a]		627.80	90
[Tc(N)(PSiso)$_2$]	24,33[b]; 19.15[c]	25.13[b]; 19.21[c]	0.4[b]; 0.14[c]	3.99	466.53	95
[Tc(N)(PSme)$_2$]	3.8[b]			1.85	355.33	95
[Tc(N)(PSibu)$_2$]	35.2[b]; 33.56[c]	35.49[b];33.80[c]	0.35[c]	5.45	523.65	94
[Tc(N)(PStbu)$_2$]	35.05[b]	35.37[b]		6.28	523.65	85
[Tc(N)Cl(PScy)(PPh$_3$)]			0.3[a]		668.15	
[Tc(N)Cl(PSiso)(PPh$_3$)]	30.36	30.56[b]	mix		586.93	23.2
[Tc(N)Cl(PSibu)(PPh$_3$)]	33.84[c]	29.93−34.05[c]			616.07	32.1
[Tc(N)(PScy)(DTC1)]	26.10[a]	26.20[a]	0.5[a]	5.7	519.67	92
[Tc(N)(PSiso)(DTC1)]	14.38[c]	14.75[c]	0.37[b]; 0.28[c]	3.28	438.10	92
[Tc(N)(PSiso)(DTC2)]	25.35[c]	25.55[c]	0.64[b]		466.72	90
[Tc(N)(PSiso)(DTC3)]	14.13[c]	14. 38[c]	0.42[b]	3.76	436.65	94
[Tc(N)(PSibu)(DTC3)]	25,68[c]	25.83[c]	0.26[c]	4.39	464.52	92
[Tc(N)(PSiso)(DTC4)]	9.56[c]	9.82 [c]	0.24[b]	3.69	479.61	93
[Tc(N)(PScy)(PSS1)]			0.31[a]; 0.21[d]		554.34	94
[Tc(N)(PSiso)(PSS1)]		22.05[c]	0.18[a]; 0.68[b]		475.46	95
[Tc(N)(PScy)(PSS2)]			0.27[a]; 0.12[d]		550.60	56
[Tc(N)(PSiso)(PSS2)]	24.52[c]	24.74[c]	0.3[b]	4.47	472.51	90
[Tc(N)(PSiso)(DTCOX1)]			0.47[c]		442.43	72
[Tc(N)(PSiso)(DTCOX2)]		31.1[c]	0.71[b]		486.49	88
[Tc(N)(PSiso)(SN)]		5.85[d]	0.65[e]		323.33	83
[Tc(N)(PSibu)(SN)]		11.29[d]	0.78[e]		394.47	85
[Tc(N)(PSiso)(SN−Cys)]		8.54; 9.58[d]	0.65, 0.43[e]		396.40	82
[Tc(N)(PSibu)(SN−Cys)]		18.36; 20.55[d]	0.80, 0.64[e]		467.54	80
[Tc(ECD)]				2.44		
[Tc(N)(DTC1)$_2$]	10.04[a]	10.1[a]; 20.8[c]	0.85[b]; 0.8[c]		409.73	95
[Tc(N)(DTC2)$_2$]		31.93[c]	0.90[b]		465.84	90
[Tc(N)(DTC3)$_2$]		18.67[c]	0.71[b]		405.71	93
[Tc(N)(DTC4)$_2$]		9.12[c]	0.17[b]		491.70	90
[Tc(N)(PSS1)$_2$]		30.87[c]	0.45[a]; 0.92[b]; 0.9[d]		483.31	95
[Tc(N)(PSS2)$_2$]		31.38[c]	0.41[a]; 0.75[b]		477.41	40
[Tc(N)(DTCOX1)$_2$]			0.9[f]		418.41	90
[Tc(N)(DTCOX2)$_2$]		39.11[c]	1[b]		506.52	95

HPLC: [a]Reverse-phase C18 precolumn (Beckman Ultrasphere ODS 4.6 × 45 mm) and a reverse-phase C18 column (Beckman Ultrasphere ODS 4.6 × 250 mm); A = H_2O, B = CH_3CN; 0−20 min, B, 70% (isocratic), 20−22 min, B, 100% (gradient), 22−40 min, B, 100% (isocratic), 40−45 min, B, 70% (gradient). [b]A = NH_4Ac 0.01 M pH 7, B = CH_3CN; 0−20 min, B, 60% (isocratic), 20−30 min, B, 100% (gradient), 30−40 min, B, 100% (isocratic), 40−45 min, B, 60% (gradient). [c]Reverse-phase, C18 precolumn (Waters Symmetry Shield) (3.9 × 20 mm, 5 μm), and a reverse phase C18 column (Waters Symmetry Shield) (4.6 × 250 mm, 5 μm). A = NH_4Ac 0.01 M pH 7, B = CH_3CN; 0−20 min, B, 60% (isocratic), 20−30 min, B, 100% (gradient), 30−40 min, B, 100% (isocratic), 40−45 min, B, 60% (gradient). [d]A = NH_4Ac 0.01 M pH 7, B = CH_3CN; 0−20 min, B, 50% (isocratic), 20−30 min, B, 100% (gradient), 30−40 min, B, 100% (isocratic), 40−43 min, B, 50% (gradient). TLC: [a]RP-C18, CH_3CN/H_2O (90/10); [b]SiO_2, EtOH/$CHCl_3$/C_6H_6 (0.1/2/1.5); [c]SiO_2, CH_2Cl_2; [d]SiO_2, CH_2Cl_2/toluene (1/1); [e]SiO_2, $CHCl_3$/MeOH (98/2); [f]SiO_2, EtOH/$CHCl_3$/C_6H_6 (0.01/2/1.5).

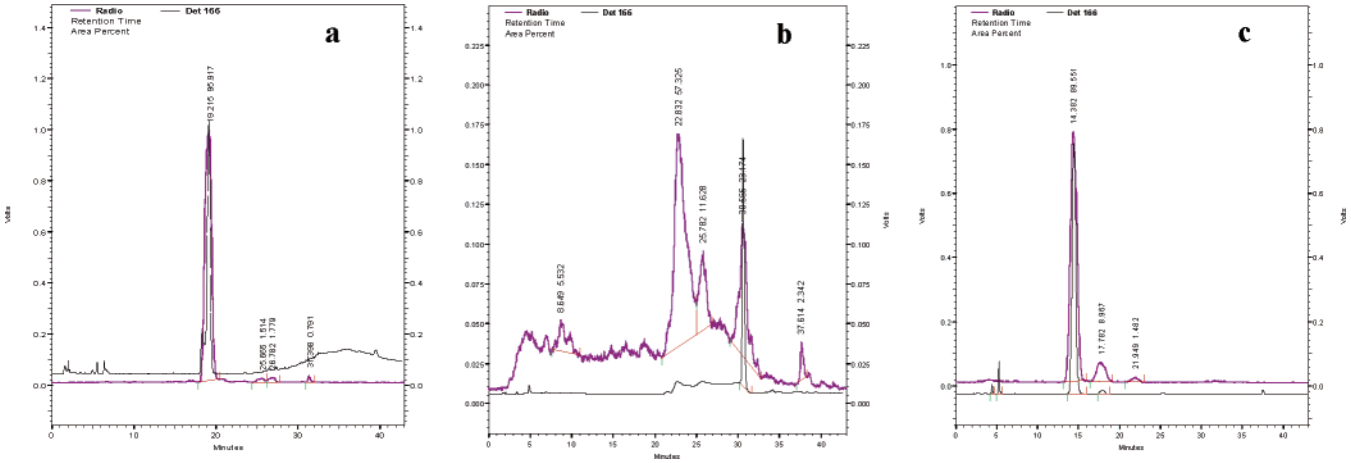

Figure 3. RP-HPLC comparison of (a) [^{99m}Tc(N)(PSiso)$_2$] with [^{99g}Tc(N)(PSiso)$_2$]; (b) [^{99m}Tc(N)Cl(PSiso)PPh$_3$] with [^{99g}Tc(N)Cl(PSiso)PPh$_3$]; (c) [^{99m}Tc(N)(DTC3)(PSiso)] with [^{99g}Tc(N)(DTC3)(PSiso)].

solution with 20% of EtOH and utilized for in vitro and in vivo studies or, alternatively, with a physiological solution containing 0.5 mg/mL of β-HPC.

Stability Studies. *In Vitro Stability*. The in vitro stability of the complexes was evaluated by monitoring the radiochemical purity (RCP) at different time points using the following procedures. In a propylene test tube 50 μL of HPLC purified Tc-99m complex were added to (a) 950 μL of saline, (b) 450 μL of phosphate buffer (0.10 M, pH 7.4), and (c) 950 μL of β-HPC saline solution (0.1−0.5 mg/mL). The resulting mixture was incubated at 37 °C for 24 h. RCP was determined by TLC and HPLC chromatography at 15 min, 1, 3, and 24 h.

Serum Stability. In a propylene test tube 100 μL of HPLC purified Tc-99m complex was added to 900 μL of rat serum and incubated at 37 °C. At 15 min, 1 and 3 h aliquots (200 μL) of the solution were withdrawn, diluted with 800 μL of

phosphate buffer (0.2 M, pH 7.4), and loaded onto an OASIS HLB extraction cartridge previously conditioned with MeOH (1 mL) and equilibrated with water (1 mL). The cartridge was rinsed with MeOH 5% (3 mL), and 90% of the starting activity was eluted with 1 mL of MeOH. Aliquots (100 μL) of this fraction were analyzed by HPLC chromatography.

Glutathione (GSH) and Cysteine Challenge. An aliquot (50 μL) of a freshly prepared aqueous solution of GSH (10 mM) or, alternatively, of L-cysteine (10 mM, 1 mM) was added to a propylene test tube, containing phosphate buffer (250 μL, 0.2 M, pH 7.4), water (100 μL), and Tc-99m complex (100 μL). The mixture was vortexed and incubated at 37 °C for 24 h. A control reaction adding an equal volume of water instead of GSH or cysteine solution was conducted in parallel. At 15, 30 min, 1, 3, and 24 h aliquots of the reaction mixture were analyzed by TLC and HPLC chromatography.

Determination of Log k'_0 Values. Log k'_0 values of complexes were determined by HPLC as described elsewhere (*13*) and compared with the Log k'_0 values of the commercially available cerebral agent [^{99m}Tc]-ECD, obtained under the same chromatographic conditions. The results are reported in Table 1. It has been previously shown that the Log k'_0 values are highly correlated with their Log *P* values as an expression of the lipophilic character molecules.

Log k'_0 is obtained from Log k', where k' is the capacity factor measuring the partitioning of the compound between a nonpolar stationary phase and a polar mobile phase. The Log k' values were determined here using methanol and phosphate buffer (0.02 M, pH 7.4) at various compositions. An analysis of the relationship between Log k' and mobile phase composition gave extrapolated Log k' values at 0% organic solvent composition (Log K'_0) as a measure of the activity partitioning between the hydrophobic stationary phase and water. The Log k'_0 values were extrapolated from the linear part of the curve Log $k' = a + bC$, where C is the methanol concentration and Log k'= Log-$(t_r - t_0)/t_0$.

The elution time (t_0) for an unretained component was considered to be equal to the elution time for $Na^{99g}TcO_4$. For each compound, retention data were measured by using a minimum of four different methanol concentrations in the mobile phase. Each measurement was replicated at least three times.

Animal Studies. Biodistribution was carried out in rats. Before injection, Tc-99m complexes were purified using the procedure outlined above. After purification, the activity recovered was further diluted with a saline solution containing β-HPC 0.1 mg/mL to obtain a final solution that was 2% in ethanol content. Female Sprague−Dawley rats weighing 180−200 g were anesthetized with an intraperitoneal injection of a mixture of Zoletil (40 mg kg^{-1}) and Xilazine (2 mg kg^{-1}). A jugular vein was surgically exposed and 100 μL (300−370 kBq) of the solution containing the radioactive complex were injected. The animals ($n = 3$) were sacrificed by cervical dislocation at different times postinjection. The blood was withdrawn from the heart with a syringe immediately after sacrifice and quantified. Organs were excised, rinsed in saline, weighed and the activity counted in a NaI well counter. Results were expressed as percentage of injected dose per gram (%ID/g).

RESULTS

Synthesis of Disubstituted [^{99m}Tc(N)(R_2PS)$_2$] Compounds. Neutral disubstituted [^{99m}Tc(N)(R_2PS)$_2$] nitrido compounds were prepared, in high yield (>90%), through a two-step procedure (methods 1, 2). The first step involved the preliminary conversion of the starting [$^{99m}TcO_4$]$^-$ into a mixture of prereduced species containing the [Tc(N)]$^{2+}$ multiple bound. The second step, which took place in basic media, required the addition of 0.25−1 mg of the bidentate phosphino-thiol ligand (R_2PSH).

Scheme 1

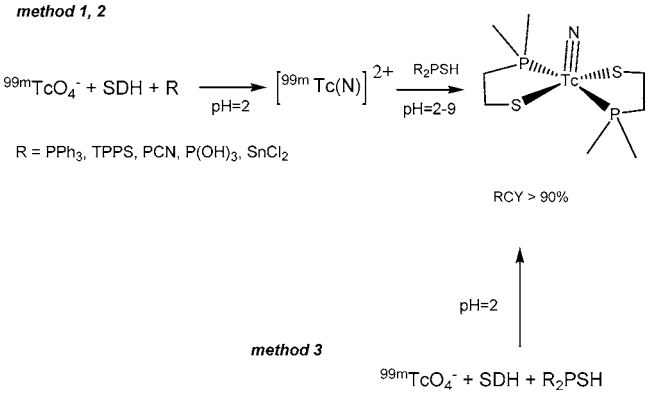

Table 2. Variation of % RCY in Formation of [^{99m}Tc(N)(R_2PS)$_2$] Complexes, at Different Times, as Function of pH, Temperature, and Amount of R_2PSH Ligand

			[Tc(N)(PScy)$_2$] (% RCY)		
PScyH (mg)	pH	temp (°C)	15 min	30 min	60 min
0.050	9	RT	73.0	78.0	91.0
0.050	7	RT	60.4	78.5	87.2
0.050	5	RT	57.3	69.0	85.8
0.050	2	RT	−	−	−
0.050	2	100	40.5	57.9	85.0
1	2	RT	85.0	65.1	94.9
			[Tc(N)(PSiso)$_2$] (% RCY)		
PSisoH (mg)	pH	temp (°C)	15 min	30 min	60 min
0.025	9	RT	73.0	75.0	71.0
0.025	7	RT	86.4	88.5	87.2
0.025	5	RT	84.2	87.2	87.4
0.025	2	RT	−	−	−
0.025	2	100	40.5	57.9	85.0
1	9	RT	78.1	80.1	78.9
1	2	RT	95.0	95.1	94.9

The reaction was carried out using different procedures depending on the reducing agents, the source of nitride (N^{3-}), and the pH employed (Scheme 1).

Coordination of R_2PSH was achieved at basic pH after 15 min at 100 °C. Lower temperatures (50 °C) required prolonged reaction times. Acidic media caused the reaction to be incomplete; in particular when SDH and PPh_3 were used to produce the intermediate nitrido compounds, different species were obtained (vide infra). Following this latter procedure, the influence of pH, temperature, and concentration of R_2PSH on the RCY formation of [^{99m}Tc(N)(R_2PS)$_2$] (R = C_6H_{11} and CH-$(CH_3)_2$) was monitored at different times. The results are illustrated in Table 2.

Alternatively, due to the intrinsic reducing power of the phosphino-thiol ligands, disubstituted symmetrical compounds may be obtained directly with a one-step procedure (method 3) using these ligands as reducing and coordinating agents. In this case an increased amount of R_2PSH (ca. 1−2 mg) was required to guarantee a radiochemical yield >85%. However, this reduction−substitution procedure gave low yield of formation (<70%) when applied to PS*me*H or PS*tbu*H ligands.

Synthesis of Monosubstituted Intermediate [^{99m}Tc(N)-(R_2PS)Cl(PPh_3)] Compounds. The monosubstituted compounds [^{99m}Tc(N)(R_2PS)(PPh_3)]$^+$ were prepared through a two step procedure, as reported in Scheme 2.

The first step involved the reduction of pertechnetate with PPh_3, in acidic media at 100 °C and in the presence of a donor of nitride (N^{3-}) (SDH). A mixture of labile PPh_3-containing intermediate nitrido complexes was obtained. In the second step the monosubstituted asymmetrical compounds [^{99m}Tc(N)(R_2PS)-

Scheme 2

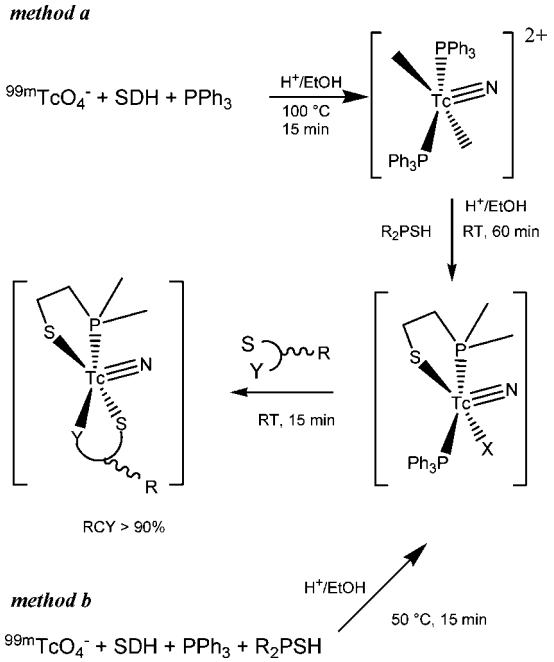

$(PPh_3)]^+$ (R = C_6H_{11}, $CH(CH_3)_2$, and $CH_2CH(CH_3)_2$) were generated, at room temperature, through a ligand exchange reaction by adding a specific amount (10^{-4} mmol) of the selected bidentate phosphino-thiol. Proton concentration was found to be critical in obtaining a quantitative conversion of the mixture of intermediate nitrido complexes into the $[^{99m}Tc(N)(R_2PS)(PPh_3)]^+$ species (Table 2). In fact, as previously described, when the preparation was carried out in basic media, the yield of $[^{99m}Tc(N)(R_2PS)(PPh_3)]^+$ was endangered due to the formation of the corresponding symmetric disubstituted complexes $[^{99m}Tc(N)(R_2PS)_2]$.

Alternatively, the monosubstituted compounds could be obtained in 15 min at 50 °C through a one-step procedure by adding pertechnetate to a vial containing SDH and PPh_3 at low pH (pH = 2) and 10^{-4} mmol of R_2PSH.

A systematic study was performed under the optimized pH and R_2PSH concentrations in order to evaluate the role of the PPh_3 in the formation of monosubstituted complexes compared to the use of other tertiary phosphines. The results indicated that PPh_3 (used as both reducing and coordinating agent) gave better yields compared to other tertiary phosphines (PCN, TPPS, $P(CH_2OH)_3$) or compared to the classical reducing agent tin chloride. These alternative phosphines were selected considering their solubility in hydro-alcoholic solution and their electronic and steric properties.

For all alternative phosphines, the HPLC analysis revealed the formation of $[^{99m}Tc(N)(R_2PS)_2]$ as main products, further underlying the key role of PPh_3 in controlling $[^{99m}Tc(N)(PS)(PPh_3)]^+$ formation and stabilization. The molecular structure of this monosubstituted complex has been schematically drawn in Scheme 2. It is composed of a terminal Tc≡N multiple bond coordinated to a phosphino-thiol ligand (R_2PS) through the neutral phosphorus and deprotonated sulfur thiol atoms and a tertiary phosphine PPh_3. The residual position, in the square pyramid arrangement, is available for the coordination of monodentate ligands such as Cl^-, OH^-, and H_2O (X), present in physiological solution. This hypothesis was confirmed by the comparison of the HPLC profiles of various $[^{99m}Tc(N)X(R_2PS)(PPh_3)]^{+/0}$ (R= C_6H_{11}, $CH(CH_3)_2$, and $CH_2CH(CH_3)_2$) complexes with those of the corresponding $[^{99g}Tc(N)Cl(R_2PS)(PPh_3)]$ compounds prepared with the long-lived isotope Tc-99g (Figure 3b) which showed a mixture of different compounds. One of them was characterized as the neutral $[^{99m}Tc(N)Cl(R_2PS)(PPh_3)]$ species (RCY < 30%). At macroscopic level, these $[^{99g}Tc(N)Cl(R_2PS)(PPh_3)]$ intermediate complexes were prepared by reacting the precursor $[^{99g}Tc(N)Cl_2(PPh_3)_2]$ with the R_2PSH ligand in dichloromethane solution and were characterized by elemental analysis and spectroscopic methods (*22*). In addition, the synthesis and the chemical structure of the $[^{99g}Tc(N)Cl[(C_6H_{11})_2PS](PPh_3)]$ prototype complex has been previously reported (*21*). The X-ray analysis showed a square pyramidal geometry with the nitrido at the apex and the remaining coordinating atoms (P, S, P, Cl) at the base of the pyramid.

At nanomolar level, despite the unfeasibility in identifying the remaining species, the mixture containing the monosubstituted complexes was easily and quantitatively converted into the corresponding final mixed compounds $[^{99m}Tc(N)(R_2PS)(S\text{^}Y)]$ by reaction with the appropriate bidentate S^Y ligand (see below). This behavior suggests that the mixture of intermediate compounds possesses the same $[^{99m}Tc(N)(R_2PS)]^+$ moiety.

Attempts to prepare similar monosubstituted $[^{99m}Tc(N)X(R_2PS)(PPh_3)]^{+/0}$ compounds using PS*me*H and PS*tbu*H failed. The less sterically hindered PS*me*H ligand led only to the formation of the stable disubstituted symmetrical compound $[^{99m}Tc(N)(PSme)_2]$. Meanwhile, the bulkiest PS*tbu*H yielded unstable species which rapidly converted in to the disubstituted $[^{99m}Tc(N)(S\text{^}Y)_2]$ complexes after addition of the bidentate S^Y ligand. This behavior can be attributed to the ligand bulkiness which decreases its binding ability, owing to the increased congestion around the binding face of the P atom. This fact indicates that a careful choice of the bulkiness is necessary to control the formation of $[^{99m}Tc(N)X(R_2PS)(PPh_3)]^{+/0}$.

Synthesis of Asymmetrical $[^{99m}Tc(N)(R_2PS)(S\text{^}Y)]$ Compounds. The preparation of asymmetric $[^{99m}Tc(N)(R_2PS)(S\text{^}Y)]$ was carried out following the procedure reported in Scheme 2. Table 1 summarizes the chromatographic properties and the RCY values obtained for the corresponding hetero-complexes. RCY data showed the ability of S^Y ligands, containing different combinations of heteroatom (S, N, O), to form the final complexes. The results indicated that [S^-,S] ligands such as dithiocarbamate, dithiophosphinate, and dithiocarboxylate exhibited a high selectivity in displacing the monodentate ligands (X^- and PPh_3) from the $[^{99m}Tc(N)X(R_2PS)(PPh_3)]^{+/0}$ intermediate compound. A quick and quantitative conversion into neutral asymmetrical nitrido species occurred within 15 min at room temperature by using a small amount (1−0.025 mg) of the bidentate [S^-, S] ligand.

Analogously, encouraging preliminary results were found using monoanionic bidentate ligands having [S^-, NH_2] as coordinating pairs such as cysteamine (SN) or L-cysteine ethyl ester (SN-Cys). Also in these cases, neutral species of the type $[^{99m}Tc(N)(R_2PS)(S\text{^}NH_2)]$ were isolated after 15 min at 60 °C, by adding 1 mg of the bidentate [S^-, NH_2] ligand to the intermediate species. The $[^{99m}Tc(N)(R_2PS)(SN\text{-}Cys)]$ complex was formed as a mixture of two isomeric forms (60/40 ratio) due to the relative syn or anti orientation of the pendant lateral group with respect to the Tc≡N multiple bond. On the contrary, no reactivity toward the $[^{99m}Tc(N)X(R_2PS)(PPh_3)]^{+/0}$ species was observed for bidentate ligands carrying [O^-, S] or [S^-, O] pair of coordinating atoms. The chemical identity of ^{99m}Tc-complexes was determined by HPLC comparison of their chromatographic properties with those of the corresponding Tc-99g complexes (see Table 1 and Figure 3c).

The Log k_0' values of some representative compounds as measure of the relative lipophilicity of the complexes were calculated by reverse phase HPLC using various mixtures of methanol/phosphate buffer (pH 7.4) as eluant and compared with

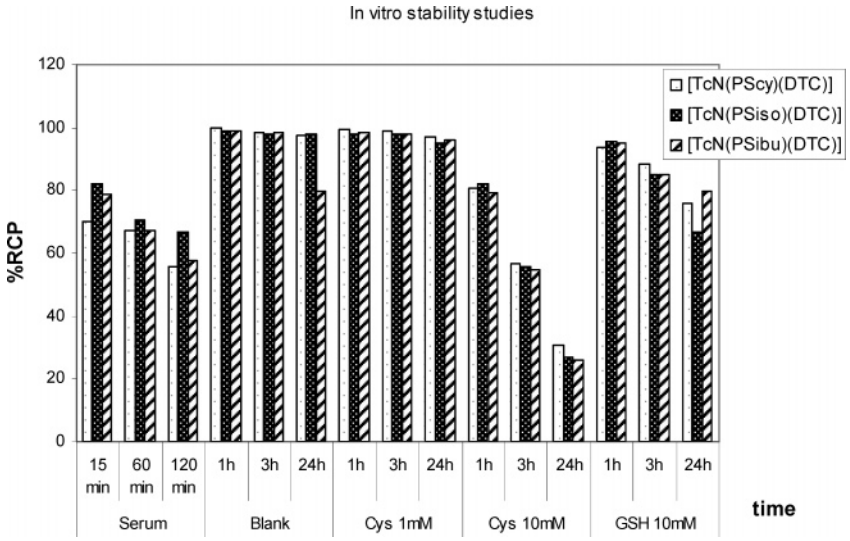

Figure 4. In vitro stability studies of some representative [^{99m}Tc(N)(DTC)(R_2PS)] asymmetrical compounds.

Log k_0' of the commercially available perfusion agent [^{99m}Tc]-ECD measured under the same experimental conditions.

Stability Studies. Neutral disubstituted symmetrical compounds [^{99m}Tc(N)(R_2PS)$_2$] were found stable under all investigated conditions. Neutral asymmetrical [^{99m}Tc(N)(R_2PS)(S^Y)] compounds were stable for 24 h, after HPLC purification, in ethanol solution or in aqueous solution containing 15% EtOH. Transformation of mixed complexes into more hydrophilic compounds was observed after dilution with saline or phosphate buffer (0.02 M, pH 7.4), to obtain a final solution containing 5% EtOH. The corresponding RCP evaluated by TLC and HPLC chromatography was reduced to 50% at 1 h. In these latter conditions a remarkable increase of the stability (RCP 90% after 24 h) in aqueous solution was achieved by adding a small amount of β-HPC (0.5 mg/mL) to the complex solution.

In Vitro Stability Studies with Serum and Challenge with Glutathione or Cysteine. The stability of all complexes in serum and toward transchelation with GSH and cysteine were investigated. The complexes were found stable after serum incubation at 37 °C for 2 h. More specifically, after 15 min of incubation about 5−15% of the starting activity was associated to the plasma proteins, while the remaining activity matched the initial product. After 2 h the activity associated to the proteins was generally increased to 20%, and the HPLC profile revealed the presence of traces of some more hydrophilic compounds near the initial complex.

No significant changes in RCPs of the [^{99m}Tc(N)(R_2PS)$_2$] complexes were observed in challenge experiments, after 24 h of incubation at 37 °C with cysteine and GSH, whereas a slight difference in stability was observed for [^{99m}Tc(N)(R_2PS)(S^Y)] complexes. The results are showed in Figure 4.

No considerable change of RCP was observed after incubation at 37 °C with an excess of GSH. However a more hydrophilic compound was observed after incubation with an excess of Cys (10 mM) as consequence of a tranchelation reaction between the S^Y ligands and Cys. Nevertheless, studies carried out with 1 mM of Cys showed a reduction of the transchelation rate of the complexes which therefore return to stability.

Biodistribution Studies. Biodistribution studies of neutral symmetrical and asymmetrical disubstituted compounds were evaluated in female Sprague−Dawley rats. The experiments were carried out in compliance with the international laws for the conducting of animal experimentation. Purification of the radiolabeled compound before injection was necessary in order to remove excess of cold ligands and any radiochemical impurity formed during the labeling procedure. The radiochemical purity and stability of the purified compounds were verified with HPLC prior to in vivo administration, as well as during the utilized period, to guarantee >90% purity of the injected radiolabeled compounds. Tissue distribution data of neutral disubstituted symmetrical compounds [^{99m}Tc(N)(R_2PS)$_2$] are summarized in Table 3.

Our results show that the substituents at the phosphorus atom of the R_2PSH ligand influence the biodistribution pattern. Notable differences were observed in blood, liver, and kidney accumulations and especially in the brain uptake. For all these compounds a rapid blood clearance is generally observed. The high liver uptake suggests that the hepatobiliary system is the major route of excretion of the administered agents.

In detail, the [^{99m}Tc(N)(PS*iso*)$_2$] complex revealed the highest brain uptake (1.28 ± 0.02% ID/g) at 2 min postinjection (p.i.), with a significant brain-to-blood ratio (B/bl = 4), though, the initial high brain uptake was followed by a rapid wash-out and at 20 min p.i. the brain activity dropped to 0.20 ± 0.02% ID/g. The more lipophilic [^{99m}Tc(N)(PS*tbu*)$_2$] complex showed initial brain uptake (0.71 ± 0.02% ID/g; 2 min p.i.), but a slower brain elimination (0.23 ± 0.06% ID/g; 60 min p.i.), indicating that by increasing the lipophilicity of the complex it is possible to reduce the wash-out from the brain tissue.

Biodistribution of some representative neutral [^{99m}Tc(N)(R_2PS)(S^S)] mixed compounds are summarized as % of dose/g in Table 4. The data show that, at 2 min p.i., all the investigated compounds were distributed throughout the body with a similar pattern, independently from the nature of the two bidentate ligands. The complexes exhibited a rapid blood clearance and, despite their high lipophilicity, the radioactivity was eliminated through the liver and intestines as well as the kidneys and the urine.

A significant initial high extraction by the myocardial tissue was observedfor all [^{99m}Tc(N)(R_2PS)(S^S)] compounds (in the range 5.48 ± 0.09%ID/g; 2.48 ± 0.35% ID/g) followed by a rapid wash-out (0.55 ± 0.09% ID/g; 0.29 ± 0.01% ID/g).

All investigated complexes show a transient but significant initial brain uptake at 2 min p.i. with the activity in the range 0.20 ± 0.01% ID/g and 0.91 ± 0.06% ID/g. A brain-to-blood ratio > 1 was observed at 2 and 10 min p.i., demonstrating that these compounds quickly diffuse across the BBB, probably through passive diffusion due to their lipophilicity.

DISCUSSION

A systematic investigation on the reactivity of bidentate phosphino-thiol ligands (R_2PSH where R = alkyl groups) toward

Table 3. Biodistribution of Some Representative Disubstituted [Tc(N)(R_2PS)$_2$] Compounds, as % Dose/g in Rats (n = 3) at Different Times

	[^{99m}Tc(N)(PSme)$_2$]			[^{99m}Tc(N)(PSiso)$_2$]		
organ	0 min	2 min	20 min	0 min	2 min	20 min
blood	1.94± 0.82	0.90 ± 0.21	0.44 ± 0.03	0.59± 0.14	0.32 ± 0.04	0.23 ± 0.01
brain	0.64± 0.02	0.65 ± 0.02	0.19 ± 0.03	1.18 ± 0.17	1.28 ± 0.09	0.08 ± 0.01
heart	2.96 ± 0.19	0.98 ± 0.12	0.56± 0.01	2.44 ± 1.03	1.36 ± 0.39	0.28 ± 0.04
lungs	1.92 ± 0.04	0.90 ± 0.09	0.59 ± 0.02	1.46 ± 0.24	0.90 ± 0.13	0.35 ± 0.06
liver	0.86± 0.03	1.62 ± 0.20	1.19 ± 0.08	1.73 ± 0.30	2.95 ± 0.40	1.81 ± 0.30
kidneys	4.05 ± 0.96	1.32 ± 0.22	0.87 ± 0.03	3.43 ± 0.91	1.56 ± 0.42	0.56 ± 0.13
intestine	1.35 ± 0.43	1.14 ± 0.22	2.20± 0.26	1.47 ± 0.43	2.48 ± 0.50	13.69 ± 6.10
muscle	0.13± 0.04	0.34 ± 0.07	0.45 ± 0.02	0.15 ± 0.03	0.17 ± 0.05	0.25 ± 0.05
brain/blood	0.33	0.72	0.43	2.00	4.00	0.35
	[^{99m}Tc(N)(PSibu)$_2$]			[^{99m}Tc(N)(PStbu)$_2$]		
organ	0 min	2 min	20 min	0 min	2 min	20 min
blood	1.38 ± 0.23	0.32 ± 0.04	0.20 ± 0.06	2.80 ± 0.77	1.06 ± 0.13	0.43 ± 0.01
brain	0.20 ± 0.04	0.15 ± 0.01	0.09 ± 0.01	0.83 ± 0.01	0.71 ± 0.02	0.36 ± 0.08
heart	2.90 ± 0.08	1.97 ± 0.08	0.62 ± 0.03	3.60 ± 0.75	1.93 ± 0.03	0.97 ± 0.23
lungs	1.94 ± 0.23	1.14 ± 0.15	0.45 ± 0.04	3.27 ± 0.89	1.62 ± 0.02	0.83 ± 0.16
liver	2.68 ± 0.41	4.43 ± 0.26	2.75 ± 0.09	4.75 ± 0.78	7.02 ± 0.62	5.23 ± 0.95
kidneys	2.24 ± 0.01	1.94 ± 0.11	0.47 ± 0.01	4.25 ± 0.53	3.03 ± 0.37	1.16 ± 0.22
intestine	0.58 ± 0.04	1.74 ± 0.06	10.91 ± 3.63	1.68 ± 0.17	4.30 ± 0.18	13.9 ± 3.03
muscle	0.28 ± 0.06	0.37 ± 0.18	0.41 ± 0.06	0.48 ± 0.12	0.65 ± 0.06	0.50 ± 0.04
brain/blood	0.14	0.47	0.45	0.29	0.66	0.83

Table 4. Biodistribution of Some Representative Asymmetrical [Tc(N)(S^Y)(R_2PS)] Compounds, as %Dose/g, in Rats (n = 3) at Different Times

	[^{99m}Tc(N) (PScy) (DTC1)]				[^{99m}Tc(N) (PSiso)(DTC1)]		
organ	0 min	2 min	10 min	20 min	0 min	2 min	20 min
blood	1.52± 1.13	0.23 ± 0.05	0.16 ± 0.03	0.15 ± 0.03	4.24 ± 1.90	0.33 ± 0.02	0.17 ± 0.02
brain	0.26± 0.03	0.20 ± 0.01	0.18 ± 0.03	0.10 ± 0.01	0.31± 0.04	0.56 ± 0.03	0.08 ± 0.01
heart	5.48 ± 0.09	3.79 ± 0.52	1.88 ± 0.06	0.55± 0.07	2.48 ± 0.35	1.24 ± 0.07	0.29 ± 0.01
liver	3.89± 0.22	5.53 ± 1.0.35	5.43 ± 0.90	4.52 ± 1.06	0.18 ± 0.04	3.81 ± 0.09	2.98 ± 0.09
kidneys	4.42 ± 0.47	4.29 ± 0.55	2.58 ± 0.05	1.25 ± 0.26	1.26 ± 0.21	1.87 ± 0.03	0.56 ± 0.02
intestine	1.45 ± 0.01	1.50 ± 0.30	0.29±0.25	5.87±0.43	0.33 ± 0.06	1.57 ± 0.07	4.38 ± 0.91
brain/blood	0.166	0.87	1.13	0.66	0.07	1.69	0.47
	[^{99m}Tc(N) (PSiso)(DTC4)]				[^{99m}Tc(N) (PSiso)(PSS2)]		
organ	0 min	2 min	20 min		0 min	2 min	20 min
blood	1.14 ± 0.59	0.27 ± 0.07	0.17 ± 0.03		0.99± 0.35	0.53 ± 0.02	0.36 ± 0.05
brain	0.61 ± 0.28	0.96 ± 0.14	0.13 ± 0.02		0.83 ± 0.09	0.70 ± 0.04	0.26 ± 0.01
heart	4.81 ± 0.73	1.92 ± 0.47	0.36 ± 0.03		3.70 ± 0.66	2.05 ± 0.36	0.44 ± 0.01
liver	0.42 ± 0.20	3.94 ± 1.85	3.30 ± 0.33		1.84 ± 0.69	3.89 ± 0.52	4.90 ± 0.25
kidneys	2.22 ± 1.29	2.37 ± 0.57	0.68 ± 0.03		4.73 ± 0.96	2.39 ± 0.40	1.00 ± 0.10
intestine	1.40 ± 1.08	3.90 ± 2.59	7.61 ± 2.22		1.77 ± 0.16	2.29 ± 0.35	5.60 ± 0.59
brain/blood	0.54	3.56	0.76		0.84	1.32	0.72
	[^{99m}Tc(N) (PSiso)(DTC3)]				[^{99m}Tc(N) (PSibu)(DTC3)]		
organ	0 min	2 min	20 min		0 min	2 min	20 min
blood	0.58 ± 0.09	0.25 ± 0.06	0.20 ± 0.05		1.42 ± 0.40	0.30 ± 0.02	0.26 ± 0.01
brain	0.86 ± 0.06	0.91 ± 0.06	0.11 ± 0.03		1.11 ± 0.14	0.76 ± 0.11	0.23 ± 0.01
heart	4.78 ± 0.76	1.25 ± 0.43	0.39 ± 0.08		4.02 ± 1.37	2.17 ± 0.61	0.80 ± 0.01
liver	1.63 ± 0.74	3.20 ± 0.39	3.34 ± 0.20		1.99 ± 0.66	4.19 ± 0.72	3.71 ± 0.24
kidneys	4.04 ± 0.40	1.61 ± 0.14	0.65 ± 0.10		5.54 ± 1.21	2.93 ± 0.31	1.05 ± 0.08
intestine	1.60 ± 0.13	2.18 ± 0.21	5.53 ± 0.14		1.35 ± 0.38	1.78 ± 0.15	4.59 ± 3.63
brain/blood	1.48	3.64	0.55		0.78	2.53	0.88

nitrido-^{99m}Tc precursors led to the preparation of pentacoordinate symmetrical [^{99m}Tc(N)(R_2PS)$_2$] and asymmetrical [^{99m}Tc(N)-(R_2PS)(S^Y)] complexes. [^{99m}Tc(N)(R_2PS)$_2$] complexes were prepared following the methods reported in Scheme 1. The best labeling procedure involved ligand-exchange reactions performed in basic media (methods 1, 2) using a very low amount of phosphino-thiol ($\sim 10^{-4}$ mmol). The basic pH was essential in guaranteeing the quantitative formation of the disubstituted products, indicating that the coordination of the R_2PSH ligand probably occurred through the initial nucleophilic attachment of the deprotonated thiol sulfur to the metal center. Lower radiochemical yields were obtained using the R_2PSH ligand as both a reducing and coordinating agent (one-step procedure, method 3), because of the concomitant formation of the corresponding Tc(III) compounds [^{99m}Tc(R_2PS)$_3$] (*20*).

The chemical identity of [^{99m}Tc(N)(R_2PS)$_2$] complexes was established by HPLC comparison with the corresponding compounds prepared at macroscopic level with the long-lived isotope Tc-99g (Figure 3a). The remarkable in vitro stability of the disubstituted compounds is determined by the combination of two π-acceptor (P) and two π-donor (S^-) atoms around the $[Tc(N)]^{2+}$ core which confer high thermodynamic stability and kinetic inertness.

Biological evaluation of these agents showed encouraging results. The [^{99m}Tc(N)(PS*iso*)$_2$] compound showed the best brain uptake of the series with a significant brain-to-blood ratio (B/bl = 4) at 2 min p.i. (Table 3). However, the initial high brain uptake was followed by a rapid wash-out, and at 20 min p.i. brain activity dropped to 1/6 of its initial value. Data collected for the more lipophilic [^{99m}Tc(N)(PS*tbu*)$_2$] species revealed that

it was possible to modulate the kinetic of the wash-out, increasing the permanence of the complex in the tissue.

These results suggested that the diffusion across the BBB was a reversible process for this class of complexes, and that these compounds moved freely in and out of the brain. This behavior could be attributed to the absence of an efficient trapping mechanism that prevents the complex from crossing the BBB in the opposite direction. In connection, while the lipophilicity of $[Tc(N)(R_2PS)_2]$ symmetrical compounds can be modified by varying the substituents on the phosphorus donor or on the R_2PSH backbone, the introduction of pendant groups that could be involved in trapping mechanisms required instead quite complicated and difficult synthesis.

Considering the recent demonstration that other disubstituted complexes of the type $[^{99m}Tc(N)(S\text{^}Y)_2]$, where S^Y is a dithiocarbamate (DTC) or a dithiophosphinate (PSS) ligand, showed an appreciable accumulation in the cerebral tissue (*25*, *27*, *28*), we decided to design a new class of CNS agents which combined the biological properties of $[^{99m}Tc(N)(S\text{^}Y)_2]$ and $[^{99m}Tc(N)(R_2PS)_2]$ compounds through the preparation of mixed pentacoordinate species of the type $[^{99m}Tc(N)(R_2PS)(S\text{^}Y)]$. In these complexes the co-ligand S^Y offered the possibility of being modified with an appropriate functional group designed for trapping mechanism in order to increase the brain retention for longer time intervals.

The possibility of introducing only one R_2PSH ligand onto a $[Tc(N)]^{2+}$ group was accomplished with bulky aliphatic substituents to the phosphine phosphorus under particular reaction conditions. In fact, the existence of a monosubstituted phosphino thiolato complex $[^{99g}Tc(N)Cl(R_2PS)(PPh_3)]$ has already been demonstrated at macroscopic level using the encumbering 2-(dicyclohexylphosphino)ethanethiol (PS*cy*H) ligand (*21*). The subsequent replacement of the monodentate chloride and PPh_3 ligands with a mononegative chelate (S^Y) such as dithiocarbamate (DTC) permitted the preparation of neutral disubstituted asymmetrical complexes of the type $[^{99g}Tc(N)(R_2PS)(DTC)]$. They represent prototypes of a new class of complexes characterized by the presence of the $[Tc(N)(R_2PS)]^+$ building block (*22*).

Identical asymmetrical monosubstituted $[^{99m}Tc(N)Cl(R_2PS)(PPh_3)]$ and disubstituted $[^{99m}Tc(N)(R_2PS)(DTC)]$ species were efficiently prepared at tracer level, following the procedures indicated in Scheme 2. The acidic medium was essential in obtaining the monosubstituted compounds. In fact, high proton concentration prevented the thiol group of the R_2PSH ligand from being deprotonated, thus reducing its affinity toward the metal center. On the contrary, as described above, basic conditions favored the substitution of chlorine and PPh_3 ligands giving the substitution inert $[^{99m}Tc(N)(R_2PS)_2]$ symmetrical complexes.

In addition, the use of PPh_3 was also found to be a key factor in the redox synthesis and in the stabilization of the monosubstituted compounds. In particular in the one step procedure (method b), the complex was obtained though a redox-exchange reaction, by adding pertechnetate to a vial containing SDH, PPh_3 and the R_2PSH, in the presence of H^+. Despite the recognized ability of the phosphino thiol ligands to work both as reducing and coordinating agents, the small amount ($\sim 10^{-4}$ mmol) of R_2PSH used in this preparation was not enough to guarantee reduction of the pertechnetate. Thus, reduction was performed by PPh_3 that simultaneously acts with R_2PSH as coordinating agent to form $[^{99m}Tc(N)Cl(R_2PS)(PPh_3)]$ compounds.

Addition of the appropriate bidentate mononegative ligand (S^Y) to the reaction vial containing the monosubstituted species (15 min, at room temperature) gave the final neutral $[^{99m}Tc(N)(R_2PS)(S\text{^}Y)]$ complexes in high yield. These results suggest that the monosubstituted $[Tc(N)Cl(R_2PS)(PPh_3)]$ complex represents the key intermediate for the synthesis of this new class of mixed technetium species.

In general, the intermediate complex prefers to react with S^Y ligands having 'soft' σ-,π-donor combinations such as $[S^-, S]$ or $[S^-, NH_2]$ pairs, whereas ligands containing at least one 'hard' σ-donor atom, such as $[O^-, S]$ or $[S^-, O]$ combinations, do not react at all. The ability to form the $[^{99m}Tc(N)(R_2PS)(S\text{^}Y)]$ species ($R = CH(CH_3)_2$), expressed as % of RCY, is as follows:

$$DTC[94\%] > PSS[90\%] > DTCOX[88\%] > SN[85\%] \geq SN\text{-}Cys[83\%]$$

In vitro stability studies demonstrated that these mixed agents were stable for hours in aqueous solution in the presence of β-HPC and inert toward tranchelation in the presence of GSH (10 mM) or cysteine (1 mM). This indicates that the combination of π-acceptor and π-donor coordinating atoms is responsible for the stability and kinetic inertness of the resulting mixed complexes in this case as well. No significant interaction with the serum protein was observed.

In vivo biodistribution data of some representative $[^{99m}Tc(N)(R_2PS)(S\text{^}Y)]$ compounds displayed a similar pattern, comparable to those exhibited by the symmetrical $[^{99m}Tc(N)(PSiso)_2]$ complex. All investigated compounds showed a transient brain uptake and encouraging B/bl ratio >1, indicating that this class of mixed complexes retains the ability to freely cross the intact BBB. The initial brain uptake of these tracers was apparently driven by their lipophilic character as we have already demonstrated for the disubstituted compounds. Data collected for the complexes having a Log k_0' value around 4.4 ($[^{99m}Tc(N)(PSibu)(DTC3)]$ and $[^{99m}Tc(N)(PSiso)(PSS2)]$) revealed that the kinetic of the wash-out from the brain tissue was decreased.

Prolonged brain retention must still be achieved, but the possibility of introducing specific groups onto the S^Y ligand in mixed complexes allows for the designing of updated agents which may be subject to the trapping mechanism inside the cerebral tissue. Studies aimed toward this goal are currently in progress (*29*).

CONCLUSIONS

This study devises a general procedure for the preparation of a new class of nitrido asymmetrical Tc-99m complexes containing two different bidentate ligands bound to the same $[Tc(N)]^{2+}$ core, which could be used to design either essential or target specific imaging agents.

This procedure is based on the chemical property of a new monosubstituted $[Tc(N)Cl(R_2PS)(PPh_3)]$ species which represents the key intermediate for the development of a new class of neutral pentacoordinate asymmetrical nitrido compounds of the type $[Tc(N)(R_2PS)(S\text{^}Y)]$, characterized by the presence of a Tc≡N terminal group, an *ancillary* P^S ligand and a bidentate mononegative co-ligand (S^Y), such as a dithiocarbamate. In these complexes the phosphino-thiol ligand stabilizes the metal oxidation state, whereas the S^Y chelate, designed to carry a functional group or a bioactive molecule, completes the metal coordination sphere.

The molecular weight of the $[Tc(N)(R_2PS)]^+$ building block (about 300 Da) allows the molecular weight of the final compound to be maintained within the limit required to cross the BBB. Moreover, the bidentate ligand S^Y may be used to carry additional functional groups which are useful for the trapping mechanism such as 'pH shift', enzymatic degradation mechanism, and receptor specific interactions, to increase brain retention for longer time intervals.

The flexibility of this system due to the possibility of changing the substituents at the P atoms and/or the bidentate ligand may

be utilized to design a wide range of Tc≡N mixed compounds and to modulate their biological properties. The discovery that the amino acid cysteine exhibited encouraging coordinating properties toward the $[Tc(N)(R_2PS)]^+$ intermediate suggests the use of this chelating system for incorporating a short peptide in a Tc-99m asymmetrical complex.

ACKNOWLEDGMENT

The authors are grateful to Mr. Mariano Schiavon for his assistance in the animal studies.

LITERATURE CITED

(1) Kung, H. F., Kung, M. P., and Choi, S. R. (2003) Radiopharmaceuticals for Single-Photon Emission Computed Tomography Brain Imaging. *Sem. Nucl. Med. 33*, 2−13.

(2) Kung, H. F., Yu, C. C., Billings, J., Molnar, M., and Blau, M. (1985) Synthesis of New Bis(Aminoethanethiol) (BAT) Derivatives: Possible Ligands for 99mTc Brain Imaging Agents. *J. Med. Chem. 28*, 1280−1284.

(3) Hom, R. K., and Katzenellenbogen, J. A. (1997) Technetium-^{99m}Tc-Labeled Receptor-Specific Small-Molecule Radiopharmaceuticals: Recent Developments and Encouraging Results. *Nucl. Med. Biol. 24*, 485−498.

(4) Boschi, A., Uccelli, L., Duatti, A., Bolzati, C., Refosco, F., Tisato, F., Romagnoli, R., Baraldi, P. G., Varani, K., and Borea, P. A. (2003) Asymmetrical Nitrido Tc-99m Heterocomplexes as Potential Imaging Agents for Benzodiazepine Receptors. *Bioconjugate Chem. 14*, 1279−1288.

(5) Alberto, R., Schibli, R., Waibel, R., Abram, U., and Schubiger, A. P. (1999) Basic aqueous chemistry of $[M(OH_2)_3(CO)_3]^+$ (M = Re, Tc) directed towards radiopharmaceutical application. *Coord. Chem. Rev. 190*−*192*, 901−919.

(6) Egli, A., Alberto, A., Tannahill, L., Schibli, R., Abram, U., Schaffland, A., Waibel, R., Tourwe', D., Jeannin, L., Iterbeke, K., and Schubiger, P. A. (1999) Organometallic ^{99m}Tc-aquaion labels peptide to an unprecedent high specific activity. *J. Nucl. Med. 40*, 1913−1917.

(7) Spies H., Fietz Th., Glaser M., Pietzsch H. J., and Johannsen, B. (1995) The '$n + 1$' concept in the synthesis strategy of novel technetium and rhenium tracer. In *Technetium and Rhenium in Chemistry and Nuclear Medicine 4* (Nicolini, M., Bandoli, G., and Mazzi, U., Eds.) pp 243−246, SGEditoriali, Padova, Italy.

(8) Johannsen, B., Berger, R., Brust, P., Pietzsch, H. J., Scheunemann, M., Seifert, S., Spies, H., and Syher, R. (1997) Structural modification of receptor-binding technetium-99m complexes in order to improve brain uptake. *Eur. J. Nucl. Med. 24*, 316−319.

(9) Bolzati, C., Boschi, A., Duatti, A., Prakash, S., Uccelli, L., Refosco, F., Tisato, F., and Bandoli, G. (2000) Geometrically Controlled Selective Formation of Nitrido Technetium(V) Asymmetrical Heterocomplexes with Bidentate Ligands. *J. Am. Chem. Soc. 122*, 4510−4511.

(10) Bolzati, C., Boschi, A., Uccelli, L., Tisato, F., Refosco, F., Cagnolini, A., Duatti, A., Prakash, S., Bandoli, G., and Vittadini, A. (2002) Chemistry of the strong electrophilic metal fragment $[^{99}Tc(N)(PXP)]^{2+}$ (PXP = Diphosphine ligand). A novel tool for the selective labeling of small molecules. *J. Am. Chem. Soc. 124*, 11468−11479.

(11) Boschi, A., Bolzati, C., Benini, E., Malagò, E., Uccelli, L., Duatti, A., Piffanelli, A., Refosco, F., and Tisato, F. (2001) A novel approach to the high-specificic-activity labeling of small peptides with the technetium-99m fragment $[^{99m}Tc(N)(PXP)]^{2+}$ (PXP = Diphosphine ligand). *Bioconjugate Chem. 12*, 1035−1042.

(12) Boschi, A., Bolzati, C., Uccelli, L., Duatti, A., Benini, E., Refosco, F., Tisato, F., and Piffanelli, A. (2002) A class of asymmetrical nitrido ^{99m}Tc heterocomplexes as heart imaging agents with improved biological properties. *Nucl. Med. Commun. 23*, 689−693.

(13) Boschi, A., Uccelli, L., Bolzati, C., Duatti, A., Sabba, N., Moretti, E., Di Domenico, G., Zavattini, G., Refosco, F., and Giganti, M. (2003) Biological Evaluation of monocationic Asymmetrical Nitride Tc-99m Heterocomplexes Showing high Heart Uptake and Improved Imaging Properties. *J. Nucl. Med. 44*, 806−814.

(14) Hatada, K., Riou, L. M., Ruiz, M., Yamamichi, Y., Duatti, A., Lima, R. L., Goode, A. R., Watson, D. D., George A., Beller, G. A., and Glover, D. K. (2004) ^{99m}Tc-N-DBODC5, a New Myocardial Perfusion Imaging Agent with Rapid Liver Clearance: Comparison with ^{99m}Tc−Sestamibi and ^{99m}Tc-Tetrofosmin in Rats. *J. Nucl. Med. 45*, 2095−2101.

(15) Bolzati, C., Benini, E., Cazzola, E., Jung, C. M., Tisato, F., Refosco, F., Pietzsch, H. J., Spies, H., Uccelli, L., and Duatti, A. (2004) Synthesis, Characterization and Biological Evaluation of Neutral Nitrido Technetium(V) Mixed Ligand Complexes Containing Dithiolates and Aminodiphosphines. A Novel System for Linking Technetium to Biomolecules. *Bioconjugate Chem. 15*, 628−637.

(16) Bolzati, C., Refosco, F., Cagnolini, A., Tisato, F., Boschi, A., Duatti, A., Uccelli, L., Dolmella, A., Marotta, E., and Tubaro, M. (2004) Synthesis, Solution- State and Solid-State Structural Characterization on Monocationic Nitrido Heterocomplex $[M(N)(DTC)(PNP)]^+$ (M = ^{99}Tc, Re; DTC = Dithiocarbammate; PNP = Heterodiphosphine) *Eur. J. Inorg. Chem.* 1902−1913.

(17) Tisato, F., Refosco, F., Porchia, M., Bolzati, C., Bandoli, G., Dolmella, A., Duatti, A., Boschi, A., Jung, C. M., Pietzsch, H. J., and Kraus, W. (2004) The Crucial Role of the Diphosphine Heteroatom X in the Stereochemistry and Stabilization of the Substitution-Inert $[M(N)(PXP)]^{2+}$ Metal Fragments (M = Tc, Re; PXP = Diphosphine Ligand) *Inorg. Chem. 43*, 8617−8625.

(18) Bolzati, C., et al. Unpublished data.

(19) Bolzati, C., Boschi, A., Uccelli, L., Malagò, E., Bandoli, G., Tisato, F., Refosco, F., Pasqualini, R., and Duatti, A. (1999) Synthesis of a Novel Class of Trigonal Bipyramidal Nitrido Tc(V) Complexes with Phosphino-thiol Ligands. Crystal Structure of $[^{99g}Tc(N)(L1)_2]$ [L1 = 2-(Diphenylphosphino)-ethanethiolato] and $[^{99g}Tc(N)(L5)_2]$ [L5 = 2-(Diphenylphosphino)-propanethiolato]. *Inorg. Chem. 38*, 4473−4479.

(20) Bolzati, C., Uccelli, L., Boschi, A., Malagò, E., Duatti, A., Tisato, F., Refosco, F., Pasqualini, R., and Piffanelli, A. (2000) Synthesis of a Novel Class of Nitrido Tc-99m Radiopharmaceutical with Phosphino-Thiol Ligands Showing Transient Heart Uptake. *J. Nucl. Med. Biol. 27*, 369−374.

(21) Bolzati, C., Malagò, E., Boschi, A., Cagnolini, A., Porchia, M., and Bandoli, G. (1999) Symmetric bis-substituted and asymmetric mono-substituted nitridotechnetium complexes with heterofunctionalized phosphino-thiolate ligands. *New J. Chem. 23*, 807−809.

(22) Bolzati, C., *et al.*, manuscript in preparation.

(23) Duatti, A., Marchi, A., and Pasqualini, R. (1990) Formation of the Tc≡N multiple bond from ammonium pertechnetate with S-methyl dithiocarbazate and its application to the preparation of technetium-99m radiopharmaceuticals. *J. Chem. Soc., Dalton Trans.* 3729−3733.

(24) Pasqualini, R., Duatti, A., Bellande, E., Comazzi, V., Brucato, V., Hoffschir, D., Fagret, D., and Comet, M. (1994) Bis(dithiocarbamato) nitrido technetium-99m radiopharmaceuticals: a class of neutral myocardial imaging agents. *J. Nucl. Med. 35*, 334−341.

(25) Bellande, E., Comazzi, V., Laine, J., Lecayon, M., Pasqualini, R., Duatti, A. and Hoffschir, D. (1995) Synthesis and biodistribution of nitrido technetium-99m radiopharmaceuticals with dithiophosphinate ligands: a class of brain imaging agents. *Nucl. Med. Biol. 22*, 315−320.

(26) Demaimay, F., Noiret, N., Roucoux, A., Patin, H., Bellande, E., Pasqualini, R., and Moisan, A. (1997)New bis(dithiocarboxylato)-nitridotechnetium-99m radiopharmaceuticals for leucocyte labelling: *In vitro* and *In vivo* studies. *Nucl. Med. Biol. 24*, 439−445.

(27) Pasqualini, R., Bellande, E., Comazzi, V., Lainé, J., Lécayon, M., Hoffschir, D., and Duatti, A. (1993) Synthesis of a neutral TcN-dithiocarbamate complex bearing ester groups: A new potential imaging agent for cerebral perfusion. *J. Nucl. Med* 34, 18 P. No 63 abstract.

(28) Zhang, J., Wang, X., and Li, C. Y., (2002) Synthesis and biodistribution of a new ^{99m}Tc nitrido complex for cerebral imaging. *J. Nucl. Med. Biol. 29*, 665−669.

(29) Bolzati, C., *et al.*, manuscript in preparation.

BC050358Q

Surface-Assisted Delivery of Fluorescent Groups to hGST A1-1 and a Lysine Mutant

Johan Viljanen, Lotta Tegler, Jenny Larsson, and Kerstin S. Broo*

IFM, Department of Organic Chemistry, Linköping University S-581 83 Linköping, Sweden. Received September 13, 2005

Human glutathione transferase (hGST) A1-1 and a lysine mutant (A216K) can both be rapidly and site-specifically acylated on Y9 and K216, respectively, using a range of thiolesters of glutathione (GS-thiolesters) as modifying reagents. The present investigation was aimed at developing a method with which to deliver a fluorescent acyl group from a solid support under conditions compatible with standard protein purification schemes. A number of fluorescent GS-thiolesters with modified peptide backbones were therefore prepared and tested for reactivity toward hGST A1-1 and the A216K mutant. Substitutions at the α-NH_2 part of the glutathione backbone were not tolerated by the proteins. However, two fluorescent reagents that carry a biotin moiety at the C-terminal part of glutathione were found through MALDI-MS experiments to react in solution with Y9 of the wild-type protein and one reagent with K216 of A216K. The reaction can take place in the presence of glutathione and even in a crude *E. coli* lysate of cells expressing A216K. Delivery of the fluorescent group to Y9 or K216 was possible using NeutrAvidin (NA) beads that had been preincubated with biotinylated reagent. Alternatively, excess reagent can be removed by a brief incubation with NA beads. We have thus now developed a system for protein labeling with easy removal of excess and used up low-molecular weight reagent. This strategy can conceivably be utilized in future protein purification and labeling experiments.

INTRODUCTION

Following the completion of the HUGO project (*1*, *2*), proteomic research has become an even more expansive field (*3*). There is thus a considerable need for tools that can aid in expression, purification, and analysis of old and new proteins. A popular method is to express a protein linked to a dependable fusion-protein partner (*4*, *5*). In our protein reengineering efforts, we have focused on extending the repertoire of protein scaffolds by chemical modification to introduce an artificial group (*6*−*8*). This new methodology could conceivably be exploited in protein fusion and protein purification applications.

We use the glutathione transferases (GSTs, EC 2.5.1.18)[1,2] as scaffolds, and on the basis of the results from our previous studies (*6*−*8*), we have focused on human glutathione transferase (hGST) A1-1 (Figure 1), which is easy to express in a high yield, displays a high stability, is easy to purify, and is relatively tolerant to mutations. A number of crystal structures of the GSTs have been published, and there is thus an extensive knowledge of structure−activity relationships (*9*). The GSTs are detoxication enzymes (phase II) that catalyze the nucleophilic addition of the thiol of glutathione (GSH, Scheme 1) to a wide range of hydrophobic electrophilic molecules (*10*−*13*). The proteins form homo- or heterodimers (*12*, *14*) and the fold of the N-terminal part of the proteins where GSH binds (G-site) is very similar throughout the classes (*10*, *15*). The differences between the isoenzymes are mostly situated in the promiscuous hydrophobic binding sites (H-sites) that provide a broad and overlapping substrate specificity (*16*). In the alpha class the catalytic function is dependent on a conserved tyrosine residue in the G-site that aids in the ionization of GSH to form the more reactive thiolate ion (*10*). The modular features of the GSTs are close to ideal from a protein engineering aspect with specific binding of GSH in the G-site combined with an

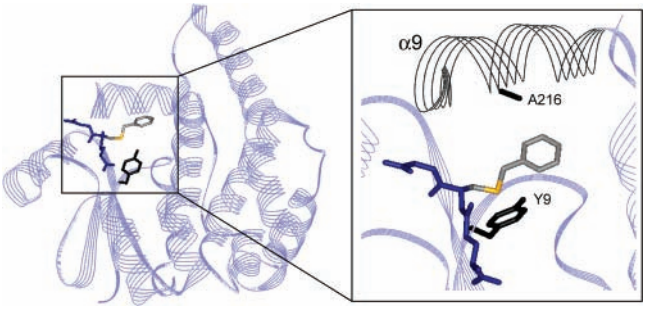

Figure 1. A close-up of the crystal structure (1GUH) of wt hGST A1-1 in a complex with *S*-benzylglutathione (*15*). The targeted positions (Y9 and A216) are shown in "stick" representation, and the flexible helix 9 (α9) is also indicated in the figure. The protein is dimeric but shown here as a monomer for reasons of clarity of presentation.

Scheme 1

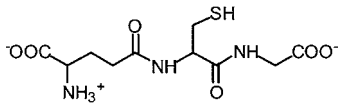

GSH

* To whom correspondence should be addressed. Phone: +46-13-28 66 71, Fax +46-13-12 25 87, E-mail: kerbr@ifm.liu.se.

[1] Abbreviations: ACN, acetonitrile; A216K-Cou, coumarin-labeled A216K.; Boc-Glu-OtBu, *N*-α-t-Boc-L-glutamic acid α-*tert*-butyl ester; C18, octadecyl; CDNB, 1-chloro-2,4-dinitrobenzene; DIPCIDI, *N*,*N*′-diisopropylcarbodiimide; DIPEA, *N*,*N*-diisopropylethylamine, DMF, dimethylformamide; Fmoc-Cys(Mmt)-OH, *N*-α-Fmoc-*S*-*p*-methoxytrityl-L-cysteine; Fmoc-Cys(t-Bu-thio)-OH, *N*-α-Fmoc-*S*-*tert*-butylthio-L-cysteine; FRET, fluorescence resonance energy transfer; GSH, glutathione, γ-Glu-Cys-Gly; GST, glutathione transferase; hGST A1-1, GST A1-1 isoform from human; HOBt, *N*-hydroxybenzotriazole·H_2O; G-site, glutathione-binding site; GS-thiolester, thiolester of glutathione; HPLC, high performance liquid chromatography; H-site, hydrophobic electrophile binding site; MALDI-MS, matrix-assisted laser desorption mass spectrometry; NA, immobilized NeutrAvidin; NaP_i, sodium phosphate; TFA, trifluoroacetic acid; TOF, time-of-flight; UV, ultraviolet; wt, wild-type.

[2] This nomenclature is derived from that recommended by Mannervik, B. et al. (1992) *Biochem. J. 282 (Pt 1)*, 305−6.

10.1021/bc0502762 CCC: $33.50 © 2006 American Chemical Society
Published on Web 03/01/2006

Scheme 2

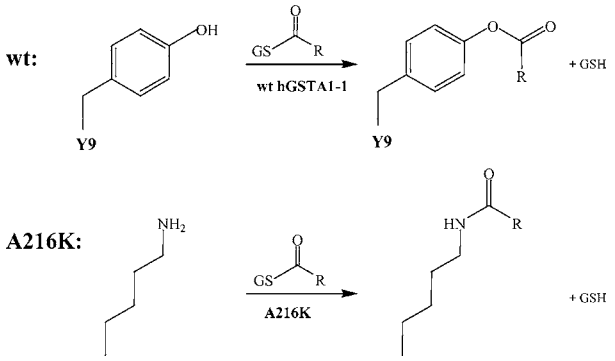

adjacent, promiscuous H-site. This, together with the robustness of the proteins, singles out the GSTs as exceptional candidates for chemical reengineering purposes.

Previously, we reported that hGST A1-1 (Figure 1) can be site-specifically acylated on a single tyrosine residue (Y9) using thiolesters of glutathione (GS-thiolesters, Scheme 2) (*6*). Out of a total of 20 GS-thiolesters tested, 15 are accepted by hGST A1-1 (*7*), and this is thus a very versatile reaction. We then produced a mutant (A216K) of hGST A1-1 that can be rapidly and site-specifically modified at the introduced lysine residue to form a stable amide linkage with a range of acyl groups (Scheme 2) (*8*). The reaction can take place in the presence of GSH and even in a crude *E. coli* lysate. The acylation reaction is very versatile, fast, and site-directed toward one residue in the protein (Y9 or K216) with minimal side reactions. This is due to the glutathione-based backbone of the reagents that orient the thiolester functionality in close proximity to the reactive residues while the adjacent, promiscuous H-site accepts a large variety of acyl groups. Using an appropriate GS-thiolester reagent, we can thus chemically reengineer folded protein scaffolds with the goal of obtaining new function.

To create an even more user-friendly acylating reagent, we wanted to investigate the possibility of surface-assisted delivery of the acyl group to the folded protein scaffold. If the acyl group could be delivered from a solid support or if a solid support could be used to mop up excess reagent, the need for purification of the protein conjugate from excess reagent after labeling would be removed. Because of the physiological importance of the GSTs, alot of work has been put into investigating the substrate requirements, both for GSH (*17*−*19*) and also for the electrophile (*16*). It has been found that even though the binding of GSH by the GSTs is quite specific, some changes of the peptide are accepted (*18*). Alterations of the unusual γ-Glu part of the tripeptide are generally not accepted whereas the GSTs seem to be tolerant to some changes at the C-terminal glycyl-moiety (*18, 19*). However, since neither the A216K mutant nor our particular type of reaction has been studied in this respect, we decided to synthesize a series of fluorescent GS-thiolesters where the GSH moiety was altered either at the α-NH_2 group (Scheme 3) or at the glycine residue (GSC-thiolesters, Scheme 4).

MATERIALS AND METHODS

All chemicals and reagents used were of the highest purity available. The tripeptides were synthesized using solid-phase Fmoc-chemistry, and protected amino acids were purchased from Novabiochem (Darmstadt, Germany) or Bachem Holding AG (Weil am Rhein, Germany). The fluorescent acyl groups were purchased from Sigma-Aldrich, Inc. (St. Louis, MO) or Molecular Probes, Inc. (Eugene, OR). NHS-activated Sepharose was purchased from Amersham Biosciences (Uppsala, Sweden) and EZ-LinkPEO-Iodoacetyl Biotin and Immobilized NeutrAvidin (NA) gel were purchased from Pierce Biotechnology, Inc.

Scheme 3

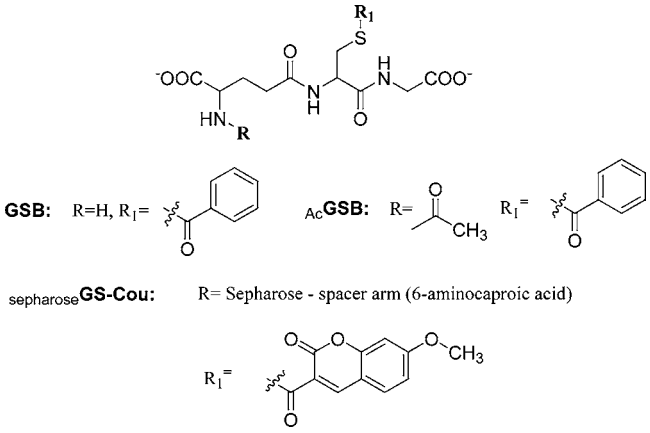

(Rockford, IL). All solid-phase syntheses were carried out in a VacMaster (International Sorbent Technology). The HPLC experiments were carried out using a Kromasil C_8-column (4.6 mm × 250 mm, Supelco inc.) or a Grace Vydac Everest C18 column (4.6 mm × 150 mm) attached to a Varian system with a ProStar 230 Delivery System, a ProStar 330 Photodiode Array Detector, controlled by the Varian LC Software. All mass spectra were recorded using a MALDI-TOF MS (Voyager System 4212, Applied Biosystems) with detection in the positive mode. The UV measurements were performed using a Varian Cay 100 Scan UV-visible spectrophotometer and the results analyzed with the CaryWin UV software.

Attachment of GS-Cou to NHS-Activated Sepharose and Incubation with hGST A1-1. The tripeptide GS-Cou was attached to NHS-activated Sepharose (Amersham Biosciences) in accordance with the protocol supplied by the manufacturer. The substitution level was 16−23 μmol/mL drained gel, and the thiolester was added in a 3.5 times excess over activated groups. The reaction was performed at 25 °C for 3 h. Unreacted NHS groups on the gel were then blocked, and the gel was washed again in accordance with the protocol to remove excess GS-Cou. The derivatized gel fluoresced under a UV lamp (λ = 337 nm). The gel was stored in buffer (0.1 M NaPi, pH 7) at +4 °C until used in the experiments.

The wt protein hGST A1-1 was added to the $_{\text{sepharose}}$GS-Cou gel with the immobilized thiolester in a ratio of protein:thiolester of 1:20 assuming a 100% yield in the derivatization reaction. The mixture was allowed to incubate at 25 °C for 5 h, and the protein was then eluted with a quick spin in a tabletop centrifuge. The eluted protein was digested with *Staphylococcus aureus* V-8 Protease (see below), and the peptide fragments were analyzed with MALDI-MS.

Synthesis of $_{\text{Ac}}$GSB. To synthesize $_{\text{Ac}}$GSB, GSB (2 mM) was incubated with 20 equivalents of sulfosuccinimidyl-acetate in 0.1 M NaP_i, pH 7.0 at r.t. After 30 min another 20 equivalents of sulfosuccinimidyl acetate was added to the reaction mixture. The reaction was followed by analytical reversed phase HPLC using a GraceVydac, Everest C-18 column (4.6 × 150 mm) with a shallow gradient of ACN:H_2O from 20 to 90% ACN. The identity of the product was confirmed with MALDI-MS (Voyager System 4212, Applied Biosystems) using an α-cyano-4-hydroxycinnamic acid matrix with detection in the positive mode. The acetylated product was purified by reversed phase HPLC.

Synthesis of γ-Glu-Cys-Cys (GSC). The tripeptide γ-Glu-Cys-Cys was synthesized using Fmoc-chemistry, starting from Fmoc-Cys(t-Bu-thio)-Wang-resin (0.5 g, 0.51 mmol/g). The two thiol groups in the peptide were orthogonally protected with the Mmt- and t-Bu-thio group to enable selective deprotection. Deprotection of the Fmoc groups was carried out using 20%

Scheme 4

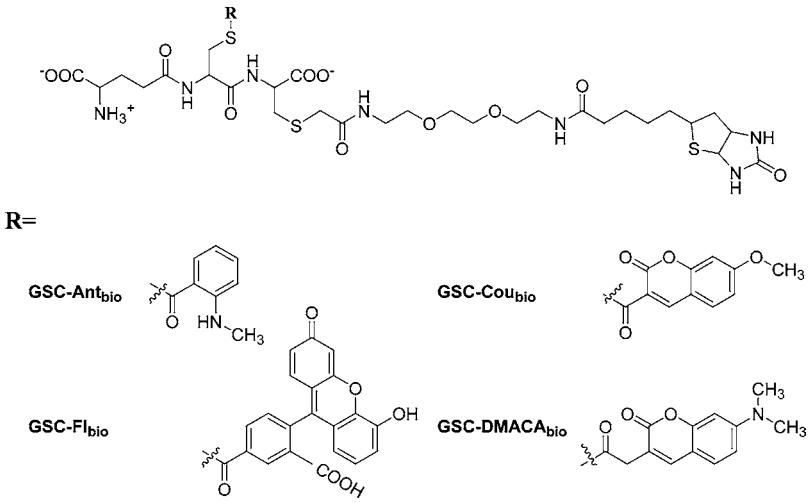

piperidine in DMF. Couplings of Fmoc-Cys(Mmt)-OH and subsequently Boc-Glu-OtBu were performed in DMF using amino acid:HOBt:TBTU:DIPEA (3:5:5:6), with coupling times of 1−2 h. The deprotection and coupling steps were monitored by Kaiser tests (*20*), to estimate the amount of free amino groups. After completed synthesis, the polymer was washed thoroughly with DMF and DCM and dried under vacuum.

Synthesis of C-Terminally Biotinylated GSC-thiolesters. The tripeptides were synthesized in parallel, each on a 0.025 mmol scale, starting with 56 mg of protected γ-Glu-Cys-Cys -polymer for each tripeptide. The t-Bu-thio group was removed using β-mercaptoethanol:DMF (1:1) overnight. The coupling of EZ-LinkPEO-iodoacetyl biotin was performed in DMF with 6 equivalents of DIPEA. The Mmt group was removed with DCM:TFA:TIS (97:1:2) 3 × 6 mL with shaking for 2 min. The couplings of the different acyl groups were performed in DMF using a cocktail of acid:DIPCIDI:HOBt:DIPEA (2:3:3:6) with addition of a catalytic amount of 4-pyrrolidinopyridine. After 1 h, the solutions were removed, an additional batch of coupling-cocktail was added, and the couplings then proceeded overnight.

For each peptide, total deprotection and simultaneous cleavage from the solid support was achieved with TFA:H_2O (97.5:2.5), with occasional shaking for 2 h. The mixtures were filtered into preweighed centrifuge tubes, and the polymers were washed with small amounts of TFA. The volumes were then reduced to less than 0.5 mL, and the peptides were precipitated with cold diethyl ether. The peptide precipitates were collected by centrifugation and washed twice with diethyl ether, dried, dissolved in 0.1% TFA, and lyophilized. If a peptide was hard to dissolve in water, ACN was added before lyophilization. The peptides were purified using reversed phase HPLC on a C8-column or a C18-column with a gradient of ACN:H_2O from 20 to 90% ACN. The identities of the products were confirmed with MALDI-TOF MS using a α-cyano-4-hydroxycinnamic acid matrix with detection in the positive mode. The measured masses of the GSC-thiolesters were in good agreement with the calculated masses.

Site-Directed Mutagenesis, Protein Expression, and Purification. The mutant A216K was prepared by site-directed mutagenesis using the Quik-Change kit (Stratagene) as described elsewhere (*8*). The purity was confirmed by SDS−PAGE, and the concentration was determined spectrophotometrically using $\epsilon_{280} = 24\,700\ M^{-1}\cdot cm^{-1}$ (*21*). The fluorescence spectra of hGST A1-1 and A216K (1 μM each in 100 mM NaPi, pH 7.0) were collected using a Hitachi f-4500 fluorescence spectrophotometer, with excitation at 280 nm and emission scanning between 310 and 380 nm as described elsewhere (*8*).

The activities of the GSTs (*8*) were tested with a standard assay (*22*) containing 1 mM each of 1-chloro-2,4-dinitrobenzene (CDNB) and GSH (pH 6.5 in 0.1 M NaP_i at 30 °C). The proteins were stored in NaP_i buffered solutions containing NaCl and 10% glycerol at −80 °C or −20 °C until used in the experiments.

Modification Reactions in Solution. A typical modification was performed in the following way: 0.54 μL of protein (0.372 mM stock solution) was diluted with 15.5 μL of buffer (0.1 M NaP_i, pH 7.0), and the reaction was initiated by adding 4 μL of reagent (0.5 mM stock solution). The reaction was allowed to proceed at 25°C from 1 min up to 24 h. To control the temperature, the incubations were performed in an Eppendorf Master cycler gradient.

Modification Reactions in an *E. coli* Lysate. A lysate was prepared from *Escherichia coli* BL21(DE3) cells (Novagen) containing the vector pET-21a(+) with the A216K gene inserted (*8*). The cells were grown in 20 mL of 2 x YT medium to an OD_{600} of 0.6, induced with IPTG, and incubated at 37 °C for 3.5 h. The cells were harvested by centrifugation and resuspended in 250 μL of 0.1 M NaPi, pH 7, and lysed by freezing at −80 °C and thawing four times. The modification reactions were carried out by adding GS-thiolester (100 μM) to 2.5 μL of the cell lysate and the mixtures were then incubated for 5 h at 25 °C. The lysate itself was also analyzed by MALDI-MS to identify lysate-specific peaks. In the lysate experiments, all mixtures were acidified using 0.1% TFA and citrate was added (see below) prior to MALDI-MS analyses.

Proteolytic Digestion and MALDI-MS Analysis of Modified GSTs. The digestions were performed in the following way: 5 μL of modification mixture was diluted with 15 μL of buffer (75 mM NH_4OAc, pH 4), and the reaction was started by addition of 1 μL of *Staphylococcus aureus* V-8 Protease (1 μg/μL stock solution in 75 mM NH_4OAc, pH 4) from Pierce Biotechnology, Inc.. The mixture was then incubated at 25 °C for 2 h. A control reaction was also performed for each protein, containing unmodified protein, buffer, and protease. Cleaving with this protease results in fragments that contain K216 (K_{216}-RKIFRF) and Y9 (AEKPKLHY$_9$FNARGRME, one missed cleavage).

After proteolysis, an equal amount of 0.1% TFA (eg., 20 μL to 20 μL reaction mixture) was added to the digestion mixture to quench and acidify the sample. Following incubation, 0.5 μL of the reaction mixture was mixed with 0.5 μL of saturated α-cyano-4-hydroxycinnamic acid matrix, and 0.5 μL of citrate (10 mg/mL) was also added to quench salts from the buffers. The samples were then analyzed by MALDI-TOF MS (Voyager 4212, Applied Biosystems) with detection in the positive mode.

The Rate of the Reaction between A216K and GSC-Cou$_{bio}$. A216K (10 μM) was incubated with 100 μM GSC-Cou$_{bio}$ in 0.1 M NaPi buffer, pH 7, at 25 °C, and samples were withdrawn at various time points starting at $t = 0$ min. The samples were immediately quenched with 0.1% TFA and stored at −20 °C until digestion at pH 4 and analysis using MALDI-MS. The data were analyzed by dividing the *m*/*z* peak resulting from the modified fragment containing K216 by that of the respective (unmodified + modified) fragment.

Modification Reactions Using Premodified NA Gel. Loading of the tripeptides on to the NA gel (Pierce Biotechnology, binding capacity ≥20 μg biotin/mL gel) was performed in buffer (0.1 M NaPi, pH 7) with the tripeptide in two times excess over the available biotin-binding sites. After a brief incubation, the gel was washed with 5× the double volume of the gel with buffer and stored in buffer at 4 °C until used in the experiments.

The modification reactions with premodified gel were typically performed with 50 μL of premodified NA gel (containing approximately 4.1 nmol tripeptide) and 100 μL of hGST A1-1 in buffer (0.1 M NaPi, pH 7), with hGST A1-1 concentration ranging from 1 to 25 μM. The reaction was allowed to proceed at 25 °C for up to 5 h with occasional gentle mixing. Alternatively, the temperature was lowered to 4 °C after 5 h and the protein eluted the following day. The labeled protein was eluted with 100 μL of buffer and the sample diluted to 200 μL before fluorescence measurements.

Modification Reactions Using NA Gel as Scavenger. After completed modification in solution, 1.5 equiv of NA beads (binding capacity ≥ 20 μg biotin/ mL gel) was added to the reaction mixture. The gel had been preequilibrated with 0.1 M NaP$_i$, pH 7.1, containing 0.15 M NaCl in VacMaster (International Sorbent Technology) tubes. After incubation with the gel (from 10 min up to 1 h), the labeled protein was eluted from the gel by a brief spin in a tabletop centrifuge.

Fluorescence Measurements of Labeled Proteins. In the experiments where the acyl group was delivered from the solid support, the fluorescence measurements were performed using a Hitachi F-4500 fluorescence spectrophotometer. The coumarin-labeled proteins were analyzed with excitation at 350 nm, and emission spectra were collected between 370 and 600 nm with a slit width of 5/5 nm. All measurements were performed in 0.1 M NaPi, pH 7.

In the experiments where the gel was used as a scavenger, the fluorescence spectra were recorded with an ISA spex FluoroMax-2apparatus (Jobin Yvon, Longjumeau, France). All spectra were recorded in 0.1 M NaPi, pH 7, with excitation at 360 nm using 2-nm excitation and emission slits, at 20 °C in a 1-cm quartz cuvette.

HPLC Analysis of Labeled A216K. A216K (10 μM) was incubated with GSC-Cou$_{bio}$ (100 μM) in 0.1 M NaPi buffer (total volume 500 μL), pH 7, at 25 °C for 5 h. After completed modification (verified by MALDI-MS) 25 μL were removed and injected on a C18 column using a gradient from 100% buffer A (buffer A: 10% ACN, 90% H_2O, 0.1% TFA; buffer B: 90% ACN, 10% H_2O, 0.1% TFA) to 30% buffer A over 30 min. The rest of the modification mixture was then incubated with NA-gel for 1 h and A216-Cou was eluted with N_2(g). In this experiment, the dilution factor resulting from the gel treatment was estimated to be roughly 3 and 75 μL of the eluate was therefore injected on the HPLC column using the same gradient.

Determination of the Yield from the Gel Treatment. GSC-Cou$_{bio}$ (200 μM) was incubated with A216K (20 μM) in 0.1 M NaPi buffer, pH 7, for 5 h at 25 °C. The extent of the reaction was confirmed to be >99% by MALDI-MS. The reaction mixture was then spilt into three different samples, and the fractions were treated in parallel with NA gel in the same manner as described above. The volumes of the eluted samples were carefully estimated with automatic pipets. The protein concentration in each sample was determined by UV measurements at 280 nm, and the fluorescence spectra were then recorded after diluting 100 μL of eluate with 400 μL of buffer (0.1 M NaP$_i$, pH 7.0).

Table 1. Modification Reactions with α-NH$_2$-Substituted GS-thiolesters

GS-thiolester	hGST A1−1[a]	A216K[b]
GSB	yes[c]	yes[d]
$_{Ac}$GSB	no	no

[a] Yes and no corresponds to modified or not modified Y9 fragment. [b] Yes and no corresponds to modified or not modified K216 fragment. [c] From reference 6. [d] From reference 8.

The A216K Concentration in Unknown Samples. The concentration studies were performed in the following way: 100 μM GSC-Cou$_{bio}$ was incubated with A216K (1 and 10 μM) in 0.1 M NaPi buffer, pH 7. Two separate modification mixtures were also prepared with A216K concentrations unknown to the person performing the subsequent steps. These two samples contained 100 μM GSC-Cou$_{bio}$ and A216K (5 and 9 μM) in buffer. All samples were incubated at 25 °C for 5 h. The samples were then treated with NA gel, and the protein mixtures were eluted by a quick spin in a tabletop centrifuge. The dilution factors from the gel treatment were estimated by careful use of calibrated automatic pipets. The samples were then diluted and the fluorescence spectra recorded as described above.

Addition of GSH to A216K-Cou. GSC-Cou$_{bio}$ (100 μM) was incubated with A216K (10 μM) in 0.1 M NaPi buffer, pH 7, for 5 h at 25 °C. The extent of the reaction was confirmed to be >95% by MALDI-MS. After incubation and elution by centrifugation, the concentration of A216K in the eluted sample was found to be 4.2 μM using the absorbance at 280 nm and $\epsilon_{280} = 24\ 700\ M^{-1}\cdot cm^{-1}$ (*21*). The absorbance of the coumarin probe was negligible at this wavelength. The sample was split in two fractions and the samples diluted with NaPi buffer, pH 7, to final concentrations of 0.84 and 0.25 μM, respectively. The fluorescence spectra of the A216K-Cou samples were then recorded using $\lambda_{exc} = 280$ nm and $\lambda_{exc} = 360$ nm, respectively. Increasing amounts of GSH (1, 10, 50, 100, and 500 equiv) were then added to the cuvettes using a stock solution of 3 mM in 0.1 M NaPi buffer.

RESULTS

Modification Reactions Using GS-thiolesters and GSC-thiolesters. The outcome of adding the GS-thiolesters and GSC-thiolesters to hGST A1-1 and A216K was investigated by MALDI-MS. Each reagent (100 μM) was incubated with protein (10 μM) at 25 °C for 5 h. The samples were then analyzed by MALDI-MS following proteolytic digestion. To simplify subsequent analyses we used *S. aureus* V-8 protease since it cleaves after glutamic acid residues (and aspartic acid depending on reaction conditions) and is thus unaffected by a potential lysine modification. In general, if a residue becomes covalently modified, the mass of the fragment containing this residue will increase with the mass of the corresponding acid minus the mass of water (Scheme 2). For control purposes, the proteins were also digested after incubation in buffer without addition of any reagent.

Both the A216K mutant and the wt protein were unaffected by the addition of the α-NH$_2$ acetylated GSB analogue $_{Ac}$GSB (Table 1). We also tried to acylate the wt protein by incubating hGST A1-1 with sepharose-linked GS-Cou (Scheme 3) but could not detect any modified protein in the eluate after proteolytic digestion and MALDI-MS analysis. This negative result was also backed up by the lack of fluorescence of the eluted protein.

Table 2. Modification Reactions with GSC-thiolesters

	hGST A1−1[a]		A216K[b]	
acyl group	GS-thiolester	GSC-thiolester$_{bio}$	GS-thiolester	GSC-thiolester$_{bio}$
Ant	yes[c]	yes	no	no
Cou (GS-4[d])	yes[c]	yes	yes[d]	yes
Fl	yes[c]	no	no[d]	no
DMACA	n.m.[e]	no	n.m.[e]	no

[a] Yes and no corresponds to modified or not modified Y9 fragment. [b] Yes and no corresponds to modified or not modified K216 fragment. [c] From reference 7. [d] From reference 8. [e] n.m. = not measured.

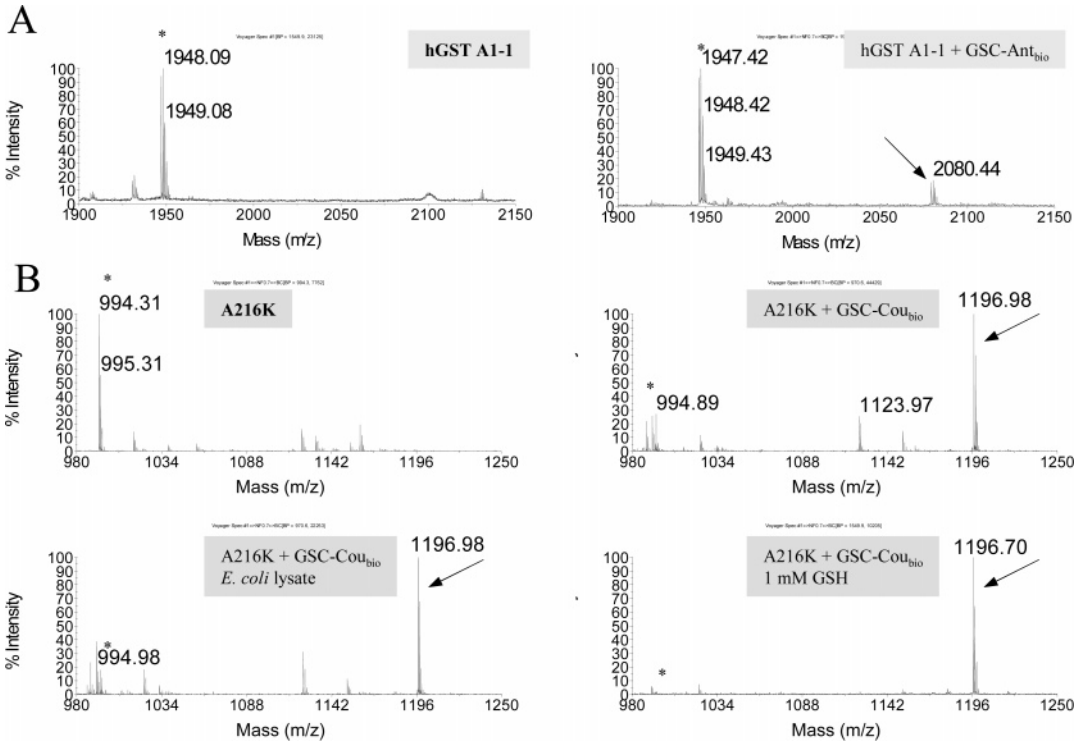

Figure 2. MALDI-MS spectra of proteolytic (*S. aureus* V-8) peptide fragments from (A) hGST A1-1 and hGST A1-1 (10 μM) incubated with GSC-Ant$_{bio}$ (100 μM) for 5 h and; (B) A216K and A216K (10 μM) incubated with GSC-Cou$_{bio}$ (100 μM) for 5 h in buffer, in buffer with 1 mM GSH, and in an *E. coli* lysate of cells expressing A216K. The *m*/*z* interval containing the Y9 (A1-1) or K216 (A216K) fragment is shown in the figure. Parent fragments are indicated with asterisks and modified fragments are highlighted with arrows.

However, the wt protein could be modified at the Y9 residue with two of the C-terminally altered GSC-thiolesters (Scheme 4) and the A216K mutant reacted with one of the GSC-reagents (Table 2 and Figure 2). A positive classification corresponds to more than 10% modified fragment relative to the parent fragment (unmodified fragment). This threshold was set because MALDI-MS is not a quantitative technique and also because the reaction conditions are not optimized for each individual reagent and protein combination (*7*).

The Rate of the Reaction between A216K and GSC-Cou$_{bio}$. The rate of the reaction between A216K and GSC-Cou$_{bio}$ was estimated from semiquantitative MALDI-MS experiments. The reagent (100 μM) was added to A216K (10 μM in 0.1 M NaPi, pH 7), time points were withdrawn, and the samples were quenched with 0.1% TFA. To enhance the resolution compared to whole-protein analysis, the mixtures were subjected to proteolytic digestion before MALDI-MS analysis. The resulting peptide fragments were analyzed, and the ratio (modified K216 fragment/(modified K216 fragment + unmodified K216 fragment)) was plotted vs time (Figure 3). About 85% of the K216 fragment is modified after 1 h (Figure 3).

Modification Reactions in the Presence of GSH and in an *E. coli* Lysate. The reagent GSC-Cou$_{bio}$ (100 μM) was added to lysed BL-21 (DE3) cells expressing A216K and to a buffer (0.1 M NaPi, pH 7) containing A216K (10 μM) and GSH (1 mM), and both mixtures were incubated at 25 °C for 5 h. We found (Figure 2) that GSC-Cou$_{bio}$ was able to modify K216 in lysed *E. coli* cells directly after expression. The modification reaction could also be carried out in a buffer containing GSH (Figure 2).

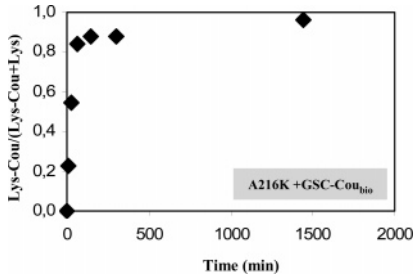

Figure 3. Semiquantitative analysis of the reaction between A216K (10 μM) and GSC-Cou$_{bio}$ (100 μM) obtained from MALDI-MS experiments. Samples were withdrawn at the indicated time points, quenched with 0.1% TFA and treated with protease (*S. aureus* V-8). The ratio of modified K216 fragment divided by the total amount of fragment (K216 + modified K216 fragment) is plotted vs time.

Modification Reactions Using Premodified NA Beads. To test the ability of delivery of coumarin to hGST A1-1 and A216K from a solid support, GSC-Cou$_{bio}$ was preincubated with NA gel in buffer (0.1 M NaPi, pH 7). After a brief incubation, the gel was washed with buffer. The beads fluoresced under a UV lamp (λ = 337 nm) (Figure 4A). As a control, the gel was

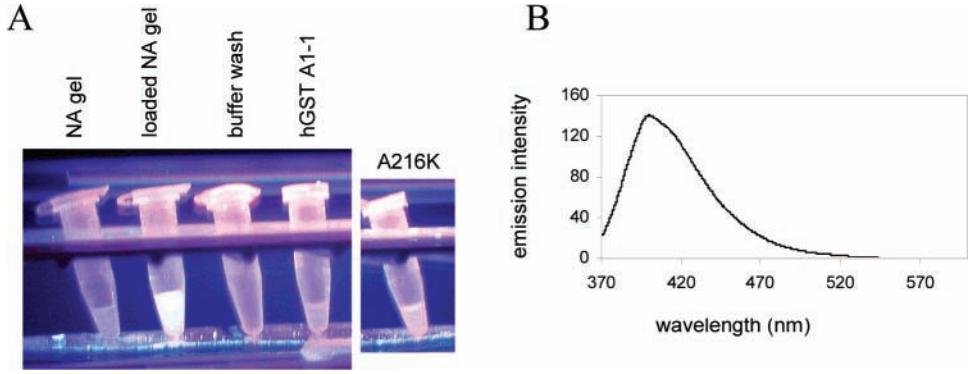

Figure 4. An illustration of the experiments with premodified (GSC-Cou_{bio}) NA gel. (A) A photography (under UV lamp, $\lambda = 337$ nm) showing the NA gel, the NA gel after incubation with GSC-Cou_{bio}, buffer washes, and the eluted hGST A1-1 after a 5 h incubation with the derivatized gel. The cut out shows eluted A216K after a similar treatment. (B) Fluorescence measurements ($\lambda_{exc} = 350$ nm) of eluted labeled hGST A1-1 in buffer at pH 7.

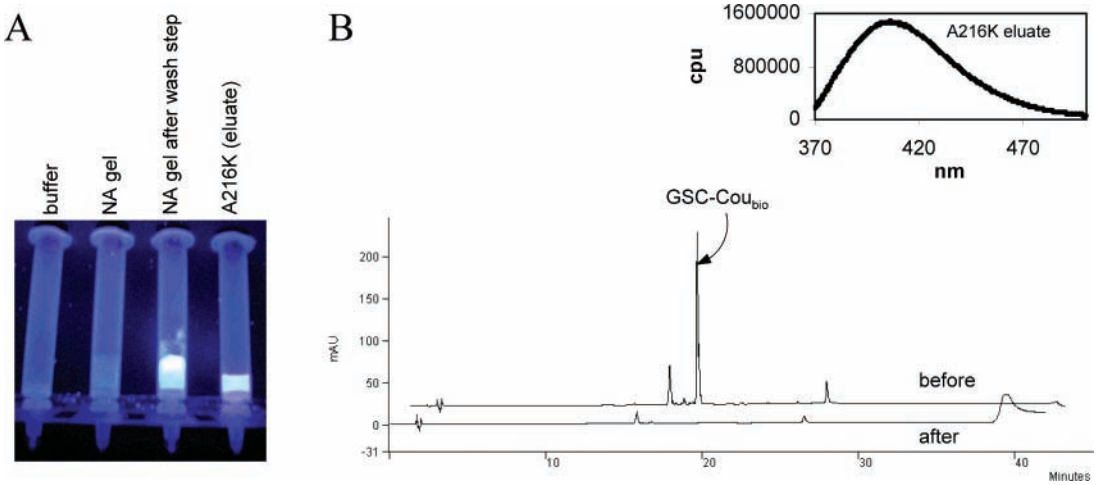

Figure 5. An illustration of the experiments where NA gel was used as a scavenger. (A) A photography (under UV lamp, λ=337 nm) showing A216K (10 μM) that had been preincubated with GSC-Cou_{bio} (100 μM) for 5 h. The mixture was then incubated with NA gel and the labeled protein finally removed from the gel by centrifugation. (B) HPLC chromatograms ($\lambda = 355$ nm) from the labeling mixture before and after the scavenging step. The inset shows the fluorescence spectrum ($\lambda_{exc} = 360$ nm) of the labeled A216K after elution.

washed with buffer prior to adding the protein solution, and no leaking from the gel could be observed (Figure 4A).

The NA gel (approximately 4.1 nmol GSC-thiolester) was then incubated with hGST A1-1 or A216K in buffer with protein concentration ranging from 1 to 25 μM. The reactions were allowed to proceed at 25 °C for 5 h with occasional gentle mixing. The protein solutions were then eluted from the gel by centrifugation in a tabletop centrifuge (Figure 4A) and the samples subjected to fluorescence measurements after dilution. The protein-containing samples did show the typical coumarin fluorescence (Figure 4B, Supporting Information).

Using NA Beads as Scavenger after Labeling. The NA gel was also used as a scavenger to remove excess and used up reagent. In a pilot experiment GSC-Cou_{bio} (100 μM) and A216K (10 μM) were incubated in a buffered solution (0.1 M NaPi, pH 7) at 25 °C for 5 h, and we used MALDI-MS to verify that the reaction had gone to completion. The mixture was then applied to NA beads that had been preequilibrated in buffer. The gel was added in excess (1.5 equiv) over the amount of biotin in solution to mop up used up and surplus GSC-Cou_{bio}. The labeling mixture was incubated for 45 min with the beads, and the protein solution was then separated from the gel by a brief spin in a tabletop centrifuge (Figure 5). The eluate was then analyzed by reversed phase HPLC to check the efficiency of the scavenging step. We found that the treatment with the gel had quantitatively removed residual reagent (Figure 5B). A fluorescence spectrum of A216-Cou was recorded (Figure 5B, inset), and it displayed the typical coumarin spectrum.

To test the yield and repeatability of the gel-treatment step, GSC-Cou_{bio} (200 μM) was incubated with A216K (20 μM) for 5 h at 25 °C. The extent of the reaction was confirmed to be >99% by MALDI-MS. The mixture was then spilt into three different samples (100 μL each), and the resulting fractions treated separately with NA gel. The volumes of the eluted samples were 165, 157, and 190 μL. From UV measurements (*21*) (280 nm) we found that the protein concentrations in these samples were 3.9, 4.2, and 3.6 μM, respectively. The samples thus contained $6.6 \pm 0.2 \times 10^{-10}$ mol which corresponds to a 3% difference in the different samples after gel treatment.

Measurement of A216K Concentration Using GSC-Cou_{bio} and NA Beads. A diagnostic test of the ability to measure the A216K concentration in a sample was carried out by incubating GSC-Cou_{bio} (100 μM) with two known (1 and 10 μM) and two unknown (5 and 9 μM but unknown to the person performing the subsequent steps) concentrations of A216K. All samples were incubated at 25 °C for 5 h and treated with NA gel, and the protein solutions were eluted by a quick spin in a tabletop centrifuge. The fluorescence spectra were then recorded (Figure 6), and using the intensities at 407 nm from the samples with known concentrations of A216K, the concentrations of labeled A216K in the unknown samples were calculated to be 4.8 and 9.1 μM with the dilution factors taken into account.

Addition of GSH to A216K-Cou. To test the ability of labeled A216K to bind GSH, GSC-Cou_{bio} (100 μM) was incubated with A216K (10 μM) for 5 h at 25 °C, conditions that result in >95% labeling. Excess probe was then removed

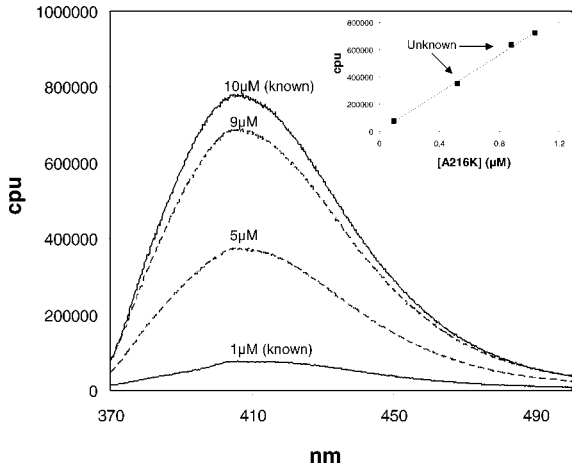

Figure 6. Fluorescence spectra (λ_{exc} = 360 nm) resulting from incubating two known (1 and 10 μM) and two unknown (5 and 9 μM, dotted lines) concentrations of A216K with GSC-Cou_{bio} (100 μM) for 5 h with subsequent treatment with NA beads. The inset shows the intensity of the signal at 407 nm plotted vs concentration of protein. The two unknown samples are highlighted with arrows.

by NA gel treatment. The fluorescence spectra of A216K-Cou with (1, 10, 50, 100, and 500 equiv) and without GSH were then recorded using λ_{exc} = 280 nm (excitation of W21) and also λ_{exc} = 360 nm (direct excitation of the coumarin probe). We found that adding GSH to the labeled protein quenched the fluorescence of A216-Cou (Figure 7). This was true both for direct excitation of the coumarin probe and also in the case of FRET from W21 to the coumarin probe.

DISCUSSION

The versatility, speed, and site-selectivity of the covalent modification reaction between Y9 of hGST A1-1 and K216 of the A216K mutant and numerous GS-thiolesters (*6*−*8*) encouraged us to try to construct an even more user-friendly labeling reagent with a handle that could be used to mop up excess reagent. Since it is difficult to predict which reagent (if any) that would work we prepared a minilibrary of four GS-thiolesters with biotinylated GSH moieties in the hope that at least one would be a reagent in the labeling reaction. Biotin was chosen because of the multitude of commercially available, protein-friendly products that utilize the highly specific and extraordinarily strong biotin−streptavidin interaction ($K_a = 10^{15}$ M^{-1}) (*23*). If successful, we would thus not be confined to a single system. The thiol-reactive biotin derivative that we used is commercially available, is water-soluble, and has an extended arm to allow for optimal interactions with the biotin-binding pocket of streptavidin and its analogues. Since the biotin tag is situated in the leaving group (i.e. the GSH moiety), this allows for both potential delivery of the acyl group from a streptavidin-covered surface to the protein and also for the use of a streptavidin-containing surface to mop up residual reagent in a fashion akin to the use of polymer-bound scavengers in organic synthesis. In addition, we also synthesized α−NH_2-modified reagents since such alterations have been shown to increase the stability of GSH analogues in a physiological environment (*24*, *25*). This was done despite indications that such modifications would not be tolerated (*26*).

Substitutions at the Glycine Position Are Tolerated but Not α-NH_2 Substitutions. We have previously found that the α-NH_2 group of GS-thiolesters can be reacted with NHS-esters leaving the thiolester linkage intact (*27*). This finding was utilized in the manufacturing of the α-NH_2-derivatized substances. Unsurprisingly, sepharose-linked GS-Cou (Scheme 3) was not able to modify hGST A1-1. To rule out any specific deleterious interactions with the linker or the sepharose gel, control experiments were performed where the α-NH_2 group was simply acylated. The well characterized reagent GSB was used in these experiments since it has been highly successful as a labeling reagent for both hGST A1-1 and A216K. The proteins however also rejected the resulting reagent $_{Ac}$GSB, and we could thus conclude that alterations of this part of the GSH backbone are not a viable route to user-friendly labeling reagents.

We were however pleased to observe that two of the biotinylated GSC-thiolesters based on the peptide γ-Glu-Cys-Cys were successful in labeling hGST A1-1 (Table 2). One of these (GSC-Cou_{bio}) was also a reagent for the A216K mutant. Our results are in agreement with previously published data that suggest that using C-terminally modified GSH analogues are to some extent accepted by GSTs in the natural detoxication reaction (*18*). Our results also suggest that other C-terminally altered GS-thiolester analogues might be accepted by the proteins. It is not surprising that the A216K mutant is more selective than the wt protein since this is in accordance with our previous studies using a 20-membered GS-thiolester library (*8*). We have thus now produced a fluorescent reagent, GSC-Cou_{bio}, with a biotin handle that can modify either Y9 (wt hGST A1-1) or K216 (A216K). Two types of residues are thus targeted, and this increases the flexibility of the system in a potential protein fusion scheme since, if desired, the ester bond formed with the wt protein can be quickly and gently broken simply by addition of GSH (*7*) whereas the amide bond formed with K216 in the mutant is very robust.

A Fast Labeling Reaction of A216K Using GSC-Cou_{bio}. In our previous studies (*8*) we found that the reaction between A216K and GS-4 (i.e. GS-Cou, Scheme 3, Table 2) is fast since it takes approximately 10 min for the reaction to reach 50% completion. Interestingly, the modification of the GSH moiety actually seems to add positive binding interactions since the reaction between A216K and GSC-Cou_{bio} appears to be even faster. This is highly gratifying considering the advantages resulting from the added biotin functionality.

K216 Can Be Modified in a Cell Lysate Using GSC-Cou_{bio}. We have been able to modify both Y9 (*6*) and K216 (*8*) in protein-doped *E. coli* lysates before using GS-thiolesters with the normal GSH backbone. Gratifyingly, using GSC-Cou_{bio} we were able to modify K216 in an *E. coli* lysate of cells expressing A216K. This is ideal in a potential application with A216K as a fusion partner since a combination of GSC-Cou_{bio} and streptavidin-based products should create a clean signal from A216K-Cou. This system could then be used for optimization of protein expression in an easy format. The product in the reaction between A216K and GSC-Cou_{bio} is a stable amide linkage, and the conjugate can thus be handled "roughly" without bothering about the stability. A diagnostic of this is also the inertness toward GSH in the labeling mixture.

Direct Labeling with GSC-Cou_{bio} Using NA Gel. It was indeed possible to deliver the acyl group from a solid support. This significantly simplifies the handling of the labeling reaction. However, it is not easy to control the extent of the reaction in this format. In a potential application such as measurement of fusion protein concentration one would want to be sure that the reaction has gone to completion, and it is laborious and time-consuming to remove samples for MALDI-MS analysis during incubation. We therefore turned to the use of the gel as a scavenger instead.

Excess GSC-Cou_{bio} Can Be Removed Using NA Gel as Scavenger. It is common for example in solid-phase peptide synthesis to use scavengers to quench reactive species when the peptide is cleaved from the solid support. These scavengers are also commercially available attached to a solid support to

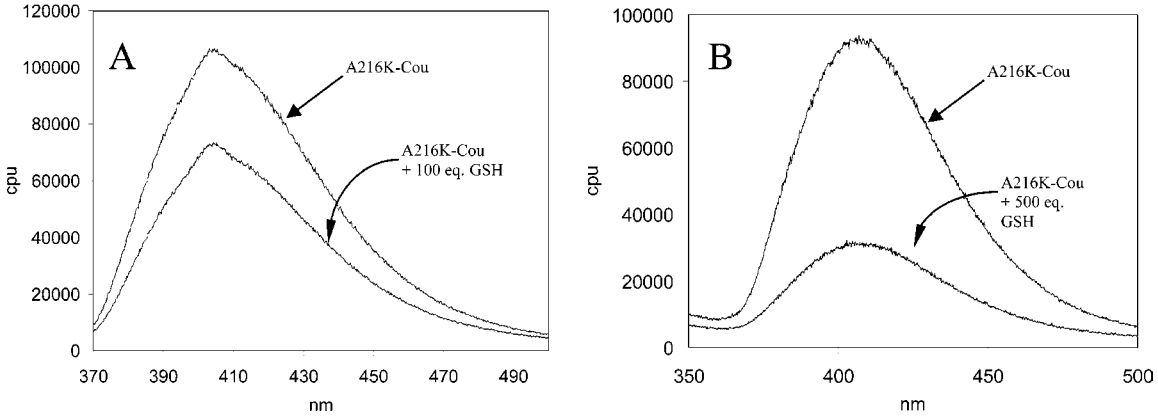

Figure 7. Fluorescence spectra resulting from adding (A) GSH (100 equiv) to A216K-Cou (250 nM) with excitation at 360 nm (e.g. the coumarin probe) and (B) GSH (500 equiv) to A216K-Cou (800 nM) with excitation at 280 nm (e.g. W21). The emission signal in Figure 7B is thus a result of FRET from W21 to the coumarin probe.

facilitate the workup of the soluble product. With this in mind, we performed the labeling reaction in solution so that we could verify that the reaction had gone to completion and then used the gel as a scavenger. Gratifyingly, from HPLC experiments we found that this step completely removed excess and used up reagent. This is a significant improvement in the handling of the labeling reaction since it is no longer necessary to purify the labeled protein with extended dialysis or size exclusion chromatography. We also found that the yield from the NA step was repeatable within 3%, a satisfactory result considering that the handling of the gel has not been optimized. These results in combination with the finding that A216K can be derivatized directly after expression further add to the value of the reaction. Using our setup with centrifugation as elution method, there is however a (repeatable) loss of protein during the gel treatment on the order of 50%. From SDS−PAGE experiments, it appears as if the protein adheres both to the beads and the filter (Supporting Information). Since the loss is repeatable and none of the steps have yet been optimized with respect to handling of protein mixtures and yield, we do not believe that this will be a problem.

The Concentration of A216K Can Be Determined Using GSC-Cou$_{bio}$ and NA Beads. Since the HPLC experiments (Figure 5B) show that the reagent is quantitatively removed, the fluorescence intensity at 407 nm is a result of the concentration of A216K-Cou in the sample. This inspired us to perform an experiment with known (as calibration) and unknown amounts of A216K, and we found that the concentration of A216K in a sample can be determined using a combination of GSC-Cou$_{bio}$ and NA beads. The calculated amounts of A216K in the unknown samples were within 5% of the actual concentrations. Since the handling of the steps has not been optimized, we find a 5% variation to be satisfactory. On the basis of the intensities of the fluorescence signals, we estimate that we can measure protein concentrations at least in the upper nanomolar range.

Both A216K and A216K-Cou Can Bind GSH. When a protein is expressed in the fusion format, it is frequently done to facilitate expression and purification. With this in mind, a fusion protein partner should be able to bind an affinity gel. From measuring the kinetics of the mutant A216K, we know that it catalyzes the conjugation reaction between GSH and CDNB with about 30% of wt hGST A1-1 activity (*8*). To catalyze the reaction A216K must bind GSH, hence it should be possible to find an affinity gel that binds A216K and fusion protein constructs thereof.

By adding GSH to A216K-Cou, we also know that the labeled protein binds GSH since the coumarin-fluorescence was quenched upon addition of GSH. To further verify that GSH binds in the G-site, even though the probe could occupy some of the available space, we also measured the effect of adding GSH by exciting W21 (λ_{exc} = 280 nm), a well-known reporter of events taking place in the active site of hGST A1-1 (*28*). The transferred fluorescence from W21 to the coumarin probe was also quenched upon addition of GSH in agreement with binding of GSH in the G-site. Thus, A216K, both in its unlabeled and labeled form, binds GSH. This is of course very useful in a protein fusion scheme since a partner could potentially be purified using commercially available glutathione-based protein purification products.

CONCLUSIONS

We have designed protein-labeling reagents that attach a fluorescent probe in a site-specific manner. The reaction is quantitative, fast, creates a stable amide bond and can be performed directly in an *E. coli* lysate after expression. The reagents have a biotin handle to mop up excess reagent. The lysine mutant A216K is expressed in a high yield, is easy to purify, and binds GSH both labeled and in its free form. A216K can easily be perceived as a fusion protein partner that in combination with this new type of reagent could be quite useful in protein expression and labeling systems.

ACKNOWLEDGMENT

This work was financially supported by The Wenner-Gren Foundation, The Carl-Trygger Foundation, the Knut and Alice Wallenberg Foundation, and the Swedish Research Council.

Supporting Information Available: An SDS−PAGE gel of the lysate (expressing A216K) used in the MALDI-MS experiments. Fluorescence spectrum of GSC-Cou$_{bio}$. An SDS−PAGE gel showing the eluate from the NA beads, the NA beads, and the filter. This material is available free of charge via the Internet at http://pubs.acs.org/BC.

LITERATURE CITED

(1) Lander, E. S., Linton, L. M., Birren, B., Nusbaum, C., Zody, M. C., Baldwin, J., Devon, K., Dewar, K., Doyle, M., FitzHugh, W., Funke, R., Gage, D., Harris, K., Heaford, A., Howland, J., Kann, L., Lehoczky, J., LeVine, R., McEwan, P., McKernan, K., Meldrim, J., Mesirov, J. P., Miranda, C., Morris, W., Naylor, J., Raymond, C., Rosetti, M., Santos, R., Sheridan, A., Sougnez, C., Stange-Thomann, N., Stojanovic, N., Subramanian, A., Wyman, D., Rogers, J., Sulston, J., Ainscough, R., Beck, S., Bentley, D., Burton, J., Clee, C., Carter, N., Coulson, A., Deadman, R., Deloukas, P., Dunham, A., Dunham, I., Durbin, R., French, L., Grafham, D., Gregory, S., Hubbard, T., Humphray, S., Hunt, A., Jones, M., Lloyd, C.,

McMurray, A., Matthews, L., Mercer, S., Milne, S., Mullikin, J. C., Mungall, A., Plumb, R., Ross, M., Shownkeen, R., Sims, S., Waterston, R. H., Wilson, R. K., Hillier, L. W., McPherson, J. D., Marra, M. A., Mardis, E. R., Fulton, L. A., Chinwalla, A. T., Pepin, K. H., Gish, W. R., Chissoe, S. L., Wendl, M. C., Delehaunty, K. D., Miner, T. L., Delehaunty, A., Kramer, J. B., Cook, L. L., Fulton, R. S., Johnson, D. L., Minx, P. J., Clifton, S. W., Hawkins, T., Branscomb, E., Predki, P., Richardson, P., Wenning, S., Slezak, T., Doggett, N., Cheng, J. F., Olsen, A., Lucas, S., Elkin, C., Uberbacher, E., Frazier, M., et al. (2001) Initial sequencing and analysis of the human genome. *Nature 409*, 860−921.

(2) Venter, J. C., Adams, M. D., Myers, E. W., Li, P. W., Mural, R. J., Sutton, G. G., Smith, H. O., Yandell, M., Evans, C. A., Holt, R. A., Gocayne, J. D., Amanatides, P., Ballew, R. M., Huson, D. H., Wortman, J. R., Zhang, Q., Kodira, C. D., Zheng, X. H., Chen, L., Skupski, M., Subramanian, G., Thomas, P. D., Zhang, J., Gabor Miklos, G. L., Nelson, C., Broder, S., Clark, A. G., Nadeau, J., McKusick, V. A., Zinder, N., Levine, A. J., Roberts, R. J., Simon, M., Slayman, C., Hunkapiller, M., Bolanos, R., Delcher, A., Dew, I., Fasulo, D., Flanigan, M., Florea, L., Halpern, A., Hannenhalli, S., Kravitz, S., Levy, S., Mobarry, C., Reinert, K., Remington, K., Abu-Threideh, J., Beasley, E., Biddick, K., Bonazzi, V., Brandon, R., Cargill, M., Chandramouliswaran, I., Charlab, R., Chaturvedi, K., Deng, Z., Di Francesco, V., Dunn, P., Eilbeck, K., Evangelista, C., Gabrielian, A. E., Gan, W., Ge, W., Gong, F., Gu, Z., Guan, P., Heiman, T. J., Higgins, M. E., Ji, R. R., Ke, Z., Ketchum, K. A., Lai, Z., Lei, Y., Li, Z., Li, J., Liang, Y., Lin, X., Lu, F., Merkulov, G. V., Milshina, N., Moore, H. M., Naik, A. K., Narayan, V. A., Neelam, B., Nusskern, D., Rusch, D. B., Salzberg, S., Shao, W., Shue, B., Sun, J., Wang, Z., Wang, A., Wang, X., Wang, J., Wei, M., Wides, R., Xiao, C., Yan, C., et al. (2001) The sequence of the human genome. *Science 291*, 1304−51.

(3) Phillips, C. I., and Bogyo, M. (2005) Proteomics meets microbiology: technical advances in the global mapping of protein expression and function. *Cell Microbiol. 7*, 1061−76.

(4) Korf, U., Kohl, T., van der Zandt, H., Zahn, R., Schleeger, S., Ueberle, B., Wandschneider, S., Bechtel, S., Schnolzer, M., Ottleben, H., Wiemann, S., and Poustka, A. (2005) Large-scale protein expression for proteome research. *Proteomics, 5*, 3571−80.

(5) Sassenfeld, H. M. (1990) Engineering proteins for purification. *Trends Biotechnol. 8*, 88−93.

(6) Håkansson, S., Viljanen, J., Broo, K. S. (2003) Programmed delivery of novel functional groups to the alpha class glutathione transferases. *Biochemistry 42*, 10260−10268.

(7) Viljanen, J., Tegler, L., and Broo, K. S. (2004) Combinatorial chemical reengineering of the alpha class glutathione transferases. *Bioconjugate Chem 15*, 718−27.

(8) Hederos, S., Karlsson, B., Tegler, L., and Broo, K. S. (2005) Ligand-directed labeling of a single lysine residue in hGST A1-1 mutants. *Bioconjugate Chem 16*, 1009−18.

(9) Ketterer, B. (2001) A bird's eye view of the glutathione transferase field. *Chem. Biol. Interact. 138*, 27−42.

(10) Sheehan, D., Meade, G., Foley, V. M., and Dowd, C. A. (2001) Structure, function and evolution of glutathione transferases: implications for classification of nonmammalian members of an ancient enzyme superfamily. *Biochem. J. 360*, 1−16.

(11) Strange, R. C., Spiteri, M. A., Ramachandran, S., and Fryer, A. A. (2001) Glutathione-S-transferase family of enzymes. *Mutat. Res. 482*, 21−6.

(12) Armstrong, R. N. (1997) Structure, catalytic mechanism, and evolution of the glutathione transferases. *Chem. Res. Toxicol. 10*, 2−18.

(13) Mannervik, B. (1996) Evolution of glutathione transferases and related enzymes for the protection of cells against electrophiles. *Biochem. Soc. Trans. 24*, 878−80.

(14) Pettigrew, N. E., and Colman, R. F. (2001) Heterodimers of glutathione S-transferase can form between isoenzyme classes pi and mu. *Arch. Biochem. Biophys. 396*, 225−30.

(15) Sinning, I., Kleywegt, G. J., Cowan, S. W., Reinemer, P., Dirr, H. W., Huber, R., Gilliland, G. L., Armstrong, R. N., Ji, X., Board, P. G., and et al. (1993) Structure determination and refinement of human alpha class glutathione transferase A1-1, and a comparison with the Mu and Pi class enzymes. *J. Mol. Biol. 232*, 192−212.

(16) Hayes, J. D., and Pulford, D. J. (1995) The glutathione S-transferase supergene family: regulation of GST and the contribution of the isoenzymes to cancer chemoprotection and drug resistance. *Crit. Rev. Biochem. Mol. Biol. 30*, 445−600.

(17) Adang, A. E., Duindam, A. J., Brussee, J., Mulder, G. J., and van der Gen, A. (1988) Synthesis and nucleophilic reactivity of a series of glutathione analogues, modified at the gamma-glutamyl moiety. *Biochem. J. 255*, 715−20.

(18) Adang, A. E., Meyer, D. J., Brussee, J., Van der Gen, A., Ketterer, B., and Mulder, G. J. (1989) Interaction of rat glutathione S-transferases 7−7 and 8−8 with gamma-glutamyl- or glycyl-modified glutathione analogues. *Biochem. J. 264*, 759−64.

(19) Adang, A. E., Brussee, J., van der Gen, A., and Mulder, G. J. (1990) The glutathione-binding site in glutathione S-transferases. Investigation of the cysteinyl, glycyl and gamma-glutamyl domains. *Biochem. J. 269*, 47−54.

(20) Kaiser, E., Colescott, R. L., Bossinger, C. D., and Cook, P. I. (1970) Color test for detection of free terminal amino groups in the solid-phase synthesis of peptides. *Anal.Biochem. 34*, 595−8.

(21) Gustafsson, A., and Mannervik, B. (1999) Benzoic acid derivatives induce recovery of catalytic activity in the partially inactive Met208Lys mutant of human glutathione transferase A1-1. *J. Mol. Biol. 288*, 787−800.

(22) Habig, W. H., and Jakoby, W. B. (1981) Assays for differentiation of glutathione S-transferases. *Methods Enzymol. 77*, 398−405.

(23) Wilchek, M., and Bayer, E. A. (1988) The avidin−biotin complex in bioanalytical applications. *Anal. Biochem. 171*, 1−32.

(24) Ouwerkerk-Mahadevan, S., and Mulder, G. J. (1998) Inhibition of glutathione conjugation in the rat in vivo by analogues of glutathione conjugates. *Chem. Biol. Interact. 111−112*, 163−76.

(25) Adang, A. E., Brussee, J., van der Gen, A., and Mulder, G. J. (1991) Inhibition of rat liver glutathione S-transferase isoenzymes by peptides stabilized against degradation by gamma-glutamyl transpeptidase. *J. Biol. Chem. 266*, 830−6.

(26) Adang, A. E., Brussee, J., Meyer, D. J., Coles, B., Ketterer, B., van der Gen, A., and Mulder, G. J. (1988) Substrate specificity of rat liver glutathione S-transferase isoenzymes for a series of glutathione analogues, modified at the gamma-glutamyl moiety. *Biochem. J. 255*, 721−4.

(27) Hederos, S., Broo, K. S., Jakobsson, E., Kleywegt, G. J., Mannervik, B., and Baltzer, L. (2004) Incorporation of a single His residue by rational design enables thiol-ester hydrolysis by human glutathione transferase A1-1. *Proc. Natl. Acad. Sci. U. S. A. 101*, 13163−7.

(28) Dirr, H. W., and Wallace, L. A. (1999) Role of the C-terminal helix 9 in the stability and ligandin function of class alpha glutathione transferase A1-1. *Biochemistry 38*, 15631−40.

BC0502762

Surface-Assisted Delivery of Fluorescent Groups to hGST A1-1 and a Lysine Mutant.

Viljanen, J., Tegler, L., Larsson, J., and Broo, K.S.*

Supporting Information

Table of Contents:

Page 1
An SDS-PAGE gel of the *E. coli* lysate (expressing A216K) used in the MALDI-MS experiments

Page 2
Fluorescence measurements of GSC-Cou_{bio}

Page 2
An SDS-PAGE gel showing the eluate from the NA beads, the NA beads and the filter.

Below: An SDS-PAGE gel showing the lysate from *E. coli* bacteria expressing A216K.

1 2 3

1. 10 μl cell lysate
2. 5 μl cell lysate
3. 2 μl cell lysate

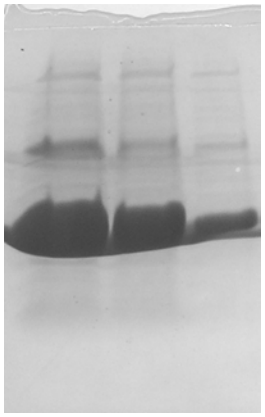

Below: Fluorescence measurements (λ_{exc} = 350 nm) of GSC-Cou_{bio} (0.75 µM) in buffer at pH 7.

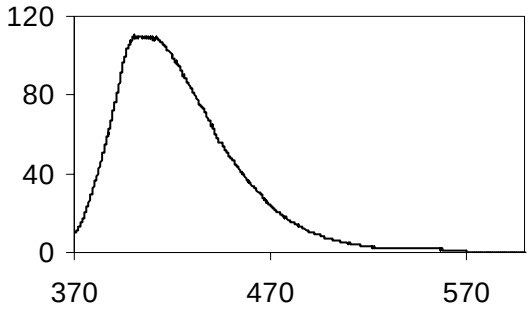

Below: An SDS-PAGE gel showing the eluate from the NA beads, the NA beads and the filter.

1. The filter from the vac-master.
2. The solution after incubation with the NA gel.
3. Protein eluate after washes.
4. The NA gel.

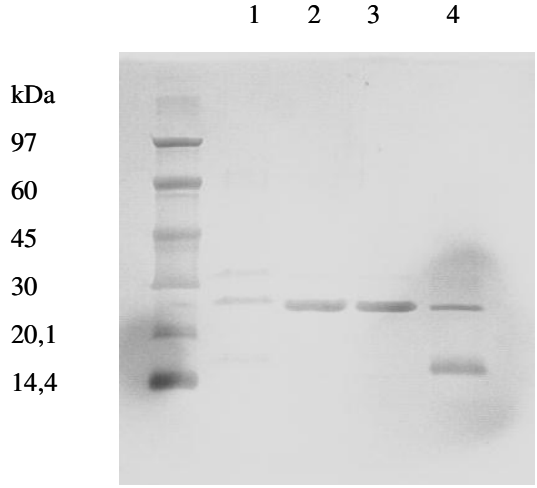

Micelles as Intermediates in the Preparation of Protein−Liposome Conjugates

Jennifer Takasaki and Steven M. Ansell*

Inex Pharmaceuticals Corporation, 100-8900 Glenlyon Parkway, Burnaby, BC, V5J 5J8, Canada. Received February 24, 2005; Revised Manuscript Received November 21, 2005

A method for preparing protein−liposome conjugates based on micelles as intermediates was developed. Ovalbumin was thiolated with 2-IT and conjugated to the surface of micelles composed of a maleimide-derivatized active lipid and a micelle-forming lipid. These micelles were then incubated with liposomes, allowing the micelle components to exchange into the liposome bilayers. Using this technique we were able to demonstrate that it was possible to saturate the surface of the micelle with protein and use this property to control the level of conjugation. Titration of these protein−micelle conjugates into liposome solutions resulted in reproducible batches of protein−liposome conjugates. Chemical cross-linking could be observed in some cases; however, this was controllable through selection of reagent concentrations. The effects of parameters such as thiolation levels, micelle lipid composition, active lipid structure, micelle-forming lipid structure, and micelle/liposome/protein ratios were examined. The method represents a general approach to the preparation of well defined and reproducible protein−liposome-based drug formulations.

INTRODUCTION

The attachment of proteins to the surface of liposomes in order to alter their in vivo behavior is an area of continuing interest. These proteins might serve a wide range of functions, with the most common application being use as targeting vectors (*1*) for liposomal drug delivery systems. More currently, interest is increasing in the use of liposome surface-bound proteins and peptides as antigens in immunological applications (*2*−*4*).

Traditionally proteins have been conjugated to liposomes using maleimide−sulfhydryl coupling chemistry (*5*). Typically the protein is thiolated using a heterobifunctional cross-linker and subsequently coupled to the surface of liposomes containing a maleimide lipid as one of the lipid components. In most reports the reagent SPDP[1] has been used as the cross-linker. More recently a few reports using 2-IT have appeared (*6*, *7*).

Early work in the field involved coupling proteins directly onto the surface of the liposome. Many problems were experienced with this approach due to cross-linking reactions between protein−liposome conjugates and additional liposomes, leading to aggregation (*8*). Since size is an important parameter in determining the clearance behavior in vivo (*9*), these liposome−protein conjugates often suffered from poor pharmacokinetics in vivo. Many years ago we resolved this problem by incorporating small amounts of PEG−lipids in the liposome formulations to act as steric barriers to inhibit the cross-linking reaction (*10*). However, including these "steric barrier" molecules in the bilayer also reduced the overall conjugation efficiency of the protein to the bilayer surface.

This problem was partially resolved by using maleimide lipids (or other reactive lipids) in which the reactive function and the lipid anchor were separated by a PEG chain (*11*). The steric inhibition of the conjugation step seen in our early work was partially abolished when the reactive function was placed outside of the steric barrier created by the PEG−lipids in the formulation. Recently work done in Allen's laboratory has demonstrated that maleimide- or hydrazide-PEG−lipids in pure or mixed micelles could be reacted with thiolated or oxidized proteins, respectively. The products from those reactions could then be exchanged into bilayers when they were mixed with conventional liposomes (*12*).

We believe that the critical aspect of these recent publications is not that the protein is conjugated to the terminus of a PEG−lipid, but rather the fact that the process is based on a micelle intermediate. By performing the actual conjugation reaction remote from the liposome surface we can potentially obtain a system that has a high degree of reproducibility. In fact it may not be necessary to have the PEG tether present at all, if the reaction is done under the appropriate conditions.

With this hypothesis in mind we set out to explore the range of utility of micelle-based conjugation methods and to characterize the parameters that might affect the outcome of those reactions. We determined that micelle-based reactions can be performed on a wide range of micelle compositions, and in fact that large steric barrier molecules are unnecessary and frequently undesirable components in the formulation. The conditions that lead to aggregation were characterized, allowing us to develop formulations with minimal aggregation without resorting to the use of additional steric barrier molecules. Application of this micelle-based technology led to the development of reproducible, simple, and scaleable methods for preparing liposome−protein conjugates.

There are two general methods which can be used for preparing liposomes with proteins attached to their surfaces. Ultimately the protein is conjugated to a lipid anchor, and this

* To whom correspondence should be addressed. 201−2010 Weighth Ave, Vancouver, B. C., V6J 1W5, Canada. Phone (604) 733-1231. E-mail: ansell2010@shaw.ca.

[1] Abbreviations: 2-IT, 2-iminithiolane; SPDP, *N*-succinimidyl 3-(2-pyridyldithio)propionate; PEG, poly(ethylene glycol); POPC, 1-palmitoyl-2-oleoyl-*sn*-glycero-3-phosphocholine; chol, cholesterol; DSPE-MPB, *N*-4′-(4″-maleimidophenyl)butanoyl-1,2-distearoyl-*sn*-glycero-3-phosphoethanolamine; DSPE-ATTA2-MPA, *N*-(*N*′-(*N*″-(3‴-maleimidopropionoyl)-14″-amino-3″,6″,9″,12″-tetraoxatetradecanoyl)-14′-amino-3′,6′,9′,12′-tetraoxatetradecanoyl)-1,2-distearoyl-*sn*-glycero-3-phosphoethanolamine; OGP, octyl β-D-glucopyranoside; CHAPS, 3-[(3-cholamidopropyl)dimethylammonio]-1-propane sulfonate; HBS, HEPES-buffered saline; DTT, 1,4-dithio-DL-threitol; ATTA, 14-amino-3,6,9,12-tetraoxatetradecanoic acid; DSPE, 1,2-distearoyl-*sn*-glycero-3-phosphoethanolamine; DCC, *N*,*N*′-dicyclohexylcarbodiimide; NHS, *N*-hydroxysuccinimide; TFA, triflouroacetic acid; MePEGS-2000-DSPE, *N*-(4′-*O*-(ω-monomethoxypoly(ethylene glycol)$_{2000}$)succinoyl)-1,2-distearoyl-*sn*-glycero-3-phosphoethanolamine.

10.1021/bc050051r CCC: $33.50 © 2006 American Chemical Society
Published on Web 01/12/2006

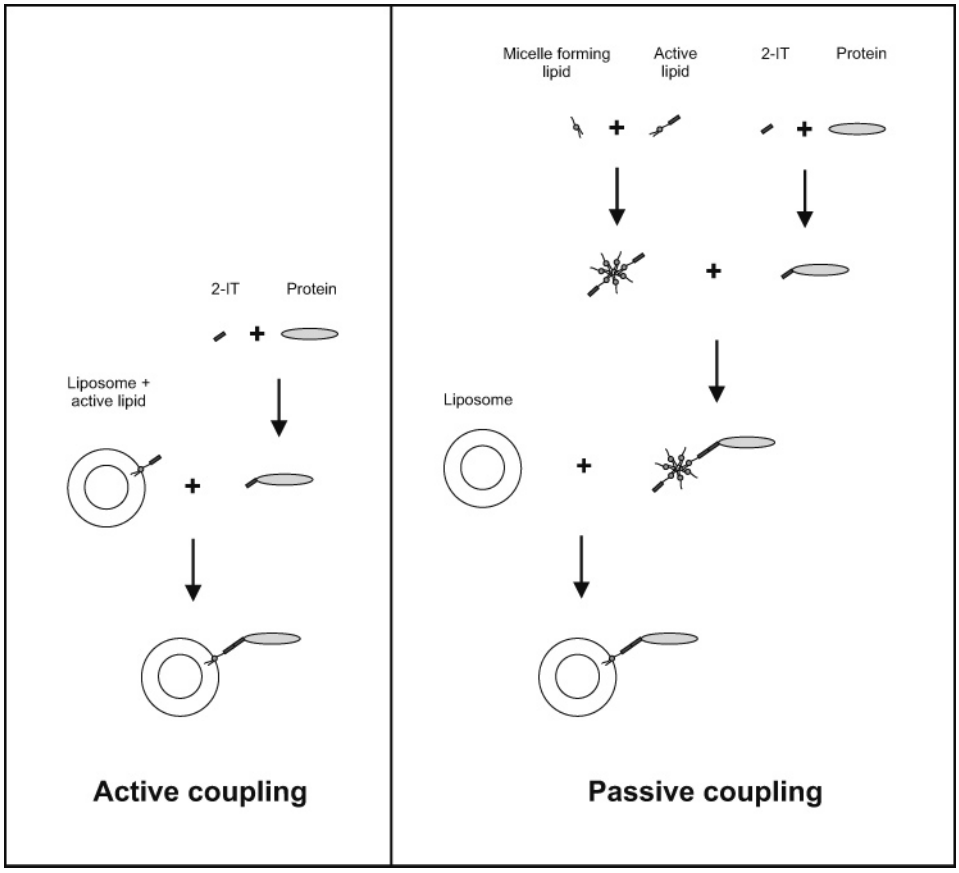

Figure 1. Examples of protocols involving active and passive coupling techniques. In this work active coupling refers to methods in which the lipid−protein conjugation reaction occurs at the liposome surface, and passive coupling refers to methods in which the lipid−protein conjugation reaction occurs remote from the liposome surface.

can be done either at the surface of a preformed liposome with the appropriate active lipid already present, or it can be done remotely and then introduced to the liposome at a later point, using a variety of methods. We are using the terms "active" and "passive" coupling in this work when referring to the two types of conjugate formation. Examples of these two types of coupling procedures are presented in Figure 1.

"Active coupling" applies to procedures where the chemical linkage occurs at the liposome surface. There are a number of ways to produce a liposome with an active lipid incorporated in the membrane structure. For example, liposomes could be prepared directly where the active lipid is one of the component lipids (*8*). Alternatively, liposomes could be prepared without the active lipid present. The active lipid may then be exchanged into the outer leaflet of the bilayer from micelles. Both methods would result in liposomes with reactive functions on their surfaces, available for conjugation with a suitably derivatized protein. The former method is the one generally used in the literature for the preparation of protein−liposome conjugates.

"Passive coupling" applies to procedures where the protein is conjugated to the lipid anchor away from the liposome surface. Generally in such reactions a micelle serves as the platform for performing the conjugation reaction since lipids and proteins are usually not soluble in the same solvents. Once formed, the protein−lipid conjugate could then be incorporated into the bilayer during liposome formation, either by cohydration of dried lipid/conjugate, or by detergent dialysis. Alternatively, the micelles on which the conjugates were formed could be exchanged into preformed liposomes (*12*). We have used the latter method as our starting point for this work.

EXPERIMENTAL PROCEDURES

Materials. DSPE was obtained from Genzyme Pharmaceuticals, Cambridge, MA. DSPE-MPB was obtained from Northern lipids Inc, Vancouver, Canada. 2-IT was obtained from Sigma-Aldrich.

Synthesis of 11-Azido-3,6,9-trioxaundecanol 1. A solution of tetraethylene glycol (1.2 kg) and methanesulfonyl chloride (400 mL) in benzene (2 L) was cooled in an ice bath. Triethylamine (716 mL) was slowly added with stirring. The reaction mixture was stirred at room temperature for 2 h and filtered and the solvent removed on a rotovap. The oil was diluted with water (100 mL). Saturated sodium bicarbonate solution was then added until the solution tested neutral using pH paper. The mixture was diluted with ethanol (1.6 L). Sodium azide (270 g) was then slowly added as a slurry in water (500 mL). The reaction mixture was heated to 60 °C with stirring for 2 h. Water (5 L) was added to the reaction mixture, and the resultant solution was washed with diethyl ether. The aqueous fraction was then extracted with dichloromethane (3 passes, 500 mL). The combined organic fraction was washed with water (250 mL), which in turn was extracted with methylene chloride (250 mL). The combined methylene chloride fractions were dried over anhydrous magnesium sulfate and filtered, and the solvent was removed on a rotovap, yielding ∼400 g of **1**.

Synthesis of 14-Azido-3,6,9,12-tetraoxatetradecanoic Acid 2. Finely powdered potassium bromoacetate was prepared by neutralizing a solution of bromoacetic acid in water with potassium hydroxide and lyophilizing the resultant solution. A portion of this product (270 g) was added to a solution of **1** (252 g) in toluene (750 mL) in a water-jacketed reactor. The suspension was vigorously stirred with a mechanical stirrer at 45 °C, and four portions of sodium hydroxide pellets (4 × 40

g) were added at 15 min intervals. The reaction was allowed to proceed for an hour and then quenched by the addition of water (500 mL). The two phases were allowed to separate and the aqueous phase run off. The toluene phase was washed with 5% sodium hydroxide. The two aqueous phases were combined and washed with methylene chloride. The resultant aqueous phase was acidified to ~pH 3−4, and extracted with methylene chloride. The organic fraction was dried over magnesium sulfate and filtered and the solvent removed on a rotovap, yielding crude **2** as a pale yellow oil (~120 g).

Synthesis of Ethyl *N*-(*N*′-BOC-14′-amino-3′,6′,9′,12′-tetraoxatetradecanoyl))-14-amino-3,6,9,12-tetraoxatetradecanoate 4. Ethyl *N*-(14′-amino-3′,6′,8′,12′-tetraoxatetradecanoyl)-14-amino-3,6,9,12-tetraoxatetradecanoate **3** was prepared as previously described (*13*). A solution of **3** (30 g) in methylene chloride (100 mL) was treated with di-*tert*-butyl dicarbonate (13.2 g) and triethylamine (8.5 mL) at room temperature for 1 h. The solution was washed with dilute hydrochloric acid, dried over anhydrous magnesium sulfate,and filtered and the solvent removed on a rotovap. Yields ~30 g of **4** as a colorless oil.

Synthesis of *N*-(*N*′-(*N*″-(*tert*-Butoxycarbonyl)-14″-amino-3″,6″,9″,12″-tetraoxatetradecanoyl)-14′-amino-3′,6′,9′,12′-tetraoxatetradecanoyl)-1,2-distearoyl-*sn*-glycero-3-phosphoethanolamine 5. A solution of **4** (5 g) in aqueous sodium carbonate (4.5 g in 100 mL) was warmed at 60 °C for 30 min with stirring. The solution was washed with methylene chloride, acidified to ~pH 3 with hydrochlorics acid, and extracted with methylene chloride. The organic phase was dried over magnesium sulfate and filtered and the solvent removed. The residue was dissolved in alcohol free chloroform (50 mL). *N*-Hydroxysuccinimide (1.65 g) was added, followed by a solution of dicyclohexylcarbodiimide (2.90 g) in alcohol free chloroform (50 mL). The solution was stirred at room temperature for 20 min and then filtered. 1,2-Distearoyl-*sn*-glycero-phosphethanolamine (DSPE, 4.5 g) was added, and the solution was heated in a water bath at 60 °C until the DSPE had dissolved. Triethylamine (3 mL) was added and the solution stirred at room temperature for 1 h. The solution was filtered, diluted with water, and extracted with methylene chloride. The organic phase was washed with dilute hydrochloric acid and dried over anhydrous magnesium sulfate and the solvent removed on a rotovap. The product was purified using a preparative HPLC, yielding **5** as a colorless solid (7.6 g).

Synthesis of *N*-(*N*′-(*N*″-(3‴-Maleimidopropionoyl)-14″-amino-3″,6″,9″,12″-tetraoxatetradecanoyl)-14′-amino-3′,6′,9′,12′-tetraoxatetradecanoyl)-1,2-distearoyl-*sn*-glycero-3-phosphoethanolamine. 6. Trifluoroacetic acid (4 mL) was added to solid **5** (2.75 g) and stirred at room temperature for 30 min. The excess trifluoroacetic acid was removed on a rotovap and the residue dissolved in distilled water (50 mL), neutralized with aqueous sodium hydroxide, and extracted with methylene chloride. The organic fractions were dried over anhydrous magnesium sulfate and filtered and the solvent removed. 3-Maleimidopropanoic acid (0.41 g) was dissolved in chloroform (20 mL) and treated with NHS (0.42 g) and DCC (0.71 g). The solution was stirred at room temperature for 20 min and filtered. The filtrate was added to a solution of the previously obtained crude product in chloroform (30 mL). Triethylamine (2 mL) was added and the solution stirred at room temperature for 1 h. The solution was filtered, diluted with water, and extracted with methylene chloride. The organic fractions were washed with dilute hydrochloric acid, dried over anhydrous magnesium sulfate, and filtered, and the solvent was removed. The residue was purified by HPLC, taken up in benzene, and lyophilized, yielding **6** (1.7 g) as an off white powder. The product appeared as a single spot on TLC analysis and showed no evidence of primary amines when stained with a flouresc-amine/acetone solution and viewed under UV light.

Preparation of Liposomes. Lipid mixtures composed of POPC/chol (55:45) were dissolved in chloroform. On larger scales the solvent was removed in a round-bottomed flask on a rotovap at 50 °C. In small scale preparations the solvent was removed by blowing nitrogen into the sample tube while warming the solution in a water bath. The resulting thin film was dried on a lyophilizer and rehydrated in HBS, for a final lipid concentration of 25 mM. The lipid solution was then passed 10 times through 2 × 100 nm stacked filters using an extrusion device (Northern Lipids Inc., Vancouver, Canada) at 45 °C.

Preparation of Micelle−Ovalbumin Conjugates. Ovalbumin was dissolved in HBS at a concentration of 30 mg/mL. An aliquot of from a freshly prepared stock solution of 2-IT in HBS (prepared at a concentration such that the total volume added to the albumin did not exceed 5%) corresponding to 1−5 equiv (depending on the particular experiment) was added to the ovalbumin solution and the mixture stirred at room temperature for 0.5 h.

Lipid mixtures were prepared by combining an active lipid (DSPE-MPB or DSPE-ATTA2-MPA) and a micelle-forming lipid (DSPE-ATTA4, OGP, or CHAPS). The lipid was dissolved in 1 part of ethanol, with warming if required, and diluted sequentially with 1 part of HBS, with vortexing and warming, until a total of 9 parts HBS had been added. The total volume should was such that the final concentration of lipid was approximately 10 mM. Any residual solid materials were removed by filtration through 0.22 micron filters.

An aliquot of freshly prepared thiolated ovalbumin was added to freshly prepared maleimide-micelles in the appropriate ratio. In most cases this corresponded to 3000 g protein/mol micelle lipid. The micelle−protein mixture was allowed to stir at room temperature overnight. It was then either used immediately without additional purification, or stored at 5 °C for use at a later date.

Incubation of Protein−Micelles with Liposomes. Liposomes were mixed with ovalbumin−micelle conjugates in proportions appropriate for the particular experiment. Typically the standard preparation used a 1:19 micelle/liposome lipid ratio, corresponding to an initial protein/final lipid ratio of 150 g/mol when using the typical 3000 g protein/mol micelle lipid reagent. The liposome−micelle mixtures were incubated in a water bath at 60 °C for 30 min and then passed down a Sepharose CL-4B column (0.8 mL of sample/25 mL bed volume) using HBS as the running buffer.

Assays. Lipid was assayed by determining the phosphate content as previously described (*14*). The protein content of the final liposome−protein conjugates was determined using a modified micro-BCA assay as previously described (*14*), with negative controls being performed where possible to correct for background interference. Protein/lipid ratios in this work are expressed either as g protein/mol micelle-forming lipid, or as g protein/mol final lipid. The first quantity relates to the ratio of protein to lipid present in the initial micelles, while the second quantity refers to the ratio of protein to the total lipid present in the final liposomes. Particle size was measured using a Nicomp 380 submicron particle sizer.

RESULTS

The basic design of the process is outlined in Figure 1. The passive conjugation method can be divided into three parts, which can be performed separately. These are (1) preparation of the liposomes, (2) preparation of micelle−protein conjugates, and (3) incubation of the liposomes with the micelle−protein conjugates. This contrasts with the active conjugation method also outlined in Figure 1, where the liposome preparation and

protein derivatization need to be done more or less simultaneously due to the chemical instability of some of the reagents used. The more flexible time constraints associated with the passive conjugation method make it a more attractive choice from the perspective of scalability. This was an important consideration if this technology is to be used in commercial products which are generally prepared in very large quantities.

It needs to be kept in mind however that while the "passive conjugation" terminology is being applied to the entire process, the actual conjugation is taking place in the micelle step, whereas the final assembly of the system is mediated through purely physical exchange processes. The apparent coupling efficiency on the micelle surface is implied by the level of protein on the surface of the final liposome composition. It is necessary for the micelles to equilibrate with the liposomes for that to be true. Generally a 1 h incubation is sufficient to equilibrate most systems, but in some cases, for example in liposomes with high levels of securely anchored steric barrier molecules, longer incubation times may be required to equilibrate the system.

Presence of Ethanol and Detergents in the Final Formulation. Since the presence of ethanol and/or detergents in the final formulation might affect the integrity of various components during the assembly or after assembly of the final liposome system, it is necessary to ensure that the levels of these materials remain with acceptable limits. Many proteins will denature in the presence of organic solvent. Typically we limit the ethanol content of any solution that proteins might be dissolved in to 5%. In this protocol we mix equal volumes of a thiolated protein solution with a micelle solution. The micelle solution was generally prepared by diluting an ethanolic solution of lipid in buffer. To limit the final ethanol concentration to 5% we needed to prepare the micelles using 1 part of ethanolic lipid solution to 9 parts of buffer solution. The final lipid concentration of the protein−micelle solution was 5 mM. The final ethanol content in the liposome solution can be controlled using the initial liposome concentration. Typically liposomes are prepare with lipid concentrations in the range 10−50 mM. The reference formulation protocol used a 1:19 micelle/liposome lipid ratio, i.e. 10 mM and 50 mM liposome solutions would be treated with 2/19ths and 10/19ths the volume of protein−micelles. This would result in final ethanol concentrations of ∼0.5−1.7%. It might be necessary to use lower initial liposome concentrations if this level of ethanol is a problem in any particular system.

The stereotypical micelle formulation in this work was composed of an active lipid and a micelle-forming lipid in a 1:4 ratio and were added to liposomes in a 1:19 lipid ratio. This means that the final active lipid content of the protein−liposome system is 1%, and the final micelle lipid content is 4%. These values are well within the range used in typical "targeted" or "steric barrier" liposome formulations. These ratios were chosen to ensure that this was the case.

Thiolation of the Protein. One of the most commonly used methods of preparing protein conjugates involves the use of the maleimide−sulfhydryl coupling reaction. Usually the protein is derivatized with a heterobifunctional cross-linker based either on a maleimide or protected sulfhydryl. This is then reacted with a substrate bearing the complementary reactive function. Most of the literature dealing with liposome−protein conjugation reactions involves modifying the protein with SPDP, deprotecting the sulfhydryl with DTT, and then reacting the product with liposomes containing lipids bearing a maleimide function.

Initially we used this chemistry when preparing our micelle−protein conjugates. The use of SPDP presents a number of problems however. The cross-linker generally reacts with the protein in high yield, but the need to deprotect the sulfhydryl with DTT is a major issue, particularly when trying to scale-up the reaction. The DTT treatment is time sensitive, since it may damage intramolecular disulfide bonds in the protein as well as performing the deprotection of the introduced sulfhydryl group. While this can be controlled to some extent by performing the reaction at lower pH, the reaction needs to be stopped relatively quickly (∼15 min) to prevent significant damage to the disulfide bonds. The reaction is stopped by passing the reaction mixture down a gel column to remove the DTT and exchange the buffer back to pH 7. These constraints make the method unsuitable for large scale preparations. Another disadvantage with the method is that if the DTT is not completely separated from the protein, it may be present in sufficient quantities to quench the reaction with the activated liposomes.

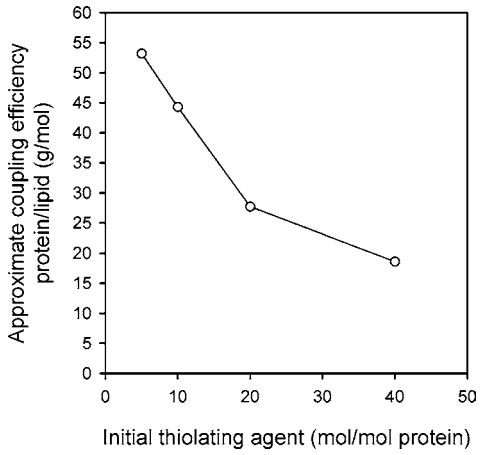

Figure 2. The effect of increasing the 2-iminothilone/protein ratio on the coupling efficiency. Ovalbumin was thiolated using 5−40 equiv of 2-iminothiolane. The resultant thiolated protein solution was used without workup and incubated with DSPE-ATTA2-MPA/DSPE-ATTA4 (1:4 ratio) micelles at 3000 g protein/mol micelle lipid. The protein−micelle conjugates were exchanged into POPC/chol (55:45) liposomes at a 1:19 mol/mol ratio by incubation at 60 °C for 1 h. The liposomes were recovered by passing the solution down a sepharose CL-4B column. Final amounts of protein coupled are represented as g protein/mol total lipid.

A less commonly used thiolating agent is 2-IT. The advantage of using 2-IT is that it is a cyclic reagent that exposes the sulfhydryl group when it reacts with amino functions on proteins. This means that it is not necessary to exchange the buffers or use a specific deprotection reagent, and in principle it may not be necessary to remove excess 2-IT before use of the thiolated protein. 2-IT has been used previously to conjugate proteins to liposomes (*6*, *7*). In those studies it was used in a 20-fold excess, with unreacted reagent being removed by gel filtration before the conjugation of the thiolated protein with liposomes.

Since we were interested in minimizing the amount of processing required during the process, we wanted to determine if 2-IT could be used in the passive conjugation protocol without an intermediate gel filtration step to remove unreacted 2-IT. An experiment was conducted where 2-IT was titrated into an ovalbumin solution, and the resultant thiolated product conjugated to DSPE-ATTA2-MPA/DSPE-ATTA4 micelles. The conjugation efficiency was determined by incubation of the ovalbumin−micelles with POPC/chol liposomes at an initial protein/final lipid ratio of 150 g/mol. Unconjugated protein and micelles were removed by gel filtration though sepharose CL-4B and the recovered liposome fraction analyzed for lipid and protein content. The results are presented in Figure 2.

Interestingly it was found that as the ratio of 2-IT relative to ovalbumin increased, the apparent coupling efficiency decreased. This behavior is likely due to the omission of the gel filtration step for removal of unreacted 2-IT prior to incubation with the maleimide micelles. Hydrolysis of the excess 2-IT in solution probably resulted in quenching of some of the maleimide

functionality, inhibiting the slower protein−micelle conjugation reaction. The best conjugation efficiency was seen at about 5 equiv of 2-IT. Following this experiment we used 5 equiv of 2-IT as our baseline in further optimization studies.

Synthesis of Lipids Used. Most of the original protein−liposome conjugation studies reported in the literature used simple lipids derivativatized with a cross-linker to introduce the reactive function. One of the most commonly used lipids is DSPE-MPB. After the development of PEG−lipids as steric barrier molecules in liposomes, some researchers began conjugating proteins to the ends of PEG−lipids in an attempt to get systems with good conjugation efficiencies and favorable pharmacokinetic properties. Maleimide-capped PEG−lipids were good candidates for the first application of micelle-based conjugation techniques in the preparation of liposome−protein conjugates.

We were interested in investigating the relationship between the size of the tether in the active lipid and the size of the hydrophilic domain in the micelle-forming lipid in terms of their effects on coupling efficiency. PEG lipids are not ideal for this since they are polymers composed of a wide range of molecular sizes. We have recently developed PEG like molecules based on repeating units of 14-amino-3,6,9,12-tetraoxatetradecanoic acid (ATTA) (*13*). These ATTA derivatives are suitable for investigating the effects of the relative headgroup size of the active and micelle-forming lipids on the conjugation efficiency since they can be tailored to exact sizes.

The synthesis of the ATTA monomer was performed using a modified version of a literature procedure (*15*). 11-Azido-3,6,9-trioxundecanol **1** was prepared by partially mesylating tetra(ethylene glycol), treating the product with sodium azide and recovering the product through a series of selective extraction procedures. Crude **1** was then treated with a suspension of finely powdered potassium bromoacetate and sodium hydroxide pellets in toluene. The literature method used DMF as the solvent; however, we found this to be unsuitable due to decomposition of the solvent under the reaction conditions, which caused considerable problems. The most effective results were obtained with lyophilized potassium bromoacetate. Other methods of preparing the potassium bromoacetate yielded granular forms of the salt, which were found to be relatively ineffective in the reaction. Synthesis of ATTA2 and ATTA4 were performed as previously described (*13*).

The primary active lipid used in this work was DSPE-ATTA2-MPA. This was prepared by reducing the azido group of ATTA2 to the amine **3** and protecting the amino function using a BOC group to form **4**. The carboxyl group was then deprotected by basic hydrolysis to form the acid **5**. This was conjugated to DSPE using DCC/NHS chemistry. The BOC protecting group was removed with TFA and the amino function derivatized with MPA using DCC/NHS chemistry. The product **6** was purified by HPLC. Excessive workup of the product should be avoided since this results in hydrolysis and other side reactions with the maleimide group, reducing yields and complicating purification. The storage conditions for the product were important. Over time an unknown material insoluble in organic solvents and water began to form. We believe that this material is a polymer stemming from ring opening of nearby maleimide functions by maleamic acid contaminants. Maleamic acids are much less reactive than maleimides, and excessive presence of those compounds can lead to an apparent loss of activity of the active lipid. Material stored as a lyophilized powder was generally sufficiently stable to be used for up to 4−5 months with noticeable loss of coupling activity. New batches were prepared every 4−6 months. However, material stored as gums formed by evaporating solutions directly using rotovaps usually became unusable within weeks. It is important

Scheme 1. The Synthesis of DSPE-ATTA2-MPA

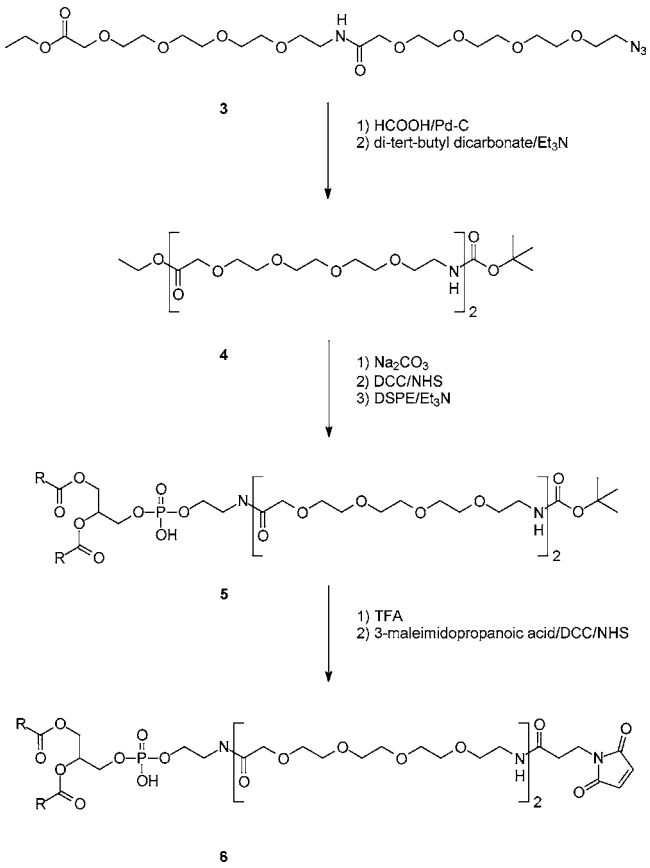

that active lipids be stored in a cool dry location once lyophilized and, if significantly below room temperature, be allowed to equilibrate to room temperature to prevent water from condensing on the product. An outline of the synthesis is shown in Scheme 1.

It is not practical to synthesize a fresh batch of active lipids prior to each micelle formulation experiment. Consequently any polymerized material formed in the active lipid stocks on storage were removed from the micelles by filtration through 0.22 micron filters. The presence of the impurity can be observed through the appearance of a "haze" in the lipid ethanol and in micelle solution after dilution with buffer. It is necessary to remove this material since it potentially could interfere in size determination measurements. The problem becomes increasingly pronounced as the sample ages. Properly stored reagents were typically effective with minimal insolubles for 4−5 months after synthesis. Material much older than that tended to generate significant amounts of insoluble materials and showed noticeably lower conjugation efficiencies. Whenever using maleimide-based active lipids in formulations of this sort, it is advisable to perform small test runs periodically to ensure that the lipid activity is at an acceptable level.

A number of micelle-forming lipids were used in this work. Some of them were commercially obtained but a number of them were based on our ATTAn templates and synthesized in house. These included DSPE-ATTAn, where $n = 1$, 2, and 4. The synthesis of these lipids was performed as described previously (*16*).

Effect of Micelle Lipid Structure. The use of micelle-mediated passive coupling techniques have been reported in a number of publications (*6*, *7*). All of these reports use lipid-PEG−maleimide conjugates as the active lipids and PEG−lipids as micelle-forming lipids.

There are a number of good reasons for diluting the active lipid with a micelle-forming lipid, even if the active lipid forms

micelles in isolation. First, the active lipid is typically a relatively high cost component in formulations. It is highly unlikely that a large molecule such as a protein can be coupled to every maleimide on pure micelles; therefore, much of the active lipid in those cases is wasted. In principle it should be possible to dilute the active lipid out with another lower cost micelle-forming lipid. Second, it should be remembered that maleimide functions are active molecules, which might cause issues in pharmaceutical applications if they are present in high levels.

The previously reported work had used DSPE-PEG-2000 as the micelle-forming lipid, and DSPE-PEG-2000-maleimide as the active lipid, in a 4:1 ratio. In that particular case the active group is presented approximately at the surface of the PEG shroud above the micelle; consequently, there should be little inhibition of reaction with proteins. Such systems are expected to exhibit at least some degree of cross-linking since both the micelles and the thiolated protein are multivalent species. Traditionally when doing similar reactions at liposome surfaces, PEG lipids are included to inhibit these cross-linking reactions, based on the principle that, at some ideal concentration range, the PEG is dense enough to inhibit the approach of a liposome−protein conjugate but not the protein by itself. Since both approaches were being presented as "improvements" over previous technology, we asked the question: what effect does the relative size of the hydrophilic domain of the two lipids present have on coupling efficiency using the micelle based passive conjugation method?

To answer this question we designed an experiment where we used micelles composed of a 1:4 ratio of DSPE-ATTA2-MPA:micelle-forming lipid, where the micelle-forming lipid was one of the following: DSPE-ATTA1, DSPE-ATTA2, DSPE-ATTA4, MePEGS-2000-DSPE, and MePEGS-5000-DSPE. The ATTA1, ATTA2, and ATTA4 correspond approximately to PEG 250, 500, and 1000 in size. A micelle-forming lipid was required in this case since the active lipid used, DSPE-ATTA2-MPA, did not form a micellar solution by itself. DSPE-ATTA1 was found not to be an effective micelle-forming lipid and was dropped from the study. The four remaining lipid compositions were hydrated by first dissolving the lipids in ethanol and then diluting the solution with nine parts of buffer, such that the final lipid concentration was 10 mM.

Previously reported studies on the phase behavior of pure mono methoxy PEG−lipids have shown that MePEG-350-DSPE forms bilayer phases on hydration, whereas the MePEG-750, MePEG-2000, and MePEG-5000 analogues form micellar phases (*17*). It is likely that DSPE-ATTA1 forms a bilayer phase, while DPSE-ATTA4 forms a micelle phase. It is not immediately clear what form DSPE-ATTA2 adopts, but when fully hydrated it forms a clear solution suggesting that it forms micelles.

The MePEGS-5000-DSPE system hydrated very readily, with the other systems showing some signs of nonhydrated material as the size of the micelle-forming lipid headgroup decreased. In the case of the DSPE-ATTA2 system the solution exhibited thermotropic behavior, forming a gel at room temperature which reverted to micellar form on being heated in a 60 °C water bath. The micelles thus formed were incubated with previously thiolated ovalbumin at a protein/micelle lipid ratio of 3000 g/mol. The reaction was allowed to proceed overnight at room temperature. Interestingly, once reacted with the thiolated protein, the DSPE-ATTA2 micelles no longer exhibited the thermotropic behavior previously seen.

Each sample was then divided into two parts. One-half was mixed directly with liposomes in a 1:19 ratio and incubated at 60 °C for 30 min. The solution was then run down a sepharose CL-4B column to remove any excess protein or micelles from the sample. The second half of the micelle/protein solutions were filtered through 0.22 micron filters and then treated in the same way as the first half. Protein content was assessed using a modified BCA assay (*10*) and lipid content with a molybdate assay (*10*). The samples were also sized with a Nicomp 380 particle sizer. The results of the experiment are shown in Figure 3.

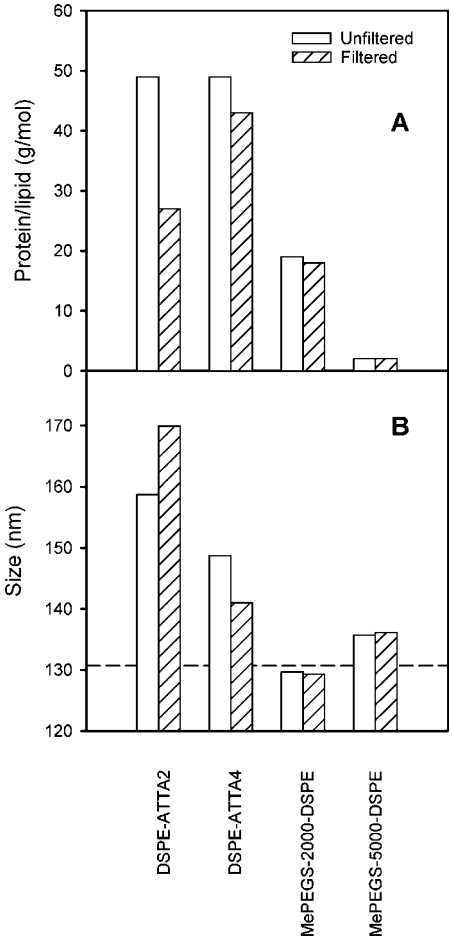

Figure 3. The effect of the micelle-forming lipid headgroup size on coupling efficiency in passive coupling protocols. Ovalbumin was thiolated with 5 equiv of 2-IT and incubated with DSPE-ATTA2-MPA/micelle-forming lipid (1:4) micelles in a 3000 g/mol ratio. The micelle-forming lipids used were as denoted on the figure. The protein−micelle conjugates were incubated with POPC/chol (55:45) liposomes in a 1:19 mol/mol ratio. Panel A: Final bound protein/lipid ratio (g/mol) where the protein−micelle conjugates were filtered before incubation with the liposomes (crossed bars), or added directly to the liposomes without pretreatment (open bars). Panel B: Size increases of liposomes after incubation with the protein−micelle conjugates. The dotted line represents the original size of the liposomes.

The first observation made was that filtering the micelle−protein conjugates prior to incubation with the liposomes had little effect on coupling efficiency except for the DSPE-ATTA2 systems, which showed a marked drop. There was a slight increase in turbidity as the micelle-forming lipid headgroup decreased in size, which was removed by the filtration step. This suggested that cross-linking increased as the headgroup size decreased, which is not a surprising finding. Similar trends were observed with the particle sizing data for the final liposome constructs.

Aggregation of the liposomes is indirectly linked to cross-linking in the micelle solutions since it is mediated by proteins that have two or more lipid anchors attached at distal ends. Thus, when one lipid anchor inserts into the liposome membrane, the distal anchor is available to insert into another liposome, inducing aggregation. Multiple distal derivatization of the protein

occurs when a protein conjugated to one micelle surface is able to access and react with another micelle surface. Clearly, increasing the size of the micelle-forming lipid inhibits this cross-linking as evidenced by the particle sizing data. However, increasing headgroup size also inhibits the conjugation reaction, resulting in decreasing conjugation efficiencies. PEG5000 essentially stopped the reaction, suggesting that the maleimide group was inaccessible. Significant inhibition is also seen with PEG2000. ATTA2 and ATTA4 have similar conjugation efficiencies, capping at approximately 50 g/mol, which, as we will show later, corresponds to the saturation of the micelle surface.

The apparent coupling efficiency for the filtered DSPE-ATTA2 micelles is lower than the unfiltered sample due to the removal of aggregated micelle−protein constructs. This in turn is reflected in the sizing data where the protein−liposomes generated from the filtered sample are larger than those from the unfiltered sample. This apparent contradiction is likely due to the removal of the most severely aggregated liposomes during the gel filtration step, resulting in a selective recovery of smaller liposomes.

The trend of decreased coupling efficiency as the extent of the steric barrier coverage of the surface of the micelle increases is similar to the behavior seen when conjugating protein to PEGylated liposomes using active coupling methods (*18*). In that experiment protein is conjugated to the surface of liposomes containing varying amounts of PEG2000 lipids in the membrane. As the level of PEG2000 increases, the conjugation efficiency drops off to a background level at ∼6 mol %. At this point the protein can no longer access the surface due to steric inhibition.

The results of these experiments demonstrate that a wide range of micelle compositions are possible provided that the micelle-forming lipid headgroup does not become so large that it prevents access of the protein to the maleimide group. The primary issues to consider in developing optimal reaction/formulation conditions are aggregation and reaction efficiency.

Zero Length Micelle-Forming Lipids. The fact that the passive coupling protocol worked with the DSPE-ATTA2 system posed new questions: How small is it possible for the micelle-forming lipid to be and still comprise a working formulation? How small is it possible for the active lipid to be and still comprise a working formulation? To answer these questions we designed an experiment where we used either DSPE-MPB or DSPE-ATTA2-MPA as the active lipids, and DSPE-ATTA4, OGP, and CHAPS as the micelle-forming lipids, six systems in all. The DSPE-ATTA2-MPA/DSPE-ATTA4 system was used as a reference point. Thiolated protein corresponding to a range of initial protein/final lipid ratios (based on final lipid, after mixture of the protein−micelles to the liposomes) from 50 to 500 g/mol was added to sets of micelle samples from each formulation group (since the final micelle/liposome lipid ratio is 1:19, this corresponded to protein/micelle lipid ratios of 1000−10000 g/mol micelle lipid). The protein−micelles (42 in all) were added to liposome samples and treated as described earlier. Lipid, protein, and size analyses were performed for each system. The results for the DSPE-ATTA2-MPA/OGP system data set are presented in Figure 4. Results for the other five systems can be seen in the Supporting Information.

We used the usual hydration method for preparing the micelles. This involved dissolving the lipid in ethanol and diluting the resultant solution in 9 parts buffer, such that the final concentration was ∼10 mM. This worked well in most cases, except for the CHAPS systems. CHAPS formed a gel-like solid in ethanol but formed micelles readily enough when the buffer was added. All systems formed micelles during the hydration process. Two systems showed thermotropic gel

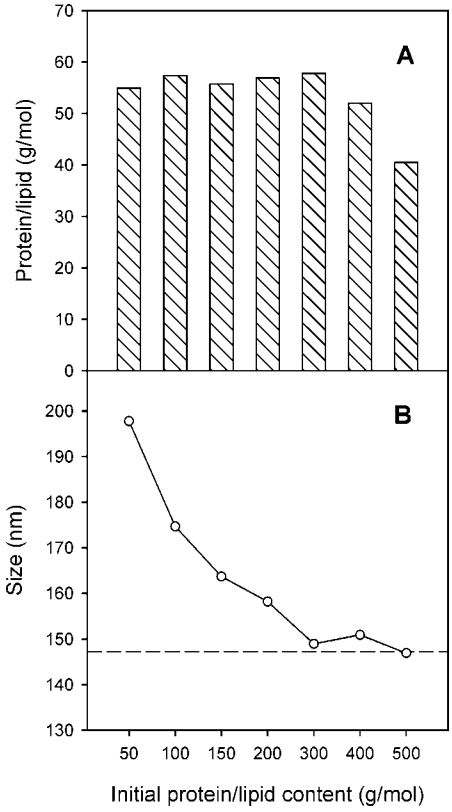

Figure 4. The effect of increased protein/micelle lipid ratio. Micelles were composed of DSPE-ATTA2-MPA/OGP (1:4). Ovalbumin was thiolated with 2-IT in a 1:5 ratio and incubated with micelles at various protein/lipid ratios. The initial protein/lipid content is expressed as g ovalbumin/mol total lipid for convenience, the initial protein/micelle lipid (g/mol) ratio is 20× the number shown. Liposomes were based on POPC/chol (55:45), and were treated with protein−micelles in a 1:19 micelle/liposome lipid ratio. Panel A: Protein bound to liposomes as a function of the initial protein content. Panel B: Final liposome size as a function of the initial protein content. The dashed line represents the size of the precursor liposomes.

formation behavior, namely the DSPE-MPB formulation with OGP and CHAPS. Gel formation was heaviest in the latter case. However, both systems could be redissolved into a micellar solution on warming in a 60 °C water bath. It is likely that this behavior is due to transient hydrophobic interactions between the maleimide groups in the absence of some sort of steric barrier molecule on the micelle surface.

Addition of thiolated ovalbumin in various ratios resulted in abolition of the thermotropic behavior mentioned above. The reaction was allowed to proceed overnight at room temperature. The systems containing CHAPS at 50 g/mol (initial protein/final total lipid) showed heavy aggregation, with light aggregation at 100 g/mol (initial protein/final total lipid). No aggregation was observed at higher ratios. Light aggregation was also seen in the DSPE-MPB/OGP system at 50 g/mol (initial protein/final total lipid). Slight turbidity was seen in a number of other formulations at 50 g/mol (initial protein/final total lipid) but could be dispersed on heating. The heavy aggregation observed in some of the systems was likely caused by cross-linking between the micelles, resulting in proteins which have been derivatized with hydrophobic anchors on distal ends of the molecule. Such molecules are undesirable when associated with liposome surfaces due to their ability to cause cross-linking and aggregation of the liposomes. The enhanced aggregation observed in the CHAPS systems at lower initial protein/lipid ratios is probably due to ionic interactions between the CHAPS and protein. At higher initial protein concentrations this effect is no longer seen, most likely as a result of conjugated protein

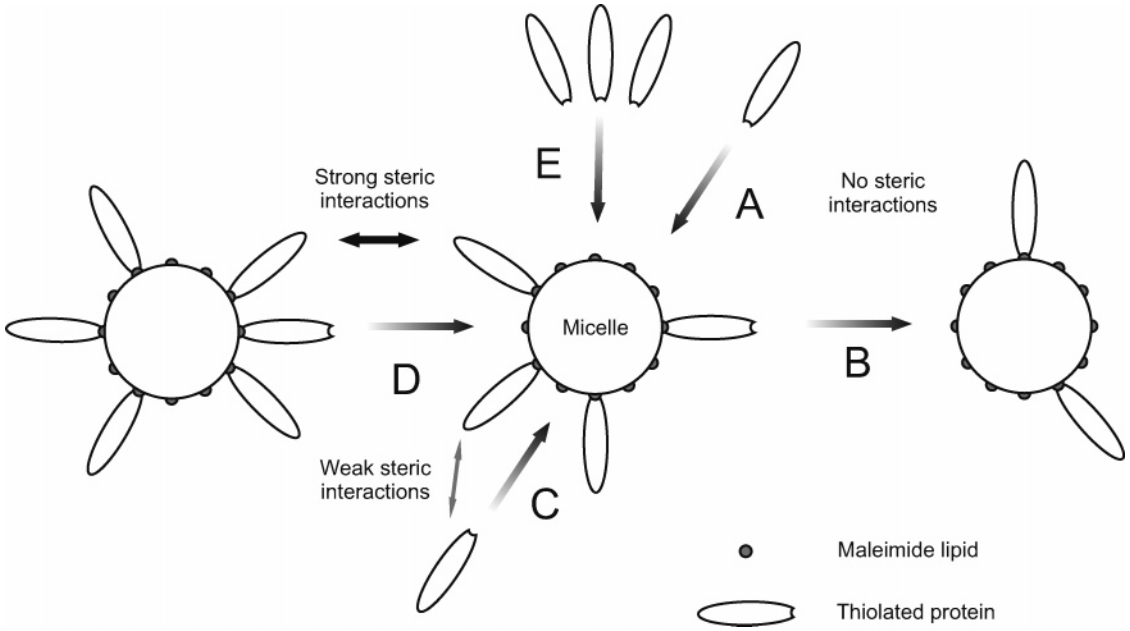

Figure 5. Mechanism for the inhibition of aggregation. A. Single macro-molecules can access unprotected surfaces readily. B. Surfaces without sufficient density of protein can undergo cross-linking reactions. C. Single macromolecules can access protected surfaces. D. Modified surfaces cannot access other modified surfaces readily, inhibiting cross-linking. E. Increasing concentration of free protein relative to other surfaces increases the rate of reaction of single protein conjugation

acting as a steric barrier molecule on the liposome surface, inhibiting further cross-linking reactions.

Figure 4 (and the related Supporting Information) show several interesting trends. In many cases the coupling efficiency increases to somewhere between 50 and 60 g/mol (initial protein/final total lipid) and then plateaus out. At high ratios it begins to decline. This would suggest that the micelle surfaces are being saturated at some point between 50 and 60 g/mol (initial protein/final total lipid), and that attempting to achieve higher ratios would reduce coupling efficiency. The particle sizing data (Figure 4 panel B) showed a steady decline in aggregation levels until around 200−300 g/mol (initial protein/final total lipid). We chose 150 g/mol (initial protein/final total lipid) as the standard initial protein/final lipid ratio, since it saturated the micelle surface at reasonable coupling efficiencies with relatively minor size increases due to aggregation. The apparent decline in coupling efficiency seen at high initial protein/final lipid ratios is probably due to the advent of maleimide quenching by excess hydrolyzed 2-IT which is still present in the thiolated protein solution.

Another interesting observation was that the saturation level of the DSPE-MPB micelles appeared to be somewhat lower than the DSPE-ATTA2-MPA systems (Supporting Information). This is not surprising since the area available for protein coverage is determined by the radius of the maleimide functionality, which is somewhat larger in the case of DSPE-ATTA2-MPA than DSPE-MPB. A smaller radius means less reactive surface area and hence a lower saturation level.

These results suggest a general model for preparing protein−micelle conjugates. Both the micelles and the proteins are multifunction entities. Micelles have a great many copies of maleimide on their surface, while the ovalbumin has on average up to five sulfhydryl groups. This means that once a thiolated protein has reacted with the surface of a micelle, it may still be available for reaction to another micelle. Once a protein is conjugated to a micelle however, the probability of it reacting with another micelle is smaller than the free protein alone due to steric hindrance.

As the surface concentration increases, the protein starts to act as a steric barrier molecule in its own right and eventually stops aggregation reactions. In situations where the initial free protein/micelle ratio is large, the rapid coating of the micelles prevents further aggregation reactions. Alternatively, where the initial free protein/micelle ratio is smaller, aggregation can still occur (Figure 5). This suggests that the degree of aggregation in a particular system can be controlled simply by adjusting the initial protein/lipid ratio. There is a limit to how far this can be taken though, since coupling efficiency is likely to be an issue with many proteins, particularly those in limited supply. For most of our work we selected 150 g/mol (initial protein/final total lipid) as our baseline standard, since aggregation was reasonable and coupling efficiency acceptable (∼35%).

If this mechanism is correct, we can predict that changing other parameters should also have effects on coupling efficiency and aggregation. These include the active lipid content of the micelles, initial 2-IT concentration, and the initial protein/final lipid ratio.

Effects of Changes to the Active Lipid Content. If the proposed mechanism is correct, we would expect that alterations to the active lipid content should affect the coupling efficiency. A micelle surface concentration of 1000 g/mol (initial protein/micelle lipid) corresponds to 0.022 mol protein/mol lipid. This implies that there is one protein for every 45−50 lipid molecules in the micelle. Our baseline formulation used a micelle composition of active lipid/micelle-forming lipid in a 1:4 ratio; in other words there is one protein for every 9−10 active lipid molecules. That would imply that the surface is being saturated, rather than the reactive functions on the surface, since this appears to be the upper limit of conjugation in these systems.

We designed an experiment in which the active lipid content in the micelles was changed, but the total amount of micellar lipid relative to liposome lipid was held constant. Thiolated protein was incubated with various samples of micellar lipid in a 3000 g/mol ratio (or 150 g initial protein/mol final lipid) and then treated with POPC/chol liposomes in a 1:19 lipid ratio. The results are shown in Figure 6. As expected reducing the amount of active lipid in the micelles resulted in reduced aggregation. However, coupling efficiency is also adversely affected, falling off as the active lipid content drops.

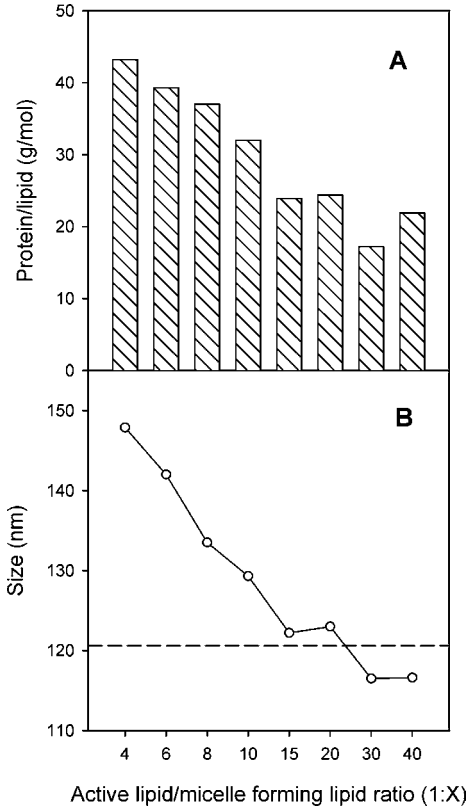

Figure 6. The effect of reducing the active lipid content while keeping the micelle/liposome lipid ratio constant. Micelles were composed of DSPE-ATTA2-MPA/OGP (1:X). Ovalbumin was thiolated with 2-IT in a 1:5 ratio and incubated with micelles at 3000 g protein/mol micelle lipid. Liposomes were based on POPC/chol (55:45), and were treated with protein−micelles in a 1:19 micelle/liposome lipid ratio, for an initial protein/total lipid content of 150 g/mol. Panel A: Final bound protein content as a function of active lipid content in the micelles. Panel B: Final liposome size. The dashed line represents the size of the precursor liposomes.

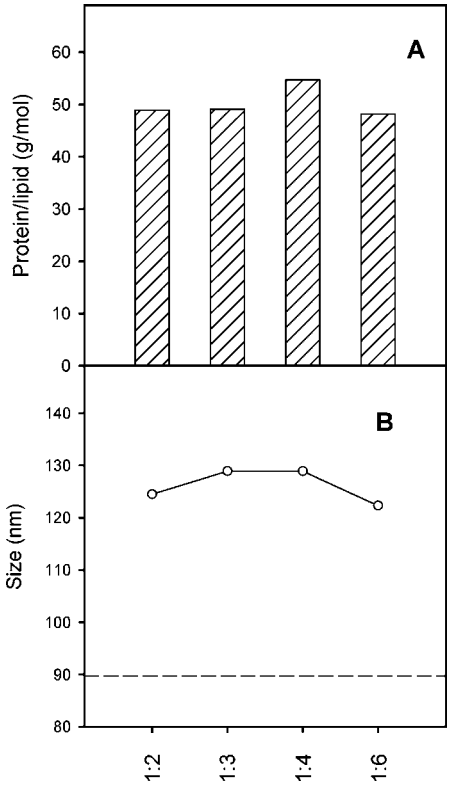

Figure 7. The effect of reducing the micelle lipid content while keeping the active lipid/liposome lipid at 1%. Micelles were composed of DSPE-ATTA2-MPA/OGP (1:X). Ovalbumin was thiolated with 2-IT in a 1:5 ratio and incubated with micelles at 15000 g protein/mol active lipid. Liposomes were based on POPC/chol (55:45) and treated with micelles such that the initial protein/total lipid content was 150 g/mol. Panel A: Final bound protein content. Panel B: Final liposome size. The dashed line represents the size of the precursor liposomes.

A second experiment was done in which the active lipid/micelle-forming lipid ratio was changed, but with the total amount of micelles added to the liposomes normalized against the active lipid. The final active lipid content was 1%. The results are presented in Figure 7. We had expected that the amount of conjugated protein would increase as the amount of micelle-forming lipid increased, since this should have resulted in more micelles with a corresponding increase in the reaction surface. In fact there were relatively small changes in the conjugation efficiency, with no clear change in particle size. This would imply that either the surface area of the micelles was remaining approximately constant, or that the reaction efficiency on the surface was decreasing as the micelle number increased. The most probable explanation is that both the micelle number and the reactive radius in the context of this experiment are being determined largely by the active lipid. The results suggest that the protocol is relatively insensitive to changes in the micelle lipid composition, at least within the data range covered by the experiment.

Effects of 2-IT Ratio on Aggregation. An alternative method for reducing cross linking reactions is to reduce or minimize the number of additional sulfhydryl groups in the thiolated protein. To investigate the effect of the number of cross-linking groups we titrated in 2-IT corresponding to 1−5 equiv per protein, with 5 equiv being our baseline system. The experiment was performed at two initial protein/final lipid ratios, namely 50 and 200 g/mol (initial protein/final total lipid). The results of the experiment are presented in Figure 8. As expected, decreasing the amount of cross-linker used decreased the level of aggregation. Surprisingly, however, reducing the amount of cross-linker used did not dramatically affect coupling efficiency, although a slight drop-off could usually be seen at the lowest cross-linker content, even in the 50 g/mol (initial protein/final total lipid) system.

Reducing the Initial Protein Content below the Saturation Level. Since the micelle surface was apparently becoming saturated at a protein/micelle lipid ratio of ∼1000 g/mol, we ran an experiment in which the initial protein content was titrated into micelles below the saturation level. The results are presented in Figure 9 (P/L is represented as initial protein/final lipid). The apparent coupling efficiency in this particular experiment is 60−70% for all the data points, except for the final one at 100 g/mol where it has fallen off to 45%. This would indicate that the surface of the micelle is saturated at approximately 1000 g/mol (protein/micelle lipid), which is consistent with the result previously obtained. The limit to the apparent coupling efficiency at 60−70% in this experiment suggests that at least some of the protein is not thiolated, or is thiolated in areas of the protein that are not available for reaction. Modest changes to the sizes of the liposomes were observed after incubation with the protein−micelle conjugates, suggesting that the liposomes were more prone to cross-linking reactions as the protein content decreased. Again, this is to be expected if protein bound on the surface of the micelles acted as a steric barrier, since reducing the protein on the surface should increase the probability of a successful cross-link reaction.

Titration of Protein−Micelles into Liposomes. A solution of protein−micelles with an initial protein/micelle lipid ratio of 3000 g/mol was prepared and titrated into liposomes (Figure 10). At this concentration, coupling efficiency is typically 30−

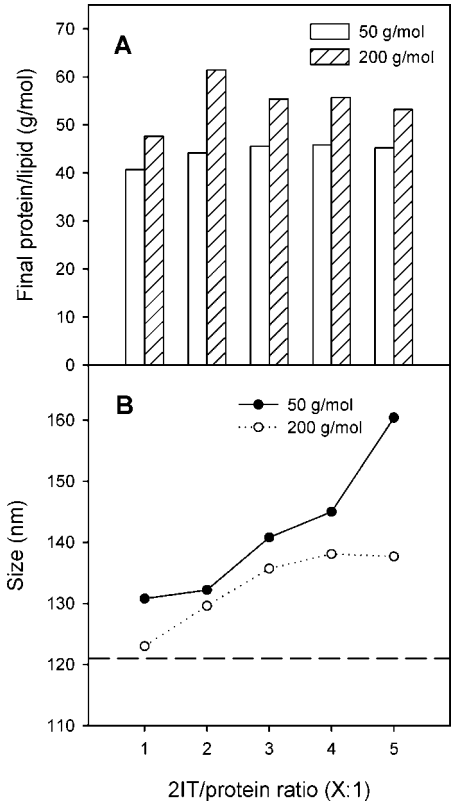

Figure 8. The effect of the 2-IT/ovalbumin ratio. Micelles were composed of DSPE-ATTA2-MPA/OGP (1:4). Ovalbumin was incubated with 1−5 equiv of 2-IT and incubated with micelles at 1000 g/mol or 4000 g/mol. Liposomes were based on POPC/chol (55:45) and incubated with micelles in a 19:1 lipid ratio, so that the initial protein/total lipid content was either 50 or 200 g/mol. Panel A: Final bound protein content as a function of the initial 2-IT/ovalbumin ratio. Panel B: Final liposome size. The dashed line represents the size of the precursor liposomes.

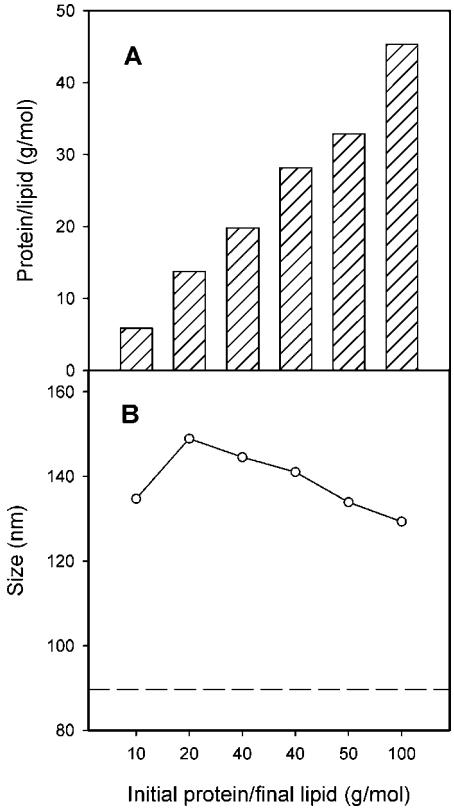

Figure 9. The effect of low initial protein/lipid ratios. Ovalbumin was incubated with 5 equiv of 2-IT and added to micelles composed of DSPE-ATTA2-MPA/OGP (1:4) at protein/micelle lipid ratios of 200−2000 g/mol. Liposomes based on POPC/chol (55:45) were incubated with micelles in a 19:1 lipid ratio, for initial protein/total lipid ratios of 10−100 g/mol. Panel A: Final bound protein content as a function of initial protein added. Panel B: Final liposome size. The dashed line represents the size of the precursor liposomes.

40%. The protein content associated with the final liposome formulations increased in proportion to the amount added. This value tended to fall off at very high levels of added micelles. Figure 10 shows a slight fall off in association efficiency at 300 g/mol (initial protein/final total lipid); however, at this point the ratio of liposome/micelle lipid is 10:1. At these levels the detergent itself may start to affect the system in significant ways. We have titrated the micelles into liposomes to much higher levels (see Supporting Information) and start to see a marked decline in association efficiency, together with a fall in the levels of liposome aggregation at very high micelle contents. Those results suggest that the liposome surfaces might be becoming saturated at those levels, but it is difficult to draw conclusions since at those detergent levels, the surfactants must be playing a role.

The levels of aggregation observed in Figure 10 is approximately the same for all the systems studied. This is not surprising since the cross-linking reaction occurs during the micelle−protein incubation, and the same micelle−protein solution was used to prepare all of the final liposome formulations. The systems should show equivalent levels of aggregation provided that the surface of the liposomes was not saturated.

Reproducibility of the Conjugation Process. One of the primary problems when using active coupling protocols for preparing protein−liposome conjugates is controlling parameters such as conjugation efficiency. This problem is exacerbated in some cases by the presence of steric barrier molecules on the surface of some liposome formulations, since even small changes in the concentration of these molecules can have significant effects on the accessibility of the liposome surface to the reactive face of the protein. In principle the passive conjugation process should result in far more reproducible formulations since the amount of protein−lipid conjugates formed can be regulated by saturation of the micelle surface. The protein micelles can then be titrated into liposomes at specific concentrations, allowing the user to accurately tailor the particular composition of a protein−liposome formulation.

To test this idea we designed an experiment in which three separate sets of protein solutions were thiolated using the same 2-IT stock solution. The three thiolate protein solutions were then incubated with three separately prepared maleimide-containing micelle solutions. Aliquots of these three solutions were then treated with POPC/chol liposomes as usual. The final micelle−liposome incubation was repeated 4 days later using the same protein−micelle and liposome solutions. After final workup and analysis, the results plotted and presented in Figure 11. The experiment served to demonstrate that relatively reproducible results can be obtained if a standard protocol is followed.

DISCUSSION

The primary focus of our laboratory is the development of liposome-based drug delivery systems that are practical candidates for commercialization as pharmaceutical products. Two areas of interest to us have long been the development of a functional “targeted” formulation and artificial vaccines. In both cases, to develop viable products based on these concepts we have considered it important that we have techniques for conjugating proteins of interest to these systems that are both robust and reproducible.

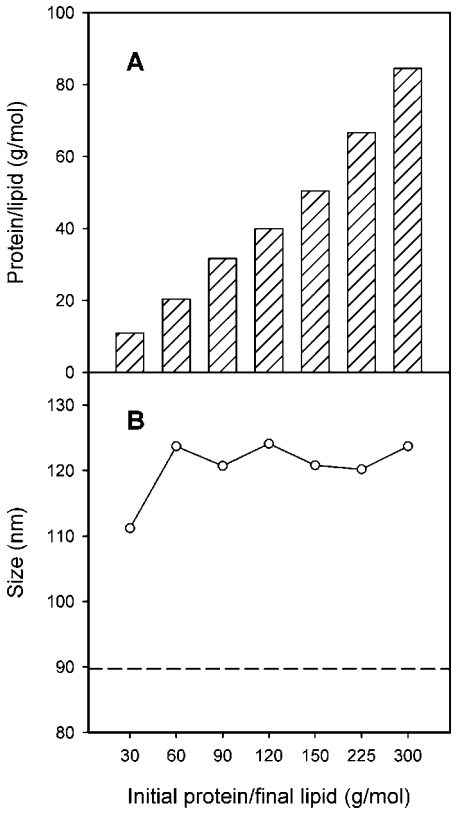

Figure 10. Titration of ovalbumin/micelles conjugates into POPC/chol (55:45) liposomes. Ovalbumin was incubated with 5 equiv of 2-IT and added to micelles composed of DSPE-ATTA2-MPA/OGP (1:4) in a 3000 g protein/mol micelle lipid ratio. Aliquots of ovalbumin/micelles were added to liposomes such that the initial protein/total lipid ratio was as indicated in the figure. Panel A: Final bound protein content as a function of the initial protein/lipid ratio. Panel B: Final liposome size. The dashed line represents the size of the precursor liposomes.

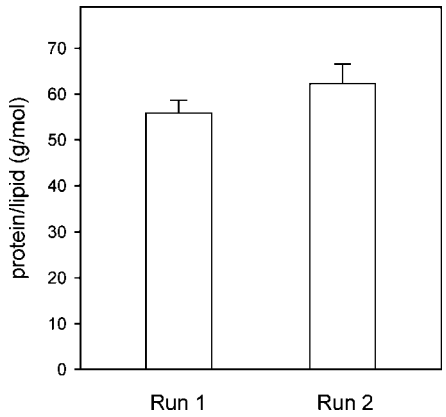

Figure 11. Reproducibility of the passive coupling procedure. Three separate ovalbumin solutions were treated with 2-IT in a 1:5 ratio. Aliquots of the thiolated ovalbumin were added independently to three separately prepared micelle solutions (DSPE-ATTA2-MPA/DSPE-ATTA4; 1:4) at 3000 g protein/mol micelle lipid. Aliquots of the three micelle−ovalbumin conjugate solutions were added to POPC/chol liposomes (55:45; a single stock solution was used) at an initial protein/total lipid ratio of 150 g/mol. After a few days of storage the micelle−ovalbumin/liposome incubations were repeated a second time using the same liposome and micelles stock solutions.

Drugs encapsulated in liposomes largely assume the pharmacokinetic characteristics of the liposomes themselves, with the primary variable being the leakage rate of the drug in vivo. This creates limitations in the utility of these systems however, since liposomes distribute in vivo in specific ways. It has long been an objective of many groups in the field to alter this distribution through the attachment of targeting functions on the surface of liposomes, such that they would accumulate in a specific tissue or a specific cell type. Much of this work has focused on the use of proteins such as antibodies to achieve this goal.

Many problems have been experienced in these studies however. It is often difficult to determine if a "targeted" liposome has truly reached the target in vivo, since in many cases access to the target requires extravasation to take place first. Extravasation then becomes the rate-limiting step, making it difficult to distinguish between actual targeting and non specific association. In addition, many of the proteins used in these studies have natural effector functions, or are recognized as foreign by the immune system when attached to liposomes.

One of the issues faced when comparing different studies or experiments is that very often the levels of conjugated protein vary considerably. This is partly the result of the intrinsic variability in conducting multistep reactions on proteins and partly due to aggregation reactions and/or steric inhibition of reactions on liposome surfaces due to the presence of steric barrier molecules. The development of the work discussed in this paper was motivated to address these issues and provide a conjugation system that was both reproducible and technically simple.

The other area of interest to us in this field was the synthesis of artificial vaccines. While working on the development of liposome-encapsulated oligonucleotides (*19*) we discovered that these formulations had powerful immunostimulatory effects (*20*). We also made the serendipitous discovery that a subset of these formulations which included nonexchangeable PEG−lipids as part of the lipid composition showed dramatic increases in liposome clearance rates on repeat administrations. This was later shown to be due to an induced immune response to the PEG (*21*), a molecule which is normally thought of as nonimmunogenic. Following this discovery we were able to show that greatly enhanced immune responses to protein was achieved when they were conjugated to the surface of these oligonucleotide−liposome particles.[2]

Originally we conjugated proteins to these particles using active coupling methods. It was difficult to get reproducible results with these methods however, necessitating the development of more controllable methods of conjugation. Although the nature of the particle is very different from those used in drug targeting applications, the fundamental issues involved in performing a protein−particle conjugation are much the same. The same techniques should be applicable to both applications. This need led to the development of the general technique described in this paper.

Active conjugation methods tend to suffer from a number of serious drawbacks. The most important of these are reaction control, aggregation, and conjugation efficiency. When conjugating a protein to the surface of a liposome, both entities have multiple sites of possible reaction. In the absence of any sort of controlling mechanism, this leads to cross-linking of liposomes and the formation of liposome aggregates. These aggregates are rapidly cleared in vivo and are considered pharmaceutically undesirable. The formation of the aggregates can be suppressed by including steric barrier molecules in the formulation or by controlling the relative concentrations of the reactants. However, these methods lead to the suppression of the reaction through either steric inhibition or by competition

[2] Yuan, Z. N., Brodsky, I., Ansell S. M., Klinuk, S.K, and Semple, S. C. (2004) Systemic and mucosal immune responses induced by liposomes with surface-coupled antigen and high levels of encapsulated immunostimulatory oligonucleotides. Unpublished data.

from hydrolysis reactions. This manifests itself through generally low and variable coupling efficiencies.

The basic problem with active conjugation is that we are performing two processes simultaneously, namely: (a) associating the protein with the liposome; and (b) forming a lipid−protein conjugate. Since a number of variables affect this process, we end up with a system that is intrinsically difficult to control. The simplest and most obvious solution to the problem is to separate the procedure into two steps, and this is what we do with the passive conjugation method. The lipid protein−conjugate is formed externally from the liposome, after which it is exchanged into the liposome bilayer.

In this particular case we are using a micelle as a substitute surface to perform the reaction on. As can be seen from the data in Figure 4, once you reach a certain point it is no longer possible to increase the amount of protein associated with the micelles since the surface has been saturated with protein. This property allows us to prepare a reagent in which the amount of lipid−protein conjugate available for association with the liposomes is determined primarily by the micelle surface area. This can then be titrated into a preformed liposome solution and incubated under appropriate conditions until the protein−lipid conjugates exchanges into the liposome bilayer. The method allows us to make protein−liposome conjugates with a precision not previously possible.

Reports in the literature have used similar techniques to prepare protein−liposome conjugates (*6*, *7*). In those cases the active lipid used was a phospholipid−PEG−maleimide derivative. Placing the reactive function on the end of a PEG chain effectively dramatically increases the micellar radius of reaction, meaning that considerably more protein is required to saturate the micelle surface. Since saturation of the micelle surface is advantageous for reproducible results, the active lipids we have used here (DSPE-MPB and DSPE-ATTA2-MPA) should be more effective than PEG-based analogues.

The issue of aggregation of the final protein−liposome conjugates is not immediately solved by the approach described here since the micelles can still undergo cross-linking reactions in much the same way liposomes do. However, there are methods for controlling this process. With active coupling protocols this would be achieved by including a steric barrier lipid in the liposome composition. This results in systems where the reaction at a liposome surface with a free protein is more likely than with the much larger protein−liposome conjugate, because of interactions between the steric barrier lipids in the respective liposomes. The same principle applies for micelles, except that in this case the conjugated protein acts as the steric barrier molecule. As the initial protein content increases above the amount needed for saturation, the faster rate of reaction for the free protein would result in increased inhibition of the slower cross-linking reaction and consequent reduction in cross-linking. This is reflected indirectly in the sizing data for the final liposome conjugate.

This means that aggregation can be minimized by increasing the initial protein−lipid ratio. The price paid is a lower coupling efficiency. This might be acceptable if the protein is inexpensive or readily available, but in many cases this may not be true and consequently the cost aspect may a factor to consider when designing the specifics of the process used. An alternative approach to the problem is to reduce the probability of cross-linking occurring by reducing the amount of one of the reactive functions. This can be done by reducing the active lipid content in the micelles, or by reducing the level of thiolation in the protein. As can be seen in Figures 6 and 8, both of these approaches work, albeit with lowered coupling efficiency in some cases. The process works by making the cross-linking reaction less likely than the primary conjugation reaction.

In conclusion we have demonstrated that micelle-based passive coupling techniques are highly effective for the preparation of well defined protein−liposome techniques, and that a wide range of micelle-forming and active lipids can be used for this purpose. The ideal system to use would be one in which a relatively large excess of initial protein was used. The active lipid chosen should have a relatively nonexchangeable lipid anchor, such as DSPE, and preferably have a short tether between the lipid anchor and the maleimide function. A micelle-forming lipid should be present to dilute out some of the reactive lipid and to facilitate micelle formation where necessary. A range of micelle-forming lipids are suitable; however, the hydrophilic headgroup should not be so large that it inhibits the reaction through steric interactions. The application of these techniques to the preparation of protein−lipid-antisense complexes will be described in a later work.

Supporting Information Available: Experimental details. This material is available free of charge via the Internet at http://pubs.acs.org.

LITERATURE CITED

(1) Supra, P., and Allen, T. M. (2003) Ligand-targeted liposomal anticancer drugs. *Prog. Lipid Res. 42*, 439−462.

(2) Fortin, A., Shahum, E., Krzysztof, K., and Therien, H. M. (1996) Differential activation of cell-mediated immune functions by encapsulated and surface-linked liposomal antigens. *Cell. Immunol. 169*, 208−217.

(3) Vannier, W. E., and Snyder, S. L, (1988) Antibody responses to liposome-associated antigen. *Immunol. Lett. 19*, 59−64.

(4) Guan, H. H., Budztnski, W., Koganty, R. R., Krantz, M. J., Reddish, M. A., Rogers, J. A., Longenecker, B. M., and Samuel, J. (1998) Liposomal formulations of synthetic MUC1 peptides: effects of encapsulation versus surface display of peptides on immune responses. *Bioconjugate Chem. 9*, 451−458.

(5) Hermanson, G. T. (1996) *Bioconjugate Techniques*, Academic Press, San Diego.

(6) Iden, D. L., and Allen, T. M. (2001) In vitro and in vivo comparison of immunoliposomes made by conventional coupling techniques with those made by a new post-insertion approach. *Biochim. Biophys. Acta 1513*, 207−216.

(7) Supra, P., and Allen, T. M. (2004) Improved outcome when B-cell lymphoma is treated with combinations of immunoliposomal anticancer drugs targeted to both CD19 and CD20 epitopes. *Clin Cancer Res. 10*, 2530−257.

(8) Loughrey, H. C., Wong, K. F., Choi, L. S., Cullis, P. R., and Bally, M. B. (1990) Protein-liposome conjugates with defined size distributions. *Biochim. Biophys. Acta 1028*, 73−81.

(9) Juliano, R. L., and Stamp, L. (1975) The effect of particle size and charge on the clearance rates of liposomes and liposome encapsulated drugs. *Biochem. Biophys. Res. Commun. 63*, 651−685.

(10) Harasym, T. O., Tardo, P., Longman, S. A., Ansell, S. M., Bally, M. B., Cullis, P. R., and Choi, L. S. L. (1995) Poly(ethylene glycol)-modified phospholipids prevent aggregation during covalent conjugation of proteins to liposomes. *Bioconjugate Chem. 6*, 187−194.

(11) Blume, G., Cevc, G., Crommelin, M. D., Bakker-Woudenberg, I. A., Kluft, C., and Storm, G. (1993) Specific targeting with poly(ethylene glycol)-modified liposomes: coupling of homing devices to the ends of the polymeric chains combines effective target binding with long circulation times. *Biochim. Biophys. Acta 1149*, 180−184.

(12) Ishida, T., Iden, D. L., and Allen, T. M. (1999) A combinatorial approach to producing sterically stabilized (Stealth) immunoliposomal drugs. *FEBS Lett. 460*, 129−133.

(13) Dhawan, R., Kadijk, M. G. A., Joikinen, T. J., Feng, M., and Ansell, S. M. (2000) Synthesis of polyamide oligomers based on 14-amino-3, 6, 9, 12-tetraoxatetradecanoic acid. *Bioconjugate Chem. 11*, 14−21.

(14) Ansell, S. M., Tardi, P. G., and Buchkowsky, S. S. (1996) 3-(2-Pyridyldithio)propioic acid hydrazide as a cross-linker in the formation of liposome−antibody conjugates. *Bioconjugate Chem. 7*, 490−496.

(15) Schwabacher, A. W., Lane, J. W., Scheisher, M. W., Leigh, K. M., and Johnson, C. W. (1998) Desymmetrization reactions: efficient preparation of unsymmetrical substituted linker molecules. *J. Org. Chem. 63*, 1727−1729.

(16) Ansell, S. M., Kojic, L. D., Hankins, J. S., Sekirov, L. Boey, A., Lee. D. K., Bennett, A. R., Klimuk, S. K., Harasym, T. O., Dos Santos, N., and Semple, S. C. (1999) Application of oligo-(14-amino-3, 6, 9, 12-tetraoxatetradecanoic acid) lipid conjugates as steric barrier molecules in liposomal formulations. *Bioconjugate Chem. 10*, 653−666.

(17) Kenworthy, A. K., Simon, S. A., and McIntosh, T. J. (1995) Structure and phase behaviour of lipid suspensions containing phospholipids with covalently attached poly(ethylene glycol). *Biophys. J. 68*, 1903−1920.

(18) Ansell, S. M., Harasym, T. O., Tardi, P. G., Buchkowsky, S. S., Bally, M. B., and Cullis, P. R. (2000) Antibody conjugation methods for active targeting of liposomes. In *Drug Targeting: Strategies, Principles and Applications* (Francis, G. E., and Delgado, C., Eds.) pp 51−68, Chapter 4, Humana Press, Totowa, NJ.

(19) Semple, S. C., Klimuk, S. K., Harasym, T. O., Dos Santos, N., Ansell, S. M., Wong, K. F., Maurer, N., Stark, H., Cullis, P. R., Hope, M. J., and Scherrer, P. (2001) Efficient encapsulation of antisense oligonucleotides inlipid vesicles using ionizable aminolipids: formation of novel small multilamellar vesicle structures. *Biochim. Biophys. Acta 1510*, 152−166.

(20) Mui, B., Raney, D. G., Semple, S. C., and Hope, M. J. (2001) Immune stimulation by a CpG-containing oligodeoxynucleotide enhanced when encapsulated and delivered in lipid particles. *J. Pharmacol. Exp. Ther. 298*, 1185−1192.

(21) Semple, S. C., Harasym, T. O., Clow, K., Ansell, S. M., Klimuk, S. K., and Hope, M. J. (2004) Immunogenicity and rapid clearance of lipososmes containing polyethylene glycol-lipid conjugates and nucleic acid. *J. Pharmacol. Exp. Ther. 312*, 1020−1026.

BC050051R

List of supplementary data for manuscript entitled "Micelles as intermediates in the preparation of protein-liposome conjugates"

Figure S.1. Related data for figure 6 in the manuscript. Micelles composed of DSPE-ATTA2-MPA/DSPE-ATTA4 (1:4)

Figure S.2. Related data for figure 6 in the manuscript. Micelles composed of DSPE-ATTA2-MPA/CHAPS (1:4)

Figure S.3. Related data for figure 6 in the manuscript. Micelles composed of DSPE-MPB/DSPE-ATTA4 (1:4)

Figure S.4. Related data for figure 6 in the manuscript. Micelles composed of DSPE-MPB/OGP (1:4)

Figure S.5. Related data for figure 6 in the manuscript. Micelles composed of DSPE-MPB/CHAPS (1:4)

Figure S.6. Titration of protein-micelles into liposomes

S.7. Comments regarding the assays used and reproducibility

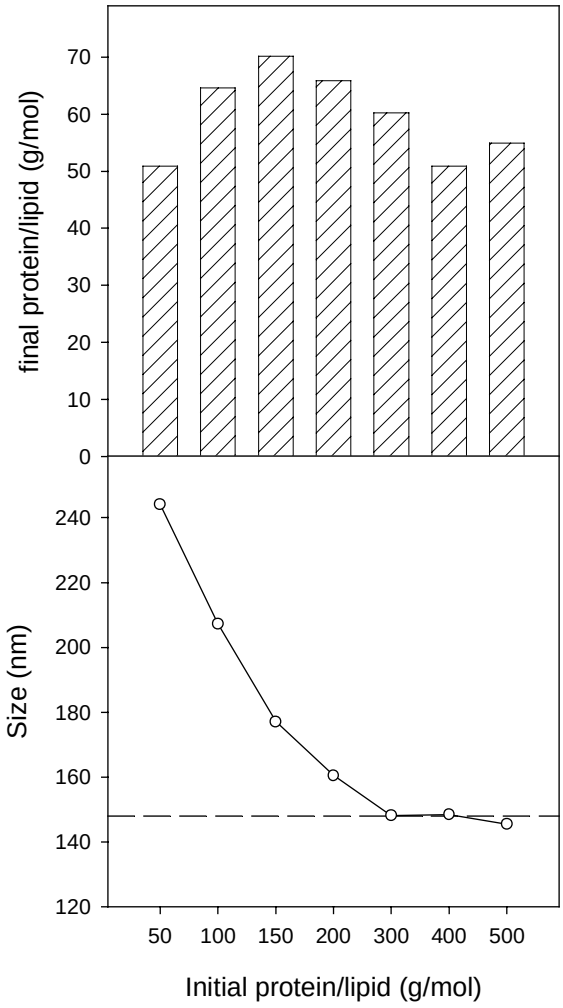

Figure S.1. Related data for figure 6 in the manuscript. Micelles composed of DSPE-ATTA2-MPA/DSPE-ATTA4 (1:4)

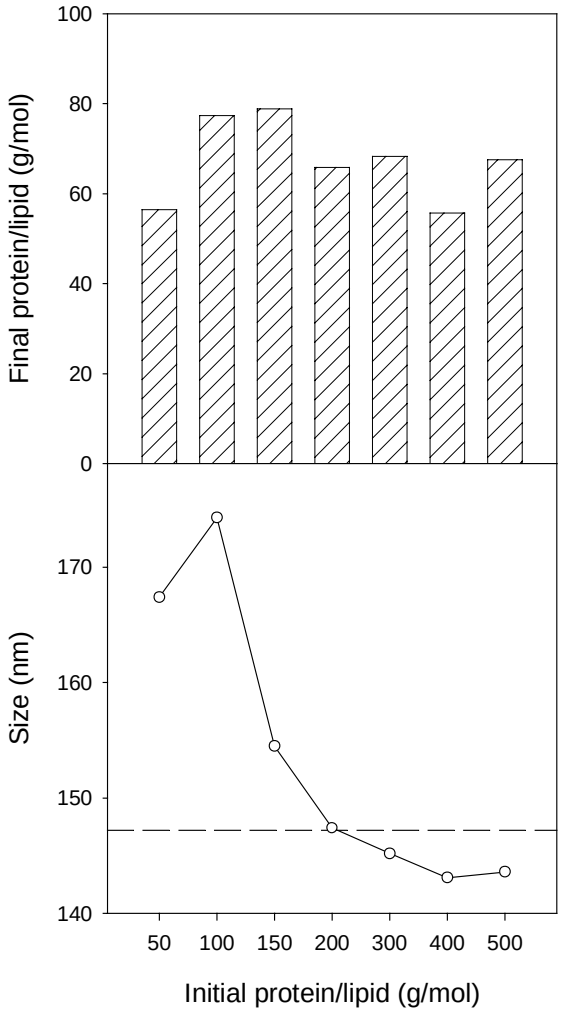

Figure S.2. Related data for figure 6 in the manuscript. Micelles composed of DSPE-ATTA2-MPA/CHAPS (1:4)

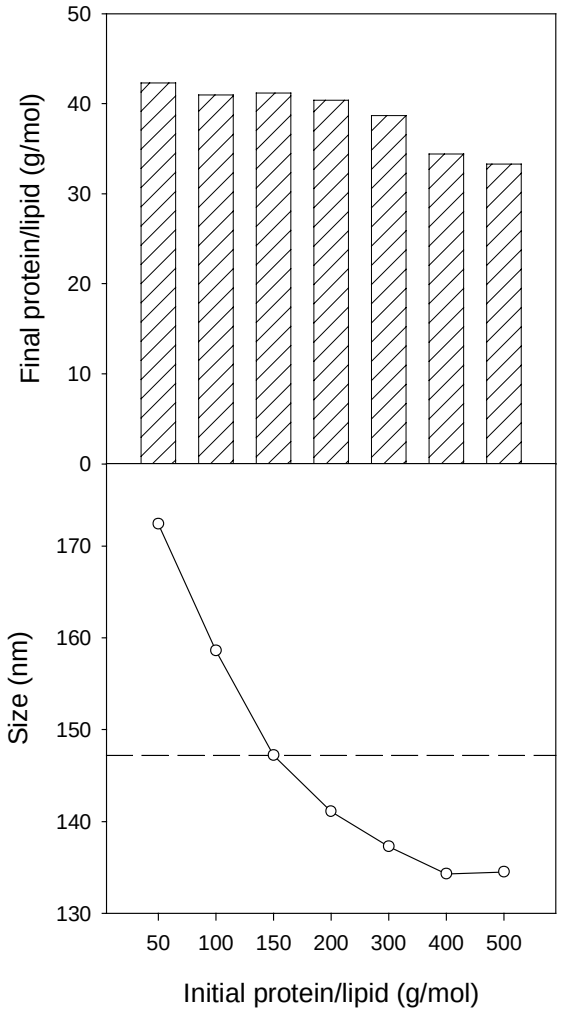

Figure S.3. Related data for figure 6 in the manuscript. Micelles composed of DSPE-MPB/DSPE-ATTA4 (1:4)

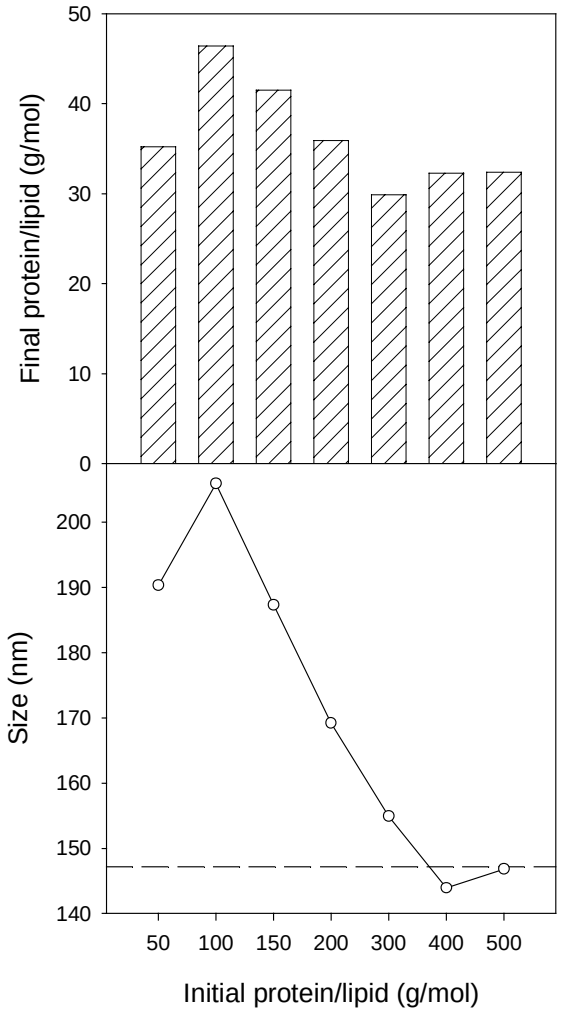

Figure S.4. Related data for figure 6 in the manuscript. Micelles composed of DSPE-MPB/OGP (1:4)

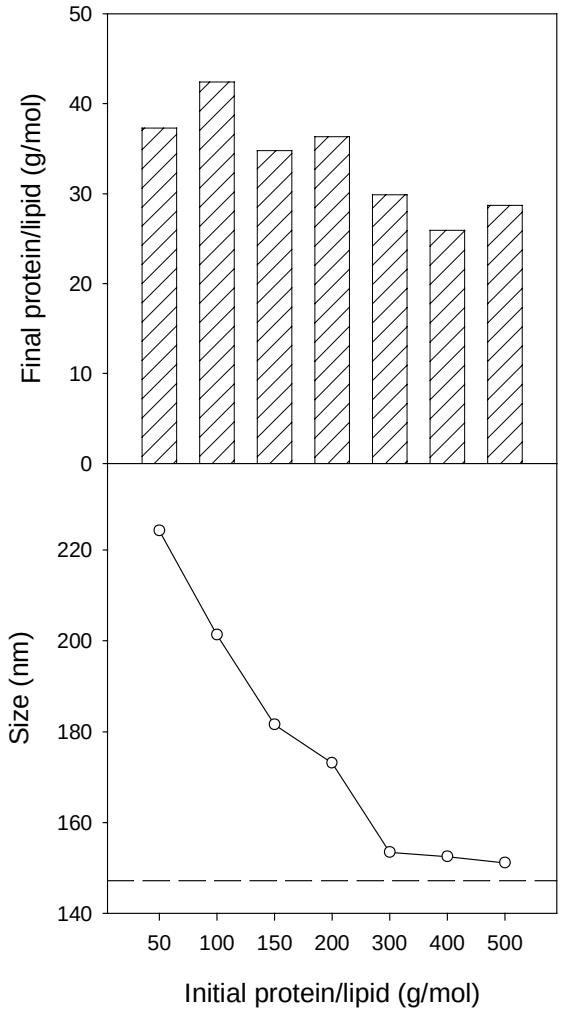

Figure S.5. Related data for figure 6 in the manuscript. Micelles composed of DSPE-MPB/CHAPS (1:4)

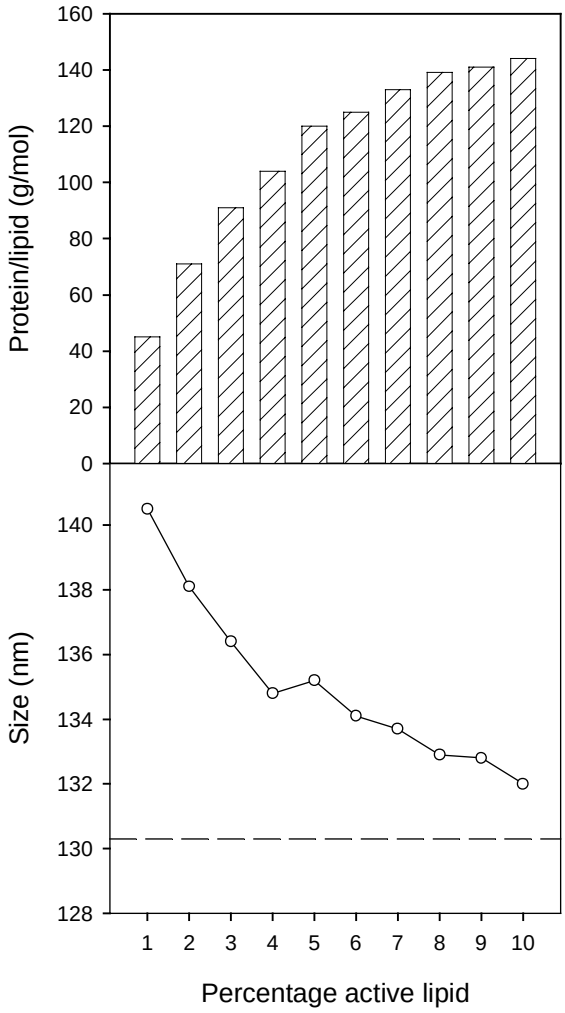

Figure S.6. Titration of protein-micelles into liposomes. Ovalbumin was coupled to DSPE-ATTA2-MPA/OGP (1:4) micelles in a 3000 g protein/mol micelle lipid ratio. Aliquots of these micelles were added to POPC/cholesterol (55:45) liposomes, such that the % of active lipid relative to the liposome lipid was as shown above. Sample processing and workup protocols were conducted as described generally in the manuscript methods section. Protein, lipid and particle sizing assays were conducted as described in the manuscript. Each % active lipid added corresponds to 5% total micelle lipid, ie between 5 and 50% micelle lipid is added to the liposomes.

S.7. Comments regarding the assays used and reproducibility

The passive method has a relatively high level of reproducibility provided that experimental conditions are kept constant and provided that analytical methods are accurate. However, there are potential sources of variability in terms of the numbers that are generated in different experiments. Much of this stems from the assay that is used to determine protein content. Basically it involves a chemical colorimetric assay using a standard curve performed with reagents from Pierce's BCA assay kit. The standard curve itself is generated using a set of BSA standards. These standards are prepared by first diluting 50 µl of a kit stock solution with 950 µl of buffer to prepare a working stock solution. Aliquots ranging from 25 to 200 µl are then taken from this stock to prepare the standard curve samples. Any pipetting errors in this series of dilutions will result in deviations from the true concentration, both in terms of the slope of the standard curve and scatter of the data points making up the curve. The actual samples were analyzed in triplicate, for both the protein assay and the phosphate assay. Consequently, while data within a particular experiment is reasonable consistent, data between experiments may show some variability.

In addition to issues involving uncertainty with the slope of standard curve, the lipids used to produce liposomes can generate varying levels of background interference independent of the presence of protein. Usually this interference is small relative to the assay numbers with normal liposomes (typically 1-3 g/mol), but it can be fairly large in some cases with SALP lipids (up to around 5-6 g/mol). The reported number can deviated from the true value somewhat depending on whether or not results are corrected for background. The background and the associated uncertainty places constraints on the sensitivity of the BCA assay as well as the accuracy.

The BCA assay is far from ideal, but under the circumstances it was the most reliable method available to us. We attempted using flourescamine based assays, but found that the standard curve varied considerably depending on what exactly was used to produce it. Standard curves were generated using ovalbumin, albumin and thiolated ovalbumin, and yielded different results in each case for test samples, apparently all inaccurate based on comparisons with values determined using extinction coefficients. The BCA assay on the other hand, generated concentration results consistent with that obtained using extinction coefficients irrespective of which standard curve was used. Florescamine should be more sensitive in principle, but it was limited by the lack of material suitable for generating an appropriate standard curve.

Probably the best assay method to use would be one based on labeled protein, but that was not available for this work.

A second factor affecting the absolute results was the slow degradation of maleimide reagents on storage. Over a period of months the materials start to form insoluble products that we believe are polymers formed from intermolecular trans-acylation reactions initiated by maleamic acid impurities present in the samples. This results in polymeric materials which are unreactive and cause formulation issues, collectively

reducing conjugation efficiency. If properly stored, materials would perform consistently for 4-5 months, after which degradation of performance (in the form of coupling efficiency) would start to become apparent. Normally we would synthesize fresh reagents before this happened, but some data sets were generated with older material, and consequently absolute coupling efficiencies in those cases are lower than normal.

However, since general conclusions drawn from this work were made within data sets, and not between data sets, we believe that these discrepancies do not impact the overall message. Comparing data between sets is probably of dubious validity, but within data sets it is reasonably consistent. For example, in figure 6 the coupling efficiency is somewhat lower than what we would normally expect, but the message that the micelles can be titrated proportionally into SALP in a concentration dependant manner is still valid.

Methods for the Preparation of Protein−Oligonucleotide−Lipid Constructs

Jennifer Takasaki, Sameersingh G. Raney, Ghania Chikh, Laura Sekirov, Irina Brodsky, Ying Tam, and Steven M. Ansell*

Inex Pharmaceuticals Corporation, 100-8900 Glenlyon Parkway, Burnaby, BC, V5J 5J8, Canada. Received February 24, 2005; Revised Manuscript Received November 21, 2005

A mixture of ionizable cationic lipids, steric barrier lipids, and colipids is used to encapsulate oligonucleotide DNA in lipidic particles called SALP. This material is under development as an adjuvant for vaccines. Previously we have shown that coupling the antigen directly to the surface of SALP can lead to enhanced immunological responses in vivo. Two different methods for preparing ovalbumin−SALP were assessed in this work. Originally the conjugates were prepared by treating SALP containing a maleimide-derivatized lipid with thiolated ovalbumin, a method we refer to as active coupling. This reaction was found to be difficult to control and generally resulted in low coupling efficiencies. The issues relating to this approach were characterized. We have recently developed alternative techniques based on first coupling ovalbumin to a micelle and then incubating the resultant product with SALP, methods we refer to as passive coupling. We have shown that this method allows accurate control of the levels of protein associated SALP and does not suffer from surface saturation effects seen with the active coupling method that places maximum limits on the amount of protein that can be coupled to the SALP surface. The products from the passive coupling protocol are shown to have activity comparable to those derived from the active coupling protocol in investigations of in vivo immune responses.

INTRODUCTION

As part of a program for the development of drug delivery systems, an efficient means of formulating oligonucleotides in lipidic particles (*1*, *2*) has been developed. These particles were formed through a self-assembly process after addition of an ethanolic solution of lipids to a solution of the oligonucleotide in a citrate buffer at pH ∼4.0. The lipids used included cholesterol, a bilayer-forming phospholipid (typically DSPC or POPC), a protonatable amino lipid, and a steric barrier lipid. Addition of the lipid solution to the buffer resulted in protonation of the amino lipid and formation of bilayer structures. The anionic oligonucleotide associates with these charged bilayer structures as they assemble, resulting in the formation of lipidic particles entrapping the oligonucleotide. The steric barrier lipid, typically a PEG−lipid, acts to moderate the rate of particle formation, regulating growth and inhibiting aggregation of particles. After the initial dilution, the preparation is extruded through a high-pressure filtration device and the external buffer replaced with one at pH ∼7.0 (usually HBS). At this pH the amino lipids are neutral. The final product is a lipidic particle that is stable in solution, with physical and pharmacokinetic properties much like liposomes of similar size. We refer to these particles as SALP (stabilized antisense lipid particles).[1]

During the biological characterization of SALP, a number of interesting observations were made. First, during early studies aimed at the investigation of the role played by the steric barrier molecule's relative exchangeability on pharmacokinetic behavior, we noted that certain formulations would be rapidly cleared in vivo when administered on a repeat dose schedule (*3*). This effect was only observed with formulations with (a) PEG-lipids that did not exchange rapidly out of the bilayer on administration in vivo and (b) more than a certain level of encapsulated oligonucleotide. Further studies demonstrated that the clearance behavior was due to an immune response to PEG, and that this immune response was induced by the encapsulated oligonucleotide.

Other studies with these oligonucleotide−lipid particles demonstrated that they were capable of potent enhancement of the immune stimulation associated with the CpG motif in oligonucleotides (*4*). This sequence had been shown to cause activation of macrophages, dendritic cells and B-cells, and release of various cytokines (*5*).

These observations led us to investigate the use of SALP as adjuvants for vaccines. Initially we mixed the SALP with an antigen and found that coupling the antigen directly to the surface of the particle resulted in an enhanced biological response.[2] These initial formulations were prepared using the classical protein-liposome coupling technique (*6*), namely derivatizing the protein with SPDP and coupling the resultant product (after deprotection) to SALP which had a maleimide lipid included in its composition.

From a production point of view, the process of coupling a thiolated protein to the surface of a liposome or lipid particle is fraught with difficulty. Coupling efficiency tends to be variable

* To whom correspondence should be addressed. Phone (604) 733-1231. E-mail: ansell2010@shaw.ca.

[1] Abbreviations: SALP, stabilized antisense lipid particles; DSPC, 1,2-distearoyl-*sn*-glycero-3-phosphocholine; POPC, 1-palmitoyl-2-oleoyl-*sn*-glycero-3-phosphocholine; PEG, poly(ethylene glycol); HBS, hEPES-buffered saline; DSPE-ATTA2-MPA, *N*-(*N*′-(*N*″-(3‴-maleimidopropionoyl)-14″-amino-3″,6″,9″,12″-tetraoxatetradecanoyl)-14′-amino-3′,6′,9′,12′-tetraoxatetradecanoyl)-1,2-distearoyl-*sn*-glycero-3-phosphoethanolamine; ATTA, 14-amino-3,6,9,12-tetraoxatetradecanoic acid; OVA, ovalbumin; MePEGS-2000-mCer, 1-*O*−(4′-*O*-(ω-monomethoxypoly(ethylene glycol)$_{2000}$)succinoyl)-*N*-myristoylsphingosine; MePEGS-2000-DMG, 3-*O*-(4′-*O*-(ω-monomethoxypoly(ethylene glycol)$_{2000}$)succinoyl)-1,2-dimyristoyl-*sn*-glycerol; DSPE-MPB, *N*-4′-(4″-maleimidophenyl)butanoyl-1,2-distearoyl-*sn*-glycero-3-phosphoethanolamine; chol, cholesterol; DODMA, *N*,*N*-dimethyl-2,3-dioleyloxypropylamine; OGP, octyl β-D-glucopyranoside.

[2] Yuan, Z. N., Brodsky, I., Ansell S. M., Klimuk, S.K, and Semple, S. C. (2005) Systemic and mucosal immune responses induced by liposomes with surface-coupled antigen and high levels of encapsulated immunostimulatory oligonucleotides. Unpublished data.

10.1021/bc050052j CCC: $33.50 © 2006 American Chemical Society
Published on Web 01/12/2006

and aggregation is a frequent problem (*7*). To study and characterize the in vivo effects of these particles we required systems that were reproducible and controllable; consequently, we required more robust methods of preparing these materials.

A number of groups in recent years have attempted to solve many of the original problems associated with conjugating proteins directly to liposome surfaces by moving the point of attachment from the liposome surface to the end of PEG tethers (*16, 17*). In theory this should allow efficient conjugation while still allowing a formulation to have a PEG coating on the surface. However, by moving the reactive radius outside the steric barrier domain many of the advantages of such barriers in terms of aggregation control are potentially lost. In addition to this problem there are a number of other reasons why these systems are unsuitable for use in our particles. First, if a PEG based active lipid is used with an active coupling protocol, most of the active lipid would not conjugate to a protein and would still be present as free PEG attached to the surface. Since these compounds have relatively nonexchangeable anchors by design they would remain associated with the particle in vivo sufficiently long to generate an immune response in their own right. This would limit the use of the particle as a generic platform for vaccines since the application of one formulation in a patient would generate an immune response to the platform and would presumable render any other formulations useless in that patient.

A second potential negative of the PEG tether approach relates to the exchangeability of the lipid−protein molecule once attached to the surface. The association-dissociation of a lipid−macromolecule from a bilayer surface is determined in part by the increase in freedom of motion of the macromolecule. PEG generally has considerable freedom of motion in solution, whereas most proteins and oligosaccharides are relatively rigid. Consequently, the exchange rates of PEG−lipids are much more sensitive to constraints on their freedom of motion than most biological macromolecules. Introducing a PEG tether between a macromolecule and a lipid anchor is expected to adversely affect the retention of the macromolecule in vivo, and this effect should become worse as the length of the tether increases.

Finally, we were concerned with the chemical stability of the maleimide functions used in the active lipids during processing. These compounds are susceptible to hydrolysis, forming ring-opened maleamic acids which are fairly unreactive in the coupling reaction. This is not normally a major concern when preparing research quantities of various formulations since they can be prepared fast enough, but will be an issue for large scale preparations where processing times are usually significantly longer than lab scale.

We have recently characterized general methods for an alternative method of preparing similar constructs, wherein the protein is coupled to a micelle, and the micelle lipids exchanged into liposome bilayers.[3] These methods were found to be reproducible and controllable. In this work we describe the adaptation of these micelle-based methods to the production of protein−SALP particles, demonstrate the advantages of the new method, and show that constructs prepared by the micelle method are at least as efficacious as those prepared by traditional methods.

EXPERIMENTAL PROCEDURES

Materials. Ovalbumin (grade V), cholesterol, and OGP were obtained from Sigma. MePEGS-2000-DMG (*14*) and DSPE-ATTA2-MPA[3] were synthesized in our laboratories as described elsewhere. DPSC was obtained from Northern Lipids Inc., Vancouver. SIINFEKL peptide was synthesized on contract by Commonwealth Biotechnologies Inc., Richmond, VA. The oligonucleotides used were synthesized on contract by Trilink Biotech, San Diego, CA. CD8-FITC and TCR-cychrome were obtained from BDPharMingen, San Diego. Phycoerythrin-coupled H-2Kb-SIINFEKL tetramers were synthesized on contract by Beckman Coulter Immunomics, San Diego, CA.

Synthesis of DODMA. DODMA was synthesized using an adaptation of a previously described method (*15*). Briefly, a solution of 3-(dimethylamino)-1,2-propanediol in benzene was treated with an excess of potassium hydride with stirring for 1 h under argon. Oleyl bromide (1.5 equiv) was then added and the solution refluxed for 3 h. After workup, the product was isolated from the crude reaction mixture by column chromatography.

Preparation of SALP. Solutions containing 26 μmol of lipid in 0.4 mL of ethanol and 4 mg of oligonucleotide in 0.6 mL of citrate buffer were warmed to 60 °C. The ethanol solution was then slowly added to the buffer while vortexing. The resultant suspension was passed 10 times through 2 × 100 nm filters using a pressurized extruding device. The SALP was then passed down a Sepharose CL-4B column in HBS to remove external oligonucleotide and to exchange the buffer. The quantities used were adjusted in proportion when larger amounts of material were required.

Preparation of Micelle−Ovalbumin Conjugates. Ovalbumin was dissolved in HBS at a concentration of 30 mg/mL. An aliquot of from a stock solution of 2-iminothiolane in HBS corresponding to 1−5 equiv (depending on the particular experiment) was added to the ovalbumin solution and the mixture stirred at room temperature for 0.5 h. The solution was used without further purification.

Lipid composed of the DSPE-ATTA2-MPA and a micelle-forming lipid (DSPE-ATTAn, where $n = 2$, 4, 8, or OGP) were weighed and combined. The lipid was dissolved in 1 part of ethanol, with warming if required, and diluted sequentially with 1 part of HBS, with vortexing and warming, until a total of 9 parts HBS had been added. The total volume should was such that the final concentration of lipid was approximately 10 mM. Any residual solid materials were removed by filtration through 0.22 micron filters.

An aliquot of freshly prepared thiolated ovalbumin was added to freshly prepared maleimide−micelles in the appropriate ratio. In most cases this corresponded to 3000 g protein/mol micelle lipid. The micelle−protein mixture was allowed to stir at room temperature overnight. It was then either used immediately without additional purification or stored at 5 °C for use at a later date.

Incubation of Protein−Micelles with SALP. SALP was mixed with ovalbumin−micelle conjugates in proportions appropriate for the particular experiment. Typically the standard preparation used a 1:19 micelle/SALP lipid ratio, corresponding to an initial protein/total lipid ratio of 150 g/mol. The SALP−micelle mixtures were incubated in a water bath at 60 °C for 30 min and then passed down a Sepharose CL-4B column (0.8 mL of sample/25 mL bed volume) using HBS as the running buffer.

Assays. Lipid was assayed by determining the phosphate content as previously described (*8*). Samples containing oligonucleotide were analyzed for lipid content after processing as follows. An aliquot of the formulation (usually 100−250 μL) was diluted with 750 μL CHCl3/MeOH (1:2 vol/vol) in a 13 × 100 mm tube and vortexed for 1−2 min. A few drops of additional methanol were added if the solution was still turbid. Water (250 μL) and CHCl3 (250 μL) were then added and the solution vortexed for 1−2 min. The sample was then centrifuged at 3000 rpm for 10 min. The upper phase was carefully removed. An aliquot of water/methanol (1:1: 300 μL) was then added

[3] Takasaki, J., and Ansell, S. M. (2005) Micelles as intermediates in the preparation of protein-liposome conjugates. Unpublished data.

and the solution vortexed for 1−2 min. The solution was centrifuged at 300 rpm for 5 min and the upper layer carefully removed. The organic fraction was washed with water/methanol a further two times in the same manner. The organic fraction was first dried down under a nitrogen stream and then under vacuum. The lipid assay was then carried out as previously described.

The protein content of the final liposome−protein conjugates was determined using a modified micro-BCA assay as previously described (*8*), with negative controls being performed where possible to check for background interference. Particle size, where determined, was measured using a Nicomp 380 submicron particle sizer.

Oligonucleotide content was determined by diluting a 20 μL sample with 250 μL of distilled water, 1200 μL of methanol, and 500 μL of chloroform and determining absorbance at 260 nm relative to a similarly treated sample of HBS buffer. The oligonucleotide concentration was calculated using the equation $[\text{oligo (mg/mL)}] = 3.41 \times A_{260}$

Immunization Protocols. 6- to 8-week-old female C57BL6 (H-2b) and BalbC (H-2d) mice were purchased from Harlan (Indianapolis, IN). All animal studies were completed using protocols that were approved by the institution's animal care committee, and the methods used are consistent with the current guidelines of the Canadian Council of Animal Care. Mice (C57BL6 for cellular response and BalbC for humoral response; five animals in each test group) were immunized by injection sc with 100 μL of HBS alone or containing either 66 μg of ovalbumin, 66 of μg ovalbumin mixed with 100 μg of free 6295PS, 66 μg of ovalbumin mixed with 100 μg of 6295PS encapsulated in SALP, 73 μg of ovalbumin passively coupled to SALP containing 100 μg of 6295PS or 60 μg of ovalbumin actively coupled to SALP containing 100 μg of 6295PS.

Mice received injections on day 0 and 7 for investigation of immunological cellular responses. Spleens were harvested 7 days after the last immunization and a cell suspension was generated for the tetramer assay.

Mice received injections on day 0 and 14 for investigation of the humoral response. Blood was recovered by cardiac puncture after 42 days, placed in EDTA tubes, and centrifuged (4 °C, 2000 rpm, 10 min) to obtain plasma. The pooled plasma was examined for antibody induction by ELISA.

Tetramer Assay. Specific CD8 T cells raised against the SIINFEKL epitope were assessed using a modified tetramer assay (*9*) as described by the manufacturer (Beckman-Coulter, Immunomics, San Diego, CA). Briefly, this consisted of incubation of 2×10^6 spleen cells with 1 μL of phycoerythrin-coupled H-2K^b-SIINFEKL-tetramers for 1 h at room temperature. Samples were then labeled with anti-mouse CD8-FITC and TCR-Cychrome (BD PharMingen, San Diego, CA) for 20 min at 4 °C. After two washes with PBS 2% FBS, samples were analyzed using FACSort and CellQuest software (Beckton-Dickinson).

Humoral Immunogenicity Studies. Ovalbumin-specific mouse IgG was detected and quantified by end-point dilution ELISA assay on samples of plasma pooled together from individual animals. Briefly, a solid phase of ovalbumin (100 μL of 10 μg/mL per well, overnight at 4 °C) was used to capture ovalbumin specific antibody from plasma samples serially diluted with 2% BSA−PBS. The antibody was then detected by treatment with horseradish peroxidase-conjugated rabbit anti-mouse IgG (1:3000 in PBS−BSA-2%; 100 μL/well), followed by incubation with TMB liquid substrate system (200 μL/well, 30 min at room temperature, light protected). The reaction was stopped by addition of 100 μL/well of 0.5 M sulfuric acid and the absorbance measured at 450 nm on an Elisa plate reader. End point dilution titers were defined as the highest dilution of ovalbumin specific antibodies detected in plasma that resulted in absorbance value (OD_{450}) two times greater than that of naive animal, with a cut off value of 0.1.

RESULTS

We have drawn a distinction between coupling protocols where the conjugation reaction takes place at the liposome surface (active coupling) or at some point remote from the liposome surface (passive coupling).[3] The traditional method of producing protein−liposome conjugates is an active coupling process in which a protein is first thiolated and then incubated with liposomes containing maleimide-derivatized lipids.

Our first preparations of protein−SALP constructs were made using an active coupling protocol. The model antigen used in these studies was ovalbumin. The thiolation of the ovalbumin in the initial studies was performed using the reagent SPDP in HBS at pH 7.4. Once the protein had been derivatized, the protecting group had to be removed using DTT at pH 4.4. The external buffer was then replaced with HBS at pH 7.4 in preparation for the conjugation reaction. This process involves a large number of steps, and in later work the thiolation process was greatly simplified by using the reagent 2-iminothiolane (2-IT).[3]

The original SALP formulation had been developed with 10 mol % of the steric barrier lipid MePEGS-2000-Mcer as part of the lipid composition. The high levels of steric barrier lipids in these formulations presented a problem, since it is known that PEG−lipids in the bilayer inhibit the liposome−protein reactions required for preparing the construct. Most earlier work in the field of liposome−protein constructs had relied on zero length cross-linker active lipids, such as DSPE-MPB (*6*). In our work we have used an alternative lipid, DSPE-ATTA2-MPA. DSPE-ATTA2-MPA has a maleimide cap which is less susceptible to hydrolysis than that in DSPE-MPB and a cross-linker roughly equivalent to a 500 MW PEG in size. This lipid was chosen since aliphatic maleimides are supposedly more stable in aqueous solution than aromatic versions and since the small tether should provide greater accessibility of the reactive function on the bilayer surface.

Effect of PEG−Lipids on SALP Stability and Coupling Efficiency. Earlier work showed that the presence of PEG−lipids on a liposome surface inhibits the lipid−protein reaction, causing saturation of the surface to occur at lower concentrations. This effect results in a steady fall off in conjugation efficiency as the surface concentration of PEG rises, bottoming out at roughly 6 mol % PEG (*18*). However, significant amounts of PEG are required in SALP formulations to stabilize the construct during formation and prevent aggregation. Since these two requirements are mutually exclusive, we needed to determine what the minimum amount of PEG for a stable formulation of SALP actually was. A formulation experiment was conducted in which SALP was prepared with varying amounts of PEG−lipid in the composition. The stability of the final product was assessed by doing particle sizing and seeing which samples showed evidence of aggregation (Figure 1). All samples showed roughly equivalent encapsulation efficiencies (50−70%), suggesting that particle formation was equivalent in all cases. However, particle sizes were uniform until the PEG concentration dropped to ∼2 mol %, at which point the particle size started to increase. The conclusion was that the minimum required PEG concentration in a SALP formulation was ∼2%.

Previous work had shown that the range of PEG concentration that allowed effective conjugation in liposomes was 0−5 mol %. The cross-linker we were using in the current studies (DSPE-ATTA2-MPA) was rather larger than the cross-linker used in the earlier work, so it was not immediately obvious to what extent the SALP PEG−lipid would inhibit the coupling reaction.

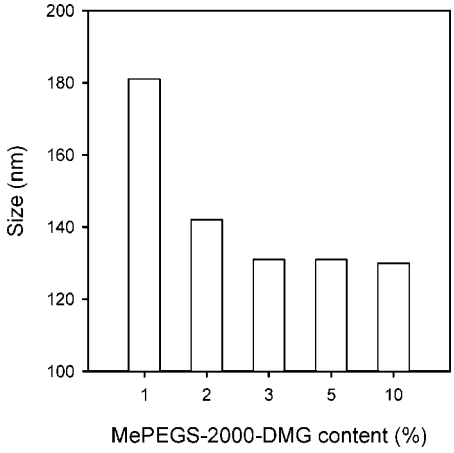

Figure 1. The effect of steric barrier lipid concentration on the stability of SALP particles. SALP composed of DSPC/chol/DODAP/MePEGS-2000-DMG ((25 + *n*):45:20:(10 − *n*); where *n* = 0, 5, 7, 8, and 9) was prepared with 6295 oligonucleotide encapsulated at an initial oligo/lipid ratio of 0.15 g/mol. Encapsulation efficiencies ranged from 50 to 70%. Physical stability is assessed by the size of the product as determined using a Nicomp.

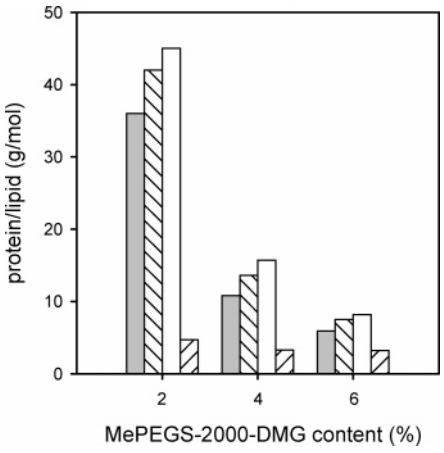

Figure 2. The effect of steric barrier molecules on coupling efficiencies when conjugating ovalbumin to SALP using the active conjugation method. Ovalbumin derivatized with 5 equiv of SPDP was treated with SALP composed of DSPC/chol/DODAP/MePEGS-2000-DMG/DSPE-ATTA2-MPA ((34 − *n*):45:20:*n*:1; *n* = 2, 4, 6%). Initial protein/lipid ratios were 100 g/mol (solid bars), 200 g/mol (hatched left bars) and 400 g/mol (open bars). A negative control, where SALP (*n* = 2) was incubated with underivatized ovalbumin, was included (hatched right bars).

We designed an experiment to determine what the effect of the SALP PEG concentration on coupling efficiency was. Ovalbumin was thiolated with 5 equiv of SPDP and conjugated to SALP containing 2, 4 or 6 mol % MePEGS-2000-DMG. Protein aliquots corresponding to an initial protein/lipid ratio of 100, 200, and 400 g/mol were incubated with samples of each SALP formulation, respectively. In addition, a negative control was performed for each SALP formulation, where the SALP was incubated with nonthiolated ovalbumin at 100 g/mol and worked up as usual. The results can be seen in Figure 2. Clearly the coupling efficiency drops off dramatically as the SALP PEG concentration increases. Increasing the initial protein/lipid ratio has only a small effect on the overall amount of protein coupled to the SALP surface, presumably since the surface is approaching saturation under these conditions. The response seen in the negative controls is due to background interference in the protein assay used.

The implication of the experiments presented in Figures 1 and 2 is that for active coupling protocols the competing requirements that the levels of PEG in SALP be high enough to inhibit aggregation but low enough to allow reasonable coupling efficiencies means that in general anyone using these sorts of coupling protocols has a very narrow range of PEG concentration to work with. Small uncertainties in the PEG concentration might have dramatic effects on the coupling efficiency. In addition, the surface saturation effect caused by the presence of the steric barrier molecules during coupling means that the amount of protein that can be conjugated to the surface is relatively small. These limitations mean that the active coupling protocol is unattractive from a production point of view.

Effect of PEG−Lipids and Micelle-Forming Lipids on the Passive Conjugation Protocol. In a companion report we have described the characterization of a passive coupling technique in which the protein is first coupled to the surface of a micelle and then exchanged into liposome bilayers.[3] This method has a number of advantages over active coupling when applied to SALP. First, since the coupling reaction is performed at the micelle surface, the presence of PEG−lipids in SALP will not interfere. It should be possible to obtain a range of reproducible levels of protein at the SALP surface since the protein−lipid conjugates can be titrated into the liposomes. The lack of interference from the SALP PEG−lipids would also mean that in principle it should be possible to obtain much higher levels of protein on the SALP surface, if required. The second advantage of the passive conjugation method is that it separates the SALP formulation step from the protein−lipid coupling step. When using the active conjugation method it is necessary to have both the SALP preparation and the protein thiolation process occurring simultaneously because of the potential for competing side reactions to quench the reactive functionality of the reagent. This presents potential logistical problems when scaling the process up since larger scale processes tend to take longer periods of time. With the passive conjugation method the two components can be prepared independently and combined at the appropriate time.

We conducted a study looking at the effects of various micelle-forming lipids and different PEG−lipid levels in SALP when using the passive conjugation method. SALP was prepared with 2, 4, and 10% PEG−lipid as part of the composition. The 2% formulation represented the lower limit for physical stability as determined in Figure 1. The 10% formulation represented the "classical" SALP particle, whereas the 4% one was our guess at the "ideal" SALP formulation for passive conjugation methods. A POPC/chol liposome formulation was also included in the data set to serve as a control. Micelles were prepared using DSPE-ATTA2-MPA as the active lipid in a 1:4 ratio with the micelle-forming lipid. The micelle-forming lipids used in this study were DSPE-ATTA2, DSPE-ATTA4 and DSPE-ATTA8. The results are shown in Figure 3.

DSPE-ATTA4 was found to be the best micelle-forming colipid in the group studied for Figure 3, similar to earlier work with POPC/chol liposomes.[3] DSPE-ATTA2 generally gave somewhat lower coupling efficiencies; however, this is likely due to the tendency of DSPE-ATTA2-MPA/DSPE-ATTA2 micelles to show some thermotropic behavior at room temperature. The much larger DSPE-ATTA8 resulted in sharply lower coupling efficiencies. This is comparable to the results we had seen earlier with MePEGS-2000-DSPE liposomes and is likely a result of steric inhibition of the micelle−protein reaction. The SALP formulations generally resulted in slightly lower final protein/lipid ratios than regular control liposomes. The reason for this is not clear, but it might be related to the fact that SALP frequently forms multilamellar structures, which would result in a lower particle protein/lipid ratio. The most interesting aspect of this experiment was the observation that the PEG level in the SALP did not appear to affect the final protein/lipid ratio. This is sharp contrast to the active coupling method, where 10

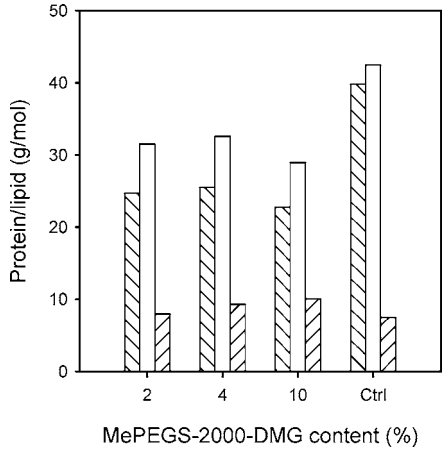

Figure 3. The effect of steric barrier molecules on coupling efficiencies when conjugating ovalbumin to SALP using the passive conjugation method. Ovalbumin was thiolated with 5 equiv of SPDP and conjugated to DSPE-ATTA2-MPA/DSPE-ATTAn (1:4) micelles in a 3000 g/mol protein/lipid ratio. DSPE-ATTAn used were as follows: $n = 2$, hatched left bars; $n = 4$, open bars; and $n = 8$, hatched right bars. Micelles were incubated with DSPC/chol/DODAP/MePEGS-2000-DMG ((25 + n):45:20:(10 − n); $n = 0, 6, 8$) SALP or POPC/chol (55:45) liposomes ("Ctrl" in the figure) at 150 g/mol protein/lipid. The SALP was prepared using 6295 PS oligonucleotide at a 0.15 oligo/lipid ratio.

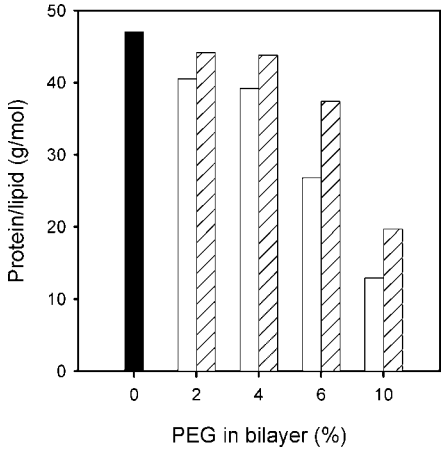

Figure 4. The effect of the exchangeability of PEG−lipids in liposomes on the passive coupling protocol. Ovalbumin was thiolated with 5 equiv of 2-IT and conjugated to DSPE-ATTA2-MPA/OGP (1:4) micelles in a 3000 g/mol protein/lipid ratio. Micelles were incubated with POPC/chol/PEG-lipid (55 − n:45:n; $n = 0, 2, 4, 6, 10$) liposomes at 150 g/mol protein/lipid. PEG-lipids used included MePEGS-2000-DSPE (open bars) and MePEGS-2000-DMG (hatched right bars). The solid bar is the 0% PEG-lipid sample.

mol % of PEG would effectively shut down the conjugation reaction.

This raised an interesting question, since we knew that PEG was capable of preventing surface conjugation reactions by inhibiting access of the protein to the reactive surface. The most reasonable explanation of the difference was that once coupled to a lipid anchor, the protein−lipid conjugate would behave like any other steric barrier molecule and would compete for a place on the liposome surface with the PEG−lipids already there. Given enough time an equilibrium should be reached based on the thermodynamic states of the molecules at the surface or in solution. If this is true, then less exchangeable PEG−lipids should still inhibit exchange of the protein−lipid conjugates from micelles, while exchangeable analogues are competed off. To determine if this is the case we set up an experiment where protein−micelles were incubated with POPC/chol liposomes with varying amounts of MePEGS-2000-DSPE (non exchangeable) or MePEGS-2000-DMG (exchangeable). The results are shown in Figure 4.

In this experiment PEG−lipids start to inhibit association of the protein−lipid conjugates with the liposomes when levels exceed 4 mol %. The effect is more pronounced with the nonexchangeable PEG−lipid but takes place with both species. Presumably SALP formulations, which contain MePEGS-2000-DMG, do not anchor the PEG−lipid as well as a POPC/chol liposome since no such drop-off is observed at high PEG−lipid concentrations. It is likely however, that the effect may still take place in SALP formulations to a greater or lesser extent based depending on the conditions of the final formulation step. With that in mind it is advisable to use a 4 mol % PEG SALP formulation.

Comparison between the Active and Passive Coupling Protocols. An additional experiment was performed to characterize the surface saturation effect when using the active coupling protocol. SALP containing 2 mol % MePEGS-2000-DSPE and 1 mol % DSPE-ATTA2-MPA was coupled to ovalbumin which had been thiolated with 2 or 5 equiv of 2-IT. Each data set was repeated with initial protein/lipid ratios ranging from 50 to 300 g/mol. The same two thiolated ovalbumin solutions were used to prepare ovalbumin−micelle reagents, which in turn were used to prepare protein−SALP conjugates under our standard passive conjugation conditions.

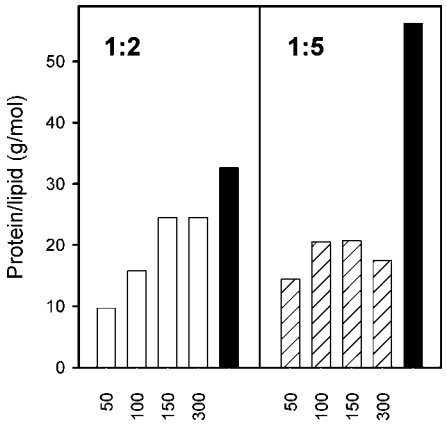

Figure 5. Comparison of active and passive coupling protocols. Ovalbumin was thiolated with 2 or 5 equiv of 2-IT. Thiolated ovalbumin (2 equiv of 2-IT: open bars; 5 equiv of 2-IT: hatched right bars) was coupled to DSPC/chol/DODMA/MePEGS-2000-DMG/DSPE-ATTA2-MPA (32:45:20:2:1) SALP at initial protein/lipid ratios of 50, 100, 150 and 300 g/mol. The same two thiolated ovalbumin solutions were coupled to DSPE-ATTA2-MPA/OGP (1:4) micelles in a 3000 g/mol protein/micelle lipid ratio. These micelles were incubated with DSPC/chol/DODMA/MePEGS-2000-DMG (31:45:20:4) SALP at 150 g/mol protein/final lipid, with the final results shown as the solid bars. All SALP was prepared with 6295 PS oligonucleotide at 0.15 g/mol oligo/lipid.

The results are shown in Figure 5. It is clear that saturation of the surface is occurring at relatively low levels, since increasing the initial thiolated protein concentration has minimal effects on the final surface protein concentration. In addition the maximum surface concentration is quite low. In contrast the passive conjugation samples showed much higher levels of bound protein.

The passive conjugation efficiency is largely regulated by saturation of the micelle surface. This means that it is possible to prepare relatively uniform samples if an excess of initial protein is used. Since the SALP PEG concentration does not inhibit association of the protein−lipid with the SALP surface (unlike the reaction inhibition seen with active coupling protocols), it should be possible to accurately titrate a specific amount of protein into a SALP formulation. We conducted an experiment where an ovalbumin−micelle reagent was prepared and then titrated into a SALP formulation. The results are shown

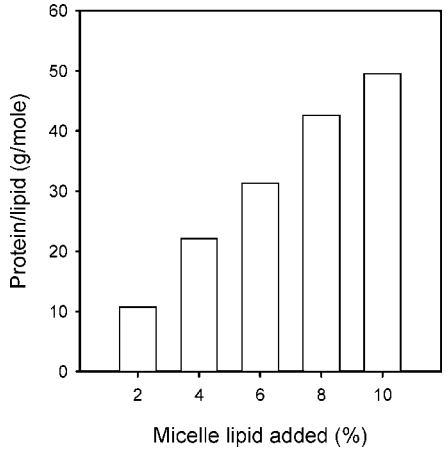

Figure 6. Titration of ovalbumin−micelles into SALP. Ovalbumin was thiolated with 5 equiv of 2-IT and coupled to DSPE-ATTA2-MPA/OGP (1:4) micelles at 3000 g/mol protein/lipid. Portions of this ovalbumin−micelle solution corresponding to 2, 4, 6, 8 and 10% of the SALP lipids were added to DSPC/chol/DODMA/MePEGS-2000-DMG (31:45:20:4) SALP prepared using 6295 PS oligonucleotide at 0.15 g/mol oligo/lipid.

in Figure 6. As expected, the final protein−lipid ratio shows a uniform rate of increase in the surface protein levels in proportion to the amount of the reagent added to the SALP. The implication of this experiment is that not only is it possible to prepare SALP with relatively high levels of protein on the surface, it is also feasible to prepare samples with predetermined levels. This aspect is very important if the mechanism of in vivo action is to be properly characterized.

Stability and Reproducibility during Formulation. Analysis of the oligonucleotide content of the samples in Figure 6 before and after incorporation with the micelles indicated that the treatment did not cause loss of entrapped oligonucleotide. However, since the micelles are detergents, it is likely that at some point sufficient detergent will be present to disrupt the integrity of the SALP particles. We have not determined what this point actually is, at best we can say that treatment with up to 10 mol % micelles will not disrupt the SALP. It may be possible to go significantly higher than this, provided that excess micelle-forming lipid is removed through some means, such as by dialysis.

As a final demonstration of the utility of the method we performed a reproducibility study using the passive coupling protocol. Three sets of protein−micelles were prepared independently and incubated with samples taken from a single batch of SALP (Figure 7). After workup the products were assayed for size, protein/lipid ratio, and oligonucleotide/lipid ratio. The three samples were reassayed after one week of storage at 5 °C. The purpose of the experiment was to demonstrate that material prepared according to standard conditions would yield consistent results. This turned out to be the case in terms of levels of bound protein. The specific conditions used for the coupling generally result in limited aggregation. This aggregation is caused by proteins on the bilayer surface that have been derivatized by more than one lipid anchor. If one of the three batches included protein which was derivatized to a greater or lesser degree than the other batches, it would be reflected in a change in size even though the levels of bound protein were the same. The size differences between the three data sets was minimal, indicating that the protein in all three data sets was largely in the same state. Storage of the samples for a week did not appear to adversely affect the integrity of the constructs. These results suggest that the method potentially has a high degree of reproducibility and result in relatively stabile constructs.

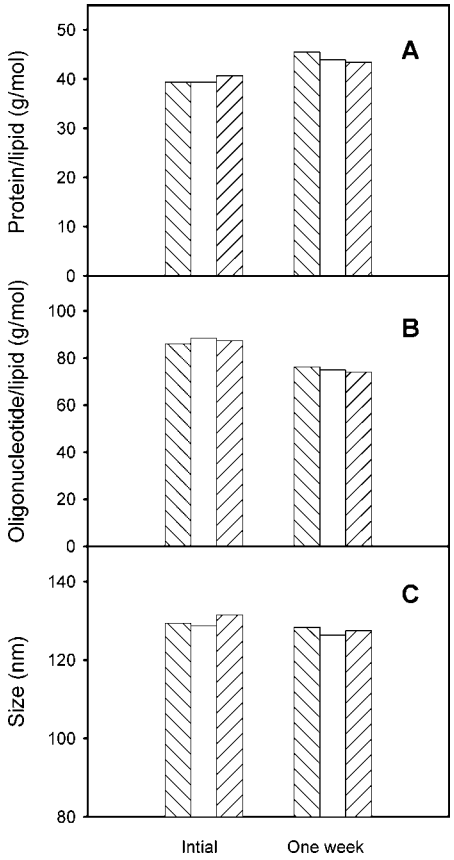

Figure 7. Reproducibility of the passive coupling protocol when preparing protein−SALP conjugates. Three separate ovalbumin solutions were thiolated with 5 equiv of 2-IT and coupled to three individual DSPE-ATTA2-MPA/OGP (1:4) micelle solutions at 3000 g/mol protein/lipid. These three sets of solutions were incubated at 150 g/mol protein/lipid with samples of a single DSPC/chol/DODMA/MePEGS-2000-DMG (31:45:20:4) SALP batch prepared using 6295 PS oligonucleotide at 0.15 g/mol oligo/lipid. The samples were analyzed at the time of production and again after one week of storage at 5 °C.

The effects of the structure of the oligonucleotide was also studied. SALP was prepared using the following oligonucleotides: 6295 PS (5′-TAACGTTAGGGGCAT-3′; phosphothioate chemistry); 6295 PO (5′-TAACGTTAGGGGCAT-3′; phosphodiester chemistry); 5001 PS (5′-AACGTT-3′; phosphothioate chemistry); and 2006 PS (5′-TCGTCGTTTTGTCGTTTTCT-CGTT-3′; phosphothioate chemistry). The structure of an oligonucleotide plays a role in the encapsulation efficiency, and a wide range was observed in this case (75%, 47%, 13%, and 27%, respectively). All four SALP formulations were treated with the same protein−micelle reagent (initial protein/lipid ration of 150 g/mol) as usual. All four formulations showed similar levels of conjugated protein, with minimal size changes compared to the original SALP controls. The results demonstrate that the coupling process produces similar products irrespective of the structure of the oligonucleotide used.

In Vivo Immunological Behavior. In a companion report[2] we have shown that coupling an antigen to the surface of SALP results in enhanced humoral responses in vivo compared to a sample where the antigen and SALP were mixed but not coupled. The material used in that study was conjugated using the active coupling protocol. While it is reasonable to presume that the antigen−SALP conjugate prepared by the passive conjugation protocol would be equivalent, we needed to demonstrate that this was indeed the case. An experiment was conducted to compare the basic in vivo cellular and humoral responses to treatment with ovalbumin−SALP prepared by the two methods.

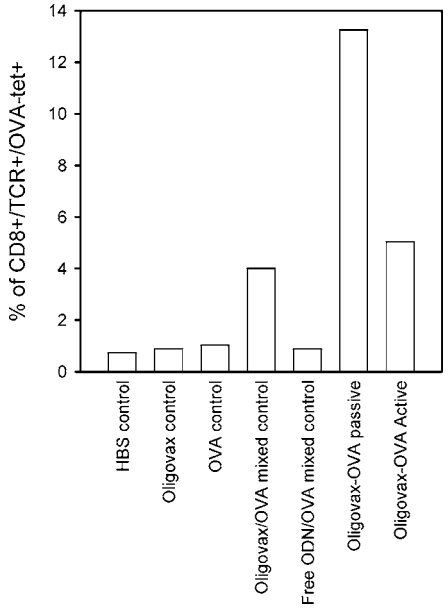

Figure 8. Assessment of cellular response induced against OVA antigen delivered coupled with SALP-6295 PS either with active or passive protocol. Mice were immunized sc at day 0 and 7 (see Materials and Methods) with either HBS, OVA protein (66 μg), OVA (66 μg) mixed with free 6295PS (100 μg), OVA (66 μg) mixed with 6295PS (100 μg) encapsulated in SALP, OVA (73 μg) passively coupled to SALP containing 6295PS (100 μg), or OVA (60 μg) actively coupled to SALP containing 6295PS (100 μg). Seven days after the last injection spleens were assessed for CD8 T cell induced against SIINFEKL epitope using the tetramers assay. *Y*-axis report % of CD8+/TCR+/OVA-tet+ among gated lymphocytes.

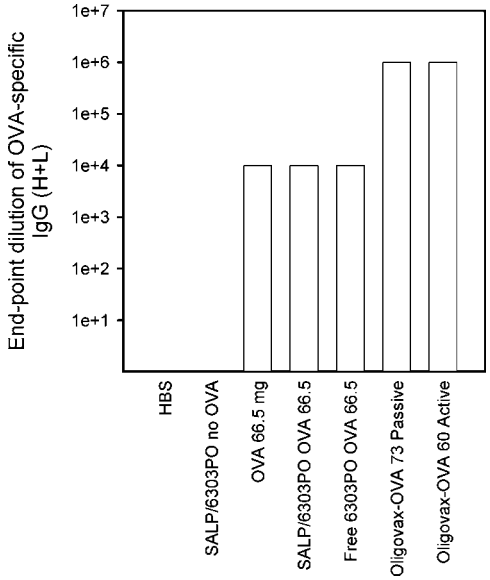

Figure 9. The effect of coupling on humoral immunonogenicity. Plasma obtained six weeks upon SC prime-boost immunization with ovalbumin mixed (66 μg), actively (73 μg), or passively coupled (60 μg) with 100 μg of free or SALP encapsulated 6295PS ODN. IgG levels measured by end-point dilutions ELISA. Data points represent the Mean value from group of four animals.

C57BL6 mice were injected with various controls and ovalbumin-6295 SALP conjugates prepared by the active and passive techniques on days 0 and 7. The spleens were recovered after a further 7 days and the level of CD8 T cells specific for an epitope derived from ovalbumin (SIINFEKL) determined by flow cytometry. The results are shown in Figure 8. As expected, the negative controls (HBS, SALP, and ovalbumin individually) show similar background levels of response. Mixing free oligonucleotide with ovalbumin did not cause proliferation of specific T cells, whereas oligonucleotide encapsulated in SALP and mixed with ovalbumin did. A similar response was seen with ovalbumin−SALP conjugates prepared using the active conjugation method. A much stronger response was observed when the ovalbumin−SALP sample prepared by the passive conjugation protocol was tested. The reason for the difference is not clear at this point. All the samples were normalized to the oligonucleotide content on administration, and consequently protein and lipid content may not be entirely comparable. We plan to do more detailed studies with these systems to determine which formulation parameters affect efficacy and will report that data when it becomes available. In the meantime, however, for the purposes of this work we can state that the passive coupled conjugate is at least as effective as the active coupled material in the stimulation of SIINFEKL reactive T-cell proliferation.

In a second in vivo experiment samples and controls were injected into BalbC mice to investigate humoral responses to the formulations. The treatment was repeated after two weeks and the blood from the animals recovered after a further four weeks. Plasma was recovered from the pooled blood and the level of ovalbumin specific IgG determined using a serial dilution ELISA assay. The results are shown in Figure 9. The negative controls (HBS and SALP) produced no response, as expected. Positive controls (ovalbumin, SALP + ovalbumin, and oligonucleotide + ovalbumin) generated similar responses. The two ovalbumin−SALP conjugates (prepared by the active and passive conjugation methods, respectively) produced responses 2 orders of magnitude greater than the positive controls. This demonstrated the increased efficacy associated with coupled systems as opposed to mixed analogues. More importantly, it shows that the products derived from the two methods are more or less equivalent in terms of inducing a humoral response.

DISCUSSION

Active coupling protocols have been widely used to produce protein−liposome conjugates. While these methods are relatively straightforward to use on lab scales, they suffer from a number of problems. These range from the lack of fine control over the reaction to logistical problems on scale-up. More recent work (*10, 11*) has shown that passive coupling protocols may greatly simplify the logistics of scaling a preparation up. Using these ideas as a lead we have demonstrated that, with proper selection of materials and appropriate experiment design, it is possible to prepare protein−liposome conjugates with a relatively high degree of precision using passive coupling protocols. In addition, the passive coupling protocols greatly simplify many of the workup processes involved in the production of the final conjugate.

SALP type formulations are particularly troublesome to deal with when using the active coupling protocol since the formulation requires relatively large amounts of PEG lipid in order to stabilize the particle. This has two effects, namely that it is very difficult to reproduce a specific level of coupled protein, and the surface becomes saturated at relatively low levels. The passive coupling technique solves many of these problems since it separates the process of forming the protein−lipid conjugate from the process of forming the protein−particle conjugate.

The initial coupling event in the passive conjugation process occurs at the surface of a micelle, which acts as a surrogate for the SALP surface. Since the micelle has a much smaller surface area than the final SALP particle, it is possible to saturate this surface with protein and then use the resultant protein−micelles as a reagent for preparing the final protein−SALP conjugate. By saturating the micelle surface we are effectively placing an upper limit on the amount of protein that can in principle

associate with the micelles, and this fact allows us to produce micelles with reproducible protein/lipid ratios.

A second advantage of using micelles in this manner is that once formed, the protein−lipid conjugate in the micelle essentially becomes yet another steric barrier lipid when exposed to SALP and consequently can compete for spots on the surface of the SALP with the endogenous PEG−lipids. Once there it would be subject to the same thermodynamic influences that determine exchange rates, namely the enthalpy component derived from association of the lipid anchor with bilayer lipids (drives association with the bilayer) and the entropy factor associated with an increase in freedom of motion of the macromolecule on dissociation into free solution (drives disassociation from the bilayer). The PEG−lipids used in SALP are based on an uncharged dimyristoyl lipid anchor (DMG) and as such dissociate from the bilayer very readily (*12*, *13*). The protein−lipid conjugates, on the other hand, use DSPE as a lipid anchor. DSPE is known to provide a much stronger association with the bilayer than DMG. In addition, even though proteins are much larger than the PEG molecules used as steric barrier molecules, they are relatively rigid in free solution and consequently do not have the same entropy contributions that PEG−lipids do. The result of this is that these DSPE−protein conjugates should compete out the PEG−DMG on the SALP surface, producing much higher levels of protein on the surface than would be possible using active conjugation methods.

The effect of constraining freedom of motion of macromolecules on liposome surfaces has been shown in work carried out a number of years ago by Silvius (*12*). He studied interbilayer exchange rates using fluorescent labeled PEG lipids which made up 0.5 mol % of the donor membranes. In that work it was noted that including 4% of unlabeled PEG−lipid significantly increased the off rate of the fluorescent label, thereby providing strong evidence for the effect of steric interactions between individual PEG molecules. Silvius also showed that rigid macromolecule−lipids, such as the protein transferrin and dextrans in the size range 10−70 kDa, had much lower off rates than PEG analogues (2 kDa and 5 kDa) even though they are considerably larger in size. Also, while the off rate for PEG lipids showed a clear relationship to polymer size, rigid polymers such as dextran did not. The data presented by Silvius is consistent with the arguments made in this work.

By being able to control both the amount of protein associated with the micelles, and the amount of the protein−micelles titrated into SALP, we were able to demonstrate that it was possible to produce a series of protein−SALP samples with accurate protein/lipid ratios. In doing so we have opened the door for future studies investigating the role that the relative amounts of protein/lipid/oligonucleotide play in in vivo efficacy. From a production point of view this technology allows us to produce sophisticated formulations with an unparalleled degree of accuracy. The separation of the SALP formation, protein−lipid conjugate formation, and protein−SALP formulation into three distinct and independent steps greatly improves the logistics of scale-up.

Finally, we have shown that the in vivo efficacy of the product produced by the passive coupling protocol is at least as good as that of the material produced by the active coupling process.

Supporting Information Available: Experimental details. This material is available free of charge via the Internet at http://pubs.acs.org.

LITERATURE CITED

(1) Semple, S. C., Klimuk, S. K., Harasym, T. O., Dos Santos, N., Ansell, S. M., Wong, K. F., Maurer, N., Stark, H., Cullis, P. R., Hope, M. J., and Scherrer, P. (2001) Efficient encapsulation of antisense oligonucleotides in lipid vesicles using ionizable aminolipids: formation of novel small multilamellar vesicle structures. *Biochim. Biophys. Acta 1510*, 152−166.

(2) Maurer, N., Wong, K. F., Stark, H., Louie, L., McIntosh, D., Wong, T., Scherrer, P., Semple, S. C., and Cullis, P. R. (2001) Spontaneous entrapment of polynucleotides upon electrostatic interaction with ethanol-destabilized cationic liposomes. *Biophys. J. 80*, 2310−2326.

(3) Semple, S. C., Harasym, T. O., Clow, K., Ansell, S. M., Klimuk, S. K., and Hope, M. J. (2004) Immunogenicity and rapid clearance of liposomes containing polyethylene glycol-lipid conjugates and nucleic acid. *J. Pharmacol. Exp. Ther. 312*, 1020−1026.

(4) Mui, B., Raney, S. G., Semple, S. C., and Hope, M. J. (2001) Immune stimulation by a CpG-containing oligodeoxynucleotide is enhanced when encapsulated and delivered in lipid particles. *J. Pharmacol. Exp. Ther. 298*, 1185−1192.

(5) Krieg, A. M., Yi, A. K., and Hartman, G. (1999) Mechanisms and therapeutic applications of immune stimulatory CpG DNA. *Pharmacol. Ther. 84*, 113−120.

(6) Loughrey, H. C., Choi, L. S., Cullis, P. R., and Bally, M. B. (1990) Optimized procedures for the coupling of proteins to liposomes. *J. Immunol. Methods 132*, 25−35.

(7) Harasym, T. O., Tardi, P., Longman, S. A., Ansel, S. M., Bally, M. B., Cullis, P. R., and Choi, L. S. L. (1995) Poly (ethylene glycol)-modified phospholipids prevent aggregation during covalent conjugation of proteins to liposomes. *Bioconjugate Chem. 6*, 187−194.

(8) Ansell, S. M., Tardi, P. G., and Buchkowsky, S. S. (1996) 3-(2-pyridyldithio)propioinc acid hydrazide as a cross linker in the formation of liposome-antibody conjugates. *Bioconjugate Chem. 7*, 490−496.

(9) Gallimore, A., Glithero, A., Godkin, A., Tissot, A. C., Pluncktun, A., Elliott, T., Hengartner, H., and Zinkernagel, R. (1998) Induction and exhaustion of lymphocytic choriomeningitis virus-specific cytotoxic T lymphocytes visualized using soluble tetrameric major histocompatibility complex class I-peptide complexes. *J. Exp. Med. 187*, 1383−1393.

(10) Iden, D. L., and Allen, T. M. (2001) In vitro and in vivo comparison of immunoliposomes made by conventional coupling techniques with those made by a new post-insertion approach. *Biochim. Biophys. Acta 1513*, 207−216.

(11) Supra, P., and Allen, T. M. (2004) Improved outcome when B-cell lymphoma is treated with combinations of immunoliposomal anticancer drugs targeted to both CD19 and CD20 epitopes. *Clin Cancer Res. 10*, 2530−257.

(12) Silvius, J. R., and Zuckermann, M. J. (1993) Interbilayer transferr of phospholipids-anchored macromolecules via monomer diffusion. *Biochemistry 32*, 3153−3161.

(13) Rex, S., Zuckerman, M. J., Lafleur, M., and Silvius, J. R. (1998) Experimental and monte carlo simulation studies of the thermodynamics of polyethylene glycol chains grafted to lipid bilayers. *Biophys. J. 75*, 2900−2914.

(14) Ambegia, E., Ansell, S., Cullis, P., Heyes, J., Palmer, L., and MacLachlan, I. (2005) Stabilized plasmid-lipid particles containing PEG-diacylglycerols exhibit extended circulation lifetimes and tumor selective gene expression. *Biochim. Biophys. Acta 1669*, 155−163.

(15) Eppstein, D. A., Felgner, P. L., Gadek, T. R., Jones, G. H., and Roman, R. N. (1990) N[ω,(ω-1)-dialkyloxy]- and N-[ω,(ω-1)-dialkenyloxy]-alk-yl-N,N,N-tetrasubstituted ammonium lipids and uses therefore. US Patent 4,897,355.

(16) Hansen, C. B., Kao, G. Y., Moase, E. H., Zalipsky, S., and Allen, T. (1995) Attachment of antibodies to sterically stabilized liposomes: evaluation, comparison and optimization of coupling procedures. *Biochim. Biophys. Acta 1239*, 133−144.

(17) Kirpotin, D., Park, J. W., Hong, K., Zalipsky, S., Li, W. L., Carter, P., Benz, C. C., and Papahadjopoulos D. (1997) Sterically stabilized anti-HER2 immunoliposomes: design and targeting to human breast cancer cells in vitro. *Biochemistry 36*, 66−75.

(18) Ansell, S. M., Harasym, T. O., Tardi, P. G., Buchkowsky, S. S., Bally, M. B., and Cullis P. R. (2000) Antibody conjugation methods for active targeting of liposomes. In *Drug Targeting: Strategies, Principles and Applications* (Francis, G. E., and Delgado, C., Eds.) pp 51-68, Chapt. 4, Humana Press, Totowa, NJ.

BC050052J

List of supplementary data for manuscript entitled "Methods for the preparation of protein-oligonucleotide-lipid constructs"

S.1. Comments regarding the assays used and reproducibility.

S.2. Structures of lipids used in this work.

S.1. Comments regarding the assays used and reproducibility

The passive method has a relatively high level of reproducibility provided that experimental conditions are kept constant and provided that analytical methods are accurate. However, there are potential sources of variability in terms of the numbers that are generated in different experiments. Much of this stems from the assay that is used to determine protein content. Basically it involves a chemical colorimetric assay using a standard curve performed with reagents from Pierce's BCA assay kit. The standard curve itself is generated using a set of BSA standards. These standards are prepared by first diluting 50 µl of a kit stock solution with 950 µl of buffer to prepare a working stock solution. Aliquots ranging from 25 to 200 µl are then taken from this stock to prepare the standard curve samples. Any pipetting errors in this series of dilutions will result in deviations from the true concentration, both in terms of the slope of the standard curve and scatter of the data points making up the curve. The actual samples were analyzed in triplicate, for both the protein assay and the phosphate assay. Consequently, while data within a particular experiment is reasonable consistent, data between experiments may show some variability.

In addition to issues involving uncertainty with the slope of standard curve, the lipids used to produce liposomes can generate varying levels of background interference independent of the presence of protein. Usually this interference is small relative to the assay numbers with normal liposomes (typically 1-3 g/mol), but it can be fairly large in some cases with SALP lipids (up to around 5-6 g/mol). The reported number can deviated from the true value somewhat depending on whether or not results are corrected for background. The background and the associated uncertainty places constraints on the sensitivity of the BCA assay as well as the accuracy.

The BCA assay is far from ideal, but under the circumstances it was the most reliable method available to us. We attempted using flourescamine based assays, but found that the standard curve varied considerably depending on what exactly was used to produce it. Standard curves were generated using ovalbumin, albumin and thiolated ovalbumin, and yielded different results in each case for test samples, apparently all inaccurate based on comparisons with values determined using extinction coefficients. The BCA assay on the other hand, generated concentration results consistent with that obtained using extinction coefficients irrespective of which standard curve was used. Florescamine should be more sensitive in principle, but it was limited by the lack of material suitable for generating an appropriate standard curve.

Probably the best assay method to use would be one based on labeled protein, but that was not available for this work.

A second factor affecting the absolute results was the slow degradation of maleimide reagents on storage. Over a period of months the materials start to form insoluble

products that we believe are polymers formed from intermolecular trans-acylation reactions initiated by maleamic acid impurities present in the samples. This results in polymeric materials which are unreactive and cause formulation issues, collectively reducing conjugation efficiency. If properly stored, materials would perform consistently for 4-5 months, after which degradation of performance (in the form of coupling efficiency) would start to become apparent. Normally we would synthesize fresh reagents before this happened, but some data sets were generated with older material, and consequently absolute coupling efficiencies in those cases are lower than normal.

However, since general conclusions drawn from this work were made within data sets, and not between data sets, we believe that these discrepancies do not impact the overall message. Comparing data between sets is probably of dubious validity, but within data sets it is reasonably consistent. For example, in figure 6 the coupling efficiency is somewhat lower than what we would normally expect, but the message that the micelles can be titrated proportionally into SALP in a concentration dependant manner is still valid.

S.2. Structures used in this work

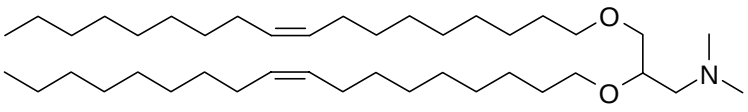

DODMA

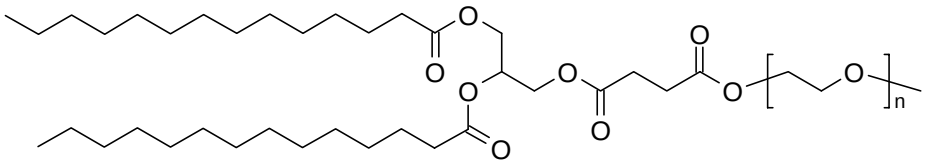

MePEGS-2000-DMG

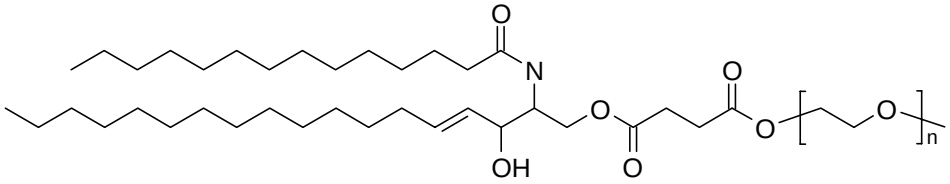

MePEGS-2000-Mcer

Development of Saxitoxin-Conjugated Affinity Gels

Ryuichi Watanabe, Ritsumi Samusawa-Saito, and Yasukatsu Oshima*

Laboratory of Bioorganic Chemistry, Graduate School of Life Sciences, Tohoku University, Sendai 981-8555, Japan.
Received December 21, 2004; Revised Manuscript Received January 25, 2006

Saxitoxin (STX) and its analogues accumulated in bivalves cause food poisoning through the blockade of sodium channels in the nervous system. In the current studies, STX-conjugated agarose gels as affinity chromatography reagents were prepared for investigation of the fate of the toxins in natural environments and in the human body. A carboxyl moiety was introduced through positions C11 and C13 to leave the most characteristic part of the molecule intact. Two types of synthesized derivatives, 11-(2-carboxyethylthio)saxitoxin and 13-*O*-hemisuccinyldecarbamoylsaxitoxin, were successfully conjugated to Sepharose 4B in high yield. Affinity gels containing 500 nmol of STX or decarbamoylsaxitoxin per milliliter of gel were accomplished by masking the residual amino groups by acetylation. Finally, the STX-conjugated affinity gel was effective for concentrating STX-binding proteins from pufferfish and bullfrog plasma.

INTRODUCTION

The human health syndrome known as paralytic shellfish poisoning is caused by the consumption of shellfish containing high levels of saxitoxin (STX) and its numerous analogues (Chart 1). The STXs are originally produced by certain dinoflagellates, such as *Alexandrium* spp. (e.g., *A. catenella, A. tamarense,* and *A. minutum*), *Pyrodinium bahamense* var. *compressa*, and *Gymnodinium catenatum* (*1*−*5*). Also, some freshwater cyanobacteria (*Aphanizomenon flos-aquae*, *Anabaena circinalis* and *Lyngbya wollei*) are known to produce these toxins (*6*−*9*).

Filter feeding mollusks accumulate these toxins when they feed on these microalgae. The toxins are subsequently introduced into aquatic food chains. The toxicity levels and persistence of toxins in bivalves vary greatly according to the species of mollusk and the physiological conditions (*10*). Actual mechanisms of accumulation and depuration of toxins by bivalves have not been clarified, but circumstantial evidence strongly suggests that macromolecules play a role in the transportation or bioaccumulation of highly ionized toxins in marine animals.

STXs comprise three classes of tetrahydropurine derivatives: carbamate, *N*-sulfocarbamoyl, and decarbamoyl toxins (Chart 1). The toxicity of the STXs is attributed to the reversible blockage of voltage-gated sodium channels on excitable cells. The STXs bind to site 1 on the channels, blocking channel opening and thereby interfering with neurotransmission at neuronal synapses and skeletal muscle (*11*). All the STX analogues bind to the same receptor site, although affinities differ greatly. On the basis of structure−activity studies of STXs, 7,8,9-guanidino and geminal diols at C12 are most important for receptor binding. The carbamoyl side chain also contributes to binding, and introduction of a N-sulfonate results in low binding affinity, probably due to ionic interaction with the channel protein. Furthermore, N1-hydroxy and 11-hydroxysulfate moieties of both stereochemistries have little effect on the binding affinity (*12*, *13*).

In addition to sodium channel proteins and artificially induced antibodies (*14*−*16*), some other macromolecules have an affinity for STX. Toxin-transforming enzymes have been found in dinoflagellates (*17*) and mollusks (*18*−*20*). In addition, saxiphilin, a soluble circulatory protein related to transferrin and found in vertebrates and arthropods, binds to STX (*21*). However, the function of the protein in the organisms has not been clarified. During studies on the mechanism of tetrodotoxin accumulation by pufferfish, Yamashita et al. (*22*) found a STX-tetrodotoxin binding protein (PSTBP) in *Fugu pardalis* plasma that has a higher affinity for STX than tetrodotoxin.

A radioisotope assay with tritium-labeled STX has been the most sensitive and commonly used method for isolating and characterizing STX-binding proteins; however, this reagent is not commercially available, partly due to the designation of STX as a schedule one chemical by the United Nations Chemical Weapon Convention. Other methods developed for the analysis of toxins in shellfish have not always been effective for research on the above macromolecules, mainly due to their lack of sensitivity. Therefore, development of new research tools is essential for advancing the understanding of STX binding macromolecules and their role in determining the fate of the toxins in animals and controlling toxin kinetics in humans (*23*, *24*).

In this paper, we describe the development of STX-conjugated affinity gels for tracking and purifying macromolecules that interact with the STXs. The binding sites available after conjugation were carefully chosen to leave the most characteristic part of the molecule intact and thereby maintain its affinity for the sodium channel. Two types of affinity gels were prepared and tested with biological materials known to contain STX-binding proteins.

EXPERIMENTAL PROCEDURES

Chemicals and Organisms. Gonyautoxins 2 and 3 (GTX2/3), and C1/C2 were prepared as mixture of epimers from a mass culture of the freshwater cyanobacteria *Anabaena circinalis* TA04 strain (CSIRO, Hobart, Australia) (*25*). STX was purified from the spiny oyster *Spobylus butreli* collected in the Palau Islands (*3*). EAH-Sepharose 4B was purchased from Amersham Pharmacia Biotech (Uppsala, Sweden). Centrifugal filter devices, Ultrafree-MC (30 000 Da cutoff) and Ultrafree-CL (30 000 Da cutoff), were obtained from Amicon (Bedford, USA). The Micro-BCA protein assay kit was from Pierce (Rockford, USA). 1-Ethyl-3-(3-dimethylaminopropyl)-carbodiimide hydrochloride

* Corresponding author. Yasukatsu Oshima. Tel: +81-22-717-8814. Fax: +81-22-717-8817. E-mail: oshimay@mail.tains.tohoku.ac.jp.

10.1021/bc049699e CCC: $33.50 © 2006 American Chemical Society
Published on Web 02/23/2006

Chart 1. Structure of Saxitoxin and Its Analogues[a]

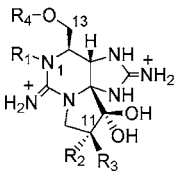

R_1	R_2	R_3	R_4 ; H_2N O	^-O_3S H N O	H
H	H	H	STX	GTX5	dcSTX
OH	H	H	neoSTX	GTX6	dcneoSTX
OH	OSO_3^-	H	GTX1	C3	dcGTX1
H	OSO_3^-	H	GTX2	C1	dcGTX2
H	H	OSO_3^-	GTX3	C2	dcGTX3
OH	H	OSO_3^-	GTX4	C4	dcGTX4

[a] STX: saxitoxin; GTX: gonyautoxin; dc: decarbamoyl-.

(EDC) and 2-(*N*-morpholino)-ethanesulfonic acid (MES) were from Dojindo Lab (Kumamoto, Japan). All other reagents used were analytical grade and purchased from Wako Pure Chemicals (Osaka, Japan) unless otherwise stated.

The Neuro 2A cell line (American Type Culture Collection, Manassas, USA) for the neuroblastoma cell assay was obtained from Dainippon Pharmaceuticals (Tokyo, Japan). Plasma from the pufferfish *F. pardalis* and purified STX-binding protein (PSTBP) were gifts from Professor Mari Yotsu-Yamashita of Tohoku University, Japan. Bullfrogs, *Rana catesbeiana*, were collected in Miyagi Prefecture, Japan, in August 2001.

HPLC Analysis of the Toxins and Derivatives. Saxitoxins were analyzed by postcolumn fluorescent derivative high-performance liquid chromatography (FD-HPLC) as reported previously (*26*). Detection of the STX derivatives, 11-(2-carboxylethylthio)-saxitoxin (CET-STX) and 13-*O*-hemisuccinyl-decarbamoylsaxitoxin (HS-dcSTX), was performed with a slightly modified mobile phase (1 mM sodium 1-heptane-sulfonate in 35 mM ammonium phosphate, pH 3.5) and postcolumn oxidizing reagent (0.6% of hydrogen peroxide in 50 mM potassium phosphate buffer [KPB], pH 9.0) on a Mightysil RP-8 GP column (150 × 4.6 mm; Kanto Chemicals, Tokyo, Japan).

Spectral Analysis. Electrospray ionization mass spectra were recorded in positive ion mode with a TSQ 700 mass spectrometer (Finnigan Mat, San Jose, USA) using 10% methanol at a flow rate of 0.1 mL/min. High resolution-fast atom bombardment (HR-FAB) mass spectra were measured with a JEOL JMS-700 spectrometer in positive ion mode using glycerol as a matrix. NMR spectra were measured with an INOVA 600 spectrometer (Varian, Palo Alto, USA) at 20 °C, and chemical shifts are given on a δ (ppm) scale with 2.06 ppm of CHD_2COOD as an internal standard.

Preparation of Carboxyl STX Derivatives. Preparation of CET-STX was carried out using the reaction described by Sato et al. (*27*). Lyophilized GTX 2/3 (47 μmol) was dissolved in 5 mL of 50 mM KPB (pH 7.4) containing 500 mM 3-mercapto-propionic acid. The mixture was stirred at 70 °C for 1 h, and the reaction was terminated with 1.0 M acetic acid. The reaction mixture was applied to a Bio Gel P-2 (Bio-Rad, Hercules, USA) column using 50 mM acetic acid as a mobile phase. Fractions containing CET-STX were further purified with Hitachi gel 3011-C (Hitachi, Tokyo, Japan) using 0.8 M acetic acid as a mobile phase.

Preparation of HS-dcSTX was performed using C1/C2 as starting material as follows. Lyophilized C1/C2 (36 μmol) was dissolved in 5 mL of 100 mM KPB (pH 7.0) and stirred at 75 °C for 50 min. Decarbamoylgonyautoxin 2 and 3 (dcGTX2/3) formed by the reaction were separated from unreacted C1/C2 using a Bio Gel P-2 (Bio-Rad) column with 50 mM acetic acid as a mobile phase. Lyophilized dcGTX2/3 (17 μmol) was dissolved in 5 mL of a 1:1 mixture of β-mercaptoethanol and 100 mM KPB (pH 6.0) and then heated at 60 °C for 1 h. The resulting dcSTX was purified using a Bio Gel P-2 (Bio-Rad) column with 50 mM acetic acid as a mobile phase. Lyophilized dcSTX (4 μmol) was dissolved in 5 mL of saturated sodium bicarbonate solution and mixed with 200 mg (2 mmol) of succinic anhydride. The solution was stirred at ambient temperature for 24 h, and the reaction was terminated with acetic acid. HS-dcSTX was purified by column chromatography using a Bio-Rex 70 (Bio-Rad) column with stepwise elution of 0.05 and 0.8 M acetic acid, followed by a Hitachi gel 3011-C (Hitachi) column with isocratic elution of 0.8 M acetic acid.

Coupling of STX Derivatives to EAH-Sepharose 4B Gel. Prior to use, EAH-Sepharose 4B was washed with 100 vol of distilled water and 100 vol of 50 mM MES buffer, pH 6.5. To 1 mL of EAH-Sepharose 4B suspended in 50 mM MES buffer (pH 6.5) in a 4-mL vial, 800 μL of 0.83 mM CET-STX and 700 μL of 678 mM EDC in the same buffer were added. The suspension was mixed gently on a revolution mixer (Asahi Techno Glass, Tokyo, Japan) at room temperature for 24 h. Next, the gel was washed sequentially with 6 vol of 50 mM MES buffer (pH 6.5), 6 vol of 0.1 M acetic acid containing 0.5 M NaCl, and 6 vol of distilled water. The gel was then suspended in an equal volume of 0.5 M acetate buffer, pH 7.4. Unreacted amino moieties on the gel were masked by acetylation with acetic anhydride on ice for 30 min. The gel was washed with 6 vol of distilled water, resuspended with 50 mM MES buffer (pH 6.5), and stored at 4 °C.

To 1 mL of EAH-Sepharose 4B in a 4-mL vial, 450 μL of 3 mM HS-dcSTX, 700 μL of 678 mM EDC, and 350 μL of 87 mM *N*-hydroxysuccinimide (NHS) were added. The suspension was rotated with revolution mixer (Asahi Techno Glass, Tokyo, Japan) at 4 °C for 24 h. The resulting dcSTX-affinity gel was washed and acetylated as described above.

Neuroblastoma Cell Bioassay of STX Derivatives. The sodium channel binding activity of intermediate derivatives (CET-STX and HS-dcSTX) was measured by the method of Manger et al. (*28*). Serial dilutions of the standard STX or the derivatives were made with complete medium containing 500 μM ouabain (Sigma, St. Louis, USA) and 20 μM veratridine (Sigma). To each well on a 96-well microplate, 100 μL of the diluted toxins and 100 μL of 5×10^5 cells/mL were added. After the plate was incubated for 20 h under 5% CO_2 at 37 °C, 50 μL of medium containing 0.74 mM 2,3-bis[2-methoxy-4-nitro-5-sulfonyl]-2H-tetrazolium-5-carboxanilide (Sigma) and 9 nM phenazine methosulfate (Sigma) was added. Cell viability was calculated by measuring the absorbance at 490 nm after 4 h incubation with an IMMUNO-MINI NJ-2300 microplate reader (Nalge Nunc International, Rochester, USA). The tests were performed in triplicate.

Measurement of Gel-Immobilized STX and dcSTX. To evaluate the amount of STX bound to the CET-STX gel, 50 μL of the gel was boiled for 10 min in 500 μL of 1 M 2-mercaptoethanol in 50 mM KPB, pH 7.0. STX released by this reaction was assessed by direct injection into FD-HPLC. The amount of dcSTX bound to the HS-dcSTX gel was determined by boiling 50 μL of gel in 500 μL of 1 M HCl for 10 min. The dcSTX released from the gel was then determined by FD-HPLC.

Scheme 1. Preparation of Saxitoxin-Conjugated Affinity Gels[a]

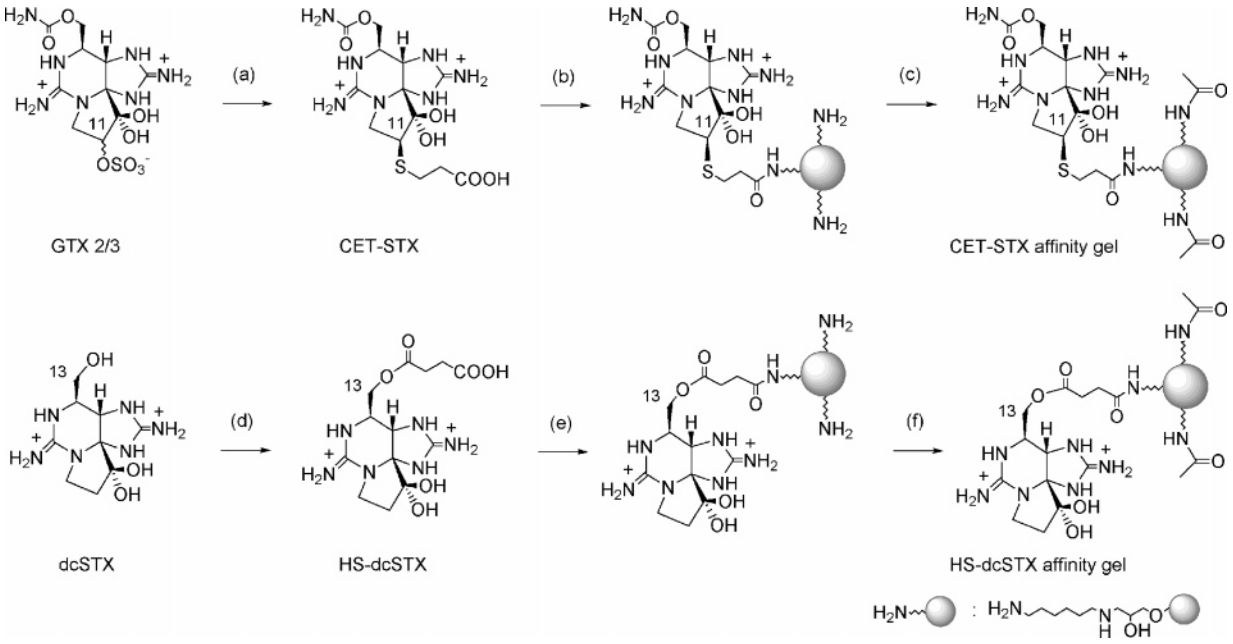

[a] (a) MPA/KPB, pH 7.0, 70 °C, 60 min, (b) EAH-Sepharose 4B, EDC/MES, pH 6.5, room temperature, 24 h, (c) $(CH_3CO)_2O$/acetate buffer, pH 7.4, on ice, 30 min, (d) succinic anhydride/saturated $NaHCO_3$ aqueous, room temperature, 60 min, (e) EAH-Sepharose 4B, EDC, NHS/MES, pH 6.5, 4 °C, 24 h, (f) $(CH_3CO)_2O$/acetate buffer, pH 7.4, on ice, 30 min. GTX: gonyautoxin; CET-STX: 11-(2-carboxyethylthio)saxitoxin; HS-dcSTX: 13-*O*-hemisuccinyldecarbamoylsaxitoxin.

Stability of the STX-Conjugated Affinity Gels. One milliliter of STX-conjugated affinity gels was suspended in one of the following buffers and kept at 4 °C in the dark: 50 mM acetate buffer, pH 4.5; 50 mM succinate buffer, pH 5.5; 50 mM MES buffer, pH 6.5; or 50 mM HEPES buffer, pH 7.5. An aliquot of each suspension was taken out at various times and used to assess the amount of bound toxin as described above.

Preparation of Plasma from Pufferfish and Bullfrog. The plasma protein fraction from the pufferfish *F. pardalis* was obtained according to the method of Yotsu-Yamashita et al. (*22*). Tetrodotoxin was removed from the plasma by washing it several times with 50 mM acetate buffer (pH 5.0) using an Ultrafree-CL (30 000 Da cutoff) with centrifugation at 4500*g* at 4 °C for 30 min. Finally, plasma proteins were dissolved in 50 mM Tris-HCl buffer, pH 7.4. Bullfrog plasma was prepared according to the modified method of Li et al. (*29*). Bullfrogs were anesthetized with diethyl ether. Blood was taken from the systemic arch into a heparinized syringe and was centrifuged for 5 min at 1500*g* at 4 °C. The plasma was stored at −80 °C until use.

Chromatography on the STX-Conjugated Affinity Gels. A 1.5-mL sample of each type of STX-conjugated affinity gel was equilibrated with 50 mM Tris-HCl buffer (pH 7.4) and packed in a plastic column (40 × 7 mm). Pufferfish and bullfrog plasma protein solutions were applied to the column and eluted with 50 mM Tris-HCl (pH 7.4) containing different concentrations of NaCl and finally with 50 mM acetate buffer (pH 5.0) at a flow rate of 0.2 mL/min. The elution was monitored with a diode array detector (Shimadzu, Tokyo, Japan), and 0.5 mL of each fraction was collected. The acetylated gel as control was also performed with the same chromatographic procedure.

Protein Assay and Electrophoresis of the Fractions. Aliquots of fractions were concentrated with Ultrafree-MC (30 000 Da) at 4500*g* at 4 °C for 10 min. Retained proteins were washed with 100 μL of 10 mM Tris-HCl buffer (pH 7.4) and then dissolved in 30 μL of the same buffer. The amount of protein in the concentrated mixture was determined using a Micro BCA Protein Assay kit (Pierce) with bovine serum albumin as the standard. SDS−PAGE was performed on a 7.5% polyacrylamide gel according to the method of Laemmli (*30*). Gels were stained with Coomassie brilliant blue R-250.

Measurement of STX Binding Activity in the Fractions. Aliquots (5 to 100 μL) of each fraction were concentrated with Ultrafree-MC as above. The residue remaining was dissolved in 30 μL of 10 mM Tris-HCl buffer (pH 7.4) containing 330 pmol of STX and then kept on ice for 10 min. After ultrafiltration, the amount of STX in the filtrate was quantified by FD-HPLC. The amount of STX bound to proteins was calculated by subtracting the amount in the filtrate from the control without proteins.

RESULTS

Preparation of Carboxyl Derivatives of STX and their Na Channel-Binding Activities. STX-conjugated affinity gels were prepared according to the strategy shown in Scheme 1. For the first step of reactions, GTX2/3 was reacted with 3-mercaptopropionic acid to introduce carboxylic moiety into the toxin by the unique substitution reaction (*27*). Using 47 μmol of a GTX2/3 mixture, we obtained 19 μmol of CET-STX in 40% yield. A molecular formula of $C_{13}H_{22}O_6N_7S$ was obtained by HR-FAB MS ($[M + H]^+$ 404.1355; $\Delta = +0.3$ mmu). Figure 1 shows the ^{1}H NMR spectra taken in both D_2O and D_2O/H_2O (1:1) containing 4% CD_3COOD, with assigned HMBC and NOESY correlations. Methylene protons at δ 2.94 to 3.06 and 2.74 indicated the replacement of the hydroxysulfate of GTX2/3 with a carboxyethylthio moiety. The HMBC correlation from H-1′ to C-11 indicated that the position of substitution was at C-11. H-11 was not observed in D_2O by complete exchange to deuterium in solvent through keto−enol equilibration, but observed as triplet at δ 3.65 in D_2O/H_2O. The coupling constant was 9.3 Hz, close to that of ($^3J_{10\alpha,11}$ 8−9 Hz) of GTX3, which has a 11β-hydroxysulfate (*31*), indicating that the substituent was in a β-configuration. The long-range correlation signal between H-10α (δ 4.15) and H-11 in the NOESY experiment also supported this stereochemical assignment.

As another way to introduce carboxyl moiety into STX skeleton, dcSTX was succinylated. HS-dcSTX was obtained in

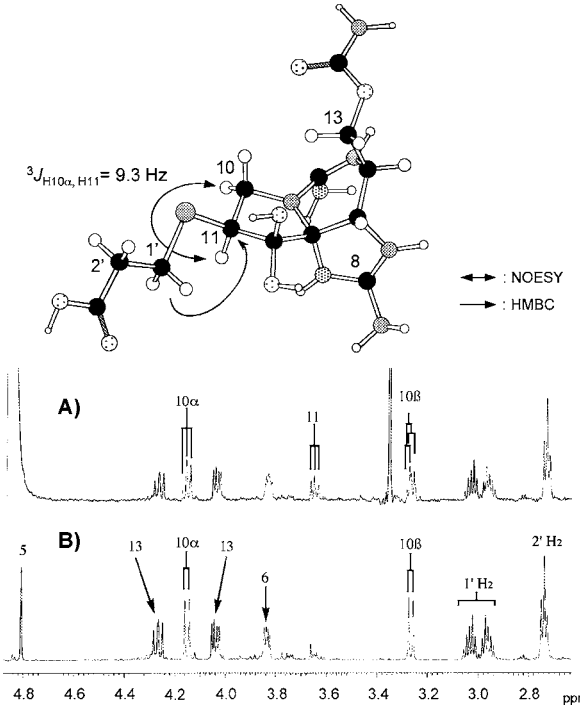

Figure 1. ^{1}H NMR spectra and structure of 11-(2-carboxyethylthio)-saxitoxin. These spectra were measured in 4% CD_3COOD/D_2O:H_2O (1:1) (A) and 4% CD_3COOD/D_2O (B) at 600 MHz. In the structure, observed HMBC and NOESY correlations are shown only around C11.

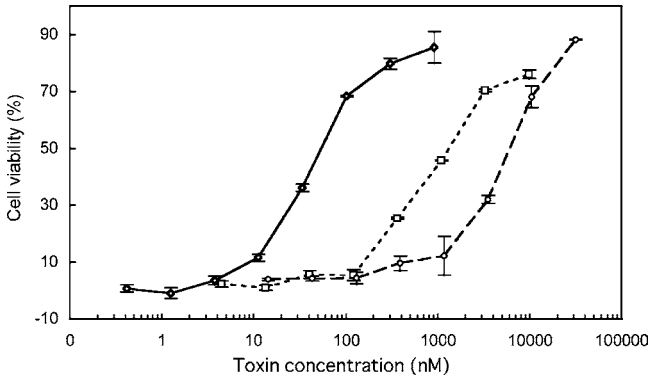

Figure 2. Dose−response curve of neuroblastoma assay. ◇: STX, □: CET-STX, ○: HS-dcSTX.

a yield of 53%. A molecular formula of $C_{13}H_{21}O_6N_6$ ([M + H]$^+$ 357.1524; Δ = +0.2 mmu) was confirmed by HR-FAB mass spectroscopy, and the following signals were observed in^{1}H NMR (4% CD_3COOD/D_2O, 600 MHz): δ (ppm), 4.77 (1H, s, H-5), 4.40 (1H, dd, J = 11.7, 9.4 Hz, H-13), 4.11 (1H, dd, J = 11.7, 5.4 Hz, H-13), 3.87 (1H, dd, J = 9.4, 5.4 Hz, H-6), 3.80 (1H, d, J = 9.9 Hz, H-10α), 3.58 (1H, d, J = 9.9 Hz, H-10β), and 2.70 (4H, m, succinate). The parameters were identical to those reported for this compound by Koehn et al. (*32*), with a 0.5 ppm difference due to the use of different standards.

Figure 2 shows dose−response curves of CET-STX and HS-dcSTX together with the control STX in the Neuro 2A cell bioassay. The Hill coefficients calculated from the curves were identical for the three compounds (1.23), suggesting that the action of two derivatives on the cell were similar to that of STX. The EC_{50} values of STX, CET-STX, and HS-dcSTX were 40, 888, and 6530 nM, respectively.

Preparation of STX-Conjugated Affinity Gels and Their Stability. After several preliminary experiments with different reaction conditions, CET-STX and HS-dcSTX were effectively

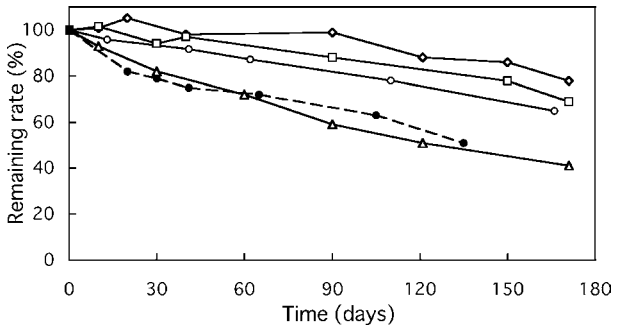

Figure 3. Stability of CET-STX affinity gel. The remaining STX on a CET-STX affinity gel was plotted as % of 0 day. The gel was stored at 4 °C in the following buffers: pH 4.5 (◇): 50 mM acetate buffer, pH 5.5 (□): 50 mM succinate buffer, pH 6.5 (○): 50 mM MES buffer, pH 7.5 (△): 50 mM HEPES buffer was plotted against time after preparation. CET-STX was stored at 4 °C in 50 mM MES buffer at pH6.5 (●).

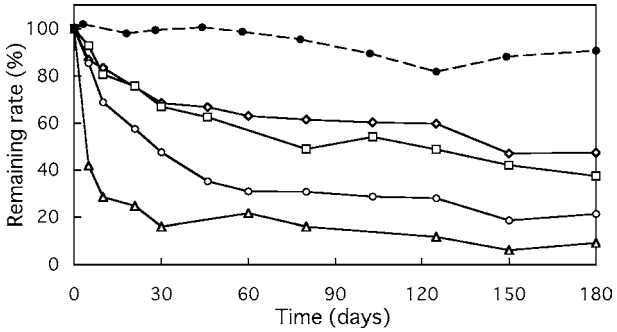

Figure 4. Stability of the HS-dcSTX affinity gel. The remaining dcSTX on the HS-dcSTX affinity gel was plotted as % of 0 day. Symbols for buffers are the same as in Figure 3.

bound to EAH-Sepharose 4B. Use of MES buffer and 0.6−0.7 μmol of CET-STX per 1 mL of gel were found to be optimal, resulting in a 90% yield of reaction. During acetylation step for masking amino residues, a small portion of STX was released from the gel, but 90% remained intact. The amount of STX bound to 1 mL of the final product (CET-STX affinity gel) was estimated to be 500 nmol, which is equivalent to coupling of 4−7% of the amino groups on the gel based on the reported value of 7−12 μmol of amino groups/mL in EAH-Sepharose 4B.

Addition of NHS was essential for the coupling of HS-dcSTX to EAH-Sepharose 4B, and the derivative was quantitatively introduced into the gel. However, more dcSTX was released by acetylation than in the case of CET-STX. The concentration of dcSTX bound to the final gel (HS-dcSTX affinity gel) was 510 nmol/mL gel, which is equivalent to 4−7% of the amino groups in the gel.

Masking of amino residues by acetylation reduced the ionic binding of proteins as demonstrated by testing with bovine serum albumin. In this case, acetylation reduced nonspecific protein binding by 99% (data not shown).

The stability of the affinity gels during storage was tested at various pHs. CET-STX gels gradually lost their toxin moieties during storage at 4 °C in a pH-dependent manner. The gels were more stable at lower pH, and more than 80% of toxins were retained at pH 4.5 after 6 months (Figure 3). HS-dcSTX gels were less stable, and approximately 50% of the toxin was lost after 6 months, even at pH 4.5 (Figure 4).

Chromatography of Pufferfish and Bullfrog Plasma on the STX-Conjugated Affinity Gels. To evaluate the binding activities of the STX-conjugated gels, pufferfish and bullfrog plasma preparations, which are known to contain STX-binding proteins, were subjected to chromatography on the columns.

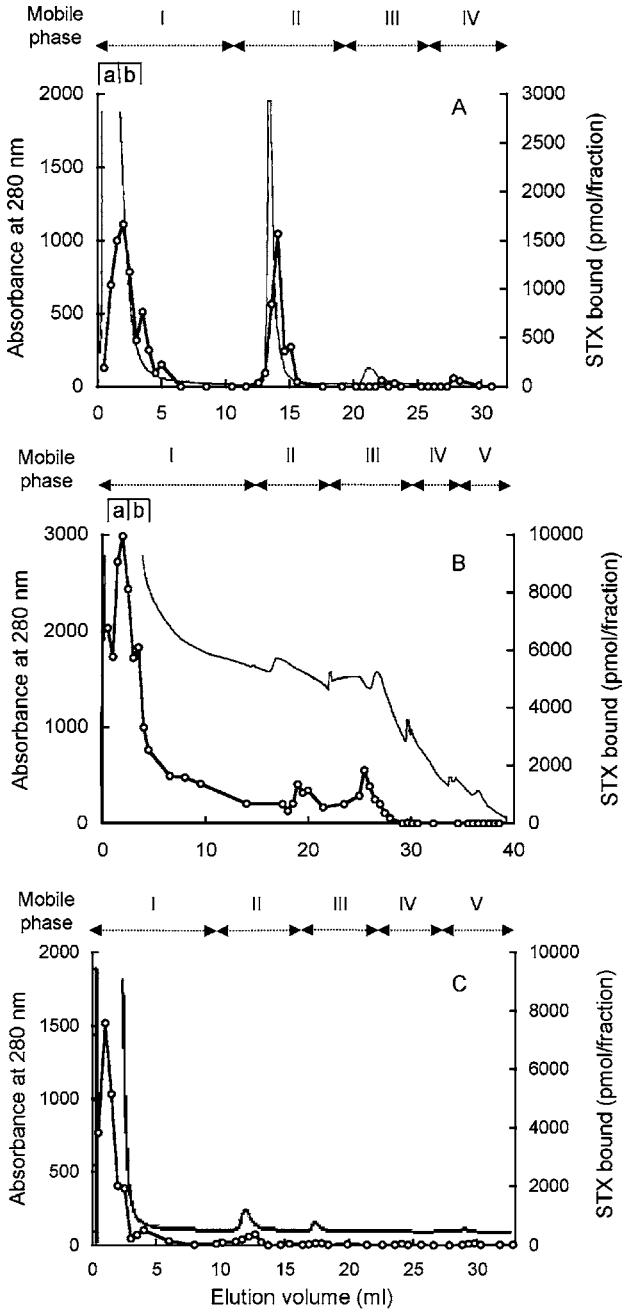

Figure 5. Chromatograms of pufferfish or bullfrog plasma on STX-conjugated affinity gels. The elution of protein and STX binding activity was monitored by the absorbance at 280 nm and the amount of STX bound to protein (○), respectively. (A) Pufferfish plasma on CET-STX affinity gel eluted with I: 50 mM Tris-HCl buffer (pH 7.4), II: 50 mM Tris-HCl buffer (pH 7.4) containing 500 mM NaCl, III: 50 mM Tris-HCl buffer (pH 7.4) containing 1 M NaCl, IV: 50 mM acetate buffer (pH 5.0) as mobile phases at a flow rate of 0.2 mL/min. (B) Bullfrog plasma on the CET-STX affinity gel eluted with I: 50 mM Tris-HCl buffer (pH 7.4), II: 50 mM Tris-HCl buffer (pH 7.4) containing 50 mM NaCl, III: 50 mM Tris-HCl buffer (pH 7.4) containing 500 mM NaCl, IV: 50 mM Tris-HCl buffer (pH 7.4) containing 1 M NaCl, V: 50 mM acetate buffer (pH 5.0) as mobile phases at a flow rate of 0.2 mL/min. (C) Bullfrog plasma on HS-dcSTX affinity gel. Eluting condition is the same as B.

Figure 5 shows chromatograms of pufferfish plasma (panel A) and bullfrog plasma (panel B) on CET-STX affinity gel and bullfrog plasma on a HS-dcSTX affinity gel column (panel C). SDS−PAGE of the corresponding fractions from A and B are shown in Figure 6. Distribution of STX-binding activity and specific activities of each fraction are summarized in Table 1. Several fractions, especially in flow-through fraction, showed

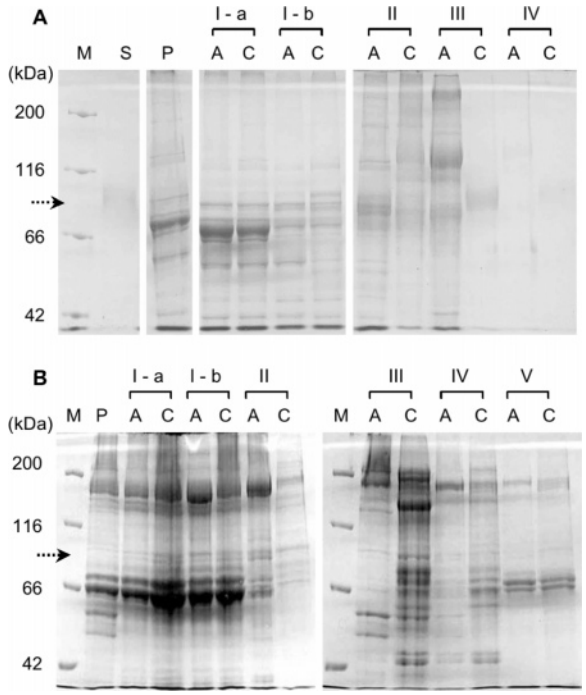

Figure 6. SDS−PAGE of fractions from CET-STX affinity column chromatography. (A) Pufferfish plasma. M: marker, S: standard PSTBP, P: pufferfish plasma, A: acetylated gel as control, C: CET-STX affinity gel, I−IV: fractions in Figure 5A. (B) Bullfrog plasma. M: marker, P: bullfrog plasma, A: acetylated gel as control, C: CET-STX affinity gel I−V: fractions in Figure 5B. Each arrow indicates the bands corresponding to PSTBP (A) and the reported molecular weight of saxiphilin (B) (90.8 kDa), respectively.

higher STX-binding activity than the estimated activity (approximately 440 pmol for pufferfish plasma and 150 pmol for bullfrog plasma). This finding implies the activity includes nonspecific binding activity.

When 400 μL (12−14 mg of protein) of pufferfish plasma was chromatographed on the CET-STX gel (Figure 5A), or the acetylated gel as control, a large proportion of the STX-binding activity (65% of the total recovered) was found in the unbound fraction (I), and 30% was eluted with buffer containing 0.5 M NaCl (II). Although only 5% of the STX-binding activity was detected in the affinity gel, the 1 M NaCl fraction (III) showed a specific activity of 7 nmol/mg of protein. This 40-fold increase in specific activity was similar to the original report of PSTBP purification with 4 steps (*22*), although a different method was used for the evaluation of binding activity in the previous study. Like the PSTBP standard, this purified fraction shows a single broad band at around 90 kDa on SDS−PAGE (Figure 6A). In contrast, this band was not detected in the lane of the acetylated gel. From SDS−PAGE, PSTBP was selectively concentrated on fraction III by the CET-STX affinity gel.

Bullfrog plasma (400 μL, containing 25−30 mg protein) was also applied to the CET-STX affinity gel column (Figure 5B) or the acetylated gel. Most of the STX-binding activity (84%) was found in the unbound fraction (I), and 7 and 9%, respectively, were found in the 0.05 and 0.5 M NaCl fractions (II and III). The latter two fractions showed specific activities of 12 and 17 nmol/mg of protein, respectively, corresponding to 109- and 159-fold purifications of the activity in the original plasma preparations. Fractions II and III in the affinity gel showed several bands on SDS−PAGE including a 91-kDa band corresponding to the reported molecular weight of saxiphilin in bullfrog (*29*) (Figure 6B). These bands other than saxiphilin were also detected in the control, suggesting that these are nonspecific binding to this affinity gel.

Table 1. Saxitoxin Binding Activities in Each Fraction from CET-STX Affinity Chromatography

pufferfish plasma				bullfrog plasma			
fraction no.	NaCl (M) in buffer[a]	activity[b] (%)	specific activity (nmol/mg of protein)	fraction no.	NaCl (M) in buffer*	activity[b] (%)	specific activity (nmol/mg of protein)
original			0.14	original			0.11
I	0.00	65.0	0.82	I	0.00	84.1	2.22
II	0.50	29.0	2.11	II	0.05	6.9	11.69
III	1.00	5.3	6.98	III	0.50	9.0	17.04
IV		0.7	5.31	IV	1.00	0.0	0.34
				V		0.0	0.00

[a] In 50 mM Tris HCl buffer, pH 7.4. Eluting buffer of fraction IV for pufferfish plasma and fraction V for bullfrog plasma was 50 mM acetate buffer, pH 5.0. [b] Percent of total recovered STX binding activity (pmol).

HS-dcSTX affinity gel was tested only for bullfrog plasma due to unavailability of pufferfish plasma. The gels did not show any interaction with saxiphilin in bullfrog, which accounted for almost all the activity in the first fraction (Figure 5C).

DISCUSSION

The first step in our strategy for the preparation of STX-conjugated affinity gels was the introduction of carboxylic acids at positions C-11 or C-13 of STX, leaving two guanidine groups and the *gem*-diols at C-12 intact (Scheme 1). Using the methods described here, CET-STX could be prepared in sufficient yields for the first time. Preparation of HS-dcSTX has been reported previously (*32*), but our reaction in sodium bicarbonate solution gave a much higher yield. Both derivatives were shown to maintain Na channel-binding activity, although we observed a 1 order of magnitude reduction for CET-STX and 2 orders of magnitude reduction for HS-dcSTX. A low affinity of HS-dcSTX for the Na channel-binding site might be due to an ionic repulsion between the carboxylic acid and the receptor site, similar to that between the channel and the N-sulfocarbamoyl group of the toxin (*33*). This repulsion is expected to be reduced by the formation of an amido bond with the EAH-Sepharose 4B gel.

CET-STX obtained was exclusively composed of 11-β epimer, despite the use of a 11-hydroxysulfate epimeric mixture (GTX2/3) as the starting material. A similar result was reported for glutathione derivatives of GTX1/4 (*27*). This might be a reflection of the highly favored energetic stability of the β- rather than the α-configuration because a keto−enol equilibration can be observed by substitution of 11-α H with solvent deuterium.

For the second step, the derivatives were effectively coupled to an agarose gel with amino groups under aqueous conditions. The reaction yields were as high as 90%, and two derivatives could be introduced into affinity gels at a concentration of 500 nmol/mL of gel. The STX skeleton was separated from agarose by 15 bonds (Scheme 1). The length was expected to be enough as a spacer.

A preliminary test using known STX binding proteins showed that the affinity gels would be useful for the purification of active proteins. A high degree of purification could be achieved in the NaCl-eluted fraction. In fact, especially for the CET-STX gel, nearly pure PSTBP was obtained in just one chromatographic step. A large proportion of activity in the first unbound fraction might be the result of nonspecific binding with native STX, since this affinity gel possessed enough binding capability to interact with the active proteins (approximately 440 pmol in pufferfish and 150 pmol in bullfrog) present in plasma preparations.

Several proteins were observed by SDS−PAGE in the 0.5 and 1.0 M NaCl fractions (Figure 6A). These proteins were also detected in the acetylated gel, suggesting that the affinity gel interacted with proteins other than the active protein, mainly due to the masked moiety of the gel. Such nonspecific binding would be inevitable and however could be reduced by treating crude extract with ammonium sulfate, dialysis, or column chromatography, or by using the affinity gel conjugated to more toxins. Therefore, those steps will improve the interaction between active proteins and toxins without being disturbed by nonspecific binding. Further, the comparison of the elution profile between the affinity gel and the acetylated gel is effective and necessary to find unidentified active proteins. Experiments are also necessary to clarify whether these were actual STX-binding proteins or were merely bound by nonspecific hydrophobic or ionic binding to the unmasked amino groups remaining on the gels.

the HS-dcSTX affinity gel showed no interaction with saxiphilin, probably because it was hindered by the introduced side chain. It was also expected from the reported binding characteristic of saxiphilin, which showed much lower affinity to GTX5 (N-sulfonate derivative) than did STX or dcSTX (*34*). However, it is important to have affinity gels with different toxin structures because unidentified STX-binding proteins might have diverse modes of interaction with the toxin.

The high reaction yields for introducing carboxyl-conjugated STX derivatives in the gels are noteworthy because the reaction can be utilized to prepare STX-conjugated proteins. In the past, direct coupling using formaldehyde (*35*) was widely used for the preparation of antigens or toxin-linked enzymes for the development of an enzyme-linked immunosorbent assay for STX groups. However, the established protocol using formaldehyde has fundamental problems due to the uncertain binding between toxins and proteins and to the large consumption of toxins. Therefore, this coupling reaction of carboxyl-conjugated STX derivatives may solve these problems.

We established the preparation of two types of toxin-conjugated affinity gels in short steps and in high yields under aqueous conditions. They are expected to be a new research tool to elucidate the mechanism of transportation or bioaccumulation in marine organisms. Screening of toxin-binding proteins in bivalve mollusk using these affinity gels is underway.

ACKNOWLEDGMENT

We are grateful to Professor Mari Yotsu-Yamashita, Graduate School of Agricultural Science, Tohoku University, for providing pufferfish plasma and PSTBP. We also thank Dr Susan Blackburn, CSIRO Hobart, Australia, for permitting us to use the *Anabaena circinalis* culture strain. This study was supported by a Grant-in-Aid from the Ministry of Education, Culture, Sports, Science and Technology, Japan.

LITERATURE CITED

(1) Oshima, Y., Bolch, C. J., and Hallengraeff, G. M. (1992) Toxin composition of resting cysts of *Alexandrium tamarense* (dinophyceae). *Toxicon 30*, 1539−1544.

(2) Chang, F. H., Anderson, D. M., Kulis, D. M., and Till, D. G. (1997) Toxin production of *Alexandrium minutum* (Dinophyceae) from the bay of plenty, New Zealand. *Toxicon 35*, 393−409.

(3) Harada, T., Oshima, Y., Kamiya, H., and Yasumoto, T. (1982) Confirmation of paralytic shellfish toxins in the dinoflagellate *Pyrodinium bahamense* var. *compressa* and bivalves in Palau. *Nippon Suisan Gakkaishi 48*, 821−825.
(4) Takatani, T., Morita, T., Anami, A., Akaeda, H., Kamijo, Y., Tsutsumi, K., and Noguchi, T. (1998) Appearance of *Gymnodinium catenatum* in association with the toxification of bivalves in kamae, Oita prefecture, Japan. *J. Food Hyg. Soc. Jpn. 39*, 275−280.
(5) Oshima, Y., Blackburn, S. I., and Hallengraeff, G. M. (1993) Comparative study on paralytic shellfish toxin profiles of the dinoflagellate *Gymnodinium catenatum* from three different countries. *Mar. Biol. 116*, 471−476.
(6) Mahmood, N. A., and Carmichael, W. W. (1986) Paralytic shellfish poisons produced by the freshwater cyanobacterium *Aphanizomenon Flos-aquae* NH-5. *Toxicon 24*, 175−186.
(7) Negri, A. P., Jones, G. J., and Hindmarsh, M. (1995) Sheep mortality associated with paralytic shellfish poisons from the cyanobacterium *Anabaena circinalis. Toxicon 33*, 1321−1329.
(8) Carmichael, W. W., Evans, W. R., Yin, Q. Q., Bell, P., and Moczydlowski, E. (1997) Evidence for paralytic shellfish poisons in the freshwater cyanobacterium *Lyngbya wollei* (Farlow ex Gomot) comb. nov. *Appl. Environ. Microbiol. 63*, 3104−3110.
(9) Pomati, F., Sacchi, S., Rossetti, C., Giovannardi, S., Onodera, H., Oshima, Y., and Neilan, B. A. (2000) The freshwater cyanobacterium *Planktothrix* sp. FP1: molecular identification and detection of paralytic shellfish poisoning toxins. *J. Phycol. 36*, 553−562.
(10) Bricelj, V. M., and Shumway, S. E. (1998) Paralytic shellfish toxins in bivalve mollusks: occurrence, transfer kinetics, and biotransformation. *Rev. Fish. Sci. 6*, 315−383.
(11) Cestéle, S., and Catterall, W. A. (2000) Molecular mechanisms of neurotoxin action on voltage-gated sodium channels. *Biochimie 82*, 883−892.
(12) Kao, C. Y. (1993) Paralytic shellfish poisoning. *Algal toxins in seafood and drinking water* (Falconer, I. R., Ed.) pp 75−86, Chapter 4, Academic Press, San Diego.
(13) Kao, C. Y. (1986) Structure−activity re1ations of tetrodotoxin, saxitoxin, and analogues. *Ann. N. Y. Acad. Sci. 479*, 52−67.
(14) Kawatsu, K., Hamano, Y., Sugiyama, A., Hashizume, K., and Noguchi, T. (2002) Development and application of an enzyme immunoassay based on a monoclonal antibody against gonyautoxin components of paralytic shellfish poisoning toxins. *J. Food Prot. 65*, 1304−1308.
(15) Bürk, C., Usleber, E., Dietrich, R., and Märtlbauer, E. (1995) Production and characterization of antibodies against neosaxitoxin utilizing a novel immunogen synthesis procedure. *Food Agric. Immunol. 7*, 315−322.
(16) Kralovec, J. A., Laycock, M. V., Richards, R., and Usleber, E. (1996) Immobilization of small molecules on solid matrixes: a novel approach to enzyme-linked immunosorbent assay screening for saxitoxin and evaluation of anti-saxitoxin antibodies. *Toxicon 34*, 1127−1140.
(17) Sako, Y., Yoshida, T., and Uchida, A. (2001) Purification and characterization of sulfotransferase specific to N-21 of saxitoxin and gonyautoxin 2+3 from the toxic dinoflagellate *Gymnodinium catenatum* (Dinophyceae). *J. Phycol. 37*, 1044−1051.
(18) Sullivan, J. J., Iwaoka, W. T., and Liston, J. (1983) Enzymatic transformation of PSP toxins in the littleneck clam (*Protothaca staminea*). *Biochem. Biophys. Res. Commun. 114*, 465−472.
(19) Shimizu, Y., and Yoshioka, M. (1981) Transformation of paralytic shellfish toxins as demonstrated in scallop homogenates. *Science 212*, 547−549.
(20) Oshima, Y. (1995) Chemical and enzymatic transformation of paralytic shellfish toxins in marine organisms. *Harmful Marine Algal Blooms* (Lassus, P., Arzul, G., Erard, E., Gentien. P., Marcaillou, C., Eds.) pp 475−480, Lavoisier, Paris.
(21) Mahar, J., Lukacs, G. L., Li, Y., Hall, S., and Moczydlowski, E. (1991) Pharmacological and biochemical properties of saxiphilin, a soluble saxitoxin-binding protein from the bullfrog (*Rana catesbeiana*). *Toxicon 29*, 53−71.
(22) Yotsu-Yamashita, M., Sugimoto, A., Terakawa, T., Shoji, Y., Miyazawa, T., and Yasumoto, T. (2001) Purification, characterization and cDNA cloning of a novel soluble saxitoxin and tetrodotoxin binding protein from plasma of the pufferfish *Fugu pardalis*. *Eur. J. Biochem. 268*, 5937−5946.
(23) Andrinolo, D., Michea, L. F., and Lagos, N. (1997) Toxic effects, pharmacokinetics and clearance of saxitoxin, a component of paralytic shellfish poison (PSP) in cats. *Toxicon 37*, 447−464.
(24) Gessner, B. D., Bell, P., Doucette, G. J., Moczydlowski, E., Poli, M. A., Dolah, F. V., and Hall, S. (1997) Hypertension and identification of toxin in human urine and serum following a cluster of mussel-associated paralytic shellfish poisoning outbreaks. *Toxicon 35*, 711−722.
(25) Onodera, H., Oshima, Y., Watanabe, M. F., Watanabe, M., Bolch, C. J., Blackburn, S., and Yasumoto, T. (1996) Screening of paralytic shellfish toxins in freshwater cyanobacteria and chemical confirmation of the toxins in cultured *Anabaena circinalis* from Australia. *Harmful and toxic algal blooms* (Yasumoto, T., Oshima, Y., Fukuyo, Y., Eds.) pp 563−566, IOC-UNESCO, Paris.
(26) Oshima, Y. (1995) Postcolumn derivatization liquid chromatography method for paralytic shellfish toxins. *J. AOAC Int. 78*, 528−532.
(27) Sato, S., Sakai, R., and Kodama, M. (2000) Identification of thioether intermediates in the reductive transformation of gonyautoxins into saxitoxins by thiols. *Bioorg. Med. Chem. Lett. 10*, 1787−1789.
(28) Manger, R. L., Leja, L. S., Lee, S. Y., Hungerford, J. M., and Wekell, M. M. (1993) Tetrazolium-based cell bioassay for marine toxins active on voltage sensitive sodium channels, semiautomated assay for saxitoxins, brevetoxins, and ciguatoxins. *Anal. Biochem. 214*, 190−194.
(29) Li, Y., and Moczydlowski, E. G. (1991) Purification and partial sequencing of Saxiphilin, a saxitoxin-binding protein from bullfrog, reveals homology to transferrin. *J. Biol. Chem. 266*, 15481−15487.
(30) Laemmli U. K. (1970) Cleavage of structural proteins during the assembly of the head bacteriophage T4. *Nature 227*, 680−685
(31) Wichmann, C. F., Niemczura, W. P., Schnoes, H. K., Hall, S., Reichardt, P. B., and Darling, S. D. (1981) Structures of two novel toxins from *Protogonyaulax*. *J. Am. Chem. Soc. 103*, 6977−6978.
(32) Koehn, F. E., Ghazarossian, V. E., Schantz, E. J., Schnoes, H. K., and Strong, F. M. (1981) Derivatives of Saxitoxin. *Bioorg. Chem. 10*, 412−428.
(33) Shimizu, Y. (1984) Paralytic shellfish poisons. *Progress in the chemistry of organic natural products 45*, 235−264.
(34) Llewellyn, L. E., Bell, P. M., and Moczydlowski, E. G. (1997) Phylogenetic survey of soluble saxitoxin-binding activity in pursuit of the function and molecular evolution of saxiphilin, a relative of transferrin. *Proc. R. Soc. London B 264*, 891−902.
(35) Usleber, E., Dietrich, R., Bürk, C., Schneider, E., and Märtlbauer, E. (2001) Immunoassay methods for paralytic shellfish poisoning toxins. *J. AOAC Int. 84*, 1649−1656.

BC049699E

Cationic Nucleoside Lipids for Gene Delivery

Pauline Chabaud,[†] Michel Camplo,[†] Dominique Payet,[⊥] Guillaume Serin,[||] Louis Moreau,[‡] Philippe Barthélémy,*[,‡] and Mark W. Grinstaff[§]

Groupe de Chimie Organique et des Matériaux Moléculaires (UMR-CNRS 6114), Faculté des Sciences de Luminy, case 901, 13288 Marseille Cedex 09, France, INSERM U386, Université Victor Segalen Bordeaux 2, 146 rue Léo Saignat 33076 Bordeaux Cedex, France, Laboratoire de Chimie Biologique UMR A408 Faculté des sciences d'Avignon 33, rue Louis Pasteur, 84000 Avignon, France, Centre d'Immunologie de Marseille Luminy, Parc scientifique de Luminy, 13288 Marseille, Cedex 9, France, Oncodesign, Parc de la Toison d'Or, 28 rue Louis de Broglie, 21000 Dijon, France, and Departments of Biomedical Engineering and Chemistry, Boston University, Boston, Massachusetts 02215. Received June 7, 2005; Revised Manuscript Received January 4, 2006

A novel uridine-based nucleo-lipid, DOTAU (*N*-[5′-(2′,3′-dioleoyl)uridine]-*N*′,*N*′,*N*′-trimethylammonium tosylate) was prepared by using a convenient four-step synthetic pathway. From the preliminary physicochemical studies (quasielastic light scattering and light microscopy), this amphiphilic structure forms supramolecular organizations in aqueous solution. In addition, in the presence of nucleic acids, transmission electronic microscopy experiments (TEM) and small angle X-ray scattering (SAXS) reveal the formation of multilamellar structures similar to lipoplexes (cationic liposome−DNA complexes) with cationic lipids. The formation of a complex was confirmed by fluorescence spectroscopic assays involving ethidium bromide. Transfection assays of mammalian cell lines (HeLa and MCF-7) indicate that DOTAU can transfect efficiently an expression vector (pEGFP) encoding GFP. Proliferation assays realized on these cell lines show that DOTAU does not inhibit cell proliferation and is less toxic than the commercial Lipofectamine 2000.

INTRODUCTION

The transport of nucleic acids through a cell membrane for subsequent transcription is fundamental for the delivery of therapeutic genes (*1*−*3*). Viruses are efficient vectors for transportation of DNA, but there are risks associated with their clinical application (*4*). Consequently, there is significant basic and clinical interest in nonviral vectors, and a large variety of synthetic gene-delivery systems have been investigated including cationic lipids, dendritic macromolecules, and linear polymers (*5*−*12*).

New cationic lipids have been synthesized and evaluated for plasmid DNA delivery (*13*) since the discovery of *N*-[1-(2,3-dioleyloxy)propyl]-*N*,*N*,*N*-trimethylammonium chloride (DOTMA)[1] as a cationic transfecting agent (*5*, *14*). In general, cationic lipids are attractive materials for this application because (1) of their reduced cytotoxicity compared to viral vectors, (2) of their well-defined structure (compared to linear polymers), (3) tuneable chemical structure, and (4) ease of synthesis. Four primary motivations for this research are to improve the transfection activity or modulate the level of gene expression, reduce the cytotoxicity, broaden the scope of the nucleic acid payload, and expand the repertoire of chemical structures under investigation. Consequently, numerous structural features have been altered on the basic cationic lipid structure, leading to compositions such as DOTAP (*N*-[1-(2,3-dioleoyloxy)propyl]-*N*′,*N*′,*N*′-trimethylammonium chloride) which are now commercially available and under clinical evaluation (Figure 1) (*15*). Among the chemical variants/alterations of the lipid structure explored, the incorporation of natural moieties such as cholesterol, oleic acids, and amino acids or multicationic charges have been investigated. Currently, all the synthetic vectors used relay on either electrostatic interactions or electrostatic and hydrophobic interactions for DNA binding and supramolecular assembly formation required for gene delivery. We are interested in molecular interactions such as hydrogen bonding and $\pi-\pi$ stacking to further modulate the interactions between DNA and the synthetic vector. Within this framework, hybrid molecules bearing both nucleic acid units and amphiphilic moieties would be the simplest prototype. To the best of our knowledge, there are no previous examples of synthetic gene carriers derived from cationic nucleoside-based lipids. Herein, we describe a promising nucleic acid vector based on a cationic amphiphilic uridine. We report the synthesis, physicochemical studies, cytotoxicity, and in vitro transfection results of this new nucleoside-based lipid (DOTAU, Figure 1).

MATERIALS AND METHODS

General Experiments and Analytical Conditions. Unless noted otherwise, all starting materials were obtained from Aldrich and were used without further purification, and the solvents were redistilled over calcium chloride, calcium hydride, potassium hydroxide, or sodium according to the solvent used.

* To whom correspondence should be addressed. E-mail: barthelemy@bordeaux.inserm.fr.

[†] Groupe de Chimie Organique et des Matériaux Moléculaires (UMR-CNRS 6114).

[‡] Laboratoire de chimie biologique UMR A408 Faculté des sciences d'Avignon 33 and Université Victor Segalen Bordeaux 2.

[⊥] Centre d'Immunologie de Marseille Luminy.

[||] Oncodesign.

[§] Boston University.

[1] Abbreviation: TEM (transmission electron microscopy); SAXS (small-angle X-ray scattering); CT DNA (calf thymus DNA); GFP (green fluorescent protein); FACS (fluorescence activated cell sorter); DOTAP, (*N*-[1-(2,3-dioleoyloxy)propyl]-*N*′,*N*′,*N*′-trimethylammonium chloride) or DOTAP (*16*); DOTAU, *N*-[5′-(2′,3′-dioleoyl)uridine]-*N*′,*N*′,*N*′-trimethylammonium tosylate; DCC, dicyclohexylcarbodiimide; DCU, dicyclohexylurea; DMAP, (dimethylamino)pyridine; DCM, methylene dichloride; DMF, dimethylformamide; TEA, triethylamine; THF, tetrahydrofuran; SUV, small unilamellar vesicles; BrdU, 5-bromo-2′-deoxyuridine; LIPO, Lipofectamine 2000; EB, ethidium bromide; NBA, 3-nitrobenzyl alcohol.

10.1021/bc050162q CCC: $33.50 © 2006 American Chemical Society
Published on Web 02/08/2006

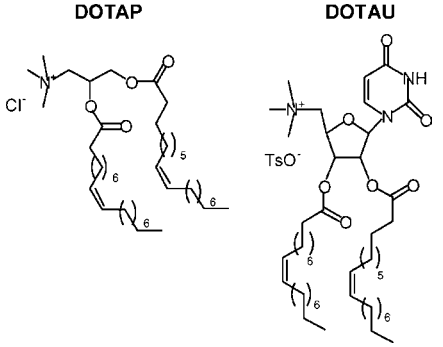

Figure 1. Chemical structures of DOTAP (*N*-[1-(2,3-dioleoyloxy)-propyl]-*N*′,*N*′,*N*′-trimethylammonium chloride) and DOTAU (*N*-[5′-(2′,3′-dioleoyl)uridine]-*N*′,*N*′,*N*′-trimethylammonium tosylate).

All compounds were characterized using standard analytical and spectroscopic techniques such as ^{1}H, ^{13}C, and ^{31}P NMR spectroscopy (apparatus Bruker Avance DPX-300, ^{1}H at 300.13 MHz, ^{13}C at 75.46 MHz, and ^{31}P at 121.49 MHz) and mass spectrometry (Instrument JEOL SX 102, NBA matrix). The NMR chemical shifts are reported in ppm relative to tetramethylsilane for ^{1}H and ^{13}C. The ^{1}H NMR coupling constants, *J*, are reported in Hz. TEM microscopy experiments were performed on a Philips CM 10 (negative staining with ammonium molybdate 1% in water, Cu/Pd carbon coated grids). A Wyatt QELS system was used to obtain the Rh. Silica gel 60 (particle size: 40−60 μm) was employed for flash chromatography. Thin layer chromatograms were performed with aluminum plates coated with silica gel 60 F_{254} (Merck). Varian silica gel reverse phase C18 Mega BE-C18, 2GM 12 mL, and Sephadex LH-20 (25−100 μm) were used for quantitative chromatography. ^{13}C chemical shifts were determined by HMQC.

2′,3′-*O*-Isopropylideneuridine, 1. To a stirring solution of uridine (1.5 g, 6.14 mmol) in dry acetone (135 mL) was added a catalytic amount of H_2SO_4 dropwise, at room temperature. After being stirred for 2 h, the solution became clear and was quenched with $BaCO_3$ until neutralization. The heterogeneous mixture was filtered on a Celite pad, and the filtrate was evaporated under reduced pressure. The crude product was immediately purified by flash column chromatography (CH_2Cl_2/MeOH: 90/10) to give **1** (1.24 g, 71%) as a white solid. mp = 161 °C. ^{1}H NMR (D_3CCOCD_3): δ 7.84 (1H, d, J = 8.06 Hz), 5.92 (1H, d, J = 2.69 Hz), 5.62 (1H, d, J = 8.06 Hz), 4.92 (2H, 2 × dd, J = 2.76 Hz, 6.3 Hz and J = 3.24 Hz, 6.3 Hz), 4.19 (q, 1H, J = 3.47 Hz), 3.78 (2H, t, J = 3.70 Hz), 1.54 (3H, s), 1.34 (1H, s). ^{13}C (D_3CCOCD_3): δ 163.64, 152.00, 142.71, 114.28, 102.67, 93.04, 87.63, 85.14, 81.59, 62.74, 29.55 FAB MS *m*/*z*: 285 (M + 1), 307(M + 23).

2′,3′-*O*-Isopropylidene-5′-*O*-tosyluridine, 2. 2′,3′-*O*-Isopropylideneuridine **1** (1.2 g, 4.22 mmol) was dissolved in dry pyridine (15 mL), and the solution was cooled to 0 °C. Tosyl chloride (2.4 g, 12.67 mmol) was added in small portions. After the addition, the solution which was allowed to warm to room temperature, was stirred overnight, and was quenched with methanol. The resulting mixture was stirred for 30 min, diluted with CH_2Cl_2, and successively washed with brine, aqueous $NaHCO_3$ 5% w/v, and brine. The organic layer was dried on Na_2SO_4, filtered, and concentrated under reduced pressure. The residue was purified by flash column chromatography (cyclohexane/EtOAc: 50/50) to give **2** (1.32 g, 71%) as a white solid. mp = 67 °C. ^{1}H NMR ($CDCl_3$): δ 9.48 (1H, s), 7.75 (2H, d, J = 8.29 Hz), 7.32 (2H, d, J = 7.98 Hz), 7.23 (1H, d, J = 8.13 Hz), 5.71 (1H, d, J = 8.06 Hz), 5.63 (1H, d, J = 2.05 Hz), 4.93 (1H, dd, J = 2.05 Hz, 6.40 Hz), 4.78 (1H, dd, J = 3.63 Hz, 6.40 Hz), 4.32 (1H, m), 4.27 (2H, m), 2.43 (3H, s), 1.53 (3H, s), 1.32 (3H, s). ^{13}C ($CDCl_3$): δ 163.41, 150.10, 145.42, 142.41, 132.59, 130.03, 128.09, 114.79, 102.83, 94.96, 85.16, 84.45, 80.94, 69.45, 27.15, 23.31, 21.81 FAB-MS *m*/*z* 439 (M + 1).

2′,3′-Dioleyl-5′-*O*-tosyluridine, 3. At 0 °C, 2′,3′-*O*-isopropylidene-5′-*O*-tosyluridine **2** (200 mg, 0.46 mmol) was dissolved in 3.5 mL of an aqueous trifluoroacetic acid/H_2O (6/1) solution and stirred for 1 h at 0°C. The solvents were coevaporated with methanol under reduced pressure, and the residue was dried in vacuo. The crude product was dissolved in 10 mL of CH_2Cl_2, and the solution was cooled to 0 °C. Dicyclohexylcarbodiimide (388 mg, 1.88 mmol), (dimethylamino)pyridine (230 mg, 1.88 mmol), and oleic acid (531 mg, 1.88 mmol) were added, and the mixture was stirred at room temperature overnight. DCU was then filtered through a Celite pad, and the filtrate was successively washed with aqueous 2 N HCl and aqueous saturated $NaHCO_3$ solutions. The organic layer was dried on Na_2SO_4, filtered, and evaporated under reduced pressure. The crude product was purified by flash column chromatography (cyclohexane/EtOAc: 90/10 to 70/30) to give **3** (349 mg, 82%) as an oil which solidify upon standing. ^{1}H NMR (DMSO-d_6): δ 7.80 (2H, d, J = 8.37 Hz), 7.62 (1H, d, J = 8.21 Hz), 7.48 (2H, d, J = 8.06 Hz), 5.83 (1H, d, J = 5.05 Hz), 5.70 (1H, d, J = 8.06 Hz), 5.21−5.49 (6H, m), 4.17−4.40 (3H, m), 2.24−2.30 (4H, m), 1.88−2.00 (8H, m), 1.17−1.39 (44H, m), 0.80−0.87 (6H, m) ^{13}C NMR (DMSO-d_6): 171.48, 162.84, 150.098, 145.06, 141.45, 131.83, 130.00, 129.38, 129.37, 127.62, 102.26, 88.16, 78.63, 71.42, 69.03, 33.626, 31.22, 29.02, 28.80, 28.64, 28.58, 28.44, 28.39, 28.3, 26.5, 24.16, 22.02, 21.01, 13.79 FAB MS *m*/*z*: 927 (M + 1), 949 (M + 23).

Tosylate Salt of 2′,3′-Dioleyl-5′-(trimethylammonio)uridine, 4. Anhydrous trimethylamine (1 mL) was transferred to a pressure tube cooled at −50 °C via a syringe. Next, anhydrous acetonitrile (2 mL) and a solution of **3** (200 mg, 0.46 mmol) in dry THF (2 mL) were added. The tube was sealed and heated in an oil bath at 50 °C during 48 h and then cooled to −20 °C and opened. The solvents were evaporated under reduced pressure to give **4** (229 mg, quantitative) as a white solid. ^{1}H NMR (DMSO-d_6): δ 8.06 (1H,d, J = 8.13 Hz), 7.69 (2H, d, J = 8.06 Hz), 7.32 (2H, d, J = 7.90 Hz), 6.09 (1H, d, J = 4.27 Hz), 5.92 (1H, d, J = 9.80 Hz), 5.60−5.67 (1H, m), 5.52 (6H, m), 4.00 (2H, broad s), 3.34 (9H, s), 2.29−2.34 (4H, m), 1.91−2.02 (8H, m), 1.13−1.35 (44H, m), 0.82−0.86 (6H, m). ^{13}C NMR (DMSO-d_6): δ 172.00, 162.93, 150.10, 145.71, 142.35, 137.44, 129.38, 127.92, 125.40, 102.30, 89.13, 74.73, 70.89, 70.41, 66.53, 52.99, 33.25, 31.21, 28.20−29.20, 26.49, 24.20, 22.01, 20.01, 14.00 FAB MS *m*/*z*: 815 (M cation). (**4**+H_2O) Anal. Cal. C, 65.77; H, 9.33; N, 4.18. Found Cal. C, 65.22; H, 9.51; N, 4.61.

Materials. pEGFP-N3 (Clontech) plasmid was amplified in *E. coli* and purified with endotoxin free plasmid preparation kit (Qiagen). Calf thymus DNA (CAS regist. no. 91080-16-9) and ethidium bromide (EB) were obtained from Sigma. EB was weighed, and a stock solution (0.6 mg/mL) was prepared in distilled water and filtered (0.22 μm) water. The buffer solutions were also prepared in distilled and filtered (0.22 μm) water, and the buffers were pH adjusted to 7.4 with 0.1 N NaOH. A stock solution (1 mL) of calf thymus DNA (1 mg/mL) for the fluorescence exclusion assay and for TEM and SAXS studies was dissolved in Tris buffer: 20 mM Tris, 100 mM NaCl, 10 μM EDTA, pH 7.4.

Exclusion Assay. Five micrograms (5 μL of 1 mg/mL solution) of DNA and a varying amount of lipid (dependent on the lipid/DNA ratio required) were diluted to 1000 μL with buffer (Tris buffer: 20 mM Tris, 100 mM NaCl, 10 μM EDTA, pH 7.4). The solutions were mixed on a benchtop vortex and incubated for 60 min at room temperature. Each solution was then diluted to 3 mL with buffer. Immediately prior to the

analysis, 3 μL of an ethidium bromide (EB) solution (0.6 mg/mL, 1.3 mM) was added, the sample was mixed on a benchtop vortex, and the fluorescence was measured (λ_{exc} = 546 nm, λ_{em} = 600 nm; 1 cm path length glass cuvette, slit width 3 nm). The fluorescence was expressed as the percentage of the maximum fluorescence signal when EB was bound to the DNA in the absence of lipid. All assays were run in triplicate.

Transmission Electronic Microscopy. Samples containing lipoplexes were obtained from the mixture of 3 mg/mL of extruded (50 nm) liposome and 1.25 mg/mL DNA solutions (Tris buffer: 20 mM Tris, 100 mM NaCl, 10 μM EDTA, pH = 7.4). Before TEM imaging, the mixture was incubated for 5 h at 4 °C. TEM microscopy experiments were realized on a Philips CM 10 (negative staining with ammonium molybdate 1% in water, Cu/Pd carbon coated grids).

X-ray Diffraction. A typical procedure for lipoplex formation with DOTAU and CT-DNA in a Tris buffer (20 mM Tris, 100 mM NaCl, 10 μM EDTA, pH = 7.4) is described. The samples were prepared from 10 mg/mL of extruded (50 nm) liposome solutions (33 μL) and 10 mg/mL DNA solution (20 μL), in 53 μL of buffer. The mixture was incubated for 5 h at 4 °C and then centrifuged in an eppendorf tube. The supernatant was removed, and the pellet was suspended in 50 μL of buffer. Lipoplexes were studied by placing a small amount of this suspension in a sealed quartz capillary (diameter 1 mm) and then placing the capillary in a sample holder. SAXS measurements were conducted at the University of Montpellier II, Laboratoire GDPC, on a diffraction system equipped with a two-dimensional position-sensitive area detector. The sample-to-detector distance was 30 cm, source: "Rigaku" copper rotating anode working at 40 kV, 100 mA, monochromator confocal Max Flux Osmic optic. Diffraction patterns were obtained using an image plate 2D detector. The low angle reflections were in accordance with Bragg's law $2d \sin \theta = h\lambda$, where λ is the wavelength (1.54 Å), d is the repeat period, h is the number of the diffraction order, and θ is the Bragg angle.

Cell Culture and Transfection. The human epitheloid carcinoma Hela cells and the human breast adenocarcinoma MCF-7 cells were maintained in Dulbecco's modified Eagle's medium (DMEM) supplemented with 10% fetal bovine serum (FBS). Cells were grown on plastic tissue dishes at 37 °C in a 5% CO_2 containing atmosphere. One day before transfection, cells were seeded in 24-well plates (1×10^5 cells/well), to reach 70−90% confluency at the time of the transfection. Just prior to transfection, the complete medium was replaced by serum-free DMEM (350 μL/well). DOTAU and DOTAP solutions at 1 mg/mL in water or Lipofectamine 2000 (Invitrogen) were mixed with DNA (2.5 μg/well) in serum-free medium. Various liposome/DNA ratios were tested. The lipoplexes were formed at room temperature during 20 min and then loaded on cells which were incubated at 37 °C. At 4 h posttransfection, 350 μL of DMEM supplemented with 20% FBS was added to the cells. Cells were analyzed 48 h after transfection.

Flow Cytometry. The transfection efficiency was defined by the expression of the green fluorescent protein (GFP). After transfection, cells were detached from the plastic dish with trypsin/EDTA and then resuspended in PBS. Then single-cell suspensions were analyzed by flow cytometry using a fluorescence-activated cell sorter (FACS) Becton-Dickinson model BD-LSR II device and the FlowJo software.

Proliferation Assay. Proliferation in cell population was defined using the 5-bromo-2′-deoxyuridine (BrdU) labeling and detection kit III (Roche) accordingly to the manufacturer recommendations. Briefly, after 48 h of incubation with the liposomes, the cells cultured in 96-well plates were incubated during 3 h with BrdU, fixed with ethanol, and incubated with an anti-BrdU monoclonal antibody labeled with peroxidase. Upon addition of its substrate, the peroxidase catalyzes a colored reaction which was quantified by the measure of the absorbance at 405 nm.

Scheme 1. Synthetic Route to DOTAU[a]

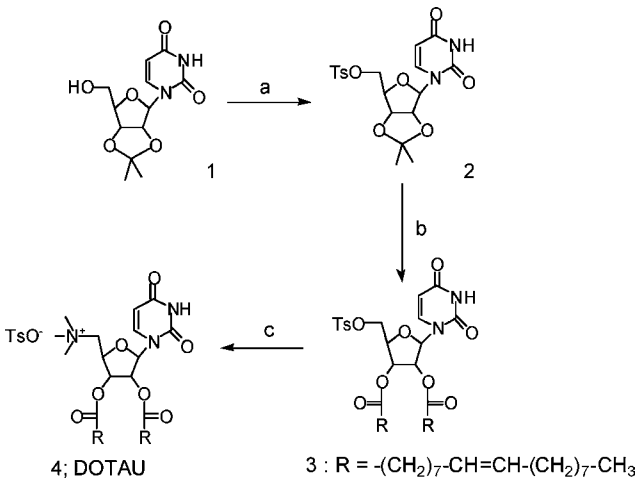

[a] Conditions: (a) TsCl, pyridine, 14 h, rt, 71%; (b) TFA/H_2O, 1 h, 0 °C then oleic acid, DCC, DMAP, CH_2Cl_2, 14 h, rt, 82%; (c) NMe_3.HCl, THF, CH_3CN, 48 h, quant.

RESULTS AND DISCUSSION

Lipid−DNA interactions control many of the steps in the path to efficient gene transfection. There are two primary mechanisms for a lipid to interact with DNA. The lipid can possess one or more cationic charges that interact with the negatively charged phosphate backbone of DNA, as is typical. Alternatively, the lipid possesses a functional group for nonionic interactions with DNA (e.g., Watson−Crick/Hoogsteen hydrogen-bonding and base $\pi-\pi$ stacking) to form a lipid/DNA supramolecular assembly (*17*). Both of these interaction features can be combined in one molecular structure to affect the binding between DNA and the lipid. Thus, we prepared a new lipid possessing a DNA unit (e.g., nucleobase), a cationic ammonium group, and hydrophobic oleyl chains connected by an ester linkage to the ribose hydroxyls. The amphiphilic polar head bears a cationic charge to ensure formation of a stable DNA complex. The cationic charge is required, since our previous studies on a noncationic derivative of **4**, which possesses a phosphocholine group, does not strongly bind DNA (*18*). This is not entirely unexpected, given that the binding constant for a single U−U base−base interaction in a non-hydrogen bonding organic solvent (e.g., $CHCl_3$), is estimated to be less than 10^2 M^{-1} and orders of magnitude weaker than known cationic lipids such as DOTAP binding to DNA in water (*19*). Lipid **4** also possesses a hydrophobic section, which entails two oleyl chains. These chains were selected since previous studies have shown that this chain length and unsaturation was the most efficient for gene transfer in the cationic lipid family (*20*). Herein, we report the synthesis of 2′,3′-dioleyl-5′-(trimethylammonio)-uridine (DOTAU), the lipoplex formed between DNA and DOTAU, cytotoxicity, and successful in vitro gene delivery.

Synthesis. A nucleoside-based cationic lipid derived from uridine was synthesized as shown in Scheme 1. After preparation of the uridine acetonide **1** in acidic conditions, this intermediate was treated with tosyl chloride in pyridine to afford the 5′-tosylate nucleoside derivative, **2**. Hydrolysis of the acetonide protecting group followed by a coupling reaction with oleic acid using the standard reagent DCC to the 2′ and 3′ secondary alcohols of **2** afforded the intermediate **3**. Next, **3** was transferred to a pressure tube and treated for 2 days with trimethylamine in acetonitrile to give the final lipid product, **4**. Importantly,

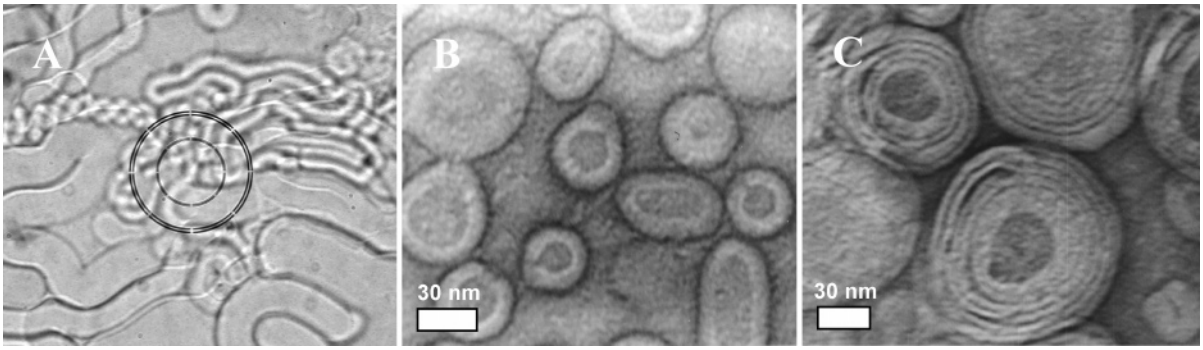

Figure 2. (A) Light micrograph of DOTAU "worm-like" structures upon hydration (internal circle is 14 μm, method A). (B) TEM images of SUV obtained after extrusion of DOTAU through a 50 nm filter. (C) TEM micrograph of DOTAU lipoplexes resulting from the incubation of CT-DNA.

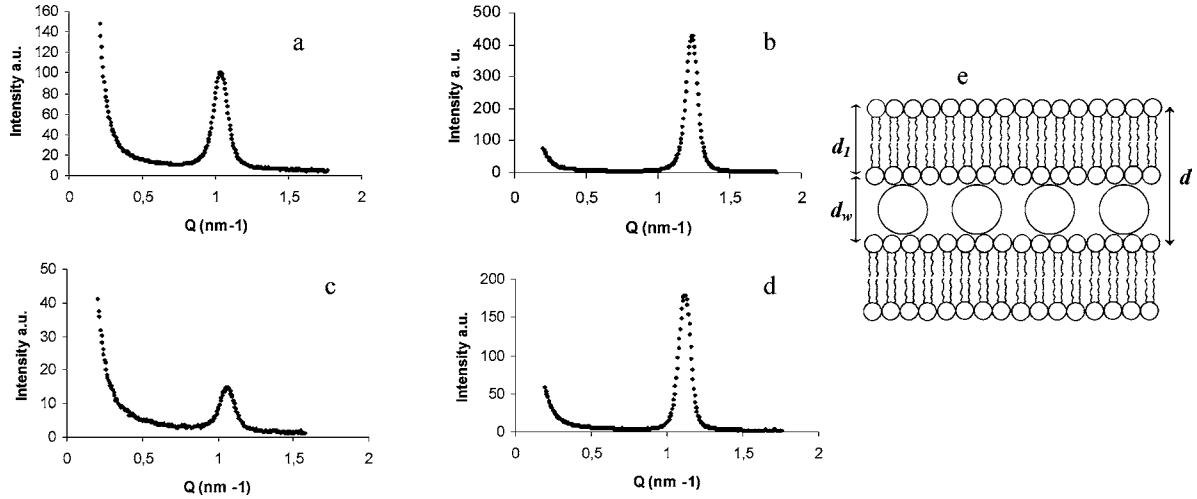

Figure 3. SAXS profiles of (a) CT-DNA/DOTAU, (b) poly A/DOTAU, (c) CT-DNA/DOTAP, and (d) poly A/DOTAP complexes showing Bragg peaks at Q (0.1041 Å^{-1}), Q (0.1241 Å^{-1}), Q (0.1061 Å^{-1}), and Q (0.1131 Å^{-1}), and corresponding lamellar repeat distances d of 6.0 nm, 5.0, 5.9, and 5.6 nm, respectively. SAXS measurements realized on samples containing only DOTAU in the absence of nucleic acids (data not shown) give a repeat period of 4.6 $\pm$ 0.2 nm. (e) Schematic drawing of a CL-DNA complex in the L_α^C phase, displaying a condensed multilamellar structure with DNA rods intercalated between lipid bilayers. The key length scales are the bilayer spacing d and the interaxial DNA spacing dDNA.

the synthetic strategy developed allows easy access in four steps to only one stereoisomer of the lipid.

Supramolecular Assembly Studies. The supramolecular structures formed by **4** in aqueous solution with and without DNA were studied by light and transmission electronic microscopy (TEM). Lipid **4** was observed to self-assemble at room temperature into liposome-like structures in aqueous solutions. Under these conditions, at room temperature, the oleyl chains are in a "fluid" state. This result is consistent with that reported previously for phosphocholine uridine derivatives (*18*). Interestingly, the presence of both a nucleobase and a cationic charge on the molecular structure does not prohibit the formation of lamellar phases. Depending on the procedure used, different sizes of liposomes ranging from 60 nm to 15 μm can be prepared. Light microscopy and TEM experiments were initially performed on samples without DNA. Solid lipid material can be hydrated directly on a glass slide (method A). Under this experimental setup, hydration was followed visually under a microscope and vesicular organization and/or multilamellar systems were observed. A light micrograph of supramolecular organizations forming on a hydrated thin film of DOTAU is shown in Figure 2. Another typical procedure (method B) to form self-assembled structures involves extrusion. In this procedure, 3 mg of the lipid was first dissolved in 1 mL of buffer (Tris buffer: 20 mM Tris, 100 mM NaCl, 10 μM EDTA, pH 7.4). After 20 min of agitation at room temperature, the liposomes were extruded through a polycarbonate filter (50 nm) 10 times at 21 °C to obtain small unilamellar vesicles (SUV). Particle sizing using a QELS showed supramolecular organizations of approximately 60 nm. The presence of this SUV population was confirmed by TEM experiments (see Figure 2b). TEM experiments were also performed on samples prepared with DNA. For this experiment, a SUV population of the lipid was prepared as described above, and then these vesicles were incubated for 5 h in the presence of calf thymus DNA (CT-DNA). TEM micrographs of the DNA−lipid supramolecular assemblies exhibited a typical multilamellar structure called a lipoplex as shown in Figure 2c. The apparent size of the bilayer was estimated to be roughly 6−7 nm, suggesting that the DNA macromolecules are entrapped within the organized structures.

SAXS Studies. To further characterize the molecular organization within the DNA supramolecular assemblies, small-angle X-ray scattering (SAXS) experiments were performed with lipid **4** in the presence of either calf thymus double stranded or polyadenylic acid single strand DNA. For lamellar lipoplexes, the repeat distance of the lipid−DNA multilayer d is related to the membrane thickness d_1 and solvent thickness containing DNA in the intermembrane space d_w via the expression: $d = d_w + d_1$ (Figure 3e). Data collected from several SAXS experiments at room temperature show that CT-DNA/lipid complexes arrange into L_α^C lamellar phases. For reference, supramolecular assemblies of DOTAP/CT-DNA and DOTAU/CT-DNA at 20 °C possess lamellar repeat periods d of 5.9 $\pm$ 0.2 nm and 6.0 $\pm$ 0.2 nm, respectively (Figure 3c and 3a). A priori, since DOTAU possesses a larger polar head volume than DOTAP, such a result indicates that the uracil moiety of DOTAU does not increase the d_w distance. It can be postulated that the uracil is closely associated to the DNA double helix.

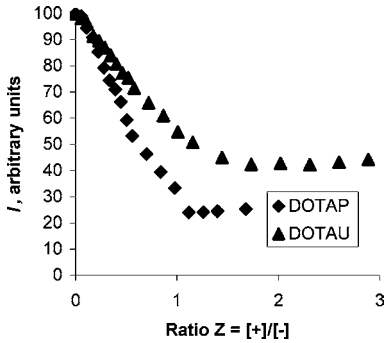

Figure 4. EB exclusion assays with DOTAP and DOTAU in the presence of CT-DNA (fluorescence intensity versus charge ratio).

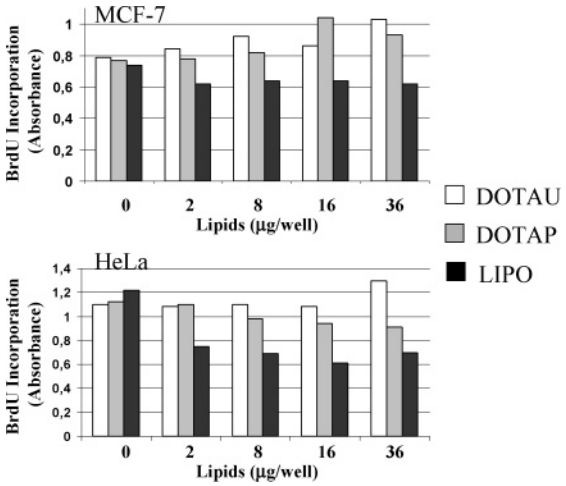

Figure 5. Effects of nucleoside lipids on cell proliferation. MCF-7 (top) and HeLa cells (bottom) were incubated with various quantities of lipids then BrdU was added to the cells.

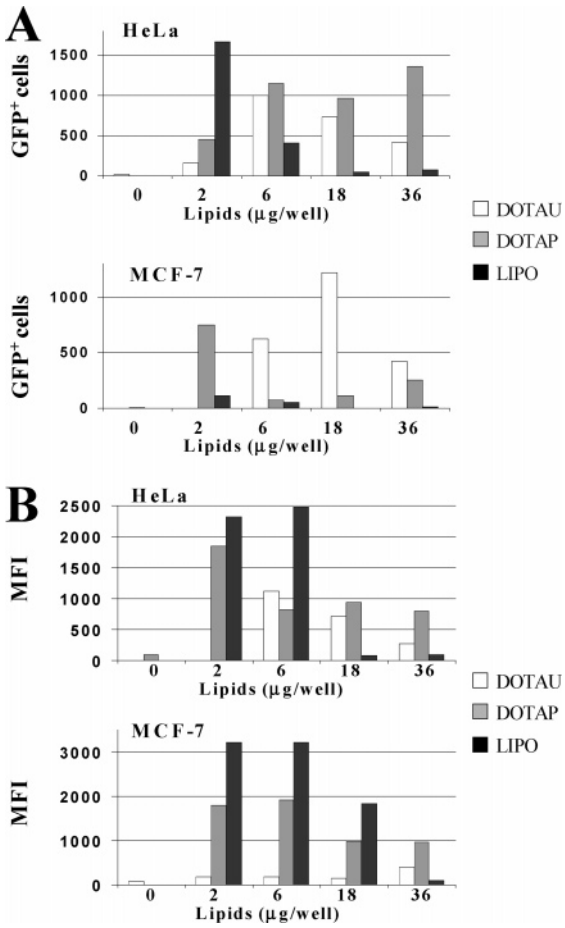

Figure 6. Transfection efficiency of nucleoside lipids. The pEGFP vector (2.5 μg) was transiently transfected into HeLa (top histograms) or MCF-7 cells (bottom histograms) using various quantities of lipotransfectant. After transfection, cells were analyzed by FACS. In part A, the number of GFP positive cells is reported. The MFI of GFP positive cells is reported in part B.

As expected, the distance *d* decreases when a poly A single strand is added to the liposome solutions, indicating more compact structures, which are likely due to smaller d_w distances. Interestingly, the DOTAU/poly A lipoplexes exhibit a repeat period of $d = 5.0 \pm 0.2$ nm (Figure 3b), which is 0.6 nm smaller than DOTAU/poly A lipoplexes ($d = 5.6 \pm 0.2$ nm) (Figure 3d). In that case, the smaller *d* value observed may be attributed to tighter association involving the uracil base of DOTAU and adenine of the poly A single strand. The infrared spectrum of the DOTAU/poly A lipoplex in the KBr pellet shows a carbonyl stretch at 1712 cm^{-1} for the C_2═O uracil-associated stretching vibration and both C═N and C═C ring vibrations characteristic of adenine upon duplexation in RNA (*21*), confirming U−A hydrogen bonding in the DOTAU/poly A complex.

Ethidium Bromide Exclusion Assays. The formation of the DNA−lipid complexes was also studied using an ethidium bromide (EB) exclusion assay (*22*). The binding affinity of the nucleoside-based lipid to CT-DNA was investigated by the fluorescence titration of EB with a premixed solution of DNA and various concentrations of lipid **4**. In the presence of DNA, the fluorescence emission of EB is enhanced relative to that in water as a result of EB intercalation between the DNA base pairs (*23*). The subsequent addition of lipids to the DNA-EB solution results in lipid binding to DNA and displacement of EB from the DNA helix to water, which yields a decrease in fluorescence intensity. As expected, the fluorescence intensity decreases rapidly for DOTAU and DOTAP (Figure 4). The binding curves for DOTAP and DOTAU indicate that 1:1 and 1:1.5 charge complexes are formed, respectively, between DNA and the lipids. The residual fluorescence intensity of 45% measured for DOTAU above a charge ratio of 1.5 indicates that certain portions of DNA are still exposed to EB (*24*). In the same conditions, DOTAP induces a residual fluorescence intensity of 20%. These results would suggest that DOTAU exhibits a lesser ability to condense DNA compare to DOTAP.

Cell Proliferation. The effect on mammalian cell lines proliferation of the nucleoside lipids was compared to a commercially available transfectant, Lipofectamine 2000 (LIPO). As shown in Figure 5, the incorporation of BrdU into HeLa or MCF-7 DNA is not affected by DOTAU or DOTAP, as the absorbance does not decrease in the presence of these cationic lipids. In contrast, in both cell types, the incorporation of BrdU decreases in the presence of Lipofectamine 2000. The effect is much stronger in HeLa cells than in MCF-7 cells as the absorbance is respectively reduced by 50% and 15% in the presence of Lipofectamine 2000. These proliferation assays show that the nucleoside lipids do not inhibit cell proliferation and appear to be less toxic than the commercial Lipofectamine 2000.

Transfection. To investigate the efficiency of DOTAU to transfer DNA into cells, we performed transient transfection assay of mammalian cell lines (HeLa and MCF-7). The transfected DNA is an expression vector (pEGFP) encoding GFP which fluorescence can be detected by FACS. Various quantities of cationic lipids were mixed with 2.5 μg of pEGFP, and then lipoplexes were incubated with HeLa or MCF-7 cells. Single-cell suspensions were analyzed by FACS. The GFP negative and positive gates were defined using the control experiment

carried out in absence of lipoplex. In each experiment 5000 cells were sorted, the results are shown in Figure 6 and in Supporting Information Figure 1. DOTAU is efficient for transfection at a concentration of 6 μg/well. At a concentration of 36 μg/well, approximately 400 cells are GFP positive. With DOTAP, 2 μg/well is the best concentration to transfect MCF-7 cells. Higher quantities are necessary to transfect 20% of Hela cells; however, an equivalent transfection efficiency is obtained with concentrations of 6, 18, and 36 μg/well. In comparison, the commercial Lipofectamine 2000 is efficient only at 2 μg/well, while higher quantities induce a strong decrease of transfection efficiency. Therefore, it appears that the nucleoside lipid is efficient in a wider range of concentration compared to Lipofectamine 2000; likely this feature might be linked to the low cell toxicity of these products. It must be underlined that ongoing transfection studies on nucleolipid analogues have shown similar results with high transfection efficiency only at high charge ratios. The mean fluorescence intensities (MFI) defined for GFP positive cells reveal that the level of GFP expression with a higher MFI value correlated with a high GFP expression. Surprisingly, transfection carried out with DOTAU is characterized by low MFI values (around 1000 for Hela cells and 400 for MCF-7). DOTAP and Lipofectamine 2000 lead respectively to medium MFI values (around 1900) and high MFI values (around 3000) (Figure 6). This study reveals that cells transfected using DOTAU express GFP at a low level. For the moment we can only speculate about the basis of this observation. One possibility is that DOTAU/DNA lipoplex might contain less DNA molecules than the lipoplex formed with DOTAP or Lipofectamine 2000. Another possibility is that the vectors do not reach the nuclei where DNA is transcribed because DOTAU/DNA lipoplex might dissociate in the cytoplasm instead of the nuclei. Only at higher nucleolipid concentrations compared to Lipofectamine 2000 can we observe increased transfection efficiencies. Further studies are in progress to confirm these hypotheses.

CONCLUSION

The results obtained by SAXS, TEM studies, ethidium bromide exclusion assays, and FTIR clearly indicate that the cationic nucleolipid DOTAU interacts with both DNA double helix and polyadenylic acid single strand. Transfection assays of mammalian cell lines (HeLa and MCF-7) reveal that DOTAU can efficiently transfect a high number of cells with a low level of gene expression by cells (compare to DOTAP and Lipofectamine). This aspect could be of interest in the case of gene overexpression; the possibility of this novel nucleolipid to tune gene expression could be exploited when transfection of toxic proteins is needed, for example. The proliferation assays realized on the same cell lines show that the nucleoside lipid DOTAU does not inhibit cell proliferation and is less toxic than the commercial Lipofectamine 2000. In summary, the data reported here suggest that the presence of a nucleoside moiety on the cationic lipid has an impact on the lipoplex efficiency and cell toxicity. The results collected for this biocompatible lipid suggest its potential use as a transfection reagent for mammalian cells and in vitro applications for gene therapy. Further cell biology experiments, such as cellular uptake studies and intracellular trafficking experiments aimed at understanding subcellular localizations of the nucleolipid/DNA complexes, are planned to gain better mechanistic insights into the origin of the contrasting transfection profiles of these novel nucleolipids.

ACKNOWLEDGMENT

This research was supported by the Army Research Office (Grant DAAD 19-02-1-0386) and the "Association pour la Recherche sur le Cancer" (ARC). The authors would like to thank Dr. Philippe Genne and Dr. Nicolas Guilbaud of the Oncodesign company (Dijon, France), Dr. Stephen J. Lee (ARO, US Army), Dr. Carla A. H. Prata (Boston University), Dr. Philippe Dieudonné (University of Montpellier, France), and Prof. Mohamed El Maataoui (University of Avignon, France).

Supporting Information Available: FACS details. This material is available free of charge via the Internet at http://pubs.acs.org.

LITERATURE CITED

(1) Morgan, R. A., and Anderson, W. F. (1993) Human gene therapy. *Annu. Rev. Biochem. 62*, 191−217.

(2) Bennett, C. F., Chiang, M. Y., Chan, H., Shoemaker, J. E., and Mirabelli, C. K. (1992) Cationic lipids enhance cellular uptake and activity of phosphorothioate antisense oligonucleotides. *Mol. Pharm. 41*, 1023−1033.

(3) Debs, R. J., Freedman, L. P., Edmunds, S., Gaensler, K. L., Duzgunes, N., and Yamamoto, K. R. (1990) Regulation of gene expression in vivo by liposome-mediated delivery of a purified transcription factor. *J. Biol. Chem. 265*, 10189−10192.

(4) Marshall E. (2000) FDA Halts All Gene Therapy Trials at Penn. *Science* 287, 565−567.

(5) Felgner, P. L., Gadek, T. R., Holm, M., Roman, R., Chan, H. W., Wenz, M., Northrop, J. P., Ringold, G. M., and Danielsen, M. (1987) Lipofection: a highly efficient, lipid mediated DNA-transfection procedure. *Proc. Natl. Acad. Sci. U.S.A. 84*, 7413−7417.

(6) Leventis, R., and Silvius, J. R. (1990) Interactions of mammalian cells with lipid dispersions containing novel metabolizable cationic lipids. *Biochim. Biophys. Acta 1023*, 124−132.

(7) Gao, X., and Huang, L. (1991) A novel cationic liposome reagent for efficient transfection of mammalian cells. *Biochem. Biophys. Res. Commun. 179*, 280−285.

(8) Rose, J. K., Buonocore, L., and Whitt, M. A. (1991) A new cationic liposome reagent mediating nearly quantitative transfection of animal cells. *Biotechniques 10*, 520−525.

(9) Barthel, F., Remy, J. S., Loeffler, J. P., and Behr, J. P. (1993) Gene transfer optimization with lipospermine-coated DNA. *DNA Cell Biol. 12*, 553−560.

(10) Solodin, I., Brown, C. S., Bruno, M. S., Chow, C. Y., Jang, E. H., Debs, R. J., and Heath, T. D. (1995) A novel series of amphiphilic imidazolinium compounds for in vitro and in vivo gene delivery. *Biochemistry 34*, 13537−13544.

(11) Akao, T., Nakayama, T., Takeshia, K., and Ito, A. (1994) Design of a new cationic lipid with efficient DNA transfection ability. *Biochem. Mol. Biol. Int. 34*, 915−920.

(12) Bichko, V., Netter, H. J., and Taylor, J. (1994) Introduction of hepatitis delta virus into animal cell lines via cationic liposomes. *J. Virol. 68*, 5247−5252.

(13) Gao, X., and Huang, L. (1995) Cationic liposome-mediated gene transfer. *Gene Ther. 2*, 710−22.

(14) Rolland, A. P. (1998) From genes to gene medicines: recent advances in nonviral gene delivery. *Crit. Rev. Ther. Drug Carrier Syst. 15*, 143−98.

(15) Choi, J. S., Lee, E. J., Jang, H. S., and Park, J. S. (2001) New cationic liposomes for gene transfer into mammalian cells with high efficiency and low toxicity. *Bioconjugate Chem. 12*, 108−113 and references herein.

(16) Godbey, W. T., and Mikos, A. G. (2001) Recent progress in gene delivery using non-viral transfer complexes *J. Controlled Release. 72*, 115−125.

(17) Kim, Y. H., Gihm, S. H., Park, C. R., Lee, K. H., Kim, T. W., Kwon, I. C., Chung, H., and Jeong, S. Y. (2001) Structural characteristics of size-controlled self-aggregates of deoxycholic acid-modified chitosan and their application as a DNA delivery carrier. *Bioconjugate Chem. 12*, 932−938.

(18) Moreau, L., Barthélémy, P., El Maataoui, M., and Grinstaff, M. W. (2004)Supramolecular Assemblies of Nucleoside-based Lipids. *J. Am. Chem. Soc. 126*, 7533−7539.

(19) Pozharski, E., and MacDonald, R. C. (2002) Thermodynamics of Cationic Lipid-DNA Complex Formation as Studied by Isothermal Titration Calorimetry. *Biophys J. 83*, No. 1, 556-565.
(20) Regelin, A. E., Fankhaenel, S., Gürtesch, L, Prinz, C., von Kiedrowski, G., Massing, U. (2000) Biophysical and lipofection studies of DOTAP analogs. *Biochim. Biophys. Acta 1464*, 151−164.
(21) Banyay, M., Sarkar, M.; Gräslund, A. (2003) A library of IR bands of nucleic acids in solution *Biophys. Chem. 104*, Issue 2, 477−488.
(22) Geall, A. J., and Blagbrough, I. S. (2000) Rapid and sensitive ethidium bromide fluorescence quenching assay of polyamine conjugate-DNA interactions for the analysis of lipoplex formation in gene therapy. *J. Pharm. Biomed. Anal.* 22, 849−859.
(23) LePecq, J. B., and Paoletti, C. (1967) A fluorescent complex between ethidium bromide and nucleic acids. Physical-chemical characterization *J. Mol. Biol. 27*, 87−106.
(24) Faneca, H., Simões S., and Pedroso de Lima, M. C. (2002) Evaluation of lipid-based reagents to mediate intracellular gene delivery. *Biochim. Biophys. Acta 1567*, 23−33.

BC050162Q

Cationic Nucleoside Lipids derived for Gene Delivery

Supporting Information

Pauline Chabaud,[†] *Michel Camplo,* [†] *Dominique Payet,*[#] *Guillaume Serin,* [¶]

Louis Moreau,[‡] *Philippe Barthélemy,*[*‡] *and Mark W. Grinstaff*[§]

[†] Groupe de Chimie Organique et des Matériaux Moléculaires (UMR-CNRS 6114). Faculté des Sciences de Luminy, case 901, 13288 Marseille cedex 09, France. [‡] Laboratoire de Chimie Biologique UMR A408 Faculté des sciences d'Avignon 33, rue Louis Pasteur, 84000 Avignon, France. [#] Centre d'Immunologie de Marseille Luminy, Parc scientifique de Luminy, 13288 Marseille, cedex 9, France. [¶] Oncodesign, Parc de la Toison d'Or, 28 rue Louis de Broglie, 21000 Dijon, France.[§] Departments of Biomedical Engineering and Chemistry, Boston University, Boston MA 02215, USA.

Figure 1: Facs graphs of MCF-7 (A) and HeLa (B) cells transfected with DOTAU (first lane) DOTAP (second lane) and Lipofectamine 2000 (third lane) at various lipids concentration 0, 2, 6, 18 and 36 μg/well. For all graphs: on the x-axis is reported the fluorescence intensity of GFP, on the y-axis the cell number; in the left gate are the GFP negative cells and in the right gate are the GFP positive cells

DOTAU DOTAP Lipofectamine 2000

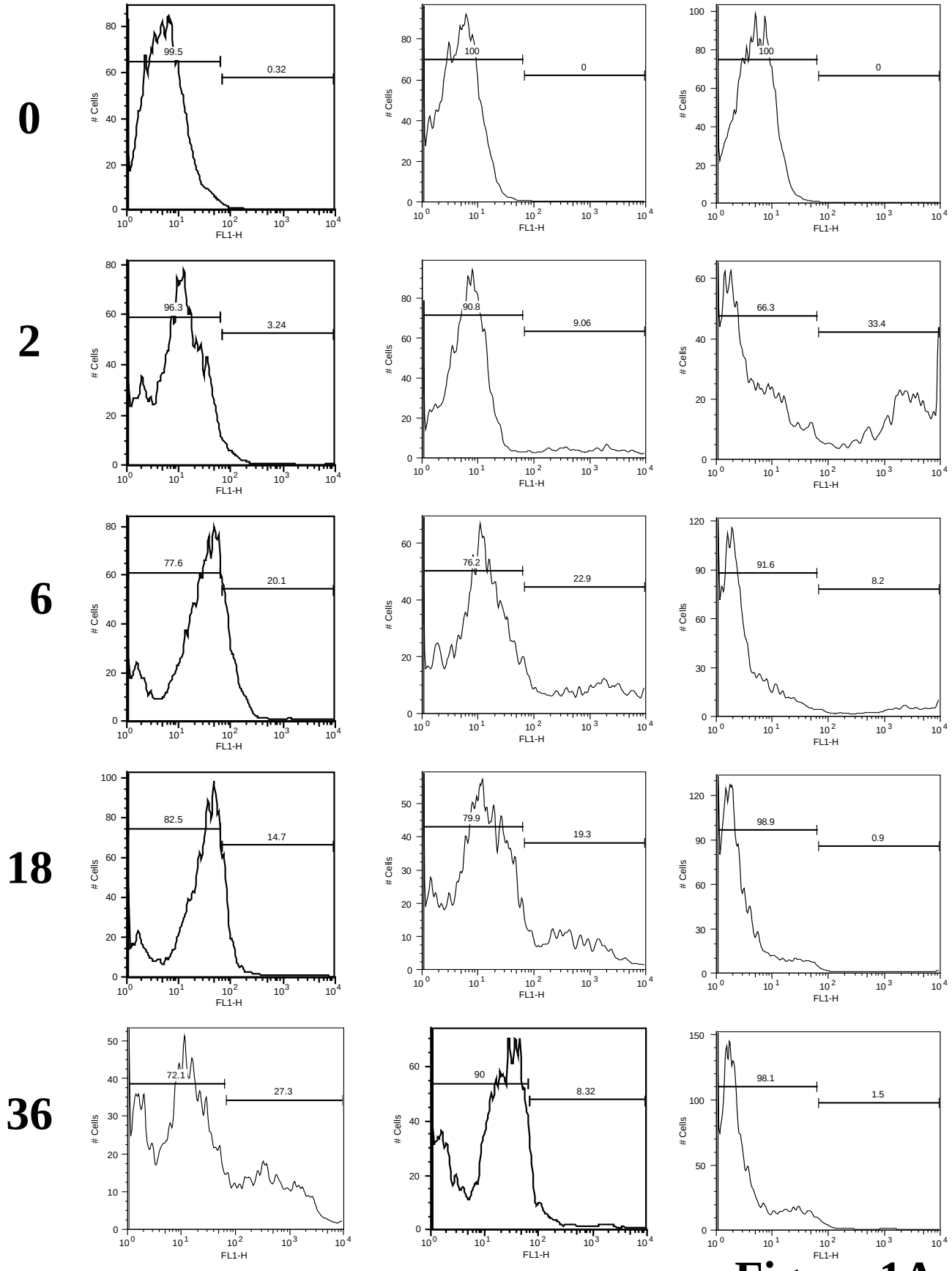

Figure 1A

DOTAU DOTAP Lipofectamine 2000

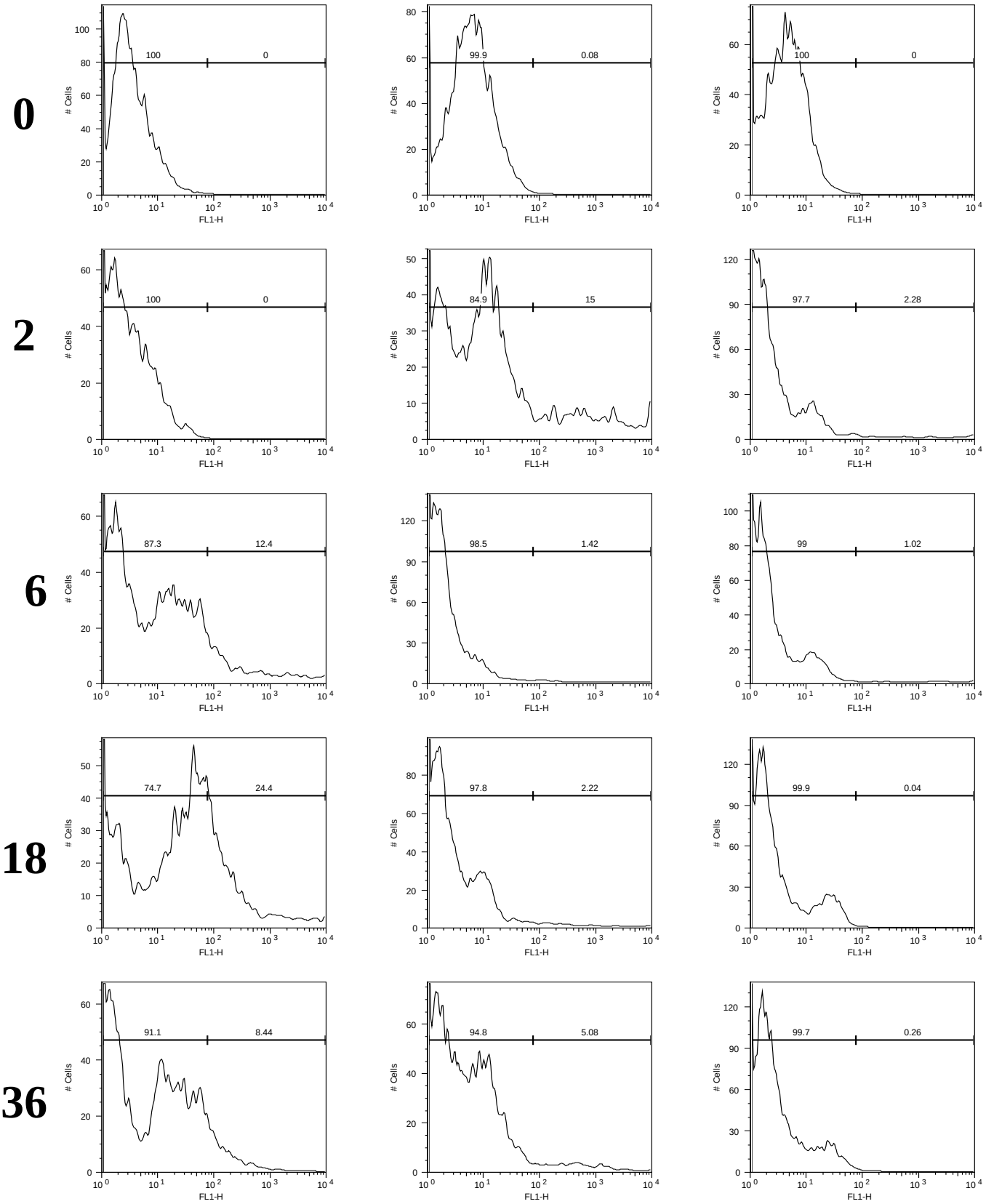

Figure 1B

A Novel Ternary Ligand System Useful for Preparation of Cationic ^{99m}Tc-Diazenido Complexes and ^{99m}Tc-Labeling of Small Biomolecules

Young-Seung Kim, Zhengjie He, Wen-Yuan Hsieh, and Shuang Liu*

Department of Industrial and Physical Pharmaceuticals, Division of Nuclear Pharmacy, Purdue University, 575 Stadium Drive, West Lafayette, Indiana 147907-205. Received September 7, 2005; Revised Manuscript Received December 5, 2005

This report describes a novel ternary ligand system composed of a phenylhydrazine, a crown ether-containing dithiocarbamate (DTC), and a PNP-type bisphosphine (PNP). The combination of three different ligands with ^{99m}Tc results in cationic ^{99m}Tc-diazenido complexes, $[^{99m}Tc(NNAr)(DTC)(PNP)]^+$, with potential radiopharmaceuticals for heart imaging. Synthesis of cationic ^{99m}Tc-diazenido complexes can be accomplished in two steps. For example, the reaction of phenylhydrazine with $^{99m}TcO_4^-$ at 100 °C in the presence of excess stannous chloride and 1,2-diaminopropane-*N*,*N*,*N*′,*N*′-tetraacetic acid (PDTA) results in the $[^{99m}Tc(NNPh)(PDTA)_n]$ intermediate, which then reacts with sodium *N*-(dithiocarbamato)-2-aminomethyl-15-Crown-5 (L4) and *N*,*N*-bis[2-(bis(3-ethoxypropyl)phosphino)ethyl]ethoxyethylamine (PNP6) at 100 °C for 15 min to give the complex, $[^{99m}Tc(NNPh)(L4)(PNP6)]^+$ in high yield (>90%). Cationic complexes $[^{99m}Tc(NNPh)(DTC)(PNP)]^+$ are stable for ≥6 h. Their composition was determined to be 1:1:1:1 for Tc:NNPh:DTC:PNP using the mixed-ligand experiments on the tracer (^{99m}Tc) level and was further confirmed by the ESI-MS spectral data of a model compound $[Re(NNPh)(L4)(L6)]^+$. It was found that both DTCs and bisphosphines have a significant impact on the lipophilicity of their cationic ^{99m}Tc-diazenido complexes. Results from a ^{99m}Tc-labeling efficiency experiment showed that 4-hydrazinobenzoic acid (HYBA) might be useful as a bifunctional coupling agent for ^{99m}Tc-labeling of small biomolecules. However, the ^{99m}Tc-labeling efficiency of HYBA is much lower than that of 6-hydrazinonicotinic acid (HYNIC) with tricine and trisodium triphenylphosphine-3,3′,3″-trisulfonate (TPPTS) as coligands.

INTRODUCTION

Abrams and co-workers first reported the use of arylhydrazines, including 4-hydrazinobenzoic acid (HYBA) and 6-hydrazinonicotinic acid (HYNIC), as bifunctional coupling agents (BFCs) for ^{99m}Tc-labeling of polyclonal IgG (*1*, *2*). Since then, HYNIC has been used for the ^{99m}Tc-labeling of antibodies (*3*, *4*), chemotactic peptides (*5*−*8*), somatostatin analogues (*9*−*14*), antisense oligonucleotides (*15*, *16*), folate receptor ligands (*17*), and polypeptides (*18*, *19*). The advantage of HYNIC is its high labeling efficiency (*20*, *21*). Since HYNIC occupies only one coordination site, coligands are needed to complete the Tc coordination sphere (Figure 1). The use of coligands, such as glucoheptonate and tricine, allows easy modification of hydrophilicity and pharmacokinetics of ^{99m}Tc-labeled biomolecules. The use of HYNIC for ^{99m}Tc-labeling of small biomolecules has recently been reviewed (*22*−*26*).

For the last several years, we have been using a ternary ligand system (Figure 1: HYNIC, tricine, and TPPTS) for the ^{99m}Tc-labeling of chemotactic peptides (*27*, *28*) and LTB_4 receptor antagonists (*29*−*31*), integrin $\alpha_v\beta_3$ antagonists (*32*), and GPIIb/IIIa receptor antagonists (*33*−*37*) in attempt to develop new target-specific radiopharmaceuticals. It was found that this ternary ligand system forms very stable ^{99m}Tc complexes $[^{99m}Tc(HYNIC-BM)(tricine)(TPPTS)]$ (BM = biomolecule) with high specific activity (>20000 mCi/μmol). Through a series of mixed ligand experiments, the composition of these ternary ligand ^{99m}Tc complexes was determined to be 1:1:1:1 for Tc:HYNIC−BM:tricine:TPPTS and has been confirmed by LC-MS at both the tracer (^{99m}Tc) and macroscopic (^{99}Tc) levels (*38*, *39*). Like phosphines, pyridine analogues (Figure 1) were also used as coligands for ^{99m}Tc-labeling of biomolecules (*40*−*42*). Unlike phosphines, pyridine analogues are much smaller and more amendable for further derivatization. Despite the

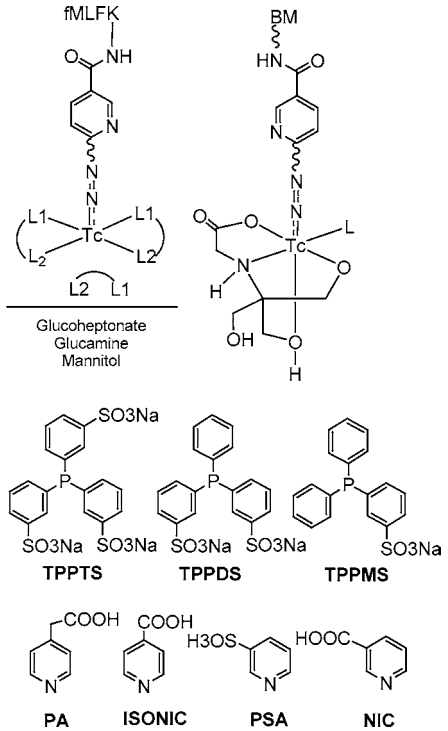

Figure 1. Binary and ternary ligand ^{99m}Tc complexes of HYNIC-conjugated biomolecules (HYNIC−BM). The combination of HYNIC, tricine, and a phosphine or pyridine analogue results in a versatile ternary ligand system that forms ternary ligand ^{99m}Tc complexes $[^{99m}Tc(HYNIC-BM)(tricine)(TPPTS)]$ (BM = biomolecule) with extremely high solution stability.

* To whom correspondence should be addressed. Civil Engineering Building, Room 1275, School of Health Sciences, Purdue University, 550 Stadium Mall Dr., West Lafayette, IN 47907. Phone: 765-494-0236; Fax 765-496-1377; E-mail: lius@pharmacy.purdue.edu.

10.1021/bc0502715 CCC: $33.50 © 2006 American Chemical Society
Published on Web 01/17/2006

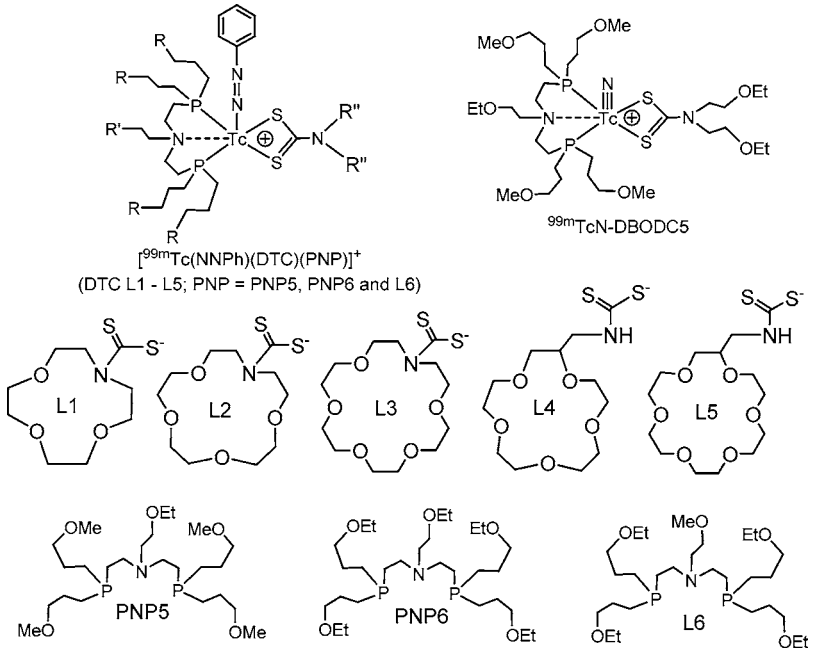

Figure 2. Structures of crown ether-containing dithiocarbamates (crowned DTCs), bisphosphine coligands, ^{99m}TcN-DBODC5, and cationic ^{99m}Tc-diazenido complexes.

success of HYNIC, very little has been reported on the use of HYBA as a BFC for the ^{99m}Tc-labeling of small biomolecules, and the cationic ^{99m}Tc(III)-diazenido complexes as radiotracers for scintigraphic imaging.

It is well-documented that arylhydrazines form highly stable Tc(III)-hydrazino and Tc(III)-diazenido complexes (*43*−*53*). To understand the coordination chemistry of HYNIC with Tc, a number of heteroatom-containing arylhydrazines, such as 2-hydrazinopyridine (HYPY), have been used as model compounds for preparation of their Tc(III) and Re(III) complexes with various coligands (*54*−*62*). It was found that the binding modality and number of HYPY ligands in Tc(III)/Re(III) complexes depend on the nature and availability of coligands. Like HYPY, phenylhydrazine analogues also bind strongly to Tc(III) to form the Tc(III)-diazenido core. Cationic complexes $[^{99}Tc(NNPh\text{-}R)(PP)_2Cl]^+$ (R = H, CH_3, Cl, and NO_2; PP = bisphosphine) have been reported (*45*−*47*). However, it is not clear if they are able to maintain their cationic character in biological system since the chloride ligand may become dissociated to form the dicationic species $[^{99m}Tc(NNPh\text{-}R)(PP)_2]^{2+}$ at the tracer (^{99m}Tc) level.

Recently, we found that the combination of phenylhydrazine with a crown ether-containing dithiocarbamate (DTC) and a PNP bisphosphine (PNP) and resulted in a novel ternary ligand system that forms stable cationic complexes, $[^{99m}Tc(NNPh)(DTC)(PNP)]^+$ (Figure 2: DTC = L1−L5; PNP = PNP5, PNP6, and L6), in high yield. The ether-containing bisphosphines and crown ether-containing DTCs are used for three purposes: (1) to stabilize the ^{99m}Tc-diazenido core, (2) to control the cationic character of the ^{99m}Tc-diazenido complexes, and (3) to balance their lipophilicity so that the heart uptake and target-to-background (T/B) ratios can be optimized systematically. We are interested in HYBA for its potential as a BFC for the ^{99m}Tc-labeling of small biomolecules, and cationic complexes $[^{99m}Tc(NNPh)(DTC)(PNP)]^+$ for their potential as new radiopharmaceuticals in myocardial perfusion imaging.

In this report, we present the use of this ternary ligand system for preparation cationic ^{99m}Tc-diazenido complexes and for the ^{99m}Tc-labeling of HYBA. The main objective of this study is: (1) to explore radiolabeling conditions for preparation of cationic ^{99m}Tc-diazenido complexes, (2) to study the impact of both DTC and bisphosphine coligands on the lipophilicity of cationic ^{99m}Tc-diazenido complexes, and (3) to demonstrate the utility of HYBA as a BFC for the ^{99m}Tc-labeling of small biomolecules. This study represents the first to use the crown ether-containing DTCs for modifying the lipophilicity of cationic ^{99m}Tc radiotracers. Results from biodistribution and imaging studies on cationic ^{99m}Tc-diazenido complexes in rats will be reported in a separate communication elsewhere (*63*).

EXPERIMENTAL SECTION

Instruments and Methods. Chemicals and reagents were purchased from Sigma/Aldrich (St. Louis). NMR (^{1}H and ^{13}C) spectral data were recorded on a 300 MHz Bruker spectrometer, and chemical shifts are reported as δ in ppm relative to TMS. ^{31}P NMR spectra were recorded on a 300 MHz Bruker spectrometer using 85% phosphoric acid as the external reference. Mass spectral data were collected on a Finnigan LCQ mass spectrometer, School of Pharmacy, Purdue University. Elemental analysis was performed by Dr. H. Daniel Lee using a Perkin-Elmer Series III analyzer, Department of Chemistry, Purdue University. *N*,*N*-Bis(ethoxyethyl)dithiocarbamate (DBODC) was prepared according to the literature method (*64*−*66*).

Radio-HPLC Method 1 used a LabAlliance semi-prep HPLC system with a β-Ram IN-US detector, and a Zorbax C_8 column (4.6 mm × 150 mm, 100 Å pore size). The flow rate was 1 mL/min. The mobile phase was isocratic with 30% solvent A (25 mM NH_4OAc buffer, pH = 6.8) and 70% solvent B (methanol) at 0−5 min, followed by a gradient from 70% solvent B at 5 min to and 90% solvent B at 20 min. Radio-HPLC Method 2 was almost identical to method 1 except the mobile phase was isocratic with 30% solvent A (25 mM NH_4OAc buffer, pH = 6.8) and 70% solvent B (methanol) at 0−10 min, followed by a slow gradient from 70% solvent B at 10 min to and 90% solvent B at 20 min. The radio-HPLC Method 3 was slightly different from Method 1, and used an isocratic mobile phase with 50% solvent A (25 mM NH_4OAc buffer, pH = 6.8) and 50% solvent B (methanol) at 0−5 min, followed by a gradient from 50% solvent B at 5 min to and 90% solvent B at 20 min.

General Procedure for Synthesis of the Crown Ether-Containing DTCs. To an ice-cold solution of aminomethyl

crown ether or aza-crown ether (2.0 mmol) and sodium hydroxide (0.08 g, 2.0 mmol) in 6 mL of ethanol was added dropwise carbon disulfide (0.30 g, 2.0 mmol). The mixture was stirred at 0−5 °C for 2−3 h, during which a white precipitate was formed. To the reaction mixture was added 40 mL of diethyl ether with vigorous stirring. The supernatant was decanted and discarded. The white precipitate was washed twice with diethyl ether (2 × 10 mL) and dried under vacuum overnight to give the final product.

Sodium *N*-(Dithiocarbamato)-1-aza-12-crown-4 (L1): The yield was 92%. ^{1}H NMR (D_2O): 4.22 (t, 4H, J = 5.1 Hz), 3.83 (t, 4H, J = 5.1 Hz), and 3.59 (m, 8H). ^{13}C NMR (D_2O, DMSO-d_6 as internal reference): 212.7 (C═S), 71.8, 71.2, 70.8, and 56.8 (crown ether ring carbons). Anal. (Calcd) for $C_9H_{16}NO_3S_2Na$: C, 39.52 (39.54); H, 6.11 (5.90); N, 4.81 (5.12).

Sodium *N*-(Dithiocarbamato)-1-aza-15-crown-5 (L2): The yield was 67%. ^{1}H NMR (D_2O): 4.13 (t, 4H, J = 5.7 Hz), 3.77 (t, 4H, J = 5.7 Hz), and 3.56 (m, 12H). ^{13}C NMR (D_2O, DMSO-d_6 as internal reference): 212.8 (C═S), 71.4, 71.2, 70.8, 69.8, and 57.7 (crown ether ring carbons). Anal. (Calcd) for $C_{11}H_{20}NO_4S_2Na$: C, 41.58 (41.62); H, 6.48 (6.35); N, 4.44 (4.41).

Sodium *N*-(Dithiocarbamato)-1-aza-18-crown-6 (L3): The yield was 84%. ^{1}H NMR (D_2O): 4.19 (t, 4H, J = 6.0 Hz), 3.70 (t, 4H, J = 6.0 Hz), and 3.52 (m, 16H). ^{13}C NMR (D_2O, DMSO-d_6 as internal reference): 205.7 (C═S), 71.9, 70.9 (m), 69.5, 56.7 (crown ether ring carbons). Anal. (Calcd) for $C_{13}H_{24}NO_5S_2Na$: C, 43.12 (43.20); H, 6.92 (6.69); N, 3.77 (3.88).

Sodium *N*-(Dithiocarbamato)-2-aminomethyl-15-crown-5 (L4): The yield was 99%. ^{1}H NMR (D_2O): 3.80−3.72 (m, 2H), 3.64−3.45 (m, 17H), and 3.41 (m, 2H). ^{13}C NMR (D_2O, DMSO-d_6 as internal reference): 214.0 (C═S), 78.1, 72.0, 71.1, 71.0, 70.8, 70.7, 70.6, 70.5, 70.4, 70.3 (crown ether carbons), and 49.4 (CH_2N). Anal. (Calcd) for $C_{12}H_{22}NO_5S_2Na$: C, 41.22 (41.48); H, 6.53 (6.38); N, 3.82 (4.03).

Sodium *N*-(Dithiocarbamato)-2-aminomethyl-18-crown-6 (L5): The yield was 95%. ^{1}H NMR (D_2O): 3.78 (m, 2H), 3.66−3.40 (m, 21H), and 3.37 (m, 2H). ^{13}C NMR (D_2O, DMSO-d_6 as internal reference): δ 197.0 (C═S), 78.5, 72.0, 71.5, 71.0, 70.9, 70.8 (m), 70.2, 70.0 (crown ether carbons), and 47.7 (CH_2N). Anal. (Calcd) for $C_{14}H_{26}NO_6S_2Na$: C, 41.22 (41.25); H, 6.51 (6.43); N, 3.19 (3.44).

General Procedure for Preparation of Bisphosphines (PNP5, PNP6, and L6). N-Substituted Bis(2-Diethoxyphosphorylethyl)amine (1). A mixture of the primary amine (2.0 mmol) and excess diethyl vinylphosphonate (4.4−6.0 mmol) in 10 mL of ethanol was refluxed for 7−12 days. The solvent and excess vinylphosphonate were evaporated under reduced pressure, and the crude product was purified by column chromatography using silica gel as the solid phase and a mixture of CH_2Cl_2−methanol (20:1 = v:v) as the mobile phase.

***N*-Methoxyethyl-*N*,*N*-Bis(2-Diethoxyphosphorylethyl)amine (1a):** The yield was 77%. ^{1}H NMR ($CDCl_3$): 4.09 (m, OCH_2CH_3, 8H), 3.44 (t, J = 5.7 Hz, CH_3OCH_2, 2H), 3.33 (s, CH_3OCH_2, 3H), 2.82 (dt, J = 7.7, 8. Hz, NCH_2CH_2P, 4H), 2.64 (t, J = 5.7 Hz, OCH_2CH_2, 2H), 1.92 (m, NCH_2CH_2P, 4H), 1.32 (t, J = 7.0 Hz, OCH_2CH_3, 12H). ^{13}C NMR ($CDCl_3$): 70.7, 61.4 (d, J = 6.2 Hz), 58.8, 52.2, 46.9, 23.1 (d, J = 136.4 Hz), 16.3 (d, J = 5.8 Hz). ^{31}P NMR ($CDCl_3$): 28.6 ppm.

***N*-Ethoxyethyl-*N*,*N*-Bis(2-Diethoxyphosphorylethyl)amine (1b).** The yield was 74%. ^{1}H NMR ($CDCl_3$): 4.08 (m, OCH_2CH_3, 8H), 3.49 (t, J = 5.7 Hz, $CH_3CH_2OCH_2$, 2H), 3.47 (q, J = 7.0 Hz, $CH_3CH_2OCH_2$, 2H), 2.81 (dt, J = 7.7, 8.1 Hz, NCH_2CH_2P, 4H), 2.64 (t, J = 5.7 Hz, OCH_2CH_2, 2H), 1.93 (m, NCH_2CH_2P, 4H), 1.32 (t, J = 7.0 Hz, OCH_2CH_3, 12H), 1.18(t, J = 7.0 Hz, $CH_3CH_2OCH_2$, 3H). ^{13}C NMR ($CDCl_3$): 68.7, 66.4, 61.4 (d, J = 6.2 Hz), 52.3, 47.1, 23.3 (d, J = 136.3 Hz), 16.4 (d, J = 5.8 Hz), 15.1. ^{31}P NMR ($CDCl_3$): 28.7 ppm.

N-Substituted Bis(2-Phosphinoethyl)amine (2). *All manipulations were carried out under nitrogen atmosphere using standard Schlenk line.* A solution of the bisphosphonate **1** (2.0 mmol) in 5 mL of anhydrous THF was added dropwise into a stirred suspension of lithium aluminum hydride (8.0 mmol) in 5 mL of anhydrous THF. After the initial exothermal reaction subsided, the reaction mixture was heated under reflux for 16 h. The reaction mixture was cooled to room temperature, and 20 mL of ether was added into it. The excess lithium aluminum hydride was hydrolyzed by cautious addition of 3% sodium hydroxide solution (2−3 mL). The ethereal layer was separated from the precipitate via cannula transfer. Another 20 mL of ether was used to wash the precipitate. The combined ether layers were dried over anhydrous sodium sulfate, then filtered, and evaporated to afford the desired product **2** as colorless liquid. This crude product was used in next step reaction without further purification and characterization.

N-Substituted *N*,*N*-Bis[2-(Bis(3-Ethoxypropyl)phosphino)-ethyl]amine (PNP5, PNP6, and L6). Bisphosphine **2** (1.0 mmol), allylethyl or allylmethyl ether (9.0 mmol), and VAZO 67 (1,1′-azobis-(cyclohexanecarbonitrile), 0.2 mmol) were dissolved in 5 mL of ethanol, and the resulting mixture was heated to reflux for 20 h. Volatiles were removed under vacuum, and the residue was mixed thoroughly with 3 mL of 6 M hydrochloric acid. The resulting mixture was extracted twice with diethyl ether (2 × 10 mL), and the ethereal layer was discarded via cannula transfer. The pH of the aqueous layer was adjusted >12 using 20% (w/w) sodium hydroxide solution. The aqueous layer was extracted three times with ether (3 × 10 mL). The combined ether layers were dried over anhydrous sodium sulfate, filtered, and then acidified with 4 M hydrogen chloride in dioxane until there was no more white precipitate. The supernant solution was separated from the precipitate and discarded. The precipitate was washed with diethyl ether (2 × 10 mL) and dried under vacuum to afford the desired product (PNP5, PNP6, and L6) as a colorless viscous oil. Since all bisphosphines are extremely air-sensitive under basic conditions, they were isolated as the hydrochloride salts, and stored under inert atmosphere all the time.

***N*-Ethoxyethyl-*N*,*N*-bis[2-(bis(3-methoxypropyl)phosphino)ethyl]amine (PNP5).** The yield was 84%. ^{1}H NMR ($CDCl_3$): 4.10−3.20 (m, $CH_3CH_2OCH_2CH_2N$, NCH_2CH_2P, CH_2OCH_3, 22H), 3.35(s, $PCH_2CH_2CH_2OCH_3$, 12H), 2.63 (m, $PCH_2CH_2CH_2$, 8H), 1.99 (m, $PCH_2CH_2CH_2$, 8H), 1.18(t, J = 7.0 Hz, $CH_3CH_2OCH_2CH_2N$, 3H). ^{31}P NMR ($CDCl_3$): 10.4 ppm. ESI-M: m/z = 497 ($[M + H]^+$).

***N*-Ethoxyethyl-*N*,*N*-bis[2-(bis(3-ethoxypropyl)phosphino)-ethyl]amine (PNP6).** The yield was 74%. ^{1}H NMR ($CDCl_3$): 4.10−3.20 (m, $CH_3CH_2OCH_2CH_2N$, NCH_2CH_2P, $CH_2OCH_2CH_3$, 30H), 2.62 (m, $PCH_2CH_2CH_2$, 8H), 2.05 (m, $PCH_2CH_2CH_2$, 8H), 1.20 (t, J = 6.9 Hz, OCH_2CH_3, 12H), 1.18 (t, J = 7.0 Hz, $CH_3CH_2OCH_2CH_2N$, 3H). ^{31}P NMR ($CDCl_3$): 11.5 ppm. ESI-M: m/z = 553 ($[M + H]^+$).

***N*-Methoxyethyl-*N*,*N*-bis[2-(bis(3-ethoxypropyl)phosphino)ethyl]amine (L6):** The yield was 68%. ^{1}H NMR ($CDCl_3$): 4.00−3.20 (m, OCH_2CH_2N, NCH_2CH_2P, $CH_2OCH_2CH_3$, 28H), 3.38 (s, CH_3O, 3H), 2.72 (m, $PCH_2CH_2CH_2$, 8H), 2.01 (m, $PCH_2CH_2CH_2$, 8H), 1.20 (t, J = 7.0 Hz, OCH_2CH_3, 12H). ^{31}P NMR ($CDCl_3$): 12.0 ppm. ESI-MS: m/z = 539 ($[M + H]^+$).

General Procedure for Preparation of ^{99m}Tc-Diazenido Complexes. To a 5 mL vial was added 1.0 mL of 0.5 M NH_4-OAc buffer containing PDTA (5 mg/mL) and arylhydrazine (1 mg/mL), followed by addition of 0.5 mL $Na^{99m}TcO_4$ solution (~20 mCi) in saline, and 20 μL $SnCl_2$ solution (1 mg/mL) in 1.0 N HCl. The reaction mixture was heated at 100 °C for 10 min to form the ^{99m}Tc-diazenido intermediate. To the reaction mixture above was added 0.5 mL of the solution containing

the DTC chelator (2 mg) and bisphosphine (2 mg). The vial was heated at 100 °C for another 10−15 min. After cooling to room temperature, a sample of the resulting solution was analyzed by ITLC and radio-HPLC. In all cases, the ^{99m}Tc-colloid formation was minimal.

Determination of Log *P* Values of Cationic ^{99m}Tc-Diazenido Complexes. The Log *P* values of cationic ^{99m}Tc-diazenido complexes were determined using the following procedure: the cationic ^{99m}Tc-diazenido complex was prepared and purified by HPLC. HPLC mobile phases were evaporated under reduced pressure and the residue was dissolved in a mixture of equal volume (3 mL:3 mL) *n*-octanol and 25 mM phosphate buffer (pH = 7.4). After vertex for at least 20 min, samples (in triplets) from *n*-octanol and aqueous layers were counted in a gamma counter (Beckman Gama 8000). The *P* values was calculated using the following equation: P = (activity concentration in *n*-octanol)/(activity concentration in aqueous layer). For comparison, we also determined the log *P* values of ^{99m}Tc-Sestamibi and ^{99m}TcN-DBODC5.

Solution Stability of Cationic ^{99m}Tc-Diazenido Complexes. For the solution stability in kit matrix, cationic ^{99m}Tc-diazenido complexes were prepared and were analyzed by radio-HPLC at 0, 1, 2, 3, and 6 h post-labeling. For the stability in diluted solutions, the cationic ^{99m}Tc-diazenido complex was prepared, and the resulting solution was diluted to 10−20 μCi/mL. Samples of the dilute solution were analyzed by radio-HPLC at 0, 1, 2, 3, and 6 h. For the cysteine challenging experiment, the cationic ^{99m}Tc-diazenido complex was prepared, and the reaction mixture was mixed with an equal volume of a cysteine solution (1 mg/mL). Samples of the resulting solution were analyzed by radio-HPLC at 0, 1, 2, 3, and 6 h.

Composition Studies of Cationic ^{99m}Tc-Diazenido Complexes. Number of DTCs. To a 5 mL vial was added 1.0 mL of 0.5 M NH_4OAc buffer containing PDTA (5 mg/mL) and phenylhydrazine (1 mg/mL), 0.5 mL of $Na^{99m}TcO_4$ solution (∼10 mCi), and 20 μL $SnCl_2$ solution (1 mg/mL) in 1.0 N HCl. The mixture was heated at 100 °C for 10 min. To the mixture above was added DBODC (2 mg), L4 (2 mg), L5 (2 mg), and PNP5 (2 mg) in 0.5 mL of 50% ethanol. The vial was heated at 100 °C for 15 min. After cooling to room temperature, a sample of the resulting solution was analyzed by radio-HPLC.

Number of Bisphosphines. To a 5 mL vial was added 1.0 mL of 0.5 M NH_4OAc buffer containing PDTA (5 mg/mL) and phenylhydrazine (1 mg/mL), 0.5 mL of $Na^{99m}TcO_4$ solution (∼10 mCi), and 20 μL $SnCl_2$ solution (1 mg/mL) in 1.0 N HCl. The mixture was heated at 100 °C for 10 min. To the mixture above was added L4 (2 mg), PNP5 (2 mg), and PNP6 (2 mg) in 0.5 mL of 50% ethanol. The vial was heated at 100 °C for another 15 min. After cooling, a sample of the resulting solution was analyzed by radio-HPLC.

^{99m}Tc-Labeling Efficiency of HYBA. To a 5 mL vial was added 1.0 mL of 0.5 M NH_4OAc buffer containing PDTA (5 mg/mL) and HYBA (1−100 μg/mL), followed by addition of 0.5 mL $Na^{99m}TcO_4$ solution (∼10 mCi) in saline, and 20 μL $SnCl_2$ solution (1 mg/mL) in 1.0 N HCl. The mixture was heated at 100 °C for 10 min. To the mixture were added L4 (2 mg) and PNP6 (2 mg) in 0.5 mL of saline. The vial was heated at 100 °C for 15 min. After cooling to room temperature, a sample of the resulting mixture was analyzed by radio-HPLC.

Preparation of [Re(NNPh)(L4)(L6)]$^{+}$. $[ReCl_2(NNPh)(PPh_3)_2(CH_3CN)]$ was prepared directly from $[^nNBu_4][ReO_4]$ according to the literature method (*67*). To a 10 mL vial were added $[ReCl_2(NNPh)(PPh_3)_2(CH_3CN)]$ (18.5 mg, 0.02 mmol), 2.0 mL of chloroform, 1.0 mL of 0.5 M NH_4OAc buffer (pH = 5.0), and 2 mL of ethanol solution containing L6 (25 mg, 0.046 mmol). The reaction mixture was heated at 100 °C for 10 min to form the $[ReCl_2(NNPh)(L6)]$ intermediate. To the reaction mixture above was added 0.5 mL of the 0.5 M NH_4OAc buffer solution containing L4 (20 mg, 0.062 mmol). The vial was heated at 100 °C for another 10−15 min. After removal of volatiles, the residue was dissolved in 6 mL of methanol and water mixture (70:30 = v:v). The resulting solution was subjected to HPLC purification. The HPLC method used a LabAlliance semi-prep HPLC system equipped with a LabAlliance UV/visible detector (model 500, λ = 254 nm) and a Zorbax C_{18} semi-prep column (9.4 mm × 250 mm, 300 Å pore size). The flow rate was 2.5 mL/min. The mobile phase was isocratic with 30% solvent A (water) and 70% solvent B (methanol) at 0 − 5 min, followed by a gradient from 70% solvent B at 5 min to and 90% solvent B at 20 min. The fraction at ∼15 min due to the cationic complex $[Re(NNPh)(L4)(L6)]^+$ was collected. The combined fractions were combined and lyophilized to give a brown oil. The HPLC concordance experiment was performed by co-injecting HPLC-purified $[Re(NNPh)(L4)(L6)]^+$ and $[^{99m}Tc(NNPh)(L4)(L6)]^+$.

RESULTS AND DISCUSSION

^{99m}Tc-Diazenido Complex Design. It is well-documented that arylhydrazines form highly stable Tc(III)-diazenido complexes when appropriate coligands are used (*43*−*53*). Since aryldiazenido is monodentate, triphenylphosphine (Ph_3P), *N*,*N*′-bis(salicylidene)ethane (salen), *N*,*N*-dimethyldithiocarbamate (DMDC), and 1,2-bis(diphenylphosphino)ethane (DPPE) have been used as coligands to stabilize the Tc(III)-diazenido core. For example, the complex $[^{99m}Tc(NNPh)(DPPE)_2Cl]^+$ has a slight distorted octahedral coordination geometry with the PhNN and chloride occupying the *trans*-axial sites, and the P-donors from two DPPTE coligands occupying four equatorial sites. $[^{99m}Tc(NNC_6H_4)(salen)(Ph_3P)]^+$ also has a distorted octahedral coordination geometry with salen and Ph_3P as coligands (*48*). In the complex $[^{99}Tc(NNC_6H_4Cl)(DMDC)_2(Ph_3P)]$, PhNN and Ph_3P are monodentate, and two DMDC chelators occupy the other four remaining coordination sites of technetium (*46*).

Recently, Duatti's group reported a series of cationic ^{99m}Tc-nitrido complexes with ether-containing DTC and PNP-type bisphosphine coligands (*64*−*66*). It was found that the cationic complex $[ReN(DEDC)(PNP2)]^+$ (DEDC = *N*,*N*-diethyldithiocarbamate; PNP2 = bis[(2-diphenylphosphino)ethyl]methoxyethylamine) had a distorted octahedral coordination geometry with the amine-N atom weakly bonded to the Tc (*64*, *66*). The combination of DTC and bisphosphine coligands is critical in maintaining the cationic character of Tc-nitrido complexes. On the basis of these findings, we propose that the combination use of phenylhydrazine, a bisphosphine, and a DTC might result in a ternary ligand system that forms cationic complexes, $[^{99m}Tc(NNPh)(DTC)(PNP)]^+$ (Figure 2: DTC = L1−L5; and PNP = PNP5, PNP6, and L6), with potential as radiopharmaceuticals for heart imaging. This new ternary ligand system may also be useful for the ^{99m}Tc-labeling of small biomolecules.

Choice of DTCs and Bisphosphines. During the development of ^{99m}Tc-Sestamibi, it was discovered that ether groups in isonitriles greatly improved biodistribution properties of the radiotracer (*68*−*72*). Studies on the Q-series of cationic ^{99m}Tc complexes also show that ether groups from the phosphine coligands improve excretion kinetics of radiotracers (*73*−*75*). The results from biodistribution studies showed that ether groups from DTC and bisphosphine coligands play a significant role in heart uptake and excretion kinetics of cationic ^{99m}Tc-nitrido complexes (*76*−*78*). For example, ^{99m}Tc-N-DBODC5 (Figure 1) is rapidly extracted by the rat myocardium and is retained in the heart for a long time. The liver activity is almost completely eliminated into intestine at 60 min postinjection. The heart/liver ratio was higher than that of ^{99m}Tc-Sestamibi and ^{99m}Tc-Tetrofosmin (*76*, *77*). In contrast, ^{99m}TcN-DBODC6 has a lower

Scheme 1. Synthesis of Crowned DTCs (L1−L5)

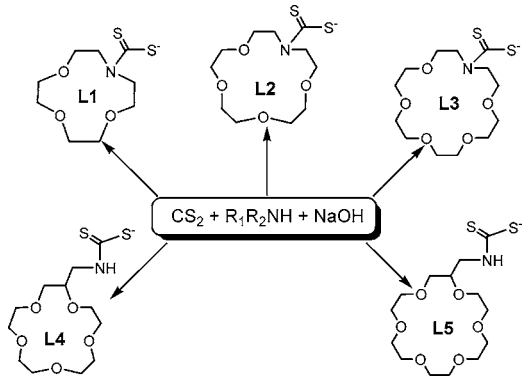

Scheme 2. Synthesis of the Bisphosphines (PNP5, PNP6, and L6)

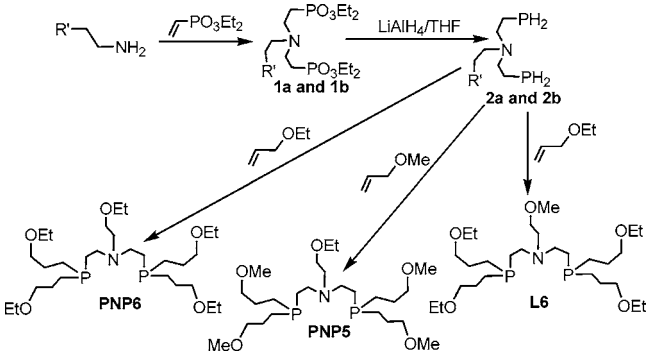

heart uptake and much lower target-to-background (T/B) ratios than ^{99m}TcN-DBODC5 due to its high lipophilicity (*76, 77*), even though they share the same bidentate DBODC chelator. These results clearly show that it is possible to design cationic ^{99m}Tc radiotracers with a high heart uptake and fast liver clearance by *balancing* their lipophilicity with the ether- or crown ether-containing groups. That is why in this study we use the ether-containing bisphosphines (PNP5, PNP6, and L6) and the crown ether-containing DTCs (L1−L5) as coligands to prepare cationic complexes $[^{99m}Tc(NNPh)(DTC)(PNP)]^+$ (DTC = L1−L5; PNP = PNP5, PNP6, and L6).

Synthesis of L1 − L5. The crown containing DTCs (L1−L5) were synthesized according to Scheme 1. Aza-crown ethers (1-aza-12-crown-4, 1-aza-15-crown-5, 1-aza-18-crown-6) and aminomethyl-crown ethers (2-aminomethyl-15-crown-5 and 2-aminomethyl-18-crown-6) are commercially available from Aldrich/Sigma. The aza-crown or aminomethyl-crown ether reacts with carbon disulfide in the presence of sodium hydroxide to give the corresponding DTC as its sodium salt in high yield (80−90%). L1−L5 were purified by recrystallization from a mixture of ethanol and diethyl ether and were characterized by NMR (^{1}H and ^{13}C) and elemental analysis.

Synthesis of PNP5, PNP6, and L6. PNP5, PNP6, and L6 were prepared according to the literature method (*64, 66*) using 2-methoxyethylamine and 2-ethoxyethylamine as starting materials (Scheme 2). The primary amine reacted with excess diethyl vinylphosphonate to produce the bisphosphonate intermediate $ROCH_2CH_2N(CH_2CH_2PO_3Et_2)_2$ (**1a**: R = Me, and **1b**: R = Et), which was then reduced with $LAlH_4$ in anhydrous THF to afford the bisphosphine intermediate $ROCH_2CH_2N(CH_2CH_2PH_2)_2$ (**2a**: R = Me, and **2b**: R = Et). The reaction of **2** with excess allylmethyl or allylethyl ether in the presence of a radical initiator, such as VAZO 67, produced PNP5, or PNP6 and L6. Since they are very air-sensitive under basic conditions, all PNP-type bisphosphines (PNP5, PNP6, and L6) were isolated as hydrochloride salts, and should be stored under inert atmosphere at all times. PNP5, PNP6, and L6 were characterized by NMR (^{1}H and ^{31}P) and ESI-MS.

Synthesis and Characterization of Cationic ^{99m}Tc-Diazenido Complexes. Cationic complexes $[^{99m}Tc(NNPh)(DTC)(PNP)]^+$ (DTC = L1−L5; PNP = PNP5, PNP6, and L6) were prepared according to Scheme 3. First, $^{99m}TcO_4^-$ reacted with phenylhydrazine in the presence of excess stannous chloride and PDTA to give the $[^{99m}Tc(NNPh)(PDTA)]^-$ intermediate, which reacted with a DTC and a PNP to form the cationic complex $[^{99m}Tc(NNPh)(DTC)(PNP)]^+$ (DTC = L1−L5; PNP = PNP5, PNP6, and L6), which were analyzed using reversed HPLC method. The HPLC retention times are listed in Table 1. Figure 3 shows a typical HPLC chromatograms for cationic complexes $[^{99m}Tc(NNPh)(L2)(PNP6)]^+$ and $[^{99m}Tc(NNPh)(L4)(PNP6)]^+$. The RCP was 80−90% with one or two small peaks (5−12%) as the main radioimpurities (Figure 3) for the synthesized cationic ^{99m}Tc-diazenido complexes. The amount of radioimpurities is largely dependent upon the quality of the bisphosphine while changing the DTC has little impact on the amount of these radioimpurities. Therefore, it is reasonable to believe that the radioimpurities are caused by the partial oxidation of the bisphosphine during preparation.

We tried to use HYPY to replace phenylhydrazine for preparation of cationic complexes $[^{99m}Tc(HYPY)(L4)(L)]^+$ (L = PNP5, PNP6, and L6) and found that the resulting mixture often contains several ^{99m}Tc-containing species (Figure SI) most likely due to the fact that HYPY itself is a bidentate chelator and may compete with bisphosphines as coligands for ^{99m}Tc-bonding. In addition, HYPY has several bonding modalities with the Tc(III) and Re(III) (*61, 62*).

PDTA is a transferring ligand to stabilize the $[^{99m}Tc(NNPh)(PDTA)]^-$ intermediate. The PDTA concentration in each vial can be varied from 2 to 10 mg/vial. Lower PDTA level (<1.0 mg/vial) often results in a significant amount of ^{99m}Tc-colloid. PDTA can be replaced by other polyaminocarboxylates, such as ethylenediamine-*N*,*N*-diacetic acid (EDDA), ethylenediamine-*N*,*N*,*N*′,*N*′-tetraacetic acid (EDTA), and *N*-(2-hydroxyethyl)-ethylenediamine-*N*,*N*′,*N*′-triacetic acid (HEDTA). However, replacing PDTA with tricine always results in formation of several ^{99m}Tc-containing species in the reaction mixture (Figure SII).

The new ternary ligand system is composed of three different ligands (phenylhydrazine, DTC, and a PNP bisphosphine), all of which can influence the yield and purity of their cationic ^{99m}Tc-diazenido complexes. For example, the DTC and bisphosphine levels in each vial can be varied from 0.5 to 5.0 mg/vial. In all cases, cationic complexes $[^{99m}Tc(NNPh)(DTC)(PNP)]^+$ (DTC = L1−L5; PNP = PNP5, PNP6, and L6) can be prepared in high yield (RCP = 80−90%). Lower DTC and bisphosphine levels (<0.1 mg/vial) often result in incomplete reaction with the $[^{99m}Tc(NNPh)(PDTA)]^-$ intermediate. The level of phenylhydrazine can be varied in the range of 0.5−2.0 mg using PDTA as the transferring ligand. Lower phenylhydrazine concentration will results in a significant amount of more hydrophilic radioimpurities as demonstrated by the radiolabeling efficiency experiments.

The ^{99m}Tc-Labeling Efficiency of HYBA. For HYBA to be useful as a BFC, it must show a high ^{99m}Tc-labeling efficiency. In this study, we used PDTA (5 mg/vial) as the transferring ligand. The concentration of DTC and bisphosphine coligands was 2.0 mg/vial. It was found that the RCP for $[^{99m}Tc(HYBA)(L4)(PNP6)]$ was still >90% when the HYBA concentration is 100 μg/vial (6.85×10^{-7} mole, FW = 146) for 10 mCi of $^{99m}TcO_4^-$ ($\sim 7 \times 10^{-11}$ mole of ^{99m}Tc and ^{99}Tc for 24 h generator). The HYBA/Tc ratio is about 10000:1 under the radiolabeling conditions used in this study. This specific activity (~15 Ci/mmol) is much lower than that obtained with

Scheme 3. Synthesis of Cationic Complexes [^{99m}Tc(NNPh)(DTC)(PNP)]$^+$ (DTC = L1−L5; PNP = PNP5, PNP6, and L6)

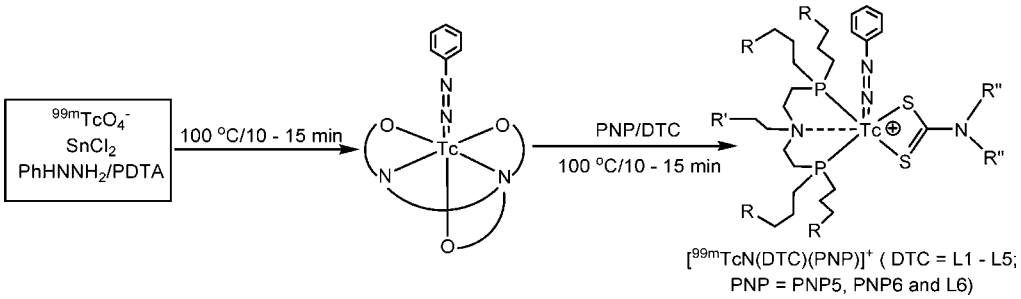

Table 1. The RCP Data and Radio-HPLC Retention Times of Cationic ^{99m}Tc-Nitrido Complexes

compound	radiochem purity (%)	HPLC retention time (min)[a]	log *P* value
^{99m}Tc−Sestamibi	>98	16.5	1.29 ± 0.15
^{99m}TcN-DBODC5	>90	16.2	1.10 ± 0.07
[^{99m}Tc(NNPh)(L1)(PNP5)]$^+$	>90	10.7	0.11 ± 0.05
[^{99m}Tc(NNPh)(L2)(PNP5)]$^+$	>90	10.5	−0.22 ± 0.04
[^{99m}Tc(NNPh)(L3)(PNP5)]$^+$	>90	9.9	−0.24 ± 0.07
[^{99m}Tc(NNPh)(L4)(PNP5)]$^+$	>90	10.5	−0.38 ± 0.07
[^{99m}Tc(NNPh)(L5)(PNP5)]$^+$	>90	9.0	−0.58 ± 0.06
[^{99m}Tc(NNPh)(L1)(PNP6)]$^+$	>90	16.7	1.39 ± 0.01
[^{99m}Tc(NNPh)(L2)(PNP6)]$^+$	>90	16.3	1.33 ± 0.22
[^{99m}Tc(NNPh)(L3)(PNP6)]$^+$	>90	15.3	1.13 ± 0.01
[^{99m}Tc(NNPh)(L4)(PNP6)]$^+$	>90	16.5	1.34 ± 0.03
[^{99m}Tc(NNPh)(L5)(PNP6)]$^+$	>90	14.6	0.91 ± 0.03
[^{99m}Tc(NNPh)(L1)(L6)]$^+$	>85	16.7	1.35 ± 0.20
[^{99m}Tc(NNPh)(L2)(L6)]$^+$	>85	16.2	1.04 ± 0.01
[^{99m}Tc(NNPh)(L3)(L6)]$^+$	>85	15.8	0.92 ± 0.05
[^{99m}Tc(NNPh)(L4)(L6)]$^+$	>85	15.5	1.09 ± 0.10
[^{99m}Tc(NNPh)(L5)(L6)]$^+$	>90	13.5	0.63 ± 0.03

[a] The HPLC retention times were obtained using Method 1.

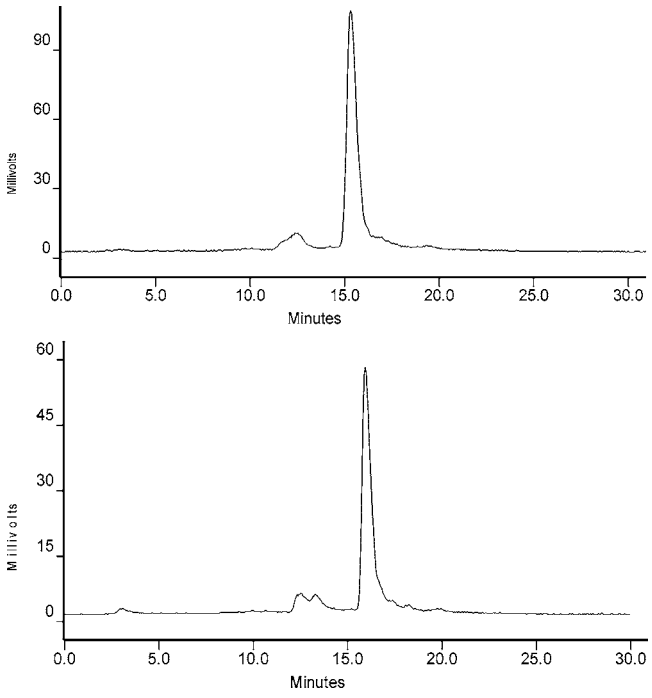

Figure 3. Typical radio-HPLC chromatograms (Method 1) for cationic complexes [^{99m}Tc(NNPh)(L2)(PNP6)]$^+$ and [^{99m}Tc(NNPh)(L4)(PNP6)]$^+$. Small radioimpurity peaks at ~12.5 min are most likely caused by the partial oxidation of the bisphosphine during preparation.

HYNIC with the BFC, tricine, and TPPTS as coligands (*34*, *40*). The low ^{99m}Tc-labeling efficiency of HYBA may also be caused by the use of PDTA as the transferring ligand that forms the [^{99m}Tc(NNPh)(PDTA)]$^-$ intermediate with low reactivity toward ligand exchange (*1*, *2*, *34*, *40*). It is important to note that HYBA is just a BFC without the attached biomolecule, and the radiolabeling conditions have not been optimized yet. Our future research will focus on improvement of ^{99m}Tc-labeling efficiency of this novel ternary ligand system (HYBA-BM, DTC, and bisphosphine) by varying radiolabeling conditions (pH, buffering agents, transferring ligand, and reaction time or temperature), as well as the component levels.

Stability of Cationic ^{99m}Tc-Diazenido Complexes. High solution stability is a requirement for a useful cationic ^{99m}Tc radiotracer. In this experiment, we studied the solution stability of cationic complexes [^{99m}Tc(NNPh)(L4)(PNP)]$^+$ (PNP = PNP5, PNP6, and L6). It was found that they all remain stable for more than 6 h both in the kit matrix and after HPLC purification. The cysteine challenge experiment was also performed for cationic complexes [^{99m}Tc(NNPh)(L4)(PNP)]$^+$ (PNP = PNP5, PNP6, and L6). They are all relatively stable (>6 h) in the presence of cysteine (1.0 mg/mL) at ambient temperature. These results are consistent with their extremely high in vivo metabolic stability in rats (Figure SIII).

Log *P* Values of Cationic ^{99m}Tc-Diazenido Complexes. In addition to the charge, lipophilicity plays a significant role in the heart uptake of cationic ^{99m}Tc radiotracers. Therefore, we determined the partition coefficient constants by measuring the distribution of the HPLC purified cationic ^{99m}Tc-diazenido complexes in a mixture of equal volume *n*-octanol and 25 mM phosphate buffer (pH = 7.4). HPLC purification was needed to minimize possible interference from other radioimpurities. The log *P* values are summarized in Table 1. As the number of the ether linkage increases, the lipophilicity of cationic ^{99m}Tc-diazenido complexes decreases (lower log *P* value), indicating that the crown ether groups have a significant impact on the lipophilicity of cationic ^{99m}Tc-diazenido complexes. Like the crown ether-containing DTCs, bisphosphine coligands also have a significant impact on the lipophilicity of their cationic ^{99m}Tc-diazenido complexes. For example, cationic complexes [^{99m}Tc(NNPh)(DTC)(PNP6)]$^+$ (DTC = L1−L5) are much more lipophilic than [^{99m}Tc(NNPh)(DTC)(PNP5)]$^+$ (DTC = L1−L5) due to the presence of four ethoxypropyl groups in PNP6 instead of four methoxypropyl groups in PNP5. It is very interesting to note that substituents on the aromatic benzene ring have little impact on the lipophilicity of their cationic ^{99m}Tc-diazenido complexes, which explains why we had difficulties in determining the number of phenyldiazenido ligands in cationic ^{99m}Tc-diazenido complexes.

Examination of the heart uptake mechanism of ^{99m}Tc-Sestamibi indicates that the cationic charge and lipophilicity are important for its accumulation and retention in myocardium (*68*−*72*). If the ^{99m}Tc radiotracer is too lipophilic (log *P* >1.5), it often shows a high protein binding and slow liver clearance. If the ^{99m}Tc radiotracer is too hydrophilic (log *P* <0), it tends to have a low heart uptake and fast heart washout. In both cases, the heart/liver ratio is low due to either high liver uptake or fast myocardial washout (*74*, *75*). In this study, we use crown ether-containing DTCs and ether-containing bisphosphines to

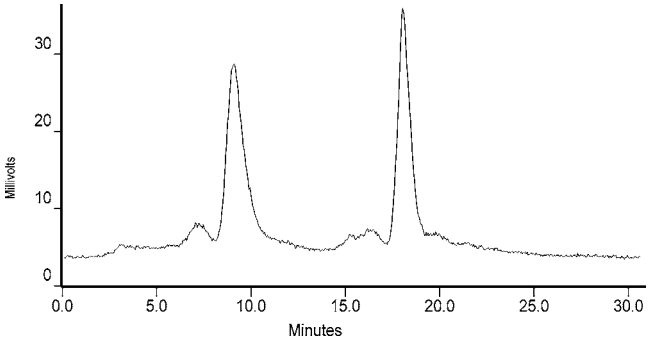

Figure 4. A typical radio-HPLC chromatogram (Method 2) of the reaction mixture containing cationic complexes $[^{99m}Tc(NNPh)(L4)(PNP5)]^+$ and $[^{99m}Tc(NNPh)(DBODC)(PNP5)]^+$.

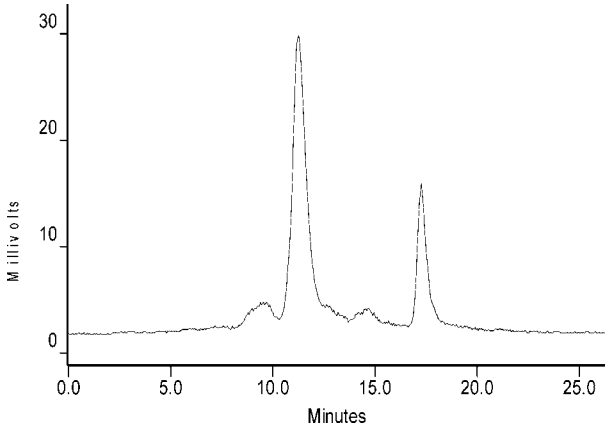

Figure 5. Radio-HPLC chromatogram (Method 1) of the reaction mixture containing cationic complexes $[^{99m}Tc(NNPh)(L4)(PNP5)]^+$ (left) and $[^{99m}Tc(NNPh)(L4)(PNP6)]^+$.

balance the lipophilicity of cationic ^{99m}Tc-diazenido complexes so that their heart uptake and excretion kinetics can be optimized in a systematic fashion. We are interested cationic ^{99m}Tc-diazenido complexes with the log *P* values similar to that of ^{99m}TcN-DBODC5, which was reported to have the best heart-to-liver ratio (*76*−*78*). On the basis of log *P* values (Table 1), we believe that $[^{99m}Tc(NNPh)(L4)(L6)]^+$ might show a heart uptake and heart/liver ratio equivalent to those of ^{99m}TcN-DBODC5 due to their almost identical log *P* values (1.10 ± 0.07 for $[^{99m}Tc(NNPh)(L4)(L6)]^+$ and 1.09 ± 0.10 for ^{99m}TcN-DBODC5). Recent results (Figure SIV) from imaging and biodistribution studies support this hypothesis.

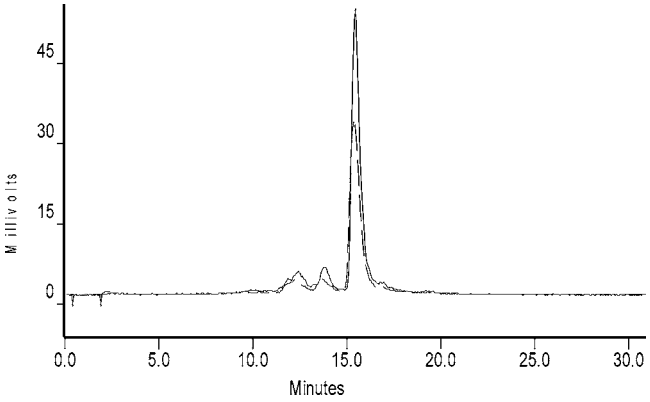

Figure 6. Typical radio-HPLC chromatograms (Method 1) for cationic complexes $[^{99m}Tc(NNPh)(L2)(L6)]^+$ (solid line) and $[^{99m}Tc(NNPh\text{-}2,5\text{-}Me_2)(L4)(L6)]^+$ (dashed line). Small radioimpurity peaks at ∼12.5 min are most likely caused by the partial oxidation of the bisphosphine during preparation.

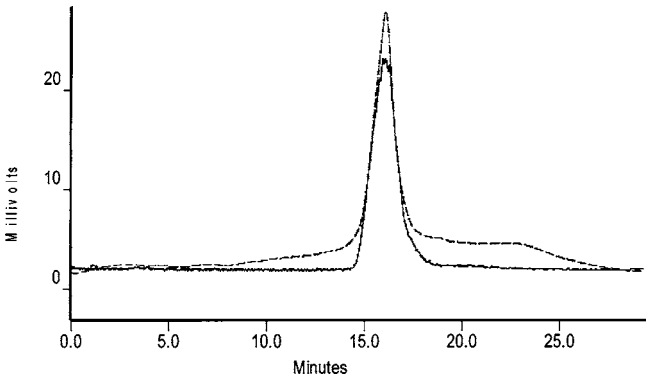

Figure 7. The HPLC concordance (Method 1) for the HPLC-purified $[Re(NNPh)(L4)(L6)]^+$ (dashed line) and $[^{99m}Tc(NNPh)(L4)(L6)]^+$ (solid line).

Composition Studies of Cationic ^{99m}Tc-Diazenido Complexes. The mixed-ligand experiment was performed to determine the composition of cationic ^{99m}Tc-diazenido complexes according to the procedure described in our previous report (*40*). In the first experiment, we used PNP5 as the bisphosphine coligand, L4 and DBODC as the competing chelators. After radiolabeling, the reaction mixture was analyzed by radio-HPLC. If only one DTC is bonded to the Tc, the HPLC chromatogram should show two peaks: one from $[^{99m}Tc(NNPh)(L4)(PNP5)]^+$ and the other from $[^{99m}Tc(NNPh)(DBODC)(PNP5)]^+$. If there

Scheme 4. Synthesis of $[Re(NNPh)(L4)(L6)]^+$

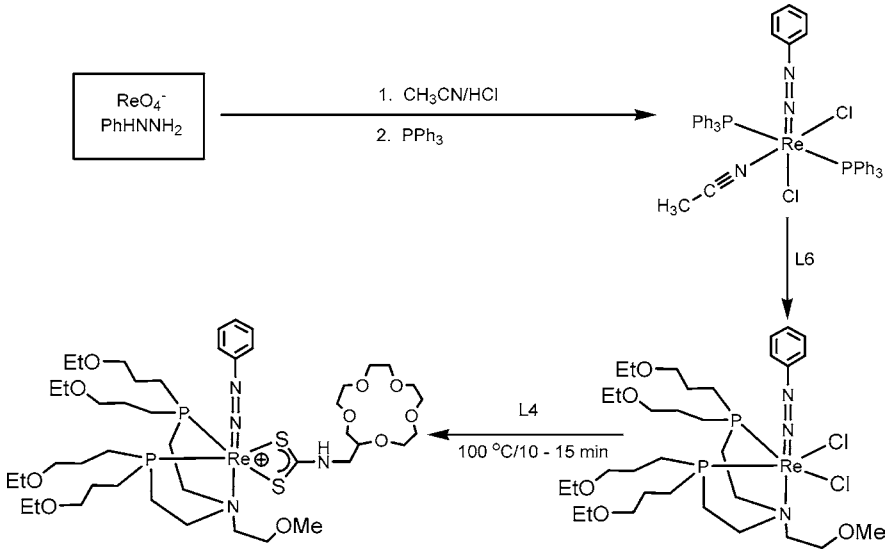

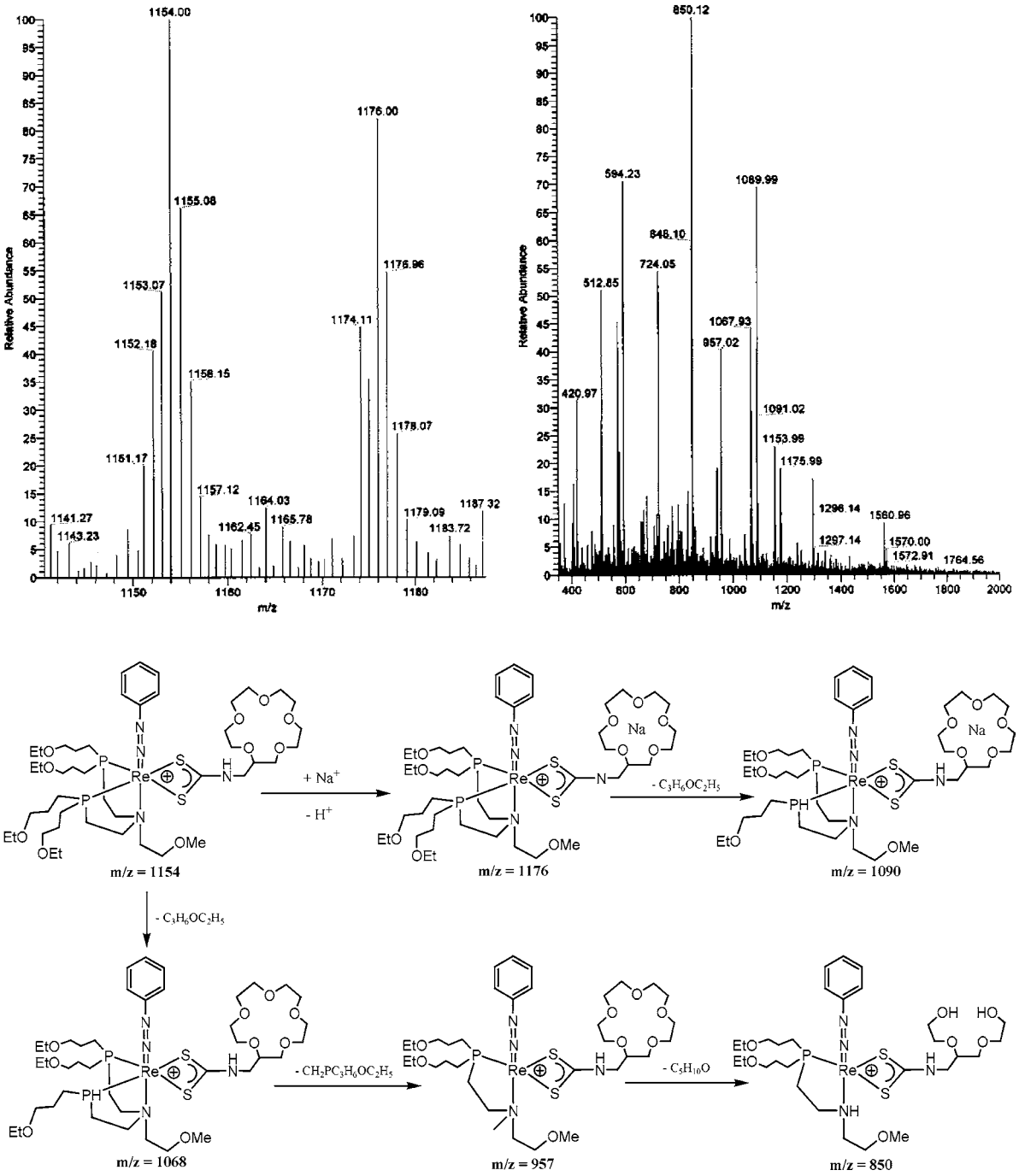

Figure 8. ESI mass spectrum (top) and the proposed fragmentation pattern (bottom) for the cationic complex $[Re(NNPh)(L4)(L6)]^+$.

were two DTC chelators bonded to the Tc, a third peak from the mixed-ligand complex, $[^{99m}Tc(NNPh)(L4)(DBODC)(PNP5)]^+$. The presence of only two radiometric peaks in the HPLC chromatogram (Figure 4) clearly shows that there is only one DTC in cationic complexes $[^{99m}Tc(NNPh)(DTC)(PNP)]^+$.

The number of bisphosphine ligands in $[^{99m}Tc(NNPh)(DTC)(PNP)]^+$ was determined in a similar fashion using L4 as the DTC chelator, and PNP5 and PNP6 as competing coligands. Figure 5 shows the typical radio-HPLC chromatogram of the resulting reaction mixture. The peaks at 11.5 min is due to the cationic complex $[^{99m}Tc(NNPh)(L4)(PNP5)]^+$, and the peak at 17.5 min is from the cationic complex $[^{99m}Tc(NNPh)(L4)(PNP6)]^+$. This clearly demonstrates that there is only one bisphosphine coligand in cationic complexes $[^{99m}Tc(NNPh)(DTC)(PNP)]^+$.

We made many attempts to determine the number of phenyldiazenido ligands in cationic complexes $[^{99m}Tc(NNPh)(DTC)(PNP)]^+$ using phenylhydrazine, 4-methoxyphenylhydrazine, 4-chlorophenylhydrazine, 4-methylphenylhydrazine, and 2,5-dimethylphenylhydrazine as competing ligands. Regardless of the DTC and bisphosphine coligands, cationic complexes $[^{99m}Tc(NNPh\text{-}R)(DTC)(PNP)]^+$ (R = H, Cl, OCH_3, and 2,5-Me_2) all showed very similar HPLC retention times. For example, cationic complexes $[^{99m}Tc(NNPh)(L4)(PNP6)]^+$ and $[^{99m}Tc(NNPh\text{-}2,5\text{-}Me_2)(L4)(PNP6)]^+$ have almost identical HPLC retention time (Figure 6). Thus, it is impossible to separate them using chromatographic conditions described in this study.

On the basis of the results from three mixed-ligand experiments and their similarity to cationic ^{99m}Tc-nitrido complexes, we believe that the cationic complexes $[^{99m}Tc(NNPh)(DTC)(PNP)]^+$ most likely have a distorted coordination geometry with one monodentate phenyldiazenido ligand, one bidentate DTC, and one bisphosphine coligand.

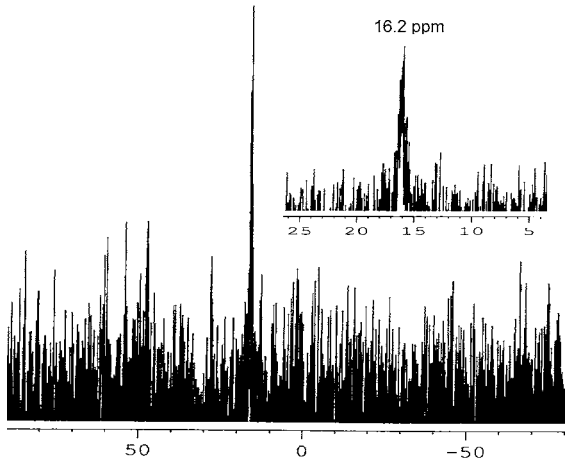

Figure 9. The ^{31}P NMR spectrum of $[Re(NNPh)(L4)(L6)]^+$.

Synthesis of $[Re(NNPh)(L4)(L6)]^+$. To further confirm the findings in the mixed ligand experiments, we decided to prepare $[Re(NNPh)(L4)(L6)]^+$ as a model compound for the cationic complexes $[^{99m}Tc(NNPh)(DTC)(PNP)]^+$. Attempts to synthesize $[Re(NNPh)(L4)(L6)]^+$ from the direct reaction of $[^nNBu_4][ReO_4]$ using the procedure for $[^{99m}Tc(NNPh)(DTC)(PNP)]^+$ were not successful due to difficulty in the reduction of Re(VII) to Re(III), which reflects the significant difference in the redox chemistry of Re and Tc. Thus, we used $[ReCl_2(NNPh)(PPh_3)_2(CH_3CN)]$ as the starting material, and the substitution reaction was carried out in a mixture of chloroform, ethanol, and 0.5 N ammonium acetate buffer (pH = 5.0) according to Scheme 4. The acetonitrile and two PPh_3 ligands in $[ReCl_2(NNPh)(PPh_3)_2(CH_3CN)]$ were first replaced by L6 to give the intermediate complex $[ReCl_2(NNPh)(L6)]$, which was then reacted with L4 to give the cationic complex $[Re(NNPh)(L4)(L6)]^+$ in very low yield (<20% by UV/vis at λ = 254 nm), which is in sharp contrast to the high radiochemical purity (>95%) of the cationic complex $[^{99m}Tc(NNPh)(L4)(L6)]^+$ at the tracer level. After HPLC purification, only 1−2 mg of [Re(NNPh)(L4)(L6)]Cl was obtained for the HPLC concordance experiment, and spectroscopic characterization (ESI-MS, ^{1}H and ^{32}P NMR).

HPLC Concordance Experiment. We performed the HPLC concordance experiment using the HPLC-purified $[Re(NNPh)(L4)(L6)]^+$ and $[^{99m}Tc(NNPh)(L4)(L6)]^+$. Figure 7 shows the HPLC concordance of cationic complexes $[Re(NNPh)(L4)(L6)]^+$ (dashed line) and $[^{99m}Tc(NNPh)(L4)(L6)]^+$ (solid line). It is quite clear that they share the same composition due to their identical HPLC retention times.

Spectroscopic Characterization of $[Re(NNPh)(L4)(L6)]^+$. The ES-MS spectrum (Figure 8) shows the expected molecular ion at m/z = 1154 for $[Re(NNPh)(L4)(L6)]^+$ and 1176 for $[M + Na]^+$. On the basis of fragmentation patterns reported for cationic Re(V)-nitrido complexes, $[ReN(DTC)(PNP)]^+$ (*64*, *66*), we were able to identify several molecular fragments (Figure 8). The ^{31}P NMR spectrum (Figure 9) of $[Re(NNPh)(L4)(L6)]^+$ clearly shows a singlet at ∼16 ppm, which is almost identical to that (16.3 ppm) of the complex [Re(NPh)(O,O-cat)(PNMeP)]Cl (O,O-cat = catechol; PNMeP = bis[(2-diphenylphosphino)ethyl]methylamine) in the same solvent (*79*). The ESI-MS and NMR spectral data are completely consistent with our conclusion that the cationic complexes $[^{99m}Tc(NNPh)(DTC)(PNP)]^+$ contain one phenyldiazenido ligand, one bidentate DTC, and one bisphosphine coligand. More detailed structural and spectroscopic characterization of cationic Re(III)-diazenido complexes is still in progress.

CONCLUSIONS

This report describes the discovery of a new ternary ligand system for the ^{99m}Tc-labeling of small biomolecules and for preparation of cationic complexes $[^{99m}Tc(NNPh)(DTC)(PNP)]^+$ with potential as radiopharmaceuticals for heart imaging. The cationic ^{99m}Tc-diazenido complexes can be prepared in two steps with high yield and have very high solution stability. Their composition was determined to be 1:1:1:1 for Tc:NNPh:DTC:PNP through the mixed-ligand experiments on the tracer (^{99m}Tc) level and was further confirmed by the ESI-MS and NMR spectral data of a model compound $[Re(NNPh)(L4)(L6)]^+$.

Apparently, this new ternary ligand system offers several advantages. The cationic complexes $[^{99m}Tc(NNPh)(DTC)(PNP)]^+$ have high solution stability. Since no post-labeling chromatographic purification is needed for cationic Tc-diazenido complexes, the new ternary ligand system is amendable for the development of a kit formulation. All cationic complexes $[^{99m}Tc(NNPh)(DTC)(PNP)]^+$ show only one radiometric peak in their HPLC chromatograms due to the "symmetric" nature of the Tc chelate. Their hydrophilicity can be modified by the choice of DTC and bisphosphine coligands. The toxicity of the crown ether-containing DTCs and phenylhydrazine should be minimal since they are used in small amount (<1 mg/25 mCi or 13 μg/kg if injected into a 75 kg patient).

It is important to note that LD_{50} values of crown ethers does not apply to the crown ether-containing DTCs because the N-functionalization will change their toxicity significantly. It is also important to emphasize that the formulation for preparing cationic ^{99m}Tc-diazenido complexes has not been optimized. Once a promising agent is identified, efforts will be made to optimize the formulation so that each components in the kit matrix can be minimized while maintaining the high RCP for the selected cationic complex $[^{99m}Tc(NNPh)(DTC)(PNP)]^+$.

ACKNOWLEDGMENT

This work is supported, in part, by Purdue University, Bristol-Myers Squibb Medical Imaging Inc., and research grants AHA0555659Z (S.L.) from the Greater Midwest Affiliate of American Heart Association, R21 EB003419 (S.L.) from National Institute of Biomedical Imaging and Bioengineering (NIBIB), and BCTR0503947 (S.L.) from Susan G. Komen Breast Cancer Foundation.

Supporting Information Available: The radio-HPLC chromatograms of cationic ^{99m}Tc-diazenido complexes, metabolic stability data, and planar images of rats administered with ∼600 μCi of the cationic complex $[^{99m}Tc(NNPh)(L4)(L6)]^+$. These materials are available free of charge at http://pubs.acs.org.

LITERATURE CITED

(1) Abrams, M. J., Juweid, M., tenKate, C. I., Schwartz, D. A., Hauser, M. M., Gaul, F. E., Fuccello, A. J., Rubin, R. H., Strauss, H. W., and Fischman, A. J. (1990) Technetium-99m-human polyclonal IgG radiolabeled via the hydrazino nicotinamide derivative for imaging focal sites of infection in rats. *J. Nucl. Med. 31,* 2022−2028.

(2) Schwartz, D. A., Abrams, M. J., Hauser, M. M., Gaul, F. E., Larsen, S. K., Rauh, D., and Zubieta, J. (1991) Preparation of hydrazino-modified proteins and their use for the synthesis of ^{99m}Tc-protein conjugates. *Bioconjugate Chem. 2,* 333−336.

(3) Ultee, M. E., Bridger, G. J., Abrams, M. J., Longley, C. B., Burton, C. A., Larsen, S. K., Henson, G. W., Padmanabhan, S., Gaul, F. E., and Schwartz, D. A. (1997) Tumor imaging with technetium-99m-labeled hydrazinonicotinamide-Fab′ conjugates. *J. Nucl. Med. 38,* 133−138.

(4) Bridger, G. J., Abrams, M. J., Padmanabhan, S., Gaul, F. E., Larsen, S., Henson, G. W., Schwartz, D. A., Longley, C. B., Burton, C. A., and Ultee, M. E. (1996) A comparison of cleavable and noncleavable

hydrazinopyridine linkers for the ^{99m}Tc-labeling of Fab′ monoclonal antibody fragments. *Bioconjugate Chem. 7*, 255−264.
(5) Babich, J. W., Solomon, H., Pike, M. C., Kroon, D., Graham, W., Abrams, M. J., Tompkins, R. G., Rubin, R. H., and Fischman, A. J. (1993) Technetium-99m labeled hydrazino nicotinamide derivatized chemotactic peptide analogs for imaging focal sites of bacterial infection. *J. Nucl. Med. 34*, 1964−1974.
(6) Babich, J. W. and Fischman, A. J. (1995) Effect of co-ligand on the biodistribution of ^{99m}Tc-labeled hydrazino nicotinic acid derivatized chemotactic peptides. *Nucl. Med. Biol. 22*, 25−30.
(7) Babich, J. W., Graham, W., Barrow, S. A., and Fischman, A. J. (1995) Comparison of the infection imaging properties of a ^{99m}Tc labeled chemotactic peptide with ^{111}In IgG. *Nucl. Med. Biol. 22*, 643−648.
(8) Babich, J. W., Coco, W. G., Barrow, S., Fischman, A. J., Femia, F. J., and Zubieta, J. (2000) ^{99m}Tc-labeled chemotactic peptides: influence of coligand on distribution of molecular species and infection imaging properties. Synthesis and structural characterization of model complexes with the {Re(η^2-HNNC$_5$H$_4$N)(η^1-NNC$_5$H$_4$N)} core. *Inorg. Chim. Acta 309*, 123−136.
(9) Decristoforo, C. and Mather, S. J. (1999) ^{99m}Tc-labeled peptide-HYNIC conjugates: effects of lipophilicity and stability on biodistribution. *Nucl. Med. Biol. 26*, 389−396.
(10) Decristoforo, C. and Mather, S. J. (1999) Preparation, ^{99m}Tc-labeling, and in vitro characterization of HYNIC and N_3S modified RC-160 and [Tyr^3]Octreotide. *Bioconjugate Chem. 10*, 431−438.
(11) Decristoforo, C. and Mather, S. J. (1999) Technetium-99m somatostatin analogues: effect of labeling methods and peptide sequence. *Eur. J. Nucl. Med. 26*, 869−876.
(12) Decristoforo, C., Melendez-Alafort, L., Sosabowski, J. K., and Mather, S. J. (2000) ^{99m}Tc-HYNIC-[Tyr^3]-octreotide for imaging somatostatin-receptor-positive tumors: preclinical evaluation and comparison with ^{111}In-Octreotide. *J. Nucl. Med. 41*, 1114−1119.
(13) Bangard, M., Béhé, M., Guhlke, S., Otte, R., Bender, H., Maecke, H. R., and Biersack, H. J. (2000) Detection of somatostatin receptor-positive tumours using the new ^{99m}Tc-tricine-HYNIC-D-Phe^1-Tyr^3-octreotide: first results in patients and comparison with ^{111}In-DTPA-D-Phe^1-octreotide. *Eur. J. Nucl. Med. 27*, 628−637.
(14) Decristoforo, C., Mather, S. J., Cholewinski, W., Donnemiller, E., Riccabona, G. and Moncayo, R. (2000) ^{99m}Tc-EDDA/HYNIC-TOC: a new ^{99m}Tc-labeled radiopharmaceutical for imaging somatostatin receptor-positive tumors: first clinical results and intrapatient comparison with ^{111}In-labeled octreotide derivatives. *Eur. J. Nucl. Med. 27*, 1318−1325.
(15) Zhang, Y.-M., Liu, N., Zhu, Z.-H., Rusckowski, M., and Hnatowich, D. J. (2000) Influence of different chelators (HYNIC, MAG_3 and DTPA) on tumor cell accumulation and mouse biodistribution of technetium-99m labeled antisense DNA. *Eur. J. Nucl. Med. 27*, 1700−1707.
(16) Hnatowich, D. J., Winnard, P. Jr., Virzi, F., Fogarasi, M., Santo, T., Smith, C. L., Cantor, C. R., and Rusckowski, M. (1995) Technetium-99m labeling of DNA oligonucleotides. *J. Nucl. Med. 36*, 2306−2314.
(17) Guo, W. J., Hinkle, G. H., and Lee, R. J. (1999) ^{99m}Tc-HYNIC-folate: a novel receptor-based targeted radiopharmaceutical for tumor imaging. *J. Nucl. Med. 40*, 1563−1569.
(18) Ono, M., Arano, Y., Mukai, T., Uehara, T., Fujioka, Y., Ogawa, K., Namba, S., Nakayama, M., Saga, T., Konishi, J., Horiuchi, K., Yokoyama, A. and Saji, H. (2001) Plasma protein binding of ^{99m}Tc-labeled hydrazino nicotinamide derivatized polypeptides and peptides. *Nucl. Med. Biol. 28*, 155−164.
(19) Ono, M., Arano, Y., Mukai, T., Fujioka, Y., Ogawa, K., Uehara, T., Saga, T., Konishi, J., and Saji, H. (2001) ^{99m}Tc-HYNIC-derivatized ternary ligand complexes for ^{99m}Tc-labeled peptides with low in vivo protein binding. *Nucl. Med. Biol. 28*, 215−224.
(20) Liu, S., Edwards, S. D., Harris, A. R., and Singh, P. R. (1997) ^{99m}Tc-labeling kinetics of four thiol-containing chelators and 2-hydrazinopyridine: factors influencing their radiolabeling efficiency. *Appl. Radiat. Isot. 48*, 1103−1111.
(21) Edwards, D. S. and Liu, S. (1997) ^{99m}Tc-labeling of hydrazinonicotinamide modified highly potent small molecules: Problems and solutions. *Transition Metal Chem. 22*, 425−426.
(22) Liu, S., Edwards, D. S., and Barrett, J. A. (1997) ^{99m}Tc-labeling of highly potent small peptides. *Bioconjugate Chem. 8*, 621−636.
(23) Liu, S. and Edwards, D. S. (1999) ^{99m}Tc-labeled small peptides as diagnostic radiopharmaceuticals. *Chem. Rev. 99*, 2235−2268.
(24) Liu, S. and Edwards, D. S. (2001) New Radiopharmaceuticals for imaging infection and inflammation. *Drugs Future 26*, 375−382.
(25) Liu, S. (2005) HYNIC derivatives as bifunctional coupling agents for ^{99m}Tc-labeling of small biomolecules. *Topics Curr. Chem. 252*, 117−153.
(26) Liu, S., Robinson, S. P., and Edwards, D. S. (2003) Integrin $\alpha_v\beta_3$ directed radiopharmaceuticals for tumor imaging. *Drugs Future 28*, 551−564.
(27) Edwards, D. S., Liu, S., Ziegler, M. C., Harris, A. R., Crocker, A. C., Heminway, S. J., Barrett, J. A., Bridger, G. J., Abrams, M. J., and Higgins, J. D. (1999) RP463: A stabilized technetium-99m complex of a hydrazino nicotinamide derivatized chemotactic peptide for infection imaging. *Bioconjugate Chem. 10*, 884−891.
(28) van der Laken, C. J., Boerman, O. C., Oyen, W. J., van de Ven, M, T. P., Edwards, D. S., Barrett, J. A., van der Meer, J. W., and Corstens, F. H. (1997) Technetium-99m-labeled chemotactic peptides in acute infection and sterile inflammation. *J. Nucl. Med. 38*, 1310−1315.
(29) van Eerd, J. E. M., Oyen, W. J. G., Harris, T. D., Rennen, H. J. J. M., Edwards, D. S., Liu, S., Ellars, C. E., Corstens, F. H. M., and Boerman, O. C. (2003) A bivalent leukotriene B4 antagonist for scintigraphic imaging of infectious foci. *J. Nucl. Med. 44*, 1087−1091.
(30) Brouwers, A. H., Laverman, P., Boerman, O. C., Oyen, W. J. G., Barrett, J. A., Harris, T. D., Edwards, D. S., and Corstens, F. H. M. (2000) A ^{99}Tc^m-labeled leukotriene B4 receptor antagonist for scintigraphic detection of infection in rabbits. *Nucl. Med. Commun. 21*, 1043−1050.
(31) Liu, S., Edwards, D. S., Ziegler, M. C., Harris, A. R., Williams, N. E., and Edwards, D. S. (2002) ^{99m}Tc-labeling of a hydrazinonictotinamide-conjugated LTB_4 receptor antagonist useful for imaging infection and inflammation. *Bioconjugate Chem. 13*, 881−886.
(32) Liu, S., Edwards, D. S., Ziegler, M. C., Harris, A. R., Hemingway, S. J., and Barrett, J. A. (2001) ^{99m}Tc-Labeling of a hydrazinonictotinamide-conjugated vitronectin receptor antagonist useful for imaging tumors. *Bioconjugate Chem. 12*, 624−629.
(33) Liu, S., Edwards, D. S., Looby, R. J., Harris, A. R., Poirier, M. J., Barrett, J. A., Heminway, S. J., and Carroll, T. R. (1996) Labeling a hydrazinonicotinamide-modified cyclic IIb/IIIa receptor antagonist with ^{99m}Tc using aminocarboxylates as co-ligands. *Bioconjugate Chem. 7*, 63−71.
(34) Edwards, D. S., Liu, S., Barrett, J. A., Harris, A. R., Looby, R. J., Ziegler, M. C., Heminway, S. J., and Carroll, T. R. (1997) A new and versatile ternary ligand system for technetium radiopharmaceuticals: water soluble phosphines and tricine as coligands in labeling a hydrazino nicotinamide-modified cyclic glycoprotein IIb/IIIa receptor antagonist with ^{99m}Tc. *Bioconjugate Chem. 8*, 146−154.
(35) Edwards, D. S., Liu, S., Harris, A. R., Poirier, M., and Ewels, B. A. (1999) ^{99m}Tc-labeling of hydrazones of a hydrazinonicotinamide conjugated cyclic peptide. *Bioconjugate Chem. 10*, 803−807.
(36) Liu, S., Edwards, D. S., Harris, A. R., Ziegler, M. C., Poirier, M. J., Ewels, B. A., DiLuzio, W. R., and Hui, P. (2001) Towards developing a non-$SnCl_2$ formulation for RP444: a new radiopharmaceutical for thrombus imaging. *J. Pharm. Sci. 90*, 114−123.
(37) Edwards, D. S., Liu, S., Harris, A. R., Poirier, M. J., and Ewels, B. A. (1999) ^{99m}Tc-labeling hydrazones of a hydrazinonicotinamide conjugated cyclic peptide. *Bioconjugate Chem. 10*, 803−807.
(38) Liu, S., Edwards, D. S., Harris, A. R., Heminway, S. J., and Barrett, J. A. (1999) Technetium complexes of a hydrazinonicotinamide-conjugated cyclic peptide and 2-hydrazinopyridine: Synthesis and characterization. *Inorg. Chem. 38*, 1326−1335.
(39) Liu, S., Ziegler, M. C., and Edwards, D. S. (2000) Radio-LC-MS for the characterization of ^{99m}Tc-labeled bioconjugates. *Bioconjugate Chem. 11*, 113−117.
(40) Liu, S., Edwards, D. S., and Harris, A. R. (1998) A novel ternary ligand system for technetium radiopharmaceuticals for ^{99m}Tc-labeling of hydrazino nicotinamide-modified biologically active molecules using imine-N containing heterocycles as coligands. *Bioconjugate Chem. 9*, 583−595.
(41) Purohit, A., Liu, S., Casebier, D., and Edwards, D. S. (2003) Phosphine-containing HYNIC-derivatives as potential bifunctional

chelators for ^{99m}Tc-labeling of small biomolecules. *Bioconjugate Chem. 14*, 720−727.
(42) Purohit, A., Liu, S., Ellars, C. E., Casebier, D., Haber, S. B., and Edwards, D. S. (2004) Pyridine-containing HYNIC-derivatives as potential bifunctional chelators for ^{99m}Tc-labeling of small biomolecules. *Bioconjugate Chem. 15*, 728−737.
(43) Nicholson, T. and Zubieta, J. (1985) The synthesis and structural characterization of $[ReCl_2(PPh_3)_2(NNHCOPh)(NHNHCOPh)]\cdot 1/2Et_2O$, a complex exhibiting linear hydrazido(2-) ligation and end-on hydrazido(1-) ligation. *J. Chem. Soc., Chem. Commun. 6*, 367.
(44) Dilworth, J. R., Harrison, S. A., Walton, D. R. M., and Schweda, E. (1985) Preparation and protonation of $[ReBr(N_2Ph)_2(PPh_3)_2]$. Structure of $[ReBr_2(NNPh)(NNHPh)(PPh_3)_2]$, a complex with a hydrazido(2-) ligand with a large angular distortion. *Inorg. Chem. 24*, 2594−2595.
(45) Archer, C. M., Dilworth, J. R., Jobanputra, P., Thompson, R. M., McPartlin, M., Povey, D. C., Smith, G. W., and Kelly, J. D. (1990) Development of new technetium cores containing technetium−nitrogen multiple bonds. Synthesis and characterization of some diazenido-, hydrazido- and imido- complexes of technetium. *Polyhedron 9*, 1497−1502.
(46) Archer, C. M., Dilworth, J. R., Jobanputra, P., Thompson, R. M., McPartin, M., and Hiller, W. (1993) Technetium diazenido complexes. Part 1. Synthesis and structures of $[TcCl(NNC_6H_4Cl\text{-}4)_2(PPh_3)_2]$ and $[TcCl(NNPh)(Ph_2PCH_2CH_2PPh_2)_2][PF_6]\cdot H_2O$. *J. Chem. Soc., Dalton Trans.* 897−904.
(47) Dilworth, J. R., Jobanputra, P., Thompson, R. M., Povey, D. C., Archer, C. M., and Kelly, J. D. (1994) Technetium diazenido complexes. Part 2. Substitution chemistry of $[TcCl(NNC_6H_4Cl\text{-}4)_2(PPh_3)_2]$ and the synthesis of technetium diazenido-complexes directly from $[NH_4][TcO_4]$. *J. Chem. Soc., Dalton Trans.* 1251−1256.
(48) Dilworth, J. R., Jobanputra, P., Thompson, R. M., Archer, C. M., Kelly, J. D., and Hiller, W. (1991) Crystal structure of a diazenido-dithiocarbamate complex of technetium, $[Tc(NNC_6H_4Cl)((CH_3)_2NCS_2)_2(PPh_3)]$. *Z. Naturforsch. 46*, 449−452.
(49) Nicholson, T. and Zubieta, J. (1987) Synthesis and characterization of a rhenium-dioxygen complex. The crystal and molecular structure of $[ReCl_2(PPh_3)_2(NNCO_2Me)(O_2)]$, a precursor in the synthesis of organosulfinato complexes of rhenium. *Inorg. Chim. Acta 134*, 191−193.
(50) Nicholson, T., Lombardi, P., and Zubieta, J. (1987) Monomeric five-coordinate rhenium diazenido and hydrazido complexes with aromatic thiolate ligands: X-ray structures of $[Re(NNC_6H_4\text{-}4\text{-}Br)_2(SC_6H_3\text{-}2,5\text{-}Me_2)(PPh_3)_2]$ and $[ReO(NNMePh)(SPh)_3]$, and of the synthetic precursor $[Re(NNC_6H_4\text{-}4\text{-}Br)_2Cl(PPh_3)_2]$. *Polyhedron 6*, 1577−1585.
(51) Nicholson, T. and Zubieta, J. (1988) Complexes of rhenium with benzoylazo and related ligands. Crystal and molecular structures of the "green chelate" benzoylazo complex $[ReCl_2(PPh_3)_2(NNCOC_6H_4\text{-}p\text{-}Cl)](N_\alpha, O)$, of the analogous 1-azophthalazine chelate complex $[ReCl_2(PPh_3)_2(NNC_8H_5N_2)](N_\alpha, N_1)$, and of the *cis*-dichloro organodiazenido complexes of the type $[ReCl_2(PPh_3)_2(NNR)L]$ (L = $NCCH_3$, NH_3 and C_5H_5N). A comparison to the structure of the *trans*-dichloro dimethylformamide derivative $[ReCl_2(PPh_3)_2(NNCO_2CH_3)(Me_2NCHO)]$. The structural characterization of the mixed hydrazido(1-) hydrazido(2-) complexes $[ReCl_2(PPh_3)_2(NNHR)(NHNHR')]$, (R = R′ = $-COC_6H_5$; R = $-COC_6H_5$, R′ = $-CO_2CH_3$). *Polyhedron 7*, 171−185.
(52) Dilworth, J. R., Jobanputra, P., Miller, J. R., Parrott, S. J., Chen, Q. and Zubieta, J. (1993) The cleavage of the N- - -N bond of N,N-disubstituted hydrazines on rhenium. The preparation, reactions and X-ray crystal structures of $[ReCl_2(NH_3)(NNCOC_6H_4\text{-}4\text{-}R)(PPh_3)_2]$ (R = H, −OMe, $-NO_2$), $[ReCl_3(NNPh_2)(PPh_3)_2]$, $[ReCl_2(N)(NNPh_2)(PPh_3)]$ and $[ReCl(N)(Me_2CNNCOPh)(PPh_3)_2]$. *Polyhedron 12*, 513−522.
(53) Coutinho, B., Dilworth, J. R., Jobanputra, P., Thompson, R. M., Schmid, S., Strähle, J., and Archer, C. M. (1995) Mono- and bis-diazenido complexes of rhenium(III) containing bidentate ditertiary phosphine ligands. The crystal and molecular structures of $[Re(NNC_6H_4Me\text{-}4)(Ph_2PCH_2CH_2PPh_2)_2][PF_6]\cdot 2dmf$, $[Re(NNC_6H_4Cl\text{-}4)(Me_2PCH_2CH_2PMe_2)_2][PF_6]$ and $[ReCl(NNC6H4Me\text{-}4)(Me_2PCH_2CH_2PMe_2)_2][PF_6]$. *J. Chem. Soc., Dalton Trans.* 1663−1669.
(54) Abrams, M. J., Larsen, S. K., Shaikh, S. N., and Zubieta, J. (1991) Investigations of technetium-organohydrazine coordination chemistry. The crystal and molecular structures of $[TcCl_2(C_8H_5N_4)(PPh_3)_2]\cdot 0.75C_7H_8$ and $[TcNCl_2(PPh_3)_2]\cdot 0.25CH_2Cl_2$. *Inorg. Chim. Acta 185*, 7−15.
(55) Nicholson, T., Hirsch-Kuchma, M., Freiberg, E., Davison, A., and Jones, A. G. (1998) The reaction chemistry of a technetium(I) nitrosyl complex with potentially chelating organohydrazines: the X-ray crystal structure of $[TcCl_2(NO)(HN{=}NC_5H_4N)(PPh_3)]$. *Inorg. Chim. Acta 279*, 206−209.
(56) Rose, D. J., Maresca, K. P., Nicholson, T., Davison, A., Jones, A. G., Babich, J., Fischman, A., Graham, W., DeBord, J. R. D., and Zubieta, J. (1998) Synthesis and Characterization of Organohydrazino Complexes of Technetium, Rhenium, and Molybdenum with the $\{M(\eta^1\text{-}HxNNR)(\eta^2\text{-}HyNNR)\}$ Core and Their Relationship to Radiolabeled Organohydrazine-Derivatized Chemotactic Peptides with Diagnostic Applications. *Inorg. Chem. 37*, 2701−2716.
(57) Nicholson, T., Cook, J., Davison, A., Rose, D. J., Maresca, K. P., Zubieta, J. A. and Jones, A. G. (1996) The synthesis and characterization of $[MCl_3(N{=}NC_5H_4NH)(HN{=}NC_5H_4N)$ from $[MO_4]^-$ (where M = Re, Tc) organodiazenido, organodiazene-chelate complexes. The X-ray structure of $[ReCl_3(N{=}NC_5H_4NH)(HN{=}NC_5H_4N)]$. *Inorg. Chim. Acta 252*, 421−426.
(58) Nicholson, T., Cook, J., Davison, A., Rose, D. J., Maresca, K. P., Zubieta, J. A., and Jones, A. G. (1996) The synthesis, characterization and X-ray crystal structure of the rhenium organodiazenido, organodiazene complex $[ReCl_2(PPh_3)(N{=}NC_5H_4N)(HN{=}NC_5H_4N)]$. *Inorg. Chim. Acta 252*, 427−430.
(59) Hirsch-Kuchma, M., Nicholson, T., Davison, A., Davis, W. M., and Jones, A. G. (1997) Synthesis and characterization of rhenium(III) and technetium(III) organohydrazide chelate complexes. Reactions of 2-hydrazinopyridine with complexes of rhenium and technetium. *Inorg. Chem. 36*, 3237−3241.
(60) Nicholson, T., Hirsch-Kuchma, M., Davison, A., and Jones, A. G. (1998) The synthesis and characterization of a technetium(III) isodiazene complex. The X-ray crystal structure of $[TcCl_3(N{=}NPh_2)(PPh_3)_2]$. *Inorg. Chim. Acta 271*, 191−194.
(61) Hirsch-Kuchma, M., Nicholson, T., Davison, A., and Jones, A. G. (1997) Group 7 'organohydrazide' chemistry: classification of ligand type based on crystal structural data.*J. Chem. Soc., Dalton Trans.* 3189−3192.
(62) Hirsch-Kuchma, M., Nicholson, T., Davison, A., Davis, W. M., and Jones, A. G. (1997) The synthesis and characterization of technetium and rhenium hydrazinopyrimidine chelate complexes. *J. Chem. Soc., Dalton Trans.* 3185−3188.
(63) Liu, S., He, Z. J., and Hsieh, W. Y. A crown ether-containing cationic ^{99m}Tc-diazenido complex showing high heart uptake and rapid liver clearance in rats: comparison with ^{99m}Tc-Sestamibi and ^{99m}TcN-DBODC5. *Nucl. Med. Biol.*, submitted.
(64) Bolzati, C., Refosco, F., Cagnolini, A., Tisato, F., Boschi, A., Duatti, A., Uccelli, L., Dolmella, A., Marotta, E., and Tubaro, M. (2004) Synthesis, solution-state and solid-state structural characterization of monocationic nitrido heterocomplexes $[M(N)(DTC)(PNP)]^+$ (M = ^{99}Tc and Re; DTC = dithiocarbamate; PNP = heterodiphosphane). *Eur. J. Inorg. Chem.* 1902−1913.
(65) Bolzati, C., Boschi, A., Duatti, A., Prakash, S., and Uccelli, L. (2000) Geometrically controlled selective formation of nitrido technetium(V) asymmetrical heterocomplexes with bidentate ligands. *J. Am. Chem. Soc. 122*, 4510−4511.
(66) Bolzati, C., Boschi, A., Uccelli, L., Tisato, F., Refosco, F., Cagnolini, A., Duatti, A., Prakash, S., Bandoli, G., and Vittadini, A. (2002) Chemistry of the strong electrophilic metal fragment $[^{99}Tc(N)(PXP)]^{2+}$ (PXP = diphosphine ligand). A novel tool for the selective labeling of small molecules. *J. Am. Chem. Soc. 124*, 11468−11479.
(67) Cowley, A. R., Dilworth, J. R. and Donnelly, P. S. (2003) A monodiazenide complex from perrhenate: toward a new core for rhenium radiopharmaceuticals. *Inorg. Chem. 42*, 929−931.
(68) Jones, A. G., Abrams, M. J., Davison, A., Brodack, J. W., Toothaker, A. K., Adelstein, S. J. and Kassis, A. I. (1984) Biological studies of a new class of technetium complexes: the hexakis(alkylisonitrile)technetium(I) cations. *Int. J. Nucl. Biol. 11*, 225−234.
(69) Carvalho, P. A., Chiu, M. L., Kronauge, J. F., Kawamura, M., Jones, A. G., Holman, B. L., and Piwnica-Worms, D. (1992) Subcellular distribution and analysis of technetium-99m-MIBI in isolated perfused rat hearts. *J. Nucl. Med. 33*, 1516−1521.

(70) Iskandrian, A. S., Heo, J. Y., Kong, B., Lyons, E., and Marsch, S. (1989) Use of technitium-99m Isonitrile (RP-30A) in assessing left ventricular perfusion and function at rest and during exercise in coronary artery disease and comparison with coronary arteriography and exercise thallium-201 SPECT imaging. *Am. J. Cardiol. 64*, 270−275.

(71) Mousa, S. A., Cooney, J. M., and Williams, S. J. (1987) Flow-distribution characteristics of Tc-99m-Hexakis-2-methoxy-2-methylpropyl isonitrile in animal-models of myocardial-ischemia and perfusion (abstract). *J. Am. Coll. Cardiol. 9*, A137.

(72) Crane, P., Laliberte, R., Heminway, S., Thoolen, M., and Orlandi, C. (1993) Effect of mitochondrial viability and metabolism on technetium-99m-sestamibi myocardial retention. *Eur. J. Nucl. Med. 20*, 20−25.

(73) Marmion, M. E., Woulfe, S. R., Neumann, W. L., Nosco, D. L. and Deutsch, E. (1999) Preparation and characterization of technetium complexes with Schiff-base and phosphine coordination. 1. Complexes of technetium-99 g and −99m with substituted $acac_2$en and trialkyl phosphines (where $acac_2$en = N,N′-ethylenebis[acetylacetone iminato]). *Nucl. Med. Biol. 26*, 755−770; references therein.

(74) Lisic, E. C., Heeg, M. J. and Deutsch, E. (1999) $^{99m}Tc(L-L)_3^+$ complexes containing ether analogs of DMPE. *Nucl. Med. Biol. 26*, 563−571.

(75) Tisato, F., Maina, T., Shao, L. R., Heeg, M. J., and Deutsch, E. (1996) Cationic $[^{99m}Tc^{III}(DIARS)_2(SR)_2]^+$ complexes as potential myocardial perfusion imaging agents (DIARS = *o*-phenylenebis(dimethylarsine); SR^- = thiolate). *J. Med. Chem. 39*, 1253−1261.

(76) Boschi, A., Bolzati, C., Uccelli, L., Duatti, A., Benini, E., Refosco, F., Tisato, F., and Piffanelli, A. (2002) A class of asymmetrical nitrido ^{99m}Tc heterocomplexes as heart imaging agents with improved biological properties. *Nucl. Med. Commun. 23*, 689−693.

(77) Boschi, A., Uccelli, L., Bolzati, C., Duatti, A., Sabba, N., Moretti, E., Di Domenico, G., Zavattini, G., Refosco, F., and Giganti, M. (2003) Synthesis and biologic evaluation of monocationic asymmetrical ^{99m}Tc-nitride heterocomplexes showing high heart uptake and improved imaging properties. *J. Nucl. Med. 44*, 806−814.

(78) Hatada, K., Riou, L. M., Ruiz, M., Yamamichi, Y., Duatti, A., Lima, R. L., Goode, A. R., Watson, D. D., Beller, G. A., and Glover, D. K. (2004) ^{99m}Tc-N-DBODC5, a new myocardial perfusion imaging agent with rapid liver clearance: comparison with ^{99m}Tc-Sestamibi and ^{99m}Tc-Tetrofosmin in rats. *J. Nucl. Med. 45*, 2095−2101.

(79) Porchia, M., Tisato, F., Refosco, F., Bolzati, C., Cavazza-Ceccato, M., Bandoli, G., Dolmella, A. (2005) New approach to the chemistry of technetium(V) an rhenium(V) phenylimido complexes: novel $[M(NPh)PNP]^{3+}$ and metal fragments (M = Tc, Re; PNP = aminodiphosphine) suitable for the synthesis of stable mixed-ligand compounds. *Inorg. Chem. 44*, 4766−4776.

BC0502715

Supporting Materials for the Manuscript Entitled

"A Novel Ternary Ligand System Useful for Preparation of Cationic ^{99m}Tc-Diazenido Complexes and ^{99m}Tc-Labeling of Small Biomolecules" by Young-Seung Kim, Zhengjie He, Wen-Yuan Hsieh, and Shuang Liu*

Figure SI. Typical radio-HPLC chromatogram (**Method 3**) of the reaction mixture containing the cationic complex $[^{99m}Tc(HYPY)(L4)(L6)]^+$. The large difference in retention times of two main peaks suggests that they might be two different compounds with completely different compositions.

Figure SII. Typical radio-HPLC chromatogram (**Method 1**) of the reaction mixture containing the cationic complex $[^{99m}Tc(NNPh)(L4)(L6)]^+$ prepared using PDTA (top) or tricine (bottom) as transferring ligands. The large difference in retention times of two main peaks suggests that they might not be the same compound and have different compositions.

Figure SIII. Radio-HPLC chromatograms of the cationic complex $[^{99m}Tc(NNPh)(L6)(L4)]^+$ in the kit matrix before injection (A), in the urine at 30 min postinjection (B), in the urine at 120 min postinjection (C), and in feces at 120 min postinjection (D). Each rat was administered with about 600 μCi of $[^{99m}Tc(NNPh)(L6)(L4)]^+$. Based on these results, it is quite clearly that the cationic ^{99m}Tc-diazenido complexes would have very high *in vivo* stability with little metabolism in rats under anesthesia.

Figure SIV. Planar images (no decay correction) of the Sprague-Dawley rats administered with ~600 μCi of $[^{99m}Tc(NNPh)(L4)(L6)]^+$ (left) and ^{99m}TcN-DBODC5 (right). Both rats were placed side-by-side so that they are compared in a direct fashion. Arrows indicate the location of the heart, liver and salivary gland (as determined by ex-vivo gamma counting).

Figure SV. ^{1}H NMR of the cationic complex $[Re(NNPh)(L4)(L6)]^+$.

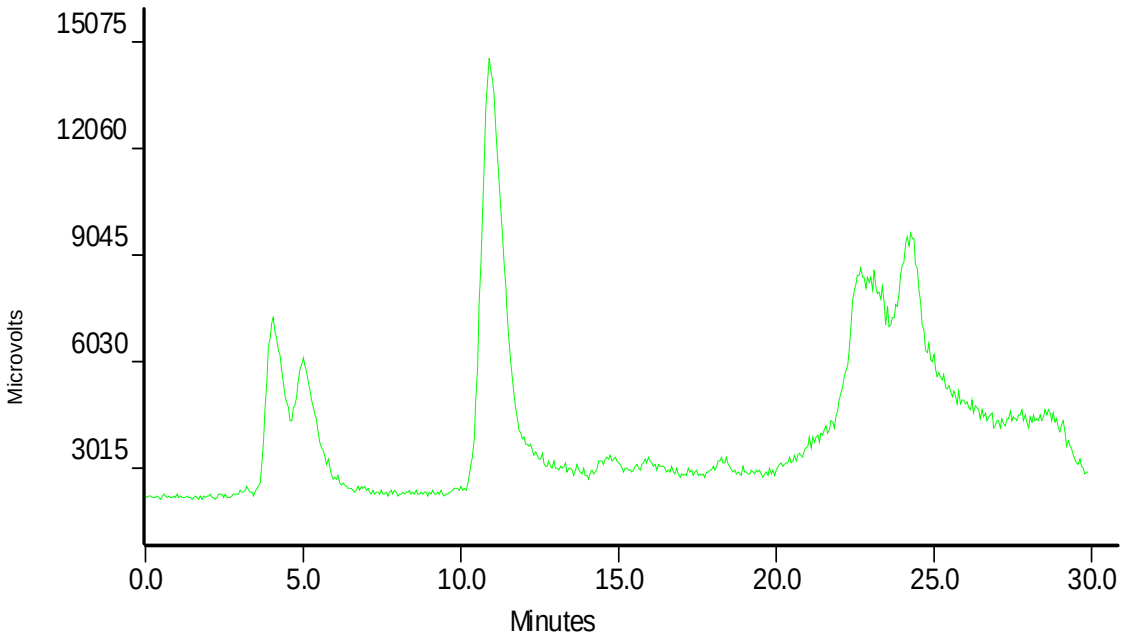

Figure SI. Typical radio-HPLC chromatogram (**Method 3**) of the reaction mixture containing the cationic complex $[^{99m}Tc(HYPY)(L4)(L6)]^{+}$. The large difference in retention times of two main peaks suggests that they might be two different compounds with completely different compositions.

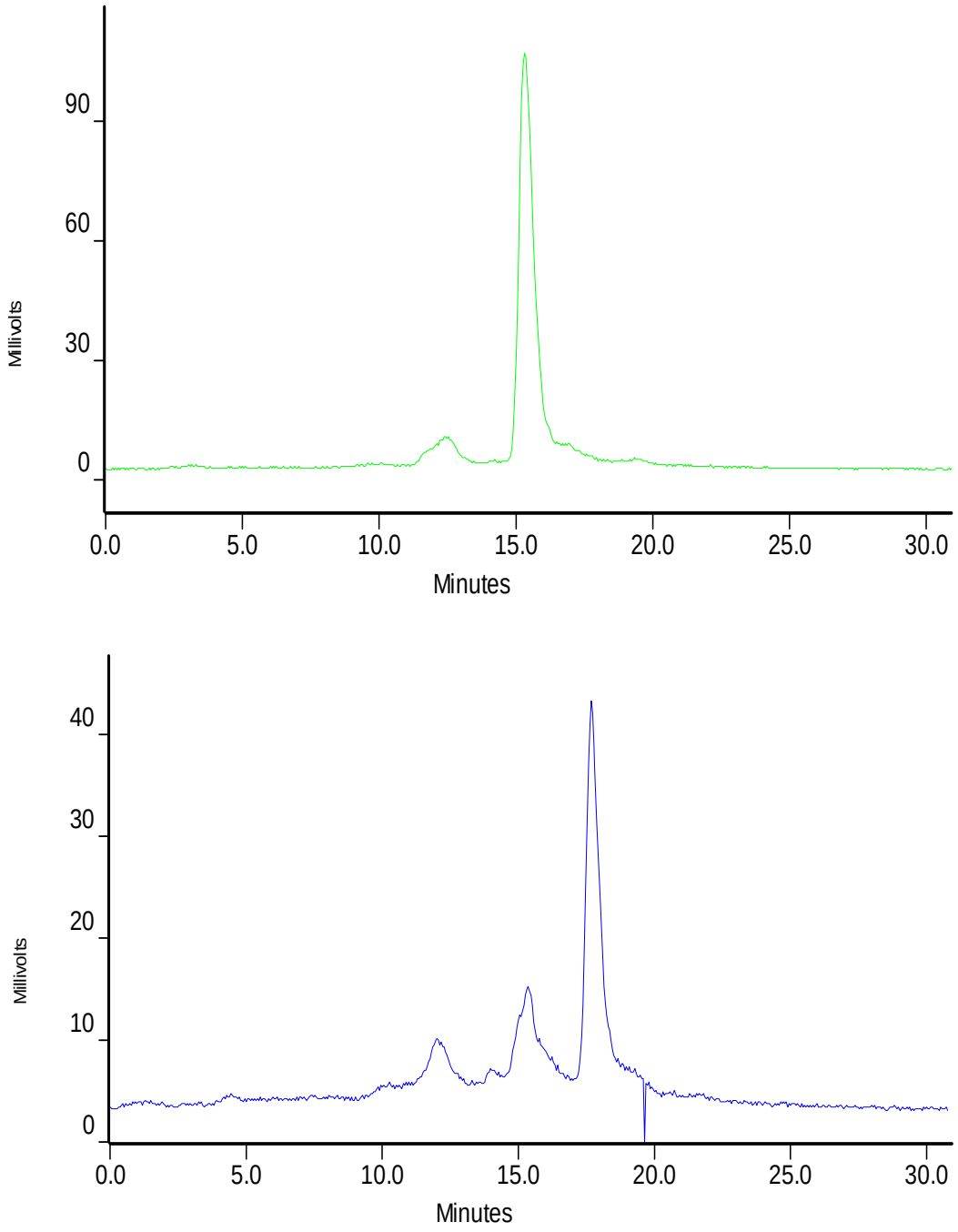

Figure SII. Typical radio-HPLC chromatogram (**Method 1**) of the reaction mixture containing the cationic complex $[^{99m}Tc(NNPh)(L4)(L6)]^{+}$ prepared using PDTA (top) or tricine (bottom) as transferring ligands. The large difference in retention times of two main peaks suggests that they might not be the same compound and have different compositions.

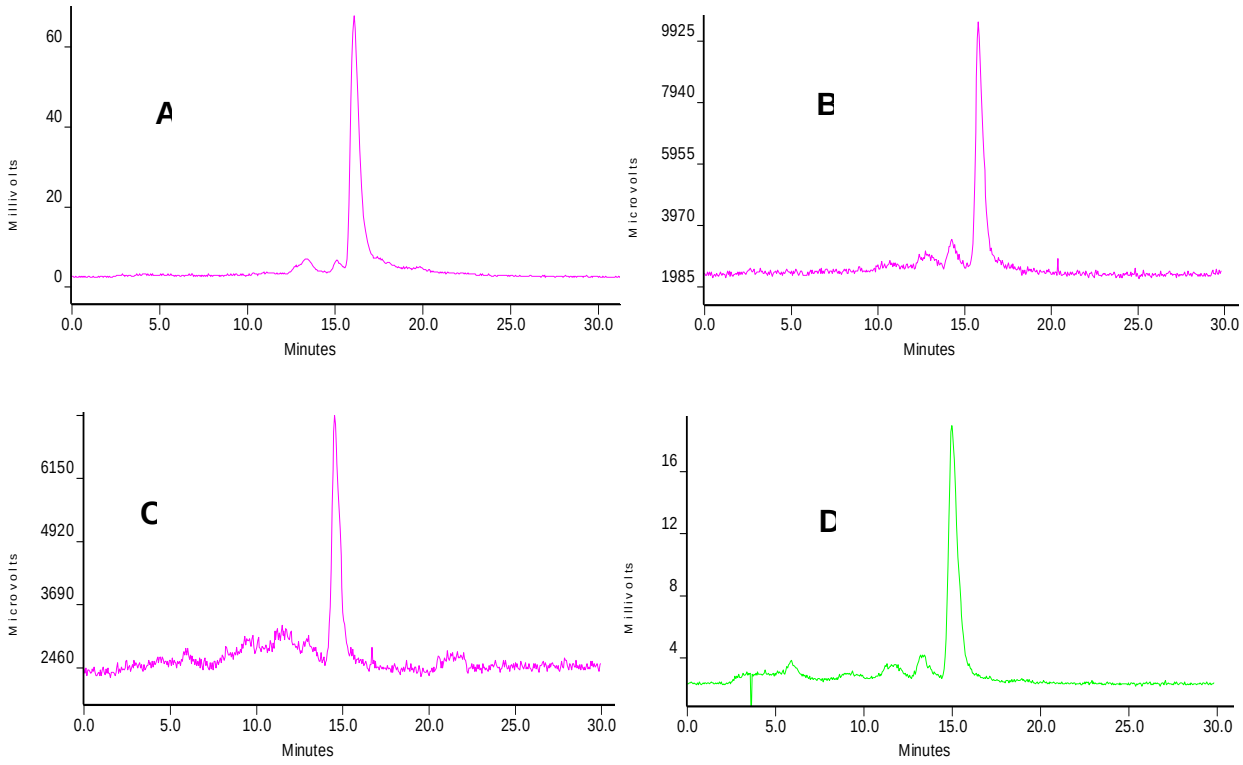

Figure SIII. Radio-HPLC chromatograms of the cationic complex $[^{99m}Tc(NNPh)(L6)(L4)]^+$ in the kit matrix before injection (A), in the urine at 30 min postinjection (B), in the urine at 120 min postinjection (C), and in feces at 120 min postinjection (D). Each rat was administered with about 600 μCi of $[^{99m}Tc(NNPh)(L6)(L4)]^+$. Based on these results, it is quite clearly that the cationic ^{99m}Tc-diazenido complexes would have very high *in vivo* stability with little metabolism in rats under anesthesia.

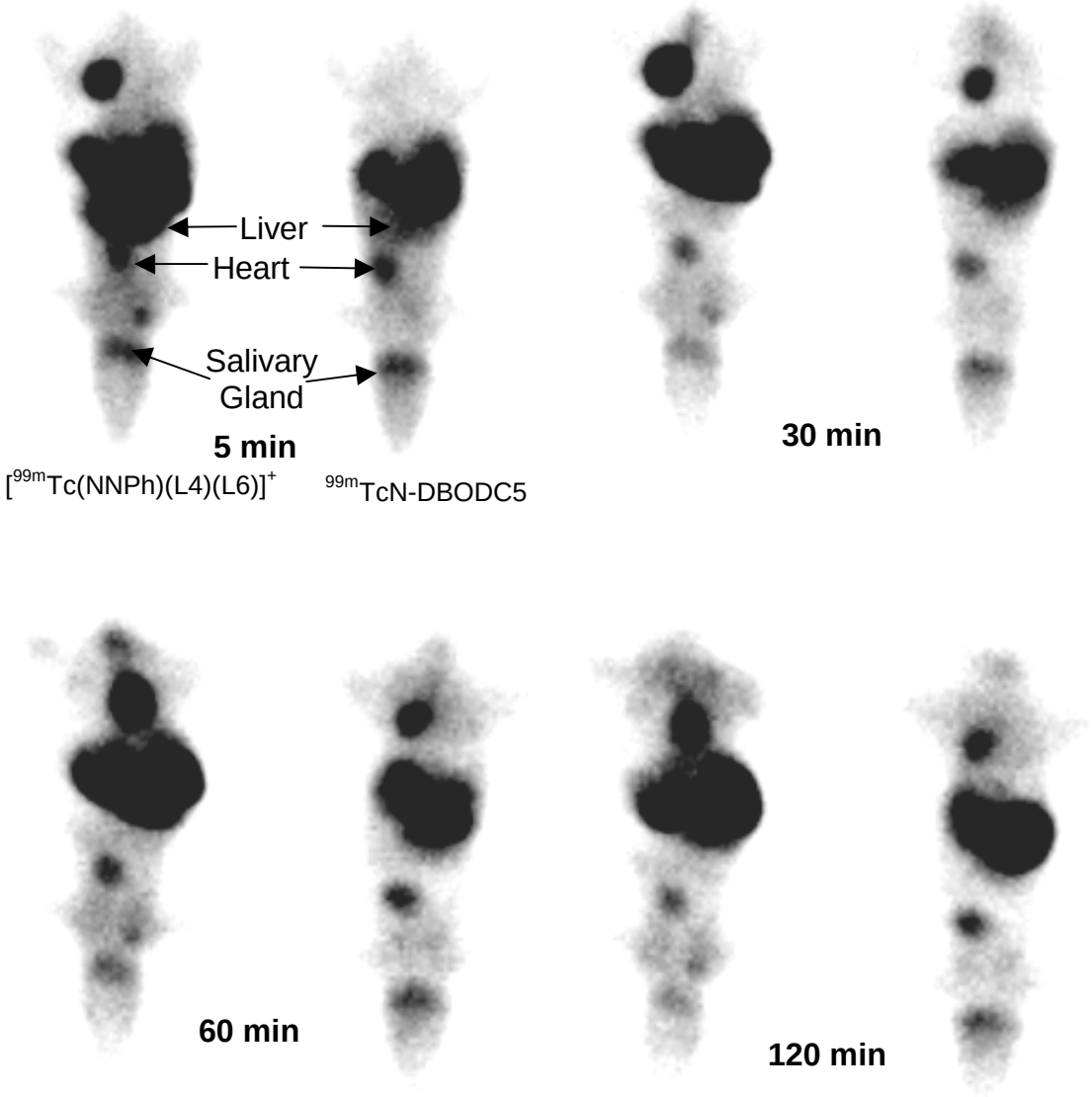

Figure SIV. Planar images (no decay correction) of the Sprague-Dawley rats administered with ~600 μCi of $[^{99m}Tc(NNPh)(L4)(L6)]^+$ (left) and ^{99m}TcN-DBODC5 (right). Both rats were placed side-by-side so that they are compared in a direct fashion. Arrows indicate the location of the heart, liver and salivary gland (as determined by ex-vivo gamma counting).

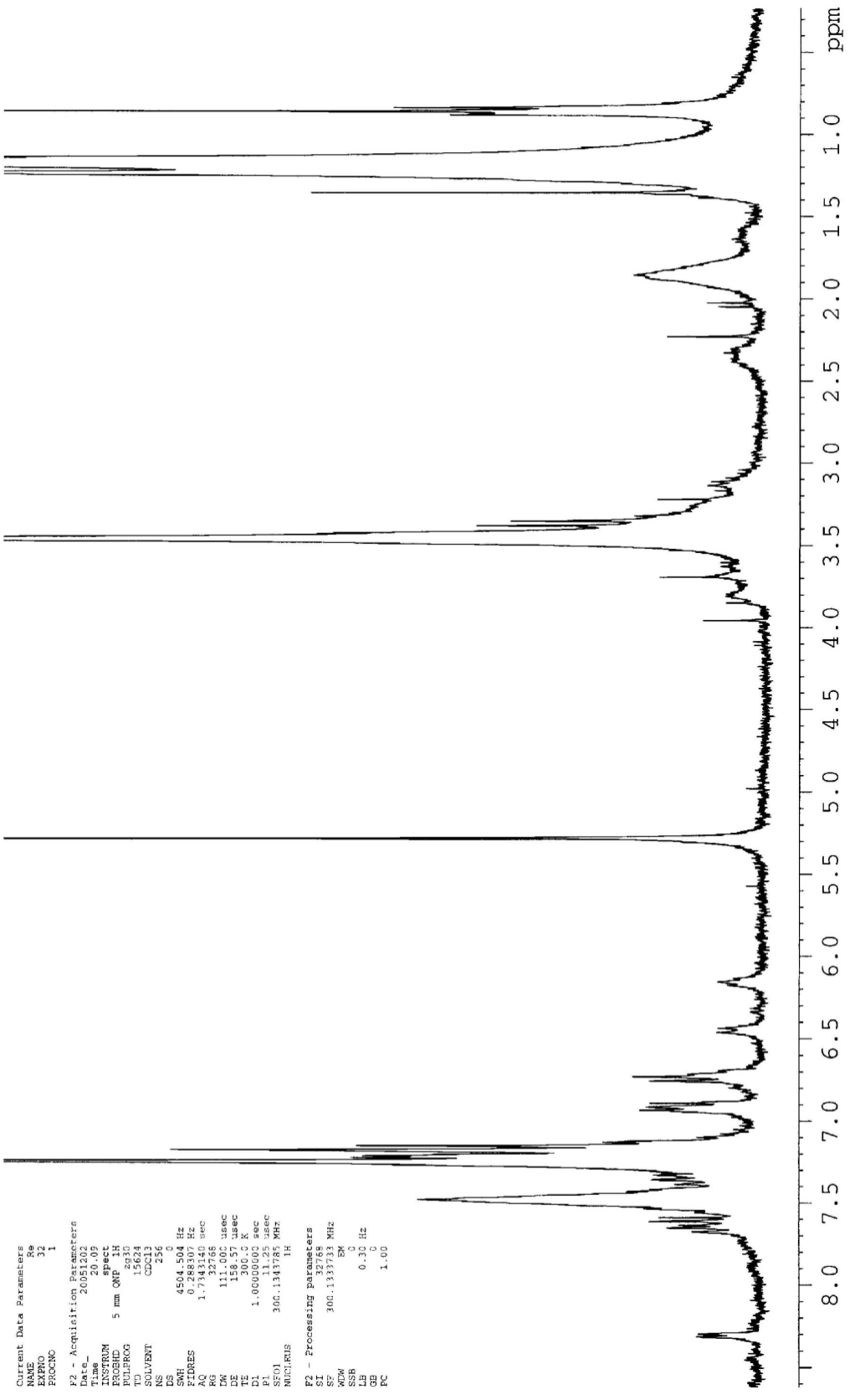

Figure SV. ^{1}H NMR of the cationic complex [Re(NNPh)(L4)(L6)]$^{+}$.

Radiolanthanide-Labeled Monoclonal Antibody CC49 for Radioimmunotherapy of Cancer: Biological Comparison of DOTA Conjugates and ^{149}Pm, ^{166}Ho, and ^{177}Lu

Huma Mohsin,[†] Fang Jia,[‡] Geethapriya Sivaguru,[‡] Michael J. Hudson,[§] Tiffani D. Shelton,[∥] Timothy J. Hoffman,[∥] Cathy S. Cutler,[⊥] Alan R. Ketring,[⊥] Phillip S. Athey,[▽] Jaime Simón,[▽] R. Keith Frank,[▽] Silvia S. Jurisson,[†,⊥,#] and Michael R. Lewis*[,‡,∥,#,⊗]

Department of Chemistry, and Department of Veterinary Medicine and Surgery, University of Missouri−Columbia, Columbia, Missouri 65211, Department of Biology, University of Maryland Baltimore County, Baltimore, Maryland 21250, Research Service, Harry S. Truman Memorial Veterans' Hospital, Columbia, Missouri 65201, University of Missouri Research Reactor, University of Missouri−Columbia, Columbia, Missouri 65211, Dowpharma, The Dow Chemical Company, Freeport, Texas 77541, and Nuclear Science and Engineering Institute, and Department of Radiology, University of Missouri−Columbia, Columbia, Missouri 65211. Received August 1, 2005; Revised Manuscript Received February 1, 2006

The radiolanthanides ^{149}Pm, ^{166}Ho, and ^{177}Lu have decay characteristics suitable for radioimmunotherapy (RIT) of cancer. *N*-Hydroxysulfosuccinimidyl DOTA (DOTA-OSSu) and methoxy-DOTA (MeO-DOTA) were conjugated to the anti-TAG-72 monoclonal antibody CC49 for radiolabeling with ^{149}Pm, ^{166}Ho, and ^{177}Lu. While both DOTA conjugates could be labeled to high specific activity with ^{177}Lu, MeO-DOTA afforded superior conjugate stability, radiolabeling, and radiochemical purity. Pilot biodistributions in nude mice bearing LS174T human colon carcinoma xenografts demonstrated that MeO-DOTA afforded higher tumor uptake and lower kidney retention of ^{177}Lu than DOTA-OSSu. The in vitro stability of ^{149}Pm-, ^{166}Ho-, and ^{177}Lu-MeO-DOTA−CC49 was evaluated using serum and hydroxyapatite assays. Serum stability of radiolanthanide-labeled MeO-DOTA−CC49 followed a trend based on the coordination energies of the radiometals, with ^{177}Lu showing the highest stability after 96 to 168 h at 37 °C. In contrast, MeO-DOTA−CC49 labeled with all three radiolanthanides was >92% stable to hydroxyapatite challenge for 168 h at 37 °C. Comprehensive biodistributions of ^{149}Pm-, ^{166}Ho-, and ^{177}Lu-MeO-DOTA−CC49 were obtained in LS174T-bearing nude mice. Maximum tumor uptakes were 100.0% ID/g for ^{149}Pm at 96 h, 69.5% ID/g for ^{166}Ho at 96 h, and 132.4% ID/g for ^{177}Lu at 168 h. Normal organ uptakes were generally low, except in the liver, spleen, and kidney at early time points. By 96 to 168 h postinjection, nontarget organ uptake decreased to approximately 7% ID/g (kidney), 12% ID/g (spleen), and 20% ID/g (liver) for each radiolanthanide. When labeled with ^{149}Pm, ^{166}Ho, and ^{177}Lu, MeO-DOTA−CC49 has potential for RIT of colorectal cancer and other carcinomas.

INTRODUCTION

Radiolabeled monoclonal antibodies (mAbs) have shown great promise for cancer therapy. Recently, two commercial preparations of radiolabeled mAbs have been approved by the United States Food and Drug Administration for radioimmunotherapy (RIT)[1] of relapsed or refractory B-cell non-Hodgkin's lymphoma (*1*, 2). Targeted radiopharmaceuticals are well suited to the therapy of this disease, as tumors are well vascularized for the delivery of the mAbs, and lymphocytes are exquisitely sensitive to radiation injury. However, targeting of solid tumors with therapeutic radiopharmaceuticals has been far less effective in producing lasting remissions or tumor control. The slow plasma clearance properties of radiolabeled mAbs result in prolonged exposure of the bone marrow to ionizing radiation. This requires limiting the dose to the tumor to keep marrow exposure below 150 to 200 rad (1.5 to 2.0 Gy). Creation of stable fragments of mAbs has improved clearance kinetics but yielded decreased tumor antigen binding affinity and altered biodistributions, often with unacceptably high kidney doses (*3*).

An alternative strategy is to label mAbs with radionuclides having emission characteristics that are more effective for solid tumor therapy. The radiolanthanides ^{149}Pm, ^{166}Ho, and ^{177}Lu (Table 1) possess a range of half-lives and β^- energies for RIT applications. They also emit low abundance γ rays with energies suitable for tracking radiolabeled mAbs in vivo and estimating radiation dosimetry. Furthermore, these radiolanthanides can be

* To whom correspondence should be addressed: Michael R. Lewis, Ph.D., Department of Veterinary Medicine and Surgery, College of Veterinary Medicine, 379 E. Campus Dr., University of Missouri−Columbia, Columbia, MO 65211. Phone: (573) 814-6000, ext. 3703. Fax: (573) 814-6551. E-mail: LewisMic@missouri.edu.

[†] Department of Chemistry, University of Missouri−Columbia.

[‡] Department of Veterinary Medicine and Surgery, University of Missouri−Columbia.

[§] University of Maryland Baltimore County.

[∥] Harry S. Truman Memorial Veterans' Hospital.

[⊥] University of Missouri Research Reactor, University of Missouri−Columbia.

[▽] The Dow Chemical Company.

[#] Nuclear Science and Engineering Institute, University of Missouri−Columbia.

[⊗] Department of Radiology, University of Missouri−Columbia.

[1] Abbreviations: % ID/g, percent injected dose per gram of tissue; % ID/organ, percent injected dose per organ; AUC, area under the curve; BSA, bovine serum albumin; CC49, second generation anti-TAG-72 mAb; DOTA, 1,4,7,10-tetraazacyclododecane-*N*,*N*′,*N*″,*N*‴-tetraacetic acid; DOTA−CC49, CC49 conjugated with DOTA-OSSu; DOTA-OSSu, *N*-hydroxysulfosuccinimidyl DOTA; DTPA, diethylenetriaminepentaacetic acid; GF−HPLC, gel filtration HPLC; HA, hydroxyapatite; MeO-DOTA, methoxy-DOTA; MeO-DOTA−CC49, CC49 conjugated with MeO-DOTA; PA-DOTA, 1,4,7,10-tetraaza-*N*-(1-carboxy-3-(4-aminophenyl)propyl)-*N*′,*N*″,*N*‴-tris(acetic acid)cyclododecane; RIC, radioimmunoconjugate; RIT, radioimmunotherapy; TAG-72, tumor-associated glycoprotein-72.

10.1021/bc0502356 CCC: $33.50 © 2006 American Chemical Society
Published on Web 02/23/2006

Table 1. Decay Characteristics and DOTA log K_{ML} Values for ^{149}Pm, ^{166}Ho, and ^{177}Lu

radiometal	$T_{1/2}$ (h)	β^- MeV (%)	γ keV (%)	log K_{ML} (M^{3+}-DOTA)
^{149}Pm	53.1	0.784 (9) 1.06 (90)	286 (3.1)	22.87
^{166}Ho	26.9	1.76 (47) 1.84 (52)	81 (5.4)	24.83
^{177}Lu	159.6	0.497 (90)	208 (11)	25.34

obtained readily from a nuclear reactor, by both direct neutron capture and indirect methods (*4*).

Bifunctional derivatives of 1,4,7,10-tetraazacyclododecane-*N*,*N*′,*N*″,*N*‴-tetraacetic acid (DOTA) have been used often to label mAbs with lanthanide radionuclides and other radiometals. We previously developed a facile, water-soluble method (*5*, *6*) for conjugating mAbs with *N*-hydroxysulfosuccinimidyl DOTA (DOTA-OSSu). Conjugates of several antibodies prepared with DOTA-OSSu have been labeled to high specific activity, high radiochemical purity, and high stability with ^{111}In and ^{90}Y (*5*−*7*), as well as ^{64}Cu (*8*−*10*). However, modified structures of DOTA, such as methoxy-DOTA (MeO-DOTA, Figure 1), may have improved binding kinetics and stability for radiolanthanides. Methoxy-DOTA has four amine and four carboxylic acid coordination sites available to bind the radionuclide, while the benzyl isothiocyanate moiety is available off one of the carboxylate arms for conjugation.

CC49 (*11*) is a second generation murine IgG_1 mAb that has been shown to react with the disaccharide sialyl Tn epitope on the extracellular antigen tumor-associated glycoprotein-72, or TAG-72. TAG-72 is expressed on ∼85% of human adenocarcinomas such as colon, breast, pancreatic, ovarian, prostate, non-small cell lung, and gastric cancers (*12*−*21*). Both ^{131}I- and ^{177}Lu-labeled CC49 have been evaluated for RIT in tumor-bearing mice (*22*, *23*) and patients (*24*−*29*). These studies demonstrated excellent tumor targeting and elimination of established tumors in rodent models.

The objective of the present studies was to obtain comparative biodistributions of CC49 labeled with ^{149}Pm, ^{166}Ho, and ^{177}Lu in nude mice bearing LS174T human colon carcinoma xenografts. CC49 conjugates were prepared using DOTA-OSSu and MeO-DOTA, and the stabilities and tumor-targeting properties of the radioimmunoconjugates were evaluated in vitro and in vivo. When labeled with ^{177}Lu, MeO-DOTA was superior to DOTA in terms of CC49 conjugate stability, radiolabeling, radiochemical purity, and biodistributions. The favorable and comparable biodistributions and tumor targeting properties exhibited by the three radiolanthanides allowed the current work to be extended to preclinical RIT studies with each radionuclide.

EXPERIMENTAL PROCEDURES

General. The radiolanthanides were obtained as $^{149}PmCl_3$, $^{166}HoCl_3$, and $^{177}LuCl_3$ in 0.05 M HCl from the University of Missouri Research Reactor (MURR, Columbia, MO). DOTA was purchased from Macrocyclics (Dallas, TX), and MeO-DOTA was provided by the Dow Chemical Company (Dowpharma, Freeport, TX). Chelex 100 (Analytical Grade, 100−200 mesh, sodium form) was purchased from Bio-Rad (Hercules, CA). All solutions were prepared using ultrapure water (18 MΩ-cm resistivity).

CC49 was produced from the hybridoma cell line provided by Dr. Jeffrey Schlom at the National Cancer Institute (Bethesda, MD). Hybridoma cells were grown in a CELLine CL 1000 bioreactor (Integra Biosciences AG, Chur, Switzerland) in serum-free medium (GIBCO Hybridoma-SFM, Invitrogen, Carlsbad, CA) with ORIGEN (Hybridoma Cloning Factor, IGEN International, Inc., Gaithersburg, MD) for 38 days, and

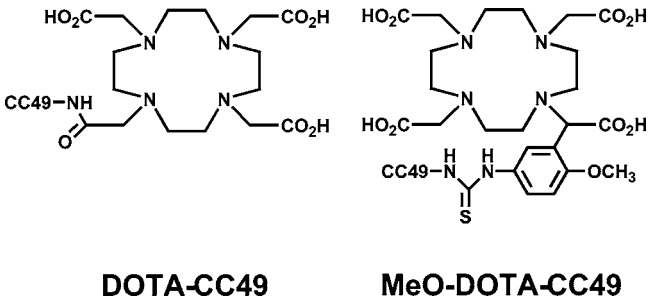

Figure 1. Structures of chelator−mAb conjugates DOTA−CC49 and MeO-DOTA−CC49.

supernatant from the cell side was harvested every 3−4 days. CC49 was purified from the supernatant by Protein G affinity chromatography, using a 10-mL UltraLink Immobilized Protein G column (Pierce, Rockford, IL). The column was washed with 0.1 M sodium acetate, pH 6.0, and eluted with 0.1 M glycine, pH 3.0, after which collected fractions were neutralized with 1 M Tris, pH 8.0. The pooled fractions containing purified mAb were dialyzed against of 1 L of 10 mM NaH_2PO_4/150 mM NaCl, pH 7.5, containing approximately 1 g of Chelex 100, for 72 h at 4 °C, with two buffer changes. This procedure afforded typical yields of 85 to 100 mg of CC49. CC49 concentration was measured by absorbance at 280 nm ($\epsilon = 1.5 \times 10^5$ M^{-1} cm^{-1}; A_{280} at 1 mg/mL = 1.4).

The purity of the radioimmunoconjugates was confirmed by gel filtration HPLC (GF−HPLC), using a Waters (Milford, MA) Delta 600 chromatograph equipped with a manual Rheodyne injector, a 2487 dual wavelength UV detector, a Packard 500TR Flow Scintillation Analyzer with a LQ flow cell for ^{149}Pm, ^{166}Ho, and ^{177}Lu, a Waters busSAT/IN analog-digital interface, and the Waters Millennium 32 software package. A Superose 12 HR 10/30 (Amersham Pharmacia, Torrance, CA) column (300 × 10 mm), an isocratic mobile phase of 100 mM NaH_2PO_4/0.05% NaN_3, pH 6.8, and a flow rate of 0.5 mL/min were used. Scintillation counting was performed on a Wallac 1480 Wizard 3″ automated gamma counter (PerkinElmer Life Sciences, Gaithersburg, MD).

Antibody Conjugation. An aliquot of 6.03 mg of CC49 was conjugated with the bifunctional chelating agent *N*-hydroxysulfosuccinimidyl DOTA (DOTA-OSSu) at a 20:1 molar ratio of DOTA-OSSu:mAb, as described previously (*5*). For methoxy-DOTA (MeO-DOTA) conjugation, a modification of the method of Sumerdon et al. (*30*) was used. Briefly, an aliquot of 6.03 mg of CC49 in 1 mL of 10 mM NaH_2PO_4/150 mM NaCl, pH 7.4, was dialyzed against 1 L of 0.1 M Na_2HPO_4, pH 7.5, containing approximately 1 g of Chelex 100, for 18 to 24 h at 4 °C, and then against 1 L of 0.1 M $NaHCO_3/Na_2HPO_4$, pH 8.5, containing approximately 1 g of Chelex 100, for 48 h at 4 °C, with one buffer change. CC49 was conjugated with MeO-DOTA at a MeO-DOTA:mAb molar ratio of 20:1. The reaction mixture was incubated for 3 h at 37 °C and then dialyzed against 0.25 M ammonium acetate, pH 7.0, containing approximately 1 g of Chelex 100, at 4 °C for 144 h, with five buffer changes. The DOTA−CC49 and MeO-DOTA−CC49 conjugate concentrations were measured by absorbance at 280 nm. The average number of chelates per antibody was determined using an ^{111}In isotopic dilution assay method, using a previously published procedure (*5*).

Radiolanthanide Labeling. Modifications of the methods previously described by Lewis et al. (*5*, *31*) were used to radiolabel DOTA−CC49 and MeO-DOTA−CC49. An initial radiolabeling ratio of 5 μCi/μg was used. In the ^{177}Lu labeling reaction, 59.6 μL of 1.0 M ammonium acetate, pH 4.5, was added to 2.0 mCi of $^{177}LuCl_3$ in 2.0 μL of 0.05 M HCl, followed by 400 μg of DOTA−CC49 or MeO-DOTA−CC49 in 65.6 μL

of 0.25 M ammonium acetate, pH 7.0. The reaction mixture was incubated at 43 °C for 1 h, and diethylenetriaminepentaacetic acid (DTPA), pH 6.0, was added to a final concentration of 1 mM. The reaction mixture was allowed to stand for 15 min at room temperature and then purified using a Bio-Spin 6 column (Bio-Rad) equilibrated with 10 mM Na_2HPO_4/150 mM NaCl, pH 7.5. Prior to purification, radiometal labeling efficiency and specific activity were determined by GF−HPLC. After spin column purification, the specific activity of the mAb was adjusted to 1 μCi/μg, by dilution with unmodified CC49. Radiochemical purity was then determined by GF−HPLC. For ^{166}Ho and ^{149}Pm labeling, similar conditions were used as for ^{177}Lu, except the ^{149}Pm solution contained 2.0 mCi in 6.0 μL of 0.05 M HCl.

Immunoreactivity Determination. A modification of a previously described method (*5*) was used. Briefly, a dilution of the purified radiolabeled CC49 conjugate, containing approximately 200 000 cpm of radioactivity, was mixed with a 20-fold molar excess of bovine submaxillary mucin type I-S (Sigma; St. Louis, MO) in 150 μL of 1% human serum albumin/10 mM NaH_2PO_4/150 mM NaCl, pH 7.4. A control sample was prepared in an identical manner, except that mucin type I-S was not added. The reaction mixtures were incubated at 37 °C for 15 min with continuous end-over-end mixing, after which aliquots of 100 μL were analyzed by GF-HPLC, as described above. Immunoreactivity was calculated as the percentage of the total radioactivity shifted to complexes with apparent molecular weights higher than that of the mAb.

Serum Stability Studies. An aliquot of 1 mCi of ^{177}Lu-DOTA−CC49 or ^{177}Lu-, ^{166}Ho-, or ^{149}Pm-MeO-DOTA−CC49 was added to 1 mL of mouse serum, clarified by centrifugation at 16 110*g* for 15 min and stabilized with 10 μL of 10% NaN_3. Serum samples were analyzed by GF−HPLC, as described above, after incubation at 37 °C for 1, 4, 24, 48, 96, and 168 h.

Hydroxyapatite Stability Studies. Hydroxyapatite stability studies were performed according to a previously published procedure (*32*). Reaction mixtures containing 300 μL of HA-Ultrogel (Sigma, 40% w/w aqueous ethanol suspension, particle size 60−180 μm), 100 μL of bovine serum albumin (BSA) to give a final concentration of 2.5%, 800 μL of 50 mM Tris with 0.01 M $CaCl_2$, and 10 to 20 μCi of radiolabeled MeO-DOTA−CC49 were incubated in 1.5-mL conical polypropylene tubes with continuous mixing at 37 °C. Each day for 7 days, one reaction mixture was separated into liquid and solid phases. The tubes were centrifuged in an Eppendorf 5415D centrifuge (Brinkmann Instruments, Westbury, NY) at 10 000 rpm for 1 min. The liquid phase was removed. The solid sample was washed with 1 mL of water and recentrifuged at 10 000 rpm for 1 min. The liquid wash was removed from the tube. The solid phase was dissolved in 1.3 N HNO_3. The liquid phase, wash, and solid phase were counted in a gamma counter. The percentage of radioactivity in the liquid phase of the sample was calculated by combining the liquid phase and wash and dividing by the total counts in the three parts (liquid, wash, and solid). The solid phase was calculated by taking the counts in the solid phase and dividing by the total counts.

Biodistribution Studies. All experiments were conducted in compliance with the guidelines established by the Animal Care and Use Committee of the University of Missouri−Columbia Animal Care Quality Assurance Office. Outbred female nu/nu mice (4 to 6 weeks of age) were implanted subcutaneously (sc) in the hind flank with 2×10^6 LS174T human colon cancer cells in 0.15 mL of Hank's Balanced Salt Solution. After 14 days, tumors had grown to 100−400 mg, with a mean weight of 175 mg. Mice were then injected intravenously (iv) via the tail vein with 60 μCi/60 μg of ^{177}Lu-DOTA−CC49 or ^{177}Lu-, ^{166}Ho-, or ^{149}Pm-MeO-DOTA−CC49.

Table 2. Serum Stability (mean ± SD)[a] of Radiolanthanide-Labeled MeO-DOTA−CC49 and ^{177}Lu-DOTA−CC49

	MeO-DOTA[b]			DOTA[b]
time (h)	^{149}Pm	^{166}Ho	^{177}Lu	^{177}Lu
0	99.2 ± 1.3	98.7 ± 0.9	99.2 ± 1.2	98.3 ± 2.9
1	99.0 ± 1.8	98.6 ± 1.1	99.6 ± 0.7	98.3 ± 2.9
4	98.1 ± 3.2	98.1 ± 1.4	100.0 ± 0.0	98.2 ± 3.1
24	97.4 ± 3.7	98.4 ± 1.4	98.1 ± 2.1	96.7 ± 3.2
48	96.7 ± 4.0	97.7 ± 1.4	99.3 ± 1.2	97.2 ± 3.6
96	93.7 ± 2.5	93.9 ± 0.7	96.5 ± 0.9	97.3 ± 4.0
168	91.6 ± 0.5	n.d.[c]	98.0 ± 2.4	94.3 ± 3.0

[a] The standard deviations (SD) represent variances of three separate experiments. [b] $n = 3$. [c] n.d. = not determined.

For ^{149}Pm- and ^{177}Lu-labeled CC49, biodistributions were obtained at 15 min, 1, 4, 24, 48, 96, and 168 h postinjection. For ^{166}Ho-MeO-DOTA−CC49, biodistributions were obtained at the same time points out to 96 h postinjection. Tissues harvested included blood, lung, liver, spleen, kidney, muscle, fat, heart, bone, uterus, ovaries, bladder, stomach, small intestine, large intestine, tumor, and carcass. Tissues were drained of blood, weighed, and counted in the gamma counter with a standard of the injected dose, such that decay-corrected uptakes were calculated as the percent injected dose per gram of tissue (% ID/g) and the percent injected dose per organ (% ID/organ).

Statistical Analysis. To compare biodistributions between ^{149}Pm-, ^{166}Ho-, and ^{177}Lu-MeO-DOTA−CC49, one-way analysis of variance (ANOVA) using statistical software SPSS 12.0.1 (Chicago, IL) was performed. Differences at the 95% confidence level ($p < 0.05$) were considered significant.

RESULTS

Conjugation of DOTA and MeO-DOTA to CC49 and Radiolanthanide Labeling. The reactions of *N*-hydroxysulfosuccinimidyl-DOTA (DOTA-OSSu) and methoxy-DOTA (MeO-DOTA) with mAb CC49 are expected to produce amide and thiourea linkages, respectively, between chelators and the ϵ-amino group of lysine residues and/or the *N*-termini of polypeptide chains (Figure 1). Both bifunctional chelating agents were reacted with CC49 at a molar ratio of 20:1. The average number of chelates per antibody was 5.53 for DOTA−CC49, as determined by an ^{111}In isotopic dilution assay (*5*, *33*). In comparison, the average number of chelates per antibody for MeO-DOTA−CC49 was 2.51. Reaction with purified antigen and GF−HPLC analysis demonstrated that the immunoreactivity of the DOTA and MeO-DOTA conjugates of CC49 were 97%. The nonreactive fraction (3%) consisted of incompletely assembled mAb species, which were minor byproducts of hybridoma production.

The average labeling efficiency of DOTA−CC49 with ^{177}Lu was 70.8% at a ratio of 5 μCi/μg, and purification by gel filtration spin column chromatography afforded a radiochemical purity of 95% as determined by GF−HPLC. At a 5 μCi/μg ratio, the MeO-DOTA−CC49 conjugate gave average labeling yields of 76.8%, 63.5%, and 68.0%, respectively, with ^{149}Pm, ^{166}Ho, and ^{177}Lu. For each radiolanthanide, radiochemical purity of MeO-DOTA−CC49 was >98.0% after purification, as determined by GF−HPLC. Surprisingly, the radiolabeling efficiency of DOTA−CC49 dropped precipitously and reproducibly to near zero values within two months of storage at either 4 °C or −70 °C. In contrast, after more nine months at 4 °C the MeO-DOTA conjugate could be labeled with all three radiolanthanides with efficiencies up to 80% at 5 μCi/μg.

In Vitro Stability Studies. The stability of ^{177}Lu-DOTA−CC49 in mouse serum was 94.3 ± 4.0% after 168 h at 37 °C (Table 2), a value significantly lower ($p = 0.0067$) than that of

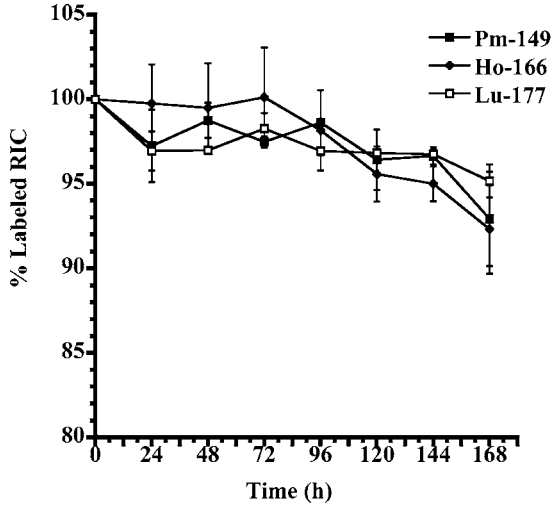

Figure 2. Percentages of ^{149}Pm, ^{166}Ho, and ^{177}Lu bound to MeO-DOTA−CC49 as a function of time of incubation with hydroxyapatite at 37 °C. Error bars represent standard deviations (SD) of three separate experiments.

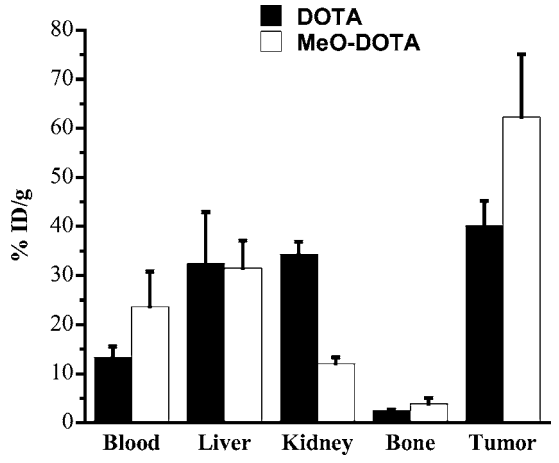

Figure 3. Comparison of ^{177}Lu-DOTA−CC49 and ^{177}Lu-MeO-DOTA−CC49 biodistributions ($n = 5$) in blood, liver, kidney, bone, and LS174T tumor at 24 h postinjection. Error bars represent standard deviations (SD).

^{177}Lu-MeO-DOTA−CC49 (98.0 ± 2.4%). In the case of the MeO-DOTA conjugate (Table 2), the serum stabilities at 96 h were statistically identical for ^{149}Pm (93.7 ± 2.5%) and ^{166}Ho (93.9 ± 0.7%), both lower than the corresponding value for ^{177}Lu (96.5 ± 0.9%). The ^{177}Lu-labeled MeO-DOTA conjugate was more stable than ^{149}Pm-MeO-DOTA−CC49 at 168 h ($p = 0.02$) and more stable than ^{166}Ho-MeO-DOTA−CC49 at 48 h ($p = 0.02$) and 96 h ($p = 0.03$). The radiolanthanides lost from DOTA−CC49 and MeO-DOTA−CC49 were invariably observed as low molecular weight species. Hydroxyapatite stability studies were also conducted, based on a previously published in vitro method for predicting the in vivo stability of radiolanthanide chelates (*32*). In the hydroxyapatite studies (Figure 2), the MeO-DOTA conjugate was 92.3 ± 2.6% stable with ^{166}Ho, 92.9 ± 2.8% stable with ^{149}Pm, and 95.2 ± 1.0% stable with ^{177}Lu for 168 h at 37 °C. The only statistically significant difference observed was between ^{177}Lu and ^{166}Ho at 168 h, which was marginal at $p = 0.048$.

Biodistribution Studies. Pilot ^{177}Lu biodistribution studies in nude mice bearing LS174T human colon carcinoma xenografts were conducted to compare CC49 conjugates of DOTA and MeO-DOTA. Uptakes in the major organs of interest at 24 h postinjection are shown in Figure 3. For ^{177}Lu-MeO-DOTA−CC49, substantially lower kidney uptake was observed, concomitant with considerably higher LS174T tumor uptake and slower blood clearance. With ^{177}Lu, the MeO-DOTA conjugate displayed superior conjugate and radiolabeling stability and more favorable biodistribution properties at 24 h postinjection. Therefore, MeO-DOTA−CC49 was selected for further in vivo evaluation using all three radiolanthanides.

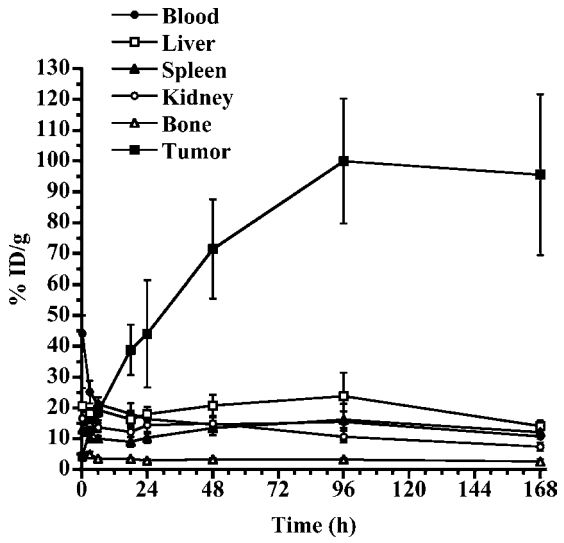

Figure 4. Biodistribution ($n = 5$) of ^{149}Pm-MeO-DOTA−CC49 in LS174T-bearing nude mice. Error bars represent standard deviations (SD).

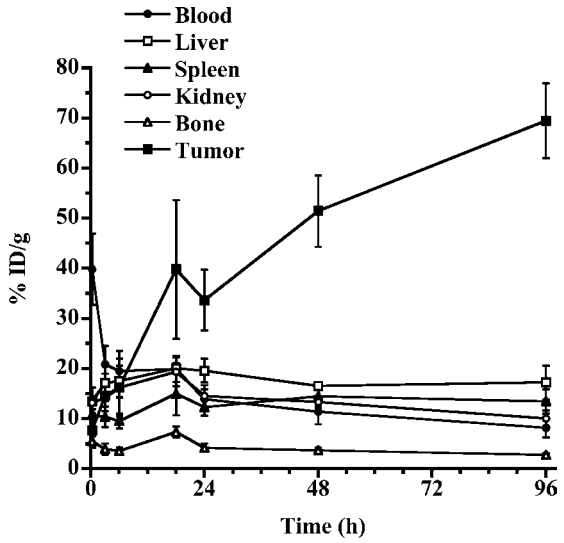

Figure 5. Biodistribution ($n = 5$) of ^{166}Ho-MeO-DOTA−CC49 in LS174T-bearing nude mice. Error bars represent standard deviations (SD).

Comprehensive biodistributions of ^{149}Pm- and ^{177}Lu-MeO-DOTA−CC49 were obtained in the LS174T mouse model at 15 min, 1, 4, 24, 48, 96, and 168 h postinjection. Biodistributions for ^{166}Ho-MeO-DOTA−CC49 were obtained at the same time points out to 96 h postinjection. The results obtained for ^{149}Pm-, ^{166}Ho-, and ^{177}Lu-MeO-DOTA−CC49 are given in Figures 4, 5, and 6, respectively. MeO-DOTA−CC49 exhibited extremely high tumor uptake for each of the radiolanthanides. The highest tumor uptake of ^{166}Ho-MeO-DOTA−CC49 was 69.5% ID/g at 96 h, which was significantly lower ($p < 0.05$) than the tumor uptake of ^{149}Pm- and ^{177}Lu-MeO-DOTA−CC49 (100.0% and 95.4%, respectively) at the same time point. Maximum tumor uptake of ^{177}Lu-MeO-DOTA−CC49, 132.4% ID/g, was observed at 168 h postinjection. This value was significantly higher than the maximum uptake observed for ^{166}Ho− ($p = 0.001$) and ^{149}Pm-MeO-DOTA−CC49 ($p = 0.001$).

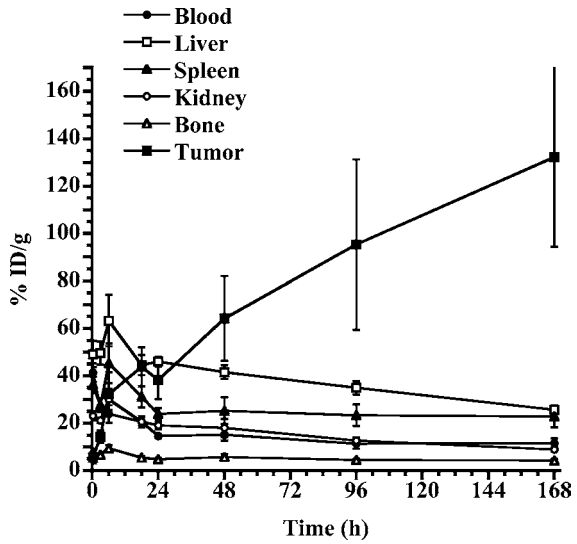

Figure 6. Biodistribution ($n = 5$) of ^{177}Lu-MeO-DOTA−CC49 in LS174T-bearing nude mice. Error bars represent standard deviations (SD).

Normal organ uptakes were generally below uniform distribution, except for initial uptakes of ^{177}Lu in the liver (63.3% ID/g), spleen (45.3% ID/g), and kidney (30.0%). Nontarget organ uptakes of ^{177}Lu decreased significantly ($p < 0.05$) with time to approximately 7% ID/g (kidney), 12% ID/g (spleen), and 20% ID/g (liver) at 96 to 168 h. Corresponding uptakes of ^{149}Pm and ^{166}Ho remained essentially constant at these values throughout the course of the studies. Blood levels of radiolanthanide-labeled MeO-DOTA−CC49 decreased significantly ($p < 0.05$) from approximately 21 to 27% ID/g at 3 h to 8 to 15% ID/g at 96 h. Bone uptakes of all three radiolanthanides decreased significantly ($p < 0.05$) from 4.89 to 7.66% ID/g at 15 min to 2.65 to 4.51% ID/g by 96 h. Small intestinal uptakes peaked at 1.33 to 2.52% ID/g at 6 h, and large intestinal uptakes reached maximum values of 1.33 to 2.48% ID/g by 6 h (data not shown).

Tumor-to-Blood Time−Activity Ratios of ^{149}Pm-, ^{166}Ho-, and ^{177}Lu-MeO-DOTA−CC49. The biodistributions of ^{149}Pm-, ^{166}Ho-, and ^{177}Lu-MeO-DOTA−CC49 were used to generate tumor and blood time-activity curves for the three radioimmunoconjugates. Physical decay was included to calculate percent injected activity per gram of tissue (% IA/g). The ratio of areas under the curves (AUCs) was used to estimate the anticipated "therapeutic index" of each agent. For ^{149}Pm-MeO-DOTA−CC49, the tumor AUC was 4405% IA/g−h, and the blood AUC was 1177% IA/g−h, affording a tumor-to-blood ratio of 3.74. Using ^{166}Ho-MeO-DOTA−CC49, lower values were obtained, yielding a tumor AUC of 1329% IA/g−h, a blood AUC of 596% IA/g−h, and a tumor-to-blood ratio of 2.23. MeO-DOTA−CC49 labeled with ^{177}Lu gave the highest results, with a tumor AUC of 9166% IA/g−h, a blood AUC of 1778% IA/g−h, and a tumor-to-blood ratio of 5.15.

DISCUSSION

The present studies evaluated the anti-TAG-72 monoclonal antibody CC49 conjugated with two bifunctional chelating agents, DOTA-OSSu and MeO-DOTA, for labeling with lanthanide radionuclides. Over the past several years, numerous groups have developed a large number of C- and N-substituted analogues of DOTA for antibody conjugation. Using DOTA-OSSu, we have had success targeting mouse xenografts with a variety of mAbs and radiometals (*5*−*10*). Conversely, MeO-DOTA may have better binding and in vivo distribution properties for radiolanthanides. A recent study compared anti-TAG-72 mAb B72.3 conjugated to MeO-DOTA, an octadentate C-substituted DOTA derivative, and a heptadentate DOTA attached by conversion of one of the carboxylate groups to an amide linker (*34*). In non-tumor-bearing mice, ^{177}Lu-labeled MeO-DOTA-B72.3 showed the lowest lung and spleen uptake of the three conjugates, suggesting reduced formation of colloidal radiometal hydroxides in vivo. Bone uptake of ^{177}Lu-MeO-DOTA-B72.3 was lower than that of amide-linked DOTA and comparable to that of C-substituted DOTA, indicating high chelate stability. Blood clearance of ^{177}Lu-MeO-DOTA-B72.3 was also faster than that of the C-substituted conjugate. Another advantage of MeO-DOTA is that it is the product of a convergent synthesis, which is considerably more straightforward than those of many C-substituted DOTA analogues.

Several mAbs (cT84.66, cBR96, and NR-LU-10) have been conjugated with DOTA-OSSu to give immunoconjugates that labeled reproducibly to high specific activity and high stability with ^{111}In, ^{90}Y, and ^{64}Cu (*5*−*10*). One preparation of DOTA-cT84.66 (*5*) has afforded near quantitative labeling and immunoreactivity after more than nine years of storage at 4 °C (*8, 9*). In contrast, the DOTA−CC49 conjugate was not stable for extended storage at 4 °C, and after approximately two months, ^{177}Lu labeling gave consistently irreproducible results. This finding was unusual and suggested that the choice of mAb and bifunctional chelating agent may be important for developing stable and high specific activity radiolanthanide immunoconjugates for RIT applications. However, at present we have no logical explanation for the instability of DOTA−CC49 upon storage. Unlike the DOTA conjugate, MeO-DOTA−CC49 could be labeled with ^{149}Pm, ^{166}Ho, and ^{177}Lu stably and with reproducibly high specific activity, even after more than nine months of storage at 4 °C.

For initial comparisons of the in vivo properties of two ^{177}Lu chelate conjugates, pilot biodistributions in the major organs were obtained for ^{177}Lu-DOTA−CC49 and ^{177}Lu-MeO-DOTA−CC49 in LS174T-bearing nude mice at 24 h postinjection. When labeled with ^{177}Lu, MeO-DOTA−CC49 showed lower kidney uptake, slower blood clearance, and higher LS174T tumor uptake. For CC49, MeO-DOTA was a more robust bifunctional chelating agent for stable conjugation and reproducible, efficient labeling than DOTA. Therefore, MeO-DOTA−CC49 was chosen for further evaluation in vitro and in vivo using ^{149}Pm, ^{166}Ho, and ^{177}Lu.

To assess the in vitro stability of radiolanthanide-labeled CC49, studies were conducted in mouse serum and a hydroxyapatite model. In serum, the small degree of radiometal dissociation from the conjugate resulted only in lower molecular weight constituents in serum out to 96 to 168 h at 37 °C, consistent with other published reports evaluating ^{111}In-, ^{90}Y-, and ^{64}Cu-labeled mAbs (*5, 6, 8*−*10*). Relative to initial radiochemical purity, the serum stability of ^{177}Lu-DOTA−CC49 was statistically equivalent to ^{177}Lu-MeO-DOTA−CC49 over a 96-h period. Only at 168 h was the MeO-DOTA conjugate more stable than the DOTA conjugate when labeled with ^{177}Lu. Because of the lanthanide contraction, lutetium has the smallest radius and highest coordination energy of the three radiometals and is likely to be bound more tightly by the MeO-DOTA chelator. MeO-DOTA−CC49 was most stable in serum when labeled with ^{177}Lu, followed by ^{166}Ho and ^{149}Pm. However, radiolanthanides do not bind with high affinity to any major serum proteins. At longer time points in the serum stability studies, equilibria likely exist between the radiolanthanide chelate conjugates and the free radiometals. Over an extended period, the serum stability curves began to reach asymptotes for all three radioimmunoconjugates. This asymptotic behavior was characteristic of equilibrium conditions, under which thermodynamic stability of the radiolanthanide−mAb conjugates would be expected to prevail.

However, the in vivo stability of radiolanthanide-labeled CC49 is likely to depend on kinetic, rather than thermodynamic, properties. Therefore, a hydroxyapatite matrix (*32*) was used as an in vitro model to predict the relative in vivo stabilities of ^{149}Pm-, ^{166}Ho-, and ^{177}Lu-MeO-DOTA−CC49. Hydroxyapatite is a major constituent found in the extracellular matrix of bone. As calcium mimics, free lanthanides deposit and become fixed in bone, presumably by a hydroxyapatite-mediated mechanism. In contrast to the serum stability studies, hydroxyapatite binding showed that ^{149}Pm-, ^{166}Ho-, and ^{177}Lu-MeO-DOTA−CC49 were ≥92% stable for up to 168 h at 37 °C. The difference in stability of ^{149}Pm-, ^{166}Ho-, and ^{177}Lu-labeled CC49 in hydroxyapatite versus serum may reflect differences in kinetic versus thermodynamic stability, as measured respectively by the two assays. Dissociation of radiolanthanides from mAb conjugates in vivo will likely result in substantial accumulation in the skeleton. In the present studies, the high stabilities of ^{149}Pm-, ^{166}Ho-, and ^{177}Lu-MeO-DOTA−CC49 to hydroxyapatite challenge paralleled the low bone uptakes of the three radiometals in LS174T-bearing nude mice. Bone uptakes were not statistically significant between the radiometals ($p > 0.05$), and by 96 h values for all three radiolanthanide immunoconjugates were <5% ID/g.

Given its high concentration in LS174T xenografts and the presence of multiple epitopes per molecule, TAG-72 represents a high capacity tumor target, and high specific activity of labeling CC49 is not necessary to achieve high tumor uptake. Empirically, a specific activity 1 μCi/μg, compared to approximately 4 μCi/μg, slightly improved the tumor uptake and normal tissue biodistribution of ^{177}Lu-MeO-DOTA−CC49 in the LS174T mouse model (data not shown). It is well-documented that TAG-72 is secreted into the blood of patients and correlates strongly with tumor antigen expression (*35*). In LS174T-bearing mice, TAG-72 could be shed into circulation, and the use of higher specific activity of CC49 may result in greater accumulation of immune complexes in the liver and spleen. It is possible that lowering the specific activity reduced the uptake in these organs and concomitantly increased tumor uptake. However, the slightly improved tumor uptake and reticuloendothelial clearance of lower specific activity ^{177}Lu-MeO-DOTA−CC49 was based on a limited number of pilot biodistributions and may not be statistically significant. Further studies of the relationship between the specific activity of radiolanthanide-labeled CC49 and its biodistribution properties are warranted.

Relative to the DOTA conjugate, an increased amount of ^{177}Lu from MeO-DOTA−CC49 was observed in the blood at 24 h. A possible explanation for this result is the decreased kidney uptake of ^{177}Lu from MeO-DOTA−CC49. However, the dose-limiting toxicity of conventional RIT is usually myelosuppression caused by slow blood clearance, raising the question as to whether the use of MeO-DOTA may augment this toxicity. Conversely, the higher kidney uptake of DOTA−CC49 might result in increased renal toxicity, although it is likely that bone marrow will remain the dose-limiting tissue. We have performed preliminary RIT studies of ^{149}Pm-, ^{166}Ho-, and ^{177}Lu-MeO-DOTA−CC49 in LS174T-bearing nude mice (*36*). No overt signs of systemic toxicity were observed in any of these animals, and among six-month survivors, no microscopic evidence of liver, kidney, or spleen toxicity was found at necropsy. The results of these studies will be reported in greater detail in the future. However, the respective maximum tolerated doses of ^{149}Pm-, ^{166}Ho-, and ^{177}Lu-MeO-DOTA−CC49 have not yet been determined. Dose escalation studies will be performed in order to identify the dose-limiting toxicities of these RIT agents, as well as ^{177}Lu-DOTA−CC49.

In vivo, free lanthanides also accumulate in the liver as a result of metabolic processing. Although relatively high liver uptake was observed for all three radiolanthanides, this phenomenon was more likely attributable to antibody metabolism and not chelate instability. Chelate instability would be expected to result in high bone uptake, which was not observed for ^{149}Pm-, ^{166}Ho-, and ^{177}Lu-MeO-DOTA−CC49. Monoclonal antibody clearance and metabolism occurs predominantly through reticuloendothelial organs, primarily the liver and spleen. Antibodies are bound and internalized by asialoglycoprotein receptors in liver cells, resulting in concomitant radiometal retention in that organ for prolonged periods (*37*). In the present studies significantly higher liver uptake of ^{177}Lu-MeO-DOTA−CC49 was observed versus ^{166}Ho- ($p = 0.001$) and ^{149}Pm-MeO-DOTA−CC49 ($p = 0.001$). No significant difference in liver uptake was observed between ^{166}Ho- and ^{149}Pm-MeODOTA−CC49. Both ^{149}Pm- and ^{177}Lu-MeO-DOTA−CC49 exhibited a decrease in liver uptake with time, while ^{166}Ho-MeO-DOTA−CC49 showed an increase in liver accumulation with time. Regardless of this trend, ^{177}Lu-MeO-DOTA−CC49 had the highest liver uptake and retention of the three radiolanthanides. Spleen uptakes of ^{149}Pm-, ^{166}Ho-, and ^{177}Lu-MeO-DOTA−CC49 were above uniform distribution and remained relatively constant over time for all three radiolanthanides. In addition to reticuloendothelial clearance of mAbs, positively charged metabolites of radiometal chelates bind to the negatively charged brush border of the renal proximal tubule, leading to kidney retention. Therefore, it was not surprising that MeO-DOTA−CC49 also displayed relatively high renal uptakes of ^{149}Pm, ^{166}Ho, and ^{177}Lu. However, radioactivity in the kidneys decreased appreciably over time for each radiolanthanide.

In the biodistribution studies, the major tissue of uptake for ^{149}Pm-, ^{166}Ho-, and ^{177}Lu-MeO-DOTA−CC49 was the tumor. The maximum tumor uptake of ^{177}Lu-MeO-DOTA−CC49 was 132.4% ID/g at 168 h. This result compares extremely favorably to the work of Schlom et al. (*23*), who observed an 81.1% ID/g uptake in subcutaneous LS174T xenografts in nude mice 168 h after injection of ^{177}Lu−PA-DOTA−CC49 (1 μCi/μg). However, direct comparisons between the work of Schlom et al. and the results reported here should be made with caution. PA-DOTA was conjugated to CC49 by a prelabeling strategy, in which essentially every conjugate was complexed with lutetium. In the present work, a postlabeling approach was used, such that at 1 μCi/μg, 1 of 24 MeO-DOTA−CC49 molecules was complexed with lutetium, one of three conjugates was complexed with holmium, and 1 of 395 conjugates was complexed with promethium, based on the respective specific activities of the radiolanthanides (*4*). Pre- and postlabeling strategies produce inherently different products that are likely to have different in vivo distribution properties. Furthermore, the average tumor weight in the experiments performed by Schlom *et* al. (*23*) was 30 mg, as opposed to 175 mg in the studies presented here. It is likely that larger tumors will exhibit lower antibody uptake, in % ID/g, than smaller tumors. For the larger tumors established in the present work, the uptake of ^{177}Lu-MeO-DOTA−CC49 was the highest of any radiopharmaceutical we have evaluated to date.

The maximum tumor uptake of MeO-DOTA−CC49 occurred in approximately two half-lives for ^{149}Pm, approximately four half-lives for ^{166}Ho, and approximately one half-life for ^{177}Lu. The time of maximum tumor uptake in conventional RIT relative to the half-life of the radionuclide could have a significant effect on therapeutic efficacy. As the half-life decreases, more radioactive decays will occur in the blood before the long-circulating mAb localizes to the tumor. As expected, the blood uptake of all three MeO-DOTA conjugates was initially high but slowly cleared to 8 to 12% ID/g by 96 to 168 h.

As a result, the tumor-to-blood AUC ratios, or anticipated "therapeutic indices," followed the trend ^{177}Lu > ^{149}Pm > ^{166}Ho. In subsequent RIT studies (*36*), it was determined that the most significant endpoint was time to progression to an LS174T tumor burden of 1 g. Using this endpoint, it was found that the therapeutic efficacy of ^{177}Lu-MeO-DOTA−CC49 was statistically superior to that of the ^{149}Pm conjugate, which in turn was statistically greater than that of the ^{166}Ho conjugate. These results suggest that, given the relatively long tumor targeting and clearance kinetics of intact radiolabeled antibodies, the physical half-life of the radionuclide should be well matched to the biological half-life of the targeting agent.

CONCLUSION

MeO-DOTA−CC49 labeled with the lanthanide radionuclides ^{149}Pm, ^{166}Ho, and ^{177}Lu showed extremely high tumor uptake and generally favorable biodistribution properties in nude mice bearing LS174T human colon carcinoma xenografts. The high tumor-specific targeting of each of these agents warrants further investigation for RIT of adenocarcinomas. However, the different physical half-lives and β^- particle energies of the radiolanthanides, as well as the different clearance properties of the radioimmunoconjugates, may have important effects on radiation dosimetry, toxicity, and therapeutic efficacy. The results of RIT studies of ^{149}Pm-, ^{166}Ho-, and ^{177}Lu-MeO-DOTA−CC49 in the LS174T mouse model have been presented in preliminary form (*36*) and will be reported in more detail soon.

ACKNOWLEDGMENT

This research, under Award Number DAMD 17-02-1-0103, was supported by the Department of Defense Prostate Cancer Research Program, which is managed by the U.S. Army Medical Research and Materiel Command. This work was also funded by Grant URB-01-015 from the University of Missouri Research Board and a grant from the University of Missouri College of Veterinary Medicine Committee on Research. The authors would like to thank Dr. Jeffrey Schlom for providing the CC49 hybridoma cell line, as well as Dr. Christopher Johnson for assistance with statistical software SPSS 12.0.1. We also acknowledge the support of the U.S. Department of Veterans Affairs, for providing resources and the use of facilities at the Harry S. Truman Memorial Veterans' Hospital in Columbia, MO.

Supporting Information Available: Tables of mean percent injected dose per gram of tissue (% ID/g) with standard deviations (SD) of ^{149}Pm-, ^{166}Ho-, and ^{177}Lu-MeO-DOTA−CC49 for all tissues and time points evaluated. This material is available free of charge via the Internet at http://pubs.acs.org.

LITERATURE CITED

(1) Vose, J. M., Wahl, R. L., Saleh, M., Rohatiner, A. Z., Knox, S. J., Radford, J. A., Zelenetz, A. D., Tidmarsh, G. F., Stagg, R. J., and Kaminski, M. S. (2000) Multicenter phase II study of iodine-131 tositumomab for chemotherapy-relapsed/refractory low-grade and transformed low-grade B-cell non-Hodgkin's lymphomas. *J. Clin. Oncol. 18*, 1316−1323.

(2) Witzig, T. E., Gordon, L. I., Cabanillas, F., Czuczman, M. S., Emmanouilides, C., Joyce, R., Pohlman, B. L., Bartlett, N. L., Wiseman, G. A., Padre, N., Grillo-Lopez, A. J., Multani, P., and White, C. A. (2002) Randomized controlled trial of yttrium-90-labeled ibritumomab tiuxetan radioimmunotherapy versus rituximab immunotherapy for patients with relapsed or refractory low-grade, follicular, or transformed B-cell non-Hodgkin's lymphoma. *J. Clin. Oncol. 20*, 2453−2463.

(3) Goldenberg, D. M. (2002) Targeted therapy of cancer with radiolabeled antibodies. *J. Nucl. Med. 43*, 693−713.

(4) Lewis, M. R., Zhang, J., Jia, F., Owen, N. K., Cutler, C. S., Embree, M. F., Schultz, J., Theodore, L. J., Ketring, A. R., Jurisson, S. S., and Axworthy, D. B. (2004) Biological comparison of ^{149}Pm-, ^{166}Ho-, and ^{177}Lu-DOTA-biotin pretargeted by CC49 scFv-streptavidin fusion protein in xenograft-bearing nude mice. *Nucl. Med. Biol. 31*, 213−223.

(5) Lewis, M. R., Kao, J. Y., Anderson, A.-L. J., Shively, J. E., and Raubitschek, A. (2001) An improved method for conjugating monoclonal antibodies with *N*-hydroxysulfosuccinimidyl DOTA. *Bioconjugate Chem. 12*, 320−324.

(6) Lewis, M. R., Raubitschek, A., and Shively, J. E. (1994) A facile, water-soluble method for modification of proteins with DOTA. Use of elevated temperature and optimized pH to achieve high specific activity and high chelate stability in radiolabeled immunoconjugates. *Bioconjugate Chem. 5*, 565−576.

(7) Williams, L. E., Lewis, M. R., Bebb, G. G., Clarke, K. G., Odom-Maryon, T. L., Shively, J. E., and Raubitschek, A. A. (1998) Biodistribution of ^{111}In- and ^{90}Y-labeled DOTA and maleimido-cysteineamido-DOTA conjugated to chimeric anti-carcinoembryonic antigen antibody in xenograft-bearing nude mice: comparison of stable and chemically labile linker systems. *Bioconjugate Chem. 9*, 87−93.

(8) Bryan, J. N., Jia, F., Mohsin, H., Sivaguru, G., Miller, W. H., Anderson, C. J., Henry, C. J., and Lewis, M. R. (2005) Comparative uptakes and biodistributions of internalizing vs. noninternalizing copper-64 radioimmunoconjugates in cell and animal models of colon cancer. *Nucl. Med. Biol. 32*, 851−858.

(9) Bryan, J. N., Lewis, M. R., Henry, C. J., Owen, N. K., Zhang, J., Mohsin, H., Jia, F., Sivaguru, G., and Anderson, C. J. (2004) Development of a two-antibody model for the evaluation of copper-64 radioimmunotherapy. *Vet. Comp. Oncol. 2*, 82−90.

(10) Lewis, M. R., Wang, M., Axworthy, D. B., Theodore, L. J., Mallett, R. W., Fritzberg, A. R., Welch, M. J., and Anderson, C. J. (2003) In vivo evaluation of pretargeted ^{64}Cu for tumor imaging and therapy. *J. Nucl. Med. 44*, 1284−1292.

(11) Muraro, R., Kuroki, M., Wunderlich, D., Poole, D. J., Colcher, D., Thor, A., Greiner, J. W., Simpson, J. F., Molinolo, A., Noguchi, P., and Schlom, J. (1988) Generation and characterization of B72.3 second generation monoclonal antibodies reactive with the tumor-associated glycoprotein 72 antigen. *Cancer Res. 48*, 4588−4596.

(12) Battista, P., Muraro, R., Mammarella, S., Curia, M. C., Colasante, A., Rosini, S., Lesti, G., Sacco, R., French, D., Frati, L., and Costantini, R. M. (1990) Complementary reactivities of anti-carcinoembryonic antigen and antitumor-associated glycoprotein 72 monoclonal antibodies in lung carcinomas. *Cancer Res. 50*, 6987−6994.

(13) Johnston, W. W., Szpak, C. A., Thor, A., and Schlom, J. (1986) Phenotypic characterization of lung cancers in fine needle aspiration biopsies using monoclonal antibody B72.3. *Cancer Res. 46*, 6462−6470.

(14) Lyubsky, S., Madariaga, J., Lozowski, M., Mishriki, Y., Schuss, A., Chao, S., and Lundy, J. (1988) A tumor-associated antigen in carcinoma of the pancreas defined by monoclonal antibody B72.3. *Am. J. Clin. Pathol. 89*, 160−167.

(15) Mazur, M. T., and Shultz, J. J. (1990) Prostatic adenocarcinoma. Evaluation of immunoreactivity to monoclonal antibody B72.3. *Am. J. Clin. Pathol. 93*, 466−470.

(16) Nuti, M., Mottolese, M., Viora, M., Donnorso, P. R., Schlom, J., and Natali, P. G. (1986) Use of monoclonal antibodies to human breast tumor associated antigens in fine needle aspirate cytology. *Int. J. Cancer 37*, 493−498.

(17) Nuti, M., Yoshio, A., Teramato, Y. A., Mariani-Costantini, R., Horan Hand, P., Colcher, D., and Schlom, J. (1982) A monoclonal antibody (B72.3) defines patterns of distribution of a novel tumor-associated antigen in human mammary carcinoma cell populations. *Int. J. Cancer 29*, 539−545.

(18) Ohuchi, N., Thor, A., Nose, M., Fujita, J., Kyogoku, M., and Schlom, J. (1986) Tumor-associated glycoprotein (TAG-72) detected in adenocarcinomas and benign lesions of the stomach. *Int. J. Cancer 38*, 643−650.

(19) Stramignoni, D., Bowen, R., Atkinson, B. F., and Schlom, J. (1983) Differential reactivity of monoclonal antibodies with human colon adenocarcinomas and adenomas. *Int. J. Cancer 31*, 543−552.

(20) Thor, A., Ohuchi, N., Szpak, C. A., Johnston, W. W., and Schlom, J. (1986) Distribution of oncofetal antigen tumor-associated glycoprotein-72 defined by monoclonal antibody B72.3. *Cancer Res. 46*, 3118−3124.

(21) Xu, M., Real, F. X., Welt, S., Schussler, M. H., Oettgen, H. F., and Old, L. J. (1989) Expression of TAG-72 in normal colon, transitional mucosa, and colon cancer. *Int. J. Cancer 44*, 985−989.

(22) Schlom, J., Eggensperger, D., Colcher, D., Molinolo, A., Houchens, D., Miller, L. S., Hinkle, G., and Siler, K. (1992) Therapeutic advantage of high-affinity anticarcinoma radioimmunoconjugates. *Cancer Res. 52*, 1067−1072.

(23) Schlom, J., Siler, K., Milenic, D. E., Eggensperger, D., Colcher, D., Miller, L. S., Houchens, D., Cheng, R., Kaplan, D., and Goeckeler, W. (1991) Monoclonal antibody-based therapy of a human tumor xenograft with a ^{177}lutetium-labeled immunoconjugate. *Cancer Res. 51*, 2889−2896.

(24) Alvarez, R. D., Partridge, E. E., Khazaeli, M. B., Plott, G., Austin, M., Kilgore, L., Russell, C. D., Liu, T., Grizzle, W. E., Schlom, J., LoBuglio, A. F., and Meredith, R. F. (1997) Intraperitoneal radioimmunotherapy of ovarian cancer with ^{177}Lu−CC49: A phase I/II study. *Gynecol. Oncol. 65*, 94−101.

(25) Divgi, C. R., Scott, A. M., Dantis, L., Capitelli, P., Siler, K., Hilton, S., Finn, R. D., Kemeny, N., Kelsen, D., Kostakoglu, L., Schlom, J., and Larson, S. M. (1995) Phase I radioimmunotherapy trial with iodine-131-CC49 in metastatic colon carcinoma. *J. Nucl. Med. 36*, 586−592.

(26) Meredith, R. F., Partridge, E. E., Alvarez, R. D., Khazaeli, M. B., Plott, G., Russell, C. D., Wheeler, R. H., Liu, T., Grizzle, W. E., Schlom, J., and LoBuglio, A. F. (1996) Intraperitoneal radioimmunotherapy of ovarian cancer with lutetium-177-CC49. *J. Nucl. Med. 37*, 1491−1496.

(27) Mulligan, T., Carrasquillo, J. A., Chung, Y., Milenic, D. E., Schlom, J., Feuerstein, I., Paik, C., Perentesis, P., Reynolds, J., Curt, G., Goeckeler, W., Fordyce, W., Cheng, R., Riseberg, D., Cowan, K., and O'Shaughnessy, J. (1995) Phase I study of intravenous ^{177}Lu-labeled CC49 murine monoclonal antibody in patients with advanced adenocarcinoma. *Clin. Cancer Res. 1*, 1447−1454.

(28) Murray, J. L., Macey, D. L., Kasi, L. P., Rieger, P., Cunningham, J., Bhadkamkar, V., Zhang, H. Z., Schlom, J., Rosenblum, M. G., and Podoloff, D. A. (1994) Phase II radioimmunotherapy trial with ^{131}I-CC49 in colorectal cancer. *Cancer 73*, 1057−1066.

(29) Tempero, M., Leichner, P., Dalrymple, G., Harrison, K., Augustine, S., Schlom, J., Anderson, J., Wisecarver, J., and Colcher, D. (1997) High-dose therapy with iodine-131-labeled monoclonal antibody CC49 in patients with gastrointestinal cancers: a phase I trial. *J. Clin. Oncol. 15*, 1518−1528.

(30) Sumerdon, G. A., Rogers, P. E., Lombardo, C. M., Schnobrich, K. E., Melvin, S. L., Hobart, E. D., Tribby, I. I. E., Stroupe, S. D., and Johnson, D. K. (1990) An optimized antibody-chelator conjugate for imaging of carcinoembryonic antigen with indium-111. *Nucl. Med. Biol. 17*, 247−254.

(31) Lewis, M. R., Boswell, C. A., Laforest, R., Buettner, T. L., Ye, D., Connett, J. M., and Anderson, C. J. (2001) Conjugation of monoclonal antibodies with TETA using activated esters: biological comparison of ^{64}Cu-TETA-1A3 with ^{64}Cu−BAT-2IT-1A3. *Cancer Biother. Radiopharm. 16*, 483−494.

(32) Li, W. P., Ma, D. S., Higginbotham, C., Hoffman, T., Ketring, A. R., Cutler, C. S., and Jurisson, S. S. (2001) Development of an in vitro model for assessing the in vivo stability of lanthanide chelates. *Nucl. Med. Biol. 28*, 145−154.

(33) Meares, C. F., McCall, M. J., Reardan, D. T., Goodwin, D. A., Diamanti, C. I., and McTigue, M. (1984) Conjugation of antibodies with bifunctional chelating agents: isothiocyanate and bromoacetamide reagents, methods of analysis, and subsequent addition of metal ions. *Anal. Biochem. 142*, 68−78.

(34) Mohsin, H., Fitzsimmons, J., Hoffman, T., Lever, S., and Jurisson, S. (2004) Preparation and biological evaluation of ^{111}In, ^{177}Lu, and ^{90}Y labeled DOTA analogs conjugated to B72.3 antibody. *J. Nucl. Med. 45*, 457P.

(35) Guadagni, F., Roselli, M., Cosimelli, M., Spila, A., Cavaliere, F., Tedesco, M., Arcuri, R., Abbolito, M. R., Casale, V., Pericoli, M. N., Vecchione, A., Casciani, C. U., Greiner, J. W., and Schlom, J. (1996) Correlation between tumor-associated glycoprotein 72 mucin levels in tumor and serum of colorectal patients as measured by the quantitative CA 72−4 immunoassay. *Cancer Res. 56*, 5293−5298.

(36) Mohsin, H., Sivaguru, G., Jia, F., Bryan, J. N., Cutler, C. S., Ketring, A. R., Athey, P. S., Simón, J., Frank, R. K., Theodore, L. J., Axworthy, D. B., Jurisson, S. S., and Lewis, M. R. (2005) Comparison of pretarget and conventional CC49 radioimmunotherapy using ^{149}Pm, ^{166}Ho and ^{177}Lu. *J. Labelled Compd. Radiopharm. 48*, S21.

(37) Kukis, D. L., Novak-Hofer, I., and DeNardo, S. J. (2001) Cleavable linkers to enhance selectivity of antibody-targeted therapy of cancer. *Cancer Biother. Radiopharm. 16*, 457−467.

BC0502356

SUPPORTING INFORMATION

Bioconjugate Chemistry

Radiolanthanide-Labeled Monoclonal Antibody CC49 for Radioimmunotherapy of Cancer: Biological Comparison of DOTA Conjugates and ^{149}Pm, ^{166}Ho, and ^{177}Lu

Huma Mohsin, Fang Jia, Geethapriya Sivaguru, Michael J. Hudson, Tiffani D. Shelton, Timothy J. Hoffman, Cathy S. Cutler, Alan R. Ketring, Phillip S. Athey, Jaime Simón, R. Keith Frank, Silvia S. Jurisson, and Michael R. Lewis*

Table 3. Biodistribution (mean % ID/g ± s.d.) of ^{149}Pm-MeO-DOTA-CC49 in nude mice bearing LS174T human colorectal carcinoma xenografts.[a]

Tissue	15 min	3 h	6 h	18 h	24 h	48 h	96 h	168 h
Blood	44.2 ± 5.72	25.2 ± 3.69	21.3 ± 2.27	18.1 ± 3.45	16.4 ± 2.42	14.7 ± 2.23	15.5 ± 5.80	10.8 ± 0.98
Lung	15.7 ± 3.32	10.6 ± 1.89	8.41 ± 0.46	6.72 ± 0.87	6.78 ± 0.98	6.93 ± 1.31	5.16 ± 0.49	5.15 ± 1.09
Liver	20.6 ± 5.84	18.2 ± 1.72	19.4 ± 2.06	16.4 ± 2.77	18.0 ± 2.36	20.8 ± 3.52	23.9 ± 7.57	14.1 ± 1.76
Spleen	13.0 ± 1.96	10.0 ± 1.22	10.1 ± 0.86	9.04 ± 1.61	10.4 ± 1.70	13.5 ± 2.25	16.2 ± 2.71	12.2 ± 1.60
Kidney	16.7 ± 2.06	14.2 ± 1.66	13.7 ± 1.51	12.3 ± 1.72	14.4 ± 2.70	15.0 ± 2.41	10.7 ± 1.93	7.43 ± 1.37
Bladder	2.78 ± 0.65	2.51 ± 0.50	4.03 ± 0.59	7.43 ± 0.78	5.39 ± 0.87	7.33 ± 1.51	5.28 ± 1.51	4.17 ± 1.56
Muscle	1.04 ± 0.14	1.06 ± 0.09	1.08 ± 0.17	1.30 ± 0.16	1.45 ± 0.20	1.22 ± 0.22	0.75 ± 0.09	0.91 ± 0.10
Fat	2.54 ± 0.74	1.78 ± 0.18	2.12 ± 0.45	2.96 ± 0.16	2.19 ± 0.13	1.35 ± 0.39	2.43 ± 0.43	1.60 ± 0.25
Heart	10.5 ± 2.02	9.17 ± 0.17	6.37 ± 0.50	5.05 ± 0.91	3.52 ± 0.30	3.56 ± 0.39	3.03 ± 0.40	3.51 ± 0.98
Bone	4.89 ± 0.76	4.90 ± 0.95	3.58 ± 0.33	3.44 ± 0.38	2.90 ± 0.41	3.31 ± 0.52	3.22 ± 0.44	2.65 ± 0.73
Uterus	5.27 ± 1.09	4.42 ± 0.70	7.71 ± 1.77	8.29 ± 0.90	6.15 ± 0.79	5.03 ± 0.86	6.61 ± 0.98	6.73 ± 0.69
Ovaries	9.35 ± 1.69	9.63 ± 1.33	8.32 ± 1.19	8.66 ± 2.09	7.43 ± 0.98	6.70 ± 1.19	6.90 ± 0.35	14.0 ± 4.46
Stomach	0.50 ± 0.18	1.20 ± 0.18	1.13 ± 0.21	0.98 ± 0.18	1.27 ± 0.27	0.87 ± 0.19	0.63 ± 0.18	0.31 ± 0.06
Sm. Int	1.42 ± 0.29	1.63 ± 0.13	1.67 ± 0.25	1.50 ± 0.29	1.44 ± 0.30	1.34 ± 0.32	1.11 ± 0.05	0.67 ± 0.16
Lg. Int	0.59 ± 0.18	1.16 ± 0.20	1.34 ± 0.08	1.27 ± 0.27	1.14 ± 0.20	1.27 ± 0.24	0.92 ± 0.15	0.74 ± 0.20
Tumor	4.14 ± 1.42	12.7 ± 3.47	18.7 ± 2.62	38.9 ± 8.15	44.1 ± 17.4	71.6 ± 16.0	100.0 ± 20.3	95.7 ± 26.2

[a] n = 5.

Table 4. Biodistribution (mean % ID/g ± s.d.) of ^{166}Ho-MeO-DOTA-CC49 in nude mice bearing LS174T human colorectal carcinoma xenografts.[a]

Tissue	15 min	3 h	6 h	18 h	24 h	48 h	96 h
Blood	39.8 ± 7.16	20.9 ± 3.63	19.5 ± 4.03	19.9 ± 2.60	13.9 ± 1.99	11.4 ± 7.16	8.15 ± 1.93
Lung	12.3 ± 2.83	8.74 ± 1.67	7.91 ± 1.55	14.7 ± 2.36	6.44 ± 1.18	5.55 ± 0.28	4.85 ± 1.09
Liver	13.4 ± 2.78	17.1 ± 3.60	17.5 ± 3.13	20.1 ± 0.99	19.5 ± 2.37	16.5 ± 0.73	17.2 ± 3.38
Spleen	10.7 ± 1.11	10.4 ± 2.07	9.50 ± 1.53	15.0 ± 4.29	12.3 ± 1.74	14.5 ± 2.38	13.5 ± 2.44
Kidney	13.2 ± 1.28	14.2 ± 2.66	16.2 ± 1.97	19.4 ± 2.89	14.5 ± 2.13	13.3 ± 0.79	10.0 ± 1.61
Bladder	2.60 ± 0.73	3.65 ± 0.69	2.76 ± 0.64	6.85 ± 2.27	6.13 ± 1.77	7.14 ± 2.40	4.05 ± 0.79
Muscle	0.70 ± 0.13	1.16 ± 0.30	0.99 ± 0.07	2.28 ± 0.55	1.14 ± 0.10	1.19 ± 0.28	0.80 ± 0.19
Fat	1.19 ± 0.27	1.91 ± 0.53	1.36 ± 0.28	2.51 ± 0.38	1.61 ± 0.48	1.58 ± 0.65	2.96 ± 0.53
Heart	4.55 ± 0.86	3.11 ± 1.05	4.53 ± 0.78	7.84 ± 2.08	3.71 ± 0.88	3.20 ± 0.69	2.13 ± 0.43
Bone	5.45 ± 1.08	3.93 ± 1.08	3.52 ± 0.66	7.33 ± 1.11	4.22 ± 0.81	3.70 ± 0.50	2.77 ± 0.30
Uterus	2.78 ± 0.58	4.99 ± 0.59	4.10 ± 1.09	8.68 ± 1.74	5.49 ± 1.50	4.37 ± 0.98	4.02 ± 0.92
Ovaries	10.5 ± 3.51	13.0 ± 5.91	7.30 ± 1.44	15.3 ± 2.04	9.91 ± 3.28	9.26 ± 2.16	7.16 ± 1.67
Stomach	0.34 ± 0.13	0.64 ± 0.23	1.02 ± 0.33	0.92 ± 0.17	0.89 ± 0.11	0.21 ± 0.05	0.56 ± 0.10
Sm. Int	0.90 ± 0.09	1.22 ± 0.23	1.33 ± 0.14	1.49 ± 0.18	1.16 ± 0.16	0.68 ± 0.16	0.74 ± 0.10
Lg. Int	0.41 ± 0.07	0.98 ± 0.15	1.21 ± 0.06	1.27 ± 0.19	1.23 ± 0.22	0.69 ± 0.20	0.75 ± 0.15
Tumor	7.63 ± 3.42	14.6 ± 4.40	16.2 ± 5.78	39.8 ± 13.8	33.7 ± 6.04	51.4 ± 7.12	69.5 ± 7.47

[a] n = 5.

Table 5. Biodistribution (mean % ID/g ± s.d.) of ^{177}Lu-MeO-DOTA-CC49 in nude mice bearing LS174T human colorectal carcinoma xenografts.[a]

Tissue	15 min	3 h	6 h	18 h	24 h	48 h	96 h	168 h
Blood	41.4 ± 3.82	26.5 ± 1.14	23.9 ± 3.74	20.7 ± 1.86	14.7 ± 0.85	15.1 ± 2.31	11.4 ± 2.01	11.7 ± 2.02
Lung	28.4 ± 3.06	12.5 ± 1.36	16.7 ± 2.19	9.43 ± 1.49	7.54 ± 1.43	7.20 ± 1.41	6.75 ± 0.68	5.54 ± 1.60
Liver	49.3 ± 5.53	49.7 ± 4.95	63.3 ± 10.8	44.6 ± 4.25	46.1 ± 2.07	41.5 ± 2.90	35.0 ± 2.92	25.7 ± 1.79
Spleen	36.3 ± 3.39	27.7 ± 2.95	45.4 ± 8.36	31.2 ± 4.41	23.9 ± 2.60	25.4 ± 5.72	23.3 ± 4.50	22.9 ± 4.50
Kidney	23.2 ± 1.82	21.2 ± 1.11	30.0 ± 4.48	20.6 ± 2.36	19.1 ± 1.67	18.1 ± 3.87	12.8 ± 1.30	8.96 ± 0.84
Bladder	5.68 ± 0.24	2.41 ± 0.42	7.59 ± 1.16	6.20 ± 0.89	4.95 ± 0.87	6.16 ± 1.36	5.86 ± 0.66	5.77 ± 1.43
Muscle	1.26 ± 0.21	1.58 ± 0.27	1.65 ± 0.19	1.94 ± 0.34	1.48 ± 0.17	1.37 ± 0.12	1.20 ± 0.20	0.87 ± 0.11
Fat	3.47 ± 0.66	2.62 ± 0.87	2.23 ± 0.65	1.75 ± 0.16	1.74 ± 0.21	3.12 ± 0.58	1.79 ± 0.30	1.37 ± 0.15
Heart	15.0 ± 1.83	9.41 ± 1.04	10.1 ± 1.10	6.41 ± 0.81	5.02 ± 0.53	5.60 ± 0.50	5.37 ± 0.86	4.54 ± 0.43
Bone	7.66 ± 0.60	6.70 ± 0.52	9.49 ± 1.26	5.43 ± 0.81	4.77 ± 0.65	5.80 ± 1.02	4.51 ± 0.49	4.31 ± 0.60
Uterus	4.83 ± 1.00	5.81 ± 0.42	4.74 ± 0.45	7.86 ± 1.20	5.17 ± 0.81	5.66 ± 1.02	7.64 ± 0.40	5.42 ± 1.07
Ovaries	8.27 ± 0.77	5.47 ± 0.89	8.42 ± 1.96	7.95 ± 0.62	7.56 ± 1.61	8.71 ± 1.61	6.42 ± 1.84	10.8 ± 3.38
Stomach	0.45 ± 0.30	0.94 ± 0.17	1.55 ± 0.39	0.48 ± 0.15	1.29 ± 0.09	0.88 ± 0.17	0.88 ± 0.14	0.72 ± 0.19
Sm. Int	1.86 ± 0.20	2.27 ± 0.24	2.52 ± 0.23	1.82 ± 0.18	1.53 ± 0.17	1.49 ± 0.22	1.27 ± 0.27	1.11 ± 0.19
Lg. Int	0.65 ± 0.07	1.47 ± 0.15	2.48 ± 0.20	2.18 ± 0.36	2.07 ± 0.36	1.29 ± 0.23	1.27 ± 0.13	0.94 ± 0.13
Tumor	5.46 ± 2.43	14.4 ± 2.60	32.4 ± 9.03	43.8 ± 8.19	38.3 ± 8.14	64.3 ± 17.9	95.4 ± 35.9	132.4 ± 37.9

[a] n = 5.

Toward a Carbohydrate-Based HIV-1 Vaccine: Synthesis and Immunological Studies of Oligomannose-Containing Glycoconjugates

Jiahong Ni, Haijing Song, Yadong Wang, Nicholas M. Stamatos, and Lai-Xi Wang*

Institute of Human Virology, University of Maryland Biotechnology Institute, University of Maryland, Baltimore, Maryland 21201. Received September 20, 2005; Revised Manuscript Received January 19, 2006

Human antibody 2G12 is a broadly neutralizing antibody that exerts its anti-HIV activity by targeting a novel oligomannose cluster on HIV-1 gp120. It was previously demonstrated that synthetic oligomannose clusters could mimic the carbohydrate epitope of 2G12 and showed enhanced antigenicity (Wang L. X. et al. (2004) *Chem.* Biol. *11*, 127). This paper describes the synthesis of oligomannose-containing glycoconjugates that include either a carrier protein or a universal T-helper epitope peptide to provide an effective immunogen. It was shown that the synthetic neoglycoconjugates containing oligomannose clusters could be recognized by the human antibody 2G12. Rabbit immunization studies revealed that only a small fraction of antibodies raised by the glycoconjugates was directed to the carbohydrate antigens, with the majority of the IgG type antibodies being directed to the linkers in the conjugates. The anti-sera showed weak cross-reactivity to HIV-1 gp120.

INTRODUCTION

An effective protective vaccine against HIV-1 is believed to be the best hope to end the worldwide epidemic of HIV/AIDS. However, development of an effective HIV-1 vaccine has faced many challenges (*1*−*3*). To achieve maximal protection, both cellular immunity and humoral immunity are likely to be required for an effective HIV vaccine (*4*, *5*). While cytotoxic T lymphocyte (CTL) response is important to reduce HIV-1 infection by destroying the infected cells (*6*), CTL alone cannot prevent or eliminate HIV infection. On the other hand, passive immunization with some broadly neutralizing monoclonal antibodies such as 2F5, 2G12, and 4E10 has repeatedly demonstrated in animal models that these neutralizing antibodies can provide sterilizing immunity when present at sufficient concentrations (*7*−*9*). Therefore, eliciting broadly neutralizing antibodies remains a high priority in designing a preventive HIV vaccine. Unfortunately, attempts to create immunogens capable of eliciting broadly neutralizing antibodies have been largely unsuccessful (*4*, *10*, *11*). This situation urges the exploration of new vaccine approaches. Among the several broadly neutralizing antibodies so far identified from AIDS patients (*10*−*15*), the human monoclonal antibody 2G12 is of particular interest, as it targets a unique carbohydrate antigenic structure on HIV-1 gp120 (*15*). Recent biochemical and structural studies suggest that the epitope of 2G12 consists of a novel cluster of oligomannose residues on the "silence face" of the HIV-1 envelope glycoprotein gp120 (*16*−*19*).

Glycosylation with multiple high-mannose type N-glycans was found to be a common feature of the envelope glycoprotein gp120 of different HIV-1 strains so far analyzed (*20*−*23*). Such a high-density oligomannose clustering structure is rare for normal human glycoproteins. Thus a vaccine based on this unique antigenic structure may raise specific antibodies that would not be cross-reactive to normal human glycoproteins. Indeed, phase I clinical trials of the carbohydrate-specific antibody 2G12, together with another broadly neutralizing antibody 2F5, showed that 2G12 are safe and well tolerated in humans (*24*, *25*). The results suggest that targeting the oligomannose cluster on HIV-1 gp120 constitutes a feasible vaccine approach. As the first step toward this goal, several groups have performed 2G12-binding studies with structurally defined oligomannoses and/or related synthetic oligosaccharide clusters in order to define the antigenic structure (*26*−*30*). The binding studies indicated that the terminal Manα1,2Man unit was essential for 2G12 recognition but the Manα1,2Man unit alone was not sufficient for an effective binding to 2G12. In addition, it was shown that the full-size Man9 had the highest affinity to 2G12 among several natural high-mannose oligosaccharides, and the synthetic mannose tetrasaccharide corresponding to the D1 arm of Man9 showed comparable affinity to the antibody as that of the Man9 moiety (*26*). Using synthetic oligomannose clusters, we have further demonstrated that template-assembled oligomannose clusters are better mimics of the 2G12 epitope (*27*, *28*). For example, the galactose-based tetravalent Man9-cluster (Tetra-Man9) was 73-fold and 5000-fold more effective in binding to 2G12 than the monomeric $Man_9GlcNAc$ and Man_6-GlcNAc, respectively (*27*). These results suggest that the synthetic oligomannose cluster Tetra-Man9 may serve as a reasonable starting point for designing a carbohydrate-based HIV-1 vaccine. Since carbohydrate antigens alone are poorly immunogenic and are unable to raise T-cell dependent, IgG-type antibody responses, a conventional means to solve this problem is to conjugate the carbohydrate antigen to a strong T-helper epitope, e.g., a carrier protein, as exemplified by numerous studies on carbohydrate-based cancer vaccines (*31*). We describe in this paper the synthesis of conjugate vaccines in which Man9 and the oligomannose clusters are conjugated either to keyhole limpet hemocyanin (KLH) or to a universal T-helper epitope from tetanus toxoid (TT) (Figure 1). The glycoconjugates were used to immunize rabbits. The antigenicity and the immunogenicity of the synthetic glycoconjugates were investigated.

EXPERIMENTAL PROCEDURES

General Methods. ^1H NMR spectra were recorded on a 300 MHz machine with Me_4Si (δ 0) as the internal standard. The ESI-MS spectra were measured on a Micromass ZQ-4000 single

* To whom correspondence should be addressed: Institute of Human Virology, University of Maryland Biotechnology Institute, University of Maryland, 725 W. Lombard St., Baltimore, MD 21201. Telephone: 410-706-4982. Fax: 410-706-5068. E-mail: wangx@umbi.umd.edu.

10.1021/bc0502816 CCC: $33.50 © 2006 American Chemical Society
Published on Web 02/21/2006

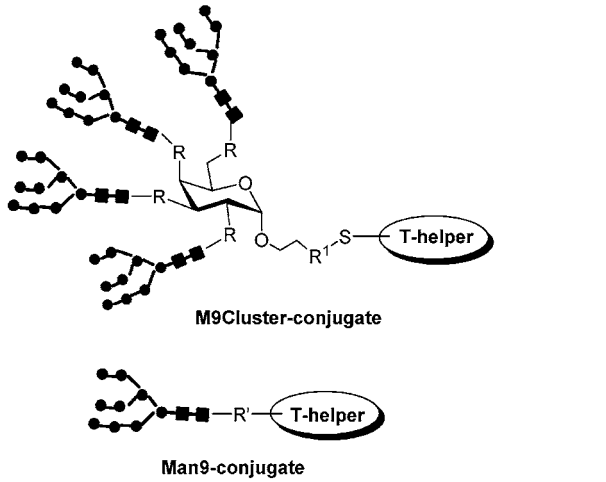

● = Mannose; ■ = GlcNAc; R, R' = spacer; T-helper = KLH or TT peptide

Figure 1. Schematic depiction of the designed glycoconjugate vaccine.

quadruple mass spectrometer. TLC was performed on glass plates coated with silica gel 60 F254 by visualizing the spots with UV light (254 nm) irradiation, 10% ethanolic sulfuric acid (for carbohydrates), ninhydrin spraying (for amines), and/or iodine coloration (for allyl groups). Flash column chromatography was performed on silica gel 60 (230−400 mesh). Photoaddition reaction was carried out in a quartz flask under N_2. Analytical HPLC was carried out with a Waters 626 HPLC instrument on a Waters Nova-Pak C18 column (3.9 × 150 mm) at 40 °C. The column was eluted with a linear gradient of MeCN−water containing 0.1% TFA at a flow rate of 1 mL/min with UV (214 nm) detection: Method A, 0−50% MeCN in 25 min; Method B, 0−90% MeCN in 25 min. Preparative HPLC was performed on a Waters 600 HPLC instrument equipped with a Waters C18 column (Symmetry 300, 19 × 300 mm). The column was eluted with a suitable gradient of MeCN−water containing 0.1% TFA at 12 mL/min.

2′-Azidoethyl 2,3,4,6-tetra-*O*-allyl-α-D-galactopyranoside (2). A solution of 2-azidoethyl α-D-galactopyranoside (**1**) (0.96 g, 3.85 mmol) in anhydrous DMF (5 mL) was added dropwise to a stirred suspension of sodium hydride (60% dispersion in mineral oil, 1.23 g, 30.80 mmol) in anhydrous DMF (30 mL). After being stirred for 30 min at room temperature, the reaction mixture was cooled to 0 °C, and then allyl bromide (3.70 g, 30.80 mmol) was added dropwise. The resulting mixture was stirred for 1 h at 0 °C and for 3 h at room temperature. After the mixture was cooled with an ice bath, the excess sodium hydride was quenched by the slow addition of methanol (5 mL). The volatile was evaporated to dryness, and then the residue was mixed with ethyl acetate (200 mL) and washed with brine (3 × 50 mL). The organic phase was dried over Na_2SO_4, filtered, and concentrated at a reduced pressure. The residue was purified by flash chromatography (hexane/EtOAc 80:20) to give compound **2** (1.39 g, 88%). R_f 0.46 (hexane/EtOAc 80:20); ^{1}H NMR (300 MHz, $CDCl_3$/TMS): δ 6.05−5.84 (m, 4 H, OCH_2CH═CH_2), 5.36−5.14 (m, 8 H, OCH_2CH═CH_2), 4.95 (d, 1 H, J = 3.2 Hz, H-1), 4.39 (dd, 1 H, J = 12.6, 5.5 Hz, $OCHHCH$═CH_2),), 4.26 (dd, 1 H, J = 12.6, 5.2 Hz, $OCHHCH$═CH_2), 4.22−4.06 (m, 4 H, OCH_2CH═CH_2), 4.04−3.98 (m, 2 H, OCH_2CH═CH_2), 3.96 (dd, 1 H, J = 6.6, 6.4 Hz, H-5),), 4.01−3.80 (m, 3 H, H-2, H-4 and $OCHHCH_2N_3$), 3.75 (dd, 1 H, J = 10.1, 2.8, H-3), 3.67 (ddd, 1 H, J = 10.8, 5.9, 3.9 Hz, $OCHHCH_2N_3$), 3.62−3.51 (m, 3 H, H-6, H-6′, and OCH_2CHHN_3), 3.38 (ddd, 1 H, J = 13.2, 5.6, 3.9 Hz, OCH_2CHHN_3); ESI-MS (*m*/*z*): 432.41 $(M + Na)^+$.

2′-(6-*tert*-Boc-Aminohexoic-amido)-ethyl 2,3,4,6-Tetra-*O*-allyl-α-D-galactopyranoside (3). To a stirred mixture of azide **2** (269.9 mg, 0.66 mmol) was added *N*-Boc-6-aminocaproic acid (191.6 mg, 0.83 mmol) in toluene (10 mL) *n*-Bu_3P (167.6 mg, 0.83 mmol) dropwise. After being stirred at room temperature for 3 h and then at 100 °C for 18 h, the resulting mixture was cooled to room temperature, and the solvent was evaporated at reduced pressure. The residue was purified by flash column chromatography (CH_2Cl_2/MeOH 95:5) to give compound **3** (180.9 mg. 46%), R_f 0.44 (CH_2Cl_2/MeOH, 95:5); ^{1}H NMR ($CDCl_3$/TMS): δ 6.63 (t, 1 H, J = 6.4 Hz, N*H*), 6.02−5.82 (m, 4 H, OCH_2CH═CH_2), 5.36−5.14 (m, 8 H, OCH_2CH═CH_2), 4.90 (d, 1 H, J = 3.2 Hz, H-1), 4.60 (t, 1 H, J = 6.2 Hz, N*H*Boc-*t*), 4.38 (dd, 1 H, J = 11.7, 5.8 Hz, $OCHHCH$═CH_2), 4.27 (dd, 1 H, J = 11.7, 5.8 Hz, $OCHHCH$═CH_2), 4.22−3.94 (m, 6 H, $OCHHCH$═CH_2), 3.90−3.78 (m, 3 H, H-2, H-4, $OCHHCH_2$-NH), 3.76−3.66 (m, 3 H, H-3, H-5, $OCHHCH_2NH$), 3.58 (d, 2 H, J = 6.2 Hz, H-6, H-6′), 3.52−3.38 (m, 2 H, OCH_2CH_2NH), 3.14−3.06 (m, 2 H, $(O)CCH_2CH_2CH_2CH_2CH_2NHBoc$-*t*), 2.15 (t, J = 7.1 Hz, 2 H, $(O)CCH_2CH_2CH_2CH_2CH_2NHBoc$-*t*), 1.72−1.55 (m, 2 H, $(O)CCH_2CH_2CH_2CH_2CH_2NHBoc$-*t*), 1.44 (s, 9 H, H−Boc-*t*), 1.43−1.30 (m, 2 H, $(O)CCH_2CH_2CH_2CH_2CH_2$-$NHBoc$-*t*), 0.94 (p, J = 6.7 Hz, 2 H, $(O)CCH_2CH_2CH_2CH_2$-CH_2NHBoc-*t*); ESI-MS (*m*/*z*): 619.32 $(M + Na)^+$, 597.27 $(M + H)^+$, 497.30 $(M - Boc + H)^+$.

2′-(6-*tert*-Boc-Aminohexoic-amido)-ethyl 2,3,4,6-Tetra-*O*-(6-amino-3-thiahexyl)-α-D-galactopyranoside (4). To a solution of compound **3** (173.0 mg, 0.29 mmol) and AIBN (20.0 mg) in methanol (15 mL) in a Quartz flask was added cysteamine hydrochloride (263.6 g, 2.32 mmol). After being degassed by bubbling N_2 into solution for 30 min, the resulting mixture was stirred and irradiated (UV, 254 nm) under N_2 for 24 h. The volatile was evaporated under reduced pressure, and the residue was purified by gel filtration on Sephadex G-15 column (2.5 × 75 cm) using water as eluent. Fractions containing the product were pooled and lyophilized to give compound **4** (859.5 mg, 82%). ^{1}H NMR (D_2O): δ 5.09 (d, 1 H, J = 3.4 Hz, H-1), 4.04−3.33 (m, 16 H, H-2, H-3, H-4, H-5, H-6, H-6′, $OCH_2CH_2CH_2S$, and OCH_2CH_2NH), 3.26−3.14 (m, 10 H, $SCH_2CH_2CH_2NH_2HCl$, and OCH_2CH_2NH), 3.04 (t, 2 H, J = 6.4 Hz, $(CH_2)_4CH_2NHBoc$-*t*), 2.90−2.82 (m, 8 H, SCH_2-$CH_2CH_2NH_2HCl$), 2.74−2.62 (m, 8 H, $OCH_2CH_2CH_2S$), 2.25 (t, J = 6.8 Hz, 2 H, $(O)CCH_2CH_2CH_2CH_2CH_2NHBoc$-*t*), 1.96−1.80 (m, 8 H, $OCH_2CH_2CH_2S$), 1.66−1.55 (m, 2 H, (O)-$CCH_2CH_2CH_2CH_2CH_2NHBoc$-*t*), 1.41 (s, 9 H, H−Boc-*t*), 1.38−1.26 (m, 2 H, $(O)CCH_2CH_2CH_2CH_2CH_2NHBoc$-*t*), 0.88 (p, J = 6.2 Hz, 2 H, $(O)CCH_2CH_2CH_2CH_2CH_2NHBoc$-*t*); ESI-MS (*m*/*z*): 927.44 $(M - 4HCl + Na)^+$, 905.53 $(M - 4HCl + H)^+$, 453.51 $(M - 4HCl + 2H)^{2+}$, 403.37 $(M - 4HCl - Boc + 2H)^{2+}$.

2′-(6-*tert*-Boc-Aminohexoic-amido)-ethyl 2,3,4,6-Tetra-*O*-(6-(6-maleimido-hexanamido)-3-thiahexyl)-α-D-galactopyranoside (5). To a stirred solution of *N*-succimidyl 6-maleimidohexanoic acid ester (50.2 mg, 162.90 μmol) in THF (3 mL) at 0−5 °C was added a solution of **4** (21.4 mg, 20.36 μmol) in 0.1 M aqueous solution of $NaHCO_3$ (1.0 mL). The resulting mixture was stirred for 1 h at 0−5 °C, then diluted with $CHCl_3$ (50 mL) and washed with brine (3 × 10 mL). The organic phase was dried over Na_2SO_4, filtered, and concentrated. The residue was purified by flash chromatography (CH_2Cl_2/MeOH 95:5) to give compound **5** (14.9 mg, 44%); R_f 0.57 (CH_2Cl_2/MeOH 90:10); ^{1}H NMR ($CDCl_3$/TMS): δ 6.70 (s, 8 H, C*H*═C*H*), 6.62 (t, 1 H, J = 6.4 Hz, N*H*), 6.36−6.16 (m, 4 H, N*H*), 4.89 (d, 1 H, J = 3.0 Hz, H-1), 4.80−4.68 (t, 1 H, J = 6.0 Hz, N*HBoc*-*t*), 3.94−3.84 (m, 2 H, $OCH_2CH_2CH_2$), 3.80−3.34 (m, 32 H, H-2, H-3, H-4, H-5, H-6, H-6′, $OCH_2CH_2CH_2S$, SCH_2CH_2NH, $(CH_2)_4CH_2N$, and OCH_2CH_2NH), 3.18−3.08 (m, 2 H, $(CH_2)_4CH_2$-NHBoc-*t*), 2.74−2.55 (m, 16 H, $OCH_2CH_2SCH_2CH_2NH$), 2.28−2.14 (m, 10 H, $(O)CCH_2CH_2CH_2CH_2CH_2$), 1.94−1.78

(m, 8 H, $OCH_2CH_2CH_2SCH_2CH_2N$), 1.74−1.54 (m, 20 H, $OCCH_2CH_2CH_2CH_2CH_2N$), 1.44 (s, 9 H, H−Boc-*t*), 1.40−1.24 (m, 10 H, $(O)CCH_2CH_2CH_2CH_2CH_2N$, $(O)CCH_2CH_2CH_2CH_2CH_2NHBoc$-*t*); ESI-MS (*m*/*z*): 1699.79 $(M + Na)^+$, 1677.73 $(M + H)^+$, 839.52 $(M + 2H)^{2+}$, 789.55 $(M - Boc + 2H)^{2+}$.

The Oligomannose Cluster Carrying a Boc-Protected Amino Group (6). To a solution of the SH-tagged oligomannose Man9GlcNAc2Asn-SH (18.0 mg, 8.69 μmol) (*27*) in a phosphate buffer (pH 6.6, 50 mM, 3.0 mL) and acetonitrile (3.0 mL) was added a solution of the scaffold **5** (1.83 mg, 1.09 μmol) in DMF (104 μL). The resulting mixture was shaken gently at room-temperature overnight. The mixture was lyophilized to dryness, and the ligation product was purified by preparative reverse-phase HPLC to yield the tetravalent oligomannose derivative **6** (10.9 mg, 68%): analytical HPLC (Method A), $t_R = 16.71$ min; ESI-MS: 2492.39 $(M + 4H)^{4+}$, 1994.05 $(M + 5H)^{5+}$, 1974.11 $(M - Boc + 5H)^{5+}$, 1961.41 $(M - Man + 5H)^{5+}$, 1941.74 $(M - Boc\text{-}Man + 5H)^{5+}$, 1929.31 $(M - 2Man + 5H)^{5+}$.

Oligomannose Cluster Carrying a Free Amino Group (7). A solution of the Boc-containing oligomannose cluster **6** (10.0 mg, 1.00 μmol) in a mixture of TFA, acetonitrile, and water (10/10/1, v/v, 2 mL) was shaken at room temperature for 2 h. The mixture was lyophilized to dryness, and the residue was purified by preparative HPLC to give the oligomannose cluster **7** (8.9 mg, 90%): Analytical HPLC (Method A), $t_R = 14.63$ min; ESI-MS (*m*/*z*): 2467.33 $(M + 4H)^{4+}$, 1973.97 $(M + 5H)^{5+}$, 1941.80 $(M - Man + 5H)^{5+}$, 1909.30 $(M - 2Man + 5H)^{5+}$.

Maleimido-Functionalized Oligomannose Cluster (8). Compound **7** (8.5 mg, 0.86 μmol) was dissolved in a mixed solvent of a phosphate buffer (pH 7.4, 50 mM) and acetonitrile (2/1, v/v, 1.5 mL). To the solution was added *N*-succimidyl 6-maleimidohexanoic ester (2.7 mg, 8.60 μmol) in acetonitrile (0.5 mL). The reaction mixture was stirred at room temperature for 2 h and then lyophilized to dryness. The residue was purified by preparative HPLC to yield the desired maleimido-functionalized oligomannose cluster (**8**) (5.9 mg, 68%): Analytical HPLC (Method A), $t_R = 16.36$ min; ESI-MS (*m*/*z*): 2516.45 $(M + 4H)^{4+}$, 2013.27 $(M + 5H)^{5+}$, 1980.75 $(M - Man + 5H)^{5+}$, 1948.22 $(M - 2Man + 5H)^{5+}$.

Biotinylated Oligomannose Cluster (9). Compound **7** (2.2 mg, 0.22 μmol) was dissolved in a mixed solvent of a phosphate buffer (pH 7.4, 50 mM) and acetonitrile (2/1, v/v, 1.0 mL). Then NHS-LS-biotin (5 equiv) was added, and the mixture was stirred at room temperature for 2 h. The mixture was lyophilized, and the residue was purified by preparative HPLC to give the M9Cluster-X-biotin (**9**) (1.88 mg, 84%): Analytical HPLC (Method A), $t_R = 15.81$ min; ESI-MS: 2552.52 $(M + 4H)^{4+}$, 2041.77 $(M + 5H)^{5+}$, 2009.205 $(M - Man + 5H)^{5+}$, 1977.50 $(M - 2Man + 5H)^{5+}$.

Oligomannose Cluster/T-Helper Peptide Conjugate (10). A mixture of the maleimido-M9Cluster (**8**) (2 mg, 0.2 μmol) and the cysteine-containing tetanus toxoid peptide (TT-peptide) CGQYIKANSKFIGITEL (*32*) (0.76 mg, 0.4 μmol) in a mixed solvent containing phosphate buffer (pH 6.6, 50 mM) and acetonitrile (1/1, 1 mL) was kept at room temperature for 2 h with gentle shaking. The reaction mixture was lyophilized to dryness. The residue was subject to preparative RP-HPLC to give the glycopeptide M9Cluster-Pep (**10**) (1.9 mg, 79%): Analytical HPLC (Method B), $t_R = 11.49$ min; ESI-MS: 2389.39 $(M + 5H)^{5+}$, 2357.21 $(M - Man + 5H)^{5+}$, 1991.38 $(M + 6H)^{6+}$, 1964.55 $(M - Man + 6H)^{6+}$, 1707.08 $(M + 7H)^{7+}$, 1684.01 $(M - Man + 7H)^{7+}$.

Oligomannose Cluster/KLH Conjugate (11). A mixture of thiolated KLH (10 mg), prepared according to the reported procedure (*33*), and the maleimido-M9Cluster 8 (2.2 mg) in a mixed solvent of phosphate buffer (pH 6.6, 50 mM) and acetonitrile (1/1, 3 mL) containing EDTA (5 mM) was incubated at room temperature for 4 h with gentle shaking. Then a solution of cysteine (0.1 M, 100 μL) in a phosphate buffer was added to quench any residual maleimide on KLH. The solution was lyophilized, and the conjugate M9Cluster-KLH (**11**) was isolated by gel filtration on a Sephadex G-15 column equilibrated and eluted with a phosphate buffer (10 mM, pH 7.2). The carbohydrate content was measured by anthrone assay, and the protein content was measured using BioRad dye reagent according to the manufacturer's instructions.

Man9/T-Helper Peptide Conjugate (13). A mixture of the maleimido-Man9 (*34*) (2.5 mg, 1.14 μmol) and the cysteine-containing tetanus toxoid peptide (TT-peptide) (5.4 mg, 2.8 μmol) in a mixed solvent containing phosphate buffer (pH 6.6, 50 mM) and acetonitrile (1/1, 1 mL) was kept at room temperature for 2 h with gentle shaking. The reaction mixture was lyophilized and the residue was subject to preparative RP-HPLC to give the glycopeptide Man9-Pep (**13**) (3.7 mg, 81%): Analytical HPLC (Method B), $t_R = 11.37$ min; ESI-MS: 1359.27 $(M + 3H)^{3+}$, 1305.27 $(M - Man{+}3H)^{3+}$, 1251.27 $(M - 2Man{+}3H)^{3+}$, 1019.73 $(M + 4H)^{4+}$, 979.24 $(M - Man{+}4H)^{4+}$, 938.62 $(M - 2Man{+}4H)^{4+}$.

Man9/KLH Conjugate (14). A mixture of thiolated KLH (5 mg) and the maleimido-Man9 (1.5 mg) in a mixed solvent of phosphate buffer (pH 6.6, 50 mM) and acetonitrile (1/1, 2 mL) containing EDTA (5 mM) was incubated at room temperature for 4 h with gentle shaking. Then a solution of cysteine (0.1 M, 50 μL) in a phosphate buffer was added to quench any residual maleimide on KLH. The solution was lyophilized, and the conjugate Man9-KLH (**14**) was isolated by gel filtration on a Sephadex G-15 column equilibrated and eluted with a phosphate buffer (10 mM, pH 7.2). The carbohydrate content was measured by anthrone assay and the protein content was measured using BioRad dye reagent according to the manufacturer's instructions.

Biotinylated Man9 (15). A mixture of Man9GlcNAc2Asn (3 mg, 1.5 μmol) and NHS-LS-biotin (4.5 μmol) in a mixed solvent of phosphate buffer (pH 7.4, 50 mM) and acetonitrile (2/1, v/v, 1.0 mL) was stirred at room temperature for 3 h. The mixture was lyophilized and the residue was purified by preparative HPLC to give the Man9-X-biotin (**15**) (2.17 mg, 62%): Analytical HPLC (Method A), $t_R = 8.97$ min; ESI-MS: 2337.60 $(M + H)^+$, 1169.16 $(M + 2H)^{2+}$, 1088.40 $(M - Man + 2H)^{2+}$, 1007.12 $(M - 2Man + 2H)^{2+}$, 926.09 $(M - 3Man + 2H)^{2+}$, 845.12 $(M - 4Man + 2H)^{2+}$, 764.02 $(M - 5Man + 2H)^{2+}$.

Rabbit Immunizations. New Zealand white rabbits (two rabbits per group) were used for the immunization studies. One milligram of respective glycoconjugate in 500 μL of water was emulsified with 500 μL of complete Freunds' adjuvant (CFA). The emulsions were used for immunizing rabbits (two rabbits per group) subcutaneously. The rabbits were then boosted three times at days 14, 28, and 56, with each rabbit receiving at the intervals 0.5 mg of each glycoconjugate in 500 μL water emulsified with 500 μl of incomplete Freunds' adjuvant (IFA). The rabbits were bled 10 days after the last boosting and the sera were obtained for the assays.

Virus Neutralization Assay. The neutralizing activity of the sera was examined by the previously described method (*35*). Briefly, HIV-1_{IIIB} (100 $TCID_{50}$) was preincubated with serial dilutions of the rabbit anti-sera in RPMI 1640 containing 15% FCS for 45 min at 37 °C. Then 1.5×10^5 PHA-activated PBMCs were added, and the mixture were incubated for 24 h at 37 °C. The infected cells were washed five times with the complete medium to remove unabsorbed virus and residual antibody. Cells were resuspended in the complete medium containing IL-2 and were distributed into wells of a 96-well

Scheme 1. Synthesis of Maleimide- and Biotin-tagged Oligomannose Clusters[a]

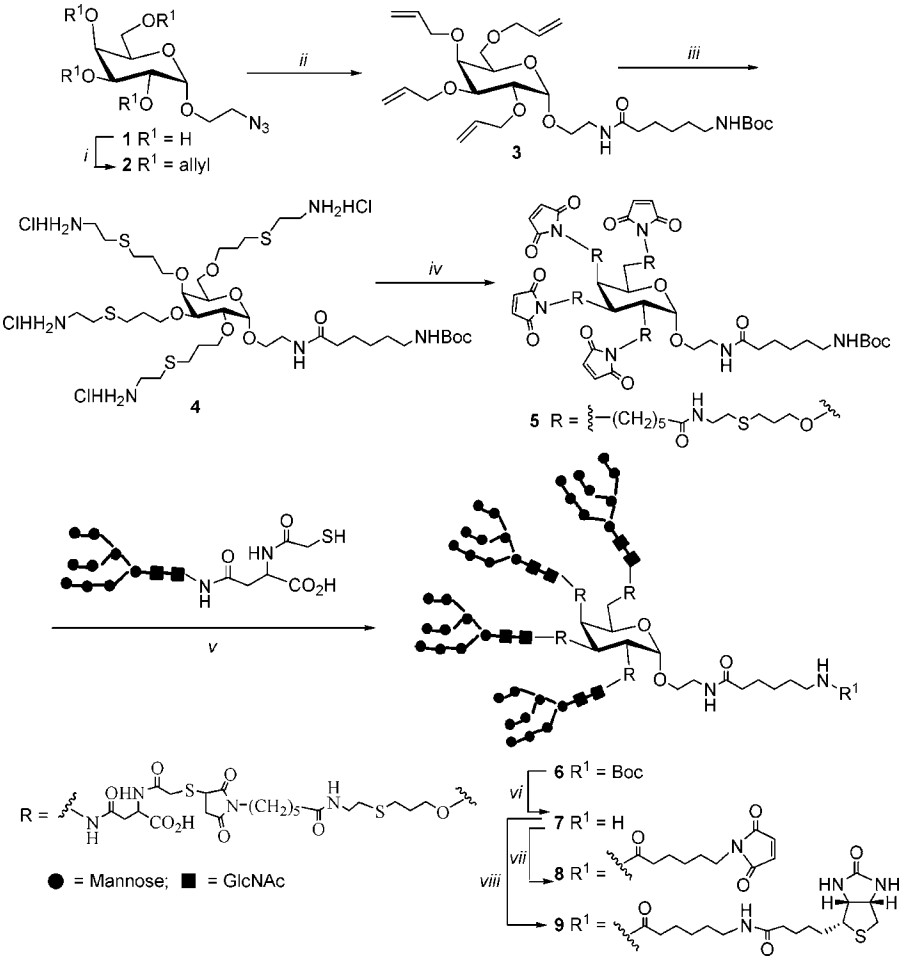

[a] Reaction conditions: (i) allyl bromide, NaH, DMF, 88%; (ii) *N*−Boc-6-aminocaproic acid, Bu_3P, toluene, 46%; (iii) cysteamine hydrochloride, AIBN, MeOH, UV (254 nm), 82%; (iv) 6-maleimidohexanoic acid *N*-hydroxysuccinimide ester, THF, 0.1 M $NaHCO_3$, 44%; (v) phosphate buffer (pH 6.6, 50 mM)/MeCN (1:1, v/v), 68%; (vi) TFA/MeCN/H_2O (10:10:1, v/v), 90%; (vii) 6-maleimidohexanoic acid *N*-hydroxylsuccimide ester, phosphate buffer (pH 7.4, 50 mM)/MeCN (1:1, v/v), 68%; (viii) NHS-LC-biotin, phosphate buffer (pH 7.4)/MeCN, 84%.

tissue plate. Aliquots were taken from the culture on day 4 and 6. Viral growth was determined by measuring HIV-1 p24 antigen released into the culture medium by ELISA. The extent of neutralization activity was determined by measuring and comparing the p24 antigens released from the cells that were infected by the virus in the presence and absence of the rabbit sera or antibody. Human antibody 2G12 was used as a positive control for the neutralizing activity.

Enzyme-Linked Immunosorbent Assay (ELISA). For biotinylated antigens (Man9-X-biotin, M9Cluster-x-biotin, G−X-biotin, and GCluster-X-biotin), the 96-well ELISA microtiter plates were first coated with 8 μg/mL Neutravidin (streptavidin) in PBS and incubated at 4°C overnight. After washings with PBS/0.5% Tween-20, nonspecific binding was blocked with 5% (w/v) BSA in PBS at room temperature for 1 h. Plates were washed, and then 5 μg/mL of the respective biotinylated antigen in 1% BSA was added. Plates were incubated at 37 °C for 1 h. The plates were again washed, and rabbit sera were added in a 1:2 or 1:3 serial dilution in 1% BSA/PBS. The plates were incubated at 37°C for 2 h and washed. To the plates was added a solution (100 μL) of 1:2000 diluted horseradish peroxidase (HRP)-conjugated goat anti-rabbit IgG (H & L) in 1% BSA/PBS. After incubation for 1 h at 37 °C, the plates were washed again and a solution of 3,3′,5,5′-tetramethylbenzidine (TMB) was added. Color was allowed to develop for 5 min, and the reaction was then quenched by adding a solution of 0.5 M H_2SO_4 to each well. The optical density was then measured at 450 nm. For testing the cross-reactivity of the sera to HIV-1 gp120, 10 μg/mL of HIV-1 (BAL) gp120 (produced in human H9 cell lines) was coated to the 96-well plates, and antibody titers were measured as described above. For testing the binding of the synthetic glycoconjugates with human antibody 2G12, the 96-well microtiter plates were incubated with 10 μg/mL of Man9-KLH and M9Cluster-KLH, and then the plates were titrated against a serial dilution of human antibody 2G12 (obtained from the NIH AIDS Research and Reference Reagent Program) starting at 10 μg/mL. After washings, the plates were incubated with a solution (100 μL) of 1:3000 diluted horseradish peroxidase (HRP)-conjugated goat anti-human IgG in 1% BSA/PBS. Color was developed and the OD_{450} was read.

RESULTS AND DISCUSSION

Synthesis. The construction of the glycoconjugate vaccines requires chemoselective conjugation of the galactose-based oligomannose cluster (Tetra-Man9) to a carrier protein or to a T-helper epitope peptide. For this purpose, the galactose scaffold was modified at the aglycon portion so that a suitable functional group could be selectively generated at later stage for ligation without influencing the integrity of the assembled oligomannose cluster. The synthesis started with the 2-azidoethyl α-D-galactoside (**1**), which was prepared by reaction of D-galactose with 2-chloroethanallyl alcohol under the catalysis of $BF_3{\cdot}Et_2O$ with subsequent displacement of the chloride with azide (*34*). Treatment of **1** with sodium hydride and allyl bromide in *N*,*N*-dimethylformamide gave the O-allylated 2-azidoethyl galacto-

Scheme 2. Synthesis of Oligomannose Cluster-Peptide/Protein Conjugates

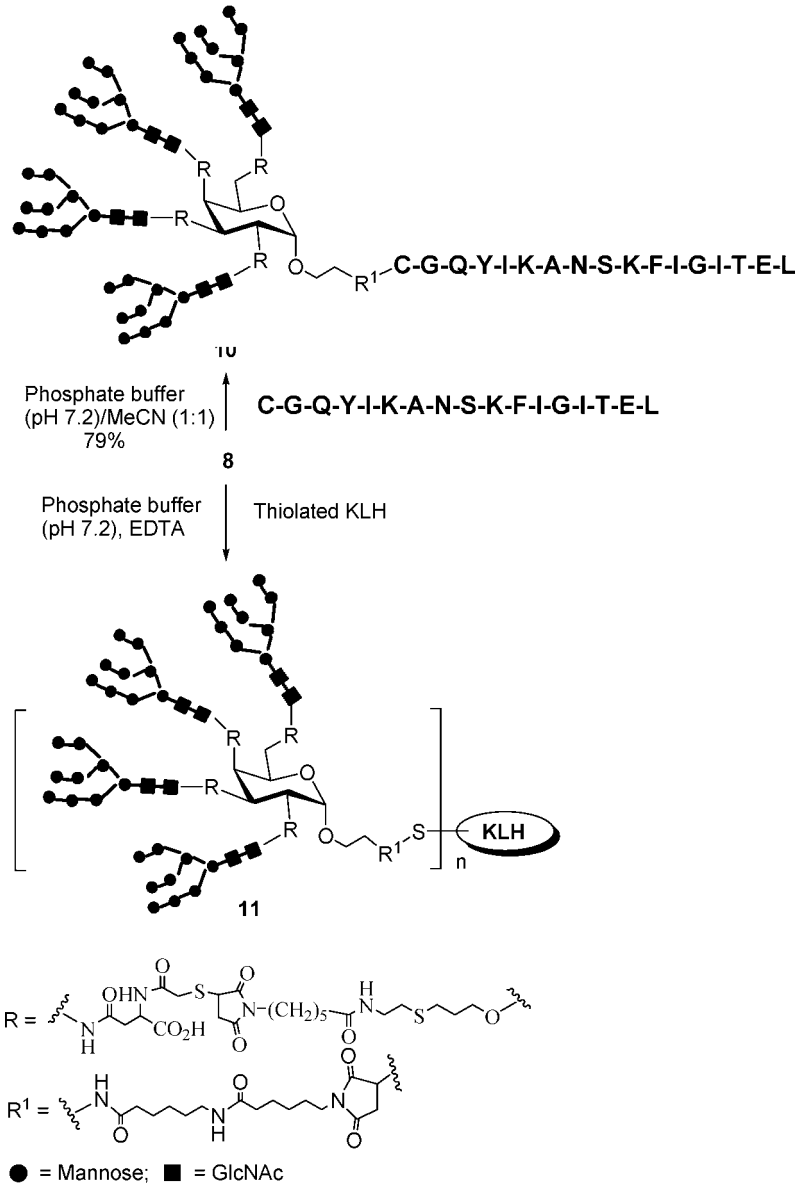

side **2**. Reaction of **2** with *N*-Boc-6-aminocarproic acid in the presence of tributylphosphine gave the derivative **3**. Introduction of four maleimido groups was achieved via a two-step conversion: the photoaddition of cysteamines to the allyl functional groups in **3** to give compound **4**, and subsequent elongation of the spacer by reaction of the free amino groups with the active ester of 6-maleimidohexanoic acid to provide the maleimido derivative **5** (Scheme 1). The ligation of the maleimido-functionalized scaffold with the SH-tagged Man9GlcNAc2Asn, which was prepared according to the literature (*27*), was performed in phosphate buffer (pH 6.6) containing MeCN to give the oligomannose cluster **6** in 68% yield, which was purified by HPLC and characterized by ESI-MS. The *N*-Boc group was selectively removed by treatment with TFA−MeCN−H_2O (10:10:1, v/v) to yield compound **7** that carries a free amino group. Treatment of **7** with 6-maleimidohexanoic acid *N*-hydroxylsuccinimide ester gave the maleimido-functionalized oligomannose cluster **8** in 68% yield. Selective biotinylation of **7** with active ester NHS-LC−biotin afforded the biotin-tagged oligomannose cluster (M9Cluster-X-biotin) (**9**) in 84% yield, which would be used as the coating antigen (Scheme 1).

The synthesis of the oligomannose cluster-containing glycoconjugates was achieved through the chemoselective ligation of the maleimido-functionalized oligomannose cluster (**8**) with the respective thiol-species under a mild aqueous condition. Briefly, chemoselective ligation between maleimide **8** and the T-helper peptide CGQYIKANSKFIGITEL from tetanus toxoid (aa830−844) (*32*) in a phosphate buffer (pH 6.6) containing MeCN gave the glycopeptide conjugate **10** (M9Cluster-Pep) in 79% yield, which was purified by HPLC and characterized by ESI-MS. On the other hand, treatment of **8** with thiolated KLH (*33*) in a phosphate buffer gave the KLH conjugate **11**, M9Cluster-KLH, which was isolated by gel filtration (Scheme 2). The corresponding Man9-containing glycopeptide conjugate **13**, Man9-Pep, was synthesized by chemoselective ligation between maleimido-functionalized Man9 (**12**) (*34*) and the TT-peptide (81% yield). Reaction of the maleimide-Man9 (**12**) with the thiolated KLH afforded the Man9-KLH conjugate **14** (Scheme 3). The carbohydrate contents of the KLH conjugates were determined by carbohydrate and protein assays. The synthetic M9Cluster-KLH (**11**) was determined to contain 15% carbohydrate, whereas the Man9-KLH (**13**) contained 19% carbohydrate. Finally, the coating antigen, Man9-X-biotin (**15**), was synthesized by treatment of Man9GlcNAc2Asn with NHS-LC-biotin (Scheme 3).

Binding of the Synthetic Glycoconjugates to Antibody 2G12. The 2G12 binding ability of the synthetic glycoconjugates

Scheme 3. Synthesis of Man9-KLH, Man9-Peptide, and Man9-Biotin Conjugates[a]

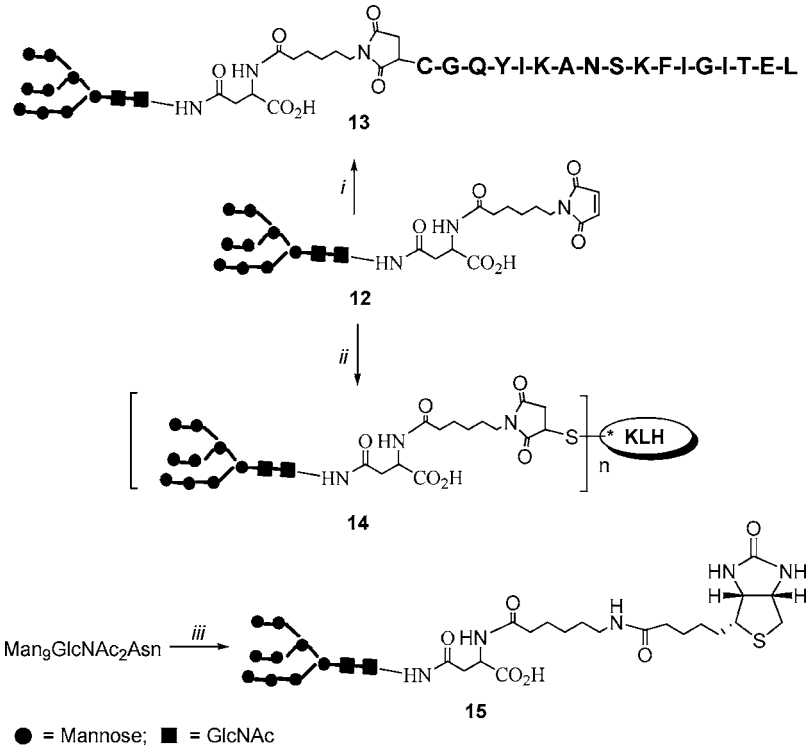

[a] Reaction conditions: (i) Cys-tagged T-helper peptide, phosphate buffer (pH 6.6)/MeCN (1:1, v/v), 81%; (ii) thiolated KLH, phosphate buffer (pH 7.2), EDTA; (iii) NHS-LC-biotin (Pierce), phosphate buffer (pH 7.4, 50 mM)/MeCN (1:1, v/v), 62%.

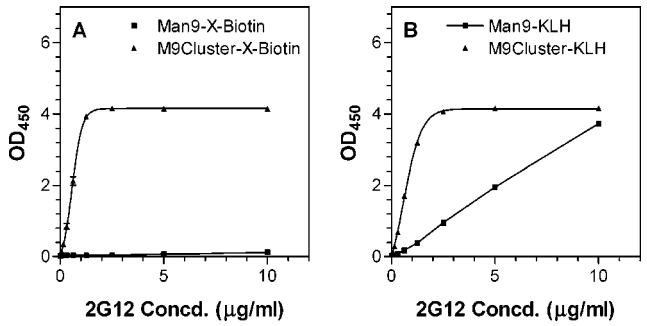

Figure 2. Binding of antibody 2G12 to synthetic glycoconjugates. A, binding to biotinylated Man9 and Man9 cluster; B, binding to KLH-conjugated Man9 and Man9 cluster.

was estimated by ELISAs. For the binding assays, the biotinylated coating antigens, M9Cluster-X-biotin (**9**) and Man9-X-biotin (**15**), were immobilized on streptavidin plates, whereas the KLH conjugates (**11**) and (**14**) were coated directly to the plastic microtiter plates. The plates were then titrated with serial dilutions of antibody 2G12 (Figure 2). As shown in Figure 2A, the Man9-cluster was readily recognized by antibody 2G12 at an apparent EC50 of ca. 0.8 μg/mL under the assay condition. However, the immobilized monomeric Man9 was unable to catch 2G12 in the solution when the concentration of 2G12 was below 10 μg/mL. The results are consistent with the previous observations that synthetic Man9-clusters are much better antigens than the monomeric Man9 oligomannose (*27*, *28*, *30*). Interestingly, the synthetic Man9-KLH conjugate, which contains 19% Man9 (by weight), was able to bind to 2G12 (EC50 at ca. 6 μg/mL) (Figure 2B), demonstrating certain clustering effect of the Man9 moieties within the conjugate. The 2G12-binding ability of M9Cluster-KLH is about the same as that of the M9Cluster-X-biotin under the same binding conditions (Figure 2, panels A and B). The results suggest that the mild chemoselective conjugation between the M9Cluster-maleimide and the thiolated KLH did not affect the structural integrity of the oligomannose cluster.

Immunization Studies. We next evaluated the immunogenicity of the synthetic glycoconjugates in rabbits. Pre-sera were taken before the immunization and the anti-sera were collected after four immunizations (priming and three boosts). The sera were first tested against the respective antigen-X-biotin as the coating antigen. The ELISA results were summarized in Table 1. It was found that the KLH conjugates raised higher IgG type antibody titers than the corresponding peptide conjugates. Particularly, the M9Cluster-KLH raised unusually high antibody titer (> 1:100 000). To examine the possibility that the antibodies might be raised against the linkers rather than the carbohydrate antigens, we prepared the corresponding biotin-tagged linkers (linker-X-biotin) by treatment of the biotin-tagged glycoconjugates with endo-β-*N*-acetyl-glucosaminidase from *Arthrobacter* (Endo-A). Endo-A is known to be able to remove the high-mannose type N-glycan (here, Man9GlcNAc) from gly-

Table 1. ELISA Antibody Titers against the Respective Coating Antigens[a]

	synthetic immunogens			
coating antigens	Man9-KLH	M9Cluster-KLH	Man9-Pep	M9Cluster-Pep
Man9-X-biotin	960	n.d.[b]	640	n.d.[b]
G-X-biotin	460	n.d.[b]	480	n.d.[b]
M9Cluster-X-biotin	n.d.[b]	163,840	n.d.[b]	2560
G-Cluster-X-biotin	n.d.[b]	81,920	n.d.[b]	1280

[a] The antibody titer was defined as the highest dilutions of the sera that yielded an absorbance (OD_{450}) of 0.2 in the ELISA. [b] Not determined.

Table 2. ELISA Antibody Titers against HIV-1 gp120[a]

	synthetic immunogens			
rabbit sera	Man9-KLH	M9Cluster-KLH	Man9-Pep	M9Cluster-Pep
pre-sera[b]	80	60	60	80
anti-sera	120	150	80	120

[a] The antibody titer was defined as the highest dilutions of the sera yielded an absorbance (OD_{450}) of 0.2 in the ELISA. [b] The pre-sera were the sera taken from each of the rabbit group before immunizations.

coconjugates by cleaving the N-glycans at the GlcNAcβ1,-4GlcNAc linkage (*36*, *37*). As monitored by HPLC coupled with ESI-MS analysis, we found that incubation of the Man9-X-biotin and the Man9Cluster-X-biotin with Endo-A could completely remove the Man9 portions from the conjugates, giving the corresponding GlcNAc-X-biotin (G-X-biotin) and GlcNAcCluster-X-biotin (G-cluster-X-biotin), respectively. When the G-X-biotin and G-Cluster-X-biotin were used as the coating antigens on a streptavidin plate, the ELISA assay revealed that the majority of the antibodies generated were in fact directed to the linkers, although a small fraction of the antibodies might be raised against the carbohydrate antigen (Table 1). The results suggest that the oligomannose (Man9) and the corresponding clustered oligomannose antigens were poorly immunogenic even when conjugated to KLH (a strong immune-stimulating carrier protein) or to the TT-peptide (a universal T-helper epitope). On the other hand, the fact that the majority of antibody responses were directed to the linkers strongly suggests that the choice of an appropriate linker in making the glycoconjugate vaccines is of primary importance for raising sufficient antibody responses against the weakly immunogenic carbohydrate antigen. Recently, an excellent study has also demonstrated that a maleimide-functionalized linker significantly suppressed the immunogenicity of a tumor-associated carbohydrate antigen in its KLH conjugate (*38*), resulting in low antibody titers specific for the carbohydrate antigen.

We also tested reactivity of the rabbit sera toward HIV-1 envelope glycoprotein gp120 (BAL gp120 expressed in human H9 cell lines) (Table 2). It was found that the rabbit pre-sera showed a significant background of cross-reactivity to the HIV-1 gp120. Nevertheless, the anti-sera clearly showed an enhanced reactivity to HIV-1 gp120 above the background of the pre-sera (Table 2), which might be contributed from the oligomannose-specific antibodies in the anti-sera. A preliminary HIV-neutralization assay indicated that, at 1:10 dilution, none of the rabbit anti-sera demonstrated HIV-1 neutralizing activities. The results implicated that either the glycoconjugates failed to raise any neutralizing antibodies under the immunization protocol or, if any, the neutralizing antibodies might be generated only at very low levels insufficient to show neutralizing activities.

CONCLUSION

The recent characterization of the neutralizing epitope of the broadly neutralizing antibody 2G12 as a novel oligomannose cluster on the envelope glycoprotein gp120 has implicated the possibility of developing a carbohydrate-based HIV-1 vaccine. The present work represents the first attempt to create such a vaccine by synthesizing oligomannose- and oligomannose cluster-containing glycoconjugates. The synthetic oligomannose cluster could be recognized by the human antibody 2G12 in binding studies. Preliminary immunization studies suggested that moderate carbohydrate-specific antibodies were raised by the glycoconjugate immunogens, but the majority of antibody responses were directed to the linkers. In addition, the anti-sera were weakly cross-reactive to HIV-1 gp120, but the carbohydrate-specific antibodies in the anti-sera generated by our current immunization protocol have not reached the level that could neutralize HIV-1 infection. The results implicated the poor immunogenicity of the carbohydrate antigens and, again, attested to the difficulties of raising neutralizing antibodies against HIV-1 in general. It is suggested that the next step should focus on enhancing the immunogenicity of the HIV-1 carbohydrate antigen, such as synthesizing more effective glycoconjugate immunogen (better linkers and more effective built-in adjuvant), optimizing the immunization protocols, and emphasizing fundamental studies on B cell immunology to break the immune tolerance on the HIV-1 carbohydrate antigens.

ACKNOWLEDGMENT

We thank Prof. Anthony L. DeVico, Prof. George K. Lewis, Dr. Shibo Jiang, and Dr. Robert Powell for helpful discussions during the work. The human antibody 2G12 was obtained from the National Institutes of Health (NIH)'s AIDS Research and Reference Reagent Program. The work was supported by the National Institutes of Health (NIH grant R21 AI054354).

Supporting Information Available: The HPLC profiles and ESI-MS spectra of the synthetic, homogeneous glycopeptides. This material is available free of charge via the Internet at http://pubs.acs.org/BC.

LITERATURE CITED

(1) McMichael, A. J., and Hanke, T. (2003) HIV vaccines 1983−2003. *Nat. Med. 9*, 874−880.

(2) Pantaleo, G., and Koup, R. A. (2004) Correlates of immune protection in HIV-1 infection: what we know, what we don't know, what we should know. *Nat. Med. 10*, 806−810.

(3) Gallo, R. C. (2005) The end or the beginning of the drive to an HIV-preventive vaccine: a view from over 20 years. *Lancet 366*, 1894−1898.

(4) Nabel, G. J. (2001) Challenges and opportunities for development of an AIDS vaccine. *Nature 410*, 1002−1007.

(5) Calarota, S. A., and Weiner, D. B. (2003) Present status of human HIV vaccine development. *Aids 17* Suppl 4, S73−84.

(6) McMichael, A. J., and Rowland-Jones, S. L. (2001) Cellular immune responses to HIV. *Nature 410*, 980−987.

(7) Shibata, R., Igarashi, T., Haigwood, N., Buckler-White, A., Ogert, R., Ross, W., Willey, R., Cho, M. W., and Martin, M. A. (1999) Neutralizing antibody directed against the HIV-1 envelope glycoprotein can completely block HIV-1/SIV chimeric virus infections of macaque monkeys. *Nat. Med. 5*, 204−210.

(8) Mascola, J. R., Stiegler, G., VanCott, T. C., Katinger, H., Carpenter, C. B., Hanson, C. E., Beary, H., Hayes, D., Frankel, S. S., Birx, D. L., and Lewis, M. G. (2000) Protection of macaques against vaginal transmission of a pathogenic HIV-1/SIV chimeric virus by passive infusion of neutralizing antibodies. *Nat. Med. 6*, 207−210.

(9) Baba, T. W., Liska, V., Hofmann-Lehmann, R., Vlasak, J., Xu, W., Ayehunie, S., Cavacini, L. A., Posner, M. R., Katinger, H., Stiegler, G., Bernacky, B. J., Rizvi, T. A., Schmidt, R., Hill, L. R., Keeling, M. E., Lu, Y., Wright, J. E., Chou, T. C., and Ruprecht, R. M. (2000) Human neutralizing monoclonal antibodies of the IgG1 subtype protect against mucosal simian-human immunodeficiency virus infection. *Nat. Med. 6*, 200−206.

(10) Burton, D. R., Desrosiers, R. C., Doms, R. W., Koff, W. C., Kwong, P. D., Moore, J. P., Nabel, G. J., Sodroski, J., Wilson, I. A., and Wyatt, R. T. (2004) HIV vaccine design and the neutralizing antibody problem. *Nat. Immunol. 5*, 233−236.

(11) Zolla-Pazner, S. (2004) Identifying epitopes of HIV-1 that induce protective antibodies. *Nat. Rev. Immunol. 4*, 199−210.

(12) Parker, C. E., Deterding, L. J., Hager-Braun, C., Binley, J. M., Schulke, N., Katinger, H., Moore, J. P., and Tomer, K. B. (2001) Fine definition of the epitope on the gp41 glycoprotein of human immunodeficiency virus type 1 for the neutralizing monoclonal antibody 2F5. *J. Virol. 75*, 10906−10911.

(13) Zwick, M. B., Labrijn, A. F., Wang, M., Spenlehauer, C., Saphire, E. O., Binley, J. M., Moore, J. P., Stiegler, G., Katinger, H., Burton, D. R., and Parren, P. W. (2001) Broadly neutralizing antibodies targeted to the membrane-proximal external region of human

immunodeficiency virus type 1 glycoprotein gp41. *J. Virol. 75*, 10892−10905.

(14) Saphire, E. O., Parren, P. W., Pantophlet, R., Zwick, M. B., Morris, G. M., Rudd, P. M., Dwek, R. A., Stanfield, R. L., Burton, D. R., and Wilson, I. A. (2001) Crystal structure of a neutralizing human IGG against HIV-1: a template for vaccine design. *Science 293*, 1155−1159.

(15) Trkola, A., Purtscher, M., Muster, T., Ballaun, C., Buchacher, A., Sullivan, N., Srinivasan, K., Sodroski, J., Moore, J. P., and Katinger, H. (1996) Human monoclonal antibody 2G12 defines a distinctive neutralization epitope on the gp120 glycoprotein of human immunodeficiency virus type 1. *J. Virol. 70*, 1100−1108.

(16) Sanders, R. W., Venturi, M., Schiffner, L., Kalyanaraman, R., Katinger, H., Lloyd, K. O., Kwong, P. D., and Moore, J. P. (2002) The mannose-dependent epitope for neutralizing antibody 2G12 on human immunodeficiency virus type 1 glycoprotein gp120. *J. Virol. 76*, 7293−7305.

(17) Scanlan, C. N., Pantophlet, R., Wormald, M. R., Ollmann Saphire, E., Stanfield, R., Wilson, I. A., Katinger, H., Dwek, R. A., Rudd, P. M., and Burton, D. R. (2002) The broadly neutralizing anti-human immunodeficiency virus type 1 antibody 2G12 recognizes a cluster of alpha1−2 mannose residues on the outer face of gp120. *J. Virol. 76*, 7306−7321.

(18) Calarese, D. A., Scanlan, C. N., Zwick, M. B., Deechongkit, S., Mimura, Y., Kunert, R., Zhu, P., Wormald, M. R., Stanfield, R. L., Roux, K. H., Kelly, J. W., Rudd, P. M., Dwek, R. A., Katinger, H., Burton, D. R., and Wilson, I. A. (2003) Antibody domain exchange is an immunological solution to carbohydrate cluster recognition. *Science 300*, 2065−2071.

(19) Calarese, D. A., Lee, H. K., Huang, C. Y., Best, M. D., Astronomo, R. D., Stanfield, R. L., Katinger, H., Burton, D. R., Wong, C. H., and Wilson, I. A. (2005) Dissection of the carbohydrate specificity of the broadly neutralizing anti-HIV-1 antibody 2G12. *Proc. Natl. Acad. Sci. U.S.A. 102*, 13372−13377.

(20) Geyer, H., Holschbach, C., Hunsmann, G., and Schneider, J. (1988) Carbohydrates of human immunodeficiency virus. Structures of oligosaccharides linked to the envelope glycoprotein 120. *J. Biol. Chem. 263*, 11760−11767.

(21) Leonard, C. K., Spellman, M. W., Riddle, L., Harris, R. J., Thomas, J. N., and Gregory, T. J. (1990) Assignment of intrachain disulfide bonds and characterization of potential glycosylation sites of the type 1 recombinant human immunodeficiency virus envelope glycoprotein (gp120) expressed in Chinese hamster ovary cells. *J. Biol. Chem. 265*, 10373−10382.

(22) Mizuochi, T., Matthews, T. J., Kato, M., Hamako, J., Titani, K., Solomon, J., and Feizi, T. (1990) Diversity of oligosaccharide structures on the envelope glycoprotein gp 120 of human immunodeficiency virus 1 from the lymphoblastoid cell line H9. Presence of complex-type oligosaccharides with bisecting N− acetylglucosamine residues. *J. Biol. Chem. 265*, 8519−8524.

(23) Zhu, X., Borchers, C., Bienstock, R. J., and Tomer, K. B. (2000) Mass spectrometric characterization of the glycosylation pattern of HIV-gp120 expressed in CHO cells. *Biochemistry 39*, 11194−11204.

(24) Armbruster, C., Stiegler, G. M., Vcelar, B. A., Jager, W., Michael, N. L., Vetter, N., and Katinger, H. W. (2002) A phase I trial with two human monoclonal antibodies (hMAb 2F5, 2G12) against HIV-1. *Aids 16*, 227−233.

(25) Stiegler, G., Armbruster, C., Vcelar, B., Stoiber, H., Kunert, R., Michael, N. L., Jagodzinski, L. L., Ammann, C., Jager, W., Jacobson, J., Vetter, N., and Katinger, H. (2002) Antiviral activity of the neutralizing antibodies 2F5 and 2G12 in asymptomatic HIV-1-infected humans: a phase I evaluation. *Aids 16*, 2019−2025.

(26) Lee, H. K., Scanlan, C. N., Huang, C. Y., Chang, A. Y., Calarese, D. A., Dwek, R. A., Rudd, P. M., Burton, D. R., Wilson, I. A., and Wong, C. H. (2004) Reactivity-based one-pot synthesis of oligomannoses: defining antigens recognized by 2G12, a broadly neutralizing anti-HIV-1 antibody. *Angew. Chem., Int. Ed. 43*, 1000−1003.

(27) Wang, L. X., Ni, J., Singh, S., and Li, H. (2004) Binding of high-mannose-type oligosaccharides and synthetic oligomannose clusters to human antibody 2G12: implications for HIV-1 vaccine design. *Chem. Biol. 11*, 127−134.

(28) Li, H., and Wang, L. X. (2004) Design and synthesis of a template-assembled oligomannose cluster as an epitope mimic for human HIV-neutralizing antibody 2G12. *Org. Biomol. Chem. 2*, 483−488.

(29) Adams, E. W., Ratner, D. M., Bokesch, H. R., McMahon, J. B., O'Keefe, B. R., and Seeberger, P. H. (2004) Oligosaccharide and glycoprotein microarrays as tools in HIV glycobiology; glycan-dependent gp120/protein interactions. *Chem. Biol. 11*, 875−881.

(30) Dudkin, V. Y., Orlova, M., Geng, X., Mandal, M., Olson, W. C., and Danishefsky, S. J. (2004) Toward fully synthetic carbohydrate-based HIV antigen design: on the critical role of bivalency. *J. Am. Chem. Soc. 126*, 9560−9562.

(31) Danishefsky, S. J., and Allen, J. R. (2000) From the Laboratory to the Clinic: A Retrospective on Fully Synthetic Carbohydrate-Based Anticancer Vaccines. *Angew. Chem., Int. Ed. 39*, 836−863.

(32) Panina-Bordignon, P., Tan, A., Termijtelen, A., Demotz, S., Corradin, G., and Lanzavecchia, A. (1989) Universally immunogenic T cell epitopes: promiscuous binding to human MHC class II and promiscuous recognition by T cells. *Eur. J. Immunol. 19*, 2237−2242.

(33) Ragupathi, G., Koganty, R. R., Qiu, D., Lloyd, K. O., and Livingston, P. O. (1998) A novel and efficient method for synthetic carbohydrate conjugate vaccine preparation: synthesis of sialyl Tn-KLH conjugate using a 4-(4-N-maleimidomethyl) cyclohexane-1-carboxyl hydrazide (MMCCH) linker arm. *Glycoconjugate J. 15*, 217−221.

(34) Ni, J., Singh, S., and Wang, L. X. (2003) Synthesis of maleimide-activated carbohydrates as chemoselective tags for site-specific glycosylation of peptides and proteins. *Bioconjugate Chem. 14*, 232−238.

(35) Stamatos, N. M., Mascola, J. R., Kalyanaraman, V. S., Louder, M. K., Frampton, L. M., Birx, D. L., and VanCott, T. C. (1998) Neutralizing antibodies from the sera of human immunodeficiency virus type 1-infected individuals bind to monomeric gp120 and oligomeric gp140. *J. Virol. 72*, 9656−9667.

(36) Takegawa, K., Yamabe, K., Fujita, K., Tabuchi, M., Mita, M., Izu, H., Watanabe, A., Asada, Y., Sano, M., Kondo, A., Kato, I., and Iwahara, S. (1997) Cloning, sequencing, and expression of Arthrobacter protophormiae endo- beta-N-acetylglucosaminidase in Escherichia coli. *Arch. Biochem. Biophys. 338*, 22−28.

(37) Fujita, K., Miyamura, T., Sano, M., Kato, I., and Takegawa, K. (2002) Transfer of high-mannose-type oligosaccharides to disaccharides by endo-b−*N*-acetylglucosaminidase from Arthrobacter protophormiae. *J. Biosci. Bioeng. 93*, 614−617.

(38) Buskas, T., Li, Y., and Boons, G. J. (2004) The immunogenicity of the tumor-associated antigen Lewis(y) may be suppressed by a bifunctional cross-linker required for coupling to a carrier protein. *Chem. Eur. J. 10*, 3517−3524.

BC0502816

SUPPORTING INFORMATION FOR

Toward a carbohydrate-based HIV-1 vaccine: Synthesis and immunological studies of oligomannose-containing glycoconjugates

Jiahong Ni, Haijing Song, Yadong Wang, Nicholas M. Stamatos, and Lai-Xi Wang*

Institute of Human Virology, University of Maryland Biotechnology Institute, University of Maryland, Baltimore, MD 21201, USA

Running title: Carbohydrate-based HIV-1 vaccine

CONTENTS:

Figure S1. HPLC profile of the glycopeptide Man9Cluster-Pep……....S2

Figure S2. ESI-MS spectrum of the synthetic glycopeptide Man9Cluster-Pep……..……S3

Figure S3. HPLC profile of the synthetic glycoconjugate Man9-Pep……..…S4

Figure S4. ESI-MS spectrum of the synthetic glycopeptide Man9-Pep…….…….S5

Figure S1. HPLC profile of the glycopeptide Man9Cluster-Pep (**10**)

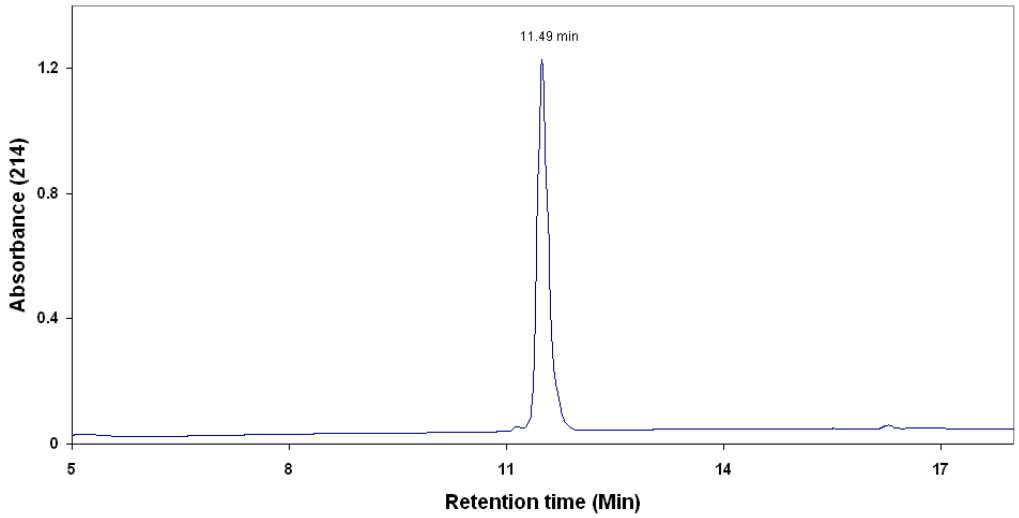

Analytical HPLC was carried out with a Waters 626 HPLC instrument on a Waters Nova-Pak C18 column (3.9x150 mm) at 40 ^{o}C. The column was eluted with a linear gradient (0-90%) of MeCN containing 0.1% TFA within 25 min at a flow rate of 1 mL/min with UV (214 nm) detection.

Figure S2. ESI-MS spectrum of the glycopeptide Man9Cluster-Pep (**10**)

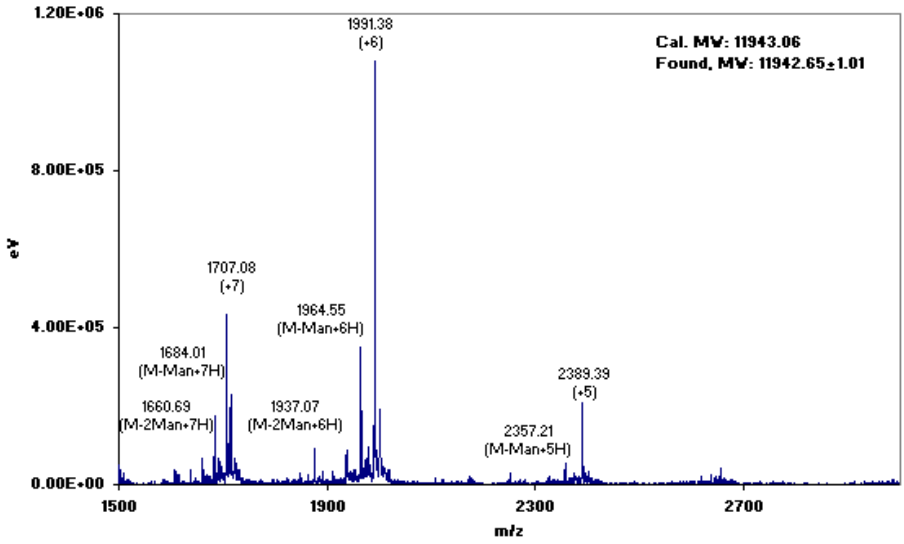

Figure S3. HPLC profile of the glycopeptide Man9Cluster-Pep (**13**)

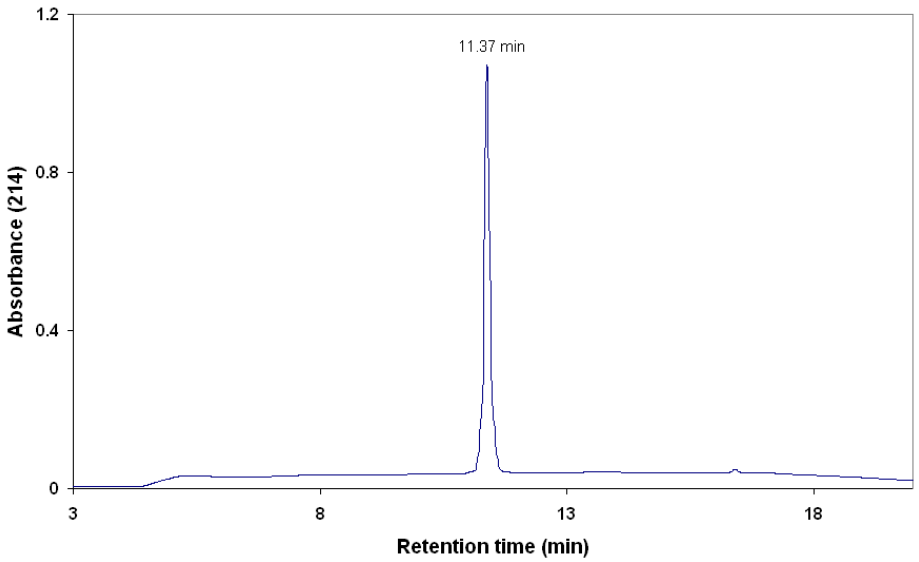

Analytical HPLC was carried out with a Waters 626 HPLC instrument on a Waters Nova-Pak C18 column (3.9x150 mm) at 40 ^{o}C. The column was eluted with a linear gradient (0-90%) of MeCN containing 0.1% TFA within 25 min at a flow rate of 1 mL/min with UV (214 nm) detection.

Figure S4. ESI-MS spectrum of the glycopeptide Man9Cluster-Pep (**13**)

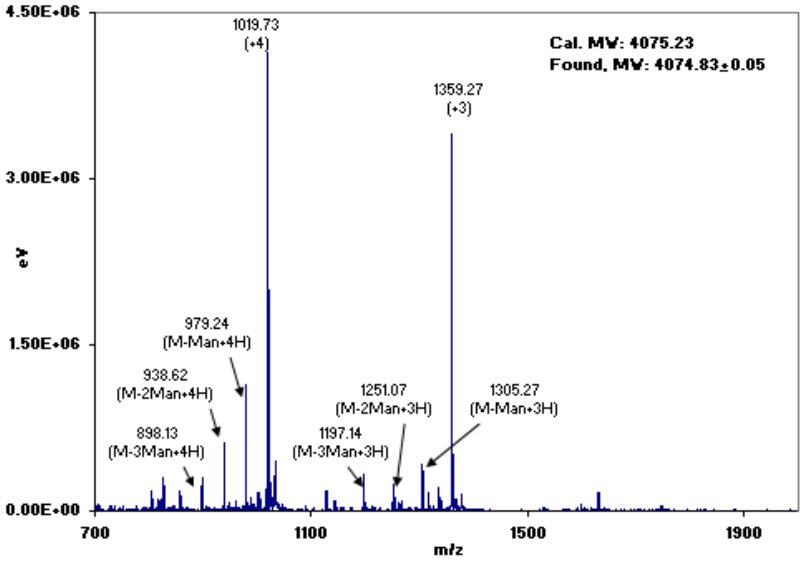

Kinetics of Amine Modification of Proteins

George P. Smith[†]

Division of Biological Sciences, Tucker Hall, University of Missouri, Columbia, Missouri 65211-7400. Received October 14, 2005; Revised Manuscript Received December 23, 2005

A simple kinetic model for coupling small molecules such as biotin to proteins with amine-reactive reagents such as *N*-hydroxysuccinimide esters is developed. It predicts the reagent concentration required to modify a protein at a given concentration to a specified number of modified amines per molecule. By optimizing the model's three adjustable kinetic parameters, its predictions can be brought into close agreement with empirical data for modification of IgG, serum albumin, and other proteins over a wide range of protein and reagent concentrations. Data for modification of one protein can be used to approximate the results for modification of another protein with the same reagent under the same reaction conditions.

INTRODUCTION

A typical protein has numerous surface-exposed α- and ϵ-amino groups; in their unprotonated form they are strong nucleophiles that can be efficiently modified by a number of electrophilic reagents under mild, non-denaturing conditions to yield stable adducts. Although it sometimes happens that a few modifiable amino groups lie in or near functional sites—for example, the antigen-binding sites of an antibody—many more lie elsewhere on the surface of the molecule. Random modification of a few of these groups with small molecules is therefore unlikely to functionally inactivate more than a small fraction of the molecules. For these reasons, amine modification has become the most commonly used method of coupling small groups such as biotin or fluorescent dyes to proteins (reviewed in ref *1*). To exploit this simple coupling technology fully, it is necessary to control the level of amine modification. Increasing the number of coupled groups per protein molecule far beyond the required number unnecessarily incurs the risk of inactivating a significant fraction of the target proteins. The purpose of this paper is to help researchers achieve this goal by developing a simple mathematical model of modification kinetics.

It is obviously desirable that the reaction solution be as free as practicable of competing nucleophiles such as primary and secondary amines, but depletion of the reagent by hydrolysis is inevitable in aqueous solution, at a rate that depends on the particular reagent, pH, temperature, and buffer composition. In this regard, the protein itself must be considered a buffer component, quite apart from its modifiable amines. Protein-dependent hydrolysis would include futile modifications (e.g., of histidine) leading to unstable adducts that are rapidly hydrolyzed to regenerate the original nucleophile. In light of these considerations, hydrolysis will be divided into two additive components: a protein-independent component, the rate of which is independent of protein concentration; and a protein-dependent component, the rate of which is proportional to protein concentration, which is assumed to be effectively constant throughout the course of the reaction even though the content of modifiable amines diminishes.

Figure 1 shows a typical modification reaction, which will serve as an exemplar in this work: biotinylation with the *N*-hydroxysuccinimide (NHS) ester NHS−PEO_4−biotin. Nucleophilic attack on the activated carbonyl by a protein amino group displaces the NHS leaving group and couples the biotin-containing moiety to the protein through a stable amide bond. Competing with this modification reaction is hydrolysis, which releases the NHS leaving group and a nonreactive carboxyl.

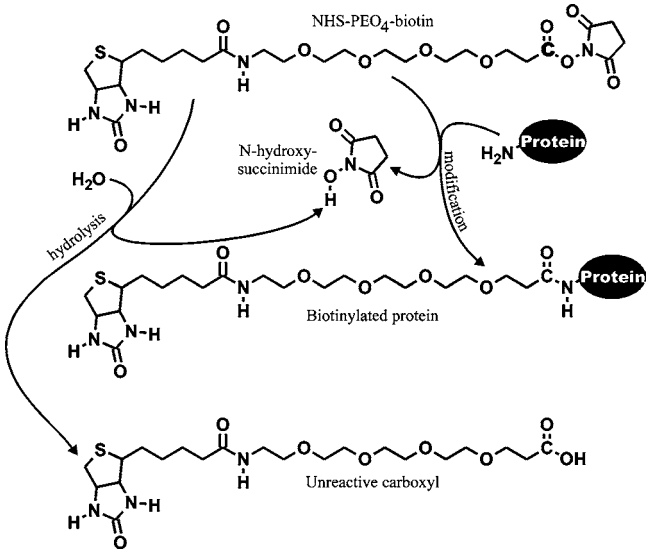

Figure 1. Modification of protein amines with the *N*-hydroxysuccinimide (NHS) ester, NHS−PEO_4−biotin. The electrophilic carbonyl carbon attacked by the nucleophile (protein amine or water) is printed in bold type.

Despite their name, amine-reactive reagents are not entirely selective for amines. In particular, free (non-disulfide-bonded) cysteine thiols in their unprotonated form are stronger nucleophiles and, if accessible on the protein surface, are readily modified by most amine-reactive reagents. The resulting thio adducts are generally much more susceptible than amine adducts to nucleophilic attack by neighboring nucleophiles on the protein itself or by nucleophilic solutes, but in the absence of such nucleophiles can be sufficiently stable in aqueous solution to be operationally indistinguishable from amine adducts. For the sake of simplicity in what follows the term "amine" will be used to refer to all stably modifiable nucleophiles, even though in some cases a few thiols or other nucleophilic groups might be included.

[†] Telephone (573) 882-3344; e-mail smithgp@missouri.edu.

10.1021/bc0503061 CCC: $33.50 © 2006 American Chemical Society
Published on Web 02/16/2006

EXPERIMENTAL PROCEDURES

Biotinylation. Immunoglobulin G (IgG) was purified by protein G chromatography from human serum after prior solvent/detergent (SD) treatment essentially as described (*2*) and by protein A chromatography from rabbit serum with and without SD treatment. The IgGs were dialyzed against phosphate-buffered saline (PBS), pH 7.2 (0.15 M NaCl, 0.1 M NaH_2PO_4, pH adjusted to 7.2 with NaOH), and quantified spectrophotometrically, assuming an absorbance of 1.4 at 280 nm for a 1 mg/mL solution (*3*) and a molecular mass of 150 kDa. Bovine serum albumin (BSA; Sigma Chemical Co., St. Louis, MO; catalog no. A7906) was dissolved in water at a concentration of 726 μM, as determined spectrophotometrically assuming a molar extinction coefficient of 44 022 at 280 nm.

In each of 16 reactions, 1 mg of human IgG was reacted with various concentrations of NHS−PEO_4−biotin reagent in final volumes ranging from 100 μL to 7.1 mL. To accomplish this, the protein was diluted in PBS, pH 7.2, to a calculated volume slightly less than the final volume; a 2 mg (3.4 μmol) portion of the reagent (No-Weigh NHS−PEO_4−biotin; Pierce Chemical Co., Rockford, IL) was dissolved in 100 μL of dimethyl sulfoxide and diluted to the desired concentration in PBS, pH 7.2; working as rapidly as feasible, the diluted reagent was pipetted into the reaction vessels in sufficient volumes to give the desired final volumes and reagent concentrations; the vessels were vortexed immediately and incubated overnight (16−20 h) at room temperature. After the addition of PBS, pH 7.2, to the biotinylated IgG (Bio-IgG) samples as necessary to bring the total volume to 7.1 mL, they were concentrated to ∼50 μL by four concentration cycles on centrifugal ultrafiltration devices with a molecular mass cutoff of 30 kDa (Centricon; Millipore Corp., Bellerica, MA) and freed of uncoupled biotin by four cycles of dilution with 1.8 mL of TBS, pH 8 (0.15 M NaCl, 50 mM Tris-HCl, pH 8.0) and concentration to ∼50 μL on the same ultrafiltration devices. The final Bio-IgG retentates (in ∼50 μL) were diluted with 400 μL of TBS, pH 8, and quantified spectrophotometrically; the yield of Bio-IgG was ∼80% of the starting IgG. Reactions with rabbit IgG and BSA were carried out similarly.

Measuring Biotinylation Level. Most biotin assays rely on competition between the analyte (the biotin to be quantified) and another ligand for binding to avidin or streptavidin. Protein-coupled biotins, unlike free biotins, cannot react freely with all four biotin-binding sites on a tetrameric avidin or streptavidin molecule because of steric hindrance. Moreover, multivalent biotinylation can lead to formation of aggregates with uncertain effects on the results. These uncertainties can be reduced if the biotin analyte is released from the protein by acid hydrolysis or proteolytic digestion prior to quantitation (*1*, *4*, *5*). The biotinylation levels reported here were measured by inhibition ELISA after first digesting the biotinylated protein extensively with proteinase K and filtering the digest through a centrifugal ultrafiltration device with a molecular mass cutoff well below the size of intact proteinase K (molecular mass = 27 kDa).

In 2.2 mL microtubes, 2 μL of SDS/DTE (5% SDS, 10 mM dithioerythritol in TBS, pH 8) was mixed with 16 μL of TBS, pH 8, containing a known amount (∼30 μg) of biotinylated protein; after heating to 95−100 °C for 5 min, cooling to room temperature, and brief centrifugation to drive condensation to the bottom, 2 μL of 20 mg/mL proteinase K stock solution [a 1:1 v/v mixture of glycerol and 40 mg/mL proteinase K in 0.3 M NaCl, 0.1 M *N*-(2-hydroxyethyl)piperazine-*N*′-(2-ethanesulfonic acid), pH adjusted to 7.5 with NaOH; stored at −20 °C] was added (enzyme/substrate weight ratio = 1.3), and the tube was incubated at 50 °C for 30 min. After brief centrifugation, the digests were heated to 95−100 °C for 5 min, briefly centrifuged again, diluted with 1.8 mL of TBS, pH 7.5 (0.15 M NaCl, 50 mM Tris-HCl, pH 7.5), and filtered through a Centricon ultrafiltration device with a molecular mass cutoff of 10 kDa. A less extensive proteinase K digestion of biotinylated protein (enzyme/substrate weight ratio = 0.02; 37 °C for 24 h) is sufficient to release the bulk of the biotin in the form of free biotin and much of the remainder as small biotinylated peptide fragments (*5*). In accord with that finding, a pilot experiment in which fluoresceinated IgG and BSA were digested and filtered in the same way as our biotinylated proteins showed quantitative recovery of fluorescence in the filtrate and no detectable retention in the retentate (data not shown).

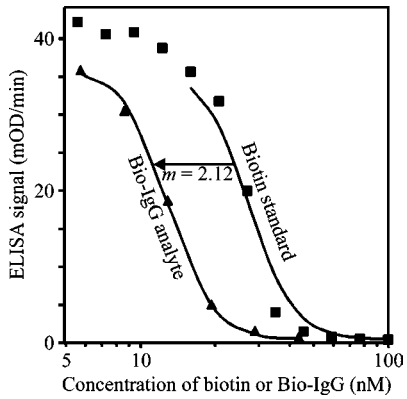

Figure 2. Biotin quantitation by inhibition ELISA. Analyte (filtered protein K-digested Bio-IgG) and biotin standard at known concentrations were tested for the ability to inhibit binding of an alkaline phosphatase conjugate of streptavidin (AP−SA) to biotinylated BSA immobilized on ELISA wells, as described in the text. All ELISA signals from a given ELISA dish were fitted to an empirical equation of the form $y = B + S/[1 + (mc/C)^N]$, where y = predicted ELISA signal (dependent variable), c = concentration of biotin or Bio-IgG inhibitor (independent variable), m = modification level (number of biotins per molecule; $m = 1$ for the biotin standard; m = a single positive number for all dilutions of a given Bio-IgG analyte), and B, S, C, and N are unknown "nuisance" parameters assumed to be constant for all 96 wells of a single ELISA dish. The modification level m for each Bio-IgG analyte and the four nuisance parameters were adjusted to minimize the root-mean-squared (RMS) deviation of the empirically measured ELISA signals from the theoretical ELISA signals predicted by the above equation. ELISA signals >35 mOD/min were excluded as being less accurate and informative than lower signals. On a semilogarithmic plot like the one shown, all curves of ELISA signal y as a function of inhibitor concentration c will have the same shape, but will be shifted to the left relative to the curve for the biotin standard ($m = 1$) by the increment $\log(m)$. The optimal value of m determined in this way for a given Bio-IgG sample was taken as the estimate of its biotinylation level. The modification levels for biotinylated proteins other than Bio-IgG were determined similarly.

Inhibition ELISA (detailed in the next paragraph) quantifies the ability of the analytes (filtered proteinase K digests) and of a free biotin standard to block binding of an alkaline phosphatase conjugate of streptavidin (AP−SA; Jackson ImmunoResearch Laboratories, West Grove, PA) to immobilized biotin in the wells of a 96-well ELISA dish. To minimize the effects of steric hindrance on the association rate, the AP−SA was preincubated with analyte or biotin for 30 min before being loaded into the biotin-coated wells.

The wells of the ELISA dish were first coated overnight at 4 °C with 200 μL of TBS, pH 7.5, containing nonbiotinylated BSA at 100 μg/mL and biotinylated BSA (Sigma; nominally 10 biotins/molecule) at 2 μg/mL. Meanwhile, using TBS/Tween (TBS, pH 7.5, supplemented with 0.5% v/v Tween 20) as diluent, serial dilutions of a free biotin standard at concentrations ranging from 1.95 to 100 nM and of the proteinase K filtrates equivalent to biotinylated protein concentrations ranging from 0.2 to 45 nM were set up. In the wells of a round-bottom 96-well dish (not the ELISA dish) were mixed 50 μL portions of the biotin and filtrate dilutions and 150 μL portions of a 200

Table 1. Derivation of Equation 1

variables (units in parentheses)
- t = time since the start of the modification reaction (s)
- $a = a(t)$ = concentration of unmodified (but modifiable) amines remaining at time t (μM)
- A = initial concentration of modifiable amines before any modification (μM); $A = a(0)$
- P = concentration of protein (μM)
- M = number of modifiable amines per protein molecule (dimensionless); $A = P \times M$
- $m = m(t)$ = number of modified amines per protein at time t (dimensionless); $m(t) = [A - a(t)]/P = M - a(t)/P$; $m(0) = 0$
- $r = r(t)$ = concentration of amine-modifying reagent remaining at time t (μM)
- R = initial concentration of reagent before modification or hydrolysis (μM); $R = r(0)$
- k_m = second-order modification rate constant ($\mu M^{-1}\ s^{-1}$)
- k_h = first-order protein-independent hydrolysis rate constant (s^{-1})
- Q = second-order protein-dependent hydrolysis rate constant ($\mu M^{-1}\ s^{-1}$)

differential equations from the mass-action law
- $da/dt = -k_m a r$
- $dr/dt = -k_m a r - (k_h + QP)r$

dividing the second equation by the first yields an easily solved differential equation relating r to a:
- $dr/da = 1 + [(k_h + QP)/k_m](1/a)$

eq 1 of the text is the solution to this equation when the reaction goes to completion ($r = 0$)

ng/mL dilution of AP−SA (also in TBS/Tween diluent); the dish was incubated for 30 min at room temperature. As that incubation was ending in the round-bottom dish, the ELISA dish was washed with a plate washer and 150 μL portions were pipetted from the wells of the round-bottom dish into the corresponding wells of the ELISA dish, which was incubated for 30 min at room temperature to allow AP−SA to bind the immobilized biotinylated BSA. The ELISA dish was washed extensively on a plate washer, and the wells were filled with 150 μL portions of substrate solution: a fresh mixture of 20 mL of 1 M diethanolamine, pH adjusted to 9.8 with HCl, 20 μL of 1 M $MgCl_2$, and 200 μL of 50 mg/mL *p*-nitrophenyl phosphate (stored at −20 °C). The difference between the optical density (OD) at 405 and that at 490 nm was read at 3 min intervals over a 57 min period on a kinetic plate reader at room temperature to obtain a slope (mOD/min) for each well (1 mOD corresponds to an OD of 1/1000), which was taken as the ELISA signal; for slopes up to at least 50 mOD/min, time dependence is linear, with correlation coefficients usually exceeding 0.995.

Figure 2 shows an example of an inhibition ELISA with the filtered proteinase K digest of a Bio-IgG sample. As can be seen in the graph, the equivalent Bio-IgG concentration required to reach a given level of inhibition was 2.12 times lower than the concentration of free biotin required to reach the same inhibition level; the modification level of this Bio-IgG sample is therefore estimated at 2.12 biotins/molecule. Duplicate measurements (on separate ELISA dishes) with all biotinylated protein samples gave closely similar numbers with few exceptions.

The inhibition data for the free biotin standard in Figure 2 deviate slightly but systematically from the theoretical curve, indicating that protein-derived biotins are not entirely equivalent kinetically to free biotins. A plausible explanation is that a few biotins remain coupled to small peptide fragments even after extensive proteinase K digestion, as noted above (*5*). Such peptide-coupled biotins may well bind streptavidin with somewhat altered kinetics compared to free biotin because of steric hindrance, thus accounting for the slight deviations in Figure 2. Still, there is no reason to believe such peptides are so abundant and so kinetically different from biotin as to lead to large errors in biotin content estimates. Complete acid hydrolysis has been advocated as a method for releasing all protein-coupled biotin in the form of free biotin (*5*); however, as measured by inhibition ELISA, that method yielded only 66% as much biotin from a Bio-IgG sample as did proteinase K digestion, possibly because some biotin was destroyed or altered in the acid (*6*). In any case, modest errors in biotin level (on the order of 33%, say) are seldom of practical importance and do not undermine the conclusions of this paper—especially if, as seems likely, they apply proportionally across all samples (see below under eq 2).

RESULTS AND DISCUSSION

Mathematical Model. If one makes the simplifying assumptions that all amines react independently and identically, depletion of the target amines and amine-reactive reagent from their respective initial concentrations is described by the differential equations in Table 1. At completion of the reaction those equations have the solution

$$R = \left[m - \frac{Q}{k_m}\ln\left(1 - \frac{m}{M}\right)\right]P - \frac{k_h}{k_m}\ln\left(1 - \frac{m}{M}\right) \qquad (1)$$

where M = total number of modifiable amines per protein molecule, m = average number of amines modified per protein molecule at completion of the reaction, R = reagent concentration, P = protein concentration, k_m = second-order modification rate constant, k_h = first-order protein-independent hydrolysis rate constant, and Q = second-order protein-dependent hydrolysis rate constant (derivation in Table 1).

According to eq 1, the reagent concentration R required to achieve a given modification level m is a linear function of the protein concentration P, with slope $[m - (Q/k_m)\ln(1 - m/M)]$ and intercept $-(k_h/k_m)\ln(1 - m/M)$ (both expressions are always positive, because the logarithm is negative). It is obvious from this expression that the ratio of reagent to protein, R/P, is not an adequate description of reaction conditions, contrary to common practice in protein chemistry. Indeed, in circumstances when the intercept term of eq 1 dominates, either because the protein concentration P is low or because protein-independent hydrolysis is relatively fast compared to modification, the reagent concentration required is independent of protein concentration. To fully describe the conditions of a modification reaction, therefore, both the reagent concentration R and the protein concentration P must be individually specified (along with buffer composition and pH, temperature, and time of reaction).

In most applications, the fraction of available amines modified m/M will be small (less than ~20%, say), in which circumstances $-\ln(1 - m/M) \approx m/M$ and eq 1 can be approximated by

$$R \approx \left[\left(1 + \frac{Q}{k_m M}\right)P + \frac{k_h}{k_m M}\right]m \quad \text{when } \frac{m}{M} \ll 1 \qquad (2)$$

In a typical modification reaction, therefore, the reagent concentration R required to achieve modification level m at fixed

protein concentration P will be nearly proportional to m. In these circumstances, proportional errors in measuring m lead only to the same proportional errors in R.

The mass-action law that underlies eq 1 is silent on the values of the three kinetic parameters Q/k_m, k_h/k_m, and M—or, when eq 2 applies, the two parameters Q/k_mM and k_h/k_mM. Those parameter values must be estimated empirically by adjusting their values to optimize the fit of eq 1 (or eq 2) to experimentally measured modification levels. It is vital that those experimental measurements span a wide range of protein concentrations, because modification at a single protein concentration is essentially governed by a single proportionality constant—the quantity in square brackets in eq 2—and cannot be used to constrain two or three separate parameters.

Biotinylation as an Example of Amine Modification. Conjugating biotin to proteins opens up a wealth of techniques that exploit the extremely rapid and stable binding of biotin to avidin and streptavidin (reviewed in refs *1* and *7*). For most of these purposes, a modification level of 2−3 biotins per molecule is fully sufficient and stands very little chance of interfering with the biological activity of most modified proteins. Biotinylation of human IgG with NHS−PEO_4−biotin (Figure 1) will serve as the chief example of amine modification in this paper.

Sixteen human IgG samples at concentrations ranging from 0.953 to 67.6 μM (from 143 μg/mL to 10.1 mg/mL) were biotinylated overnight at room temperature with NHS−PEO_4−biotin at various concentrations in PBS, pH 7.2, and freed of uncoupled biotin as described under Experimental Procedures. The biotin contents of the resulting biotinylated IgGs (Bio-IgGs) were quantified by proteinase K digestion and duplicate inhibition ELISA as described under Experimental Procedures. The measured biotinylation levels m were fitted to eq 1 by adjusting the kinetic parameters to optimize agreement with the data. A series of four biotinylation reactions with BSA were likewise fitted to eq 1, yielding an independent set of optimal parameter values. In Figure 3 those optimized IgG and BSA parameter values (reported in the caption) are used to plot the predicted reagent concentration R required to achieve various modification levels m as a function of protein concentration P (IgG in the upper part of the graph, BSA in the lower part); in a linear plot these isomodification contours would be straight lines, as explained above under eq 1. Superimposed on the theoretical contour curves are the data on which they are based. For each biotinylation reaction, the open symbol marks the actual concentrations of protein and reagent, whereas the associated horizontal bars plot the reagent concentration R that according to eq 1 would theoretically be required to achieve the biotinylation levels m actually measured for that sample (one bar for each of the duplicate determinations). The closeness of the bars to each other testifies to the excellent reproducibility of the biotin determinations; the closeness of the bars to their corresponding open symbols testifies to the excellent fit between the observed data and the theoretical calculations over a wide range of protein and reagent concentrations. Also included in the upper part of Figure 3 (but not considered in optimizing the IgG parameter values) are four reactions with rabbit IgG; here, too, the observed biotinylation levels closely match the predictions of eq 1. This graph illustrates dramatically how eq 1 allows results of a handful of pilot experiments to be parlayed into reliable projections covering a broad continuous range of concentrations of the same protein and the same reagent under the same reaction conditions.

As Figure 3 shows, eq 1 (or, when applicable, its corollary eq 2) applies in form to biotinylation of both IgG and BSA, although the optimal parameter values are different for the two proteins as will be detailed in the next subsection. It is probable that eq 1 will likewise apply in form to almost any amine

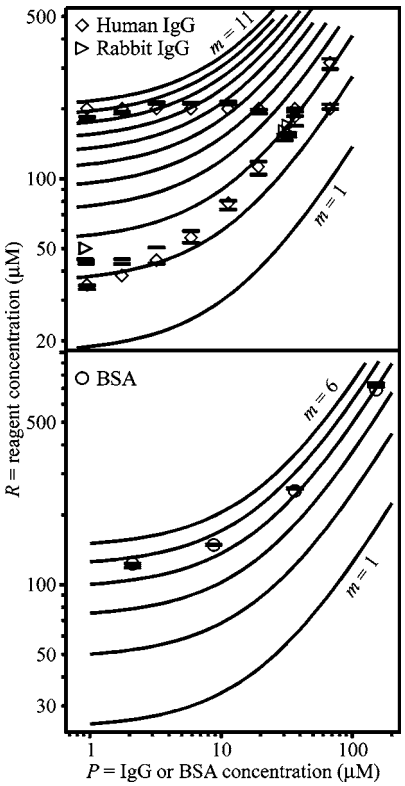

Figure 3. Graph of NHS−PEO_4−biotin concentration R required to biotinylate human and rabbit IgGs (upper part) and BSA (lower part) to various modification levels m as a function of protein concentration P. The theoretical curves are iso-modification contours for $m = 1-11$, calculated according to eq 1 (IgG) or eq 2 (BSA) with the following optimized parameter values: $k_h/k_m = 2274$ μM, $Q/k_m = 25.60$, and $M = 128.9$ accessible amines per molecule for IgG; and $k_h/k_mM = 24.1$ μM per accessible amine and $Q/k_mM = 0$ for BSA. The open symbols plot the protein and reagent concentrations for each reaction; the associated pair of horizontal bars represent the duplicate results for that reaction, as explained in the text.

modification reaction that goes to completion, because it appeals only to basic principles of mass action that successfully describe the great majority of chemical interconversions. In accord with this supposition, for example, Larson et al. (*8*) found that the degree of modification of IgG at constant concentration with amine-reactive poly(ethylene glycol) (PEG) polymer chains was directly proportional to the concentration of the PEGylating reagent, as predicted by eq 2. The mathematical model's most vulnerable assumption is kinetic homogeneity of the accessible aminess, but it is not necessary for that assumption to be literally true for eq 1 to be empirically useful: all that is required is that there exist compromise values of the parameters that give a reasonable approximation to the overall kinetic behavior of the amines. Equation 1 may be much less successful if extended to high degrees of modification, when the homogeneity assumption would be more severely challenged, but in most applications calling for the kinetic predictability afforded by eq 1, only modest modification levels are of practical interest.

The ratio $[(Q/k_mM)P)/((k_h/k_m)M] = QP/k_h$ gauges the relative contribution of protein-dependent and protein-independent hydrolysis to consumption of the reagent. For IgG that ratio reaches 0.75 at the highest IgG concentrations P, when hydrolysis as a whole is relatively unimportant compared to modification, but declines proportionally at lower IgG concentrations as hydrolysis comes to dominate. For BSA the ratio vanishes altogether. The data therefore do not support the existence of a significant protein-dependent route for hydrolysis of NHS−PEO_4−biotin. When protein-mediated hydrolysis is negligible and the modification level m is modest compared to the total number of

Table 2. Dependence of the Kinetic Parameters of Equation 1 on Reagent, Protein, and Reaction Conditions and Sensitivity of Predictions of Equation 1 to Variations in Those Parameters[a]

	expected dependence of parameter on			
parameter	reagent	protein	conditions	sensitivity of reaction kinetics to variations in parameter
k_h	strong	none	strong	strong
k_m	strong	none	strong	strong
M	weak	proportional to amines?	strong	strong
Q	strong	proportional to MW?	strong	weak

[a] See text for details.

accessible amines *M*, eq 2 reduces further to the single-parameter approximation

$$R \approx \left(P + \frac{k_h}{k_m M}\right)m \quad \text{when } \frac{m}{M} \ll 1 \text{ and } \frac{QP}{k_h} \ll 1 \qquad (3)$$

It is entirely possible that protein-dependent hydrolysis may be much more important for amine-reactive reagents other than NHS−PEO_4−biotin, however—particularly when the reactive function is something other than an NHS ester.

It is evident from Figure 3 that at the lowest protein concentrations *P* explored the curves are nearly horizontal because consumption of reagent by modification of protein amines or protein-mediated hydrolysis is negligible compared to consumption by non-protein-mediated hydrolysis. In those circumstances eq 3 further simplifies to the approximation

$$R \approx \left(\frac{k_h}{k_m M}\right)m \quad \text{when } \frac{m}{M} \ll 1 \text{ and } \left(1 + \frac{Q}{k_m M}\right)P \ll \frac{k_h}{k_m M} \qquad (4)$$

and it is not necessary to know the protein concentration accurately to modify it to a specified level. This case underscores the inadequacy of reagent/protein ratio *R*/*P* alone as a description of the conditions of a modification reaction, as emphasized in the previous subsection (Mathematical Model).

Applicability to Different Proteins, Reagents, and Conditions. The three parameters of eq 1 are composed of four fundamental parameters that arise directly from the underlying kinetic model and that respond in different ways to changes in the protein, reagent, and reaction conditions (pH, buffer composition, and temperature). The parameters k_h and k_m, respectively, gauge the susceptibility of the reagent to protein-independent hydrolysis and its intrinsic reactivity with an accessible amine; they are therefore specific to the reagent but independent of the protein. In contrast, *M* gauges the total number of accessible amines on the protein molecule; it is therefore specific to the protein and may also depend somewhat on the reagent to the degree that the reagent's structure affects its access to amines. For a given reagent *M* should vary roughly in proportion to the total number of amines, although of course there will be excursions from this trend because of variations in protein shape and other properties. Finally, *Q* parametrizes the rate of protein-dependent hydrolysis and, in general, may depend on both reagent and protein. This mode of hydrolysis is presumably due to various surface groups on the protein, and because the nature of those groups is unknown, the best guess is that *Q* for a given reagent is roughly proportional to total protein molecular mass. All four fundamental parameters might depend strongly on pH and temperature, but probably only weakly on buffer composition provided no strong nucleophiles are included. These theoretical dependencies are summarized in the second, third, and fourth columns of Table 2. The last column of the table summarizes the sensitivity of reaction kinetics (*R* as calculated from eq 1) to variation in the four kinetic parameters. The value of each parameter was halved and doubled relative to its optimal value for the IgG data, keeping the other three parameters constant, and the resulting overall deviations from the original values of *R* were scored. This sensitivity analysis reveals that halving or doubling *Q* changes the theoretical predictions of eq 1 only slightly, reflecting the finding that protein-dependent hydrolysis is minor or nonexistent (see above). In contrast, halving or doubling the other three parameters drastically changes the predictions of eq 1 in at least some circumstances.

Because eq 1 is based on an oversimplification of the true kinetic situation (particularly the simplifying assumption that all modifiable amines are kinetically homogeneous), the parameter values that optimize the fit to actual data may represent compromise values in which the theoretical dependencies in Table 2 are somewhat blurred. For example, the optimal value of the parameter *M* for IgG in Figure 3, 129 modifiable amines per molecule, certainly cannot be interpreted literally, in that it greatly exceeds the number of accessible IgG amines [~30 as determined at saturating concentrations of another NHS ester, *N*-succinimidyl *S*-acetylthioacetate (*1*)], and indeed exceeds the total number of amines in a typical IgG (~90). Because the conditions of eq 2 apply to a good approximation for most of the IgG reactions, the overall fit of eq 1 to the IgG data can evidently be improved by exaggerating the value of *M* substantially while keeping the ratios Q/k_mM and k_h/k_mM roughly the same. The improvement is slight: the best fit to the data with *M* fixed at 30 is nearly as good as the overall best fit. Despite these reservations to the theoretical parameter dependencies, though, it is reasonable to accept them as first approximations in extrapolating results from one combination of protein, reagent, and reaction conditions to another. For instance, whatever the discrepancy between the optimal value of *M* for IgG and that protein's actual content of modifiable amines, when one is extrapolating from IgG to other proteins, it is reasonable to assume that *M* scales as the total amine content to a first approximation. The BSA data in Figure 3 provide an opportunity to test the validity of such projections. Because BSA has 44% of the molecular mass and 66.7% of the total amine content of IgG, parameters k_h/k_mM and Q/k_mM for biotinylation of BSA are projected to be $(k_h/k_m)/M \approx 2274/0.667 \times 129 = 26.4\ \mu M$ per accessible amine and $(Q/k_m)/M \approx (0.44 \times 25.6)/(0.667 \times 129) = 0.13$ per accessible amine. Actual results for BSA biotinylation optimally fit values of 24.1 and 0 for those parameters, respectively (Figure 3 caption). The agreement for the first parameter (24.1 predicted, 26.5 observed) is quite close, whereas the discrepancy for the second (0.13 predicted, 0 observed) is of little significance because protein-dependent hydrolysis seems to be very minor. By the same token, the observed BSA modification levels were only 11−19% higher than those projected on the basis of the IgG results. The BSA data thus suggest that results for modification of one protein can be used to make reasonable predictions about modification of another with the same reagent under the same reaction conditions. Such extrapolations—especially if supported by a handful of additional proteins—are of great practical usefulness because they bypass the need for preliminary investigation of modification kinetics for each new protein to be modified (provided great precision is not required). For modifications such as biotinylation that are difficult to quantify accurately (see Experimental Procedures), a great deal of effort can thereby be saved. For proteins in very short supply, valuable material can be spared. It remains to be ascertained if other additional useful generalizations will emerge from further investigation with additional reagents, proteins, and reaction conditions.

ACKNOWLEDGMENT

Robert Davis provided excellent technical assistance in this work, which was supported by U.S. National Institutes of Health Grant GM41478 to the author and National Cancer Institute Center Grant P50-CA-10313-01 to Wynn A. Volkert.

LITERATURE CITED

(1) Hermanson, G. T. (1996) *Bioconjugate Techniques*; Academic Press, San Diego, CA.

(2) Kouzmitcheva, G. A., Petrenko, V. A., and Smith, G. P. (2001) Identifying diagnostic peptides for Lyme disease through epitope discovery. *Clin. Diagn. Lab. Immunol. 8*, 150−160.

(3) Mandy, W. J., and Nisonoff, A. (1963) Effect of reduction of several disulfide bonds on the properties and recombination of univalent fragments of rabbit antibody. *J. Biol. Chem. 238*, 206−213.

(4) Bayer, E. A., and Wilchek, M. (1990) Protein biotinylation. *Methods Enzymol. 184*, 138−160.

(5) Rao, S. V., Anderson, K. W., and Bachas, L. G. (1997) Determination of the extent of protein biotinylation by fluorescence binding assay. *Bioconjugate Chem. 8*, 94−98.

(6) Mock, D. M., Mock, N. I., and Langbehn, S. E. (1992) Biotin in human milk: methods, location, and chemical form. *J. Nutr. 122*, 535−545.

(7) Wilchek, M., and Bayer, E. A., Eds. (1990) *Avidin−Biotin Technology*. *Methods in Enzymology*; Vol. 184, Academic Press, New York.

(8) Larson, R. S., Menard, V., Jacobs, H., and Kim, S. W. (2001) Physicochemical characterization of poly(ethylene glycol)-modified anti-GAD antibodies. *Bioconjugate Chem. 12*, 861−869.

BC0503061

Synthesis, Photophysical Effects, and DNA Targeting Properties of Oxazole Yellow−Peptide Bioconjugates

Martin Thompson*

Department of Chemistry, Michigan Technological University, 1400 Townsend Drive, Houghton, Michigan 49931. Received October 17, 2005; Revised Manuscript Received January 19, 2006

The design of a dsDNA-sensitive fluorescent bioconjugate capable of targeting a specific DNA sequence with high efficiency is described. The bioconjugate has the molecular recognition features of the polypeptide from a DNA-binding protein and the dsDNA-dependent fluorescence of an intercalating dye. The DNA sequence selectivity of the probe was characterized, as were the changes in photophysical properties of the dye upon covalent linkage to the peptide to assess whether such bioconjugates could function as molecular probes of gene sequences. The oxazole yellow−peptide bioconjugate exhibits DNA recognition and binding affinity comparable to the native Hin recombinase protein. Examination of photophysical effects to dye conjugation indicates a negligible affect on the fluorescence quantum yield. Fluorescence studies indicate this molecular probe is useful to determine the presence of a given DNA target sequence and gives negligible fluorescence in the absence of a given target site. Using the synthetic route described here, bioconjugates could be designed using different combinations of DNA recognition polypeptides and cyanine dyes to generate an array of sequence specific and wavelength specific probes.

INTRODUCTION

Small molecular mimics of DNA-binding proteins have previously been shown to be useful as synthetic nucleases (*1*−*4*), inhibitors of protein interactions (*5*−*7*), and transcriptional activators (*8*). In fact, recent studies indicate thiazole orange−peptide bioconjugates can act as synthetic nucleases via two competing mechanisms, which depend on environmental conditions (*4*). The functionality responsible for targeting in the bulk of such studies is derived from a segment of a DNA-binding protein comprising the protein−DNA interface (*3*, *9*). Using short polypeptides as recognition molecules, however, has the drawback that alone they bind with low affinity. This is largely because many of the native protein−DNA contacts at the interface, including numerous electrostatic interactions between backbone phosphates and positively charged side chains located in nearby regions of the protein, are lost. To develop molecular probes of DNA sequence and structure, these peptide−dye bioconjugates need to be highly sequence-specific due to the low ratio of specific to nonspecific sites in genomic DNA, and bind with sufficiently high affinity to ensure it remains bound long enough to be a useful probe of its local environment.

The sequence specific DNA targeting region of a native DNA-binding protein can be excised from the full-length protein without altering its molecular recognition features. This means that short peptides can be constructed with strategically positioned fluorophores to generate sequence specific molecular probes capable of being highly fluorescent when bound to a DNA target site, yet effectively invisible in the absence of this site. Such polypeptides can readily be made using solid-phase synthesis in conjunction with specific chemistries required to add non-native functional probes at specific positions along the peptide chain. The resulting bioconjugates spatially orient the probe and optimize its interaction with DNA (*3*, *4*, *10*, *11*). Furthermore, this approach overcomes time-consuming and low yield strategies, such as cloning using standard molecular biology techniques, followed by the incorporation of mutant side chains to conjugate fluorophores or other reporter groups at specific positions within the protein sequence. Oftentimes, cysteines are used for the selective incorporation of non-native reporter groups. This requires several workup steps and can significantly decrease yields due to oxidative cross-linking of free thiols into disulfide linkages. The strategy described here is a direct synthesis strategy that avoids such low yield workup steps and results in high yield, high purity preparations of fluorescent DNA targeting probes.

The polypeptide used in these studies was derived from the Hin recombinase of *Salmonella typhimurium.* Hin belongs to the invertase class of DNA-cleaving enzymes that catalyzes the inversion of a 1-kb segment of the chromosome to control flagellin gene expression by switching the orientation of the promoter (*12*). The Hin proteins bind as dimers to attain high affinity and high site selectivity by targeting left (hixL) and right (hixR) DNA sites that flank the invertible segment. Structural information about the Hin protein shows that it uses a helix-turn-helix motif to position a helix in the major groove at the hix target site (*13*). Hin interacts with the hixL half-site with higher affinity than the right half-site and therefore is used as the cognate site throughout these studies.

The intercalating dye used in this work is the cyanine dye oxazole yellow (YO)[1], which exhibits increased emission enhancement upon intercalation into dsDNA (*14*, *15*). Intercalation between the DNA bases forces the cyanine dye to adopt a planar conformation, which has a longer-lived excited state than the free (not DNA bound) dye. This feature makes the cyanine dyes ideal for use as a molecular probe of DNA, as it is effectively invisible when not bound to DNA. Oxazole yellow is widely used in cytology as a DNA stain due to its emission

* To whom correspondence should be addressed. Tel.: 906-487-3522, Fax: 906-487-2061, E-mail: mthomps@mtu.edu.

[1] Abbreviations used: YO, oxazole yellow; HIN, polypeptide derived from hin recombinase; TMS, trimethylsilane; DMF, dimethylformamide; MALDI-TOF, matrix-assisted laser desorption ionization time-of-flight; CT, calf thymus; HPLC, performance liquid chromatography; SPPS, solid-phase peptide synthesis; TFA, trifluoroacetic acid; DCM, dichloromethane

10.1021/bc050307t CCC: $33.50 © 2006 American Chemical Society
Published on Web 02/18/2006

Scheme 1. Reaction Scheme for Synthesis of the Carboxylic Acid Derivative of Oxazole Yellow

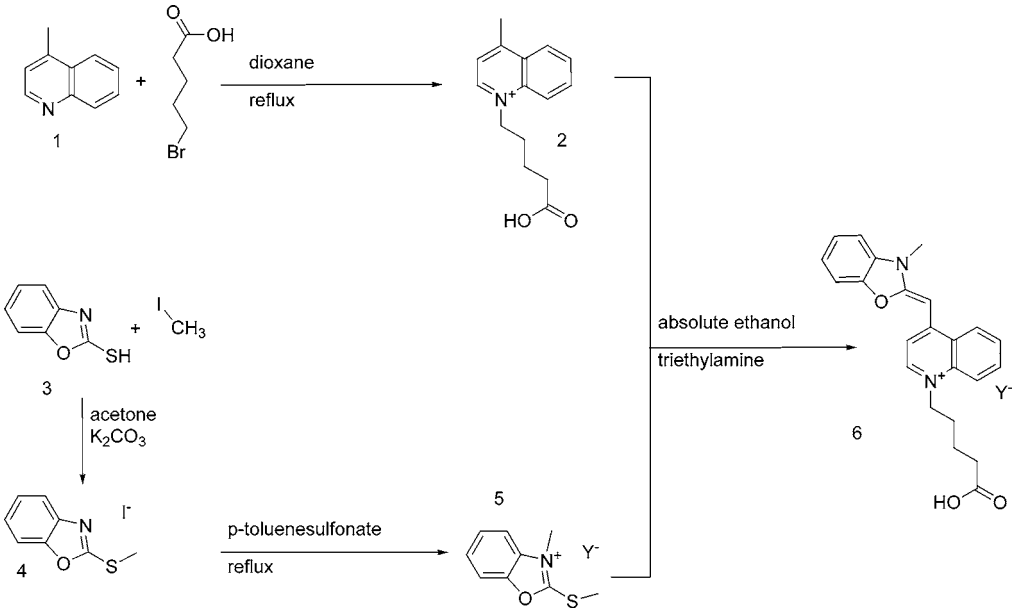

enhancement of up to 2000-fold in going from a free to a DNA-bound state (*14*).

Solid phase peptide synthesis (SPPS) was used to couple the cyanine dye oxazole yellow at a strategically positioned lysine within an amino acid sequence derived from Hin recombinase (HIN). The oxazole yellow−Hin recombinase (YOHIN) bioconjugate probe has been prepared and characterized to understand the effects of peptide conjugation on dye photophysics, and to assess whether such probes would be useful as DNA sequence and wavelength sensitive stains. Fluorescence analysis is also used to characterize probe sensitivity to mutant hixL sequences to determine the extent to which the peptide moiety reproduces the binding features of the native protein. From design to functional application, synthetic bioconjugates represent an opportunity to develop systematically rational strategies for site-specific nucleic acid targeting by small readily made complexes. Furthermore, by using different combinations of DNA recognition polypeptides and cyanine dyes, groups of bioconjugates could potentially be synthesized with custom-made sequence and wavelength specificities.

EXPERIMENTAL PROCEDURES

Materials. Lepidine, 5-bromovaleric acid, 2-mercaptobenzoxazole, dipotassium carbonate, trimethyloxonium tetrafluoroborate, *p*-toluenesulfonate, iodomethane, acetone, dichloromethane, dioxane, anhydrous ethanol, and triethylamine were purchased from Aldrich (Milwaukee, WI) and used without further purification, except dioxane, which was distilled prior to use. F-moc amino acids and peptide synthesis reagents were purchased from Advanced Chemtech (Louisville, KY). The F-moc-Lys (Mtt)-OH was purchased from Anaspec (San Jose, CA).

Instrumentation. NMR spectra were recorded on a Varian 400 MHz spectrometer using a deuterated solvent and were referenced to TMS. Peptides were synthesized on a 9050 peptide synthesizer (Millipore, Bedford, MA). Purification of synthetic peptides was performed using high-performance liquid chromatography (HPLC). Bioconjugate characterization was performed using matrix-assisted laser desorption ionization-time-of-flight (MALDI-TOF) mass spectrometry with α-cyanohydroxycinnamic acid as matrix. Absorbance measurements were made on a Cary V spectrophotometer (Varian Instruments, Palo Alto, CA). Steady-state fluorescence measurements were performed on a Quantamaster-6/2003 Spectrofluorometer in T-format, with a 75W xenon lamp and analyzed with Felix32 Fluorescence Analysis Software (PTI, Canada).

Synthesis and Characterization of Carboxylic Acid Derivative of Oxazole Yellow. The synthesis of a carboxylic acid derivative of YO for use in SPPS of the bioconjugate was adapted from published procedures (*4*, *16*) and is shown in detail in Scheme 1. The YO derivative and intermediates were purified on silica gel 60−200 mesh using a 2:2:1 (v/v) acetic acid:water:ethyl acetate solvent solution characterized by ^{1}H NMR using a deuterated solvent (DMSO-d_6), referenced to tetramethylsilane (TMS) and confirmed with MALDI-TOF mass spectrometry.

Synthesis of 4-methyl-1-(4′-carboxybutyl)quinolinium (2) was performed by refluxing lepidine (1, 1.4 mL, 11 mmol) and 5-bromovaleric acid (5.7 g, 32 mmol) in 30 mL of distilled dioxane under nitrogen overnight. The reaction mixture was allowed to cool to room temperature and filtered. The precipitate was washed twice with 10 mL of dioxane followed by 50 mL of petroleum ether to yield 2.6 g (70%) of pure 4-methyl-1-(4′-carboxybutyl)quinolinium bromide (**2**). MALDI-TOF gave a molecular weight (*m*/*z*) of 244.9 (244.3, calculated for $C_{15}H_{18}NO_2^+$). ^{1}H NMR (400 MHz, DMSO-d_6) δ 1.42−1.52(m, 2H, CH_2), 1.87−1.97 (m, 2H, CH_2), 2.21 (t, J = 7.79 Hz, 2H, CH_2), 3.09 (s, 3H, CH_3), 4.93 (t, J = 7.39 Hz, 2H, NCH_2), 8.10−8.20 (m, 2H, Ar), 8.12−8.20 (m, 1H, Ar), 8.71−8.90 (m, 2H, Ar), 9.66 (d, J = 5.83 Hz, 1H, Ar).

Synthesis of 2-methylmercapto-3-methylbenzoxazole (5) was performed in a two-step reaction by first mixing 2-mercaptobenzoxazole (3, 2.0 g, 11 mmol), iodomethane (8.0 mL, 55 mmol), and K_2CO_3 (1.0 g, 7 mmol) in 100 mL of acetone for 60 min at 70 °C. Reaction mixture was filtered hot, and filtrate was dried in vacuo. Recrystallization from ethanol:diethyl ether gave 1.3 g (40%) of pure 2-methylmercaptobenzoxazole iodide (*4*). Next, 2-methylmercaptobenzoxazole (4, 1.0 g, 3 mmol) and trimethyloxonium tetrafluoroborate (1.1 g, 3.3 mmol) of were mixed in 50 mL of dichloromethane in a nitrogen environment for 5 h at room temperature. Precipitation with diethyl ether was followed by filtration and yielded 3.5 g (90%) of pure 2-methylmercapto-3-methylbenzoxazole (*5*). MALDI-TOF gave a molecular weight (*m*/*z*) of 179.8 (180.2, calculated for $C_9H_{10}NOS^+$). ^{1}H NMR (400 MHz, DMSO-d_6) δ 3.31 (s, 3H, SCH_3), 3.91 (s, 3H, NCH_3), 7.50−7.61 (m, 1H, Ar), 7.84−

7.88 (m, 1H, Ar), 8.00 (d, $J = 8.82$ Hz, 1H, Ar), 8.61 (d, $J = 7.66$ Hz, 1H, Ar).

Alternate synthesis of 2-methylmercapto-3-methylbenzoxazole (5) was performed by reflux of 2-methylmercaptobenzoxazole (4, 1.0 g, 3 mmol) in *p*-methyltoluenesulfonate (10 mL, 66 mmol) under nitrogen for 60 min. The reaction mixture was allowed to cool to room temperature, filtered, and washed with diethyl ether. Recrystallization from ethanol:diethyl ether gave 1.5 g (70%) of pure 2-methylmercapto-3-methylbenzoxazole tosylate (*5*). MALDI-TOF gave a molecular weight (*m*/*z*) of 180.5 (180.2, calculated for $C_9H_{10}NOS^+$).

Synthesis of Carboxylic Acid Derivative of Oxazole Yellow (6). 1-(4-Carboxybutyl)-4-[(3-methylbenzoxazol-2(3*H*)-ylidene)-methyl]quinolinium was synthesized by mixing 4-methyl-1-(4-carboxybutyl)quinolinium bromide (**2**, 1.0 g, 3 mmol) and 2-methylmercapto-3-methylbenzoxazole (**5**, 1.0 g, 3 mmol) in 30 mL of absolute ethanol with slight heating for 5 min. To this solution, triethylamine (840 μL, 6 mmol) was added causing the reaction mixture to immediately turn a deep red color. Heating was discontinued and the reaction allowed to stir for 60 min. Product was precipitated by addition of 150 mL of diethyl ether. Recrystallization from acetone:diethyl ether gave 1.4 g (80% yield) of pure 1-(4-carboxybutyl)-4-[(3-methylbenzoxazol-2(3*H*)-ylidene)methyl]quinolinium (**6**). MALDI-TOF gave a molecular weight (*m*/*z*) of 375.8 (375.5, calculated for $C_{23}H_{23}N_2O_3^+$). ^{1}H NMR (400 MHz, DMSO-d_6) δ 1.27−1.41 (m, 2H, CH_2), 1.87−1.99 (m, 2H, CH_2), 2.22 (t, $J = 7.93$ Hz, 2H, CH_2), 4.13 (s, 3H, NCH_3), 4.54 (t, $J = 7.54$ Hz, 2H, NCH_2), 6.91 (s, 1H, CH), 7.18 (d, $J = 7.62$ Hz, 1H, Ar), 7.61−7.66 (m, 1H, Ar), 7.57−7.67 (m, 1H, Ar), 7.71−7.85 (m, 2H, Ar), 8.01−8.11 (m, 1H, Ar), 8.26 (d, $J = 7.29$ Hz, 1H, Ar), 8.45 (d, $J = 7.83$ Hz, 1H, Ar), 8.62 (d, $J = 7.38$ Hz, 1H, Ar), 8.87 (d, $J = 8.81$ Hz, 1H, Ar).

Peptide Bioconjugate Synthesis and Characterization. All labeled and nonlabeled peptides were synthesized on PAL-PEG-PS resin by automated solid-phase peptide synthesis using F-moc protection and *O*-(7-azabenzotriazol-1-yl)-*N*,*N*,*N*^{9},*N*^{9}-tetramethyluronium hexafluorophosphate (HATU) coupling chemistry. The carboxylic acid derivative of the cyanine dye is attached to a F-moc-Lys (Mtt)-OH, which can be inserted anywhere in the polypeptide sequence and selectively deprotected. The Mtt protective group is removed by a mild treatment with 1% trifluoroacetic acid (TFA) in dichloromethane (DCM), leaving all other protective groups requiring 90% TFA for removal to remain intact. This process was performed by exchanging the solvent from *N*′,*N*′-dimethylformamide (DMF) to DCM, followed by washing the resin-bound peptide with the 1% TFA in DCM solution. Because Mtt removal results in a deep yellow change in color, the TFA/DCM wash was continued until no further color change was observed. After solvent exchange back to DMF, the carboxylic acid derivative of the appropriate dye was coupled to the lysine using HATU activated coupling chemistry. This dye attachment protocol was carried out either immediately after addition of F-moc-Lys (Mtt)-OH or after completion of the normal peptide synthesis. Peptides were purified by RP-HPLC on a Zorbax C8 column (9.4 mm × 25 cm) (Agilent Tech.,Palo Alto, CA) using a flow rate of 1 mL/min and a water (0.1% TFA)−acetonitrile (0.1% TFA) gradient from 20 to 60% acetonitrile over 40 min. Identities of the peptides were confirmed MALDI-TOF mass spectrometry. Stock solution concentrations of all peptide samples were determined using a Bradford Assay with BSA as a reference.

Oligonucleotide Sample Preparation. All oligonucleotides were synthesized on a DNA synthesizer using phosphoramidite chemistry and gel purified on a 12% denaturing polyacrylamide gel. Bands were cut out and recovered by soaking the crushed gel pieces in 50 mM Tris, (pH 8.0) 100 mM NaCl buffer for 4−6 h. Extractions were combined and the urea and salts removed by spin filtration or a Sephadex G-15 size exclusion column (Aldrich). Concentrations for purified single-stranded oligonucleotides were calculated from 260 nm absorbance using an extinction coefficient calculated from the nearest neighbor method (*17*, *18*). Oligonucleotides were annealed using the same molar equivalent of each oligonucleotide. The oligonucleotide sequences used in these studies are shown in Figure 1.

A

139 190

[YO]-GRPRAIN<u>KHEQEQISR</u>LLEK<u>GHPRQQLAII</u>F<u>GIGVSTL</u>YRYFPASSIKKRMN

B

HIN1: 5'-TCTAGATGGCCACG<u>TTATCAAA</u>AACACTATGTCGCACGGC-3'

HIN2: 5'-TCTAGATGGCCACG<u>TTAC</u><u>CAAA</u>AACACTATGTCGCACGGC-3'

HIN3: 5'-TCTAGATGGCCACG<u>TTGC</u><u>CAAA</u>AACACTATGTCGCACGGC-3'

HIN4: 5'-TCTAGATGGCCACG<u>TCGCT</u><u>AAA</u>AACACTATGTCGCACGGC-3'

Figure 1. Peptide and oligonucleotide sequences used in this study. (A) The primary sequence of the oxazole yellow−Hin recombinase (YOHIN) bioconjugate used in these studies. The amino acid sequence derived from residues 139−190 of the native Hin recombinase was tethered to the cyanine dye oxazole yellow (shown in brackets). The underlined residues are those having α-helical secondary structure. (B) Oligonucleotides used in this study are 35-bases in length and derived from the native hixL recognition site. Native hixL sequence (HIN) is underlined. Note that as the binding site is progressively lost in going from HIN1 to HIN4, only native bases are underlined to highlight the sequence variation.

Determination of Spectral Properties. Absorbance spectra were taken over a concentration range of 0.5 to 5 μM for all samples under the indicated conditions. The DNA samples used were 1 to 10 μM dsDNA (2-fold molar excess was used for each measurement) that contained the appropriate cognate site. Samples for the free dyes were prepared by dilution of a dimethyl sulfoxide (DMSO) stock solution into the indicated solvent or aqueous buffer. Measurements were made in polypropylene cuvettes to minimize surface adsorption of the cyanine dyes in aqueous solutions. Serial dilutions were taken to ensure adherence to the Beer−Lambert law. The calculation of the extinction coefficient was performed by plotting absorbance versus concentration for different dilutions giving the slope, which is equivalent to the extinction coefficient.

Samples for determination of the quantum yield contained 50 to 500 nM conjugate in 20 mM Tris, (pH 7.6) 100 mM NaCl with 500 nM of the appropriate cognate DNA to ensure complete binding of the conjugate. Fluorescence quantum yields (Φ_F) for these samples were determined relative to fluorescein in 0.1 M NaOH ($\Phi_F = 0.90$) by integration of corrected emission spectra (*19*). Solutions used for fluorescence quantum yield determination for the conjugates were made to have the same absorbance (ca. 0.03) at absorbance maximum for each dye. The relative emission quantum yields were calculated as described by Demas and Crosby (*20*).

Fluorescence lifetime measurements were made using the time-correlated single photon counting method. The fundamental output from a Spectra Physics Tsunami laser was doubled by a Spectra Physics Model 3980 frequency doubler and pulse selector. The excitation rate was 4 MHz, pulse width 2 ps, average power ca. 1.1 W. A microchannel plate photomultiplier (Hamamatsu R2809U-11) was used to detect the fluorescence emission after passing the emission through a polarizer set at the magic angle with respect to excitation and through a single grating monochromator. The instrument response time was ca. 60 ps (full width at half maximum), as verified by scattering from Ludox AS-40. The spectrometer was controlled by software based on a Lab View program from National Instruments. Lifetime analysis was performed using the same samples and buffers as described above for the steady-state measurements

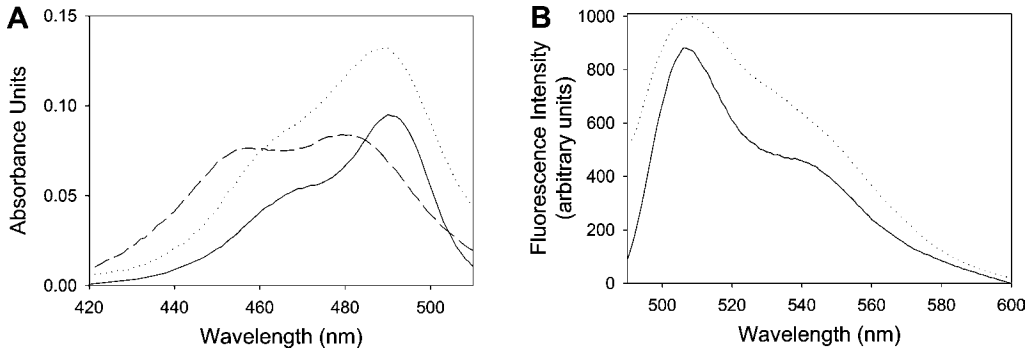

Figure 2. Comparison of the effect of conjugation on the spectral properties for the YOHIN bioconjugate in the presence and absence of the HIN1−DNA sequence. (A) Absorbance spectra used a concentration 2 μM for YOHIN in the absence (dashed line) and presence (solid line) of 4 μM DNA. (B) Fluorescence spectra of 50 nM of the bioconjugate (solid line) and 100 nM HIN1−DNA. Unconjugated oxazole yellow (dotted line) in the presence of DNA is shown in A and B for comparison. Excitation of the dyes are at 480 nm.

except that samples contained 100 nM YOHIN, and 200 nM DNA and no titrations were performed. Excitation of samples was at 440 nm and emission detection was at 510 nm. Fluorescence decays were analyzed by fitting to a sum of exponential decay terms convoluted with the measured instrument response function. This was done either at single measurement wavelengths or simultaneously to data taken at several emission wavelengths (*21*, *22*). The values for amplitude and lifetime are solved using MATLAB by use of an application called ASUFIT, which deconvolutes the individual lifetime components and their respective amplitudes.

Steady-state fluorescence measurements were performed as reverse titrations as described previously (*4*, *9*). Reverse titrations using 1 to 5 nM of the peptide−dye bioconjugate were performed by varying the concentration of nonlabeled DNA. Excitation was at 480 nm and emission detection at 510 nm for oxazole yellow samples. Measurements were carried out in 20 mM Tris (pH 7.6), 100 mM NaCl. Each measurement was performed at least three times and curves were fit as previously described (*4*). For fluorescence spectra, excitation was at 480 nm and emission spectra were taken from 500 to 600 nm with a 1 nm bandwidth on the excitation and emission monochromator.

RESULTS AND DISCUSSION

Bioconjugate Synthesis. Synthesis of the oxazole yellow−peptide bioconjugate using SPPS requires a carboxylic acid derivative of oxazole yellow to be synthesized (Scheme 1). Lepidine was reacted with bromovaleric acid to make the quaternary amine. The resulting charged quinolinium (**2**) was allowed to react with 2-methylmercapto-3-methylbenzoxazole (**5**), generating the carboxylic acid derivative of oxazole yellow (**6**). This product was characterized by ^{1}H NMR and mass spectrometry, indicating the desired products (see Experimental Procedures). The carboxylic acid derivative of YO was coupled to the ϵ-amine of a lysine strategically incorporated at the indicated position in the peptide sequence (Figure 1). This unique lysine has the Mtt protective group, which can be selectively deprotected to yield the free ϵ-amine of its side chain. To this lysine the HATU activated dye is coupled, forming an amide linkage between the lysine side chain and the dye. For HIN peptide samples without conjugated YO, the dye was simply not added. The amino acid sequence of the DNA-binding region of Hin recombinase (HIN) used in this study is shown in Figure 1. An HPLC analysis of purified bioconjugate and unlabeled HIN peptide showed only one peak in each respective chromatograph, which confirms the purity of these preparations. The expected mass of the purified YOHIN bioconjugate (oxazole yellow conjugated to the Hin DNA binding region) is 6522.3, and a sharp peak in its mass spectrum is observed for the singly charged species at (m/e) = 6523.8. The solid-phase synthesis of the bioconjugate was successful in giving a high-purity product in high yield with no detectible residual dye. This is important, as these dyes have an inherent affinity for intercalation into DNA, making any residual free dye a complication in interpreting results.

Spectral Profile. The spectral features of the peptide−bioconjugate are attributed exclusively to YO in the visible spectrum. Variations in YO photophysics are dependent on environmental changes resulting from peptide attachment. Absorbance spectra of the peptide bioconjugate in the presence and absence of DNA was examined to determine if DNA binding effects by YO behaves similar to when it is unconjugated (Figure 2). The visible absorbance spectrum of purified YOHIN in the absence of DNA shows two roughly equivalent peaks at 460 and 479 nm. After a 10 min incubation of YOHIN with DNA containing the HIN1 sequence, the absorbance maxima redshifts to 490 nm, with a much less pronounced shoulder to the blue side of the peak. The unconjugated YO shows a similar redshift upon DNA intercalation to 489 nm and a less prominent shoulder at 471 nm. This redshift in going from a highly solvated unbound YO dye to a less solvated, DNA intercalated state was also observed for other cyanine dyes, such as thiazole orange, indicating the environmentally sensitive spectral features are an inherent property of the cyanine family of dyes. It was previously shown that free thiazole orange underwent an approximately 10 nm redshift, with an increase in the absorbance maxima upon DNA addition (*23*). Figure 2 shows comparable effects of DNA-binding by dye, suggesting the dye is intercalated in both the unconjugated and bioconjugate form.

Based on the observed differences in the absorption profiles of unconjugated and conjugated YO, extinction coefficients for the YOHIN bioconjugate were determined in the absence and presence of DNA containing the HIN1 sequence. The extinction coefficient changes from 40 500 to 45 700 M^{-1} cm^{-1} upon DNA binding, representing an increase of more than 10%. This increase in the oscillator strength accompanies the observed 479 to 490 nm redshift that occurs upon DNA intercalation by the dye (Figure 2A). For comparison, the extinction coefficient of unconjugated YO decreases by approximately 20% in going from methanol to a Tris buffer (66 000 to 52 000 M^{-1} cm^{-1}). When incubated with DNA in an aqueous buffer, the unconjugated YO shows a slight increase in the extinction coefficient to 52 900 M^{-1} cm^{-1} that accompanies the aforementioned redshift upon DNA intercalation.

Next, fluorescence analysis was performed to characterize the photophysical effects of dye−peptide linkage on the fluorescence properties of the bioconjugate. The fluorescence

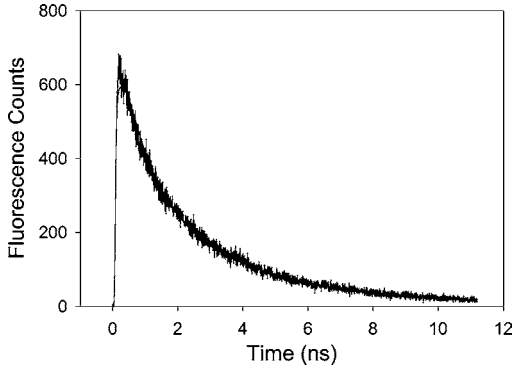

Figure 3. Time correlated single photon counting measurement of YOHIN bioconjugate bound to HIN1−DNA. Samples of 100 nM YOHIN bioconjugate preincubated for 10 min with 200 nM HIN1−DNA were examined using 440 nm excitation and 510 nm emission detection.

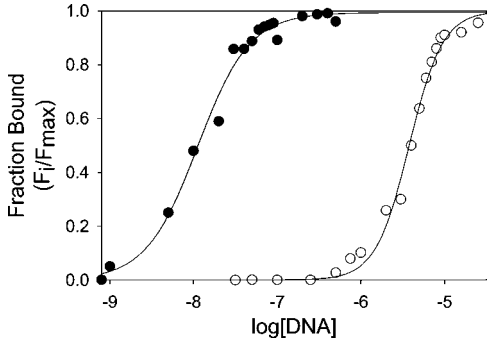

Figure 4. Fluorescence titrations of unconjugated and conjugated YO. Fluorescence measurements are given as a fraction of total fluorescence (F_i/F_{max}) versus the HIN1−DNA concentration. Total fluorescence from 1 nM YOHIN (●) and YO (○) when titrated with increasing concentrations of HIN1 is plotted and fit to a two-state binding model (*4*).

spectra for YOHIN is taken after 10 min incubation with DNA containing the HIN1 site (Figure 2B). The fluorescence spectra for the unconjugated or peptide conjugated dye is comparable, although there is a decrease in the signal intensity and shape of the spectral profile. For the cyanine dye-based probes, samples measured in the absence of DNA had very low fluorescence counts that were not significantly above the background (data not shown). The quantum yields for the YO and YOHIN were estimated by using fluorescein as a reference. The fluorescence quantum yield of HIN1−DNA-bound YOHIN bioconjugate is 0.37. The YOHIN in the absence of DNA shows negligible fluorescence, as is the case for the unconjugated YO (data not shown). The unconjugated YO was also determined to establish a basis of comparison to the known literature values and was found to be the comparable ($\Phi_F = 0.437$) within experimental error. The quantum yield for unconjugated YO intercalated into CT-DNA was previously determined to be 0.44 (*15*). For comparison, the fluorescence quantum yield for the unconjugated oxazole yellow in the absence of DNA was shown to be 4.8×10^{-4}. If it is assumed that the unbound bioconjugate exhibits the same low fluorescence quantum yield observed for the unbound YO, then the emission enhancement is approximately 770 for the DNA-bound YOHIN. The emission enhancement of unconjugated YO bound to CT-DNA was determined to be 920 (*15*), which is a difference of roughly 15%. This is a rather modest effect when compared to fluorescein, which shows a 50% decrease in quantum yield upon conjugation (*24*) and rhodamine, which is known to exhibit solvent, pH, and conjugation-dependent changes in its photophysical properties (*25*).

The fluorescence lifetimes are measured for the YOHIN conjugate bound to HIN1−DNA. Average lifetimes are calculated by summing the products of the emission lifetimes and their corresponding relative emission amplitudes. The lifetime values were determined from a global fit of three sets of spectra for each sample taken over the emission wavelength range of 510 to 530 nm (Figure 3). The fluorescence lifetimes and relative amplitudes of the emission decay fits (shown in parentheses) are 0.75 ns (0.58) and 3.14 ns (0.42), to give an average fluorescence lifetime of 1.92 ns. Unconjugated YO exhibits a lifetime of 2.22 ns when bound to CT-DNA, although sequence-dependent variations were also observed. YO has fluorescence lifetimes of 2.16 ns and 3.19 ns when intercalated into $d(AT)_6$ and $d(GC)_6$ sequences, respectively (*15*). The decrease in lifetime upon conjugation may reflect sequence-dependent effects, as the peptide forces the dye to intercalate at a narrowly defined region, two to three bases flanking the peptide binding site (*4*) or may be due to the peptide forcing the dye into binding modes that have lower quantum yields (*23*).

In summary, the photophysical properties of the dye are comparable for the unconjugated YO and YOHIN bioconjugate because the interaction of the dye with DNA is predominantly due to intercalation in both cases. The small decrease in the fluorescence quantum yield and lifetime compared to the unconjugated YO may be due to two reasons; the sequence-dependent photophysical properties previously observed (*15*), or the existence of two different DNA-binding modes by YO. The existence of a sub-population of bioconjugates where the dye moiety is bound to the DNA via electrostatic interactions was shown to be the case for a single zinc finger attached to thiazole orange (*4*, *26*). This external binding mode is known to be fluorescent, but with a lower quantum yield because rotation about the central methine bridge is more accessible than is the case for fully intercalated dye (*23*). This may be an additional mode with which the dye of the bioconjugate interacts with DNA and may explain the slight decrease in fluorescence quantum yield and lifetime. Single molecule studies support this notion of multiple DNA-binding modes by the dye, suggesting that the bound peptide moiety might force the dye to bind by intercalation or electrostatic interaction with the backbone (*26*, *27*). If the YO moiety of the YOHIN bioconjugate has two binding modes and fluorescence quantum yield varies with each binding mode (*23*), then the emission enhancement would depend on the relative populations of each binding mode.

DNA Targeting Properties. The equilibrium dissociation constants (K_D) were determined for the unconjugated YO and the YOHIN bioconjugate with the HIN1−DNA sequence. Binding data indicates a significant enhancement in the affinity of the bioconjugate for dsDNA over the dye alone (Figure 4). Together, the YOHIN bioconjugate has a $K_D \sim 10$ nM, indicating the contribution of both moieties. Individually, the HIN bound to HIN1−DNA has a $K_D \sim 120$ nM and the dye alone has a $K_D \sim 2$ μM. The dissociation constant is larger than the product of the individual dissociation constants from the polypeptide and the oxazole yellow, indicating that the binding of YO and HIN in the YOHIN bioconjugate is noncooperative. The binding event may act noncooperatively because both the dye and the peptide individually alter the structure of DNA. The dye has been shown to untwist the DNA approximately 20° (*28*), which may adversely affect peptide binding. Conversely, the crystal structure of the hixL-bound Hin recombinase shows the recognition helix alters base stacking at the protein−DNA interface (*13*, *29*). It is possible these structural perturbations force the dye to adopt alternate binding modes.

The interaction of YOHIN with cognate and noncognate DNA sequences, designed based on several mutant sequences known to adversely affect binding of the native Hin recombinase, was

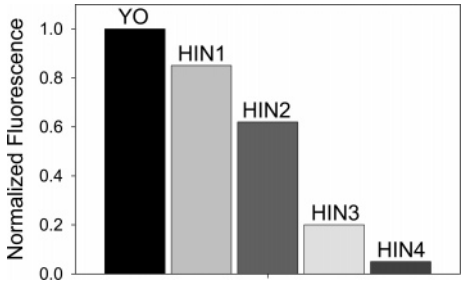

Figure 5. Total fluorescence intensity measurements of YOHIN incubated with the indicated HIN sequence. Measurements were performed at ambient temperature using concentrations of 20 nM YOHIN and 50 nM HIN−DNA in 20 mM Tris (pH 7.6), 100 mM NaCl. All data were normalized to the fluorescent counts for 20 nM unconjugated YO incubated with the HIN1−DNA sequence.

measured by steady-state fluorescence spectroscopy. The goal here was to determine if the bioconjugate reproduces the sequence-specificity of the native protein and to assess its usefulness as a suitable fluorescent probe for the detection of specific DNA sites. YOHIN was incubated with one of four HIN sequences; the appropriate native DNA-binding site or one of three mutated binding sites to quantify the relative fluorescence intensity of each (Figure 5). At 20 nM bioconjugate, the native DNA-binding site gives the highest fluorescence intensity with a progressive decrease in the fluorescence intensity as mutations in the binding site accumulate. These sequence-dependent variations in fluorescence are consistent with previous binding studies of the native Hin protein, which show roughly a 40% decrease in protein−DNA complex formation for the point mutation given in HIN2 (*12*, *30*, *31*). A thymine is mutated to a cytosine in HIN2, causing a critical contact with the thymine methyl to be lost. For comparison, the bioconjugate shows a 35% decrease in fluorescence counts in binding HIN2 versus the HIN1 cognate site. Fluorescence signal is progressively lost, as mutations accumulate in the region of the cognate site known to form the major groove−Hin contact interface (*13*, *31*, *32*). Nonspecific binding of HIN4 by YOHIN showed roughly 5% of the fluorescence signal observed for the cognate HIN1 sites.

The fact that the YOHIN bioconjugate reproduces the binding features of native Hin recombinase indicates the peptide moiety drives site recognition. This is in agreement with similar studies using polyamides, short peptides, single zinc fingers or helix-turn-helix motifs as the DNA-targeting element, which show the cyanine dye makes significant contributions to binding affinity but exerts negligible effects on sequence specificity (*4*, *33*, *34*). This is, in part, because the monomeric form of the dye has no sequence preference and intercalates with equal affinity to d(AT), d(GC), and poly(G)-poly(C) repeats as it does to calf-thymus DNA (*23*).

Determination of nonspecific binding at HIN4−DNA concentrations 10-, 50-, and 100-times higher show less than 50% of the maximum fluorescence intensity observed with the cognate site (data not shown). Similarly, 100 times the bioconjugate concentration was required to reach greater than 90% of the total fluorescence observed for YOHIN bound to HIN1−DNA. Unconjugated YO showed no sequence-dependent change in fluorescence intensity. The HIN conjugated dye is only able to intercalate DNA and emit fluorescence signal when the peptide is bound with high affinity to its native cognate site. The fluorescence from YOHIN incubated in the presence of DNA containing the target sequence is comparable in intensity to the same amount of the intercalating dye bound to DNA. This implies that the fluorescence yield and the level of occupancy of the dye on the DNA in the assembled bioconjugate DNA complex is comparable to that observed for unconjugated dye bound to DNA. The range of concentrations used in the screen described above limits the amount of nonspecific binding and makes the bioconjugate a very sensitive probe of sequence within the nanomolar concentration range.

In summary, the fluorescent intercalating dye, oxazole yellow (YO), has been tethered to the ϵ-amine of a lysine specifically positioned within the amino acid sequence of the HIN recombinase DNA-recognition region. YO has been shown to be several orders of magnitude more fluorescent upon intercalation into DNA, making it a very sensitive probe of DNA interaction (*14*, *23*). Here, we have used the DNA recognition features of the polypeptide to control DNA-sequence targeting and the ability of the dye to fluoresce only when bound to DNA. These studies reveal three main points: first, the photophysical properties of the probe show a small effect on the fluorescence lifetime and quantum yield upon conjugation to the peptide, second, the dye is only able to intercalate DNA and emit appreciable fluorescence signal when the peptide is bound with high affinity to its native cognate site, and third, that the specificity of the probe reproduces the molecular recognition features of the native protein. The roughly 10% loss of emission enhancement upon conjugation of YO to the peptide is most likely due to sub-populations of the dye adopting different DNA-binding modes known to have a lower quantum yield. In fact, recent single molecule measurements of a thiazole orange−histone H3 bioconjugate reconstituted into nucleosomes suggest that there may be multiple binding configurations of the dye molecule (*7*). Also, at low concentrations it seems the dye of the bioconjugate is unable to intercalate with noncognate DNA, indicating the peptide moiety is the driving force determining DNA-sequence specificity. For the YOHIN bioconjugate studied here, there is a 10-fold contribution to the HIN binding affinity by YO. While covalent attachment of oxazole yellow to the Hin recombinase DNA-binding region has been shown to greatly increase the DNA-binding affinity, it does not adversely effect the sequence specificity. The results of this work indicate that by using the strategy described here, bioconjugates could be designed using different combinations of DNA recognition polypeptides and cyanine dyes to generate an array of sequence specific and wavelength specific probes.

ACKNOWLEDGMENT

We thank Dr. Neal Woodbury for discussion and providing samples used in this study and Dr. Dan Brune for assistance with the peptide synthesizer.

LITERATURE CITED

(1) Taylor, J. S., Schultz, P. G., and Dervan, P. B. (1984) DNA Affinity Cleaving, Sequence Specific Cleavage of DNA by Distamycin−EDTA-Fe(II) and EDTA-Dystamcin-Fe(II). *Tetrahedron 40*, 457−465.

(2) Sluka, J. P., Horvath, S. J., Bruist, M. F., Simon, M. I., and Dervan, P. B. (1987) Synthesis of a Sequence Specific DNA-Cleaving Peptide. *Science 238*, 1129−1132.

(3) Oakley, M. G., Turnbull, K. D., and Dervan, P. B. (1994) Synthesis of a Hybrid Protein Containing the Iron-Binding Ligand of Bleomycin and the DNA-Binding Domain of Hin. *Bioconjugate Chem. 5*, 242−247.

(4) Thompson, M., and Woodbury, N. W. (2000) Fluorescent and Photochemical Properties of a Single Zinc Finger Conjugated to a Fluorescent DNA-binding Probe. *Biochemistry 39*, 4327−4338.

(5) Rajski, S. R., and Barton, J. K. (2000) DNA-Mediated Electron Transfer: A Sensitive Probe of DNA-Protein Interactions. *J. Biomol. Struct. Dyn. 11*, 285−295.

(6) Heyduk, T., and Lee, J. C. (1990) Application of fluorescence energy transfer and polarization to monitor Escherichia Coli cAMP receptor protein and lac promoter interaction. *Proc. Natl. Acad. Sci. U.S.A. 87*, 1744−1748.

(7) Babendure, J., Bash, R., LoVullo, D., Schiefer, T. K., Williams, M., Daniel, D. C., Thompson, M., Taguchi, A. K. W., Lohr, D.,

and Woodbury, N. W. (2003) Development of a fluorescent probe for the study of nucleosome assembly and dynamics. *Anal. Biochem. 317*, 1−11.
(8) Gearhart, M., Dickinson, L., Ehley, J., Melander, C., Dervan, P., Wright, P., and Gottesfeld, J. (2005) Inhibition of DNA binding by human estrogen-related receptor 2 and estrogen receptor alpha with minor groove binding polyamides. *Biochemistry 44*, 4196−4203.
(9) Thompson, M., and Woodbury, N. W. (2001) Thermodynamics of specific and non-specific DNA binding by two DNA binding domains conjugated to fluorescent probes. *Biophys. J. 81*, 1793−1804.
(10) Graham, K. S., and Dervan, P. B. (1990) Structural Motif of the DNA Binding Domain of gd-Resolvase Characterized by Affinity Cleaving. *J. Biol. Chem. 265*, 16534−16540.
(11) Shin, J. A., Ebright, R. H., and Dervan, P. B. (1991) Orientation of the lac repressor DNA binding domain in complex with the left lac operator half site characterized by affinity cleaving. *Nucl. Acids Res. 19*, 5233−5236.
(12) Hughes, K. T., Gaines, P. C. W., Karlinsey, J. E., Vinayak, R., and Simon, M. I. (1992) Sequence specific interaction of the Salmonella Hin recombinase in both major and minor grooves of DNA. *EMBO J. 11*, 2695−2705.
(13) Feng, J. A., Johnson, R. C., and Dickerson, R. E. (1994) Hin Recombinase bound to DNA: The origin of specificity in major and minor groove interactions. *Science 263*, 348−355.
(14) Lee, L., Chen, C.-H., and Chiu, L. (1986) Thiazole Orange: A New Dye for Reticulocyte Analysis. *Cytometry 7*, 508−517.
(15) Netzel, T. L., Nafisi, K., Zhao, M., Lenhard, J. R., and Johnson, I. (1995) Base-Content Dependence of Emission Enhancements, Quantum Yields, and Lifetimes for Cyanine Dyes Bound to Double-Strand DNA: Photophysical Properties of Monomeric and Bichromophoric DNA Stains. *J. Phys. Chem., B 99*, 17936−17947.
(16) Rye, H. S., and Glazer, A. N. (1995) Interaction of dimeric intercalating dyes with single-stranded DNA. *Nucl. Acids Res. 23*, 1215−1222.
(17) Rychlik, W., Spencer, W., and Rhoads, R. (1990) Optimization of the annealing temperature for DNA amplification in vitro. *Nucl. Acids Res. 18*, 6409−6412.
(18) Breslaur, K., Frank, R., Blocker, H., and Marky, L. (1986) Predicting DNA duplex stability from the base sequence. *Proc. Natl. Acad. Sci. U.S.A. 83*, 3746−3750.
(19) Ozaki, H., and McLaughlin, L. W. (1992) The estimation of distances between specific backbone-labeled sites in DNA using fluorescence resonance energy transfer. *Nucl. Acids Res. 20*, 5205−5214.
(20) Demas, J. N., and Crosby, G. A. (1971) The measurement of photoluminescence quantum yields. *J. Phys. Chem., B 75*, 991−1024.
(21) Peloquin, J., Williams, J., Lin, X., Alden, R., Taguchi, A., Allen, J., and Woodbury, N. (1994) Time-dependent thermodynamics during early electron-transfer in reaction centers from rhodobacter-sphaeroides. *Biochemistry 33*, 8089−8100.
(22) Taguchi, A., Stocker, J., Alden, R., Causgrove, T., Peloquin, J., Boxer, S., and Woodbury, N. (1992) Biochemical characterization and electron-transfer reactions of sym1, a rhodobacter-capsulatus reaction center symmetry mutant which affects the initial electron-donor. *Biochemistry 31*, 10345−10355.
(23) Nygren, J., Svanvik, N., and Kubista, M. (1998) The Interactions Between the Fluorescent Dye Thiazole Orange and DNA. *Biopolymers 46*, 39−51.
(24) Haugland, R. P. (2002) *Handbook of Fluorescent Probes and Research Products, Ninth Edition.* (Gregory, J., Ed.) pp 7−78, Chapter 1, Molecular Probes, Inc., Eugene, OR.
(25) Neckers, D. C., and Valdes-Aguilera, O. M. (1993) Photochemistry of Xanthine Dyes. *Advances in* Photochemistry. Volume 18 (Volman, D. H., Ed.) pp 315−399, Wiley-Interscience.
(26) Daniel, D. C., Thompson, M., and Woodbury, N. W. (2000) Fluorescence intensity fluctuations of individual labeled DNA fragments and a DNA binding protein in solution at the single molecule level: A comparison of photobleaching, diffusion, and binding dynamics. *J. Phys. Chem., B 104*, 1382−1390.
(27) Daniel, D. C., Thompson, M., and Woodbury, N. W. (2002) DNA-Binding Interactions and Conformational Fluctuations of Tc3 Transposase DNA Binding Domain Examined with Single Molecule Fluorescence Spectroscopy. *Biophys. J. 82*, 1654−1666.
(28) Spielmann, H., Wemmer, D., and Jacobsen, J. (1995) Solution structure of a DNA complex with the fluorescent bis-intercalator TOTO determined by NMR-spectroscopy. *Biochemistry 34*, 8542−8553.
(29) Komeiji, Y., and Uebayasi, M. (1999) Change in conformation by DNA-peptide association: Molecular dynamics of the Hin recombinase-hixL complex. *Biophysical J. 77*, 123−138.
(30) Lim, H. M., Hughes, K. T., and Simon, M. I. (1992) The Effects of Symmetrical Recombination Site Hixc on Hin Recombinase Function. *J. Biol. Chem. 267*, 11183−11190.
(31) Glasgow, A. C., Bruist, M. F., and Simon, M. I. (1989) DNA-binding properties of the Hin recombinase. *J. Biol. Chem. 264*, 10072−10082.
(32) Chiu, T. K., Sohn, C., Dickerson, R. E., and Johnson, R. C. (2002) Testing water-mediated DNA recognition by the Hin recombinase. *EMBO J. 21*, 801−814.
(33) Carreon, J. R., Mahon, K. P., and Kelley, S. O. (2004) Thiazole orange-peptide conjugates: Sensitivity of DNA binding to chemical structure. *Org. Lett. 6*, 517−519.
(34) Fechter, E. J., Olenyuk, B., and Dervan, P. B. (2005) Sequence-specific fluorescence detection of DNA by polyamide-thiazole orange conjugates. *J. Am. Chem. Soc. 127*, 16685−16691.

BC050307T

Identification of CD21-Binding Peptides with Phage Display and Investigation of Binding Properties of HPMA Copolymer−Peptide Conjugates

Hui Ding,[†] Wolfgang M. Prodinger,[‡] and Jindřich Kopeček*[,†,§]

Departments of Pharmaceutics and Pharmaceutical Chemistry, and Bioengineering, University of Utah, Salt Lake City, Utah 84112, and Department of Hygiene, Microbiology and Social Medicine, Innsbruck Medical University, Innsbruck, Austria. Received November 3, 2005; Revised Manuscript Received January 19, 2006

Cancer targeting with peptides has become promising with the emergence of combinatorial peptide techniques such as phage display. Using phage display under stringent screening conditions, we selected five distinct peptides that specifically recognized the CD21 receptor, a cell surface marker of malignant B cell lymphoma. Two highly hydrophobic sequences were excluded (RLAYWCFSGLFLLVC and PVAAVSFVPYLVKTY). The binding affinity toward CD21 of the other three selected peptides (RMWPSSTVNLSAGRR, PNLDFSPTCSFRFGC, and GRVPSMFGGHFFFSR) was analyzed with fluorescence quenching. Their dissociation constants were determined to be within the micromolar range. On the basis of the results of phage ELISA, competitive phage ELISA, and fluorescence quenching, the binding sites of the three selected peptides were found to reside within the first four short consensus repeats of CD21 (SCR1−4). The peptide RMWPSSTVNLSAGRR (**P1**) was bound to the *N*-(2-hydroxypropyl)methacrylamide (HPMA) copolymer, a potential drug carrier for chemotherapeutic agents, and the surface binding properties of HPMA copolymer−**P1** conjugates were investigated. Specific interactions were observed between HPMA copolymer−**P1** conjugates and surface-bound receptor. Binding of HPMA copolymer−**P1** conjugates was directly related to the amount of surface (MaxiSorp plate) bound receptor, and the binding of the conjugates could be inhibited by the application of a 3−4 orders-of-magnitude excess of free peptide over the peptide concentration in conjugates. The enhanced binding of polymer-bound peptide was ascribed to multivalent interactions between the HPMA copolymer−**P1** conjugate and the surface-bound CD21 receptor.

INTRODUCTION

Cancer therapy has entered a new era since the introduction of monoclonal antibodies (mAbs) for the treatment of various cancers (*1*−*4*). To date, nearly 10 monoclonal drugs have been approved by the United States Food and Drug Administration; examples include Rituxan (*5*) (Anti-CD20 mAb), Herceptin (*6*) (anti-Her2/*neu* mAb), and Bexxar (*7*) (^{131}I labeled Anti-CD20 mAb). mAbs alone may affect antitumor activity through the mechanisms of antibody-dependent cellular cytotoxicity and complement-dependent cytotoxicity. mAbs have also been extensively used to specifically deliver cytotoxic agents to tumor sites, due to the highly specific interaction between mAbs and their corresponding tumor antigens (*4*). Compared with conventional chemotherapy, therapy with immunoconjugates (targeting mAbs conjugated with anticancer drugs) results in significantly enhanced tumor-killing activity with minimal side effects (*8*).

An alternate approach is targeting with receptor-binding peptides (*9*). Because of their small molecular size, precise control of their chemical makeup and their chemical stability provides a variety of choices to construct sophisticated targeting arrangements, such as graft, starlike, and dendritic structures.

Peptide targeting has become feasible due to the advent of combinatorial peptide library techniques (*10*, *11*), such as phage display (*12*, *13*). Phage display is a powerful technique for bioscreening: by engineering the DNA structure of phage, a phage peptide library is constructed, so that millions of different peptides are displayed on the phage capsid and are accessible for interaction with target proteins. Peptides with desired properties can be selected and identified with appropriate screening methods. Phage display has been extensively used for epitope mapping (*14*), vaccine discovery (*15*), and ligand identification (*16*). There are also many successful examples using phage display to identify peptide ligands for cancer targeting (*11*, *17*). Proteins uniquely expressed or overexpressed by cancer cells can provide suitable targets. Although library screening with purified proteins is the most straightforward method, when the target protein is known and has been isolated, successful screening has been reported using targets other than purified proteins, such as in vitro screening with cancer cells (*18*), tumor tissues (*19*, *20*), and even directly applied to the entire cancer patient's body (*21*).

With phage display, peptides targeting the CD21 receptor, a surface marker for malignant B cell lymphoma phenotyping, may be selected (*22*). CD21 receptor (complement receptor 2, CR2) is a 145-kDa transmembrane glycoprotein that is expressed primarily on mature B lymphocytes, epithelial cells, thymocytes, and follicular dendritic cells (*23*). The extracellular region consists of 15−16 short consensus repeats (SCRs),[1] of which SCR1 and SCR2 are responsible for the interaction with several natural ligands, such as C3d, C3dg, and Epstein Barr virus (EBV). The expression of CD21 on B and T lymphocytes is upregulated by infection with the lymphocytotropic virus EBV and HTLV (*24*, *25*). CD21 receptor mediates internalization through endocytosis (*26*); therefore, it is regarded as a suitable target for the treatment of lymphoma with chemotherapy. Two different forms of CD21 receptors, soluble CD21 (sCD21) (*27*) and recombinant short CD21 (rsCR2.1−4) (*28*), were used in this work. sCD21 is a 135-kDa protein generated from shedding

[†] Department of Pharmaceutics and Pharmaceutical Chemistry, University of Utah.

[§] Department of Bioengineering, University of Utah.

[‡] Innsbruck Medical University.

* To whom correspondence should be addressed. Phone: (801) 581-4532. Fax: (801) 581-3674. E-mail: Jindrich.Kopecek@m.cc.utah.edu.

10.1021/bc0503162 CCC: $33.50 © 2006 American Chemical Society
Published on Web 03/01/2006

and cleavage of the extracellular portion of CD21 receptor, while rsCR2.1−4 is a recombinant short CD21 receptor containing SCR1−4. Both sCD21 and rsCR2.1−4 are fully functional in interaction with ligands that specifically bind to SCR1−4.

Our goal is to select high-affinity peptide ligands of CD21 receptor, determine their biorecognizability, and use them as targeting moieties in a potential anticancer drug delivery system. A well-characterized polymer for delivery of cancer therapeutics is the water-soluble synthetic polymer, poly[*N*-(2-hydroxypropyl)methacrylamide] (PHPMA). The advantages of using HPMA copolymer as a drug carrier include (*29*): improved physical properties of polymer−drug conjugates such as enhanced drug solubility, elongated blood circulation time, passive accumulation in solid tumors, and the potential to overcome efflux-pump related multidrug resistance (MDR) (*30*, *31*). To enhance targeting efficiency, it is possible to incorporate several peptide ligands into one HPMA copolymer macromolecule (*32*), thus increasing the apparent binding affinity through multivalent interactions (*33*).

Targeting peptides have been used previously to direct HPMA copolymers to tumor sites. A nonapeptide (EDPGFFNVE) (*34*), a portion of EBV virus envelope glycoprotein gp350/220, assumed to be responsible for the binding of EBV virus to CD21 receptor (*34*), has been incorporated into HPMA copolymer. The cytotoxicity of peptide-targeted HPMA copolymer−doxorubicin conjugates was dependent on the amount of peptide per macromolecule (*32*, *35*, *36*). In vitro studies by Nan et al. revealed that cellular uptake of HPMA copolymer increased significantly after it was modified with the peptide, WHYPWFQNWAMA, which targets human squamous cell carcinoma of the head and neck (*37*). In vivo studies with HPMA copolymer containing the integrin-targeting peptide, KACDCRGDCFCG, demonstrated not only passive accumulation of polymer conjugate at the tumor site, but also active targeting of polymer conjugate mediated by the peptide (*38*). The work described above suggested that HPMA copolymers equipped with peptides as targeting moieties may work as a promising approach to targeted chemotherapy.

In this work, peptide ligands recognizable by CD21 receptor were selected with phage display. Specific binding between selected peptides and CD21 receptor was confirmed by phage ELISA, and the binding affinities were determined with fluorescence quenching. To evaluate the efficiency of targeting lymphoma with selected peptides, we synthesized HPMA copolymer−peptide **P1** (RMWPSSTVNLSAGRR) conjugates. Specific interactions were verified between HPMA copolymer−peptide conjugates and surface-bound CD21 receptor using ELISA experiments. We further investigated the effect of the spacer between the peptide and polymer, and the effect of peptide content per macromolecule upon surface binding of HPMA copolymer−**P1** conjugate.

EXPERIMENTAL PROCEDURES

Materials. *Escherichia coli* strain K91 kan and the fuse-5 15-mer phage library (*39*) were gifts from Dr. G. P. Smith (University of Missouri, Columbia). HB5 anti-CD21 mAb was a gift from Dr. A. Tang. sCD21 (*35*) and rsCR2.1−4 (*28*) were prepared as previously described. 2-Chlorotrityl chloride resin, hydroxymethylbenzoic acid (HMBA) resin, and all N-α-Fmoc protected amino acids were purchased from Novabiochem.

Screening of CD21 Specific Binding Phage with fUSE5 15-mer Phage Library. MaxiSorp plate (NUNC, Denmark) was coated with 200 μL (20 μg/mL) of sCD21 receptor at 4 °C overnight and blocked with 4% skim milk for 2 h at room temperature. The plate was then washed with 0.1% Tween/PBS. Before exposing the phage to the receptor, the plate was preblocked by incubation with 2% BSA in PBS for 15 min. Approximately 10^{12} phage virions were incubated with receptor-coated plate for 3 h. The nonspecific bound phage was removed with stringent washing: washing with TPBS (pH 7.4) 15 times, followed by washing with TPBS (pH 5.0) 5 times, and finally washing with PBS 5 times. The bound phage was eluted with glycine hydrochloride buffer (0.1 M HCl, pH adjusted to 2.2 with glycine). The eluted phage was neutralized with 1 M Tris-buffer (pH 9.1) and amplified. An additional three rounds of selection were performed as described above with decreased phage incubation time: 1 h, 30 and 15 min, respectively. In the fourth round of selection, to minimize the selection of nonspecific bound phage caused by nonspecific elution with glycine hydrochloride buffer, the bound phage was eluted with 4 μg of sCD21 receptor in 200 μL of PBS. After the fourth round of selection, 21 randomly chosen phage clones were tested with preliminary phage ELISA and the DNA of nine phage clones with the highest binding was sequenced using the primer 5′-TCCACAGACAGCCCTCATAG-3′.

Phage ELISA and Competitive Phage ELISA. Receptors sCD21 and rsCR2.1−4 (200 ng in 100 μL of PBS) were coated onto a MaxiSorp plate by incubation overnight at 4 °C. The plate was blocked with 2% BSA in PBS for 2 h at room temperature. Phage **P1** ($\sim 1 \times 10^7$ virion/mL) was incubated in the plate for 1 h at room temperature. The plate was then washed eight times with TPBS. After washing, horseradish peroxidase (HRP)/anti-M13 mAb conjugate (Pharmacia Biotech, Uppsala, Sweden) was diluted 1:5000 with 1% BSA/TPBS and incubated in the plate for 1 h. Again, the plate was washed five times with TPBS, followed by incubation with HRP substrate (ImmunoPure TMB Substrate kit, PIERCE Biotech. Inc.), a mixture of 3,3′,5,5′-tetramethylbenzidine (TMB) and peroxide solution, for 30 min. The reaction was stopped by addition of 100 μL of 1 N H_2SO_4, and the absorbance was read using a microplate reader at 450 nm and background subtraction at 630 nm.

For the competitive phage ELISA, the plate surface was coated with sCD21 and blocked with 2% BSA. Phage **P1** was preincubated with different amounts of (competitor) rsCR2.1−4 (0, 0.45, 0.9, 1.35, and 1.8 μg, respectively, in 100 μL of TPBS containing 1% BSA) for 30 min before the mixture was placed in sCD21 coated plate; there, the mixtures of phage and rsCR2.1−4 were incubated with surface-bound sCD21. The detection of bound phage was the same as that used for the phage ELISA.

Synthesis of Peptides. Peptides, RMWPSSTVNLSAGRR (**P1**), PNLDFSPTCSFRFGC (**P2**), and GRVPSMFGGHFFFSR (**P3**), were synthesized manually on a solid support of 2-chlorotrityl chloride resin using standard Fmoc chemistry. The synthesized peptides were cleaved from resin with a mixture of TFA/H_2O/phenol/TIS (88:5:5:2, v/v/w/v) for 4 h at room

[1] Abbreviations: A, 8-amino-3,6-dioxaoctanoic acid; A2, dimer of A; AIBN, 2,2′-azobisisobutyronitrile; BSA, bovine serum albumin; DIPEA, *N*,*N*-diisopropylethylamine; DMSO, dimethyl sulfoxide; ELISA, enzyme linked immunosorbent assay; Fmoc, 9-fluorenylmethoxycarbonyl; HMBA, hydroxymethylbenzoic acid; HPMA, *N*-(2-hydroxypropyl)methacrylamide; HRP, horseradish peroxidase; NHS, *N*-hydroxysuccinimide ester; MA, methacryloyl; MA-GG-OH, *N*-methacryloylglycylglycine; MALDI-TOF MS, matrix-assisted laser desorption/ionization time-of-flight mass spectrometry; NP, EDPGFFNVE; P, HPMA copolymer backbone; P^B, HPMA copolymer backbone labeled with a PEG_{3400}-biotin graft; **P1**, RMWPSSTVNLSAGRR; **P2**, PNLDFSPTCSFRFGC; **P3**, GRVPSMFGGHFFFSR; **P4**, RLAYWCFSGLFLLVC; **P5**, PVAAVSFVPYLVKTY; PBS, phosphate-buffered saline; PEG, poly(ethylene glycol); PHPMA, polyHPMA; rsCR2.1−4, recombinant short (truncated) CD21 receptor containing SRCs 1−4; SCR, short consensus repeat; sCD21, soluble CD21 receptor; TFA, trifluoroacetic acid; TIS, triisopropylsilane; TMB, 3,3′,5,5′-tetramethylbenzidine; TPBS, PBS containing 0.1% Tween 20.

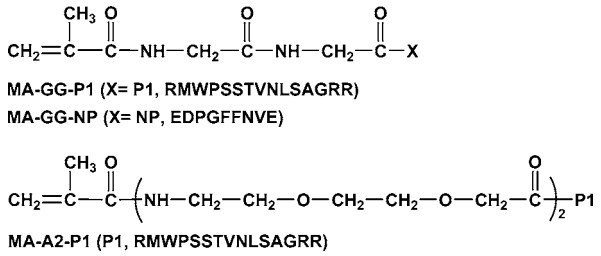

Figure 1. Structures of peptide monomers.

temperature. All synthesized peptides were purified with RP-HPLC and verified with MALDI-TOF MS. MALDI-TOF MS calculated for **P1** (MH^+) 1717.88, found 1718.25; MALDI-TOF MS calculated for **P2** (MH^+) 1702.73, found 1702.78; MALDI-TOF MS calculated for **P3** (MH^+) 1728.84, found 1728.89.

Fluorescent Labeling of rsCR2.1−4. To a solution of rsCR2.1−4 in 200 μL of PBS (0.5 mg/mL), 20 μL of 1 M $NaHCO_3$ (pH 9.0), and 23.3 μL of FITC in DMSO (10 mg/mL) was added, and the reaction was stirred for 5 h at room temperature in the dark. To remove free FITC, the reaction mixture was diluted to 0.5 mL with PBS and immediately applied to a PD-10 column (Amersham Biosciences) preequilibrated with PBS buffer. The concentration of the fluorescently labeled protein and labeling efficiency were determined using UV spectrometry.

Determination of Peptide Binding Constants with Fluorescence Quenching. A series of mixtures of the labeled receptor rsCR2−FITC at 0.02 μM, and peptides, **P1**, **P2**, and **P3**, at different concentrations were prepared in 150 μL of PBS. The mixtures were incubated at room temperature for 5 h. The fluorescence intensity of each sample was measured in duplicates with a LS-55 luminescence spectrometer (Perkin-Elmer) with excitation and emission wavelengths of 495 and 515 nm, respectively. The fluorescence background caused by the peptides was negligible within the concentration range used. The association constant was estimated by fitting the quenching data to eq 1 with software KaleidaGraph (version 3.0) (*40*).

$$Q = \frac{Q_m K_a [P]}{1 + K_a [P]} \quad (1)$$

$$Q = \frac{F_0 - F}{F} \quad (2)$$

where Q is the quenching value defined in eq 2, and Q_m represents maximal fluorescence quenching, K_a is the association constant of peptide binding, and $[P]$ is the concentration of free peptide. F_0 and F are fluorescence intensities of fluorescently labeled rsCR2.1−4 in the absence and presence of peptide ligands, respectively.

Synthesis of Peptide Monomers (MA-GG-P1, MA-A2-P1, MA-GG-NP). Peptide monomers MA-GG-**P1**, MA-A2-**P1** and MA-GG-NP (see structures in Figure 1) were synthesized on HMBA resin using standard Fmoc chemistry. After the last amino acid residue of **P1** (or NP) was attached on the resin, the peptides were extended with additional spacers: a GG spacer was added by coupling with MA-GG-OH (*N*-methacryloylglycylglycine); A2 spacer was added by coupling with two repeats of Fmoc-A (9-fluorenylmethoxycarbonyl-8-amino-3,6-dioxaoctanoic acid, Peptides International) and capped with methacryloyl chloride. All peptide monomers were purified with RP-HPLC and were verified with MALDI-TOF MS. MALDI-TOF MS calculated for MA-GG-**P1** (MH^+) 1898.97, found 1898.93; MALDI-TOF MS calculated for MA-A2-**P1** (MH^+) 2076.06, found 2076.11; MALDI-TOF MS calculated for MA-GG-NP ($M + Na^+$) 1257.50, found 1257.54.

Synthesis of MA-PEG_{3400}-biotin and biotin-PEG-P1. *Synthesis of MA-PEG-biotin. N*-(3-Aminopropyl)methacrylamide hydrochloride (MA-NH_2) (2.7 mg) was dissolved in 200 μL of DMF and 6.7 μL of *N*,*N*-diisopropylethylamine (DIPEA) was added. The temperature of the solution was lowered to 0 °C with an ice bath. Biotin-PEG_{3400}-NHS (PEG, poly(ethylene glycol), mol wt 3400; NHS, *N*-hydroxysuccinimide ester; Nektar Therapeutics) dissolved in 200 μL of DMF was added dropwise. The reaction was kept at 0 °C for 30 min and then left overnight at room temperature. Then, the crude product was diluted 1:1 with water and MA-PEG_{3400}-biotin purified on a PD-10 column. Molecular weight as determined by MALDI-TOF MS was M_w = 3.89 kDa; M_n = 3.86 kDa; M_w/M_n = 1.01.

*Synthesis of biotin-PEG-***P1**. Peptide **P1** (5 mg) was dissolved in 0.5 mL of 0.1 M $NaHCO_3$ (pH 8.5). The temperature was lowered to 0 °C with an ice bath. A DMF solution of biotin-PEG-NHS (5 mg in 100 μL) was added dropwise to the peptide solution. The reaction was kept 0 °C for 30 min and then left overnight at room temperature. The solvent was removed by evaporation, and the biotin-PEG_{3400}-**P1** was purified with RP-HPLC. The identity of biotin-PEG_{3400}-**P1** was confirmed by MALDI-TOF MS. Molecular weight as determined by MALDI-TOF MS was M_w = 5.31 kDa; M_n = 5.29 kDa; M_w/M_n = 1.01.

Synthesis of Biotin-Labeled HPMA Copolymer−Peptide Conjugates (Figure 2). The synthesis of HPMA copolymer−peptide conjugate P^B-GG-**P1** (P^B is HPMA copolymer backbone labeled with a PEG_{3400}-biotin graft) is described as an example: HPMA (11.7 mg), MA-GG-**P1** (10 mg), MA-PEG_{3400}-biotin (3 mg) (molar ratio, 93:6:1), and initiator AIBN (1.6 mg) were dissolved in 155 μL of DMSO in a glass ampule. The solution was bubbled with nitrogen for 10 min and polymerized in the sealed ampule at 50 °C for 24 h. After the reaction was finished, the reaction solution was diluted to 3 mL with H_2O and dialyzed against water in dialysis tubing with molecular cutoff of 12−14 kDa for 3 days. After dialysis, the polymer water solution was lyophilized. P^B, P^B-A2-**P1**, and P^B-GG-NP were synthesized similarly, except that P^B contains no peptide. The polymers were analyzed with size-exclusion chromatography on an ÄKTA FPLC system (Pharmacia). The content of peptide was determined by amino acid analysis, and the content of biotin was determined with an EZ Biotin Quantitation kit (PIERCE Biotech. Inc.).

ELISA of HPMA Copolymer−Peptide Conjugates. The receptor rsCR2.1−4 (150 ng) was coated onto a MaxiSorp plate by overnight incubation at 4 °C. The plate was blocked with 4% milk at room temperature for 1.5 h, washed with TPBS, and incubated with HPMA copolymer−peptide conjugates (0.02 μM) for 30 min. Then, the plate was washed eight times with TPBS, followed by incubation with streptavidin/HRP (Zymed Laboratories) for 30 min. The plate was washed 5 times with TPBS; then TMB substrate was added to the plate and incubated for 30 min. The absorbance was read at 450/630 nm.

For the inhibitive ELISA of P^B-GG-**P1**, plate surface was coated with rsCR2.1−4 (150 ng) and blocked with 4% milk. Different concentrations of free peptide **P1** (0−100 μM) were preincubated with surface-bound rsCR2.1−4 in 100 μL of TPBS for 15 min. Then, P^B-GG-**P1** was added to each plate well (final concentration 0.02 μM) and incubated for 30 min. The bound P^B-GG-**P1** was detected as described above.

RESULTS

Identification of Peptide Ligands for CD21 Receptor. Peptide ligands for the CD21 receptor were selected with a 15-mer phage library based on the phage vector fUSE 5 using sCD21 as the target molecule. To select specifically bound phage and exclude nonspecifically bound phage, a stringent biopanning process was performed including several measures: extensive

Table 1. Screening Results of CD21 Receptor Binding Phages

selected phage	sequence	occurrence
P1	R M W P S S T V N L S A G R R	4
P2	P N L D F S P T C S F R F G C	1
P3	G R V P S M F G G H F F F S R	1
P4	R L A Y W C F S G L F L L V C	2
P5	P V A A V S F V P Y L V K T Y	1

washing with TPBS (pH 7.4) (*41*), stringent washing with TPBS (pH 5.0) (*41*), decreasing the incubation time in each round of selection (*42*), and elution with sCD21 at the last round selection (*42*). After four rounds of selection, a preliminary phage ELISA of 21 individual phage colonies was performed, and the DNA of the nine phages with the highest binding was sequenced (Table 1). Five different sequences were obtained; four phages shared the sequence RMWPSSTVNLSAGRR (**P1**) and two shared the sequence RLAYWCFSGLFLLVC (**P4**). It is interesting to note that two sequences, PNLDFSPTCSFRFGC (**P2**) and **P4**, contained two cysteine residues. The distance between the two cysteines are five (**P2**) and eight (**P4**) amino acid residues, respectively. Consequently, the formation of cyclic peptide structures with constrained conformations is more probable than cross-linking. Except for **P1**, all sequences of selected peptides, **P2**−**P4**, consisted mostly of hydrophobic residues, which may participate in hydrophobic interactions with the CD21 receptor. However, the five sequences did not show obvious homology with each other.

Phage ELISA and Competitive Phage ELISA. The binding affinity of the selected peptides toward the CD21 receptor was first verified by phage ELISA with sCD21 and rsCR2.1−4 (Figure 3). As expected, all the selected phages were found to bind to sCD21 specifically, and all showed little binding to the surface in the absence of receptor. Since rsCR2.1−4 represents only the first four SCRs of the whole CD21 receptor, it was unexpected that all the selected phages bound to rsCR2.1−4, indicating that the binding sites of selected peptides are all localized in this region (Figure 3). Furthermore, the binding of the different phages to sCD21 correlated very well with their binding to rsCR2.1−4. Even though phage **P4** showed the highest signal in the presence of CD21 receptors, it also showed significant binding to the surface in the absence of CD21

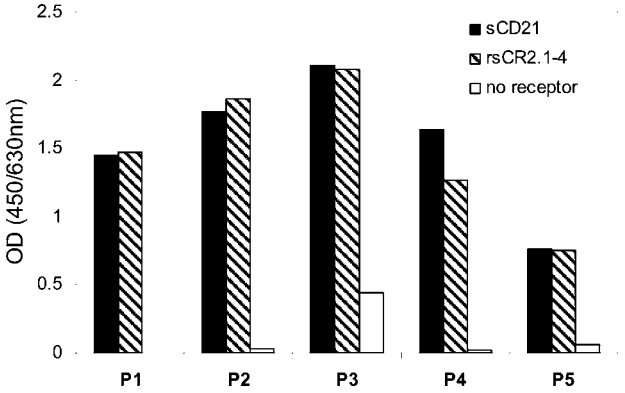

Figure 3. The specificity of selected phage with different sequences was confirmed by phage ELISA. The plate surface was coated with two different forms of CD21 receptor, sCD21 and rsCR2.1−4. The absorbance was compared with the control surface without receptor.

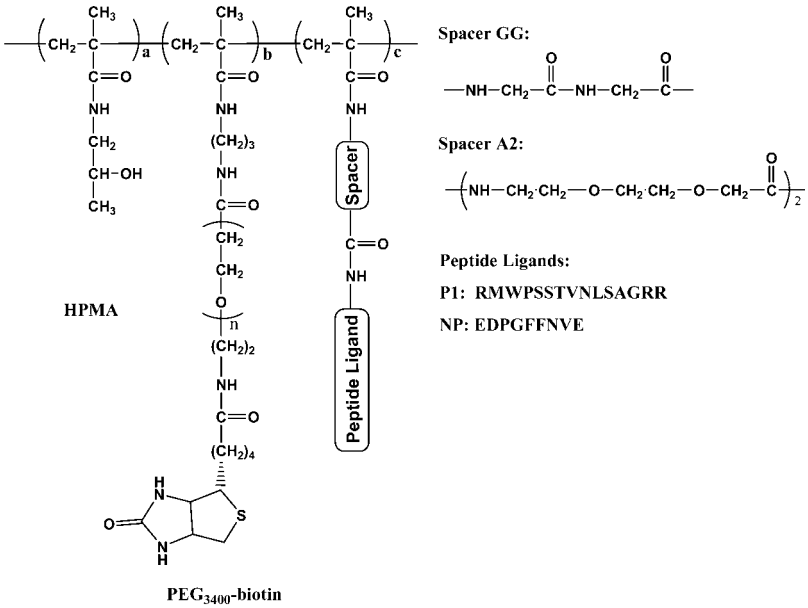

Structure of conjugate[a]	Polymer Backbone	Peptide	Spacer[a]	Peptide position
P[B]	PHPMA	N/A	N/A	N/A
P[B]-GG-**P1**	PHPMA	**P1**	GG	Grafts[b]
P[B]-A2-**P1**	PHPMA	**P1**	A2	Grafts[c]
P[B]-GG-NP	PHPMA	NP	GG	Grafts[b]
Biotin-PEG$_{3400}$-**P1**	PEG$_{3400}$	**P1**	N/A	Chain end[d]

[a]HPMA copolymer backbone labeled with a PEG$_{3400}$-biotin graft; [b]peptide attached to the HPMA copolymer backbone via GG side-chains; [c]peptide attached to the HPMA copolymer backbone via A2 (dimer of 8-amino-3,6-dioxaoctanoic acid) side-chains; [d]peptide attached to the carboxy end of PEG.

Figure 2. Structures of HPMA copolymer−**P1** conjugates and PEG−**P1** conjugate. HPMA copolymer−peptide conjugates consist of three components: an HPMA copolymer backbone, a PEG-biotin graft used as a label for immunoassay, and peptide ligands with spacers of different lengths, GG and A2. Each polymer chain of the HPMA copolymer−peptide conjugates contains several copies of peptide, while each polymer chain of biotin-PEG$_{3400}$-**P1** contains only one peptide.

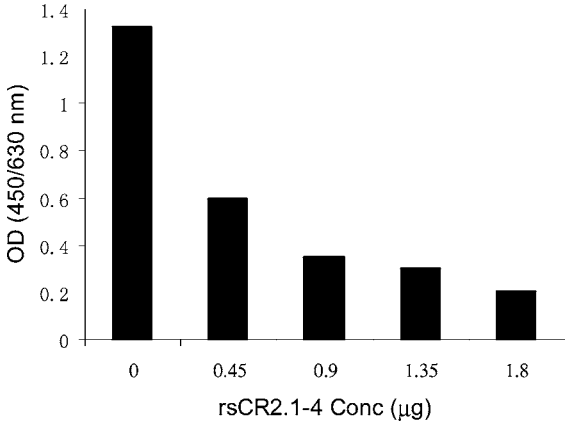

Figure 4. Competitive phage ELISA. Different amounts of rsCR2.1−4 were used to compete with surface-bound sCD21 for binding to phage **P1**.

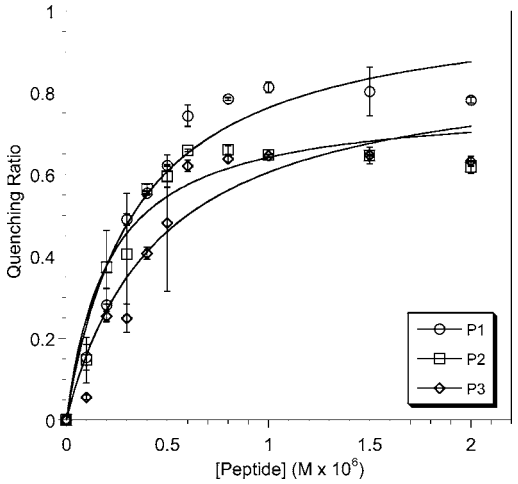

Figure 5. Fluorescence quenching of fluorescein labeled rsCR2.1−4 as a function of peptide concentration. Data are depicted as mean ± standard deviation from duplicate measurements.

receptor, which possibly is a result of the three consecutive phenylalanine residues in its structure.

We further verified that the binding sites of selected peptides are within the first four SCRs using competitive phage ELISA. Using phage **P1** as an example, whole receptor sCD21 was immobilized on a MaxiSorp plate surface and rsCR2.1−4 was co-incubated with **P1** as a competitor to surface-bound sCD21. As shown in Figure 4, with increasing concentration of competitor the number of phage bound to sCD21 decreased, as indicated by the decreasing ELISA signal. The binding of sCD21 with **P1** was inhibited by rsCR2.1−4, which confirmed that the binding site of **P1** is within first four SCRs. This result provided a basis for using rsCR2.1−4 for the binding constant determination of the selected peptides.

Binding Constant Determination with Fluorescence Quenching. The rsCR2.1−4 receptor was fluorescently labeled with FITC, and it was found that the extent of labeling had a significant effect on the fluorescence quenching effect. When the labeling of rsCR2.1−4 was low (F/P $\approx$ 1), the quenching effect was not apparent (data not shown). When the labeling of rsCR2.1−4 was high (F/P $\approx$ 5), the quenching effect was pronounced—over 80% quenching was observed, as shown in Figure 5.

Our previous studies of the binding kinetics of peptide LVLLTRE (a peptide derived from one-bead one-compound peptide library, to be published) with rsCR2.1−4-FITC indicated that at least 3 h are needed to reach equilibrium. Therefore, the peptides were incubated with the receptor for 5 h, before measuring the fluorescence intensity. The association constants of peptides **P1**, **P2**, and **P3** were determined to be 2.9×10^6 M^{-1}, 4.7×10^6 M^{-1}, and 2.2×10^6 M^{-1}, respectively (Figure 5). **P2** (PNLDFSPTCSFRFGC) contains two cysteine residues and can form a cyclic structure. To evaluate the impact of conformation constrain on biorecognition, the binding affinities of cyclic **P2** and linear **P2** were compared. Linear **P2** in reduced form showed poor aqueous solubility. Its quenching study was carried out with the assistance of a small amount of DMF for solubilization. The binding constant of linear **P2** was estimated to be 2×10^6 M^{-1} (data not shown). Therefore, the cyclic structure of **P2** enhanced the binding about 2-fold when compared with linear **P2**.

Synthesis and Characterization of HPMA Copolymer−Peptide Conjugates. All HPMA copolymer conjugates were synthesized by copolymerization of monomers of HPMA, peptide, and biotin. The composition of the synthesized polymers is summarized in Table 2. The weight-average molecular weight was determined with size-exclusion chromatography on a Sepharose 6B column calibrated with PHPMA standards. The concentration of the peptide monomers, MA-GG-**P1** and MA-A2-**P1**, in the feed was 6 mol %, but only about 1 mol % of peptide-containing comonomer was incorporated into the copolymer. Peptide monomer, MA-GG-NP, possessed a better incorporation efficiency: 2.6 mol % of peptide monomer was incorporated to a content identical to the feed composition. We synthesized P^B-GG-NP using a feed composition of 4% MA-GG-NP, so that the content of NP in P^B-GG-NP was comparable to the content of peptide **P1** in conjugates P^B-GG-**P1** and P^B-A2-**P1**. (One may speculate that the difference of incorporation efficiency relates to the length of the peptide; however, more experiments would be needed to verify this hypothesis.) The copolymers were labeled with biotin by incorporation of a small amount of the MA-PEG_{3400}-biotin comonomer. Biotin was used to detect surface-bound conjugates in the ELISA experiments. Only 1 mol % of MA-PEG_{3400}-biotin was used in the monomer feed, and approximately 0.3−0.4% of biotin-containing comonomer was incorporated into the HPMA copolymer (Table 2). This corresponds to about one biotin per macromolecule.

ELISA of Peptide HPMA Copolymer Binding to Surfaces with Different Amounts of rsCR2.1-4. Two experiments were performed to evaluate the impact of peptide conjugation with HPMA copolymers on biorecognition by the CD21 receptor, including (a) the dependence of binding on receptor surface density and (b) competitive inhibition with free peptide **P1**. For the receptor density dependent study, MaxiSorp plate was coated with different amounts of rsCR2.1−4 (0−640 ng), and the binding of P^B-GG-**P1** (0.02 μM) was detected with ELISA using biotin/streptavidin/HRP as the reporting system. To minimize the nonspecific interaction between plate surface and polymer−peptide conjugate, we tried several blocking agents and found that 4% milk produced the lowest background. We are aware that milk may contain some amount of endogenous biotin, which may interact with the biotin/streptavidin/HRP detection system; however, in our experiment, this did not seem to be a problem. If the endogenous biotin were to interact with the detection system, it can be masked with egg white and milk (*43*).

The binding of P^B-GG-**P1** to surface-bound receptor was directly related to the receptor density: the higher the receptor density, the higher the amount of surface-bound P^B-GG-**P1** (Figure 6). These data indicate a specific interaction between P^B-GG-**P1** and surface-bound receptor. This experiment also provided the binding profile of P^B-GG-**P1**, so that an optimum amount of receptor density could be identified. In the final surface binding experiments, 150 ng of rsCR2.1−4 was used to coat the surface.

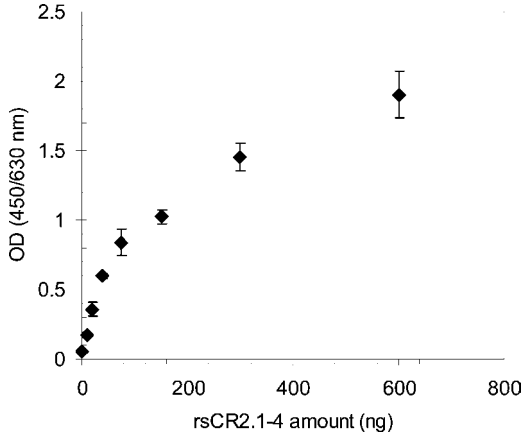

Figure 6. The relationship between the binding of P^B-GG-**P1** and amount of surface coating receptor. Data are depicted as mean ± standard deviation from duplicate measurements.

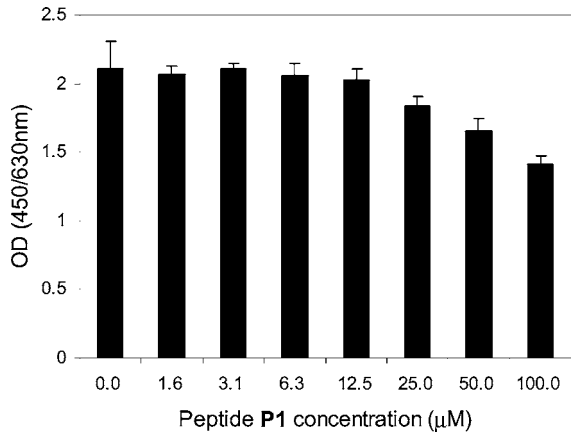

Figure 7. Inhibition of P^B-GG-**P1** binding to surface-bound receptor by free peptide **P1**. The data represent mean ± standard deviation from duplicate measurements.

Competitive Inhibition of Binding with Free Peptide. To further demonstrate the binding specificity of HPMA copolymer−peptide conjugate and CD21 receptor, we investigated binding of conjugate P^B-GG-**P1** (0.02 μM) in the presence of different concentrations of free peptide **P1** (0−100 μM). Free **P1** was able to inhibit the binding of P^B-GG-**P1** at concentrations higher than 25 μM (Figure 7). However, no apparent inhibition was observed when the concentration of free peptide was below 6.25 μM, and the inhibition was only 25% even at the **P1** concentration of 100 μM. This fact implied that the binding affinity of P^B-GG-**P1** is much higher than that of free peptide, given that binding concentration of P^B-GG-**P1** was only 0.02 μM. One could expect that the biorecognition (binding) of the peptide in a polymer conjugate may decrease due to the sterical hindrance of the polymer backbone on the formation of the ligand−receptor complex. However, the binding affinity of the HPMA copolymer-bound peptide was enhanced (Figure 7). The enhanced binding could be ascribed to the effect of multivalent interactions between P^B-GG-**P1** and surface-bound receptor. Each polymer chain of P^B-GG-**P1** contained about 4.4 grafted peptides (Table 2A). With the appropriate receptor density on the surface, multivalent interactions between P^B-GG-**P1** and receptor apparently occurred, resulting in a binding affinity enhanced by 3−4 orders of magnitude. A separate experiment, described below, was devoted to clarify the effect of multivalent interactions on the binding of HPMA copolymer−peptide conjugates.

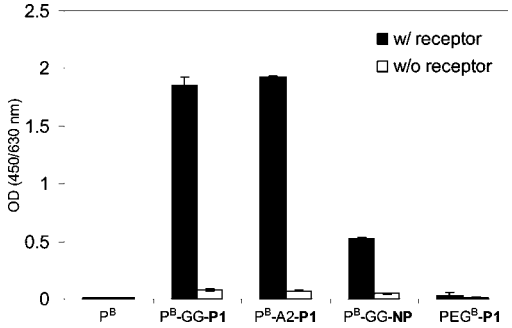

Figure 8. ELISA results of different polymer−peptide conjugates binding to surface-bound receptor. Data are depicted as mean ± standard deviation from duplicate measurements.

Surface Binding of the Conjugates with Varying Structure. Biotin-labeled HPMA copolymer−**P1** conjugates, differing in the structure and length of the spacer separating the peptide and the HPMA copolymer backbone, were synthesized (Table 2A), and their binding to CD21 was evaluated. Two spacers, namely, GG (glycylglycine) and A2 (dimer of 8-amino-3,6-dioxaoctanoic acid), and two peptides, **P1** and NP were used. As controls, biotin-labeled HPMA copolymer (no peptide) and biotin-labeled PEG-**P1** conjugate were evaluated.

P^B (HPMA copolymer containing no peptide) did not show any binding to the surface with or without receptor. As in experiments described above, HPMA copolymer containing the peptide ligand **P1** (P^B-GG-**P1**) demonstrated receptor-specific binding (Figure 8). Polymer conjugate (P^B-GG-NP) containing

Table 2. Composition of (A) Various Polymer−Peptide Conjugates and (B) HPMA Copolymer−P1 Conjugates with Different Contents of P1

(A) Various Polymer−Peptide Conjugates[a]

conjugates	structure	M_w[c] (kDa)	Pd[d]	peptide (mol %)[e]	peptide no./chain	biotin (mol %)[f]
P^B	PHPMA−(PEG−biotin)	63.2	1.7	0	0	0.4
P^B−GG−**P1**	PHPMA−(GG−**P1**)−(PEG−biotin)	47.1	1.4	1.3	4.4	0.36
P^B−A2−**P1**	PHPMA−(A2−**P1**)−(PEG−biotin)	55.6	1.5	1.1	4.3	0.36
P^B−GG−NP	PHPMA−(GG−NP)−(PEG−biotin)	60.3	1.3	1.2	5.2	0.35
PEG^B−**P1**	biotin−PEG_{3400}−**P1**	5.3	1	N/A	1	N/A

(B) HPMA Copolymer−**P1** Conjugates with Different Contents of **P1**[b]

conjugates	feed composition (HPMA/biotin/**P1**)	M_w[c] (kDa)	Pd[d]	peptide (mol %)[e]	peptide no./chain	biotin (mol %)[f]
P^B−GG−**P1**A	98.5:1:0.5	67.1	1.6	0.07	0.3	0.28
P^B−GG−**P1**B	98:1:1	81.1	1.5	0.15	0.8	0.40
P^B−GG−**P1**C	97:1:2	79.4	1.6	0.31	1.7	0.37
P^B−GG−**P1**D	95:1:4	65.2	1.5	0.98	4.5	0.31
P^B−GG−**P1**E	93:1:6	47.1	1.4	1.3	4.4	0.37

[a] P^B HPMA copolymer backbone labeled with a PEG_{3400}−biotin graft. [b] P^B HPMA copolymer backbone labeled with a PEG_{3400}−biotin graft. [c] M_w: weight-average molecular weight as determined with size exclusion chromatography. [d] Pd: polydispersity, ratio of weight-average molecular weight over number-average molecular weight. [e] Determined with amino acid analysis. [d] Determined with EZ Biotin Quantitation kit.

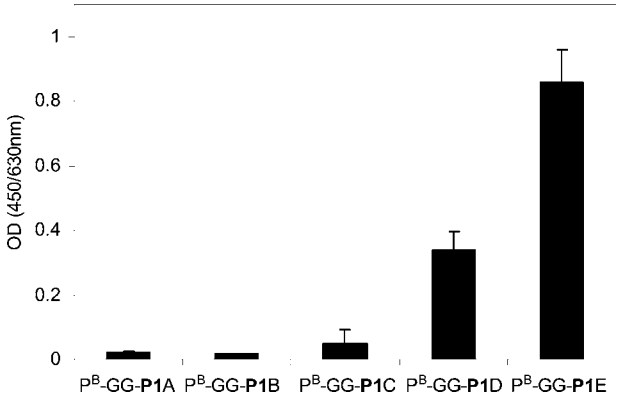

Figure 9. The binding of HPMA copolymer−**P1** conjugates (P^B-GG-**P1**A-E; containing different amounts of peptide **P1**) to the CD21 receptor. For composition of copolymers, see Table 2B. Data are depicted as mean ± standard deviation from duplicate measurements.

a nonapeptide (EDPGFFNVE) ligand of CD21 receptor reported by literature (*34*), also demonstrated specific binding to CD21 receptor, however, to a lesser degree compared with P^B-GG-**P1**.

The binding of biotin-labeled PEG-**P1** conjugate (PEG^B-**P1**) was also evaluated. PEG^B-**P1** is composed of a 3400-Da poly(ethylene glycol) macromolecule with one terminus modified with peptide **P1** and the other with biotin. However, no appreciable binding of PEG^B-**P1** to receptor was detected (Figure 8). This conjugate (PEG^B-**P1**) contains only one peptide per macromolecule. Consequently, it interacts with the receptor only in a monovalent manner. In contrast, each polymer chain of P^B-GG-**P1** has 4−5 copies of peptide **P1**, thus capable of multivalent interactions with surface-bound receptor. This difference in biorecognition may be attributed to the difference in the binding mode (multivalent vs monovalent interactions).

The Effect of Peptide Accessibility on the Binding Affinity. Both PHPMA and the peptide may influence the physical properties of HPMA copolymer−peptide conjugates. PHPMA itself is water-soluble; its conformation in solution is a random coil (*44*). When hydrophobic moieties are attached to HPMA copolymer side chains, the conformation of the macromolecule in the solution may change as a result of intramolecular and/or intermolecular association of side chains (*45*). On the other hand, the polymer backbone, due to its constant mobility, may have a shielding effect on the accessibility of peptide to the target. To investigate this possibility, the peptide **P1** was conjugated to HPMA copolymer via two different spacers, GG and A2 (Figure 1). Spacer A2 is four times as long as spacer GG. It is also more flexible because the amide bonds limit the flexibility of GG. Therefore, the peptide in P^B-A2-**P1** may be better exposed and should have more accessibility than that in P^B-GG-**P1**. However, no obvious binding differences between P^B-GG-**P1** and P^B-A2-**P1** were observed (Figure 8). This suggests that in both conjugates, peptide **P1** was sufficiently exposed for interaction with the target receptor, and the spacer effect was minimal. Because **P1** is a peptide 15 amino acid residues long, the results do not eliminate possible spacer effects using shorter peptides.

Demonstration of Multivalent Interaction in Surface Binding. To evaluate the relationship between the amount of peptides per macromolecule and biorecognition, biotin-labeled HPMA copolymers containing different amounts of GG-**P1** side chains were synthesized (Table 2B), and their binding properties were determined. When the peptide content of conjugates (P^B-GG-**P1**A and P^B-GG-**P1**B) was low, less than one peptide per polymer chain, the binding of the conjugates was negligible (Figure 9). Conjugate P^B-GG-**P1**C (1.7 peptide per polymer chain) showed minimal binding; however, both P^B-GG-**P1**D (4.5 peptide per polymer chain) and P^B-GG-**P1**E (4.4 peptide per polymer chain) demonstrated extraordinary binding. Although the number of peptide grafts per macromolecule in P^B-GG-**P1**D and P^B-GG-**P1**E was similar, the latter showed much better binding than P^B-GG-**P1**D. This may be explainable by the higher mol % of peptide in P^B-GG-**P1**E (the difference is due to the lower molecular weight of conjugate P^B-GG-**P1**E than that of P^B-GG-**P1**D). The above results demonstrated the importance of multivalent interaction in the binding of HPMA copolymer−peptide conjugates to the CD21 receptor.

DISCUSSION

Identification of CD21 Ligands with Phage Display. Two forms of CD21 receptor, soluble CD21 (sCD21) and recombinant short CD21 rsCR2.1−4 were prepared. SCD21 contains the whole extracellular portion of CD21 receptor, while rsCR2.1−4 only the first four SCRs. sCD21, about four times as large as rsCR2.1−4, is expected to have more binding sites than rsCR2.1−4. Therefore, biopanning with whole sCD21 should select peptides not only binding to SCR1−4, but also to SCR5−16. Since the goal was to find suitable peptide ligands for the CD21 receptor, sCD21 was used, instead of rsCR2.1−4, for phage display, to find the best peptide binders of the whole CD21 receptor. Surprisingly, all peptide ligands selected with sCD21 also bound to SCR1−4 as indicated by phage ELISA with rsCR2.1−4 and competitive phage ELISA, demonstrating that the binding sites of all selected peptides were located within the first four SCRs. Several factors might contribute to this result: SCR1−4 is well exposed and accessible for interaction with phage; SCR1−4 consists of binding sites most suitable for peptide binding; peptides binding outside of SCR1−4 are relatively weaker and cannot withstand stringent screening.

Another feature of selection results is the lack of obvious homology among all of the selected peptides, which implies that SCR1−4 is not the only antigenic region, but also a multi-antigenic region. It has several distinctive binding sites, which was verified by epitope mapping with different antibodies. Although the epitopes of anti-CD21 antibodies, FE8 (*46*), OKB7 (*47*), mAb171 (*48*), and mAb1048 (*48*) are all located in SCR1−2, they are distinct from each other. The binding sites of C3d and EBV have been extensively studied, but the results had been controversial until the X-ray crystallographic structure of C3d-CD21 complex was published (*49*). There is evidence that the binding sites of C3d and EBV are far from each other (*50*). Therefore, it was not surprising that the selected peptides exhibited no homology. Moreover, the phage display results further confirmed that the CD21 receptor is multi-antigenic.

Affinity Analysis by Fluorescence Quenching. Fluorescence spectrometry is most suited for protein−ligand interactions with dissociation constants in the range 10^{-4} to 10^{-8} M. The formation of the protein−ligand complex usually induces a conformational change of the protein and an alteration of the microenvironment of the fluorophore. Some fluorescence parameters such as anisotropy and intensity are sensitive to such changes, and the variation of fluorescence intensity upon the formation of protein−ligand complex can be used for affinity analysis (*51*).

By comparing on the crystal structure of both free CD21 (SCR1−2) (*50*) and the complex (*49*) of CD21 (SCR1−2) and C3d, it was found that the binding of C3d with CD21 is an induced-fitting process. Not only does the conformation of the local binding site change upon binding, but the global conformation also changes (*50*). This implies that the CD21 receptor (or at least SCR1−2) is a relatively flexible protein. The conformational change of CD21 receptor upon binding with ligands should be detectable with fluorescence spectrometry. The recombinant short CD21 receptor, rsCR2.1−4, was used

for affinity analysis by fluorescence quenching. It is a much smaller molecule compared to the whole CD21 receptor. With a smaller molecule, the change of fluorescence parameters is more sensitive to conformational change. Although selected peptides are only 15 amino acid residues long, their interaction with rsCR2.1−4 induced enough conformational change to be detected by fluorescence quenching. The dissociation constants of three synthesized peptides were determined to be within the micromolar range, which is typical for most phage display results (*11*). We are aware that the binding affinity of selected peptides might be affected, to some extent, by the labeling of rsCR2.1−4 with FITC.

Synthesis of HPMA Copolymer−Peptide Conjugates. There are two different ways to synthesize HPMA copolymer−peptide conjugates: polymer-analogous reactions and copolymerization. In polymer-analogous reaction, a HPMA copolymer precursor containing, e.g., reactive *p*-nitrophenyl ester groups at side chain termini is prepared first, followed by the attachment of the peptide to the HPMA copolymer precursor by aminolysis of the active ester (*32*). However, this approach has some limitations, as the peptide should have only one free amino group to achieve site-specific conjugation. This can be inconvenient because most peptides usually contain more than one reactive group; therefore, protection during synthesis is required. In comparison, copolymerization using peptide-containing monomers with HPMA, in an appropriate solvent, does not present this limitation. Because **P1** contains three arginine residues and one amino group reactive toward the active ester of the HPMA copolymer precursor, P^B-GG-**P1** was prepared by the copolymerization of HPMA, MA-GG-**P1**, and MA-PEG-biotin in DMSO (a good solvent).

Affinity Analysis of Polymer-Bound Peptides. Several different targeting moieties have been incorporated into HPMA copolymers, including lectins (*52*), antibodies (*53*), and antibody fragments (*54*). Successful targeting with peptides will undoubtedly expand the application of HPMA copolymer as an anticancer drug carrier. Therefore, it is necessary to examine the biorecognizability of selected peptides after they are conjugated with HPMA copolymer. We chose peptide **P1** for this purpose, since **P1** is quite soluble in water, thus avoiding the possible complications caused by inter/intramolecular hydrophobic interactions.

When multiple copies of a peptide are incorporated into a polymer-based drug delivery system, the properties of both the peptides and the polymer may change accordingly. On one hand, the targeting efficiency of the peptides may be partially masked by the polymer. On the other hand, the polymer structure may be influenced by the composition of peptides, especially when peptides contain a large number of hydrophobic or charged residues. Therefore, the interaction between the HPMA copolymer−peptide conjugates and the surface-bound receptor was investigated. It was found that conjugation of **P1** with HPMA copolymer did not impair its binding affinity toward the CD21 receptor as demonstrated by receptor-dependent surface binding and inhibition experiments using free peptide. On the basis of the binding results of P^B-GG-**P1** and P^B-GG-NP, the selected peptide **P1** showed better recognizability than the previously reported nonapeptide (NP) when incorporated into HPMA copolymer−peptide conjugates (*32*).

By changing the spacer from GG to GFLG, the binding affinity of HPMA copolymer−peptide NP conjugates increased as determined by the whole cell binding assay (*32*, *36*), implying that extended spacer length may improve the interaction between the NP and the cell surface receptor. However, in our experiment, the spacer effect (A2 is four times as long as GG) was not significant. It was noted that **P1** is a 15-amino-acid peptide and NP is a 9-amino-acid peptide. It was speculated that length of peptide ligands may account for the spacer effect on different HPMA copolymer−peptide conjugates—the longer the peptide length, the less the spacer effect.

The enhanced surface binding affinity of P^B-GG-**P1** compared with free peptide and PEG^B-**P1** suggested multivalent interactions of HPMA copolymer conjugates. Because each PEG chain contained only one peptide, while each HPMA copolymer chain contained 4−5 copies of peptide, HPMA copolymer−peptide conjugates are capable of multivalent interaction with surface-bound receptor. This multivalent effect was also observed in inhibitive ELISA by free peptide: noticeable inhibition was observed only when free peptide concentration was 3−4 orders of magnitude higher than peptide concentration in conjugates. The binding affinity test with peptide conjugates of different peptide contents confirmed the importance of multivalent interaction in the surface binding of HPMA copolymer−peptide conjugates. Also shown in whole cell binding assays, the binding affinity of HPMA copolymer NP conjugates increased with the increase of NP content in the conjugates (*32*, *36*). This observation is directly correlated to our results in this work: multivalent interaction played an important role on the binding of HPMA copolymer not only in our plate surface model but also in the cell surface system. Therefore, HPMA polymer−peptide conjugates are beneficial to recognize a target, which is capable of multivalent interaction.

A soluble form of CD21, shed from the cell membrane, may compete with the binding of HPMA copolymer−peptide conjugates to lymphoma cells, thus reducing its targeting specificity. This fact further strengthens the importance of the multivalent capability of HPMA−peptide conjugates; if multivalent interactions are achievable with the membrane-bound receptor, then the competition by the soluble receptor will be significantly minimized.

CONLUSIONS

Five peptide sequences were identified as ligands for CD21 receptor using phage display. The binding affinity of selected peptides was confirmed by phage ELISA, and the binding constants of three peptides were determined with fluorescence quenching. Using surface binding studies, it was demonstrated that the peptide RMWPSSTVNLSAGRR (**P1**) retained its recognizability by the CD21 receptor after its incorporation into HPMA copolymer. The specificity of its recognition was confirmed with competitive inhibition by free peptide. The spacer effect for this peptide in the HPMA copolymer conjugates was minimal. The importance of multivalent interaction for biorecognition of HPMA copolymer−peptide conjugates toward the CD21 receptor was confirmed.

ACKNOWLEDGMENT

This work was supported in part by NIH Grants CA88047 and CA51578 from the National Cancer Institute. We thank Dr. G. P. Smith for providing the fUSA-5 15-mer phage library, Dr. A. Tang for valuable discussions and the gift of HB5 anti-CD21 mAb, and J. Callahan for carefully revising the manuscript.

LITERATURE CITED

(1) Stern, M., and Herrmann, R. (2005) Overview of monoclonal antibodies in cancer therapy: present and promise. *Crit. Rev. Oncol. Hematol. 54*, 11−29.

(2) Cersosimo, R. J. (2003) Monoclonal antibodies in the treatment of cancer, Part 1. *Am. J. Health Syst. Pharm. 60*, 1531−1548.

(3) Cersosimo, R. J. (2003) Monoclonal antibodies in the treatment of cancer, Part 2. *Am. J. Health Syst. Pharm. 60*, 1631−41; quiz 1642−1643.

(4) Adams, G. P., and Weiner, L. M. (2005) Monoclonal antibody therapy of cancer. *Nat. Biotechnol. 23*, 1147−1157.
(5) James, J. S., and Dubs, G. (1997) FDA approves new kind of lymphoma treatment. Food and Drug Administration. *AIDS Treat. News*, 2−3.
(6) Goldenberg, M. M. (1999) Trastuzumab, a recombinant DNA-derived humanized monoclonal antibody, a novel agent for the treatment of metastatic breast cancer. *Clin. Ther. 21*, 309−318.
(7) Friedberg, J. W., and Fisher, R. I. (2004) Iodine-131 tositumomab (Bexxar): radioimmunoconjugate therapy for indolent and transformed B-cell non-Hodgkin's lymphoma. *Exp. Rev. Anticancer Ther. 4*, 18−26.
(8) Wu, A. M., and Senter, P. D. (2005) Arming antibodies: prospects and challenges for immunoconjugates. *Nat. Biotechnol. 23*, 1137−1146.
(9) Stefanidakis, M., and Koivunen, E. (2004) Peptide-mediated delivery of therapeutic and imaging agents into mammalian cells. *Curr. Pharm. Des. 10*, 3033−3044.
(10) Liu, R., Enstrom, A. M., and Lam, K. S. (2003) Combinatorial peptide library methods for immunobiology research. *Exp. Hematol. 31*, 11−30.
(11) Landon, L. A., and Deutscher, S. L. (2003) Combinatorial discovery of tumor targeting peptides using phage display. *J. Cell Biochem. 90*, 509−517.
(12) Smith, G. P. (1985) Filamentous fusion phage: novel expression vectors that display cloned antigens on the virion surface. *Science 228*, 1315−1317.
(13) Smith, G. P., and Petrenko, V. A. (1997) Phage Display. *Chem. Rev. 97*, 391−410.
(14) Chen, Y. C., Delbrook, K., Dealwis, C., Mimms, L., Mushahwar, I. K., and Mandecki, W. (1996) Discontinuous epitopes of hepatitis B surface antigen derived from a filamentous phage peptide library. *Proc. Natl. Acad Sci U.S.A. 93*, 1997−2001.
(15) Matthews, L. J., Davis, R., and Smith, G. P. (2002) Immunogenically fit subunit vaccine components via epitope discovery from natural peptide libraries. *J. Immunol. 169*, 837−846.
(16) Takenaka, I. M., Leung, S. M., McAndrew, S. J., Brown, J. P., and Hightower, L. E. (1995) Hsc70-binding peptides selected from a phage display peptide library that resemble organellar targeting sequences. *J. Biol. Chem. 270*, 19839−19844.
(17) Aina, O. H., Sroka, T. C., Chen, M. L., and Lam, K. S. (2002) Therapeutic cancer targeting peptides. *Biopolymers 66*, 184−199.
(18) Shukla, G. S., and Krag, D. N. (2005) Phage display selection for cell-specific ligands: development of a screening procedure suitable for small tumor specimens. *J. Drug Target. 13*, 7−18.
(19) Shukla, G. S., and Krag, D. N. (2005) Selection of tumor-targeting agents on freshly excised human breast tumors using a phage display library. *Oncol. Rep. 13*, 757−764.
(20) Kolonin, M., Pasqualini, R., and Arap, W. (2001) Molecular addresses in blood vessels as targets for therapy. *Curr. Opin. Chem. Biol. 5*, 308−313.
(21) Arap, W., Kolonin, M. G., Trepel, M., Lahdenranta, J., Cardo-Vila, M., Giordano, R. J., Mintz, P. J., Ardelt, P. U., Yao, V. J., Vidal, C. I., Chen, L., Flamm, A., Valtanen, H., Weavind, L. M., Hicks, M. E., Pollock, R. E., Botz, G. H., Bucana, C. D., Koivunen, E., Cahill, D., Troncoso, P., Baggerly, K. A., Pentz, R. D., Do, K. A., Logothetis, C. J., and Pasqualini, R. (2002) Steps toward mapping the human vasculature by phage display. *Nat. Med. 8*, 121−127.
(22) Timens, W. (2000) Cd21. *J. Biol. Regul. Homeostatic Agents 14*, 292−294.
(23) Prodinger, W. M. (1999) Complement receptor type two (CR2, CR21): a target for influencing the humoral immune response and antigen-trapping. *Immunol. Res. 20*, 187−194.
(24) Calender, A., Billaud, M., Aubry, J. P., Banchereau, J., Vuillaume, M., and Lenoir, G. M. (1987) Epstein−Barr virus (EBV) induces expression of B-cell activation markers on in vitro infection of EBV-negative B-lymphoma cells. *Proc. Natl. Acad. Sci. U.S.A. 84*, 8060−8064.
(25) McNearney, T. A., Ebenbichler, C. F., Totsch, M., and Dierich, M. P. (1993) Expression of complement receptor 2 (CR2) on HTLV-1-infected lymphocytes and transformed cell lines. *Eur. J. Immunol. 23*, 1266−1270.
(26) Hess, M. W., Schwendinger, M. G., Eskelinen, E. L., Pfaller, K., Pavelka, M., Dierich, M. P., and Prodinger, W. M. (2000) Tracing uptake of C3dg-conjugated antigen into B cells via complement receptor type 2 (CR2, CD21). *Blood 95*, 2617−2623.
(27) Fremeaux-Bacchi, V., Kolb, J. P., Rakotobe, S., Kazatchkine, M. D., and Fischer, E. M. (1999) Functional properties of soluble CD21. *Immunopharmacology 42*, 31−37.
(28) Prodinger, W. M., Schoch, J., Schwendinger, M. G., Hellwage, J., Parson, W., Zipfel, P. F., and Dierich, M. P. (1997) Expression in insect cells of the functional domain of CD21 (complement receptor type two) as a truncated soluble molecule using a baculovirus vector. *Immunopharmacology 38*, 141−148.
(29) Kopeček, J., Kopečková, P., Minko, T., and Lu, Z. (2000) HPMA copolymer-anticancer drug conjugates: design, activity, and mechanism of action. *Eur. J. Pharm. Biopharm. 50*, 61−81.
(30) Minko, T., Kopečková, P., and Kopeček, J. (1999) Chronic exposure to HPMA copolymer-bound adriamycin does not induce multidrug resistance in a human ovarian carcinoma cell line. *J. Control. Release 59*, 133−148.
(31) Minko, T., Kopečková, P., and Kopeček, J. (1999) Comparison of the anticancer effect of free and HPMA copolymer-bound adriamycin in human ovarian carcinoma cells. *Pharm. Res. 16*, 986−996.
(32) Tang, A., Kopečková, P., and Kopeček, J. (2003) Binding and cytotoxicity of HPMA copolymer conjugates to lymphocytes mediated by receptor-binding epitopes. *Pharm. Res. 20*, 360−367.
(33) Mammen, M., Choi, S. K., and Whitesides, G. M. (1998) Polyvalent interactions in biological systems: implications for design and use of multivalent ligands and inhibitors. *Angew. Chem., Int. Ed. 37*, 2754−2794.
(34) Nemerow, G. R., Houghten, R. A., Moore, M. D., and Cooper, N. R. (1989) Identification of an epitope in the major envelope protein of Epstein−Barr virus that mediates viral binding to the B lymphocyte EBV receptor (CR2). *Cell 56*, 369−377.
(35) Tang, A., and Kopeček, J. (2002) Presentation of epitopes on genetically engineered peptides and selection of lymphoma-targeting moieties based on epitope biorecognition. *Biomacromolecules 3*, 421−431.
(36) Omelyanenko, V., Kopečková, P., Prakash, R. K., Ebert, C. D., and Kopeček, J. (1999) Biorecognition of HPMA copolymer-adriamycin conjugates by lymphocytes mediated by synthetic receptor binding epitopes. *Pharm. Res. 16*, 1010−1019.
(37) Nan, A., Ghandehari, H., Hebert, C., Siavash, H., Nikitakis, N., Reynolds, M., and Sauk, J. J. (2005) Water-soluble polymers for targeted drug delivery to human squamous carcinoma of head and neck. *J. Drug Target. 13*, 189−197.
(38) Line, B. R., Mitra, A., Nan, A., and Ghandehari, H. (2005) Targeting tumor angiogenesis: comparison of peptide and polymer-peptide conjugates. *J. Nucl. Med. 46*, 1552−1560.
(39) Scott, J. K., and Smith, G. P. (1990) Searching for peptide ligands with an epitope library. *Science 249*, 386−390.
(40) Lin, M., and Nielsen, K. (1997) Binding of the Brucella abortus lipopolysaccharide O-chain fragment to a monoclonal antibody. Quantitative analysis by fluorescence quenching and polarization. *J. Biol. Chem. 272*, 2821−2827.
(41) Tur, M. K., Huhn, M., Sasse, S., Engert, A., and Barth, S. (2001) Selection of scFv phages on intact cells under low pH conditions leads to a significant loss of insert-free phages. *Biotechniques 30*, 404−8, 410, 412−3.
(42) Mourez, M., Kane, R. S., Mogridge, J., Metallo, S., Deschatelets, P., Sellman, B. R., Whitesides, G. M., and Collier, R. J. (2001) Designing a polyvalent inhibitor of anthrax toxin. *Nat Biotechnol 19*, 958−961.
(43) Miller, R. T., and Kubier, P. (1997) Blocking of endogenous avidin-binding activity in immunohistochemistry: The use of egg whites. *Appl. Immunohistochem. 5*, 63−66.
(44) Bohdanecký, M., Bažilová, H., and Kopeček, J. (1974) Poly[N-(2-hydroxypropyl)methacrylamide]. II. Hydrodynamic properties of dilute solutions. *Eur. Polym. J. 10*, 405−10.
(45) Kopeček, J., Kopečková, P., and Koňák, C. (1997) Biorecognizable polymers: design, structure, and bioactivity. *J. Macromol. Sci. − Pure Appl. Chem. A34*, 2103−2117.
(46) Prodinger, W. M., Schwendinger, M. G., Schoch, J., Kochle, M., Larcher, C., and Dierich, M. P. (1998) Characterization of C3dg binding to a recess formed between short consensus repeats 1 and 2 of complement receptor type 2 (CR2; CD21). *J. Immunol. 161*, 4604−4610.

(47) Martin, D. R., Marlowe, R. L., and Ahearn, J. M. (1994) Determination of the role for CD21 during Epstein−Barr virus infection of B-lymphoblastoid cells. *J. Virol. 68*, 4716−4726.
(48) Guthridge, J. M., Young, K., Gipson, M. G., Sarrias, M. R., Szakonyi, G., Chen, X. S., Malaspina, A., Donoghue, E., James, J. A., Lambris, J. D., Moir, S. A., Perkins, S. J., and Holers, V. M. (2001) Epitope mapping using the X-ray crystallographic structure of complement receptor type 2 (CR2)/CD21: identification of a highly inhibitory monoclonal antibody that directly recognizes the CR2−C3d interface. *J. Immunol. 167*, 5758−5766.
(49) Szakonyi, G., Guthridge, J. M., Li, D., Young, K., Holers, V. M., and Chen, X. S. (2001) Structure of complement receptor 2 in complex with its C3d ligand. *Science 292*, 1725−1728.
(50) Prota, A. E., Sage, D. R., Stehle, T., and Fingeroth, J. D. (2002) The crystal structure of human CD21: Implications for Epstein−Barr virus and C3d binding. *Proc. Natl. Acad. Sci. U.S.A. 99*, 10641−10646.
(51) Roy, S. (2004) Fluorescence quenching methods to study protein-nucleic acid interactions. *Methods Enzymol. 379*, 175−187.
(52) Wróblewski, S., Berenson, M., Kopečková, P., and Kopeček, J. (2001) Potential of lectin-N−(2-hydroxypropyl)methacrylamide copolymer-drug conjugates for the treatment of pre-cancerous conditions. *J. Control. Release 74*, 283−293.
(53) Omelyanenko, V., Kopečková, P., Gentry, C., Shiah, J. G., and Kopeček, J. (1996) HPMA copolymer-anticancer drug-OV-TL16 antibody conjugates. 1. influence of the method of synthesis on the binding affinity to OVCAR-3 ovarian carcinoma cells in vitro. *J. Drug Target. 3*, 357−373.
(54) Lu, Z. R., Kopečková, P., and Kopeček, J. (1999) Polymerizable Fab′ antibody fragments for targeting of anticancer drugs. *Nat. Biotechnol. 17*, 1101−1104.

BC0503162

Study of the Interaction between Actin and Antitumor Substance Aplyronine A with a Novel Fluorescent Photoaffinity Probe

Takeshi Kuroda, Kiyotake Suenaga, Akira Sakakura, Tomohisa Handa, Kazuhito Okamoto, and Hideo Kigoshi*

Department of Chemistry, University of Tsukuba, 1-1-1 Tennoudai, Tsukuba, Ibaraki 305-8571, Japan. Received November 11, 2005; Revised Manuscript Received February 9, 2006

The interaction between actin and aplyronine A, a potent antitumor and actin-depolymerizing substance of marine origin, was investigated by photoaffinity labeling experiments. Photoaffinity probes consisting of a side-chain portion of aplyronine A as a ligand, a diazirine moiety as a photoaffinity group, and a fluorophore as a detecting group were synthesized. Photolabeling experiments between actin and the probe were carried out. Actin was successfully photolabeled by the fluorescent probe and visualized clearly. The present results provide the first chemical evidence for the direct interaction between actin and the side-chain portion of aplyronine A.

INTRODUCTION

Aplyronine A (**1**) (Figure 1) is a 24-membered macrolide isolated from the sea hare *Aplysia kurodai*. Aplyronine A (**1**) exhibits strong cytotoxicity and exceedingly potent antitumor activities in vivo against P388 murine leukemia (T/C = 545%, 0.08 mg/kg), Lewis lung carcinoma (T/C = 556%, 0.04 mg/kg), Ehrlich carcinoma (T/C = 398%, 0.04 mg/kg), colon 26 carcinoma (T/C = 255%, 0.08 mg/kg), and B16 melanoma (T/C = 201%, 0.04 mg/kg) (*1*−*5*). Aplyronine A (**1**) has been found to inhibit the polymerization of globular actin (G-actin) to fibrous actin (F-actin) and to depolymerize F-actin to G-actin by severing (*6*). Actin is one of the most abundant and common proteins in the cytoskeleton and regulates various cell functions. It is worth noting that actin is related to tumor metastasis and invasion into the basement membrane (*7*). Although several actin-depolymerizing compounds, such as mycalolide B and cytochalasin D (Figure 2), have been found to be cytotoxic in vitro (*8*), the antitumor activities in vivo of these compounds have not been reported. Thus, aplyronine A (**1**) is interesting from the viewpoint of the mode of antitumor activity.

Details of the structure−actin-depolymerizing activity relationships of aplyronine A (**1**) were investigated using natural and synthetic analogues (*9*, *10*): the side chain portion of aplyronine A (**1**) is essential for actin-depolymerizing activity, and compound **2**, which consists only of the side-chain portion of aplyronine A (**1**), exhibits strong activity, considering the size of the molecule. Therefore, compound **2** is suitable for analysis of the interaction between aplyronine A (**1**) and actin. Even though aplyronine A (**1**) has been found to exhibit actin-depolymerizing activity, little is known of its interactions with actin at the molecular level. Recently, X-ray structure analyses of complexes of actin and several actin-depolymerizing macrolides possessing side chain portions similar to that of aplyronine A (**1**) were reported (*11*). We are now interested in the binding manner between aplyronine A (**1**) and actin and its relationships to biological activities. Insight into specific residue interactions has been gained through the use of photoaffinity probes.

The photoaffinity labeling experiment has become a powerful method in postgenomic science, as confirmed by the identification of target proteins of biologically active compounds and elucidation of their binding sites (*12*). The design of a photoaffinity probe requires the following three components: (i) a ligand that binds strongly and specifically with a target protein; (ii) a photoaffinity group that forms a stable covalent bond between the ligand and its target protein (*13*); (iii) a detective group to make the labeled products easy to be detected. Radioisotopes or biotin are frequently used for the third demand (*14*, *15*). However, radioisotopes are environmentally problematic, and biotin requires highly expensive reagents for detection. Recently, non-RI and nonbiotin photoaffinity labeling methods have been developed (*16*). In this report, we describe the design of a fluorescent probe and an analysis of the interaction between aplyronine A (**1**), an antitumor substance, and actin.

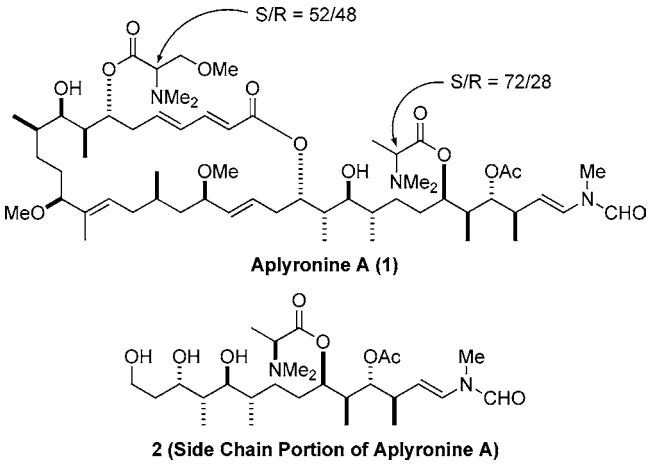

Figure 1. Structure of aplyronine A (**1**) and compound **2**, the side-chain portion of aplyronine A (**1**).

EXPERIMENTAL SECTION

General. Compound **2**, a side-chain portion of aplyronine A (**1**), and activated ester **5** were prepared as previously described (*10*, *13*). Aplyronine A (**1**) was isolated from the sea hare *Aplysia kurodai* by the method described previously (*1*). Actin for photoaffinity labeling experiments was obtained from Cytoskeleton Inc. Pyrenyl actin for measurement of actin-depolymerizing activity was prepared by the method described previously (*6*). Other chemicals and solvents were the best grade available and were used as received from commercial sources. ^{1}H NMR spectra were recorded on a JEOL JNM-EX-270 (270

* To whom correspondence should be addressed. Telephone and Fax: +81-29-853-4313. E-mail: kigoshi@chem.tsukuba.ac.jp.

10.1021/bc050324i CCC: $33.50 © 2006 American Chemical Society
Published on Web 02/25/2006

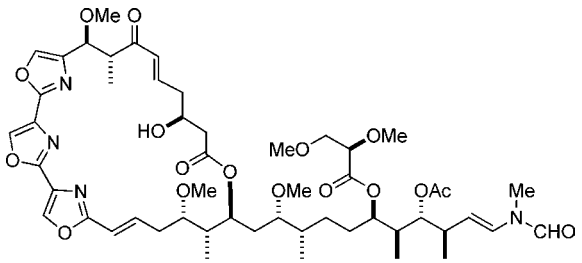

Mycalolide B (myB)

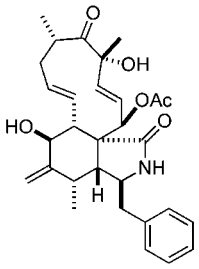

Cytochalasin D (CD)

Figure 2. Structure of mycalolide B (myB) and cytochalasin D (CD).

MHz) instrument. Proton chemical shifts are reported as parts per million (δ) relative to internal tetramethylsilane ($\delta = 0.00$ ppm) or solvent signals ($\delta = 3.31$ ppm for CHD_2OD, 7.26 ppm for $CHCl_3$). Mass spectra were measured with Applied Biosystems QStar pulser i instrument.

6-*tert*-Butoxycarbonylamino-2-[4-(3-trifluoromethyl-3*H*-diazirin-3-yl)benzoylamino]hexanoic Acid Methyl Ester. To a solution of activated ester **5** (42.7 mg, 137 μmol) and H-Lys(Boc)-OMe·HCl (77.8 mg, 262 μmol) in dichloromethane (0.5 mL) was added triethylamine (55 μL) at room temperature. After being stirred at room temperature for 2 h, the reaction mixture was concentrated. The residual oil was chromatographed on aluminum oxide (1 g, dichloromethane) to give the desired product (59.7 mg, 92%) as a colorless oil. ^{1}H NMR (270 MHz, $CDCl_3$) δ 7.73 (d, $J = 8.4$ Hz, 2 H), 7.11 (d, $J = 8.4$ Hz, 2 H), 6.93 (br d, $J = 6.8$ Hz, 1 H), 4.59−4.12 (m, 2 H), 3.64 (s, 3 H), 2.98 (m, 2 H), 1.90−1.15 (m, 6 H), 1.25 (s, 9 H); MS (ESI) *m*/*z* 495.2 $(M + Na)^+$; HRMS calcd for $C_{21}H_{27}F_3N_4NaO_5$ $(M + Na)^+$: 495.1831 Found 495.1858.

Carboxylic Acid 6. To a solution of 6-*tert*-butoxycarbonylamino-2-[4-(3-trifluoromethyl-3*H*-diazirin-3-yl)benzoylamino]hexanoic acid methyl ester (8.2 mg, 17 μmol) in dioxane (0.17 mL) was added a 0.50 M solution of lithium hydroxide in water (0.17 mL, 85 μmol) at room temperature. After being stirred at room temperature for 2 h, the mixture was diluted with brine (1 mL), acidified with 1 M aqueous sulfuric acid to pH 1, and extracted with ether (5 × 1 mL). The combined extracts were dried (sodium sulfate) and concentrated to give carboxylic acid **6** (7.9 mg, 100%). ^{1}H NMR (270 MHz, CD_3OD) δ 7.94 (d, $J = 8.4$ Hz, 2 H), 7.35 (d, $J = 8.4$ Hz, 2 H), 4.57 (dd, $J = 4.6$, 8.9 Hz, 1 H), 2.94 (t, $J = 5.9$ Hz, 2 H), 1.95−1.06 (m, 6 H), 1.39 (s, 9 H); MS (ESI) *m*/*z* 503.1 $(M-H + 2Na)^+$; HRMS calcd for $C_{20}H_{24}F_3N_4Na_2O_5$ $(M - H + 2Na)^+$: 503.1494, Found 503.1497.

Probe 3. To a mixture of compound **2** (5.1 mg, 9.6 μmol), carboxylic acid **6** (16.0 mg, 35.0 μmol), 4-(dimethylamino)-pyridine (8.5 mg, 70 μmol), and (±)-camphorsulfonic acid (8.1 mg, 35 μmol) was added a 0.35 M solution of dicyclohexylcarbodiimide in dichloromethane (0.10 mL, 35 μmol) at room temperature. The mixture was stirred at room temperature for 1 day and diluted with dichloromethane (0.5 mL) and trifluoroacetic acid (0.5 mL) at 0 °C. The mixture was stirred at 0 °C for 30 min and filtered. The filtrate was concentrated and purified by column chromatography on ODS (1 g, 60% MeOH) to give a crude amine. To a solution of the amine in *N*,*N*-dimethylformamide (0.1 mL) were added triethylamine (0.1 mL) and fluorescein-4-isothiocyanate (7.8 mg, 10 μmol) at room temperature. The mixture was stirred at room temperature for 4 h and concentrated. The residue was purified by preparative HPLC (Develosil ODS-HG-5 20 × 250 mm, 70% MeOH-0.1% TFA, 5 mL/min, detection at UV 470 nm, t_R 32.3−36.7 min) to give probe **3** (2.8 mg, 23% from ester **6**) as a yellow oil. ^{1}H NMR (270 MHz, $CDCl_3$−CD_3OD = 3:1) δ 8.20 (s, 0.7 H, CHO), 8.05−7.95 (m, 1.3 H, CHO, fluorescein), 7.83 (d, $J =$ 8.3 Hz, 2 H, aryldiazirine), 7.78 (m, 1 H, fluorescein), 7.19 (d, $J = 8.3$ Hz, 2 H, aryldiazirine), 7.04 (d, $J = 8.4$ Hz, 1 H, fluorescein), 6.63 (d, $J = 2.4$ Hz, 2 H, fluorescein), 6.59 (d, J = 8.6 Hz, 2 H, fluorescein), 6.46 (dd, $J = 2.4$, 8.6 Hz, 2 H, fluorescein), 6.50 [7.07] (m, 1 H, C34), 5.05−4.88 (m, 2 H), 4.70−4.53 (m, 2 H), 3.57 (m, 2 H), 2.96 [3.02] (s, 3 H, enamide NMe), 2.85 [2.80] (br s, 6 H, NMe_2), 2.50 (m, 1 H), 1.95 [2.02] (s, 3 H, CH_3COO), 2.00−1.70 (m, 3 H), 1.70−1.40 (m, 15 H), 1.00−0.70 (m, 12 H). Signals of five protons (dimethylalanine-α, C21, C23, and C25) were overlapped with the solvent signals. The minor counterparts of doubled signals in the ratios of 2:1 are in brackets; MS (ESI) *m*/*z* 630.7 $(M + 2H)^{2+}$; HRMS calcd for $C_{63}H_{77}F_3N_7O_{15}S$ $(M + H)^+$: 1260.5151, Found 1260.5165.

2-Benzoylamino-6-*tert*-butoxycarbonylaminohexanoic Acid Methyl Ester. To a solution of H-Lys(Boc)-OMe·HCl (0.10 g, 0.35 mmol) in dichloromethane (1.0 mL) were added a triethylamine (0.40 mL) and benzoyl chloride (0.17 mL, 1.5 mmol) at room temperature. After being stirred at room temperature for 5 h, the mixture was concentrated. The residual oil was chromatographed on silica gel (5 g, hexanes−ethyl acetate−methanol = 30:1:1→15:1:1→14:1:1→12:1:1→10:1:1) to give the desired product (85 mg, 67%) as a colorless oil. ^{1}H NMR (270 MHz, $CDCl_3$) δ 7.82 (d, $J = 7.0$ Hz, 2 H), 7.57−7.39 (m, 3 H), 6.96 (br d, $J = 7.6$ Hz, 1 H), 4.84−4.76 (m, 2 H), 3.76 (s, 3 H), 3.15−3.05 (m, 2 H), 2.00−1.70 (m, 2 H), 1.60−1.25 (m, 4 H), 1.40 (s, 9 H); MS (ESI) *m*/*z* 387.2 $(M + Na)^+$; HRMS calcd for $C_{19}H_{29}N_2NaO_5$ $(M + Na)^+$: 387.1896, Found 387.1877.

2-Benzoylamino-6-*tert*-butoxycarbonylaminohexanoic Acid. To a solution of 2-benzoylamino-6-*tert*-butoxycarbonylaminohexanoic acid methyl ester (85 mg, 0.24 mmol) in dioxane (4.8 mL) was added a 0.50 M solution of lithium hydroxide in water (2.2 mL, 1.1 mmol) at room temperature. After being stirred at room temperature for 1 h, the mixture was diluted with brine (10 mL), acidified with 1 M hydrochloric acid to pH 1, and extracted with ethyl acetate (6 × 20 mL). The combined extracts were washed with brine (20 mL) and concentrated to give the desired product (79 mg, 96%). ^{1}H NMR (270 MHz, CD_3Cl) δ 10.3 (br s, 1 H), 7.71 (m, 2 H), 7.40−7.15 (m, 4 H), 4.85−4.65 (m, 2 H), 3.02 (m, 2 H), 2.05−1.65 (m, 2 H), 1.55−1.25(m, 4 H), 1.31 (s, 9 H); MS (ESI) *m*/*z* 351.2 $(M + H)^+$; HRMS calcd for $C_{18}H_{27}N_2O_5$ $(M + H)^+$: 351.1920, Found 351.1954.

Compound 4. To a mixture of compound **2** (1.8 mg, 3.4 μmol), 2-benzoylamino-6-*tert*-butoxycarbonylaminohexanoic acid (2.4 mg, 6.8 μmol), 4-(dimethylamino)pyridine (3.4 mg, 27 μmol), and (±)-camphorsulfonic acid (3.0 mg, 14 μmol) was added a 0.2 M solution of dicyclohexylcarbodiimide in dichloromethane (70 μL, 14 μmol) at room temperature. The mixture was stirred at room temperature for 40 h, washed with aqueous sodium bicarbonate (3 mL), and concentrated. The residual oil was purified by column chromatography on silica gel (500 mg, dichloromethane-acetone-methanol = 2:1:0→1:1:0→10:10:1→5:5:1→1:1:1) to give compound **4** (1.6 mg, 55% from compound **2**) as a colorless oil. ^{1}H NMR (270 MHz, $CDCl_3$) δ 8.29 [8.08] (s, 1 H, CHO), 7.82 (d, $J = 6.8$ Hz, 2 H), 7.55−7.40 (m, 3 H), 6.87 (br s, 1 H), 6.51 [7.16] (d, $J = 14.3$ [15.3] Hz, 1 H, C34), 5.05−4.90 (m, 2 H), 4.80−4.50 (m, 3 H), 4.44 (m, 1 H), 4.29

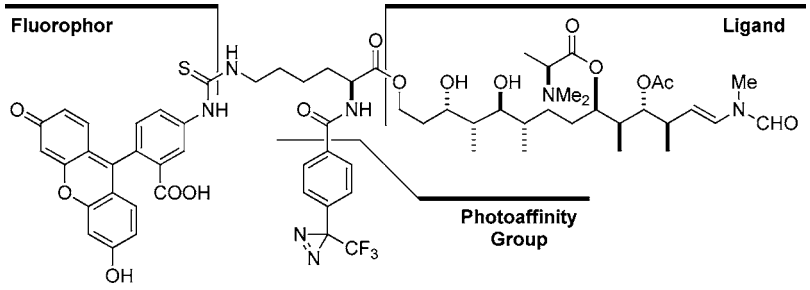

Figure 3. Designing of the fluorescent photoaffinity probe **3**.

(m, 1 H), 4.08 (m, 1 H), 3.34 (m, 2 H), 3.10 (m, 2 H), 3.04 [3.08] (s, 3 H, enamide NMe), 2.70 (m, 1 H), 2.18 [2.13] (s, 6 H, NMe_2), 1.95 [2.02] (s, 3 H, CH_3COO), 2.00−1.40 (m, 18 H), 1.40 (s, 9 H), 1.00−0.70 (m, 12 H). The minor counterparts of doubled signals in the ratios of 2:1 are in brackets; MS (ESI)-*m/z* 863.5 $(M + H)^+$; HRMS calcd for $C_{45}H_{75}N_4O_{12}$ $(M + H)^+$: 863.5382, Found 863.5373.

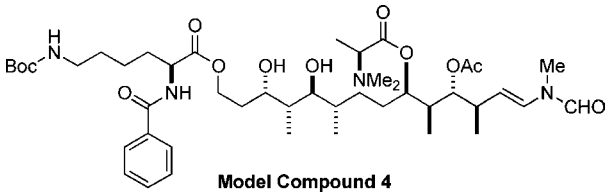

The Actin-Depolymerizing Activity. The actin-depolymerizing activity of compounds was measured as previously described (*6*) with minor modifications. To the 3.7 μM solution of actin (0.30 mL, containing 10% pyrenyl actin) in G-buffer was added a 0.15 M solution of $MgCl_2$ (2.0 μL), and the mixture was stirred at room temperature for 1 h to polymerize G-actin to F-actin. To the solution of F-actin were added various concentrations of compounds in dimethyl sulfoxide (2.0 μL) with stirring, and the time course of depolymerization was continuously monitored by measuring fluorescence of pyrenyl actin (10% of total actin) with a fluorometer (HITACHI, F-4000, equipped with a magnetic stirrer) at 25 °C at 365 nm excitation and 407 nm emission wavelengths. The IC_{50} values were concentration required to depolymerize F-actin to 50% of its control amplitude. The values were the average of three assays, and the errors were calculated in SD values.

Photoaffinity Labeling Experiments. Photoaffinity labeling of actin with probe **3** was performed as previously reported for similar photoaffinity labeling experiments (*16*) with minor modifications. An 11 μM solution of actin (44 μL, 0.48 nmol, Cytoskeleton Inc., final concentration was 10 μM) in G-buffer (2.0 mM Tris-HCl, 0.20 mM $CaCl_2$, 0.50 mM β-mercaptoethanol, 0.20 mM ATP, pH 8.0) was incubated with various concentrations of solutions of probe **3** in dimethyl sulfoxide (4.0 μL; 120, 240, 480, 960 μM; final concentration, 10, 20, 40, 80 μM, respectively) in Eppendorf tubes at 0 °C for 1 h. For competition studies, an 11 μM solution of actin (44 μL, 0.48 nmol) in G-buffer was incubated with various concentrations of solutions of probe **3** in dimethyl sulfoxide (2.0 μL; 240, 480, 960, 1900 μM; final concentration, 10, 20, 40, 80 μM, respectively) and 2.4 mM solution of aplyronine A in dimethyl sulfoxide (2.0 μL, final concentration 100 μM) in Eppendorf tubes at 0 °C for 1 h. The samples were irradiated with a handhold 365 nm UV lamp at 0 °C for 15 min, and SDS−PAGE sample buffer was added. After SDS−PAGE, the gels were subjected to laser-scanning with a fluorescent imaging analyzer (BIO-RAD, molecular imager FX, excitation and detection filter for FITC) followed by CBB-stained.

SEC−HPLC Analysis. A 100 μM solution of actin (48 μL, 4.8 nmol, Cytoskeleton Inc.) in G-buffer (2.0 mM Tris-HCl, 0.20 mM $CaCl_2$, 0.50 mM β-mercaptoethanol, 0.20 mM ATP, pH 8.0) was incubated with 1.3 mM solution of probe **3** in dimethyl sulfoxide (2.0 μL; final concentration, 100 μM) in an Eppendorf tube at 0 °C for 1 h. The sample was irradiated with a handhold 365 nm UV lamp at 0 °C for 15 min. To the mixture was added 10 mM solution of aplyronine A in dimethyl sulfoxide (2.0 μL, final concentration, 400 μM), and the mixture was incubated at 0 °C for 1 h. The resulting mixture was analyzed by HPLC (TOSOH TSK-GEL $G2000SW_{XL}$ 7.8 × 300 mm, 0.1 M phosphate buffer−10% dimethyl sulfoxide, 1.0 mL/min, detection at UV 254 nm, fluorescence at 480 nm excitation, 540 nm emission).

RESULTS

The designed probe **3** is shown in Figure 3. Probe **3** includes the side-chain portion of aplyronine A (**1**) as a ligand, an aryldiazirine group as a photoaffinity group, and a fluorescein group as a fluorescent detective group (*17*). Although a few photoaffinity probes that possess a fluorophore have been reported (*18*), fluorescence quenching often occurs. To avoid loss of the photoadducts due to weakened fluorescence, the fluorescein group, which has a high quantum yield and strong fluorescent intensity, was selected for the detective group.

Probe **3** was readily synthesized from compound **2** in three steps (Scheme 1). Because the fluorophore was introduced to the probe molecule in the very last step of the synthetic route, the fluorescent probe could be easily customized by optimizing the fluorophors (solubility, exiting or emission wavelength, molecular size, etc.). Acylation of H-Lys(Boc)-OMe·HCl with activated ester **5** (*19*) followed by hydrolysis afforded carboxylic acid **6** (95% in two steps). Condensation between compound **2** (*10*) and **6** followed by removal of the *t*-butoxycarbonyl (Boc) group and thioamidation with fluorescein-4-isocyanate (FITC) provided probe **3** (23% from **6**). The fluorescence quenching of the fluorescein likely occurred by the photoaffinity group, but the fluorescence was strong enough to be detected with a fluorophotometer or fluorescent imaging analyzer. Probes that have the other fluorophore such as pyrene or NBD (*20*, *21*) were also synthesized, but their solubility in water was low and their fluorescence intensities were very weak. Therefore, the fluorescein probe **3** was chosen for the photolabeling experiment.

Prior to a photoaffinity labeling study, the ability of the probe to interact with actin should be evaluated. However, the activity of the probe **3** could not be determined in a pyrenyl-actin assembly assay (*6*) due to the fluorescence of **3** itself. Therefore, model compound **4**, which lacks a fluorophore, was synthesized, and its activity was evaluated. Synthesis of the model compound **4** was accomplished by the following procedure. Acylation of H-Lys(Boc)-OMe·HCl with benzoyl chloride, hydrolysis of methyl ester, and esterification with compound **2** afforded the model compound **4** (35% in three steps).

Scheme 1[a]

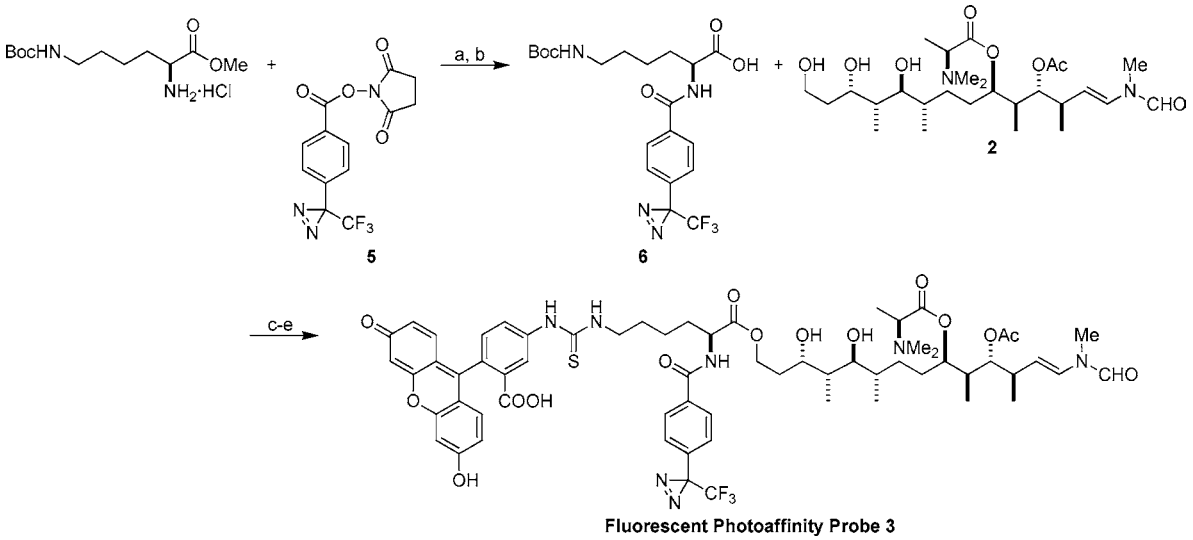

[a] (a) Et_3N, CH_2Cl_2, rt, 96%, (b) LiOH, dioxane, H_2O, rt, 99%, (c) DCC, DMAP, CSA, CH_2Cl_2, rt, (d) TFA, CH_2Cl_2, 0 °C, (e) FITC, Et_3N, DMF, rt, 23% (three steps).

Table 1. Actin-Depolymerizing Activity of Aplyronine A (1), 2, and 4

compounds	actin-depolymerizing activity[a]	
	IC_{50} (μM)[b]	relative potency[c]
aplyronine A (**1**)	1.6 ± 0.1	100
2	7.9 ± 1.5	20
4	9.7 ± 1.7	16

[a] Activity was monitored by measuring the fluorescence intensity of pyrenyl actin (*6*). [b] IC_{50} indicates the concentration required to depolymerize F-actin (3.7 μM) to 50% of its control amplitude, the value is the average of three assays, and the errors are given in SD values. [c] The relative potencies were calculated from the IC_{50} values of the compound (aplyronine A = 100).

The actin-depolymerizing activities of model compound **4**, aplyronine A (**1**), and its analogue **2** are shown in Table 1. Model compound **4** retained the activity comparable to that of analogue **2**. This result indicates that the potent activity of analogue **2** was not influenced by the functionalization of its primary hydroxyl group. These findings suggest that probe **3** holds promise for use in photolabeling studies.

Using the fluorescent photoaffinity probe **3**, we carried out the photoaffinity labeling experiment (*12*). Probe **3** was incubated in various concentrations with actin for 1 h at 0 °C in the absence or presence of aplyronine A (**1**). The mixtures were photoirradiated using a portable UV-lamp, denatured, and then subjected to SDS-polyacrylamide gel electrophoresis (SDS−PAGE) using 12.5% polyacrylamide gels in the Laemmli buffer system (*22*). The gels were directly visualized by laser scanning in a fluorescent imaging analyzer (Figure 4). Actin was successfully photolabeled, and labeled-actin was clearly visualized. The intensity of fluorescent bands of the labeled-actin increased with an increase in the dose of **3** (lane 1, 3, 5, 7). All of the fluorescent signals were decreased by coincubation with excess amounts of aplyronine A (**1**, lane 2, 4, 6, 8), indicating that the photolabeling proceeded specifically at the aplyronine A (**1**) binding site.

Inhibition study with other actin depolymerizing reagents, mycalolide B and cytochalasin D, was preformed. Although mycalolide B possesses a side-chain portion, which is very similar to that of aplyronine A (**1**), it exhibits only cytotoxicity in vitro, and no antitumor activity in vivo was reported. Cytochalasin D depolymerizes actin by a capping mechanism different from that of aplyronine A (**1**) (*8*). Probe **3** (20 μM) was incubated with actin (10 μM) for 1 h at 0 °C in the absence

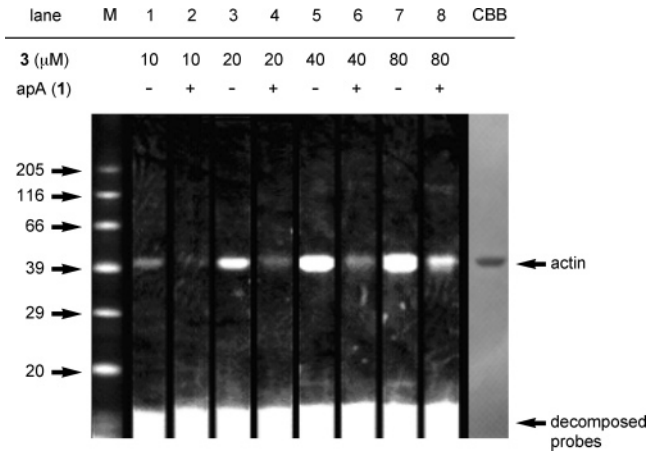

Figure 4. SDS−PAGE analysis of actin (10 μM) photolabeled in various concentrations of probe **3** in the absence (−) or presence (+) of aplyronine A (100 μM). For comparison, Coomassie brilliant blue (CBB)-stained actin is shown in the rightmost lane. The fluorescent signal was visualized by laser-scanning of the electrophoresed gel with a fluorescent imaging analyzer (BIO-RAD, molecular imager FX, and an excitation and detection filter for FITC). Lane M shows the fluorescent high molecular weight marker (Sigma).

or presence of additives (aplyronine A, mycalolide B, or cytochalasin D, 100 μM). The mixtures were photoirradiated and subjected SDS−PAGE analysis as stated above (Figure 5). Mycalolide B inhibited the photolabeling as well as aplyronine A (**1**, lane 2, 3); however, cytochalasin D did not inhibit it (lane 4).

The photoirradiated mixtures were also analyzed using size-exclusion chromatography (SEC) (Figure 6). Generally, the peak of actin was broadened due to the equilibrium between F-actin and G-actin in the column. To obtain a sharp peak for G-actin, the mixtures were coincubated with 100 μM aplyronine A (**1**), a potent actin-depolymerizing reagent, for 20 min at room temperature, before SEC analysis. Analytical conditions were chosen so that the probe was dissolved in the moving phase and a peak of G-actin, the molecular weight of which is 42 kDa, was completely separated from the other side products. The photolabeled actin exhibited fluorescence, as shown in the chromatographic profile. The photolabeled actin (retention time = 7.0−8.0 min) was unseparable from the intact actin (retention time = 7.0−8.0 min) in this condition but fully

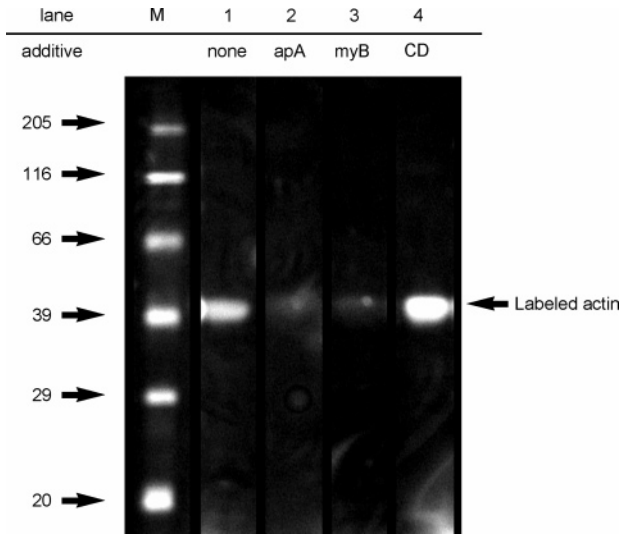

Figure 5. SDS−PAGE analysis of actin (10 μM) photolabeled with probe **3** (20 μM) in the absence or presence of well-known actin depolymerizing reagents: aplyronine A (apA, 100 μM), mycalolide B (myB, 100 μM, wako), and cytochalasin D (CD, 100 μM, wako). Visualization was performed in the same way as described above in the Figure 4. Lane M shows the fluorescent high molecular weight marker (Sigma).

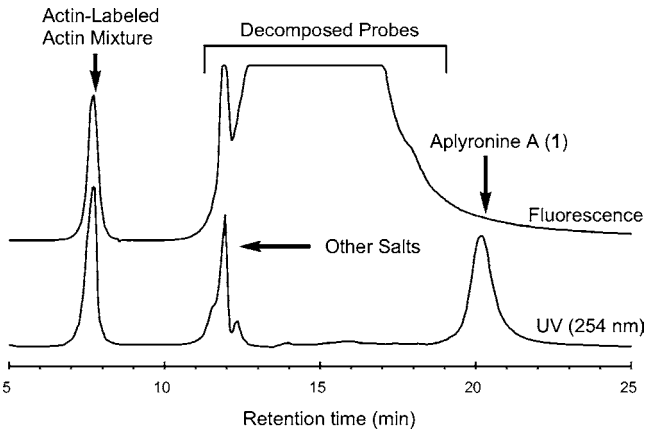

Figure 6. Size-exclusion chromatogram of the photoirradiated mixture with actin (100 μM) and probe **3** (100 μM), in 0.1 M phosphate buffer−10% DMSO (detect with UV 254 nm absorption, fluorescence at 480 nm excitation, 540 nm emission). TOSOH TSK-GEL G2000SW$_{XL}$ 7.8 × 300 mm was used. Aplyronine A (**1**) (400 μM) was added to the mixture prior to injection to depolymerize actin to obtain a sharp peak of monomer actin on a chromatographic profile. The retention times of 7.0 min to 8.0 min and beyond 11.0 min correspond to molecular weights of 40 kDa and below 1 kDa, respectively.

resolved from the decomposed probe and other salts (retention time = 11.0−20.0 and 11.0−13.0 min, respectively).

DISCCUSION

Actin was successfully photolabeled with probe **3**. The coincubated study showed that aplyronine A (**1**) competitively inhibits the binding of the probe **3** to actin. Therefore, probe **3**, which possesses the side-chain portion of aplyronine A (**1**), bound to actin specifically at the aplyronine A (**1**) binding site. These results indicate that the side-chain portion of aplyronine A (**1**) has actin-binding ability, which is consistent with the fact that the side-chain portion of aplyronine A (**1**) plays a key role in the actin-depolymerizing activity (*10*). The present results provide the first chemical evidence for a direct interaction between actin and the side-chain portion of aplyronine A (**1**). Furthermore, mycalolide B inhibited the binding of **3** to actin, whereas cytochalasin D did not. This result indicated that mycalolide B binds to actin at the same site as the probe **3**, and cytochalasin D is irrelevant to binding between the probe **3** and actin. Therefore, it is reasonable to suppose that aplyronine A (**1**) and mycalolide B bind to actin at the same site by using the similar side-chain portion.

Thus, we developed a fluorescent photoaffinity probe. Although a few instances have been reported for the successful visualization of photolabeled proteins with fluorescence, some posttreatments have been often required to visualize the adducts. Because probe **3** possesses a fluorescent group ab initio, labeled actin was visualized directly on polyacrylamide gels or HPLC without any posttreatments. Combination of a fluorescent group and a photoaffinity group was essential to gaining a high fluorescent intensity. The fluorescein group gave the best result due to its high quantum yield, fluorescent intensity, and solubility in water.

Although removal of a decomposed probe from a labeled protein mixture was often problematic, separation of the actin and labeled-actin mixture from the decomposed probe was completely achieved by SEC−HPLC. Exploring the HPLC condition revealed that a broad actin peak can be shifted to a sharp G-actin peak by the addition of aplyronine A as an actin-depolymerizing agent. The separated mixture can be subjected to enzymatic digestion, HPLC, and mass spectroscopic analysis to identify the binding site of the aplyronine A (**1**) against actin.

In conclusion, we have obtained chemical evidence that actin directly interacts with the side-chain portion of aplyronine A (**1**) based on a photolabeling experiments with fluorescent probe **3**. The photolabeled actin was visualized by electrophoresis and analytical SEC with satisfactory sensitivity. This fluorescent probe system can be successfully employed in photoaffinity labeling studies from both an economical and environmental perspective. Aplyronine A (**1**) was found to bind to actin not at the cytochalasin D binding site but at the mycalolide B binding site. It is interesting that aplyronine A (**1**) exhibits antitumor activity in vivo, in spite that aplyronine A (**1**) binding site is same as that of mycalolide B, whose in vivo antitumor effect has not been reported. Further analyses of the labeled actin are underway in an effort to identify the specific amino acid residues and to identify the aplyronine A (**1**) binding manner.

ACKNOWLEDGMENT

We would like to thank Emeritus Professor Kiyoyuki Yamada for his helpful discussions and comments. We are also grateful to Professors Hiroshi Ozaki and Masatoshi Hori for their donation of actin and their helpful advice and discussions. We would like to thank Professor Hideyuki Shigemori and Dr. Kosumi Yamada for their generous assistance with the electrophoretic analysis. This study was supported in part by the 21st Century COE program and Grants-in-Aid for Scientific Research from Ministry of Education, Culture, Sports, Science, and Technology, Shorai Foundation for Science and Technology, The Asahi Glass Foundation, Suntory Institute for Bioorganic Research, University of Tsukuba Research Projects, TARA project (University of Tsukuba), and Research Fellowships of the Japan Society for the Promotion of Science for Young Scientists (JSPS) to T.K.

LITERATURE CITED

(1) Yamada, K., Ojika, M., Ishigaki, T., Yoshida, Y. (1993) Aplyronine A, a potent antitumor substance, and the congeners aplyronines B and C isolated from the sea hare *Aplysia kurodai*. *J. Am. Chem. Soc. 115*, 11020−11021.

(2) Ojika, M., Kigoshi, H., Ishigaki, T., Yamada, K. (1993) Further studies on Aplyronine A, an antitumor substance isolated from the sea hare *Aplysia kurodai*. *Tetrahedron Lett. 34*, 8501−8504.

(3) Ojika, M., Kigoshi, H., Ishigaki, T., Nishiwaki, M., Tsukada, I., Mizuta, K., Yamada, K. (1993) Studies on the stereochemistry of aplyronine A − determination of the stereochemistry of the C21−C34 fragment. *Tetrahedron Lett. 34*, 8505−8508.

(4) Ojika, M., Kigoshi, H., Ishigaki, T., Tsukada, I., Tsuboi, T., Ogawa, T., Yamada, K. (1994) Absolute stereochemistry of aplyronine A, a potent antitumor substance of marine origin. *J. Am. Chem. Soc. 116*, 7441−7442.

(5) Kigoshi, H., Suenaga, K., Mutou, T., Ishigaki, T., Atsumi, T., Ishiwata, H., Sakakura, A., Ogawa, T., Ojika, M., Yamada, K. (1996) Aplyronine A, a potent antitumor substance of marine origin, aplyronines B and C, and artificial analogues: Total synthesis and structure−cytotoxicity relationships. *J. Org. Chem. 61*, 5326−5351.

(6) Saito, S., Watabe, S., Ozaki, H., Kigoshi, H., Yamada, K., Fusetani, N., Karaki, H. (1996) Novel actin depolymerizing macrolide aplyronine A. *J. Biochem. 120*, 552−555.

(7) Staff, C. A. (2001) An introduction to cell migration and invasion. *Scand. J. Clin. Lab. Invest. 61*, 257−268.

(8) Yeung, S. K., Paterson, I. (2002) Actin-binding marine macrolides: total synthesis and biological importance. *Angew. Chem., Int. Ed. 41*, 4632−4653.

(9) Suenaga, K., Kamei, N., Okugawa, Y., Takagi, M., Akao, A., Kigoshi, H., Yamada, K. (1997) Cytotoxicity and actin depolymerizing activity of aplyronine A, a potent antitumor macrolide of marine origin, and the natural and artificial analogs. *Bioorg., Med. Chem. Lett. 7*, 269−274.

(10) Kigoshi, H., Suenaga, K., Takagi, M., Akao, A., Kanematsu, K., Kamei, N., Okugawa, Y., Yamada, K. (2002) Cytotoxicity and actin-depolymerizing activity of aplyronine A, a potent antitumor macrolide of marine origin, and its analogs. *Tetrahedron 58*, 1075−1102.

(11) Klenchin, V. A., Allingham, J. S., King, R., Tanaka, J., Marriott, G., Rayment, I. (2003) Trisoxazole macrolides toxins mimic the bindng of actin-capping proteins to actin. *Nature Struct. Biol. 10*, 1058−1063.

(12) Kotzybal-Hibert, F., Kapfer, I., and Geoldner, M. (1995) Recent Trends in Photoaffinity Labeling. *Angew. Chem., Int. Ed. Engl. 34*, 1296−1312.

(13) Nassal, M. (1983) 4-(1-Azi-2,2,2-trifluoroethyl)benzoic acid, a highly photolabile carbine generating label readily fixable to biochemical agents. *Liebigs Ann. Chem.* 1510−1523.

(14) Yoshida, E., Nakayama, H., Hatanaka, Y., Kanaoka, Y. (1990) Photoaffinity labeling of the electroplax sodium channel with tetrodotoxin derivatives. II. Comparison of the photoreactivity of different photoactivable groups in the tetrodotoxin binding site. *Chem. Pharm. Bull. 38*, 982−987.

(15) Hatanaka, Y., Kanaoka, Y. (1998) Biotinyl diazirine photophore: an approach to highresolution photoaffinity labeling for probing receptor−ligand interface. *Heterocycles 47*, 625−632.

(16) Hosoya, T., Hiramatsu, T., Ikemoto, T., Nakanishi, M., Aoyama, H., Hosoya, A., Iwata, T., Maruyama, K., Endo, M., Suzuki, M. (2004) Novel bifunctional probe for radioisotope-free photoaffinity labeling: compact structure comprised of photospecific ligand ligation and detectable tag anchoring units. *Org. Biomol. Chem. 2*, 637−641.

(17) Maeda, H., Ishida, N., Kawaguchi, H., Tuzimura, K. (1967) Reaction of fluorescein-isothiocyanate with proteins and amino acids. *J. Biochem. 65*, 777−783.

(18) Kurono, M., Isobe, M. (2004) Synthesis and physical nature of fluorescent photoaffinity probe for the bioorganic studies on tautomycin, a protein phosphatase type 1 selective inhibitor. *Chemistry Lett. 33*, 452−453.

(19) Strømgaard, K., Saito, R. D., Shindou, H., Ishii, S., Shimizu, T., Nakanishi, K. (2002) Ginkgolide derivatives for photolabeling studies: preparation and pharmacological evaluation. *J. Med. Chem. 45*, 4038−4046.

(20) Ghosh, B. P., Whitehouse, W. M. (1968) 7-chloro-4-nitrobenzo-2-oxa-1,3-diazole: a new fluorigenic reagent for amino acids and other amines. *Biochem. J. 108*, 155−156.

(21) Fager, S. R., Kutina, B. C., Abrahamson, W. E. (1973) The use of chloride (7 chloro-4-nitrobenzo-2-oxa-1,3-diazole) in detecting amino acids and as an N-terminal reagent. *Anal. Biochem. 53*, 290−294.

(22) Laemmli, U. K. (1970) Cleavage of structural proteins during the assembly of the head of bacteriophage T4. *Nature 227*, 680−685.

BC050324I

Synthesis and Characterization of a Hemoglobin−Ribavirin Conjugate for Targeted Drug Delivery

Steve Brookes, Pieter Biessels, Nancy F. L. Ng, Caroline Woods, David N. Bell,* and Gord Adamson

Hemosol Corporation, 2585 Meadowpine Boulevard, Mississauga, Ontario, Canada L5N 8H9. Received November 17, 2005; Revised Manuscript Received January 26, 2006

A novel conjugate of human hemoglobin (Hb) and the nucleoside analogue ribavirin (RBV) was synthesized to demonstrate the utility of Hb as a biocompatible drug carrier for improved drug delivery in the treatment of liver disease. RBV is used in combination with interferon for the treatment of hepatitis C, but its side effects can result in dose limitation or discontinuation of treatment. Targeted delivery of RBV may help to prevent or minimize its toxicity. The hemoglobin−ribavirin conjugate (Hb−RBV) was designed to release bioactive drug upon endocytosis by cells and tissues involved in extracellular Hb catabolism and clearance. Ribavirin-5′-monophosphate (RBV-P) was prepared from RBV and activated as the 5′-monophosphorimidazolide (RBV-P-Im) for reaction with carbonmonoxyhemoglobin to yield Hb−RBV consisting of multiple RBV drugs covalently attached as physiologically labile phosphoramidates via their 5′-hydroxyl groups. A molar drug ratio of six to eight RBV molecules per Hb tetramer was obtained with near complete haptoglobin (Hp) binding of the drug modified Hb maintained. The conjugate complex (Hp−Hb−RBV) was selectively taken up *in vitro* by cells that express the hemoglobin−haptoglobin receptor, CD163. Recovered ribavirin enzymatically cleaved from Hb−RBV showed equipotent antiproliferative activity compared to control unconjugated RBV against human HepG2 and mouse AML12 liver cell lines. Based upon the reported high level of Hb uptake in the liver, Hb−RBV may be useful in the treatment of certain liver diseases, as well as inflammatory disorders associated with CD163-positive macrophages.

INTRODUCTION

Many therapeutic drugs do not achieve optimal efficacy due to systemic toxicity and side effects that require dose reduction, or due to inherent limitations in drug stability, half-life, and solubility (*1*). Targeted drug delivery to diseased tissues is one strategy for improving drug efficacy and reducing systemic side effects. One common targeting strategy employs chemical conjugation of drugs to a ligand capable of binding to specific cell surface receptors. The premise is that, following internalization and metabolism of the ligand−drug conjugate, the attached drug is released intracellularly to exert its therapeutic effect (*2*). Examples of ligands that have been used for targeted drug delivery include transferrin, hormones, growth factors, lectins, folic acid, carbohydrates, asialoglycoproteins, glycoproteins, and antibodies (*1*−*3*). In addition, natural and non-natural agents such as liposomes, polymers, and modified carbohydrates (*4*−*6*) have been used to target drugs through tissue-specific clearance pathways for the particular macromolecular carrier.

We have developed a novel drug targeting strategy using hemoglobin (Hb) as a natural carrier to target the delivery of drugs to the liver by taking advantage of the natural Hb clearance pathways. Hemoglobin is the most abundant blood protein and consists of two α and two β chains ($\alpha_2\beta_2$) which are noncovalently associated within erythrocytes (red blood cells) as a 64.5 kDa tetramer (*7*, *8*). The main function of Hb is to bind oxygen in the lungs for delivery to respiring tissues (*7*). Extracellular Hb released as a result of red blood cell deterioration and senescence dissociates into two 32 kDa $\alpha\beta$ dimers (*8*) which are rapidly and essentially irreversibly bound ($K_D < 10^{-15}$ M) by the plasma protein haptoglobin (Hp) (*9*−*12*). Three major organs are known to take up and degrade Hb−Hp complexes: liver, spleen, and bone marrow, with the liver being the principal (>70%) site of Hb catabolism (*9*, *13*, *14*). The liver was confirmed recently as the principal site of Hb uptake; radiolabeled Hb was found primarily in the liver following Hb dosing at near Hp-saturating levels in rats (*15*). Multiple mechanisms exist for liver uptake of Hb. Hepatocyte receptors for Hb−Hp complexes have been reported (*16*, *17*) to account for the majority of liver uptake. Liver macrophages (Kupffer cells) specifically recognize and internalize Hb−Hp complexes via Hb−Hp scavenger receptors such as CD163 (*18*, *19*). This receptor is expressed by cells of the monocyte/macrophage lineage, with Kupffer cells expressing the highest levels of CD163 mRNA (*20*). Cellular expression of CD163 is also elevated in association with certain liver diseases and inflammatory disorders (*19*, *21*). In addition to the specific receptor-mediated uptake by hepatocytes and Kupffer cells, Hb is taken up by the liver through Hp-independent mechanisms (*22*) and via uptake into transendothelially located hepatocytes through open fenestrations in the sinusoidal endothelial cells (*23*). By using Hb as a drug carrier, the natural mechanisms of Hb clearance can be utilized to selectively transport therapeutic drugs to the liver for the treatment of both liver and macrophage-associated diseases.

Ribavirin (RBV) is a nucleoside analogue currently approved for use in combination with interferon-α for the treatment of chronic hepatitis C virus (HCV) infection, and most recently in combination with PEGylated forms of interferon-α (*24*, *25*). The major toxic side effect of RBV therapy is a dose-dependent hemolytic anemia in approximately 10% of the treatment-eligible population which results from high drug accumulation in red blood cells (*26*). Accordingly, RBV is contraindicated for certain subpopulations of HCV patients with concurrent medical disease. We have selected RBV as a model drug for conjugation to Hb to demonstrate the feasibility of Hb-based drug delivery.

* Corresponding author. Telephone: (905) 286-6207. Fax: (905) 286-0603. E-mail address: dbell@hemosol.com.

10.1021/bc0503317 CCC: $33.50 © 2006 American Chemical Society
Published on Web 02/21/2006

RBV is both an antiviral agent and an immunomodulator (*27*), making it an ideal choice for targeted delivery to cells of the liver for the treatment of viral infections and inflammatory disorders. Increased drug potency may result from increased RBV bioavailability through targeted delivery. An additional benefit may be realized through a reduction in side effects such as hemolytic anemia in susceptible patients. Fiume and coworkers have demonstrated reduced toxicity of RBV through coupling of the drug to lactosaminated poly-L-lysine, a carrier polymer that is specific for asialoglycoprotein receptors on hepatocytes (*28*, *29*).

We describe the synthesis, characterization, and physical properties of a novel Hb−ribavirin conjugate designed for targeted delivery and release of bioactive drug within cells capable of taking up and internalizing the drug conjugate. We have chosen phosphoramidate conjugation chemistry (*30*, *31*) because of the labile nature of this linkage within the endosomal compartment, thereby allowing release of free drug following endocytosis.

EXPERIMENTAL PROCEDURES

Materials. All chemicals, proteins, and enzymes used were purchased from Sigma-Aldrich (Oakville, ON, Canada) unless otherwise indicated. Ribavirin (1-β-D-ribofuranosyl-1,2,4-triazole-3-carboxamide) was obtained from Inter-Chemical Ltd. (Shenzhen, China). Pure human Hb was derived from expired whole blood according to established procedures at Hemosol Corp. (*32*) and used in the carbonmonoxy form (COHb). Human Hp (mixed phenotype) was from Athens Research and Technology, Inc. (Athens, GA). Human plasma was obtained from informed donors, and mouse plasma was obtained from Balb/c mice (Charles River, St. Constant, QC, Canada). Alexa Fluor 488 was purchased from Molecular Probes (Cedarlane Laboratories, Ltd., Hornby, ON, Canada). Phosphate buffered saline (PBS), AIMV, fetal bovine serum (FBS), Dulbecco's modified eagle medium (DMEM), insulin transferrin selenium supplement (ITSS), and Ham's F12 culture media were all purchased from Invitrogen (Burlington, ON, Canada). Lactated Ringer's solution (Ringer's Lactate) was purchased from Abbott Laboratories (Montreal, QC, Canada). Chinese hamster ovary (CHO), human hepatoma HepG2, and mouse hepatocyte AML12 cells were from the American Type Culture Collection (ATCC, Manassas, VA). The bromodeoxyuridine (BrdU) cell proliferation enzyme-linked immunosorption assay (ELISA) kit was from Roche (Mississauga, ON, Canada). Electrospray ionization (EI) and matrix-assisted laser desorption ionization (MALDI) mass spectral analyses were performed at the Proteomic and Mass Spectrometry Centre, Faculty of Medicine, University of Toronto (Toronto, ON, Canada). ^{31}P NMR (121.5 Hz) analyses were performed at the Department of Chemistry, University of Toronto.

Cell Lines and Culture Conditions. HepG2 (ATCC HB-8065) human hepatoma and mouse AML12 (CRL-2254) hepatocyte cells were cultured in DMEM/Ham's F12 supplemented with 10% FBS, ITSS, and dexamethasone. Chinese hampster ovary (CHO) cells expressing human CD163 (variant 1, CHO/CD163) were cultured in Ham's F12 supplemented with 10% FBS.

HPLC Analyses. All high performance liquid chromatography (HPLC) analyses were performed using a Beckman HPLC Gold system. Anion exchange chromatography was performed on a Poros H/HQ (4.6 mm × 100 mm) column, using a pH gradient of 8.3−6.3 over 10 min (25 mM Tris pH 8.3 buffer, 25 mM bisTris pH 6.3 buffer) at a flow rate of 4 mL/min, with absorbance monitoring at 280 nm (to detect total protein) and 414 nm (to detect only heme protein). C_4 reverse-phase HPLC was performed on a Vydac C_4 column (4.6 mm × 250 mm) using a gradient of 20−60% acetonitrile in water containing 0.1% trifluoroacetic acid (TFA) over 90 min, at a flow rate of 0.9 mL/min, and absorbance was measured at 220 nm (*33*). C_{18} reverse-phase HPLC was performed on a C_{18} Phenomenex Luna column (4.6 mm × 250 mm) eluted with water (0.1% TFA), pH 2.9, at a flow rate of 1 mL/min, and absorbance was measured at 210 and 254 nm. Size-exclusion chromatography (SEC) was performed using a Pharmacia Superdex 200 column (10 mm × 310 mm) eluted with 0.5 M magnesium chloride in 25 mM Tris buffer, pH 7.2, at a flow rate of 0.4 mL/min, and absorbance was measured at 280 nm (to detect total protein) and 414 nm (to detect only heme protein).

Synthesis of Ribavirin-5′-monophosphate. Ribavirin-5′-monophosphate (RBV-P) was prepared by reaction of RBV with phosphorus oxychloride ($POCl_3$) and trimethyl phosphate (TMP) according to the method of Allen (*34*), with progress of the reaction monitored by C_{18} reverse-phase HPLC. RBV (2 mmol) was reacted with $POCl_3$ (8 mmol) and purified water (2 mmol) in 8.3 mL of TMP. Following completion of the reaction (5 h), the product was poured over 20 g of ice and 2 N sodium hydroxide solution was added to bring the pH up to 3. The product was allowed to hydrolyze overnight at room temperature. The hydrolyzed product was extracted with 2 × 20 mL portions of chloroform. The product RBV-P in chloroform was mixed with 10 g of fine charcoal (100−400 mesh). The reaction mixture/charcoal slurry was centrifuged at 2000*g* for 15 min, and the supernatant was recovered. The wash steps were repeated until no inorganic phosphate (P_i) could be detected in the supernatant by C_{18} reversed-phase HPLC or by the Ames method (*35*). The charcoal was extracted three times with ethanol/water/ammonium hydroxide (10:10:1), and the pooled extract was evaporated to dryness. The resulting RBV-P ammonium salt was converted to the free acid by ion exchange using BioRAD AG 50W-X2 (H form) resin and elution of product with water according to the method by Streeter (*36*). The isolated yield after purification was 70%. The RBV-P was characterized using two assays: C_{18} reverse-phase HPLC quantification of the RBV released by enzymatic cleavage using acid phosphatase (acid phosphatase assay, described below), and quantification of total inorganic phosphate (P_i) by the Ames method (*35*). EI mass spectral analysis: $m/z = 323.2$ (calculated 324). ^{31}P NMR (D_2O): δ 0.95 ppm.

Synthesis of Ribavirin-5′-phosphorimidazolide. Purified RBV-P was converted to ribavirin-5′-monophosphorimidazolide (RBV-P-Im) according to the procedure of Fiume (*30*, *31*) with slight modifications. The reaction was performed under dry nitrogen using anhydrous solvents. RBV-P (324 mg, 1 mmol) was dissolved in 10 mL of *N*,*N*′-dimethylformamide (DMF). Carbonyldiimidazole (CDI, 5 mmol) dissolved in 5 mL of DMF was added to the RBV-P solution with stirring, followed by addition of 5 mmol of imidazole freshly predissolved in 5 mL of DMF. The reaction mixture was stirred at room temperature for 45 min followed by removal of the DMF by evaporation. The resulting waxy solid was dissolved in 2 mL of ethanol, followed by precipitation of the RBV-P-Im product by slow addition of 20 mL of ether. The precipitate was washed twice with ether, and residual ether was evaporated using a gentle stream of dry nitrogen. The RBV-P-Im was isolated in >90% yield and used immediately for conjugation to Hb. EI mass spectral analysis: $m/z = 373.2$ (calculated 374). ^{31}P NMR (D_2O) analysis: δ 20.3 ppm, trace P_i (3.3 ppm), and pyrophosphate (−10.3 ppm).

Conjugation of Ribavirin-5′-phosphorimidazolide to Hemoglobin. COHb (6.67 μmol, 430 mg) (4.3 mL of a 100 mg/mL solution in purified water) was mixed with 1 mmol of RBV-P-Im dissolved in 8.6 mL of 0.1 M sodium bicarbonate, pH 9.5, buffer (150:1 ratio of RBV-P-Im to Hb). The pH of the

reaction mixture was maintained at pH 9.5−9.6 over the first hour by addition of 0.2 M sodium carbonate solution as required. After the pH of the reaction mixture had stabilized, the reaction vessel was charged with carbon monoxide (CO) for 15 min and the reaction was allowed to continue under positive CO pressure with mixing at 37 °C for 96 h. The degree of Hb modification was monitored by anion exchange HPLC. The final reaction mixture was purified by dialysis (10 kDa molecular weight cutoff) against Ringer's Lactate (3 × 0.5 L exchanges), sterile filtered (0.2 μm filter), charged with CO, and stored at −80 °C. The final Hb concentration following the reaction was 15 mg/mL.

Determination of Molar Drug Ratio (MDR). The RBV/Hb molar drug ratio (MDR) in the hemoglobin−ribavirin conjugate (Hb−RBV) was determined by C_{18} reverse-phase HPLC quantification of RBV released by enzymatic cleavage using the acid phosphatase assay (described below), and determination of total inorganic phosphate (P_i) using the Ames inorganic phosphate assay (described below). The molar concentration of Hb was determined using the Drabkin's assay (Sigma Diagnostics). The MDR was also assessed by MALDI mass spectrometry. Hb−RBV MALDI mass spectra were analyzed in the *m*/*z* range corresponding to 15−20 kDa to identify [α globin + *n*] or [β globin + *n*] peaks, where the mass of the α globin chains was measured as 15145 g/mol, β globin chains were measured as 15869 g/mol, and *n* is the calculated number of attached RBV-P (307 g/mol).

Acid Phosphatase Assay. RBV-P analysis: 20 μL of 30 μmol/mL RBV-P (0.6 μmol) was diluted into 0.3 mL of 1 mM sodium acetate buffer, pH 4.8, containing 3 units of acid phosphatase (type IV-S, potato). Conjugate analysis: 20 μL of 15 mg/mL Hb−RBV in Ringer's Lactate solution (0.3 mg, 5 nmol) was diluted into 0.3 mL of 1 mM sodium acetate buffer, pH 4.8, containing 3 units of acid phosphatase. The mixtures were incubated at 37 °C for 2 h. Precipitates were removed by centrifugation through a Centricon concentrator (Amicon, 10 kDa molecular weight cutoff), and RBV in the supernatant was quantified by C_{18} reverse-phase HPLC against standard calibration curves of RBV and Hb + RBV admixture solutions also treated with acid phosphatase.

Inorganic Phosphate Assay. Total inorganic phosphate (P_i) was determined using the Ames method (*35*) using potassium phosphate solutions as standards. 80 μL of 10% magnesium nitrate in ethanol was used for analysis of 5 nmol of the Hb−RBV sample (25 μL of ∼15 mg/mL Hb−RBV solution). Samples were ashed over an open flame in a test tube and then hydrolyzed with 0.4 mL of 0.5 M hydrochloric acid solution in a 100 °C water bath for 2 h. The samples were filtered to remove precipitates and adjusted back to 0.4 mL with water. 1.0 mL of the Ames color reagent (prepared by mixing 1 part 10% ascorbic acid solution with 6 parts of 0.42% ammonium molybdate in 1.0 N sulfuric acid solution) was added and incubated at 37 °C for 45 min. The absorbances of the samples were measured at 820 nm, and the P_i concentration was determined using a standard curve generated from the phosphate standards.

Haptoglobin-Binding Assay. Hb−RBV (500 μL of a 1 mg/mL solution in PBS, 7.7 nmol) was mixed with a 10% molar excess of human Hp (85 μL of a 10 mg/mL solution in PBS, 8.5 nmol), at room temperature for 1 h to allow complex formation of Hb−RBV with the added Hp. The extent of Hb−RBV binding to Hp was determined by SEC analysis of the mixture. Hb-containing species were detected at 414 nm. Hp-bound complexes appear as high molecular weight early-eluting species, predominantly 164 kDa, but up to as high as 400 kDa due to the heterogeneous molecular weight of the mixed phenotype polymerized Hp (*10*, *11*). Noncomplexed Hb species appear as late-eluting low molecular weight species (∼32 kDa) due to dissociation of the tetrameric $\alpha_2\beta_2$ Hb into $\alpha\beta$ dimers under the high salt elution conditions. The Hb−Hp complex, however, is stable under the dissociating elution conditions. The extent of Hb−RBV binding to Hp was determined by comparing the amount of Hp-bound early-eluting Hb species to the amount of nonbound late-eluting Hb species remaining in the Hp-containing incubation mixture injected.

Stability Assay. Approximately 15 nmol of Hb−RBV (1 mg in 75 μL of PBS) was mixed with an equal volume of freshly prepared plasma (human and mouse) and adjusted to a final volume of 0.2 mL with PBS. Samples were removed for analysis after incubation at 37 °C for 0.5, 1, and 2 h. Samples were centrifuged through a Centricon concentrator (Amicon, 10 kDa molecular weight cutoff), and the filtrate was analyzed for RBV by C_{18} reverse-phase HPLC. Plasma samples were prepared with known amounts of Hb and RBV as standards to achieve a RBV standard curve against which released RBV in the incubated samples could be measured by comparing HPLC peak areas. The standards were processed and analyzed identically and in parallel to account for any loss of RBV due to plasma protein binding and removal from the supernatant. Percent release was estimated by dividing the measured RBV concentration determined at each time point by the initial conjugated RBV concentration (calculated by multiplying the amount of Hb−RBV treated (15 nmol) by the MDR determined from the acid phosphatase and Ames' assays, and dividing by the volume of the sample, 0.2 mL). The amount of RBV released in plasma over time was compared with the known MDR to assess conjugate stability.

Labeling Haptoglobin with Alexa Fluor 488. Hp was fluorescently labeled (fHp) with Alexa Fluor 488 (a dye containing an amine-reactive carboxylic acid tetrafluorophenolate ester tethering functionality) to allow characterization of cell binding and uptake of Hp−Hb−RBV *in vitro*. Human Hp (500 μL of a 2 mg/mL solution in PBS) was labeled according to the Alexa Fluor 488 kit procedure, and the extent of the labeling was determined using the formula below:

$$\text{moles of fluor/moles of Hp} = (A_{495\text{fHp}} - A_{495\text{Hp}})/\epsilon_{\text{F495}} \times d/C_{\text{Hp}}$$

where ϵ_{F495} is the published extinction coefficient for the fluor (71 000 $\text{cm}^{-1}\cdot\text{M}^{-1}$, Molecular Probes, Inc., Eugene, OR), *d* is the assay dilution factor, C_{Hp} is the concentration of the labeled Hp sample, and $A_{495\text{fHp}}$ and $A_{495\text{Hp}}$ are the measured absorbance values for fHp and Hp, respectively. Typically, 2−3 fluors were attached per Hp to give fluorescently labeled Hp (fHp).

Hp−Hb Cell Internalization Assay. To evaluate uptake of Hp−Hb−RBV by cells expressing a known Hb−Hp receptor (CD163), internalization assays were performed using wild type CHO cells (CHO/WT) and proprietary CHO cells stably transfected with CD163 variant 1 (CHO/CD163). Both cell types were incubated with Alexa Fluor 488-labeled Hp (fHp) complexed with either Hb or Hb−RBV. The flow cytometry analysis procedure was adapted from the method published by Schaer et al. (*37*). CHO/WT and CHO/CD163 cells were plated in media overnight in a 24-well plate at 1 × 10^5 cells/well. fHp−Hb and fHp−Hb−RBV complexes were prepared fresh for the assay by combining fHp with Hb and Hb−RBV at a 1.1:1 molar ratio and incubated for 1 h at room temperature in the dark prior to dilution to the appropriate concentrations (spanning a Hb concentration range from 0 to 100 μg/mL) with AIMV culture medium. The cell culture medium was removed, and the cells were rinsed with PBS. 200 μL aliquots of fHp, fHp−Hb, and fHp−Hb−RBV in AIMV were added to the wells and incubated for 1 h at 37 °C. The labeling medium was removed from the cells, and the cells were washed with PBS. The cells were removed from the wells using trypsin and transferred to a

Scheme 1. Hemoglobin−Ribavirin Conjugate Synthesis

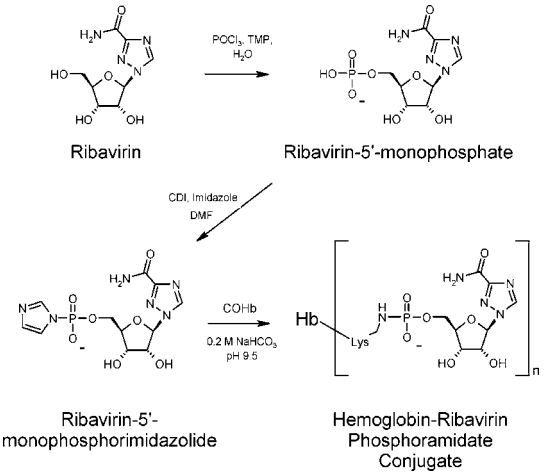

5 mL polypropylene flow tube. PBS was combined with the cells in the tube, and the cells were pelleted at 1500 rpm at 4 °C for 10 min. The supernatant was removed, and the cells were resuspended in 500 μL of PBS in flow tubes. Fluorescent intensity was measured by flow cytometry. FL-1% is the percentage of cells within the sampled population fluorescing above baseline, and X-mean is the mean relative fluorescence of the cell population on a logarithmic scale expressed as relative fluorescence units (RFU). A high X-mean indicates that the cells are highly fluorescent and is related to the amount of fluor taken up in the form of fHp.

Recovery of Ribavirin from Hb−RBV. RBV was cleaved from Hb−RBV by enzymatic hydrolysis and isolated for evaluation of bioactivity. Hb−RBV (500 μL of a 15 mg/mL solution in PBS, ∼120 nmol, 7.5 mg) was treated with 100 U of acid phosphatase in a final volume of 2 mL of 0.2 M sodium acetate buffer, pH 4.8, at 37 °C for 3 h. The reaction mixture was centrifuged through a Centricon concentrator (Amicon, 10 kDa molecular weight cutoff) to remove precipitated Hb, and the supernatant was analyzed by C_{18} HPLC (according to the acid phosphatase assay) to quantify the amount of RBV and then was lyophilized and reconstituted in PBS prior to *in vitro* activity evaluation.

***In Vitro* Ribavirin Bioactivity Assay.** RBV recovered from acid phosphatase cleavage of Hb−RBV was evaluated for bioactivity in an *in vitro* cell proliferation assay using a BrdU incorporartion cell proliferation ELISA. Human HepG2 and mouse AML12 cells were plated at a density of 4×10^4 cells/well in flat bottom 96-well plates. The cells were allowed to grow for 24 h, at which time they were treated in quadruplicate with RBV or RBV cleaved from Hb−RBV. Cells were incubated for 6 h at 37 °C over a dose range of 0−200 μM RBV. Following incubation, the medium was removed, fresh medium containing BrdU was added to the wells, and the incubation was continued for 18 h to allow for incorporation of BrdU into the DNA. The extent of BrdU incorporation is a measure of cell proliferation and was determined by ELISA using an antibody directed to BrdU according to the kit protocol. The growth inhibitory effect of RBV with respect to dose was expressed as a percent of control with untreated cells set as 100% proliferation.

RESULTS

Synthesis of Hb−RBV. The preparation of Hb−RBV is shown in Scheme 1. The synthesis of RBV-P was carried out using $POCl_3$ in TMP to phosphorylate the 5′-hydroxyl group of RBV according to the procedure by Fiume (*30*, *31*). More than 95% of RBV was modified according to C_{18} reverse-phase HPLC, where RBV-P had an earlier-eluting peak than RBV. Figure 1 is a normalized overlay of the C_{18} chromatograms of purified RBV-P, RBV, and inorganic phosphate (P_i) byproduct, illustrating the different retention times. Instead of using a charcoal column to separate RBV-P from inorganic phosphate, the reaction solution was mixed with charcoal to adsorb RBV-P, and then the charcoal containing RBV-P was washed/centrifuged several times. This resulted in sufficient P_i removal compared to product loss. Washing was stopped when P_i was no longer detected in the supernatants using the indicator from the Ames inorganic phosphate assay (*35*) or by C_{18} HPLC. The ammonium salt of RBV-P was extracted from the charcoal with ethanol/water/ammonium hydroxide, converted to its free acid form, and lyophilized. Analysis of the recovered RBV-P showed it to contain less than 5% of unmodified RBV. The product was also evaluated using acid phosphatase to convert the RBV-P to RBV, which was quantified by C_{18} HPLC analysis. This assay indicated more than 90% of the purified product RBV-P could be cleaved into RBV and P_i. The Ames inorganic phosphate assay was used to determine the purity of the RBV-P as measured by free P_i liberated upon pyrolysis. The measured phosphate accounted for >95% of the theoretical phosphate content. The overall yield from RBV after charcoal purification was 60%. This product was used in the next step to form the 5′-monophosphorimidazolide, RBV-P-Im.

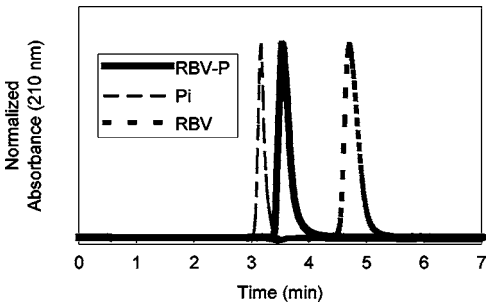

Figure 1. Overlaid C_{18} chromatography profiles of RBV, P_i byproduct, and RBV-P, illustrating how reaction progress was monitored based on elution time.

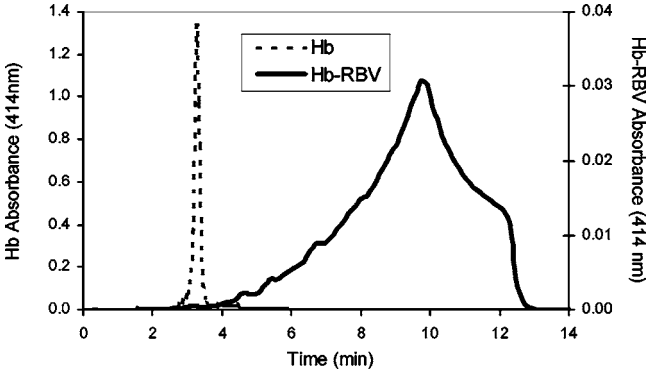

Figure 2. Anion exchange chromatographic profile of Hb−RBV showing the conjugate eluting later than native Hb (concentration-equivalent injection) due to a greater net negative charge on the Hb imparted by attached RBV.

Synthesis of the intermediate RBV-P-Im was achieved by activating RBV-P with CDI and imidazole followed by evaporation of DMF solvent. Numerous precipitations from ethanol with ether yielded an off-white powder after drying. RBV-P-Im was conjugated to Hb immediately and without further purification.

Reacting RBV-P-Im in a 150-fold molar excess over Hb (COHb) with the pH held constant at 9.5 was found to provide the highest ratio of RBV to Hb in the final conjugate. Anion exchange chromatographic analysis (Figure 2) indicated a lowering and broadening of the Hb isoelectric point, consistent

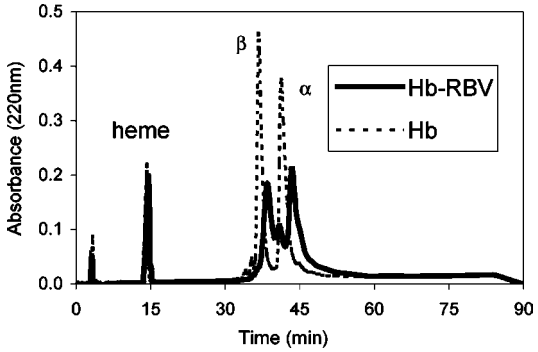

Figure 3. C_4 reverse-phase HPLC profile of Hb−RBV showing the shift in retention time of the individual globin chains due to conjugation of RBV to native Hb chains.

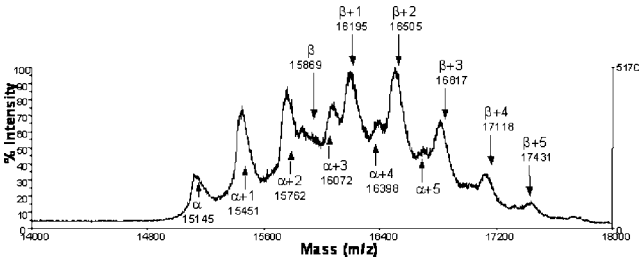

Figure 4. MALDI mass spectral analysis of the Hb−RBV conjugate showing several [α globin + *n*] and [*β* globin + *n*] peaks, where *n* is the calculated number of RBV-P attached. The average MDR estimated from this distribution is between 4 and 12.

Table 1. Hb−RBV Molar Drug Ratio (MDR)

	RBV conc	Hb conc	MDR
acid phosphatase assay	100 μM	16 μM	6
inorganic phosphate assay	2.36 mM	0.29 mM	8

with addition of multiple negatively charged RBV-P moieties to the protein resulting in increased retention time. Greater than 95% of the starting Hb was modified in the reaction. C_4 reverse-phase HPLC analysis (Figure 3) showed modification of both the α and *β* chains, as indicated by a shift of the peaks to slightly longer retention times and by peak broadening. The molar drug ratio (MDR) of the product mixture was calculated by dividing either the acid phosphatase-cleaved RBV concentration (acid phosphatase assay) or the P_i concentration (Ames inorganic phosphate assay) by the Hb concentration (Drabkin's assay), taking into account any dilutions. The MDR was found to be between 6 and 8 RBV moieties attached per hemoglobin tetramer (Table 1). MALDI mass spectral analysis (Figure 4) indicated the attachment of 1−3 RBV drugs per α or *β* globin chain (the [α + *n*] and [*β* + *n*] peaks were within 0.2% of the expected values based on 307 g/mol RBV-P incremental mass additions). This corresponds to a MDR distribution of 4−12 if the α and *β* monomers were recombined in the Hb $\alpha_2\beta_2$ tetrameric form and is consistent with the average 6−8 MDR determined by the acid phosphatase and Ames assays, which give the ratio per $\alpha_2\beta_2$ tetramer. SEC analysis of Hb−RBV under high magnesium chloride salt conditions that dissociate 64.5 kDa $\alpha_2\beta_2$ Hb into 32 kDa $\alpha\beta$ dimers revealed the conjugate mixture to contain predominantly 32 kDa material (82%) eluting at 41 min, as well as some 64.5 kDa material (18%) that appeared as an earlier-eluting 38.5 min shoulder on the 32 kDa 41 min peak (Figure 5).

Binding of Hb−RBV to Hp. Approximately 90% of the Hb−RBV mixture bound to human Hp (mixed phenotype), which accounted for all of the 32 kDa Hb−RBV species (Figure 5) but only some of the 64.5 kDa Hb−RBV species. The lower molecular weight Hb−RBV species moved completely to an earlier elution time by SEC analysis, indicating Hp-binding, whereas most of the higher molecular weight Hb−RBV species did not change elution time, indicating no Hp-binding. Incubation overnight did not increase binding of this species to Hp. The non-Hp-bound, high molecular weight Hb−RBV can be removed by preparative SEC due to the 10 min difference in elution times; however, this was not done for any of the MDR or *in vitro* analyses described in this report.

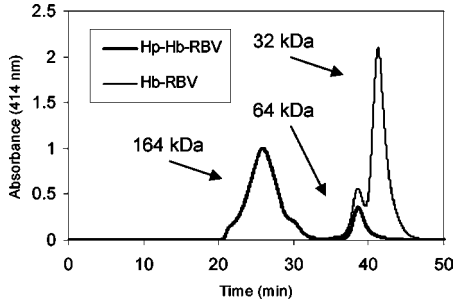

Figure 5. Overlaid SEC profiles of Hb−RBV and Hp−Hb−RBV showing a shift of all of the 32 kDa Hb−RBV to higher molecular weight upon Hp-binding, but only some of the 64 kDa Hb−RBV.

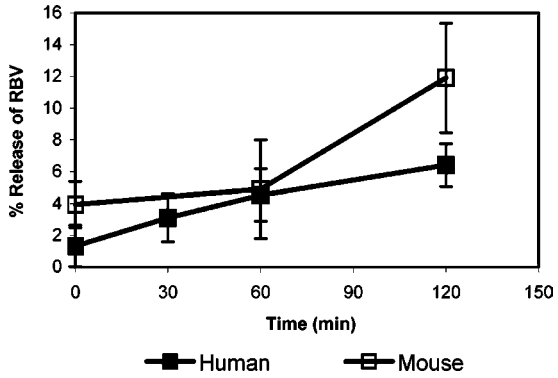

Figure 6. Release of RBV from Hb−RBV in human and mouse plasma after 2 h (mean ± std dev).

Stability of Hb−RBV in Plasma. The stability of Hb−RBV in fresh human and mouse plasma was tested *in vitro* to provide an estimate of its expected stability in circulation *in vivo*. Incubation of the Hb−RBV in plasma resulted in increasing levels of free RBV with the same elution time as that of RBV control by C_{18} reversed-phase HPLC. There was no evidence of release of RBV−P from the conjugate. Hb−RBV was more stable in human plasma in this experiment, with release of only 6 ± 1.3% of the conjugated RBV load compared to 12 ± 3.4% release in the mouse plasma after 2 h (Figure 6).

$CD163^+$ Cell-Specific Uptake of Hb−RBV. Fluorescent labeling of Hp for cell uptake studies did not interfere with Hb-binding when analyzed by SEC (data not shown). At 50 μg/mL (Hb) incubation concentration, a 100% FL-1 (percent of cells fluorescing) was measured for the CHO/CD163 cells with Hb and Hb−RBV, indicative of binding of fluor (in the form of fHp-bound Hb complexes) to the transfected cells. Much lower FL-1 values were observed for all the CHO/WT cell samples and the CHO/CD163 cells incubated with fHp, indicative of minimal binding. X-mean (relative brightness of the fluorescent cells as measured by RFU) increased in a linear fashion over time for the CHO/CD163 cells, indicating binding and uptake (data not shown), in contrast to the case of CHO/WT cells, which showed only low nonspecific binding and no uptake. Figure 7 shows the results of uptake after 1 h by CHO/WT and CHO/CD163 cells incubated with 50 μg/mL fHp-bound Hb, 50 μg/mL fHp-bound Hb−RBV, or fHp control (80 μg/mL; the concentration of fHp bound to Hb and Hb−RBV in the 50 μg/mL Hb samples). CHO/WT cells did not take up fHp,

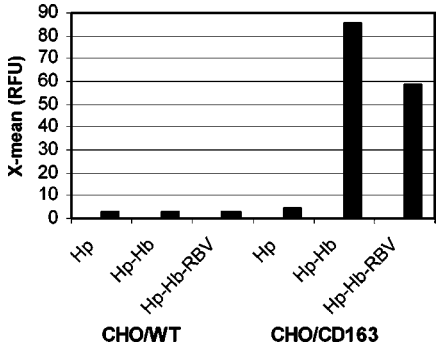

Figure 7. Relative fluorescence uptake (RFU) of fHp, fHp−Hb, and fHp−Hb−RBV into CHO/WT and CHO/CD163 at 50 μg/mL Hb (80 μg/mL Hp) after 1 h.

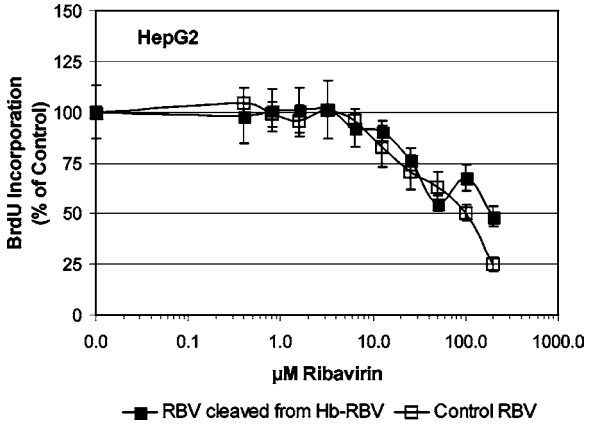

Figure 8. Antiproliferative activity of RBV control and RBV enzymatically cleaved from Hb−RBV against human HepG2 cells. Determined by measuring the extent of BrdU incorporation relative to control untreated cells (mean ± std dev).

fHp−Hb, or fHp−Hb−RBV complexes above the background level. CHO/CD163 transfectants bound and internalized fHp−Hb (85 RFU) and fHp−Hb−RBV (60 RFU) but did not internalize fHp, indicating that binding was specific for Hp−Hb complexes and occurred only in cells expressing the Hp−Hb receptor (CD163).

Bioactivity of Hb−RBV. The bioactivity of RBV released from Hb−RBV by enzymatic hydrolysis was assessed using the known antiproliferative activity of RBV (*27*, *38*) in an *in vitro* cell proliferation assay based on BrdU incorporation into DNA by actively dividing HepG2 cells. Proliferation of HepG2 cells was decreased by RBV in a concentration-dependent manner (Figure 8). RBV posthydrolysis and control unmodified RBV had similar dose-response curves, demonstrating that the conjugated RBV could be released in active form through enzymatic action. The antiproliferative activities of the control and cleaved RBV were also assessed in mouse AML12 cells, yielding similar dose-response curves (Figure 9).

DISCUSSION

A novel conjugate of human Hb and RBV was prepared to demonstrate the utility of Hb as a biocompatible carrier for improved drug delivery for the treatment of liver disease and diseases affecting Hb−Hp receptor bearing cells. Ribavirin is a drug currently approved for use in the treatment of HCV, but it suffers from dose-limiting toxicity associated with its systemic biodistribution. A Hb−RBV conjugate was prepared with releasable bioactive drug through stepwise synthesis from purified human Hb and RBV. RBV was first phosphorylated at its 5′-hydroxyl and subsequently activated to a phosphorimidazolide and reacted with COHb to yield a phosphoramidate

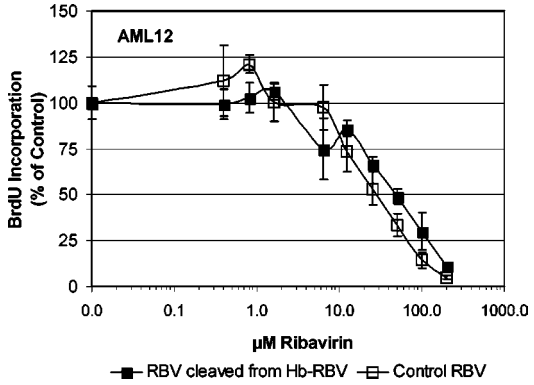

Figure 9. Antiproliferative activity of RBV control and RBV enzymatically cleaved from Hb−RBV against mouse AML12 cells. Determined by measuring the extent of BrdU incorporation relative to control untreated cells (mean ± std dev).

attachment of ribarivin to amino groups on hemoglobin. The attachment chemistry is similar to that developed by Baddiley (*39*), Staab (*40*), and Fiume (*30*, *31*). Hb was maintained in the carbonmonoxy ligation state instead of the oxygenated or deoxygenated state to prevent heme oxidation, methemoglobin formation, and protein precipitation under the reaction conditions. Sites of drug attachment include some of the approximately 40 surface lysine residues of Hb and possibly terminal amino groups of the globin chains. Several lysine residues on the α and β globin chains of Hb, as well as the β globin valine (Val1) amino termini, have been shown to be reactive toward a range of amine-directed Hb modifiers (*41*), supporting the selection of an amino group-directed chemistry to achieve a high molar drug ratio. The MDR of the Hb−RBV conjugate was determined to be 6−8 RBVs per Hb tetramer with little unmodified hemoglobin remaining after 96 h of reaction. It is important that all Hb molecules contain some drug to minimize competition of the unmodified Hb for binding to Hp and cell receptors. Native Hb−Hp may be a more effective competitor for cell receptors than the Hp−Hb−RBV complex and may explain the difference in CHO/CD163 cell binding and uptake for these two species (see CHO/CD163 cell uptake data and explanation below).

The Hb−RBV formulation consists of two species: (1) a Hb that dissociates into two 32 kDa Hb−RBV $\alpha\beta$ dimers under dissociating conditions (magnesium chloride containing buffer) and binds Hp despite the extensive modification by RBV, and (2) an ~64 kDa Hb−RBV species that does not dissociate and which essentially does not bind Hp. The sequence homology of haptoglobin is highly conserved across species (*42*), and cross-species compatibility of Hb−Hp binding has been demonstrated in our lab using rat Hp and human Hb (unpublished data). In addition, Hp has been shown to bind a range of modified Hbs (*43*, *44*), providing evidence for the ability of Hp to accommodate a variety of Hb surface features. However, Hp does not bind Hb cross-linked between the α globin chains but does bind Hb cross-linked between the β globin chains (*44*, *45*). The high molecular weight Hb component that does not bind Hp as observed on SEC under dissociating conditions is most likely cross-linked across the α chains, while the fraction that binds Hp is most likely cross-linked across the β chains. It is possible that Hb subunit cross-linking can occur through the secondary 3′ and 5′ hydroxyl groups of RBV, a consequence of ribavirin-3′,5′-diphosphate (RBV-P_2) and ribavirin-3′,5′-diphosphorimidazolide (RBV-[P-Im]$_2$) formation during the activation of RBV which is carried through to the conjugation step. Supporting this concept is the observation of a lone contaminant with $m/z = 403$ identified in the MALDI mass spectrum of RBV-P, corresponding to RBV-P_2, with a calculated

mass of 404 g/mol. The α chains are easily cross-linked by molecules of this size (*44*), which explains why most of the fraction did not bind Hp. Retention of Hp-binding by the Hb−drug conjugates is important for CD163-mediated cellular uptake since this receptor has been reported to bind and internalize complexes of Hb and Hp. However, multiple mechanisms including direct uptake of free Hb (*22*) and cross-linked Hb (*15*) appear to be necessary to account for the high capacity of the liver for Hb uptake. For subsequent *in vitro* and *in vivo* studies, residual cross-linked Hb−RBV was readily removed from the Hp−Hb−RBV complex using preparative SEC based upon the ∼100 kDa size difference. SEC purification was not performed on the initial formulations used in the characterization experiments presented in this report. However for *in vivo* studies, it is important that all Hb−RBV is bound to Hp to minimize rapid renal clearance of unbound 32 kDa Hb (*46*, *47*). Aside from eliminating renal clearance, Hp complexation helps to selectively target Hb−Hp receptor bearing cells such as liver macrophages and aids in overall liver targeting (*9*−*12*). The Hb−RBV conjugate was sufficiently stable in plasma to allow for efficient liver clearance, which is expected to occur within minutes of administration (half-life of clearance on the order of 9−12 min)(*9*−*12*). It is expected that most of the conjugate would be rapidly taken up by liver cells and metabolized before significant release of free drug into plasma could occur as a result of conjugate degradation.

To investigate receptor binding and uptake of Hb−drug conjugates, CHO cells expressing CD163 (CHO/CD163) were constructed. The Hp−Hb−RBV conjugate complex was taken up by CHO/CD163 cells but not by wild type cells lacking CD163 (CHO/WT). Fluorescent labeling of Hp did not impair Hb-binding and did not appear to prevent recognition and uptake by CD163. On the other hand, CD163 did not internalize fluorescently labeled Hp as an individual entity. These data indicate that Hb−RBV is specifically bound and internalized by Hb−Hp receptor bearing cells and provide evidence for the receptor-mediated uptake of Hp−Hb−RBV by cells that express CD163, primarily cells of the monocyte/macrophage lineage (*48*). The CD163 membrane protein has been identified as the macrophage scavenger receptor for Hb−Hp complexes, as part of a Hb uptake and iron recovery pathway (*18*, *21*). A similar receptor or process may mediate the uptake of Hb−Hp by hepatocytes; however, a related receptor has not yet been identified. Tissue macrophages are ideal targets for Hb-based drug delivery, particularly with conjugated RBV due to the known presence of CD163 on such cells. Several studies have shown that RBV alters the Th1/Th2 cytokine expression ratio during an immune response (*27*).

In the design of the Hb−RBV conjugate, a linkage was used that would be cleavable by lysosomal enzymes. A phosphoramidate linkage was employed due to the lability of phosphoramidates *in vivo* (*30*, *31*, *39*, *40*). As a model of cellular metabolism, RBV was enzymatically hydrolyzed and cleaved from the Hb−RBV conjugate using acid phosphatase *in vitro*. Released RBV was shown to retain bioactivity similar to that of unmodified RBV against HepG2 and AML12 cells, indicating active drug would be released following exposure of the Hb−RBV to hydrolytic enzymes in the lysosome following endocytosis (*49*). Also, nonphosphorylated RBV was detected by HPLC in this simulation of lysosomal release of drug. However, drug activity is expected from release of either RBV or RBV-P (phosphorylated form).

One mechanism by which RBV exerts its antiviral effect is through conversion to RBV-P, which inhibits inosine monophosphate dehydrogenase, resulting in reduced guanosine triphosphate (GTP) levels, thereby allowing RBV to ultimately compete against GTP in the host cell for incorporation into growing viral RNA (*38*, *50*, *51*). Successive phosphorylation steps ultimately lead to the RBV-5′-triphosphate nucleotide (*52*), which exerts antiviral activity through inhibition of viral RNA polymerase and causes mutations through error-prone replication when incorporated into growing viral RNA in place of GTP (*51*). Presumably, it is this form of RBV that is responsible for the antiproliferative effect on HepG2 and AML12 cells reported here.

Due to the dual immunomodulatory and antiviral mode of action of RBV, a Hb−RBV conjugate is expected to be suitable for the treatment of HCV infection, a viral disease affecting both hepatocytes and macrophages. Recent studies have already demonstrated the enhanced activity of the drug conjugate in a model of acute viral hepatitis, in which significantly lower amounts of conjugated RBV provided improved outcomes relative to the case of free RBV (*53*).

As a protein−drug conjugate, it is anticipated that Hb−RBV would be administered intravenously. As an injectable form of targeted RBV, Hb−RBV may serve as a more potent source of RBV that is particularly suited to acute stages of viral infection or the prevention of HCV recurrence following liver transplant, when free RBV cannot be used due to unacceptably high toxicity. RBV conjugated to Hb is in essence sequestered and prevented from entering red blood cells, thus minimizing the associated toxicities of systemic administration of the drug while targeting the drug to the cells of the liver where therapeutic benefit may be greatest. Thus, treatment of hepatitis C patients with Hb−RBV may reduce the dose-limiting toxicity of hemolytic anemia (*26*, *54*, *55*). Further work is being conducted to determine the clinical potential of this novel conjugate.

LITERATURE CITED

(1) Francis, G. E., and Delgado, C. (2000) *Drug targeting. Strategies, principles, and applications*. Humana Press, Inc., Totowa, NJ.
(2) Rihova, B. (1998) Receptor-mediated targeted drug or toxin delivery. *Adv. Drug Delivery Rev. 29*, 273−289.
(3) Moghimi, S. M., and Rajabi-Siahboomi, A. R. (2000) Recent advances in cellular, sub-cellular and molecular targeting. *Adv. Drug Delivery Rev. 41*, 129−133.
(4) Goyal, P., Goyal, K., Vijaya Kumar, S. G., Singh, A., Katare, O. P., and Mishra, D. N. (2005) Liposomal drug delivery systems−clinical applications. *Acta Pharm. 55*, 1−25.
(5) Ambade, A. V., Savariar, E. N., and Thayumanavan, S. (2005) Dendrimeric micelles for controlled drug release and targeted delivery. *Mol. Pharm. 2*, 264−272.
(6) Uekama, K. (2004) Design and evaluation of cyclodextrin-based drug formulation. *Chem. Pharm. Bull. (Tokyo) 52*, 900−915.
(7) Perutz, M. F. (1978) Hemoglobin structure and respiratory transport. *Sci. Am. 239*, 92−125.
(8) Shaeffer, J. R., McDonald, M. J., Turci, S. M., Dinda, D. M., and Bunn, H. F. (1984) Dimer-monomer dissociation of human hemoglobin A. *J. Biol. Chem. 259*, 14544−14547.
(9) Nagel, R. L., and Gibson, Q. H. (1971) The binding of hemoglobin to haptoglobin and its relation to subunit dissociation of hemoglobin. *J. Biol. Chem. 246*, 69−73.
(10) Javid, J. (1978) Human haptoglobins. *Curr. Top. Hematol. 1*, 151−192.
(11) Dobryszycka, W. (1997) Biological functions of haptoglobin−new pieces to an old puzzle. *Eur. J. Clin. Chem. Clin. Biochem. 35* (9), 647−654.
(12) Nagel, R. L., and Gibson, Q. H. (1967) Kinetics and mechanism of complex formation between hemoglobin and haptoglobin. *J. Biol. Chem. 242* (15), 3428−3434.
(13) Keene, W. R., and Jandl, J. H. (1965) The sites of hemoglobin catabolism. *Blood 26*, 705−719.
(14) Hershko, C., Cook, J. D., and Finch, C. A. (1972) Storage iron kinetics. II. The uptake of Hb iron by hepatic parenchymal cells. *J. Lab. Clin. Med. 80*, 624.
(15) Ship, N. J., Toprak, A., Lai, R. P., Tseng, E., Kluger, R., and Pang, K. S. (2005) Binding of acellular, native and cross-linked human hemoglobins to haptoglobin: enhanced distribution and

clearance in the rat. *Am. J. Physiol.: Gastrointest. Liver Physiol. 288*, G1301−G1309.
(16) Okuda, M., Tokunaga, R., and Taketani, S. (1992) Expression of haptoglobin receptors in human hepatoma cells. *Biochim. Biophys. Acta 1136*, 143−9.
(17) Zuwala-Jagiello, J., and Osada, J. (1998) Internalization study using EDTA-prepared hepatocytes for receptor-mediated endocytosis of haemoglobin-haptoglobin complex. *Int. J. Biochem. Cell Biol. 30*, 923−31.
(18) Kristiansen, M., Graversen, J. H., Jacobsen, C., Sonne, O. Hoffman, H. J., Law, S. K. A., and Moestrup, S. K. (2001) Identification of the haemoglobin scavenger receptor. *Nature 409*, 198−201.
(19) Hiraoka, A., Horiike, N., Akbar, S. M. F., Michitaka, K., Matsuyama, T., and Onji, M. (2005) Expression of CD163 in the liver of patients with viral hepatitis. *Pathol., Res. Pract. 201*, 379−384.
(20) Schaer, D. J., Boretti, F., S., Hongegger, A., Poehler, D., Linnscheid, P., Staege, H., Muller, C., Schoedon, G., and Schaffner, A. (2001) Molecular cloning and characterization of the mouse CD163 homologue, a highly glucocorticoid-inducible member of the scavenger receptor cysteine-rich family. *Immunogenetics 53*, 170−177.
(21) Moestrup, S. K., and Moller, H. J. (2004) CD163: a regulated hemoglobin scavenger receptor with a role in the anti-inflammatory response. *Ann. Med. 36*, 347−354.
(22) Weinstein, M. B., and Segal, H. L. (1984) Uptake of free hemoglobin by rat liver parenchynmal cells. *Biochem. Biophys. Res. Commun. 123*, 489−496.
(23) Scherphof, G. L., Koning, G., Bartsch, M., Yan, X., and Kamps, J. (2002) Targeting liposomes and lipoplexes to cells in the liver. *Cell. Mol. Biol. Lett. 7*, 251−254.
(24) Lauer, G., and Walker, B. D. (2001) Hepatitis C virus infection. *N. Engl. J. Med. 345*, 41−52.
(25) Manns, M. P., McHutchison, J. G., Gordon, S. C., Rustgi, V. K., Shiffman, M., Reindollar, R., Goodman, Z. D., Koury, K., Ling, M.-H., Albrecht, J. K., and the International Hepatitis Interventional Therapy Group. (2001) Peginterferon alfa-2b plus ribavirin compared with interferon alfa-2b plus ribavirin for initial treatment of chronic hepatitis C: a randomized trial. *Lancet 358*, 958−965.
(26) Takaki, S., Tsubota, A., Hosaka, T., Akuta, N., Someya, T., Kobayashi, M., Suzuki, F., Suzuki, Y., Saitoh, S., Arase, Y., Ikeda, K., and Kumada, H. (2004) Factors contributing to ribavirin dose reduction due to anemia during interferon alfa2b and ribavirin combination therapy for chronic hepatitis C. *J. Gastroenterol. 39*, 668−673.
(27) Lau, J. N. J., Tam, R. C., Liang, T. J., and Hong, Z. (2002) Mechanism of action of ribavirin in combination treatment of chronic HCV infection. *Hepatology 35*, 1002−1009.
(28) Di Stefano, G., Bignamini, A., Busi, C., Colonna, F. P., and Fiume, L. (1997) Enhanced accumulation of ribavirin and its metabolites in liver versus erythrocytes in mice administered with the liver targeted drug. *Ital. J. Gastroenterol. Hepatol. 29*, 420−426.
(29) Fiume, L., Di Stefano, G., Busi, C., Incitti, F., Rapicetta, M., Farina, C., Gervasi, G. B., and Bonino, F. (1998) Coupling to lactosaminated poly-L-lysine reduces the toxic effects of ribavirin on red blood cells. *J. Hepatol. 29*, 1032−1033.
(30) Polichetti, A., Viti, V., Barone, P., Colonna, F., and Fiume, L. (1992) Prony-Householder method applied to ^{31}P NMR signals: II. Study of conjugates of ara-AMP with lactosaminated albumin. *Phys. Med. Biol. 37*, 1−12.
(31) Fiume, L., Busi, G. Di Stefano, G., and Mattioli, A. (1993). Coupling of antiviral nucleoside analogues to lactosaminated human albumin by using the imidazolides of their phosphoric esters. *Anal. Biochem. 212*, 407−411.
(32) Pliura, D., Wiffen, D., Ashraf, S., and Magnin, A. (1995) Displacement chromatography process. United States Patent 5,439,591.
(33) Jones, R. T. (1994) Structural characterization of modified hemoglobins. *Methods Enzymol. 231*, 322−343.
(34) Allen, L. B., Boswell, K. H., Khwaja, T. A., Meyer, R. R., Sidwell, R. W., and Witkowski, J. T. (1978) Synthesis and antiviral activity of some phosphates of the broad-spectrum antiviral nucleosides, 1-β-D-ribofuranosyl-1,2,4-triazole-3-carboxamide (Ribavirin). *J. Med. Chem. 21*, 742−746.
(35) Ames, B. (1966) Assay of inorganic phosphate, total phosphate and phosphatases. In *Methods in Enzymology* (Neufeld, E., and Ginsburg, V., Eds.) Vol. 8, pp 115−118, Academic Press, New York/London.
(36) Streeter, D. G., Witkowski, J. T., Khare, G. P., Sidwell, R. W., Bauer, R. J., Robins, R. K., and Simon, L. N. (1973) Mechanism of action of 1-β-D-ribofuranosyl-1,2,4-triazole-3-carboxamide (virazole), a new broad spectrum antiviral agent. *Proc. Natl. Acad. Sci. 70*, 1174−1178.
(37) Schaer, D. J., Boretti, F. S., Schoedon, G., and Schaffner, A. (2002) Induction of the CD163-dependent haemoglobin uptake by macrophages as a novel anti-inflammatory action of glucocorticoids. *Br. J. Haematol. 119*, 239−243.
(38) Tam, R. C., Lau, J. Y., and Hong, Z. (2001) Mechanisms of action of ribavirin in antiviral therapies. *Antivir. Chem. Chemother. 12*, 261−272.
(39) Baddiley, J., Buchanan, J. G., and Letters, R. (1956) Phosphorylation through glyoxalines (imidazoles) and its significance in enzymic transphosphorylation. *J. Chem. Soc*., 2812−2817.
(40) Staab, H. A., Scaller, H., and Cramer, F. (1959) An imidazolide of phosphoric acid. *Angew. Chem. 71*, 736.
(41) Manning, J. M. (1994) *Methods Enzymol. 231*, 225−246.
(42) Lim, S.-K., Ferraro, B., Moore, K., and Halliwell, B. (2001) Role of haptoglobin in free hemoglobin metabolism. *Redox Report 6*, 219−227.
(43) Adamson, J. G., Wodzinska, J. M., and Moore, M. S. C. (2002) Hemoglobin-haptoglobin complexes. United States Patent 6,479,637.
(44) Benesch, R. E., Ikeda, S., and Benesch, R. (1976) Reaction of haptoglobin with hemoglobin covalently cross-linked between the alpha beta dimers. *J. Biol. Chem. 251*, 465−470.
(45) Panter, S. S., Vandegriff, K. D., Yan, P. O., and Regan, R. F. (1994) Assessment of hemoglobin-dependent neurotoxicity: alpha-alpha cross-linked hemoglobin. *Artif. Cells, Blood Substitutes, Immobilization Biotechnol. 22*, 399−413.
(46) Baker, S., and Dodds, S. (1925) Obstruction of the renal tubules during the excretion of hemoglobin. *Br. J. Exp. Pathol. 6*, 247−260.
(47) Lieberthal, W. (1997) Renal effects of hemoglobin-based blood substitutes. In *Red cell substitutes: basic principles and clinical application* (Rudolph, A. S., Feuerstein, G., and Rabinovici, R., Eds.) pp 189−217, Marcell Dekker, New York.
(48) Nguyen, T. T., Schwartz, E. J., West, R. B., Warnke, R. A., Arber, D. A., and Natkunam, Y. (2005) Expression of CD163 (hemoglobin scavenger receptor) in normal tissues, lymphomas, carcinomas, and sarcomas is largely restricted to the monocyte/macrophage lineage. *Am. J. Surg. Pathol. 29* (5), 617−624.
(49) Limet, J. N., Quintart, J., Otte-Slachmuylder, C., and Schneider, Y. J. (1982) Receptor mediated endocytosis of hemoglobin-haptoglobin, galactosylated serum albumin and polymeric IgA by the liver. *Acta Biol. Med. Ger. 41*, 113−124.
(50) *Goodman & Gilman's The Pharmacological Basis of Therapeutics*, 9th ed. (Gilman, A. G., Ed.), McGraw-Hill, Inc., Toronto, 1996.
(51) Crotty, S., Cameron, C. E., and Andino, R. (2001) RNA virus error catastrophe: direct molecular test by using ribavirin. *Proc. Natl. Acad. Sci. U.S.A. 98*, 6895−6900.
(52) Page, T., and Connor, J. D. (1990) The metabolism of ribavirin in erythrocytes and nucleated cells. *Int. J. Biochem. 22*, 379−383.
(53) Levy, G., Adamson, G., Phillips, M. J., Scrocchi, L., Fung, L., Biessels, P., Ng, N. F., Ghanekar, A., Rowe, A., Ma, M. X., Levy, A., Koscik, C., He, W., Gorczynski, R., Brookes, S., Woods, C., McGilvray, I. D., and Bell, D. (2005) Targeted delivery of ribavirin improves outcome to murine hepatitis virus induced fulminant hepatitis through enhanced anti-viral activity. *Hepatology* (submitted manuscript).
(54) Glue, P. (1999) The clinical pharmacology of ribavirin. *Semin. Liver Dis. 19* (Suppl. 1), 17−24.
(55) Nakao, M., Nakao, T., and Yamazoe, S. (1960) Adenosine triphosphate and maintenance of shape of the human red cells. *Nature 187*, 945−946.

BC0503317

Development of Contrast Agents Targeted to Macrophage Scavenger Receptors for MRI of Vascular Inflammation

Björn Gustafsson,‡ Susan Youens,‡ and Angelique Y. Louie*

Department of Biomedical Engineering, University of California, Davis, California 95616. Received January 25, 2006; Revised Manuscript Received February 7, 2006

Atherosclerosis is a leading cause of death in the U.S. Because there is a potential to prevent coronary and arterial disease through early diagnosis, there is a need for methods to image arteries in the subclinical stage as well as clinical stage using various noninvasive techniques, including magnetic resonance imaging (MRI). We describe a development of a novel MRI contrast agent targeted to plaques that will allow imaging of lesion formation. The contrast agent is directed to macrophages, one of the earliest components of developing plaques. Macrophages are labeled through the macrophage scavenger receptor A, a macrophage specific cell surface protein, using an MRI contrast agent derived from scavenger receptor ligands. We have synthesized and characterized these contrast agents with a range of relaxivities. In vitro studies show that the targeted contrast agent accumulates in macrophages, and solution studies indicate that micromolar concentrations are sufficient to produce contrast in an MR image. Cell toxicity and initial biodistribution studies indicate low toxicity, no detectable retention in normal blood vessels, and rapid clearance from blood. The promising performance of this contrast agent targeted toward vascular inflammation opens doors to tracking of other inflammatory diseases such as tumor immunotherapy and transplant acceptance using MRI.

INTRODUCTION

Atherosclerosis-related diseases are a leading cause of death and impairment in the United States. According to the American Heart Association, cardiovascular disease affects over 70 million people and was the cause of 38.0% of all deaths in 2002. Over half of these deaths were due to coronary disease, which is primarily diagnosed by X-ray angiography. Researchers are investigating use of MRI angiography as a nonionizing alternative (*1, 2*). Nontargeted roentgen graphic visualization of the blood vessels after injection of a radioopaque substance, or MR angiogram with blood pool contrast agents, can reveal only the vessel lumen and silhouette of lesions that impinge upon the lumen (*3*). The appreciation that a considerable atherosclerosis burden, including plaques vulnerable to rupture or susceptible to erosion, can be accommodated in the vessel wall without impingement on the lumen has led to a new imperative for direct plaque imaging (*4*). In fact, 4−16% of patients suffer from "silent" lesions that do not restrict blood flow but are still vulnerable to rupture (*5*).

One of the earliest cellular components of plaques are macrophages (*6*). Macrophages are attracted to lesions where they take up and accumulate oxidized and other modified low-density lipoproteins (LDLs) from the bloodstream. Over time they become filled with lipid-laden droplets so as to appear foamy under microscope, and they are then termed "foam cells" (*2*). The formation of foam cells is a key event in atherogenesis, and the massive uptake of modified LDLs by macrophages is believed to be mediated by scavenger receptors (*7, 8*). The scavenger receptors are a diverse family of receptors; one of the best studied has been the class A receptor (*9*−*11*). Scavenger receptor class A (SR-A) is primarily expressed by mature macrophages, including Kupffer cells, and alveolar, splenic, and some other tissue macrophages. Class A scavenger receptors are present in high numbers on macrophages, and in vessel lumens they are unique to macrophages, i.e., they are not expressed by endothelial cells lining normal vessels (*12, 13*). SR-A is expressed on the endothelial lining of the liver, on adrenal sinusoids, and on the high endothelial cells of the postcapillary venules in the lymph nodes; but, immunohistochemical staining analysis could not detect SR-A expression in the aortic endothelium of cows, mice, and humans (*13*). SR-A is strongly localized in the cap and interiorly in lesions at all stages (*14, 15*). This makes the receptors an attractive target for a diagnostic or therapeutic agent.

SR-A has broad ligand specificity for a diverse array of polyanionic macromolecules, such as maleylated bovine serum albumin (mal-BSA), oxidized LDL, malondialdehyde modified LDL, and polyinosinic acid (*7, 16*−*20*). Recognition is not dependent upon specific amino acid sequence or carbohydrate structures. Because of their role in inflammation, SR-A receptors are not down regulated with ligand concentration, mediate very efficient and rapid internalization of bound ligand, and repeatedly recycle through the endosomal compartment (*21, 22*), illustrating desirable traits as targets for labeling. Potentially efficient delivery of the contrast agent to plaque sites is also suggested by the significantly increased vascular permeability in the sites of plaque inflammation and relatively small size of the maleylated BSA macromolecule (8 nM (*23*)). We describe here the synthesis and characterization of MRI contrast agents based on scavenger receptor ligands conjugated to multiple Gd-DOTA groups. The ligand maleylated BSA was selected due to its strong affinity and specificity for the SR-A receptor (*20, 24, 25*). The results presented here demonstrate targeting of macrophages in culture using the contrast agents, low toxicity on cells, and negligible labeling of normal arteries.

EXPERIMENTAL PROCEDURES

Synthesis of mal-BSA (Gd-DOTA)$_n$. Covalent linkage coupling of protein to *p*-isothiocyanatobenzyl-1,4,7,10-tetraazacyclododecane-1,4,7,10-tetraacetic acid (*p*-SCN-Bz-DOTA) fol-

* Corresponding author. Phone: (530) 752-7134, fax: (530) 754-5739, e-mail: aylouie@ucdavis.edu.

‡ These authors contributed equally toward this work.

10.1021/bc060018k CCC: $33.50 © 2006 American Chemical Society
Published on Web 02/28/2006

lows closely as described in Mirzadeh et al. (*26*). A typical preparation proceeded as follows: a suspension of bovine serum albumin (10 mg/ml solution, Acros Organics, Belgium, distributed by Fisher Scientific) was dissolved in 16 mL of 0.1 mM of sodium bicarbonate (pH 8.5). To this albumin solution a 60 molar excess of *p*-SCN-Bz-DOTA·4HCl (20 mg/mL, Macrocyclics, TX) suspended in dimethyl sulfoxide (DMSO) was added in 100 μL to 200 μL aliquots with rapid stirring at room temperature. The pH was monitored continuously during the additions and adjusted by dropwise addition of 1 M sodium bicarbonate (pH 9.0). Once the reaction had reached completion, as shown by no further change in pH, the mixture was stirred an additional 36 h at room temperature, yielding 18 DOTA per BSA molecule. An aliquot was removed, exhaustively dialyzed in ddH_2O, and lypophilized for analysis by ionized matrix assisted laser desorption ionization mass spectrometry (MALDI-MS). The same 36 h incubation with decreasing DOTA:BSA ratios (45:1, 30:1, 15:1) yielded 15, 10, and 5 DOTA per BSA, respectively. In addition, increasing incubation time to 47 h for the 60:1 synthesis resulted in 22 DOTA per BSA. The remaining solution was dialyzed in 50 000 MW pore bags (SpectraPor 7) for 12 h, in 0.1 M of sodium bicarbonate (pH 8.5) at 4 °C and then maleylated following the method of Butler and Hartley (*27*). Maleyl groups were incorporated into the BSA molecule using the remaining free lysylamines. The reaction of maleic anhydride with amines is competitive with hydrolysis of the reagent in water; therefore, 600 molar excess of solid maleic anhydride was added in small quantities to the buffered well stirred BSA $(DOTA)_n$ protein solution. The pH was monitored continuously and adjusted by the addition of solid sodium carbonate. Reaction was complete when no further acid is liberated, and the maleylated protein was recovered by dialysis. An aliquot of product was removed for analysis by MALDI-MS. Typically this yielded maximal coverage of maleic blocking groups on the protein molecule in excess of the 37 groups needed for its activation as a recognized ligand.

The resulting solution was dialyzed in 50 000 MW pore bags and exchanged to 0.1 M of sodium citrate (pH 6.6) no more than 9 h at 4 °C, with minimum of four changes of buffer. The dialyzed maleylated albumin−DOTA solution was then treated with 1.2 molar excess (Gd:DOTA) of gadolinium chloride solution added dropwise while stirred. The pH was maintained between 6.6 and 7.0 using aliquots of 1 M sodium citrate. After the pH was stabilized, the sample was stirred for an additional 24 h at room temperature. The mal-BSA $(Gd\text{-}DOTA)_n$ complex was purified by an exhaustive dialysis (SpectraPor 7) at 4 °C with minimally six changes of ddH_2O water within a 36 h period at 4 °C. The purified solution of mal-BSA $(Gd\text{-}DOTA)_n$ was then lyophilized, stored, and desiccated, at 4 °C. Gadolinium content was determined using ICP-MS. We have found that similar results can be obtained by purification using standard desalting columns (Bio-Rad, Dallas TX) rather than dialysis, with less loss of product.

Synthesis of FITC-mal-BSA. BSA was maleylated by the method of Butler and Hartley (*27*), desalted to remove unreacted maleic anhydride, and then lyophilized. The product was resuspended in PBS, pH 7.4. The extent of acylation of the protein amino groups was determined using *o*-phthalaldehyde (OPA) fluorescent protein assay according to a method modified from Roth (*28, 29*). FITC labeling followed a modified protocol from Molecular Probes. Due to differential accessibility of lysines on the BSA molecule and the increased blocking of free amines by maleyl groups, fluorescent labeling required increasing stoichiometric ratios of FITC to mal-BSA with higher degree of maleylation. Therefore FITC:protein ratios of 2:1, 5:1, 10:1, 20:1, and 30:1 were employed for BSA maleylated at 0%, 8−20.5%, 29−69%, 82%, and 89%, respectively. Briefly, FITC (10 mg/mL in DMSO) was added to mal-BSA in small aliquots over the course of 1 h at room temperature while stirred. The pH was maintained at 8.5 using aliquots of fresh 1 M sodium bicarbonate solution. After completion of the reaction, as indicated by no further changes in pH, unreacted FITC was removed using a standard desalting column. Absorbance spectroscopy against a BSA standard was used to determine the protein concentration and fluorophore:protein ratio, using 68000 cm^{-1} M^{-1} as the molar extinction coefficient of the dye at pH 8.0 at 494 nm. Resulting fluorophore-to-protein ratios (f/p) were as follows: 1.14 for BSA, 1.85 for 8% maleylated, 1.09 for 20.5% maleylated, 1.15 for 29% maleylated, 1.24 for 43% maleylated, 1.04 for 54% maleylated, 1.57 for 69% maleylated, and 1.34 for 89% maleylated.

Mass Spectrometry. Mass Spectrometery (Finnigan LCQ Deca XP Plus Ion Trap Mass Spectrometer) was used to identify the proportion of chelates to maleyl groups conjugated to the protein molecule and to determine final molecular weight of the contrast agent. Samples were ionized by matrix-assisted laser desorption ionization (MALDI) and the resulting ions analyzed by a mass analyzer hybrid of quadrupole and time-of-flight (TOF). Serum albumin, which is characterized by a broad, low intensity peak susceptible to noise, reduces the method accuracy to an estimated ±500Da.

ICP-MS. To verify the incorporation of gadolinium to DOTA chelators and purification success, inductively coupled plasma mass spectrometry (ICP-MS) was utilized for analysis of gadolinium content. Quadrupole ICP-MS (Agilent Technologies 7500a) is capable of analyzing a large number of elements with detection sensitivity at the ppb-ppt level. Samples were prepared in 10 mL vials of 3% nitric acid. All samples were prepared in triplicate. Indium solution was spiked into all solutions (i.e. calibration standards and samples) as an internal standard in order to correct instrumental drift during analysis. Isotopes ^{157}Gd and ^{115}In were used for determination.

Magnetic Resonance Measurements. *Relaxivity at 0.6 T.* Relaxivity data was measured using a GE-NMR CSI-2 system with a Tecmag console and a 450 mm clear bore horizontal magnet operating at 0.6 T. Experiments were performed at room temperature (25 °C). A typical 180° pulse was 15 μs, and the reproducibility of the T_1 data was within 3%. Spin−lattice relaxation times were measured using an inversion recovery technique with least-squares fitting applied to the semilog representation of 10 to 12 inversion times ranging from 50 to 3000 ms in an exponential fashion. In all samples, the region of interest was evaluated for a 100 μL NMR tube volume containing contrast agent, typically ranged between 0.1 mM to 1 mM gadolinium, dissolved in distilled, deionized water, pH 7.0 (Gibco, Ultrapure).

Imaging and Relaxivity at 7 T. Relaxivity and MR cell studies were also performed using Bruker Avance Biospec system (Billericia, MA) equipped with a 95 mT/m max gradient set and 72 mm ID coil operating at 300 MHz, at ambient temperature (25 °C). MR measurements were carried out using freshly harvested lysed cells in suspensions of distilled water. Imaging was performed with a T_1-weighted saturation recovery sequence with differing repetition times and an echo delay time of 16 ms, and a flip angle of 90° was used for imaging. The T_2 effects are minimized through the use of a short TE. In all experiments, the FOV was 6 cm × 6 cm, matrix size was 256 × 256 and slice thickness was 1 mm. From the images a T_1 map was calculated using Paravision System software.

Cell Studies. Agents were prepared as described and employed in cell assays. All agents used for cell studies were 60% maleylated unless otherwise noted, and the number of gadolinium per molecule of agent is indicated by the subscript

'*n*' in $(Gd\text{-}DOTA)_n$. Although the gadolinium content for the probes used may differ from figure to figure, all controls were matched to the gadolinium content of the experiment group, so the data are self-consistent.

Dependence of Cellular Uptake on Degree of Maleylation. P388D1 cells (ATCC.com) were maintained in RPMI 1640 supplemented with L-glutamine and 10% fetal bovine serum (FBS). For the uptake experiments cells at 70−80% confluency in 35 mm dishes were incubated with 100 μg/mL FITC-mal-BSA in medium supplemented with lipoprotein-deprived serum (LPDS) for 1 h at 37 °C. LPDS was substituted for fetal bovine serum to remove competing modified lipoproteins (e.g. oxidized LDL) and maximize the cell's SR-A receptor expression during experimentation. All samples were prepared in triplicate unless otherwise noted. After incubation cells are washed three times with PBS and placed in warmed PBS for confocal imaging. Cells dishes were imaged using a BioRad upright confocal microscope.

Cellular Uptake. P388D1 cells on 48 well plates were incubated with increasing concentrations of mal-BSA $(Gd\text{-}DOTA)_n$ where $n = 10$ or 15 for 1 h. After incubation, the wells were washed twice and then cells were lysed by addition of ddH_2O and imaged by MRI at 7 T. Typical preparations consisted for 3×10^5 cells lysed in 150 μL of water. Gd content for each well was assessed by ICP-MS.

Specificity of Uptake. To verify that uptake was specific, cells were incubated with either mal-BSA or control of BSA labeled with Gd-DOTA. BSA is not recognized by the scavenger receptor. The mal-BSA and BSA agents used here were prepared as matched pairs, with synthesis proceeding through the addition of Gd-DOTA and then splitting the product to two samples, one of which was subjected to maleylation (for mal-BSA). Equal Gd-DOTA load was confirmed by mass spectroscopy and ICP-MS. Cells were incubated for 1 h at 37 °C and then washed twice and lysed for imaging as described above.

To verify that cellular uptake was receptor specific, competition experiments were conducted and characterized by MRI and ICP-MS. Cells in 48-well plates were incubated with 200 μM contrast agent ($n = 22$) in the presence of unlabeled mal-BSA or BSA as control in 0, 0.1, 1, 10, and 20-fold excess concentrations. BSA was used as nontargeted control in a separate set of wells.

Cytotoxicity Studies. *Cell Culture.* Mouse fibroblast 3T3 cells were cultured as a monolayer in high glucose DMEM (Cellgro) and supplemented with 10% calf bovine serum (v/v) and 5 mM L-glutamine. Exponentially growing cultures were maintained in a humidified atmosphere of 5% CO_2 at 37 °C.

MTT Assay. The MTT assay performed in this study was a modification of the procedure described by Carmichael (*30*). 3T3 cells at 10 000 cells/well were plated in a 96-well plate. The MTT assay was performed after a 24 h adhesion time. Cytotoxicity was then assessed for mal-BSA $(Gd\text{-}DOTA)_{15}$ and chlorpromazine, for comparison. The assays were carried out in parallel and in triplicate. Cells were counted and plated evenly in a 96-well plate. After a 24 h adhesion time, varying concentrations of mal-BSA $(Gd\text{-}DOTA)_{15}$ (0, 45, 90, 225, and 445 μM) or chlorpromazine (0, 10, 25, 50, and 100 μM) were placed on the cells. After a 4 and 24 h agent exposure time at 37 °C, the MTT assay was performed. After the appropriate incubation times, media was removed from the wells, replaced with 100 μL of fresh media containing 1.0 mM MTT (Invitrogen), and incubated for 3 h at 37 °C. To dissolve the insoluble MTT formazan crystals, 75 μL of media was removed and 50 μL of DMSO was added to the wells. The plate was incubated at 37 °C for an additional 10 min. Well solutions were mixed thoroughly just before absorbance measurement with a Tecan Safire^2 UV/Vis spectrophotometer. Triplicate assays were performed at all drug concentrations. Chlorpromazine was obtained from MP Biomedicals Inc. Mal-BSA $(Gd\text{-}DOTA)_{15}$ was synthesized in the lab as previously described.

Biodistribution Studies. To determine in vivo accumulation sites of the agent and to study the blood clearance dynamics, mal-BSA $(Gd\text{-}DOTA)_{15}$ was labeled with a positron emitter, i.e. ^{64}Cu ($T_{1/2} = 12.7$ h: β^+: 0.653 MeV, 17.4%; β^-: 0.578 MeV, 39%), and biodistribution studies on rats were performed by positron emission tomography (PET). Under isoflorane anaesthesia three male rats (Sprague−Dawley and Fisher), ~200−230 g, were injected via the tail vein with 889, 1045, and 816 μCi, respectively, of the ^{64}Cu-labeled compound in 0.3 mL of PBS buffer followed by a 0.5 mL saline flush. Blood samples were drawn at five approximate time points between 2 and 200 min postinjection, and activity was measured. At 1, 4, 24, and 48 h postinjection, the animals were scanned on a MicroPET II (developed at UCD) or a Siemens Preclinical Imaging Focus 120. An ^{18}FDG calibration scan was also performed in order to determine the absolute values of the radioactive dose in affected organs. At 2, 15, 33, 60, and 200 min postinjection, blood samples (mass between 0.013 and 0.089 g) were collected via tail nicking and activity counted by a Perkin-Elmer Wizard 1470 Automatic Gamma Counter with an energy window setting of 425−640 keV. The raw data are acquired and the unreconstructed images produced by the software MicroPET Manager 2.2.4.0 (MPM) (Concorde Microsystems Inc. (now Siemens Preclinical Solutions)). The emission images ($128 \times 128 \times 359$; pixel size 0.60 mm) were then iteratively MAP reconstructed (field of view 3.85 cm) using the MPM plus the MicroPET MAP Files 1.0.3.0. For analysis of the images, ASIPro 6.0.5.0 was used.

Synthesis of ^{64}Cu-Labeled mal-BSA $(Gd\text{-}DOTA)_{15}$. A typical procedure incorporated 1 mCi of activity to 0.1 mM of contrast agent: the mal-BSA $(Gd\text{-}DOTA)_{15}$ and required amount of $^{64}Cu^{2+}$-solution were dissolved in 0.25 M NH_4OAc (pH 7) separately. The solutions were added together and incubated at 40 °C for 30 min. The resulting solution was then purified according to Penefsky (*31*).

RESULTS AND DISCUSSION

There are theoretically 60 free amines on BSA through which Gd-DOTA could be conjugated; however, some fraction of these must be occupied by maleyl groups for recognition by the scavenger receptor. The number of maleyl groups incorporated, however, must be balanced with the number of Gd-DOTA that must be attached to achieve significant contrast enhancement. To evaluate the minimum number of maleyl groups to satisfy receptor recognition we synthesized a series of mal-BSA molecules with varying degrees of maleylation. Significant conformation changes with maleylation are believed to facilitate access to lysines that are buried in unmodified BSA (*32*). These molecules were also tagged with FITC and applied to macrophages in culture to assess uptake. As shown in Figure 1 optimal uptake is achieved with greater than 80% of the free amines modified by maleyl groups. Figure 1 present confocal images for cells incubated for 1 h with mal-BSA from 0 to 89% maleylation carrying ~1 FITC per molecule. Confocal images were obtained on a BioRad system using 488 nm excitation. Significant increases in fluorescence intensity are observed as the degree of maleylation is increased, indicating increased uptake. Although optimal at 80% maleylation, cellular internalization is still significant for 40−80% maleylated molecules. These results are consistent with previous studies performed

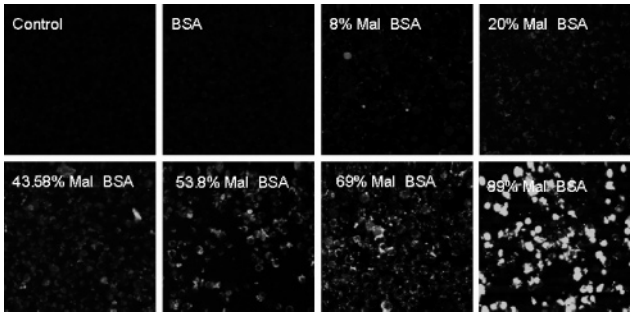

Figure 1. Macrophage uptake is dependent on degree of maleylation. Cells were incubated with FITC-labeled derivatives of mal-BSA bearing different numbers of maleyl groups. Signal intensity increases with increasing maleylation, with significant uptake at greater than 50% maleylation. Optimal uptake is observed for 80% maleylation and above.

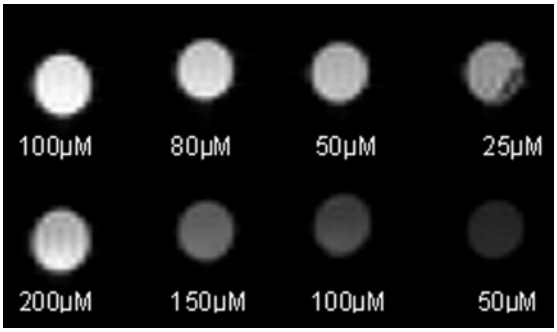

Figure 2. Contrast enhancement correlates with number of Gd-DOTAs bound. Solutions of mal-BSA $(Gd\text{-}DOTA)_n$ with $n = 10$ (bottom row) or 18 (top row) in distilled, deionized water, pH 7.0, were imaged at 7 T at ambient temperature (25 °C). Signal intensity increases as concentration increases (from right to left), and greater signal intensity is observed for the more heavily labeled agent. Contrast enhancement is observed for concentrations greater than 25−50 μM.

using radiolabeled ligands (*33*). In a study with rat endothelial sinusoidal liver cells, SR-A uptake activity correlated with different degrees of BSA modification labeled with ^{125}I (*33*). Scavenger receptor mediated endocytosis (uptake) of maleylated BSA indicated that 60% maleylation, or >37 lysyl amino residues, sharply increased ligand activity. Radioligand data supported that all lysyl amino groups are accessible for maleylation or DOTA conjugation. Based on the results of Figure 1, subsequent labeling with Gd-DOTA was performed on 60% maleylated BSA in order to maximize the number of free-amines for Gd-DOTA conjugation. At 60% maleylation, there should be up to 24 available free amines for conjugation of Gd-DOTA groups.

Additions of increasing numbers of DOTA groups to mal-BSA $(Gd\text{-}DOTA)_n$ increased the number of paramagnetic centers, improving the relaxivity of the contrast agent as shown in Table 1. Observed relaxivities for the mal-BSA contrast agents are summarized in Table 1. Incorporation of DOTA groups was verified by mass spectrometry, and Gd content was analyzed by ICP-MS. Close agreement between the DOTA:BSA ratio, determined by mass spectroscopy, and Gd:BSA ratio, determined by ICP-MS, suggests formation of the Gd:DOTA chelate with no nonspecific binding to the protein despite reported affinity sites for gadolinium on the BSA molecule (*34*). Relaxivity of mal-BSA (Gd-DOTA) increases with increasing Gd-DOTA per molecule and then plateaus at >15 Gd/molecule, attaining a maximum of 33 $mM^{-1}\ s^{-1}$. The relaxivity values are comparable to those for literature reported and commercial agents such as isothiocyanato-benzyl-diethylenetriamine-pentaacetic acid (ITCB-DTPA-Gd), albumin (30.3 $mM^{-1}\ s^{-1}$ at 29 MHz, 24 °C) (*35*), and MS-325, a Gd chelate that reversibly and noncovalently binds native albumin with relaxivity at maximum loading of albumin equal to 33 $mM^{-1}\ s^{-1}$ and relaxivity under in vivo conditions of 17.3 $mM^{-1}\ s^{-1}$ (*36*). Relaxivities for mal-BSA $(Gd\text{-}DOTA)_{>15}$ are significantly higher than those reported for a related albumin-$(Gd\text{-}DTPA)_{19}$ (14.9 $mM^{-1}\ s^{-1}$ at 10.7 MHz, 37 °C) (*37*) or for Magnevist, a small molecule gadolinium chelate (3.4 $mM^{-1}\ s^{-1}$ at 42 MHz, 37 °C). The reported values for the albumin compounds were obtained a slightly higher temperature and with different field strength instruments, so the values are not directly translatable. However, these results show that the relaxivities for the prepared agents are on the order or better than expected values. R_1 values are also improved over free Gd-DOTA preparations such as Magnevist. Conjugation of Gd-DOTA to larger molecules is known to increase relaxivity by reducing rotational correlation time (*38*). This has been observed for lipophilic Gd-DOTP and Gd-DOTA complexes that bind to albumin (*39*, *40*), as well as for other Gd-DOTA conjugates (*41*, *42*).

MR images of solutions of the contrast agent at 7 T demonstrated that these levels of labeling with Gd-DOTA were sufficient to affect contrast at physiologically reasonable concentrations. As shown in Figure 2 contrast was increased in a concentration dependent manner by the Gd-DOTA conjugates, with greater enhancement by more heavily labeled molecules. Figure 2 presents mal-BSA that has been conjugated to 18 or 10 Gd-DOTA, and greater contrast is seen with 18 attached Gd-DOTA for the top row of solutions, as expected. For the 18 Gd-DOTA molecule, significant contrast enhancement is seen for concentrations greater than 50 μM.

Uptake by cells was assessed on P388D1 macrophages in culture. Cells were incubated with 15 and 10 Gd-DOTA labeled mal-BSA for 1 h and then lysed for MR imaging. As shown in Figure 3 macrophages show increasing contrast in an MRI image with increasing concentration of the Gd-DOTA-labeled compounds. Incubation with greater than 50 μM of either labeled agent was sufficient to produce observable contrast in the MR image. Results from ICP-MS indicate that femtomoles of gadolinium could be found inside a cell after 1 h incubation.

That uptake by cells is specific was confirmed by incubating cells with mal-BSA carrying 22 Gd-DOTA, or with a Gd-DOTA matched BSA control. These control molecules were prepared from the same batch of Gd-DOTA-labeled BSA but were not maleylated for scavenger receptor recognition. Images at 7 T, Figure 4, from incubated cells show that there is no uptake of the BSA compound (bottom row) while the maleylated partner

Table 1. Relaxivities of Prepared Agents Compared to Other Reported Agents. Relaxivities Increase with Increasing Gd-DOTA Incorporation, Reaching an Apparent Plateau above 15 Gd/Molecule

contrast agent	r_1 per Gd ($mM^{-1}\ s^{-1}$)	temp and field strength	molecular weight BSA-DOTA only (Da)	final molecular weight (Da)	Gd ion per DOTA
Mal-BSA $(Gd\text{-}DOTA)_{22}$	29.1	RT, 26 MHz	79142	85898.7	19.8
Mal-BSA $(Gd\text{-}DOTA)_{18}$	33.4	RT, 26 MHz	76607.5	82317.2	11.9
Mal-BSA $(Gd\text{-}DOTA)_{15}$	31.2	RT, 26 MHz	74844.5	82455	14
Mal-BSA $(Gd\text{-}DOTA)_{10}$	20.0	RT, 26 MHz	71702.2	77490.6	6.7
Mal-BSA $(Gd\text{-}DOTA)_6$	12.2	RT, 26 MHz	69535.6	75954.1	4.4
Mal-BSA $(Na\text{-}DOTA)_6$	0.09	RT, 26 MHz	69535.6	−	0

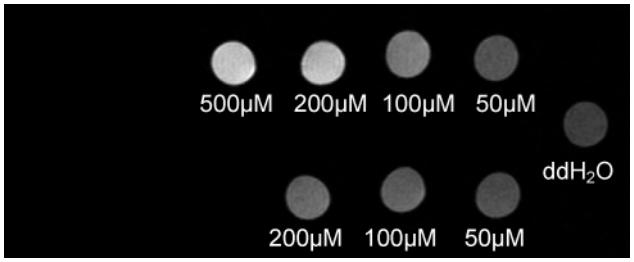

Figure 3. Mal-BSA (Gd-DOTA)$_n$ is taken up by macrophages. P388D1 cells were incubated with $n = 15$ (top row) or $n = 10$ (bottom row) mal-BSA (Gd-DOTA)$_n$ for 1 h then imaged at 7 T. Contrast increases in a concentration dependent manner (right to left) indicating uptake of the contrast agent by the cells. Contrast enhancement is observed for an application of as low as 50 μM contrast agent to the cells (top row, rightmost column). Actual T_1 values were, left-right: (top row) = 0.84 s, 0.96 s, 1.49 s. 2.33 s; (bottom row) = 1.79 s, 1.96 s, 2.51 s; (water) = 3.44 s.

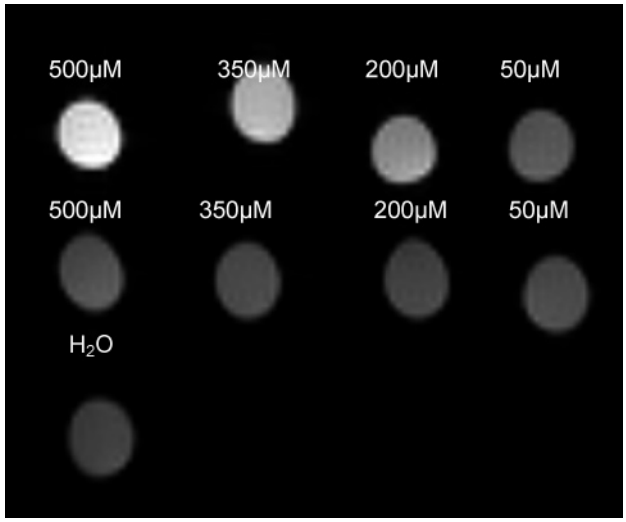

Figure 4. Uptake of mal-BSA (Gd-DOTA)$_n$ is specific. P388D1 cells were incubated with either mal-BSA (Gd-DOTA)$_n$ or a matched BSA control, $n = 22$ for both. Cells were imaged at 7 T. Macrophages demonstrate uptake of the maleylated agent (top row) but do not recognize the nonmaleylated control (middle row). Contrast enhancement after uptake of mal-BSA (Gd-DOTA)$_{22}$ is observable for as little as 25 μM of the agent applied to cells. Actual T_1 values were, left-right: (top row) = 0.58 s. 0.89 s, 1.46 s, 2.53 s; (bottom row) = 2.81 s, 2.90 s, 3.09 s, 2.85 s; (water) = 3.50 s.

is taken up in a concentration dependent manner (top row). Specificity of uptake was further confirmed by competition studies in which cells were incubated with a fixed concentration of mal-BSA (Gd-DOTA)$_{15}$ and increasing excess of unlabeled mal-BSA. If uptake were receptor-mediated, the excess unlabeled ligand should compete for uptake. Nonspecific uptake is strictly concentration-dependent and would not be affected by additional ligands in the solution. Receptor-mediated uptake is confirmed by the results seen in Figure 5: increasing amounts from 0 to 20-fold excess competitor reduce uptake as expected for a receptor-mediated process.

One of the primary concerns regarding the use of biomolecules labeled with gadolinium chelates as contrast agents is whether sufficient amounts of gadolinium can be accumulated in sites of interest to be visible on an MR image (*43*). The final amount of contrast agent required to produce sufficient contrast in an MRI scan depends on a host of factors including the precise pulse sequence and parameters used for acquisition (*2, 23*). Nevertheless, this issue has been studied by a number of investigators, and estimations can be made. One of the earliest theoretical models for the minimum amount of Gd(III) complex, of a given relaxivity, to produce detectable contrast enhancement

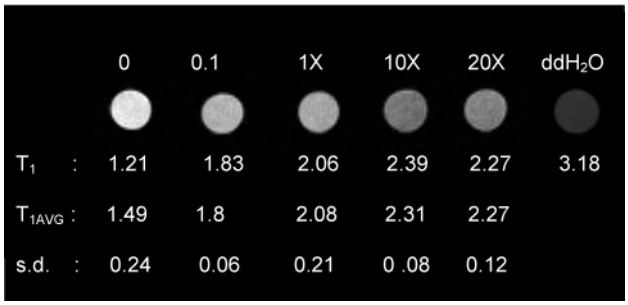

Figure 5. Uptake of mal-BSA (Gd-DOTA)$_n$ is receptor-mediated. P388D1 cells were incubated with a fixed concentration of mal-BSA (Gd-DOTA)$_{15}$ and increasing molar excesses of unlabeled mal-BSA. Representative samples are shown with molar excesses of competitor as indicated above each sample. Actual T_1 values for the image appear below each sample, as well as average and standard deviation T_1 for triplicate repeats. All values are given in seconds. Cells were imaged at 7 T. Increasing molar excess of unlabeled agent inhibits uptake of the labeled agent and reduced signal in the image. T_1 decreases dramatically with molar excess of competitor. Competition by unlabeled ligand confirms that uptake of the contrast agent is receptor-mediated.

was tested against microinjections of Gd(III) into Xenopus eggs (*44*). These trials established that measurable contrast was visualized when the concentration of agent in the egg is on the order of 10−100 μM (at 500 MHz). The Xenopus embryo system is unique, and while similar to some types of human tissue, the eggs are quite fatty and are different from many tissues of interest in mammals. More recent empirical results at 7 T have shown that for contrast agents with relaxivities in the range of 5−7 mM^{-1} s^{-1}, the minimum amount of Gd(III) to produce contrast is on the order of 2×10^9 molecules per cell; while for an agent with relaxivity on the order of 80 mM^{-1} s^{-1} (20 MHz) contrast is observed for concentrations on the order of 4×10^7 Gd(III) per cell (*45*). These observations were made using apoferritin as a carrier for the Gd(III), which is taken up by receptors found on the cell surface at a density of 4×10^4 per cell, $K_d = 1$ nM.

Relaxivities are also field-dependent. NMRD curves for Gd-DOTA show that relaxivity does not change much up to about 2 MHz and then begins to fall off rapidly, so the relaxivity at typical clinical field strengths (1.5−3 T) should actually be a bit higher than that observed on typical research instruments (4.7−11.7 T) (*40*). Thus, the amount of Gd-DOTA required would be less at lower field strengths. We estimated that the relaxivity for our multilabeled mal-BSA molecules would be similar to that observed for Gd-labeled albumin (26:1 Gd:albumin) = 192 mM^{-1} s^{-1} (per mM agent) at 4.7 T (*46*). At 1.5 T this value would be higher. With this estimate of relaxivity, based on the criteria just described, the amount of Gd(III) required to produce contrast at 1.5 T should be less than 4×10^7 molecules per cell.

The scavenger receptor is a high affinity (pM−nM, depending upon ligand) receptor present in high numbers on macrophages, on the order of 5×10^5 receptors per cell P388D1 (*18, 25, 47, 48*). Thus, ~20−80 Gd(III) must be taken up per receptor during the course of incubation (depending on cell type used) to reach the concentrations required per cell. Scavenger receptors uptake and process modified lipoproteins through a classic coated pit pathway, similar to the LDL pathway, wherein the receptor takes up ligand, brings ligand into the cell, dissociates from the ligand, and recycles back to the surface in a highly efficient manner. The scavenger receptor has an estimated $t_{1/2}$ for internalization of the ligand−receptor complex of 2.8−4 min (*22*). Recycling of receptors in the scavenger receptor pathway has not been fully characterized, but in the LDL pathway, receptors recycle on the order of 10 min (*49−51*). If this is similar for the scavenger receptor pathway then 500 000

receptors can uptake $\sim 3 \times 10^6$ ligands per hour. Based on the values given above, this would be sufficient for contrast with 13:1 Gd:ligand complex and 1 h incubation. As our results show, modification with 10 and greater Gd-DOTA per mal-BSA was sufficient to produce contrast with micromolar applications to cells. Moreover, the cell densities used for these studies is on the order of that found for macrophages in isolated human plaques, indicating that these imaging results will be applicable to the in vivo case (*52*−*56*).

There are number of examples in the literature of efficient cellular uptake of Gd(III) complexes using Gd-DOTA-derived molecules (*57*−*60*). More recent efforts have sought to maximize the load of Gd delivered per receptor by tethering carrier molecules to dendridic polymers containing high numbers of Gd(III) (*61*). Uptake through the folate receptor has been demonstrated by this means as has avidin−biotin antibody-based targeting (*59, 62, 63*). Again, definitive measurement of the amount of Gd required to produce contrast depends on the imaging parameters employed, and these must also be evaluated when testing the new contrast agents. But on the basis of the approximate calculations shown here, and these similar studies in the literature, we predicted that MRI contrast could be achieved for the scavenger receptor system using feasible ratios of Gd:ligand, and this was confirmed by the results reported here.

Recent literature has investigated MRI contrast agents targeted to other molecular markers in plaque, but these tend to be geared for imaging of more advanced stages of disease. For example, 5-HT-DOTA(Gd) targets myeloperoxidase (MPO), a heme-containing enzyme secreted by a number of neutrophils, for selective imaging of MPO activity in a model system (*64*). Myeloperoxidase secretion has been correlated with plaque instability. The described agent is a serotonin derivative of Gd-DOTA that polymerizes after oxidation by myeloperoxidase-catalyzed reduction of hydrogen peroxide. Polymerization resulted in increased relaxivity attributed to decrease in rotational correlation time and demonstrated contrast enhancement in the presence of at least 650 U of enzyme. This agent is geared toward more advanced plaques that would have significant secretion of MPO and may be vulnerable to rupture. Other examples in the literature describe the use of Gd-DTPA-labeled fibrin binding peptides to label thrombi in animal models (*65, 66*). Each agent carries four gadolinium chelates and binds to mural thrombi, rather than atherosclerotic plaque. Thrombosis occurs after plaque rupture, and these agents are designed to aid in guiding thrombolytic therapy.

Fewer reports describe MRI agents able to detect earlier stages of disease. One example is low-density lipoprotein (LDL) complexed with manganese-mesoporphyrin (MnMeso) (*67*). These agents are also targeted to macrophages in that the modified LDL was demonstrated to be taken up by foam cell cultures. However, the MnMeso is not covalently bound to the lipoprotein and therefore may transfer off LDL to other plasma proteins and lipoproteins. In addition, there is concern about possible cardiotoxicity and accumulation of Mn^{2+} agents in the brain after intravenous injection (*68, 69*). Dextran-coated iron oxide nanoparticles have also been observed to be taken up by macrophages in plaques, due to the phagocytic nature of the cells to engulf particles (*70*). However these rely on nonspecific uptake of the nanoparticles, which is an inefficient process, outside of the liver, and the agent must be delivered in severalfold excess of standard clinical doses in order to accumulate enough contrast agent in the plaque after clearance through by renal system.

A possible limitation to administering mal-BSA $(Gd\text{-}DOTA)_n$ in a clinical setting is possible humoral immune response to this macrocyclic chelated agent (*71, 72*). By targeting macrophages, we are in effect aiming for increased recognition by these immune cells. However, our aim is for internalization of mal-BSA and removal from blood without negative systemic effects. Studies on methods to increase immunogenicity of antigens for vaccine development have examined maleylation (*21*). In those studies, immunogenicity, i.e. uptake by macrophages, of maleylated antigens was increased compared to unmodified antigens upon repeated injections in mice without adjuvants present (*21*). Upon repeated exposure, animals exposed to mal-BSA shows higher serum anti-immunogen antibody concentration than those exposed to BSA. In addition, maleylation disrupts native B cell epitopes on the antigens, for example, maleylated diphtheria toxoid (DT) is not recognized by antibodies to native DT. New epitopes seem to be created that can cross-react between various maleylated proteins regardless of amino acid sequence. It is likely then that the epitopes are purely maleylation dependent. While mice produced antibodies against the antigen, no systemic toxicity was reported. Possible toxic or other negative immune responses of mal-BSA require further study. The scavenger receptor recognizes a number of different ligands (*9*−*11, 13*), and these can also be investigated as carriers should mal-BSA prove undesirable in vivo.

From the MTT cell toxicity studies, dose−response curves suggest that mal-BSA $(Gd\text{-}DOTA)_{15}$ has a low toxicity when compared to chlorpromazine, as shown in Figures 6A and 6B. Chlorpromazine is a phenothiazine drug, primarily used as a psychotropic agent since the 1950s, with a low toxicity (*73*−*75*). Its toxicity has been well documented, and therefore it has been employed as a standard in toxicity assays (*74*−*76*). The EC_{50} can be interpolated from these plots and used to directly compare the toxicity of mal-BSA $(Gd\text{-}DOTA)_{15}$ to chlorpromazine. From Figure 6A, EC_{50} is not reached at even the highest concentration tested for 4-h incubations with mal-BSA $(Gd\text{-}DOTA)_{15}$. For 24 h incubations, EC_{50} was found to be 40 μM. Both values are less toxic than those found for chlorpromazine, Figure 6B, which showed $EC_{50} = 84$ μM for 4 h, and $EC_{50} = 24$ μM for 24 h incubations, respectively.

Biodistribution studies show a very fast clearance from the bloodstream. More than 97% of the injected dose of radiolabeled contrast agent is cleared out within 2 min as seen in Figure 7. From the PET studies of biodistribution it was found that the main sites for accumulation are the liver, kidneys, and the urinary bladder. The highest accumulation is in the liver (Figure 8). After 1 h about 50% of the injected dose remains in the liver. During the next 3 h the activity drops to 30% of the injected dose. This is equivalent to 30 μM agent in the liver after 1 h and 18 μM after 4 h. The activity then remains stable at 18 μM (Figure 9). Comparing these accumulated concentrations to the concentrations from the cell toxicity studies, $EC_{50} = 40$ μM for 24 h incubation, suggests that in these experiments in vivo accumulation is at less than toxic levels. Accumulation observed in the other organs is even less and thus also below toxic EC_{50}. For the kidneys, about 1% of the injected dose is found in each kidney, and the levels are stable for the duration of the whole experiment. In the urinary bladder 2.5% of the injected dose remains after 1 h; this clears to approximately 0.2−0.5% of injected dose during the first 24 h and falls to undetectable levels after 48 h. By comparison, the blood pool agent albumin$(Gd\text{-}DTPA)_{30}$ is largely retained in the intravascular space with a half-life of 88 min after intravenous injection and can remain in the bloodstream and extravascular compartment two weeks after injection (*77, 78*). These undesirably long retention times have precluded its use in the clinic.

In conclusion, we describe the preparation, characterization, and successful in vitro targeting of a paramagnetic contrast agent, mal-BSA $(Gd\text{-}DOTA)_n$, for use in MRI. This novel contrast agent builds upon previously reported studies on anionic

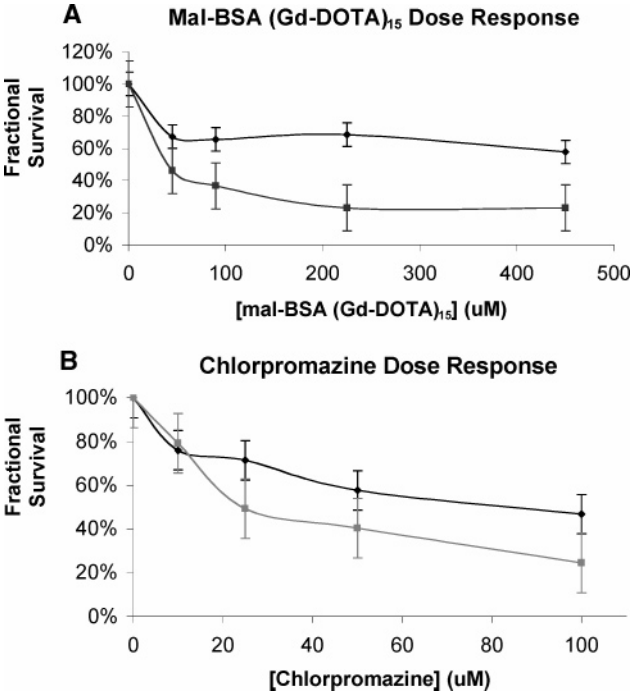

Figure 6. Toxicity of mal-BSA. Cytotoxicity was assessed for mal-BSA $(Gd\text{-}DOTA)_{15}$ and chlorpromazine as a positive control. The assays were carried out in parallel and in triplicate. Cells were counted and plated evenly in a 96-well plate. After a 24-h adhesion time, varying concentrations of mal-BSA $(Gd\text{-}DOTA)_{15}$ (0, 45, 90, 225, and 445 μM) or chlorpromazine (0, 10, 25, 50, and 100 μM) were placed on the cells. After a 4 and 24 h agent exposure time at 37 °C the MTT assay was performed. Dose−response curves at 4 (black) and 24 (gray) hours are shown for mal-BSA $(Gd\text{-}DOTA)_{15}$ (Figure 6A) and chlorpromazine (Figure 6B). For 4 h mal-BSA incubation, toxic dose EC_{50} is not reached for the concentrations of agent tested ($EC_{50} > 450$ μM). For the 24 h mal-BSA, $EC_{50} = 40$ μM. This is in contrast with chlorpromazine with $EC_{50} = 84$ μM for 4 h incubation and $EC_{50} = 24$ μM for 24 h incubation. Toxicity of mal-BSA (Gd-DOTA) is less that that of the chlorpromazine standard. Error bars reflect standard error.

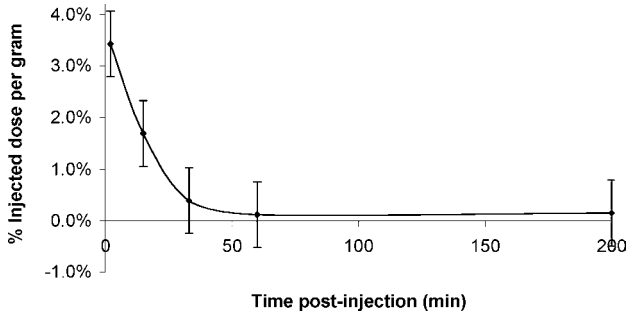

Figure 7. Blood clearance. Blood samples were collected by tail nicking at 2, 15, 33, 60, and 200 min postinjection of contrast agent and quantitated by gamma counting. Clearance from the blood is rapid with ~97% of the injected agent cleared out from the bloodstream after 2 min; 0.5% of injected dose remaining after 30 min and undetectable levels in the blood after 1 h. Error bars reflect standard error.

modifications of BSA and knowledge of the SR-A receptor. Mal-BSA $(Gd\text{-}DOTA)_n$ has physical properties that permit localization to the target and demonstrated high specific uptake of agent by macrophages; also low toxicity and fast clearance dynamics are shown. The synthesis process outlined here allows controllable degrees of maleylation and paramagnetic labeling of known lysines on the BSA molecule. Mal-BSA $(Gd\text{-}DOTA)_n$ demonstrated relaxation effects comparable to or better than similar commercial and experimental plaque-targeted or albumin-based agents. An optimal payload of 22 Gd-DOTA with mal-BSA $(Gd\text{-}DOTA)_{22}$ showed contrast effects comparable to

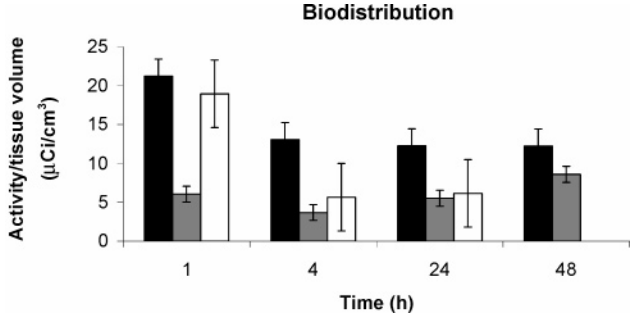

Figure 8. Biodistribution in the rat model. Primary sites of accumulation of the agent in normal tissues are in liver (black), kidneys (gray), and urinary bladder (white). Clearance from kidneys is rapid in first hour. Signal from bladder falls to negligible levels by 48 h. Error bars reflect standard error.

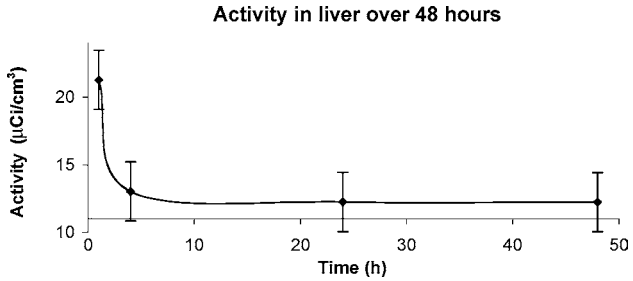

Figure 9. Liver pharmacokinetics. The clearance of the agent from the liver is initially rapid. The activity per tissue volume of the agent decreased over 60% the first 4 h after injection. Calculated corresponding concentration of the agent falls to 18 μM after 4 h, well below the EC_{50} found for macrophages in culture ($EC_{50} > 450$ μM for 4 h, $EC_{50} = 40$ μM for 24 h). Error bars reflect standard error.

albumin $(Gd\text{-}DTPA)_{30}$, which is used as a standard to evaluate performances of novel intravascular agents (*79*−*82*).

Though further studies are required to evaluate immunogenicity of the agent, the high specificity of mal-BSA $(Gd\text{-}DOTA)_n$ shows promise for reducing dosage of administration and toxicity compared to high dose nonspecific contrast agents currently employed in the clinic. Future work includes isolating the regional domains of maleylated BSA that afford targeting in order to circumvent immune responses that may be provoked by full length protein. Through the modification with other diagnostic agents, such as the ^{64}Cu positron emitter or fluorophores, this carrier system shows potential to act as a multimodality imaging agent for diagnosis and study of atherosclerotic and restenotic lesions.

ACKNOWLEDGMENT

The authors thank National Institutes of Health (EB000993-01A1) and the Whitaker Foundation (RG-02-0740) for their support of this work; Dr. Jeff Walton for assistance with MRI, Dr. Ryoji Shiraki for assistance with ICP-MS, David Kukis for assistance with radioactive labeling, Chris Griesemer for assistance with animal studies, Lily Wong for her assistance with chemical coupling and tissue culture, and Christina Takanishi and Edgar Sanchez for assistance with cell toxicity studies.

LITERATURE CITED

(1) Desai, M. Y., and Bluemke, D. A. (2005) Atherosclerosis imaging using MR imaging: current and emerging applications. *Magn. Reson. Imaging Clin. N. Am. 13*, 171−80, vii.

(2) Rogers, W. J., Prichard, J. W., Hu, Y. L., Olson, P. R., Benckart, D. H., Kramer, C. M., Vido, D. A., and Reichek, N. (2000) Characterization of signal properties in atherosclerotic plaque components by intravascular MRI. *Arterioscler. Thromb. Vasc. Biol. 20*, 1824−30.

(3) Fayad, Z. A. (2003) MR imaging for the noninvasive assessment of atherothrombotic plaques. *Magn. Reson. Imaging Clin. N. Am. 11*, 101−13.

(4) Choudhury, R. P., Fuster, V., and Fayad, Z. A. (2004) Molecular, cellular and functional imaging of atherothrombosis. *Nat. Rev. Drug Discovery 3*, 913−25.

(5) Ruygrok, P., Webster, M., deValk, V., vanEs, G., Ormiston, J., Morel, M., and Serruys, P. (2001) Clinical and angiographic factors associated with asymptomatic restenosis after percutaneous coronary intervention. *Circulation 104*, 2289.

(6) Ross, R. (1993) The pathogenesis of atherosclerosis: a perspective for the 1990s. *Nature 362*, 801−809.

(7) Platt, N., and Gordon, S. (2001) Is the class A macrophage scavenger receptor (SR-A) multifunctional? − The mouse's tale. *J. Clin. Invest. 108*, 649−54.

(8) Van Berkel, T. J., Van Eck, M., Herijgers, N., Fluiter, K., and Nion, S. (2000) Scavenger receptor classes A and B. Their roles in atherogenesis and the metabolism of modified LDL and HDL. *Ann. N. Y. Acad. Sci. 902*, 113−26; discussion 126−7.

(9) Sakai, M., Kobori, S., Miyazaki, A., and Horiuchi, S. (2000) Macrophage proliferation in atherosclerosis. *Curr. Opin. Lipidol. 11*, 503−9.

(10) Silverstein, R., and Febbraio, M. (2000) CD36 and atherosclerosis. *Curr. Opin. Lipidol. 11*, 482−491.

(11) Trigatti, B., Rigotti, A., and Braun, A. (2000) Cellular and physiological roles of SR−BI, a lipoprotein receptor which mediates selective lipid uptake. *Biochim. Biophys. Acta*, 276−286.

(12) Hughes, D., Fraser, I., and Gordon, S. (1995) Murine macrophage scavenger receptor: In vivo expression and function as receptor for macrophage adhesion in lymphoid and nonlymphoid organs. *Eur. J. Biochem. 25*, 466−473.

(13) de Winther, M. P., van Dijk, K. W., Havekes, L. M., and Hofker, M. H. (2000) Macrophage scavenger receptor class A: A multifunctional receptor in atherosclerosis. *Arterioscler. Thromb. Vasc. Biol. 20*, 290−7.

(14) Nakata, A., Nakagawa, Y., Nishida, M., Nozaki, S., Miyagawa, J., Nakagawa, T., Tamura, R., Matsumoto, K., Kameda-Takemura, K., Yamashita, S., and Matsuzawa, Y. (1999) CD36, a novel receptor for oxidized low-density lipoproteins, is highly expressed on lipid-laden macrophages in human atherosclerotic aorta. *Arterioscler. Thromb. Vasc. Biol. 19*, 1333−9.

(15) Linton, M., and Fazio, S. (2001) Class A scavenger receptors, macrophages and atherosclerosis. *Curr. Opin. Lipidol. 12*, 489−495.

(16) Krieger, M., and Herz, J. (1994) Structures and functions of multiligand lipoprotein receptors- macropahge scavenger receptors and LDL receptor-related protein (LRP). *Ann. Rev. Biochem. 63*, 601−637.

(17) De Rijke, Y. B., Biessen, E. A., Vogelezang, C. J., and van Berkel, T. J. (1994) Binding characteristics of scavenger receptors on liver endothelial and Kupffer cells for modified low-density lipoproteins. *Biochem. J. 304* (Pt 1), 69−73.

(18) Gough, P. J., and Gordon, S. (2000) The role of scavenger receptors in the innate immune system. *Microbes Infect. 2*, 305−11.

(19) Horiuchi, S., Sakamoto, Y., and Sakai, M. (2003) Scavenger receptors for oxidized and glycated proteins. *Amino Acids 25*, 283−92.

(20) Ottnad, E., Via, D. P., Frubis, J., Sinn, H., Friedrich, E., Ziegler, R., and Dresel, H. A. (1992) Differentiation of binding sites on reconstituted hepatic scavenger receptors using oxidized low-density lipoprotein. *Biochem. J. 281* (Pt 3), 745−51.

(21) Abraham, R., Singh, N., Mukhopadhyay, A., Basu, S. K., Bal, V., and Rath, S. (1995) Modulation of immunogenicity and antigenicity of proteins by maleylation to target scavenger receptors on macrophages. *J. Immunol. 154*, 1−8.

(22) Fong, L., and Le, D. (1999) The processing of ligands by class A scavenger receptor is dependent on signal information located in the cytoplasmic domain. *J. Biol. Chem. 274*, 26808−26816.

(23) Artemov, D. (2003) Molecular magnetic resonance imaging with targeted contrast agents. *J. Cell Biochem. 90*, 518−24.

(24) Rhainds, D., Falstrault, L., Tremblay, C., and Brissette, L. (1999) Uptake and fate of class B scavenger receptor ligands in HepG2 cells. *Eur. J. Biochem. 261*, 227−35.

(25) Haberland, M. E., Tannenbaum, C. S., Williams, R. E., Adams, D. O., and Hamilton, T. A. (1989) Role of the maleyl-albumin receptor in activation of murine peritoneal macrophages in vitro. *J. Immunol. 142*, 855−62.

(26) Mirzadeh, S., Brechbiel, M. W., Atcher, R. W., and Gansow, O. A. (1990) Radiometal labeling of immunoproteins: covalent linkage of 2-(4-isothiocyanatobenzyl)diethylenetriaminepentaacetic acid ligands to immunoglobulin. *Bioconjugate Chem. 1*, 59−65.

(27) Butler, P., and Hartley, B. (1972) Maleylation of proteins. *Methods Enzymol. 25*, 191−199.

(28) Benson, J. R., and Hare, P. E. (1975) O-phthalaldehyde: fluorogenic detection of primary amines in the picomole range. Comparison with fluorescamine and ninhydrin. *Proc. Natl. Acad. Sci. U.S.A. 72*, 619−22.

(29) Roth, M. (1971) Fluorescence reaction for amino acids. *Anal. Chem 43*, 880−2.

(30) Carmichael, J., Degraff, W. G., Gazdar, A. F., Minna, J. D., Mitchell, J. B. (1987) Evaluation of a tetrazolium-based semiautomated colorimetric assay: assessment of chemosensitivity testing. *Cancer Res. 47*, 936−942.

(31) Penefsky, H. S. (1977) Reversible binding of Pi by beef-heart mitochondrial adenosine- triphosphatase. *J. Biol. Chem. 252*, 2891−2899.

(32) Islam, M., Qamar, S., and Tayyab, S. (1994) Involvement of lysine residues of goat serum albumin in high-affinity binding of bilirubin. *Biochim. Biophys. Acta 1205*, 171−7.

(33) Horiuchi, S., Takata, K., Araki, N., and Morino, Y. (1989) Regional ligand domain is involved in scavenger receptor-mediated recognition of maleyl-albumin by rat sinusoidal liver cells. *J. Mol. Recognit. 2*, 56−62.

(34) Ohyoshi, E., and Kohata, S. (1993) The binding of Yb(III) and Gd(III) to bovin serum albumin by a competitive spectrophotometry. *J. Inorg. Biochem. 52*, 157−63.

(35) Niemi, P., Koskinen, S., and Reisto, T. (1991) Tissue relaxation enhancement after intravenous administration of (ITCB-DTPA)-gadolinum conjugated albumin, an intravascular magnetic resonance imaging contrast agent. *Invest. Radiol. 26*, 674−80.

(36) Corot, C., Violas, X., Robert, P., Gagneur, G., and Port, M. (2003) Comparison of different types of blood pool agents (P792, MS325, USPIO) in a rabbit MR angiography-like protocol. *Invest. Radiol. 38*, 311−9.

(37) Ogan, M. D., Schmiedl, U., Moseley, M. E., Grodd, W., Paajanen, H., and Brasch, R. C. (1987) Albumin labeled with Gd-DTPA. An intravascular contrast-enhancing agent for magnetic resonance blood pool imaging: preparation and characterization. *Invest. Radiol. 22*, 665−71.

(38) Meyer, D., Schaefer, M., and Bonnemain, B. (1988) Gd-DOTA, a potential MRI contrast agent. Current status of physicochemical knowledge. *Invest. Radiol. 23* (Suppl 1), S232−5.

(39) Caravan, P., Greenfield, M., Li, Z., and Sherry, A. (2001) The Gd3+ complex of a fatty acid analogue of DOTP binds to multiple albumin sites with variable water relaxivities. *Inorg. Chem. 40*, 6580−6587.

(40) Caravan, P., Ellison, J., McMurry, T., and Lauffer, R. (1999) Gadolinium (III) chelates as MRI contrast agents: Structure, dynamics, and applications. *Chem. Rev. 99*, 2293−2352.

(41) Anelli, P., Bertini, I., Fragai, M., Lattuada, L., Luchinat, C., and Parigi, G. (2000) Sulfonamide-functionalized gadolinium DTPA complexes as possible contrast agents for MRI: a relaxometric investigation. *Eur. J. Biochem.*, 625−630.

(42) Nivorozhkin, A., Kolodziej, A., Caravan, P., Greenfield, M., Lauffer, R., and McMurry, T. (2001) Enzyme-activated Gd3+ magnetic resonance imaging contrast agents with a prominent receptor-induced magnetization enhancement. *Angew. Chem., Int. Ed. 40*, 2903−2906.

(43) Nunn, A. D., Linder, K. E., and Tweedle, M. F. (1997) Can receptors be imaged with MRI agents? *Q. J. Nucl. Med. 41*, 155−62.

(44) Ahrens, E., Rothbacher, U., Jacobs, R., and Fraser, S. (1998) A model for MRI contrast enhancement using T1 agents. *Proc. Natl. Acad. Sci. U.S.A. 95*, 8443−8448.

(45) Aime, S., Furllano, L., and Crich, S. (2002) Comparmentalization of a gadolinium complex in the apoferritin cavity: a route to obtain high relaxivity contrast agent for magnetic resonance imaging. *Angew. Chem. Int. Ed. 41*, 1017−1019.

(46) Dafni, H., Israely, T., Bhujwalla, Z., Benjamin, L., and Neeman, M. (2002) Overexpression of vascular endothelial growth factor 165 drives peritumor interstitial convection and induces lymphatic drain: Magnetic Resonance Imaging, confocal microscopy, and histological tracking of triple-labeled albumin. *Cancer Res. 62*, 6731−6739.

(47) Ward, D., Ajioka, R., and Kaplan, J. (1989) Cohort movement of different ligands and receptors in the intracellular endocytic pathway of alveolar macrophages. *J. Biol. Chem. 264*, 8164−8170.

(48) Ottnad, E., Via, D. P., Sinn, H., Friedrich, E., Ziegler, R., and Dresel, H. A. (1990) Binding characteristics of reduced hepatic receptors for acetylated low-density lipoprotein and maleylated bovine serum albumin. *Biochem. J. 265*, 689−98.

(49) Goldstein, J., Brown, M., Anderson, R., Russell, D., and Schneider, W. (1985) Receptor-mediated endocytosis. *Ann. Rev. Cell Biol. 1*.

(50) Murphy, J., Tedbury, P., HomerVanniasinkam, S., Walker, J., and Ponnambalam, S. (2005) Biochemistry and cell biology of mammalian scavenger receptors. *Atherosclerosis 182*, 1−15.

(51) Harwood, H., and Pellarin, L. (1997) Kinetics of low-density lipoprotien receptor activity in Hep-G2 cells: derivation and validation of a Briggs-Haldane-based kinetic model for evaluating receptor-mediated endocytotic processes in which receptors recycle. *Biochem. J. 323*, 649−659.

(52) Lendon, C., Davies, M., Born, G., and Richardson, P. (1991) Atherosclerotic plaque caps are locally weakened when macrophages density is increased. *Atherosclerosis 87*, 87−90.

(53) Celletti, F., Waugh, J., Amabile, P., Brendolan, A., Hilfiker, P., and Dake, M. (2001) Vascular endothelial growth factor enhances atherosclerotic plaque progression. *Nat. Med. 7*, 425−429.

(54) McCarthy, M. J., Loftus, I. M., Thompson, M. M., Jones, L., London, N. J., Bell, P. R., Naylor, A. R., and Brindle, N. P. (1999) Angiogenesis and the atherosclerotic carotid plaque: an association between symptomatology and plaque morphology. *J. Vasc. Surg. 30*, 261−8.

(55) Lastas, A., Graziene, V., Barkauskas, E., Salkus, G., and Rimkevicius, A. (2004) Carotid artery atherosclerotic plaque: clinical and morphological-immunohistochemical correlation. *Med. Sci. Monit. 10*, CR606−14.

(56) Schmitz, S. A., Taupitz, M., Wagner, S., Coupland, S. E., Gust, R., Nikolova, A., and Wolf, K. J. (2002) Iron-oxide-enhanced magnetic resonance imaging of atherosclerotic plaques: postmortem analysis of accuracy, inter-observer agreement, and pitfalls. *Invest. Radiol. 37*, 405−11.

(57) Oyewumi, M., Yokel, R., Jay, M., Coakley, T., and Mumper, R. (2004) Comparison of celluptake, biodistribution and tumor retention of folate-covered and PEG-coated gadolinium nanoparticles in tumor-bearing mice. *J. Controlled Release 95*, 613−626.

(58) Allen, M. J., MacRenaris, K. W., Venkatasubramanian, P. N., and Meade, T. J. (2004) Cellular delivery of MRI contrast agents. *Chem. Biol. 11*, 301−7.

(59) Aime, S., Cabella, C., Colombatto, S., Crich, S., Gianolio, E., and Maggioni, F. (2002) Insights into the use of paramagnetic Gd(III) complexes in MR-molecular imaging investigations. *J. Mag. Res. Imaging 16*, 394−406.

(60) Alauddin, M., Louie, A., Shahinian, A., Meade, T., and Conti, P. (2003) Receptor mediated uptake of a radiolabeled contrast agent sensitive to b-galactoside activity. *Nucl. Med. Biol. 30*, 261−265.

(61) Margerum, L., Campion, B., Koo, M., Shargill, N., Lai, J., Marumoto, A., and Sontum, P. (1997) Gadolinium(III) DO3A macrocycles and poly(ethylene glycol) coupled to dendrimers. Effect of molecular weight on physical and biological properties of macromolecular magnetic resonance imaging contrast agents. *J. Alloys Compd. 249*, 185−190.

(62) Kobayashi, H., Kawamoto, S., Star, R., Waldmann, T., Brechbiel, M., and Choyke, P. (2003) Activated clearance of a biotinylated macromolecular MRI contrast agent from the blood pool using an avidin chase. *Bioconjugate Chem. 14*, 1044−1047.

(63) Wiener, E., Konda, S., Shadron, A., Brechbiel, M., and Gansow, O. (1997) Targeting dendrimer-chelates to tumors and tumor cells expressing the high-affinity folate receptor. *Invest. Radiol. 32*, 748−754.

(64) Chen, J. W., Pham, W., Weissleder, R., and Bogdanov, A., Jr. (2004) Human myeloperoxidase: a potential target for molecular MR imaging in atherosclerosis. *Magn. Reson. Med. 52*, 1021−8.

(65) Botnar, R. M., Perez, A. S., Witte, S., Wiethoff, A. J., Laredo, J., Hamilton, J., Quist, W., Parsons, E. C., Jr., Vaidya, A., Kolodziej, A., Barrett, J. A., Graham, P. B., Weisskoff, R. M., Manning, W. J., and Johnstone, M. T. (2004) In vivo molecular imaging of acute and subacute thrombosis using a fibrin-binding magnetic resonance imaging contrast agent. *Circulation 109*, 2023−9.

(66) Spuentrup, E., Buecker, A., Katoh, M., Wiethoff, A., Parsons, E., Botnar, R., Weisskoff, R., Graham, P., manning, W., and Gunther, R. (2005) Molecular magnetic resonance imaging of coronary thrombosis and pulmonary emboli with a novel fibrin-targeted contrast agent. *Circulation 111*, 1377−1382.

(67) Mitsumori, L., Ricks, J., Rosenfeld, M., Schmiedl, U., and Yuan, C. (2004) Development of a lipoprotein based molecular imaging MR contrast agent for the noninvasive detection of early atherosclerotic disease. *Int. J. Cardiovasc. Imaging 20*, 561−567.

(68) Crossgrove, J., and Zhang, W. (2004) Maganese toxicity upon overexposure. *NMR Biomed. 17*, 544−553.

(69) Gallez, B., Baudelet, C., Adline, J., Geurts, M., and Delzenne, N. (997) Accumulation of manganese in the brain of mice after intravenous injection of manganese-based contrast agents. *Chem. Res. Toxicol. 10*, 360−363.

(70) Ruehm, S., Corot, C., Vogt, P., Kolb, S., and Debatin, J. (2001) Magnetic resonance imaging of atherosclerotic plaque with ultrasmall superparamagnetic particles of iron oxide in hyperlipidemic rabbits. *Circulation 103*, 415−422.

(71) Baxter, A. B., Melnikoff, S., Stites, D. P., and Brasch, R. C. (1991) AUR Memorial Award 1991. Immunogenicity of gadolinium-based contrast agents for magnetic resonance imaging. Induction and characterization of antibodies in animals. *Invest. Radiol. 26*, 1035−40.

(72) Perico, M. E., Chinol, M., Nacca, A., Luison, E., Paganelli, G., and Canevari, S. (2001) The humoral immune response to macrocyclic chelating agent DOTA depends on the carrier molecule. *J. Nucl. Med. 42*, 1697−703.

(73) Frotschl, R., Weickardt, S., Stazewski, S., Kaufman, G., and Kasper, P. (2005) Effects of chlorpromazine with and without UV irradiation on gene expression of HepG2 cells. *Mutat. Res. 575*.

(74) Petruska, J., Frank, D., Freeman, G., Evans, E., and Macdonald, J. (2002) Toxicity and carcinogenicity studies of chlorpromazine hydrochloride and p-cresidine in the p53 heterozygous mouse model. *Toxicol. Pathol. 30*, 696−704.

(75) Adams, C. (2005) Chlorpromazine for schizophrenia: A Cochran systematic review of 50 years of randomized controlled studies. *BMC Med. 3*, 15.

(76) Andres, M., Repetto, G., Sanz, P., and Repetto, M. (1999) Biochemical effects of chlorpromazine on mouse neuroblastoma cells. *Vet. Human Toxicol. 5*, 273−278.

(77) Schmiedl, U., Ogan, M., Paajanen, H., Marotti, M., Crooks, L. E., Brito, A. C., and Brasch, R. C. (1987) Albumin labeled with Gd-DTPA as an intravascular, blood pool-enhancing agent for MR imaging: biodistribution and imaging studies. *Radiology 162*, 205−10.

(78) Turetschek, K., Huber, S., Floyd, E., Helbich, T., Roberts, T. P., Shames, D. M., Tarlo, K. S., Wendland, M. F., and Brasch, R. C. (2001) MR imaging characterization of microvessels in experimental breast tumors by using a particulate contrast agent with histopathologic correlation. *Radiology 218*, 562−9.

(79) Turetschek, K., Huber, S., Helbich, T., Floyd, E., Tarlo, K. S., Roberts, T. P., Shames, D. M., Wendland, M. F., and Brasch, R. C. (2002) Dynamic MRI enhanced with albumin-(Gd-DTPA)30 or ultrasmall superparamagnetic iron oxide particles (NC100150 injection) for the measurement of microvessel permeability in experimental breast tumors. *Acad. Radiol. 9* (Suppl 1), S112−4.

(80) Preda, A., Novikov, V., Moglich, M., Turetschek, K., Shames, D. M., Brasch, R. C., Cavagna, F. M., and Roberts, T. P. (2004)

MRI monitoring of Avastin antiangiogenesis therapy using B22956/1, a new blood pool contrast agent, in an experimental model of human cancer. *J. Magn. Reson. Imaging 20*, 865−73.

(81) Preda, A., Novikov, V., Moglich, M., Floyd, E., Turetschek, K., Shames, D. M., Roberts, T. P., Corot, C., Carter, W. O., and Brasch, R. C. (2005) Magnetic resonance characterization of tumor microvessels in experimental breast tumors using a slow clearance blood pool contrast agent (carboxymethyldextran-A2-Gd-DOTA) with histopathological correlation. *Eur. Radiol. 15*, 2268−75.

(82) Li, K. L., Wilmes, L. J., Henry, R. G., Pallavicini, M. G., Park, J. W., Hu-Lowe, D. D., McShane, T. M., Shalinsky, D. R., Fu, Y. J., Brasch, R. C., and Hylton, N. M. (2005) Heterogeneity in the angiogenic response of a BT474 human breast cancer to a novel vascular endothelial growth factor-receptor tyrosine kinase inhibitor: assessment by voxel analysis of dynamic contrast-enhanced MRI. *J. Magn. Reson. Imaging 22*, 511−9.

BC060018K

TECHNICAL NOTES

Preparation of LL-37-Grafted Titanium Surfaces with Bactericidal Activity

Matthias Gabriel,*,† Kamran Nazmi,‡ Enno C. Veerman,‡ Arie V. Nieuw Amerongen,‡ and Andrej Zentner†

Departments of Orthodontics and Oral Biochemistry, Academic Centre for Dentistry Amsterdam (ACTA), The Netherlands.
Received March 23, 2005; Revised Manuscript Received December 12, 2005

Modification of material surfaces aimed at bestowing them with antimicrobial properties is a promising approach in the development of new biomaterials. Antimicrobial peptides (AMPs) are an attractive alternative to conventional antibiotics because of lack of toxicity, inherently high selectivity, and absence of immune response. As the antimicrobial mode of action of the AMP cathelin LL37 is formation of pores and disruption of microbial membrane, the purpose of the present study was to develop and test a method of covalent immobilization of LL37 on titanium surface. The application of a flexible hydrophilic poly(ethylene glycol) spacer and selective N-terminal conjugation of LL37 resulted in a surface peptide layer which was capable of killing bacteria on contact.

INTRODUCTION

Bacterial contamination may cause serious complications of implant surgery. Implant removal is usually the only treatment option because the biofilm mode of bacterial growth on the implant surface protects the microorganisms from the immune response and antibiotic treatment. There is a substantial interest in developing biomaterials with inherent properties, which would not only prevent bacterial adherence and colonization but would also be capable of killing microorganisms. Previous studies (*1*, *2*) have described bactericidal activity of quaternary ammonia salts covalently bound to biomaterial surfaces. Another approach to prevent microbial contamination would be the application of antimicrobial peptides (AMPs) (*3*, *4*). These peptides play an important role in the innate and adaptive immune system of various organisms and have a broad-spectrum activity against bacteria and fungi, while exhibiting low cytotoxicity. AMPs share a number of common molecular features: they are maximally 40−50 amino acid residues long, are rich in cationic amino acid residues, and form an amphiphilic α-helix in which clusters of hydrophobic and cationic amino acids are spatially separated. These characteristics promote their binding and insertion into the negatively charged phospholipid bilayers of bacteria and fungi, and disruption and impairment of vital membrane functions. Although the exact mechanisms by which AMPs kill bacteria are not precisely understood, it has been shown that peptide−lipid interactions leading to membrane permeation, possibly via transient formation of membrane-associated pores, might play an important role. An attractive advantage of AMPs over conventional antibiotics is the fact that they do not evoke immune response. In this study we have explored the potential use of the AMP cathelin LL37, a cryptic peptide obtained by enzymic cleavage of its precursor cathelicidin which is stored in granulocytes (*5*). The aim of this study was to render LL37 indiffusible by means of covalent immobilization while retaining its antimicrobial activity. Titanium (Ti) was chosen as implant material because methods of binding of biologically active molecules to a titanium surface by means of silanization are readily available (*6*, *7*). The limited information on the precise mechanisms of bactericidal action of LL37 made several assumptions necessary. First, to permit effective bactericidal activity, immobilized LL37 needs to be conjugated to a rather long and flexible spacer molecule enabling lateral diffusion of the peptide molecules in the lipid double layer of the microbial membrane. Second, the α-helices need a parallel arrangement in order to ensure interactions within the peptide molecules and enable formation of membrane pores. Functionalized poly(ethylene glycol) (PEGs) molecules are appropriate for this purpose and have the beneficial side-effect of rendering coated surfaces nonadhesive (*8*). A method of exclusive N-terminal coupling was developed for the purpose of the parallel alignment of immobilized peptide molecules.

EXPERIMENTAL SECTION

Materials. Ti was purchased from Alfa Aesar (Karlsruhe, Germany). Heterobifunctional PEGs were obtained from Nektar Therapeutics (San Carlos, CA). Sulfosuccinimidyl 4-(4,4′-dimethoxytrityl)butyrate (sulfo-SDTB) and *N*-maleimidopropionic acid succinimide ester (NHS-Prop-Mal) were bought from Pierce (Etten-Leur, The Netherlands). Propidium iodide and general chemicals were from Sigma (Zwijndrecht, The Netherlands). Organic solvents were dried over 3 Å molecular sieves if necessary.

Peptide Synthesis. Fmoc-protected amino acids were purchased from NovaBiochem (Läufelingen, Switzerland). Peptides were synthesized using Fmoc chemistry on a MilliGen 9050 peptide synthesizer (MilliGen/Biosearch, Bedford, MA) and purified by reversed phase HPLC JASCO HPLC System (Jasco, Tokyo, Japan) as previously reported (*9*). The peptide LL37 with the amino acid sequence LLGDFFR KSKEKIGKEF KRIVQRIKDF LRNLVPRTES was used in the native form or with an additional N-terminal cysteine residue (Cys-LL37).

Silanization. Ti platelets of 10 × 10 mm^2 size were cut from 2 mm thick foil. One side of each platelet was ground with

* Corresponding author: M. Gabriel, Department of Orthodontics, Academic Centre for Dentistry Amsterdam (ACTA), Louwesweg 1, 1066 EA Amsterdam, The Netherlands. E-mail: mat.gabriel@web.de, Tel.: +31-20-5188 481, Fax.: +31-20-5188 566.

† Department of Orthodontics.

‡ Department of Oral Biochemistry.

10.1021/bc050091v CCC: $33.50 © 2006 American Chemical Society
Published on Web 01/17/2006

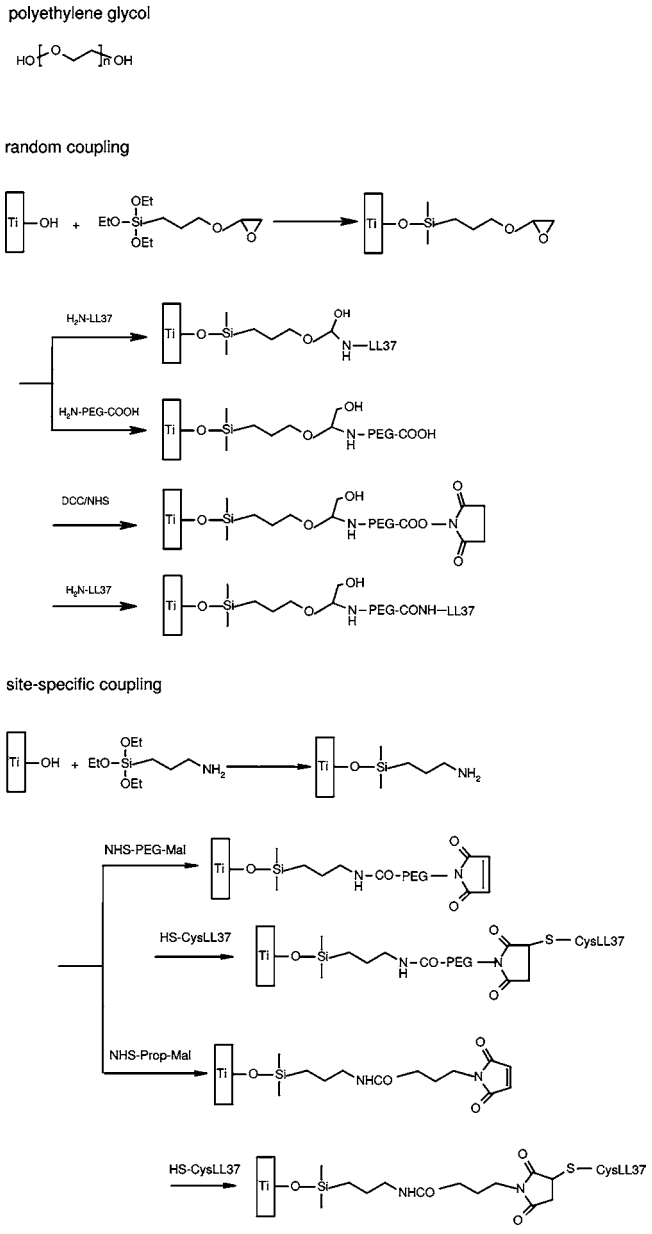

Figure 1. Reaction schemes of the conjugation methods.

600- and 1200-grid sandpaper and cleaned by etching in a solution of 9% $NH_4F{\cdot}HF$ (w/v), 8.5% H_2SO_4 (v/v), and 0.5% urotropin (w/v) in deionized water for 2 min at room temperature. Passivation was accomplished by treatment with a 1:1 mixture of 30% H_2O_2 and concentrated H_2SO_4 (Piranha solution) for 1 h (*6*). Ti specimens were silanized with a solution of 2% 3-aminopropyl triethoxysilane (amino silane) and glycidyloxypropyl triethoxysilane (epoxy silane), respectively, in dry toluene for 18 h at room temperature. After being washed with toluene and methanol, the silanized samples were cured at 80 °C for 1 h.

Direct and Spacer-Mediated Random Binding. Figure 1 shows schematically various coupling reactions. Epoxy-silanized platelets were incubated for 3 h with 0.5 mg/mL LL37 in 10 mM carbonate buffer, pH 8.5, for 2 h at room temperature. Subsequently they were washed with buffer containing 0.1% Tween-20 followed by washing with water and drying. To produce spacer-mediated coupling, the specimens were first covalently coated (PEGylated) using α-amino-ω-carboxy-PEG hydrochloride (H_2N-PEG-COOH) (MW 5400, 0.2 mg/mL) in dry dimethylformamide (DMF) for 2 h, rinsed thoroughly with DMF, and dried. A mixture of 0.1 M dicyclohexyl carbodiimide (DCC) and 0.1 M NHS-Prop-Mal in dry DMF was prepared, and the PEGylated samples were incubated for another 2 h. After washing with DMF, Ti samples were treated with peptide solution in the same manner as described for directly immobilized peptide, followed by washing as above.

Table 1. Surface Density of Immobilized Peptide As Estimated by the Sulfo-SDTB Method

peptide	surface density, mol/cm^2
Ti-LL37	1.11×10^{-10}
Ti-CysLL37	7.86×10^{-11}
Ti-PEG-LL37	1.42×10^{-10}
Ti-PEG-CysLL37	1.47×10^{-10}

Direct and Spacer-Mediated Site-directed Binding. Selective N-terminal coupling of Cys-LL37 was performed using a two-step procedure. First, direct binding of the peptide was achieved by treating amino-silanized Ti with NHS-Prop-Mal, 0.1 M in DMSO, for 4 h at room temperature. Second, after being washed with DMSO, the samples were reacted with Cys-LL37 (0.5 mg/mL in PBS pH 7.3) for 3 h. They were then rinsed with buffer and water and dried. Amino-silanized Ti was treated with a solution of α-*N*-hydroxysuccinimidyl-ω-maleimidyl-PEG (NHS-PEG-Mal) in dry DMF (0.2 mg/mL) similarly to the protocol described above. Incubation with Cys-LL37 (0.5 mg/mL in PBS, pH 7.3) was performed for 2 h, followed by washing steps. This procedure results in a Michael-type coupling of the peptide to the PEG spacer exclusively at the N-terminus of the peptide (*15*).

Estimation of Surface Density of Amino Groups. LL37 contains six lysine residues at positions 8, 10, 12, 15, 18 and 25 (*4*). Together with the N-terminus the peptide provides seven primary amino groups available for modification. Assuming that only one of these moieties is involved in the conjugation, seven amino groups are left for binding with a colorimetric reagent. The density of immobilized peptide was estimated using the sulfo-SDTB test according to manufacturer's instructions. One milliliter of a solution containing 3 mg sulfo-SDTB, first dissolved in 0.5 mL of DMSO, then in 50 mL of carbonate buffer (10 mM, pH 8.5) was pipetted into wells of 24-well microtiter plates containing Ti specimens and incubated for 1 h. Subsequently the specimens were washed thrice with buffer. An addition of 400 μL of 35% hypochloric acid to each well resulted in color formation measured photometrically at $\lambda =$ 498 nm. Concentration of released dye and, therefore, of surface amino groups was calculated with $\epsilon = 70\,000$ cm^2/mol for the chromophore (*12*).

Bacterial Killing Assay. *E. coli* (strain K12) was grown overnight in brain−heart infusion (BHI; Becton, Dickinson Microbiology Systems, Sparks, MD). Bacteria were harvested by centrifugation and grown in BHI to a density of $OD_{570} =$ 0.8. After a second centrifugation step, bacteria were resuspended in 10 mM phosphate buffer (pH 7.5), and 100 μL of bacterial suspension, containing 6 μM of propidium iodide (PI), was added to each well with pretreated or uncoated titanium platelets. Enhancement of PI fluorescence caused by intercalation of PI into the DNA of dead cells (*11*) was monitored after 30 min as a measure of bacterial death. Excitation at $\lambda = 520$ nm and emission at $\lambda = 620$ nm was measured using a microtiter plate reader (Fluostar Galaxy BMG Laboratories, Offenburg, Germany).

RESULTS

The determination of surface concentration of immobilized peptide yielded by the sulfo-SDTB method is shown in Table 1. The values were calculated from the optical densities on the basis of the assumption that each peptide molecule was conjugated by only one primary amino group. Within the limits

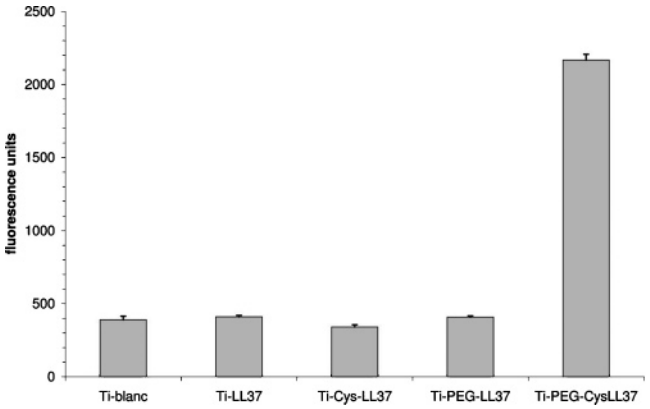

Figure 2. Fluorescence detection of bactericidal activity.

of this method, different coupling efficiencies were observed. PI permeabilization assay was used to estimate the extent of *E. coli* death at the various titanium surfaces. Ti samples with exclusively N-terminally spacer-conjugated Cys-LL37 (Ti-PEG-CysLL37) expressed antimicrobial activity against *E. coli*, as shown by the enhanced PI fluorescence (Figure 2). In contrast, compared to untreated Ti, no killing was observed when bacteria were exposed to Ti with randomly immobilized peptide, both with and without the use of a spacer (Ti-PEG-LL37, Ti-LL37). In addition, directly N-terminally bound LL37 (Ti-CysLL37) showed no killing activity under the conditions of the present study.

DISCUSSION

Immobilization of AMPs as accomplished in the present study is a novel approach toward endowing material surfaces with bactericidal properties. In the present study silanization was used as a versatile method of covalent binding of biologically active molecules to Ti. Various multistep procedures of binding the peptide to Ti were tested in order to meet the aim of developing a method which would optimally preserve the antibacterial activity of the AMP LL37. The amine-reactive NHS-group and the thiol-reactive maleimide-moiety were chosen for site-specific conjugation (*15*).

The amounts of surface-bound AMP-molecules were estimated by means of the sulfo-SDTB test (*12*), which in the case of LL37 was facilitated by the relative abundance of amino groups on the basic peptide. The measurements obtained were within 1 order of magnitude, suggesting that the mere presence of properly immobilized peptide molecules was responsible for the observed bactericidal activity, and that the latter was independent of the relative peptide concentration on Ti surfaces. As for a successful operation, this assay deals with very low absolute amounts of functional groups on the target molecules. These measurements represent only a rough estimate restricting a direct comparison between the various coupling strategies.

Assuming that the potential bactericidal mechanism of the helical AMP LL37 is its interaction with the bacterial membrane, lateral mobility of peptide molecules is required. This assumption was confirmed indirectly by the absence of bactericidal activity of directly immobilized LL37 (Figure 2) and the finding that only the peptide properly bound to the PEGylated Ti surface was capable of killing *E. coli* on contact. Such an orientation necessary for the above lateral mobility was achieved by the use of long flexible spacer molecule PEG.

At least two features seem to be essential for effective bactericidal activity. First, the assumed necessity of a long spacer with a flexible molecular chain granting lateral mobility of surface-bound AMP and facilitating interactions with bacterial membrane seems to be confirmed by the observations made in the present work. Second, only N-terminal conjugation permits appropriate parallel orientation of the peptide helices, which is required for interaction among the peptide molecules and between the peptides and the lipid double layer during membrane pore formation. Presumably, C-terminal immobilization of the peptide might have similar effects. A positive side-effect of PEGylation is the intrinsic antiadhesiveness of the treated surface (*14, 15*), which is also applicable to other hydrophilic spacer molecules (*13*). Further work is warranted to test these assumptions and to expand and if necessary, modify the biomedical application of the present method of antibacterial surface modification to a wider range of pathogenic microorganisms.

LITERATURE CITED

(1) Isquith, A. J., Abbott, E. A., and Walters, P. A. (1972) Surface-bonded antimicrobial activity of an organosilicon quaternary ammonium chloride. *Appl. Microbiol. 2,* 859−63.

(2) Tiller, J. C., Liao, C. J., Lewis, K., and Klibanov, A. M. (2001) Designing surfaces that kill bacteria on contact. *Proc. Natl. Acad. Sci. U.S.A. 98,* 5981−5.

(3) Boman, H. G. (2003) Antibacterial peptides: basic facts and emerging concepts. *J. Intern. Med.* 254, 197−215.

(4) Nieuw Amerongen, A. van, Bolscher, J. G., and Veerman, E. C. (2004) Salivary proteins: protective and diagnostic value in cariology? *Caries Res. 38,* 247−53.

(5) Zanetti, M., Gennaro, R., and Romeo, D. (1995) Cathelicidins: a novel protein family with a common proregion and a variable C-terminal antimicrobial domain. *FEBS Lett. 374,* 1−5.

(6) Nanci, A., Wuest, J. D., Peru, L., Brunet, P., Sharma, V., Zalzal, S., and McKee, M. D. (1998) Chemical modification of titanium surfaces for covalent attachment of biological molecules. *J. Biomed. Mater. Res.* 40, 324−35.

(7) Rezania, A., Johnson, R., Lefkow, A. R., and Healy, K. E. (1999) Bioactivation of metal oxide surfaces. 1. Surface characterization and cell response. *Langmuir 15,* 6931−6939.

(8) Harris, L. G., Tosatti, S., Wieland, M., Textor, M., and Richards, R. G. (2004) Staphylococcus aureus adhesion to titanium oxide surfaces coated with non-functionalized and peptide-functionalized poly(L-lysine)-grafted-poly(ethylene glycol) copolymers. *Biomaterials 25,* 4135−48.

(9) Groenink, J., Ruissen, A. L., Lowies, D., van 't Hof, W., and Veerman, E. C., Nieuw Amerongen, A. V. (2003) Degradation of antimicrobial histatin-variant peptides in Staphylococcus aureus and Streptococcus mutans. *J. Dent. Res. 82,* 753−7.

(10) Bosch, J. A., Veerman, E. C., Turkenburg, M., Hartog, K., Bolscher, J. G., and Nieuw Amerongen, A. V. (2003) A rapid solid-phase fluorimetric assay for measuring bacterial adherence, using DNA-binding stains. *J. Microbiol. Methods 53,* 51−6.

(11) Miyamoto, D., Watanabe, J., and Ishihara, K. (2004) Effect of water-soluble phospholipid polymers conjugated with papain on the enzymatic stability. *Biomaterials 25,* 71−6.

(12) Penzol, G., Armisen, P., Fernandez-Lafuente, R., Rodes, L., and Guisan, J. M. (1998) Use of dextrans as long and hydrophilic spacer arms to improve the performance of immobilized proteins acting on macromolecules. *Biotechnol. Bioeng. 60,* 518−23.

(13) Massia, S. P., and Stark, J. (2001) Immobilized RGD peptides on surface-grafted dextran promote biospecific cell attachment. *J. Biomed. Mater. Res. 56,* 390−9.

(14) Piehler, J., Brecht, A., Valiokas, R., Liedberg, B., and Gauglitz, G. (2000) A high-density poly(ethylene glycol) polymer brush for immobilization on glass-type surfaces. *Biosens. Bioelectron. 15,* 473−81.

(15) Hermanson, G. T. (1996) *Bioconjugate Techniques,* pp 139, 148, Academic Press, San Diego.

BC050091V

An Efficient, Convenient Solid-Phase Synthesis of Amino Acid-Modified Peptide Nucleic Acid Monomers and Oligomers

Baghavathy S. Balaji,[†] Fabio Gallazzi,[‡] Fang Jia,[†] and Michael R. Lewis*[,†,§,||,⊥]

Department of Veterinary Medicine and Surgery, Molecular Biology Program, Department of Radiology, and Nuclear Science and Engineering Institute, University of Missouri—Columbia, Columbia, Missouri 65211, and Research Service, Harry S. Truman Memorial Veterans' Hospital, Columbia, Missouri 65201. Received July 22, 2005; Revised Manuscript Received December 12, 2005

An efficient and highly versatile method for the synthesis of amino acid-modified peptide nucleic acid (PNA) monomers is described. By using solid-phase Fmoc techniques, such monomers can be assembled readily in a stepwise manner and obtained in high yield with minimal purification. Protected neutral hydrophilic, acidic, and basic amino acids were coupled to 2-chlorotrityl chloride resin. Following Fmoc removal, innovative conditions for the key step, reductive alkylation with *N*-Fmoc-aminoacetaldehyde, were developed to circumvent problems encountered with previously reported methods. Activation and coupling of pyrimidine and purine nucleobases to the resulting secondary amines afforded amino acid-modified PNA monomers. The mild reaction conditions utilized were compatible with sensitive and labile functional groups, such as *tert*-butyl ethers and *tert*-butyl esters. PNA monomers were obtained in 36−42% overall yield and very high purity, after cleavage and purification. Using standard solid-phase Fmoc chemistry, two of these monomers were incorporated with high coupling efficiency into a variety of modified PNA oligomers, including four tetradecamers designed to target *bcl-2* mRNA. Such modified oligomers have the potential to enhance water solubility and cell portability, while maintaining hybridization affinity and promoting favorable biodistribution properties.

INTRODUCTION

Peptide nucleic acids (PNAs)[1] are DNA-like molecules having unique binding properties to either single-stranded DNA and RNA or double-stranded DNA (*1*, *2*). In recent years, much attention has been focused on synthetic (*3*−*5*), biomedical (*6*−*9*), and bioconjugate (*10*−*12*) applications of PNAs. The major advantage of using PNAs for DNA and RNA hybridization and targeting is due to the presence of an uncharged, achiral, acyclic amide backbone composed of (2-aminoethyl)glycine units. This structural feature can give rise to considerable conformational flexibility, as well as stability toward degradation by nucleases and proteases (*2*). These properties, coupled with high sequence specificity (*13*, *14*), make PNAs important molecules for various biological applications such as gene silencing (*7*, *15*, *16*). However, the poor water solubility and extremely low cellular uptake of PNAs necessitated incorporation of modifications that can enhance cell portability (*17*−*19*).

We recently synthesized and evaluated several fluorescent and radiometal-labeled cell-permeating peptide−PNA conjugates for targeting the B-cell lymphoma/leukemia-2 (*bcl-2*) gene at the mRNA expression level (*20*, *21*). While the use of a cell-permeating peptide resulted in efficient internalization of *bcl-2* antisense PNA in tumor cells in vitro, such a peptide delivery vehicle is likely to have little or no in vivo specificity. We subsequently prepared an ^{111}In-labeled anti-*bcl-2* PNA conjugated to a peptide receptor ligand designed for in vivo tumor targeting (*22*). When labeled with ^{111}In, this PNA−peptide conjugate is zwitterionic but has sufficient water solubility for in vitro and in vivo applications. However, evaluation of a corresponding PNA conjugate complementary to the large splice variant of the B-cell lymphoma/leukemia-X gene (*bcl-X$_L$*) was limited by its extremely poor water solubility (*23*).

At present, it is not possible to predict the water solubility of a PNA−peptide conjugate a priori. Nielsen, Buchardt, and co-workers showed that replacing some of the glycine residues of PNA with hydrophilic or charged amino acids (*24*) improved water solubility. The incorporation of positively charged amino acids, such as D-lysine, afforded modified PNAs with superior

* To whom correspondence should be addressed: Michael R. Lewis, Ph.D., Department of Veterinary Medicine and Surgery, College of Veterinary Medicine, 379 E. Campus Dr., University of Missouri—Columbia, Columbia, MO 65211, Phone: (573) 814-6000, ext. 3703, Fax: (573) 814-6551, e-mail: LewisMic@missouri.edu.

[†] Department of Veterinary Medicine and Surgery, University of Missouri—Columbia.

[‡] Molecular Biology Program, University of Missouri—Columbia.

[§] Department of Radiology, University of Missouri—Columbia.

[||] Nuclear Science and Engineering Institute, University of Missouri—Columbia.

[⊥] Harry S. Truman Memorial Veterans' Hospital.

[1]Abbreviations: % ID/g, percent injected dose per gram of tissue; *bcl-2*, B-cell lymphoma/leukemia-2 gene; *bcl-X$_L$*, large splice variant of B-cell lymphoma/leukemia-X gene; Bhoc, benzhydryloxycarbonyl; Bn, benzyl; Boc, *tert*-butyloxycarbonyl; Bz, benzoyl; Cbz, benzyloxycarbonyl; DCE, dichloroethane; DCM, dichloromethane; DhbtOH, 3-hydroxy-1,2,3-benzotriazin-4(3*H*)-one; DIC, *N*,*N*′-diisopropylcarbodiimide; DIPEA, diisopropylethylamine; DMF, *N*,*N*-dimethylformamide; DMT, 4,4′-dimethoxytriphenylmethyl; EDCI, 1-ethyl-3-[3-(dimethylamino)propyl]carbodiimide; ESI-MS, electrospray ionization mass spectrometry; Fmoc, (9*H*-fluoren-9-ylmethoxycarbonyl); Fmoc-Cl, Fmoc chloride; Fmoc-OSu, Fmoc succinimidyl carbonate; G$_S$, serine-derivatizedbenzyl-protected guanine PNA residue; HATU, 2-(7-aza-1*H*-benzotriazol-1-yl)-1,1,3,3-tetramethyluronium hexafluorophosphate; HBTU, *O*-(benzotriazol-1-yl)-1,1,3,3-tetramethyluronium hexafluorophosphate; HOBT, 1-hydroxybenzotriazole; IBX, *o*-iodoxybenzoic acid; NMP, 1-methyl-2-pyrrolidinone; PNA, peptide nucleic acid; PyBOP, benzotriazol-1-yl-oxytripyrrolidinophosphonium hexafluorophosphate; T$_D$, aspartic acid derivatized thymine PNA residue; T$_K$, lysine-derivatized thymine PNA residue; T$_S$, serine-derivatized thymine PNA residue; TBTU, *O*-(benzotriazol-1-yl)-1,1,3,3-tetramethyluronium tetrafluoroborate; tBu, *tert*-butyl; TFA, trifluoroacetic acid; THF, tetrahydrofuran; TMOF, trimethyl orthoformate.

10.1021/bc0502208 CCC: $33.50 © 2006 American Chemical Society
Published on Web 02/18/2006

hybridization affinity for single-stranded DNA (*24*). However, a recent in vivo study indicated that radiometal-labeled PNAs accumulate in the kidneys of tumor-bearing mice (*25*). Conjugation of these PNAs to a tumor-targeting peptide improved renal clearance (*26*), but kidney uptake persisted out to 24 h postinjection. Another recent report demonstrated that a ^{64}Cu-labeled antisense PNA, conjugated to a cell-permeating peptide with high positive charge density, could be used to image mouse tumor xenografts, albeit with renal uptake as high as 280% ID/g (*27*). On the basis of these findings, we reasoned that judicious incorporation of neutral hydrophilic and/or negatively charged residues may enhance water solubility and cell portability of radiolabeled PNAs, while maintaining hybridization affinity and promoting renal clearance. Though our goal was to make thymine monomers (**1**, **2**) as our lead compounds, we also synthesized additional monomers with a basic amino acid (**3**, lysine) and containing a purine nucleobase (**4**, guanine), to show the versatility and robustness of this methodology.

There are a number of strategies available for synthesis of side chain-modified PNA monomers (*10*, *28*−*33*). Modifications can be made either on the glycine unit or on the aminoethyl unit. When oligomers are synthesized from these modified monomers, the presence of bulky side chains on the aminoethyl unit may pose difficulties during coupling reactions and may also exert steric hindrance on base pair formation. Moreover, preparation of N-protected, 2-substituted aminoacetaldehyde requires two steps from the commercially available amino acid, sometimes affording low yields and/or unstable products (*34*, *35*). Another approach uses a Mitsunobu reaction between the N-protected amino acid and N-protected β-amino alcohols (*28*). In this method, every step requires chromatographic purification, and the incorporation of carboxylic acid functionalities such as aspartic acid is not compatible with reduction using Vitride or sodium borohydride. Thus, the present work focused on modifications of the glycine unit, where most of the appropriately protected starting materials are commercially available, and a simple N-protected aminoacetaldehyde can be employed for synthesis of the aminoethyl unit.

A very recent report describes the solution phase synthesis of a single, modified PNA monomer having glutamic acid as the amino acid derivative (*33*). The formation of the pseudopeptide backbone was attempted using two methods, reductive N-alkylation or Mitsunobu condensation. It was found that the second method afforded higher yields and fewer byproducts. However for this route, the amine nitrogen on the pseudopeptide backbone had to be protected with an *N*-*o*-nitrobenzenesulfonyl group.

Recently it was shown that modified PNA monomers and oligomers can be synthesized readily on a solid support, using Fukuyama−Mitsunobu alkylation of the desired α-amino acid, followed by acylation with the desired nucleobase-acetic acid derivative (*36*). However, in this case even thymine has to be protected in order to be used in the synthesis.

The overall goal of the present work was to develop a robust synthetic method for introduction of amino acid-modified residues into PNA oligomers. The construction of oligomers with these modifications first required an efficient synthesis of appropriate PNA monomers. We report herein a facile solid-phase synthesis of various PNA monomers prepared from different amino acid derivatives and containing either a pyrimidine or a purine as the nucleobase.

We initially chose to synthesize modified derivatives of thymine for two reasons. First, protected nucleobase-acetic acid derivatives for adenine, guanine, and cytosine are not readily available from commercial sources. Second, the thymine derivative requires no protecting group using the conditions employed here. In addition, PNA hybridization stability can be highly sensitive to amino acid modifications, particularly at internal sequence positions (*24*). Judicious incorporation of a neutral or negatively charged hydrophilic side chains at or near the end of a duplex structure, such as the C-terminal thymine complimentary to the start codon of mRNA, may yield more water soluble PNA oligomers without abrogating target binding.

The solid-phase strategy described here affords higher yields and higher purity crude products than analogous solution-phase methods. Unlike previously reported solid-phase methods, the mild conditions utilized are compatible with 9*H*-fluoren-9-ylmethoxycarbonyl (Fmoc) PNA and peptide chemistry. To show the generality of the newly developed method, we also synthesized a lysine derivative of thymine and a serine derivative of guanine. In addition, we showed that two of these monomers can be incorporated efficiently into a variety of PNA oligomers in various sequence positions.

EXPERIMENTAL PROCEDURES

General. All reagents were HPLC or peptide synthesis grade. *N*-α-Fmoc-L-Ser(OtBu)-OH, *N*-α-Fmoc-L-Asp(OtBu)-OH, *N*-α-Fmoc-L-Lys(Boc)-OH, and 2-cholorotrityl chloride resin were obtained from Novabiochem (San Diego, CA). *N*-α-Fmoc-ethanolamine and thymine-1-acetic acid were purchased from Aldrich (Milwaukee, WI). PNA monomers Fmoc-A(Bhoc)-OH, Fmoc-C(Bhoc)-OH, Fmoc-G(Bhoc)-OH, and Fmoc-T-OH, as well as Fmoc-XAL PEG PS resin, were obtained from Applied Biosystems (Foster City, CA). All laboratory glassware was washed with a mixed acid solution (*37*) and thoroughly rinsed with ultrapure water (18 MΩ-cm resistivity). Manual reaction vessels were obtained from Chemglass, Inc. (Vineland, NJ). ^{1}H NMR analysis of purified monomers was performed using a Bruker DRX 300 MHz spectrometer (Bruker BioSpin, Westmont, IL), and elemental analysis was performed by Atlantic Microlab (Norcross, GA). ESI-MS analyses were performed on a Finnigan TSQ7000 mass spectrometer (Thermo Finnigan, San Jose, CA). A Waters (Milford, MA) NovaPak C18 column (3.9 × 300 mm) was used for LC-MS analysis.

Analytical and preparative reversed-phase HPLC were performed on a Waters 600 chromatograph equipped with a Waters Delta 600 pump, a Rheodyne 7725i injector, Waters 2487 dual wavelength UV detector, Waters 600 controller, and the Empower Pro software package (Build No. 1154). A Phenomenex (Torrance, CA) C-18 Jupiter column (4.6 × 250 mm, 5 μm, 300 Å) was used for analytical HPLC. For preparative HPLC, a Phenomenex Jupiter Proteo column (21.2 × 250 mm, 10 μm, 90 Å) was used. The flow rate was maintained at 1.0 mL/min for analytical runs and at 3.0 mL/min for preparative purification. The wavelengths used for UV detection were 214 and 280 nm for analytical HPLC and 280 nm for preparative HPLC, respectively. Eluents used in all runs consisted of solvent A (0.1% TFA/H_2O) and solvent B (0.1% TFA/CH_3CN). Two different gradients were used: (1) "Analytical Gradient": sequential linear from 30% to 80% solvent B in 40 min (step 1) and 80% to 95% solvent B in 10 min (step 2), or 30% to 80% solvent B in 40 min (step 1) and 80% to 95% solvent B in 20 min (step 2); or (2) "Prep Gradient" (optimized for preparative purification of monomers): sequential linear from 35% to 65% solvent B in 60 min (step 1), 65% to 80% solvent B in 30 min (step 2), and 80% to 100% solvent B in 10 min (step 3).

Monomer Synthesis. Syntheses of PNA monomers having serine, aspartic acid, or lysine derivatives were performed manually, using Fmoc chemistry and 2-chlorotrityl chloride resin at a substitution level of 0.6 mmol/g. All reactions were carried out at room temperature.

Amino Acid Coupling. In a typical experiment, 350 mg of the resin was charged to the reaction vessel. The resin was

washed with DCM (4 × 3 mL), DMF (2 × 3 mL), and DCM/NMP (1:1, 2 × 3 mL). A preactivated mixture of 215 mg (561 μmol) of *N*-α-Fmoc-L-Ser(OtBu)-OH or 230 mg (559 μmol) of *N*-α-Fmoc-L-Asp(OtBu)-OH or 262 mg (560 μmol) of *N*-α-Fmoc-L-Lys(Boc)-OH and 389 μL (289 mg, 2.24 mmol) of DIPEA, dissolved in 3 mL of 1:1 DCM/NMP, was charged to the reaction vessel, and a stream of argon was used for mixing. After 45 min the activation and coupling reactions were repeated, and the resin was washed with DCM/NMP (1:1, 3 × 3 mL), DCM/CH_3OH/DIPEA (17:2:1, 2 × 3 mL), and DMF (3 × 3 mL). A solution of 25% piperidine in 3 mL of DMF was charged to the reaction vessel and Fmoc removal was carried out for 30 min. The deprotection reaction was repeated, and the resin was washed with DMF (3 × 3 mL) and TMOF (2 × 3 mL).

***N*-Fmoc-aminoacetaldehyde Coupling.** *o*-Iodoxybenzoic acid (IBX) was synthesized according to the literature procedure (*38*). *N*-Fmoc-ethanolamine was oxidized using IBX (*39*), and the corresponding aldehyde, *N*-Fmoc-aminoacetaldehyde, was obtained as a single pure product in 90−95% yield. The aldehyde (81 mg, 282 μmol) was dissolved in TMOF (3 mL) and charged to the resin. A small amount (∼0.3−0.5 mL) of DMF was added to increase the solubility of the aldehyde. After 40 min, a few drops of acetic acid were added, followed by sodium (triacetoxy)borohydride (60 mg, 283 μmol), and the resulting suspension was mixed under argon for 20 min. The resin was washed with TMOF (2 × 3 mL) and DMF (3 × 3 mL).

Nucleobase Coupling. In the case of the L-serine monomer, thymine-1-acetic acid (81 mg, 440 μmol) or benzyloxypurine-9-acetic acid (132 mg, 441 μmol) was activated with 71 mg of DhbtOH (436 μmol) and 69 μL of DIC (55 mg, 437 μmol) in 3 mL of DMF. This mixture was added to the resin, and the resulting suspension was mixed under argon for 6−8 h. The activation and coupling steps were repeated using benzyloxypurine-9-acetic acid. For the L-aspartic acid monomer, the activation and coupling steps were also repeated. Then the resin was washed with DMF (3 × 3 mL) and DCM (3 × 3 mL).

Cleavage and Purification of *S*-3-*tert*-Butyloxy-2-{2*N*-[(9*H*-fluoren-9-ylmethoxycarbonyl)aminoethyl]-2-[(thymine-1-acetyl)-amino]}-propanoic Acid (1), *S*-3-*tert*-Butyloxycarbonyl-2-{2*N*-[(9*H*-fluoren-9-ylmethoxycarbonyl)aminoethyl]-2-[(thymine-1-acetyl)-amino]}-propanoic Acid (2), *S*-6-*tert*-Butyloxycarbonylamino-2-{2*N*-[(9*H*-fluoren-9-ylmethoxycarbonyl)aminoethyl]-2-[(thymine-1-acetyl)-amino]}-hexanoic Acid (3), and *S*-3-*tert*-Butyloxy-2-{2*N*-[(9*H*-fluoren-9-ylmethoxycarbonyl)aminoethyl]-[2-(2-amino-6-benzyloxypurine-9-acetyl)-amino]}-propanoic Acid (4). A small amount of each resin was removed from the reaction mixture and washed with DMF, DCM, and CH_3OH. The final products were cleaved from the resin using 0.5% TFA in DCM for 30 min and precipitated using diethyl ether. The precipitate was dissolved in CH_3CN:H_2O (1:1) and analyzed by HPLC ("Analytical Gradient") to confirm completion of nucleobase coupling. The remainder of the resin was then washed, and the final products were cleaved and isolated by precipitation as described above. The side chain-modified PNA monomers were purified by either preparative HPLC ("Prep Gradient") or flash chromatography on silica gel, using DCM:CH_3OH (10:1) as the mobile phase. After purification, 60.0 mg (42.2%) of **1** (T_S) was obtained as a white powder. ^{1}H NMR (300 MHz, $CDCl_3$) δ 1.08 (s, 9H), 1.76 (s, 3H), 2.87 (br, 1H), 3.37−3.40 (m, 2H), 3.50 (s, 2H), 3.76−3.82 (m, 2H), 3.88−3.90 (m, 1H), 4.11−4.17 (m, 2H), 4.37 (d, 1H), 4.58 (d, 1H), 4.69 (br, 1H), 6.15 (s, 1H), 6.78 (s, 1H), 7.20−7.23 (m, 2H), 7.30−7.33 (m, 2 H), 7.49−7.52 (m, 2H), 7.66−7.70 (m, 2H), 10.2 (br, 1H). ESI-MS *m*/*z* calcd for $C_{31}H_{36}N_4O_8$ $(M + H)^+ = 593.7$, found 537.2 $(M + H - tBu)^+$, 593.2 $(M + H)^+$, 615.1 $(M + Na)^+$. Anal. ($C_{31}H_{36}N_4O_8 \cdot CH_2Cl_2$): C, H, N.

Chromatographic purification afforded 48.0 mg (36.8%) of **2** (T_D) as a white powder. ^{1}H NMR (300 MHz, $CDCl_3$) δ 1.40 (s, 9H), 1.77 and 1.85 (2s, 3H), 2.78−2.87 (m, 2H), 3.01−3.20 (m, 2H), 3.46 (s, 1H), 3.57 (s, 1H), 3.79−3.82 (d, 1H), 3.95 (br, 1H), 4.09−4.20 (m, 1H), 4.37 (d, 1H), 4.52−4.54 (m, 1H), 4.72 (d, 1H), 5.83 (s, 1H), 6.81 and 6.86 (2s, 1H), 7.19−7.21 (m, 2H), 7.30−7.37 (m, 2 H), 7.48−7.54 (m, 2H), 7.62−7.73 (m, 2H), 10.62 (br, 1H). ESI-MS *m*/*z* calcd for $C_{32}H_{36}N_4O_9$ $(M + H)^+ = 621.7$, found 565.1 $(M + H - tBu)^+$, 621.4 $(M + H)^+$, 643.3 $(M + Na)^+$. Anal. ($C_{32}H_{36}N_4O_9 \cdot CH_2Cl_2 \cdot 1/2 (CH_3CH_2)_2O$): C, H, N.

Chromatographic purification afforded 68.0 mg (38.0%) of **3** (T_K) as a white powder. ^{1}H NMR (300 MHz, $CDCl_3$) δ 1.31 (t, 1H), 1.46 and 1.49 (2s, 9H), 1.59 (s, 1H), 1.76 (s, 1H), 1.82 and 1.86 (2s, 3H), 1.92−2.03 (m, 1H), 2.72 (br, 1H), 2.94 (s, 1H), 3.10 (s, 2H), 3.28 and 3.37 (m, 2H), 3.49 (s, 1H), 3.67 (br, 1H), 3.82 (m, 1H), 4.20 (d, 1H), 4.39, (d, 1H), 4.66 (d, 1H), 4.82 (m, 1H), 6.12 (s, 1H), 6.98 (s, 1H), 7.27−7.29 (m, 2H), 7.35−7.42 (m, 2 H), 7.53−7.62 (m, 2H), 7.70−7.82 (m, 2H), 10.52 (br, 1H). ESI-MS *m*/*z* calcd for $C_{35}H_{43}N_5O_9$ $(M + H)^+ = 678.7$, found 579.2 $(M + H - Boc)^+$, 700.1 $(M + Na)^+$. Anal. ($C_{35}H_{43}N_5O_9 \cdot CF_3CO_2H$): C, H, N.

Chromatographic purification afforded 64.0 mg (36.2%) of **4** (G_S) as a white powder. ^{1}H NMR (300 MHz, $CDCl_3$) δ 1.14−1.17 and 1.22−1.23 (d, 9H), 2.84−3.04 (m, 1H), 3.08−3.20 (m, 1H), 3.45−3.79 (m, 2H), 3.80 (t, 1H), 3.91 (s, 1H), 4.06 (s, 1H), 4.12−4.25 (m, 2H), 4.31 (s, 1H), 4.55 (dd, 1H), 4.90 and 4.96 (s, 1H), 5.05 (q, 1H), 5.49−5.57 (m, 2H), 6.30 (s, 1H), 7.26−7.29 (m, 4H), 7.32−7.41 (m, 4H), 7.42−7.49 (m, 2H), 7.51−7.58 (m, 2H), 7.64−7.71 (m, 1H), 7.73−7.78 (m, 2H), 10.62 (br, 1H). ESI-MS *m*/*z* calcd for $C_{38}H_{41}N_7O_7$ $(M + H)^+ = 708.8$, found 708.3 $(M + H)^+$. Anal. ($C_{38}H_{41}N_7O_7 \cdot 2 CF_3CO_2H$): C, H, N.

Synthesis of Model PNA Tetramers (5−11). Syntheses of PNA tetramers using **2** were performed according to a previously published procedure (*20*), using Fmoc-XAL PEG PS resin at a substitution level of 0.15 mmol/g. Compound **2** was incorporated into tetramers **5** ($AAGT_D$; T_D = aspartic acid derivatized thymine residue), **6** (GAT_DA), **7** (AT_DCG), **8** (T_DACA), **9** (AT_DGC), **10** ($AGAT_D$), and **11** (T_DCAA) on a 1 μmol scale. After cleavage, deprotection, precipitation with diethyl ether, and lyophilization, 0.8−1.0 mg (68−86%) of **5**−**11** were obtained as white powders. ESI-MS (**5**) *m*/*z* calcd $(M + 2H)^{2+} = 592.4$, found 592.4; (**6**) *m*/*z* calcd $(M + 2H)^{2+} = 593.4$, found 592.2; (**7**) *m*/*z* calcd $(M + 2H)^{2+} = 581.4$, found 580.2; (**8**) *m*/*z* calcd $(M + 2H)^{2+} = 573.4$, found 572.2; (**9**) *m*/*z* calcd $(M + 2H)^{2+} = 580.9$, found 580.4; (**10**) *m*/*z* calcd $(M + 2H)^{2+} = 592.9$, found 592.6; (**11**) *m*/*z* calcd $(M + 2H)^{2+} = 572.9$, found 572.4.

Synthesis of *bcl-2* Antisense Tetradecamers (12−15). Compounds **1** and **2** were each incorporated into sequence positions 1 or 8 of four *bcl-2* antisense PNA tetradecamers: **12** ($CCAGCGTGCGCCAT_S$; T_S = serine derivatized thymine residue), **13** ($CCAGCGT_SGCGCCAT$), **14** ($CCAGCGTGCGCCAT_D$), and **15** ($CCAGCGT_DGCGCCAT$). The syntheses were carried out on a 5 μmol scale, using Fmoc-XAL PEG PS resin at a substitution level of 0.15 mmol/g and modifications of a method reported previously (*20*). After cleavage, Bhoc deprotection, and precipitation with diethyl ether, the N-terminal Fmoc-protected tetradecamers were purified by preparative reversed-phase HPLC, using a sequential linear gradient of 5% to 15% solvent B in 10 min (step 1), 15% to 55% solvent B in 40 min (step 2), 55% to 75% solvent B in 30 min (step 3), 75% to 85% solvent B in 20 min (step 4), 85% to 95% solvent B in 20 min (step 5), and 95% to 100% solvent B in 10 min

Scheme 1

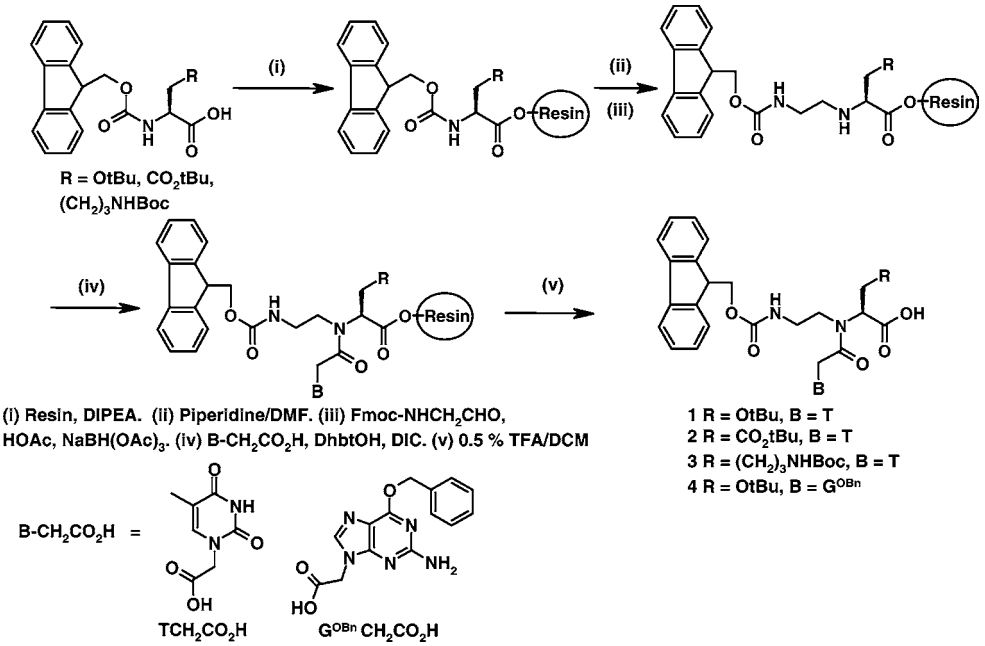

(step 6). The fractions corresponding to the major products were collected, pooled, and lyophilized. Fmoc removal was carried out in 25% piperidine in DMF for 30 min at room temperature, after which the products were isolated by precipitation with diethyl ether and dried to give 1.2−1.3 mg (6.3−6.8%) of **12**−**15** as white powders. ESI-MS (**12**) *m*/*z* calcd $(M + 3H)^{3+} = 1268.9$, $(M + 4H)^{4+} = 951.7$; found, 1268.2, 951.7; (**13**) *m*/*z* calcd $(M + 3H)^{3+} = 1268.9$, $(M + 4H)^{4+} = 951.7$; found, 1268.4, 951.6; (**14**) *m*/*z* calcd $(M + 3H)^{3+} = 1278.2$, $(M + 4H)^{4+} = 958.7$; found, 1277.8, 958.5; (**15**), *m*/*z* calcd $(M + 3H)^{3+} = 1278.2$, $(M + 4H)^{4+} = 958.7$; found, 1277.3, 958.3.

RESULTS AND DISCUSSION

Initially the solution-phase synthesis previously reported for similar amino acid-modified PNA monomers (*11*) was attempted. To obtain the desired products, protection and deprotection of the C-terminus was mandatory, most steps required chromatographic purification of the intermediates, and the overall yields were <15%. Some of the intermediate deprotection conditions (e.g., TFA) are optimized for Boc chemistry and are likely to result in unwanted removal of the tBu protecting group from the serine and aspartic acid derivatives used. Moreover, Fmoc removal under solution-phase conditions was complicated by persistent contamination of the desired products with excess piperidine. Although alternative Fmoc deprotection conditions have been reported (*40*), they cannot be applied to amino acids bearing the acid labile tBu protecting group. For these reasons, an alternate solid-phase method (Scheme 1) was developed to overcome the inherent shortcomings of solution-phase synthesis.

To develop a mild method, compatible with even tBu side chain protection, 2-chlorotrityl resin was used for the present synthesis. The initial step in the synthesis was coupling of the first submonomer unit, namely the fully protected chiral amino acid to 2-chlorotrityl chloride resin. Initial coupling was carried out at an amino acid loading capacity of 0.6 mmol/g in DCM/NMP (1:1). The reaction was carried out for two 45-min cycles, after which the Fmoc group was cleaved using a standard procedure (*41*).

The incorporation of the aminoethyl unit can be achieved by two simple methods: (1) Mitsunobu coupling of an N-protected ethanolamine or (2) reaction of an N-protected aminoacetaldehyde followed by reduction. The first method is well documented (*36*), but DMT, which has been used as a protecting group for the aminoethyl unit (*36*), is not compatible with 2-chlorotrityl resin. A strong base is also required, and this coupling can lead to dialkylation, which is a very common side reaction (*33*). Therefore, reductive alkylation with an N-protected aminoacetaldehyde was utilized in the present synthesis. The presence of tBu side chain protection on serine and aspartic acid was incompatible with Boc protection of the N-terminus. A number of compatible N-protecting groups are available, such as Cbz, Bn, Bz, and Fmoc (*42*). However, most of these protecting groups require metal-catalyzed removal or strong acidic conditions, with the exception of Fmoc. For the preparation of PNA−peptide conjugates labeled with metallic radionuclides (*20*−*22*), the presence of trace metal contamination from a metal-catalyzed deprotection could severely inhibit radiometal incorporation. Therefore, Fmoc protection was the most logical choice for preparation of the aminoethyl synthon. Fmoc-*N*-aminoacetaldehyde is not commercially available, and reports using this compound (*11*) did not specify how it was prepared. An attempt was made to synthesize Fmoc-*N*-aminoacetaldehyde from N-protected aminoacetaldehyde dimethyl acetal. Introduction of Fmoc was attempted using two reagents, Fmoc succinimidyl carbonate (Fmoc-OSu) and Fmoc chloride (Fmoc-Cl). The use of Fmoc-Cl resulted in the formation of numerous products, and obtaining the desired N-protected aminoacetaldehyde was difficult. When Fmoc-OSu was employed, the desired product was obtained in pure form and 90−95% yield within 30 min. All attempts to deprotect the resulting N-protected dimethyl acetal under well-established conditions, e.g., HCl, silica gel/DCM, or TFA (*43*) in various solvents failed to give the desired Fmoc-*N*-aminoacetaldehyde. In another route, Fmoc-glycine was converted to Weinreb amide and reduced using lithium aluminum hydride (*44*). Though the desired product was obtained, the workup was cumbersome and the yields were low, necessitating a third approach. In this reaction, Fmoc-aminoethanol was easily oxidized to the corresponding aldehyde in nearly quantitative yield, using IBX in ethyl acetate (*39*). The various syntheses of *N*-Fmoc-aminoacetaldehyde attempted are shown in Scheme 2.

The next reaction sequence, solid-phase aldehyde condensation followed by reduction, was initially met with poor yields.

Scheme 2

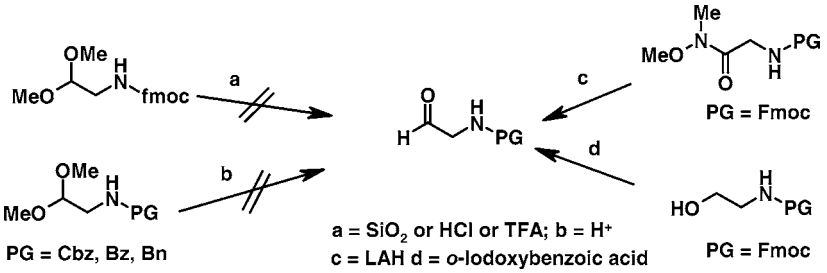

Table 1. Comparison of Different Reducing Agents and Solvents for Reductive Alkylation Using Fmoc-NHCH$_2$CHO

solvent	reducing agent	% yield[a]
THF	$NaBH_3CN$	61
DMF	$NaBH_3CN$	53
TMOF	$NaBH_3CN$	68
DCE	$NaBH_3CN$	34
THF	$NaBH(OAc)_3$	62
DMF	$NaBH(OAc)_3$	55
TMOF	$NaBH(OAc)_3$	88
DCE	$NaBH(OAc)_3$	40

[a] Based on Fmoc evaluation.

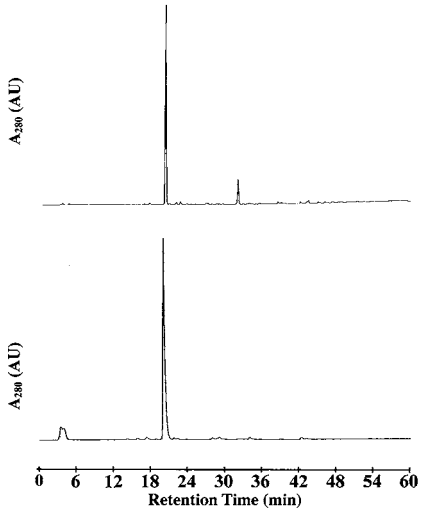

Figure 1. Analytical reversed-phase HPLC chromatograms of crude (top) and purified (bottom) **1**, using Analytical Gradient conditions. The peak at a retention time of 20.9 min represents the desired product, while the peak at 18.1 min represents the unreacted secondary amine precursor. The small peaks in the chromatogram of the purified product are injection artifacts.

It was found that methanol, which is commonly used in analogous solution-phase synthesis, was not compatible with 2-chlorotrityl resin. A systematic investigation was carried out to optimize the solid-phase reductive alkylation. First, to make the imine formation complete, the aldehyde was allowed to react with the amine for 40 min, and then the reducing agent was added. A mild reducing agent, sodium cyanoborohydride, was employed, and the use of sodium (triacetoxy)borohydride was also evaluated. Reactions with various combinations of the two reducing agents and several solvents, including DCE, THF, DMF, and TMOF, were carried out. On the basis of quantitation of Fmoc incorporation on the resin, it was found that the sodium (triacetoxy)borohydride in TMOF gave optimal results for this step (Table 1). Although a previously published synthesis reported no product formation using Fmoc-aminoacetaldehyde (*45*), systematic modification of the reaction conditions made it possible to obtain the desired product on the resin in typical yields of 80−90%. Appropriate precautions, such as measuring amino acid loading of the resin, sufficient reaction time, and use of inert atmosphere, were essential to reduce the most common side reaction, dialkylation. To the best of our knowledge, this is the first reported solid-phase reductive alkylation using *N*-Fmoc-aminoacetaldehyde.

Finally, thymine-1-acetic acid was activated under various conditions, using uronium or phosphonium salts, and was coupled to the secondary amine on the solid support. It was found that coupling conditions based on anhydride formation using DIC (*46*), TBTU/PyBOP (*47*), HOBT/HBTU (*48*), and HOBT/EDCI (*49*) were ineffective. However, DhbtOH/DIC or HATU (*50*) afforded efficient coupling of thymine-1-acetic acid to the secondary amine. In the case of the serine derivative, a single coupling gave the crude product in high purity (Figure 1, top). For the aspartic acid (Figure 2, top) and lysine (Figure 3, top) derivatives, two couplings of activated thymine-1-acetic acid were required to obtain optimal yields of the desired product, although 5−10% of unreacted secondary amine remained. In the case of guanine, benzyloxypurine-9-acetic acid was synthesized according to the literature method (*51*). That work also provides potential routes to amino acid-modified cytosine and adenine PNA monomers, using modifications of the present methods. The protected guanine nucleobase was attached to the protected (aminoethyl)serine intermediate, using the same coupling conditions twice. The final products were cleaved from the resin using 0.5% TFA in DCM and precipitated with diethyl ether. These products could be isolated in typical overall yields of 36−42%, after purification by preparative reversed-phase HPLC or flash chromatography on normal silica. As determined by analytical reversed-phase HPLC, these

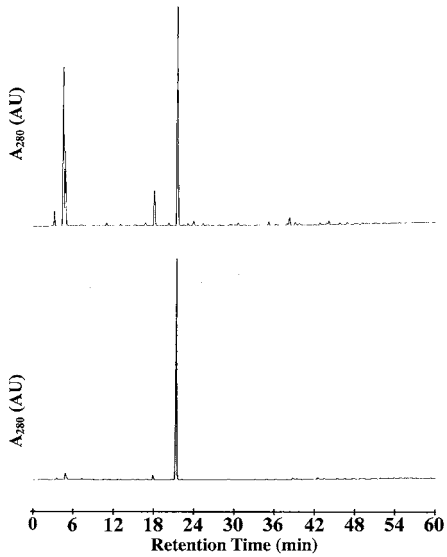

Figure 2. Analytical reversed-phase HPLC chromatograms of crude (top) and purified (bottom) **2**, using Analytical Gradient conditions. The peak at a retention time of 22.0 min represents the desired product, while the peak at 18.7 min represents the unreacted secondary amine precursor. The other small peaks in the chromatogram of the purified product are injection artifacts.

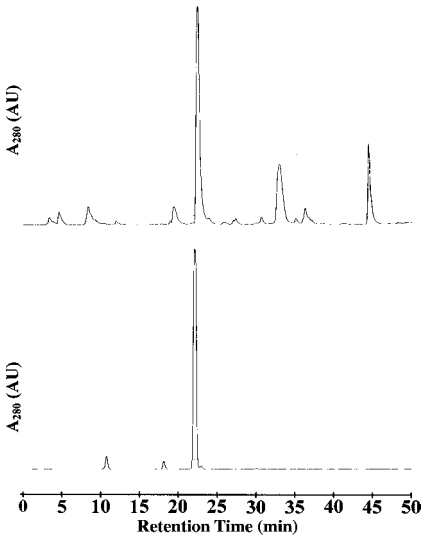

Figure 3. Analytical reversed-phase HPLC chromatograms of crude (top) and purified (bottom) **3**, using Analytical Gradient conditions. The peak at a retention time of 22.1 min represents the desired product, while the peak at 18.7 min represents the unreacted secondary amine precursor. The other small peaks in the chromatogram of the purified product are injection artifacts.

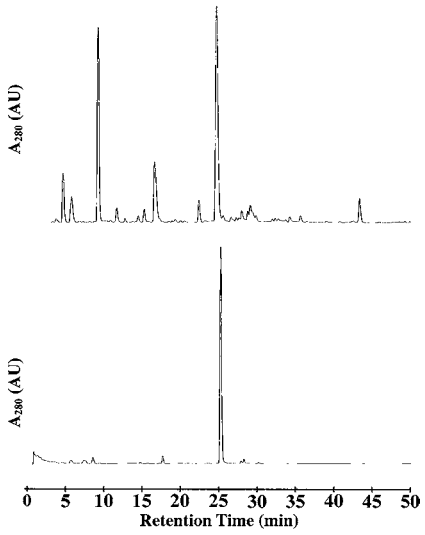

Figure 4. Analytical reversed-phase HPLC chromatograms of crude (top) and purified (bottom) **4**, using Analytical Gradient conditions. The peak at a retention time of 25.2 min represents the desired product, while the peak at 18.1 min represents the unreacted secondary amine precursor. The other small peaks in the chromatogram of the purified product are injection artifacts.

methods yielded **1** in near quantitative purity (Figure 1, bottom), **2** in 98.6% purity (Figure 2, bottom), **3** in 98.0% purity (Figure 3, bottom), and **4** in 98.8% purity (Figure 4, bottom). In the case of **2**, **3**, and **4**, the only impurity (1.2−2.0%) after HPLC or flash chromatography purification was the secondary amine precursor. All compounds could be purified to homogeneity using a subsequent reversed-phase separation.

Using compound **2**, PNA tetramers were synthesized in which the position of an aspartic acid derivatized thymine residue (T_D) was varied in seven model sequences: $AAGT_D$ (**5**), GAT_DA (**6**), AT_DCG (**7**), T_DACA (**8**), AT_DGC (**9**), $AGAT_D$ (**10**), and T_DCAA (**11**). Compound **2** was incorporated into all four sequence positions, from the C-terminus to the N-terminus (including direct coupling on the resin) and attached to a cytosine residue, an adenine residue, or a guanine residue. After cleavage, deprotection, and precipitation, the purity of each of the crude products was >95% by reversed-phase HPLC analysis

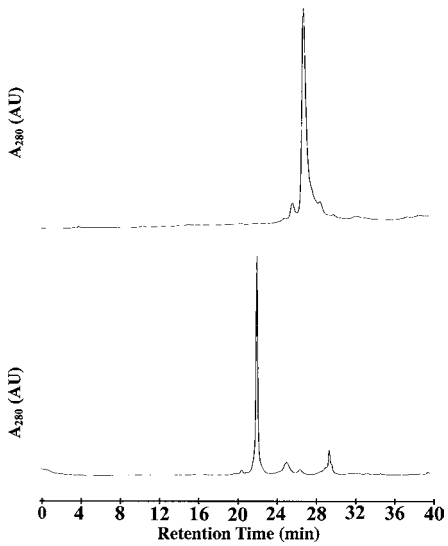

Figure 5. Analytical reversed-phase HPLC chromatograms of serine derivatized tetradecamers **12** ($CCAGCGTGCGCCAT_S$, top) and **13** ($CCAGCGT_SGCGCCAT$, bottom), using a sequential linear gradient of 5% to 25% solvent B in 20 min (step 1), 25% to 45% solvent B in 10 min (step 2), and 45% to 95% solvent B in 10 min (step 3). The peaks at a retention times of 26.9 min (top) and 22.2 min (bottom) represent the desired products.

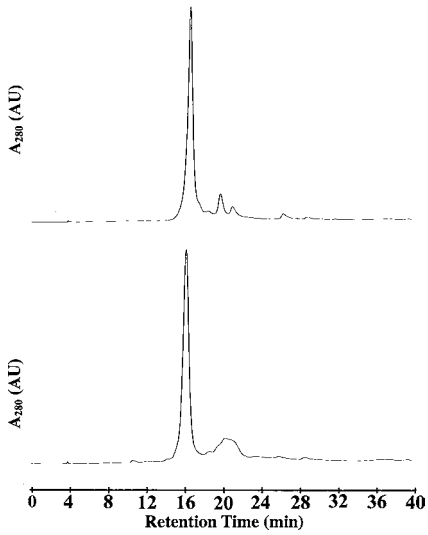

Figure 6. Analytical reversed-phase HPLC chromatograms of aspartic acid derivatized tetradecamers **14** ($CCAGCGTGCGCCAT_D$, top) and **15** ($CCAGCGT_DGCGCCAT$, bottom), using a sequential linear gradient of 5% to 25% solvent B in 20 min (step 1), 25% to 45% solvent B in 10 min (step 2), and 45% to 95% solvent B in 10 min (step 3). The peaks at a retention times of 16.8 min (top) and 16.3 min (bottom) represent the desired products.

(data not shown). The high purity of the tetramer preparations indicated that the coupling efficiency of **2** was comparable to that of commercially available glycine monomers. For each of the tetramers, ESI-MS analysis was consistent with the structures of the desired products.

Finally, four tetradecamers, complementary to the translational start sequence of *bcl-2* mRNA, were synthesized using compounds **1** and **2**. A serine (T_S) or an aspartic acid (T_D)-derivatized thymine residue was incorporated at the C-terminus (position 1) or coupled to a guanine residue in position 8 of the respective tetradecamers: $CCAGCGTGCGCCAT_S$ (**12**), $CCAGCGT_SGCGCCAT$ (**13**), $CCAGCGTGCGCCAT_D$ (**14**), and $CCAGCGT_DGCGCCAT$ (**15**). After cleavage, Bhoc deprotection, HPLC separation, Fmoc removal, and precipitation, reversed-phase HPLC analysis of **12** (Figure 5, top), **13** (Figure

5, bottom), **14** (Figure 6, top), and **15** (Figure 6, bottom) indicated that the purity of each of the modified oligomers was approximately 90%. ESI-MS of the major products was consistent with the structures of the respective tetradecamers. Minor impurities (~10%) present in the tetradecamer preparations may represent truncated species not removed by preparative reversed-phase HPLC. However, these syntheses demonstrated that two of these amino acid-modified monomers (T_S and T_D) can be incorporated with high efficiency into PNAs sufficiently long for statistically unique targeting in the human RNA pool (*52*).

CONCLUSION

We have developed a convenient, efficient, and high yielding synthesis of amino acid-modified PNA monomers requiring minimal purification using solid-phase techniques. Amino acids represented neutral hydrophilic (serine), acidic (aspartic acid), and basic (lysine) residues, and the nucleobases included a pyrimidine (thymine) and a purine (protected guanine), to afford a wide variety of compounds. Furthermore, we have synthesized several PNA tetramers and *bcl-2* antisense tetradecamers in which two of these modified residues have been incorporated into various sequence positions, with coupling efficiencies comparable to those of commercially available glycine analogues. Studies evaluating the water solubility and DNA hybridization properties of PNAs containing these amino acid modifications are currently in progress.

ACKNOWLEDGMENT

This work was supported by NIH Grant CA103130 from the National Cancer Institute. The authors also acknowledge the Department of Veterans Affairs, for providing resources and the use of facilities at the Harry S. Truman Memorial Veterans' Hospital in Columbia, MO.

Supporting Information Available: ESI mass spectra and ^{1}H NMR spectra of compounds **1**−**4**, as well as ESI mass spectra of compounds **12**−**15**. This material is available free of charge via the Internet at http://pubs.acs.org.

LITERATURE CITED

(1) Nielsen, P. E., Egholm, M., Berg, R. H., and Buchardt, O. (1991) Sequence-selective recognition of DNA by strand displacement with a thymine-substituted polyamide. *Science 254*, 1497−1500.
(2) Nielsen, P. E., and Haaima, G. (1997) Peptide nucleic acid (PNA). A DNA mimic with a pseudopeptide backbone. *Chem. Soc. Rev. 26*, 73−78.
(3) Uhlmann, E., Peyman, A., Breipohl, G., and Will, D. W. (1998) PNA: synthetic polyamide nucleic acids with unusual binding properties. *Angew. Chem., Int. Ed. 37*, 2796−2823.
(4) Di Giorgio, C., Pairot, S., Schwergold, C., Patino, N., Condom, R., Farese-Di Giorgio, A., and Guedj, R. (1999) Liquid-phase synthesis of polyamide nucleic acids (PNA). *Tetrahedron 55*, 1937−1958.
(5) Maison, W., Schlemminger, I., Westerhoff, O., and Martens, J. (2000) Multicomponent synthesis of novel amino acid-nucleobase chimeras: a versatile approach to PNA-monomers. *Bioorg. Med. Chem. 8*, 1343−1360.
(6) Nielsen, P. E. (2000) Peptide nucleic acids: on the road to new gene therapeutic drugs. *Pharmacol. Toxicol. 86*, 3−7.
(7) Wang, G., and Xu, X. S. (2004) Peptide nucleic acid (PNA) binding-mediated gene regulation. *Cell Res. 14*, 111−116.
(8) Doyle, D. F., Braasch, D. A., Simmons, C. G., Janowski, B. A., and Corey, D. R. (2001) Inhibition of gene expression inside cells by peptide nucleic acids: effect of mRNA target sequence, mismatched bases, and PNA length. *Biochemistry 40*, 53−64.
(9) Kaihatsu, K., Huffman, K. E., and Corey, D. R. (2004) Intracellular uptake and inhibition of gene expression by PNAs and PNA−peptide conjugates. *Biochemistry 43*, 14340−14347.
(10) Sforza, S., Tedeschi, T., Corradini, R., Ciavardelli, D., Dossena, A., and Marchelli, R. (2003) Fast, solid-phase synthesis of chiral peptide nucleic acids with a high optical purity by a submonomeric strategy. *Eur. J. Org. Chem.*, 1056−1063.
(11) Hamzavi, R., Dolle, F., Tavitian, B., Dahl, O., and Nielsen, P. E. (2003) Modulation of the pharmacokinetic properties of PNA: preparation of galactosyl, mannosyl, fucosyl, *N*-acetylgalactosaminyl, and *N*-acetylglucosaminyl derivatives of aminoethylglycine peptide nucleic acid monomers and their incorporation into PNA oligomers. *Bioconjugate Chem. 14*, 941−954.
(12) Matysiak, S., Reuthner, F., and Hoheisel, J. D. (2001) Automating parallel peptide synthesis for the production of PNA library arrays. *BioTechniques 31*, 896−904.
(13) Egholm, M., Buchardt, O., Christensen, L., Behrens, C., Freier, S. M., Driver, D. A., Berg, R. H., Kim, S. K., Norden, B., and Nielsen, P. E. (1993) PNA hybridizes to complementary oligonucleotides obeying the Watson−Crick hydrogen-bonding rules. *Nature 365*, 566−568.
(14) Lomakin, A., and Frank-Kamenetskii, M. D. (1998) A theoretical analysis of specificity of nucleic acid interactions with oligonucleotides and peptide nucleic acids (PNAs). *J. Mol. Biol. 276*, 57−70.
(15) Pooga, M., and Langel, U. (2001) Targeting of cancer-related proteins with PNA oligomers. *Curr. Cancer Drug Targets 1*, 231−239.
(16) Mier, W., Eritja, R., Mohammed, A., Haberkorn, U., and Eisenhut, M. (2003) Peptide-PNA conjugates: targeted transport of antisense therapeutics into tumors. *Angew. Chem., Int. Ed. 42*, 1968−1971.
(17) Koppelhus, U., and Nielsen, P. E. (2003) Cellular delivery of peptide nucleic acid (PNA). *Adv. Drug Delivery Rev. 55*, 267−280.
(18) Li, X., Zhang, L., Lu, J., Chen, Y., Min, J., and Zhang, L. (2003) Signal peptide mimics conjugated to peptide nucleic acid: a promising solution for improving cell membrane permeability. *Bioconjugate Chem. 14*, 153−157.
(19) Braasch, D. A., and Corey, D. R. (2002) Novel antisense and peptide nucleic acid strategies for controlling gene expression. *Biochemistry 41*, 4503−4510.
(20) Gallazzi, F., Wang, Y., Jia, F., Shenoy, N., Landon, L. A., Hannink, M., Lever, S. Z., and Lewis, M. R. (2003) Synthesis of radiometal-labeled and fluorescent cell-permeating peptide-PNA conjugates for targeting the *bcl-2* proto-oncogene. *Bioconjugate Chem. 14*, 1083−1095.
(21) Lewis, M. R., Jia, F., Gallazzi, F., Wang, Y., Zhang, J., Shenoy, N., Lever, S. Z., and Hannink, M. (2002) Radiometal-labeled peptide-PNA conjugates for targeting *bcl-2* expression: preparation, characterization, and in vitro mRNA binding. *Bioconjugate Chem. 13*, 1176−1180.
(22) Jia, F., Gallazzi, F., Lever, S. Z., Hannink, M., and Lewis, M. R. (2005) Synthesis and *in vitro* evaluation of ^{111}In-DOTA-anti-*bcl-2*−PNA-Tyr^3-octreotate in chronic lymphocytic leukemia cells. *J. Labeled Cpd. Radiopharm. 48*, S286.
(23) Gallazzi, F., Jia, F., Balaji, B. S., Hannink, M., Lever, S. Z., and Lewis, M. R. (2004) Synthesis of radiometal-labeled, receptor-targeted anti-bcl-xL PNA conjugates. Abstract Number NUCL-4, 228th American Chemical Society National Meeting, Philadelphia, PA.
(24) Haaima, G., Lohse, A., Buchardt, O., and Nielsen, P. E. (1996) Peptide nucleic acids (PNAs) containing thymine monomers derived from chiral amino acids: hybridization and solubility properties of D-lysine PNA. *Angew. Chem., Int. Ed. Engl. 35*, 1939−1941.
(25) Rao, P. S., Tian, X., Qin, W., Aruva, M. R., Sauter, E. R., Thakur, M. L., and Wickstrom, E. (2003) Tc-99m-peptide-peptide nucleic acid probes for imaging oncogene mRNAs in tumours. *Nucl. Med. Commun. 24*, 857−863.
(26) Tian, X., Aruva, M. R., Qin, W., Zhu, W., Duffy, K. T., Sauter, E. R., Thakur, M. L., and Wickstrom, E. (2004) External imaging of CCND1 cancer gene activity in experimental human breast cancer xenografts with ^{99m}Tc-peptide-peptide nucleic acid-peptide chimeras. *J. Nucl. Med. 45*, 2070−2082.
(27) Sun, X., Fang, H., Li, X., Rossin, R., Welch, M. J., and Taylor, J.-S. (2005) MicroPET imaging of MCF-7 tumors in mice via unr mRNA-targeted peptide nucleic acids. *Bioconjugate Chem. 16*, 294−305.
(28) Falkiewicz, B., Kolodziejczyk, A. S., Liberek, B., and Wisniewski, K. (2001) Synthesis of achiral and chiral peptide nucleic acid (PNA) monomers using Mitsunobu reaction. *Tetrahedron 57*, 7909−7917.

(29) Dueholm, K. L., Petersen, K. H., Jensen, D. K., Egholm, M., Nielsen, P. E., and Buchardt, O. (1994) Peptide nucleic acid (PNA) with a chiral backbone based on alanine. *Bioorg. Med. Chem. Lett. 4*, 1077−1080.

(30) Zhang, L., Min, J., and Zhang, L. (1999) Studies on the synthesis and properties of new PNA analogs consisting of L- and D-lysine backbones. *Bioorg. Med. Chem. Lett. 9*, 2903−2908.

(31) Falkiewicz, B. (2002) Application of Mitsunobu reaction to solid-phase peptide nucleic acid (PNA) monomer synthesis. *Nucleosides Nucleotides Nucleic Acids 21*, 883−889.

(32) Li, Y., Jin, T., and Liu, K. (2001) Synthesis and binding affinity of a chiral PNA analogue. *Nucleosides Nucleotides Nucleic Acids 20*, 1705−1721.

(33) Prokhorov, D. I., Kirillova, Y. G., Boyarskaya, N. P., Tevyashova, A. N., Esipova, O. V., Zvonkova, E. N., and Shvets, V. I. (2005) Synthesis of thymine-containing monomers of negatively charged peptide nucleic acids. *Pharm. Chem. J. 39*, 323−328.

(34) Lubell, W. D., and Rapoport, H. (1987) Configurational stability of N-protected α-amino aldehydes. *J. Am. Chem. Soc. 109*, 236−239.

(35) Jurczak, J., and Golebiowski, A. (1989) Optically active N-protected α-amino aldehydes in organic synthesis. *Chem. Rev. 89*, 149−164.

(36) Viirre, R. D., and Hudson, R. H. E. (2001) Optimization of a solid-phase synthesis of a PNA monomer. *Org. Lett. 3*, 3931−3934.

(37) Thiers, R. E. (1957) Contamination in trace element analysis and its control. *Methods Biochem. Anal. 5*, 273−335.

(38) Frigerio, M., Santagostino, M., and Sputore, S. (1999) A user-friendly entry to 2-iodoxybenzoic acid (IBX). *J. Org. Chem. 64*, 4537−4538.

(39) More, J. D., and Finney, N. S. (2002) A simple and advantageous protocol for the oxidation of alcohols with *o*-iodoxybenzoic acid (IBX). *Org. Lett. 4*, 3001−3003.

(40) Leggio, A., Liguori, A., Napoli, A., Siciliano, C., and Sindona, G. (2000) New strategies for an efficient removal of the 9-fluorenylmethoxycarbonyl (Fmoc) protecting group in the peptide synthesis. *Eur. J. Org. Chem.*, 573−575.

(41) Carpino, L. A., and Han, G. Y. (1972) 9-Fluorenylmethoxycarbonyl amino-protecting group. *J. Org. Chem. 37*, 3404−3409.

(42) Sheppard, R. (2003) The fluorenylmethoxycarbonyl group in solid-phase synthesis. *J. Pept. Sci. 9*, 545−552.

(43) Greene, T. W., and Wuts, P. G. M. (1999) Protection for the carbonyl group. *Protective Groups in Organic Synthesis*, 3rd ed., pp 299−302, Chapter 4, John Wiley & Sons, New York.

(44) Falkiewicz, B., Kowalska, K., Kolodziejczyk, A. S., Wisniewski, K., and Lankiewicz, L. (1999) Synthesis of new chiral peptide nucleic acid (PNA) monomers by a simplified reductive amination method. *Nucleosides Nucleotides 18*, 353−361.

(45) Davis, P. W., and Swayze, E. E. (2000) Automated solid-phase synthesis of linear nitrogen-linked compounds. *Biotechnol. Bioeng. 71*, 19−27.

(46) Chan, W. C., and White, P. D. (2003) Basic procedures. *Fmoc Solid-Phase Peptide Synthesis. A Practical Approach* (Chan, W. C., and White, P. D., Eds.) p 56, Chapter 3, Oxford University Press, New York.

(47) Knorr, R., Trzeciak, A., Bannwarth, W., and Gillessen, D. (1989) New coupling reagents in peptide chemistry. *Tetrahedron Lett. 30*, 1927−1930.

(48) Neuner, P., and Monaci, P. (2002) New Fmoc pseudoisocytosine monomer for the synthesis of a bis-PNA molecule by automated solid-phase Fmoc chemistry. *Bioconjugate Chem. 13*, 676−678.

(49) Wang, W., and Nan, F. (2003) First total synthesis of leucamide A. *J. Org. Chem. 68*, 1636−1639.

(50) Carpino, L. A. (1993) 1-Hydroxy-7-azabenzotriazole. An efficient peptide coupling additive. *J. Am. Chem. Soc. 115*, 4397−4398.

(51) Dueholm, K. L., Egholm, M., Behrens, C., Christensen, L., Hansen, H. F., Vulpius, T., Petersen, K. H., Berg, R. H., Nielsen, P. E., and Buchardt, O. (1994) Synthesis of peptide nucleic acid monomers containing the four natural nucleobases: thymine, cytosine, adenine, and guanine and their oligomerization. *J. Org. Chem. 59*, 5767−5773.

(52) Summerton, J. (1999) Morpholino antisense oligomers: the case for an RNase H-independent structural type. *Biochim. Biophys. Acta 1489*, 141−158.

BC0502208

Efficient Monitoring of Enzymatic Conjugation Reaction by Surface-Enhanced Laser Desorption/Ionization Time of Flight Mass Spectrometry for Process Optimization

Teresa Freire,[†] Jacques D'Alayer,[‡] and Sylvie Bay*[,†]

Unité de Chimie Organique URA CNRS 2128 and Plate-forme d'Analyse et de Microséquençage des Protéines, Institut Pasteur, 25-28 rue du Dr. Roux, 75724 Paris, Cedex 15, France. Received September 5, 2005; Revised Manuscript Received January 16, 2006

Efficient analysis of bioconjugation reactions is one the most challenging task for optimizing and eventually achieving the reproducible production of large amount of conjugates. In particular, the complexity of some reaction mixtures precludes the use of most of the existing methods, because of the presence of large amounts of contaminants. As an alternative method, we used surface-enhanced laser desorption/ionization time-of-flight mass spectrometry (SELDI-TOF MS) for monitoring an in vitro enzymatic transglycosylation of *N*-acetylgalactosamine (GalNAc) residues to a recombinant mucin protein MUC6. For this reaction, catalyzed by the uridine 5′-diphospho-*N*-acetylgalactosamine:polypeptide *N*-acetylgalactosaminyltransferases (ppGalNAc-Ts), we used either a recombinant ppGalNAc-T1 or a mixture of ppGalNAc-Ts contained in MCF7 tumor cell extracts. In the present study, we show that SELDI-TOF MS offers unique advantages over the traditional methodologies. It is a rapid, accurate, sensitive, reproducible, and very convenient analytical method for monitoring the course of a bioconjugation, even in heterogeneous samples such as cell extracts. SELDI-TOF MS proved very useful for optimizing the reaction parameters of the transglycosylation and for achieving the large scale preparation of Tn antigen-glycosylated mucins for antitumor immunotherapy applications.

INTRODUCTION

Bioconjugation technology has been widely used in nearly every discipline of life sciences research (*1*, *2*). One of the application areas is the preparation of hapten−carrier conjugates for immunization purposes, antibody production, and vaccine research. Indeed, small hapten molecules such as carbohydrates cannot elicit an efficient immune response on their own. To make them immunogenic, they must be coupled to a suitable carrier molecule, typically a protein. The characteristics of the resulting conjugate play a critical role in the intensity and the quality of the immune response. In particular, several groups have reported the influence of the hapten density on the level, the specificity, and the affinity of the produced antibodies (*3*−*6*). Careful follow-up of the conjugation is therefore very important to achieve the reproducible production of conjugates.

Different approaches are commonly employed to analyze these conjugates and to ascertain their optimal preparation. The choice of the method depends on the physicochemical properties of both hapten and carrier, as well as on the cross-linking strategy. The most frequently used procedures involve mass spectrometry, sometimes associated with high performance liquid chromatography (HPLC) (*4*, *6*−*8*), gel filtration (*2*), absorption (*9*) and fluorescence (*6*, *7*) spectroscopy, gel electrophoresis (*5*, *6*, *8*), and colorimetric assay for reactions involving sulfhydryl groups (*10*), amino groups (*11*), or carbohydrate residues (*12*). Although efficient, these existing methods suffer from several drawbacks. First, they often require further treatment of the samples, they are time-consuming, and they are not easy to perform when multiple samples are to be analyzed. Moreover, they are usually not very accurate and only give a rough estimate of the conjugate's molecular mass and integrity. Finally, the complexity of some reaction mixtures (cell extracts, sera, tissue homogenates, etc.) can affect the effectiveness of the analysis adversely, due to the presence of large amounts of other compounds (lipids, detergents, salts, other proteins, etc.).

Therefore, there is a need for rapid and sensitive analytical methods for monitoring bioconjugation reactions, particularly with complex and heterogeneous samples. Additionally, such efficient methods are essential in development, for optimizing the process and scaling up the production of the conjugates, while ensuring a batch-to-batch consistency.

ProteinChip array technology or surface-enhanced laser desorption/ionization time-of-flight mass spectrometry (SELDI-TOF MS) allows the analysis of complex protein mixtures by combining two powerful techniques: chromatography and mass spectrometry. After selective retention on a chip surface, the compounds of interest are subsequently analyzed by a laser desorption/ionization mass spectrometer. This technique has been successfully used in many fields such as biomarker discovery, study of biomolecular interactions, protein profiling, analysis of posttranslational modifications, etc. (*13*, *14*).

As compared to these applications, very few examples have been described so far showing the use of SELDI-TOF for the monitoring of a reaction (whether chemical or enzymatic) or for the analysis of the resulting product. Recently, the direct analysis of peptides or proteins after either enzymatic digestion (*15*−*17*) or limited acid hydrolysis (*18*) has been successfully performed on-chip, with the aim of identifying protein sequences. On-chip enzymatic reactions and subsequent characterization have also been performed in order to study posttranslational modifications. Using this method, the degree of glycosylation of a recombinant antibody has been monitored with a deglycosylation procedure using PNGase F (*19*) and the

* Corresponding author. Tel: (33) 1 45 68 83 98; Fax: (33) 1 45 68 84 04; e-mail: sbay@pasteur.fr.

[†] Unité de Chimie Organique URA CNRS 2128.

[‡] Plate-forme d'Analyse et de Microséquençage des Protéines.

10.1021/bc0502661 CCC: $33.50 © 2006 American Chemical Society
Published on Web 02/24/2006

phosphorylation state of a peptide or a protein has been evaluated after the action of a kinase (*20*) or a phosphatase (*21*). This last example included a time course study. In another characterization study, Hubalek et al. (*41*) have described the analysis of biotinylated tryptic peptides after digestion of biotinylated recombinant human monoamine oxidases and subsequent purification on an affinity column. Similarly, a peptide enzymatically released from a synthetic peptide related to the proteinase-activated receptor 2 was identified by SELDI-TOF MS (*22*). Interestingly, SELDI-TOF MS has also allowed the course of the autoactivation process of a bacterial protein to be followed, directly from the culture supernatant (*23*). Finally, the utility of SELDI-TOF MS has been demonstrated for monitoring the attachment of bacterial oligosaccharides to a protein, by a conjugation method using squaric acid diester chemistry (*24*, *25*). However, the reaction was a chemical ligation in a simple mixture composed of the synthetic linker-derivatized oligosaccharide, the protein carrier, and the buffer. To our knowledge, SELDI-TOF MS has never been used for monitoring an in vitro enzymatic conjugation reaction in a complex mixture.

Among the hapten molecules, carbohydrates are of particular interest since they are part of bacterial determinants, and they are also tumor-associated antigens (TAA). As a result, a large number of carbohydrate−protein conjugates have been developed as vaccines against infectious diseases (*26*) and cancer (*27*). In previous works, we and others have prepared various conjugates displaying the Tn antigen (α-D-GalNAc−Ser/Thr) (*28*−*30*) which is a carbohydrate TAA overexpressed in breast, lung, prostate, and colon cancers (*31*, *32*). The resulting glycopeptides (*28*) or glycoproteins (*29*, *30*) have been shown to be highly promising vaccine candidates for targeting cancers. However, the preparation of such conjugates relies on multistep tedious syntheses and/or time-consuming purifications. To circumvent these difficulties, we developed an enzymatic approach for producing a protein glycoconjugate with a high Tn density.

Tn-mucins are attractive targets for antitumor immunotherapy since carbohydrates have been shown to be an essential part of tumor-associated structures within the mucins (*33*). As the protein backbone, we chose the MUC6 gastric mucin (*34*) which has been described in different tumors, including lung (*35*, *36*) and breast (*37*, *38*) carcinomas. This mucin is a natural substrate of the uridine 5′-diphospho-*N*-acetylgalactosamine:polypeptide *N*-acetylgalactosaminyltransferases (ppGalNAc-Ts, EC 2.4.1.41) which are the enzymes responsible for the Tn antigen synthesis in vivo.

To achieve the large scale preparation of MUC6-Tn conjugates for antitumor immunotherapy, we performed the in vitro enzymatic GalNAc antigen transfer onto the mucin acceptor. We describe herein the monitoring of the conjugation by SELDI-TOF MS and we show that this method is very rapid and efficient for optimizing the reaction parameters, including in complex mixtures.

EXPERIMENTAL PROCEDURES

MUC6 Cloning and Expression in *E. coli*. A cDNA clone containing one tandem repeat of MUC6 was isolated from total cDNA of MCF7 breast cancer cells by RT-PCR and cloned into pGem-T (Promega, France). The PCR products were designed to encode a half tandem repeat (87 amino acids) that were amplified with *Pfu* DNA polymerase and the primers MUC6-F, 5′-cgggatccTCCACCTCCTTGGTGACT-3′ and MUC6-2R 5′-ggaagcttATTAGGATGGTGTGTGGA-3′ (lowercase characters indicate restriction sites for *BamH*I and *Hind*III in the forward and reverse primers, respectively). Following digestion with *BamH*I and *Hind*III, each product was cloned into the pET28a(+) vector (Novagen, Fontenay-sous-Bois, France), so as to encode for a protein carrying a six-histidine tail at the N-terminus. *E. coli* DH5α transformants were selected on LB plates containing 50 μg/mL kanamycin, and the positive clones were confirmed by PCR and sequencing. Plasmids were purified from selected clones and used to transform *E. coli* BLi5 chemically competent cells. The recombinant was expressed in *E. coli* BLi5 by induction with 1 mM IPTG and purified over Ni^{2+}-nitriloacetic acid columns under denaturing conditions according to the manufacturer's (Qiagen, Germany) instructions. The MUC6 protein was characterized by amino acid analysis (AAA), SELDI-TOF MS, and electrospray mass spectrometry (ESMS: 12148.05; calculated: 12147.45). These analyses, together with a N-terminal sequencing, show that the protein lacks the N-terminal methionine residue.

Breast Cancer Cell Line Extracts. Breast cancer cell line MCF7 was grown to 90% confluence in Dulbecco's modified Eagle's medium (Life Technologies, Inc.) with 10% fetal bovine serum, 1 mM pyruvate, and 2 mM glutamine and 5% CO_2 at 37 °C. After trypsinization, cells were washed three times with phosphate-buffered saline (PBS), resuspended in 250 mM sucrose, and homogeneized. Cells were then centrifuged at 3000*g* for 10 min at 4 °C. The resulting supernatant was again centrifuged at 100000*g* for 1 h at 4 °C. The pellet was resuspended in 0.1 M imidazole pH 7.2 and 0.1% Triton X-100. Cell extracts were aliquoted and stored at −80 °C. Protein concentration was determined by the BCA method (Sigma Chemical Co., St Louis, MO).

Recombinant Bovine Polypeptide GalNAc Transferase 1. A soluble form of the bovine ppGalNAc-T1 (ppGalNAc-T1), kindly given by F. Piller and V. Piller, was expressed in the yeast *Pichia pastoris* KM71H strain (Invitrogen, Cergy Pontoise, France) using the pPICZαA expression vector (Invitrogen). The recombinant ppGalNAc-T1 (from amino acids 52 to 559) carrying a N-terminal 6His-tag was expressed (induction in 0.5% methanol for 120 h) and purified on Ni-NTA-agarose (Qiagen, Hilden, Germany). The specific activity of the recombinant ppGalNAc-T1 was tested as previously described (*39*) and estimated to 3 U/mg protein (1 unit transfers 1 μmole of GalNAc per min at 37 °C to the acceptor peptide $[STP]_5$).

In vitro GalNAc Transfer to MUC6 Protein. Microsome fractions of MCF7 breast cancer cells were incubated at 37 °C for 48 h with uridine 5′-diphospho-*N*-acetylgalactosamine (UDP-GalNAc) and purified recombinant MUC6 (40−80 μM) in 50 mM imidazole pH 7.2 containing 50 mM $MnCl_2$ and 0.1% Triton-X100. When recombinant ppGalNAc-T1 was used, the MUC6 purified protein (40−80 μM) was incubated with UDP-GalNAc in 50 mM MES, pH 6.5 for 24 h at 37 °C. Aliquots were taken at different times and frozen at −20 °C. The different reaction conditions are detailed in Table 1. The resulting MUC6-Tn were purified using Ni-NTA-agarose (Qiagen, Hilden, Germany) (only when cell extracts were used) and then subjected to reversed phase HPLC using a Perkin-Elmer pump system with an UV detector at 230 nm. The column was a Symmetry 300 C18 (5 μm, 300 Å, 3.9 × 250 mm) (Waters, France). Elution was carried out with a linear gradient of 10−60% acetonitrile in 0.1% trifluoracetic acid in water at a flow rate of 1 mL/min (over 30 min). The peak was collected and then lyophilized. The MUC6-Tn glycoproteins were characterized by amino acid analysis and SELDI-TOF MS.

Reaction Monitoring by SELDI-TOF. The SELDI-TOF mass spectrometer was purchased from Ciphergen Biosystems (Fremont, CA). IMAC30 ProteinChip array surfaces were activated with 100 mM $NiCl_2$ at room temperature for 15 min and then washed with water and PBS. Spots were incubated with total glycosylation mix aliquots for 40 min at room temperature using the Bioprocessor system and then washed

Table 1. Conditions of the Tranglycosylation Reactions and the Average GalNAc Amount of the Resulting Conjugates

figure	panel	UDP-GalNAc amount (equiv)[a]	enzyme amount (μg of protein/10 μg mucine)	observed average molecular mass (Da)[c]	change in mass (ΔM)	average GalNAc amount/mucin ($\Delta M/M_g$)[d]
1	A	0	1 (ppGalNAc-T1)	12144.3	-	-
1	B	2	0.01 (ppGalNAc-T1)	13170.0	1025.7	5 (5.05)
1	C	2	0.04 (ppGalNAc-T1)	13778.8	1634.5	8 (8.04)
1	D	2	0.2 (ppGalNAc-T1)	15018.2	2873.9	14 (14.14)
1	E	2	1 (ppGalNAc-T1)	16036.1	3891.8	19 (19.15)
1	F	1	1 (ppGalNAc-T1)	15806.6	3662.3	18 (18.02)
1	G	0.5	1 (ppGalNAc-T1)	15598.8	3454.5	17 (17.0)
3	A	0	130 (MCF7 cell extracts)[b]	12144.8	-	-
3	B	2	130 (MCF7 cell extracts)[b]	17037.3	4892.5	24 (24.08)

[a] The molar equivalent amount is expressed as compared to potential *O*-glycosylation sites (47 serine and threonine residues). [b] 65 μg was added at the beginning of the reaction and then at 24 h. [c] The average molecular mass of the neoglycoconjugate was calculated from the medium peak which is marked with an arrow on Figures 1 and 3. [d] Calculated average mass of GalNAc $M_g = 203.193$ Da.

Scheme 1. Enzymatic Transglycosylation of GalNAc from UDP−GalNAc to the MUC6 Mucin Using Either Recombinant ppGalNAc-T1 or MCF7 Tumor Cell Extracts

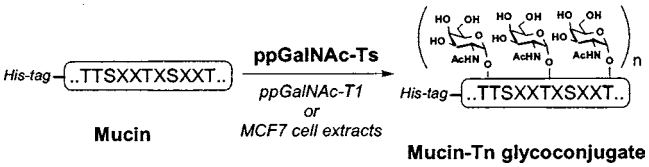

with 0.1% Triton-X100 in PBS (2 × 5 min), PBS (3 × 2 min), and 5 mM HEPES (2 × 5 min). The matrix (2 × 0.6 μL of sinapinic acid saturated in 50% acetonitrile/0.5% TFA) was applied on each spot and allowed to air-dry. Chips were then read in the PBS II Reader, and each array spot was laser-sampled. Spectra were generated at a laser setting of 220 with a detector sensitivity of 8 and an acceleration energy of 20 kV. The laser intensity at these values corresponds to ~8 μJ. Optimization range of the time lag focusing was set between 10 and 20 kDa. The instrument was externally calibrated with bovine ubiquitin (8564.8 Da), bovine cytochrome C (12230.9 Da), and bovine β-lactoglobulin (18363.3 Da) (all from Ciphergen Biosystems) with the matrix and the settings as described above for the MUC6 samples. Spectra were treated using the Ciphergen ProteinChip software 3.2.1.

RESULTS AND DISCUSSION

The recombinant MUC6 protein was subjected to the transglycosylation reaction from the carbohydrate activated donor UDP-GalNAc in the presence of the enzyme, either a recombinant ppGalNAc-T1 (*39*) or a mixture of ppGalNAc-Ts contained in MCF7 tumor cell extracts (Scheme 1). Small aliquots of the reaction were withdrawn at different times and directly analyzed by SELDI-TOF MS after immobilization on the ProteinChip surface through immobilized metal affinity capture (IMAC30). The reaction progress was monitored by the shift to higher masses, caused by the transfer of GalNAc residues, as compared with the mass of the starting material (Figures 1 and 3). The spectra displayed a set of peaks showing the incremental molecular masses of the conjugates and allowing to determine the average hapten−protein stoichiometry, as well as the distribution of the conjugates. The transglycosylation reactions were studied under various experimental conditions (Table 1).

The ppGalNAc-T1 was shown to catalyze very efficiently the in vitro transfer of GalNAc residues onto the MUC6 protein (Figure 1). The extent of transfer was first analyzed with 2 equiv of UDP-GalNAc donor (the molar equivalent amount refers to the potential *O*-glycosylation sites, i.e., the total serine and threonine residues) and variable amounts of the recombinant ppGalNAc-T1, after 24 h incubation. As shown in Figure 1

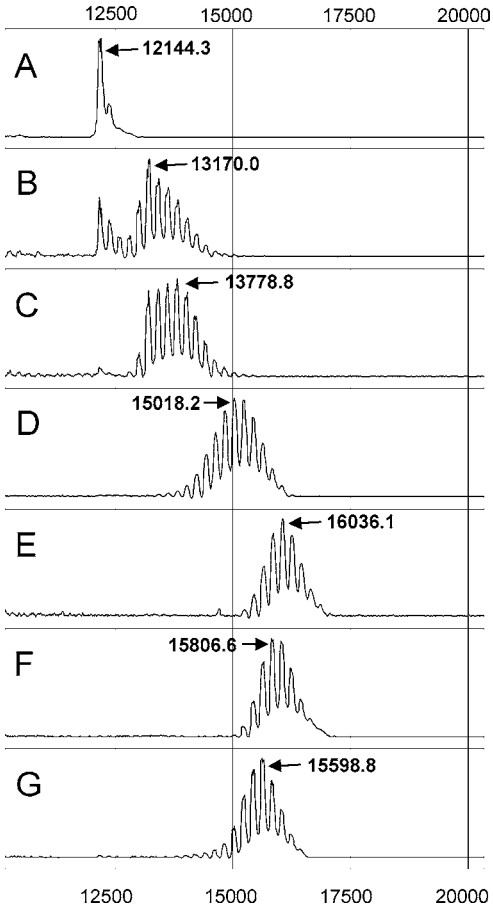

Figure 1. SELDI-TOF MS analysis of the progress of the GalNAc transglycosylation on MUC6 (molecular mass: 12144.3 Da, Panel A) using ppGalNAc-T1, depending on the donor (panels B−E) or the enzyme amount (panels E−G). The panel A (incubation reaction without UDP-GalNAc) served as a control for the starting material, i.e., the nonglycosylated MUC6 protein. The average mass/charge (*m*/*z*) values (in daltons) are shown in each panel on the medium peak marked with an arrow. The conditions of the tranglycosylation reactions, and the average GalNAc amount of the resulting conjugates are given in the Table 1.

(Panels B−E), the addition of enzyme results in a pronounced and progressive spectra shift showing significant increase in glycosylation with an average Tn amount from 5 (Panel B) to 19 (Panel E). Further addition of enzyme alone or enzyme together with UDP-GalNAc did not significantly improve the transfer (data not shown). Likewise, longer incubation period than 24 h did not produce any observable increase in molecular mass, showing that a maximum Tn level has been reached, at least under these experimental conditions (data not shown).

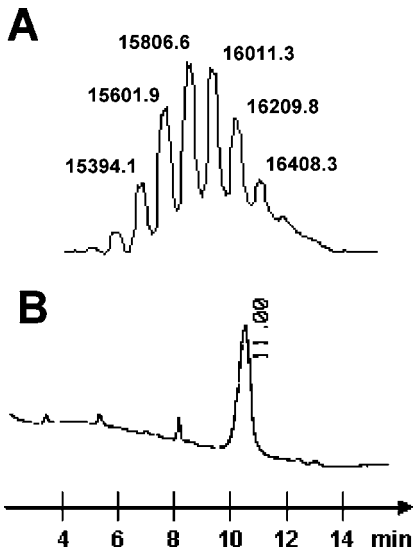

Figure 2. Comparison of the resolution by SELDI-TOF MS and HPLC analysis. Products from the experiment of Figure 1F (1 equiv of UDP-GalNAc and 1 μg of ppGalNAc-T1/10 μg of MUC6) were analyzed by SELDI-TOF MS (A) and reversed-phase HPLC (B). Enlarged SELDI-TOF mass spectrum shows the mass increment details (*m*/*z* values in daltons). Chromatographic conditions: Waters Symmetry C18 (5 μm, 300 Å, 3.9 × 250 mm), flow rate of 1 mL/min, gradient with water (0.1% trifluoracetic acid)/acetonitrile (10−60%) over 30 min.

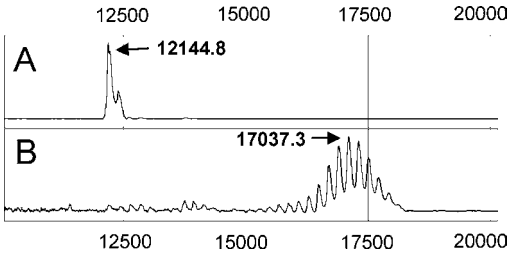

Figure 3. SELDI-TOF MS analysis of the conjugation reaction using MCF7 tumor cell extracts. The panel A (incubation reaction without UDP-GalNAc) served as a control for the starting material, i.e., the nonglycosylated MUC6 protein. The average mass/charge (*m*/*z*) values (in daltons) are shown in both panels on the medium peak marked with an arrow. The conditions of the tranglycosylation reaction, and the average GalNAc amount of the resulting conjugate are given in the Table 1.

The effect of the amount of donor is presented in Figure 1E−G. When lower quantities of UDP-GalNAc were used, the SELDI-TOF MS profile was found to be comparable, although a slight decrease in transfer was observed with 0.5 equiv of donor (Figure 1G).

To produce large amounts of conjugates while saving the expensive donor UDP-GalNAc, we chose the experimental conditions of Figure 1F for scaling up the reaction (1 equiv of UDP-GalNAc and 1 μg of enzyme/10 μg of MUC6). When the transglycosylation was performed on semipreparative quantities (mg range of mucin), the number of transferred GalNAc residues was found to be virtually the same as the one obtained at the analytical level (data not shown). As a result, the preparation of milligrams of neoglycoconjugates has been achieved, and the evaluation of their immunological properties will be reported separately (T. Freire et al., *Glycobiology*, in press).

Enlargement of the representative spectrum with the selected conditions (Figure 1F) shows the mass increment details (Figure 2A). The difference between each peak corresponds to the expected average mass of a single GalNAc residue (203.193 Da), demonstrating that SELDI-TOF MS allows a good resolution, at least in this molecular mass range. In contrast, the reverse phase HPLC profile did not show any separation of the different species (Figure 2B).

SELDI-TOF MS was then applied to the analysis of a transglycosylation in complex mixtures, by using the ppGalNAc-Ts contained in extracts from MCF7 tumor cells (Figure 3). The mass distribution obtained with the crude mixture was similar to the one observed with the recombinant enzyme. However, the transfer rate was better since an average density of 24 Tn/protein molecule was achieved after 48 h of reaction and two additions of cell extracts (Figure 3B). With the ppGalNAc-T1 and the cell extracts, the maximum Tn level was found to be, respectively, 40% and 51% of the potential glycosylation sites. The fact that the maximum Tn-protein stoichiometry was higher in this last case suggests that the additional GalNAc may have been transferred by other ppGalNAc-Ts that are present in the cell extracts. Interestingly, the presence of numerous contaminants in the cell extracts hardly affect the signal-to-noise ratio, showing that SELDI-TOF can be useful for such complex analysis.

We show here that the monitoring of a chemical conjugation reaction can be done for an enzymatic reaction in a crude and complex mixture (cell extracts) without any interference from contaminants, although such monitoring with simple samples has been reported previously by P. Kováč and co-workers (*24*, *25*). These results imply that SELDI-TOF MS is a powerful tool for monitoring a bioconjugation reaction. Indeed, this technique provides a very efficient alternative to the traditional analysis methods.

First, it is a sensitive and accurate method since the conjugates could be efficiently analyzed from as few as 10 ng (1 pmol range), at least in the molecular mass range of 10000−20000 with mass increments of approximately 203 Da. The traditional protein carriers which are used for immunization purposes have usually higher molecular mass, from approximately 60000 Da (bovine serum albumin or BSA, diphtheria toxoid) to several million Da (keyhole limpet hemocyanin or KLH). The accuracy and resolution of SELDI-TOF MS will be most probably limited in these higher molecular mass ranges, in particular for the KLH. This will also depend on the molecular mass of the hapten. To overcome these problems, the use of Zip Tip pipette tips can be considered. This method involves a microscale cleanup of the sample which then can be applied to high performance mass spectrometers (MALDI or electrospray), allowing efficient analyses in the high molecular weight range. However it is noteworthy that, for low molecular weights, ProteinChip array technology remains simpler since it allows the purification step and the mass analysis on the same device. This eliminates the need for a transfer step and results in an optimal recovery of the sample.

Second, SELDI-TOF MS is very rapid since it can be performed directly on the crude reaction without the need to purify or to derivatize the sample prior to analysis. In addition, the fact that several samples can be easily analyzed in parallel can be very valuable for studying the impact of various conditions on the efficiency of the conjugation. SELDI-TOF MS is therefore potentially very useful for high-throughput optimization strategies. Finally, the present study indicates that SELDI-TOF MS is suitable for analyzing complex crude samples from in vitro enzymatic conjugations. It may thus be directly applicable to the monitoring of intracellular reactions performed in vivo. Such analyses have already been reported on crude fermentation or cell culture sources in order to optimize recombinant protein production (*19*, *40*) or to analyze the secretion and autoactivation of a bacterial protein (*23*). Similar studies on mucin proteins are currently underway in the laboratory.

ACKNOWLEDGMENT

The authors are thankful to V. Piller and F. Piller for providing the recombinant ppGalNAc-T1 and to C. Leclerc for the critical review of the manuscript. We gratefully acknowledge financial support from the Association pour la Recherche sur le Cancer and the ECOS France-Uruguay Program. T.F. was financed by la Ligue Nationale contre le Cancer, la Fondation pour la Recherche Médicale, and a Vasant and Kusum Joshi grant.

LITERATURE CITED

(1) Niemeyer, C. M. (2004) Bioconjugation protocols: Strategies and methods. *Methods in Molecular Biology*, Volume 283, Humana Press, Totowa, NJ.

(2) Hermanson, G. T. (1996) *Bioconjugate techniques*, Academic Press, New York.

(3) Houen, G., Olsen, D. T., Hansen, P. R., Petersen, K. B., and Barkholt, V. (2003) Preparation of bioconjugates by solid-phase conjugation to ion exchange matrix-adsorbed carrier proteins. *Bioconjugate Chem. 14*, 75−79.

(4) Oda, M., Sato-Nakamura, N., and Azuma, T. (2004) Molecular characterization of monovalent and multivalent hapten-protein conjugates for analysis of the antigen−antibody interaction. *Anal. Biochem. 333*, 365−371.

(5) Pawlowski, A., Kallenius, G., and Svenson, S. B. (2000) Preparation of pneumococcal capsular polysaccharide-protein conjugate vaccines utilizing new fragmentation and conjugation technologies. *Vaccine 18*, 1873−1885.

(6) Singh, K. V., Kaur, J., Varshney, G. C., Raje, M., and Suri, C. R. (2004) Synthesis and characterization of hapten-protein conjugates for antibody production against small molecules. *Bioconjugate Chem. 15*, 168−173.

(7) Weller, M. G., Diemer, M., Wersching, C., Niessner, R., and Sochor, H. (2003) Development of antibodies for the detection of *N*-acetyl-glufosinate. *J. Agric. Food Chem. 51*, 6668−6675.

(8) Adamczyk, M., Gebler, J. C., and Mattingly, P. G. (1996) Characterization of protein-hapten conjugates. 2. Electrospray mass spectrometry of bovine serum albumin-hapten conjugates. *Bioconjugate Chem. 7*, 475−481.

(9) Pauillac, S., Naar, J., Mouratou, B., and Guesdon, J. L. (2002) Application of a modified version of Habeeb's trinitrophenylation method for the characterization of hapten-protein conjugates in a reversed micellar medium. *J. Immunol. Methods 263*, 75−83.

(10) Riddles, P. W., Blakeley, R. L., and Zerner, B. (1979) Ellman's reagent: 5,5′-dithiobis(2-nitrobenzoic acid)- -a reexamination. *Anal. Biochem. 94*, 75−81.

(11) Sashidhar, R. B., Capoor, A. K., and Ramana, D. (1994) Quantitation of epsilon-amino group using amino acids as reference standards by trinitrobenzene sulfonic acid. A simple spectrophotometric method for the estimation of hapten to carrier protein ratio. *J. Immunol. Methods 167*, 121−127.

(12) Manzi, A. E., and Varki, A. (1993) Glycobiology. *A Practical Approach*, Oxford University Press, New York.

(13) Tang, N., Tornatore, P., and Weinberger, S. R. (2004) Current developments in SELDI affinity technology. *Mass Spectrom. Rev. 23*, 34−44.

(14) Issaq, H. J., Veenstra, T. D., Conrads, T. P., and Felschow, D. (2002) The SELDI-TOF MS approach to proteomics: protein profiling and biomarker identification. *Biochem. Biophys. Res. Commun. 292*, 587−592.

(15) Caputo, E., Moharram, R., and Martin, B. M. (2003) Methods for on-chip protein analysis. *Anal. Biochem. 321*, 116−124.

(16) Cool, D. R., and Hardiman, A. (2004) C-terminal sequencing of peptide hormones using carboxypeptidase Y and SELDI-TOF mass spectrometry. *Biotechniques 36*, 32−34.

(17) Merchant, M., and Weinberger, S. R. (2000) Recent advancements in surface-enhanced laser desorption/ionization-time-of-flight-mass spectrometry. *Electrophoresis 21*, 1164−1177.

(18) Lin, S., Tornatore, P., King, D., Orlando, R., and Weinberger, S. R. (2001) Limited acid hydrolysis as a means of fragmenting proteins isolated upon ProteinChip array surfaces. *Proteomics 1*, 1172−1184.

(19) Cleverley, S., Bengio, S., Boschetti, E., and Spencer, J. (2003) Direct "on-chip" protein-expression monitoring. *Genet. Eng. News 23*, 2.

(20) Cardone, M. H., Roy, N., Stennicke, H. R., Salvesen, G. S., Franke, T. F., Stanbridge, E., Frisch, S., and Reed, J. C. (1998) Regulation of cell death protease caspase-9 by phosphorylation. *Science 282*, 1318−1321.

(21) Vorderwülbecke, S., Cleverley, S., Weinberger, S. C., and Wiesner, A. (2005) Protein quantification by the SELDI-TOF-MS-based ProteinChip System system. *Nature Methods 2*, 393−395.

(22) Dulon, S., Leduc, D., Cottrell, G. S., D'Alayer, J., Hansen, K. K., Bunnett, N. W., Hollenberg, M. D., Pidard, D., and Chignard, M. (2005) *Pseudomonas aeruginosa* elastase disables PAR2 in repiratory epithelial cells. *Am. J. Respir. Cell Mol. Biol. 32*, 411−419.

(23) Boyle, M. D., Romer, T. G., Meeker, A. K., and Sledjeski, D. D. (2001) Use of surface-enhanced laser desorption ionization protein chip system to analyze streptococcal exotoxin B activity secreted by *Streptococcus pyogenes*. *J. Microbiol. Methods 46*, 87−97.

(24) Chernyak, A., Karavanov, A., Ogawa, Y., and Kovac, P. (2001) Conjugating oligosaccharides to proteins by squaric acid diester chemistry: rapid monitoring of the progress of conjugation, and recovery of the unused ligand. *Carbohydr. Res. 330*, 479−486.

(25) Saksena, R., Chernyak, A., Karavanov, A., and Kovac, P. (2003) Conjugating low molecular mass carbohydrates to proteins. 1. Monitoring the progress of conjugation. *Methods Enzymol. 362*, 125−139.

(26) Ada, G., and Isaacs, D. (2003) Carbohydrate-protein conjugate vaccines. *Clin. Microbiol. Infect. 9*, 79−85.

(27) Danishefsky, S. J., and Allen, J. R. (2000) From the laboratory to the clinic: a retrospective on fully synthetic carbohydrate-based anticancer vaccines. *Angew. Chem., Int. Ed. 39*, 836−863.

(28) Lo-Man, R., Vichier-Guerre, S., Perraut, R., Dériaud, E., Huteau, V., BenMohamed, L., Diop, O. M., Livingston, P. O., Bay, S., and Leclerc, C. (2004) A fully synthetic therapeutic vaccine candidate targeting carcinoma-associated Tn carbohydrate antigen induces tumor specific antibidies in non-human primates. *Cancer Res. 64*, 4987−4994.

(29) Kuduk, S. D., Schwarz, J. B., Chen, X.-T., Glunz, P. W., Sames, D., Ragupathi, G., Livingston, P. O., and Danishefsky, S. J. (1998) Synthetic and immunological studies on clustered modes of mucin-related Tn and TF O-linked antigens: the preparation of a glycopeptide-based vaccine for clinical trials against prostate cancer. *J. Am. Chem. Soc. 120*, 12474−12485.

(30) Slovin, S. F., Ragupathi, G., Musselli, C., Olkiewicz, K., Verbel, D., Kuduk, S. D., Schwarz, J. B., Sames, D., Danishefsky, S., Livingston, P. O., and Scher, H. I. (2003) Fully synthetic carbohydrate-based vaccines in biochemically relapsed prostate cancer: clinical trial results with alpha-N-acetylgalactosamine-O-serine/threonine conjugate vaccine. *J. Clin. Oncol. 21*, 4292−4298.

(31) Springer, G. F. (1984) T and Tn, general carcinoma autoantigens. *Science 224*, 1198−1206.

(32) Freire, T., and Osinaga, E. (2003) Immunological and biomedical relevance of the Tn antigen. *Immunology* (Spain) *22*, 27−38.

(33) Grinstead, J. S., Koganty, R. R., Krantz, M. J., Longenecker, B. M., and Campbell, A. P. (2002) Effect of glycosylation on MUC1 humoral immune recognition: NMR studies of MUC1 glycopeptide-antibody interactions. *Biochemistry 41*, 9946−9961.

(34) Toribara, N. W., Roberton, A. M., Ho, S. B., Kuo, W. L., Gum, E., Hicks, J. W., Gum, J. R., Jr., Byrd, J. C., Siddiki, B., and Kim, Y. S. (1993) Human gastric mucin. Identification of a unique species by expression cloning. *J. Biol. Chem. 268*, 5879−5885.

(35) Hamamoto, A., Abe, Y., Nishi, M., Fujimori, S., Ohnishi, Y., Yamazaki, H., Oida, Y., Miyazaki, N., Inada, K., Ueyama, Y., Iwasaki, M., Inoue, H., and Nakamura, M. (2005) Aberrant expression of the gastric mucin MUC6 in human pulmonary adenocarcinoma xenografts. *Int. J. Oncol. 26*, 891−896.

(36) Nishiumi, N., Abe, Y., Inoue, Y., Hatanaka, H., Inada, K., Kijima, H., Yamazaki, H., Tatematsu, M., Ueyama, Y., Iwasaki, M., Inoue, H., and Nakamura, M. (2003) Use of 11p15 mucins as prognostic factors in small adenocarcinoma of the lung. *Clin. Cancer Res. 9*, 5616−5619.

(37) De Bolos, C., Garrido, M., and Real, F. X. (1995) MUC6 apomucin shows a distinct normal tissue distribution that correlates with Lewis antigen expression in the human stomach. *Gastroenterology 109*, 723−734.

(38) Pereira, M. B., Dias, A. J., Reis, C. A., and Schmitt, F. C. (2001) Immunohistochemical study of the expression of MUC5AC and MUC6 in breast carcinomas and adjacent breast tissues. *J. Clin. Pathol. 54*, 210−213.
(39) Duclos, S., Da Silva, P., Vovelle, F., Piller, F., and Piller, V. (2004) Characterization of the UDP-N-acetylgalactosamine binding domain of bovine polypeptide alphaN-acetylgalactosaminyltransferase T1. *Protein Eng. Des. Sel. 17*, 635−646.
(40) Savage, C. (2003) Ciphergen segments proteomics applications. *Genet. Eng. News 23*, 1.
(41) Hubalek, F., Pohl, J., and Edmondson, D. E. (2003) Structural comparison of human monoamine oxidases A and B: mass spectrometry monitoring of cysteine reactivities. *J. Biol. Chem. 278*, 2612−2618.

BC0502661

MAY/JUNE 2006
Volume 17, Number 3

© Copyright 2006 by the American Chemical Society

Bioconjugate Chemistry

COMMUNICATIONS

Single-Drug Multiligand Conjugates: Synthesis and Preliminary Cytotoxicity Evaluation of a Paclitaxel−Dipeptide "Scorpion" Molecule

Ahmad Safavy,*,§ Kevin P. Raisch,§ Damien Matusiak,⊥ Saloni Bhatnagar,§ and Lawrence Helson‡

Department of Radiation Oncology and the Comprehensive Cancer Center, University of Alabama at Birmingham, Birmingham, Alabama 35294, Department of Medicine, University of Illinois at Chicago and Jessie Brown Veterans Administration Medical Center, Chicago, Illinois 60612, and Tapestry Pharmaceuticals, Boulder, Colorado 80301. Received July 26, 2005; Revised Manuscript Received March 7, 2006

To improve the targeting properties of receptor-directed drug-peptide conjugates, a multiligand approach was proposed and a model "scorpion" conjugate (**6**, Figure 1), consisting of two peptide "claws" and a paclitaxel (PTX) "tail", was synthesized. The cell surface receptor-directed peptide used in this single-drug multiligand (SDML) model was a segment of the amphibian peptide bombesin (BBN) which had the $Y^6Q^7W^8A^9V^{10}G^{11}H^{12}L^{13}M^{14}$-$NH_2$ sequence, designated here as BBN[6−14] (**2**, Figure 2). Due to the lipophilic nature of both PTX and BBN-[6−14], compound **6** had a low water solubility. To enhance the solubility, PEG derivatives of this conjugate were prepared with the polymer inserted either in the claws or in the tail regions. In a preliminary random screening, conjugate **6** showed superior cytotoxic activity in several GRPR-positive human cancer cell lines as compared to free PTX and two single-drug single-ligand (SDSL) conjugates. In a receptor blocking experiment, addition of excess unconjugated BBN[6−14] ligand reduced the cytotoxicity of conjugate **6**, indicating the receptor-mediated mechanism of drug delivery. The PEG-derived conjugates showed activities which were intermediate between SDSL and the SDML congeners. Also, an increase in the number of the PEG segments lowered cytotoxicity, possibly due to steric hindrance against ligand−receptor binding. Taken together, these results demonstrate the potential of the multiligand approach in the design of receptor-targeting conjugates for tumor-specific drug delivery.

INTRODUCTION

Targeted delivery of antitumor agents is an active and promising area of oncology research (*1*, *2*). Two of the main classes of *targeting* molecules used for the delivery of cytotoxic agents are MAbs[1] (*3*, *4*) and tumor cell surface receptor-directed

* Correspondence to Ahmad Safavy, Ph.D., University of Alabama at Birmingham, Department of Radiation Oncology, 1530 3rd Ave. South, 674 Wallace Tumor Institute, Birmingham, Alabama 35294-6832. E-mail: Safavy@uab.edu.

§ University of Alabama at Birmingham.

⊥ University of Illinois at Chicago and Jessie Brown Veterans Administration Medical Center.

‡ Tapestry Pharmaceuticals.

[1] Abbreviations: BBN, bombesin; Boc, (*tert*)-butyloxycarbonyl; DCM, dichloromethane; DIEA, *N*,*N*-diisopropyl ethylamine; EEDQ, (2-ethoxy-1-ethoxycarbonyl)-1,2-dihydroquinoline; ESMS, electrospray mass spectrometry; Fmoc, fluorenylmethoxycarbonyl; MAbs, monoclonal antibodies; MALDI, matrix-assisted laser desorption/ionization; NHS, *N*-hydroxysuccinimidyl ester; PEG, poly(ethylene glycol); PTX, paclitaxel; SDML, single-drug multiligand; SDSL, single-drug single-ligand; TA, thioanisole; TBST, Tris-buffered saline Tween-20; TFA, trifluoroacetic acid; TIPS, triisopropylsilane.

10.1021/bc050224c CCC: $33.50 © 2006 American Chemical Society
Published on Web 04/06/2006

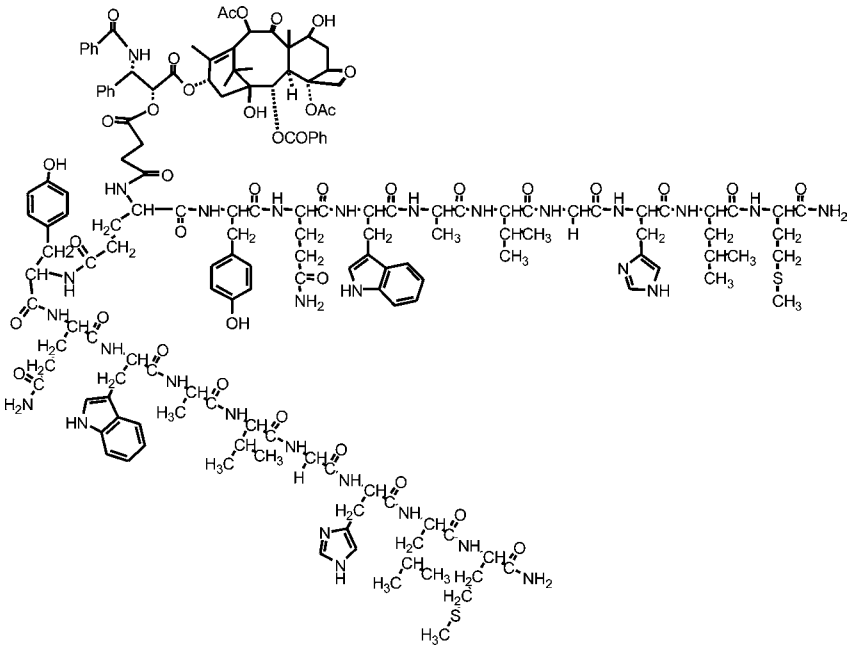

Figure 1. Structure of the PTX-di-BBN[6−14] "scorpion" conjugate **6**.

small-molecule peptides (SMPs) (*5*, *6*). The interest in the use of SMPs for drug targeting is related to their better tumor penetration and faster circulatory clearance when compared to the large MAb molecules. Although the use of SMPs in oncology started mainly with radiolabeled analogues (*7*−*9*), research on the development of drug-conjugated SMPs has also attracted interest. To this end, peptides targeting a variety of tumor cell membrane receptors with different drugs have been evaluated (*10*, *11*). An SDSL-type PTX-BBN conjugate (structure **1**) was recently reported by our group which showed a higher cytotoxic activity against a human non small cell lung cancer cell line, and as compared to the unconjugated PTX (*12*).

As therapeutic agents, peptide conjugates may suffer from short circulation half-lives, and thereby, low tumor uptake (*13*, *14*). This, in turn, may prevent the tumor tissue from receiving a therapeutically significant dose of the drug.

By analogy to the divalent antigen-binding feature of MAbs, which along with their long circulation times account for their characteristic high tumor uptake, we hypothesized that doubling the number of the peptide segments of an SDSL conjugate might improve the tumor targeting ability of the molecule. This hypothesis may be supported by the previously reported investigations on receptor-directed multivalent peptide and protein ligands (*15*−*17*). The improvement was expected to be the result of an increase in the frequency of ligand−receptor collisions and/or an augmented stability of the ligand−receptor complex. This communication reports on the synthesis of a PTX-derived SDML peptide conjugate as well as on its cytotoxic activity against some human cancer cell lines. To evaluate only the effect of the ligand multiplicity on the overall activity, the drug:conjugate molar ratio was kept at 1 and equal to that in the previously reported SDSL (*12*). The SDML conjugates are part of a study on the design, synthesis, and evaluation of multidrug multiligand drug conjugates currently underway in this laboratory.

EXPERIMENTAL PROCEDURES

Peptide Synthesis. The tyrosylbombesin (BBN[6−14], **2**) used in this work was synthesized by standard solid-phase peptide synthesis methods using Rink amide resin and the Fmoc protocol. After TFA cleavage, the peptide was purified by reversed-phase HPLC and identified by ESMS.

For all products, reversed-phase (RP) HPLC analysis/purification were performed with a Beckman System Gold instrument consisting of a SG 125 solvent module and a SG 166 UV/vis detector, operated by Beckman 32 Karat Version 5.0 software. For analytical HPLC, a 4.6 × 250 mm C18 column (Vydac, Hesperia, CA), and for preparative runs, a Vydac 2.5 × 25 Cm C8 column, were used. Columns were eluted with 0.1% TFA/water (solvent A) and a 10% to 90% gradient of 0.1:60:40, TFA:CH_3CN:H_2O (v/v) (solvent B). Analytical retention times (t_R) in minutes are reported with the corresponding percent purities in parentheses.

Paclitaxel-2′-hemisuccinate was prepared as described previously (*18*).

PTXGlu(BBN[6−14])$_2$, 6. To a solution of Boc-Glu (**3**, Fluka, Milwaukee, WI, 3.4 mg, 13.8 μmol) in dry DMF were added solutions of BBN[6−14] (**2**, 36.7 mg, 27.6 μmol) and HOBT (5.6 mg, 41.4 μmol) in the same solvent. Under argon, DIEA (20 μL) and then DCC (23 mg, 111.5 μmol) were added and the solution was stirred at ambient temperature for 48 h. A second and a third addition of **2** (19.5 mg, 14.7 μmol), HOBT (1.6 mg, 11.8 μmol), and DCC (7 mg, 34 μmol) were made and stirring continued for 48 h. Product formation was monitored by peak separation and identification by RP-HPLC and ESMS, respectively. On reaction completion, the Boc protection of the intermediate **4** was removed by adding 3 mL of a deblocking cocktail consisting of 5:1:1:0.5, v/v, TFA:DCM:TIPS:TA, and incubation at ambient temperature for 1 h. The intermediate product **5** was purified by preparative RP-HPLC. Yield: 28 mg (87.5%); HPLC, t_R: 18.8 min (96%); ESMS: 1159 (M + 2H), 773 (M + 3H).

Compound **5** (20 mg, 7.52 μmol) was dissolved in dry DMF, and the vessel was cooled in an ice bath under dry argon. PTXSX (13.3 mg, 15.6 μmol), NHS (5.4 mg, 46.9 μmol), and EEDQ (7.7 mg, 31.2 μmol) were added in sequence and the solution was stirred at 4 °C for 24 h. The final product **6** was purified by RP-HPLC. Yield: 23.5 mg (89.8%); HPLC, t_R: 24.4 min (93%); ESMS: 1627 (M + 2H), 1085 (M + 3H).

PTXGlu(OH)YBBN[6−14], 9. The same procedure as for **6** was used except that equal molar amounts of Boc-Glu, DCC, and BBN[6−14] were used with no HOBT. The peptide was added 1 h after the addition of DCC. The intermediate conjugate **7** was not isolated and was converted directly to the deprotected

Table 1. Analytical Data for PEG-Derived Scorpion Conjugates

conjugate	MW_{cal}[a]	MW_{mal}[b]	t_R (min)[c]	% purity[d]
PTX**PEG**Glu(BBN[6−14])$_2$, **13**	5500	5532	24.3	>86
PTX(**PEG**Glu)$_2$(BBN[6−14])$_2$, **16**	10250	10118	22.9	99
PTXGlu(**PEG**BBN[6−14])$_2$, **20**	10250	10172	24.2	99

[a] Calculated average MW based on the average MW of the starting material PEG **10**. [b] MALDI average MW. [c] HPLC retention time. [d] By HPLC.

Scheme 1

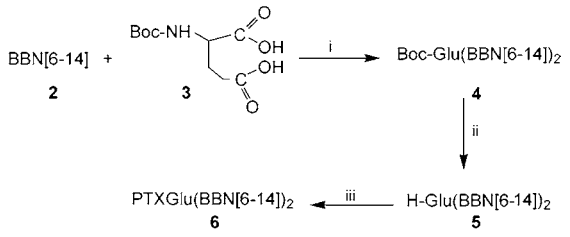

(i) HOBT , DCC , DIEA, DMF; (ii) TFA:DCM:TA:TIPS, (iii) PTXSX,NHS, EEDQ, DMF

derivative **8**. The latter conjugate and the final product **9** were purified by RP-HPLC. **8**: Yield: 1.85 mg (37.7%); HPLC, t_R: 19.3 min (95%); ESMS: 1232 (M + H), 616 (M + 2H) **9**: Yield: 1.3 mg (89.8%); HPLC, t_R: 24.0 min (85%); ESMS: 2167 (M + H), 1084 (M + 2H).

General Procedure for PEG Conjugation. Fmoc-PEG-NHS, the *N*-Fmoc-protected NHS ester of amino-PEG carboxylic acid, with an average MW of ∼3400 (Nektar, Huntsville, AL) was used as the solubilizing linker. The peptide component (1 equiv) was added in dry DMF to the solution of Fmoc-PEG-NHS (**10**, 1.2 equiv) followed by the addition of DIEA (1 equiv) at 0 °C. On reaction completion, piperidine (as 50% DMF solution, v/v) was added and the mixture was incubated for 20 min at ambient temperature. The intermediate conjugates **11**, **12**, **14**, **15**, and **17**−**19** were purified by dialysis against water and were identified by MALDI MS. The final products were purified by RP-HPLC and identified by MALDI MS. The analytical data for these PEG conjugates are shown in Table 1.

PTX Conjugation. All PTX couplings (including that for conjugate **21**) were carried out according to the procedure of Scheme 1 (last step), described above for the synthesis of conjugate **6**.

Quantitative Immunohistochemistry. All reagents were supplied as a kit by DAKO (Carpentaria, CA). Cells were plated on two-well permonox chamber slides (Nalge Nunc International, Rochester, NY) at a density of 25 000 cells/well and allowed to grow in defined media. Cells were fixed in 3.7% formaldehyde in PBS for 20 min at 37 °C, followed by rinsing and permeabilizing with TBST. Immunohistochemistry was performed using a two-step indirect immunoperoxidase technique. Cells were incubated in 0.03% H_2O_2 solution and were rinsed with water and TBST in sequence. The primary (rabbit anti-GRPR) antibody was applied for 1 h at room temperature before rinsing with TBST. The secondary antibody (Labeled Polymer Rabbit HRP) was added with incubation for 30 min. After TBST rinse, the cells were incubated with DAB+Chromogen for 5 min, rinsed with water, and counterstained for 2 min with hematoxylin. Slides were washed with TBST and covered. Control cells were processed identically except that they were not exposed to the primary antibody. Slides were cover-slipped using pristine mount (Invitrogen, Carlsbad, CA).

Chromogen abundance was quantified by quantitative immunohistochemistry as previously described (*19*, *20*). Briefly, images were acquired using a Diagnostic Instruments SPOT RT

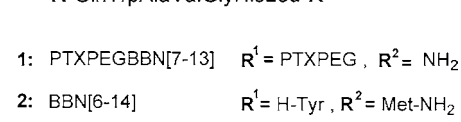

Figure 2. Structures of different GRPR-directed bombesin-derived peptides.

Scheme 2

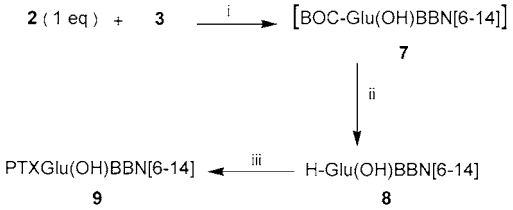

(i) DCC, DIEA, DMF; (ii) TFA:DCM:TA:TIPS; (iii) PTXSX, NHS, EEDQ, DMF

Digital Scanning Camera (Sterling Heights, MI) attached to a Nikon E600 microscope (Stamford, CT). The amount of chromogen per pixel was determined by subtracting the mathematical energy (E_M) of the control slide from that in the homologous region of the experimental slide exposed to primary antibody. Chromogen quantity (E_M) is expressed as energy units per pixels (eu/pix).

Cytotoxicity Assays. Tumor cells were grown as monolayers in 25-cm^2 tissue culture flasks using their respective cell culture medium. All media contained 10% fetal bovine serum. Incubation was at 37 °C under a 5% CO_2:air atmosphere (standard conditions) for 5 days. The cells were harvested when in mid-log growth, and their concentration was determined using a Coulter particle counter. An aliquot of the cell suspension was diluted in culture medium for delivery to a 96-well plastic plate at a range of 3000 to 10 000 per 100 μL media. Twenty-four hours later, sextuplicate wells were inoculated with either 100 μL per well of medium (controls), or 100 μL of medium containing PTX or a conjugate. Concentrations were adjusted to deliver 0.1 μg/mL of PTX equivalent to all treatment groups. After 1 h incubation, the wells were aspirated and refilled with 200 μL conjugate-free medium. Following an additional 120 h incubation under standard conditions, and removal of the floating nonviable cells by aspiration, the plate-attached viable cells were counted and normalized to the percent of untreated controls. The extent of cytotoxicity in treated wells as compared to the controls, were calculated using a Magellin software program (Dynex Technology, Chantilly, VA).

Receptor-Blocking Assay. Tumor cells were cultured, in sextuplicate, in 96-well plates as described above. After a 24 h incubation, 100 μL of medium containing DMSO (control), or 100 μL of medium containing PTX, **6**, BBN[6−14], BBN[6−14]+PTX, or BBN[6−14]+**6** was added to sextuplicate wells. Additions were such that a 120 nM of PTX or **6**, and 2400 nM of BBN[6−14] were delivered to each well. The BBN[6−14]+PTX or BBN[6−14]+**6** were mixed immediately prior to the addition of the agents to their respective wells. After 1 h incubation at 37 °C, the medium was removed, the cells were washed 1× with PBS, and 200 μL drug-free medium was added to each well. Following an additional 120 h incubation period, the cells were washed 1× with PBS, then detached with trypsin-EDTA and counted with a hemacytometer (Hausser Scientific, Horsham, PA). The cell counts were normalized to the percent of untreated control cells. The data were statistically analyzed using Microsoft Excel Software (Microsoft Corporation, Redmond, WA).

Table 2. Cytotoxicity[a] of PTX-Di-BBN SDML Conjugates in Different Human Cancer Cell Lines as Compared to Those of PTX and Mono-Ligand Conjugates[b,c]

conjugate	structure	SKNAS[d]	FADU	MO59J	JNPRSLT1	HuTu-80
6	PTXGlu(BBN[6−14])$_2$	87 ± 4.9	89 ± 2.8	64 ± 4.2	86 ± 1.6	93 ± 0.93
		(59 ± 3.0)	(87 ± 2.3)	(58 ± 4.0)	(31 ± 7.8)	(77 ± 11.3)
9	PTXGlu(OH)BBN[6−14]	43 ± 10.4				
		(59 ± 3.0)				
13	PTXPEGGlu(BBN[6−14])$_2$	70 ± 2.8			55 ± 8.1	90 ± 0.9
		(55 ± 4.8)			(26 ± 2.3)	(84 ± 4.1)
16	PTX(PEG)$_2$Glu(BBN[6−14])$_2$	23 ± 4.5	33 ± 6.0			
		(67 ± 3.4)	(51 ± 7.0)			
20	PTXGlu(PEGBBN[6−14])$_2$		56 ± 6.5	50 ± 4.2	16 ± 6.1	29 ± 11.1
			(87 ± 2.3)	(58 ± 4.0)	(31 ± 7.8)	(77 ± 11.3)
21[e]	PTXBBN[6−14]	22 ± 3.9	26 ± 3.5			16 ± 1.7
		(51 ± 2.2)	(85 ± 2.8)			(85 ± 0.02)

[a] Defined as %growth inhibition = 100% − %viable treated cells ± SD; the untreated controls were normalized to 100%. [b] See footnote 3. [c] Numbers in parentheses refer to %inhibition induced by unconjugated PTX at equimolar concentrations and in the same experiment. [d] SKNAS, neuroblastoma; FADU, squamous cell tumor of the pharynx; MO59J, glioblastoma multiform; JNPRSLT1, desmoplastic small cell tumor; HuTu-80, intestinal tumor. All of human origin. [e] Prepared the same procedure as used for the synthesis of **6** from **5**.

Scheme 3

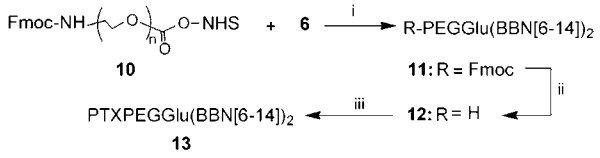

(i) DIEA, DMF; (ii) 30% piperidine/DMF; (iii) PTXSX, NHS, EEDQ, DMF

Scheme 4

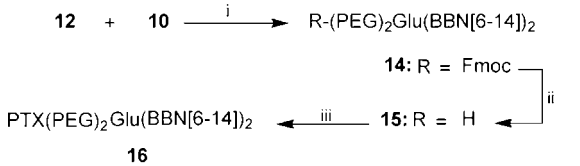

(i) DIEA, DMF; (ii) 30% piperidine/DMF; (iii) PTXSX, NHS, EEDQ, DMF

Scheme 5

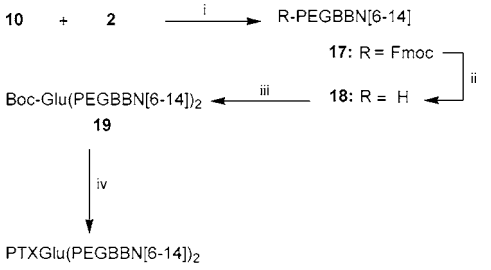

(i) DIEA, DMF; (ii) 30% piperidine/DMF; (iii) **3**, HOBT, DCC, DIEA, DMF; (iv) a: TFA:DCM:TA:TIPS; b: PTXSX, NHS, EEDQ, DMF

RESULTS AND DISCUSSION

The amino acid sequence of the peptide used in this work (BBN[6−14], **2**, Figure 2) made possible the solution-phase synthesis of the final conjugates without side-chain protection.[2]

As the central branching scaffold, N^{α}-(*tert*)-butyloxycarbonyl-L-glutamic acid (Boc-Glu, **3**, Scheme 1) was used to which the BBN[6−14] segments were connected. A standard DCC/HOBT coupling reaction worked satisfactorily although some condition manipulations seemed to improve both the yield of product recovery and the product purity. Briefly, starting with a 2:1 mole ratio of **2**:**3**, and a larger excess of HOBT/DCC with respect to Boc-Glu, it was noticed that a gradual increase in the molarities of **2** and the reagents resulted in better product yields. Removal of the Boc protection from compound **4**, and condensation of the bis-peptide **5** with an equivalent of paclitaxel-2′-hemisuccinate, afforded the target conjugate **6**. A mono-BBN conjugate (compound **9**) was also prepared for studying the effect of BBN duplicity on cytotoxicity. Synthesis of this product was through the formation of Boc-Glu cyclic anhydride followed by the α-addition of BBN[6−14]. The preferential α-opening of the anhydride by the peptide was presumably due to the presence of the electron-withdrawing Boc group (*21*). Chromatographic and mass spectrometric analyses indicated formation of only one major product.

The low water solubility of paclitaxel has been one of the disadvantages of this drug, which has necessitated the use of solubilizing excipients (e.g., cremophore EL, a poly-ethoxylated castor oil) in the clinically used formulations (*22*, *23*). These additives have been reported to be the cause of allergic reactions and posttreatment toxicities (*22*, *23*). We, and others, have reported the use of PEG as a solubilizing attachment to PTX (*24*) and its peptide conjugate (*12*). In the latter case, PEG was inserted between the drug and the peptide segments resulting in high overall aqueous solubility. Here, a PEG amino acid (from Fmoc-PEG-NHS, **10**, Schemes 3−5) was used as the solubilizing linker. Furthermore, to study the effect of positional isomerism on both solubility and biological activity, the PEG linker was inserted, separately, in both the claws and the tail regions. Conjugates with one (**13**, Scheme 3) or two (**16**, Scheme 4, and **20**, Scheme 5) PEG linkers were synthesized. It should be noted that addition of only one PEG to each claw (conjugate **20**) results in the formation of a regioisomer of compound **16**. Analytical data for these readily water-soluble derivatives are presented in Table 1.

Prior to the cytotoxicity experiments, the cell lines were screened for the presence of BBN-related receptors (BBNRs). Immunohistochemistry assays demonstrated the presence of GRP receptors, the mammalian counterpart of BBNR (*25*, *26*) in four of the cell lines (Figure 3). The results of cytotoxicity assays (Table 2) indicated a superior activity for the scorpion conjugate, as compared to both free PTX and the mono-BBN-[6−14] control (conjugate **21**) in all tested cell lines.[3] The MO59J cells, with the lowest GRPR expression (35 000 eu/pix), showed a weaker response to the di-BBN conjugate than did the other, high-density lines. The human squamous cell tu-

[2] Numbering based on the native bombesin sequence. This sequence includes an N-terminal tyrosine residue. Although not relevant to this report, the tyrosine would serve as a radioiodination site for the synthesis of radiolabeled analogues.

[3] Selection of the cell lines of Table 2 is for elucidating the general trend of cytotoxicity of the conjugates. The cell lines have different sensitivity towards PTX, and therefore each column of the table has to be viewed individually.

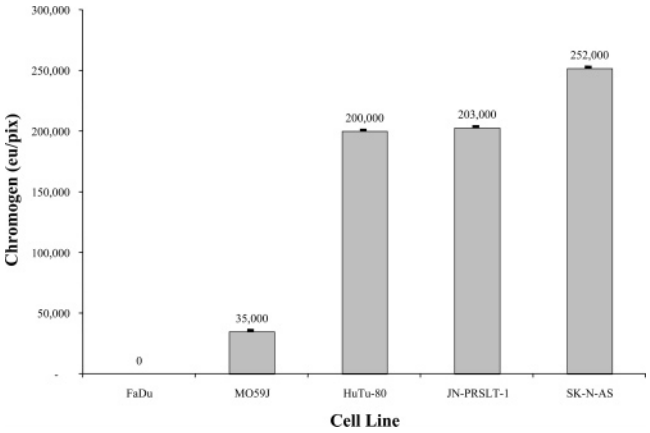

Figure 3. Density of GRPR expression in different human cancer cell lines as determined by immunohistochemistry. Each bar is the mean of values from four independent experiments. Error bars are too small to be visible.

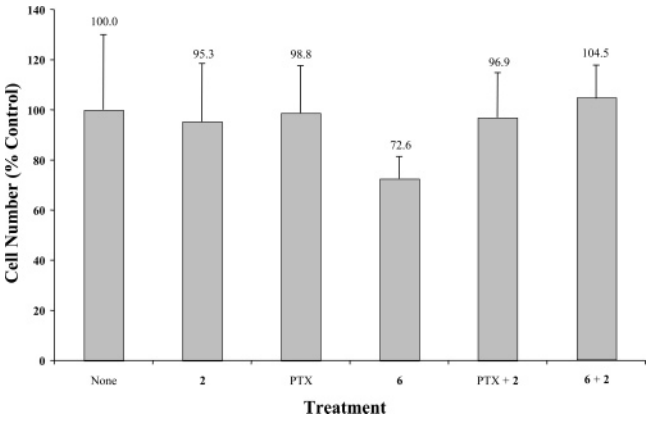

Figure 4. Reduction of PTXGlu(BBN[6−14])$_2$ (**6**) cytotoxicity due to receptor blockage by excess BBN[6−14] (**2**) in JNPRSLT1 human desmoplastic small cell tumor. Each bar shows the percentage of viable cells after treatment. The untreated controls were normalized to 100%.

mor of the pharynx, FADU, does not express BBN/GRP receptors (Figure 3) but is highly sensitive to paclitaxel. To verify the receptor-mediated drug delivery of conjugate **6**, a blocking experiment was carried out using the JN-PRSLT-1 cell line (GRPR 203 000 eu/pix). Addition of a 20-fold molar excess of the free BBN[6−14] ligand (structure **2**) reduced the cytotoxicity of **6** by about 45%whereas it did not have a significant effect on PTX cytotoxicity (Figure 4). On the other hand, when no-GRPR FADU cells were used, both PTX and conjugate **6**, with or without the blocker **2**, killed the cells to the same extent (Figure 5), presumably due to the extreme sensitivity of this cell line to PTX. And for reasons not clear at this time, this sensitivity is reflected in the cytotoxicity of **6** but not with any other conjugate of Table 2.

Activity enhancement due to the simultaneous presence of two BBN moieties in the same molecule was also demonstrated by the low relative cytotoxicity of **9**. It should be noted that the higher activity of conjugate **9** against the other mono-BBN compound (**21**) might be due to a higher water solubility of the former under the experimental conditions. Separation of the ligand segment from the bulky PTX by the Glu spacer in **9** also might have reduced the PTX-resulted steric hindrance (SH) and facilitated the peptide−receptor binding.

Addition of one PEG spacer to the tail region (compound **13**) lowered the activity probably due to a more crowded environment around the molecule, and thereby, jeopardizing conjugate−receptor interactions (e.g., collision), in this case due to the large size of the PEG segments relative to those of the

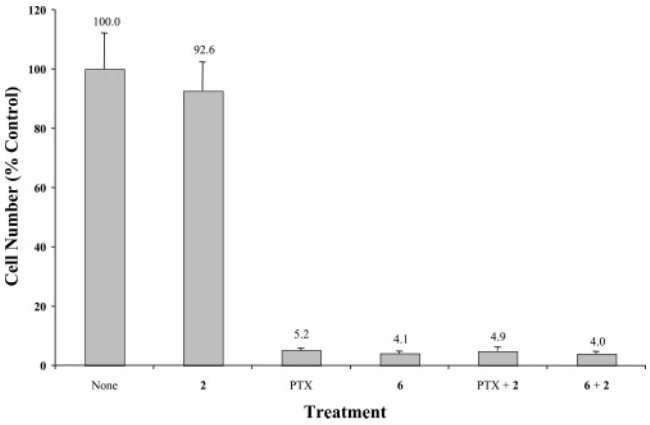

Figure 5. Indiscriminate killing of FaDu cells by PTX and PTXGlu-(BBN[6−14])$_2$ (**6**) in the presence and absence of the blocker peptide BBN[6−14] (**2**) due to extreme PTX sensitivity to this cell line. Each bar shows the percentage of viable cells after treatment. Treated cell numbers normalized to the untreated control.

Table 3. Conjugate:PTX Cytotoxicity Ratios for PTX-Di-BBN SDMLCs in Different Human Cancer Cell Lines as Compared to Those of Free PTX and Mono-Ligand Conjugate[a]

conjugate	structure	SKNAS	FADU	MO59J	JNPR-RLT1	HuTu-80
6	PTXGlu(BBN[6−14])$_2$	1.5	1.02	1.1	2.8	1.2
9	PTXGlu(OH)BBN[6−14]	0.73				
13	PTXPEGGlu(BBN[6−14])$_2$	1.3			2.1	1.1
16	PTX(PEG)$_2$Glu(BBN[6−14])$_2$	0.34	0.65			
20	PTXGlu(PEGBBN[6−14])$_2$		0.64	0.86	0.52	0.38
21	PTXBBN[6−14]	0.43	0.31			0.19

[a] Calculated from values of Table 2.

peptide moieties. This SH-caused deactivating effect was more apparent when addition of a second PEG in conjugate **16** led to a considerably lower activity.

Incorporation of PEG segments into the claws (compound **20**) caused deactivation with respect to both **6** and free PTX. At the same time, conjugate **20** was more cytotoxic than its regioisomer **16**, indicating that a regional separation between the PEG segments, even when located in the proximity of the ligands, had less of a deactivating effect than a tandem arrangement.

An outline of the cytotoxicity results, in the form of conjugate-to-PTX activity ratios, is shown in Table 3.

Advantage of a multiligand approach in the design of receptor-targeted drug delivery molecules was demonstrated in this work by the synthesis of a di-bombesin−paclitaxel conjugate. With the exception of the highly PTX-sensitive FaDu cells, the SDML conjugate showed enhanced cytotoxicity when screened against both the unconjugated drug and mono-ligand conjugates, in a panel of GRPR-positive human cancer cell lines. The cytotoxicity was reduced with receptor blocking by the free ligand and increased with increases in GRPR density. On the basis of these results, further investigation of these conjugates, including antitumor activity studies, is warranted and is underway in this laboratory.

ACKNOWLEDGMENT

Valuable assistance and contributions of Dr. Madhavi Chander and Mark Jones (Tapestry Pharmaceuticals), Marion C. Kirk, D. Ray Moore, Landon Wilson (UAB Comprehensive Cancer Center Mass Spectrometry Core Facility), and David Fisher (UAB Medical Education and Design Services) is greatly acknowledged.

LITERATURE CITED

(1) Guillemard, V., and Saragovi, H. U. (2004) Novel approaches for targeted cancer therapy. *Curr. Cancer Drug Targets 4*, 313−26.

(2) Ranson, M., and Jayson, G. (2005) Targeted antitumour therapy—future perspectives. *Br. J. Cancer 92 Suppl 1*, S28−31.

(3) Green, M. C., Murray, J. L., and Hortobagyi, G. N. (2000) Monoclonal antibody therapy for solid tumors. *Cancer Treat. Rev. 26*, 269−286.

(4) Lin, M. Z., Teitell, M. A., and Schiller, G. J. (2005) The evolution of antibodies into versatile tumor-targeting agents. *Clin. Cancer Res. 11*, 129−138.

(5) Garrett, M. D., and Workman, P. (1999) Discovering novel chemotherapeutic drugs for the third millennium. *Eur. J. Cancer 35*, 2010−30.

(6) Stefanidakis, M., and Koivunen, E. (2004) Peptide-mediated delivery of therapeutic and imaging agents into mammalian cells. *Curr. Pharm. Des. 10*, 3033−44.

(7) Fischman, A. J., Babich, J. W., and Strauss, H. W. (1993) A ticket to ride: Peptide radiopharmaceuticals. *J. Nucl. Med. 34*, 2253−2263.

(8) Rogers, B. E., Manna, D. D., and Safavy, A. (2004) In vitro and in vivo evaluation of a ^{64}Cu-labeled polyethylene glycol-bombesin conjugate. *Cancer Biother. Radiopharm. 19*, 25−34.

(9) Safavy, A., Khazaeli, M. B., Qin, H., and Buchsbaum, D. J. (1997) Synthesis of bombesin analogues for radiolabeling with Rhenium-188. *Cancer (Suppl) 80*, 2354−2359.

(10) Burkhart, D. J., Kalet, B. T., Coleman, M. P., Post, G. C., and Koch, T. H. (2004) Doxorubicin-formaldehyde conjugates targeting alphavbeta3 integrin. *Mol. Cancer Ther. 3*, 1593−604.

(11) Chau, Y., Tan, F. E., and Langer, R. (2004) Synthesis and characterization of dextran-peptide-methotrexate conjugates for tumor targeting via mediation by matrix metalloproteinase II and matrix metalloproteinase IX. *Bioconjugate Chem. 15*, 931−41.

(12) Safavy, A., Raisch, K. P., Khazaeli, M. B., Buchsbaum, D. J., and Bonner, J. A. (1999) Paclitaxel derivatives for targeted therapy of cancer: Toward the development of smart taxanes. *J. Med. Chem. 42*, 4919−4924.

(13) Weiner, R. E., and Thakur, M. L. (2005) Radiolabeled peptides in oncology: role in diagnosis and treatment. *BioDrugs 19*, 145−63.

(14) Zhang, H., Chen, J., Waldherr, C., Hinni, K., Waser, B., Reubi, J. C., and Maecke, H. R. (2004) Synthesis and evaluation of bombesin derivatives on the basis of pan-bombesin peptides labeled with indium-111, lutetium-177, and yttrium-90 for targeting bombesin receptor-expressing tumors. *Cancer Res. 64*, 6707−15.

(15) Jones, D. S. (2005) Multivalent compounds for antigen-specific B cell tolerance and treatment of autoimmune diseases. *Curr. Med. Chem. 12*, 1887−904.

(16) Kok, R. J., Schraa, A. J., Bos, E. J., Moorlag, H. E., Asgeirsdottir, S. A., Everts, M., Meijer, D. K., and Molema, G. (2002) Preparation and functional evaluation of RGD-modified proteins as alpha(v)-beta(3) integrin directed therapeutics. *Bioconjugate Chem. 13*, 128−35.

(17) Terskikh, A. V., Le Doussal, J. M., Crameri, R., Fisch, I., Mach, J. P., and Kajava, A. V. (1997) "Peptabody": A new type of high avidity binding protein. *Proc. Natl. Acad. Sci. U.S.A. 94*, 1663−1668.

(18) Deutsch, H., Glinski, J., Hernandez, M., Haugwitz, R., Narayanan, V., Suffness, M., and Zalkow, L. (1989) Synthesis of congeners and prodrugs: Water soluble prodrugs of taxol with potent antitumor activity. *J. Med. Chem. 32*, 788−792.

(19) Matkowskyj, K. A., Cox, R., Jensen, R. T., and Benya, R. V. (2003) Quantitative immunohistochemistry by measuring cumulative signal strength accurately measures receptor number. *J. Histochem. Cytochem. 51*, 205−14.

(20) Matkowskyj, K. A., Schonfeld, D., and Benya, R. V. (2000) Quantitative immunohistochemistry by measuring cumulative signal strength using commercially available software photoshop and matlab. *J. Histochem. Cytochem. 48*, 303−12.

(21) Lloyd-Williams, P., Albericio, F., and Giralt, E. (1997) *Chemical approaches to the synthesis of peptides*, CRC Press, Boca Raton, FL.

(22) Dorr, R. T. (1994) Pharmacology and toxicology of Cremophor EL diluent. *Ann. Pharmacother. 28*, S11−S14.

(23) Sharma, A., Mayhew, E., Bolcsak, L., Cavanaugh, C., Harmon, P., Janoff, A., and Bernacki, R. J. (1997) Activity of paclitaxel liposome formulations against human ovarian tumor xenografts. *Int. J. Cancer 71*, 103−107.

(24) Greenwald, R., Pendri, A., and Bolikal, D. (1995) Highly water soluble-taxol derivatives: 7-poly(ethylene glycol) carbamates and carbonates. *J. Org. Chem. 60*, 331−336.

(25) Cuttitta, F., Carney, D. N., Mulshine, J., Moody, T. W., Fedorko, J., Fischler, A., and Minna, J. D. (1985) Bombesin-like peptides can function as autocrine growth factors in human small-cell lung cancer. *Nature 316*, 823−6.

(26) Kroog, G. S., Jensen, R. T., and Battey, J. F. (1995) Mammalian bombesin receptors. *Med. Res. Rev. 15*, 389−417.

BC050224C

Fast Water-Exchange Gd^{3+}-(DO3A-like) Complex Functionalized with Aza-15-Crown-5 Showing Prolonged Residence Lifetime in Vivo

Cong Li,[†] Ying-Xia Li,[‡] Ga-Lai Law,[†] Kwan Man,[§] Wing-Tak Wong,*[,†] and Hao Lei*[,‡]

Department of Chemistry and Open Laboratory of Chemical Biology of the Institute of Molecular Technology for Drug Discovery and Synthesis, Department of Surgery, The University of Hong Kong, Pokfulam Road, Hong Kong, and State Key Laboratory of Magnetic Resonance and Atomic and Molecular Physics, Wuhan Institute of Physics & Mathematics, The Chinese Academy of Sciences, Wuhan, P. R. China . Received January 7, 2006; Revised Manuscript Received March 17, 2006

A bis-hydrated Gd^{3+} complex based on tris acetic acid-1,4,7,10-tetraazacyclododecane (DO3A) that was functionalized with aza-15-crown-5 demonstrated a nearly optimal water-exchanging rate ($k_{ex} = 3.1 \times 10^7\ s^{-1}$) and low acute cytotoxicity. Efficient magnetic resonance signal intensity enhancements and prolonged residence lifetime induced by this small molecular complex in vivo were demonstrated even with one-fifth of the standard dosage used in the clinic.

Small molecular gadolinium complexes, such as Gd-DOTA (Dotarem), and its derivatives, are widely used as magnetic resonance imaging (MRI) contrast agents (CAs) to aid the diagnosis of pathologies by enhancing the morphology and functionality of the tissue with the advantage of low inherent toxicity (*1*). However, their pharmacokinetic properties, especially the transient retention lifetime in the blood pool, result in their poor performance in cardiovascular and tumor imagings (*2*). Additionally, these small complexes demonstrate relatively low relaxivity, so a high dosage is required to achieve a satisfactory signal enhancement. To overcome the problems, Gd^{3+} complexes were covalently bound to macromolecules, such as proteins (*3*), antibodies (*4*), dendrimers (*5*), and micellar aggregates (*6*) because their large sizes not only lead to the confinement and a long circulation lifetime in the vasculature (*7*) but also improve the relaxivity by increasing their rotational correlation time τ_R (*8*). Unfortunately, the increasing toxicity induced by the slow clearance rate and the inefficient delivery of these macromolecules to the targeting sites seriously limit their applications (*5*, *7*, *9*). In response to the problems, Lu et al. designed the biodegradable macromolecular agents, in which a Gd^{3+} complex was grafted with poly(ethylene glycol) (PEGs) through the disulfide bond (*10*, *11*). After the imaging, Gd^{3+} chelates can be released from the macromolecules and excreted in time through the cleavage of the disulfide bond by disulfide−thiols exchange. However, because of the low concentration of endogenous thiols in human plasma, multiple administrations of extraneous thiols are needed to keep the efficient cleavage of the disulfide bond. For the above reasons, innovative designs for MRI contrast agents with high relaxivity and moderate excretion rates in vivo are needed.

PEGs are nontoxic and nonantigenic polymers that have been widely used in the modification of biomolecules to improve their biocompatibility and pharmacokinetics (*12*). Covalently bound PEGs not only promote the passive accumulation of the conjugates into the tumors (*13*) but also decrease their clearance rate from the circulation system (*14*). Crown ethers as artificial molecules have been extensively investigated in supramolecular chemistry (*15*). What attracts us here are their well-known amphiphilicity (*16*), identical building block (ethylene glycol) as PEGs, and much smaller molecular weights as compared to PEGs. Considering these properties of crown ethers, a compromise between a prolonged circulation lifetime and low inherent toxicity is expected after functionalization of the crown ether moiety to the Gd^{3+} chelates.

In this communication, we report the synthesis and preliminary evaluation of the crown ether functionalized Gd^{3+} complex. Tris acetic acid-1,4,7,10-tetraazacyclodecane (DO3A) was chosen as the chelate here because its Gd^{3+} complexes not only demonstrated a satisfactory thermodynamic stability [$\log K = 22.0$, 298 K] (*17*), but also a maximum of two binding sites is left for water molecules, which makes their relaxivity increase substantially because the inner-sphere proton relaxivity is proportional to the q values (*8*, *18*). Meanwhile, aza-15-crown-5 was selected because of its moderate ring size and the modification availability of the secondary amine.

The synthesis of **LnL1** is depicted in Scheme 1. Mono-crown ether alkylated cyclen **1a** (*19*) was prepared straightforwardly with high yield according to our previous method. **1a** reacted with excess *tert*-butyl bromoacetate to afford **1b**. Following a deprotection step, the resulting ligands **L1** were treated with $Ln_2(CO_3)_3$ to give the desired Gd^{3+}, Tb^{3+}, and Eu^{3+} complexes. To clarify the effect of the pendant crown ether to relaxivity and other relaxometric parameters, Ln^{3+} complexes of DO3A grafted with ethylamine **LnL2** as control molecules were prepared (*20*, *21*). The luminescent lifetimes of **TbL1** ($\tau_{H_2O} = 1.39$ ms, $\tau_{D_2O} = 2.94$ ms) and **TbL2** ($\tau_{H_2O} = 1.25$ ms, $\tau_{D_2O} = 3.05$ms) were measured in H_2O and D_2O, respectively, and both of their hydration numbers q were given as 2 (*22*).

The water proton relaxivity r_{1p} of **GdL1** and **GdL2** at 20 MHz, 25 °C was measured as 9.5 and 5.9 $mM^{-1}\ s^{-1}$, respectively at pH 7.0. Significantly, the r_{1p} of **GdL1** nearly doubled compared with its parent complex Gd-DO3A (5.7 $mM^{-1}\ s^{-1}$) (*23*). A main reason that determines the lower relaxivity of small molecular complexes compared to their theoretical prediction is their water/proton residence lifetime

* To whom correspondence should be addressed. (W.-T.W.) Tel.: +852 2859 2157. Fax: +852 2547 2933. E-mail: wtwong@hkucc.hku.hk. (H.L.) Tel. +86 27 8719 8542. Fax: +86 27 8719 9291. E-mail: leihao@wipm.ac.cn.

[†] Department of Chemistry, The University of Hong Kong.

[‡] Wuhan Institute of Physics & Mathematics, The Chinese Academy of Sciences.

[§] Department of Surgery, The University of Hong Kong.

10.1021/bc060003m CCC: $33.50 © 2006 American Chemical Society
Published on Web 04/15/2006

Scheme 1. Synthesis Procedure of LnL1[a]

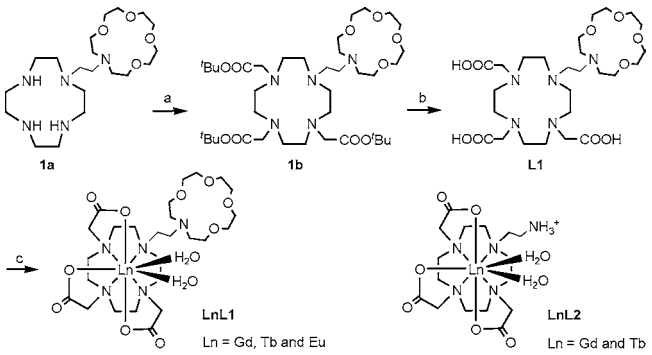

[a] Reagents and conditions: (a) 3.3 equiv of *tert*-butyl bromoacetate, Na_2CO_3/THF-H_2O, r.t., 4 h, 84%; (b) TFA/CH_2Cl_2, r.t., 2 h, 96%; (c) $Ln_2(CO_3)_3$, H_2O, 70 °C, 10 h, Ln = Gd, Tb, and Eu. Yields of the lanthanide complexes range from 88−95%.

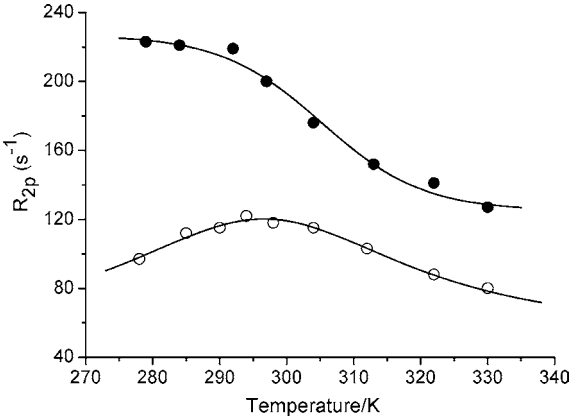

Figure 1. VT-^{17}O NMR transverse relaxation rate of **GdL1** and **GdL2** at 2.1 T, 25 °C, pH 7.0. **GdL1**, filled circle; **GdL2**, open circle.

τ_M (τ_M is the reciprocal of the water exchange rate, k_{ex}) is far from optimal values (*8*). Therefore, many efforts have been dedicated to investigating ligand systems for Gd^{3+} ion by optimizing the water exchange rate k_{ex} (*24*, *25*). To clarify the unusually high r_{1p} of **GdL1**, the measurement of the water ^{17}O NMR transverse relaxation rate, R_2, at variable temperature (VT), which allows a precise assessment of the water residence lifetime τ_M, was conducted. The VT ^{17}O NMR curve of **GdL1** (Figure 1) demonstrated that it is a typical system within the fast exchange regime. The τ_M value of 32 ns ($k_{ex} = 3.1 \times 10^7$ s^{-1}) for **GdL1** at 25 °C was provided by analyzing the curve in terms of the Swift-Connick equation (*3*). Notably, this τ_M value is rather rare for a neutral complex and very close to its optimal range of 20−30 ns (*24*). τ_M is generally determined by several factors including steric crowding at the water binding site, the overall charge of the complex as well as the geometry of the complex. In comparison to **GdL2** (τ_M = 240 ns, $k_{ex} = 4.2 \times 10^6$ s^{-1}, Figure 1) and Gd-DO3A (τ_M = 159 ns, $k_{ex} = 6.3 \times 10^6$ s^{-1}) (*23*), the fast water exchange rate of **GdL1** could arise from the increasing negative charge density and steric congestion around the Gd^{3+} ion upon the approach of the crown ether, which promotes the departure of the bound water molecules. Therefore, the fast water-exchanging rate of **GdL1** should be an important reason for its high relaxivity.

Besides the relaxivity, another important factor to evaluate the potential application of Gd^{3+} complexes as MRI contrast agent is their toxicity, which is generally caused by the free gadolinium ion. To determine the cytotoxic effect of **GdL1**, an MTT assay (*26*) (MTT = 3-(4,5-dimethythiazol-2-yl)-2,5-diphenyltetrazolium bromide) was performed on the human nontumotigenic immortalized liver cell line (MIHA) (*27*). In this work, the commercial available MRI contrast agent, Gd-DOTA, and Gd-DO3A with two bound water molecules were used as the control molecules under the same condition. The experimental results demonstrated that the cell's proliferation and viability were not obviously affected after incubating from 1 to 24 h, while the concentration of **GdL1** ranged from 0.5 to 10 mM (Figure 2, Figure S1, Supporting Information). Additionally, the morphology of live MIHA cells in response to 100 μM **GdL1** was monitored by laser scanning confocal microscopy after 1, 2, 8, and 24 h incubation at 37 °C (Figure S2, Supporting Information). Compared to the cells in the control experiments, no obvious morphological changes of the MIHA cell were detected. The MTT assay showed that the acute cytotoxicity of **GdL1** is quite low in the concentration range required for obtaining the detectable MR signal.

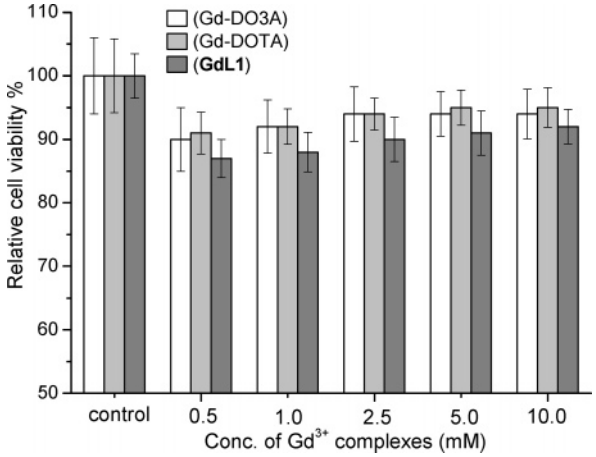

Figure 2. Results obtained from the MTT assay showing the effect of Gd-DOTA (white bars), Gd-DO3A (light gray bars), and **GdL1** (gray bars) on MIHA cells. The viability (%) refers to the growth inhibition induced by the Gd^{3+} complex in comparison to the cells in the absence of Gd^{3+} complex. Error bars represent the standard deviation (± SD) on a triplicate analysis (n = 3).

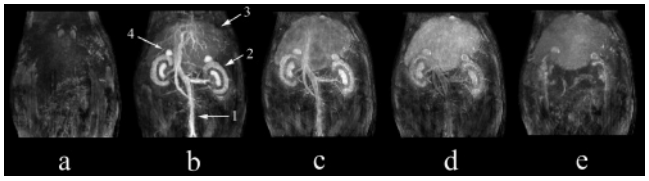

Figure 3. 3D maximum intensity projection T_1-weighted MR images of a rat at preinjection (a), 4 (b), 30 (c), 100 (d), and 200 (e) min after administration of **GdL1** (0.04 mmol/kg). In panel b, the MR signal in abdominal aorta (1), kidney (2), liver (3), and adrenal gland (4) was enhanced significantly and attained their maximum at different times.

In vivo T_1-weighted images were acquired after the administration of **GdL1**, Gd-DOTA, and the liver-specific CA Gd-BOPTA (MultiHance) to anesthetized rats. Figure 3 shows the three-dimensional (3D) maximum intensity projection (MIP) abdomen images of a rat before and after intravenous injection of **GdL1** at 0.04 mmol/kg. MR signals in the kidney, liver, adrenal gland, and abdominal aorta were enhanced significantly. Time dependent MR signal intensity enhancements (IEs) after administration of different CAs were demonstrated in Figure 5. **GdL1** offered much higher vascular and renal contrast enhancements than commercial available Gd-DOTA under the same dosage (Figure 5A,B). The IEs in the abdominal aorta from **GdL1** remained strong in the first 30 min, and still visible at 45−100 min (Figures 3 and 5A), while the enhancement in kidney cortex was even longer; obvious renal IEs lasted for more than 3 h (Figures 4A and 5B). Comparatively, the IEs induced by Gd-DOTA in the blood vessel and kidney vanished completely in less than 15 and 40 min, respectively. To clarify the prolonged resident lifetime of **GdL1** in vasculature, the titration

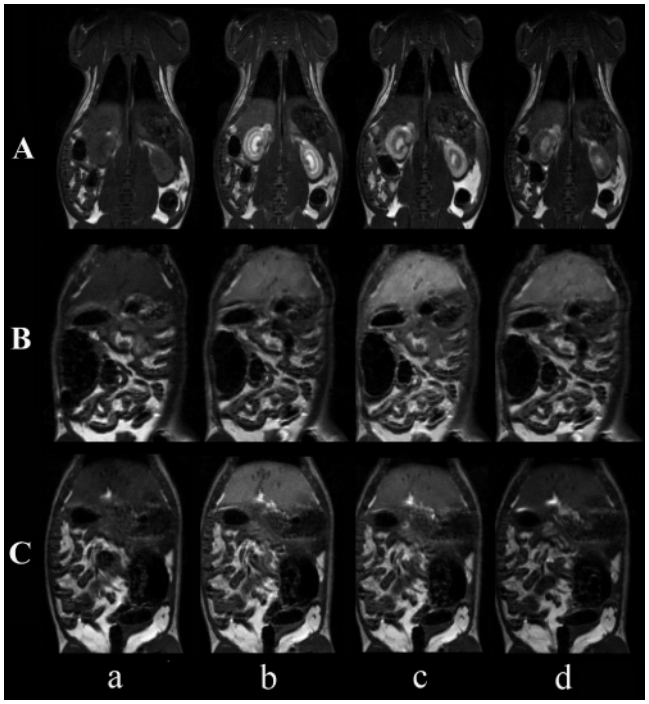

Figure 4. 2D axial T_1-weighted renal and hepatic MR images of rats before (a) and 10 (b), 100 (c) and 200 (d) min after the administration of **GdL1** (A, B) and Gd-BOPTA (C) in the dosage of 0.04 mmol/kg.

of human serum albumin (HSA) to this complex was conducted at pH 7.4 (Figure S3, Supporting Information). The r_{1p} (20 MHz, 25 °C) of **GdL1** increased substantially with the concentration of HSA, and the binding constant K_a of 3009 M^{-1} was measured. This result implied that the nonspecific binding between the amphiphilic crown ether moiety and serum proteins resulted in the prolonged resident lifetime of **GdL1** in vasculature (*28*).

Pronouncedly different time courses of hepatic IEs were observed between **GdL1** and Gd-BOPTA (Figures 4B,C and 5C). IE induced by Gd-BOPTA reached its maximum within the first 10 min, while the peak value of **GdL1** appeared in 80−100 min after administration. Notably, the significant hepatic IEs induced by **GdL1** was sustained for more than 4 h. Moreover, it is worth mentioning that the vascular, renal, and hepatic enhancements of **GdL1** reached their maximal values at different time windows, which implies this complex can be used to image multiple organs successively after the single injection. Even though the mechanism of extended residence lifetime of **GdL1** in liver parenchyma is not very clear, the experimental results suggest that, like the pendant phenyl group in Gd-BOPTA, amphiphilic crown ether can enhance the passive accumulation of **GdL1** in the reticuloendothelial system (RES). Moreover, the uptake of this complex by hepatocytes, and following biliary excretion, may be other reasons for the prolonged hepatic IE (*29*). Dosage-dependent MR signal IE behaviors induced by these three complexes were also investigated (Figure S4, Supporting Information). Even in 0.02 mmol/kg, one-fifth of the standard dosage used in the clinic, bishydrated **GdL1** achieved higher and longer IEs in blood vessel, kidney, and liver compared to two other commercial available CAs. Additionally, it is noteworthy that all rats recovered spontaneously from anesthesia after the MRI studies, which further indicates that **GdL1** has no acute fatal toxicity at the dosage used.

In conclusion, this work describes a fast water-exchange Gd^{3+}-DO3A complex showing efficient MR signal enhancements, an extended excretion rate, and low acute cytotoxicity. The relaxometric and in vivo imaging studies demonstrate the crown ether moiety as a functional group is a potential choice

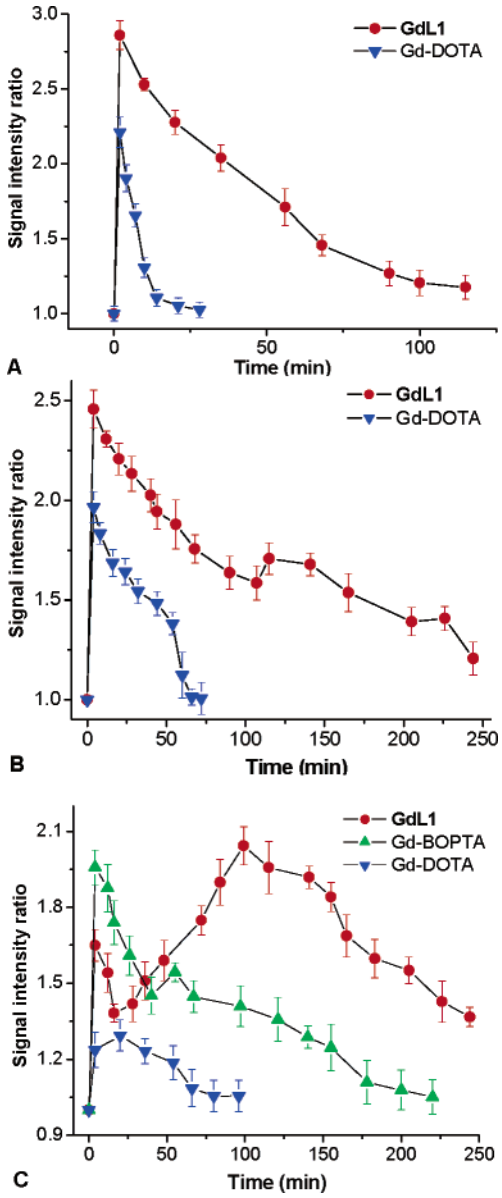

Figure 5. Time-dependent abdominal aortic (**A**), renal (**B**), and hepatic (**C**) IEs induced by **GdL1**, Gd-DOTA, and Gd−BOPTA at the dosage of 0.04 mmol/kg. Error bars represent the standard deviation (± SD) on a triplicate analysis ($n = 3$).

to realize the compromise between the prolonged excretion rate and the low toxicity of MRI contrast agents.

ACKNOWLEDGMENT

The authors thank the Hong Kong Research Grants Council (HKU 7119/00P and HKU 7116/02P) and Natural Science Foundation of China (10234070 and 30370419). This work was also supported by the Area of Excellence Scheme of the University Grants Committee (Hong Kong). We are grateful to Prof. M. Botta and his student S. Avedano for their assistance with the relaxometric measurements.

Supporting Information Available: Details of chemical synthesis and characterization, time-dependent MR IEs at different dosages, and cytotoxicity studies. This material is available free of charge via the Internet at http://pubs.acs.org.

LITERATURE CITED

(1) Caravan, P., Ellison, J. J., McMurry, T. J., and Lauffer, R. B. (1999) Gadolinium(III) chelates as MRI contrast agents: structure, dynamics, and applications. *Chem. Rev. 99*, 2293−2352.

(2) Weinmann, H. J., Ebert, W., Misselwitz, B., and Schmitt-Willich, H. (2003) Tissue-specific MR contrast agents. *Eur. J. Radiol. 46*, 33−44.

(3) Aime, S., Chiaussa, M., Digilio, G., Gianolio, E., and Terreno, E. (1999) Contrast agents for magnetic resonance angiographic applications: ^{1}H and ^{17}O NMR relaxometric investigations on two gadolinium(III) DTPA-like chelates endowed with high binding affinity to human serum albumin. *J. Bioinorgate Chem. 4*, 766−774.

(4) Marecos, E., Weissleder, R., and Bogdanov, A., Jr. (1998) Antibody-mediated versus nontargeted delivery in a human small cell lung carcinoma model. *Bioconjugate Chem. 9*, 184−191.

(5) Kobayashi, H., Kawamoto, S., Jo, S. K., Jr., Bryant, H. L., Brechbiel, M. W., and Star, R. A. (2003) Macromolecular MRI contrast agents with small dendrimers: pharmacokinetic differences between sizes and cores. *Bioconjugate Chem. 14*, 388−394.

(6) Accardo, A., Tesauro, D., Roscigno, P., Gianolio, E., Paduano, L., D'Errico, G., Pedone, C., and Morelli, G. (2004) Physicochemical properties of mixed micellar aggregates containing CCK peptides and Gd complexes designed as tumor specific contrast agents in MRI. *J. Am. Chem. Soc. 126*, 3097−3107.

(7) Artemov, D. (2003) Molecular magnetic resonance imaging with targeted contrast agents. *J. Cell. Biochem. 90*, 518−524.

(8) Aime, S., Botta, M., Fasano, M., and Terreno, E. (1998) Lanthanide (III) chelates for NMR biomedical applications. *Chem. Soc. Rev. 27*, 19−29.

(9) Franano, F. N., Edwards, W. B., Welch, M. J., Brechbeil, M. W., Gansow, O. A., and Duncan, J. R. (1995) Biodistribution and metabolism of targeted and nontargeted protein chelate gadolinium complexes: Evidence for gadolinium dissociation in vitro and in vivo. *Magn. Reson. Imaging 13*, 201−214.

(10) Mohs, A. M., Wang, X., Goodrich, K. C., Zong, Y., Parker, D. L. and Lu, Z. R. (2004) PEG-*g*-poly(GdDTPA-*co*-L-cystine): A biodegradable macromolecular blood pool contrast agent for MRI imaging. *Bioconjugate Chem. 15*, 1424−1430.

(11) Mohs, A. M., Zong, Y., Guo, J., Parker, D. L., and Lu, Z. R. (2005) PEG-*g*-poly(GdDTPA-*co*-L-cystine): Effect of PEG chain length on in vivo contrast enhancement in MRI. *Biomacromolecules 6*, 2305−2311.

(12) Harris, J. M., and Chess, R. B. (2003) Effect of pegylation on pharmaceuticals. *Nat. Rev. Drug Discov. 2*, 214−221.

(13) Veronese, F. M., Schiavon, O., Pasut, G., Mendichi, R., Andersson, L., Tsirk, A., Ford, J., Wu, G., Kneller, S., Davies, J., and Duncan, R. (2005) PEG-doxorubicin conjugates: influence of polymer structure on drug release, in vitro cytotoxicity, biodistribution, and antitumor activity. *Bioconjugate Chem. 16*, 775−784.

(14) Weissleder, R., Jr., Bogdanov, A., Tung, C. H., and Weinmann, H. J. (2001) Size optimization of synthetic graft copolymers in vivo angiogenesis imaging. *Bioconjugate Chem. 12*, 213-219.

(15) Gokel, G. W. (1991) *Crown Ethers and Cryptands*, The Royal Society of Chemistry: Cambridge, England.

(16) Stott, P. E., Bradshaw, J. S., and Parish, W. W. (1980) Modified crown ether catalysts. 3. Structural parameters affecting phase transfer catalysis by crown ethers and a comparison of the effectiveness of crown ethers to that of other phase transfer catalysts. *J. Am. Chem. Soc. 102*, 4810−4815.

(17) Bianchi, A., Calabi, L., Giorgi, C., Losi, P., Mariani, P., Paoli, P., Rossi, P., Valtancoli, B., Virtuani, M. (2000) Thermodynamic and structural properties of Gd^{3+} complexes with functionalized macrocyclic ligands based upon 1,4,7,10-tetraazacyclododecane. *J. Chem. Soc., Dalton Trans.* 697−705.

(18) Merbach, A. E., and Tóth, É. (2001) *The Chemistry of Contrast Agents in Medical Magnetic Resonance Imaging*, Wiley-VCH, Weinheim, Germany.

(19) Li, C., and Wong, W. T. (2002) A convenient method for the preparation of mono *N*-alkylated cyclams and cyclens in high yields. *Tetrahedron Lett. 43*, 3217−3220.

(20) Mishra, A. K., and Chatal, J. F. (2001) Synthesis of macrocyclic bifunctional chelating agents: 1,4,7-tris(carboxymethyl)-10-(2-aminoethyl)-1,4,7,10-tetraazacyclododecane and 1,4,8-tris(carboxymethyl)-11-(2-aminoethyl)-1,4,8,11-tetraazacyclotetradecane. *New J. Chem. 25*, 336−339.

(21) Li, C., and Wong, W. T. (2004) Luminescent heptadentate Tb^{3+} complex with pendant aza-15-crown-5 showing recognition of lactate and salicylate in aqueous solution. *Tetrahedron Lett. 45*, 6055−6058.

(22) Beeby, A., Clarkson, I. M., Dickins, R. S., Faulkner, S., Parker, D., Royle, L., de Sousa, A. S., Williams, J. A. G., and Woods, M. (1999) Non-radiative deactivation of the excited states of europium, terbium and ytterbium complexes by proximate energy-matched OH, NH and CH oscillators: animproved luminescence method for establishing solution hydration states. *J. Chem. Soc., Perkin Trans. 2*, 493−504.

(23) Aime, S., Botta, M., Crich, S. G., Giovenzana, G., Pagliarin, R., Sisti, M., Terreno, E. (1998) NMR relaxometric studies of Gd(III) complexes with heptadentate macrocyclic ligands. *Magn. Reson. Chem. 36*, S200−S208.

(24) Raymond, K. N., and Pierre, V. C. (2005) Next Generation, high relaxivity gadolinium MRI agents. *Bioconjugate Chem. 16*, 3−8.

(25) Doble, D. M. J., Botta, M., Wang, J., Aime, S., Barge, A., Raymond, K. N. (2001) Optimization of the relaxivity of MRI contrast agents: Effect of poly(ethylene glycol) chains on the water-exchange rates of Gd^{III} complexes. *J. Am. Chem. Soc. 123*, 10758−10759.

(26) The rationale to use the MTT assay (MTT = 3-(4,5-dimethythiazol-2-yl)-2,5-diphenyltetrazolium bromide) was because water-soluble MTT can be reduced by mitochondrial dehydrogenases of living cells into water-insoluble purple formazan. The conversion never occurs in dead cells. The formazan can be dissolved by DMSO, and the resulting solution can be measured spectrophotometrically for the quantification of cell viability. See Lee T. K., Man, K., Ho, J. W., Sun, C. K., Ng, K. T., Wang, X. H., Wong, Y. C., Ng, I. O., Xu, R., and Fan, S. T. (2004) FTY720 induces apoptosis of human hepatoma cell lines through PI3-K-mediated Akt dephosphorylation. *Carcinogenesis 25*, 2397−2405.

(27) MIHA is a human immortalized liver cell and regarded as a normal liver cell for the in vitro culture model. See Brown, J. J., Parashar, B., Moshage, H., Tanaka, K. E., Engelhardt, D., Rabbani, E., Roy-Chowdhury, N., and Roy-Chowdhury, J. (2000) A long-term hepatitis B viremia model generated by transplanting nontumorigenic immortalized human hepatocytes in Rag-2-deficient mice. *Hepatology 31*, 173−181.

(28) Caravan, P., Cloutier, N. J., Greenfield, M. T., McDermid, S. A., Dunham, S. U., Bulte, J. W. M., Amedio, J. C., Jr., Looby, R. J., Supkowski, R. M., Horrocks, Jr. W. DeW., McMurry, T. J., and Lauffer, R. B. (2002) The interaction of MS-325 with human serum albumin and its effect on proton relaxation rates. *J. Am. Chem. Soc. 124*, 3152−3162.

(29) Pavone, P., Patrizio, G., Buoni, C., Tettamanti, E., Passariello, R., Musu, C., Tirone, P., and Felder, E. (1990) Comparison of Gd-BOPTA with Gd-DTPA in MR imaging of rat liver. *Radiology 176*, 61−64.

BC060003M

Carbohydrate-Labeled Fluorescent Microparticles and Their Binding to Lectins

Timothy L. Kelly, Michael C. W. Lam, and Michael O. Wolf*

Department of Chemistry, University of British Columbia, Vancouver, British Columbia, Canada, V6T 1Z1. Received November 23, 2005; Revised Manuscript Received February 17, 2006

The preparation of micrometer-sized, cross-linked poly(*p*-phenyleneethynylene) (PPE) beads to which simple monosaccharides are attached is reported. Mannose, glucose, and galactose derivatives have been synthesized. The fluorescence properties, size distribution, and morphology of these microparticles have been elucidated through fluorimetry, fluorescence confocal microscopy, and scanning electron microscopy. Protein binding assays were carried out using Concanavalin A tagged with the fluorophore Texas Red, and the resultant bioconjugates were imaged using confocal microscopy. The microparticles are shown to exhibit efficient binding to lectins and may have potential application as fluorescent probes, biocapture agents, or column packing material for affinity chromatography.

The binding of proteins to cell surface carbohydrates is of critical importance in molecular biology and mediates a wide variety of responses, including inflammation (*1*), viral attack on host cells (*2*), and blood antigenicity (*3*). This versatility in function makes carbohydrates attractive additions to many synthetic molecules and polymers and can lend them the capacity for biocompatibility and biorecognition. The interaction of carbohydrate-binding proteins (lectins) with sugars is multivalent (*4*). Monomeric interactions are typically weak, whereas presenting the lectin with an array of carbohydrate ligands results in significant enhancement in the binding. Thus, there is a growing interest in neoglycopolymers as multivalent ligands which can inhibit viral agglutination, act as biological sensors, and serve as models for complex biological processes (*5, 6*).

The preparation of micrometer or nanometer diameter particles that have been labeled with carbohydrates is of particular interest. This geometry offers an advantage over linear or dendritic structures in that it more closely mimics the cell surface that is the natural substrate for lectins. As such, multivalent carbohydrate liposomes (*7*−*10*), magnetic beads (*11*, *12*), quantum dots (*12*−*14*), and polymer beads (*15*) have all been explored with the aim of elucidating fundamental properties of molecular biology. π-Conjugated neoglycopolymers are also particularly useful as multivalent ligands for lectins; owing to their electrical conductivity and luminescence, they can act as signal transduction elements in biological probes and sensors. Linear sugar-functionalized poly(*p*-phenyleneethynylene)s (PPEs) have recently been prepared as fluorescence based sensors for *E. coli* bacteria, as well as a number of proteins (*16*−*21*). Similarly, Charych describes polythiophene-based biosensors for both *E. coli* and influenza virus (*22*). Additionally, the formation of conjugated networks through cross-linking has been shown to lead to enhanced charge-transfer properties (*23*). Combination of the functional properties of sugar-substituted π-conjugated cross-linked polymers with the advantages of a micro- or nanoscale spherical geometry is therefore an attractive target.

In this Communication, we report the preparation of spherical cross-linked PPE beads having diameters in the range 0.5−5 μm. Preparation of the glycoside monomers **1a**−**c** was accomplished by coupling the α-D-sugar trichloroacetimidates with 1,4-diiodo-2,5-hydroquinone using boron trifluoride diethyl etherate as a catalyst. This yields **1a**−**c** with complete inversion of stereochemistry, and no evidence for either the α-anomer or mixed α−β-anomer was found in the ^{1}H NMR spectrum. The stereochemistry was confirmed by the $J_{H1-H2} = 3$ Hz coupling constant in **1a** and the $J_{H1-H2} = 8$ Hz coupling constant in **1b** and **1c**. Subsequent reaction of **1a**−**c** with 1,4-diethynyl-2,5-dimethoxybenzene (**2**) and 1,2,4-tribromobenzene (**3**) under Sonogashira conditions (Scheme 1) forms cross-linked, insoluble polymers. To prepare micrometer-sized beads **4a**−**c**, the polymerization was carried out in an emulsion of toluene/diisopropylamine in an aqueous solution of sodium dodecyl sulfate (SDS) (*24*). The polymerization is templated by the formation of the organic micelles, and the SDS helps to stabilize smaller micelles of micrometer dimensions. The particles were washed with copious quantities of toluene and methanol in order to remove both oligomers and linear polymer. Subsequent treatment with ca. 0.5 M sodium methoxide in methanol

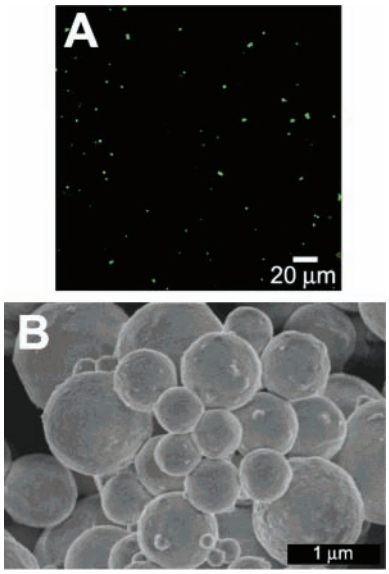

Figure 1. (A) Fluorescence confocal micrograph (*Z*-axis projection) of **4c**, exciting at 488 nm. (B) Scanning electron micrograph of **4c** showing a cluster of polymer beads. Results for **4a** and **4b** are similar.

* Corresponding author. Phone: (604) 822-1702. Fax: (604) 822-2847. E-mail: mwolf@chem.ubc.ca.

10.1021/bc050339g CCC: $33.50 © 2006 American Chemical Society
Published on Web 04/07/2006

Scheme 1. Polymerization under Sonogashira Conditions To Form Cross-Linked PPE Microparticles[a]

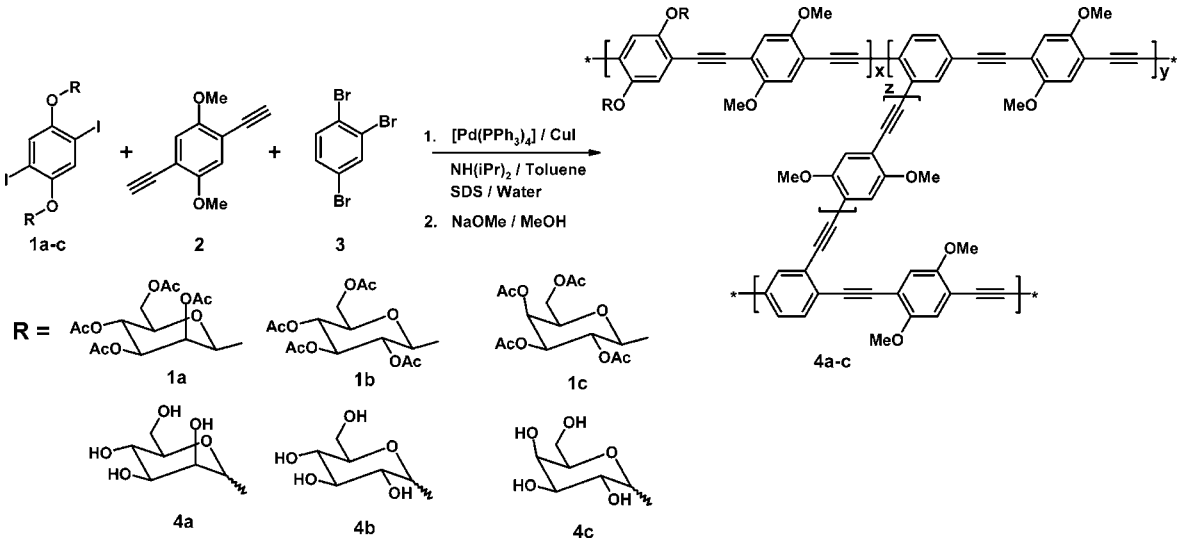

[a] R = β-D-mannose tetraacetate (**1a**), β-D-glucose tetraacetate (**1b**), β-D-galactose tetraacetate (**1c**), D-mannose (**4a**), D-glucose (**4b**), and D-galactose (**4c**).

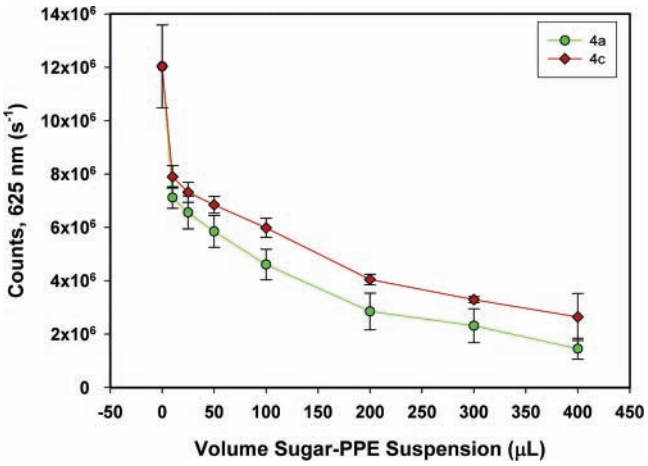

Figure 2. Plot showing the extraction of Concanavalin A-Texas Red conjugate by the mannose-modified (**4a**, green circles) and galactose-modified (**4c**, red diamonds) microparticles. Data are averaged from binding assays on two separate preparations of microparticles.

removes the acetate protecting groups on the precursors to polymers **4a**−**c**. Successful removal of the acetate groups is evidenced by the absence of the distinctive carbonyl stretch in the infrared spectrum (prior to deprotection, a distinctive carbonyl stretch at 1751 cm^{-1} was observed. After treatment with sodium methoxide, this signal disappeared).

Once deprotected, the particles are readily redispersed in polar solvents such as water or methanol by either vigorous shaking or sonication. Analysis of particle size by laser scanning confocal microscopy (Figure 1) shows a mean particle diameter of ≈4.9 μm. This number reflects the formation of aggregates in solution. When evaluated by scanning electron microscopy, the mean particle diameter was found to be ≈0.8 μm. As expected for polymers derived from the PPE backbone, **4a**−**c** were found to be emissive as suspensions in water and organic solvents, although only very weakly in the dry solid state. The emission band is centered at 560 nm in methanol, which is markedly red-shifted compared to linear PPEs in dilute solution (*18, 21*). Bunz and co-workers have shown that aggregation of alkyl-PPEs in solvent/nonsolvent mixtures or in thin films results in a substantial bathochromic shift of the emission spectrum (*25*). In this case, the short methoxy substituents are not long enough to prevent interchain aggregation, and both hydrogen bonding of the carbohydrate groups and cross-linking of the chains may encourage this phenomenon. While the emission spectra of the microparticles prepared by Weder (*24*) show no such shift, this is likely due to the bulkier 2-ethylhexyl and *n*-octyl substituents, which lead to a more porous bead structure that is readily swollen by organic solvents.

To probe the versatility of these PPE beads for potential biosensor, biocapture, or affinity chromatography application, their binding to lectins was examined. Suspensions (1 mg/mL) of **4a** (mannose-modified) and **4c** (galactose-modified) were prepared in 0.1 M PBS buffer (pH 7.2) containing 1 mM $CaCl_2$ and 1 mM $MnCl_2$, the cofactors required for the lectin Concanavalin A (*4*). Similarly, a 1 mg/mL stock solution of Concanavalin A−Texas Red (ConA-TR) conjugate was prepared

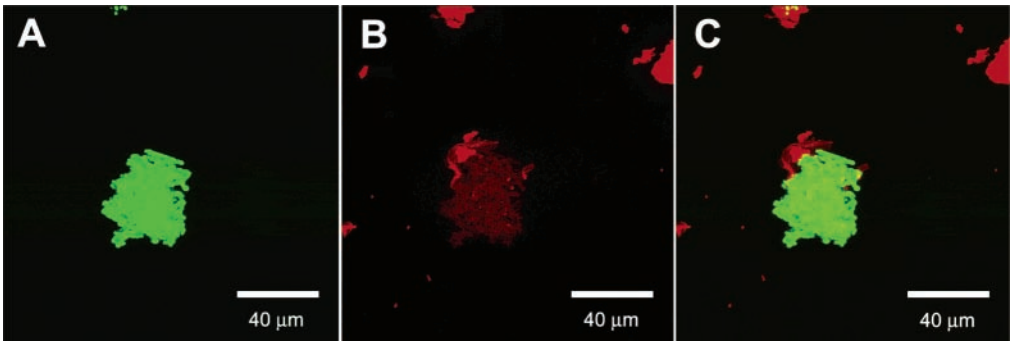

Figure 3. Fluorescence confocal micrographs (*Z*-axis projection). (A) 488 nm excitation, showing a cluster of mannose microparticles after incubation with ConA-TR. (B) 568 nm excitation, showing the presence of the tagged protein. (C) Merged image.

in the same matrix. Aliquots (100 μL) of the ConA-TR solution were mixed with varying amounts (0−400 μL) of the polymer suspensions. All samples were diluted to a total of 500 μL with PBS. After incubating for 4 h at room temperature, the samples were centrifuged at 7500 rpm for 5 min, and the supernatant was removed. The isolated supernatants were then analyzed for protein content by a fluorescence assay at 625 nm (quantifying Texas Red emission). As seen in Figure 2, there is clearly an extraction of the protein from the supernatant as compared to the blank (0 μL of polymer suspension), which is greater for **4a** compared to **4c**. Data in Figure 2 is averaged between two different preparations of microparticles. If multiple assays on a single batch of particles are performed, the results show less variability, suggesting that batch-to-batch differences in particle size distribution are significant. While Concanavalin A should exhibit no binding affinity toward galactose, there is clearly a nonspecific interaction present (*19*). This may be due to nonspecific van der Waals interactions, hydrogen bonding, or protein adsorption on the polymer bead.

Glucose also binds to Concanavalin A with a binding affinity lower than that of mannose, and the glucose microparticles (**4b**) were also investigated for their binding to lectin. Significant batch-to-batch differences in binding were observed. Additionally, **4b** showed an increased propensity for aggregation and sedimentation compared to **4a** and **4c**. Zeta potential measurements (ζ = −14, −30, and −11 mV for **4a**, **4b**, and **4c**, respectively) suggest a greater surface charge density for **4b**. At present this anomalous behavior is not understood, and the binding data is not included in Figure 2.

A competition experiment was also carried out, where 100 μL of ConA-TR solution, 200 μL of polymer suspension, and 200 μL of a 0.3 M D-mannose solution were incubated under identical conditions to those described above. For both **4a** and **4c** there was an increase in fluorescence intensity (20% and 9% respectively) of the supernatant, indicating a decrease in binding. The free sugar effectively competes for protein binding sites, and aqueous sugar solutions could presumably be used to remove bound protein from a sample of polymer.

The isolated protein-polymer bioconjugates were washed twice with 200 μL aliquots of fresh PBS buffer and suspended in 50 μL of PBS. Fluorescence confocal microscopy is used to confirm the binding to the microparticles; it shows colocalization of the polymer beads with the Texas Red fluorophore. Additionally, there appears to be some degree of aggregation among the individual polymer beads upon lectin binding. This phenomenon is quite similar to cellular agglutination, which is mediated by the multivalent character of lectins; by binding sugar residues on more than one cell, the proteins link the cells together in large aggregates (*4*). Owing to the similar size of these microparticles (ca. 5 μm) and erythrocytes (ca. 7 μm), their highly fluorescent properties, and their surface carbohydrate residues, these beads may prove to be useful models in the study of agglutination and other important biological processes. The mannose-substituted polymer beads may also form clusters with *E. coli* bacteria in a manner analogous to the mannosylated-PPE of Swager (*17*), making them useful as fluorescent tags for pathogens.

In conclusion, we have prepared sugar-substituted, cross-linked PPE microparticles by a templated Pd-catalyzed cross-coupling reaction. The polymer beads are fluorescent and exhibit a substantial bathochromic shift in the emission spectrum compared to linear, alkyl-substituted PPEs. Binding to the lectin Concanavalin A was demonstrated, with some evidence of agglutination, forming the basis of a potential blood erythrocyte mimic. These particles also hold promise as a high surface area packing material for the purification of lectins by affinity chromatography, and in biocapture and tagging applications for pathogenic agents such as *E. coli*, influenza, or ricin.

ACKNOWLEDGMENT

The authors thank the Natural Sciences and Engineering Research Council of Canada SRO program for financial support and for a scholarship (T.L.K.).

Supporting Information Available: Synthetic procedures and spectroscopic data. This material is available free of charge via the Internet at http://pubs.acs.org.

LITERATURE CITED

(1) Rosen, S. D., and Bertozzi, C. R. (1994) The selectins and their ligands. *Curr. Opin. Cell Biol. 6*, 663−673.
(2) Karlsson, K.-A. (1995) Microbial recognition of target-cell glycoconjugates. *Curr. Opin. Struct. Biol. 5*, 622−635.
(3) Khan, F., Khan, R. H., Sherwani, A., Mohmood, S., and Azfer, M. A. (2002) Lectins as markers for blood grouping. *Med. Sci. Monit. 8*, RA293−RA300.
(4) Lis, H., and Sharon, N. (1998) Lectins: Carbohydrate-Specific Proteins that Mediate Cellular Recognition. *Chem. Rev. 98*, 637−674.
(5) Bertozzi, C. R., and Kiessling, L. L. (2001) Chemical glycobiology. *Science 291*, 2357−2364.
(6) Wong, S. Y. C. (1995) Neoglycoconjugates and their applications in glycobiology. *Curr. Opin. Struct. Biol. 5*, 599−604.
(7) Kingery-Wood, J. E., Williams, K. W., Sigal, G. B., and Whitesides, G. M. (1992) The agglutination of erythrocytes by influenza virus is strongly inhibited by liposomes incorporating an analog of sialyl gangliosides. *J. Am. Chem. Soc. 114*, 7303−7305.
(8) Reichert, A., Nagy, J. O., Spevak, W., and Charych, D. (1995) Polydiacetylene Liposomes Functionalized with Sialic Acid Bind and Colorimetrically Detect Influenza Virus. *J. Am. Chem. Soc. 117*, 829−830.
(9) Spevak, W., Foxall, C., Charych, D. H., Dasgupta, F., and Nagy, J. O. (1996) Carbohydrates in an Acidic Multivalent Assembly: Nanomolar P−Selectin Inhibitors. *J. Med. Chem. 39*, 1018−1020.
(10) Sun, X.-L., Kanie, Y., Guo, C.-T., Kanie, O., Suzuki, Y., and Wong, C.-H. (2000) Syntheses of C-3-modified sialyl-glycosides as selective inhibitors of influenza hemagglutinin and neuraminidase. *Eur. J. Org. Chem.*, 2643−2653.
(11) Rye, P. D., and Bovin, N. V. (1997) Selection of carbohydrate-binding cell phenotypes using oligosaccharide-coated magnetic particles. *Glycobiology 7*, 179−182.
(12) Sun, X.-L., Cui, W., Haller, C., and Chaikof, E. L. (2004) Site-specific multivalent carbohydrate labeling of quantum dots and magnetic beads. *ChemBioChem 5*, 1593−1596.
(13) Robinson, A., Fang, J.-M., Chou, P.-T., Liao, K.-W., Chu, R.-M., and Lee, S.-J. (2005) Probing lectin and sperm with carbohydrate-modified quantum dots. *ChemBioChem 6*, 1899−1905.
(14) Osaki, F., Kanamori, T., Sando, S., Sera, T., and Aoyama, Y. (2004) A Quantum Dot Conjugated Sugar Ball and Its Cellular Uptake. On the Size Effects of Endocytosis in the Subviral Region. *J. Am. Chem. Soc. 126*, 6520−6521.
(15) Basu, A., and Kahne, D. (2003) Overcoming degeneracy in carbohydrate recognition. *Angew. Chem., Int. Ed. 42*, 2504−2506.
(16) Babudri, F., Colangiuli, D., Di Lorenzo, P. A., Farinola, G. M., Omar, O. H., and Naso, F. (2003) Synthesis of poly(aryleneethynylene)s bearing glucose units as substituents. *Chem. Commun.* 130−131.
(17) Disney, M. D., Zheng, J., Swager, T. M., and Seeberger, P. H. (2004) Detection of Bacteria with Carbohydrate-Functionalized Fluorescent Polymers. *J. Am. Chem. Soc. 126*, 13343−13346.
(18) Erdogan, B., Wilson, J. N., and Bunz, U. H. F. (2002) Synthesis and Mesoscopic Order of a Sugar-Coated Poly(*p*-phenyleneethynylene). *Macromolecules 35*, 7863−7864.
(19) Kim, I.-B., Dunkhorst, A., and Bunz, U. H. F. (2005) Nonspecific Interactions of a Carboxylate-Substituted PPE with Proteins. A Cautionary Tale for Biosensor Applications. *Langmuir 21*, 7985−7989.

(20) Kim, I.-B., Wilson, J. N., and Bunz, U. H. F. (2005) Mannose-substituted PPEs detect lectins: A model for Ricin sensing. *Chem. Commun.* 1273−1275.

(21) Lavigne, J. J., Broughton, D. L., Wilson, J. N., Erdogan, B., and Bunz, U. H. F. (2003) "Surfactochromic" Conjugated Polymers: Surfactant Effects on Sugar-Substituted PPEs. *Macromolecules 36*, 7409−7412.

(22) Baek, M.-G., Stevens, R. C., and Charych, D. H. (2000) Design and synthesis of novel glycopolythiophene assemblies for colorimetric detection of influenza virus and E. coli. *Bioconjugate Chem. 11*, 777−788.

(23) Weder, C. (2005) Synthesis, processing and properties of conjugated polymer networks. *Chem. Commun.* 5378−5389.

(24) Hittinger, E., Kokil, A., and Weder, C. (2004) Synthesis and characterization of cross-linked conjugated polymer milli-, micro-, and nanoparticles. *Angew. Chem., Int. Ed. 43*, 1808−1811.

(25) Halkyard, C. E., Rampey, M. E., Kloppenburg, L., Studer-Martinez, S. L., and Bunz, U. H. F. (1998) Evidence of Aggregate Formation for 2,5-Dialkylpoly(*p*-phenyleneethynylenes) in Solution and Thin Films. *Macromolecules 31*, 8655−8659.

BC050339G

ARTICLES

Extension of the Single Amino Acid Chelate Concept (SAAC) to Bifunctional Biotin Analogues for Complexation of the $M(CO)_3^{+1}$ Core (M = Tc and Re): Syntheses, Characterization, Biotinidase Stability, and Avidin Binding

Shelly James,[†] Kevin P. Maresca,[#] Damian G. Allis,[†] John F. Valliant,[‡] William Eckelman,[#] John W. Babich,[#] and Jon Zubieta*[,†]

Department of Chemistry, Syracuse University, Syracuse, New York 13244, Department of Chemistry, McMaster University, Hamilton, Ontario Canada L8S 4M1, and Molecular Insight Pharmaceuticals, 160 Second Street, Cambridge, Massachusetts 02142. Received October 8, 2005; Revised Manuscript Received February 3, 2006

Biotin and avidin form one of the most stable complexes known ($K_D = 10^{-15}$ M^{-1}) making this pairing attractive for a variety of biomedical applications including targeted radiotherapy. In this application, one of the pair is attached to a targeting molecule, while the other is subsequently used to deliver a radionuclide for imaging and/or therapeutic applications. Recently, we reported a new single amino acid chelate (SAAC) capable of forming stable complexes with $Tc(CO)_3$ or $Re(CO)_3$ cores. We describe here the application of SAAC analogues for the development of a series of novel radiolabeled biotin derivatives capable of forming robust complexes with both Tc and Re. Compounds were prepared through varying modification of the free carboxylic acid group of biotin. Each ^{99m}Tc complex of SAAC−biotin was studied for their ability to bind avidin, susceptibility to biotinidase, and specificity for avidin in an in vivo avidin-containing tumor model. The radiochemical stability of the ^{99m}Tc$(CO)_3$ complexes was also investigated by challenging each ^{99m}Tc-complex with large molar excesses of cysteine and histidine at elevated temperature. All compounds were radiochemically stable for greater than 24 h at elevated temperature in the presence of histidine and cysteine. Both [^{99m}Tc$(CO)_3$(**L6**)]$^{+1}$ [**TcL6**; **L6** = biotinylamidopropyl-*N*,*N*-(dipicolyl)amine] and [^{99m}Tc$(CO)_3$(**L12a**)]$^{+1}$ (**TcL12**; **L12** = *N*,*N*-(dipicolyl)biotinamido-Boc-lysine; **TcL12a**; **L12a** = *N*,*N*-(dipicolyl)biotinamide-lysine) readily bound to avidin whereas [^{99m}Tc$(CO)_3$(**L9**)]$^{+1}$ [**TcL9**; **L9** = *N*,*N*-(dipicolyl)biotinamine] demonstrated minimal specific binding. **TcL6** and **TcL9** were resistant to biotinidase cleavage, while **TcL12a**, which contains a lysine linkage, was rapidly cleaved. The highest uptake in an in vivo avidin tumor model was exhibited by **TcL6**, followed by **TcL9** and **TcL12a**, respectively. This is likely the result of both intact binding to avidin and resistance to circulating biotinidase. Ligand **L6** is the first SAAC analogue of biotin to demonstrate potential as a radiolabeled targeting vector of biotin capable of forming robust radiochemical complexes with both ^{99m}Tc and rhenium radionuclides. Computational simulations were performed to assess biotin-derivative accommodation within the binding site of the avidin. These calculations predict that deformation of the surface domain of the binding pocket can occur to accommodate the transition metal−biotin derivatives with negligible changes to the inner-β-barrel, the region most responsible for binding and retaining biotin and its derivatives. The biological activity and biodistribution of the technetium complexes **TcL6**, **TcL9**, and **TcL12a** were examined in an avidin tumor model. In the avidin bead tumor localization model, **TcL6** demonstrated the most favorable localization with a 7:1 ratio of avidin bead implanted muscle versus normal muscle, while **TcL9** exhibited a 2:1 ratio. However, **TcL9** displayed no specificity for avidin.

INTRODUCTION

Biotin is a water-soluble member of the B-complex group of vitamins and is commonly referred to as vitamin H. The molecule acts as a carrier of CO_2 in the pyruvate carboxylase reaction, where biotin is linked to the ϵ-amino group of a lysine residue in the enzyme (*1*, *2*). Biotin is necessary for both metabolism and growth in humans, particularly in the production of fatty acids, antibodies, digestive enzymes, and in niacin (vitamin B-3) metabolism (*3*, *4*). Biotin has nine host molecules with which it is associated, including pyruvate carboxylase, β-methylcrotonyl-CoA carboxylase, propinyl-CoA carboxylase, and acetyl-CoA-carboxylase in humans. Biotin is also bound by avidin, a homotetrameric glycoprotein (molecular weight ~ 63 000 Da), each monomer of which binds a single biotin molecule. The noncovalent interaction between avidin and biotin is the strongest binding between a ligand and a protein known ($K_d = 10^{-15}M^{-1}$), resulting in important applications in immunology, bioanalytical chemistry (*5*), and targeted radiotherapy of cancer (*6*). These observations suggest that the effective linking of biotin to the radionuclides ^{99m}Tc and ^{186,188}Re would provide applications to imaging (*7*−*10*) and radiotherapy (*11*), respectively.

We have described the design of a family of bifunctional chelators from natural amino acids or synthetic analogues (single

* To whom correspondence should be addressed. Fax: (315) 443-4070. E-mail: jazubiet@syr.edu.
[†] Syracuse University.
[‡] McMaster University.
[#] Molecular Insight Pharmaceuticals.

10.1021/bc050297w CCC: $33.50 © 2006 American Chemical Society
Published on Web 04/14/2006

amino acid chelates, SAAC), which provide for robust coordination of the $\{M(CO)_3\}^{+1}$ (M = Tc, Re) core and a linker group for attachment to biomolecules (*12*). It was further demonstrated that the SAAC−Re complexes could be incorporated within peptide sequences using an automated peptide synthesizer (*13*). These successful applications of the technology have encouraged us to extend the general approach to other biomolecules.

A variety of biotin derivatives incorporating a tridentate chelator for binding of $\{M(CO)_3\}^{+1}$ (M = ^{99m}Tc and ^{186,188}Re) have been prepared. These M(I)-tricarbonyl cores were chosen because of their useful properties for the development of radiopharmaceuticals (*14*−*16*). For instance, the precursor complexes to the radioconjugates, *fac*-$[M(CO)_3(H_2O)_3]^{+1}$, may be readily prepared in a kit formulation. The aqua ligands of the precursor complexes are readily substituted by a variety of donor groups. Moreover, the *fac*-$\{M(CO)_3\}^{+1}$ core is chemically robust, low-spin d^6, providing a useful platform for further chemical development. The organometallic nature of the M(I)-tricarbonyl cores combined with the tridentate chelate dipicolylamine (dpa), yields a highly stable metal complex which is a prerequisite for effective in vivo radiotargeting (*17*).

In this contribution, we discuss the syntheses and characterizations of novel biotin-chelate derivatives and of their $\{^{99m}Tc(CO)_3\}^{+1}$ and $\{Re(CO)_3\}^{+1}$ complexes, their stability toward biotinadase, their affinity and specificity for avidin, the ^{99m}Tc-labeling and the stability of the ^{99m}Tc conjugates toward cysteine and histidine challenges and the biodistribution of the radiolabeled compounds in an avidin tumor model. In addition, molecular modeling studies have been undertaken to explore the derivatized biotin−avidin interactions and to assess the structural implications of the work presented in this paper.

EXPERIMENTAL PROCEDURES

General. All reactions were performed under an inert atmosphere of argon, unless otherwise noted. Solvents and chemicals obtained from commercial sources were analytical grade or better and used without further purification. D-Biotin was purchased from Aldrich Chemical Co. (Milwaukee, WI). Avidin was purchased from Pierce Biotechnology (Rockford, IL) and used as a solution diluted with PBS to pH 7.2 as noted in the literature reference (*18*). All experiments were performed in duplicate or triplicate to ensure reproducibility.

Spectroscopy. ^{13}C NMR and ^{19}F NMR spectra were obtained on a Bruker Avance system at 500 and 300 MHz, respectively. Proton chemical shifts are expressed as parts per million versus tetramethylsilane in deuterated solvent. ^{13}C NMR data were obtained on a Bruker Avance 75 MHz system versus a C of the deuterated solvent. IR spectra were obtained as solutions dissolved in methanol and run on a Perkin-Elmer Paragon 1000 FT-IR spectrophotometer. HRMS data were obtained on a 3-Tesla Fourier Transform mass spectrometer with an ESI source in positive ion mode. Mass spectrometry samples were prepared in MeOH/THF with added NaCl. Melting points were obtained on a Barnstead International apparatus and are uncorrected.

Chromatography. Silica gel chromatography was performed using silica gel purchased from EM Science (Gibbstown, NJ), silica gel 60 Geduran, 40−63 μm. Alumina chromatography was performed using alumina purchased from Aldrich (Milwaukee, WI). Alumina used was weakly acidic aluminum oxide, activated Brockmann I standard grade 150 mesh, 58 Å. In addition, basic aluminum oxide, activated, 150 mesh, 58 Å was used as noted in the experimental descriptions.

SYNTHETIC PROCEDURES

2,3,5,6-Tetrafluorophenyl Trifluoroacetate (1). Compound **1** was prepared by following literature procedure (*19*).

Dipicolyl Propyl Phthalimide (2). Bromopropyl phthalimide (10.4 g, 38.8 mmol) was added to dry THF (85 mL) in a 100-mL round-bottom flask. Tetrabutylammonium iodide (2.9 g, 7.8 mmol) was added, and the clear, light yellow solution was stirred for 5 min at room temperature. Dipicolylamine (7.0 mL, 38.8 mmol) was added, followed by Na_2CO_3 (16.4 g, 155.0 mmol). After the sample was refluxed for 10 min, the solution turned a dark orange color. The mixture was heated to reflux overnight to give a dark, red-brown suspension which was filtered and the residue evaporated to a dark, red-brown oil. The oil was passed through a silica gel column with $CHCl_3$/MeOH (40:1) to yield a clear, orange oil isolated in 60% yield after purification. ^{1}H NMR ($CDCl_3$, δ, 300 MHz): 1.93 (t, J = 7.2 Hz, 2H), 2.64 (m, 2H), 3.68−3.74 (m, 2H), 7.11 (t, J = 6.3 Hz, 2H), 7.53, (d, 7.8 Hz, 2H), 7.62 (t, J = 7.8 Hz, 2H), 7.60−7.70 (m, 2H), 7.82 (dd, J_A = 5.3 Hz, J_B = 3.2 Hz, 2H), 8.48 (d, J = 4.2 Hz, 2H); ^{13}C NMR ($CDCl_3$,? δ, 75 MHz): 26.2, 36.2, 51.5, 60.3, 76.8, 121.9, 123.1, 132.1, 133.9, 136.4, 148.9, 159.6, 168.3; HRMS calcd for $C_{23}H_{22}N_4O_2Na^+$ 409.1635, found 409.1640; IR (MeOH): 1396 and 1700 cm^{-1}.

***N,N*-Dipicolyl Propylamine (4).** Dipicolyl propyl phthalimide (**2**) (10.3 g, 27.1 mmol) was added to EtOH (39 mL) in a 100-mL round-bottom flask. Hydrazine monohydrate (1 mL) was added, resulting in a clear orange solution that was heated to reflux for 3 h, whereupon HCl (35 mL, 12 M) was added. The solution was allowed to reflux an additional 2 h. Addition of HCl (12 M) to the cooled solution provided a light yellow precipitate. After partitioning between deionized water and $CHCl_3$, the aqueous layer was made basic with 1 M NaOH and extracted with $CHCl_3$. The clear, light yellow chloroform layer was dried over magnesium sulfate, filtered, and evaporated to yield a clear, light yellow-orange oil. Column chromatography over silica gel with CH_2Cl_2/MeOH (95:5) provided the product as a clear, light yellow oil in 90% yield. ^{1}H NMR ($CDCl_3$, δ, 300 MHz): 2.04 (t, J = 6.5 Hz, 2H), 2.75 (t, J = 5.57 Hz, 2H), 3.80 (s, 4H), 7.1 (dd, J_A = 6.3 Hz, J_B = 5.4 Hz, 2H), 7.31 (d, 7.2 Hz, 2H), 7.62 (t, 7.8 Hz, 2H), 8.69 (d, J = 5.1 Hz, 2H); ^{13}C NMR ($CDCl_3$, δ, 75 MHz): 31.4, 40.6, 52.0, 60.7, 122.1, 123.0, 136.5, 149.2, 160.0; HRMS calcd for $C_{15}H_{20}N_4H^+$ 257.1761, found 257.1746.

Biotin TFP-ester (5). Biotin TFP-ester was prepared using a modified literature procedure (*20*).

Biotinylamido-propyl (Dipicolyl)amine (L6). Biotin TFP-ester (**5**) (1.2 g, 2.9 mmol) was dissolved in DMF (10 mL) in a 25-mL round-bottom flask. Dipicolyl propylamine (**4**) (0.5 mL, 2.9 mmol) and NEt_3 (0.5 mL, 3.2 mmol) were added to (**5**) at room temperature, and the resulting clear, light yellow solution was heated to 50 °C and stirred overnight. The solution was then evaporated to give a dark green, sticky oil. The oil was evaporated in vacuo at 70 °C to give a hard, glassy greenish-white powder, which was washed with THF at room temperature (4 × 10 mL) to yield a white residue in >95% yield, mp 135−136 °C. ^{1}H NMR (DMSO-d_6, δ, 300 MHz): 1.2−1.7 (m, 8H), 2.02 (t, J = 7.2 Hz, 2H), 2.4−2.6 (m, 2H), 2.55 (d, J = 12.6 Hz), 2.81 (dd, J_A = 12.3 Hz, J_B = 4.8 Hz, 1H), 3.02−3.06 (m, 3H), 3.72 (s, 4H), 4.13 (m, 1H), 4.31 (m, 1H), 6.40 (d, J = 21.0 Hz, 2H), 7.25 (dd, J_A = 5.9 Hz, J_B = 5.9 Hz, 2H), 7.50 (d, J = 7.8 Hz, 2H), 7.76 (dd, J_A = 6.9 Hz, J_B = 6.9 Hz, 2H), 8.48 (d, J = 4.5 Hz, 2H); ^{13}C NMR (DMSO-d_6, δ, 75 MHz): 25.3, 26.7, 28.0, 28.2, 35.2, 36.7, 51.4, 55.4, 59.2, 59.6, 61.0, 79.2, 122.1, 122.6, 136.5, 148.7, 159.4, 162.7, 171.9; HRMS calcd for $C_{25}H_{34}N_6O_2SNa^+$: 505.2356, found: 505.2359; IR (MeOH): 1647 and 1699 cm^{-1}.

Biotinamide (7) and Biotinamine (8). Biotinamide and biotinamine were prepared by the literature methods (*21a*−*c*).

N,N-(Dipicolyl)biotinamine (L9). Biotinamine (**8**) (203 mg, 0.9 mmol) was added to DCE (11 mL) to give a clear, light

yellow-brown solution. Pyridine carboxaldehyde (0.2 mL, 1.8 mmol) was added, and the solution was stirred at room temperature for 30 min. Addition of $Na(OAc)_3BH$ (954 mg, 4.5 mmol), followed by holding at reflux overnight, provided a dark brown solution. The reaction was quenched with saturated $NaHCO_3$ solution (20 mL) and extracted with CH_2Cl_2 (5 × 20 mL). The combined organic phases were evaporated and purified on a silica gel column with CH_2Cl_2 (95:5) to yield a fluffy, light yellow powder in 55% yield. ^{1}H NMR ($CDCl_3$, δ, 300 MHz): 1.2−1.7 (m, 10H); 2.5 (t, J = 7.5 Hz, 2H); 2.90 (dd, J_A = 13.2 Hz, J_B = 4.8 Hz, 1H); 3.00 (d, J = 13.2 Hz, 1H); 3.1−3.2 (m, 1H); 3.73 (s, 4H); 4.2−4.3 (m, 1H); 4.7−4.8 (m, 1H); 7.22 (t, J = 6.9 Hz, 2H); 7.56 (d, J = 7.8 Hz, 2H); 7.73 (t, J = 8.1 Hz, 2H); 8.37 (d, J = 4.8 Hz, 2H); ^{13}C NMR ($CDCl_3$, δ, 75 MHz): 27.8, 28.3, 29.6, 30.1, 37.9, 55.6, 56.9, 60.9, 61.1, 124.0, 125.0, 138.8, 149.5, 160.8, 161.6; HRMS calcd for $C_{22}H_{29}N_5OSNa^+$: 434.1985, found 434.2008; IR (MeOH): 1702 cm^{-1}.

Biotin-Boc-lysine-OH (10) and Biotin-Boc-lysine-TFP ester (11). Biotin-Boc lysine and biotin-Boc-lysine-TFP ester were prepared by a modified literature procedure (*21a*−*c*).

***N*,*N*-(Dipicolyl)biotinamide-Boc-lysine (L12).** Biotin-Boc-lysine-TFP ester (**11**) (597 mg, 0.96 mmol) was added to a 10 mL round-bottom flask with DMF (4 mL). To the clear, light yellow solution was added Na_2CO_3 (204 mg, 1.92 mmol), followed by (**4**) (250 mg, 0.96 mmol). The solution was then heated to 40 °C and stirred overnight. After heating overnight, the clear, light brown solution was evaporated to dryness. The light brown powder was then purified by column chromatography on neutral alumina with CH_2Cl_2:MeOH (90:10), 1% NEt_3 and the product isolated in 85% yield. ^{1}H NMR ($CDCl_3$, δ, 300 MHz): 1.3−1.7 (m, 21H); 2.13 (t, J = 7.2 Hz, 2H); 2.54 (t, J = 6.6 Hz, 2H); 2.62 (d, J = 12.6 Hz, 1H); 2.86 (dd J_A = 12.6 Hz, J_B = 4.8 Hz, 1H); 3.1−3.2 (m, 1H); 3.73 (s, 4H); 4.2−4.3 (m, 1H); 3.9 (m, 1H); 4.30 (dd, J_A = 7.8 Hz, J_B = 5.1 Hz, 1H); 7.23 (t, J = 5.4 Hz, 2H); 7.54 (d, J = 7.8 Hz, 2H); 7.74 (t, J = 7.8 Hz, 2H); 8.39 (d, J = 4.8 Hz, 1H); ^{13}C NMR ($CDCl_3$, δ, 75 MHz): 24.0, 27.0, 28.0, 29.0, 30.0, 31.0, 32.0, 34.0, 37.0, 39.0, 40.0, 41.0, 54.0, 56.0, 57.0, 61.0, 62.0, 64.0, 81.0, 124.0, 125.0, 139.0, 150.0, 158.0, 161.0, 167.0, 175.0, 176.0; HRMS calcd for $C_{36}H_{54}N_8O_5SNa^+$: 733.3830, found 733.3818.

Biotinol (13). Biotinol was prepared using a reported procedure (*21a*,*c*).

[Re(CO)$_3$(L6)]Br (ReL6). The clear colorless solution obtained by dissolving **L6** (68 mg, 0.16 mmol) in CH_2Cl_2 (1 mL) was placed in a 10-mL round-bottom flask. $[NEt_4]_2[Re(CO)_3Br_3]$ (123 mg, 0.16 mmol) was added at room temperature. The resulting white slurry was heated to reflux for 3 h, then stirred at room-temperature overnight. The clear light yellow solution, mixed with a small amount of white precipitate, was evaporated to dryness and purified by chromatography with CH_2Cl_2/MeOH (95:5) over acidic alumina, giving the product in quantitative yield, mp: 70−71 °C. ^{1}H NMR ($CDCl_3$, δ, 300 MHz): 1.4−1.9 (m, 6H), 2.2−2.5 (m, 4H), 2.75 (d, J = 12 Hz, 1H), 2.88 (dd, J_A = 12 Hz, J_B = 4.5 Hz, 1H), 3.1−3.3 (m, 2H), 3.51 (m, 1H), 3.7−3.8 (m, 2H), 4.30−4.34 (m, 1H), 4.46−4.53 (m, 1H), 4.75 (dd, J_A = 18.9 Hz, J_B = 18.9 Hz, 2H), 5.37 (dd, J_A = 18.0 Hz, J_B = 12.0 Hz, 2H), 7.29−7.33 (m, 2H), 7.91 (dd, J_A = 4.4 Hz, J_B = 4.4 Hz, 2H), 8.8 (m, 2H); ^{13}C NMR (DMSO-d_6, δ, 75 MHz): 26.4, 27.0, 29.6, 29.9, 37.0, 37.7, 41.3, 57.2, 61.6, 63.4, 68.9, 69.8, 124.9, 127.0, 141.8, 153.2, 162.1, 166.0, 176.4, 196.5, 197.4; HRMS calcd for (M-Br) $C_{28}H_{34}BrN_6O_5ReS$: 753.1863, found: 753.1863; IR (MeOH): ν(C═O) of $\{Re(CO)_3\}^+$ unit: 1920 and 2028 cm^{-1}; ν(C═O) urea: 1691 cm^{-1}.

[Re(CO)$_3$(L9)]Br (ReL9). $[Re(CO)_3(H_2O)_3]Br$ was added to a clear, pale yellow solution of **L9** (35.0 mg, 0.08 mmol) in MeOH (3 mL) and the solution was heated to reflux overnight. A bright yellow precipitate of **ReL9** was obtained by slow evaporation of the solution in quantitative yield, mp: 202−204 °C. ^{1}H NMR (DMSO-d_6, δ, 300 MHz): 1.4−1.8 (m, 6 H), 1.8−2.0 (m, 2H), 2.67 (d, J = 12.9 Hz), 2.91 (dd, J_A = 12.6 Hz, J_B = 5.1 Hz), 3.3 (s, 4H), 3.8 (m, 2H), 4.30−4.34 (m, 1H), 4.46−4.53 (m, 1H), 7.30 (t, J = 6.1 Hz, 2H), 7.48 (d, J = 7.5 Hz), 7.8−7.9 (m, 2H), 8.80 (d, J = 5.1 Hz, 2H); ^{13}C NMR (DMSO-d, δ, 75 MHz): 26.3, 27.8, 29.8, 30.2, 41.2, 57.2, 61.9, 63.7, 69.0, 72.1, 124.9, 127.0, 141.8, 153.2, 162.4, 196.6, 197.4; HRMS calcd for (M-Br) $C_{25}H_{29}N_5O_4ReS^+$: 682.1492, found 682.1518; IR (MeOH): 1920 and 2028 cm^{-1}.

[Re(CO)$_3$(L12)]Br (ReL12). $[Re(CO)_3(H_2O)_3]Br$ (41 mg, 0.10 mmol) was added to a clear, pale yellow solution of **L12** (100 mg, 0.09 mmol) in MeOH (1 mL), and the solution was heated to reflux overnight. A pale yellow precipitate of **ReL12** was obtained by slow evaporation of the solution. The light yellow powder was then columned over weakly acidic alumina using CH_2Cl_2/MeOH (90:10) to yield a fine, fluffy light yellow powder quantitatively, mp: 191−192 °C. ^{1}H NMR (DMSO-d_6, δ, 300 MHz): 1.3−1.7 (m, 6 H), 2.13 (t, J = 7.2 Hz, 2H), 2.54 (t, J = 6.6 Hz, 2H), 2.64 (d, J = 12.6 Hz, 1H), 2.87 (dd, J_A = 12.6 Hz, J_B = 4.8 Hz, 1H), 3.1−3.2 (m, 1H), 3.25 (s, 4H), 4.24 (m, 1H), 4.43 (dd, J_A = 7.8 Hz, J_B = 5.1 Hz, 1H), 7.23 (t, J = 5.4 Hz, 2H), 7.54 (d, J = 7.8 Hz), 7.74 (t, J = 7.8 Hz, 2H), 8.40 (d, J = 4.8 Hz, 2H); ^{13}C NMR (CD_3OD, δ, 75 MHz): 24.5, 26.3, 27.0, 28.9, 29.6, 29.9, 30.2, 33.0, 36.9, 37.7, 40.1, 41.2, 56.7, 57.2, 61.7, 63.5, 68.0, 69.8, 80.5, 124.8, 127.1, 141.8, 153.3, 158.0, 162.3, 166.2, 176.0, 196.5, 197.3; HRMS calcd for $C_{39}H_{54}BrN_8O_8ReSH^+$: 981.3343, found 981.3369.

Technetium Chemistry. ^{99m}Tc is a γ-emitting radionuclide. Standard safety precautions were adhered to throughout the investigation.

Technetium-99m was obtained as $Na^{99m}TcO_4$ in saline, from a commercial ^{99}Mo/^{99m}Tc generator (Cardinal Health). Technetium-99m (^{99m}Tc) is a γ emitter (140 keV) with a half-life of 6 h. Complexes were characterized using HPLC (Varian Prostar 510; column: Vydac C18 (25 cm × 4.6 mm); gradient elution: 5−95%B from 3 to 21 min at 1 mL/min for 30 min; mobile phase: A = triethylammonium phosphate pH 2.5 and B = methanol; UV detector: Varian model 345 set at 254 nm; radioactivity detector: NaI(Tl) gamma detector, Bicron Friske Tech)

$[^{99m}Tc(CO)_3(H_2O)_3]^{+1}$ 22 was prepared using the following general procedure: 1.0 mL of $^{99m}TcO_4^-$ from a commercial generator (50−200 mCi) was added to commercially available Isolink kits (Mallinckrodt). The solution was heated in an oil bath at 100 °C for 30 min. The solution was then cooled for 5 min, vented, and 1 N HCl (150 μL) was added to neutralize the solution.

In a sealed vial, $[^{99m}Tc(CO)_3(H_2O)_3]^{+1}$ was mixed with the biotin derivative (**L6**, **L9,** and **L12**; 0.01 mg dissolved in 0.5 mL of methanol) and heated at 100 °C for 30 min. After the sample was cooled, the reaction mixture was analyzed by reverse phase-HPLC. The $[Tc(CO)_3(LX)]^{+1}$ complexes, **TcL6**, **TcL9**, and **TcL12a**, were then purified by HPLC as described above. The compound $[^{99m}Tc(CO)_3\{N,N$-(dipicolyl)biotinamido-lysine$)]^{+1}$ (**TcL12a**) was also prepared by heating $[^{99m}Tc(CO)_3\{N,N$-(dipicolyl)biotinamido-Boc-lysine$)]^{+1}$ (**TcL12**) in methanol in the presence of TFA at 100° C for an additional 30 min to effect the deprotection of the derivatized lysine.

^{99m}Tc Challenge Experiments. To test the stability of the metal complexes, the isolated ^{99m}Tc-biotin complexes (**TcL6**, **TcL9**, and **TcL12a**; 100 μL in 10% ethanol/saline) were incubated with 1 mL of 100 mM of cysteine and histidine in PBS pH 7.2 at 37 °C for 18 h. Aliquots of the incubation

mixtures were analyzed by HPLC to determine the degree of decomposition.

IN VITRO STUDIES

Biotinidase Resistance. Mouse blood (diluted 1:10 in PBS, pH 7.2) was used as a source of biotinidase to test the susceptibility of the ^{99m}Tc-biotin conjugates (**TcL6**, **TcL9**, and **TcL12a**). The HPLC isolated complexes were dried under N_2 and dissolved in 10% ethanol in saline. The HPLC-isolated ^{99m}Tc-complex (50 μL) was added to a vial containing 1 mL of diluted mouse plasma and incubated at 37 °C for 2 h. Biotinidase activity was quenched by adding 4-(hydroxymercuric)benzoic acid sodium salt in water (200 μL of 1 mg/mL solution). Subsequently, a molar excess of avidin (100 μL of 4.8 mg/8 mL water solution) was added and incubated at 37 °C for a further 30 min. The solutions were then filtered using a 30 kDa M. W. cutoff filter (Centricon YM-30). Each filter was washed three times with 1 mL of PBS pH 7.2 to ensure transfer from the membrane. The activity retained by the filter was assumed to be intact and avidin bound Tc-biotin complex. The degree of cleavage was determined as the percent radioactivity in the filtrate as compared to the total radioactivity, which was assayed using an automated gamma counter (LKB model 1282, Wallac Oy, Finland). A control for each complex was performed by adding the 4-(hydroxymercuric)benzoic acid sodium salt in water (200 μL of 1 mg/mL solution) to the mouse serum prior to addition of the Tc-biotin complex. In addition, each Tc-biotin complex was tested for binding to the filter membrane alone. Membranes were pretreated by exposure to a solution of lysine followed by washing with sterile water. Each ^{99m}Tc-biotin complex, **TcL6**, **TcL9**, and **TcL12a** was tested six times.

The filtrate was analyzed by HPLC to determine the presence of intact Tc-biotin complex. For **TcL6** and TcL9, the small amount of activity in the filtrate was shown to elute with a retention time consistent with the original complexes. For **TcL12a** > 80% of the activity eluted with retention times significantly different than the original complex.

Avidin Binding. Avidin binding was determined by incubating the HPLC-isolated ^{99m}Tc-complex (50 μL) with avidin (4.8 mg/ 8 mL water) for 30 min, followed by filtration through a 30 kDa MW cutoff filter (Centricon YM-30), and washing three times with 1 mL of PBS pH 7.2. Avidin binding was determined as the percent radioactivity retained on the filter as compared to the total radioactivity.

Protein Binding. To determine the degree of nonspecific protein binding of the complexes a 50 μL aliquot of HPLC-isolated ^{99m}Tc-complexes (in 10% ethanol in saline) were mixed with 1 mL of human serum albumin (10% in PBS pH = 7.2) and incubated for 2 h at 37 °C. The proteins were then precipitated using acetonitrile and separated using centrifugation. The protein pellet was washed twice with PBS. The pellet and washes were counted using a gamma counter and the percent protein binding was calculated as percent activity in the pellet compared to the total activity.

Biotin Competitive Binding Assay. To determine the specific avidin binding of the Tc-biotin complexes, we initially mixed radiolabeled biotin complexes with cold biotin at varying concentrations and then incubated the biotin solutions with fixed amounts of avidin. An aliquot of the HPLC-isolated ^{99m}Tc-complexes (2 μL) was added to varying concentrations of biotin in water (0, 4.7, 9.4, 36.4, 80.5, 133.3, 200 μM). A 2 μL aliquot of the Tc-biotin complex/cold biotin solutions was added to an aqueous solution of avidin (250 μL; 1×10^{-5} M). This allowed for a range in stoichiometry from 0.1:1 to 40:1. The solutions were incubated at 37 °C for 30 min, then filtered using a 30 kDa MW cutoff filter (Centricon YM-30). The filters were washed twice with 2 mL of PBS pH 7.2. Binding was determined as the percent activity remaining on the filter as compared to the total activity (filter + filtrate). All three ^{99m}Tc-biotin complexes, **TcL6**, **TcL9** and **TcL12a**, were tested in duplicate. A control was performed using 2 μL of the ^{99m}Tc-complexes added to 500 μL of water. The samples of the control were treated to the same filtration, washing, and assaying techniques as the other samples. The control ensured there was no significant binding of the complexes to the regenerated cellulose of the Centricon YM-30 filters.

IN VIVO STUDIES

Biodistribution in the Avidin Bead Tumor Model. To assess the ability of these new biotin derivatives to target avidin in vivo, we have used an artificial tumor model of agarose beads coated with avidin injected intramuscularly, which has been previously described (*23*, *24*). Avidin coated beads (Sigma-Aldrich as avidin acrylic beads: 200−400 units/g of resin, with 1 unit binding 1.0 μg of biotin), were injected intramuscularly 24 h prior to injection of the ^{99m}Tc-labeled biotin derivatives in male rats (Sprague Dawley, at 180−200 g each, Charles River Laboratories, Burlington, MA). Groups of five rats were sacrificed at 2 and 24 h after intravenous injection of the ^{99m}Tc-labeled biotin derivatives. Tissue samples were taken including a sample of the "tumor" bearing muscle, weighed wet, and counted for radioactivity using an automated γ-counter (LKB Model 1282, Wallac Oy, Finland). An aliquot of the injected dose was also counted to allow for calculation of the percent of the injected dose in each tissue sample. The data were analyzed using Stat-View, running the application A Nova.

COMPUTATIONAL STUDIES

Molecular Mechanics/Molecular Dynamics. Molecular mechanics (MM) and molecular dynamics (MD) simulations (300 K) were performed with the program NAMD2 (*25a*). Version 22 of the CHARMM protein force field [CHARMM22] (*25b*) was used in all simulations for the avidin and was the basis for the generation of parameters of the biotin derivatives. The avidin−biotin complex starting geometry was taken from the PDB (*26*) crystal structure of its unique dimer, 1AVD (segment A), available in ref *27*. A previous study of the unbinding of biotin from avidin (*28*) saw the generation of a custom set of force field parameters and charge distributions (at the HF/6-31G* level of theory, see below) that were used in all biotin and biotin derivative MM/MD calculations. The avidin−biotin complex was studied by MM/MD simulations prior to the biotin-derivative calculations to determine what binding pocket changes occurred in the absence of crystal waters, crystallographic forces, etc., as a means of benchmarking all subsequent changes resulting from biotin modification. VMD (*29*), the graphical interface to NAMD, was used for visualization and image rendering.

The biotin−Re complexes were parametrized with the intent of reproducing molecular geometry to examine the effect of steric bulk on the binding pocket. Consequently, these biotin−Re force field parameters are an amalgam of standard CHARMM22 parameters and those generated from previous parametrization studies of transition metal complexes (*30*) based on the requirement of accounting for all of the bond, angle, and dihedral angle parameters needed to describe their molecular geometries. The molecular geometries and charge distributions of the biotin-Re pendant groups were calculated at the Restricted Hartree−Fock (RHF) level of theory with the PC-GAMESS version (*31*) of the GAMESS−US quantum chemistry package (*32*). The 6-31G* basis set (*33*) was used for all main group atoms, while the Re coordination center was treated with the

Scheme 1

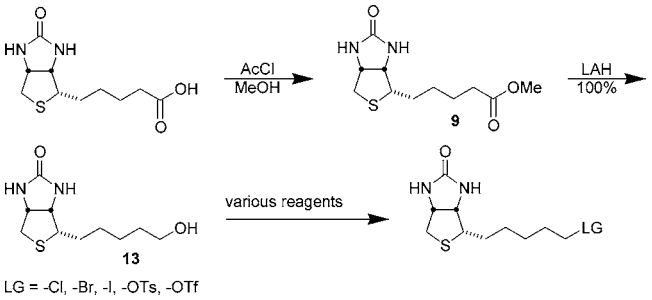

SBKJC effective core potential (*34*). Full details of the computational studies are provided in the Supporting Information.

RESULTS AND DISCUSSION

Syntheses and Characterization. The literature detailing strategies for the derivatization of biotin is extensive (*35*−*39a*−*g*). A common procedure exploits reduction of the carboxylate function of biotin to the alcohol, followed by substitution with a variety of leaving groups, as illustrated in Scheme 1. However, attempts to displace the leaving groups with the potentially tridentate chelator dipicolylamine resulted in no reaction or decomposition, possibly due to the insolubility of the derivatives in common organic solvents.

Biotin was successfully derivatized using the reaction route outlined in Scheme 2. Biotin-TFP-ester (**5**) was treated with dipicolylpropylamine (**4**) to provide biotinylamide-propyl-(dipicolyl)amine (**L6**). Alternatively, treatment of **5** with ammonium hydroxide provided biotinamide (**7**), which was then reduced with LAH to give the biotinamine (**8**). Reductive amination of **15** with the appropriate aldehydes (*40*) provided *N*,*N*-(dipicolyl)biotinamine (**L9**), as shown in Scheme 3. Similarly, the reaction of biotin-Boc-lysine-OH (**10**), prepared by the addition of Boc-lysine to biotin-TPF ester (**5**), with tetrafluorophenol and EDC provided biotin-Boc-lysine-TPF ester (**11**), which upon addition of dipicolylpropylamine (**11**) gave *N*,*N*-(dipicolyl)biotinamido-Boc-lysine (**L12**), as shown in Scheme 4.

While a number of ^{99}Tc-biotin complexes have been described previously (*41*−*48*), the chemistry of the {M(CO)$_3$} core remains largely unexplored (*49*, *50*). The rhenium tricarboxyl complexes of **L6**, **L9**, and **L12** were prepared by reactions of the ligands with [NEt$_4$]$_2$[Re(CO)$_3$Br$_3$] (*51*) or [Re(H$_2$O)$_3$(CO)$_3$]-Br (*52a*,*b*) to give [Re(CO)$_3$(**L6**)]Br (**ReL6**), [Re(CO)$_3$(**L9**)]Br (**ReL9**), [Re(CO)$_3$(**L12**)]Br (**ReL12**), respectively. It is noteworthy that the use of [Re(H$_2$O)$_3$(CO)$_3$]Br provides a much improved synthetic route as [NEt$_4$]$^{+1}$ containing byproducts are avoided, consequently obviating extensive purification procedures. The complexes were characterized by ^{1}H and ^{13}C NMR, IR, HMQC and by high-resolution mass spectrometry. A comparison of the ^{1}H NMR spectra of **ReL6**, **ReL9**, and **ReL12** with those for the biotin-chelates **L6**, **L9**, and **L12** shows that the chemical shift of the protons associated with the chelate are influenced strongly by the Re(I) core. Similarly, the ^{13}C NMR spectra of complexes **ReL6**, **ReL9**, and **ReL12** exhibited two additional peaks downfield in the 195−198 ppm region in a 2:1 ratio, assigned to the carbon atoms of the carbonyl ligands, a pattern reflecting the local symmetry of the complexes. The remaining carbonyl groups of the biotin-chelate showed no major changes from the free ligand to the complexes. Thus, the biotin ring carbonyl is observed in the 163−166 ppm region for **L6**, **L9**, and **L12** and in the range 162−167 ppm for **ReL6**, **ReL9,** and **ReL12**. The complex **ReL6** and the ligand **L6** exhibit

Scheme 2

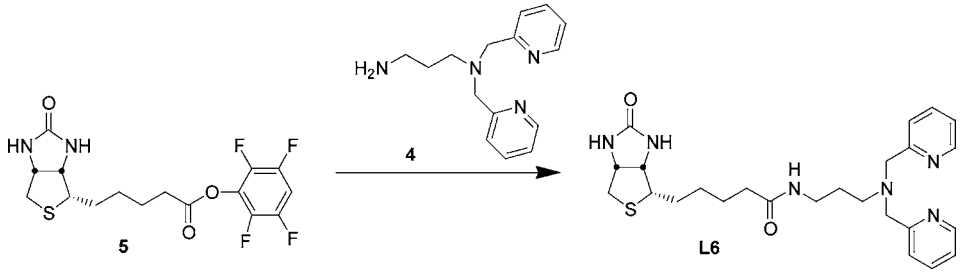

Scheme 3

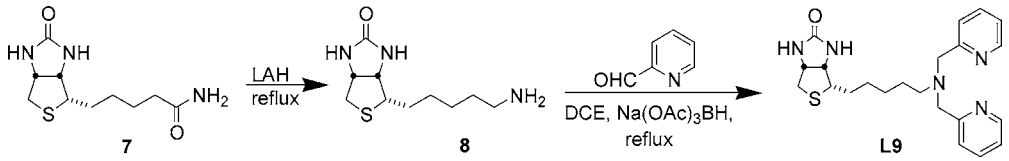

Scheme 4

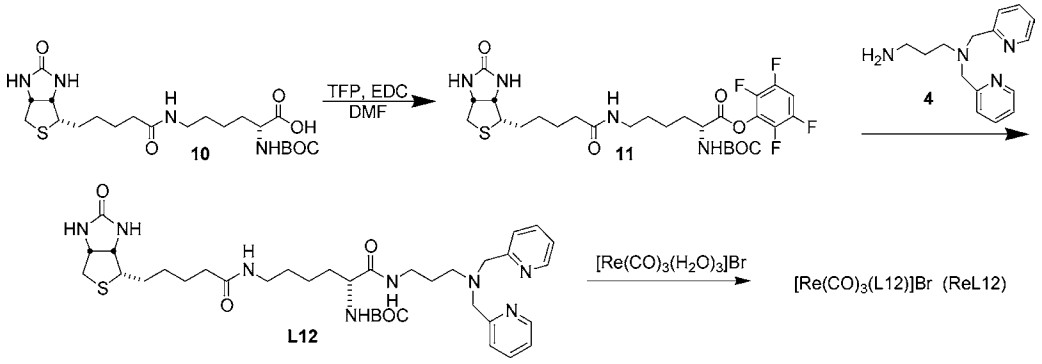

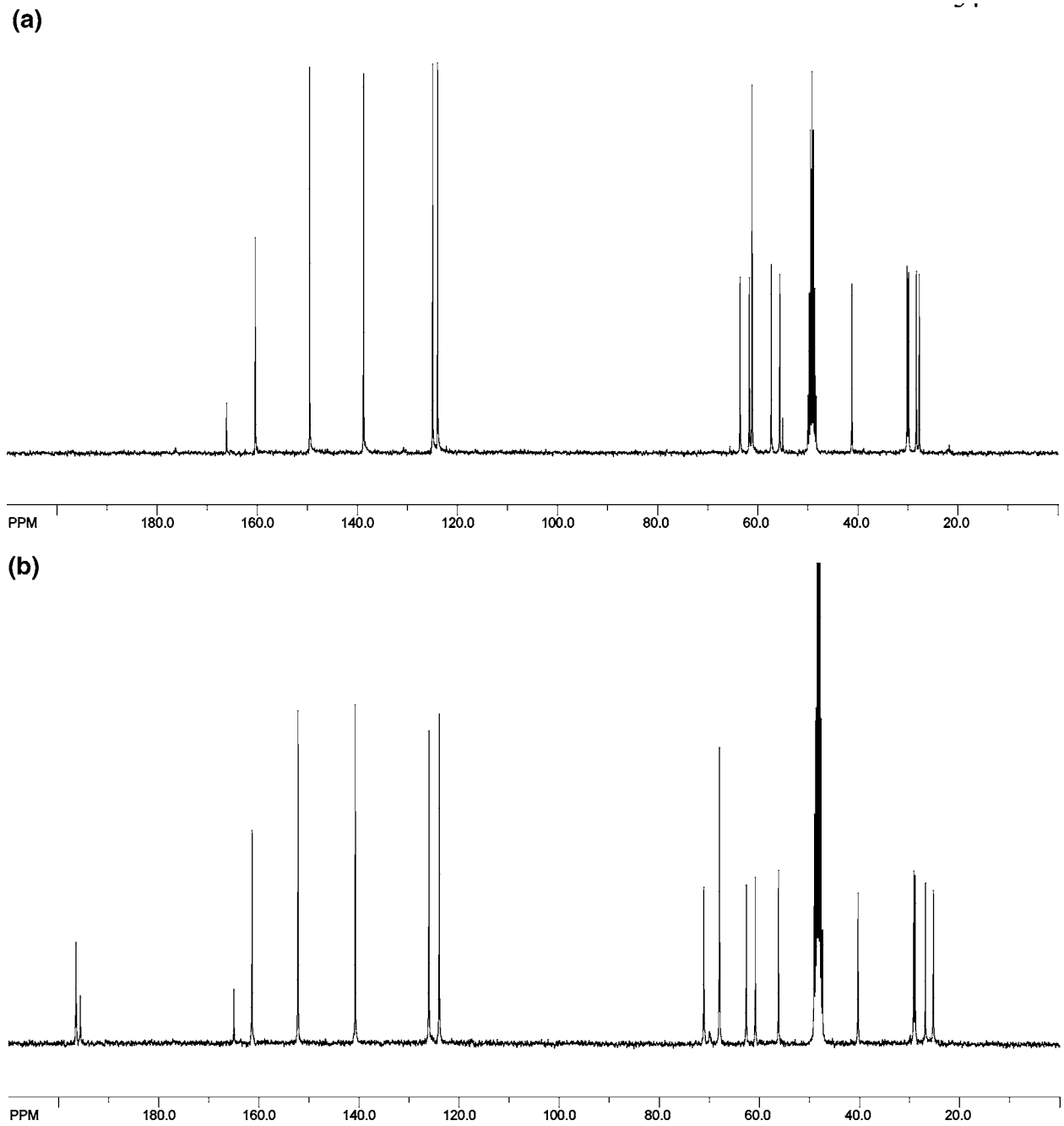

Figure 1. The ^{13}C NMR spectra of (a) **L9** and (b) **ReL9**.

cis/trans isomers associated with the amide carbonyl at 177 and 171.5 ppm, respectively. As shown in Figure 1, for **L9** and **ReL9**, only the carbon atoms in close proximity to the Re center exhibited significant shifts. The high-resolution mass spectra of the complexes, obtained in MeOH/THF were also consistent with the proposed structures.

The $[^{99m}Tc(CO)_3(H_2O)_3]^{+1}$ was mixed with the appropriate biotin derivatives **L6**, **L9**, and **L12** (0.01 mg) in 0.5 mL of methanol. The sealed vial was heated at 100 °C for an additional 30 min. After cooling of the sample, the reaction was checked for purity via HPLC, and methanol was used to elute the products. Purity, analyzed via C18 HPLC, showed >95% radiochemical purity. The radiochemical yields for all the derivatives was > 85%. The Tc-99m labeling was achievable using as low as 2 μg/mL. The ^{99m}Tc-complexes were completely stable in the presence of excess cysteine and histidine at elevated temperature over 18 h. An example of the labeling stability is depicted in Figure 2a,b, which demonstrates the HPLC purified complex **TcL9** pre- and postincubation at 37 °C with 1 mL of mouse plasma for 18 h, respectively.

IN VITRO RESULTS

Biotinidase Resistance of the ^{99m}Tc Complexes. One of several important criteria for successful design of radiolabeled biotin compounds as pretargeting agents in the treatment of cancer (*53a*−*c*) or as radioimaging agents (*54a*,*b*) is the stability of the biotin derivatives toward the enzyme biotinidase, as well as the affinity and specificity biotin displays for avidin.

Biotinidase is an enzyme present in both serum and tissues of animals in nanomolar concentrations (*55*), which is believed to be responsible for cleavage of the biotin amide bond of biocytin to release biotin for recycling in the system after peptidase degradation of biotin containing carboxylase enzymes (*56*). Previous investigations of the biotinidase activity toward amide bonds have revealed that the enzyme is not specific for

biocytin but readily cleaves biotin amide bonds present in other compounds as well (*18*).

We have studied the effect of biotinidase on three novel biotin $\{^{99m}Tc(CO)_3\}^{+1}$ complexes, **TcL6**, **TcL9**, and **TcL12a**. The complex **TcL6**, a biotin propyl amide complex, would potentially be susceptible to biotinidase activity due to the presence of the amide moiety but retain avidin binding affinity and specificity through the retention of the carboxyl group of the amide bond (*47*). The complex **TcL9** was prepared as the corresponding tertiary amine derivative, which would not be expected to undergo cleavage by biotinidase due to the lack of an amide bond and the robust nature of the tertiary amine toward biotinidase. The third complex investigated, **TcL12a**, as the lysine amide derivative, was expected to behave in a fashion similar to **TcL6**, exhibiting high avidin affinity and specificity as well but susceptible to biotinidase cleavage. The biotin derivatives were radiolabeled to a high degree of radiochemical purity (>95%) allowing for the evaluation of biotinidase cleavage of the biotin ^{99m}Tc complexes radiometrically.

The radiometric assay is based on the hydrolysis of the biotin amide bond, which results in separation of the biotin from the $\{^{99m}Tc(CO)_3(chelate)\}^{+1}$ fragment. The measurement of the degree of biotinidase cleavage was performed as described in the literature (*18*). The measurements were performed using Centricon 30K cutoff regenerated cellulose filters. The presence of radioactivity on the filter (still avidin bound) or in the filtrate (cleavage occurred) determined the percent of biotinidase cleavage. Consequently, lack of avidin binding radioactivity correlated with biotinadase cleavage.

The complex, **TcL6**, was stable to biotinidase activity, with approximately 82% of the activity associated with avidin binding after exposure to biotinidase. We have assumed that the radioactivity retained on the filter is associated with the avidin and therefore is the intact **TcL6** complex. HPLC analysis of the filtrate also demonstrated intact **TcL6**. Steric hindrance has been implicated as a factor in inhibiting biotinidase cleavage when the biotin derivatives are substituted at the position α to the carbonyl functionality, with sterically bulky substituents providing the greatest amount of biotinidase resistance, and less sterically demanding substituents providing little or no protection from biotinidase degradation (*37*). Presumably, the steric bulk of the $\{^{99m}Tc(CO)_3\}^{+1}$ core in **TcL6** prevents ready access to the biotinidase enzyme responsible for amide bond cleavage, in an effect analogous to α-substitution.

Complex **TcL9**, as predicted, was entirely biotinidase resistant (>90%), since **TcL9** does not possess an amide bond susceptible to cleavage. Consequently, **TcL9** provided a convenient internal control for the absence of biotinidase activity. Complex **TcL12a**, the biocytin analogue, was susceptible to biotinidase cleavage, with >80% cleaved. The side chain of the lysine, in contrast to **TcL6**, may provide a degree of conformational flexibility allowing greater access to the biotin amide bond, and resulting in more facile cleavage by biotinidase than that observed for **TcL6**.

Avidin Binding. The ^{99m}Tc-biotin complexes **TcL6**, **TcL9**, and **TcL12a** were also evaluated for affinity and specificity for avidin binding, as well as nonspecific binding to human serum albumin. Determination of the affinity was performed using a modification of a previously described method. The radiolabeled compounds were incubated in the presence of avidin for a period of 30 min, followed by centrifugation through a 30 K filter, and washing with 1 mL of PBS pH 7.2 three times. The radioactivity of both the filter (potentially avidin bound) and filtrate (nonbound) fractions were then counted. The percent binding of **TcL6**, **TcL9** and **TcL12a** were 92% ± 2, 93% ± 2, and 100% ± 2, respectively.

Competitive Binding Assay. Determination of the competitive binding of the radiolabeled biotin derivatives is crucial in evaluating efficacy of the complexes as potential therapeutic and diagnostic agents. Since D-biotin is present in the human body naturally, the competitive binding ratios of the radiolabeled ^{99m}Tc-biotin complexes in the presence of D-biotin were measured.

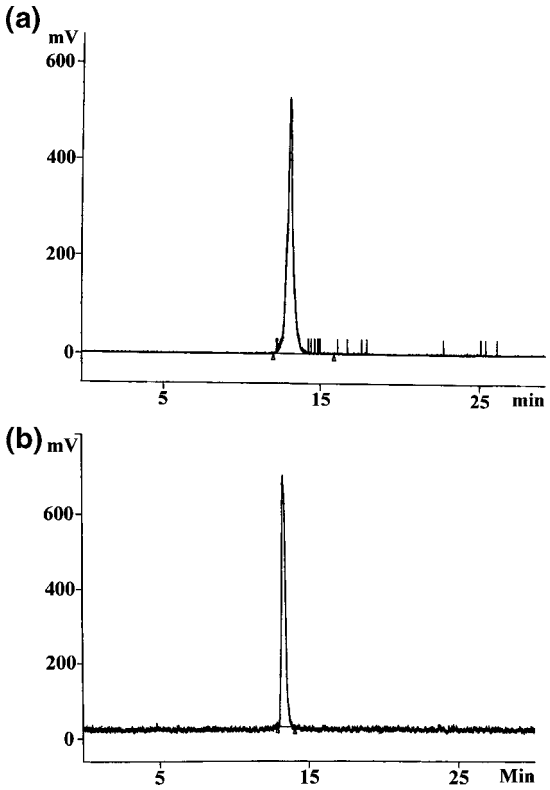

Figure 2. Radiochromatograms of HPLC purified **TcL9** (a) pre- and (b) postincubation at 37 °C with 1 mL of mouse plasma for 18 h.

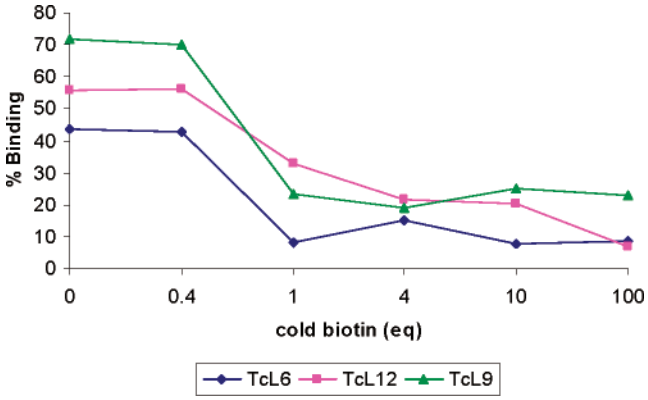

Figure 3. The saturation behavior of **TcL6**, **TcL9**, and **TcL12a**, expressed as percent binding of the radiolabeled compound as a function of the equivalents of "cold" biotin concentration.

Equivalent affinities of radiolabeled biotin and D-biotin for avidin would result in 50% molar activity bound to avidin at the saturation point of avidin, which is four molar equivalents, since avidin is capable of binding four biotin molecules. The saturation behavior of all three radiolabeled ^{99m}Tc-biotin complexes, shown in Figure 3, is similar in terms of profile, with **TcL6**, the biotin DPA amide complex, being displaced by D-biotin when between one and four equivalents of D-biotin are added. Compound **TcL9**, the biotin tertiary amine, reaches the dissociation point at approximately four equivalents of added D-biotin, and **TcL12a**, the biotin lysine derivative, achieves the saturation point between four and 10 equivalents of added D-biotin. Both **TcL6** and **TcL12a**, the biotin compounds

Table 1. Comparative Biodistribution of the ^{99m}Tc−Biotin Derivatives: %ID/g[a]

	2 h			24 h		
organ/tissue	TcL9	TcL12a	TcL6	TcL9	TcL12a	TcL6
blood	0.510 ± 0.356	0.070 ± 0.006	0.034 ± 0.003	0.007 ± 0.003	0.064 ± 0.001	0.008 ± 0.001
heart	0.024 ± 0.001	0.088 ± 0.007	0.034 ± 0.002	0.014 ± 0.002	0.065 ± 0.003	0.013 ± 0.001
lungs	0.065 ± 0.005	0.102 ± 0.008	0.068 ± 0.006	0.031 ± 0.010	0.066 ± 0.002	0.023 ± 0.006
liver	0.385 ± 0.04	1.283 ± 0.100	0.765 ± 0.054	0.085 ± 0.006	0.881 ± 0.121	0.209 ± 0.026
spleen	0.047 ± 0.001	0.091 ± 0.005	0.052 ± 0.002	0.029 ± 0.004	0.056 ± 0.004	0.015 ± 0.001
kidneys	0.432 ± 0.028	2.813 ± 0.484	0.998 ± 0.109	0.163 ± 0.012	1.430 ± 0.509	0.191 ± 0.016
adrenals	0.027 ± 0.007	0.056 ± 0.014	0.034 ± 0.011	0.014 ± 0.003	0.032 ± 0.007	0.012 ± 0.002
stomach	0.066 ± 0.020	0.247 ± 0.108	0.166 ± 0.006	2.957 ± 0.736	0.442 ± 0.284	0.037 ± 0.026
GI	0.837 ± 0.180	2.493 ± 0.784	1.184 ± 0.307	1.105 ± 0.281	0.168 ± 0.083	0.068 ± 0.021
testes	0.014 ± 0.001	0.023 ± 0.002	0.021 ± 0.001	0.007 ± 0.001	0.014 ± 0.001	0.006 ± 0.001
SK muscle	0.014 ± 0.002	0.046 ± 0.007	0.022 ± 0.005	0.009 ± 0.001	0.051 ± 0.005	0.007 ± 0.001
bone	0.042 ± 0.004	0.308 ± 0.015	0.023 ± 0.003	0.008 ± 0.002	0.041 ± 0.001	0.009 ± 0.001
brain	0.005 ± 0.0002	0.009 ± 0.001	0.005 ± 0.0004	0.003 ± 0.001	0.007 ± 0.003	0.004 ± 0.0004
infected muscle	0.032 ± 0.004	0.055 ± 0.004	0.107 ± 0.019	0.015 ± 0.001	0.055 ± 0.004	0.051 ± 0.004
infected/normal muscle	2.3	1.2	4.9	1.7	1.1	7.3

[a] Mean ± standard error of the mean from $n = 5$ rats per time point.

containing the carboxyl functional group, maintain the highest binding to avidin, with the tertiary amine complex **TcL9** exhibiting the greatest diminution of competitive avidin binding in the presence of D-biotin.

IN VIVO RESULTS

Biotin Biodistribution in the Avidin Bead Model for Tumor Localization. The avidin bead model has been utilized previously (*23*, *24*) as an effective tumor model to simulate biotin binding to pretargeted avidin in vivo. The model allowed us to explore the affinity and specificity of the three new ^{99m}Tc-biotin conjugates for avidin in vivo as well as allowing determination of the biodistribution the ^{99m}Tc-complexes. Each of the three ^{99m}Tc-biotin derivatives afforded good labeling yields (>95%) and were easily purified via HPLC. Table 1 shows the results of the biodistribution experiments obtained at 2 and 24 h postinjection of the ^{99m}Tc-radiolabeled biotin derivatives **TcL6**, **TcL9**, and **TcL12a**.

For compound **TcL6**, the tissue with the highest concentration at 2 h p.i. was the GI tract followed by the kidneys > liver > stomach > lungs > heart = blood. At 24 h, the highest concentration was found in the liver followed by kidneys > GI tract > stomach > spleen. The activity in the avidin "tumor" was the highest of the three complexes studied. Radioactive concentrations in this tissue were approximately five times that of normal muscle (4.9:1). At 24 h, the concentration had dropped by approximately 50%, but the ratios improved to 7.3:1 against normal muscle.

For compound **TcL9**, the tissues with the highest concentration at 2 h p.i. were the GI tract followed by the blood > kidneys > liver > bone > stomach = lungs. At 24 h p.i. the activity in the stomach had increased and was the highest, followed by the GI tract > kidneys > liver. The activity in the avidin "tumor" was approximately twice that of the normal muscle at 2 h (2.3:1), but activity washed out in both tissues resulting in a slightly lower ratio at 24 h (1.7:1).

For compound **TcL12a**, the highest concentration at 2 h postinjection was found in the kidney followed by the GI tract > liver > stomach > lungs. At 24 h p.i., the tissue with the highest concentration was the kidneys followed by the liver > stomach > GI tract. The activity in the avidin "tumor" was similar to normal muscle (1.2:1) and the concentration remained virtually unchanged at 24 h (1.1:1).

COMPUTATIONAL RESULTS

Molecular Modeling. Molecular mechanics/molecular dynamics (MM/MD) calculations were performed to consider the binding of the Re/Tc−biotin complexes with avidin. The MM/MD calculations began from the crystallographic coordinates of the avidin−biotin tetrameric complex (*27*). The modeling of these Re/Tc complexes from the coordinates of the avidin/unsubstituted biotin crystal structure then assumes that binding for these complexes occurs in a manner consistent with the unsubstituted biotin (i.e., retention of the hydrogen-bonding framework between the biotin ureido and thiophene rings and the avidin inner β-barrel pocket). Accommodation of biotin derivatives with avidin structural changes (*57*), as well as the binding of biotin itself to avidin (*27*), has been considered previously by experimental and computational methods. With the assumption that the binding of the Re/Tc−biotin derivatives within the avidin β-barrel is similar to that observed in the crystal structure for the unsubstituted biotin, the MM/MD calculations provide a means for examining structural changes to the binding pocket expected to occur due to the steric bulk of the Re/Tc complexes. Further, these MM/MD results can be used as predictive tools for the identification of structural modifications to the Re/Tc−biotin derivatives that might improve the binding properties of these molecules.

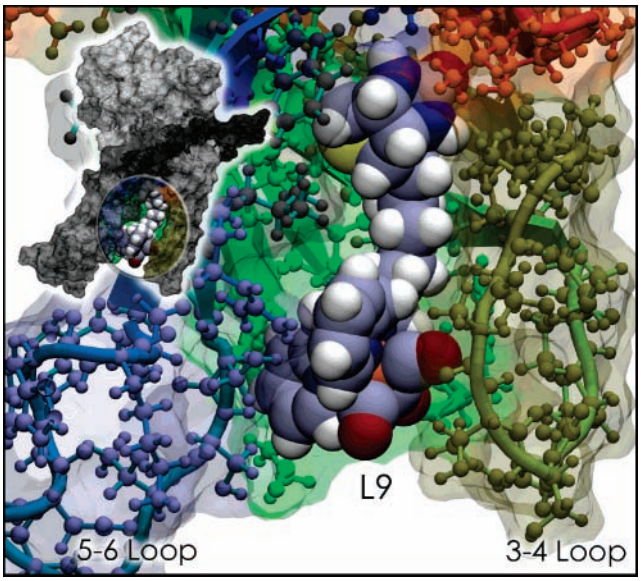

Figure 4. The biotin−Re ligand bound within the avidin−biotin binding pocket. The entire avidin−biotin−Re complex is shown (inset) with the binding pocket highlighted. The biotin−Re ligand is shown in van der Waals representation. The 3−4 loop is at bottom-right (gold).

Figure 4 shows a MM minimum energy structure of the biotin−Re complex **L9** bound to avidin. Significant differences between this structure and the avidin/biotin structure are, as

expected, localized to the 3−4 (Figure 4, gold) and 5−6 (Figure 4, blue) avidin loops, the sites of steric interactions with the Re coordination complex. The specific flex of the 3−4 loop is familiar to theoretical and experimental studies, as its motion is the only major structural change to occur upon biomolecule binding to biotin (*25*) and, from theoretical studies, the only significant motion required in the modeling of the unbinding of biotin from avidin (*28*). The ureido/thiophene biotin binding pocket within the avidin β-barrel is nearly identical in arrangement to that of the unsubstituted biotin/avidin complex. Both the **L9**/avidin and biotin/avidin MM structures differ from the crystal structure slightly for reasons that can be attributed to packing interactions between avidin proteins in the tetrameric crystal complex. With the retention of the ureido/thiophene binding pocket within the avidin β-barrel, the Re tail of derivative **L9** does not clear the external binding pocket of the avidin. The calculations indicate that the hydrocarbon tail of **L9** is long enough to position the Re complex within the 3−4/5−6 loop pocket and beyond the more constrained interior of the avidin β-barrel. A complete description of the binding interactions between biotin and avidin, the differences between the crystal and MM/MD avidin/biotin structures, and an analysis of the role of steric bulk on the change in avidin structure for other functionalized biotin molecules are provided in Supporting Information.

CONCLUSIONS

By exploiting the tridentate chelate concept of the single amino acid chelate approach (SAAC), we prepared a series of biotin derivatives capable of forming robust complexes with both technetium and rhenium. The ligands **L6**, **L9**, and **L12** (biotinylamidepropyl-*N*,*N*-(dipicolyl)amine, *N*,*N*-(dipicolyl)biotinamine, and *N*,*N*-(dipicolyl)biotinamido-Boc-lysine, respectively) were obtained by appropriate modification of the free carboxylic group of biotin. The Re complexes $[Re(CO)_3(\mathbf{L6})]Br$, $[Re(CO)_3(\mathbf{L9})]Br$, and $[Re(CO)_3(\mathbf{L12})]Br$ were prepared from $[NEt_4]_2[Re(CO)_3Br_3]$ and characterized by ^1H and ^{13}C NMR and mass spectroscopy. The corresponding $\{^{99m}Tc(CO)_3\}^{+1}$ core complexes **TcL6**, **TcL9**, and **TcL12a** were also prepared. The ^{99m}Tc complexes were stable in cysteine and histidine challenges. **TcL6** and **TcL9** were resistant to biotinidase activity, while the biocytin analogue **TcL12a** was susceptible to cleavage. The complexes **TcL6** and **TcL12a** bound readily to avidin, while **TcL9** showed minimal specificity in avidin binding. Molecular mechanics/molecular dynamics simulations are consistent with these results, since deformation of the surface domain can occur so as to accommodate the metal complexes of the biotin derivatives with negligible changes to the inner β-barrel, the most significant domain for binding biotin and its derivatives. Using an in vivo avidin tumor model, **TcL6** demonstrated the highest uptake followed by **TcL9** and **TcL12a**, respectively. Consequently, the ligand **L6** represents an example of a SAAC analogue of biotin showing potential as a radiolabeled targeting vector of biotin that forms robust radiochemical complexes with ^{99m}Tc.

ACKNOWLEDGMENT

This work was supported in part by a grant from the National Institutes of Health, National Institutes of Allergy and Infectious Diseases, STTR 1R41 A10044080-01. Mr. Eric Zelman and Apple Computers are thanked for their provision of resources for the theoretical work.

Supporting Information Available: The full details of the computational studies, together with an extensive discussion of the results. This material is available free of charge via the Internet at http://pubs.acs.org.

LITERATURE CITED

(1) Attwood P. V., and Wallace J. C. (2002) Chemical and catalytic mechanisms of carboxyl transfer reactions in biotin-dependent enzymes, *Acc. Chem. Res. 35*, 113−120.
(2) McCormick, D. B. (2001) Bioorganic mechanisms important to coenzyme functions, *Clinical Nutrition in Health and Disease 3* (Handbook of Vitamins, 3rd ed.) pp 199−212, Marcel Dekker, Inc., New York.
(3) Pacheco-Alvarez, D., Solorzano-Vargas, R. S., and Del Rio, A. L. (2002) Biotin in metabolism and its relationship to human disease. *Arch. Med. Res. 33*, 439−447.
(4) McMahon, R. J. (2002) Biotin in metabolism and molecular biology. *Annu. Rev. Nutr. 22*, 221−239.
(5) Wilchek, M., and Bayer, E. A., Eds. (1990) *Methods in Enzymology 184*: *Avidin−Biotin Technology*, Elsevier, Amsterdam.
(6) Boerman, O. C, van Schaijk, F. G, Oyen, W. J G., and Corstens, F. H M (2003) Pretargeted radioimmunotherapy of cancer: progress step by step. *J. Nucl. Med. 44*, 400−11.
(7) Hom, R. K., and Katzenellenbogen, J. A. (1997) Technetium-99m-labeled receptor-specific small-molecule radiopharmaceuticals: recent developments and encouraging results. *Nucl. Med. Biol. 24*, 485−498.
(8) Liu, S., and Edwards, D. S. (2002) Fundamentals of receptor-based diagnostic metalloradiopharmaceuticals. *Top. Curr. Chem. 222 (Contrast Agents II)*, 259−278.
(9) Schibli, R., and Schubiger, P. A. (2002) Current use and future potential of organometallic radiopharmaceuticals. *Eur. J. Nucl. Med. Mol. Imaging 29*, 1529−1542.
(10) Dilworth, J. R., and Parrott, S. J. (1998) The biomedical chemistry of technetium and rhenium. *Chem. Soc. Rev. 27*, 43−55.
(11) Blower, P. J., and Prakash, S. (1999) The chemistry of rhenium in nuclear medicine. *Persp. Bioinorg. Chem. 4*, 91−143.
(12) Banerjee, S. R., Levadala, M. K., Lazarova, N., Wei, L., Valliant, J. F., Stephenson, K. A., Babich, J. W., Maresca, K. P., and Zubieta, J. (2002) Bifunctional Single Amino Acid Chelates for Labeling of Biomolecules with the $\{Tc(CO)_3\}^+$ and $\{Re(CO)_3\}^+$ Cores. Crystal and Molecular Structures of $[ReBr(CO)_3(H_2NCH_2C_5H_4N)]$, $[Re(CO)_3\{(C_5H_4NCH_2)_2NH\}]Br$, $[Re(CO)_3\{(C_5H_4NCH_2)_2NCH_2CO_2H\}]Br$, $[Re(CO)_3\{X(Y)NCH_2CO_2CH_2CH_3\}]Br$ (X = Y = 2-pyridylmethyl; X = 2-pyridylmethyl, Y = 2-(1-methylimidazolyl)methyl; X = Y = 2-(1-methylimidazolyl)methyl), $[ReBr(CO)_3\{(C_5H_4NCH_2)NH(CH_2C_4H_3S)\}]$, and $[Re(CO)_3\{(C_5H_4NCH_2)N(CH_2C_4H_3S)(CH_2CO_2)\}]$. *Inorg. Chem. 41*, 6417−6425.
(13) Stephenson, K. A., Zubieta, J., Banerjee, S. R., Levadala, M. K., Taggart, L., Ryan, L., McFarlane, N., Boreham, D. R., Maresca, K. P., Babich, J. W., and Valliant, J. F. (2004) A new strategy for the preparation of peptide-targeted radiopharmaceuticals based on an Fmoc-lysine-derived single amino acid chelate (SAAC). Automated solid-phase synthesis, nmr characterization, and in vitro screening of fMLF(SAAC)G and fMLF[(SAAC-$Re(CO)_3)^+$]G. *Bioconjate Chem. 15*, 128−136.
(14) Mundwiler, S., Candreia, L., Haefliger, P., Ortner, K., and Alberto, R. (2004) Preparation of No−carrier-added technetium-99m complexes via metal-assisted cleavage from a solid phase. *Bioconjate Chem. 15*, 195−202.
(15) Wald, J., Alberto, R., Ortner, K., and Candreia, L. (2001) Aqueous one-pot synthesis of derivatized cyclopentadienyl-tricarbonyl complexes of ^{99m}Tc with an in situ CO source: Application to a serotonergic receptor ligand. *Angew. Chem., Int. Ed. 40*, 3062−3066.
(16) Alberto, R. (2004) *Technetiumin Comprehensive Coordination Chemistry II 5*, 127−270.
(17) Banerjee, S. R., Maresca, K. P., Francesconi, L., Valliant, J., Babich, J. W., and Zubieta, J. (2005) New directions in the coordination chemistry of (99m)Tc: a reflection on technetium core structures and a strategy for new chelate design. *Nucl. Med. Biol. 32(1)*: *1−20*.
(18) Wilbur, D. S., Hamlin, D. K., Chyan, M.-K., Kegley, B. B., and Pathare, P. M. (2001) Biotin reagents for antibody pretargeting. 5. Additional studies of biotin conjugate design to provide biotinidase stability. *Bioconjate Chem. 12*, 616−623.
(19) Gamper, H. B., Reed, M. W., Cox, T., and Virosco, J. S.; Adams, A. D.; Gall, A. A.; Scholler, J. K., and Meyer, R. B. (1993) Facile preparation of nuclease resistant 3′ modified oligodeoxynucleotides, *Nucleic Acids Res. 21*, 145−150.

(20) Wilbur, S., Hamlin, D. K., Vessella, R. L., Stray, J. E., Buhler, K. R., Stayton, P. S., Klumb, L. A., Pathare, P. M., and Weerawarna, S. A. (1996) Antibody fragments in tumor pretargeting. Evaluation of biotinylated Fab′ colocalization with recombinant streptavidin and avidin. *Bioconjate Chem. 7*, 689−702.

(21) (a) Wilbur, S., Chyan, M. K., Pathare, P. M., Hamlin, D. K., Frownfelter, M. B., and Kegley, B. B. (2000) Biotin reagents for antibody pretargeting. 4. Selection of biotin conjugates for in vivo application based on their dissociation rate from avidin and streptavidin. *Bioconjate Chem. 11*, 569−583. (b) Sundberg, S. A., Barrett, R. W., Pirrung, M., Lu, A. L., Kiangsoontra, B., and Holmes, C. P. (1995) Spatially-addressable immobilization of macromolecules on solid supports. *J. Am. Chem. Soc. 117*, 12050−12057. (c) Alves, A. M., Holland, D., and Edge, M. D. (1989) A chemical method of labeling oligodeoxyribonucleotides with biotin: A single step procedure using a solid-phase methodology. *Tetrahedron Lett. 30*, 3089−3092.

(22) Alberto, R., Ortner, K., Wheatley, N., Schibli, R., and Schubiger, A. P. (2001) Synthesis and properties of boronocarbonate: A convenient in situ CO source for the aqueous preparation of $[^{99m}Tc(OH_2)_3(CO)_3]^+$. *J. Am. Chem. Soc. 123*, 3135−3136.

(23) Virzi, F., Fritz, B., Rusckowski, M., Gionet, M., Misra, H., and Hnatowich, D. J. (1991) New indium-111 labeled biotin derivatives for improved immunotargeting. *Nucl. Med. Biol. 18*, 719−726.

(24) Rusckowski, M., Fogarasi, M., Fritz, B., and Hnatowich, D. (1997) Effect of endogenous biotin on the applications of streptavidin and biotin in mice. *Nucl. Med. Biol. 24*, 263−268.

(25) (a) Kalé, L., Skeel, R., Bhandarkar, M., Brunner, R., Gursoy, A., Krawety, N., Phillips, J., Shinozaki, A., Varadarajan, K., and Schulten, K. (1999) NAMD2: Greater scalability for parallel molecular dynamics. *J. Comput. Phys. 151*, 283−312. (b) Brooks, B. R., Bruccoleri, R. E., Olafson, B. D., States, D. J., Swaminathan, S. and Karplus, M., Charmm: A program for macromolecular energy, minimization, and dynamics calculations (1983) *J. Comp. Chem. 4*, 187−217.

(26) Berman, H. M., Westbrook, J., Feng, Z., Gilliland, G., Bhat, T. N., Weissig, H., Shindyalov, I. N., and Bourne, P. E. (2000) The protein data bank. *Nucl. Acids Res. 28*, 235−242.

(27) Pugliese, L., Coda, A., Malcovati, M., and Bolognesi, M. (1993) Three-dimensional structure of the tetragonal crystal form of egg-white avidin in its functional complex with biotin at 2.7 Å resolution. *J. Mol. Biol. 231*, 698−710.

(28) Izrailev, S., Stepaniants, S., Balsera, M., Oono, Y., and Schulten, K. (1997) Molecular dynamics study of unbinding of the avidin−biotin complex. *Biophys. J. 72*, 1568−1581.

(29) Humphrey, W., Dalke, A., and Schulten, K. (1996) VMD − Visual Molecular Dynamics, *J. Mol. Graphics 14*, 33−38.

(30) As the transition metal relevant to imaging agents, complexes containing Tc have received more attention and, subsequently, force field parametrization. The procedure for transition metal force field parameter generation is described in detail in Norrby, P.-O., and Brandt, P. (2001) Deriving force field parameters for coordination complexes. *Coord. Chem. Rev. 212*, 79−109. Specific force field parameters for Tc modified for the Re complexes were taken, in part, from Cundari, T. R., and Fu, W. (2000) Genetic algorithm optimization of a molecular mechanics force field for technetium. *Inorg. Chim. Acta 300−302*, 113−124.

(31) Granovsky, A. A. Available from http://classic.chem.msu.su/gran/gamess/index.html.

(32) Schmidt, M. W., Baldridge, K. K., Boatz, J. A., Elbert, S. T., Gordon, M. S., Jensen, J. H., Koseki, S., Matsunaga, N., Nguyen, K. A., Su, S., Windus, T. L., Dupuis, M., and Montgomery, J. A. (1993) General atomic and molecular electronic structure system, *J. Comput. Chem. 14*, 1347−1363.

(33) Hehre, W. J., Ditchfield, R., and Pople, J. A. (1972) Self-consistent molecular orbital methods. XII. Further extensions of Gaussian-type basis sets for use in molecular orbital studies of organic molecules, *J. Chem. Phys. 56*, 2257−2261.

(34) Stevens, W. J., Krauss, M., Basch, H., and Jasien, P. G. (1992) Relativistic compact effective potentials and efficient, shared-exponent basis sets for the third-, fourth-, and fifth-row atoms, *Can. J. Chem. 70*, 612−630.

(35) Wilbur, D. S., Hamlin, D. K., Chyan, M. K., Kegley, B. B., and Pathare, P. M. (2001) Biotin reagents for antibody pretargeting. 5. Additional studies of biotin conjugate design to provide biotinidase stability, *Bioconjugate Chem. 12*, 616−623.

(36) Wilbur, S. D., Hamlin, D. K., Chyan, M. K., Kegley, B., Quinn, J., and Vessella, R. L. (2004) Biotin reagents in antibody pretargeting. 6. Synthesis and in vivo evaluation of astatinated and radioiodinated aryl- and nido-carboranyl-biotin derivatives. *Bioconjate Chem. 15*, 601−616.

(37) Rudolf, B., Makowska, M., Domagala, A., Rybarczyk-Pirek, A., and Zakrzewski, J. (2003) Metallo-carbonyl conjugates of biotin and biocytin. *J. Organomet. Chem. 668*, 95−100.

(38) Booth, C., Bushby, R. J., Cheng, Y., Evans, S. D., Liu, Q., and Zhang, H. (2001) Synthesis of novel biotin anchors. *Tetrahedron 57*, 9859−9866.

(39) (a) Allart, B., Lehtolainen, P., Yla-Herttuala, S., Martin, J. F., and Selwood, D. L. (2003) A stable bis-allyloxycarbonyl biotin aldehyde derivative for biotinylation via reductive alkylation: Application to the synthesis of a biotinylated doxorubicin derivative. *Bioconjate Chem. 14*, 187−194. (b) Lindegren, S., Andersson, H., Jacobsson, L., Back, T., Skarnemark, G., and Karlsson, B. (2002) Synthesis and biodistribution of ^{211}At-labeled, biotinylated, and charge-modified poly-L-lysine: Evaluation for use as an effector molecule in pretargeted intraperitoneal tumor therapy. *Bioconjugate Chem. 13*, 502−509. (c) Rudolf, B., Makowska, M., Domagala, A., Rybarczyk-Pirek, A., and Zakrzewski, J. (2003) Metallo-carbonyl conjugates of biotin and biocytin. *J. Organometallic Chem. 668*, 95−100. (d) Angus, D., Kiefel, M., and von Itzstein, M. (2000) The synthesis of biotinylated carbohydrates as probes for carbohydrate-recognizing proteins. *Bioorg. Med. Chem. 8*, 2709−2718. (e) Evans, K., Kane, C., and Tice, C. (2002) Synthesis of biotin conjugates of the antifungal compound cymoxanil. *Pest Manage. Sci. 58*, 392−396. (f) Booth, C., Bushby, R., Cheng, Y., Evans, S., Liu, Q., and Zhang, H. (2001) Synthesis of novel biotin anchors. *Tetrahedron, 57*, 9859−9866. (g) Torreggiani, A., Bottura, G., and Fini, G. (2000) Interaction of biotin and biotinyl derivatives with avidin: conformational changes upon binding. *J. Raman Spectrosc. 31*, 445−450.

(40) Levadala, M. K., Banerjee, S. R., Maresca, K. P., Babich, J. W., and Zubieta, J. (2004) Direct reductive alkylation of amino acids: synthesis of bifunctional chelates for nuclear imaging. *Synthesis, 11*, 1759−1766.

(41) Medina, L. A., Klipper, R., Phillips, W. T., and Goins, B. (2004) Pharmacokinetics and biodistribution of [111In]-avidin and [99mTc]-biotin-liposomes injected in the pleural space for the targeting of mediastinal nodes. *Nucl. Med. Biol. 31*, 41−51.

(42) Chinol, M., De Cobelli, O., Trifiro, G., Scardino, E., Bartolomei, M., Verweij, F., Papi, S., Matei, D. V., and Paganelli, G. (2003) Localization of avidin in superficial bladder cancer: a potentially new approach for radionuclide therapy. *Eur. Urol. 44*, 556−559.

(43) Phillips, W. T., Medina, L. A., Klipper, R., and Goins, B. (2002) A novel approach for the increased delivery of pharmaceutical agents to peritoneum and associated lymph nodes. *J. Pharm. Exp. Ther. 303*, 11−16.

(44) Lo, K. K−W., Hui, W.-K., and Ng, D. C−M., (2002) Novel rhenium(I) polypyridine biotin complexes that show luminescence enhancement and lifetime elongation upon binding to avidin. *J. Am. Chem. Soc. 124*, 9344−9345.

(45) Laverman, P., Zalipsky, S., Oyen, W. J., Dams, E. T., Storm, G., Mullah, N., Corstens, F. H., and Boerman, O. C. (2000) Improved imaging of infections by avidin-induced clearance of 99mTc-biotin-PEG liposomes. *J. Nucl. Med. 41*, 912−918.

(46) Correa-Gonzalez, L., Arteaga de Murphy, C., Ferro-Flores, G., Pedraza-Lopez, M., Murphy-Stack, E., Mino-Leon, D., Perez-Villasenor, G., Diaz-Torres, Y., and Munoz-Olvera, R. (2003) Uptake of 153Sm-DTPA-bis-biotin and 99mTc-DTPA-bis-biotin in rat AS-30D-hepatoma cells. *Nucl. Med. Biol. 30*, 135−140.

(47) Pollok, J. M., Schultes, B., and Oehr, P. (1990) Labeling of a biotin-derivative by technetium-99m, its purification, and binding-capacity to avidin. *NucCompact 21*, 36−37.

(48) Paganelli, G., Magnani, P., Zito, F., Lucignani, G., Sudati, F., Truci, G., Motti, E., Terreni, M., Pollo, B., and Giovanelli, M. (1994) + Pre-targeted immunodetection in glioma patients: tumour localization and single-photon emission tomography imaging of [99mTc]-PnAO-biotin. *Eur. J. Nucl. Med. 21*, 314−321.

(49) Lo, K. K−W., and Hui, W.-K. (2005) Design of rhenium(I) polypyridine biotin complexes as a new class of luminescent probes for avidin. *Inorg. Chem. 44*, 1992−2002.

(50) Lo, K. K−W., and Tsang, K. H−K. (2004) Bifunctional luminescent rhenium(I) complexes containing an extended planar diimine ligand and a biotin moiety. *Organometallics 23*, 3062−3070.

(51) Alberto, R., Egli, A., Abram., U., Hegetschweiler, K., Gramlich, V., and Schubiger, P. A. (1994) Synthesis and reactivity of $[NEt_4]_2[ReBr_3(CO)_3]$. Formation and structural characterization of the clusters $[NEt_4][Re_3(\mu 3\text{-}OH)(\mu\text{-}OH)_3(CO)_9]$ and $[NEt_4][Re_2(\mu\text{-}OH)_3(CO)_6]$ by alkaline treatment. *J. Chem. Soc., Dalton Trans*, 2815−20.

(52) (a) Lazarova, N., James, S., and Zubieta, J. (2004) A convenient synthesis, chemical characterization and reactivity of $[Re(CO)_3(H_2O)_3]Br$. The crystal and molecular structure of $[Re(CO)_3(CH_3CN)_2Br]$. *Inorg. Chem. Commun. 7/9*, 1023. (b) Alberto, R., Schibli, R., Schubiger, A. P., Abram, U., Pietzsch, H.-J., and Johannsen, B. (1999) First application of *fac*-$[^{99m}Tc(OH_2)_3(CO)_3]^+$ in bioorganometallic chemistry: Design, structure, and in vitro affinity of a 5-HT1A receptor ligand labeled with ^{99m}Tc. *J. Am. Chem.* Soc. *121*, 6076−6077.

(53) (a) Zhu, H., Jain, R. K., and Baxter, L. T. (1998) Tumor pretargeting for radioimmunodetection and radioimmunotherapy. *J. Nucl. Med. 39*, 65−76. (b) Wilbur, D. S., Hamlin, D. K., Vessela, R. L., Stray, J. E., Buhler, K. R., Stayton, P. S., Klumb, L. A., Pathare, P. M., and Weerawarna, S. A. (1996) Antibody fragments in tumor pretargeting. Evaluation of biotinylated Fab′ colocalization with recombinant streptavidin and avidin. *Bioconjugate Chem. 7*, 689−702. (c) Sung, C., and van Osdol, W. W. (1995) Tumor pretargeting: almost the bottom line. *J. Nucl. Med. 36*, 876−879.

(54) (a) Garlick, R. K., and Giese, R. W. (1988) Avidin binding of radiolabeled biotin derivatives. *J. Biol. Chem. 263*, 210−215. (b) Arterburn, J. B., Rao, K. V., Goreham, D. M., Valenzuela, M. V., and Holguin, M. S. (2000) Functionalized rhenium(V) organoimido complexes as potential radiopharmaceuticals. 2. Synthesis, structural characterization, and reactivity of *N*-succinimidyl ester derivatives with amines. *Organometallics 19*, 1789−1795.

(55) Wolf, B., and McVoy, J. S. (1983) A sensitive radioassay for biotinidase activity: deficient activity in tissues of serum biotinidase-deficient individuals. *Clin. Chim. Acta 135*, 275−281.

(56) Hymes, J., Fleischhauer, K., and Wolf, B. (1997) Biotinidase in serum and tissues, *Methods Enzymol. 279*, 422−434.

(57) Pazy, Y.; Kulik, T.; Bayer, E. A.; Wilcheck, M.; Livnah, O. (2002) Ligand exchange between proteins. Exchange of biotin and biotin derivatives between avidin and streptavidin. *J. Biol. Chem. 277*, 30892−30900.

BC050297W

Isostructural Re and ^{99m}Tc Complexes of Biotin Derivatives for Fluorescence and Radioimaging Studies

Shelly James,[†] Kevin P. Maresca,[‡] John W. Babich,[‡] John F. Valliant,[§] Laurie Doering,[#] and Jon Zubieta*[,†]

Department of Chemistry, Syracuse University, Syracuse, New York 13244, Department of Chemistry, McMaster University, Hamilton, Ontario, Canada L8S 4M1, and Department of Pathology and Molecular Medicine, McMaster University, Hamilton, Ontario Canada L8S 4M1, and Molecular Insight Pharmaceuticals, 160 Second Street, Cambridge, Massachusetts 02142. Received October 8, 2005; Revised Manuscript Received March 13, 2006

The reaction of biotinamine with two equivalents of 2-quinoline aldehyde in the presence of $Na(OAc)_3BH$ in dichloroethane provides *N*,*N*-bis(methylquinoline)biotinamine (**L1**), a molecule displaying a tridentate donor terminus which has proven effective in coordinating to the $\{M(CO)_3\}^+$ core (M = Tc, Re). Reaction of **L1** with $(NEt_4)_2[Re(CO)_3Br_3]$ yields $[Re(CO)_3(L1)]Br$, a compound with an absorbance at 350 nm and luminescence emission maxima at 425 and 580 nm. The luminescence lifetime of 11.4 μs, which is associated with the 580 nm emission, is sufficiently prolonged to enable time-gating techniques to be used during in vitro imaging studies and to overcome interference from endogenous fluorescence. Exposure of avidin beads to $\{Re(CO)_3(L1)]Br$ resulted in binding, which was qualitatively imaged using fluorescence microscopy. The ^{99m}Tc analogue $[^{99m}Tc(CO)_3(L1)]^{+1}$ was prepared by reacting **L1** with $[^{99m}Tc(CO)_3(H_2O)_3]^{+1}$ and purified by HPLC. The ^{99m}Tc complex is chemically robust and resistant to cysteine and histidine challenges. This study demonstrates that complementary fluorescent and radioactive biotin-derived probes may be readily prepared to allow direct correlation of in vitro and in vivo molecular imaging studies.

Biotin, a water-soluble member of the B-complex group of vitamins commonly referred to as vitamin H, binds to the homotetrameric glycoprotein avidin with one of the strongest known binding constants between a ligand and a protein ($K_d = 10^{-15}$ M^{-1}) (*1*). The high K_d has been used in a number of applications to biochemistry, immunology, bioanalytical chemistry (*2*), and targeted cancer radiotherapy (*3*). The effective linking of biotin to the radionuclides ^{99m}Tc and ^{186,188}Re would create new applications in nuclear imaging (*4*−*8*) and to radiotherapy (*9*), respectively. This is particularly true of the ^{99m}Tc conjugate because of the undisputed use of the isotope.

The development of radiopharmaceuticals is often hampered by the inability to image the behavior of these compounds at the cellular and subcellular level. This is problematic when attempting to determine mechanisms responsible for cellular specificity and localization. While visualization in vitro may be accomplished by substitution of the radiolabel with a fluorescent dye (*10*), in the case of biotin−fluorophore conjugates, such as pyrene, fluorescein, or tetramethylrhodamine, the fluorophore and radionuclide prosthetic groups have very different structures. Consequently, binding to avidin results in fluorescence quenching unless lengthy spacers are introduced between the biotin and the fluorophore units (*11*). The optimal system would exploit isostructural metal-based luminescent and radioactive prosthetic groups.

Re(I) complexes are attractive as luminescent probes, because of their useful photophysical properties, which include long lifetimes, polarized emission, and large Stoke's shift (*12*−*16*). These properties have been exploited recently in the conjugation of biotin to the $\{Re(CO)_3\}^{+1}$ core in $[Re(CO)_3(phen)(py\text{-}CH_2\text{-}NH\text{-}biotin)](PF_6)$ where phen is 1,10-phenanthroline and py-CH_2-NH-biotin is *N*-[(*N*-pyridyl)methyl biotinamide] (*17*). However, a potential disadvantage of this design is the monodentate coordination mode of the biotin derivative to the $\{Re(CO)_3\}^{+1}$ core, requiring a bidentate coligand to satisfy the coordination requirements of the rhenium(I) core.

Since the coordination chemistry of the group 7 congeners technetium and rhenium is similar, it should be possible to design an appropriate multidentate ligand that forms a robust Re fluorescent complex and a stable ^{99m}Tc complex. The ligand should also be linkable to the biotin so as to allow images obtained on a fluorescent microscope to be correlated with in vivo radioimaging studies since the two probe structures are identical.

Our recent design of Tc(I)/Re(I) binding bifunctional chelates based on natural or synthetic amino acid-derived bis(pyridyl)-amines, referred to as single amino acid chelates (SAAC) (*18*), provided inert complexes with the $\{M(CO)_3\}^{+1}$ core (M = Tc, Re) (*19*). Encouraged by these results, we modified the chelate terminus to provide a bis(quinolylmethyl)amine donor set, which resulted in a ligand whose Re complex is fluorescent and retains the ability to bind ^{99m}Tc (*20*). On the basis of these results, we have prepared *N*,*N*-bis(quinolylmethyl)biotinamine (**L1**) and its complexes with the $\{^{99m}Tc(CO)_3\}^{+1}$ and $\{Re(CO)_3\}^{+1}$ cores. The fluorescent properties of $[Re(CO)_3(L1)]^{+1}$ are described, as well as the uptake of the Re complex by avidin beads.

EXPERIMENTAL PROCEDURES

General. All reactions were performed under an inert atmosphere of argon, unless otherwise noted. Solvents and chemicals obtained from commercial sources were analytical grade or better and used without further purification. D-Biotin was purchased from Aldrich Chemical Co. (Milwaukee, WI). Avidin was purchased from Pierce Biotechnology (Rockford, IL) and used as a solution diluted with PBS to pH = 7.2 as noted in the literature reference (*21*). Avidin beads were purchased from Aldrich Chemical Co. (Milwaukee, WI). All experiments were performed in duplicate or triplicate to ensure

* To whom correspondence should be addressed. E-mail: jazubiet@syr.edu. Fax: (315) 443-4070.

[†] Syracuse University.

[§] McMaster University, Department of Chemistry.

[‡] Molecular Insight Pharmaceuticals.

[#] McMaster University, Department of Pathology and Molecular Medicine.

10.1021/bc050298o CCC: $33.50 © 2006 American Chemical Society
Published on Web 04/14/2006

reproducibility. Melting points were obtained on a Barnstead International apparatus and are uncorrected.

Chromatography. Silica gel was purchased from EM Science (Gibbstown, NJ), silica gel 60 Geduran, 40−63 μm. Alumina chromatography was performed using alumina purchased from Aldrich (Milwaukee, WI): weakly acidic, activated Brockmann I standard grade 150 mesh, 58 Å. In addition, basic aluminum oxide, activated, 150 mesh, 58 Å was used as noted in the experimental descriptions.

HPLC Chromatography. Purification of **TcL1** was achieved through the use of HPLC purification and the following solvent system: Solvent A: TEAP (0.05 M) (tetraethylammonium phosphate buffer) adjusted to pH 2−2.5 with 1 M HCl; and Solvent B: MeOH.

Spectroscopy. ^{1}H NMR spectra were obtained on a Bruker Avance system, at 300 and 500 MHz. Proton chemical shifts are expressed as parts per million versus tetramethylsilane. ^{13}C NMR data were obtained on a Bruker Avance 75 MHz system using trimethylsilane or the protonated fraction of the deuterated solvent as the reference standards. IR spectra were obtained in methanol solution using a Perkin-Elmer Paragon 1000 FT-IR spectrophotometer for data collection. HRMS data were obtained on a 3-Tesla Fourier Transform mass spectrometer with an ESI source in positive ion mode. Mass spectrometry samples were prepared in MeOH/THF containing NaCl.

Fluorescence and UV Spectroscopy. Samples were flushed with nitrogen before use. All absorbance spectra were recorded using a Varian CARY 500 bio UV−visible spectrophotometer. Measurements were performed in double-beam mode baseline corrected in matched quartz cuvettes. A concentrated stock solution of the complex [Re(CO)$_3$(L1)]Br was prepared to give a 0.2 M solution in methanol. Emission spectra, lifetime and quantum yield data used steady-state measurements with a Jobin Yvon-SPEX Fluorolog-3 model 212 T-format spectrofluorimeter (ISA Instrument Int. Edison, NJ). Emission was monitored from 400 to 700 nm with an excitation wavelength of 366 nm in 1-nm increments with an integration time of 0.25 s and bandwidths of 5 nm. Methanol solutions of the rhenium compounds were prepared with optical densities no higher than 0.1 at 366 nm. The POPOP (1,4-bis(5-phenyl-2-oxazolyl)-benzene) standard was used to measure the quantum yield and was prepared in a concentration of 0.1 M and diluted to an optical density of 0.01 measured at 366 nm.

Synthetic Procedures. *N,N-Bis(methylquinoline)biotinamine (L1).* Biotin TPF ester (**1**), biotinamide (**2**), and biotinamine (**3**) were prepared following literature methods (*22*). Biotinamine (**3**) (171 mg, 0.74 mmol) was added to DCE (9 mL) in a 25-mL round-bottom flask. Quinoline aldehyde (236 mg, 1.1 mmol) was introduced, followed by Na(OAc)$_3$BH (784 mg, 3.7 mmol). The resulting blood red solution was heated to reflux overnight. The mixture was quenched with saturated Na_2CO_3 solution (5 mL) and extracted with CH_2Cl_2 (5 × 5 mL). The solution was evaporated to a red-brown oil, and the product, a light brown colored solid (341 mg, 60% yield) was eluted from a silica gel column using CH_2Cl_2/MeOH (95:5). ^{1}H NMR (CD_3OD, δ, 300 MHz): 0.9−1.4 (m, 6H), 1.4−1.6 (m, 4H), 2.5−2.6 (m, 3H), 2.74 (dd, J_A = 12 Hz, J_B = 4.8 Hz), 2.8−2.9 (m, 1H), 3.83 (s, 4H), 4.02 (dd, J_A = 7.8 Hz, J_B = 4.2 Hz), 4.29 (dd, J_A = 7.5 Hz, J_B = 4.8 Hz), 7.4−7.5 (m, 2H), 7.6−7.7 (m, 2H), 7.56 (t, J = 7.5 Hz, 1H), 7.68 (d, J = 8.4 Hz, 2H), 8.13 (d, J = 8.4 Hz, 2H); ^{13}C NMR (CD_3OD, δ, 75 MHz): 27.8, 28.1, 29.7 30.0 41.4, 54.9, 55.7, 57.2, 61.5, 62.2, 63.4, 122.6, 127.7, 128.9, 129.90, 131.0, 138.4, 148.2, 162.0, HRMS calc for $C_{30}H_{33}N_5OSNa^+$: 534.2298, found 534.2282; IR(MeOH): 1703 cm^{-1}. Melting point: 235−236 °C.

[Re(CO)$_3$(L1)]Br. (ReL1). $(NEt_4)_2[Re(CO)_3Br_3]$ (62 mg, 0.08 mmol) was added to **L1** (34.0 mg, 0.07 mmol) in methanol (4 mL) in a 10-mL round-bottom flask. The clear, light brown solution was held at reflux overnight, and the red-brown solution obtained was evaporated to give a dark red-brown powder that was purified by column chromatography using CH_2Cl_2/MeOH (95:5) over weakly acidic alumina, giving a quantitative yield of the Re complex.

^{1}H NMR (CD_3OD, δ, 300 MHz): 1.4−1.7 (m, 4H), 1.7−1.8 (m, 2H), 1.9−2.1 (m, 2H), 2.65 (d, J = 12 Hz, 1H), 2.87 (dd, J_A = 12 Hz, J_B = 4,9 Hz, 1H), 3.19 (m, 1H), 3.3 (s, 2H), 3.8 (dd, J_A = 8.3 Hz, J_B = 8.3 Hz), 4.26 (dd, J_A = 8.0 Hz, J_B = 4.35 Hz), 4.45 (dd, J_A = 7.8 Hz, J_B = 4.2 Hz), 7.60 (d, J = 7.8 Hz, 2H), 7.65 (t, J = 7.5 Hz, 2H), 7.83 (t, J = 7.8 Hz, 2H), 7.97 (d, J = 7.2 Hz, 2H), 8.46 (d, J = 9.9 Hz, 2H), 8.51 (d, J = 8.7 Hz, 2H); ^{13}C NMR (CD_3OD, δ, 75 MHz): 27.3, 27.9, 29.8, 30.2, 41.2, 57.2, 61.8, 63.6, 69.5, 121.0, 129.6, 129.7, 130.0, 131.1, 134.2, 143.1, 148.3, 166.3, 195.7, 197.3. Melting point: decomposes above 200 °C.

[Tc(CO)$_3$(L1)]Cl. (TcL1). (a) $[^{99m}Tc(H_2O)_3(CO)_3]^{+1}$ was prepared by minor modification of the literature procedure: a 10-mL sealed tubing vial containing the followed lyophilized formulation: 13 mg of L-tartaric acid, 7.6 mg of KBH_4, 20 mg of lactose, borate buffer at pH = 11.6, and CO in the headspace, was added to1.5 mL (20.5 mCi) of $^{99m}TcO_4^-$ from a commercial generator (50−200 mCi). The vial was shaken vigorously for 30 s and placed in a boiling water bath for 30 min. The solution was cooled for 5 min, and 1 N HCl (150 μL) added to the cooled solution. The ^{99m}Tc reagent (500 μL) was purified using reverse HPLC (C-18 column with a 0.05 M TEAP buffer adjusted to a pH = 2.25 and a MeOH gradient HPLC method). HPLC retention time for $\{^{99m}Tc(CO)_3(H_2O)_3\}^{+1}$: 4.0 min. (b) The reaction of $\{^{99m}Tc(CO)_3(H_2O)_3\}^{+1}$ (650 MBq (17.5 mCi) with **L1** (450 μg) 100 °C for 30 min afforded **TcL1** in 95% yield.

HPLC purification of **TcL1** was performed on a Varian instrument using a NUCLEOSIL column 300−5μ, C-18 analytical column. All solvents were HPLC grade and filtered prior to use in the HPLC system. A gradient method was utilized to purify the ^{99m}Tc complexes, with the following gradient elution conditions: 0−3 min: 100% A; 3−6 min: 100% A to 75% A; 6−9 min: 67% A; 9−20 min: 100% B; 22−25 min: 100% B; 25−30 min: 100% A. The total run time was 30 min, with an injection loop of 100 μL. The flow rate was 1.0 mL/min with 30 μL of compound injected. Detectors were β-ram (γ-detector) with 10 μL loop (1 s dwell time) and a UV/vis detector which was set at λ = 254 nm.

^{99m}Tc Labeling Studies. The concentration of the ^{99m}Tc compound **TcL1** was determined to be 36 μCi in 500 μL of 10 mM HCl (pH = 2). Na[$^{99m}TcO_4$], $[^{99m}Tc(CO)_3(H_2O)_3]$Cl, and the Re complex [Re(CO)$_3$(L1)]Br were introduced as standards under the operating conditions of the HPLC run. Na[TcO_4] retention time was noted as 11.2 min, while retention time for $[^{99m}Tc(CO)_3(H_2O)_3]^{+1}$ was 4.5 min and that of [Re(CO)$_3$(L1)]Br was 22.9 min. The retention time for **TcL1** was 22.0 min. The uncomplexed **L1** was also injected and had a retention time of 20.3 min. Radiochemical yield for all ^{99m}Tc complexes was >95%. Quantitative recovery of the complex **TcL1** was achieved by HPLC chromatography.

Avidin Binding. Avidin binding was determined by incubating the HPLC-isolated ^{99m}Tc-complex (50 μL) with avidin (4.8 mg/8 mL water) for 30 min, followed by filtration through a 30 kDa MW cutoff filter (Centricon YM-30), and washing three times with 1 mL of PBS pH 7.2. Avidin binding was determined as the percent radioactivity retained on the filter as compared to the total radioactivity.

Lipophilicity. 100 μL of compound **TcL1** (20.2 μCi) was placed in 10% EtOH/0.9 saline solution and added to a 1:1 solution of 1-octanol: PBS (pH = 7.2) for a total volume of 4 mL. The 1-octanol:PBS solution had been incubated for 24 h

Scheme 1

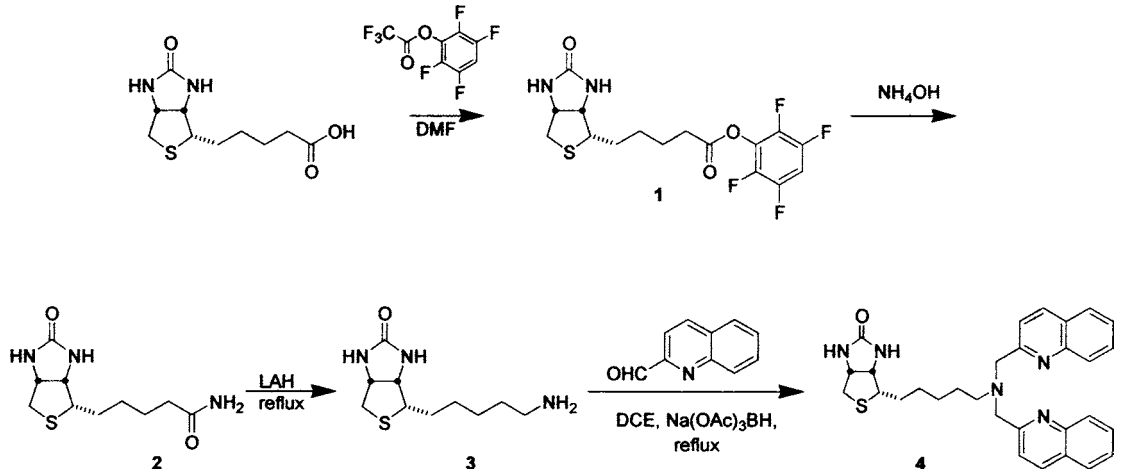

before use. The solution was then shaken for 5 min on an automixer and then vortexed for 30 s. After allowing the solution to settle into two distinct layers for a period of 5 min, 0.5 mL samples were removed from both the 1-octanol layer and the PBS layer. These samples were then placed into 0.5 mL of PBS buffer (pH = 7.2), shaken on the automixer for 5 min, and then vortexed for 30 s. 100 μL of the 1-octanol layer and the PBS layer were subsequently injected into the HPLC and the cpm recorded using a NaI detector. Three samples were studied to ensure reproducibility. The log *P* value represents the average of the three experimental values.

Qualitative Binding on Avidin Beads. The rhenium complex $[Re(CO)_3(L1)]Br$ was incubated with avidin beads at 37 °C for 30 min (0.5 mL beads diluted in 5 mL PBS pH = 7.2).

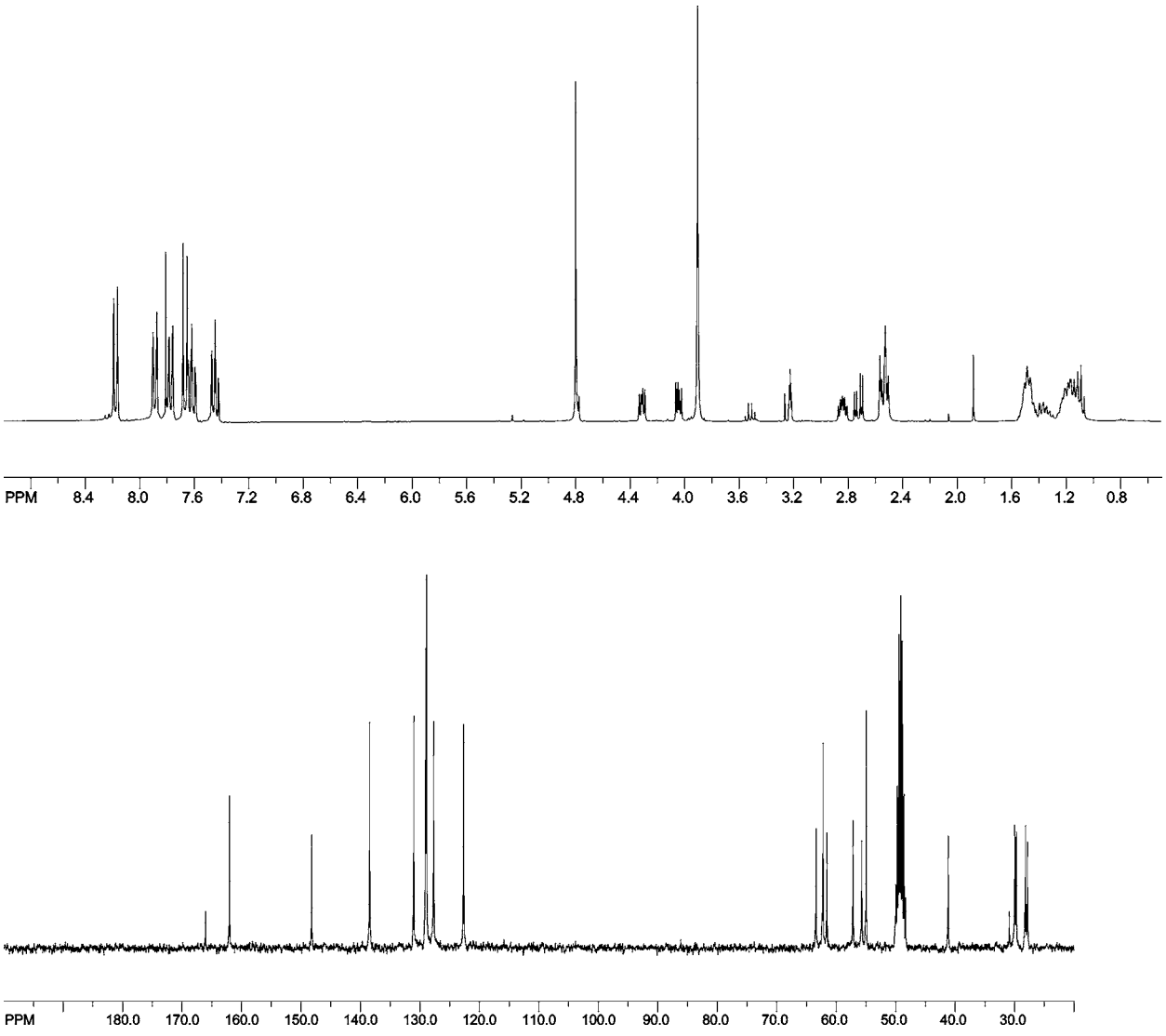

Figure 1. The ^{1}H NMR of **L1** (300 MHz, CD_3OD (top) at room temperature; the ^{13}C NMR of **L1** (75 MHz, CD_3OD) (bottom) at room temperature.

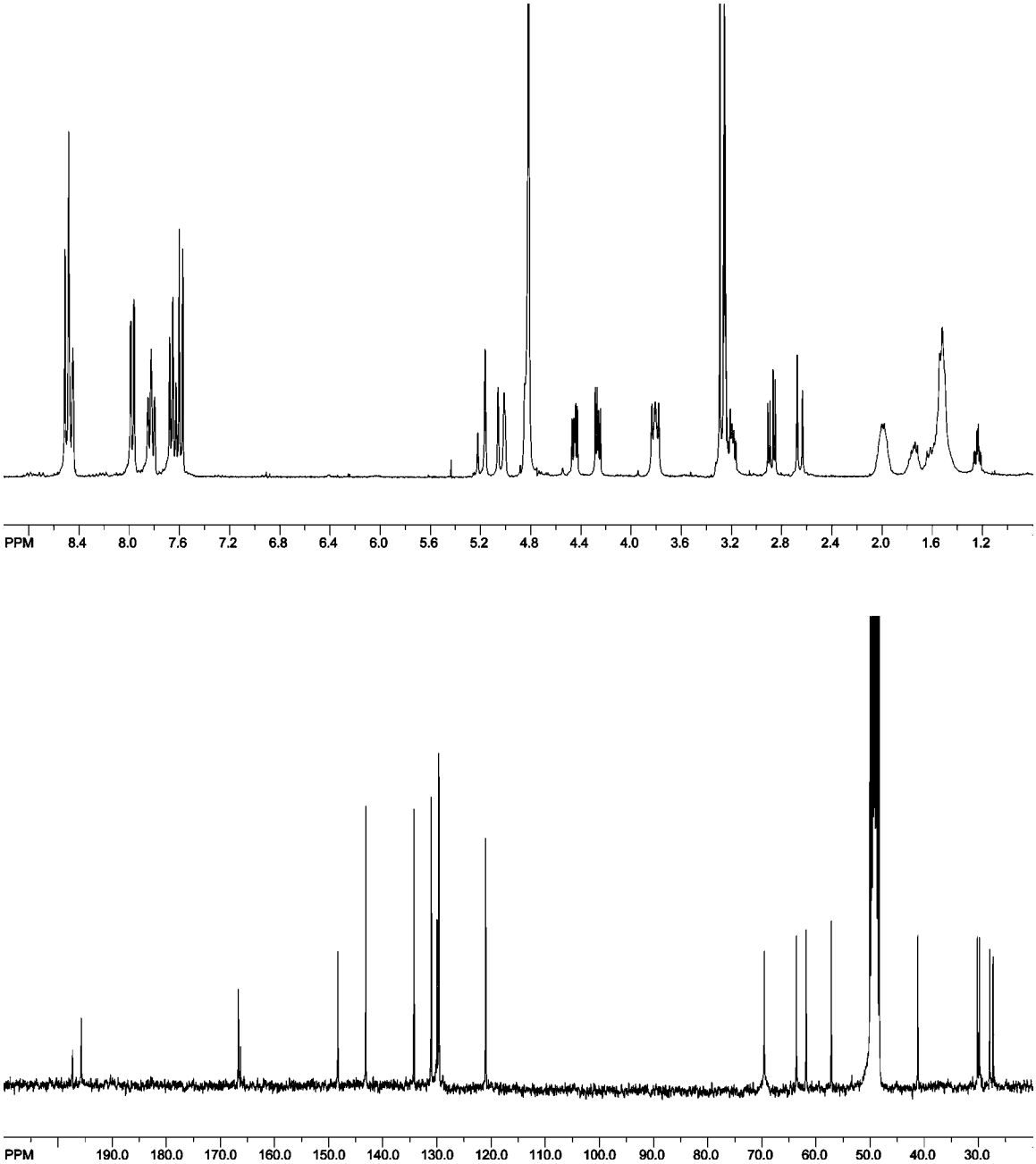

Figure 2. The ^{1}H NMR of **ReL1** (300 MHz, CD_3OD) (top) at room temperature; the ^{13}C NMR of **ReL1** (75 MHz, CD_3OD)(bottom) at room temperature.

Fluorescence microscopy images were taken prior to washing the beads 4× with PBS (pH = 7.4), followed by centrifuging and decanting. Fluorescence microscopy images were then recorded once again. The avidin beads with the bound rhenium complex were then subjected to a biotin challenge with an excess of biotin (>1000×) for a period of 30 min at a temperature of 37 °C, followed by reexamination by fluorescence microscopy.

RESULTS AND DISCUSSION

The ligand synthesis was performed as outlined in Scheme 1. The biotin TFP ester was prepared by the transesterification reaction of biotin with 2,3,5,6-tetrafluorophenyl trifluoroacetate in DMF and was subsequently treated with NH_4OH to give the biotinamide (**2**). Reduction of **2** with LAH gave biotinamine (**3**), which upon reductive alkylation with two equivalents of 2-quinolinecarboxaldehyde provided the ligand **L1** (*23*), whose ^{1}H and ^{13}C NMR spectra are shown in Figure 1. The reaction of **L1** with $(NEt_4)_2[Re(CO)_3Br_3]$ in methanol yielded a dark red-

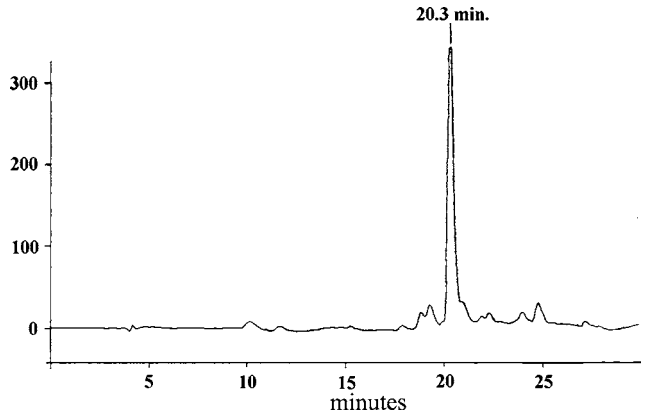

Figure 3. HPLC radiochromatogram of ^{99m}**TcL1**. The HPLC retention time (UV detector) for the corresponding rhenium compound **ReL1** was 19.9 min.

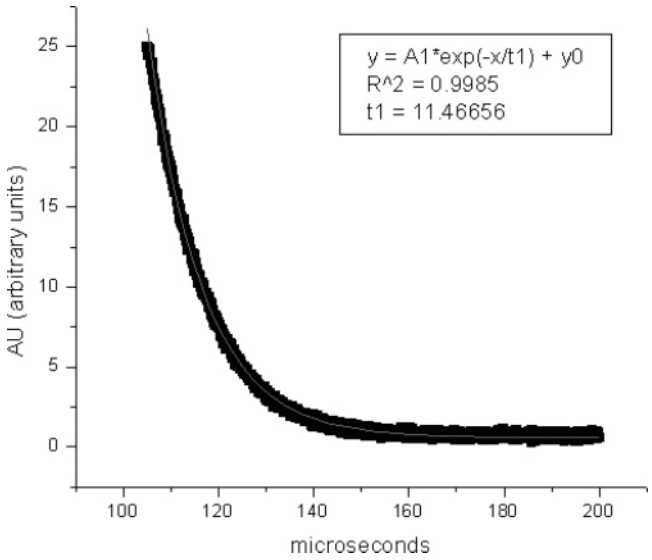

Figure 4. Emission decay trace for **ReL1** in methanol, monitored at 580 nm after 366 nm excitation. Monoexponential fit to the emission decay gave a lifetime of $\tau = 11.4$ μs.

brown powder of **[Re(CO)$_3$L1]Br** (**ReL1**) in quantitative yield. The ^{99m}Tc analogue of **ReL1** was prepared by the reaction of an aqueous solution of $[^{99m}Tc(CO)_3(H_2O)_3]^{+1}$ with **L1** to give $[^{99m}Tc(CO)_3L1]^{+1}$ in 95% radiochemical yield and >85% radiochemical purity.

The rhenium complex was characterized by ^{1}H and ^{13}C NMR spectroscopy, as shown in Figure 2. Comparison of the ^{1}H NMR spectra of **L1** with that of complex **ReL1** shows that the protons associated with the chelating groups are most strongly influenced by coordination of the $\{Re(CO)_3\}^{+1}$ core. In comparison to that of **L1**, the ^{13}C NMR spectrum of $\{Re(CO)_3\}^{+1}$ exhibits two additional peaks at 195.7 and 197.3 ppm in a 2:1 ratio, assigned to the carbon atoms of the carbonyl ligands. The pattern reflects the local C_{2v} symmetry of the $\{Re(CO)_3\}^{+1}$ facial subunit.

The ^{99m}Tc analogue **TcL1** was prepared by reacting **L1** with $[^{99m}Tc(CO)_3(H_2O)_3]^{+1}$, which had been prepared from $^{99m}TcO_4^-$ using a modified literature procedure. **TcL1** was purified by HPLC on a C-18 analytical column and exhibited a single radioactive peak after purification with a retention time consistent with that of the rhenium complex **ReL1** (Figure 3).

The ^{99m}Tc-biotin complex **TcL1** was also evaluated for avidin affinity binding. Determination of the affinity was performed using a modification of a previously described method. The radiolabeled compound was incubated in the presence of avidin for a period of 30 min, followed by centrifugation through a 30 K filter and washing with 1 mL of PBS pH 7.2 three times. The radioactivity of both the filter (potentially avidin bound) and the filtrate (nonbound) fractions was then counted. The percent binding of **TcL1** was 96% $\pm$ 2.

Although factors other than lipo(hydro)philicity can affect the biodistribution profile of bioconjugate materials such as **TcL1**, high lipophilicity can result in predominantly hepatobiliary excretion patterns and high background activities, with concomitant low in vivo target-to-nontarget ratios. However, the route of excretion, whether hepatobiliary or urinary tract, seems to correlate with the log $P_{o/w}$ value of the reagent. In general, compounds may be grouped by log $P_{o/w}$ values into three categories: low, log $P_{o/w} \leq 1.5$; moderate, $1.5 \leq \log P_{o/w} \leq 4$; and high, log $P_{o/w} \geq 4$ (*24*). The log $P_{o/w}$ was determined to be 1.10, which corresponds to relatively modest lipophilicity. Consequently, the **TcL1** is expected to exhibit only modest hepatobiliary retention. Furthermore, the chemistry of the biotin subunit of the conjugate lends itself to derivatization, which

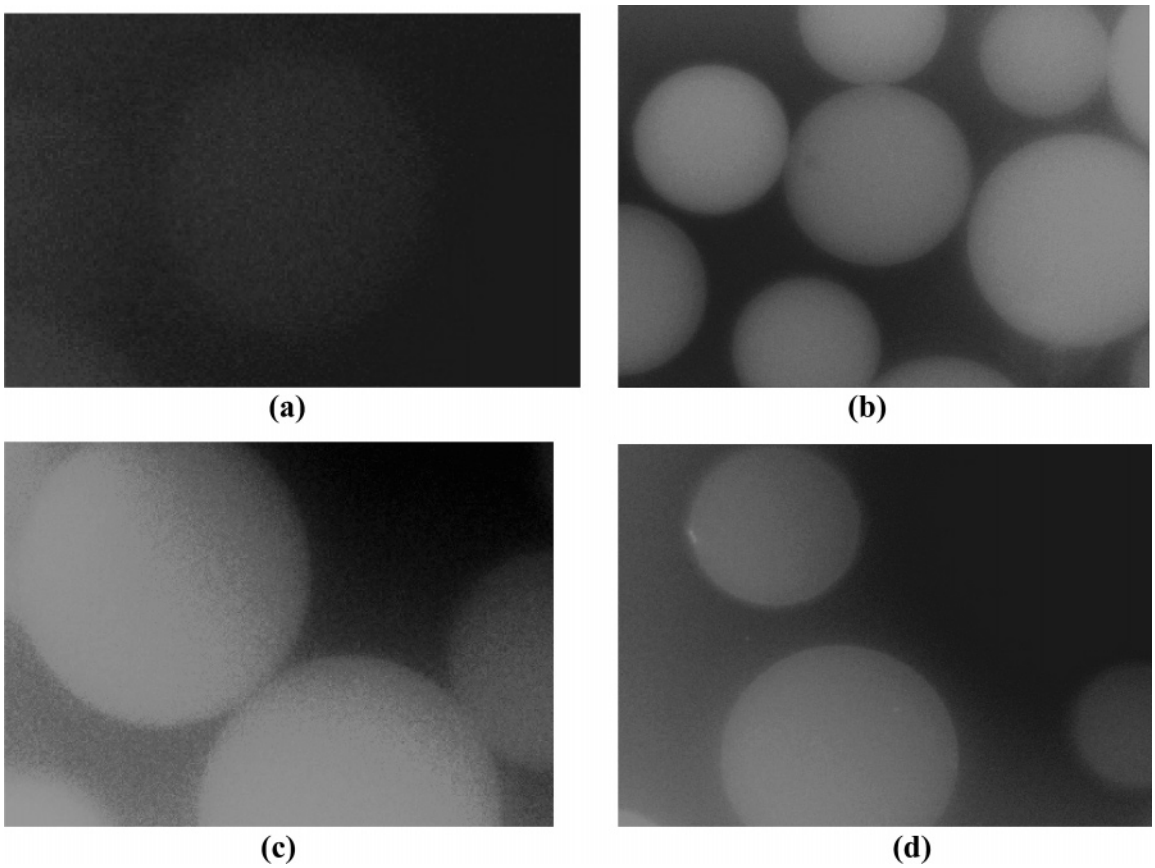

Figure 5. Fluorescence microscopy images of (a) avidin beads; (b) $[Re(CO)_3(L1)]^+$ bound to the avidin beads; (c) avidin bound-$[Re(CO)_3(L1)]^+$ after washing with PBS (pH = 7.4); (d) avidin bound-$[Re(CO)_3(L1)]^+$ after challenging with a 10^3-fold excess of biotin.

would allow the introduction of hydrophilic residues such as a carboxylate group.

Compound **ReL1** displays an appreciable absorbance in the UV and blue regions of the UV−visible spectrum with a peak absorbance at 350 nm. The emission spectrum shows that the rhenium probe has two distinct transitions giving rise to luminescence intensities at 420 and 580 nm. The emission at 580 nm has a lifetime of 11.4 μs (Figure 4), depending upon the solvent and amount of oxygen present. The sensitivity to oxygen is common for an emission that likely originates from a triplet metal-to-ligand charge transfer (^{3}MLCT) excited state (*25*). The quantum yield for **ReL1** of 0.0059 in MeOH under nitrogen is low but not significantly different from yields reported for other transition metal based fluorescent probes (*25*).

Having established that **ReL1** has the necessary properties to be used as a fluorescent probe, the binding of **ReL1** to avidin was studied using fluorescence microscopy. The background autofluorescence of the avidin beads was imaged initially (Figure 5a), followed by **ReL1** incubated with the avidin beads (30 min at 37 °C) (Figure 5b). The avidin beads bound to **ReL1** were subsequently washed with water (4×), centrifuged, decanted, and once again imaged under the fluorescence microscope (Figure 5c) to remove excess unbound luminescent probe from the avidin beads and leave behind only the biotin probe that was bound to the avidin beads. **ReL1**-bound avidin beads were then incubated with >1000-fold excess of biotin for 30 min at 37 °C and imaged (Figure 5d). The images demonstrate that there was no appreciable change in the fluorescence after washing or challenging with excess biotin, confirming that **ReL1** binds effectively to avidin and that the complex has the appropriate fluorescence properties to be used for in vitro microscopy.

CONCLUSIONS

Biotin has been derivatized to provide a tridentate *N*,*N*-bis(pyridylmethyl)amino terminus that is able to coordination the $\{M(CO)_3\}^{+1}$ core (M = Re, ^{99m}Tc). The rhenium complex $[Re(CO)_3(L1)]Br$ possesses the appropriate fluorescence properties to be used for in vitro fluorescence microscopy studies. The biotin ligand **L1** can also be labeled with ^{99m}Tc in high yield to provide a robust complex, **TcL1**. The log $P_{o/w}$ value of **TcL1** is 1.10, suggesting that the compound is only modestly lipophilic and should not exhibit unduly high hepatic retention. The study demonstrates that **L1** or its derivatives may be exploited for the preparation of complementary fluorescent and radioactive biotin probes. These reagents can then be used to perform correlated in vitro and in vivo imaging studies, such that work in isolated cells and studies carried out in living organisms may be compared. Of course, this presupposes that the partition coefficient of the bioconjugate meaningfully correlates with the lipophilicity and hepatic retention of the compound, such that in vivo target-to-nontarget ratios are useful.

LITERATURE CITED

(1) Green, N. M. (1975) Avidin. *Adv. Protein Chem. 29*, 85−133.

(2) Wilchek, M., and Bayer, E. A., Eds. (1990) *Methods in Enzymology 184: Avidin−Biotin Technology*, Elsevier, Amsterdam.

(3) Boerman O. C., van Schaijk, F. G., Oyen, W. J. G., and Corstens, F. H. M. (2003) Pretargeted radioimmunotherapy of cancer: progress step by step. *J. Nucl. Med. 44*, 400−411.

(4) Hom, R. K., and Katzenellenbogen, J. A. (1997) Technetium-99m-labeled receptor-specific small-molecule radiopharmaceuticals: recent developments and encouraging results. *Nucl. Med. Biol. 24*, 485−498.

(5) Liu, S., and Edwards, D. S. (2002) Fundamentals of receptor-based diagnostic metalloradiopharmaceuticals. *Topics Curr. Chem. 222 (Contrast Agents II)*, 259−278.

(6) Schibli, R., and Schubiger, P. A. (2002) Current use and future potential of organometallic radiopharmaceuticals. *Eur. J. Nucl. Med. Mol. Imaging 29*, 1529−1542.

(7) Dilworth, J. R., and Parrott, S. J. (1998) The biomedical chemistry of technetium and rhenium. *Chem. Soc. Rev. 27*, 43−55.

(8) Alberto, R. (2004) Technetium, in *Comprehensive Coordination Chemistry II* (McCleverty, J. A., Meyer, T. J., Eds.) Vol. 5, p 127, Elsevier, New York.

(9) Blower, P. J., and Prakash, S. (1999) The chemistry of rhenium in nuclear medicine. *Persp. Bioinorg. Chem. 4*, 91−143.

(10) Gallazzi, F., Wang, Y., Jia, F., Shenoy, N., Landon, L. A., Hannink, M., Lever, S. Z., and Lewis, M. R. (2003) Synthesis of radiometal-labeled and fluorescent cell-permeating peptide-PNA conjugates for targeting the bcl-2 proto-oncogene. *Bioconjate Chem. 14*, 1083−1095.

(11) Gruber, H. J., Hahn, C. D., Kada, G., Riener, C. K., Harms, G. S., Ahrer, W., Dax, T. G., and Knaus, H. G. (2000) Anomalous fluorescence enhancement of Cy3 and Cy3.5 versus anomalous fluorescence loss of Cy5 and Cy7 upon covalent linking to IgG and noncovalent binding to avidin. *Bioconjate Chem. 11*, 696−704.

(12) Guo, X. Q., Castellano, F. N., Li, L., and Lakowicz, J. R. (1998) Use of a long-lifetime Re(I) complex in fluorescence polarization immunoassays of high-molecular-weight analytes. *Anal. Chem. 70*, 632−637.

(13) Shen, Y., Maliwal, B. P., and Lakowicz, J. R. (2001) Long-lived luminescent Re(I) complexes containing cis-carbonyl and bidentate phosphine ligands. *J. Fluoresc. 11*, 315−318.

(14) Lo, K. K.-W., Hui, W.-K., Ng, D. C.-M., and Cheung, K.-K. (2002) Synthesis, characterization, photophysical properties, and biological labeling studies of a series of luminescent rhenium(I) polypyridine malemide complexes. *Inorg. Chem. 41*, 40−46.

(15) (a) Wrighton, M., and Morse, D. L. (1974) Nature of the lowest excited state in tricarbonylchloro-1,10-phenanthrolinerhenium(I) and related complexes. *J. Am. Chem. Soc. 96*, 998−1003. (b) Sullivan, B. P. (1989) Large solvatochromism of metal-to-ligand charge-transfer transitions in organometallic complexes of rhenium(I). *J. Phys. Chem. 93*, 24−26. (c) Tapolsky, G., Duesing, R., and Meyer, T. J. (1990) Synthetic control of excited-state properties in ligand-bridged complexes of rhenium(I). Intramolecular energy transfer by an electron-transfer/energy-transfer cascade. *Inorg. Chem. 29*, 2285−2297. (d) Zipp, A. P., Sacksteder, L. A., Streich, J., Cook, A., Demas, J. N., and DeGraff, B. A. (1993) Luminescence of rhenium(I) complexes with highly sterically hindered diimine ligands. *Inorg. Chem. 32*, 5629−5632. (e) Stufkens, D. J., and Vlcek, A., Jr. (1998) Ligand-dependent excited-state behavior of Re(I)- and Ru(II) carbonyl-diimine complexes. *Coord. Chem. Rev. 177*, 127−179.

(16) (a) Chen, P., Curry, M., and Meyer, T. J. (1989) Effects of conformational change in the acceptor on intramolecular electron transfer. *Inorg. Chem. 28*, 2271−2280. (b) Yam, V. W.-W., Lau, V., Chor, Y., and Cheung, K.-K. (1995) Synthesis, photophysics and photochemistry of novel luminescent rhenium(I) photoswitchable materials. *J. Chem. Soc., Chem. Commun. 11*, 1195. (c) Wallace, L., Woods, C., and Rillema, D. P. (1995) Structure and luminescence properties of $[Re(4,7\text{-dimethyl-}1,10\text{-phenanthroline})(CO)_3py]^+$ in a solid matrix. *Inorg. Chem. 34*, 2875−2882. (d) Lucia, L. A., Abboud, K., and Schanze, K. S. (1997) Outer sphere metal-to-ligand charge transfer in organometallic ion pairs. *Inorg. Chem. 36*, 6224−6234. (e) Yam, V. W.-W., Lo, K. K.-W., Cheung, K.-K., and Kong, R. Y.-C. (1997) Deoxyribonucleic acid binding and photocleavage studies of rhenium(I) dipyridophenazine complexes. *J. Chem. Soc., Dalton Trans.: Inorg. Chem. 12*, 2067−2072. (f) Kunkely, H., and Vogler, A. (2000) Photocleavage of the 1,3-dimethyluracil cyclobutane dimer sensitized by (1,10-phenanthroline)tricarbonylrhenium(I) chloride. Self-inhibition by the monomer. *Inorg. Chem. Commun. 3*, 188−190. (g) Yam, V. W,-W., Lo, K. K.-W., Cheung, K.-K., and Kong, R. Y.-C. (1995) Synthesis, photophysical properties and DNA binding studies of novel luminescent rhenium(I) complexes. X-ray crystal structure of $[Re(dppn)(CO)_3(py)](OTf)$. *J. Chem. Soc., Chem. Commun. 11*, 1191−1193. (h) Thornton, N. B., and Schanze, K. S. (1993) A chromophore-quencher-based luminescence probe for DNA. *Inorg. Chem. 32*, 4994−4995. (i) Stoeffler, H. D., Thornton, N. B., Temkin, S. L., and Schanze, K. S. (1995) Unusual photophysics of a rhenium(I) dipyridophenazine complex in homogeneous solution and bound to DNA. *J. Am. Chem. Soc. 117*, 71190−7128.

(17) Lo, K. K.-W., Hui, W.-K., and Ng, D. C.-M. (2002) Novel rhenium(I) polypyridine biotin complexes that show luminescence enhancement and lifetime elongation upon binding to avidin. *J. Am. Chem. Soc. 124*, 9344−9345.

(18) Banerjee, S. R., Levadala, M. K., Lazarova, N., Wei, L., Valliant, J. F., Stephenson, K. A., Babich, J. W., Maresca, K. P., and Zubieta, J. (2002) Bifunctional single amino acid chelates for labeling of biomolecules with the $\{Tc(CO)_3\}^+$ and $\{Re(CO)_3\}^+$ cores. Crystal and molecular structures of $[ReBr(CO)_3(H_2NCH_2C_5H_4N)]$, $[Re(CO)_3\{(C_5H_4NCH_2)_2NH\}]Br$, $[Re(CO)_3\{(C_5H_4NCH_2)_2NCH_2CO_2H\}]Br$, $[Re(CO)_3\{X(Y)NCH_2CO_2CH_2CH_3\}]Br$ (X = Y = 2-pyridylmethyl; X = 2-pyridylmethyl, Y = 2-(1-methylimidazolyl)methyl; X = Y = 2-(1-methylimidazolyl)methyl), $[ReBr(CO)_3\{(C_5H_4NCH_2)NH(CH_2C_4H_3S)\}]$, and $[Re(CO)_3\{(C_5H_4NCH_2)N(CH_2C_4H_3S)(CH_2CO_2)\}]$. *Inorg. Chem. 41*, 6417−6425.

(19) Waibei, R., Alberto, R., Willude, J., Finnern, R., Schibli, R., Stichelberger, A., Egli, A., Abram, U., Mach, J. P., Pluckthern, A., and Schubiger, P. A. (1999) Stable one-step technetium-99m labeling of His-tagged recombinant proteins with a novel Tc(I)-carbonyl complex. *Nat. Biotechnol. 17*, 897−901.

(20) Stephenson, K. A., Banerjee, S. R., Besanger, T., Sogbein, O. O., Levadala, M. K., McFarlane, N., Lemon, J. A., Boreham, D. R., Maresca, K. P., Brennan, J. D., Babich, J. W., Zubieta, J., and Valliant, J. F. (2004) Bridging the gap between in vitro and in vivo imaging: isostructural Re and 99mTc complexes for correlating fluorescence and radioimaging studies. *J. Am. Chem. Soc. 126*, 8598−8599.

(21) (a) Di Bilio, A. M., Crane, B. R., Wehbi, W. A., Kiser, C. N., Abu-Omar, M. M., Carlos, R. M., Richards, J. H., Winkler, J. R., and Gray, H. B. (2001) Properties of photogenerated tryptophan and tyrosyl radicals in structurally characterized proteins containing rhenium(I) tricarbonyl diimines. *J. Am. Chem. Soc. 123*, 3181−3182. (b) Guo, X. Q., Castellano, F. N., Li, L., Szmacinski, H., Lakowicz, J. R., and Sipior, J. (1997) A long-lived, highly luminescent Re(I) metal−ligand complex as a biomolecular probe. *Anal. Biochem. 254*, 179−186. (c) Guo, X. Q., Castellano, F. N., Li, L., and Lakowicz, J. R. (1998) Use of a long-lifetime Re(I) complex in fluorescence polarization immunoassays of high-molecular-weight analytes. *Anal. Chem. 70*, 632−637. (d) Dattelbaum, J. D., Abugo, O. O., and Lakowicz, J. R. (2000) Synthesis and characterization of a sulfhydryl-reactive rhenium metal−ligand complex. *Bioconjate Chem. 11*, 533−536.

(22) (a) Wilbur, S., Hamlin, D. K., Vessella, R. L., Stray, J. E., Buhler, K. R., Stayton, P. S., Klumb, L. A., Pathare, P. M., and Weerawarna, S. A. (1996) Antibody fragments in tumor pretargeting. Evaluation of biotinylated fab′ colocalization with recombinant streptavidin and avidin. *Bioconj. Chem. 7*, 689−702. (b) Wilbur, S., Chyan, M. K., Pathare, P. M., Hamlin, D. K., Frownfelter, M. B., and Kegley, B. B. (2000) Biotin Reagents for antibody pretargeting. 4. Selection of biotin conjugates for in vivo application based on their dissociation rate from avidin and streptavidin. *Bioconjate Chem. 11*, 569−583. (c) Sundberg, S. A., Barrett, R. W., Pirrung, M., Lu, A. L., Kiangsoontra, B., and Holmes, C. P. (1995) Spatially addressable immobilization of macromolecules on solid supports. *J. Am. Chem. Soc. 117*, 12050−12057. (d) Alves, A. M., Holland, D., and Edge, M. D. (1989) A chemical method of labeling oligodeoxyribonucleotides with biotin: a single step procedure using a solid-phase methodology. *Tetrahedron Lett. 30*, 30889−3092.

(23) Levadala, M. K., Banerjee, S. R., Maresca, K. P., Babich, J. W., and Zubieta, J. (2004) Direct reductive alkylation of amino acids: synthesis of bifunctional chelates for nuclear imaging. *Synthesis* 1759−1766.

(24) Singh, B. N. (2005) A quantitative approach to probe the dependence and correlation of food-effect with aqueous solubility, dose/solubility ratio and partition coefficient (log *P*) for orally active drugs administered as intermediate-release formulations. *Drug Dev. Res. 65*, 55−75 and references therein.

(25) Lees, A. J. (1987) Luminescence properties of organometallic complexes. *Chem. Rev. 87*, 711−743.

BC050298O

Effects of Cell-Permeating Peptide Binding on the Distribution of ^{125}I-Labeled Fab Fragment in Rats

Shouju Kameyama,*,† Mayo Horie,† Takeo Kikuchi,† Takao Omura,† Toshihide Takeuchi,‡ Ikuhiko Nakase,‡ Yukio Sugiura,‡ and Shiroh Futaki‡,§

Research Planning, Bipha Corporation, Chitose, Hokkaido 066-0051, Japan, Institute for Chemical Research, Kyoto University, and PRESTO, JST, Uji, Kyoto 611-0011, Japan. Received August 24, 2005; Revised Manuscript Received January 5, 2006

The peptides comprising the sequence of HIV-1 Tat protein (positions 48−60), Antennapedia (positions 43−58), and HIV-1 Rev protein (positions 34−50) are known to be cell-permeating. In this study, we examined how the distribution of Fab fragments in rats is affected by conjugation with these peptides. Fab fragment was iodinated by a chloramine-T method and then chemically conjugated with cell-permeating peptide. The complex of ^{125}I-Fab and cell-permeating peptide was administered to male rats intravenously at a dose of 1 mg/kg, and whole-body autoradiography was performed at 4 and 24 h after administration. The patterns of distribution of ^{125}I-Fab exhibited remarkable variation depending on the cell-permeating peptide used. In particular, at 4 h, high concentrations of radioactivity were observed in the spleen, adrenal gland, renal medulla, and liver with Rev peptide−Fab complex, in the liver and spleen with Tat peptide−Fab complex, and in the spleen, adrenal gland, and liver with Antennapedia peptide−Fab complex. Even at 24 h, high concentrations of radioactivity were still observed in the spleen and renal medulla of rat with Rev peptide−Fab complex, and in the spleen and renal cortex of rat with Antennapedia peptide−Fab complex. These findings demonstrate that the patterns of distribution of peptide−^{125}I-Fab complexes can be modulated by selection of cell-penetrating peptides. Moreover, the patterns of retention of peptide−^{125}I-Fab complexes in internal organs also differed at 24 h after administration. These findings provide valuable information for the development of novel antibody pharmaceuticals and therapeutic systems.

INTRODUCTION

Antibodies are used in a variety of diagnostic methods and treatments for their high specificity and affinity to antigens. Their specificity of binding to viruses and bacteria, in particular, is associated with the prevention of viral and bacterial proliferation and infection, and antibody preparations are already available as therapeutic pharmaceuticals. However, although they are effective in blood, lymph, and similar tissues, antibodies are incapable of penetrating into cells and tissues and are thus nearly ineffective against latent viruses and bacteria.

Recently, a method of delivering high-molecular-weight proteins into cells using a cell-permeating peptide was developed, and the intracellular delivery of various proteins is now being studied (*1*−*9*). One of the most well-known cell-permeating peptides is that derived from positions 48−60 of Tat protein, a transcription regulator protein of HIV-1 (TAT). Antennapedia-derived peptide corresponding to positions 43−58 (ANP) has also been widely used (*10*−*12*). We have shown that the RNA binding site (positions 34−50: REV) of the HIV-1 Rev protein, which is involved in the cytosolic transport of viral mRNA, can act as a cell-permeating peptide (*13*−*15*). We are seeking to develop an innovative pharmaceutical by conjugating the REV peptide to an antibody. Although many individual studies of these cell-permeating peptides have been performed, there have been few comparative studies of them. In particular, there have been almost no such studies of the effects of attachment of these cell-permeating peptides to binding partner proteins on patterns of distribution in vivo.

In this study, we used REV, TAT, and ANP peptides as cell-permeating peptides. As a binding partner protein, we employed a Fab fragment (Fab), a functional low-molecular-weight antibody component. Each cell-permeating peptide was conjugated to iodinated Fab, radioisotope-labeled with ^{125}I in advance, and each complex was intravenously administered to rats. The patterns of distribution of complexes were examined by whole-body autoradiography (ARG), a method commonly used to examine the kinetics of labeled drugs in animals. The Fab was prepared from a polyclonal antibody (*16*), and each conjugate of cell-permeating peptide and Fab was prepared by a convenient method based on chemical modification (*13*).

EXPERIMENTAL PROCEDURES

General Procedures. The native Fab was prepared from a commercially available polyclonal antibody preparation (Venoglobulin-IH, Mitsubishi Pharma) using the ImmunoPure Fab Preparation Kit (Pierce). Cell-permeating peptides were synthesized using solid-phase methods at the Peptide Institute (Osaka, Japan). We employed REV, TAT, and ANP peptides as cell-permeating peptides, as shown in Table 1. The purities of these peptides were 95% or more as determined by HPLC. Matrix-assisted laser desorption ionization time-of-flight mass spectrometry (MALDI-TOFMS) was measured using an Applied Biosystems Voyager-DE STR.

Preparation of Cell-Permeating Peptide−^{125}I-Fab. The Fab was first labeled with ^{125}I by the chloramine-T method (*17*, *18*). Iodinated Fab (^{125}I-Fab) was adjusted to 1 mg/mL with nonlabeled Fab solution. One hundred twenty micrograms of *N*-(6-maleimidocaproyloxy) succinimide ester (EMCS) (1 molar equiv to Fab) was added to 1 mL of ^{125}I-Fab solution, and this

* Corresponding author. Mailing address: 1007-124, Izumisawa, Chitose, Hokkaido, 066-0051, Japan. Phone: +81-72-856-9389. Fax: +81-72-864-2341. E-mail: Kameyama.Shouju@mm.m-pharma.co.jp.
† Bipha Corporation.
‡ Kyoto University.
§ PRESTO, JST.

10.1021/bc050258k CCC: $33.50 © 2006 American Chemical Society
Published on Web 04/25/2006

Table 1. Cell-Permeating Peptides Used in This Study

peptide	amino acid sequence	purity (%)[a]
REV (HIV-1 Rev (34−50))	NH_2-TRQARRNRRRRWRERQR-GC-$CONH_2$	98.2
TAT (HIV-1 Tat (48−60))	NH_2-GRKKRRQRRRPPQ-C-$CONH_2$	98.0
ANP (Antennapedia (43−58))	NH_2-RQIKIWFQNRRMKWKK-GC-$CONH_2$	95.6

[a] HPLC conditions: column, Zorbax 300SB-C18 (4.6 mm i.d. × 150 mm); eluant, 1−60% CH_3CN/ 0.1% TFA (25 min); temperature, 50 °C; flow rate, 1.0 mL/min; detection, 220 nm.

mixture was gently stirred at room temperature for 2 h. The free EMCS was removed with a PD-10 column (Amersham) previously equilibrated with phosphate-buffered saline (PBS). Subsequently, the column effluent was concentrated by centrifugation using Microprep (Millipore), and this concentrate was adjusted to a final volume of 1 mL with PBS. One molar equivalent of REV, TAT, or ANP peptide (230 μL) was added to this reaction mixture, and the mixture was gently stirred at room temperature for 2 h. After excess peptide was removed using a PD-10 column, the protein fraction was concentrated by centrifugation using Microprep to obtain the complexes of REV, TAT, or ANP peptide with ^{125}I-Fab (REV−^{125}I-Fab, TAT−^{125}I-Fab, ANP−^{125}I-Fab). Each peptide−^{125}I-Fab complex was adjusted to a final protein concentration of 1 mg/mL and stored below −30 °C until use.

Radiochemical Purity of Cell-Permeating Peptide-Conjugated ^{125}I-Fab. The radiochemical purity of test substances was determined by radio-HPLC before administration. The analytical column used was a POROS R2/10 (PerSeptive Biosystems), with a nonlabeled complex used to confirm retention time. Subsequently, an aliquot of the dosing solution was separated and assayed for radioactivity before administration. After this mixed solution was centrifuged (3000 rpm, 15 min, 4 °C), the supernatant was removed, and the sediment was assayed for radioactivity. The ratio of the concentration of radioactivity of the TCA sediment fraction to that of the entire dosing solution was calculated. Radioactivities were determined using a γ counter (Cobra 5005, PerkinElmer).

Incorporation of Cell-Permeating Peptide-Conjugated ^{125}I-Fab into HeLa Cells. HeLa cells (in 24-well plates) were grown to subconfluence. After replacement of culture medium with 500 μL per well of fresh MEM medium, the cells were incubated at 37 °C for 3 h. Subsequently, 5 μL of peptide−^{125}I-Fab was added and the cells were incubated at 37 °C for 30 min. After washing three times with PBS, 200 μL of trypsin-EDTA solution was added to each well and incubated at 37 °C for at least 15 min to completely detach the cells. The cells and cell lysate were recovered from each well into a polystyrene tube, and radioactivity was determined using a γ counter (COBRA Quantum, PerkinElmer).

Preparation of Fluorescein-REV−Fab and Microscopic Observation. The fluorescently labeled conjugates of Fab with cell-penetrating peptides were prepared similarly to cell-permeating peptide−^{125}I-Fab conjugates. One hundred twenty micrograms of EMCS, together with 305 μg of fluorescein-5(6)-carboxamidocaproic acid *N*-hydroxy succinimide ester (FLUOS), was added to 1 mL of nFab solution (1 mg/mL), and this mixture was gently stirred at room temperature for 2 h. Free EMCS and FLUOS were removed with a PD-10 column (eluate, PBS). The first main peak was concentrated by centrifugation using Microprep, and this concentrate was adjusted to a final volume of 1 mL with PBS. One molar equivalent of REV peptide (230 μL) to EMCS was added to this reaction mixture, and the mixture was gently stirred at room temperature for 2 h. After excess peptide was removed using a PD-10 column, the protein fraction was concentrated by centrifugation using Microprep to obtain the conjugates of fluorescein-REV peptide with nFab (fluorescein-REV−Fab). Fluorescein-REV−Fab was stored below −30 °C until use.

For microscopic assay, 2×10^5 cells were plated into 35-mm glass-bottomed dishes (Iwaki) and cultured for 48 h. After complete adhesion, the culture medium was exchanged. The cells were then incubated at 37 °C with fresh medium (200 μL) containing the fluorescein-REV−Fab. The cells were washed five times with cold PBS. Distribution of fluorescein-REV−Fab in live cells was analyzed using a confocal scanning laser microscope FV300 (Olympus) equipped with a 40 × objective without fixation.

Determination of Concentrations of Radioactivity in Blood. At 0.25, 0.5, 1, 3, 6, and 24 h after administration of test substance, blood (approximately 0.4 mL) was drawn from the caudal vein using a glass capillary with an inner wall treated with 500 units/mL heparin sodium in physiological saline. A 0.1 mL portion of each blood sample was separated for determination of blood concentrations and transferred to a polystyrene tube, and the radioactivity in the sample was determined using a γ counter. Subsequently, 1 mL of physiological saline and 1 mL of 20% trichloroacetic acid (TCA) were added to the assayed sample, and this solution was subjected to centrifugation (3000 rpm, 15 min, 4 °C). After the supernatant was removed, 1 mL of physiological saline was added to the sediment, followed by centrifugation in the same manner. The supernatant was removed, and the radioactivity in the TCA sediment fraction was determined.

Whole-Body ARG. Animals receiving test substance were killed by ether anesthesia at 4 h after administration. After each animal body was clipped, an approximately 3% carboxymethylcellulose sodium salt (CMC-Na) solution was filled in the oral cavity, nasal cavities, earholes, and anus, and the animal was quickly frozen in a hexane−dry ice bath. The tail and extremities were then amputated, and the body was preserved in wrap at −20.4 to −17.0 °C for at least 24 h. An approximately 3% CMC-Na solution was applied to the body surface of the frozen fixed rat. Subsequently, the body was embedded in an approximately 5% CMC-Na solution and frozen in a hexane-dry ice bath to obtain a frozen block. Frozen sections 30 μm in thickness were prepared using a cryomicrotome. The sections were obtained in a median plane, in 2 planes containing kidney and other major tissues. Each section was freeze-dried at approximately −20 °C. The dry sections were applied to base paper and covered with Mylar film. The sections for ARG were brought into close contact with an imaging plate (IP), and exposed in a shield box for 12 h. After completion of exposure, the images were scanned using a bioimaging analyzer, and whole-body ARGMs were generated (gradation, 65536; resolution, 50 μm; sensitivity, 4000; latitude, 5, IP; BAS-MS2040). Images obtained by whole-body ARG were analyzed on a relative basis using the Image Gauge software program (version 3.46, Fuji Photo Film).

RESULTS

Preparation of Cell-Permeable Peptide−Fab Conjugates. When the in vivo distribution of cell-permeable peptide−Fab conjugates is examined, contamination of free Fab in the conjugates may make the analysis of results difficult, since the methods of biodistribution of conjugates may differ from that of free Fab. We therefore first established conditions in which no free Fab remained in the conjugates, with use of various amounts of the cross-linking agent EMCS and the peptides (Figure 1). SDS−PAGE of REV−Fab and nFab showed that the ranges of molecular weights of the conjugates shifted depending on the amounts of cross-linking agent (EMCS) and

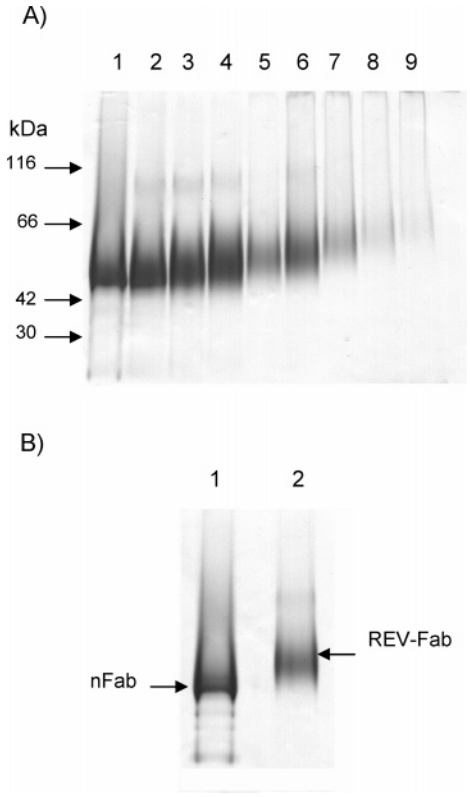

Figure 1. SDS−PAGE of REV peptide and Fab conjugate. (A) Lanes 1−9 correspond to conjugates prepared by the treatment of nFab with 0, ×1.5, ×3, ×6, ×12 (1/2 sample volume), ×12, ×24, ×36, and ×48 equiv of EMCS and REV peptide, respectively, at room temperature for 2 h. When ×12 equiv of these are employed, substantially no free Fab is observed in the sample (B). Lane 1, nFab, and lane 2, REV−Fab, correspond to samples prepared by the same conditions as samples administered to rats. A 4−12% gradient gel (NOVAX) was employed for the analysis.

Table 2. Stoichiometric Ratios of Fab and Cell-Permeable Peptide Conjugates

	molecular weight			
		complex[b]		stoichiometric ratio (*B*/*A*)
samples	peptide[a] (*A*)	main	diff[c] (*B*)	
nFab		48 000		
REV−Fab	2 597	61 000	13 000	5.0
TAT−Fab	1 821	57 000	9 000	4.9
ANP−Fab	2 406	60 000	12 000	5.0

[a] Molecular weight determined by electrospray ion mass spectroscopy (ESIMS). [b] Molecular weight determined by TOFMS. [c] The difference of molecular weight between peptide−Fab and nFab.

the peptides employed (Figure 1A). We selected use of ×12 equiv of EMCS and peptides each to Fab for preparation of the conjugates, with which no notable bands corresponding to unmodified nFab were observed on SDS−PAGE (Figure 1B). Since the cationic cell-penetrating peptides may neutralize the negative charges of SDS and may affect the mobility of samples in the gel, we further analyzed the molecular weights of the conjugates using MALDI-TOFMS.

Table 2 shows the stoichiometric ratios of cell-penetrating peptides and Fab in the conjugates prepared using the same conditions as determined above, which were also employed for chemical conjugation of ^{125}I-Fab in subsequent study. The average peptide:Fab ratios were thus estimated to be about 5:1 for each conjugate. In addition, no notable signals corresponding to the free Fab were observed (data not shown).

Cellular Uptake of Fluorescently Labeled REV−Fab Conjugate in HeLa Cells. Figure 2 shows results of confocal microscopic observation of HeLa cells treated with the fluorescently labeled REV−Fab conjugate (1 M) at 37 °C for 1 h. Significant internalization of the conjugate was observed, whereas internalization of the free, unconjugated Fab was poor.

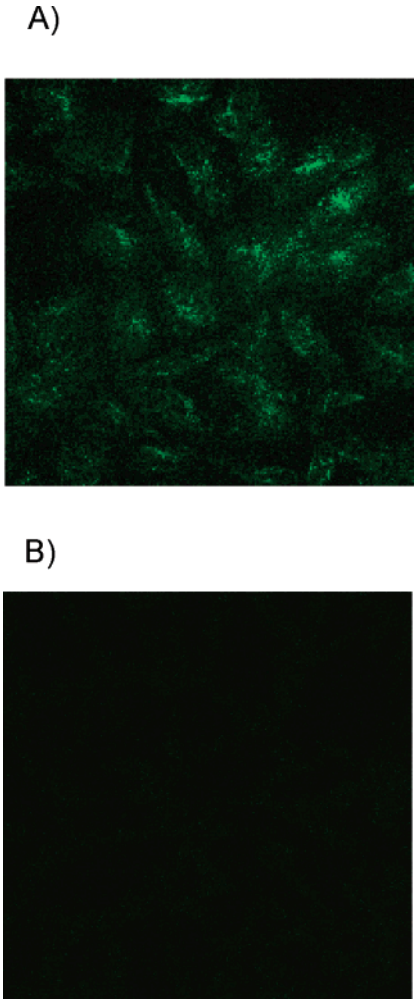

Figure 2. The cellular uptake of the fluorescently labeled REV−Fab conjugate by HeLa cells. The cells were observed without fixation. (A) Fluorescently labeled REV−Fab. (B) Fluorescently labeled nFab.

Table 3. Radiochemical Purities of the Cell-Permeable Peptide-Conjugated ^{125}I-Fabs

	radioactivity	radiochemical purity	
sample	(MBq mg^{-1} mL^{-1})	HPLC (%)	TCA insoluble (%)[a]
^{125}I-Fab	1.27	97.3	95.1
REV−^{125}I-Fab	1.45	98.5	96.5
TAT−^{125}I-Fab	1.49	98.4	96.2
ANP−^{125}I-Fab	1.27	98.5	94.3

[a] HPLC conditions: column, POROS R2/10 (4.6 mm diameter × 50 mm length); eluant, 1−100% CH_3CN/0.1% TFA (5.5 min); temperature, 23 °C; flow rate, 3.0 mL/min; detection, 280 nm.

Radiochemical Purity of Peptide−^{125}I-Fab Complexes. Table 3 shows the concentrations of radioactivity in and radiochemical purities of the samples given to rats. Rev peptide conjugated ^{125}I-Fab (REV−^{125}I-Fab), Tat peptide conjugated ^{125}I-Fab (TAT−^{125}I-Fab), and Antennapedia peptide conjugated ^{125}I-Fab (ANP−^{125}I-Fab) each had radiochemical purities above 97% as determined by HPLC. The radiochemical purities of the TCA sediment fractions of these samples were also 94% or higher.

Incorporation of Cell-Permeating Peptide Conjugated with ^{125}I-Fab into HeLa Cells. REV−^{125}I-Fab, TAT−^{125}I-Fab, ANP−^{125}I-Fab, or ^{125}I-Fab was added to the culture medium

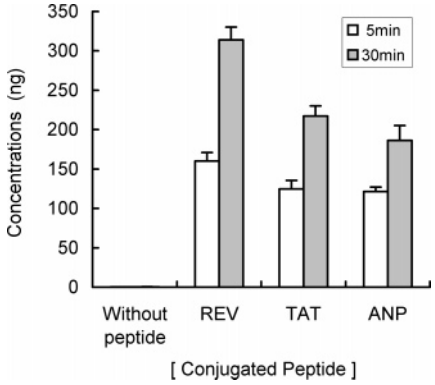

Figure 3. Effects of peptide binding on cellular uptake of ^{125}I-Fabs in HeLa cells. Values are the mean ± SD of the results for 4 wells.

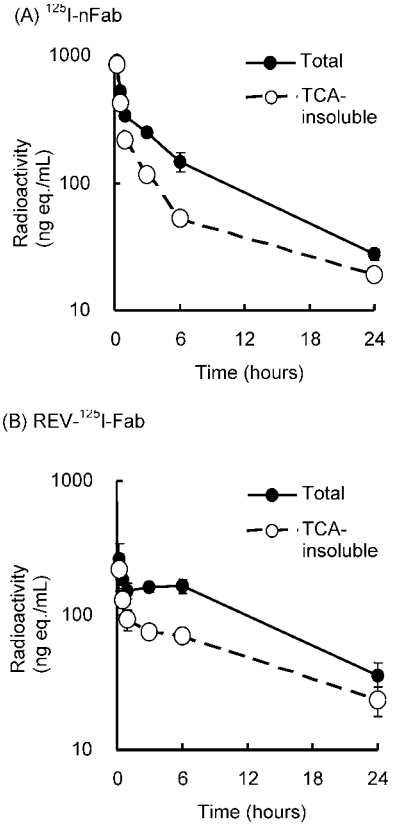

Figure 4. Concentrations of radioactivity in blood after intravenous administration of ^{125}I-Fab or REV−^{125}I-Fab to male rats. Values are the mean ± SD of results for 3 animals.

for HeLa cells, and uptake into cells was determined. Figure 3 shows findings for these peptides at 5 and 30 min after addition of samples. The level of incorporation of ^{125}I-Fab was very low at both times. On the other hand, the cell-permeating, peptide-conjugated Fabs each exhibited high intracellular incorporation. The order of cellular uptake was REV−^{125}I-Fab > TAT−^{125}I-Fab ≥ ANP−^{125}I-Fab at both time points.

Concentrations of Radioactivity in Blood Following Intravenous Administration. Figure 4 shows the time course of radioactive concentration in rat blood following intravenous administration of ^{125}I-Fab or REV−^{125}I-Fab. We measured the concentrations of radioactivity in whole blood and the TCA-insoluble fractions. ^{125}I-Fab without cell-permeating peptide exhibited a slow biphasic decline in concentration of radioactivity. On the other hand, a rapid decrease in concentration of radioactivity was observed for REV−^{125}I-Fab as early as within 1 h after administration, though the rate of decline subsequently slowed, with a plateau at 3 to 6 h after administration.

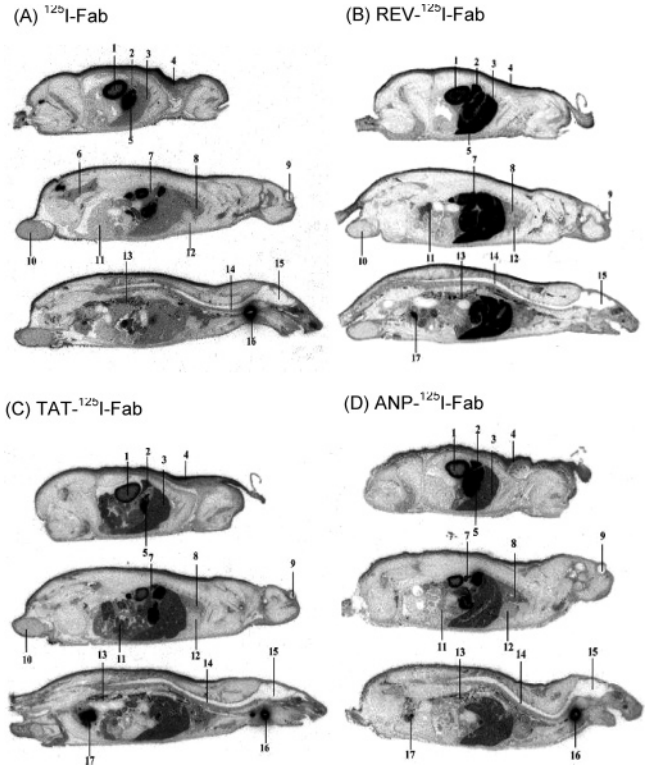

Figure 5. Whole-body autoradiograms at 4 h after intravenous administration of peptide−^{125}I-Fab complexes to rats: 1, kidney; 2, spleen; 3, liver; 4, skin; 5, gastric contents; 6, bone marrow; 7, adrenal gland; 8, lung; 9, eyeball; 10, testis; 11, intestinal contents; 12, heart; 13, blood; 14, spinal cord; 15, brain; 16, thyroid gland; 17, urinary bladder.

Whole-Body ARG. Single intravenous administration of REV−^{125}I-Fab, TAT−^{125}I-Fab, ANP−^{125}I-Fab, or ^{125}I-Fab to male rats was performed, and whole-body ARGMs were generated 4 and 24 h later. At 4 h after administration of ^{125}I-Fab, particularly high radioactivity was observed in the thyroid, renal cortex, and gastric contents, and relatively high radioactivity in the skin. However, little radioactivity was detected in the brain or spinal cord (Figure 5A). At 24 h after administration, particularly high radioactivity was observed in the thyroid and relatively high radioactive concentrations were observed in the renal cortex, gastric contents, and skin, but almost no radioactivity was detected in any other tissue (Figure 6A).

In the case of REV−^{125}I-Fab, particularly high radioactivity was observed in the spleen, adrenal gland, and liver at 4 h after administration, and relatively high radioactivity was observed in the renal medulla (Figure 5B). At 24 h after administration, relatively high radioactivity was observed in the spleen and renal medulla (Figure 6B). For TAT−^{125}I-Fab, particularly high radioactivity was observed in intestinal contents at 4 h after administration, and relatively high radioactivities were observed in the liver, spleen, and small intestinal contents (Figure 5C). At 24 h after administration, relatively high radioactivity was observed in intestinal contents, but almost no radioactivity was observed in any other tissue (Figure 6C). At 4 h after administration of ANP−^{125}I-Fab, relatively high radioactivities were observed in the spleen, adrenal gland, and liver (Figure 5D). At 24 h after administration, relatively high radioactivity was observed in the spleen and renal cortex (Figure 6D).

DISCUSSION

Whole-body ARG has been used for accurate analysis of the kinetics of labeled drugs and bioactive proteins in animals, and it yields precise findings useful for characterizing patterns of

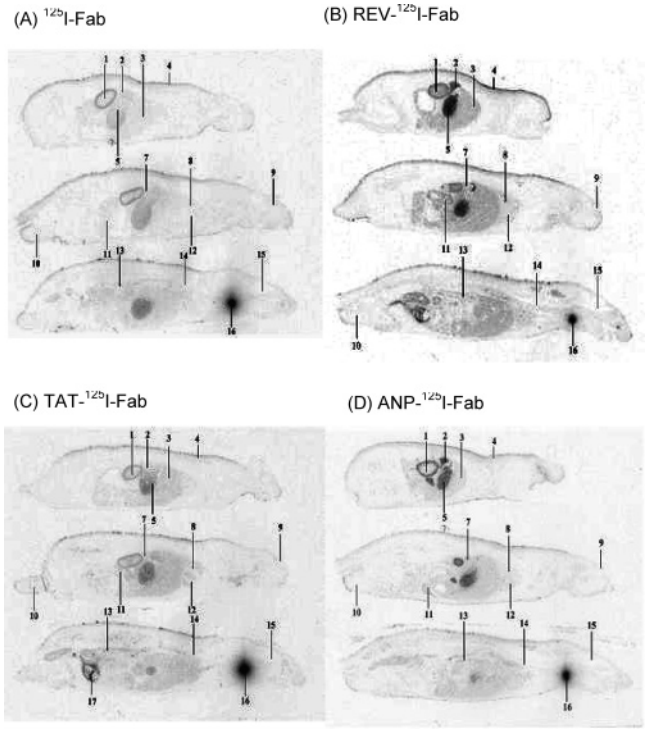

Figure 6. Whole-body autoradiograms at 24 h after intravenous administration of peptide−^{125}I-Fab complexes to rats: 1, kidney; 2, spleen; 3, liver; 4, skin; 5, gastric contents; 7, adrenal gland; 8, lung; 9, eyeball; 10, testis; 11, intestinal contents; 12, heart; 13, blood; 14, spinal cord; 15, brain; 16, thyroid gland; 17, urinary bladder.

distribution as well. Development of new antibody pharmaceuticals with the potential for penetration into cells is a challenge in antibody therapy. Determination of in vivo patterns of distribution is a very important part of this development. We therefore examined the patterns of distribution of peptide−antibody complexes in rat using whole-body ARG. In the present study, we used REV, TAT, and ANP peptides as cell-permeating peptides, which were chemically conjugated to Fab as an antibody component. The patterns of distribution of the complexes were compared with each other.

Contamination by free, unmodified Fab would make assessment of biodistribution of the peptide conjugates difficult due to the presence of two radioiodinated species (^{125}I-Fab and peptide−^{125}I-Fab); in this case, the biodistribution profiles of each peptide−^{125}I-Fab conjugate would be the sum of those of the two radiolabeled species. We therefore established conditions in which free Fab should not contaminate cell-permeating peptide−Fab conjugates in significant amounts (Figure 1). TOFMS analysis revealed that each peptide−Fab conjugate had a peptide:Fab stoichiometric ratio of about 5:1. Therefore, the differences in biodistribution of conjugates can be attributed to the nature of each peptide.

It would be ideal to use conjugates for which carrier peptides are modified to specific sites with a predefined stoichiometry. Generally speaking, it is not easy to obtain these by chemical modification. They may be obtained using genetically engineered proteins. However, considering the lack of information on antibody delivery using peptide carriers, we decided to employ chemical modification as a first step in our study.

Confocal microscopic observation of HeLa cells showed that cellular uptake of Fab was promoted by conjugation with the cell-permeating peptides. Others have reported similar observations (*23, 24*). Using ^{125}I-labeled Fab, we then examined the cellular uptake of REV−^{125}I-Fab, TAT−^{125}I-Fab, ANP−^{125}I-Fab, and unconjugated ^{125}I-Fab by HeLa cells. Each complex of ^{125}I-Fab conjugated with a cell-permeating peptide was rapidly incorporated into HeLa cells, though ^{125}I-Fab was not. These results are consistent with those of previous microscopic studies using fluorescently labeled conjugates (*12, 13*), suggesting that radioisotope labeling did not decrease the cellular permeability of these peptides.

We subsequently performed whole-body ARG for cell-permeating peptides conjugated to ^{125}I-Fab following intravenous administration to rats. The times for performance of whole-body ARG were determined based on the time courses of blood concentration of radioactivity following intravenous administration. ^{125}I-Fab exhibited a slow biphasic decline in the blood, whereas REV−^{125}I-Fab initially exhibited a rapid decline in blood following intravenous administration and then slowly entered a continuous phase about 3 to 6 h after administration. This initial rapid reduction in radioactivity in blood may be due to the quick penetration of REV−^{125}I-Fab into tissue.

One of the most successful studies of in vivo delivery using TAT and other cell-penetrating peptides is that by Schwarze et al. (*4*), who reported that intraperitoneal injection of conjugate of TAT and β-galactosidase to mouse resulted in distribution of the conjugates to various tissues including brain. They included tissue distributions at 4 h after administration. There have been several other in vivo studies, the majority of which present distributions in the body from 1 to 24 h (*20, 21, 25*−*27*). In order to compare our results with the preceding findings, we performed whole-body ARG at 4 and 24 h. The latter time point was also selected to assess the duration of the conjugates in tissues; this information is very important for designing effective delivery systems with low toxicity.

Conjugation of the cell-permeating peptides yielded remarkable changes in distributions of ^{125}I-Fab. At 4 h after administration, nonconjugated ^{125}I-Fab was present in the thyroid, gastrointestinal contents, renal cortex, and skin. On the other hand, peptide-conjugated ^{125}I-Fabs were distributed not only to these organs but to others as well, including the liver, spleen, and adrenal gland. Interestingly, distinct patterns of penetration were observed for each of the cell-permeating peptides. For REV−^{125}I-Fab, the highest concentrations of radioactivity were observed in the liver, spleen, and adrenal gland. TAT−^{125}I-Fab was nearly unobservable in the adrenal gland, although it was observed in the liver and spleen. The pattern of tissue distribution of ANP−^{125}I-Fab in tissues was similar to that of REV−^{125}I-Fab, though REV−^{125}I-Fab was characterized by greater penetration into the liver, spleen, and adrenal gland.

On whole-body ARG at 24 h after administration, the earliest elimination was observed for TAT−^{125}I-Fab, the levels of which had decreased nearly to those of ^{125}I-Fab in almost all organs examined. The finding of high levels of radioactivity in intestinal and gastric contents suggests that TAT−^{125}I-Fab might be excreted in the form of low-molecular-weight components. For REV−^{125}I-Fab, high retention compared to that of ^{125}I-Fab was observed in the spleen and renal medulla. Retention of ANP−^{125}I-Fab was observed in the spleen and renal cortex. These differences among peptides in localization and retention of Fab conjugates in vivo provide valuable information for the development of organ-specific antibody delivery systems.

The distribution of TAT−^{125}I-Fab at 4 h after administration in this study was similar to those of [99mTc]Tat peptide and ^{125}I-scFV−Cys-TAT in previous studies. Previous studies on the distribution of TAT peptide alone or complexes of it with proteins have revealed accumulation in the liver and spleen (*4, 19*−*22*), consistent with the present findings. It should be noted, however, that although relatively high pulmonary penetration was observed in previous studies, almost no pulmonary accumulation of TAT−^{125}I-Fab was observed in this study. This difference in findings might be due in part to differences among studies in binding partner proteins used or in methods used for

conjugation. In addition, although the existence of β-galactosidase activity in brain was reported by Schwarze et al. (*4*), none of the Fab conjugates tested in this study exhibited high levels of accumulation in brain or spinal cord. Schwarze et al. administered test samples intraperitoneally, whereas we employed the intravenous route for administration. This difference in route of administration might have affected passage through the blood−brain barrier.

In conclusion, this study has clearly demonstrated that appropriate selection of cell-penetrating peptides yields differences in in vivo distribution of Fab, with large changes in distribution observed in organs such as the liver, spleen, adrenal gland, and kidney. Moreover, conjugation of Fabs with cell-penetrating peptides was found to have profound effects on retention of such Fabs in internal organs. Further study using cell-penetrating peptides, especially on the effects of peptide: Fab stoichiometry and the precise kinetics/time course of biodistribution, will provide valuable information for the development of novel antibody pharmaceuticals and therapeutic systems.

ACKNOWLEDGMENT

We are grateful to Dr. Takatoshi Nakamura (Shin Nippon Biomedical Lab., Japan) for helpful discussions.

LITERATURE CITED

(1) Fawell, S., Seery, J., Daikh, Y., Moore, C., Chen, L. L., Pepinsky, B., and Barsoum, J. (1994) Tat-mediated delivery of heterologous proteins into cells. *Proc. Natl. Acad. Sci. U.S.A. 91*, 664−668.

(2) Vives, E., Brodin, P., and Lableu, B. (1997) A truncated HIV-1 tat protein basic domain rapidly translocates through the plasma membrane and accumulates in the cell nucleus. *J. Biol. Chem. 272*, 16010−16017.

(3) Nagahara, H., Vocero-Ajkbani, A. M., Snyder, E. L., Ho, A., Latham, D. G., Lissy, N. A., Becker-Hapak, M., Ezheevsky, S. A., and Dowdy, S. F. (1998) Transduction of full-length TAT fusion proteins into mammalian cells: TAT-p27^{Kip1} induces cell migration. *Nat. Med. 4*, 1449−1452.

(4) Schwarze, S. R., Ho, A., Vocero-Akbani, A., and Dowdy, S. F. (1999) In vivo transduction: delivery of a biological active protein into mouse. *Science 285*, 1569−1572.

(5) Lee, H. J., and Pardridge, W. M. (2001) Pharmacokinetics and delivery of tat and tat-protein conjugates to tissues in vivo. *Bioconjugate Chem. 12*, 995−999.

(6) Richard, J. P., Melokov, K., Vives, E., Ramos, C., Verbeure, B., Gait, M. J., Chemomordik, L. V., and Lebleu, B. (2003) Cell-penetrating peptides. A reevaluation of the mechanism of cellular uptake. *J. Biol. Chem. 278*, 585−590.

(7) Lindsay, M. A. (2002) Peptide-mediated cell delivery: application in protein target validation. *Curr. Opin. Pharmacol. 2*, 587−594.

(8) Gait, M. J. (2003) Peptide-mediated cellular delivery of antisense oligonucleotides and their analogs. *Cell. Mol. Life Sci. 60*, 844−853.

(9) Zhao, M., and Weissleider, R. (2004) Intracellular cargo delivery using tat peptide and derivatives. *Med. Res. Rev. 24*, 1−12.

(10) Derossi, D., Joliot, A. H., Chassaing, G., and Prochiantz, A. (1994) The third helix of the Antennapedia homeodomain translocates through biological membranes. *J. Biol. Chem. 269*, 10444−10450.

(11) Williams, E. J., Dunican, D. J., Green, P. J., Howell, F. V., Derossi, D., Walsh, F. S., and Doherty, P. (1997) Selective inhibition of growth factor-stimulated mitogenesis by a cell-permeable Grb2-binding peptide. *J. Biol. Chem. 272*, 22349−22354.

(12) Derossi, D., Chassaing, G., and Prochiantz, A. (1998) Trojan peptides: the penetratin system for intracellular delivery. *Trends Cell Biol. 8*, 84−87.

(13) Futaki, S., Suzuki, T., Ohashi, W., Yagami, T., Tanaka, S., Ueda, K., and Sugiura, Y. (2001) Arginine-rich peptides: an abundant source of membrane-permeable peptides having potential as carriers for intracellular protein delivery. *J. Biol. Chem. 276*, 5836−5840.

(14) Suzuki, T., Futaki, S., Niwa, M., Tanaka, S., Ueda, K., and Sugiura, Y. (2002) Possible Existence of Common Internalization Mechanisms among Arginine-rich Peptides. *J. Biol. Chem. 277*, 2437−2443.

(15) Futaki, S., Goto, S., Suzuki, T., Nakase, I., and Sugiura, Y. (2003) Structural variety of membrane permeable peptides. *Curr. Protein Pept. Sci. 4*, 87−96.

(16) Mage, M. G. (1980) Preparation of Fab fragments from IgGs of different animal species. *Methods Enzymol. 70*, 142−150.

(17) Sonoda, S., and Schlamowitz, M. (1970) Studies of 125I trace labeling of immunoglobulin G by chloramine-T. *Immunochemistry 7*, 885−898.

(18) Stavrou, D., Mellert, W., Bilzer, T., Senekowitsch, R., Keiditsch, E., and Mehraein, P. (1985) Radioimmunodetection of gliomas by administration of radiolabelled monoclonal antibodies. Experimental data. *Anticancer Res. 5*, 147−156.

(19) Polyakov, V., Sharma, V., Dahlheimer, J. L., Pica, C. M., Luker, G. D., and Piwnica-Worms, D. (2000) Novel Tat-Peptide Chelates for Direct Transduction of Techetium-99m and Rhenium into Human Cells for Imaging and Radiotherapy. *Bioconjugate Chem. 11*, 762−771.

(20) Niesner, U., Halin, C., Lozzi, L., Gunthert, M., Neri, P., Wunderli-Allenspach, H., Zardi, L., and Neri, D. (2002) Quantitation of the tumor-targeting properties of antibody fragments conjugated to cell-permeating HIV-1 tat peptides. *Bioconjugate Chem. 13*, 729−736.

(21) Wunderbaldinger, P., Josephson, L., and Weissleder, R. (2002) Tat Peptide Directs Enhanced Clearance and Hepatic Permeability of Magnetic Nanoparticles. *Bioconjugate Chem. 13*, 264−268.

(22) Bullok, K. E., Dyszlewski, M., Prior, J. L., Pica, C. M., Sharma, V., and Piwnica-Worms D. (2002) Characterization of novel Histidine-tagged tat-peptide complexes dual-labeled with ^{99m}Tc-tricarbonyl and fluorescein for scintigraphy and fluorescence microscopy. *Bioconjugate Chem. 13*, 1226−1237.

(23) Stein, S., Weiss, A., Adermann, K., Lazarovici, P., Hochman, J., and Wellhoner, H. (1999) A disulfide conjugate between anti-tetanus antibodies and HIV (37-72) Tat neutralizes tetanus toxin inside chromaffin cells. *FEBS Lett. 458*, 383−386.

(24) Pooga, M., Kut, C., Kihlmark, M., Hallbrink, M., Ferneus, S., Raid, R., Land, T., Hallberg, E., Bartfai, T., and Langel, U. (2001) Cellular translocation of proteins by transportan. *FASEB J. 15*, 1451−1453.

(25) Jain, M., Chauhan, S. C., Singh, A. P., Venkatraman, G., Colcher, D., and Batra, S. K. (2005) Penetratin improves tumor retention of single-chain antibodies: A novel step toward optimization of radioimmunotherapy of solid tumors. *Cancer Res. 65*, 7840−7846.

(26) Lee, H. J., and Pardridge, W. M. (2001) Phramacokinetiks and delivery of tat and tat-protein conjugates to tissues in vivo. *Bioconjugate Chem. 12*, 995−999.

(27) Hong, G., Bazin-Redureau, M. I., and Scherrmann, J. M. G. (1999) Pharmacokinetics and organ distribution of cationized colchicine-specific IgG and Fab fragments in rats. *J. Pharm. Sci. 88*, 147−153.

BC050258K

Synthesis and Grafting of Thioctic Acid−PEG−Folate Conjugates onto Au Nanoparticles for Selective Targeting of Folate Receptor-Positive Tumor Cells

Vivechana Dixit,[†] Jeroen Van den Bossche,[‡] Debra M. Sherman,[#] David H. Thompson,*[,‡] and Ronald P. Andres*[,†]

School of Chemical Engineering, Department of Chemistry, Life Science Microscopy Facility, Purdue University, West Lafayette, Indiana 47907. Received November 22, 2005; Revised Manuscript Received February 16, 2006

This paper reports the creation of Au nanoparticles (AuNP) that are soluble in aqueous solution over a broad range of pH and ionic strength values and that are capable of selective uptake by folate receptor positive (FR+) cancer cells. A novel poly(ethylene glycol) (PEG) construct with thioctic acid and folic acid coupled on opposite ends of the polymer chain was synthesized for targeting the AuNP to FR+ tumor cells via receptor-mediated endocytosis. These folic acid−PEG−thioctic acid conjugates were grafted onto 10-nm-diameter Au particles in aqueous solution. The resulting folate−PEG-coated nanoparticles do not aggregate over a pH range of from 2 to 12 and at electrolyte concentrations of up to 0.5 M NaCl with particle concentrations as high as 1.5×10^{13} particles/mL. Transmission electron microscopy was used to document the performance of these coated nanoparticles in cell culture. Selective uptake of folate−PEG grafted AuNPs by KB cells, a FR+ cell line that overexpress the folate receptor, was observed. AuNP uptake was minimal in cells that (1) do not overexpress the folate receptor, (2) were exposed to AuNP lacking the folate−PEG conjugate, or (3) were co-incubated with free folic acid in large excess relative to the folate−PEG grafted AuNP. Understanding this process is an important step in the development of methods that use targeted metal nanoparticles for tumor imaging and ablation.

INTRODUCTION

Current anticancer agents suffer from several limitations—they are typically highly toxic and are often nonspecific in that they accumulate within normal as well as tumor cells. In many cases, they also have limited bioavailability due to poor solubility and limited stability in vivo, leading to short half-lives and rapid clearance from the body. An ideal solution to these problems would be to deliver biologically effective concentrations of the therapeutic agent(s) to the cancer cells with high specificity. One approach to this ultimate goal could be achieved by attaching the agents to the surface of a gold nanoparticle (AuNP)[1] that is small enough to be transported through the circulatory system, is not rapidly cleared from the body, and is selectively targeted to cancer cells.

AuNPs are the most chemically stable of metal nanoparticles. They have been studied as "soluble" gold since the fifth or fourth century B.C. both for their aesthetic and for their curative properties. In ancient times, they were used in the manufacture of ruby glass and in the treatment of a wide range of diseases (*1*). The use of AuNP in modern biology dates to their application as immunological staining agents for electron microscopy (*2*), wherein the AuNP are functionalized by simple covalent attachment or physisorption of an antibody or enzyme to the particle surface prior to exposure to tissue sections.

Recently, AuNPs have become the subject of increased interest in the context of the emerging fields of nanoscience and nanotechnology due to the ease of synthesizing monolayer-protected AuNP. These inorganic−organic constructs typically have a core−shell morphology consisting of a gold core, as small as 1−2 nm in diameter, surrounded by a covalently attached monolayer of organic molecules. The organic shell passivates the metallic core and imparts steric stabilization to the nanoparticles, permitting their manipulation as stable organic compounds. Recent reviews provide a compilation of the methods used to fabricate monolayer-protected AuNPs and highlight some of their important applications (*3*, *4*).

AuNPs must be water-soluble over a wide range of pH values and electrolyte concentrations to successfully target tumor cells. They must also resist recognition and subsequent removal by macrophages associated with the reticuloendothelial system. We anticipated that water solubility and biocompatibility could be achieved by coating the Au core with a biomedically accepted, water-soluble polymer such as poly(ethylene glycol) (PEG), since PEGylation of proteins (*5*) and liposomes (*6*−*9*) is known to increase their bioavailability, improve their pharmacokinetics, and decrease their immunogenicity.

One method of covalently attaching PEG chains to AuNP is through the use of a thiol-terminated PEG. Foos et al. (*10*) used this approach to synthesize water-soluble AuNP. Tshikhudo et al. (*11*) also synthesized water-soluble AuNP by terminating the PEG chain with an alkanethiol. The use of a short alkane chain between the Au surface and the PEG chain is thought to produce a dense, ordered "brush" morphology on the Au surface. Tokumitsu et al. (*12*) observed a conformational transition when alkanethiol-terminated PEG chains are grafted to a flat Au substrate, consistent with the theoretical predictions of Szleifer (*13*). The PEG chains exist in a so-called "mushroom" regime at low coverages; however, as the coverage increases, they undergo a transition to a more extended conformation (i.e., the "brush" regime) away from the surface. From the standpoint of producing stable AuNPs for in vivo use, chemisorption of PEG is preferred over physisorption. It is not clear, however, whether a more ordered PEG layer anchored by alkanethiol adsorption

* Corresponding authors. (R.P.A.) E-mail: Ronald@ecn.purdue.edu. Voice: 765-494-4047. Fax: 765-494-0805. (D.H.T.) E-mail: davethom@purdue.edu. Fax: 765-496-2592.

[†] School of Chemical Engineering.

[‡] Department of Chemistry.

[#] Life Science Microscopy Facility.

[1] Abbreviations: Poly(ethylene glycol) (PEG), folate−PEG1500−thioctamide-modified gold nanoparticles (F−PEG1500−T:AuNP), folate receptor (FR), folate receptor positive (FR+), gold nanoparticles (AuNP), mPEG2000−thioctamide-modified gold nanoparticles (mPEG2000−T:AuNP).

10.1021/bc050335b CCC: $33.50 © 2006 American Chemical Society
Published on Web 05/03/2006

Scheme 1. Schematic Representation of the PEG-Modified AuNP Used and Their Exposure to FR+ and FR− Cells.

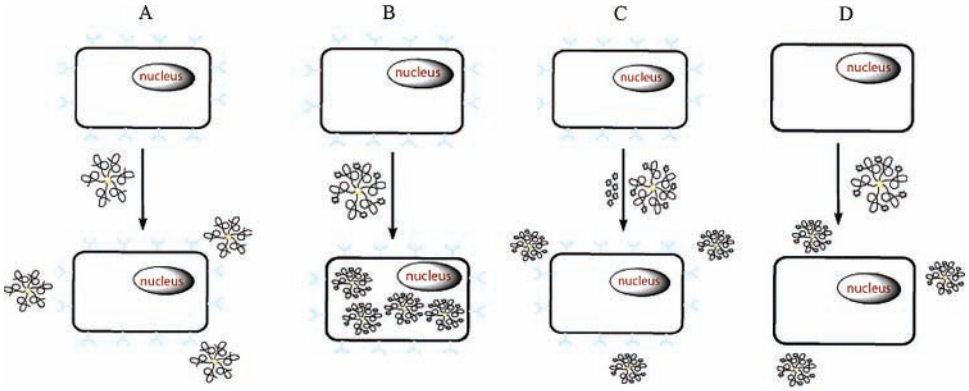

A: fR+ cells exposed to mPEG2000-T:Au NP
B: fR+ cells exposed to F-PEG1500-T:Au NP
C; fR+ cells exposed to F-PEG 1500-T:Au NP in presence of excess folate
D: fR- cells exposed to F-PEG1500-T:Au NP

on gold or a more amorphous monolayer provided by direct disulfide termination of the PEG chain is more desirable for imparting water solubility and biocompatibility to the Au nanoparticles.

A second method for covalently attaching PEG chains to AuNP is by replacing the terminal thiol substituent with a disulfide moiety. Mangenay et al. (*14*) have shown that hydrophilic polymers that are end-capped with a disulfide can be efficiently grafted onto citrate-stabilized AuNPs in aqueous solution. This is the method adopted in the present study. Thioctic acid was chosen as the grafting agent due to its low cost, simple coupling chemistry, and ease of handling relative to thiol-based conjugates.

Folic acid was chosen as the targeting agent. Folate is an essential precursor for the synthesis of nucleic acids and some amino acids, is not produced endogenously by mammalian cells, and requires internalization by cells via either receptor-mediated endocytosis or a carrier-based uptake mechanism (*15*−*17*). The folic acid receptor (FR)-based mechanism constitutes a particularly useful target for tumor-specific drug delivery because it is upregulated in many human cancers, including malignancies of the ovary, brain, kidney, breast, and lung. The FR density also appears to increase as the stage/grade of the cancer increases (*18*). An additional feature of FR that is particularly attractive for intravenous drug delivery strategies is the fact that FR generally becomes accessible to the vascular epithelium only after malignant transformation. This is because FR is selectively expressed on the apical membrane surface of normal polarized epithelial cells and is, therefore, protected from FR-directed therapeutics delivered in the plasma. Upon epithelial cell transformation, however, cell polarity is lost and FR becomes accessible to targeted drugs in blood circulation (*19*). The folate receptor has a high affinity for folic acid ($K_d \sim 0.1$ nM), which results in high uptake by FR+ cells, even at low folate loadings on the therapeutic agent (*17*, *19*). Because of these attractive characteristics, folate conjugation has become a widely used strategy for targeting liposomes (*20*−*25*), plasmid complexes (*26*−*33*), nanoparticles (*34*−*36*), polymer micelles (*37*), and other polymer constructs (*38*) for selective uptake by tumor cells.

The 10 nm AuNPs chosen for this study were a compromise between providing a reasonable surface area for attachment of PEG chains while at the same time enabling rapid nanoparticle penetration into solid tumors based on the enhanced permeation and retention effect (e.g., EPR) (*39*, *40*). The AuNPs were purchased as a citrate-stabilized aqueous colloid. Two PEG polymers were synthesized for grafting onto AuNPs, a mPEG−thioctic acid conjugate (mPEG2000−T) for steric stabilization and a folic acid−PEG−thioctic acid conjugate (F−PEG1500−T) that would enable both steric stabilization and tumor cell targeting. After the AuNPs were modified with either of these conjugates, they were monitored for colloidal stability by absorption spectroscopy. KB cells were then treated with either the mPEG−thioctic acid-modified AuNP (mPEG2000−T:AuNP) or the folate−PEG1500−thioctic acid-modified AuNP (F−PEG1500−T:AuNP) constructs (Scheme 1) and their capacity for internalization observed using TEM.

EXPERIMENTAL PROCEDURES

Materials and Methods. Size selected (10 nm) gold colloid was obtained from Ted Pella Inc. (Redding, CA). mPEG-NH_2 was purchased from Nektar Therapeutics (Huntsville, AL); all other chemicals were purchased from Sigma-Aldrich (St. Louis, MO) and used as received. All reactions were performed under anhydrous conditions and under an Ar atmosphere unless otherwise mentioned. All solvents were reagent grade and were distilled from CaH_2 under Ar before use. NMR spectra were recorded on Varian 200 or 300 MHz spectrometers using ^1H solvent peaks as internal reference. Column chromatography was typically performed on 230−400 mesh silica gel using HPLC grade eluents. Thin-layer chromatography was performed using Baker-flex IB−F plates (J. T. Baker) and visualized using UV, I_2 adsorption, $KMnO_4$/heat, and/or H_2SO_4/heat.

Synthesis of Functionalized PEG Polymers. *Synthesis of mPEG-NH−thioctamide (mPEG2000−T).* mPEG2000-NH_2 (1 g, 0.50 mmol) and NHS-activated thioctic acid (287 mg, 1 mmol; prepared as described by Ponpipom et al. (*41*) were dissolved in 20 mL anhydrous CH_2Cl_2. Triethylamine (1 mL, 6.9 mmol) was then added dropwise, and the resulting solution was stirred for 3 days at reflux. After cooling of the reaction to 25 °C, the mixture was evaporated, redissolved in 1 mL of CH_2Cl_2, and precipitated from a 1:1 Et_2O/hexane mixture at −20 °C. After filtration, the product was isolated via silica gel chromatography using 9:1 $CHCl_3$/MeOH as eluent. The white powder was determined to be pure by NMR analysis (>95% purity) Yield: 63%, R_F: 0.48 (9:1 $CHCl_3$/MeOH, I_2 stain), ^1H NMR ($CDCl_3$, 300 MHz): 6.32 (br s, 1H), 3.89 (t, 2H), 3.74−3.55 (m, 200H), 3.19 (m, 3H), 2.51 (m,2H), 2.37 (t, 2H), 2.23 (t, 2H), 1.96 (m, 3H), 1.7 (m, 8 H), 1.50 (m, 4H).

Synthesis of NH_2-PEG1500-NHBoc. NH_2-PEG1500-NH_2 (5 g, 3 mmol) in 50 mL anhydrous MeOH was added to a solution of Boc_2O (0.7 g, 3 mmol). Et_3N (1 mL, 6.9 mmol) was then added in dropwise fashion, and the resulting solution was stirred overnight at reflux. After cooling of the reaction to 25 °C, the

mixture was evaporated, dissolved in 5 mL of CH_2Cl_2, and precipitated from a 1:1 Et_2O/hexane mixture at −20 °C. After filtration, the product was isolated via silica gel chromatography using 89:10:1 $CHCl_3$/MeOH/NH_4OH as eluent. The off-white powder was determined to be pure by NMR (>95%). Yield: 27%, R_F: 0.3 (89:10:1 $CHCl_3$/MeOH/NH_4OH, I_2 stain), ^1H NMR ($CDCl_3$, 300 MHz): 5.03 (s, 3H), 3.75−3.52 (m, 150H), 3.21 (q, 2H), 2.1 (s, 3H), 1.76 (m, 2H), 1.44 (s, 9H).

Synthesis of tBocNH-PEG1500-NH−thioctamide. H_2N-PEG1500-NHBoc (1 g, 0.62 mmol) and NHS-thioctate (400 mg, 1.2 mmol) were dissolved in 10 mL CH_2Cl_2, and 1 mL of Et_3N was added dropwise. This mixture was stirred at reflux for 3 days, after which it was evaporated, redissolved in 1 mL of CH_2Cl_2, and precipitated from 1:1 Et_2O/hexane at −20 °C. After filtration, the product was purified by silica gel chromatography using 95:5 $CHCl_3$/MeOH as eluent. The off-white powder was pure by NMR (>95%) Yield: 61%, R_F: 0.25 (95:5 $CHCl_3$/MeOH, I_2 stain), ^1H NMR ($CDCl_3$, 300 MHz): 4.28 (t, 2H), 3.92−3.45 (m, 150H), 3.28 (m, 3H), 2.78 (s, 2H), 2.52 (m, 1H), 2.41 (t, 1H), 2.0−1.65 (m, 14H), 1.49 (s, 9H).

Synthesis of NH_2-PEG1500-NH−thioctamide. Boc-NH-PEG1500-NH−thioctamide (610 mg) was dissolved in 10 mL of a 1:1 (vol/vol) solution of TFA in CH_2Cl_2. This mixture was stirred at 25 °C for 3 h after which the solvent was evaporated. The recovered solid was redissolved in 1 mL of CH_2Cl_2 and precipitated from a 1:1 Et_2O/hexane mixture at −20 °C. The isolated solid was pure by TLC analysis. Yield: 98%, R_F: 0.14 (89:10:1 $CHCl_3$/MeOH/NH_4OH, I_2 stain), ^1H NMR ($CDCl_3$, 300 MHz): 4.24 (t,2H), 3.88−3.41 (m, 150H), 3.2 (q, 4H), 2.48 (m, 2H), 2.36 (t, 2H), 2.0 (m, 3H), 1.91 (m,1H), 1.67 (m, 3H), 1.5 (m,2H), 0.80 (s,1H).

Synthesis of Folate−NH-PEG-NH−thioctamide (F−PEG-1500−T). Thioctic acid−NH-PEG1500-NH_2 (200 mg, 0.11 mmol) and folic acid (100 mg, 0.20 mmol) were dissolved in 5 mL of anhydrous DMSO. Pyridine (500 μL) was added dropwise to this mixture, followed by DCC (100 mg, 0.6 mmol). The solution was stirred overnight at 70 °C, then cooled to 25 °C, and 50 mL of Et_2O was added. The precipitated product was redissolved and reprecipitated from 1:1 Et_2O/hexane at −20 °C, and the solid was further purified via silica gel chromatography using a 20:79:1 to 50:49:1 MeOH/CH_2Cl_2/NH_4OH step gradient elution. After purification, the isolated product was redissolved in CH_2Cl_2 and filtered through a PFTE filter to remove dissolved Si gel. The filtered solution was then evaporated and dissolved in 60:30:10 benzene/CH_2Cl_2/MeOH and lyophilized to give a yellow powder (>95% pure by NMR). Yield: 59%, R_F: 0.44 (50:49:1 MeOH/CH_2Cl_2/NH_4OH, I_2/UV visualization), ^1H NMR (DMSO, 300 MHz): 8.67 (d, 1H), 8.32 (br s, 1H), 7.92−7.85 (m, 2H), 7.72 (d, 1H), 7.64 (d, 1H), 7.43 (s, 1H), 7.20 (br s, 2H), 6.95 (q, 2H), 6.70 (t, 2H), 4.5 (t,3H), 4.18 (t, 2H), 3.80−3.11 (m, 150h), 2.70 (s, 1H), 2.49 (m, 2H), 2.37 (t, 2H), 2.29 (t, 1H), 2.20−1.80 (m, 4H), 1.64 (m, 5H), 1.44 (m, 2H), 1.30 (s, 1H).

Grafting of Functionalized PEG Polymers onto AuNP. All glassware was cleaned with aqua regia and rinsed with DI water. Citrate-stabilized gold colloid solution (3 mL, used as supplied at ~5.7×10^{12} particles/mL) was adjusted to pH 9−11 using 0.5 M NaOH. The AuNP suspension was then combined with 3 mL of 0.25 mM mPEG2000−T or F−PEG1500−T, and the solution was stirred at 25 °C for 16−18 h. The resulting suspension was split into two equal volumes and centrifuged twice at 13,000 rpm for 60 min at 8 °C with decantation of the supernatant and redispersion of the particles in DI water. The two rinsed samples of AuNP were then recombined in 1 mL of DI water.

The UV−Vis spectra of the AuNP in DI water were measured using a Jasco V-550 spectrophotometer operating at a resolution of 1 nm with a 400 nm/min scan rate. The concentration of nanoparticles in the final suspension was in the range 1.0×10^{13} to 1.5×10^{13} particles/mL as determined by absorption spectroscopy.

TEM Characterization of AuNP Samples. AuNP samples were prepared for TEM analysis by placing a drop of the colloidal solutions on Formvar+C-coated Cu TEM grids and air-drying the grid at 25 °C. The samples were viewed with a Philips CM-10 TEM using 80 kV accelerating voltage.

Cell Culture and AuNP Treatment. KB cells, a human cancer cell line of nasopharyngeal origin that is known to overexpress folate receptors, were cultured in folate-deficient Dulbecco's modified Eagle medium (FD-DMEM) supplemented with 10% heat inactivated fetal calf serum, 2 mM L-glutamine, and penicillin/streptomycin for 3 weeks to establish a folate deficiency. The folate-deficient KB cells were then subcultured in 75 cm^2 flasks at 37 °C in a 5% CO_2 atmosphere. Cells were used during the log phase of growth and discarded after the sixth passage.

WI-38 cells, a normal embryonic human diploid cell line, were used as a control. These cells were cultured in FD-DMEM supplemented with 10% heat inactivated fetal calf serum, 2 mM L-glutamine, and penicillin/streptomycin for 3 weeks. The WI-38 cells were subcultured in 75 cm^2 flasks at 37 °C in a 5% CO_2 atmosphere. Cells were used during the log phase of growth and discarded after the sixth passage.

Both the KB and the WI-38 cells were plated at ~250,000 cells/well in six-well plates and incubated for 48 h. At this point, 100 μL of AuNP solution (~1.5×10^{13} particles/mL; sterilized by filtration through a 0.22 μm filter) was added to three of the wells. After a 1 h incubation period, 100 μL of nanoparticle solution was added to the remaining three wells, and all were incubated for an additional 1 h before rinsing with fresh media to remove free AuNP before fixation.

TEM Imaging of AuNP Uptake by Cells. TEM imaging was used to evaluate the cellular uptake of AuNP. Gold intensification was used to enhance the observability of the 10 nm AuNPs followed by osmium fixation to delineate the cell membranes. Gold enhancement, unlike silver intensification, is not degraded by exposure to osmium tetroxide.

The samples were processed in a PELCO model 3450 microwave equipped with variable wattage, a Coldspot temperature regulator, and vacuum chamber (Ted Pella, Inc., Redding, CA). Processing times and wattage (P1 = 233 W, P2 = 345 W) are noted for each step. Cells were fixed in 2% glutaraldehyde in 0.1 M cacodylate buffer (pH 7.4) containing 2 mM $MgCl_2$, 1 mM $CaCl_2$, 40 mM NaCl (P1: 1 min hold > 40 s on > 3 min hold). Samples were then washed with buffer three times followed by a water wash (P1: 40 s each). Cells were scraped from the wells and pelleted by centrifugation.

Samples were incubated for 2 min at 25 °C in GoldEnhance kit #2113 (Nanoprobes, Inc. Yaphank, NY) formulated according to kit directions to increase the size of the gold particles. Following a water wash (P1: 40 s), the pellets were post-fixed in reduced osmium (1% OsO_4 + 1.5% $K_4Fe(CN)_6$) for two 40 s cycles at P1). The samples were then enrobed with 1.5% agarose (Sigma Type VII) and processed further as tissue blocks.

Sample blocks were dehydrated through a graded ethanol series (P1: 30, 50, 70, 90 and 100%, two cycles each, 40 s per change), followed by propylene oxide (P1 × 40 s). They were then infiltrated in propylene oxide (LX-112 resin mix, 3:1, 1:1 for 30 min each followed by overnight in 1:3 mix plus accelerator on a rotator at 25 °C). Blocks were embedded in LX-112 resin mixture (Ladd Research Industries, Williston, VT) and polymerized at 60°C for 48 h.

Ultrathin sections (~100 nm) were picked up on Formvar+C coated 100 mesh Cu grids. The samples were viewed with a

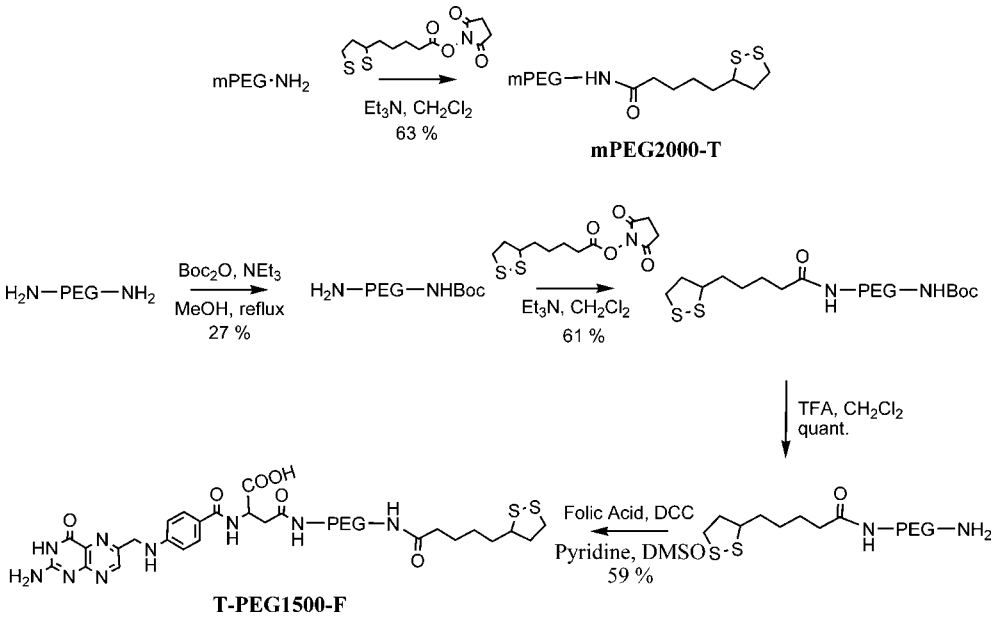

Figure 1. Synthetic schemes for mPEG2000−T and F−PEG1500−T.

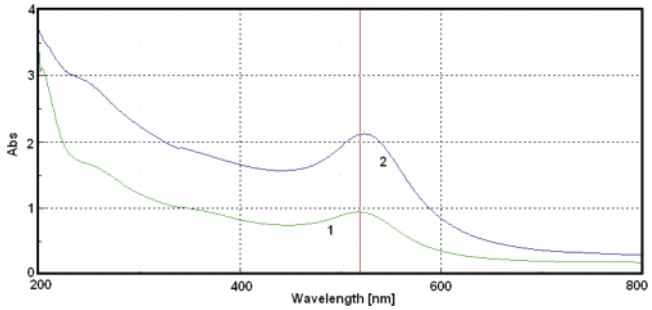

Figure 2. Absorption spectra of colloidal suspensions of 10 nm diameter AuNPs: (1) citrate capped AuNPs; (2) T−PEG−F coated AuNPs.

Philips CM-10 TEM using 80 kV accelerating voltage. TEM negatives were scanned at 600 dpi and image processed using Adobe Photoshop.

RESULTS AND DISCUSSION

The methods developed for both mPEG−thioctamide (mPEG-2000−T) and folate−PEG−thioctamide (F−PEG1500−T) enable the synthesis of these constructs on the gram scale (Figure 1). Boc-protection of NH_2-PEG1500-NH_2 was found to be necessary since initial attempts at the direct synthesis of monosubstituted PEG-thioctamide resulted in inseparable mixtures. Boc protection results in a mixture of products that is easier to separate and produces acceptable yields of mono-Boc protected PEG. Coupling of this intermediate with NHS-thioctate, followed by deprotection and coupling with folic acid gives the desired F−PEG1500−T in reasonable yield.

Initial attempts at grafting the thioctic acid-functionalized polymers onto citrate-capped AuNP under a wide variety of conditions and concentrations in aqueous solution proved unsuccessful. However, it was found that efficient displacement of citrate by the thioctic acid functionalized polymers could be achieved by adjusting the solution pH to 9−11 with NaOH.

UV−Vis absorption spectra for the 10-nm-diameter, citrate-stabilized AuNP, with and without a chemisorbed F−PEG-1500−T coating in deionized H_2O, are presented in Figure 2. These spectra have a strong absorption feature at ∼520 nm due to the characteristic surface plasmon resonance of AuNPs (*3*). The height of this feature is proportional to the concentration of AuNPs in solution, while peak position and width are indicative of the size, size distribution, aggregation, and surface coating of the particles. Figure 2 shows that there is minimal broadening of the peak and only a small red-shift in the position of the maximum when the citrate-capped particles are coated with F−PEG1500−T. This is an indication that the AuNPs are not aggregated in solution. Adding HCl, NaOH, or NaCl to an aqueous suspension of the AuNP (∼1.5×10^{13} particles/mL) does not markedly affect the UV−Vis spectra (i.e., cause particle aggregation) over a pH range of 2−12 and an electrolyte concentration range of 0−0.5 M NaCl. Aqueous suspensions of AuNP within these ranges of pH and electrolyte concentration are observed to be stable for up to a year as determined by their absorption spectra.

Figure 3 shows TEM micrographs illustrating the diameter and size distribution of the citrate-capped AuNPs and F−PEG-1500−T:AuNPs. Although the nanoparticles aggregate due to surface tension as the water evaporates during sample preparation, the Au cores of the particles do not coalesce and fuse. Analysis of the mean diameter and size distribution of these two AuNP preparations shows that the Au cores of the F−PEG1500−T coated particles are similar to those of the citrate-capped particles. These data indicate that AuNP integrity is unaffected by F−PEG1500−T grafting.

Of the two known mechanisms of folic acid transport into cells, only the receptor-mediated endocytosis pathway enables the uptake of folate conjugates by mammalian cells (*42*) (Scheme 2). A series of experiments were undertaken to determine whether the 10-nm-diameter F−PEG1500−T:AuNPs are selectively internalized by FR+ tumor cells. The nanoparticles were added to the cell cultures at a particle concentration of ∼5×10^{11} particles/mL or a loading of ∼6×10^6 AuNPs/cell, and the cells were incubated for periods of 1 and 2 h. After the incubation period, the cells were rinsed with FD-DMEM, chemically fixed, washed, and processed as described in the Experimental Section prior to TEM analysis.

KB cells were incubated with mPEG−T:AuNP as a control to establish that (1) nontargeted PEG-coated AuNPs are not internalized and that (2) AuNPs not taken up by the cells are eliminated in the washing process. Figure 4A shows a typical micrograph of a KB cell exposed to mPEG-T:AuNP. Only an occasional Au nanoparticle was observed inside the cells, which

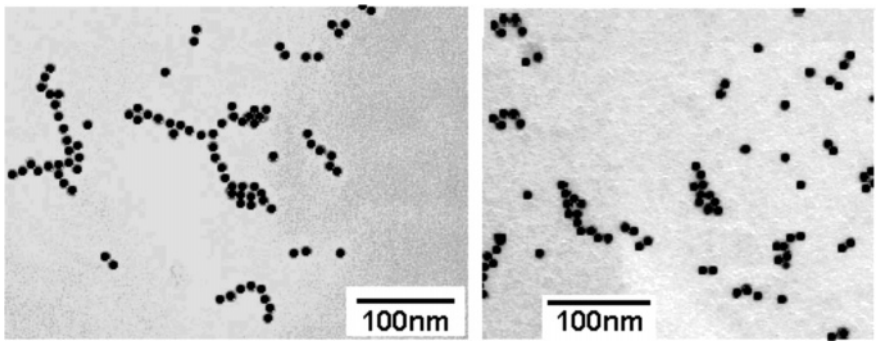

Figure 3. TEM micrographs of 10 nm diameter Au nanoparticles: left micrograph citrate-capped AuNPs; right micrograph T−PEG−F-coated AuNPs.

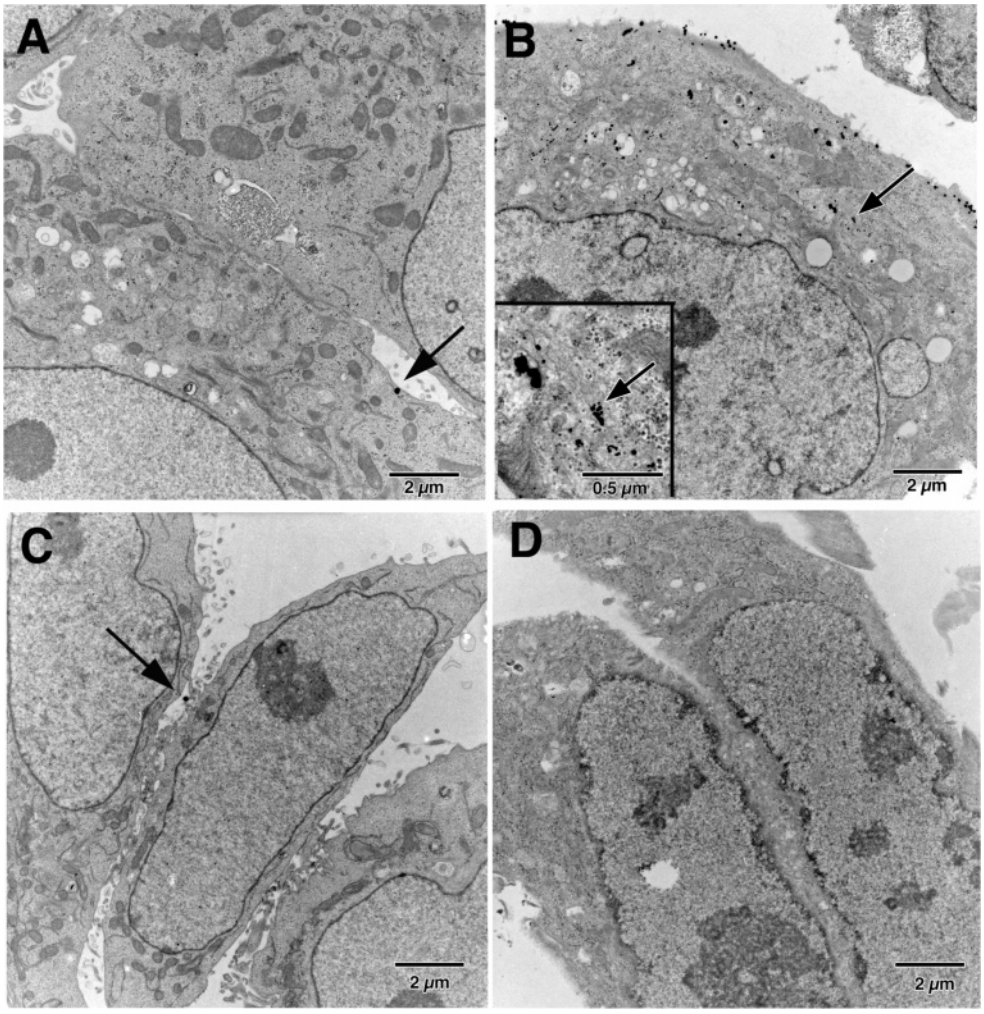

Figure 4. TEM Micrographs of thin sections of cells that were incubated for 2 h with various AuNP constructs. Magnification of primary images is 6000×; the inset is shown at 28000×. (A) KB cells incubated with mPEG2000−T:AuNP. Occasionally, AuNP are found adjacent to the cell plasma membrane (arrow), but most are removed by washes during sample preparation. (B) KB cells incubated with F−PEG1500−T:AuNP. Region corresponding to the higher magnification inset is denoted by the arrow which shows significant uptake of nanoparticles throughout the cytoplasm. (C) KB cells incubated with F−PEG−T:AuNP in the presence of excess folic acid. (D) WI-38 cells incubated with F−PEG−T:AuNP.

was presumably internalized via nonspecific adsorption to the cell surface. The number of nanoparticles observed outside the cell membrane was also extremely small as indicated by the single AuNP imaged in Figure 4A. These data support the expectation that mPEG2000−T-coated particles are not internalized to a significant extent by KB cells. The absence of a specific binding event between the mPEG2000−T:AuNPs and the folate receptor on the surface of these cells prevents their uptake, enabling their facile removal from the cells by washing.

Figure 4B shows a typical micrograph of a KB cell that was incubated with F−PEG−T:AuNPs. After both 1 and 2 h of exposure, about 20% of the KB cells were found to contain a large number of the folate functionalized nanoparticles. The intracellular distribution of the nanoparticles was similar to that observed with folate-targeted liposomes (*21*), i.e., localization within lysosomes near the nucleus and within endosomes distributed throughout the endosomal pathway. It should be noted that gold intensification of AuNPs enclosed inside the cells resulted in a nonuniform particle size distribution and caused particles adjacent to each other to coalesce as seen in

Scheme 2. Conceptual Diagram of Folate Receptor-Mediated Binding, Internalization, Endosomal Acidification, Intracellular Trafficking, and Endosomal Escape of F−PEG1500−T:AuNP by Folate Receptor-Positive Cells (*43*).

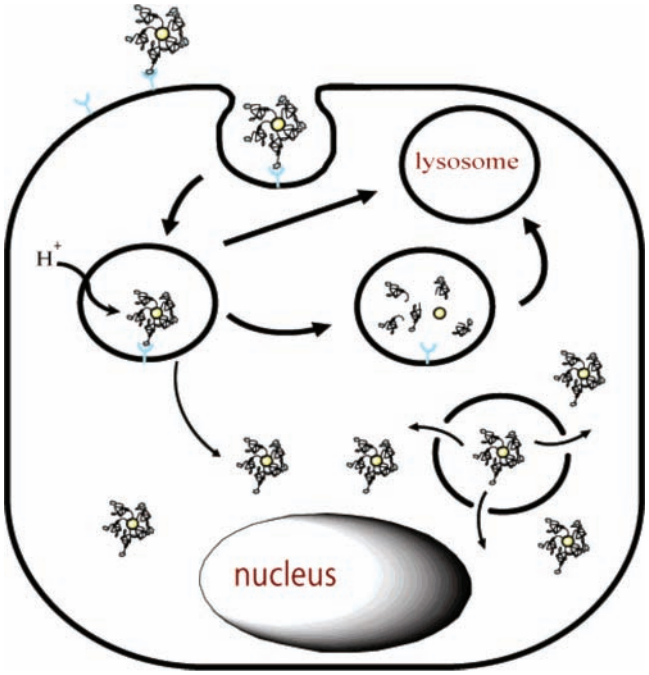

the high magnification inset in Figure 4B. This phenomenon and the random nature of the sectioning process made accurate estimation of the AuNP density within the cells difficult. However, by taking multiple high magnification images, it was possible to estimate the particle density in the thin sections. Assuming these thin sections to be 100 nm thick, this analysis yields an estimated density of $0.25-1.0 \times 10^{15}$ nanoparticles/mL of cell volume, which is 2−3 orders of magnitude greater than the particle density in the growth medium. Variations in the incubation times (e.g., 1, 2, or 12 h) of the cells with F−PEG1500−T:AuNP did not appear to affect the number of particles internalized.

Two additional control experiments lend further support for the uptake of F−PEG1500−T:AuNP via receptor-mediated endocytosis. When F−PEG1500−T/AuNP were incubated with KB cells in a medium that was augmented with free folate (i.e., 2 μM folic acid added to the FD-MEM during nanoparticle incubation with the cells), the KB cells did not internalize the nanoparticles (see Figure 4C). Furthermore, it was observed that WI-38 cells rarely internalized any of the particles when incubated with F−PEG1500−T:AuNP (see Figure 4D). Since the WI-38 cells lack the folate receptor, they are incapable of internalizing significant amounts of the folate-functionalized nanoparticles.

CONCLUSIONS

Poly(ethylene glycol) conjugates bearing either methoxy and thioctic acid or folic acid and thioctic acid substituents at opposing ends of the polymer have been synthesized. These conjugates have been grafted onto 10-nm-diameter Au nanoparticles, via the thioctic acid moiety. The PEG−folate-coated nanoparticles are soluble in water over a pH range of 2−12 and electrolyte concentration range of 0−0.5 M and exhibit selective uptake by a folate receptor positive (FR+) cell line when the AuNP construct contains folic acid. These sterically stabilized nanoparticles may have potential uses in targeted drug delivery to FR+ cancer cells.

It is interesting to note that only about 20% of the KB cancer cells exposed to the F−PEG1500−T/AuNP actively took up the particles. However, these cells took them up in large numbers. It is not clear whether this is related to the metabolic state of the cells during the initial exposure to the particles or to other physiological reasons unique to this type of cell. Additional experiments will be done to increase the uptake efficiency and further develop the responsiveness of the system.

ACKNOWLEDGMENT

We would like to acknowledge the use of the Life Science Microscopy Facility and the expertise of Chia-Ping Huang in preparation of samples for TEM. Dr. Vivechana Dixit performed the AuNP coating, spectroscopy, and stability studies. Mr. Jeroen Van den Bossche performed the PEG syntheses and the cell culture experiments. This study was supported by the Showalter Trust.

LITERATURE CITED

(1) Antonii, F. *Panacea Aurea-Auro Potabile*, Bibiopolio Frobeniano, Hamburg, 1618.
(2) Faulk, W. P., and Taylor, G. M. (1971) Immunocolloid method for electron microscope. *Immunochemistry 8*, 1081.
(3) Daniel, M.-C., and Astruc, D. (2004) Gold nanoparticles: Assembly, supramolecular chemistry, quantum-size-related properties, and applications toward biology, catalysis, and nanotechnology. *Chem. Rev. 104*, 293−346.
(4) Goodman, C. M., and Rotello, V. M. (2004) Biomacromolecule surface recognition using nanoparticles. *Mini-Rev. Org. Chem. 1*, 103−114.
(5) Abuchowski, A., Vanes, T., Palczuk, N., and Davis, F. (1977) Alteration of immunological properties of bovine serum-albumin by covalent attachment of polyethylene-glycol. *J. Biol. Chem. 252*, 3578−3581.
(6) Klibanov, A. L., Maruyama, K., Torchilin, V. P., Huang, L (1990) Amphipathic poly(ethylene glycol)s effectively prolong the circulation time of liposomes. *FEBS Lett 268*, 235−7.
(7) Allen, T. M., Hansen, C., Martin, F., Redemann, C.; Yau-Young A. (1991) Liposomes containing synthetic lipid derivatives of poly-(ethylene glycol) show prolonged circulation half-lives in vivo. *Biochim. Biophys. Acta 1066*, 29−36.
(8) *Stealth Liposomes* (Lasic, D., Martin, F., Eds.) CRC Press, Boca Raton, FL, 1995.
(9) Gabizon, A., Shmeeda H., and Barenholz, Y. (2003) Pharmacokinetics of pegylated liposomal doxorubicin − Review of animal and human studies. *Clin. Pharmacokin. 42*, 419−436.
(10) Foos, E. E., Snow, A. W., Twigg, M. E., and Ancona, M. G. (2002) Thiol-terminated di-, tri-, and tetraethylene oxide functionalized gold nanoparticles: A water-soluble, charge-neutral cluster. *Chem. Mater. 14*, 2401−2408.
(11) Tshikhudo, T. R., Wang, Z., and Brust, M. (2004) Biocompatible gold nanoparticles. *Mater. Sci. Technol. 20*, 980−984.
(12) Tokumitsu, S., Liebich, A., Herrwerth, S., Eck, W., Himmelhaus, M., and Grunze, M. (2002) Grafting of alkanethiol-terminated poly-(ethylene glycol) on gold. *Langmuir 18*, 8862−8870.
(13) Carignano, M. A., and Szleifer, I. (2003) Controlling surface interactions with grafted polymers. *Interface Sci. 11*, 187−197 and references therein.
(14) Mangeney, C., Ferrage, F., Aujard, I., Marchi-Artzner, V., Jullien, L., Ouari, O., Rekai, E. D., Laschewsky, A., Vikholm, I., and Sadowski, J. W. (2002) Synthesis and properties of water-soluble gold colloids covalently derivatized with neutral polymer monolayers. *J. Am. Chem. Soc. 124*, 5811−5821.
(15) *Folate and Human Development* (Massaro, E. J., Rogers, J. M., Eds.) p 376, Humana Press, NJ, 2002.
(16) Kamen, B. A., and Smith, A. K. (2004) A review of folate receptor alpha cycling and 5-methyltetrahydrofolate accumulation with an emphasis on cell models in vivo. *Adv. Drug Delivery Rev. 56*, 1085−1097.
(17) Sabharanjak, S., and Mayor, S. (2004) Folate receptor endocytosis and trafficking. *Adv. Drug Delivery Rev. 56*, 1099−1109.
(18) Parker, N., Turk, M. J., Westrick, E., Lewis, J. D., Low, P. S., and Leamon, C. P. (2005) Folate receptor expression in carcinomas

and normal tissues determined by a quantitative radioligand binding assay. *Anal. Biochem. 338*, 284−293.
(19) Elnakat, H., and Ratnam, M. (2004) Distribution, functionality, and gene regulation of folate receptor isoforms: implications in targeted therapy. *Adv. Drug Delivery Rev. 56*, 1067−1084.
(20) Rui, Y., Wang, S., Low, P. S., and Thompson, D. H. (1998) Diplasmenylcholine-folate liposomes: an efficient vehicle for intracellular drug delivery. *J. Am. Chem. Soc. 120*, 11213−11218.
(21) Qualls, M. M., and Thompson, D. H. (2001) Synergistic phototoxicity of chloroaluminum phthalocyanine tetrasulfonate delivered via acid-labile diplasmenylcholine-folate liposomes. *Intl J. Cancer 93*, 384−392.
(22) Pan, X. Q., Wang, H., and Lee, R. J. (2002) Boron delivery to a murine lung carcinoma using folate receptor targeted liposomes. *Anticancer Res. 22*, 1629−1633.
(23) Gabizon, A., Horowitz, A. T., Goren, D., Tzemach, D., Shmeeda, H. and Zalipsky, S. (2003) In vivo fate of folate-targeted poly-(ethylene glycol) liposomes in tumor-bearing mice. *Clin. Cancer Res. 9*, 6551−6559.
(24) Leamon, C. P., Cooper, S. R. and Hardee, G. E. (2003) Folate-liposome-mediated antisense oligodeoxynucleotide targeting to cancer cells: evaluation in vitro and in vivo. *Bioconjugate Chem. 14*, 738−747.
(25) Boomer, J. A., Qualls, M. M., Inerowicz, H. D., Haynes, R. H., Patri, G. V. S., Kim, J.-M. and Thompson, D. H., unpublished results.
(26) Gottschalk, S., Cristiano, R. J., Smith, L. C., and Woo, S. L. C. (1994) Folate receptor mediated DNA delivery into tumor cells: potosomal disruption results in enhanced gene expression. *Gene Ther. 1*, 185−191.
(27) Mislick, K. A., Baldeschwieler, J. D., Kayyem, J. F., and Meade, T. J. (1995) Transfection of folate -polylysine DNA complexes: evidence for lysosomal delivery. *Bioconjugate Chem. 6*, 512−515.
(28) Li, S., and Huang, L. (1997) Targeted delivery of antisense oligodeoxynucleotides by LPDII. *J. Liposome Res. 7*, 63−75.
(29) Benns, J. M., Maheshwari, A., Furgeson, D. Y., Mahato, R. I., and Kim, S. W. (2001) Folate-PEG-folate-graft-polyethylenimine-based gene delivery. *J. Drug Targeting 9*, 123−139.
(30) Dauty, E., Remy, J. S., Zuber, G., and Behr, J.-P. (2002) Intracellular delivery of nanometric DNA particles via the folate receptor. *Bioconjugate Chem. 13*, 831−839.
(31) Zhou, W., Yuan, X., Wilson, A., Yang, L., Mokotoff, M., Pitt, B., and Song, L. (2002) Efficient intracellular delivery of oligonucleotides formulated in folate receptor-targeted lipid vesicles. *Bioconjate Chem. 13*, 1220−1225.
(32) Quintana, A., Raczka, E., Piehler, L., Lee, I., Myc, A., Majoros, I., Patri, A. K., Thomas, T., Mule, J., and Baker, J. R. (2002) Design and function of a dendrimer-based therapeutic nanodevice targeted to tumor cells through the folate receptor. *Pharm. Res. 19*, 1310−1316.
(33) Ward, C. M., Pechar, M., Oupicky, D., Ulbrich, K., and Seymour, L. W. (2002) Modification of pLL/DNA complexes with a multivalent hydrophilic polymer permits folate-mediated targeting in vitro and prolonged plasma circulation in vivo. *J. Gene Med. 4*, 536−547.
(34) Turek, J. J., Leamon, C. P., and Low, P. S. (1991) Endocytosis of folate-protein conjugates: ultrastructural localization in KB cells. *J. Cell. Sci. 106*, 423−430.
(35) Zhang, Y., Kohler, N., and Zhang, M. (2002) Surface modification of superparamagnetic magnetite nanoparticles and their intracellular uptake. *Biomaterials 23*, 1553−1561.
(36) Stevens, P. J., Sekido, M., and Lee, R. J. (2004) A folate receptor-targeted lipid nanoparticle formulation for a lipophilic paclitaxel prodrug. *Pharm. Res. 21*, 2153-2157.
(37) Lee, E. S., Na, K., and Bae, Y. H. (2003) Polymeric micelle for tumor pH and folate-mediated targeting. *J. Controlled Release 91*, 103−113.
(38) Aronov, O., Horowitz, A. T., Gabizon, A., and Gibson, D. (2003) Folate-targeted PEG as a potential carrier for Carboplatin analogues. Synthesis and in vitro studies. *Bioconjugate Chem. 14*, 563−574.
(39) Jain, R. K. (2001) Delivery of molecular medicine to solid tumors: lessons from in vivo imaging of gene expression and function. *J. Controlled Release 74*, 7−25.
(40) Maeda, H. (2001) The enhanced permeability and retention (EPR) effect in tumor vasculature: the key role of tumor-selective macromolecular drug targeting. *Adv. Enzyme Regul. 41*, 189−207.
(41) Ponpipom, M. M., Bugianesi, R. L., and Blake, T. J. Inhibition of delayed hypersensitivity reactions by cinnamyl 1-thioglycosides (1987) *J. Med. Chem. 30*, 705−710.
(42) Low, P. S., and Antony, A. C. (2004) Folate receptor-targeted drugs for cancer and inflammatory diseases. *Adv. Drug Delivery Rev. 56*, 1055−1058.
(43) Leamon, C. P., and Reddy, J. A. (2004) Folate-targeted chemotherapy. *Adv. Drug Delivery Rev. 56*, 1127−1141.

BC050335B

Rapid Production of Functionalized Recombinant Proteins: Marrying Ligation Independent Cloning and in Vitro Protein Ligation

Susanna Kushnir,[†,‡] Yoann Marsac,[†,‡] Reinhard Breitling,[§] Igor Granovsky,[#] Vera Brok-Volchanskaya,[#] Roger S. Goody,[‡] Christian F. W. Becker,[‡] and Kirill Alexandrov*[,‡,§]

Department of Physical Biochemistry, Max-Planck-Institute for Molecular Physiology, Otto-Hahn-Strasse 11, 44227 Dortmund, Germany; Jena Bioscience GmbH, Löbstedter Strasse 78, 07749 Jena, Germany; and Department of Molecular Biology, Institute of Biochemistry and Physiology of Microorganisms, Russian Academy of Sciences, Institutskaya str. 5, Pushchino 142290, Moscow Region, Russia. Received November 7, 2005; Revised Manuscript Received April 5, 2006

Functional genomics and proteomics have been very active fields since the sequencing of several genomes was completed. To assign a physiological role to the newly discovered coding genes with unknown function, new generic methods for protein production, purification, and targeted functionalization are needed. This work presents a new vector, pCYSLIC, that allows rapid generation of *Escherichia coli* expression constructs via ligation-independent cloning (LIC). The vector is designed to facilitate protein purification by either Ni-NTA or GSH affinity chromatography. Subsequent proteolytic removal of affinity tags liberates an N-terminal cysteine residue that is then used for covalent modification of the target protein with different biophysical probes via protein ligation. The described system has been tested on 36 mammalian Rab GTPases, and it was demonstrated that recombinant GTPases produced with pCYSLIC could be efficiently modified with fluorescein or biotin in vitro. Finally, LIC was compared with the recently developed In-Fusion cloning method, and it was demonstrated that In-Fusion provides superior flexibility in choice of expression vector. By the application of In-Fusion cloning Cys-Rab6A GTPase with an N-terminal cysteine residue was generated employing unmodified pET30a vector and TVMV protease.

INTRODUCTION

Sequencing of several pro- and eukaryotic genomes and the subsequent advent of structural and functional genomics projects have created a need for a spectrum of new protein analysis methods. Although traditional biochemistry includes investigation of a few selected proteins often studied by individually tailored assays, the postgenomic era requires the study of hundreds of proteins simultaneously. This calls for standardization and automation of protein generation and handling methods. The obligatory first step in protein research, namely, in vivo protein expression, was greatly facilitated by the development of rapid cloning techniques based on recombination systems such as Gateway or ligation-independent cloning (LIC) (*1*). Both of these systems are employed to almost equal extent in high-throughput cloning projects because, whereas the LIC approach relies on cheap generic reagents, the more expensive Gateway method is simpler and faster when genes must be moved among several vectors (*2*). A disadvantage shared by both methods is the necessity to design vectors carrying recombination sites, which often leads to the introduction of unwanted sequences to or elimination of wanted sequences from the open reading frame. A newly introduced system called In-Fusion has the potential for avoiding this problem. In this system an undisclosed enzyme recombines linearized vector with a PCR product flanked by homology regions of 15 nucleotides to 5′ and 3′ ends of the vector (*3*).

The combination of rapid cloning approaches with various tag systems allows rapid isolation of resulting recombinant proteins for subsequent structural or functional investigations (*4*). Whereas in structural studies proteins are directly used for crystallization or NMR studies, the functional assays require further derivatization of proteins to provide a generic and easily detectable readout for their activity. Although the methods applied vary widely, two modifications dominate: immobilization and covalent labeling with affinity groups, fluorophores, or isotopes. Although the molecular toolbox currently available to researchers is filled with reporter groups suitable for protein research, the methods for their conjugation to polypeptides are far less developed. This is largely due to the lack of chemistries that enable the modification of proteins at defined sites with a predictable outcome. The two most commonly used approaches that are based on chemical coupling to sulfhydryl groups or to primary amines result in different labeling patterns on different proteins as a consequence of the unique content and distributions of cysteine and lysine residues in a given protein. A recently developed approach referred to as expressed protein ligation (EPL) provides a possible solution to this problem (*5*). In this approach proteins are expressed in C-terminal fusion with an intein domain and an affinity tag. The resulting fusion proteins can be separated from the proteins of the expression host on an affinity matrix. Treatment of the immobilized protein with a high concentration of thiol leads to the cleavage of the peptide bond between intein and target protein. The cleaved protein carries a thioester group on the C terminus that can be coupled to a peptide (or, in fact, any molecule) bearing a cysteine at its N terminus according to the method of native chemical ligation to generate a native peptide bond at the coupling site (Figure 1) (*6*). Although this approach was successfully used for protein engineering, its shortcomings are related to the necessity of expressing a large fusion protein that may influence the solubility and folding of the target protein and the different efficiencies of intein splicing due to the influence of the flanking

* Corresponding author [telephone (+49)-0231-1332356; fax (+49)-0231-1331651; e-mail kirill.alexandrov@mpi-dortmund.mpg.de].
[†] Both authors contributed equally.
[‡] Max-Planck-Institute for Molecular Physiology.
[§] Jena Bioscience GmbH.
[#] Russian Academy of Sciences.

10.1021/bc050320d CCC: $33.50 © 2006 American Chemical Society
Published on Web 04/27/2006

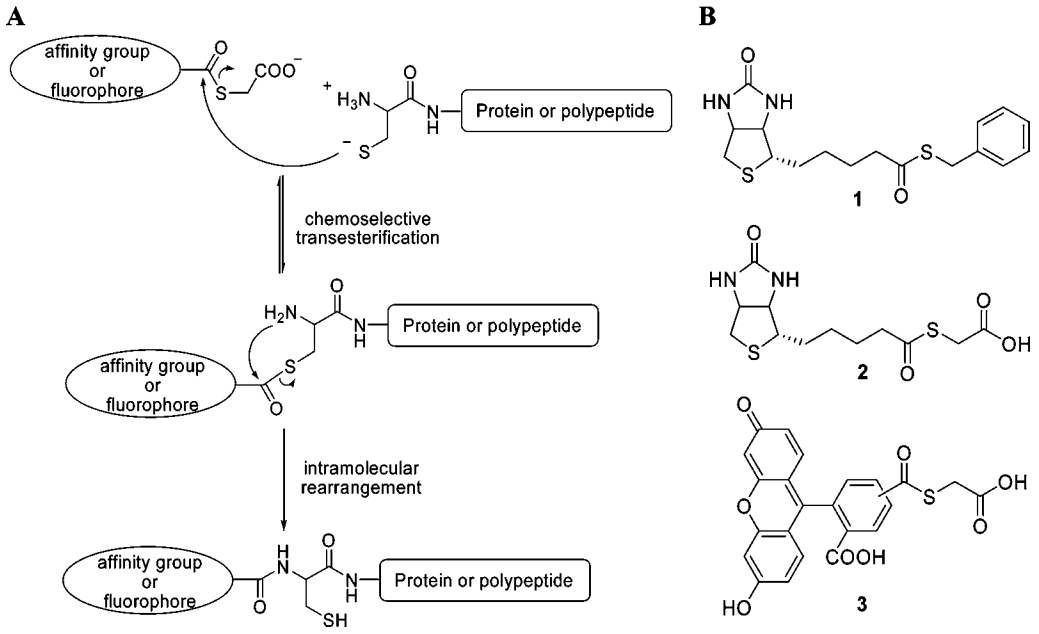

Figure 1. (A) Mechanism of the protein labeling reaction in analogy to native chemical ligation. (B) Thioester labeling reagents: biotin benzylthioester **1**, biotin mercaptoacetic acid thioester **2**, 5(6)-(mercaptoacetic acid)fluorescein thioester **3**.

residues of the target protein (*7*). An alternative configuration was proposed whereby a thioester-conjugated functionality such as a fluorophore is coupled onto the N-terminal cysteine of a recombinant protein (*8*). However, generation of recombinant proteins with N-terminal cysteine is not straightforward. In some cases cysteine on position 2 becomes N-terminal upon methionine cleavage by aminopeptidase of the expression host, although the efficiency varies among proteins (*9*). In an alternative configuration an N-terminal cysteine is created by self-cleavage of an intein domain fused N-terminally to the target protein. As in the case of C-terminally fused intein domains, cleavage does not always occur with the desired efficiency. Finally, the N-terminal cysteine residue can be generated by proteolytic cleavage of a properly engineered protease cleavage site. Among proteases that were shown to tolerate cysteine at the +1 position of the cleavage site are factor X, Precision protease, and TEV proteases (*10*, *11*). The latter protease became particularly popular due its high processivity, selectivity, and related ease of recombinant production, which promoted interest in other proteases of plant viruses such as TVMV (*12*). In this work we compare LIC and In-Fusion cloning for rapid production of recombinant proteins with N-terminal cysteine mediated by TEV and TVMV proteases.

EXPERIMENTAL PROCEDURES

Construction of pCYSLIC Vector. The His−GST tag fusion gene was amplified using oligonucleotides Xba-GAT_for TAGATCCTCTAGAAATAATTTTGTTTAACTTTAAG AAGGAG and TEV_LIC_rev TTATTATCCCATATGGGTATACATTACCCAATAATA TTGAAAATAAAGATTTTCATCAGCCATACTTAC that encode the TEV protease recognition sequence and *Xba*I and *Ssp*I restriction sites. The resulting PCR product was digested with *Xba*I and *Ssp*I and ligated into plasmid pMCSG7 linearized with the same enzymes (*13*). The integrity of the GST ORF and LIC site of the resulting pCYSLIC vector was verified by sequencing using T7 promoter and T7 terminator primers.

Cloning of Rab6A into pCYSLIC Vector. To amplify Rab6A ORF, oligonucleotide primers 5′-AAAATCTTTATTTTCAATGCATGTCCACGGGCGGAGACT-3′ and 5′-TTATCCACTTCCAATGTTAGCAGGAACAGCCTCCTTCA-3′ were used. The primers are complementary to the 5′- or 3′-ends of the ORF, respectively, at 3′-ends and to sequences flanking the *Ssp*I site of the pCYSLIC vector at 5′-ends (underlined). Both PCR fragments of 663 bp and *Ssp*I-digested pCYSLIC vector were purified by electrophoresis in 1% agarose gel and isolated with QIAquick gel extraction kit (Qiagene). Five hundred nanograms of vector DNA and 50 ng of the PCR fragment were treated with 0.7 unit of T4 DNA polymerase in the presence of 2.5 mM dGTP and 2.5 mM dCTP, respectively, at 22 °C for 30 min. The enzyme was inactivated by heating at 75 °C for 20 min. Thirty nanograms of vector DNA and 10 ng of PCR fragment were mixed in a total volume of 3 μL (molar ratio of vector to fragment approximately 1:3) and incubated at 22 °C for 10 min. Then 1 μL of 25 mM EDTA was added, and incubation was continued for another 10 min. *Escherichia coli* Top10 competent cells were transformed with the above mixture, followed by selection on LB agar supplemented with 60 μg/mL ampicillin. Ten recombinant clones were picked and screened by PCR with primers complementary to the vector sequences upstream and downstream of the insert. All 10 screened clones contained the insert of interest. The integrity of the open reading frame was verified by sequencing.

In-Fusion Cloning of TVMV-Rab6A into the pET30a Vector. The open reading frame of Rab6A was amplified with the primers TVMV_Rab6_p30_dir AAGGCCATGGCTGATGAGACCGTTCGCTTTCAGTGCATGTCCACGGGCGGAGACTTCG and TVMV_Rab6_p30_rev GAATTCGGATCCGATTCAGCAGGAACAGCCTCCTTCAC containing the 15 bp region of homology to the pET30a vector upstream and downstream of the *Eco*RV site. The 3′ primer also contains the recognition sequence for TVMV protease, where the S residue in the sequence E-T-V-R-F-Q-S is substituted by cysteine. The PCR product was gel purified and mixed in 1:1 molar ratio with pET30a vector linearized by the *Eco*RV enzyme and incubated with In-Fusion reaction mix (BD Bioscience) for 30 min at room temperature. The reaction mixture was transformed into Fusion-Blue Competent Cells, and recombinant clones were selected on LB agar plates supplemented with 30 mg/L kanamycin.

Cloning, Expression, and Purification of Mammalian RabGTPases. For cloning of a library of mammalian RabGTPases the oligonucleotides were designed to start with the sequence AAAATCTTTATTTTCAATGC followed by the nucleotides encoding the target protein. The antisense primers

start with the sequence AATAGGTGAAGGTTAC followed by the complement of stop codon and the C terminus of the target protein. The cDNAs for mammalian RabGTPases were obtained from RZPD GmbH and used as templates for PCR reactions. PCR products were then treated with T4 polymerase and annealed with the pCYSLIC vector. The mixture was transformed into *E. coli* Top10 competent cells, and the positive clones were identified as described above. The sequence of the inserts was verified by sequencing with specific primers.

Test protein expressions were performed in BL21(DE3)RIL cells (Stratagene) cultured in 2 mL of LB medium supplemented with 100 μg/mL ampicillin and 34 μg/mL chloramphenicol. The cells were grown at 37 °C to OD_{600} = 0.5, and protein expression was induced by the addition of 1 mM IPTG for 4 h at 37 or 20 °C. To determine the amount and solubility of the recombinant protein, the cells were disrupted by sonication and cell debris was removed by centrifugation. The total cellular lysates, the cells debris, and supernatants were analyzed by SDS−PAGE followed by Coomassie Blue staining.

For large-scale purification cultures were pregrown to OD_{600} = 0.5 in 1−10 L of LB, and protein expression was induced by the addition of 0.1 mM IPTG for 12 h at 20 °C. Cells were resuspended in buffer A containing 50 mM NaH_2PO_4, pH 8.0, 0.3 M NaCI with 1 mM PMSF, and 2 mM BME and lysed using a fluidizer (Microfluidics Corp.). Clarified lysates were loaded onto a 5 mL Hi-Trap Ni column (Amersham) equilibrated with buffer A. The protein was eluted with a gradient of 10−150 mM imidazole in buffer A. The fractions containing recombinant protein were pooled, and TEV or TVMV protease was added at 1:20 molar ratio. The resulting mixture was dialyzed against protease cleavage buffer: 25 mM NaH_2PO_4, pH 8.0, 2 mM EDTA, and 2 mM BME for 12 h at 4 °C. Next, the excess EDTA was quenched by the addition of excess $MgCl_2$, and cleaved 6His-GST-tag, His-tagged protease, and impurities were removed from the dialyzed mixture by passing it over an Ni−NTA column. The collected flow-through was concentrated in Centricon 10 concentrators up to ≈8 mL and loaded onto a gel filtration column (Superdex-75) equilibrated with 25 mM Hepes, pH 7.2, 40 mM NaCl, 2 mM $MgCl_2$, 10 μM GDP, and 2 mM DTE. The fractions were concentrated with Centriprep 10, frozen, and stored at −80 °C.

Expression vectors pRK1035_TVMV and pRK1037_TEV were a generous gift of D. Waugh. Expression and purification of the enzymes were performed essentially as described previously (*12*).

Biotin and Fluorescein Thioester Synthesis. Biotin benzylthioester **1** was prepared according to a procedure described by Schuler and Pannell (*8*). To a cooled mixture (0 °C) of 2.0 M trimethylaluminum (10 mL; 20 mmol) in heptane and anhydrous dichloromethane (40 mL) was slowly added benzyl mercaptan (2.35 mL; 20 mmol). The reaction mixture was allowed to warm to room temperature over a 20−30 min period. Twenty milliliters of this solution was added to a solution of biotin succinimidyl ester (110 mg; 0.322 mmol) in anhydrous DMF (5 mL). After 2 h of stirring at room temperature, the solvents were removed and the remaining yellow oil was dissolved in dichloromethane. Wet silica gel was added to the solution to quench the excess aluminum complex. After evaporation, the crude product was purified by flash chromatography ($CHCl_3$/MeOH, 95:5). Fractions containing the biotin benzylthioester were pooled, evaporated, and dried under vacuum to give a white powder (109.5 mg; 0.312 mmol; 97% yield): ^{1}H NMR ($CDCl_3$, 400 MHz) δ 7.24−7.14 (m, 5H, Ph), 4.45−4.41 (m, 1H), 4.23−4.20 (m, 1H), 4.04 (s, 2H), 3.08−3.03 (m, 1H), 2.83 (dd, 1H, J = 4.8 Hz, J = 12.8 Hz), 2.65 (dd, 1H, J = 0.4 Hz, J = 12.8 Hz), 2.52 (t, 2H, J = 7.4 Hz), 1.70−1.55 (m, 4H), 1.44−1.31 (m, 2H); ^{13}C NMR ($CDCl_3$, 100 MHz) δ 198.7, 163.7, 137.6−127.1, 61.9, 60.1, 55.3, 43.3, 40.5, 33.1, 28.1, 25.4; MALDI-TOF MS, calcd for $C_{17}H_{22}N_2O_2S_2$ $(M + H)^+$ 351.5067, found 351.5827.

Synthesis of the water-soluble biotin **2** and 5(6)-carboxyfluorescein **3** thioesters was performed as described by Tolbert et al. (*14*), using *tert*-butyl mercaptoacetate (*15*). D-Biotin thioester **2**: ^{1}H NMR ($(CD_3)_2CO$, 400 MHz) δ 5.95 (s large, 1H, NH), 5.89 (s large, 1H, NH), 3.85 (dd, 1H, J = 4.8 Hz, J = 8.0 Hz), 3.68 (ddd, 1H, J = 5.2 Hz, J = 8.0 Hz), 3.22 (s, 2H), 2.64 (ddd, 1H, J = 4.8 Hz, J = 6.4 Hz, J = 8.0 Hz), 2.37 (dd, 1H, J = 5.2 Hz, J = 12.4 Hz), 2.17 (t, 2H, J = 7.4 Hz), 2.12 (d, 1H, J = 12.4 Hz), 1.20−1.10 (m, 4H), 1.06−0.85 (m, 2H); MALDI-TOF MS, calcd for $C_{12}H_{18}N_2O_4S_2$ $(M + H)^+$ 319.0786, found 319.2774. 5-(and -6)-carboxyfluorescein-thioester **3**: ^{1}H NMR ($CDCl_3$, 400 MHz) δ 8.74 (s, 1H), 8.73 (s, 1H), 8.10 (d, 1H), 8.09 (d, 1H), 7.27 (s, 1H), 7.25 (s, 1H), 6.88 (d, 4H), 6.63−6.58 (m, 4H), 6.56−6.50 (m, 4H), 3.84 (s, 4H); MALDI-TOF MS, calcd for $C_{23}H_{14}O_8S$ $(M + H)^+$ 451.0487, found 451.2801.

Labeling of Peptides and Proteins with Biotin and Fluorescein Thioesters. *Peptide Labeling.* The RBD[1] peptide (5 mg) was dissolved in 375 μL of a buffer containing 6 M GdmCl and 100 mM sodium phosphate, pH 7.5, and 4% thiophenol was added. The biotin benzylthioester **1** was dissolved in DMF at a concentration of 15 mM, and then 50 μL was added to the peptide solution. The reaction mixture was vortexed and incubated at room temperature. The reaction progress was monitored by analytical reversed phase HPLC.

Protein Labeling. A solution of Cys-Rab6A protein (8.0 μL; 531 μM) in 50 mM NaP_i, 1 mM $MgCl_2$, and 100 μM GDP, pH 7.5, was mixed with 30 mM TCEP, 200 mM MesNa in 100 mM NaP_i buffer (4.5 μL), and a 5 mM solution of water-soluble thioester **2** or **3** in 100 mM NaP_i buffer (1.5 μL) at pH 8.0. The reaction mixture was vortexed and incubated at room temperature (22 °C). In the case of the 5(6)-carboxyfluorescein thioester, 1 μL of 3 mM labeling reagent **3** in 100 mM NaP_i buffer at pH 8.0 was added each 8 h. In the case of the biotin thioester, 1 μL of 3 mM labeling reagent **2** in 100 mM NaP_i buffer at pH 8.0 was added once after 12 h.

HPLC and Mass Spectrometry. HPLC analysis of peptides and proteins was performed with an analytical RP-C4-column (Vydac) at a flow rate of 1 mL/min over 30 min with a gradient from 5 to 65% (v/v) buffer B (acetonitrile, 0.08% TFA) in buffer A (water, 0.1% TFA). Peptide and protein masses were determined by electrospray ionization mass spectrometry on an LCQ Advantage Max (Finnigan) operating in positive ion mode.

RESULTS AND DISCUSSION

Construction of pCYSLIC Vector and Preparation of Recombinant Cys-Rab6A GTPase. To design a generic vector suitable for rapid construction of a large number of expression constructs that yield recombinant polypeptides selectively derivatizable with a range of chemical entities, we attempted to combine recent advances in molecular cloning and protein chemistry. The proposed vector should contain sequence(s) coding for one or two affinity tags operably linked to a site for LIC, which should allow rapid in-frame cloning of PCR-amplified genes. The expressed polypeptide should be readily isolatable by, preferably, a single-step chromatography and then be amenable to site-directed modification with a range of chemical groups. The functional assembly that satisfies the above-described requirements is presented in Figure 2. The gene of interest is cloned via LIC after a tandem of the 6His-GST tag and the TEV protease cleavage site. Use of the tandem tag

[1] Amino acids 96−131 from the Ras-binding domain of cRaf-1 carrying a C-terminal His6 tag.

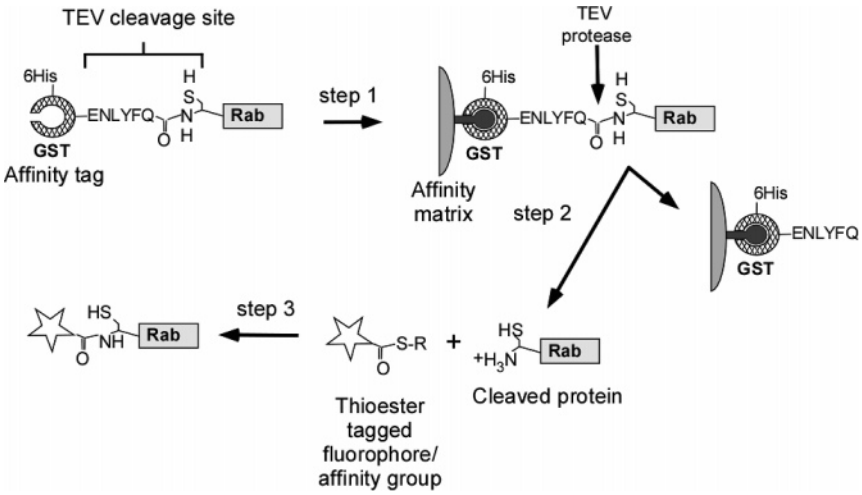

Figure 2. Principal scheme for generic generation of N-terminal cysteine in recombinant proteins and its subsequent labeling via in vitro protein ligation: step 1, isolation of the fusion protein on the affinity matrix; step 2, cleavage of the fusion protein with TEV protease and separation of the target protein; step 3, ligation of the thioester-tagged functional group to the N-terminal cysteine of the target protein.

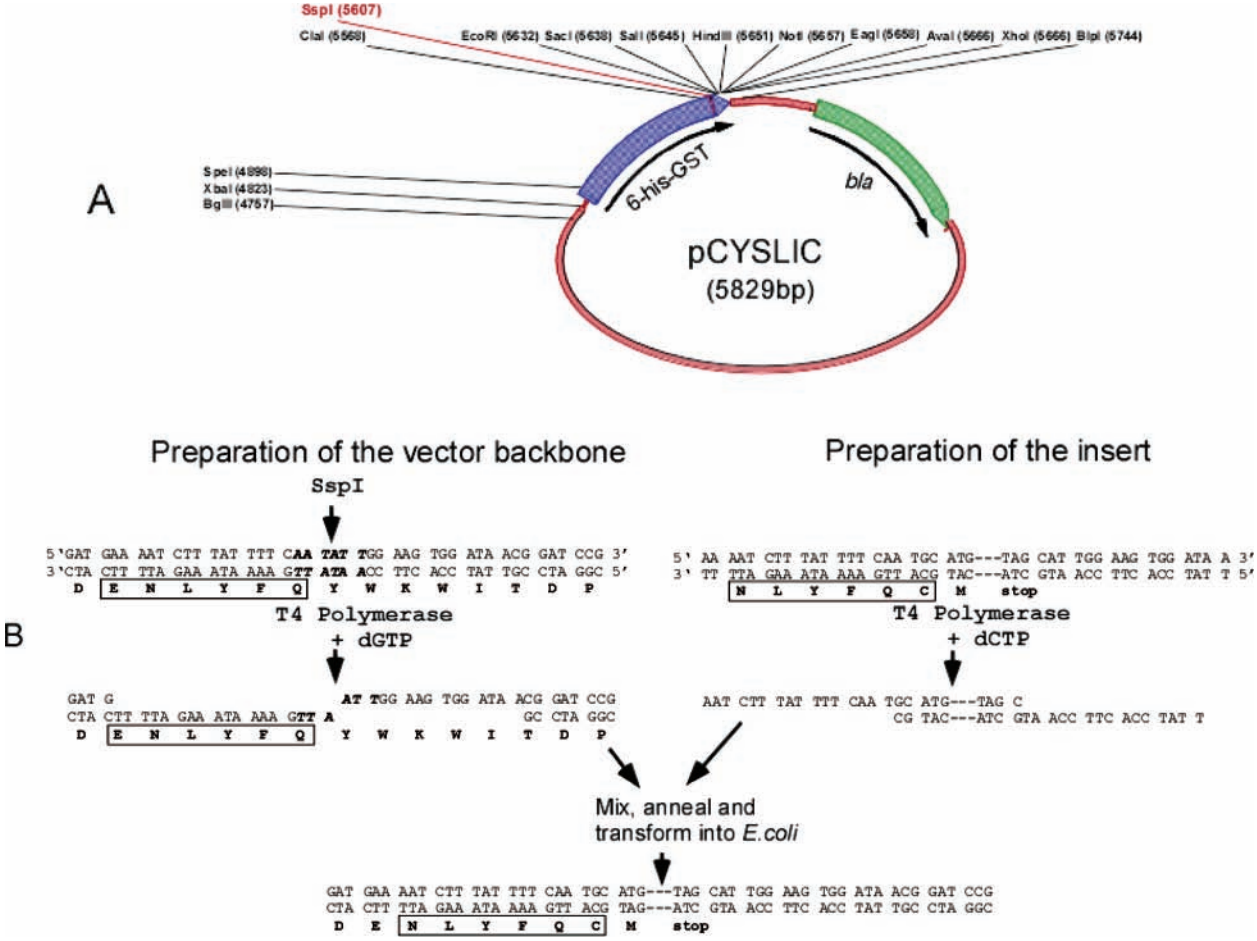

Figure 3. (A) Map of pCYSLIC vector. The unique restriction sites before and after the 6-His-GST fusion gene are shown. (B) Organization of the LIC site of pCYSLIC vector and the PCR product and the flowchart of cloning reaction. The TEV protease cleavage site is boxed.

allows two-step affinity purification if the target protein is not sufficiently pure after the first purification step. The TEV protease cleavage site is modified in such a way that upon cleavage a cysteine is left on the N terminus of the resulting polypeptide that can be used for ligation of molecules bearing the reactive thioester group. To construct such a vector, we combined *E. coli* expression vector pGATEV, which contains tandem 6His-GST tags followed by a TEV protease cleavage site (*16*), and pMCSG7 vector that combines a LIC cloning site with a 6His tag removable via TEV cleavage (*13*). The resulting vector was termed pCYSLIC (Figure 3A). For cloning of a gene of interest into this vector the backbone is digested with blunt cleaving *Ssp*I enzyme and treated with T4 polymerase in the presence of dGTP (Figure 3B). This results in the formation of long (14−18 nucleotides) overhangs that are then used for capturing the insert. The gene of interest is PCR amplified with the primers containing a sequence complementary to the regions flanking the *Ssp*I site of the pCYSLIC (Figure 3B). The PCR products are treated with T4 polymerase in the presence of dCTP leading to the formation of single-stranded regions complemen-

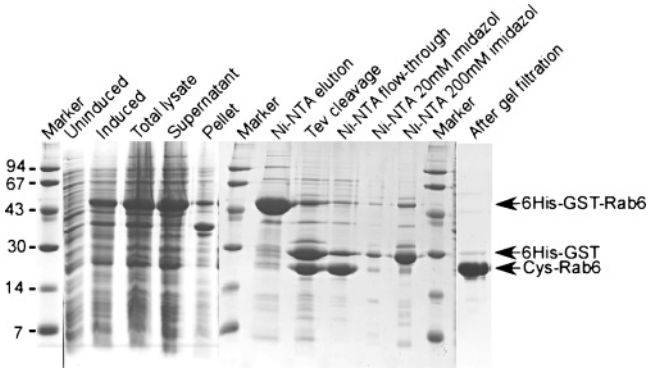

Figure 4. Expression and purification of the Cys-Rab6A using pCYSLIC vector. Aliquots of *E. coli* culture, cell lysates, and purification steps were resolved on 15% SDS−PAGE and stained with Coomassie Blue stain. The positions of fusion protein and cleavage products are indicated by arrows.

tary to those of the backbone. The backbone and the insert are mixed and transformed into the *E. coli* strain. The resulting clones are screened by colony PCR for the presence of the desired insert.

To test the vector we PCR amplified the ORF of human GTPase Rab6A and cloned it using the above-described approach into the pCYSLIC vector. The efficient cloning depended on the high quality of backbone linearization with the *Ssp*I enzyme, which was achieved by increasing the enzyme to DNA ratio as described before (*13*) (Experimental Procedures). Following the optimization a cloning efficiency of >90% was routinely achieved. The resulting pCYSLIC−Rab6A vector was introduced into *E. coli* BL21(DE3) RIL strain, and the suspension culture was induced with IPTG as described under Experimental Procedures. As can be seen in Figure 4 6His-GST-Rab6A was highly overexpressed and found predominantly in the soluble fraction. Chromatography of the supernatant on Ni−NTA resin resulted in >70% pure 6His-GST-Rab6A

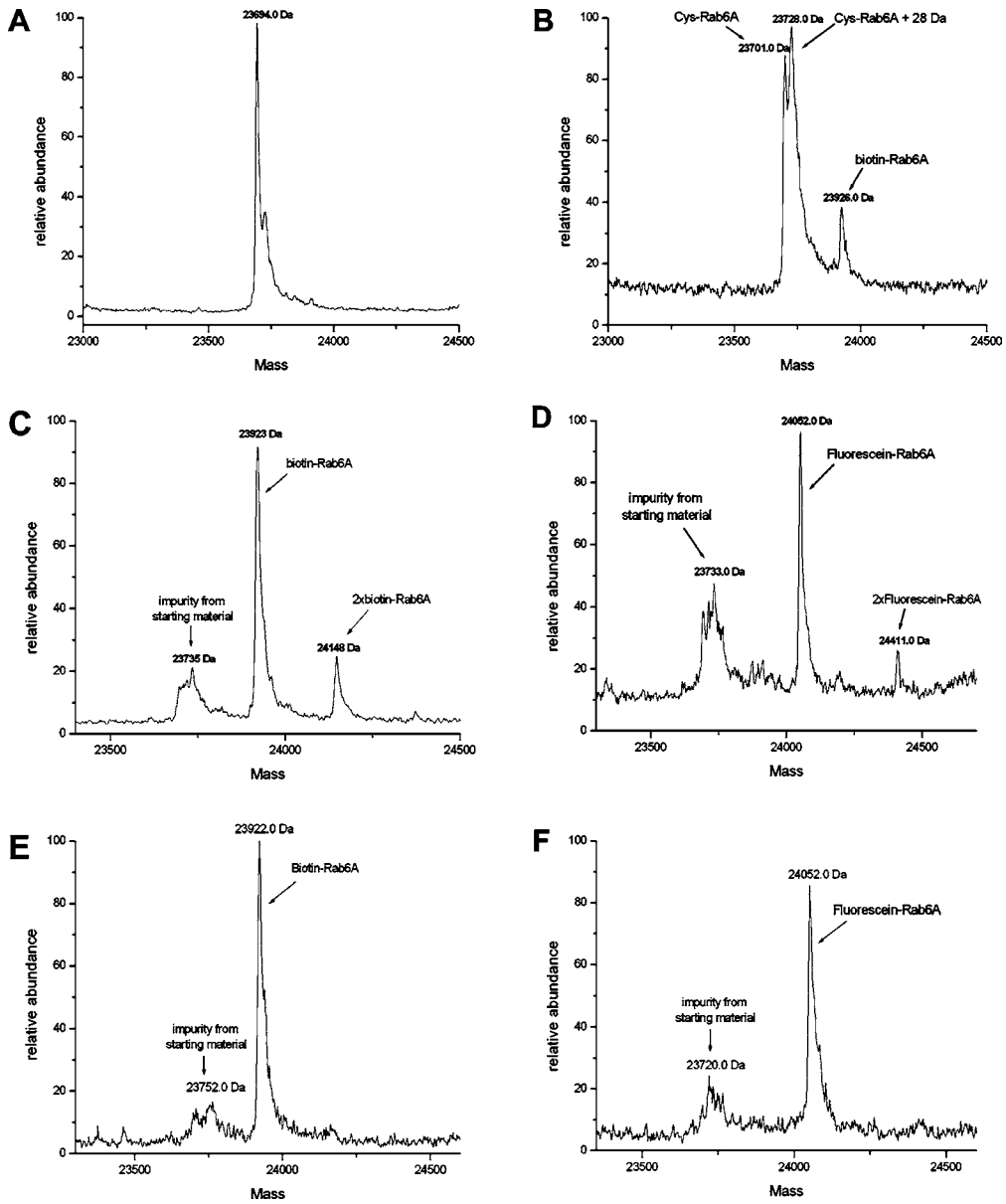

Figure 5. ESI-MS spectra of cleaved and labeled Rab6A protein: (A) deconvoluted mass spectrum of Cys-Rab6A, calculated molecular mass 23695.9 Da; (B) deconvoluted mass spectrum of Cys-Rab6A after 24 h of reaction with **1** at room temperature in a non-denaturing buffer (20 mM sodium phosphate, 1 mM $MgCl_2$, 100 μM GDP, pH 7.5) and 5−10% of DMF; (C) deconvoluted mass spectrum of Cys-Rab6A labeled with biotin thioester **2** after 24 h at 22 °C; (D) deconvoluted mass spectrum of Cys-Rab6A labeled with 5(6)-carboxyfluorescein thioester **3** after 24 h at 22 °C; (E) deconvoluted mass spectrum of Cys-Rab6A labeled with biotin thioester **2** after 3 h of hydroxylamine (50 mM) treatment; (F) deconvoluted mass spectrum of Cys-Rab6A labeled with fluorescein thioester **3** after 3 h of hydroxylamine (50 mM) treatment.

protein. To remove the tags and to liberate the N-terminal cysteine, the sample was dialyzed against 25 mM NaP_i, pH 8.0, 2 mM EDTA, and 2 mM BME at 4 °C in the presence of TEV protease. The cleavage reaction was monitored by SDS−PAGE and typically reached >80% completion after 12 h. The cleaved 6His-GST fusion and TEV protease were removed by passing the mixture over Ni−NTA resin (Figure 4). The obtained Rab6 was >80% pure and migrated on the size exclusion chromatography as a single peak with an apparent molecular mass of ≈25 kDa, indicating that the protein was properly folded (not shown).

Synthesis of and Labeling with Biotin and Fluorescein Thioesters. Having developed an expression system for rapid generation of pure proteins competent for in vitro chemical ligation, a strategy for their rapid and site-selective modifications with various labels was devised. This labeling procedure is based on the nucleophilic attack of the cysteine thiol group on the thioester moiety of the labeling molecules and subsequent formation of an amide bond, as described for linking peptide segments via native chemical ligation (*6*) (Figure 1). However, reaction conditions and obtainable yields depend heavily on the nature of the label and the protein used. We sought to develop a general procedure for the synthesis of labeling reagents carrying a thioester and to identify conditions that ensure site-specific monolabeling of peptides/proteins in high yields without side reactions. In a first set of experiments we used a biotin benzylthioester **1** that was synthesized following a two-step reaction procedure presented first by Schuler and Pannell for conversion of a fluorescent dye into its thioester derivative (*8*). The benzylthioester **1** was obtained at very high yield (97%) from a biotin succinimidyl ester derivative. An aluminum complex, prepared from a stoichiometric mixture of trimethylaluminum and benzyl mercaptan, was allowed to react with the biotin succinimidyl ester at room temperature, generating **1** (Figure 1). Initially this water-insoluble compound was applied in organic solvents such as DMF, DMSO, THF, or dioxane to ligation reactions with Rab6A (Cys-Rab6A calculated mass = 23695.9 Da, ESI-MS observed mass = 23694.0 Da). To avoid precipitation of **1**, a concentration of 5−10% DMF was used during our initial experiments, reacting Rab6A and **1** under denaturing or native conditions in the presence of 4% thiophenol. Mass spectrometry indicated the formation of a side product (protein mass + 28 Da) and of the expected biotin labeled protein (calculated mass = 23922.2 Da, ESI-MS observed mass = 23926.0 Da; Figure 5). Optimization of reaction conditions [longer reaction times, use of MesNa (2-mercaptoethanesulfonic acid, sodium salt) instead of thiophenol] did not lead to complete conversion of Rab6A to the biotinylated species, possibly indicating a modification of the N-terminal cysteine residue of Rab6A. Such a modification would prevent any reaction with **1**. The replacement of DMF by other organic solvents such as DMSO, THF, or dioxane led to a decrease in labeling efficiency, probably due to less efficient solubilization of **1**. However, the occurrence of the nonreactive side product was prevented. To exclude the possibility that the observed phenomenon was protein-specific, a similar series of experiments was performed with the N-terminal cysteine containing the 42 amino acid peptide RBD96-131/His_6-tag (*17*). The results corroborated those obtained with the Rab6A protein, including the low efficiency of the reaction, under either denaturing (6 M GdmCl) or native conditions, and the formation of a side product (peptide mass + 28). To overcome the problems encountered with the largely water-insoluble compound **1**, we decided to prepare water-soluble thioester labeling reagents. Synthetic access to such compounds has been established by Tolbert et al. (*14*), using *tert*-butyl mercaptoacetate (*15*), and we obtained water-soluble biotin and 5(6)-carboxyfluorescein thioesters with yields of

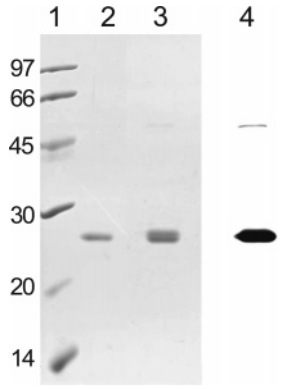

Figure 6. SDS−PAGE analysis of Rab6A labeling with 5(6)-carboxyfluorescein: lane 1, protein marker; lane 2, Cys-Rab6A; lane 3, fluorescein-Rab6A; lane 4, fluorescence scan of Cys-Rab6A labeled at λ_{ex} = 473 nm and λ_{em} = 510 nm.

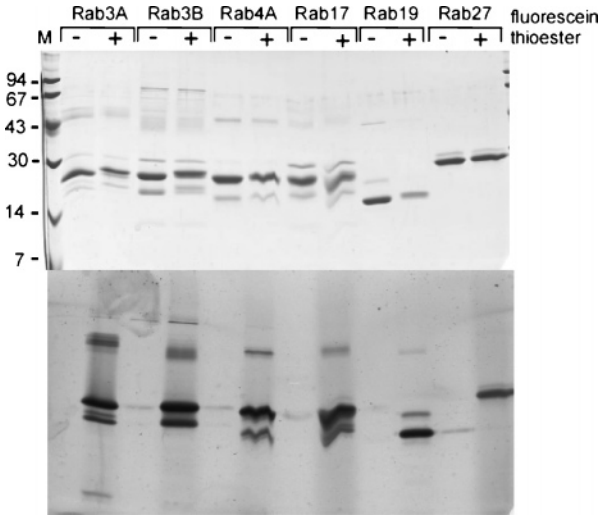

Figure 7. SDS−PAGE analysis of six Rab proteins before and after ligation with 5(6)-carboxyfluorescein thioester. The reactions were carried out and analyzed as in Figure 4. The bottom panel represents the fluorescent scan of the gel, whereas the top panel shows the same gel stained with Coomassie Blue. The high molecular weight fluorescent bands represent GTPase dimers.

between 22 and 45% following their procedure. In the first ligation experiment using 1.78 mM **3** and a 370 μM solution of Rab6A in the presence of β-mercaptoethanol (1 mM) and 2-mercaptoethanesulfonic acid (25 mM), we observed low labeling yields of Rab6A and the occurrence of a small fraction of doubly labeled Rab6A protein. The latter was rationalized as thioester exchange between cysteine side chains in the protein and the labeling reagents **2** and **3**. Different reaction conditions using various amounts of MesNa as an inducer of thioester exchange, TCEP as an additional reducing agent, or a combination of both reagents were tested without significant reduction in unspecific labeling. Such multiple labeling essentially defeats the potential advantages of using native chemical ligation for protein labeling. Optimization of the labeling conditions to suppress the unwanted multiple labeling revealed a marked cysteine reactivity difference of biotin and carboxyfluorescein thioesters. We observed that regular additions, approximately every 8 h for carboxyfluorescein thioester **3** (final concentration = 1 mM) and once after 12 h for biotin thioester **2** (final concentration = 1 mM), produced almost only monolabeled protein within 24 h. The reaction progress was monitored by LC-MS, and the respective deconvoluted mass spectra showed in each case the formation of the monolabeled protein as the major product (calculated molecular mass = 23922.2 Da, Rab6A + **2** and 24054.2 Da Rab6A + **3**; observed molecular mass =

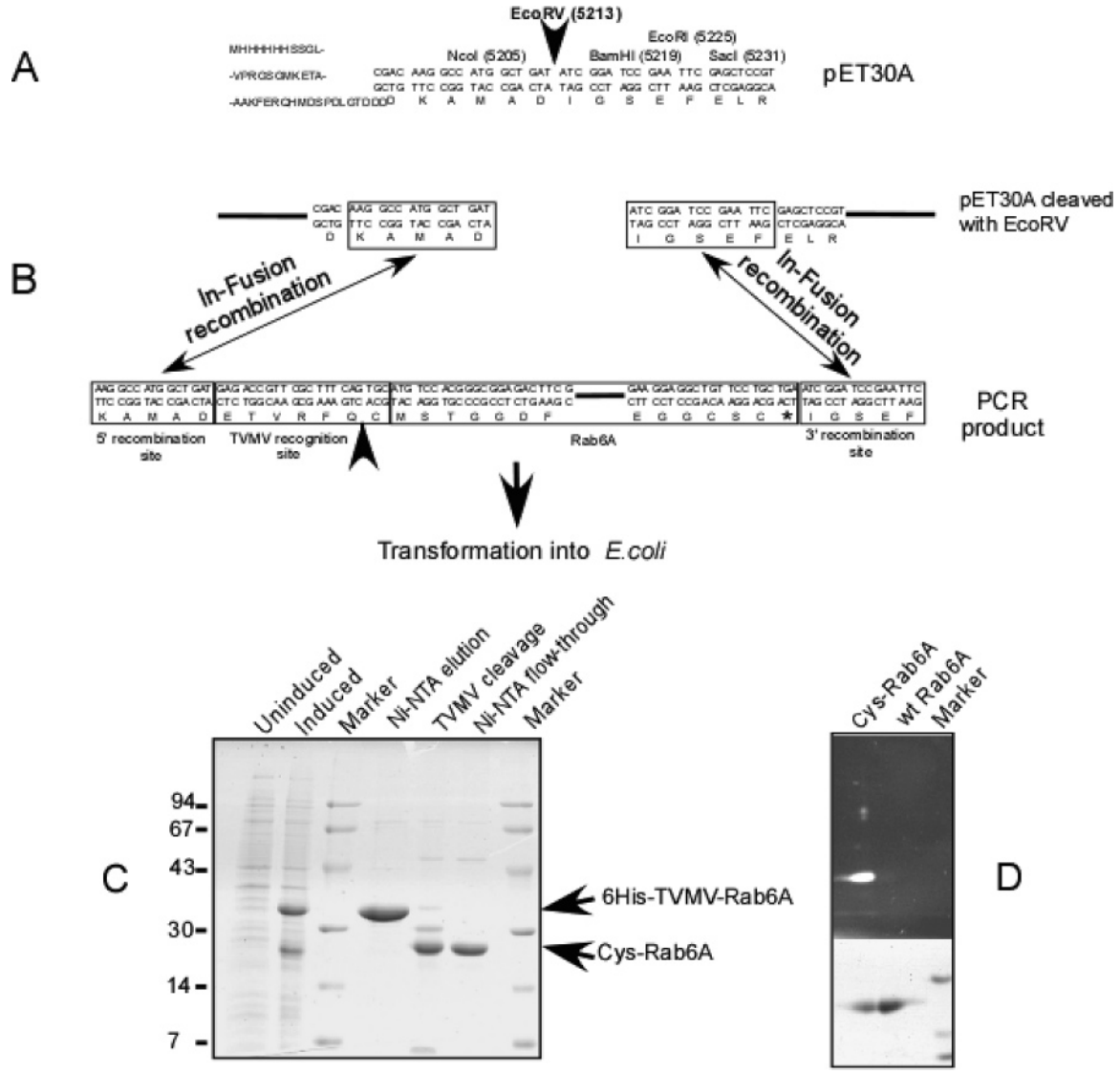

Figure 8. Use of In-Fusion cloning for generation of the 6His-TVMV-Rab6A fusion protein: (A) multicloning site of the pET30A vector (the *Eco*RV site used for vector linearization is marked by an arrow); (B) flowchart of cloning reaction and design of the PCR product; (C) expression in *E. coli*, purification and cleavage of 6His-TVMV-Rab6A with TVMV protease; (D) ligation of TVMV-processed Cys-Rab6A protein with 5(6)-carboxyfluorescein thioester. The samples were processed as in Figure 7.

23922.0 and 24052.0 Da, respectively), as well as the impurity already contained in the starting material and a small peak belonging to the dilabeled protein (calculated molecular mass = 24148.5 Da + **2** and 24412.5 Da + **3**; observed molecular mass = 24146.0 and 24411.0 Da, respectively; Figure 5). In cases when the dilabeled product interferes with the intended use of the labeled protein, the additional label that is attached to the protein via a thioester bond can be efficiently removed by treatment with hydroxylamine (50 mM in aqueous buffer, 3 h).

Cloning, Expression, Purification, and Labeling of Mammalian Rab GTPases. To establish the general applicability of the designed vector and the labeling procedure on a larger set of test proteins, we chose to clone a subset of mammalian RabGTPases into the pCYSLIC vector. We amplified 39 ORFs of RabGTPases and cloned them into the pCYSLIC vector. The cloning procedure was very robust with typical cloning efficiency of >90%. The resulting clones were verified by sequencing and tested for expression in BL21(DE3)RIL strains at 37 and 20 °C (see Supporting Information). Approximately 50% of the proteins were either completely or partially soluble at 20 °C. We purified a subset composed of Rab3A, Rab3B, Rab4A, Rab19, and Rab27 to >70% purity by Ni−NTA chromatography followed by subsequent cleavage of GST tag with TEV protease. Incubation of the purified proteins with carboxyfluorescein thioester resulted in the formation of a fluorescent product easily detectable by SDS−PAGE. Labeling of most proteins resulted in a slight (≈0.5 kDa) decrease in electrophoretic mobility of the ligation product, which suggests that the majority of the protein was labeled efficiently (Figure 6). Proteins retained their solubility, indicating that labeling does not significantly affect protein folding or solubility.

Use of In-Fusion Cloning for Production of Proteins Containing N-Terminal Cysteine. The described approach based on LIC cloning is both sufficiently inexpensive and flexible to be adapted to an automated cloning platform. However, similar to most recombination-based cloning methods, it precludes the use of vectors not adapted to the chosen cloning method. Ideally one would like to be able to use any selection of vectors, particularly in cases when the protein displays folding or solubility problems. The recently introduced In-Fusion cloning procedure potentially provides a way to clone a PCR fragment into any linearized vector. We decided to test whether this approach could also be used for the rapid generation of the recombinant proteins with N-terminal cysteines. To this end, we chose a pET30a vector that features an N-terminal 6His tag

and is commonly used for the expression of recombinant proteins. We decided to incorporate into recombinant Rab6A a cleavage site for TVMV polymerase, which has not been previously used for the generation of an N-terminal cysteine residue. Hence, we included a modified recognition sequence of TVMV polymerase into the primers, which would result in substitution of the serine in the recognition sequence ETVRFQS by cysteine (cleavage normally occurs between Q and S). The primer design and recombination cloning procedure are depicted in Figure 8A−C and described under Experimental Procedures. The recombinant clones were readily obtained, and the fusion protein was expressed in *E. coli*, purified, and cleaved with recombinant TVMV protease under conditions used for TEV protease (Figure 8C). The cleavage was very efficient, demonstrating that TVMV could well tolerate S→C substitution in the cleavage site. Following a second purification by Ni−NTA, the protein was already >85% pure and could be used directly for downstream applications. To ensure that the generated N-terminal cysteine was functional in the ligation reaction, we incubated the recombinant protein with carboxyfluorescein thioester as described above. As can be seen in Figure 8D, this resulted in specific labeling of Rab6A.

CONCLUSIONS

In the current work we present a new *E. coli* expression vector pCYSLIC that allows rapid cloning of PCR fragments via ligation-independent cloning in frame with the 6-His-GST tag. The affinity tags were easily removed with TEV protease, leaving an N-terminal cysteine that was subsequently used to label the proteins with carboxyfluorescein and biotin via in vitro protein ligation reaction. The developed combination of inexpensive rapid cloning, purification, and functionalization procedures provides an advance in protein expression and derivatization. We compared this method to the recently developed In-Fusion cloning approach and demonstrated that, although more expensive, the In-Fusion cloning provides superior cloning vector flexibility compared with other cloning methods. We also showed that TVMV protease can be employed for the generation of recombinant proteins with N-terminal cysteine.

ACKNOWLEDGMENT

We acknowledge N. Lupilova, S. Thuns, and M. Terbeck for invaluable technical assistance. The pMCSG7 vector was kindly provided by M. I. Donnelly. We are grateful to F. Barr for the cDNAs of Rab6A and to D. Waugh for the gift of expression vectors for TVMV and TEV proteases. This work was supported in part by Grant DFG AL 484/7-2 to K.A.

Supporting Information Available: Expression and solubility test of RabGTPases cloned and expressed in pCYSLIC vector. This material is available free of charge via the Internet at http://pubs.acs.org.

LITERATURE CITED

(1) Yokoyama, S. (2003) Protein expression systems for structural genomics and proteomics. *Curr. Opin. Chem. Biol. 7*, 39−43.

(2) Hartley, J. L., Temple, G. F., and Brasch, M. A. (2000) DNA cloning using in vitro site-specific recombination. *Genome Res. 10*, 1788−1795.

(3) Benoit, R. M., Wilhelm, R. N., Scherer-Becker, D., and Ostermeier, C. (2006) An improved method for fast, robust, and seamless integration of DNA fragments into multiple plasmids. *Protein Express. Purif. 45*, 66−71.

(4) Waugh, D. S. (2005) Making the most of affinity tags. *Trends Biotechnol. 23*, 316−320.

(5) Muir, T. W. (2003) Semisynthesis of proteins by expressed protein ligation. *Annu. Rev. Biochem. 72*, 249−289.

(6) Dawson, P. E., Muir, T. W., Clark-Lewis, I., and Kent, S. B. (1994) Synthesis of proteins by native chemical ligation. *Science 266*, 776−779.

(7) Zhang, A., Gonzalez, S. M., Cantor, E. J., and Chong, S. (2001) Construction of a mini-intein fusion system to allow both direct monitoring of soluble protein expression and rapid purification of target proteins. *Gene 275*, 241−252.

(8) Schuler, B., and Pannell, L. K. (2002) Specific labeling of polypeptides at amino-terminal cysteine residues using Cy5-benzyl thioester. *Bioconjugate Chem. 13*, 1039−1043.

(9) Gentle, I. E., De Souza, D. P., and Baca, M. (2004) Direct production of proteins with N-terminal cysteine for site-specific conjugation. *Bioconjugate Chem. 15*, 658−663.

(10) Cotton, G. J., and Muir, T. W. (2000) Generation of a dual-labeled fluorescence biosensor for Crk-II phosphorylation using solid-phase expressed protein ligation. *Chem. Biol. 7*, 253−261.

(11) Tolbert, T. J., and Wong, C. H. (2002) New methods for proteomic research: Preparation of proteins with N-terminal cysteines for labeling and conjugation. *Angew. Chem. Int. Ed. 41*, 2171−2174.

(12) Tozser, J., Tropea, J. E., Cherry, S., Bagossi, P., Copeland, T. D., Wlodawer, A., and Waugh, D. S. (2005) Comparison of the substrate specificity of two potyvirus proteases. *FEBS J. 272*, 514−523.

(13) Stols, L., Gu, M., Dieckman, L., Raffen, R., Collart, F. R., and Donnelly, M. I. (2002) A new vector for high-throughput, ligation-independent cloning encoding a tobacco etch virus protease cleavage site. *Protein Express. Purif. 25*, 8−15.

(14) Tolbert, T. J., Franke, D., and Wong, C. H. (2005) A new strategy for glycoprotein synthesis: ligation of synthetic glycopeptides with truncated proteins expressed in *E. coli* as TEV protease cleavable fusion protein. *Bioorg. Med. Chem. 13*, 909−915.

(15) Woulfe, S. R., and Miller, M. J. (1986) The synthesis of substituted [[3(*S*)-(acylamino)-2-oxo-1-azetidinyl]thio]acetic acids. *J. Org. Chem. 51*, 3133−3139.

(16) Kalinin, A., Thoma, N. H., Iakovenko, A., Heinemann, I., Rostkova, E., Constantinescu, A. T., and Alexandrov, K. (2001) Expression of mammalian geranylgeranyltransferase type-II in *Escherichia coli* and its application for in vitro prenylation of Rab proteins. *Protein Express. Purif. 22*, 84−91.

(17) Becker, C. F. W., Hunter, C. L., Seidel, R. P., Kent, S. B. H., Goody, R. S., and Engelhard, M. (2001) A sensitive fluorescence monitor for the detection of activated Ras: total chemical synthesis of site-specifically labeled Ras binding domain of c-Raf1 immobilized on a surface. *Chem. Biol. 8*, 243−252.

BC050320D

Structure−Function Engineering of Interferon-β-1b for Improving Stability, Solubility, Potency, Immunogenicity, and Pharmacokinetic Properties by Site-Selective Mono-PEGylation

Amartya Basu, Karen Yang, Maoliang Wang, Sam Liu, Ramesh Chintala, Thomas Palm, Hong Zhao, Ping Peng, Dechun Wu, Zhenfan Zhang, Jack Hua, Ming-Ching Hsieh, John Zhou, Gerald Petti, Xiguang Li, Ahsen Janjua, Magda Mendez, Jun Liu, Clifford Longley, Zhihua Zhang, Mary Mehlig, Virna Borowski, Manickam Viswanathan, and David Filpula*

Enzon Pharmaceuticals, 20 Kingsbridge Road, Piscataway, New Jersey 08854-3969. Received November 9, 2005; Revised Manuscript Received February 22, 2006

Recombinant interferon-beta-1b (IFN-β-1b) is used clinically in the treatment of multiple sclerosis. In common with many biological ligands, IFN-β-1b exhibits a relatively short serum half-life, and bioavailability may be further diminished by neutralizing antibodies. While PEGylation is an approach commonly employed to increase the blood residency time of protein therapeutics, there is a further requisite for molecular engineering approaches to also address the stability, solubility, aggregation, immunogenicity and in vivo exposure of therapeutic proteins. We investigated these five parameters of recombinant human IFN-β-1b in over 20 site-selective mono-PEGylated or multi-PEGylated IFN-β-1b bioconjugates. Primary amines were modified by single or multiple attachments of poly(ethylene glycol), either site-specifically at the N-terminus, or randomly on the 11 lysines. In two alternate approaches, site-directed mutagenesis was independently employed in the construction of designed IFN-β-1b variants containing either a single free cysteine or lysine for site-specific PEGylation. Optimization of conjugate preparation with 12 kDa, 20 kDa, 30 kDa, and 40 kDa amine-selective PEG polymers was achieved, and a comparison of the structural and functional properties of the IFN-β-1b proteins and their PEGylated counterparts was conducted. Peptide mapping and MALDI-TOF mass spectrometric analysis confirmed the attachment sites of the PEG polymer. Independent biochemical and bioactivity analyses, including antiviral and antiproliferation bioassays, circular dichroism, capillary electrophoresis, flow cytometric profiling, reversed phase and size exclusion HPLC, and immunoassays demonstrated that the functional activities of the designed IFN-β-1b conjugates were maintained, while the formation of soluble or insoluble aggregates of IFN-β-1b was ameliorated. Immunogenicity and pharmacokinetic studies of selected PEGylated IFN-β-1b compounds in mice and rats demonstrated both diminished IgG responses, and over 100-fold expanded AUC exposure relative to the unmodified protein. The results demonstrate the capacity of this macromolecular engineering strategy to address both pharmacological and formulation challenges for a highly hydrophobic, aggregation-prone protein. The properties of a lead mono-PEGylated candidate, 40 kDa PEG_2−IFN-β-1b, were further investigated in formulation optimization and biological studies.

INTRODUCTION

Human interferon-beta (IFN-β[1]) is produced in many cell types in response to viral infection or exposure to double stranded RNA (*1*, *2*). Following binding of this glycoprotein to a heterodimeric cell receptor, IFNAR-1/IFNAR-2, a cascade of signaling events leads to expression of IFN-β inducible genes which modulate antiviral, antiproliferative, and immunomodulatory functions (*3*−*6*). Three recombinant IFN-β therapeutics are presently marketed for the treatment of the relapsing-remitting form of multiple sclerosis (*7*−*12*). IFN-β-1a preparations are glycosylated products expressed in mammalian cells and are similar to the 166 amino acid native human protein. IFN-β-1b is a nonglycosylated protein expressed in *E. coli*; it also differs from the human protein in that it lacks the N-terminal methionine and has a Cys17Ser substitution (*13*−16). These structural alterations may correlate with an apparent reduced bioactivity in vitro and an increase in neutralizing antibodies for patients treated with IFN-β-1b when compared with IFN-β-1a (*17*−*22*). While both of the Type I interferons, IFN-α and IFN-β, which bind to a common IFNAR-1/IFNAR-2 receptor (*23*−*25*), have proven to be among the most successful biotechnology products, the major obstacle to clinical development has not been biological potency. Rather, the physicochemical properties of these very potent compounds have led to challenges in frequent dosing, formulation, and immunogenicity. Among the human therapeutic cytokines, IFN-β-1b is a prime example of a hydrophobic protein difficult to purify and formulate, owing to the propensity of the molecule to form aggregates. The marketed IFN-β-1b product, Betaseron, is a lyophilized powder containing human serum albumin as an excipient. Clinical pharmacokinetic studies have demonstrated that IFN-β-1b has a very short terminal serum half-life and the

* To whom correspondence should be addressed. Tel: 732-980-4941. Fax: 732-885-2950. E-mail: david.filpula@enzon.com.

[1] Abbreviations: ALD, aldehyde; AUC, area under the curve; ELISA, enzyme-linked immunosorbent assay; HAc, acetic acid; HRP, horseradish peroxidase; HSA, human serum albumin; IFN-β-1b, interferon beta-1b; im, intramuscular; iv, intravenous; mAb, monoclonal antibody; mPEG, monomethoxy-PEG; MRT, mean retention time; MW, molecular weight; NHS, *N*-hydroxysuccinimide; PBS, phosphate-buffered saline; PEG, poly(ethylene glycol); PEG_2, branched PEG; RP, reversed phase; sc, subcutaneous; SC, succinimidyl carbonate; SE-HPLC, size-exclusion-high performance liquid chromatography; SPA, succinimidyl propionate; $t_{1/2}$, serum half-life; TFA, trifluoroacetic acid; T-PEG, thiazolidine-2-thione PEG; U-PEG, branched PEG; X-US-PEG, extended branched PEG.

10.1021/bc050322y CCC: $33.50 © 2006 American Chemical Society
Published on Web 05/03/2006

low serum concentrations challenge the limits of assay detection following subcutaneous administration (*14*, *26*).

The goals of the present study were to design IFN-β-1b molecules exhibiting (1) prolonged solubility in the absence of detergents, (2) diminished formation of protein aggregates, (3) diminished immunogenicity, (4) improved in vivo potency, and (5) tailored pharmacokinetic profiles with alternate routes of administration. We wished to employ bioconjugate and protein engineering approaches to investigate the performance of a series of designed IFN-β-1b compounds synthesized by site-specific or site-selective surface modification. PEGylation, the covalent attachment of poly(ethylene glycol) polymers to compounds, has become one of the best validated drug delivery methods for extension of serum half-life (*27*−*38*) and at least six PEGylated protein therapeutics are now on the market (*39*). Two PEGylated interferon-α products are included in this category (*40*−*45*) and initial progress on PEG−IFN-β-1a has been reported (*34*, *46*, *47*), but a general strategy for creating tailored PEGylated IFN-β-1b has not been developed after the1990 patent disclosure of Katre and Knauf (*48*). Conjugates composed of PEG and receptor-binding ligands frequently exhibit diminution or even loss of bioactivity, and these compounds may also demonstrate substantial product heterogeneity. In general, activated PEG polymers reactive with primary amines have been employed in multiple attachments with catabolic enzymes and other macromolecules which recognize small substrates. In comparison, PEGylation of cytokines, hormones, and other small protein ligands represents a greater challenge for enhancing clinical potency due to the opposing effects of reduced receptor binding affinity and prolonged conjugate circulating lives (*49*−*52*). A receptor binding site may constitute a large proportion of the ligand surface area; for example, 960 Å^2 of accessible surface is buried in each binding interface of the IFN-γ/IFN-γRα complex (*53*). Furthermore, reactive amines are prevalent moieties on the scaffold and contact regions of essentially all natural cytokine sequences (*2*). Consequently, extensive random conjugations may be inactivating either through direct attachment to receptor-binding contact residues or as a result of transient steric hindrance and diffusional constraints from the long polymer strands.

To investigate this macromolecular engineering approach, we expressed purified and re-engineered recombinant IFN-β-1b through construction of 20 disparate conjugate preparations with 12 kDa, 20 kDa, 30 kDa, and 40 kDa PEG polymers and performed a comparison of the structural and functional properties of the purified IFN-β-1b proteins and their PEGylated counterparts. Physicochemical analysis of selected mono-PEGylated IFN-β-1b compounds verified their composition, while several cell based assays, immunoassays, and chromatographic methods confirmed that the conjugates demonstrated superior monomeric stability and maintained functional activity dependent on microenvironment. Pharmacokinetic studies of the conjugates in rodents demonstrated that the circulating lives of the PEGylated IFN-β-1b proteins could be tailored with correspondence to the polymer molecular mass, reaching circulating times comparable to the major blood proteins for the conjugate compounds employing 40 kDa branched PEG polymers. These investigations demonstrate a practical approach for engineering IFN-β-1b, and perhaps other similar hydrophobic proteins, to achieve improved physical stability as well as improved pharmacological properties.

EXPERIMENTAL PROCEDURES

Materials. Recombinant human IFN-β-1b (30 MIU/mg) was supplied by Enzon Pharmaceuticals (Piscataway, NJ). Betaseron was purchased from the pharmacy. All activated PEG polymers were supplied by Enzon Pharmaceuticals, except mPEG2-ButyrALD-40 kDa-PEG, mPEG-SPA-20 kDa and mPEG2-NHS-40 kDa, which were purchased from Nektar Therapeutics (San Carlos, CA). Hiload Superdex 200, HiPrep 26/10, and PD-10 desalting columns were supplied by Amersham BioSciences (now GE Healthcare, Piscataway, NJ), and Poros HS was supplied by Applied Biosystems (Foster City, CA). Precast 4−20% Tris-glycine SDS PAGE gels and the gel running buffer were obtained from Invitrogen (Carlsbad, CA). Encephalomyocarditis virus (EMCV; VR-129B) and Vero cells (CCL-81) were from ATCC. Titrisol iodine solution was obtained from EM Science (Gibbstown, NJ).

IFN-β-1b Genetic Constructions. The synthetic genes for human IFN-β-1b and protein variants were constructed from the published sequence (*13*). Recombinant proteins were expressed in *E. coli* BL21(DE3), refolded, and purified to near homogeneity as previously described (*54*, *55*). The inclusion of 0.05% Zwittergent 3−14 in column and formulation buffers was needed to maintain protein solubility. DNA sequence confirmation of all IFN-β genes was performed on an ABI PRISM 310 Genetic Analyzer. Generation of lysine-free variants of IFN-β-1b followed the reported protocol (*52*).

PEGylation of IFN-β-1b. IFN-β-1b (0.8 mg/mL; 5−50 mL) in 100 mM sodium phosphate, 0.05% Zwittergent 3−14, 2 mM EDTA, pH 7.8, was conjugated with activated PEG polymers with PEG mass of 12 kDa, 20 kDa, 30 kDa, and 40 kDa. In random PEGylation of primary amines, PEG-NHS or PEG-T compounds were dissolved in 0.1 mM HAc (or in H_2O for T-PEG). With fast stirring without generating foam, the PEG solution was added at 0.5−1.0 g/min to a final 10-fold molar excess over protein. The reaction was conducted at 25 °C for 60 min for PEG-NHS, or 120 min for PEG-T, quenched by adding glycine to a final molar ratio of 50:1 (glycine:PEG), and filtered through a 0.2 μm membrane before the column purification.

N-Terminal PEGylation: IFN-β-1b (0.8 mg/mL) was reacted with ALD-PEG polymers at a 1:10 reaction molar ratio in 100 mM sodium acetate, pH 5.2, at 25 °C for 3 h. 1 M sodium cyanoborohydride in PEGylation buffer was added to the reaction to a final concentration of 15 mM. The reaction was conducted at 25 °C for 16 h.

Purification of PEG−IFN-β-1b. The PEGylation reaction (5 mL; 0.8 mg protein/mL) was purified by Superdex 200 High Load chromatography with a 10 mM sodium phosphate, pH 7.3, 0.05% Zwittergent running buffer at a flow rate of 2 mL/min. In the second step, 8 mL of peak fractions were loaded onto an HS-50 column with 10 mM sodium phosphate, pH 7.3, 5% mannitol running buffer. The PEG−IFN-β-1b was eluted with 1 M NaCl in equilibration buffer at 2 mL/min and 2 mL/fraction over a period of 40 min. Fractions identified on SDS−PAGE were combined and the pH of the sample was immediately adjusted to 3.7 with HAc. It was then dialyzed using a 30k-MW-cutoff membrane against 5% mannitol, 3 mM HAc, pH 3.7 at 4 °C for 12 h. The fractions were diafiltered on Amicon membranes to a final concentration of 0.5−1 mg/mL in 3 mM HAc, pH 3.7, 5% mannitol. The endotoxin levels of the IFN-β-1b conjugates were <1 EU/mg; contamination of *E. coli* proteins was below 0.002% by immunoassay (Cygnus Technologies); Zwittergent and SDS were undetectable by RP-HPLC using an ELSD detector (detection limit: 0.01%) and acridine-orange (detection limit: 0.001%), respectively.

Analytical Characterization of IFN-β-1b and PEG−IFN-β-1b. Protein concentrations were determined by UV absorbance at 280 nm, with an IFN-β-1b extinction coefficient of 1.5 mL/mg.cm. The concentration was also confirmed by the bicinchoninic acid assay (BCA) using a BSA standard.

Western blot analysis was performed with anti-huIFN-β rabbit antiserum as a primary antibody and goat anti-rabbit HRP was

used as a secondary antibody with a TMBM peroxidase substrate. Iodine staining of SDS PAGE gels was performed after gels were rinsed with distilled water and placed in 5% barium chloride solution. After 10 min of gentle mixing, the gels were again rinsed with water and placed in 0.1 M Titrisol iodine solution for color development.

Mass values of IFN-β-1b and PEG−IFN-β-1b conjugates were determined by matrix-assisted laser desorption ionization−time-of-flight mass spectrometry (MALDI-TOF; Bruker Daltronics OmniFlex NT) using an internal standard with similar molecular weight on the α-cyano-4-hydroxycinnamic acid (CHCA) matrix. Apparent molecular weights (Stoke radius) of the compounds were estimated using Superdex 200 HR 10/30 Gel Filtration column chromatography. Additionally, analysis of molecular masses on 4−20% SDS−PAGE gels was performed using protein and PEG-protein standards.

Peptide mapping was performed by published procedures (*57*).The PEG−IFN-β-1b (0.2 mg) was denatured and reduced in 6 M guanidine HCl, 1 mM EDTA, 5 mM DTT, then alkylated with iodoacetamide prior to digestion with TPCK-treated trypsin. The trypsin generated peptide mixture was fractionated by size exclusion chromatography (Superdex 75) with HPLC-grade water and analyzed by SDS−PAGE and iodine staining. The unique iodine-stained fraction was subjected to protein sequencing analysis (PROCISE, Applied Biosystems). Alternatively, the PEG-peptide fragments were isolated on RP-HPLC and subsequently subjected to sequencing. The percent isomer was calculated by dividing the amount of each isomer by the total amount of isomers in the first cycle of sequencing. Lys-C digested fragments from either IFN-β-1b or PEG−IFN-β-1b were also separated on RP-HPLC and identified by LC-MS. PEG-peptides were identified by comparative analysis.

Circular dichroism (CD) and the determination of enthalpy of folding were conducted as described (*58*). All samples were analyzed at 0.1 mg/mL in 5 mM acetic acid. Spectra were collected at 25 °C. Data were analyzed using the neural network software CDNN (*59*).

Flow cytometry for comparative analysis of fluorescence intensity was conducted on FACSCalibur as previously described (*28*). A549 cells were incubated sequentially with IFN-β-1b, rat anti IFN-β-1b or anti PEG−IFN-β-1b plasma, and PE conjugated goat anti- rat IgG polyclonal antibody (BD Biosciences).

Biacore analysis was performed as described (*28*). IFN-β-1b was immobilized on a CM5 chip and the preimmunized and postimmunized rat serum (1:100) were analyzed for antibodies against IFN-β-1b.

RP-HPLC. RP-HPLC was used to determine conjugate purity and stability. A Vydac C4 column was run at 55 °C. Samples (0.5 mg/mL in 5% mannitol, 3 mM HAc, pH 3.7) were analyzed using a 45−60% gradient over 25 min at 0.8 mL/min of buffer A (0.1% TFA in H_2O) and buffer B (0.1% TFA in acetonitrile).

SE-HPLC. Superdex 200 HR was used to analyze formation of soluble aggregates of the PEG−IFN-β conjugates. The mobile phase was composed of 100 mM sodium phosphate, pH 6.8, at 24 °C. Evaporative Light Scattering Detection (ELSD; Sedere, Inc.) allowed free PEG detection.

Antiviral Assays of IFN-β-1b. Specific antiviral activity from the cytopathic effect of IFN-β-1b was assayed by published methods (*60*) using Vero cells and EMCV virus, which were cultivated as recommended by the ATCC supplier. Vero cells were distributed on 96-well microtiter plates (20000 cells/well) in 0.05 mL of culture medium. Serial dilutions of 0.05 mL of the IFN-β samples were added and incubated at 37 °C, 5% CO_2, for 24 h. EMCV (200 pfu/20 μL) was added to each well at 25 °C for 30 min and then incubated at 37 °C for 24 h. After the addition of 20 μL of 10 mg/mL 3-(4,5-dimethyl-2-thiazoyl)-2,5-diphenyl-2*H*-tetrazolium bromide (MTT; Promega, Madison, WI) dye solution to each well, incubation was continued for 4 h; then 100 μL of stop solution (1.2 N HCl in 2-propanol) was added to each well, and the plate was read at 570 nm in a 96-well plate reader (Molecular Devices, Sunnyvale, CA) to determine EC_{50} values, as analyzed with Softmax Pro software. Native IFN-β-1b and PEGylated IFN-β-1b were analyzed in triplicate on each plate. Conversion of mass to antiviral units was attained using specific activity of the parent compound (native or PEG−IFN-β-1b). A549 cells were also used in antiviral assays in this procedure.

Antiproliferation Assay. A549 cells were seeded in 96-well plates, 4000 cells/well, in 100 μL complete Ham's F12K medium containing 2 mM L-glutamine, 1.5 g/L sodium bicarbonate, and 10% fetal bovine serum. IFN-β-1b compounds were added to the cells (in triplicate) in serial dilutions, initiating at 125 ng/mL, which is equivalent to 4000 Units/mL of Betaseron activity. Cells were allowed to grow for 4 days, and cell proliferation was measured by the MTT assay.

Pharmacokinetic Analysis of PEG−IFN-β-1b in Mice. C57BL/6 mice (7−8 week, female) were supplied by Sprague Dawley Harlan (Madison, WI). Mice (5/group) were injected subcutaneously, intramuscularly, and intravenously with 100 μL per mouse (0.2 mg protein/kg) of IFN-β-1b, or its PEGylated conjugates. Following sedation with 0.09% avertin, sampling of blood was undertaken via the retro-orbital sinus into vials containing EDTA. At 2, 15, 30, and 60 min, the mice were bled 100 μL, and at 4, 24, 48, 72, and 96 h, the mice were terminally bled by cardiac puncture. The plasma was collected following centrifugation of the blood at 5000 rpm at 4 °C for 5 min and immediately frozen on dry ice. The concentrations of the compounds were analyzed by both antiviral activity and by ELISA. The data were modeled using WinNonlin software (WinNonlin Pharsight, Mountain View, CA) to determine pharmacokinetic parameters using a two compartment, bolus, first-order elimination model for the intravenous samples. The correlation between the observed and predicted model time point values was ≥95%.

Pharmacokinetic Analysis of PEG−IFN-β-1b in Rats. Sprague Dawley (Harlan) rats (150−300 g; 3/group) were injected subcutaneously, intramuscularly, or intravenously with 150 μL per rat (0.1−0.6 mg/kg) of IFN-β-1b, or its PEGylated conjugates. Following sedation with 30% O_2/70% CO_2, sampling of blood (250 μL) was undertaken via the retro-orbital plexus into vials containing EDTA, at times prior to compound administration and at 2 min, 60 min, 2 h, 4 h, 8 h, 24 h, and daily for 3 additional days. The plasma was collected following centrifugation of the blood at 5000 rpm at 4 °C for 5 min and immediately frozen on dry ice. The concentrations of the compounds were analyzed by both antiviral activity and by ELISA. The data were modeled using WinNonlin software (WinNonlin Pharsight, Mountain View, CA) by noncompartmental analysis with AUC estimated by the linear trapezoidal rule to determine pharmacokinetic parameters.

Immunogenicity of IFN-β-1b and PEG−IFN-β-1b in Rats. Sprague Dawley (Harlan) rats weighing 150−300 g (three in a group) were injected intramuscularly with either buffer, native IFN-β-1b (0.1 mg/kg), or NHS 40 kDa PEG_2−IFN-β-1b (0.1 mg protein/kg). Injections were given once per week for five weeks, and the plasma samples were collected before the next injection and at the end of the sixth week. Rat plasma antibodies were analyzed by direct ELISA, indirect ELISA, flow cytometry, Biacore, and antiviral neutralization assays.

Direct ELISA: As previously described (*61*), IFN-β-1b coated the microtiter plates (400 ng/50 μL). Rat anti IFN-β-1b or anti PEG−IFN-β-1b plasma was added in 1:2 serial dilutions. The secondary antibody was HRP conjugated rabbit anti rat IgG

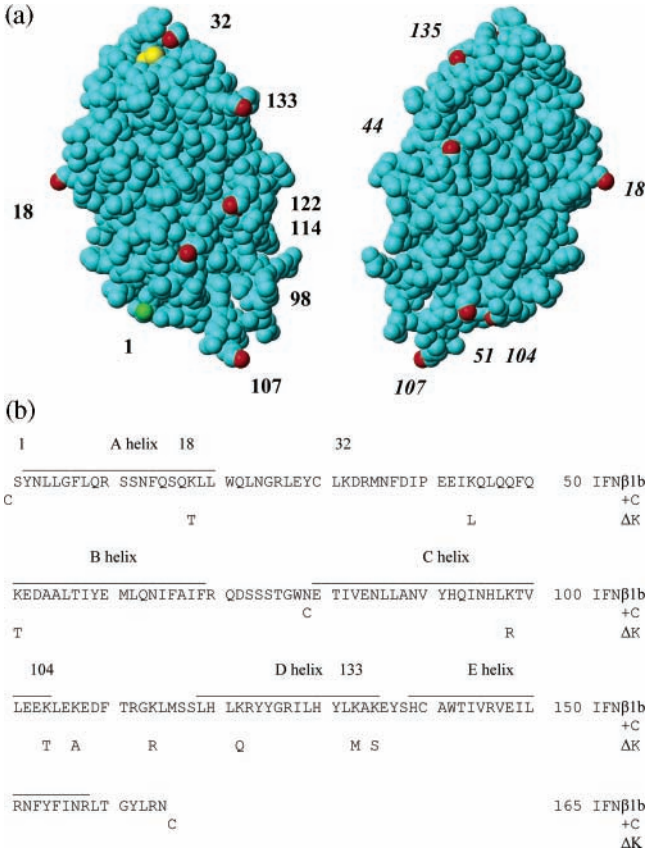

Figure 1. (A) Two views of the human IFN-β model based on the IFN-β-1a crystal structure (PDB File Name 1AU1). The space-filling model is shown from two different angles, rotated by 180°. The 11 lysines are numbered and highlighted with nitrogen in red. The right-hand model uses italics numbering for clarity. The N-terminal serine-1 amino group is green and the disulfide (S−S) bond between cysteine-30 and cysteine-140 is shown in yellow. Lysine-114 is not readily visible in this figure. (B) Amino acid sequence of 165-residue IFN-β-1b is shown with five helix structures. Locations of primary sites of PEGylation at lysines or the N-terminus are shown by numbering above the sequence. Below the sequence are shown site-specific mutant proteins corresponding to sites of single free cysteine insertion (+C) at either the N-terminus, C-terminus, or position 79. Also shown on the bottom line are the sequence substitutions in a lysine depleted variant protein (ΔK).

(Jackson Labs; 1:5000) with TMB peroxidase substrate (Moss, Inc.). Plates were read at 450 nm. The control mAb MMHB-3 was obtained from R&D Systems.

Indirect ELISA: The microtiter plates were coated with the capture antibody, anti- huIFN-β mAb (R&D Systems) at 200 ng/50 μL per well. After blocking, either 4 ng or 20 ng of the two test compounds, IFN-β-1b and NHS 40 kDa PEG_2−IFN-β-1b, were added in alternate wells and incubated 12 h at 4 °C. After washing, rat plasma samples were added in 1:2 serial dilutions, beginning at 1:100 or 1:1000 dilutions for IFN-β-1b or NHS 40 kDa PEG_2−IFN-β-1b, respectively. After 12 h incubation at 4 °C and plate washing with PBS, 0.05% Tween-20, pH 7.4, 50 μL of HRP conjugated goat anti rat IgG (1:5000; Jackson Labs) was added and after 2 h incubation at 22 °C and plate washing, TMBE−100 substrate (Moss, Inc.) was incubated for 20 min and the plates were read at 450 nm.

RESULTS AND DISCUSSION

Recombinant Human IFN-β-1b and Site-Selective PEGylation Strategy. A structural view of IFN-β-1b architecture is shown in Figure 1A and 1B (*13, 15*). In our investigations of PEGylation of this protein, we wished to examine multiple approaches which would include attachment of PEG polymers at several different positions on the protein surface. Other investigated parameters would include PEG size, PEG linker, and number of polymer attachments per protein. The key characteristics under evaluation for improved performance would include blood residency time, potency, solubility, aggregation, and immunogenicity. To minimize the potential for PEG polymer strands to sterically block the receptor-binding sites, our preferred designs place single attachments of PEG either (1) site-specifically at the N-terminus, (2) site-selectively on lysines in a stochastic mixture of mono-PEGylated products, or (3) site-specifically in engineered attachment sites. Several linear or branched electrophilic mPEG polymers of 12, 20, 30, and 40 kDa were included in the investigations of lysine modification, whereas, PEG-aldehyde was employed for N-terminal modification. Di- and tri-PEGylated IFN-β-1b proteins were also prepared for comparison to the preferred mono-PEGylated compounds.

Previous studies of PEGylation of IFN-α and IFN-β-1a demonstrate the utility in either random or site-specific modification with one large PEG polymer per protein (*40*, *41*, *43*, *46*). Since IFN-β-1b exhibits only about 35% sequence identity with the IFN-α family, and lacks the N-glycan, N-terminal methionine, and free thiol of IFN-β-1a, there may be limited guidance in the PEGylation approach for IFN-β-1b from these prior studies with other interferons.

Chart 1 displays the structures of the amine selective PEG polymers used in this study. These reagents react with primary amines with release of either the *N*-hydroxysuccinimide (NHS) or thiazolidine-2-thione (T) leaving group to form an acylated product. One example of bioconjugation of UA-PEG to primary amines is shown in Scheme 1. As shown in Figure 1A, eleven lysines and the N-terminal α-amine are available for modification by the well characterized activated PEG compounds such SC−PEG (*33*), XUS−PEG (*35*), T-PEG (*36*), and various NHS derivatives (*29*, *40*, *50*). ALD-PEG polymers may be employed to construct PEG conjugates selectively modified at low pH at the N-terminus, forming secondary amines by reduction with sodium cyanoborohydride (*37*, *46*). Mono-PEGylation of proteins using random amine-directed chemistries commonly produces positional isomers, which are conjugate mixtures with single PEG attachments at different sites on the protein surface. We conducted trypsin or Lys-C peptide mapping analysis, amino acid sequence analysis, LC/MS, and MALDI-TOF or SELDI-TOF MS on two of the most promising mono-PEGylated conjugates, which employed the branched 40 kDa PEG_2−NHS or 40 kDa PEG_2-ALD polymers, to evaluate preferred linkage sites. Figure 1B summarizes the major sites of attachment for these derivatives.

The 40 kDa ALD PEG_2 selectively modified the N-terminus; minor alternate sites (<15%) were not identified. Conjugation with the 40 kDa NHS PEG_2 polymer produced at least five major positional isomers corresponding to positions S1 plus K18 (42%), K104 (18%), K32 (15%), and K133 (14%), and other sites (11%). The N-terminal sequence analyses indicated that K18 was a slightly more preferred PEGylation site than the alpha amine of serine-1 on this N-terminal peptide. The structure of IFN-β-1a shows that the lysines with the most solvent exposed amino groups are K18, K107, and K133. Two of these lysines were shown in these analyses to be PEGylated in NHS 40 kDa PEG_2−IFN-β-1b. K107 is located within a tripeptide Lys-C fragment that eluted very early during C18 RP-HPLC, and this precluded a conclusive determination for this position. The available data suggest that K107, although well exposed, may be a minor site for PEGylation in this compound.

Using systematic mutational mapping of IFN-β-1a, Runkel et al. (*3*, *4*) proposed binding sites for the type I IFN (IFNAR-

Chart 1. Amine-Selective PEG Reagents

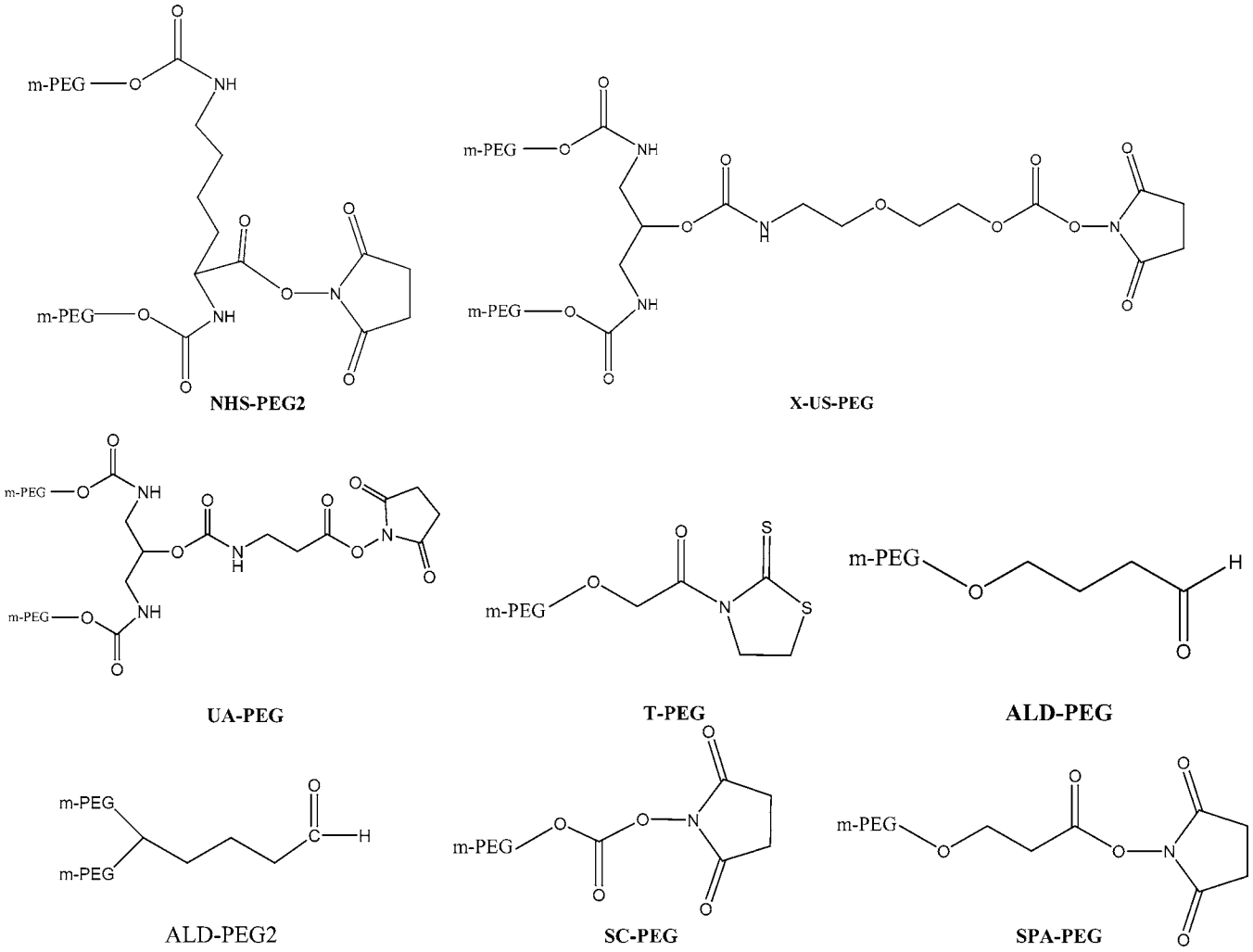

Scheme 1. Reaction of UA-PEG with Amine of Protein To Form an Amide Linkage

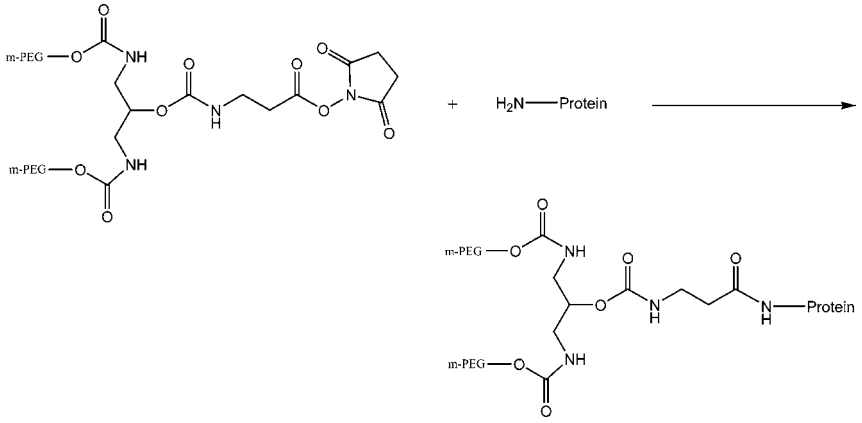

1/IFNAR-2) receptor from Daudi cells. For example, K18, K32, K122, and K133 are located in the general proximity of the binding site for IFNAR-2 and PEGylation at these sites might compromise the efficiency of receptor binding to PEG−IFN-β-1b. For the purpose of our present investigations, the observed differences in distribution of positional isomers in these two conjugates provide a basis for subsequent comparison of functional properties in relationship to structural differences.

We also examined two alternate, entirely site-specific PEGylation approaches for PEG−IFN-β-1b engineering that were both found to be unsatisfactory in our investigations. A recent trend in PEGylation has been the generation of site-specific modification with a single large polymer (*40*, *43*, *49*). Designed protein variants containing one free cysteine may be effectively conjugated to maleimide activated polymers (*28*). We designed three such variants of IFN-β-1b wherein the free cysteine is engineered at either the N-terminus, the C-terminus, or at position 79, which is occupied by the N-glycan in the native protein (Figure 1B). All proteins were expressed and purified in similar yields and bioactivities, compared to IFN-β-1b. However, a completely site-specific modification with maleimide PEG polymers, by our previous protocol (*28*), proved to be challenging due to the lability of the protein disulfide (C30−C140) under reducing conditions. Although conducting the

Table 1. Composition and Antiviral Activity of PEG−IFN-β-1b Conjugates

compound	IFN-β (%)[a]	mono PEG−IFN-β (%)[a]	di PEG−IFN-β (%)[a]	tri PEG−IFN-β (%)[a]	antiviral activity (%)[b]
native IFN-β−1b	100	0	0	0	100
mono NHS-40k-PEG_2−IFN	1	96	3	0	24
mono NHS-40k-PEG_2−IFN	1	97	2	0	22
mono NHS-40k-PEG_2−IFN	0.6	99	0	0.4	31
di NHS-40k-PEG_2−IFN	0	1	96	3	<1
mono ALD-20k-PEG−IFN	3	94	3	0	66
mono ALD-30k-PEG−IFN	0	99	1	0	58
mono ALD-40k-PEG_2−IFN	2	96	2	0	19
mono ALD-40k-PEG_2−IFN	0	99	0.6	0.4	25
mono T-12k-PEG−IFN	1	80	19	0	62
di T-12k-PEG−IFN	1	13	78	8	41
mono T-20k-PEG−IFN	1	96	3	0	55
di T-20k-PEG−IFN	0	8	84	8	23
mono UA-24k-PEG−IFN	1	94	3	2	43
mono UA-40k-PEG−IFN	0	96	3	1	35
mono XUS-40k-PEG−IFN	1	96	2	1	21
mono SC-12k-PEG−IFN	3	87	10	0	71
di SC-12k-PEG−IFN	1	12	82	5	26
tri SC-12k-PEG−IFN	0	0	4	96	1
mono SPA-20k-PEG−IFN	2	92	6	0	68
mono SPA-20k-PEG−IFN	1	94	5	0	63
di SPA-20k-PEG−IFN	0	4	91	5	21

[a] Following purification as described in Experimental Procedures of mono-, di-, and tri-PEG−IFN-β-1b derivatives, which contain one, two, or three PEG attachments per protein, respectively, the purified compounds were analyzed by SE-HPLC. The molar percent of each species in the purified compounds is based on SE-HPLC peak integration. In some cases, independent lots of a compound are shown. [b] The percent of antiviral activity per protein retained in the purified conjugates relative to native IFN-β-1b (30 MIU/mg = 100%).

conjugation reaction at acidic pH or with mild reducing reagents improved the maintenance of the disulfide linkage, the overall yield and complete site specificity of attachment were determined to be insufficient (data not shown).

Another reported approach for site-specific modification was described by Yamamoto et al. (*52*), wherein lysine depleted muteins were screened, thus producing variants with one or a few available primary amines. Our attempts to use this protocol with IFN-β-1b variants demonstrated limited success. Most variant proteins lost antiviral activity or maintained an unacceptably low residual activity such as the mutein shown in Figure 1B which retained only 1% of the native bioactivity. Therefore, we focused our detailed investigations of PEGylated IFN-β-1b on conventional amine selective chemistries under controlled reaction conditions.

PEGylation of IFN-β-1b. Amine directed PEGylation reactions and purification of either mono-PEGylated or di-PEGylated IFN-β-1b conjugates are described in Experimental Procedures. Seven previously described linker designs (*33*, *35*, *36*, *37*, *40*) were investigated including NHS, X-US, UA, T, SC, SPA and ALD. Four PEG masses were examined including 12 kDa, 20 kDa, 30 kDa, and 40 kDa. Table 1 summarizes the purity and bioactivity of the PEGylated IFN-β-1b derivatives investigated in a first screen of compounds. Isolation of mono-PEGylated derivatives was possible from the starting conjugate mixtures, with native IFN-β-1b and di- and tri-PEGylated conjugates present as either trace impurities or as significant species, depending on the conjugate category. The purification of the multi-PEGylated derivatives allowed an initial examination of the correlation of degree of modification with bioactivity. Figure 2 presents one representative SDS−PAGE analysis, including Coomassie Blue, Western, and iodine staining, of mono-PEGylated IFN-β-1b compounds with 12 kDa, 20 kDa, or 40 kDa polymers.

Relative to native IFN-β-1b, the mono-PEGylated compounds retained excellent activity. The retention of about 20−70% of antiviral activity in these derivatives compares favorably to the marketed PEGylated IFN-α drugs, PEG-INTRON and Pegasys, where in vitro antiviral activities are about 28% or 7% of the unmodified protein, respectively (*40*, *45*). It is apparent that the conjugates with the highest molecular weight 40 kDa PEG polymers have lower antiviral activity in vitro. There is no apparent distinction between different linkers and bioactivity within the mono-PEGylated derivatives. A significant observa-

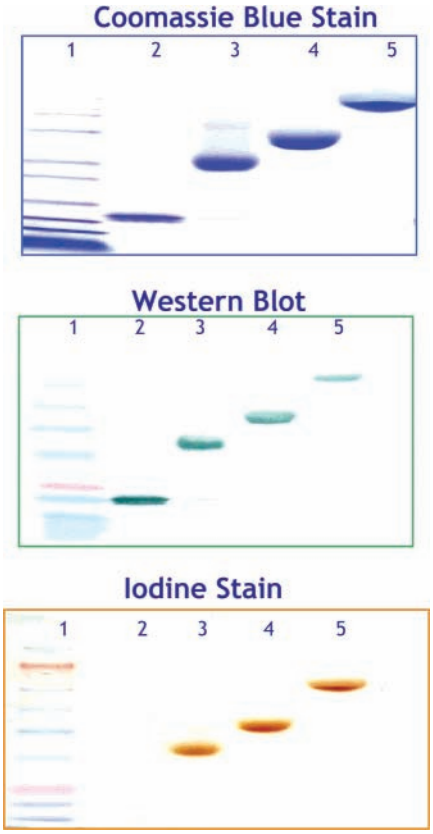

Figure 2. SDS−PAGE analysis of mono-PEGylated IFN-β-1b compounds. Molecular weight markers (lane 1), IFN-β-1b (lane 2), SC 12 kDa PEG−IFN-β-1b (lane 3), SPA 20 kDa PEG−IFN-β-1b (lane 4), and NHS 40 kDa PEG_2−IFN-β-1b (lane 5) are shown. The samples were denatured by heating at 85 °C for 3 min in the presence of 12 mM β-mercaptoethanol. Protein was identified by Coomassie Blue staining or Western staining with anti-huIFN-β mAb; PEG was detected by iodine staining.

Table 2. Molecular Mass of PEG−IFN-β-1b Compounds

compound	MALDI-TOF	SEC[a]	SEC PEG std[b]	SDS−PAGE	calculated[c]
native IFN-β−1b	19876	20000	n.a.	20000	19878
mono SC-12k-PEG−IFN-β	32000	401000	36000	39000	32000
di SC-12k-PEG−IFN-β	40000	430000	38000	54000	44000
mono T-20k-PEG−IFN-β	40000	401000	36000	51000	40000
mono SPA-20k-PEG−IFN-β	40000	430000	38000	50000	40000
di SPA-20k-PEG−IFN-β	60000	874000	65000	110000	60000
mono ALD-20k-PEG−IFN-β	40000	317000	31000	49000	40000
mono ALD-30k-PEG−IFN-β	50000	596000	49000	60000	50000
mono ALD-40k-PEG_2−IFN-β	60000	894000	66000	115000	60000
mono NHS-40k-PEG_2−IFN-β	60000	876000	65000	120000	60000

[a] Molecular weight determined with protein standard markers. [b] Molecular weight determined with PEG polymer standard markers. [c] Molecular weight determined from DNA sequence plus estimated polymer mass.

tion from this study is the reduced or abolished in vitro bioactivity for the multi-PEGylated IFN-β-1b compounds. Attachment of two 40 kDa branched polymers, or attachment of three 12 kDa linear polymers diminished antiviral activities by about 100-fold. Independent analysis of bioactivity of the compounds by an anti-proliferation assay on A549 cells provided similar results (data not shown).

One especially interesting conjugate is the SPA 2 × 20 kDa di PEGylated IFN-β-1b compound, which does retain 21% of native antiviral activity. This conjugate is analogous to the branched 40 kDa PEG modified protein, except the two 20 kDa polymers are at disparate sites rather than at a common attachment position. Therefore, comparison of biological properties of these two conjugate types will be instructional. In addition to the isolation of conjugate species, the purification protocol was also able to remove free PEG polymers, SDS, and Zwittergent, as verified by light scattering detection, acridine orange assays, and RP-HPLC, respectively. Additional purity analysis of these conjugates, including analysis of endotoxin (<1 EU/mL) and *E. coli* protein contaminants (<15 ppm), were conducted prior to in vivo studies.

As shown in Table 2, MALDI-TOF MS confirmed the predicted molecular mass of IFN-β-1b and PEG−IFN-β-1b compounds, and gel filtration analysis demonstrated the capacity of PEGylated proteins to markedly expand in hydrodynamic volume resulting in a predicted molecular weight about 14-fold greater than the calculated mass in the case of the conjugates with single 40 kDa branched polymer attachments. Use of PEG polymer or PEG-protein standards also allowed an approximate measurement of mass with SEC or SDS−PAGE methods, respectively. An evaluation of the preliminary compounds in Table 1 and Table 2 was the basis for selection of several of these conjugates for further analytical and pharmacological investigations.

Stability, Solubility, and Aggregation Analysis. Marketed interferon-β drugs have encountered formulation challenges for this aggregation prone protein; Betaseron, Avonex, and Rebif are formulated with human serum albumin either as powder or in solution. One of the potential benefits of PEGylation for an exceptionally hydrophobic protein such as IFN-β-1b, which is particularly susceptible to aggregation, is increasing the solubility and stability of the conjugate molecule. This attribute was immediately apparent in our investigations of PEGylated IFN-β-1b conjugates. When native IFN-β-1b was formulated in aqueous solution in the absence of a surfactant, such as Zwittergent 3−14, the protein rapidly and quantitatively precipitated as insoluble aggregates within 7 days at neutral pH, whereas the 40 kDa PEGylated IFN-β-1b remained soluble during this duration. Using the selected formulation buffer (3 mM HAc, pH 3.7, 5% mannitol), we found that the NHS 40 kDa PEG_2−IFN-β-1b compound retained the initial antiviral bioactivity (8.5 MIU/mg ± 20%) for 6 months when stored in aqueous solution at 4 °C.

However, we wished to perform a stringent analysis of the physical behavior of PEG−IFN-β in stability studies in order to also examine the extent of formation of soluble aggregates of the bioconjugate. We used RP-HPLC to examine the physical integrity and purity of the conjugates, and SE-HPLC to examine the appearance of soluble aggregates in the PEG−IFN-β-1b preparations. As shown in Figure 3A and 3B, the chromatographic analyses distinguished the mono-PEGylated protein from both degradation products and aggregates. As shown in Table 3, the NHS 40 kDa PEG_2−IFN-1b compound (0.1 mg protein/ml) demonstrated no formation of soluble aggregates during 37-day storage at 4 °C at pH 3.7−4.0. However, storage at higher pH (5.0−8.5) resulted in increasing formation of soluble aggregates with higher pH. We further examined the stability of PEGylated IFN-β-1b compounds in plasma and confirmed no significant loss of antiviral activity in rat plasma incubated at 37 °C for 72 h for the seven conjugates used in subsequent in vivo studies. There was a trend toward better in vitro solubility and stability of the IFN-β-1b conjugates with increasingly higher molecular weight polymers. This may be compared to the successful formulation of the relatively more soluble IFN-α proteins with PEG polymers of intermediate size. Additionally, we examined the rate of degradation of IFN-β-1b and PEG-modified counterparts in rat liver and kidney extracts at 37 °C. The rates of degradation of the PEGylated proteins were approximately 15% of the native protein based on antiviral activity measurements (data not shown).

Finally, we wanted to examine the conformational and structural integrity of the PEGylated IFN-β-1b in a direct comparison to the native protein. In circular dichroism analysis of the NHS 40 kDa PEG_2−IFN-β-1b compound and native IFN-β-1b (0.1 mg/mL), the CD spectra were indistinguishable. As shown in Figure 3C, in additional studies of thermal unfolding of the helices (α helix content ∼ 60%), the thermal stability of the protein and conjugate were very similar and the thermal unfolding of the helices was uncooperative in character. The melting temperatures of IFN-β-1b (T_m = 61.8 °C) and two independent preparations of 40 kDa PEG_2−IFN-β-1b (T_m = 63.2 °C; T_m = 63.5 °C) were virtually identical. The CD data confirm that PEGylation does not impart a notable alteration in secondary structure or thermal stability of the IFN-β-1b protein.

Pharmacokinetic Analysis in Mice and Rats. A hallmark of the beneficial effects of PEGylation is an increased blood residency time of the bioconjugates. Pharmacokinetic properties of the IFN-β-1b and PEGylated IFN-β-1b compounds were determined in both mice and rats using antiviral bioassays for quantitation. While immunoassay methods for detection of total compound produced comparable results for the PEGylated derivatives, native IFN-β-1b cleared too rapidly for detection by ELISA. Three routes of administration—intravenous, subcutaneous, and intramuscular—were examined in both rats and mice. A comparison of the PK profiles in mice of native IFN-β-1b and the amine directed mono-PEGylated conjugates with

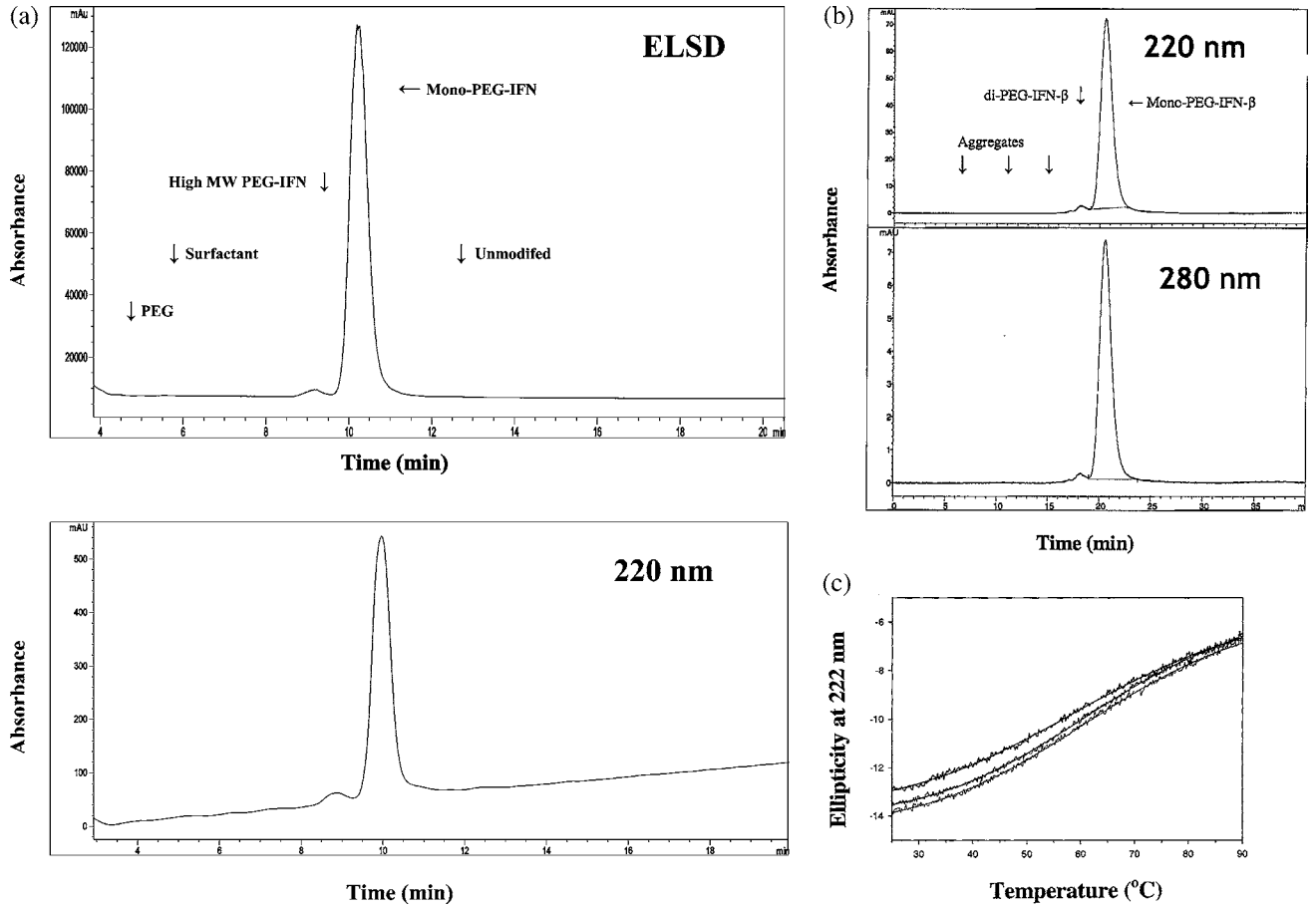

Figure 3. Analyses of physical integrity of PEG−IFN-β-1b. (A) RP-HPLC of NHS 40 kDa PEG_2−IFN-β-1b (0.48 mg/mL in 5% mannitol, 3 mM HAc, pH 3.7) on Vydac C4 at 55 °C with diode array and evaporative light scattering detectors. Upper graph is ELSD scan; lower graph is generated by a 220 nm UV detector. Buffer A: 0.1% TFA in H_2O; buffer B: 0.1% TFA in acetonitrile; gradient: 45−60% over 25 min; flow rate: 0.80 mL/min. Elution times of each species are shown. (B) SE-HPLC of NHS 40 kDa PEG_2−IFN-β-1b (0.88 mg protein/mL in 5% mannitol, 3 mM HAc, pH 3.7) on Superdex 200 HR at 24 °C. Running buffer is 100 mM sodium phosphate, pH 6.8; flow rate is 0.50 mL/min. Elution times of each species are shown. UV detectors scanned 220 nm (upper) and 280 nm (lower). (C) Circular dichroism analysis of IFN-β-1b (upper curve) and two independent preparations of NHS 40 kDa PEG_2−IFN-β-1b (lower two curves) in thermal denaturation investigations. Samples were 0.1 mg/mL (protein) in 5 mM HAc buffer, pH 3.7; CD was conducted at 25 °C. Ellipticity at 222 nm as a function of temperature (°C) is shown.

Table 3. Effect of Buffer pH of 40 kDa PEG_2−IFN-β-1b on Aggregation[a]

buffer	concentration, mM	pH	protein (mg/mL)	T (°C)	time (day)	aggregation (%)
acetic acid	3	3.7	0.1	4	37	0.0
citrate	5	4.0	0.1	4	37	0.0
citrate	5	5.0	0.1	4	37	3.5
citrate	5	6.0	0.1	4	37	4.1
phosphate	5	7.4	0.1	4	37	6.7
phosphate	5	8.5	0.1	4	37	57.3
H_2O		6.5	0.1	4	37	4.7

[a] Percent aggregates of mono-PEGylated NHS-40k-PEG_2−IFN were measured by SE-HPLC.

either NHS 40 kDa PEG_2, SPA 20 kDa PEG, or SC 12 kDa PEG polymers is shown in Figure 4A. Total exposure of the protein is markedly enhanced through PEGylation, and the rank order of exposure increased with increasing PEG mass. In Figure 4B, a similar trend is observed with the mono-PEGylated compounds employing aldehyde linkers. Greatest exposure is observed with the branched 40 kDa ALD-PEG polymer, while the native IFN-β-1b exposure is marginal. In all sets of PK experiments, a second control using Betaseron was included to confirm the comparability of the PK profile of the experimental IFN-β-1b protein (data not shown). As shown in Figure 4C, the mouse PK profile exhibited a similar outcome in side-by-side comparison of the 40 kDa PEG conjugates, including mono-PEGylated derivatives of NHS−PEG_2, ALD-PEG_2, UA-PEG, XUS−PEG, and a di-PEGylated derivative of SPA-20 kDa polymers. Native IFN-β-1b cleared rapidly from the mice, whereas each of the high molecular weight conjugates exhibited very similar absorption and elimination curves. Mice were administered 0.2 mg protein/kg of all compounds, or about 4 μg of interferon protein per mouse. Since the PEGylated IFN-β-1b compounds do not contain equivalent antiviral activity compared the native interferon, as shown in Table 1, the PEGylated conjugates were actually under-dosed relative the native control, with respect to units of activity. In some cases, subsequent conversions of units of bioactivity to ng of protein were performed with an internal standard for specific activity for each individual compound, corresponding to the analyzed sample administered to the animal. Table 4 presents representative pharmacokinetic parameters from the subcutaneous administration route in mice. All PEGylated conjugates exhibit an expanded area under the curve, relative to unmodified protein, of about 14-fold to 173-fold, which increases with polymer mass. The times of maximal concentration by the sc route were delayed in all of the PEGylated compounds by several hours relative to native IFN-β-1b.

The PEG_2-40 kDa polymers demonstrated exceptionally good performance and were selected for detailed studies in PK studies in rats. Figure 5A shows the side-by-side comparison of PK profiles of PEGylated IFN-β-1b compounds with 40 kDa mass

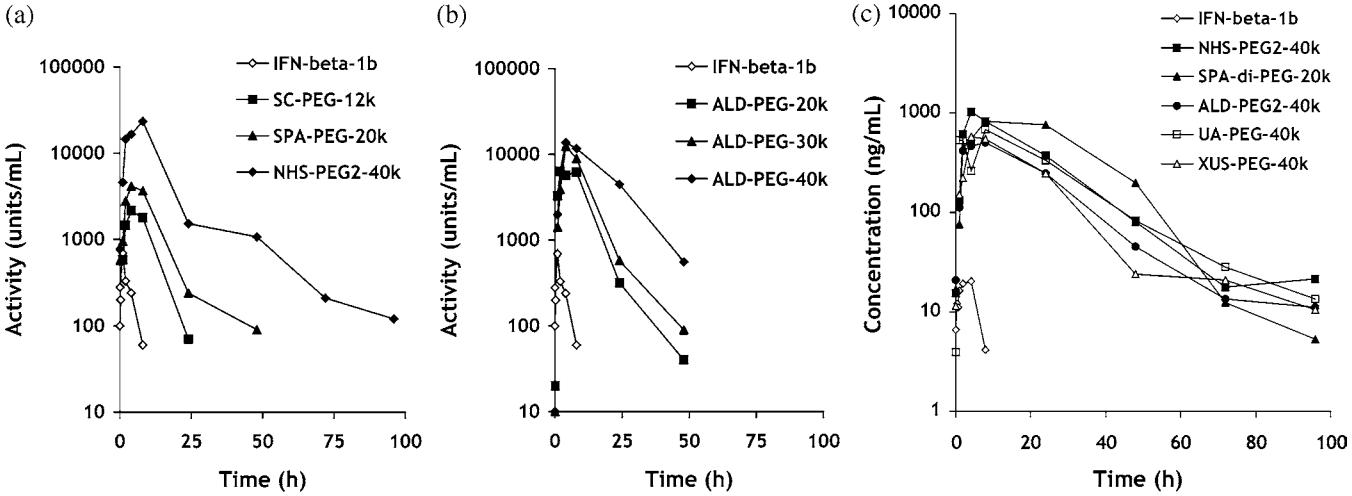

Figure 4. Pharmacokinetics of IFN-β-1b and mono-PEGylated IFN-β-1b in mice. (A) Subcutaneous administration at 0.2 mg protein/kg for IFN-β-1b (open diamonds), NHS 40 kDa PEG_2−IFN-β-1b (closed diamonds), SPA 20 kDa PEG−IFN-β-1b (closed triangles), SC 12 kDa PEG−IFN-β-1b (closed boxes). Antiviral activity of plasma samples was measured at the indicated times post-administration. (B) PK profile of IFN-β-1b (open diamonds), ALD 40 kDa PEG_2−IFN-β-1b (closed diamonds), ALD 30 kDa PEG−IFN-β-1b (closed triangles), ALD 20 kDa PEG−IFN-β-1b (closed boxes) at 0.2 mg/kg dose following sc administration. (C) PK profile of IFN-β-1b (open diamonds), NHS 40 kDa PEG_2−IFN-β-1b (closed boxes), ALD 40 kDa PEG_2−IFN-β-1b (closed circles), X-US 40 kDa PEG−IFN-β-1b (open triangles), UA 40 kDa PEG−IFN-β-1b (open boxes) and di-PEGylated SPA 2 × 20 kDa PEG−IFN-β-1b (closed triangles) at 0.2 mg/kg dose following sc administration.

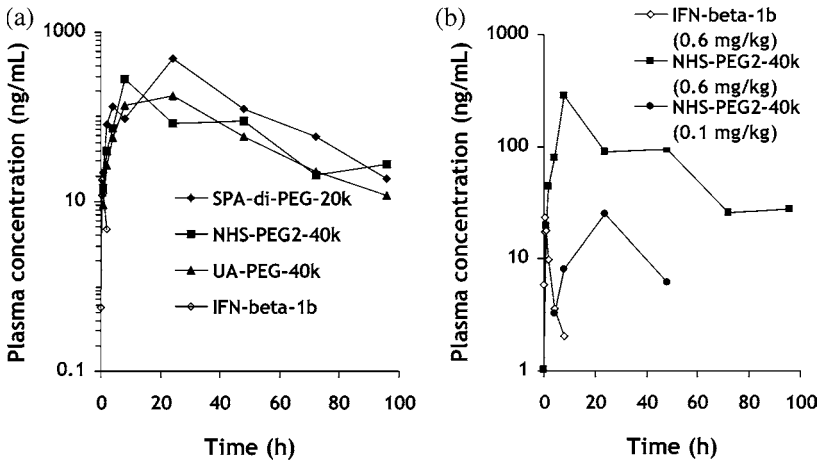

Figure 5. Pharmacokinetics of IFN-β-1b and mono-PEGylated IFN-β-1b in rats. (A) Subcutaneous administration at 0.6 mg protein/kg for IFN-β-1b (open diamonds), NHS 40 kDa PEG_2−IFN-β-1b (closed boxes), UA 40 kDa PEG−IFN-β-1b (closed triangles), and di-PEGylated SPA 2 × 20 kDa PEG−IFN-β-1b (closed diamonds). Antiviral activity of plasma samples was measured at the indicated times post-administration. (B) Dose−response for NHS 40 kDa PEG_2−IFN-β-1b at 0.6 mg protein/kg (closed boxes) or 0.1 mg protein/kg (closed circles) following sc administration. Unmodified IFN-β-1b (0.6 mg/kg) is also shown (open diamonds).

Table 4. Pharmacokinetic Parameters in Mice[a]

compound	route	dose (mg/kg)	AUC (h·U/mL)	T_{max} (h)
IFN-β−1b	sc	0.2	2040	0.9
NHS-40k-PEG_2−IFN	sc	0.2	352740	6.3
SC-12k-PEG−IFN	sc	0.2	27920	5.1
SPA-12k-PEG−IFN	sc	0.2	58180	3.7
ALD-20k-PEG−IFN	sc	0.2	88680	4.4
ALD-30k-PEG−IFN	sc	0.2	157100	5.9
ALD-40k-PEG_2−IFN	sc	0.2	258440	7.3
di SPA-20k-PEG−IFN	sc	0.2	103854	13.0

[a] PK parameters of mono-PEGylated IFN-β-1b compounds and di-PEGylated SPA (2 × 20 kDa) PEG−IFN-β-1b compound were determined by using a two-compartment, first-order input, first-order elimination model. AUC, area under the curve; T_{max}, time of maximal concentration postadministration.

of PEG polymers per protein, but with three different linker chemistries and conformations. The two mono-PEGylated compounds, PEG_2-40 kDa and PEG-UA-40 kDa, employ an NHS ester on a branched polymer and generate an amide linkage, while the di-PEGylated IFN-β-1b compound uses a 20 kDa PEG with an SPA linker, and two random amide linkages with 20 kDa PEG polymers are formed in this PEG−IFN-β-1b compound. The PK results are comparable for these three compounds, which all demonstrated much greater exposure than the unmodified interferon. A dose−response investigation in rats, shown in Figure 5B, demonstrated that the AUC exposure of 40 kDa PEG_2−IFN-β-1b was relative to the administered dose. Rats receiving 0.1 mg/kg or 0.6 mg/kg of this compound displayed an AUC difference of 9-fold. Table 5 summarizes key PK parameters for two representative mono-PEGylated 40 kDa PEG−IFN-β-1b compounds administered to rats via the three routes of injection. Both molecules demonstrated comparable overall performance as sc or im administered compounds. Both bioconjugates displayed comparable terminal half-lives (18−23 h in sc route), while exhibiting an expanded Tmax (24−48-fold increase via sc) and increased Cmax (9−19-fold increase via sc) relative to the native protein. Similarly, the clearance via the sc route for the two PEGylated conjugates was diminished 125−210-fold relative the unmodified interferon. PK parameters for the di-PEGylated SPA-20 kDa-PEG−

Table 5. Pharmacokinetic Parameters in Rats[a]

compound	route	dose (mg/kg)	half-life (h)	AUC (h.U/mL)	CL (mL/h) × (μg/U)	T (h)	C_{max} (U/mL)
IFN-β−1b	iv	0.6	1.1	26210	0.0057	nd	nd
NHS-40k-PEG_2−IFN	iv	0.6	9.4	751328	0.0002	nd	nd
UA-40k-PEG−IFN	iv	0.6	12.0	687389	0.0002	nd	nd
IFN-β−1b	sc	0.6	2.4	324	0.3990	1.0	95
NHS-40k-PEG_2−IFN	sc	0.6	23.8	72014	0.0019	24	1829
UA-40k-PEG−IFN	sc	0.6	18.1	42938	0.0032	48	798
IFN-β−1b	im	0.6	2.3	805	0.1500	0.5	136
NHS-40k-PEG_2−IFN	im	0.6	15.2	164920	0.0009	8.0	4909
UA-40k-PEG−IFN	im	0.6	14.4	76782	0.0019	8.0	2990

[a] PK parameters of the mono-PEGylated IFN-β-1b compounds: AUC, area under the curve; CL, total body clearance; T_{max}, time of maximal concentration; C_{max}, maximal concentration; nd, not determined.

Table 6. Bioavailability of IFN-β-1b and PEG−IFN-β-1b Conjugate in Mice and Rats

		dose (mg/kg)		bioavailability (%)	
compound	species	sc	im, iv	sc	im
IFN-β−1b	mouse	0.2	0.1	15	30
NHS-40k-PEG_2−IFN-β-1b	mouse	0.2	0.1	22	42
IFN-β−1b	rat	0.6	0.6	1	3
NHS-40k-PEG_2−IFN-β-1b	rat	0.6	0.6	10	22

IFN-β-1b compound were similar to the conjugates with a single branched 40 kDa polymer (data not shown). The specific choice of preferred linker for the branched (2 × 20) kDa design might ultimately be based on practical considerations, such as ease and costs of synthesis.

One highlighted comparison of the three routes of administration with regard to bioavailability, based on total AUC exposure of activity units, is shown in Table 6. Bioavailability was superior for the 40 kDa PEG_2−IFN-β-1b conjugate compared to IFN-β-1b. The difference was greatest in rats where the bioconjugate exhibited 8-fold and 7-fold better bioavailability by sc and im routes, respectively. The overall bioavailability by im injection was excellent, which suggests this parenteral route might be an alternative to the currently used sc administration of Betaseron in patients. The enhanced exposure of the PEGylated IFN-β-1b compounds is expected to provide a much more potent drug than unmodified IFN-β-1b, with respect to AUC effects per mg of protein.

Immunogenicity in Rats. Immunogenicity is a central concern in the development and drug monitoring of protein therapeutics, including PEGylated proteins. Binding antibodies are commonly encountered, and neutralizing antibodies versus Betaseron and other IFN-β compounds have been reported (*17*−*22*). Measurement of the antibody response to a protein therapeutic is challenging. First, immunogenicity in animals is not sufficiently predictive of immunogenicity in humans. Second, an antidrug immune response may dissipate over time. Third, it is difficult to develop the perfect analytical method to measure an antibody response, since immunoassays normally measure titers, and the detection sensitivity of immunoassays will vary based in part on the affinity of the serum antibodies and test reagents. With these limitations in mind, we examined the immune response to IFN-β-1b and four PEGylated (40 kDa PEG) IFN-β-1b compounds in rats.

Rats received 0.1 mg/kg once weekly im injections of the compounds for six weeks. Rat plasma samples were collected each week and analyzed by direct ELISA, indirect ELISA, flow cytometry, Biacore, or antiviral activity neutralization. As shown in Figure 6A, the rat IgG response to the four PEGylated IFN-β-1b compounds was markedly diminished in week two through week six compared to the IgG response to unmodified IFN-β-1b. In this immunoassay, native IFN-β-1b coated the plates and the bound rat IgG was specifically detected by anti rat IgG reagents. Measurement of the antigen specific IgG antibody levels by direct ELISA was based on a control mAb versus human IFN-β. Direct ELISA analysis however demonstrated a similarity in IgM response for all compounds (data not shown). The rat plasma samples were also examined in an alternate capture ELISA format as shown in Figure 6B. Either IFN-β-1b or PEG−IFN-β-1b was captured on an anti human IFN-β mAb immobilized on the plate, and the plasma samples were analyzed on the plates for IFN-β-1b or PEG−IFN-β-1b binding IgG antibodies. High titers of IgG versus IFN-β-1b were produced in rats injected with the unmodified protein at week six, whereas much lower titers of IgG versus 40 kDa PEG_2−IFN-β-1b were produced in rats injected with the PEG conjugate. Most interestingly, the rat IgG antibodies versus native IFN-β-1b did not demonstrate significant binding to PEG−IFN-β-1b, whereas rat IgG versus PEG−IFN-β-1b did demonstrate significant binding to native IFN-β-1b. Since these ELISA plates were coated with an anti human IFN-β mAb, however, any rat plasma IgG directed against a common epitope to the immobilized anti−IFN-β mAb would likely be undetected in this immunoassay.

To further evaluate low affinity IFN-β-1b binding IgG, we performed analysis of the rat plasma samples by flow cytometry using cell line A549, which was incubated first with IFN-β-1b, and then with rat plasma and phycoerythrin conjugated anti-rat IgG reagents. As shown in Figure 6C, fluorescence measurements demonstrated that total IgG bound was greater in the plasma from rats injected with native IFN-β-1b. In Biacore analysis, IFN-β-1b was immobilized on the chip surface. Measurement of total bound antibodies, including IgM and low affinity IgG, also exhibited a trend to reduced titers in the plasma from rats injected with the PEGylated IFN-β-1b conjugate when compared to plasma from rats administered the unmodified protein (data not shown). Antiviral bioassays were employed to examine the capacity of the rat plasma samples to neutralize IFN-β-1b activity in cell culture. Neutralizing antibodies were detected at six weeks in plasma from rats injected with either the native or PEGylated protein, although the plasma from native IFN-β-1b produced a higher titer antibody response (data not shown). Also, rat antibodies raised versus either native or PEGylated IFN-β-1b were capable of neutralizing either the native or PEGylated interferon compounds.

Possibly, the immunoassay designs in Figures 6A and 6B detect a high affinity IgG response in the treated rats, whereas the remaining assays reflect the total high/low affinity IgG and IgM response. One concern for mono-PEGylated proteins is the potential for enhancement of the host immune response due to the large prolongation in blood residency time of the protein (*46*). This effect was not demonstrated in any of our studies. Rather, it seems possible that the solubilized and shielded PEGylated IFN-β-1b may be an inferior antigen for dendritic cells in sc or im administration compared to the aggregation-prone native protein. Further studies in primates and humans are needed to address the question of immunogenicity of these experimental compounds.

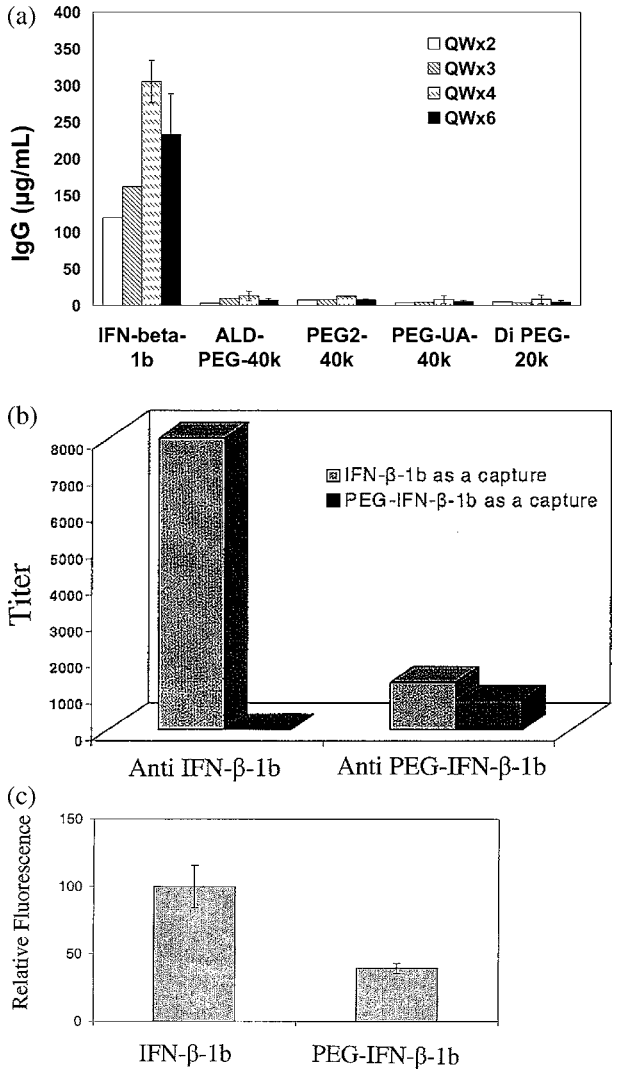

Figure 6. Immunogenicity of IFN-β-1b and PEGylated IFN-β-1b in rats. (A) IgG response, following weekly im injections (0.1 mg/kg), at weeks 2, 3, 4, and 6 to IFN-β-1b and four PEG−IFN-β-1b conjugates. QW × 2, QW × 3, QW × 4, and QW × 6 correspond to once per week dosing at weeks 2, 3, 4, and 6, respectively. IgG (μg/mL) were estimated based on a standard curve with anti-huIFN-β mAb MMHB-3. IFN-β-1b and PEG−IFN-β-1b compounds were coated on ELISA plates prior to incubation with rat plasma and anti-rat IgG-HRP conjugate. (B) Indirect (capture) ELISA assay of IgG response in rats to IFN-β-1b and NHS 40 kDa PEG_2−IFN-β-1b at week 6. Anti-huIFN-β mAb was immobilized on the plate to capture either native or PEGylated protein. Plasma from the rats injected with either of these two test articles were incubated independently on microtiter wells with the captured native or PEG IFN-β-1b, followed by detection with anti-rat IgG-HRP reagent. (C) Flow cytometry with relative fluorescence intensity results for A549 cells incubated with native IFN-β-1b, then incubated with rat plasma versus either native IFN-β-1b or NHS 40 kDa PEG_2−IFN-β-1b, and phycoerythrin-conjugated anti-rat IgG mAb.

CONCLUSIONS

We describe investigations of the physical and functional properties of mono-PEGylated IFN-β-1b compounds. Employment of PEGylation strategies for drug delivery often focus on one specific desired improvement in the drug features, and this is most often a need for improved circulating life. Our present studies illustrate the capacity of attachment of a PEG polymer to IFN-β-1b to improve five key attributes in the bioconjugate. In comparison to the unmodified protein, PEG−IFN-β-1b compounds exhibit better solubility, less propensity to insoluble and soluble aggregation, expanded in vivo exposure of bioactive protein, prolonged blood residency, and a reduced IgG response versus the bioconjugate. Many other protein ligands that have been proposed as therapeutics encounter similar challenges and these PEGylation strategies may be applicable in addressing formulation, stability, and pharmacology difficulties in other incommodious hydrophobic proteins. Our studies also illustrate both the difficulties in site-specific modification of engineered proteins and the ability to construct markedly differing bioconjugates, such as with either the 40 kDa mono-PEGylated NHS−PEG_2 and ALD-PEG_2 derivatives or the di-PEGylated SPA-(2 × 20 kDa) derivative, that nonetheless exhibited notably similar physical and biological properties. The mono-PEGylated IFN-β-1b compounds with a branched 40 kDa polymer appear especially beneficial with regard to prolonged blood circulation and in vitro stability. Of several promising bioconjugates in this study, we chose to further investigate the 40 kDa PEG_2−IFN-β-1b compounds in ongoing pharmacokinetic and pharmacodynamic studies in primates.

ACKNOWLEDGMENT

We thank Steve Youngster, Qing Dong, Lisa Hwang, Eun Jang, and Julia Zhu for performance of MALDI-TOF and LC-MS. We are also grateful to Anju Dang and Massy Rajabzadeh of Ciphergen, Inc. for assistance with SELDI-TOF-MS analysis. We thank Uli Grau and Pascal Bailon for their encouragement and support and Jack Lipman and Ivan Horak for a critical review of the manuscript.

LITERATURE CITED

(1) Theofilopoulos, A. N., Baccala, R., Beutler, B., and Kono, D. H. (2005) Type I interferons (α/β) in immunity and autoimmunity. *Annu. Rev. Immunol. 23*, 307−336.

(2) Meager, A. (1998) Interferons alpha, beta, and omega. In *Cytokines* (Mire-Sluis, A. R., and Thorpe, R., Eds.) pp 361−389, Academic Press, San Diego.

(3) Runkel, L., deDios, C., Karpusas, M., Betzenhauser, M., Muldowney, C., Zafari, M., Benjamin, C. D., Miller, S., Hochman, P. S., and Whitty, A. (2000) Systematic mutational mapping of sites on human interferon-β-1a that are important for receptor binding and functional activity. *Biochemistry 39*, 2538−2551.

(4) Runkel, L., deDios, C., Karpusas, M., Baker, D., Li, Z., Zafari, M., Betzenhauser, M., Muldowney, C., Miller, S., Redlich, P. N., Grossberg, S. E., Whitty, A., and Hochman, P. S. (2001) Mapping of IFN-beta epitopes important for receptor binding and biologic activation: comparison of results achieved using antibody-based methods and alanine substitution mutagenesis. *J. Interferon Cytokine Res. 21*, 931−941.

(5) Arduini, R. M., Strauch, K. L., Runkel, L. A., Carlson, M. M., Hronowski, X., Foley, S. F., Young, C. N., Cheng, W., Hochman, P. S., and Baker, D. P. (1999) Characterization of a soluble ternary complex formed between human interferon-beta-1a and its receptor chains. *Protein Sci. 8*, 1867−1877.

(6) Mager, D. E., Neuteboom, B., Efthymiopoulos, C., Munafo, A., and Jusko, W. J. (2003) Receptor-mediated pharmacokinetics and pharmacodynamics of interferon-β1a in monkeys. *J. Pharmacol. Exp. Ther. 306*, 262−270.

(7) Durelli, L., Verdun, E., Barbero, P., Bergui, M., Versino, E., Ghezzi, A., Montanari, E., Zaffaroni, M., and the Independent Comparison of Interferon (INCOMIN) Trial Study Group. (2002) Every-other-day interferon beta-1b versus once-weekly interferon beta-1a for multiple sclerosis: results of a 2-year prospective randomized multicentre study (INCOMIN). *Lancet 359*, 1453−1460.

(8) Bertolotto, A., Deisenhammer, F., Gallo, P., and Sørensen, P. S. (2004) Immunogenicity of interferon beta: differences among products. *J. Neurol. 251*, II/15-II/24.

(9) Runkel, L., Meier, W., Pepinsky, R. B., Karpusas, M., Whitty, A., Kimball, K., Brickelmaier, M., Muldowney, C., Jones, W., and Goelz, S. E. (1998) Structural and functional differences between

glycosylated and nonglycosylated forms of human interferon-beta (IFN-beta). *Pharm. Res*. *15*, 641−649.
(10) Antonetti, F., Finocchiaro, O., Mascia, M., Terlizzese, M. G. and Jaber, A. (2002) A comparison of the biologic activity of two recombinant IFN-beta preparations used in the treatment of relapsing-remitting multiple sclerosis. *J. Interferon Cytokine Res*. *22*, 1181−1184.
(11) Horowski, R. (2002) Multiple sclerosis and interferon beta-1b, past, present and future. *Clin. Neurol. Neurosurg. 104*, 259−264.
(12) Williams, G. J. and Witt, P. L. (1998) Comparative study of the pharmacodynamic and pharmacologic effects of Betaseron and AVONEX. *J. Interferon Cytokine Res. 18*, 967−975.
(13) Mark, D. F., Lu, S. D., Creasey, A. A., Yamamoto, R. and Lin, L. S. (1984) Site-specific mutagenesis of the human fibroblast interferon gene. *Proc. Natl. Acad. Sci. U.S.A. 81*, 5662−5666.
(14) Chiang, J., Gloff, C. A., Yoshizawa, C. N. and Williams, G. J. (1993) Pharmacokinetics of recombinant human interferon-beta ser in healthy volunteers and its effect on serum neopterin. *Pharm. Res. 10*, 567−572.
(15) Karpusas, M., Nolte, M., Benton, C. B., Meier, W., Lipscomb, W. N., and Goelz, S. (1997) The crystal structure of human interferon β at 2.2-Å resolution. *Proc. Natl. Acad. Sci. U.S.A. 94*, 11813−11818.
(16) Karpusas, M., Whitty, A., Runkel, L., and Hochman P. (1998) The structure of human interferon-β: implications for activity. *CMLS. Cell. Mol. Life Sci. 54*, 1203−1216.
(17) Bertolotto, A., Gilli, F., Sala, A., Capobianco, M., Malucchi, S., Milano, E., Melis, F., Marnetto, F., Lindberg, R. L. P., Bottero, R., Di Sapio, A., and Giordana, M. T. (2003) Persistent neutralizing antibodies abolish the interferon β bioavailability in MS patients. *Neurology 60*, 634−639.
(18) Sorensen P. S., Ross C., Clemmesen, K. M., Bendtzen, K., Frederiksen, J. L., Jensen, K., Kristensen, O., Petersen, T., Rasmussen, S., Ravnborg, M., Stenager, E., Koch-Henriksen, N., and the Danish Multiple Sclerosis Study Group. (2003) Clinical importance of neutralizing antibodies against interferon beta in patients with relapsing-remitting multiple sclerosis. *Lancet 362*, 1184−1191.
(19) Bitsch, A., Dressel, A., Meier, K., Bogumil, T., Deisenhammer, F., Tumani, H., Kitze, B., Poser, S., and Weber, F. (2004) Autoantibody synthesis in primary progressive multiple sclerosis patients treated with interferon beta-1b. *J. Neurol. 251*, 1498−1501.
(20) Hartung, H.-P., Schellekens, H., and Munschauer III, F. E. (2004) Neutralizing antibodies to interferon beta in patients with multiple sclerosis: scientific background and clinical implications. *J. Neurol. 251*, II/1−II-3.
(21) Reske, D., Walser, A., Haupt, W. F., and Petereit, H.-F. (2004) Long-term persisting interferon beta-1b neutralizing antibodies after discontinuation of treatment. *Acta Neurol. Scand. 109*, 66−70.
(22) Yeung, V. P., Chang, J., Miller, J., Barnett, C., Stickler, M. and Harding, F. A. (2004) Elimination of an immunodominant $CD4^+$ T cell epitope in human IFN-β does not result in an in vivo response directed at the subdominant epitope. *J. Immunol*. *172*, 6658−6665.
(23) Runkel, L., Pfeffer, L., Lewerenz, M., Monneron, D., Yang, C. H., Murti, A., Pellegrini, S., Goelz, S., Uzé, G., and Mogensen, K. (1998) Differences in activity between α and β type I interferons explored by mutational analysis. *J. Biol. Chem. 273*, 8003−8008.
(24) Goldman, L. A., Zafari, M., Cutrone, E. C., Dang, A., Brickelmeier, M., Runkel, L., Benjamin, C. D., Ling, L. E. and Langer, J. A. (1999) Characterization of antihuman IFNAR-1 monoclonal antibodies: epitope localization and functional analysis. *J. Interferon Cytokine Res*. *19*, 15−26.
(25) David, M. (2002) Signal transduction by Type I interferons. *BioTechniques 33*, S58−S65.
(26) Khan, O. A., Xia, Q., Bever, C. T. Jr., Johnson, K. P., Panitch, H. S., and Dhib-Jalbut, S. S. (1996) Interferon beta-1b serum levels in multiple sclerosis patients following subcutaneous administration. *Neurology*, *46*, 1639−1643.
(27) Greenwald, R. B. (2001) PEG drugs: an overview. *J. Controlled Release 74*, 159−171.
(28) Yang, K., Basu, A., Wang, M., Chintala, R., Hsieh, M.-C., Liu, S., Hua, J., Zhang, Z., Zhou, J., Li, M., Phyu, H., Petti, G., Mendez, M., Janjua, H., Peng, P., Longley, C., Borowski, V., Mehlig, M., and Filpula, D. (2003) Tailoring structure−function and pharmacokinetic properties of single-chain Fv proteins by site-specific PEGylation. *Protein Eng. 16*, 761−770.
(29) Lee, L. S., Conover, C., Shi, C., Whitlow, M., and Filpula, D. (1999) Prolonged circulating lives of single-chain Fv proteins conjugated with poly(ethylene glycol): a comparison of conjugation chemistries and compounds. *Bioconjugate Chem. 10*, 973−981.
(30) Greenwald, R. B., Yang, K., Zhao, H., Conover, C. D., Lee, S., and Filpula, D. (2003) Controlled release of proteins from their poly-(ethylene glycol) conjugates: drug delivery systems employing 1,6-elimination. *Bioconjugate Chem*. *14*, 395−403.
(31) Greenwald, R. B., Choe, Y. H., McGuire, J., and Conover, C. D. (2003) Effective drug delivery by PEGylated drug conjugates. *Adv. Drug Delivery Rev*. *55*, 217−250.
(32) Greenwald, R. B., Zhao, H., Yang, K., Reddy, P., and Martinez, A. (2004) A new aliphatic amino prodrug system for the delivery of small molecules and proteins utilizing novel PEG derivatives. *J. Med. Chem. 47*, 726−734.
(33) Miron, T. and Wilchek, M. (1993) A simplified method for the preparation of succinimidyl carbonate poly(ethylene glycol) for coupling to proteins. *Bioconjugate Chem. 4*, 568−569.
(34) Roberts, M. J., Bentley, M. D., and Harris, J. M. (2002) Chemistry for peptide and protein PEGylation. *Adv. Drug Delivery Rev. 54*, 459−476.
(35) Martinez, A., Pendri, A., Xia, J. and Greenwald, R. B. (1997) Branched poly(ethylene glycol) linkers. *Macromol. Chem. Phys*. *198*, 2489−2498.
(36) Greenwald, R. B., Pendri, A., Martinez, A., Gilbert, C., and Bradley, P. (1996) PEG thiazolidine-2-thione, a novel reagent for facile protein modification: conjugation of bovine hemoglobin. *Bioconjugate Chem*. *7*, 638−641.
(37) Kinstler, O. B., Brems, D. N., Lauren, S. L., Paige, A. G., Hamburger, J. B., and Treuheit, M. J. (1996) Characterization and stability of N-terminally PEGylated rhG-CSF. *Pharm. Res*. *13*, 996−1002.
(38) Wang, M., Lee, L. S., Nepomich, A., Yang, J.-D., Conover, C., Whitlow, M. and Filpula, D. (1998) Single-chain Fv with manifold *N*-glycans as bifunctional scaffolds for immunomolecules. *Protein Eng*. *11*, 1277−1283.
(39) Harris, J. M. and Chess, R. B. (2003) Effect of PEGylation on pharmaceuticals. *Nat. Rev. Drug Discovery 2*, 214−221.
(40) Bailon, P., Palleroni, A., Schaffer, C. A., Spence, C. L., Fung, W. J., Porter, J. E., Ehrlich, G. K., Pan, W., Xu, Z. X., Modi, M. W., Farid, A., Berthold, W., and Graves, M. (2001) Rational design of a potent, long-lasting form of interferon: a 40 kDa branched polyethylene glycol-conjugated interferon α-2a for the treatment of hepatitis C. *Bioconjugate Chem. 12*, 195−202.
(41) Grace, M., Youngster, S., Gitlin, G., Sydor, W., Xie, L., Westreich, L., Jacobs, S., Brassard, D., Bausch, J., and Bordens, R. (2001) Structural and biologic characterization of pegylated recombinant IFN-α2b. *J. Interferon Cytokine Res. 21*, 1103−1115.
(42) Foser, S., Schacher, A., Weyer, K. A., Brugger, D., Dietel, E., Marti, S., and Schreitmuller, T. (2003) Isolation, structural characterization, and antiviral activity of positional isomers of monopegylated interferon α-2a (PEGASYS). *Protein Expr. Purif. 30*, 78−87.
(43) Rosendahl, M. S., Doherty, D. H., Smith, D. J., Carlson, S. J., Chlipala, E. A., and Cox, G. N. (2005) A long-acting, highly potent interferon α-2 conjugate created using site-specific PEGylation. *Bioconjugate Chem. 16*, 200−207.
(44) Peleg-Shulman, T., Tsubery, H., Mironchik, M., Fridkin, M., Schreiber, G., and Shechter, Y. (2004) Reversible PEGylation: a novel technology to release native interferon α2 over a prolonged time period. *J. Med. Chem*. *47*, 4897−4904.
(45) Wang, Y.-S., Youngster, S., Grace, M., Bausch, J., Bordens, R. And Wyss, D. F. (2002) Structural and biological characterization of pegylated recombinant interferon alpha-2b and its therapeutic implications. *Adv. Drug Delivery Rev. 54*, 547−570.
(46) Pepinsky, R. B., Lepage, D. J., Gill, A., Chakraborty, A., Vaidyanathan, S., Green, M., Baker, D. P., Whalley, E., Hochman, P. S., and Martin, P. (2001) Improved pharmacokinetic properties of a polyethylene glycol-modified form of interferon-β-1a with preserved *in vitro* bioactivity. *J. Pharmacol. Exp. Ther. 297*, 1059−1066.
(47) Mager, D. E., Neuteboom, B., and Jusko, W. J. (2005) Pharmacokinetics and pharmacodynamics of PEGylated IFN-β 1a following subcutaneous administration in monkeys. *Pharm. Res. 22*, 58−61.

(48) Katre, N. and Knauf, M. J. (1990) Solubilization of immunotoxins for pharmaceutical compositions using polymer conjugation. U. S. Patent Number 4,917, 888.

(49) Chapman, A. P. (2002) PEGylated antibodies and antibody fragments for improved therapy: a review. *Adv. Drug Delivery Rev. 54*, 531−545.

(50) Clark, R., Olson, K., Fuh, G., Marian, M., Mortensen, D., Teshima, G., Chang, S., Chu, H., Mukku, V., Canova-Davis, E., Somers, T., Cronin, M., Winkler, M., and Wells, J. A. (1996) Long-acting growth hormones produced by conjugation with poly(ethylene glycol). *J. Biol. Chem. 271*, 21969−21977.

(51) Pettit, D. K., Bonnert, T. P., Eisenman, J., Srinivasan, S., Paxton, R., Beers, C., Lynch, D., Miller, B., Yost, J., Grabstein, K. H., and Gombotz, W. R. (1997) Structure−function studies of interleukin 15 using site-specific mutagenesis, poly(ethylene glycol) conjugation, and homology modeling. *J. Biol. Chem. 272*, 2312−2318.

(52) Yamamoto, Y., Tsutsumi, Y., Yoshioka, Y., Nishibata, T., Kobayashi, K., Okamoto, T., Mukai, Y., Shimizu, T., Nakagawa, S., Nagata, S., and Mayumi, T. (2003) Site-specific PEGylation of a lysine-deficient TNF-α with full bioactivity. *Nat. Biotechnol. 21*, 546−552.

(53) Walter, M. R., Windsor, W. T., Nagabhushan, T. L., Lundell, D. J., Lunn, C. A., Zauodny, P. J., and Narula, S. K. (1995) Crystal structure of a complex between interferon-γ and its soluble high-affinity receptor. *Nature 37*, 230−235.

(54) Lin, L. S., Yamamoto, R. and Drummond, R. J. (1986) Purification of recombinant human interferon beta expressed in *Escherichia coli*. *Methods Enzymol. 119*, 183−192.

(55) Russell-Harde, D., Knauf, M., and Croze, E. (1995) The use of zwittergent 3−14 in the purification of recombinant human interferon-β ser^{17} (Betaseron). *J. Interferon Cytokine Res. 15*, 31−37.

(56) Smith, P. K., Krohn, R. I., Hermanson, G. T., Mallia, A. K., Gartner, F. H., Provenzano, M. D., Fujimoto, E. K., Goeke, N. M., Olson, B. J. and Klenk, D. C. (1985) Measurement of protein using bicinchoninic acid. *Anal. Biochem. 150*, 76−85.

(57) Carrey, E. A. (1989) Peptide mapping. In *Protein Structure: A Practical Approach* (Creighton, T. E., Ed.) pp 117−144, Oxford University Press, Oxford.

(58) Greenfield, N. J., Montelione, G. T., Farid, R. S., and Hitchcock-DeGregori, S. E. (1998) The structure of the N-terminus of striated muscle alpha-tropomyosin in a chimeric peptide: nuclear magnetic resonance structure and circular dichroism studies. *Biochemistry 37*, 7834−7843.

(59) Bohm, G., Muhr, R., and Jaenicke, R. (1992) Quantitative analysis of protein far UV circular dichroism spectra by neural networks. *Protein Eng. 5*, 191−195.

(60) Familletti, P. C., Rubinstein, S. and Pestka, S. (1981) A convenient and rapid cytopathic effect inhibition assay for interferon. *Methods Enzymol. 78*, 387−394.

(61) Garrison, T. L., Hung, F., Izotova, L., Schwartz, B., Lavoie, T. and Lee-Own, F. V. (2002) ELISA measurement of interferons. *Biotechniques 33*, S98−S100.

BC050322Y

A Molecular Toolkit for Highly Insulating Tethered Bilayer Lipid Membranes on Various Substrates

Vladimir Atanasov, Petia P. Atanasova, Inga K. Vockenroth, Nikolaus Knorr, and Ingo Köper*

Max Planck Institute for Polymer Research, Ackermannweg 10, 55128 Mainz, Germany. Received November 16, 2005; Revised Manuscript Received March 1, 2006

Tethered bilayer lipid membranes (tBLMs) are promising model architectures that mimic the structure and function of natural biomembranes. They provide a fluid, stable, and electrically sealing platform for the study of membrane related processes, specifically, the function of incorporated membrane proteins. This paper presents a generic approach toward the synthesis of functional tBLMs adapted for application to various surfaces. The central element of a tethered membrane consists of a lipid bilayer. Its proximal layer is covalently attached via a spacer unit to a solid support, either gold or silicon oxide. The membranes are characterized optically by using surface plasmon resonance spectroscopy (SPR) or ellipsometry and electrically by using electrochemical impedance spectroscopy (EIS). The bilayer membranes obtained show high electrical barrier properties and can be used to incorporate and study small membrane proteins in a functional form.

INTRODUCTION

Model membrane systems mimic properties of a natural biomembrane. One type of model system, solid supported bilayer membranes, provides an architecture that is accessible to many (surface-) analytical methods. Thus, they can easily be used as biotic−abiotic interfaces in various biosensing applications (*1*−*4*). In the last years, tBLMs have proved to be a powerful tool for producing solid supported membranes. They consist of a lipid bilayer with the proximal layer at least to some extend covalently attached to a solid support. If this substrate is an electrode, electrical characterization of the system is possible. To be considered as a suitable model system, such architectures should possess specific key features of a natural membrane. One requirement is that the membrane must serve as a barrier between an inner- and an outer-membrane environment. This implies that the leakage of small molecules and ions across the lipid bilayer is prevented. Transport processes should only be governed by protein function and not be due to defects in the bilayer structure. Additionally, some lateral fluidity or mobility is necessary to allow for the incorporation and proper function of membrane proteins.

As schematically depicted in Figure 1, the proximal layer of a tBLM can be divided into three distinct parts: (a) the lipid with a linking unit to (b) the spacer group and (c) the anchoring moiety.

In previous tBLM architectures, either saturated (*5*, *6*) or unsaturated (*7*−*9*) alkyl chains have been used as lipid tails. However, these lipids suffer from relatively high transition temperatures (e.g., the transition temperature of dipalmitoyl phosphatidylcholine is 41.5 °C (*10*)) and thus do not form fluid bilayer membranes at room temperature. To reduce the Krafft temperature (T_K), it is common to use branched alkyl chains. T_K is the critical temperature above which the solubility of the surfactant rapidly increases and micelles are formed. To modify this behavior, branched chains have been investigated by varying the branching types, including various short iso and antesio branches (*11*). Although the chain branching consistently lowers the T_K values, this is often not sufficient for the formation of fluid membranes, particularly for long alkyl chains. Highly branched alkyl chains show different properties. The most studied lipids are based on phytanyl with T_K values below 0 °C (*4*, *12*−*14*). The phytanyl functionality consists of a highly branched 3,7,11,15-tetramethylhexadecyl group. This moiety is well-known from extremophiles or archaea to form stable and fluid membranes in harsh environments (*15*).

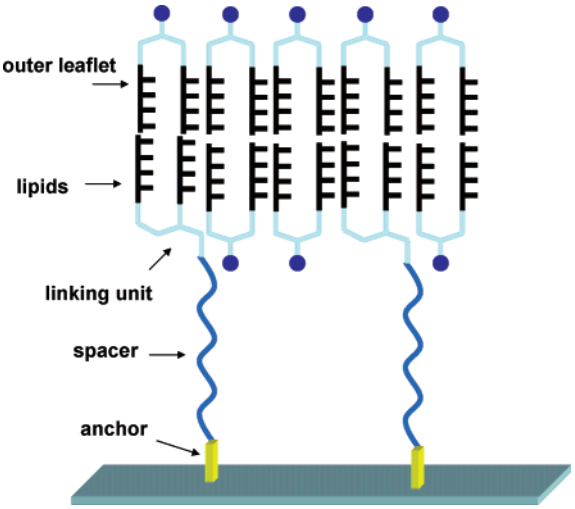

Figure 1. Schematic tBLM architecture. The proximal leaflet is formed by self-assembly of the anchor lipids, while the distal layer is completed by vesicle fusion. Defects and voids in the proximal leaflet might be filled during the fusion process.

The hydrocarbon tail of the lipid is coupled to a polar headgroup. Since this linkage is in a dynamic interfacial region in an aqueous suspension, even small changes of this moiety can significantly modulate the aggregation properties. Among various linkage functionalities such as oxyethylenes (*9*, *16*), sulfides (*13*), and 2-hydroxymethylglycerol (*17*), the glycerol linker is used most often (*12*). In natural lipids, this stable moiety occurs in a defined *sn*-2 stereochemistry configuration.

The spacer unit separates the lipid layer from the solid substrate while serving as a polymer cushion that compensates for surface roughness effects, protects embedded biomaterial from touching the surface (and thus losing their functionality

* Corresponding author. E-mail: ingo.koeper@mpip-mainz.mpg.de. Tel: +49-6131-379164. Fax: +49-6131-370503.

10.1021/bc050328n CCC: $33.50 © 2006 American Chemical Society
Published on Web 04/13/2006

due to denaturation), and provides an ion reservoir underneath the membrane. Various materials such as oligosaccharides (*18*), polymers based on acrylamide and its derivatives (*19*), ethylene glycol esters/amides of succinic acid/succinamide (*20*), and poly(ethylene glycol) (*21*, *22*) have been proposed. These moieties form a hydrophilic layer between the lipid membrane and the substrate surface. This reservoir shows a gellike structure that is permeable to ionic species (*17*). The characteristics of this reservoir have an important effect on the electrical properties of the tBLM (*23*).

Finally, surface immobilization of the lipid-spacer molecule is achieved by an anchor group, which forms, by matching chemistry, a covalent bond with the surface. Several anchor groups have been tested on gold surfaces, most of them are based on gold−sulfur interactions (*4*, *14*, *24*). Gold substrates are interesting because they can be used as an electrode for electrical read-outs as well as for many other surface analytical techniques. However, most devices in the microelectronics and semiconductor field are silicon-based. These substrates, as well as the large number of silica-like substrates (glass, metallic oxides, etc.) are easily accessible, if not commercially available. They can also be integrated into standard microelectronics fabrications processes.

Tamm et al. presented tBLMs on silicon oxide substrates using PEG−phospholipid conjugates with a triethoxisilane anchor group. The polymer-supported membrane (the PEG cushion has 77 repeat units) was used for detailed investigation on the lateral diffusion of proteins and lipids (*25*) and to study the vertical distances of the bilayer from the substrate (*26*). Investigations were carried out by using fluorescence recovery after photobleaching measurements and fluorescence interference−contrast microscopy. Similarly, Rossi et al. have presented a model membrane system with large polymeric spacer groups that can be anchored on a amino-silane treated glass substrate (*27*). Lateral mobility could be observed using fluorescence techniques. However, in both cases, no electrochemical measurements have been reported.

We present here a generic approach, a molecular toolkit that allows for the systematic modification of certain key components of tethered membrane architectures. Starting from a universal precursor molecule, different anchor groups that are suitable either for noble metal surfaces (e.g., Au, Ag, Pt, Cu, Fe, Ni, or Hg) or for oxide surfaces (e.g., SiO_x) can be added. The lipid headgroup consists of a diphytanyglycerol unit, while a short oligo(ethylene glycol) forms the spacer. The length of the spacer unit can easily be modified. These anchor lipids form stable bilayer membranes with high electrical sealing properties. The tBLMs can serve as a matrix for the functional incorporation of membrane proteins.

EXPERIMENTAL PROCEDURES

Electrochemical Impedance Spectroscopy (EIS). Measurements were conducted using an IM6 spectrometer (Zahner Electrics) or an AUTOLAB PGSTAT 12 impedance spectrometer. Three electrode measurements were performed in Teflon cells with the substrates as the working electrode, a coiled platinum wire as the counter electrode, and DRIREF-2 reference electrodes (World Precision Instruments). Spectra were recorded for frequencies between 2 mHz and 1 MHz at a controlled potential with an AC modulation amplitude of 10 mV. Raw data were analyzed using the ZVIEW software package (version 2.70, Scribner Associates). The Teflon cells have a buffer volume of 0.5 mL for the silicon oxide substrates and 1 mL for the gold substrates and an electrochemically active area on the substrates of 0.385 and 0.2 cm^2, respectively. The data obtained is fit using an equivalent circuit of capacitors and resistances. The final values are normalized to the electrode surface area.

Contact Angle Measurements. Contact angles were determined using a DSA 10 contact angle measuring system (Krüss, Germany). Software (Drop Shape Analysis, version 1.8) was employed to analyze the drops created by the sessile-drop method.

Ellipsometry. Measurements were carried out using an EP^3 ellipsometer (Nanofilm, Göttingen, Germany) with a 532 nm laser source. The angle of incidence was 70° for measurements in air and 60° for measurements in a fluid cell. Thickness values were fit with the EP^3View v2.01 software using a layer model with the following parameters: $n = 4.17$ and $k = 0.049$ for Si, $n = 1.4605$ and $k = 0$ for SiO_x, $n = 1.50$ and $k = 0$ for the monolayers, and $n = 1.45$ and $k = 0$ for the bilayer.

Surface Plasmon Resonance Spectroscopy (SPR). A setup in Kretschmann configuration, built in-house, with a 632 nm He/Ne laser was used. In the scan mode, reflectivity changes are monitored as a function of the angle of incidence of the incoming laser beam. In the kinetic mode, reflectivity changes occurring at a fixed angle are monitored as a function of time.

SPR spectra were analyzed using a three layer model including the prism, gold, and the thiolipid monolayer. After vesicle fusion, a fourth layer corresponding to the outer leaflet of the bilayer was added. The refractive indices for the mono- and bilayer were $n = 1.489$ and $n = 1.423$, respectively.

Analytical Instrumentation. ^1H and ^{13}C NMR spectra were recorded on a Brucker DXP 250 MHz NMR spectrometer. If not otherwise stated, NMR spectra were recorded at ambient conditions at 250 and 62.5 MHz for ^1H and ^{13}C NMR, respectively. The spectra were calibrated to the solvent signal as follows: 7.24 (^1H) and 77.0 (^{13}C) ppm for $CDCl_3$ and 5.23 (^1H) and 54.0 (^{13}C) ppm for CD_2Cl_2. Mass spectroscopy was performed using a VG ZAB2-SE-FPD Spectrofield spectrometer. IR spectra were measured on a Nicolet 730 FTIR spectrometer using an endurance diamant-ATR.

Chemicals. (±)-3-Benzyloxy-1,2-propanediol, tetra(ethylene glycol), and allylbromide (all purchased from Fluka) were dried over an A3 molecular sieve. Triethylamine (TEA, Acros) and tetrahydrofuran (THF, Fisher) were dried over CaH_2 and potassium−benzophenone complex, respectively. Trichlorosilane (Acros), triethoxysilane (Lancaster), thioacetic acid (Acros), and chlorodimethylsilane (Lancaster) were distilled prior to use. *p*-Toluenesulfonyl chloride (TosCl, Acros), platinum on activated charcoal (Pt/C, Fluka), hexachloroplatinic acid (H_2PtCl_6, Fluka), platinum-divinyltetramethyldisiloxane complex as 2.1−2.4% solution in hexane (ABCR), 2,2'-azobis(2-methylpropionitrile) (AIBN, Acros), hexamethyldisilazane (Fluka), and 1,2-di-*O*-phytanoyl-*sn*-glycero-3-phosphocholine (DphyPC) (Avanti Polar Lipids) were used as received.

Synthesis. We will describe the synthetic steps depicted in Scheme 1, especially the final modifications of the anchor groups. Most reactions were carried out until complete consumption of the starting material as monitored by thin-layer chromatography (TLC) using a THF/petrolether (1:4) elution system.

Precursor Synthesis, ***9.*** The synthesis of the precursor molecule has been previously described (28). The synthetic pathway is depicted in Scheme 1. The product can be obtained at high purity. ^1H NMR ($CDCl_3$) δ_H, ppm: 5.9 (m, $-CH{=}CH_2$), 5.3−5.1 (m, $-CH{=}CH_2$), 4.0 (d, $-OCH_2CH{=}CH_2$), 3.6−3.4 (overlapping signals $CH_{(2)}O-$), 1.5 (m, C*H*), 1.2 (overlapping signals $-CH_2-$), 0.8 (t, CH_3). ^{13}C NMR (CD_2Cl_2) δ_C, ppm: 135.5, 116.8, 78.4, 72.4, 71.7, 71.2, 70.9, 70.2, 70.0, 69.0, 39.8, 37.8, 37.2, 33.2 30.3, 28.4, 25.2, 24.8, 22.9, 22.8, 19.9. IR (ATR): 2952, 2925, 2868, 1462, 1377, 1300, 1250, 1107, 1043, 995, 992, 879, 735 cm^{-1}. Field desorption mass spectrum (FD-MS) (*m*/*z*) 869.8 (M^+), calcd ($C_{54}H_{108}O_7$)

Scheme 1. Reaction Pathway for the Synthesis of Lipids with Different Anchor Groups via a Unique Precursor Molecule (9)

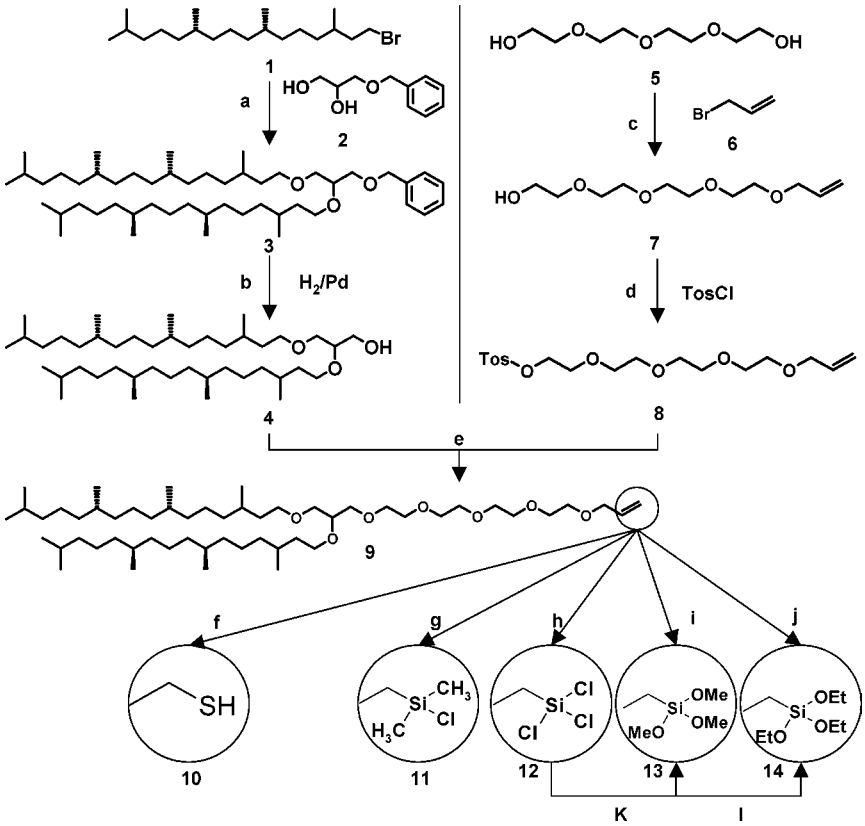

= 869.43; 1737.9 ($M + M^+$), calcd ($2\times C_{54}H_{108}O_7$) = 1738.86; 2607.7 ($2M + M^+$), calcd ($3\times C_{54}H_{108}O_7$) = 2608.29 (see Figure 2).

*Synthesis of the Thiol Anchored Lipid **10** (Step f).* The conversion of a double bond to a mercapto group is a two step process: (a) radical addition of thioacetic acid to the double bond and (b) hydrolysis of the thioester to a thiol (*29*, *30*). (a) A mixture of **9** (1.85 g), thioacetic acid (1.97 g), and azobisisobutyronitrile (AIBN) (7 mg) in toluene (6 mL) was degassed and heated to 70 °C for 24 h. The reaction was monitored by TLC (R_f of the product = 0.35) of aliquots taken from the reaction mixture. After completion of the reaction, toluene and the remaining thioacetic acid were evaporated, and the residue was purified by flash chromatography (FC) (eluent THF/petroleum ether = 1:6). Yield: 1.53 g (76%). ^{1}H NMR ($CDCl_3$) δ_H, ppm: 3.6−3.4 (overlapping signals C$H_{(2)}$O−), 2.9 (t, −CH_2S−), 2.3 (s, −SC(O)CH_3), 1.8 (p, −OCH$_2$CH_2CH$_2$S−), 1.5 (m, CH), 1.2 (overlapping signals −CH_2−), 0.8 (t, −CH_3). ^{13}C NMR ($CDCl_3$) δ_C, ppm: 77.9, 71.5, 70.9, 70.6, 70.2, 70.0, 69.6, 68.9, 39.4, 37.4, 36.7, 32.8, 30.6, 29.9, 29.8, 29.6, 28.0, 26.0, 24.8, 24.5, 24.4, 22.7, 22.6, 19.7. FD-MS (*m*/*z*): 945.4 (M^+), calcd ($C_{56}H_{112}O_8S$) = 945.58.

(b) The product of step a (1.53 g) was treated with NaOH (1 M in water, 6.3 mL) in THF (40 mL) for 24 h at 50 °C. After completion as seen by TLC (R_f(**10**) = 0.53), the THF was evaporated, and the mixture was extracted with methylene chloride. The extracts collected were dried over $CaCl_2$, the methylene chloride was evaporated, and the residue was purified by FC (THF/petroleum ether = 1:4). Yield: 0.98 g (70%). ^{1}H NMR ($CDCl_3$) δ_H, ppm: 3.6−3.4 (overlapping signals −C$H_{(2)}$O−), 2.7 (t, −CH_2S−), 1.9 (p, −OCH$_2$CH_2CH$_2$S−), 1.5 (m, −CH), 1.2 (overlapping signals −CH_2−), 0.8 (t, −CH_3). ^{13}C NMR (CD_2Cl_2) δ_C, ppm: 78.4, 71.7, 71.2, 70.9, 70.6, 70.2, 69.6, 69.0, 68.1, 39.7, 37.8, 37.1, 35.8, 33.2, 30.5, 30.3, 29.7, 28.4, 26.0, 25.1, 24.8, 24.7, 22.8, 22.7, 19.8. IR (ATR): br 2952, 2925, 2865, s 1462, s 1377, s 1292, s 1248, s 1111, s 1070, s 916, s 860, s 737 cm^{-1}. FD-MS (*m*/*z*): 1804.5 ($M + M^+$)− dimerization due to oxidation, calcd for **10** ($C_{54}H_{110}O_7S$) = 903.54; calcd for dimer ($C_{108}H_{218}O_{14}S_2$) = 1805.06.

*Synthesis of **11** and **12** (Steps g and h) (31).* A reaction mixture of freshly distilled chlorosilane (see table below), Pt-catalyst, and **9** was refluxed under inert atmosphere until complete consumption of **9** (R_f(**9**) = 0.58, R_f(**11**, **12**) = 0.00). The mixture was filtered (0.2 μm PTFE) in a glovebox, and the residual chlorosilane was evaporated.

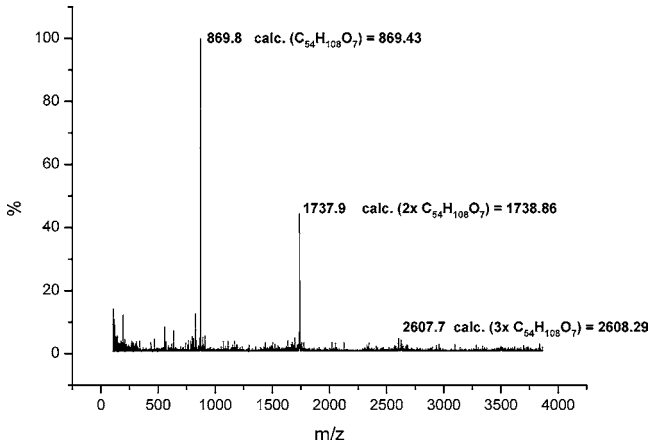

Figure 2. FD-MS spectrum of **9**. The formation of doublets and triplets occur during analysis with the spectrometer.

no.	chlorosilane (mL)	Pt catalyst (mg)	**9** (g)	time (h)	yield (g, %)
11	chlorodimethylsilane (10)	H_2PtCl_6 (100)	1.1	20	1.0, 82
12	trichlorosilane (10)	Pt/C (2%Pt) (100)	2.1	48	2.3, 95

*Characterization of **11**.* ^{1}H NMR (CD_2Cl_2) δ_H, ppm: 3.6−3.4 (overlapping signals −C$H_{(2)}$O−), 1.5 (m, −CH), 1.4−1.0

(overlapping signals $-CH_2-$), 0.8 (t, $-CH_3$), 0.4 (s, Si$-CH_3$). ^{13}C NMR (CD_2Cl_2) δ_C, ppm: 78.5, 73.8, 71.9, 71.4, 71.1, 70.7, 70.4, 69.2, 40.0, 38.0, 37.9, 37.4, 37.3, 33.4, 30.5, 28.6, 25.4, 25.0, 23.9, 23.0, 20.0, 15.8, 1.9. IR (ATR): br 2952, 2923, 2868, s 1462, s 1377, s 1299, s 1253, s 1108, s 941, s 845, s 845, s 735 cm^{-1}. FD-MS (*m*/*z*): 945.9 (M^+), calcd ($C_{56}H_{116}O_8Si$) = 945.63; 1874.2 ($M + M^+ - HCl$)—condensation product due to hydrolysis of **11**, calcd ($C_{112}H_{230}O_{15}Si_2$) = 1873.24.

Characterization of ***12.*** ^{1}H NMR (CD_2Cl_2) δ_H, ppm: 3.6−3.4 (overlapping signals $-CH_{(2)}O-$), 1.8 (m, $-SiCH_2CH_2$) 1.5 (m, $-CH$), 1.2 (overlapping signals $-CH_2$), 0.8 (t, $-CH_3$). ^{13}C NMR (CD_2Cl_2) δ_C, ppm: 78.5, 72.0, 71.9, 71.4, 71.1, 70.8, 70.6, 70.4, 69.2, 39.9, 38.1, 38.0, 37.9, 37.4, 37.3, 33.4, 30.5, 28.6, 25.4, 25.0, 23.3, 23.0, 21.5, 20.1, 20.0. IR (ATR): br 2952, 2924, 2867, s 1462, s 1377, s 1299, s 1250, s 1109, s 939, s 839, s 760, s 733, s 696, s588 cm^{-1}. FD-MS: characterization was not possible due to condensation reaction during the analysis.

Synthesis of ***13*** *and* ***14*** *(Steps i and j) (32).* Pt-complex (2.1−2.4% Pt), acetic acid, and **9** were added to freshly distilled trialkyloxysilane and refluxed under inert atmosphere (see table below). The reaction was monitored by TLC (R_f(**13**) = 0.48, R_f(**14**) = 0.53) of aliquots taken from the reaction mixture. After complete consumption of **9**, the mixture was filtered (0.2 μm PTFE) in a glovebox, and the remaining alkyloxysilane was evaporated.

no.	alkyloxysilane (mL)	Pt complex (μL)	acetic acid (μL)	**9** (g)	time (h)	yield (g, %)
13	trimethoxysilane (5)	1	3	0.52	48	0.55, 92
14	triethoxysilane (10)	1	3	1.10	72	0.94, 72

Alternative Synthesis of ***13*** *and* ***14*** *(Steps k and l) (33).* Compound **12** diluted in toluene (2 mL, see table below) was added dropwise to an ice-cold mixture of alcohol, triethylamine, and toluene (3 mL) under inert atmosphere, and the reaction was left at RT overnight. The mixture was filtered (0.2 μm PTFE) in a glovebox, and the solvent was evaporated.

no.	**12** (g)	alcohol (μL)	triethylamine (μL)	yield (g, %)
13	0.24	methanol (57)	128	0.23, 98
14	0.20	ethanol (66)	106	0.18, 96

Both synthetic routes for **13** (i and k) and **14** (l and j) led to products with identical characteristics.

Characterization of ***13.*** ^{1}H NMR δ_H, ppm: 3.6−3.4 (overlapping signals $-CH_{(2)}O$), 3.5 (s, $-SiOCH_3$), 1.5 (m, $-CH$), 1.2 (overlapping signals $-CH_2$), 0.8 (t, $-CH_3$), 0.6 (t, $-SiCH_2$). ^{13}C NMR δ_C, ppm: 77.9, 73.4, 71.5, 70.8, 70.6, 70.0, 68.9, 50.5, 39.4, 37.4, 36.7, 32.8, 29.9, 28.0, 24.8, 24.5, 24.4, 22.7, 22.6, 19.7, 5.2. IR (ATR): br 2950, 2925, 2867, s 1461, s 1377, s 1301, s 1248, s 1194, s 1087, s 945, s 885, s 835, s 737 cm^{-1}. FD-MS (*m*/*z*): 1011.8 ($M + Na^+$), calcd ($C_{57}H_{118}O_{10}Si$) = 991.66.

Characterization of ***14.*** ^{1}H NMR δ_H, ppm: 3.8 (q, $-SiOCH_2$-CH_3), 3.6−3.4 (overlapping signals $-CH_{(2)}O$), 1.5 (m, $-CH$), 1.2 (overlapping signals $-CH_2$), 0.8 (t, $-CH_3$), 0.6 (t, $-SiCH_2$). ^{13}C NMR δ_C, ppm: 77.9, 73.6, 71.4, 70.8, 70.6, 70.0, 68.9, 58.3, 39.3, 37.4, 36.7, 32.8, 29.9, 28.0, 24.8, 24.5, 22.9, 22.7, 22.6, 19.7, 18.3, 6.4. IR (ATR): br 2952, 2925, 2868, s 1462, s 1377, s 1365, s 1296, s 1450, s 1105, s 1061, s 955, s 795, s 775 cm^{-1}. FD-MS (*m*/*z*): 1056.2 ($M + Na^+$), calcd ($C_{60}H_{124}O_{10}$-Si) = 1033.74.

tBLM Assembly. Monolayers of the different compounds were obtained via self-assembly. The thiol-based tBLMs were prepared on template stripped gold slides as described previously (*24*). In short, 50 nm of gold is evaporated on a clean silicon wafer and glued to a clean glass slide using an epoxy glue. After curing, the silicon is stripped away, and the clean gold substrate is immersed for 24 h into an ethanolic self-assembly solution containing **10** (0.2 mg/mL). The substrates are thoroughly cleaned with ethanol and dried in a nitrogen stream.

The chlorosilane-based (**11** and **12**) tBLMs were prepared in a self-assembly process on highly boron p-doped (0.01 Ω cm) silicon single crystal (100) wafers as described by Purrucker et al. (*34*). In short, **11** and **12** were assembled by immersion of the silicon wafer in a solution of the respective lipid in toluene (typically 2−40 mM) for 24 h. Et_3N was used as a promoter and acid scavenger. For **11**, dried substrates were used. The surface reaction of **12** requires a small amount of water at the substrate (*35*). The electrical backside contact of the wafer is made by a 250 nm thick aluminum electrode.

First attempts using self-assembly of the alkoxysilanes (**13** and **14**) did not result in homogeneous mono- or bilayers. Further investigations will be made using Langmuir−Blodgett−Kuhn techniques.

RESULTS AND DISCUSSION

Syntheses. From a chemical point of view, our approach consists of the synthesis of a "universal" lipid precursor. It possesses all advantages of diphytanyl glycerol, that is, it forms fluid membranes under ambient conditions. The tethering spacer consists of tetra(ethylene glycol), because this moiety prevents the nonspecific adsorption of proteins to surfaces (*36*−*38*), does not absorb to lipid bilayers (*39*), and interacts only minimally with quartz and glass surfaces (*40*). A terminal C═C double bound can be transformed in a few steps into thiol, chlorosilane, and alkyloxysilane anchors (see Scheme 1).

We have previously published briefly the synthesis of the lipid precursor **9** as well as the synthesis of the lipids with chlorosilane anchors (*28*). The formation of tBLMs on silicon substrates and the functional incorporation of two different proteins have been reported. In the present study, we extend the chemical modification of the lipid anchor to thiols and alkoxysilanes for tBLM architectures on gold as well as on silicon substrates. Furthermore, the general synthetic strategy is discussed in more detail.

Lipid Precursor, ***9.*** The preparation of the lipid precursor **9** was achieved by the parallel synthesis of the hydrophobic lipid part (diphytanyl glycerol, **4**) and the tetra(ethylene glycol) tethering unit with a double bond **8**, followed by a Williamson reaction between both (Scheme 1, step e). The structure of the lipid precursor **9** could be shown by ^{1}H NMR and ^{13}C NMR; the purity is characterized by FD-MS. The related signal integrals at 5.9 and 5.3 ppm in ^{1}H NMR and 135.5 and 116.8 ppm in ^{13}C NMR show the double bond functional group. This will be important for the next steps, since the modification of the double bond functionality leads to the different anchor groups. A sequence of signals related to single, double, and triple *m*/*z* values of 870.2 (the calculated molecular weight of **9** is 869.43) are observed by FD-MS, as shown in Figure 2. This sequence may be due to the high affinity between the phytanyl chains. These physical interactions seem to be the main reason for the stability of membranes containing this residue. A similar sequence of signals was observed in the FD mass spectra of **1**, **3**, and **4** where phytanyl units were present. The formation of dimeric and trimeric macromolecules in terms of chemical interactions during the synthesis of the lipid precursor can be excluded because of the absence of any additional signals in ^{1}H NMR and ^{13}C NMR. However, the chemical interactions during the FD-MS measurements might be due to the high reactivity of the ionized lipid molecules that can undergo a number of chemical interactions (*41*). Thus, the purity of the lipid precursor **9** was determined to be higher than 98%.

*Lipids with −SH Anchor, **10**.* The transformation of a double bond into a thiol via thioacetals is a well-known reaction (*30*, *42*). The reaction applied to our precursor lipid **9** leads to lipids with thiol anchors that can be used for tBLMs on gold surfaces. The complete conversion of the double bond to the thioacetal in the first step is shown indirectly by the disappearance of the ^{1}H (5.9 and 5.2 ppm) and ^{13}C NMR (135.5 and 116.8 ppm) signals corresponding to the double bond functionality. Additionally, signals at 2.3 in ^{1}H NMR and 28.0 ppm in ^{13}C NMR appeared. These signals are related to the methyl protons of the thioacetal groups. After FC isolation of **10**, FD-MS was used to determine the structure. A single peak with $m/z = 1804.5$ corresponds to a dimer of **10** (calculated molecular weight of 903.54), which is formed through oxidation of **10**. The mechanism for the oxidation of thiols is a well-established process (*42*) resulting in −S−S− bridge formation and dimerization. The dimers are surface active and efficiently self-assemble on gold surfaces.

*Lipids with $-Si(CH_3)_2Cl$ or $-SiCl_3$ Anchors **11** and **12**.* Herein, we discuss the preparation of both lipids in more detail to understand their structure and chemical behavior and compare them with the other lipids (**10**, **13**, and **14**). Both lipids were prepared similarly using a hydrosilylation reaction in the presence of the corresponding hydrosilane (dimethylchlorosilane for **11** and trichlorosilane for **12**) and a platinum-based catalyst (see Scheme 1, steps g and h). The hydrosilane is in large excess of the precursor lipid **9** and also serves as reaction medium. The use of a heterogenic catalyst, such as platinum over charcoal (Pt/C), requires longer reaction times (48 h) and larger amounts of the catalyst than using homogenic catalysts, such as hexachloroplatinic acid and platinum-divinyltetramethyldisiloxane complex. However, the heterogenic catalyst can easily be separated from the reaction mixture either by filtration or by centrifugation. It should be pointed out that due to extremely high reactivity of chlorosilanes with protic substances (water, acids, alcohols, amines, etc.), the presence of chlorosilane groups drastically reduces the number of suitable purification and analytical methods (e.g., flash chromatography). Thus, most of the purification steps, for example, filtration through 0.2 μm PTFE filter to remove the solid residues such as catalyst or three-dimensional networks obtained by hydrolization of trichlorosilanes, were carried out in a glovebox. Excess of chlorosilanes, their dimers, and their trimers and of HCl (products of hydrolization of the chlorosilanes) could be removed in a vacuum (1×10^{-3} mbar). However, this does not purify the products (**11** and **12**) from unreacted **9.** Therefore, the reactions are stopped only after complete consumption of the starting material. The reaction progress can be monitored either by TLC, FD-MS, or ^{1}H NMR. The final products may still contain dimers, trimers, and oligomers of **11** and **12**, as well as the main side products for both reactions, which is the lipid precursor with hydrogenated double bonds (isolated by FC). Because they will not interact with the substrate, the presence of saturated lipid precursors in the final product will not significantly influence the self-assembly process. Dimers, trimers, or 2D-oligomers of **12** that possess available chlorosilane anchors can effectively self-assemble on a substrate.

The relatively fast hydrolysis of **12** to 1D-, 2D-, and 3D-oligomers causes the main difficulty during the analysis of the compound. It was impossible to detect any structure related fragments by FD-MS. Therefore, the disappearance of the proton signals corresponding to the double bond functionality of **9** by ^{1}H NMR and the drop of the retention factor (R_f) from 0.58 for **9** to 0.00 for **12** indirectly prove the termination of the reaction. In the case of **11**, FD-MS was more informative; dimers obtained by condensation reaction between hydrolyzed and nonhydrolyzed **11** were detected. The presence of signals at 0.39 ppm corresponding to methylsilane protons in the ^{1}H NMR were direct proof that the chlorodimethylsilane functionality was gained. Additionally, an indirect proof of the presence of chlorosilane anchors is accomplished by the formation of chemically adsorbed monolayers on silicon oxide surfaces, as well as by further modification of the trichlorosilane groups to alkoxysilanes.

Table 1. Surface Properties (Contact Angles (CA, deg) and Layer Thickness (nm)) of the Different Monolayers[a]

	static CA	advancing CA	receding CA	modeled thickness	thickness (ellipsometry)	thickness (SPR)
10	104 ± 3	105 ± 2	98 ± 3	4.5	*b*	3.3 ± 0.2
11	72 ± 4	86 ± 4	59 ± 3	4.6	1.3 ± 0.5	*b*
12	87 ± 4	91 ± 5	66 ± 4	4.6	1.8 ± 0.6	*b*

[a] An approximation of fully stretched molecules is used to model the system. [b] Not applicable.

*Lipid with $-Si(OCH_3)_3$ or $-Si(OC_2H_5)_3$ Anchors, **13** and **14**.* The lipids **13** and **14** were obtained by applying either hydrosilylation of **9** with trimethoxysilane or triethoxysilane (Scheme 1, steps i and j (*32*)) or substitution of chlorine of the trichlorosilanated lipid **12** with methanol or ethanol (Scheme 1, steps k and l (*33*)). Since hydrosilylation occurs similarly in the cases of chlorosilanes and alkoxysilanes, the alternative method, that is, substitution of trichlorosilane anchors of **12** with alcohols, is much simpler and faster once **12** is obtained. Moreover, the method indirectly proves the quantitative content of trichlorosilyl anchors in **12**. Similarly to **11** and **12**, the hydrolization of **13** and **14** in ambient conditions renders the quantitative analysis of the structures difficult, especially in the case of **13**, which hydrolyzes faster than **14** (*43*). However, FD-MS, ^{1}H NMR, and ^{13}C NMR directly prove the presence of the methoxy- (**13**) and ethoxysilane (**14**) anchors.

Indeed, both chlorosilanes (**11** and **12**) and alkoxysilanes (**13** and **14**) were prepared as lipids with appropriate anchors for silicon oxide surfaces. However, the different anchors differ in their hydrolyzation rates and, therefore, require individual immobilization techniques. Chlorosilanated lipids should be suitable for less homogeneous metal oxides (e.g., poorly oxidized metal) or less reactive (e.g., chemically modified) surfaces due to their high reactivity but poor control over the hydrolization process. On the other hand, alkoxysilanes hydrolyze more slowly, allowing a better control of the immobilization process. Additionally, the aggressive chlorosilanes can cause problems when adsorbed on surfaces obtained by layer deposition (e.g., plasma polymerized silicones or indium tin oxide (ITO) deposited on silicon wafers). Due to their high affinity for silicon oxide, these surface layers may get peeled off the substrate.

We obtained self-assembled monolayers using the chlorosilanated lipids **11** and **12**. Further experiments with **13** and **14** will be performed using Langmuir−Blodgett−Kuhn techniques and published separately.

tBLM Formation and Characterization. The hydrophobic character of the different self-assembled monolayers was investigated using contact angle measurements. The results in Table 1 show that all samples possess relatively high contact angles. In our experiments, this is a prerequisite to allow for successful fusion of vesicles.

Compound **10** forms a well-ordered monolayer, as can be seen by the small difference in advancing and receding contact angles. The further assembly and membrane formation of **10** is investigated by SPR. The formation of the outer leaflet of the lipid membrane by fusion with vesicles (50 nm by extrusion) results in an angular shift of the plasmon resonance. The kinetic scan recorded at 57.7° (Figure 3) shows the exponential character of the process, which reaches equilibrium after about 160 min. After 3 h, the vesicle fusion is completed at the final

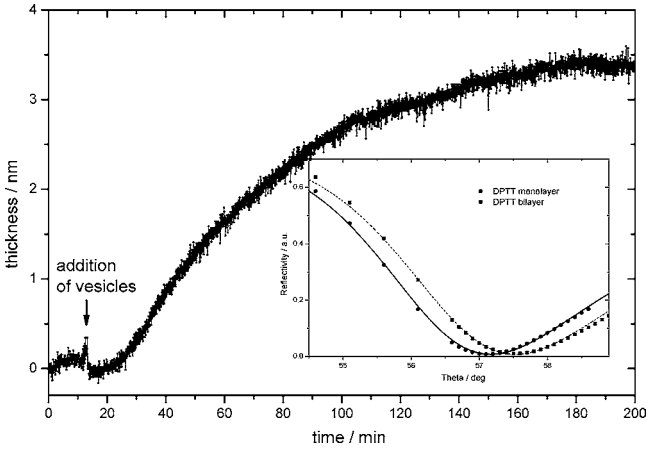

Figure 3. SPR scans for vesicle fusion experiments on a monolayer of **10**. The curve shows the evolution of the bilayer thickness with time. The inset shows the corresponding angular shift in the SPR curve before and after the addition of the vesicles.

Table 2. Electrical Properties of the Different tBLMs[a]

	R, MΩ cm^2	*C*, μF cm^{-2}
10	3.6 ± 1.1	1.1 ± 0.03
11	1.5 ± 1.1	0.88 ± 0.04
12	0.5 ± 0.5	0.78 ± 0.03

[a] The EIS data has been fit by an equivalent circuit. The values for the resistance and capacitance corresponding to the bilayer are listed.

thickness of the bilayer (6.7 nm). The inset in Figure 3 shows the angular scans before and after vesicle fusion. The fit parameters are summarized in Table 1. The optical properties of the bilayers composed of the lipids **11** and **12** were characterized using ellipsometry.

As shown in Table 1, the experimental thickness values of the different monolayers (as measured from SPR or ellipsometry) and the theoretical thickness differ significantly. The latter are obtained for a model of a densely packed layer of fully stretched molecules. This lack of agreement between measured and calculated thickness might be due to an incomplete coverage of the surface. This assumption is supported by a hysteresis in advancing and receding contact angles, revealing a rather inhomogeneous surface in the case of the silane-based monolayers. Furthermore, the hydrophobic tails have a tilted conformation and the ethylene glycol units adopt a helical structure, as seen by IR spectroscopy (Lipkowski, unpublished results).

By fusion of small unilamellar vesicles with monolayers of **10**, **11**, and **12**, we were able to create bilayers and investigate their electrical properties using electrochemical impedance spectroscopy. The spectra were analyzed using a passive equivalent model circuit of resistors and capacitances. For membranes based on **11** and **12**, a model with two RC elements in series with a feed resistance was used (R(RC)(RC)). Whereas for the thiol **10**, one RC element in series with a capacitor and a feed resistance was sufficient (R(RC)C). The values we obtained were normalized to the electrode surface area and are listed in Table 2.

The lower the capacitance is, the higher the charge separation. Here, the silane-based tBLMs show better electrical properties. However, the resistance values show an opposite trend, as the thiol-based tBLM shows the highest membrane resistance. The dense packing of the lipids is in agreement with the results from the contact angle measurements.

Due to the high electrical resistances our membranes allow minimal leakage across the membrane. Therefore, we were able to show the functional incorporation of ion carriers and ion channels (*37*).

CONCLUSION

We developed a new synthetic strategy for the systematic study of tethered bilayer lipid membranes. A toolkit-like approach using a precursor strategy allows for the synthesis of anchor lipids with various end groups. We showed the synthesis of a thiol anchor and four different silane anchors and their ability to form monolayers on gold or silicon oxide surfaces. These monolayers can be used to form highly insulating bilayers offering a synthetic platform for the incorporation of membrane proteins. This approach can be used as a central element in biosensing applications when the coupling of biological elements to electronics is needed. Furthermore, the synthetic strategy allows adaptation of the lipids to various kinds of surface architectures by matching anchor groups. Similarly, spacer units of various types or of different lengths can be easily included in the synthesis to facilitate protein incorporation.

This generic approach should allow for the design of tBLMs individually adapted to various substrates and biological compounds, for example, ion channels, receptors, and membrane proteins.

ACKNOWLEDGMENT

Sven Ingebrandt is acknowledged for providing silicon wafers. Partial financial support came from the Defense Advanced Research Projects Agency (DARPA) through the MOLDICE program. I.K. acknowledges support from the Laboratoire Européen Associé (LEA) on "Polymers in Confined Geometries".

LITERATURE CITED

(1) Sackmann, E., and Tanaka, M. (2000) Supported membranes on soft polymer cushions: fabrication, characterization and applications. *Trends Biotechnol. 18*, 58−64.

(2) Sackmann, E. (1996) Supported membranes: Scientific and practical applications. *Science 271*, 43−48.

(3) Hillebrandt, H., Tanaka, M., and Sackmann, E. (2002) A novel membrane charge sensor: Sensitive detection of surface charge at polymer/liquid composite films on Indium Tin oxide electrodes. *J. Phys. Chem. B 106*, 477−486.

(4) Cornell, B. A., Braach-Maksvytis, V. L. B., King, L. G., Osman, P. D. J., Raguse, B., Wieczorek, L., and Pace, R. J. (1997) A biosensor that uses ion-channel switches. *Nature 387*, 580−583.

(5) Krueger, S., Meuse, C. W., Majkrzak, C. F., Dura, J. A., Berk, N. F., Tarek, M., and Plant, A. L. (2001) Investigation of Hybrid Bilayer Membranes with Neutron Reflectometry: Probing the Interactions of Melittin. *Langmuir 17*, 511−521.

(6) Glazier, S. A., Vanderah, D. J., Plant, A. L., Bayley, H., Valincius, G., and Kasianowicz, J. J. (2000) Reconstitution of the Pore-Forming Toxin r-Hemolysin in Phospholipid/18-Octadecyl-1-thiahexa(ethylene oxide) and Phospholipid/*n*-Octadecanethiol Supported Bilayer Membranes. *Langmuir 16*, 10428−10435.

(7) Tian, L., Yam, L., Wang, J., Tat, H., and Uhrich, K. E. (2004) Core cross-linkable polymeric micelles from PEG-lipid amphiphiles as drug carriers. *J. Mater. Chem. 14*, 2317−2324.

(8) Morigaki, K., Baumgart, T., Jonas, U., Offenhaeusser, A., and Knoll, W. (2002) Photopolymerization of Diacetylene Lipid Bilayers and Its Application to the Construction of Micropatterned Biomimetic Membranes. *Langmuir 18*, 4082−4089.

(9) Bhattacharya, S., and Dileep, P. V. (2004) Cationic Oxyethylene Lipids. Synthesis, Aggregation, and Transfection Properties. *Bioconjugate Chem. 15*, 508−519.

(10) Pantusa, M., Bartucci, R., Marsh, D., and Sportelli, L. (2003) Shifts in chain-melting transition temperature of liposomal membranes by polymer-grafted lipids. *Biochim. Biophys. Acta 1614*, 165−170.

(11) Mannock, D. A., Lewis, R. N. A. H., and McElhaney, R. N. (1990) The chemical synthesis and physical characterization of 1,2-di-O-acyl-3-O-(-D-glucopyranosyl -sn-glycerols), an important class of membrane glycolipids. *Chem. Phys. Lipids 55* (3), 309−321.

(12) Joo, C. N., Shier, T., and Kates, M. (1968) Characterization and synthesis of mono- and diphytanyl ethers of glycerol. *J. Lipid Res. 9*, 782−788.
(13) Sita, L. R. (1993) Covalent Highly Stereoselective Syntheses of (3R,7R,11R)- and (3S,7R,11R)-3,7,11,15-Tetramethylhexadecanoic Acid (Phytanic Acid) and Corresponding 3,7,11,15-Tetramethylhexadecan-1-ols. *J. Org. Chem. 58*, 5285−5287.
(14) Schiller, S. M., Naumann, R., Lovejoy, K., Kunz, H., and Knoll, W. (2003) Archaea Analogue Thiolipids for Tethered Bilayer Lipid Membranes on Ultrasmooth Gold Surfaces. *Angew. Chem., Int. Ed. 42*, 208−211.
(15) Woese, C. R., and Fox, G. E. (1977) Phylogenetic Structure of the Prokaryotic Domain: The Primary Kingdoms. *Proc. Natl. Acad. Sci. U.S.A. 74*, 5088−5090.
(16) Stewart, L. C., and Kates, M. (1989) Synthesis and characterization of deuterium-labeled dihexadecylglycerol and diphytanylglycerol phospholipids. *Chem. Phys. Lipids 50*, 23−42.
(17) Cornell, B. A., Krishna, G., Osman, P. D., Pace, R. D., and Wieczorek, L. (2001) Tethered-bilayer lipid membranes as a support for membrane-active peptides. *Biochem. Soc. Trans. 29*, 613−617.
(18) Hato, M. (2001) Synthetic glycolipid/water system. *Curr. Opin. Colloid Interface Sci. 6*, 268−276.
(19) Theato, P., Zentel, R., and Schwarz, S. (2002) Synthesis of end-functionalized lipopolymers and their characterization with regard to polymer-supported lipid memebrane. *Macromol. Biosci. 2*, 378−394.
(20) Burns, C. J., Field, L. D., Morgan, J., Petteys, B. J., Prashar, J., Ridley, D. D., Sandanayake, K. R. A. S., and Vignevich, V. (2001) Componenets for tethered bilayer membranes: synthesis of hydrophilically substituted phytanol derivatives. *Aust. J. Chem. 54*, 431−438.
(21) Sharma, M. K., Jattani, H., and Lane M. Gilchrist, J. (2004) Bacteriorhodopsin Conjugates as Anchors for Suppported Membranes. *Bioconjugate Chem. 15*, 942−947.
(22) Munro, J. C., and Frank, C. W. (2004) In situ formation and characterization of poly(ethylene glycol)-supported lipid bilayers on gold surface. *Langmuir 20*, 10567−10575.
(23) Krishna, G., Schulte, J., Cornell, B. A., Pace, R. J., and Osman, P. D. (2003) Tethered Bilayer Membranes Containing Ionic Reservoirs: Selectivity and Conductance. *Langmuir 19*, 2294−2305.
(24) Naumann, R., Schiller, S. M., Giess, F., Grohe, B., Hartmann, K. B., Kärcher, I., Köper, I., Lübben, J., Vasilev, K., and Knoll, W. (2003) Tethered lipid bilayer on ultraflat gold surface. *Langmuir 19*, 5435−5443.
(25) Wagner, M. L., and Tamm, L. K. (2000) Tethered Polymer-Supported Planar Lipid Bilayers for Reconstitution of Integral Membrane Proteins: Silane-Poly(ethylene glycol)-Lipid as a Cushion and Covalent Linker. *Biophys. J. 79*, 1400−1414.
(26) Kiessling, V., and Tamm, L. K. (2003) Measuring Distances in Supported Bilayers by Fluorescence Interference-Contrast Microscopy: Polymer Supports and SNARE Proteins. *Biophys. J. 84*, 408−418.
(27) Rossi, C., Homand, J., Bauche, C., Hamdi, H., Ladant, D., and Chopineau, J. (2003) Differential Mechanisms for Calcium-Dependent protein/membrane association as evidenced from SPR-binding studies on supported biomimetic membranes. *Biochemistry 42*, 15273−15283.
(28) Atanasov, V., Knorr, N., Duran, R. S., Ingebrandt, S., Offenhäusser, A., Knoll, W., and Köper, I. (2005) Membrane on a Chip. A functional tethered lipid bilayer membrane on silicon oxide surfaces. *Biophys. J. 89*, 1780−1788.
(29) Mumbauer, P. D., Carey, D. H., and Ferguson, G. S. (1995) Organic Chemistry at Polymer Surfaces To Promote Adhesion to Gold and Copper: Surface-Modified Polybutadiene Having Functional Groups Containing Sulfur. *Chem. Mater. 7*, 1303−1314.
(30) Romani, F., Passaglia, E., Aglietto, M., and Ruggeri, G. (1999) Functionalization of SBR copolymer by free radical addition of thiols. *Macromol. Chem. Phys. 200*, 524−530.
(31) Prucker, O., Naumann, C. A., Rühe, J., Knoll, W., and Frank, C. W. (1999) Photochemical Attachment of Polymer Films to Solid Surfaces via Monolayers of Benzophenone Derivatives. *J. Am. Chem. Soc. 121*, 8766−8770.
(32) Mamoru, T., and Kasumi, T. (1999) *Method for making compounds containing hydrocarbonoxysilyi groups by hydrosilylation using hydrido (hydrocarbonoxy) silane compounds*, Dow Corning Asia, Ltd., Tokyo, JP.
(33) Hosomi, A., Kohra, S., Ogata, K., Yanagi, T., and Tominagat, Y. (1990) Pentacoordinate Allylsiliconates in Organic Synthesis: Synthesis of Triethylammonium Bis(catecho1ato)allylsiliconates and Selective Allylation of Aldehydes. *J. Org. Chem. 55*, 2415−2420.
(34) Purrucker, O., Hillebrand, H., Adlkofer, K., and Tanaka, M. (2001) Deposition of highly resistive lipid bilayer on silicon−silicon dioxide electrode and incorporation of gramicidin studied by ac impedance spectroscopy. *Electrochim. Acta 47*, 791−798.
(35) Silberzan, P., Léger, L., Ausserre, D., and Benattar, J. J. (1991) Silanation of Silica Surfaces. A New Method of Constructing Pure or Mixed Monolayers. *Langmuir 7*, 1647−1651.
(36) Lee, J. H., Lee, H. B., and Andrade, J. D. (1995) Blood compatibility of poly(ethylene oxide) surfaces. *Prog. Polym. Sci. 20*, 1043−1079.
(37) Du, H., Chandaroy, P., and Hui, S. W. (1997) Grafted poly-(ethylene glycol) on lipid surfaces inhibits protein adsorption and cell adhesion. *Biochim. Biophys. Acta 1326*, 236−248.
(38) Prime, K. L., and Whitesides, G. M. (1991) Self-assembled organic monolayers: model systems for studing adsorption of proteins at surfaces. *Science 252*, 1164−1167.
(39) Arnold, K., Zschoernig, O., Barthel, D., and Herold, W. (1990) Exclusion of poly(ethylene glycol) from liposome surfaces. *Biochim. Biophys. Acta 1022*, 303−310.
(40) Ariga, K., Shin, J. S., and Kunitake, T. (1995) Interaction af lipid monolayers with aqueous neutral polymers and the consequent monolayer stabilization and improved Langmuir−Blodgett transfer. *J. Colloid Interface Sci. 170*, 440−448.
(41) Sabino, A. A., Eberlin, M. N., Moraes, L. A. B., and Laali, K. K. (2003) Gas-phase chemistry of the 2-*tert*-butyl-3-phenylphosphirenylium cation: novel onium ions by nucleophilic attack at phosphorus and de novo P-spiro bicyclic phosphonium ions via [4 + 2+] cycloaddition with dienes. *Org. Biomol. Chem. 1*, 395−400.
(42) Padeken, H.-G., and Klamann, D. (1985) In *Methoden der Organischen Chemie*, Organische Schwefel − Verbindungen., (Gundremann, K. D., and Hümke, K., Eds.) Vol. E11, pp 38−62, Georg Thieme Verlag, Stuttgart, New York.
(43) Kozerski, G. E., Gallava, R. H., and Ziemelis, M. J. (2003) Investigation of trialkoxysilane hydrolysis kinetics using liquid chromatography with inductively coupled plasma atomic emission spectrometric detection and nonlinear regression modeling. *Anal. Chim. Acta 489*, 103−114.

BC050328N

Bioconjugatable Porphyrins Bearing a Compact Swallowtail Motif for Water Solubility

K. Eszter Borbas,[‡] Pawel Mroz,[§,†] Michael R. Hamblin,[§,†,⊥] and Jonathan S. Lindsey*[,‡]

Department of Chemistry, North Carolina State University, Raleigh, North Carolina 27695-8204, Wellman Center for Photomedicine, Massachusetts General Hospital, Boston, Massachusetts 02114-2605, Department of Dermatology, Harvard Medical School, Boston, Massachusetts 02115-6092, and Harvard-MIT Division of Health Sciences and Technology, Cambridge, Massachusetts 02142-1323. Received November 22, 2005; Revised Manuscript Received March 18, 2006

A broad range of applications requires access to water-soluble, bioconjugatable porphyrins. Branched alkyl groups attached at the branching site to the porphyrin meso position are known to impart high organic solubility. Such "swallowtail" motifs bearing a polar group (hydroxy, dihydroxyphosphoryl, dihydroxyphosphoryloxy) at the terminus of each branch have now been incorporated at a meso site in *trans*-AB-porphyrins. The incorporation of the swallowtail motif relies on rational synthetic methods whereby a 1,9-bis(*N*-propylimino)dipyrromethane (bearing a bioconjugatable tether at the 5-position) is condensed with a dipyrromethane (bearing a protected 1,5-dihydroxypent-3-yl unit at the 5-position). The two hydroxy groups in the swallowtail motif of each of the resulting zinc porphyrins can be transformed to the corresponding diphosphate or diphosphonate product. A 4-(carboxymethyloxy)phenyl group provides the bioconjugatable tether. The six such porphyrins reported here are highly water-soluble (≥20 mM at room temperature in water at pH 7) as determined by visual inspection, UV−vis absorption spectroscopy, or ^{1}H NMR spectroscopy. Covalent attachment was carried out in aqueous solution with the unprotected porphyrin diphosphonate and a monoclonal antibody against the T-cell receptor CD3ϵ. The resulting conjugate performed comparably to a commercially available fluorescein isothiocyanate-labeled antibody with Jurkat cells in flow cytometry and fluorescence microscopy assays. Taken together, this work enables preparation of useful quantities of water-soluble, bioconjugatable porphyrins in a compact architecture for applications in the life sciences.

INTRODUCTION

A large and growing number of applications in the life sciences require porphyrinic macrocycles that are water-soluble and are suited for conjugation in a variety of formats. The applications encompass flow cytometry, cellular and whole-organism imaging, sensing, photodynamic therapy, biomimetic catalysis, and radical scavenging. The success of these applications relies on a host of factors, including (1) significant solubility in aqueous saline solutions, thereby avoiding intermolecular aggregation (and excited-state quenching), (2) minimal nonspecific binding to cellular components, (3) incorporation of a single reactive group for conjugation, thereby avoiding cross-linking and the formation of product mixtures, and (4) robust synthesis affording ample quantities for experimentation.

The large hydrophobic face of a porphyrinic macrocycle presents a challenge to water solubilization. Traditional approaches to achieve water solubility of porphyrins have largely relied on uroporphyrin (*1*−*5*), *meso*-tetrakis[4-(*N*-methyl)-pyridinium]porphyrin (*6*), and *meso*-tetrakis(4-sulfophenyl)-porphyrin (*6*) (Chart 1). More recent approaches have entailed attachment of the following motifs to the porphyrin via a *meso*-aryl group: oligo(ethylene glycol) (OEG) chains (*7*, *8*), OEG dendrimers (*9*), glycosyl units (*10*), alkyl polyamine chains (*11*), branched polycarboxy units (*12*), or malonate groups (*13*). Solubilizing groups that do not incorporate an aryl group include 1,2-dihydroxyethyl at the porphyrin meso position (*14*) and a variety of substituents attached to the β-position of a sapphyrin (*15*). A lengthy review of water-soluble porphyrins has been prepared by Hambright (*6*). Each solubilizing group has merit; however, many are not compatible with bioconjugation reactions, and others are so large (mass >10-times that of the porphyrin) as to limit the scope of desired experiments.

The presence of a bioconjugatable group is essential for attachment of water-soluble porphyrins to substances ranging from nanoparticles to biological targeting agents. Indeed, porphyrinic molecules have been attached to diverse molecular entities such as peptides (*16*−*19*), estrogen (*20*), acridine (*21*), bovine serum albumin (*22*), antibodies (*23*−*27*), transferrin (*28*), epidermal growth factor (*29*, *30*), low-density lipoprotein (*31*), nucleic acids (*32*), and polymers such as polylysine (*33*) or poly(vinyl alcohol) (*29*, *30*). In some cases, the bioconjugation is carried out in organic solution, whereas in others aqueous media are employed. Regardless of medium, the choice of bioconjugatable group must enable conjugation to be carried out without interference with the functional groups that afford water solubility.

To meet the objectives stated above requires a water solubilization unit that is (1) compact, (2) synthetically accessible, preferably amenable for use in the building-block synthesis of meso-substituted porphyrins, and (3) compatible with bioconjugation procedures. Anionic substituents are particularly attractive in the water solubilization motif to minimize nonspecific binding to cellular components. A chief challenge is to solubilize the rather hydrophobic porphyrinic macrocycle so as to suppress cofacial interaction, a likely mechanism for aggregation and precipitation. We recently found that branched-

* Corresponding author. Phone: (919) 515-6406. Fax: (919) 513-2830. E-mail: jlindsey@ncsu.edu.
[‡] North Carolina State University.
[§] Massachusetts General Hospital.
[†] Harvard Medical School.
[⊥] Harvard-MIT Division of Health Sciences and Technology.

10.1021/bc050337w CCC: $33.50 © 2006 American Chemical Society
Published on Web 04/28/2006

Chart 1

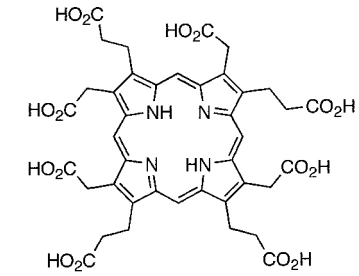

Uroporphyrin III

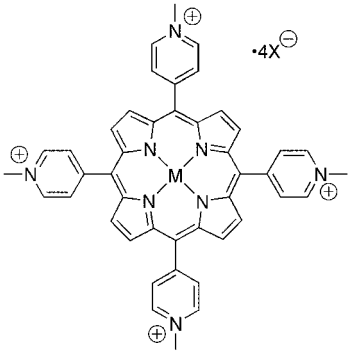

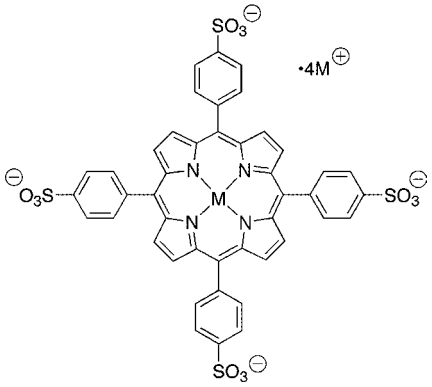

alkyl groups (e.g., tridec-7-yl) known as "swallowtail" substituents are very effective at imparting a high level of organic solubility to porphyrins (Figure 1) (*34*, *35*). The hydrocarbon chains of the swallowtail motif project over both faces of the macrocycle, suppressing $\pi-\pi$ interactions between porphyrin rings (*34*). Such hydrocarbon swallowtails were shown earlier to impart excellent solubility in organic media to perylene dyes, which otherwise are quite insoluble (*36*). We expected that swallowtail moieties modified with polar end groups could render porphyrins water-soluble. The swallowtail groups do not include a meso-aryl substituent and hence are compact, helping limit the overall molecular weight of the porphyrinic compound.

In this paper, we report the synthesis of *trans*-AB-porphyrins bearing one conjugatable group and one swallowtail motif. The presence of two small meso substituents affords a minimalist design suited for diverse applications. The swallowtail motif is a pent-3-yl group bearing a polar group (dihydroxyphosphoryl, dihydroxyphosphoryloxy) at each terminus. The conjugatable group is either 4-bromophenyl or 4-(carboxymethyloxy)phenyl. The solubility of the porphyrins has been examined in aqueous media. The bromo substituent is not directly useful for bioconjugation but can be substituted in Pd-mediated reactions. In addition, the porphyrin bearing the bromo substituent can serve as a benchmark for assessing the extent to which the swallowtail motifs are responsible for water solubilization without the polar, ionizable carboxylic acid. The favorable properties of the

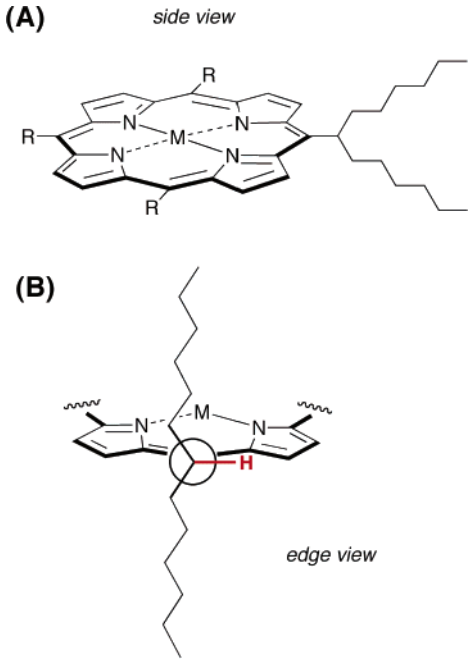

Figure 1. (A) Porphyrin bearing one swallowtail substituent and (B) Newman projection showing the alkyl chains of the swallowtail substituent above and below the plane of the porphyrin.

porphyrin allowed the facile preparation of soluble nonaggregated protein conjugates. The biological activity of the conjugated porphyrin was established by the stringent method of intracellular fluorescent staining using a monoclonal antibody against the epsilon invariant chain of the human T-cell receptor CD3, and assessing the performance by flow cytometry and fluorescence microscopy. This work establishes the foundation for the rational synthesis of porphyrins for applications where water solubility and bioconjugation are required.

EXPERIMENTAL PROCEDURES

General Methods. ^{1}H NMR (300 MHz) and ^{13}C NMR (75 MHz) spectra were recorded in $CDCl_3$ unless noted otherwise. Bulb-to-bulb distillation was performed using a standard-size Kugelrohr apparatus. Absorption spectra and fluorescence spectra were collected at room temperature in CH_2Cl_2 unless noted otherwise. Infrared absorption spectra were recorded as thin films. Hydrophobic porphyrins were analyzed in neat form by laser desorption mass spectrometry (LD-MS) (*37*). The water-soluble porphyrins were analyzed by direct infusion of water/methanol (40:60) solutions by atmospheric pressure electrospray ionization mass spectrometry (ESI-MS). Both in LD-MS and ESI-MS analyses, positive ions were detected unless noted otherwise. Melting points are uncorrected. Solvents were dried according to standard procedures. LDA was generated in situ (*38*). The mouse IgG1 anti-human CD3 intracellular ϵ-chain (clone UCHT) (*39*) and the same antibody derivatized with a fluorescein-isothiocyanate (FITC) label, were obtained from BD Biosciences (San Jose, CA). All other materials were used as received from commercial sources. Molecular mechanics calculations were carried out using PCMODEL for Windows version 7.50.00 (Serena Software).

Chromatography. Preparative chromatography was performed using silica (230−400 mesh) or alumina (80−200 mesh). Thin-layer chromatography was performed on silica or alumina. Samples were visualized by UV light (254 and 365 nm), Br_2 vapor, or $KMnO_4/K_2CO_3$. Dipyrromethanes and compounds **2**−**4** and **6a** were analyzed by GC as described previously (*40*). Reversed-phase preparative column chromatography was carried out using C-18-coated silica and eluants based on water admixed

with methanol. Analytical RP-HPLC was carried out using an ODS C-18 column (5 μm, 125 mm × 4 mm), flow rate = 1 mL/min, detection at 254, 410, and 417 nm, and the following elution program with solvents A (water containing 0.1% TFA) and B (acetonitrile containing 0.1% TFA): 0−2 min, 0% B; 2−20 min, 0→90% B; 20−23 min, 90% B.

2-(*tert*-Butyldimethylsilyloxy)ethyl Bromide (2). Following a published procedure (*41*), 2-bromoethanol (10.0 mL, 141 mmol) was added to a mixture of imidazole (12.5 g, 184 mmol) and *tert*-butyldimethylsilyl chloride (21.1 g, 140 mmol) in anhydrous DMF (25 mL). The reaction mixture was stirred at room temperature for 12 h. Water and diethyl ether were added. The phases were separated. The aqueous phase was extracted with diethyl ether. The organic phase was washed with water and brine. The solution was dried (Na_2SO_4). Evaporation of the solvent followed by bulb-to-bulb distillation (40−45 °C, 0.05 mmHg) yielded a colorless liquid (32.5 g, 97%): IR (film, ν_{max} cm^{-1}) 2951, 2859, 1471; ^{1}H NMR δ 0.07 (s, 6H), 0.89 (s, 9H), 3.36−3.41 (m, 2H), 3.85−3.90 (m, 2H); ^{13}C NMR δ −5.06, 18.49, 26.04, 33.45, 63.74; EI-MS 137/139, 181/183; Anal. ($C_8H_{19}BrOSi$) C, H.

3-Cyano-1,5-bis(*tert*-butyldimethylsilyloxy)pentane (3). A solution of HMPA (12.0 mL) and LDA (33.5 mmol) in dry THF (39 mL) at −78 °C under argon was treated with acetonitrile (1.75 mL, 33.5 mmol). The solution was stirred for 30 min. Then, **2** (6.82 g, 29.0 mmol) in THF (30 mL) was added dropwise. Stirring was continued for 2 h, after which a second portion of LDA (33.5 mmol in 39 mL THF) was added. The solution was stirred for 30 min, after which **2** (6.82 g, 29.0 mmol) in THF (30 mL) was added dropwise. The reaction was allowed to proceed for 2 h. Saturated aqueous NH_4Cl was added, and the mixture was allowed to reach room temperature. Diethyl ether was added, the phases were separated, and the aqueous layer was extracted with diethyl ether. The organic phase was washed with water and brine, dried over Na_2SO_4, and concentrated. Chromatography [silica, petroleum ether/diethyl ether (40:1)] afforded a colorless liquid (7.79 g, 77%): IR (film, ν_{max} cm^{-1}) 2953, 2859, 1738, 1472; ^{1}H NMR δ 0.07 (s, 12H), 0.89 (s, 18H), 1.76−1.83 (m, 4H), 3.03−3.13 (m, 1H), 3.73−3.83 (m, 4H); ^{13}C NMR δ −5.24, 18.45, 24.82, 26.09, 35.32, 60.08, 122.15; EI-MS 115, 142/144, 156/157, 182/184, 198; Anal. ($C_{18}H_{39}NO_2Si_2$) C, H, N.

3-Formyl-1,5-bis(*tert*-butyldimethylsilyloxy)pentane (4). Following a published procedure (*41*), a solution of **3** (3.65 g, 10.2 mmol) in dry toluene (52 mL) at −78 °C under argon was treated with DIBALH (12 mmol, 8.3 mL, 1.5 M solution in toluene). The reaction was allowed to proceed for 1 h. Water (2.6 mL) was added, and the mixture was allowed to reach room temperature. Aqueous NaOH (2.6 mL, 4.0 M solution) was added, and stirring was continued for 15 min. Water (7.8 mL) was added, and the suspension was stirred for a further 15 min. The reaction mixture was dried with a large quantity of Na_2SO_4. The dried solution was concentrated at reduced pressure and chromatographed [silica, petroleum ether/diethyl ether (20:1)], affording a colorless liquid (2.70 g, 73%): IR (film, ν_{max} cm^{-1}) 2955, 2859, 1729, 1708, 1472; ^{1}H NMR δ 0.01 (s, 12H), 0.87 (s, 18H), 1.64−1.74 (m, 2H), 1.85−1.96 (m, 2H), 2.50 (m, 1H), 3.57−3.68 (m, 4H), 9.65 (d, J = 2.4 Hz, 1H); ^{13}C NMR δ −5.27, 18.45, 26.09, 32.15, 46.40, 60.80, 204.74; EI-MS 171/172, 141, 97, 75; Anal. ($C_{18}H_{40}O_3Si_2$) C, H; C calcd, 59.94; found, 58.15.

5-[1,5-Bis(*tert*-butyldimethylsilyloxy)pent-3-yl]dipyrromethane (5). Following a standard procedure (*40*), aldehyde **4** (4.61 g, 12.8 mmol) was dissolved in dry pyrrole (89.1 mL, 1.28 mmol), and the solution was flushed with argon for 10 min. $InCl_3$ (285 mg, 1.28 mmol) was added, and the reaction was allowed to proceed for 3 h. The reaction was quenched by addition of powdered NaOH (1.54 g, 38.5 mmol). The mixture was stirred for 45 min. The mixture was filtered. The filtrate was concentrated at reduced pressure. The residue was chromatographed [silica, ethyl acetate/CH_2Cl_2/hexanes (1:2:7)] affording a viscous, pale yellow liquid (5.87 g, 96%): IR (film, ν_{max} cm^{-1}) 3427, 1639; ^{1}H NMR δ 0.09 (s, 12H), 0.94 (s, 18H), 1.35−1.44 (m, 2H), 1.71−1.78 (m, 2H), 2.41−2.43 (m, 1H), 3.64−3.77 (m, 4H), 4.38 (d, J = 4.2 Hz, 1H), 6.03 (app s, 2H), 6.13−6.16 (m, 2H), 6.65−6.66 (m, 2H), 8.45−8.55 (br, 2H); ^{13}C NMR δ −5.08, 18.65, 26.29, 35.13, 35.37, 40.41, 62.18, 107.03, 108.27, 116.45, 132.25; LD-MS obsd 475.6; FAB-MS obsd 476.3255, calcd 476.3254 ($C_{26}H_{48}N_2O_2Si_2$); Anal. C, H, N.

5-(1,5-Dihydroxypent-3-yl)dipyrromethane (5-(OH)$_2$). A solution of **5** (3.81 g, 8.01 mmol) in THF (30 mL) was treated with TBAF (4.61 g, 17.6 mmol). The reaction was allowed to proceed until the starting material could not be detected by TLC [alumina, CH_2Cl_2/MeOH (97:3)]. The solvent was evaporated. The residue was dissolved in a mixture of ethyl acetate and water. The aqueous layer was extracted with ethyl acetate. The organic phase was washed with water and dried (Na_2SO_4). The solvent was removed, and the residue was chromatographed [neutral alumina, CH_2Cl_2/MeOH (2→10%)] to afford an off-white viscous oil (1.60 g, 89%): ^{1}H NMR δ 1.43−1.50 (m, 2H), 1.68−1.79 (m, 2H), 2.39−2.43 (m, 3H), 3.59−3.75 (m, 4H), 4.21 (d, J = 5.4 Hz, 1H), 6.04 (d, J = 0.9 Hz, 2H), 6.13−6.16 (m, 2H), 6.65−6.66 (m, 2H), 8.40−8.55 (br, 2H); ^{13}C NMR δ 25.88, 34.86, 35.60, 41.79, 61.25, 106.77, 108.38, 117.03, 131.84; FAB-MS obsd 248.1528, calcd 248.1525 ($C_{14}H_{20}N_2O_2$); Anal. C calcd, 67.71; found, 66.59; H calcd, 8.12; found, 8.62; N calcd, 11.28; found, 10.34.

5-[1,5-Bis(dimethoxyphosphoryloxy)pent-3-yl]dipyrromethane (5-(P)$_2$). A solution of **5-(OH)$_2$** (950 mg, 4.24 mmol) in CH_2Cl_2 (16 mL) was treated with DMAP (1.18 g, 9.67 mmol) followed by slow addition of a solution of dimethyl chlorophosphate (1.06 mL, 9.83 mmol) in CH_2Cl_2 (11 mL). The reaction mixture was stirred at room temperature for 8 h. The crude mixture was diluted with CH_2Cl_2 and water. The aqueous layer was extracted with CH_2Cl_2. The organic layer was washed with water. The organic layer was dried (Na_2SO_4), concentrated, and chromatographed [silica, CH_2Cl_2/MeOH (2→5%)], affording a pale yellow oil (1.19 g, 61%): IR (film, ν_{max} cm^{-1}) 3320, 1567; ^{1}H NMR δ 1.57−1.64 (m, 2H), 1.84−1.90 (m, 2H), 2.19 (m, 1H), 3.72 (s, 6H), 3.76 (s, 6H), 4.02 (q, J = 8.4 Hz, 4H), 4.28 (d, J = 5.1 Hz, 1H), 6.00−6.01 (m, 2H), 6.10−6.13 (m, 2H), 6.67−6.69 (m, 2H), 8.79 (br, 2H); ^{13}C NMR δ 31.16, 32.54, 32.62, 35.21, 40.76, 54.55, 54.65, 66.29, 106.85, 108.32, 117.22, 130.88; FAB-MS obsd 464.1480, calcd 464.1477 ($C_{18}H_{30}N_2O_8P_2$); Anal. C, H, N. Data for **5-(P/OH)**. TLC analysis of the crude mixture revealed the presence of a more polar component, which was isolated as an off-white oil: IR (film, ν_{max} cm^{-1}) 3320, 1566, 1450; ^{1}H NMR δ 1.45−1.87 (m, 4H), 2.44−2.46 (m, 1H), 3.66 (t, J = 5.1 Hz, 2H), 3.75 (s, 3H), 3.78 (s, 3H), 3.95−4.19 (m, 2H), 4.26 (d, J = 4.8 Hz, 1H), 6.03 (app s, 2H), 6.14 (app s, 2H), 6.68 (app s, 2H), 8.64 (br, 2H); ^{13}C NMR δ 33.07, 34.84, 35.23, 41.33, 54.67, 54.73, 61.02, 66.65, 66.71, 106.65, 106.96, 108.26, 108.34, 111.76, 117.08, 117.15, 131.27, 131.69; EI-MS 157/158, 230/231; FAB-MS obsd 356.2, calcd 356.2 ($C_{16}H_{25}N_2O_5P$); Anal. ($C_{16}H_{25}N_2O_5P\cdot 0.5CH_3OH$) C, H, N.

4-(*tert*-Butoxycarbonylmethoxy)benzaldehyde (6a). A solution of 4-hydroxybenzaldehyde (2.44 g, 20.0 mmol) in dry acetonitrile (8.0 mL) was treated with powdered, dried K_2CO_3 (3.04 g, 22.0 mmol) and NaI (304 mg, 2.00 mmol). The mixture was refluxed under argon for 30 min. *tert*-Butyl bromoacetate (1.48 mL, 1.95 g, 10.0 mmol) was added dropwise, and the reflux was continued for 12 h. Water and CH_2Cl_2 were added,

and the phases were separated. The aqueous layer was extracted with CH_2Cl_2. The organic phase was washed with water. The organic layer was dried (Na_2SO_4). Evaporation of the solvent and chromatography of the oily residue [silica, ethyl acetate/hexanes (3:7)] afforded a white, crystalline solid (2.18 g, 92%): mp 56−57 °C; IR (film, ν_{max} cm^{-1}) 1762, 1752, 1685, 1600; ^{1}H NMR δ 1.48 (s, 9H), 4.60 (s, 2H), 6.99 (d, J = 8.7 Hz, 2H), 7.84 (d, J = 8.7 Hz, 2H), 9.89 (s, 1H); ^{13}C NMR δ 28.25, 65.76, 83.17, 115.08, 130.82, 132.18, 163.00, 167.37, 190.98; EI-MS 105/107, 135, 193/194, 236/237; FAB-MS obsd 237.1120, calcd 237.1127 [(M + H)$^+$, M = $C_{13}H_{16}O_4$]; Anal. C, H.

5-[4-(*tert*-Butoxycarbonylmethoxy)phenyl]dipyrromethane (7a). Following a standard procedure (*40*), aldehyde **6a** (2.07 g, 8.78 mmol) was dissolved in dry pyrrole (56.0 mL, 880 mmol), and the solution was flushed with argon for 10 min. $InCl_3$ (666 mg, 0.800 mmol) was added, and the reaction was allowed to proceed for 3 h. The reaction was quenched by addition of powdered NaOH (977 mg, 24.4 mmol). The mixture was stirred for 45 min. The mixture was filtered. The filtrate was concentrated at reduced pressure. Chromatography [silica, ethyl acetate/CH_2Cl_2/hexanes (1:2:7)] afforded a pale yellow oil (2.73 g, 88%): IR (film, ν_{max} cm^{-1}) 1744, 1608; ^{1}H NMR δ 1.49 (s, 9H), 4.49 (s, 2H), 5.42 (s, 1H), 5.90 (app s, 2H), 6.15 (d, J = 2.7 Hz, 2H), 6.69 (app s, 2H), 6.83 (d, J = 9.0 Hz, 2H) 7.12 (d, J = 9.0 Hz, 2H), 7.93 (br, 2H); ^{13}C NMR δ 28.30, 43.35, 65.96, 82.66, 107.32, 108.61, 114.91, 117.40, 129.70, 132.96, 135.33, 157.13, 168.32; EI-MS 145, 229/230, 295/296, 352; FAB-MS obsd 352.1800, calcd 352.1787 ($C_{21}H_{24}N_2O_3$); Anal. H, N; C calcd, 71.57; found, 71.00.

5-[4-(*tert*-Butoxycarbonylmethoxy)phenyl]-1,9-diformyldipyrromethane (8a). Following a standard procedure (*42*), a solution of **7a** (2.66 g, 7.55 mmol) in DMF (7.53 mL) was cooled to 0 °C under argon, and phosphorus oxychloride (1.48 mL, 16.2 mmol) was added. The mixture was allowed to reach room temperature. Stirring was continued for 1 h. The solution was poured into aqueous sodium hydroxide (80 mL of 10 wt % solution) and was extracted into ethyl acetate (5 × 80 mL). The organic phases were combined, washed with water and brine, dried (Na_2SO_4), and concentrated. Chromatography [neutral alumina, CH_2Cl_2/MeOH (0.5→1%)] gave a pale brown solid (1.36 g, 45%): mp 84−85 °C (dec); IR (film, ν_{max} cm^{-1}) 1754, 1599; ^{1}H NMR δ 1.47 (s, 9H), 4.48 (s, 2H), 5.52 (s, 1H), 6.03 (d, J = 3.9 Hz, 2H), 6.81−6.85 (m, 4H), 7.15 (d, J = 8.4 Hz, 2H), 9.21 (s, 2H), 10.20−10.80 (br, 2H); ^{13}C NMR δ 28.48, 43.79, 65.94, 82.90, 111.64, 115.23, 12.36, 129.79, 132.90, 141.88, 162.82, 168.13, 179.17; FAB-MS obsd 408.1668, calcd 408.1685 ($C_{23}H_{24}N_2O_5$); Anal. H, N; C calcd, 67.63; found, 66.43.

Dibutyl[5-[4-(*tert*-butoxycarbonylmethoxy)phenyl]-1,9-diformyl-5,10-dihydrodipyrrinato]tin(IV) (8aSnBu$_2$). Following a standard method (*43*), a solution of **8a** (1.79 g, 4.39 mmol) in CH_2Cl_2 (3.6 mL) was treated with TEA (1.83 mL) and dibutyltin dichloride (1.33 g, 4.38 mmol). The solution was stirred at room temperature for 1 h. The reaction mixture was concentrated at reduced pressure. Chromatography [silica, CH_2Cl_2/TEA (99:1)] gave a dark orange oil (0.79 g, 28%): IR (film, ν_{max} cm^{-1}) 1753, 1599; ^{1}H NMR δ 0.70−0.79 (m, 6H), 1.10−1.57 (m, 23H), 4.46 (s, 2H), 5.46 (s, 1H), 6.11 (d, J = 3.3 Hz, 2H), 6.79 (d, J = 3.3 Hz, 2H), 7.03−7.06 (m, 2H), 9.15 (s, 2H); ^{13}C NMR δ 13.71, 13.78, 24.14, 24.56, 26.26, 26.50, 27.29, 27.33, 28.27, 66.01, 22.64, 82.60, 115.04, 124.11, 129.42, 136.85, 138.11, 152.52, 157.11, 168.21, 178.79; FAB-MS obsd 641.2004, calcd 641.2037 [(M + H)$^+$, M = $C_{31}H_{40}N_2O_5Sn$]; Anal. C, H, N.

5-[4-(*tert*-Butoxycarbonylmethoxy)phenyl]-1,9-bis(*N*-propylimino)dipyrromethane (9a). A solution of **8a** (1.49 g, 3.64 mmol) in THF (12 mL) was treated with propylamine (6.0 mL). The solution was stirred at room temperature for 1 h. The volatile components were evaporated. The crude product was dried at reduced pressure, affording a pale brown solid (quantitative): mp 119−121 °C; IR (film, ν_{max} cm^{-1}) 1755, 1639; ^{1}H NMR δ 0.88 (t, J = 7.5 Hz, 6H), 1.48 (s, 9H), 1.55−1.62 (m, 4H), 3.37 (t, J = 6.6 Hz, 4H), 4.47 (s, 2H), 5.36 (s, 1H), 5.88 (d, J = 3.6 Hz, 2H), 6.32 (d, J = 3.6 Hz, 2H), 6.81 (d, J = 8.7 Hz, 2H), 7.09 (d, J = 8.7 Hz, 2H), 7.88 (s, 2H); ^{13}C NMR δ 12.04, 24.51, 28.29, 43.76, 62.90, 66.01, 82.58, 109.31, 114.55, 114.96, 129.68, 130.39, 134.24, 136.73, 151.68, 157.21, 168.26, 20.98; FAB-MS obsd 491.3026, calcd. 491.3022 [(M + H)$^+$, M = $C_{29}H_{38}N_4O_3$]; Anal. C, H, N.

Zn(II) 5-[1,5-Bis(*tert*-butyldimethylsilyloxy)pent-3-yl]-15-[4-(*tert*-butoxycarbonylmethoxy)phenyl]porphyrin (Zn10a). A solution of **9a** (132 mg, 0.269 mmol) and **5** (142 mg, 0.298 mmol) in toluene (30.0 mL) was treated with $Zn(OAc)_2$ (550 mg, 3.00 mmol). The mixture was refluxed for 18 h open to the air. The toluene was evaporated. The residue was chromatographed (silica, CH_2Cl_2) to give a purple solid (62.0 mg, 24%): ^{1}H NMR δ −0.19 (s, 12H), 0.75 (s, 18H), 1.62 (s, 9H), 3.03−3.12 (m, 2H), 3.25−3.37 (m, 2H), 3.56−3.71 (m, 4H), 4.80 (s, 2H), 5.93 (m, 1H), 7.29−7.33 (m, 2H), 8.12−8.15 (m, 2H), 9.10−9.12 (m, 2H), 9.38−9.40 (m, 2H), 9.46−9.50 (m, 2H), 9.91 (d, J = 4.8 Hz, 1H), 10.04 (d, J = 5.1 Hz, 1H), 10.25 (s, 2H); LD-MS obsd 908.4; FAB-MS obsd 908.3694, calcd 908.3707 ($C_{49}H_{64}N_4O_5Si_2Zn$); λ_{abs} (log ϵ) 408 (4.64), 538 (3.68) nm; λ_{em} (λ_{exc} 408 nm) 580, 634 nm.

Zn(II) 5-(4-*tert*-Butoxycarbonylmethoxyphenyl)-15-(1,5-dihydroxypent-3-yl)porphyrin (Zn11a). A solution of **Zn10a** (48.7 mg, 0.0536 mmol) was dissolved in THF containing TBAF (3.0 mL of 1.0 M solution, water content ∼5%). The reaction mixture was cooled in an ice−water bath, and the reaction was allowed to proceed for 1 h. Then, the mixture was poured into ethyl acetate, and the organic phase was washed with water. The aqueous layer was extracted with ethyl acetate. The organic phase was washed with water and dried (Na_2SO_4). The sample was concentrated. Anhydrous zinc acetate (200 mg, 1.09 mmol) was added, and the mixture was stirred at room temperature for 15 min. Chromatography [neutral alumina, CH_2Cl_2/MeOH (2→10%)] afforded a bright purple solid (31.8 mg, 78%): ^{1}H NMR (THF-d_8) δ 1.53 (s, 9H), 2.95−2.99 (m, 2H), 3.19−3.24 (m, 2H), 3.48−3.52 (m, 4H), 4.74 (s, 2H), 5.71 (m, 1H), 7.21 (d, J = 7.8 Hz, 2H), 8.05 (d, J = 7.8 Hz, 2H), 8.95 (s, 2H), 9.24 (s, 2H), 9.32−9.33 (m, 2H), 9.69−9.70 (m, 1H), 9.80−9.81 (m, 1H), 10.06 (s, 2H); LD-MS obsd (−) 678.7; FAB-MS obsd 680.1963, calcd 680.1977 ($C_{37}H_{36}N_4O_5Zn$); λ_{abs} (log ϵ) 411 (5.22), 540 (4.34) nm; λ_{em} (λ_{exc} 411 nm) 583, 635 nm.

Zn(II) 5-(4-*tert*-Butoxycarbonylmethoxyphenyl)-15-[1,5-bis(dimethoxyphosphoryloxy)pent-3-yl]porphyrin (Zn12a). A solution of **9a** (211 mg, 0.431 mmol) and **5c** (200 mg, 0.431 mmol) in toluene (46 mL) was treated with anhydrous zinc acetate (0.810 g, 4.43 mmol). The mixture was refluxed open to the air for 18 h. The mixture was concentrated to dryness. The crude product was dried and chromatographed [silica, CH_2Cl_2/EtOAc (0→20%) then CH_2Cl_2/methanol (0→2%)], affording a deep red solid (87.0 mg, 22%): ^{1}H NMR δ 1.63 (s, 9H), 2.81−3.00 (m, 14H), 3.19−2.28 (m, 2H), 3.33−3.37 (m, 4H), 4.80 (s, 2H), 5.48−5.55 (m, 1H), 7.28−7.31 (m, 2H), 8.11−8.16 (m, 2H), 9.05−9.06 (m, 2H), 9.27−9.38 (m, 3H), 9.41−9.42 (m, 1H), 9.55−9.61 (m, 2H), 10.08 (s, 1H), 10.16 (s, 1H); LD-MS obsd 896.8; FAB-MS obsd 896.1970, calcd 896.1930 ($C_{41}H_{46}N_4O_{11}P_2Zn$); λ_{abs} (log ϵ) 412 (4.96), 541 (4.12) nm; λ_{em} (λ_{exc} 412 nm) 591, 638 nm.

5-[4-(Carboxymethoxy)phenyl]-15-[1,5-bis(dimethoxyphosphoryloxy)pent-3-yl]porphyrin (12a). A solution of **Zn12a** (41.9 mg, 0.0468 mmol) in CH_2Cl_2 (1.5 mL) was treated with

TFA (1.5 mL). The solution was stirred at room temperature for 3 h. The volatile components were evaporated. The dark green residue was dissolved in CH_2Cl_2. The solution was washed with water. The aqueous phase was extracted with CH_2Cl_2. The organic phase was washed with water, dried (Na_2SO_4), and concentrated, affording a dark green solid (29.6 mg, 76%): ^{1}H NMR δ 3.05−3.33 (m, 16H), 3.81−4.03 (m, 4H), 4.71 (s, 2H), 5.76 (m, 1H), 7.38 (d, J = 8.7 Hz, 2H), 8.02 (d, J = 8.7 Hz, 2H), 8.98−8.99 (m, 2H), 9.31−9.35 (m, 2H), 9.44−9.51 (m, 2H), 9.63−9.65 (m, 2H), 9.81−9.83 (m, 2H), 10.27 (s, 2H); LD-MS 778.6 $(M + H)^+$, 801.7 $(M + Na)^+$, 815.7 $(M + K)^+$; FAB-MS obsd 779.2247, calcd 779.2247 [$(M + H)^+$, M = $C_{37}H_{40}N_4O_{11}P_2$]; λ_{abs} 407, 505 nm; λ_{em} (λ_{exc} 407 nm) 635, 699 nm.

Cu(II) 5-(4-(Carboxymethoxy)phenyl)-15-[1,5-bis(dimethoxyphosphoryloxy)pent-3-yl]porphyrin (Cu12a). A solution of **12a** (16 mg, 0.021 mmol) in $CHCl_3$/CH_3OH (5.0 mL, 9:1 v/v) was treated with $Cu(OAc)_2 \cdot H_2O$ (42 mg, 0.21 mmol). The solution was stirred at room temperature for 12 h. Water was added to the reaction mixture. The phases were separated. The aqueous layer was extracted with CH_2Cl_2. The organic phase was washed with water, dried (Na_2SO_4), and concentrated, affording a dark orange solid (17 mg, 98%): LD-MS obsd 862.7, calcd 862.1 [$(M + Na)^+$, M = $C_{37}H_{38}CuN_4O_{11}P_2$]; λ_{abs} (log ϵ) 405 (4.47), 530 (2.50) nm.

5-(4-(Carboxymethoxy)phenyl)-15-[1,5-bis(dihydroxyphosphoryloxy)pent-3-yl]porphyrin (13a). A thoroughly dried sample of **12a** (11.8 mg, 0.0151 mmol) was dissolved in dry CH_2Cl_2 (2.0 mL) and then treated with TMS−Br (100 μL, 0.760 mmol). The reaction mixture was stirred at room temperature for 3 h under argon. The volatile components were evaporated at reduced pressure. The residue was dissolved in MeOH (3.0 mL). The solution was stirred for 1 h at room temperature. The volatile components were evaporated. The residue was dissolved in MeOH (3 mL). The solution was stirred for 1 h. The sample was concentrated. The solid residue was dissolved in ∼0.5 mL of dilute aqueous NaOH (0.1 M) and was diluted to ∼3 mL with water. The resulting solution was chromatographed [silica C-18, water/MeOH (0→50%)] to afford a dark red solid (8.20 mg, 76%): ^{1}H NMR (D_2O) δ 3.61 (m, 4H), 3.95 (m, 2H), 4.33 (m, 2H), 5.04 (s, 2H), 5.89 (m, 1H), 7.57 (d, J = 7.8 Hz, 2H), 7.94−7.97 (m, 2H), 8.91 (m, 2H), 9.28−9.34 (m, 2H), 9.78−9.82 (m, 2H), 10.24−10.33 (m, 4H); ESI-MS obsd (+) 362.1 $(M + 2H)^{2+}$, 723.1 $(M + H)^+$, 745.1 $(M + Na)^+$, (−) 721.1 $(M - H)^-$, calcd 722.15 (M = $C_{33}H_{32}N_4O_{11}P_2$); λ_{abs} 402, 506 nm; λ_{em} (λ_{exc} 402 nm) 628, 688 nm; HPLC t_R = 9.83 min.

Cu(II) 5-(4-(Carboxymethoxy)phenyl)-15-[1,5-bis(dihydroxyphosphoryloxy)pent-3-yl]porphyrin (Cu13a). A thoroughly dried sample of **Cu12a** (28.7 mg, 0.034 mmol) was dissolved in dry CH_2Cl_2 (1.5 mL) and then treated with TMS−Br (111 μL, 0.84 mmol). The reaction mixture was stirred at room temperature for 3 h under argon. The volatile components were evaporated at reduced pressure. The residue was dissolved in MeOH (3.0 mL). The solution was stirred for 1 h at room temperature. The mixture was concentrated. The solid residue was dissolved in ∼0.5 mL of dilute aqueous NaOH (0.1 M) and was diluted to ∼3 mL with water. Chromatography [silica C-18, water/MeOH (0→50%)] afforded an orange solid (12.2 mg, 12.2%, 46%): ESI-MS obsd (−) 782.4, 391.0, calcd 784.0, 391.5 [$(M - H)^-$, $(M - 2H)^{2-}$, M = $C_{33}H_{30}CuN_4O_{11}P_2$], also obsd 796.2 (M + methylene)$^+$; λ_{abs} 402, 530 nm.

5-(4-(*tert*-Butoxycarbonylmethoxy)phenyl)-15-(1,5-dibromopent-3-yl)porphyrin (14a). A sample of **Zn11a** was thoroughly dried by treatment overnight under vacuum (0.05 mmHg) at room temperature. Following a standard method (*44*), a solution of the dried sample of **Zn11a** (35.6 mg, 57 μmol) in dry CH_2Cl_2 (12 mL) was treated with CBr_4 (53.5 mg, 0.16 mmol). The solution was cooled in an ice−water bath for 10 min. Triphenylphosphine (84 mg, 0.32 mmol) was added. The solution was allowed to warm to room temperature. The reaction was allowed to proceed at room temperature for 12 h. Water was added, and the phases were separated. The aqueous phase was extracted with CH_2Cl_2. The organic phase was washed with water. The organic layer was dried (Na_2SO_4). Chromatography (silica, CH_2Cl_2) afforded a dark green solid (38.7 mg, 91%): ^{1}H NMR δ −2.86 (s, 1H), −2.82 (s, 1H), 1.64 (s, 9H), 3.24−3.39 (m, 6H), 3.65−3.75 (m, 2H), 4.85 (s, 2H), 5.83 (m, 1H), 7.35 (d, J = 8.1 Hz, 2H), 8.18 (d, J = 8.1 Hz, 2H), 9.08−9.11 (m, 2H), 9.37−9.60 (m, 5H), 9.98 (d, J = 4.2 Hz, 1H), 10.30 (s, 2H); LD-MS obsd 745.1; FAB-MS obsd 742.1166, calcd 742.1154 ($C_{37}H_{36}Br_2N_4O_3$); λ_{abs} (log ϵ) 407 (5.00), 503 (4.15) nm; λ_{em} (λ_{exc} 407 nm) 635, 701 nm.

5-(4-(*tert*-Butoxycarbonylmethoxy)phenyl)-15-[1,5-bis(dimethoxyphosphoryl)pent-3-yl]porphyrin (15a). A sample of **14a** (38.7 mg, 0.0521 mmol) was dissolved in $P(OCH_3)_3$ (10.0 mL). The solution was refluxed under argon for 1.5 days. The $P(OCH_3)_3$ was evaporated at reduced pressure. The residue was chromatographed [silica, CH_2Cl_2/MeOH (0→5%)] to yield a dark purple solid (24.6 mg, 65%): ^{1}H NMR δ 1.64 (s, 9H), 3.15 (m, 2H), 3.32−3.36 (m, 2H), 3.43 (s, 3H), 3.47 (s, 6H), 3.50 (s, 3H), 3.81−3.87 (m, 4H), 4.84 (s, 2H), 5.44 (m, 1H), 7.35 (d, J = 8.1 Hz, 2H), 8.17 (d, J = 8.1 Hz, 2H), 9.10 (s, 2H), 9.40 (s, 2H), 9.50−9.51 (m, 2H), 9.73−9.74 (m, 2H), 10.30−10.31 (m, 2H); LD-MS obsd 803.7; FAB-MS obsd 803.2983, calcd 803.2975 ($C_{41}H_{48}N_4O_9P_2$); λ_{abs} (log ϵ) 407 (4.90), 504 nm; λ_{em} (λ_{exc} 407 nm) 636 nm, 702 nm. Varying amounts of a less polar purple solid (**15a-Br**) were isolated along with small amounts of the starting material **14a** (limited characterization). Data for **15a-Br**: ^{1}H NMR δ 0.86−0.95 (m, 1H), 1.65 (s, 9H), 1.91−2.00 (m, 1H), 3.13−3.40 (m, 6H), 3.44 (s, 3H), 3.48 (s, 3H), 3.55−3.85 (m, 2H), 4.83 (s, 2H), 5.51−5.61 (m, 1H), 7.34 (d, J = 8.1 Hz, 2H), 8.17 (d, J = 8.1 Hz, 2H), 9.08−9.10 (m, 2H), 9.37−9.41 (m, 2H), 9.49−9.51 (m, 2H), 9.67−9.68 (m, 1H), 9.84−9.85 (m, 1H), 10.30 (s, 2H); LD-MS obsd 773.6, calcd 773.2 [$(M + H)^+$, M = $C_{39}H_{42}BrN_4O_6P_2$]; λ_{abs} 407, 502 nm; λ_{em} (λ_{exc} 407 nm) 634, 702 nm.

5-(4-(Carboxymethoxy)phenyl)-15-[1,5-bis(dihydroxyphosphoryl)pent-3-yl]porphyrin (16a). A solution of **15a** (19 mg, 0.024 mmol) in anhydrous $CHCl_3$ (2 mL) was flushed with argon for 10 min. Bromotrimethylsilane (400 μL, 3.03 mmol) was added, and the solution was refluxed for 4 h. The reaction mixture was allowed to cool to room temperature. The volatile components were evaporated. The residue was dissolved in MeOH (3 mL). The solution was stirred at room temperature for 1 h. The volatile components were evaporated. Aqueous NaOH (0.3 mL, 0.1 M) was added. The mixture was diluted to ∼3 mL with distilled water. The resulting solution was chromatographed (C-18 silica, H_2O/MeOH gradient) to yield a red solid (9.8 mg, 58%): ^{1}H NMR (D_2O) δ 1.31−1.36 (m, 2H), 2.10−2.15 (m, 2H), 3.16−3.62 (m, 4H), 5.03 (s, 2H), 5.60−5.72 (m, 1H), 7.55−7.60 (m, 2H), 7.82−7.96 (m, 2H), 8.82−8.94 (m, 2H), 9.32−9.40 (m, 2H), 9.84−9.93 (m, 2H), 10.35−10.48 (m, 4H); ESI-MS obsd 691.1 $(M + H)^+$, 346.1 $(M + 2H)^{2+}$, 713.2 $(M + Na)^+$, calcd 690.2 (M = $C_{33}H_{32}N_4O_9P_2$); λ_{abs} (H_2O) 402, 506 nm; λ_{em} (λ_{exc} 402 nm) 627, 688 nm; HPLC t_R = 9.37 min.

Zn(II) 5-(4-(Carboxymethoxy)phenyl)-15-[1,5-bis(dihydroxyphosphoryl)pent-3-yl]porphyrin (Zn16a) (by in Situ Metalation of 16a). A solution of **15a** (10.4 mg, 0.013 mmol) in anhydrous $CHCl_3$ (2 mL) was flushed with argon for 10 min. Bromotrimethylsilane (300 μL, 2.27 mmol) was added, and the solution was refluxed for 4 h. The reaction mixture was allowed to cool to room temperature. The volatile components were evaporated. The residue was dissolved in MeOH (2 mL). The

solution was stirred at room temperature for 1 h. The solvent was evaporated. Aqueous NaOH (0.3 mL, 15 wt %) was added. The sample was diluted with distilled water (3 mL). The mixture was treated with $Zn(OAc)_2$ (55 mg, 0.301 mmol) for 1 h. A second portion of aqueous NaOH (0.3 mL, 15 wt %) was added. The resulting solution was chromatographed [C-18 silica, water/MeOH (0→50%)] to yield a bright purple solid (9.1 mg, 93%): ^{1}H NMR (D_2O) δ 1.17−1.30 (m, 2H), 2.01−2.15 (m, 2H), 3.38−3.49 (m, 4H), 5.05 (s, 2H), 5.72 (s, 1H), 7.74 (d, J = 6.9 Hz, 2H), 8.37 (d, J = 6.9 Hz, 2H), 9.33 (app s, 2H), 9.71 (app s, 2H), 9.85−9.95 (m, 2H), 10.36−10.38 (m, 1H), 10.44−10.46 (m, 1H), 10.57 (s, 1H), 10.60 (s, 1H); ESI-MS obsd 376.9 $(M + 2H)^{2+}$, 753.0 $(M + H)^+$, 774.9 $(M + Na)^+$, calcd 752.0779 ($M = C_{33}H_{30}N_4O_9P_2Zn$); λ_{abs} (H_2O) 409, 544 nm; λ_{em} (λ_{exc} 409 nm) 590, 641 nm; HPLC t_R = 9.83 (27%), 12.10 (73%) min.

5-(4-Bromophenyl)dipyrromethane (7b). This compound was previously prepared by a less efficient method (*45*). Following a standard procedure (*40*), 4-bromobenzaldehyde (5.55 g, 30.0 mmol) was dissolved in dry pyrrole (208 mL, 3.00 mol), and the solution was flushed with argon for 10 min. $InCl_3$ (666 mg, 3.00 mmol) was added, and the reaction was allowed to proceed for 90 min. The reaction was quenched by addition of powdered NaOH (3.60 g, 90.0 mmol). The mixture was stirred for 45 min. The mixture was filtered. The filtrate was concentrated at reduced pressure. Chromatography [silica, ethyl acetate/CH_2Cl_2/hexanes (1:2:7)] afforded a pale yellow solid (8.29 g, 92%): mp 120−122 °C; IR (film, ν_{max} cm^{-1}) 1487; ^{1}H NMR δ 5.43 (s, 1H), 5.88−5.89 (m, 2H), 6.15−6.16 (m, 2H), 6.70−6.71 (m, 2H), 7.06−7.08 (m, 2H), 7.42−7.44 (m, 2H), 7.88−7.93 (br, 2H); ^{13}C NMR δ 43.66, 107.65, 108.80, 112.61, 117.73, 121.08, 130.36, 131.92, 141.40; EI-MS 145, 234/236, 300/302; FAB-MS obsd 300.0257, calcd 300.0262 ($C_{15}H_{13}BrN_2$); Anal. C, H, N.

5-(4-Bromophenyl)-1,9-diformyldipyrromethane (8b). Following a standard procedure (*42*), a solution of **7b** (1.51 g, 5.00 mmol) in DMF (5.00 mL) was cooled to 0 °C under argon, and phosphorus oxychloride (980 μL) was added. The mixture was allowed to reach room temperature. Stirring was continued for 1 h. The solution was poured into aqueous sodium hydroxide (50 mL of 10 wt % solution) and was extracted into ethyl acetate (5 × 50 mL). The organic phases were combined, washed with water and brine, dried (Na_2SO_4), and chromatographed [neutral alumina, CH_2Cl_2/MeOH (0.5→1%)] to afford a pale brown solid (1.43 g, 80%): mp 79−80 °C (dec); IR (film, ν_{max} cm^{-1}) 1645, 1485; ^{1}H NMR δ 5.54 (s, 1H), 6.03−6.05 (m, 2H), 6.85−6.87 (m, 2H), 7.17 (d, J = 7.1 Hz, 2H), 7.46 (d, J = 7.1 Hz, 2H), 9.18 (s, 2H), 10.60−10.70 (br, 2H); ^{13}C NMR δ 44.14, 112.07, 121.89, 122.68, 130.48, 132.27, 132.93, 138.63, 141.61, 179.37; FAB-MS obsd 356.0173, calcd 356.0160 ($C_{17}H_{13}BrN_2O_2$); Anal. C, H, N.

Dibutyl[5-(4-bromophenyl)-1,9-diformyl-5,10-dihydrodipyrrinato]tin(IV) (8bSnBu$_2$). Following a standard procedure (*43*), a solution of **8b** (1.55 g, 4.35 mmol) in CH_2Cl_2 (3.5 mL) was treated with TEA (1.82 mL) and dibutyltin dichloride (1.32 g, 4.34 mmol). The solution was stirred at room temperature for 1 h. The reaction mixture was concentrated at reduced pressure. Chromatography [silica, CH_2Cl_2/TEA (99:1)] gave a crystalline pink solid (0.410 g, 16%): mp 115−117 °C; IR (film, ν_{max} cm^{-1}) 1601; ^{1}H NMR δ 0.70−0.80 (m, 6H), 1.12−1.59 (m, 12H), 5.49 (s, 1H), 6.13 (d, J = 3.9 Hz, 2H), 7.00 (d, J = 8.1 Hz, 2H), 7.06 (d, J = 3.9 Hz, 2H), 7.39 (d, J = 8.1 Hz, 2H), 9.17 (s, 2H); ^{13}C NMR δ 13.72, 13.79, 24.16, 24.70, 26.25, 27.27, 27.37, 44.83, 112.62, 115.63, 121.09, 124.12, 130.01, 132.05, 138.24, 142.88, 151.45, 179.09; FAB-MS obsd 589.0500, calcd. 589.0513 [$(M + H)^+$, $M = C_{25}H_{29}BrN_2O_2Sn$]; Anal. C, H, N.

5-(4-Bromophenyl)-1,9-bis(*N*-propylimino)dipyrromethane (9b). Following a standard procedure (*42*), a solution of **8b** (488 mg, 1.37 mmol) in THF (4.6 mL) was treated with propylamine (2.25 mL, 27.4 mmol). The solution was stirred at room temperature for 1 h. The volatile components were evaporated, and the crude product was dried at reduced pressure, affording a pale brown solid: mp 136−138 °C; IR (film, ν_{max} cm^{-1}) 1634, 1485; ^{1}H NMR δ 0.85−0.89 (m, 6H), 1.52−1.55 (m, 4H), 3.31−3.39 (m, 4H), 5.36 (s, 1H), 5.88 (app s, 2H), 6.34 (app s, 2H), 7.05 (d, J = 7.1 Hz, 2H), 7.40 (d, J = 7.1 Hz, 2H), 7.90 (s, 2H), 8.80−9.05 (br, 2H); ^{13}C NMR δ 12.04, 24.53, 44.00, 62.77, 109.44, 114.62, 121.10, 130.35, 130.69, 131.74, 136.07, 140.59, 151.84; FAB-MS obsd 439.1503, calcd 439.1497 [$(M + H)^+$, $M = C_{23}H_{27}BrN_4$]; Anal. C, H, N.

Zn(II) 5-(4-Bromophenyl)-15-[1,5-bis(*tert*-butyldimethylsilyloxy)pent-3-yl] porphyrin (Zn10b). A solution of **9b** (132 mg, 0.269 mmol) and **5a** (142 mg, 0.298 mmol) in toluene (30.0 mL) was treated with $Zn(OAc)_2$ (550 mg, 3.00 mmol). The mixture was refluxed for 18 h open to the air. The mixture was concentrated, and the resulting residue was chromatographed (silica, CH_2Cl_2) to give a purple solid (62.0 mg, 24%): ^{1}H NMR δ −0.07 (s, 12H), 0.96 (s, 18H), 3.13−3.15 (m, 2H), 3.37−3.44 (m, 2H), 3.67−3.81 (m, 4H), 6.03 (m, 1H), 7.82−7.90 (m, 4H), 8.78−8.80 (m, 2H), 9.04−9.10 (m, 2H), 9.39−9.42 (m, 1H), 9.48−9.50 (m, 2H), 9.93−9.97 (m, 2H), 10.05−10.14 (m, 2H); ^{13}C NMR δ −0.11, 23.45, 23.80, 31.50, 43.96, 50.83, 67.50, 111.18, 111.46, 116.12, 123.12, 127.61, 129.08, 135.31, 136.46, 137.19, 137.34, 141.40, 147.07, 152.87, 154.27, 154.68, 155.94, 155.12, 155.52, 157.57, 174.92; LD-MS obsd 853.7; FAB-MS obsd 856.2232, calcd 856.2182 ($C_{43}H_{53}BrN_4O_2Si_2Zn$); λ_{abs} 409, 539 nm; λ_{em} (λ_{exc} 409 nm) 578, 633 nm.

Zn(II) 5-(4-Bromophenyl)-15-(1,5-dihydroxypent-3-yl)porphyrin (Zn11b). A sample of **Zn10b** (54 mg, 0.063 mmol) was dissolved in dry THF (1.26 mL) containing 1.0 M TBAF (1.3 mmol, 10.0 equiv), and the reaction mixture was stirred overnight at room temperature. The THF was evaporated. The residue was dissolved in ethyl acetate. The solution was washed with water. The aqueous layer was extracted with ethyl acetate. The organic phase was washed with water and brine, dried over Na_2SO_4, and concentrated. LD-MS indicated demetalation (obsd *m*/*z* 563), whereupon the solid was dissolved in $CHCl_3$/MeOH (10 mL, 9:1) and $Zn(OAc)_2$ (195 mg, mmol) was added. The mixture was stirred at room temperature for 1 h. The mixture was concentrated and chromatographed [neutral alumina, CH_2Cl_2/methanol (2→10%)], affording a bright red solid (34.5 mg, 87%): ^{1}H NMR (THF-d_8) δ 3.04−3.10 (m, 2H), 3.24−3.28 (m, 2H), 3.28−3.62 (m, 4H), 5.96 (m, 1H), 7.95 (d, J = 8.1, 2H), 8.14 (d, J = 8.1 Hz, 2H), 8.98−8.99 (m, 2H), 9.37−9.38 (m, 2H), 9.42−9.46 (m, 2H), 9.93 (d, J = 4.5 Hz, 1H), 10.05 (d, J = 4.5 Hz, 1H), 10.19−10.20 (m, 2H); LD-MS obsd 627.2 $(M - H)^-$; FAB-MS obsd 628.0424, calcd 628.0452 ($C_{31}H_{25}BrN_4O_2Zn$); λ_{abs} (CH_2Cl_2/MeOH, 97.5:2.5) (log ϵ) 408 (4.89), 538 nm; λ_{em} (λ_{exc} 408 nm) 589, 643 nm.

Zn(II) 5-(4-Bromophenyl)-15-[1,5-bis(dimethoxyphosphoryloxy)pent-3-yl]porphyrin (Zn12b). Method A: A solution of **Zn11b** (30.0 mg, 0.048 mmol) in dry pyridine (1.0 mL) was cooled in an ice−water bath. Dimethyl chlorophosphate (168 μL, 225 mg, 1.56 mmol) was added, and stirring was continued with cooling for 2 h. The reaction mixture was allowed to reach room temperature. The reaction was allowed to proceed for a further 12 h. The sample was poured into CH_2Cl_2 and was washed with brine. The aqueous layer was extracted with CH_2Cl_2. The organic phase was washed with brine and dried (Na_2SO_4). LD-MS analysis of the crude mixture indicated partial demetalation (obsd *m*/*z* 782), whereupon the residue was dissolved in $CHCl_3$/MeOH (15 mL, 9:1) and $Zn(OAc)_2$ (230 mg, 1.26 mmol) was added. The mixture was stirred at room temperature for 2 h. Chromatography [silica,

CH_2Cl_2/methanol (1→2%)] afforded a deep red solid (12.5 mg, 30%): ^{1}H NMR δ 2.75 (s, 3H), 2.78 (s, 3H), 2.84 (s, 3H), 2.88 (s, 3H), 3.18 (m, 6H), 2.75−2.88 (m, 2H), 5.42 (m, 1H), 7.90 (d, J = 8.1 Hz, 2H), 8.07 (d, J = 8.1 Hz, 2H), 9.00−9.02 (m, 2H), 9.26−9.62 (m, 6H), 10.09 (s, 1H), 10.21 (s, 1H); LD-MS obsd 842.5; FAB-MS obsd 844.0444, calcd 844.0405 ($C_{35}H_{35}BrN_4O_8P_2Zn$); λ_{abs} (log ϵ) 411 (4.92), 541 (4.01) nm; λ_{em} (λ_{exc} 411 nm) 587, 636 nm.

Method B: A solution of **9b** (247 mg, 0.50 mmol) and **5c** (247 mg, 0.53 mmol) in toluene (58 mL) was treated with anhydrous zinc acetate (1.03 g, 5.65 mmol). The mixture was refluxed open to the air for 18 h. The mixture was concentrated, dried, and chromatographed [silica, CH_2Cl_2/methanol (0→2%)], affording a deep red solid (95.5 mg, 21%) with the same physical properties (^{1}H NMR, LD-MS, λ_{abs}) as the sample obtained by method A.

5-(4-Bromophenyl)-15-[1,5-bis(dimethoxyphosphoryloxy)-pent-3-yl]porphyrin (12b). A solution of **Zn12b** (50.6 mg, 0.0600 mmol) in CH_2Cl_2 (2 mL) was treated with TFA (2 mL). The solution was stirred at room temperature for 30 min. The volatile components were evaporated. The dark green residue was dissolved in CH_2Cl_2. The solution was washed with water. The aqueous phase was extracted with CH_2Cl_2. The organic phases were combined and washed with water. The organic layer was dried (Na_2SO_4). Chromatography [silica, CH_2Cl_2/MeOH (97:3)] afforded a deep purple solid (46.0 mg, 98%): ^{1}H NMR δ 3.22−3.24 (m, 2H), 3.42−3.51 (m, 2H), 3.90−3.99 (m, 14H), 4.01−4.11 (m, 2H), 5.75−5.92 (m, 1H), 7.94−7.96 (m, 2H), 8.11−8.13 (m, 2H), 9.00−9.05 (m, 2H), 9.38−9.43 (m, 2H), 9.45−9.52 (m, 2H), 9.67−9.68 (m, 1H), 9.84−9.85 (m, 1H), 10.30 (s, 1H), 10.32 (s, 1H); LD-MS obsd (−) 782.8; FAB-MS obsd 782.1257, calcd 782.1270 ($C_{35}H_{37}BrN_4O_8P_2$); λ_{abs} 405, 504 nm; λ_{em} (λ_{exc} 405 nm) 635, 700 nm.

Cu(II) 5-(4-Bromophenyl)-15-[1,5-bis(dimethoxyphosphoryloxy)pent-3-yl]porphyrin (Cu12b). A solution of **12b** (16.5 mg, 0.0211 mmol) in $CHCl_3$/CH_3OH (5 mL, 9:1 v/v) was treated with $Cu(OAc)_2 \cdot H_2O$ (42.0 mg, 0.231 mmol). The solution was stirred at room temperature for 12 h. The volatile components were evaporated, and the residue was suspended in a small volume of CH_2Cl_2. Chromatography [silica, CH_2Cl_2/MeOH (95:5)] afforded an orange solid (17.6 mg, 99%): LD-MS obsd 846.7 $(M + H)^+$; FAB-MS obsd 843.0443, calcd 843.0410 ($C_{35}H_{35}BrCuN_4O_8P_2$); λ_{abs} 405, 504 nm.

5-(4-Bromophenyl)-15-(1,5-bis[dihydroxyphosphoryloxy)-pent-3-yl]porphyrin (13b). A thoroughly dried sample of **12b** (23 mg, 0.031 mmol) was dissolved in dry CH_2Cl_2 (1.0 mL) and then treated with TMS−Br (25 μL, 0.19 mmol). The reaction mixture was stirred at room temperature for 3 h under argon. The volatile components were evaporated at reduced pressure. The residue was dissolved in MeOH (3.0 mL). The solution was stirred for 1 h at room temperature. The methanol was evaporated. The resulting solid was dissolved in aqueous NaOH (0.3 mL, 0.1 M) and diluted to ∼3 mL with water. The solution was chromatographed [silica C-18, water/MeOH (0→50%)] to afford a red solid (9.6 g, 43%): ^{1}H NMR (D_2O) δ 3.63−3.68 (m, 4H), 3.67−3.99 (m, 2H), 4.30−4.35 (m, 2H), 5.91−5.96 (m, 1H), 7.40 (d, J = 6.3 Hz, 2H), 7.75 (d, J = 6.3 Hz, 2H), 8.44−8.51 (m, 2H), 8.99−9.02 (br, 1H), 9.13−9.16 (br, 1H), 9.79−9.87 (m, 2H), 10.15−10.18 (m, 1H), 10.33−10.40 (m, 3H); ESI-MS obsd (+) 726.3 $(M + H)^+$, 748.8 $(M + Na)^+$, (−) 724.9 $(M - H)^-$, calcd 726.1 ($M = C_{31}H_{29}BrN_4O_8P_2$); λ_{abs} (H_2O) 400, 504 nm; λ_{em} (λ_{exc} 400 nm) 624, 686 nm; HPLC t_R = 13.80 min.

Cu(II) 5-(4-Bromophenyl)-15-[1,5-bis(dihydroxyphosphoryloxy)pent-3-yl]porphyrin (Cu13b). A thoroughly dried sample of **Cu12b** (16.5 mg, 0.019 mmol) was dissolved in dry CH_2Cl_2 (800 μL) and then treated with TMS−Br (18 μL, 0.136 mmol). The reaction mixture was stirred at room temperature for 3 h under argon. The solvents were evaporated at reduced pressure. The residue was dissolved in MeOH (3.0 mL). The solution was stirred for 1 h at room temperature. The methanol was evaporated. The resulting solid was dissolved in aqueous NaOH (0.3 mL, 0.1 M) and diluted to ∼3 mL with water. The solution was concentrated and chromatographed [silica C-18, water/MeOH (0→50%)] to afford a red solid (10.1 mg, 68%): ESI-MS (−) obsd 786.1 $(M - H)^-$, calcd 787.0 ($M = C_{31}H_{27}BrCuN_4O_8P_2$), also obsd 800.1 (M + methylene)$^+$, 814.2 (M + 2methylene)$^+$; λ_{abs} (H_2O) 400, 528 nm.

5-(4-Bromophenyl)-15-(1,5-dibromopent-3-yl)porphyrin (14b). A sample of **Zn11b** was thoroughly dried by treatment overnight under vacuum (0.05 mmHg) at room temperature. Following a standard method (*44*), a solution of the dried sample of **Zn11b** (52 mg, 83 μmol) in dry CH_2Cl_2 (20 mL) was treated with CBr_4 (84 mg, 0.25 mmol). The solution was cooled in an ice−water bath for 10 min. Triphenylphosphine (132 mg, 0.504 mmol) was added. The solution was allowed to warm to room temperature. Water was added, and the phases were separated. The aqueous phase was extracted with CH_2Cl_2. The organic phase was washed with water. The organic layer was dried (Na_2SO_4). Chromatography (silica, CH_2Cl_2) afforded a dark green solid (44.5 mg, 78%): ^{1}H NMR δ −2.90 (s, 1H), −2.85 (s, 1H), 0.86−0.95 (m, 2H), 3.17−3.39 (m, 6H), 3.65−3.74 (m, 2H), 5.81−5.94 (m, 1H), 7.94 (d, J = 8.1 Hz, 2H), 8.11 (d, J = 8.1 Hz, 2H), 9.02−9.06 (m, 2H), 9.36−9.42 (m, 2H), 9.45−9.47 (m, 1H), 9.51−9.52 (m, 1H), 9.58−9.60 (m, 1H), 9.99 (d, J = 4.8 Hz, 1H), 10.30 (s, 2H); LD-MS 688.1; FAB-MS obsd 690.9700, calcd 690.9708 ($C_{31}H_{25}N_4Br_3$); λ_{abs} (log ϵ) 406 (4.96), 503 (4.01) nm; λ_{em} (λ_{exc} 407 nm) 633, 700 nm.

5-(4-Bromophenyl)-15-[1,5-bis(dimethoxyphosphoryl)pent-3-yl]porphyrin (15b). A solution of **14b** (33 mg, 0.047 mmol) was dissolved in $P(OCH_3)_3$ (8.0 mL). The solution was refluxed under argon for 2.5 days. The $P(OCH_3)_3$ was evaporated. The residue was chromatographed [silica, CH_2Cl_2/MeOH (0→5%)] to yield a dark purple solid (26 mg, 72%): ^{1}H NMR δ −2.93 (s, 1H), −2.85 (s, 1H), 1.35−1.42 (m, 2H), 1.86−2.03 (m, 2H), 3.12−3.50 (m, 16H), 5.30−5.46 (m, 1H), 7.95 (d, J = 8.1 Hz, 2H), 8.12 (d, J = 8.1 Hz, 2H), 9.04−9.05 (m, 2H), 9.41−9.51 (m, 4H), 9.74−9.75 (m, 2H), 10.31−10.33 (m, 2H); LD-MS obsd 749.1 $(M - H)^-$; FAB-MS obsd 751.1454, calcd 751.1450 [$(M + H)^+$, $M = C_{35}H_{37}BrN_4O_6P_2$); λ_{abs} 406, 503 nm; λ_{em} (λ_{exc} 406 nm) 633, 699 nm. Varying amounts of a less polar purple solid (**15b-Br**) were isolated along with small amounts of the starting material **14b** (limited characterization). Data for **15b-Br**: ^{1}H NMR δ 0.74−0.99 (m, 2H), 3.14−3.41 (m, 6H), 3.45 (s, 3H), 3.49 (s, 3H), 3.69−3.80 (m, 2H), 5.63−5.63 (m, 1H), 7.95 (d, J = 7.5 Hz, 2H), 8.12 (d, J = 7.5 Hz, 2H), 9.04−9.05 (m, 2H), 9.39−9.42 (m, 2H), 9.49−9.52 (m, 2H), 9.69 (d, J = 4.2 Hz, 1H), 9.86 (d, J = 4.2 Hz, 1H), 10.31−10.32 (m, 2H); LD-MS obsd 718.3, calcd 720.1 ($C_{33}H_{31}Br_2N_4O_3P$); λ_{abs} 406, 502 nm; λ_{em} (λ_{exc} 406 nm) 633, 699 nm.

5-(4-Bromophenyl)-15-[1,5-bis(dihydroxyphosphoryl)pent-3-yl]porphyrin (16b). A solution of **15b** (11 mg, 0.015 mmol) in anhydrous $CHCl_3$ (2 mL) under argon was treated with TMS−Br (300 μL, 2.27 mmol). The sample was refluxed for 4 h. The mixture was concentrated, and the residue was dissolved in MeOH (3 mL). The mixture was stirred for 1 h. Evaporation of the solvent yielded a dark green solid, which was dissolved in dilute aqueous NaOH. Chromatography (C-18 silica, water/MeOH gradient) yielded a dark red solid (6.1 mg, 60%): ^{1}H NMR (D_2O) δ 0.88−0.97 (m, 2H), 1.70−1.84 (m, 2H), 2.96−3.08 (m, 2H), 3.09−3.24 (m, 2H), 5.21−5.33 (m, 1H), 6.80−6.87 (br, 2H), 7.26−7.38 (br, 2H), 7.91−7.95 (m, 2H), 8.36−8.40 (br, 1H), 8.52−8.61 (br, 1H), 9.35 (br, 1H), 9.48 (br, 1H), 9.62 (br, 1H), 9.82 (br, 1H), 9.95 (s, 1H), 10.03 (s, 1H); LD-

MS obsd 693.8, ESI-MS obsd 695.0 $(M + H)^+$, 717.0 $(M + Na)^+$, 348.0 $(M + 2H)^{2+}$, calcd 694.1 ($M = C_{31}H_{29}BrN_4O_6P_2$); λ_{abs} (H_2O) 400, 504 nm; λ_{em} (λ_{exc} 400 nm) 625, 687 nm; HPLC $t_R = 13.48$ min.

Zn(II) 5-(4-Bromophenyl)-15-[1,5-bis(dihydroxyphosphoryl)pent-3-yl]porphyrin (Zn16b). A solution of **15b** (18.9 mg, 0.025 mmol) in anhydrous $CHCl_3$ (2 mL) under argon was treated with TMS−Br (200 μL, 1.51 mmol). The reaction mixture was refluxed for 4 h. The volatile components were evaporated, and the residue was dissolved in MeOH (3 mL). The mixture was stirred for 1 h. The mixture was treated with aqueous NaOH (0.2 mL of 15 wt % solution). $Zn(OAc)_2 \cdot 2H_2O$ (125 mg, 0.57 mmol) was added, and stirring was continued for 1 h. The mixture was concentrated, treated with 0.1 mL of aqueous NaOH followed by 3 mL of water, and chromatographed [C-18 silica, water/MeOH (0→50%)], affording a deep purple solid (7.7 mg, 41%): ^{1}H NMR (D_2O) δ 0.72 (dd, $J_1 = 13.2$ Hz, $J_2 = 15.6$ Hz, 2H), 1.64 (dd, $J_1 = 14.4$ Hz, $J_2 = 14.1$ Hz, 2H), 2.96−3.22 (br, 4H), 5.36 (br, 1H), 7.65−7.74 (m, 4H), 8.76 (m, 2H), 9.17 (m, 1H), 9.49 (m, 1H), 9.53 (m, 1H), 10.01 (m, 1H), 10.09 (m, 1H), 10.14 (m, 1H), 10.20 (m, 1H); ESI-MS obsd 755.7 $(M + H)^+$, 380.2 $(M + 2H)^{2+}$, calcd 756.0 ($M = C_{31}H_{27}BrN_4O_6P_2Zn$); λ_{abs} 409, 542 nm; λ_{em} (λ_{exc} 409 nm) 589, 640 nm; HPLC $t_R = 9.86$ (17%), 15.51 (83%) min.

***meso*-Tetrakis[1,5-bis(*tert*-butyldimethylsilyloxy)pent-3-yl]porphyrin (17).** Following a standard procedure (*34*), a solution of **4** (360 mg, 1.00 mmol) and pyrrole (70.0 μL, 1.00 mmol) in $CHCl_3$ (100 mL) was treated with NaCl (1.46 g, 25.0 mmol). The mixture was flushed with argon for 10 min. The reaction was initiated with $BF_3 \cdot OEt_2$ (41 μL, 0.30 mmol). Stirring was continued overnight. DDQ (172 mg, 0.758 mmol) was added, and the reaction mixture was stirred for 1 h. The solvent was removed at reduced pressure. Chromatography [silica, hexanes/CH_2Cl_2 (1:1)] yielded a dark purple solid (41 mg, 10%): ^{1}H NMR δ −2.46 (br, 2H), −0.15 (s, 48H), 0.86 (s, 72H), 2.88−2.92 (m, 8H), 3.11−3.16 (m, 8H), 3.61−3.69 (m, 16H), 5.57 (m, 4H), 9.49 (m, 4H), 9.66 (m, 4H); ^{13}C NMR δ −0.00, 23.72, 31.45, 35.18, 45.22, 50.33 (br), 67.33, 116.15, 174.86; LD-MS 1631.9; FAB-MS obsd 1631.0, calcd 1631.1 ($C_{88}H_{166}N_4O_8Si_8$); λ_{abs} 421, 522 nm; λ_{em} (λ_{exc} 421 nm) 665, 732 nm.

Zn(II) *meso*-Tetrakis[1,5-bis(*tert*-butyldimethylsilyloxy)pent-3-yl]porphyrin (Zn17). A solution of **17** (20 mg, 0.012 mmol) in $CHCl_3$/MeOH (5 mL, 9:1) was treated with $Zn(OAc)_2 \cdot 2H_2O$ (100 mg, 0.5 mmol). The reaction mixture was stirred at room temperature for 2 h. The volatile components were evaporated. Chromatography (silica, CH_2Cl_2) afforded a dark red solid (15.6 mg, 78%): ^{1}H NMR δ −0.19 (s, 48H), 0.84 (s, 72H), 2.92−2.98 (m, 8H), 3.17−3.21 (m, 8H), 3.61−3.68 (m, 16H), 5.65 (m, 4H), 9.49 (m, 4H), 9.66−9.68 (m, 4H); LD-MS 1686.9; FAB-MS obsd 1695.0, calcd 1692 ($C_{88}H_{164}N_4O_8Si_8Zn$); λ_{abs} 422, 556 nm; λ_{em} (λ_{exc} 422 nm) 606, 657 nm.

16a−anti-CD3ϵ. A mixture of **16a** (1.50 mg, 2.17 μmol) and EDCI (4.13 mg, 21.6 μmol) in PBS (50 μL) was added to a solution of IgG1 anti-human CD3 intracellular ϵ-chain (clone UCHT) (*39*) (125 μg in 50 μL PBS). The reaction was allowed to proceed at room temperature for 2 h. PBS (2.4 mL) was added to the reaction mixture, and the conjugate was isolated by chromatography (PD-10 size exclusion column, 1 mL fractions, PBS). The antibody conjugate was characterized by sodium dodecyl sulfate−polyacrylamide gel electrophoresis in a 5% nonreducing gel giving a single red fluorescent band migrating at 150 kDa. Absorption spectroscopy comparing predominant absorption by the antibody ($\lambda_{280\ nm}$) and porphyrin absorption ($\lambda_{410\ nm}$) indicated an average labeling efficiency of approximately two porphyrins per antibody.

Biological Experiments. Jurkat cells (human T-cell lymphoma, ATCC no. TIB-152) and murine Lewis lung carcinoma (LLC) cells (ATCC no. CRL-1642) were cultured in RPMI with L-glutamine and $NaHCO_3$ supplemented with 10% heat inactivated fetal bovine serum and penicillin (100 U/mL) and streptomycin (100 μg/mL) (all from Sigma, St Louis, MO) at 37 °C in a 5% CO_2 humidified atmosphere in 75 cm^3 tissue culture flasks (BD Falcon, Franklin Lakes, NJ). On the day of the experiment, when cells reached 80% confluence, the cells were washed with phosphate-buffered saline (PBS). The LLC cells were harvested with 2 mL of 0.25% trypsin−EDTA solution (Sigma), centrifuged, and counted with a hemocytometer, then resuspended in Cytofix/Cytoperm solution (BD Biosciences) and incubated for 30−40 min at 4 °C to permeabilize the membranes. The cells were washed twice in perm/wash buffer (BD Biosciences) and incubated at room temperature for 20−30 min with porphyrin conjugate **16a−anti-CD3ϵ** or a control antibody, FITC-conjugated anti-CD3ϵ IgG1 or FITC-conjugated IgG1 isotype (Sigma). Control cells were incubated with nothing. After incubation, cells were washed twice with perm/wash buffer. Flow cytometry analysis was performed using a FACSCalibur flow cytometry instrument (BD Biosciences) with laser excitation at 488 nm. Fluorescence emission was counted in several channels including FL1 (530 ± 30 nm) and FL3 (670-nm long pass) channels. For fluorescence microscopy, cells were seeded on glass slides by centrifugation and then analyzed with an Axiophot microscope (Carl Zeiss Inc, Thornwood, NY) fitted with a Spot camera and RT software, v 3.5 (Diagnostic Instruments, Stirling Heights, MI). Images were captured with a 40× objective and filter sets: FITC excitation 480−500 nm, emission 520−580 nm; rhodamine excitation 480−500 nm, emission 635-nm long pass.

Chart 2

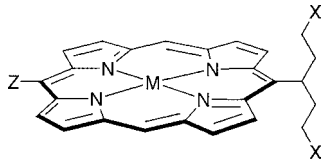

X: polar terminal group
Z: bioconjugatable handle
M: metal ion

RESULTS AND DISCUSSION

1. Synthesis. The target porphyrins are of the *trans*-AB-type, bearing one swallowtail substituent, one bioconjugatable group, and no substituents at the flanking meso positions (Chart 2). We recently developed two rational routes to *trans*-AB-porphyrins: (1) reaction of a 1,9-bis(*N*,*N*-dimethylaminomethyl)-dipyrromethane and a dipyrromethane in the presence of zinc acetate in ethanol followed by oxidation with DDQ (*46*) and (2) reaction of a 1,9-bis(imino)dipyrromethane and a dipyrromethane in the presence of zinc acetate in ethanol (*42*). Both routes directly afford zinc porphyrins; the latter method was employed herein. The dipyrromethanes bearing appropriate substituents for preparing the target porphyrins are available via a one-flask reaction of an aldehyde and excess pyrrole (*39*).

A. Dipyrromethanes. The synthesis of a dipyrromethane bearing a swallowtail diol is shown in Scheme 1. The synthesis begins with 2-bromoethanol. Some early intermediates in the synthesis have been described in the literature but without complete characterization data (*41*). The complete synthesis is described as follows.

2-Bromoethanol (**1**) was protected by reaction with *tert*-butyldimethylsilyl chloride (TBDMS−Cl) in a mixture of imidazole and DMF. Aqueous workup followed by bulb-to-bulb distillation afforded the TBDMS-protected species **2** in 97% yield. A swallowtail nitrile was described by de Groot as a side-

Scheme 1

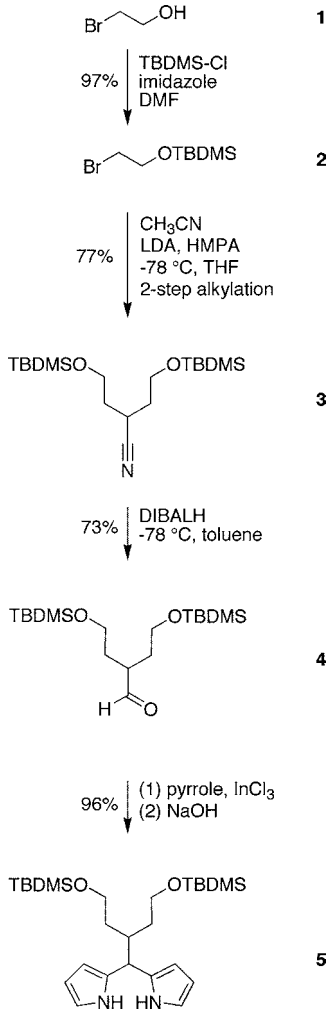

product in the alkylation of acetonitrile (*41*). We modified the de Groot method by changing the ratios of reactants and by performing sequential alkylation in a two-step one-flask process. Thus, treatment of acetonitrile with LDA in the presence of HMPA followed by alkylating agent **2** and repetition of this deprotonation/alkylation sequence afforded the dialkylated nitrile as the major product. Silica column chromatography gave **3** in 77% yield, along with mono- and trialkylated nitriles and a small amount of recovered **2**. Reduction of **3** with DIBALH at −78 °C in toluene gave **4** in 73% yield. Aldehyde **4** reacted with excess pyrrole in the presence of $InCl_3$ to give the 5-substituted dipyrromethane **5** in 96% yield as a pale yellow, viscous oil.

The bioconjugatable site was constructed from 4-hydroxybenzaldehyde by O-alkylation with *tert*-butyl bromoacetate. The alkylation proceeded smoothly in anhydrous acetonitrile in the presence of potassium carbonate and a catalytic amount of sodium iodide, affording **6a** as a white, crystalline solid in excellent yield. The aldehyde **6a** was reacted with excess pyrrole in the presence of $InCl_3$ followed by silica column chromatography to give dipyrromethane **7a** as a pale yellow, viscous liquid in 88% yield (Scheme 2). Vilsmeier formylation of **7a** followed by basic workup and chromatography on neutral alumina gave the 1,9-diformyldipyrromethane **8a**. Yields were generally low (25−45%), presumably because of the sensitivity of the *tert*-butyl ester to the formylation conditions. For characterization purposes, the dibutyltin complex, **8aSnBu**$_2$, was prepared by derivatization of **8a** with dibutyltin dichloride in a standard reaction (*43*). A similar sequence of reactions led from 4-bromobenzaldehyde (**6b**) via the dipyrromethane **7b** (*45*) to 1,9-diformyldipyrromethane **8b**. Yields were comparable to those

Scheme 2

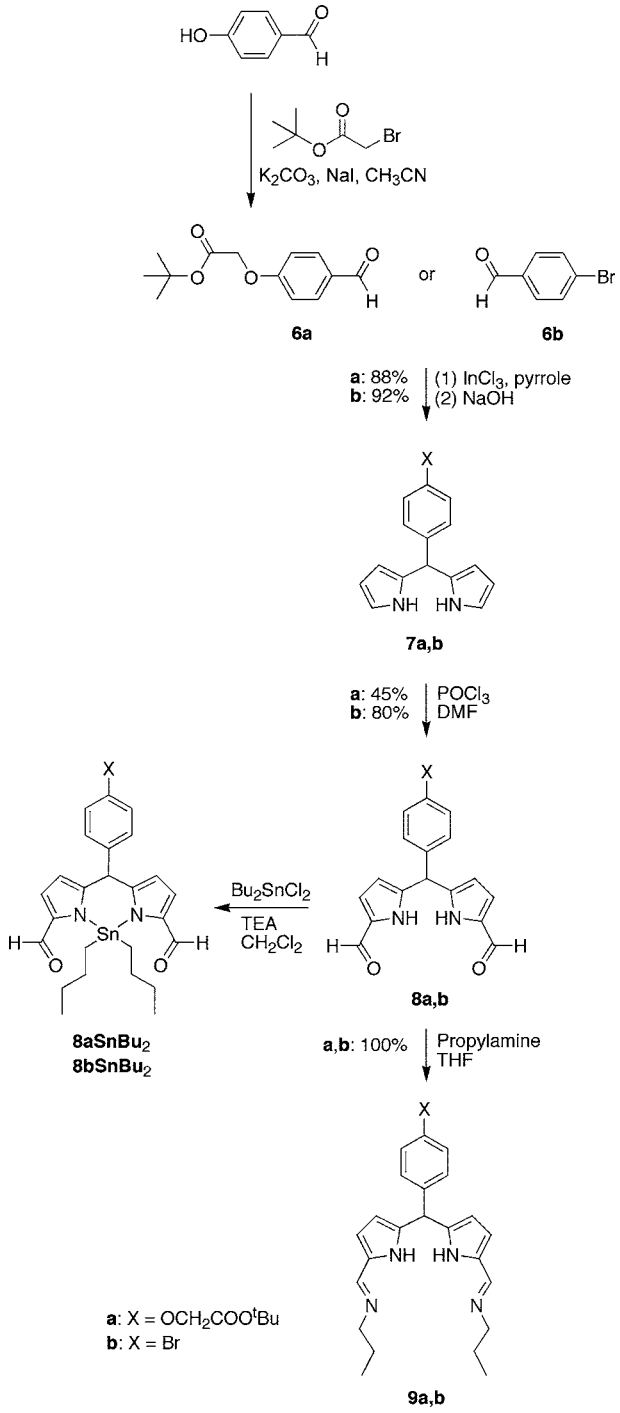

obtained for the *tert*-butyl ester derivatives, with the exception of the Vilsmeier formylation, which proceeded in excellent yield. Treatment of **8a** or **8b** with excess propylamine at room temperature quantitatively afforded the bis-imine **9a** or **9b**, respectively.

B. Porphyrin Diphosphates. The condensation of the swallowtail dipyrromethane **5** and the bis(imino)dipyrromethane **9a** or **9b** was carried out in the presence of a 10-fold excess of anhydrous zinc acetate in refluxing dry toluene open to the air (Scheme 3). In the original publication (*42*), ethanol was the solvent of choice for porphyrin formation. Ethanol proved to be an excellent solvent for the synthesis of the 4-bromophenyl-substituted zinc porphyrin (**Zn10b**), affording the desired product in 24−27% yield. However, under the same conditions only very small amounts of **Zn10a** were isolated. The main

Scheme 3

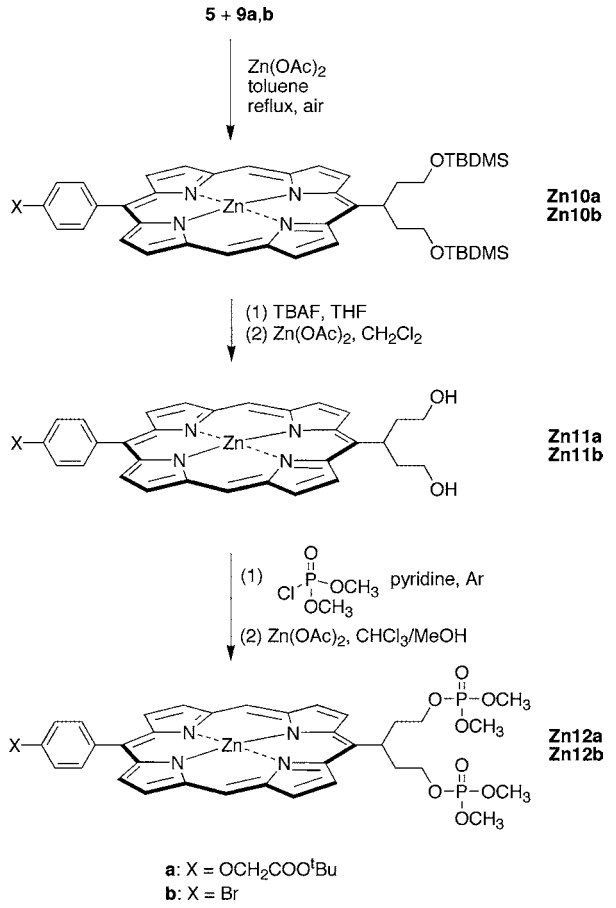

side reaction was hydrolysis of the *tert*-butyl ester. Also, some transesterification by the solvent occurred (either directly or via the free acid), as shown by LD-MS analysis of the crude reaction mixture and by ^{1}H NMR analysis of the pure porphyrin. Therefore, small-scale trial reactions were carried out in a number of solvents to find a substitute for ethanol. The use of chloroform resulted both in very low yields and in extensive scrambling (i.e., formation of other porphyrin products owing to fragmentation of dipyrromethane units and subsequent undesired recombination processes). Upon reaction in dry toluene, scrambling was not observed, and both **Zn10a** and **Zn10b** could be isolated after straightforward silica column chromatography. Treatment of **Zn10a** or **Zn10b** with TBAF in THF cleaved the TBDMS protecting groups and also caused some demetalation of the zinc porphyrin, in each case affording a mixture of the zinc chelate and the free base porphyrin as shown by LD-MS. Remetalation with zinc acetate followed by chromatography on neutral alumina gave the zinc porphyrin diol **Zn11a** or **Zn11b** in >80% yield. It was important to limit the reaction time for conversion of **Zn10a** to **Zn11a**, because prolonged exposure under these conditions resulted in hydrolysis of the *tert*-butyl ester group.

Porphyrin diols **Zn11a** and **Zn11b** are highly polar and are only sparingly soluble in most organic solvents. Reaction of **Zn11a** with dimethyl chlorophosphate in anhydrous pyridine gave no **Zn12a**, whereas similar reaction with **Zn11b** gave a very low yield of **Zn12b**. The poor yields are presumably due to the combination of low solubility and low reactivity on the part of the porphyrin diol starting materials. We assumed that incorporation of the dimethoxyphosphoryl groups at an earlier stage could provide a more efficient process.

Our attempts to introduce the phosphate groups to aldehyde **4** were unsuccessful. Phosphorylation of the hydroxy groups

Scheme 4

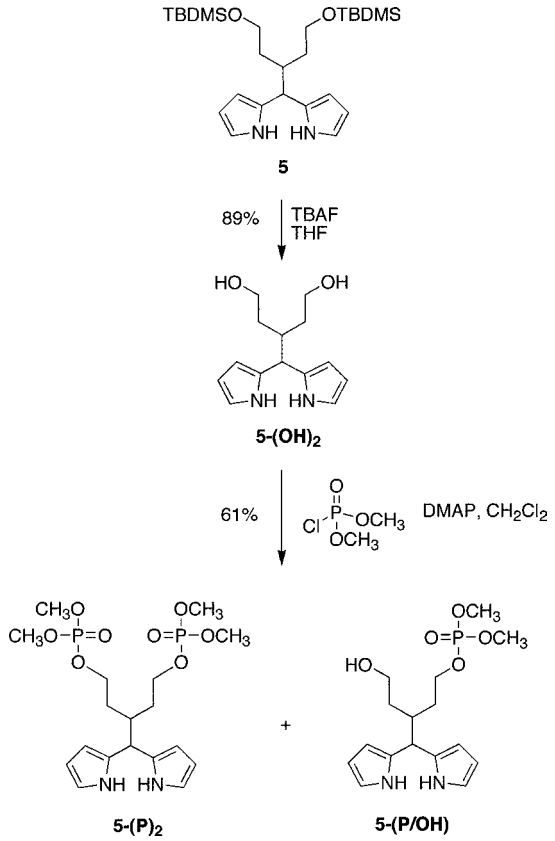

of aldehyde **4** appeared attractive, but deprotection of **4** afforded the monocyclic hemiacetal and the bicyclic acetal of the corresponding 3-formylpentane-1,5-diol as an approximately 1:2 equilibrium mixture. None of the free diol was observed by ^{1}H NMR spectroscopy. Therefore, the phosphate groups were introduced at the dipyrromethane stage (Scheme 4). Treatment of the TBDMS-protected swallowtail dipyrromethane **5** with TBAF in THF at room temperature resulted in cleavage of the protecting groups. Aqueous−organic workup followed by chromatography on neutral alumina gave the dipyrromethane diol **5-(OH)$_2$** as a pale yellow oil in 89% yield. The dipyrromethane diol **5-(OH)$_2$** was reacted with dimethyl chlorophosphate in anhydrous CH_2Cl_2 to give the bis(dimethoxyphosphoryloxy)dipyrromethane **5-(P)$_2$** as a yellow oil in 61% yield. The monophosphate derivative **5-(P/OH)** was also isolated (20−30% yield) and could be transformed to **5-(P)$_2$**. Alternatively, **5-(P/OH)** could prove useful if a second functional group is to be introduced into the swallowtail moiety.

Reaction of **5-(P)$_2$** with bis-imine **9a** or **9b** in anhydrous toluene in the presence of zinc acetate furnished the corresponding zinc porphyrin **Zn12a** or **Zn12b** in ∼15% yield (Scheme 5). The spectroscopic yields of **Zn12a** and **Zn12b** were higher (30−45%) than the isolated yields. Two problems were encountered in handling the porphyrin diphosphate compounds **Zn12a** and **Zn12b**: (1) hydrolysis of the phosphates during purification, and (2) hydrolysis of the phosphates during "standard" conditions for methyl ester hydrolysis (*47, 48*). A lengthy series of experiments indicated that the loss of phosphate was facilitated by the presence of the centrally coordinated zinc atom (see Supporting Information for experiments and results). In summary, zinc porphyrins bearing phosphate-terminated swallowtail groups were not obtained for the pent-3-yl groups examined. Accordingly, we turned our attention to free base and copper analogues of the porphyrin diphosphates. Copper is strictly four-coordinate and was not expected to facilitate phosphate hydrolysis.

Scheme 5

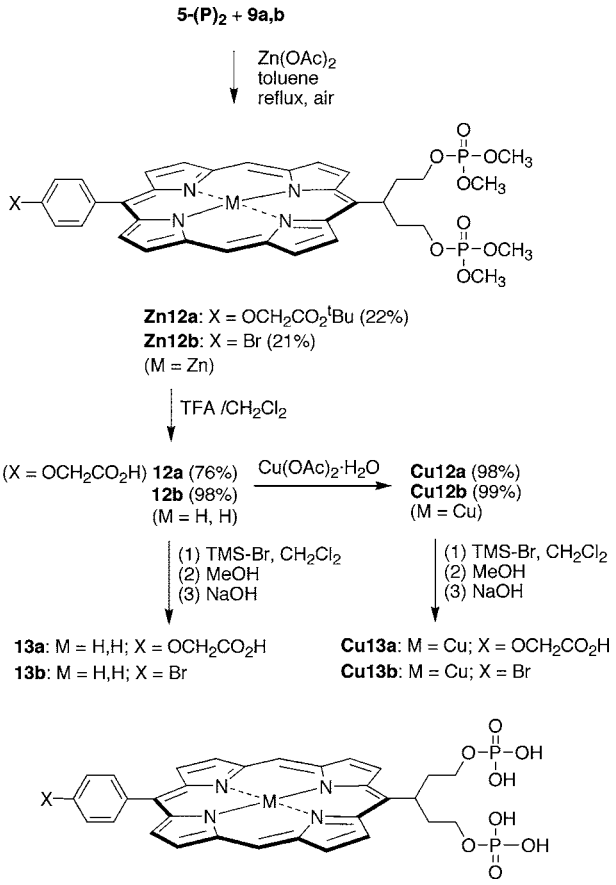

The free base porphyrins **12a** and **12b** were prepared by demetalation of **Zn12a** and **Zn12b**, respectively, by treatment with a 1:1 mixture of TFA and CH_2Cl_2. The demetalation was essentially complete within 15 min (as determined by absorption spectroscopy), but **Zn12a** was allowed to react further to allow for the quantitative cleavage of the *tert*-butyl ester. The resulting free base porphyrins **12a** and **12b** maintained the phosphate protecting groups although **12a** contained a free carboxylic acid. Treatment of **12a,b** with copper acetate afforded the corresponding copper porphyrins (**Cu12a,b**). Compounds **Cu12a** and **Cu12b** were characterized by LD-MS, FAB-MS, and absorption spectroscopy (but not ^{1}H NMR spectroscopy because of the broadened spectra of copper porphyrins).

Cleavage of the phosphate protecting groups in the free base porphyrins (**12a,b**) and copper porphyrins (**Cu12a,b**) was carried out using TMS−Br. Porphyrin **12b** reacted smoothly with a slight excess of TMS−Br in dry CH_2Cl_2 at room temperature. Subsequent treatment with aqueous NaOH and reversed-phase column chromatography yielded the desired porphyrin diphosphate **13b** in excellent yield. The carboxylate-functionalized **12a** required a larger excess of TMS−Br, whereupon the desired fully deprotected carboxy-porphyrin diphosphate **13a** was obtained in 76% yield, along with a second fraction containing fully deprotected **13a** and monomethyl-**13a**. Increasing the amount of TMS−Br, the reaction time, or the temperature resulted in conversion of **12a** to the dibromo-substituted **14a**.

It is noteworthy that the copper complexes were only partially deprotected by the same amount of TMS−Br as used for the corresponding free base porphyrins. ESI-MS showed the dimethyl and monomethyl **Cu13a,b** as the major products. Increasing the amount of TMS−Br resulted in almost complete demetalation and a reduction in the deprotection yield. Small quantities of **Cu13a** and **Cu13b** could be isolated, but the samples were only partially characterized. Moreover, neither

Scheme 6

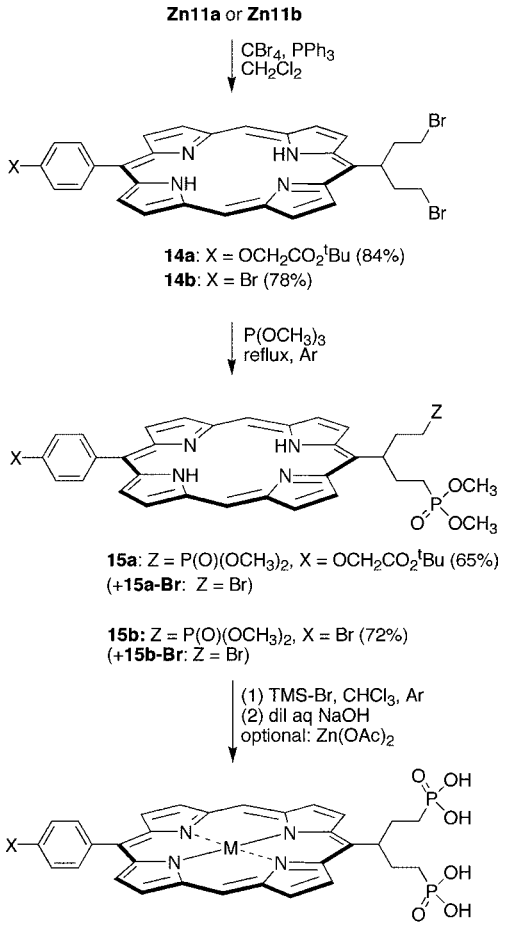

	X	M
16a	CH_2CO_2H	H,H
16b	Br	H,H
Zn16a	CH_2CO_2H	Zn
Zn16b	Br	Zn

diol **11a** nor **11b** (nor copper chelates thereof) was observed by LD-MS or ESI-MS during the deprotection reaction, by contrast with the case of the zinc chelates (**Zn12a,b** and **Zn13a,b**) where central metal atom coordination promoted hydrolysis. In summary, the free base and copper porphyrin diphosphates were prepared without the complications of loss of phosphate encountered with the corresponding zinc chelates.

C. Porphyrin Diphosphonates. For in vivo studies, the phosphate groups may be susceptible to cleavage by phosphatases. Therefore, porphyrin diphosphonates, which are stable to phosphatases, were prepared from the porphyrin diols **Zn11a** and **Zn11b** (Scheme 6). Montforts has reported the conversion of a porphyrin alcohol to the corresponding bromide upon reaction with CBr_4 and triphenylphosphine (*44*). Similar treatment of a thoroughly dried sample of **Zn11a** or **Zn11b** in anhydrous CH_2Cl_2 with CBr_4 at 0 °C followed by excess triphenylphosphine afforded the corresponding free base dibromo-porphyrin **14a** or **14b** in excellent yield. During the chromatographic purification of the products, a very nonpolar bluish-green compound was isolated, in addition to the desired **14a** or **14b**. This compound was not characterized due to lack of material (<1 mg) and its instability, but absorption spectroscopy suggested that it was a chlorin species (λ_{abs} 414, 641 nm). It is possible that the triphenylphosphine could reduce one of the porphyrin pyrrole rings, giving rise to the chlorin. Refluxing **14a** or **14b** in neat $P(OCH_3)_3$ under an inert

atmosphere for 36 h afforded **15a** or **15b** in moderate to good yield as a dark red solid. The reaction also produced the intermediate monobromo, monophosphonate porphyrins (**15a-Br**, **15b-Br**). Although conditions have been optimized for the production of **15a** and **15b**, it is possible that the intermediates could be obtained in good yields and serve as starting points for the introduction of two different polar groups into one molecule.

The cleavage of the phosphonate protecting groups (and the *tert*-butyl ester for **15a**) was investigated by treatment of **15a** or **15b** with TMS−Br beginning with the conditions we had employed earlier for cleaving porphyrin phosphonates (*49*, *50*). The phosphonate groups are more robust than phosphate groups (vide supra) and will tolerate use of excess reagent at higher temperature for prolonged reaction times. The use of excess TMS−Br in refluxing chloroform under argon gave good results, affording the free acids after methanolysis of the silyl intermediates. The resulting green solids were insoluble in a number of organic solvents and water. Addition of small quantities of dilute aqueous base (NaOH or $NaHCO_3$) rendered the porphyrins water-soluble. Treatment of the basic porphyrin solutions (prior to purification) with zinc acetate resulted in formation of the corresponding zinc chelates. Purification of each free base or zinc porphyrin was achieved by reversed-phase column chromatography upon elution with water/methanol. Removal of the solvent followed by freeze-drying of the aqueous samples yielded the desired porphyrin (**16a**, **16b**, **Zn16a**, and **Zn16b**) in good to excellent yield.

2. Characterization and Water Solubility. All of the hydrophobic porphyrins were analyzed by LD-MS, FAB-MS, ^{1}H NMR spectroscopy (except copper chelates), and absorption and emission spectroscopy. In certain cases O*H*, N*H*, and COO*H* signals were not observed owing to broadening, exchange with the solvent, or coincidence with the solvent peak. All of the deprotected porphyrin diphosphates and porphyrin diphosphonates were characterized by ^{1}H NMR spectroscopy, ESI-MS, and absorption and emission spectroscopy. Each ESI-MS spectrum exhibited a strong peak due to the parent molecule (protonated and sodium adduct in the positive-ion mode; deprotonated in the negative-ion mode), with no peaks owing to partially deprotected porphyrins. Each deprotected free base porphyrin sample was found to be homogeneous upon examination by reversed-phase HPLC, while the zinc chelates eluted as two separate peaks. The front peak (minor) had the same t_R as the corresponding free base porphyrin. Because the elution mixture contains TFA, partial demetalation during chromatography is likely. The free base porphyrins were not observed by ESI-MS, ^{1}H NMR spectroscopy, or absorption or emission spectroscopies (see Experimental Procedures section).

All of the porphyrin diphosphates and porphyrin diphosphonates examined herein were readily soluble in water across a wide pH range and exhibited sufficient solubility to enable ^{1}H NMR measurements in D_2O. Although good-quality ^{1}H NMR spectra were obtained at room temperature, the resolution increased substantially upon increasing the temperature to 60 °C. The higher temperature also enabled observation of the OCH_2 signal in the carboxylic acid, which at room temperature was coincident with the water signal. gCOSY experiments carried out on the porphyrin diphosphonates enabled the partial assignment of the signals.

Determination of the upper limit of water solubility was not possible given the amount of material in hand and the relatively high solubility encountered. Indeed, in each case examined, 8−10 mg of pure porphyrin (**13a**, **13b**, **16a**, **16b**, **Zn16a**, **Zn16b**) completely dissolved in 500 μL of distilled water, consistent with a concentration of ≥20 mM. The aqueous solutions are stable for days at room temperature when shielded from the light. Precipitation was not observed either with the naked eye or by absorption spectroscopy.

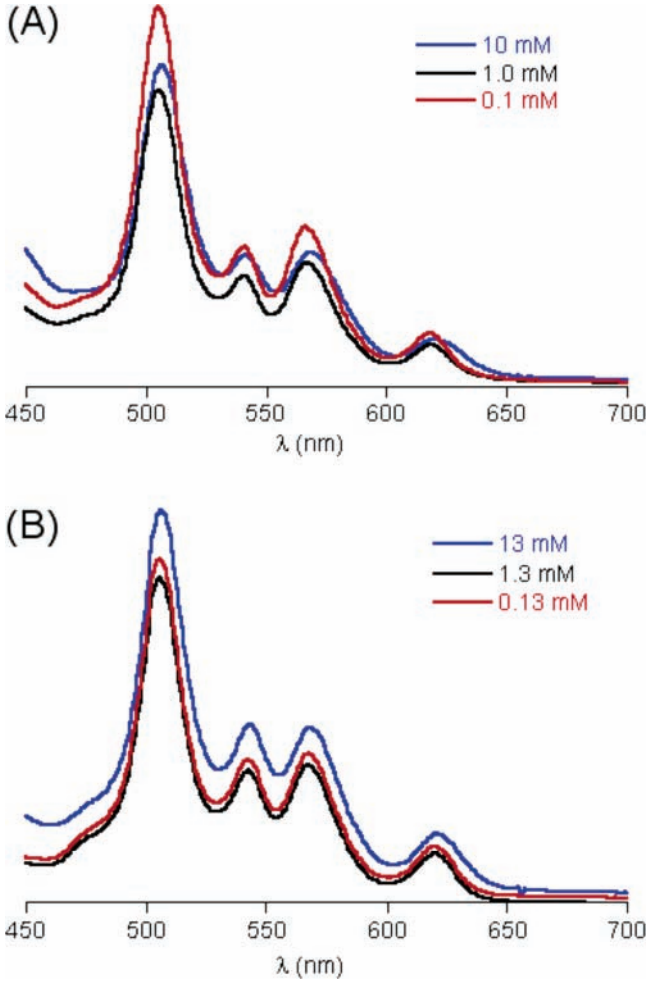

Figure 2. (A) Absorption spectra of porphyrin **16b**: (blue) $c \approx 10$ mM, $l = 0.1$ mm; (black) $c \approx 1$ mM, $l = 1$ mm; (red) $c \approx 0.1$ mM, $l = 10$ mm. (B) Absorption spectra of porphyrin **13a**: (blue) $c = 13$ mM, $l = 0.1$ mm; (black) $c = 1.3$ mM, $l = 1$ mm; (red) $c = 0.13$ mM, $l = 10$ mm.

A standard method for the detection of aggregation of porphyrin solutions is based on the comparison of absorption spectra at different concentrations. In the absence of aggregation, the absorption spectrum recorded at concentration c_1 and path length l_1 should be unaltered upon 10-fold dilution and simultaneous increase of l_1 to $10l_1$. For this purpose, a stock solution of each of the least polar water-soluble porphyrin (**16b**) and the most polar water-soluble porphyrin (**13a**) was prepared. The concentration ([**16b**] ≈ 10 mM, [**13a**] = 13.4 mM) was such that $A \approx 0.6$ for the visible absorption band near 505 nm. Then aliquots of both samples were diluted by 10-fold and 100-fold, and the absorption spectrum was recorded for each sample. For the most concentrated sample of **16b**, peak broadening in the 450−700 nm region indicated some aggregation at a concentration of ~10 mM. The absorption spectra of the 1 mM and the 0.1 mM samples were not broadened, consistent with a nonaggregated sample at these concentrations (Figure 2A). By contrast, no band broadening was observed for **13a** over a concentration of 0.13−13.4 mM (Figure 2B).

3. Structural Studies. The success of the hydrocarbon swallowtails in the lipophilization of extended aromatic systems has been explained by projection of the alkyl groups above and below the plane of the macrocycle, which prevents $\pi-\pi$ stacking and aggregation (Figure 1). Molecular mechanics calculations were carried out on a series of swallowtail por-

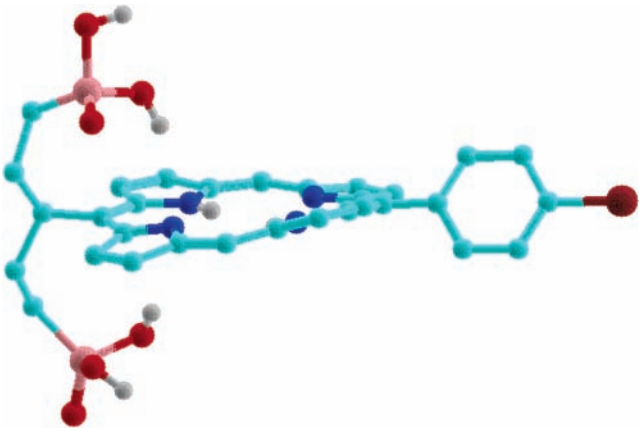

Figure 3. MMX-calculated gas-phase geometry of porphyrin **16b** bearing dimethoxyphosphoryl end groups. Hydrogens on carbons are omitted for clarity.

Scheme 7

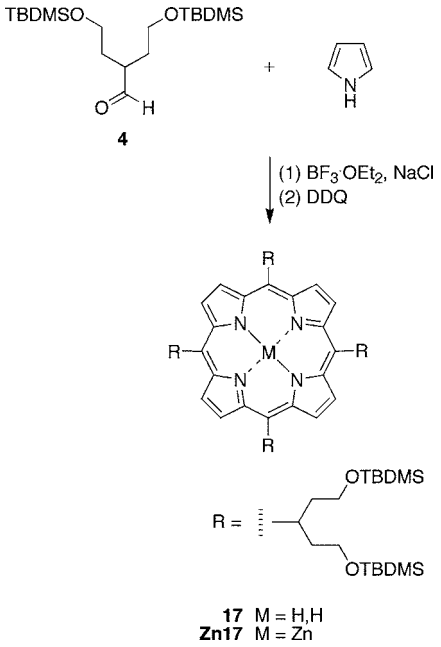

phyrins wherein the swallowtail substituents were hydrophobic or terminated with polar substituents, including neutral or ionic groups. In all cases, the calculated geometries showed the projection of the substituents above and below the plane of the macrocycle. The geometry calculated for an ionic-functionalized swallowtail porphyrin is shown in Figure 3.

We carried out ^{1}H NMR studies (1 and 2D NMR, VT NMR) of a series of swallowtail porphyrins that were synthesized in this work as well as a porphyrin bearing a single hydrocarbon swallowtail group (*34*) to gain further insight concerning conformation of the swallowtail groups. An A_4-swallowtail porphyrin (**17**) was synthesized from **4** upon condensation with pyrrole via a standard procedure (*34*) followed by oxidation with DDQ. The corresponding chelate, **Zn17**, was prepared by metalation with zinc acetate (Scheme 7). The results are as follows.

The ^{1}H NMR spectrum of each A_4-swallowtail porphyrin in $CDCl_3$ (**17** and **Zn17**) contains two broad apparent singlets (~9.67 and ~9.49 ppm) in the aromatic region each with integration of 4. For an A_4-porphyrin with four magnetically equivalent substituents, the eight β-protons would resonate as *one* singlet in the aromatic region with an integration of eight. The signal corresponding to the CH protons of the swallowtail motifs (the branch site $C^{1'}H$) appears as a broad, structureless

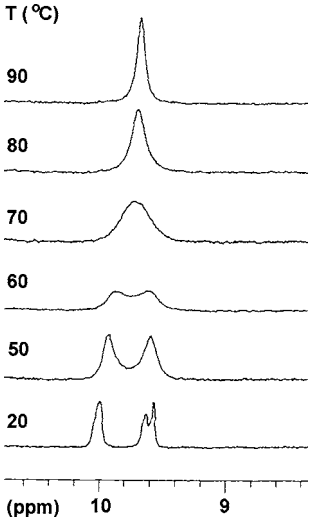

Figure 4. Changes in the β-proton signals in porphyrin **17** with increasing temperature.

multiplet (~5.56 ppm). NOESY experiments revealed that the two types of aromatic protons giving rise to the broad apparent singlets were closely juxtaposed and also that the one giving rise to the 9.67 ppm signal is close to $C^{1'}H$ (see Supporting Information). The spectra are consistent with restricted motion of the swallowtail substituent at the site of attachment to the porphyrin.

At room temperature in toluene-d_8, the spectrum of **17** was similar to that recorded in $CDCl_3$, although the signal at higher field consisted of two overlapping broad singlets. Increasing the temperature resulted in the broadening of the two aromatic signals (9.60 and 9.93 ppm). At ~70 °C, the two signals collapsed into one broad singlet (9.77 ppm), which eventually became a sharp singlet (9.72 ppm, 90 °C) with an integration of 8 (Figure 4). A similar but less pronounced sharpening was observed for the broad singlet at −1.72 ppm (NH) and the multiplet of $C^{1'}H$ (5.88 ppm) (see Supporting Information). The spectra at elevated temperature are consistent with a dynamic averaging on the NMR time scale of the conformation at the swallowtail branching site. On the basis of a coalescence temperature of 60 or 70 °C, an energy of activation of 68 or 70 kJ/mol is calculated for rotation of the swallowtail motif about the porphyrin meso carbon and the branch carbon $C^{1'}$.

The *trans*-AB-porphyrins examined (**Zn10b** and **Zn12b**) have nominally lower symmetries than the A_4-porphyrins **17** and **Zn17**. A *trans*-AB-porphyrin with simple A and B substituents is expected to exhibit signals in the aromatic region stemming from the four distinct porphyrin β-positions and the unsubstituted meso position. However, the ^{1}H NMR spectra of all swallowtail *trans*-AB-porphyrins (**Zn10a,b**−**Zn12a,b**, **12a,b**−**16a,b**, and **Zn16a,b**) studied in this work were more complex. Typically, two separate meso-proton signals were observed (at ~10.0 and 10.1 ppm). The four β-protons on the pyrrole units flanking the swallowtail substituents gave four doublets: a pair around 9.7 and 9.5 ppm with different coupling constants, and a pair at ~9.30 ppm (overlapping). In one case examined (**Zn12b**), increasing the temperature again simplified the spectrum, whereupon (1) the two meso-proton signals collapsed into one singlet (~100 °C, δ 10.03 ppm) and (2) the doublets corresponding to the two protons flanking the swallowtail group broadened out and moved closer to each other, although in the available temperature range (up to 100 °C) the doublets remained separate signals. Similarly to the A_4-porphyrin, NOESY experiments on **Zn12b** showed the proximity between $C^{1'}H$ and one of either swallowtail-flanking β-pyrrolic protons. Two of the four $C^{2'}H_2$ protons are pointing toward the other

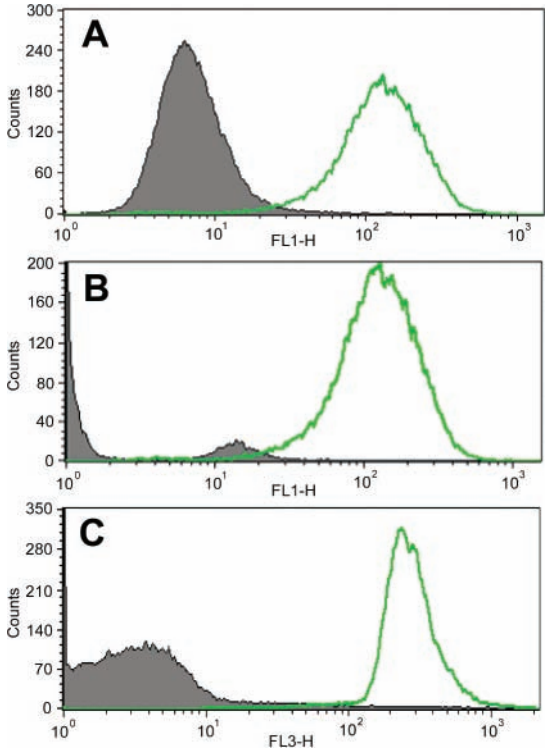

Figure 5. FACS analysis histograms: (A) green fluorescence (FL1) obtained with Jurkat cells stained with FITC−anti-CD3ϵ (open curve) or FITC isotype IgG1 (shaded curve); (B) green fluorescence obtained with Jurkat cells (open curve) or LLC cells (shaded curve) stained with FITC−anti-CD3ϵ; (C) red fluorescence (FL3) obtained with Jurkat cells (open curve) or LLC cells (shaded curve) stained with **16a**−**anti-CD3ϵ**.

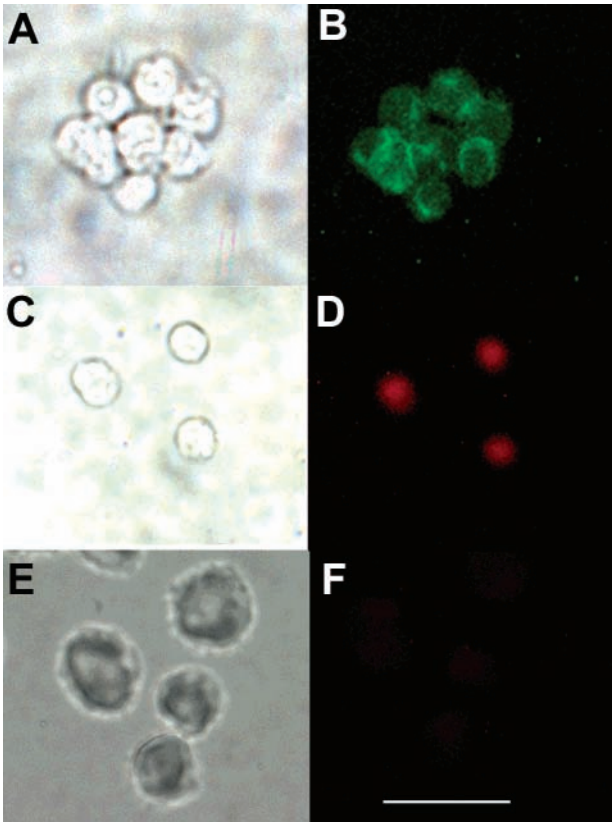

Figure 6. Fluorescence microscopy. The top panel shows Jurkat cells stained with FITC−anti-CD3ϵ under (A) bright field illumination or (B) green fluorescence detection. The middle panel shows Jurkat cells stained with **16a**−**anti-CD3ϵ** under (C) bright field illumination or (D) red fluorescence detection. The bottom panel shows LLC cells stained with **16a**−**anti-CD3ϵ** under (E) bright field illumination or (F) red fluorescence detection. The scale bar is 50 μm.

swallowtail-flanking β-proton (see Supporting Information). NOESY experiments carried out on a porphyrin bearing a single all-hydrocarbon swallowtail group (*34*) indicated a similar configuration.

These results suggest that the swallowtail alkyl groups not only preferentially occupy positions out-of-plane with the porphyrin ring but at room temperature are hindered in their rotation around the carbon−carbon single bond between the porphyrin meso position and the swallowtail branching site (i.e., $C^5-C^{1\prime}H$). The $C^{1\prime}H$ is more or less in the plane of the porphyrin macrocycle. This conformation results in the two sets of β-protons and the two different meso-proton signals. At increased temperature, the rotational barrier is more easily surmounted and the time-averaged C_2 symmetry of the porphyrin is restored. This geometry undoubtedly helps suppress cofacial interaction between porphyrin molecules at room temperature, thereby increasing solubility. The results of the NMR experiments are consistent with previous observations obtained via EPR spectroscopy (*34*) and provide additional evidence concerning the conformation of the swallowtail porphyrins in solution.

4. Bioconjugation Studies. The availability of water-soluble porphyrins each bearing a single bioconjugatable tether opens a number of applications in the life sciences. The porphyrin carboxylate **16a** was used to label a monoclonal antibody (IgG). The labeling was carried out in aqueous solution using the water-soluble carbodiimide reagent EDCI. Purification was achieved in aqueous solution via size exclusion chromatography. Absorption spectroscopy of the purified conjugate (**16a-anti**−**CD3ϵ**) indicated an average loading of two porphyrins per antibody. It is noteworthy that no precipitation was observed during conjugation or purification or on standing during the three-week period over which biological experiments were carried out.

The performance of the conjugate was examined for staining an intracellular epitope using both flow cytometry and fluorescence microscopy. The use of dye-tagged monoclonal antibodies for staining both extracellular and intracellular epitopes is well established. In the present case, we employed the human T-cell lymphoma cell line, Jurkat cells, for which monoclonal antibodies (and FITC-labeled analogues) against the CD3ϵ chain are available. The flow cytometry results upon intracellular staining are shown in Figure 5. Panel A demonstrates that Jurkat cells bind anti-CD3ϵ but do not bind IgG1 isotype control, thus confirming the expression of intracellular CD3ϵ on Jurkat cells and the lack of Fc receptors that can nonspecifically bind IgG molecules via Fc regions. Panel B demonstrates that the epithelial cancer cells LLC do not bind FITC−anti-CD3ϵ, consistent with their known lack of T-cell receptors. Panel C shows that Jurkat cells bind porphyrin conjugate **16a**−**anti-CD3ϵ** in an analogous fashion to the commercially available FITC−anti-CD3ϵ, thereby showing that porphyrin conjugation did not adversely affect the antigen recognition domain of the antibody. The TCR-negative LLC cells are also negative to **16a**−**anti-CD3ϵ**, thereby demonstrating the lack of any non-bound porphyrin present in the conjugate preparation that could have also bound nonspecifically to receptor-negative cells.

The specificity and functionality of the porphyrin conjugate **16a**−**anti-CD3ϵ** was assessed by fluorescence microscopy as shown in Figure 6. Panels A and B show the green fluorescence staining of Jurkat cells with FITC−anti-CD3ϵ. Panels C and D show the red fluorescence staining of Jurkat cells with the porphyrin conjugate **16a**−**anti-CD3ϵ**. Note that while the pattern of porphyrin staining is equally specific for target cells as the FITC counterpart, the subcellular pattern is somewhat different and appears to be more concentrated in the middle of the cell

for unknown reasons. Panels E and F show that the receptor-negative LLC cells give no red staining with **16a**−**anti-CD3ϵ**, a result that is consistent with the FACS data reported above.

OUTLOOK

A compact water-solubilizing motif has been developed for use with porphyrinic macrocycles. The water-solubilizing motif consists of a short, branched alkyl chain ("swallowtail") with polar end groups (phosphate, phosphonate) and does not include any aryl moieties. Incorporation of only one such swallowtail motif (based on a 1,5-disubstituted pent-3-yl group) at the meso position suffices to impart high aqueous solubility (≥20 mM) to a *trans*-AB-porphyrin, where the other meso substituent consists of a bioconjugatable group. The alkyl groups project above and below the hydrophobic porphyrinic macrocycle, thereby suppressing cofacial aggregation. The versatile synthetic chemistry for manipulating swallowtail substituents should facilitate their use as compact water-solubilizing motifs with a variety of porphyrinic macrocycles. The ability to carry out bioconjugations in aqueous solution is exceptionally valuable for use with diverse biomolecules. The requirement for only one swallowtail motif to achieve water solubility opens up a great deal of latitude in the design of porphyrinic-based molecular architectures for diverse applications in the life sciences.

ACKNOWLEDGMENT

This work was supported by the NIH (Grant GM36238 to J.S.L. and Grant CA/AI838801 to M.R.H.). Mass spectra were obtained at the Mass Spectrometry Laboratory for Biotechnology at North Carolina State University. Partial funding for the facility was obtained from the North Carolina Biotechnology Center and the NSF.

Supporting Information Available: Description of experiments concerning the hydrolytic lability of zinc porphyrin diphosphates, VT-NMR data for **Zn12b** and **17**, NOESY data for **Zn12b** and **17**, and evidence concerning water solubility of **Zn16b**. This material is available free of charge via the Internet at http://pubs.acs.org.

LITERATURE CITED

(1) Mauzerall, D. (1962) The photoreduction of porphyrins: Structure of the products. *J. Am. Chem. Soc. 84*, 2437−2445.
(2) Mauzerall, D. (1962) The photoreduction of uroporphyrin: Effect of pH on the reaction with EDTA. *J. Phys. Chem. 66*, 2531−2533.
(3) Mauzerall, D. (1965) Spectra of molecular complexes of porphyrins in aqueous solution. *Biochemistry 4*, 1801−1810.
(4) Carapellucci, P. A., and Mauzerall, D. (1975) Photosynthesis and porphyrin excited-state redox reactions. *Ann. New York Acad. Sci. 244*, 214−238.
(5) Feitelson, J., and Mauzerall, D. (2002) Enthalpy and electrostriction in the electron-transfer reaction between triplet zinc uroporphyrin and ferricyanide. *J. Phys. Chem. B 106*, 9674−9678.
(6) Hambright, P. (2000) Chemistry of water soluble porphyrins, in *The Porphyrin Handbook. Volume 3: Inorganic, Organometallic and Coordination Chemistry* (Kadish, K. M., Smith, K. M., and Guilard, R., Eds.) pp 129−210, Chapter 18, Academic Press, San Diego, CA.
(7) Grahn, M. F., Giger, A., McGuinness, A., de Jode, M. L., Stewart, J. C. M., Ris, H.-B., Altermatt, H. J., and Williams, N. S. (1999) mTHPC polymer conjugates: The in vivo photodynamic activity of four candidate compounds. *Lasers Med. Sci. 14*, 40−46.
(8) Hornung, R., Fehr, M. K., Walt, H., Wyss, P., Berns, M. W., and Tadir, Y. (2000) PEG-*m*-THPC-mediated photodynamic effects on normal rat tissues. *Photochem. Photobiol. 72*, 696−700.
(9) Zingg, A., Felber, B., Gramlich, V., Fu, L., Collman, J. P., and Diederich, F. (2002) Dendritic iron(II) porphyrins as models for hemoglobin and myoglobin: Specific stabilization of O_2 complexes in dendrimers with H-bond-donor centers. *Helv. Chim. Acta 85*, 333−351.
(10) Schell, C., and Hombrecher, H. K. (1999) Synthesis and investigation of glycosylated mono- and diarylporphyrins for photodynamic therapy. *Bioorg. Med. Chem. 7*, 1857−1865.
(11) Lamarche, F., Sol, V., Huang, Y.-M., Granet, R., Guilloton, M, and Krausz, P. (2002) Synthesis and biological evaluation of polyamine-porphyrin conjugates as potential agents in photodynamic therapy (PDT). *J. Porphyrins Phthalocyanines 6*, 130−134.
(12) Subbarayan, M., Shetty, S. J., Srivastava, T. S., Noronha, O. P. D., Samuel, A. M., and Mukhtar, H. (2001) Water-soluble ^{99m}Tc-labeled dendritic novel porphyrins tumor imaging and diagnosis. *Biochem. Biophys. Res. Commun. 281*, 32−36.
(13) Jee, J.-E., Eigler, S., Hampel, F., Jux, N., Wolak, M., Zahl, A., Stochel, G., and van Eldik, R. (2005) Kinetic and mechanistic studies on the reaction of nitric oxide with a water-soluble octa-anionic iron(III) porphyrin complex. *Inorg. Chem. 44*, 7717−7731.
(14) Cornia, M., Valenti, C., Capacchi, S., and Cozzini, P. (1998) Synthesis, characterisation and conformational studies of lipophilic, amphiphilic and water-soluble C-*glyco*-conjugated porphyrins. *Tetrahedron 54*, 8091−8106.
(15) Král, V., Davis, J., Andrievsky, A., Kralová, J., Synytsya, A., Poucková, P., and Sessler, J. L. (2002) Synthesis and biolocalization of water-soluble sapphyrins. *J. Med. Chem. 45*, 1073−1078.
(16) Bisland, S. K., Singh, D., and Gariépy, J. (1999) Potentiation of chlorin e6 photodynamic activity in vitro with peptide-based intracellular vehicles. *Bioconjugate Chem. 10*, 982−992.
(17) de Luca, S., Tesauro, D., di Lello, P., Fattorusso, R., Saviano, M., Pedone, C., and Morelli, G. (2001) Synthesis and solution characterization of a porphyrin-CCK8 conjugate. *J. Pept. Sci. 7*, 386−394.
(18) Chaloin, L., Bigey, P., Loup, C., Marin, M., Galeotti, N., Piechaczyk, M., Heitz, F., and Meunier, B. (2001) Improvement of porphyrin cellular delivery and activity by conjugation to a carrier peptide. *Bioconjugate Chem. 12*, 691−700.
(19) Sibrian-Vazquez, M., Jensen, T. J., Fronczek, F. R., Hammer, R. P., and Vicente, M. G. H. (2005) Synthesis and characterization of positively charged porphyrin−peptide conjugates. *Bioconjugate Chem. 16*, 852−863.
(20) James, D. A., Swamy, N., Paz, N., Hanson, R. N., and Ray, R. (1999) Synthesis and estrogen receptor binding affinity of a porphyrin-estradiol conjugate for targeted photodynamic therapy of cancer. *Bioorg. Med. Chem. Lett. 9*, 2379−2384.
(21) Karagianis, G., and Reiss, J. A. (1995) Preparation and characterization of porphyrin-acridine conjugates as bifunctional antitumor agents. *Aust. J. Chem. 48*, 1693−1705.
(22) Sutton, J. M., Clarke, O. J., Fernandez, N., and Boyle, R. W. (2002) Porphyrin, chlorin, and bacteriochlorin isothiocyanates: Useful reagents for the synthesis of photoactive bioconjugates. *Bioconjugate Chem. 13*, 249−263.
(23) Bedel-Cloutour, C. H., Maneta-Peyret, L., Pereyre, M., and Bezian, J.-H. (1991) Synthesis of a monoclonal antibody-indium-111-porphyrin conjugate. *J. Immunol. Methods 144*, 35−41.
(24) Bhalgat, M. K., Roberts, J. C., Mercer-Smith, J. A., Knotts, B. D., Vessella, R. L., and Lavallee, D. K. (1997) Preparation and biodistribution of copper-67-labeled porphyrins and porphyrin-A6H immunoconjugates. *Nucl. Med. Biol. 24*, 179−185.
(25) Birchler, M, Viti, F., Zardi, L., Spiess, B., and Neri, D. (1999) Selective targeting and photocoagulation of ocular angiogenesis mediated by a phage-derived human antibody fragment. *Nat. Biotechnol. 17*, 984−988.
(26) Vrouenraets, M. B., Visser, G. W. M., Loup, C., Meunier, B., Stigter, M., Oppelaar, H., Stewart, F. A., Snow, G. B, and van Dongen, G. A. M. S. (2000) Targeting of a hydrophilic photosensitizer by use of internalizing monoclonal antibodies: A new possibility for use in photodynamic therapy. *Int. J. Cancer 88*, 108−114.
(27) Oseroff, A. R., Ara, G., Ohuoha, D., Aprille, J., Bommer, J. C., Yarmush, M. L., Foley, J., and Cincotta, L. (1987) Strategies for selective cancer photochemotherapy: Antibody-targeted and selective carcinoma cell photolysis. *Photochem. Photobiol. 46*, 83−96.

(28) Cavanaugh, P. G. (2002) Synthesis of chlorin *e*6-transferrin and demonstration of its light-dependent *in vitro* breast cancer cell killing ability. *Breast Cancer Res. Treat. 72*, 117−130.
(29) Gijsens, A., and De Witte, P. (1998) Photocytotoxic action of EGF-PVA-Sn(IV)chlorin e_6 and EGF-dextran-Sn(IV)chlorin e_6 internalizable conjugates on A431 cells. *Int. J. Oncol. 13*, 1171−1177.
(30) Gijsens, A., Missiaen, L., Merlevede, W., and de Witte, P. (2000) Epidermal growth factor-mediated targeting of chlorin e_6 selectively potentiates its photodynamic activity. *Cancer Res. 60*, 2197−2202.
(31) Schmidt-Erfurth, U., Diddens, H., Birngruber, R., and Hasan, T. (1997) Photodynamic targeting of human retinoblastoma cells using covalent low-density lipoprotein conjugates. *Br. J. Cancer 75*, 54−61.
(32) Frau, S., Bernadou, J., and Meunier, B. (1997) Nuclease activity and binding characteristics of a cationic "manganese porphyrin−bis(benzimidazole) dye (Hoechst 33258)" conjugate. *Bioconjugate Chem. 8*, 222−231.
(33) Soukos, N. S., Hamblin, M. R., and Hasan, T. (1997) The effect of charge on cellular uptake and phototoxicity of polylysine chlorin e_6 conjugates. *Photochem. Photobiol. 65*, 723−729.
(34) Thamyongkit, P., Speckbacher, M., Diers, J. R., Kee, H. L., Kirmaier, C., Holten, D., Bocian, D. F., and Lindsey, J. S. (2004) Swallowtail porphyrins: Synthesis, characterization and incorporation into porphyrin dyads. *J. Org. Chem. 69*, 3700−3710.
(35) Thamyongkit, P., and Lindsey, J. S. (2004) Synthesis of swallowtail-substituted multiporphyrin rods. *J. Org. Chem. 69*, 5796−5799.
(36) Langhals, H., Ismael, R., and Yürük, O. (2000) Persistent fluorescence of perylene dyes by steric inhibition of aggregation. *Tetrahedron 56*, 5435−5441.
(37) Srinivasan, N., Haney, C. A., Lindsey, J. S., Zhang, W., and Chait, B. T. (1999) Investigation of MALDI-TOF mass spectrometry of diverse synthetic metalloporphyrins, phthalocyanines, and multiporphyrin arrays. *J. Porphyrins Phthalocyanines 3*, 283−291.
(38) Marshall, J. A., Andrews, R. C., and Lebioda, L. (1987) Synthetic studies on cembranolides. Stereoselective total synthesis of isolobophytolide. *J. Org. Chem. 52*, 2378−2388.
(39) Callard, R. E., Smith, C. M., and Beverley, P. C. (1982) Phenotype of human T helper and suppressor cells in an in vitro specific antibody response. *Eur. J. Immunol. 12*, 232−236.
(40) Laha, J. K., Dhanalekshmi, S., Taniguchi, M., Ambroise, A., and Lindsey, J. S. (2003) A scalable synthesis of meso-substituted dipyrromethanes. *Org. Process Res. Dev. 7*, 799−812.
(41) Vader, J., Sengers, H., and de Groot, A. (1989) The stereoselective syntheses of substituted furo[2,3b]furans (part II). *Tetrahedron 45*, 2131−2142.
(42) Taniguchi, M., Balakumar, A., Fan, D., McDowell, B. E., and Lindsey, J. S. (2005) Imine-substituted dipyrromethanes in the synthesis of porphyrins bearing one or two *meso* substituents. *J. Porphyrins Phthalocyanines 9*, 554−574.
(43) Tamaru, S.-I., Yu, L., Youngblood, W. J., Muthukumaran, K., Taniguchi, M., and Lindsey, J. S. (2004) A tin-complexation strategy for use with diverse acylation methods in the preparation of 1,9-diacyldipyrromethanes. *J. Org. Chem. 69*, 765−777.
(44) Wedel, M., Walter, A., and Montforts, F.-P. (2001) Synthesis of metalloporphyrins and metallochlorins for immobilization on electrode surfaces. *Eur. J. Org. Chem*. 1681−1687.
(45) Lee, C.-H., and Lindsey, J. S. (1994) One-flask synthesis of *meso*-substituted dipyrromethanes and their application in the synthesis of *trans*-substituted porphyrin building blocks. *Tetrahedron 50*, 11427−11440.
(46) Fan, D., Taniguchi, M., Yao, Z., Dhanalekshmi, S., and Lindsey, J. S. (2005) 1,9-Bis(*N*,*N*-dimethylaminomethyl)dipyrromethanes in the synthesis of porphyrins bearing one or two *meso* substituents. *Tetrahedron 61*, 10291−10302.
(47) Zhang, D., and Poulter, C. D. (1993) Biosynthesis of archaebacterial ether lipids. Formation of ether linkages by prenyltransferases. *J. Am. Chem. Soc. 115*, 1270−1277.
(48) Xu, Y., and Prestwich, G. D. (2002) Concise synthesis of acyl migration-blocked 1,1-difluorinated analogues of lysophosphatidic acid. *J. Org. Chem. 67*, 7158−7161.
(49) Muthukumaran, K., Loewe, R. S., Ambroise, A., Tamaru, S.-I., Li, Q., Mathur, G., Bocian, D. F., Misra, V., and Lindsey, J. S. (2004) Porphyrins bearing arylphosphonic acid tethers for attachment to oxide surfaces. *J. Org. Chem. 69*, 1444−1452.
(50) Loewe, R. S., Ambroise, A., Muthukumaran, K., Padmaja, K., Lysenko, A. B., Mathur, G., Li, Q., Bocian, D. F., Misra, V., and Lindsey, J. S. (2004) Porphyrins bearing mono or tripodal benzylphosphonic acid tethers for attachment to oxide surfaces. *J. Org. Chem. 69*, 1453−1460.

BC050337W

Fractionation of Serum Components Using Nanoporous Substrates

David Geho,*[,†,⊗] Mark Ming-Cheng Cheng,[∥] Keith Killian,[†] Mark Lowenthal,[†] Sally Ross,[⊥] Kristina Frogale,[†] Jasper Nijdam,[∥] Nicholas Lahar,[†] Don Johann,[†] Paul Herrmann,[†] Gordon Whiteley,[⊥] Mauro Ferrari,[§] Emanuel Petricoin,[‡,⊗] and Lance Liotta[†,⊗]

Laboratory of Pathology, FDA-NCI Clinical Proteomics Program, National Cancer Institute, National Institutes of Health, Bethesda, Maryland 20892, Center for Biologics Evaluation and Research, FDA-NCI Clinical Proteomics Program, Food and Drug Administration, Bethesda, Maryland 20892, Davis Heart and Lung Research Institute, The Ohio State University, 473 West 12th Avenue, Columbus, Ohio 43210, Comprehensive Cancer Center, The Ohio State University, 1381 Kinnear Road, Suite 100, Columbus, Ohio 43212, and Clinical Proteomics Laboratory, SAIC-Frederick, Inc., Gaithersburg, Maryland 20878.
Received November 22, 2005; Revised Manuscript Received March 29, 2006

Numerous previously uncharacterized molecules resident within the low molecular weight circulatory proteome may provide a picture of the ongoing pathophysiology of an organism. Recently, proteomic signatures composed of low molecular weight molecules have been identified using mass spectrometry combined with bioinformatic algorithms. Attempts to sequence and identify the molecules that underpin the fingerprints are currently underway. The finding that many of these low molecular weight molecules may exist bound to circulating carrier proteins affords a new opportunity for fractionation and separation techniques prior to mass spectrometry-based analysis. In this study we demonstrate a method whereby nanoporous substrates may be used for the facile and reproducible fractionation and selective binding of the serum-based biomarker material, including subcellular proteins found within the serum. Aminopropyl-coated nanoporous silicon, when exposed to serum, can deplete serum of proteins and yield a serum with a distinct, altered MS profile. Additionally, aminopropyl-coated, nanoporous controlled-pore glass beads are able to bind a subset of serum proteins and release them with stringent elution. The eluted proteins have distinct MS profiles, gel electrophoresis profiles, and differential peptide sequence identities, which vary based on the size of the nanopores. These material surfaces could be employed in strategies for the harvesting and preservation of labile and carrier-protein-bound molecules in the blood.

INTRODUCTION

Since the introduction of the microscope along with laboratory methods revolutionized medical pathology practice, technologic advancement has unveiled increasingly sensitive and insightful views of disease processes. Following in this rich tradition of constant integration of new technologies, modern pathology is currently evaluating the applicability of novel testing methods for patient-based diagnostics. One such method rests on technical advances resulting in more sensitive mass spectrometry instruments. These instruments are currently being used to mine patient body fluid and tissue samples for potential diagnostic signatures (*1*). These efforts are part of a new discipline, namely tissue proteomics, wherein the measurements of a multiplexed combination of molecules within the patient tissues are being analyzed and correlated with disease states and outcomes. Because of the potential increase in both specificity and sensitivity using a combination marker approach, it may be possible to detect potentially lethal diseases in early stages when they are more curable.

* To whom correspondence should be addressed. Paul Herrmann, M.D., Ph.D., Laboratory of Pathology, National Cancer Institute, Rm. 2A33, Bldg. 10, 10 Center Dr., Bethesda, MD 20892. E-mail: herrmanp@mail.nih.gov.

[†] Laboratory of Pathology, FDA-NCI Clinical Proteomics Program.

[‡] Center for Biologics Evaluation and Research, FDA-NCI Clinical Proteomics Program.

[§] Davis Heart and Lung Research Institute, The Ohio State University.

[∥] Comprehensive Cancer Center, The Ohio State University.

[⊥] SAIC-Frederick, Inc.

[⊗] Current address: Center for Applied Proteomics and Molecular Medicine, George Mason University, Manassas, VA 20110.

Proteomic fingerprinting methods utilizing mass spectrometry coupled to bioinformatics analysis have yielded clues about the existence of potential diagnostic information content within the low molecular weight range of the blood and tissue proteome (*2*−*9*). Now that this information archive has been uncovered by these initial studies, efforts are underway to sequence and characterize the underlying components of these disease-related fingerprints.

The molecules that coalesce to form a diagnostic portrait are likely diverse small proteins, and protein fragments, shed by numerous tissues into the interstitial fluid with an equilibrium established between cells and the intravascular compartment. The constant synthesis and degradation of proteins by cells within the body should reflect the overall state of health, and some of the synthesized proteins and fragments are expected to be present within the serum. The expressed proteome within a host, in fact, represents a complex interplay between all cells (normal and diseased cells). It is for this reason that the body fluids such as serum are thought to be a rich source of information for the discovery of biomarkers and the development of diagnostic tests. Recent work indicates that the low molecular molecules that have comprised the previously described disease fingerprints actually exist bound to larger carrier molecules (*10*). In particular, high abundance carrier proteins such as albumin have been found to bind lower molecular weight proteomic species that could serve as potential biomarkers (i.e. proteolytic fragments of BRCA2) (*11*). On the basis of these findings, isolation of low molecular weight molecules as well as the resident carrier proteins that harbor them and protect them from renal clearance is now a primary object in MS-based tissue proteomics for discovery and sequencing of new biomarkers.

10.1021/bc0503364 CCC: $33.50 © 2006 American Chemical Society
Published on Web 05/03/2006

A more comprehensive and expansive analysis of the carrier protein-bound low molecular weight proteome requires the development of novel fractionation methods. Fabrication of nanoporous material surfaces is one strategy for methodically parsing the various subsets of proteins and protein fragments present within the circulation (*12*). These types of materials have the ability to be modified and functionally manipulated through specific chemical derivitization such that selective and custom binding and fractionation can ensue. Moreover, nanoporosity dramatically increases the surface areas of the system such that the selective fractionation and binding occurs with potentially higher efficiency and speed.

In this report, we describe the use of nanoporous material surfaces as a fractionation tool for serum-based analysis and biomarker discovery. Nanoporous silicon wafers are used to selectively deplete serum of a fraction of proteins. By the use of controlled-pore nanoporous glass beads, distinct subsets of the proteome are harvested from serum for subsequent elution and evaluation. Within these subsets subcellular proteins are identified, lending credence to the hypothesis that the serum reflects cellular pathology. The types of materials utilized hold significant promise as the next generation of fractionation and separation tools are developed for proteomic analysis and biomarker discovery. Future studies will focus on using these fractionation techniques to isolate low abundance molecules from the serum.

EXPERIMENTAL PROCEDURES

Serum Samples. The serum sample consisted of a reference pool from normal donors that was stored at −80 °C.

Chemicals. Acetonitrile (ACN) (HPLC grade), ammonium bicarbonate (NH_4HCO_3), iodoacetamide (97%), methanol (99+%), and dithiothreitol (DTT) were purchased from Sigma-Aldrich Co. (St. Louis, MO). Formic acid (88%) and acetic acid (glacial) were purchased from Mallinckrodt Baker (Phillipsburg, NJ). H_2O was doubly distilled in house with Kontes High Purity Water System. Porcine sequencing grade modified trypsin was purchased from Promega (Madison, WI).

Other Materials. Bovine serum albumin purchased from (Sigma-Aldrich Co, St. Louis, MO). SYPRO Ruby protein gel stain purchased from Molecular Probes (Eugene, OR). Precast 4−12% Bis-tris 1D gels, LDS sample and running buffers, antioxidant, and the prestained Benchmark protein ladder were purchased from Invitrogen Co. Fused silica is from Polymicro Technologies (Phoenix, AZ).

Nanoporous Silicon Wafer Fabrication. Boron-doped, (100) oriented silicon wafers (from Silicon Quest Inc) with resistivity $< 0.005\ \Omega\cdot$cm were used as the substrates. Wafers were cleaned in a piranha solution (H_2SO_4:H_2O = 1:1) at 120 °C for 30 min. This was followed by oxide removal in HF:H_2O = 1:10 and rinsing in deionized water. The porous silicon surfaces were prepared by electrochemical etching in a homemade Teflon cell. The wafers sit on the Teflon cell base with aluminum foil (0.1 mm thick) underneath to provide the electrical contact. A platinum mesh was positioned in the cell cavity as a counter electrode. The electrolyte was a 1:1 mixture by volume of 49% HF and ethanol. A constant current density 72 mA/cm^2 was applied for 65 s. Immediately after porous silicon formation, the sample was rinsed in deionized water and placed under vacuum to remove the moisture. The porous silicon was silanized in 10% APTES (aminopropyltriethoxysilane) in toluene. To remove the air bubbles from the nanopores, the porous silicon was placed under vacuum for 3 min. The reaction solution was refluxed for 3 h at room temperature in a sealed dish. The porous silicon was rinsed several times with toluene and acetone and dried in a N_2 flow. The Barret−Joyner−Halenda (BJH) model applied to the nitrogen desorption branch of the isotherms indicated a pore size distribution centered at 2−20 nm (data not shown) (*13*−*16*).

Partial Depletion of Serum Proteins Using a Nanoporous Silicon Wafer. Aminopropyl-coated nanoporous silicon wafers were placed in 1.5 mL tubes and washed four times in deionized water. Pooled serum samples (500 μL), diluted 1:5 in deionized water, were then applied to the wafers and the mixtures incubated at room temperature for 1.5 h. Following this incubation, the diluted serum supernatants were removed and stored for later MS analysis at −80 °C. For controls, diluted serum samples were frozen as well. As a further control, the wafers were also incubated with deionized water in place of diluted serum.

Proteomic Harvesting Using Nanoporous Controlled-Pore Glass Beads. Aminopropyl-coated controlled-pore glass beads, with pore sizes of 70 or 17 nm, were purchased from Sigma (St. Louis, MO). For each experiment, 10 mg of beads was measured into 1.5 mL tubes. The beads were washed four times in deionized water. Pooled serum, diluted 1:5 in deionized water, was then applied to the bead samples and the mixtures incubated at room temperature for 1.5 h. Following this incubation, the diluted serum supernatants were removed and saved. The beads were then washed two times using 1 mL of deionized water. Following this wash, 500 μL of elution buffer (5 mL of acetonitrile, 5 mL water, 10 μL of trifluoroacetic acid) was applied to the samples, which were then rotated for 0.5 h at room temperature. The eluant was then collected and stored for later MS analysis at −80 °C.

Mass Spectrometry Analyses. Low resolution mass spectrometry-generated spectral profiles were used as a generalized unbiased readout to assess fractionation performance. Weak cation exchange SELDI chips were processed using a Biomek 2000 bioprocesser (WCX2 ProteinChips, Ciphergen Biosystems, Inc.). HCl (10 mM, 100 μL) was applied to the chip followed by a 5-min incubation. The HCl was then removed via aspiration and was followed by a 1-min incubation with 100 μL of water. The water was aspirated and freshwater applied for an additional 1 min. This was followed by the addition of 100 μL of 10 mM ammonium acetate with 0.1% Triton X, applied to the chip for a 5 min incubation. The ammonium acetate mixture was then aspirated and discarded followed by another application of the ammonium acetate mixture for an additional 5-min incubation. After these preparative steps, the chips were dried with the assistance of a vacuum. Sample (5 μL) (such as serum) was then applied to the chip spots and incubated for 55 min. The chips were washed three times with 150 μL of phosphate buffered saline followed by 150 μL of water. The chips were then vacuum-dried and 1.0 μL of a 30% solution of cinnaminic acid in 50% (v/v) acetonitrile/0.5% trifluoroacetic acid was applied to each protein spot, twice with drying between applications. The chips were then assayed using a PBS-II mass spectrometer (Ciphergen Biosystems, Inc.). The spectrum for each spot was collected using the following protocol settings: detector voltage was 1800 V, focus mass was 6000 Da, the high mass limit was 20000 Da, the sensitivity gain was set to 5, the laser intensity was 145, 15 laser shots were taken per position, and the number of positions ranged from 20 to 80 incrementing every five positions. A protocol was created which processed all of the samples identically.

Protein Sequencing Studies. *Protein Assay.* Bead-fractionated samples from 17 μm and 70 μm pore beads were assayed by a traditional Bradford assay using bovine serum albumin (BSA) standard ranging from 200 ug/mL to 1 mg/mL monitored at 595 nm on a UV−Vis spectrophotometer (Spectromax Plus 384, Molecular Devices).

*1D Gel Separation and Digestion.*Amounts of 15 μg of each bead fractionated sample and 3 μL of raw serum were diluted

in 30 μL of LDS sample buffer and boiled for 5 min at 95 °C. The fractions were run on a 1D precast gel (4−12% Bis-tris) to isolate desired molecular weight regions of the complex protein mixture. The gel was washed thoroughly with ddH_2O, fixed in a 50% methanol/ 10% acetic acid solution for 30 min, stained with Sypro ruby stain overnight, and destained in ddH_2O for 3 h prior to UV excitation and visualization. The gel was sliced into 1 mm^2 gel regions, and the gel bands were destained in 50% methanol. Gel bands were reduced and alkylated with 10 mM DTT and 55 mM iodoacetamide, incubated at 4°C for 1 h in trypsin (20 ng/μL), and allowed to digest overnight (16 h) at 37 °C in 25 mM NH_4HCO_3. The following morning, proteins were extracted from the gel with repeated incubations of 70% ACN/5% formic acid solution.

μLC/MS/MS Analysis. The samples were lyophilized to near dryness and reconstituted in 6.5 μL of HPLC buffer A (94.9% H_2O, 5.0% ACN, 0.1% FA) for mass spec analysis. Microcapillary reverse phase LC/MS/MS analysis was performed with Dionex's LC Packings liquid chromatography system coupled online to a ThermoFinnigan LCQ Classic ion trap mass spectrometer (San Jose, CA) with a modified nanospray source. Reverse phase separations were performed with an in-house, slurry packed capillary column. The C_{18} silica-bonded column is 75 μm i.d., 360 μm o.d., 10 cm long fused silica packed with 5 μm beads with 300 Å pores (Vydac, Hesperia, CA). A μ-precolumn PepMap, 5 mm, C_{18} cartridge (Dionex) acts as a desalting column. Sample is injected in μL pick-up mode and washed with Buffer A for five minutes prior to a linear gradient elution with Buffer B (95% ACN/ 5% H_2O/ 0.1% formic acid) up to 85% over 95 min at a flow rate of 200 nL/ minute. Full MS scans are followed by four MS/MS scans of the most abundant peptide ions (in a data dependent mode), and collision-induced dissociation (CID) is performed at a collision energy of 38% with the ion spray voltage set to 2.00 kV, capillary voltage, and temperature to 22.80 V and 180 °C, respectively.

Data Analysis. Data analysis was performed by searching MS/MS spectra against the European Bioinformatics Institute of the nonredundant proteome set of Swiss-Prot, TrEMBL and Ensembl entries through the Sequest Bioworks Browser (ThermoFinnigan). Peptides were considered legitimate hits after filtering the correlation scores (refer below) and manual inspection of the MS/MS data. The criteria used to filter data in this manuscript are at least as stringent as most literature citations.

charge	X_{corr}	DeltaCN	ions	Rsp
+1	>1.9	>0.1	>50%	=1
+2	>2.5	>0.1	>50%	=1
+3	>3.5	>0.1	>50%	=1

Accepted peptide hits are required to have an X_{corr} ranking = 1 relative to all other peptides in the database.

RESULTS

Serum Depletion Using Nanoporous Silicon. One strategy for fractionating serum is to deplete the serum of a portion of its protein content, followed by analysis of the remaining protein species (Figure 1A). To try this approach, a nanoporous substrate was produced out of silicon with pore sizes ranging from 2 to 20 nm. Nanoporous silicon wafers possessing an asymmetric surface were incubated with pooled serum samples. After an 1.5 h incubation, the wafers were removed and the remaining proteins within the serum were subjected to MS evaluation (Figure 1B). Of note, the emergence of a new ion peak pattern from surface-enhanced laser desorption ionization (SELDI) mass spectrometry resulted from this fractionation technique. In fact, the entire spectra appeared dramatically different compared to unfractionated serum alone. In the case of this depletion experiment, two peaks within the MS spectra were markedly changed. More specifically, a peak at 8122 *m*/*z* was significantly enhanced in the depleted sample, when compared with the native serum sample. On the other hand, the 8927 *m*/*z* peak was markedly diminished within the depleted sample, when compared with its dominance in native serum. Thus, the incubation followed by the removal of the nanoporous particles altered the spectral qualities of the serum, enhancing the profile of a previously minor peak into the dominating area of intensity.

Molecular Harvesting Using Nanoporous Controlled-Pore Glass. As an alternative to measuring depleted serum for proteomic signatures, a bead harvesting strategy was developed for isolating molecular species for subsequent elution and profiling (Figure 2A). Similar aminopropyl-coated glass beads with distinct pore sizes (17 nm versus 70 nm) were incubated with serum for selective molecular isolation and release. Nitrogen adsorption and desorption isotherm analysis was used to characterize surface area and pore volume (data not shown) (*13*−*16*). The surface area of the 17 nm beads is 30.8 m^2/g and the pore volume is 0.032 cm^3/g. For 70 nm beads, the surface area is 130.5 m^2/g and the pore volume is 0.93 cm^3/g. While surface treatments and composition of the particles was similar, the surface area and pore volumes were distinct, allowing for comparison of their respective fractionation properties. Following incubation with serum, the beads were gently washed with water, and then the bound molecules were eluted using the elution buffer. The eluted species were then analyzed via SELDI MS and compared with the spectra of unfractionated serum (Figure 2B). Visual inspection of the 17 nm bead eluate revealed a unique MS spectral portrait when compared with unprocessed serum. A marked difference at the *m*/*z* of 7762 was noted when comparing the harvested sample and the native serum. While the 8927 *m*/*z* peak dominates the spectral landscape in normal serum, it is the 7762 *m*/*z* peak that assumes the dominant role in the harvested subset.

To assess the effect that the nanopore size and surface area played in the generation of unique spectral signatures, a 70 nm pore-sized controlled pore glass bead was used in an identical experiment. Strikingly, a different SELDI MS spectra resulted using the larger pore-sized controlled-pore glass beads (Figure 3). At 6629 *m*/*z*, a new major peak that dominated the spectral pattern eluted from the beads. The normal serum peak at the same *m*/*z* was barely discernible. In contrast, the 8927 peak in normal serum assumed a minor status within the set of proteins eluted from the larger pore beads.

To further characterize the molecular components eluted from either the 17 nm pore-sized or 70 nm pored-sized beads, 15 μg of protein from each sample was run on a 4−12% Bis-Tris SDS−PAGE gel followed by staining with Sypro Ruby Red (Figure 4). Throughout the molecular weight spectrum, distinct differences were noted between the eluates from the two types of beads. This finding was consistent with the marked differences noted in the SELDI-based analysis. Analysis of the molecular content of the eluants via one-dimensional electrophoresis provided additional visual confirmation that the beads were differentially fractionating the molecular content of serum.

To further characterize differences between the eluants from the 17 nm pore-sized beads and the 70 nm pore-sized beads, bands from a SDS−PAGE gel were excised and the protein content of the gel slices were digested using trypsin. The resulting peptide fragments were analyzed using electrospray ionization mass spectrometry. Following interrogation of the spectral data, peptide identities were assigned to the proteomic content of the gel (Figure 5). While there was some overlap of the peptide species identified between the 17 nm pore-sized beads and the 70 nm pore-sized beads (six peptides shared),

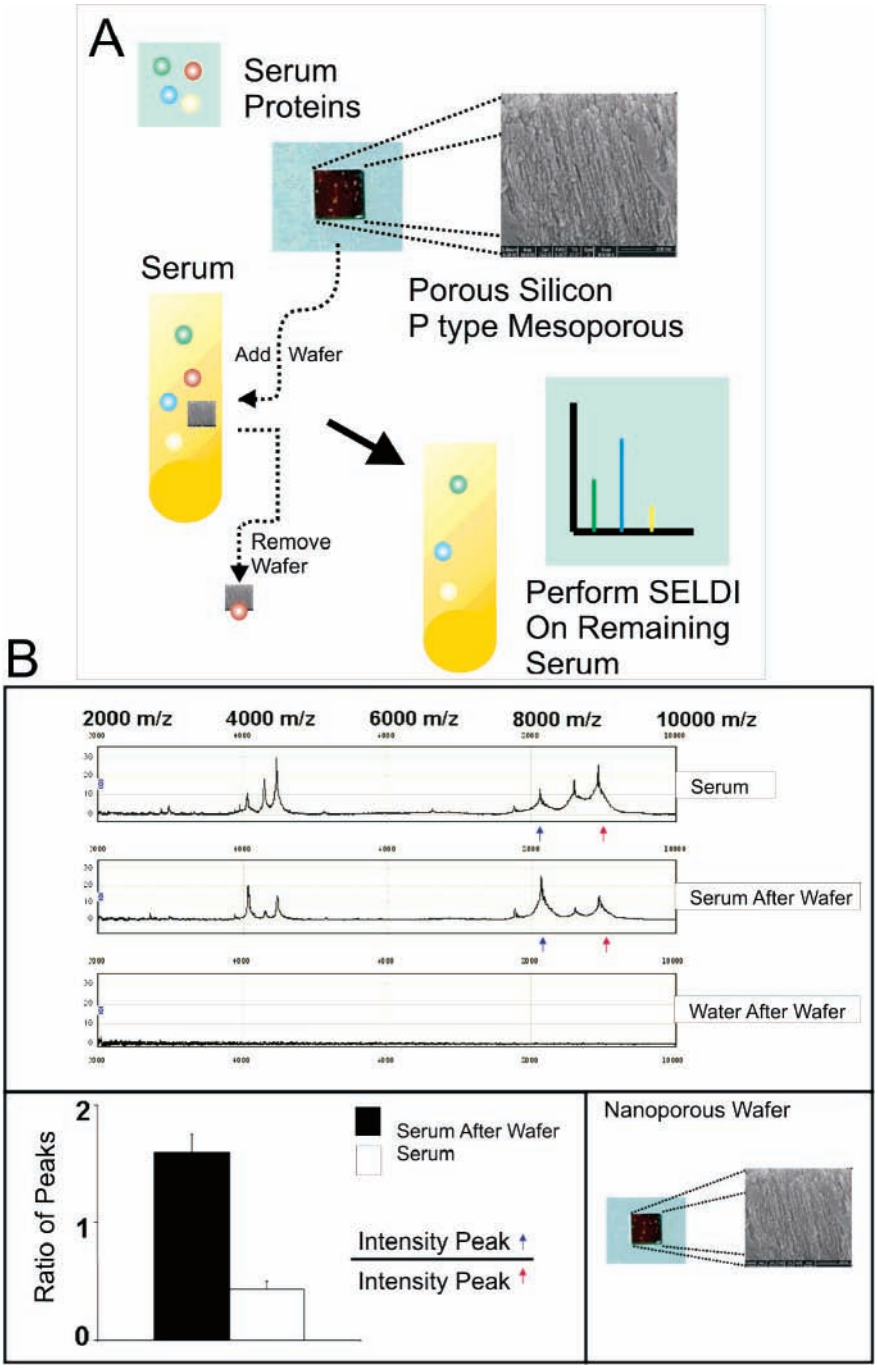

Figure 1. Serum depletion using nanoporous materials. (A) Strategy for partial depletion of serum using nanoporous silicon wafers. Porous silicon wafers are generated and incubated with serum. After an incubation period, the wafers are removed and the remaining serum sample is spotted on a weak cation exchange chip for SELDI analysis and compared to MS spectra from control serum not exposed to the wafer. (B) MS analysis of serum partially depleted using a nanoporous silicon wafer. Serum is incubated with a nanoporous silicon wafer coated with aminopropyl groups. Following incubation, the serum is bound to a weak cation exchange chip and then undergoes MS analysis. MS fingerprints are obtained. Native serum is compared with serum after wafer depletion. A dominant peak is present in serum (red arrow) that overshadows a smaller peak within a similar *m*/*z* range (blue arrow). In the serum partially depleted of its proteomic content by incubation with the nanoporous wafer, the peak designated by the blue arrow assumes a dominant profile when compared to the peak marked with the red arrow. When the ratio of relative peak intensity is compared between the blue and red peaks, a marked shift is demonstrated between native serum and serum after depletion using the nanoporous silicon wafer.

differences were observed, indicating that significant fractionation had occurred. Thus, three distinct analyses indicate that the glass beads with different pore sizes offer a means of fractionating serum components.

DISCUSSION

Proteomic profiling using mass spectrometry coupled with bioinformatics data mining approaches has revealed a complex and exciting information archive, contained within the low molecular weight range of the circulatory proteome, which may contain important diagnostic information. Nanoporous material surfaces, such as the silicon wafer and the controlled pore glass beads used in the present study, provide a new strategic means to fractionate and manipulate biologic information contained within body fluids such as serum. A systematic evaluation of nanoporous material surfaces combining MS analysis with bioinformatic interrogation may reveal certain fractionation schemes with enhanced disease detection properties, identify

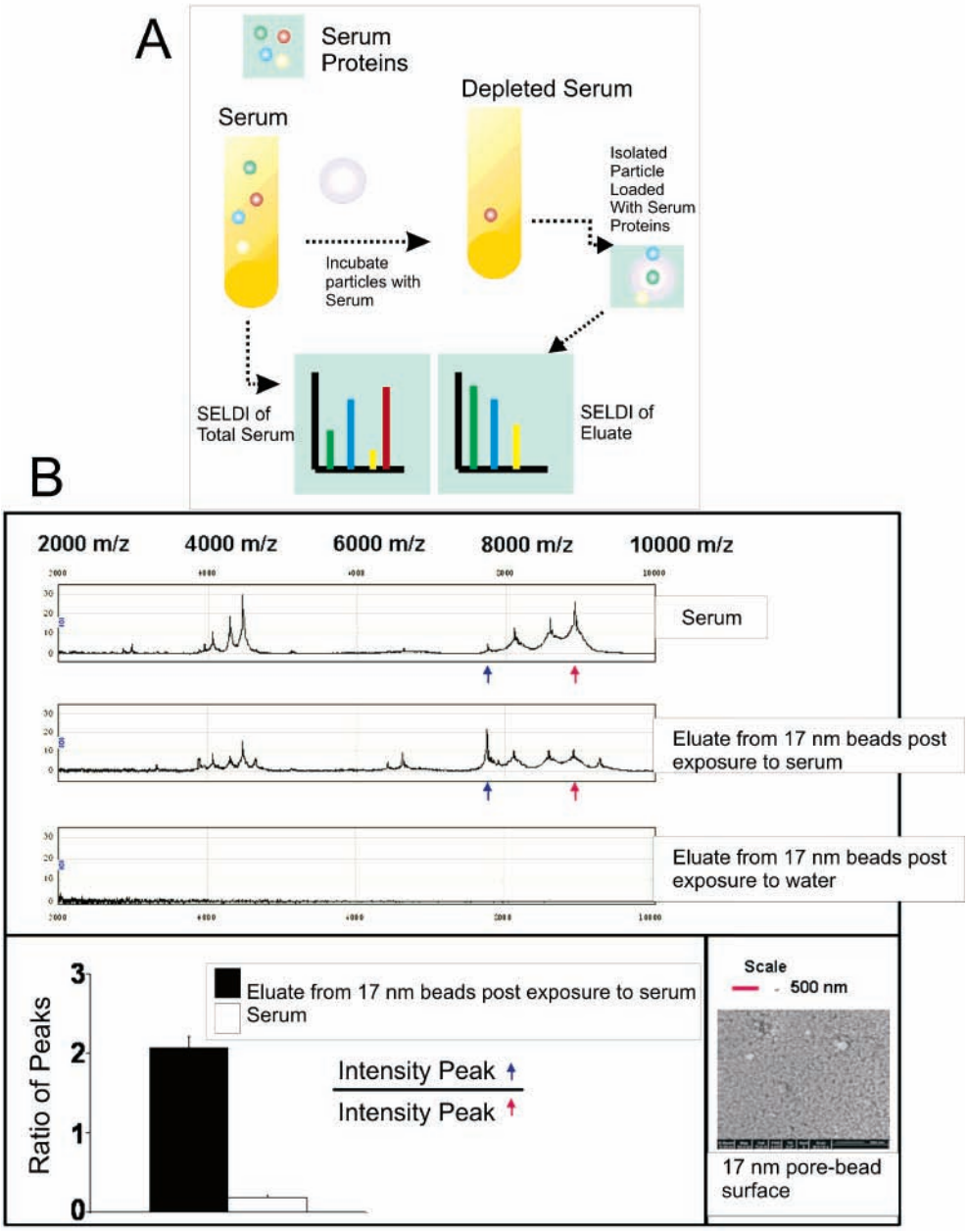

Figure 2. Harvesting molecules from serum using nanoporous glass beads. (A) Strategy for harvesting molecules from serum using nanoporous glass beads. Glass beads coated with aminopropyl groups are incubated with serum. After an incubation period, the beads are removed, washed, and bound molecules are eluted and spotted on a weak cation exchange chip for SELDI analysis and compared to MS spectra from control serum. (B) MS analysis of molecules harvested by nanoporous beads. Serum is incubated with glass beads coated with aminopropyl groups. Following incubation, the serum is bound to a weak cation exchange chip and then undergoes MS analysis. MS profiles are obtained. Native serum is compared with molecules harvested using 17 nm beads. A dominant peak is present in serum (red arrow) that overshadows a smaller peak within a similar *m*/*z* range (blue arrow). In the eluted sample, the peak designated by the blue arrow assumes a dominant profile when compared to the peak marked with the red arrow. When the ratio of relative peak intensity is compared between the blue and red peaks, a marked shift is demonstrated between native serum and molecules harvested and subsequently eluted from the beads.

an expanded set of molecules for workup and provide a more facile and robust means for purification, fractionation, and peptide/protein sequencing of the molecules themselves.

To that end, in this study, fractionation of serum using material surfaces with nanopores can result in significantly altered spectral profiles, altered 1-D electrophoretic profiles, and differential sequence identities. Each of these parameters suggest that a significant, unique fractionation had occurred using either the 17 nm pore-sized beads or the 70 nm pore-sized beads. Of note, while six of the peptide species identified by ESI MS were harvested using either of the bead types, there were distinct peptides that were isolated using only one type of the beads. The sequenced peptides included highly abundant plasma proteins as well as lower abundance species. In addition, subcellular protein species not traditionally associated with serum were identified. Using the 70 nm pore-sized beads, the protein named mediator of RNA polymerase II transcription subunit 8 homologue was isolated. In the 17 nm pore-sized bead fraction, histone 4 and golgi autoantigen were harvested. The presence of these molecular species, not traditionally thought of as serum proteins, supports the hypothesis that fragments of organismal proteins make their way into the serum and provide a potential portrait of the overall state of the organism.

The serum and circulatory proteome is a mixture of high and low abundance molecules, with most biomarkers that carry important diagnostic information thought to reside in the lower abundance region of the concentration range. Certainly, a challenge for tissue proteomics is the development of tools to

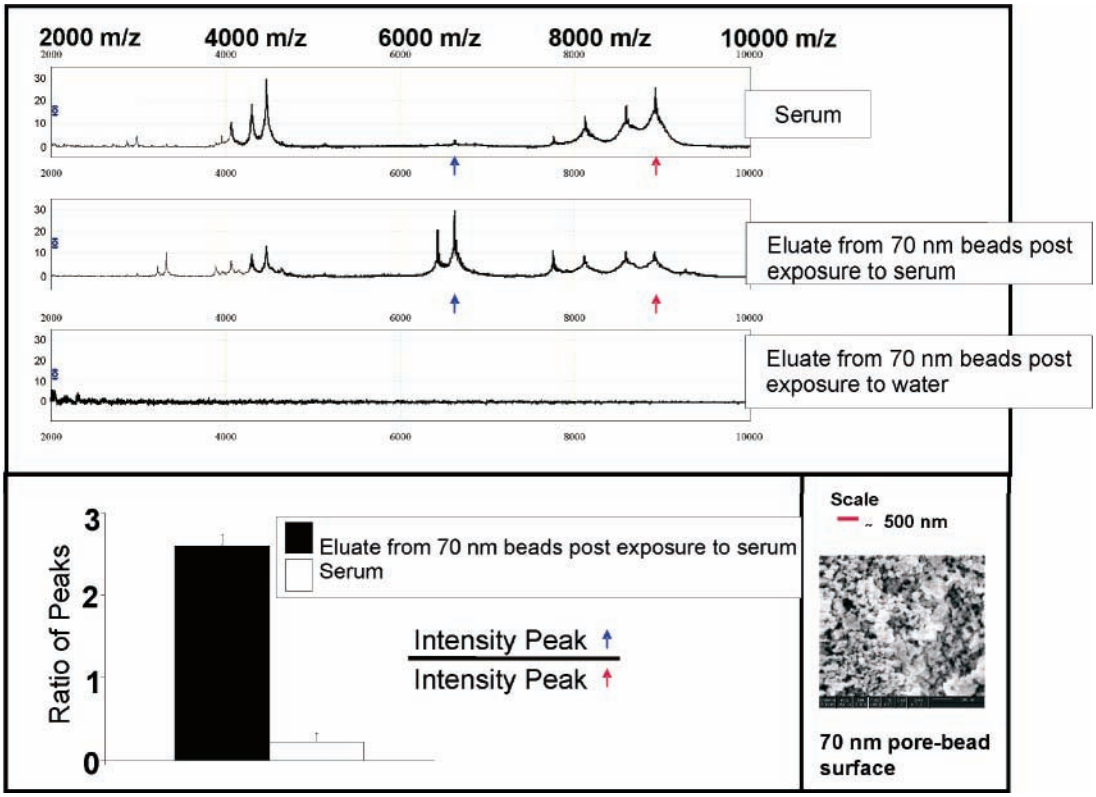

Figure 3. MS analysis of molecules harvested by 70 nm porous beads. Serum is incubated with glass beads with 70 nm pores and with coated aminopropyl groups. Following incubation, the serum is bound to a weak cation exchange chip and then undergoes MS analysis. MS profiles are obtained. Native serum is compared with molecules harvested using 70 nm beads. A dominant peak is present in serum (red arrow) that overshadows a smaller peak within a similar *m*/*z* range (blue arrow). In the eluted sample, the peak designated by the blue arrow assumes a dominant profile when compared to the peak marked with the red arrow. When the ratio of relative peak intensity is compared between the blue and red peaks, a marked shift is demonstrated between native serum and molecules harvested and subsequently eluted from the beads.

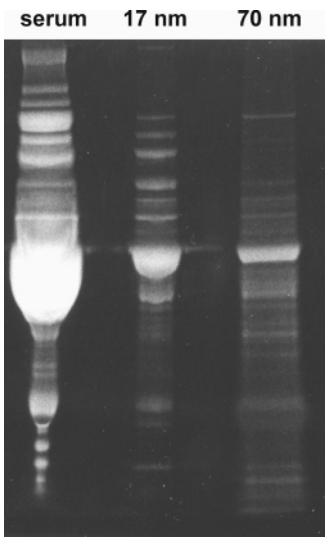

Figure 4. SDS−PAGE analysis of molecules eluted from 17 nm pore-sized glass beads and 70 nm pore-sized glass beads. These are compared with diluted, unfractionated serum.

rapidly identify these low abundance molecules in complex biological samples. One approach is to develop flow through surfaces or depletion architectures for rapid, robust, and facile fractionation and selective purification. Material surfaces such as those used in the assays presented here are amenable to physicochemical modification whereby distinct pore sizes and charge characteristics can be added to the pore surfaces. These discriminatory properties would allow fine-tuning of the fractionation of proteins within the serum.

In the present study, the serum proteins were fractionated via noncovalent associations with the material surfaces. It is becoming increasingly apparent that low molecular weight, low abundance molecules are carried by high abundance serum proteins. In the future, it will be important to use methods such as those described above to capture and immobilize carrier proteins. For example, reactive groups could be added to the material surfaces that immobilize differentially isolated carrier proteins in order to further refine the fractionation properties of the substrate. Through immobilizing high abundance molecules such as albumin onto the highly porous, size-selective material surfaces, it may be possible to subsequently elute lower abundance molecules from the immobilized carrier proteins. It is likely that such an approach could maximize the retrieval of low abundance molecular information. Further studies are required to evaluate the relative abundance distribution over the molecular weight distribution using a fractionation strategy similar to the one described above. Similar strategies have been employed for discrimination of DNA molecules (*17*−*19*). The present study represents an initial step in the use of material surfaces to parse high and low abundance molecules into more manageable groupings.

These experiments reveal that fractionation of serum using material surfaces with nanopores can result in significantly altered spectral profiles.. Assessment of the power of this approach will require continued optimization of the methodologies such that a series of manipulations could dramatically expand the low molecular weight portrait observed. In the present study, incubation of the serum proteins with the substrates was performed under physiologic conditions. In this setting, it is likely that the low molecular weight serum molecules that are potential biomarkers remain bound to the

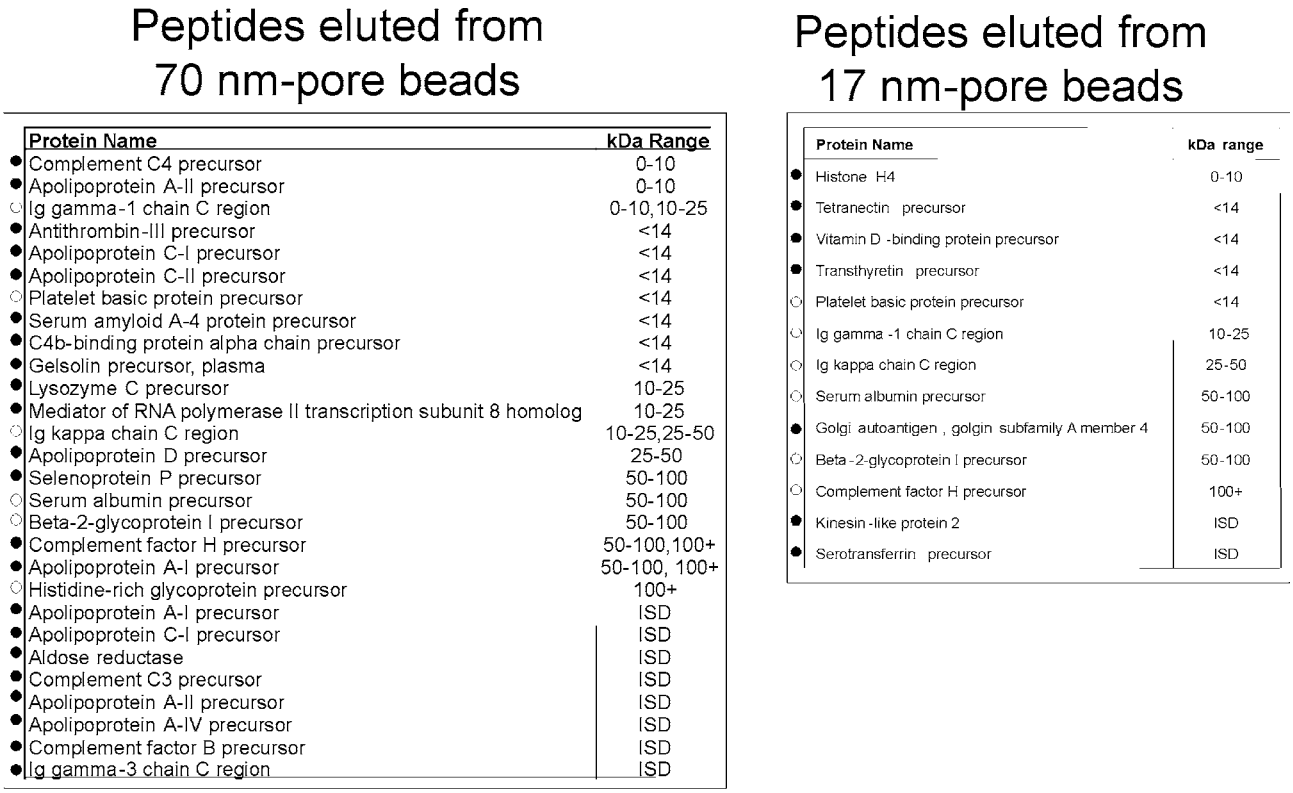

Figure 5. Peptide sequencing results showing protein sequences obtained from eluents of 17 nm pore-sized glass beads and 70 nm pore-sized glass beads. Black circles indicate peptide sequences unique to either the 17 or 70 nm pore-sized glass beads. The open circles indicate peptide sequences shared by the 17 and 70 nm pore-sized glass beads. The kDa ranges indicate the 1D gel slice size range from which the peptides were extracted prior to MS analysis.

high abundance proteins, like albumin, that carry them in serum. As an alternative approach, the serum proteins could be denatured through heat or pH treatment, which would disrupt the noncovalent association of the low molecular weight proteins from the larger carrier proteins. Liberated low molecular weight species could then more freely percolate into the pores of the particles, potentially enhancing the fractionation of the serum molecules. The solvents used as eluents could likewise be expanded in future studies. For example, a spectrum of salt concentrations could be tested in eluants in order to determine the optimal conditions for eluting low molecular weight species of interest.

One potential use for such surfaces is in collection devices for serum samples at the clinic. As labile molecules in the serum increasingly become interesting as biomarkers, standardized collection procedures will have to be initiated. Nanoporous substrates may offer one means of sequestering labile small molecules in a format readily adaptable to serum collection procedures. In this type of application, the specialized nanoporous substrate becomes akin to specialized tissue fixatives which are chosen in select cases to preserve specific tissue properties for subsequent visualization.

Because silicon can be fashioned into micron-sized particles, nanoporous substrates could be developed that would be in the size range of blood cells. These particles may be designed with a range of pore sizes and other physicochemical properties for fractionation of abundant serum proteins and the low molecular weight cargo they carry. As an added feature, the micron-sized particles could be coded with a discriminating tag, such as a metallic tag or quantum dot. Such a strategy would allow blood to be harvested and the particles isolated from the blood cells through a sorting or enrichment process (*20*−*22*). While these particles might initially be used in blood collection tubes, an eventual utilization might include infusion of the particles for longer term in vivo monitoring (*23*). Ultimate approval for this type of strategy would of course require biocompatibility and toxicity profiling of the particles, not unlike the safety profiling carried out for infused radiocontrast agents and indwelling medical devices.

This present study demonstrates the feasibility of nanoporous-based separation and fractionation as a means to selectively fractionate, purify, and analyze the circulatory proteome. The ultimate objective is to design a new method that will allow for the rapid isolation and sequence identification of new low molecular weight biomarkers for disease detection and risk stratification. Further analysis of this approach in specific disease states will be required to fully characterize the utility of these approaches. Additional pore sizes, surface modifications, and carrier protein (e.g. albumin) immobilization strategies will be screened as well for their abilities to achieve expanded and robust fractionation and purification of low molecular weight species.

ACKNOWLEDGMENT

This project has been funded in part with Federal Funds from the National Cancer Institute, National Institutes of Health, under Contract No. NO1-CO-12400. This research was supported in part by the Intramural Research Program of the NIH, National Cancer Institute, Center for Cancer Research.

LITERATURE CITED

(1) Rosenblatt, K. P., Bryant-Greenwood, P., Killian, J. K., Mehta, A., Geho, D., Espina, V., Petricoin, E. F., III, and Liotta, L. A. (2004) Serum proteomics in cancer diagnosis and management. *Annu Rev Med 55*, 97−112.

(2) Petricoin, E. F., Ardekani, A. M., Hitt, B. A., Levine, P. J., Fusaro, V. A., Steinberg, S. M., Mills, G. B., Simone, C., Fishman, D. A., Kohn, E. C., and Liotta, L. A. (2002) Use of proteomic patterns in serum to identify ovarian cancer. *Lancet 359*, 572−7.

(3) Petricoin, E. F., III, Ornstein, D. K., Paweletz, C. P., Ardekani, A., Hackett, P. S., Hitt, B. A., Velassco, A., Trucco, C., Wiegand, L., Wood, K., Simone, C. B., Levine, P. J., Linehan, W. M., Emmert-Buck, M. R., Steinberg, S. M., Kohn, E. C., and Liotta, L. A. (2002) Serum proteomic patterns for detection of prostate cancer. *J Natl Cancer Inst 94*, 1576−8.

(4) Hingorani, S. R., Petricoin, E. F., Maitra, A., Rajapakse, V., King, C., Jacobetz, M. A., Ross, S., Conrads, T. P., Veenstra, T. D., Hitt, B. A., Kawaguchi, Y., Zhou, Y., Johann, D., Liotta, L., Crawford, H. C., Putt, M. E., Jacks, T., Konieczny, S. F., Wright, C. E., Hruban, R. E., Lowry, A. M., and Tuveson, D. A. (2003) Preinvasive and invasive ductal pancreatic cancer and its early detection in the mouse. *Cancer Cell 4*, 437−450.

(5) Paweletz, C. P., Gillespie, J. W., Ornstein, D. K., Simone, N. L., Brown, M. R., Cole, K. A., Wang, Q.-H., Huang, J., Hu, N., Yip, T.-T., Rich, W. E., Kohn, E. C., Linehan, W. M., Weber, T., Taylor, P. Emmert-Buck, M. R., Liotta, L. A., and Petricoin, E. F. (2000) Rapid protein display profiling of cancer progression directly from human tissue using a protein biochip. *Drug Dev. Res. 49*, 34−42.

(6) Chaurand, P., and Caprioli, R. M., (2002) Direct profiling and imaging of peptides and proteins from mammalian cells and tissue sections by mass spectrometry. *Electrophoresis 23*, 3125−35.

(7) Stoeckli, M., Chaurand, P., Hallahan, D. E., and Caprioli, R. M. (2001) Imaging mass spectrometry: a new technology for the analysis of protein expression in mammalian tissues. *Nat. Med. 7*, 493−6.

(8) Yanagisawa, K., Shyr, Y., Xu, B. J., Massion, P. P., Larsen, P. H., White, B. C., Roberts, J. R., Edgerton, M., Gonzalez, A., Nadaf, S., Moore, J. H., Caprioli, R. M., and Carbone, D. P. (2003) Proteomic patterns of tumour subsets in nonsmall-cell lung cancer. *Lancet 362*, 433−9.

(9) Schwartz, S. A., Weil, R. J., Johnson, M. D., Toms, S. A., and Caprioli, R. M. (2004), Protein profiling in brain tumors using mass spectrometry: feasibility of a new technique for the analysis of protein expression. *Clin. Cancer Res. 10*, 825−7.

(10) Mehta, A. I., Ross, S., Lowenthal, M., Fusaro, V. A., Fishman, D. A., Petricoin, E., and Liotta, L. (2003) Biomarker amplification by serum carrier protein binding. *Disease Markers 19*, 1−10.

(11) Lowenthal, M. S., Mehta, A. I., Frogale, K., Bandle, R. W., Araujo, R. P., Hood, B. L., Veenstra, T. D., Conrads, T. P., Goldsmith, P., Fishman, D., Petricoin, E. F., III, and Liotta, L. A. (2005) Analysis of albumin-associated peptides and proteins from ovarian cancer patients. *Clin Chem, 51*, 1933−45.

(12) Geho, D. H., Lahar, N., Ferrari, M., Petricoin, E. F., and Liotta, L. A. (2004) Opportunities for nanotechnology-based innovation in tissue proteomics. *Biomed Microdevices 6*, 231−9.

(13) Barrett, E. P., Joyner, L. G., and Halenda, P. P. (1951) The Determination of Pore Volume and Area Distributions in Porous Substances. I. Computations from Nitrogen Isotherms. *Journal of the American Chemical Society*, *73*, 373−380.

(14) Ravikovitch P. I., Wei, D., Chueh, W. T., Haller, G. L., and Neimark, A. V. (1997) Evaluation of pore structure parameters of MCM-41 catalyst supports and catalysts by means of nitrogen and argon adsorption. *Journal of Physical Chemistry B*, *101* : 3671−3679.

(15) Gelb, L. D., and Gubbins, K. E, (1999) Pore size distributions in porous glasses: A computer simulation study. *Langmuir 15*: 305−308.

(16) Kruk, M., Jaroniec, M., Kim, J. H., and Ryoo, R. (1999) Characterization of highly ordered MCM-41 silicas using X-ray diffraction and nitrogen adsorption. *Langmuir 15*, 5279−5284.

(17) Wang, H., and Branton, D.(2001) Nanopores with a spark for single-molecule detection. *Nat Biotechnol 19*, 622−3.

(18) Meller, A., Nivon, L., Brandin, E., Golovchenko, J., and Branton, D. (2000) Rapid nanopore discrimination between single polynucleotide molecules. *Proc Natl Acad Sci U S A 97*, 1079−84.

(19) Howorka, S., Cheley, S., and Bayley, H. (2001) Sequence-specific detection of individual DNA strands using engineered nanopores. *Nat Biotechnol 19*, 636−9.

(20) Han, M., Gao, X., Su, J. Z., and Nie, S. (2001) Quantum-dot-tagged microbeads for multiplexed optical coding of biomolecules. *Nat Biotechnol 19*, 631−5.

(21) Nicewarner-Pena, S. R., Freeman, R. G., Reiss, B. D., He, L., Pena, D. J., Walton, I. D., Cromer, R., Keating, C. D., and Natan, M. J. (2001) Submicrometer metallic barcodes. *Science 294*, 137−41.

(22) Bruchez, M., Jr., Moronne, M., Gin, P., Weiss, S., and Alivisatos, A. P. (1998) Semiconductor nanocrystals as fluorescent biological labels. *Science 281*, 2013−6.

(23) Liotta, L. A., Ferrari, M., and Petricoin, E. (2003) Clinical proteomics: written in blood. *Nature 425*, 905.

BC0503364

Near-Infrared Fluorescent Deoxyglucose Analogue for Tumor Optical Imaging in Cell Culture and Living Mice

Zhen Cheng,[†] Jelena Levi,[†] Zhengming Xiong,[†,‡] Olivier Gheysens,[†] Shay Keren,[†] Xiaoyuan Chen,[†] and Sanjiv Sam Gambhir*[,†]

Molecular Imaging Program at Stanford (MIPS), Departments of Radiology and Bioengineering, Bio-X Program, Stanford University, Stanford, California, 94305-5344, and Department of Pediatrics, Tongji Medical College, Huazhong University of Science and Technology and Tongji Hospital, Wuhan 430030, China. Received December 2, 2005; Revised Manuscript Received February 26, 2006

2-Deoxy-2-[^{18}F]fluoro-D-glucose ([^{18}F]FDG) has extensively been used for clinical diagnosis, staging, and therapy monitoring of cancer and other diseases. Nonradioactive glucose analogues enabling the screening of the glucose metabolic rate of tumors are of particular interest for anticancer drug development. A nonradioactive fluorescent deoxyglucose analogue may have many applications for both imaging of tumors and monitoring therapeutic efficacy of drugs in living animals and may eventually translate to clinical applications. We found that a fluorescent 2-deoxyglucose analogue, 2-[*N*-(7-nitrobenz-2-oxa-1,3-diazol-4-yl)amino]-2-deoxy-D-glucose (2-NBDG), can be delivered in several tumor cells via the glucose transporters (GLUTs). We therefore conjugated D-glucosamine with a near-infrared (NIR) fluorphor Cy5.5 and tested the feasibility of the Cy5.5−D-glucosamine (Cy5.5−2DG) conjugate for NIR fluorescence imaging of tumors in a preclinical xenograft animal model. Cy5.5−2DG was prepared by conjugating Cy5.5 monofunctional *N*-hydroxysuccinimide ester (Cy5.5−NHS) and D-glucosamine followed by high-performance liquid chromatography purification. The accumulation of Cy5.5−2DG and Cy5.5−NHS in different tumor cell lines at 37 and 4 °C were imaged using a fluorescence microscope. Tumor targeting and retention of Cy5.5−2DG and Cy5.5−NHS in a subcutaneous U87MG glioma and A375M melanoma tumor model were evaluated and quantified by a Xenogen IVIS 200 optical cooled charged-coupled device system. Fluorescence microscopy imaging shows that Cy5.5−2DG and Cy5.5−NHS are taken up and trapped by a variety of tumor cell lines at 37 °C incubation, while they exhibit marginal uptake at 4 °C. The tumor cell uptake of Cy5.5−2DG cannot be blocked by the 50 mM D-glucose, suggesting that Cy5.5−2DG may not be delivered in tumor cells by GLUTs. U87MG and A375M tumor localization was clearly visualized in living mice with both NIR fluorescent probes. Tumor/muscle contrast was clearly visible as early as 30 min postinjection (pi), and the highest U87MG tumor/muscle ratios of 2.81 ± 0.10 and 3.34 ± 0.23 were achieved 24 h pi for Cy5.5−2DG and Cy5.5−NHS, respectively. While as a comparison, the micropositron emission tomography imaging study shows that [^{18}F]FDG preferentially localizes to the U87MG tumor, with resulting tumor/muscle ratios ranging from 3.89 to 4.08 after 30 min to 2 h postadministration of the probe. In conclusion, the NIR fluorescent glucose analogues, Cy5.5−2DG and Cy5.5−NHS, both demonstrate tumor-targeting abilities in cell culture and living mice. More studies are warranted to further explore their application for optical tumor imaging. To develop NIR glucose analogues with the ability to target GLUTs/hexokinase, it is highly important to select NIR dyes with a reasonable molecular size.

INTRODUCTION

Positron emission tomography (PET)[1] has become a generally accepted technique for preclinical and clinical noninvasive imaging of diseases, especially cancer (*1*−*3*). Tracers enabling the targeting of specific cellular and molecular processes are major driving forces that have contributed to the rapid progress of PET imaging. One of these tracers, 2-deoxy-2-[^{18}F]fluoro-D-glucose ([^{18}F]FDG), is very widely used in tumor diagnosis, staging, and monitoring therapeutic response. Currently, the majority (∼95%) of clinical PET scans use [^{18}F]FDG (*1*).

The molecular targets for [^{18}F]FDG are glucose transporters (e.g., GLUT1) and hexokinase. [^{18}F]FDG can first be recognized and transported into the cells by glucose transporters, which are located on the cell membrane, and it is then phosphorylated by hexokinase to form 2-deoxy-2-[^{18}F]fluoro-D-glucose-6-phosphate ([^{18}F]FDG-6-phosphate). Because [^{18}F]FDG lacks a hydroxyl group in the 2 position, [^{18}F]FDG-6-phosphate cannot be further metabolized and this polar compound is metabolically trapped inside the cells (*3*, *4*). The rationale for using [^{18}F]FDG as a general tumor marker relies on the fact that tumor cells often exhibit an increased glucose metabolism and an upregulation of GLUT and hexokinase compared to non-neoplastic cells (*5*). The preferential accumulation of [^{18}F]FDG metabolites inside tumor cells compared to that in surrounding normal tissues makes the detection of tumors using PET possible. [^{18}F]FDG can not only be used in diagnosis and staging of cancer but also is a powerful tool for monitoring disease recurrence and therapeutic efficacy (*6*−*8*). A recent excellent example of the

* To whom correspondence should be addressed: Molecular Imaging Program at Stanford Departments of Radiology and Bioengineering, Bio-X Program, 318 Campus Dr., Clark Center, E-150 Stanford University, Stanford, CA 94305. Telephone: 650-725-2309. Fax: 650-724-4948. E-mail: sgambhir@stanford.edu.

[†] Stanford University.

[‡] Huazhong University of Science and Technology and Tongji Hospital.

[1] Abbreviatons: NIRF, near-infrared fluorescence; Cy5.5−2DG, Cy5.5−D-glucosamine; [^{18}F]FDG, 2-deoxy-2-[^{18}F]fluoro-D-glucose; HPLC, high-performance liquid chromatography; PET, positron emission tomography; pi, postinjection.

10.1021/bc050345c CCC: $33.50 © 2006 American Chemical Society
Published on Web 04/21/2006

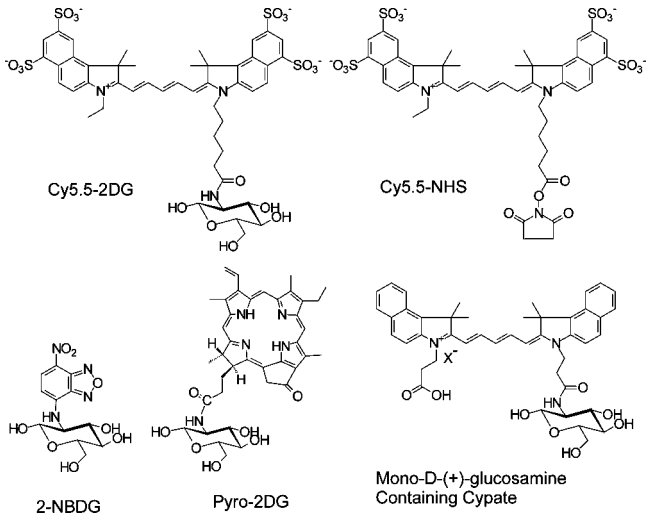

Figure 1. Schematic structures of Cy5.5−2DG, Cy5.5−NHS, 2-NBDG, Pyro−2DG, and mono-D-(+)-glucosamine-containing cypate.

latter is the use of [^{18}F]FDG−PET for monitoring treatment effects of imatinib mesylate (STI-571) on gastrointestinal stromal tumors (*9*, *10*). The success of [^{18}F]FDG−PET for metabolic imaging of disease has prompt scientist to develop glucose analogues labeled with less costly or therapeutic isotopes such as ^{99m}Tc and $^{186/188}$Re (*11*, *12*). Recently, it was reported that ^{99m}Tc-labeled ethylenedicysteine−deoxyglucose (ECDG) can potentially be used for tumor imaging (*11*). However, further investigations are required to reveal the mechanism responsible for the accumulation of this probe in tumors, as well as to identify the specific molecular targets interacting with ^{99m}Tc-ECDG.

Although radionuclide imaging has several advantages, including intrinsically high sensitivity, capability of quantitation, and clinical translation, it often suffers from relatively low spatial resolution, high cost, and limited radiation to personnel. Moreover, PET imaging often requires an on-site cyclotron and a radiochemistry laboratory to produce short half-life radionuclides and radiolabeled agents. Therefore, optical imaging (bioluminescence and fluorescence imaging) has emerged as an attractive imaging modality to study the biological/molecular events in both cell culture and small living subjects. Optical imaging does not involve any ionizing radiation; it is inexpensive and highly sensitive and allows for a high throughput screening because the acquisition times for obtaining a good image using optical imaging can be as short as seconds (*13*, *14*). Because of the strong tissue penetration ability of light in the near-infrared (NIR) region (650−900 nm wavelengths), near-infrared fluorescence (NIRF) imaging has emerged as a powerful tool for small animal imaging. Many studies have demonstrated that it is a viable method to noninvasively monitor disease states at the molecular level, localize cancer, and even assess the antitumor efficacy of new therapeutic drugs (*15*−*18*).

Considering the extensive applications of [^{18}F]FDG in nuclear medicine and the rapid advancement in optical imaging, the development of NIRF deoxyglucose analogues may serve as novel probes with the ability to evaluate the glucose metabolic rate of tumors. These probes could be useful for (a) the accurate detection of abnormalities such as tumors and (b) the noninvasive monitoring of the therapeutic efficacy of drugs in living small animals. It was reported that a fluorescent derivative of 2-deoxyglucose, 2-[*N*-(7-nitrobenz-2-oxa-1,3-diazol-4-yl)amino]-2-deoxy-D-glucose (2-NBDG) (excitation, 475 nm; emission, 550 nm) can be delivered and trapped in cells via the GLUT/hexokinase pathway. Several studies demonstrated that the uptake of 2-NBDG (structure shown in Figure 1) can be inhibited by D-glucose but not L-glucose in different organisms (*19*−*23*). 2-NBDG can then be further metabolized to 2-NBDG-6-phosphate in *Escherichia coli* cells, which was confirmed by mass spectrometry (*21*). These results highlight the possibility of preserving the GLUT/hexokinase-targeting ability of the glucose analogues when they are conjugated with a bulk NIR fluorescent group at position 2 of deoxyglucose. A pyropheophorbide derivative of 2-deoxyglucose, Pyro−2DG (excitation, 667 nm; emission, 679 and 720 nm; structure shown in the Figure 1), was synthesized and also proven to be useful as both a tumor-targeted NIRF imaging probe and a photodynamic therapy agent for the treatment of tumors. Preliminary confocal fluorescence microscopy studies further shows that the uptake of Pyro−2DG in 9 L of glioma cells can be inhibited by 50 mM D-glucose, suggesting that Pyro−2DG is a substrate of GLUTs (*24*). Another interesting report tethered multiple D-(+)-glucosamines with cypate, a NIR chromophore core, to generate multivalent carbocyanine molecular beacons (structure of mono-D-(+)-glucosamine-containing cypate shown in the Figure 1). Biodistribution studies in tumor-bearing mice show that all of the NIR fluorescent glucosamine derivatives localized in the tumor. However, it is not clear whether their uptake and trapping in the tumor is through the GLUT/hexokinase pathway (*25*, *26*).

In this study, we first investigated the tumor cell uptake of 2-NBDG and the specificity of 2-NBDG toward GLUTs. We found that 2-NBDG is delivered and trapped in tumors cells via the GLUT, which is consistent with the recent literature (*27*). The NIR fluorescent dye Cy5.5 has been proven to be a very useful fluorochrome for labeling biomolecules for in vivo optical imaging by several groups (*28*−*35*). Encouraged by the specific tumor cell uptake of 2-NBDG, we conjugated Cy5.5 monofunctional *N*-hydroxysuccinimide (NHS) ester (Cy5.5−NHS) and D-glucosamine to prepare a Cy5.5−D-glucosamine (Cy5.5−2DG) conjugate (see their structure in the Figure 1) and tested its feasibility for NIRF imaging of tumors in preclinical xenograft tumor models. As a comparison, Cy5.5−NHS was also tested for its tumor-targeting ability in vitro and in vivo. Furthermore, [^{18}F]FDG as a radioactive probe was utilized to image mice bearing U87MG tumors with microPET. We demonstrate the tumor specificity and long-lasting tumor accumulation of both fluorescent agents in human primary tumor cells in mouse xenografts.

EXPERIMENTAL PROCEDURES

Materials and General Methods. Cy5.5−NHS was purchased from Amersham Biosciences (Piscataway, NJ). All other reagents were obtained from Sigma−Aldrich Chemical Co. (St. Louis, MO). Matrix-assisted laser desorption/ionization time-of-flight mass spectrometry (MALDI−TOF−MS) was performed by Stanford Protein and Nucleic Acid Biotechnology Facility, Stanford University, Stanford, CA. A Dionex Summit high-performance liquid chromatography (HPLC) system (Dionex Corporation, Sunnyvale, CA) equipped with a 170U 4-channel UV−vis absorbance detector was used for purification and analysis of the Cy5.5-labeled compound. UV detection wavelengths were 218, 280, and 590 nm for all of the experiments. Both semipreparative (Zorbax SB-C18, 9.4 × 250 mm) and analytical (Dionex Acclaim 120 C18, 4.6 × 250 mm) reversed-phase HPLC columns were used. The mobile phase was solvent A, 0.1% trifluoroacetic acid (TFA) in water, and solvent B, 0.1% TFA in acetonitrile (CH_3CN).

Synthesis and Characterization of Cy5.5−2DG. D-Glucosamine (30.2 mg) was dissolved in 302 μL of H_2O to make a concentration of 463.7 mM in solution. D-Glucosamine (34.5 μL, 16.0 μmol), sodium phosphate buffer (Na_2HPO_4 at pH 9.0, 0.1 M, 805.5 μL), and Cy5.5−NHS (1.81 mg, 1.60 μmol) dissolved in 160 μL of H_2O were then mixed together. After

overnight incubation at 4 °C in the dark, the reaction was quenched by adding 100 μL of 1% TFA. The crude product was then injected onto a semipreparative HPLC column [the flow rate was 3.0 mL/min, with the mobile phase starting from 5% solvent B (0.1% TFA in CH_3CN) and 95% solvent A (0.1% TFA in water) (0−3 min), to 65% solvent B and 35% solvent A at 33 min, and then going to 85% solvent B and 15% solvent A (33−36 min), maintaining this solvent composition for another 3 min (36−39 min) and returning to the initial solvent composition by 42 min]. Fractions containing Cy5.5−2DG conjugate (retention time of 14.3 min) were collected, lyophilized, and identified by MALDI−TOF−MS. The chemical purity of the product was determined by analytical HPLC (same gradient as used for semipreparative HPLC; flow rate of 1.0 mL/min). The product was redissolved in saline at a concentration of 1 mg/mL and stored in the dark at −80 °C until use. The absorbance spectrum of Cy5.5−2DG was rerecorded on an Agilent 8453 UV−visible ChemStation (Agilent Technologies, Wilmington, DE), and the fluorescence spectrum of Cy5.5−2DG was measured on a Fluoromax-3 fluorophotometer (JOBIN YVON/HORIBA, Edison, NJ).

Cell Lines and Tumor Xenografts. U87MG human glioblastoma cells, C6 rat glioma cells, A375M human melanoma cells, B16F10 murine melanoma cells, and MDA-MB-435 human breast cancer cells were all obtained from American Type Culture Collection (Manassas, VA). U87MG, C6, A375M, and B16F10 cells were cultured in Dulbecco's modified Eagle high glucose medium supplemented with 10% fetal bovine serum (FBS) and 1% penicillin−streptomycin (DMEM, Invitrogen Life Technologies, Carlsbad, CA). MDA-MB-435 was cultured in Leibovitz's L-15 medium with 2 mM L-glutamine supplemented with 0.01 mg/mL insulin, 10% FBS, and 1% penicillin−streptomycin (Invitrogen Life Technologies, Carlsbad, CA) in CO_2-free atmosphere. All the other cell lines were maintained in a humidified atmosphere of 5% CO_2 at 37 °C, with the medium changed every other day. A confluent monolayer was detached with trypsin and dissociated into a single-cell suspension for further cell culture.

Animal procedures were performed according to a protocol approved by the Stanford University Administrative Panels on Laboratory Animal Care (A-PLAC). Female athymic nude mice (*nu/nu*), obtained from Charles River Laboratories, Inc. (Cambridge, MA) at 4−6 weeks of age, were subcutaneously injected in the right shoulder with 5×10^6 U87MG glioblastoma cells suspended in 100 μL of phosphate-buffered saline (PBS, 0.01 mol/L; pH 7.4). When the tumors reached 0.4−0.6 cm in diameter (14−21 days after implantation), the tumor-bearing mice were subjected to in vivo imaging studies. In addition, 6-week-old Fox chase ICR scid (severe combined immunodeficient) mice were inoculated with 4×10^6 A375M human melanoma cells. A total of 3−4 weeks post-inoculation, the mice bearing A375M tumors were ready for further studies.

Fluorescence Microscopy and Cell-Uptake Studies of 2-NBDG. For fluorescence microscopy studies, U87MG cells (1×10^5) were cultured on 35 mm MatTek glass-bottom culture dishes (catalog number, P35G-0-14-C; Ashland, MA). After 24 h, the cells were washed with PBS and then incubated at 37 °C in the presence of 10 μM 2-NBDG for 10 min. After the incubation period, cells were washed 3 times with ice-cold PBS. The fluorescence signal of the cells was recorded using an Axiovert 200M fluorescence microscope (Carl Zeiss MicroImaging, Inc., Thornwood, NY) equipped with a GFP filter set (exciter, HQ 475/20 nm; emitter, HQ 540/30 nm). An AttoArc HBO 100 W microscopic illuminator was used as a light source for fluorescence excitation. Images were taken using a thermoelectrically cooled charged-coupled device (CCD) (Micromax, model RTE/CCD-576, Princeton Instruments, Inc., Trenton, NJ) and analyzed using MetaMorph Software version 6.2r4 (Molecular Devices Corporation, Downingtown, PA). The effect of D-glucose or L-glucose on 2-NBDG accumulation in U87MG cells was also examined. In these studies, cells were preincubated with medium containing either 50 mM D-glucose or L-glucose for 0.5 h at 37 °C. Cells were then incubated with 10 μM 2-NBDG for 10 min at 37 °C. After incubation, U87MG cells were washed 3 times with ice-cold PBS and subjected to fluorescence microscopy imaging.

The inhibition effect of D-glucose or L-glucose on 2-NBDG uptake in U87MG cells was also assessed by the measurement of the fluorescence intensity of cell lysates. Briefly, the cultured U87MG human glioblastoma cells were trypsinized, washed twice with PBS, and suspended at 10×10^6 cells/mL in PBS. Cells (1.0×10^6) were preincubated with either 10 or 50 mM D-glucose or 50 mM L-glucose for 30 min and then incubated with 50 μM 2-NBDG for another 1 h at 37 °C. The cells were centrifuged (at 250*g*) for 3 min and washed 3 times with cold PBS. Cell pellets were then lysed with 150 μL of cold spectral-grade water, following by freezing in dry ice. The frozen cell solution was thawed and centrifuged at 12000*g* for 5 min. The fluorescence intensity of 100 μL of cell lysate was measured on a Fluoromax-3 fluorophotometer.

Fluorescence Microscopy Studies of Cy5.5−2DG and Cy5.5−NHS. Fluorescence microscopy imaging was performed to study the uptake of Cy5.5−2DG and Cy5.5−NHS by several tumor cell lines such as U87MG, C6, A375M, B16F10, and MDA-MB-435, as well as to exam the effect of D-glucose or L-glucose on 2-NBDG accumulation in U87MG cells. The procedure described in the above section was followed in this experiment, except that 100 nM Cy5.5−2DG or Cy5.5−NHS was used for incubation with cells and a Cy5.5 filter set was used in the fluorescence microscope for the collection of the fluorescence signal.

Optical Imaging of Tumors in Mice. In vivo fluorescence imaging was performed with an IVIS 200 small animal imaging system (Xenogen, Alameda, CA). A Cy5.5 filter set was used for acquiring Cy5.5−2DG and Cy5.5−NHS fluorescence in vivo. Identical illumination settings (lamp voltage, filters, f/stop, field of views, binning) were used for acquiring all images, and fluorescence emission was normalized to photons per second per centimeter squared per steradian (p s^{-1} cm^{-2} sr^{-1}). Images were acquired and analyzed using Living Image 2.5 software (Xenogen, Alameda, CA). Mice bearing either U87MG or A375M ($n = 3$ for each imaging probe) were injected via the tail vein with 0.5 nmol of Cy5.5−2DG or Cy5.5−NHS and subjected to optical imaging at various time points postinjection (pi). For scid mouse bearing A375M tumor, the fur covered the tumor and the lower right flank was shaved to reduce light absorbance and scattering. All NIR fluorescent images were acquired using 1 s exposure time (f/stop = 4) and displayed in the same scale of fluorescent intensity.

Fluorescence Microscopy Imaging of Fresh Tissue Slides. After optical imaging, the mice bearing U87MG were euthanized 24 h pi of the fluorescent probe. Tumors were dissected, placed in tissue holders, then filled with Tissue-Tek Optimal Cutting Temperature Compound (Sakura Finetek USA, Inc., Torrance, CA), and immediately frozen in dry ice. They were sectioned into 200 μm transverse slices using a tissue slicer. Fluorescence microscopy imaging of fresh tissue slides was then performed to determine the localization and distribution of the probe in the tumor. The images were taken with a 10× objective.

MicroPET Imaging of the U87MG Tumor. PET imaging of tumor-bearing mice was performed on a microPET R4 rodent model scanner (Concorde Microsystems, Inc., Knoxville, TN). The mice bearing U87MG glioblastoma were injected with 5.55 MBq (150 μCi) of [^{18}F]FDG. At 30, 60, and 120 min pi, the

mice were anesthetized with 2% isoflurane and placed in the prone position near the center of the field of view of a microPET scanner (Siemens, Inc.). The 5-min static scans were obtained, and the images were reconstructed by a two-dimensional ordered subsets expectation maximum (OSEM) algorithm. Regions of interest (ROIs) were then drawn over the tumor on decay-corrected whole-body coronal images. The counts per pixel per minute were obtained from the ROI and converted to counts per milliliter per minute by using a calibration constant. When a tissue density of 1 g/mL was assumed, the ROI values were converted to counts per gram per minute. An image ROI-derived percentage ID per gram of tissue (%ID/g) was then determined by dividing the counts per gram per minute with the injected dose (ID).

Data Processing and Statistics. All of the data are given as the mean ± standard deviation (SD) of *n* independent measurements. Statistical analysis was performed using a Student's *t* test. Statistical significance was assigned for p values <0.05. For determining tumor contrast, maximum fluorescence intensities (p s^{-1} cm^{-2} sr^{-1}) of the tumor area at the right shoulder of the animal (*T*) and of the area at the right flank [normal tissue (*N*)] were calculated by the ROI function of Living Image software integrated with Igor (Wavemetrics, Lake Oswego, OR). Dividing *T* by *N* yielded the contrast between the tumor tissue and the normal tissue.

RESULTS AND DISCUSSION

NIRF imaging is emerging as a powerful tool for noninvasive imaging diseases in preclinical models. It also has a great potential for clinical use in providing both real-time surgical information and functional/molecular information of the disease. NIRF probes with the capability of imaging specific molecular targets and events are therefore under active investigation. Our research was intended to develop NIR fluorescent glucose analogues for imaging tumor metabolism in living subjects. Although several NIR 2-deoxyglucose analogues, which are able to accumulate in the tumors, were successfully synthesized recently (*24*−*26*), whether these compounds are delivered and trapped in tumor cells via the GLUTs/hexokinase pathway remains to be answered. Moreover, the ability of these NIR 2-deoxyglucose analogues to imaging tumor metabolism in small animals has not been demonstrated yet.

It was reported that 2-NBDG could be incorporated by glucose-transporting systems in living cells. More recently, it was found that 2-NBDG can accumulate into malignant tumor cells such as the MCF-7 breast cancer cells and the HepG2 liver cancer cells (*27*). In this work, the cell uptake of 2-NBDG by U87MG was also examined using fluorescence microscopy imaging. It was found that 2-NBDG did accumulate in the cytoplasm of U87MG cells (a and d of Figure 2A). We also found that this fluorescent glucose analogue showed good uptake in several other tumor cell lines such as C6, A375M, B16F0, and MDA-MB-435 (data not shown). More importantly, the uptake of 2-NBDG by U87MG was significantly inhibited by 10 and 50 mM D-glucose ($p < 0.05$) but not by 50 mM L-glucose (parts A and B of Figure 2), strongly indicating that the uptake of 2-NBDG is likely mediated by glucose transporters. However, the short excitation and emission wavelengths (excitation, 475 nm; emission, 550 nm) of 2-NBDG limit its applications for imaging small living subjects.

Encouraged by these results, we hypothesized that conjugation of D-glucosamine with a carefully designed NIRF dye may generate a fluorescence deoxyglucose analogue, which can be still recognized by GLUTs and hexokinase. Therefore, Cy5.5−2DG was synthesized and evaluated in both cell culture and mice, because of the longer excitation/emission wavelengths of Cy5.5 and its easy availability. Synthesis of Cy5.5−2DG was

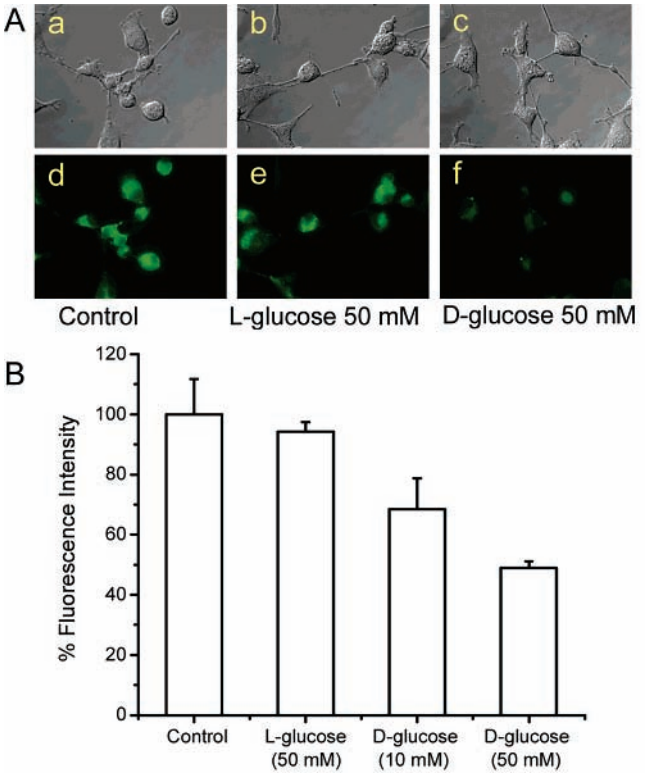

Figure 2. (A) Light (top) and fluorescence (bottom) images of U87MG cells. The cells were incubated with 10 μM 2-NBDG for 10 min at 37 °C in the absence of D-glucose or L-glucose (a and d) and presence of 50 mM L-glucose (b and e) and 50 mM D-glucose (c and f). The images show that 2-NBDG accumulates in the cytoplasm of cells and that the 2-NBDG fluorescence in cells can be competitively inhibited by D-glucose but not by L-glucose. (B) Significant inhibition of the 2-NBDG uptake by U87MG cells by 10 and 50 mM D-glucose ($p < 0.05$) but not by 50 mM L-glucose, as measured by fluorescence intensity with a spectrofluorometer.

achieved through conjugation of Cy5.5−NHS ester with the 2-amino group of the D-glucosamine. The desired products were purified by semipreparative HPLC. The retention time on analytical HPLC for Cy5.5−2DG was found to be 15.2 min. The yield of the Cy5.5−2DG conjugate was typically over 70%. The purity of Cy5.5−2DG was over 95% from analytical HPLC analysis. The purified Cy5.5−2DG was characterized by MALDI−TOF−MS. Cy5.5−2DG: *m/z* 1078.26 for $[M + H]^+$ ($C_{47}H_{56}N_3O_{18}S_4$, calculated molecular weight = 1078.24). The absorption and fluorescence emission characteristics of Cy5.5−2DG (λ_{ab} = 675 nm, λ_{em} = 695 nm) were identical to those of free Cy5.5, as apparent from the spectra measured in H_2O (Figure 3). The stability of Cy5.5−2DG was further evaluated by incubation of the compound with mouse serum for 1 h. No dissociation of Cy5.5 from the Cy5.5−2DG conjugate was found by using HPLC analysis, suggesting the good serum stability of Cy5.5−2DG.

Fluorescence microscopy imaging studies were performed to investigate the cell uptake of Cy5.5−2DG in different tumor cell lines. It was found that Cy5.5−2DG does accumulate in several tumor cell lines such as A375M, B16F10, C6, U87MG, and MDA-MB-435 at 37 °C, while the uptake at 4 °C was minimal. This result indicates that the cellular uptake of Cy5.5−2DG is due to an active and temperature-dependent process, instead of simple passive diffusion. To further elucidate whether its cell uptake is related to GLUTs, Cy5.5−2DG was incubated with either 50 mM D-glucose or L-glucose. However, Cy5.5−2DG localizes within U87MG cells with similar fluorescence intensity in the presence and absence of 50 mM D-glucose and L-glucose. D-Glucose failed to block the cell uptake of Cy5.5−

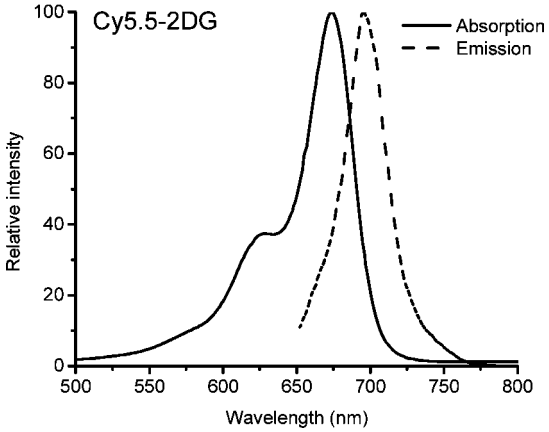

Figure 3. Absorption (675 nm) and emission fluorescence (695 nm) spectra of Cy5.5−2DG in water.

2DG, suggesting that GLUTs are not likely the transporter system responsible for Cy5.5−2DG uptake. To determine whether Cy5.5−2DG is a substrate for hexokinase, Cy5.5−2DG was incubated with glucose reagent (Infinity Glucose Reagent, ThermoDMA, Louisville, CO) at 37 °C for 3 min (*12*). From MALDI−TOF−MS analysis, we were not able to observe the formation of phosphorylated Cy5.5−2DG (data not shown). Cy5.5−2DG does not seem to mimic glucose/deoxyglucose phosphorylation. More studies are needed to pinpoint the uptake and retention mechanism of Cy5.5−2DG in cells.

For a comparison, Cy5.5−NHS was used as a control for staining the tumor cell lines. Fluorescence microscopy imaging studies demonstrate that Cy5.5−NHS can label these tumor cell lines as well as Cy5.5−2DG at 37 °C and also shows a negligible fluorescence signal when incubated at 4 °C. In a previous study (*28*), it was reported that very little Cy5.5−NHS accumulates in two breast cancer cell lines, MDA-MB-648 and MDA-MB-435. This is likely due to different filter settings and detection sensitivity of the fluorescence microscopes used in our study compared to the published study. In that paper, a 775/845 nm (excitation/emission) filter was equipped to obtain Cy5.5 fluorescence images. However, a Cy5.5 filter set (exciter, 650/20 nm; emitter, 675/35 nm) was used in our study. Considering that the maximum excitation and emission wavelengths of Cy5.5 dye are 675 and 694 nm respectively, the 775/845 nm filter set is not the proper setting, and one is unlikely to observe enough Cy5.5 fluorescence signal using such a filter.

Whole-body optical imaging of subcutaneous tumor xenografted mice was then performed by using an IVIS200 system to monitor in vivo biodistribution of Cy5.5−2DG and Cy5.5−NHS. As shown in Figure 4A, the subcutaneous U87MG tumor could be clearly distinguished from the surrounding background tissue from 30 min up to 24 h pi of either 0.5 nmol of Cy5.5−2DG or Cy5.5−NHS. Quantitative analysis of these images was performed, and the fluorescence intensities in the tumor and normal tissues as a function of time for Cy5.5−2DG and Cy5.5−NHS are depicted in parts B and C of Figure 4, respectively. It was found that both probes exhibited fast tumor targeting characteristics in vivo. The tumor uptake of Cy5.5−2DG and Cy5.5−NHS reached a maximum 30 min pi and slowly washed out over time. A similar pattern was found for the uptake of both probes in normal tissue. At all time points pi (0.5−24 h), there is no statistical significant difference in tumor and normal tissue uptake between Cy5.5−2DG and Cy5.5−NHS ($p > 0.05$) (parts B and C of Figure 4). The fluorescence intensity ratio between the tumor and normal tissue

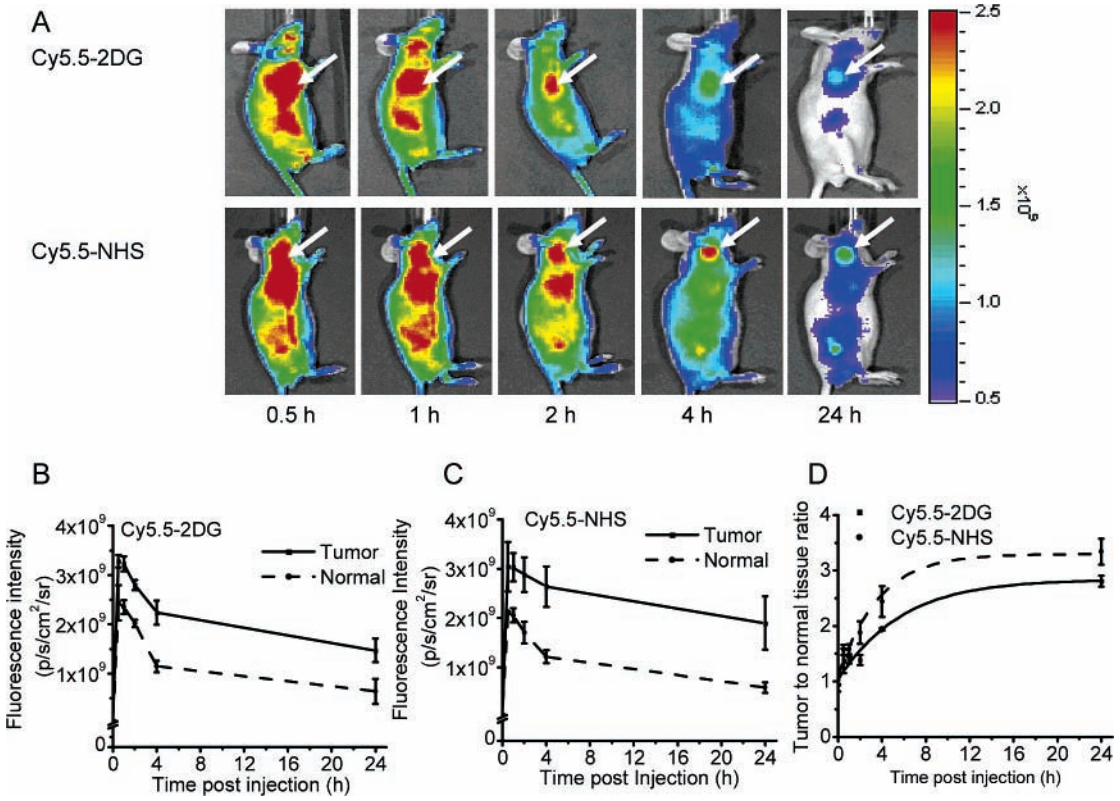

Figure 4. (A) In vivo fluorescence imaging of subcutaneous U87MG glioblastoma tumor-bearing nude mice after intravenous injection of 0.5 nmol of Cy5.5−2DG (top) or Cy5.5−NHS (bottom). The position of the tumor is indicated by an arrow. The fluorescence signal from probes was pseudo-colored red. Quantification and kinetics of in vivo targeting charactereristics of Cy5.5−2DG (B) and Cy5.5−NHS (C). The fluorescence intensity was recorded as photons per second per centimeter squared per steradian (p s^{-1} cm^{-2} sr^{-1}). Tumor fluorescence was higher than that in the normal tissue. (D) Tumor contrast (tumor/normal tissue ratio) as a function of time postadministration of Cy5.5−2DG (■, —) and Cy5.5−NHS (◆, ···). The tumor/normal tissue ratio of Cy5.5−NHS at 4 and 24 h pi is significantly higher than that of Cy5.5−2DG ($p < 0.05$).

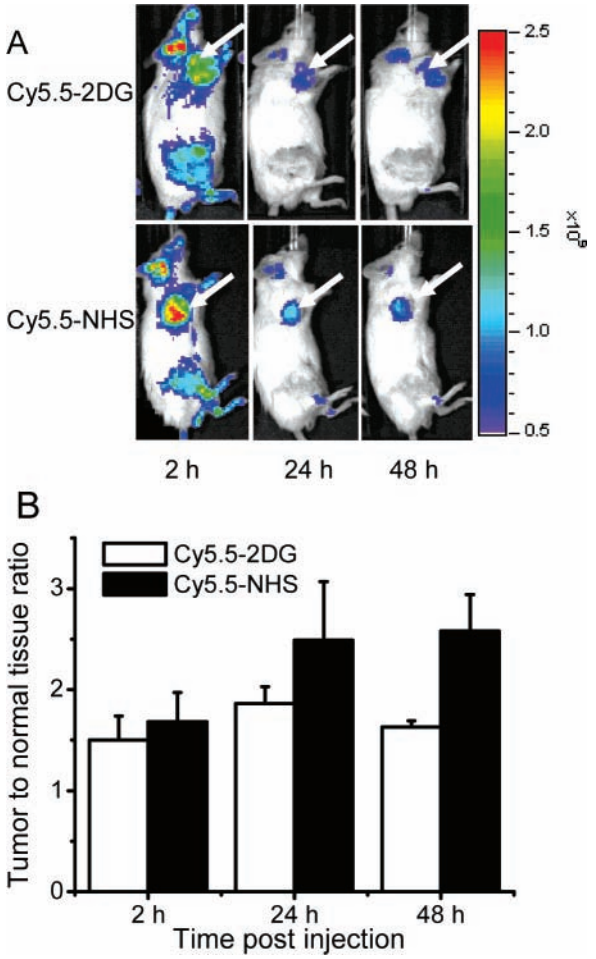

Figure 5. (A) In vivo NIRF images of subcutaneous A375M melanoma bearing scid mice after intravenous injection of 0.5 nmol of Cy5.5−2DG (top) and Cy5.5−NHS (bottom). The position of the A375M tumor is indicated by an arrow. The fluorescence signal from NIRF probes was pseudo-colored red. The tumor can be clearly visualized at 2−48 h pi. (B) Tumor/normal tissue ratio at 2, 24, and 48 h postadministration of Cy5.5−2DG (□) and Cy5.5−NHS (■). The tumor contrast of Cy5.5−NHS at 48 h pi is significantly higher than that of Cy5.5−2DG ($p < 0.05$).

(*T*/*N*) for Cy5.5−2DG (represented by −) and Cy5.5−NHS (represented by ···) was calculated and shown in Figure 4D. Cy5.5−NHS shows a significantly higher *T*/*N* ratio than Cy5.5−2DG at later time points (4 and 24 h) ($p < 0.05$). For example, *T*/*N* ratios for Cy5.5−2DG and Cy5.5−NHS are found to be 2.81 ± 0.10 and 3.34 ± 0.23, respectively, at 24 h pi. U87MG tumor tissues from the mice 24 h after administration of fluorescent probes were then taken out and sliced for NIRF imaging. Fluorescence and brightfield images for the tumor slices of mice injected with Cy5.5−2DG and Cy5.5−NHS were obtained. It was found that both probes accumulate in the tumor cells, and the fluorescence intensity is similar in both samples.

The tumor-targeting abilities in living subjects of Cy5.5−2DG and Cy5.5−NHS were also evaluated in the A375M xenografted mouse model. Figure 5A shows typical NIR fluorescence images of scid mice bearing subcutaneous A375M melanoma tumor after intravenous (iv) injection of 0.5 nmol of probe. Similar to the distribution in the U87MG mouse, both Cy5.5−2DG and Cy5.5−NHS show higher uptake in the tumor compared to normal tissue uptake. Moreover, a significant difference in *T*/*N* is observed between Cy5.5−2DG and Cy5.5−NHS at 48 h pi ($p = 0.01$). The *T*/*N* ratios for Cy5.5−2DG and Cy5.5−NHS at 48 h are 1.63 ± 0.06 and 2.58 ± 0.36, respectively (Figure 5B).

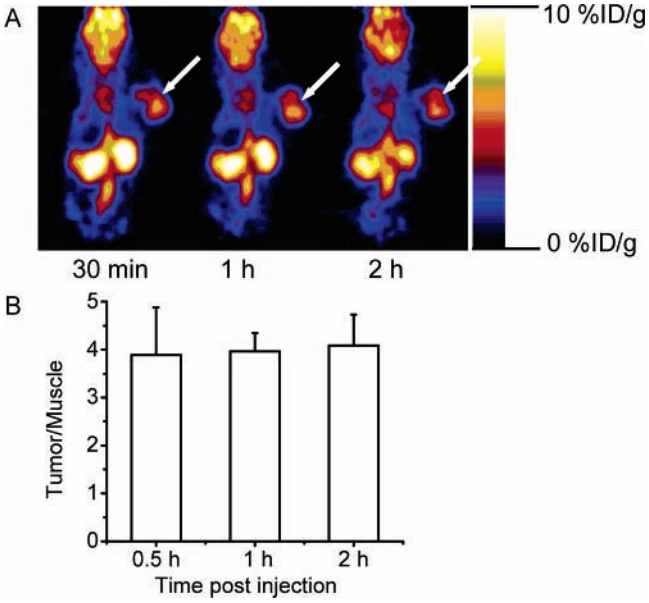

Figure 6. (A) Decay-corrected whole-body coronal microPET images of the nude mouse bearing human U87MG tumor at 30 min, 1 h, and 2 h (5-min static image) pi of 5.55 MBq (150 μCi) of [^{18}F]FDG. The position of the U87MG tumor is indicated by an arrow. (B) Tumor/normal tissue ratio at 30 min, 1 h, and 2 h pi of [^{18}F]FDG, with uptake values for organs derived from a multiple time-point microPET study. ROIs are shown as the mean %ID/g ± SD ($n = 3$).

The radioactive deoxyglucose analogue, [^{18}F]FDG, was then used to image the nude mice bearing human U87MG using microPET. [^{18}F]FDG preferentially localizes and is retained in U87MG tumors, as clearly shown in Figure 6A. The tumor/muscle ratios are 3.89 ± 0.99, 3.96 ± 0.39, and 4.08 ± 0.65, at 30 min, 1 h, and 2 h pi of the probe. Obviously, the tumor contrast for [^{18}F]FDG at these time points is significantly higher than that of Cy5.5−2DG (*T*/*N* ratios at 30 min to 2 h pi are all below 2, as shown in Figure 4D). This is probably caused by (1) the conjugation of D-glucose with a big fluorophor Cy5.5, resulting in a compound with reduced cell uptake and/or retention, and (2) autofluorescence of normal tissue, increasing the background signal. Furthermore, in comparison to optical imaging, [^{18}F]FDG−microPET is able to quantify the probe accumulation in most organs of interest such as the brain, heart, kidney, etc. However, except for the disadvantages as described in the Introduction, PET imaging can only monitor the [^{18}F]-FDG distribution up to several half-lives of F-18, while optical imaging can observe the Cy5.5−2DG NIR signal in living mice even several days pi.

The small animal optical imaging data shows that both Cy5.5−2DG and Cy5.5−NHS can accumulate very well in U87MG and A375M tumor models. Even 4 days pi of the probes, the tumor showed the high fluorescent signal and could be clearly visualized (data not shown). Another preliminary study also revealed that Cy5.5−2DG and Cy5.5−NHS can localize in the MDA-MB-435 tumor in an orthotopic tumor model (data not shown). Although it is not clear how Cy5.5−2DG and Cy5.5−NHS localize and are retained in the tumor, their high specificity, high accumulation, and retention in tumors will likely make them very useful in (1) labeling cancer cells for cell trafficking and (2) in vivo staining of tumors such as breast cancer, melanoma, and glioma for guidance of tumor surgery and radiation therapy in conjunction with proper optical imaging systems, etc. Moreover, conjugation of Cy5.5−NHS with cancer chemotherapeutical drugs or radionuclides such as F-18 may generate novel tumor-targeting agents.

The in vivo tumor-seeking ability of Cy5.5−NHS documented here is very different from the results reported previously

(*28*). In that paper, the authors did not observe any significant difference between the uptake in the tumor region and normal tissue region pi of Cy5.5−NHS. This inconsistency may be due to several factors such as the depth and size of the tumor, different settings of the optical imaging system, and the amount of dye injected (2.9 nmol/mouse in their report versus 0.5 nmol/mouse in our study), etc. Our finding also highlights the importance of a complete separation of free Cy5.5−NHS and Cy5.5-labeled biomolecules (peptides, antibodies, etc.) to avoid any false-positive results.

On the basis of our data reported here and previous literature (*19*−*23*), 2-NBDG has been proven to be a substrate of GLUTs, while Cy5.5−2DG is not a substrate of GLUTs. Considering that Cy5.5 is a much larger molecule than the 2-[*N*-(7-nitrobenz-2-oxa-1,3-diazol-4-yl)amino] (NBD) moiety (Figure 1), it is likely that the size of the fluorophor in the 2 position is the reason that Cy5.5−2DG cannot be delivered and trapped in tumor cells via the GLUT/hexokinase pathway. It looks like the resulting conjugate no longer behaves like D-glucose if the dye gets too large. These results clearly suggest the importance of selection of NIR dyes for the preparation of NIRF D-glucose analogues.

In conclusion, the NIRF glucose analogues, Cy5.5−2DG and Cy5.5−NHS, both demonstrate tumor-targeting abilities in cell culture and living mice but not through the GLUT/hexokinase pathway. More studies are warranted to further explore these two imaging probes for optical tumor imaging in cell culture and living subjects.

ACKNOWLEDGMENT

We thank Dr. Bengang Xing for technical assistance on fluorescent microscopy imaging. This work was supported, in part, by the National Cancer Institute (NCI) Small Animal Imaging Resource Program (SAIRP) Grant R24 CA93862 and NCI *In Vivo* Cellular Molecular Imaging Center (ICMIC) Grant P50 CA114747 (to S. S. G.).

LITERATURE CITED

(1) Gambhir, S. S. (2002) Molecular imaging of cancer with positron emission tomography. *Nat. Rev. Cancer 2*, 683−693.

(2) Nabi, H. A., and Zubeldia, J. M. (2002) Clinical applications of ^{18}F-FDG in oncology. *J. Nucl. Med. Technol. 30*, 3−9.

(3) Wahl, R. (1996) Positron emission tomography: Applications in oncology. In *Nuclear Medicine* (Henkin, R. V., Boles, M. A., Dillehay, G. L., et al., Eds.) pp 1524−1545, Mosby, St. Louis, MO.

(4) Kaarstad, K., Bender, D., Bentzen, L., Munk, O. L., and Keiding, S. (2002) Metabolic fate of ^{18}F-FDG in mice bearing either SCCVII squamous cell carcinoma or C3H mammary carcinoma. *J. Nucl. Med. 43*, 940−947.

(5) Warburg, O. (1931) *The Metabolism of Tumors*, pp 129−169, Richard R. Smith, Inc., New York.

(6) Wahl, R. L., Zasadny, K., Helvie, M., Hutchins, G. D., Weber, B., and Cody, R. (1993) Metabolic monitoring of breast cancer chemohormonotherapy using positron emission tomography: Initial evaluation. *J. Clin. Oncol. 11*, 2101−2111.

(7) Lapela, M., Eigtved, A., Jyrkkio, S., Grenman, R., Kurki, T., Lindholm, P., Nuutinen, J., Sutinen, E., Solin, O., Bjornskov, I., Bretlau, P., Friberg, L., Holm, S., Jensen, M., Sand Hansen, H., and Minn, H. (2000) Experience in qualitative and quantitative FDG PET in follow-up of patients with suspected recurrence from head and neck cancer. *Eur. J. Cancer 36*, 858−867.

(8) Akhurst, T., Downey, R. J., Ginsberg, M. S., Gonen, M., Bains, M., Korst, R., Ginsberg, R. J., Rusch, V. W., and Larson, S. M. (2002) An initial experience with FDG−PET in the imaging of residual disease after induction therapy for lung cancer. *Ann. Thorac. Surg. 73*, 259−264.

(9) Gayed, I., Vu, T., Iyer, R., Johnson, M., Macapinlac, H., Swanston, N., and Podoloff, D. (2004) The role of ^{18}F-FDG PET in staging and early prediction of response to therapy of recurrent gastrointestinal stromal tumors. *J. Nucl. Med. 45*, 17−21.

(10) Joensuu, H., Roberts, P. J., Sarlomo-Rikala, M., Andersson, L. C., Tervahartiala, P., Tuveson, D., Silberman, S., Capdeville, R., Dimitrijevic, S., Druker, B., and Demetri, G. D. (2001) Effect of the tyrosine kinase inhibitor STI571 in a patient with a metastatic gastrointestinal stromal tumor. *N. Engl. J. Med. 344*, 1052−1056.

(11) Schibli, R., Dumas, C., Petrig, J., Spadola, L., Scapozza, L., Garcia-Garayoa, E., and Schubiger, P. A. (2005) Synthesis and in vitro characterization of organometallic rhenium and technetium glucose complexes against Glut 1 and hexokinase. *Bioconjugate Chem. 16*, 105−112.

(12) Yang, D. J., Kim, C. G, Schechter, N. R., Azhdarinia, A., Yu, D. F., Oh, C. S., Bryant, J. L., Won, J. J., Kim, E. E., and Podoloff, D. A. (2003) Imaging with ^{99m}Tc ECDG targeted at the multifunctional glucose transport system: Feasibility study with rodents. *Radiology 226*, 465−473.

(13) Massoud, T. F., and Gambhir, S. S. (2003) Molecular imaging in living subjects: Seeing fundamental biological processes in a new light. *Genes Dev. 17*, 545−580.

(14) Ntziachristos, V., Bremer, C., and Weissleder, R. (2003) Fluorescence imaging with near-infrared light: New technological advances that enable in vivo molecular imaging. *Eur. Radiol. 13*, 195−208.

(15) Mahmood, U., and Weissleder, R. (2003) Near-infrared optical imaging of proteases in cancer. *Mol. Cancer Ther. 2*, 489−496.

(16) Achilefu, S. (2004) Lighting up tumors with receptor-specific optical molecular probes. *Technol. Cancer Res. Treat. 3*, 393−409.

(17) Sevick-Muraca, E. M., Houston, J. P., and Gurfinkel, M. (2002) Fluorescence-enhanced, near-infrared diagnostic imaging with contrast agents. *Curr. Opin. Chem. Biol. 6*, 642−650.

(18) Hawrysz, D. J., and Sevick-Muraca, E. M. (2000) Developments toward diagnostic breast cancer imaging using near-infrared optical measurements and fluorescent contrast agents. *Neoplasia 2*, 388−417.

(19) Yamada, K., Nakata, M., Horimoto, N., Saito, M., Matsuoka, H., and Inagaki, N. (2000) Measurement of glucose uptake and intracellular calcium concentration in single, living pancreatic β-cells. *J. Biol. Chem. 275*, 22278−22283.

(20) Yoshioka, K., Takahashi, H., Homma, T., Saito, M., Oh, K. B., Nemoto, Y., and Matsuoka, H. (1996) A novel fluorescent derivative of glucose applicable to the assessment of glucose uptake activity of *Escherichia coli*. *Biochim. Biophys. Acta 1289*, 5−9.

(21) Yoshioka, K., Saito, M., Oh, K. B., Nemoto, Y., Matsuoka, H., Natsume, M., and Abe, H. (1996) Intracellular fate of 2-NBDG, a fluorescent probe for glucose uptake activity, in *Escherichia coli* cells. *Biosci. Biotechnol. Biochem. 60*, 1899−1901.

(22) Lloyd, P. G., Hardin, C. D., and Sturek, M. (1999) Examining glucose transport in single vascular smooth muscle cells with a fluorescent glucose analog. *Physiol. Res. 48*, 401−410.

(23) Oh, K. B., and Matsuoka, H. (2002) Rapid viability assessment of yeast cells using vital staining with 2-NBDG, a fluorescent derivative of glucose. *Int. J. Food Microbiol. 76*, 47−53.

(24) Zhang, M., Zhang, Z., Blessington, D., Li, H., Busch, T. M., Madrak, V., Miles, J., Chance, B., Glickson, J. D., and Zheng, G. (2003) Pyropheophorbide 2-deoxyglucosamide: A new photosensitizer targeting glucose transporters. *Bioconjugate Chem. 14*, 709−714.

(25) Ye, Y., Bloch, S., and Achilefu, S. (2004) Polyvalent carbocyanine molecular beacons for molecular recognitions. *J. Am. Chem. Soc. 126*, 7740−7741.

(26) Ye, Y., Bloch, S., Kao, J., and Achilefu, S. (2005) Multivalent carbocyanine molecular probes: Synthesis and applications. *Bioconjugate Chem. 16*, 51−61.

(27) O'Neil, R. G., Wu, L., and Mullani, N. (2005) Uptake of a fluorescent deoxyglucose analog (2-NBDG) in tumor cells. *Mol. Imaging Biol. 7*, 1−5.

(28) Ke, S., Wen, X., Gurfinkel, M., Charnsangavej, C., Wallace, S., Sevick-Muraca, E. M., and Li, C. (2003) Near-infrared optical imaging of epidermal growth factor receptor in breast cancer xenografts. *Cancer Res. 63*, 7870−7875.

(29) Ballou, B., Fisher, G. W., Deng, J. S., Hakala, T. R., Srivastava, M., and Farkas, D. L. (1998) Cyanine fluorochrome-labeled antibod-

ies in vivo: Assessment of tumor imaging using Cy3, Cy5, Cy5.5, and Cy7. *Cancer Detect. Prev. 22*, 251−257.

(30) Chen, X., Conti, P. S., and Moats, R. A. (2004) In vivo near-infrared fluorescence imaging of integrin $\alpha_v\beta_3$ in brain tumor xenografts. *Cancer Res. 64*, 8009−8014.

(31) Ntziachristos, V., Schellenberger, E. A., Ripoll, J., Yessayan, D., Graves, E., Bogdanov, A., Jr., Josephson, L., and Weissleder, R. (2004) Visualization of antitumor treatment by means of fluorescence molecular tomography with an annexin V−Cy5.5 conjugate. *Proc. Natl. Acad. Sci. U.S.A. 101*, 12294−12299.

(32) Law, B., Curino, A., Bugge, T. H., Weissleder, R., and Tung, C. H. (2004) Design, synthesis, and characterization of urokinase plasminogen-activator-sensitive near-infrared reporter. *Chem. Biol. 11*, 99−106.

(33) Hansch, A., Frey, O., Hilger, I., Sauner, D., Haas, M., Schmidt, D., Kurrat, C., Gajda, M., Malich, A., Brauer, R., and Kaiser, W. A. (2004) Diagnosis of arthritis using near-infrared fluorochrome Cy5.5. *Invest. Radiol. 39*, 626−632.

(34) Ballou, B., Fisher, G. W., Waggoner, A. S., Farkas, D. L., Reiland, J. M., Jaffe, R., Mujumdar, R. B., Mujumdar, S. R., and Hakala, T. R. (1995) Tumor labeling in vivo using cyanine-conjugated monoclonal antibodies. *Cancer Immunol. Immunother. 41*, 257−263.

(35) Cheng, Z., Wu, Y., Xiong, Z. M., Gambhir, S. S., and Chen, X. (2005) Near-Infrared fluorescent RGD peptides for optical imaging of integrin $\alpha_v\beta_3$ expression in living mice. *Bioconjugate Chem. 16*, 1433−1441.

BC050345C

A Blue-Green Absorbing Cross-Linker for Rapid Photoswitching of Peptide Helix Content

Lei Chi, Oleg Sadovski, and G. Andrew Woolley*

Department of Chemistry, University of Toronto, 80 Saint George Street, Toronto, ON M5S 3H6, Canada. Received December 23, 2005; Revised Manuscript Received March 15, 2006

Azobenzene derivatives can be used to reversibly photoregulate secondary structure when introduced as intramolecular bridges in peptides and proteins. Here we report the design, synthesis, and characterization of a disubstituted *N*,*N*-dialkyl azobenzene derivative that absorbs near 480 nm in aqueous solution and relaxes with a half-life of ∼50 ms at room temperature. The wavelength of maximum absorbance and the rate of thermal relaxation are solvent-dependent. An increase in the percentage of organic solvent leads, in general, to a blue shift in the absorbance maximum and a slowing of the relaxation rate. In accordance with the design, the thermal relaxation of the azobenzene cross-linker from cis to trans causes an increase in the helix content of one peptide where the linker is attached via cysteine residues spaced at *i*, *i* + 11 positions and a decrease in helix content of another peptide with cysteine residues spaced at *i*, *i* + 7. This cross-linker design thus expands the possibilities for fast photocontrol of peptide and protein structure.

INTRODUCTION

Reversible optical control of protein structure and function offers the possibility of probing and manipulating individual proteins within the complex environment of a living cell (*1*, *2*). Azobenzene, in particular, has been a popular choice as a photoswitching chromophore due to its robust photophysical properties and relative ease of synthesis (*3*, *4*). However, there is no wavelength at which only one azobenzene isomer absorbs; the absorption spectra of trans and cis forms overlap extensively. Thus, irradiation typically produces photostationary states composed of at most ∼80% cis or ∼95% trans isomers (*5*, *6*). This fact limits the degree of photoswitching that is possible; For example, the fraction of cis isomer can be changed from ∼5% to 80% (16-fold) or trans from ∼20% to 95% (∼5-fold) (*6*). Thermal isomerization, in contrast, yields >99.99% trans isomer (*7*). Therefore, if thermal isomerization is used to reset the switch, a much greater fold change in the cis isomer is then possible.

The half-life for thermal cis-to-trans isomerization of unmodified azobenzene is on the order of 3−4 days at room temperature (*6*). If one wished to probe a dynamic process in a living cell using thermal reversion to reset the switch, this half-life would likely be too long. Many cellular signaling processes, such as the actions of kinases and phosphatases, operate on the time frame of seconds to minutes (e.g., refs *8* and *9*). Indeed naturally occurring photoswitchable proteins reset in the dark in seconds or less (*10*, *11*).

Several groups have shown that the rate of thermal isomerization of azobenzenes can be varied substantially by altering the nature of substituents on the aromatic rings (e.g., refs *12*−*15*). Previously we reported the design and synthesis of thiol-reactive azobenzene derivatives bearing alkyl, amide, carbamate, and urea substituents that could be used to manipulate peptide secondary structure (*7*). The fastest of these, the urea-substituted compounds, relaxed with a half-life of ∼10 s at room temperature. While significantly faster than the parent compounds, these photoswitches may still be too slow for certain applications such as probing calcium signaling in myocytes or reversibly modulating neural activity with switchable ion channels (*9*, *16*).

In addition to a requirement for rapid thermal relaxation, a critical design feature of such photoswitches is the effective end-to-end distance and how this changes upon isomerization. The urea- and carbamate-substituted compounds, in particular, can accommodate a wide range of end-to-end distances in their cis states, a feature that may limit their effect on the conformation of an attached peptide or protein (*17*). A smaller number of bonds between the azo moiety and the peptide backbone would be likely to maximize the conformational switching effect.

Finally, the wavelength that causes photoisomerization can be of considerable practical importance if one wishes to achieve photocontrol in a biological context. Short wavelength UV light is damaging to proteins and nucleic acids (*18*). Wavelengths in the 330−370 nm range (where current azobenzene-based photoswitches operate), while compatible with biological systems (*1*, *2*), are less able to penetrate cells and tissues than longer wavelengths (*19*). Longer wavelength switches would also make possible the incorporation of separately addressable photoswitches into a single protein.

With these considerations in mind, we designed the thiol reactive dialkylamino-substituted azobenzene-based photoswitch **1**. We report here the synthesis and characterization of this new photoswitch.

EXPERIMENTAL PROCEDURES

All chemicals were purchased from Sigma-Aldrich Chemical Co. except if specified otherwise. All ^{1}H and ^{13}C NMR spectra were recorded using a Varian Unity 400 or a Varian Gemini 300 spectrometer. High-resolution mass spectra were obtained either by electron impact (EI) or electrospray (ESI) ionization. Peptide mass spectra were obtained either by ESI or matrix-assisted laser desorption (MALDI) ionization.

Synthesis of the Cross-Linker. *2-[Ethyl-(4-{4-[ethyl-(2-hydroxy-ethyl)-amino]-phenylazo}-phenyl)-amino]-ethanol (**3**).* Ten grams (36 mmol) of 4-(ethyl(2-hydroxyethyl)amino)-benzenaminium hydrogensulfate (**2**) was mixed with 100 mL of ethyl acetate, and a saturated solution of sodium bicarbonate was added (∼15 mL). The reaction mixture turned a red color,

* E-mail: awoolley@chem.utoronto.ca. Telephone/fax: (416) 978-0675.

10.1021/bc050363u CCC: $33.50 © 2006 American Chemical Society
Published on Web 04/18/2006

and after the evolution of carbon dioxide was complete, the organic layer was separated. The water layer was extracted with ethyl acetate (3 × 50 mL), and the combined organic layers were dried with Na_2SO_4. The water layer was then mixed with ethanol (∼ 5 mL) and filtered through a pad of Na_2SO_4 and Al_2O_3. The pad was washed with CH_2Cl_2 (∼100 mL). The CH_2Cl_2 solution was combined with the ethyl acetate fractions, and the combined solution was evaporated, then dissolved again in CH_2Cl_2 and dried with Na_2SO_4. Removal of CH_2Cl_2 gave 4 g of the free amine of **2** (62% yield).

A mixture of 2-((4-aminophenyl)(ethyl)amino)ethanol (**2**; 4 g, 22 mmol) and manganese dioxide (20 g) was refluxed in dry benzene (200 mL) for 4 h. Removal of residual manganese dioxide and the solvent gave a residue, which was chromatographed on alumina. Elution with benzene gave 2.3 g of **3** (29% yield) as a slurry. ^{1}H NMR (300 MHz, $CDCl_3$) δ ppm: 1.20 (t, J = 7.3 Hz, 6 H, $2CH_3$), 3.40−3.60 (m, 8 H, 4 CH_2), 3.90 (t, J = 5.9 Hz, 4 H, $2CH_2$), 6.80 (d, J = 9.1 Hz, 4 H, $4CH_{arom}$), 7.8 (d, J = 9.1 Hz, 3 H, $4CH_{arom}$). MS (ESI): calcd (MH+) $C_{20}H_{29}N_4O_2$ 357.47; obsd 357.2.

*N-(2-Bromoethyl)-4-((4-((2-bromoethyl)(ethyl)amino)phenyl)-diazenyl)-N-ethylbenzenamine (**4**).* Methanesulfonyl chloride (0.65 mL, 8.4 mmol) was added in small portions to a stirred solution of **3** (1 g, 2.8 mmol) and TEA (1.56 mL, 11 mmol) in dry THF (50 mL) under N_2 maintained at 0 °C. After being stirred for 1 h at 0 °C and 24 h at room temperature, the mixture was poured into cold water and extracted with CH_2Cl_2. The organic extract was washed with cold water, dried, and concentrated under reduced pressure. LiBr (1.2 g, 14 mmol) was added over the course of 15 min to a solution of the residue so obtained in acetone (100 mL), and the mixture was stirred for 48 h at room temperature. It was then poured into water (400 mL) and extracted with CH_2Cl_2. The organic extract was washed with water, dried, and purified by silica gel chromatography (CH_2Cl_2/hexane, 1:1) to yield **4** (0.9 g, 67%). ^{1}H NMR (300 MHz, $CDCl_3$) δ ppm: 1.20 (t, J = 7.0 Hz, 6 H, $2CH_3$), 3.40−3.60 (m, 8 H, $4CH_2$), 3.70−3.80 (m, 4 H, $2CH_2$), 6.7 (d, J = 9.3 Hz, 4 H), 7.8 (d, J = 9.3 Hz, 4 H). ^{13}C NMR (300 MHz, $CDCl_3$) δ ppm: 12.72, 28.24, 45.74, 52.43, 111.39, 124.39, 144.33, 148.15. HRMS (ESI): calcd (MH+) $C_{20}H_{27}N_4Br_2$ 481.0596; obsd 481.0608.

*Methanethiosulfonic Acid S-{2-[Ethyl-(4-{4-[ethyl-(2-methanesulfonylsulfanyl-ethyl)-amino]-phenylazo}-phenyl)-amino]-ethyl} Ester (**1**).* Compound **4** (0.1 g, 0.2 mmol) and sodium methanethiosulfonate (80 mg, 0.6 mmol) were dissolved in dry DMF (10 mL) under Ar and heated to 60 °C. After 18 h of stirring at this temperature, the DMF was evaporated under reduced pressure. The crude product was dissolved in EtOAc and filtered, and the filtrate was evaporated under reduced pressure. Chromatography on silica (EtOAc/hexanes 1:1, R_f = 0.36) gave **1** (30 mg, 33%), as a brown-yellow solid. ^{1}H NMR (400 MHz, $CDCl_3$) δ ppm: 1.25 (t, J = 7 Hz, 6.H, $2CH_3$), 3.30−3.45 (m, 10 H, $2CH_2$, $2CH_3$), 3.5 (q, J = 7.3 Hz, 4 H, 2 CH_2), 3.80 (t, J = 7.Hz, 4 H $2CH_2$), 6.8 (d, J = 9 Hz, 4 H), 7.8 (d, J = 9 Hz, 4 H). ^{13}C NMR (300 MHz, $CDCl_3$) δ ppm: 12.53, 33.39, 45.78, 50.55, 50.72, 111.78, 124.45, 144.45, 148.20. HRMS (ESI): calcd (MH+) $C_{22}H_{33}N_4S_4O_4$ 545.1379; obsd 545.1390.

Peptide Cross-Linking. Peptides FK-11 (acetyl-EACAREAAAREAACRQ-amide) and JRK-7 (acetyl-EACARVAibAACEAAARQ-amide) were prepared using standard Fmoc-based solid-phase synthetic methods as described previously (*20*). Intramolecular cross-linking of cysteine residues was performed for FK-11 as follows: 2.0 mg (1.2 μmol) of FK-11 was dissolved in a total volume of 3.8 mL of a solvent consisting of 1.0 mL of 10 mM Tris·Cl, 1 mM EDTA buffer (pH 8.0) and 2.8 mL of DMSO. This solution was stirred, and 200 μL of a 14.5 mM solution of the linker **1** in DMSO was added dropwise. Then the mixture was left to stir for 2 h protected from light. The modified peptide was purified by Bio-gel P4 gel-filtration chromatography, followed by HPLC [Zorbax 300SB-C3 column; 20−80% acetonitrile/H_2O (+0.1% trifluoroacetic acid) linear gradient over the course of 30 min; elution at 54% acetonitrile]. The peptide molecular composition was confirmed by ESI-MS (calculated for $C_{85}{}^{13}C_2H_{139}N_{31}O_{24}S_4$ = 2133.5 Da; observed = 2133.4 Da).

For JRK-7, 0.5 mg (0.3 μmol) of peptide was dissolved in a total volume of 1.8 mL of a solvent consisting of 0.5 mL of 10 mM Tris·Cl, 1 mM EDTA buffer (pH 8.0) and 1.3 mL of THF. This solution was stirred, and 200 μL of a 3.65 mM solution of the linker **1** in THF was added dropwise. Then the mixture was left to stir for 2 h protected from light. The modified peptide was purified by HPLC [Zorbax 300SB-C3 column; 20−70% acetonitrile/H_2O (+0.1% trifluoroacetic acid) linear gradient over the course of 25 min; elution at 65% acetonitrile]. The peptide molecular composition was confirmed by electrospray ionization MS (calculated for $C_{85}H_{136}N_{28}O_{22}S_4$ = 2030.5 Da; observed = 2030.4 Da).

The glutathione derivative of **1** was prepared as follows: 2.8 mg (9.1 μmol) of glutathione was dissolved in a total volume of 4.5 mL of a solvent consisting of 1.5 mL of 10 mM Tris·Cl, 1 mM EDTA buffer (pH 8.0) and 3.0 mL of THF. This solution was stirred, and 200 μL of a 9.0 mM solution of the linker **1** in THF was added dropwise. Then the mixture was left to stir overnight protected from light. The modified peptide was purified by Bio-gel P4 gel-filtration chromatography, followed by HPLC [Zorbax 300SB-C18 column; 20−70% acetonitrile/H_2O (+0.1% trifluoroacetic acid) linear gradient over the course of 30 min; elution at 48% acetonitrile]. The peptide molecular composition was confirmed by electrospray ionization MS (calculated for $C_{40}H_{58}N_{10}O_{12}S_4$ = 999.2 Da; observed = 999.1 Da).

UV/Vis Spectra and Photoisomerization. Ultraviolet absorbance spectra were obtained using either a Perkin-Elmer Lambda 2 spectrophotometer or a diode array UV−vis spectrophotometer (Ocean Optics Inc., USB2000) coupled to a temperature-controlled cuvette holder (Quantum Northwest, Inc.). The latter arrangement was used to determine thermal relaxation rates of cross-linked species. Irradiation of the sample (at 90° to the light source and detector used for the absorbance measurements) was carried out using a xenon lamp (450 W) coupled to a double monochromator with slits at 16 nm and 16 nm. Rates of thermal cis-to-trans isomerization were measured for a series of temperatures by monitoring absorbance at 480 nm after irradiation to convert a percentage of the solution to the cis isomer. All curves could be fit well by single-exponential decay kinetics. Solution conditions are described in the figure legends.

For rapid (<1 s) measurements of thermal relaxation, photoisomerization was accomplished by irradiating thermostated cross-linked peptide solutions in a 10 cm path length, quartz, water-jacketed cell mounted in a microsecond flash photolysis apparatus operating in a manual single-shot mode. An Osram model XBO W/1 150-W xenon lamp was used as a continuous monitoring light source. The light that passed through the cell was focused by an Oriel model 77250 grating monochromator set at a wavelength of 480 nm, then detected by an Oriel model 7068 photomultiplier. Signals were displayed on a Tektronix 2225 50 MHz oscilloscope. The digitized outputs were fed into a PC computer for data analysis.

A molar extinction coefficient for the cross-linker of 16 200 $cm^{-1}\,M^{-1}$ at 480 nm (in 10% acetone/90% MeOH) was determined by quantitative NMR with CH_2Cl_2 as a reference material. Approximately 3 mg of cross-linker was dissolved in acetone-d_6, followed by addition of a known number of moles

Scheme 1

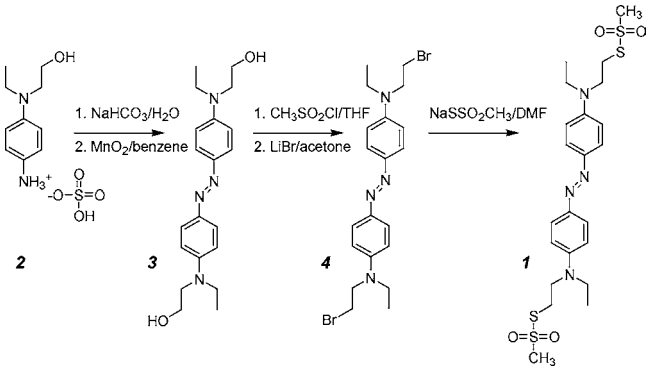

of CH_2Cl_2. The concentration of the cross-linker was then calculated by comparing the areas of the methylene resonance of CH_2Cl_2 with the area of the aromatic ring signals of **1**. The molar extinction coefficient of **1** at 480 nm (maximum absorbance) was then calculated using the concentration, the UV absorbance, and the path length of the cuvette.

Circular Dichroism Measurements. Circular dichroism (CD) measurements were performed on a Jasco model J-710 spectropolarimeter. Peptide concentrations were determined using a molar extinction coefficient for the cross-linker of 16 200 cm^{-1} M^{-1} at 480 nm. For fast CD measurements, the instrument was set to time-drive mode. A scan time of 8 min with a 2-s step resolution and 1-s response was used. All samples were dissolved in 75% MeOH/25% pH 7.0 sodium phosphate buffer. The temperature of the sample was 10 °C, and the nitrogen flow rate was increased 2-fold to minimize condensation on the cuvette. Samples in cuvettes were flashed 40 times with an Elinchrome EL1000 flash lamp (flash power 1000 W•s, flash duration 1 ms) passed through a water cell to block short-wavelength UV as well as IR radiation, then transferred immediately into the spectropolarimeter for the measurement.

Molecular Modeling. Models of cis and trans cross-linkers were built using HyperChem (v.7, Hypercube Inc.) with the linker terminated with methyl groups representing the β carbon of cysteine in the cross-linked peptide and minimized using the Amber99 force field. Restraints were added to the azo bond for the cis conformation (force constant 50). The bonds labeled a, b, c, and d between the rings and the nitrogen atoms (Figure 5) were treated as being in conjugation with the rings for the trans isomer, whereas only bonds labeled a and d were treated as delocalized in the cis isomer (b and c were treated a normal single bonds). For the trans isomer, four MD runs of 50 ns each were performed using the Amber99 force field and using different starting torsion angles of the bonds labeled a, b, c, and d (180,180,180,180; 0,180,180,180; 180,180,0,180; 0,180,0,-180). Similarly, for the cis isomer, four MD runs of 50 ns each were performed using starting torsion angles of the bonds labeled a, b, c, and d of 180,48,48,180; 0,48,48,180; 180,48,−133,-180; and 0,180,−133,180. Constant energy MD was performed in vacuo with a distance-dependent dielectric and 1−4 scale factors of 0.833 for electrostatic and 0.5 for van der Waals interactions, a step size of 1 fs, and 300 K as the simulation temperature. Trajectories were analyzed to verify that numerous torsion angle changes occurred for all single bonds during the course of the simulation to ensure that conformational space was adequately sampled. All points histograms were then produced for the S−S distance during the full set of simulations for each isomer. S−S distance ranges in the peptides were calculated using FOLDTRAJ as described previously (*21*).

RESULTS AND DISCUSSION

Design and Synthesis of the Cross-Linker. Based on previous studies (*15*), we expected that an azobenzene derivative with a dialkylamino substituent in the para position would exhibit a wavelength of maximal absorption substantially longer than alkyl- and amide-substituted azobenzene derivatives, together with a faster thermal relaxation rate. We therefore wished to prepare a dialkylamino-substituted derivative that was symmetrical (to avoid the formation of different isomers upon protein conjugation), contained a minimum number of single bonds connecting the azo group with the peptide backbone, and was thiol reactive.

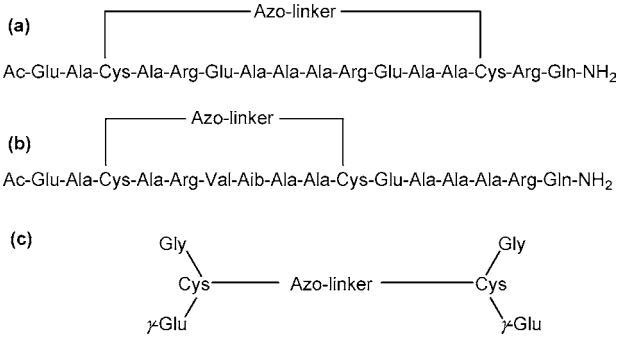

Figure 1. Primary sequences of the cross-linked peptides examined in this study: (a) FK-11 (azo-linker **1** reacted via cysteine residues spaced *i*, *i* + 11); (b) JRK-7 (azo-linker **1** reacted via cysteine residues spaced *i*, *i* + 7); (c) cross-linked glutathione.

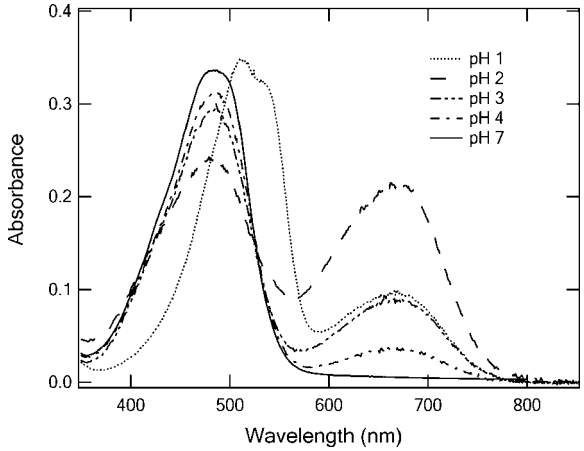

Figure 2. UV−vis spectra of the cross-linked FK-11 peptide (∼30 μM) in aqueous buffer at series of pH values.

These considerations, together with the fact of the commercial availability of **2**, led us to the design of **1** (Scheme 1). Oxidation of **2** produced the symmetrical azo derivative **3**, which was subsequently converted to the dibromo derivative **4**. High reactivity and selectivity toward cysteine residues was then achieved by introducing methanethiosulfonyl groups. These groups enable reversible attachment of the cross-linker to peptides and proteins via disulfide linkages (*22*).

The cross-linker (**1**) was then reacted with the peptides shown in Figure 1. Reaction with FK-11 and JRK-7 produces an intramolecular cross-link between cysteine residues spaced *i*, *i* + 11 and *i*, *i* + 7, respectively. As a control, the cross-linker was also reacted with two molecules of the small tripeptide glutathione, which is too short to exhibit substantial secondary structure in solution. The cross-linked peptides were purified by HPLC and characterized by mass spectrometry.

UV Spectra: pH and Solvent Dependence. Figure 2 shows UV spectra of the cross-linked FK-11 peptide in aqueous buffer at a series of pH values. At pH values of 5 and above, a single maximum near 480 nm was observed. This value is at approximately 100 nm longer wavelengths than amide-substituted azobenzenes investigated previously. As the pH is lowered below 5, a second absorption band emerges at ∼680

Scheme 2

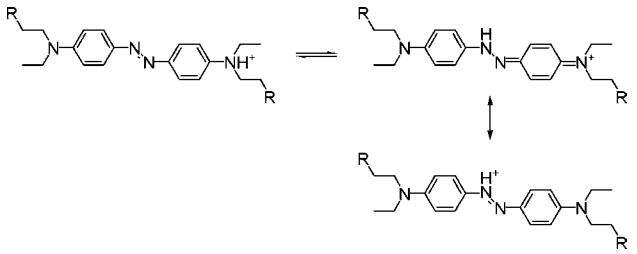

nm giving the solution a strong green color. Sawicki (*23*) and Jaffé (*24*) have studied the effect of ring substitutions on the pK_a's of azobenzene derivatives in detail. Based on their data, the singly protonated form of the cross-linker is expected to be a tautomeric equilibrium of the species shown in Scheme 2.

Lowering the pH below ~1.5 causes a further qualitative shift in the absorbance spectrum (Figure 2) consistent with the presence of a doubly protonated species (*23, 24*). Protonated forms of the cross-linker do not appear to isomerize. Thus the effective pH range of this cross-linker is pH 5 and above. Since most biological systems of interest operate in the region of pH 7, this pH sensitivity is not likely to present any difficulty.

Although this photoswitch is designed to be used with proteins in aqueous solution, the local environment of the switch will be determined primarily by the nature of the protein side chains near the cross-linking site. Amino-substituted azobenzenes, in contrast to alkyl- or amide-substituted species, are expected to be quite sensitive to local solvation (*15*). To ascertain the possible effects of local hydrophobicity, we examined the effects of modifying overall solvent polarity on the UV−vis spectra and thermal isomerization rates of peptide−cross-linker conjugates. Figure 3 shows UV absorbance spectra of cross-linked FK-11 with added organic cosolvents. As the percentage of methanol or DMSO is increased, the wavelength of maximal absorbance becomes shorter. In addition, fine structure in the spectra becomes more pronounced. Similar trends are observed for the glutathione-linked species (Figure 3).

For the JRK-7 cross-linked peptide, a more complicated solvent dependence is observed. Figure 4 shows spectra obtained in aqueous buffer (pH 7) with increasing fraction of methanol or DMSO. As the percentage of methanol or DMSO is increased from 0 to 50%, a bathochromic shift of absorption can be observed, and the fine structure in the spectra becomes less pronounced. Then, as the percentage of methanol or DMSO is increased from 50% to 100%, the spectra undergo a hypsochromic shift, and the fine structure becomes obvious again.

Similar solvent-induced effects on the electronic absorption spectra of related azobenzene derivatives have been observed previously (e.g., refs *15*, *25*, and *26* and references therein). Increased solvent polarity has been proposed to stabilize enhanced dipolar character in the excited state relative to the ground state. Chromophores in some cross-linked peptides (e.g., JRK-7) may experience especially complex local solvation processes compared to chromophores in bulk solution. Dipolar character similar to that in the excited state has been proposed to exist also in the transition state for isomerization (*25*). Thus increased solvent polarity may stabilize this transition state and increase the rate of isomerization. We therefore studied the effects of solvent polarity on isomerization rates.

Kinetics of Isomerization. The kinetics of thermal relaxation from cis to trans was studied for each peptide under a variety of solvent conditions at 25 °C. Cis isomers were produced by a brief exposure to 480 nm light. Recovery of the trans isomer

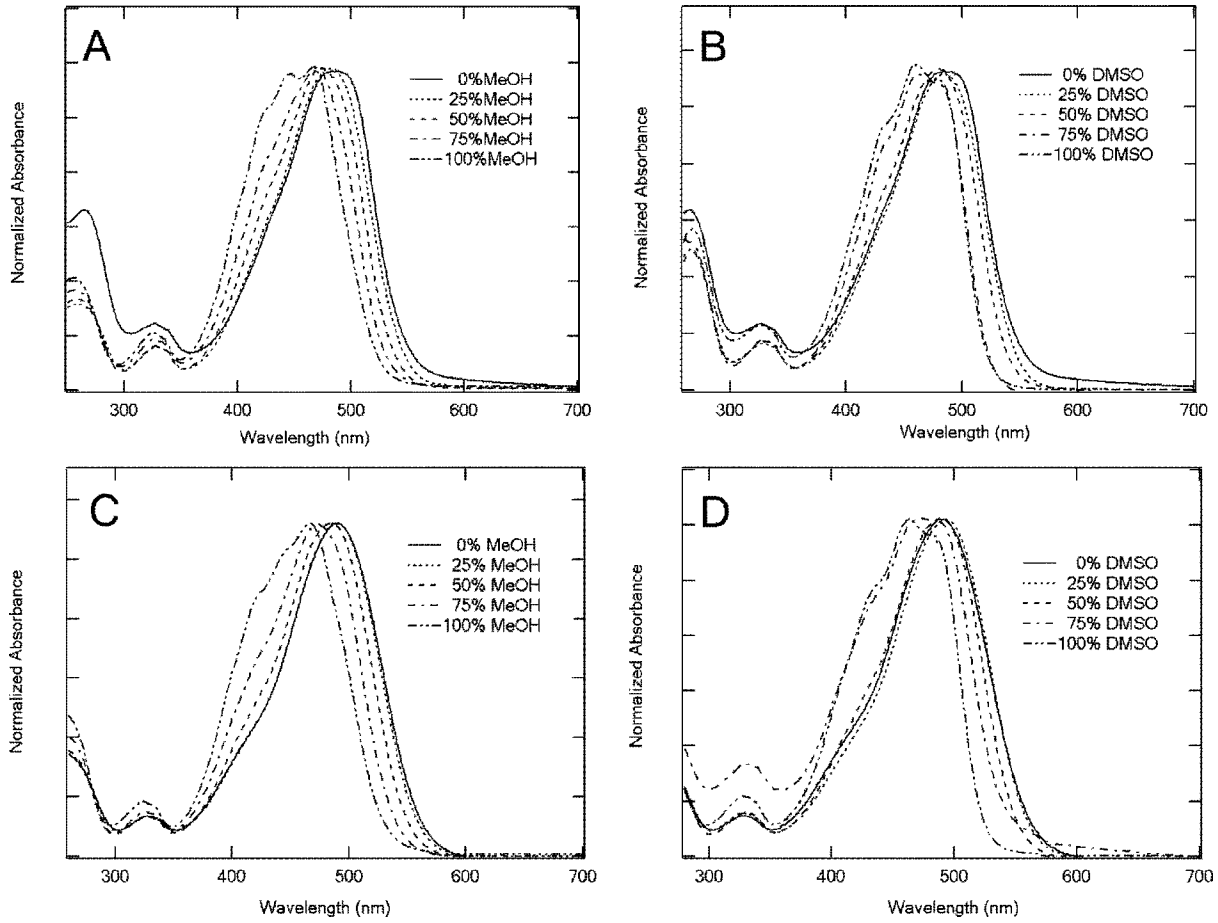

Figure 3. UV−vis spectra of the cross-linked FK-11 peptide (~70 μM) in aqueous buffer, pH 7, with added methanol (A) or DMSO (B) and for the glutathione-linked azo compound (~35 μM) in aqueous buffer, pH 7, with added methanol (C) or DMSO (D).

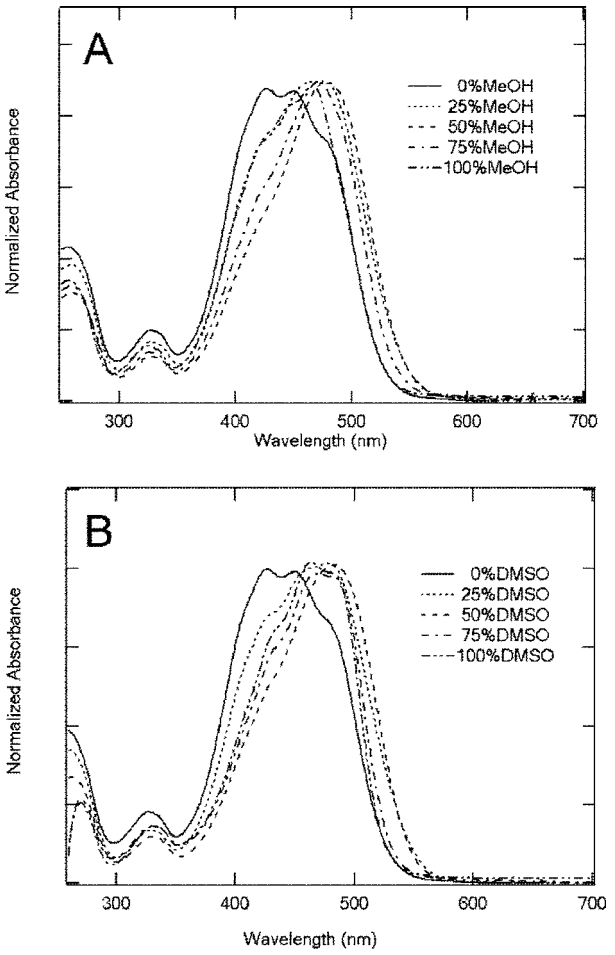

Figure 4. UV−vis spectra of the cross-linked JRK-7 peptide (~50 μM) in aqueous buffer, pH 7, with added methanol (A) or DMSO (B).

Table 1

organic solvent content (%)	$\tau_{1/2}$ (s) of cross-linked FK-11		$\tau_{1/2}$ (s) of cross-linked JRK-7		$\tau_{1/2}$ (s) of azobenzene glutathione derivative	
	DMSO	MeOH	DMSO	MeOH	DMSO	MeOH
0	0.076		0.0065		0.025	
25	2.4	1.1	4.2	2.2		
50	24.0	8.2	18.0	12.1	13.7	3.1
75	57.3	24.1	55.7	24.1	49.6	18.7
100	99.7	6.2	83.2	15.0	89.2	0.9

was measured by monitoring recovery of 480 nm absorbance over time using a low-intensity light source as desribed in the Experimental Procedures section. Half-lives were calculated by fitting absorbance vs time curves to the standard expression for a single-exponential decay process. These data are collected in Table 1.

In general, the half-lives of cis cross-linked FK-11 and JRK-7 become longer with increasing percentages of organic solvents. In 100% methanol, however, faster relaxation is observed in each case. The half-lives observed in aqueous buffer (between 10 and 100 ms) are the shortest recorded to date for a designed conformational switch (*3*, *7*). The half-live observed for JRK-7 was particularly short (6.5 ms). This may indicate that the local peptide environment of JRK-7 helps to stabilize the dipolar transition state for isomerization or that conformational preferences of the peptide act to destabilize the cis conformation of the cross-linker or both. To estimate the activation energy involved for cis to trans isomerization of the peptide systems in aqueous solution, we measured relaxation rates as a function of temperature. Calculated activation energies were as follows:

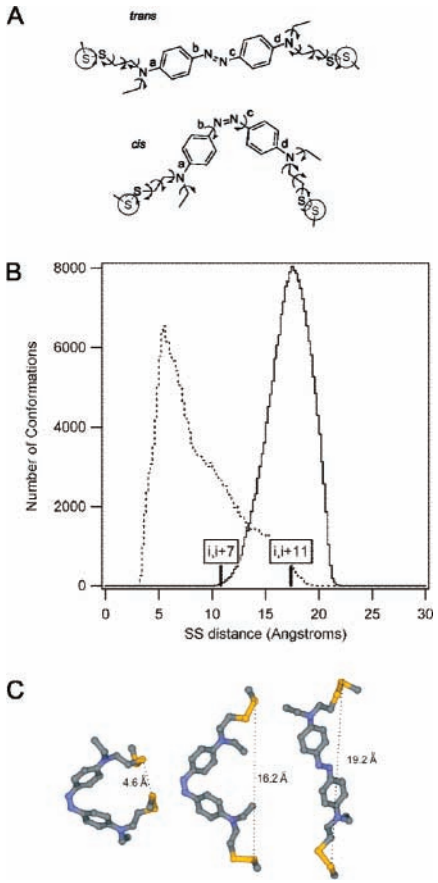

Figure 5. (A) Trans and cis forms of the cross-linker structure used for molecular dynamics simulations. Bonds labeled a−d were constrained as described in the Experimental Procedures section. (B) Probability distributions of distances between S atoms (circled in panel A) derived from the molecular dynamics simulations (cis (···), trans (—); distances between cysteine S atoms in ideal α-helices spaced *i, i* + 7 and *i, i* + 11 in the primary sequence are indicated. (C) Some representative structures and S−S distances observed during the simulations. Cis forms show a wider range of S−S distances.

cross-linked-FK11 is 6.5 ± 0.5 kcal/mol (27 ± 2 kJ/mol); cross-linked JRK-7 is 5.5 ± 1.4 kcal/mol (23 ± 6 kJ/mol); the cross-linked glutathione derivative is 6.5 ± 0.3 kcal (27 ± 1 kJ/mol).

Conformational Analysis of the Cross-Linker and Effects of Photoisomerization. To estimate the effects of the cross-linker on the conformational properties of attached peptides or proteins, we first examined the conformational properties of the cross-linker itself in cis and trans conformations. In particular, the range of end-to-end distances exhibited by the cross-linker provides a good first approximation for predicting its effect on conformational ensembles of helical peptides (*17*, *21*). Simplified models of **1** attached to a peptide (where the β position of a cysteine side chain is represented by a methyl group) in cis and trans conformation were built using HyperChem (Hypercube Inc.).

Figure 5a shows these structures together with the restraints that were added during molecular dynamics simulations. Sulfur−sulfur distances together with all bond torsion angles were monitored. Figure 5b shows histograms of the S−S distances for cis and trans isomers together with some representative structures (Figure 5c). The trans isomer has a most-probable end to end distance of ~18 Å (and a range from 11 to 21 Å), whereas the cis isomer shows a more complex distribution with a most probable distance of ~6 Å but is compatible with distances from ~4 to ~17 Å. When a peptide with cysteine residues spaced *i, i* + 11 is in an α-helical conformation, the distance between S atoms of the cysteine side chains is 17.4 Å.

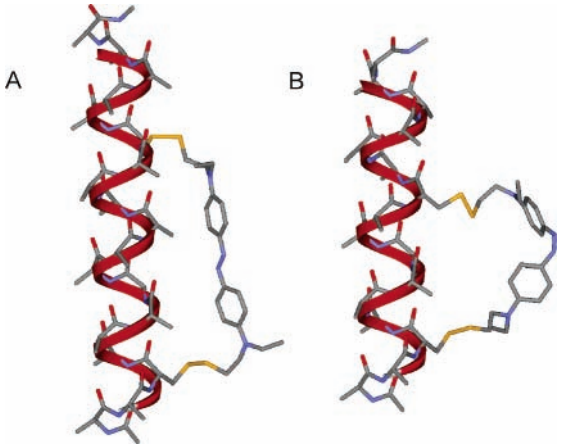

Figure 6. Molecular models of trans cross-linked FK-11 (A) and cis cross-linked JRK-7 (B) in a helical conformation.

When a peptide with cysteine residues spaced i, $i + 7$ is in an α-helical conformation, the distance between S atoms of the cysteine side chains is 10.8 Å (*17*, *21*). Based on observed effects with previous cross-linkers, one would predict that the trans form of the cross-linker (**1**) would be compatible with a helical conformation of FK-11 (Figure 6) and that isomerization from trans to cis would decrease the helical content. Conversely, a trans conformation of the cross-linker should be incompatible with standard helix formation for JRK-7 but isomerization from trans to cis should make helix formation more likely (Figure 6).

To test these predictions, we performed CD studies of the two cross-linked peptides in 75% methanol as described in the Experimental Procedures section. Under these solvent conditions, the cross-linked peptides isomerize slowly enough to monitor using a conventional CD instrument. The half-lives observed without an organic cosolvent are too short to permit CD measurements with a standard commercial instrument. We expect similar conformational behavior in aqueous solution although the magnitude of the helix content changes will likely be different.

Figure 7 shows the effects of photoisomerization on peptide conformation. For the FK-11 peptide, relaxation of the cross-linker from cis to trans after a light flash is expected to increase helicity. Consistent with this expectation, the CD signal at 225 nm recovers from a less negative to a more negative value (Figure 7A). Conversely, for the JRK-7 peptide, relaxation of the cross-linker from cis to trans after a light flash is expected to decrease helicity. Likewise, the CD signal at 225 nm recovers from a more negative to a less negative value (Figure 7B). The magnitudes of the observed changes are not particularly significant since they depend on the precise solvent composition, the temperature, and the time elapsed between the flash and the beginning of the measurement. From the time dependence of the signal however, the half-lives of cis forms of cross-linked FK-11 and JRK-7 can be calculated to be 80 ± 14 and 81 ± 6 s, respectively. These values are comparable to the time constants estimated from the UV data in Table 1 (∼40 s) assuming that the activation energy of the two peptides in 75% methanol is the same as that in phosphate buffer (pH 7.0).

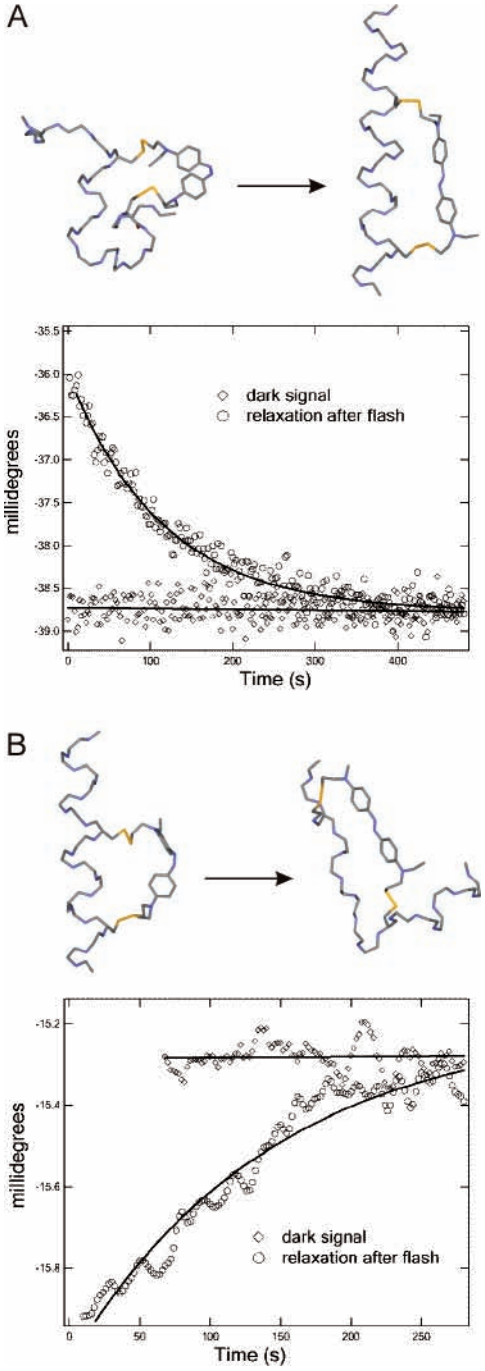

Figure 7. Time-dependent circular dichroism (CD) signal at 225 nm of (A) cross-linked FK-11 (∼25 μM, 1 cm cell) and (B) cross-linked JRK-7 (∼100 μM, 0.1 cm cell) observed after conversion of a percentage of each peptide to the cis isomer. In panel A, relaxation from cis-to-trans is associated with an increase in peptide helix content. In panel B, relaxation from cis-to-trans is associated with a decrease in peptide helix content. Solvent conditions were 75% methanol in 10 mM sodium phosphate buffer, pH 7.0, 10 °C.

SUMMARY

We have designed and synthesized a new methanethiosulfonate (MTS)-bearing thiol-reactive azobenzene cross-linker that is able to reversibly control the helical content of attached peptides. Its effects on helix content can be predicted by comparing the range of S−S distances in the intrinsic conformational ensemble of the peptide with the range compatible with the chemical structure of the linker. The wavelength for trans-to-cis photoswitching is ∼100 nm longer (λ_{max} = 480 nm) than cross-linkers previously described, and the half-life of the cis state (10−100 ms) is comparable to the time scale of many protein-based dynamic processes in biochemical systems. This switch may therefore prove useful as a tool for probing dynamic processes in biochemical systems using light.

ACKNOWLEDGMENT

We are grateful to Prof. Jerry Kresge for the use of his flash photolysis apparatus. This work has been supported by Natural Sciences and Engineering Research Council of Canada.

LITERATURE CITED

(1) Volgraf, M., Gorostiza, P., Numano, R., Kramer, R. H., Isacoff, E. Y., and Trauner, D. (2006) Allosteric control of an ionotropic glutamate receptor with an optical switch. *Nat. Chem. Biol. 2*, 47−52.

(2) Banghart, M., Borges, K., Isacoff, E., Trauner, D., and Kramer, R. H. (2004) Light-activated ion channels for remote control of neuronal firing. *Nat. Neurosci. 7*, 1381−1386.

(3) Renner, C., Kusebauch, U., Loweneck, M., Milbradt, A. G., and Moroder, L. (2005) Azobenzene as photoresponsive conformational switch in cyclic peptides. *J. Pept. Res. 65*, 4−14.

(4) Ulysse, L., and Chmielewski, J. (1994) The synthesis of a light-switchable amino acid for inclusion into conformationally mobile peptides. *Bioorg. Med. Chem. Lett. 4*, 2145−2146.

(5) Rau, H. (1990) Photoisomerization of Azobenzenes, in *Photochemistry and Photophysics* (Rabek, J. F., Ed.) pp 119−141, CRC Press Inc., Boca Raton, FL.

(6) James, D. A., Burns, D. C., and Woolley, G. A. (2001) Kinetic characterization of ribonuclease S mutants containing photoisomerizable phenylazophenylalanine residues. *Protein Eng. 14*, 983−991.

(7) Pozhidaeva, N., Cormier, M. E., Chaudhari, A., and Woolley, G. A. (2004) Reversible photocontrol of peptide helix content: adjusting thermal stability of the cis state. *Bioconjugate Chem. 15*, 1297−1303.

(8) Bhalla, U. S. (2004) Signaling in small subcellular volumes. I. Stochastic and diffusion effects on individual pathways. *Biophys. J. 87*, 733−744.

(9) Bers, D. M., and Guo, T. (2005) Calcium signaling in cardiac ventricular myocytes. *Ann. N. Y. Acad. Sci. 1047*, 86−98.

(10) Lanyi, J. K. (2004) Bacteriorhodopsin. *Annu. Rev. Physiol. 66*, 665−688.

(11) Genick, U. K., Soltis, S. M., Kuhn, P., Canestrelli, I. L., and Getzoff, E. D. (1998) Structure at 0.85 Å resolution of an early protein photocycle intermediate. *Nature 392*, 206−209.

(12) Talaty, E. R., and Fargo, J. C. (1967) Thermal cis−trans isomerization of substituted azobenzenes: a correction of the literature. *Chem. Commun. (London)*, 65−66.

(13) Le Fevre, R. J. W., and Northcott, J. (1953) The effects of substituents and solvents on the cis−trans change of azobenzene. *J. Chem. Soc.*, 867−870.

(14) Forber, C. L., Kelusky, E. C., Bunce, N. J., and Zerner, M. C. (1985) Electronic spectra of cis- and trans-azobenzenes: consequences of ortho substitution. *J. Am. Chem. Soc. 107*, 5884−5890.

(15) Nishimura, N., Sueyoshi, T., Yamanaka, H., Imai, E., Yamamoto, S., and Hasegawa, S. (1976) Thermal cis-to-trans isomerization of substituted azobenzenes II. Substituent and solvent effects. *Bull. Chem. Soc. Jpn. 49*, 1381−1387.

(16) Wulff, P., and Wisden, W. (2005) Dissecting neural circuitry by combining genetics and pharmacology. *Trends Neurosci. 28*, 44−50.

(17) Burns, D. C., Flint, D. G., Kumita, J. R., Feldman, H. J., Serrano, L., Zhang, Z., Smart, O. S., and Woolley, G. A. (2004) Origins of helix−coil switching in a light-sensitive peptide. *Biochemistry 43*, 15329−15338.

(18) Kulms, D., and Schwarz, T. (2002) Molecular mechanisms involved in UV-induced apoptotic cell death. *Skin Pharmacol. Appl. Skin Physiol. 15*, 342−347.

(19) Cullander, C. (1994) Imaging in the far-red with electronic light microscopy: requirements and limitations. *J. Microsc. 176* (Part 3), 281−286.

(20) Flint, D. G., Kumita, J. R., Smart, O. S., and Woolley, G. A. (2002) Using an azobenzene cross-linker to either increase or decrease peptide helix content upon trans-to-cis photoisomerization. *Chem. Biol. 9*, 391−397.

(21) Woolley, G. A. (2005) Photocontrolling peptide α helices. *Acc. Chem. Res. 38*, 486−493.

(22) Smith, D. J., Maggio, E. T., and Kenyon, G. L. (1975) Simple alkanethiol groups for temporary blocking of sulfhydryl groups of enzymes. *Biochemistry 14*, 766−771.

(23) Sawicki, E. (1957) Physical properties of the aminoazobenzene dyes. IV. The position of proton addition, *J. Org. Chem. 22*, 365−367.

(24) Yeh, S., and Jaffe, H. (1959) Tautomeric equilibria. VI The structure of the conjugate acid of p-(dimethylamino)-azobenzene. *J. Am. Chem. Soc. 81*, 3283−3287.

(25) Nishimura, N., Tanaka, T., Asano, M., and Sueishi, Y. (1986) A volumetric study on the thermal cis-to-trans isomerization of 4-(dimethylamino)4′-nitroazobenzene and 4, 4′-bis(dialkylamino)-azobenzenes: Evidence of an inversion mechanism. *J. Chem. Soc., Perkin Trans. 2*, 1839−1845.

(26) Airinei, A., Rusu, E., and Dorohoi, D. (2001) Solvent influence on the electronic absorption spectra of some azoaromatic compounds. *Spectrosc. Lett. 34*, 65−74.

BC050363U

pH-Responsive Three-Layered PEGylated Polyplex Micelle Based on a Lactosylated ABC Triblock Copolymer as a Targetable and Endosome-Disruptive Nonviral Gene Vector

Motoi Oishi,[†] Kazunori Kataoka,*[,‡,#] and Yukio Nagasaki*[,†]

Tsukuba Research Center for Interdisciplinary Materials Science (TIMS), University of Tsukuba, 1-1-1 Ten-noudai, Tsukuba, Ibaraki 305-8573, Japan, Department of Materials Engineering, Graduate School of Engineering, The University of Tokyo, 7-3-1 Hongo, Bunkyo-ku, Tokyo 113-8656, Japan, and Division of Clinical Biotechnology, Center for Disease Biology and Integrative Medicine, Graduate School of Medicine, The University of Tokyo, 7-3-1 Hongo, Bunkyo-ku, Tokyo 113-0033, Japan. Received December 24, 2005; Revised Manuscript Received February 21, 2006

Nonviral vectors for gene therapy have recently received an increased impetus because of the inherent safety problems of the viral vectors, while their transfection efficiency is generally low compared to the viral vectors. The lack of the ability to escape from the endosomal compartments is believed to be one of the critical barriers to the intracellular delivery of noviral gene vectors. This study was devoted to the design and preparation of a novel ABC triblock copolymer for constructing a pH-responsive and targetable nonviral gene vector. The copolymer, lactosylated poly(ethylene glycol)-*block*-poly(silamine)-*block*-poly[2-(*N*,*N*-dimethylamino)ethyl methacrylate] (Lac-PEG-PSAO-PAMA), consists of lactosylated poly(ethylene glycol) (A-segment), a pH-responsive polyamine segment (B-segment), and a DNA-condensing polyamine segment (C-segment). The Lac-PEG-PSAO-PAMA spontaneously associated with plasmid DNA (pDNA) to form three-layered polyplex micelles with a PAMA/pDNA polyion complex (PIC) core, an uncomplexed PSAO inner shell, and a lactosylated PEG outer shell, as confirmed by ^{1}H NMR spectroscopy. Under physiological conditions, the Lac-PEG-PSAO-PAMA/pDNA polyplex micelles prepared at an N/P (number of amino groups in the copolymer/number of phosphate groups in pDNA) ratio above 3 were found to be able to condense pDNA, thus adopting a relatively small size ($<$ 150 nm) and an almost neutral surface charge ($\zeta \sim +5$ mV). The micelle underwent a pH-induced size variation (pH = 7.4, 132.6 nm $\rightarrow$ pH = 4.0, 181.8 nm) presumably due to the conformational changes (globule-rod transition) of the uncomplexed PSAO chain in response to pH, leading to swelling of the free PSAO inner shell at lowered pH while retaining the condensed pDNA in the PAMA/pDNA PIC core. Furthermore, the micelles exhibited a specific cellular uptake into HuH-7 cells (hepatocytes) through asialoglycoprotein (ASGP) receptor-mediated endocytosis and achieved a far more efficient transfection ability of a reporter gene compared to the Lac-PEG-PSAO/pDNA and Lac-PEG-PAMA/pDNA polyplex micelles composed of the diblock copolymers and pDNA. The effect of hydroxychloroquine as an endosomolytic agent on the transfection efficiency was not observed for the Lac-PEG-PSAO-PAMA/pDNA polyplex micelles, whereas the nigericin treatment of the cell as an inhibitor for the endosomal acidification induced a substantial decrease in the transfection efficiency, suggesting that the protonation of the free PSAO inner shell in response to a pH decrease in the endosome might lead to the disruption of the endosome through buffering of the endosomal cavity. Therefore, the polyplex micelle composed of ABC (ligand-PEG/pH-responsive segment/DNA-condensing segment) triblock copolymer would be a promising approach to a targetable and endosome disruptive nonviral gene vector.

INTRODUCTION

Nonviral vectors for gene therapy have recently received increased attention because of the concerns over the safety issues of viral vectors, including immunogenicity, oncogenicity, and potential virus recombination (*1*−*3*). Most of the nonviral vectors developed so far, however, show low transfection efficiency compared to the viral vectors, because the latter have evolved multi-functionality to overcome the critical barrier to efficient gene delivery by directing the specific cellular uptake and enhancing transport to the cytoplasm from the endosomal compartment. Recently, a new class of nonviral gene vectors has been developed based on the supramolecular assembly between plasmid DNA (pDNA) and poly(ethylene glycol) (PEG)-*block*-polyamine copolymers (polyplex micelles) (*4*−*10*). Because of the highly dense PEG shell surrounding the polyion complex (PIC) core, the polyplex micelles exhibited excellent solubility in aqueous media, high tolerability toward nuclease degradation, and minimal interaction with biological components, including proteins and cells, compared to the other conventional polyplex and lipoplex systems. Furthermore, ligand-installed polyplex micelles prepared from lactosylated PEG-*block*-poly[2-(*N*,*N*-dimethylamino)ethyl methacrylate] copolymer and pDNA showed an increase in the cellular uptake through a receptor-mediated endocytosis process compared to those without lactose (ligand) moieties (*11*). To observe an appreciable effect of the ligand molecules on gene expression, however, the presence of hydroxychloroquine (100 μM) as an endosomolytic agent (*12*, *13*) has so far been required. This indicates that endosomal escape should be the most critical

* To whom correspondence should be addressed. (Y.N.) Phone: +81-29-853-5749. Fax: +81-29-853-5749. E-mail: nagasaki@nagalabo.jp; (K.K.) Phone +81-3-5841-7139. Fax: +81-3-5841-7139. E-mail: kataoka@bmw.t.u-tokyo.ac.jp.

[†] Tsukuba Research Center for Interdisciplinary Materials Science (TIMS), University of Tsukuba.

[‡] Department of Materials Engineering, The University of Tokyo.

[#] Division of Clinical Biotechnology, The University of Tokyo.

10.1021/bc050364m CCC: $33.50 © 2006 American Chemical Society
Published on Web 04/15/2006

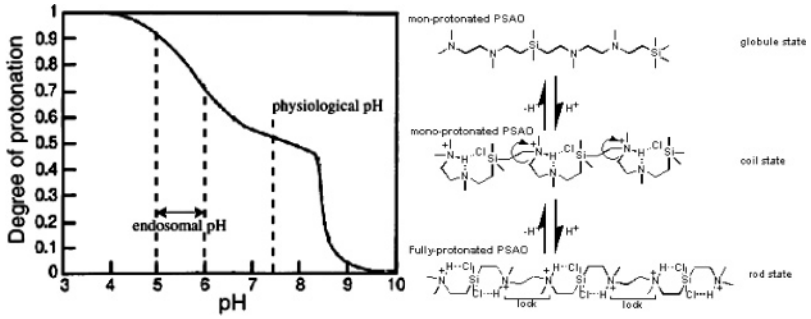

Figure 1. Change in the protonation degree of poly(silamine) (PSAO) with pH accompanying the conformation transition (globule-coil-rod).

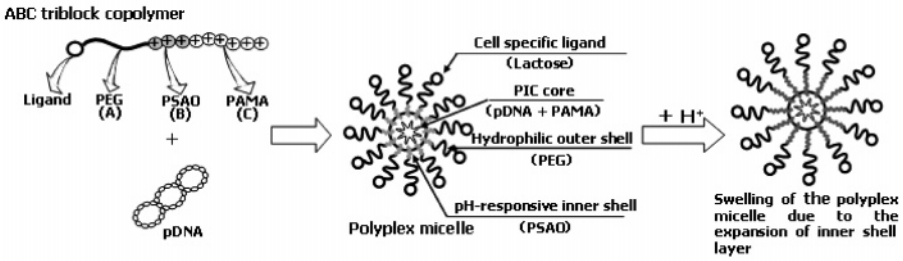

Figure 2. Schematic illustration of the formation of the three-layered polyplex micelle composed of the ABC triblock copolymer and pDNA.

barrier to intracellular gene delivery by polyplex micelles (*14*−*16*). Therefore, approaches are needed to devise polyplex micelles with a function to escape from the endosome where the pH is 1.4−2.4 units lower than the physiological pH of 7.4 (*17*−*20*). In this regard, poly(ethylenimine) (PEI) derivatives are of interest as a pH-responsive polyamine component to accomplish endosomal escape by taking advantage of their substantially lowered value of apparent pK_a (∼5.5) ("buffer or proton-sponge effect") (*21*). However, the buffer effect of the PEI segment occurs only when an excess of amino groups with respect to DNA phosphate groups (high N/P ratio) is present in the system, where a considerable amount of the amino groups in PEI is in the free-base form. This fact strongly suggests that free PEI, which is not complexed with pDNA, is likely to play a crucial role in the buffer effect, because amino groups in the PEI/pDNA polyplex generally undergo facilitated protonation due to the zipper effect or the neighboring group effect during the polyion complexation (over-protonation) to decrease the buffering capacity (*22*). Therefore, a strategy is needed to satisfy the prevention of overprotonation of the pH-responsive polyamine segment in the polyplex, as well as the achievement of efficient condensation of pDNA into the PIC core to exert efficient stability. Worth noting in this regard is a concomitant incorporation of the polyamine segment with a high pK_a and one with a low pK_a into a single PEG-based strand, as an ABC triblock copolymer (*23*). A polyamine segment with a high pK_a as the C block preferentially forms a polyion complex with phosphate groups in pDNA (DNA-condensation segment), whereas the pH-responsive polyamine segment (B block) with a comparatively low pK_a, located between the PEG segment (A block) and the pDNA-condensation segment (C block), is expected to retain a substantial fraction of unprotonated amino groups (free-base) even in the polyplex due to the low protonation ability. As a consequence, the polyion complexation between such an ABC triblock copolymer and pDNA may lead to the formation of a three-layered polyplex micelle possessing an unprotonated pH-responsive polyamine segment as an intermediate layer to function as a buffering moiety for facilitated endosomal escape.

We herein synthesized a novel ABC triblock copolymer composed of a targetable and biocompatible polymer segment, a pH-responsive polyamine segment, and a DNA-condensing polyamine segment to form a three-layered polyplex micelle: lactosylated PEG-*block*-poly(silamine) (PSAO) -*block*-poly[2-(*N*,*N*-dimethylamino)ethyl methacrylate] (PAMA) [Lac-PEG-PSAO-PAMA]. Here, PSAO was selected as the pH-responsive polyamine segment showing two-step protonation (Figure 1, pK_{a1} = 8.6 and pK_{a2} = 5.8) along with a unique conformational transition at the critical pH (*24*−*29*). The unprotonated PSAO is insoluble in water, assuming a globular conformation with high flexibility, whereas fully protonated PSAO is soluble in water, assuming a rodlike conformation with rigid and expanded polymer strands. Such a unique conformational transition (rod-globule transition) can be explained by the rotational hindrance around the polymer chain due to the protonation of the amino groups along with the counteranion binding to the Si atoms (Figure 1). On the other hand, PAMA (pK_a = 7.2) is known to condense pDNA to form a compact structure, the size of which is less than 200 nm under physiological conditions (*8*, *30*, *31*). This fact suggests that polyion complexation between the Lac-PEG-PSAO-PAMA and pDNA may form a targetable and endosome disruptive polyplex micelle with a well-defined three-layered structure (Figure 2).

EXPERIMENTAL SECTION

Materials. 2,2′-Azobisisobutyronitrile (AIBN), dicyclohexylcarbodiimide (DCC), *N*-hydroxysuccinimide (NHS), and nigericin (NR) were purchased from Wako and used without further purification. Asialofetuine (ASF) and hydroxychloroquine sulfate (HCQ) were purchased from Sigma and Acros Organics, respectively. Potassium naphthalene was used as a THF solution, whose concentration was determined by titration. Water was purified using a Milli-Q instrument (Millipore). 2-Propanol and diethyl ether (Et_2O) were used as received without further purification. Lysotraker Red DND-99 was purchased from Molecular Probes. Plasmid DNA (pDNA) encoding firefly luciferase (pGL3-Luc, Promega; 5256 bpa) was amplified using EndoFree Plasmid Maxi or Mega kits (QIAGEN). The DNA concentration was determined by reading the absorbance at 260 nm.

Polymer Analysis. ^{1}H NMR (400 MHz) spectra were obtained in $CDCl_3$, DMSO-d_6, or D_2O (pD = 7.4 and 4.0) with 0.15 M NaCl using a JEOL EX400 spectrometer. Chemical shifts were reported in ppm relative to $CDCl_3$ (δ7.26, ^{1}H), DMSO-d_6 (δ 2.50, ^{1}H), or D_2O buffer (δ 4.76, ^{1}H). Size exclusion chromatography (SEC) was performed using a TOSO

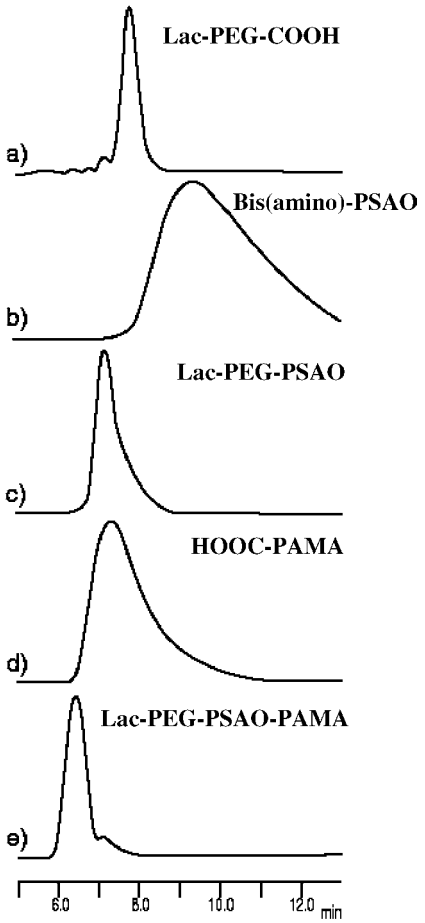

Figure 3. SEC chromatograms of the (a) Lac-PEG-COOH, (b) bis-(amino)-PSAO, (c) Lac-PEG-PSAO block copolymer, (d) HOOC-PAMA, and (e) Lac-PEG-PSAO-PAMA triblock copolymer.

HLC-8020 equipped with an internal refractive index (RI) detector (RID-6A) with the combination of TSK $G4000_{HR}$ and $G3000_{HR}$ columns using THF as the eluent.

Synthesis of Lactose-PEG-*block*-PSAO. Bis(amino)-PSAO was synthesized according to our previous report (*24*−*29*). The Lac-PEG-COOH (0.100 g, 16 μmol) and an excess amount of bis(amino)-PSAO (1.244 g 800 μmol, M_n = 1550, DP = 6) were dissolved in $CHCl_3$ (5.0 mL) together with DCC (6.3 mg, 32 μmol) and NHS (2.3 mg, 20 μmol). The reaction mixture was stirred at room temperature for 72 h. To remove the unreacted bis(amino)-PSAO and other chemicals, the reaction mixture was poured into Et_2O (200 mL). The obtained polymer was further purified by reprecipitation into Et_2O (200 mL) and then freeze-dried with benzene to obtain the lactose-PEG-*b*-PSAO (0.102 g, 83% yield). Figures 3c and 4a, respectively, show the SEC chromatogram and ^{1}H NMR spectrum of Lac-PEG-PSAO with assignment. SEC M_n = 7170, M_w/M_n = 1.15 (calcd. M_n = 7850); ^{1}H NMR ($CDCl_3$, in Figure 4a) δ 0.10 (s, 36H, H_k), 0.63−0.79 (m, 24H, H_j), 1.02 (t, J = 7.3 Hz, 36H, H_i), 1.10 (t, J = 7.1 Hz, 3H, H_i''), 1.16 (t, J = 7.1 Hz, 3H, H_i'), 1.77−2.02 (m, 4H, H_d+H_f), 2.42 (t, J = 7.1 Hz, 2H, H_g), 2.47−2.62 (m, 80H, H_h), 2.62−2.73 (m, 2H, H_c), 3.61 (s, 617H, H_a+H_b+H_e)

Synthesis of Lactose-PEG-*block*-PSAO-*block*-PAMA. A PAMA homopolymer bearing a carboxylic acid group at the α-end (HOOC-PAMA) was synthesized via anionic polymerization of 2-(*N*,*N*-dimethylamino)ethyl methacrylate (*32*) using the allyl alcohol/potassium-naphthalene initiator system, followed by the radical addition of 3-mercaptopropionic acid in the presence of AIBN. The Lac-PEG-PSAO (0.051 g, 7.8 μmol) and an excess amount of HOOC-PAMA bearing a carboxylic acid group at the α-end (0.5017 g, 88.5 μmol, M_n = 5670, DP = 35) were dissolved in $CHCl_3$ (5.0 mL) together with DCC (3.2 mg, 16 μmol) and NHS (1.6 mg, 10 μmol). The reaction mixture was stirred at room temperature for 72 h. To remove the unreacted HOOC-PAMA and other chemicals, the polymer was recovered by precipitation into cold 2-propanol (−15 °C, 200 mL) and centrifuged for 45 min at 6000 rpm. Further purification was carried out by dialyzing against distilled, deionized water (cutoff MW 3500) and then freeze-dried to obtain Lac-PEG-PSAO-PAMA (0.0383 g, 37% yield). Figures 3e and 4b, respectively, show the SEC chromatogram and ^{1}H NMR spectrum of Lac-PEG-PSAO-PAMA with assignment. SEC M_n = 10850, M_w/M_n = 1.29 (calcd. M_n = 13450); ^{1}H NMR ($CDCl_3$, in Figure 4b) δ 0.10 (s, 36H, H_d), 0.63−0.79 (m, 24H, H_c), 0.80−1.16 (m, 94H, H_g), 1.02 (t, J = 7.3 Hz, 42H, H_e), 1.16−2.17 (m, 64H, H_f), 2.23 (s, 185H, H_j), 2.37−2.84 (m, 143H, H_b + H_i), 3.61 (s, 617H, H_a), 4.08 (s, 62H, H_h).

Light Scattering Measurements of Polyplex Micelles. To prepare stock solutions, specific amounts of each of the block copolymers (Lac-PEG-PSAO-PAMA, Lac-PEG-PSAO, and Lac-PEG-PAMA) were dissolved in 10 mM Tris-HCl buffer (pH 7.4) or distilled, deionized water, followed by adjustment of the pH to 7.4. Both solutions were filtered through a 0.1-μm filter to remove dust prior to the measurement. For the dynamic light scattering (DLS) measurements as a function of pH, the Lac-PEG-PSAO-PAMA copolymer in distilled water at pH 7.4 including 0.15 M NaCl was mixed with pDNA at an N/P ratio of 3 [N/P = (amino group in the block copolymer)/(phosphate groups in pDNA)] at pH 7.4 to obtain the final concentration of 33.3 μg/mL of pDNA in the solution. The sample solutions were adjusted to the desired pH using small aliquots of 0.1 or 0.01 M HCl, and the DLS was measured at each pH point (pH = 7.0, 6.5, 6.0, 5.5, 5.0, 4.5, and 4.0).

For the DLS measurements of the samples prepared at various N/P ratios, the block copolymer in 10 mM Tris-HCl buffer (pH 7.4) was mixed with pDNA at various N/P ratios (N/P = 1, 2, 3, 4, 5, 7, and 10), followed by the addition of 10 mM Tris-HCl buffer (pH 7.4) including 0.3 M NaCl to adjust the pDNA concentration (33.3 μg/mL) and the ionic strength of the solution to physiological conditions (0.15 M NaCl).

A light-scattering spectrometer (DLS-7000, Photal, Otsuka Electronics) equipped with a 75 mW Ar-laser that produces a vertically polarized incident beam at λ_0 = 488 nm was used in the present study for the DLS measurements.

During the DLS measurements, the autocorrelation function was analyzed using the cumulant method in which

$$g^{(1)}(\tau) = \exp[-\bar{\Gamma}\tau + (\mu_2/2)\tau^2 - (\mu_3/3!)\tau^3 + \cdots] \quad (1)$$

yielding an average characteristic line width of $\bar{\Gamma}$. The z-averaged diffusion coefficient was obtained from the $\bar{\Gamma}$ based on the following equations:

$$\bar{\Gamma} = Dq^2 \quad (2)$$

$$q = (4\pi n/\lambda)\sin(\theta/2) \quad (3)$$

where q is the magnitude of the scattering vector, n is the refractive index of the solvent, and θ is the detection angle. The hydrodynamic radius, d, can then be calculated using the Stokes−Einstein equation:

$$d = k_B T/(6\pi\eta D) \quad (4)$$

where k_B is the Boltzmann constant, T is the absolute temperature, and η is the viscosity of the solvent. Also, the polydispersity index (PDI = μ_2/Γ^2) was derived from eq 1.

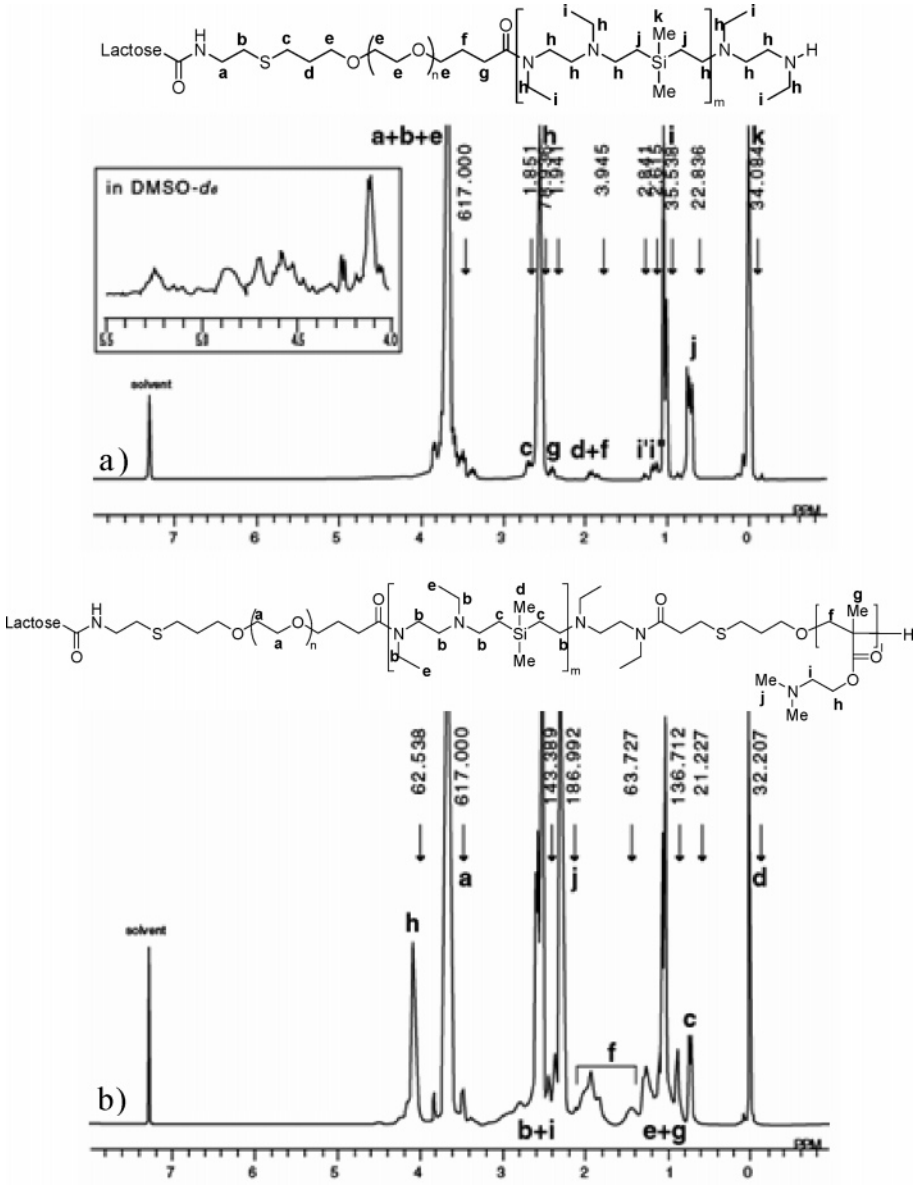

Figure 4. [1]H NMR spectra of (a) Lac-PEG-PSAO diblock copolymer and (b) Lac-PEG-PSAO-PAMA triblock copolymer.

Zeta-Potential Measurements. Laser-Doppler electrophoresis measurements of the polyplex micelles were carried out in 10 mM Tris-HCl buffer (pH 7.4) without NaCl (ELS-600, Photal, Otsuka Electronics). From the determined electrophoretic mobility, the zeta-potential (ζ) was calculated according to the Smoluchouski equation as follows:

$$\zeta = 4\pi n\eta\mu u/\epsilon \qquad (5)$$

where η is the viscosity of the solution, u is the electrophoretic mobility, and ϵ is the dielectric constant of the solvent.

Ethidium Bromide Exclusion Assay. The polyplex micelle solutions at various N/P ratios were mixed with ethidium bromide (EtBr) solution, and the final concentration was adjusted to [pDNA] = 20 μg/mL and [EtBr] = 0.4 μg/mL. The fluorescence of the intercalated EtBr was measured on a spectrofluorometer (F-2500, Hitachi) by exciting at 510 nm while monitoring emission at 590 nm.

Agarose Gel Retardation Studies. Aliquots (10 μL) of the above polyplex micelle solutions with various N/P ratios were mixed with 13 μL of running buffer of 3.3 mM Tris-AcOH with 1.0 mM EDTA2Na (pH 7.4) and loaded onto a 0.9 wt % agarose gel (50 V, 2 h). The amount of pDNA was adjusted to 0.3 μg of pDNA/lane. After EtBr (0.5 μg/mL) staining for 1 h, retardation of pDNA was visualized under UV irradiation.

Cell Culture. HuH-7 human cancer cells, derived from a hepatocarcinoma cell line, were obtained from the Cell Resource Center for Biomedical Research, Institute of Development, Aging and Cancer, Tohoku University. The cells were grown in Dulbecco's modified Eagle's medium (DMEM) supplemented with 10% FBS, 100 units/mL penicillin, and 100 μg/mL streptomycin at 37 °C in a humidified 5% CO_2 atmosphere.

Fluorescent Microscopy. Fluorescein isothiocyanate (FITC)-labeled pDNA was prepared using a Label IT nucleic acid labeling kit (Panvera). HuH-7 cells were seeded at a density of 5×10^5 cells/dish in a 35-mm glass bottom dish (Iwaki, Japan) and kept overnight at 37 °C in 5% CO_2 atmosphere. The Lac-PEG-PSAO-PAMA/pDNA polyplex micelles (N/P = 3) were added at a pDNA concentration of 30 μg/mL and incubated at 37 °C in 5% CO_2 atmosphere in the presence or absence of ASF (10 mg/mL) for 60 min. The cells were washed with phosphate buffered saline (PBS) three times and imaged directly in the cell culture medium using an Olympus IX70 with an appropriate filter.

Confocal Fluorescent Microscopy. HuH-7 cells were seeded at a density of 5×10^5 cells/dish in a 35-mm glass bottom dish

Scheme 1. Synthetic Route of Lac-PEG-PSAO-PAMA Block Copolymer

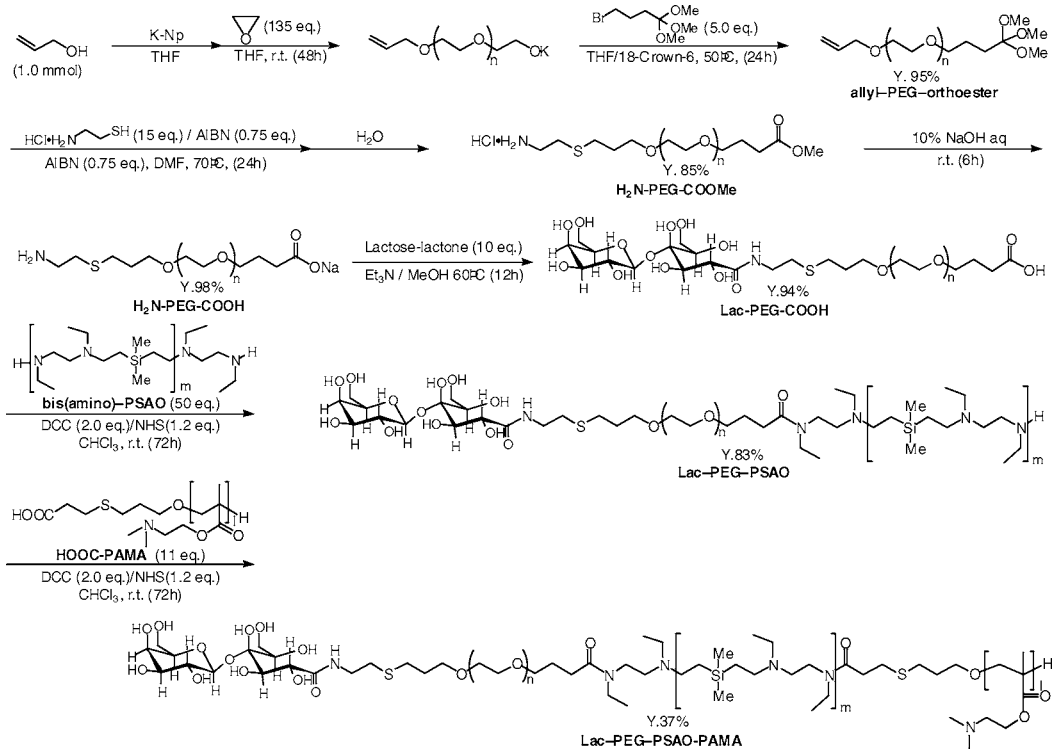

(Iwaki, Japan) and kept overnight at 37 °C in 5% CO_2 atmosphere. The Lac-PEG-PSAO-PAMA/pDNA and the Lac-PEG-PAMA/pDNA polyplex micelles (N/P = 3) containing FITC-labeled pDNA were added at a pDNA concentration of 30 μg/mL and incubated at 37 °C in 5% CO_2 atmosphere in the presence of Lysotraker Red DND-99 (50 nM) for 30 and 120 min. The cells were washed with PBS three times and imaged directly in the cell culture medium using an Olympus IX81 equipped with a confocal IX2-DSU system and an appropriate filter.

Transfection to HuH-7 Cells. HuH-7 cells were plated in a 24-well plate (5×10^4 cells/well) to reach about 50% confluence after 24 h at transfection, and the medium was then changed to fresh DMEM with 10% FBS (225 μL/well). For each well, the polyplex micelles or B-PEI/pDNA polyplexes at various N/P ratios (25 μL/well) were added with a pDNA concentration of 30 μg/mL. After 24 h incubation, the transfection medium was changed to fresh DMEM with 10% FBS, and the cells were further incubated for 24 h. For the preincubation study with serum, a medium containing 20% FBS was added to the solution of the polyplex micelles or B-PEI/pDNA polyplexes and incubated at 37 °C for 6 h prior to the transfection study. The cells were lysed, and the luciferase activity of the lysate was monitored with the a Luciferase Assay kit (Promega) and ARVOSX-1 (PerkinElmer). The results were expressed as light units per milligram of cell protein determined by a micro BCA assay kit (Pierce).

RESULTS AND DISCUSSION

Synthesis of Lactosylated Poly(ethylene glycol)-*block*-poly(silamine)-*block*-poly[2-(*N*,*N*-dimethlyamino)ethyl methacrylate] Triblock Copolymer. A synthetic route to lactosylated poly(ethylene glycol)-*block*-poly(silamine)-*block*-poy[2-(*N*,*N*-dimethlyamino)ethyl methacrylate] (Lac-PEG-PSAO-PAMA) triblock copolymer is shown in Scheme 1. A heterobifunctional PEG bearing an allyl group at the α-end and an ortho ester group at the ω-end (allyl-PEG-ortho ester) was synthesized via the anionic ring-opening polymerization of ethylene oxide using the allyl alcohol /potassium-naphthalene initiator system, followed by termination with trimethyl 4-bromoorthobutyrate in the presence of 18-Crown-6. The radical addition of 2-aminoethanethiol hydrochloride to the allyl-PEG-ortho ester quantitatively afforded an amine-PEG-methoxycarbonyl (H_2N-PEG-COOMe). Conversion of the ortho ester group into a methoxycarbonyl group (COOMe) occurred due to the hydrolysis of the ortho ester group during the purification (dialysis) process. The H_2N-PEG-COOMe was then converted into an amine-PEG-carboxylic acid (H_2N-PEG-COOH) by hydrolysis with 10% NaOHaq. The SEC (data not shown), ^{1}H NMR, and MALDI-TOF MS analyses (see Supporting Information) revealed that the determined molecular weight of the H_2N-PEG-COOH (SEC: $M_n = 6200$, $M_w/M_n = 1.04$, TOF-MS: $M_n = 6190$, $M_w/M_n = 1.03$) agrees well with the calculated value (calcd. $M_n = 6130$), and an amino group and carboxylic acid group were quantitatively introduced into the α-end and ω-end of PEG, respectively, to confirm the successful synthesis of allyl-PEG-ortho ester and H_2N-PEG-COOMe. The introduction of a lactose group to the amine end of H_2N-PEG-COOH was performed by reaction with an excess amount of lactose-lactone (*33*). In the ^{1}H NMR spectrum of Lac-PEG-COOH, the degree of lactose functionality was determined to be 72% (see Supporting Information).

To obtain the lactosylated PEG-PSAO block copolymer, bis-(amino)-PSAO ($M_n = 1550$, the degree of polymerization (DP) = 6) was prepared as reported previously by the anionic polyaddition of dimethyldivinylsilane with *N*,*N*′-diethylethylenediamine in the presence of a catalytic amount of *n*-BuLi in THF at 60 °C (*24*−*29*). The conjugation of the Lac-PEG-COOH with bis(amino)-PSAO was performed by activating the terminal carboxylic acid of Lac-PEG-COOH using dicyclohexylcarbodiimide (DCC) and *N*-hydroxysuccinimide (NHS). A large excess (50 equiv) of the bis(amino)-PSAO was used to suppress the formation of triblock coplymer viz., Lac-PEG-PSAO-PEG-Lac. After the conjugation reaction, unconjugated bis(amino)-PSAO and other chemicals were removed by precipitation into Et_2O. Figures 3c and 4a, respectively, show the SEC chromatogram and ^{1}H NMR spectrum of the Lac-PEG-PSAO block

Table 1. Diameter (d), PDI (μ_2/Γ^2), and Zeta-Potential (ζ) of the Lac-PEG-PSAO-PAMA/pDNA, Lac-PEG-PAMA/pDNA, and Lac-PEG-PSAO/pDNA Polyplex Micelles Prepared at Various N/P Ratios

	Lac-PEG-PSAO−PAM A polyplex micelles		Lac-PEG-PAMA polyplex micelles		Lac-PEG-PSAO polyplex micelles	
N/P ratio	DLS[a] d (nm) /PDI (μ_2/Γ^2)	zeta-potential[b] (mV)	DLS[a] d (nm)/ PDI (μ_2/Γ^2)	zeta-potential[b] (mV)	DLS[a] d (nm)/ PDI (μ_2/Γ^2)	zeta-potential[b] (mV)
1	200.3/0.23	−4.3	196.5/0.24	−3.8	178.9/0.24	−5.8
2	175.4/0.23	+3.6	180.9/0.22	+3.8	166.6/0.20	−1.2
3	149.1/0.14	+4.7	147.0/0.14	+4.6	157.0/0.17	+0.6
4	147.2/0.17	+5.3	141.5/0.17	+4.8	163.4/0.22	+1.7
5	147.4/0.13	+5.1	140.0/0.19	+4.7	140.1/0.12	+2.3
7	146.8/0.18	+5.5	141.6/0.14	+5.0	144.7/0.19	+2.5
10	145.5/0.18	+5.4	136.1/0.12	+4.8	145.2/0.17	+2.4

[a] Conditions for DLS measurements: detection angle, 90°; solvent, 10 mM Tris-HCl, pH 7.4, including 0.15 M NaCl; temperature, 37 °C. [b] Conditions for zeta-potential measurements: solvent, 10 mM Tris-HCl, pH 7.4; temperature, 25 °C.

copolymer with assignments. As seen in the SEC chromatograms (Figure 3), Lac-PEG-PSAO (Figure 3c) gave a unimodal peak at a high molecular weight position (i.e., shorter elution time) compared to the Lac-PEG-COOH (M_n = 6300, M_w/M_n = 1.05, Figure 3a) and bis(amino)-PSAO (M_n = 1550, M_w/M_n = 2.01, Figure 3b). Note that the unreacted Lac-PEG-COOH and bis(amino)-PSAO were not observed in the SEC chromatogram (Figure 3c) of the Lac-PEG-PSAO (obsd. M_n = 7150, M_w/M_n = 1.15, calcd. M_n = 7850). In the ^{1}H NMR spectrum (Figure 4a), the peaks corresponding to both of the PEG and PSAO segments were clearly observed, consistent with the formation of a diblock copolymer. Note that the peaks corresponding to the terminal lactose moiety were also observed at δ 4.0−5.3 ppm in the ^{1}H NMR spectrum in DMSO-d_6. From the integral ratio between the PEG-backbone protons (3.7 ppm -OCH_2CH_2-) and the methyl protons of PSAO segment (0.1 ppm, $SiMe_2$), the DP of the PSAO segment in the block copolymer was calculated to be 5.67, which is in good accordance with that of the starting bis(amino)-PSAO (DP = 6).

To obtain the Lac-PEG-PSAO-PAMA triblock copolymer, the conjugation of the Lac-PEG-PSAO diblock copolymer and HOOC-PAMA was performed in a manner similar to the conjugation of Lac-PEG-COOH and bis(amino)-PSAO. After the conjugation reaction, unconjugated HOOC-PAMA and other chemicals were removed by precipitation into cold 2-propanol, followed by centrifugation. Figures 3e and 4b, respectively, show the SEC chromatogram and ^{1}H NMR spectrum of the Lac-PEG-PSAO-PAMA triblock copolymer with assignments. The Lac-PEG-PSAO-PAMA (Figure 3e, M_n = 10850, M_w/M_n = 1.29, calcd. M_n = 13450) had a shorter elution time compared to the Lac-PEG-PSAO (M_n = 7170, M_w/M_n = 1.15, Figure 3c) and HOOC-PAMA (M_n = 5670, M_w/M_n = 1.50, DP = 35, Figure 3d), indicating an increased molecular weight due to the formation of the triblock polymer. Nevertheless, a slight portion of unreacted Lac-PEG-PSAO and/or HOOC-PAMA seems to still remain (about 10%) in the sample as indicated by the small accompanying peak appearing after the main fraction (Figure 3e). In thethe ^{1}H NMR spectrum (Figure 4b), the peaks corresponding to the PEG, PSAO, and PAMA segments were clearly observed, suggesting the formation of a triblock copolymer. From the integral ratio between the PEG-backbone protons (3.7 ppm -OCH_2CH_2-) and methylene protons of the PAMA segment (4.08 ppm, -COOCH_2CH_2N(CH_3)$_2$), the DP of the PAMA segment was calculated to be 31.3 (DP of starting PAMA = 35). This result indicates that the purity of the triblock copolymer was 89%.

Furthermore, Lac-PEG-PSAO (M_{nPEG} = 6300, DP_{PSAO} = 6, number of amino groups = 12) and Lac-PEG-PAMA (M_{nPEG} = 6300, DP_{PAMA} = 55, number of amino groups = 55) diblock copolymers were prepared in a similar manner as the controls for the Lac-PEG-PSAO-PAMA (M_{nPEG} = 6300, DP_{PSAO} = 6, DP_{PAMA} = 35, total number of amino groups = 47).

Physicochemical Characterization of Polyplex Micelles. The obtained triblock (Lac-PEG-PSAO-PAMA) and diblock (Lac-PEG-PAMA and Lac-PEG-PSAO) copolymers form polyplex micelles through the mixing with pDNA based on electrostatic interaction. The size and surface charge of the polyplex micelles (Lac-PEG-PSAO-PAMA/pDNA, Lac-PEG-PAMA/pDNA, and Lac-PEG-PSAO/pDNA) was respectively evaluated by dynamic light scattering (DLS) and Laser-Doppler electrophoresis measurements at various N/P ratios, as summarized in Table 1. In the DLS measurements, the diameter (d) and polydipersity index (PDI; μ_2/Γ^2) of all the polyplex micelles decreased with increasing N/P ratios and reached plateau values of ca. 150 nm and 0.2, respectively, at an N/P ratio higher than 5. Concomitantly, as the N/P ratios increased, the zeta-potential (ζ) of all the polyplex micelles gradually shifted from a negative value ($\zeta < 0$) to a positive value ($\zeta > 0$). Nevertheless, the zeta-potential of all the polyplex micelles retained only a slightly positive value (ζ = +5 mV) even when the N/P ratio was increased to 10, suggesting the formation of a PEG corona surrounding the PIC core. These phenomena are consistent with the DNA condensation (coil-globule transition) upon complexation with the polycation segment in the block copolymers (*5*, *9*, *10*). It should also be noted that the N/P ratio to induce complete DNA condensation substantially shifted to a higher value from a stoichiometric mixing ratio (N/P = 1). A similar tendency was observed for the polyplex micelle from the PEG-PAMA block copolymer and pDNA (*4*).

To further clarify the behavior of DNA condensation, the quenching of the fluorescence intensity of the DNA intercalating dye, EtBr, was observed under physiological conditions for all of the polyplex micelles. Note that cationic EtBr is excluded from the DNA minor groove with the progress of the charge neutralization and the subsequent condensation of DNA due to the interaction with polycations, and therefore, this characteristic of EtBr is frequently utilized to estimate the degree of DNA condensation through complexation with a polycation. The profiles are shown in Figure 5a. In line with a trend in the hydrodynamic diameter and zeta-potential variations as shown in Table 1, the fluorescence intensity of EtBr decreased with increasing N/P ratios for all of the polyplex micelles, and the quenching of the fluorescence still continued even in the region of N/P > 1, suggesting that DNA condensation was not completely finished at the stoichiometric mixing ratio (N/P = 1) and that a nonstoichiometric complex may form in the range of N/P > 1. It should be noted that the amino groups of both PAMA and PSAO segments are incompletely protonated at physiological pH (= 7.4) because of their relatively lowered pKa values (PAMA: pK_a = 7.2, and PSAO: pK_{a1} = 8.6, pK_{a2} = 5.8). This may be a reason for the shift of the DNA-condensation point from a stoichiometric mixing ratio (N/P = 1). It should also be noted that a 35% decrease in fluorescence intensity compared to the initial value was observed for Lac-PEG-PSAO, whereas a decrease is more significant (50∼55%)

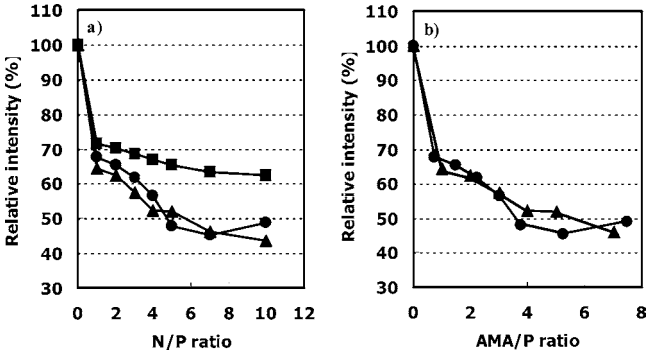

Figure 5. Ethidium bromide (EtBr) exclusion assay for the Lac-PEG-PSAO-PAMA/pDNA (circle), Lac-PEG-PAMA/pDNA (triangle), and Lac-PEG-PSAO/pDNA (square) systems. (a) Change in relative fluorescence intensity with the N/P ratio. (b) Change in relative fluorescence intensity with the AMA/P unit ratio ([amino groups in the PAMA segment]/[phosphate group in the pDNA]) (solvent, 10 mM Tris-HCl buffer including 0.15 M NaCl (pH 7.4); temperature, 37 °C).

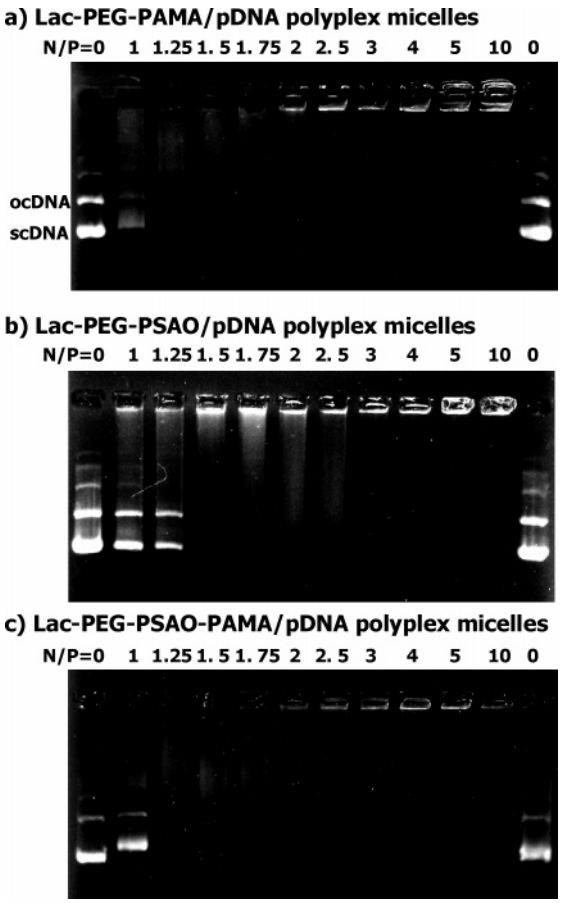

Figure 6. Agarose gel electrophoresis of the (a) Lac-PEG-PAMA/pDNA, (b) Lac-PEG-PSAO/pDNA, and (c) Lac-PEG-PSAO-PAMA/pDNA polyplex micelles prepared at various N/P ratios.

for Lac-PEG-PAMA and Lac-PEG-PSAO-PAMA, and their fluorescence intensities of Lac-PEG-PSAO-PAMA were almost identical when the N/P ratio was converted to the AMA/P ([amino groups in the PAMA segment]/[phosphate group in the pDNA]) unit ratio (Figure 5b), suggesting that the PAMA segment may preferentially take part in the complexation with DNA in the Lac-PEG-PSAO-PAMA/pDNA system, bearing the PSAO segment in the free form.

To evaluate the stability of the polyplex micelle, an agarose gel retardation assay at various N/P ratios was carried out. As shown in Figure 6, two topologically different forms of pDNA, i.e., supercoiled (scDNA) and open circular (ocDNA), were clearly observed in the absence of the block copolymer (at N/P = 0). In the cases of Lac-PEG-PSAO-PAMA/pDNA and Lac-PEG-PAMA/pDNA polyplex micelles, pDNA migration was completely retarded at an N/P ratio ≥ 1.5 (Figure 6a,c). Alternatively, a higher N/P ratio (≥ 3) was required for the complete retardation of pDNA for Lac-PEG-PSAO/pDNA polyplex micelles (Figure 6b). Presumably, excess cationic component may be needed for the Lac-PEG-PSAO block copolymer with a shorter cationic segment to induce effective DNA stabilization.

The polyplex micelle from Lac-PEG-PSAO-PAMA and pDNA was characterized by ^{1}H NMR spectroscopy in D_2O containing 0.15 M NaCl at pD = 7.4. Figure 7f shows the ^{1}H NMR spectrum of the polyplex micelle prepared at N/P = 3, where the residual molar ratio of the protonated PAMA segment in the block copolymer, calculated from the pK_a value, to the phosphate groups in pDNA is estimated to be unity at physiological pH (= 7.4). Note that the DNA condensation process was almost completed at N/P = 3, as shown in Table 1. Obviously, the peaks from the PAMA segment, which were clearly observed in the spectrum of the free polymers (Figure 7c), nearly disappeared upon complexation with pDNA (Figure 7f), whereas the peaks from the PSAO segment were still clearly observed in the spectrum. The selective disappearance of PAMA peaks upon complexation strongly suggests that the PAMA segment predominantly forms a PIC with pDNA to cause significant peak broadening. On the other hand, observation of the peaks from the PSAO segment even in the spectrum of the polyplex micelle suggests the presence of the uncomplexed PSAO fraction. Eventually, these results are consistent with the formation of the three-layered structure of the polyplex micelle with a PAMA/pDNA PIC core, a free PSAO inner shell, and a lactosylated PEG outer shell, as illustrated in Figure 2. In sharp contrast to the Lac-PEG PSAO-PAMA/pDNA system, peaks corresponding to polyamine segments (PAMA and PSAO) completely disappeared in the NMR spectra of the polyplex micelles from diblock copolymers (Lac-PEG-PAMA/pDNA (Figure 7d) and Lac-PEG-PSAO/pDNA (Figure 7e)) due to the limited molecular motion in the complex form.

pH Response of the Polyplex Micelles. To estimate the effect of the environmental pH on the hydrodynamic diameter of the polyplex micelles, the Lac-PEG-PSAO-PAMA/pDNA, Lac-PEG-PSAO/pDNA, and Lac-PEG-PAMA/pDNA polyplex micelles were prepared in 0.15 M NaClaq (pH 7.4) at N/P = 3. By decreasing the pH from 7.4 to 4.0, the diameter (d) of the Lac-PEG-PSAO-PAMA/pDNA and Lac-PEG-PSAO/pDNA polyplex micelles proportionally increases with a unimodal distribution ($\mu_2/\Gamma^2 < 0.25$), reaching a 2.7-times larger hydrodynamic volume at pH 4.0 compared to that at pH 7.4, as shown in Figure 8. On the contrary, there was negligible change in the hydrodynamic diameter of the Lac-PEG-PAMA/pDNA polyplex micelle with decreasing pH from 7.4 to 4.0. This pH-induced size variation observed for the system containing the PSAO segment is most likely to be related to the conformational changes in the PSAO chain due to progressive protonation with decreasing pH. In the ^{1}H NMR spectrum of the Lac-PEG-PAMA/pDNA polyplex micelle (N/P = 3) at pD = 4.0, the peaks from the PAMA segment almost disappeared, indicating that pDNA was still condensed even at pD = 4.0 by the PAMA segment (see Supporting Information). Furthermore, the ^{1}H NMR spectrum of the Lac-PEG-PSAO-PAMA/pDNA polyplex micelle at pD = 4.0 shows only the peaks assigned to the PSAO segment along with the PEG segment, suggesting the three-layered structure even at pD = 4.0 (see Supporting Information). This result supports the plausible scheme that the globule-to-rod conformational changes in the uncomplexed PSAO segment in the three-layered Lac-PEG-PSAO-PAMA/pDNA polyplex

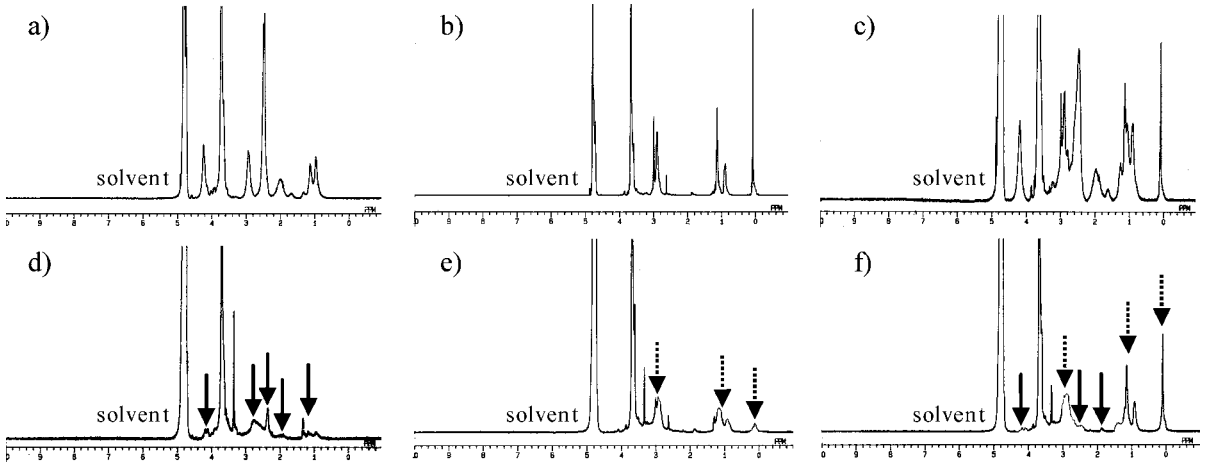

Figure 7. ^{1}H NMR spectra of (a) the Lac-PEG-PAMA block copolymer at pD = 7.4, (b) the Lac-PEG-PSAO block copolymer at pD = 7.4, (c) Lac-PEG-PSAO-PAMA triblock copolymer at pD = 7.4, (d) the Lac-PEG-PAMA/pDNA polyplex micelle at pD = 7.4, (e) the Lac-PEG-PSAO/pDNA polyplex micelle at pD = 7.4, and (f) the Lac-PEG-PSAO-PAMA/pDNA polyplex micelle at pD = 7.4 in D_2O containing 0.15 M NaCl at 37 °C. The solid and dotted arrows indicate the peaks corresponding to the PAMA segment and PSAO segment, respectively.

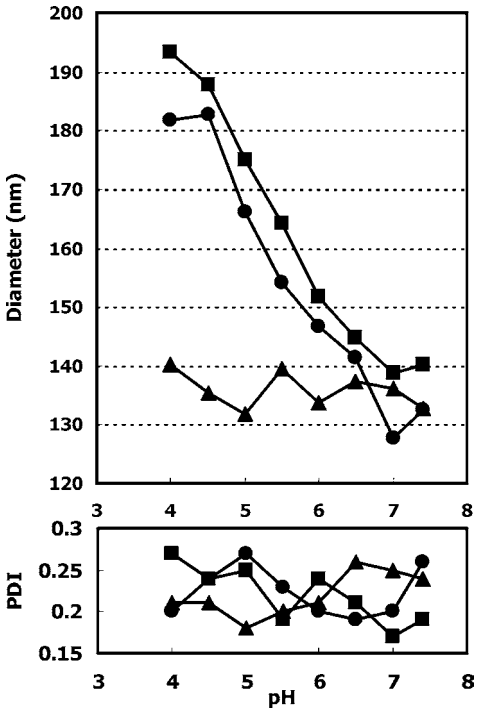

Figure 8. pH vs diameter (d) and PDI (μ_2/Γ^2) of the Lac-PEG-PSAO-PAMA/pDNA (circle), Lac-PEG-PAMA/pDNA (triangle), and Lac-PEG-PSAO/pDNA (square) polyplex micelles at N/P = 3 (angle, 90°; solvent, distilled water including 0.15 M NaCl; temperature, 37 °C).

micelle may induce the selective expansion of the PSAO inner shell while retaining the condensed pDNA in the PAMA/pDNA PIC core, leading to the remarkable pH-induced size variation. However, the observed size variation is clearly too large compared with the calculated PSAO length as the fully stretched chains for coil-state (pH 7.4) and rod-state (pH 4.0), indicating that the expansion of the PSAO inner shell is not sufficient to account for the size variation of the micelles. Although other possible factors probably exist, we believe that the expansion of the PSAO inner shell is one of the factor for the size variation of the micelles. On the other hand, the peaks from the PSAO segment clearly appeared in the ^{1}H NMR spectrum of the Lac-PEG-PSAO/pDNA polyplex micelle at pD = 4.0, suggesting that the conformational changes (globule-rod transition) of the complexed PSAO segment in the Lac-PEG-PSAO/pDNA polyplex micelle presumably leads to the formation of a loose PIC core (see Supporting Information). Apparently, the high rigidity of the protonated PSAO chain in the lower pH region should be unfavorable for triggering the DNA condensation upon complexation. As a consequence, a loose complex may form between pDNA and the PSAO segment without condensation in the lower pH region, showing an appreciable size increase.

Evaluation of the Biological Efficacy of the Polyplex Micelles. The cytotoxicity of the Lac-PEG-PSAO-PAMA, Lac-PEG-PAMA, and Lac-PEG-PSAO block copolymers against HuH-7 cells (hepatocytes) was studied using an MTT assay (see: Supporting Information). The viability of cells treated with the Lac-PEG-PSAO block copolymer was less than 20% at a polymer concentration of 100 μg/mL (IC_{50} < 30 μg/mL). In contrast, cells incubated with Lac-PEG-PSAO-PAMA or Lac-PEG-PAMA retained 65∼70% viability relative to controls even at concentrations up to 100 μg/mL. This result indicates that the inclusion of PSAO segment into the Lac-PEG-PSAO-PAMA triblock copolymer seems to substantially reduce its inherent cytotoxicity.

To examine whether the lactose moiety (galactose terminal) on the surface of Lac-PEG-PSAO-PAMA/pDNA polyplex micelle is recognized by the asialoglycoprotein (ASGP) receptors existing on the HuH-7 cells (*34*, *35*), the cellular association and internalization of the polyplex micelle (N/P = 3) with fluorescein isothiocyanate (FITC)-labeled pDNA were visualized under a fluorescence microscope at 60 min of incubation in the presence and absence of asialofetuine (ASF). Note that the ASF is known to function as a competitive inhibitor for the ASGP receptor-mediated endocytosis (*36*). The cellular association and internalization of the Lac-PEG-PSAO-PAMA/pDNA polyplex micelle to HuH-7 cells in the absence of ASF were clearly observed as shown in Figure 9b,d. On the contrary, substantially reduced cellular association and internalization of the micelles were observed in the presence of ASF as shown in Figure 9a,c. This result indicates that the cellular association and internalization of the Lac-PEG-PSAO-PAMA/pDNA polyplex micelle occur mainly through the ASGP receptor-mediated process, which is inhibited in the presence of ASF (*37*).

To estimate the transfection ability of the Lac-PEG-PSAO-PAMA/pDNA, Lac-PEG-PAMA/pDNA, and Lac-PEG-PSAO/pDNA polyplex micelles with various N/P ratios, a transfection study using HuH-7 cells was carried out in the presence of 10% FBS. A pGL-3 control plasmid DNA encoding firefly luciferase was used as a reporter gene. In addition, the B-PEI/pDNA polyplex was used as a control vector at the optimal N/P ratio of 10 to show the highest transfection efficacy. As shown in Figure 10, the transfection efficiency of the Lac-PEG-PSAO-

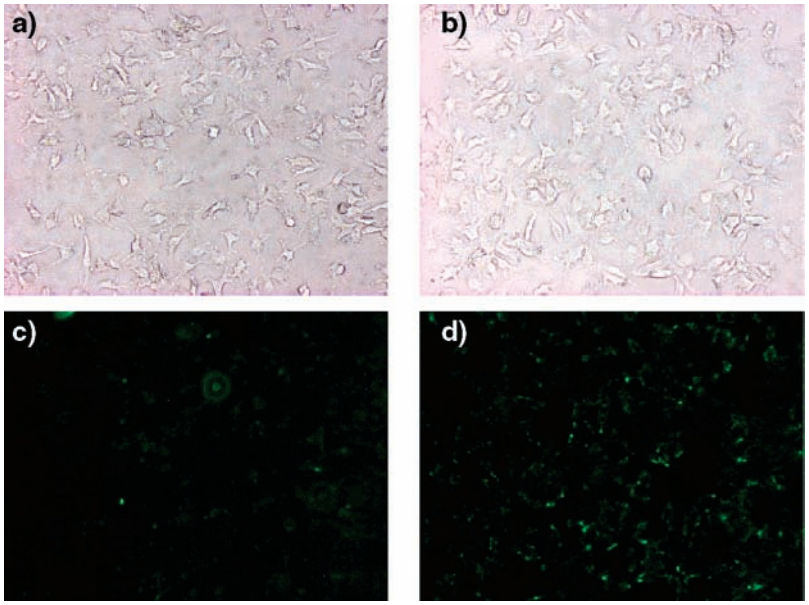

Figure 9. Association and internalization to HuH-7 cells of the Lac-PEG-PSAO-PAMA/pDNA polyplex micelles prepared at N/P = 3 after 60 min incubation. (a) ASF (+) (phase-contrast image), (b) ASF (−) (phase-contrast image), (c) ASF (+) (fluorescent image), and (d) ASF (−) (fluorescent image).

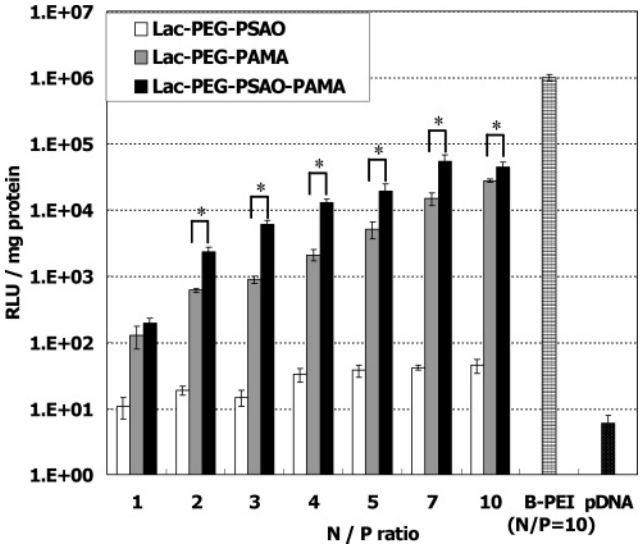

Figure 10. Transfection efficiency to HuH-7 cells of the Lac-PEG-PSAO-PAMA/pDNA, Lac-PEG-PAMA/pDNA, and Lac-PEG-PSAO/pDNA polyplex micelles prepared at various N/P ratios with a fixed pDNA amount. The plotted data are the average of triplicate experiments ± SD ($P^* < 0.05$).

PAMA/pDNA and Lac-PEG-PAMA/pDNA polyplex micelles was substantially improved with an increasing N/P ratio. In particular, 1 order of magnitude increase in transfection efficiency was achieved by increasing the N/P ratio from 1 to 2 ($P < 0.05$), corresponding to the formation of a stable polyplex structure judging from the agarose gel retardation assay, seen in Figure 6. Alternatively, the Lac-PEG-PSAO/pDNA polyplex micelles exhibited only limited transfection efficiency, presumably due to the low DNA condensing capacity of the PSAO chain as indicated from the results of the EtBr exclusion assay shown in Figure 5. Thus, polyplex micelles formed from Lac-PEG-PSAO may not be stable enough to be tolerated in the culture medium containing a substantial amount of serum proteins. Of interest, the transfection efficiency of the Lac-PEG-PSAO-PAMA/pDNA polyplex micelles always revealed a higher transfection efficiency than the Lac-PEG-PAMA/pDNA polyplex micelles in the range of N/P ratios between 2 and 10 ($P < 0.05$).

To determine whether the difference in the transfection efficiency between the Lac-PEG-PSAO-PAMA/pDNA and Lac-PEG-PAMA/pDNA polyplex micelles is related to the endosomal escape function, confocal microscope experiments were performed on the HuH-7 cells treated with the polyplex micelles containing FITC-labeled pDNA. Cells were co-incubated with LysoTracker Red DND-99 probe, which specifically stains acidic organelles such as endosomes and lysosomes. Thus, the colocalization of the polyplex micelles and the LysoTracker Red probe in an acidic compartment (endosome and lysosome) should be detected as yellow (or orange) fluorescence due to the merging of green and red colors. In the case of the Lac-PEG-PAMA/pDNA polyplex micelles (Figure 11a,b), the yellow and red fluorescences were observed without isolated green fluorescence even after a 120-min incubation, indicating that the polyplex micelles localized in the endosomes and/or lysosomes with the LysoTracker Red probe. The Lac-PEG-PSAO-PAMA/pDNA polyplex micelles localized in the endosomes and/or the lysosomes with the LysoTracker Red probe after a 30 min incubation (Figure 11c), as suggested by the partially yellow fluorescence. At 120 min of incubation, diffused green fluorescence was observed in the cytoplasm (Figure 11d), indicating that the Lac-PEG-PSAO-PAMA/pDNA polyplex micelles gradually escaped from the endosomes and/or lysomes into the cytoplasm in a time-dependent manner. These results suggest that both the PAMA segment as a DNA-condensing polycation and the PSAO segment as the buffering moiety may synergistically contribute to enhance the transfection efficiency of the Lac-PEG-PSAO-PAMA/pDNA polyplex micelles. Although the Lac-PEG-PSAO-PAMA/pDNA polyplex micelles showed 1 order of magnitude lower transfection efficiency than the B-PEI/pDNA polyplex at N/P = 10 ($P < 0.05$), this value may still be appreciable considering that the polyplexe micelles have hydrophilic and neutral PEG palisades on their surface to shield the cationic character.

To verify that the improved transfection ability of the Lac-PEG-PSAO-PAMA/pDNA polyplex micelles is a result of the facilitated endosomal escape function as well as the enhanced cellular uptake through ASGP-mediated endocytosis, the transfection study at N/P = 3, 5, and 10 was carried out in the presence or the absence of hydroxychloroquine (HCQ) as an endosomolytic agent, nigericin (NR) (*38*) as an inhibitor of the

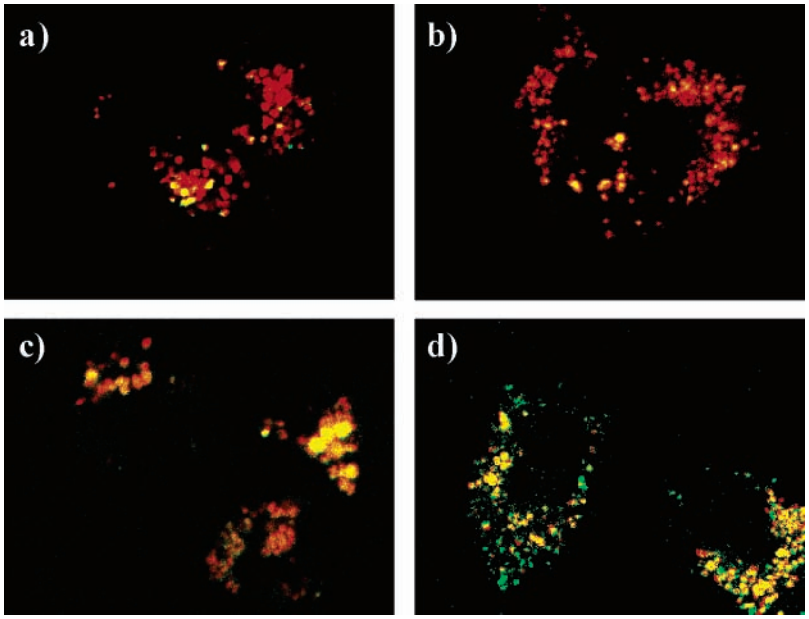

Figure 11. Confocal fluorescent microscope images of the HuH-7 cells in the presence of Lysotracker Red DND-99 and polyplex micelles prepared at N/P = 3 with FITC-labeled pDNA. (a) Lac-PEG-PAMA/pDNA polyplex micelles (incubation time: 30 min), (b) Lac-PEG-PAMA/pDNA polyplex micelles (incubation time: 120 min), (c) Lac-PEG-PSAO-PAMA/pDNA polyplex micelles, (incubation time: 30 min), (d) Lac-PEG-PSAO-PAMA/pDNA polyplex micelles (incubation time: 120 min). These images are the typical image of triplicate experiments.

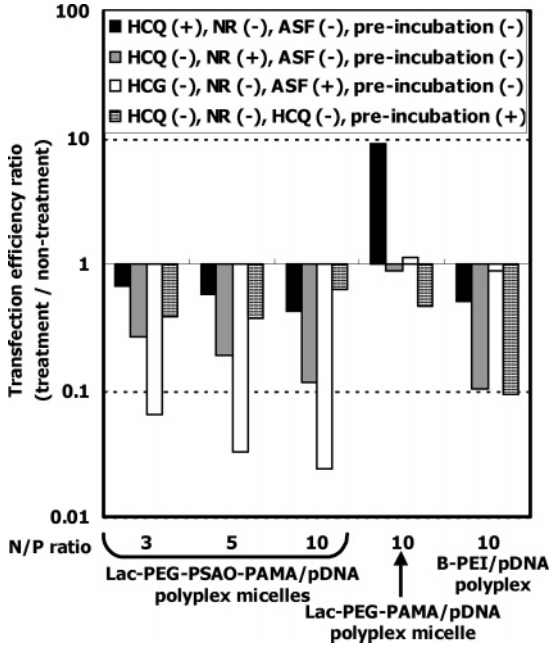

Figure 12. Effect of the HCQ (100 μM), NR (5 μM), ASF (4 mg/mL), and 20% serum preincubation on the transfection efficiency to HuH-7 cells of the Lac-PEG-PSAO-PAMA/pDNA polyplex micelle, Lac-PEG-PAMA/pDNA polyplex micelle, and B-PEI/pDNA polyplex as a function of N/P ratios at a fixed pDNA amount. Transfection efficiency ratio is described as [value of RLU/mg of protein treated with additive (HCQ, NR, and ASF)]/[value of RLU/mg of protein in Figure 11]. The plotted data are the average of triplicate experiments ± SD.

endosomal acidification, and ASF as an inhibitor of the ASGP-mediated endocytosis. As shown in Figure 12, HCQ treatment (100 μM) had no contribution in increasing the transfection efficiency for the Lac-PEG-PSAO-PAMA/pDNA polyplex micelles and the B-PEI/pDNA polyplex compared with the Lac-PEG-PAMA/pDNA polyplex micelle (about 1 order of magnitude increase in transfection efficiency), whereas it showed an appreciable decrease in the transfection efficiency in the presence of NR (5 μM) for the Lac-PEG-PSAO-PAMA/pDNA polyplex micelles and the B-PEI/pDNA polyplex. This is in line with the assumption that the Lac-PEG-PSAO-PAMA/pDNA polyplex micelles may be equipped with an endosome escaping function due to the unprotonated pH-responsive PSAO segment in the polyplex micelles.

A significant decrease in the transfection efficiency of the Lac-PEG-PSAO-PAMA/pDNA polyplex micelles was observed in the presence of ASF, consistent with the results of cellular uptake, as shown in Figure 9. Alternatively, no effect of ASF was observed even for the Lac-PEG-PAMA/pDNA polyplex micelle, suggesting that the endosomal escape may be the most critical barrier to intracellular gene delivery by Lac-PEG-PAMA/pDNA polyplex micelle. Thus, it may be reasonable to conclude that an appreciable fraction of the Lac-PEG-PSAO-PAMA/pDNA polyplex micelles is taken up into HuH-7 cells through the ASGP receptor-mediated endocytosis process mediated by the cluster of the large number of lactose moieties on the surface of the polyplex micelles, followed by the effective disruption of the endosome by the buffer effect of the unprotonated pH-responsive PSAO segment in the polyplex micelles.

It is well-known that components of the serum may interact with the polyplex to induce its structure change, resulting in decreasing transfection efficiency. Thus, we examined the effect of the 20% serum preincubation for 6 h on the transfection efficiency of Lac-PEG-PSAO-PAMA/pDNA, Lac-PEG-PAMA/pDNA polyplex micelles, and B-PEI/pDNA polyplexes. As shown in Figure 12, 1 order of magnitude decrease in the transfection efficiency was observed for B-PEI/pDNA polyplexes after preincubation with 20% serum probably due to the nonspecific interaction of the cationic polyplexes with negatively charged biomacromolecules, inducing the decrease in the cellular uptake. In a sharp contrast, the polyplex micelle sytems still retained sufficient transfection efficiency toward HuH-7 cells even after preincubation with 20% serum. The almost neutral surface charge ($\zeta \sim +5$ mV in Table 1) of the Lac-PEG-PSAO-PAMA/pDNA polyplex micelles with the highly lactosylated PEG outer shell surrounding the PIC core and the PSAO inner shell may induce the micelles to tolerate serum components, allowing the cellular specific interaction through ASGP receptor-mediated endocytosis to retain efficiency even after the serum preincubation.

CONCLUSIONS

In conclusion, this study demonstrates the pH-responsive nature of novel three-layered polyplex micelles composed of a lactosylated-PEG-PSAO-PAMA triblock copolymer and pDNA, aimed at the development of a targetable and endosome-disruptive gene delivery system. The Lac-PEG-PSAO-PAMA triblock copolymer bearing a PAMA segment as the DNA-condensing polyamine and a PSAO segment as the pH-responsive polyamine was successfully synthesized. The Lac-PEG-PSAO-PAMA triblock copolymer, thus prepared, spontaneously associated with pDNA to form three-layered polyplex micelles with a PAMA/pDNA PIC core, a free PSAO inner shell, and a lactosylated PEG outer shell, as confirmed by ^{1}H NMR spectroscopy. Under physiological conditions, the Lac-PEG-PSAO-PAMA/pDNA polyplex micelles prepared at an N/P ratio above 3 were found to be able to condense pDNA (EtBr assay), thus forming polyplex micelles with a relatively small size ($<$ 150 nm, DLS measurements), and an almost neutral surface charge ($\zeta \sim +5$ mV, zeta-potential measurements). The Lac-PEG-PSAO-PAMA/pDNA polyplex micelle formed at N/P = 3 exhibited a pH-induced size variation (pH = 7.4, 132.6 nm $\rightarrow$ pH = 4.0, 181.8 nm) corresponding to the conformational changes (globule-rod transition) in the uncomplexed PSAO chain in response to pH. The swelling of the free PSAO inner shell is likely to occur in this process while retaining the condensed PIC core composed of the PAMA segment and pDNA. The fluorescence microscopic observation revealed that the interaction of the polyplex micelle entrapping FITC-labeled pDNA with HuH-7 cells was significantly reduced in the presence of ASF compared to the condition without ASF, suggesting that ASGP receptor-mediated endocytosis would be a major route of the cellular uptake of the Lac-PEG-PSAO-PAMA/pDNA polyplex micelles. Furthermore, the Lac-PEG-PSAO-PAMA/pDNA polyplex micelles exhibited more efficient transfection ability than Lac-PEG-PSAO/pDNA and Lac-PEG-PAMA/pDNA polyplex micelles. Presumably, the Lac-PEG-PSAO-PAMA/pDNA polyplex micelles might have an endosomal escape function, and thus, hydroxychloroquine as an endosomolytic agent was not required to observe appreciable transfection. Several important factors are likely to be synergistically involved in the pronounced transfection efficiency of the Lac-PEG-PSAO-PAMA/pDNA polyplex micelles, such as minimal interaction with serum proteins, enhancement of the cellular uptake through ASGP receptor-mediated endocytosis, and effective transport to the cytoplasm from the endosomal compartment (endosomal escape). Therefore, the polyplex micelle composed of the ABC triblock copolymer, thus described here, would be a promising vector for smart gene delivery.

ACKNOWLEDGMENT

This work was supported by the Core Research for Evolutional Science and Technology (CREST) from the Japan Science and Technology Agency [JST]. We thank Professor Dr. Teiji Tsuruta for helpful comments on the preparation of the manuscript and Hiroshi Ogawa for the excellent experimental support.

Supporting Information Available: Other experimental procedures and results including synthesis of PEGs, the ^{1}H NMR spectrum of polyplex micelles at pD 4.0, and the MTT assay. This material is available free of charge via the Internet at http://pubs.acs.org.

LITERATURE CITED

(1) Yang, Y., Li, Q., Ertl, H. C., and Wilson, J. M. (1995) Cellular and humoral immune response to viral antigens create barrier to lung-directed gene therapy with recombinant adenoviruses. *J. Virol. 69*, 2004−2015.

(2) Yang, Y., Li, Q., Ertl, H. C., and Wilson, J. M. (1994) MHC class I-restricted cytotoxic T lymphocytes to viral antigens destroy hepatocytes in mice infected with E1-deleted recombinant adenoviruses. *Immunity 1*, 433−442.

(3) Gunter, K. C., Khan, A. S., and Noguchi, P. D. (1993) The safety of retroviral vectors. *Hum. Gene Ther. 4*, 643−645.

(4) Wakebayashi, D., Nishiyama, N., Itaka, K., Miyata, K., Yamasaki, Y., Harada, A., Koyama, H., Nagasaki, Y., and Kataoka, K. (2004) Polyion complex micelles of pDNA with acetal-poly(ethylene glycol)-poly(2-(dimethylamino)ethyl methacrylate) block copolymer as the gene carrier system: physicochemical properties of micelles relevant to gene transfection efficacy. *Biomacromolecules 5*, 2128−2136.

(5) Itaka, K., Yamauchi, K., Harada, A., Nakamura, K., Kawaguchi, H., and Kataoka, K. (2003) Polyion complex micelles from plasmid DNA and poly(ethylene glycol)-poly(L-lysine) block copolymer as serum-tolerable polyplex system: physicochemical properties of micelles relevant to gene transfection efficiency. *Biomaterials 24*, 4495−4506.

(6) Itaka, K., Yamauchi, K., Harada, A., Nakamura, K., Kawaguchi, H., and Kataoka, K. (2002) Evaluation by fluorescence resonance energy transfer of the stability of nonviral gene delivery vectors under physiological conditions. *Biomacromolecules 3*, 841−845.

(7) Harada-Shiba, M., Yamauchi, K., Harada, A., Takamisawa, I., Shimokado, K., and Kataoka, K. (2002) Polyion complex micelles as vectors in gene therapy-pharmacokinetics and in vivo gene transfer. *Gene Therapy 9*, 407−417.

(8) Kataoka, K., Harada, A., Wakebayashi, D., and Nagasaki, Y. (1999) Polyion complex micelles with reactive aldehyde groups on their surface from plasmid DNA and end-functionalized charged block copolymers. *Macromolecules 32*, 6892−6894.

(9) Katayose, K., and Kataoka, K. (1998) Remarkable increase in nuclease resistance of plasmid DNA through supramolecular assembly with poly(ethylene glycol)-poly(L-lysine) block copolymer. *J. Pharm. Sci. 87*, 160−163.

(10) Katayose, S., and Kataoka, K. (1997) Water-soluble polyion complex associates of DNA and poly(ethylene glycol)-poly(L-lysine) block copolymer. *Bioconjugate Chem. 8*, 702−707.

(11) Wakebayashi, D., Nishiyama, N., Yamasaki, Y., Itaka, K., Kanayama, N., Harada, A., Nagasaki, Y., and Kataoka, K. (2004) Lactose-conjugated polyion complex micelles incorporating plasmid DNA as a targetable gene vector system: their preparation and gene transfecting efficiency against cultured HepG2 cells. *J. Control. Release 95*, 653−664.

(12) van de Wetering, P., Cherng, J. Y., Talsma, H., Crommelin, D. J. A., and Hennink, W. E. (1998) 2-(Dimethylamino)ethyl methacrylate based (co)polymers as gene transfer agents. *J. Control. Release 53*, 145−153.

(13) Cherng, J. Y., Van de Wetering, P., Tslsma, H.; Crommelin, D. J. A., and Hennink, W. E. (1996) Effect of size and serum proteins on transfection efficiency of poly ((2-dimethylamino)ethyl methacrylate)-plasmid nanoparticles. *Pharm. Res. 13*, 1038−1042.

(14) Brown, M. D., Schatslein, A. G., and Uchegbu, I. F. (2001) Gene delivery with synthetic (non viral) carriers. *Int. J. Pharm. 229*, 1−21.

(15) Nishikawa, M., and Huang, L. (2001) Nonviral vectors in the new millennium: delivery barriers in gene transfer. *Hum. Gene Ther. 12*, 861−870.

(16) Lloyd, J. B. (2000) Lysosome membrane permeability: implications for drug delivery. *Adv. Drug Deliv. Rev. 41*, 189−200.

(17) Gruenberg, J. (2001) The endocytic pathway: a mosaic of domains. *Nat. Rev.: Mol. Cell. Biol. 2*, 721−730.

(18) Clague, M. J. (1998) Molecular aspects of the endocytic pathway. *Biochem. J. 336*, 271−282.

(19) Mukherjee, S., Ghosh, R. N., and Maxfield, F. R. (1997) Endocytosis. *Physiol. Rev. 77*, 759−803.

(20) Duncan, R. (1992) Drug-polymer conjugates: potential for improved chemotherapy. *Anti-Cancer Drugs 3*, 175−210.

(21) Boussif, O., Lezoualc, F., Zanta, M. A., Mergny, M. D., Scherman, D., Demeneix, B., and Behr, J. P. (1995) A versatile vector for gene

and oligonucleotide transfer into cells in culture and in vivo: polyethylenimine. *Proc. Natl. Acd. Sci. U.S.A. 92*, 7297−7301.
(22) Kabanov, A. V., Bronich, T. K., Kabanov, V. A., Yu, K., and Eisenberg, A. (1998) Soluble stoichiometric complexes from poly-(*N*-ethyl-4-vinylpyridinium) cations and poly(ethylene oxide)-*block*-polymethacrylate anions. *Macromolecules 29*, 6797−6802.
(23) Fukushima, S., Miyata, K., Nishiyama, N., Kanayama, N., Yamasaki, Y., and Kataoka, K. (2005) PEGylated polyplex micelles from triblock catiomers with spatially ordered layering of condensed pDNA and buffering units for enhanced intracellular gene delivery. *J. Am. Chem. Soc. 127*, 2810−2811.
(24) Nagasaki, Y., Luo, L. B., Tsuruta, T., and Kataoka, K. (2001) Novel pH-sensitive poly(silamine) hydrogel microsphere possessing a stable skin layer. *Macromol. Rapid Commun. 22*, 1124−1127.
(25) Luo, L. B., Kato, M., Tsuruta, T., Kataoka, K., and Nagasaki, Y. (2000) Stimuli-sensitive polymer gels that stiffen upon swelling. *Macromolecules 33*, 4992−4994.
(26) Nagasaki, Y., Kazama, K., Honzawa, E., Kato, M., Kataoka, K., and Tsuruta, T. (1996) A hydrogel with rubber elasticity transition. *Macromol. Symp. 109*, 27−40.
(27) Nagasaki, Y., Kazama, K., Honzawa, E., Kato, M., Kataoka, K., and Tsuruta, T. (1995) Rubber elasticity transition of poly(silamine) induced by ionic interactions. *Macromolecules 28*, 8870−8871.
(28) Nagasaki, Y., Honzawa, E., Kato, M., and Kataoka, K. (1994) Novel stimuli-sensitive telechelic oligomers. pH and temperature sensitivities of poly(silamine) oligomers. *Macromolecules 27*, 4848−4850.
(29) Nagasaki, Y., Honzawa, E., Kato, M., Kihara, Y., and Tsuruta, T. (1992) Novel synthesis of a macromonomer having organosilyl and amino groups. *J. Macromol. Sci., Pure Appl. Chem. A29*, 457−470.
(30) van de Wetering, P., Schuurmans-Nieuwenbroek, N. M. E., Hennink, W. E., and Storm. G. (1999) Comparative transfection studies of human ovarian carcinoma cells in vitro, ex vivo and in vivo with poly(2-(dimethylamino)ethyl methacrylate)-based polyplexes. *J. Gene Med. 1*, 156−165.
(31) Cherng, J. Y., Talsma, H., Verrijik, R., Crommelin, D. J., and Hennink, W. E. (1999) The effect of formulation parameters on the size of poly-((2-dimethylamino)ethyl methacrylate)-plasmid complexes. *Eur. J. Pharm. Biopharm. 47*, 215−224.
(32) Nagasaki, Y., Sato, Y., and Kato, M. (1997) A novel synthesis of ssemitelechelic functional poly(methacrylate)s through an alcoholate-initiated polymerization. Synthesis of poly[2-(N,N-diethylaminoethyl) methacrylate] macromonomer. *Macromol. Rapid Commun. 18*, 827−835.
(33) Kitano, H., Shoda, K., and Kosaka, A. (1995) Galactose-containing amphiphiles prepared with a lipophilic radical initiator. *Bioconjugate Chem. 6*, 131−134.
(34) Hashida, M., Takemura, S., Nishikawa, M., and Takakura, Y. (1998) Targeted delivery of plasmid DNA complexed with galactosylated poly(L-lysine). *J. Controlled Release 53*, 301−310.
(35) Stockert, R. J. (1995) The asialoglycoprotein receptor: relationships between structure, function, and expression. *Physiol. Rev. 75*, 591−609.
(36) Zanta, M. A., Boussif, O., Adib, A., and Behr, J. P. (1997) In vitro gene delivery to hepatocytes with galactosylated polyethylenimine. *Bioconjugate Chem. 8*, 839−844.
(37) Plank, C., Mechter, K., Szoka, F. C., Jr., and Wagner, E. (1996) Activation of the complement system by synthetic DNA complexes: a potential barrier for intravenous gene delivery. *Hum. Gene Ther. 7*, 1437−1446.
(38) Uherek, C., Fominaya, J., and Wels, W. (1998) A modular DNA carrier protein based on the structure of diphtheria toxin mediates target cell-specific gene delivery. *J. Biol. Chem. 273*, 8835−8841.

BC050364M

Synthesis of a Biotin Derivative of Iberiotoxin: Binding Interactions with Streptavidin and the BK Ca^{2+}-Activated K^+ Channel Expressed in a Human Cell Line

Jon-Paul Bingham,[†] Shumin Bian,[‡] Zhi-Yong Tan,[§] Zoltan Takacs,[#] and Edward Moczydlowski*[,†]

Department of Biology, Clarkson University, Potsdam, New York 13699, Department of Cellular and Molecular Physiology, Yale University School of Medicine, New Haven, Connecticut 06520, Department of Internal Medicine, University of Iowa, Iowa City, Iowa 52242, and The Department of Pediatrics, University of Chicago, Chicago, Illinois 60637. Received January 6, 2006; Revised Manuscript Received March 14, 2006

Iberiotoxin (IbTx) is a scorpion venom peptide that inhibits BK Ca^{2+}-activated K^+ channels with high affinity and specificity. Automated solid-phase synthesis was used to prepare a biotin-labeled derivative (IbTx−LC-biotin) of IbTx by substitution of Asp19 of the native 37-residue peptide with *N*-ϵ-(D-biotin-6-amidocaproate)-L-lysine. Both IbTx−LC-biotin and its complex with streptavidin (StrAv) block single BK channels from rat skeletal muscle with nanomolar affinity, indicating that the biotin-labeled residue, either alone or in complex with StrAv, does not obstruct the toxin binding interaction with the BK channel. IbTx−LC-biotin exhibits high affinity (K_D = 26 nM) and a slow dissociation rate ($k_{off} = 5.4 \times 10^{-4}$ s^{-1}) in a macroscopic blocking assay of whole-cell current of the cloned human BK channel. Titration of IbTx−LC-biotin with StrAv monitored by high performance size exclusion chromatography is consistent with a stoichiometry of two binding sites for IbTx−LC-biotin per StrAv tetramer, indicating that steric interference hinders simultaneous binding of two toxin molecules on each of the two biotin-binding faces of StrAv. In combination with fluorescent conjugates of StrAv or anti-biotin antibody, IbTx−LC-biotin was used to image the surface distribution of BK channels on a transfected cell line. Fluorescence microscopy revealed a patch-like surface distribution of BK channel protein. The results support the feasibility of using IbTx−LC-biotin and similar biotin-tagged K^+ channel toxins for diverse applications in cellular neurobiology.

INTRODUCTION

The human genome contains at least 75 different genes for K^+ channel proteins as cataloged by the International Union of Pharmacology (Gutman et al., 2003). These membrane proteins are classified into seven distinct subfamilies (K_V1-6, K_V8, K_V9; K_V7; K_V10-12; $K_{Ca}1$, $K_{Ca}4$, $K_{Ca}5$; $K_{Ca}2$, $K_{Ca}3$; K_{2P}; K_{ir}) based on phylogenetic analysis of sequence similarity that reflects common structural relationships. From a parallel evolutionary perspective, at least 60 different peptide toxins that target K^+ channels have thus far been discovered in scorpion venoms (Zhu et al., 2004). Sequence analysis of these toxin peptides has identified at least 12 subfamiles of scorpion K^+ toxins that block various members of the K^+ channel family in a complex pattern of selective and overlapping specificity (Tytgat et al., 1999; Rodriguez de la Vega et al. 2003). Evidently, over the course of evolution, scorpion species have waged a biological arms race to produce an ever more diverse array of venom peptide toxins that recognize a similarly diverse variety of K^+ channel proteins in the interplay of natural selection.

This natural peptide library constitutes an important resource for biomolecular engineering of derivatives of K^+ channel toxins with numerous basic and clinical applications. For example, fluorescent and biotin-labeled derivatives of such peptides have already been used for cellular localization, flow cytometry analysis, and single-molecule microscopy of various K^+ channels (Roibtaille et al., 1993; Schütz et al., 2000; Pragl et al., 2002; Jimenez-Gonzalez et al., 2003; Beeton et al., 2004; Hafadi et al., 2005). The growing database of X-ray crystal structures of K^+ channel proteins (MacKinnon, 2003; Gulbis and Doyle, 2004) and NMR structures of K^+ toxins (Bontems et al., 1992; Johnson and Sugg, 1992; Renisio et al., 1999; Rodriguez de la Vega et al., 2003) provides a unique vantage point for molecular modeling and design of toxin derivatives engineered for specific applications.

Converting a collection of natural peptide toxins into a practical toolbox of molecular probes requires concerted efforts to develop optimal methods for synthesis and pharmacological assay of activity, affinity, and stability of the designed molecules. Toward this goal, we have synthesized and characterized a biotin-derivative of iberiotoxin (IbTx[1]), a toxin from the Indian red scorpion, *Mesobuthus tamulus* (formerly known as *Buthus tamulus*) (Galvez et al., 1990; Strong et al., 2001), for use as a probe in molecular and cellular studies of the large conductance Ca^{2+}-activated K^+ channel ($K_{Ca}1.1$). $K_{Ca}1.1$ is also called the BK channel, the maxi K_{Ca} channel, or HSlo, the latter term designating the human α-subunit protein that forms the channel tetramer (Wallner et al., 1995). The BK channel is synergistically activated by membrane depolarization and intracellular Ca^{2+} and is known to function in neurotransmitter release at

* Corresponding author. Tel.: 315-268-6641; fax: 315-268-7118; e-mail: emoczydl@clarkson.edu.

[†] Clarkson University.

[‡] Yale University School of Medicine, Department of Cellular and Molecular Physiology.

[§] University of Iowa, Department of Internal Medicine.

[#] University of Chicago, Department of Pediatrics.

[1] Abbreviations: BK, large conductance Ca^{2+}-activated K^+ channel; ChTx, charybdotoxin; DIC, differential interference contrast microscopy; IbTx, iberiotoxin; HPLC, high-pressure liquid chromatography; HPSEC, high performance size exclusion chromatography; HSlo, human BK channel; IbTx−LC-biotin, iberiotoxin-D19K-LC-biotin; TFA, trifluoracetic acid, Acm; acetamidomethyl.

10.1021/bc060002u CCC: $33.50 © 2006 American Chemical Society
Published on Web 04/25/2006

nerve terminals, regulation of smooth muscle contractility, and auditory functions of cochlear hair cells (Toro et al., 1998; Orio et al., 2002; Hafadi et al., 2005).

IbTx (αKTx1.3) is a 37-residue peptide with three disulfide bonds that belongs to the same K^+ toxin subfamily as charybdotoxin (ChTx or αKTx1.1), an extensively studied model of K^+ toxin-channel interaction (Galvez et al., 1990; Miller, 1995; Tenenholz et al., 2000). Whereas ChTx blocks various K^+ channels of both K_V and K_{Ca} gene families, IbTx appears to be a specific, high-affinity inhibitor of HSlo and other mammalian BK channels (Galvez et al., 1990; Rodriguez de la Vega et al., 2003). Extensive studies of the structure−activity relationships of ChTx, IbTx, K_V channels, BK channels, and the prokaryotic K^+ channel, KcsA, have led to a detailed model of the complex of IbTx docked to the external vestibule of the BK channel (Lucchesi et al., 1989; Giangiacomo et al., 1993; Goldstein et al., 1994; Stampe et al., 1994; Doyle, D. A. et al., 1998; MacKinnon et al., 1998; Mullmann et al., 1999; Cui et al., 2001; Gao and Garcia, 2003; Yu et al., 2005). Guided by this trove of information, we describe a direct method for synthesizing IbTx−LC-biotin and characterize its biochemical interactions with respect to block of BK channels, binding to streptavidin (StrAv), and cellular imaging of BK channels by fluorescence microscopy.

EXPERIMENTAL PROCEDURES

Materials. Streptavidin, Alexa488-streptavidin, Alexa488-anti-biotin antibody, and biotin-4-fluorescein were obtained from Molecular Probes (Eugene, OR). The Fmoc derivatives of *N*-ϵ-(D-biotin-6-amidocaproate)-L-lysine and *S*-acetamidomethyl-L-cysteine were purchased from Anaspec (AnaSpec, San Jose CA).

Synthesis and Purification of IbTx−LC-Biotin. Automated peptide synthesis based on the linear sequence of IbTx was performed via solid-phase Fmoc coupling chemistry by the Keck Peptide Facility at Yale Medical School (New Haven, CT). In place of the native Asp residue at position 19, *N*-ϵ-(D-biotin-6-amidocaproate)-L-lysine was substituted to produce the toxin derivative illustrated in Figure 1. Cleavage from the support resin and removal of protecting groups were accomplished using trifluoroacetic acid (TFA). Molecular mass determined by MALDI MS for the reduced product after cleavage, ether extraction, and lyophilization was MH^+ 4588.0 Da vs the theoretical monoisotopic mass of 4587.1 Da. A portion of the crude product (20 mg) was sonicated in 40 mL of buffer (2 M urea, 0.1 M NaCl, 0.1 M glycine, pH 7.8) and allowed to oxidize in air by stirring at 22 °C for 18 h. Final purification was achieved by C18 reverse-phase HPLC first on a semipreparative column followed by a narrow-bore Vydac C18 column both using a linear separation gradient of 0.01% TFA/Aq to 60% CH_3CN in 0.08% TFA/Aq over 60 min. UV absorption was monitored at 223 nm. Electrospray mass spectroscopy of pure oxidized peptides was performed on a Thermo Finnigan spectrometer. Peptide concentration of IbTx−LC-biotin was determined from integrated area of the HPLC peak (absorbance monitored at 280 nm) of the sample relative to that of a reference standard of synthetic IbTx previously quantified by amino acid analysis.

IbTx-D19C-Acm was synthesized in a similar manner by automated Fmoc solid-phase chemistry. In place of the native Asp residue at position 19, *S*-acetamidomethyl-L-cysteine was substituted to produce the toxin derivative. IbTx-D19C-Acm was oxidized, purified and quantified, as described above.

Planar Bilayer Assay. Single-channel recording of BK channels from rat skeletal muscle in planar lipid bilayers was performed as previously described (Favre and Moczydlowski, 1999). The recording solution was 200 mM KCl, 10 mM Mops-KOH, pH 7.4 on both sides of the bilayer, with 0.2 mM $CaCl_2$ on the intracellular side and 0.1 mM EDTA plus 0.1 mg/mL bovine serum albumin on the extracellular side as defined by native asymmetry of the channel.

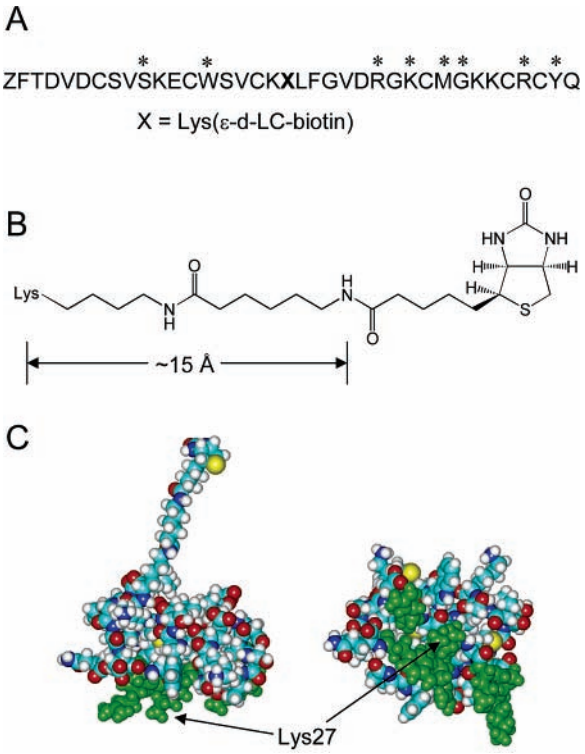

Figure 1. Design strategy and molecular model of IbTx−LC-biotin. (A) Sequence of synthetic IbTx−LC-biotin showing substitution of native residue D19 with Lys(ϵ-D-LC-biotin). Asterisks (*) mark eight residues important for toxin binding to BK channels. (B) Chemical structure of the side chain of the biotin derivative showing the ~15 Å linker between the Lys α-carbon atom and the biotin moiety buried in the complex with streptavidin. (C) Molecular model of IbTx−LC-biotin. Left panel is a side view of a model of the IbTx derivative with the BK channel binding surface at the bottom and the biotin-derivative side chain at the top. A 90° rotation of the latter structure back into the plane of the paper was used to generate the image for the right panel, which shows green colored residues (marked * in A) at the toxin−channel interface.

Whole-Cell Electrophysiology. HEK293 transformed human embryonic kidney cells were stably transfected using G418 selection with a pcDNA3 vector encoding a His_6-Flag-epitope-tagged version of the human BK channel (HSlo) originally cloned by Wallner et al. (1995). The tagged version of HSlo (kindly supplied by Dr. Andrew Tinker, University College London) contained the N-terminal tag sequence, MVHHHH-HHDYKDDDDK, linked directly to the second amino acid (D2) of the native HSlo sequence. HEK293/HSlo cells were grown in DMEM medium (Gibco) supplemented with 10% fetal bovine serum, 10 000 U/mL penicillin/streptomycin (Gibco), and 0.6 mg/mL Geneticin (G418, from Gibco) at 37 °C in a humidified atmosphere of 5% CO_2 in air. Cells were seeded on small chips of glass cover slips coated with polylysine 2−4 days prior to patch-clamp recording.

Whole-cell patch recording was performed using a low volume cell recording chamber (RC24E, Warner Instruments) mounted on a Nikon TE200 inverted microscope. The recording chamber was continuously perfused at 0.5 mL/min with control and various bath solutions containing toxins and inhibitors. Patch pipets with a resistance of 1−2 MΩ were fabricated from glass capillaries (Kimax-51, Fisher Scientific) with a PP-83 puller (Narishige). Whole-cell current was measured at room temperature with an Axon 200B amplifier controlled by PC-based Clampex software (Axon Instruments) for voltage pulse delivery

and digital current acquisition. Currents were low pass filtered at 5 kHz and corrected for capacitance transients and leak current using a negative P/5 pulse protocol. The composition of standard pipet (intracellular) solution with 500 nM free Ca^{2+} (Strobaek et al., 1996) was 150 mM KCl, 1 mM $MgCl_2$, 1 mM $CaCl_2$, 1.3 mM EGTA, 10 mM Hepes-KOH, pH 7.2. The bath solution contained 145 mM NaCl, 5 mM KCl, 2 mM $CaCl_2$, 2 mM $MgCl_2$, 10 mM Hepes-KOH, pH 7.4 and various peptide toxins or 1 μM paxilline (Sigma) as described.

Streptavidin Binding Interaction. Streptavidin (StrAv) concentration was standardized by the method of Kada et al. (1999) based on fluorescence quenching of biotin-4-fluorescein (e.g., Figure 6A), a ligand known to bind stoichiometrically to four sites of StrAv and avidin with high affinity. Sequential additions (5 nM) of biotin-4-fluorescein were made to a stirred cuvette containing ~11 nM StrAv in 100 mM NaCl, 50 mM Hepes-NaOH, pH 7.3. Fluorescence emission spectra excited at 484 nm were recorded 5 min after each addition of biotin-4-fluorescein using a QuantaMaster-4 spectrofluorimeter (Photon Technology International, Lawrenceville, NJ). The concentration of biotin-4-fluorescein was based on the reported extinction coefficient of 68 000 $M^{-1}cm^{-1}$ at 494 nm (Haugland, 2002).

Complex formation between standardized IbTx−LC-biotin and StrAv was analyzed by high performance size-exclusion chromatography using a Phenomenex BioSep-SEC-S 2000 column (300 × 7.5 mm) with buffer delivery and detection controlled by a Waters Alliance 2695 HPLC system equipped with a 995 photodiode array detector (wavelength scan at 200−400 nm). The column was equilibrated with buffer (100 mM NaCl, 50 mM Hepes-NaOH, pH 7.3) and run isocratically at a flow rate of 0.5 mL/min. Dextran blue (~2000 kDa) and uridine (244.2 Da) were used to determine the void volume and column volume, respectively. Fixed samples of IbTx−LC-biotin (250 pmol) were incubated for 24 h in separate vials containing increasing amounts of StrAv ranging from 0 to 375 pmol in 18 μL of running buffer. Each sample was separately injected on the column and monitored by absorbance at 280 nm. Binding of IbTx−LC-biotin (5 kDa molecular mass) to StrAv (52.8 kDa molecular mass) was followed by the decrease in area of the IbTx−LC-biotin peak and appearance of peaks corresponding to bound and free StrAv eluting at a higher mass range as observed upon increasing addition of StrAv (e.g., Figure 5).

Fluorescence Microscopy. Native HEK293 cells and stably transfected HEK293/HSlo cells were grown either in tissue culture flasks for labeling of cells in suspension or on cover slips coated with poly-D-lysine in a 12-well culture plate for attached-cell labeling. Cells grown on cover slips were washed once with 125 mM NaCl, 25 mM NaP_i, pH 7.4 (PBS) followed by an optional endogenous biotin-blocking protocol following kit instructions (E-21390) from Molecular Probes. Cover slips were next incubated in PBS containing 1 mg/mL bovine serum albumin (BSA) and 50 to 100 nM IbTx−LC-biotin for 30 min at room temperature and then washed three times in PBS. This step was followed by incubation in the dark for 20 min at room temperature in the same buffer containing either 3 μg/mL Alexa488-StrAv or 4 μg/mL Alexa488-anti-biotin antibody. A final wash step, three times in PBS, was performed before observing cells using a Nikon Eclipse TE2000-E inverted epifluorescence microscope. Incubation and wash conditions were similar for labeling dissociated cells removed from tissue culture flasks by gentle pipetting except that the washing steps were performed by low-speed microcentrifugation. Labeled cells were either observed directly or after fixation with 2% formaldehyde in PBS for 20 min followed by washing in PBS and mounting on glass slides using VectaShield mounting media (Vector Laboratories). Digital Images were captured using with a Hamumatsu Orca CCD camera and IPLab acquisition software (Scanalytics).

RESULTS

Design and Synthesis of a Biotin Derivative of IbTX. Similar to other αKTx1 toxins such as ChTx and Lq2 (Bontems et al., 1992; Renisio et al., 1999), the three-dimensional (3D) solution structure of IbTx (sequence given in Figure 1A) is characterized by a short α-helix at residues 13−21 and a two-stranded antiparallel β-sheet comprised of residues 25−36 (Johnson and Sugg, 1992). Three disulfide bonds between Cys residues 7−28, 13−33, and 17−35 tightly constrain the structure of αKTx1 toxins and render them quite resistant to denaturation by heating and other treatments in the folded, oxidized state (Smith et al., 1986). Structure−activity studies including mutagenesis, X-ray crystallography, NMR, Brownian dynamics simulation, and molecular modeling approaches have yielded a rather detailed picture of the probable molecular basis of interaction of αKTx1 toxins with various K^+ channels (Goldstein et al., 1994; Stampe et al., 1994; Doyle et al., 1998; Tenenholz et al., 2000; Cui et al., 2001; Schroeder et al., 2002; Gao and Garcia, 2003; Yu et al., 2005). Binding of αKTx1 toxins is primarily determined by molecular interactions between critical residues that lie on the β-sheet face of the toxin and particular residues within the outer vestibule of K^+ channels. K^+ channel residues critical for toxin binding lie either in the "turret" formed by an extracellular linker between the outer membrane helix (M1 or S5) and the so-called pore helix, or in a second extracellular linker between the selectivity filer and the inner membrane helix (M2 or S6) (MacKinnon et al., 1998; Gao and Garcia, 2003). Eight residues predicted to lie on the interaction surface of IbTX (S10, W14, R25, K27, M29, G30, R34, Y36) are marked with asterisks in Figure 1A. Modification of these latter residues typically lowers the affinity of the αKTx1 toxin−channel interaction, requiring the identification of other noncritical residues for toxin derivatization.

On the basis of the observation that certain residue substitutions on the toxin surface opposite to the channel interaction surface do not interfere with blocking activity, Shimony et al. (1994) identified residue R19 near the C-terminal end of the α-helical region of charybdotoxin as a favorable site for derivatization. Using a "spinster cysteine" strategy, *N*-[^{3}H]ethylmaleimide derivatives of the R19C mutant of charydotoxin and a D19C mutant of IbTx have previously been developed as radioligands used in binding assays for Shaker and BK K^+ channels (Shimony et al., 1994; Sun et al., 1994; Knaus et al., 1996).

We followed a similar approach in this work by substituting *N*-ε-(D-biotin-6-amidocaproate)-L-lysine [Lys(ε-D-LC-biotin)] in place of native residue D19 of IbTx in automated solid-phase synthesis of IbTx−LC-biotin. Figure 1B illustrates the chemical structure of the unnatural amino acid side chain substituted at residue 19 of IbTx−LC-biotin and also denotes the ~15 Å chemical linker between the α-carbon atom of the peptide backbone and the carboxy tail of the biotin moiety that is virtually buried upon binding to streptavidin (Henrickson et al., 1989). Lys(ε-D-LC-biotin) was selected as the replacement residue to evaluate the use of biotin−avidin labeling technology for biochemical and cellular studies of BK channels. As illustrated in Figure 1C, a plausible extended conformation of a molecular model of IbTx−LC-biotin shows that the biotin-tagged side chain is physically well separated from the channel-interaction surface of the toxin. We expected that the relatively long linear linker of this particular biotin-amino acid derivative (17 atoms from the peptide backbone to the biotin ring) may facilitate unhindered binding of streptavidin or avidin to the toxin-channel complex.

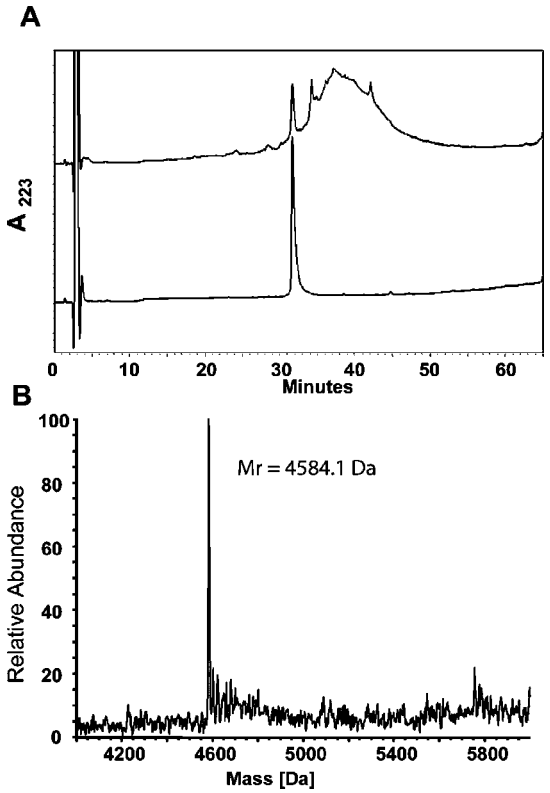

Figure 2. Purification and mass analysis of IbTx−LC-biotin. (A) Reverse phase HPLC chromatogram of crude oxidized (top trace) and purified (bottom trace) synthetic IbTx−LC-biotin. Samples were run on a Vydac C18 column and eluted with a linear gradient of buffer A to buffer B (A = 0.1% TFA, B = 60% CH_3CN in 0.08% TFA, over 60 min). (B) Electrospray MS analysis of pure oxidized IbTx−LC-biotin demonstrating a deconvoluted average mass of 4584.1 Da.

After automated synthesis and cleavage from the resin were performed, the crude peptide product was solubilized in folding buffer at pH 7.8, allowed to oxidize in air for 18 h, and analyzed by reverse phase HPLC as described in Experimental Procedures. The HPLC chromatogram exhibited a broad peak of heterogeneous product superimposed upon a major sharp peak at 32 min that comprised about ∼5% of the total material (Figure 2, top trace). Purification of this latter peak yielded about ∼1 mg of pure IbTx−LC-biotin per 100 mg of the crude synthetic product (Figure 2A, lower trace). Electrospray mass spectroscopy of the latter peak confirmed the identity of oxidized IbTx−LC-biotin, with an observed deconvoluted mass of 4584.1 Da (Figure 2B) compared to a theoretical average mass of 4584.5 Da predicted for the sequence in Figure 1A with three disulfide bonds.

Electrophysiological Assays of BK Channel Block by IbTX−Biotin. We first investigated the biological activity of synthetic IbTx−LC-biotin by the planar bilayer assay method (Miller et al., 1985; Smith et al., 1986; Lucchesi et al., 1989). Addition of IbTx−LC-biotin to the external side of bilayers containing single BK channels resulted in the appearance of discrete long-lived blocked states characteristic of αKTx1 toxins such as ChTx, Lq2, and IbTx (Miller et al., 1985; Lucchesi et al., 1989; Candia et al., 1992; Giangiacomo et al., 1992). As illustrated in Figure 3A, under control conditions (200 mM symmetrical KCl, 0.2 mM internal Ca^{2+}, holding voltage = +30 mV) in the absence of toxin, typical current records of a single BK channel from rat skeletal muscle exhibit a high probability of opening with the majority of brief closures lasting less than 1 s. Long silent periods ranging from seconds to minutes observed after addition of 4 nM IbTx−LC-biotin to the external side of a single BK channel (Figure 3B) correspond to blocking

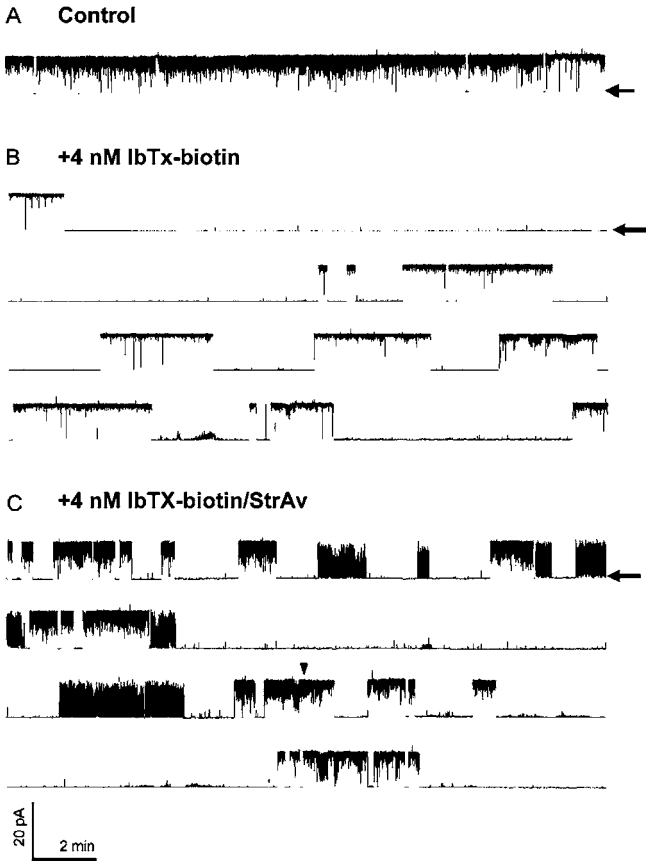

Figure 3. Bilayer assay of BK_{Ca} channel block by IbTx−LC-biotin in the absence and presence of StrAv. (A) Current record of a single BK_{Ca} channel from rat skeletal muscle under control conditions in the absence of toxin. (B) Record of a BK_{Ca} channel with 4 nM IbTx−LC-biotin on the external side. (C) Record of a BK_{Ca} channel in the presence of 4 nM IbTx−LC-biotin plus 16 nM StrAv on the external side. A small triangle in the third line marks where data are spliced from another bilayer recorded under identical conditions. Control conditions: Holding voltage = +30 mV. The solution on both sides of the bilayer was 10 mM Mops-KOH, pH 7.4, 200 mM KCl. The internal solution also contained 200 μM $CaCl_2$, and the external solution contained 0.2 mM EDTA plus 0.1 mg/mL bovine serum albumin. Arrows to the right indicate zero current level or the closed state of the channel. Low conductance noise superimposed on IbTx-blocked events in Figure 3B,C is due to activity of extraneous, non-BK channels occasionally observed in planar bilayer recordings.

events or residence times of single toxin molecules similar to those produced by native IbTx (Candia et al., 1992; Giangiacomo et al., 1992). To test whether IbTx−LC-biotin retains blocking activity after complex formation with StrAv, we preincubated IbTx−LC-biotin with a 4-fold excess of StrAv tetramer and tested the mixture on single BK channels. As illustrated in Figure 3C, single channel records in the presence of 4 nM complex of IbTx−LC-biotin /StrAv exhibit long-lived blocked events similar to those produced by IbTx alone, demonstrating that the toxin-StrAv complex is fully capable of binding to the toxin receptor site on BK channels.

Single-channel analysis of IbTX-blocking kinetics is technically rather difficult due to the long duration of IbTx-blocked state events; however, we estimated kinetic parameters with limited sets of blocking events pooled from several single-channel bilayers using a standard analysis for a one-site blocking reaction (Moczydlowski, 1992; Favre and Moczydlowski, 1999). For IbTx−LC-biotin, this analysis yields the following kinetic constants: $k_{off} = 4.7 \times 10^{-3}$ s (dissociation rate constant), $k_{on} = 1.9 \times 10^{6}$ $s^{-1}M^{-1}$ (association rate constant), and $K_D = 2.5$ nM (equilibrium dissociation constant). The corresponding values estimated for the complex of IbTx−LC-biotin and StrAv

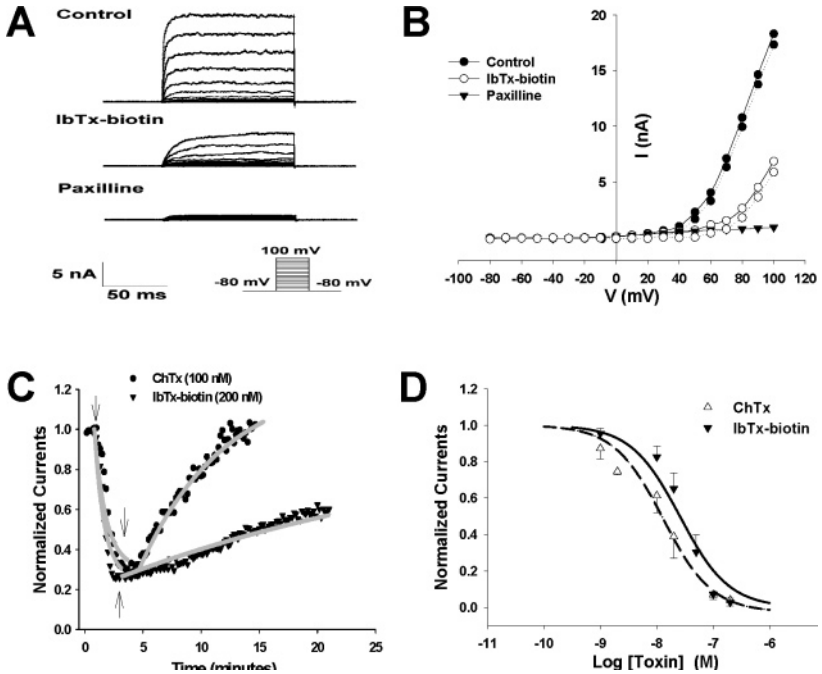

Figure 4. Electrophysiological assay of IbTx−LC-biotin and ChTx on the whole-cell current of HSlo expressed in HEK293 cells. (A) Effect of IbTx−LC-biotin and paxilline on whole-cell currents. Top panel shows a family of current traces elicited by stepping membrane voltage from a holding potential of −80 mV up to +100 mV in consecutive steps of +10 mV for a duration of 100 ms. Middle and bottom panels were recorded after addition of 100 nM IbTx−LC-biotin and 1 μM paxilline, respectively, to the extracellular bathing solution. (B) Plot of whole-cell current from panel A at the end of the 100 ms depolarization vs the step voltage. Solid and dotted lines for control and 100 nM IbTx−LC-biotin correspond to current values before and after subtraction of background current measured in the presence of 1 μM paxilline, respectively. (C) Time course of inhibition by toxins and recovery after perfusion. Peak current was monitored by 50 ms voltage steps from −80 mV to +50 mV once every 10 s. IbTx−LC-biotin (200 nM) or ChTx (100 nM) was added to the extracellular perfusion solution at the time of the first arrow and replaced by toxin-free solution at the time of the second arrow. Data points are normalized to the first few points before addition of toxin. Solid lines overlays are fits to an exponential time course. (D) Titration curves of toxin inhibition. HSlo current at steady state in the presence of various concentrations of IbTx−LC-biotin or ChTx is normalized to values measured before toxin addition. Data are fit to a single-site inhibition isotherm ($I_{norm} = K_D/(K_D + [\text{toxin}])$ with K_D values of 26 nM for IbTx−LC-biotin and 13 nM for ChTx.

are $k_{off} = 8.5 \times 10^{-3}$ s^{-1}, $k_{on} = 3.4 \times 10^6$ s^{-1} M^{-1}, and $K_D = 2.5$ nM. Although these kinetic parameters have large uncertainties in the range of 12−60%, they imply that the complex of IbTx−LC-biotin and StrAv has somewhat faster dissociation and association rates in comparison to IbTx−LC-biotin but retains an equilibrium binding affinity in the low nanomolar range, similar to that of native IbTx (Candia et al., 1992; Giangiacomo et al., 1992).

We next investigated the effect of IbTx−LC-biotin in a macroscopic assay of whole-cell currents of the cloned human BK channel (HSlo) stably expressed in the HEK293 cell line. Using an intracellular solution containing 500 nM free Ca^{2+}, BK currents are activated at voltages more positive than +40 mV under these conditions (Figure 4A,B). Greater than 95% of outward K^+ current recorded in this cell line is sensitive to inhibition by 1 μM paxilline (Figure 4A,B), a potent inhibitor of mammalian BK channels (Knaus et al., 1994; Strobaek et al., 1996). Addition of 200 nM IbTx−LC-biotin to the bath solution substantially inhibits BK current (Figure 4A,B), and such inhibition is slowly reversed by perfusion with toxin-free solution (Figure 4C). The titration curve of steady-state inhibition of peak outward BK current by IbTx−LC-biotin is well described by one-site behavior with a K_D of 26 nM (Figure 4D). By fitting the time course of development of IbTx−LC-biotin and washout with a single exponential and assuming one-site kinetics (Figure 4C), we obtained values of apparent rate constants, $k_{on} = 9.9 \times 10^4$ s^{-1} M^{-1} and $k_{off} = 5.1 \times 10^{-4}$ s^{-1}, which are respectively, 19- and 9-fold slower than the corresponding rate constants measured for the bilayer experiments of Figure 3. Inhibition of whole-cell BK current by native ChTx in this assay system exhibited a K_D value of 13 nM (Figure 4D), and apparent rate constants of $k_{on} = 1.3 \times 10^5$ s^{-1} M^{-1} and $k_{off} = 3.2 \times 10^{-3}$ s^{-1} (Figure 4C). These results demonstrate that synthetic IbTx−LC-biotin is a potent inhibitor of the cloned HSlo BK channel with a slower dissociation rate than charybdotoxin, as originally observed for blocking interactions of the native toxins (Candia et al., 1992; Giangiacomo et al., 1992; Stampe et al., 1994).

Binding Interaction of IbTx−LC-Biotin with Streptavidin. To characterize complex formation between IbTx−LC-biotin and StrAv, a fixed amount of IbTx−LC-biotin (250 pmol) was preincubated for 24 h with increasing amounts of tetrameric StrAv ranging from 0 to 375 pmol, and the resulting samples were analyzed by size exclusion chromatography. Superimposed absorbance profiles of the separate chromatography runs from this experiment are shown in Figure 5. In the absence of StrAv (mass ∼ 52 800 kDa), IbTx−LC-biotin (mass = 4.6 kDa) runs as a single peak (22.2 min) that elutes near the total column volume (12.4 mL; 24.8 min; 0.5 mL/min flow rate). Preincubation of the synthetic toxin with a low amount of StrAv results in a decrease in the absorbance of peak corresponding to the free toxin and the appearance of a higher mass peak (at 17.2 min) that corresponds to complex(es) of IbTx−LC-biotin and StrAv. As shown in Figure 5, at a molar ratio greater than 0.5 mole of StrAv tetramer per mole of IbTx−LC-biotin, a new peak is observed corresponding to the elution time (18.1 min) of free, uncomplexed StrAv. This observation indicates that the StrAv tetramer binds a maximum of two molecules of IbTx−LC-biotin under the conditions of this experiment in comparison to the theoretical capacity of four molecules corresponding to the four known biotin sites on the tetrameric protein (Hendrickson et al., 1989; Green, 1990). This surprising result was verified by measuring the concentration of total biotin binding sites in the commercial StrAv preparation using a method based on

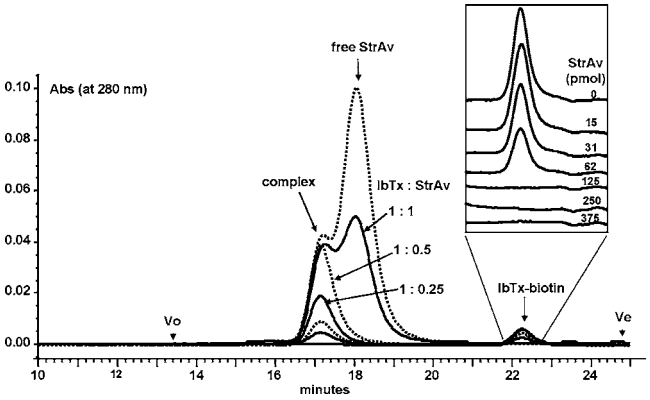

Figure 5. Analysis of complex formation between IbTx−LC-biotin and StrAv by size exclusion chromatography. A fixed amount of IbTx−LC-biotin (250 pmol) was incubated with increasing amounts of StrAv in the range of 0 to 375 pmol, and samples were subjected to HPSEC as described in Experimental Procedures. Overlayed consecutive traces of the absorbance profile are alternated using solid and dashed lines for the sake of clarity. The inset shows seven traces underlying the peak corresponding to unbound IbTx−LC-biotin that have been enlarged and vertically displaced. Triangles mark column calibrations: Vo, void volume; Ve, column volume.

fluorescence quenching of biotin-4-fluorescein (Kada et al., 1999). As shown in Figure 6A, this method reliably gives the total number of biotin binding sites in a StrAv sample from the break point of the fluorescence titration with biotin-4-fluorescein. On the basis of the standardized concentration of StrAv tetramer, titration experiments of IbTx−LC-biotin and StrAv (Figure 5) clearly demonstrate an equivalence point of two binding sites for IbTx−LC-biotin per molecule of StrAv tetramer (Figure 6B).

This result implies that binding of one molecule of IbTx−LC-biotin sterically interferes with binding of another IbTx−LC-biotin molecule on the StrAv tetramer. In fact, such "anti-cooperative" binding has been previously observed for titration of StrAv with certain long chain derivatives of biotin-fluorescein (Gruber et al., 1998). This unusual behavior is attributed to the particular 3D relationship of biotin binding sites in StrAv. The quaternary structure of StrAv tetramer consists of a dimer of dimers, with two adjacent biotin sites on neighboring StrAv monomers located within ~19 Å of each other on each of two separate faces of the tetramer (Hendrickson et al., 1989; Green, 1990; Freitag et al., 1997). Biotin derivative molecules with long chain linkers have a propensity to interfere with pairwise binding of each other across the two separate binding faces of the tetramer. In the present situation, the potential likelihood of this behavior can be appreciated by comparing the space filling models of StrAv and IbTx−LC-biotin (Figure 6D). The molecular models show that the dimensions of IbTx−LC-biotin are comparable to the distance of separation of two biotin binding sites across the binding face of the tetramer. Steric interference or physical occlusion of an unoccupied site by a toxin molecule bound to an adjacent site may explain the 2:1 binding stoichiometry observed for titration of IbTx−LC-biotin with StrAv. Figure 6A also shows that preincubation of 11 pmol of StrAv with 3 equiv (33 pmol) of IbTx−LC-biotin is sufficient to completely block binding of biotin-4-fluorescein to StrAv as shown by the lack of a detectable linear region of quenched fluorescence. This latter result implies that binding of IbTx−LC-biotin also interferes with binding of the smaller biotin-4-fluorescein molecule to an adjacent biotin site on StrAv.

Cellular Imaging of BK Channels with IbTx−LC-Biotin. The interactions with StrAv and BK channels described above suggest that IbTx−LC-biotin may be useful for studies of the cellular localization of BK channels by fluorescence microscopy. To evaluate IbTX−LC-biotin as an imaging probe, HEK293 cells stably expressing a version of the human BK channel,

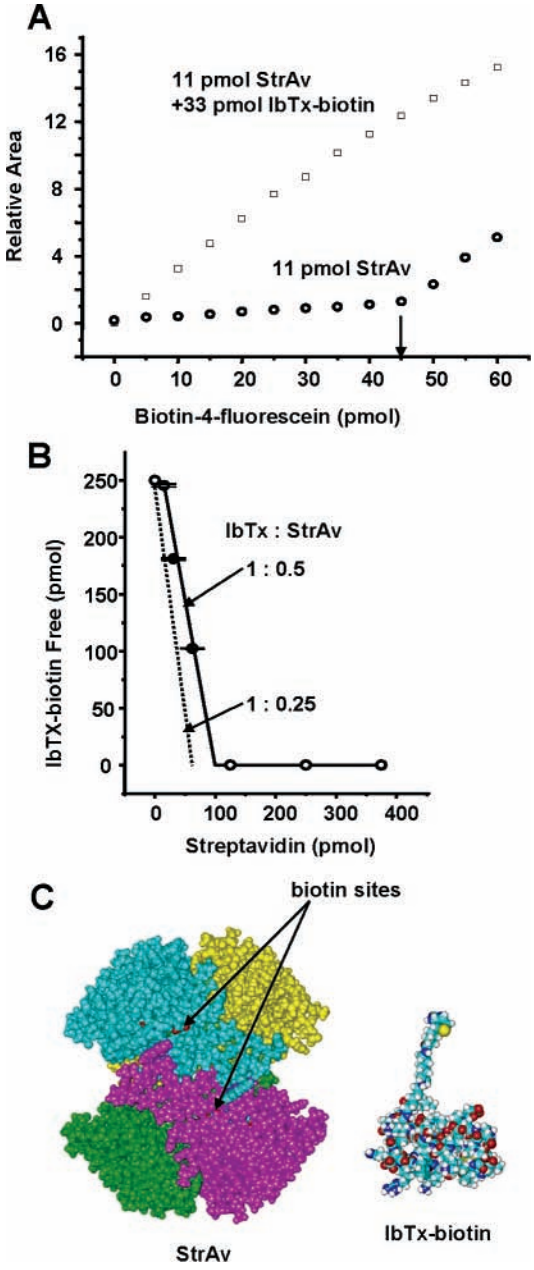

Figure 6. Stoichiometry of IbTx−LC-biotin binding to StrAv. (A) Fluorescence titration of 11 pmol of StrAv with biotin-4-fluorescein. Open circles, StrAv alone; open squares, StrAv preincubated with 33 pmol of IbTx−LC-biotin. The arrow indicates the equivalence point at ~44 pmol of biotin-4-fluorescein. (B) Titration of IbTx−LC-biotin with increasing StrAv. Peak areas corresponding to free IbTx−LC-biotin for various samples in Figure 4 were normalized to the control taken in the absence of StrAv and plotted versus the amount of added StrAv. Titration data are consistent with an equivalence point near 125 pmol of StrAv or a molar ratio of 1:0.5 for IbTx−LC-biotin/StrAv. Dashed line shows theoretical expectation for four IbTx−LC-biotin binding sites per StrAv. (C) Space-filling molecular models of StrAv complex with biotin on the left (structure 1SWE from Protein Data Bank) and IbTx−LC-biotin on the right at the same scale. Arrows mark the location of two adjacent biotin sites on the front face of the StrAv tetramer.

HSlo, were sequentially incubated with 100 nM IbTx−LC-biotin and 10 μg/mL StrAv conjugated with Alexa488, a fluorophore with spectral properties similar to fluorescein (Panchuk-Voloshina et al., 1999). The labeled cells were washed, fixed, and examined with a 100× oil immersion objective in an inverted fluorescence microscope. As shown by comparison of fluorescence and DIC (differential interference contrast) imaging of cells on processed coverslips, virtually all of the HEK293/

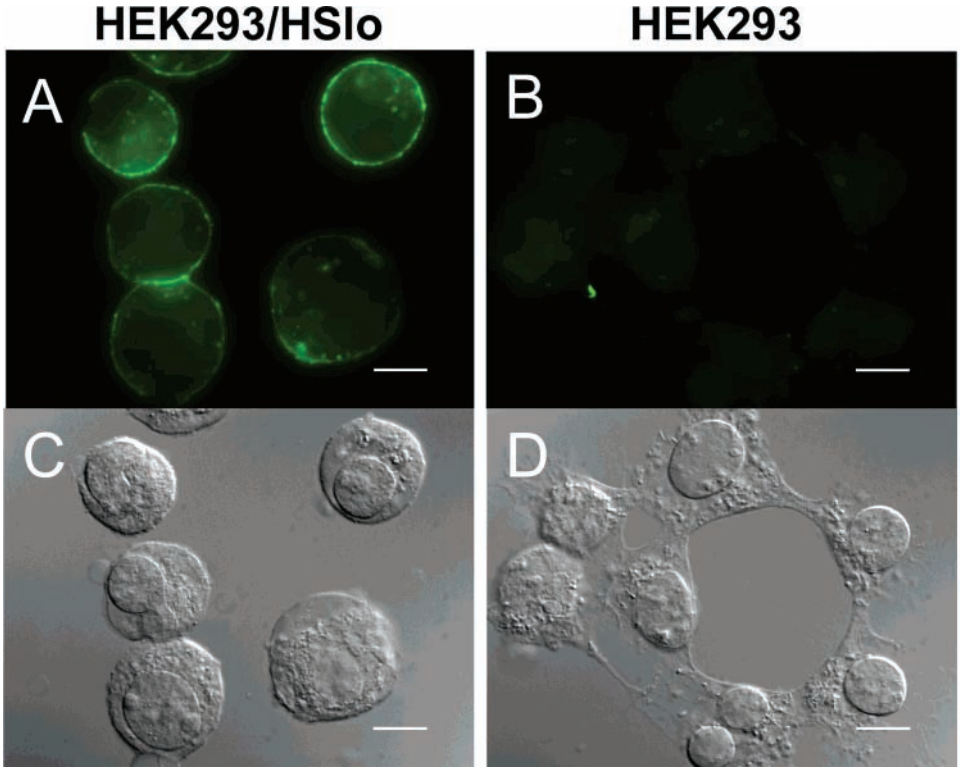

Figure 7. Fluorescence microscopy of transfected cells expressing HSlo using IbTx−LC-biotin. (A, C) Stably transfected HEK293/HSlo cells. (B, D) Untransfected HEK293 cells. (A, B) Fluorescence images acquired under identical conditions. (C, D) DIC image of the same fields in A and B, respectively. Cells grown on coverslips were processed for microscopy by incubation with 100 nM IbTx−LC-biotin, then washed and incubated with 10 μg/mL Alexa488-StrAv, washed again, fixed in 2% formaldehyde, and viewed using a 100× oil immersion objective as described in Experimental Procedures. Scale bar = 10 μm.

HSlo cells exhibited intense fluorescence on the perimeter of the plasma membrane (Figure 7A,C) consistent with the G418 antibiotic selection procedure for growth of cells stably transfected with the pcDNA3 vector containing the HSlo gene. In contrast, the plasma membrane of control untransfected HEK293 cells processed for imaging in an identical manner (Figure 7B,D) showed only faint and diffuse background fluorescence, consistent with weak nonspecific adsorption of the labeling reagents and the fact that this fibroblast-like cell line has very low levels of endogenous BK current (Yu et al., 1998).

Analysis of 0.5 μm Z-sections of single cell images by fluorescence deconvolution enhancement showed that virtually all the fluorescence signal in HEK293/HSlo cells is localized to the cell surface, consistent with membrane impermeability and lack of cellular uptake of the imaging reagents under the labeling conditions. Supplementary Figure 1 (Supporting Information) is a movie file that shows a series of consecutive two-dimensional (2D) 0.5 μm Z-sections through a single HEK293/HSlo cell labeled with IbTX−LC-biotin/Alexa488-StrAv, imaged by fluorescence microscopy, and processed by deconvolution enhancement. This visualization method reveals a nonrandom distribution of fluorescence on the cell plasma membrane. Supplementary Figure 2A−C (Supporting Information) contains movie files of HEK293/HSlo cells imaged in a similar fashion, reconstructed in three dimensions by software, and displayed by rotation of the reconstructed fluorescence image of the cell or cell pairs. These data also show a punctate-like distribution of fluorescence on the cell surface. A similar patch-like surface distribution of BK channels was also observed by processing fixed HEK293/HSlo cells for fluorescence microscopy with an anti-Flag antibody that recognizes the extracellular Flag epitope on the tagged HSlo channel (not shown). Thus, the patch-like surface distribution of BK channels observed by IbTX−LC-biotin labeling is not a peculiar feature of the toxin-labeling method. The patch-like distribution of BK channels revealed in these experiments indicates that cellular mechanisms operating in this transfected cell line result in preferential clustering of BK channels on the membrane surface. Clustering and co-localization of BK channels with various signal-transduction proteins has previously been observed described in diverse cell types (Alioua et al., 2002; Eghbali et al., 2003; Liu et al., 2004) and is thought to be an important mechanism for coupling of BK channel activity to specific cellular functions.

In certain histochemical applications, StrAv-based labeling techniques are prone to background signals due to nonspecific adsorption and endogenous biotin (Haugland, 2002). To test for this possibility, we used a commercial biotin-blocking procedure according to the manufacturer's instructions (Molecular Probes; Eugene, OR) but found that this treatment made little difference in the background fluorescence (not shown). To further examine the specificity and versatility of IbTx−LC-biotin imaging, a number of additional control experiments were performed. As shown in Figure 8A,B, fluorescence labeling of HEK293/HSlo cells by 50 nM IbTx−LC-biotin and 3 μg/mL Alexa488-StrAv is effectively blocked by 5 μM IbTX-D19C-Acm, a nonbiotinylated derivative of IbTx. This result shows that excess untagged IbTx effectively competes with BK channel labeling by IbTx−LC-biotin, demonstrating that the fluorescence signal is specific for IbTx-binding sites. The latter experiment was performed with unfixed cells demonstrating potential utility in live cell applications where fixation treatments are to be avoided. Figure 8C,D shows results of a similar control experiment where IbTx−LC-biotin was simply omitted in the labeling procedure, again demonstrating specificity for the BK channel toxin. As an alternative to the use of StrAv, the experiment of Figure 8E,F shows that a commercially available monoclonal antibody, Alexa488-antibiotin antibody, is also effective as a secondary fluorescent reagent in visualizing IbTx−LC-biotin bound to BK channels expressed on the cell surface.

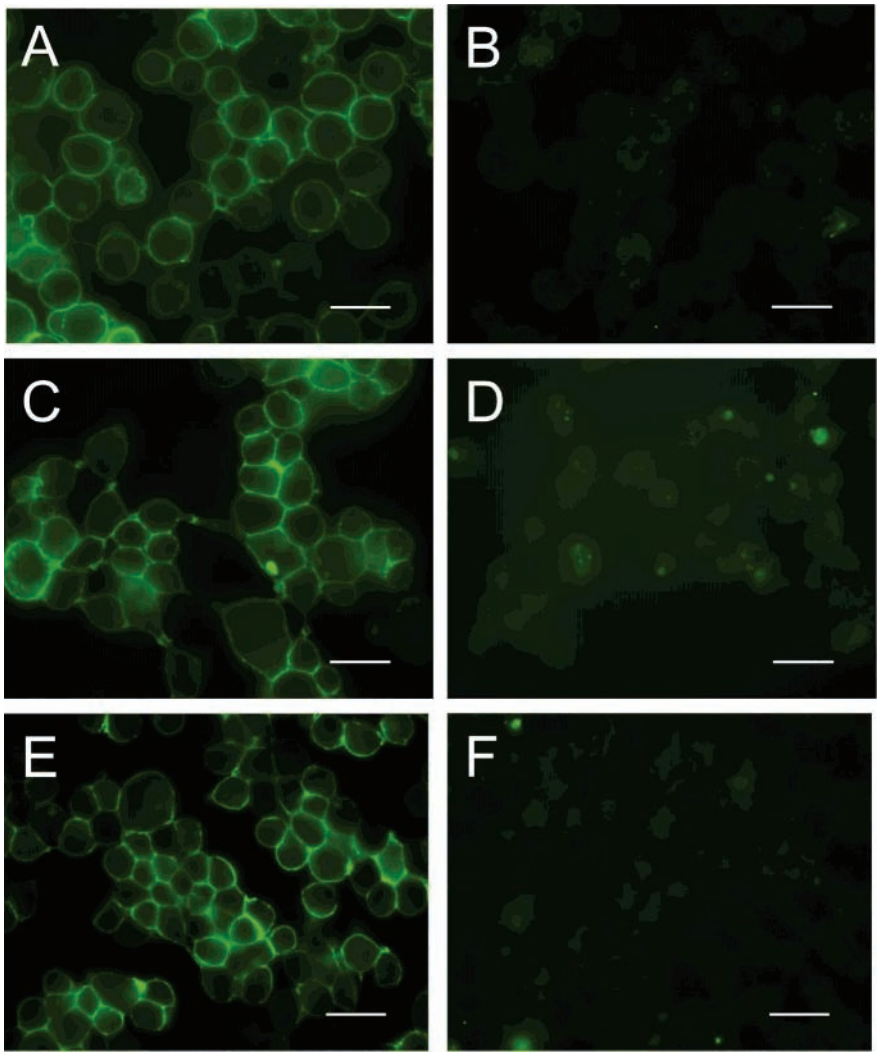

Figure 8. Specificity of fluorescence labeling by IbTx−LC-biotin assessed by various controls. (A, B) Live (unfixed) HEK293/HSlo cells after processing with 50 nM IbTx−LC-biotin and 3 μg/mL Alexa488-StrAv. Control coverslip in B was treated identically to A except that 5 μM IbTx-D19C-Acm was added before exposure to IbTx−LC-biotin. (C, D) HEK293/HSlo cells after processing with 50 nM IbTx−LC-biotin, 3 μg/mL Alexa488-StrAv, and fixation with 2% formaldehyde. Control coverslip in D was treated identically to C except that IbTx−LC-biotin was omitted. (E, F) HEK293/HSlo cells after processing with 50 nM IbTx−LC-biotin, 4 μg/mL Alexa488-antibiotin antibody, and fixation with 2% formaldehyde. Control coverslip in F was treated identically to E except that IbTX−LC-biotin was omitted. Cells were processed for microscopy and viewed with a 40× oil immersion objective as described in Experimental Procedures. Scale bar = 30 μm.

DISCUSSION

The growing inventory of natural K^+ channel peptide toxins discovered in venoms of insects, scorpions, spiders, sea anemones, cone snails, and snakes has motivated efforts to develop radioactive and fluorescent derivatives of these molecules for applications in biochemistry and neuroscience. K^+ channel toxins from scorpions are attractive candidates for probe development due to their small size (<40 residues) and selective affinity for particular members of the K^+ channel family. Peptide toxins and mutant toxin derivatives can be readily produced by synthetic gene technology and recombinant expression in *Escherichia coli* (Park et al., 1991; Koschak et al., 1997); however, this approach involves numerous steps required to express, cleave, and purify the recombinant toxins. Alternatively, numerous disulfide-linked toxins such as ChTx and IbTx have also been produced by automated peptide synthesis (e.g., Sugg et al., 1990; Toth et al., 1995). The latter methodology permits direct incorporation of non-native amino acids during linear synthesis of the peptide as illustrated here by substitution of Lys-ϵ-D-LC-biotin at position 19 of the IbTx sequence. Biotin tags or fluorescent labels may also be coupled to peptide toxins by appropriate chemical modification reactions [(e.g., alkylation of the thiol group of a spinster cysteine (Shimony et al., 1994)] after synthesis and oxidation of paired disulfides. However, a practical coupling strategy requires high-yield labeling reactions and efficient purification of the bioactive derivative. Improvements in biomolecular engineering, i.e., design, synthesis, and labeling of K^+ channel toxins, are needed to make these promising molecular tools more widely available to researchers in the field of ion channel biology.

Interesting findings previously reported with ChTx labeled with a biotin moiety at the N-terminus (Robitaille et al., 1993), IbTx randomly labeled with rhodamine red succinimidyl ester at native Lys residues (Jimenez-Gonzalez et al., 2003) or IbTx-D19C labeled with Alexa488 (Hafidi et al., 2005) warrant further development of ChTx and IbTx derivatives for fluorescence imaging applications in native cells and tissues. In this respect, the goal of the present work was to synthesize a derivative of IbTx with a biotin tag at a "backside" residue and to characterize its relevant activities under defined model conditions. The results indicate that synthetic IbTx−LC-biotin avidly binds to mammalian BK channels as demonstrated by

its blocking activity against rat muscle BK channels in planar bilayers (Figure 3) and human BK channels expressed in a cultured cell line (Figure 4).

Previous studies have shown that measured equilibrium constants for block and binding of charybdotoxin and IbTx are strongly dependent upon the ionic strength of the extracellular assay medium (Anderson et al., 1988; Garcia-Calvo et al., 1991; Vasquez et al., 1989; Koschak et al., 1997) and the association of particular isoforms of four known accessory beta subunits with the BK channel alpha subunit in native tissues (Hanner et al., 1997; Wallner et al., 1999; Giangiacomo et al., 2000; Meera et al., 2000). For example, when the BK channel is coexpressed with the β1 subunit, the dissociation rate of ChTx is slowed by ~10-fold (Hanner et al., 1997; Gianciacomo et al., 2000). Thus, the performance of IbTx−LC-biotin in particular imaging applications may be expected to be strongly dependent upon the cellular preparation and the specific conditions of labeling. In transfected HEK293 cells, we find that incubation of cells with 50 nM IbTx−LC-biotin is sufficient to obtain high-quality fluorescence imaging (Figure 8), but use of lower toxin concentrations may be possible. It may also be possible to further improve the specific fluorescence signal by exposing cells to a low concentration of IbTx−LC-biotin in combination with paxilline, an alkaloid that acts to enhance binding of scorpion toxins to BK channels by an allosteric mechanism (Knaus et al., 1994; Hanner et al., 1997; Koschak et al., 1997). The absolute affinity of a probe molecule for specific receptor sites is an important factor in fluorescence imaging, since the greater the difference between specific and nonspecific binding to cell membranes, the greater the signal-to-noise ratio in visualization of receptor localization.

Our results generally support the use of biotin-StrAv methodology as a feasible approach to toxin-based imaging and localization of K^+ channels. Placement of a biotin-tag with a long chain linker on backside residue 19 of IbTx preserves both specific binding to the BK channel and efficient access to two of the four biotin sites of StrAv. A potential advantage of this method is the ability to combine IbTx−LC-biotin with a wide array of detection methods accessible through commercially available conjugates of StrAv and avidin including numerous fluorophores, enzyme conjugates, nanogold particles, and quantum dots (Woldin et al., 1999; Haugland, 2002; Watson et al., 2003). Since fluorescent conjugates of StrAv typically contain multiple fluorophores per StrAv molecule (Panchuk-Voloshina et al. 1999), this detection method may provide greater sensitivity than IbTx probes directly coupled to a single fluorophore. The apparent restriction of IbTx−LC-biotin binding to one site on each of the two binding faces of the StrAv tetramer would be expected to limit or prevent 2D cross-linking of BK channels via multiple interactions with a single tetravalent StrAv molecule. The latter issue, also a problem with bivalent antibodies, may be of concern in situations where observation of natural clustering of BK channels is of special interest. In cellular preparations where StrAv-based secondary detection results in excessive background fluorescence, visualization of bound IbTx−LC-biotin with fluorescent anti-biotin antibody (Figure 8E) may provide a satisfactory alternative.

In summary, we have described synthesis of a novel biotin-derivative of IbTx that has high binding affinity for both mammalian BK channels and StrAv. The combination of IbTx−LC-biotin and Alexa488-StrAv can be used to image the surface distribution of BK channels on stably transfected HEK293 cells. Such images reveal a nonrandom, patch-like distribution of BK channels indicative of an endogenous mechanism for BK channel clustering. Further improvements in design, synthesis, and imaging protocols for scorpion toxin probes may be expected to enhance research on numerous aspects of the cell biology of K^+ channels.

ACKNOWLEDGMENT

This work was supported by a Scientist Development Award from the American Heart Association (0530204N) to J-P.B.; NIH Grant P01 NS42202 and a Grant-in-Aid from the American Heart Association (0150058N) to E.G.M.

Supporting Information Available: Supplementary Figure 1: Z-section series of a single HEK293/HSlo cell labeled with IbTx−LC-biotin and Alexa488-StrAv. Successive Z-sections of the cell can be viewed as a movie in avi format; supplementary Figure 2A−C: three-dimensional reconstruction of HEK293/HSlo cells labeled with IbTx−LC-biotin and Alexa488-StrAv. Rotation of the three-dimensional cell image can be viewed by playing the .avi files in a media viewer such as Windows Media Player or QuickTime Player. This material is available free of charge via the Internet at http://pubs.acs.org.

LITERATURE CITED

(1) Alioua, A., Mahajan, A., Nishimaru, K., Zarei, M. M., and Stefani, E. (2002) Coupling of s-Src to large conductance voltage- and Ca^{2+}-activated K^+ channels as a new mechanism of agonist-induced vasoconstriction. *Proc. Nat. Acad. Sci. U.S.A. 99*, 14560−14565.

(2) Anderson, C. S., MacKinnon, R., Smith, C., and Miller, C. (1988) Charybdotoxin block of single Ca^{2+}-activated K^+ channels: effects of channel gating, voltage, and ionic strength. *J. Gen. Physiol. 91*, 317−333.

(3) Beeton, C., Wulff, H., Singh, S., Botsko, S., Crossley, G., Gutman, G. A., Cahalan, M. D., Pennington, M., and Chandy, G. K. (2003) A novel fluorescent toxin to detect and investigate Kv1.3 channel up-regulation in chronically activated T lymphocytes. *J. Biol. Chem. 278*, 9928−9937.

(4) Bontems, F., Gilquin, B., Roumestand, Menez, A., and Toma, F. (1992) Analysis of side chain organization on a refined model of charybdotoxin: structural and functional implications. *Biochemistry 31*, 7756−7764.

(5) Candia, S., Garcia, M. L., and Latorre, R. (1992) Mode of action of iberiotoxin, a potent blocker of the large conductance Ca^{2+}-activated K^+ channel. *Biophys. J. 63*, 583−590.

(6) Cui, M., Shen, J., Briggs, J. M., Luo, X., Tan, X., Jiang, H., Chen, K., and Ji, R. (2001) Brownian dynamics simulations of the interaction between scorpion toxin Lq2 and potassium ion channel. *Biophys. J. 80*, 1659−1669.

(7) Doyle, D. A., Morais-Cabral, J., Pfuetzner, R. A., Kuo, A., Gulbis, J. M., Cohen, S. L., Chait, B. T., and MacKinnon, R. (1998) The structure of the potassium channel: molecular basis of K^+ conduction and selectivity. *Science 280*, 69−77.

(8) Eghbali, M., Toro, L., and Stefani, E. (2003) Diminished surface clustering and increased perinuclear accumulation of large conductance Ca^{2+}-activated K^+ channel in mouse myometrium with pregnancy. *J. Biol. Chem. 278*, 45311−45317.

(9) Favre, I., and Moczydlowski, E. (1999) Simultaneous binding of basic peptides at intracellular sites on a large conductance Ca^{2+}-activated K^+ channel. *J. Gen. Physiol. 113*, 295−320.

(10) Freitag, S., Le Trong, I., Klumb, L., Stayton, P. S., and Stenkamp, R. E. (1997) Structural studies of the streptavidin binding loop. *Protein Sci. 6*, 1157−1166.

(11) Galvez, A., Gimenez-Gallego, G., Reuben, J. P., Roy-Contancin, L. Feigenbaum, P., Kaczorowski, G. J., and Garcia, M. L. (1990) Purification and characterization of a unique, potent, peptidyl probe for the high conductance calcium-activated potassium channel from venom of the scorpion *Buthus tamulus*. *J. Biol. Chem. 265*, 11083−11090.

(12) Gao, Y.-D., and Garcia, M. L. (2003) Interaction of agitoxin2, charybdotoxin, and iberiotoxin with potassium channels: selectivity between voltage-gated and maxi-K channels. *Proteins: Struct. Funct. Genet. 52*, 146−154.

(13) Garcia-Calvo, M., Vazquez, J., Smith, M., Kaczorowski, G. J., and Garcia, M. L. (1991). Characterization of the solubilized

charybdotoxin receptor from bovine aortic smooth muscle. *Biochemistry 30*, 11157−11164.
(14) Giangiacomo, K. M., Garcia, M. L., and McManus, O. B. (1992) Mechanism of iberiotoxin block of the large-conductance calcium-activated potassium channel from bovine aortic smooth muscle. *Biochemistry 31*, 6719−6727.
(15) Giangiacomo, K. M., Sugg, E. E., Garcia-Calvo, M., Leonard, R. J., McManus, O. B., Kaczorowski, G. J., and Garcia, M. L. (1993) Synthetic charybdotoxin-iberiotoxin chimeric peptides define toxin binding sites on calcium-activated and voltage-dependent potassium channels. *Biochemistry 32*, 2363−2370.
(16) Giangiacomo, K. M., Fremont, V., Mullmann, T. J., Hanner, M., Cox, R. H., and Garcia, M. L. (2000) Interaction of charybdotoxin S10A with single maxi-K channels: kinetics of blockade depend on the presence of the β1 subunit. *Biochemistry 39*, 6115−6122.
(17) Goldstein, S. A. N., Pheasant, D. J., and Miller, C. (1994) The charybdotoxin receptor of a Shaker K^+ channel: peptide and channel residues mediating molecular recognition. *Neuron 12*, 1377−1388.
(18) Green, N. M. (1990) Avidin and streptavidin. *Methods Enzymol. 184*, 51−67.
(19) Gruber, H. J., Kada, Marek, M., and Kaiser, K. (1998) Accurate titration of avidin and streptavidin with biotin-fluorophore conjugates in complex, colored biofluids. *Biochim. Biophys. Acta 1381*, 203−212.
(20) Gulbis, J. M., and Doyle, D. A. (2004) Potassium channel structures: do they conform? *Curr. Opin. Struct. Biol. 14*, 440−446.
(21) Gutman, G. A., Chandy, K. G., Adelman, J. P., Aiyar, J., Bayliss, D. A., Clapham, D. E., Covarriubias, M., Desir, G. V., Furuishi, K., Ganetzky, B., Garcia, M. L., Grissmer, S., Jan, L. Y., Karschin, A. Kim, D., Kuperschmidt, S., Kurachi, Y., Lazdunski, M., Lesage, F., Lester, H. A., McKinnon, D., Nichol, C. G., O'Kelly, I., Robbins, J., Robertson, G., Rudy, B., Sanguinetti, M., Seino, S., Stuehmer, W., Tamkun, M. M., Vandenberg, C. A., Wei, A., Wulff, H., and Wymore, R. S. (2003) International Union of Pharmacology. XLI. Compendium of voltage-gated ion channels: potassium channels. *Pharmacol. Rev. 55*, 583−586.
(22) Hafadi, A., Beurg, M., and Dulon, D. (2005) Localization and developmental expression of BK channels in mammalian cochlear hair cells. *Neuroscience 130*, 475−484.
(23) Hanner, M., Schmalhofer, W. A., Munujos, P., Knaus, H.-G., Kaczorowski, G. J., and Garcia, M. L. (1997) The β subunit of the high conductance calcium-activated potassium channel contributes to the high-affinity receptor for charybdotoxin. *Proc. Natl. Acad. Sci. U.S.A. 94*, 2853−2858.
(24) Haugland, R. P. (2002) *Handbook of Fluorescent Probes and Research Products*, 9th ed., Molecular Probes, Eugene, OR.
(25) Hendrickson, W. A., Pähler, A., Smith, J. L., Satow, Y., Merritt, E. A., and Phizackerley, R. P. (1989) Crystal structure of core streptavidin determined from multiwavelength anomalous diffraction of synchrotron radiation. *Proc. Natl. Acad. Sci. U.S.A. 86*, 2190−2194.
(26) Jimenez-Gonzalez, C., McLaren, G. J., and Dale, N. (2003) Development of Ca^{2+}-channel and BK-channel expression in embryos and larvae of *Xenopus laevis*. *Eur. J. Neurosci. 18*, 2175−2187.
(27) Johnson, B. A., and Sugg, E. E. (1992) Determination of the three-dimensional structure of iberiotoxin in solution by ^{1}H nuclear magnetic resonance spectroscopy. *Biochemistry 31*, 8151−8159.
(28) Kada, G., Falk, and Gruber, H. J. (1999) Accurate measurement of avidin and streptavidin in crude biofluids with a new, optimized biotin-fluorescein conjugate. *Biochim. Biophys. Acta 1427*, 33−43.
(29) Knaus, H.-G., McManus, O. B., Lee, S. H., Schmalhofer, W. A., Garcia-Calvo, M., Helms, L. M. H., Sanchez, M., Giangiacomo, K., Reuben, J. P., Smith, A. B., Kaczorowski, G. J., and Garcia, M.. L. (1994) Tremorgenic indole alkaloids potently inhibit smooth muscle high-conductance calcium-activated potassium channels. *Biochemistry 33*, 5819−5928.
(30) Knaus, H.-G., Schwarzer, C., Koch, R. O. A., Eberhart, A., Kaczorowski, G. J., Glossman, H., Wunder, F., Pongs, O., Garcia, M. L., and Sperk, G. (1996) Distribution of high-conductance Ca^{2+}-activated K^+ channels in rat brain: targeting to axons and nerve terminals. *J. Neurosci. 16*, 955−963.
(31) Koschak, A., Koch, R. O., Liu, J., Kaczorowski, G. J., Reinhart, P. H., Garcia, M. L., and Knaus, H.-G. (1997) [^{125}I]Iberiotoxin-D19Y/Y36F, the first selective, high specific activity radioligand for high-conductance calcium-activated potassium channels. *Biochemistry 36*, 1943−1952.
(32) Liu, G., Shi, J., Yang, L., Cao, L., Park, S. M., Cui, J., and Marx, S. O. (2004) Assembly of a Ca^{2+}-dependent BK channel signaling complex by binding to β2 adrendergic receptor. *EMBO J. 23*, 2196−2205.
(33) Lucchesi, K., Ravindran, A., Young, H., and Moczydlowski, E. (1989) Analysis of the blocking activity of charybdotoxin homologues and iodinated derivatives against Ca^{2+}-activated K^+ channels. *J. Membr. Biol. 109*, 269−281.
(34) MacKinnon, R. (2003) Potassium channels. *FEBS Lett. 555*, 62−65.
(35) MacKinnon, R., Cohen, S. L., Kuo, A., Lee, A., and Chait, B. T. (1998) Structural conservation in prokaryotic and eukaryotic potassium channels. *Science 280*, 106−109.
(36) Meera, P., Wallner, M., and Toro, L. (2000) A neuronal β subunit (KCNMB4) makes the large conductance, voltage- and Ca^{2+}-activated K^+ channel resistant to charybdotoxin and iberiotoxin. *Proc. Natl. Acad. Sci. U.S.A. 97*, 5526−5567.
(37) Miller, C. (1995) The charybdotoxin family of K^+ channel-blocking peptides. *Neuron 15*, 5−10.
(38) Miller, C., Moczydlowski, E., Latorre, R., and Phillips, M. (1985) Charybdotoxin, a protein inhibitor of single Ca^{2+}-activated K^+ channels from mammalian skeletal muscle. *Nature 313*, 316−318.
(39) Moczydlowski, E. (1992) Analysis of drug action at single-channel level. *Methods Enzymol. 207*, 791−806.
(40) Mullmann, T. J., Munojos, P., Garcia, M. L., and Giangiacomo, K. M. (1999) Electrostatic mutants in iberiotoxin as a unique tool for probing the electrostatic structure of the maxi-K channel outer vestibule. *Biochemistry 38*, 2395−2402.
(41) Orio, P., Rojas, P., Ferreira, G., and Latorre, R. (2002) New disguises for an old channel: maxiK channel β-subunits. *News Physiol. Sci. 17*, 156−161.
(42) Panchuk-Voloshina, N., Haugland, R. P., Bishop-Stewart, J., Bhalgat, M. K., Millard, P. J., Mao, F., Leung, W.-Y., and Haugland, R. P. (1999) Alexa dyes, a series of new fluorescent dyes that yield exceptionally bright, photostable conjugates. *J. Histochem. Cytochem. 47*, 1179−1188.
(43) Park, C.-S., Hausdorff, S., and Miller, C. (1991) Design, synthesis, and functional expression of a gene for charybdotoxin, a peptide blocker of K^+ channels. *Proc. Natl. Acad. Sci. U.S.A. 88*, 2046−2050.
(44) Pragl, B., Koschak, A., Trieb, M., Obermair, G., Kaufmann, W. A., Gerster, U., Blanc, E., Hahn, C., Prinz, H., Schütz, G., Darbon, H., Gruber, H. J., and Knaus, H.-G. (2002) Synthesis, characterization, and application of Cy-dye and Alexa-dye-labeled hongotoxin$_1$ analogues: the first high affinity fluorescence probes for voltage-gated K^+ channels. *Bioconjugate Chem. 13*, 416−425.
(45) Renisio, J.-G., Lu, Z., Blanc, E., Jin, W., Lewis, J. H., Bornet, O., and Darbon, H. (1999) Solution structure of potassium channel-inhibiting scorpion toxin Lq2. *Proteins: Struct. Funct. Genet. 34*, 417−426.
(46) Robitaille, R., Garcia, M. L., Kaczorowski, G. J., and Charlton, M. P. (1993) Functional colocalization of calcium and calcium-gated potassium channels in control of transmitter release. *Neuron 11*, 645−655.
(47) Rodriguez de la Vega, R., Merino, E., Becerril, B., and Possani, L. (2003) Novel interactions between K^+ channels and scorpion toxins. *Trends Pharmacol. Sci. 24*, 222−227.
(48) Schroeder, N., Mullmann, T. J., Schmalhofer, W. A., Gao, Y.-D., Garcia, M. L., Giangiacomo, K. M. (2002) Glycine 30 in iberiotoxin is a critical determinant of its specificity for maxi-K versus K_V channels. *FEBS Lett. 527*, 298−302.
(49) Schütz, G. J., Pasushenko, V. P., Gruber, H. J., Knaus, H.-G., Pragl, B., and Schindler, H. (2000) 3D imaging of individual ion channels in live cells at 40 nm resolution. *Single Mol. 1*, 25−31.
(50) Shimony, E., Sun, T., Kolmakova-Partensky, L., and Miller, C. (1994) Engineering a uniquely reactive thiol into a cysteine-rich peptide. *Protein Eng. 7*, 503−507.
(51) Smith, C., Phillips, M., and Miller, C. (1986) Purification of charybdotoxin, a specific inhibitor of the high-conductance Ca^{2+}-activated K^+ channel. *J. Biol. Chem. 261*, 14607−14613.

(52) Stampe, P., Kolmakova-Partensky, L., and Miller, C. (1994) Intimations of K^+ channel structure from a complete functional map of the molecular surface of charybdotoxin. *Biochemistry 33*, 443−450.

(53) Strobaek, D., Christophersen, P., Holm, N. R., Moldt, P., Ahring, P. K., Johansen, T. E., and Olesen, S.-P. (1996) Modulation of the Ca^{2+}-dependent K^+ channel, hslo, by the substituted diphenylurea NS1608, paxilline, and internal Ca^{2+}. *Neuropharmacology 35*, 903−914.

(54) Strong, P. N., Clark, G. S., Armugam, A., De-Allie, F. A., Joseph, J. S., Yemul, V., Deshpande, J. M., Kamat, R., Gadre, S. V., Gopalakrishnakone, P., Kini, R. M., Owen, D. G., and Jeyaseelan, K. (2001). Tamulustoxin: a novel potassium channel blocker from the venom of the Indian red scorpion *Mesobuthus tamulus*. *Arch. Biochem. Biophys. 385*, 138−144.

(55) Sugg, E. E., Garcia, M. L., Reuben, J. P., Patchett, A. A., and Kaczorowski, G. J. (1990) Synthesis and structural characterization of charybdotoxin, a potent peptidyl inhibitor of the high conductance Ca^{2+}-activated K^+ channel. *J. Biol. Chem. 265*, 18745−18748.

(56) Sun, T., Aghazadeh, A., and Miller, C. (1994) High-level expression and functional reconstitution of Shaker K^+ channels. *Biochemistry 33*, 9992−9999.

(57) Tenenholz, T. C., Klenk, K. C., Matteson, D. R., Blaustein, M. P., and Weber, D. J. (2000) Structural determinants of scorpion toxin affinity: the charybdotoxin (α-KTX) family of K^+ channel blocking peptides. *Rev. Phys. Biochem. Pharmacol. 140*, 135−180.

(58) Toro, L., Wallner, M., Meera, P., and Tanaka, Y. (1998) Maxi-K_{Ca}, a unique member of the voltage-gated K channel superfamily. *News Physiol. Sci. 13*, 112−117.

(59) Toth, G. K., Pataricza, J., Janaky, T. Mak, M., Zarandi, M., Papp, J. G., and Penke, B. (1995) Synthesis of two peptide scorpion toxins and their use to investigate the aortic tissue regulation. *Peptides 16*, 1167−1172.

(60) Tytgat, J., Chandy, G., Garcia, M. L., Gutman, G. A., Martin-Eauclaire, M.-F., van der Walt, J. J., and Possani, L. D. (1999) A unified nomenclature for short-chain peptides isolated from scorpion venoms: α-KTx molecular subfamilies. *Trends Pharmacol. Sci. 20*, 444−447.

(61) Vazquez, J., Feigenbaum, P, Katz, G., King, V. F., Reuben, J. P., Roy-Contancin, L., Slaughter, R. S., Kaczorowski, G. J., and Garcia, M. L. (1989) Characterization of high affinity binding sites for charybdotoxin in sarcolemmal membranes from bovine aortic smooth muscle. *J. Biol. Chem. 264*, 20902−20909.

(62) Wallner, M., Meera, P., Ottolia, M., Kaczorowski, G. J., LaTorre, R., Garcia, M. L., Stefani, E., and Toro, L. (1995) Characterization of and modulation by a β-subunit of a human maxi K_{Ca} channel cloned from myometrium. *Recept. Channels 3*, 185−199.

(63) Wallner, M., Meera, P., and Toro, L. (1999) Molecular basis of fast inactivation in voltage and Ca^{2+}-activated K^+ channels: a transmembrane β-subunit homolog. *Proc. Nat. Acad. Sci. U.S.A. 96*, 4137−4142.

(64) Watson, A., Wu, X., and Bruchez, M. (2003) Lighting up cells with quantum dots. *Biotechniques 34*, 296−303.

(65) Woldin, C. N., Hing, F. S., Lee, J., Pilch, P. F, and Shipley G. G. (1999) Structural studies of the detergent-solubilized and vesicle-reconstituted insulin receptor. *J. Biol. Chem. 274*, 34981−34992.

(66) Yu, S. P., Kerchner, G. A. (1998) Endogenous voltage-gated potassium channels in human embryonic kidney (HEK293) cells. *J. Neurosci. Res. 52*, 612−617.

(67) Yu, L., Sun, C., Song, D., Shen, J., Xu, N., Gunasekera, A., Hajduk, P. J., and Olejniczak, E. T. (2005) Nuclear magnetic resonance structural studies of a potassium channel-charybdotoxin complex. *Biochemistry 44*, 15834−15841.

(68) Zhu, S., Huys, I., Dyason, K., Verdonck, F., and Tytgat, J. (2004) Evolutionary trace analysis of scorpion toxins specific for K-channels. *Protein Struct. Funct. Bioinform. 54*, 361−370.

BC060002U

Diethylenetriaminepentaacetic Acid−Gadolinium (DTPA-Gd)-Conjugated Polysuccinimide Derivatives as Magnetic Resonance Imaging Contrast Agents

Ha Young Lee,[†,‡] Hye Won Jee,[‡] Sung Mi Seo,[‡] Byung Kook Kwak,[§] Gilson Khang,[†] and Sun Hang Cho*[,‡]

Department of Advanced Organic Materials Engineering, Chonbuk National University, Jeonju, Jeonbuk, Republic of Korea, Nanobiomaterials Laboratories, Korea Research Institute of Chemical Technology, Daejeon, Republic of Korea, and College of Medicine, Chung-Ang University, Seoul, Republic of Korea. Received January 23, 2006; Revised Manuscript Received March 19, 2006

Biocompatible polysuccinimide (PSI) derivatives conjugated with diethylenetriaminepentaacetic acid gadolinium (DTPA-Gd) were prepared as magnetic resonance imaging (MRI) contrast agents. In this study, we synthesized PSI derivatives incorporating methoxy-poly(ethylene glycol) (mPEG) as hydrophilic ligand, hexadecylamine as hydrophobic ligand, and DTPA-Gd as contrast agent. PSI was synthesized by the polycondensation polymerization of aspartic acid. All the synthesized materials were characterized by proton nuclear magnetic resonance (^{1}H NMR). Critical micellization concentrations were determined using fluorescent probes (pyrene). Micelle size and shape were measured by electro-photometer light scattering (ELS) and atomic force microscopy (AFM). The formed micelle size ranged from 100 to 300 nm. The T1-weighted MR images of the phantom prepared with PSI−mPEG-C_{16}−(DTPA-Gd) were obtained in a 3.0 T clinical MR imager, and the conjugates showed a great potential as MRI contrast agents.

INTRODUCTION

Magnetic resonance imaging (MRI) utilizes a strong magnetic field to image the human body (*1*). Recently, MRI contrast agents have been used specifically to improve the image contrast between normal and pathological tissue. These MRI contrast agents must have contrast enhancing ability, high stability, and favorable pharmacokinetic properties (*2*).

Several poly(amino acid) derivatives have been investigated as a type of delivery system (*3*, *4*). Particularly, polysuccinimide (PSI) is one of the most promising particle carriers since it was demonstrated to possess suitable physicochemical characteristics for development of macromolecular prodrugs, due to the biocompatibility, biodegradability, and the ease of synthesis and functionalization (*5*−*11*).

Micellization of biologically active substances prepared by advanced bioconjugation technology is a useful method to increase the solubility, stability, and bioavailability of lipophilic drugs and nutrients (*12*, *13*). The rational design of polymeric bioconjugates represents a key issue to achieve derivatives that have the desired physicochemical and biopharmaceutical properties. Therefore, the introduction a of specific pendant group in the polymer backbone is often carried out to modify the carrier properties (*14*−*16*). Especially, the polymeric micelle system can offer some advantages such as wide applicability to drugs and small particle size (*17*−*19*).

Polymeric micelles having hydrophilic/hydrophobic groups were prepared by conjugating a hydrophilic methoxy-poly (ethylene glycol) (mPEG) and a hydrophobic group to PSI, a biodegradable polymer, that is known to be excreted by the kidney (*20*, *21*). The size of micelles with different molecular weights of mPEG and lengths of hydrophobic chains was measured by electro-photometer light scattering (ELS).

We also attached an MRI contrast agent, Gd-DTPA, to the polymeric micelles, PSI. Diethylenetriaminepentaacetic acid (DTPA) is a very efficient chelating agent for lanthanide metal ions. Due to its contrast enhancement and high stability in vivo, a DTPA complex has been clinically used as a contrast agent in MRI (*22*, *23*), but because this DTPA-Gd complex has a low molecular weight and is removed rapidly from the blood pool, the study has been directed toward stable DTPA-Gd complexes that can circulate for a longer time in blood (*24*, *25*).

In this study, we synthesized PSI−mPEG-C_{16}−(DTPA-Gd) which formed a micelle. The size diameter of the micelles was 100−300 nm which is suitable for a particle carrier to be well incorporated into the internal organs (*26*, *27*). Furthermore, we investigated the potential of PSI−mPEG-C_{16}−(DTPA-Gd) as a MRI contrast agent by an MRI test of the phantom.

EXPERIMENTAL PROCEDURES

Materials. D,L-Aspartic acid and hexadecylamine were purchased from Aldrich Co., Milwaukee, WI. Methoxy-poly-(ethylene glycol)-amine [mPEG-NH_2, number-average molecular weight (M_n) ≈ 5000] was purchased from Fluka, Buchs, Switzerland. Reagents for DTPA preparation were obtained from Fluka and Aldrich. Phosphoric acid, sulfolane, *N*,*N*-dimethylformamide (DMF), methyl alcohol (MeOH), and diethyl ether were commercially available and were used without further purification. Omniscan was purchased from Guerbet Co., Germany.

Synthesis of Polysuccinimide (PSI). Polysuccinimide was synthesized by a polycondensation reaction. A suspension of D,L-aspartic acid (25 g, 0.188 mol) and phosphoric acid (9.4 mmol) in sulfolane (80 g) was stirred at 160 °C under a nitrogen atmosphere. After 24 h, the reaction solution was precipitated by into MeOH. PSI was filtered, washed with MeOH, and dried under vacuum.

Synthesis of Poly(succinimide-ethylene glycol) (PSI−mPEG). A solution of mPEG-NH_2 (0.1×10^{-4} mol) in DMF (5 mL) was added dropwise to a solution of PSI (2.5×10^{-4}

* To whom correspondence should be addressed. Tel: + 82-42-860-7222. Fax: + 82-42-860-7228. E-mail: shcho@krict.re.kr.
† Chonbuk National University.
‡ Korea Research Institute of Chemical Technology.
§ Chung-Ang University.

10.1021/bc060014f CCC: $33.50 © 2006 American Chemical Society
Published on Web 05/02/2006

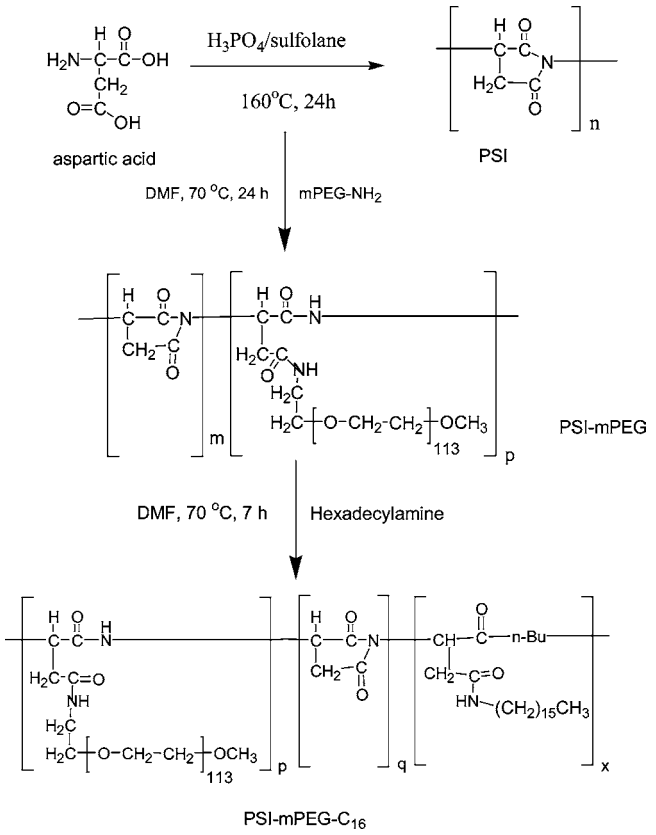

Figure 1. The overall synthetic scheme of PSI−mPEG-C_{16} from poly(aspartic acid).

mol) in DMF (50 mL). The mixture was stirred at 70 °C, under a nitrogen atmosphere. After 24 h, the reaction solution was precipitated and filtered with ethyl ether for removal of DMF and unreacted materials. The filtered PSI−mPEG was washed with ether and dried under vacuum.

Synthesis of PSI−mPEG-C_{16}. A solution of hydrophobic ligand, hexadecylamine (2×10^{-4} mol), in DMF (5 mL) was dropped to a solution of PSI−mPEG (2.5×10^{-4} mol) in DMF (30 mL). The mixture was stirred at 70 °C under a nitrogen atmosphere. After 7 h, the reaction solution was precipitated and filtered with ethyl ether. The filtered PSI−mPEG-C_{16} was washed with ethyl ether and dried under vacuum. The distribution of micelle size was experimentally evaluated.

Synthesis of PSI−mPEG-C_{16}−(DTPA-Gd). Lysine-DTPA *tert*-butyl ester was prepared according to the method reported in the literature (*22*). The solution of DTPA (3.75×10^{-4} mol) in DMF (5 mL) was added dropwise to a solution of PSI−mPEG-C_{16} (2.5×10^{-4} mol) in DMF (20 mL). The mixture was stirred at room temperature. After 18 h, ethyl ether was added. The precipitate was filtered, washed with ethyl ether, and dried under vacuum. The dried residue was dissolved in formic acid and stirred at 100 °C to perform the deprotection of *tert*-butyl group, according to the literature (*1*). After 3−5 h, the reaction solution was evaporated under vacuum condition. The residue was dissolved in water and stirred at room temperature for 3 h. Thereafter, the mixture was filtered and lyophilized.

To support gadolinium in PSI−mPEG-C_{16}-DTPA, a solution of $GdCl_3$ (1.5×10^{-3} mol) in water (5 mL) was added dropwise to a solution of PSI−mPEG-C_{16}−DTPA (1.5×10^{-3} mol) in water (30 mL), maintaining the solution mixture at pH 7−8. After 1 h, the reaction mixture containing PSI−mPEG-C_{16}−(DTPA-Gd) was precipitated by addition of acetonitrile and was filtered. The filtered solid was washed with ethyl ether and dried under vacuum.

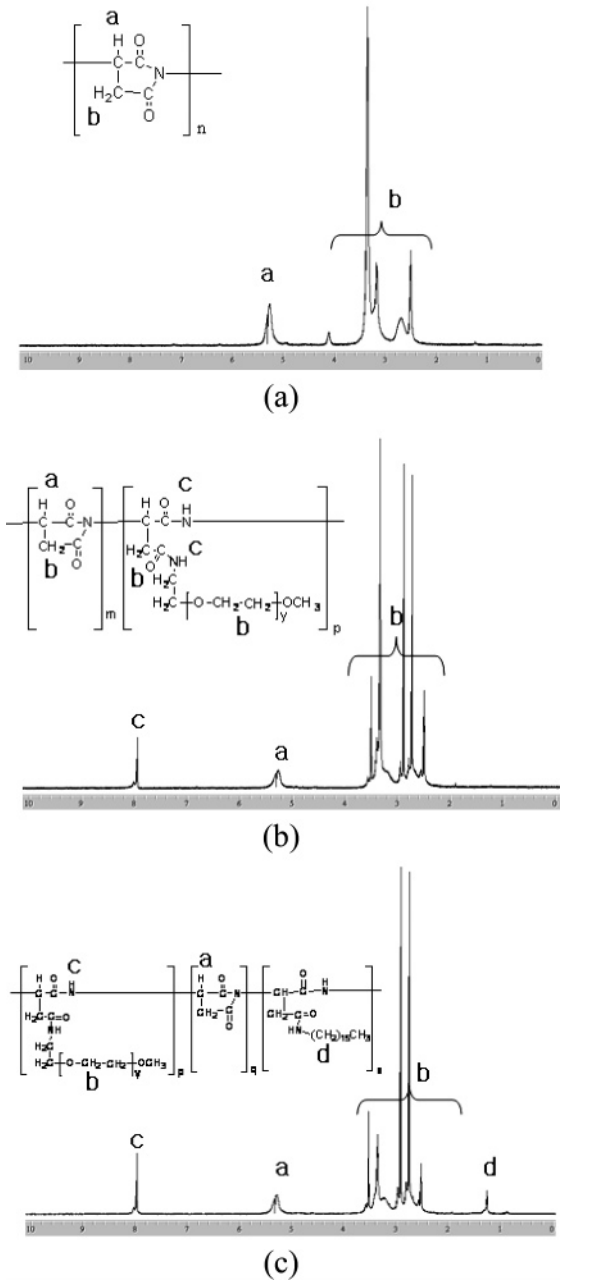

Figure 2. ^{1}H NMR spectra of (a) PSI, (b) PSI−mPEG, and (C) PSI−mPEG-C_{16}.

Table 1. Degree of Derivatization (DD) of mPEG and C_{16}

sample	mPEG DD (mol %)	C_{16} DD (mol %)
PSI−mPEG	13.5	-
PSI−mPEG- C_{16}	14.7	1.37

Characterization Analysis. The molecular weight of PSI was confirmed by GPC ((PL-GPC220, Polymer Laboratory, England) analysis. GPC had two columns (10 μm, MIXED-B $\times$2. 50 nm), and DMF (Aldrich) was used as mobile phase. Polystyrene (Showa Denko, Japan) was used as the standard sample. The flow rate was 1 mL/min. The results of polymerization were confirmed by ^{1}H NMR (Bruker 300, 500 MHz). Dimethyl sulfoxide (DMSO, Aldrich) was used as solvent. The size of micelles and shape were confirmed by ELS (ELS-8000, Otsuka Electronics, Japan) and AFM (Nanoscope IV). Also, Gd incorporation and Gd content were confirmed by EA, EDS, and ICP-AES. Fluorescence studies were carried out using a F-4500 fluorescence spectrophotometer (Hitachi Co. Ltd., Japan).

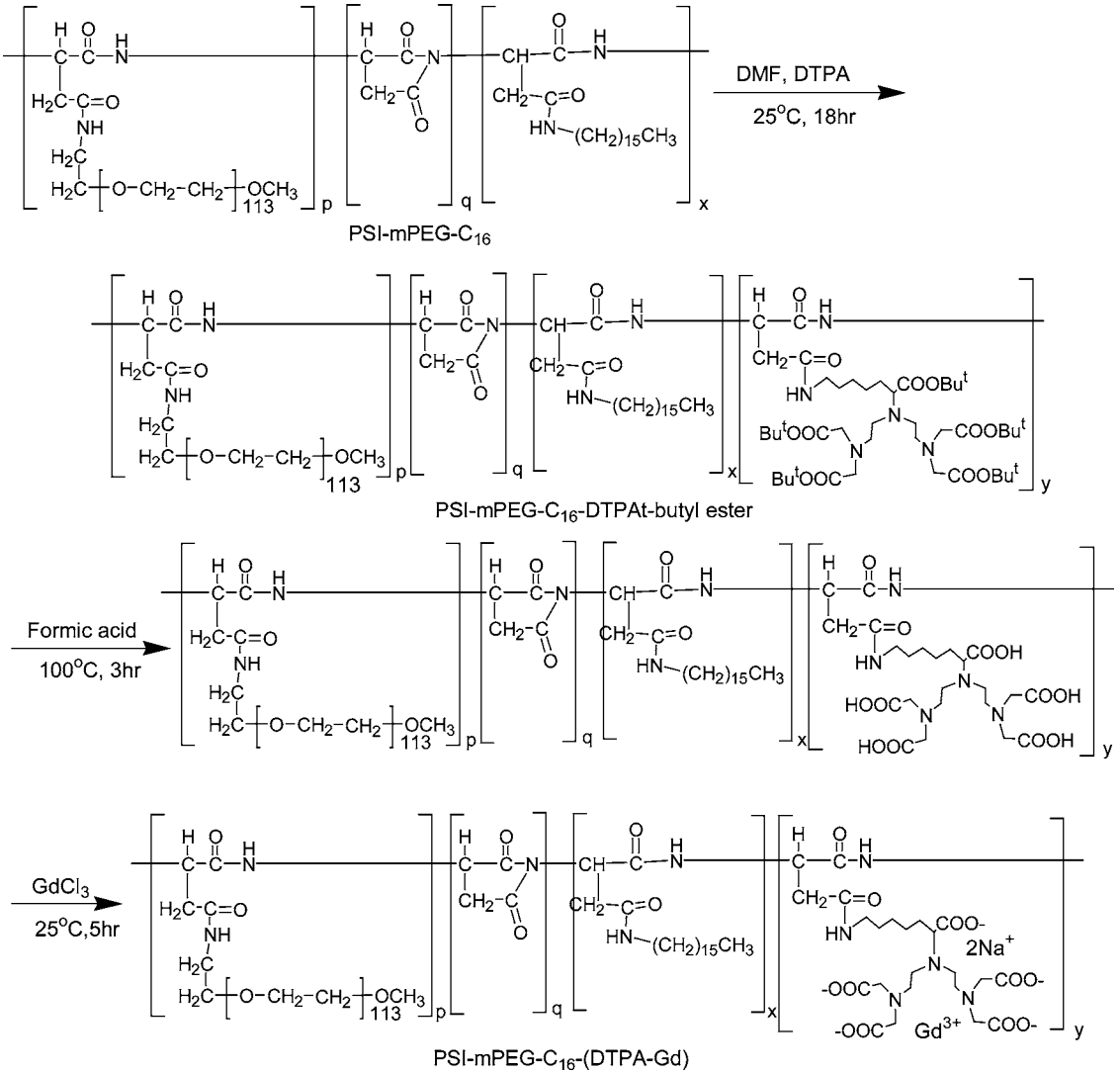

Figure 3. The overall synthetic scheme of PSI−mPEG-C_{16}−(DTPA-Gd) from PSI−mPEG-C_{16}.

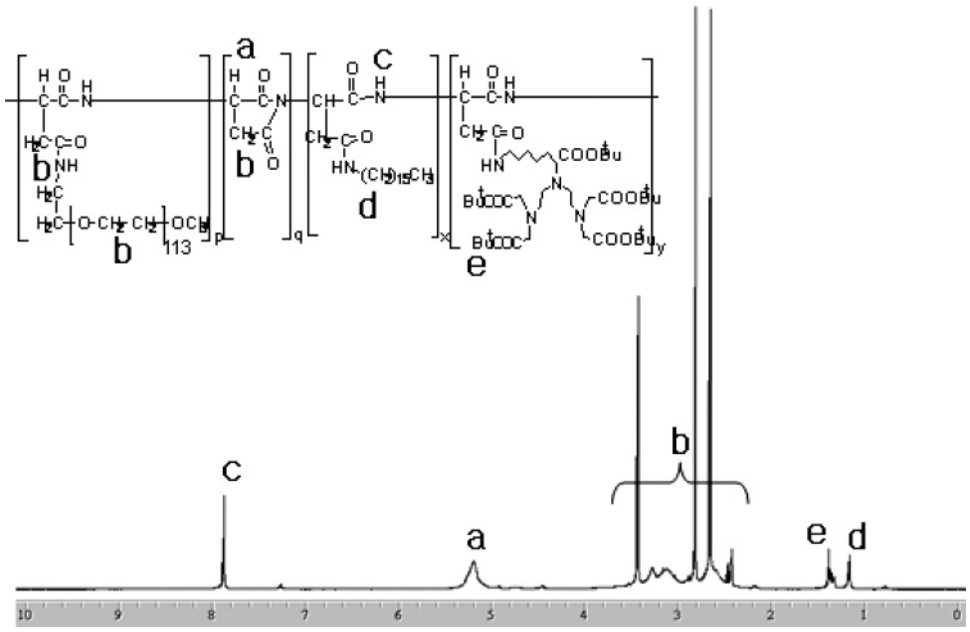

Figure 4. ^{1}H NMR spectrum of PSI−mPEG-C_{16}−DTPA *tert*-butyl ester.

Table 2. Elemental Analysis of Complex

complex	element	elemental anal. average (%)
PSI-mPEG-C_{16}−DTPA	nitrogen	8.911348
	carbon	44.71717
	hydrogen	6.167405
PSI−mPEG-C_{16}−(DTPA-Gd)	nitrogen	4.997967
	carbon	22.12623
	hydrogen	2.562378

In Vitro Contrast Effect Measurement. In vitro MR imaging test was performed with a 3.0T magnet at Philips Achieva 3.0T MRI (Philips Co., Netherlands). The T1-weighted MR images of the prepared compounds and a commercially available contrast agent, Omniscan, were obtained. MR images were taken with different concentrations of Gd solution (1×10^{-3} M Gd/L to 5×10^{-6} M Gd/L). The experimental condition was as follows: TR (recycle time) = 9.6 ms, TE (echo delay time) = 4.6 ms, flip angle: 8.0, field of view: 10×5 cm^2.

RESULTS AND DISCUSSION

Synthesis and Characterization of PSI−mPEG-C_{16}. To prepare the micelle-formed MRI contrast agent with Gd, at first, PSI, PSI−mPEG, and PSI−mPEG-C_{16} were sequentially synthesized following the literature (*28*). The overall synthetic route of PSI−mPEG-C_{16} is shown in Figure 1. PSI was synthesized by the polycondensation polymerization of aspartic acid. The yield and weight average molecular weight of PSI were 80% and 21000 by GPC measurement.

^{1}H NMR spectra of PSI, PSI−mPEG, and PSI−mPEG-C_{16} are shown in Figure 2a−c. In the PSI spectra, the signals at 5.04 ppm were assigned to the methyne proton (a) of the repeating succinimide unit and the signals at 2.5−3.5 ppm were assigned to the methylene protons (b) (*29*).

The degree of derivatization (DD) of PEG was determined by ^{1}H NMR and was calculated by comparing the integral of the NH peak at δ 7.9 that appears during the opening of the ring when being combined with PEG to the integral of the peak at δ 5.04 assigned to protons that belong to the PSI unit.

The DD of C_{16} was calculated by comparing the integral of the CH_2 peak at δ 1.2 of hexadecylamine to the integral of the peak at δ 5.04 to protons that belong to the PSI unit (*28*). The DD values of PSI−mPEG and PSI−mPEG-C_{16} are reported in Table 1.

Synthesis and Characterization of PSI−mPEG-C_{16}−(DTPA-Gd). The overall synthetic route of PSI−mPEG-C_{16}−(DTPA-Gd) from PSI−mPEG-C_{16} is shown in Figure 3. DTPA used as a chelating agent was combined with PSI−mPEG-C_{16}, and Gd was incorporated into the complex. Figure 4a,b shows ^{1}H NMR analysis data of PSI−mPEG-C_{16}−DTPA and PSI−mPEG-C_{16}−(DTPA-Gd). These spectra show the existence of a *tert*-butyl peak at 1.2−1.8 ppm before formic acid treatment. Incorporation of Gd into the polymer chain was confirmed by EDS (energy dispersive spectroscopy) analysis and EA (elemental analysis) data. Table 2 showed that the content of C, H, N decreased after incorporation of Gd. Figure 5 showed that the peak of Gd appeared after incorporation of Gd. The content of Gd was measured by ICP (Table 3). The results showed that a moderately consistent amount of Gd was incorporated in the polymer from two different batches, because the binding site of PSI involved in the conjugation of DTPA was limited.

Critical Micelle Concentration (CMC). The CMC of PSI−mPEG, PSI−mPEG-C_{16}, and PSI−mPEG-C_{16}-(DTPA-Gd) were determined using pyrene emission (*30, 31*). The concentrations of sample solution were varied from 1×10^{-5} to 1 mg/mL. The ratio I_3/I_1 of the intensities of the first ($\lambda_1 \approx 335$ nm) and the third ($\lambda_3 \approx 338$ nm) vibronic band is a sensitive measure for pyrene. This ratio increases with increasing hydrophobicity in the core because pyrene is expected to be distributed in hydrophobic regions of a self-organized system in solution due to low water solubility. Figure 6 shows the fluorescence emission spectra of pyrene incorporated into PSI−mPEG, PSI−mPEG-C_{16}, and PSI−mPEG-C_{16}−(DTPA-Gd) in water, respectively. The ratio I_3/I_1 increases rapidly, indicating that interactions between pyrene and the hydrophobic core are occurring and pyrene is in the micellar core. The critical micelle concentration (CMC) was determined by the interception of two straight lines. This CMC data indicate that the CMC values increase with increasing hydrophilic groups such as PEG and DTPA-Gd and that all prepared copolymers form micelles.

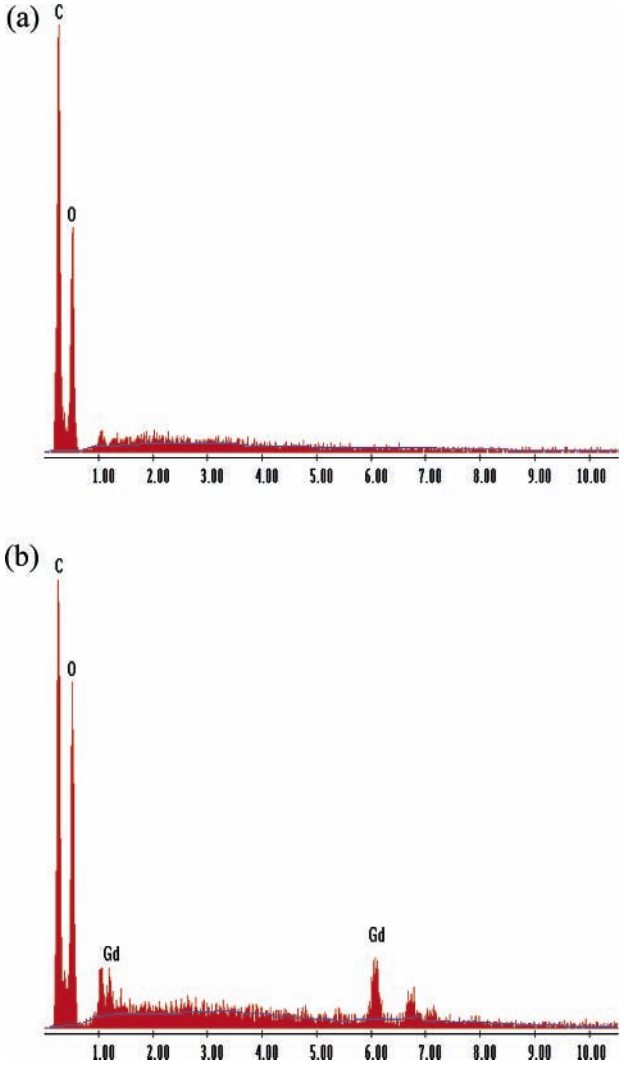

Figure 5. The analysis of gadolinium chelating measured by EDS: (a) PSI−mPEG-C_{16}−DTPA, (b) PSI−mPEG-C_{16}−(DTPA-Gd).

Table 3. Concentration Analysis of Gadolinium in Final Product by Inductively Coupled Plasma−Atomic Emission Spectrometer (ICP-AES)

DTPA content ratio of final product	gadolinium concentration (%)
batch 1	29
batch 2	26.9

Size Distribution. The size effect of micelles with different molecular weights of mPEG is shown in Figure 7. This result shows that the size of micelles is decreased as the molecular weight is increased. The decrease in micelle size could be due to increased hydrophilicity when more mPEG units are added.

The size effect of micelle with the length of alkyl chain is shown in Figure 8. This result showed that the size of micelles increased as the length of hydrophobic chain increased. Figure

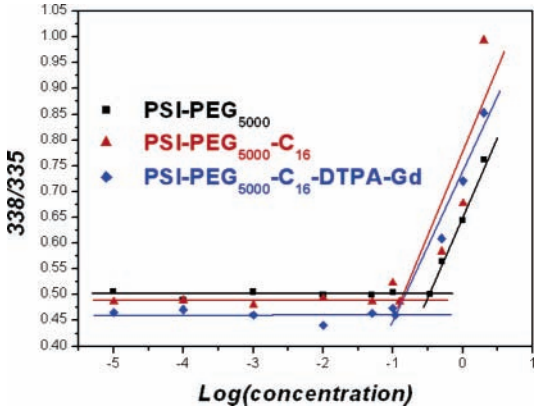

Figure 6. Change of intensity ratio (I_{338}/I_{335}) versus the concentration of PSI−mPEG, PSI−mPEG-C_{16},and PSI−mPEG-C_{16}−(DTPA-Gd).

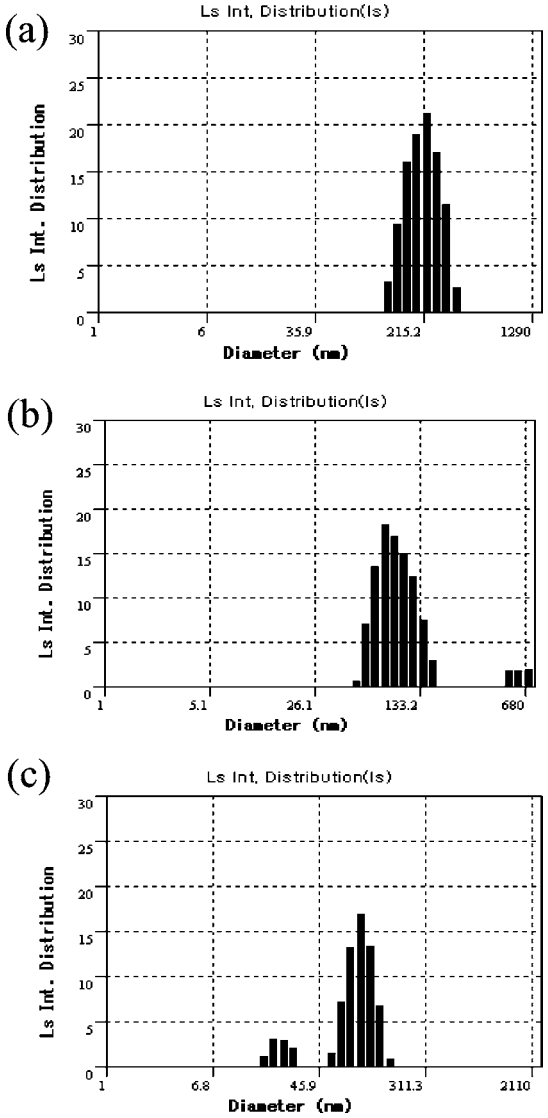

Figure 7. The size of micelles with different molecular weight of mPEG by ELS analysis: (a) PSI−$mPEG_{2000}$ micelles average size: 212.3 nm, (b) PSI−$mPEG_{5000}$ micelles average size: 129.3 nm, and (c) PSI−$mPEG_{10000}$ micelles average size: 97 nm.

9 shows the AFM image of micelles. The formed micelles had a spherical shape, and the diameter of micelle ranged from 100 to 300 nm.

In Vitro MRI Test. T1-weighted MR images of the phantom are shown in Figure 10. In the phantom image, when the concentration of Gd was above 9.4×10^{-4} M, the image contrast

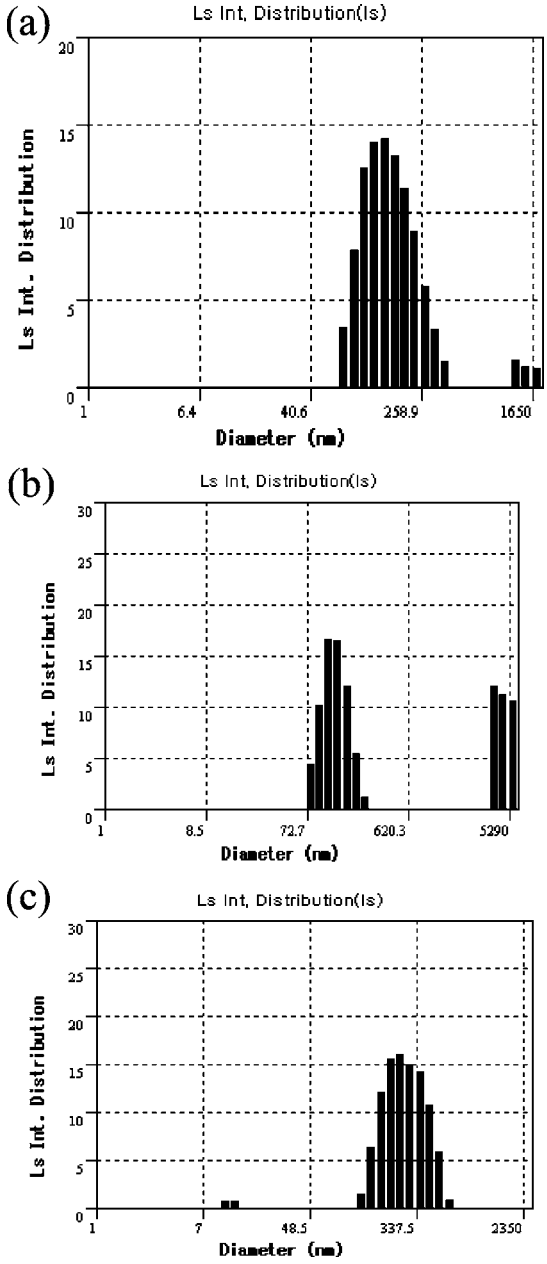

Figure 8. The size distribution of micelles with different hydrophobic ligand lengths by ELS analysis; (a) PSI−$mPEG_{5000}$-C_8 micelles average size: 238 nm, (b) PSI−$mPEG_{5000}$-C_{14} micelles average size: 288 nm and (c) PSI−$mPEG_{5000}$-C_{18} micelles average size: 342 nm.

showed similar patterns, but when the concentration of Gd was below this amount, the image contrast seemed better than that of Omniscan. Table 4 shows relaxivity values according to different concentrations of Gd. From these data, we can know that the signal intensity value of PSI−mPEG-C_{16}−(DTPA-Gd) in 1.2×10^{-4} M (Gd) is similar with the signal intensity value of Omniscan in 4.7×10^{-4} M (Gd). These results showed that the prepared sample had better contrast imaging at a lower concentration than that of Omniscan.

CONCLUSION

In this study, we have prepared PSI micelle conjugates by combining PSI with a hydrophilic chain, a hydrophobic chain, and a contrast agent. We have tested the compounds to determine its potential use as a carrier and a contrast agent. First, PSI with various molecular weights was synthesized through condensation polymerization with different reaction

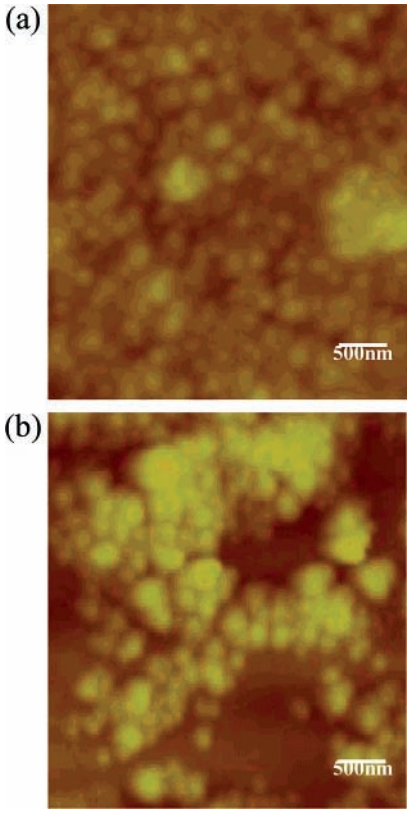

Figure 9. The shape of micelles measured by AFM: (a) PSI−mPEG micelles, (b) PSI−mPEG-C_{16} micelles.

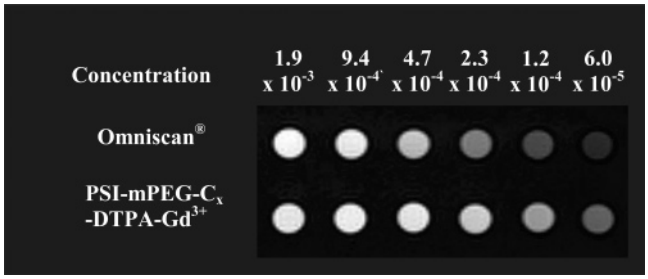

Figure 10. Contrast effect of the phantom measured by MRI.

Table 4. Signal Intensity Value with Different Concentrations of Gd Measured by MRI

Gd concn (M)	signal intensity of Omniscan	signal intensity of PSI−mPEG-C_{16}−(DTPA-Gd)
1.9×10^{-3} M	1992.17	2112.12
9.4×10^{-4} M	1724.86	2043.92
4.7×10^{-4} M	1468. 42	1912.2
2.3×10^{-4} M	1096	1812.43
1.2×10^{-4} M	771.05	1430.12
6.0×10^{-5} M	580.96	1043.42

times and catalyst contents using aspartic acid and catalyst. The synthesized PSI was combined with the hydrophilic mPEG, the hydrophobic chain, and the contrast agent, and the variation of micelle size was measured with different molecular weights of hydrophilic group and different lengths of hydrophobic chain. The size of micelles was confirmed by ELS and AFM. The diameter of micelles was 100−300 nm. In vitro, the prepared micelles showed the enhancement of MRI contrast over five times of commercially available products. From these results, it was concluded that PSI conjugates possessing mPEG, a hydrophobic ligand, and DTPA-Gd might be exploited as carriers and contrast agents due to their biocompatibility, good stability, and good contrast imaging.

ACKNOWLEDGMENT

This work was supported by KMOCIE(10011394).

LITERATURE CITED

(1) Lattuada, L., and Lux, G. (2003). Synthesis of Gd-DTPA-cholesterol: a new lipophilic gadolinium complex as a potential MRI contrast agent. *Tetrahedron Lett. 44*, 3893−3895.

(2) Rongved, P., Fritzell, T. H., Strande, P., and Klaveness, J. (1996) Polysaccharides as carriers for magnetic resonance imaging contrast agents: synthesis and stability of a new amino acid linker derivative. *Carbohydate Res. 287*, 77−89.

(3) Tomida, M., Nakato, T., Kuramochi, M., Shibata, M., Matsunami, S., and Kakuchi, T. (1996) Novel method of synthesizing poly-(succinimide) and its copolymeric derivatives by acid-catalysed polycondensation of L-aspartic acid. *Polymer 37*, 4435−4437.

(4) Tomida, M., Nakato, T., Matsunami, S., and Kakuchi, T. (1997) Convenient synthesis of high molecular weight poly(succinimide) by acid-catalysed polycondensation of L-aspartic acid. *Polymer 38*, 4733−4736.

(5) Hayashi, T., and Iwatsuki, M. (1990) Biodegradation of copoly-(L-aspartic acid/L-glutamic acid) in vitro. *Biopolymers 29*, 549−557.

(6) Jain, G. L., and Ray, R. A. (1981) Syntheses and characterization of random copolymers of aspartic acid with lactic acid and glycolic acid. *Macromol. Chem. 182*, 2557−2561.

(7) Giammona, G., Carlisi, B., and Palazzo, S. (1987) Reaction of poly-(N-hydroxyethyl)-DL-aspartamide with derivatives of carboxylic acids. *J. Polym. Sci. Polym. Chem. 25*, 2813−2818.

(8) Giammona, G., Carlisi, B., Pitarresi, G., Cavallaro, G., and Liveri, V. T. (1992) Water-soluble copolymers of an antiviral agent: synthesis and their interaction with a biomembrane model. *J. Controlled Release 22*, 197−204.

(9) Giammona, G., Puglisi, G., Cavallaro, G., Spadaro, A., and Pitarresi, G. (1995) Chemical stability and bioavailability of acyclovir coupled to poly(N-2-hydroxyethyl)-dl-aspartamide. *J. Controlled Release 33*, 261−271.

(10) Giammona, G., Cavallaro, G. Fontana, G. Guidi, G. D., and Giuffrida, S. (1996) Macromolecular prodrug of diflunisal. II. Investigations of in vitro release and of photochemical behaviour. *Eur. J. Pharm. Sci.* 4, 273−282.

(11) Palmer, W. K., Emeson, E. E., and Johnston, T. P. (1998) Poloxamer 407-induced atherogenesis in the C57BL/6 mouse. *Atherosclerosis 136*, 115−123.

(12) Lasic, D. (1992) Mixed micelles in drug delivery. *Nature 355*, 279−280.

(13) Torchilin, V. P. (2001) Structure and design of polymeric surfactant-based drug delivery systems. *J. Controlled Release 73*, 137−172.

(14) Kwon, G. S., and Okano, T. (1996) Polymeric micelles as new drug carriers. *Adv. Drug Delivery Rev. 21*, 107−116.

(15) Kataoka, K., Harada, A., and Nagasaki, Y. (2001) Block copolymer micelles for drug delivery: design, characterization and biological significance. *Adv. Drug Delivery Rev. 47*, 113−131.

(16) Kwon, G. S., and Kataoka, K. (1995) Block copolymer micelles as long-circulating drug vehicles. *Adv. Drug Delivery Rev. 16*, 295−309.

(17) Yokoyama, M., Satoh, A., Sakurai, Y., Okano, T., Matsumura, Y., Kakizoe, T., and Kataoka, K. (1998) Incorporation of water-insoluble anticancer drug into polymeric micelles and control of their particle size. *J. Controlled Release 55*, 219−229.

(18) Jones, M. C., and Leroux, J. C. (1999) Polymeric micelles: a new generation of colloidal drug carriers. *Eur. J. Pharm. Biopharm. 48*, 101−111.

(19) Lavasanifar, A., Samuel, J., and Kwon, G. S. (2002) Poly(ethylene oxide)-block-poly(L-amino acid) micelles for drug delivery. *Adv. Drug Dev. Rev. 54*, 169−190.

(20) Choi, H. S., Khang, G., Shin, H., Rhee, J. M., and Lee, H. B. (2002) Preparation and characterization of fentanyl-loaded PLGA microspheres: in vitro release profiles. *Int. J. Pharm. 195*, 234−203.

(21) Cavallaro, G., Licciardi, M., Giammona, G., Caliceti, P., and Semenzato, A., Salmaso, S. (2003) Poly(hydroxyethylaspartamide) derivatives as colloidal drug carrier systems. *J. Controlled Release 89*, 285−295.

(22) Anelli, L., Fedeli, F., Gazzotti, O., Lattuada, L., Lux, G., and Rebasti, F. (1999) L-Glutamic acid and L-lysine as useful building block for the preparation of bifunctional DTPA-like ligands. *Bioconjugate Chem. 10*, 137−140.

(23) Weiner, E. C., Brechbiel, M. W., Brothers, H., R Magin, L., Gansow, O. A., Tomalia, D. A., and Lauterbur, P. C. (1994) Dendrimer-based metal chelates: a new class of magnetic resonance imaging contrast agents. *Magn. Reson. Med. 31*, 1−8.

(24) Boden, N., Bushby, R. J., Clarckson, S., Evans, S. D., Knowles, P. F., and Marsh, A. (1997) The design and synthesis of simple molecular tethers for binding biomembranes to a gold surface. *Tetrahedron 53*, 10939−10952.

(25) Vu, H., Schmaltz, H., T., and Jayaraman, K. 5 (1994) Synthesis and properties of cholesteryl-modified triple-helix forming oligonucleotides containing a triglycyl linker. *Bioconjugate Chem. 5*, 666−668.

(26) Bailey, A. G., Hashish, A. H., and Williams, T. J. (1998) Drug delivery by inhalation of charged particles. *J. Electrost. 44*, 3−10.

(27) Allen, C., and Maysinger, D. A. (1999) Eisenberg, Nano-engineering block copolymer aggregates for drug delivery. *Colloid Surfaces 16*, 3−27.

(28) Caliceti, P., Quarta, S. M., Veronese, F. M., Cavallaro, G., Pedone, E., and Giammona, G. (2001) Synthesis and biopharmaceutical characterisation of new poly(hydroxyethylaspartamide) copolymers as drug carriers. *Biochim. Biophys. Acta, Gen. Subjects 1528*, 177−186.

(29) Chen, H., Chen, T., Hu, J., and Wang, C. (2005) Nano aggregates of biodegradable amphiphilic poly(hydroxyethyl aspartamide-*co*-propyl aspartamide) grafted with poly(d, l-lactide). *Colloids Surf., A 268*, 24−29.

(30) Zhang, Y., Lam, Y. M., and Tan, W. S. (2005) Poly(ethylene oxide)-poly(propylene oxide)-poly(ethylene oxide)-*g*-poly(vinylpyrrolidone): Association behavior in aqueous solution and interaction with anionic surfactants. *J. Colloid Interface Sci. 285*, 74−79.

(31) Wu, Y., Zheng, Y., Yang, W., Wang, C., Hu, J., and Fu, S. (2005) Synthesis and characterization of a novel amphiphilic chitosan-polylactide graft copolymer. *Carbohyd. Polym. 59*, 165−171.

BC060014F

Combination Cancer Therapy by Hapten-Targeted Prodrug-Activating Enzymes and Cytokines

Kuo-Hsiang Chuang,[†,‡,§] Chiu-Min Cheng,[‡,§] Steve R. Roffler,[∥] Yu-Lin Lu,[⊥] Shiu-Ru Lin,[#] Jaw-Yuan Wang,[#] Wen-Shyong Tzou,[▽] Yu-Cheng Su,[†] Bing-Mae Chen,[∥] and Tian-Lu Cheng*[,†,#]

Faculty of Biomedical Science and Environmental Biology, Kaohsiung Medical University, Kaohsiung, Taiwan, Institute of Medicine, Kaohsiung Medical University, Kaohsiung, Taiwan, Institute of Biomedical Sciences, Academia Sinica, Taipei, Taiwan, Chia Nan University of Pharmacy and Science, Tainan, Taiwan, MedicoGenomic Research Center, Kaohsiung Medical University, Kaohsiung, Taiwan, and Institute of Bioscience and Biotechnology, National Taiwan Ocean University, Keelung, Taiwan. Received January 23, 2006; Revised Manuscript Received March 30, 2006

Combination therapy can help overcome limitations in the treatment of heterogeneous tumors. In the current study, we examined whether multiple therapeutic agents could be targeted to anti-dansyl single-chain antibodies (DNS scFv) that were anchored on the plasma membrane of cancer cells. Functional DNS scFv could be stably expressed on CT-26 colon cancer cells both in vitro and in vivo. Dansyl moieties were covalently attached to recombinant β-glucuronidase (βG) and interleukin 2 (IL-2) via a flexible poly(ethylene glycol) linker to form DNS−PEG−βG and DNS−PEG−IL-2 conjugates. The conjugates displayed enzymatic and splenocyte-stimulatory activities, respectively, that were similar to those of the unmodified proteins. The conjugates selectively bound CT-26 cells that expressed anti-DNS scFv (CT-26/DNS cells) but not CT-26 cells that expressed control scFv (CT-26/phOx cells). DNS−PEG−βG preferentially activated a glucuronide prodrug (BHAMG) of *p*-hydroxy aniline mustard at CT-26/DNS cells in culture and accumulated in subcutaneous CT-26/DNS tumors after intravenous administration. Systemic administration of DNS−PEG−IL-2 or DNS−PEG−βG and BHAMG significantly delayed the growth of CT-26/DNS but not control CT-26/phOx tumors. Combination treatment with DNS−PEG−βG and BHAMG followed by DNS−PEG−IL-2 therapy significantly suppressed the growth of CT-26/DNS tumors as compared to either single-agent regimen. These results show that at least two DNS-modified therapeutic agents can be selectively delivered to DNS scFv receptors in vitro and in vivo, allowing combination therapy of DNS scFv-modified tumors.

INTRODUCTION

Conventional cancer treatment is often limited by unacceptable toxicity to normal tissues and associated side effects (*1*, *2*). Methods to selectively target therapeutic agents to tumor cells can improve treatment efficacy and reduce the exposure of normal tissues to cytotoxic agents. Antibody-directed enzyme prodrug therapy (ADEPT), in which an immunoenzyme is employed to preferentially activate prodrugs at cancer cells, has demonstrated advantages for tumor therapy in animal models including high accumulation of drug in tumors (*3*), bystander killing of antigen-negative tumor cells (*4*), and improved efficacy compared with conventional chemotherapy with reduced side effects (*5*). Our previous results also demonstrated that an immunoenzyme composed of monoclonal antibody RH1 conjugated to β-glucuronidase could target rat AS30D hepatocellular carcinoma tumors and specifically convert a glucuronide prodrug (BHAMG[1]) of *p*-hydroxy aniline mustard to active *p*-hydroxy aniline mustard (pHAM) (*6*, *7*). Rats cured of malignant hepatocellular carcinoma ascites by ADEPT with BHAMG possessed long-lasting protective immunity to subsequent tumor challenges, suggesting that ADEPT can synergize with the immune system to provide increased therapeutic efficacy (*6*, *7*). The immunogenicity of synergistic malignancies can also be increased by targeting cytokines to the tumor microenvironment (*8*). For example, antibody−IL-2 fusion proteins can effectively suppress tumor growth (*9*) and amplify the T cell mediated immune responses induced by cancer vaccines (*10*, *11*). Based on these findings, an attractive therapeutic strategy can be envisioned in which the major bulk of tumors is reduced by ADEPT and targeted immunocytokine therapy is then employed to potentiate the immune response generated during prodrug therapy, thereby eliminating residual and disseminated disease.

One approach to target therapeutic agents to tumors is to create artificial anti-hapten receptors on cancer cells that can bind to hapten-derivatized molecules. We previously demonstrated that expression on tumor cells of a membrane-anchored

* Corresponding author.: Mailing address: Faculty of Biomedical and Environmental Biology, Kaohsiung Medical University, 100 Shih-Chuan 1st Road, Kaohsiung, Taiwan. Tel: +886-7-3121101-2697. Fax: +886-7-3227508. E-mail: tlcheng@kmu.edu.tw.

† Faculty of Biomedical Science and Environmental Biology, Kaohsiung Medical University.

‡ Institute of Medicine, Kaohsiung Medical University.

§ Equal contribution.

∥ Academia Sinica.

⊥ Chia Nan University of Pharmacy and Science.

MedicoGenomic Research Center, Kaohsiung Medical University.

▽ National Taiwan Ocean University.

[1] Abbreviations: DNS scFv, anti-dansyl single chain antibody; phOx scFv, anti-4-ethoxymethylene-2-phenyl-2-oxazoline-5-one single chain antibody; CT-26/DNS, CT-26 cells that express membrane DNS scFv; CT-26/phOx, CT-26 cells that express membrane phOx scFv; DNS, dansyl (5-dimethylamino-1-naphthalenesulfonyl); phOx, 4-ethoxymethylene-2-phenyl-2-oxazoline-5-one; PEG, poly(ethylene glyol); DNS−PEG, PEG modified with a dansyl moiety; DNS−PEG−βG, *Escherichia coli* β-glucuronidase modified with DNS−PEG; DNS−PEG−IL-2, interleukin 2 modified with DNS−PEG; pHAM, *p*-hydroxyaniline mustard; BHAMG, tetra-*n*-butylammonium salt of glucuronide *p*-hydroxyaniline mustard.

10.1021/bc0600160 CCC: $33.50 © 2006 American Chemical Society
Published on Web 04/21/2006

scFv with specificity for the hapten 4-ethoxymethylene-2-phenyl-2-oxazoline-5-one (phOx) allowed selective trapping of phOx-derivatized βG at the cells for activation of glucuronide prodrugs (*12*). phOx, however, is unstable in serum, resulting in the progressive loss of phOx antigenicity. In contrast, a bivalent dansyl probe [$(DNS)_2$-DTPA-^{111}In] was stable in serum and could be specifically bound by tumor cells that expressed DNS scFv receptors in vitro and in vivo (*13*). The DNS moiety is therefore more suitable for in vivo hapten-directed targeting.

In the present study, we wished to test the hypothesis that multiple therapeutic agents can be simultaneously targeted to cells expressing anti-hapten receptors. This was examined by expressing DNS scFv receptors on CT-26 colorectal cancer cells and attaching DNS molecules to recombinant βG and IL-2 via flexible poly(ethylene glycol) spacers (Figure 1a). We then tested the hypotheses that (1) DNS-modified molecules could be selectively bound by anti-DNS scFv on cells, (2) accumulation of DNS-modified βG at DNS scFv-positive cells would allow activation of glucuronide prodrugs, (3) DNS-modified IL-2 could stimulate splenocyte proliferation at receptor-positive cells, and (4) treatment of established tumors with hapten-modified βG for prodrug activation in combination with hapten-modified IL-2 could provide improved therapeutic efficacy as compared with either individual treatment regimen. The results of our study show that hapten-directed therapy does allow more than one therapeutic agent to be targeted to tumors for combination cancer therapy.

EXPERIMENTAL PROCEDURES

Reagents. The syntheses of pHAM and BHAMG have been described (*14*). Recombinant βG containing a his-tag was purified by metal chelate chromatography on His-Bind resin (Novagen) as described (*15*). Recombinant mouse IL-2 was produced in *Pichia pastoris* (kindly provided by Dr. Mi-Hua Tao, Institute of Biomedical Sciences, Academia Sinica, Taipei) and purified by metal chelate chromatography on His-Bind resin (Novagen, San Diego, CA). Dansyl chloride, dansyl cadaverine, fluorescamine, and *p*-nitrophenyl-β-D-glucuronide were purchased from Sigma-Aldrich Chemical Co. (St. Louis, MO). PEG_{3400}-disuccinimidyl succinamide (3400 Da) was purchased from Nektar Therapeutics (Birmingham, AL). Dansyl chloride and 4-ethoxymethylene-2-phenyl-2-oxazoline-5-one (phOx) were linked to fluorescein via a diaminopentane spacer to generate phOx-FITC and dansyl-FITC as described (*12*). The anti-poly(ethylene glycol) antibody, E11 (IgG_1), which binds to the repeating ($O-CH_2-CH_2$) subunits of the PEG backbone and can detect and clear PEG-modified proteins, has been described (*16*).

Cells and Animals. CT-26 colon carcinoma cells were obtained from the American Type Culture Collection (Manassas, VA). Cells were cultured in DMEM supplemented with 10% heat-inactivated bovine calf serum, 100 units/mL penicillin and 100 μg/mL streptomycin. BALB/c mice were obtained from the National Laboratory Animal Center, Taipei, Taiwan. Animal experiments were performed in accordance with institute guidelines.

Transfection of Receptor Transgenes. pLNCX-DNS-B7 and pLNCX-phOx-B7 plasmids encode membrane-bound scFv with specificity for DNS and phOx, respectively (*12*). To produce pseudotyped retroviruses, pLNCX-DNS-B7 and pLNCX-phOx-B7 were cotransfected in GP2-293 cells (Clontech, Mountainview, CA) with pVSVG (Clontech), which expresses the G protein of vesicular stomatitis virus (VSV) under the transcriptional control of the cytomegalovirus immediate early gene promoter. Two days after transfection, the culture medium was filtered, mixed with 8 μg/mL Polybrene and added to CT-26 colon carcinoma cells. The cells were selected in G418 and sorted on a flow cytometer to generate CT-26/DNS and CT-26/phOx cells that expressed similar levels of DNS or phOx scFv receptors, respectively.

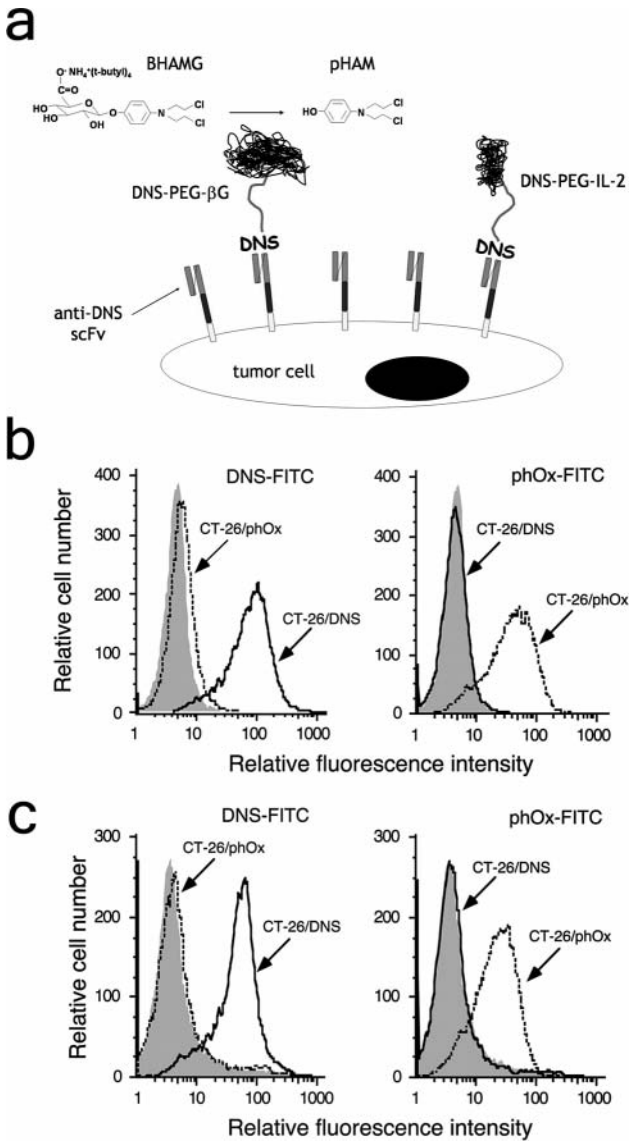

Figure 1. Combination cancer therapy by hapten-targeted prodrug-activating enzymes and cytokines. (a) Anti-DNS scFv expressed on the surface of tumor cells can bind and trap DNS−PEG−βG on the cells. The glucuronide prodrug BHAMG can then be selectively hydrolyzed to the active alkylating agent pHAM at the tumor cells. Likewise, binding of DNS−PEG−IL-2 to anti-DNS scFv on the cancer cells can also allow accumulation of the cytokine at the tumor site to boost tumor immunity. (b) The immunofluorescence of CT-26 (shaded curve), CT-26/DNS cells (solid line), and CT-26/phOx (dashed line) cells is shown after staining with 1 μM DNS−FITC (left panel) or phOx-FITC (right panel). (c) Established CT-26 (shaded curve), CT-26/DNS (solid line), and CT-26/phOx (dashed line) tumors were excised from BALB/c mice and disaggregated by collagenase treatment. The cells were cultured for 24 h and stained with DNS−FITC (left panel) or phOx-FITC (right panel), and the immunofluorescence of the cells was measured on a flow cytometer.

Functional Expression of scFv Receptors in Vitro and in Vivo. Five million CT-26/DNS or CT-26/phOx cells were incubated with 1 μM phOx-FITC or DNS-FITC at 4 °C for 1 h. After removal of unbound probe by extensive washing, the surface immunofluorescence of viable cells was measured on a FACScaliber flow cytometer (Becton Dickinson, Mountain View, CA) and fluorescence intensities were analyzed with

Flowjo V3.2 (Tree Star, Inc., San Carlos, CA). In vivo expression of scFv receptor was examined by injecting BALB/c mice sc with 2×10^6 CT-26/DNS or CT-26/phOx cells. After 14 days, tumors (200−300 mm^3) were resected, cut into small fragments, and digested with 0.5 mg/mL collagenase in Hanks balanced saline solution containing Ca^{2+} and Mg^{2+} for 1 h at room temperature. The cells were cultured in complete medium for 24 h before the surface expression of scFv receptors was measured in a FACScaliber flow cytometer.

Generation and Characterization of DNS−PEG−βG and DNS−PEG−IL-2. PEG_{3400}-disuccinimidyl succinamide (SSA_2-PEG) was reacted with dansyl cadaverine at a molar ratio of 2:1 in CH_2Cl_2 containing 0.1% triethylamine at room temperature for 1 h. The resulting DNS−PEG_{3400}-succinimidyl succinamide (DNS−PEG_{3400}-SSA) was detected under UV illumination, eluted from silica gel with dichloromethane−methanol (9:1 v/v), and then dried (*16*). βG and IL-2 were passed through a Sephadex G-25 column equilibrated with 0.1 M $NaHCO_3$, pH 7.5 and then concentrated by ultrafiltration to 1 mg/mL. DNS−PEG_{3400}-SSA (2.5 w/w βG, 2 w/w IL-2) was added for 2 h at room temperature. One-tenth volume of a saturated solution of glycine (pH 8.0) was added to stop the reaction. Unreacted PEG was removed by gel filtration on a Sephacryl S-200 HR column. Protein concentrations were determined by the bicinchoninic acid assay (Pierce, Rockford, IL) with bovine serum albumin used as the reference protein. The number of PEG molecules introduced in the proteins was estimated by measuring amine groups before and after PEG modification with fluorescamine. After 7 min of reaction, the fluorescence was measured on a Fluostar Galaxy fluorometer with an excitation wavelength of 390 nm and emission at 475 nm (*17*). An average of 3.5 and 2.5 DNS_{3400}−PEG chains were attached to βG and IL-2 to form DNS−PEG−βG and DNS−PEG−IL-2 conjugates, respectively. The catalytic activity of DNS−PEG−βG was assayed by measuring hydrolysis of *p*-nitrophenol β-D-glucuronide; the absorbance of *p*-nitrophenol was measured in a microtiter plate reader (Molecular Devices, Menlo Park, CA) at 405 nm (*18*). The activity of DNS−PEG−IL-2 was assayed by measuring splenocyte proliferation. 10^6 splenocytes/well were incubated with DNS−PEG−IL-2 or IL-2 (1 μg/mL) in 96-well microtiter plates for 24, 48, 72, and 96 h. Splenocyte proliferation was assayed by the luminescence ATP detection assay system according to the manufacturer's instructions (Perkin-Elmer Life and Analytical Sciences, Boston, MA).

Binding of DNS−PEG−βG and DNS−PEG−IL-2 to anti-DNS scFv Receptors. CT-26/DNS and CT-26/phOx cells were incubated with DNS−PEG−βG (1 μg/mL), DNS−PEG−IL-2 (1 μg/mL), or PBS at 4 °C for 1 h. The cells were washed twice with cold PBS and sequentially stained with rabbit anti-βG serum (1:1000), rabbit anti-mIL-2 serum (1:1000), or rabbit normal serum at 4°C for 1 h, washed twice with cold PBS, and incubated with FITC-conjugated goat anti-rabbit antibody (5 μg/mL) at 4 °C for 1 h. The cells were then washed twice with cold PBS, and the surface immunofluorescence of 10 000 viable cells was measured on a FACSCaliber flow cytometer.

Specific Activation of BHAMG by DNS−PEG−βG. 10^6 CT-26/DNS or CT-26/phOx cells were seeded overnight in 96-well microtiter plates. DNS−PEG−βG (5 μg/mL) was added to the cells at room temperature for 1 h before the cells were washed twice with PBS and graded concentrations of *p*-hydroxyaniline mustard (pHAM) or BHAMG were added to the cells in triplicate for 24 h at 37 °C. The cells were subsequently incubated until hour 48 in fresh medium. Cell viability was determined by the ATPlite luminescence ATP detection assay system (Perkin-Elmer). Results are expressed as percent inhibition of luminescence as compared to untreated cells by the following formula:

$$\% \text{ inhibition} = 100 \times \frac{\text{sample luminescence} - \text{background luminescence}}{\text{control luminescence} - \text{background luminescence}}$$

Specific Stimulation of Splenocytes by DNS−PEG−IL-2. DNS−PEG−IL-2 (1 μg/mL) was incubated with CT-26, CT-26/DNS, or CT-26/phOx cells in 96-well microtiter plates at room temperature for 1 h. The cells were treated with pHAM (100 μM) for 2 h at 37 °C to inhibit cellular proliferation and then washed twice with PBS. 10^6 BALB/c splenocytes were added to the wells for 24, 48, 72, or 96 h. Proliferation of splenocytes was measured by the ATPlite luminescence ATP detection assay system.

In Vivo Clearance of DNS−PEG−βG. Groups of 3 BALB/c mice bearing established CT-26/DNS (right flank) or CT-26/phOx (left flank) tumors were iv injected with 150 μg of βG or DNS−PEG−βG at time zero. Blood samples (30 μL) were removed at 0.17, 1.5, 4, 7, 11, 23 h before iv injection at hour 24 of 150 μg of mAb E11 to accelerate the clearance of DNS−PEG−βG from the circulation. Additional blood samples were taken at subsequent times (3.5, 6, 24 h), and the serum concentration of DNS−PEG−βG was measured by a βG enzyme microassay as described (*18*). Sample concentrations were calculated by comparison of absorbance values with a standard curve constructed from known concentrations of DNS−PEG−βG or βG.

Tumor Localization of DNS−PEG−βG. BALB/c mice bearing established CT-26/DNS (right flank) or CT-26/phOx (left flank) tumors were iv injected with 150 μg of DNS−PEG−βG. After 24 h, mice were iv injected with 150 μg of mAb E11 to accelerate the clearance of DNS−PEG−βG. After 3.5 h, the tumors were excised, embedded in Tissue-Tek OCT in liquid nitrogen, and cut into 10 μm sections. Tumor sections were stained for βG activity with the β-glucuronidase reporter gene staining kit (Sigma). Briefly, the sections were placed in fixation solution (10 mM MES, pH 5.6, with 300 mM mannitol and 0.3% formaldehyde) at room temperature for 45 min, washed three times with wash solution (10 mM sodium phosphate, pH 7.0, with 0.2 mM EDTA), and stained with 5-bromo-4-chloro-3-indolyl-β-D-glucuronide (X-GlcA) at 37 °C for 3 h. The sections were then stained with nuclear fast red (Sigma) as a counterstain. All sections were examined on an upright microscope (Olympus BX41, Japan).

Cocktail Therapy. Groups of 5 BALB/c mice were sc injected in the right flank with 10^6 CT-26/DNS or CT-26/phOx cells. After 7 days, the mice were iv injected with PBS or 150 μg of DNS−PEG−βG. Twenty-four hours later, the mice were iv injected with 150 μg of E11 to accelerate the clearance of DNS−PEG−βG. Mice were iv injected 4 h later with three fractionated doses of 15 mg/kg BHAMG at 1 h intervals. Control groups of tumor-bearing mice were treated with BHAMG (15 mg/kg × 3), or PBS alone. All groups of BHAMG-treated mice were iv injected 24 h later with three fractionated doses of 15 mg/kg BHAMG at 1 h intervals. On day 10, specific groups of mice were ip injected with 20 000 units of DNS−PEG−IL-2. These mice received a total of 5 rounds of DNS−PEG−IL-2 over 10 days. Tumor volumes (length × width × height × 0.5) and body weight were measured twice a week.

Data Analysis. Statistical significance of differences between mean values was estimated with Excel (Microsoft, Redmond, WA) using the independent *t*-test for unequal variances.

RESULTS

Surface Display of Functional Anti-Dansyl scFv Receptors. The retroviral vectors pLNCX-DNS-eB7 and pLNCX-phOx-

eB7 encode membrane-anchored forms of DNS scFv and phOx scFv receptors in which anti-DNS or anti-phOx scFv is fused to the Ig-like C type domain, the transmembrane, and the cytoplasmic tail of murine CD80 (*12*). CT-26 colon cancer cells were infected with recombinant retroviral particles, selected in G418, and sorted for high expression of DNS or phOx scFv receptors to obtain stable CT-26/DNS and CT-26/phOx cell lines. The surface expression and antigen-binding activity of the receptors were examined by immunofluorescence staining using DNS−FITC or phOx−FITC probes. These probes contain a single hapten moiety (DNS or phOx) linked to a fluorescein residue. DNS−FITC bound to CT-26/DNS cells but not to CT-26/phOx cells whereas phOx−FITC displayed the opposite cellular specificity (Figure 1b). These results demonstrate that functional scFv receptors were expressed on the surface of CT-26 cells with retention of hapten-binding specificity.

The expression of DNS and phOx scFv receptors in vivo was examined by recovering single cells from established CT-26/DNS and CT-26/phOx tumors and then measuring the expression of the receptors on the recovered cells by staining with DNS−FITC or phOx−FITC. Similar levels of DNS and phOx receptors were detected on the cells as compared with cells maintained in culture, demonstrating that functional receptors were stably expressed in vivo (Figure 1c).

Characterization of DNS and PEG Modified Proteins. DNS moieties were covalently attached to βG and IL-2 via a flexible poly(ethylene glycol) linker to minimize steric barriers between DNS and the DNS scFv receptors on cells. Addition of PEG to proteins can also prolong their circulation half-life and improve in vivo stability. An average of 3.5 and 2.5 molecules of DNS−PEG_{3400} were attached to each molecule of βG or IL-2 to form DNS−PEG−βG and DNS−PEG−IL-2, respectively. The electrophoretic mobilities of DNS−PEG−βG and DNS−PEG−IL-2 were slower than those of unmodified βG and IL-2 as determined by SDS−PAGE, demonstrating successful conjugation of DNS−PEG_{3400} to βG and IL-2 (Figure 2a). The bioactivity of the conjugates was assayed by measuring the hydrolysis of *p*-nitrophenol-β-D-glucuronide by DNS−PEG−βG or the stimulation of splenocyte proliferation by DNS−PEG−IL-2. Both conjugates displayed activities similar to those of the unmodified proteins (Figure 2b,c). The ability of DNS−PEG−βG and DNS−PEG−IL-2 to bind to DNS scFv receptors was examined by incubating the conjugates with CT-26/DNS and CT-26/phOx cells and then staining the cells with rabbit anti-βG or anti-IL-2 antibodies followed with FITC-conjugated second antibodies. Both DNS−PEG−βG and DNS−PEG−IL-2 bound to CT-26/DNS cells (Figure 3, upper panel) but not to control CT-26/phOx cells (Figure 3, lower panel), demonstrating that DNS−PEG-modified proteins could specifically bind DNS scFv receptors.

Specific Bioactivity of DNS−PEG−βG and DNS−PEG−IL-2. To examine whether targeting DNS−PEG−βG to DNS scFv receptors could allow selective activation of the glucuronide prodrug BHAMG to pHAM at cancer cells, CT-26/DNS and CT-26/phOx cells were incubated with DNS−PEG−βG, washed, and then exposed to BHAMG or pHAM. The rate of cellular ATP synthesis after drug treatment was measured as an index of cell viability. The IC_{50} value of BHAMG to both CT-26/DNS and CT-26/phOx cells was >2000 μM, demonstrating that prodrug displayed low toxicity to these cells (Figure 4a). CT-26/DNS cells that were preincubated with DNS−PEG−βG were sensitive to BHAMG with an IC_{50} value of 6.25 μM, similar to the IC_{50} value observed when the cells were treated with pHAM (IC_{50} = 5.72 μM), showing that DNS−PEG−βG efficiently converted BHAMG to pHAM at CT-26/DNS cells (Figure 4a, upper panel). By contrast, incubation of CT-26/phOx cells with DNS−PEG−βG before addition of BHAMG did not result in additional cell killing as compared to cells treated with BHAMG alone (Figure 4a, lower panel), demonstrating that prodrug activation required specific capture of DNS−PEG−βG by DNS scFv receptor-positive cells.

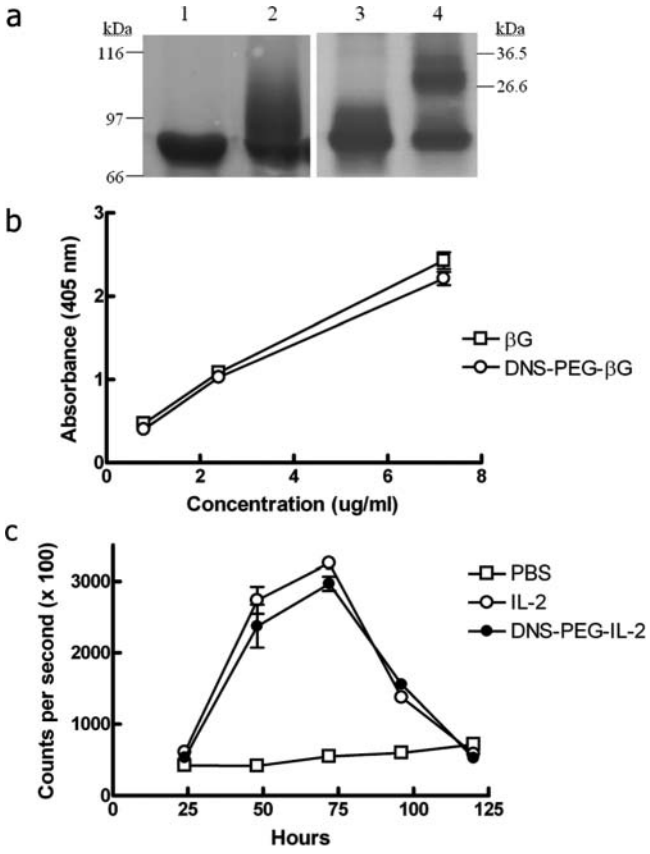

Figure 2. Biological activity of DNS−PEG-modified βG and IL-2. (a) Proteins were electrophoresed on a reducing 10% SDS polyacrylamide gel and stained with Coomassive Blue R-250. Lane 1: βG. Lane 2: DNS−PEG−βG. Lane 3: IL-2. Lane 4: DNS−PEG−IL-2. (b) The catalytic activities of unmodified βG (□) and DNS−PEG−βG (○) were measured by monitoring the release of *p*-nitrophenol from *p*-nitrophenol-β-D-glucuronide at 405 nm (n = 3; bars SE). (c) Splenocytes were incubated with 1 μg/mL DNS−PEG−IL-2 (●), IL-2 (○), or medium (□) before cellular proliferation was assayed by the luminescence ATP detection assay system (n = 3; bars, SE).

We also examined whether DNS−PEG−IL-2 that was captured on cells by DNS scFv receptors could stimulate splenocyte proliferation. CT-26/DNS and CT-26/phOx cells were incubated with DNS−PEG−IL-2, washed twice with PBS, and then incubated with murine splenocytes. Figure 4b shows that incubation of DNS−PEG−IL-2 with CT-26/DNS cells, but not CT-26/phOx cells, induced splenocyte proliferation, demonstrating that DNS−PEG−IL-2 targeted to DNS scFv receptors retained T cell stimulatory activity.

In Vivo DNS−PEG−βG Clearances and Localization. We previously showed that the PEG modification of βG prolonged serum half-life, reduced spleen uptake, and enhanced tumor localization of antibody−βG conjugates (*15*). The long serum half-life of PEG-modified βG, however, prevents administration of prodrug when maximal tumor accumulation of the immunoconjugate is achieved. Intravenous anti-PEG antibodies can accelerate the clearance of PEG-modified proteins from the circulation and allow earlier administration of prodrug (*15*). DNS−PEG−βG displayed an initial serum half-life of 4.4 ± 0.2 h as compared to 0.84 ± 0.03 h for unmodified βG. Intravenous administration of the anti-PEG mAb E11 rapidly reduced the concentration of DNS−PEG−βG in blood by 37-fold (2.6 to 0.07 μg/mL) within 3.5 h after administration (Figure

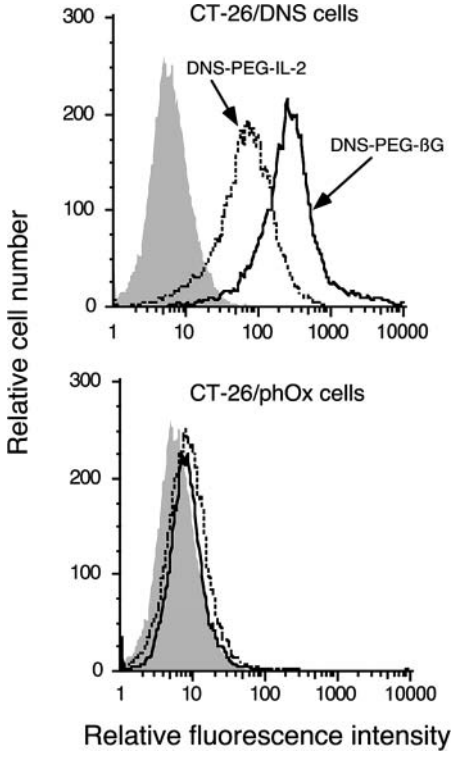

Figure 3. Specificity of DNS−PEG−βG and DNS−PEG−IL-2. CT-26/DNS (upper panel) or CT-26/phOx (lower panel) cells were incubated with DNS−PEG−βG (open curve), DNS−PEG−IL-2 (dashed line), or PBS (solid line). Cells were washed and stained with rabbit anti-βG, anti-IL-2 antibody, or PBS followed by FITC-conjugated second antibody. The surface immunofluorescence of viable cells was measured on a flow cytometer.

5a). The localization of DNS−PEG−βG in CT-26/DNS and CT-26/phOx tumors after E11-accelerated clearance was examined by staining tissue sections for βG activity. CT-26/DNS tumor sections clearly displayed βG activity (Figure 5b, right panel) whereas only background activity was observed in CT-26/phOx tumors (Figure 5b, left panel), demonstrating that βG was selectively retained in CT-26/DNS tumors after E11-mediated clearance of DNS−PEG−βG.

In Vivo Antitumor Activity. The antitumor activity of prodrug treatment in combination with DNS−PEG−IL-2 was examined in BALB/c mice bearing 50−100 mm^3 CT-26/DNS or CT-26/phOx tumors. Prodrug therapy consisted of an intravenous bolus of DNS−PEG−βG, clearance with mAb E11, and fractionated intravenous administration of BHAMG on days 8 and 9. Starting on day 10, some mice received 20 000 units of DNS−PEG−IL-2 every 2 days over 10 days. Groups of tumor-bearing mice were also treated with DNS−PEG−IL-2 alone, BHAMG, or PBS. Figure 6 shows that targeted prodrug therapy ($p \leq 0.005$) or DNS−PEG−IL-2 therapy ($p \leq 0.005$) significantly delayed the growth of CT-26/DNS tumors but not control CT-26/phOx tumors as compared to therapy with BHAMG or PBS. Combined treatment with prodrug and DNS−PEG−IL-2 further significantly ($p < 0.001$) delayed CT-26/DNS tumor growth as compared to each individual treatment and cured one of 5 mice. No significant weight loss was observed in any of the treatment groups (data not shown).

DISCUSSION

This report evaluated simultaneous targeting of hapten-derivatized therapeutic molecules to anti-hapten scFv receptor-positive cells for combination cancer therapy. Our results demonstrate that functionally active DNS−PEG-derivatized βG and IL-2 could specifically bind to DNS scFv receptors on

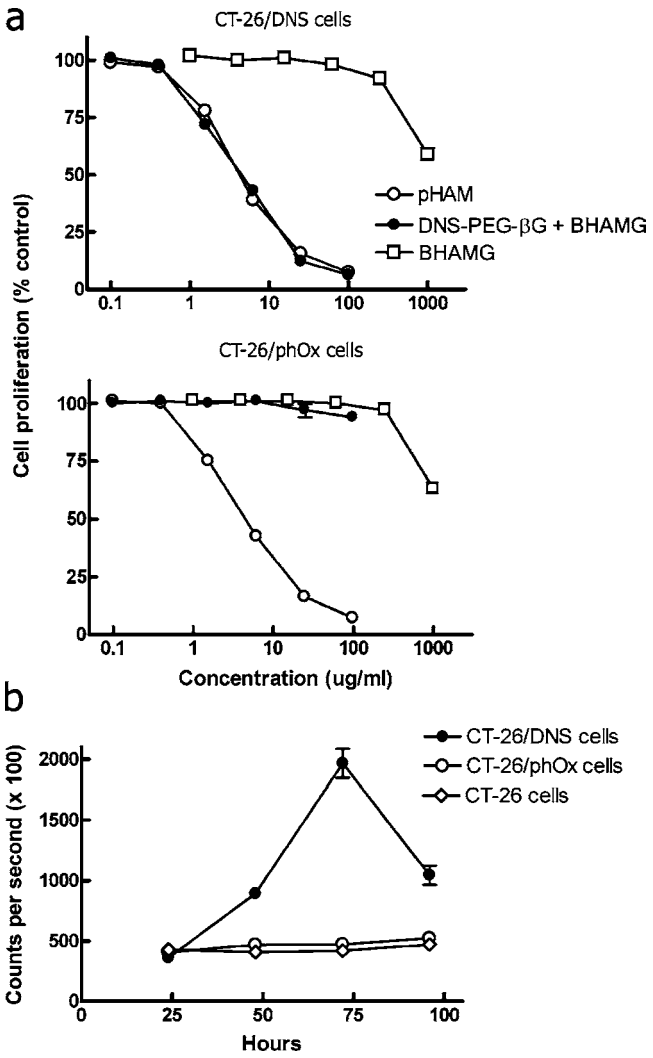

Figure 4. Specific bioactivity of DNS−PEG−βG and DNS−PEG−IL-2. (a) Specific activation of BHAMG at DNS positive cells. CT-26/DNS (upper panel) and CT-26/phOx (lower panel) cells were treated with graded concentrations of pHAM (○), BHAMG (□), or DNS−PEG−βG followed by BHAMG (●). Results show the cell viability of treated cells as compared to untreated cells ($n = 3$; bars, SE). (b) Specific stimulation of splenocytes by DNS−PEG−IL-2. CT-26/DNS (●), CT-26/phOx (○), and CT-26 (◇) cells were incubated with DNS−PEG−IL-2 and then treated with pHAM to inhibit cellular proliferation, washed, and then coincubated with murine splenocytes. The rate of cellular ATP synthesis was measured as an index of splenocyte proliferation. Bars, SE of triplicate determinations.

cancer cells to selectively convert the glucuronide prodrug BHAMG to pHAM and stimulate the proliferation of splenocytes, respectively. Combination treatment of established CT-26/DNS scFv receptor-positive tumors by prodrug therapy and DNS−PEG−IL-2 significantly suppressed tumor growth as compared to treatment with prodrug therapy or DNS−PEG−IL-2 alone. Our results therefore show that two therapeutic molecules can be targeted to tumor cells to increase therapeutic efficacy.

Successful targeting of hapten-derivatized molecules requires efficient expression of functional DNS scFv receptors on cells as well as prolonged retention of the hapten-derivatized molecules at the cells. The B7-1 TM and cytosolic tail employed to anchor the DNS scFv receptors on cells allow enhanced surface expression and reduced shedding of chimeric scFv receptors in vitro and in vivo (*19*, *20*). The anti-DNS scFv possesses high affinity ($K_D = 1.4 \times 10^{-8}$ M^{-1}) for DNS (*21*), allowing prolonged retention of DNS-modified molecules on

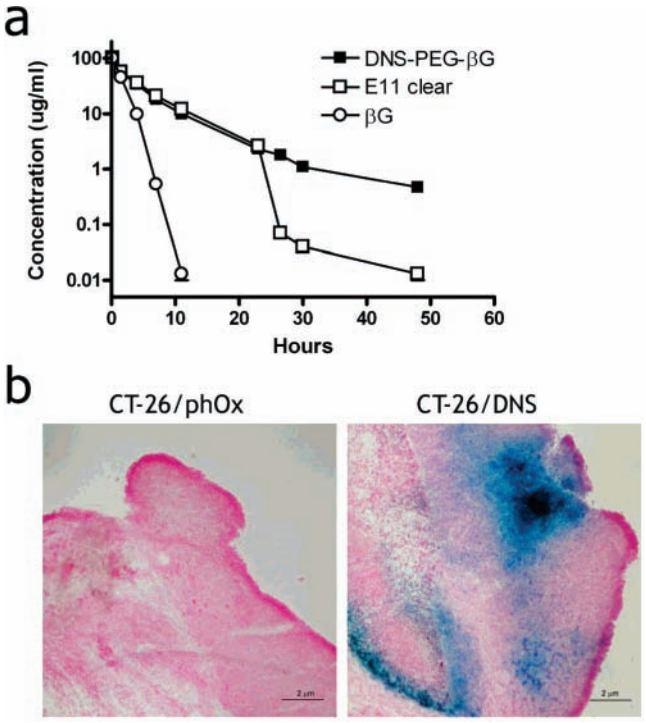

Figure 5. In vivo clearance and localization of DNS−PEG−βG. (a) Groups of 3 BALB/c mice bearing 100−200 mm^3 CT-26/DNS or CT-26/phOx tumors were iv injected with 150 μg of βG (○) or DNS−PEG−βG (□, ■) at time zero. PBS (■) or 150 μg of mAb E11 (□) was administered at 24 h, and the serum concentration of DNS−PEG−βG was measured. (b) Specific localization of DNS−PEG−βG. Twenty-four hours after injection of DNS−PEG−βG, mice were iv injected with E11 mAb to clear DNS−PEG−βG; 3.5 h later, CT-26/phOx (left) and CT-26/DNS (right) tumors were excised and sections were stained with X-GlcA for βG activity and counterstained with nuclear fast red. Magnification: ×40.

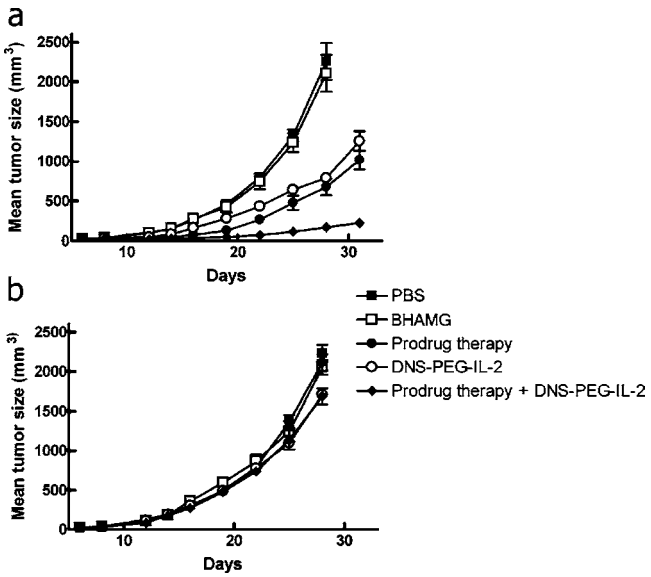

Figure 6. Cocktail therapy of CT-26/DNS tumors. Groups of 5 BALB/c mice bearing CT-26/DNS (a) or CT-26/phOx (b) tumors were iv injected with PBS (■), BHAMG (□), DNS−PEG−IL-2 (○), DNS−PEG−βG and BHAMG (●), or DNS−PEG−βG, BHAMG, and then DNS−PEG−IL-2 (◆) as described in Experimental Procedures. Bars, SE.

the cell surface. Surface localization of DNS−PEG−βG is important for efficient activation of hydrophilic glucuronide prodrugs (*22*) and bystander killing (*4*). IL-2 also requires surface localization for efficient stimulation of immune cells (*23*).

The specificity and stability of the hapten is also critical for the successful localization of hapten-modified molecules to anti-hapten scFv receptors on cells. We previously employed phOx for hapten-directed enzyme−prodrug therapy (HDEPT) but found that phOx is susceptible to hydrolysis in serum, resulting in the progressive loss of phOx antigenicity (*12*). DNS is a small molecule which has been extensively employed to derivatize proteins. $(DNS)_2$−DTPA−^{111}In was stable in serum at 37 °C for 24 h and specifically bound to B16-F1 cells that expressed DNS scFv receptors in vitro and in vivo (*13*), indicating DNS-derivatized molecules possess sufficient stability and specificity to allow effective targeting to DNS receptors in vivo. The results of the current study support the notion that DNS is suited for in vitro and in vivo targeting applications.

Effective localization of hapten-modified ligands requires ensuring adequate half-lives of the therapeutic agents in vivo. PEG modification of βG can extend its serum half-life, decrease normal tissue uptake, and increase tumor uptake of antibody−βG−PEG conjugates for targeted activation of glucuronide prodrugs (*24*). Our present results showed that DNS−PEG-modified βG exhibited more than 5-fold increase in serum half-life as compared with unmodified βG. PEG modification was also critical for retention of enzymatic activity and for attachment of multiple DNS moieties on the proteins. Direct linkage of 3.7 DNS molecules to βG resulted in the loss of 80% of enzyme activity (unpublished results) whereas attachment of 3.5 DNS−PEG molecules to βG allowed retention of over 90% of enzyme activity. The large size of the hydrophilic DNS−PEG_{3400} molecules may retard interactions with lysines in the active site of βG, resulting in less damage to enzyme activity. Attachment of DNS through a PEG spacer may also allow more conformational flexibility in binding of DNS to the anti-DNS scFv receptors on cells, thereby promoting multivalent interactions between the DNS-modified proteins and the scFv receptors. Multivalent binding is highly desirable. For example, Cortens and colleagues reported that in a two-step approach for radioimmunotargeting of cancers, the tumor uptake of bivalent DTPA−^{111}In was better than that of monovalent DTPA−^{111}In due to increased avidity (*25*). Similarly, we found increased uptake of a divalent $(DNS)_2$−DTPA−^{111}In probe by anti-DNS scFv receptors on B16/DNS tumors (*13*). The ability to attach multiple DNS groups on βG and IL-2 with retention of nearly full biological activity is therefore an important advantage of using PEG as a spacer.

The slow clearance of PEG-modified conjugate from the circulation can cause low tumor-to-blood ratios that delay prodrug injection. Antibody−βG−PEG conjugates can be rapidly cleared from the circulation and uptake of conjugate in the liver can be induced by systemic administration of an IgM anti-PEG antibody without affecting the accumulation of the conjugate in tumors (*24*). In the present study, we found that the clearance of DNS−PEG−βG from the blood could be accelerated by systemic administration of an IgG anti-PEG antibody. High concentrations of DNS−PEG−βG can therefore be maintained in the blood to maximize tumor accumulation until anti-PEG antibody is given shortly before prodrug administration.

PEG-modified IL-2 has been demonstrated to possess a markedly prolonged circulating half-life and increased antitumor potency as compared to unmodified IL-2 (*26*, *27*). For example, Morrison et al. showed that specifically targeting antibody−IL-2 to cancer cells can provide a specific and effective T cell response capable of eliminating tumors (*28*), and Zimmerman et al. showed that a lower dose and less frequent administration of PEG−IL-2 could provide the same tumor-growth-inhibiting effect compared with IL-2 (*29*). In our study, DNS−PEG−IL-2 required tumor-targeting to exhibit antitumor activity since CT-

26/phOx tumors were completely refractory to DNS−PEG−IL-2 (Figure 6b).

Combination cancer treatment by chemotherapy and immunotherapy is attractive because the treatments have different mechanisms of action and toxicities, possess potential therapeutic synergies, and have general applicability to many cancer types (*30*). It was not evident a priori, however, that combination therapy with IL-2 and BHAMG would produce additional therapeutic benefits over each individual agent since alkylating agents such as pHAM, the hydrolysis product of BHAMG, can induce dose-limiting leukopenia (*31*), which could in turn antagonize the effects of IL-2 therapy. We previously showed that treatment of rats bearing established malignant hepatocellular carcinoma ascites by ADEPT with BHAMG produced only a limited reduction in white blood cell numbers as compared to treatment with pHAM (*6*), suggesting that local generation of alkylating agents at the tumor site may spare bone-marrow progenitors and allow initiation of an antitumor immune response against antigens released from dying tumor cells. An important finding of this study was that ADEPT did not cure tumor-bearing rats depleted of $CD4^+$ and $CD8^+$ T cells, demonstrating that T cells provide substantial antitumor activity in ADEPT with BHAMG therapy (*7*). In addition, Lode, H.N et al. also showed that tumor-targeted IL-2 amplifies T cell mediated immune responses (*10*). Based on these results, T cells likely play an important role in the combination treatment with DNS−PEG−βG and BHAMG followed by DNS−PEG−IL-2 therapy.

In summary, our results demonstrate that selectively targeted DNS−PEG−βG/BHAMG to reduce the bulk of tumors and subsequent DNS−PEG−IL-2 therapy to potentiate the immune response resulted in improved therapeutic efficacy. A major strength of hapten-directed targeting is the ability to employ multiple agents that possess different mechanisms of actions. Importantly, a single small anti-DNS scFv receptor gene can be employed for gene-expression imaging (*13*) as well as for delivering multiple therapeutic agents for the combination therapy of tumors.

ACKNOWLEDGMENT

This study was supported by grants from the National Research Program for Genomic Medicine, National Science Council, Taipei, Taiwan (NSC92-3112-B-037-001 and NSC91-2320-B-037-046), and the Genomic and Proteomic Program, Academia Sinica, Taipei, Taiwan (94M007-2).

LITERATURE CITED

(1) Moulder, S. L., and Roth, B. J. (2001) Systemic chemotherapy for urothelial transitional cell carcinoma: an overview of toxicity. *Semin. Urol. Oncol. 19*, 194−201.

(2) Lowenthal, R. M., and Eaton, K. (1996) Toxicity of chemotherapy. *Hematol. Oncol. Clin. North Am. 10*, 967−90.

(3) Wallace, P. M., MacMaster, J. F., Smith, V. F., Kerr, D. E., Senter, P. D., and Cosand, W. L. (1994) Intratumoral generation of 5-fluorouracil mediated by an antibody-cytosine deaminase conjugate in combination with 5-fluorocytosine. *Cancer Res. 54*, 2719−23.

(4) Cheng, T. L., Wei, S. L., Chen, B. M., Chern, J. W., Wu, M. F., Liu, P. W., and Roffler, S. R. (1999) Bystander killing of tumour cells by antibody-targeted enzymatic activation of a glucuronide prodrug. *Br. J. Cancer 79*, 1378−85.

(5) Kerr, D. E., Schreiber, G. J., Vrudhula, V. M., Svensson, H. P., Hellstrom, I., Hellstrom, K. E., and Senter, P. D. (1995) Regressions and cures of melanoma xenografts following treatment with monoclonal antibody beta-lactamase conjugates in combination with anticancer prodrugs. *Cancer Res. 55*, 3558−63.

(6) Chen, B. M., Chan, L. Y., Wang, S. M., Wu, M. F., Chern, J. W., and Roffler, S. R. (1997) Cure of malignant ascites and generation of protective immunity by monoclonal antibody-targeted activation of a glucuronide prodrug in rats. *Int. J. Cancer 73*, 392−402.

(7) Chen, B. M., Cheng, T. L., Tzou, S. C., and Roffler, S. R. (2001) Potentiation of antitumor immunity by antibody-directed enzyme prodrug therapy. *Int. J. Cancer 94*, 850−8.

(8) Lode, H. N., Xiang, R., Perri, P., Pertl, U., Lode, A., Gillies, S. D., and Reisfeld, R. A. (2000) What to do with targeted IL-2. *Drugs Today 36*, 321−36.

(9) Lode, H. N., Xiang, R., Varki, N. M., Dolman, C. S., Gillies, S. D., and Reisfeld, R. A. (1997) Targeted interleukin-2 therapy for spontaneous neuroblastoma metastases to bone marrow. *J. Natl. Cancer Inst. 89*, 1586−94.

(10) Lode, H. N., Xiang, R., Duncan, S. R., Theofilopoulos, A. N., Gillies, S. D., and Reisfeld, R. A. (1999) Tumor-targeted IL-2 amplifies T cell-mediated immune response induced by gene therapy with single-chain IL-12. *Proc. Natl. Acad. Sci. U.S.A. 96*, 8591−6.

(11) Niethammer, A. G., Xiang, R., Ruehlmann, J. M., Lode, H. N., Dolman, C. S., Gillies, S. D., and Reisfeld, R. A. (2001) Targeted interleukin 2 therapy enhances protective immunity induced by an autologous oral DNA vaccine against murine melanoma. *Cancer Res. 61*, 6178−84.

(12) Cheng, T. L., Liao, K. W., Tzou, S. C., Cheng, C. M., Chen, B. M., and Roffler, S. R. (2004) Hapten-directed targeting to single-chain antibody receptors. *Cancer Gene Ther. 11*, 380−8.

(13) Roffler, S. R., Wang, H. E., Yu, H. M., Chang, W. D., Cheng, C. M., Lu, Y. L., Chen, B. M., and Cheng, T. L. (2006) A membrane antibody receptor for noninvasive imaging of gene expression. *Gene Ther. 13*, 412−20.

(14) Roffler, S. R., Wang, S. M., Chern, J. W., Yeh, M. Y., and Tung, E. (1991) Anti-neoplastic glucuronide prodrug treatment of human tumor cells targeted with a monoclonal antibody-enzyme conjugate. *Biochem. Pharmacol. 42*, 2062−5.

(15) Cheng, T. L., Chen, B. M., Chan, L. Y., Wu, P. Y., Chern, J. W., and Roffler, S. R. (1997) Poly(ethylene glycol) modification of beta-glucuronidase-antibody conjugates for solid-tumor therapy by targeted activation of glucuronide prodrugs. *Cancer Immunol. Immunother. 44*, 305−15.

(16) Cheng, T. L., Cheng, C. M., Chen, B. M., Tsao, D. A., Chuang, K. H., Hsiao, S. W., Lin, Y. H., and Roffler, S. R. (2005) Monoclonal antibody-based quantitation of poly(ethylene glycol)-derivatized proteins, liposomes, and nanoparticles. *Bioconjugate Chem. 16*, 1225−31.

(17) Stocks, S. J., Jones, A. J., Ramey, C. W., and Brooks, D. E. (1986) A fluorometric assay of the degree of modification of protein primary amines with polyethylene glycol. *Anal. Biochem. 154*, 232−4.

(18) Wang, S. M., Chern, J. W., Yeh, M. Y., Ng, J. C., Tung, E., and Roffler, S. R. (1992) Specific activation of glucuronide prodrugs by antibody-targeted enzyme conjugates for cancer therapy. *Cancer Res. 52*, 4484−91.

(19) Liao, K. W., Chou, W. C., Lo, Y. C., and Roffler, S. R. (2001) Design of transgenes for efficient expression of active chimeric proteins on mammalian cells. *Biotechnol. Bioeng. 73*, 313−23.

(20) Liao, K. W., Lo, Y. C., and Roffler, S. R. (2000) Activation of lymphocytes by anti-CD3 single-chain antibody dimers expressed on the plasma membrane of tumor cells. *Gene Ther. 7*, 339−47.

(21) Coloma, M. J., and Morrison, S. L. (1997) Design and production of novel tetravalent bispecific antibodies. *Nat. Biotechnol. 15*, 159−63.

(22) Cheng, T. L., Chou, W. C., Chen, B. M., Chern, J. W., and Roffler, S. R. (1999) Characterization of an antineoplastic glucuronide prodrug. *Biochem. Pharmacol. 58*, 325−8.

(23) Chang, M. R., Lee, W. H., Choi, J. W., Park, S. O., Paik, S. G., and Kim, Y. S. (2005) Antitumor immunity induced by tumor cells engineered to express a membrane-bound form of IL-2. *Exp. Mol. Med. 37*, 240−9.

(24) Cheng, T. L., Chen, B. M., Chern, J. W., Wu, M. F., and Roffler, S. R. (2000) Efficient clearance of poly(ethylene glycol)-modified immunoenzyme with anti-PEG monoclonal antibody for prodrug cancer therapy. *Bioconjugate Chem. 11*, 258−66.

(25) Boerman, O. C., Kranenborg, M. H., Oosterwijk, E., Griffiths, G. L., McBride, W. J., Oyen, W. J., de Weijert, M., Oosterwijk-Wakka, J., Hansen, H. J., and Corstens, F. H. (1999) Pretargeting

of renal cell carcinoma: improved tumor targeting with a bivalent chelate. *Cancer Res. 59*, 4400−5.
(26) Feng, X. S. (1993) [In vivo antitumor activities of polyethylene glycol modified recombinant interleukin 2 (PEG-rIL-2) against murine hepatoma]. *Zhonghua Zhongliu Zazhi 15*, 256−8.
(27) Menzel, T., Schomburg, A., Korfer, A., Hadam, M., Meffert, M., Dallmann, I., Casper, S., Kirchner, H., Poliwoda, H., and Atzpodien, J. (1993) Clinical and preclinical evaluation of recombinant PEG-IL-2 in human. *Cancer Biother. 8*, 199−212.
(28) Penichet, M. L., Harvill, E. T., and Morrison, S. L. (1997) Antibody-IL-2 fusion proteins: a novel strategy for immune protection. *Hum. Antibodies 8*, 106−18.
(29) Chapes, S. K., Simske, S. J., Sonnenfeld, G., Miller, E. S., and Zimmerman, R. J. (1999) Effects of spaceflight and PEG-IL-2 on rat physiological and immunological responses. *J. Appl. Physiol. 86*, 2065−76.
(30) Lake, R. A., and Robinson, B. W. (2005) Immunotherapy and chemotherapy—a practical partnership. *Nat. Rev. Cancer 5*, 397−405.
(31) Fleming, R. A. (1997) An overview of cyclophosphamide and ifosfamide pharmacology. *Pharmacotherapy 17*, 146S−154S.

BC0600160

Efficient DNA Alkylation by a Pyrrole-Imidazole CBI Conjugate with an Indole Linker: Sequence-Specific Alkylation with Nine-Base-Pair Recognition

Toshikazu Bando, Shunta Sasaki, Masafumi Minoshima, Chikara Dohno, Ken-ichi Shinohara, Akihiko Narita, and Hiroshi Sugiyama*

Department of Chemistry, Graduate School of Science, Kyoto University, Sakyo, Kyoto 606-8501, Japan. Received January 30, 2006; Revised Manuscript Received April 6, 2006

Conjugates **7**, **8**, and **10** of *N*-methylpyrrole (Py)-*N*-methylimidazole (Im) polyamides and 1,2,9,9a-tetrahydrocyclopropa[1,2-*c*]benz[1,2-*e*]indol-4-one (CBI) with a 5-amino-1*H*-indole-2-carbonyl linker were synthesized by Fmoc solid-phase synthesis and a subsequent liquid-phase coupling procedure. The DNA alkylating abilities of conjugates **7**, **8**, **6b**, and **10** were examined using Texas Red-labeled PCR fragments and high-resolution denaturing gel electrophoresis. CBI conjugates **7** and **8** exhibited highly efficient sequence-specific DNA alkylation comparable with previous CBI conjugates with a vinyl linker. In particular, conjugate **10**, with a 10-ringed hairpin Py-Im polyamide, alkylated at the adenine of 5′-ACAAATCC**A**-3′. Introduction of an indole linker greatly facilitated the synthesis of sequence-specific alkylating Py-Im polyamides.

INTRODUCTION

DNA is often the target of anticancer agents, which covalently bond to or oxidatively damage bases and deoxyriboses. DNA alkylating agents, which include well-known anticancer drugs such as cyclophosphamide and mitomycin C, are used routinely in cancer treatment. However, these drugs are extremely toxic because they attack normal cells and cause severe adverse effects. One intriguing question to consider is whether the introduction of sequence selectivity to an alkylating agent can improve its efficacy as an anticancer agent (*1*−*3*). To address this question, we have developed various types of sequence-specific alkylating agents by conjugating alkylating agents and *N*-methylpyrrole (Py)-*N*-methylimidazole (Im) polyamides and have investigated their DNA alkylating activity and biological functions (*4*, *5*). Importantly, the insertion of a vinyl linker between Segment A of DU-86 (*6*) and the Py-Im polyamides dramatically enhances DNA alkylating reactivity (*7*−*10*) and cytotoxicity against human cancer cell lines by more than 100-fold compared with compounds with no vinyl linker (*11*, *12*). Alkylation of the coding region of the template strand by Py-Im polyamides with vinyl linkers effectively terminates transcription, producing truncated mRNA (*13*). We have also demonstrated that alkylating Py-Im polyamides, such as **1a**, causes gene silencing of GFP in mammalian cells (*14*). These results encouraged us to test alkylating Py-Im polyamides in animal studies, such as in xenografts of human cancers. For this purpose, we changed the alkylating moiety to 1,2,9,9a-tetrahydrocyclopropa[1,2-*c*]benz[1,2-*e*]indol-4-one (CBI), which can be synthesized from commercially available naphthalene-1,3-diol or 4-amino-1-naphthol (*15*−*18*). We demonstrated that CBI conjugate **1b** tethered to Py-Im hairpin polyamides with a vinyl linker have higher sequence-specific DNA alkylating activity and cell toxicity than does CPI conjugate **1a** (Figure 1**)** (*19*). More recently, we found that CBI conjugate **1b** specifically alkylates at adenines, despite having a binding orientation similar to the corresponding CPI conjugate **1a** (*20*). Additional sequence specificity relative to CPI conjugates will be useful for biological applications.

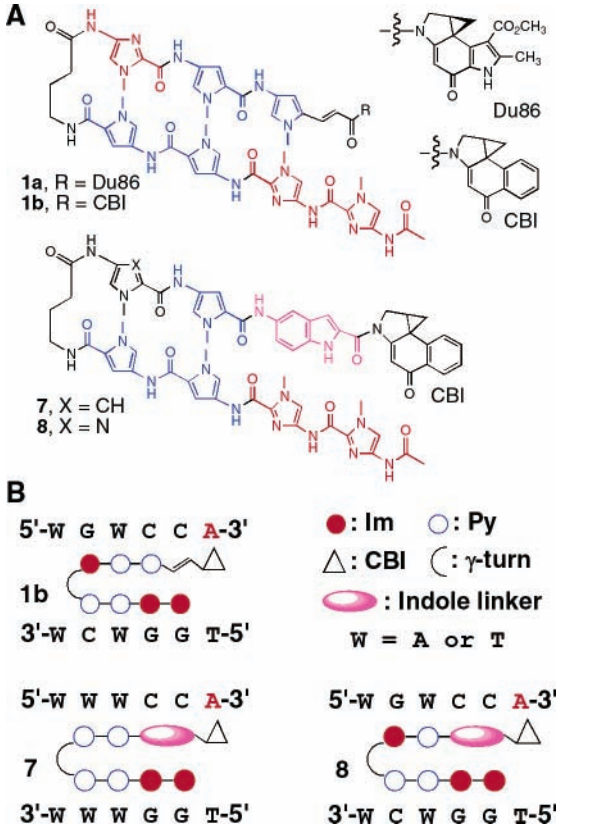

Figure 1. (A) Structures of compounds **1a**,**b**, **7**, and **8**. (B) Schematic representations of the DNA alkylation of the specific sequence by compounds **1b**, **7**, and **8**.

Here we report the synthesis and evaluation of hairpin Py-Im polyamide−CBI conjugates **7**, and **8** and seco-CBI conjugates **6b** and **10**, which specifically alkylate DNA. In particular, compound **10**, with a 10-ringed hairpin Py-Im polyamide specifically alkylated at adenine of the targeted nine-base-pair matching sequence, 5′-ACAAATCC**A**-3′ at nanomolar concentrations.

[a] Reaction conditions: (i) Fmoc solid-phase synthesis then 1 N NaOH, DMF; (ii) HATU, $^{i}Pr_2NEt$, DMF then **3**, $^{i}Pr_2NEt$, DMF; (iii) **5**, EDCI, $NaHCO_3$, DMF; (iv) 5% aq. $NaHCO_3$: DMF = 1:1.

10.1021/bc060022w CCC: $33.50 © 2006 American Chemical Society
Published on Web 04/27/2006

EXPERIMENTAL PROCEDURES

Materials. Reagents and solvents were purchased from standard suppliers and used without further purification. Abbreviations of some reagents: $^{i}Pr_2NEt$, *N*,*N*-diisopropylethylamine; DMF, *N*,*N*-dimethylformamide; HATU, *O*-(7-azabenzotriazole-1-yl)-1,1,3,3-tetramethyluronium; EDCI, 1-ethyl-3-(3-dimethylaminopropyl)carbodiimide hydrochloric salt. NMR spectra were recorded with a JEOL JNM-A 500 nuclear magnetic resonance spectrometer, and tetramethylsilane was used as the internal standard. Proton NMR spectra were recorded in parts per million (ppm) downfield relative to tetramethylsilane. Electrospray ionization mass spectrometry (ESI-MS) and electrospray ionization time-of-flight mass spectrometry (ESI-TOFMS) were produced on a API 150 (PE SCIEX) and BioTOF II (Bruker Daltonics) mass spectrometer. Polyacrylamide gel electrophoresis was performed on a HITACHI 5500-S DNA sequencer. Ex Taq DNA polymerase and Suprec-02 purification cartridges were purchased from Takara Co.; the Thermo Sequenase core sequencing kit and loading dye (dimethylformamide with fuschin red) from Amersham Co. Ltd; 5′-Texas Red-modified DNA oligomer from Proligo Co. Ltd; and 50% Long Ranger gel solution from FMC Bioproducts.

AcImImPyPy-γ-ImPy-CO_2H (2b). AcImImPyPy-γ-ImPy-CO_2-oxime resin was synthesized in a stepwise reaction by Fmoc solid-phase protocol (Fmoc$PyCO_2H$, Fmoc$ImCO_2H$, FmocγCO_2H, HATU, DIEA, DMF). A sample of resin was cleaved with alkali conditions (1 N NaOH in DMF, 1 h, 55 °C) and purified by HPLC using a Chemcobond 5-ODS-H column (0.1% AcOH/CH_3CN 0−100% linear gradient, 0−30 min, 254 nm), to produce **2b** (20 mg, 23%) as a yellow powder. ^{1}H NMR (500 MHz, DMSO-d_6) δ 10.32 (s, 1H; NH), 10.29 (s, 1H; NH), 10.23 (s, 1H; NH), 10.00 (s, 1H; NH), 9.91 (s, 1H; NH), 9.32 (s, 1H; NH), 8.02 (s, 1H; NH), 7.56 (s, 1H; Im-H), 7.50 (s, 1H; Im-H), 7.45 (s, 1H; Py-H), 7.44 (s, 1H; Im-H), 7.27 (s, 1H; Py-H), 7.16 (s, 1H; Py-H), 7.14 (s, 1H; Py-H), 6.92 (s, 1H; Py-H), 6.89 (s, 1H; Py-H), 4.00 (s, 3H; NCH_3), 3.97 (s, 3H; NCH_3), 3.93 (s, 3H; NCH_3), 3.84 (s, 3H; NCH_3), 3.81 (s, 3H; NCH_3), 3.79 (s, 3H; NCH_3), 3.19 (m, 2H; CH_2), 2.34 (m, 2H; CH_2), 2.03 (s, 3H; $COCH_3$), 1.78 (m, 2H; CH_2); ESI-TOFMS *m*/*e* calcd for $C_{39}H_{45}N_{16}O_9$ [M^+ + H] 881.35, found 881.36. A synthetic protocol similar to that used for the preparation of compound **2b** was followed to prepare compound **2a** using Fmoc solid-phase protocol.

H_2N-Indole-CO_2H (3). Compound **3** was synthesized by two stepwise reactions from commercially available ethyl 5-nitroindole-2-carboxylate (hydrolysis by 1 N aq. NaOH, then hydrogenation by hydrogen gas catalyzed by palladium−carbon), which was used in the next coupling step without further purification. ^{1}H NMR (500 MHz, DMSO-d_6) δ 11.22 (s, 1H; NH), 7.11 (d, 1H, *J* = 8.5 Hz; CH), 6.75 (d, 1H, *J* = 2.0 Hz; CH), 6.67 (s, 1H; CH), 6.65 (dd, 1H, *J* = 2.0, 8.5 Hz; CH), 3.31 (brs, 2H; NH_2 and H_2O); ESI-TOFMS *m*/*e* calcd for $C_9H_9N_2O_2$ [M^+ + H] 177.06, found 177.02.

AcImImPyPy-γ-ImPy-Indole-CO_2H (4b). To a solution of compound **2b** (3.5 mg, 4.0 μmol) in DMF (0.1 mL) was added $^{i}Pr_2NEt$ (1.4 μL, 8.0 μmol) and HATU (1.4 mg, 3.7 μmol), The reaction mixture was stirred for 4 h at room temperature. After the conversion from **2b** to activated ester was confirmed by HPLC and ESI-MS analysis, **3** (1.3 mg, 7.4 μmol) and $^{i}Pr_2NEt$ (1.3 μL, 7.5 μmol) were added to the reaction vessel. The reaction mixture was stirred for overnight at room temperature under N_2 atmosphere. Evaporation of the solvent gave a yellow residue by filtration, which was washed with chloroform (2 mL × 2) and water (2 mL × 2) to produce **4b** (3.0 mg, 73%) as a yellow powder. **4b** was used in the next step without further purification. ^{1}H NMR (500 MHz, DMSO-d_6) δ 11.33 (brs, 1H; NH), 10.34 (s, 1H; NH), 10.33 (s, 1H; NH), 10.27 (s, 1H; NH), 9.92 (s, 2H; NH), 9.73 (s, 1H; NH), 9.32 (brs, 1H; NH), 8.01 (brt, 1H; NH), 7.94 (s, 1H; CH), 7.56 (s, 1H; Im-H), 7.50 (s, 1H; Im-H), 7.46 (s, 1H; Im-H), 7.40 (brd, 1H, *J* = 8.5 Hz; CH), 7.31 (brd, 1H, *J* = 8.5 Hz; CH), 7.30 (d, 1H, *J* = 1.5 Hz; Py-H), 7.26 (d, 1H, *J* = 1.5 Hz; Py-H), 7.17 (d, 1H, *J* = 1.5 Hz; Py-H), 7.16 (s, 2H; Py-Hx2), 6.90 (d, 1H, *J* = 1.5 Hz; Py-H), 6.85 (brs, 1H; CH), 4.00 (s, 3H; NCH_3), 3.97 (s, 3H; NCH_3), 3.95 (s, 3H; NCH_3), 3.85 (s, 3H; NCH_3), 3.84 (s, 3H; NCH_3), 3.80 (s, 3H; NCH_3), 3.20 (dt, 2H, *J* = 6.0, 7.5 Hz; CH_2), 2.36 (t, 2H, *J* = 7.5 Hz; CH_2), 2.04 (s, 3H; $COCH_3$), 1.79 (qu, 2H, *J* = 7.5 Hz; CH_2); ESI-TOFMS *m*/*e* calcd for $C_{48}H_{51}N_{18}O_{10}$ [M^+ + H] 1039.40, found 1039.39.

AcImImPyPy-γ-ImPy-Indole-seco-CBI (6b). To a solution of compound **4b** (9.5 mg, 9.2 μmol) in DMF (0.4 mL) was added seco-CBI **5** (2.1 mg, 9.2 μmol), EDCI (3.5 mg, 18.3 μmol) and $NaHCO_3$ (1.5 mg, 18.3 μmol). The reaction mixture was stirred for 3 h at room temperature. Evaporation of the solvent gave a yellow residue, which was subjected to column chromatography (silica gel, 5−10% MeOH in CH_2Cl_2, gradient elution) to produce compound **6b** (4.4 mg, 3.5 μmol: 38% yield) as a yellow powder. ESI-TOFMS *m*/*e* calcd for $C_{61}H_{61}ClN_{19}O_{10}$ [M^+ + H] 1254.51; found 1254.45.

AcImImPyPy-γ-ImPy-Indole-CBI (8). To a solution of compound **6b** (1.1 mg, 0.9 μmol) in DMF (0.1 mL) was added 5% aqueous $NaHCO_3$ (0.1 mL). The reaction mixture was stirred for 1 h at room temperature. Evaporation of the solvent gave a brown residue, which was subjected to column chromatography (silica gel, 5−10% MeOH in CH_2Cl_2, gradient elution) to produce compound **8** (1.1 mg, 0.9 μmol: quantitative yield) as a brown powder. After further purification by HPLC using a Chemcobond 5-ODS-H column (0.1% AcOH/CH_3CN 0−50% linear gradient, 0−40 min, 254 nm), **8** was used in the DNA alkylation reaction.^{1}H NMR (500 MHz, DMSO-d_6) δ 11.77 (s, 1H; NH), 10.32 (s, 1H; NH), 10.29 (s, 1H; NH), 10.26 (s, 1H; NH), 9.95 (s, 1H; NH), 9.92 (s, 1H; NH), 9.82 (s, 1H; NH), 9.33 (s, 1H; NH), 8.08 (s, 1H; CH), 8.01 (brs, 1H; NH), 8.00 (d, *J* = 7.5 Hz, 1H; CH), 7.60 (t, *J* = 7.5 Hz, 1H; CH), 7.56 (s, 1H; CH), 7.53 (d, *J* = 8.5 Hz, 1H; CH), 7.50 (s, 1H; CH), 7.46 (s, 1H; CH), 7.43 (t, *J* = 7.5 Hz, 1H; CH), 7.42 (s, 1H; CH), 7.31 (s, 1H; CH), 7.27 (s, 1H; CH), 7.24 (d, *J* = 8.5 Hz, 1H; CH), 7.22 (s, 1H; CH), 7.19 (s, 1H; CH), 7.16 (d, *J* = 7.5 Hz, 1H; CH), 7.06 (s, 1H; CH), 6.95 (s, 1H; CH), 6.89 (s, 1H; CH), 4.62 (dd, *J* = 10.0, 5.0 Hz, 1H; NCH_2), 4.48 (d, *J* = 10.0 Hz, 1H; NCH_2), 4.00 (s, 3H; NCH_3), 3.97 (s, 3H; NCH_3), 3.95 (s, 3H; NCH_3), 3.86 (s, 3H; NCH_3), 3.84 (s, 3H; NCH_3), 3.80 (s, 3H; NCH_3), 3.20 (m, 2H; CH_2), 2.90 (m, 1H; CH), 2.35 (m, 2H; CH_2), 2.03 (s, 3H; $COCH_3$), 1.79 (m, 2H; CH_2), 1.76 (dd, *J* = 7.5, 5.0 Hz, 1H; CH), 1.70 (t, *J* = 5.0 Hz, 1H; CH); ESI-TOFMS *m*/*e* calcd for $C_{61}H_{60}N_{19}O_{10}$ [M^++H] 1218.48, found 1218.48.

AcImImPyPy-γ-PyPy-Indole-CBI (7). A synthetic procedure similar to that used for the preparation of compound **8** was followed to prepare compound **7**, with a yield of 6% for two steps from **2a**. After further purification by HPLC using a Chemcobond 5-ODS-H column (0.1% AcOH/CH_3CN 0−50% linear gradient, 0−40 min, 254 nm), **8** was used in the DNA alkylation reaction. ESI-MS *m*/*e* calcd for $C_{62}H_{61}N_{18}O_{10}$ [M^+ + H] 1217.5, found 1217.4.

AcImImPy-β-PyPyIm-γ-PyPyP-β-Py-CO_2H (9). AcImImPy-β-PyPyIm-γ-PyPyPy-β-$PyCO_2$-oxime resin was synthesized in a stepwise reaction by Fmoc solid-phase protocol. A sample of resin was cleaved with alkali conditions (1 N NaOH in DMF, 1 h, 55 °C) and purified by HPLC using a Chemcobond 5-ODS-H column (0.1% AcOH/CH_3CN 0−100% linear gradient, 0−30 min, 254 nm), to produce **9** (31 mg, 21%) as a yellow powder. ^{1}H NMR (400 MHz, DMSO-d_6) δ 10.29 (s, 1H), 10.26 (s, 1H), 10.24 (s, 1H), 9.90 (s, 1H), 9.89 (s, 1H), 9.87 (s, 1H),

9.86 (s, 1H), 9.85 (s, 1H), 9.81 (s, 1H), 9.34 (s, 1H), 8.07 (s, 1H), 8.03 (s, 1H), 8.01 (s, 1H), 7.55 (s, 1H), 7.49 (s, 1H), 7.48 (s, 1H), 7.31 (s, 1H), 7.28 (s, 1H), 7.23 (s, 1H), 7.23 (s, 1H), 7.22 (s, 1H), 7.18 (s, 1H), 7.15 (s, 1H), 7.06 (s, 1H), 7.02 (s, 1H), 6.96 (s, 1H), 6.88 (s, 1H), 6.86 (s, 1H), 6.82 (s, 1H), 6.65 (s, 1H), 3.99 (s, 3H), 3.97 (s, 3H), 3.93 (s, 3H), 3.84 (s, 3H), 3.83 (s, 3H), 3.82 (s, 3H), 3.81 (s, 3H), 3.80 (s, 3H), 3.79 (s, 3H), 3.78 (s, 3H), 3.43 (m, 6H), 2.50 (m, 4H), 2.27 (m, 2H), 2.03 (s, 3H), 1.81 (m, 2H); ESI-TOFMS *m*/*e* calcd for $C_{69}H_{79}N_{26}O_{15}$ [M^+ + H] 1511.61; found 1511.63.

AcImImPy-β-PyPyIm-γ-PyPyPy-β-Py-Indole-seco-CBI (10). A synthetic procedure similar to that used for the preparation of compound **6b** was followed to prepare compound **10**, with a yield of 14% for two steps from **9**. After further purification by HPLC using a Chemcobond 5-ODS-H column (0.1% AcOH/CH_3CN 0−50% linear gradient, 0−40 min, 254 nm), **10** was used in the DNA alkylation reaction. ESI-TOFMS *m*/*e* calcd for $C_{91}H_{95}ClN_{29}O_{16}$ [M^+ + H] 1884.71; found 1884.70.

Preparation of 5′-Texas Red-Modified DNA Fragments. The 5′-Texas Red-modified 537-bp DNA fragment, λ-DNA F10960*-11496, was prepared by polymerase chain reaction (PCR) with 5′-TexasRed-modified-ATCAGGGCAACTCAACCCTGTCC-3′ (λ-DNA forward, 10960−10982) and 5′-CAGGACGACCAATATCCAGC-3′ (λ-DNA reverse, 37007−37026). The 5′-Texas Red-modified 488-bp DNA fragment, λ-DNA F30990*-31477, was prepared by polymerase chain reaction (PCR) with 5′-Texas Red-modified-TGCATTCCGTGGTTGTCATACC-3′ (λ-DNA forward, 30990−31011) and 5′-GCATTATGTCGTGATTGAGC-3′ (λ-DNA reverse, 17045−17064). Fragments were purified by filtration using Suprec-02, and their concentrations were determined by UV absorption. The asterisk indicates Texas Red modification and the nucleotide numbering starts with the replication site.

High-Resolution Gel Electrophoresis. The 5′-Texas Red-labeled DNA fragments (10 nM) were alkylated by various concentration of **7**, **8**, and **6b** in 10 μL of 5 mM sodium phosphate buffer (pH 7.0) containing 10% DMF at 23 °C for 15 h. The reaction was quenched by the addition of calf thymus DNA (1 mM, 1 μL) and heating for 5 min at 90 °C. The DNA was recovered by vacuum centrifugation. The pellet was dissolved in 8 μL of loading dye (formamide with fuschin red), heated at 94 °C for 20 min, and then immediately cooled to 0 °C. A 2-μL aliquot was subjected to electrophoresis on a 6% denaturing polyacrylamide gel using a Hitachi 5500-S DNA Sequencer.

Molecular Modeling Studies. Density functional calculations were performed at the B3LYP/6-31G* level utilizing Spartan 04 (Wave function, Irvine, CA) program. Energy minimizations of d(ATACAAATCCAAT)/d(ATTGGATTTGTAT)-**11** were performed with the Discover (Accelrys, San Diego, CA) program using CFF force-field parameters. The starting structure was built on the basis of the NMR structure of the ImPyPy-γ-PyPyPy-d(CGCTAACAGGC)/d(GCCTGTTAGCG) complex (*21*) and the Duo-Dist-octamer complex (*22*). The connecting parts between them were built using standard bond lengths and angles. The CBI unit of the assembled initial structure was energy minimized using a distance-dependent dielectric constant of $\epsilon = 4r$ (r stands for the distance between atoms i and j) and with convergence criteria having an RMS gradient of less than 0.001 kcal/mol Å. Eighteen Na cations were placed at the bifurcating position of the O−P−O angle at a distance of 2.51 Å from the phosphorus atom. The resulting complex was soaked in a 10-Å layer of water. The whole system was minimized without any constraint, to the stage where the RMS was less than 0.001 kcal/mol Å.

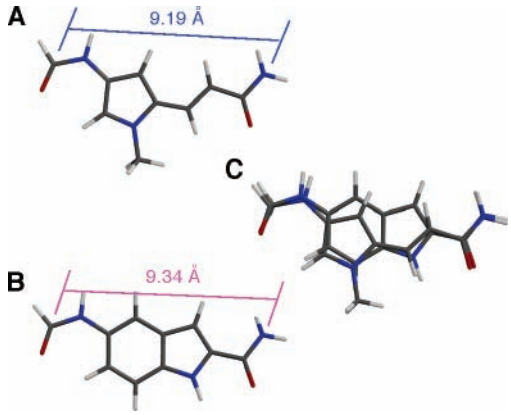

Figure 2. Geometry optimized structures of (*E*)-3-(4-formamido-1-methyl-1*H*-pyrrol-2-yl)acrylamide (A) and 5-formamido-1*H*-indole-2-carboxamide (B) and their superimposition (C) obtained by density functional calculation at the B3LYP/6-31G* level.

RESULTS AND DISCUSSION

Molecular Design of Linker Unit. A vinyl linker between the Py-Im polyamides and CBI moiety is highly advantageous for DNA alkylation, as it facilitates highly specific DNA alkylation by adjusting the position of the CBI moiety in the minor groove. However, the vinyl linker moiety has certain disadvantages in the molecular design of alkylating Py-Im polyamides, as it is relatively unstable under acidic and basic conditions, and it suffers from low chemical yields. Because ethyl 3-(4-amino-*N*-methyl-pyrrol-2-yl)acrylate is extremely unstable, Py-Im polyamides prepared by a solid phase method cannot easily be employed in the synthesis of alkylating agents which possess vinyl linkers. Therefore, we synthesized various alkylating Py-Im polyamides by a combination of time-consuming liquid-phase coupling reactions.[4] To overcome these problems, we searched for a new linker that could provide almost the same geometry as Py with a vinyl linker and is stable.

We chose a 5-amino-1*H*-indole-2-carbonyl linker (indole linker) as the new linker, because amide linkages of this unit are approximately superimposable with Py with a vinyl linker. Similarity of structures between 5-formamido-1*H*-indole-2-carboxamide and (*E*)-3-(4-formamido-1-methyl-1*H*-pyrrol-2-yl)-acrylamide was estimated by density functional calculation at the B3LYP/6-31G* level (Figure 2). We expected that Py-Im polyamide-indole−CBI conjugates **7** and **8** would alkylate DNA in a sequence-specific fashion (Figure 1b). Indole linker unit has already been used in the synthesis of derivatives of CC-1065 (*23*).

Synthesis of Hairpin Py-Im Polyamide−CBI Conjugates with Indole Linker, 7 and 8. Conjugates **7** and **8** were synthesized as shown in Scheme 1. The six-ring Py-Im polyamides **2a** and **2b**, both of which have terminal carboxylic acid groups, were prepared by Fmoc solid-phase synthesis using an oxime resin (*24*−*26*), and purified by reversed-phase HPLC. Indole linker unit **3** was synthesized by hydrolysis of commercially available ethyl 5-nitro-1*H*-indole-2-carboxylate, followed by reduction using palladium−carbon and H_2 gas. The carboxylic acids **2a** and **2b** were converted to activating esters with HATU and $^iPr_2NEt$, followed by coupling with **3** to give **4a** and **4b**. The DNA alkylating moiety, seco-CBI **5**, was prepared according to procedures from the literature (*16*). Conjugates **6a** and **6b** were synthesized by the coupling of **4a** and **4b** with seco-CBI **5** using EDCI and $NaHCO_3$. Treatment of **6a** and **6b** with aqueous 5% $NaHCO_3$ provided **7** and **8**, respectively. Use of Fmoc solid phase synthesis greatly facilitates the synthesis of alkylating Py-Im polyamides. For example, conjugate **8** was synthesized with an overall yield of 6.4%. In contrast, conjugate **1b** with a vinyl linker, prepared by the 22

Scheme 1 [a]

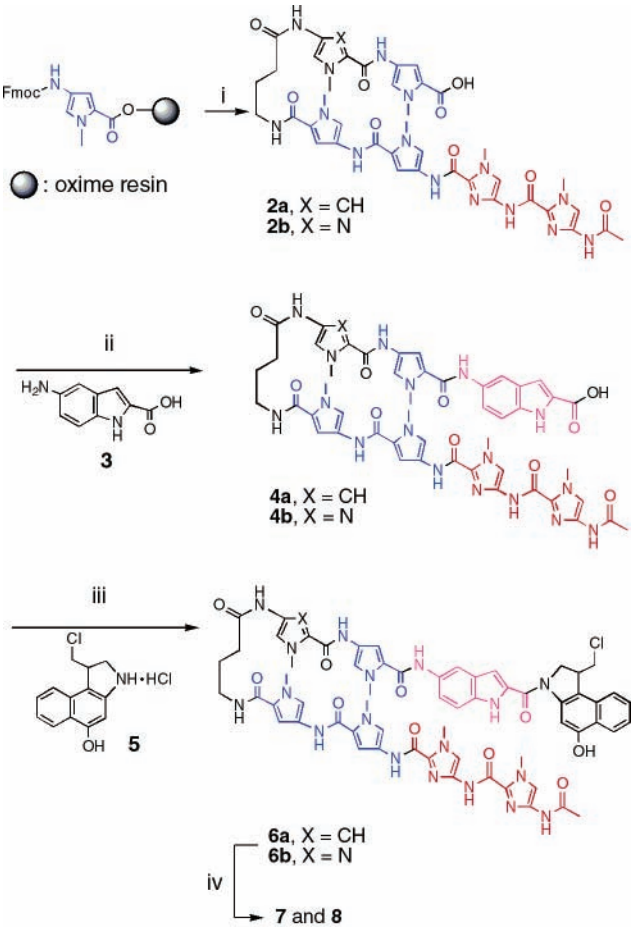

steps of a convergent liquid-phase synthesis, gave an overall yield of 0.1% (*19*). The purity and identity of conjugates **7** and **8** were verified by reversed-phase analytical HPLC and ESI-TOF mass spectrometry.

Evaluation of DNA Alkylating Activity. Sequence-selective alkylation by compounds **7**, **8**, and **6b** was investigated using the 5′-Texas Red-labeled 537 bp DNA fragments λ-DNA F10960*-11496 using an automated DNA sequencer. Alkylation was carried out at 23 °C for 15 h, followed by quenching by the addition of calf thymus DNA. The samples were heated at 94 °C under neutral conditions for 20 min. The alkylation sites were visualized by thermal cleavage of the DNA strand at the alkylated sites. Under these heating conditions, all the purine N3 alkylated sites in the DNA almost quantitatively produced cleavage bands on the gel. Sequencing analysis of the alkylated DNA fragments after heat treatment is shown in Figure 3. The conjugates with indole linkers, **7** and **8**, produced discrete cleavage bands at nanomolar concentrations. Efficient alkylation by **7** occurred at site 1, 5′-AATCC**A**-3′, and site 2, 5′-TAACC**A**-3′, only at a concentration of 10 nM (lane 3). Similarly, alkylation by **8** was observed at the four match sites, 3−6, 5′-WGWCC**A**-3′ (W = A or T; lanes 7−10) with no alkylation at the mismatch site. These results clearly indicate that **7** and **8** efficiently alkylate DNA in a sequence-specific fashion at nanomolar concentrations, as does **1b** (*19*), and the indole moiety acts as an appropriate substitute for the vinyl linker.

We confirmed that seco-CBI conjugate **6b**, which is quantitatively converted to **8** under basic conditions, efficiently alkylates DNA at target sequences, 5′-WGWCC**A**-3′ (lanes 12−14), as does CBI conjugate **8**. It is assumed that **6b** readily converts to **8** in aqueous buffered solution. Analogous in situ cyclization to reactive aziridines for DNA alkylation was found

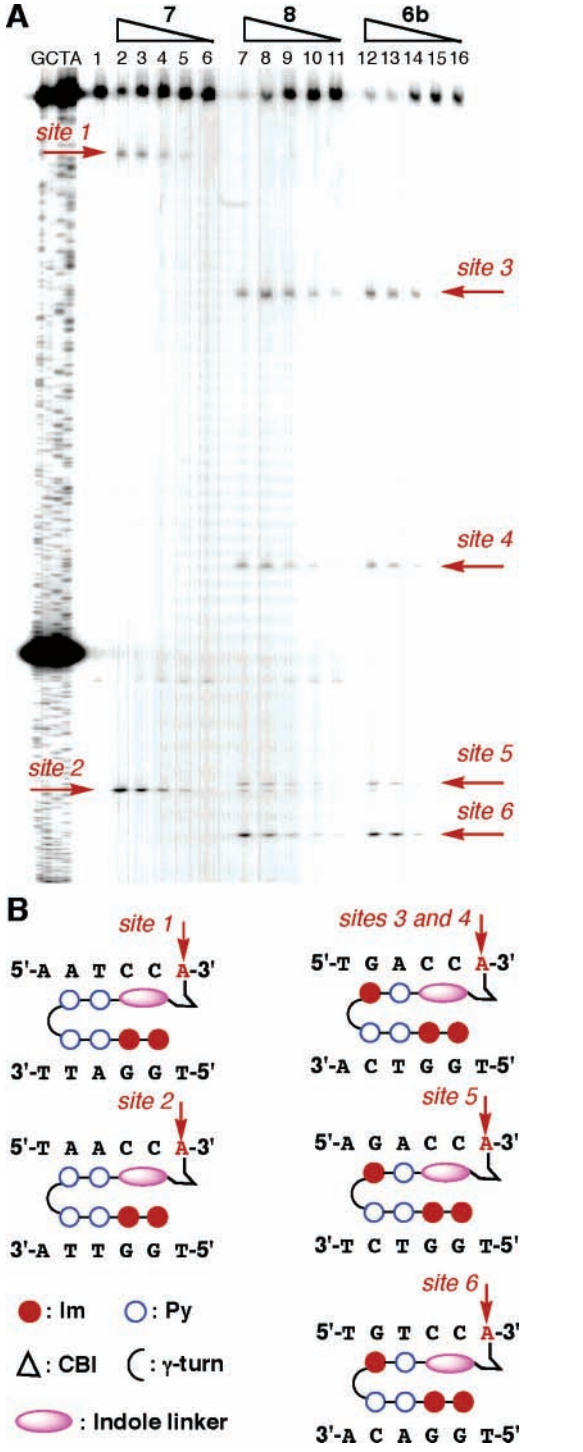

Figure 3. (A) Thermally induced strand cleavage of the 5′-Texas Red-labeled 537 bp DNA fragment λ-DNA F10960*-11496 by conjugates **7**, **8**, and **6b** at 23 °C for 15 h: Lane 1 = DNA control; Lanes 2−6 = 20, 10, 5, 2, and 1 nM of **7**; Lanes 7−11 = 20, 10, 5, 2, and 1 nM of **8**; Lanes 12−16 = 20, 10, 5, 2, and 1 nM of **6b**. (B) Schematic representation of the recognition of matching sequences by **7** and **8**. The arrows indicate the site of alkylation by **7** and **8**.

for both mitomycin C and nitrogen mustard (*23*). In addition, this result is consistent with the previous results for Py-Im derivatives with seco-CBI (*27*).

Synthesis and Evaluation of DNA Alkylating Activity using seco-CBI Conjugate 10. Toward the goal of sequence-specific alkylating agents that target specific genes, alkylating polyamides that recognize longer sequences are desirable. Thus, we designed and synthesized seco-CBI conjugate **10** by coupling of carboxylic acid **9**, prepared by Fmoc solid-phase synthesis

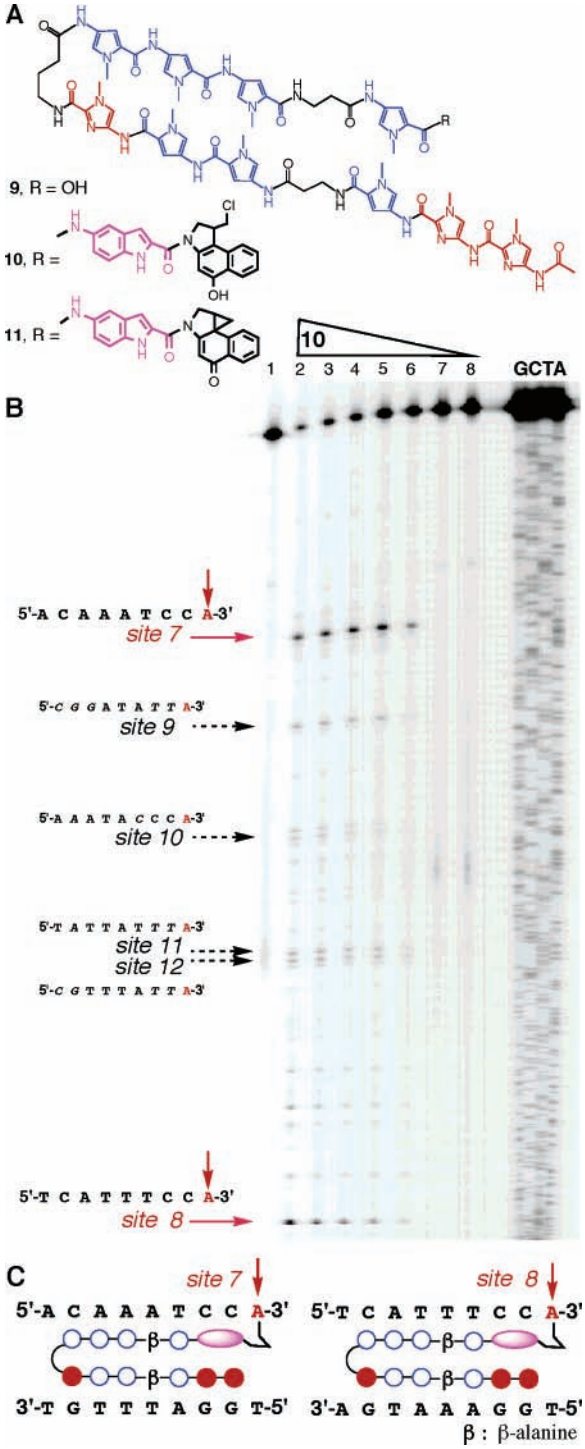

Figure 4. (A) Chemical structures of compound **9**, **10**, and **11**. (B) Thermally induced strand cleavage of the 5′-Texas Red-labeled 488 bp DNA fragment, λ-DNA F30990*-31477, by conjugate **10** at 37 °C for 15 h: Lane 1 = DNA control; Lanes 2−8 = 1000, 800, 600, 400, 200, 100, and 50 nM of **10**. Sites 7 and 8 = match sequences, sites 9−12 = mismatch sequences. (C) Schematic representation of the recognition in matching sequences by **10**. The arrows indicate the site of alkylation. The alkylating base is shown in red bold, and the mismatch-binding base is shown in italics.

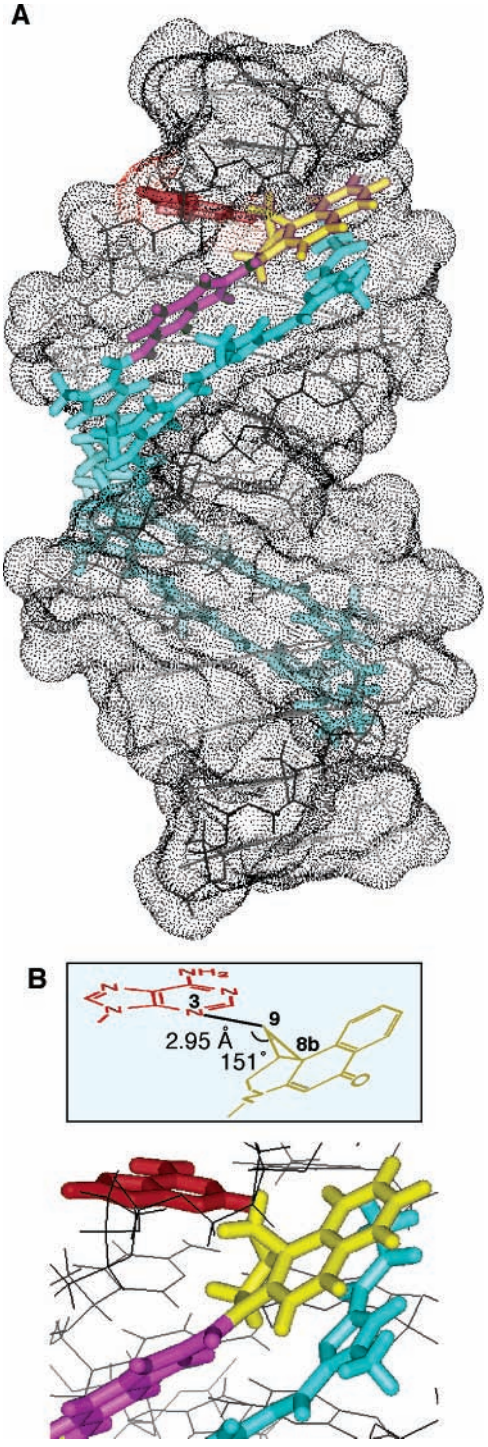

Figure 5. The energy-minimized structure of d(ATACAAATCCAAT)/d(ATTGGATTTGTAT)-**11** (A). The alkylating base is shown in orange and the minor-groove-binding Py-Im polyamide is shown in blue. The indole linker is shown in purple, and the CBI moiety is shown in yellow. Schematic representation of distance and angle of N3 of adenine and CBI (B).

in 21% yield, with **3** and successively with seco-CBI **5** (Figure 4a). It is important to note that the synthesis of the larger polyamide proceeded as smoothly as for **7** and **8**. Sequencing gel analysis clearly indicated that the seco-CBI conjugate **10** alkylated predominantly at the adenine of the nine-base-pair matching sequence 5′-ACAAATCC**A**-3′ (site 7) and 5′-TCATTTCC**A**-3′ (site 8, lanes 2−6), together with faint mismatch alkylations at the A of 5′-*CGG*ATA*TT***A**-3′ (site 9), 5′-A*A*ATA*CCC***A**-3′ (site 10), 5′-T*A*TTATT*TT***A**-3′ (site 11) and 5′-*CG*TTTA*TT***A**-3′ (site 12). It is assumed that **10** readily converts to **11** under the reaction conditions. Differences in reaction rates for each sequence can be a consequence of many associated factors, which require further investigation for detailed understanding. To the best of our knowledge, the present result is the first example of the sequence-specific Py-Im alkylating polyamide recognizing a nine-base-pair sequence.

Model of Binding of 11 to Target Oligonucleotides. To gain an insight into the location of the seco-CBI conjugate **10** in the DNA minor groove, we constructed the d(ATACAAATCCA$_{11}$AT)/d(ATTGGATTTGTAT)-**11** complex, which is based on the predictable structure of the CBI conjugate in the DNA minor groove. The energy-minimized structures suggest that binding of **11** to the minor groove of d(ATACAAATCCA$_{11}$AT)/d(ATTGGATTTGTAT) is located in close proximity to the nucleophilic N3 of the A$_{11}$ residues: 2.95 Å, with the angle of the N3−C9−C8b bond = 151° (Figure 5). The similar binding orientations of the vinyl-linked CPI and CBI conjugates would indicate induction of alkylation at a specific nine-base-pair sequence.

CONCLUSIONS

We have successfully synthesized Py-Im hairpin polyamide CBI conjugates **7** and **8**, and the corresponding seco-CBI conjugates with indole linker, **6a** and **b**, together with the longer alkylating conjugate **10** using Fmoc solid phase synthesis and a subsequent liquid phase coupling procedure. We have evaluated these DNA alkylating polyamides in detail using high-resolution denaturing gel electrophoresis employing DNA fragments. The results clearly indicate that Py-Im CBI conjugates **7**, **8**, **6b**, and **10** efficiently alkylate at specific DNA sequences. Importantly, the selectivity and the efficiency of DNA alkylation by **8** were as good as those of the corresponding CBI conjugate **1b**. In particular, we have clearly demonstrated successful sequence-specific DNA alkylation by the seco-CBI conjugate **10**, which alkylates a specific nine-base-pair sequence, 5′-ACAAATCC**A**-3′. Furthermore, introduction of an indole linker greatly facilitated the synthesis of sequence-specific alkylating Py-Im polyamides. To open the next door toward the goal of developing antitumor agents, the design of new indole−CBI conjugates will allow further biological studies.

ACKNOWLEDGMENT

This work was supported by a Grant-in-Aid for Priority Research from the Ministry of Education, Culture, Sports, Science, and Technology, Japan.

LITERATURE CITED

(1) Denison, C., and Kodadek, T. (1998) Small-molecule-based strategies for controlling gene expression. *Chem. Biol. 5*, R129−145.
(2) Hurley, L. H. (2002) DNA and its associated processes as targets for cancer therapy. *Nat. Rev. Cancer. 2*, 188−200.
(3) Baraldi, P. G., Bovero, A., Fruttarolo, F., Preti, D., Tabrizi, M. A., Pavani, M. G., and Romagnoli, R. (2004) DNA minor groove binders as potential antitumor and antimicrobial agents. *Med. Res. Rev. 24*, 475−528.
(4) Dervan, P. B. (2001) Molecular recognition of DNA by small molecules. *Bioorg. Med. Chem. 9*, 2215−2235.
(5) Dervan, P. B., and Edelson, B. S. (2003) Recognition of the DNA minor groove by pyrrole-imidazole polyamides. *Curr. Opin. Struct. Biol. 13*, 284−299.
(6) Nagamura, S., Asai, A., Kanda, Y., Kobayashi, E., Gomi, K., and Saito, H. (1996) Synthesis and antitumor activity of duocarmycin derivatives: modification of segment A of duocarmycin B2. *Chem. Pharm. Bull. 44*, 1723−1730.
(7) Tao, Z.-F., Saito, I., and Sugiyama, H. (2000) Highly cooperative DNA dialkylation by the homodimer of imidazole-pyrrole diamide-CPI conjugate with vinyl linker. *J. Am. Chem. Soc. 122*, 1602−1608.
(8) Bando, T., Iida, H., Saito, I., and Sugiyama, H. (2001) Sequence-specific DNA interstrand cross-linking by imidazole-pyrrole CPI conjugate. *J. Am. Chem. Soc. 123*, 5158−5159.
(9) Bando, T., Narita, A., Saito, I., and Sugiyama, H. (2002) Molecular design of pyrrole-imidazole hairpin polyamide for effective DNA alkylation. *Chem.-Eur. J. 8*, 4781−4790.
(10) Bando, T., Narita, A., Saito, I., and Sugiyama, H. (2003) Highly efficient Sequence-specific DNA interstrand cross-linking by pyrrole/imidazole CPI conjugates. *J. Am. Chem. Soc. 125*, 3471−3485.
(11) Bando, T., Iida, T., Tao, Z.-F., Narita, A., Fukuda, N., Yamori, T., and Sugiyama, H. (2003) Sequence-specificity, reactivity and antitumor activity of DNA alkylating pyrrole-imidazole diamides. *Chem. Biol. 10*, 751−758.
(12) Bando, T., Narita, A., Iwai, A., Kihara, K., and Sugiyama, H. (2004) C−H to N substitution dramatically alters the sequence-specific DNA alkylation, cytotoxicity, and expression of human cancer cell lines. *J. Am. Chem. Soc. 126*, 3406−3407.
(13) Oyoshi, T., Kawakami, W., Narita, A., Bando, T., and Sugiyama, H. (2003) Inhibition of transcription at a coding sequence by alkylation polyamide. *J. Am. Chem. Soc. 125*, 4752−4754.
(14) Shinohara, K., Narita, A., Oyoshi, T., Bando, T., Teraoka, H., and Sugiyama, H. (2004) Sequence-specific gene silencing in mammalian cells by alkylating pyrrole-imidazole polyamides. *J. Am. Chem. Soc. 126*, 5113−5118.
(15) Boger, D. L., Ishizaki, T., Kitos, P. A., and Suntornwat, O. (1990) Synthesis of *N*-(*tert*-butyloxycarbonyl)-CBI, CBI, CBI−CDPI1, and CBI-CDPI2: enhanced functional analogues of CC-1065 incorporating the 1,2,9,9a-tetrahydrocyclopropa[c]benz[*e*]indol-4-one (CBI) left-hand subunit. *J. Org. Chem. 55*, 5823−5832.
(16) Boger, D. L., Yun, W. Y., and Teegarden, B. R. (1992) An improved synthesis of 1, 2, 9, 9a-tetrahydrocyclopropa[c]benz[*e*]-indol-4-one (CBI): a simplified analog of the CC-1065 alkylation subunit. *J. Org. Chem. 57*, 2873−2876.
(17) Boger, D. L., and McKie, J. A. (1995) An efficient synthesis of 1, 2, 9, 9a-tetrahydrocyclopropa[c]benz[*e*]indol-4-one (CBI): an enhanced and simplified analog of the CC-1065 and duocarmycin alkylation subunits. *J. Org. Chem. 60*, 1271−1275.
(18) Kastrinsky D. B., and Boger, D. L. (2004) Effective asymmetric synthesis of 1,2,9,9a-tetrahydrocyclopropa[c]benz[*e*]indol-4-one (CBI). *J. Org. Chem. 69*, 2284−2289.
(19) Bando, T., Narita, A., Asada, K., Ayame, H., and Sugiyama, H. (2004) Enantioselective DNA alkylation by a pyrrole-imidazole S−CBI conjugate. *J. Am. Chem. Soc. 126*, 8948−8955.
(20) Bando, T., Narita, A., Sasaki, S., and Sugiyama, H. (2005) Specific adenine alkylation by pyrrole-imidazole CBI conjugates. *J. Am. Chem. Soc. 127*, 13890−13895.
(21) de Clairac, R. P. L., Geierstanger, B. H., Mrksich, M., Dervan, P. B., and Wemmer, D. E. (1997) NMR characterization of hairpin polyamide complexes with the minor groove of DNA. *J. Am. Chem. Soc. 119*, 7909−7916.
(22) Sugiyama, H., Lian, C. Y., Isomura, M., Saito, I., and Wang, A. H.-J. (1996) Distamycin A modulates the sequence specificity of DNA alkylation by duocarmycin A. *Proc. Natl. Acad. Sci. U.S.A. 93*, 14405−14410.
(23) Wolkenberg S. E., and Boger, D. L. (2002) Mechanisms of in situ activation for DNA-targeting antitumor agents. *Chem. Rev. 102*, 2477−2495.
(24) Baird, E. E., and Dervan, P. B. (1996) Solid-phase synthesis of polyamides containing imidazole and pyrrole amino acids. *J. Am. Chem. Soc. 118*, 6141−6146.
(25) Wurtz, N. R., Turner, J. M., Baird, E. E., and Dervan, P. B. (2001) Fmoc solid-phase synthesis of polyamides containing pyrrole and imidazole amino acids. *Org. Lett. 3*, 1201−1203.
(26) Belitsky, J. M., Nguyen, D. H., Wurtz, N. R., and Dervan, P. B. (2002) Solid-phase synthesis of DNA binding polyamides on oxime resin. *Bioorg. Med. Chem. 10*, 2767−2774.
(27) Chang A. Y., and Dervan, P. B. (2000) Strand selective cleavage of DNA by diastereomers of hairpin polyamide-*seco*-CBI conjugates. *J. Am. Chem. Soc. 122*, 4856−4864.

BC060022W

Folate Immobilized and PEGylated Adenovirus for Retargeting to Tumor Cells

In Kyung Oh, Hyejung Mok, and Tae Gwan Park*

Department of Biological Sciences, Korea Advanced Institute of Science and Technology, 373-1 Guseong-dong, Yuseong-gu, Daejeon 305-701, Korea. Received February 4, 2006

The surface of adenovirus (ADV) was modified with folate−poly(ethylene glycol) (FOL−PEG) conjugate to overcome the inherent problems associated with viral gene therapy. The ADV coding the green fluorescent protein (GFP) gene was used to immobilize PEG or FOL−PEG conjugate on the viral surface to comparatively evaluate their extents of retargeting and immune response, as compared to those of naked ADV. The FOL−PEG immobilized ADV exhibited a greatly enhanced level of GFP expression than naked or PEG immobilized ADV for a folate receptor overexpressing cell line (KB cells), but not for a folate receptor deficient cell line (A549 cells), suggesting that the retargeting of ADV could be achieved by immobilizing FOL−PEG conjugate. The ADV immobilized with PEG or FOL−PEG also significantly lowered innate immune response, as judged from the amount of interleukin 6 released from macrophage cells.

INTRODUCTION

Gene therapy employs a variety of viral and nonviral vectors. An ideal vector system for practical in vivo applications is yet to be used. Viral vectors show very high transfection efficiency, but have inherent safety problems mainly relating to undesirable immune responses. In contrast, nonviral vectors mostly using cationic lipids and polymers exhibit relatively lower gene transfection efficiencies than the viral vectors, but elicit little immune reactions. Adenovirus (ADV) has been used extensively for gene therapy (*1*). The ADV, which can carry foreign DNA of a relatively big size (*2*), normally exhibits high transduction and gene expression efficiencies in many human dividing and nondividing cells, compared to other available viral vectors (*3*). The knob domain of fiber proteins protruded on the viral surface forms a high-affinity complex with a host cell surface receptor protein (coxsackie-adenovirus receptor (CAR)) (*4*). CAR-mediated viral infection is known to be a major route of cellular uptake for many types of cells expressing CAR on the surface (*4*). This limits the versatility of ADV vectors for target-specific gene therapy. They have to be administered locally with repeated injections to maintain a long-term sustainable effect. Most ADV vectors derived from serotype 5 have defective replication abilities, also requiring repetitive administrations. As a result, serious innate and adaptive immune responses are provoked (*5*).

Several strategies were introduced to overcome the immune response problems of ADV vectors: use of immunosuppressants (*6*), coadministration of interferon γ or interleukin 12 (*7*), and the use of ablative agents (*8*). Recently, a new approach for minimizing the immune response from ADV was explored with use of poly(ethylene glycol) (PEG) (*9*−*13*). PEG modification (PEGylation) is a well-established technique for therapeutic peptides and proteins that need prolonged circulation in the bloodstream (*9*). Additionally, it is known that PEGylated proteins elicit immune responses to a lesser extent. It was previously shown that PEGylated ADV could retain considerable transfection efficiency even in the presence of ADV-neutralizing antibodies (*14*−*16*) and exhibited prolonged resistance in the blood (*17*). However, PEGylated ADV still transfected cells in a nonspecific manner via a CAR-mediated viral infection mechanism. To solve this problem, genetically modified ADV expressing cell recognizable peptide and protein ligands on the surface were constructed to achieve cell-specific retargeting (*7*, *17*, *29*)

In this study, the surface of ADV having a GFP gene was immobilized with folate (FOL) as a retargeting moiety using a PEG spacer. It was postulated that the immobilized PEG could minimize the innate immune response problem to some extent, and the FOL moiety at the distal end of the PEG chain could redirect the ADV to FOL receptor overexpressing tumor cells in a specific manner. FOL receptors are overexpressed in many cancerous cells (*18*−*19*), which was exploited for specifically targeting anticancer agents, gene, and imaging agents to the tumor cells by using FOL-conjugated nanoparticulate carriers (*20*−*22*). In our previous studies, FOL−PEG conjugates were attached to nonviral cationic polymers to promote cell-specific gene transfection efficiency (*23*−*27*). To this end, FOL−PEG conjugate was synthesized and immobilized on the surface of ADV to comparatively evaluate the extent of cell-specific GFP transfection using FOL receptor overexpressing and deficient cell lines. The extent of immune response elicited by the surface modified ADV was also analyzed by determining the amount of interleukin 6 released from macrophage cells.

MATERIALS AND METHODS

Materials. ADV containing the GFP gene was obtained from QBIOgene (AD5.CMV5-GFP) (Montreal, Canada). Hetero-bifunctional poly(ethylene glycol) derivative (NH_2-PEG-COOH, MW 3400), methoxy-PEG-NHS (MW 3400), and fluorescein-PEG-NHS (MW 3400) were purchased from Nektar (Huntsville, AL). Folate (FOL, MW 440), dicyclohexylcarbodiimide (DCC), *N*-hydroxysuccinimide (NHS), DMSO, acetone, $CsCl_2$, sucrose, fluorescamine, and Triton-X 100 were purchased from Sigma (St. Louis, MO). Cell culture media and materials were products of Gibco-BRL (Grand Island, NY). HEK293 cells, A549 cells, and RAW 264.1 macrophage cells were purchased from the Korea Cell Line Bank (Seoul, Korea), and KB cells (CCL-17) were purchased from ATCC (Manassas, VA). All other chemicals were of analytical grade.

Methods. Synthesis of FOL−PEG-COOH Conjugate. FOL−PEG-COOH conjugate was synthesized according to the previous method (*23*). Briefly, FOL was activated with di-

* Corresponding author: Tel: +82-42-869-2621, Fax: +82-42-869-2610, e-mail: tgpark@kaist.ac.kr.

10.1021/bc060030c CCC: $33.50 © 2006 American Chemical Society
Published on Web 04/14/2006

cyclohexylcarbodiimide (DCC) and *N*-hydroxysuccinimide (NHS) at a 1:2:2 molar ratio in DMSO for 12 h under nitrogen atmosphere and filtered with a syringe filter (pore size: 0.2 μm). A hetero-bifunctional poly(ethylene glycol) derivative (NH_2-PEG-COOH, MW 3400) was added to the solution at a molar ratio of 15:1 (FOL:PEG). After reaction for 4 h under nitrogen atmosphere, the reactants were precipitated with acetone and centrifuged to remove free FOL residues. FOL−PEG-COOH conjugate in the supernatant was dialyzed against deionized water (SpectraPor6, MW cutoff: 1000) and freeze-dried. FOL conjugation to PEG chain was confirmed by ^{1}H NMR and matrix-assisted time-of flight mass spectrometer (MALDI-TOF, Bruker, Germany).

ADV Preparation. For expansion of ADV, 1.2×10^7 HEK293 cells were plated in a 150 mm tissue culture dish. The media used was Dulbecco's Modified Eagle Medium (DMEM) with 10% fetal bovine serum (FBS) and penicillin G sodium at 100 U/mL and streptomycin sulfate at 100 μg/mL. After reaching 60% of confluency, 1×10^{10} of ADV particles (pts) was added and continued to cultivate at 37 °C under humidified 5% CO_2 atmosphere. When over 60% of the cells were detached from the culture plate (about 30 h after virus infection), the cells were collected and lysed. The cell suspension was frozen in a liquid nitrogen bath and thawed at 37 °C three times to break up the cells. The cell lysate was centrifuged at 1500*g* for 10 min, and the supernatant containing infected adenoviral particles was collected. ADV particles were isolated using $CsCl_2$ gradient ultracentrifugation according to the established procedure (*28*). The number of ADV particles was determined by a spectrophotometer. The ADV solution was diluted to an appropriate ADV concentration with 10 mM Tris pH 8.1 and A_{260} of the diluted solution was measured. To determine the approximate number of viral particles (pts) per mL, the following equation was used: $A_{260} \times$ dilution factor $\times 10^{12} =$ pts/mL. Phosphate-buffered saline (PBS) solution containing 3% (w/v) sucrose was used as a blank (*28*).

PEGylation of ADV (ADV−PEG−FOL, ADV−PEG, and ADV−PEG−FITC). Various amounts (10^0−$10^{7.8}$ pmol) of FOL−PEG-COOH conjugate were dissolved in 3 mL of PBS solution with 5% (w/v) sucrose and preactivated with EDC and NHS (1:10:10; molar ratio of FOL−PEG-COOH/EDC/NHS) for 1 h at room temperature. To the solution, 6.02×10^{11} pts of ADV (PEG: ADV = 10^0−$10^{7.8}$:1, molar ratio) suspended in 5% sucrose/PBS solution (pH 8.1) were added to produce FOL−PEG immobilized ADV (ADV−PEG−FOL). For preparing PEGylated ADV (ADV−PEG) and FITC−PEGylated ADV (ADV−PEG-FITC), methoxy-PEG-NHS, and fluorescein-PEG-NHS were used to conjugate to ADV, respectively. After reacting for 4 h at room temperature, PEGylated ADVs were dialyzed against 3% (w/v) sucrose/PBS solution (SpectraPor 6, MW cutoff: 50 000) at 4 °C and kept at −20 °C until use.

Determination of Degree of PEGylation. An amine reactive dye, fluorescamine, was dissolved in acetone at a concentration of 7 mg/mL. One hundred microliters of fluorescamine solution was added to 900 μL of PBS containing 1.0×10^{11} pts of ADV, mixed immediately, and incubated in the dark for 15 min. The fluorescence intensity was detected by spectrofluorometer (excitation wavelength at 390 nm and emission wavelength at 475 nm). PEG-diamine (Sigma, MW: 3550) was used to construct a calibration curve.

Determination of Size and Surface Charge. The sizes and surface charges of ADV, ADV−PEG, and ADV−PEG−FOL were measured using a dynamic light scattering instrument (Zeta plus, Brookhaven, New York) equipped with a He−Ne laser at a wavelength of 632.2 nm.

Cellular Uptake of PEGylated ADV. HEK 293 cells were cultured in 10% FBS media (DMEM). Cells were maintained at 37 °C in a humidified 5% CO_2 incubator. The cells at a seeding density of 2×10^5 were plated in a four-chamber tissue culture slide well containing 1 mL of 10% FBS media. After 24 h, the cell culture medium was replaced with 500 μL of 2% FBS media containing ADV−PEG-FITC. The seeding density of ADV−PEG-FITC was 2000 pts per cell. After 4 h incubation, the cells were washed twice with PBS. To visualize the cell cytoplasm, 500 μL of 5 μM CellTracker Probe (Molecular Probes C34552, Eugene, OR) dissolved in serum-free medium was added to each well and incubated for 20 min. The cells were washed with PBS and fixed with 1% formaldehyde in PBS for 20 min at room temperature. ADV−PEG-FITC particles present within the cells and the dye stained cytoplasm were visualized by confocal laser microscopy (LSM510, Zeiss Pascal, Jena, Germany) at excitation wavelengths of 488 and 543 nm, respectively

Cell Transfection. FOL receptor overexpressing epithelial cancer cells (KB cells) and FOL receptor deficient lung carcinoma cells (A549 cells) were cultured in FOL free RPMI1640 medium. Each cell culture medium was supplemented with 10% FBS, 100 U/mL penicillin G sodium and 100 μg/mL streptomycin sulfate. KB and A549 cell lines were seeded on a six-well-plate at a cell density of 3×10^5 cells/well. After 1 day, the culture media was replaced with 2% FBS media (FOL free RPMI) and 1.2×10^9 pts of ADV, ADV−PEG, and ADV−PEG−FOL were added to each well. After 2 days, the cells were treated with 1% (w/v) Triton-X 100 for cell lysis and centrifuged at 14 000 rpm to remove cell fragments. The supernatant was used for detection of GFP expression (excitation at 488 nm and emission at 520 nm). For counting the number of cells transfected, the cells incubated for 2 days after transfection were washed with PBS and fixed with 1% formaldehyde in PBS for 20 min at room temperature and visualized by confocal laser microscopy (LSM510, Zeiss Pascal, Jena, Germany) at excitation wavelengths of 488 and 543 nm, respectively.

Assay of Immune Response. RAW 264.1 macrophage cells were seeded on a six-well-plate at a cell density of 1×10^6/well containing RPMI1640 supplemented with 10% FBS, 100 U/mL penicillin G sodium, and 100 μg/mL streptomycin sulfate. After 1 day, the culture media was replaced with 2 mL of fresh media containing 2×10^{10} pts of ADV, ADV−PEG, and ADV−PEG−FOL. After 24 h, level of interleukin-6 in the culture media was determined by ELISA (R&D Quantikine, M6000B, MN). DNA was isolated from cells using a DNeasy tissue kit (Qiagen, CA). The total DNA amount from the cultivated macrophage was determined by measuring absorbance at 260 nm. To qualitatively determine the amount of viral particles within the cells, polymerase chain reaction (PCR) was performed on the extracted DNA from RAW 264.1 cells with viral hexon primers having forward sequence (5′-GAACAAGC-GAGTGGTGGCTC-3′) and reverse sequence (5′-CATTGCG-GTGGTGGTTAA-3′) (Bioneer, Daejeon, Korea) and using *rTaq* polymerase (Takara, Seongnam, Korea), according to the protocol (*29*). The operating parameters used were 1 cycle at 50 °C for 2 min, 1 cycle at 95 °C for 10 min, and 23 cycles at 95 °C for 15 s and 6 °C for 1 min. The PCR products were checked by 12% polyacrylamide gel electrophoresis.

RESULTS

FOL−PEG conjugate was synthesized by activating a γ-carboxylic acid in FOL with DCC/NHS and conjugating to a primary amine group of a hetero-bifunctional PEG derivative (NH_2-PEG-COOH) as reported previously (*23*). The resultant FOL−PEG-COOH conjugate was analyzed by ^{1}H NMR and MALDI-TOF. The ^{1}H NMR data suggested that the conjugation percent of FOL was almost 100% (data not shown) and the

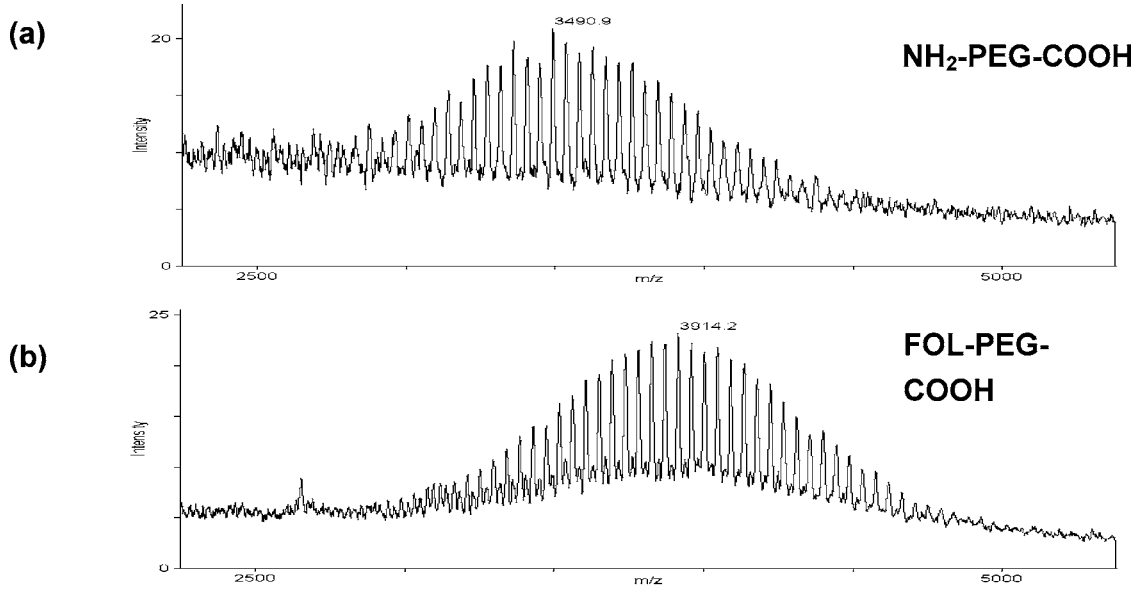

Figure 1. MALDI-TOF spectra of (a) NH_2−PEG-COOH and (b) FOL−PEG-COOH conjugate

Scheme 1. Scheme of ADV−PEG−FOL Conjugation

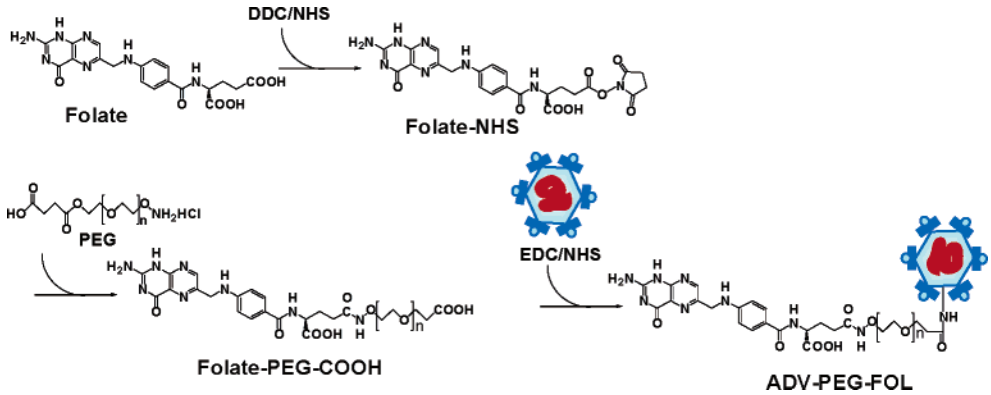

MALDI-TOF result indicated that FOL−PEG-COOH conjugate was successfully synthesized without any contaminants. As shown in Figure 1, the FOL−PEG-COOH conjugate shows a maximum peak at 3914.2 Da, while NH_2−PEG-COOH exhibits at 3490.9 Da. The difference of 423.3 Da before and after the FOL conjugation was matched with the molecular weight of conjugated FOL (423 Da), indicating that FOL was indeed conjugated to the amino terminus of the PEG derivative without any side products. FOL−PEG-COOH was then immobilized on the surface of ADV using EDC and NHS coupling agents. Figure 2 shows the reaction percent of surface amine groups of ADV with increasing amount of FOL−PEG-COOH in the feed. The number of ADV pts for PEG immobilization was fixed at 6.02×10^{11}. The total concentration of surface amine groups of ADV was determined by a fluorescamine assay. To calculate the percent immobilization of FOL−PEG on the surface of ADV, the remnant amount of surface amine groups after PEG immobilization was determined. It can be seen that the PEGylation degree of ADV increases with increasing amount of FOL−PEG-COOH in the feed. Since an excess PEGylation degree to ADV could critically damage the structure and function of ADV such as viral infection and gene expression, an optimum PEGylation degree is highly desirable to attain maximized gene expression (*9*, *31*). From preliminary GFP expression experiments using ADV with different PEGylation degrees, it was found that FOL−PEG immobilized ADV prepared from using 1×10^5 pmol FOL−PEG-COOH in the feed, corresponding to 24.1 ± 6.5% FOL−PEG immobilization out of total surface amine groups, showed the highest GFP expression. Thus, ADV with about 24.1 ± 6.5% PEGylation was selected for further experiments.

The size and surface zeta potential value of PEGylated ADV samples were measured by dynamic light scattering (DLS), as shown in Figure 3. The effective diameters of naked ADV, ADV, with PEG conjugation (ADV−PEG), and ADV with FOL−PEG conjugation (ADV−PEG−FOL) were 71.8 ± 13.8, 144.6 ± 17.9, and 148.5 ± 14.7 nm, respectively. The surface charge values of ADV, ADV−PEG, and ADV−PEG−FOL

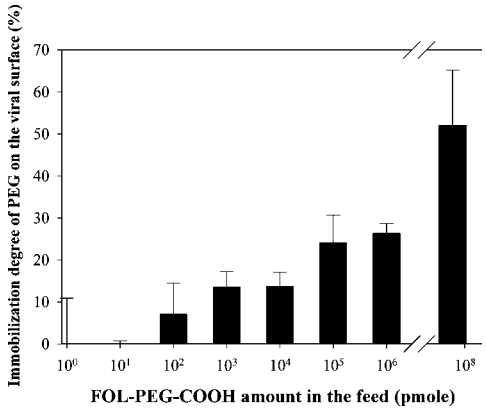

Figure 2. PEGylation degree of ADV immobilized with different amounts of NH2−PEG-COOH in the feed. 6.02×10^{11} particles of ADV was used for PEGylation. Unreacted free amine groups in ADV were determined by fluorescamine assay to calculate the PEGylation degree.

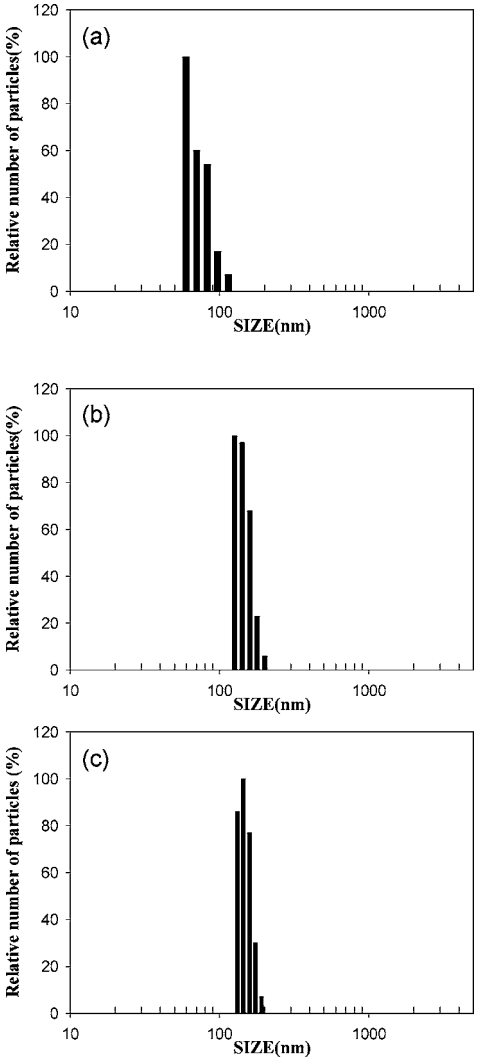

Figure 3. Size distribution of PEGylated ADV particles. The size and surface charge values of (a) ADV, (b) ADV−PEG, (c) ADV−PEG−FOL. PEGylation degree was 24.1 ± 6.1%.

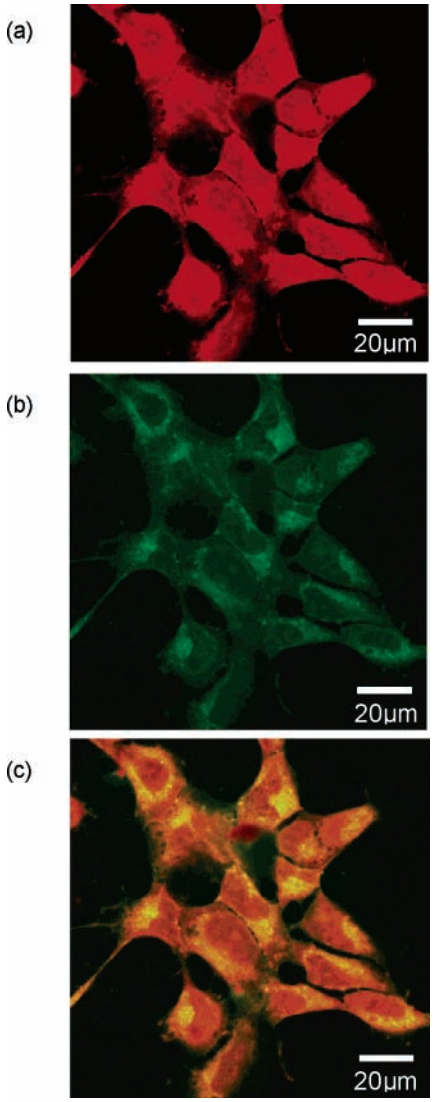

Figure 4. Cellular uptake of PEGylated ADV observed by confocal laser scanning microscopy. (a) Cells stained with a cell-tracker dye (red color), (b) ADV particles labeled with FITC (green color), and (c) a merged image of parts a and b.

were −20.3 ± 2.4, −7.0 ± 1.2, and −4.2 ± 1.7 mV, respectively. The PEGylated ADV had larger sizes than the naked ADV due to the increased hydrodynamic volume of immobilized PEG chains on the surface. They also had less negative surface charge values because immobilized neutral PEG chains on the surface masked the highly negative surface charge of naked ADV. The DLS results provided clear evidence that ADV was indeed PEGylated on the surface. However, it was not obvious why the sizes of ADV−PEG and ADV−PEG−FOL were about two times larger than that of naked ADV. It was likely that ADV dimer species were formed by noncovalent aggregation during the PEGylation process.

To visualize cellular uptake of PEGylated ADV, a FITC-labeled PEG derivative (FITC-PEG-NHS) was conjugated to ADV. The resultant ADV−PEG-FITC was transfected into HEK293 cells. Figure 4a shows a confocal laser microscopic view of cells treated with Celltracker that specifically stains the cytoplasm in red color. Figure 4b shows the cells stained with green color, resulting from the presence of ADV−PEG-FITC in the cytoplasm. In a merged image as shown in Figure 4c, it can be clearly seen that yellow ADV−PEG-FITC particles are located in the cell cytoplasm.

ADV, ADV−PEG, and ADV−PEG−FOL were transfected to FOL receptor overexpressing KB cells and FOL receptor deficient A549 cells. Figure 5 shows comparative GFP expression levels between the two cells determined by counting the number of transfected cells (Figure 5a) and measuring the fluorescence intensity after cell lysis (Figure 5b). The GFP expression percent of ADV−PEG decreased to 62.3 ± 6.1% and 43.4 ± 8.1% compared to that of ADV for KB and A549 cells, respectively. However, ADV−PEG−FOL exhibited fully recovered GFP expression percent as similar as that of ADV for KB cells, but not for A549 cells. In terms of GFP expression level by measuring total fluorescence intensity of transfected cells, ADV−PEG decreased to 66.7 ± 9.3% and 23.3 ± 5.5% compared to that of ADV for KB and A549 cells, respectively. In contrast, ADV−PEG- FOL increased to 145 ± 4.6% for KB cells, but decreased to 7.6 ± 0.4% for A549 cells. The above results suggest that ADV−PEG−FOL could be taken up by KB cells by FOL receptor-mediated endocytosis, but not by CAR-mediated endocytosis.

To determine comparatively the extent of immune response, ADV, ADV−PEG, and ADV−PEG−FOL were infected to macrophage cells (RAW264.1), and the release amount of interleukin-6 (IL-6) was measured (Figure 6 (a)). IL-6 is one of the important cytokines secreted from macrophage cells, and the secreted amount is directly related to the extent of immune response. The released IL-6 amounts were normalized to the total DNA amount extracted from RAW264.1 cells infected with ADV, ADV−PEG, and ADV−PEG−FOL. Untreated cells

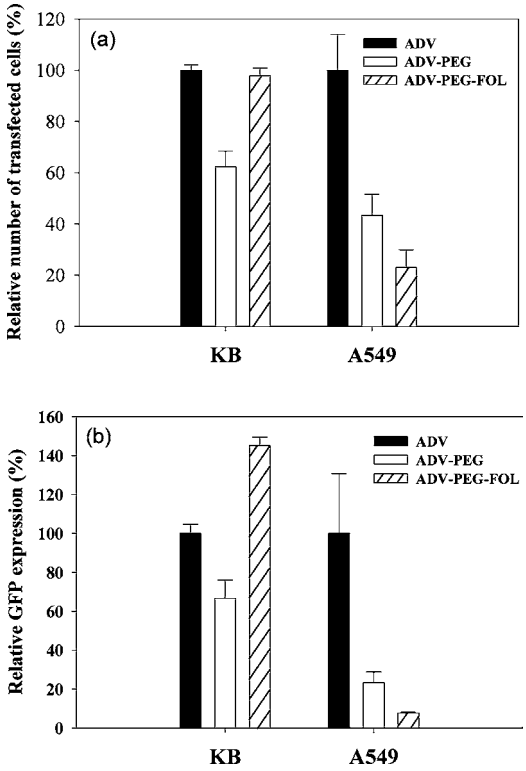

Figure 5. Quantitative measurement of GFP expression levels as determined from (a) the number of transfected cells and (b) from total fluorescent intensity of GFP in the transfected cells.

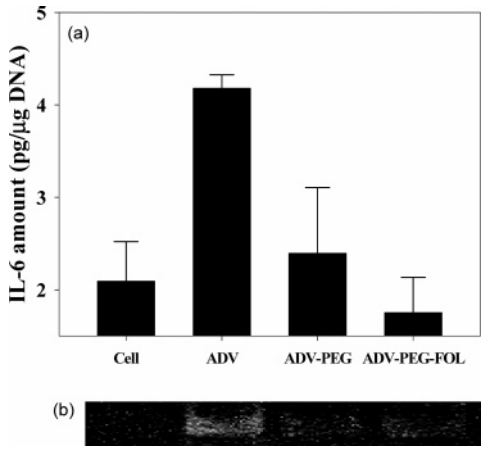

Figure 6. (a) The amount of IL-6 released from RAW264.1 macrophage cells after infection with ADV, ADV−PEG, and ADV−PEG−FOL. (b) PCR results for hexon DNA in ADV present within the macrophage cells. The amount of ADV taken up by macrophages corresponds to the band intensity.

released IL-6 to a concentration of 2.1 ± 0.4 pg/μg DNA after 24 h, while the cells cultured with ADV released 4.1 ± 0.1 pg/μg DNA. This indicates that ADV alone elicited immune response to some extent. However, IL-6 amounts for cells cultured with PEGylated ADV were much lower than that for ADV. The IL-6 amount for ADV−PEG was 2.4 ± 0.7 pg/μg DNA and that for ADV−PEG−FOL was 1.7 ± 0.4 pg/μg DNA. The reduced amounts of IL-6 released from macrophage cells suggest the PEGylated ADV could minimize the adverse immune response problems often associated with ADV gene therapy. Figure 6b shows viral hexon DNA bands amplified by PCR. The amount of viral hexon DNA fragments in the cell extract was qualitatively determined to indirectly correlate with the amount of viral particles within the macrophage cells. ADV−PEG and ADV−PEG−FOL had weaker band intensities than naked ADV, suggesting that they were taken up lesser than ADV by the stealth effect of PEG chains on the viral surface. Thus, the lower levels of IL-6 for ADV−PEG and ADV−PEG−FOL were attributed to the reduced extent of phagocytosis by macrophage cells.

DISCUSSION

PEGylation is a well-known technique for modification of peptide and protein drugs to prolong circulation time in the blood and minimize immune response. More recently, PEG has been used to decorate the surface of various nanoparticulate drug and gene carriers. To achieve retargeting of ADV while concomitantly reducing immune reactions, the surface of ADV was immobilized with FOL−PEG-COOH conjugate. FOL−PEG-COOH was synthesized and confirmed by MALDI-TOF analysis (Figure 1). It was previously reported that PEGylated ADV reduced transfection efficiency because the inherent CAR-mediated cellular uptake mechanism of ADV is hampered as a result of PEGylation (*9*, *31*). Surface immobilized PEG chains on ADV were likely to prevent the initial docking event of ADV to CAR on the host cell membrane. It is important to select an optimal PEGylation degree for maximizing gene transfection efficiency while substantially reducing the extent of immune response. With increased PEGylation degree on ADV, the extent of immune response would be reduced, but the gene transfection efficiency would be lowered substantially at the same time. An excessive PEGylation of the viral surface could also change the conformation of a viral surface capsid protein, which might prevent viral DNA from being delivered to the nucleus. The capsid protein plays an important role in dismantling the viral envelope structure for releasing DNA. Hence, the structural damage of the capsid protein by PEGylation could additionally lower the transfection efficiency. This means that excessively PEGylated ADV would result in not only a reduced extent of cellular uptake, but also a lower level of DNA release from the viral envelope within the cells. From this reason, PEGylation degree was preoptimized to approximately 1×10^5 PEG chains per viral particle for further gene transfection experiments. This corresponds to 24.1 ± 6.5% PEGylation based total amine groups on the ADV surface (Figure 2). After PEGylation, the size of ADV−PEG−FOL changed from 71.8 ± 13.8 nm to 148.5 ± 14.7 nm with increasing surface zeta potential values. It was likely that less negatively charged PEGylated ADV particles were prone to aggregation forming dimeric ADV particles. Cellular entrance of PEGylated ADV was examined by using ADV−PEG-FITC. It is known that within minutes after infection, ADV can escape from the endosome and translocate along microtubule tracks at a rate of 2 μm/s, converge at the perinuclear envelope, and undergo further dismantling for transport of viral DNA into the nucleus (*34*). Figure 4 shows that ADV−PEG-FITC particles are located primarily around the nucleus. The cellular entry of ADV−PEG-FITC was likely to occur via a nonspecific endocytic mechanism since CAR-mediated cellular entry was blocked to some extent due to PEGylation. In this study, FOL was used as a cancer targeting moiety for ADV. As shown in Figure 5, GFP expression levels of ADV−PEG and ADV−PEG−FOL were significantly different for KB and A549 cells. For KB cells, ADV−PEG−FOL showed similar or greater GFP expression levels than ADV, whereas for A549 cells, it showed decreased GFP expression levels. ADV−PEG−FOL could fully recover the loss of GFP gene expression by ADV−PEG only for KB cells, but not for A549 cells. This result clearly reveals that ADV could be delivered in a more specific manner to target cells and tissues without undergoing a CAR-mediated viral infection mechanism. Retargeting of ADV is feasible by conjugating an appropriate targeting moiety on the surface without compromising gene

transfection efficiency. Generally, ADV is administered repeatedly into a local site for clinical practices. The chromosome of genetically engineered ADV does not integrate into the host genome, thus repeated administration is often needed. This leads to serious immune response that is the biggest hurdle to practical applications of ADV for therapeutic treatments. PEGylated ADV could be one viable strategy in diminishing innate immune response as previously reported. There are several studies on PEGylated ADV to circumvent the immune response problems (*3*, *9*, *31*). In this study, a targeting moiety was conjugated to the distal end of PEG chain to provide an additional opportunity for retargeting of ADV. Chemical modification of the ADV surface with a targeting moiety is a more straightforward and versatile method than genetic modification of ADV surface with cell-recognizable proteins such as antibodies. One of the advantages of nonviral vector systems using cationic polymers and lipids are their ease of chemical modification with various targeting moieties with/without immobilizing PEG chains. The current study extended such surface modification strategies to ADV viral vectors for attaining only the merits from viral and nonviral vectors. To further validate the current findings and extend applications for other viral vectors, in vivo animal experiments are definitely required in the future.

CONCLUSIONS

We demonstrated that ADV was immobilized with a FOL−PEG conjugate on the surface to retarget the surface engineered ADV to FOL-receptor overexpressing cells and to reduce innate immune response. The two most serious problems for viral gene delivery vectors, targeting and immune response, could be partially overcome by immobilization of FOL−PEG conjugate on the viral surface. PEGylated ADV decorated with specific cell-recognizable targeting ligands could be potentially applied for many clinical applications in gene therapy.

ACKNOWLEDGMENT

This research was financially supported by a grant from the Ministry of Science and Technology (M1041403002-05N1403-00200), Republic of Korea

LITERATURE CITED

(1) Pfeifer, A., and Verma, I. M. (2000) Gene Therapy: promises and problems. *Annu. Rev. Genomics Hum. Genet. 2*, 117−211.

(2) Hunt, K. K., and Vorburger, S. A. (2002) Gene therapy: hurdles and hopes for cancer treatment. *Science 297*, 415−416.

(3) Eto, Y., Gao, J. Q., Sekiguchi, F., Kurachi, S., Katayama, K., Maeda, M., Kawasaki, K., Mizuguchi, H., Hayakawa, T., Tsutsumi, Y., Mayumi, T., and Nakagawa, S. (2005) PEGylated adenovirus vectors containing RGD peptides on the tip of PEG show high transduction efficiency and antibody evasion ability. *J. Gene Med. 7*, 604−612.

(4) Bergelson, J. M., Cunningham, J. A., Droguett, G., Kurt-Jones, E. A., Krithivas, A., Hong, J. S., Horwitz, M. S., Crowell, R. L., and Finberg, R. W. (1997) Isolation of a common receptor for Coxsackie B viruses and adenoviruses 2 and 5. *Science 275*, 1320−1323.

(5) Fields, B. N., (1996) *Adenoviruses: the viruses and their replication. fields virology*, 3rd ed., pp 2111−2148, Lippincott-Raven Publishers, Philadelphia.

(6) Engelhardt, J. F., Ye, X., Doranz, B., and Wilson, J. M. (1994) Ablation of E2A in recombinant adenoviruses improves transgene persistence and decreases inflammatory response in mouse liver. *Proc. Natl. Acad. Sci. U.S.A. 91*, 6196−6200.

(7) Yang, Y., and Wilson, J. M. (1995) Recombinant IL-12 prevents formation of blocking IgA antibodies to recombinant adenovirus and allows repeated gene therapy to mouse lung. *Nat. Med. 1*, 890−893.

(8) Dai, Y., Schwarz, E. M., Gu, D., Zhang, W. W., Sarvetnick, N., and Verma, I. M. (1995) Cellular and humoral immune responses to adenoviral vectors containing factor IX gene: tolerization of factor IX and vector antigens allows for long-term expression. *Proc. Natl. Acad. Sci. U.S.A. 92*, 1401−1405.

(9) O'Riordan, C. R., Lachapelle, A., Delgado, C., Parkes, V., Wadsworth, S. C., and Smith, A. E. Francis GE. (1999) PEGylation of adenovirus with retention of infectivity and protection from neutralizing antibody in vitro and in vivo. *Hum. Gene Ther. 10*, 1349−1358.

(10) Croyle, M. A., Yu, Q. C., and Wilson, J. M. (2000) Development of a rapid method for the PEGylation of adenoviruses with enhanced transduction and improved stability under harsh storage conditions. *Hum. Gene Ther. 11*, 1713−1722.

(11) Croyle, M. A., Chirmule, N., Zhang, Y., and Wilson, J. M. (2001) "Stealth" adenoviruses blunt cell-mediated and humoral immune responses against the virus and allow for significant gene expression upon readministration in the lung. *J. Virol. 75*, 4792−4801.

(12) Croyle, M. A., Le, H. T., Linse, K. D., Cerullo, V., Toietta, G., Beaudet, A., and Pastore, L. (2005) PEGylated helper-dependent adenoviral vectors: highly efficient vectors with an enhanced safety profile. *Gene Ther. 12*, 579−587.

(13) Croyle, M. A., Callahan, S. M., Auricchio, A., Schumer, G., Linse, K. D., Wilson, J. M., Brunner, L. J., and Kobinger, G. P. (2004) PEGylation of a vesicular stomatitis virus G pseudotyped lentivirus vector prevents inactivation in serum. *J. Virol. 78*, 912−921.

(14) Jooss, K., Ertl, H. C., and Wilson, J. M. (1998) Cytotoxic T-lymphocyte target proteins and their major histocompatibility complex class I restriction in response to adenovirus vectors delivered to mouse liver. *J. Virol. 72*, 2945−2954.

(15) Yang, Y., Jooss, K. U., Su, Q., Ertl, H. C., and Wilson, J. M. (1996) Immune responses to viral antigens versus transgene product in the elimination of recombinant adenovirus-infected hepatocytes in vivo. *Gene Ther. 3*, 137−144.

(16) Yang, Y., and Wilson, J. M. (1995) Clearance of adenovirus-infected hepatocytes by MHC class I-restricted CD4+ CTLs in vivo. *J. Immunol. 155*, 2564−2570.

(17) Yang, Y., Greenough, K., and Wilson, J. M. (1996) Transient immune blockade prevents formation of neutralizing antibody to recombinant adenovirus and allows repeated gene transfer to mouse liver. *Gene Ther. 3*, 412−420.

(18) Ross, J. F., Chaudhuri, P. K., and Ratnam, M. (1994) Differential regulation of folate receptor isoforms in normal and malignant tissues in vivo and in established cell lines. Physiologic and clinical implications. *Cancer 73*, 2432−2443.

(19) Wu, M., Gunning, W., and Ratnam M. (1999) Expression of folate receptor type α in relation to cell type, malignancy, and differentiation in ovary, uterus, and cervix. *Cancer Epidemiol. Biomarkers Prev. 8*, 775−782.

(20) Zhao, X. B., and Lee, R. J. (2004) Tumor-selective targeted delivery of genes and antisense oligodeoxyribonucleotides via the folate receptor. *Adv. Drug. Delivery Rev. 56*, 1193−1204.

(21) Beale, P., and Clarke, S. (1999) Tomudex: clinical development. *Antifolate Drugs in Cancer Chemotherapy*, pp 167−181, Humana Press Inc., Totowa, NJ.

(22) Konda, S. D., Aref, M., Brechbiel, M., and Wiener, E. C. (2000) Development of a tumor-targeting MR contrast agent using the high-affinity folate receptor: work in progress. *Invest. Radiol. 35*, 50−57.

(23) Yoo, H. S., and Park, T. G. (2004) Folate receptor targeted biodegradable polymeric doxorubicin micelles. *J. Controlled Release 96*, 273−283.

(24) Yoo, H. S., and Park, T. G. (2004) Folate-receptor-targeted delivery of doxorubicin nano-aggregates stabilized by doxorubicin-PEG-folate conjugate. *J. Controlled Release 100*, 247−256.

(25) Kim, S. H., Jeong, J. H., Chun, K. W., and Park, T. G., (2005) Target-specific cellular uptake of PLGA nanoparticles coated with poly(L-lysine)-poly(ethylene glycol)-folate conjugate. *Langmuir 21*, 8852−8857.

(26) Kim, S. H., Jeong, J. H., Cho, K. C., Kim, S. W., and Park, T. G. (2005) Target-specific gene silencing by siRNA plasmid DNA complexed with folate-modified poly(ethylenimine). *J. Controlled Release 104*, 223−232.

(27) Cho, K. C., Kim, S. H., Jeong, J. H., and Park, T. G. (2005) Folate receptor-mediated gene delivery using folate-poly(ethylene glycol)-poly(L-lysine) conjugate. *Macromol. Biosci. 5*, 512−519.

(28) p*Silencer adeno 1.0-CMV-Adenoviral siRNA expression vector system-Catalog # 5790, Instruction manual*, Ambion, *pp 37*−*39*.

(29) Curiel, D. T. (1999) Strategies to adapt adenoviral vectors for targeted delivery. *Ann. N. Y. Acad. Sci. 886*, 158−171.

(30) Enjalbal, C., Ribiere, P., Lamaty, F., Yadav-Bhatnagar, N., Martinez, J., and Aubagnac, J. L. (2005) MALDI-TOF MS analysis of soluble PEG based multistep synthetic reaction mixtures with automated detection of reaction failure. *J. Am. Soc. Mass Spectrom. 16*, 670−678.

(31) Mok, H., Palmer, D. J., Ng, P., and Barry, M. A. (2005) Evaluation of poly(ethylene glycol) modification of first-generation and helper-dependent adenoviral vectors to reduce innate immune responses. *Mol. Ther. 11*, 66−79.

(32) Pearce, O. M., Fisher, K. D., Humphries, J., Seymour, L. M., Smith, A., and Davis, B. G. (2005) Glycoviruses: chemical glycosylation retargets adenoviral gene transfer. *Angew. Chem., Int. Ed. 44*, 1057−1061.

(33) Alemany, R., and Curiel, D. T. (2001) CAR-binding ablation does not change biodistribution and toxicity of adenoviral vectors. *Gene Ther. 8*, 1347−1353.

(34) Medina-Kauwe, L. K. (2003) Endocytosis of adenovirus and adenovirus capsid proteins. *Adv. Drug Delivery Rev.* 14; 55, 1485−1496.

BC060030C

Interaction of Polycationic Polymers with Supported Lipid Bilayers and Cells: Nanoscale Hole Formation and Enhanced Membrane Permeability

Seungpyo Hong,[||,#,†] Pascale R. Leroueil,[⊥,#,†] Elizabeth K. Janus,[§,#] Jennifer L. Peters,[#] Mary-Margaret Kober,[⊥,#] Mohammad T. Islam,[#] Bradford G. Orr,[‡,⊗,#] James R. Baker, Jr.,[#] and Mark M. Banaszak Holl[‡,§,||,⊥,#,*]

Programs in Applied Physics, Biophysics, and Macromolecular Science and Engineering, Departments of Chemistry and Physics, and Michigan Nanotechnology Institute for Medicine and Biological Sciences, University of Michigan, Ann Arbor, Michigan 48109. Received March 27, 2006; Revised Manuscript Received April 5, 2006

Interactions of polycationic polymers with supported 1,2-dimyristoyl-sn-glycero-3-phosphocholine (DMPC) lipid bilayers and live cell membranes (KB and Rat2) have been investigated using atomic force microscopy (AFM), cytosolic enzyme assays, confocal laser scanning microscopy (CLSM), and a fluorescence-activated cell sorter (FACS). Polycationic polymers poly-L-lysine (PLL), polyethylenimine (PEI), and diethylaminoethyl-dextran (DEAE-DEX) and sphere-like poly(amidoamine) (PAMAM) dendrimers are employed because of their importance for gene and drug delivery. AFM studies indicate that all the polycationic polymers cause the formation and/or expansion of preexisting defects in supported DMPC bilayers in the concentration range of 1−3 μg/mL. By way of contrast, hydroxyl-containing neutral linear poly(ethylene glycol) (PEG) and poly(vinyl alcohol) (PVA) do not induce hole formation or expand the size of preexisting defects in the same concentration range. All polymers tested are not toxic to KB or Rat2 cells up to a 12 μg/mL concentration (XTT assay). In the concentration range of 6−12 μg/mL, however, significant amounts of the cytosolic enzymes lactate dehydrogenase (LDH) and luciferase (LUC) are released. PEI, which possesses the greatest density of charged groups on its chain, shows the most dramatic increase in membrane permeability. In addition, treatment with polycationic polymers allows the small dye molecules propidium idodide (PI) and fluorescein (FITC) to diffuse in and out of the cells. CLSM images also show internalization of PLL labeled with FITC dye. In contrast, controls of membrane permeability using the neutral linear polymers PEG and PVA show dramatically less LDH and LUC leakage and no enhanced dye diffusion. Taken together, these data are consistent with the hypothesis that polycationic polymers induce the formation of transient, nanoscale holes in living cells and that these holes allow a greatly enhanced exchange of materials across the cell membrane.

INTRODUCTION

The water soluble synthetic polycationic polymers poly-L-lysine (PLL), polyethylenimine (PEI), diethylaminoethyl-dextran (DEAE-DEX), and polyamidoamine (PAMAM) dendrimers have been employed in a variety of gene and drug delivery system applications (*1*−*3*). The generally accepted mechanism for internalization of these polymers is polycation-mediated endocytosis, a three-step process composed of binding with phospholipids and/or glycolipids in the membrane, internalization into cells, and exit from the endosome (*4*−*7*). Having particular interest in the first step of the process, several research groups have used model systems including phosphatidylethanolamine containing anionic vesicles to study the membrane/particle interaction (*8*−*10*). Studies of model systems have provided good evidence for membrane disruption caused by cationic macromolecules such as PEI, PAMAM dendrimers, and poly-(*N*-ethyl-4-vinylpyridinium bromide) as measured by changes in fluorescence intensity of artificial vesicles containing dyes such as fluorescein (FITC) after exposure to the polycations (*10*−*12*). Several reports using living cell membranes have also demonstrated increased membrane permeability as determined by cytotoxicity (cytosolic enzyme leakage such as LDH) using assay techniques (*13*, *14*). However, no clear connection has been made between proposed models and in vitro studies.

We recently reported that positively charged PAMAM dendrimers cause membrane disruption (dendroporation), allowing the diffusion of molecules in and out of cells (*15*). This in vitro result is in good agreement with the proposed hole formation mechanism, as suggested by atomic force microscopy (AFM) on a supported 1,2-dimyristoyl-sn-glycero-3-phosphocholine (DMPC) model membrane (*16*−*19*). On the basis of our previous results, we wanted to explore if nanoscale hole formation could be caused by less exotic polycationic polymers such as PEI, PLL, and DEAE-DEX which are substantially cheaper and more commonly used materials than the PAMAM dendrimers. The key hypotheses we address in this paper are as follows:

(1) Commercially available polycationic polymers, PEI, PLL, and DEAE-DEX cause nanoscale hole formation in supported lipid bilayers.

(2) Commercially available polycationic polymers, PEI, PLL, and DEAE-DEX cause substantial permeability of the cell plasma membrane allowing enhanced enzyme and dye diffusion.

(3) Under the same conditions, neutral linear polymers (PEG and PVA) do not cause nanoscale hole formation in supported lipid bilayers nor do they generate comparable enhancements in cell membrane permeability.

In this study, we employed AFM to observe the effect of

* To whom correspondence should be addressed. Phone: (734) 763-2283. Fax: (734) 763-2307. E-mail: mbanasza@umich.edu.

‡ Program in Applied Physics.

§ Program in Biophysics.

|| Program in Macromolecular Science and Engineering.

⊥ Department of Chemistry.

⊗ Department of Physics.

Michigan Nanotechnology Institute for Medicine and Biological Sciences.

† Both authors provided the same contribution for this work.

10.1021/bc060077y CCC: $33.50 © 2006 American Chemical Society
Published on Web 05/02/2006

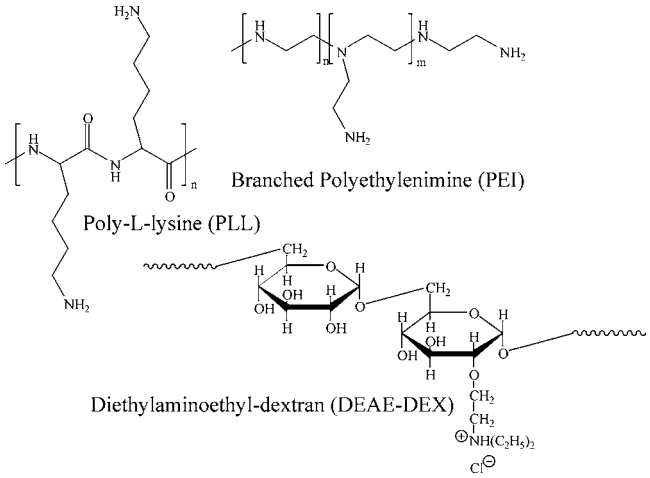

Figure 1. Chemical structures of commercially available polycationic polymers used in this study.

polymers upon supported DMPC lipid bilayers. Polymer interactions with cells in vitro were investigated in terms of morphological studies using confocal laser scanning microscopy (CLSM) as well as toxicological studies using XTT, lactate dehydrogenase (LDH), and luciferase (LUC) assays and flow cytometry. AFM studies revealed that the presence of polycationic polymers induces nanoscale hole formation and/or the expansion of preexisting defects in the supported DMPC bilayers. The presence of polycationic polymers in the cell medium made the cell membrane permeable to molecules such as cytosolic enzymes (LDH and LUC), propidium iodide (PI), and FITC. These results directly support the three hypotheses described above and suggest an alternative model to polycation-mediated endocytosis for the transport of materials across cell membranes in the presence of polycationic polymers.

EXPERIMENTAL PROCEDURES

Materials and Measurement of Molar Masses. PLL, PLL−FITC conjugate (PLL−FITC), PEI, and DEAE-DEX were purchased from Sigma-Aldrich. G5 PAMAM dendrimers were synthesized and then conjugated with FITC at the Michigan Nanotechnology Institute for Medicine and Biological Sciences, University of Michigan (*15*). DMPC lipids were provided by Avanti Lipids, Alabaster, AL. Chemical structures of the polycationic polymers used in this paper are illustrated in Figure 1.

The molar mass moments and molar mass distribution of each polymer sample was measured using gel permeation chromatography (GPC). The number average molar mass (M_n) and polydispersity index (PDI), a commonly used measure of the breadth of the molar mass distribution defined as the ratio of the weight and number average molar masses (M_w/M_n), of individual samples are listed in Table 1. GPC experiments were performed using an Alliance Waters 2690 separation module (Waters Corp., Milford, MA) equipped with a Waters 2487 UV absorbance detector (Waters Corp.), a Wyatt Dawn DSP laser photometer (Wyatt Technology Corp., Santa Barbara, CA), an Optilab DSP interferometric refractometer (Wyatt Technology Corp.), and TosoHaas TSK-Gel Guard PHW 06762 (75×7.5 mm, 12 μm), G 2000 PW 05761 (300 × 7.5 mm, 10 μm), G 3000 PW 05762 (300 × 7.5 mm, 10 μm), and G 4000 PW (300 × 7.5 mm, 17 μm) columns. Column temperatures were maintained at 25 ± 0.2 °C with a Waters temperature control module. Citric acid buffer (0.1 M) with 0.025% sodium azide in water was used as a mobile phase. The pH of the mobile phase was adjusted to 2.74 using NaOH, and the flow rate was maintained at 1 mL/min. Sample concentration was approximately 2 mg/mL, and an injection volume of 100 μL was used for all samples. Molar mass moments of the polymers were determined using Astra software (version 4.7) (Wyatt Technology Corp.).

Preparation and AFM Observation of Supported DMPC Lipid Bilayers. A 0.67 mg/mL suspension of small, unilamellar vesicles (SUVs) was prepared as previously reported (*15, 16, 20*). Supported lipid bilayers were formed by depositing 80 μL of liposome suspension on a 1 × 1 cm^2 piece of freshly cleaved mica. After an incubation time of approximately 20 min, the sample was gently rinsed with water to remove excess lipids and placed in the AFM for imaging as described in previous studies. All AFM measurements were performed in tapping mode on a Nanoscope IIIa Multimode scanning probe microscope from Digital Instruments (DI, Veeco Metrology Group, Santa Barbara, CA). The AFM was equipped with a liquid cell (DI) and a silicon nitride cantilever (DI model NPS, spring constant 0.32 N/m, length 100 μm) operating at a drive frequency of 6−9 kHz. After taking an initial image of the bilayer, approximately 20 μL of polymer solution was injected into the liquid cell. All solutions were prepared using high purity water (Nerl Diagnostics, East Providence, RI). The temperature inside the liquid cell was 28 °C and therefore above the gel to liquid transition temperature of supported DMPC bilayers.

Cell Lines. The KB and Rat2 cell lines were purchased from the American Type Tissue Collection (ATCC, Manassas, VA) and grown continuously as a monolayer at 37 °C and 5% CO_2 in RPMI 1640 medium (Mediatech, Herndon, VA) and Dulbecco's modified Eagle's medium (DMEM, Gibco, Eggenstein, Germany), respectively. The Rat2 cell line was transfected to permanently express the LUC gene using PAMAM dendrimer-mediated gene transfection as previously described (*15, 21, 22*). The LUC expressing Rat2 cells are noted as Rat2pLUC. The RPMI 1640 and DMEM media were supplemented with penicillin (100 units/mL), streptomycin (100 μg/mL), and 10% heat-inactivated fetal bovine calf serum (FBS) before use.

XTT, LUC, and LDH Assays and Flow Cytometry. Cytotoxicity of the polycationic polymers was assessed with a 2,3-bis(2-methoxy-4-nitro-5-sulfophenyl)-5-[(phenylamino)carbonyl]-*2H*-tetrazolium hydroxide (XTT) assay kit (Cell Proliferation Kit II, Roche Molecular Biochemicals, Mannheim, Germany). KB and Rat2 cell lines (at a concentration of 5 × 10^4 cells/well) were prepared as monolayers in 96 well plates, followed by incubation with polymers in phosphate-buffered saline (PBS) with Ca^{2+} and Mg^{2+} at 37 °C under 5% CO_2 for 4.5 h. Polymer solutions (supernatants) were removed and followed by washing with PBS twice. Mitochondrial activities in the cells were then measured using the assay kit.

The LDH and LUC activities in the cell supernatant after 3 h incubation were respectively analyzed using an LDH assay kit (Promega Co., Madison, WI) and a chemiluminescence assay(Promega Co., Madison, WI) as previously described (*15*). The measured LDH and LUC activities were either recalculated by percentage to the activities of cell lysates of intact cells (% LDH released) or adjusted for the protein concentration of the sample (relative light unit (RLU)/mg protein). Flow cytometry was also performed according to our report (*15*). Fluorescence signal intensities were measured by a Coulter EPICS/XL MCL Beckman-Coulter flow cytometer and data were analyzed using Expo32 software (Beckman-Coulter, Miami, FL).

CLSM Observation. A concentration of 2 × 10^4 cells/mL of Rat2 cells was seeded on MatTek glass bottom Petri dishes (35 mm) and incubated at 37 °C under 5% CO_2 for 24 h. The DMEM was removed and 2 mL of each PLL−FITC and dendrimer−FITC conjugates in PBS (Ca^{2+}, Mg^{2+}) solution was added into the appropriate dish. The dishes were incubated with added solutions at 37 °C under 5% CO_2 for 1 h. The conjugate-

Table 1. Physicochemical Properties of Polycations Used in This Study

polymer	M_n (PDI)[a]	order of amines (deg)	charge/monomer ratio[b]	zeta potential (mV)[c]	shape of chain
PLL	11210 (1.67)	1, 2	0.007519	17.59 ± 0.39	linear, flexible
PLL−FITC	23620 (1.06)	1, 2	0.007519	-	linear, flexible
PEI	78220 (3.44)	1, 2, 3	0.02290	45.18 ± 16.84	branched, flexible
DEAE-DEX	18490 (32.90)	3	0.00218	30.44 ± 2.71	linear, intramolecular cross-linking
G5-NH_2	26530 (1.02)	1, 3	0.00885	19.24 ± 16.63	sphere-like
PEG	16290 (1.22)	N/A	N/A	−1.07 ± 1.10	linear, flexible
PVA	28490 (1.57)	N/A	N/A	−0.68 ± 1.36	linear, inter-/intramolecular H bonding

[a] Measured by GPC. [b] Theoretical number of charged groups per molecular weight of polymeric monomer. [c] Measured by zeta potential/particle sizer NICOMP 380 ZLS (PSS·NICOMP, Santa Barbara, CA). The maximum count rate was 5 MHz and the measurements were carried out for 5 min. All the polymer samples were at a concentration of 1 mg/mL, pH 7.4, and measurements for each polymer were repeated five times.

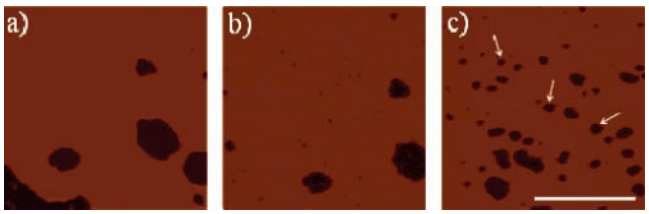

Figure 2. AFM images of supported DMPC lipid bilayers upon exposure to poly-L-lysine (PLL). 20 μL of 10 μg/mL PLL injected following image a, resulting in a final concentration of ~1.0 μg/mL in the AFM liquid cell. Total time between a and c is approximately 50 min. White arrows indicate formation of several new holes in the lipid bilayers caused by PLL. Bar: 500 nm. Z-scale: 20 nm.

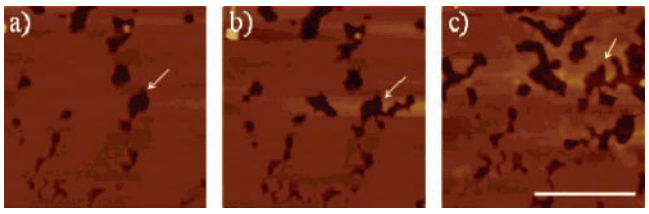

Figure 3. AFM images of supported DMPC lipid bilayers upon exposure to poly(ethylenimine) (PEI). 20 μL of 5 μg/mL PEI injected following image a, resulting in a final concentration of ~0.5 μg/mL. An additional 20 μL of 10 μg/mL was injected after b, resulting in a final concentration of ~1.5 μg/mL. Total time between a and c is approximately 40 min. Note that there is no new hole formation but instead the preexisting defects are expanded. One of the preexisting defects and expansion of the defect is indicated by white arrows in each image. Bar: 500 nm. Z-scale: 20 nm.

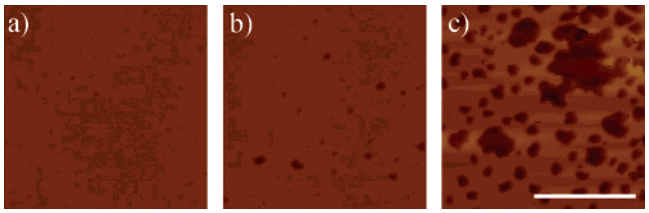

Figure 4. AFM images of supported DMPC lipid bilayers upon exposure to diethylaminoethyl-dextran (DEAE-DEX). 50 μL of 5 μg/mL DEAE-DEX injected following image a, resulting in a final concentration of ~1.3 μg/mL. Total time between a and c is approximately 90 min. Unlike that PLL and PEI create or expand defects in the lipid bilayers, DEAE-DEX induces membrane thinning. The newly formed defects are 2−4 nm deep instead of complete removal of the lipid bilayers (~4−5 nm deep). Bar: 500 nm. Z-scale: 20 nm.

containing solutions were removed, and the resulting cell monolayer was washed with PBS. Cells were fixed with 2% formaldehyde in the PBS (Ca^{2+}, Mg^{2+}) at room temperature for 10 min, followed by washing with PBS twice. Confocal and differential interference contrast (DIC) images were taken on an Olympus FV-500 confocal microscope using a 40×, 1.2 NA oil immersion objective. For the confocal images, the 488 nm line of an argon ion laser was used for excitation and the emission was filtered at 505 nm.

RESULTS

Polycation-Induced Hole Formation on Aqueous Supported DMPC Lipid Bilayers. The polycation polymers used in this study (PLL, PEI, and DEAE-DEX) were all shown to disrupt DMPC-supported lipid bilayers. Several controls were performed for the AFM study. Before the introduction (through injection) of polymers into the solution containing the aqueous supported lipid bilayers, the bilayers were imaged alone for 8 to 10 min. These preimaging steps were done to ensure that the bilayers were stable and that preexisting defects that appeared were not due to the act of imaging itself. A blank injection of water (the solvent in which the polymers were dissolved) was completed and resulted in no change to the bilayer over the course of a normal imaging session (60 to 90 min). This shows that the injection itself is not responsible for the formation of defects. Finally, injections of 1 μg/mL of poly(ethylene glycol) (PEG) and poly(vinyl alcohol) (PVA), two neutral polymers, were performed and resulted in no change to the supported bilayers over normal imaging time.

Images taken using AFM show the three polycationic polymers (PEI, PLL, and DEAE-DEX) disrupt DMPC supported lipid bilayers. Figures 2, 3, and 4 are representative data sets of the polycationic polymers and DMPC lipid bilayer interactions. Although there is some variation, several repetitions were completed for each polymer confirming that the degrees of membrane/polymer interactions are qualitatively similar. Following the addition through injection of PLL into the AFM liquid cell at a final concentration of ~ 1 ug/mL (Figure 2), new defects in the bilayer are formed. The depth of these defects in the membrane is primarily in the range of 4.0−4.8 nm. Addition of PEI onto the bilayer, however, results in mostly the expansion of preexisting defects (Figure 3). These expanded defects have measured 4.4 to 5.1 nm in depth which is consistent with the removal of a full bilayer. Interestingly, the introduction of DEAE-DEX to supported DMPC bilayers results in only 2−4 nm deep depressions.

Cytotoxicity of Polycation and Polycation-Induced Enzyme Leakage. The cytotoxicity of the polymers was determined using an XTT assay (Figure 5). The relative cell viability was calculated as:

$$[OD_{492nm}]_{sample}/[OD_{492nm}]_{control} \times 100$$

The assay results show that the polymers are not cytotoxic up to a 12 μg/mL concentration (>80% cell viability) for both KB and Rat2 cells. Based on these data, the assays performed to investigate the cytosolic enzyme release were carried out in polymer concentrations of 6 and 12 μg/mL. Within this range, the polymers are noncytotoxic, so the observed enzyme release can be ascribed to an increase in cell membrane permeability as opposed to general lysis due to cell death.

The effect of positively charged polymers on the cell membranes was investigated in terms of cytosolic enzyme release from the cells using LDH and LUC assay techniques.

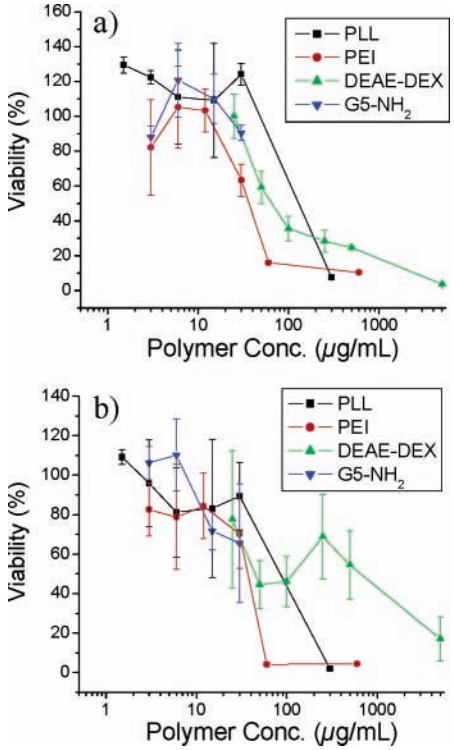

Figure 5. Cell viability determined by XTT assay of (a) KB and (b) Rat2 cells after incubation with PLL, PEI, DEAE-DEX, and G5-NH_2 PAMAM at 37 °C for 4.5 h. Note that all the polymers are not cytotoxic up to a concentration of 12 μg/mL.

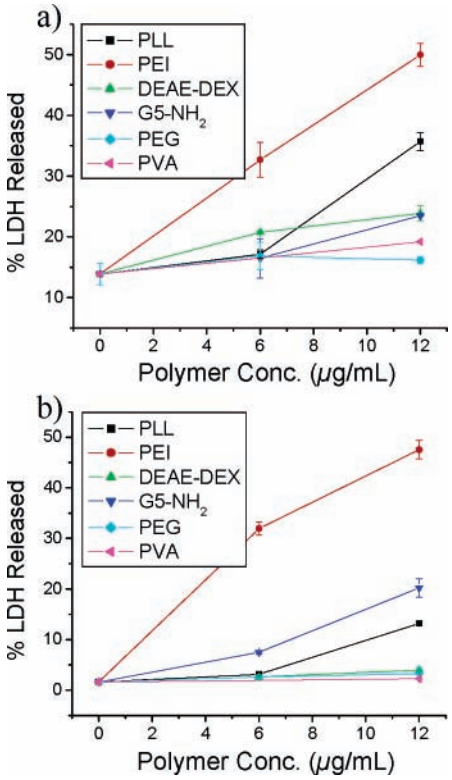

Figure 6. Dose-dependent LDH release from (a) KB and (b) Rat2 cell lines incubated with PLL, PEI, DEAE-DEX, G5-NH_2 PAMAM, PEG, and PVA at 37 °C for 3 h. All the polycationic polymers induce LDH leakage but the neutral polymers PEG and PVA do not cause any significant leakage.

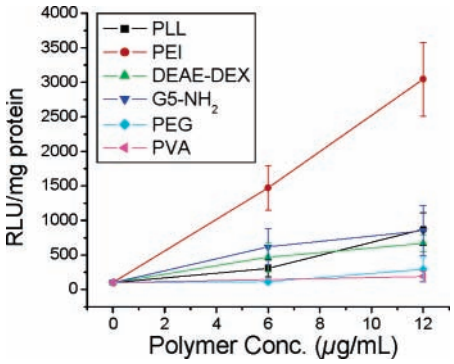

Figure 7. Dose-dependent luciferase (LUC) release from Rat2pLUC cell line incubated with PLL, PEI, DEAE-DEX, G5-NH_2 PAMAM, PEG, and PVA at 37 °C for 3 h. Before the incubation, Rat2 cells were transfected by PAMAM dedrimer-mediated cell transfection to express LUC in their cytosols. As seen in the LDH assay data in Figure 6, all the polycationic polymers used in this study also cause LUC leakage but the neutral polymers do not.

As the polymer concentration increases, the amounts of both LDH and LUC released increased as illustrated in Figures 6 and 7. Induced membrane permeability as measured by LDH release shows a degree of cell type (KB and Rat2) dependence as shown in Figure 6. In both cell types (Figure 6), however, PEI induced more LDH leakage as compared to the other polycationic polymers. This is not surprising because PEI possesses a much greater charge/monomer ratio (see Table 1) as compared to the other polymers. G5-NH_2 and PLL cause similar amount of LDH release and the least LDH was released from the cells after exposure to DEAE-DEX among the polycationic polymers, particularly in the case of the Rat2 cells. PEG and PVA did not cause enzyme leakage. LUC release from Rat2pLUC exhibits a trend similar to the LDH release from cells seen as discussed above (Figure 7).

Binding and Internalization of PLL−FITC. PLL−FITC conjugate was used for direct observation by CLSM. This experiment was carried out to compare the internalization behavior of common commercial polycationic polymers to that of dendrimeric G5-NH_2. Figure 8 shows that PLL−FITC is internalized into the Rat2 cells resulting in strong fluorescence of FITC from inside the cells. In particular, the intracellular location of the internalized conjugates appears to exclude the nucleus. This internalization behavior is particularly interesting because penetration of the polymers into the nucleus should be avoided for nontoxic gene delivery as it may alter the DNA sequence. G5-Ac−FITC, which remains neutral in water due to the conversion of all the surface primary amines groups to acetamide groups, is not internalized as shown in Figure 8e, allowing the conjugate to be used as a negative control (*15*). The DIC image is provided to show that an appropriate cell density was used (Figure 8f).

Diffusion of Small Molecules through the Permeabilized Membranes. It is known that PI and fluorescein diacetate (FDA) can be employed as indicators of diffusion-in and out, respectively (*15*, *23*). PI is readily internalized into cells with disrupted membranes but is excluded from cells with intact membranes. In contrast, FDA is able to traverse intact membranes and is then converted to fluorescein (FITC) by endogenous esterase in cells. The resulting FITC is unable to travel across intact membranes but is able to traverse permeabilized membrane. Therefore, it is assumed that PI fluorescence should increase and FITC fluorescence should decrease with increasing membrane permeability. Figure 9a shows the increase in PI signal intensity induced following the incubation of KB cells with the polycationic polymers. The greatest PI intensity increase is seen using PEI, followed by G5, DEAE-DEX, and PLL. Charge neutral PVA and PEG do not induce PI internalization.

On the other hand, FITC fluorescence intensities are decreased after exposure to the polycationic polymers in a concentration-dependent manner (Figure 9b). The largest amount of intensity

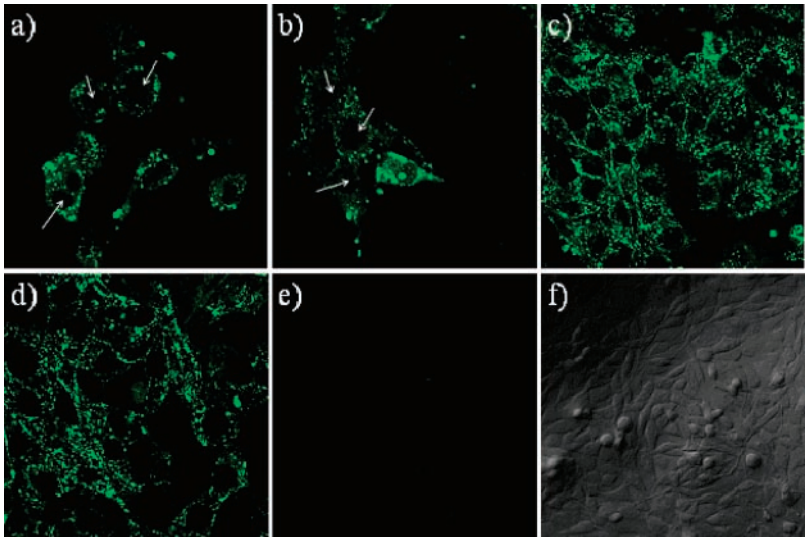

Figure 8. Confocal microscopy images of Rat2 cells incubated with (a) 6 μg/mL PLL−FITC and (b) 12 μg/mL PLL−FITC conjugates. (c) A zoomed-out image of b. Rat2 cells incubated with (d) 6 μg/mL G5-NH_2−FITC and (e) 12 μg/mL G5-Ac−FITC conjugates. (f) Differential interference contrast (DIC) image. Image f illustrates that there are a sufficient number of cells at the focal plane although nothing can be seen in fluorescence image e. Note that the green fluorescence from either PLL−FITC or G5-NH_2−FITC does not occur from within cell nuclei which are indicated by several white arrows. The location of the nuclei and the exclusion of the polycationic polymers were confirmed in previously published work using DAPI staining of the nucleus (*15*).

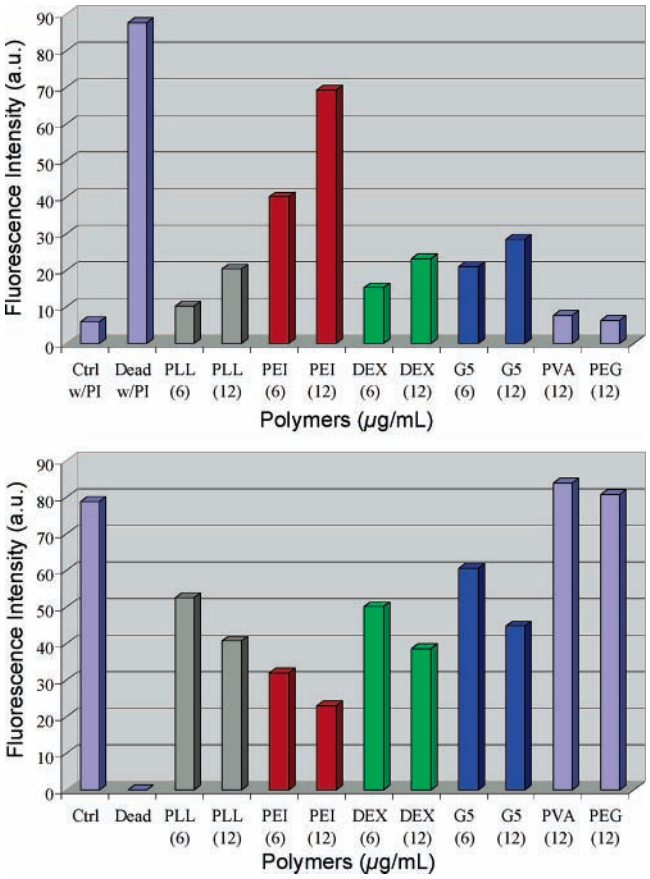

Figure 9. Fluorescence intensity of (a) propidium iodide (PI) and (b) fluorescein (FITC) from KB cells measured by flow cytometer. Note that fluorescence intensity of PI should increase while that of FITC should decrease with increase of membrane permeability. All the polycationic polymers cause an increase of PI fluorescence intensities and a decrease of FITC fluorescence. However, the neutral polymers do not cause such changes.

drop is observed in the PEI case, although DEAE-DEX, PLL, and G5 also show a decrease in FITC fluorescence intensity. As expected, PVA and PEG do not induce FITC escape.

DISCUSSION

Evidence for Hole Formation by Polycationic Polymers PEI, PLL, and DEAE-DEX. We previously reported nanoscale hole formation on both supported lipid bilayers and cellular membranes induced by positively charged PAMAM dendrimers (*15*−*19*). In this study we test the possibility of extending the proposed mechanism of dendrimer/membrane interactions, i.e., hole formation by sphere-like PAMAM dendrimers, to the more common and inexpensive polycationic polymers PEI, PLL, and DEAE-DEX. Polycationic polymer-induced disruption of various supported phospholipid bilayers including dioleoyl phosphatidyl choline (DOPC), dioleoyl phosphatidyl serine (DOPS), 1-palmitoyl-2-oleoyl-sn-glycero-3-phosphatidic acid (POPA), and their mixtures has been reported using various methods. These techniques include quartz crystal microbalance with dissipation, leakage assay, ^{31}P NMR, and electrophoretic mobility (*9*, *10*, *24*). Furthermore, polycationic polymer-induced permeabilization of living cell membranes has also been observed in vitro using enzyme assays and flow cytometry (*13*, *15*). In this paper, we correlate two separate types of studies (model membrane and in vitro studies) by performing simultaneous experiments at similar conditions to provide a better understanding of polymer/membrane interactions.

There are two basic types of disruption seen in AFM images: membrane hole formation and membrane thinning. 'Membrane hole formation' is the complete removal of the lipid bilayer from the mica surface, resulting in defects of 4 to 5 nm in depth. The apparent discrepancy between the expected depth for a removal of a full bilayer, 5 nm, and the depths experimentally measured in this study can be explained by the varying degrees of polymer adsorption to the surface of the mica. 'Membrane thinning', which could result from the reorientation of lipids or the removal of a layer of lipid from the lipid bilayer, yields depressions ranging between approximately 2 and 3 nm (*25*−*28*).

Although the effect of each of the polymers used in the study varies in degree, each of these commercial polycationic polymers induce disruption of the bilayers as shown in the AFM images (Figures 2−4). This study is consistent in terms of observing bilayer disruption but differs in both the type of disruption and concentration dependence as compared with the previous studies which examined the interaction of positively charged dendrimers

with a DMPC-supported lipid bilayers (*16*). Our in vitro study shows enzyme (LDH with MW 135−140 kDa and ∼4.3 nm in radius and LUC with MW 61 kDa and ∼2.7 nm in radius) leakage out of the cells, polymer internalization into the cells, and diffusion in and out of small molecular probes (PI and FITC respectively) through the living cell membranes (Figures 6−9) which are also consistent with our previous report using cationic PAMAM dendrimers (*15*). Therefore, it is clear that PEI, PLL, and DEAE-DEX also cause the formation of defects in both supported lipid bilayers and cell membranes.

Relationship between Polymer Properties and Membrane Permeabilization. As modern biotechnology tends toward the adaptation of biocompatible polymers for advanced biomedical applications, a fundamental understanding of these polymers, particularly in physiological conditions, should be obtained. In this paper, we try to provide a better understanding of the relationship between physical properties of polymers and biological membranes. GPC measurement enables us to rank hydrodynamic radii of the polycationic polymers in the following order: DEAE-DEX > PEI > PLL > G5 PAMAM. According to our AFM and in vitro studies, however, the size of the polymers does not seem to markedly affect their ability to induce hole formation in the membranes. Instead, it was found that the degree of membrane permeability is strongly dependent on the number of formal charges on the polymer chain. As shown in Table 1, PEI has the greatest density of charged groups on its single polymeric chain among the polymers used in this study. Not surprisingly, a significantly high amount of LDH and LUC was released in both cell lines after incubation with PEI. Furthermore, changes in fluorescence in PI and FITC as a result of interactions between PEI and cells were greater than changes induced by the other polycationic polymers. This indicates that charge interactions play a key role in inducing changes of membrane permeability, i.e., nanoscale hole formation. Our data on PLL, DEAE-DEX, and G5-NH_2, however, suggests that electrostatic interactions are not the only factor contributing to the effectiveness of polymer-induced nanoporation. Although PLL has an order of magnitude higher charge/monomer ratio than DEAE-DEX and G5-NH_2, the difference among those polymers in terms of enzyme leakage, PI internalization, and FITC escape is not remarkable. One possible explanation is that efficacy of hole formation is dependent on the architecture of polymers. That is, sphere-like (PAMAM), branched (PEI), or ring-containing (DEAE-DEX) molecular structures are likely more effective than linear polymers (PLL) at increasing membrane permeability. Mecke et al. also suggested that the macromolecular architecture is an important factor in the polymer/membrane interactions (*16*).

Taken as whole, it is found that the common, commercial polycationic polymers PEI, PLL, and DEAE-DEX result in the formation of defects on supported lipid bilayers, enzyme leakage out of cells, polymer internalization into cells, and diffusion in and out of small molecular probes (PI and FITC) through cell membranes. Our results directly support our hypotheses: (1) commercially available polycationic polymers, PEI, PLL, and DEAE-DEX cause nanoscale hole formation in supported lipid bilayers, (2) commercially available polycationic polymers, PEI, PLL, and DEAE-DEX cause substantial permeability of the cell plasma membrane leading to enzyme and dye diffusion, and (3) charge-neutral linear polymers do not induce hole formation in supported lipid bilayers or induce a significant change in membrane permeability. The proposed hypotheses are also consistent with our previous study using PAMAM dendrimers (*15*). An interesting addition to hypothesis 1 was raised by the DEAE-DEX experiments showing membrane thinning. Polycationic polymers appear capable of both nanoscale hole formation and membrane thinning events. Our data suggest that these polycationic polymer agents may be internalized into cells through the nanoscale holes generated in the membranes and that this is also a route of internalization for other materials.

In summary, we directly observe that polycationic polymers induce hole formation in supported lipid bilayers. Our in vitro results showing that polycationic polymers permeabilize living cell membranes allowing for the diffusion of molecules in and out, are consistent with a hole-formation mechanism (*15*, *16*). Once the concentration is above the nontoxic range (up to ∼12 μg/mL), the polymers cause substantial membrane damage resulting in cell death. From this point of view, these polycationic polymers are not ideal as biocompatible drug or gene delivery agents. Instead, charge-neutral polymers that do not cause nanoscale hole formation and cell membrane permeabilization would likely serve as a better choice when paired with a targeting moiety (*29*−*31*).

ACKNOWLEDGMENT

This project has been funded with federal funds from the National Cancer Institute, National Institutes of Health, under contract no. N01-CO-27173.

LITERATURE CITED

(1) Cho, Y. W., Kim, J. D., and Park, K. (2003) Pollycation gene delivery systems: escape from endosomes to cytosol. *J. Pharm. Pharmacol. 55*, 721−734.

(2) Davis, M. E. (2002) Nonviral gene delivery systems. *Curr. Opin. Biotechnol. 13*, 128−131.

(3) Segura, T., and Shea, L. D. (2001) Materials for nonviral gene delivery. *Annu. Rev. Mater. Res. 31*, 25−46.

(4) Rolland, A. P. (1998) From genes to gene medicines: Recent advances in nonviral gene delivery. *Crit. Rev. Ther. Drug 15*, 143−198.

(5) Behr, J. P. (1993) Synthetic Gene-Transfer Vectors. *Acc. Chem. Res. 26*, 274−278.

(6) Boussif, O., Lezoualch, F., Zanta, M. A., Mergny, M. D., Scherman, D., Demeneix, B., and Behr, J. P. (1995) A Versatile Vector For Gene And Oligonucleotide Transfer Into Cells In Culture And In−Vivo − Polyethylenimine. *Proc. Natl. Acad. Sci. U.S.A. 92*, 7297−7301.

(7) Kopatz, I., Remy, J. S., and Behr, J. P. (2004) A model for nonviral gene delivery: through syndecan adhesion molecules and powered by actin. *J. Gene Med. 6*, 769−776.

(8) Purohit, G., Sakthivel, T., and Florence, A. T. (2001) Interaction of cationic partial dendrimers with charged and neutral liposomes. *Int. J. Pharm. 214*, 71−76.

(9) Yaroslavov, A. A., Kuchenkova, O. Y., Okuneva, I. B., Melik-Nubarov, N. S., Kozlova, N. O., Lobyshev, V. I., Menger, F. M., and Kabanov, V. A. (2003) Effect of polylysine on transformations and permeability of negative vesicular membranes. *BBA-Biomembranes 1611*, 44−54.

(10) Zhang, Z. Y., and Smith, B. D. (2000) High-generation polycationic dendrimers are unusually effective at disrupting anionic vesicles: Membrane bending model. *Bioconjugate Chem. 11*, 805−814.

(11) Karoonuthaisiri, N., Titiyevskiy, K., and Thomas, J. L. (2003) Destabilization of fatty acid-containing liposomes by. polyamidoamine dendrimers. *Colloid. Surface. B 27*, 365−375.

(12) Kozlova, N. O., Bruskovskaya, I. B., Okuneva, I. B., Melik-Nubarov, N. S., Yaroslavov, A. A., Kabanov, V. A., and Menger, F. M. (2001) Interaction of a cationic polymer with negatively charged proteoliposomes. *BBA-Biomembranes 1514*, 139−151.

(13) Fischer, D., Li, Y. X., Ahlemeyer, B., Krieglstein, J., and Kissel, T. (2003) In vitro cytotoxicity testing of polycations: influence of polymer structure on cell viability and hemolysis. *Biomaterials 24*, 1121−1131.

(14) Benns, J. M., Mahato, R. I., and Kim, S. W. (2002) Optimization of factors influencing the transfection efficiency of folate-PEG-folate-graft-polyethylenimine. *J. Controlled Release 79*, 255−269.

(15) Hong, S., Bielinska, A. U., Mecke, A., Keszler, B., Beals, J. L., Shi, X. Y., Balogh, L., Orr, B. G., Baker, J. R., and Banaszak Holl,

M. M. (2004) Interaction of poly(amidoamine) dendrimers with supported lipid bilayers and cells: Hole formation and the relation to transport. *Bioconjugate Chem. 15*, 774−782.

(16) Mecke, A., Uppuluri, S., Sassanella, T. M., Lee, D.-K., Ramamoorthy, A., Baker, J. R., Orr, B. G., and Banaszak Holl, M. M. (2004) Direct Observation of Lipid Bilayer Disruption by Polyamidoamine Dendrimers. *Chem. Phys. Lipids 132*, 3−14.

(17) Mecke, A., Lee, D. K., Ramamoorthy, A., Orr, B. G., and Banaszak Holl, M. M. (2005) Membrane thinning due to antimicrobial peptide binding: An atomic force microscopy study of MSI-78 in lipid bilayers. *Biophys. J. 89*, 4043−4050.

(18) Mecke, A., Lee, D. K., Ramamoorthy, A., Orr, B. G., and Banaszak Holl, M. M. (2005) Synthetic and natural polycationic polymer nanoparticles interact selectively with fluid-phase domains of DMPC lipid bilayers. *Langmuir 21*, 8588−8590.

(19) Mecke, A., Majoros, I. J., Patri, A. K., Baker, J. R., Banaszak Holl, M. M., and Orr, B. G. (2005) Lipid bilayer disruption by polycationic polymers: The roles of size and chemical functional group. *Langmuir 21*, 10348−10354.

(20) Mecke, A., Lee, I., Baker, J. R., Banaszak Holl, M. M., and Orr, B. G. (2004) Deformability of poly(amidoamine) dendrimers. *Eur. Phys. J. E 14*, 7−16.

(21) Bielinska, A., KukowskaLatallo, J. F., Johnson, J., Tomalia, D. A., and Baker, J. R. (1996) Regulation of in vitro gene expression using antisense oligonucleotides or antisense expression plasmids transfected using starburst PAMAM dendrimers. *Nucleic Acids Res. 24*, 2176−2182.

(22) Bielinska, A. U., KukowskaLatallo, J. F., and Baker, J. R. (1997) The interaction of plasmid DNA with polyamidoamine dendrimers: mechanism of complex formation and analysis of alterations induced in nuclease sensitivity and transcriptional activity of the complexed DNA. *BBA-Gene Struct. Expr. 1353*, 180−190.

(23) Umebayashi, Y., Miyamoto, Y., Wakita, M., Kobayashi, A., and Nishisaka, T. (2003) Elevation of plasma membrane permeability on laser irradiation of extracellular latex particles. *J. Biochem. 134*, 219−224.

(24) Rossetti, F. F., Reviakine, I., Csucs, G., Assi, F., Voros, J., and Textor, M. (2004) Interactions between poly(L-Lysine)-*g*-poly(ethylene glycol) and Supported Phospholipid Bilayers. *Biophys. J. 86*, 174A−174A.

(25) Harroun, T. A., Heller, W. T., Weiss, T. M., Yang, L., and Huang, H. W. (1999) Experimental evidence for hydrophobic matching and membrane-mediated interactions in lipid bilayers containing gramicidin. *Biophys. J. 76*, 937−945.

(26) Heller, W. T., Waring, A. J., Lehrer, R. I., Harroun, T. A., Weiss, T. M., Yang, L., and Huang, H. W. (2000) Membrane thinning effect of the beta-sheet antimicrobial protegrin. *Biochemistry 39*, 139−145.

(27) Ludtke, S., He, K., and Huang, H. (1995) Membrane thinning caused by magainin 2. *Biochemistry 34*, 16764−16769.

(28) Mazzuca, C., Stella, L., Venanzi, M., Formaggio, F., Toniolo, C., and Pispisa, B. (2005) Mechanism of membrane activity of the antibiotic trichogin GA IV: A two-state transition controlled by peptide concentration. *Biophys. J. 88*, 3411−3421.

(29) Quintana, A., Raczka, E., Piehler, L., Lee, I., Myc, A., Majoros, I., Patri, A. K., Thomas, T., Mule, J., and Baker, J. R. (2002) Design and function of a dendrimer-based therapeutic nanodevice targeted to tumor cells through the folate receptor. *Pharm. Res. 19*, 1310−1316.

(30) Kukowska-Latallo, J. F., Candido, K. A., Cao, Z. Y., Nigavekar, S. S., Majoros, I. J., Thomas, T. P., Balogh, L. P., Khan, M. K., and Baker, J. R. (2005) Nanoparticle targeting of anticancer drug improves therapeutic response in animal model of human epithelial cancer. *Cancer Res. 65*, 5317−5324.

(31) Thomas, T. P., Patri, A. K., Myc, A., Myaing, M. T., Ye, J. Y., Norris, T. B., and Baker, J. R. (2004) In vitro targeting of synthesized anti body-conjugated dendrimer nanoparticles. *Biomacromolecules 5*, 2269−2274.

BC060077Y

A Peripheral Benzodiazepine Receptor Targeted Agent for In Vitro Imaging and Screening

H. Charles Manning,[†,‡] Sarah M. Smith,[†] Michelle Sexton,[†,§,||] Sarah Haviland,[†] Mingfeng Bai,[†] Kristin Cederquist,[†] Nephi Stella,[§] and Darryl J. Bornhop*[,†]

Department of Chemistry, Vanderbilt University, Nashville, Tennessee 37235, Vanderbilt University Institute of Imaging Science and Department of Radiology and Radiological Sciences, Nashville, Tennessee 37235, Department of Pharmacology, Psychiatry, and Behavioral Science, University of Washington, Seattle, Washington 98195, and Department of Basic Sciences, School of Naturopathic Medicine, Bastyr University, Seattle, Washington 98028. Received January 26, 2006; Revised Manuscript Received March 24, 2006

We developed a molecular imaging agent (MIA), a conjugable form of PK11195 (conPK11195) coupled to a lissamine dye (Liss−ConPK11195), which targets the peripheral benzodiazepine receptor (PBR). To determine that our compound specifically binds to this 18 kDa protein, primarily expressed on the mitochondria, we performed classic binding studies on live MDA-MB-231 breast cancer cells and measured fluorescence in cell fractions of C6 glioma cells. We found that conPK11195 conjugated to the fluorophore retained significant binding to its target. Here we demonstrate the utility of the agent for in vitro imaging of live cells by specific binding to the protein of interest.

INTRODUCTION

Molecular imaging (MI) has the potential to revolutionize biological investigations and diagnostic medicine. For example, discrete intracellular molecular events can be followed in vitro in real time (*1*, *2*), and MI agents allow the in vivo study of disease progression and therapeutic efficacy monitoring (*3*−*5*). Numerous ligands have been functionalized for nuclear imaging such as autoradiography (*6*) and positron emission tomography (PET) (*7*), yet synthetic complexity, short half-life of radioligands, and expense of the detection methodologies are limitations to these applications of molecular imaging. Immunohistochemistry continues to be a valuable tool for cellular scale imaging in vitro, but the numerous steps involved in this technique make this a somewhat tedious process. The development of targeted imaging agents for in vitro screening of protein expression as well as in vitro therapy efficacy monitoring is an emerging concept in MI. Fluorescent agents with high specificity and attractive spectroscopic properties are therefore needed in the biomedical research community.

The peripheral benzodiazepine receptor (PBR), reported to be expressed primarily by mitochondria (*8*, *9*), is known to be associated with numerous biological functions including regulation of cellular proliferation, immunomodulation, regulation of cholesterol transport and steroidogenesis, and apoptosis (*10*). The precise biological relevance and clinical significance of PBR in disease progression has remained somewhat elusive, yet the overexpression in cancer (*11*, *12*) and neurodegenerative disease (*13*−*15*) is well-documented as is its correlation with metastasis and poor clinical prognosis (*16*−*18*).

Several exogenous PBR ligands have been developed which bind PBR with high affinity, including PK11195 (*19*), DAA1106 (*20*, *21*), and Ro5-4864 (*22*). Both ^{3}H- and ^{11}C-PK11195 have been used for human imaging of glioma (*23*−*26*), neurodegenerative disease (*27*), and stroke (*28*).

Papadopolous et al. reported an agent for in vitro analysis, NBD-FGIN 1-27, utilizing a fluorophore (NBD) that is not optimal for in vitro imaging (*29*). With the principal excitation and emission wavelengths for NBD (7-nitro-2,1,3-benzoxadiazole) at 466 nm and 536 nm, respectively (*30*), the effective signal-to-noise ratio for detection in cells and tissues tends to be limited by autofluorescence and scatter, especially when compared to longer wavelength dyes (*1*). Furthermore, the fluorescence sensitivity of NBD agents is limited by relatively low ($\sim$8000 L mol^{-1} cm^{-1}) aqueous phase molar extinction coefficients (*30*). More recently, Chen et al has prepared PBR targeted photodynamic therapy (PDT) probes based on pyropheophorbide metal complexes (*31*). These probes appear to have utility for therapeutic purposes, but the potential for performing imaging with these compounds is less clearly defined (*31*).

We recently reported another PBR targeted MI agent, a lanthanide chelate (Ln-PK11195) (*32*, *33*). This agent is unique because it has the potential to provide both an optical and MR signature depending on the metal ion that is chelated (i.e. Eu^{3+} for optical and Gd^{3+} for MR) (*34*). While we demonstrated optical microscopy of live cells using the europium chelate (*34*), excitation of the sensitizing antenna at 320 nm is unattractive due to the high energy of UV radiation, and the attenuated transmission through glass optical trains of standard microscopes limits the usefulness of this agent.

To address this limitation, we have prepared Liss−ConPK11195, which has a relatively high molar extinction coefficient, thus allowing improved sensitivity for microscopy imaging and high-throughput screening detection in multiwell plates. Here we report the synthesis and spectroscopic characterization of Liss−ConPK11195, demonstrate specific binding in live cells, and confirm the intracellular location by isolation of the mitochondrial fraction.

EXPERIMENTAL PROCEDURES

Synthesis and Spectroscopic Characterization of Liss−ConPK11195. Lissamine−Rhodamine B sulfonyl chloride was

* Corresponding author. Mailing address: Vanderbilt University, 7300 Stevenson Center, Nashville, TN 37235. Tel: 615.322.4226. Fax: 615.343.1234. E-mail: Darryl.Bornhop@Vanderbilt.Edu.

† Department of Chemistry, Vanderbilt University.

‡ Vanderbilt University Institute of Imaging Science and Department of Radiology and Radiological Sciences.

§ University of Washington.

|| Bastyr University.

10.1021/bc060020b CCC: $33.50 © 2006 American Chemical Society
Published on Web 05/03/2006

purchased from Molecular Probes. Conjugable PK11195 (as previously reported (*33*)) was dissolved in dry chloroform along with 1 equiv of triethylamine (TEA). Next, 1.5 equiv of Lissamine−Rhodamine B sulfonyl chloride was added in one part. The vessel was purged with argon, and the reaction was allowed to continue overnight. Formation of the product was monitored via thin-layer chromatography (TLC) ($R_f = 0.8$, 9:1 chloroform/methanol). Purification of the product was achieved using column chromatography on silica, eluting with a 30:1:0.1 mixture of chloroform, methanol, and aqueous ammonia. Absorbance was measured using a Shimadzu 1700 spectrophotometer, and fluorescence was recorded using a PTI fluorometer.

^{1}H NMR ($CDCl_3$): δ 1.31 (t, 12H), 1.42 (m, 2H), 1.54 (m, 2H), 1.67 (bs, 4H), 2.90 (q, 2H), 3.39 (m, 2H), 3.57 (q, 8H), 6.70 (d, 2H), 6.87 (d, 2H), 7.20 (m, 3H), 7.46−7.57 (m, 6H), 7.65 (m, 1H), 7.73 (m, 1H), 8.03 (d, 1H), 8.22 (t, 1H), 8.36 (d, 1H), 8.63 (s, 1H), 8.73 (s, 1H).

ESI MS+ (calcd: found): (921.32: 922.45 and 944.44 M + Na^+).

Tissue Culture. C6 glioma cells were cultured in Dulbecco's modified Eagle medium (DMEM)−F12 medium (Gibco/Invitrogen) supplemented with 0.1% gentamicin sulfate (Biowhittaker). Standard medium pH was adjusted to 7.4. Cells were maintained in a tissue culture incubator (Forma Scientific) at 37 °C, 5% CO_2. MDA-MB-231 cells were cultured in closed cap flasks, with 90% Leibovitz's L-15 medium, supplemented with 2 mM L-glutamine and 10% fetal bovine serum.

PBR Binding Affinity Determinations. A standard fluorescence calibration curve for Liss−ConPK11195 was prepared using a Beckman Coulter DTX 880 plate reader and found linear over the concentration range 0−10 μM. Twenty-four hours prior to performing the binding experiments, MDA-MB-231 cells were plated into NUNC 96 well (optical) plates at a density of 4×10^4 cells (80% confluence). To measure specific binding, cells were incubated in triplicate for 30 min with standard dilutions of Liss−ConPK11195 (0, 1 μM, 3.2 μM, 10 μM, 32 μM) without and with excess (10 μM "cold") unlabeled DAA1106 (prepared as previously reported) (*35*). The plate was subsequently rinsed with MEM/Cellgro and read on the plate reader. When the values for the nonspecific binding were subtracted from the total, the specific binding signal was revealed. These data were analyzed by Scatchard analysis using Graphpad Prism software.

Live Cell Imaging. Cells were plated in MaTek dishes and incubated with the imaging agent by first aspirating the growth media and then adding media containing the contrast agent. Incubation concentrations ranged from 1 nM to 100 μM, although concentrations above 10 μM seemed to produce nonspecific staining in the microscopy experiments (data not shown). The cells were incubated with the imaging agent for 45 min at 37 °C, 5% CO_2 as previously reported (*29*). At the end of the incubation time, cells were rinsed with fresh medium three times and imaged.

PBR Functional Displacement of Liss−ConPK11195. Forty-eight hours prior to imaging, 2.5×10^4 C6 glioma cells were plated into MaTek dishes and propagated at 37 °C under 5% CO_2. The cells were either incubated for 45 min with 1 μM Liss−ConPK11195 or coincubated for 45 min with 1 μM Liss−ConPK11195 and 100 μM PK11195 (Sigma-Aldrich). The cells were subsequently rinsed with saline to remove any unbound contrast agent, and then imaged using fluorescence microscopy. The cellular fluorescence intensity was evaluated by measuring the gray scale intensities of individual cells from multiple assays. A one-way ANOVA (Prism 4.0) at the 95% confidence level was used to indicate the statistical significance of the data.

Microscopy. Microscopy was performed using a Nikon TE 2000-U inverted microscope, coupled to a Q-Imaging Retiga-EXi camera. Image acquisition was controlled using Metamorph (version 6.2). The optical train used to image Liss−ConPK11195 consisted of a mercury lamp and a Texas Red filter set (Chroma, excitation 575 nm × 20 nm, emission 625 nm × 50 nm). Confocal microscopy was performed using a Zeiss LSM510 confocal microscope, 543 nm excitation line and emission collected through a 620 nm × 50 nm filter.

Mitochondrial Fractionation Assay. Cellular Disruption. A total of ninety (90) 10 cm culture flasks of C6 glial cells were propagated to near confluency. Half of the plates (45) were incubated with 1 μM Liss−ConPK11195 for 45 min, and the other half (45) were left unincubated as control. At the end of the incubation time, each plate of cells was rinsed with approximately 5 mL of ice-cold disruption buffer ("H" buffer, 5 mM HEPES, 0.21 M D-mannitol, 0.07 M sucrose, 2 mM benzamidine, 2 mM α-toluenesulfonyl fluoride, 4 mM magnesium chloride, pH 7.4) (5×), and then the monolayer was scraped from the surface of the dish. The combined scrapings from the labeled and unlabeled plates were separately resuspended in ice-cold disruption buffer to yield 10 mL total volume. The cells were then ruptured by 50 strokes with a glass homogenizer, type A pestle. The homogenates were centrifuged at 200*g* for 1 min. The resulting pellet was then rehomogenized in ice-cold disruption buffer (diluted to 1/4 strength) and centrifuged at 200*g* for 1 min. Next, the supernatants were combined and centrifuged at 200*g* for 1 min. The resulting supernatant was filtered through four layers of cheesecloth and centrifuged at 0.6K × *g* for 20 min (fraction 1). The resulting supernatant was then centrifuged at 10K × *g* for 2 h, and the pellet (fraction 2) was separated from the supernatant (fraction 3).

Mitochondrial Fluorescence Assay. Fluorescence measurements were made using a PTI fluorimeter and standard quartz cuvettes. A fluorescence calibration curve was prepared using increasing concentrations of Liss−ConPK11195 solution in PBS (1−20 nm). Samples (1.5 mg/mL) from fractions 1 and 2 were prepared by diluting the pellet 100:1 in PBS. Fraction 3 was run neat. Samples were excited at 571 nm, and the emission was scanned from 580 nm to 630 nm. The principal emission band was found at 585 nm, and the reported fluorescence values are from said wavelength.

Corrected Mitochondrial Activity. Succinate dehydrogenase activity was assayed via the colorimetric reduction of iodonitrotetrazolium (INT) chloride using a protocol previously reported (*36*). Briefly, to prepare the enzyme solution, a 20 μL protein suspension (1.5 mg/mL verified by the Bradford assay) was added to 500 μL of freshly prepared INT reagent (~35 °C) and absorbance was continuously monitored at 500 nm for 10 min (triplicate measurement). The INT reagent without succinate, subtracted from the sample rates, served as a control. The specific activity was calculated according to the following equation: units/mL = ΔA/min × 5.18. A one-way ANOVA (Prism 4.0) at the 95% confidence level was used to indicate the statistical significance of the data. INT reagent = 100 mM triethanolamine, 0.5 mM EDTA, 2 mM INT, 12 g/L Tween 20, 20 mM succinic acid.

RESULTS AND DISCUSSION

We synthesized a PBR targeted MI agent, Liss−ConPK11195, by labeling our previously reported conjugable PK11195 ligand (*33*) with Lissamine−Rhodamine B sulfonyl chloride (Scheme 1). The agent was easily purified using standard column chromatography on silica gel. To determine whether the structure/function relationship of the dye was changed upon coupling, we measured the absorbance and fluorescence properties of Liss−ConPK11195 in aqueous media (Figure 1). The absorption maximum was centered at 571 nm, and emission was centered at 585 nm, similar to that of the

Scheme 1. Synthesis of Liss−ConPk11195

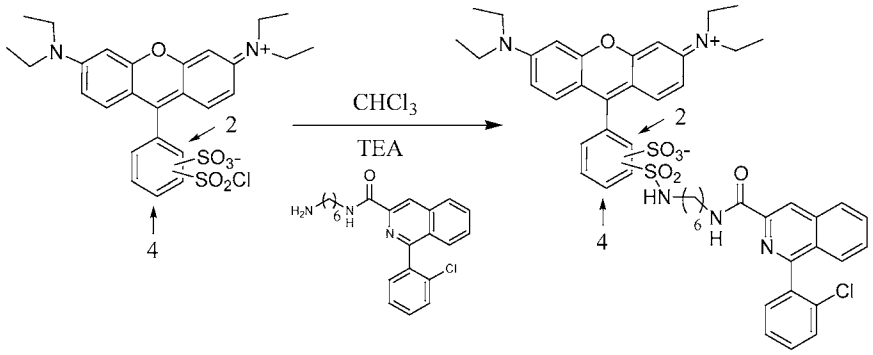

free dye. The molar extinction coefficient for Liss−ConPK11195 was determined to be 35 000 L mol^{-1} cm^{-1} in water, enabling sensitive detection of the imaging agent and demonstrating that conjugation did not significantly alter the function of the dye. While the absorbance and emission bands for Liss−ConPK11195 do not show as large a Stokes shift as the previously reported lanthanide chelate agent−PBR agent (*33*), it does have spectral characteristics leading to utility for fluorescence microscopy and commercially available fluorescence plate readers.

We next determined that conjugation of the dye to the ligand did not prevent binding to the target and that it was specific for PBR. We performed a classic binding assay in a multiwell plate in a live-cell format. Binding affinity (K_d) of Liss−ConPK11195 to PBR was calculated to be 1 μM (data not shown). While this value is higher than expected for an unperturbed PK11195 analogue, the imaging work shown here and by others (*31*) demonstrates that PBR targeted agents with micromolar binding affinities still have utility for cellular targeting applications. It is likely that the presence of the bulky, charged fluorophore and the minor structural differences between PK11195 and the conjugable PK11195 analogue contribute to a reduced binding affinity (*33*).

Fluorescence microscopy was used to characterize the cellular uptake and distribution of Liss−ConPK11195 in PBR overexpressing C6 glioma and MDA-MB-231 breast cancer cells. We first incubated live C6 glioma cells with the imaging agent (10 μM) and then rinsed the cells and imaged them using an epi-illumination fluorescence microscope. As controls, we imaged a similar population of cells with Lissamine after incubation with the free dye (nontargeted, 10 μM) and another population of unincubated cells to evaluate the level of autofluorescence. As seen in Figure 2A−D, both controls (unlabeled (A, B) and free Lissamine labeled (C, D) C6 cells) lack fluorescence, while cells incubated with Liss−ConPK11195 (Figure 2E,F) show perinuclear fluorescence. Fluorescence was also easily detected by microscopy in C6 cells at a concentration of 100 nM (data not shown). MDA-MB-231 breast cancer cells were imaged identically with a 100 nM concentration Liss−ConPK11195 yielding bright perinuclear fluorescence (Figure 3). Controls were the same as with the C6 cells and are shown in Figure 3A−D.

Confocal microscopy verified that Liss−ConPK11195 was internalized in C6 cells labeled with the MI agent as previously described. Fluorescence appeared to be perinuclear while no fluorescence was visualized on the cell surface (Figure 4). These images are consistent with previous reports describing the

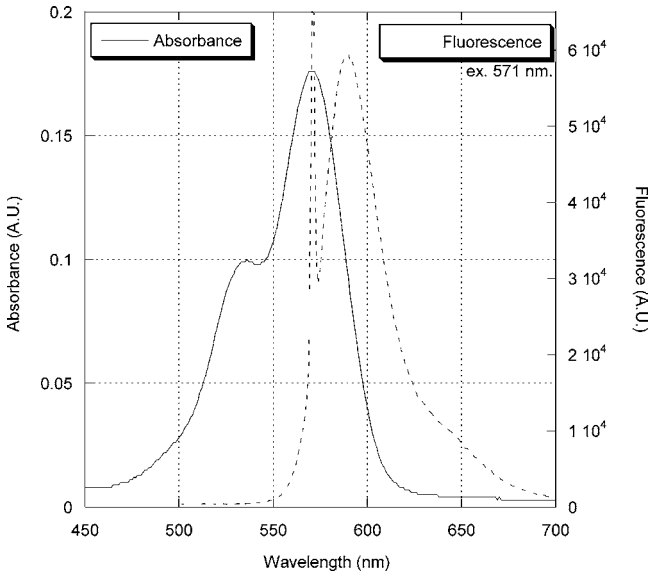

Figure 1. Liss−ConPK11195 aqueous spectroscopy (agent concentration = 5 μM).

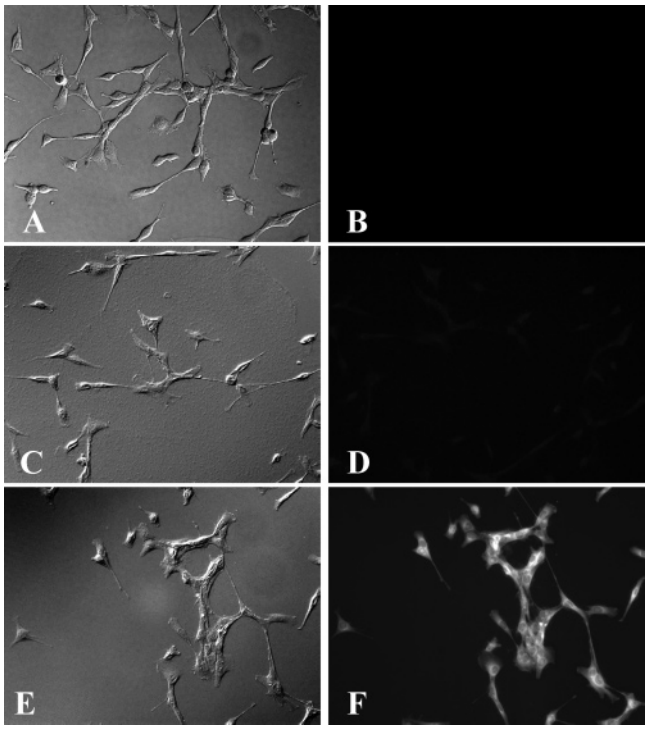

Figure 2. Fluorescent labeling studies of PBR in C6 glioma cells using Liss-PK11195. C6 cells were cultured on glass coverslips and incubated with either 10μM Lissamine free dye or Liss−ConPK11195 at 37 °C for 30 min. (A) Whitelight DIC image, unlabeled control. (B) Fluorescence image, unlabeled control. (C) Whitelight DIC image, cells incubated with 10 μM Lissamine free dye. (D) Fluorescence image, Lissamine control. (E) Whitelight DIC image, cells incubated with 10 μM Liss−ConPK11195. (F) Fluorescence image, cells incubated with Liss−ConPK11195.

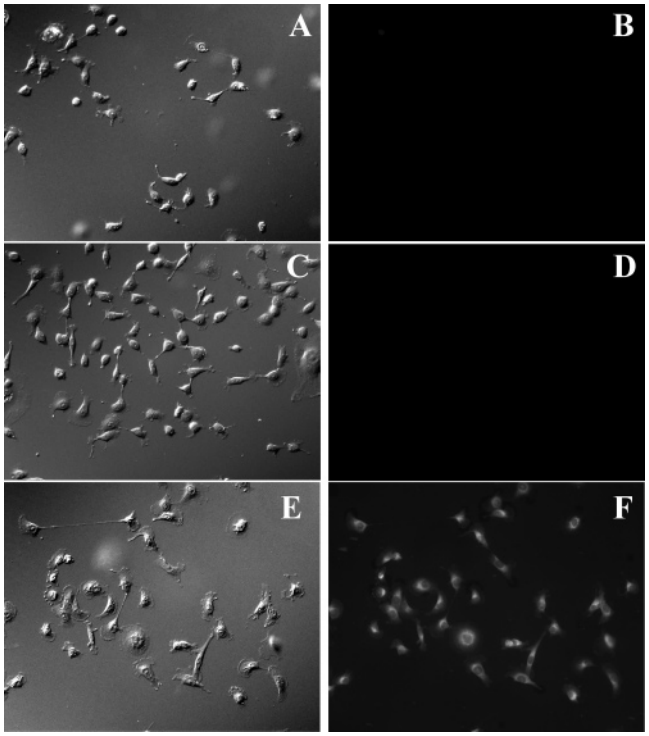

Figure 3. Fluorescent labeling studies of PBR in MDA-MB-231 cells using Liss−ConPK11195. MDA-MB-231 cells were cultured on glass coverslips and incubated with either 100 nM Lissamine free dye or Liss−ConPK11195 at 37 °C for 30 min. (A) Whitelight DIC image, unlabeled control. (B) Fluorescence image, unlabeled control. (C) Whitelight DIC image, cells incubated with 100 nM Lissamine free dye. (D) Fluorescence image, Lissamine control. (E) Whitelight DIC image, cells incubated with 100 nM Liss−ConPK11195. (F) Fluorescence image, cells incubated with Liss−ConPK11195.

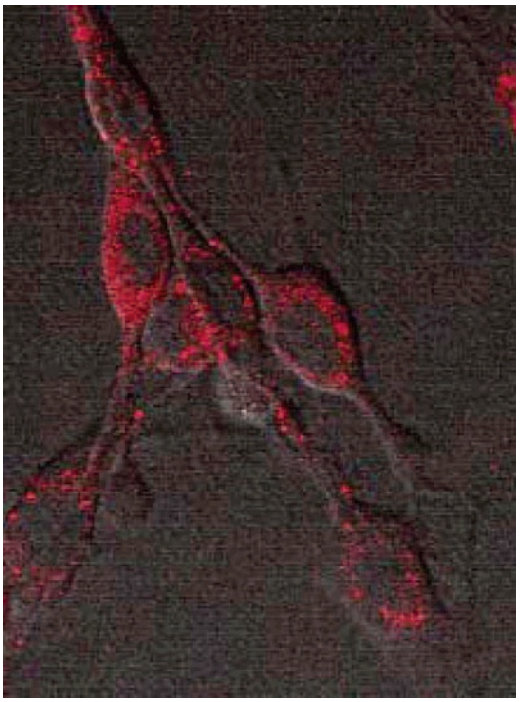

Figure 4. Confocal imaging of PBR in C6 rat glioma cell line. C6 cells were labeled with 1 μM Liss−ConPK11195 and imaged using a Zeiss confocal microscope. False color fluorescence image/DIC overlay demonstrating typical cellular morphology and predominately perinuclear fluorescence.

primary intracellular location of PBR and immuohistochemical PBR staining (*29*).

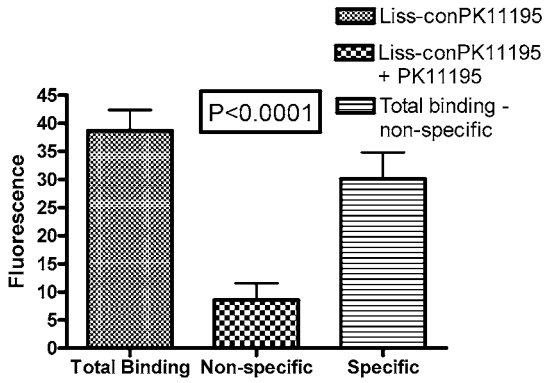

Figure 5. Live cell fluorescence displacement of 1 μM Liss−ConPK11195 with 100-fold excess PK 11195 in C6 glioma cells. Left bar: total binding. Middle bar: nonspecific binding. Right bar: specific binding. Autofluorescence was subtracted from each value. *P* value was calculated via one-way ANOVA, comparing fluorescence intensity of total, nonspecific, and specific binding.

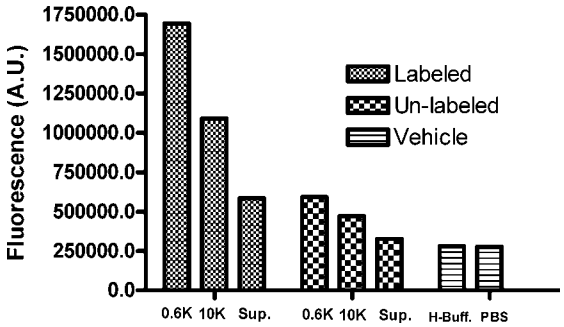

Figure 6. Fluorescence intensity from C6 cellular fractionations, 10K $\times$ *g*, 0.6K $\times$ *g*, and supernatant. Bars represent fluorescence intensity from labeled, unlabeled, and vehicle (control) samples.

An optical competitive binding assay was performed with live C6 glioma cells using excess "cold" PK11195 as the competitor with the dye. Labeled, unlabeled, and PK11195 challenged cells were imaged with fluorescence microscopy. Conservation of imaging settings, including integration time, binning, and magnification, gave a direct comparison of the cells labeled under the various medium conditions, and we quantified the displacement by subtracting the nonspecific binding from the total binding. Figure 5 shows total, specific, and nonspecific binding, with the statistical significance of all three measurements verified by one-way ANOVA analysis ($P < 0.0001$).

Cellular fractionation (*37*) confirmed the observations of the intracellular localization made by microscopy. A standard fluorimeter was used to measure fluorescence in mitochondrial and cytosolic cell fractions. C6 glioma cells were incubated with and without (control) Liss−ConPK11195, rinsed, and then mechanically disrupted. Lysates were then purified using a protocol that yields two mitochondrial-rich fractions (0.6K $\times$ *g* and 10K $\times$ *g*) (*37*). Next, we measured the relative fluorescence emission (excitation 571 nm, emission 580−630 nm) of all the cellular fractions collected (cytosol, 0.6K $\times$ *g* fraction, and 10K $\times$ *g* fraction). Liss−ConPK11195 fluorescence was detected in all three fractions with significant binding in the 0.6K $\times$ *g* and the 10K $\times$ *g* mitochondrial fractions (Figure 6). Fluorescence in the cytosolic fraction (supernatant) was detectable, yet miniscule in comparison to the other fractions measured, and suggests either nonspecific binding or binding to another protein in the cytosolic fraction. Fluorescence values for unlabeled cells and vehicle (as control) represent the bacK $\times$ ground signal and indicate some autofluorescence at the measured wavelength. Mitochondrial content of the assayed fractions was confirmed by measuring succinate dehydrogenase

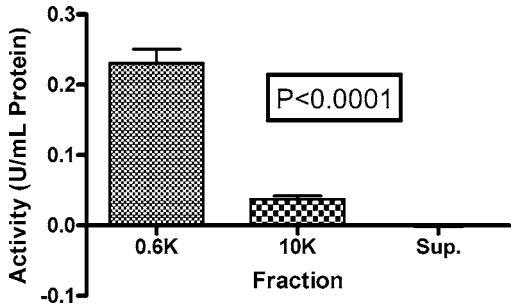

Figure 7. Corrected specific succinate dehydrogenase (mitochondrial) activity (U/mL) for the three assayed cellular fractions. Value represents the difference between the experimental and control (nonspecific) activities for each sample. *P* value calculated via one-way ANOVA.

activity (Figure 7). As expected, the mitochondrial fractions had statistically significant succinate dehydrogenase activity compared to the cytosolic fraction ($P < 0.0001$).

CONCLUSIONS

In this report we have demonstrated the synthesis, spectroscopic, and biological characterization of a novel optical molecular imaging agent targeting PBR. Liss−ConPK11195 specifically binds to PBR and displays attractive optical properties for live cell fluorescence microscopic imaging and high-throughput plate reader assays. While immunofluorescence has been a valuable technique for measuring proteins of interest in fixed cells, live cell molecular imaging has the potential to be translated to rapid high-throughput screening of therapies and to in vivo imaging. With molecular imaging being used increasingly in medical diagnostics, it is important to identify potential agents for reporting physiological processes such as protein expression. Here we show that simple synthetic chemistry can be used to enhance in vitro studies of disease processes, by targeting PBR expression with an optical imaging agent.

ACKNOWLEDGMENT

The authors would like to acknowledge Dr. Vassilios Papadopoulos for helpful discussions and assistance with the mitochondrial assay.

LITERATURE CITED

(1) Weissleder, R., and Mahmood, U. (2001) Molecular imaging. *Radiology 219*, 316−333.

(2) Gaietta, G., Deerinck, T. J., Adams, S. R., Bouwer, J., Tour, O., Laird, D. W., Sosinsky, G. E., Tsien, R. Y., and Ellisman, M. H. (2002) Multicolor and electron microscopic imaging of connexin trafficking. *Science 296*, 503−507.

(3) Tung, C. H., Mahmood, U., Bredow, S., and Weissleder, R. (2000) In vivo imaging of proteolytic enzyme activity using a novel molecular reporter. *Cancer Res. 60*, 4953−4958.

(4) McIntyre, J. O., and Matrisian, L. M. (2003) Molecular imaging of proteolytic activity in cancer. *J. Cell. Biochem. 90*, 1087−1097.

(5) Wu, J. C., Sundaresan, G., Iyer, M., and Gambhir, S. S. (2001) Noninvasive optical imaging of firefly luciferase reporter gene expression in skeletal muscles of living mice. *Mol. Ther. 4*, 297−306.

(6) Myers, R., Manjil, L. G., Cullen, B. M., Price, G. W., Frackowiak, R. S. J., and Cremer, J. E. (1991) Macrophage and Astrocyte Populations in Relation to [H-3] Pk 11195 Binding in Rat Cerebral-Cortex Following a Local Ischemic Lesion. *J. Cereb. Blood Flow Metab. 11*, 314−322.

(7) Maeda, J., Suhara, T., Zhang, M. R., Okauchi, T., Yasuno, F., Ikoma, Y., Inaji, M., Nagai, Y., Takano, A., Obayashi, S., and Suzuki, K. (2004) Novel peripheral benzodiazepine receptor ligand [C-11]DAA1106 for PET: An imaging tool for glial cells in the brain. *Synapse 52*, 283−291.

(8) Anholt, R. R. H., Pedersen, P. L., Desouza, E. B., and Snyder, S. H. (1986) The Peripheral-Type Benzodiazepine Receptor−Localization to the Mitochondrial Outer-Membrane. *J. Biol. Chem. 261*, 576−583.

(9) Basile, A. S., and Skolnick, P. (1986) Subcellular-Localization of Peripheral-Type Binding-Sites for Benzodiazepines in Rat-Brain. *J. Neurochem. 46*, 305−308.

(10) Casellas, P., Galiegue, S., and Basile, A. S. (2002) Peripheral benzodiazepine receptors and mitochondrial function. *Neurochem. Int. 40*, 475−486.

(11) Miettinen, H., Kononen, J., Haapasalo, H., Helen, P., Sallinen, P., Harjuntausta, T., Helin, H., and Alho, H. (1995) Expression of Peripheral-Type Benzodiazepine Receptor and Diazepam-Binding Inhibitor in Human Astrocytomas−Relationship to Cell-Proliferation. *Cancer Res. 55*, 2691−2695.

(12) Han, Z., Slack, R. S., Li, W., and Papadopoulos, V. (2003) Expression of peripheral benzodiazepine receptor (PBR) in human tumors: relationship to breast, colorectal, and prostate tumor progression. *J. Recept. Signal Transduction Res. 23*, 225−238.

(13) Messmer, K., and Reynolds, G. P. (1998) Increased peripheral benzodiazepine binding sites in the brain of patients with Huntington's disease. *Neurosci. Lett. 241*, 53−56.

(14) Rao, V. L. R., Dogan, A., Bowen, K. K., and Dempsey, R. J. (2000) Traumatic brain injury leads to increased expression of peripheral-type benzodiazepine receptors, neuronal death, and activation of astrocytes and microglia in rat thalamus. *Exp. Neurol. 161*, 102−114.

(15) Banati, R. B. (2002) Visualising microglial activation in vivo. *Glia 40*, 206−217.

(16) Hardwick, M., Fertikh, D., Culty, M., Li, H., Vidic, B., and Papadopoulos, V. (1999) Peripheral-type benzodiazepine receptor (PBR) in human breast cancer: Correlation of breast cancer cell aggressive phenotype with PBR expression, nuclear localization, and PBR-mediated cell proliferation and nuclear transport of cholesterol. *Cancer Res. 59*, 831−842.

(17) Hardwick, M., Rone, J., Han, Z. Q., Haddad, B., and Papadopoulos, V. (2001) Peripheral-type benzodiazepine receptor levels correlate with the ability of human breast cancer MDA-MB-231 cell line to grow in SCID mice. *Int. J. Cancer 94*, 322−327.

(18) Maaser, K., Grabowski, P., Sutter, A. P., Hopfner, M., Foss, H. D., Stein, H., Berger, G., Gavish, M., Zeitz, M., and Scherubl, H. (2002) Overexpression of the peripheral benzodiazepine receptor is a relevant prognostic factor in stage III colorectal cancer. *Clin. Cancer Res. 8*, 3205−3209.

(19) Benavides, J., Quarteronet, D., Imbault, F., Malgouris, C., Uzan, A., Renault, C., Dubroeucq, M. C., Gueremy, C., and Lefur, G. (1983) Labeling of Peripheral-Type Benzodiazepine Binding-Sites in the Rat-Brain by Using [Pk-H-3 11195, an Isoquinoline Carboxamide Derivative−Kinetic-Studies and Autoradiographic Localization. *J. Neurochem. 41*, 1744−1750.

(20) Chaki, S., Funakoshi, T., Yoshikawa, R., Okuyama, S., Okubo, T., Nakazato, A., Nagamine, M., and Tomisawa, K. (1999) Binding characteristics of [H-3]DAA1106, a novel and selective ligand for peripheral benzodiazepine receptors. *Eur. J. Pharmacol. 371*, 197−204.

(21) Culty, M., Silver, P., Nakazato, A., Gazouli, M., Li, H., Muramatsu, M., Okuyama, S., and Papadopoulos, V. (2001) Peripheral benzodiazepine receptor binding properties and effects on steroid synthesis of two new phenoxyphenyl-acetamide derivatives, DAA1097 and DAA1106. *Drug Dev. Res. 52*, 475−484.

(22) File, S. E., and Pellow, S. (1983) Ro5-4864, a Ligand for Benzodiazepine Micromolar and Peripheral Binding-Sites−Antagonism and Enhancement of Behavioral-Effects. *Psychopharmacology 80*, 166−170.

(23) Starosta-Rubinstein, S., Ciliax, B., Penney, J., McKeever, P., and Young, A. (1987) Imaging of a glioma using peripheral benzodiazepine receptor ligands. *Proc. Natl. Acad. Sci. U.S.A. 84*, 891−895.

(24) Junck, L., Olson, J. M. M., Ciliax, B. J., Koeppe, R. A., Watkins, G. L., Jewett, D. M., Mckeever, P. E., Wieland, D. M., Kilbourn, M. R., Starostarubinstein, S., Mancini, W. R., Kuhl, D. E., Greenberg, H. S., and Young, A. B. (1989) Pet Imaging of Human Gliomas with Ligands for the Peripheral Benzodiazepine Binding-Site. *Ann. Neurol. 26*, 752−758.

(25) Pappata, S., Cornu, P., Samson, Y., Prenant, C., Benavides, J., Scatton, B., Crouzel, C., Hauw, J. J., and Syrota, A. (1991) Pet Study of Carbon-11-Pk 11195 Binding to Peripheral Type Benzodiazepine Sites in Glioblastoma—a Case-Report. *J. Nucl. Med. 32*, 1608−1610.

(26) Miyazawa, N., Hamel, E., and Diksic, M. (1998) Assessment of the peripheral benzodiazepine receptors in human gliomas by two methods. *J. Neuro-Oncol. 38*, 19−26.

(27) Banati, R. B., Newcombe, J., Gunn, R. N., Cagnin, A., Turkheimer, F., Heppner, F., Price, G., Wegner, F., Giovannoni, G., Miller, D. H., Perkin, G. D., Smith, T., Hewson, A. K., Bydder, G., Kreutzberg, G. W., Jones, T., Cuzner, M. L., and Myers, R. (2000) The peripheral benzodiazepine binding site in the brain in multiple sclerosis—Quantitative in vivo imaging of microglia as a measure of disease activity. *Brain 123*, 2321−2337.

(28) Wang, D. C., Fryer, T., Price, C., Cleij, M., Aigbirhio, F., Green, H., Clark, J., Menon, D., Warburton, L., and Baron, J. C. (2004) Effect of CBV correction on ischaemic stroke [11C]-PK11195 binding potential values produced using a simplified reference tissue model. *Neuroimage 22*, T96−T97.

(29) Kozikowski, A. P., Kotoula, M., Ma, D. W., Boujrad, N., Tuckmantel, W., and Papadopoulos, V. (1997) Synthesis and biology of a 7-nitro-2,1,3-benzoxadiazol-4-yl derivative of 2-phenylindole-3-acetamide: A fluorescent probe for the peripheral-type benzodiazepine receptor. *J. Med. Chem. 40*, 2435−2439.

(30) Shilova, N. V., and Bovin, N. V. (2003) Fluorescent labels for the analysis of mono- and oligosaccharides. *Russ. J. Bioorg. Chem. 29*, 309−324.

(31) Chen, Y., Zheng, X., Dobhal, M. P., Gryshuk, A., Morgan, J., Dougherty, T. J., Oseroff, A., and Pandey, R. K. (2005) Methyl pyropheophorbide-a analogues: Potential fluorescent probes for the peripheral-type benzodiazepine receptor. Effect of central metal in photosensitizing efficacy. *J. Med. Chem. 48*, 3692−3695.

(32) Manning, H. C., Bai, M. F., Anderson, B. M., Lisiak, R., Samuelson, L. E., and Bornhop, D. J. (2005) Expeditious synthesis of 'P'-protected macrocycles en route to lanthanide chelate metal complexes. *Tetrahedron Lett. 46*, 4707−4710.

(33) Manning, H. C., Goebel, T., Marx, J. N., and Bornhop, D. J. (2002) Facile, efficient conjugation of a trifunctional lanthanide chelate to a peripheral benzodiazepine receptor ligand. *Org. Lett. 4*, 1075−1078.

(34) Manning, H. C., Goebel, T., Thompson, R. C., Price, R. R., Lee, H., and Bornhop, D. J. (2004) Targeted molecular imaging agents for cellular-scale bimodal imaging. *Bioconjugate Chem. 15*, 1488−1495.

(35) Okubo, T., Yoshikawa, R., Chaki, S., Okuyama, S., and Nakazato, A. (2004) Design, synthesis, and structure-activity relationships of novel tetracyclic compounds as peripheral benzodiazepine receptor ligands. *Bioorg. Med. Chem. 12*, 3569−3580.

(36) Munujos, P., Collcanti, J., Gonzalezsastre, F., and Gella, F. J. (1993) Assay of Succinate-Dehydrogenase Activity by a Colorimetric-Continuous Method Using Iodonitrotetrazolium Chloride as Electron-Acceptor. *Anal. Biochem. 212*, 506−509.

(37) Olson, J. M., Mcneel, W., Young, A. B., and Mancini, W. R. (1992) Localization of the Peripheral-Type Benzodiazepine Binding-Site to Mitochondria of Human Glioma-Cells. *J. Neuro-Oncol. 13*, 35−42.

BC060020B

Annexin A5-Functionalized Bimodal Lipid-Based Contrast Agents for the Detection of Apoptosis

Geralda A. F. van Tilborg,*[,†] Willem J. M. Mulder,[†] Niko Deckers,[‡] Gert Storm,[§] Chris P. M. Reutelingsperger,[‡] Gustav J. Strijkers,[†] and Klaas Nicolay[†]

Biomedical NMR, Department of Biomedical Engineering, Eindhoven University of Technology, P.O. Box 513, 5600 MB Eindhoven, The Netherlands, Department of Biochemistry, Cardiovascular Research Institute Maastricht, University of Maastricht, P.O. Box 616, 6200 MD Maastricht, The Netherlands, and Utrecht Institute for Pharmaceutical Sciences, Department of Pharmaceutics, Utrecht University, 3508 TB Utrecht, The Netherlands. Received February 1, 2006; Revised Manuscript Received April 11, 2006

Apoptosis, or programmed cell death, plays an important role in the etiology of a variety of diseases, including cancer and myocardial infarction. Visualization of apoptosis would allow both early detection of therapy efficiency and evaluation of disease progression. To that aim, we synthesized two types of lipid-based bimodal contrast agents that enable the detection of apoptotic cells with both MRI and optical techniques. MR contrast was provided either by entrapment of iron oxide particles within pegylated micelles or by incorporation of Gd-DTPA-bis(stearylamide) (Gd-DTPA-BSA) lipids within the lipid bilayer of pegylated liposomes. The resulting contrast agents were approximately 10 and 100 nm in diameter, respectively. Additional fluorescent lipids were incorporated in the lipid (bi)layer of the contrast agents to allow parallel detection with optical methods. Multiple human recombinant annexin A5 molecules were covalently coupled to introduce specificity for apoptotic cells. Both annexin A5-conjugated contrast agents were shown to significantly increase the relaxation rates of apoptotic cell pellets compared to untreated control cells and apoptotic cells that were treated with nonfunctionalized nanoparticles. Increased relaxation rates were confirmed to originate from association of the contrast agents to apoptotic cells by confocal microscopy. The targeted nanoparticles presented in this study, which differ both in size and in magnetic properties, may have applications for the in vivo detection of apoptosis.

INTRODUCTION

Apoptosis, or programmed cell death, is an important feature of normal tissue development and homeostasis. Deregulation of the apoptotic program plays a key role in a variety of diseases, including cancer, autoimmune diseases, neurodegenerative diseases, atherosclerosis, and myocardial infarction (*1*, *2*). Therefore the apoptotic pathway appears to be a promising target for therapeutic purposes. Stimulation of the apoptotic program is, for example, used for tumor treatment (*3*) by irradiation or cytotoxic chemotherapy, whereas myocardial infarct size due to reperfusion injury was shown to be reduced by early application of anti-apoptotic treatment (*4*). Visualization of apoptosis is therefore of great importance for the early detection of therapy efficiency and the evaluation of disease progression.

Traditionally the detection of apoptosis has been based on changes in the morphology and the cytoplasmic compartment of the cell (*5*). More recently several studies have been performed in which translocation of the phospholipid phosphatidylserine (PS) was used for the detection of apoptosis (*6*). PS is exposed on the outer leaflet of the apoptotic cell membrane for recognition by surface proteins on macrophages and fibroblasts, which subsequently engulf these cells prior to lysis (*7*). The expression of PS can also be exploited as a marker for apoptosis that can be detected by annexin A5 or synaptotagmin I conjugates (*8*). Both proteins bind with high affinity to PS in the presence of Ca^{2+}. Several fluorescent annexin A5 conjugates have been successfully used for the detection of apoptosis in vitro (*8*, *9*) and in vivo (*10*, *11*). Radiolabeled annexin A5 was shown to enable the in vivo visualization of apoptosis in animal models (*12*), as well as in patients with acute myocardial infarction (*13*).

Both nuclear and optical techniques allow the detection of contrast agents at nano- to picomolar concentrations. However optical imaging techniques suffer from limited tissue penetration depth, whereas nuclear techniques provide images with a low spatial resolution against a poor anatomical background. Magnetic resonance imaging (MRI) allows the noninvasive detection of MR contrast agents in the micro- to millimolar concentration range in high spatial resolution anatomical images throughout the complete living animal. Conjugation of annexin A5 to cross-linked iron oxide particles (CLIO) was shown to enable the detection of apoptosis with MRI both in vitro (*14*) and in vivo (*15*). As an alternative to annexin A5, the C_2 domain of synaptotagmin I was conjugated to either superparamagnetic iron oxide particles (SPIO) or multiple Gd-DTPA molecules (*16*). Additional labeling of MRI contrast agents with fluorescent dyes would allow for colocalization of the detected contrast agent in MR images at the macroscopic level and at the cellular level with optical techniques. Several bimodal probes have been proposed that have one or multiple fluorescent dyes conjugated to either low molecular weight MR contrast agents, gadolinium-tetraazacyclododecanetetraacetic acid (Gd-DOTA) (*17*), or high molecular weight MR contrast agents, for example, complexes of polymers and gadolinium-dietjylenetriaminepentaacetric acid (Gd-DTPA) (*17*, *18*), paramagnetic liposomes (*19*, *20*), or iron oxide particles (*21*, *22*).

Here we present the synthesis of two types of lipid-based nanoparticulate contrast agents, which differ both in size and

* To whom correspondence should be addressed. Fax: +31 40 243 2598. E-mail: g.a.f.v.tilborg@tue.nl.

[†] Eindhoven University of Technology.

[‡] University of Maastricht.

[§] Utrecht University.

10.1021/bc0600259 CCC: $33.50 © 2006 American Chemical Society
Published on Web 05/04/2006

magnetic properties. The first bimodal nanoparticle is based on liposomes of ~100 nm diameter in which both paramagnetic lipids, Gd-DTPA-bis(stearylamide) (Gd-DTPA-BSA), and fluorescent lipids are incorporated in the lipid bilayer. The second bimodal nanoparticle of ~10 nm was prepared by enclosure of hydrophobic iron oxide particles in a fluorescent lipid containing micellular shell. The resulting nanoparticles can be referred to as positive and negative MR contrast agents, respectively. Amphiphiles with a functional headgroup were incorporated in the lipid layer(s) of both contrast agents to allow the covalent coupling of multiple recombinant annexin A5 proteins for targeting. In addition, the contrast agents were pegylated for improved bioavailability and circulation time (*23*).

In this study, apoptotic Jurkat cells were incubated with both annexin A5-functionalized nanoparticles to determine their ability to detect apoptosis with MRI and fluorescence microscopy in vitro.

EXPERIMENTAL PROCEDURES

Materials. 1,2-Distearoyl-*sn*-glycero-3-phosphocholine (DSPC), cholesterol, 1,2-distearoyl-*sn*-glycero-3-phosphoethanolamine-*N*-[methoxy(poly(ethylene glycol))-2000] (PEG2000−DSPE), 1,2-distearoyl-*sn*-glycero-3-phosphoethanolamine-*N*-[maleimide-(poly(ethylene glycol))2000] (Mal−PEG2000−DSPE), and 1,2-dioleoyl-*sn*-glycero-3-phosphoethanolamine-*N*-(carboxyfluorescein) (PE−carboxyfluorescein) were obtained from Avanti Polar Lipids (Albaster, AL). Gd-DTPA-bis(stearylamide) (Gd-DTPA-BSA) was purchased from Gateway Chemical Technology (St. Louis, MO). An ultrastable colloidal suspension of oleic acid coated magnetite (Fe_3O_4) particles of 3−15 nm in toluene carrier liquid (ferrofluid) was obtained from the University "Polytehnica" of Timisoara (Romania). Liposomes were sized with a Lipofast Extruder (Avestin, Canada). Polycarbonate filters that were required for liposome extrusion were obtained from Costar (Cambridge, MA). Dynamic light scattering (DLS) was performed with a Malvern 4700 system using an argon-ion laser (488 nm) operating at 10.4 mW (Uniphase) and PCS (photon correlation spectrometry) software for Windows, version 1.34 (Malvern, U.K.).

N-2-Hydroxyethylpiperazine-*N*′-2-ethanesulfonic acid (HEPES) and ethylenediaminetetraacetic acid (EDTA) (Titriplex) were purchased from Merck (Darmstadt, Germany). An iron standard solution ($Fe(NO_3)_3$) was obtained from Merck. All other chemicals were of analytic grade or of the best grade available.

Preparation of Bimodal Lipid-Based Contrast Agents. *Preparation of Superparamagnetic Micelles.* Water-insoluble iron oxide particles were coated with phospholipids (Figure 1A) according to a modified procedure previously described for quantum dots (*24*). Typically, 20 μL of oleic acid coated iron oxide particles (magnetite) in toluene (50 g of magnetite/100 mL) with a mean diameter of 5 nm were diluted in 1 mL of chloroform. A chloroform solution containing 95 μmol of PEG2000−DSPE and 5 μmol of Mal−PEG2000−DSPE, of which the latter allowed conjugation of annexin A5 to the distal ends of the PEG chains, was added to the iron oxide particle solution. For fluorescence microscopy and flow cytometry, 1 mol % PE−carboxyfluorescein was added as well. The solvent was evaporated to dryness by rotary evaporation, and the obtained mixed film was heated to 65 °C. Next, the film was hydrated with a 65 °C HEPES buffer (20 mM HEPES, 135 mM NaCl, pH 6.7). This suspension was vigorously vortexed and heated to 65 °C until a clear solution was obtained, indicative of a small size for the formed aggregates. Thereafter, the sample was centrifuged (1 h at 500 000*g*) to separate micelles with a magnetite core from empty micelles. The supernatant was removed gently, and the pellet was resuspended in 1 mL HEPES buffer and filtered through a 200 nm polycarbonate filter. The mean size was determined to be approximately 10 nm with dynamic light scattering.

Preparation of Paramagnetic Liposomes. Paramagnetic liposomes were prepared by lipid film hydration (Figure 1B) of a lipid mixture that typically contained a total lipid amount of 100 μmol. Gd-DTPA-BSA, DSPC, cholesterol, PEG2000−DSPE, and Mal−PEG2000−DSPE were added at a molar ratio of 0.75/1.1/1/0.075/0.075. Mal−PEG2000−DSPE was included for conjugation of annexin A5 to the distal ends of the PEG chains. The lipid mixture was dissolved in chloroform/methanol 1:1 (v/v) and 0.1 mol % PE−carboxyfluorescein was added to allow the detection of the paramagnetic liposomes with flow cytometry and fluorescence microscopy. The solvent was subsequently removed by rotary evaporation, followed by additional drying under nitrogen. The completely dried lipid film was hydrated in 4 mL of HEPES-buffered saline (20 mM HEPES and 135 mM NaCl, pH 6.7) at 65 °C. The resulting large multilamellar vesicles were downsized by extrusion at 65 °C through a stack of two 200 nm filters (four times), followed by extrusion through a stack of two 100 nm filters (10 times). The mean size was determined to be approximately 100 nm with dynamic light scattering.

Annexin A5-Functionalized Nanoparticles. *Annexin A5-cys.* Recombinant human annexin A5 was labeled with fluorescein−isothiocyanate (Amersham Biosciences). To allow easy coupling of annexin A5 to maleimide-functionalized biomolecules, a variant of annexin A5 was engineered having a single cysteine residue in the N-terminal tail (annexin A5-cys). The PS and apoptotic cell binding properties of annexin A5-cys are identical to those of recombinant human annexin A5 as was measured by ellipsometry (*25*) and flow cytometry (*26*), respectively.

Coupling of Annexin A5-cys. Annexin A5-cys was conjugated to the maleimide groups of both Mal−PEG2000−DSPE-containing contrast agents by sulfhydryl−maleimide coupling. Prior to conjugation, annexin A5-cys was reactivated by cleavage of sulfide bridges with 10 mM DTT at 37 °C. After 1.5 h, 10 mM EDTA was added to stop this reaction. DTT and EDTA were subsequently removed by dialysis of 1 mL of activated annexin A5-cys in a 12−14 kD MWCO membrane (Pierce) against 1000 mL of dialysis buffer (25 mM Hepes, 140 mM NaCl, 1 mM EDTA, pH 7.4). Dialysis was performed overnight at 4 °C followed by a change of the dialysis buffer to continue dialysis of the activated annexin A5-cys for another 4 h at room temperature.

For the superparamagnetic micelles, 100 μg of purified activated annexin A5-cys was added per micromole of total lipid, whereas for the paramagnetic liposomes 25 μg of purified activated annexin A5-cys was added per micromole of total lipid. Coupling was performed overnight at 4 °C. The resulting mixture was ultracentrifuged (2 times, 45 min at 60 000 rpm) to separate the annexin A5-conjugated contrast agents from unbound annexin A5-cys.

Contrast Agent Characterization. *Cryo Transmission Electron Microscopy.* Size and morphology of the lipid-based nanoparticles were measured with cryo transmission electron microscopy (cyro-TEM). Suspensions of the contrast agents were vitrified according to a procedure previously described by Frederik and Hubert (*27*). The vitrified specimens were stored under liquid nitrogen and observed at 103 K (Gatan 626 cryoholder) in a Philips CM12 microscope, operating at 120 kV.

Nanoparticle Concentration. The concentration of the paramagnetic liposomes used for in vitro targeting experiments was based on the total lipid concentration, which was determined by phosphate analysis according to Rouser (*28*) after destruction with perchloric acid. The concentration of the superparamagnetic micelles that were used for the in vitro targeting experiments

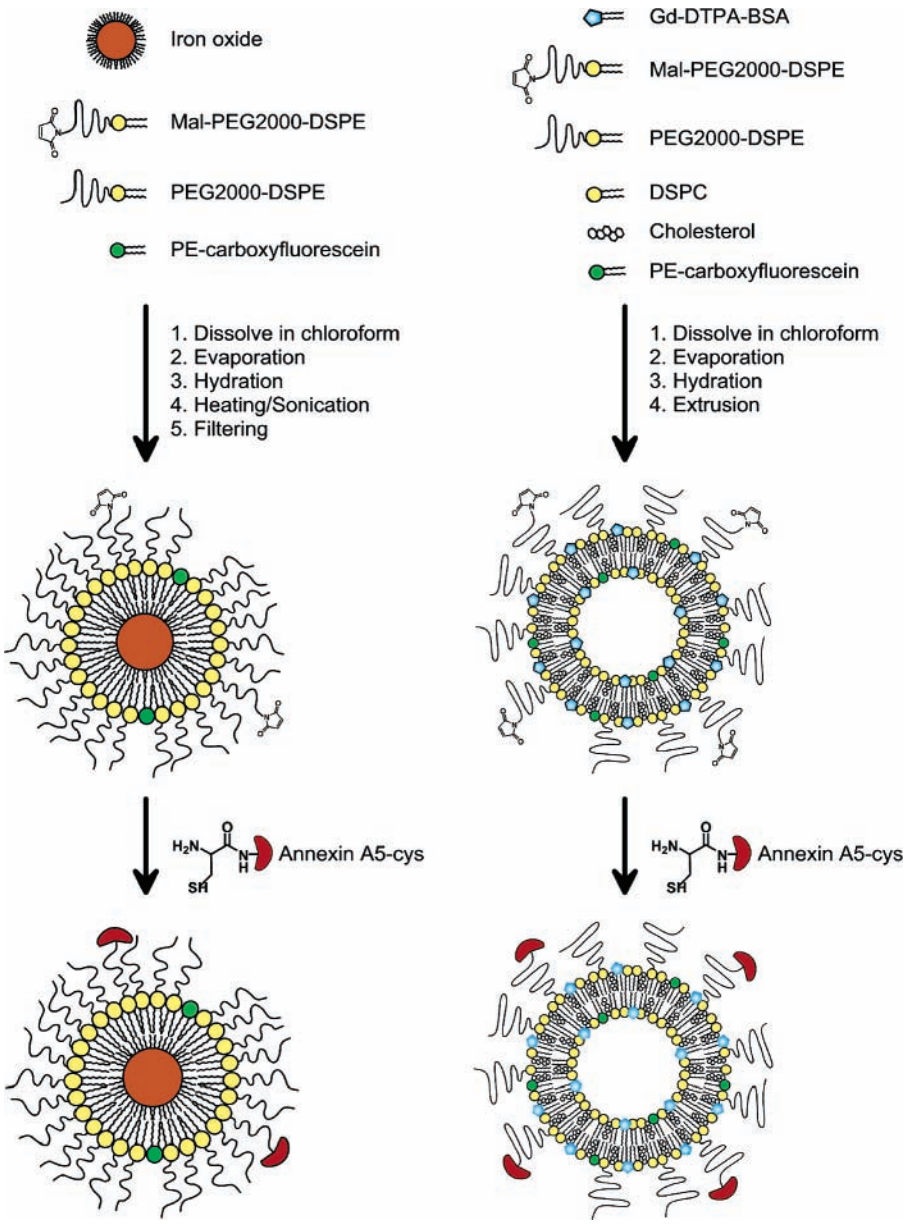

Figure 1. Preparation of annexin A5-functionalized superparamagnetic micelles (left) and annexin A5-functionalized paramagnetic liposomes (right). In both systems, fluorescent lipids were incorporated in the lipid layer for fluorescence microscopy or flow cytometry. MR contrast was obtained by incorporation of superparamagnetic iron oxide in the micellular core (left) or by incorporation of paramagnetic Gd-DTPA-BSA in the lipid bilayer of the liposomes (right). Both contrast agents were functionalized with annexin A5.

was based on the total iron content, which was measured with atomic absorption spectrometry (Philips, PU 9100X). For atomic absorption spectrometry (AAS) measurements, the micellular iron oxide particles were destructed in 100 μL of perchloric acid at 180 °C and subsequently diluted to a volume of 1.5 mL with ultrapure water. The same procedure was followed for calibration samples containing known amounts of iron from the iron standard solution ($Fe(NO_3)_3$).

Relaxivities. The ability of an MR contrast agent to reduce the intrinsic T_1 or T_2 relaxation times of water is generally described by the so-called molar relaxivities r_1 and r_2, respectively, which are expressed in units of $(mM^{-1}\ Gd)\cdot s^{-1}$ or $(mM^{-1}\ Fe)\cdot s^{-1}$. Relaxivities r_1 and r_2 of both lipid-based contrast agents were measured in HEPES-buffered saline (20 mM HEPES and 135 mM NaCl, pH 7.4) at room temperature (RT) with a tabletop 20 MHz NMR spectrometer (Bruker, Minispec). T_1-relaxation times were measured with an inversion recovery sequence. A CPMG sequence was used for T_2 measurements. To determine the r_1 and r_2 of the lipidic paramagnetic nanoparticles, the gadolinium concentration was measured with NMR using the following procedure. Liposomes were destructed with perchloric acid at 180 °C. The resulting mixture was evaporated to dryness and dissolved in a known volume of ultrapure water. The gadolinium concentration was determined from calibration samples containing known amounts of $GdCl_3$ for which the same protocol was performed. Concentrations obtained with this procedure were essentially identical to the values that were measured with inductively coupled plasma atomic emission spectroscopy (ICP-AES). Iron concentrations of the superparamagnetic micellular iron oxide particles were measured by AAS, as described above.

Specificity of the Nanoparticles for Phosphatidylserine. *Ellipsometry.* The PS binding properties of the annexin A5-conjugated lipidic nanoparticles were measured by ellipsometry as described in ref *25*. Briefly, a silicium plate was coated with a bilayer of PS and phosphatidylcholine (PC) in a molar ratio of 20:80. Binding of the nanoparticles to this surface was assessed in binding buffer (10 mM HEPES, 150 mM NaCl, 5 mM KCl, 1 mM $MgCl_2$, 2.5 mM $CaCl_2$, pH 7.4) and monitored by continuously measuring the polarization angle of the reflected

elliptically polarized light. Once the polarization angle reached its steady state, 5 mM EDTA was added to investigate Ca^{2+} dependency.

In Vitro Targeting. *Cell Culture.* The T-lymphoma cell line Jurkat (ATCC) was grown in RPMI 1640 medium (Gibco), which was supplemented with 10% fetal calf serum and a mixture of antibiotics (100 units mL^{-1} penicillin, 0.1 mg mL^{-1} streptomycin (Biochrom AG)). Cells were grown at 37 °C in a humidified atmosphere and 5% CO_2. To induce apoptosis, Jurkat cells were resuspended to 10^6 cells mL^{-1} of medium and treated with 200 ng mL^{-1} anti-Fas (CD95 human monoclonal antibody, Beckman Coulter B.V.) for 3 h at 37 °C in a humidified atmosphere and 5% CO_2, which initiates apoptosis in approximately 40−50% of the cells.

Flow Cytometry. Flow cytometry measurements (Coulter EPICS-XL-MCL) were performed to determine whether the cell population was successfully stimulated to undergo apoptosis. For flow cytometry, 25 000 cells were resuspended in 250 μL of binding buffer and incubated with annexin A5−FITC (250 ng/mL) during 5 min. Cell populations containing ≥30% apoptotic cells were used to measure binding of both the nonfunctionalized and the annexin A5-conjugated nanoparticles.

MRI and Confocal Laser Scanning Microscopy. Apoptotic Jurkat cells were incubated with both nonfunctionalized and annexin A5-conjugated contrast agents to study the ability of these contrast agents to change the relaxation times of apoptotic cells. Each sample contained approximately 5×10^6 cells to obtain a loosely packed pellet that was sufficient for slice-planning in MRI experiments. Experiments were performed as follows. After stimulation with anti-Fas, cells were harvested and resuspended to 10^6 cells mL^{-1} of binding buffer or HEPES-buffered saline that was supplemented with EDTA (25 mM HEPES, 140 mM NaCl, and 5 mM EDTA, pH 7.4). Annexin A5-conjugated superparamagnetic micelles or paramagnetic liposomes were added to a final concentration of 5 μg mL^{-1} iron or 0.2 mM total lipid, respectively. Control cells were either treated with equivalent amounts of nonfunctionalized contrast agents or not exposed to contrast agents at all. All cell samples were incubated with the contrast agents for 30 min on a rollerbench at room temperature. Subsequently each sample was washed 3 times (5 min, 300 g) in a buffer that was identical to the buffer in which the incubation was performed. All samples were subsequently resuspended in a 4% paraformaldehyde solution (pH 8), which was prepared either in binding buffer or in HEPES-buffered saline that was supplemented with 5 mM EDTA. The cells were allowed to settle as a loosely packed pellet in a 250 μL PCR tube overnight at 4 °C.

MRI on Apoptotic Cell Pellets. MRI on cell pellets was performed at 6.3 T (Bruker, BioSpec), using a 3 cm send and receive birdcage coil (Rapid Biomedical). A maximum of four samples were measured at once in a custom-made sample holder to prevent artifacts from B_1 inhomogeneities. A T_2-weighted image of a pellet of cells that were incubated with superparamagnetic micelles was obtained with a multislice spin−echo sequence (TE 14.7 ms, TR 6000 ms). For quantification of T_2-relaxation times a series of T_2-weighted images with 20 echo times in the range of 4−200 ms was obtained with a multislice spin−echo sequence (TR 6000 ms). All T_2-weighted images were obtained with a slice thickness of 1 mm, field of view 1.5 $\times$ 2.5 cm^2, matrix size of 64 $\times$ 64, and four averages. A T_1-weighted image of a pellet of cells that were treated with paramagnetic liposomes was obtained with a multislice spin−echo sequence (TE 4.3 ms, TR 950 ms). For quantification of T_1-values, a series of FLASH images were obtained after inversion of the longitudinal magnetization (segmented IR). Images were obtained with a slice thickness of 1 mm, field of view 3 $\times$ 3 cm^2, matrix size of 128 $\times$ 128, 16 segments, TE 1.5 ms, TR 3 s, α 15°, and four averages. A total of 50 images were obtained following inversion with the following parameters: first inversion delay 73.5 ms, separation time 48 ms, and inversion repetition 20 s.

Pixel-by-pixel T_2 and T_1 maps were reconstructed from the acquired T_2- and T_1-weighted images, respectively, using a nonlinear least-squares data fitting procedure by the Gauss−Newton method programmed in Matlab. T_1 maps were corrected for saturation as described by Haase et al. (*29*). Average T_2 and T_1 values within the cell pellets were determined in a region of interest typically containing 10 pixels.

Confocal Laser Scanning Microscopy. Confocal microscopy (Axiovert 100M, Zeiss) was performed on cells that were previously used for MR experiments to enable localization of the lipid-based contrast agents at the cellular level.

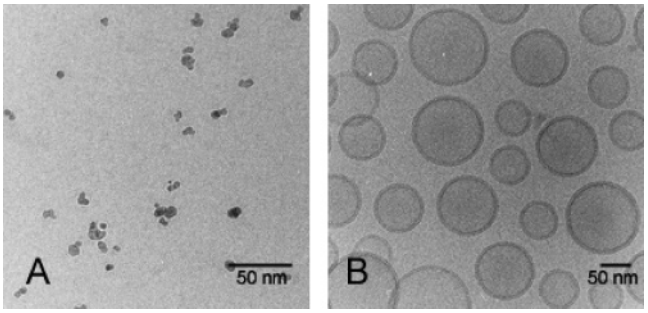

Figure 2. Cryo-TEM images of superparamagnetic micelles (A) and paramagnetic liposomes (B).

Table 1. Relaxivities r_1 and r_2 Expressed in (mM^{-1} Fe) s^{-1} or (mM^{-1} Gd) s^{-1} for the Superparamagnetic Micelles and Paramagnetic Liposomes, Respectively[a]

	r_1	r_2	r_2/r_1
superparamagnetic micelles	13.3	159.6	12.0
paramagnetic liposomes	4.1	6.8	1.7

[a] Measurements were performed at 20 MHz and room temperature.

RESULTS

Characterization of the Contrast Agents. Morphology and size of the contrast agents that were prepared following the schematic overview given in Figure 1 were studied with cryo transmission electron microscopy (Figure 2). In cryo-TEM images of the superparamagnetic micellular contrast agent, single nanoparticles could be discriminated of which only their iron oxide core with a diameter of approximately 5 nm was visible (Figure 2A). The total diameter of the conjugate was measured to be approximately 10 nm with dynamic light scattering. The resulting micellular iron oxide particle showed a relatively high r_2/r_1 ratio (Table 1), which is typical for negative MR contrast agents. The paramagnetic liposomal contrast agents were confirmed to be spherical bilayer particles that were sized to a diameter of approximately 100 nm (Figure 2B). An r_2/r_1 ratio of approximately 1.7 (Table 1) was found for these particles, indicating that these contrast agents are very well applicable as T_1-reducing agents.

Specificity of the Nanoparticles for Phosphatidylserine. *Binding to PS/PC Bilayers.* Wild-type annexin A5 was shown to bind to the PS/PC-coated silicium plate in the ellipsometry setup in the presence of 2.5 mM Ca^{2+} (Figure 3). Nonfunctionalized paramagnetic liposomes showed no significant binding to an identical PS/PC bilayer, whereas the polarization angle changed approximately 6° due to binding of the annexin A5-conjugated liposomes in the presence of Ca^{2+} (Figure 3). Addition of EDTA caused an immediate drop of the polarization angle for both the wild-type annexin A5 and the annexin A5-conjugated liposomes, which confirmed specific, Ca^{2+}-depend-

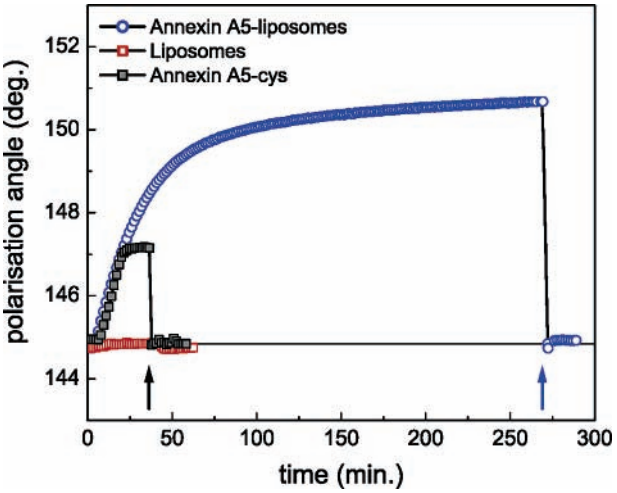

Figure 3. Ellipsometry measurement of binding of annexin A5-cys (black square), nonfunctionalized paramagnetic liposomes (red square), or annexin A5-functionalized paramagnetic liposomes (blue circle) to a PS/PC (20:80) bilayer in the presence of 2.5 mM Ca^{2+}. EDTA (5 mM) was added at the time points indicated by the arrows.

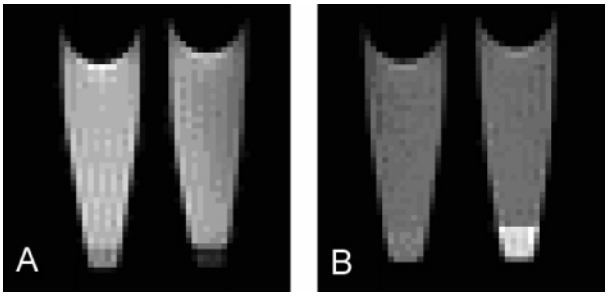

Figure 4. MR images of loosely packed cell pellets: (A) T_2-weighted spin-echo image of a pellet of apoptotic cells that were incubated with annexin A5-functionalized superparamagnetic micelles (right) or not exposed to contrast agents (left), TE 14.7 ms, TR 6000 ms; (B) T_1-weighted spin-echo image of apoptotic cells that were incubated with paramagnetic annexin A5-liposomes (right) or not exposed to contrast agents (left), TE 4.3 ms, TR 950 ms.

ent binding to PS (*25*). Ellipsometry measurements of superparamagnetic micelles were impossible because of the magnetic properties of the contrast agent.

MRI of Apoptotic Cell Pellets. Apoptotic cells that were incubated with annexin A5-functionalized superparamagnetic micelles in the presence of Ca^{2+} appeared as a hypointense pellet compared to untreated control cells in the T_2-weighted MR image (Figure 4A). In contrast, apoptotic cells that were incubated with annexin A5-conjugated paramagnetic liposomes appeared as a hyperintense pellet compared to control cells in a T_1-weighted MR image (Figure 4B). Relaxation times that were measured within all cell pellets were expressed as relaxation rates R_1 and R_2, that is, inverse relaxation times, since both relaxation rates are linearly dependent on the contrast agent concentration. The relaxation rate R_2 of apoptotic cells was shown to be approximately 172% increased after incubation with annexin A5-funtionalized micellular iron oxide particles in the presence of Ca^{2+}, whereas an increase of only 19% was measured in the presence of EDTA (Figure 5A). Nonfunctionalized superparamagnetic micelles were also shown to minimally increase the intrinsic R_2 of apoptotic cells.

The R_1 of apoptotic cells was shown to be approximately 258% increased after incubation with annexin A5-conjugated paramagnetic liposomes in the presence of Ca^{2+} compared to untreated apoptotic cells (Figure 5B). An increase of approximately 22% was observed after incubation with nonfunctionalized liposomes, both in the presence of Ca^{2+} and EDTA.

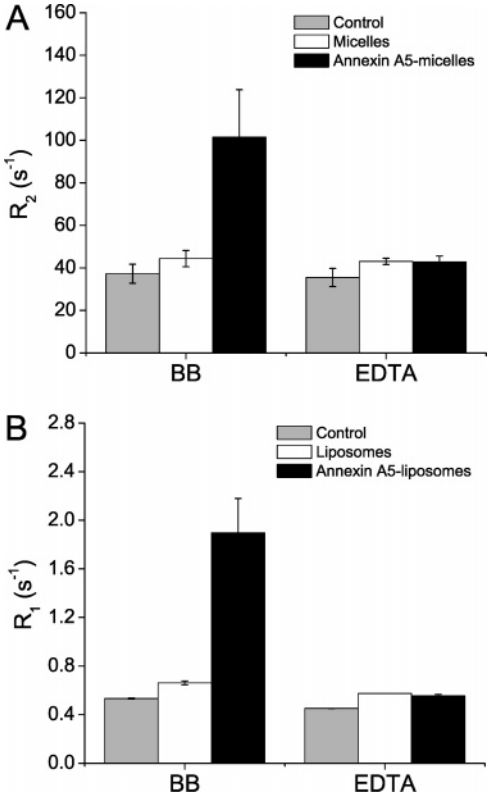

Figure 5. Relaxation rates within the cell pellets. R_2 or R_1 values were obtained for apoptotic Jurkat cells that were either untreated (control), incubated with 5 μg of Fe/mL of annexin A5-functionalized superparamagnetic micelles (A), incubated with 0.2 μmol of lipid/mL of annexin A5-functionalized paramagnetic liposomes (B), or incubated with their corresponding nonfunctionalized contrast agents (A,B). Cells were incubated for 30 min either in the presence of Ca^{2+} (BB) or in the presence of EDTA (EDTA). Error bars represent the standard deviation for $n = 3$.

A similar minimal increase was measured for apoptotic cells that were incubated with annexin A5-conjugated paramagnetic liposomes in the presence of EDTA. Since Ca^{2+} is required for both annexin A5 conjugates to significantly increase the relaxation rates of apoptotic cells, it may be concluded that both contrast agents bind to the exposed negatively charged phospholipids.

Confocal Laser Scanning Microscopy of Apoptotic Cell Pellets. Confocal transmission and fluorescence images of all cell samples were obtained to determine the spatial location of the contrast agents that contributed to the measured relaxation rates within the pellets. Apoptotic cells that were incubated with nonfunctionalized superparamagnetic micelles showed presumably unspecific association of these contrast agents to less than 1% of the cells (Figure 6A). On the other hand, annexin A5-funtionalized superparamagnetic micelles were found to be associated to a relatively large fraction of cells (Figure 6B). In confocal fluorescence images of apoptotic cells that were treated with nonfunctionalized liposomes, no contrast agents were observed to be associated with apoptotic cells (Figure 6C). However, some remaining liposomal aggregates were found occasionally, probably due to insufficient washing of the cell preparation. In contrast, annexin A5-conjugated paramagnetic liposomes were observed to be massively associated with apoptotic cells (Figure 6D). These observations were confirmed by flow cytometry measurements, which showed significant binding of the annexin A5-conjugated paramagnetic liposomes to apoptotic Jurkat cells, whereas little association was observed for the nonfunctionalized liposomes (Figure 3).

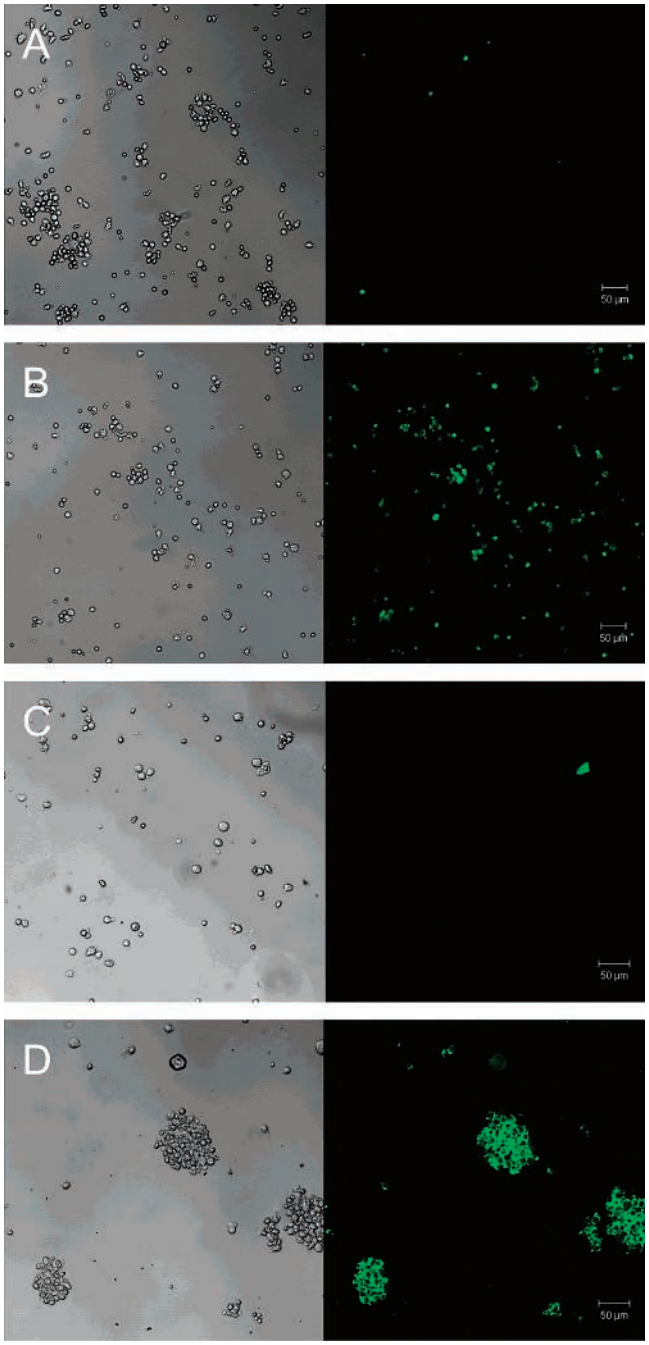

Figure 6. Confocal transmission (left) and fluorescence images (right) of fixed apoptotic Jurkat cells after incubation with superparamagnetic micelles (A, B) or paramagnetic liposomes (C, D) for 30 min in the presence of Ca^{2+}. Images were acquired after treatment with both nonfunctionalized (A, C) and annexin A5-functionalized (B, D) lipid-based contrast agents.

DISCUSSION

In this study, we presented two types of lipid-based bimodal nanoparticles that were functionalized with the protein annexin A5 for targeting to apoptotic cells. Both annexin A5-functionalized contrast agents were shown to bind specifically to apoptotic cells as confirmed by MRI and confocal laser scanning microscopy.

No typical bilayer structure was found in the cryo-TEM images of the superparamagnetic micelles (*30*), suggesting that the oleic acid coated superparamagnetic particles were enclosed by a lipid monolayer. The resulting superparamagnetic micelles were measured to be ~10 nm in diameter by DLS, whereas their core diameter was found to be ~5 nm in cryo-TEM images (Figure 2A). This suggests that each micelle contains approximately one magnetite particle, which provides the contrast agents with a relatively large r_2/r_1 ratio of 12.0 compared to r_2/r_1 ratios of 2.2 that were measured for other small iron oxide particles at the same field strength, including AMI 227 and MION-46 (*31*). r_2/r_1 ratios of the magnitude reported here suggest that the magnetite particles were aggregated (*32*). However, nonaggregated superparamagnetic micelles were predominantly found on the cryo-TEM images. Whether this high r_2/r_1 ratio was caused by the use of a micellular coating consisting of 100% PEG polymers, instead of the commonly used dextran coating remains to be investigated. Altogether the micellular iron oxide preparation may be classified as an ultrasmall and extremely potent T_2-reducing contrast material. Conjugation of annexin A5 to the micellular iron oxide particles was shown to specifically decrease the T_2 of apoptotic cell pellets by approximately 70% (Figure 5A), which was clearly visible on a T_2-weighted MR image (Figure 3A). Schellenberger et al. previously showed the ability of annexin A5−CLIO to specifically reduce the T_2 relaxation times of apoptotic cells (*21*, *33*). Additional coupling of the near-infrared fluorophore Cy5.5 allowed successive near-infrared imaging (*21*). As an alternative to covalent coupling of annexin A5 to iron oxide particles, Jung et al. presented a two-step approach, where biotinylated C_2A domain of synaptotagmin I was subsequently labeled with streptavidin−SPIO nanoparticles (*16*). This approach was successfully used to reduce the T_2 relaxation times of apoptotic cells in vitro; however its in vivo application is expected to suffer from the immunogenecity of streptavidin. The mean size of the used streptavidin−SPIO label is 20−30 nm (*16*), whereas the mean size of the annexin A5−CLIO−Cy5.5 was measured to be approximately 50 nm (*21*). Consequently the application of these particles for molecular imaging purposes of extravascular targets may be limited by their size. The mean size of the superparamagnetic micelles presented in this study was determined to be approximately 10 nm, which is at least 2 times smaller than the iron oxide particles that were previously described for the detection of apoptosis. Consequently the micellular iron oxide particles are thought to show facilitated extravasation compared to these iron oxide particles.

It was shown by Kim et al. that the size of magnetomicelles scales with the number of iron oxide particles entrapped in the micellular core, which was determined by the starting ratio between the concentration of magnetite particles and the polymers (*34*). In this manner, the size of the contrast agents may be optimized for the target of interest. In addition, the incorporation of multiple iron oxide particles in the micellular core could also be used to enhance the magnetic properties of the superparamagnetic micelles presented here. Alternatively, multiple superparamagnetic particles with a hydrophilic coating could be entrapped inside the internal water compartment of liposomes. The resulting particles can be sized to approximately 40 nm and are often referred to as magnetoliposomes (*35*). Magnetomicelles and magnetoliposomes that show sufficient magnetism could be simultaneously used as MRI contrast agents and for magnetic-nanoparticle-induced hyperthermia (*36*). As an alternative to magnetothermal therapy a mixture of magnetite particles and hydrophobic drugs could be incorporated in the micellular core to allow targeted therapy with particles that can be detected both with MRI and with optical imaging.

Targeted molecular imaging of sparsely expressed receptors in tissues, where positive contrast is preferred due to intrinsic T_1 and T_2 relaxation times, requires amplification strategies because of the relatively low relaxivities of T_1-reducing ions, including Gd^{3+}. Therefore it is advantageous to use liposomes in which a large payload of paramagnetic lipids can be incorporated in the bilayers, resulting in efficient T_1- and T_2-

shortening lipidic nanoparticles (*37*). Minor differences were observed between the ionic relaxivity r_1 and r_2 of Gd-DTPA and that of Gd-DTPA-BSA incorporated in the liposomal bilayer. However, the molar relaxivities r_1 and r_2, expressed in $(mM^{-1}$ nanoparticle$)\cdot s^{-1}$, are tremendously increased compared to free Gd-DTPA due to the large payload of Gd-DTPA-BSA (~40 000/liposome). Consequently, for annexin A5−Gd-DTPA conjugates with a 1:1 stoichiometry, the concentration of annexin A5 should be at least 400-fold higher than for annexin A5-conjugated paramagnetic liposomes to produce comparable changes in the relaxation times of apoptotic cells, assuming that a maximum of 100 annexin A5-cys proteins were conjugated to each liposome. An alternative gadolinium-based contrast agent for the detection of apoptosis was presented by Jung et al., who conjugated a maximum of about 100 Gd-DTPA molecules to one biotinylated C_2A domain of the protein synaptotagmin I through biotin−avidin interaction (*16*). Only a small decrease in T_1 was observed for apoptotic cells after incubation with this contrast agent, indicating that further amplification strategies are desirable to obtain significant contrast enhancement of apoptotic tissue in T_1-weighted images.

Besides diagnostics, these contrast agents could also be used for therapeutic applications by additional incorporation of water-soluble drugs inside the liposomal lumen. Pegylated liposomes have been successfully used as drug carriers, which has primarily found its clinical application in tumor treatment (*38*). Incorporation of anti-apoptotic drugs in the annexin A5-conjugated paramagnetic liposomes presented here would allow for the combination of multimodal detection of apoptotic cells and anti-apoptotic treatment. In cases of reversible PS exposure, these cells could be rescued from dying. Since liposomes are approximately 100 nm in size, these particles can only be used to target the extravascular space in tissue with enhanced permeability or intravascular compartments. Alternatively the size of the nanoparticles could be reduced by incorporation of Gd-DTPA-BSA lipids in a micellular lipid monolayer to allow the multimodal detection of more extravascular targets. Hydrophobic drugs can be additionally incorporated in the micellular core for targeted therapy (*39*).

The bimodal lipid-based contrast agents that were designed as efficient T_1- or T_2-reducing agents could be localized at the subcellular level with fluorescence microscopy due to additional incorporation of fluorescent lipids in the lipid (bi)layer. However, flow cytometry experiments with the annexin A5-functionalized superparamagnetic micelles were hindered by their relatively weak fluorescent signal, which was also observed on the confocal fluorescence images. Nevertheless the contrast agent could be detected on the confocal fluorescence images since no autofluorescence was observed for cells in 4% paraformaldehyde solution. Unfortunately, their spatial location was difficult to define based on these images. The fluorescent headgroups that were incorporated in the micellular lipid layer for fluorescence microscopy and flow cytometry were in close proximity to the iron oxide core, which might induce fluorescent quenching. Josephson et al. also observed extensive fluorescent quenching after attachment of fluorescein to magnetic nanoparticles (*40*). Therefore, the fluorescent moiety should be positioned at a more distant location from the iron oxide core, for example, by covalent coupling of the fluorophores to the distal ends of PEG polymers. It was shown by Nitin et al. that fluorescent properties of Texas Red were maintained after conjugation to PEG phospholipids that were incorporated in micellular coated iron oxide nanoparticles (*41*).

The obtained confocal fluorescence images of the annexin A5-conjugated paramagnetic liposomes suggest that these contrast agents are only found on the outer leaflet of the cell membrane. Since Jurkat cells have a relatively large nucleus additional staining for cell membrane markers should be performed to confirm exclusive binding of the contrast agents to the cell membrane. Cells with associated annexin A5-conjugated paramagnetic liposomes were mainly found to be clustered, which was already observed during the incubation period of 30 min. It is known that contrast agent clustering may alter its T_1- and T_2-reducing ability compared to more homogeneously distributed contrast agents. Therefore the r_2/r_1 ratio of cell-associated annexin A5-conjugated paramagnetic liposomes was measured (van Tilborg, unpublished observations). An r_2/r_1 ratio of approximately 6 was found for homogeneously distributed annexin A5-conjuated paramagnetic liposomes in HEPES buffer at 6.3 T, whereas an r_2/r_1 ratio of approximately 39 was measured in a 4% paraformaldehyde solution at 6.3 T after association of the annexin A5-conjugated paramagnetic liposomes to apoptotic cells. Whether this increase results only from clustering or also from cell association per se should be further investigated. In contrast to annexin A5-conjugated paramagnetic liposomes, no cell aggregation was observed in the presence of annexin A5-functionalized micellular iron oxide particles.

In this study, it was shown that a fraction of apoptotic cells >30% within the region of interest could be easily detected with MRI using the described annexin A5-conjugated lipid-based nanoparticles in vitro. The fraction of apoptotic cells found in vivo varies from <1% in viable tissue to 4% in tumor tissue. These values may be increased to approximately 20% in diseased tissue, including cardiomyocytes in intact myocardial tissue that were exposed to transient ligation of the left descending coronary artery (LAD) during 30 min (*10*). Sosnovik et al. observed local abnormal contractility within a well-defined area of the mouse myocardium after transient ligation of the LAD. Intravenously injected annexin A5−CLIO−Cy5.5 (2 mg of Fe/kg) was shown to reduce the T_2* relaxation time within this region up to 39% (*22*). Furthermore, irradiation or cytotoxic chemotherapy was shown to locally increase the apoptotic fraction in tumor tissue up to 30%. In this animal model, the intravenous administration of 20 mg of Fe/kg of synaptotagmin I-conjugated SPIO was found to decrease the signal intensity up to 15% in well-defined areas of the tumor (*15*). Consequently, the increased apoptotic fraction within diseased or successfully treated tumor tissue should also be detectable with the annexin A5-functionalized lipid-based contrast agents presented here if a sufficient dose of the contrast agent can be targeted to the tissue of interest. Since both nanoparticles are pegylated, they are expected to exhibit improved circulation times and bioavailability, which has been extensively studied for similar lipid-based aggregates in which no MR contrast agent was incorporated (*42*, *43*).

The nanoparticles that were prepared for this study are examples of lipid-based bimodal contrast agents that differ both in size and in magnetic properties. Consequently these contrast agents are suitable for all kinds of diagnostic MR imaging applications, varying from magnetic resonance angiography (MRA) to molecular and cellular imaging. The superparamagnetic micellular contrast agent is relatively small and is therefore expected to be suitable for the visualization of both intravascular and extravascular targets. In contrast, extravasation of the paramagnetic liposomes is limited by their size, which makes the contrast agent best suited for targeting intravascular receptors. Interestingly, with these systems, diagnostics could be extended to targeted therapeutic applications either by additional incorporation of drugs or alternatively by exploitation of the magnetic properties of the micellular iron oxide particles for so-called magnetothermal therapy.

ACKNOWLEDGMENT

This study was financially supported by the BSIK program entitled Molecular Imaging of Ischemic Heart Disease (Project Number BSIK03033) and the European Union Network of Excellence Diagnostic Molecular Imaging (EC - FP6-project DiMI, LSHB-CT-2005-512146). The authors thank Mircea V. Rasa for helping us find suitable iron oxide particles for this study and for reading the manuscript. We thank Peter M. Frederik and Paul H. Bomans from the EM unit of the University of Maastricht for the acquisition of the TEM images and Cécile Lejeune for the ellipsometry measurements.

LITERATURE CITED

(1) Haunstetter, A., and Izumo, S. (1998) Apoptosis: Basic Mechanisms and Implications for Cardiovascular Disease. *Circ. Res. 82*, 1111−1129.

(2) Carson, D. A., and Ribeiro, J. M. (1993) Apoptosis and Disease. *Lancet 341*, 1251−1254.

(3) Brown, J. M., and Attardi, L. D. (2005) The Role of Apoptosis in Cancer Development and Treatment Response. *Nat. Rev. Cancer 5*, 231−237.

(4) Gao, F., Tao, L., Yan, W., Gao, E., Liu, H. R., Lopez, B. L., Christopher, T. A., and Ma, X. L. (2004) Early Anti-Apoptosis Treatment Reduces Myocardial Infarct Size After a Prolonged Reperfusion. *Apoptosis 9*, 553−559.

(5) Van Cruchten, S., and Van den, B. W. (2002) Morphological and Biochemical Aspects of Apoptosis, Oncosis and Necrosis. *Anat., Histol., Embryol. 31*, 214−223.

(6) van Engeland, M., Nieland, L. J., Ramaekers, F. C., Schutte, B., and Reutelingsperger, C. P. (1998) Annexin V-Affinity Assay: a Review on an Apoptosis Detection System Based on Phosphatidylserine Exposure. *Cytometry 31*, 1−9.

(7) Fadok, V. A., de Cathelineau, A., Daleke, D. L., Henson, P. M., and Bratton, D. L. (2001) Loss of Phospholipid Asymmetry and Surface Exposure of Phosphatidylserine Is Required for Phagocytosis of Apoptotic Cells by Macrophages and Fibroblasts. *J. Biol. Chem. 276*, 1071−1077.

(8) Reutelingsperger, C. P., Dumont, E., Thimister, P. W., van Genderen, H., Kenis, H., van de, E. S., Heidendal, G., and Hofstra, L. (2002) Visualization of Cell Death in Vivo With the Annexin A5 Imaging Protocol. *J. Immunol. Methods 265*, 123−132.

(9) Koopman, G., Reutelingsperger, C. P., Kuijten, G. A., Keehnen, R. M., Pals, S. T., and van Oers, M. H. (1994) Annexin V for Flow Cytometric Detection of Phosphatidylserine Expression on B Cells Undergoing Apoptosis. *Blood 84*, 1415−1420.

(10) Dumont, E. A., Reutelingsperger, C. P., Smits, J. F., Daemen, M. J., Doevendans, P. A., Wellens, H. J., and Hofstra, L. (2001) Real-Time Imaging of Apoptotic Cell-Membrane Changes at the Single-Cell Level in the Beating Murine Heart. *Nat. Med. 7*, 1352−1355.

(11) Petrovsky, A., Schellenberger, E., Josephson, L., Weissleder, R., and Bogdanov, A., Jr. (2003) Near-Infrared Fluorescent Imaging of Tumor Apoptosis. *Cancer Res. 63*, 1936−1942.

(12) Blankenberg, F. G., Katsikis, P. D., Tait, J. F., Davis, R. E., Naumovski, L., Ohtsuki, K., Kopiwoda, S., Abrams, M. J., Darkes, M., Robbins, R. C., Maecker, H. T., and Strauss, H. W. (1998) In Vivo Detection and Imaging of Phosphatidylserine Expression During Programmed Cell Death. *Proc. Natl. Acad. Sci. U.S.A. 95*, 6349−6354.

(13) Hofstra, L., Liem, I. H., Dumont, E. A., Boersma, H. H., van Heerde, W. L., Doevendans, P. A., De Muinck, E., Wellens, H. J., Kemerink, G. J., Reutelingsperger, C. P., and Heidendal, G. A. (2000) Visualisation of Cell Death in Vivo in Patients With Acute Myocardial Infarction. *Lancet 356*, 209−212.

(14) Schellenberger, E. A., Hogemann, D., Josephson, L., and Weissleder, R. (2002) Annexin V−CLIO: a Nanoparticle for Detecting Apoptosis by MRI. *Acad. Radiol. 9* (Suppl 2), S310−S311.

(15) Zhao, M., Beauregard, D. A., Loizou, L., Davletov, B., and Brindle, K. (2001) M. Non-Invasive Detection of Apoptosis Using Magnetic Resonance Imaging and a Targeted Contrast Agent. *Nat. Med. 7*, 1241−1244.

(16) Jung, H. I., Kettunen, M. I., Davletov, B., and Brindle, K. M. (2004) Detection of Apoptosis Using the C2A Domain of Synaptotagmin I. *Bioconjugate Chem. 15*, 983−987.

(17) Huber, M. M., Staubli, A. B., Kustedjo, K., Gray, M. H., Shih, J., Fraser, S. E., Jacobs, R. E., and Meade, T. J. (1998) Fluorescently Detectable Magnetic Resonance Imaging Agents. *Bioconjugate Chem. 9*, 242−249.

(18) Modo, M., Cash, D., Mellodew, K., Williams, S. C., Fraser, S. E., Meade, T. J., Price, J., and Hodges, H. Tracking Transplanted Stem Cell Migration Using Bifunctional, Contrast Agent-Enhanced, Magnetic Resonance Imaging. *Neuroimage 17*, 803−811.

(19) Mulder, W. J., Strijkers, G. J., Griffioen, A. W., van Bloois, L., Molema, G., Storm, G., Koning, G. A., and Nicolay, K. (2004) A Liposomal System for Contrast-Enhanced Magnetic Resonance Imaging of Molecular Targets. *Bioconjugate Chem. 15*, 799−806.

(20) Mulder, W. J., Strijkers, G. J., Habets, J. W., Bleeker, E. J., van der Schaft, D. W., Storm, G., Koning, G. A., Griffioen, A. W., and Nicolay, K. (2005) MR Molecular Imaging and Fluorescence Microscopy for Identification of Activated Tumor Endothelium Using a Bimodal Lipidic Nanoparticle. *FASEB J. 19*, 2008−2010.

(21) Schellenberger, E. A., Sosnovik, D., Weissleder, R., and Josephson, L. (2004) Magneto/Optical Annexin V, a Multimodal Protein. *Bioconjugate Chem. 15*, 1062−1067.

(22) Sosnovik, D. E., Schellenberger, E. A., Nahrendorf, M., Novikov, M. S., Matsui, T., Dai, G., Reynolds, F., Grazette, L., Rosenzweig, A., Weissleder, R., and Josephson, L. (2005) Magnetic Resonance Imaging of Cardiomyocyte Apoptosis With a Novel Magneto-Optical Nanoparticle. *Magn. Reson. Med. 54*, 718−724.

(23) Needham, D., McIntosh, T. J., and Lasic, D. D. (1992) Repulsive Interactions and Mechanical Stability of Polymer-Grafted Lipid Membranes. *Biochim. Biophys. Acta 1108*, 40−48.

(24) Dubertret, B., Skourides, P., Norris, D. J., Noireaux, V., Brivanlou, A. H., and Libchaber, A. (2002) In Vivo Imaging of Quantum Dots Encapsulated in Phospholipid Micelles. *Science 298*, 1759−1762.

(25) Andree, H. A., Reutelingsperger, C. P., Hauptmann, R., Hemker, H. C., Hermens, W. T., and Willems, G. M. (1990) Binding of Vascular Anticoagulant Alpha (VAC Alpha) to Planar Phospholipid Bilayers. *J. Biol. Chem. 265*, 4923−4928.

(26) Vermes, I., Haanen, C., Steffens-Nakken, H., and Reutelingsperger, C. (1995) A Novel Assay for Apoptosis. Flow Cytometric Detection of Phosphatidylserine Expression on Early Apoptotic Cells Using Fluorescein Labeled Annexin V. *J. Immunol. Methods 184*, 39−51.

(27) Frederik, P. M., and Hubert, D. H. (2005) Cryoelectron Microscopy of Liposomes. *Methods Enzymol. 391*, 431−448.

(28) Rouser, G., Fkeischer, S., and Yamamoto, A. (1970) Two-Dimensional Then Layer Chromatographic Separation of Polar Lipids and Determination of Phospholipids by Phosphorus Analysis of Spots. *Lipids 5*, 494−496.

(29) Deichmann, R., and Haase, A. (1992) Quantification of T1 Values by Snapshot-Flash NMR Imaging. *J. Magn. Reson, 96*, 608−612.

(30) de Cuyper, M., and Joniau, M. (1988) Magnetoliposomes. Formation and Structural Characterization. *Eur. Biophys. J. 15*, 311−319.

(31) Allkemper, T., Bremer, C., Matuszewski, L., Ebert, W., and Reimer, P. (2002) Contrast-Enhanced Blood-Pool MR Angiography With Optimized Iron Oxides: Effect of Size and Dose on Vascular Contrast Enhancement in Rabbits. *Radiology 223*, 432−438.

(32) Josephson, L., Lewis, J., Jacobs, P., Hahn, P. F., and Stark, D. D. (1988) The Effects of Iron Oxides on Proton Relaxivity. *Magn. Reson. Imaging 6*, 647−653.

(33) Schellenberger, E. A., Bogdanov, A., Jr., Hogemann, D., Tait, J., Weissleder, R., and Josephson, L. (2002) Annexin V−CLIO: a Nanoparticle for Detecting Apoptosis by MRI. *Mol. Imaging 1*, 102−107.

(34) Kim, B. S., Qiu, J. M., Wang, J. P., and Taton, T. A. (2005) Magnetomicelles: Composite Nanostructures from Magnetic Nanoparticles and Cross-Linked Amphiphilic Block Copolymers. *Nano Lett. 5*, 1987−1991.

(35) Bulte, J. W., de Cuyper, M., Despres, D., and Frank, J. A. (1999) Short- Vs. Long-Circulating Magnetoliposomes As Bone Marrow-Seeking MR Contrast Agents. *J. Magn Reson. Imaging 9*, 329−335.

(36) Ito, A., Shinkai, M., Honda, H., and Kobayashi, T. (2005) Medical Application of Functionalized Magnetic Nanoparticles. *J. Biosci. Bioeng. 100*, 1−11.

(37) Kabalka, G. W., Buonocore, E., Hubner, K., Davis, M., and Huang, L. (1988) Gadolinium-Labeled Liposomes Containing Paramagnetic Amphipathic Agents: Targeted MRI Contrast Agents for the Liver. *Magn. Reson. Med. 8*, 89−95.

(38) Torchilin, V. P. (2005) Recent Advances With Liposomes As Pharmaceutical Carriers. *Nat. Rev. Drug Discovery 4*, 145−160.

(39) Nishiyama, N., Okazaki, S., Cabral, H., Miyamoto, M., Kato, Y., Sugiyama, Y., Nishio, K., Matsumura, Y., and Kataoka, K. (2003) Novel Cisplatin-Incorporated Polymeric Micelles Can Eradicate Solid Tumors in Mice. *Cancer Res. 63*, 8977−8983.

(40) Josephson, L., Kircher, M. F., Mahmood, U., Tang, Y., and Weissleder, R. (2002) Near-Infrared Fluorescent Nanoparticles As Combined MR/Optical Imaging Probes. *Bioconjugate Chem. 13*, 554−560.

(41) Nitin, N., LaConte, L. E., Zurkiya, O., Hu, X., and Bao, G. (2004) Functionalization and Peptide-Based Delivery of Magnetic Nanoparticles As an Intracellular MRI Contrast Agent. *J. Biol. Inorg. Chem. 9*, 706−712.

(42) Lukyanov, A. N., Hartner, W. C., and Torchilin, V. P. (2004) Increased Accumulation of PEG-PE Micelles in the Area of Experimental Myocardial Infarction in Rabbits. *J. Controlled Release 94*, 187−193.

(43) Allen, T. M., Hansen, C., Martin, F., Redemann, C., and Yau-Young, A. (1991) Liposomes Containing Synthetic Lipid Derivatives of Poly(Ethylene Glycol) Show Prolonged Circulation Half-Lives in Vivo. *Biochim. Biophys. Acta 1066*, 29−36.

BC0600259

Evaluation of Cell-Penetrating Peptides (CPPs) as Vehicles for Intracellular Delivery of Antisense Peptide Nucleic Acid (PNA)

Nadia Bendifallah,[†] Frank Winther Rasmussen,[§] Vladimir Zachar,[#] Peter Ebbesen,[#] Peter E. Nielsen,[†,§] and Uffe Koppelhus*[,†,#]

Center for Biomolecular Recognition, Department of Medical Biochemistry and Genetics, Biochemistry Laboratory B, The Panum Institute, University of Copenhagen, Blegdamsvej 3c, DK-2200 Copenhagen N, Denmark; Pantheco A/S, Bøge Allé 3, DK-2970 Hørsholm, Denmark; and Laboratory for Stem Cell Research, Institute for Health Technologies, Aalborg University, Fredrik Bajers Vej 3B, DK-9220 Aalborg Ø, Denmark. Received September 21, 2005; Revised Manuscript Received March 22, 2006

Cell-penetrating peptides (CPPs) are characterized by their ability to be internalized in mammalian cells. To investigate the relative potency of CPPs as carriers of medicinally relevant cargo, a positive read-out assay based on the ability of a peptide nucleic acid (PNA) oligomer to promote correct expression of a recombinant luciferase gene was employed. Seven different CPPs were included in the study: Transportan, oligo-arginine (R_{7-9}), pTat, Penetratin, KFF, SynB3, and NLS. The CPP−PNA conjugates were synthesized by different conjugation chemistries: continuous synthesis, maleimide coupling, and ester or disulfide linkage. Under serum-free conditions PNA−SS-Transportan-amide (ortho)−PNA was found to be the most potent conjugate, resulting in maximum luciferase signal at a concentration of 1−2 μM. (D-Arg)$_9$−PNA showed optimal efficacy at 5 μM but gave rise to only one-third of the luciferase signal obtained with the Transportan conjugate. The pTat− and KFF−PNA conjugates showed significantly lower efficacy. The penetratin−, SynB3−. and NLS−PNA conjugates showed only minimal or no activity. Serum was found to have a drastic negative impact on CPP-driven cellular uptake. PNA−SS-Transportan-acid (ortho) and (D-Arg)$_9$−PNA were least sensitive to the presence of serum. Both the chemical nature and, in the case of Transportan, the position of the peptide PNA coupling were found to have a major impact on the transport capacity of the peptides. However, no simple relationship between linker type and antisense activity of the conjugates could be deduced from the data.

INTRODUCTION

Over the past decade a group of cell-penetrating peptides (CPPs) have been identified. CPPs are characterized by their ability to become internalized by mammalian cells and, in some cases, to cotransport macromolecules to the cellular interior. Proteins, peptides, oligonucleotides, and other macromolecules with a therapeutic potential related to intracellular processes are prospective cargos for CPPs. The most intensively studied CPPs include protein-derived peptides such as pTat, pAntp (Penetratin), and VP22 and synthetic or chimeric peptides such as oligo-arginine and Transportan, respectively (*1*−*7*).

The mechanism underlying the translocation of CPPs across the lipid bilayer of mammalian cells is yet not fully understood. Initially, a "passive" passage over the membrane based on a temperature- and energy-independent "physicochemical" mechanism was suggested (*8*−*10*). However, later studies strongly suggested that (at least some of) the peptides designated CPPs are internalized in cells by classic endocytotic pathways (*11*−*13*), and most recently evidence for multiple pathways has emerged (*14*, *15*). Thus, further investigations on the mechanism of CPPs are warranted.

Another largely unresolved aspect of CPPs is their (relative) potency as transport vehicles for therapeutically relevant macromolecules. Due to the large diversity in application, cell type, and methodology, it is not possible to make a relevant comparison of the CPPs based on meta-analysis of the many data reported. Moreover, only a few studies (comprising only a few CPPs) have been concerned with a direct comparison of CPP performance (*2*, *5*, *11*, *16*−*19*).

Therefore, to establish data on the relative efficacy of some of the most prominent CPPs, we employed a transgenic reporter cell line, pLuc 705 HeLa, in which a PNA targeted to an aberrant splice site in luciferase mRNA is known to induce correct splicing and thus produce a positive read-out signal in the form of increased luciferase activity (*20*, *21*). We use this assay to evaluate the potency of seven different CPPs as vehicles for intranuclear delivery of PNA. We chose to analyze pTat, pAntp (Penetratin), and Transportan, as these peptides are some of the most widely used CPPs that have also been employed in earlier studies with PNA (*11*, *22*, *23*). We also included oligo-arginine, KFF, SynB3, and NLS. Oligo-arginine peptides have been shown to be potent cellular delivery vehicles for morpholino oligomers (*2*). Like PNA oligomers, morpholino oligomers have uncharged backbones. KFF has been shown to induce cellular uptake of PNA in prokaryotic cells (*24*, *25*), but data from eukaryotic cells are lacking. SynB3 has been claimed to enhance passage of the blood−brain barrier of conjugated molecules such as doxorubicin (*26*) and morphine-6-glucuronide (*27*) but has not previously been tested as a cellular vehicle for PNA. NLS was included in the study as earlier papers have claimed this peptide to promote PNA translocation over the plasma cell membrane (*28*). NLS is not usually perceived as having capacity to transgress membranes other than the nucleolemma. In addition to the PNA−peptide conjugates, we tested a PNA−biotin

* Corresponding author [e-mail uffek@hst.aau.dk; fax (+45) 9635 7816].

[†] University of Copenhagen.

[§] Pantheco A/S. Present address: Novozymes A/S, Krogshoejvej 36, DK-2880 Bagsvaerd, Denmark.

[#] Aalborg University.

10.1021/bc050283q CCC: $33.50 © 2006 American Chemical Society
Published on Web 04/15/2006

conjugate. This was done to assess the surprising finding that biotin by itself can promote cellular uptake of conjugated PNA (*29*).

EXPERIMENTAL PROCEDURES

Synthesis of PNAs and Peptide−PNA Conjugates. PNA oligomers and peptide−PNA conjugates were synthesized on an MBHA[1] resin LL (100−200 mesh, 0.40−0.80 mmol/g, Novabiochem), which was downloaded to approximately 0.15 mmol/g by the first building block. The remaining sites were capped using the capping mixture described below. The compounds were typically synthesized on 100 mg of resin using a standard peptide Bo protocol: deprotection (TFA/DCM/anisole 50:45:5, 2−3 min), DCM wash, DMF wash, base wash (DIEA/DCM 5:95), DMF wash, coupling (30 min), DMF wash, DCM wash, capping (Ac_2O/Et_3N/DCM 5:10:85, 1 min), DCM wash, DMF wash, and DCM wash.

The couplings were performed with a volume of 0.9 mL of a preactivated (1 min) mixture of PNA monomer (3.6 equiv), NMM (7.2 equiv), and HBTU (3.5 equiv) in DMF or NMP. For natural amino acids, the concentrations were doubled for all three reagents, and cysteine was activated in situ. The couplings were monitored by the Kaiser test and repeated until complete.

Cleavage. The compounds were cleaved from the resin using a low-high TFMSA protocol.

- The *N*-terminal Boc-group was removed with TFA/DCM/anisole (50:45:5, 2 min).
- If a formyl protective group on tryptophan was present, it was cleaved with piperidine/DMF (10:90, 120 min).
- The side-chain protective groups were removed with TFA/dimethyl sulfide/*m*-cresol/TFMSA (55:30:10:5, 60 min).
- The resin was washed with TFA/DCM/anisole (50:45:5).
- The compounds were cleaved from the resin using TFMSA/TFA/*m*-cresol (2:8:1, 90 min). For cysteine-containing compounds, ethanedithiol was added to prevent oxidation. Alternatively, the cleavage procedure was performed under nitrogen.

The liquid phase, plus TFA (0.5 mL) from washing the resin, was added to diethyl ether (8 mL), when the product precipitated. It was isolated by centrifugation (3000 min^{-1}, −4 °C), washed with diethyl ether (8 mL), and dissolved in H_2O (4 mL).

Formation of Disulfide Linkage between Peptide and PNA. The formation of a disulfide-linked peptide−PNA conjugate was performed by a solution-phase reaction between a peptide with a 3-nitro-2-pyridinesulfenyl (Npys) activated cysteine and a cysteine-conjugated PNA. Npys-peptides were obtained from K. J. Ross-Petersen (Copenhagen, Denmark).

The conjugation was performed in thoroughly degassed solvents to prevent oxidation of the cysteine−PNA. The Npys-activated peptide (10 mM, NMP, 130 μL, 1.3 equiv) was added to the cysteine−PNA (1.0 mM, NMP/H_2O 1:1, 1000 μL) followed by the addition of acetate buffer (1.0 M, pH 5.0, 100 μL). The mixture was heated to 37 °C for 4 h, then quenched with TFA/H_2O (5:95, 200 μL), and diluted with H_2O to a volume of 5.0 mL. A yellow color during the reaction indicates the cleavage of the Npys group upon reaction with another cysteine.

PNA−peptide maleimide conjugates were prepared as previously described (*30*) using a cysteine-modified peptide, which was reacted with a maleimide-modified PNA. The latter was prepared by reacting the terminal amino group of purified PNA oligomers with an *N*-hydroxysuccinimide cyclohexylmaleimide reagent. Ester-rontaining conjugates were prepared from PNAs containing a glycyl(hydroxymethyl)benzoic acid unit at the N terminus (*31*).

Purification, Solubility, and Stability. Preparative chromatography was performed using a Gilson FAST Prep HPLC system equipped with a Vydac C18 column (10 μm, 22 × 250 mm) or a YMC column (10 μm, 10 × 50 mm) for disulfide-containing compounds. Fractions were analyzed on a Waters Alliance HT 2790 HPLC system using a YMC C18 column (3 μm, 2 × 150 mm). Electrospray mass spectra were recorded using an Agilent 1100 single-quadrupole LC-MS instrument. MALDI-TOF mass spectra were obtained on a Kratos MALDI II instrument.

Synthesized products were in general purified using a preparative Vydac column and a 0.1% TFA/H_2O/ethanol gradient (5−40%) over 7 column volumes. Compounds containing a disulfide bridge between the PNA and the peptide part of the molecule did, however, not elute very well from the Vydac column, and a method using a YMC column and a 0.5% HOAc/H_2O/acetonitrile gradient (5−40%) over 9 column volumes was therefore introduced. Purity of collected fractions was measured by analytical HPLC, and correct masses were verified by LC-MS and/or MALDI-TOF. The calculated masses and the masses found by MALDI-TOF mass spectrometry and the purities determined by analytical HPLC are listed for each conjugate in Table 1. With two exceptions all conjugates were found to be at least 90% pure. SynB3 was 86% pure. Transportan-6 was only 60% pure. HPLC analysis showed one major closely eluting and inseparable impurity. Therefore, the concentration of this conjugate is probably overestimated throughout the study. We comment on this when relevant under Results.

All conjugates were soluble in water to concentrations of at least 50 μM. No sign of insolubility (precipitation) was seen when the conjugates were added to the cell media at the test concentrations (up to 10 μM).

All conjugates were found to be highly stable in water. The only exceptions were the conjugates containing the ester linkage, which we have shown earlier to have a half-life of approximately 6 h at pH 7.4 at 37 °C (*31*). Stock solutions of ester-linked conjugates were prepared just before addition to culture. This procedure ensured minimal breakdown of the conjugates before they were applied in the assay.

Cellular Uptake Experiments Using the Positive Readout Reporter Cell Line, pLuc705 HeLa. The pLuc705 HeLa cell line was purchased from Gene Tools (Philomath, OR). pLuc 705 HeLa cells are derived by stable integration of the pLuc705 plasmid into HeLa S2 cells as described in Kang et al. (*20*). The plasmid has luciferase downstream and out-of-frame with a dominant splice mutation in the β-globin intron position 705. The recombinant luciferase gene is under control of the immediate early cytomegalovirus promoter. Binding of PNA (of sequence H-CCT CTT ACT CCA GTT ACA-NH_2) to a region covering the splice mutation results in restoration of wild-type splicing, which generates a transcript with luciferase in-frame (*21*, *31*).

pLuc 705 HeLa cells were grown in Dulbecco's modified Eagle's medium (DMEM) supplemented with penicillin/streptomycin (10 μg/mL) (antibiotics) and 10% fetal calf serum (Gibco, Invitrogen, Taastrup, Denmark). Cell cultures were maintained at 37 °C in a humidified atmosphere containing 5% CO_2 (standard conditions). For transfection with the PNA conjugates, the cells were seeded in a 96-well microtiterplate (Nunc, Invitrogen, Roskilde, Denmark) in a volume of 200 μL and at cell densities of (50−100) × 10^3 cells/mL unless otherwise stated. The following day the semiconfluent cells were prepared for uptake experiments. This was done by washing

[1] Abbreviations: DCM, dichloromethane; DIEA, diisopropylethylamine; DMF, dimethylformamide; HBTU, *O*-(1*H*-benzotriazole-1-yl)-*N*,*N*,*N*′,*N*′-tetramethyluronium hexafluorophosphate; MBHA, methylbenzhydrylamin; NMP, *N*-methylpyrrolidone; TFA, trifluoroacetic acid; TFMSA, trifluoromethanesulfonic acid.

Table 1. CPP−PNA Conjugates Used in This Study: Nomenclature and Structure[a]

conjugate	designation	sequence of peptide	linkage	position of PNA N terminus	purity (%)	MW (calcd)	MW (found)
PNA−SMCC-Transportan	Transportan-1	CGWTLNSAGYLLGKINLKALAALAKKIL−$CONH_2$	III	N terminus of peptide	98	8073	8073
PNA(E)−SMCC-Transportan	Transportan-2	CGWTLNSAGYLLGKINLKALAALAKKIL−$CONH_2$	II	N terminus of peptide	95	8410	8424
PNA−SS-Transportan	Transportan-3	CGWTLNSAGYLLGKINLKALAALAKKIL−$CONH_2$	IV	N terminus of peptide	95	7955	7964
PNA−SMCC-Transportan (ortho)	Transportan-4	GWTLNSAGYLLGK(ϵC)INLKALAALAKKIL−$CONH_2$	III	ϵ N of K_{13}	90	8072	8094[b]
PNA(E)−SMCC-Transportan (ortho)	Transportan-5	GWTLNSAGYLLGK(ϵC)INLKALAALAKKIL−$CONH_2$	II	ϵ N of K_{13}	60[c]	8410	8413
PNA−SS-Transportan-amide (ortho)	Transportan-6	GWTLNSAGYLLGK(ϵC)INLKALAALAKKIL−$CONH_2$	IV	ϵ N of K_{13}	97	7812	7823
PNA−SS-Transportan -acid (ortho)	Transportan-7	GWTLNSAGYLLGK(ϵC)INLKALAALAKKIL−COOH	IV	ϵ N of K_{13}	95	7813	7825[b]
$(D\text{-Arg})_7$−PNA	Arg (7)	RRRRRRR−	I	C terminus of peptide	90	5916	5915
$(D\text{-Arg})_8$−PNA	Arg (8)	RRRRRRRR−	I	C terminus of peptide	90	6072	6068
$(D\text{-Arg})_9$−PNA	Arg (9)-1	RRRRRRRRR−	I	C terminus of peptide	90	6228	6234
PNA−SMCC−$(D\text{-Arg})_9$	Arg (9)-2	CRRRRRRRRR−$CONH_2$	III	N terminus of peptide	98	6656	6662
PNA(E)−SMCC-$(D\text{-Arg})_9$	Arg (9)-3	CRRRRRRRRR−$CONH_2$	II	N terminus of peptide	95	6992	6993
pTat (48−60)−PNA	Tat-1	GRKKRRQRRRPPQ−	I	C terminus of peptide	90	6612	6611
PNA(E)−SMCC-pTat (48−60)	Tat-2	CGRKKRRQRRRPPQ−$CONH_2$	II	N terminus of peptide	98	7329	7329
PNA−SMCC-pTat (48−57)	Tat-3	CGRKKRRQRRR−$CONH_2$	III	N terminus of peptide	95	6792	6797
PNA−SMCC-Penetratin	Penetratin	CRQIKIWFQNRRMKWKK−$CONH_2$	III	N terminus of peptide	98	7480	7486
PNA−SS-SynB3	SynB3	CRRLSYSRRRF−$CONH_2$	IV	N terminus of peptide	86	6365	6367
NLS−PNA	NLS	PKKKRKV−	I	C terminus of peptide	98	5775	5774
KFF−PNA	KFF	KFFKFFKFFK−	I	C terminus of peptide	95	6306	6306

[a] The calculated (calcd) masses and the masses found by MALDI-TOF mass spectrometry and the purity found by HPLC are listed for each of the conjugates. Also, the position of the N terminus of the PNA with respect to the conjugated peptide is listed for each of the conjugates. [b] These PNAs yielded relatively weak MALDI signals and less sharp peaks. [c] Two closely migrating and inseparable peaks (absorbing at 260 nm) were observed. However, the MALDI spectrum did not indicate the presence of any other large molecular weight component.

the cells once in fresh DMEM containing antibiotics but no serum (serum-free DMEM) and adding 80−90 μL of the serum-free DMEM (unless otherwise stated) to the cells afterward. The cells were then incubated at standard conditions for 1−2 h before the cells were given CPP−PNA conjugates in the concentrations mentioned in the text. Typically, the cells were given 2−10 μL of a 100 μM stock. All additions were made in at least triplicates. Control cells were given sterilized water in volumes similar to each different volume of added CPP−PNA stock. This was done to avoid any misinterpretations due to volume effects. After 2−4 h, 10 μL of fetal calf serum was added to all cultures. After incubation at standard conditions for 16−20 h, luciferase activity was measured by use of the Stedy-Glo Luciferase Assay System (Promega, Ramcon A/S, Birkerød, Denmark) and a Victor^2 Multilabel Counter (Wallac, Perkin-Elmer Danmark A/S, Allerød, Denmark) according to the manufacturer's instructions.

Cell viability was assessed by indirect ATP measurements performed on cells run in parallel and treated exactly as the cells used for luciferase determinations. ATP was determined by use of the ATPlite assay (Perkin-Elmer Danmark A/S) according to the manufacturer's instructions.

RESULTS

The 19 PNA−peptide conjugates used in this study are listed in Table 1. As can be seen from the table, Transportan was studied in seven different configurations. These configurations comprise six conjugates in which PNA is linked to either a cysteine at the amino (N) terminus or at the ϵ N of lysine 13 (ortho position) of Transportan (amide) by a maleimide, an ester, or a disulfide linkage, respectively. In addition, a conjugate was prepared from the free carboxylic acid form of Transportan in which PNA is linked to the ortho (Lys13) position via a disulfide linkage. The different chemical linkers employed are depicted in Figure 1.

Oligo-arginine−PNA conjugates were prepared by continuous solid-phase synthesis. Furthermore, two arginine (9) conjugates were made through maleimide coupling. The pTat(48−60)−PNA conjugates were prepared via direct synthesis or ester maleimide conjugation, respectively. The truncated pTat(48−57)−PNA conjugate was prepared via maleimide coupling. The Penetratin−PNA conjugate was also prepared using maleimide conjugation. The SynB3 conjugate was prepared from disulfide coupling, and NLS− and KFF−PNA conjugates were prepared via continuous synthesis.

It is noted that maleimide and disulfide conjugation, as performed, links the PNA (N terminus) to the N terminus of the peptide, whereas continuous synthesis links the PNA (N terminus) to the C terminus of the peptide.

The antisense activity of the PNA−peptide conjugates was studied in the pLuc 705 HeLa cells (see Experimental Procedures). This cell line has successfully been exploited to quantitatively study the potency of antisense agents, and we have recently used it in a comprehensive study on transfection of modified and unmodified PNA (*32*). This study emphasized the value of the pLuc 705 HeLa cells as a model system for a precise, reproducible, and quantitative assessment on cellular uptake and nuclear delivery of PNA. However, it also pointed out that the assay is sensitive to even little (and sometimes uncontrollable) variations in cell density, cell viability, and luciferase assay performance. These factors influence assay performance in a way that is mainly reflected in the absolute luciferase activities. Therefore, to increase the transparency of the data, the results in this paper are not given as absolute luciferase signals. Instead, luciferase expression resulting from treatment of the cells with a conjugate was in each case normalized to the basal luciferase expression found in control cells. Control cells were given sterilized water in volumes similar to the volumes of conjugate solution added to the test cultures. Essentially, this presentation should eliminate errors due to variations in cell density and mRNA expression level as well as variations in the luciferase assay performance. It is important to point out that the resulting normalized ratios [called the relative luciferase signals (RLS)] must not be perceived as absolute and are most likely not directly comparable in different experiments. A direct (head-to-head) experimental evaluation of two conjugates is necessary to make an optimal evaluation of the relative activity. However, we found it useful to always include one or two "reference" conjugates (Tat-1 and/or Transportan-6) in a given experiment. Thereby, the relative

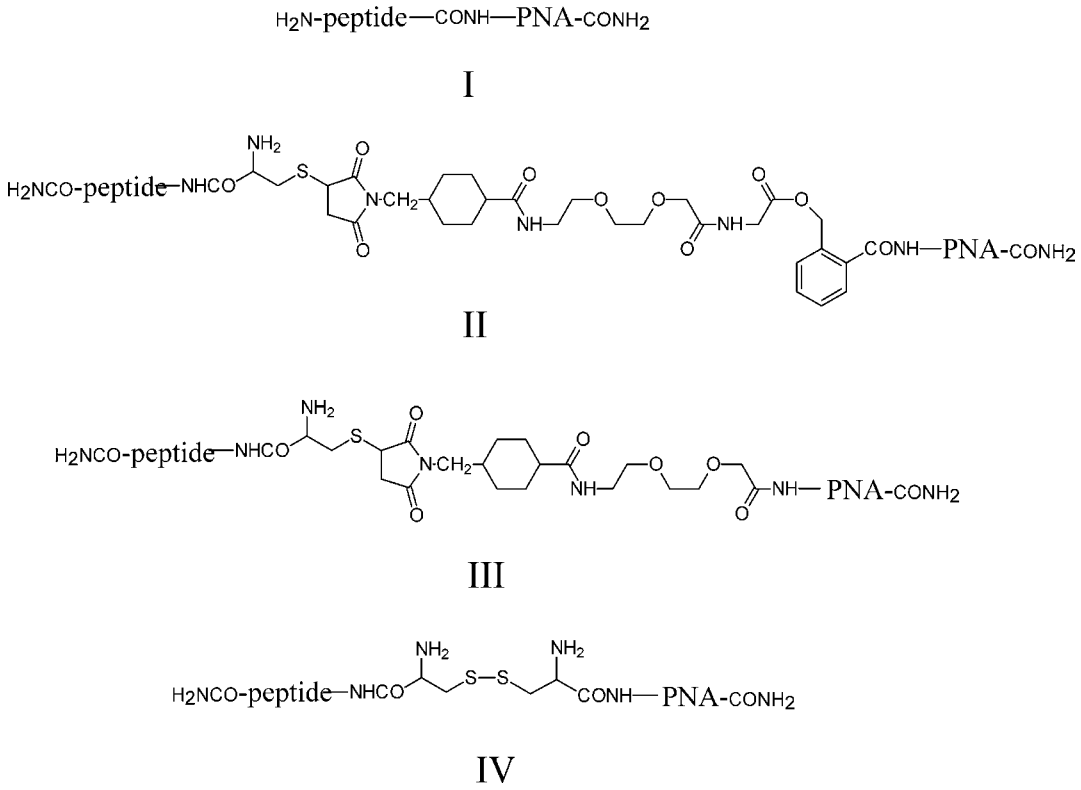

Figure 1. The structure and length of the four different linkers resulting from direct synthesis (I), ester maleimide (II), stable maleimide (III), and disulfide conjugation (IV), respectively.

activity of two different conjugates not tested in the same experiment could still be estimated from their relative activity compared to one or two of the reference conjugates.

Effect of Serum on the Relative Activity of the Conjugates. At an early stage of the study, serum was found to have a profound (inhibitory) effect on the efficiency of the CPP−PNA conjugates. However, the effect was not equally strong with respect to all of the conjugates. This indicates that the relative activity of the peptides as carriers for PNA depends on the presence or absence of serum. Therefore, these two different situations must be evaluated separately. The data shown in Figure 2 illustrate this finding. In this experiment a number of conjugates are evaluated during conditions varying only with respect to serum. Thus, the cells in this experiment were seeded, incubated, washed, incubated with the conjugates, and analyzed for luciferase activity in complete parallel in a 96-well microtiterplate. The only difference is that half of the cells were given serum-free medium, whereas the other half of the cells were given medium containing 10% fetal calf serum before addition of the conjugates. The cells in serum-free medium were then given serum to a concentration of 10% after approximately 2 h. In this experiment we studied four of the most frequently used CCPs, penetratin, Tat-peptide, Arg9, and Transportan (either as the C-terminal amide or as the free carboxylic acid). In the absence of serum, 2 μM Transportan-6 resulted in a RLS of approximately 130, that is, 4−70 times higher than that obtained with Transportan-7, Arg(9)-1, Tat-1, or Penetratin (left part of Figure 2). At 4 μM the antisense activities of Transportan-7 and Transportan-6 were equal, possibly indicating saturation of the effect for Transportan-6.

The right side of the Figure 2 shows the results obtained with the same conjugates when the cells were not allowed serum-free conditions during the first hours of incubation. It is seen that serum dramatically reduces the activity of the two Transportan conjugates as compared to serum-free conditions. However, the results also show that the amide derivative of the Transportan conjugate (Transportan-6) is more sensitive than

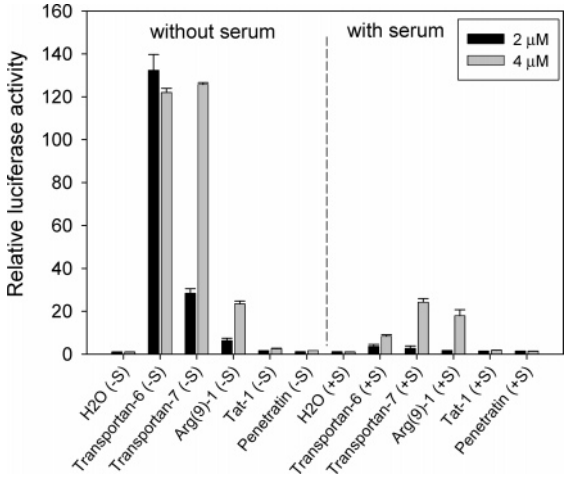

Figure 2. Effect of serum on the antisense activity of five different CPP−PNA conjugates. The indicated conjugates were tested in pLuc 705 HeLa under conditions varying only with respect to the concentration of serum (either 0 or 10%) during the first 2 h after addition of the conjugates. For details see the text. All samples were tested in triplicates. Control cultures were given sterilized water in volumes equal to the volumes (2 and 4 μL, respectively) of conjugate solutions added to obtain the test concentrations. Luciferase activities were normalized to the relevant controls and are given as the average values ± standard deviations.

the free acid derivative (Transportan-7) to the inhibitory effect of serum. Furthermore, the oligo-arginine conjugate [Arg(9)-1] was found to be even less sensitive than Transportan-7 to the inhibitory effect of serum. The little uptake seen with Tat-1 and Penetratin (at 2 and 4 μM) was almost completely suppressed by the presence of serum.

Relative Activity of the Conjugates in the Presence of Serum. A number of experiments were performed to further evaluate the relative efficiency of the conjugates during conditions with constant presence of serum. Two of these experiments

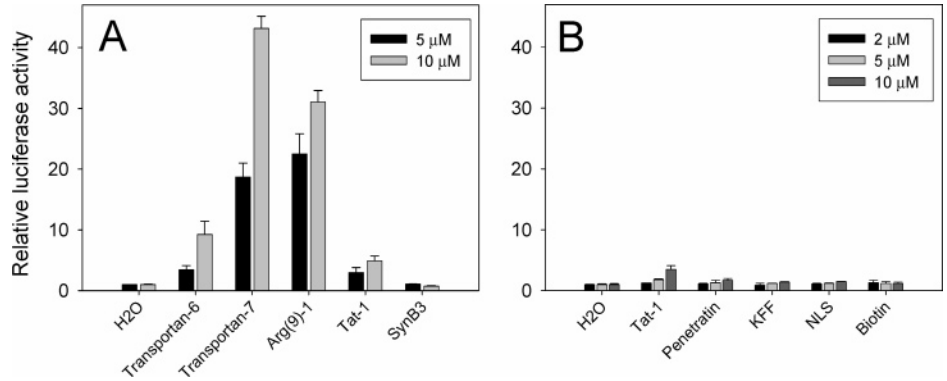

Figure 3. Relative antisense activity of different CPP−PNA conjugates tested in the presence of 10% serum. Panels A and B represent two separate experiments in which the indicated CPP−PNA conjugates (and biotin-PNA) were tested head-to-head. For details see the text. All samples were tested in triplicates. Control cultures were given sterilized water in volumes equal to the volumes (2, 5, and 10 μL, respectively) of conjugate solutions added to obtain the test concentrations. Luciferase activities were normalized to the relevant controls and are given as the average values ± standard deviations.

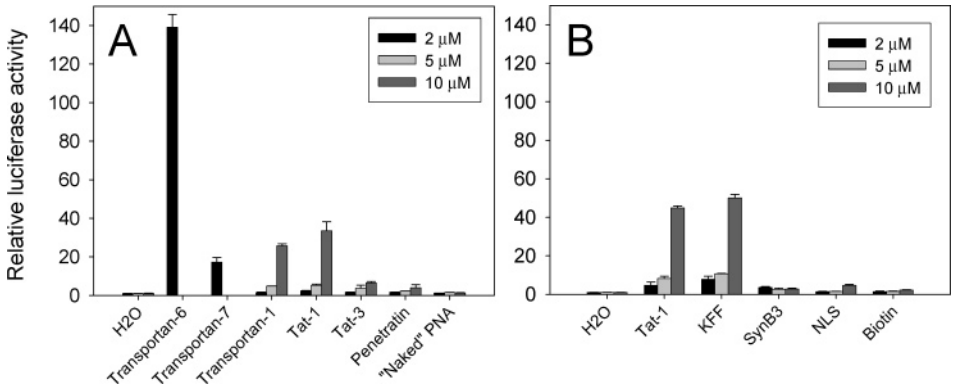

Figure 4. Relative antisense activity of different CPP−PNA conjugates tested during serum-free conditions. Panels A and B represent two separate experiments in which the indicated CPP−PNA conjugates (and biotin-PNA and unmodified PNA) were tested head-to-head. For details see the text. All samples were tested in triplicates. Control cultures were given sterilized water in volumes equal to the volumes (2, 5, and 10 μL, respectively) of conjugate solutions added to obtain the test concentrations. Luciferase activities were normalized to the relevant controls and are given as the average values ± standard deviations.

are summarized in Figure 3. Panels A and B of Figure 3 represent two separate experiments evaluating a number of conjugates at concentrations up to 10 μM. From Figure 3A it is seen that the relative activities of Transportan-6, Transportan-7, and Arg(9)-1 are maintained when these conjugates are tested at higher concentrations than employed in the experiment presented in Figure 2. Furthermore, the results show that among the tested peptides, only Transportan-6, Transportan-7, and oligo-arginine conjugates resulted in RLS above 10 in the presence of serum.

If the cells were not washed and given fresh serum but rather kept in conditioned medium and the conjugates were tested directly in this medium, activities were in general found to be considerably higher (approximately 2-fold) than seen when the conjugates were tested in the presence of fresh serum/medium (results not shown). However, the highest activities were always observed when CPP−PNA conjugates were allowed to act during a period of 2−4 h in serum-free medium (serum-free conditions). We therefore focused the rest of the study on such conditions.

Relative Activity of the Conjugates under Serum-free Conditions. In Figure 4 are shown two separate experiments comparing the antisense activity of a number of CPP−PNA conjugates tested under serum-free conditions. Note that Transportan-6 and Transportan-7 were tested at only 2 μM, whereas all other conjugates in these experiments were tested at 2, 5, and 10 μM. It is immediately clear from these data that Transportan-6 is—by far—the most potent conjugate among the ones tested. Not only Transportan-6, but also Tat-1, was used as internal reference in most of the experiments. From Figure 4A, it is seen that 10 μM Tat-1 induces a RLS of 34, corresponding to one-fourth of the saturating luciferase signal (SLS). Thus, a 5 times higher concentration of pTat results in a 4 times lower activity when compared to Transportan-6. Even at 5 μM, we found almost no activity of pTat-1. This is consistent with an earlier study in which we were unable to trace fluorescein-labeled pTat−PNA (and penetratin−PNA) conjugate to the nucleus when applied in concentrations of 2 μM [instead, we found a massive uptake to vesicular compartments (endosomes) in the cytoplasm] (*11*).

It is seen from Figure 4B that the activity of the KFF conjugate is comparable to that of the Tat-1. Furthermore, it is seen that the Penetratin and the SynB3 conjugates along with the NLS and the truncated Tat conjugates induced only very limited luciferase activation even at concentrations of 10 μM. Comparison with data from a recent publication (also performed in the pLuc HeLa cell system) indicate that the relative activities found for oligo-arginine, pTat, and Penetratin in the present study reflect a general order of strength between these peptides rather than being a special case relating to PNA as the cargo. It was found for phosphorodiamidate morpholino oligomers (PMO) that the arginine-9 peptide constitutes a more potent delivery vehicle than pTat, which in turn was more efficient than penetratin. Transportan was not included in the PMO study (*2*). The biotin conjugate showed practically no activity above background. Most interestingly, the Transportan-1 conjugate is dramatically less active than the Transportan-6 and Transportan-7 conjugates (Figure 4A). This indicates that the position

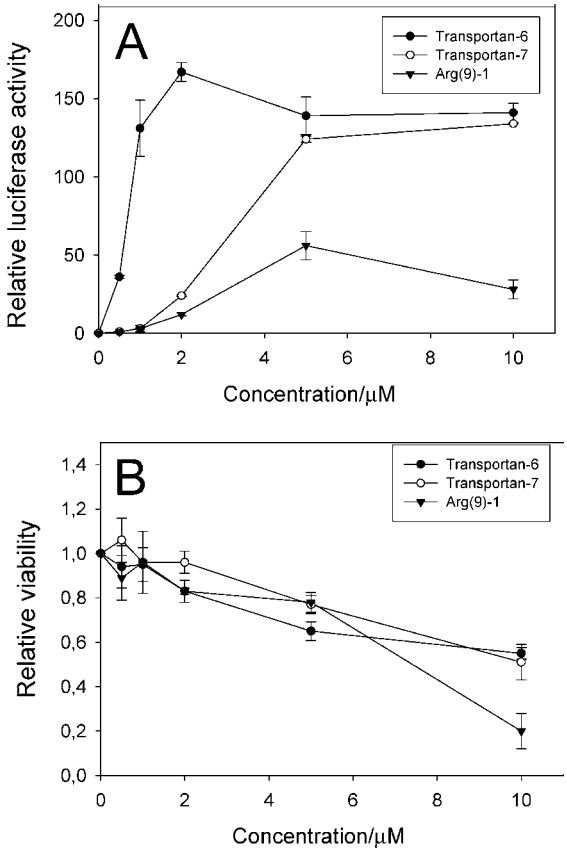

Figure 5. Antisense activity and toxicity of Transportan-6, Transportan-7, and Arg(9)-1 tested during serum-free conditions. The three conjugates were tested head-to-head in the pLuc 705 HeLa cells in concentrations between 0.5 and 10 μM (A). Cell viability was determined in parallel cultures by indirect ATP determinations (B). For details see the text. Control cultures were given sterilized water in volumes equal to the volumes (0.5, 1, 2, 5, and 10 μL, respectively) of conjugate solutions added to obtain the test concentrations. Luciferase activities and cell viability were normalized to the control cultures. All samples were tested in triplicates, and results are given as the average values ± standard deviations.

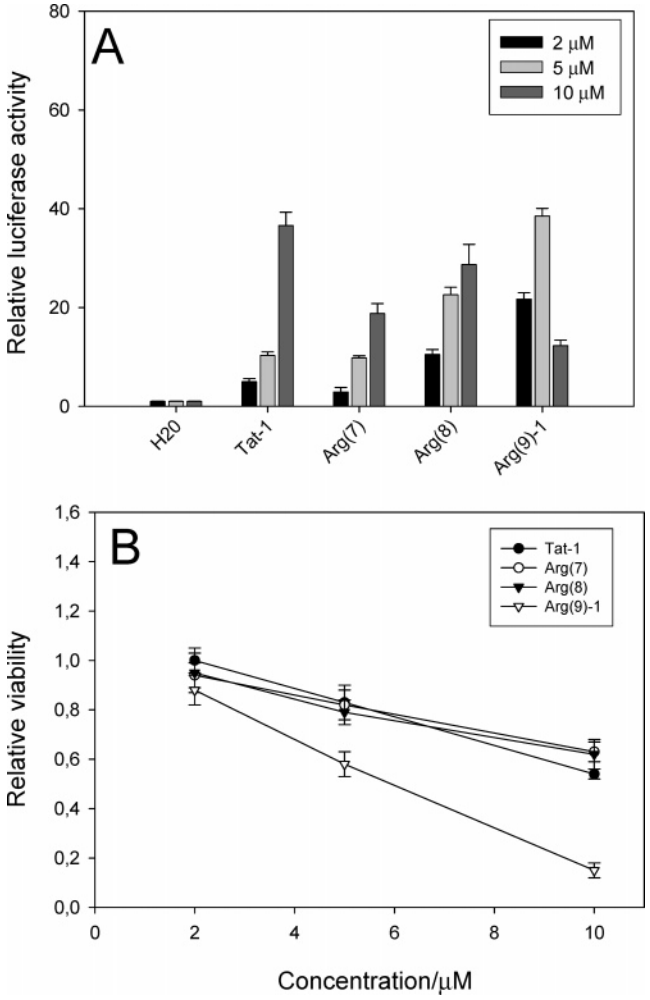

Figure 6. Antisense activity and toxicity of oligo-arginine-PNA conjugates. Arg(6), Arg(7), Arg(8), and Arg(9)-1 (and pTat-1) were tested head-to-head in the pLuc 705 HeLa cells in the indicated concentrations (A). Cell viability was determined in parallel cultures by indirect ATP determinations (B). For details see the text. Control cultures were given sterilized water in volumes equal to the volumes of conjugate solutions added to obtain the test concentrations. Luciferase activities and cell viability were normalized to the control cultures. All samples were tested in triplicates, and results are given as the average values ± standard deviations.

and/or chemical nature of the linker between the peptide and the PNA is of critical importance for activity/cellular uptake. This point is elaborated in much more detail in the separate experiments described later (Figures 7 and 8).

Relative Efficacy and Toxicity of Transportan-6, Transportan-7, and Arg(9)-1. The experiments shown in Figure 4 did not include any of the oligo-arginine conjugates. However, parallel experiments showed Transportan-6, Transportan-7, and Arg(9)-1 to have the highest activities among all of the tested conjugates. Therefore, additional experiments were performed to make a precise comparison among these three conjugates. In Figure 5 are shown the results of testing Transportan-6, Transportan-7, and Arg(9)-1 under serum-free conditions at concentrations up to 10 μM. The viability data on fully parallel cultures (Figure 5B) are based on indirect ATP determinations and reflect the number of living cells. The results clearly demonstrate that Transportan-6 is the most potent conjugate of the three and also show that all three conjugates exhibit significant cellular toxicity above 3−5 μM.

In the experiment shown in Figure 5, maximum activity for Transportan-6 was found at a concentration of 2 μM. In other experiments the maximum value for Transportan-6 was found to be at 1 μM. This was typically the case when the serum-free incubation time was prolonged (>3 h). If serum-free incubation times were shortened (<2 h), then maximum uptake values were found at higher concentrations (see Figure 8). This indicates that the cellular uptake as a prerequisite for antisense activity is time-dependent. It is noteworthy that the maximum luciferase activity obtained with the Arg(9)-1 conjugate is only approximately one-third of that obtained with the Transportan conjugates (Figure 5A). Most likely, this difference reflects a higher relative toxicity of the Arg-9 peptide at higher concentrations (Figure 5B).

Relative Activity and Toxicity of Different Oligo-arginine Conjugates. Initial screening of a series of oligo-arginine conjugates showed Arg(9)-1 to have the highest potency. The result of a direct comparison between Arg(7), Arg(8), and Arg(9)-1 is shown in Figure 6. Clearly, increasing the number of arginine residues results in more active conjugates, as also recently concluded in a parallel study with morpholino-type antisense agents (*2*). It is noteworthy that very similar toxicity is observed for conjugates with seven or eight arginine residues. However, when the number of arginine reaches nine, the toxicity seen at concentrations of 5 and 10 μM was significantly higher for Arg(9)-1 than for the rest of the conjugates. Thus, the data convincingly show that increasing the number of arginine residues in the poly-arginine peptides correlates with increased antisense activity, but also to some extent with increased toxicity (and at some point toxicity appears to become a limiting factor

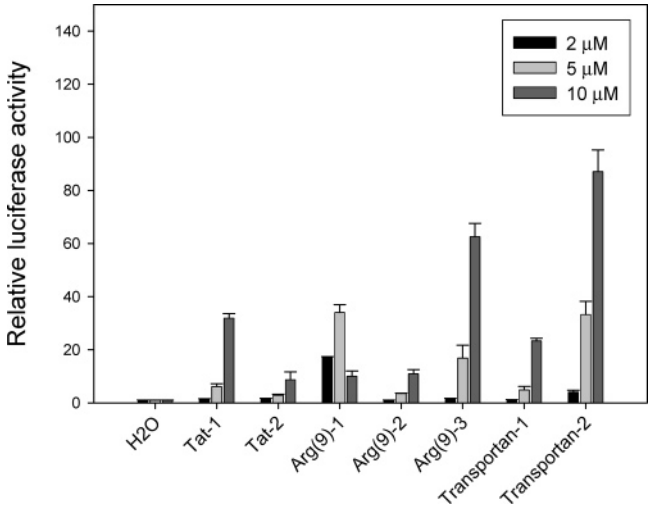

Figure 7. Effect of a biolabile ester linker on CPP−PNA antisense activity. Three ester-linked conjugates [pTat-2, Arg(9)-3, and Transportan-2] were tested in the pLuc 705 HeLa cells head-to-head with conjugates of the same CPP/PNA composition but prepared from either continuous synthesis [Tat-1 and Arg(9)-1] or stable maleimide coupling [Arg(9)-2 and Transportan-1]. For details see the text. Control cultures were given sterilized water in volumes equal to the volumes (2, 5, and 10 μL, respectively) of conjugate solutions added to obtain the test concentrations. Luciferase activities were normalized to the relevant controls and are given as the average values ± standard deviations.

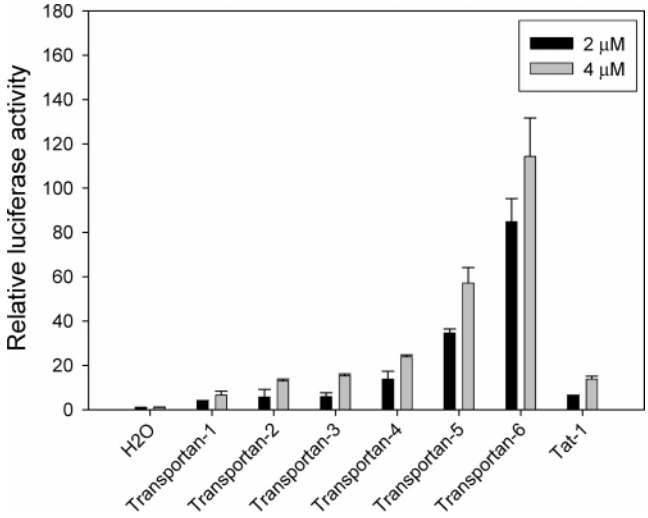

Figure 8. Effect of linker type and linker position in Transportan−PNA conjugates. Six different Transportan−PNA conjugates were tested head-to-head in the pLuc 705 HeLa cells. PNA is linked to the amino (N) terminus of Transportan (end position) or to the ϵ N of lysine 13 of Transportan (ortho position) by either stable maleimide (Transportan-1 and -4), by ester-maleimide (Transportan-2 and -5), or by disulfide linkage (Transportan-3 and -6). The conjugates were tested in concentrations of 2 and 4 μM and were allowed to incubate at serum-free conditions for only a relatively short period of time (1.5 h versus normally 2−4 h). These conditions were chosen to accurately reveal the differences in antisense activity reflecting both uptake potency and kinetics between the conjugates. For details see the text. Control cultures were given sterilized water in volumes equal to the volumes (2, 5, and 10 μL, respectively) of conjugate solutions added to obtain the test concentrations. Luciferase activities were normalized to the relevant controls and are given as the average values ± standard deviations.

for the activity of the poly-arginine conjugates). The problem of toxicity is most serious in the case of oligo-arginine peptides of more than eight arginine residues

Effect of a Biolabile Ester Linker on Uptake Efficiencies. Recently, we have found that conjugation of fatty acids to PNA via an ester-linkage increased antisense activity of PNA−lipid conjugates by a factor of 2 compared to similar conjugates not containing the ester linker. The ester linker is biolabile as it was shown to be cleaved by intracellular esterases (*31*). Inspired by these findings, we set out to investigate whether incorporation of this ester linker would also improve activities of CPP−PNA conjugates compared to CPP−PNA conjugates linked via a more biostable linkage. For this purpose, three ester-containing conjugates were made: pTat(48−60)-ester−PNA (Tat-2), Transportan-ester−PNA (Transportan-2) in which PNA is linked to the N terminus of the peptide, and (D-arginine)$_9$-ester−PNA [Arg(9)-3].

The data of Figure 7 show the results of an experiment designed to compare the three ester-linked conjugates with control conjugates of the same CPP/PNA composition but not containing the ester linkage and prepared by continuous synthesis [Tat-1 and Arg(9)-1] or maleimide coupling [Arg(9)-2 and Transportan-1]. From a comparison of the results with Tat-1 and Tat-2 it is seen that linking PNA to the Tat peptide through the ester linker apparently reduced performance about 2-fold compared to the continuous synthesis construct. However, continuous synthesis results in conjugates having the peptide and PNA in identical orientations (N terminus of PNA is bound directly to the C terminus of the peptide), whereas maleimide and disulfide coupling (via a cysteine residue in the N terminus of the PNA) results in conjugates having the peptide and PNA in opposite orientations. Therefore, when the Tat-1 and Tat-2 conjugates were compared, the orientation of the peptide was also reversed, and this could affect the activity as well.

The results with the three Arg(9) conjugates address this question. First of all, it is seen that conjugating the arginine(9) peptide and the PNA via the maleimide coupling [Arg(9)-2] severely reduces the activity compared to continuous synthesis [Arg(9)-1]. As observed for the Tat−PNA conjugates the ester-linked arginine conjugate [Arg(9)-3] is also less potent than the Arg(9)-1 conjugate prepared by continuous synthesis [the relatively high activity of Arg(9)-3 at 10 μM compared to Arg(9)-1 was due to less toxicity of the Arg(9)-3 conjugate compared to Arg(9)-1 at this concentration (results not shown)]. However, the ester-linked conjugate Arg(9)-3 is considerably (4−5-fold) more active than the chemically comparable nonester control Arg(9)-2 conjugate, differing only by the absence of the ester amino acid moiety. This result strongly emphasizes the advantage of including the biolabile (ester) linkage between the antisense oligomer and the carrier peptide.

This conclusion is supported by the finding that linking PNA to the N terminus of Transportan by an ester linker results in a much more efficient conjugate than that obtained from stable maleimide conjugation of PNA to the same end of Transportan (Figure 7). (Due to the length of the peptide, and the associated synthetic difficulties, a PNA−Transportan conjugate was not prepared by continuous synthesis.)

Direct comparison of the ester-linked conjugates [Tat-2, Arg(9)-3, and Transportan-2] and the maleimide-coupled conjugates [Arg(9)-2 and Transportan-1] consistently points at Transportan to possess the highest potency for cellular transport of PNA but also indicates that conjugation chemistry and position are critical.

Influence of Linker and Position of the Linker in Transportan−PNA Conjugates. Inspired by the results obtained with the different linkers described above and the high activity seen with Transportan-6 (in which the PNA is linked via a disulfide bridge to an amino acid positioned in the middle of the peptide), we decided to make a more elaborate study on the influence of linker and position of the linker in Transportan−PNA conjugates. For this purpose we employed six Transportan−PNA conjugates: three conjugates in which PNA is linked to the amino (N) terminus of Transportan (end position) and three conjugates in which PNA is linked to the ϵ N of lysine 13 of

Transportan (ortho position) by either stable maleimide (Transportan-1 and -4), ester maleimide (Transportan-2 and -5), or disulfide linkage (Transportan-3 and -6). The results (Figure 8) show two clear tendencies. First, linking the PNA to lysine 13 of the peptide in general results in higher antisense activity (up to 4-fold) of the PNA than if PNA is linked to the N terminus of the peptide. Second, disulfide linking results in more potent compounds (about 2-fold) than ester linking, which in turn performs better than stable maleimide coupling of the PNA to the peptide. However, it should be noted that the ortho ester-linked conjugate, Transportan-5, was purified to only 60%. Therefore, the spectroscopically determined concentration of Transportan-5 was probably underestimated, and the activity of this conjugate may be closer to the activity of Transportan-6 than indicated by the results shown in Figure 8.

The reasons for the observed differences in activity due to the position and chemistry of the linkage are not obvious. In a recent study on arginine-rich CPP delivery vectors for PMO in which a number of different linker types were tested, it was concluded that linker length rather than conjugation chemistry (maleimide, ether, or disulfide) affected the antisense activity of the conjugates. Thus, a consistent and positive relationship between linker length and antisense activity was found, whereas no consistent relationship was found between conjugation type and antisense activity (*2*). However, our results do not comply with such a simple rule. In fact, we found the most active conjugates to have the shortest linkers (disulfide and direct coupling/synthesis compared to stable maleimide and ester maleimide). Taken together, our results indicate a complex dependence of the antisense activity/cellular uptake on factors such as orientation of the PNA−CPP conjugate and position and type of the linker connecting these two domains. Thus, further data are needed to decipher the important relationship between the chemical structure of CPP−cargo conjugates and cellular delivery efficacy.

Considerations Regarding the Choice of Test System. In this study we have employed a biological antisense endpoint read-out for evaluating functional cellular uptake. We find this assay to be more relevant than other methods such as confocal microscopy using fluorescently labeled PNA−CPP conjugates. Confocal microscopy implicates many modifications of the experimental procedure (such as labeling of the PNA, growth of the cells in special chambers, and fixation of the cells), and these modifications are likely to influence the observed results. Moreover, quantitative analysis by confocal microscopy is by itself associated with a large number of pitfalls, which easily may give rise to incorrect or biased results (*23*, *33*). The positive read-out offered by the pLuc 705 HeLa cell system is highly superior to analysis by confocal microscopy and therefore may stand alone in a comparative study such as the present, which emphasizes precision and relevance for antisense applications. However, this analysis is also restricted by certain inherent limitations. First of all, the assay reflects only nuclear delivery of the active antisense agents because splicing, and thus correction of aberrant splicing, is confined to the nucleus. Thus, the pLuc 705 HeLa cells cannot provide us with exact information on the extranuclear compartmentalization of the CPP−PNA constructs. This is a significant limitation. Some targets for PNA antisense such as translation and HIV reverse transcriptase may theoretically be targeted equally well or better in the cytoplasm compared to the nucleus (*34*, *35*). Another shortcoming of the test system based on pLuc 705 HeLa cells is the limited information provided on the dynamics of the cellular uptake. This limitation follows from the reporter having to be translated before it is measurable. Thus, it will take a thorough analysis of all dynamic parameters involved in the process of luciferase expression (i.e., factors such as RNA stability, translations rate, luciferase stability) to make a relevant analysis of the kinetics underlying the observed data, and still it will not be possible to decide if the active antisense probe is delivered to the nucleus within (for example) seconds or minutes.

DISCUSSION

We have employed an easily quantifiable positive read-out assay, believed to directly reflect relative cellular uptake, to compare the antisense activity of 19 different CPP−PNA conjugates. A number of clear conclusions can be drawn from the data. First, we found the activity of most of the tested CPP−PNAs to be dramatically reduced if serum was present during treatment. Two conjugates, PNA−SS-Transportan-acid (ortho) and $(D\text{-Arg})_9$−PNA, were less sensitive to serum than the rest of the conjugates. We found no correlation between the type of linkage in the conjugate and serum sensitivity.

Under conditions where the conjugates were delivered in the absence of serum for a period of 2−4 h, a transportan−PNA conjugate, Transportan-6, was found to be the most active of the tested conjugates. An oligo-arginine−PNA conjugate, Arg-(9)-1, was found to be the second most potent conjugate, showing approximately $^1/_{10}$ of the activity seen with Transportan-6. Furthermore, Arg(9)-1 was found to be more toxic than Transportan-6. pTat-1 and the KFF−PNA conjugate were the third most active conjugates, whereas the Penetratin, SynB3, NLS, and biotin conjugates showed only minimal or no activity.

A significant finding of our study is the strong dependence of delivery efficacy on the chemical nature and position of the linker. Our results strongly suggest that biologically cleavable ester and especially disulfide linkages between the delivery peptide and the antisense agent result in more active conjugates. The results also show that the molecular site of conjugation (N terminus versus C terminus or "ortho" of the peptide) can dramatically affect the antisense (and thus implicitly the cell penetration) potency of the conjugate. However, a simple relationship between the type (and position) of the linker of a CPP−PNA conjugate and its antisense activity is not obvious at this stage.

ACKNOWLEDGMENT

This work was supported by the Danish Research Council and the 6th Framework Program of the European Union (EUROXY Project). The excellent technical assistance provided by Masumeh Chavosi and Anna Bay Nielsen is greatly appreciated.

LITERATURE CITED

(1) Jarver, P., Langel, U. (2004) The use of cell-penetrating peptides as a tool for gene regulation. *Drug Discov Today 9*, 395−402.

(2) Moulton, H. M., Nelson, M. H., Hatlevig, S. A., Reddy, M. T., and Iversen, P. L. (2004) Cellular uptake of antisense morpholino oligomers conjugated to arginine-rich peptides. *Bioconjugate Chem. 15*, 290−299.

(3) Pooga, M., Kut, C., Kihlmark, M., Hallbrink, M., Fernaeus, S., Raid, R., Land, T., Hallberg, E., Bartfai, T., and Langel, U. (2001) Cellular translocation of proteins by transportan. *FASEB J. 15*, 1451−1453.

(4) Terrone, D., Sang, S. L., Roudaia, L., and Silvius, J. R. (2003) Penetratin and related cell-penetrating cationic peptides can translocate across lipid bilayers in the presence of a transbilayer potential. *Biochemistry 42*, 13787−13799.

(5) Thoren, P. E., Persson, D., Isakson, P., Goksor, M., Onfelt, A., and Norden, B. (2003) Uptake of analogs of penetratin, Tat(48−60) and oligoarginine in live cells. *Biochem. Biophys. Res. Commun. 307*, 100−107.

(6) Trehin, R., and Merkle, H. P. (2004) Chances and pitfalls of cell penetrating peptides for cellular drug delivery. *Eur. J. Pharm. Biopharm. 58*, 209−223.
(7) Vives, E. (2003) Cellular uptake [correction of utake] of the Tat peptide: an endocytosis mechanism following ionic interactions. *J. Mol. Recognit. 16*, 265−271.
(8) Prochiantz, A. (1999) Homeodomain-derived peptides. In and out of the cells. *Ann. N. Y. Acad. Sci. 886*, 172−179.
(9) Derossi, D., Chassaing, G., and Prochiantz, A. (1998) Trojan peptides: the penetratin system for intracellular delivery. *Trends Cell Biol. 8*, 84−87.
(10) Oehlke, J., Scheller, A., Wiesner, B., Krause, E., Beyermann, M., Klauschenz, E., Melzig, M., and Bienert, M. (1998) Cellular uptake of an alpha-helical amphipathic model peptide with the potential to deliver polar compounds into the cell interior non-endocytically. *Biochim. Biophys. Acta 1414*, 127−139.
(11) Koppelhus, U., Awasthi, S. K., Zachar, V., Holst, H. U., Ebbesen, P., and Nielsen, P. E. (2002) Cell-dependent differential cellular uptake of PNA, peptides, and PNA-peptide conjugates. *Antisense Nucleic Acid Drug Dev. 12*, 51−63.
(12) Ross, M. F., Filipovska, A., Smith, R. A., Gait, M. J., and Murphy, M. P. (2004) Cell-penetrating peptides do not cross mitochondrial membranes even when conjugated to a lipophilic cation: evidence against direct passage through phospholipid bilayers. *Biochem. J. 383*, 457−468.
(13) Richard, J. P., Melikov, K., Vives, E., Ramos, C., Verbeure, B., Gait, M. J., Chernomordik, L. V., and Lebleu, B. (2003) Cell-penetrating peptides. A reevaluation of the mechanism of cellular uptake. *J. Biol. Chem. 278*, 585−590.
(14) Ziegler, A., Nervi, P., Durrenberger, M., and Seelig, J. (2005) The cationic cell-penetrating peptide CPP(TAT) derived from the HIV-1 protein TAT is rapidly transported into living fibroblasts: optical, biophysical, and metabolic evidence. *Biochemistry 44*, 138−148.
(15) Thoren, P. E., Persson, D., Esbjorner, E. K., Goksor, M., Lincoln, P., and Norden, B. (2004) Membrane binding and translocation of cell-penetrating peptides. *Biochemistry 43*, 3471−3489.
(16) Hallbrink, M., Floren, A., Elmquist, A., Pooga, M., Bartfai, T., and Langel, U. (2001) Cargo delivery kinetics of cell-penetrating peptides. *Biochim. Biophys. Acta 1515*, 101−109.
(17) Saalik, P., Elmquist, A., Hansen, M., Padari, K., Saar, K., Viht, K., Langel, U., and Pooga, M. (2004) Protein cargo delivery properties of cell-penetrating peptides. A comparative study. *Bioconjugate Chem. 15*, 1246−1253.
(18) Astriab-Fisher, A., Sergueev, D., Fisher, M., Shaw, B. R., and Juliano, R. L. (2002) Conjugates of antisense oligonucleotides with the Tat and antennapedia cell-penetrating peptides: effects on cellular uptake, binding to target sequences, and biologic actions. *Pharm. Res. 19*, 744−754.
(19) Moulton, H. M., and Moulton, J. D. (2004) Arginine-rich cell-penetrating peptides with uncharged antisense oligomers. *Drug Discov. Today 9*, 870.
(20) Kang, S. H., Cho, M. J., and Kole, R. (1998) Up-regulation of luciferase gene expression with antisense oligonucleotides: implications and applications in functional assay development. *Biochemistry 37*, 6235−6239.
(21) Shiraishi, T., and Nielsen, P. E. (2004) Down-regulation of MDM2 and activation of p53 in human cancer cells by antisense 9-aminoacridine-PNA (peptide nucleic acid) conjugates. *Nucleic Acids Res. 32*, 4893−4902.
(22) Pooga, M., Soomets, U., Hallbrink, M., Valkna, A., Saar, K., Rezaei, K., Kahl, U., Hao, J. X., Xu, X. J., Wiesenfeld-Hallin, Z., Hokfelt, T., Bartfai, T., and Langel, U. (1998) Cell penetrating PNA constructs regulate galanin receptor levels and modify pain transmission in vivo. *Nat. Biotechnol. 16*, 857−861.
(23) Koppelhus, U., and Nielsen, P. E. (2003) Cellular delivery of peptide nucleic acid (PNA). *Adv Drug Deliv. Rev. 55*, 267−280.
(24) Good, L., Awasthi, S. K., Dryselius, R., Larsson, O., and Nielsen, P. E. (2001) Bactericidal antisense effects of peptide-PNA conjugates. *Nat. Biotechnol. 19*, 360−364.
(25) Eriksson, M., Nielsen, P. E., and Good, L. (2002) Cell permeabilization and uptake of antisense peptide-peptide nucleic acid (PNA) into *Escherichia coli*. *J. Biol. Chem. 277*, 7144−7147.
(26) Rousselle, C., Smirnova, M., Clair, P., Lefauconnier, J. M., Chavanieu, A., Calas, B., Scherrmann, J. M., and Temsamani, J. (2001) Enhanced delivery of doxorubicin into the brain via a peptide-vector-mediated strategy: saturation kinetics and specificity. *J. Pharmacol. Exp. Ther. 296*, 124−131.
(27) Temsamani, J., Bonnafous, C., Rousselle, C., Fraisse, Y., Clair, P., Granier, L. A., Rees, A. R., Kaczorek, M., Scherrmann, J. M. (2005) Improved brain uptake and pharmacological activity profile of morphine-6-glucuronide using a peptide-vector-mediated strategy. *J. Pharmacol. Exp. Ther. 313*, 712−719.
(28) Cutrona, G., Carpaneto, E. M., Ulivi, M., Roncella, S., Landt, O., Ferrarini, M., and Boffa, L. C. (2000) Effects in live cells of a c-myc anti-gene PNA linked to a nuclear localization signal. *Nat. Biotechnol. 18*, 300−303.
(29) Chinnery, P. F., Taylor, R. W., Diekert, K., Lill, R., Turnbull, D. M., and Lightowlers, R. N. (1999) Peptide nucleic acid delivery to human mitochondria. *Gene Ther. 6*, 1919−1928.
(30) Awasthi, S. K., and Nielsen, P. E. (2002) Synthesis of PNA−peptide conjugates. *Methods Mol. Biol. 208*, 43−52.
(31) Bendifallah, N., Kristensen, E., Dahl, O., Koppelhus, U., and Nielsen, P. E. (2003) Synthesis and properties of ester-linked peptide nucleic acid prodrug conjugates. *Bioconjugate Chem. 14*, 588−592.
(32) Rasmussen, F. W., Bendifallah, N., Zachar, V., Shiraishi, T., Fink, T., Ebbesen, P., Nielsen, P. E., and Koppelhus, U. (2006) Evaluation of transfection protocols for unmodified and modified peptide nucleic acid (PNA) oligomers. *Oligonucleotides 16*, 42−56.
(33) Pichon, C., Monsigny, M., and Roche, A. C. (1999) Intracellular localization of oligonucleotides: influence of fixative protocols. *Antisense Nucleic Acid Drug Dev. 9*, 89−93.
(34) Knudsen, H., and Nielsen, P. E. (1996) Antisense properties of duplex- and triplex-forming PNAs. *Nucleic Acids Res. 24*, 494−500.
(35) Koppelhus, U., Zachar, V., Nielsen, P. E., Liu, X., Eugen-Olsen, J., and Ebbesen, P. (1997) Efficient in vitro inhibition of HIV-1 gag reverse transcription by peptide nucleic acid (PNA) at minimal ratios of PNA/RNA. *Nucleic Acids Res. 25*, 2167−2173.

BC050283Q

Linear Topology Confers in Vivo Gene Transfer Activity to Polyethylenimines

B. Brissault,[‡] C. Leborgne,[§] C. Guis,[‡] O. Danos,[§] H. Cheradame,[‡] and A. Kichler*[,§]

Laboratoire Matériaux Polymères aux Interfaces UMR 7581, Université d'Evry, 91025 Evry Cedex, France, and Genethon - UMR 8115 CNRS, Department of Gene Transfer, BP 60, 91002 Evry Cedex, France. Received September 30, 2005; Revised Manuscript Received March 15, 2006

Although polyethylenimines (PEIs) are frequently used transfection agents, it is still unclear which of their properties are required for efficient gene delivery. This is even more striking when working in vivo since some PEIs are able to generate significant gene expression, whereas others are not. To facilitate a rational development of compounds with improved transfection activities, studies aimed at identifying the properties involved in the transfection process seem indispensable. In the present work, we investigated how transfection with linear PEI of 22 kDa allows for high reporter gene expression in lungs after intravenous injection, whereas the branched PEI of 25 kDa does not. To this end, we synthesized L-PEI derivatives that are intermediates between linear and branched PEIs. Our results show that the topology plays a crucial role in obtaining in vivo reporter gene expression, whereas the content of primary, secondary, and tertiary amines is only of minor importance.

INTRODUCTION

Introduction of nucleic acids into mammalian cells by using synthetic compounds such as cationic polymers has become a routine technology in many research fields. It allows for example the expression of a foreign or tagged protein by transfection of plasmid DNA or selective silencing of mRNAs by delivering small interfering RNAs into the target cell. However, to be useful as a gene delivery system for the treatment of human diseases, the efficiency of the currently existing nonviral transfection systems has to be significantly improved. One way to reach this goal is by synthesizing new transfection agents or by improving the performance of the currently existing ones. Alternatively, a better understanding of the molecular requirements for successful gene delivery will allow rational design of new vectors. In line with this latter approach, we undertook a detailed analysis of the key features of polyethylenimines (PEIs).[1]

PEIs belong to the most efficient synthetic gene transfer agents developed so far. Although these cationic polymers are available in a wide range of molecular weights (*1*), only two of them, namely, the linear PEI 22 kDa (L-PEI) and the branched PEI of 25 kDa (B-PEI), are commonly used as transfection reagents. Interestingly, although both polymers were described to possess high in vitro transfection efficiencies (*2, 3*), they differ profoundly in their ability to mediate in vivo gene transfer. Indeed, the L-PEI mediates in vivo reporter gene expression orders of magnitude higher than that of the branched PEI (*3*−*6*). It was largely unknown why two closely related compounds show such a difference in their in vivo transfection capacities. We therefore decided to identify the properties conferring the in vivo gene transfer capabilities of L-PEI.

To this end, we evaluated the role of the two parameters that differ between the L-PEI and the B-PEI, namely, their topology and their content of primary, secondary, and tertiary amines. We synthesized polymers presenting short amino residues grafted on the linear L-PEI backbone and containing various proportions of primary, secondary, and tertiary amino nitrogens. Our in vivo gene transfer experiments clearly demonstrate that the class of amines only plays a minor role in the transfection activity. The dominant effect for efficient in vivo gene transfer is based on the topology of the polymer.

EXPERIMENTAL PROCEDURES

Materials. Tetrahydrofuran (sds) was distilled over calcium hydride. *N*-(2-Chloroethyl)acetamide (Acros), 2-(dimethylamino)ethyl chloride hydrochloride (Aldrich), anhydrous ethyl alcohol (sds), methyl alcohol (sds), diethyl ether (sds), methylene chloride (sds), and sodium hydroxide pellets (Aldrich) were used as received. The linear PEI of 22 kDa was synthesized as described (*7*). The polyethylenimine of 25 kDa was from Aldrich. SMD2-LucΔ*I*TR (7.6 kb) is an expression plasmid encoding the firefly luciferase gene under the control of the human cytomegalovirus (CMV) immediate-early promoter.

Synthesis of Poly(ethylenimine-*co*-*N*-(2-aminoethyl)ethylenimine) (L-PEI-g-$CH_2CH_2NH_2$) (PEI-2). *N*-(2-Chloroethyl)-acetamide (1.57 g, 12.9 mmol) was dissolved in 20 mL of EtOH before dropwise addition to a solution of L-PEI (1.24 g, 0.06 mmol) in THF (20 mL) and stirred for 4 h at 65 °C. After the sample was evaporated, the product was dissolved in MeOH and precipitated by dropwise addition of diethyl ether to remove the excess of *N*-(2-chloroethyl)acetamide. The polymer was first isolated by filtration, and then dissolved in 50 mL of water with NaOH pellets (1.5 g, 37.5 mmol). The reaction mixture was stirred refluxing for 64 h. At room temperature, the product precipitated spontaneously, and after filtration and washing with water, it was dried in vacuo (952 mg, 83%).

^{1}H NMR ($CDCl_3$): δ (ppm) = 2.7 (bs, CH_2); 1.7 (bs, NH and NH_2). ^{13}C NMR ($CDCl_3$): δ (ppm) = 54.9 (NCH_2CH$_2$-NH$_2$); 52.4, 52.1 (−CH_2N(CH$_2$CH$_2$NH$_2$)CH_2-); 49.4 (−CH_2-NHCH_2-); 48.5−47.0 (−CH$_2$(H$_2$NCH$_2$CH$_2$)NCH_2CH$_2$NH-); 41.7 (NCH$_2$CH_2NH$_2$).

Synthesis of Poly(ethylenimine-*co*-N-(2-dimethylaminoethyl)ethylenimine) (L-PEI-g-$CH_2CH_2N(CH_3)_2$) (PEI-4). To a solution of L-PEI (1 g, 0.04 mmol) in EtOH (30 mL), a solution of 2-(dimethylamino)ethyl chloride hydrochloride (1.1 g, 7.64

* To whom correspondence should be addressed. E-mail: akich@genethon.fr.

‡ Laboratoire Matériaux Polymères aux Interfaces UMR 7581, Université d'Evry.

§ Genethon - UMR 8115 CNRS.

[1] Abbreviations: ACE, acetamidoethyl residues; EtOH, ethanol; MeOH, methanol; NaOH, sodium hydroxide; PEI, polyethylenimine; B-PEI, branched polyethylenimine; L-PEI, linear polyethylenimine; L-PNPEI, poly(*N*-propylethylenimine); PMeOXZ, poly methyloxazoline; THF, tetrahydrofuran.

10.1021/bc050287v CCC: $33.50 © 2006 American Chemical Society
Published on Web 04/27/2006

Scheme 1[a]

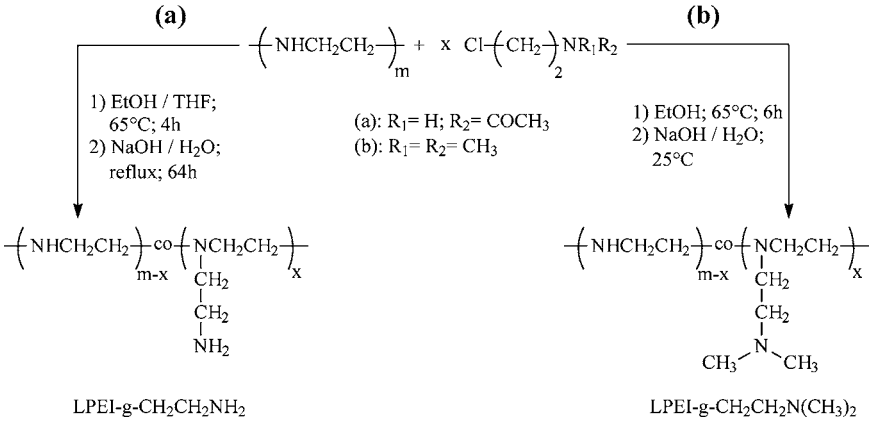

[a] Synthetic routes of (a)poly(ethylenimine-*co*-*N*-(2-aminoethyl)ethylenimine) (LPEI-*g*-$CH_2CH_2NH_2$); (b) poly(ethylenimine-*co*-*N*-(2-dimethylaminoethyl)ethylenimine) (LPEI-*g*-$CH_2CH_2N(CH_3)_2$) grafted L-PEIs copolymers.

mmol) in EtOH (10 mL) was added dropwise during 4 h at 65 °C, and the mixture was stirred at 65 °C for 2 h. The solution was concentrated on the rotavapor to precipitate a byproduct, i.e., a cyclic dimer of 2-(dimethylamino)ethyl chloride. After filtration, the organic layer was evaporated. The residue was dissolved in water at room temperature, and then NaOH pellets (1.2 g) were added for neutralization. To remove the excess NaOH and residual byproduct, the polymer was dissolved in methylene chloride, and then the organic layer was evaporated in vacuo. Yield was 457 mg (65%). ^{1}H NMR ($CDCl_3$): δ (ppm) = 2.7 (bs, CH_2); 2.2 (m, N-(CH_3)$_2$).

Cell Culture. Dulbecco's modified Eagle medium (DMEM; GIBCO-BRL) was supplemented with 2 mM L-glutamine, 100 units/mL of penicillin, 100 μg/mL streptomycin, and 10% heat-inactivated foetal calf serum (HyClone). Human hepatocarcinoma cells (HepG2 cells; American Type Culture Collection) were used for the in vitro studies.

DNA Retardation Assay. DNA binding was studied by means of agarose gel retardation assays. Plasmid DNA (1 μg) and increasing amounts of PEI were each diluted in 25 μL of 150 mM NaCl and mixed. After a period of 15 min, samples (20 μl) were electrophoresed through a 1% agarose gel using Tris-borate-EDTA buffer, and DNA was visualized after ethidium bromide staining.

Particle Size Measurements. DNA (25 μg) and the desired amount of PEI were each diluted in 625 μL of either 5% glucose, 150 mM NaCl or 0.5 HBS (75 mM NaCl, 2.5% glucose, 10 mM Hepes). After the solutions were mixed and left for 10 min at room temperature, particle size was measured using a Zetasizer nano ZS (Malvern).

Preparation of DNA Complexes. Four micrograms of plasmid DNA and the desired amount of PEI were diluted into 100 μL of 150 mM NaCl and gently mixed. DNA complexes were prepared at various N/P ratios. After 15 min of incubation, the mixture was diluted with serum-free medium to a final volume of 1 mL.

For the in vivo experiments, the DNA complexes were formulated in 5% glucose since previous work showed that in vivo PEI-mediated transfection is more efficient when complexes are prepared in glucose than in sodium chloride (*5*, *6*). DNA and PEI were each diluted in 175 μL of 5% glucose and then gently mixed. After 15 min, complexes were ready for use.

Transfection Experiments. HepG2 cells were plated in 24-well plates 1 or 2 days before use. For transfection, 0.5 mL of serum-free transfection medium was put into each well. After 3 h of incubation at 37 °C, the medium was replaced with fresh one containing 10% of serum. Luciferase activity was assayed about 30 h after transfection. Each experiment was carried out several times; within a series, experiments were done in duplicate with 2 μg of DNA per well. The transfection experiments involving bafilomycin A1 were done in the same way as described above except that the drug was added after dilution of the complexes with DMEM, just before addition of the transfection medium to the cells.

The luciferase assay was performed as described (*8*). Luciferase background was subtracted from each value, and the transfection efficiency is expressed as total light units (10 s)$^{-1}$ (mg of protein)$^{-1}$ and the values are the means of duplicates. Protein content was measured by using the BioRad protein assay (Bradford).

Cell Viability Assay. Cytotoxicity was evaluated by performing the 3-(4,5-dimethylthiazol-2-yl)-2,5-diphenyl-tetrazolium bromide (MTT; Sigma) assay. Briefly, 1 day after transfection, the cell culture medium was removed and replaced by serum-free DMEM containing 0.5 mg/mL MTT. After incubation at 37 °C for 4 h, the medium was removed, and 200 μL of DMSO was added to each well to dissolve the formazan crystals produced from the reduction of MTT by viable cells. Absorbance was then measured at 570 nm. Untreated cells were used as control.

In Vivo Experiments. Experiments were conducted with five animals/condition. A total of 350 μL of PEI/50 μg CMV-Luc solution were slowly injected into the tail vein of female Balb/C mice (6−8 weeks old, Iffa-Credo). To facilitate the injection, vasodilation was achieved by working under a heating lamp. Mice were sacrificed 20 h post-administration.

For the measurement of luciferase levels in lungs, the following protocol was used: 500 μL of lysis buffer containing a cocktail of protease inhibitors (Sigma) were added to the collected organs. Each organ was then homogenized for about 30 s with an Ultra-turrax (Ika), and the homogenate was centrifuged for 10 min at 8000*g* at 4 °C. A 5 μL aliquot of the supernatant was used for luciferase assay.

RESULTS AND DISCUSSION

Synthesis of Poly(ethylenimine-*co*-N-(2-aminoethyl)ethylenimine)s (LPEI-*g*-$CH_2CH_2NH_2$). The synthesis of the copolymers containing both ethylenimine and grafted *N*-(2-aminoethyl)ethylenimine units was carried out in two steps: introduction of 2-acetamidoethyl residues (ACE) on the L-PEI backbone followed by alkaline hydrolysis to obtain short 2-aminoethyl side groups (Scheme 1, route a). In the first step, L-PEI was mixed with *N*-(2-chloroethyl)acetamide to give grafted *N*-(2-acetamidoethyl)ethylenimine units according to the reaction conditions summarized in Table 1. After solvent evaporation and precipitation in diethyl oxide to remove

Table 1. Synthesis of Poly(ethylenimine-*co*-*N*-(2-acetamidoethyl)-ethylenimine) (L-PEI-*g*-$CH_2CH_2NHCOCH_3$) and Poly(ethylenimine-*co*-*N*-(2-dimethylaminoethyl)ethylenimine) (L-PEI-*g*-$CH_2CH_2N(CH_3)_2$) Grafted Copolymers: Reaction Conditions and Results

run	[NH][a] (mol/L)	[R−Cl] (mol/L)	solvent	temp (°C)	time (h)	yield (%)	grafting $content_{theo}$[b] (%)	grafting $content_{exp}$[c] (%)
1	0.67	0.31[d]	MeOH	25	5	38	46	0[e]
2	0.71	0.30[d]	EtOH	78	21	60	42	31[e]
3	0.66	0.31[d]	THF	65	4	65	47	13[e]
4	0.57	0.12[d]	THF/EtO (1/1)	65	8	83	21	17[e]
5	0.69	0.31[d]		65	4	61	45	30[e]
6	0.55	0.39[d]		65	15	20	71	56[e]
7	0.57	0.19[f]	EtOH	65	4	84	33	18[g]
8	0.57	0.35[f]	EtOH	65	6	20	61	6[g]
9	0.57	0.19[f]	EtOH	65	6	65	33	21[g]
10	0.58	0.18[f]	EtOH	65	48	100	31	28[g]
11	0.59	0.24[f]	EtOH	65	118	82	41	20[g]

[a] Ethylenimine units concentration of starting L-PEI. [b] Theoretical content of grafted ethylenimine units calculated from the initial concentration ratio of alkyl halide and secondary amino sites (100× [R−Cl]/[NH]). [c] Experimental content of grafted ethylenimine units calculated from ^{1}H NMR spectrum. [d] *N*-(2-Chloroethyl)acetamide concentration. [e] $Grafted_{ACE}$ ethylenimine units content. [f] 2-(Dimethylamino)ethyl chloride hydrochloride concentration. [g] $Grafted_{DMAE}$ ethylenimine units content.

unreacted *N*-(2-chloroethyl)acetamide, the polymers were collected under their protonated form. The modified L-PEIs were then analyzed by NMR spectroscopy to estimate the grafting efficiency. This conjugation experiment was conducted under various conditions of time, solvent, reaction temperature, and initial feed ratio [RCl]/[NH]. It can be noticed that a high reaction temperature was required to functionalize ethylenimine units by an acetamide side function (Table 1, run 1). ^{1}H NMR spectra of polymers collected in runs 2 and 3 revealed, besides the presence of peaks corresponding to modified L-PEI, the characteristic peaks of poly(*N*-acetylethylenimine) (PMeOXZ) at 2.1 and 3.5 ppm (*9*). The formation of this byproduct is explained by dehydrohalogenation of the chloroamide compound (favored by the presence of basic amino sites in starting and modified L-PEIs), leading to methyloxazoline monomer, which polymerizes with starting chloride agent (Supporting Information Scheme 1) (*10, 11*). To avoid this side reaction, acetamide was added dropwise to the polyamine solution in a THF/EtOH mixture making profit of the good solubility of modified L-PEIs in this medium (runs 4, 5, and 6). ^{1}H NMR spectra of poly(ethylenimine-*co*-*N*-(2-acetamidoethyl)ethylenimine)s in D_2O showed, besides the methylene protons of unreacted ethylenimine units at 2.9 ppm (H_a), two triplets and a broad singlet, respectively, at 3.7 (H_d), 3.1 (H_c), and 2.2 (H_e) ppm corresponding to 2-acetamidoethyl side groups introduced on polymer backbone (Figure 1a). Further, two new resonance peaks also appeared at 3.6 and 3.9 ppm with areas 2-fold higher than those of methylene protons (3.7, 3.1 ppm) of the amide side groups. The peak at 3.6 ppm was attributed to methylene protons near the protonated secondary amino groups (H_f), whereas resonance at 3.9 ppm was assigned to protons in α position of tertiary amines formed on L-PEI chain (H_b), probably downfield shifted by intramolecular hydrogen bond established between these nitrogens and acetamido residues. The assignments were also supported both by ^{13}C NMR and 2D-^{1}H NMR analyses (Supporting Information, Scheme 2). The experimental content of grafted acetamido (ACE) ethylenimine units in polymers was calculated by ^{1}H NMR spectroscopy from the peak integration ratio of methyl protons of 2-acetamidoethyl group (h_{He}) to the sum of those corresponding to methylene groups belonging to the L-PEI backbone ($h_{Ha} + h_{Hb} + h_{Hf}$), using the relationship: $grafted_{ACE} = (4/3)h_{He}/(h_{Ha} + h_{Hb} + h_{Hf})$ (Figure 1a).

The poly(ethylenimine-*co*-*N*-(2-acetamidoethyl)ethylenimine)s obtained in runs 4, 5, and 6 were fully hydrolyzed in alkaline conditions giving, respectively, poly(ethylenimine-*co*-*N*-(2-aminoethyl)ethylenimine) copolymers PEI-1, PEI-2, and PEI-3. The composition in the three classes of nitrogen groups of these polymers were determined from the initial contents of acetamido (ACE) and secondary amino units present in the precursor polymers (Table 2). Moreover, the ^{13}C NMR analysis of PEI-2 in $CDCl_3$ was compared to those of L-PEI and commercial B-PEI ($N_I/N_{II}/N_{III}$: 1/1/1) (Figure 2). It clearly showed the presence of methylene groups bonded, respectively, to tertiary and primary nitrogen atoms in the copolymer, thanks to the peaks observed above and below 49.4 ppm as proof of the grafted structure of the modified L-PEIs (*12*).

Synthesis of Poly(ethylenimine-*co*-*N*-2-dimethylaminoethyl)ethylenimine)s (LPEI-*g*-$CH_2CH_2N(CH_3)_2$). The synthesis of poly(ethylenimine-*co*-*N*-(2-dimethylaminoethyl)ethylenimine) copolymers was performed by direct reaction of 2-(dimethylamino)ethyl chloride hydrochloride with L-PEI (Scheme 1, route b). Several runs were carried out in EtOH solution stirred at 65 °C, using different [RCl]/[NH] feed ratios and time conditions (Table 1). As the reaction proceeded, a white precipitate appeared in the reaction medium, which was isolated by filtration. After solvent evaporation, the crude protonated grafted polymers were analyzed by ^{1}H NMR spectroscopy. The spectra showed the expected peaks corresponding to methyl protons of neutral and charged 2-dimethylaminoethyl moieties (DMAE) bonded to the L-PEI backbone, clearly distinguishible at 2.3 (H_j) and 2.8 (H_e) ppm. (Figure 1b). These resonance signals do not correspond to unreacted aminoethyl chloride since the triplet peak characteristic of methylene near of the halogen atom, usually seen at 3.7 ppm in D_2O, was absent on the spectra of the isolated polymers. The extent of polymer modification ($grafted_{DMAE}$ content) was calculated using the integrations of these peaks on one hand, and those of peaks present in the range 3−3.6 ppm ascribed to all methylene groups of compound on the other hand. Of note, the spectrum of the product obtained on run 8 showed also two peaks at 4.0 and 3.4 ppm corresponding to a non-negligible amount of a byproduct that partially precipitated in the reaction medium. To understand its formation, a NMR study of 2-(dimethylamino)ethyl chloride hydrochloride behavior in sodium hydroxide D_2O solution was performed and it showed the production of the same compound (witnessed by the same peaks increasing with time). Its chemical structure was established by mass spectroscopy as a cyclic quaternary ammonium dimer of 2-(dimethylamino)ethyl chloride formed in the medium owing to the basic character of L-PEI (Supporting Information Scheme 3). Of note, the formation of this product implies first the partial neutralization of the dimethylamino sites in the medium and also that the reaction easily undergoes on haloamine itself and consequently unfavored with L-PEI. This side reaction was reduced by dropwise addition of 2-(dimethylamino)ethyl chloride hydrochloride in the medium (runs 9, 10, and 11) leading, after neutralization, to poly(ethylenimine-*co*-*N*-(2-dimethylaminoethyl)ethylenimine) copolymers with short amino side groups, such as PEI-4 obtained from run 9, which has a secondary and tertiary amino composition rather close to the B-PEI one but without primary nitrogen groups (Table 2).

Gel Mobility Shift Assay and in Vitro Transfection Activity. To summarize the chemical part, we developed two types of grafted L-PEIs: the first series consist of modified L-PEIs characterized by the presence of different ratios of primary, secondary, and tertiary amines (Table 2). The second derivative contains only secondary and tertiary amines. Of note, PEI-2 presents almost the same ratios of I, II, and III amino groups compared to the branched PEI of 25 kDa. This particular derivative thus allows us to clearly distinguish the influence of the topology versus the content in I, II, and III amines on DNA transfection.

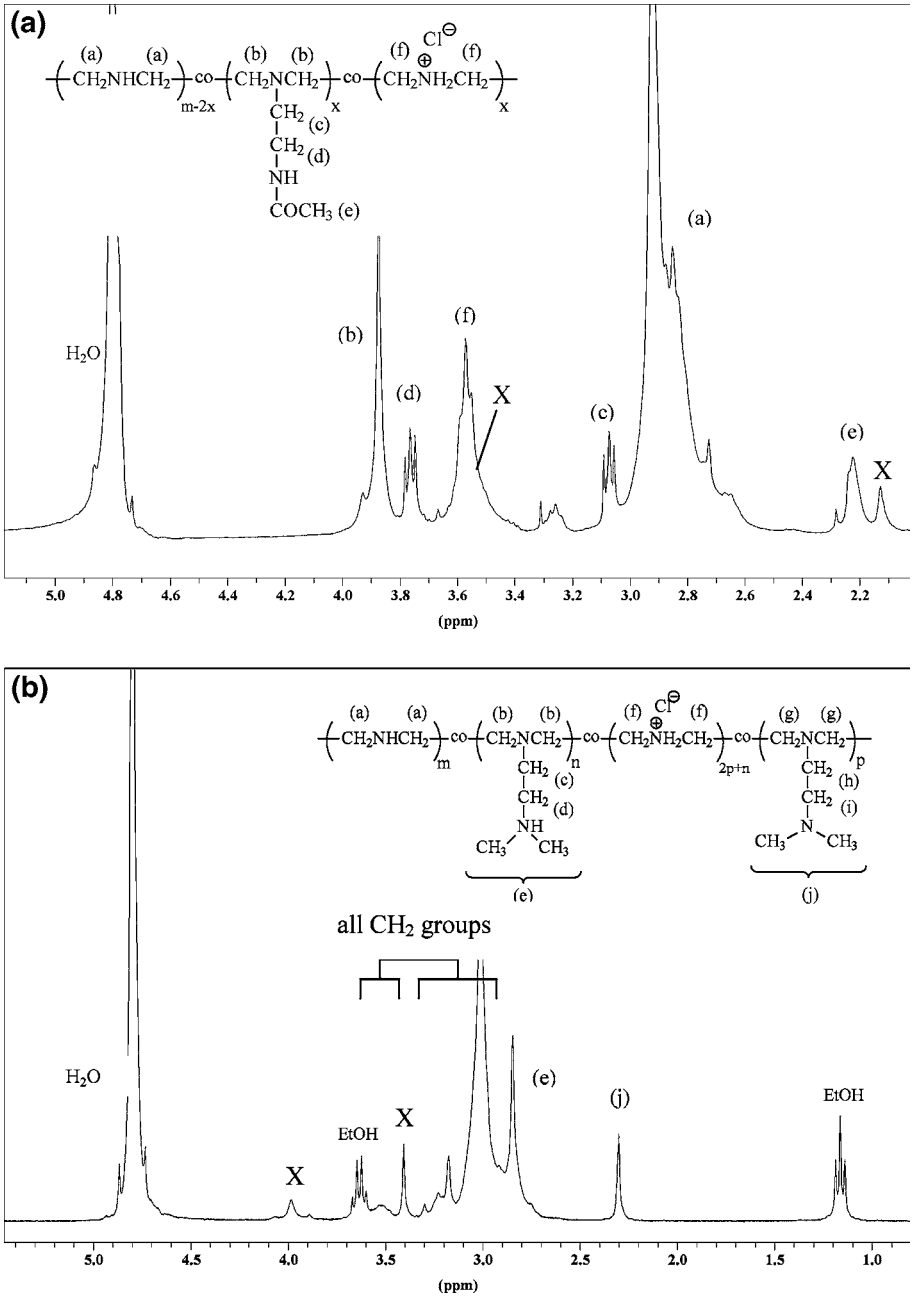

Figure 1. 300 MHz ^{1}H NMR spectra of protonated (a) L-PEI-*g*-$CH_2CH_2NHCOCH_3$ from run 3 (Table 1) (X: PMeOXZ byproduct); (b) L-PEI-*g*-$CH_2CH_2N(CH_3)_2$ from run 7 (Table 1) (X: cyclic dimer byproduct) in D_2O.

Table 2. Structure and Composition of Grafted L-PEIs Derivatives

polymer	molecular weight	grafting[a] content (%)	N_I[b] (%)	N_{II}[b] (%)	N_{III}[b] (%)
PEI-1[c]	25000	17	15	70	15
PEI-2[d]	28000	30	23	54	23
PEI-3[e]	33000	56	36	28	36
PEI-4[f]	29000	21	0	65	35
L-PEI	22000		0	100	0
B-PEI	25000		25	50	25

[a] Experimental grafted ethylenimine monomer units content in the copolymers. [b] N_I, N_{II}, and N_{III} are, respectively, the primary, secondary, and tertiary amine content of copolymers determined from NMR. [c–e] L-PEI-*g*-$CH_2CH_2NH_2$ obtained, respectively, after hydrolysis of runs 4, 5, and 6 (Table 1). [f] L-PEI-*g*-$CH_2CH_2N(CH_3)_2$ was obtained from run 9 (Table 1).

The DNA binding capacity of the grafted L-PEIs was evaluated by DNA retardation assays. The results summarized in Table 3 show that, as expected, all the derivatives were able to efficiently complex DNA. We then measured the transfection efficiency of all the polymers. Therefore, increasing amounts of PEI were complexed with a constant amount of a luciferase expression plasmid, and the resulting complexes were incubated with HepG2 cells. The luciferase assay showed that the four PEI derivatives (PEI-1 to -4) displayed similar capacities for reporter gene expression compared to the L- and B-PEI polymers (Figure 3). This confirms that the topology and the content in I, II, and III amines do not play a critical role when transfecting cell lines in vitro.

Proton Sponge Activity. We recently reported that the transfection efficiency of PEIs partly relies on their capacity to buffer endo-lysosomes (*8*)—a mechanism called proton sponge that leads to the release of DNA from the endosomes into the cytosol (*13*). Our demonstration was based on the use during transfection of drugs able to inhibit acidification of endocytic vesicles. Here, we investigated whether DNA transfection performed in the presence of bafilomycin A1, an antibiotic that selectively inhibits vacuolar type H^+-ATPases (*14*), results in

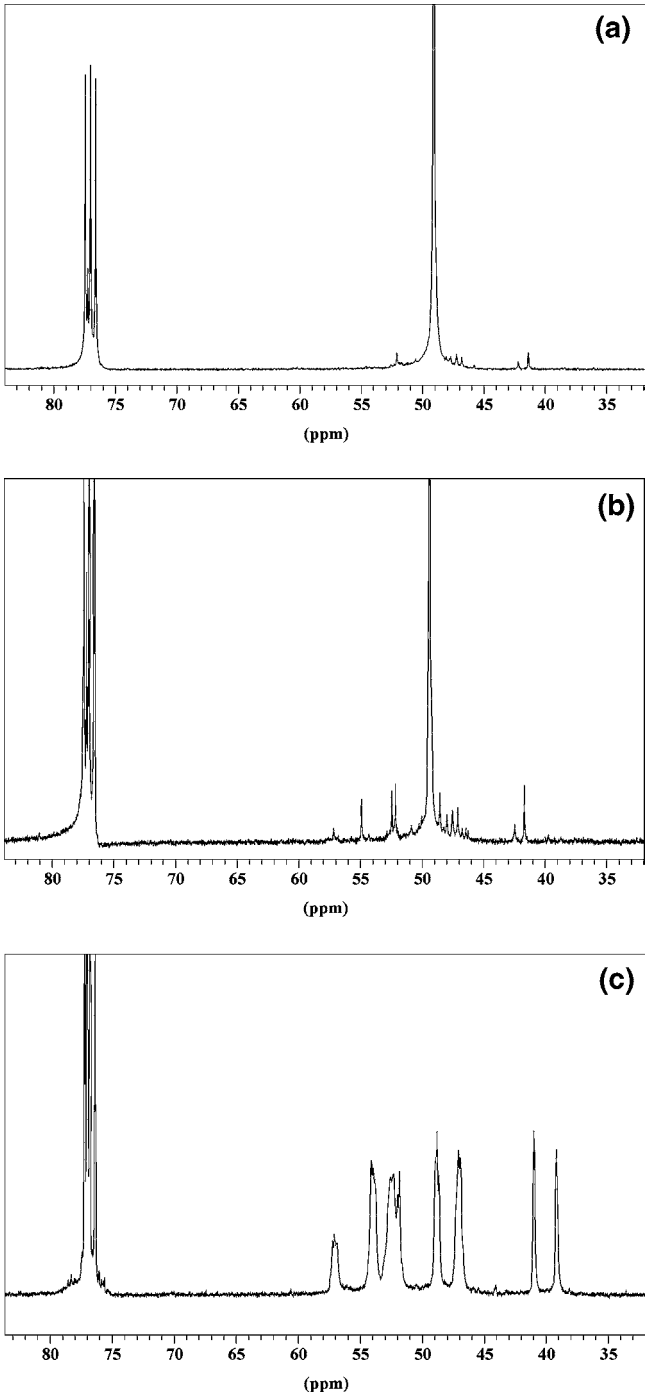

Figure 2. 300 MHz ^{13}C NMR spectra of (a) L-PEI; (b) L-PEI-*g*-CH_2-CH_2NH_2 (PEI-2) (Table 2); (c) commercial B-PEI ($N_I/N_{II}/N_{III}$: 1/1/1) in $CDCl_3$ (scans: 16000).

a similar severe drop in reporter gene expression for all the L-PEI derivatives. As shown in Figure 4a, bafilomycin A1 treatment led to luciferase levels about 100-fold lower than those obtained in the absence of drug. To ensure that the inhibition of transfection was not due to cytotoxicity of the drug, we measured the protein content and performed a MTT-based cell viability assay. The results indicate that incubation with bafilomycin A1 reduced the protein content as well as the cell viability to about 50% (Figure 4b). This latter value, however, cannot alone explain the 2 orders of magnitude decrease of reporter gene expression. Moreover, the efficiency of the monocationic lipid DOTAP, which was used as a control since its protonation state is not altered in the pH range 5−7.5, remained identical in the presence of the inhibitor, although the cytotoxicity was

Table 3. Characterization of Grafted L-PEIs/DNA Complexes

polymer	DNA retardation[a] (μg)	N/P ratio[b]	zeta potential[c] (mV)	particle size (nm)[d] 5% glucose	particle size (nm)[d] 150 mM NaCl
PEI-1	0.5	58	+17	72	895
PEI-2	0.5−1	15	+20	74	1028
PEI-3	0.5	19.5	+16	74	891
PEI-4	0.25−0.5	15	+21	72	760
L-PEI	0.5−1	13	+22	69	1178
B-PEI	0.5	13	+23	59	113

[a] Indicates the minimal amount of PEI required to completely retard 1 μg of plasmid DNA. [b] N/P ratios used for the zeta-potential and size measurements. [c] Complexes were generated in 150 mM NaCl, and the size measurement was performed about 20 min after complexes formation. [d] The size was measured 10 min after having mixed PEI with DNA.

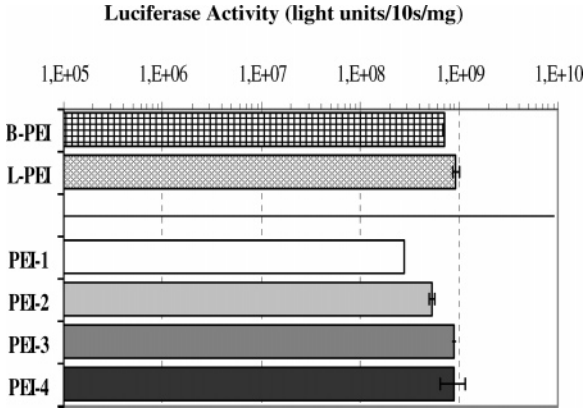

Figure 3. Evaluation of the transfection efficiency of grafted L-PEI derivatives on HepG2 cells. Increasing amounts of polymer were mixed with a constant amount of plasmid DNA (4 μg per duplicate). The complexes were incubated with the cells in serum-free culture medium for 3 h. The luciferase activity was measured 39 h thereafter. The transfection efficiency was expressed as total light units $(10\ s)^{-1}$ (mg of protein)$^{-1}$. For each compound, only the optimal condition is shown (N/P = 13 for B- and L-PEI; N/P = 11.5 for PEI-2 and PEI-4; N/P = 19.5 for PEI-3 and 58 for PEI-1).

similar compared to that observed with the polymers (Figure 4b). Taken together, these results suggest that the buffering capacities of all the PEIs are comparable.

Tail Vein Injection of PEI/DNA Complexes. Next, we evaluated the in vivo activity of PEI-2 and -4, which are the two most interesting derivatives among PEI-1 to -4 due to their amino contents. Polyplexes containing 50 μg of CMV-Luc and increasing amounts of polymer were generated and slowly injected into the tail vein. The levels of luciferase were measured in the lungs, where it is known that the expression is the highest. In agreement with the literature, the L-PEI demonstrated a 1000-fold higher transfection efficiency compared to the one displayed by the branched PEI (Figure 5). Of note, in our hands and in our conditions, we could not use N/P ratios higher than 7 with the B-PEI without inducing high mortality rates. Interestingly, the grafted L-PEIs 2 and 4 allowed for significantly higher luciferase expression compared to that with the B-PEI. In fact, PEI-2 and -4 were only 4 and 9 times less efficient than L-PEI, respectively. Taken together, these results clearly demonstrate that the topology plays a more crucial role than the content in I, II, and III amines for in vivo transfection.

Characterization of the Polyplexes. Previous work revealed that the linear PEI of 22 kDa and the branched PEI of 25 kDa show differences in some of their properties. In particular, Wightman and colleagues (*15*) found a stronger propensity of L-PEI compared to B-PEI to aggregate. This behavior may explain, to some extent, the differences observed in vivo between the two polymers. Indeed, it is known that large complexes are more efficient in mediating gene transfer than small ones (*16*),

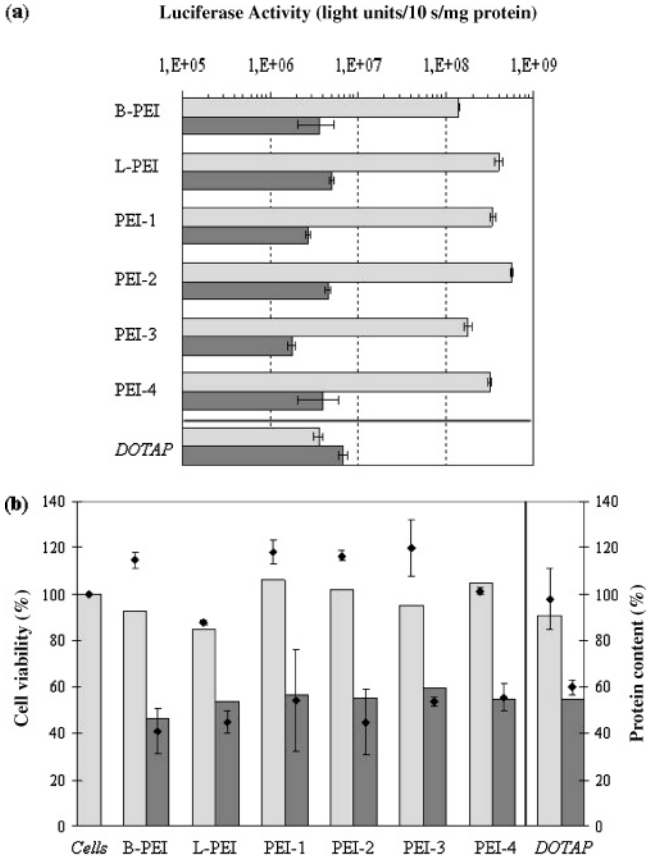

Figure 4. Effect of bafilomycin A1 on PEI-mediated transfection efficiency. HepG2 cells were transfected with PEIs (same N/P ratios as those described in legend of Figure 3) in the absence (light gray) or presence (dark gray) of 175 nM of the proton pump inhibitor bafilomycin A1. After about 3 h of incubation at 37°C, the transfection medium was removed and replaced with DMEM containing 10% of serum. (a) The luciferase activity was measured 30 h later. (b) The protein content measurements (the black diamonds represent the average of duplicates) and the MTT based cell viability assay ($n = 1$; light gray bars in the absence and dark bars in the presence of bafilomycin A1) were done as described in materials and methods.

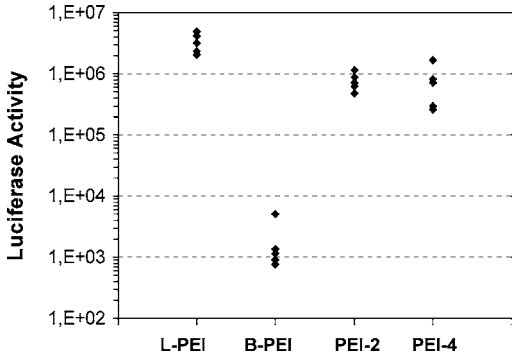

Figure 5. Evaluation of the in vivo efficiency. Complexes were prepared in 5% glucose with 50 μg of CMV-Luc mixed with increasing amounts of PEI. 350 μL of the solution was then slowly injected intravenously and 20 h postinjection, the luciferase levels were measured from the processed lungs ($n = 5$). For each compound, only the optimal condition is shown (N/P = 23 for PEI-2; N/P of 10 for PEI-4 and N/P ratios of 7 and 14 for the B- and L-PEI, respectively).

most probably because the endosomal release through the proton sponge effect is highly dependent on PEI concentration. Since the linear PEI-2 showed significant in vivo gene transfer capacity, we asked whether its aggregation properties are close to those of the L-PEI. To this end, we measured at different time points the particle size of DNA/grafted L-PEI complexes prepared in salt-free (5% glucose), in 0.5 HBS and in salt-rich

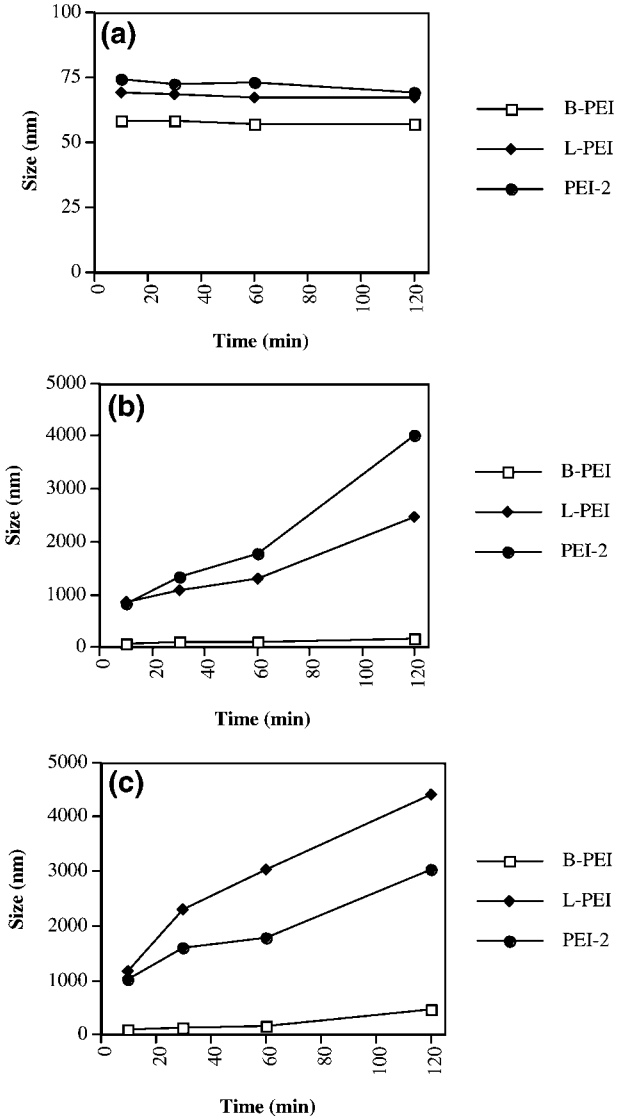

Figure 6. Measurement of particle size of complexes generated in varying salt conditions. PEI/DNA complexes (N/P = 13 for B- and L-PEI and 15 for PEI-2) were generated either in 5% glucose (a), 0.5 HBS (b) or 150 mM NaCl (c). The size of the particles was monitored at 10, 30, 60, and 120 min after complex formation.

(150 mM NaCl) conditions. In salt-free conditions L- and B-PEI, as well as PEI-2, generate stable particles with a diameter below 100 nm (Figure 6). This is in agreement with results from the literature (*15*). However, in the presence of salt, differences between the branched and the grafted/linear PEIs appeared: while the particle size of B-PEI/DNA complexes only slowly increased in size with time, complexes generated with the L-PEI and PEI-2 rapidly aggregated, and particle size became micrometric within 10 min. These results clearly show that PEI-2 shares the same aggregating properties compared to the L-PEI. Size measurements performed with the other PEI derivatives confirmed that the linear topology amplifies complex aggregation in the presence of salt (Table 3). Of note, in these assays, all the complexes had a positive surface charge, the zeta potential being around +20 mV (Table 3).

Taken together, our results show that PEI-2, like the L-PEI, generates small complexes in salt-free conditions, whereas in the presence of salt, aggregation occurs in a time-dependent manner. It is interesting to note that L-PEI/DNA complexes generated in 150 mM NaCl are significantly less efficient in vivo than particles prepared in 5% glucose (*15*). This suggests that at the time of injection the particles have to be small, but

once in the blood or once complexes reached the target tissue—mainly the lung after intravenous injection—aggregation of the complexes has to occur to obtain efficient cell transfection.

Conclusion. In the present work, we describe a way to modify linear PEIs, allowing for the introduction of primary and tertiary amino groups. DNA transfection with such compounds clearly demonstrated that the topology of a polymer plays a more critical role than the content in I, II, and III amines to obtain efficient in vivo gene transfer. Of note, we have recently shown that it is possible to synthesize linear PEI derivatives (L-PNPEIs) having high buffering capacities while being significantly less efficient than the nonmodified L-PEI (*7*). Together, these results demonstrate that even polymers that possess a linear topology and a capacity to buffer endo-lysosomes are not necessarily efficient in vivo transfection agents. Therefore, other parameters such as flexibility of the polymer, as suggested by Szoka and colleagues for dendrimers, may be of importance (*17*).

ACKNOWLEDGMENT

We would like to thank Laetitia Baudry and Thibaut Marais for technical assistance. This work was performed with the financial support of the Association Française contre les Myopathies (AFM).

Supporting Information Available: Schemes 1 and 3 show the side reactions leading to the generation of PMeOXZ and the cyclic quaternary ammonium dimer, respectively. Scheme 2 shows the 2D-^{1}H NMR spectrum of L-PEI-*g*-$CH_2CH_2NHCOCH_3$ (run 3) in D_2O. This material is available free of charge via the Internet at http://pubs.acs.org/BC.

LITERATURE CITED

(1) Kichler, A., Behr, J. P., and Erbacher, P. (1999) Polyethylenimines: a family of potent polymers for nucleic acid delivery, in *Nonviral Vectors for Gene Therapy* (Huang, L., Hung, M. C., and Wagner, E., Eds.) pp 191−206, Academic Press, San Diego.

(2) Boussif, O., Lezoualc'h, F., Zanta, M. A., Mergny, M. D., Scherman, D., Demeneix, B., and Behr, J. P. (1995) A versatile vector for gene and oligonucleotide transfer into cells in culture and in vivo: polyethylenimine. *Proc. Natl. Acad. Sci. U.S.A. 92*, 7297−7301.

(3) Zou, S. M., Erbacher, P., Remy, J. S., and Behr, J. P. (2000) Systemic linear polyethylenimine (L-PEI)-mediated gene delivery in the mouse. *J. Gene Med. 2*, 128−34.

(4) Bragonzi, A., Boletta, A., Biffi, A., Muggia, A., Sersale, G., Cheng, S. H., Bordignon, C., Assael, B. M., and Conese, M. (1999) Comparison between cationic polymers and lipids in mediating systemic gene delivery to the lungs. *Gene Ther. 6*, 1995−2004.

(5) Goula, D., Benoist, C., Mantero, S., Merlo, G., Levi, G., and Demeneix, B. A. (1998) Polyethylenimine-based intravenous delivery of transgenes to mouse lung. *Gene Ther. 5*, 1291−1295.

(6) Goula, D., Remy, J. S., Erbacher, P., Wasowicz, M., Levi, G., Abdallah, B., and Demeneix, B. A. (1998) Size, diffusibility and transfection performance of linear PEI/DNA complexes in the mouse central nervous system. *Gene Ther. 5*, 712−717.

(7) Brissault, B., Kichler, A., Guis, C., Leborgne, C., Danos, O., and Cheradame, H. (2003) Synthesis of linear polyethylenimine derivatives for DNA transfection. *Bioconjugate Chem. 14*, 581−587.

(8) Kichler, A., Leborgne, C., Coeytaux, E., and Danos, O. (2001) Polyethylenimine-mediated gene delivery: a mechanistic study. *J. Gene Med. 3*, 135−144.

(9) Guis, C., and Cheradame, H. (2000) Synthesis of polymers containing pseudohalide groups by cationic polymerization. Study of the functionalizing living cationic polymerization of 2-methyl-oxazoline in the presence of trimethylsilylazide. *Eur. Polym. J. 36*, 2581−2590.

(10) Frump, J. A. (1971) Oxazoline. Their preparation, reactions, and applications. *Chem. Rev. 71*, 483−505.

(11) Saegusa, T., Kobayashi, S., and Yamada, A. (1976) Kinetics and mechanism of isomerization polymerization of 2-methyl-2-oxazoline by benzyl chloride and bromide initiators. Effect of halogen counteranions. *Makromol. Chem. 177*, 2271−2283.

(12) Lukovkin, G. M., Pshezhetsky, V. S., and Murtazaeva, G. A. (1973) ^{13}C NMR study of structure of polyethylenimine. *Eur. Polym. J. 9*, 559−565.

(13) Demeneix, B. A., and Behr, J. P. (1996) The proton sponge: a trick the viruses didn't exploit, in *Artificial Self-Assembling Systems for Gene Delivery* (Behr, J. P., Felgner, P., Heller, R., Lehn, P., and Szoka, F. C., Eds.) pp 146−152, American Chemical Society Books, Washington, DC.

(14) Yoshimori, T., Yamamoto, A., Moriyama, Y., Futai, M., and Tashiro, Y. (1991) Bafilomycin A1, a specific inhibitor of vacuolar-type H(+)-ATPase, inhibits acidification and protein degradation in lysosomes of cultured cells. *J. Biol. Chem. 266*, 17707−17712.

(15) Wightman, L., Kircheis, R., Rossler, V., Carotta, S., Ruzicka, R., Kursa, M., and Wagner, E. (2001) Different behavior of branched and linear polyethylenimine for gene delivery in vitro and in vivo. *J. Gene Med. 3*, 362−372.

(16) Ogris, M., Steinlein, P., Kursa, M., Mechtler, K., Kircheis, R., and Wagner, E. (1998) The size of DNA/transferrin-PEI complexes is an important factor for gene expression in cultured cells. *Gene Ther. 5*, 1425−1433.

(17) Tang, M. X., Redemann, C. T., and Szoka, F. C., Jr. (1996) In vitro gene delivery by degraded polyamidoamine dendrimers. *Bioconjugate Chem. 7*, 703−714.

BC050287V

Temperature Dependent Gene Expression Induced by PNIPAM-Based Copolymers: Potential of Hyperthermia in Gene Transfer

Arkadi Zintchenko,* Manfred Ogris, and Ernst Wagner

Pharmaceutical Biology-Biotechnology, Department of Pharmacy, Ludwig-Maximilians-Universität, Butenandstr 5−13, Munich, D-81377, Germany. Received October 5, 2005; Revised Manuscript Received March 16, 2006

The objective of this work was to obtain gene delivery vectors with high efficiency induced by application of local hyperthermia. As a building construct for the polyplex particles, block copolymers were used, in which one block represents poly(ethyleneimine) (PEI) and another block a statistical copolymer of poly(*N*-isopropylacryamide) (PNIPAM) and different hydrophilic monomers (acrylamide or vinylpyrrolidinone). The block copolymers were synthesizized by radical polymerization of the corresponding monomers directly onto PEI. The complexation of DNA with these copolymers led to small, charge neutral particles, which aggregated upon increasing the temperature from 37 °C to 42 °C. This aggregation was found to be responsible for the enhanced transfection efficiency of these formulations under hyperthermic conditions. Gene expression in cells treated by hyperthermia was found to be nearly 2 orders of magnitude higher in comparison to cells transfected at physiological temperature. The mechanism by which hyperthermia influences the gene transfection efficiency is proposed.

1. INTRODUCTION

Nonviral gene delivery vectors are becoming increasingly attractive as delivery vehicles because of a great flexibility regarding the type and size of DNA delivered, their low production costs, and low immunogenicity, which enables repeated applications. However, they show rather low efficiency compared to viral vectors. Therefore, the main directions in development of nonviral vectors are to increase specificity and transfection efficiency and to decrease toxicity. Specificity can be achieved by targeting of the delivery vehicle to a specific site. The targeting strategies developed at present can be divided into two types (*1*): Targeting based on incorporation of specific cell binding ligands into the gene transfer vector enables an increased and specific accumulation of particles within the target tissue. Physical targeting is achieved by local application of an external force; this provides higher efficiency of gene expression at the site where it is applied. Physical targeting can be achieved by application of ultrasound (*2*, *3*), magnetic (*4*), or electric field (*5*, *6*), heat (*7*, *8*), and light (*9*, *10*). Regional hyperthermia is an approved method for treatment of solid tumors (*11*) by selectively heating tumor tissue to 40−44 °C. Above 42.5 °C a direct cytotoxic effect on tumor cells is observed, whereas below that temperature an immunstimulatory effect and radiation- and chemosensibilization take place. Additionally, application of heat to the targeting site increases the permeability of the tissue and allows the extravasation of macromolecular drugs, e.g. liposomes, into the interstitium (*12*, *13*). This effect can in principle also be utilized for delivery on particulate gene delivery systems, e.g. polyplexes.

Transfection studies with thermosensitive polymers were reported previously using poly(*N*-isopropylacrylamide) (PNIPAM)[1]-based copolymers. PNIPAM is a nonionic polymer, which is known to undergo hydrophilic to hydrophobic phase transition by increasing the temperature above 32 °C. The authors synthesized either statistical copolymers of NIPAM with cationic comonomer (*14*, *15*) or block copolymers with polycation (*16*). In all cases they found an increased expression of the reporter gene for the cells being incubated at room temperature during transfection. An increased transfection in these works was attributed to partial dissociation of the polyplexes and better availability of DNA for cell translation machinery. However, for practical applications the low temperature is not easy to achieve in vivo.

In this study we synthesized copolymers of PEI as a cationic block, and statistical copolymers of NIPAM with hydrophilic comonomers such as acrylamide (AAm) or vinylpyrrolidinone (VP). Hydrophilic comonomers are known to increase the transition temperature of PNIPAM depending on the monomer ratio (*17*−*19*). By their incorporation into the PNIPAM chain, the transition temperature can be easily tuned above 32 °C. Varying the copolymer composition enables adjustment of the copolymer phase transition temperature between 37 °C and 42 °C. At physiological temperatures, such copolymers being covalently attached to the surface of DNA/polycation polyplexes can shield the particles from unspecific interactions and provide their stability in a similar fashion as PEGylation of polyplexes. During hyperthermia they can destabilize the particles and lead to their aggregation. Also, PNIPAM above the phase transition point is known to destabilize liposomal membranes (*20*, *21*), which suggests that it also might enhance release of the particles from intracellular lipid vesicles such as endosomes.

Here we describe the synthesis of block copolymers between branched PEI and thermosensitive PNIPAM-based polymers. On the basis of these polymers, we obtained DNA polyplexes with temperature-dependent gene transfection efficiency.

2. EXPERIMENTAL SECTION

2.1. Materials. Ammonium persulfate (APS) was purchased from Amersham Biochemicals (Freiburg, Germany), and mercaptoethanol (ME) was purchased from Merck (Darmstadt,

* Corresponding author. Tel.: +49-89-2180-77373; fax: +49-89-2180-77791. E-mail: arkadi.zintchenko@cup.uni-muenchen.de.

[1] Abbreviations: AAm, acrylamide; APS, ammonium persulfate; DLS, dynamic light scattering; EtBr, ethidium bromide; LCST, lower critical solution temperature; ME, mercaptoethanol; NIPAM, *N*,*N*-isopropylacrylamide; PEG, poly(ethylene glycol); PEI, polyethyleneimine; TMEDA, tetramethylethylendiamine; VP, 1-vinyl-2-pyrrolidinone.

10.1021/bc050292z CCC: $33.50 © 2006 American Chemical Society
Published on Web 05/02/2006

Table 1. Copolymers and Their Characteristics

copolymer	AAm feed %	PEI wt %	cloud point, °C	copolymer	VP feed %	PEI wt %	cloud point, °C
AAm15	15	50.5	36	PVP10	10	49.6	40
AAm20	20	43.3	39	PVP15	15	48.4	43
AAm25	25	49.2	42	PVP20	20	37.8	46
AAm30	30	50.7	45				

Germany). Acrylamide (AAm), *N*,*N*-isopropylacrylamide (NIPAM), 1-vinyl-2-pyrrolidinone (VP), and branched poly(ethyleneimine) (PEI) (M_w = 25 kDa) were purchased from Aldrich (Munich, Germany). PEI22−PEG20 (PEI-22 kDa, linear form, conjugated with PEG 20kDa) was synthesized and purified as previously described in Kursa et al. (*26*).

Cell culture media, antibiotics, and fetal calf serum (FCS) were from Life Technologies (Karlsruhe, Germany). Plasmid pCMVLuc (*Photinus pyralis* luciferase under control of the CMV enhancer/promoter) described in Plank et al. (*22*) was purified with the EndoFree Plasmid Kit from Qiagen (Hilden, Germany).

2.1.1. Synthesis of the Copolymers. Copolymers poly(NIPAM-*stat*-AAm)-*block*-PEI and poly(NIPAM-*stat*-AAm)-*block*-PEI were prepared by radical copolymerization of NIPAM with AAm or VP in water using APS as initiator in the presence of PEI. PEI served as a promoter as well as a starting block. The mixture contained 0.6 g of PEI and 0.06 mol of monomer mixture. To avoid cross-linking due to recombination of radicals, ME (17.5 μL) was added to the copolymerization mixture. Argon was bubbled through the solution during 15 min to remove oxygen. The molar ratios of monomers in the feed are presented in Table 1. Thereafter APS (200 μL 5% APS w/v) was added to the reaction mixture. The amount of added APS corresponded to a molar ratio of APS/PEI of 2/1. Copolymerization was carried out at room temperature for 2 h. The final product was dialyzed against water using a cellulose acetate membrane (Roth, Karlsruhe, Germany) with a molecular weight cut off of 18 kDa for 2 days and freeze-dried. PEI content in the copolymers was determined as a number of primary amino groups by TNBS assay at 405 nm (*23*). The cloud point was determined on a fluorimeter (Varian Eclipse, Varian, Mulgrave, Australia) in HBS buffer (20 mM HEPES, pH 7.1, 150 mM NaCl) with emission and excitation wavelengths set to 500 nm.

2.2. Polyplex Formation. DNA was condensed with PEI at a molar ratio of PEI nitrogen to DNA phosphate (N/P ratio) of 6. DNA/PEI polyplexes were prepared at a final DNA concentration of 20 or 200 μg/mL by flash-mixing of plasmid DNA (1 mg/mL) with PEI or PEI copolymer (15 or 150 μg/mL PEI) in HEPES-buffered glucose (HBG, 5% glucose, 20 mM HEPES, pH 7.1). Polyplexes were allowed to stand for at least 20 min at room temperature before use.

2.3. Methods. *2.3.1. Chromatography.* Cation exchange was performed on a Macro-Prep High S, HR 10/10 column (Bio-Rad, Munich, Germany) in water, NaOH gradient from 0 to 0.1 M NaOH at a flow rate of 1 mL/min.

2.3.2. ^{1}H and ^{13}C NMR Measurements. The ^{1}H and ^{13}C NMR measurements of the copolymers were performed in D_2O on a Bruker 400 MHz instrument. To avoid any influence of the Nuclear Overhauser effect (NOE), all ^{13}C spectra used for quantitative analysis were recorded using inverse gated decoupling pulse sequences. The ratios between primary, secondary, and ternary amines was calculated as described in ref 24.

2.3.3. Ethidium Bromide (EtBr) Displacement Assay. The ability of the copolymers to condense DNA was studied using an ethidium bromide (EtBr) assay. Copolymer solution was added stepwise to plasmid DNA solution (10 μg/mL) in HBG containing EtBr (0.4 μg/mL). After each step, fluorescence intensity was monitored (λ_{ex} = 510 nm, λ_{em} = 590 nm). The fluorescence intensity of the EtBr solution in the presence of free DNA corresponded to 0% condensation, whereas the fluorescence intensity without DNA corresponded to 100% DNA condensation.

2.3.4. Measurement of Particle Size and Zeta-Potential. Particle size of transfection complexes was measured by laser-light scattering using a Malvern Zetasizer 3000HS (Malvern Instruments, Worcestershire, UK). Polyplexes were generated at DNA concentration of 20 μg/mL and subsequently diluted to 2 μg/mL prior to measurement. For estimation of surface charge, transfection complexes were diluted in 10 mM NaCl to give a final DNA concentration of 2 μg/mL and the zeta-potential was measured as previously described (*25*).

2.3.5. Cell Culture and Transfection. Neuro2A cells (ATCC CCL-131) were grown at 37 °C in a 5% CO_2 humidified atmosphere in DMEM containing Glutamax I, 20 mM HEPES, and 10% fetal calf serum (FCS). Cells were plated in 96-well plates with 1×10^4 cells per well 24 h prior to transfection. Transfection complexes containing 200 ng of pCMVL plasmid DNA were added per well in serum free medium. After 4 h of incubation (if not otherwise indicated), transfection medium was replaced by fresh culture medium. The cells were treated with hyperthermia in a cyclic regime in which 30 min heat shock at 42 °C was followed by 30 min at 37 °C. The heat shock was introduced either during incubation with complexes or after change of culture medium. The total duration of hyperthermia was between 0 and 6 h. Luciferase gene expression was measured after 24 h as described (*26*). Values are given as relative light units and represent the luciferase activity per 10^4 cells as mean ± standard deviation of at least triplicates. Two nanograms of recombinant luciferase (Promega, Mannheim, Germany) correspond to 10^7 light units.

2.3.6. In Vitro Cytotoxicity Using MTT Assay. Neuro2A cells were seeded into 96-well microtiter plates at a density of 1×10^4 cells/well. After 24 h the culture medium was replaced with 100 μL/well of serial dilutions of polymer stock solutions in DMEM. Alternatively, polyplexes with a final DNA concentration of 200 μg/mL were formed in HBG, serially diluted, and added in a fixed volume of 10 μL to the cells. After a 4 h incubation period medium was replaced by fresh culture medium. After 24 h MTT (3-(4,5-dimethylthiazol-2-yl)-2,5-diphenyltetrazolium bromide) (Sigma-Aldrich, Germany) was dissolved in phosphate-buffered saline at 5 mg/mL, and 10 μL was added to each well reaching a final concentration of 0.5 mg MTT/mL. After an incubation time of 1 h, unreacted dye with medium was removed. The purple formazan product was dissolved in 100 μL/well dimethyl sulfoxide and quantified by a plate reader (Tecan, Groedig, Austria) at 590 nm with background correction at 630 nm. The relative cell viability (%) relative to control wells containing cell culture medium without polymer was calculated by ([A] test/[A] control) × 100.

2.3.7. Covalent Labeling of Plasmid DNA and Flow Cytometry. Plasmid pCMVLuc was covalently labeled with the fluorophore Cy5 using the Label IT kit (MIRUS, Madison, WI) according to the manufacturers instructions. On average, one Cy5 molecule was bound per 50 bp.

For analysis by flow cytometry, cells were seeded in six-well plates at a density of 2×10^5 cells per well 24 h prior to transfection. Polyplexes containing Cy5-labeled DNA (20% Cy5-DNA) were added to the cells at a DNA concentration of 2 μg/well in 1 mL of fresh culture medium, and cells were harvested after 1 h incubation at 37 °C or 42 °C by treatment with collagenase solution (Invitrogen GmbH, Karlsruhe, Germany). Cell association of polyplexes was assayed using a Cyan MLE flow cytometer (DaKoCytomation, Copenhagen, Denmark). The fluorophore Cy5 was excited at 635 nm and emission was detected at 665 ± 20 nm. Data were analyzed in logarithmic mode. To discriminate between viable and dead cells and to

exclude doublets, propidium iodide was added to the cell suspension and cells were appropriately gated by forward/side scatter, pulse width, and propidium iodide fluorescence. 1×10^4 gated events per sample were collected. Median channel values ± SD of triplicates (representing the median intensity of cell-associated DNA) were determined and presented as analytical fluorescence units (AFU).

3. RESULTS AND DISCUSSION

3.1. Synthesis and Characterization of the Copolymers. The initiating system based on tetramethylethylendiamine (TMEDA) and APS is well-known from the literature and widely used in laboratory practice (i.e. for preparation of acrylamide gels). APS itself is able to decompose only at high temperature; noticeable formation of free radical is observed only at 50−60 °C. TMEDA is able to catalyze the decomposition of APS and shift the formation of radical to room temperature. Moreover, during the decomposition, a free radical is formed on one of the methyl groups of TMEDA. Thus, TMEDA serves not only as a promoter in decomposition of APS, but it is also a starting block for the further polymerization (*27*). TMEDA was found to be an optimal promoter for APS decomposition. However, the efficiencies of many similar structures were extensively studied. It was found that the increase of the distance between two amines by additional methylene groups inactivates the promoter. The substitution of methyl groups to longer aliphatic radicals in the basic structure decreases the rate of decomposition. However, the activity of the promoter is still sufficient to induce the polymerization (*28*). Since the structure of PEI is very similar to the structure of TMEDA, PEI should be able to promote the decomposition of APS, so that polymerization could start directly on the PEI chain. The advantage of this strategy is the formation of the product in one step, in comparison to the alternative way, namely synthesis of NIPAM copolymer with further conjugation to PEI molecule.

Two hydrophilic comonomers, AAm and VP, were used for NIPAM polymerization. Since the lower critical solution temperature (LCST) of pure NIPAM in water is approximately 32 °C, the introduction of hydrophilic residues into the polymer chain should increase the solubility of the final polymer. The composition of the copolymer could be adjusted in such way to obtain the optimal characteristics of the system for hyperthermic treatment, namely with a LCST between 37 °C and 42 °C.

ME was added to copolymerization mixture for control of the molecular weight of the growing chains and to avoid the cross-linking as a result of recombination of growing radicals.

The addition of APS to the reaction mixture led to heating of the sample due to the start of polymerization. In case of the polymerization of pure NIPAM the increase of the temperature of the reaction mixture was accompanied with the increase of turbidity of the solution. The temperature of the reaction mixture seems to rise in this sample above the LCST of NIPAM (32 °C), which was not the case for all other copolymers. In contrast, after the addition of APS to monomer solution without PEI this effect was not observed. Thus, PEI is indeed able to act as a promoter of APS decomposition and starting block for polymerization.

It is known from the literature that acrylates are able to react with primary and secondary amines by Michael addition. To estimate the extent of this side reaction, ^{13}C NMR spectra of copolymers were compared with the spectrum of PEI (data not shown). The primary amines are known to be more reactive in Michael addition in comparison to secondary amines. Thus, the side reaction should decrease the signals, corresponding to primary amines and increase the signals, corresponding to the secondary amines. However, no significant changes in the ratio between signals of two generations of amines were found. The ratio between primary, secondary, and ternary amines in PEI was 29/42/29%. For PVP10 the ratio 31/40/29% was found. These data are similar to those found for the same PEI sample in ref 24. Therefore, Michael addition was considered to have no influence on the structure of the copolymers.

To prove the binding of NIPAM chains to PEI, the polymer sample was applied cation exchange column under pH gradient. The collected fractions were tested for primary amines by TNBS assay. The fractions containing PEI were freeze-dried, dissolved in D_2O, and measured by ^1H NMR. The peak of methyl protons corresponding to NIPAM was found in PEI containing fractions, which indicates the formation of block copolymer. The comparison of NMR spectra of the copolymer before and after purification (δ 2.3−3.4 ppm for PEI protons and δ 1.2 for methyl group in NIPAM) reveals that about 50% of PNIPAM chains in the initial sample are not bound to PEI. For example, in case of PVP10 sample the ratio between PEI protons and NIPAM was 2.1:1 before and 4.3:1 after purification. Similar results were obtained for other copolymers. Such observation is in accordance with the mechanism of decomposition of APS in the presence of TMEDA (*27*). APS produces two radicals: one on the carbon of TMEDA, and the other is a free hydroxyl radical. Therefore, in the presence of chain transfer agent (ME) only half of the PNIPAM chains are expected to be bound to PEI. It is likely that the following dialysis did not lead to separation of the free PNIPAM chains from block copolymer.

Since free PNIPAM copolymer did not show any influence on the transfection (see Supporting Information), for all investigations the samples were used without further purification.

Different contents of hydrophilizing comonomer (AAm or VP) in the feed were used for polymerization (Table 1). The content of PEI in final copolymers (from TNBS assay) and their cloud points, attributed to the first temperature, at which the turbidity of the polymer solution starts to increase, are presented in Table 1. The cloud points of the copolymers increase with the increase of the content of hydrophilizing comonomer in the feed. Samples AAm25 and PVP10 fulfill the requirements for hyperthermic treatment, namely, their LCST is between 37 °C and 42 °C. These copolymers were used for further studies.

3.2. Complex Formation between DNA and Copolymers. It is known from the literature that block copolymers of PEI and PEG show lower ability to condense DNA in comparison to pure PEI. Therefore, at first the efficiency of DNA condensation by the copolymers was studied by EtBr displacement assay. Both, PEI and PEI copolymers behaved similarly, with 90% of EtBr exclusion at N/P 2.5 and above.

The sizes of the particles formed by mixing of PEI or of the copolymers with DNA in HBG were around 150−200 nm. However, PEI polyplexes were strongly positively charged (ζ-potential +30 mV), whereas polyplexes with copolymers were neutral (ζ-potential − 3 to +2 mV). Increasing the ionic strength of the complex solution to physiological NaCl concentration led to relatively fast aggregation of PEI polyplexes. The size of the polyplexes was already in the micrometer range, after 15 min of incubation. In contrast, copolymer polyplexes and PEGylated polyplexes remained small after addition of NaCl for at least 4 h at 37 °C. Obviously, the hydrophilic chains of the copolymer coating decrease the surface charge and sterically stabilize the particles against aggregation.

The increase of temperature to 42 °C led to relatively fast aggregation of the copolymer-based particles. Large aggregates in micrometer range could be observed already after 15 min of incubation at high temperature. The copolymer chains become hydrophobic at 42 °C and collapse, which leads to loss of colloidal stability of the particles and aggregation. In case of

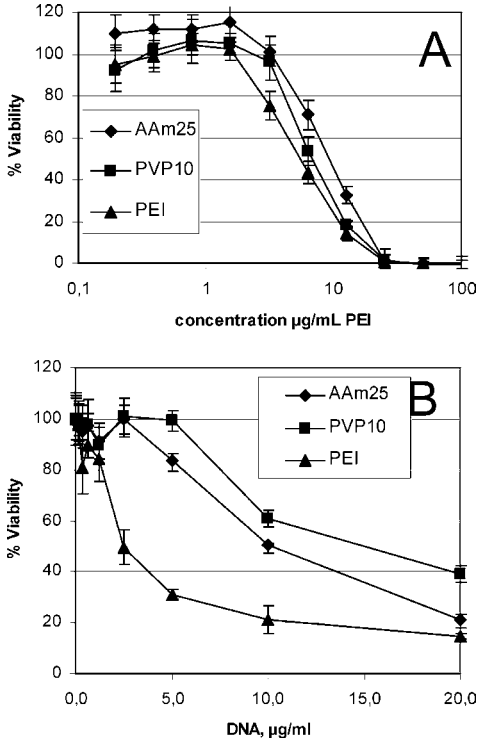

Figure 1. Cellular viability after 24 h incubation (A) with polycations, as a function of concentration in μg/mL PEI or (B) with the corresponding polyplexes N/P = 6 as a function of DNA concentration in μg/mL.

PEGylated polyplexes no significant changes in particles size after incubation at 42 °C was observed.

3.3. In Vitro Cytotoxicity Using MTT Assay. The cytotoxicity normalized to the concentration of PEI was similar for all copolymers and corresponded to the cytotoxicity of PEI (Figure 1a). However, the complexes of copolymers with DNA showed significantly lower toxicity, compared to PEI-based polyplexes (Figure 1b). Apparently, the hydrophilic shell around the particles prevents the interactions of copolymer-based polyplexes with cells and decreases the toxicity. It is necessary to note that in all gene transfection studies the final concentration of PEI in the culture medium was 1.45 μg/mL, where no toxic effects were observed.

3.4. Transfection Efficiency of Complexes. The influence of different temperature regimes on gene expression of various polyplexes was studied. Since long hyperthermic treatment is associated with high cytotoxicity (A. Zintchenko, unpublished observations), short heat shocks (30min) were repeatedly introduced (1−8 times) to cell culture followed by incubation at physiological temperature (30 min). In other words, one cycle of hyperthermia means 30 min at 42 °C and 30 min at 37 °C. No significant cytotoxicity was detected even after eight cycles.

The gene transfection efficiencies of different formulations without hyperthermia and with eight cycles hyperthermia (four during incubation with polyplexes, four after medium change, "4 + 4" regime) are presented in Figure 2. In case of pure PEI polyplexes or PEGylated PEI polyplexes, reporter gene expression is independent of hyperthermia treatment. In contrast, hyperthermia led to an increase in reporter gene expression by 2 orders of magnitude when using polyplexes formed with thermally responsive copolymers AAm25 and PVP10. Without hyperthermia the gene expression of these complexes corresponds to the moderate expression of PEGylated complexes, whereas with hyperthermia it increases to the high level of pure PEI polylexes. In case of AAm15 (the copolymer with LCST below physiological temperature), the expression is high in both

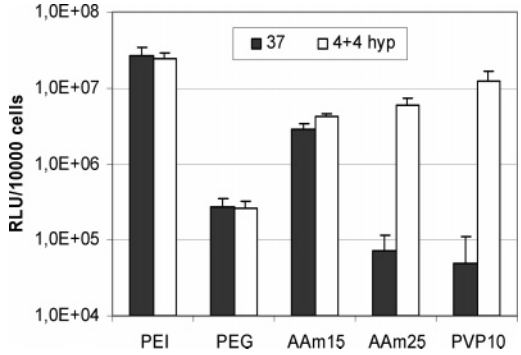

Figure 2. Luciferase gene expression after transfection with polyplexes (N/P = 6) based on pure PEI ('PEI'), PEI/PEI−PEG 90/10 ('PEG'), or copolymers AAm15, AAm25, PVP10. Black bars, no hyperthermia; white bars, four cycles of hyperthermia during incubation with complexes + four cycles after change of the medium ("4 + 4 regime").

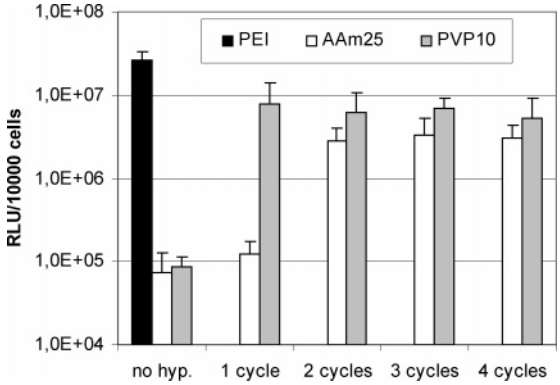

Figure 3. Luciferase gene expression after transfection with polyplexes (N/P = 6) based on PEI (black bars) or copolymers AAm25 (white bars) and PVP10 (grey bars) for a different number of hyperthermia cycles (1−4) and without hyperthermia. The hyperthermic treatment was applied during incubation of the complexes with the cells. The medium was changed after 4 h of incubation.

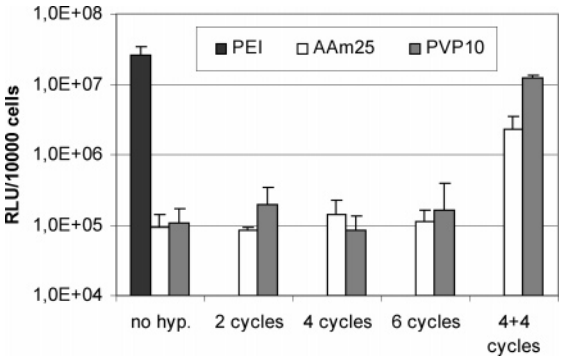

Figure 4. Luciferase gene expression after transfection with polyplexes (N/P = 6) based on PEI (black bars) and copolymers AAm25 (white bars) and PVP10 (grey bars) with different number of hyperthermia cycles (2−6) and without hyperthermia. The hyperthermic treatment was applied after the medium change. For comparison the gene expression after the "4 + 4 regime" is presented.

cases. These data demonstrate that the copolymers AAm25 and PVP10 at the temperature above LCST show thermally induced high gene transfer and are suitable for activation by local hyperthermia at a clinically relevant temperature of 42 °C.

To find out at which stage of the transfection process the hyperthermic treatment plays the most important role, the heat shock was applied to the cells either during incubation with complexes or after the change of medium (Figures 3 and 4). In case of PVP10, after one hyperthermic cycle during incubation with the complexes, the gene expression had already reached the maximum level (Figure 3). Further cycles did not increase

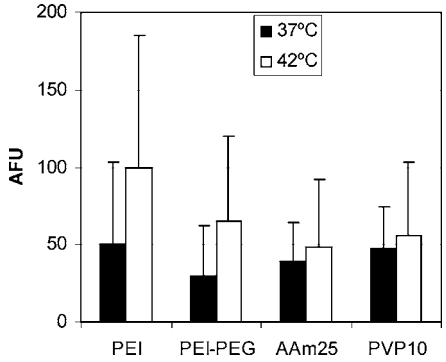

Figure 5. Median fluorescence of the cells 1 h after transfection with Cy5-labeled DNA for PEI ('PEI')-, PEI/PEI−PEG 90/10 ('PEG')-, AAm25-, and PVP10-based complexes.

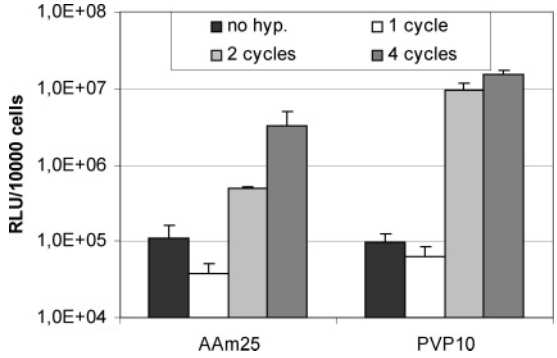

Figure 6. Luciferase gene expression after transfection with polyplexes (N/P = 6) based on PEI and copolymers AAm25 and PVP10 for a different number of hyperthermia cycles (1−4) and without hyperthermia. The hyperthermic treatment was applied during incubation of the complexes with the cells. After the indicated number of cycles, the transfection medium was replaced by fresh culture medium.

the transfection efficiency. In case of AAm25 the gene expression gradually increased during three cycles and was saturated thereafter.

In contrast, heat treatment applied after medium change did not lead to higher gene expression even after six cycles applied (Figure 4). These data allow the conclusion that the changes in the system before cellular internalization of the complex, namely particle aggregation, play the most important role. Also, it seems that the collapsed PNIPAM chains are not able to enhance the escape of particles from the endosome. Otherwise, the gene transfection efficiency would increase with the increasing number of hyperthermia cycles after medium change, acting on internalized particles.

The aggregation of the particles could lead to enhanced interaction with the cell membrane and consequently increase their cell association. Flow cytometry studies showed that cell association increases during hyperthermia (Figure 5). However, the increase is observed for all systems, even for PEI− and PEI−PEG-based polyplexes, where no temperature dependence in gene expression was observed (see above). This can be explained by the fact that only thermosensitive formulations changed their aggregation behavior after hyperthermia, whereas PEI−PEG polyplexes remained small and PEI polyplexes were already aggregated without hyperthermia leading to maximal trasngene expression (see also Figure 2). It is known from literature that PEG-PEI particles do not further aggregate inside endosomes and are therefore inefficient in terms of endosomal escape and subsequent transgene expression (*29*). Apparently the aggregation state of polyplexes is of greater importance for improved intracellular trafficking and increased transgene expression then a 2-fold increase in cell association (see also Figure 7 and discussion). Thus, the enhanced cell association during hyperthermia is not the decisive factor providing the enhanced transfection efficiency.

Nevertheless, cell association and internalization are still the important steps during transfection. The change of the transfection medium after one cycle of hyperthermia greatly decreases gene transfection efficiency (Figure 6), whereas one or two cycles of hyperthermia without medium change were sufficient to achieve elevated levels of reporter gene expression (Figure 3), as demonstrated when the incubation of cells with polyplexes was extended for a further 3 h before medium change. Hyperthermia induces aggregation of particles, but it does not enhance the rate of their uptake into the cells. Only one cycle of hyperthermia is sufficient for particles to aggregate, but the long incubation times with aggregates are still necessary to achieve a high gene expression.

4. DISCUSSION

All these observations support a mechanism by which hyperthermia can increase the transfection efficiency of thermosensitive polyplexes (see Figure 7). In the case of pure PEI-based polyplexes, initially small particles formed in HBG rapidly aggregate in culture medium. In contrast, PEGylated polyplexes are stable in culture medium and therefore remain small (*30*, *31*). Thereafter, either big (PEI) or small (PEG−PEI) particles are internalized (see also (*29*). After internalization, big aggregates are more effective in their escape from the endosomal compartment compared to small ones due to the proton sponge effect induced by PEI (*31*). Small particles, which contain less PEI material per endosome, are not able to induce sufficient osmotic pressure inside the endosome. Consequently, the endosomal release is hindered. In the case of big particles the endosomes contain remarkably more PEI material, the osmotic pressure inside is much higher and the particles are easier to release (*32*).

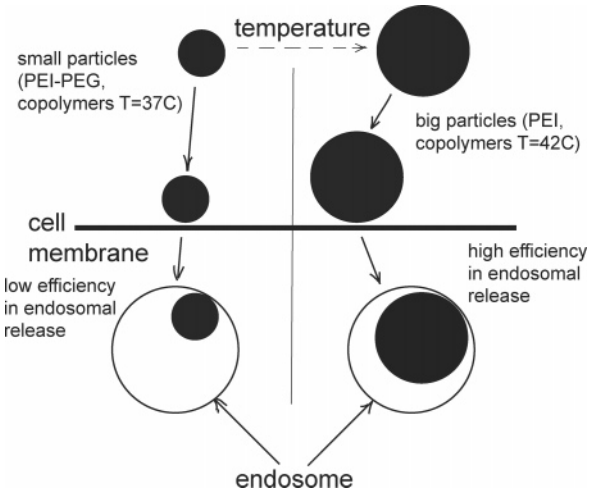

Figure 7. Schematic representation of the mechanism of cell transfection by thermosensitive polyplexes.

Thermosensitive polyplexes at physiological temperature, where hydrophilic copolymer stabilizes the particles against aggregation, acting similarly to PEGylated particles. They are small and not effective in endosomal release. At a higher temperature the shielding copolymer undergoes phase transition, becomes hydrophobic, and is not able to stabilize the particles any more. As a consequence the polyplexes aggregate and form big particles in micrometer size. Similar to pure PEI-based polyplexes, they have a higher ability to escape from the endosomal compartment. These conclusions are well supported by the observation that the levels of gene expression of the thermosensitive polyplexes without hyperthermia correspond to the level of PEGylated polyplexes. When hyperthermia during

incubation of thermosensitive polyplexes with cells is applied the gene expression level correlates with that of pure PEI-based polyplexes.

The aggregation of the thermosensitive polyplexes during hyperthermia proceeds relatively fast. One to two cycles are already sufficient to reach maximum gene expression. However, the internalization seems to be much slower. Therefore, the hyperthermia treatment together with a shorter incubation with the polyplexes dramatically decreases the gene transfection efficiency. Such results are consistent with findings with pure PEI polyplexes (*33*).

5. CONCLUSIONS

In this study we developed a transfection vector which shows enhanced gene transfection efficiency in combination with hyperthermia. We synthesized a set of different block copolymers. The PEI block is able to condense DNA, whereas the statistical copolymer of NIPAM with AAm or VP is a thermosensitive block. The latter undergoes transition from hydrophilic to hydrophobic state upon the increase of the temperature. Synthesis of block copolymers was achieved by polymerization of a NIPAM/AAm or NIPAM/VP monomer mixture directly onto PEI chains in the presence of APS. The copolymers effectively condensed DNA and formed small, charge neutral particles. Gene transfection of thermosensitive polyplexes increased by 2 orders of magnitude after hyperthermia. The reason was found to be the aggregation of the particles prior to internalization. To our knowledge this is the first report of a nonviral, polymeric gene delivery system which can be selectively activated by hyperthermia at clinically relevant temperatures.

ACKNOWLEDGMENT

This work was supported by a research fellowship to A. Zitchenko from the Alexander von Humboldt Stiftung.

Supporting Information Available: Experimental details. This material is available free of charge via the Internet at http://pubs.acs.org.

LITERATURE CITED

(1) Wagner, E., Kircheis, R., and Walker, G. F. (2004) Targeted nucleic acid deliver into tumors: new avenues for cancer therapy. *Biomed. Pharmacother 58*, 152−161.

(2) Anwer, K., Kao, G., Proctor, B., Anscombe, I., Florack, V., Earls, R., Wilson, E., McCreery, T., Unger, E., Rolland, A., and Sullivan, S. M. (2000) Ultrasound enhancement of cationic lipid-mediated gene transfer to primary tumors following systemic administration. *Gene Ther. 7*, 1833−1839.

(3) Huber, P. E., and Pfisterer, P. (2000) In vitro and in vivo transfection of plasmid DNA in the Dunning prostate tumor R3327-AT1 is enhanced by focused ultrasound. *Gene Ther. 7*, 1516−1525.

(4) Scherer, F., Anton, M., Schillinger, U., Henke, J., Bergemann, C., Kruger A., Gansbacher, B., and Plank, C. (2002) Magnetofection: enhancing and targeting gene delivery by magnetic force in vitro and in vivo. *Gene Ther. 9*, 102−109.

(5) Aihara, H., and Miyazaki, J. (1998) Gene transfer into muscle by electroporation in vivo. *Nat. Biotechnol. 16*, 867−870.

(6) Mathiesen, I. (1999) Electropermeabilization of skeletal muscle enhances gene transfer in vivo. *Gene Ther. 6*, 508−514.

(7) Chang, E., Chalikonda, S., Friedl, J., Xu, H., Phan, G. Q., Marincola, F. M., Alexander, H. R., and Bartlett, D. L. (2005) Targeting vaccinia to solid tumors with local hyperthermia. *Hum. Gene Ther. 16*, 435−444.

(8) Li, C. Y., and Dewhirst, M. W. (2002) Hyperthermia-regulated immunogene therapy. *Int. J. Hyperthermia 18*, 586−596.

(9) Prasmickaite, L., Hogset, A., Tjelle, T. E., Olsen V. M., and Berg, K. (2000) Role of endosomes in gene transfection mediated by photochemical internalisation. *J. Gene. Med. 2*, 477−488.

(10) Kloeckner, J., Prasmickaite, L., Hogset, A., Berg, K., and Wagner, E. (2004) Photochemically enhanced gene delivery of EGF receptor-targeted DNA polyplexes. *J. Drug Target. 12*, 205−213.

(11) Schlemmer, M., Lindner, L. H., Abdel-Rahman, S., and Issels, R. D. (2004) Principles, technology and indication of hyperthermia and part body hyperthermia. *Radiologe 44*, 301−309.

(12) Lindner, L. H., Eichhorn, M. E., Eibl, H., Teichert, N., Schmitt-Sody, M., Issels, R. D., and Dellian, M. (2004) Novel temperature-sensitive liposomes with prolonged circulation time. *Clin. Cancer Res. 10*, 2168−2178.

(13) Kong, G., and Dewhirst, M. W. (1999) Hyperthermia and liposomes. *Int. J. Hyperthermia 15*, 345−370.

(14) Kurisawa, M., Yokoyama, M., and Okano, T. (2000) Transfection efficiency increases by incorporating hydrophobic monomer units into polymeric gene carriers. *J. Controlled Release*, *68*, 1−8.

(15) Kurisawa, M., Yokoyama, M., and Okano, T. (2000) Gene expression control by temperature with thermo-responsive polymeric gene carriers. *J. Controlled Release 69*, 127−137.

(16) Sun, S. J., Liu, W. G., Cheng, N., Zhang, B. Q., Cao, Z. Q., Yao, K. D., Liang, D. C., Zuo, A. J., Guo, G., and Zhang, J. Y. (2005) A thermoresponsive chitosan-NIPAAm/vinyl laurate copolymer vector for gene transfection. *Bioconjugate Chem. 16*, 972−980.

(17) Yoshino, K., Kadowaki, A., Takagishi, T., and Kono, K. (2004) Temperature sensitization of liposomes by use of N-isopropylacrylamide copolymers with varying transition endotherms. *Bioconjugate Chem. 15*, 1102−1109.

(18) Yildiz, B., Isik, B., and Kis, M. (2002) Thermoresponsive poly-(N-isopropylacrylamide-*co*-acrylamide-*co*-2-hydroxyethyl methacrylate) hydrogels. *React. Funct. Polym. 52*, 3−10.

(19) Siu, M., Zhang, G. Z., and Wu, C. (2002) Effect of comonomer distribution on the coil-to-globule transition of a single AB copolymer chain in dilute solution. *Macromolecules 35*, 2723−2727.

(20) Roux, E., Francis, M., Winnik, F. M., and Leroux, J. C. (2002) Polymer based pH-sensitive carriers as a means to improve the cytoplasmic delivery of drugs. *Int. J. Pharm. 242*, 25−36.

(21) Roux, E., Zignani, M., Daigle, C., Moreau, P., Drummond, D. C., Hong, K., and Leroux J. C. (2000) pH-sensitive gel phase liposomes. *Proc. Int. Symp. Controlled Release Bioact. Mater. 27*, 215.

(22) Plank, C., Zatloukal, K., Cotten, M., Mechtler K., and Wagner, E. (1992) Gene transfer into hepatocytes using asialoglycoprotein receptor mediated endocytosis of DNA complexed with an artificial tetra-antennary galactose ligand. *Bioconjugate Chem. 3*, 533−539.

(23) Snyder, S. L., and Sobocinski, P. Z. (1975) Improved 2,4,6-trinitrobenzenesulfonic acid method for determination of amines. *Anal. Biochem. 64*, 284−288.

(24) von Harpe, A., Petersen, H., Li, Y. X., and Kissel, T. (2000) Characterization of commercially available and synthesized polyethylenimines for gene delivery. *J. Controlled Release 69*, 309−322.

(25) Kircheis, R., Wightman, L., Schreiber, A., Robitza, B., Rossler, V., Kursa, M., and Wagner, E. (2001) Polyethylenimine/DNA complexes shielded by transferrin target gene expression to tumors after systemic application. *Gene Ther. 8*, 28−40.

(26) Kursa, M., Walker, G. F., Roessler, V., Ogris, M., Roedl, W., Kircheis, R., and Wagner, E. (2003) Novel shielded transferrin-polyethylene glycol-polyethylenimine/DNA complexes for systemic tumor-targeted gene transfer. *Bioconjugate Chem. 14*, 222−231.

(27) Feng, X. D., Guo, X. Q., and Qiu, K. Y. (1988) Study of the initiation mechanism of the vinyl polymerization with the system persulfate N, N, N′,N′-tetramethylethylenediamine. *Makromol. Chem. 189*, 77−83.

(28) Guo, X. Q., Qiu, K. Y., and Feng, X. D. (1990) Studies on the kinetics and initiation mechanism of acrylamide polymerization using persulfate aliphatic diamine systems as initiator. *Makromol. Chem. 191*, 577−587.

(29) Mishra, S., Webster, P., and Davis, M. E. (2004) PEGylation significantly affects cellular uptake and intracellular trafficking of nonviral gene delivery particles. *Eur. J. Cell Biol. 83*, 97−111.

(30) Ogris, M., Brunner, S., Schuller, S., Kircheis, R., and Wagner, E. (1999) PEGylated DNA/transferrin-PEI complexes: reduced interaction with blood components, extended circulation in blood and potential for systemic gene delivery. *Gene Ther. 6*, 595−605.

(31) Ogris, M., Steinlein, P., Kursa, M., Mechtler, K., Kircheis, R., and Wagner, E. (1998) The size of DNA/transferrin-PEI complexes

is an important factor for gene expression in cultured cells. *Gene Ther. 5*, 1425−1433.
(32) Sonawane, N. D., Szoka, F. C., and Verkman, A. S. (2003) Chloride accumulation and swelling in endosomes enhances DNA transfer by polyamine-DNA polyplexes. *J. Biol. Chem. 278*, 44826−44831.
(33) Rejman, J., Bragonzi, A., and Conese, M. (2005) Role of clathrin- and caveolae-mediated endocytosis in gene transfer mediated by lipo- and polyplexes. *Mol. Ther. 12*, 468−74.

BC050292Z

A New Class of Gd-Based DO3A-Ethylamine-Derived Targeted Contrast Agents for MR and Optical Imaging

Anurag Mishra,[†] Josef Pfeuffer,[†,#] Ritu Mishra,[‡] Jörn Engelmann,[‡] Anil K. Mishra,[§] Kamil Ugurbil,[‡,⊥] and Nikos K. Logothetis[†,*]

Department for Physiology of Cognitive Processes and High-Field MR Center, Max Planck Institute for Biological Cybernetics, Spemannstrasse 38, 72076 Tübingen, Germany, Department of Radiopharmaceutical, Institute of Nuclear Medicine and Allied Sciences, Timarpur, Delhi 110054, India, and Center for Magnetic Resonance Research, University of Minnesota, 2021 Sixth Street SE, Minneapolis, Minnesota 55455. Received October 7, 2005; Revised Manuscript Received February 24, 2006

Synthetic bifunctional probes based on [4,7-bis-carboxymethyl-10-(2-aminoethyl)-1,4,7,10-tetraaza-cyclododec-1-yl]-acetic acid (DO3A-ethylamine) preloaded with gadolinium were prepared for applications in targeted magnetic resonance imaging (MRI) and optical imaging. A convenient route of synthesis is reported, which allowed conjugation of this probe with biomolecules for the preparation of model MR contrast agents for targeted imaging. The conjugated probes have the following interesting properties: (1) GdDO3A-ethylamido-biotin (**Gd-9**) can be used for targeted imaging using an avidin−biotin system. (2) The fluorescent probe GdDO3A-ethylthiourea-fluorescein (**Gd-12**) is a bimodal compound, which can be used for both MR and optical imaging. The precursors, DO3A-ethylamidopropyl-maleimide (**11**) and DO3A-ethyl-isothiocyanate (**13**) contain a highly reactive moiety, which can interact with free SH-terminals and N-terminals of biological molecules, respectively. In vitro MR relaxivity studies were performed at 300 MHz using different concentrations and chemical environments. MR relaxivity for ligand **Gd-9** at pH 7.4, r_1 was (3.32 ± 0.03) s^{-1} mM^{-1} and r_2 was (5.02 ± 0.14) s^{-1} mM^{-1}. For the mixture of **Gd-9** with avidin, at pH 7.4, relaxivity increased linearly with the avidin concentration. A relaxivity enhancement of 45% for r_1 and more than 400% for r_2 with respect to the unbound biotinylated Gd^{3+} complex was found at a ratio of 4:1. MR relaxivity for ligand **Gd-12**, r_1 was (5.36 ± 0.05) s^{-1} mM^{-1} at pH 7.4. Fluorescence microscopy and spectroscopy of **Gd-12**-labeled 3T3 mouse fibroblasts showed a concentration-dependent intracellular uptake, accompanied by a slight dose-dependent increase in toxicity up to 150 μM. MR studies on labeled cells indicated a contrast enhancement in both T_1- and T_2-weighted images by the internalized compound, with the effect being more pronounced in T_2-weighted images. Our results indicate that DO3A-ethylamine is a multipurpose precursor, from which various targeted contrast agents can be synthesized after a single-step conjugation with organic/bioorganic molecules.

INTRODUCTION

Magnetic resonance imaging (MRI) possesses an unsurpassed potential for the exploitation of intrinsic tissue and structural differences visualized as image contrast by using a wide variety of pulse sequences. Typically, MRI contrast depends on endogenous differences in water content and relaxation time in the tissue of interest. The specificity and sensitivity of MR imaging can be further enhanced by the utilization of contrast agents (CAs) based on paramagnetic metals such as gadolinium (Gd). These low molecular weight compounds distribute rapidly in blood and the extracellular fluid space and enhance image contrast by shortening the longitudinal relaxation time (T_1) and transverse relaxation time (T_2) *(1−4)*. The Gd metal ion has a high magnetic moment and long electronic relaxation times, making it most suitable for this purpose due to strong dipolar interactions with water nuclei protons. However, the introduction of paramagnetic ions directly in vivo is limited by inherent toxicity. Therefore, acyclic and macrocyclic polyamino-carboxylates are used as strong ligands to sequester the material and prevent toxicity. These ligands occupy eight of the nine available coordination sites in Gd forming kinetically and thermodynamically stable complexes *(5)*. The ninth coordination site remains available for fast exchange of coordinated water molecules with those surrounding the complex to transmit the paramagnetic relaxation effect to bulk solvent. Wide ranges of nonspecific CAs are being used in clinical applications for evaluation of physiological parameters. However, to be able to detect focal anomalies or functions, the need arises for functionalized and targeted ligands that enable the relaxivity of the CAs to indicate the function of a particular variable.

Targeted CAs localize to specific molecular targets with high affinity and specificity, thus enhancing the diversity of MR applications. They are able to recognize specific target molecules and induce an enhancement of water proton relaxation rate on binding with the target molecule *(2, 6, 7)*. A diverse variety of targeting ligands have been chemically coupled with CAs depending on the nature of final specific application of the CA. Asialoglycoproteins have been used for liver-specific application due to their high affinity for ASG receptors located uniquely on hepatocytes *(8, 9)*. Tumor selective accumulation of porphyrin-based CA is attributed to high affinity of these compounds for necrotic tissue *(10)*. DTPA-bisamide-based ligands

* To whom correspondence should be addressed. Tel: ++49-7071-601651. Fax: ++49-7071-601652. E-mail: nikos.logothetis@tuebingen.mpg.de.

[†] Department for Physiology of Cognitive Processes, Max Planck Institute for Biological Cybernetics.

[‡] High-Field MR Center, Max Planck Institute for Biological Cybernetics.

[§] Institute of Nuclear Medicine and Allied Sciences.

[#] Present address: Siemens Medical Solutions, MR Applications Development, Karl-Schall-Strasse 6, 91052 Erlangen, Germany.

[⊥] Center for Magnetic Resonance Research, University of Minnesota, MN.

10.1021/bc050295b CCC: $33.50 © 2006 American Chemical Society
Published on Web 04/26/2006

have been used for diagnosis of several types of malignancy on the basis of molecular recognition of sialic acid residues *(11)*. Monoclonal antibodies (MoAbs) and antibody fragments provide highly specific target recognition and binding for CAs. Breast cancer cells expressing Her-2/neu receptors were imaged in vivo with a two step labeling protocol using biotinylated Herceptin MoAb and avidin−GdDTPA conjugates *(12)*.

On the basis of previous reports on the synthesis and applications of targeted CAs, we have developed straightforward synthetic routes for the preparation of targeted CAs derived from DO3A-ethylamine (DO3A-EA), with potential for further conjugation with other molecules containing appropriate reactive groups.

In an effort to obtain a precursor that can enable noninvasive imaging of imperative processes in vivo using MRI, Gd-loaded DO3A-ethylamido-biotin has been synthesized by conjugating DO3A-EA with biotin. Similar systems based on DOTA after loading with metallic radionuclides such as yttrium or indium are also being explored at an in vivo level for application in radioimmunotherapy (*13*−*17*). This technology has found useful application in the medical field to localize and image cancer cells in vivo and to pretarget drugs to tumors *(18)* where MoAb−avidin/biotin act as targeting macromolecule/effector molecule pairs *(19)*. Pretargeting approach takes advantage of the fact that biotin binds strongly to the proteins avidin and streptavidin, resulting in signal amplification.

The second conjugate GdDO3A-ethylthiourea−FITC possesses fluorophore fluorescein on one arm and is intended to obtain a precursor for bimodal imaging where the macrocyclic part serves for MRvisualization and the FITC part for optical imaging. CAs intended for cell labeling can be designed from this precursor for tracking cells in vivo by MR and/or fluorescence imaging. Over the past few years, some cell therapies have developed sufficiently to enter clinical trials. However, the pace of progress toward an effective cell-based therapy has been slowed by the paucity of technology for tracking cells' fate in vivo. Recently de Vries et al. reported the use of MRI for tracking transplanted cells and obtained a detailed view of cell biodynamics in vivo (*20*−*22*). Agents based on the use of bimodal imaging have been applied to disease detection by attaching a target-specific site *(23)* or to observe cellular localization and migration *(24*−*26)*. This gives rise to the need to develop intracellular CAs that will facilitate improved contrast; the precursor presented here can serve as a template for obtaining such agents.

Additionally, to encompass the complete range of chemical reactivity, the nucleophilic "arm" of DO3A-EA was exchanged with electrophile groups, and two new precursors were designed and synthesized. The amino group of DO3A-EA was transformed to isothiocyanate, resulting in the formation of DO3A-ethyl isothiocyanate. This molecule possesses selective reactivity toward amines, thus providing the possibility of using it as a precursor for conjugation with biomolecules such as proteins, peptides and MoAbs *(27*−*30)*. The other precursor, DO3A-ethylamidopropyl-maleimide, obtained by coupling of amine with 4-maleimidobutyric acid, further enhances the diversity of application by exploiting its reactivity toward sulfydryl groups and therefore, prospects for combining with thiol-containing peptides, dendrimers, oligonucleotides *(31*−*34)*. These precursors can serve as important building blocks for designing targeted CAs with desirable traits.

EXPERIMENTAL PROCEDURES

Chemicals. All solvents and reagents were used at the purest grade commercially available without further purification/distillation. Cyclen was purchased from Strem, France. Bromoethylamine hydrobromide, *tert*-butyl bromoacetate, methyl bromoacetate, thiophosgene, trifluoroacetic acid, biotin, *N*-methylmorpholine (NMM), 1-hydroxybenzotriazole hydrate (HOBt), *N*′-(3-dimethylaminopropyl)-*N*-ethylcarbodiimide hydrochloride (EDC), *N*,*N*-dimethylformamide (extra dry), toluene, diethyl ether, and lithium hydroxide were purchased from Aldrich, Germany. Fluorescein isothiocyanate (FITC) and chloroform were purchased from Acros Organics, Germany. Sodium carbonate, 4-maleimidobutyric acid, acetonitrile (anhydrous), carbon tetrachloride, methanol, dichloromethane, *n*-hexane, ethyl acetate, gadolinium chloride hexahydrate, hydrogen chloride, silica gel 60 (70−230 mesh), sodium bicarbonate, tetrahydrofuran, sodium sulfate and potassium carbonate were purchased from Fluka, Germany. Pure water (18 MΩ cm^{-1}) was used throughout. All glass labware was washed with a mixed acid solution and thoroughly rinsed with deionized, distilled water *(35)*.

Reversed Phase High-Performance Liquid Chromatography (HPLC). HPLC was performed at room temperature on a Varian PrepStar Instrument, Australia, equipped with PrepStar SD-1 pump heads. UV absorbance was measured using a ProStar 335 photodiode array detector at 214 and 254 nm. This detector is equipped with a dual-path length flow cell which enables measurement of absorption of analytical and preparative samples without changing the flow cell. Reversed-phase analytical HPLC was performed in a stainless steel Chromsep (length 250 mm, internal diameter 4.6 mm, outside diameter 3/8 in. and particle size 8 μm) C_{18} column and preparative HPLC was performed in a stainless steel Chromsep (length 250 mm, internal diameter 41.4 mm, outside diameter 2 in. and particle size 8 μm) C_{18} column (Varian, Advanced Chromatographic Solutions). The compounds were purified using one of the following two methods. Method A: the gradient was used with the mobile phase starting from 95% solvent A (water) and 5% of solvent B (MeOH) to 70% B in 10 min, 100% B in 18 min, 100% B isocratic till 24 min and decreased to 5% B in 28 min. Alternatively, in method B, isocratic mode was maintained with mobile phase starting from 97% solvent A (water) and 3% of solvent B (MeOH) for 8 min. The flow rate generally used for analytical HPLC was 1 mL/min and for preparative HPLC 41 mL/min. All the solvents for HPLC were filtered through a nylon-66 Millipore filter (0.45 μm) prior to use.

Spectroscopy. NMR spectra were recorded on a Bruker 250 MHz system for ^{1}H and ^{13}C NMR. Mass spectra (ESI-LRMS in positive and negative ion mode) were performed on ion trap SL 1100 system (Agilent, Germany) and ESI−HRMS were performed on Bruker Daltonics Apex II FT-ICR-MS (Bruker, Germany).

Synthesis. *[4,7-Bis-carboxymethyl-10-{2-[5-(2-oxo-hexahydro-thieno[3,4-d]imidazol-4-yl)-pentanoylamino]-ethyl}-1,4,7,10-tetraaza-cyclododec-1-yl]-acetic Acid (**9**, DO3A-ethyl-amido-biotin).* A solution of **8** (0.1 g, 0.15 mmol) in 10 mL of THF:MeOH:water (3:2:2) was stirred at 0−5 °C for 15 min, and then LiOH (12 mg, 0.5 mmol) was added. The reaction mixture was stirred for 3 h at room temperature. The progress of the reaction was monitored by ESI-LRMS. After completion, the solvent was evaporated under reduced pressure and the residue was purified by preparative HPLC [method A, $\lambda = 214$ nm, retention time (t_R) = 9.4 min]. After lyophilization, 72 mg (77%) of **9** as a white solid compound was obtained. ^{1}H NMR (D_2O, 250 MHz), δ (ppm): 1.37−1.45 (m, 2H); 1.61−1.68 (m, 4H); 2.27 (t, $J = 6.87$ Hz, 2H); 2.74−3.23 (m, 14H); 3.32−3.38 (m, 9H); 3.48 (s, 3H); 3.75 (s, 3H); 4.39−4.44 (m, 1H); 4.58−4.62 (m, 1H). ^{13}C NMR (D_2O, 62.9 MHz), δ (ppm): 22.7; 25.4; 25.7; 28.0; 33.0; 33.2; 37.5; 46.1; 46.8; 48.3; 49.1; 52.7; 53.1; 54.4; 58.0; 59.8; 163.0; 169.3; 174.7. ESI−HRMS (+): calcd $C_{26}H_{45}N_7O_8S$: *m*/*z* 616.31231 $[M + H]^+$, found 616.31194 $[M + H]^+$.

*[4,7-Bis-carboxymethyl-10-{2-[4-(2,5-dioxo-2H-pyrrol-1(5H)-yl)-butanamido]-ethyl}-1,4,7,10-tetraaza-cyclododec-1-yl]-acetic Acid (**11**, DO3A-ethylamidopropyl-maleimide).* A solution of **10** (0.1 g, 0.17 mmol) in 14 mL of THF:MeOH:water (3:2:2) was stirred at 0−5 °C for 15 min, and then LiOH (20 mg, 0.83 mmol) was added. The reaction mixture was stirred for 3 h at room temperature. The progress of the reaction was monitored by ESI-LRMS. After completion, the solvent was evaporated under reduced pressure and the residue was purified by preparative HPLC (method A, $\lambda = 214$ nm, $t_R = 5.8$ min). After lyophilization, 72 mg (86%) of **11** as an off-white solid compound was obtained. ^{1}H NMR (D_2O, 250 MHz), δ (ppm): 1.80−1.94 (m, 2H); 2.37 (t, $J = 7.48$ Hz, 2H); 3.03 (t, $J = 6.10$ Hz, 2H); 3.20−3.31 (m, 10H); 3.40−3.51 (m, 15H); 3.83 (s, 4H). ^{13}C NMR (D_2O, 62.9 MHz), δ (ppm): 25.5; 35.4; 38.0; 41.0; 51.1; 51.6; 53.1; 53.7; 53.9; 54.9; 56.8; 58.9; 137.1; 173.8; 175.8; 178.3. ESI−HRMS (+): calcd $C_{24}H_{38}N_6O_9$: *m/z* 555.27730 $[M + H]^+$, found 555.27740 $[M + H]^+$.

*[4,7-Bis-carboxymethyl-10-(2-fluoresceinthioureaethyl)-1,4,7,10-tetraaza-cyclododec-1-yl]-acetic Acid (**12**, DO3A-ethylthiourea−FITC).* A solution of DO3A-EA (**7**) (0.1 g, 0.26 mmol) in 10 mL of water was stirred at room temperature, and FITC (0.11 g, 0.28 mmol) was added at pH 8.5. During stirring, pH was maintained at 8.0−8.5 by addition of 1 M Na_2CO_3. The reaction mixture was stirred for 18−20 h at room temperature in the dark. The reaction was monitored by ESI-LRMS. The reaction mixture was evaporated under reduced pressure and the residue was purified by preparative HPLC (method A, $\lambda = 254$ nm, $t_R = 6.8$ min). After lyophilization, 0.11 g (55%) of **12** as a dark orange solid compound was obtained. ^{1}H NMR (D_2O, 250 MHz), δ (ppm): 2.86−2.99 (m, 18H); 3.38−3.42 (overlapped s, 6H); 3.75 (bs, 2H); 6.52 (s, 1H); 6.53 (s, 1H); 6.55 (s, 1H); 6.59 (s, 1H); 7.16 (t, $J = 4$ Hz, 2H); 7.20 (s, 1H); 7.49 (d, $J = 6.4$ Hz, 1H); 7.66 (s,1H). ^{13}C NMR (D_2O, 62.9 MHz), δ (ppm) 43.5; 52.5; 53.2; 53.7; 53.9; 55.0; 59.9; 106.3; 115.1; 125.7; 127.7; 128.9; 132.1; 133.7; 134.2; 143.5; 161.4; 161.4; 176.8; 179.5; 179.8 183.3. ESI−HRMS (+): calcd $C_{37}H_{42}N_6O_{11}S$: *m/z* 779.27050 $[M + H]^+$, found 779.27051 $[M + H]^+$.

*[4,7-Bis-carboxymethyl-10-(2-isothiocyanatoethyl)-1,4,7,10-tetraaza-cyclododec-1-yl]-acetic Acid (**13**, DO3A-ethyl-isothiocyanate).* A solution of **7** (0.2 g, 0.5 mmol) in water (10 mL) was stirred at room temperature and thiophosgene (0.18 g, 1.5 mmol) in 5 mL of CCl_4 was added dropwise. The pH of the mixture was maintained at 7.5−8 using 1 M Na_2CO_3. The reaction was monitored by ESI-LRMS. The reaction mixture was evaporated and the residue was purified by preparative HPLC (method B, $\lambda = 214$ nm, $t_R = 2.7$ min). After lyophilization, 0.13 g (59%) of **13** as a light yellow solid was obtained. ^{1}H NMR (D_2O, 250 MHz), δ (ppm): 3.23−3.79 (m, 20H); 4.20 (br. s, 6H). ^{13}C NMR (D_2O, 62.9 MHz), δ (ppm) 42.8; 48.5; 51.4; 51.9; 52.8; 55.9; 57.9; 129.3; 178.1; 179.0. ESI−HRMS (+): calcd $C_{17}H_{29}N_5O_6S$: *m/z* 449.21768 $[M + NH_4]^+$, found 449.21790 $[M + NH_4]^+$.

Preparation of Gd Complexes. Gd complexes of DO3A-ethylamido-biotin (**Gd-9**) and DO3A-ethylthiourea−FITC (**Gd-12**) were prepared from respective solution of the ligand (1 equiv) and solution of $GdCl_3 \cdot 6H_2O$ (1.1 equiv). The reaction mixture was stirred at 50−60 °C for 12−16 h. The pH was periodically checked and adjusted to 7.0−8.0 using a solution of Na_2CO_3 (1 M) and HCl (1 N) as needed. After 12−16 h, the reaction mixture was passed through chelex-20 to trap free Gd ions, and the Gd-loaded complex was eluted. The fractions were lyophilized and white solids were obtained. The absence of free Gd^{3+} was checked with xylenol orange indicator *(36)*.

Gd-9. ESI-LRMS (−): calcd $C_{26}H_{42}GdN_7O_8S$: *m/z* 770.2; found 769.1 $[M - H]^-$.

Gd-12. ESI-LRMS (−): calcd $C_{37}H_{39}GdN_6O_{11}S$: *m/z* 932.2; found 931.3 $[M - H]^-$.

Effect of Gd-12 on Cells in Vitro. Experiments on cells were done in 96-well microplates by inoculation of NIH-3T3 mouse fibroblasts (1×10^4 cells/well) cultured in Dulbecco's Modified Eagle's Medium supplemented with 10% fetal bovine serum, 4 mM L-glutamine, 100 μg/mL streptomycin, and 100 U/mL penicillin (all purchased from Biochrom AG, Germany). After 24 h, cells were incubated with various concentrations (up to 150 μM) of **Gd-12** for an additional 18 h. After repeated cell washing with Hanks' buffered saline (Biochrom AG, Germany), cell-related FITC fluorescence (Ex 485 nm/Em 530 nm) was evaluated in a multiplate reader (BMG Labtech, Germany). Subsequently, fluorescence microscopy was performed with the same cells on a Zeiss Axiovert 40 CFL (Germany) to observe the cellular localization of **Gd-12**.

Evaluation of cytotoxicity was done by addition of propidium iodide and a detergent with subsequent fluorescent reading (Ex 530 nm/Em 645 nm). In addition, by combination of the two fluorescence readings, a correlation is established between the FITC fluorescence and the total cell number per well. Experiments were run three times each with six replicates. Statistical analysis was performed by ANOVA with Dunnett's post test. P values < 0.05 were considered significant.

MR Measurements. *Relaxivity Measurements.* Different concentrations (0.8 mM, 0.6 mM, 0.4 mM, 0.1 mM) of **Gd-9** and (1 mM, 0.7 mM, 0.4 mM, 0.1 mM) of **Gd-12** were prepared in phosphate buffer in 1.5 mL Eppendorf tubes at physiological pH to measure relaxivity.

The measurement of the relaxation rates R_1 and R_2 (longitudinal and transverse relaxation) of the **Gd-9** was performed at 300 MHz on a vertical 7 T/60 cm MRI Biospec system (Bruker Biospin, Germany), which was described recently *(37)*. Up to 16 tubes could be measured simultaneously. The relaxation rate measurements of the samples were performed at room temperature (~21 °C).

For R_1, a spin−echo saturation recovery sequence was used, varying the repetition time TR and keeping the echo time TE minimal and constant. Typical parameters were: field of view 17×6.9 cm^2, matrix 512×256, slice thickness 4 mm, SW 70 kHz, TE 15 ms, TR 40−8000 ms (logarithmic time steps, 80 images). For R_2, a multi-spin−echo sequence was used with a long TR between excitations. Similar parameters were used, but TR = 8 s and TE = 17−850 ms (linear echo time steps, 50 echoes).

MR Study of the Avidin−Gd-9 Interaction. To measure the enhancement of R_1 and R_2, MRI experiments were performed with increasing concentrations of avidin (Fluka, Germany) proportional to a constant concentration of **Gd-9** (0.4 mM) incubated for 3 h at 37 °C. The longitudinal relaxivity (r_1) and transverse relaxivity (r_2) was determined from concentration-dependent measurements of relaxation rates (R_1 and R_2) of **Gd-9**.

In Vitro MR Studies of Gd-12 with Cells. For MR imaging of cells, exponentially growing 3T3 cells were labeled with 80 and 150 μM **Gd-12** in 175 cm^2 tissue culture flasks for 18 h. After repeated washing with Hanks' buffered saline, cells were trypsinized, centrifuged, and resuspended in 1.5 mL Eppendorf tubes at 1×10^7 cells in 500 μL of complete DMEM. Cells were allowed to settle before making MR measurements. Tubes with medium only, cells without **Gd-12**, and cells resuspended in medium containing the extracellular contrast agent Magnevist (Schering, Germany) at 50 μM served as controls.

MRI of the cell pellets was also performed at 300 MHz using T_1- and T_2-weighted spin−echo sequences at room temperature (~21 °C), as in the above description.

The axial slice of interest was positioned through the cell

Scheme 1[a]

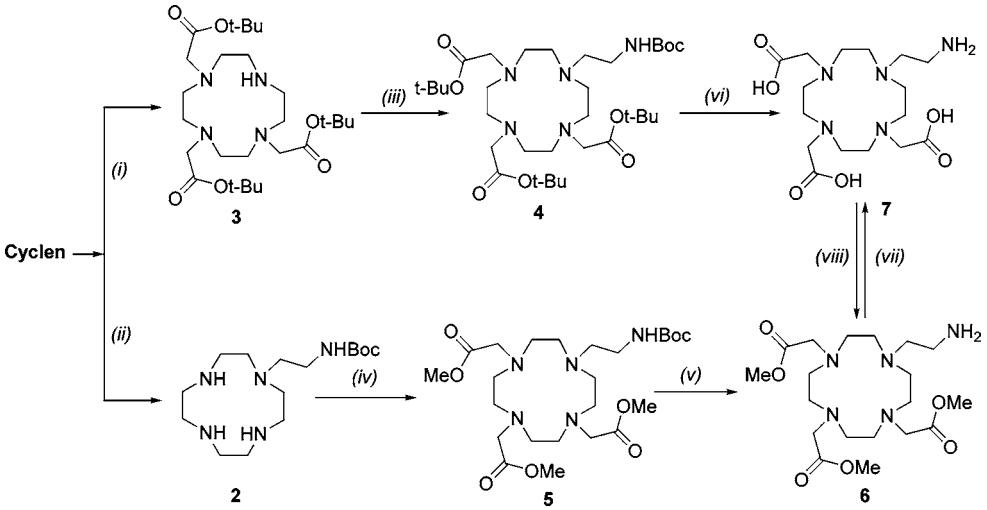

[a] Reagents and conditions: (i) *tert*-butyl bromoacetate, $NaHCO_3$, MeCN, 71%; (ii) *N*-Boc-bromoethylamine (**1**), toluene, 68%; (iii) **1**, K_2CO_3, DMF, 72%; (iv) methyl bromoacetate, Na_2CO_3, MeCN, 82%; (v) DCM, TFA, 80%; (vi) TFA, 64%; (vii) LiOH; THF:MeOH:H_2O (3:2:2), 64%; (viii) MeOH.HCl, 95%.

pellet. Experimental parameters for T_1 were as follows: field of view 17 × 6.9 cm^2, matrix 512 × 256, slice thickness 1.5 mm, SW 70 kHz, TE 14.6 ms, TR 40−6000 ms, two averages (logarithmic time steps, 80 images). For T_2, similar parameters were used, but TR = 8 s and TE = 15−675 ms (linear time steps, 45 echoes).

Sagittal images were obtained with a field of view 11.3 × 6.9 cm^2, matrix 256 × 256, slice thickness 2 mm, SW 70 kHz, TE 10.9 ms, TR 1600 ms, 4 averages for T_1 weighted images, and a field of view 12.5 × 6.8 cm^2, matrix 256 × 256, slice thickness 2 mm, SW 70 kHz, TE 90 ms, TR 8000 ms, 2 averages for T_2 weighted images.

Data Analysis. Data analysis was performed by the *fitting* to relaxivity curves with self-written routines under MATLAB 6.5 R13 (The Mathworks Inc.). For a detailed description, see Supporting Information.

RESULTS AND DISCUSSION

Synthesis of Ligands. DO3A-EA (**7**) is a bifunctional ligand *(38)*, bearing an amine group that is readily reactive toward most electrophiles such as aldehydes, carboxylic acids, and isothiocyanates to form various molecules for the development of targeted CAs. Though DO3A-EA has already been part of several synthetic schemes *(39−41)*, we report here the application of DO3A-EA in a new context, as a precursor for the synthesis of CAs to design relaxometric MRI as well as optical probes. We have developed dual synthetic routes to obtain **7** depending on the choice of protection and deprotection method (Scheme 1).

In the first route **7** was obtained from cyclen at a yield of 39% over three steps, by reaction with *tert*-butyl bromoacetate to obtain the trisubstituted product **3** *(42)*. Alkylation with **1** *(43)* gave **4** and the corresponding carboxylate derivative **7** was obtained by cleaving the *tert*-butyl groups by treatment with neat TFA at room temperature. Attempted selective deprotection of Boc group in compound **4** led to deprotection of *tert*-butyl ester groups and the formation of multiproduct mixtures. Thus, an alternative three-step route was designed also when starting from cyclen to form the methyl ester **6**. After monoalkylation of cyclen *(41)* with **1**, **2** was isolated at a yield of 63%. By alkylation with methyl bromoacetate, ligand **5** was obtained and the acid labile Boc protecting group of amine was cleaved with TFA to obtain methyl-protected ligand **6**; subsequent treatment with LiOH then gave **7**.

Scheme 2[a]

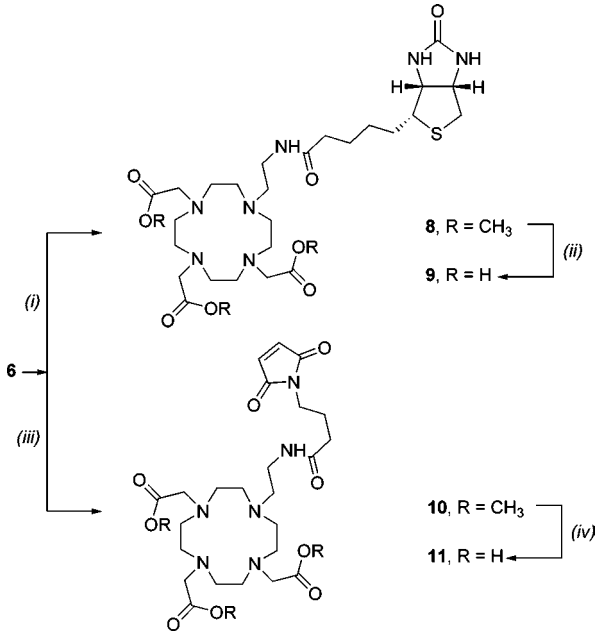

[a] Reagents and conditions: (i) biotin, NMM, HOBt, EDC, DMF, 55%; (ii) LiOH, THF:MeOH:H_2O (3:2:2), 77%; (iii) 4-maleimidobutyric acid, NMM, HOBt, EDC, DMF, 66%; (iv) LiOH, THF:MeOH:H_2O (3:2:2), 86%.

After the successful synthesis of precursors, the bioconjugate ligand **9** was synthesized in a two-step reaction (Scheme 2). Biotin-conjugated DO3A-EA compound **8** was obtained by the coupling of biotin with ligand **6** using EDC/HOBt/NMM in DMF. The choice of such mild conditions for the conjugation of biotin with DO3A-EA and amide bond formation was mandatory due to the sensitivity of biotin toward the harsh conditions (temperature etc). In the following step, ligand **9** was obtained at a yield of 77% by deprotection of methyl groups with LiOH in THF:MeOH:H_2O (3:2:2).

In a similar manner, a novel precursor **11** bearing a maleimide arm was synthesized when starting from **6** as described for biotin conjugates. It is well-known that the maleimide group reacts selectively with sulfydryl groups to form different macromolecules *(27−30)*. Two maleimide conjugates were synthesized, compound **10**, obtained from compound **6** by using 4-maleimidobutyric acid and EDC/HOBt/NMM in DMF at room

Scheme 3[a]

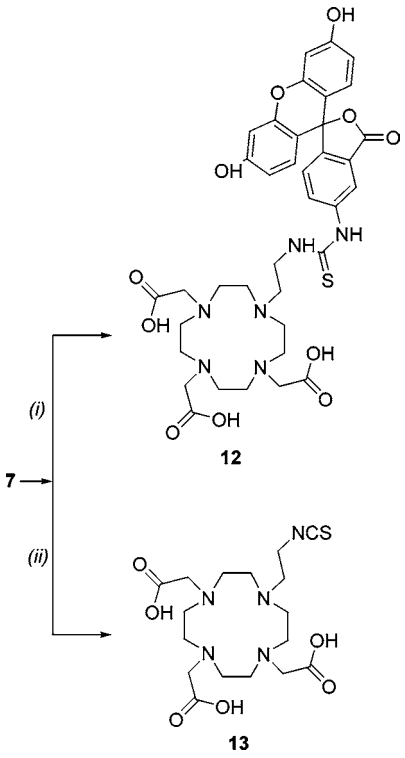

[a] Reagents and conditions: (i) FITC, water, Na_2CO_3, 55%; (ii) $CSCl_2$, water, CCl_4, 59%.

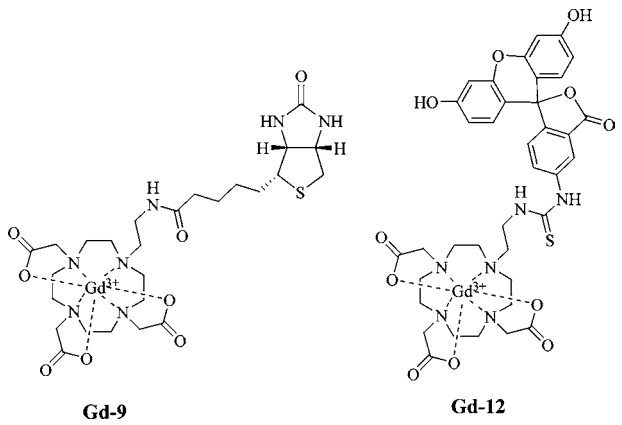

Figure 1. Structures of Gd^{3+} complexes of **9** and **12**.

temperature, and ligand **11**, obtained by deprotection of methyl groups in the presence of LiOH (Scheme 2).

Two molecules were synthesized in single step reactions when starting from **7** (Scheme 3). The first ligand **12** possessed two moieties, the fluorescence unit, and the macrocycle that can complex with paramagnetic metals which was synthesized by coupling FITC with **7** at pH 8. During the reaction, the pH was not allowed to exceed 8.5 because at pH > 9, lactone cleavage of the FITC part occurs, leading to the formation of a side product. The second molecule (**13**) was synthesized in one step by transforming the amino group into NCS with thiophosgene. The yield of the reaction was moderate (59%), although a molecule obtained this way provides possibility for further coupling with amine-containing organic and bioorganic molecules to form the desired product *(31−34)*.

Finally, Gd complexes were synthesized for ligands **9** and **12** (Figure 1). During loading Gd into biotin-containing ligand **9,** the reaction temperature was kept under 60 °C because of possible degradation of the biotin moiety. For loading Gd into FITC-containing compound **12,** the pH of the solution was

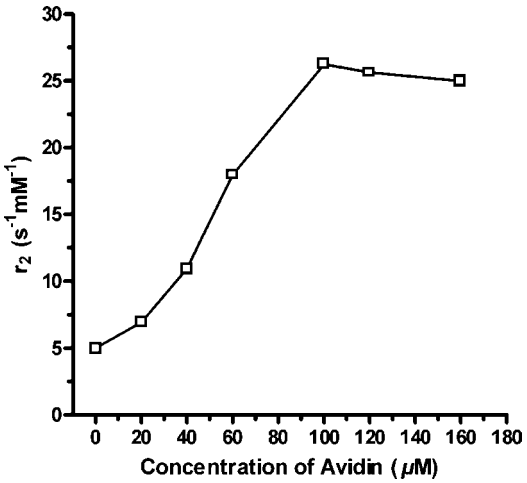

Figure 2. In vitro MR measurement of transverse relaxivity, r_2 **Gd-9** with varying concentrations of avidin. MR experiment was performed at 300 MHz (21 °C) with constant concentration of **Gd-9** (400 μM) and increasing amount of avidin in different tubes. A linear relaxation enhancement was observed up to 100 μM (0.25 equiv). At higher ratios, relaxivity r_2 remained constant. [Error for all r_2 values was less then ($\pm$ 0.6) s^{-1} mM^{-1} and is not displayed].

maintained in the range 7−8, because at lower pH, precipitation of the ligand was observed.

As a summary of the synthetic schemes described above, we would like to point out that the presented straightforward and easy synthesis, although not quite novel, is very suitable for the ready preparation of precursors in the design and preparation of targeted CAs. With the same methodology, it was possible to synthesize various targeted model probes, quite different in their behavior and potential application, which should actually be the major advantage of such approach.

BIOCHEMICAL APPLICATIONS

In Vitro Relaxometry of Gd-9. The biotin−avidin association has found widespread applications in biomolecule detection, medical diagnostics, immunoassays, cytochemistry, and nanoscience *(44−48)*. This is primarily due to the strength of the interaction between the ligand and the tetrameric protein ($K_d \approx 1.3 \times 10^{-15}$ M) which in turn allows for the cross-linking of different biotinylated molecules *(48)*.

To scrutinize the effect of binding on longitudinal and transverse relaxivities, we performed MRI experiments with increasing concentrations of avidin proportional to a constant concentration of **Gd-9** (0.4 mM). A linear enhancement in relaxivity was observed demonstrating strong binding of **Gd-9** in the biotin-binding pocket of tetrameric avidin (Figure 2). This gain in relaxivity suggests a decrease in molecular rotational correlation time τ_R. Similar to reports in the literature proposing that one avidin molecule strongly binds four equivalents of biotin *(48)*, we obtained saturation in relaxivity at ratios higher than 4:1 between **Gd-9** and avidin. MR longitudinal relaxivity, $r_1 = (3.32 \pm 0.03)$ s^{-1} mM^{-1} and transverse relaxivity, $r_2 = (5.02 \pm 0.14$ s^{-1} $mM^{-1})$ of **Gd-9** (0.4 mM) was observed at pH 7.4. The mixture of **Gd-9** and avidin showed maximum relaxivity enhancement of 45% in $r_1 = (4.82 \pm 0.09)$ s^{-1} mM^{-1} and 423% in $r_2 = (26.24 \pm 0.58)$ s^{-1} mM^{-1} relative to the unbound biotinylated Gd^{3+} complex.

In future applications, the MRI contrast sensitivity can therefore be improved by designing CAs using the above precursor, as the biotin−avidin association is expected to enhance the signal by means of in situ accumulation of the agent. Avidin has already been utilized for drug delivery through the blood−brain barrier *(49)*. This is important for future noninvasive, e.g. human research, applications, where intracranial

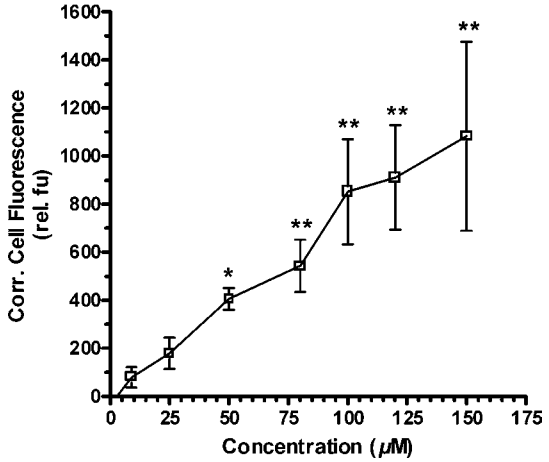

Figure 3. Increase influorescence intensity of cells labeled with different concentrations of **Gd-12**. Cells were incubated with different concentrations of **Gd-12** for 18 h, washed several times and fluorescence measured. After the addition of propidium iodide (PI) and detergent, PI fluorescence was measured to correlate the cell-bound fluorescein fluorescence with cell number resulting in corrected cell fluorescence. Values are relative fluorescence units (rel. fu) as mean ± SD ($n = 3$); *$p < 0.05$; **$p < 0.01$, statistically significant differences compared to control.

injections cannot be considered. Additionally, there is the possibility of utilizing this precursor for diagnosis and imaging using MR, based on a pretargeting approach in combination with avidin-coupled MoAbs. Pretargeted delivery of radionuclides has shown promising results in treatment of lymphoma and solid tumors but remains a sophisticated approach requiring optimization of dose and administration schedules (*14*−*16*). Although our model precursor has potential for use in MR imaging, translation to a system for in vivo application is hampered by certain drawbacks. Hydrolysis of DTPA−biotin and DOTA−biotin by endogenous biotinidase has been reported (*50*). This problem has been successfully overcome by chemically modifying the structure in order to effectively block biotinidase (*17*, *51*). In addition, endogenous biotin levels (10^{-8}−10^{-7} mol/L), immunogenicity of avidin as well as high and prolonged renal uptake markedly affect the efficacy of avidin- and streptavidin-based pretargeting strategies (*18*, *52*, *53*). Efforts are being made to develop an appropriate delivery method to overcome these problems (*54*, *55*).

In Vitro Cell Studies of Gd-12. MR relaxivity of **Gd-12** at pH 7.4 was $r_1 = (5.36 \pm 0.05)$ s^{-1} mM^{-1} and $r_2 = (7.52 \pm 0.16)$ s^{-1} mM^{-1}. In vitro studies of this Gd-loaded complex were done with NIH-3T3 mouse fibroblast cultures to demonstrate its potential for developing multifunctional CAs. **Gd-12** up to 150 μM did not show significant cytotoxicity after 18 h of incubation (propidium iodide assay), although a decrease in the number of cells was observed at concentrations > 100 μM (data not shown). However, a concentration-dependent increase in cell-related FITC fluorescence was observed, indicating cell binding/internalization of the compound (Figure 3). At concentrations higher than 50 μM this increase was statistically significant.

Fluorescence microscopy of living cells revealed a faint but detectable uptake of the compound into cells at concentrations > 50 μM. Figure 4 shows examples of cellular localization of **Gd-12** after incubation with 80 and 150 μM for 18 h and subsequent washing. Beside a faint diffused fluorescence, (asterisks), vesicles showing brighter fluorescence (arrows) were located around the nuclear area of the cells, indicating to an endosomal uptake mechanism.

Figure 5 shows the results of the MR study on 3T3 cells. The presence of Magnevist in the medium enhanced the contrast

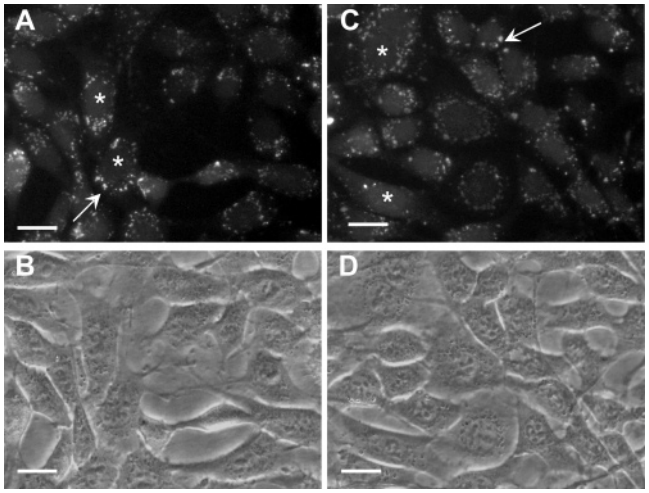

Figure 4. Optical evidence for intracellular localization of **Gd-12** in unfixed NIH 3T3 cells. Cells were incubated with 80 (A, B) and 150 μM (C, D) of **Gd-12** for 18 h as described in Materials and Methods. A and C show fluorescein fluorescence and B and D corresponding phase-contrast pictures. The scale bars represent 20 μm. Arrows point toward vesicles while asterisks indicate diffused fluorescence.

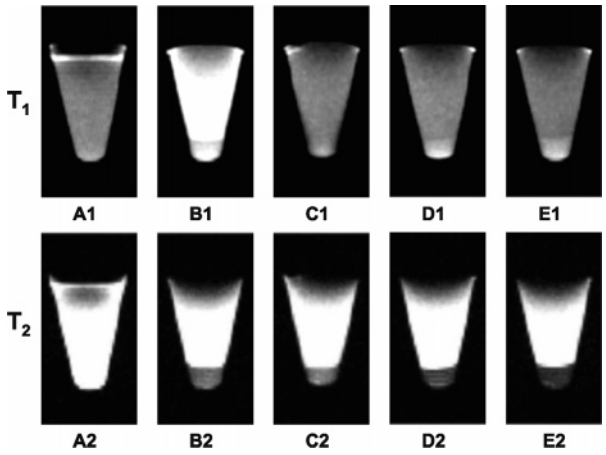

Figure 5. T_1- and T_2-weighted images of control and NIH 3T3 cell pellets labeled with **Gd-12** for 18 h. (A1-E1): T_1-weighted images. (A1) Medium only. (B1) Pelleted cells in medium with 50 μM Magnevist. (C1) Pelleted cells in medium. (D1) Pelleted cells labeled with 80 μM **Gd-12** in medium. (E1) Pelleted cells labeled with 150 μM **Gd-12** in medium. (A2-E2): Respective T_2-weighted images.

in T_1-weighted images by increasing brightness of supernatant, whereas there is almost no difference in T_2. Cells themselves induce only a minor change in T_1-weighted images in comparison to medium only. In T_2-weighted images, the cell pellet is distinguished by the darker image intensity at the bottom of the container which can be viewed also in the absence of any CA. **Gd-12**-labeled cells show a sufficient uptake of the compound to enhance contrast in T_1- and, especially, T_2-weighted images at concentrations above 80 μM. The corresponding relaxation rate R_1 in the cell layer was significantly increased in comparison to control (121% and 131% of control for 80 μM and 150 μM, respectively). A more pronounced enhancement in R_2 was observed (144% and 152% of control, respectively).

Interestingly, contrast enhancement in T_2-weighted images was found to be larger in comparison to T_1. The pronounced T_2 shortening may be caused by the accumulation of the compound in intracellular vesicles inducing local magnetic field inhomogeneities due to compartmentalization. Such behavior is generally observed in the presence of superparamagnetic particles with large magnetic moment, which also show strong compartmentalization *(56)*.

Our results indicate that this model agent is detectable inside cells by both MR and fluorescence methods. Thus, it can serve as a precursor to develop substances that can be used for bimodal (MR and fluorescence) imaging, as well as for development of intracellular contrast agents optimized for cellular internalization. In addition, this molecule can be further modulated for disease detection and diagnosis, gene/drug delivery, elucidating signaling pathways or to study biological and biochemical mechanisms *(57, 58)*. For early disease detection, a bimodal contrast agent Gd^{3+}-DTPA coupled with Oregon Green 488 containing an angiogenesis-specific site cNGR has been recently reported *(23)*. A similar dual mode approach was used by Modo et al. to investigate how neural stem cells migrated and integrated into various brain regions in the same individual over time *(24, 25)*. Aime et al. used Gd-chelate of HP-DO3A as a T_1-agent for MRI visualization, with the corresponding Eu-chelate as a reporter in fluorescence microscopy to detect localization and migration of stem cells *(26)*.

In conclusion, we report the potential of the ligand DO3A-EA as a multipurpose precursor, from which various targeted CAs can be synthesized after single step conjugation with organic molecules/biomolecules. With such methodology, two new targeted agents and two new precursors were synthesized and characterized. MR experiments verified the strong and specific interaction between biotin functionalized DO3A-EA (**Gd-9**) and avidin. Cell studies and relaxivity measurements indicate that FITC-conjugated DO3A-EA (**Gd-12**) can serve as a model to develop agents that can be used for imaging both by MR and fluorescence methods. Maleimide functionalized DO3A-EA (**11**) and DO3A-ethyl isothiocyanate (**13**) precursors having a potential for the specific binding with biomolecules via sulfydryl and amino groups, respectively, have been synthesized. Additionally, the presented precursors **7**, **11**, and **13** cover the entire range of reactivity for the coupling to electrophilic and nucleophilic groups. They possess great potential for coupling with biological molecules, proteins, vitamins, and antibodies for the simple and easy synthesis of various kinds of targeted contrast agents.

ACKNOWLEDGMENT

The authors thank Prof. Dr. Klaus Albert, Department of Organic Chemistry, University of Tübingen, for helpful discussions and providing access to the analytical facilities. The authors also thank Dr. Goran Angelovski for the help with the preparation of the manuscript and Michael Beyerlein for help with the relaxivity measurements. This work was supported by the Max-Planck Society, the Louis-Jeantet Foundation, and the Hertie Foundation.

Supporting Information Available: Synthesis of compounds **4**−**8** and **10**, data analysis for MR experiments, r_1 and r_2 measurements of **Gd-9** and **Gd-12**, and additional cytotoxicity data of **Gd-12**. This material is available free of charge via Internet at http://pubs.acs.org.

LITERATURE CITED

(1) Lauffer, R. B. (1987) Paramagnetic metal-complexes as water proton relaxation Agents for NMR imaging- theory and design. *Chem. Rev. 87*, 901−927.

(2) Caravan, P., Ellison, J. J., McMurry, T. J., and Lauffer, R. B. (1999) Gd^{3+} chelates as MRI contrast agents: Structure, dynamics, and applications. *Chem. Rev. 99*, 2293−2352.

(3) Aime, S., Botta, M., Fasano, M., and Terreno, E. (1998) Lanthanide(III) chelates for NMR biomedical applications. *Chem. Soc. Rev. 27*, 19−29.

(4) Merbach, A. E., and Toth, E. (2001) *The chemistry of contrast agents in medical magnetic resonance imaging*, Wiley, Chichester.

(5) Moreau, J., Guillon, E., Pierrard, J.-C., Rimbault, Port, M., and Aplincourt, M. (2004) Complexing mechanism of the lanthanide cations Eu^{3+}, Gd^{3+}, and Tb^{3+} with 1,4,7,10-tetrakis(carboxymethyl)-1,4,7,10-tetraazacyclododecane (DOTA)- Charactrization of three successive complexing Phases: Study of the thermodynamic and structural properties of the complexes by potentiometery, luminescence spectroscopy, and EXAFS. *Chem. Eur. J. 10*, 5218−5232.

(6) Aime, S., Botta, M., Dastru, W., Fasano, M., Panero, M., and Arnelli, A. (1993) Synthesis and characterization of a novel DTPA-like gadolinium(III) complex − A potential reagent for the determination of glycated proteins by water proton NMR relaxation measurements. *Inorg. Chem. 32*, 2068−2071.

(7) Artemov, D. (2003) Magnetic resonance imaging with targeted contrast agents. *J. Cell. Biochem. 90*, 518−524.

(8) Reamer, P., Bader, A., and Weissleder, R. (1998) Preclinical assessment of hepatocyte-targetd MR contrast agents in stable human liver cell cultures. *J. Magn. Reson. Imaging 8*, 687−689.

(9) Leveille-Webster, C., Rogers, J., and Arias, I. (1996) Use of an asialoglycoprotein receptor-targeted magnetic resonance contrast agent to study changes in receptor biology during liver regeneration and endotoxemia in rats. *Hepatology 23*, 1631−1641.

(10) Ni, Y., Marchal, G., Herijgers, P., Flameng, W., Petre, C., Ebert, W., Hilger, C. S., Pfefferer, D., Semmler, W., and Baert, A. L. (1996) Paramagnetic matalloporphyrins: From enhancers of malignant tumors to markers of myocardial infarcts. *Acad. Radiol. 3 (Suppl. 2)*, S395−S397.

(11) Frullano, L., Rohovec, J., Aime, S., Maschmeyer, T., Prata, M. I., de Lima, J. J. P., Geraldes, C. F. G. C., and Peters, J. A. (2004) Towards targeted MRI: New MRI contrast agents for sialic acid detection. *Chem. Eur. J. 10*, 5205−5217.

(12) Artemov, D., Mori, N., Ravi, R., and Bhujwalla, Z. M. (2003) Magnetic resonance molecular imaging of the Her-2/neu receptor. *Cancer Res. 63*, 2723−2727.

(13) Boerman, O. C., van Schaijk, F. G., Oyen, W. J. G., and Corstens, F. H. M. (2003) Pretargeted Radioimmunotherapy of cancer: Progress step by step. *J. Nucl. Med. 44*, 400−410.

(14) Sharkey, R. M., Karacay, H., Griffiths, G. L., Behr, T. M., Blumenthal, R. D., Mattes, M. J., Hansen, H. J., and Goldenberg, D. M. (1997) Development of a streptavidin-anti-carcinoembryonic antigen antibody, radiolabeled biotin pre-targeting method for radioimmunotherapy of colorectal cancer. Studies in a human colon cancer xenograft model. *Bioconjugate Chem. 8*, 595−604.

(15) Goodwin, D. A., Meares, C. F., and Osen, M. (1998) Biological properties of biotin-chelate conjugates for pretargeted diagnosis and therapy with the avidin/biotin system. *J. Nucl. Med. 39*, 1813−1818.

(16) Axworthy, D. B., Reno, J. M., Hylarides, M. D., Mallett, R. W., Theodore, L. J., Gustavson, L. M., Su, F.-M., Hobson, L. J., Beaumier, P. L., and Fritzberg, A. R. (2000) Cure for human carcinoma xenografts by a single dose of pretargeted yttrium-90 with negligible toxicity. *Proc. Natl. Acad. Sci. 97*, 1802−1807.

(17) Hainsworth, J., Harrison, P., and Mather, S. J. (2005) Preparation and characterization of a DOTA-lysin-biotin conjugate as an effector molecule for pretargeted radionuclidetherapy. *Bioconjugate Chem. 16*, 1468−1474.

(18) Sakahara, H., and Saga, T. (1999) Avidin−biotin system for delivery of diagnostic agents. *Adv. Drug Delivery Rev. 37*, 89−101.

(19) Goodwin, D. A., and Meares, C. F. (1997) Pretargetting. *Cancer Suppl. 80*, 2675−2680.

(20) Zitvogel, L., and Tursz, T. (2005) *In vivo* veritas. *Nat. Biotechnol. 23*, 1372−1374.

(21) de Vries, J. M., Lesterhuis, W. J., Barentsz, J. O., Verdijk, P., van Krieken, J. H., Boerman, O. C., Oyen, W. J. G., Bonenkamp, J. J., Boezeman, J. B., Adema, G. J., Bulte, J. W. M., Scheenen, T. W. J., Punt, C. J. A., Heerschap, A., and Figdor, C. G. (2005) Magnetic resonance tracking of dendritic cells in melanoma patients for monitoring of cellular therapy. *Nat. Biotechnol. 23*, 1407−1413.

(22) Tacken, P. J., de Vries, J. M., Gijzen, K., Joosten, B., Wu, D., Rother, R. P., Faas, S. J., Punt, C. J. A., Torensma, R., Adema, G. J., and Figdor, C. G. (2005) Effective induction of native and recall T-cell responses by targeting antigen to human dendritic cells via a humanized anti-DC−SIGN antibody. *Blood 106*, 1278−1285.

(23) Dirksen, A., Langereis, S., de Waal, B. F. M., van Genderen, M. H. P., Meijer, E. W., de Lussanet, Q. G., and Hackeng, T. M. (2004)

Design and synthesis of bimodal target-specific contrast agents for angiogenesis. *Org. Lett. 6*, 4857−4860.
(24) Modo, M., Cash, D., Mellodew, K., Williams, S. C. R., Fraser, S. E., Meade, T. J., Price, J., and Hodges, H. (2002) Tracking transplanted stem cell migration using bifunctional, contrast agent-enhanced, magnetic resonance imaging. *NeuroImage 17*, 803−811.
(25) Modo, M., Mellodew, K., Cash, D., Fraser, S. E., Meade, T. J., Price, J., Williams, S. C. R. (2004) Mapping transplanted stem cell migration after a stroke: a serial, in vivo magnetic resonance imaging study. *NeuroImage 21*, 311−317.
(26) Crich, S. G., Biancone, L., Cantaluppi, V., Esposito, D. D. G., Russo, S., Camussi, G., and Aime, S. (2004) Improved route for the visualization of stem cells labeled with a Gd-/Eu-chelate as dual (MRI and fluorescence) agent. *Magn. Reson. Med. 51*, 938−944.
(27) Li, M., Meares, C. F., Zhong, G.-R., Miers, L., Xiong, C.-Y. and DeNardo, S. J. (1994) Labeling monoclonol antibodies with ^{90}yttrium- and ^{111}indium-DOTA chelates: A simple and efficient method. *Bioconjugate Chem. 5*, 102−104.
(28) McCall, M. J., Diril, H., and Meares, C. F. (1990) Simplified method for conjugating macrocyclic bifunctional chelating agents to antibodies via 2-iminothiolane. *Bioconjugate Chem. 1*, 222−226.
(29) Rana, T. M., and Meares, C. F. (1990) N-terminal modification of immunoglobulin polypeptide chains tagged with isothiocyanato chelates. *Bioconjugate Chem. 1*, 357−362.
(30) Li, M., and Meares, C. F. (1993) Synthesis, metal chelate stability studies, and enzyme digestion of a peptide-linked DOTA derivative and its corresponding radiolabeled immunoconjugates. *Bioconjugate Chem. 4*, 275−283.
(31) Sieving, P. F., Watson, A. D., and Rocklage, S. M. (1990) Preparation and characterization of paramagnetic polychelates and their protein conjugates. *Bioconjugate Chem. 1*, 65−71.
(32) Herrmann, A., Mihov, G., Vandermeulen, G. W. M., Klok, H.-A., and Mullen, K. (2003) Peptide-functionalized polyphenylene dendrimers. *Tetrahedron 59*, 3925−3935.
(33) Dirksen, A., Langereis, S., de Waal, B. F. M., van Genderen, M. H. P., Meijer, E. W., de Lussanet, Q. G., and Hackeng, T. M. (2004) Design and synthesis of a bimodal target-specific contrast agent for angiogenesis. *Org. Lett. 6*, 4857−4860.
(34) Dirksen, A., Langereis, A., de Waal, B. F. M., van Genderen, M. H. P., Hackeng, T. M., and Meijer, E. W. (2005) A supramolecular approach to multivalent target-specific MRI contrast agents for angiogenesis. *Chem. Commun.* 2811−2813.
(35) Thiers, R. C. (1957) Contamination in trace element analysis and its control. *Methods Biochem. Anal. 5*, 273−335.
(36) Paull, B., and Haddad, P. R. (1999) Chelation ion chromatography of trace metal ions using metallochromic ligands. *Trac-Trends Anal. Chem. 18*, 107−114.
(37) Pfeuffer, J., Merkle, H., Beyerlein, M., Steudel, T., and Logothetis, N. K. (2004) Anatomical and functional MR imaging in the macaque monkey using a vertical large-bore 7 T setup. *Magn. Reson. Imaging 22*, 1343−1359.
(38) Subramanian, R., and Meares, C. F. (1991) Bifunctional chelating agents for radiometal-labeled monoclonal anti-bodies. *Cancer Imaging with Radiolabeled Antibodies* (Goldenberg, D. M., Ed.) pp 183−199, Kluwer Academic Pubs., Boston.
(39) Mishra, A. K. and Chatal, J. F. (2001) Synthesis of macrocyclic bifunctional chelating agents: 1,4,7-tris(carboxymethyl)-10-(2-aminoethyl)-1,4,7,10-tetraazacyclododecane and 1,4,8-tris(carboxymethyl)-11-(2-aminoethyl)-1,4,8,11-tetraazacyclotetradecane. *New J. Chem. 25*, 336−339.
(40) Gries, H., Raduechel, B., Speck, U., and Weinmann, H. J. (1988) Preparation of 1,4,7,10-tetraazacyclododecane-1,4,7-triacetates and their metal salts and complexes as diagnostic aids for X-ray and tomographic diagnoses. *(Schering A.-G., Fed. Rep. Ger.). Ger. Offen*, 11 pp. CODEN: GWXXBX DE 3625417 A1 19880211 CAN 109: 6552 AN 1988: 406552 CAPLUS.
(41) Duimstra, J. A., Femia, F. J.; Meade T. J. (2005) A gadolinium chelate for detection of β-glucuronidase: A self-immolative approach, *J. Am. Chem. Soc. 127*, 12847−12855.
(42) Pope, S. J. A., Kenwright, A. M., Heath, S. L., and Faulkner, S. (2003) Synthesis and luminescence properties of a kinetically stable dinuclear ytterbium complex with differentiated binding sites. *Chem. Commun. 13*, 1550−1551.
(43) Beylin, V. G., and Goel, O. P. (1987) A convenient synthesis of tert-butyl N-(2-bromoethyl)carbamate. *Org. Prep. And Proc. Int. 19*, 78−80.
(44) Weizmann, Y., Patolsky, F., Katz, E., and Willner, I. (2003) Amplified DNA sensing and immunosensing by the rotation of functional magnetic particles. *J. Am. Chem. Soc. 125*, 3452−3454.
(45) Rivera, V. R., Merrill, G. A., White, J. A., and Poli, M. A. (2003) An enzymatic electrochemiluminescence assay for the lethal factor of anthrax. *Anal. Biochem. 312*, 125−130.
(46) Cao, R., Gu, Z., Hsu, L., Patterson, G. D., and Armitage, B. A. (2003) Synthesis and characterization of thermoreversible biopolymer microgels based on hydrogen bonded nucleobase pairing. *J. Am. Chem. Soc. 125*, 10250−10256.
(47) Caswell, K. K., Wilson, J. N., Bunz, U. H. F., and Murphy, C. J. (2003) Preferential end-to-end assembly of gold nanorods by biotin-streptavidin connectors. *J. Am. Chem. Soc. 125*, 13914−13915.
(48) Wilchek, M., and Bayer, E. A. (1990) *Methods of Enzymology*, Vol. 184, Academic Press, San Diego.
(49) Bickel, U., Yoshikawa, T., and Pardridge, W. M. (2001) Delivery of peptides and proteins through the blood-brain barrier. *Adv. Drug Delivery Rev. 46*, 247−279.
(50) Hnatowich, D. J., Virzi, F., and Rusckowski, M. (1987) Investigation of avidin and biotin for imaging applications. *J. Nul. Med. 28*, 1294−1302.
(51) Wilbur, D. S., Hamlin, D. K., Chyan, M.-K., Brian, B. K., and Pathare, P. M. (2001) Biotin reagents for antibody pretargeting. 5. additional studies of biotin conjugate design to provide biotinidase stability. *Bioconjugate Chem. 12*, 616−623.
(52) Rusckowski, M., Fogarasi, M., Fritz, B., and Hnatowich, D. J. (1997) Effect of endogenous biotin on the applications of streptavidin and biotin in mice. *Nucl. Med. Biol. 24*, 263−268.
(53) Sharkay, R. M., Karacay, H., Griffiths, G. L., Behr, T. M., Blumenthal, R. D., Mattes, M. J., Hansen, H. J., and Goldenberg, D. M. (1997) Development of a streptavidin-anti-carcinoembryonic antigen antibody, radiolabeled biotin pretargeting method for radioimmunotherapy of colorectal cancer: studies in a human colon cancer xenograft model. *Bioconjugate Chem. 8*, 595−604.
(54) Gruaz-Guyon, A., Raguin, O., and Barbet, J. (2005) Recent advances in pretargetd radioimmunotherapy. *Curr. Med. Chem. 12*, 319−338.
(55) Foerster, G. J., Santos, E. B., Smith-Jones, P. M., Zanzanico, P., Larson, S. M. (2006) Pretargeted radioimmunotherapy with a single-chain antibody/streptavidin construct and radiolabeled DOTA-biotin: strategies for reduction of the renal dose. *J. Nul. Med. 47*, 140−149.
(56) Wang, Y.-X. J., Hussain, S. M., and Krestin, G. P. (2001) Superparamagnetic iron oxide contrast agents: physicochemical characteristics and applications in MR imaging. *Eur. Radiol. 11*, 2319−2331.
(57) Weissleder, R., and Mahmood, U. (2001) Molecular imaging. *Radiology 219*, 316−333.
(58) Hüber, M. M., Staubli A. B., Kustedjo, K., Gray, M. H. B., Shih, J., Fraser, S. E., Jacobs, R. E., and Meade, T. J. (1998) Fluorescently detectable magnetic resonance imaging agents. *Bioconjugate Chem. 9*, 242−249.

BC050295B

Nonviral Gene Carriers Based on Diblock Copolymers of Poly(2-ethyl-2-oxazoline) and Linear Polyethylenimine

Ging-Ho Hsiue,*,† Hou-Zen Chiang,‡ Chau-Hui Wang,§ and Tzuoh-Min Juang‡

Department of Chemical Engineering, National Tsing Hua University, Hsinchu, 300 Taiwan, ROC, Department of Applied Chemistry, National Chiao Tung University, Hsinchu, 300 Taiwan, ROC, and Polymer Technology Division, Union Chemical Laboratories, Industrial Technology Research Institute, Hsinchu, 300 Taiwan, ROC. Received November 4, 2005; Revised Manuscript Received December 30, 2005

Diblock copolymers that consist of poly(2-ethyl-2-oxazoline) (PEOz) and linear polyethylenimine (LPEI) were prepared for use as nonviral gene carriers. The PEOz-*b*-LPEI copolymers were synthesized by coupling PEOz with LPEI in a thiol−disulfide exchange reaction between the sulfhydryl and pyridyl disulfide terminal groups. A polymer/DNA weight ratio (P/D) of over 12 was required to enable PEOz-*b*-LPEI to condense DNA completely. The DNA-condensing capability of the diblock copolymers was increased with increasing the hydrolytic degrees of the LPEI segment. The PEOz-*b*-LPEI polyplexes were stable in 150 mM NaCl aqueous solution and had a mean diameter around 190 nm, whereas BPEI and LPEI polyplexes formed large aggregates in the range 300−500 nm. In addition, these polyplexes exhibited the sensitivity to solution pH and were dissociated in the acidic buffers (pH ≤ 5.5). The results of in vitro cell viability and luciferase assay indicated that PEOz-*b*-LPEI showed not only low cytotoxicity but also high transfection efficiency in gene expression.

INTRODUCTION

Nonviral vectors, such as liposomes and cationic polymers, have recently attracted increasing interest. They are usually considered to be safer and able to be designed with more flexible structures and chemical properties (*1*−*3*). Among the various types of polymer gene carriers, branched polyethyleneimine (BPEI) is the most effective vector for delivering genes because the BPEI/DNA polyplexes exhibit great transgene expression both in vitro and in vivo (*4*, *5*). The high transfection efficiency of BPEI is probably attributed to its large buffering capacity, which disrupts the endosomal membrane, resulting in the release of the polyplex into the cytoplasm (*6*). Additionally, linear polyethylenimine (LPEI) which can be obtained by hydrolyzing poly(2-ethyl-2-oxazoline) (PEOz) has indicated that the in vitro transfection activity of LPEI is as high as that of BPEI, but its cytotoxicity is lower (*7*).

However, the application of cationic homopolymers is hampered by their poor solubility due to charge neutralization and aggregation under physiological conditions, such as in salt or bovine serum albumin (*8*, *9*). A potential solution to these problems is to conjugate a hydrophilic polymer to the polycations. Poly(ethylene glycol) (PEG) is the polymer that is most often used for this purpose (*10*−*14*). Following complexation with plasmid DNA, the PEGylated polycation/DNA complexes exhibit neutral surface charge, low cytotoxicity, and high solubility in water. PEOz is a biocompatible and hydrophilic polymer that is ionized at acidic pH and leads to the formation of intra- and intermolecular hydrogen bond (*15*, *16*). Hence, PEOz has been investigated for use in the controlled release drug delivery systems (*16*, *17*). However, it has never been exploited as a vector in gene therapy.

The authors' previous work studied the ability of amphiphilic block copolymers that consist of LPEI and poly(L-lactide) (PLLA) to modulate the delivery of plasmid DNA (*18*). In this work, gene carriers were prepared by coupling PEOz and LPEI with various percentages of hydrolysis. The resultant diblock copolymers condensed plasmid DNA and formed micelles with core−shell structure. The physicochemical and biological characteristics of the copolymer/DNA micelles were evaluated herein.

EXPERIMENTAL SECTION

Materials. 2-Ethyl-2-oxazoline (Acros) and methyl *p*-toluenesulfonate (Aldrich) were purified by vacuum distillation over CaH_2. Acetonitrile (Tedia) was dried over CaH_2 and distilled under dry nitrogen. Potassium thioacetate, 2,2′-dithiodipyridine, and ammonia in methanol solution were purchased from Acros. 3-(4,5-Dimethylthiazol-2-yl)-2,5-diphenyltetrazolium bromide (MTT) was purchased from ICN Biomedicals, Inc. pUHC 13-3 encoding for luciferase as a reporter gene was received as a gift from Prof. Jia-Ling Yang at National Tsing Hua University, Taiwan. Dulbecco's modified Eagle's medium (DMEM), fetal bovine serum (FBS), and trypsin−EDTA were the products of Gibco-BRL. HeLa human adenocarcinoma cells were provided by Prof. Yu-Chen Hu of National Tsing Hua University, Taiwan. Dialysis tubing was obtained from Spectrum Medical Industries, Inc.

Synthesis of Poly(2-ethyl-2-oxazoline) Thioacetate (PEOz-SAc). A solution of methyl *p*-toluenesulfonate (370 mg, 1.98 mmol) and 2-ethyl-2-oxazoline (20 mL, 197.72 mmol) in dry acetonitrile (60 mL) was heated to 100 °C and stirred for 24 h in an atmosphere of nitrogen. The living PEOz polymer chains were terminated by adding potassium thioacetate (0.7 g) at 0 °C; the solution was then stirred for 24 h. The polymer solution was filtered through the silica gel and purified by precipitation in diethyl ether. After complete drying, a brown powdery product was obtained. The molecular weight and polydispersity of PEOz-SAc were determined by gel permeation chromatography (GPC). ^{1}H NMR ($CDCl_3$): $\delta = 0.98$ ppm ($N(COCH_2CH_3)$), 2.35 ($N(COCH_2CH_3)$), 3.42 ($N(COCH_2CH_3)CH_2CH_2$), 3.00 ($CH_3N(COCH_2CH_3)$), 2.92 ($CH_2CH_2S(CO)CH_3$). Elemental

* To whom correspondence should be addressed. E-mail: ghhsiue@che.nthu.edu.tw.

† National Tsing Hua University.

‡ National Chiao Tung University.

§ Industrial Technology Research Institute.

10.1021/bc050317u CCC: $33.50 © 2006 American Chemical Society
Published on Web 04/29/2006

Scheme 1. Synthetic Route of the PEOz-*b*-LPEI

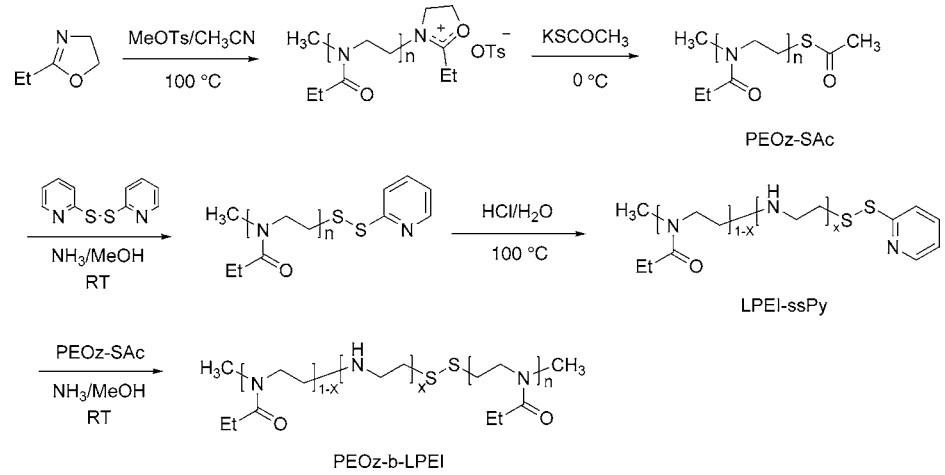

anal. (mass fraction): (C: 60.42, H: 9.08, N: 14.01, S: 0.36). Calculated: (C: 60.39, H: 9.13, N: 14.00, S: 0.32).

Synthesis of Linear Polyethylenimine Pyridyl Disulfide (LPEI-ssPy). PEOz-SAc (1 g, 0.1 mmol) and 2,2′-dithiodipyridine (111 mg, 0.5 mmol) were dissolved in ammonia/methanol solution (7 N, 20 mL). The mixture was stirred in a nitrogen atmosphere at room temperature for 24 h. After the solvent had been removed, the solid residue was redissolved in dichloromethane and then precipitated in diethyl ether several times. The purified product was vacuum-dried to yield a yellow powder. PEOz-ssPy (1 g) was heated with a mixture of concentrated hydrochloric acid (10 mL, 35%) and water (8 mL) at 100 °C for 3 h. The pH of the polymer solution was adjusted to 9−10 by adding NaOH pellets. The product was then purified by dialysis method for 3 days using cutoff dialysis tubing with a molecular weight of 3500. After completely drying in a vacuum, the viscous semisolid product was obtaied. ^{1}H NMR ($CDCl_3$): δ = 2.77 ppm ($NHCH_2CH_2$), 7.094, 7.601, 8.41 (pyridyl ring). Elemental anal. (mass fraction): (C: 57.54, H: 10.48, N: 24.31, S: 1.03). Calculated: (C: 57.47, H: 10.46, N: 24.35, S: 1.10).

Synthesis of Diblock Copolymer Poly(2-ethyl-2-oxazoline)-*block*-Linear Polyethylenimine (PEOz-*b*-LPEI). LPEI-ssPy (1 g, 0.196 mmol) and PEOz-SAc (235 mg, 0.065 mmol) were dissolved in ammonia/methanol solution (7 N, 15 mL). The reaction was carried out in a nitrogen atmosphere at room temperature for 24 h. The unreacted LPEI-ssPy and byproducts were purified by dialysis (with a molecular weight cutoff of 6000−8000) against methanol and distilled water for 3 days, respectively. After evaporation, the obtained diblock copolymer was then dried in vacuo and stored at −20 °C before use. Elemental anal. (mass fraction): (C: 58.51, H: 10.11, N: 20.31, S: 0.73). Calculated: (C: 58.56, H: 10.01, N: 20.38, S: 0.68).

Preparation of Polyplexes. An amount of 4 μg of Luciferase encoding plasmid pUHC-13−3 and the desired amount of polymer were each diluted in 100 μL of distilled water and gently mixed. The polyplex formulation was incubated at room temperature for 30 min before it was used.

Gel Retardation Assay. Various formulations of polyplexes were prepared as described above before they were loaded into the gel. The samples were electrophoresed on 1% agarose gel in 1× Tris−boric acid−EDTA (TBE) buffer at 100 mV until the 1× loading dye ran through 80% of the gel. A 1 kb DNA marker (Violet), used to determine the size of DNA, was also run. The gel was stained with 0.5 μg/mL ethidium bromide for 45 min and analyzed using an UV transilluminator.

Measurement of Particle Size and Zeta Potential. The size of the particles of the polyplexes prepared in distilled water or 150 mM NaCl was measured at 25 °C by dynamic light scattering using a Zetasizer 3000 HS from Malvern Instruments, Worcestershire, U.K. The viscosity (0.89 mPa/s) and the refractive index (1.333) of water at 25 °C were used to analyze the data. The zeta potential of the polyplexes prepared in distilled water was determined by laser Doppler anemometry in the standard capillary electrophoresis cell of the Zetasizer 3000 HS from Malvern Instruments at 25 °C. The mean values of the zeta potential were calculated from the data obtained in five runs.

pH-Sensitivity Testing. The polyplexes formed by mixing plasmid DNA and diblock copolymers were incubated in the phosphate buffer (pH 7 and 6.5) and succinate buffer (pH 6, 5.5, 5, 4.5) solutions at room temperature for 1 h. Then, the aliquots obtained from the buffer solutions were analyzed with 1% agarose gel electrophoresis.

In Vitro Cell Viability. Human cervix carcinoma HeLa cells (1×10^4 cells/well) were cultured onto a plate with 96 wells in DMEM media supplemented with 10% fetal bovine serum (FBS) in a humid atmosphere of 5% CO_2 at 37 °C for 24 h. The growth medium was replaced with a medium that contained the desired amount of polymers. Cells were incubated for 24 h, and cell viability was assayed by adding 100 μL of medium that contained 10 μL of MTT PBS solution (5 mg/mL). After incubation for 4 h, the formazan crystals were dissolved in 100 μL of DMSO. The absorbance of each well was measured using a microplate reader (Stat Fax 2100, Awareness) at a test wavelength of 570 nm and a reference wavelength of 630 nm.

In Vitro Transfection and Total Protein Assay. Human cervix carcinoma HeLa cells (2×10^5 cells/well) plated in six-well plates were incubated in DMEM media supplemented with 10% FBS in a humid atmosphere of 5% CO_2 at 37 °C for 24 h. Transfection was conducted after the cells had become approximately 80% confluent. A 2 mL volume of growth medium that contained DNA or polyplexes that contained finally 4 μg of plasmid was incubated for 48 h at 37 °C. Following transfection, the cells were washed with cold PBS and then lysed using 400 μL of 1× cell lysis buffer. The cell lysate was then transferred into eppendorf tubes and centrifuged for 15 s at 12 000 rpm. Luciferase activity was measured in relative light units (RLU), using a 96-well plate luminometer (Wallac 1420 Multilabel Counter, Perkin-Elmer) and a luciferase assay kit (Promega). The total amount of protein was measured at 595 nm using a BioRad protein assay.

RESULTS AND DISCUSSION

Synthesis of Diblock Copolymer PEOz-*b*-LPEI. Scheme 1 presents the synthesis of PEOz-*b*-LPEI. Cationic ring-opening polymerization of 2-ethyl-2-oxazoline using the monofunctional

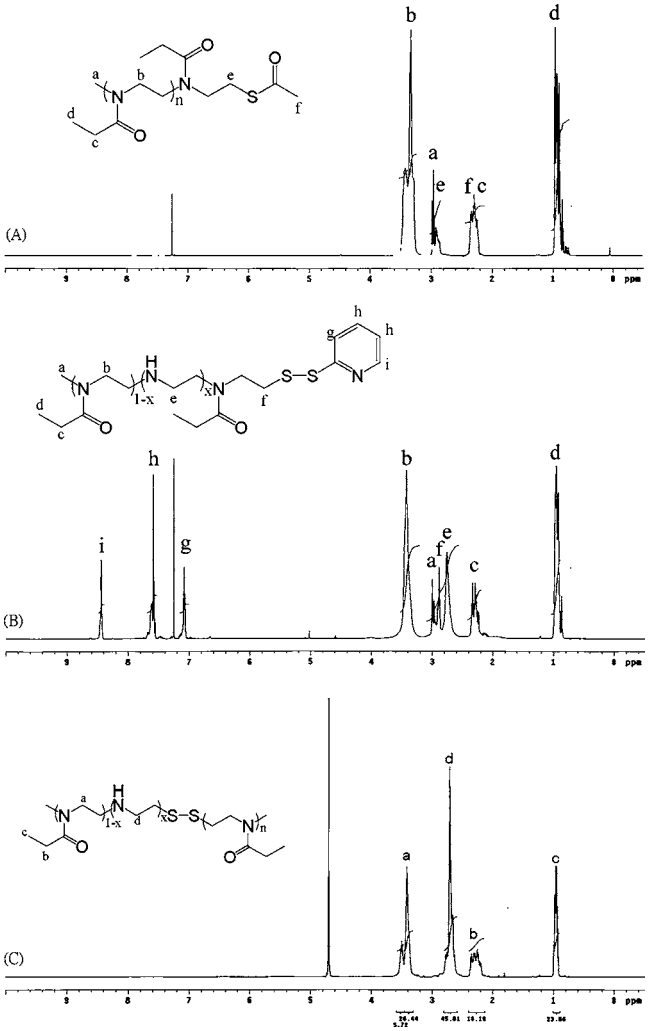

Figure 1. ^{1}H NMR spectra of (A) PEOz-SAc in $CDCl_3$, (B) LPEI-ssPy in $CDCl_3$, and (C) PEOz-*b*-LPEI in D_2O.

initiator methyl *p*-toluenesulfonate is a typical method for synthesizing PEOz (*19*, *20*). The oxazolinium salt structure of the growing polymer can readily react with nucleophiles, such as amines or water to introduce functional groups into the end of polymer chain (*21*). A thiol is used herein to couple the PEOz and LPEI via disulfide bond. However, the thiol was susceptible to oxidation to the formation of dimer; thus, the more stable form of thioacetate was desired. Adding potassium thioacetate to terminate the reaction capped the end of PEOz with the thioacetate functional group. The number average molecular weight (M_n) and polydispersity index (PDI) of PEOz-Sac determined by GPC were 10000 and 1.12, respectively. Figure 1A shows the ^{1}H NMR spectrum of PEOz-SAc dissolved in $CDCl_3$.

LPEI was prepared by the acid hydrolysis of PEOz. Because the terminal thioacetate group could be hydrolyzed as well, it was first deacetylated by treating with ammonia/methanol solution and then converted to pyridyl disulfide group by thiol−disulfide exchange reaction with 2,2′-dithiodipyridine before performing hydrolysis reaction. Figure 1B shows the ^{1}H NMR spectrum of LPEI-ssPy in $CDCl_3$. The percentage of LPEI-ssPy hydrolyzed was calculated by comparing the integral peak area of the ethylenimine groups to the *N*-propionylethylenimine groups from the ^{1}H NMR spectrum. The molecular weight of the LPEI-ssPy was estimated from the percentage of hydrolysis.

Diblock copolymers were synthesized by coupling the PEOz-SAc and LPEI-ssPy via a disulfide exchange reaction of the deprotected sulfhydryl goup of the PEOz and the pyridyl

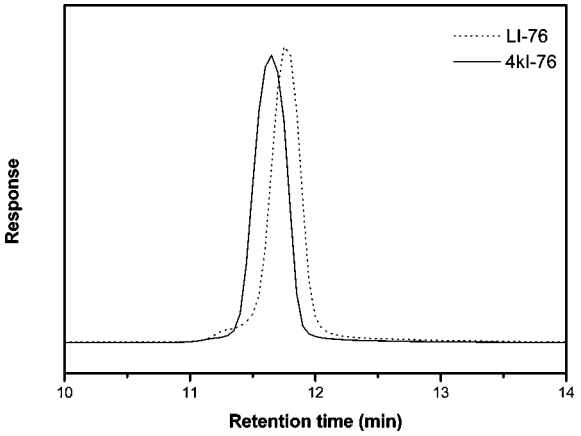

Figure 2. GPC chromatograms before and after LPEI conjugation.

Table 1. Compositions of LPEI and PEOz-*b*-LPEI

polymer	M_n (PEOz)	M_n (LPEI)	EI content (%)
L-76	-	5700	76
L-89	-	5000	89
4k-76	3600	5700	56
4k-89	3600	5000	66

disulfide group of LPEI. The disulfide bond of the diblock copolymer is cleavable intracellularly, but it is relatively stable in the extracellular milieu (*22*). Figure 1C shows the ^{1}H NMR spectrum of PEOz-*b*-LPEI in D_2O. The Mn and PDI of PEOz-SAc used in this step were 3600 and 1.18, respectively. The GPC chromatogram before and after LPEI conjugation was shown in Figure 2. The molecular weight was increased after successfully coupling PEOz and LPEI, and the unreacted polymers were completely removed. Table 1 presents the compositions of the LPEI and PEOz-*b*-LPEI. For comparison, a commercially available BPEI of 25 kDa was also evaluated in this work.

Gel Retardation Assay. Agarose gel electrophoresis was conducted to evaluate the capacity of BPEI, LPEI and PEOz-*b*-LPEI to interact with plasmid DNA. Figure 3 shows the result of gel retardation assay for polycations/DNA complexes. As the concentration of the polycation increased, the mobility of the plasmid DNA was reduced by increasing DNA condensation and compaction. BPEI was the most efficient that it could completely retard DNA migration at a polymer/DNA (P/D) ratio (w/w) of 1 while it required P/D ratios of 8 and 6 for the L-76 and L-89 to complex DNA, respectively (Figure 2A). The 4k-76 began to form polyplexes at a P/D ratio of 14, and a P/D ratio of 12 was required for 4k-89 to complex DNA completely (Figure 2B). These results demonstrated that the DNA binding capacity of LPEI increased with the hydrolytic degrees.

Particle Size and Zeta Potential. After determining the amount of the different polycations for polyplexes formation, the particle size of the polyplexes was estimated by laser light scattering. The polyplexes prepared in either an aqueous solution of physiological salt (150 mM NaCl) or in distilled water were used to measure the size of polyplex to elucidate whether the ionic strength of the media influences the stability of the polyplexes. During the measurement, we found the lowest P/D ratio for stable polyplexes formation of each polymer. The polyplexes that formed below this P/D ratio usually led to aggregation. Figure 4 presents the particle sizes of BPEI, LPEI, and PEOz-*b*-LPEI polyplexes at the lowest P/D ratio for the formation of stable polyplexes. The BPEI polyplex had a mean diameter of 100 nm in water that was reasonably consistent with the findings of Tang and Szoka (*2*). The sizes of LPEI and PEOz-*b*-LPEI polyplexes were around 190 nm. When the polyplexes were dispersed in 150 mM NaCl solution, BPEI and

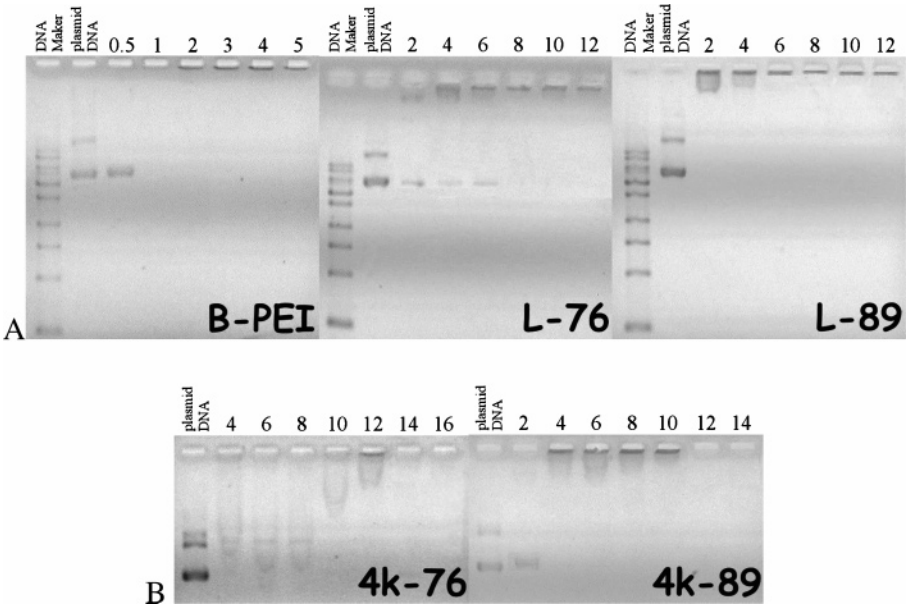

Figure 3. Gel retardation assay of the polyplexes: (A) BPEI and LPEI, (B) PEOz-*b*-LPEI. The numbers in the first row above each panel noted the P/D ratios of the complexes.

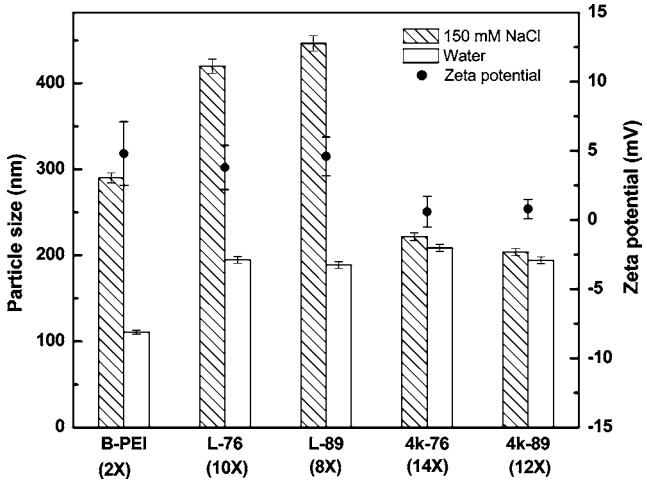

Figure 4. Particle size and zeta potential of BPEI, LPEI, and PEOz-*b*-LPEI polyplexes at the optimum P/D ratios.

LPEI polyplexes all aggregated as larger particles. However, the PEOz-*b*-LPEI polyplexes did not show any aggregation in salt-containing media.

The zeta potential of the polyplexes wasmeasured by mixing the polyplexes at the lowest P/D ratio to stabilize them. Figure 4 shows that BPEI and LPEI polyplexes all had moderate positive surface charges, but the zeta potentials of PEOz-*b*-LPEI polyplexes were almost zero. When BPEI and LPEI were mixed with DNA at a P/D ratio that was slightly less than the lowest P/D ratio for the formation of stable polyplexes, the polyplexes also had a neutral surface charge (data not shown). This result indicates that the neutral BPEI and LPEI polyplexes were prone to aggregate due to the lack of electrostatic repulsion, so the polyplexes with a positive surface charge were stable. However, the PEOz-*b*-LPEI polyplexes were stable and had a neutral surface charge probably because they possessed a core−shell structure with a hydrophobic LPEI/DNA core and a hydrophilic PEOz shell, which prevented the polyplexes from aggregating.

pH-Sensitivity Testing. The recent study conducted in our laboratory showed that the PEOz was a pH-sensitive polymer that would become a hydrogen-bonded complex at acidic buffer solutions, because of the ionization of the amide groups (*18*).

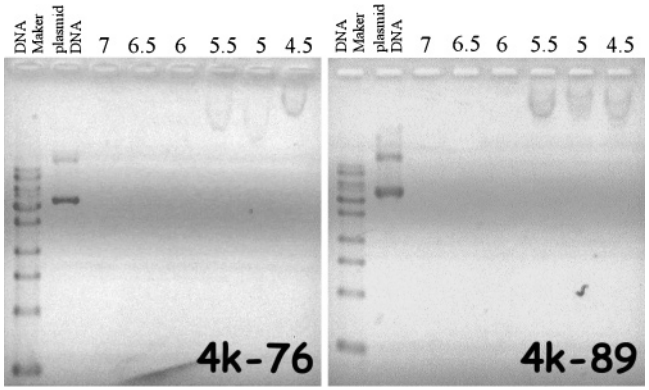

Figure 5. The pH-sensitivity of PEOz-*b*-LPEI polyplexes in various buffer solutions. The numbers in the first row above each panel noted the pH values of the buffer solutions.

The PEOz-*b*-LPEI polyplexes were incubated in buffer solutions at pH values from 7 to 4.5, to determine whether the introduction of PEOz to L-PEI made the polyplexes sensitive to pH. The integrity of the polyplexes was consistent with the analysis made by agarose gel electrophoresis. Figure 5 shows the gel electrophoresis results for PEOz-*b*-LPEI polyplexes. The 4k-76 polyplex was stable at pH $\geq$ 6, but began to dissociate at pH $\leq$ 5.5. The 4k-89 polyplex also had the same behavior as 4k-76. The LPEI polyplexes were also examined. They remained intact in all tested buffer solutions (Data not shown). These results demonstrate that the sensitivity of PEOz-*b*-LPEI polyplexes to pH does stem from the tendency of PEOz and cause the polyplexes to dissociate in acidic environments.

In Vitro Cell Viability. The in vitro cytotoxicities of the different polycations at various concentrations were quantitated by MTT assay using HeLa human cervix carcinoma cells. The wells that contained only media without polycation were treated as positive controls, with a cell viability of 100%. The relative cell viability was calculated as $[\text{Abs}]_{\text{sample}}/[\text{Abs}]_{\text{control}} \times 100$. Figure 6 compares the cell viability of HeLa cells at various polymer concentrations of BPEI, LPEI, and PEOz-*b*-LPEI, revealing that BPEI was the most toxic polycation and the cell viability was below 10% as the polymer concentration $\geq$ 0.1 mg/mL. The cell viability of LPEI declined as the hydrolyzed percentage increased, as it did in the case of PEOz-*b*-LPEI.

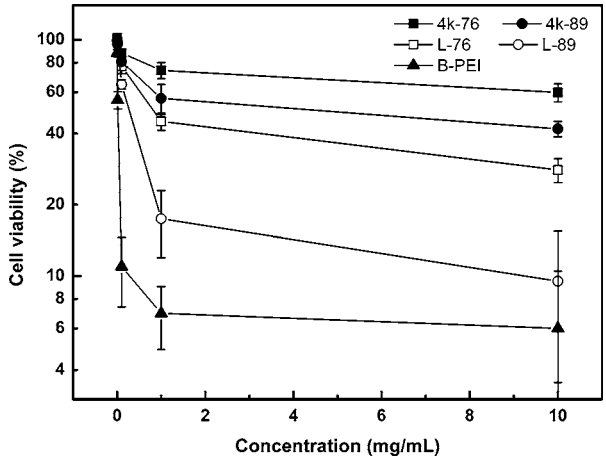

Figure 6. The cell viability of HeLa cells at various polymer concentrations ($n = 6$).

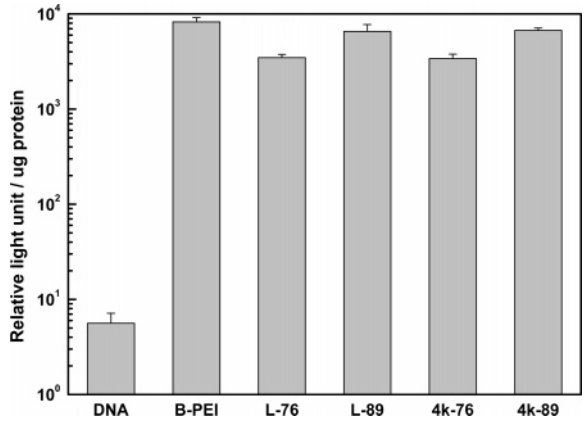

Figure 7. Luciferase gene expressions of the naked DNA, BPEI, LPEI, and PEOz-*b*-LPEI at the optimum P/D ratios ($n = 3$).

Furthermore, the PEOz-*b*-LPEI was less toxic than the corresponding LPEI. These results demonstrated that the charge density in the LPEI strongly affected cell viability. Therefore, PEOz-coupled LPEI further reduced the cationic charge density and the cytotoxicity.

In Vitro Transfection and Total Protein Assay. The total protein production, which is an indirect measure of induced toxicity, was analyzed and normalized to be expressed in relative light unit (RLU). Figure 7 presents the luciferase gene expressions of the naked DNA, BPEI, LPEI, and PEOz-*b*-LPEI at optimum P/D ratios. The results showed that all the polycationic gene carriers exhibited greater transfection efficiency than naked DNA. BPEI polyplex mediated the strongest gene expression of all polycations. The transfection efficiency of PEOz-*b*-LPEI was as high as that of LPEI. PEOz-coupling did not affect the transfection efficiency of the LPEI. Moreover, the protein production of PEOz-*b*-LPEI exceeded that of BPEI and LPEI, indicating that PEOz-*b*-LPEI polyplexes had lower cytotoxicity than others.

CONCLUSION

In this study, the pH-sensitive diblock copolymers PEOz-*b*-LPEI were synthesized by coupling PEOz with LPEI, and the physicochemical and biological characteristics were evaluated. The polyplexes of the PEOz-*b*-LPEI were shown to have neutral surface charge and stably sized particles, unlike LPEI and BPEI. These diblock copolymer polyplexes exhibited a pH-sensitivity that caused them to dissociate at pH values lower than 5.5, suggesting that they may release DNA intracellularly. The results also demonstrated that the PEOz-*b*-LPEI had low cytotoxicity and high transfection efficiency. Accordingly, the diblock copolymers have potential for application in nonviral gene therapy.

ACKNOWLEDGMENT

The authors thank the Industrial Technology Research Institute of Taiwan (ITRI) for financially supporting this research (A341XS6500). Prof. Jia-Ling Yang at the Institute of Biotechnology of National Tsing Hua University is appreciated for her assistance with luciferase expression assay.

LITERATURE CITED

(1) Han, S. O., Mahato, R. I., Sung, Y. K., and Kim, S. W. (2000) Development of biomaterials for gene therapy. *Mol.* Ther. *2*, 302−317.

(2) Tang, M. X., and Szoka, F. C. (1997) The influence of polymer structure on the interactions of cationic polymers with DNA and morphology of the resulting complexes. *Gene Ther. 4*, 823−832.

(3) Luo, D., and Saltzman, W. M. (2000) Synthetic DNA delivery systems. *Nat. Biotechnol. 18*, 33−37.

(4) Pollard, H., Remy, J. S., Loussouarn, G., Demolombe, S., Behr, J. P., and Escande, D. (1998) Polyethylenimine but not cationic lipids promotes transgene delivery to the nucleus in mammalian cells. *J. Biol. Chem. 273*, 7507−7511.

(5) Abdallah, B., Hassan, A., Benoist, C., Goula, D., Behr, J. P., and Demeneix, B. A. (1996) A powerful nonviral vector for in vivo gene transfer into the adult mammalian brain: Polyethylenimine. *Hum. Gene Ther. 7*, 1947−1954.

(6) Boussif, O., Lezoualc'h, F., Zanta, M. A., Mergny, M. D., Scherman, D., Demeneix, B., and Behr, J. P. (1995) A versatile vector for gene and oligonucleotide transfer into cells in culture and in vivo: Polyethyleneimine. *Proc. Natl. Acad. Sci. U.S.A. 92*, 7297−7301.

(7) Jeong J. H., Song S. H., Lim D. W., Lee H., and Park T. G. (2001) DNA transfection using linear poly(ethylenimine) prepared by controlled acid hydrolysis of poly(2-ethyl-2-oxazoline). *J. Controlled Release. 73*, 391−399.

(8) Kabanov, V. A., and Kabanov A. V. (1998) Interpolyelectrolyte and block ionomer complexes for gene delivery: physicochemical aspects. *Adv. Drug Delivery Rev. 30*, 49−60.

(9) Wiethoff, C. M., and Middaugh, C. R. (2003) Barriers to nonviral gene delivery. *J. Pharm. Sci. 92*, 203-217.

(10) Ogris, M., Brunner, S., Schuller, S., Kircheis, R., and Wagner, E. (1999) PEGylated DNA/ transferrin-PEI complexes: reduced interaction with blood components, extended circulation in blood and potential for systemic gene delivery. *Gene Ther. 6*, 595−605.

(11) Katayose, S., and Kataoka, K. (1997) Water-soluble polyion complex associates of DNA and poly(ethylene glycol)-poly(L-lysine) block copolymer. *Bioconjugate Chem. 8*, 702−707.

(12) Choi, J. H., Choi J. S., Suh H., and Park J. S. (2001) Effect of poly(ethylene glycol) grafting on polyethylenimine as a gene transfer vector in vitro. *Bull. Korean Chem. Soc. 22*, 46−52.

(13) Petersen, H., Fechner, P. M., Martin, A. L., Kunath, K., Stolnik, S., Roberts, C. J., Fischer, D., Davies, M. C., and Kissel, T. (2002) Polyethylenimine-graft-poly (ethylene glycol) copolymers: influence of copolymer block structure on DNA complexation and biological activities as gene delivery system. *Bioconjugate Chem. 13*, 845−854.

(14) Kichler, A., Chillon, M., Leborgne, C., and Danos, O., (2002) Frisch B. Intranasal gene delivery with a polyethylenimine-PEG conjugate. *J Controlled Release 81*, 379−388.

(15) Wang, C. H., and Hsiue, G. H. (2002) Synthesis and Characterization of Temperature/ pH Sensitive Hydrogels Based on Poly(2-ethyl-2-oxazoline) and Poly(D,L-lactide). *J. Polym. Sci., Polym. Chem. 40*, 1112−1121.

(16) Kwon, I. C., Bae, Y. H., and Kim, S. W. (1991) Electrically credible polymer gels for controlled release of drugs. *Nature 354*, 291−293.

(17) Wang, C. H., and Hsiue, G. H. New (2003) amphiphilic poly(2-ethyl-2-oxazoline)/poly(L-lactide) triblock copolymers. *Biomacromolecules 4*, 1487−1490.

(18) Wang, C. H., and Hsiue, G. H. (2003) Polymer-DNA Hybrid Nanoparticles Based on Folate-Polyethylenimine-*block*-poly(L-lactide). *Bioconjugate Chem. 16*, 391−396.

(19) Miyamoto, M., Naka, K., Tokumizu, M., and Saegusa, T. (1989) End capping of growing species of poly(2-oxazoline) with carboxylic acid: a novel and convenient route to prepare vinyl- and carboxy-terminated macromonomers. *Macromolecules 22*, 1604−1607.

(20) Woodle, M. C., Engbers, C. M., and Zalipsky, S. (1994) New amphipatic polymer−lipid conjugates forming long-circulating reticuloendothelial system-evading liposomes. *Bioconjugate Chem. 5*, 493−496.

(21) Kim, C., Lee, S. C., Kang, S. W., Kwon, I. C., and Jeong, S. Y. (2000) Phase-transition characteristics of amphiphilic poly(2-ethyl-2-oxazoline)/ poly(ϵ-caprolactone) block copolymers in aqueous solutions. *J. Polym. Sci. Part B: Polym.* Phys. *38*, 2400−2408.

(22) Meister, A., and Anderson, M. E. (1983) Glutathione *Annu. Rev. Biochem. 52*, 711−760.

BC050317U

Intracellular Cargo Delivery by an Octaarginine Transporter Adapted to Target Prostate Cancer Cells through Cell Surface Protease Activation

Elena A. Goun,[†] Rajesh Shinde,[‡] Karen W. Dehnert,[†] Angie Adams-Bond,[†] Paul A. Wender,[†] Christopher H. Contag,[‡] and Benjamin L. Franc*[,§]

Departments of Chemistry and Molecular Pharmacology, Stanford University, Stanford, California 94305, Departments of Pediatrics, Microbiology, and Immunology, and Radiology, Stanford University, Stanford, California 94305, and Department of Radiology and Bioengineering Program, University of California, San Francisco, 505 Parnassus Avenue, San Francisco, California 94143-0252. Received November 7, 2005; Revised Manuscript Received February 1, 2006

Delivery of therapeutics and imaging agents to target tissues requires localization and activation strategies with molecular specificity. Cell-associated proteases can be used for these purposes in a number of pathologic conditions, and their enzymatic activities can be exploited for activation strategies. Here, molecules based on the D-arginine octamer (r_8) protein-transduction domain (PTD, also referred to as molecular transporters) have been adapted for selective uptake into cells only after proteolytic cleavage of a PTD-attenuating sequence by the prostate-specific antigen (PSA), an extracellular protease associated with the surface and microenvironment of certain prostate cancer cells. Convergent syntheses of these activatable PTDs (APTDs) are described, and the most effective r_8 PTD-attenuating sequence is identified. The conjugates are shown to be stable in serum, cleaved by PSA, and taken up into Jurkat (human T cells) and PC3M prostate cancer cell lines only after cleavage by PSA. These APTD peptide-based molecules may facilitate targeted delivery of therapeutics or imaging agents to PSA-expressing prostate cancers.

INTRODUCTION

Targeted delivery systems are critical for refining effective molecular imaging approaches and enhancing therapeutic intervention by achieving tissue-specific localization. In oncology, a number of tumor-associated molecules have been identified, and many of these have enzymatic functions that can be exploited for cancer imaging and treatment. Prostate cancer, for example, expresses PSA, a cancer-specific enzyme that can be utilized for prodrug applications.

Currently, there is no treatment that significantly prolongs survival in the setting of metastatic prostate cancer (*1*). Androgen ablation therapy, although of substantial palliative benefit, has little impact on overall survival, and the mortality rate from prostate cancer continues to increase (*2*, *3*). The low proliferation rate of androgen-independent prostate cancer requires that standard antiproliferative chemotherapeutic agents be administered over prolonged periods risking induction of dose-limiting toxicities (*4*, *5*).

Likewise, no single imaging strategy has been identified as ideal for prostate cancer at this time. Imaging modalities that rely on anatomic changes in tissue (e.g., computed tomography, CT) lack sensitivity for small tumor-containing lymph nodes and lack selectivity for large tumor-free nodes merely reacting to local inflammation. Therefore, there has been much emphasis on the development of biologically based imaging techniques such as positron emission tomography (PET) and single photon emission computed tomography (SPECT) because they have the potential to more accurately assess nodal disease. The low metabolic rate of prostate cancer provides little uptake of the most widely utilized PET radiopharmaceutical, the glucose analogue ^{18}F-fluoro-deoxy-glucose (FDG). A few radiopharmaceuticals exploiting other molecular pathways, such as ^{11}C-acetate, have demonstrated higher levels of uptake within prostate cancer than FDG (*6*). ^{11}C-Acetate and its fluorinated counterpart, ^{18}F-fluoroacetate, are promising imaging agents for detection of prostate cancer recurrence (*7*, *8*). ^{11}C-Choline and its fluorinated counterpart, ^{18}F-fluorocholine, have also demonstrated greater uptake in prostate cancer than FDG and may be particularly useful in identifying osseous and lymph node metastases (*9*−*11*). While the relationship between their molecular target and their potential role in the choice of therapeutic management is clearer than many of the other radiopharmaceuticals, the radiolabeled androgens have not shown as high a sensitivity for prostate cancer in initial investigations (*12*−*14*). Gamma-emitting radiopharmaceuticals for SPECT, such as indium-111 (^{111}In)-radiolabeled prostate specific membrane antigen (PSMA) monoclonal antibody, have demonstrated challenges such as long blood clearance and localization times, nonspecific localization, redistribution, and poor tissue penetration (*15*−*17*).

Although many of the molecular methods currently employed in prostate cancer imaging and therapy utilize a mechanism to concentrate the delivery molecule in the cancer cell, these concentration mechanisms are often tied to a metabolic pathway that has a finite transporting capacity. Clearly, it would be useful to develop other strategies to deliver cytotoxic therapeutics or imaging agents specifically to prostate cancer cells, and exploitation of cell-selective enzymes such as PSA opens the door to unique mechanisms of delivery. Cell-specific targeting based on protease expression remains a challenge, and intracellular delivery appears to be a key in several approaches to

* To whom correspondence should be addressed. Mailing address: Benjamin Franc, M. D., Department of Radiology, University of California, San Francisco, 505 Parnassus Avenue, L340, San Francisco, CA 94143-0252. E-mail: ben.franc@radiology.ucsf.edu. Phone: (415) 353-4219. Fax: (415) 353-8571.

[†] Departments of Chemistry and Molecular Pharmacology, Stanford University.

[‡] Departments of Pediatrics, Microbiology, and Immunology, and Radiology, Stanford University.

[§] University of California, San Francisco.

10.1021/bc0503216 CCC: $33.50 © 2006 American Chemical Society
Published on Web 04/28/2006

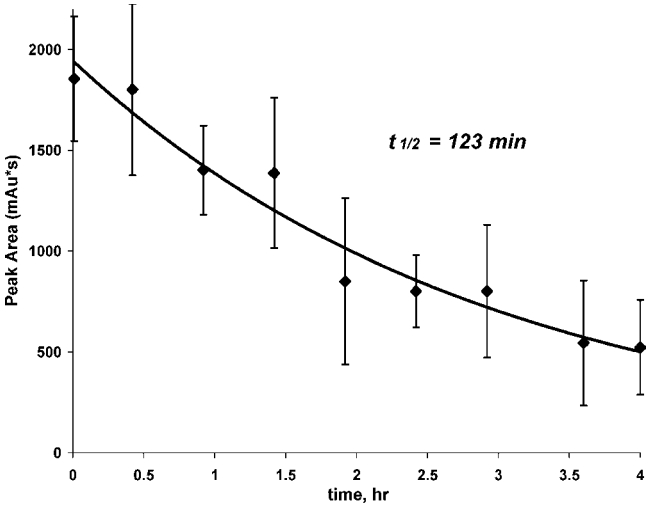

Figure 1. HPLC analysis of proteolysis of APTD by PSA. The presence of peptide **19** was plotted versus time following addition of active PSA and incubation at 37 °C giving $t_{1/2}$ = 123 min (~2 h).

imaging and therapy. Protein transduction domains (PTDs) or cell-penetrating peptides (CPPs) and more generally molecular transporters (MTs) are molecules that can be conjugated to a cargo to enable its entry as a conjugate into cells (*18*−*20*). An example of such a molecule in this rapidly emerging field of molecular transporters is the highly basic region (Tat_{49-57}, RKKRRQRRR) of the nuclear transcription activator protein (Tat) encoded by human immunodeficiency virus type 1 (HIV-1) (*21*−*23*). Our previous structure−function studies of the TAT nonamer have demonstrated that D-oligoarginine peptides as well as spaced oligoarginine peptides (rXrXrXrXrXr), guanidine-rich peptoids with 1,4-spaced side chains, guanidinylated dendrimers, and guanidinylated oligocarbamates are superior to Tat_{49-57} in cellular uptake and offer significant cost and availability advantages (*24*−*28*). Conjugates of these transporters and various probes (e.g., fluorescein) or drugs (e.g., cyclosporin A) are highly water soluble and rapidly enter cells and tissues (*25*, *28*−*30*), enabling their advancement into human trials (*25*). Cargoes ranging in size from metal chelates and fluorescent dyes (*31*, *32*) to iron oxide nanoparticles (*33*), proteins (*30*), and liposomes (*34*) can be transported into cells.

Based on a previously published mechanistic theory (*35*) of oligoarginine translocation through cell membranes, we hypothesized that conjugates in which negatively charged residues are covalently attached to an r_8 PTD would enter cells less readily, if at all. We therefore developed protransporter agents for PSA-mediated prostate cancer targeting in which r_8 PTD-containing peptides would be inactivated for cellular uptake through intramolecular complexation with attached polyanionic residues. This inactivated form would be expected to distribute systemically but would subsequently be activated for cellular uptake by PSA-mediated proteolytic cleavage at the site of prostate cancer metastases. To produce an "activatable" protein transduction domain (Figure 1, Scheme 1; APTD), an r_8 PTD would be attached to an attenuating domain (C) through a cleavable linker (CHSSKLQG) (B), a well-studied sequence selected for its balance of enzyme selectivity and cleaving kinetics (*3*, *36*, *41*−*42*). Intramolecular association of residues in C with the r_8 PTD would disfavor intermolecular association of the r_8 PTD with cell surface moieties and thereby disfavor uptake by the translocation mechanism. Tissue-selective proteolytic cleavage of B by prostate specific antigen (PSA), a protease associated with the extracellular membrane of prostate cancer cells, would eliminate internal inactivation of r_8 PTD by C, thereby enabling r_8 PTD-directed cellular entry. Together, these three components make up a complete APTD that remains

Scheme 1. Proposed Mechanism for Selective Uptake of APTDs in PSA-Expressing Prostate Cancer Cells[a]

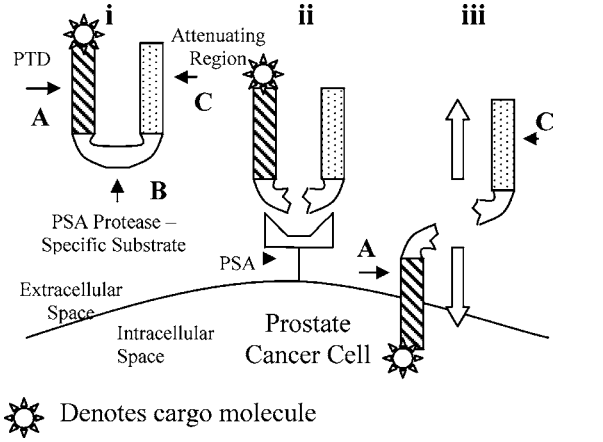

[a] (i) Intact APTD conjugate with r_8 PTD (A), PSA-protease-specific substrate linkage (B), and r_8 PTD-attenuating sequence regions (C). (ii) Upon encountering PSA associated with the surface of a prostate cancer cell, the PSA-specific substrate (B) is cleaved. (iii) Cleavage of APTD in step ii allows the fluorophor cargo-carrying r_8 PTD to enter the prostate cancer cell while the r_8 PTD-attenuating sequence remains in circulation.

extracellular until the specific peptide link is cleaved by a PSA (*37*−*39*). A similar approach based on a different protease has been recently utilized by another group to deliver imaging fluorophores into cells and squamous cell cancer xenografts in mice (*40*).

Herein, we describe the design, synthesis, and characterization of "activatable" PTDs (APTDs) that localize in cells after cleavage by PSA. The r_8 PTD-attenuating sequences were designed to disable the transmembrane transporting ability of the r_8 PTD. A variety of r_8 PTD-attenuating sequences combining charge-complementing aspartic acid residues spaced with varying numbers of glycine residues were developed. Because the critically important requirements for the attenuation component of the APTD and proteolytic release were unknown, a library of attenuated r_8 PTD peptide molecules was synthesized and the efficiency of r_8 PTD transport attenuation of various sequences was studied. These molecules were found to be cleaved by PSA and subsequently transported into Jurkat and PC3M prostate cancer cell lines. These results provide a new strategy for selective delivery of agents into prostate cancer cells and represent a new opportunity for targeted delivery of therapeutic and imaging agents based on r_8 PTDs.

EXPERIMENTAL PROCEDURES

General Methods. Unless otherwise stated, all reagents and solvents were obtained from commercial sources and used without further purification. Reverse-phase high-performance liquid chromatography (RP-HPLC) was performed with a Varian ProStar 210/215 preparative HPLC using Alltec Alltima C18, 250 mm × 22 mm, column or analytical RP-HPLC (Hewlett-Packard with Agilent 1100 series automated injector) with analytical Zorbax SB C18, 150 mm × 4.6 mm, column. The products were eluted utilizing a solvent gradient (solvent A = 0.1% trifluoroacetic acid (TFA)/H_2O; solvent B = 0.1% TFA/CH_3CN).

Matrix-assisted laser desorption/ionization time-of-flight (MALDI-TOF) mass spectrometric analysis was carried out using a Voyager-DE PRO biospectrometry workstation (PerSpective Biosystem Inc.). Ten microliters of each HPLC fraction was mixed with 20 μL of matrix solution (α-cyano-4-hydroxycinnamic acid) in 60% acetonitrile/0.1% trifluoroacetic acid/water solution. The spectra were acquired in the linear

mode, which, in general, provides values a few daltons higher than the monoisotopic mass values.

Fluorescent images were obtained using an IVIS 50 imaging system (Xenogen Corp., Alameda, CA), which consists of a cooled CCD camera detector system incorporating a xenon light source and appropriate filters for excitation and emission wavelengths. The images were acquired and processed using LivingImage 2.50 software. Flow cytometry (FACScan, Becton Dickinson, Franklin Lakes, NJ) was performed using standard FITC filters.

Automated Peptide Synthesis (Peptides 1−4). All reagents for peptide synthesis including *N*-methylpyrrolidone (NMP), diisopropylethylamine (DIEA), *N*,*N*-dimethylformamide (DMF), 1-hydroxybenzotriazole (HOBt), *O*-(benzotriazol-1-yl)-*N*,*N*,*N*′,*N*′-tetramethyluronium hexafluorophosphate (HBTU), and piperidine were purchased from Aldrich, NovaBiochem (CA), BaChem (CA), or Applied Biosystems (CA). Fmoc-protected amino acids and resins were purchased from NovaBachem or BaChem in their appropriately protected form. All automated peptide syntheses were performed on a PE Biosystems model 433A automated peptide synthesizer using the standard FastMoc coupling strategy. The peptide was assembled on Fmoc-Rink amide resin on a 0.1 or 0.25 mmol scale with all amino acids used in 4- to 10-fold excess (1 mmol).

The purity of all peptides and peptide conjugates was established as a single peak by analytical HPLC (Hewlett-Packard with Agilent 1100 series automated injector) with an analytical Zorbax SB C18, 150 mm × 4.6 mm, column at a flow rate of 1.0 mL/min in the indicated acetonitrile/water buffer containing 0.1% trifluoroacetic acid using 5−45% gradient over 15 min followed by 5 min wash at 100% acetonitrile buffer. The identity of all peptides and peptide conjugates was established using matrix-assisted laser desorption/ionization time-of-flight (MALDI-TOF) mass spectrometric analysis.

Manual Peptide Synthesis. Fmoc-Rink amide resin was mixed in DMF under nitrogen in a fritted peptide vessel (20 min). The Fmoc-protecting group was removed by mixing resin in a 20% piperidine/DMF solution (10 mL/g of resin) for 15 min (2×). The vessel was drained via vacuum and washed with DMF (3×). The chloranil resin test was performed by adding one drop of 2% acetaldehyde in DMF followed by one drop of 2% *p*-chloranil in DMF to the resin with a positive test (indicating a free amine) resulting in blue-stained beads. A small sample of resin also underwent the Kaiser resin test where two drops each of (i) 5 g of ninhydrin in 100 mL ethanol, (ii) 80 g of liquefied phenol in 20 mL of ethanol, and (iii) 0.001 M aqueous sodium cyanide (2 mL) in 98 mL of pyridine were added and the mixture was shaken to mix and heated to 120 °C for 4 min. A positive test (indicating a free primary amine) resulted in blue-colored beads.

Deprotection was repeated until the chloranil or Kaiser resin test was positive. The Fmoc-protected amino acid (5 equiv), HOBt (5 equiv), and HBTU (5 equiv) were dissolved in DMF (5 mL/g of resin) followed by the addition of DIEA (10 equiv). This mixture was added to the resin and agitated gently for 30−60 min or until a negative resin test was obtained. After coupling, the resin was washed with DMF (3×). This Fmoc deprotection and coupling sequence was repeated until the desired peptide was assembled.

Fluorescein Labeling. The fluorescent tag was attached through either the free amine of the N-terminus or a lysine side chain of the fully protected peptide while still attached to the solid support. The resin (0.1 mmol) was suspended in dry DMF in a polypropylene tube. Diisopropyl ethylamine (0.17 mL, 1 mmol, 10 equiv) and fluorescein isothiocyanate (200 mg, 0.5 mmol, 5 equiv) were added in one portion to the mixture. The solution was agitated for 18 h followed by vacuum filtration for removal of solvent. The resin was washed twice with DMF and once with DCM to remove any residual base and reagent.

Deprotection and Cleavage of Peptides. The peptide-bound resin was washed well with DCM and dried under nitrogen for several hours. The peptide was deprotected and cleaved from the solid support by exposing the resin to a solution (10 mL/0.1 mmol of peptide) of 95% TFA and 5% triisopropylsilane (TIS) for non-cysteine-containing peptides or a solution of 94% TFA, 2.5% water, 2.5% 1,2-ethane dithiol (EDT), and 1% triisopropylsilane (TIS) for cysteine-containing peptides. The mixture was placed in a polypropylene tube and mixed for 24 h at ambient temperature. After 24 h, the solution was filtered and concentrated under reduced pressure to provide a crude oil. The oil was dissolved in a minimal volume of TFA, placed in a centrifuge tube and triturated with diethyl ether. The material was pelleted via centrifugation, and the ether was removed by decanting. The pellet was washed two additional times with dry diethyl ether and dried under nitrogen. The crude peptide was dissolved in 0.1% TFA/water then purified by reverse-phase HPLC (C18 packed column; water−acetonitrile, 0.1% TFA v/v) to afford a solid after lyophilization.

Synthesis of Attenuating Sequences (Peptides 5−11). The Fmoc-Asp(OtBu)-OH or Fmoc-Gly-OH residues or both were manually attached to the resin as described above. The Boc-Cys(NPys)-OH residue was coupled using *N*,*N*′-diisopropylcarbodiimide (DIC) (5 equiv) and HOBt (6 equiv) in 80:20 DMF/dichloromethane (DCM) (5 mL). The DIEA coupling strategy could not be employed due to the base-labile nature of the 3-nitro-2-pyridinesulfenyl (Npys) protecting group. After 16 h, the peptide was washed with DMF (3×) and DCM (3×) and dried under argon for several hours. Side-chain deprotection and cleavage from the resin was achieved by mixing the resin-bound peptide in a 95:5 TFA/triisopropylsilane (TIS) solution for 5 h. Washing and purification was performed as described above.

Synthesis of the CHSSKLQG-r8-K-(FITC)NH_2 Conjugate (12). The peptide was assembled manually via solid-phase peptide synthesis on a 0.1 mmol scale using the coupling strategy described above. Amino acids Fmoc-Lys(Mtt)-OH, Fmoc-D-Arg(Pbf)-OH, Fmoc-Gly-OH, Fmoc-Gln(tBu)-OH, Fmoc-Leu-OH, Fmoc-Lys(Boc)-OH, Fmoc-Ser(OtBu)-OH, Fmoc-His-(Trt)-OH, and Fmoc-Cys(Trt)-OH (NovaBiochem, CA) were used in 4-fold excess (0.4 mmol). A solution of acetic anhydride (100 μL) and DIEA (350 μL) in DMF (2 mL) was then added, and the mixture was sparged with nitrogen gas for 1 h or until the chloranil resin test (see above) was negative indicating N-terminal acetylation. The resin was filtered via vacuum and washed with DMF (2 mL, 3×) and DCM (2 mL, 3×). A solution of TFA (1%) and TIS (3%) in DCM (96%) was then added, and the mixture was agitated under a nitrogen atmosphere for 5 min. This was repeated until a positive resin test was obtained (5×) indicating removal of the Mtt protecting group. To the free amine of the lysine side chain was added the fluorescein label according to the general procedure described above. The resin was dried for several hours under nitrogen before deprotection and cleavage (see general procedure above). Orange solid (189.7 mg, 36% yield). Analytical RP-HPLC (0.1% TFA in H_2O/CH_3CN): >98% purity. MALDI MS: calculated for $C_{111}H_{180}N_{48}O_{26}S_2$ (M + H), 2667.05; found, 2667.10.

Synthesis of the Final Attenuated Peptide Conjugates (APTD Compounds 13−19). To the attenuating peptide sequences (**5**−**11**) (4 μmol) in 0.1% TFA−water (0.5 mL) was added a solution of peptide **12** (5.3 mg, 2 μmol) in 0.1% TFA−water (1 mL). The mixture was stirred at room temperature for 24 h before quenching with ethyl acetate (2 mL). The layers were separated, and the aqueous phase was extracted and

Table 1. Library of Synthesized Peptides

no.	peptide sequence[a]	MW, calcd[b]	MW, found[b]	no.	peptide sequence[a]	MW, calcd[b]	MW, found[b]
1	r_8-K(FITC)NH_2	$C_{75}H_{123}N_{35}O_{14}S$ 1771.07	1770.11	**11**[c]	CDGGDGGDGGD	$C_{36}H_{48}N_{14}O_{21}S_2$ (M + H) 1076.98	1076.69
2	r_7-K(FITC)NH_2	$C_{69}H_{111}N_{31}O_{13}S$ 1614.88	1615.87	**12**	CHSSKLQG-r_8-K(FITC)NH_2	$C_{111}H_{180}N_{48}O_{26}S_2$ (M + H) 2667.05	2667.10
3	r_5-K(FITC)NH_2	$C_{57}H_{87}N_{23}O_{11}S$ 1302.51	1302.01	**13**	DCCHSSKLQG-r_8-K(FITC)NH_2	$C_{118}H_{191}N_{51}O_{30}S_3$ (M + H) 2900.30	2893.29
4	r_4-K(FITC)NH_2	$C_{51}H_{75}N_{19}O_{10}S$ 1146.33	1145.29	**14**	DDCCHSSKLQG-r_8-K(FITC)NH_2	$C_{122}H_{196}N_{52}O_{33}S_3$ (M + H) 3015.39	3014.96
5[c]	CD	$C_{12}H_{15}N_5O_6S_2$, (M + H) 389.41	390.46	**15**	DGDCCHSSKLQG-r_8-K(FITC)NH_2	$C_{124}H_{199}N_{53}O_{34}S_3$ (M + H) 3072.44	3072.90
6[c]	CDD	$C_{16}H_{20}N_6O_9S_2$, (M + H) 504.49	505.26	**16**	DGGDCCHSSKLQG-r_8-K(FITC)NH_2	$C_{126}H_{202}N_{54}O_{35}S_3$ (M + H) 3129.49	3129.91
7[c]	CDGD	$C_{18}H_{23}N_7O_{10}S_2$, (M + H) 561.55	562.79	**17**	DGGGDCCHSSKLQG-r_8-K(FITC)NH_2	$C_{128}H_{205}N_{55}O_{36}S_3$ (M + H) 3186.54	3187.19
8[c]	CDGGD	$C_{20}H_6N_8O_{11}S_2$, (M + H) 618.60	620.03	**18**	DGGDGGDCCHSSKLQG-r_8-K(FITC)NH_2	$C_{134}H_{213}N_{57}O_{40}S_3$ (M + H) 3358.68	3359.76
9[c]	CDGGGD	$C_{22}H_{29}N_9O_{12}S_2$, (M + H) 675.65	675.90	**19**	DGGDGGDGGDCCHSSKLQG-r_8-K(FITC)NH_2	$C_{143}H_{236}N_{59}O_{45}S_3$ (M + H) 3597.96	3597.12
10[c]	CDGGDGGD	$C_{28}H_{37}N_{11}O_{16}S_2$ (M + H) 847.79	848.93				

[a] FITC = fluorescein isothiocyanate; r_8 = arginine octamer; all other letters correspond to standard single-letter abbreviations for amino acids. [b] Without counter ions. [c] 3-Nitro-2-pyridinesulfenyl (Npys)-protected cysteine has been used for synthesis of peptides **5**−**11**.

concentrated in vacuo. The APTD conjugated peptide was purified by RP-HPLC to give the desired conjugated peptide as a bright yellow sticky solid (90−95% yield). Analytical RP-HPLC (0.1% TFA in H_2O/CH_3N): >99% purity. MALDI MS: see Table 1.

Serum Stability Studies. The serum stability of APTD conjugates was evaluated by incubation in fetal calf serum (FCS) (50% FCS/50% phosphate-buffered saline (PBS), pH 7.4) at 37 °C for 4 h using a standard protocol (*47*, *48*). The percentage of intact APTD peptide after incubation was determined by precipitation of the serum proteins with 70% acetonitrile in 0.1% TFA and separating degradation products by analytical RP-HPLC using a 15 min, 10−30% linear acetonitrile gradient (0.1% TFA/water).

Kinetic Analysis of Substrate Hydrolysis by PSA. The activity of human PSA protease (Calbiochem) was tested prior to experiments with a PSA substrate fluorogenic test kit (Mu-His-Ser-Ser-Lys-Leu-Gln-AFC, 2TFA (Mu = 4-morpholinoureidyl); Calbiochem). Subsequently, 100 μL of 50 μM PSA substrate solution in PSA buffer (50 mM Tris, pH 7.5, 150 mM NaCl) was added to 5.4 μL (concentration = 1.84 mg/mL) of enzymatically active PSA solution in the same buffer, and the mixture was incubated at 37 °C for 4 h. Buffer without PSA enzyme was used as control. Progress of the enzymatic cleavage was monitored by reverse-phase analytical HPLC. Aliquots were drawn at specific times from 0 to 4 h. Ten microliters of the sample was diluted with 90 μL of 0.1% TFA to yield pH $\approx$ 2. After filtration (0.2 μM membrane filter, Anatop Laboratory), 80 μL of the resulting samples were applied to an analytical HPLC column using a 15 min, 5−30% linear acetonitrile gradient (0.1% TFA/water). Fractions were collected manually in Eppendorf tubes (1.5 mL) and dried completely, and masses were analyzed by mass spectroscopy (MALDI).

Cell Uptake Assay: Jurkat Cells. The synthesized APTDs were each dissolved in PBS buffer (pH 7.2), and their concentrations were determined spectrophotometrically by absorption of fluorescein at 490 nm (ϵ = 67 000) (*21*). Varying concentrations (50 and 0.4 μM) of each peptide (nonattenuated CHSSKLQG-r_8-K(FITC)NH_2 (**12**, see Table 1) and all attenuated APTD forms) were added to 3×10^6 Jurkat cells (human T cell line, grown in 10% FCS and DMEM) for 5 min in microtiter plates (96 well) at 37 °C.

Peptides r_5-K(FITC)NH_2 (**3**) and r_4-K(FITC)NH_2 (**4**) were selected as controls. Previous work has shown that a minimum of six arginine residues is required for significant cell uptake to occur (*25*). Following incubation, the microtiter plates were centrifuged, and the cells were isolated, washed, and resuspended in PBS buffer containing 0.1% propidium iodide. The cells were analyzed by fluorescent flow cytometry (FACScan; Becton Dickinson), and cells stained with propidium iodide were excluded from the analysis. The data presented are the mean fluorescent signal for the 10 000 cells collected. Measurements were also made for cells exposed to APTD conjugate peptides after they were subjected to PSA-mediated cleavage. One hundred microliters of 400 μM APTD conjugate solutions in PBS buffer were incubated with 10.8 μL (concentration = 1.84 mg/mL) of enzymatically active PSA solution (Calbiochem) for ~4 h at 37 °C. Samples of each of the resulting peptide solutions were analyzed by HPLC to establish the completeness of the cleavage. Each of the cleaved APTD peptide solutions was then incubated in triplicate with Jurkat cells as described above.

Confirmation of Intracellular Uptake into PC3M Prostate Cancer Cells. Ten micromolar solutions of r8-K(FITC)NH_2 (**1**), r4-K(FITC)NH_2 (**4**), and DGGDGGDGGDCCHSSKLQG-r8-K(FITC)NH_2 (**19**) were preincubated with active PSA solution (5.4 μL, c = 1.84 mg/mL for ~4 h at 37 °C). The incubated peptides and conjugates were then added to 30 000 PC3M cells/well (200 μL total volume) for 15 min. Following incubation, the cells were washed, and the samples were visualized using fluorescence laser confocal microscopy (wavelength λ = 484

Scheme 2. Synthesis of APTD Conjugates[a]

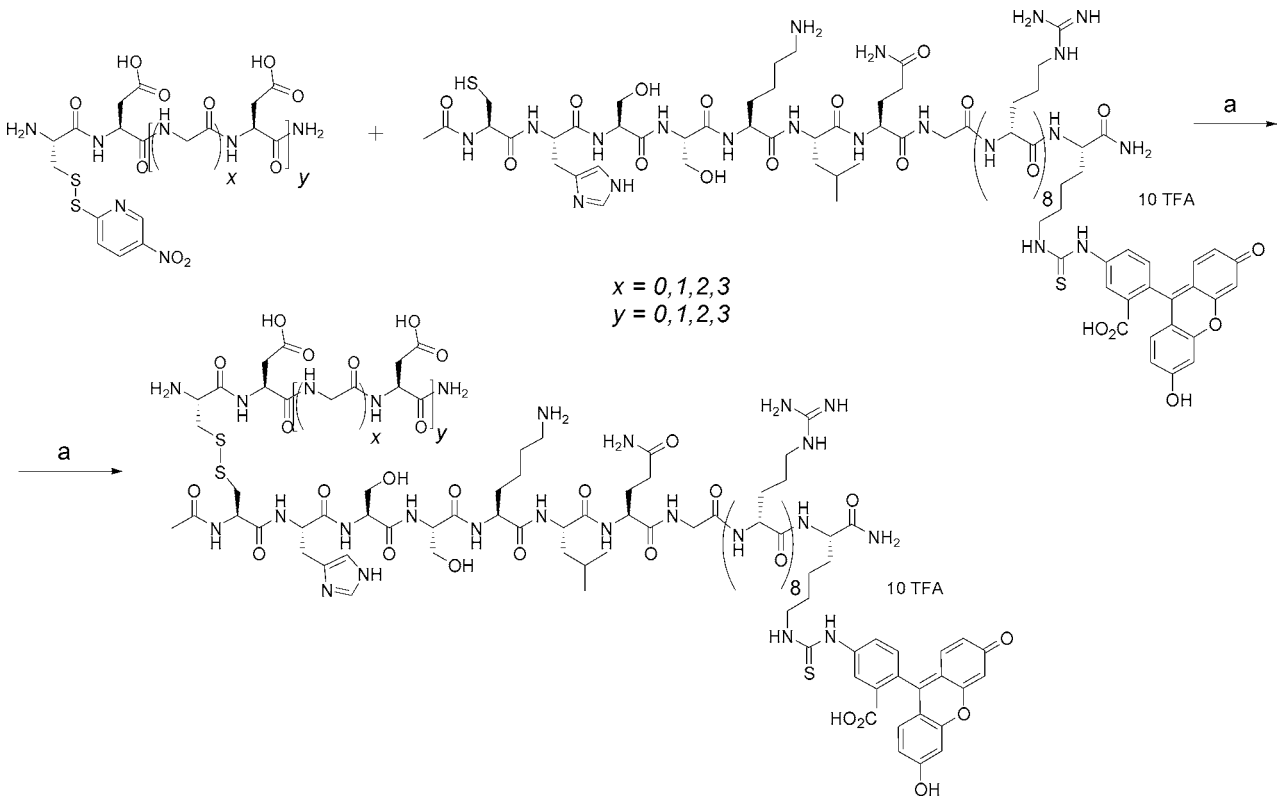

[a] (a) 0.1% TFA in deionized water, 14−24 h, 90−95%.

nm). The PC3M cells were also imaged using the IVIS fluorescent camera, and the photon flux (photons/s) was measured.

Data Analysis. All data were analyzed statistically using the Student's t-test to determine the significance of differences in cell uptake of the various peptide conjugates.

RESULTS

APTD Conjugate Library Synthesis and Purification. A peptide with sequence CHSSKLQG-r8-K, incorporating both the r_8 PTD and linking sequences separated by a single glycine spacer, was synthesized with a fluorescein isothiocyanate (FITC) fluorophore attached to a side chain of lysine at the carboxy-terminus. Multiple potential r_8 PTD-attenuating sequences of the form $C(D)_x$, $CD(GD)_x$, and $CD(GGD)_x$ ($x = 1$, 2, or 3) were synthesized, and each was subsequently conjugated to the CHSSKLQG-r_8-K(FITC)NH_2 peptide through a disulfide bond of the cysteine residues (Scheme 2). Limited peptide solubility, aggregation, or both were observed for r_8 PTD-attenuating sequences with more than four aspartate residues; therefore, the library was not expanded beyond those peptides listed in Table 1. TFA counterions were subsequently ion-exchanged for chloride ion after the disulfide coupling of the CHSSKLQG-r_8-K(FITC)NH_2 and r_8 PTD-attenuating sequences.

Serum Stability Studies. Peptide conjugates **14**−**19** (Table 1) were investigated for their stability in serum (*43*, *44*). After 4 h of incubation in serum at 37 °C, the decomposition of the peptide conjugates ranged from 1% to 5%. The most effectively attenuated APTD conjugate **19** (DGGDGGDGGDCCHSSKLQG-r8-K(FITC)NH_2) was found to be 97% intact after 4 h of incubation at 37 °C.

PSA Cleaving Studies. Following incubation in PSA-containing phosphate buffer solution, tested APTD conjugates demonstrated three distinct peaks on analytical HPLC, where one of these peaks corresponded to uncleaved APTD conjugate while the other two peaks corresponded to the expected cleavage products. Peak assignment was accomplished by collection of the new peaks following cleavage and determination of their masses by mass spectrometry (MALDI). The MALDI data indicated that proteolysis took place between glutamine and glycine residues of the PSA substrate (HSSKLQ−G), as predicted, giving products such as NH_2-DGGDGGDGGDCH-SSKLQ (MW calculated 1764.76, found 1766.12) and G-r8-K(FITC)NH_2 (MW calculated 1841.12, found 1843.38) in the case of the APTD conjugate **19** cleaving study. The time required to cleave half of the substrate varied between the APTD conjugates but was generally in the range of 1.8−2 h. Kinetics of PSA proteolysis of the most effectively attenuated APTD (peptide conjugate **19**) is shown in Figure 1. No detectable decomposition was observed after incubation of the APTD conjugates in phosphate buffer solution without PSA enzyme at 37 °C for 4 h. These data were in agreement with that previously published by other groups (*3*, *36*, *41*−*42*).

Differential APTD Uptake prior to and following PSA-Mediated Cleavage. The APTD conjugates composed of an r_8 PTD, a PSA-selective cleavage sequence (HSSKLQG), and an r_8 PTD-attenuating sequence ($CD(GGD)_x$), where $x = 2$ or 3 (compounds **18** and **19**, respectively) were incubated in PSA-containing media for 4 h prior to the introduction of either Jurkat or PC3M cells for 5 or 15 min, respectively. Flow cytometry and fluorescence laser confocal microscopy were utilized to assess intracellular peptide uptake. Control experiments consisted of cell incubation in peptide-containing media that had not been exposed to PSA, as well as incubation in solutions containing fluorescently labeled control compounds such as octamer of arginine (r_8) **1** (high uptake) and tetramer (r_4) or pentamer (r_5) of arginine (compounds **3** and **4**, insignificant uptake). The results of these studies are summarized in Figure 2, panel A (Jurkat cells) and panel B (PC3M prostate cancer cells). APTD cleavage by PSA significantly enhanced uptake in both Jurkat cells and prostate cancer cells at all time points and concentrations ($p < 0.05$);

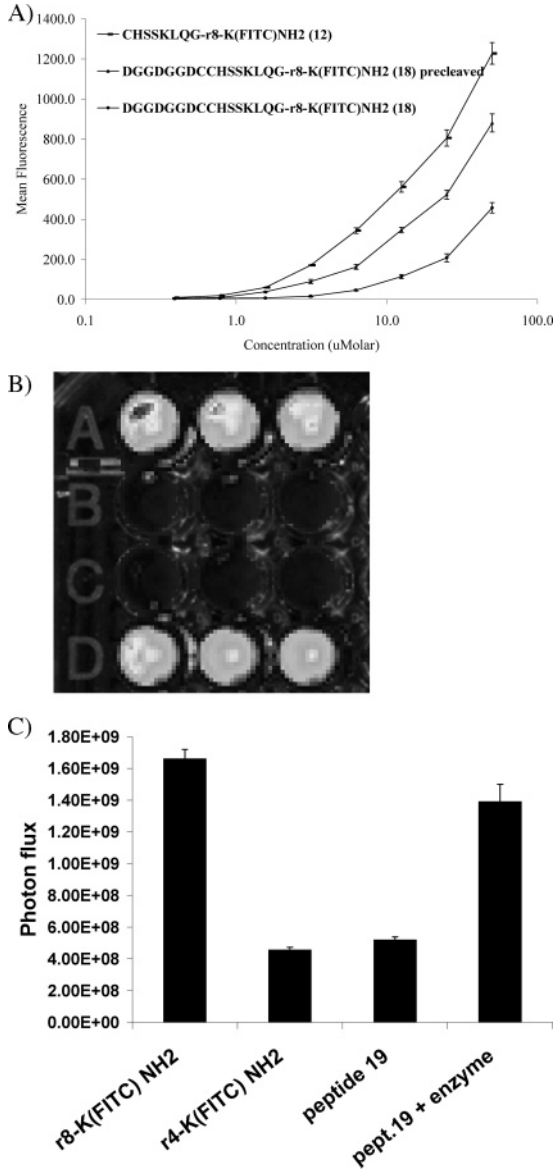

Figure 2. Comparison of cell uptake of APTD with and without prior PSA-mediated peptide cleavage: (A) Jurkat cells. Jurkat cells were incubated with each APTD conjugate solution for 5 min and washed twice. Uptake of each peptide was measured using flow cytometry. The level of cell uptake of the precleaved PSA-targeting APTD was between the levels of uptake of uncleaved APTD and r_8 PTD. Standard deviations are shown for each point; however, their magnitudes were, in many cases, less than 5% of the datapoint. (B) PC3M cells. In triplicate, row A contains r_8-K(FITC)NH_2 (**1**) positive control, row B r_4-K(FITC)NH_2 (**4**) negative control, row C DGGDGGDGGDCCH-SSKLQG-r_8-K(FITC)NH_2 (**19**), and row D DGGDGGDGGDCCH-SSKLQG-r_8-K(FITC)NH_2 (**19**) preincubated with enzymatically active PSA enzyme. This image was obtained using an IVIS 50 imaging system (Xenogen Corp., Alameda, CA) with the level of fluorescence indicated by a color scale ranging from black (no fluorescence) to white (greatest measured fluorescence). The level of fluorescence reflects the level of uptake of the APTD or nonattenuated peptide transporters (r_8 or r_4). Uptake of the PSA targeting APTD takes place only after release of r_8 PTD-attenuating sequence via PSA-specific substrate hydrolysis, as is demonstrated by fluorescence in row D but not in row C. Uptake of the cleaved APTD approaches but does not equal that of the nonattenuated r_8 PTD (row A). Panel C presents bar representation of uptake of fluorescently labeled PSA-targeting peptide **19** in PC3M prostate cancer cells with and without precleavage by PSA. FITC = fluorescein isothiocyanate; r_8 = arginine octamer; all other letters correspond to standard single-letter abbreviations for amino acids in the order from C- to N-terminus.

however, cell uptake of cleaved APTD remained significantly less than that of nonattenuated r_8 PTD ($p < 0.05$).

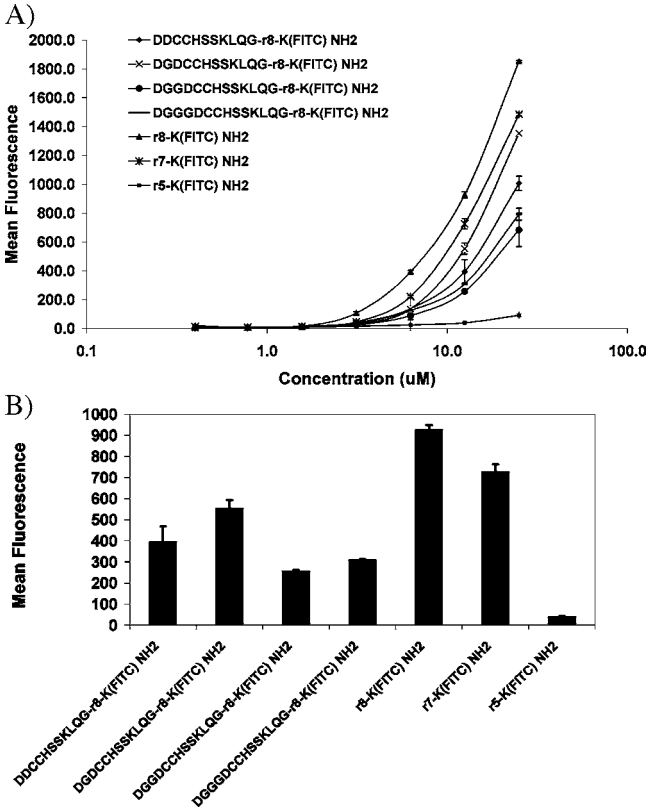

Figure 3. (A) Uptake of various concentrations of APTD conjugates incorporating r_8 PTD, a PSA enzyme-specific sequence, and one of a library of r_8 PTD-attenuating sequences composed of two aspartates spaced with different numbers of glycine residues (DD, DGD, DGGD, DGGGD). Standard deviations are shown for each point; however, their magnitudes were, in many cases, less than 5% of the datapoint. (B) Bar graph demonstrating APTD conjugate uptakes at a single concentration (20 μM), extracted from data shown in panel A. This experiment demonstrates that the number of glycine spacing residues changed the effectiveness of r_8 PTD transport attenuation by as much as 2-fold, with the order of decreasing effectiveness of 2 (greatest) > 3 > 0 > 1 ($p < 0.05$ for difference of attenuation achieved with a spacer of two glycine residues when compared to all other glycine spacer lengths).

Cell Partitioning and Attenuation/Spacing Experiments. The ability of various r_8 PTD-attenuating sequences with different spacing to prevent the r_8 PTD-containing peptide conjugates from entering cells was characterized by incubating Jurkat cells with different concentrations of APTD. The results of these experiments are presented in Figure 3A,B. All of the tested r_8 PTD-attenuating sequences significantly decreased cell uptake of the r_8 PTD transporter when compared to r_8 PTD alone at concentrations of 3 μM and above ($p < 0.01$). The r_8 PTD-attenuating sequence that included aspartic acid residues spaced with two glycines demonstrated the greatest transport-attenuating effect. The number of glycine spacing residues changed the effectiveness of attenuation by as much as 2-fold between the most and the least efficient r_8 PTD-attenuating sequence. At concentrations of 3−12 μM, the attenuation of transport activity achieved when aspartate residues were spaced with two glycine residues was significantly greater than the attenuation achieved when they were spaced by zero, one, or three residues ($p < 0.05$). Otherwise, spacing of aspartate residues with three glycine residues tended to provide greater transport attenuation than spacing with zero or one glycine residue; however, the differences in attenuation were not significant.

The level of r_8 PTD transport attenuation increased significantly with each aspartate residue added ($p < 0.05$) until three aspartate residues had been included. At most concentrations tested, the level of transport attenuation achieved by the

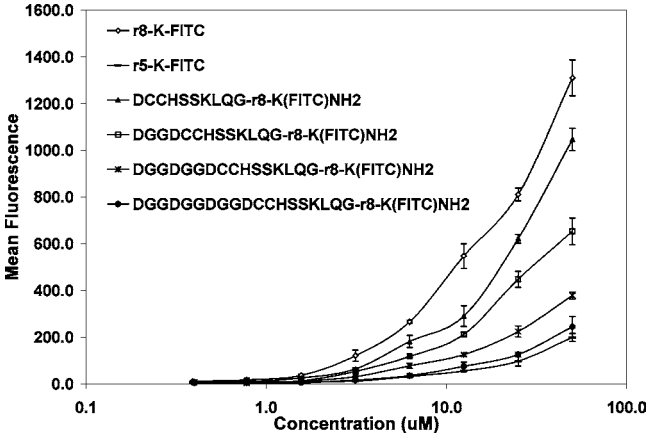

Figure 4. Characterization of the efficiency of r_8 PTD transport attenuation of APTDs with increasing number of apartates (0−4) in comparison with the control compounds r_8-K(FITC)NH_2 (**1**) (high uptake) and r_5-K(FITC)NH_2 (**3**) (no significant uptake). Abbreviations: r_8 = arginine octamer; r_5 = arginine 5-mer; all other letters correspond to standard single-letter abbreviations for amino acids.

inclusion of four aspartate residues was not significantly different from that obtained with three. The presence of four aspartates in the r_8 PTD-attenuating sequence exhibited a low level of uptake in Jurkat cells that was not significantly different from the level of uptake in r_5 and r_4 controls ($p = 0.08-0.36$) (Figure 4). Results from the APTD **19**, which demonstrated the best attenuation, were compared to r_5 and r_4 controls using PC3M cells. The results summarized in Figure 2B demonstrated similar inhibition of uptake between intact APTDs and control peptides (no significant difference).

DISCUSSION

We report the development of a group of APTD conjugates that incorporate an r_8 PTD connected to an r_8 PTD-attenuating sequence via a protease cleavable linker ([r_8 PTD-attenuating sequence]−[cleavable linker]−[r_8 PTD]). The APTD conjugates themselves do not readily enter cells because the r_8 PTD-attenuating sequence disables the r_8 PTD molecular transporter through internal complexation, but upon cleavage of the linker by a specific protease, the activity of the r_8 PTD transporter is restored and cell entry of the cargo-carrying r_8 PTD is observed. Although PTDs have been used by many investigators to facilitate the delivery of imaging agents and therapeutics in vitro and in vivo, the selective delivery of PTDs and their cargos to specific cell types is only beginning to be investigated. This initial research has mainly focused on antibody- and liposome-mediated strategies (*33*, *45*−*47*). Although antibodies have occasionally been successful in targeting tumors (*48*), their bulk hinders penetration of solid tumors and excretion of unbound reagent (*49*), and elaborate reengineering is required to minimize immunogenicity (*50*, *51*). Other investigators have recently reported the development of molecules selectively taken up by cancers expressing matrix metalloproteinase-2 (MMP-2) or MMP-9 following cleavage of the molecule to release a labeled polyarginine transporting peptide (*40*). By incorporation of the selective transporter component into the small molecule, there is greater potential for molecular delivery into deep tissues. The present work provides further evidence for the utility of this promising selective targeting strategy for cargo delivery based on the level of local protease expression. In addition, the results presented here emphasize the achievements in decreased molecular size and specific targeting that can be accomplished by careful engineering of the molecular components of APTDs.

In this study, a modular approach was taken during the design and synthesis of the APTDs, and many combinations of modules containing (1) the r_8 PTD and cleavable linker and (2) one of several r_8 PTD-attenuating sequences were tested. The r_8 PTD itself is a well-established facilitator of molecular transport across cell membranes. Although the detailed mechanisms and subcellular localization of these transporters is not fully understood and is expected to vary as a function of conjugate size, we have recently reported a mechanistic hypothesis for how water-soluble guanidinium-rich transporters attached to small cargoes (MW ca. <3000) can migrate across the nonpolar lipid membrane of a cell and enter the cytosol (*35*). The first step of this mechanism, referred to as adaptive translocation, involves the formation of bidentate hydrogen bonds between the polar, positively charged, water-soluble octamers of arginine (r_8) and negatively charged, bidentate hydrogen bond acceptor groups of endogenous membrane constituents on the cell surface (phosphates, sulfates, carboxylates), leading to the formation of membrane-soluble ion-pair complexes. This step in the mechanism of r_8 PTD-mediated cell entry provides a basis for understanding why conjugates in which negatively charged residues are covalently attached to an r_8 PTD would enter cells less readily, if at all, relative to the free r_8 PTD (*36*). At the molecular level, the attenuating effect is thought to arise through the intramolecular formation of ion pair bidentate hydrogen bond complexes between carboxylate and guanidinium groups with each complex reducing the ability of the transporter to form related intermolecular ion pair complexes as required for cell entry. We hypothesize that intramolecular affinity of the r_8 PTD and the r_8 PTD-attenuating sequence dominates over their intermolecular interaction because they are entropically constrained through the tether of the linking sequence. Thus, of the eight arginines in the r_8 PTD, only four to five arginines would be available for interaction with the membrane when as few as three or four aspartate residues are present in the r_8 PTD-attenuating sequence. We have previously found that arginine conjugates containing one to five arginine residues free for interaction with the cell membrane exhibited markedly lower uptake than conjugates of seven to nine arginines (*27*, *29*).

In the APTD strategy, such negatively charged residues can be arranged in various ways to achieve attenuation of r_8 PTD intracellular transport. The present study utilized r_8 PTD-attenuating sequences composed of aspartate residues alone or spaced with glycine residues. Those sequences incorporating aspartate and glycine residues were found to provide the greatest interference with r_8 PTD transmembrane transport. A combination of greater peptide flexibility with spacing and more optimal positioning of aspartate residues is likely to be responsible for these results because the inclusion of glycine spacers increased the effectiveness of transport attenuation. A greater number of glycines between each aspartate was not found to have a clear effect on cell uptake. These results may have been due to specific spatial orientations achieved using these various lengths of glycine spacers, or there may be an optimal degree of flexibility above which the preference for intramolecular association is lost. The r_8 PTD-attenuating sequence DGGDGGDGGD demonstrated the most effective transport attenuation of any sequence tested (APTD conjugate **19**). The level of r_8 PTD transport attenuation increased as a greater number of aspartates were incorporated into the r_8 PTD-attenuating sequence, as could be expected. The presence of four aspartates in the r_8 PTD-attenuating sequence spaced with two glycines showed as little uptake in Jurkat cells as the r_5 (**3**) or r_4 (**4**) controls, previously shown to have insignificant uptake in Jurkat cells (Figure 4) (*27*, *29*). A greater number of aspartates in the r_8 PTD-attenuating sequence resulted in aggregation and solubility problems.

Prostate cancer was chosen as a model system to demonstrate the feasibility of the APTD targeting approach. Prostate cancer

cells in humans express an abundance of PSA, which was chosen as a target protease because of its relatively specific expression by prostate cancer cells and its postulated low activity within the circulation due to potential rapid inactivation in blood by major serum protease inhibitors ACT and α_2-macroglobulin (*3*). In addition to prostate cancers, PSA is found in high concentrations in the seminal plasma, where the major proteolytic substrates for PSA are the gel-forming proteins in freshly ejaculated semen, Sg I and Sg II (*38*). Using the PSA cleavage map for Sg I and Sg II, Denmeade and co-workers have identified a peptide with the amino acid sequence His-Ser-Ser-Lys-Leu-Gln-Gly (HSSKLQG) that is selectively cleaved by PSA at the carboxylic end of glutamine with a favorable balance of kinetic and binding characteristics (*3*, *36*, *41*−*42*). The peptide sequence is a well-characterized PSA protease substrate that has been used to selectively deliver chemotherapeutics such as doxorubicin (*36*), thapsigargin (*41*), and 5-fluorouracil (*42*) as prodrugs to prostate cancer. Hence, this sequence was introduced as a linker between r_8 PTD and the r_8 PTD-attenuating sequences. In the present study, APTD constructs incorporating r_8 PTD, the HSSKLQG linker sequence, and the r_8 PTD-attenuating sequence underwent cleavage in the linker subunit during incubation with PSA. For example, the APTD conjugate DGGDGGDGGDCCHSSKLQG-r8-K(FITC)NH_2 (**19**) was cleaved into two parts (DGGDGGDGGDGGDCCHSSKLQ and G-r8-K(FITC)NH_2) by PSA, as demonstrated by HPLC and mass spectrometry. Upon cleavage from the r_8 PTD-attenuating sequence, the r_8 PTD demonstrated the ability to rapidly transport its attached cargo (FITC) into Jurkat and PC3M prostate cancer cells. This was observed from flow cytometry experiments and confirmed with laser confocal microscopy. The efficiency of this uptake approached that of nonattenuated r_8 PTD (**1**). This finding provides evidence that, once cleaved, the r_8 PTD and r_8 PTD-attenuating sequence components of the APTD molecules are capable of dissociation despite their ionic and polar attractive forces.

The APTD molecules developed in the present study provide a foundation for selective intracellular delivery of cargo to PSA-expressing prostate cancer cells. The dependence of cell uptake on the presence of PSA makes the described molecules promising candidates for the targeted delivery of therapeutics and imaging agents to prostate cancer tissues. However, studies of these molecules to date have been limited to the in vitro setting. With a focus on a cleavable sequence that is highly selective for PSA, it is anticipated that future in vivo localization of the molecules to prostate cancer will take place in a highly selective manner. However, peptide sequences designed for enzymatic cleavage can only achieve a certain level of enzyme specificity before the kinetics of their hydrolysis prevent them from being useful. Thus, while the APTD molecules were found to be stable in serum (FBS) in the present studies, there may be other enzymes present within the circulation in vivo that are capable of cleaving the APTD in a nonspecific manner. Any nonspecific cleavage of the molecule while in circulation could allow rapid intracellular localization of the r_8 PTD within the most proximal cells and could thereby both decrease the fraction of administered molecule localizing to the site of prostate cancer and increase background uptake. Future preparation for in vivo studies of these APTDs will include investigation of their stabilities in solutions of other proteases present widely within the circulation of animals and humans. Because the APTD conjugates will be tested in animal models of prostate cancer in immediate future studies, FCS was used as a model of these circulatory conditions to only grossly assess the nonspecific APTD cleavage that could be expected.

In the studies presented, a 4 h incubation of the APTD in PSA was utilized to demonstrate cell uptake of the cleaved APTD. Actual time of contact between the enzyme and the APTD in vivo may be much shorter due to factors such as blood flow and diffusion. Another potential challenge for in vivo application of the APTD strategy may be the short circulation times of peptides in general. Circulation must be long enough for a substantial fraction of the APTD to be cleaved, enabling localization in prostate cancer cells. The kinetics of APTD cleavage observed in the present study suggest that these molecules may need to be modified in future in vivo studies (e.g., through the attachment of poly[ethylene glycol]) to enable long circulation times for adequate uptake into foci of prostate cancer. However, it is difficult to extrapolate data regarding enzymatic activity from the in vitro setting to the in vivo setting where higher local concentrations of the enzyme and the optimal environment for enzymatic activity may allow more rapid substrate cleavage. Intracellular localization of the APTD following cleavage is anticipated to be rapid. In the studies presented, cells were incubated in solutions containing APTD for 5 (Jurkat) or 15 (PC3M) min with similar results. The residence time of the APTD in the extracellular matrix in vivo cannot be predicted, and in vivo studies are required to explore the impact of all of the above factors on localization of the APTD in prostate cancers. A sensitive imaging modality, such as PET or potentially SPECT, will likely be required to identify uptake of cleaved PSA-targeting APTD in vivo.

Protease-based targeting is a promising strategy in cancer therapy and imaging. This concept can be further adapted to other activation strategies such as those employing locally restricted enzymes, light, or pH gradients. The presented work demonstrates the feasibility of selective delivery of cargo to the intracellular compartments of prostate cancer cells using molecules incorporating an r_8 PTD and an r_8 PTD-attenuating sequence linked by a sequence that serves as a substrate for the PSA enzyme. Future development of these APTDs will focus on transitioning their use to in vivo models of prostate cancer.

ACKNOWLEDGMENT

This work was funded in part by grants from the National Institutes of Health (Grants CA31841 and CA31845 to P.A.W.), the Department of Defense (Grant PC040144 to B.F.), and the National Science Foundation (Center for Biophotonics Science and Technology Grant 002865-SU to C.H.C.).

LITERATURE CITED

(1) Yagoda, A., and Petrylak, D. (1993) Cytotoxic chemotherapy for advanced hormone-resistant prostate cancer. *Cancer 71*, 1098−1109.
(2) Parker, S. L., Tong, T., Bolden, S., and Wingo, P. A. (1996) Cancer statistics. *CA: Cancer J. Clin. 46*, 5−27.
(3) Denmeade, S. R., Lou, W., Lovgren, J., Malm, J., Lilja, H., and Isaacs, J. T. (1997) Specific and efficient peptide substrates for assaying the proteolytic activity of prostate-specific antigen. *Cancer Res. 57*, 4924−4930.
(4) Schulze, H., Isaacs, J. T., and Coffrey, D. S. (1987) A critical review of the concept of total androgen ablation in the treatment of prostate cancer. *Prog. Clin. Biol. Res. 243A*, 1−19.
(5) Berges, R. R., Vukanovic, J., Epstein, J. I., CarMichel, M., Cisek, L., Johnson, D. E., Veltri, R. W., Walsh, P. C., and Isaacs, J. T. (1995) Implication of cell kinetic changes during the progression of human prostatic cancer. *Clin. Cancer Res. 1*, 473−480.
(6) Oyama, N., Akino, H., Kanamaru, H., Suzuki, Y., Muramoto, S., Yonekura, Y., Sadato, N., Yamamoto, K., and Okada, K. (2002) ^{11}C-acetate PET imaging of prostate cancer. *J. Nucl. Med. 43* (2), 181−186.
(7) Matthies, A., Ezziddin, S., Ulrich, E. M., Palmedo, H., Biersack, H. J., Bender, H., and Guhlke, S.(2004) Imaging of prostate cancer metastases with ^{18}F-fluoroacetate using PET/CT. *Eur. J. Nucl. Med. Mol. Imaging. 31* (5), 797.
(8) Oyama, N., Miller, T. R., Dehdashti, F., Siegel, B. A., Fischer, K. C., Michalski, J. M., Kibel, A. S., Andriole, G. L., Picus, J., and

Welch, M. J. (2003) ^{11}C-acetate PET imaging of prostate cancer: detection of recurrent disease at PSA relapse. *J. Nucl. Med. 44* (4), 549−555.
(9) Hara, T., Kosaka, N., and Kishi, H. (1998) PET imaging of prostate cancer using carbon-11-choline. *J. Nucl. Med. 39* (6), 990−995.
(10) Kotzerke, J., Prang, J., Neumaier, B., Volkmer, B., Guhlmann, A., Kleinschmidt, K., Hautmann, R., and Reske, S. N. Experience with carbon-11 choline positron emission tomography in prostate carcinoma. *Eur. J. Nucl. Med. 27* (9), 1415−1419.
(11) DeGrado, T. R., Coleman, R. E., Wang, S., Baldwin, S. W., Orr, M. D., Robertson, C. N., Polascik, T. J., and Price, D. T. (2001) Synthesis and evaluation of ^{18}F-labeled choline as an oncologic tracer for positron emission tomography: initial findings in prostate cancer. *Cancer Res. 61* (1), 110−117.
(12) Dehdashti, F., Picus, J., Michalski, J. M., Dence, C. S., Siegel, B. A., Katzenellenbogen, J. A., and Welch, M. J. (2005) Positron tomographic assessment of androgen receptors in prostatic carcinoma. *Eur. J. Nucl. Mol. Imaging 32* (3), 344−350.
(13) Larson, S. M., Morris, M., Gunther, I., Beattie, B., Humm, J. L., Akhurst, T. A., Finn, R. D., Erdi, Y., Pentlow, K., Dyke, J., Squire, O., Bornmann, W., McCarthy, T., Welch, M., and Scher, H. (2004) Tumor localization of 16beta-^{18}F-fluoro-5alpha-dihydrotestosterone versus 18F−FDG in patients with progressive, metastatic prostate cancer. *J. Nucl. Med. 45* (3), 366−373.
(14) Bonasera, T. A., O'Neil, J. P., Xu, M., Dobkin, J. A., Cutler, P. D., Lich, L. L., Choe Y. S., Katzenellenbogen, J. A., and Welch, M. J. (1996) Preclinical evaluation of fluorine-18-labeled androgen receptor ligands in baboons. *J. Nucl. Med. 37*, 1009−1015.
(15) Manyak, M. (1998) Clinical Applications of Radioimmunoscintigraphy with Prostate-Specific Antibodies for Prostate Cancer. *Cancer Control 5*, 493−499.
(16) Manyak, M. J., Hinkle, G. H., Olsen, J. O., Chiaccherini, R. P., Partin, A. W., Piantadosi, S., Burgers, J. K., Texter, J. H., Neal, C. E., Libertino, J. A., Wright, G. L., Jr., and Maguire, R. T. (1999) Immunoscintigraphy with indium-111-capromab pendetide: evaluation before definitive therapy in patients with prostate cancer. *Urology 54*, 1058−1063.
(17) Wilder, R. B., DeNardo, G. L., and DeNardo, S. J. (1996) Radioimmunotherapy: recent results and future directions. *J. Clin. Oncol. 14*, 1383−1400.
(18) Lindgren, M., Hallbrink, M., Prochiantz, A., and Langel, U. (2000) Cell-penetrating peptides. *Trends Pharmacol. Sci. 21*, 99−103.
(19) (2002) *Cell-Penetrating Peptides: Processes and Applications* (Langel, U., Ed.) CRC Press, Boca Raton, FL.
(20) Fischer, P. M., Krausz, E., and Lane, D. P. (2001) Cellular delivery of impermeable effector molecules in the form of conjugates with peptides capable of mediating membrane translocation. *Bioconjugate Chem. 12*, 825−841.
(21) Jeang, K. T., Xiao, H., and Rich, E. A. (1999) Multifaceted activities of the HIV-1 transactivator of transcription, Tat. *J. Biol. Chem. 274*, 28837−28840.
(22) Green, M., and Loewenstein, P. M. (1988) Autonomous functional domains of chemically synthesized human immunodeficiency virus tat trans-activator protein. *Cell 55*, 1179−1188.
(23) Vives, E., Brodin, P., and Lebleu, B. (1997) A truncated HIV-1 Tat protein basic domain rapidly translocates through the plasma membrane and accumulates in the cell nucleus. *J. Biol. Chem. 272*, 16010−16017.
(24) Mitchell, D. J., Kim, D. T., Steinman, L. C., Fathman, C. G., and Rothbard, J. B. (2000) Polyarginine enters cells more efficiently than other polycationic homopolymers. *J. Pept. Res. 55*, 318−325.
(25) Wender, P. A., Mitchell, D. J., Pattabiraman, K., Pelkey, E. T., Steinman, L., and Rothbard, J. B. (2000) The design, synthesis, and evaluation of molecules that enable or enhance cellular uptake: Peptoid molecular transporters. *Proc. Natl. Acad. Sci. U.S.A. 97*, 13003−13008.
(26) Futaki, S., Suzuki, T., Ohashi, W., Yagami, T., Tanaka, S., Ueda, K., and Sugiura, Y. (2001) Arginine-rich peptides. An abundant source of membrane-permeable peptides having potential as carriers for intracellular protein delivery. *J. Biol. Chem. 276*, 5836−5840.
(27) Wender, P. A., Rothbard, J. B., Jessop, T. C., Kreider, E. L., and Wylie, B. L. (2002) Oligocarbamate Molecular Transporters: Design, Synthesis, and Biological Evaluation of a New Class of Transporters for Drug Delivery. *J. Am. Chem. Soc. 124*, 13382−13383.
(28) Chen, L., Wright, L. R., Chen, C. H., Oliver, S. F., Wender, P. A., and Mochly-Rosen, D. (2001) Molecular transporters for peptides: delivery of a cardioprotective epsilonPKC agonist peptide into cells and intact ischemic heart using a transport system, R(7). *Chem. Biol. 8*, 1123−1129.
(29) Rothbard, J. B., Garlington, S., Lin, Q., Kirschberg, T., Kreider, E., McGrane, P. L., Wender, P. A., and Khavari, P. A. (2000) Conjugation of arginine oligomers to cyclosporin A facilitates topical delivery and inhibition of inflammation. *Nat. Med. 6*, 1253−1257.
(30) Robbins, P. B., Oliver, S. F., Sheu, S. M., Goodnough, J. B., Wender, P., and Khavari, P. A. (2002) Peptide delivery to tissues via reversibly linked protein transduction sequences. *BioTechniques 33*, 190−192, 194.
(31) Bhorade, R., Weissleder, R., Nakakoshi, T., Moore, A., and Tung, C. H. (2000) Macrocyclic chelators with paramagnetic cations are internalized into mammalian cells via a HIV-tat derived membrane translocation peptide. *Bioconjugate Chem. 11*, 301−305.
(32) Bullok, K. E., Dyszlewski, M., Prior, J. L., Pica, C. M., Sharma, V., and Piwnica-Worms, D. (2002) Characterization of novel histidine-tagged Tat-peptide complexes dual-labeled with (99m)Tc-tricarbonyl and fluorescein for scintigraphy and fluorescence microscopy. *Bioconjugate Chem. 13*, 1226−1237.
(33) Lewin, M., Carlesso, N., Tung, C. H., Tang, X. W., Cory, D., Scadden, D. T., and Weissleder, R. (2000) Tat peptide-derivatized magnetic nanoparticles allow in vivo tracking and recovery of progenitor cells. *Nat. Biotechnol. 18*, 410−414.
(34) Torchilin, V. P., and Levchenko, T. S. (2003) TAT-liposomes: a novel intracellular drug carrier. *Curr. Protein Pept. Sci. 4*, 133−140.
(35) Rothbard, J. B., Jessop, T. C., and Wender, P. A. (2005) Adaptive translocation: the role of hydrogen bonding and membrane potential in the uptake of guanidinium-rich transporters into cells. *Adv. Drug Delivery Rev. 57*, 495−504.
(36) Denmeade, S. R., Nagy, A., Gao, J., Lilja, H., Schally, A. V., and Isaacs, J. T. (1998) Enzymic activation of a doxorubicin-peptide prodrug by prostate-specific antigen. *Cancer Res. 58*, 2537−2540.
(37) Sella, A., Kilbourn, R., Amato, R., Bui, C., Zukiwski, A. A., Ellerhorst, J., and Logothetis, C. J. (1994) Phase II study of ketoconazole combined with weekly doxorubicin in patients with androgen-independent prostate cancer. *J. Clin. Oncol. 12*, 683−688.
(38) Wang, M. C., Valenzuela, L. A., Murphy, G. P., and Chu, T. M. (1979) Purification of a human prostate specific antigen. *Invest. Urol. 17*, 159−163.
(39) Watt, K., Lee, P. J., M′Timkulu, T., Chan, W. P., and Loor, R. (1968) Human prostate- specific antigen: structural and functional similarity with serine proteases. *Proc. Natl. Acad. Sci. U.S.A. 83*, 3166−3170.
(40) Jiang, T., Olson, E. S., Nguyen, Q. T., Roy, M., Jennings, P. A., and Tsien, R. Y. (2004) Tumor imaging by means of proteolytic activation of cell-penetrating peptides. *Proc. Natl. Acad. Sci. U.S.A. 101*, 17867−17872.
(41) Denmeade S. R., Jakobsen, C. M., Janssen, S., Khan, S. R., Garrett, E. S., Lilja, H., Christensen, S. B., and Isaacs, J. T. (2003) Prostate-specific antigen-activated thapsigargin prodrug as targeted therapy for prostate cancer. *J. Natl. Cancer Inst. 95*, 990−1000.
(42) Mhaka, A., Denmeade, S. R., Yao, W., Isaacs, J. T., and Khan, S. R. (2002) A 5-fluorodeoxyuridine prodrug as targeted therapy for prostate cancer. *Bioorg. Med. Chem. Lett. 12*, 2459−2461.
(43) Melles, E., Bergman, T., Alvelius, G., Jonsson, A., Ekberg, K., Wahren, J., and Joernvall, H. (2003) Proinsulin C-peptide and its C-terminal pentapeptide: Degradation in human serum and schiff base formation with subsequent CO_2 incorporation. *Cell. Mol. Life Sci. 60*, 1019−1025.
(44) de Visser, M., Janssen, P. J. J. M., Srinivasan, A., Reubi, J. C., Waser, B., Erion, J. L., Schmidt, M. A., Krenning, E. P., and de Jong, M. (2003) Stabilised ^{111}In-labeled DTPA- and DOTA-conjugated neurotensin analogues for imaging and therapy of exocrine pancreatic cancer. *Eur. J. Nucl. Med. Mol. Imaging 30*, 1134−1139.
(45) Torchilin, V. P., and Lukyanov, A. N. (2003) Peptide and protein drug delivery to and into tumors: challenges and solutions. *Drug Discovery Today 8*, 259−266.
(46) Torchilin, V. P., Levchenko, T. S., Rammohan, R., Volodina, N., Papahadjopoulos-Sternberg, B., and D'Souza, G. G. (2003) Cell

transfection in vitro and in vivo with nontoxic TAT peptide-liposome-DNA complexes. *Proc. Natl. Acad. Sci. U.S.A. 100*, 1972−1977.
(47) Henry, C. (2003) Breaching Barriers. *Chem. Eng. News 81*, 35−43.
(48) Harris, M. (2004) Monoclonal antibodies as therapeutic agents for cancer. *Lancet Oncol. 5*, 292−302.
(49) Winnard, P., Jr., and Raman, V. (2003) Real time noninvasive imaging of receptor−ligand interactions in vivo. *J. Cell. Biochem. 90*, 454−463.
(50) Olafsen, T., Tan, G. J., Cheung, C. W., Yazaki, P. J., Park, J. M., Shively, J. E., Williams, L. E., Raubitschek, A. A., Press, M. F. and Wu, A. M. (2004) Characterization of engineered anti-p185HER-2 (scFv-CH3)2 antibody fragments (minibodies) for tumor targeting. *Protein Eng. Des. Sel. 17*, 315−323.
(51) Sundaresan, G., Yazaki, P. J., Shively, J. E., Finn, R. D., Larson, S. M., Raubitschek, A. A., Williams, L. E., Chatziioannou, A. F., Gambhir, S. S. and Wu, A. M. (2003) ^{124}I-labeled engineered anti-CEA minibodies and diabodies allow high-contrast, antigen-specific small-animal PET imaging of xenografts in athymic mice. *J. Nucl. Med. 44*, 1962−1969.

BC0503216

Synthesis and in Vitro/in Vivo Evaluation of Novel $^{99m}Tc(CO)_3$-Folates

Cristina Müller,[†] P. August Schubiger,[†,‡] and Roger Schibli*[,†,‡]

Center for Radiopharmaceutical Science ETH-PSI-USZ, Paul Scherrer Institute, 5232 Villigen-PSI, Switzerland, and Department of Chemistry and Applied Biosciences of the ETH Zurich, 8093 Zurich, Switzerland. Received November 10, 2005; Revised Manuscript Received March 22, 2006

Novel organometallic $^{99m}Tc(I)$-folate derivatives have been synthesized and evaluated in vitro and in vivo in order to assess the influence of the overall charge of the radioconjugates and the spacer entity on the affinity and pharmacokinetic profile. Folic acid has been functionalized at the γ-carboxylate group of the glutamate moiety with (i) a hydrophilic diethoxyethyl spacer bearing a picolylamine monoacetic acid chelate, (ii) a hexyl spacer bearing an iminodiacetic acid chelate, and (iii) a hexyl spacer with a bis(pyridylmethyl)amine chelating system. Coordination of the $^{99m}Tc(CO)_3$-core resulted in neutral complex **21**, anionic complex **22**, and cationic complex **23** in excellent yields (>90%) at ligand concentrations of 10^{-4} M. Complexes **21**−**23** were HPLC purified for in vitro and in vivo experiments. In the case of **23**, separation from the unlabeled folate analogue was incomplete, leading to low specific activity and, hence, significantly inferior in vivo uptake in folate-receptor-positive (FR-positive) organs and tissues (tumors and kidneys). Time dependent in vivo studies were performed in female, athymic nude mice bearing subcutaneous FR-positive human KB cell xenografts at 1, 4, and 24 h post injection (p.i.) of the radiotracers. Tumor uptake ranged between 1.9−2.7% ID/g, 4 h p.i. and 1.6−2.2% ID/g, 24 h p.i. for **21** and **22**, and 0.9% ID/g, 4 h p.i. and 1.1% ID/g, 24 h p.i. for **23**. Blood clearance was fast for all derivatives (≤0.2% ID/g 1 h p.i.). Significant fractions of radioactivity were found in nontargeted and FR-negative organs and tissues (particularly in the liver and the intestines/intestinal contents) at early time points p.i. Coadministration of folic acid reduced radioactivity in FR-positive tissues and organs to background levels. In conclusion, overall charge and the nature of the spacer entity seemed to have a relatively minor influence on receptor affinity and the in vivo pharmacokinetic profile of the tested radiofolates.

INTRODUCTION

The folate receptor (FR) represents a promising molecular tumor marker for selective delivery of bioactive agents, since it is overexpressed on a wide variety of cancers, but highly restricted in most normal human tissues (*1*, *2*). In the past decade the use of folic acid as a "Trojan horse" for targeting of FR-positive tumors has been effectively exemplified (*3*−*9*). Several radiolabeled folate analogues are currently under preclinical and clinical investigation for potential application in diagnostic nuclear medicine (*10*−*15*). The ^{99m}Tc radioisotope features almost ideal physical decay properties (6 h half-life, 140 keV γ-radiation) for diagnostic purposes. For that reason and because of its ready availability, ^{99m}Tc is still the most common radionuclide in routine nuclear medicine. The development of ^{99m}Tc-based folate radiotracers is therefore very attractive as a method of imaging FR-positive, malignant tissue. We recently reported the synthesis and in vitro/in vivo evaluation of folate and pteroate conjugates radiolabeled with the $[^{99m}Tc(CO)_3]^+$ core (*16*, *17*). We were able to demonstrate that these folate and pteroate conjugates fully retain their ability to bind specifically to the FR with high affinity comparable to that of folic acid. However, we noticed less favorable biodistribution of the pteroate derivative in targeted and nontargeted sites compared to folate conjugates (*17*). These findings might be ascribed to the lack of the glutamate entity and the increased lipophilicity of the pteroate derivative, which eventually leads to altered pharmacokinetic characteristics. Based on these observations, we supposed that chemical modifications would positively influence the pharmacological profile of folate derivatives in vivo.

The goal of the present study was to synthesize new folate derivatives, to assess the in vitro and in vivo behavior of the corresponding ^{99m}Tc-complexes, and to compare them with ^{99m}Tc-folate derivatives previously published by our group and others. The three novel folate analogues comprised different chelating systems and/or spacer groups, giving rise to complexes of different overall charge and with varied hydrophilic properties. The radiotracers were tested both in KB cell cultures (human nasopharyngeal cancer cell line, overexpressing the FR) and in KB tumor xenografts in athymic nude mice. Furthermore, the biodistribution of the complexes in nontargeted organs and tissues was assessed and compared.

EXPERIMENTAL PROCEDURES

Materials. Reagents and solvents for syntheses were purchased from Aldrich Chemical Co. or Fluka, Buchs, Switzerland. Solvents were dried according to standard methods. The Boc-protected α-glutamate methyl ester (Boc-Glu-OMe) was purchased from Bachem AG, Bubendorf, Switzerland. The N2-*N*,*N*-dimethylaminomethlylene-10-formylpteroic acid was generously provided by Merck Eprova AG, Schaffhausen, Switzerland. A detailed description of the synthesis and characterization of the folate derivative **20** and the corresponding Tc-99m complex **24** has been reported elsewhere (*16*). Precursor $[^{99m}Tc(CO)_3(OH_2)_3]^+$ was prepared as previously reported using the IsoLink kit (Mallinckrodt-Tyco, Petten, The Netherlands). $[Na][^{99m}TcO_4]$ was eluted from a $^{99}Mo/^{99m}Tc$ generator (Mallinckrodt-Tyco, Petten, The Netherlands) using a 0.9% saline solution. KB cells (CCL-17) were purchased from ATCC (American Type Culture Collection, Manassas, VA). Special RPMI cell culture medium (FFRPMI: without folic acid,

* Corresponding author. Phone: +41-56-310 2837. Fax: +41-56-310 2849. E-mail: roger.schibli@psi.ch.

[†] Paul Scherrer Institute.

[‡] ETH Zurich.

10.1021/bc050323q CCC: $33.50 © 2006 American Chemical Society
Published on Web 04/28/2006

vitamin B_{12}, phenol red) was purchased from Cell Culture Technologies GmbH, Gravesano/Lugano, Switzerland. HPLC analyses were performed on a Merck-Hitachi L-6200A system, equipped with an L-3000 tunable absorption detector, a Berthold LB 508 radiometric detector, and an XTerra (Waters) MS C-18 reversed phase column (5 μm, 15 cm × 4.6 mm). HPLC solvents were aqueous 0.05 M triethylammonium phosphate buffer, pH 7.0 (solvent A), and methanol (solvent B). The HPLC system started with 100% A with a linear gradient to 20% A and 80% B over 15 min followed by 5 min of 100% A with a flow rate of 1 mL/min. TLC analyses of organic syntheses were performed with silica gel 60 (F254, Merck) using CH_2Cl_2/methanol = 9/1 as an eluent. Nuclear magnetic resonance spectra were recorded on a 300 MHz Varian Gemini 2000 spectrometer. The ^{1}H and ^{13}C chemical shifts were reported relative to residual solvent protons as a reference. IR spectra were recorded on a Perkin-Elmer FT-IR 16PC using KBr pellets. MS analyses were performed with a Micromass LCT Premier (KD048, Waters) mass spectrometer (ionization mode: ESI-TOF). Radioactivity (γ-radiation of ^{99m}Tc) was measured with a γ-counter (Cobra II, model B 5003, Packard). Protein concentrations for the in vitro experiments were measured with a micro plate reader (Bio-Rad, model 550), using a Micro BCA protein assay kit (product no. 23235), Socochim.

Synthesis of Compound 1. Compound **1** was synthesized according to a previously published procedure, starting from 2,2′-(ethylenedioxyl)diethylamine (*18*). Yield: 90%. Analytical data for **1**: ^{1}H NMR ($CDCl_3$) δ 1.51 (s, 9H), 2.90−2.98 (m, 2H), 3.32−3.42 (m, 2H), 3.54−3.64 (m, 4H), 3.68 (t, 4H); ^{13}C NMR ($CDCl_3$) δ 28.5 (3C), 40.4, 41.9, 70.3 (2C), 70.4, 73.6, 79.1, 156.1; IR (KBr) 1704 cm^{-1}.

Synthesis of Compound 2. The following procedure is based on literature procedures with a slight modification (*19*). Molecular sieves and pyridine-2-carboxaldehyde (192 μL; 2.01 mmol; 1 equiv) were added to a solution of compound **1** (500 mg; 2.01 mmol; 1 equiv) in dry toluene (20 mL) and stirred for 30 min at room temperature. After 4 h reflux the solution was filtered, evaporated, and dried in a vacuum. The yellow oil of the imine was dissolved in methanol (15 mL), and the reduction was performed with $NaBH_4$ (76 mg; 2.01 mmol; 1 equiv), with stirring at room temperature for 4 h. After addition of water to quench residual $NaBH_4$, the organic solvent was removed in a vacuum. The aqueous solution was extracted three times with ethyl acetate, and the organic layer was dried over Na_2SO_4, evaporated, and dried in a vacuum to obtain a yellow oil. Yield: 86%. Analytical data for **2**: ^{1}H NMR ($CDCl_3$) δ 1.55 (s, 9H), 2.96−3.08 (m, 2H), 3.38−3.48 (m, 2H), 3.68 (t, 2H), 3.70−3.82 (m, 6H), 4.08 (s, 2H), 7.25−7.32 (m, 1H), 7.42−7.49 (m, 1H), 7.72−7.80 (m, 1H), 8.64−8.70 (m, 1H); ^{13}C NMR ($CDCl_3$) δ 28.5 (3C), 40.5, 48.9, 55.1, 60.5, 70.4 (2C), 70.7, 79.2, 122.1, 122.4, 136.6, 149.4, 156.2, 159.5; IR (KBr) 1709 cm^{-1}; MS (ESI) *m*/*z* (%) 340 [M$^+$ + H] (50), 362 [M$^+$ + Na] (100).

Synthesis of Compound 3. The following procedure is based on literature procedures with a slight modification (*19*). Compound **2** (585 mg; 1.72 mmol; 1 equiv) was dissolved in dry tetrahydrofuran (20 mL). Methyl bromoacetate (475 μL; 5.16 mmol; 3 equiv) and triethylamine (720 μL; 5.16 mmol; 3 equiv) were added, and the solution was refluxed for 4 h. After cooling to room temperature, the reaction solution was filtered and evaporated. The crude product was purified by chromatography on silica gel using CH_2Cl_2/methanol (9/1) as an eluent. After drying in a high vacuum the product **3** was obtained in 60% yield. Analytical data for **3**: ^{1}H NMR ($CDCl_3$) δ 1.56 (s, 9H), 3.12 (t, 2H), 3.38−3.48 (m, 2H), 3.65−3.70 (m, 6H), 3.72 (s, 2H), 3.76 (t, 2H), 3.84 (s, 3H), 4.20 (s, 2H), 7.28−7.36 (m, 1H), 7.68−7.75 (m, 1H), 7.78−7.86 (m, 1H), 8.64−8.70 (m, 1H); ^{13}C NMR ($CDCl_3$) δ 28.6 (3C), 40.5, 51.6, 53.6, 55.4, 60.5, 70.0, 70.3 (2C), 70,4, 79.2, 122.4, 123.6, 137.1, 148.7, 156.1, 158.9, 171.8; IR (KBr) 1740, 1708 cm^{-1}; MS (ESI) *m*/*z* (%) 434 [M$^+$ + Na] (100).

Synthesis of Compound 4. The Boc-deprotection of compound **3** (420 mg; 1.02 mmol; 1 equiv) was performed quantitatively in 6 N HCl (10 mL) at room temperature, monitored by TLC/ninhydrin. The solvent was evaporated and the compound **4**·HCl was dried in a vacuum. Analytical data for **4**: ^{1}H NMR (CD_3OD) δ 3.28−3.34 (m, 2H), 3.78−3.86 (m, 6H), 3.91 (t, 2H), 3.96 (s, 3H), 4.08 (t, 2H), 4.55 (s, 2H), 5.16 (s, 2H), 8.22−8.30 (m, 1H), 8.48−8.52 (m, 1H), 8.76−8.824 (m, 1H), 9.09−9.14 (m, 1H); ^{13}C NMR (CD_3OD) δ 39.4, 52.5, 54.4, 55.3, 55.5, 65.8, 66.6, 70.0 (2C), 127.5, 129.1, 143.5, 146.2, 146.8, 167.5; IR (KBr) 1748 cm^{-1}; MS (ESI) *m*/*z* (%) 312 [M$^+$ + H] (100).

Synthesis of Compound 5. 1-Hydroxybenzotriazole hydrate (162 mg; 1.07 mmol; 1 equiv) was added to a solution of Boc-Glu-OMe (280 mg; 1.07 mmol; 1 equiv) in dry CH_2Cl_2 to form a suspension. Addition of *N*-(3-dimethylaminopropyl)-*N*′-ethylcarbodiimide hydrochloride (226 mg; 1.18 mmol; 1.1 equiv) resulted in a transparent solution. After 4 h of stirring at room temperature, the reaction solution was extracted three times with water to remove impurities. The organic layer was dried over Na_2SO_4, evaporated, and dried in a vacuum to obtain a white solid (yield: 95%). The crude product was used directly for further coupling reactions. Compound **4**·HCl (340 mg, 1.02 mmol; 1 equiv) and *N*-ethyldiisopropylamine (348 μL; 2.04 mmol; 2 equiv) dissolved in dry *N*,*N*-dimethylformamide were added in two portions to a solution of the activated Boc-Glu-OMe (386 mg, 1.02 mmol; 1 equiv) in dry *N*,*N*-dimethylformamide. After stirring overnight at 50 °C, the solution was distilled to remove *N*,*N*-dimethylformamide. The reaction mixture was dissolved in CH_2Cl_2 and washed once with water. The organic layer was dried over Na_2SO_4, filtered, and evaporated. The crude product **5** was purified by chromatography on silica gel using CH_2Cl_2/methanol (9/1). Yield: 42%. Analytical data for **5**: ^{1}H NMR ($CDCl_3$) δ 1.55 (s, 9H), 2.02−2.16 (m, 1H), 2.22−2.36 (m, 1H), 2.38−2.46 (m, 2H), 3.06−3.14 (m, 2H), 3.51−3.60 (m, 2H), 3.59 (s, 2H), 3.62−3.72 (m, 6H), 3.72−3.78 (m, 2H), 3.83 (s, 3H), 3.84 (s, 3H), 4.19 (s, 2H), 4.33−4.46 (m, 1H), 7.29−7.38 (m, 1H), 7.65−7.72 (m, 1H), 7.78−7.87 (m, 1H), 8.62−8.72 (m, 1H); ^{13}C NMR ($CDCl_3$) δ 28.5 (3C), 32.5, 36.7, 39.5, 51.7, 52.4, 53.4, 53.6, 55.5, 60.5, 70.0 (2C), 70.4 (2C), 80.0, 122.5, 123.5, 137.2, 148.8, 159.0, 162.7, 172.0 (2C), 173.0; IR (KBr) 1744, 1712, 1662 cm^{-1}; MS (ESI) *m*/*z* (%) 555 [M$^+$ + H] (100).

Synthesis of Compound 6. Compound **5** (238 mg, 0.43 mmol; 1 equiv) was quantitatively deprotected in TFA/CH_2Cl_2 (1/9) (6 mL) at room temperature for 5 h, monitored by TLC/ninhydrin. The reaction solution was evaporated and dissolved in pure CH_2Cl_2. The crude product **6** was washed once with a saturated solution of $NaHCO_3$. The organic layer was dried over Na_2SO_4, filtered, evaporated, and dried in a vacuum. Analytical data for **6**: $C_{21}H_{34}N_4O_7$ (455.24) calcd C 55.49, H 7.54, N 12.33; found C 55.71, H 7.32, N 12.54; ^{1}H NMR (CD_3OD) δ 2.22−2.42 (m, 2H), 2.56−2.64 (m, 2H), 3.37−3.43 (m, 2H), 3.48−3.55 (m, 2H), 3.65−3.78 (m, 6H), 3.82−3.88 (m, 2H), 3.91 (s, 3H), 3.98 (s, 3H), 4.15 (s, 2H), 4.21−4.28 (m, 1H), 4.69 (s, 2H), 7.84−8.06 (m, 2H), 8.40−8.50 (m, 1H), 8.86−94 (m, 1H); ^{13}C NMR (CD_3OD) δ 25.9, 31.0, 39.1, 51.6, 52.3, 52.5, 54.6, 54.9, 56.8, 67.4, 69.1, 69.8, 69.9, 125.0, 125.2, 143.1, 143.9, 153.7, 169.3, 170.1, 172.8; IR (KBr) 1751, 1673 cm^{-1}; MS (ESI) *m*/*z* (%) 456 [M$^+$ + H] (100), 478 [M$^+$ + Na] (60).

Synthesis of Compound 9. Compound **9** was synthesized according to a previously published procedure, and the analyses

were in agreement with the literature (*18*). Yield: 80%. Analytical data for **9**: ^{1}H NMR ($CDCl_3$) δ 1.38−1.50 (m, 6H), 1.50−1.66 (m, 2H), 1.55 (s, 9H), 2.79 (t, 2H), 3.16−3.29 (m, 2H).

Synthesis of Compound 10. The following procedure is based on literature procedures with a slight modification (*19*). Methyl bromoacetate (1.30 mL; 13.87 mmol; 6 equiv) and triethylamine (1.95 mL; 13.87 mmol; 6 equiv) were added to a solution of compound **9** (400 mg; 2.31 mmol; 1 equiv) in 20 mL of dry tetrahydrofuran (20 mL) and refluxed for 4 h. After cooling to room temperature the reaction mixture was filtered and evaporated. The crude product was dissolved in CH_2Cl_2 and extracted 3 times with brine. The organic layer was dried over Na_2SO_4, evaporated, and dried in a vacuum. Yield: 95%. Analytical data for **10**: ^{1}H NMR ($CDCl_3$) δ 1.39−1.50 (m, 4H), 1.50−1.67 (m, 4H), 1.57 (s, 9H), 2.82 (t, 2H), 3.18−3.30 (m, 2H), 3.68 (s, 4H), 3.83 (s, 6H); ^{13}C NMR ($CDCl_3$) δ 26.7, 26.9, 27.9, 28.6 (3C), 30.1, 40.6, 51.7 (2C), 54.4, 55.0 (2C), 79.3, 156.1, 171.7 (2C); IR (KBr) 1747, 1712 cm^{-1}; MS (ESI) *m*/*z* (%) 383 [M^+ + Na] (90).

Synthesis of Compound 11. The Boc-deprotection of compound **10** (790 mg, 2.19 mmol; 1 equiv) was performed quantitatively in 6 N HCl (15 mL) for 2 h at room temperature, monitored by TLC/ninhydrin. The solvent was evaporated and compound **11**·HCl was dried in a vacuum. Analytical data for **11**: ^{1}H NMR (CD_3OD) δ 1.38−1.52 (m, 4H), 1.66−1.74 (m, 2H), 1.74−1.84 (m, 2H), 2.94 (t, 2H), 3.36−3.46 (m, 2H), 3.84 (s, 6H), 4.36 (s, 4H); ^{13}C NMR (CD_3OD) δ 23.4, 25.4, 26.8, 34.4, 39.1, 52.4 (2C), 53.9, 56.5 (2C), 166.4 (2C); IR (KBr) 1748 cm^{-1}; MS (ESI) *m*/*z* (%) 261 [M^+ + H] (100).

Synthesis of Compound 12. 1-Hydroxybenzotriazole hydrate (355 mg; 2.35 mmol; 1 equiv) was added to a solution of Boc-Glu-OMe (614 mg; 2.35 mmol; 1 equiv) in dry CH_2Cl_2. After addition of *N*-(3-dimethylaminopropyl)-*N*′-ethylcarbodiimide hydrochloride (497 mg; 2.59 mmol; 1.1 equiv) a transparent solution was obtained. After 4 h of stirring at room temperature, the UV-active product was detected by TLC analysis (R_f = 0.9). The reaction solution was extracted three times with water to remove impurities, and the organic layer was dried over Na_2SO_4, evaporated, and dried in a vacuum to obtain a white solid in 95% yield, used directly in the further coupling reaction. Compound **11**·HCl (650 mg, 2.19 mmol; 1 equiv) and *N*-ethyldiisopropylamine (750 μL; 4.38 mmol; 2 equiv) dissolved in dry *N*,*N*-dimethylformamide were added in two portions to a solution of the activated Boc-Glu-OMe (830 mg, 2.19 mmol; 1 equiv) in dry *N*,*N*-dimethylformamide. After 10 h at 50 °C, the solution was distilled to remove *N*,*N*-dimethylformamide and the crude product was purified by chromatography on silica gel using CH_2Cl_2/methanol (9/1) to obtain product **12**. Yield: 50%. Analytical data for **12**: ^{1}H NMR ($CDCl_3$) δ 1.28−1.38 (m, 4H), 1.43 (s, 9H), 1.45−1.53 (m, 4H), 1.86−1.98 (m, 1H), 2.11−2.21 (m, 1H), 2.22−2.28 (m, 2H), 2.72 (t, 2H), 2.18−3.27 (m, 2H), 3.56 (s, 4H), 3.70 (s, 6H), 3.73 (s, 3H), 4.12−4.38 (1H); ^{13}C NMR ($CDCl_3$) δ 26.7 (2C), 27.6, 28.5 (3C), 29.3, 29.5, 32.9, 39.6, 51.8 (2C), 52.6, 53.2, 54.3, 54.8 (2C), 80.2, 156.0, 171.6 (2C), 171.9, 172.9; IR (KBr) 1755, 1734, 1717, 1654 cm^{-1}; MS (ESI) *m*/*z* (%) 526 [M^+ + Na] (50).

Synthesis of Compound 13. Compound **12** (550 mg, 1.09 mmol; 1 equiv) was quantitatively deprotected in TFA/CH_2Cl_2 (1/9) (10 mL) at room temperature for 5 h, monitored by TLC/ninhydrin. The reaction solution was evaporated and dissolved in pure CH_2Cl_2. The crude product **13** was extracted once with a saturated solution of $NaHCO_3$. The organic layer was dried over Na_2SO_4, filtered, evaporated, and dried in a vacuum. Analytical data for **13**: $C_{18}H_{33}N_3O_7$ (403.23) calcd C 53.58, H 8.24, N 10.41; found C 53.78, H 8.04, N 10.22; ^{1}H NMR (CD_3OD) δ 1.45−1.61 (m, 4H), 1.61−1.73 (m, 2H), 1.82−1.96 (2H), 2.20−2.43 (m, 2H), 2.54−2.63 (m, 2H), 3.32 (t, 2H), 3.47−3.55 (m, 2H), 3.99 (s, 3H), 4.00 (s, 6H), 4.19−4.27 (m, 1H), 4.45 (4H); ^{13}C NMR (CD_3OD) δ 23.7, 25.8, 26.0, 26.1, 28.8, 31.0, 39.0, 52.4, 52.5 (3C), 53.8 (2C), 56.6, 166.5 (2C), 169.3, 172.6; IR (KBr) 1754, 1685, 1674 cm^{-1}; MS (ESI) *m*/*z* (%) 404 [M^+ + H] (100).

Synthesis of Compound 15. The following procedure is based on literature procedures with a slight modification (*20*−*22*). Pyridine-2-carboxaldehyde (465 μL; 4.85 mmol; 2.1 equiv) dissolved in 5 mL of dry 1, 2-dichloroethane was added to a solution of compound **9** (500 mg; 2.31 mmol; 1 equiv) in 10 mL of dry 1,2-dichloroethane and stirred for 2 h at room temperature. The reaction solution was cooled to 0 °C before slow addition of sodium triacetoxy borohydride (1125 mg; 5.31 mmol; 2.3 equiv) in portions. After 24 h of stirring at room temperature, water was added to quench residual sodium triacetoxy borohydride and the reaction mixture extracted twice with CH_2Cl_2. The organic layer was extracted with water and brine, dried over Na_2SO_4, evaporated, and dried in a vacuum. Yield: 75%. Analytical data for **15**: ^{1}H NMR ($CDCl_3$) δ 1.10−1.66 (m, 8H), 1.38 (s, 9H), 2.54−2.72 (m, 2H), 2.92−3.3.10 (m, 2H), 3.93 (s, 4H), 7.09−7.18 (m, 2H), 7.55−7.70 (m, 4H), 8.44−8.54 (m, 2H); ^{13}C NMR ($CDCl_3$) δ 26.3, 26.4, 26.7, 28.4 (3C), 29.9, 40.4, 53.8,?59.6 (2C), 79.0, 122.5 (2C), 123.8 (2C), 136.7 (2C), 149.0 (2C), 150.1, 156.0 (2C); IR (KBr) 1687 cm^{-1}; MS (ESI) *m*/*z* (%) 399 [M^+ + H] (100).

Synthesis of Compound 16. The Boc-deprotection of compound **15** (690 mg, 1.73 mmol; 1 equiv) was achieved quantitatively in 6 N HCl (15 mL) after 4 h at room temperature as determined by TLC/ninhydrin. After addition of 10 N NaOH to obtain a pH value of 5, the reaction mixture was evaporated and dried in a vacuum. Methanol was added and the mixture was filtered to remove the precipitated salt. Yield: 93%. Analytical data for **16**: ^{1}H NMR (CD_3OD) δ 1.20−1.48 (m, 4H), 1.48−1.72 (m, 4H), 2.66−2.99 (m, 2H), 2.80−2.96 (m, 2H), 4.39 (s, 4H), 7.74−7.96 (m, 2H), 8.05−8.10 (m, 2H), 8.42−8.52 (m, 2H), 8.78−8.85 (m, 2H); ^{13}C NMR (CD_3OD) δ 25.2, 25.6, 26.1, 26.9, 39.2, 54.9, 55.8 (2C), 125.8 (2C), 126.6 (2C), 142.5 (2C), 145.6 (2C), 152.8 (2C); IR (KBr) 1526, 1619 cm^{-1}; MS (ESI) *m*/*z* (%) 299 [M^+ + H] (100).

Synthesis of Compound 17. 1-Hydroxybenzotriazole hydrate (275 mg; 1.82 mmol; 1 equiv) was added to a solution of Boc-Glu-OMe (475 mg; 1.82 mmol; 1 equiv) in dry CH_2Cl_2 to form a suspension. Addition of *N*-(3-dimethylaminopropyl)-*N*′-ethylcarbodiimide hydrochloride (384 mg; 2.00 mmol; 1.1 equiv) resulted in a transparent solution. The reaction was stirred for 4 h at room temperature and monitored by TLC analysis (R_f = 0.9). The reaction solution was extracted three times with water to remove impurities. The organic layer was dried over Na_2SO_4, filtered, evaporated, and dried in a vacuum to obtain a white solid. Yield: 95%. The product was processed without further purification. Compound **16**·HCl (515 mg, 1.73 mmol; 1 equiv) and *N*-ethyldiisopropylamine (295 μL; 1.73 mmol; 1 equiv) dissolved in dry *N*,*N*-dimethylformamide were added in two portions to a solution of the activated Boc-Glu-OMe (655 mg, 1.73 mmol; 1 equiv) in dry *N*,*N*-dimethylformamide. After 16 h of stirring at room temperature, the solution was distilled to remove *N*,*N*-dimethylformamide and the crude product was purified by silica gel using CH_2Cl_2/methanol (9/1) to obtain the product **17**. Yield: 52%. Analytical data for **17**: ^{1}H NMR ($CDCl_3$) δ 1.13−1.33 (m, 4H), 1.33−1.50 (m, 2H), 1.38 (s, 9H), 1.56−1.72 (m, 2H), 1.80−1.98 (m, 1H), 2.20−2.18 (m, 1H), 2.23 (t, 2H), 2.68−2.85 (m, 2H), 3.10−3.22 (m, 2H), 3.68 (s, 3H), 4.06 (s, 4H), 4.12−4.25 (m, 1H), 7.14−7.26 (m, 2H), 7.58−7.72 (m, 4H), 8.46−8.58 (m, 2H); ^{13}C NMR ($CDCl_3$) δ 25.4, 26.2 (2C), 28.3 (3C), 28.7, 28.9, 32.6, 42.0, 52.3, 53.7, 58.6, 60.3 (2C), 79.9, 118.3 (2C), 123.2 (2C), 137.4 (2C), 148.7

(2C), 154.8 (2C), 156.0, 172.1, 172.7; IR (KBr) 1743, 1705, 1652 cm^{-1}; MS (ESI) *m/z* (%) 564 [M^+ + Na] (40), 542 [M^+ + H] (100).

Synthesis of Compound 18. Compound **17** (485 mg, 0.90 mmol; 1 equiv) was quantitatively deprotected in TFA/CH_2Cl_2 (1/9) (10 mL) at room temperature overnight as determined by TLC/ninhydrin. The reaction solution was evaporated and dissolved in pure CH_2Cl_2. The crude product **18** was washed once with a saturated solution of $NaHCO_3$. The organic layer was dried over Na_2SO_4, filtered, evaporated, and dried in a vacuum. Analytical data for **18**: $C_{24}H_{35}N_5O_3$ (441.27) calcd C 65.28, H 7.99, N 15.86; found C 65.02, H 8.19, N 16.06; ^{1}H NMR (CD_3OD) δ 1.20−1.36 (m, 4H), 1.36−1.50 (m, 2H), 1.60−1.74 (m, 2H), 2.00−2.22 (m, 2H), 2.34−2.44 (m, 2H), 2.92−3.03 (m, 2H), 3.03−3.19 (m, 2H), 3.79 (s, 3H), 4.00−4.08 (m, 1H), 4.44 (s, 4H), 7.59−7.67 (m, 2H), 7.68−7.75 (m, 2H), 8.08−8.17 (m, 2H), 8.68−8.74 (m, 2H); ^{13}C NMR (CD_3OD) δ 24.5, 25.8, 26.0 (2C), 28.6, 30.9, 38.9, 52.2, 52.3, 54.9, 56.4 (2C), 124.8 (2C), 125.0 (2C), 126.9 (2C), 141.1 (2C), 151.3 (2C), 169.1, 172.4; IR (KBr) 1753, 1672 cm^{-1}; MS (ESI) *m/z* (%) 464 [M^+ + Na] (100), 442 [M^+ + H] (60).

Synthesis of Compound 8, 14 and 19. N2-*N*,*N*-Dimethylaminomethlylene-10-formylpteroic acid **7** was activated according to Nomura et al. (*16*, *23*). Compound **6**, **13**, or **18** (1 equiv) and *N*-ethyldiisopropylamine (1.5 equiv) were dissolved in dry CH_2Cl_2 and added in two portions to a solution of **7**. The coupling reaction was stirred overnight. The reaction solution was extracted once with water; the organic layer was dried over Na_2SO_4 and filtered and the solvent evaporated. The crude product was deprotected in 1 N NaOH (10 equiv) after stirring for 5 h at room temperature, monitored via HPLC. After neutralization with 1 N HCl the pH was brought to 3 by addition of 0.1 N HCl. The yellow product precipitated on addition of ethanol. After centrifugation the crude products were washed three times with ethanol and dried in a vacuum to obtain the pure products **8**, **14**, and **19** as orange powders. Yield: 10−12%. Analytical data for **8**: $C_{33}H_{40}N_{10}O_9$ (720.30) calcd C 54.99, H 5.59, N 19.43; found C 54.56, H 6.09, N 19.93; ^{1}H NMR (DMSO) δ 1.22−1.32 (m, 2H), 1.84−1.98 (m, 1H), 1.98−2.10 (m, 1H), 2.16−2.24 (m, 2H), 2.78−2.85 (m, 2H), 3.12−3.20 (m, 2H), 3.30−3.50 (m, 6H), 3.40 (s, 2H), 3.93 (s, 2H), 4.22−4.30 (m, 1H), 4.46−4.52 (m, 2H), 6.59−6.67 (m, 2H), 7.22−27 (m, 1H), 7.46−7.50 (m, 1H), 7.62−7.68 (m, 2H), 7.74−7.78 (m, 1H), 8.44−8.50 (m, 1H), 8.64 (s, 1H); ^{13}C NMR (DMSO) δ 26.6, 31.9, 45.9, 52.9, 55.2, 56.0 (2C), 60.0, 68.9, 69.9, 69.5 (2C), 111.2 (2C), 117.7, 122.2, 122.7, 128.9 (2C), 131.1, 136.6, 148.6, 150.8, 152.0, 154.0, 157.1, 159.5, 160.9, 167.2, 168.0, 171.7, 172.3, 173.8; IR (KBr) 1701, 1684, 1643 1603 cm^{-1}; MS (ESI) *m/z* (%) 720 [M^+] (60), 743 [M^+ + Na] (100). Analytical data for **14**: $C_{29}H_{37}N_9O_9$ (655.27) calcd C 53.12, H 5.69, N 19.23; found C 53.42, H 5.88, N 19.01; ^{1}H NMR (D_2O) δ 1.22−1.72 (m, 8H), 1.98−2.40 (m, 4H), 2.75−2.90 (m, 2H), 3.00−3.10 (m, 2H), 3.70 (s, 4H), 4.25−4.38 (m, 1H), 4.57 (s, 2H), 6.70−6.80 (m, 2H), 7.55−7.62 (m, 2H), 8.67 (s, 1H); ^{13}C NMR (D_2O) δ 25.0, 26.5, 26.8, 26.9, 28.0, 34.3, 40.6, 47.1, 56.6, 57.3, 58.4 (2C), 114.1, 116.8 (2C), 130.5 (2C), 150.7, 151.0, 151.8, 152.3, 170.6, 171.0, 171.8, 171.9 (2C), 172.0, 176.8, 179.7; IR (KBr) 1718, 1681, 1650, 1636 cm^{-1}; MS (ESI) *m/z* (%) 656 [M^+ + H] (10), 328 [M^{2+} + H] (100). Analytical data for **19**: $C_{37}H_{43}N_{11}O_5$ (721.34) calcd C 61.57, H 6.00, N 21.35; found C 61.11, H 5.88, N 21.02; ^{1}H NMR (DMSO) δ 0.90−1.30 (m, 6H), 1.30−1.46 (m, 2H), 1.75−1.90 (m, 1H), 1.90−2.04 (m, 1H), 2.04−2.16 (m, 2H), 2.78−2.98 (m, 2H), 3.20−3.60 (m, 2H), 3.72 (s, 4H), 4.12−4.26 (m, 1H), 4.40 (s, 2H), 6.50−6.62 (m, 2H), 7.12−7.22 (m, 2H), 7.38−7.48 (m, 2H), 7.52−7.62 (m, 2H), 7.62−7.82 (m, 2H), 8.36−8.44 (m, 2H), 8.57 (s, 1H); ^{13}C NMR (DMSO) δ 26.6, 26.8 (2C), 29.6, 30.1 (2C), 40.7, 53.9, 54.0, 57.0, 60.2 (2C), 109.0, 111.6, 121.7 (2C), 122.5 (2C), 123.0 (2C), 128.4 (2C), 129.4 (2C), 136.9 (2C), 149.1, 151.1, 154.0, 160.0, 163.0 (2C), 166.6 (2C), 171.6, 174.2, 179.7; IR (KBr) 1718, 1684, 1631, 1613 cm^{-1}; MS (ESI): *m/z* (%) 745 [M^+ + Na] (100).

Preparation of the Radiotracers 21−24. Complexes **21−23** and complex **24** (previously reported by our group (*16*)) were prepared according to the following general procedure: $[^{99m}Tc(CO)_3(OH_2)_3]^+$ (100 μL; ~1 GBq/mL), phosphate buffered saline (PBS pH 7.4, 350 μL), and a stock solution of the corresponding derivative (**8**, **14**, **19**, **20**) in PBS (10^{-3} M, 50 μL) were placed in a sealed glass vial. After 30 min of reaction time at 75 °C the vial was cooled on ice. HPLC analyses of the complexes **21−24** revealed yields between 92% and 98%. The radiolabeled complexes **21−24** were separated from unlabeled compounds **8**, **14**, **19**, **20**) by HPLC and diluted in PBS to obtain a concentration of 1 MBq/mL for in vitro experiments or 3.7 MBq/mL for in vivo experiments, respectively.

Cell Cultures. KB cells (human, nasopharyngeal carcinoma cell line) were cultured continuously in a 150 cm^2 flask as monolayers at 37 °C in a humidified atmosphere containing 7.5% CO_2. The cells were folate-starved using a folate-deficient special RPMI 1640 medium (FFRPMI: modified RPMI 1640 medium without folic acid, vitamin B_{12} and phenol red), supplemented with 10% heat-inactivated fetal calf serum (FCS) as the only source of folate, L-glutamine, and antibiotics (penicillin 100 IU/mL, streptomycin 100 μg/mL, fungizone 0.25 μg/mL). Cell culture media such as FCS-supplemented FFRPMI are known to feature a final folate concentration of ~3 nM, i.e., a value at the low end of the physiological concentration in human serum (*24*).

Cell Preparation for in Vitro Experiments. Eighteen hours prior to each experiment, the cells were seeded in 12-well plates (8×10^5 cells/well) to form confluent monolayers overnight. The experiments were performed in triplicate.

Cell Preparation for in Vivo Experiments. For subcutaneous inoculation of the mice, subconfluent cells were harvested by treatment with EDTA (1 mM) in PBS (1×, pH 7.4). The cells were then washed once with PBS and pelleted by spinning at 1000*g* for 5 min at 20 °C. The cells were resuspended in PBS to the corresponding concentration (50×10^6 cells/mL).

Cell Binding Studies. Cell binding experiments of the folate radiotracers **21−24** were performed according to the following general procedure: Cell monolayers were rinsed twice with ice-cold PBS (pH 7.4). Pure FFRPMI medium (without FCS/L-glutamine/antibiotics, 975 μL) was added into each well. Blocking studies were performed with FFRPMI medium (475 μL) and a folic acid solution (200 μM, 500 μL). The well plates were preincubated at 37 °C for 40 min. A solution of the $^{99m}Tc(CO)_3$-labeled radiotracer (25 μL, 1 MBq/mL) was added, and the well plates were incubated again for 1 h at 37 °C. The monolayers were then washed several times. The radioactivity counted in samples washed with only PBS (pH 7.4) could be ascribed to the sum of FR-bound radiotracer on the cell surface and the internalized fraction. Cell samples, washed with stripping buffer (an aqueous solution of 0.1 M acetic acid and 0.15 M NaCl, pH 3) in order to release radiotracer from FRs on the cell surface, enabled determination of the internalized fraction of radioactivity (*25*, *26*). The monolayers were dissolved in 1 N NaOH (1 mL), transferred to 4 mL tubes, and homogenized by vortex. The radioactivity of each sample was measured with a γ-counter. The concentration of proteins was determined for each sample by a Micro BCA protein assay kit, in order to normalize measured radioactivity of the samples with respect to the averaged sample protein content. The raw data were converted from counts per minute (cpm) into percentage of total radioactivity added.

Scheme 1[a]

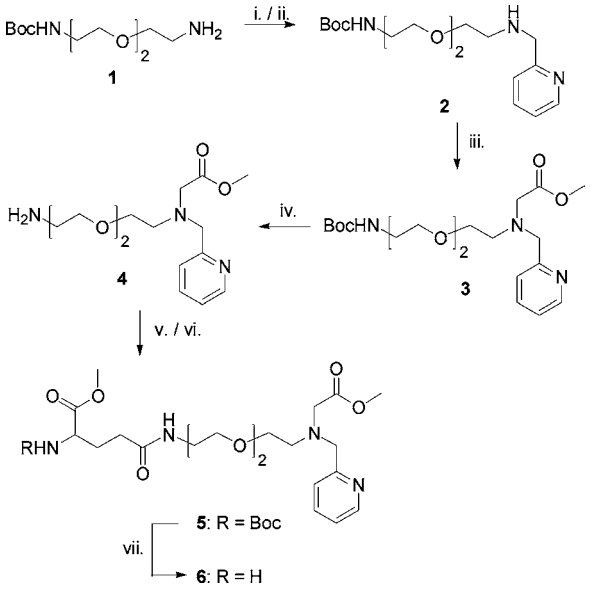

[a] (i) Pyridine-2-carboxaldehyde, toluene, reflux, 3 h; (ii) $NaBH_4$, methanol, rt, overnight; (iii) methyl bromoacetate, triethylamine, tetrahydrofuran, reflux, 5 h; (iv) HCl 6 N, rt, 3 h; (v) Boc-Glu-OMe, 1-hydroxybenzotriazole hydrate, *N*-(3-dimethylaminopropyl)-*N*′-ethylcarbodiimide hydrochloride, CH_2Cl_2, rt, 4 h; (vi) *N*-ethyldiisopropylamine, *N*,*N*-dimethylformamide, 50 °C, overnight; (vii) TFA/CH_2Cl_2 (9:1), rt, overnight.

Biodistribution Studies. Four to five week old female nude mice (CD1-Fox1n/nu) were purchased from Charles River Laboratories (Sulzfeld, Germany). Mice were housed under conditions of controlled temperature (26 °C), humidity (68%), and daily light cycle (12 h light/12 h dark). The animals were maintained on a folate-deficient rodent chow (in order to reduce their serum folate to a level near that of human serum). After an acclimation period of 5−7 days, the mice were inoculated subcutaneously with 0.1 mL of tumor cell suspension (5×10^7 cells/mL) into the subcutis of the axilla. Radiotracer distribution studies were performed 12−14 days after tumor cell inoculation. The radiotracers **21**−**24** (100 μL, 3.7 MBq/mL) were administered via a lateral tail vein. Blockade studies have been performed by coadministration of folic acid (100 ± 10 μg/mouse in 100 μL of PBS, pH = 7.4) 5 min prior to the radiotracer. At the indicated points in time, the animals were sacrificed and dissected. The selected tissues were removed and weighed, and the radioactivity was counted by a γ-counter to determine distribution of the relevant radiotracer within the test animal. The results were tabulated as percentage injected dose per gram (% ID/g) of weight tissue.

RESULTS AND DISCUSSION

Organic Syntheses. The synthetic concept described below was chosen because it leads directly and exclusively to γ-folate derivatives. Thus, cumbersome and inefficient chromatographic separation of mixtures of γ- and α-folate products (which are formed when coupling is performed directly to folic acid) could be avoided. Syntheses of various chelating systems with the spacer entities are presented in Schemes 1−3. We followed the recently published general synthetic strategy for the preparation of tridentate chelating systems with variable spacer groups comprising a terminal, primary amine functionality (*16*, *19*, *20*). Chelators and spacer entities were prepared as follows: For the synthesis of compound **2**, mono-Boc-protected 2,2′-(ethylenedioxyl)diethylamine **1** was reacted with pyridine-2-carboxyldehyde to form a Schiff base, followed by an in situ reduction using sodium borohydride. This compound was alkylated with methyl bromoacetate in the presence of base to form intermediate **3** (Scheme 1). After purification of the crude product by chromatography on silica gel, compound **3** was obtained in 60% yield. For compound **10** mono-Boc-protected diaminohexane was N-alkylated with 2 equiv of methyl bromoacetate (Scheme 2). Product **10** was obtained from an organic reaction solution after aqueous extraction. Compound **15** was synthesized by reacting mono-Boc-protected diaminohexane with 2 equiv of pyridine-2-carboxaldehyde and a slight excess of sodium triacetoxy borohydride for in situ reduction of the imine intermediate (Scheme 3). The aqueous reaction mixture was extracted with dichloromethane and washed with water and brine. Boc-deprotection of compounds **3**, **10**, and **15** was achieved in the presence of 6 N HCl to yield compounds **4**, **11**, and **16**. These intermediates were coupled to the accessible γ-carboxylate group of N_α-Boc-protected α-glutamate methyl ester using standard peptide coupling reagents (1-hydroxybenzotriazole hydrate, *N*-(3-dimethylaminopropyl)-*N*′-ethylcarbodiimide hydrochloride) to form the corresponding intermediates **5**, **12**, and **17** in good yields (Schemes 1−3). After Boc-deprotection, compounds **6**, **13**, and **18** were coupled to activated

Scheme 2[a]

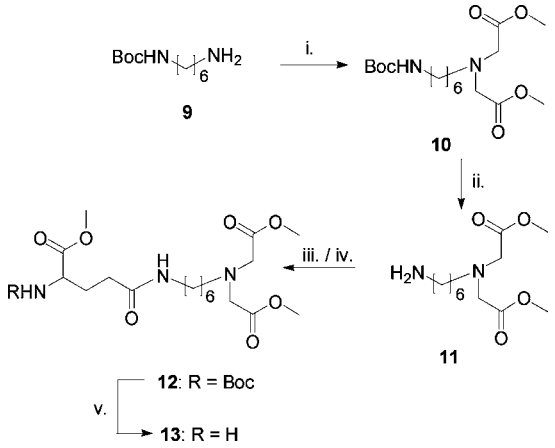

[a] (i) Methyl bromoacetate, triethylamine, tetrahydrofuran, reflux, 5 h; (ii) HCl 6 N, rt, 3 h; (iii) Boc-Glu-OMe, 1-hydroxybenzotriazole hydrate, *N*-(3-dimethylaminopropyl)-*N*′-ethylcarbodiimide hydrochloride, CH_2Cl_2, rt, 4 h; (iv) *N*-ethyldiisopropylamine, *N*,*N*-dimethylformamide, 50 °C, overnight; (v) TFA/CH_2Cl_2 (9:1), rt, overnight.

Scheme 3[a]

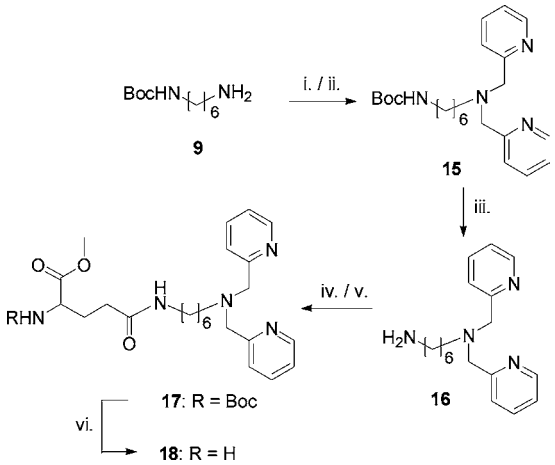

[a] (i) Pyridine-2-carboxaldehyde, $C_2H_4Cl_2$, 2 h, rt; (ii) $(CH_3COO)_3BHNa$, 0 °C to rt, 24 h; (iii) HCl 6 N, rt, 3 h; (iv) Boc-Glu-OMe, 1-hydroxybenzotriazole hydrate, *N*-(3-dimethylaminopropyl)-*N*′-ethylcarbodiimide hydrochloride, CH_2Cl_2, rt, 4 h; (v) *N*-ethyldiisopropylamine, *N*,*N*-dimethylformamide, rt, overnight; (vi) TFA/CH_2Cl_2 (9:1), rt, overnight.

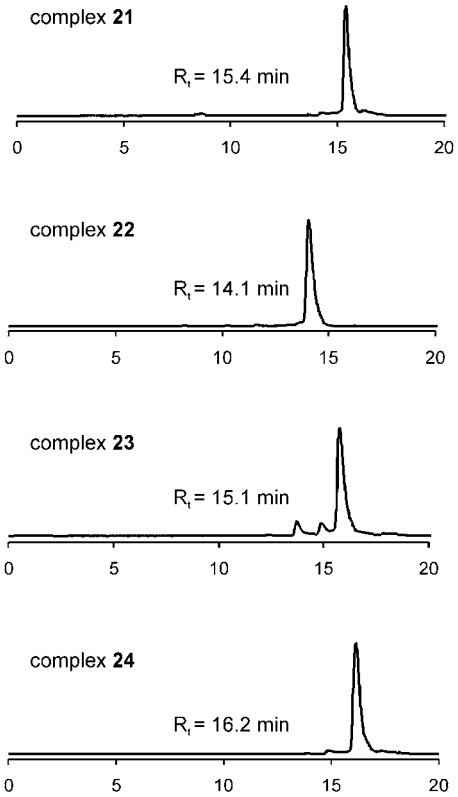

Figure 1. Radioactive HPLC-traces (γ-trace) of the $^{99m}Tc(CO)_3$-folate radiotracers 21−24, performed on an XTerra MS C-18 reversed phase column with a linear gradient (100% buffer to 80% methanol).

N2-*N*,*N*-dimethylaminomethlylene-10-formylpteroic acid (Scheme 4). Finally, all folate intermediates were fully deprotected in a single step in the presence of excess NaOH, to obtain, after 4−5 h of stirring at room temperature, the crude folate derivatives **8**, **14**, and **19**. After neutralization, followed by stepwise acidification of the aqueous solution, the pure products **8**, **14**, and **19** precipitated as yellow-orange powders and could be filtered and dried in a high vacuum.

Radiolabeling of the Folate Derivatives. Radiolabeling with $[^{99m}Tc(CO)_3(OH_2)_3]^+$ was performed at ligand concentrations of 10^{-4} M (**8**, **14**, **19**, **20**) for 30 min at 37 °C (Scheme 5). The formation of the $^{99m}Tc(CO)_3$-complexes, monitored by HPLC, showed generally a shift to longer retention times compared to the free precursor $[^{99m}Tc(CO)_3(OH_2)_3]^+$ ($R_t = \sim 7$ min) and the folate ligands (**8**, $R_t = 10.3$ min; **14**, $R_t = 10.2$ min; **19**, $R_t =$ 15.9. min; **20**, $R_t = 12.3$ min). Radiolabeling yields were >92% for all of the derivatives **21**−**24** (Figure 1). Formation of small amounts of (unidentifiable) byproducts was observed only in the case of ligand **19** and the corresponding complex **23**. Separation of the radioactive complexes from unlabeled folate derivates was necessary in order to avoid folate-receptor saturation. In the case of complexes **21**, **22**, and **24** HPLC separation was efficient. Ligand **19** and complex **23** revealed almost identical retention times. Separation was therefore difficult, hence the specific activity was significantly lower for complex **23**. This circumstance directly impaired FR targeting particularly in vivo (vide infra). The HPLC purified products showed no evidence of degradation in PBS or human plasma over a period of 24 h at 37 °C.

In Vitro Evaluation. In vitro experiments were performed with KB cells, which express a continuous, high level of FRs. In order to investigate the potential of our three novel complexes **21**−**23** and complex **24** for specific FR targeting, we performed cell binding studies (Table 1). The cells were incubated with the relevant radiotracer (**21**−**24**) at 37 °C for 1 h. After washing the cell monolayers with PBS (to remove unbound radiotracers), we found 40−55% of total radioactivity in the cell lysate, which represents FR-bound as well as cell-internalized radiotracers. Treatment of the cell monolayers with stripping buffer (pH 3) enabled the release of the radiotracers on the cell surface (specifically bound to FRs). The acid-resistant, internalized fraction of radiotracer in the cell lysates reached 13−25% of the total radioactivity. Preincubation of the cells with excess folic acid (final concentration 100 μM) for saturation of the FRs resulted in an almost complete blockade (<1% of the total added radioactivity). These studies clearly indicated high FR specificity of each of the folate radiotracers **21**−**24** and negligible unspecific cell binding. Variations with respect to percentage of bound radioactivity among the complexes were statistically not significant.

Biodistribution Studies. Time dependent biodistribution studies with the new radiotracers **21**−**23** have been performed in athymic nude mice, bearing KB cell xenografts. Compound **24** has been recently characterized by our group and was included in these studies for comparison (*17*). Data for these pre−clinical in vivo experiments are summarized in Table 2 (complexes **21**, **22**, and **24**) and Table 3 (complex **23**). Clearance from the blood pool was fast and efficient for all derivatives (≤0.2% ID/g already at 1 h p.i.). Tumor uptake of complexes **21**, **22**, and **24** ranged from 1.3% ID/g (**24**) to 2.4% ID/g (**22**) after 1 h and reached a maximum after 4 h (1.9% ID/g for **21**; 2.7% ID/g for **22**). After 24 h, more than 80% of the maximum radioactivity was retained in the tumors. A significant amount of radioactivity was localized in the kidneys. At 1 h p.i. an average of 17 ± 2% ID/g and at 24 h p.i. an average of 11 ± 4% ID/g were found in the cases of the neutral (**21**, **24**) and anionic (**22**) complexes. In the case of the cationic complex **23**, tumor uptake was only about 50% (0.91 ± 0.14% ID/g, 1 h p.i.) of that observed for the other complexes. At the same time complex **23** revealed also an approximately 50% lower uptake in the kidneys (average 7% ID/g at 1, 4, and 24 h p.i.).

Accumulation of radioactivity in the kidneys was not a surprise, since abundant FR expression in the proximal tubule cells of the kidney is widely described in the literature (*27*−*35*). This specific FR-mediated accumulation of folate radiotracers in the renal tissue is a general feature and potential drawback of radioactive folate derivatives (*10, 13, 36*). The significantly reduced uptake of complex **23** in the tumor and in the kidneys is most likely due to its low specific activity, leading to partial FR saturation with unlabeled folate ligand **19** and not because of its overall cationic charge. The absolute values of the injected dose per gram tissue for compound **23** therefore have to be interpreted with caution.

Biodistributions of all four tested complexes in other non-targeted tissues and organs were virtually identical within the standard deviations. An appreciable fraction of radioactivity was found in the liver at 1 h p.i. (e.g. 2.43 ± 0.80% ID/g for **23**; 6.53 ± 3.57% ID/g for **22**), as well as in the intestines (up to 5.01 ± 1.25% ID/g in case of **22**) and the intestinal contents (e.g. 9.31 ± 5.94% ID/g for **24** and 45 ± 34.37% ID/g for complex **21**). These data evidence a significant contribution of unspecific hepatobiliary excretion of all radiotracers independent of their physicochemical characteristics. However, clearance from these sites was efficient and at 4 h p.i. radioactivity in the liver had reached significantly lower values ranging from 2.37 ± 2.85% ID/g (complex **24**) to 0.74 ± 0.51% ID/g (complex **22**) and in the intestines from 1.58 ± 0.86% ID/g (complex **21**) to 0.71 ± 0.40% ID/g (complex **23**). Radioactivity found in other organs and tissue was generally <1% ID/g. FR-blockade experiments were performed by coadministration of folic acid at a dose of 100 ± 10 μg/mouse 5 min prior to administration of the radiotracers. These experiments showed

Scheme 4[a]

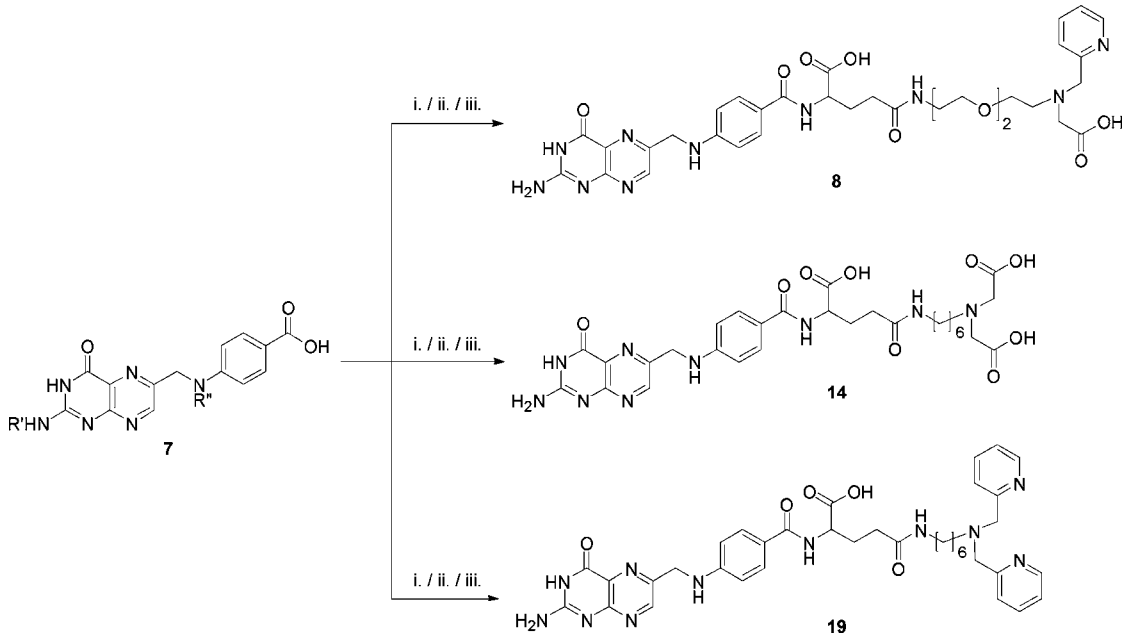

[a] R′ = CHNMe$_2$, R″ = CHO: (i) 1,1′-carbonyldiimidazole, rt, 3 h; (ii) **6**, **13**, or **18** and *N*-ethyldiisopropylamine in CH_2Cl_2, rt, overnight; (iii) NaOH, rt, 4−5 h.

Scheme 5

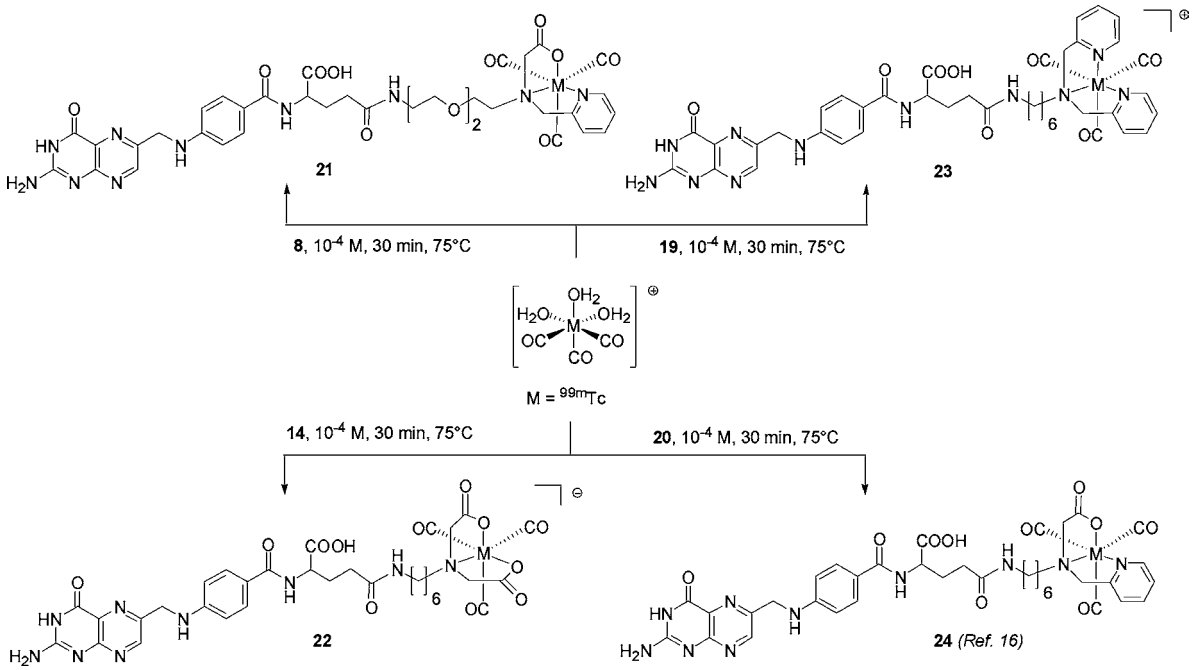

Table 1. Cell Binding Studies of the Complexes 21−24

	total cell binding [%]	internalized fraction [%]	+ excess folic acid [%]
complex **21**	40.6 ± 3.7	24.3 ± 0.8	0.06 ± 0.01
complex **22**	53.9 ± 3.9	22.2 ± 0.4	0.04 ± 0.00
complex **23**	49.0 ± 1.9	13.3 ± 0.9	0.17 ± 0.05
complex **24**	52.0 ± 2.4	13.8 ± 2.9	0.04 ± 0.00

an attenuation of radioactivity to background level in FR-positive tumors and the kidneys (Tables 2 and 3). This proved the high efficacy of all our folate derivatives to target FRs in vivo. Distribution in other organs and tissue was not significantly altered under blockade conditions.

The absolute values of the biodistribution experiments display a heterogeneous picture. None of the compounds revealed significantly and constantly superior or different results (assuming that results of **23** are an artifact due to low specific activity). We therefore reevaluated the complexes with respect to their tumor-to-nontumor ratios (tumor-to-kidney, tumor-to-blood, and tumor-to-liver) over time. This also allowed comparisons with other ^{99m}Tc-folates recently described in the literature. The highest tumor-to-kidney ratio was found at 4 h p.i. for the negatively charged compound **22** (0.26 ± 0.06). This result was significantly better than those obtained with complexes **23** and **24** (tumor-to-kidney = 0.13 ± 0.02) and the neutral complex **21** (tumor-to-kidney = 0.09 ± 0.01), featuring a diethoxyethyl spacer entity. The tumor-to-liver ratio determined for complex **22** (4.54 ± 2.06) was slightly superior to that of the other folate radiotracers. Finally, high tumor uptake

Table 2. Time-Dependent Biodistribution, Listed as % ID/g Values of Complexes 21, 22, and 24 in Athymic Female Mice with KB Xenografts

	1 h p.i.	4 h p.i.	4 h p.i. blocked[a]	24 h p.i.
		Complex **21**		
blood	0.09 ± 0.00	0.30 ± 0.29	0.00 ± 0.01	0.01 ± 0.00
heart	1.49 ± 0.23	0.48 ± 0.09	0.01 ± 0.01	0.05 ± 0.02
lung	0.48 ± 0.03	0.44 ± 0.15	0.16 ± 0.22	0.04 ± 0.02
spleen	0.19 ± 0.05	0.15 ± 0.08	0.14 ± 0.21	0.02 ± 0.00
kidney	17.71 ± 2.86	20.27 ± 1.53	0.17 ± 0.16	12.37 ± 1.93
stomach	0.84 ± 0.57	9.46 ± 15.94	0.19 ± 0.21	2.86 ± 4.54
intestines	3.59 ± 1.07	1.58 ± 0.86	0.90 ± 1.26	0.26 ± 0.18
contents of intestines	45.47 ± 34.37	15.41 ± 16.79	2.07 ± 2.89	2.07 ± 1.14
liver	4.12 ± 3.66	1.49 ± 1.61	1.96 ± 1.68	0.14 ± 0.02
muscle	0.79 ± 0.10	0.54 ± 0.15	0.13 ± 0.22	0.06 ± 0.02
bone	0.46 ± 0.03	0.29 ± 0.05	0.04 ± 0.04	0.03 ± 0.03
tumor	1.71 ± 0.22	1.89 ± 0.08	0.03 ± 0.02	1.57 ± 0.08
tumor-to-blood	19.53 ± 3.08	11.43 ± 8.68		172.91 ± 30.66
tumor-to-liver	1.19 ± 1.53	2.49 ± 1.73		11.4 ± 2.03
tumor-to-kidney	0.10 ± 0.00	0.09 ± 0.01		0.13 ± 0.02
		Complex **22**		
blood	0.16 ± 0.07	0.03 ± 0.00	0.01 ± 0.01	0.02 ± 0.01
heart	0.86 ± 0.41	0.09 ± 0.01	0.01 ± 0.01	0.05 ± 0.01
lung	0.58 ± 0.08	0.12 ± 0.01	0.01 ± 0.00	0.04 ± 0.01
spleen	0.34 ± 0.19	0.03 ± 0.01	0.00 ± 0.00	0.02 ± 0.00
kidney	19.18 ± 4.99	10.52 ± 1.92	0.08 ± 0.03	14.44 ± 4.42
stomach	0.70 ± 0.61	0.43 ± 0.56	0.05 ± 0.02	1.32 ± 1.84
intestines	5.01 ± 1.25	0.79 ± 0.35	0.36 ± 0.25	0.24 ± 0.11
contents of intestines	21.30 ± 19.49	7.48 ± 2.92	1.93 ± 1.16	0.87 ± 0.73
liver	6.53 ± 3.57	0.74 ± 0.51	0.65 ± 0.52	0.40 ± 0.23
muscle	0.94 ± 0.34	0.14 ± 0.01	0.00 ± 0.00	0.03 ± 0.00
bone	0.52 ± 0.26	0.04 ± 0.02	0.00 ± 0.00	0.00 ± 0.00
tumor	2.41 ± 0.20	2.67 ± 0.27	0.00 ± 0.00	2.18 ± 0.22
tumor-to-blood	17.57 ± 5.16	104.0 ± 7.11		137.4 ± 45.35
tumor-to-liver	0.51 ± 0.37	4.54 ± 2.06		6.77 ± 4.50
tumor-to-kidney	0.14 ± 0.04	0.26 ± 0.06		0.16 ± 0.03
		Complex **24**[b]		
blood	0.09 ± 0.02	0.04 ± 0.00	0.01 ± 0.00	0.01 ± 0.00
heart	0.85 ± 0.27	0.32 ± 0.07	0.00 ± 0.00	0.02 ± 0.02
lung	0.57 ± 0.19	0.33 ± 0.02	0.02 ± 0.02	0.03 ± 0.00
spleen	0.20 ± 0.03	0.15 ± 0.04	0.01 ± 0.01	0.01 ± 0.02
kidney	14.37 ± 1.35	18.48 ± 0.72	0.06 ± 0.01	6.90 ± 0.72
stomach	0.31 ± 0.06	0.63 ± 0.33	3.80 ± 5.46	3.70 ± 6.37
intestines	1.89 ± 0.37	1.49 ± 0.23	0.40 ± 0.45	0.76 ± 1.15
contents of intestines	9.31 ± 5.94	38.51 ± 55.88	5.54 ± 3.38	7.08 ± 11.52
liver	0.89 ± 0.31	2.37 ± 2.85	0.12 ± 0.02	0.10 ± 0.02
muscle	1.06 ± 0.33	0.54 ± 0.05	0.04 ± 0.01	0.05 ± 0.04
bone	0.76 ± 0.22	0.31 ± 0.07	0.01 ± 0.01	0.03 ± 0.04
tumor	1.30 ± 0.61	2.33 ± 0.36	0.00 ± 0.01	1.32 ± 0.17
tumor-to-blood	15.82 ± 11.29	58.0 ± 12.2		255.4 ± 115.4
tumor-to-liver	1.60 ± 0.81	2.53 ± 2.13		13.77 ± 1.90
tumor-to-kidney	0.09 ± 0.05	0.13 ± 0.02		0.19 ± 0.04

[a] Folate receptor blocked by co-injection of folic acid at a dose of 100 ± 10 μg/mouse. [b] Reference *17*.

Table 3. Time-Dependent Biodistribution, Listed as % ID/g Values of Complex 23 in Athymic Female Mice with KB Xenografts

	1 h p.i.	4 h p.i.	4 h p.i. blocked[a]	24 h p.i.
blood	0.05 ± 0.01	0.03 ± 0.01	0.01 ± 0.00	0.01 ± 0.01
heart	1.00 ± 0.28	0.20 ± 0.09	0.01 ± 0.00	0.37 ± 0.02
lung	0.26 ± 0.07	0.20 ± 0.02	0.02 ± 0.01	0.14 ± 0.02
spleen	0.13 ± 0.06	0.08 ± 0.02	0.01 ± 0.00	0.03 ± 0.01
kidney[b]	6.92 ± 1.49	7.11 ± 0.75	0.12 ± 0.01	7.76 ± 0.68
stomach	0.30 ± 0.07	0.54 ± 0.58	0.15 ± 0.07	0.57 ± 0.63
intestines	1.59 ± 0.33	0.71 ± 0.40	0.32 ± 0.30	0.14 ± 0.04
contents of intestines	15.50 ± 1.50	2.49 ± 12.10	2.63 ± 1.79	1.71 ± 2.35
liver	2.43 ± 0.80	1.72 ± 2.04	0.58 ± 0.38	0.52 ± 0.14
muscle	0.40 ± 0.11	0.27 ± 0.01	0.00 ± 0.00	0.21 ± 0.05
bone	0.26 ± 0.12	0.16 ± 0.02	0.00 ± 0.00	0.12 ± 0.02
tumor[b]	0.91 ± 0.14	0.94 ± 0.10	0.03 ± 0.01	1.10 ± 0.12
tumor-to-blood[b]	18.60 ± 3.60	29.65 ± 7.28		109.0 ± 47.25
tumor-to-liver[b]	0.42 ± 0.20	1.17 ± 0.82		2.23 ± 0.45
tumor-to-kidney	0.14 ± 0.04	0.13 ± 0.00		0.14 ± 0.01

[a] Folate receptor blocked by co-injection of folic acid at a dose of 100 ± 10 μg/mouse. [b] Low specific activity due to incomplete separation of radioactive complex **23** and nonradioactive precursor **19** is presumably responsible for low uptake of **23** in FR-positive kidneys and tumors compared to complexes **21**, **22**, and **24**.

and fast blood clearance of complex **22** gave rise also to a more favorable tumor-to-blood ratio (104.0 ± 7.11, 4 h p.i.) compared to those of the other complexes **21** (11.43 ± 8.68, 4 h p.i.) and **24** (58.0 ± 12.2, 4 h p.i.). One has to acknowledge, however,

that these trends in favor of complex **22** were less pronounced or not significant at early (1 h) and later time points (24 h) after administration of the radiotracers.

Green and co-workers published data of a presumably negatively charged DTPA-folate radiolabeled with the $^{99m}Tc(CO)_3$-core (*36*). $^{99m}Tc(CO)_3$-DTPA-folate exhibited better tumor uptake (KB cell xenografts, 3.3 ± 0.2% ID/g, 4 h, p.i.), than our derivatives but the high tumor uptake was accompanied by much higher kidney uptake. $^{99m}Tc(CO)_3$-DTPA-folate also revealed high and prolonged retention of activity in the liver (7.6 ± 0.5% ID/g, 4 h p.i.). On the other hand activity in the intestinal tract was significantly lower. The authors speculate that this might be due to clearance of $^{99m}Tc(CO)_3$-DTPA-folate from the liver back into the blood. Surprisingly such a mechanism seemed ineffective for complexes **21**−**24**. For $^{99m}Tc(CO)_3$-DTPA-folate it was also observed that coadministration of free folic acid was able to mitigate liver uptake (in addition to the tumor and the kidney uptake), which would indicate a specific, FR-mediated uptake in this organ. We observed little or no effect of free folic acid on the liver uptake of complexes **21**−**24**.

The technetium(V)−oxo folate ^{99m}Tc-EC20, which is currently in phase II clinical trials for detection of ovarian or endometrial cancer, displayed tumor-to-nontumor ratios similar to those found for our compounds (e.g. tumor-to-kidney ratios 0.12 ± 0.1; tumor-to-blood 50.6 ± 8.2; tumor-to-liver 4.83 ± 0.29, 4 h p.i.), although the absolute values for % ID/g in different tissues and organs were generally higher (*13*, *37*). Also for ^{99m}Tc-EC20 the radioactivity detected in the intestines and intestinal contents was much lower than in the case of our radiofolates.

CONCLUSION

Three novel, site-specifically modified folate derivatives have been prepared. The radiolabeling with the IsoLink precursor $[^{99m}Tc(CO)_3(OH_2)_3]^+$ was straightforward and efficient, giving rise to neutral and charged complexes in high yields. All ^{99m}Tc-complexes were successfully tested for their ability to target the FR on human KB cancer cells in vitro and in vivo. Comparative in vivo studies demonstrated that modification of the linker or chelating system does not dramatically alter the pharmacokinetic profile of the corresponding organometallic ^{99m}Tc-radiofolate. The present data suggest that overall the new $^{99m}Tc(CO)_3$-folates show competitive tumor-to-nontumor ratios compared with other ^{99m}Tc-labeled folates published in the literature. The significant hepatobiliary clearance and the resulting high fraction of radioactivity in the intestines and intestinal contents seem to be a peculiarity of our radiofolates. This is a potential drawback for clinical application. However, at the moment it is premature to draw final conclusions and further experiments are ongoing in order to assess the full potential of organometallic radiofolates for the detection of FR-positive tumors.

ACKNOWLEDGMENT

We thank Alain Blanc, Judith Stahel, and Christine De Pasquale for technical assistance. This work was financially supported by Mallinckrodt-Tyco Inc. and Merck Eprova AG.

LITERATURE CITED

(1) Leamon, C. P., and Low, P. S. (1993) Membrane folate-binding proteins are responsible for folate-protein conjugate endocytosis into cultured cells. *Biochem. J. 291*, 855−860.

(2) Leamon, C. P., and Low, P. S. (2001) Folate-mediated targeting: from diagnostics to drug and gene delivery. *Drug Discovery Today 6*, 44−51.

(3) Leamon, C. P., Pastan, I., and Low, P. S. (1993) Cytotoxicity of folate-pseudomonas exotoxin conjugates toward tumor cells—contribution of translocation domain. *J. Biol. Chem. 268*, 24847−24854.

(4) Leamon, C. P., and Low, P. S. (1994) Selective targeting of malignant cells with cytotoxin-folate conjugates. *J. Drug Targeting 2*, 101−112.

(5) Konda, S. D., Aref, M., Wang, S., Brechbiel, M., and Wiener, E. C. (2001) Specific targeting of folate-dendrimer MRI contrast agents to the high affinity fo late receptor expressed in ovarian tumor xenografts. *Magn. Reson. Mater. Phys., Biol. Med. 12*, 104−113.

(6) Lee, J. W., Lu, J. Y., Low, P. S., and Fuchs, P. L. (2002) Synthesis and evaluation of Taxol-folic acid conjugates as targeted antineoplastics. *Bioorg. Med. Chem. 10*, 2397−2414.

(7) Hofland, H. E. J., Masson, C., Iginla, S., Osetinsky, I., Reddy, J. A., Leamon, C. P., Scherman, D., Bessodes, M., and Wils, P. (2002) Folate-targeted gene transfer in vivo. *Mol. Ther. 5*, 739−744.

(8) Leamon, C. P., Cooper, S. R., and Hardee, G. E. (2003) Folate-liposome-mediated antisense oligodeoxynucleotide targeting to cancer cells: evaluation in vitro and in vivo. *Bioconjugate Chem. 14*, 738−747.

(9) Matulic-Adamic, J., Sanseverino, M., and Beigelman, L. (2002) An efficient synthesis of the ribozyme-folate conjugate. *Tetrahedron Lett. 43*, 4439−4441.

(10) Mathias, C. J., Wang, S., Waters, D. J., Turek, J. J., Low, P. S., and Green, M. A. (1998) Indium-111-DTPA-folate as a potential folate-receptor-targeted radiopharmaceutical. *J. Nucl. Med. 39*, 1579−1585.

(11) Mathias, C. J., and Green, M. A. (1998) A kit formulation for preparation of [^{111}In]In-DTPA-folate, a folate-receptor-targeted radiopharmaceutical. *Nucl. Med. Biol. 25*, 585−587.

(12) Guo, W. J., Hinkle, G. H., and Lee, R. J. (1999) ^{99m}Tc-HYNIC-folate: a novel receptor-based targeted radiopharmaceutical for tumor imaging. *J. Nucl. Med. 40*, 1563−1569.

(13) Leamon, C. P., Parker, M. A., Vlahov, I. R., Xu, L. C., Reddy, J. A., Vetzel, M., and Douglas, N. (2002) Synthesis and biological evaluation of EC20: a new folate- derived, ^{99m}Tc-based radiopharmaceutical. *Bioconjugate Chem. 13*, 1200−1210.

(14) Reddy, J. A., Xu, L. C., Parker, N., Vetzel, M., and Leamon, C. P. (2004) Preclinical evaluation of ^{99m}Tc-EC20 for imaging folate receptor-positive tumors. *J. Nucl. Med. 45*, 857−866.

(15) Ke, C. Y., Mathias, C. J., and Green, M. A. (2003) The folate receptor as a molecular target for tumor-selective radionuclide delivery. *Nucl. Med. Biol. 30*, 811−817.

(16) Müller, C., Dumas, C., Hoffmann, U., Schubiger, P. A., and Schibli, R. (2004) Organometallic ^{99m}Tc-technetium(I)- and Re-rhenium(I)-folate derivatives for potential use in nuclear medicine. *J. Organomet. Chem. 689*, 4712−4721.

(17) Müller, C., Hohn, A., Schubiger, A. P., and Schibli, R. (2006) Preclinical evaluation of novel organometallic ^{99m}Tc-folate and ^{99m}Tc-pteroate radiotracers for folate receptor-positive tumor targeting. *Eur. J. Nucl. Med. Mol. Imaging*, in press.

(18) Pons, J. F., Fauchere, J. L., Lamaty, F., Molla, A., and Lazaro, R. (1998) A constrained diketopiperazine as a new scaffold for the synthesis of peptidomimetics. *Eur. J. Org. Chem.*, 853−859.

(19) Stichelberger, A., Waibel, R., Dumas, C., Schubiger, P. A., and Schibli, R. (2003) Versatile synthetic approach to new bifunctional chelating agents tailor made for labeling with the *fac*-$[M(CO)_3]^+$ core (M = Tc, ^{99m}Tc, Re): synthesis, in vitro, and in vivo behavior of the model complex $[M(APPA)(CO)_3]$ (APPA = [(5-amino-pentyl)-pyridin-2-yl-methyl-amino]-acetic acid). *Nucl. Med. Biol. 30*, 465−470.

(20) Banerjee, S. R., Levadala, M. K., Lazarova, N., Wei, L. H., Valliant, J. F., Stephenson, K. A., Babich, J. W., Maresca, K. P., and Zubieta, J. (2002) Bifunctional single amino acid chelates for labeling of biomolecules with the $\{Tc(CO)_3\}^+$ and $\{Re(CO)_3\}^+$ cores. Crystal and molecular structures of $[ReBr(CO)_3(H_2NCH_2C_5H_4N)]$, $[Re(CO)_3\{(C_5H_4NCH_2)_2NH\}]Br$, $[Re(CO)_3\{(C_5H_4NCH_2)_2NCH_2CO_2H\}]Br$, $Re(CO)_3\{X(Y)NCH_2CO_2CH_2CH_3\}]Br$ (X = Y= 2-pyridylmethyl; X = 2-pyridyimethyl, Y = 2-(1-methylimidazolyl)methyl; X = Y=2-(1-methylimidazolyl)methyl), $[ReBr(CO)_3\{(C_5H_4NCH_2)NH(CH_2C_4H_3S)\}]$, and $[Re(CO)_3\{(C_5H_4NCH_2)N(CH_2C_4H_3S)(CH_2CO_2)\}]$. *Inorg. Chem. 41*, 6417−6425.

(21) Stephenson, K. A., Banerjee, S. R., Besanger, T., Sogbein, O. O., Levadala, M. K., McFarlane, N., Lemon, J. A., Boreham, D. R.,

Maresca, K. P., Brennan, J. D., Babich, J. W., Zubieta, J., and Valliant, J. F. (2004) Bridging the gap between in vitro and in vivo imaging: Isostructural Re and ^{99m}Tc complexes for correlating fluorescence and radioimaging studies. *J. Am. Chem. Soc. 126*, 8598−8599.

(22) Stephenson, K. A., Zubieta, J., Banerjee, S. R., Levadala, M. K., Taggart, L., Ryan, L., McFarlane, N., Boreham, D. R., Maresca, K. P., Babich, J. W., and Valliant, J. F. (2004) A new strategy, for the preparation of peptide-targeted radiopharmaceuticals based on ion of peptide-targeted an Fmoc- lysine-derived single amino acid chelate (SAAC). Automated solid-phase synthesis, NMR characterization, and in vitro screening of fMLF(SAAC)G and fMLF[(SAAC-$Re(CO)_3)^+$]G. *Bioconjugate Chem. 15*, 128−136.

(23) Nomura, M., Shuto, S., and Matsuda, A. (2000) Nucleosides and nucleotides, part 196 − Development of an efficient intermediate, α-[2-(trimethylsilyl)ethoxy]-2-*N*-[2-(trimethylsilyl)ethoxycarbonyl]-folic acid, for the synthesis of folate (γ)-conjugates, and its application to the synthesis of folate-nucleoside conjugates. *J. Org. Chem. 65*, 5016−5021.

(24) Antony, A. C., Kane, M. A., Portillo, R. M., Elwood, P. C., and Kolhouse, J. F. (1985) Studies of the role of a particulate folate-binding protein in the uptake of 5-methyltetrahydrofolate by cultured human KB cells. *J. Biol. Chem. 260*, 4911−4917.

(25) Dixon, K. H., Mulligan, T., Chung, K. N., Elwood, P. C., and Cowan, K. H. (1992) Effects of folate receptor expression following stable transfection into wild type and methotrexate transport-deficient ZR-75-1 human breast cancer cells. *J. Biol. Chem. 267*, 24140−24147.

(26) Ladino, C. A., Chari, R. V. J., Bourret, L. A., Kedersha, N. L., and Goldmacher, V. S. (1997) Folate-maytansinoids: target-selective drugs of low molecular weight. *Int. J. Cancer 73*, 859−864.

(27) Goresky, C. A., Watanabe, H., and Johns, D. G. (1963) Renal excretion of folic acid. *J. Clin. Invest. 42*, 1841.

(28) Morshed, K. M., and McMartin, K. E. (1996) In vitro characterization of renal reabsorption and secretion of folate using primary cultures of human kidney cells. *J. Nutr. Biochem. 7*, 276−281.

(29) Birn, H., Selhub, J., and Christensen, E. I. (1993) Internalization and intracellular transport of folate-binding protein in rat kidney proximal tubule. *Am. J. Physiol. 264*, C302−C310.

(30) Birn, H., Spiegelstein, O., Christensen, E. I., and Finnell, R. H. (2005) Renal tubular reabsorption of folate mediated by folate binding protein 1. *J. Am. Soc. Nephrol. 16*, 608−615.

(31) McMartin, K. E., Morshed, K. M., Hazenmartin, D. J., and Sens, D. A. (1992) Folate transport and binding by cultured human proximal tubule cells. *Am. J. Physiol. 263*, F841−F848.

(32) Selhub, J., Emmanouel, D., Stavropoulos, T., and Arnold, R. (1987) Renal folate absorption and the kidney folate binding protein. I. Urinary clearance studies. *Am. J. Physiol. 252*, F750−F756.

(33) Selhub, J., and Rosenberg, I. H. (1978) Demonstration of high-affinity folate binding activity associated with brush border membranes of rat kidney. *Proc. Natl. Acad. Sci. U.S.A. 75*, 3090−3093.

(34) Ross, J. F., Chaudhuri, P. K., and Ratnam, M. (1994) Differential regulation of folate receptor isoforms in normal and malignant tissues in-vivo and in established cell-lines—physiological and clinical implications. *Cancer 73*, 2432−2443.

(35) Parker, N., Turk, M. J., Westrick, E., Lewis, J. D., Low, P. S., and Leamon, C. P. (2005) Folate receptor expression in carcinomas and normal tissues determined by a quantitative radioligand binding assay. *Anal. Biochem. 338*, 284−293.

(36) Trump, D. P., Mathias, C. J., Yang, Z. F., Low, P. S. W., Marmion, M., and Green, M. A. (2002) Synthesis and evaluation of ^{99m}Tc$(CO)_3$-DTPA-folate as a folate-receptor-targeted radiopharmaceutical. *Nucl. Med. Biol. 29*, 569−573.

(37) Reddy, J. A., Xu, L.-C., Parker, N., Vetzel, M., and Leamon, C. P. (2004) Preclinical Evaluation of ^{99m}Tc-EC20 for Imaging Folate Receptor-Positive Tumors. *J. Nucl. Med. 45*, 857−866.

BC050323Q

Cyclic and Acyclic Oxorhenium(V)−Peptide Conjugates as New Ligands of the Human Cyclophilin hCyp-18

Cécile Clavaud, Marion Heckenroth, Charlotte Stricane, André Ménez, and Christophe Dugave*

CEA/Saclay, Département d'Ingénierie et d'Etudes des Protéines, Bâtiment 152, 91191 Gif-sur-Yvette, France. Received November 17, 2005; Revised Manuscript Received April 7, 2006

Peptide metalloconstructs display interesting conformations, activities, and resistance to proteolysis. However, introduction of a metal core close to the residues that interact with the protein might strongly affect the binding. We investigated the effects of a coordinated oxorhenium core on the binding of model peptides to cyclophilin hCyp-18, a protein implicated in important biological processes and several diseases. For this purpose, we synthesized a series of linear metalloconstructs bearing an oxorhenium(V) core (ReO^{3+}), as well as a peptide cyclized through oxorhenium(V) coordination. All these peptides contain an Ala-Pro-Xaa-*p*NA moiety (Xaa = Cys derivative) and are anticipated to bind simultaneously to the S1−S1′ and S2′−S3′ subsites of hCyp-18. Therefore, the metal core is coordinated to both the cysteine residue and exogenous or endogenous NS_2 tridentate systems. Cyclization of the peptide through metal coordination did not affect the affinity whereas bimolecular oxorhenium metalloconstructs bind hCyp-18 with a slightly better affinity than the corresponding nonmetalated peptide. Peptide labeling with a $^{99m}TcO^{3+}$ core was also carried out successfully.

INTRODUCTION

Engineered peptide metalloconstructs bearing a technetium core or a rhenium core have important applications in nuclear medicine due to their radiochemical properties (*1*, *2*), stabilized conformations, and resulting enhanced resistance to proteolysis (*3*). Technetium and rhenium both belong to the group VIIB transition metals and share common similar coordination geometries, atom size, and bond lengths. They form stable complexes with a variety of organic groups, in particular with thiolates, thioethers, amines, amides, and carboxylates, all of which may be found in peptides or in synthetic bifunctional chelating agents (BFCAs) grafted onto peptides. In a first strategy called the integrated approach, the peptide backbone plus the side chains coordinate the metal core without any exogenous motif, but metalation often results in dramatic changes in geometry and steric hindrance relative to the nonmetalated peptide and thus greatly alters its biological activity (*4*). Conversely, the peptide can bind the metal core via coordination to a BFCA grafted either onto the N-terminus or onto an amino acid side chain, provided these moieties do not interact with the biological target (*5*). The latter approach has yielded a large number of peptide and protein radiopharmaceuticals (*1*, *2*).

Several reports have described the design, synthesis, and biological characterization of peptide hormones cyclized through rhenium and technetium metal coordination (*6*). In particular, Quinn and co-workers have designed α-melanotropin (α-MSH) peptide analogues that display an enhanced affinity for the α-MSH receptor relative to the linear peptide, due to additive constraints upon metalation (*4*, *7*−*9*). A similar strategy was utilized by Gilon's research team to cyclize a GnRH analogue (*10*). Sharma et al. also reported the metal-mediated cyclization of melanocortin and tuftsin peptides (*11*). Recently, Gilon and co-workers have described the synthesis of a library of metal-cyclized somatostatin analogues (*12*).

We investigated the biochemical activity of short peptides bearing an oxorhenium(V) core coordinated via either an intermolecular (acyclic complexes) or an intramolecular (cyclic complex) NS_2/S chelating agent. These metalloconstructs all contain a minimal tripeptide sequence Ala-Pro-Xaa-*p*NA which specifically binds to cyclophilin hCyp-18, an important peptidyl prolyl isomerase which plays a critical role in protein folding and cell division and communication, and is implicated in a large number of diseases including AIDS, cancer, and neurodegenerative disorders (*13*). Introduction of a ReO^{3+}/$^{99m}TcO^{3+}$ metal core inside short ligands of cyclophilin might yield interesting substrate analogues with stabilized, biologically active conformations. Moreover, incorporation of technetium and rhenium radioisotopes might lead to the development of a new generation of radiopharmaceuticals that target hCyp-18. However, no information regarding the effect of the introduction of a rhenium complex close to the active site of hCyp-18 was available. In this study, we investigated the effect of the oxorhenium core on the binding properties of peptides derived from Suc-Ala-Ala-Pro-Phe-*p*NA **1**, a known model substrate of hCyp-18 which displays a moderate affinity for cyclophilin.

EXPERIMENTAL PROCEDURES

Materials and Methods. All reagents and solvents were purchased from Sigma-Aldrich, Fisher, or Novabiochem and were of the highest purity available. THF was distilled from sodium/benzophenone immediately prior to use. ^{99m}Tc was used as a commercial ^{99}Mo/^{99m}Tc eluate (Schering). Reaction progress and flash chromatography elution (Merck silica gel 40−63 μm) were monitored by analytical thin-layer chromatography (Merck $60F_{254}$). Spots on TLC were visualized using UV light (254 nm), and spots were revealed by ninhydrin or phosphomolybdic acid. RP-HPLC analysis and purification were conducted on a Waters 600 Millennium chromatography system coupled to a Waters diode array detector. Separations were achieved on a Vydac C^{18} column eluted with an isocratic system (100% A) from 0 to 5 min, a linear gradient system (100% A to 100% B) from 5 to 25 min, and then an isocratic system (100% B) at a flow rate of 1 mL·min^{-1} (analytical column 4.5 × 250 mm, 5

* Corresponding author. Tel: (33) 16908 5225. Fax: (33) 16908 9071. E-mail: christophe.dugave@cea.fr.

10.1021/bc050329f CCC: $33.50 © 2006 American Chemical Society
Published on Web 04/29/2006

μm) or 4 mL·min^{-1} (semipreparative column 10 × 250 mm, 10 μm) (A, 0.1% aqueous solution of trifluoroacetic acid; B, acetonitrile). ^{1}H and ^{13}C NMR spectra were recorded on Bruker AVANCE 250 and 400 NMR spectrometers; δ and J are reported in ppm relative to TMS and Hz, respectively. Electrospray mass spectrometry (ES/MS) was performed on a Quattro II (Micromass, Altricham, U.K.).

(βAla-Ala-Pro-Cys-pNA)$_2$ 2. (Boc-Cys-*p*NA)$_2$, Boc-Pro-OH, Boc-Ala-OH and Boc-βAla-OH were coupled successively by the DCC, HOBt method to give the disulfide peptide (Boc-βAla-Ala-Pro-Cys-*p*NA)$_2$. This peptide was deprotected in 4 N HCl/dioxane and purified by HPLC, to give peptide **2.** HPLC t_r = 18.6 min. ^{1}H NMR (D_2O): δ 8.12 + 7.56 (2d, J = 9.1 Hz, 8H), 4.72 (m, 2H), 4.55 (m, 2H), 4.43 (m, 2H), 3.84−3.63 (2m, 4H), 3.35−3.04 (2m, 8H), 2.66 (m, 4H), 2.27 (m, 2H), 2.04−1.87 (m, 6H), 1.31 (d, 6H). ^{13}C NMR (D_2O): δ 174.9, 174.0, 172.5, 170.9, 144.3, 143.7, 125.7, 121.2, 65.0, 61.2, 54.3, 50.0, 48.4, 39.4, 36.2, 32.3, 18.2, 24.1, 16.0. ES/MS (positive ionization): *m*/*z* 960.4 (M + H$^+$, 100%).

***N-tert*-Butyloxycarbonyl-bis(thioacetoethyl)amine 6.** Diethanolamine (21.1 g, 200 mmol) was treated with di-*tert*-butyldicarbonate (44.1 g, 200 mmol) and DIPEA (71.1 mL, 400 mmol) in methanol (250 mL) overnight at room temperature. After removal of the solvent, the residue was dissolved in ethyl acetate and the organic layer was washed successively with 10% citric acid, saturated sodium bicarbonate, and brine. The organic layer was dried over sodium sulfate, and the solvent was evaporated in vacuo. The crude product was purified by silica gel flash chromatography (eluent: ethyl acetate:hexane 10:90) to give **6** (40.6 g, 99%). ^{1}H NMR ($CDCl_3$): δ 4.27 (bs, 2H), 3.78 (bs, 4H), 3.42 (bs, 2 × 2H), 1.46 (s, 9H). ^{13}C NMR ($CDCl_3$): δ 156.59, 80.50, 61.04, 52.49, 28.58.

Diisopropylazodicarboxylate (24.87 mL, 120 mmol) was added dropwise to a solution of triphenylphosphine (31.79 g, 120 mmol) in dry THF (250 mL) at 0 °C. After formation of the white ylide precipitate, the solution was stirred for 30 min. A solution of *N-tert*-butyloxycarbonyl-diethanolamine (8.21 g, 40 mmol) in 40 mL of dry THF and thioacetic acid (9 mL, 120 mmol) were added successively. The reaction was stirred for 1 h at 0 °C and then overnight at room temperature. After reduction of the volume, the residue was washed and dried as described above. The crude product was purified twice by silica gel flash chromatography (eluent: ethyl acetate:hexane; first purification 10:90, second purification 5:95) to provide the bis-thioacetate **5** (11.1 g, 87%). ^{1}H NMR ($CDCl_3$): δ 3.40−3.35 (t, J = 6.6 Hz, 4H, 3.06−3.00 (bt, J = 7.3 Hz, 4H), 2.34 (s, 3H), 1.47 (s, 9H). ^{13}C NMR ($CDCl_3$): δ 155.2, 80.3, 47.6, 47.4, 30.7, 28.4, 27.9, 27.4. ES/MS (positive ionization): *m*/*z* 322.1 (M + H$^+$). Elemental anal. (%): calcd C (48.57), H (7.21), N (4.36), S (19.95); found C (48.49), H (7.04), N (4.42), S (20.22).

***N-tert*-Butyloxycarbonyl-bis(thioethyl)amine Disulfide 7.** Sodium methanolate (1.39 g, 25.7 mmol) was added to a solution of **6** (4.12 g, 12.8 mmol) in methanol (100 mL). The mixture was stirred over 5 days at room temperature in an open flask. The solvent was removed under reduced pressure, and the crude product was purified by silica gel flash chromatography (eluent: ethyl acetate:hexane 20:80) to provide disulfide **7** (1.96 g, 71%). ^{1}H NMR ($CDCl_3$): δ 3.75−3.68 (bq, J = 5.7 Hz, 4H), 3.02−2.93 (dt, J = 5.7 Hz, J' = 10.1 Hz, 4H), 1.47 (s, 9H). ^{13}C NMR ($CDCl_3$): δ 154.98, 79.94, 51.21, 50.77, 38.10, 28.49. ES/MS (positive ionization): *m*/*z* 236.7 (M + H$^+$). Elemental anal. (%): calcd C (45.93), H (7.28), N (5.95), S (27.25); found C (46.25), H (7.21), N (6.13), S (26.81).

***N-tert*-Butyl-bis(thioethyl)glycinate Disulfide 3a.** Compound **7** (1.96 g, 8.4 mmol) was treated with a 50:50 trifluoroacetic acid:DCM solution for 30 min. Then the solvent was evaporated in vacuo and a solution of *tert*-butyl-bromoacetate (1.9 mL, 12.6 mmol) and DIPEA (2.2 mL, 12.6 mmol) in DCM (60 mL) was added. The mixture was stirred overnight at room temperature. After removal of the solvent in vacuo the crude product was purified by silica gel flash chromatography (eluent: ethyl acetate:hexane 30:70) to provide the disulfide **3a** (1.72 g, 83%). ^{1}H NMR ($CDCl_3$): δ 3.44 (s, 2H), 3.34−3.29 (bt, J = 2.9 Hz, 4H), 2.91−2.87 (bt, J = 4.5 Hz, 4H), 1.47 (s, 9H). ^{13}C NMR ($CDCl_3$): δ170.98, 81.15, 57.24, 55.85, 39.86, 28.24. ES/MS (positive ionization): *m*/*z* 250.0 (M + H$^+$). Elemental anal. (%): calcd C (48.16), H (7.68), N (5.62), S (25.71); found C (48.22), H (7.56), N (5.55), S (25.51).

General Procedure for the Preparation of Compounds 3b and 3c. Bromoacetyl bromide (90 μL, 1 mmol) and DIPEA (190 μL, 1 mmol) were successively added to a solution of *tert*-butylamine or piperidine in DCM (10 mL) to provide the bromoacetamides **8b** and **8c**. The mixture was stirred for 30 min at 0 °C. The solvent was removed under reduced pressure. Compound **7** was treated with a 50:50 trifluoroacetic acid:DCM solution (20 mL) for 30 min. After removal of the solvent in vacuo and chase of toluene on the crude product, the residue was dissolved in methanol (5 mL). Solutions of bromoacetamide and amine resulting from the acidolysis of **7** were mixed together and treated overnight with sodium methanolate (118 mg, 2.1 mmol). After removal of the solvent in vacuo the crude product was purified by silica gel flash chromatography.

***N-tert*-Butyl-bis(thioethyl)glycinamide Disulfide 3b.** *tert*-Butylamine (106 μL, 1.03 mmol) was treated as describe above (eluent: ethyl acetate:hexane 50:50) to provide the disulfide **3b** (59 mg, 54%). ^{1}H NMR ($CDCl_3$): δ 7.35 (s, 1H), 3.36 (s, 2H), 3.31−3.23 (bt, J = 5.4 Hz) + 2.91−2.87 (bt, J = 5.9 Hz) (4H), 1.38 (s, 9H). ^{13}C NMR ($CDCl_3$): δ 169.81, 62.50, 57.48, 51.22, 39.67, 28.96. ES/MS (positive ionization): *m*/*z* 248.6 (M + H$^+$). Elemental anal. (%): calcd C (48.35), H (8.12), N (11.28), S (25.82); found C (48.41), H (8.69), N (10.97), S (25.44).

***N*-Piperidyl-bis(thioethyl)glycinamide Disulfide 3c.** Piperidine (105 μL, 1.03 mmol) was treated as describe above (eluent: ethyl acetate:hexane 50:50) to give disulfide **3c** (78 mg, 29%). ^{1}H NMR ($CDCl_3$): δ 3.57 (s, 2H), 3.57−3.48 + 3.43−3.39 (2bt, 4H), 3.39−3.29 (bt, J = 5.8 Hz) + 2.98−2.90 (bt, J = 5.8 Hz) (4H), 1.61 + 1.23 (2m, 6H). ^{13}C NMR ($CDCl_3$): δ 168.8, 57.2, 55.87, 46.5, 42.9, 39.9, 26.5, 25.8, 24.6. ES/MS (positive ionization): *m*/*z* 260.8 (M + H$^+$). Elemental anal. (%): calcd C (50.73), H (7.74), N (10.76), S (24.63); found C (50.43), H (8.09), N (10.43), S (24.22).

***N*-Bis-(thioethyl)glycine Disulfide Hydrochloride 9.** Compound **3a** (1.72 g, 6.9 mmol) was treated with 50/50 1 N HCl in acetonitrile for 1 h. After evaporation of the solvent in vacuo, toluene was chased twice over the residue. The hydrochloride salt **9**·HCl was quantitatively isolated (1.57 g, 100%). ^{1}H NMR (D_2O): δ 4.30 (s, 2H), 3.97−3.94 (bt, J = 5.6 Hz, 4H), 3.31−3.26 (bt, J = 5.9 Hz, 4H). ^{13}C NMR (D_2O): δ 169.0, 58.9, 34.6. ES/MS (positive ionization): *m*/*z* 192.9 (M +H$^+$). Elemental anal. (%): calcd C (31.37), H (5.26), N (6.10), S (27.91); found C (31.13), H (5.53), N (5.76), S (27.63).

Methyl *N*-ϵ-Bis-(thioethyl)glycyl(*N*-α-*tert*-butyloxycarbonyl)lysinate Disulfide 10. Compound **9** (101.5 mg, 0.4 mmol), HATU (205 mg, 0.6 mmol), and DIPEA (313 μL, 1.6 mmol) were added to a solution of Boc-Lys-OMe (104.1 mg, 0.4 mmol) in anhydrous DMF (14 mL), and the mixture was stirred overnight at room temperature. After removal of the solvent under reduced pressure, the crude product was purified twice by silica gel flash chromatography (eluent: dichloromethane: methanol; first purification: 95:5, second purification: 98:2) to give **10** (149.7 mg, 86%). ^{1}H NMR ($CDCl_3$): δ 7.50 (s, 1H), 5.08 (bd, 1H), 4.28 (m, 1H), 3.74 (s, 3H), 3.38 (s, 2H), 3.32−3.24 (m, 6H), 2.92−2.88 (m, 4H), 1.82−1.50 (3m, 3 × 2H),

1.44 (s, 9H). ^{13}C NMR ($CDCl_3$): δ 173.3, 156.5, 150.5, 79.9, 57.3, 52.3, 39.6, 38.6, 32.3, 29.3, 28.3, 22.7. HRMS (TOF/ES): *m*/*z* calcd for $C_{18}H_{33}N_3O_5S_2$ 435.1920; found 435.1913.

Sodium *N*-ϵ-Bis-(thioethyl)glycyl(*N*-α-*tert*-butyloxycarbonyl)lysinate Disulfide 11. Compound **10** (71.5 mg, 0.16 mmol)-was treated with lithium hydroxide (6.58 mg, 0.16 mmol) in acetonitrile:water 3:1 for 45 min. The solvent was removed to give the lithium salt **11**, which was used in the further step without purification. ES/MS (positive ionization): *m*/*z* 423.05 ($M + H^+$).

(Boc-Lys($COCH_2N(CH_2CH_2S)_2$)-Ala-Pro-Cys-*p*NA)$_2$ 13. Compound **11** was coupled with (Ala-Pro-Cys-*p*NA)$_2$ disulfide by the DCC, HOBt method to give peptide **13** (70 mg, 78%). t_r = 22.2 min. ^{1}H NMR ($CDCl_3$): δ 10.16 (s, 2H), 8.22 + 7.85 (2d, J = 9.1 Hz, 8H), 7.56 + 7.15 (2s, 2 × 2H), 5.22 (s, 2H), 4.71 (m, 2H), 4.11 (m, 4H), 3.65 (m, 4H), 3.46 (m, 8H), 3.26 (m, 8H) 3.11 (m, 4H,), 2.92 (m, 4H), 2.23−1.97 (2m, 2 × 4H), 1.91 (bd, 10H), 1.67 (m, 8H), 1.44 (s, 18H). ^{13}C NMR ($CDCl_3$): δ 157.5, 143.9, 143.7, 125.0, 119.4, 80.1, 61.7, 54.3, 49.2, 34.0, 28.3, 25.6, 24.9. ES/MS (positive ionization): *m*/*z* 356.92 (M − 2Boc + 4H$^+$, 100%).

(Lys($COCH_2N(CH_2CH_2S)_2$)-Ala-Pro-Cys-pNA)$_2$ 14. Compound **13** (70 mg, 0.04 mmol) was treated with 4 N HCl−dioxane (5 mL) for 4 h at 0 °C. After removal of the solvent in vacuo, the residue was dissolved in methanol and purified by HPLC (eluent: A, 0.1% aqueous solution of trifluoroacetic acid; B, acetonitrile; A:B 100:0 from 0 to 5 min, 10 min linear gradient from 100:0 to 70:30, 8 min isocratic 70:30, 12 min linear gradient from 70:30 to 0:100, then 0:100 for 5 min at a flow rate of 4 mL·min^{-1}) to give peptide **14** (13.0 mg, 23%), t_r = 18.6 min. ^{1}H NMR (D_2O): δ 8.24 + 7.62 (2d, J = 7.4 Hz, 8H), 7.56 + 7.15 (2s, 2 × 2H), 4.64 (m, 2H), 4.46 (bt, 2H), 4.11 (m, 2H), 3.83 (s, 6H), 3.68 (m, 4H), 3.57 (s, 8H) 3.32 (m, 4H), 3.07 (m, 12H), 2.30−2.04 (2m, 2 × 4H), 1.4 (m, 8H), 1.8 (bd, 6H). ^{13}C NMR (D_2O): δ 143.9, 143.7, 125.0, 119.4, 83.5, 61.71, 54.3, 49.2, 35.6, 28.3, 25.6, 24.9. HRMS (TOF/ES): *m*/*z* calcd for $C_{58}H_{86}N_{16}O_{14}S_6$ 1422.4988; found 1422.4978.

***β*Ala-Ala-Pro-Cys(Acm)-pNA 15.** Peptide **2** (96 mg, 0.1 mmol) was treated successively with tributylphosphine (38 μL, 2.2 equiv) in wet THF (6 mL) for 40 min. After removal of the solvent in vacuo, the crude product was treated with iodoacetamide (44 mg, 2.2 equiv) and cesium carbonate (72 mg, 0.22 equiv) in DMF (6 mL) overnight at room temperature. Purification by RP-HPLC using the standard gradient program described above gave compound **15** (40.7 mg, 38%); t_r = 15.8 min. ^{1}H NMR (CD_3CN): δ 8.19 + 7.98 (2d, 4H, J = 9.3 Hz), 6.82 (bs, 1H), 6.49 (bs, 1H), 5.94 (bs, 1H), 4.80−4.72 (m, 2H), 4.55−4.50 (m, 1H), 3.76−3.68 (m, 2H), 3.49−3.37 (m, 4H), 2.96 (s, 2H), 2.13−1.74 (2m, 4H), 1.47 (m, 2H), 1.22 (t, 3H). ^{13}C NMR (CD_3CN): δ 172.8, 171.9, 169.0, 144.0, 143.5, 124.8, 119.6, 61.2, 58.5, 53.7, 47.7, 47.6, 36.5, 36.2, 35.2, 33.9, 25.3, 24.9, 17.5. ES/MS (positive ionization): *m*/*z* 538.35 (M + H$^+$, 100%).

General Procedure for Preparation of Complexes 4a−c. Solutions of **2** and **3a−c** in methanol were treated with 10% tributylphosphine in methanol for 30 min under argon before addition of [^{n}Bu$_4$N][ReOCl$_4$] and 10% triethylamine in methanol. A brown precipitate immediately formed. After stirring for 2 h, the crude mixture was centrifuged. The precipitate was washed twice with methanol, dissolved in dimethylsulfoxide, and purified by HPLC.

Complex 4a. HPLC t_r = 21.9 min. ^{1}H NMR (D_2O): δ 8.17 + 7.68 (2d, J = 8.0 Hz, 4H), 4.96 (m, 1H), 4.56 (m, H), 4.48 (m, H), 4.22 (bs, 2H), 3.80−3.59 (m, 6H), 3.18 (m, 4H), 2.94 (m, 4H), 2.70 (m, 2H), 2.28−2.02 (m, 4H), 1.45 (s, 9H), 1.33 (m, 3H). ES/MS (positive ionization): *m*/*z* 930.2 (^{185}Re, M + H$^+$, 53%) + 932.40 (^{187}Re, M + H$^+$, 100%).

Complex 4b. HPLC t_r = 19.5 and 21.0 min. ^{1}H NMR (D_2O): δ 8.23 + 7.68 (2d, J = 7.5 Hz, 4H), 4.80 (m, 1H), 4.64 (m, 1H), 4.48 (m, 1H), 4.22 (s, 2H), 3.68−3.59 (m, 6H), 3.16 (m, 4H), 2.70 (m, 4H), 2.29 (m, 2H), 2.20−2.05 (m, 4H), 1.41 (m, 12H). ES/MS (positive ionization): (first isomer) *m*/*z* = 929.1 (^{185}Re, M + H$^+$, 53%) + 931.00 (M + H$^+$, 100%); (second isomer) *m*/*z* 929.1 (^{185}Re, M + H$^+$, 50%) + 931.00 (M + H$^+$, 100%).

Complex 4c. HPLC t_r = 18.9 and 20.5 min. ^{1}H NMR (D_2O): δ 8.26 + 7.70 (2d, J = 8.9 Hz, 4H), 4.97 (m, 1H), 4.56 (m, H), 4.47 (m, H), 4.39 (s, 2H), 4.11 (m, 2H), 3.76−3.58 (m, 8H), 3.24 (m, 6H), 3.15 (m, 2H), 2.83 + 2.70 (2m, 2 × 1H), 2.02−1.92 (m, 4H), 1.86−1.54 (bs, 6H), 1.38 (m, 3H). ES/MS (positive ionization): (first isomer) *m*/*z* = 941.2 (^{185}Re, M + H$^+$, 52%) + 943.2 (^{187}Re, M + H$^+$, 100%); (second isomer) *m*/*z* 941.2 (^{185}Re, M + H$^+$, 59%) + 943.2 (^{187}Re, M + H$^+$, 100%).

Complex 5. A solution of **14** (4.1 mg, 2.9 μmol) in methanol (115 μL) was treated with a 10% methanolic solution of tributylphosphine (15 μL) for 30 min under argon. Then methanolic solutions of [^{n}Bu$_4$N]ReOCl$_4$ (43 μL, 5.7 μmol) and 10% Et$_3$N (35 μL, 22.8 mol) were added successively. A brown precipitate immediately formed. After stirring for 2 h, the crude mixture was centrifuged. The precipitate was washed twice with methanol, then dissolved in DMSO, and purified by HPLC. t_r = 19.9 min. ^{1}H NMR (d_6-DMSO): δ 10.5 (bs, 1H), 8.23 + 7.87 (2d, J = 7.2 Hz, 4H), 7.82 (s, 1H), 4.63 (m, 1H), 4.55 (bt, 1H), 4.35−4.31 (m, 2H), 3.62 (s, 3H), 3.19 (m, 2H), 3.10−2.99 (m, 4H), 2.89 (m, 2H), 2.10−1.80 (2m, 2 × 2H), 1.56−1.53 (m, 4H), 1.15 (bd, 3H). ESMS (positive ionization): *m*/*z* 913.1 (^{185}Re, M + H$^+$, 52%) + 915.2 (^{187}Re, M + H$^+$, 100%).

Determination of Dissociation Constants (K_d). Fluorimetric determination of K_d values was done using a JASCO FP-750 spectrofluorimeter equipped with a 200 μL thermostated cell. Increasing concentrations of rhenium complexes (dissolved in DMSO) were added to solutions of hCyp-18 (1.1 μM, 180 μL) in HEPES buffer (35 mM, pH 7.8). Fluorescence at 345 nm ($\lambda_{excitation}$ = 285 nm, $\lambda_{emission}$ = 324 nm) was recorded at 20.0 ± 0.1 °C. K_d values were obtained as the fitted points of inflection from the sigmoid log *F*/*C* profiles. A concentration-dependent fluorescence enhancement was observed with CsA whereas a concentration-dependent fluorescence quenching was observed with *p*NA derivatives.

Reaction with Glutathione. A solution of complexes **4a−c** or **5** (500 μL, 50 μM) in a 35 mM HEPES buffer pH 7.4 was treated by an aqueous solution of glutathione (100 μL, 60 mM) at room temperature. For blank, distilled water was used instead of glutathione. All the solutions were purged with argon prior to use. Aliquots of the mixture (30 μL) were analyzed by RP-HPLC after 5, 15, 30, 60, and 120 min.

^{99m}Tc Radiolabeling Experiments. The [^{99m}Tc^{V}O](NS$_2$/S) mixed ligand complexes **16a−c** and **17** were obtained by ligand-exchange reaction using the [^{99m}Tc^{V}O]gluconate precursor which was produced by mixing solutions of stannous chloride (4 μL, 2 mg·mL^{-1}) in HCl 0.1 N, 50 mM gluconate (20 μL), and a [^{99m}Tc]pertechnetate solution (200 μL, 11−30 MBq) eluted from a ^{99}Mo/^{99m}Tc Elumatic III generator, Schering. The resulting [^{99m}Tc^{V}O]gluconate solution was treated for 1 h at 50 °C with disulfides **2**, **3a−c**, or **14** (100 μL of a 20 mM solution) previously reduced as reported above. Aliquots of these solutions were analyzed by RP-HPLC.

RESULTS AND DISCUSSION

Cyclophilin hCyp-18 binds a large variety of proteins and peptides that display a canonical Xaa-Pro sequence, with a marked preference when Xaa is Ala, Gly, and Glu (Figure 1) (*13*−*15*). It also accommodates short pseudopeptide analogues of compound **1** (*16*, *17*) as well as peptides derived from the

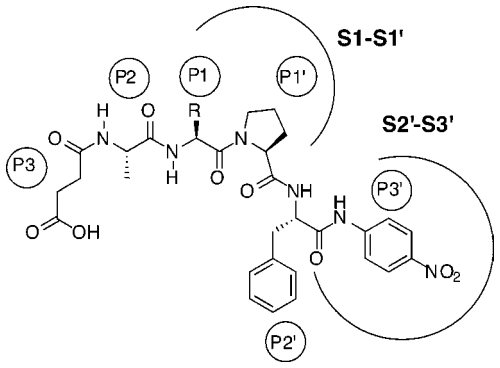

Figure 1. Structure of peptide **1** (R = CH_3) and schematic drawing of hCyp-18 subsites S1−S1′ and S2−S2′.

Scheme 1

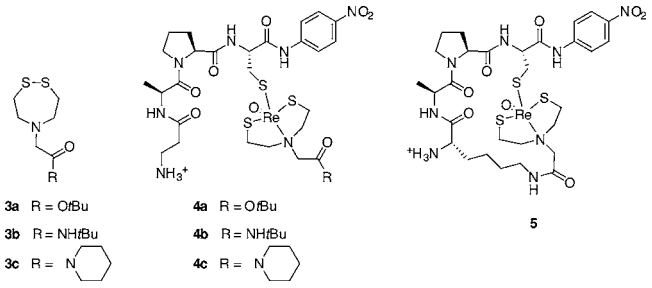

HIV-1 capsid (*18*) and cyclopeptides such as cyclosporine (*13*−*15*). hCyp-18 also binds some non-peptide compounds, in particular the macrolide sanglifehrin (*19*, *20*) and cymbimicins (*21*), as well as small molecules such as dimedone amino acid derivatives (*22*), constrained Gly-Pro mimetics (*23*), and aniline derivatives (*24*−*26*). All these compounds interact simultaneously with the two subsites S1−S1′ and S2′−S3′ and usually enhance the fluorescence of Trp121 which is located at the edge of the S2′−S3′ subsite, though peptide **1** causes a fluorescence quenching due to the presence of the *p*-nitroanilide moiety (*13*, *17*, *18*).

We investigated the potential of acyclic and cyclic metalloconstructs derived from the model tetrapeptide **1** as hCyp-18 ligands. All these peptides contain a Cys-*p*NA moiety which is anticipated to interact with the S2′−S3′ subsite via two H-bonds with Trp121 and Arg 148 (*27*, *28*) and provides the S motif for metal coordination. In cyclic metalloconstructs, the complementary tridentate chelating motif N(CH_2−CH_2−S)$_2$ (noted NS_2) is grafted onto the N-terminal sequence of the peptide (P2 position), which does not play a significant part in the binding (Scheme 1) (*29*, *30*).

We first checked that coordination of a metal core at P2′ in a linear peptide containing the Ala-Pro sequence did not interfere with the binding of the peptide to hCyp-18. For this purpose, the disulfide tetrapeptide (βAla-Ala-Pro-Cys-*p*NA)$_2$ **2** was readily prepared as a common precursor that could be connected to compounds **3a**−**c** via coordination of an oxorhenium(V) core after reduction of disulfides, in order to provide complexes **4a**−**c**. Compounds **3a**−**c** possess the NS_2 motif which is connected to 3 different substituents in order to check that variation in this position affects neither the coordination of the metal core nor the biochemical properties of the peptides (Scheme 1). We also investigated the ability of the intramolecular complex **5** to bind to hCyp-18. Compound **5**, a cyclic analogue of complexes **4a**−**c**, restricts the positioning of the rhenium core relative to the acyclic rhenium complexes.

Several syntheses of functionalized NS_2 motifs have been reported in the literature, but they necessitated the use of dangerous reagents such as ethylene sulfide (toxic) (*31*, *32*) or liquid ammonia (toxic, hazardous) (*33*). Therefore, these methods were not easily transposable to batch preparation. In particular, the double nucleophilic opening of ethylene sulfide by a variety of amines requires prolonged heating under pressure. Moreover, in our hands, the synthesis of disulfide **3a** starting from ethylene sulfide and glycine *tert*-butyl ester gave very low yields (2−5%). Results seem to depend strongly on the temperature of addition of all reactants and on the presence of polymers. Previous reports have underlined that use of excess ethylene sulfide essentially gives byproducts along with polymers resulting from the opening of ethylene sulfide by the intermediary bis-mercaptan moiety (*34*). Moreover, we found that the reaction product was not usable in further steps due to the existence of nonseparable side products (Scheme 2).

Scheme 2

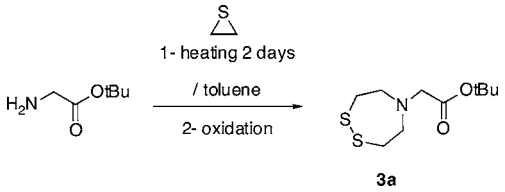

Scheme 3

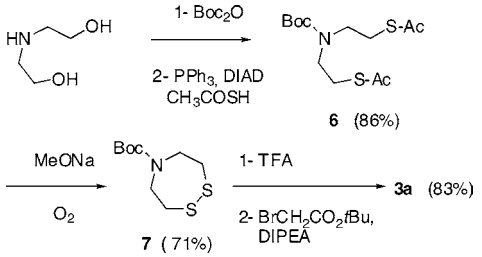

Another approach developed by Chiotellis and co-workers was based on the attractive reductive amination of 2,2′-dithiobis(2-methylpropanal) using sodium cyanoborohydride. However, this synthesis was not compatible with nonsubstituted disulfides (*35*). All these reasons prompted us to develop a simple and reproducible route to prepare large quantities of disulfides **3a**.

Selective N-protection of diethanolamine with di-*tert*-butyl dicarbonate followed by bis-thioacetylation with thioacetic acid, triphenylphosphine, and diisopropylazodicarboxylate (*36*) gave compound **6** in high yield (Scheme 3). In contrast, derivatization of the diol with 2 equiv of methanesulfonyl chloride or triphenylphosphine/carbon tetrabromide, and substitution with a salt (potassium or diisopropylethylammonium) of thioacetic acid, gave compound **6** in poor to moderate yields.

Methanolysis of the bis-thioacetate was carried out for 5 days in an open flask under high dilution conditions (Scheme 3). In fact, removal of the acetyl groups was completed in a few hours but it gave the desired disulfide mixed with the corresponding bis-thiol, which was anticipated to react irreversibly with electrophiles employed in further steps. Under these conditions, precursor **7** was isolated by silica gel flash chromatography in 71% yield. After removal of the Boc group of compound **7** with TFA, N-alkylation with *tert*-butyl bromoacetate in the presence of diisopropylamine (DIPEA) gave compound **3a** in 83% yield. The reaction was carried out reproducibly on the 25−120 mmol scale.

Compounds **3b** and **3c** were obtained as follows: after acidolysis of the Boc group of precursor **6**, treatment with bromoacyl-*tert*-butylamine **8b** and bromoacetyl-piperidine **8c** (obtained respectively by acylation of *tert*-butylamine or piperidine with bromoacetyl bromide) and sodium methanolate gave the corresponding disulfides **3b** and **3c**. Compound **3a** was also obtained by this procedure, but the yield was significantly lower than that obtained with DIPEA (Scheme 4).

Scheme 4

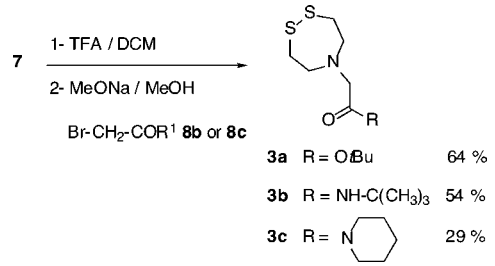

Scheme 5

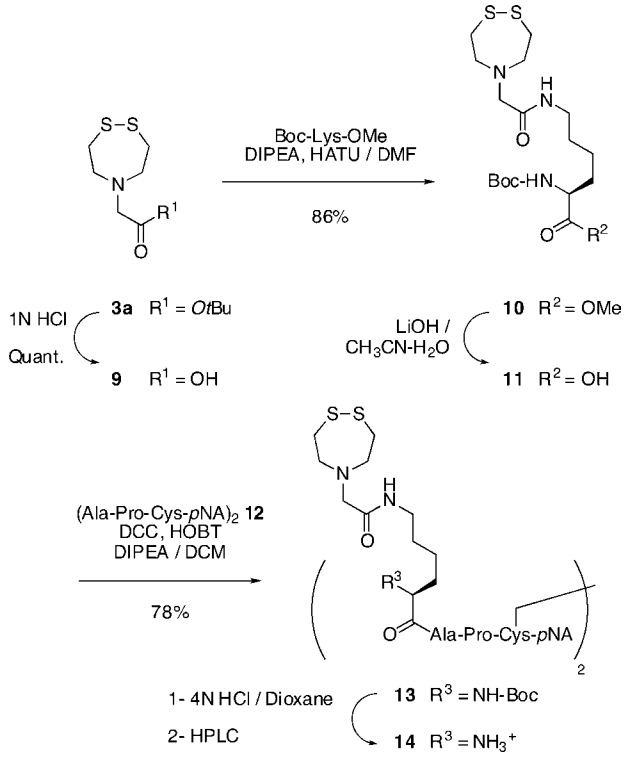

Compound **3a** was also used to synthesize peptide **14**, the precursor of the cyclic metalloconstruct **5** by the synthetic route depicted in Scheme 5. Unexpectedly, deprotection of the t*ert*-butyl group of **3a** with 50% trifluoroacetic acid in dichloromethane gave a complex mixture of compounds resulting putatively from the reaction of the disulfide with the intermediary *tert*-butyl cation. Therefore, the *tert*-butyl ester was cleaved under very mild conditions (1 N aqueous HCl in acetonitrile) to give compound **9** in quantitative yields (Scheme 5). Coupling to the side chain of Boc-lysine methyl ester with HATU in DMF gave the corresponding adduct **10** in 86% yield. In contrast, coupling with DCC afforded compound **10** in lower yields. Saponification of the methyl ester gave the modified Boc-lysine **11**, which can be used directly in peptide synthesis. Standard coupling of compound **11** with 1/2 equiv of disulfide peptide **12** led to peptide **13** in good yields. Removal of the Boc groups with a 4 N solution of hydrogen chloride in dioxane gave peptide **14**, the oxidized precursor of complex **5**, which was purified by RP-HPLC.

Complexes **4a**−**c** were assembled by reducing peptide **2** on the one hand and compounds **3a**−**c** on the other with tributylphosphine in methanol and then mixing the resulting crude products with tetrabutylammonium tetrachlorooxorhenate(V) to give the corresponding rhenium coordinates **4a**−**c**. After reduction of peptide **14** as reported above, metalation with commercial $[Bu_4N][ReOCl_4]$ (*37*) gave the peptide−oxorhenium complex **5**. All complexes precipitated and were thoroughly washed with

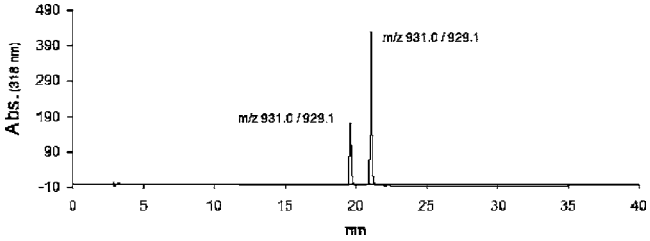

Figure 2. RP-HPLC chromatogram of peptide **2** (A) and complex **4b**: Vydac C^{18} column (5 μm, 4.6 mm, 250 mm) eluted with a binary gradient system (A, 0.1% aqueous solution of trifluoroacetic acid; B, acetonitrile; A:B 100:0 from 0 to 5 min, 25 min linear gradient from 100:0 to 0:100, then 0:100 for 5 min at a flow rate of 1 mL·min^{-1}).

methanol and dried prior to characterization by NMR and mass spectrometry. Analysis by RP-HPLC on a C^{18} column showed that compound **4a** appeared as a single peak whereas **4b** and **4c** were eluted as two peaks that had identical mass spectra, suggesting the existence of at least two diastereomers resulting from either the up or the down Re═O position relative to the peptide moiety, or from a syn/anti isomerism about the coordinated tertiary amine (Figure 2). This was not observed with the cyclic complex **5**, which gave a single but slightly shouldered peak which might correspond either to the coexistence of several diastereomers that do not separate under these conditions, or might result from a slow cis−trans isomerization about the alanyl-proline peptide bond (*38*) as suggested by the 400 MHz NMR spectrum (data not shown). In all cases, crude complexes were free of residual reduced or oxidized forms of peptides **2** or **14** as assessed by RP-HPLC and mass spectrometry analysis (Figure 3). In particular, all products' mass spectra show multipeak motifs that reflect the coexistence of ^{185}Re−^{187}Re and ^{32}S−^{34}S isotopic mixtures. In all cases, the experimental profile was identical to the calculated motif (Figure 3).

The standard fluorescence titration assay (*18*) was employed for the determination of the apparent dissociation constants (K_d) of the ligands as previously reported. Excitation of the indole moiety of Trp121 at 285 nm and recording of fluorescence at 324 nm for increasing concentrations in peptide showed a classical sigmoid curve drawn from the relation % fluorescence = *f*(log[ligand]). We first ensure that Phe to Cys change at P2′ (disulfide **2** and its thioalkylated equivalent **15**) does not perturb the binding of the peptide to hCyp-18. Peptide **15** (βAla-Ala-Pro-Cys(Acm)-*p*NA) was simply prepared by reduction of peptide **2** with tributylphosphine and quenching of the free thiol with iodoacetamide. The experiments showed that increasing the concentration of peptides **2** and **15** produces a fluorescence quenching which is very similar to that observed with the model peptide **1** (Figure 4). This suggests that these compounds interact at the S2′−S3′ subsite to produce an extinction of the Trp121 fluorescence and hence that the Phe to Cys mutation has no significant effect on the affinity. The same curve profile was observed with all oxorhenium complexes (Table 1). This clearly shows that coordination of a rhenium core at P2′ does not affect the affinity of the 4-mer peptide sequences for the protein. As anticipated, the "R" group of complexes **4a**−**c** (see Scheme 1) does not seem to influence the binding to hCyp-18 since it might protrude outside the active site. Complex **5** exhibits an affinity for hCyp-18 that is equivalent to that of peptides **1** and **14**, suggesting that the rhenium core does not perturb the binding, though the cyclic structure of the complex is assumed to maintain the metal core close to the protein structure.

A structural examination of several cyclophilin-ligand complexes, including hCyp-18:**1**, has shown that the side chain of the P2′ residue cannot interact with the protein since it stands out from the protein:ligand complex (*27*). This allows a relatively free positioning of the P2′ side chain, and, therefore, the highly polarized oxorhenium core is not anticipated to

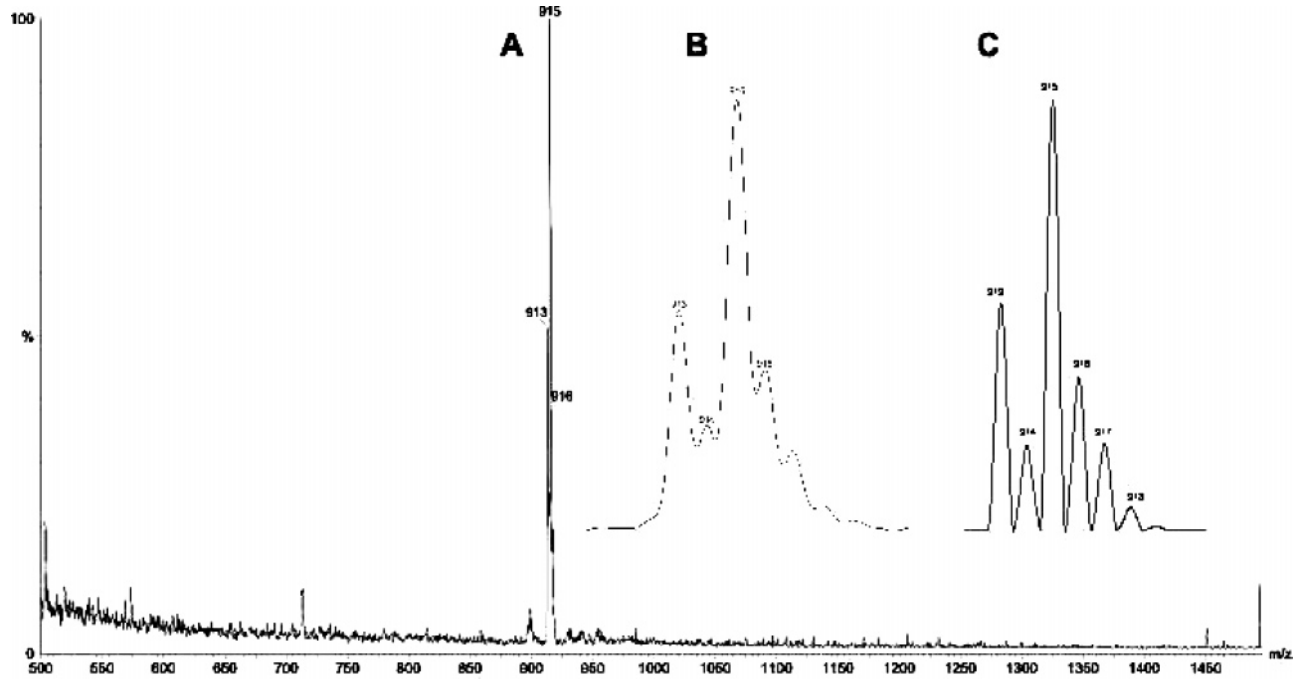

Figure 3. Electrospray mass spectrum of complex **5** (*m*/*z*): Experimental spectrum (A and B); calculated spectrum (C); the existence of several distinct signals of incremented masses relative to the theoretical values may be explained by the presence of rhenium isotopes ^{185}Re and ^{187}Re and sulfur isotopes ^{32}S and ^{34}S.

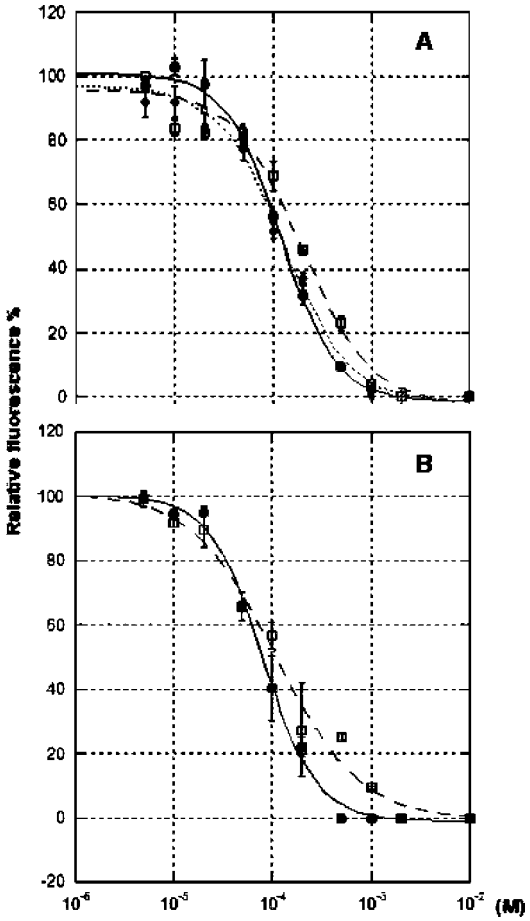

Figure 4. Fluorimetric determination of the apparent dissociation constants (K_d) of peptides **1** (■), **14** (□), and **15** (●) (A) and complexes **4a** (■) and **5** (□) (B).

interact with the protein or therefore to disturb the positioning of the peptide backbone inside the active site. In particular, Arg155 and His126 and Asn102 are located within 6−7 Å of the rhenium atom (*27*) and are not anticipated to interact directly with the metal, although deleterious effects of the oxorhenium dipole on the protein structure cannot be precluded. These results indicate that introduction of a ReO^{3+} core inside peptidic ligands of hCyp-18 does not perturb the interaction.

Table 1. RP-HPLC Retention Times[a]

compound	HPLC t_r (min)	ES/MS (*m*/*z*)[b]	K_d (μM)
1			135 ± 20
4a	21.9	932.2/930.2	81±5
4b	19.5 + 21.0	931.0/929.1 + 931.0/929.1	78 ±8
4c	18.9 + 20.5	943.2/941.2 + 943.1/941.2	75 ± 5
2	18.5	960.4	111 ± 20
15	18.9	538.35	195 ± 29
14	17.6	356.9[c]	127 ± 14
5	19.9	915.2/913.1	108 ± 2

[a] Vydac C^{18} column: 10 μM, 4.6 mm, 250 mm. Eluted with an isocratic system (100% A) from 0 to 5 min, a linear gradient system (100% A to 100% B) from 5 to 25 min, and then an isocratic system (100% B) at a flow rate of 1 mL·min^{-1} (A, 0.1% aqueous solution of trifluoroacetic acid; B, acetonitrile). ES/MS *m*/*z* values and apparent affinity constants (K_d) of complexes **4a**−**c** and **5** and peptides **1**, **2**, **14**, and **15**, calculated from fluorescence titration experiments [b] Observed as $M + H^+$. [c] Observed as $M + 4H^+$.

We also investigated the possibility that complexes **4a**−**c** and **5** might interact nonspecifically with hCyp-18. For this purpose we preincubated cyclosporin A (CsA) with hCyp-18 prior to addition of compounds **4a**−**c** and **5**. In fact, CsA, a cyclic undecapeptide, binds simultaneously to S1−S1′ and S2′−S3′ subsites and produces an enhancement of fluorescence (*39*). Therefore, CsA was anticipated to compete with the rhenium complexes. Preincubation with CsA effectively prevented binding of the complexes, and resulted in a concentration-dependent recovery of fluorescence, suggesting that compounds **4a**−**c** and **5** interact with hCyp-18 in a specific way and bind to the S1−S1′ and S2′−S3′ subsites simultaneously since they possess both a proline residue and a *p*NA moiety. We checked that these complexes also showed satisfactory stabilities when incubated with hCyp-18 for 24 h since the peptide adducts were recovered without any detectable degradation as assessed by RP-HPLC.

We investigated the resistance of complexes to thiol-contain-

ing reducing agents by treating the complexes **4a**−**c** and **5** with 1 mM glutathione (GSH) in pH 7.4 buffer. As anticipated, complexes **4a**−**c** are sensitive to GSH which replaces the βAla-Ala-Pro-Cys-*p*NA peptide to give the corresponding glutathione-containing complexes (*40*). Conversely, complex **5** is extremely resistant to glutathione, although up to 20% of the starting material is degraded in the first 5 min whereas 80% of the complex was recovered after 30 min at 20 °C. The presence of bimolecular head-to-tail complexes might account for this result, since complexation was performed with concentrated solutions. However, only one peak was observed by RP-HPLC and no other rhenium-containing species was detected by mass spectrometry. Another explanation might be the existence of multiple non-interconvertible (up/down−syn/anti−cis/trans) isomers which might differ in their resistance to GSH.

Finally, labeling of the peptides was carried out with ^{99m}Tc using standard procedures. Pertechnetate obtained from a ^{99}Mo/^{99m}Tc generator was reduced with stannous chloride at room temperature. The [^{99m}Tc^{V}O]gluconate precursor was complexed by an equimolar amount of peptide **2** and compounds **3a**−**c** previously reduced with tributyl phosphine to give complexes **16a**−**c**. Complex **17** was prepared from peptide **14** by a similar procedure. The metalated peptides **16a**−**c** and **17** were analyzed by RP-HPLC and gave elution profiles similar to those of the corresponding rhenium complexes.

In conclusion, we synthesized a series of bimolecular acyclic complexes **4a**−**c** and a cyclic peptide complex **5** through coordination of the oxorhenium core. The rhenium complexes were assayed as ligands of cyclophilin and display satisfactory stabilities under the conditions employed for the binding assay. Results clearly indicate that all complexes interact with hCyp-18 with an affinity which is equivalent to that of the substrate tetrapeptide **1** and suggest that it is possible to produce novel acyclic and cyclic cyclophilin ligands respectively by assembly or cyclization through metal coordination. The low affinity of these compounds certainly limits their use in vivo, but application of this strategy to more complex peptides such as CsA and SfA analogues might yield interesting radiopharmaceuticals to target cyclophilin.

ACKNOWLEDGMENT

We gratefully acknowledge Dr. L. Le Clainche (CEA/Saclay, DIEP) for help in radiolabeling experiments and Dr. J. Barbier and F. Beau (CEA/Saclay, DIEP) for assistance in the analysis of ^{99m}Tc complexes. We thank Dr. M. Moutiez (CEA/Saclay, DIEP) for purification of the recombinant cyclophilin hCyp-18. We are indebted to Dr. E. Zeckri (CEA/Saclay, DBJC) for NMR experiments at 400 MHz and to Dr. J. Le Gal (CEA/Saclay, DIEP) for critical reading of the manuscript.

LITERATURE CITED

(1) Dilworth, J. R., and Parrot, S. J. (1998) The Biomedical Chemistry of Technetium and Rhenium. *Chem. Soc. Rev. 27*, 43−55.

(2) Liu, S., and Edwards, D. S (1999) ^{99m}Tc-Labeled Small Peptides as Diagnostic Radiopharmaceuticals. *Chem. Rev. 99*, 2235−2268.

(3) Albrecht, M., and Stortz, P. (2005) Metallocyclopeptides: Artificial Analogues of Naturally Occurring Peptides. *Chem. Soc. Rev. 34*, 496−506.

(4) Giblin, M. F., Wang, N., Hoffman, T. J., Jurisson, S. S., and Quinn, T. P. (1998) Design and Characterization of α-Melanotropin Peptide Analogs Cyclized through Rhenium and Technetium metal Coordination. *Proc. Natl. Acad. Sci. U.S.A. 95*, 12814−12818.

(5) Stephenson, K. A., Banerjee, S. R., Sogbein, O. O., Levadala, M. K., McFarlane, N., Boreham, D. R., Maresca, K P., Babicj, J. W., Zubieta, J., and Valliant, J. F. (2005) A New Strategy for the Preparation of Peptide-Targeted Technetium and Rhenium Radiopharmaceuticals. The Automated Solid-Phase Synthesis, Characterization, Labeling, and Screening of a Peptide-Ligand Library Targeted at the Formyl Peptide Receptor. *Bioconjugate Chem. 16*, 1189−1195.

(6) Okarvi, S. M. (2004) Peptide-Based Radiopharmaceuticals: Future Tools for Diagnostic Imaging of Cancers and Other Diseases. *Med. Res. Rev. 24*, 357−397.

(7) Chen, J., Cheng, Z., Owen, N. K., Hoffman, T. J., Miao, Y., Jurisson, S. S., and Quinn, T. P. (2001) Evaluation of an ^{111}In-DOTA-Rhenium Cyclized α-MSH Analog: A Novel Cyclic-Peptide Analog with Improved Tumor-Targeting Properties. *J. Nucl. Med. 42*, 1847−1855.

(8) Cheng, Z., Chen, J., Quinn, T. P., and Jurisson, S. S. (2004) Radioiodination of Rhenium Cyclized α-Melanocyte-Stimulating Hormone Resulting in Enhanced Radioactivity Localization and Retention in Melanoma. *Cancer Res. 64*, 1411−1418.

(9) McQuade, P., Miao, Y., Yoo, J., Quinn, T. P., Welch, M. J., and Lewis, J. S. (2005) Imaging of Melanoma Using ^{64}Cu- and ^{86}Y-DOTA-ReCCMSH(Arg11), a Cyclized Peptide Analogue of α-MSH. *J. Med. Chem. 48*, 2985−2992.

(10) Barda, Y., Cohen, N., Lev, V., Ben-Aroya, N., Koch, Y., Mishani, E., Fridkin, M., and Gilon, C. (2004) Backbone Metal-Cyclization: Novel ^{99m}Tc-Labeled GnRH Analog as Potential SPECT Molecular Imaging Agent in Cancer. *Nucl. Med. Biol. 31*, 921−933.

(11) Sharma, S. D. (2001) Structurally determined cyclic metallo-constructs and applications. U.S. Patent 6,331,285.

(12) Fridkin, G., Bonasera, T. A., Litman, P., and Gilon, C. (2005) Backbone metal-cyclization: A Novel Approach for Simultaneous Peptide Cyclization and Radiolabeling. Application to the Combinatorial Synthesis of Rhenium-Cyclic Somatostatin Analogs. *Nucl. Med. Biol. 32*, 39−50.

(13) Dugave, C., and Demange, L.(2003) Cis-trans Isomerization of Organic Molecules and Biomolecules: Implications and Applications. *Chem. Rev. 103*, 2475−2532.

(14) Dugave, C. (2002) Study of the Cis-Trans Isomerization of the Amino Acyl-Prolyl Peptide Bond. Application to the Design of Novel Inhibitors of Immunophilins. *Curr. Org. Chem. 6*, 1397−1431.

(15) Dornan, J., Paylor, P., and Walkinshaw, M. D. (2003) Structures of Immunophilins and their Ligand Complexes. *Curr. Topics Med. Chem. 3*, 1392−1409.

(16) Ma, L., Hsieh-Wilson, L. C., and Schultz, P. G. (1998) Antibody catalysis of peptidyl-prolyl *cis-trans* isomerization in the folding of RNase T1, *Proc. Natl. Acad. Sci. U.S.A. 95*, 7251−7256.

(17) Demange, L., Moutiez, M., and Dugave, C.(2002) Synthesis and evaluation of Glyψ(PO_2R-N)Pro-containing pseudopeptides as novel inhibitors of the human cyclophilin hCyp-18. *J. Med. Chem. 45*, 3928−3933.

(18) Li, Q., Moutiez, M., Charbonnier, J.-B., Vaudry, K., Ménez, A., Quéméneur, E., and Dugave C. (2000) Design of a Gag pentapeptide analogue that binds human cyclophilin A more efficiently than the entire capsid protein: New insights for the development of novel anti-HIV-1 drugs. *J. Med. Chem. 43*, 1770−1779.

(19) Sedrani, R., Kallen, J., Martin Cabrejas, L. M., Papgeorgiu, C. D., Senia, F., Rohrbach, S., Wagner, D., Thai, B., Jutzi Eme, A.-M., France, J., Oberer, L., Rihs, G.; Zenke, G., and Wagner, J. (2003) Sanglifehrin-Cyclophilin Interaction: Degradation Work, Synthetic Macrocyclic Analogues, X-ray Crystal Structure, and Binding Data. *J. Am. Chem. Soc. 125*, 3849−3859.

(20) Kallen, J., Sedrani, R., Zenke, G., and Wagner, J. (2005) Structure of Human Cyclophilin A in Complex with the Novel Immunosuppressant Sanglifehrin A at 1.6 Å Resolution. *J. Biol. Chem. 280*, 21965−21971.

(21) Fehr, T., Quesniaux, V., Sanglier, J.-J., Oberer, L., Gschwind, L., Ponelle, M., Schilling, W., Wehrli, S., Enz, A., Zenke, G., and Schuler, W. (1997) Cymbimicin A and B, two Novel Cyclophilin-Binding Structures Isolated from Actinomycetes. *J. Antibiot. 50*, 893−899.

(22) Walkinshaw, M. D., Taylor, P., Turner, N. J., and Flitsch, S. L. (2002) Preparation of Dimedone Amino Acid Derivatives as Cyclophilin-Binding Compounds. World Patent WO 2002048178.

(23) Wang, H. C., Kim, K., Bakthiar, R., and Germanas, J. P. (2001) Structure−Activity Studies of Ground- and Transition-State Analogue Inhibitors of Cyclophilin. *J. Med. Chem. 44*, 2593−2600.

(24) Wu, Y.-Q., Belyakov, S., Hamilton, G. S., Limburg, D., Steiner, J. P., Vaal, M., Wei, L., and Wilkinson, D. (2002) Trisubstituted

Carbocyclic Cyclophilin-Binding Compounds and their In Vivo Neuroprotective Effects. World Patent WO 2002059080.
(25) Wu, Y.-Q., Belyakov, S., Choi, C., Limburg, D., Thomas IV, B. E.; Vaal, M., Wei, L., Wilkinson, D. E., Holmes, A.; Fuller, M., McCormick, J.; Connolly, M., Moeller, T., Steiner, J. P., and Hamilton, G. S. (2003) Synthesis and Biological Evaluation of Non-Peptidic Cyclophilin Ligands. *J. Med. Chem. 46*, 1112−1115.
(26) Steiner, J. P., and Hamilton, S. G. (2005) Non-peptidic cyclophilin binding compounds and their use. U.S. Patent 6,593,362.
(27) Zhao, Y., and Ke, H. (1996) Crystal Structure Implies That Cyclophilin Predominantly Catalyzes the Trans to Cis Isomerization. *Biochemistry 35*, 7356−7361.
(28) Zhao, Y., and Ke, H. (1996) Mechanistic Implication of Crystal Structures of the Cyclophilin-Dipeptide Complexes. *Biochemistry 35*, 7362−7368.
(29) Schiene, C., Reimer, U., Schutkowski, M., and Fischer, G. (1998) Maping the Stereospecificity of Peptidyl-Prolyl Cis-Trans Isomerases. *FEBS Lett. 432*, 202−206.
(30) Demange, L., Moutiez, M., Vaudry, K., and Dugave C., (2001) Interaction of human cyclophilin hCyp-18 with short peptides suggests the existence of two functionally independent subsites. *FEBS Lett. 505*, 191−195.
(31) Pirmettis, I. C., Papadopoulos, M. S., Mastrostamatis, S. G., Raptopoulou, C. P., Terzis, A., and Chiotellis, E. (1996) Synthesis and Characterization of Oxotechnetium(V) Mixed-Ligand Complexes Containing a Tridentate N-Substituted Bis(2-mercaptoethyl)amine and a Monodentate Thiol. *Inorg. Chem. 35*, 1685−1691.
(32) Friebe, M., Malmood, A., Spies, H., Berger, R., Johannsen, B., Mahammed, A., Eisenhut, M., Bolzati, C., Davison, A., and Jones, A. G. (2000) '3+1' Mixed-Ligand Oxotechnetium(V) Complexes with Affinity for Melanoma: Synthesis and Evaluation in Vitro and in Vivo. *J. Med. Chem. 43*, 2745−2752.
(33) Tsoukalas, CH., Pirmettis, I., Patsis, G., Papdopoulos, A., Raptopoulou, C. P., Terzis, A., Papadopoulos, M., and Chiotellis, E. (2001) Ester-Modified ^{99m}TcO[SN(R)S/S] Mixed Ligand Complexes: Synthesis and Preliminary Evaluation. *Nucl. Med. Biol. 28*, 975−982.
(34) Corbin, J., Miller, K., Pariyadath, N., Wherland, S., Bruce, L., and Stiefel, E. J. (1984) Preparation and Properties of tripodal and Linear Tetradentate Nitrogen, Sulfur-donor Ligands and their Complexes Containing the Dioxomolybdnum^{2+} Core. *Inorg. Chim. Acta 90*, 41−51.
(35) Pirmettis, I., Patsis, G., Pelecanou, M., Tsoukalas, C., Papadopoulos, A., Raptopoulou, C. P., Terzis, A., Papadopoulos, M., and Chiotellis, E. (2001) Synthesis of Oxorhenium(V) and Oxotechnetium(V) [SN(R)S/S] Mixed Ligands Complexes Containing Phenothiazine Moiety on the Tridentate SN(R)S Ligand. *Bioorg. Med. Chem. 11*, 1859−1862.
(36) Skaddan, M. B., and Katzenellenbogen, J. A. (1999) Integrated "3+1" Oxorhenium(V) Complexes as Estrogen Mimics. *Bioconjugate Chem. 10*, 119−129.
(37) Alberto, R., Schibli, R., Egli, A., Schubiger, P. A., Herrmann, W. A., Artus, G., Abram, U., and Kaden, T. A. (1995) Metal Carbonyl Synthesis XXII. Low-Pressure Carbonylation of $[MOCl_4]^-$ and $[MO_4]^-$. The Technetium (I) and Rhenium(I) Complexes $[NEt_4]_2[MCl_3(CO)_3]$. *J. Organomet. Chem. 492*, 217−224.
(38) Kálman, A., Thunecke, F., Schmidt, R., Schiller, P. W., and Horváth, C. (1996) Isolation and Identification of Peptide Conformers by Reversed-Phase High-Performance Liquid Chromatography and NMR at Low Temperature. *J. Chromatogr. A 729*, 155−171.
(39) Gastmans, M., Volckaert, G., and Engelborghs, Y. (1999) Tryptophan Microstate Reshuffling upon the Binding of Cyclosporin A to Human Cyclophilin A. *Prot.: Struct., Funct., Genet. 35*, 464.
(40) Nock, B. A., Maina, T., Yannoukakos, D., Pirmettis, I. C., Papadopoulos, M. S., and Chiotellis, E. (1999) Glutathione-Mediated Metabolism of Technetium-99m SNS/S Mixed Ligand Complexes: A Proposed Mechanism of Brain Retention. *J. Med. Chem. 42*, 1066−1075.

BC050329F

Identification of Formaldehyde-Induced Modifications in Proteins: Reactions with Insulin

Bernard Metz,*[,†,‡] Gideon F. A. Kersten,[†] Gino J. E. Baart,[†] Ad de Jong,[†] Hugo Meiring,[†] Jan ten Hove,[†] Mies J. van Steenbergen,[‡] Wim E. Hennink,[‡] Daan J. A. Crommelin,[‡] and Wim Jiskoot[‡,§]

Unit Research and Development, The Netherlands Vaccine Institute (NVI), Bilthoven, The Netherlands, Department of Pharmaceutics, Utrecht Institute for Pharmaceutical Sciences (UIPS), Faculty of Pharmaceutical Sciences, Utrecht University, Utrecht, The Netherlands, and Department of Drug Delivery Technology, Leiden/Amsterdam Center for Drug Research (LACDR), Leiden University, Leiden, The Netherlands. Received November 24, 2005; Revised Manuscript Received April 6, 2006

Formaldehyde is frequently used to inactivate, stabilize, or immobilize proteins. The treatment results in a large variety of chemical modifications in proteins, such as the formation of methylol groups, Schiff bases, and methylene bridges. The purpose of the present study was to identify the stable formaldehyde-induced modifications in a small protein. Therefore, insulin was treated with excess formaldehyde (CH_2O) or deuterated formaldehyde (CD_2O). In a separate experiment, insulin was modified by formaldehyde (CH_2O vs CD_2O) and glycine. The mixture of CH_2O-treated and CD_2O-treated insulin was digested by the proteinase Glu-C. The peptide fragments obtained were analyzed by liquid chromatography−mass spectrometry (LC-MS). Seven intramolecular cross-links were identified in formaldehyde-treated insulin. Furthermore, eight out of the sixteen potentially reactive sites of the insulin molecule were modified by incubation with formaldehyde and glycine. Both the location and the chemical nature of the modifications could be assigned based on the mass increase of potential adducts as elucidated in our previous study (B. Metz et al. (2004) *J. Biol. Chem. 279*, 6235−6243). To confirm the assigned structures, LC-MS measurements with collision-induced dissociation (LC-MS/MS) were performed on insulin fragments. The results of the LC-MS/MS analyses agreed excellently with the assignments. The study showed that arginine, tyrosine, and lysine residues were very reactive. However, eight theoretically reactive residues did not show detectable modifications, probably because of their low intrinsic reactivity, inaccessibility, or both. The asparagine, glutamine, and histidine residues were not converted in insulin. The N-termini of insulin were partly converted to the expected imidazolidinone adducts, indicating that the protein conformation affects the accessibility and reactivity of these residues. In conclusion, this study shows that, based on our current insights in the chemistry of the reactions between proteins and formaldehyde, we are able to elucidate the location and nature of formaldehyde-induced modifications in a small protein. The approach followed in this study may be generally applicable to larger formaldehyde-treated proteins, such as toxoids used in vaccines.

INTRODUCTION

In the biochemical and pharmaceutical fields, chemical modifications are often introduced in proteins to add useful properties. Chemical treatment is utilized for bioconjugation of biologicals to reduce the immunogenicity (*1*−*3*), for stabilization of biopharmaceuticals to protect against proteolytic activity (*4*−*7*), and for coupling of functional groups to proteins (*8*−*10*). Formaldehyde is one of the well-known chemicals that is frequently applied as a cross-linking agent, for example, for the preparation of vaccines (*11*−*14*), for isotope-labeling of proteins (*15*−*17*), and for studying protein−protein interactions (*18*−*20*). However, the identification of the formaldehyde-modified sites in the primary sequence of proteins is cumbersome because numerous chemical modifications occur in proteins during the treatment with formaldehyde. During the past 60 years, extensive studies have revealed that formaldehyde can modify several amino acid residues (*4*, *21*−*28*). Only a few of these articles describe investigations of formaldehyde-induced modifications in proteins (*25*−*28*), but the nature of each specific modification and the exact location of the modified residues were not identified.

* Corresponding author. Mailing address: P.O. Box 457, 3720 AL Bilthoven, The Netherlands. Phone: +31 30 27 433 73. Fax: +31 30 27 444 26. E-mail: bernard.metz@nvi-vaccin.nl.

[†] The Netherlands Vaccine Institute (NVI).

[‡] Utrecht University.

[§] Leiden University.

Table 1. Mass (Δ*m*) Increase Due to Formaldehyde Modifications of Reactive Amino Acid Residues[a]

residue	methylol Δ*m*	imine Δ*m*	formaldehyde−glycine adduct Δ*m*
arginine	30	*b*	99/198
asparagine	*b*	*b*	87
cysteine	30	*b*	*b*
glutamine	*b*	*b*	87
histidine	30	*b*	87
lysine	30	12	*b*
tryptophan	30	12	87
tyrosine	*b*	*b*	87/174
N-terminal amino acid	*b*	12	99

[a] Results from studies with peptides (*29*). [b] No modification observed.

In a recent study with model peptides, we elucidated the structures of formaldehyde-induced modifications and the intrinsic reactivity of each amino acid residue (*29*). The reaction of formaldehyde with a peptide or protein starts with the formation of unstable methylol adducts on amino and thiol groups of arginine, cysteine, histidine, lysine, and tryptophan residues (Table 1). The methylol groups partially dehydrate on lysine and tryptophan residues, yielding labile Schiff bases (Scheme 1). The Schiff base on a lysine residue can form stable cross-links with several amino acid residues, including arginine, asparagine, glutamine, histidine, tryptophan, and tyrosine. Also, our previous study confirmed other studies showing that the N-terminal residues are modified after formaldehyde treatment

10.1021/bc050340f CCC: $33.50 © 2006 American Chemical Society
Published on Web 04/28/2006

Scheme 1: The Reaction of Formaldehyde with Proteins[a]

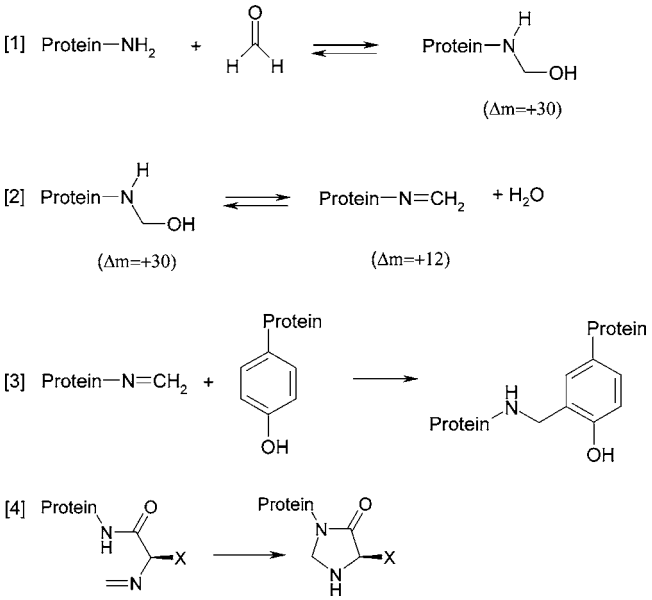

[a] The reaction starts with the formation of methylol adducts on amino groups [1]. The methylol adducts of primary amino groups are partially dehydrated, yielding labile Schiff bases [2], which can form cross-links with several amino acid residues, for example, with tyrosine [3]. After addition of formaldehyde, a 4-imidazolidinone adduct can be formed at the N-terminal site of the protein, probably via a Schiff base intermediate [4].

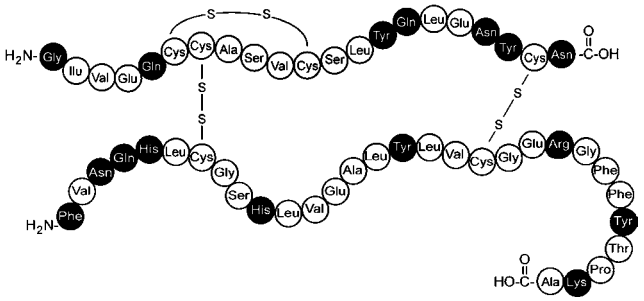

Figure 1. The primary structure of bovine insulin. The A-fragment and B-fragment of insulin are connected to each other via two disulfide bridges. Furthermore, the A-fragment has an intrachain disulfide bridge. In theory, residues given in black are reactive with formaldehyde and glycine.

resulting in an imidazolidinone (*29*−*32*). However, the effect of the protein conformation on the reactivity of amino acid residues cannot be studied in model peptides. In addition, the position and local environment of each intrinsically reactive amino acid in the protein may affect the reactivity.

The aim of the present study was to investigate whether we can elucidate formaldehyde-induced and formaldehyde/glycine-induced modifications in proteins by applying the knowledge obtained from our previous study with model peptides (*29*). For this purpose, bovine insulin was used as a model protein. Insulin is composed of two polypeptide chains: the A-chain consists of 21 amino acid residues, and the B-chain contains 30 amino acid residues; the two chains are interconnected via two disulfide linkages, Cys^{A7}−Cys^{B7} and Cys^{A20}−Cys^{B19} (Figure 1). Moreover, the A-chain contains an intrachain disulfide bridge (Cys^{A6}−Cys^{A11}). The protein can also appear in different quaternary structures, as monomers, dimers, and hexamers (*33*). For example, insulin molecules associate into hexameric complexes in the presence of two zinc ions and at a neutral pH (*34*). In this study, insulin was treated with either native formaldehyde or deuterated formaldehyde (CH_2O vs CD_2O). In a parallel experiment, formaldehyde treatments of insulin were also performed in the presence of glycine. The reaction conditions were largely based on the detoxification process of diphtheria toxin for vaccine production (*11*). After the chemical treatment, mixtures of equimolar amounts of CH_2O-treated and CD_2O-treated insulin were enzymatically digested into small peptides, which were subsequently analyzed by reversed-phase liquid chromatography, electrospray ionization mass spectrometry (LC-MS), and LC-MS measurements with collision-induced dissociation (LC-MS/MS). Using this approach, we were able to unequivocally identify the chemical nature and location of the formaldehyde-induced modifications in the protein.

Table 2. Composition of Reaction Mixtures Used in This Study

mixture	insulin, 0.35 mM (mL)	formaldehyde, 1 M (μL)	glycine, 1 M (μL)	$NaCNBH_3$, 1 M (μL)
1	3.36	320	*a*	*a*
2	3.36	320	320	*a*
3	3.36	320	*a*	320

[a] Not applicable.

MATERIALS AND METHODS

Chemicals. Formaldehyde (37% (w/v) in water with 10% methanol), formic acid (99%), glycine, potassium dihydrogen phosphate ($KH_2PO_4 \cdot 3H_2O$), and dipotassium hydrogen phosphate ($K_2HPO_4 \cdot 3H_2O$) were purchased from Merck (Amsterdam, The Netherlands). Formaldehyde-D_2 (CD_2O) was delivered from C/D/N Isotopes Inc. (Utrecht, The Netherlands). Insulin from bovine pancreas, β-lactoglobulin, DL-dithiotreitol (DTT), and sodium cyanoborohydride ($NaCNBH_3$) were obtained from Sigma (Zwijndrecht, The Netherlands). Endoproteinase Glu-C was bought from Roche Applied Science (Almere, The Netherlands).

Size-Exclusion Chromatography. Size-exclusion chromatography (SEC) was performed to determine the quaternary structure of bovine insulin prior to chemical treatment. The method used was adapted from Ahmad et al. (*35*). SEC was performed on a Waters Alliance 2695 instrument equipped with a Superdex 75 10/300GL column from GE healthcare (exclusion limit 1×10^5 Da) at a flow rate of 0.5 mL/min with detection at 280 nm. Bovine insulin (MW 5.7 kDa) was dissolved in 10 mM potassium phosphate, pH 8.5 (the buffer used for the reactions with formaldehyde), or in 20% acetic acid (in which hexameric insulin dissociates to form monomers (*35*)) to a final concentration of 0.35 mM. In addition, β-lactoglobulin (MW 36 kDa) was used as a marker. Aliquots of 200 μL were loaded on the column, which was equilibrated with 10 mM potassium phosphate, pH 7.2.

Reactions of Insulin with Formaldehyde. Three different reactions with insulin were performed in this study: (i) insulin with formaldehyde, (ii) insulin with formaldehyde and glycine, and (iii) insulin with formaldehyde and $NaCNBH_3$. For each reaction, two identical mixtures were prepared except for the type of formaldehyde: either native formaldehyde (CH_2O) or deuterium-labeled formaldehyde (CD_2O) was used. Prior to the reactions, insulin was dissolved in 10 mM potassium phosphate, pH 8.5, to a final concentration of 0.35 mM, with formaldehyde (CH_2O or CD_2O), glycine, and $NaCNBH_3$ at a concentration of 1.0 M. The compositions of the reaction mixtures are given in Table 2. The final concentration of insulin during the reaction was 0.30 mM, and the final concentrations of formaldehyde, glycine, and $NaCNBH_3$ were 80 mM. After mixing, the solution was incubated for 1 week at 35 °C. Samples were extensively dialyzed against 10 mM potassium phosphate, pH 8.5 (MWCO 1000). After incubation and dialysis, equimolar amounts of CH_2O-treated and CD_2O-treated insulin were mixed. All samples were stored at 4 °C prior to digestion with proteinase Glu-C.

Digestion by Endoproteinase Glu-C. Nontreated insulin and formaldehyde-modified insulin samples were digested by mixing 50 μL of these samples with 5 μL of 1.0 M potassium phosphate buffer, pH 9.0, 1.0 μL of 1 μg/μL endoproteinase Glu-C solution, and 44 μL of water. The mixtures were incubated for 24 h at 37 °C. To reduce disulfide bonds, 1 μL of 1.0 M DTT was added to the digests, and the samples were incubated for 1 h at 37 °C. Subsequently, the samples were stored at −20 °C prior to LC-MS analysis.

Nano-electrospray MS. Insulin was diluted to a concentration of 1 μM in water containing 5% (v/v) DMSO and 5% (v/v) formic acid. Gold-coated nano-electrospray needles (length 600−700 μm; internal diameter 1−2 μm; homemade) were loaded with 10 μL of the sample. The protein solution was analyzed by electrospray ionization mass spectrometry using a Q-TOF Ultima API mass spectrometer (Waters, England). MS scans were obtained from *m*/*z* 350 to 2000 amu. Spectra were deconvoluted using the MaxEnt 1 tool in the MassLynnx MS software (Waters).

LC-MS. Protein digests were analyzed by nanoscale reversed phase liquid chromatography electrospray ionization mass spectrometry (Q-TOF Ultima API), essentially as previously described by Meiring et al. (*36*). Briefly, each digested sample was diluted in water containing 5% (v/v) DMSO and 5% (v/v) formic acid to a concentration, corresponding to 2.5 nM of the original insulin concentration. An injection volume of 10 μL was used for analysis. Analytes were trapped on a trapping column of 15 mm (length) × 100 μm (inner diameter) with Aqua C18 (5 μm; Phenomenex) at a flow rate of 3 μL/min with 100% solvent A (0.1 M acetic acid in water) as eluent for 10 min. Then, analytes were separated by reversed phase chromatography by using a 25 cm L × 50 μm i.d. analytical column with Pepmap (5 μm; Dionex) at a flow rate of 125 nL/min. A linear gradient was started from 5% solvent B (0.1 M acetic acid in acetonitrile) to 60% solvent B in 55 min.

The digested peptides were measured in the MS mode (*m*/*z* 300−2000) to determine the masses of peptides in the mixture. The mass spectrometer was adjusted to following conditions: the electrospray voltage was set to 1.8 kV, the TOF voltage to 9.1 kV, and the MCP voltage to 2.2 kV. Peptides containing formaldehyde modifications typically appeared as mass spectral doublets as a result of the use of native (CH_2O) and deutrated (CD_2O) formaldehyde. The location and the nature of a formaldehyde-induced modification was assigned on the basis of the measured mass, the number of incorporated formaldehyde molecules, and the knowledge of potential formaldehyde adducts, the structures of which were elucidated in our previous study with synthetic model peptides (*29*). From the LC-MS results, a list of masses was compiled of formaldehyde-modified peptides, which were measured in a second run by LC-MS/MS to obtain sequence information and to verify the modified residues. Therefore, the peptides were analyzed by data-dependent scanning comprising a survey MS scan (*m*/*z* 300−2000) followed by collisional activated decomposition (CAD) of the abundant ion in the MS spectra from the compiled list. The collision energy was set between 15 and 25 V.

Accessibility of Amino Acid Residues. The accessibility of each amino acid residue was calculated from the crystal structure of bovine insulin (*37*) using a described method of Fraczkiewicz and Werner (*38*). The accessible surface area of the amino acid residues in monomeric insulin varied from 0% for completely buried residues to 100% for surface residues. Several amino acid residues were not observed as entire structural entities in the crystal structure of bovine insulin (*37*). Therefore, the accessibility of the residues Gln^{A5}, Tyr^{A14}, Gln^{A15}, Asn^{B3}, and Gln^{B4} was taken from corresponding residues in human insulin (*39*). Furthermore, for certain residues, the accessibility in the hexameric form differs from that in the monomeric form (*40*). For these residues, the accessibilities in both forms were considered because of the presence of hexameric insulin.

Table 3. List of Expected and Detected Insulin-Derived Peptides after Digestion of Insulin with Proteinase Glu-C

peptide	fragment	sequence	MH^+ (Da)[a]
		A-Fragment	
1	A^1-A^4	GIVE	417.2 (0.0)
2	A^5-A^{17}	QCCASVCSLYQLE	1446.6 (−2.0)[b]
3	$A^{18}-A^{21}$	NYCN	513.2 (0.0)
		B-Fragment	
4	B^1-B^{13}	FVNQHLCGSHLVE	1482.7 (0.0)
5	$B^{14}-B^{21}$	ALYLVCGE	867.4 (0.0)
6	$B^{22}-B^{30}$	RGFFYTPKA	1086.5 (−0.1)
		Peptides Connected with Disulfide Links	
7	A^5-A^{17} and B^1-B^{13}	QCCASVCSLYQLE FVNQHLCGSHLVE	2924.6 (0.3)
8	$A^{18}-A^{21}$ and $B^{14}-B^{21}$	NYCN ALYLVCGE	1377.6 (0.0)

[a] Eight masses were observed that could be ascribed to peptides from bovine insulin. Deviation from the calculated masses given between brackets. [b] Mass difference of 2 Da most probably due to nonreduced intrachain disulfide bridge ($C^{A6}-C^{A11}$) or reoxidized cysteine residues.

Conversion of Amino Acid Residues. The conversion (Conv) of a particular residue was estimated based on the peak areas of the modified (A_{mod}) and nonmodified peptide (A_{non}) containing that particular residue, according to the equitation $\text{Conv}\ (\%) = 100 \times A_{mod}/(A_{mod} + A_{non})$. For this estimation, it is assumed that the specific response (peak area/mole) is equal for the modified and nonmodified peptide.

RESULTS

Characterization of Untreated Insulin. Bovine insulin was chosen as a small model protein to study the possible reactions of formaldehyde with amino acid side chains of proteins. Prior to formaldehyde treatment, the composition and purity of the insulin were examined by size-exclusion chromatography (SEC) and nano-electrospray MS analysis. The protein, which can appear as monomers, dimers, and hexamers (*33*), was analyzed by SEC, which revealed one single peak with an elution time of 25.7 min (data not shown). The elution was close to that of β-lactoglobulin (ca. 21.7 min; MW of 36 kDa), indicating that the insulin dissolved in potassium phosphate buffer (pH 8.5) is completely assembled into hexamers (MW of 34 kDa). The elution time of monomeric insulin (MW of 5.7 kDa) dissolved in 20% acetic acid was 41 min.

Nano-electrospray MS analysis showed that the major compound had a mass of 5729 Da (arbitrary intensity 100%), close to the theoretical mass of bovine insulin (5730 Da). Insulin was observed as a monomeric compound by MS as a result of the low concentration and the low pH used for ionization (*41*, *42*). Also three other masses of 5659, 5792, and 5855 Da were observed with relative intensities of 9%, 33%, and 7%, respectively. The mass of 5659 Da can be ascribed to insulin lacking the alanine residue at the C-terminus of the insulin, probably as a result of a wrong cleavage of the proinsulin. The other two masses can be explained by the binding of one or two Zn^{2+} ions, each taking the position of two hydrogens ($\Delta m = 65 - 2$ Da).

Insulin was digested into small peptides by using proteinase Glu-C. This protease cleaves proteins at the C-terminal site of glutamate and aspartate residues (*43*, *44*). In theory, complete cleavage of the insulin and reduction of disulfide bridges will result in six nonoverlapping peptides (Table 3, peptides 1−6). All six expected peptides were detected. Peptide 2 was observed with a mass difference of 2 Da with regard to the expected mass, which is most probably due to nonreduced intrachain disulfide

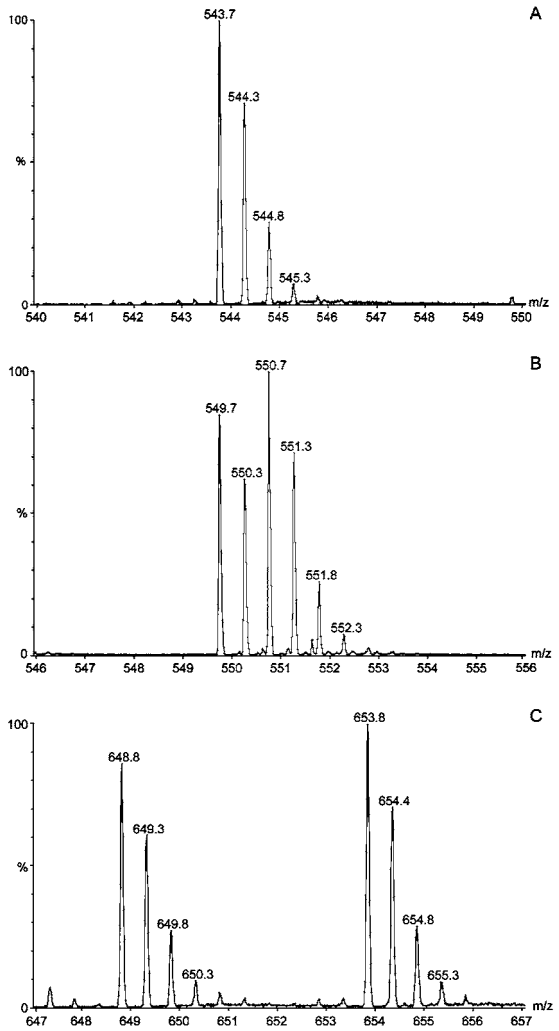

Figure 2. Examples of mass spectra of a native peptide (A), a formaldehyde-modified peptide (B), and a formaldehyde/glycine modified peptide (C). These three peptides were observed as double protonated ions (MH_2^{2+}), corresponding to (A) $MH^+ = 1086.5$ (Table 3, peptide 6), (B) $MH^+ = 1098.5$ (Table 4, peptide 4), and (C) $MH^+ = 1296.4$ (Table 5, peptide 14). From the distance between peptide pairs (B and C), the number of incorporated formaldehyde molecules can be determined. In peptides B and C, one and five formaldehyde molecules were incorporated, respectively.

bridge (Cys^{A6}−Cys^{A11}) or reoxidized cysteine residues. Also due to incomplete reduction, peptide fragments of the A- and B-chains were observed that are connected to each other with disulfide links (Table 3, peptides 7 and 8). Besides the peptides shown in Table 3, four minor peaks were observed with masses that were 16 Da heavier than the theoretical mass. Also a few masses with minor intensities were found that could not directly be related to insulin (not shown). Altogether, the digestion of insulin with proteinase Glu-C resulted in a total number of eight peptides that cover the whole protein. In principle, this permits the complete mapping of formaldehyde/glycine-induced modifications in hexameric insulin.

Formaldehyde-Induced Modifications in Insulin. In two separate samples, the insulin hexamers were treated with either CH_2O or CD_2O. The experiment was aimed to reveal intramolecular cross-links in insulin as a result of the chemical treatment. After the reaction, these two samples were mixed, digested by proteinase Glu-C, and analyzed by LC-MS (details given in Materials and Methods). This approach provided us with a method to discriminate formaldehyde-modified peptides (showing peptide pairs) from unmodified ones (no peptide pairs, see Figure 2A). Peptides containing formaldehyde modifications typically appear as mass spectral doublets because the use of CH_2O or CD_2O results in peptide pairs with mass differences of n(2 Da), where n is the number of formaldehyde residues incorporated in the peptide. Indeed the LC-MS analyses revealed seven of these peptide pairs, which eluted simultaneously from the LC column (Table 4). A representative example of a peptide pair is given in Figure 2B. The mass difference between each peptide pair was 2 or 4 Da. The total mass increment of the modified peptides, as compared to the nonmodified peptides, was 12 or 24 Da for CH_2O-treated peptides and 14 or 28 Da for CD_2O-treated peptides (Table 4). These mass increases correspond to the formation of one and two formaldehyde cross-links in the peptide ($-CH_2-$ or $-CD_2-$). So, the observed doublets could be assigned to peptides with an intrachain cross-link.

In addition, LC-MS/MS measurements were done to reveal the exact location of individual cross-links in these peptides. The MS/MS spectra showed an increased mass of 12 Da for residues Gly^{A1}, Cys^{A7}, Tyr^{A19}, Phe^{B1}, Tyr^{B16}, and Tyr^{B26}. Also a mass increment of 24 Da was observed for the residue Tyr^{B26}. Previous reactions with model peptides demonstrated that primary amino groups and thiol groups react primarily with formaldehyde and form subsequently cross-links with amino acid residues, for example, tyrosine and glutamine residues (*29*). Based on the present LC-MS/MS results and the previous study, we conclude that the intrapeptide cross-links had occurred between the Tyr^{A19} and Cys^{A20} residues, the Tyr^{B16} and Cys^{B19}, the Tyr^{B26} and Lys^{B29} residues (Figure 2) and, probably, the Gln^{A5} and Cys^{A7} residues. The formaldehyde-induced modifications of the N-terminal residues, Gly^{A1} and Phe^{B1}, are consistent with the formation of a 4-imidazolidinone, as has been described in many other studies (*31*, *32*, *45*) (Scheme 1, reaction 4).

Formaldehyde/Glycine-Induced Modifications in Insulin. In a parallel experiment, insulin hexamers were treated with either CH_2O or CD_2O in combination with glycine. In our previous paper (*29*), we showed that nine different amino acid residues in proteins are modifiable by formaldehyde and glycine (Table 1). According to that study, 16 amino acid residues in insulin can be modified (as indicated in Figure 1), provided that they are easily accessible to formaldehyde and glycine. MS analysis of intact formaldehyde-treated insulin resulted in a broad peak, demonstrating the heterogeneous character of the product (results not shown). Subsequently, the digest of modified insulin was analyzed by LC-MS. The measurements showed 21 masses from peptide pairs, each of which represents one or more formaldehyde/glycine-induced modifications (Table 5). The mass difference between the observed peptide pairs was n(2 Da), with n ranging from one to six, corresponding to the number of incorporated formaldehyde residues (CH_2O vs CD_2O). An example of a formaldehyde/glycine-modified peptide pair containing five formaldehyde residues is given in Figure 2C. All masses listed in Table 5 could be traced back as modified peptide fragments from insulin. The assignments were based on the insulin sequence and the earlier described formaldehyde modifications (*29*). Moreover, the number of incorporated formaldehyde molecules corresponded with the prediction. The resulting mass difference with the nonmodified peptides varied between 12 and 372 Da (Table 5).

LC-MS/MS measurements were performed to verify the assigned peptide sequences as listed in Table 5 and to reveal the exact location of individual modifications in the peptides. Two examples of MS/MS spectra are given in Figure 3. From the data presented in Figure 3, it appears that the formaldehyde−glycine attachments are not resistant to fragmentation during MS/MS analysis. Apparently, this fragmentation started with the loss of a part of the formaldehyde−glycine adduct from the peptide backbone, followed by backbone fragmentation.

Table 4. Insulin-Derived Peptides Containing Formaldehyde-Induced Cross-Links

peptide	MH^+ (Da)	peptide sequence[a]	fragment	no. of CH_2O[d]	Δm[e] (Da)	conversion (%)
1	429.2	**G**IVE[b]	A^1-A^4	1	12	20.7
2	525.2	N**Y**C**C**N[c]	$A^{18}-A^{21}$	1	12	35.7
3	879.2	AL$\overline{\textbf{Y}}$LV**C**GE[c]	$B^{14}-B^{21}$	1	12	1.0
4	1098.4	RG$\overline{\text{F}}$F**Y**T$\overline{\text{P}}$**K**A[c]	$B^{22}-B^{30}$	1	12	33.1
5	1110.4	RGFF$\overline{\textbf{Y}}$T$\overline{\text{P}}$**K**A[c]	$B^{22}-B^{30}$	2	24	44.8
6	1458.6	**Q**C**C**A$\overline{\text{S}}$V$\overline{\text{C}}$SLYQLE[c]	A^5-A^{17}	1	12	3.6
7	1496.6	$\overline{\text{F}}$VN$\overline{\text{Q}}$HLCGSHLVE[b]	B^1-B^{13}	1	12	32.9

[a] Modified residues marked in bold. [b] The N-terminal peptide has formed a 4-imidazolidinone adduct (Scheme 1). [c] Intrachain cross-link formed between underlined residues. [d] Number of formaldehyde residues incorporated in the peptide. [e] Mass increment as compared to nonmodified peptide.

Table 5. Insulin-Derived Peptides with Formaldehyde/Glycine-Modified Amino Acid Residues

peptide	MH^+ (Da)	peptide sequence[a]	fragment	no. of CH_2O[d]	Δm[e] (Da)	conversion[f] (%)
1	429.2	**G**IVE[b]	A^1-A^4	1	12	33.0 ± 25.9
2	525.2	N**Y**C**C**N[c]	$A^{18}-A^{21}$	1	12	31.3 ± 4.7
3	879.4	AL$\overline{\textbf{Y}}$LV**C**GE	$B^{14}-B^{21}$	1	12	2.4 ± 1.6
4	954.4	AL$\overline{\textbf{Y}}$LV$\overline{\text{C}}$GE	$B^{14}-B^{21}$	1	87	38.6 ± 3.7
5	1041.6	AL**Y**LVCGE	$B^{14}-B^{21}$	2	174	29.2 ± 5.6
6	1098.6	RGFF**Y**TP**K**A[c]	$B^{22}-B^{30}$	1	12	4.4 ± 1.5
7	1110.6	RGFF$\overline{\textbf{Y}}$TP$\overline{\textbf{K}}$A[c]	$B^{22}-B^{30}$	2	24	1.9 ± 1.2
8	1173.6	RGFF$\overline{\textbf{Y}}$TP$\overline{\text{K}}$A	$B^{22}-B^{30}$	1	87	2.7 ± 1.0
9	1185.4	**R**GFFYTPKA	$B^{22}-B^{30}$	2	99	17.7 ± 5.6
10	1197.4	**R**GFF**Y**TP**K**A[c]	$B^{22}-B^{30}$	3	111 (R, +99; Y−K, +12)	10.8 ± 4.6
11	1272.1	**R**GFF$\overline{\textbf{Y}}$TP$\overline{\text{K}}$A	$B^{22}-B^{30}$	3	186 (R, +99; Y, +87)	7.9 ± 2.0
12	1284.4	**R**GFFYTPKA	$B^{22}-B^{30}$	4	198	12.1± 1.9
13		**R**GFF**Y**TP**K**A[c]	$B^{22}-B^{30}$		198 (R, +99; Y, +87; Y−K, +12)	6.4 ± 1.5
14	1296.4	**R**GFF$\overline{\textbf{Y}}$TP$\overline{\textbf{K}}$A[c]	$B^{22}-B^{30}$	5	210 (R, +198; Y−K, +12)	8.7 ± 2.3
15	1371.1	**R**GFF$\overline{\textbf{Y}}$TP$\overline{\text{K}}$A	$B^{22}-B^{30}$	5	285 (R, +198; Y, +87)	4.7 ± 0.9
16	1383.6	**R**GFF**Y**TP**K**A[c]	$B^{22}-B^{30}$	6	279 (R, +198; Y, +87; Y−K, +12)	11.0 ± 3.6
17	1458.5	**R**GFF$\overline{\textbf{Y}}$TP$\overline{\text{K}}$A	$B^{22}-B^{30}$	6	372 (R, +198; Y, +174)	0.9 ± 0.7
18	1458.6	**Q**C**C**ASVCSLYQLE[c]	A^5-A^{17}	1	12	0.4 ± 0.4
19	1533.6	$\overline{\text{Q}}$C$\overline{\text{C}}$ASVCSL**Y**QLE	A^5-A^{17}	1	87	44.6 ± 6.4
20	1620.6	QCCASVCSL**Y**QLE	A^5-A^{17}	2	174	53.4 ± 6.7
21	1494.7	**F**VNQHLCGSHLVE[b]	B^1-B^{13}	1	12	39.6 ± 28.2
22	1581.7	**F**VNQHLCGSHLVE[b]	B^1-B^{13}	2	99	9.0 ± 6.3

[a] Modified residues marked in bold. [b] The N-terminal peptide has formed a 4-imidazolidinone adduct (Scheme 1). [c] Intrachain cross-link formed between underlined residues. [d] Number of formaldehyde residues incorporated in the peptide. [e] Mass increment as compared to nonmodified peptide. [f] Mean ± SD; $n = 3$.

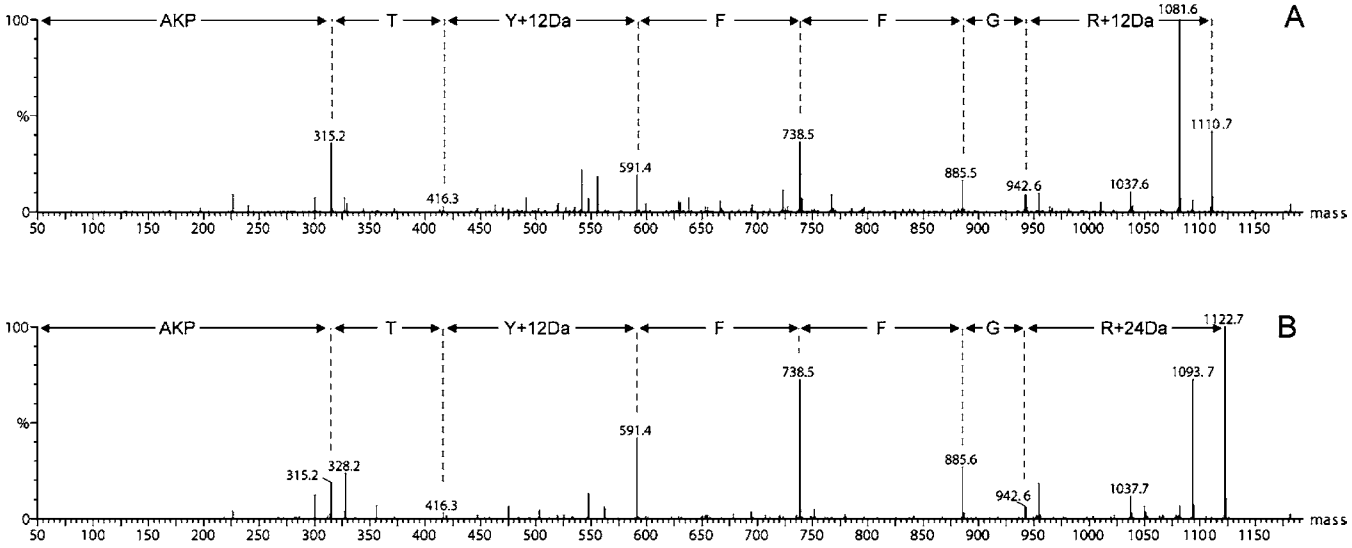

Figure 3. MS/MS analysis of two peptide fragments of insulin containing formaldehyde-induced modifications. Spectrum A is obtained from the peptide (Table 5, peptide 11, $MH^+ = 1272.1$) that contained a formaldehyde−glycine adduct on an arginine (B^{22}) and on a tyrosine (B^{26}) residue and is dominated by a y-ion series. Spectrum B is acquired from the peptide (Table 5, peptide 14, $MH^+ = 1296.4$) with an intramolecular cross-link between a tyrosine (B^{26}) and a lysine (B^{29}) residue and two formaldehyde−glycine adducts on the arginine residue.

Fortunately, a small mass tag of 12 Da was left on the modified residue and enabled the identification of the modified sites. When two formaldehyde−glycine adducts were attached to tyrosine or arginine residues (resulting in mass increments of 174 and 198, respectively), the LC-MS/MS analyses demonstrated a residual mass tag of 24 Da. All peptides were sequenced by MS/MS, and the results corresponded to the assignment based on MS data. Formaldehyde-induced modifications were observed on eight residues: Gly^{A1}, Tyr^{A14}, Tyr^{A19}, Phe^{B1}, Tyr^{B16}, Arg^{B22}, Tyr^{B26}, and Lys^{B29}. However, there was

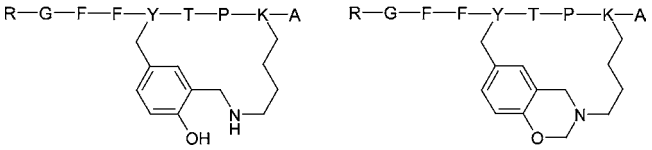

Figure 4. Formaldehyde-induced cross-links in an insulin-derived peptide (Table 4, peptide 4 and 5).

no evidence of modification of eight other residues, Gln^{A4}, Gln^{A15}, Asn^{B3}, Asn^{B3}, Asn^{B3}, Gln^{B4}, His^{B5}, and His^{B10}, although these types of residues have been shown before to be reactive with formaldehyde and glycine (*29*). The same intramolecular cross-links were expected in insulin as those observed after the reaction with formaldehyde alone. Indeed, nine insulin-derived peptides could be ascribed to peptides with an intrachain cross-link and verified by LC-MS/MS (Table 5). In summary, LC-MS/MS analyses could identify the modified amino acid residues in insulin.

Conversion and Accessibility of Formaldehyde/Glycine Modifiable Residues. In the previous section, the identification of formaldehyde/glycine-induced modifications in insulin hexamers was described. However, eight expected modifications in insulin were missing, for example, the formaldehyde−glycine adducts upon asparagine, glutamine, and histidine residues. No or little conversion observed is most probably due to poor intrinsic reactivity (*29*), poor or partial accessibility, or both in the native insulin molecule (*37*−*39*).

In this section, the accessibility and the intrinsic reactivity are compared to the conversion of the formaldehyde reactive residues. The conversion of each modified residue was calculated based on the peak areas of the formaldehyde/glycine-modified peptide and the corresponding nonmodified peptide (Table 6). The intrinsic reactivity values for each modifiable residue were previously assessed (*29*) and are also given in Table 6. Furthermore, the accessibility of each amino acid residue was calculated from the crystal structure of both monomeric and hexameric bovine insulin (*37*) using a described method of Fraczkiewicz and Werner (*38*, *39*) (Table 6).

Consistent with our previous study (*29*), it was shown that arginine and tyrosine residues were very reactive (Table 6). Nevertheless, a large variation in conversion was found between the different tyrosine residues, probably, as a result of accessibility. The most accessible tyrosine residue (Tyr^{A14}) was highly modified by formaldehyde and glycine (97%), whereas a buried residue (Tyr^{A19}) was converted in a much lesser degree (36%). Substantial conversion (59%) was observed for a fully buried tyrosine residue (Tyr^{B26}), but 32% of this conversion was due to the formation of methylene bridges between Lys^{B29} and Tyr^{B26}. A methylene bridge ($-CH_2-$) is smaller than a formaldehyde−glycine adduct, which might explain the relatively high conversion of this tyrosine residue. No modifications of asparagine, glutamine, and histidine residues were observed. The low intrinsic reactivity of these residues together with their poor accessibility (between 13% and 68%) in hexameric insulin are likely key to the absence of conversion.

Only moderate conversion of the N-terminal amino groups (residues Gly^{A1} and Phe^{B1}) into imidazolidinone adducts was observed after either formaldehyde treatment or formaldehyde−glycine treatment (Tables 4 and 6). However, high conversion was expected, because in general imidazolidinone adducts are rapidly formed by the reaction of formaldehyde with N-terminal amino groups (*29*−*32*). Therefore, the reactivity of N-terminal amino groups in insulin for formaldehyde was studied in more detail. Insulin was treated with formaldehyde (CH_2O or CD_2O) and $NaCNBH_3$ to study the accessibility to formaldehyde of the N-terminal residues Gly^{A1} and Phe^{B1}. Full accessibility would be reflected by full conversion of the N-terminal amines to dimethylated amine groups. Indeed, LC-MS analyses revealed masses corresponding to N-terminal insulin fragments of the A-chain and the B-chain with a dimethylated Gly^{A1} or a dimethylated Phe^{B1} residue as confirmed by MS/MS. Moreover, these residues, Gly^{A1} and Phe^{B1}, were completely converted (100%). We can therefore conclude that poor accessibility of the N-termini to formaldehyde was not the reason for the partial imidazolinone formation observed. Instead, the second step in the imidazolidinone formation may be hampered in the A-chain and B-chain of insulin as a result of poor access to the adjacent residues, Ile^{A2} and Val^{B2}, which take part in the reaction with formaldehyde (*20*). Indeed, according to the crystal structure, these amino acids are buried by surrounding residues: the accessibility of Ile^{A2} and Val^{B2} is 1.0% and 0.0%, respectively (*37*, *38*). These results underline the vital influence of protein conformation on the conversion of intrinsically reactive sites.

Table 6. Formaldehyde/Glycine-Reactive Residues in Insulin

residue[a]	position	expected Δm	observed Δm	accessibility[c,e] (%)	intrinsic reactivity[f] (%)	conversion[g] (%)
glycine	A^1	12/99	12	55.3 (80.1)	89	33.0 ± 25.9
glutamine	A^5	87	*h*	46.8[d] (36.1)	4	0
tyrosine	A^{14}	87/174	87/174	89.5[d] (89.1)	67	98.1 ± 0.4
glutamine	A^{15}	87	87	49.5[d] (49.5)	4	0
asparagine	A^{18}	87	87	65.4 (67.6)	4	0
tyrosine	A^{19}	87/174	87/174	20.1 (18.9)	67	31.3 ± 4.7
asparagine	A^{21}	87	87	90.1 (63.3)	4	0
phenylalanine	B^1	12/99	12/99	59.3 (86.3)	89	48.6 ± 34.5
asparagine	B^3	87	*h*	69.4[d] (36.6)	4	0
glutamine	B^4	87	*h*	64.4[d] (46.7)	4	0
histidine	B^5	87	*h*	56.6 (16.4)	7	0
histidine	B^{10}	87	*h*	76.5 (13.3)	7	0
tyrosine	B^{16}	87/174	87/174	73.0 (1.2)	67	59.4 ± 5.1
arginine	B^{22}	99/198	99/198	53.0 (59.0)	97	80.3 ± 3.9
tyrosine	B^{26}	87/174	87/174	28.0 (0.0)	67	59.4 ± 5.1
lysine	B^{29}	12/24[b]	12/24	96.6 (71.5)	*i*	32.2 ± 4.8

[a] Possible formaldehyde/glycine-reactive amino acid residues in bovine insulin are listed based on our previous study (*29*). [b] Formaldehyde treatment causes intramolecular cross-links between lysine residues and other amino residues, resulting in a mass increase of 12 or 24 Da (*29*). [c] Accessibility of amino acids in monomeric bovine insulin (see Materials and Methods for further details). [d] The accessibility of these residues was calculated based on the structure of monomeric human insulin (*48*). [e] Values given in parentheses represent the accessibility of the residue in hexameric insulin (*40*). [f] The intrinsic reactivity of each type of amino acid residue was assessed previously, except for the lysine residue (*29*). The table lists the expected conversions after a reaction time of 48 h. [g] The conversion was determined after a reaction time of 1 week (see Materials and Methods for further details). Mean ± SD; $n = 3$. [h] No change. [i] Unknown.

DISCUSSION

This study demonstrates a great diversity of chemical modifications in the model protein insulin caused by the treatment either with formaldehyde or with formaldehyde and glycine. Eight different amino acid residues were modified by the reaction of formaldehyde and glycine. Furthermore, seven distinct intrachain cross-links were identified. The results showed that arginine, tyrosine, and lysine residues were very reactive, whereas a little or no conversion was observed for asparagine, glutamine, and histidine residues, which is consistent with our earlier study with model peptides (*29*). Moreover, the data indicate that the protein conformation can have a serious effect on the reactivity of particular amino acid residues, because formaldehyde and glycine do not or only slightly convert the poorly accessible amino acids that are potentially reactive.

Insulin was used as a model protein to study the reaction of formaldehyde with amino acid residues. The protein was chosen because of its defined structure (*35*, *37*, *39*−*42*). In this study, hexameric insulin was used, which has a moderate size (34 kDa). Complete digestion of native insulin by proteinase Glu-C resulted is a small set of six peptides (Table 3). Nevertheless, after formaldehyde treatment 21 different masses were detected that could be assigned to these peptides containing different modifications (Table 5). As a consequence of the formaldehyde treatment, several modifications formed are distributed on different (monomeric) insulin molecules. This finding underscores the structural heterogeneity of formaldehyde-treated proteins, which will be even more pronounced for proteins larger than monomeric insulin.

In conclusion, we have provided a practical method to reveal the site and chemical nature of each particular formaldehyde-induced modification in proteins. The approach may be useful to study the complex modifications of larger proteins, such as the formaldehyde treatment of bacterial toxins for preparation of vaccines. The detoxification process of the bacterial toxins is of utmost importance for the antigenicity, immunogenicity, and residual toxicity of the resulting toxoid (*11*, *46*, *47*). Detailed knowledge about the chemical modifications in these antigens can help to gain a better insight into the relationship between the structure of the antigens and the safety and efficacy of the corresponding vaccines. Moreover, our strategy used to identify chemical modification sites in proteins may be applicable to many other bioconjugations.

ACKNOWLEDGMENT

We thank Wilma Witkamp, Sytse Piersma, Bert Zomer, and Anne Jan Metz for their contributions to this work. This study was, in part, supported by a grant from the "Platform Alternatieven voor Dierproeven" (the Dutch platform on alternatives to animal experiments), Grant No. 3170.0039.

LITERATURE CITED

(1) Caliceti, P., Schiavon, O., and Veronese, F. M. (2001) Immunological properties of uricase conjugated to neutral soluble polymers. *Bioconjugate Chem. 12*, 515−522.

(2) Hermeling, S., Crommelin, D. J., Schellekens, H., and Jiskoot, W. (2004) Structure-immunogenicity relationships of therapeutic proteins. *Pharm. Res. 21*, 897−903.

(3) Schellekens, H. (2002) Immunogenicity of therapeutic proteins: clinical implications and future prospects. *Clin. Ther. 24*, 1720−1740; discussion 1719.

(4) Kelly, D. P., Dewar, M. K., Johns, R. B., Wei-Let, S., and Yates, J. F. (1977) Cross-linking of amino acids by formaldehyde. Preparation and 13C NMR spectra of model compounds. *Adv. Exp. Med. Biol. 86*, 641−647.

(5) Rice, R. H., Means, G. E., and Brown, W. D. (1977) Stabilization of bovine trypsin by reductive methylation. *Biochim. Biophys. Acta 492*, 316−321.

(6) Baudys, M., Letourneur, D., Liu, F., Mix, D., Jozefonvicz, J., and Kim, S. W. (1998) Extending insulin action in vivo by conjugation to carboxymethyl dextran. *Bioconjugate Chem. 9*, 176−183.

(7) Baudys, M., Uchio, T., Mix, D., Wilson, D., and Kim, S. W. (1995) Physical stabilization of insulin by glycosylation. *J. Pharm. Sci. 84*, 28−33.

(8) Stan, A. C., Radu, D. L., Casares, S., Bona, C. A., and Brumeanu, T. D. (1999) Antineoplastic efficacy of doxorubicin enzymatically assembled on galactose residues of a monoclonal antibody specific for the carcinoembryonic antigen. *Cancer Res. 59*, 115−121.

(9) Trakselis, M. A., Alley, S. C., and Ishmael, F. T. (2005) Identification and mapping of protein−protein interactions by a combination of cross-linking, cleavage, and proteomics. *Bioconjugate Chem. 16*, 741−750.

(10) Hentz, N. G., Richardson, J. M., Sportsman, J. R., Daijo, J., and Sittampalam, G. S. (1997) Synthesis and characterization of insulin-fluorescein derivatives for bioanalytical applications. *Anal. Chem. 69*, 4994−5000.

(11) Rappuoli, R. (1997) New and improved vaccines against diphtheria and tetanus, in *New generation vaccines* (Levine, M. M., Woodrow, G. C., Kaper, J. B., and Cobon, G. S., Eds.) pp 417−435, Marcel Dekker, inc., New York.

(12) Stapleton, J. T., and Lemon, S. M. (1997) New vaccines against hepatitus A, in *New generation vaccines* (Levine, M. M., Woodrow, G. C., Kaper, J. B., and Cobon, G. S., Eds.) pp 417−435, Marcel Dekker, inc., New York.

(13) Leppla, S. H., Robbins, J. B., Schneerson, R., and Shiloach, J. (2002) Development of an improved vaccine for anthrax. *J. Clin. Invest. 110*, 141−144.

(14) Murdin, A. D., Barreto, L., and Plotkin, S. (1996) Inactivated poliovirus vaccine: past and present experience. *Vaccine 14*, 735−746.

(15) Jentoft, J. E., Jentoft, N., Gerken, T. A., and Dearborn, D. G. (1979) 13C NMR studies of ribonuclease A methylated with [13C]-Formaldehyde. *J. Biol. Chem. 254*, 4366−4370.

(16) Means, G. E., and Feeney, R. E. (1995) Reductive alkylation of proteins. *Anal. Biochem. 224*, 1−16.

(17) Gold, T. B., Smith, S. L., and Digenis, G. A. (1996) Studies on the influence of pH and pancreatin on 13C-formaldehyde-induced gelatin cross-links using nuclear magnetic resonance. *Pharm. Dev. Technol. 1*, 21−26.

(18) Kunkel, G. R., Mehrabian, M., and Martinson, H. G. (1981) Contact-site cross-linking agents. *Mol. Cell Biochem. 34*, 3−13.

(19) Jackson, V. (1999) Formaldehyde cross-linking for studying nucleosomal dynamics. *Methods 17*, 125−139.

(20) Feldman, M. Y. (1973) Reactions of nucleic acids and nucleoproteins with formaldehyde. *Prog. Nucleic Acid Res. Mol. Biol.* 131−149.

(21) Fraenkel-Conrat, H., and Mecham, D. K. (1948) The reaction of formaldehyde with proteins VII. Demonstration of intermolecular cross-linking by means of osmotic pressure measurements. *J. Biol. Chem. 177*, 477−487.

(22) Fraenkel-Conrat, H., and Olcott, H. S. (1948) Reaction of formaldehyde with proteins VI. cross-linking of amino groups with phenol, imidazole, or indole groups. *J. Biol. Chem. 174*, 827−843.

(23) Blass, J. (1966) Préparation et étude d'une base de Mannich cristallisée obtenue par action du formol sur mélange de thréonine et de dimethy-2,4-phénol. *Bull. Soc. Chim. Fr. 10*, 3120−3121.

(24) Blass, J., Bizzini, B., and Raynaud, M. (1965) Mechanisme de la détoxification par le formol. *C. R. Acad. Sci. Paris 261*, 1448−1449.

(25) Bizzini, B., and Raynaud, M. (1974) La detoxication des toxines proteiques par le formol: mecanismes supposes et nouveaux developpements [Detoxication of protein toxins by formol: supposed mechanisms and new developments]. *Biochimie 56*, 297−303.

(26) Blass, J., Bizzini, B., and Raynaud, M. (1968) Etude sur le mecanisme de la detoxification des toxines proteiques par le formol. I. Incorporation de la lysine libre radioactive dans la toxine diphterique pure, en presence du formol (detoxification dite "irreversible"). *Ann. Inst. Pasteur (Paris) 115*, 881−898.

(27) Blass, J., Bizzini, B., and Raynaud, M. (1969) Etude sur le mecanisme de la detoxification des toxines proteiques par le formol. II. Fixation quantitative du formol 14C. [Study on the mechanism of protein toxin detoxification by formol. II. Quantitative fixation of C14 formol]. *Ann. Inst. Pasteur (Paris) 116*, 501−521.

(28) Blass, B. (1964) Etat actuel de nos connaissances sur le mécanisme de la détoxification par le formol. *Biol. Méd. 53*, 202−234.
(29) Metz, B., Kersten, G. F. A., Hoogerhout, P., Brugghe, H. F., Timmermans, H. A., de Jong, A., Meiring, H., ten Hove, J., Hennink, W. E., Crommelin, D. J., and Jiskoot, W. (2004) Identification of formaldehyde-induced modifications in proteins: reactions with model peptides. *J. Biol. Chem. 279*, 6235−6243.
(30) Lin, R. C., Smith, J. B., Radtke, D. B., and Lumeng, L. (1995) Structural analysis of peptide-acetaldehyde adducts by mass spectrometry and production of antibodies directed against nonreduced protein-acetaldehyde adducts. *Alcohol: Clin. Exp. Res. 19*, 314−319.
(31) Fowles, L. F., Beck, E., Worrall, S., Shanley, B. C., and de Jersey, J. (1996) The formation and stability of imidazolidinone adducts from acetaldehyde and model peptides. A kinetic study with implications for protein modification in alcohol abuse. *Biochem. Pharmacol. 51*, 1259−1267.
(32) Heck, A. J., Bonnici, P. J., Breukink, E., Morris, D., and Wills, M. (2001) Modification and inhibition of vancomycin group antibiotics by formaldehyde and acetaldehyde. *Chemistry 7*, 910−916.
(33) Birnbaum, D. T., Dodd, S. W., Saxberg, B. E., Varshavsky, A. D., and Beals, J. M. (1996) Hierarchical modeling of phenolic ligand binding to 2Zn−insulin hexamers. *Biochemistry 35*, 5366−5378.
(34) Goldman, J., and Carpenter, F. H. (1974) Zinc binding, circular dichroism, and equilibrium sedimentation studies on insulin (bovine) and several of its derivatives. *Biochemistry 13*, 4566−4574.
(35) Ahmad, A., Millett, I. S., Doniach, S., Uversky, V. N., and Fink, A. L. (2004) Stimulation of insulin fibrillation by urea-induced intermediates. *J. Biol. Chem. 279*, 14999−15013.
(36) Meiring, H. D., Heeft, E. v. d., Hove, G. J. t., and Jong, A. d. (2002) Nanoscale LC-MS$^{(n)}$: technical design and applications to peptide and protein analysis. *J. Sep. Sci. 25*, 557−568.
(37) Badger, J., and Caspar, D. L. (1991) Water structure in cubic insulin crystals. *Proc. Natl. Acad. Sci. U.S.A. 88*, 622−626.
(38) Fraczkiewicz, R., and Braun, W. (1998) Exact and efficient analytical calculation of the accessible surface areas and their gradients for macromolecules. *J. Comput. Chem. 19*, 319−333.
(39) Smith, G. D., Ciszak, E., Magrum, L. A., Pangborn, W. A., and Blessing, R. H. (2000) R6 hexameric insulin complexed with *m*-cresol or resorcinol. *Acta Crystallogr., Sect. D: Biol. Crystallogr. 56* (Part 12), 1541−1548.
(40) O'Donoghue, S. I., Chang, X., Abseher, R., Nilges, M., and Led, J. J. (2000) Unraveling the symmetry ambiguity in a hexamer: calculation of the R6 human insulin structure. *J. Biomol. NMR 16*, 93−108.
(41) Whittingham, J. L., Scott, D. J., Chance, K., Wilson, A., Finch, J., Brange, J., and Guy Dodson, G. (2002) Insulin at pH 2: structural analysis of the conditions promoting insulin fibre formation. *J. Mol. Biol. 318*, 479−490.
(42) Nettleton, E. J., Tito, P., Sunde, M., Bouchard, M., Dobson, C. M., and Robinson, C. V. (2000) Characterization of the oligomeric states of insulin in self-assembly and amyloid fibril formation by mass spectrometry. *Biophys. J. 79*, 1053−1065.
(43) Sorensen, S. B., Sorensen, T. L., and Breddam, K. (1991) Fragmentation of proteins by S. aureus strain V8 protease. Ammonium bicarbonate strongly inhibits the enzyme but does not improve the selectivity for glutamic acid. *FEBS Lett. 294*, 195−197.
(44) Gatlin, C. L., Eng, J. K., Cross, S. T., Detter, J. C., and Yates, J. R., 3rd. (2000) Automated identification of amino acid sequence variations in proteins by HPLC/microspray tandem mass spectrometry. *Anal. Chem. 72*, 757−763.
(45) Braun, K. P., Cody, R. B., Jones, D. R., and Peterson, C. M. (1995) A structural assignment for a stable acetaldehyde-lysine adduct. *J. Biol. Chem. 270*, 11263−11266.
(46) Rappuoli, R. (1994) Toxin inactivation and antigen stabilization: two different uses of formaldehyde. *Vaccine 12*, 579−581.
(47) Metz, B., Jiskoot, W., Hennink, W. E., Crommelin, D. J. A., and Kersten, G. F. A. (2003) Physicochemical and immunochemical techniques predict the quality of diphtheria toxoid vaccines. *Vaccine 22*, 156−167.
(48) Hua, Q. X., Jia, W., Frank, B. H., Phillips, N. F., and Weiss, M. A. (2002) A protein caught in a kinetic trap: structures and stabilities of insulin disulfide isomers. *Biochemistry 41*, 14700−14715.

BC050340F

Receptor-Mediated Hepatic Uptake of M6P−BSA-Conjugated Triplex-Forming Oligonucleotides in Rats†

Zhaoyang Ye,‡ Kun Cheng,‡ Ramareddy V. Guntaka,*,§ and Ram I. Mahato*,‡

Departments of Pharmaceutical and Molecular Sciences, University of Tennessee Health Science Center, Memphis, Tennessee 38163. Received January 13, 2006; Revised Manuscript Received March 23, 2006

Excessive production of extracellular matrix, predominantly type I collagen, results in liver fibrosis. Earlier we synthesized mannose 6-phosphate−bovine serum albumin (M6P−BSA) and conjugated to the type I collagen specific triplex-forming oligonucleotide (TFO) for its enhanced delivery to hepatic stellate cells (HSCs), which is the principal liver fibrogenic cell. In this report, we demonstrate a time-dependent cellular uptake of M6P−BSA−^{33}P-TFO by HSC-T6 cells. Both cellular uptake and nuclear deposition of M6P−BSA−^{33}P-TFO were significantly higher than those of ^{33}P-TFO, leading to enhanced inhibition of type I collagen transcription. Following systemic administration into rats, hepatic accumulation of M6P−BSA−^{33}P-TFO increased from 55% to 68% with the number of M6P per BSA from 14 to 27. Unlike ^{33}P-TFO, there was no significant decrease in the hepatic uptake of $(M6P)_{20}$−BSA−^{33}P-TFO in fibrotic rats. Prior administration of excess M6P−BSA decreased the hepatic uptake of $(M6P)_{20}$−BSA−^{33}P-TFO from 66% to 40% in normal rats, and from 60% to 15% in fibrotic rats, suggesting M6P/insulin-like growth factor II (M6P/IGF II) receptor-mediated endocytosis of M6P−BSA−^{33}P-TFO by HSCs. Almost 82% of the total liver uptake in fibrotic rats was contributed by HSCs. In conclusion, by conjugation with M6P−BSA, the TFO could be potentially used for the treatment of liver fibrosis.

INTRODUCTION

Cirrhosis, the advanced stage of liver fibrosis, is the 12th leading cause of medial mortality in 2002 (*1*). To date, there are no FDA approved antifibrotic drugs (*2*). Fibrosis is characterized by excessive production of extracellular matrix (ECM) components, especially type I and III fibrillar collagens within the perivascular and interstitial space of tissues (*3, 4*). Although multiple liver cell types, including periportal and pericentral fibroblasts, produce collagen and lead to liver fibrosis, hepatic stellate cells (HSCs, also known as lipocytes, Ito cells, and perisinusoidal cells) have attracted the most attention (*5*). HSCs are distributed throughout the hepatic lobule and serve as the principal storage sites for vitamin A. Upon liver injury, infiltrating leukocytes (neutrophils, lymphocytes, and monocytes) along with resident marcrophages (Kupffer cells) release various inflammatory cytokines and growth factors, leading to activation of quiescent HSCs into actively proliferating α-smooth muscle actin (α-SMA) positive myofibroblast-like cells (*2, 6*).

Directly inhibiting the type I collagen synthesis by HSCs is a potential way to prevent liver fibrosis (*7*). Expression of type α1(I) collagen gene is regulated at the transcriptional and posttranscriptional level, producing an increase in the mRNA steady-state levels by 60−70-fold in activated HSCs compared with quiescent HSCs (*8*). Mammalian α1(I) collagen gene promoter contains two contiguous 30 bp polypurine tracts C1 and C2, located at −141 to −170 and −171 to −200 upstream from the transcription start site (*9*). Earlier we developed a triplex-forming oligonucleotide (TFO), which can form a stable triplex with the target gene sequence and inhibit the transcription of rat type α1(I) collagen gene in vitro. Therefore, this TFO molecule is a potential candidate for treating liver fibrosis.

Following systemic administration, oligonucleotides (ODNs) widely distribute throughout the body with higher uptake in the liver and kidney (*10−12*). There are several reports on targeted delivery of ODNs to hepatocytes, Kupffer cells, and liver endothelial cells (*13−15*). We have tested the in vivo distribution of the TFO molecules in normal and fibrotic rats (*16*). Almost 45% of the injected dose was deposited in the liver in normal rats, but only 35% of injected dose in fibrotic rats. The intrahepatic distribution was nonspecific, with Kupffer and endothelial cells contributing 40% of total liver uptake, HSCs contributing 40%, and heptocytes 20%.

HSCs comprise only 5−15% of all the liver cells (*17*). Mannose 6-phosphate/insulin like growth factor II (M6P/IGF II) receptor is expressed on HSCs, and its expression is up-regulated upon activation of these cells due to acute or chronic liver injury (*18, 19*). To maximize TFO delivery to the liver in general and to HSCs in particular, we recently synthesized mannose 6-phosphate−bovine serum albumin (M6P−BSA) and conjugated to type α1(I) collagen gene promoter specific TFO via a disulfide bond (*37*). Following tail vein injection into normal rats, $(M6P)_{20}$−BSA−^{33}P-TFO rapidly cleared from the circulation and accumulated mainly in the liver. TFO concentration residing in the HSCs was shown to be much higher with $(M6P)_{20}$−BSA−^{33}P-TFO than that with ^{33}P-TFO (1093 vs 215 ng/mg cell protein).

In the present study, we determined the cellular and nuclear uptake of $(M6P)_{20}$−BSA−^{33}P-TFO by HSC-T6 cells, which is an immortalized rat hepatic cell line. The effect of M6P−BSA−TFO on type α1(I) collagen gene transcription has also been determined by real time RT-PCR. We then determined the effect of number of M6P in M6P−BSA−TFO on biodistribution and hepatic uptake of M6P−BSA−^{33}P-TFO as well as the intrahepatic distribution after intravenous administration into both

† This work was supported by Grant RO1 DK064633 from the NIH and USPHS Grant 47379.

* Corresponding authors. R.I.M.: 26 S Dunlap Street, Room 413, Memphis, TN 38163; tel, (901) 448-6929; fax, (901) 448-6092; e-mail, rmahato@utmem.edu. R.V.G.: 101 Molecular Science Bldg., Memphis, TN 38163; tel, (901) 448-8230; fax, (901) 448-8462; e-mail, rguntaka@utmem.edu.

‡ Department of Pharmaceutical Sciences.

§ Department of Molecular Sciences.

10.1021/bc060006z CCC: $33.50 © 2006 American Chemical Society
Published on Web 04/29/2006

normal and fibrotic rats. Subcellular distribution of M6P−BSA−^{33}P-TFO in nuclei and cytoplasm of the liver cells was also determined at 30 min and 4 h post intravenous injection in rats.

MATERIALS AND METHODS

Materials. Bovine serum albumin (BSA) (fraction V, purity > 98%) was purchased from USB Corporation (Cleveland, OH). *p*-Nitrophenyl-α-D-mannopyranoside (pnpM), phosphorous oxide chloride, palladium (10 wt % on activated carbon), thiophosgene, 0.04% trypan blue, dimethylnitrosamine (DMN), deoxyribonuclease 1 (DNase 1) and Pronase were purchased from Sigma-Aldrich (St. Louis, MO). RNA STAT 60 reagent was purchased from Ambion RNA Diagnositics (Austin, TX). MultiScribe reverse transcriptase reagent was from Applied Biosystems Inc. (Branchburg, NJ). SYBR Green-1 dye universal master mix was from Applied Biosystems Inc. (Foster, CA). [γ-^{33}P]dATP was purchased from MP Biomedicals (Irvine, CA), and T4 polynucleotide kinase was from New England Biolabs (Beverly, MA). Soluene-350 (tissue solubilizer) and Hionic Fluor (scintillation fluid) were purchased from Perkin-Elmer (Boston, MA). Hydrogen peroxide (H_2O_2) was purchased from Fisher Chemical (Fair Lawn, NJ). Heparin was purchased from American Pharmaceutical Partners, Inc. (Los Angeles, CA). Dulbecco's modified Eagle's medium (DMEM), penicillin G (5000 unit/mL), streptomycin sulfate (5000 μg/mL), Trypsin-EDTA, and type IV collagenase were from Invitrogen Life Technologies (Carlsbad, CA). Heat-inactivated fetal bovine serum (FBS) was purchased from Altanta Biologicals (Lawrenceville, GA). Ca^{2+}/Mg^{2+}-free Hanks balanced salt solution and phenol red free Hanks balanced salt solution (Cellgro) were purchased from MediaTech (Washington, DC). Isoflurane was purchased form Baxter Pharmaceutical Products, Inc. (Deerfield, IL). Nycodenz AG was purchased from Greiner Bio-One, Inc. (Longwood, FL). All solvents and other chemicals used in this study were used as available without further treatment.

TFO, which was a 25 mer antiparallel fully phosphothioate ODN (3′-GAG GGG GGA GGA GGG AAA GGA AGG G-5′) targeting α1(I) collagen gene promoter of rats, was synthesized by The Midland Certified Reagent Company, Inc. (Midland, Texas), and the same TFO modified with a sulfhydryl group at the 3′ end (MW: 8684 Da) was synthesized by Invitrogen Life Technologies (Carlsbad, CA).

Synthesis and Characterization of M6P−BSA−TFO. We synthesized M6P−BSA and conjugated it to TFO via a disulfide bond formation as described in our recently published paper (*37*). Briefly, *p*-nitrophenyl-α-D-mannopyranoside (pnpM) (0.3 g, 1 mmol) was phosphorylated at the 6 position by reacting with phosphorous oxide chloride (0.4 mL, 4.4 mmol) in pyridine (0.4 mL, 5 mmol), acetonitrile (1 mL, 19 mmol), and water (0.04 mL, 2.2 mmol) for 1 h on an ice−water bath to give *p*-nitrophenyl-6-phospho-α-D-mannopyranoside (pnpM6P). PnpM6P (0.25 g, 0.66 mmol) was reduced with 100 mg of 10% palladium on activated carbon under H_2 (1 atm) in 20 mL of a 4:1 (v/v) methanol−water mixture for 2 h to give *p*-aminophenyl-6-phospho-α-D-mannopyranoside (papM6P). Thiophosgene (55 μL, 0.73 mmol) in 10 mL of chloroform was added to papM6P (50 mg, 0.14 mmol) in 10 mL of 0.1 M sodium carbonate buffer, pH 8.6, and the mixture was vigorously stirred for 1 h to give *p*-isothiocyanatophenyl-6-phospho-α-D-mannopyranoside (itcM6P). ItcM6P (26−75 mg) in 2.0 mL of 0.1 M sodium carbonate buffer, pH 9, and 0.15 M NaCl was added to 30 mg (0.45 μmol) of BSA in 2.0 mL of the same buffer. The reaction mixture was kept at room temperature for 18 h with stirring and then applied to a PD-10 column. All the intermediate products were verified with ^{1}H NMR and ESI-MS. The conjugates were verified on 8% sodium dodecyl sulfate−polyacryamide gel electrophoresis (SDS−PAGE). To have activated disulfide bonds for conjugation with TFOs, 20 mg of BSA or M6P−BSA was dissolved in 1 mL of 0.1 M sodium borate buffer, pH 8.6 and *N*-succinimidyl 3-(2-pyridyldithio)-propionate (SPDP) (4 mg; 12.8 μmol) in 0.65 mL of ethanol and the mixture was stirred for 20 h at room temperature. The products were purified on a PD-10 column. The sugar content and number of PDP groups coupled to M6P−BSA or BSA were determined as described previously. TFO modified with sulfhydryl group at the 3′ end was first treated with DTT to generate a 3′-thiol functional group and then reacted with 2.5 mg of $(M6P)_{20}$−BSA−PDP in glycine buffer. The product was eluted with PBS on a G75 column (1 × 25 cm). The formation of $(BSA)_{20}$−M6P−TFO conjugate was verified by electrophoresis on a 20% native polyacryamide gel at room temperature. We obtained M6P−BSA−TFO with different numbers of M6P residues (14, 20, or 27) by altering the molar ratio of itcM6P and BSA. There was one TFO molecule conjugated to M6P−BSA based on the chromatography on a G75 column. TFO was labeled by adding γ-^{33}P to the 5′-end using [γ-^{33}P]-ATP and T4 polynucleotide kinase as described (*16*).

Uptake of M6P−BSA−^{33}P-TFO by HSC-T6 Cells. Immortalized rat liver stellate cells (HSC-T6) (kindly provided by Dr. Friedman, SL, Mount Sinai School of Medicine, New York, NY) were seeded in 6-well plates at a density of 3.5 × 10^5 cells/well in 2 mL of DMEM supplemented with 10% FBS, penicillin G (100 units/ml) and streptomycin sulfate (100 μg/mL). After 24 h of incubation, the medium was removed and incubated with 1 mL of DMEM containing ^{33}P-TFO or $(M6P)_{14}$−BSA−^{33}P-TFO, $(M6P)_{20}$−BSA−^{33}P-TFO, and $(M6P)_{27}$−BSA−^{33}P-TFO (3 × 10^4 cpm, 0.4μM) at 37 °C. The cells were harvested at different time points (5, 20, 70, 120, 180, 240, 300, and 330 min) by removing the medium, washing with ice-cold PBS three times, and trypsinization. Cell pellets were digested with Soluene-350 for 4 h at 55 °C and then overnight at room temperature. After neutralization with H_2O_2, Hionic Fluor was added and the radioactivity was counted using a liquid scintillation counter. Total cellular protein was measured by BCA assay. The TFO concentration was expressed in terms of ng of TFO/μg of cell protein.

Polyacrylamide Gel Electrophoresis. To determine the amount of intact TFO taken up by HSC-T6 cells, 3.5 × 10^5 cells/well were incubated with ^{33}P-TFO or $(M6P)_{20}$−BSA−^{33}P-TFO (2 × 10^5 cpm, 0.4 μM) at 37 °C for up to 24 h. Cells were harvested at 0.5, 1, 2, 4, 8, 12, and 24 h. The cell pellet was lysed with 500 μL of 1% SDS lysis buffer (10 mM Tris-HCl, pH 7.4, 150 mM NaCl, and 1% sodium dodecyl sulfate) at 37 °C for 1 h. The lysate was centrifuged at 12000*g* for 10 min, the supernatant was collected and extracted with an equal volume of phenol/chloroform (v/v, 1/1), the extract was centrifuged for 5 min at 12000*g*, and the supernatant was collected in microcentrifuge tubes. TFO was precipitated by adding sodium acetate to 0.3 M and a 3-fold volume of 100% ethanol and keeping at −20 °C overnight. The solution was centrifuged at 12000*g* for 30 min, the supernatant was removed, and the precipitate was air-dried. The TFO pellet was redissolved in 20 μL of distilled water and analyzed by gel electrophoresis using a 20% polyacrylamide gel at 80 V for 2 h. The gel was autoradiographed for 2 days at 4 °C.

Isolation of Nuclei from HSC-T6 Cells. HSC-T6 cells (5 × 10^5 cells/well) were cultured in 6-well plates until 80% confluence. Then, $(M6P)_{20}$−BSA−^{33}P-TFO or ^{33}P-TFO (∼1.0 × 10^5 cpm, 0.4 μM) was added in 1 mL of DMEM media in the absence of FBS. At 4 h incubation at 37 °C, the cells were harvested and the nuclei were isolated from cytoplasm using Nuclei EZ PREP nuclei isolation kit (Sigma, St. Louis, MO) following the supplier's protocol. The purity and number of isolated nuclei was determined under microscopy by trypan blue

assay. Isolated nuclei and cytoplasm fraction were digested with Soluene-350 overnight. Hionic Fluor was added and the radioactivity was determined using a liquid scintillation counter. The percentage of nuclear uptake of the TFO was calculated as % of total cellular uptake.

Inhibition of Transcription in HSC-T6 Cells. HSC-T6 cells (5×10^5 cells/well) were cultured in 6-well plates until 70% confluence in DMEM containing 10% of FBS. The media were replaced with 1 mL of FBS-free DMEM containing TFO at a concentration of 0.5 μM or $(M6P)_{20}$−BSA−TFO at TFO concentrations of 0.2, 0.5, and 1 μM and incubated for 24 h at 37 °C. Cells treated with 1 mL of FBS-free DMEM were used as control. Then an additional 1 mL of DMEM containing 20% of FBS was added, and cells were incubated for another 24 h.

Cells were harvested and total RNA was isolated using RNA STAT 60 reagent. Total RNA (1 μg) was treated with DNase I and then converted to cDNA using MultiScribe reverse transcriptase reagent and random hexamers. One hundred nanograms of the cDNA was amplified by real time PCR using SYBR Green-1 dye universal master mix on ABI Prism 7700 Sequence Detection System. The forward primer specific for type α1(I) collagen mRNA was 5′-TGGTCCCAAAGGTTCTCCTGGT-3′, and the reverse primer 5′-TTAGGTCCAGGGAATCCCAT-CACA-3′. The forward and reverse primers specific for type α1(I) collagen primary mRNA were 5′-CCAGCCGCAAA-GAGTCTACATGTC-3′ and 5′-TCACCTTCTCATCCCTC-CTAA-3′, respectively. The PCR product is 234 bp. Primers (forward, 5′-GTCTGTGATGCCCTTAGATG-3′, and reverse, 5′-AGCTTATGACCCGCACTTAC-3′) specific for 18S ribosomal RNA were used as internal control for real time PCR. To confirm PCR specificity, the PCR products were subjected to a melting-curve analysis and agarose gel electrophoresis. Relative transcript levels were normalized to 18SrRNA genes. For comparison, transcript levels of control cells were set as 1 and experimental data are shown as fold decrease of control.

Induction of Liver Fibrosis. Dimethylnitrosamine (DMN) induced liver fibrosis in rats has been shown to have a pathology closely resembling that of human cirrhosis (*20*). Male Sprague−Dawley rats weighing 120−140 g (Harlan Co., San Diego, CA) were housed individually under controlled light (12/12 h) and temperature conditions and had free access to food and water. To induce liver fibrosis, DMN was injected intraperitoneally into rats at a dose of 10 mg/kg of body weight. Injections were given on the first three consecutive days of each week over a 4-week period. After the DMN injection for 4 weeks, 3 rats were killed for examination for liver fibrosis development and measurement of hydroxyproline content (*21*).

Biodistribution of M6P−BSA−^{33}P-TFO. The protocol of animal use and care was approved by the Comparative Department of the University of Tennessee Health Science Center. Male Sprague−Dawley rats weighing 150−170 g were anesthetized by inhalation of isoflurane, and then 250 μL of ^{33}P-TFO or $(M6P)_{20}$−BSA−^{33}P-TFO in saline (~2.2×10^5 cpm) was injected intravenously into rats at a dose of 0.2 mg of TFO/kg of body weight. After 30 min postinjection, blood (0.2−0.3 mL) was collected by cardiac puncture in heparinized tubes, and urine was also collected directly from the urinary bladder using a 26-gauge needle syringe. Major organs, such as liver, spleen, kidney, lung, heart, and muscle, were isolated, washed with saline, blotted dry, weighed, and stored at −86 °C. Blood was centrifuged, and plasma was separated. One hundred fifty microliters of plasma or 150−200 g of each tissue was incubated with 2 mL of solubilizer Soluene-350 for 3 h at 55 °C first and then overnight at room temperature. Two hundred microliters of 30% H_2O_2 was added to each sample, and each sample was incubated for another 30 min. Ten milliliters of Hionic Fluor scintillation fluid was added to each tissue, plasma, and urine sample, and the radioactivity of each sample was measured using a scintillation counter.

Competition in Hepatic Uptake of M6P−BSA−^{33}P-TFO. One minute before the injection of M6P−BSA−^{33}P-TFO at a dose of 0.2 mg/kg (specific activity: 1×10^6 cpm/mL), rats received 10 mg/kg of M6P−BSA. At 30 min postinjection, blood and urine were collected; other major organs were harvested as described above for radioactivity measurement.

Hepatic Cellular and Subcellular Distribution. To determine the effect of M6P on the hepatic uptake of TFOs by parenchymal cells (hepatocytes) and nonparenchymal cells (Kupffer, endothelial, and Stellate cells), the liver was perfused in situ after intravenous administration of ^{33}P-TFO or $(M6P)_{20}$−BSA−^{33}P-TFO (2×10^5 cpm) at a dose of 0.2 mg of TFO/kg of body weight as described before (*37*). Briefly, at 30 min postadministration, rats were anesthetized, 100 units of heparin was injected, the abdomen was opened, and the portal vein was cannulated with a PE-60 polyethylene tube. The liver was then perfused with 200 mL of Ca^{2+}/Mg^{2+}-free Hanks balanced salt solution and then with Hanks balanced salt solution containing 0.05% type IV collagenase and 0.1% Pronase for an additional 250 mL. All the perfusion solutions were incubated at 37 °C. After perfusion, different liver cell types were separated and radioactivity was measured as described before (*16*). The contributions of various cell types to the total liver uptake were calculated as % of total hepatic uptake.

To isolate nuclei from the whole liver cells, the livers were collected at 30 min or 4 h postinjection of ^{33}P-TFO or $(M6P)_{20}$−BSA−^{33}P-TFO (4×10^5 cpm) at a dose of 0.2 mg of TFO/kg of body weight, washed, and blotted dry. One gram of fresh liver tissue was used for isolation of nuclei using Nuclei PURE Prep nuclei isolation kit according to the supplier's protocol (Sigma-Aldrich, St Louis, MO). The purity and number of isolated nuclei were determined under microscopy by dilution in trypan blue solution. The yield of nuclei was calculated to be 40−50% by comparing the number of isolated nuclei to the starting cell number. Isolated nuclei were digested with Soluene-350 overnight. Hionic Fluor was added, and the radioactivity was determined using a liquid scintillation counter. The percentage of nuclear uptake of the TFO in the liver was calculated as % of total hepatic uptake.

Statistical Analysis. Data were expressed as the mean ± standard deviation (SD). $P < 0.05$ was considered statistically significant. Statistics were calculated based on unpaired Student's *t* test using SPSS 13.0 for windows software.

RESULTS

To enhance the cellular uptake and nuclear translocation of the TFO, we conjugated M6P−BSA to the 3′ end of the TFO via a disulfide bond. M6P−BSA−TFO was then characterized in terms of in vitro cellular and nuclear uptake and transcription inhibition of type α1(I) collagen gene in HSC-T6 cells. This was followed by biodistribution at whole body, organ (liver), and hepatic cellular and subcellular levels after intravenous injection into normal and fibrotic rats.

In Vitro Cellular and Nuclear Uptake of M6P−BSA−TFO. We have previously shown that M6P−BSA−TFO could enhance the TFO accumulation in the liver and thus concentrated TFO molecules inside HSCs compared to free TFO molecules (*37*). However, we still need to determine whether this enhanced TFO deposition is contributed to by an increase in M6P−BSA−TFO uptake by the HSCs via the M6P/IGF II receptor-mediated endocytosis. We first incubated HSC-T6 cells with ^{33}P-TFO or M6P−BSA−^{33}P-TFO for different time periods. As shown in Figure 1a, a larger amount of TFO was taken up by these cells when treated with M6P−BSA−^{33}P-TFO compared to that of ^{33}P-TFO treated cells. The TFO amount was around 1 ng/μg of

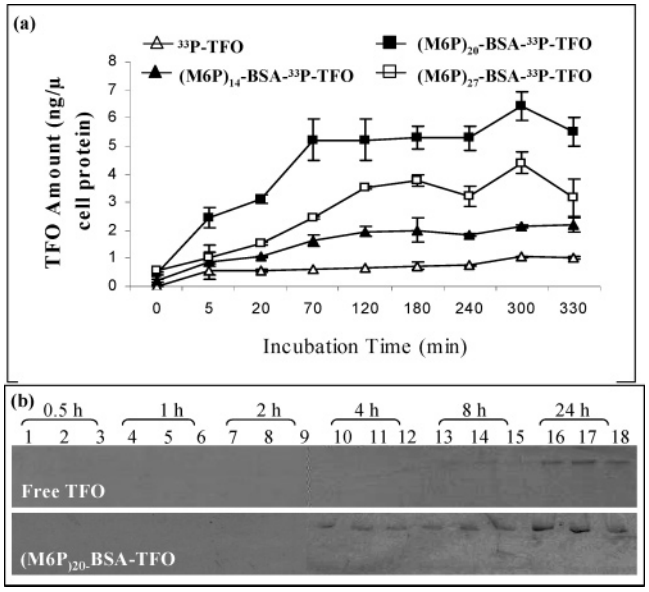

Figure 1. Cellular uptake of M6P−BSA−TFO by HSC-T6 cells. (a) Time profile of the cellular uptake of M6P−BSA−^{33}P-TFO and ^{33}P-TFO by HSC-T6 cells. HSC-T6 cells were incubated with ^{33}P-TFO or M6P−BSA−^{33}P-TFO (3×10^4 cpm, 0.4 μM) at 37 °C, and then cells were harvested at the indicated time for measurement of associated radioactivity. TFO concentration was expressed in terms of ng of TFO/μg of cell protein. Values are mean ± SD of 3 independent experiments. (b) Polyacrylamide gel electrophoresis (PAGE) of the TFO extracted from HSC-T6 cells. HSC-T6 cells were incubated with ^{33}P-TFO or (M6P)$_{20}$−BSA−^{33}P-TFO at 37 °C for up to 24 h. Cells were harvested at the indicated time and lysed with 1% SDS lysis buffer. TFO was extracted and analyzed by gel electrophoresis using a 20% polyacrylamide gel. Each time point was presented with 3 independent experiments.

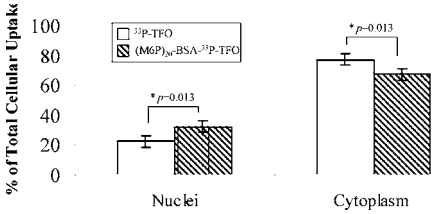

Figure 2. Subcellular distribution of (M6P)$_{20}$−BSA−^{33}P-TFO and ^{33}P-TFO in HSC-T6 cells at 4 h postincubation at 37 °C. Cells were harvested and the nuclei were isolated from the cytoplasm using Nuclei EZ PREP nuclei isolation kit (Sigma, St Louis, MO). The subcellular distribution was expressed as % of total cellular uptake, and values are mean ± SD of 3 independent experiments. Asterisk: statistically significant.

cell protein for unconjugated TFO. Conjugates with different numbers (x) of M6P residues (x = 14, 20, and 27) showed different cellular uptake, with 2, 5, and 3 ng of TFO/μg of cell protein, respectively. The optimal number of M6P for M6P−BSA−TFO is 20. The enhanced cellular uptake of the conjugates was also confirmed by polyacrylamide gel electrophoresis (Figure 1b). Bands clearly appeared at 4 h postincubation with (M6P)$_{20}$−BSA−^{33}P-TFO; however, the control TFO appeared only after 24 h of treatment. Moreover, the cellular uptake of M6P−BSA−^{33}P-TFO was time dependent (Figure 1a,b).

Since the TFO molecules have to function inside the nucleus of the hepatic stellate cells by forming a triplex with the target genomic DNA sequence (*22*), we also determined the nuclear translocation of M6P−BSA−^{33}P-TFO. As shown in Figure 2, relatively more TFO translocated into the nucleus (~32% of total cellular uptake) in the case of (M6P)$_{20}$−BSA−^{33}P-TFO compared to nonconjugated TFO molecules (~23% of total cellular uptake), possibly due to the efficient cellular uptake of M6P−BSA−^{33}P-TFO by HSC-T6 cells.

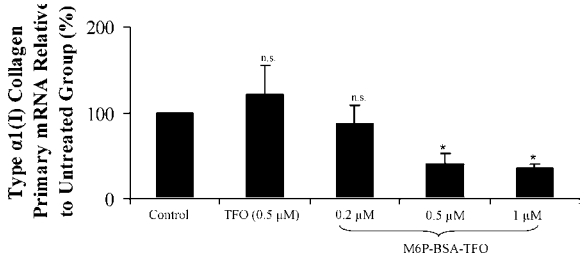

Figure 3. Relative type α1(I) collagen gene transcription in HSC-T6 cells treated with TFO or (M6P)$_{20}$−BSA−TFO by real time RT-PCR assay. HSC-T6 cells were treated with unconjugated TFO (0.5 μM) or (M6P)$_{20}$−BSA−TFO at the indicated concentrations in 1 mL of FBS-free DMEM for 24 h, and then 1 mL of DMEM containing 20% of FBS was added and incubated for another 24 h. Relative transcript levels were normalized using 18S rRNA as a housekeeping gene. Control means no treatment. Values are mean ± SD of 3 independent experiments. Asterisk: statistically significant compared to control group. n.s.: not significant.

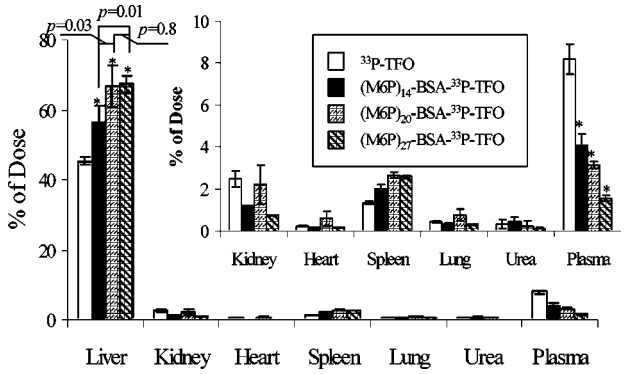

Figure 4. Effect of number of M6P per BSA on biodistribution of M6P−^{33}P−BSA−TFO in normal rats. At 30 min postinjection of M6P−BSA−^{33}P-TFO (~2.2×10^5 cpm) at a dose of 0.2 mg/kg, blood was collected by cardiac puncture and urine from the urinary bladder. Rats were sacrificed; major organs were isolated, washed with saline, blotted dry, and subjected to scintillation counting. Values are mean ± SD of 4 rats in each group. Asterisk: statistically significant comparing to naked TFO group.

Inhibition of Type α1(I) Collagen Gene Transcription. Higher cellular uptake of M6P−BSA−TFO was expected to have higher efficiency in inhibiting the transcription of type α1(I) collagen gene. We used real time RT-PCR to quantify the primary mRNA levels. It was found that at the concentration of 0.5 μM, free TFO molecules had no clear effect on the transcription inhibition. In contrast, for (M6P)$_{20}$−BSA−TFO, we observed dose-dependent transcription inhibition. Transcription product was decreased to 87% of control group at 0.2 μM, 40% at 0.5 μM, and 35% at 1 μM (Figure 3).

Effect of Number of M6P on Biodistribution of M6P−BSA−^{33}P-TFO. Since M6P is a ligand for the M6P/IGF II receptor expressed on the surface of the HSCs, the degree of M6P substitution per BSA molecule is likely to have a significant effect on the hepatic uptake and biodistribution of M6P−BSA−^{33}P-TFO. Therefore, we determined the effect of the number of M6P per BSA on the biodistribution of M6P−BSA−^{33}P-TFO. As shown in Figure 4, there was a significant increase in the amount of radioactivity in the liver compared to free TFO and as the number of M6P per BSA increased from 14 to 27, the hepatic uptake was 56.3%, 66.6%, and 67.4% for (M6P)$_{14}$−BSA−^{33}P-TFO, (M6P)$_{20}$−BSA−^{33}P-TFO, and (M6P)$_{27}$−BSA−^{33}P-TFO, respectively. However, no statistical difference was found between the (M6P)$_{20}$-^{33}P-TFO and (M6P)$_{27}$-^{33}P-TFO injected groups for the hepatic uptake (66.6% vs 67.4% of the injected dose). The amount of radioactivity in the spleen also increased (2.0%, 2.7%, and 2.6%, respectively) with increase in the number of M6P per BSA. In contrast, there was

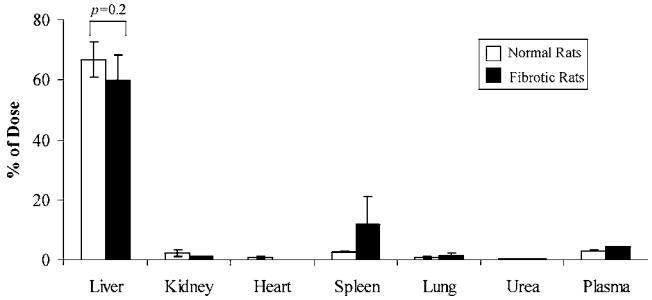

Figure 5. Effect of fibrosis on hepatic uptake of $(M6P)_{20}$−BSA−^{33}P-TFO after systemic administration into DMN-induced fibrotic rats. At 30 min postinjection of $(M6P)_{20}$−BSA−^{33}P-TFO (~2.2×10^5 cpm) at a dose of 0.2 mg/kg, blood was collected by cardiac puncture and urine from the urinary bladder. Rats were sacrificed; major organs were isolated, washed with saline, blotted dry, and subjected to scintillation counting. Values are mean ± SD of 4 rats in each group.

a significant decrease in the plasma concentration compared to free TFO, and with increase in the number of M6P per BSA, the dose in the plasma was 4.1%, 3.1%, and 1.6%, respectively. The accumulation of different M6P−BSA−TFO in heart and lung was trivial. Since there was no significant difference in the hepatic uptake of $(M6P)_{20}$−BSA−^{33}P-TFO and $(M6P)_{27}$−BSA−^{33}P-TFO (Figure 4), we selected $(M6P)_{20}$−BSA−^{33}P-TFO for further studies.

Effect of Fibrosis on Biodistribution of M6P−BSA−^{33}P-TFO. In the liver fibrosis process, activation of HSCs leads to accumulation of scar (fibril-forming) matrix, which in turn contributes to the loss of hepatocyte microvilli and sinusoidal fenestrae (*2*). These microstructural changes in the liver may prevent efficient drug delivery to HSCs.

We recently demonstrated that ^{33}P-TFO accumulation in the liver decreased from 43% in normal rats to 33% in fibrotic rats at 30 min postinjection (*16*). Therefore, we determined the biodistribution of $(M6P)_{20}$−BSA−^{33}P-TFO in DMN-induced liver fibrotic rats. As shown in Figure 5, there was no significant decrease in the hepatic uptake of $(M6P)_{20}$−BSA−^{33}P-TFO, which showed higher accumulation in both normal and fibrotic rats.

Competition in Hepatic Uptake of M6P−BSA−TFO. The role of M6P/IGF II receptor on biodistribution of M6P−BSA−^{33}P-TFO in normal and fibrotic rats was assessed by determining the effect of excess M6P−BSA on the accumulation of M6P−BSA−TFO in the liver. By administration of excess M6P−BSA, the M6P/IGF II receptor can be saturated. Prior administration of M6P−BSA caused a significant decrease in the hepatic uptake of M6P−BSA−^{33}P-TFO at 30 min postinjection, suggesting the involvement of M6P/IGF II receptor in their hepatic uptake. The hepatic uptake of $(M6P)_{20}$−BSA−^{33}P-TFO decreased from 66.6% to 41.0% in the case of normal rats (Figure 6a), but from 59.7% to 14.3% in the case of fibrotic rats (Figure 6b). When we used BSA−TFO as a control, TFO accumulation in the liver was also significantly increased. However, there was only minimal decrease in its liver accumulation due to the prior injection of excess M6P−BSA (10 mg/kg), suggesting that its hepatic uptake is not mediated by M6P/IGF II receptor-mediated endocytosis (data not shown).

Hepatic Cellular and Subcellular Localization of M6P−BSA−TFO. Upregulation of M6P/IGF II receptors during fibrosis should increase M6P−BSA−TFO uptake by the HSCs and cancel out any adverse effect created by decreased sinusoidal gap. Therefore, the intrahepatic cellular localization of M6P−BSA−TFO was compared between normal and fibrotic rats, since HSCs are quiescent in normal rats, but get activated in fibrotic rats. The liver was perfused at 30 min post tail vein injection of $(M6P)_{20}$−BSA−^{33}P-TFO and ^{33}P-TFO as described before (*16*). Hepatocytes, Kupffer and endothelial cells, and

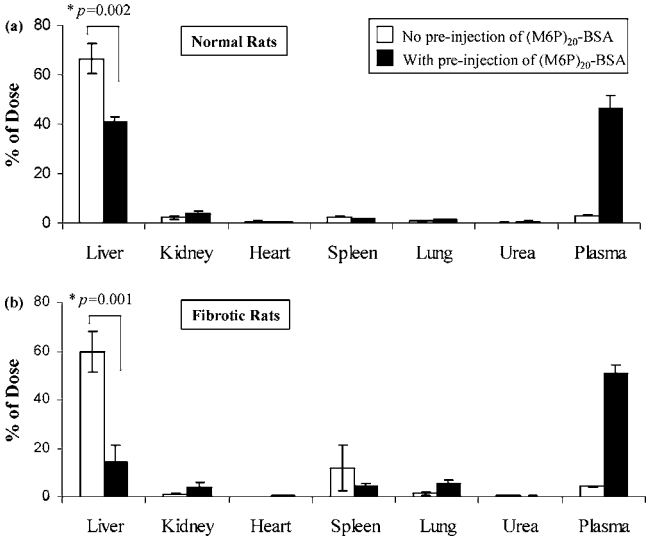

Figure 6. Inhibition of M6P−BSA on biodistribution of $(M6P)_{20}$−BSA−^{33}P-TFO in normal rats (a) and in fibrotic rats (b). $(M6P)_{20}$−BSA (10 mg/kg) was injected intravenously into rats 5 min before the injection of $(M6P)_{20}$−BSA−^{33}P-TFO in normal and fibrotic rats at a dose of 0.2 mg/kg. At 30 min postinjection, rats were sacrificed; major organs were isolated, washed with saline, blotted dry, and subjected to scintillation counting. Values are mean ± SD of 4 rats in each group. Asterisk: statistically significant.

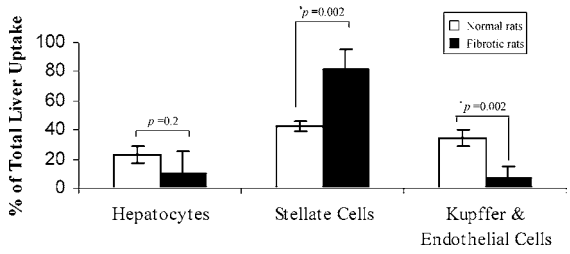

Figure 7. Intrahepatic distribution of $(M6P)_{20}$−BSA−^{33}P-TFO in normal and fibrotic rats. The liver was perfused in situ by collagenase/Pronase digestion after intravenous administration of ^{33}P-TFO or $(M6P)_{20}$−BSA−^{33}P-TFO at the dose of 0.2 mg of TFO/kg of body weight. Hepatocytes, Kupffer and endothelial cells, and stellate cells were separated, and the associated radioactivity was measured. The contribution of each cell type was expressed as % of total liver uptake. Values are mean ± SD of 5 rats in each group. Asterisk: statistically significant.

HSCs were isolated, and the amount of radioactivity in these cells was determined. Figure 7 shows the percentages of contribution by different cell types in terms of total liver uptake of $(M6P)_{20}$−BSA−^{33}P-TFO after systemic administration in normal and fibrotic rats. In normal rats, 42.3% of total liver uptake was contributed by HSCs, 34.4% by Kupffer and endothelial cells, and 23.3% by hepatocytes. In contrast, in fibrotic rats, 82.0% of the total hepatic uptake was by HSCs, only 7.4% by Kupffer and endothelial cells, and 10.6% by hepatocytes. However, in the case of free TFO, there was not much difference for HSC contribution between normal and fibrotic rats (40% versus 44%) (*16*).

To study the subcellular distribution of the conjugate in vivo, we isolated the nuclei from rat liver at 30 min or 4 h after intravenous injection of $(M6P)_{20}$−BSA−^{33}P-TFO. Fractionation by sucrose gradient gave pure and intact nuclei (Figure 8), with a recovery of 40−50%. The majority of the TFO stayed in the cytoplasm of liver cells, and the TFO in the nuclei was only 4% of the total hepatic uptake at 30 min but increased up to 6% at 4 h. However, it is important to note that only half of the cell nuclei could be isolated. Therefore, the actual nuclear distribution of the TFO should be higher than this number.

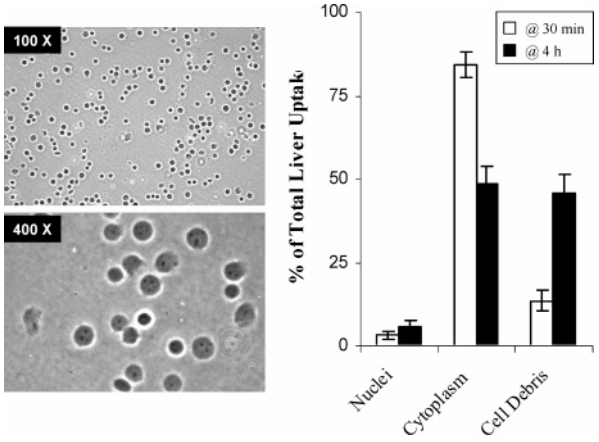

Figure 8. Subcellular distribution of $(M6P)_{20}$−BSA−^{33}P-TFO in the liver. At 30 min and 4 h after intravenous administration of $(M6P)_{20}$−BSA−^{33}P-TFO into normal rats at a dose of 0.2 mg/kg, rats were sacrificed and the livers were removed. The nuclei, cytoplasm, and cell debris were isolated from liver tissues using a sucrose gradient. Distribution in the nuclei, cytoplasm, and cell debris were given as % of the total liver uptake, and values are mean ± SD of 4 rats in each group.

DISCUSSION

Fibrosis is characterized by excessive production of ECM composed primarily of type I collagen. Antisense ODNs have been shown to inhibit type α1(I) collagen gene expression in NIH 3T3 cell in culture (*23*). Compared to quiescent HSCs, activated HSCs contain 60−70-fold more collagen α1(I) mRNA (*8*, *24*). Therefore, transfection of activated HSCs with molecular decoy and small interfering double stranded RNAs (siRNA) could significantly decrease α1(I) collagen mRNA (*24*, *25*). However, these authors did not attempt to deliver ODNs and siRNA to liver fibrogenic cells in vivo. Systemic administration of siRNA against Fas or Caspase 8 has shown some promise in controlling liver fibrosis (*26*, *27*). However, these authors used high volume hydrodynamic administration, which is not feasible in a clinical setting. Moreover, siRNA is known to have an "off-target" effect.

To avoid the use of polycations, Rajur et al. (*28*) conjugated ODNs to asialoglycoprotein via a disulfide bond. Direct conjugation of molecules to the TFO often tends to disturb the triplex-forming ability of the TFOs, which is essential for transcription inhibition. In contrast, conjugation of M6P−BSA to TFO via a disulfide bond is stable in the circulation, but will be cleaved inside the cells by glutathione and/or redox enzymes. In the current study, we used a TFO molecule, which can specifically inhibit the transcription of type α1(I) collagen gene by forming triplex at the promoter region (*9*, *29*). One of the main advantages of the TFO over antisense ODNs and siRNA is that it targets two alleles of the target gene per cell rather than the mRNA, which is usually present in hundreds or thousands of copies per cell (*22*). After intravenous administration of the TFO, 35% of the injected dose accumulated in the liver of fibrotic rats and the intrahepatic distribution was nonspecific for HSCs (*16*).

M6P is a ligand for M6P/IGF II receptor, which is upregulated in fibroblast-like cells such as activated HSCs during liver fibrosis (*18*, *19*). Coupling of M6P to albumin increased selective uptake of this modified albumin by HSCs during liver fibrosis (*30*). Conjugation of M6P to recombinant interleukin-10 (rIL-10) significantly increased the hepatic uptake of IL-10 by the liver. We synthesized M6P−BSA, conjugated to TFO via a disulfide bond, and determined the biodistribution of $(M6P)_{20}$−BSA−^{33}P-TFO after intravenous injection in normal rats (*37*). Significant increase in the hepatic uptake of the TFO was observed. Since the hepatic uptake and bioactivity of $(M6P)_x$−BSA−TFO are likely to be dependent on the dose and number of M6P per BSA, in this study, we synthesized $(M6P)_x$−BSA−TFO, where $x = 14$, 20, and 27 for both in vitro and in vivo studies.

HSC-T6 cell is a good cell culture system for studying the characteristics of activated HSCs in vitro (*31*). As shown in Figure 1, after conjugation with M6P−BSA, there was a significant increase in the TFO uptake by HSC-T6 cells. This is in a good agreement with the work of Bonfils et al. (*32*), who showed increased uptake of M6P−BSA−ODN by fibroblast-like BHK cells, which also expressed M6P/IGF II receptors. However, these authors had not tested their glycoconjugates in vivo. Also, $(M6P)_{20}$−BSA−TFO gave the highest cellular uptake, so there was an optimal number of M6P attached to BSA (Figure 1a).

For triplex formation with genomic DNA, TFO must dissociate from M6P−BSA and translocate to the nucleus. TFO molecules were shown to be efficiently getting into the nucleus varying from 18.5% to 60.6% of total cellular uptake depending on different cell lines (*33*). We determined the nuclear uptake of $(M6P)_{20}$−BSA−^{33}P-TFO at 4 h postincubation to be around 32% and higher than that of ^{33}P-TFO in HSC-T6 cells (Figure 2). The increased nuclear translocation of the TFO was not expected, since there is no apparent reason for M6P−BSA−TFO to enhance the nuclear entry of the TFO molecules. The TFO was covalently conjugated with M6P−BSA via a disulfide bond, thus upon getting inside the cells, the disulfide bonds are expected to be cleaved and TFO molecules would enter the nucleus in an unconjugated form (*37*). So, this increased nuclear translocation of TFO molecules may be due to the relatively higher and faster cellular uptake of M6P−BSA−TFO by these cells than TFO alone, as shown in Figure 1. However, we observed a much less nuclear localization of M6P−BSA−^{33}P-TFO in vivo. It was only 4% at 30 min, but increased to 6% at 4 h (Figure 8). However, these values were underestimated since we could isolate only 40−50% of the nuclei from the liver tissue. The overall nuclear translocation of the TFO in the liver is likely to be as high as 15% at 4 h.

Previously, we have reported that the TFO can form triplex with the type α1(I) collagen gene promoter sequence and inhibit the gene expression using a reporter plasmid containing the type α1(I) collagen gene promoter sequence (*9*). However, we did not show direct inhibition of type α1(I) collagen gene expression by the TFO. Since the half-life of type α1(I) collagen mRNA is 20-fold longer in activated HSCs than that of quiescent HSCs (*34*), it is impossible to detect the effect of TFO at the mRNA level in cell culture. Therefore, we designed primers specific for type α1(I) collagen primary mRNA to avoid this problem and demonstrated the gene inhibition effect of TFO. Higher cellular uptake was expected to have a more potent inhibitory effect on type α1(I) collagen gene transcription. TFO molecules did not show any inhibitory effect at 0.5 μM. In contrast, for M6P−BSA−TFO, we saw 60% inhibition at 0.5 μM and 65% at 1 μM. Thus, M6P−BSA−TFO could efficiently increase the cellular uptake of TFO and also strengthen the TFO bioactivity.

The hepatic accumulation of M6P modified human serum albumin (M6P−HSA) was shown to be dependent on the number of M6P per HSA molecule and the highest hepatic accumulation and uptake by HSCs when HSA was substituted with 28 of M6P moieties (*30*). Therefore, we substituted 14, 20, and 27 M6P moieties per BSA for TFO delivery. As shown in Figure 4, the percentage of the injected dose accumulated in the liver significantly increased with increase in M6P density. Almost 56.3% of the injected dose was accumulated in the liver for $(M6P)_{14}$−BSA−TFO, and an increase in the molar ratio of M6P:BSA to 27 resulted in an increased liver accumulation to

67.4%. Our results did not correlate well with the work of Beljaar et al. (*30*), who showed only a trivial accumulation of $(M6P)_x$−HSA in the liver when x was equal to 10 or below, but 59.2% as the hepatic uptake when x was equal to 28. This discrepancy is possibly due to the following two reasons: (i) we used M6P−BSA, since it was also shown that 52.6% accumulated in the liver for $(M6P)_{21}$−BSA (*30*); (ii) in our case, M6P−BSA was further conjugated with TFO, which is a polyanion with molecular weight of >8000Da, and must have some influence on the biodistribution of M6P−BSA. Apparently, there was a saturation in the hepatic uptake of M6P−BSA−TFO, since $(M6P)_{20}$−BSA−TFO and $(M6P)_{27}$−BSA−TFO were not significantly different in the hepatic uptake (Figure 4). This saturation was also observed for galactose modified BSA (Gal-BSA) by Staud et al. (*35*).

Since there is a concern that the fibrotic liver would prevent efficient drug delivery to the liver (*30*), we confirmed that there was no decrease in the hepatic uptake of $(M6P)_{20}$−BSA−TFO. This is in contrast to our recent findings on the biodistribution of ^{33}P-TFO, where we observed significant decrease in the hepatic uptake of ^{33}P-TFO when injected into fibrotic rats (*16*). This may be due to the fact that M6P/IGF II receptors are upregulated during fibrosis (*18*, *19*), which should increase uptake by HSCs via receptor-mediated endocytosis and cancel out any adverse effect created by decrease in sinusoidal gap.

To determine whether the hepatic accumulation of M6P−BSA−^{33}P-TFO is mediated by M6P/IGF II receptor-mediated endocytosis, we preinjected rats with excess $(M6P)_{20}$−BSA. This resulted in a significant decrease in the hepatic disposition of M6P−BSA−^{33}P-TFO, and this decrease was even more significant in fibrotic rat liver (Figure 6). This confirmed the specific receptor-mediated uptake of M6P−BSA−^{33}P-TFO. When M6P/IGF II receptor was upregulated in fibrotic rats, the hepatic accumulation was almost completely inhibited by blocking this receptor. Rachmawati et al. also demonstrated almost 50% inhibition in the hepatic uptake of M6P−IL-10 conjugate in fibrotic rats (*36*).

Finally, we should make sure the conjugate was really targeted to HSCs. We observed that 42.3% of the hepatic uptake was in the HSCs of normal rats, but increased to 82.0% in the HSCs of fibrotic rats, which means $(M6P)_{20}$−BSA−TFO not only increased TFO accumulation in the liver in general but also specifically targeted to HSCs in fibrotic rats. At the same time, the contribution of Kupffer and endothelial cells was greatly inhibited compared to that in normal rats (7.4% vs 34.4%). Unconjugated TFO was mostly taken up by Kupffer and endothelial cells, possibly through the scavenger receptors (*16*). Thus, the biodistribution of TFO was changed by conjugation with M6P−BSA.

Although we isolated nuclei from the whole liver rather than from different isolated liver cells, we assume that the nuclear translocation of the TFO of different liver cells would be similar. Since most of the TFO accumulated in the HSCs of the fibrotic rats (Figure 7), we expect that TFO concentration inside the nuclei of HSCs would be much higher for M6P−BSA−TFO than that for free TFO and thus could greatly increase the potency of TFO molecules in vivo.

In conclusion, conjugation with M6P−BSA significantly enhanced the uptake of the TFO by HSCs both in vitro and in vivo. Therefore, M6P−BSA−TFO is a suitable delivery system for targeting TFO against type α1(I) collagen gene promoter to HSCs for treating liver fibrosis.

ACKNOWLEDGMENT

This work was supported by Grant R01 DK064633 from the NIH and USPHS Grant 47379.

LITERATURE CITED

(1) Kochanek, K. D., Murphy, S. L., Anderson, R. N., and Scott, C. (2004) Deaths: final data for 2002. *Natl. Vital Stat. Rep. 53*, 1−115.
(2) Friedman, S. L. (2000) Molecular regulation of hepatic fibrosis, an integrated cellular response to tissue injury. *J. Biol. Chem. 275*, 2247−50.
(3) Knittel, T., Kobold, D., Piscaglia, F., Saile, B., Neubauer, K., Mehde, M., Timpl, R., and Ramadori, G. (1999) Localization of liver myofibroblasts and hepatic stellate cells in normal and diseased rat livers: distinct roles of (myo-)fibroblast subpopulations in hepatic tissue repair. *Histochem. Cell Biol. 112*, 387−401.
(4) Raghow, R. (1994) The role of extracellular matrix in postinflammatory wound healing and fibrosis. *FASEB J. 8*, 823−31.
(5) Rockey, D. C. (2005) Antifibrotic therapy in chronic liver disease. *Clin. Gastroenterol. Hepatol. 3*, 95−107.
(6) Maher, J. J. (2001) Interactions between hepatic stellate cells and the immune system. *Semin. Liver Dis. 21*, 417−26.
(7) Wu, C. H., Walton, C. M., and Wu, G. Y. (2000) Targeted inhibition of type I procollagen synthesis by antisense DNA oligonucleotides. *Gene Ther. Regul. 1*, 193−205.
(8) Stefanovic, B., Hellerbrand, C., Holcik, M., Briendl, M., Aliebhaber, S., and Brenner, D. A. (1997) Posttranscriptional regulation of collagen alpha1(I) mRNA in hepatic stellate cells. *Mol. Cell. Biol. 17*, 5201−9.
(9) Joseph, J., Kandala, J. C., Veerapanane, D., Weber, K. T., and Guntaka, R. V. (1997) Antiparallel polypurine phosphorothioate oligonucleotides form stable triplexes with the rat alpha1(I) collagen gene promoter and inhibit transcription in cultured rat fibroblasts. *Nucleic Acids Res. 25*, 2182−8.
(10) Sawai, K., Mahato, R. I., Oka, Y., Takakura, Y., and Hashida, M. (1996) Disposition of oligonucleotides in isolated perfused rat kidney: involvement of scavenger receptors in their renal uptake. *J. Pharmacol. Exp. Ther. 279*, 284−90.
(11) Takakura, Y., Mahato, R. I., Yoshida, M., Kanamaru, T., and Hashida, M. (1996) Uptake characteristics of oligonucleotides in the isolated rat liver perfusion system. *Antisense Nucleic Acid Drug Dev. 6*, 177−83.
(12) Agrawal, S., Temsamani, J., and Tang, J. Y. (1991) Pharmacokinetics, biodistribution, and stability of oligodeoxynucleotide phosphorothioates in mice. *Proc. Natl. Acad. Sci. U.S.A. 88*, 7595−9.
(13) Mahato, R. I., Takemura, S., Akamatsu, K., Nishikawa, M., Takakura, Y., and Hashida, M. (1997) Physicochemical and disposition characteristics of antisense oligonucleotides complexed with glycosylated poly(L-lysine). *Biochem. Pharmacol. 53*, 887−95.
(14) Bijsterbosch, M. K., Manoharan, M., Dorland, R., Waarlo, I. H., Biessen, E. A., and van Berkel, T. J. (2001) Delivery of cholesteryl-conjugated phosphorothioate oligodeoxynucleotides to Kupffer cells by lactosylated low-density lipoprotein. *Biochem. Pharmacol. 62*, 627−33.
(15) Bijsterbosch, M. K., Manoharan, M., Dorland, R., Van Veghel, R., Biessen, E. A., and Van Berkel, T. J. (2002) bis-Cholesteryl-conjugated phosphorothioate oligodeoxynucleotides are highly selectively taken up by the liver. *J. Pharmacol. Exp. Ther. 302*, 619−26.
(16) Cheng, K., Ye, Z., Guntaka, R. V., and Mahato, R. I. (2005) Biodistribution and hepatic uptake of triplex-forming oligonucleotides against type alpha1(I) collagen gene promoter in normal and fibrotic rats. *Mol. Pharm. 2*, 206−17.
(17) Beljaars, L., Olinga, P., Molema, G., de Bleser, P., Geerts, A., Groothuis, G. M., Meijer, D. K., and Poelstra, K. (2001) Characteristics of the hepatic stellate cell-selective carrier mannose 6-phosphate modified albumin (M6P(28)-HSA). *Liver 21*, 320−8.
(18) de Bleser, P. J., Jannes, P., van Buul-Offers, S. C., Hoogerbrugge, C. M., van Schravendijk, C. F., Niki, T., Rogiers, V., van den Brande, J. L., Wisse, E., and Geerts, A. (1995) Insulinlike growth factor-II/mannose 6-phosphate receptor is expressed on CCl4-exposed rat fat-storing cells and facilitates activation of latent transforming growth factor-beta in cocultures with sinusoidal endothelial cells. *Hepatology 21*, 1429−37.
(19) Weiner, J. A., Chen, A., and Davis, B. H. (1998) E-box-binding repressor is down-regulated in hepatic stellate cells during up-regulation of mannose 6-phosphate/insulin-like growth factor-II receptor expression in early hepatic fibrogenesis. *J. Biol. Chem. 273*, 15913−9.

(20) Jenkins, S. A., Grandison, A., Baxter, J. N., Day, D. W., Taylor, I., and Shields, R. (1985) A dimethylnitrosamine-induced model of cirrhosis and portal hypertension in the rat. *J. Hepatol. 1*, 489−99.
(21) Jamall, I. S., Finelli, V. N., and Que Hee, S. S. (1981) A simple method to determine nanogram levels of 4-hydroxyproline in biological tissues. *Anal. Biochem. 112*, 70−5.
(22) Stull, R. A., and Szoka, F. C., Jr. (1995) Antigene, ribozyme and aptamer nucleic acid drugs: progress and prospects. *Pharm. Res. 12*, 465−83.
(23) Laptev, A. V., Lu, Z., Colige, A., and Prockop, D. J. (1994) Specific inhibition of expression of a human collagen gene (COL1A1) with modified antisense oligonucleotides. The most effective target sites are clustered in double-stranded regions of the predicted secondary structure for the mRNA. *Biochemistry 33*, 11033−9.
(24) Stefanovic, B., Schnabl, B., and Brenner, D. A. (2002) Inhibition of collagen alpha 1(I) expression by the 5′ stem-loop as a molecular decoy. *J. Biol. Chem. 277*, 18229−37.
(25) Lindquist, J. N., Parsons, C. J., Stefanovic, B., and Brenner, D. A. (2004) Regulation of alpha1(I) collagen messenger RNA decay by interactions with alphaCP at the 3′-untranslated region. *J. Biol. Chem. 279*, 23822−9.
(26) Song, E., Lee, S. K., Wang, J., Ince, N., Ouyang, N., Min, J., Chen, J., Shankar, P., and Lieberman, J. (2003) RNA interference targeting Fas protects mice from fulminant hepatitis. *Nat. Med. 9*, 347−51.
(27) Zender, L., Hutker, S., Liedtke, C., Tillmann, H. L., Zender, S., Mundt, B., Waltemathe, M., Gosling, T., Flemming, P., Malek, N. P., Trautwein, C., Manns, M. P., Kuhnel, F., and Kubicka, S. (2003) Caspase 8 small interfering RNA prevents acute liver failure in mice. *Proc. Natl. Acad. Sci. U.S.A. 100*, 7797−802.
(28) Rajur, S. B., Roth, C. M., Morgan, J. R., and Yarmush, M. L. (1997) Covalent protein-oligonucleotide conjugates for efficient delivery of antisense molecules. *Bioconjugate Chem. 8*, 935−40.
(29) Nakanishi, M., Weber, K. T., and Guntaka, R. V. (1998) Triple helix formation with the promoter of human alpha1(I) procollagen gene by an antiparallel triplex-forming oligodeoxyribonucleotide. *Nucleic Acids Res. 26*, 5218−22.
(30) Beljaars, L., Molema, G., Weert, B., Bonnema, H., Olinga, P., Groothuis, G. M., Meijer, D. K., and Poelstra, K. (1999) Albumin modified with mannose 6-phosphate: A potential carrier for selective delivery of antifibrotic drugs to rat and human hepatic stellate cells. *Hepatology 29*, 1486-93.
(31) Vogel, S., Piantedosi, R., Frank, J., Lalazar, A., Rockey, D. C., Friedman, S. L., and Blaner, W. S. (2000) An immortalized rat liver stellate cell line (HSC-T6): a new cell model for the study of retinoid metabolism in vitro. *J. Lipid Res. 41*, 882−93.
(32) Bonfils, E., Depierreux, C., Midoux, P., Thuong, N. T., Monsigny, M., and Roche, A. C. (1992) Drug targeting: synthesis and endocytosis of oligonucleotide-neoglycoprotein conjugates. *Nucleic Acids Res. 20*, 4621−9.
(33) Cho, J. G., Kim, M. K., Oh, E. J., Yoon, E. J., Sohn, J., Park, M. K., and Park, G. H. (2002) Pharmacokinetics of (111)In-labeled triplex-forming oligonucleotide targeting human N-myc gene. *Mol. Cells 14*, 93−100.
(34) Sato, M., Suzuki, S., and Senoo, H. (2003) Hepatic stellate cells: unique characteristics in cell biology and phenotype. *Cell Struct. Funct. 28*, 105−12.
(35) Staud, F., Nishikawa, M., Takakura, Y., and Hashida, M. (1999) Liver uptake and hepato-biliary transfer of galactosylated proteins in rats are determined by the extent of galactosylation. *Biochim. Biophys. Acta 1427*, 183−92.
(36) Rachmawati, H. (2005) Chemically modified IL-10 with a liver-specific ligand: a new strategy for the treatment of liver fibrosis with a therapeutic cytokine. Ph.D. Thesis, 106−28.
(37) Ye, Z., Cheng, K., Guntaka, R. V., and Mahato, R. I. (2005) Targeted Delivery of a Triplex-Forming Oligonucleotide to Hepatic Stellate Cells. *Biochemistry 44*, 4466−76.

BC060006Z

Development and Properties of β-Glucuronide Linkers for Monoclonal Antibody−Drug Conjugates

Scott C. Jeffrey,* Jamie B. Andreyka, Starr X. Bernhardt, Kim M. Kissler, Toni Kline, Joel S. Lenox, Ruth F. Moser, Minh T. Nguyen, Nicole M. Okeley, Ivan J. Stone, Xinqun Zhang, and Peter D. Senter

Seattle Genetics, 21823 30th Drive SE, Bothell, Washington 98021. Received January 26, 2006; Revised Manuscript Received March 27, 2006

A β-glucuronide-based linker for attaching cytotoxic agents to monoclonal antibodies (mAbs) was designed and evaluated. We employed the cytotoxic auristatin derivatives MMAE (**1a**) and MMAF (**1b**) and doxorubicin propyloxazoline (DPO, **2**) to give the β-glucuronide drug-linkers **9a**, **9b**, and **17**, respectively. Cysteine-quenched derivatives of **9b** and **17** were determined to be substrates for *E. coli* β-glucuronidase, resulting in facile drug release. The β-glucuronide MMAF drug-linker **9b** was highly stable in rat plasma with an extrapolated half-life of 81 days. Each drug-linker when conjugated to mAbs c1F6 (anti-CD70) and cAC10 (anti-CD30) gave monomeric antibody−drug conjugates (ADCs) with as many as eight drugs per mAb and had high levels of immunologically specific cytotoxic activity on cancer cell lines. cAC10−**9a** displayed pronounced antitumor activity in a subcutaneous Karpas 299 lymphoma tumor model. A single dose treatment led to cures in all animals at the 0.5 mg/kg dose level and above, and the conjugate was well tolerated at 100 mg/kg. In mice with subcutaneous renal cell carcinoma xenografts, the MMAF conjugate c1F6−**9b** was tolerated at 25 mg/kg and efficacious at 0.75 mg/kg. These results demonstrate that the β-glucuronide linker system is an effective strategy for targeting cytotoxic agents providing ADCs with high degrees of efficacy at well-tolerated doses.

INTRODUCTION

Monoclonal antibody (mAb) therapies are gaining momentum as adjunct and front-line treatments for cancer. Agents such as Avastin (anti-VEGF) and Erbitux (anti-EGFR, HER1 and c-Erb-1) for colon cancer (*1*, *2*), Rituximab (anti-CD20) for non-Hodgkin's lymphoma (*3*) and Herceptin (anti-Her2) for breast cancer (*4*) provide convincing proof that mAb therapies impact disease progression and patient survival. This work has been extended by using mAbs for the delivery of cytotoxic agents to cancerous tissue (*5*−*7*), leading to the approved agents Mylotarg, Zevalin, and Bexxar.

Some considerations in making effective and well-tolerated antibody−drug conjugates (ADCs) include using highly potent drug payloads, addressing aggregation due to drug and linker hydrophobicity, circumventing issues such as multidrug resistance mechanisms and off-target toxicity, and incorporating stable linker technologies (*5*). Promising data have been reported for ADCs composed of highly potent drugs such as calicheamicins (*8*, *9*), doxorubicin (*10*−*12*), maytansinoids (*13*, *14*), taxanes (*15*), minor groove binders (*16*−*20*), and auristatins (*21*−*23*). These drugs have been attached through linkage systems comprised of hydrazones, disulfides, and peptides (*24*). Upon binding to the antigen on the surface of a cancer cells, the ADC−antigen complexes are internalized into endosomal/lysosomal compartments through a process known as receptor-mediated endocytosis. Once this occurs, the ADC is exposed to lysosomal enzymes, acidic pH, and intracellular reducing agents, all of which can be exploited for drug release (*24*).

A limitation with many hydrazone- and disulfide-based linkers is they are known to be labile in circulation, resulting in release of drug outside the targeted tissue (*12*, *14*) which can increase systemic toxicity and compromise therapeutic efficacy. We have focused our approaches on peptide-based linker strategies that provide high ADC stability (*21*). The resulting ADCs are well tolerated and efficacious, validating the development of highly stable linker technologies. Here we extend this work through the synthesis and evaluation of a novel β-glucuronic acid-based linker in which hydrolysis by the lysosomal enzyme β-glucuronidase releases active drug. We anticipated that linker systems incorporating highly hydrophilic β-glucuronides would circumvent the tendency of ADCs, particularly those incorporating hydrophobic drugs (*19*), to undergo aggregation. We were drawn to this particular mechanism for drug release based on reports indicating that β-glucuronidase is abundantly present within lysosomes and is overexpressed in some tumor types (*25*). Indeed, there have been previous examples of β-glucuronide-based prodrugs for anticancer monotherapy (*26*). One of the attractive features of such a linker system is that the enzyme activity outside cells is low, providing the possibility of high ADC stability in the systemic circulation. Our ultimate goal in developing this linker technology is to further our understanding of how linker solubility, stability, and the mechanism of drug release affect ADC activity and tolerability. Drug-linkers employing the β-glucuronide linker with the antimitotic agents monomethyl auristatin E (MMAE; **1a**) (*21*), monomethyl auristatin F (MMAF; **1b**) (*27*), and doxorubicin propyloxazoline (DPO; **2**) and the corresponding ADCs were prepared and evaluated. The resulting ADCs were found to be highly stable in plasma, well tolerated at high doses, and efficacious both in vitro and in vivo.

EXPERIMENTAL PROCEDURES

General Methods and Materials. Unless otherwise indicated, all anhydrous solvents were commercially obtained and stored in Sure-seal bottles under nitrogen. All other reagents and solvents were purchased as the highest grade available and used without further purification.

NMR spectra were recorded on Varian Mercury 400 MHz Instrument. Chemical shifts (δ) are reported in parts per million

* To whom correspondence should be addressed. Phone: 425-527-4738; Fax: 425-527-4109; E-mail: sjeffrey@seagen.com.

10.1021/bc0600214 CCC: $33.50 © 2006 American Chemical Society
Published on Web 05/03/2006

(ppm) referenced to tetramethylsilane at 0.00, and coupling constants (*J*) are reported in hertz. Low resolution mass spectral data were acquired on a Micromass ZMD mass spectrometer interfaced with an HP Agilent 1100 high performance liquid chromatography instrument (HPLC). Products were eluted on a C12 Phenomenex Synergi 2.0 × 150 mm, 4 μm, 80 Å MAX reverse phase column using a linear gradient of mobile phase B (CH_3CN with 0.05% HCO_2H) in A (0.05% aqueous HCO_2H) at 0.4 mL/min. Unless otherwise specified, the reported retention times (t_R) are those from LC-MS. High-resolution mass spectral data were obtained at the University of Washington Medicinal Chemistry Mass Spectrometry Center on a Bruker APEXIII 47e [FT(ICR)]MS. Analytical HPLC was conducted on a Waters 2695 instrument using a Waters 2996 PDA and Millenium^{32} software and a C12 Phenomenex Synergi 4.6 × 150 mm, 4 μm, 80 Å MAX reverse phase column. Products were eluted with either acidic (A) linear gradients of mobile phase B (CH_3CN with 0.05% HCO_2H; 10% to 95% over 8 min) in A (0.05% aqueous TFA), or neutral (N) linear gradients of mobile phase B (CH_3CN; 10% to 90% over 10 min, then hold at 90% for 5 min) in A (5.0 mM $NH_4H_2PO_4$) at a flow rate of 1.0 mL/min. Preparative HPLC purifications were performed on a Varian instrument equipped with C12 Phenomenex Synergy MAX-RP 4 μm 250 × 21.2 mm reversed phase column, eluting with 0.05% formic acid in a water and acetonitrile gradient at a flow rate of 4.6 mL/min (gradient 1: 10% organic for 5 min followed by a ramp up to 70% organic over 25 min; gradient 2: 10% organic for 3 min followed by a ramp up to 50% organic over 50 min). Radial chromatography was performed on a Chromatotron instrument (Harrison Research, Palo Alto, CA) on normal phase silica plates (Analtech, Newark, DE). The syntheses of MMAE (**1a**) and MMAF (**1b**) have been described (*21, 27*).

(2*S*,3*S*,4*S*,5*R*,6*S*)-Methyl 6-(2-(3-(((9*H*-Fluoren-9yl)methoxy)carbonylamino)propanamido)-4-(hydroxymethyl)-phenoxy)-3,4,5-triacetoxy-tetrahydro-2*H*-pyran-2-carboxylate. To a solution of the aniline **5** (74 mg, 0.163 mmol) in dichloromethane (6 mL) was added DIPEA (57 μL, 0.33 mmol). The acid chloride **6** (65 mg, 0.20 mmol) was added, and the mixture was stirred for 30 min. The mixture was poured into saturated aqueous sodium bicarbonate and was extracted with ethyl acetate (3 × 50 mL). The combined extracts were washed with water and brine and were dried over sodium sulfate. Filtration and concentration gave a residue that was purified via radial chromatography using 5% methanol in dichloromethane as mobile phase to give 106 mg (87%) of **11** as a white solid: ^{1}H NMR (DMSO-d_6) δ 1.98 (s, 3H), 1.99 (s, 6H), 2.52 (m, 2H) 3.27 (m, 2H), 3.32 (s, 3H), 4.20 (m, 1H), 4.26 (m, 1H), 4.39 (d, 2H, J = 6.3 Hz), 4.70 (d, 1H, J = 9.7 Hz), 5.04 (t, 1H, J = 9.6 Hz), 5.15 (m, 2H), 5.48 (t, 1H, J = 9.4 Hz), 5.54 (d, 1H, J = 7.6 Hz), 5.75 (s, 1H), 7.02 (q, 2H, J = 4.3 Hz) 7.30 (m, 2H), 7.39 (t, 4H, J = 7.72 Hz), 7.67 (d, 2H, J = 7.6 Hz), 7.80 (s, 1H), 7.87 (d, 2H, J = 7.6 Hz), 8.72 (s, 1H); LC-MS *m*/*z* (ES$^+$), 749.04 (M + H)$^+$.

(2*S*,3*S*,4*S*,5*R*,6*S*)-Methyl 6-(2-(3-(((9*H*-Fluoren-9yl)methoxy)carbonylamino)propanamido)-4-(((4-nitrophenoxy)-carbonyloxy)methyl)phenoxy)-3,4,5-triacetoxy-tetrahydro-2*H*-*pyran*-2-carboxylate (7). To a mixture of benzyl alcohol **11** (105 mg, 0.14 mmol) in DMF (4 mL) was added bis *p*-nitrophenyl carbonate (85 mg, 0.28 mmol) and DIPEA (36 μL, 0.21 mmol). The mixture was stirred for 16 h at an ambient temperature and was concentrated under reduced pressure to an oily residue. This material was dissolved in dichloromethane and aspirated directly onto a 1 mm radial Chromatotron plate and eluted with 50% ethyl acetate in hexanes followed by ethyl acetate to give 106 mg (83%) of **7** as a solid: ^{1}H NMR (*d6*-DMSO-d_6) δ 1.98 (s, 3H), 1.99 (s, 3H), 1.99 (s, 3H), 2.52 (m, 2H), 3.28 (m, 2H), 3.62 (s, 3H), 4.20 (m, 1H), 4.27 (m, 2H), 4.73 (d, 1H, J = 9.8 Hz), 5.05 (t, 1H, J = 9.6 Hz), 5.18 (t, 1H, J = 9.4 Hz), 5.21 (s, 2H), 5.49 (t, 1H, J = 10.2 Hz), 7.10 (d, 1H, J = 8.2 Hz), 7.22 (m, 1H), 7.30 (m, 2H), 7.39 (m, 4H, J = 7.0 Hz), 7.55 (d, 2H, J = 9.2 Hz), 7.67 (d, 2H, J = 5.2 Hz), 7.87 (d, 2H, J = 7.0 Hz), 7.97 (s, 1H), 8.29 (d, 2H, J = 9.0 Hz), 8.83 (s, 1H); LC-MS *m*/*z* (ES$^+$), 914.03 (M + H)$^+$.

MMAF Carbonate (8). To a mixture of the *p*-nitrophenyl carbonate **7** (30 mg, 0.033 mmol) and monomethyl auristatin F (**1**; 29 mg, 0.039 mmol) were added DMF (0.8 mL) and pyridine (0.2 mL). DIPEA (7 μL, 0.04 mmol) was added followed by HOAt (1 mg, 7 μmol). The reaction mixture was stirred for 16 h at an ambient temperature. The mixture was concentrated under reduced pressure and was chromatographed on a 1 mm Chromatotron plate, eluting with a 1 to 5% methanol in dichloromethane gradient containing 1% acetic acid. The final UV active (254 nm) band to elute was product. This gave 44% (22 mg) of **8** as a white solid that was carried forward without analytical characterization.

MMAF Glucuronide Amine. To a mixture of the MMAF carbamate (22 mg, 0.015 mmol) in methanol (1 mL) at 0 °C was added a solution of LiOH monohydrate (5.5 mg, 0.132 mmol) in water (1 mL). The mixture was stirred for 15 min at 0 °C and the reaction mixture was neutralized using acetic acid (8 μL) and was concentrated under reduced pressure: LC-MS *m*/*z* (ES$^-$), 1364.09 (M − H)$^-$, 9.78 min. The resulting material was dissolved in DMF (0.8 mL) and treated with piperidine (0.2 mL). The mixture was stirred for 5 min and concentrated under reduced pressure. The material was taken up in water and purified via preparative HPLC (gradient 1) to give 12 mg (72%) as a white solid: ^{1}H NMR (CD_3OD) δ 0.52 (d), 0.59 (d), 0.75−1.1 (m), 1.1−1.35 (m), 1.32−1.67 (m), 1.70−2.10 (m), 2.15−2.50 (m), 2.83−3.05 (m), 3.11 (s), 3.15−3.42 (m), 3.45−3.68 (m), 3.85 (m), 3.95 (m), 4.00−4.18 (m), 4.19−4.30 (m), 4.50−4.97 (m), 5.00−5.20 (m), 7.09−7.29 (m), 7.65 (d), 7.75 (d), 7.82 (d), 7.88 (d), 8.18 (d), 8.25 (m), 8.35 (d), 8.40 (d), 8.59 (d); LC-MS *m*/*z* (ES$^-$), 1144.66 (M − H)$^-$.

MMAE Glucuronide Maleimide (9a). Compound **9a** was prepared in a manner identical to **9b** starting with MMAE (**1a**) and compound **7**. Compound **9a** was obtained as a white solid: ^{1}H NMR (CD_3OD); δ 0.64−1.01 (m, 24H), 1.12 (t, J = 6.9 Hz, 3H), 1.16 (d, J = 6.5 Hz, 1H), 1.23 (m, 1H), 1.4 (m, 1H), 1.45−1.63 (m, 5H), 1.67−1.98 (m, 2H), 2.19 (m, 3H), 2.42−2.54 (m, 1H), 2.63 (m, 2H), 2.96 (m, 4H), 3.1 (s, 2H), 3.12−3.39 (m, 3H), 3.40−3.73 (m, 9H), 3.85−3.96 (m, 1H), 4.04 (m, 1H), 4.13−4.27 (m, 2H), 4.52 (m, 1H), 4.59−4.68 (m, 2H), 4.65−5.0 (m, 2H), 5.0−5.17 (m, 2H), 6.78 (s, 2H), 7.09 (m, 1H), 7.20 (m, 3H), 7.3 (m, 3H), 7.38 (d, J = 7.6 Hz, 3H), 7.75−8.01 (m, 2H), 8.26 (d, J = 9.0 Hz, 1H), 8.32 (m, 1H); LC-MS *m*/*z* (ES+) 1323.01 (M + H), 6.88 min; HRMS *m*/*z* for $C_{66}H_{97}N_8O_{20}Na_2$ (M − H + 2Na)$^+$ calcd, 1367.6615; found, 1367.6616. Supporting Information for PDA-HPLC chromatograms of **9a** under neutral (N) and acidic (A) conditions, and HRMS data.

MMAF Glucuronide Maleimide (9b). To a mixture of the amine (12 mg, 0.011 mmol) in DMF (1 mL) was added MC-OSu (**10**; 5.2 mg) followed by DIPEA (6 μL). After 15 min, the reaction mixture was concentrated under reduced pressure, was dissolved in a mixture of water and DMSO (1:1; 1 mL) and was purified via preparative HPLC (gradient 1). This gave 9.4 mg (64%) of **9b** as a white solid: ^{1}H NMR (CD_3OD) δ 0.66−1.05 (m, 22H), 1.10−1.27 (m, 9H), 1.33−1.43 (m, 2H), 1.44−1.62 (m, 6H), 1.66−2.05 (m, 5H), 2.15−2.35 (m, 4H), 2.40−2.50 (m, 2H), 2.60−2.68 (m, 2H), 2.84−2.98 (m, 9H), 3.10 (s, 2H), 3.22 (s, 2H), 3.25−3.68 (m, 12H), 3.85 (dd, J = 8.6, 2.0 Hz), 3.93 (d, J = 10 Hz), 4.05 (m, 1H), 4.13 (m, 1H), 4.22 (q, J = 10 Hz), 4.48−4.58 (m, 1H), 4.63−4.75 (m, 2H), 4.81 (d, J = 7.8 Hz, 2H), 5.02−5.17 (m, 3H), 6.77 (s, 2H),

7.10 (m, 1H), 7.15−7.29 (m, 8H), 7.82−8.01 (m, 2H), 8.16 (d, J = 8.4 Hz, 1H), 8.24 (s, 1H), 8.35 (m, 1H); LC-MS m/z (ES^+), 1337.03 $(M + H)^+$, 8.50 min; HRMS m/z for $C_{66}H_{95}N_8O_{21}Na_2$ $(M - H + 2Na)^+$ calcd, 1381.6407; found, 1381.6428. See Supporting Information for PDA-HPLC chromatograms of **9b** under neutral (N) and acidic (A) conditions, and HRMS data.

4-(*tert*-Butyldiphenylsilyloxy)butan-1-ol. To a solution of 1,4-butanediol was added sodium hydride (1.0 g of a 60% dispersion in mineral oil). This mixture was allowed to stir at an ambient temperature for 1 h, before TBDPSCl (5.0 mL, 18.2 mmol) was added. The mixture was stirred overnight at ambient temperatures, poured into water, and extracted with ether (3 × 100 mL). The combined extract was washed with water and brine and dried over sodium sulfate. Filtration and concentration gave an oily residue, which was purified via radial chromatography on a 4 mm plate eluting with 25% ethyl acetate in hexanes, followed by 50% ethyl acetate in hexane. This gave 3.36 g (56%) of desired product as clear oil. ^{1}H NMR ($CDCl_3$); δ 1.24 (s, 9H), 1.65 (m, 4h), 3.65 (m, 4H), 7.40 (m, 6H), 7.64 (d, 2H, J = 1.5 Hz).

4-(*tert*-Butyldiphenylsilyloxy)butanal. To a solution of the 4-(*tert*-butyldiphenylsilyloxy)butan-1-ol (0.5 g, 1.5 mmol) in dichloromethane (20 mL) was added Dess−Martin periodinane (775 mg, 1.83 mmol). The mixture was stirred for 1 h. The reaction mixture was poured into hexanes, and the resulting white precipitate was removed via filtration. The solution was concentrated to give a slurry, which was dissolved in dichloromethane (5 mL) and again poured into hexanes resulting in the precipitation of white solid. The solids were removed via filtration and the resulting solution was concentrated. This gave 475 mg (97%) of a clear oil: ^{1}H NMR ($CDCl_3$); δ 1.04 (s, 9H), 1.89 (m, 2H), 2.55 (m, 2H), 3.69 (t, 2H, J = 6.1 Hz)), 7.38 (m, 6H), 7.63 (d, 4H, J = 1.7 Hz), 9.79 (t, 1H, J = 1.8 Hz).

2-(3-(*tert*-Butyldiphenylsilyloxy)propyl)oxazolidine (12). A mixture of the 4-(*tert*-butyldiphenylsilyloxy)butanal (235 mg, 0.72 mmol) in benzene (3 mL) was added dropwise to a solution of hydroxy ethylamine (44 μL, 0.72 mmol) in benzene (3 mL). Powdered molecular sieves (4 Å, 600 mg) were added, and the mixture was stirred for 1.5 h, before being filtered through a 20 μm Millipore syringe filter and concentrated. This gave **12** which was used immediately in the synthesis of **13**: ^{1}H NMR (C_6D_6); δ 1.18 (s, 9H), 1.65−1.82 (m, 2H), 2.62 (m, 2H), 3.33 (dd, 3H, J = 6.1, 7.5 Hz), 3.69 (t, 3H, J = 6.1 Hz), 4.26 (t, 1H), 7.23 (dd, 6H, J = 1.9, 3.1 Hz), 7.79 (m, 4H).

3-(3-(((9*H*-Fluoren-9-yl)methoxy)carbonylamino)propanamido)-4-((2*S*,3*R*,4*S*,5*S*,6*S*)-3,4,5-triacetoxy-6-(methoxycarbonyl)-tetrahydro-2*H*-pyran-2-yloxy)benzyl 2-(3-(*tert*-Butyldiphenylsilyloxy)propyl)oxazolidine-3-carboxylate (13). To the benzyl alcohol (50 mg, 0.067 mmol) in dichloromethane (10 mL) was added pyridine (63 μL, 0.8 mmol). The mixture was cooled to −78 °C, diphosgene (16 μL, 0.134 mmol) was added, and the mixture was stirred for 1 h. Oxazolidine **12** (formed from 65 mg of 4-(*tert*-butyldiphenylsilyloxy)butanal) was added as a dichloromethane solution (3 mL) dropwise down the cooled inside wall of the reaction flask. The reaction mixture was allowed to slowly warm to −20 °C over several hours and was then poured into ethyl acetate and washed with saturated aqueous sodium bicarbonate, water, and brine. The organic phase was dried over sodium sulfate, filtered and concentrated. Purification of the resulting residue via radial chromatography (eluting with dichloromethane) provided 54 mg (70%) of **13**: ^{1}H NMR (DMSO-d_6); δ 0.95 (s, 9H), 1.55 (m, 2H), 1.63 (m, 1H), 1.82 (m, 1H), 1.98 (m, 9H), 2.4−2.52 (m, 2H), 3.27 (m, 2H), 3.54−3.66 (m, 6H), 3.70 (q, 1H, J = 10.0 Hz), 3.98 (m, 1H), 4.20 (m, 1H), 4.26 (m, 3H), 4.70 (d, 1H, J = 10.0 Hz), 4.90−5.10 (m, 4H), 5.16 (t, 1H, J = 9.6 Hz), 5.48 (t, 1H, J = 9.4 Hz), 5.57 (d, 1H, J = 7.6 Hz), 7.0−7.15 (m, 3H), 7.29 (m, 2H), 7.36−7.45 (m, 8H), 7.57 (d, 4H, J = 7.2 Hz), 7.66 (d, 2H, J = 7.2 Hz), 7.86 (d, 3H, J = 7.6 Hz), 8.75 (m, 1H); LC-MS m/z (ES^+), 1143.88 $(M + H)^+$, 13.76 min.

3-(3-(((9*H*-Fluoren-9-yl)methoxy)carbonylamino)propanamido)-4-((2*S*,3*R*,4*S*,5*S*,6*S*)-3,4,5-triacetoxy-6-(methoxycarbonyl)-tetrahydro-2*H*-pyran-2-yloxy)benzyl 2-(3-Hydroxypropyl)oxazolidine-3-carboxylate. To a mixture of the silyl ether **13** (52 mg, 0.042 mmol) in THF (2 mL) and pyridine (2 mL) was added HF-pyridine complex (400 μL). The reaction mixture was stirred for 3 h and was poured into saturated aqueous sodium bicarbonate and was extracted with ethyl acetate (3 × 100 mL). The combined extracts were washed with water and brine and dried over sodium sulfate, before filtration and concentration. The resulting oil was purified via radial chromatography on a 1 mm plate with 5% methanol in dichloromethane as eluant yielding 36 mg (86%) of a solid residue: ^{1}H NMR (CD_3OD); δ 1.55 (bs, 2H), 1.68 (m, 1H), 1.87 (m, 1H), 1.95 (s, 3H), 2.01 (m, 6H), 2.67 (oct, 2H, J = 6.8 Hz), 3.30 (m, 1H), 3.50 (m, 3H), 3.65 (m, 1H), 3.69 (m, 3H), 3.82 (q, 1H, J = 8.0 Hz), 4.01 (m, 1H), 4.23 (m, 1H, J = 7.0 Hz), 4.25−4.40 (m, 2H), 4.47 (d, 1H, J = 10.0 Hz), 5.0−5.15 (m, 3H), 5.19 (t, 1H, J = 9.8 Hz), 5.28 (dd, 1H, J = 6.0, 9.6 Hz), 5.39 (d, 1H, J = 7.6 Hz), 5.49 (m, 3H), 7.11 (m, 2H), 7.17−7.32 (m, 3H), 7.34 (t, 2H, J = 7.4 Hz), 7.62 (d, 2H, J = 7.6 Hz), 7.77 (d, 2H, J = 7.6 Hz), 8.07 (s, 1H); LC-MS m/z (ES^+), 927.87 $(M + Na^+)^+$, 9.79 min.

3-(3-(((9*H*-Fluoren-9-yl)methoxy)carbonylamino)propanamido)-4-((2*S*,3*R*,4*S*,5*S*,6*S*)-3,4,5-triacetoxy-6-(methoxycarbonyl)-tetrahydro-2*H*-pyran-2-yloxy)benzyl 2-(3-Oxopropyl)-oxazolidine-3-carboxylate (14). To a solution of the alcohol (36 mg, 0.04 mmol) in dichloromethane (3 mL) was added Dess−Martin periodinane (20 mg, 0.048 mmol). After 1 h, an additional quantity of the Dess−Martin reagent was added (20 mg) and stirring was continued for an additional hour. The reaction mixture was aspirated onto a 1 mm radial Chromatotron plate and eluted with 5% methanol in dichloromethane. This gave a quantitative yield (36 mg) of the aldehyde **14**: ^{1}H NMR (DMSO-d_6); δ 1.89 (s, 3H), 1.91 (m, 1H), 1.98 (s, 3H), 1.98 (s, 3H), 2.41 (m, 1H), 3.27 (m, 2H), 3.75 (m, 1H0, 3.61 (s, 3H), 3.77 (q, 1H, J = 7.8 Hz), 3.95 (m, 1H), 4.15−4.30 (m, 3H), 4.71 (d, 2H, J = 9.0 Hz), 4.97−5.13 (m, 4H), 5.16 (dd, 1H, J = 7.8, 9.9 Hz), 5.45 (t, 1H, J = 9.6 Hz), 5.58 (d, 1H, J = 8.0 Hz), 7.05 (d, 1H, J = 8.4 Hz), 7.12 (d, 1H, J = 7.6 Hz), 7.29 (dd, 2H, J = 5.3, 7.4 Hz), 7.39 (t, 2H, J = 7.4 Hz), 7.67 (d, 2H, J = 5.4 Hz), 8.77 (s, 1H), 9.57 (s, 1H), 11.97 (s, 1H); LC-MS m/z (ES^+), 903.96 $(M + H)^+$, 10.48 min.

3-(3-(((9*H*-fluoren-9-yl)methoxy)carbonylamino)propanamido)-4-((2*S*,3*R*,4*S*,5*S*,6*S*)-3,4,5-triacetoxy-6-(methoxycarbonyl)-tetrahydro-2*H*-pyran-2-yloxy)benzyl 2-(3-(3-Hydroxy-2-methyl-6-((3*S*)-3,5,12-trihydroxy-3-(2-hydroxyacetyl)-10-methoxy-6,11-dioxo-1,2,3,4,6,11-hexahydrotetracen-1-yloxy)-tetrahydro-2*H*-pyran-4-ylamino)propyl)oxazolidine-3-carboxylate (16). To the aldehyde **14** (36 mg, 0.04 mmol) in acetonitrile:water (2:1; 4.5 mL total) at 0 °C was added doxorubicin-HCl (**15**) followed by stirring until all the solids were dissolved. The mixture was treated with a solution of sodium cyanoborohydride (1.0 M solution in THF; 20 μL, 0.02 mmol). The reaction mixture was stirred for 2 h and the mixture was poured into water and extracted repeatedly with dichloromethane (5 × 50 mL). The combined organics were washed with water and brine and were concentrated under reduced pressure. The resulting residue was dissolved in 5% methanol in dichloromethane and was aspirated directly onto a 1 mm radial Chromatotron plate and eluted with 20% methanol in dichloromethane. The first major band was collected to give 23.6 mg (41%) of **16**: ^{1}H NMR (*d6-DMSO*); δ 1.14 (d, 3H, J

= 6.5 Hz), 1.36−1.60 (b, 2H, 1.62−1.78 (b, 2H), 1.97−1.99 (m, 9H), 2.14 (b, 3H), 2.95 (s, 3H), 3.18−3.32 (m, 2H), 3.52 (b, 1H), 3.60 (s, 3H), 3.75 (q, 1H, J = 6.8 Hz), 4.95 (bs, 1H), 3.96 (s, 3H), 4.09 (b, 1H), 4.17 (t, 1H, J = 6.5 Hz), 4.25 (d, 2H, J = 6.1 Hz), 4.54 (d, 2H, J = 6.3 Hz), 4.70 (d, 1H, J = 10.0 Hz), 4.86 (t, 1H, J = 5.9 hz), 4.92−5.07 (m, 3H), 5.15 (t, 1H, J = 8.2 Hz), 5.25 (bs, 1H), 5.04 (d, 1H, J = 2.0 Hz), 5.48 (t, 1H, J = 10.0 Hz), 5.55 (d, 1H, J = 8.0 Hz), 7.0−7.11 (m, 2H), 7.28 (m, 2H), 7.37 (t, 3H, J = 7.3 Hz), 7.65 (d, 3H, J = 7.0 Hz), 7.85 (d, 2H, J = 7.6 Hz), 8.75 (b, 1H); LC-MS *m*/*z* (ES^-), 1428.9 $(M - H)^-$, 7.9 min.

(2*S*,3*S*,4*S*,5*R*,6*S*)-6-(2-(3-Aminopropanamido)-4-((2-(3-(3-hydroxy-2-methyl-6-(3*S*)-3,5,12-trihydroxy-3-(2-hydroxyacetyl)-10-methoxy-6,11-dioxo-1,2,3,4,6,11-hexahydrotetracen-1-yloxy)-tetrahydro-2*H*-pyran-4-ylamino)propyl)oxazolidine-3-carbonyloxy)methyl)phenoxy)-3,4,5-trihydroxy-tetrahydro-2*H*-pyran-2-carboxylic Acid. To a 0 °C mixture of the doxorubicin oxazolidine **16** (30 mg, 0.021 mmol) in methanol (4 mL) was added a solution of LiOH monohydrate (8.8 mg, 0.21 mmol) in water (2 mL). The mixture was stirred for 35 min and was neutralized with acetic acid (8 μL, 0.21 mmol) to pH 7. The mixture was concentrated under reduced pressure to give a residue which was dissolved in DMF (4 mL) and treated with piperidine (1 mL). The reaction mixture was stirred for 5 min before being concentrated under reduced pressure. The residue was purified via preparative HPLC (gradient 2) to yield 6.1 mg (27%) of product: LC-MS *m*/*z* (ES^+), 1069.13 $(M + H)^+$, 5.64 min.

(2*S*,3*S*,4*S*,5*R*,6*S*)-6-(2-(3-(6-(2,5-Dioxo-2*H*-pyrrol-1(5*H*)-yl)hexanamido)propanamido)-4-((2-(3-(3-hydroxy-2-methyl-6-((3*S*)-3,5,12-trihydroxy-3-(2-hydroxyacetyl)-10-methoxy-6,11-dioxo-1,2,3,4,6,11-hexahydrotetracen-1-yloxy)-tetrahydro-2*H*-pyran-4-ylamino)propyl)oxazolidine-3-carbonyloxy)-methyl)phenoxy)-3,4,5-trihydroxy-tetrahydro-2*H*-pyran-2-carboxylic Acid (17). To a mixture of the amine (6.1 mg, 5.7 μmol) in DMF (0.2 mL) was added MC-OSu (**10**; 4 mg, 14 μmol) followed by DIPEA (3 μL, 17 μmol). The reaction mixture was concentrated under reduced pressure and then dissolved in a mixture of water and DMSO (1:1, 2 mL). The mixture was purified via reverse-phase preparative HPLC (gradient 2) to yield 2.1 mg (26%) of **17** as a red solid: ^{1}H NMR (CD_3OD); δ 1.1−1.25 (b, 2H), 1.29 (d, 3H, J = 6.6 Hz), 1.35−1.62(b, 3H), 1.65−1.90 (b, 3H), 2.02−2.13 (m, 4H), 2.67 (s, 4H, *N*-hydroxysuccinimide impurity), 3.00−3.10 (m, 4H), 3.41−3.57 (m, 3H), 3.57−3.70 (m, 3H), 3.81 (m, 2H), 3.94 (d, 1H, J = 9.6 Hz), 4.02 (b, 1H), 4.05 (s, 3H), 4.29 (q, 1H, J = 7.0 Hz), 4.71 (s, 3H), 4.73 (m, 1H), 5.06 (m, 1H), 5.12 (b, 1H), 5.49 (s, 1H), 6.78 (s, 2H), 6.82−7.09 (b, 2H), 7.57 (d, 1H, J = 6.4 Hz), 7.84 (t, 1H), J = 7.4 Hz), 7.95 (sd, 1H, J = 7.4 Hz), 8.08 (bs, 1H); LC-MS *m*/*z* (ES^-), 1260.24 $(M - H)^-$, 6.49 min.

ADC Preparation. The mAbs (>5 mg/mL) in PBS containing 50 mM sodium borate, pH 8.0, were treated with dithiothreitol (DTT; 10 mM final) or tris(2-carboxyethyl)phosphine hydrochloride (TCEP; used in the preparation of ADCs for in vivo experiments) at 37 °C for 30 min. After gel filtration (G-25, PBS containing 1mM DTPA), thiol determination using 5,5′-dithiobis(2-nitrobenzoic acid) indicated that there were approximately eight thiols per mAb (approximately four thiols per mAb with 2.25 equiv. TCEP). To the reduced mAb at 4 °C was added the maleimide drug derivatives (1.2 equiv/SH group) in ice-cold DMSO (20% v/v). After 1 h, the reactions were quenched with excess cysteine, the conjugates were concentrated by centrifugal ultrafiltration, gel filtered (G-25, PBS), and sterile filtered. The molar ratio of drug substitution was determined according to previously published methods (*23*, *28*). Size-exclusion HPLC was used to determine the levels of monomer and aggregates within each ADC, and RP-HPLC established that there was less than 0.5% unconjugated cysteine-quenched drug.

***β*-Glucuronidase Reactivity.** To water (90 μL) was added cysteine (12.5 μL of a 0.1 mM solution) and pH 9 borate buffer (12.5 μL of a 30 mM solution). This was followed by the addition of **9b** (10 μL of a 10 mM DMSO solution). HPLC inspection after 5 min revealed complete conversion to cys-**9b**. To 440 mL of PBS was added the cys-**9b** solution (50 μL; 40 nmol) followed by a solution of *E.coli* β-glucuronidase (Sigma: EC 3.2.1.31 Type IX-A; 10 μL of a 1 mg/mL solution in PBS; 3.6 μg, 13 pmol), and the reaction mixture was incubated at 37 °C. Aliquots (50 μL) were taken at t = 0, 25, 60, and 90 min and analyzed by HPLC (gradient A). Results were based on the area under the curve (AUC) of remaining cys-**9b** at each time point as a percentage of the AUC for cys-**9b** at t = 0.

Rat Plasma Stability Assay. To **9b** (2 mg, 1.5 μmol) was added the DTT solution (150 μL; 1:1 sodium borate: PBS, pH 9.0). The reaction mixture was incubated at 40 °C overnight. LC-MS revealed quantitative conversion to dihydro-**9b**. The solution of dihydro-**9b** (10 μL) was added to the sterile rat plasma (Biochemed Pharmacologicals). Aliquots (50 μL) were taken at t = 0, 2 h, 19 h, 43 h, and 7 days. The aliquots were treated with 100 μL of ice-cold methanol to precipitate plasma proteins and ultra centrifuged for 6 min. The supernatants were removed and analyzed by LC-MS (10 μL injection). The stability of dihydro-**9b** was determined by comparing the AUC for the total positive ion current (TIC^+) for materials ionizing to 732.5 Da (MMAF+H; **1b**) for each time point, relative to the t = 0 time point. Both dihydro-**9b** and free **1b** peaks displayed the 732.5 Da signal.

In Vitro Cytotoxicity Assay. Cells were collected and plated in 96-well black-sided plates at a density of 10000 cells/well in 150 μL of medium. Serial dilutions of the ADC (50 μL) were added, and incubation was carried out for 92 h at 37 °C. Resazurin (0.25 mM, 50 μL, Sigma, St. Louis, MO) in medium was added, and incubation was continued for 4 h. The plates were read on a Fusion HT microplate reader (Packard, Meriden, CT) using an excitation wavelength of 525 nm and an emission wavelength of 590 nm. Data from all assays were reduced using GraphPad Prism Version 4 for Windows (GraphPad Software, San Diego, CA). The IC_{50} concentrations compared to untreated control cells were determined using a four-parameter curve fit.

In Vitro Drug Release Assay. CD70 positive cell lines 786-O and Caki-1 were plated at 1.3×10^4 cells/cm^2 in 50 mL of medium in T-150 flasks (786-O cells in RPMI 1640, supplemented with 1 mM sodium pyruvate and 10% fetal bovine serum; Caki-1: McCoy's 5A modified and 10% FBS). When cell layers reached confluency (2−4 days), the medium was replaced and cultures were treated with 200 ng/mL ADC. Incubation was at 37 °C in a humidified 5% CO_2 atmosphere for 24 h. The cells were harvested with trypsin-EDTA and washed with ice cold PBS (approximately 2.0×10^7 viable cells per flask). Cell pellets were resuspended in 250 μL complete culture medium and extracted by mixing with two volumes of ice cold MeOH. The suspensions were kept at −20 °C for at least 30 min and centrifuged at 13200 rpm (16100*g*) for 5 min. Supernatants were evaporated by speed-vac. The resulting residues were redissolved in 110 μL of 33% MeCN and were analyzed by reverse phase HPLC coupled to time-of-flight mass spectrometry (Q-TOF).

RESULTS AND DISCUSSION

Design and Synthesis of *β*-Glucuronide Drug-Linkers. The design of the β-glucuronide linker system described here is based

Scheme 1

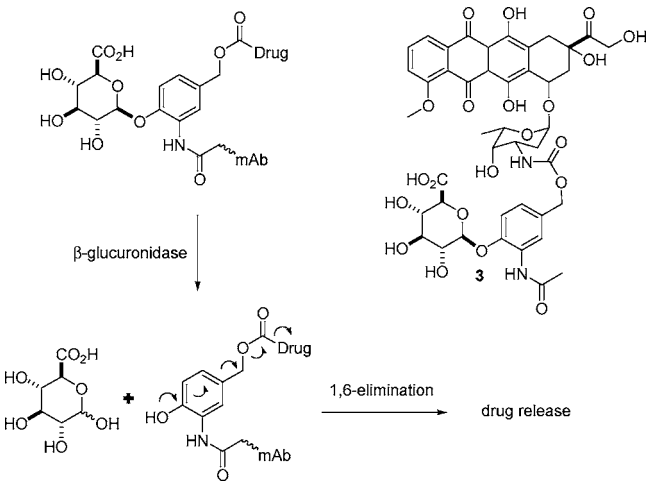

on the β-glucuronide prodrug **3** (Scheme 1) (*29*). We envisioned an antibody attachment site could be incorporated by functionalizing the aniline nitrogen with a maleimide-containing side chain. Under the action of β-glucuronidase, the drug-linker would be hydrolyzed at the glycosidic bond and undergo 1,6-elimination with loss of carbon dioxide to liberate drug. The initial ADCs based on this linker design employed the potent antimitotic drugs MMAE (*21*) (**1a**) and MMAF (*27*) (**1b**) and doxorubicin propyloxazoline (DPO; **2**), which is a labile precursor to highly potent 2-pyrrolinodoxorubicin (**4**), as shown in Scheme 2 (*30*−*32*). Compound **4** effects cell death through alkylation of double-stranded DNA (*33*).

The starting point for the synthesis of β-glucuronide drug-linker with MMAF (**1b**) was the previously described β-glucuronide **5** bearing the free aniline and hydroxy groups (Scheme 3) (*29*). This compound was acylated with the acid chloride **6** and then converted to the *p*-nitrophenyl (PNP) carbonate **7**. Reaction with MMAF (**1b**) afforded the carbamate **8**. This molecule was converted to the desired glucuronide drug-linker **9b** by first saponifying the acetate and methyl ester protecting groups with lithium hydroxide (*34*), Fmoc removal with piperidine, and capping of the resulting free amine with maleimidocaproyl *N*-hydroxysuccimidyl ester (MC-OSu; **10**). A final preparative HPLC purification afforded **9b**. The glucuronide-MMAE drug linker (**9a**) was prepared in an identical fashion starting with **5** and **1a**.

The construction of the β-glucuronide linker with DPO (**2**) required a different strategy (Scheme 4). Intermediate **11** was activated with diphosgene and then reacted with oxazoline **12** (prepared in three steps from 1,4-butanediol) to afford the desired oxazoline carbamate **13**. Removal of the silyl protecting group with fluoride was followed by oxidation to give aldehyde **14**. This compound was used in a reductive alkylation reaction with doxorubicin·HCl (**15**) to give the doxorubicin derivative **16**. Last, the β-glucuronide protecting groups and Fmoc group were removed in a two-step sequence with lithium hydroxide and piperidine, and the resulting primary amine was capped with **10** to give the desired β-glucuronide DPO linker **17**.

***β*-Glucuronidase Reactivity.** The susceptibility of this linker to enzymatic cleavage was determined by treatment of the cysteine adduct of compound **9b** with β-glucuronidase. *E. coli* β-glucuronidase (EC 3.2.1.31) rather than human enzyme was used in this study due to commercial availability. Our linker is structurally very similar to the doxorubicin prodrug **3** which was shown to be efficiently cleaved by a human lysosomal β-glucuronidase fusion protein (*29*), suggesting that our linker is likely to be a substrate for the human lysosomal enzyme as well. An HPLC assay was used to monitor the loss of cys-**9b** at 37 °C. The specific activity of the *E.coli* β-glucuronidase for cys-**9b** was 0.13 μmol/min/mg. The cleavage of β-glucuronide from cys-**9b** resulted in 1,6-elimination of MMAF (**1b**) which was identified by LC-MS. No MMAF-containing phenolic intermediates could be detected by LC-MS. Thus the 1,6-elimination appears to be rapid.

In a similar experiment with cys-**17**, treatment with β-glucuronidase yielded the 2-pyrrolinodoxorubicin (**4**) directly as confirmed by LC-MS. Controls indicated both cys-**9b** and cys-**17** were stable in the absence of β-glucuronidase. These two experiments demonstrated that the linker is a substrate for a β-glucuronidase enzyme and that the drug is readily liberated once the β-glucuronide hydrolysis occurs.

Rat Plasma Stability Assay. To determine the plasma stability of the glucuronide linker, the reactive maleimide double bond of **9b** was reduced with excess DTT to afford dihydro-**9b**. This material was added to rat plasma and incubated at 37 °C for a period of 7 days. Aliquots were taken at various time points and the plasma proteins were precipitated and centrifuged, and the supernatant was recovered. Each supernatant was analyzed by LC-MS, and the total positive ion current (TIC+) chromatogram was scanned for the masses of parent compound dihydro-**9b** and released MMAF (**1b**). After 7 days, the TIC+ for dihydro-**9b** (including the ring-opened succinimide hydrolysis adduct) was 89% of the sample taken immediately after dihydro-**9b** was injected into plasma. Free drug **1b** could be detected but was not quantified. Assuming first-order kinetics, extrapolation of these data suggest a half-life of 81 days for dihydro-**9b**. In a parallel experiment, the rat plasma stability of the maleimide reduced valine-citrulline (val-cit) dipeptide linked MMAF (*11*, *21*, *27*) was found to be 6.25 days. Thus the β-glucuronide linker system was more stable than previously reported disulfide (*14*), hydrazone (*12*), and peptide-based systems. It is possible that the stability of the β-glucuronide linker within an ADC will be increased further, as has been previously shown for another linker technology (*35*).

ADC Preparation. ADCs of **9a**, **9b**, and **17** were prepared with the chimeric mAbs cAC10 (IgG1 against the CD30 antigen) and c1F6 (IgG1 against the CD70 antigen). The CD30 antigen is found on activated B cells and is a marker for both Hodgkin's lymphoma and anaplastic large cell lymphoma (ALCL) (*22*, *36*). The CD70 antigen is overexpressed on renal cell carcinoma (RCC) lines as well as some hematologic malignancies (*37*, *38*). Conjugates of **9a**, **9b**, and **17** were prepared as described previously (*21*). Briefly, the mAbs were reduced with excess DTT or stoichiometric TCEP, purified, and treated with 1.2 equiv of drug-linker/sulfhydryl group. After 1 h, the reaction mixtures were quenched with cysteine to consume unreacted drug-linker. The conjugates were purified via gel filtration after which no free drug derivatives could be detected. As demonstrated earlier for related auristatin ADCs (*28*), the conjugates described here retained full binding activity, as assessed by flow cytometry. The cysteine residues modified during conjugation are located in the hinge region of the mAb, away from the binding domain.

Drug loading for the doxorubicin-containing conjugates cAC10−**17** and c1F6−**17** was determined by measuring the absorbance at 280 and 490 nm (doxorubicin absorbance). It was found that the cAC10 and c1F6 ADCs had 6.8 and 8.3 drugs/mAb, respectively. Due to the weak UV absorbance of the drug-linkers **9a** and **9b**, the drug per mAb ratios of the corresponding ADCs were determined through chromatographic resolution of the light and heavy chains at each drug loading level (0−1 drugs for light chains; 0−3 drugs for heavy chains) and calculation of the overall average from the peak areas at each loading level (*23*, *28*). The levels were shown to be 3.7 and 4.5 for cAC10−**9a** and c1F6−**9a**, and 7.6 and 7.0 for the cAC10−**9b** and c1F6−

Scheme 2

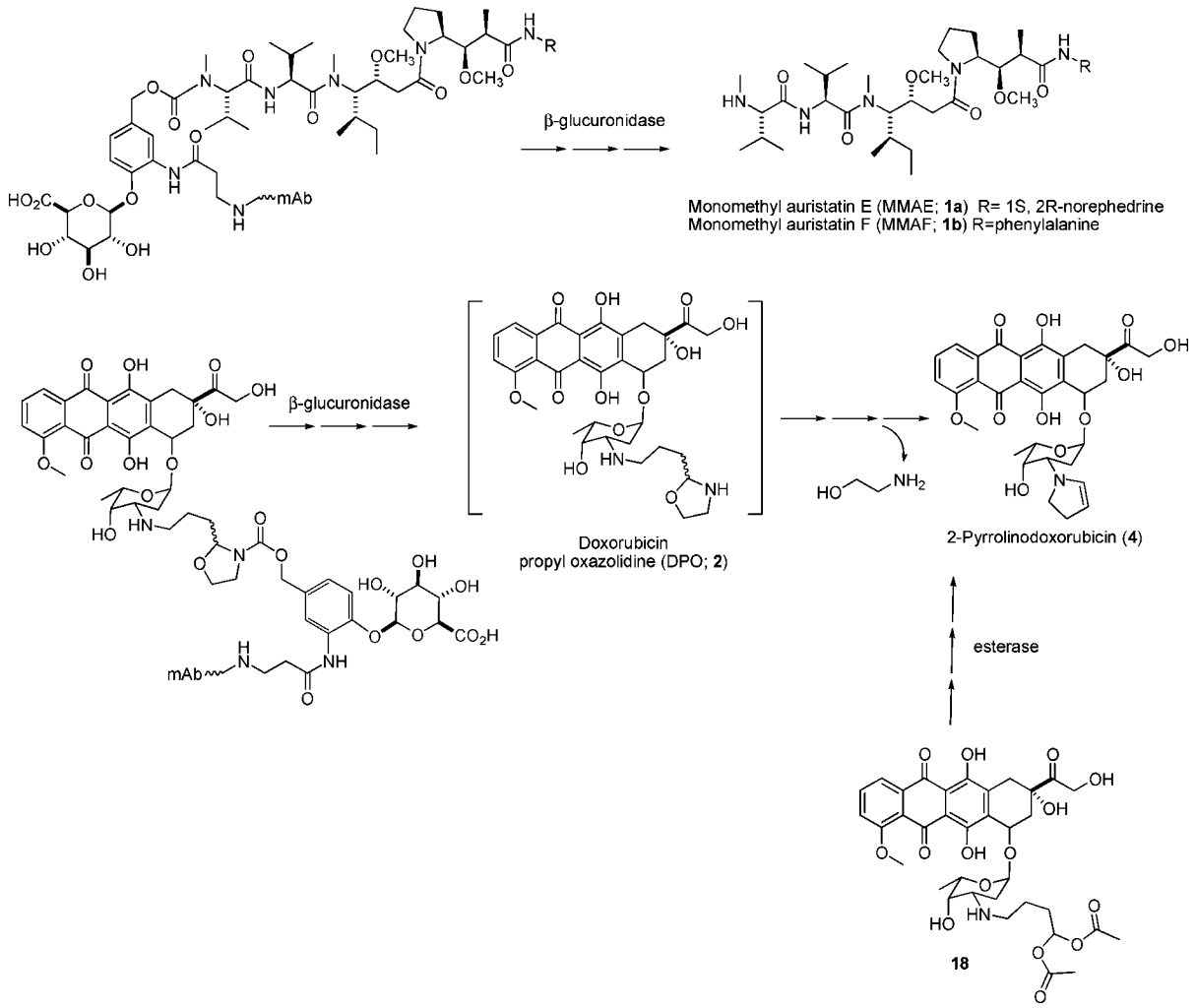

Scheme 3

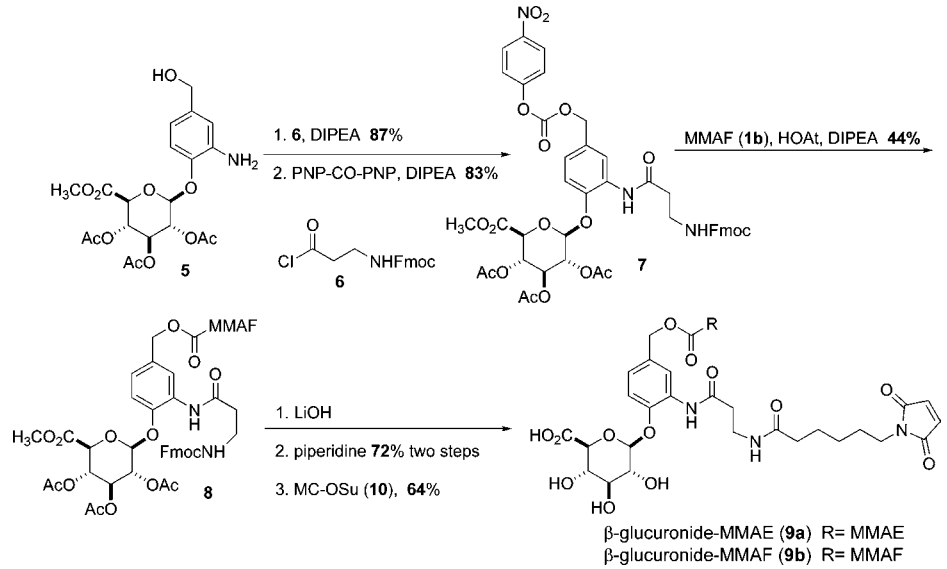

9b conjugates, respectively. The six ADCs were primarily monomeric with 2% or less aggregate being observed in the cAC10-based conjugates and 7% or less aggregate for the c1F6-based conjugates.

In Vitro Evaluation of Cytotoxic Agents and ADCs. In vitro evaluation of both MMAE (**1a**) and **18** (the esterase labile prodrug of 2-pyrrolinodoxorubicin (**4**)) revealed these compounds to be highly cytotoxic (below 0.2 nM) on the CD70+ cell lines Caki-1 and 786-O and the CD30+ line Karpas 299 (Table 1). Compound **18** proved to be 300−6500-fold more cytotoxic than doxorubicin (**15**), which is consistent with previous findings for this class of doxorubicin derivative (*30*). In contrast to **1a** and **18**, the free carboxylic acid MMAF (**1b**) was significantly less active on these cell lines with IC_{50} values

Scheme 4

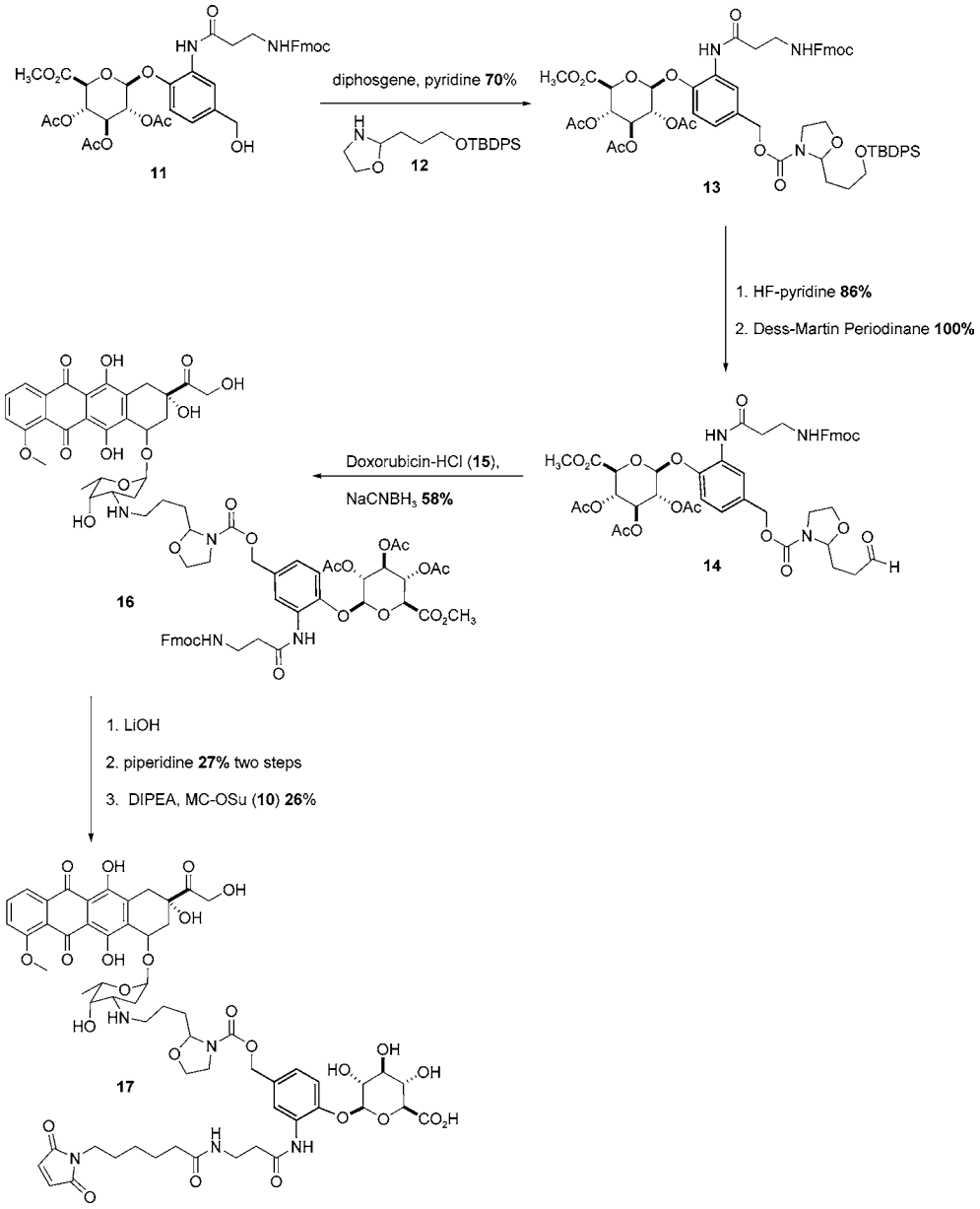

Table 1. Characterization and in Vitro Cytotoxic Activity of Free Drugs and ADCs

compound	target antigen	active drug	drug loading	% aggregation	Caki-1 (CD70+, CD30-) IC_{50} drug nM	786-O (CD70+, CD30-) IC_{50} drug nM	Karpas 299 (CD30+, CD70-) IC_{50} drug nM
1a	-	-	-	-	0.11	0.19	0.09
1b	-	-	-	-	270	300	100
15	-	-	-	-	110	65	29
18	-	**4**	-	-	0.04	0.01	0.1
c1F6−**9a**	CD70	**1a**	4.5	2	0.45	-	>30
cAC10−**9a**	CD30	**1a**	3.7	2	-	-	0.06
c1F6−**9b**	CD70	**1b**	7	7	0.08	0.2	-
cAC10−**9b**	CD30	**1b**	7.6	<1	>50	>50	0.05
c1F6−**17**	CD70	**4**	8.3	3.5	2.0	2.7	>55
cAC10−**17**	CD30	**4**	6.8	<1	>45	>45	1.2

[a] Cells were exposed to the test agents for 96 h, and viability was determined using rezasurin metabolism as a measure of cytotoxic activity. The IC_{50} values were determined compared to untreated cells.

in the 100−200 nM range. As described earlier, the negative charge associated with the carboxylate group of **1b** leads to reduced cytotoxic activity, presumably due to impaired intracellular access (*27*).

In vitro evaluation of cAC10 and c1F6 conjugates of **9a** demonstrated that the linker delivered active drug to the target cells with immunologic specificity (Figure 1). A comparison of the activity of the two conjugates on the CD30+ line Karpas 299 revealed that the anti-CD30 conjugate cAC10−**9a** titrated to an IC_{50} value of 0.06 nM (drug content), where the nonbinding conjugate c1F6−**9a** had no cytotoxic activity up to 30 nM, the highest concentration tested. The anti-CD70

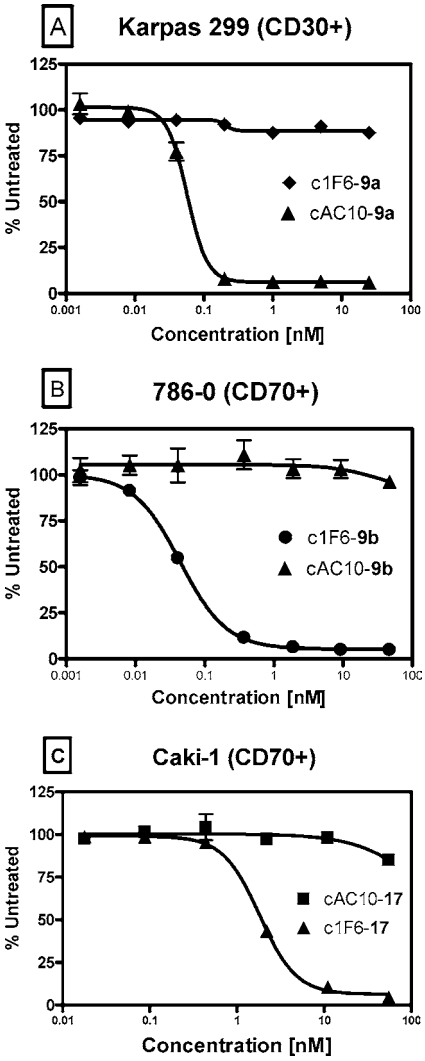

Figure 1. In vitro cytotoxic activity of ADCs on CD30+ and CD70+ cancer cell lines: (A) Karpas 299 (CD30+) ALCL cells treated with anti-CD30 ADC cAC10−**9a** and nonbinding control c1F6−**9a**. (B) 786-O (CD70+) RCC cells treated with anti-CD70 ADC c1F6−**9b** and nonbinding control cAC10−**9b**. (C) Caki-1 (CD70+) RCC cells treated with c1F6−**17** and nonbinding control cAC10−**17**. Results are shown as mean ± SD.

conjugate c1F6−**9a** was quite potent on the CD70+ cell line Caki-1 (IC_{50} 0.45 nM).

The ADCs of **9b** effectively delivered **1b** to the targeted cells. Conjugates of **9b** displayed immunologic specificity and were highly effective against the CD70+ lines Caki-1 and 786-O with IC_{50} values of 0.08 and 0.20 nM, respectively. The corresponding nonbinding cAC10−**9b** was inactive on these cell lines representing specificity levels of >250-fold. The anti-CD30 conjugate cAC10−**9b** was highly effective on the CD30+ line Karpas 299 with an IC_{50} value of 50 pM. Conjugates of doxorubicin drug-linker **17** gave the same general profile, with effective cell kill on antigen positive cell lines and specificity values >16-fold.

To determine the identity of drug released in ADC-treated cells, 786-O cells were treated with h1F6-β-glucuronide-MMAF, which was formed with a variant of **9b** in which the caproyl maleimide was replaced with a bromoacetamide (see Supporting Information). After 24 h, cell extracts were analyzed by LC-MS. The ion mass at 732.7 Da corresponds to the release of **1b** in cells treated with h1F6-β-glucuronide-MMAF while untreated cells showed no signal above background at this mass (Figure 2). The HPLC retention time of the material derived from cell extracts closely matched that of the **1b** standard (data not shown). Similar results were obtained in cells treated with h1F6-β-glucuronide-MMAE (data not shown). While efforts are ongoing to determine the efficiency of drug-release, these results suggest that β-glucuronide hydrolysis takes place within the target cell population.

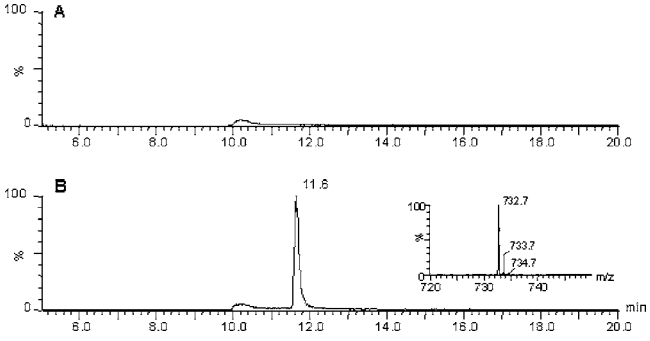

Figure 2. A. LC-MS extracted ion chromatogram (*m*/*z* 732.5 Da) of material isolated from untreated CD70+ 786-O RCC cells. B. LC-MS extracted ion chromatogram (*m*/*z* 732.5 Da) of isolate from 786-O cells treated with h1F6-β-glucuronide-MMAF ADC for 24 h. The inset shows that the mass of material at 11.6 min corresponds to free MMAF (**1b**) released inside ADC treated cells, but not present in untreated cells.

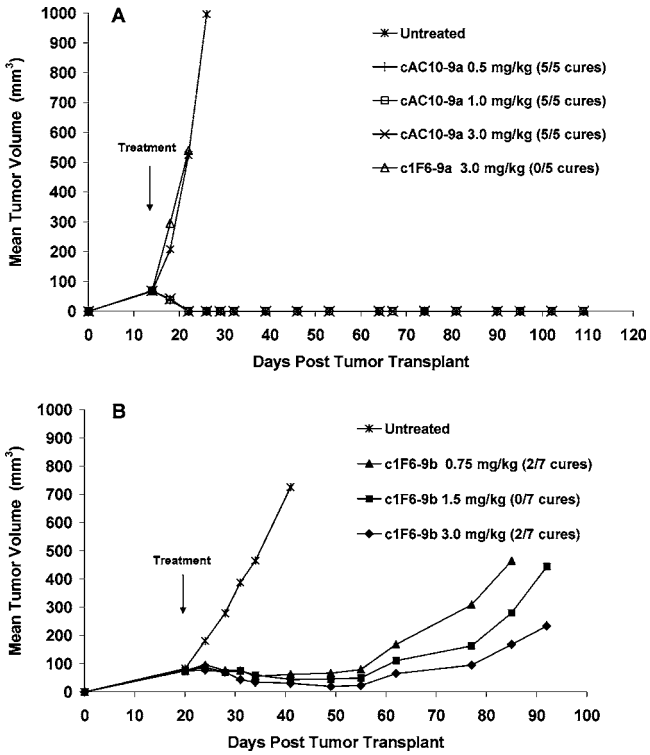

Figure 3. A. Therapy experiment with cAC10−**9a** on CD30+ Karpas 299 (ALCL) subcutaneous tumor bearing SCID mice. A single treatment (arrow: day 14) of mice with 0.5 (+), 1.0 (□), and 3.0 (×) mg/kg gave cures in 5/5 animals for each group. A dose of 3 mg/kg of nonbinding control conjugate c1F6−**9a** (△) resulted in no tumor response as with the untreated group (*). B. Therapy experiment with c1F6−**9b** on CD70+ 786-O (RCC) subcutaneous tumor bearing SCID mice. Single treatment (arrow: day 20) of mice with 0.75 (▲), 1.5 (■), and 3.0 (◆) mg/kg single dose gave tumor regressions. Cures (2/7) were seen in the 0.75 and 3 mg/kg dose groups. All animals in the untreated group (×) were sacrificed on or before day 40.

In Vivo Evaluation. ADCs of the auristatin derivatives **9a** and **9b** were evaluated for toxicity and efficacy. The maximum tolerated dose (MTD) of cAC10−**9a** (4 drugs/mAb) was determined in female Balb/c mice. cAC10−**9a** was well tolerated at 100 mg/kg, but toxic at 150 mg/kg. Conjugate c1F6−**9b** was well tolerated at 25 mg/kg, but was toxic at the 50 mg/kg dose. The MTDs of the glucuronide ADCs therefore

appear to be comparable to the corresponding peptide-linked MMAE (**1a**) (*21*) and MMAF (**1b**) (*27*) ADCs that were previously described. This was somewhat unexpected based on the increased ex vivo stability of the β-glucuronide linker in plasma. Further studies are required to determine in vivo β-glucuronide stability and potential differences in biodistribution compared to the peptide-linker ADCs. These will be the subject of further experiments. Studies to understand the difference in toxicity between MMAE and MMAF-based ADCs are currently underway.

An in vivo therapy experiment with cAC10−**9a** was undertaken in nude mice with subcutaneous Karpas 299 ALCL tumors. The animals (5 per group) were treated with a single intravenous dose of cAC10−**9a** at 0.5, 1.0, and 3 mg/kg (mAb component) on day 14 post tumor implant at which time the tumors were staged (mean = 70 mm^3) and rapidly growing. Specificity was determined using c1F6−**9a** as a nonbinding control ADC that was injected at 3 mg/kg dose. Cures were obtained in all animals treated with cAC10−**9a** at each of the three dosing levels (Figure 3A). In contrast, the nonbinding ADC c1F6−**9a** displayed no antitumor efficacy. Previous studies with unmodified cAC10 and free drug **1a** revealed no significant antitumor activity in this model (data not shown). Since the MTD of cAC10−**9a** is approximately 100 mg/kg, the therapeutic index was >200, which is as pronounced as the val-cit-MMAE ADC reported earlier (*23*).

The effects of c1F6−**9b** were determined in mice with subcutaneous 786-0 renal cell carcinoma implants. Significant levels of antitumor activity were obtained at all three dose levels (0.75, 1.5, and 3.0 mg/kg), again without any signs of toxicity or adverse events (Figure 3B). As with the c1F6−**9a** ADC, this was achieved at a small fraction of the MTD. Neither unmodified c1F6 nor free drug **1b** showed antitumor activity in this model (data not shown).

CONCLUDING REMARKS

We have described a novel β-glucuronide-based linker system for ADCs that complements previously described hydrazone, disulfide, and peptide linker technologies (*11*, *14*, *39*, *40*). The distinguishing features of the β-glucuronide linker are high aqueous solubility, serum stability, and facile drug release within antigen positive tumor cells. The high aqueous solubility of the β-glucuronide may be particularly useful for hydrophobic drugs such as DNA minor groove binders which tend to cause aggregation (*19*).

Compounds **9a**, **9b**, and **17** are the first examples of drug-linkers designed to exploit lysosomal β-glucuronide cleavage for mAb-based targeted drug delivery to cancer cells. Biological evaluation of the cAC10 and c1F6 conjugates of **9a**, **9b**, and **17** revealed them to be highly active and immunologically specific in vitro. In vivo evaluation of cAC10−**9a** showed pronounced efficacy in the Karpas 299 model, comparable to the val-cit-PABA linker system previously described (*23*). Similar trends were observed with c1F6−**9b**, an ADC that led to cures of established renal cell carcinoma xenografts in nude mice. The studies reported here demonstrate that β-glucuronide-based linkers provide well tolerated and efficacious ADCs. We are currently assessing the potential advantages of this linker technology compared to others, and are applying it to several new drug classes.

ACKNOWLEDGMENT

The authors would like to thank Steven C. Alley for his contributions to the maleimide reduction studies.

Supporting Information Available: The three-dimensional photodiode array HPLC chromatograms for compounds **9a** and **9b** under acidic and neutral conditions, as well as raw HRMS data. NMR spectra for final products **9a**, **9b** and **17**. This material is available free of charge via the Internet at http://pubs.acs.org.

LITERATURE CITED

(1) Zondor, S. D., and Medina, P. J. (2004) Bevacizumab: an angiogenesis inhibitor with efficacy in colorectal and other malignancies. *Ann. Pharmacother. 38*, 1258−64.

(2) Adams, G. P., and Weiner, L. M. (2005) Monoclonal antibody therapy of cancer. *Nat. Biotechnol. 23*, 1147−57.

(3) Plosker, G. L., and Figgitt, D. P. (2003) Rituximab: a review of its use in non-Hodgkin's lymphoma and chronic lymphocytic leukaemia. *Drugs 63*, 803−43.

(4) Emens, L. A., and Davidson, N. E. (2004) Trastuzumab in breast cancer. *Oncology (Huntingt) 18*, 1117−28; discussion 1131−2, 1137−8.

(5) Wu, A. M., and Senter, P. D. (2005) Arming antibodies: prospects and challenges for immunoconjugates. *Nat. Biotechnol. 23*, 1137−46.

(6) Meyer, D. L., and Senter, P. D. (2003) Recent Advances in Antibody Drug Conjugates for Cancer Therapy. *Annu. Rep. Med. Chem. 38*, 229−237.

(7) Lambert, J. M. (2005) Drug-conjugated monoclonal antibodies for the treatment of cancer. *Curr. Opin. Pharmacol. 5*, 543−9.

(8) Damle, N. K., and Frost, P. (2003) Antibody-targeted chemotherapy with immunoconjugates of calicheamicin. *Curr. Opin. Pharmacol. 3*, 386-90.

(9) Giles, F., Estey, E., and O'Brien, S. (2003) Gemtuzumab ozogamicin in the treatment of acute myeloid leukemia. *Cancer 98*, 2095−104.

(10) King, H. D., Staab, A. J., Pham-Kaplita, K., Yurgaitis, D., Firestone, R. A., Lasch, S. J., and Trail, P. A. (2003) BR96 conjugates of highly potent anthracyclines. *Bioorg. Med. Chem. Lett. 13*, 2119−22.

(11) Dubowchik, G. M., Firestone, R. A., Padilla, L., Willner, D., Hofstead, S. J., Mosure, K., Knipe, J. O., Lasch, S. J., and Trail, P. A. (2002) Cathepsin B-labile dipeptide linkers for lysosomal release of doxorubicin from internalizing immunoconjugates: model studies of enzymatic drug release and antigen-specific in vitro anticancer activity. *Bioconjugate Chem. 13*, 855−69.

(12) Saleh, M. N., Sugarman, S., Murray, J., Ostroff, J. B., Healey, D., Jones, D., Daniel, C. R., LeBherz, D., Brewer, H., Onetto, N., and LoBuglio, A. F. (2000) Phase I trial of the anti-Lewis Y drug immunoconjugate BR96-doxorubicin in patients with lewis Y-expressing epithelial tumors. *J. Clin. Oncol. 18*, 2282−92.

(13) Smith, S. (2001) Technology evaluation: C242-DM1, ImmunoGen Inc. *Curr. Opin. Mol. Ther. 3*, 198−203.

(14) Xie, H., Audette, C., Hoffee, M., Lambert, J. M., and Blattler, W. A. (2004) Pharmacokinetics and biodistribution of the antitumor immunoconjugate, cantuzumab mertansine (huC242-DM1), and its two components in mice. *J Pharmacol. Exp. Ther. 308*, 1073−82.

(15) Ojima, I., Geng, X., Wu, X., Qu, C., Borella, C. P., Xie, H., Wilhelm, S. D., Leece, B. A., Bartle, L. M., Goldmacher, V. S., and Chari, R. V. (2002) Tumor-specific novel taxoid-monoclonal antibody conjugates. *J. Med. Chem. 45*, 5620−3.

(16) Yasuzawa, T., Muroi, K., Ichimura, M., Takahashi, I., Ogawa, T., Takahashi, K., Sano, H., and Saitoh, Y. (1995) Duocarmycins, potent antitumor antibiotics produced by Streptomyces sp. structures and chemistry. *Chem. Pharm. Bull. (Tokyo) 43*, 378−91.

(17) Suzawa, T., Nagamura, S., Saito, H., Ohta, S., Hanai, N., Kanazawa, J., Okabe, M., and Yamasaki, M. (2002) Enhanced tumor cell selectivity of adriamycin-monoclonal antibody conjugate via a poly(ethylene glycol)-based cleavable linker. *J. Controlled Release 79*, 229−42.

(18) Suzawa, T., Nagamura, S., Saito, H., Ohta, S., Hanai, N., and Yamasaki, M. (2000) Synthesis of a novel duocarmycin derivative DU-257 and its application to immunoconjugate using poly(ethylene glycol)-dipeptidyl linker capable of tumor specific activation. *Bioorg. Med. Chem. 8*, 2175−84.

(19) Jeffrey, S. C., Torgov, M. Y., Andreyka, J. B., Boddington, L., Cerveny, C. G., Denny, W. A., Gordon, K. A., Gustin, D., Haugen, J., Kline, T., Nguyen, M. T., and Senter, P. D. (2005) Design,

synthesis, and in vitro evaluation of dipeptide-based antibody minor groove binder conjugates. *J. Med. Chem. 48*, 1344−58.
(20) Chari, R. V., Jackel, K. A., Bourret, L. A., Derr, S. M., Tadayoni, B. M., Mattocks, K. M., Shah, S. A., Liu, C., Blattler, W. A., and Goldmacher, V. S. (1995) Enhancement of the selectivity and antitumor efficacy of a CC-1065 analogue through immunoconjugate formation. *Cancer Res. 55*, 4079−84.
(21) Doronina, S. O., Toki, B. E., Torgov, M. Y., Mendelsohn, B. A., Cerveny, C. G., Chace, D. F., DeBlanc, R. L., Gearing, R. P., Bovee, T. D., Siegall, C. B., Francisco, J. A., Wahl, A. F., Meyer, D. L., and Senter, P. D. (2003) Development of potent monoclonal antibody auristatin conjugates for cancer therapy. *Nat. Biotechnol. 21*, 778−84.
(22) Francisco, J. A., Cerveny, C. G., Meyer, D. L., Mixan, B. J., Klussman, K., Chace, D. F., Rejniak, S. X., Gordon, K. A., DeBlanc, R., Toki, B. E., Law, C. L., Doronina, S. O., Siegall, C. B., Senter, P. D., and Wahl, A. F. (2003) cAC10-vcMMAE, an anti-CD30-monomethyl auristatin E conjugate with potent and selective antitumor activity. *Blood 102*, 1458−65.
(23) Hamblett, K. J., Senter, P. D., Chace, D. F., Sun, M. M., Lenox, J., Cerveny, C. G., Kissler, K. M., Bernhardt, S. X., Kopcha, A. K., Zabinski, R. F., Meyer, D. L., and Francisco, J. A. (2004) Effects of drug loading on the antitumor activity of a monoclonal antibody drug conjugate. *Clin. Cancer Res. 10*, 7063−70.
(24) Dubowchik, G. M., and Walker, M. A. (1999) Receptor-mediated and enzyme-dependent targeting of cytotoxic anticancer drugs. *Pharmacol. Ther. 83*, 67−123.
(25) Albin, N., Massaad, L., Toussaint, C., Mathieu, M. C., Morizet, J., Parise, O., Gouyette, A., and Chabot, G. G. (1993) Main drug-metabolizing enzyme systems in human breast tumors and peritumoral tissues. *Cancer Res. 53*, 3541−6.
(26) de Graaf, M., Boven, E., Scheeren, H. W., Haisma, H. J., and Pinedo, H. M. (2002) Beta-glucuronidase-mediated drug release. *Curr. Pharm. Des. 8*, 1391−403.
(27) Doronina, S. O., Mendelsohn, B. A., Bovee, T. D., Cerveny, C. G., Alley, S. C., Meyer, D. L., Oflazoglu, E., Toki, B. E., Sanderson, R. J., Zabinski, R. F., Wahl, A. F., and Senter, P. D. (2006) Enhanced activity of monomethylauristatin F through monoclonal antibody delivery: effects of linker technology on efficacy and toxicity. *Bioconjugate Chem. 17*, 114−24.
(28) Sun, M. M., Beam, K. S., Cerveny, C. G., Hamblett, K. J., Blackmore, R. S., Torgov, M. Y., Handley, F. G., Ihle, N. C., Senter, P. D., and Alley, S. C. (2005) Reduction-alkylation strategies for the modification of specific monoclonal antibody disulfides. *Bioconjugate Chem. 16*, 1282−90.
(29) Desbene, S., Van, H. D., Michel, S., Koch, M., Tillequin, F., Fournier, G., Farjaudon, N., and Monneret, C. (1998) Doxorubicin prodrugs with reduced cytotoxicity suited for tumour-specific activation. *Anticancer Drug Des. 13*, 955−68.
(30) Farquhar, D., Cherif, A., Bakina, E., and Nelson, J. A. (1998) Intensely potent doxorubicin analogues: structure−activity relationship. *J. Med. Chem. 41*, 965−72.
(31) Acton, E. M., Tong, G. L., Mosher, C. W., and Wolgemuth, R. L. (1984) Intensely potent morpholinyl anthracyclines. *J. Med. Chem. 27*, 638−45.
(32) Jeffrey, S. C., Nguyen, M. T., Andreyka, J. B., Meyer, D. L., Doronina, S. O., and Senter, P. D. (2006) Dipeptide-based highly potent doxorubicin antibody conjugates. *Bioorg. Med. Chem. Lett. 16*, 358−62.
(33) Zwelling, L. A., Altschuler, E., Cherif, A., and Farquhar, D. (1991) N−(5,5-diacetoxypentyl)doxorubicin: a novel anthracycline producing DNA interstrand cross-linking and rapid endonucleolytic cleavage in human leukemia cells. *Cancer Res. 51*, 6704−7.
(34) Leenders, R. G., Damen, E. W., Bijsterveld, E. J., Scheeren, H. W., Houba, P. H., van der Meulen-Muileman, I. H., Boven, E., and Haisma, H. J. (1999) Novel anthracycline-spacer-beta-glucuronide,-beta-glucoside, and -beta-galactoside prodrugs for application in selective chemotherapy. *Bioorg. Med. Chem. 7*, 1597−610.
(35) Walker, M. A., Dubowchik, G. M., Hofstead, S. J., Trail, P. A., and Firestone, R. A. (2002) Synthesis of an immunoconjugate of camptothecin. *Bioorg. Med. Chem. Lett. 12*, 217−9.
(36) Wahl, A. F., Klussman, K., Thompson, J. D., Chen, J. H., Francisco, L. V., Risdon, G., Chace, D. F., Siegall, C. B., and Francisco, J. A. (2002) The anti-CD30 monoclonal antibody SGN-30 promotes growth arrest and DNA fragmentation in vitro and affects antitumor activity in models of Hodgkin's disease. *Cancer Res. 62*, 3736−42.
(37) Hishima, T., Fukayama, M., Hayashi, Y., Fujii, T., Ooba, T., Funata, N., and Koike, M. (2000) CD70 expression in thymic carcinoma. *Am. J. Surg. Pathol. 24*, 742−6.
(38) Held-Feindt, J., and Mentlein, R. (2002) CD70/CD27 ligand, a member of the TNF family, is expressed in human brain tumors. *Int. J. Cancer 98*, 352−6.
(39) Toki, B. E., Cerveny, C. G., Wahl, A. F., and Senter, P. D. (2002) Protease-mediated fragmentation of p-amidobenzyl ethers: a new strategy for the activation of anticancer prodrugs. *J. Org. Chem. 67*, 1866−72.
(40) Trail, P. A., Willner, D., Lasch, S. J., Henderson, A. J., Hofstead, S., Casazza, A. M., Firestone, R. A., Hellstrom, I., and Hellstrom, K. E. (1993) Cure of xenografted human carcinomas by BR96-doxorubicin immunoconjugates. *Science 261*, 212−5.

BC0600214

Synthetic Modification of Silica Beads That Allows for Sequential Attachment of Two Different Oligonucleotides

Gali Steinberg-Tatman, Michael Huynh, David Barker, and Chanfeng Zhao*

Illumina Inc., 9885 Towne Centre Drive, San Diego, California 92121. Received January 19, 2006; Revised Manuscript Received February 22, 2006

We developed a simple and elegant synthesis strategy that enables us to attach controlled (equimolar) amounts of two different oligonucleotides onto one silica bead. The method involves addition of orthogonally protected lysine followed by activation and derivatization of each amino group with a different moiety. This sequential oligonucleotide attachment enables the use of a combinatorial scheme to generate millions of bead types, each characterized by its two oligo tags. (In our randomly assembled arrays each bead type can then be identified by a series of hybridizations of fluorescently labeled decoder oligos to the address tags.) To demonstrate feasibility of such a scheme we created over 1000 bead types, which were characterized by their two oligo tags. The method enables genotyping or gene expression assays at multiplex levels of hundreds of thousands to millions.

INTRODUCTION

DNA array technology uses microscopic arrays of DNA molecules immobilized on solid supports for biomedical analysis of gene expression, polymorphism or mutation detection, DNA sequencing and gene discovery (*1*, *2*).

Conventional microarrays are manufactured by spotting or synthesizing probes at known locations on a two-dimensional substrate (*3*−*5*).

Illumina's novel approach (*6*) enables the production of randomly assembled arrays in which the location of a probe is initially unknown (*7*). Random bead loading combined with decoding, described in detail previously (*6*), avoids the need for physical addressing of each element and thus achieves very high packing densities by using relatively simple bulk processes. The decoding process is efficient and extremely accurate (*6*). However, it requires at least one fluorescently labeled decoder oligo for each unique bead type. For very large numbers of bead types (tens to hundreds of thousands), a more practical decoding approach uses two different address oligos on each bead. This reduces the number of decoder oligos required to two times the square root of the number of unique beads. For example, to decode 1 million different bead types would require only 2000 oligo decoders. Figure 1 illustrates three potential schemes for attaching two different oligonucleotides to the same bead. In this paper, we focus on methods for groups A and B.

To enable sequential attachment of two distinct moieties to one bead, we developed an alternative chemistry scheme involving the use of orthogonally protected lysine. The two amino groups on the lysine are sequentially activated, permitting sequential addition of two different oligonucleotides. The approach is general and could be used to attach different chemical moieties to the same bead, such as an oligo and a peptide.

EXPERIMENTAL PROCEDURES

Chemical Reagents. Silica beads in water (3 μm diameter, $\sim 5 \times 10^{10}$ beads/g) were obtained from Bangs Laboratories Inc., Carmel, IN. Silanization reagent, 3-aminopropyltrimethoxysilane, was obtained from United Chemical Technologies (UCT), Bristol, PA. Succinimidyl 4-formylbenzoate (SFB) and succinimidyl hydraziniumnicotinate hydrochloride (SHNH) were obtained from Solulink, San Diego, CA. Oligonucleotides were obtained from Operon Technologies, Alameda, CA, or synthesized in house. All oligonucleotides obtained from Operon Technologies were HPLC purified. Other reagents were obtained from NovaBiochem, Aldrich, or Sigma. All solutions were prepared with OmniPur (sterile, nuclease free) water from Merck.

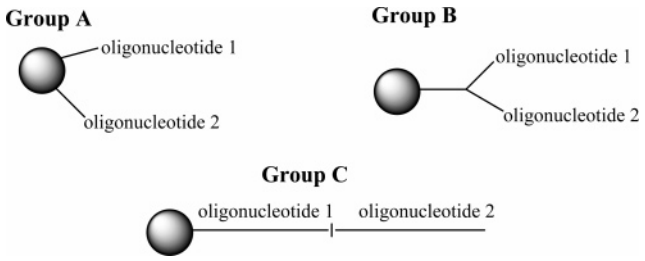

Figure 1. Potential schemes for two oligonucleotide attachment.

Surface Modifications. *Silanization.* Silica beads (1 g) were washed with 10 mL ethanol (HPLC grade). The beads were then suspended in 10 mL of ethanol followed by addition of 50 μL (0.5%) silane reagent, and shaken for 1 h at room temperature. Following silanization they were washed 5 times with 10 mL of ethanol and 3 times with 10 mL of ether, dried, and stored at room temperature. (Silanization is shown in Figure 2.)

Ninhydrin Test. Completion of various reaction steps was monitored (qualitatively) using the ninhydrin test as follows: A small amount of ninhydrin solution (10 wt % ninhydrin in ethanol) was heated to 120 °C, a smidgen of beads was added to one test tube, and another was used as reference. When primary amines were present on the beads, ninhydrin solution turned blue; otherwise, the color of the solution remained unchanged.

Chemical Modifications of Silanized Beads. Figure 2 shows the synthetic approach to sequential oligonucleotide attachment, as demonstrated in the potential scheme in Figure 1 group A.

Coupling of Fmoc and t-Boc Protected Glycines to Silanized Beads. Aminopropyl beads (100 mg) were suspended in DMF

* Author to whom correspondence should be addressed. E-mail: chanfeng@illumina.com.

10.1021/bc060012v CCC: $33.50 © 2006 American Chemical Society
Published on Web 04/25/2006

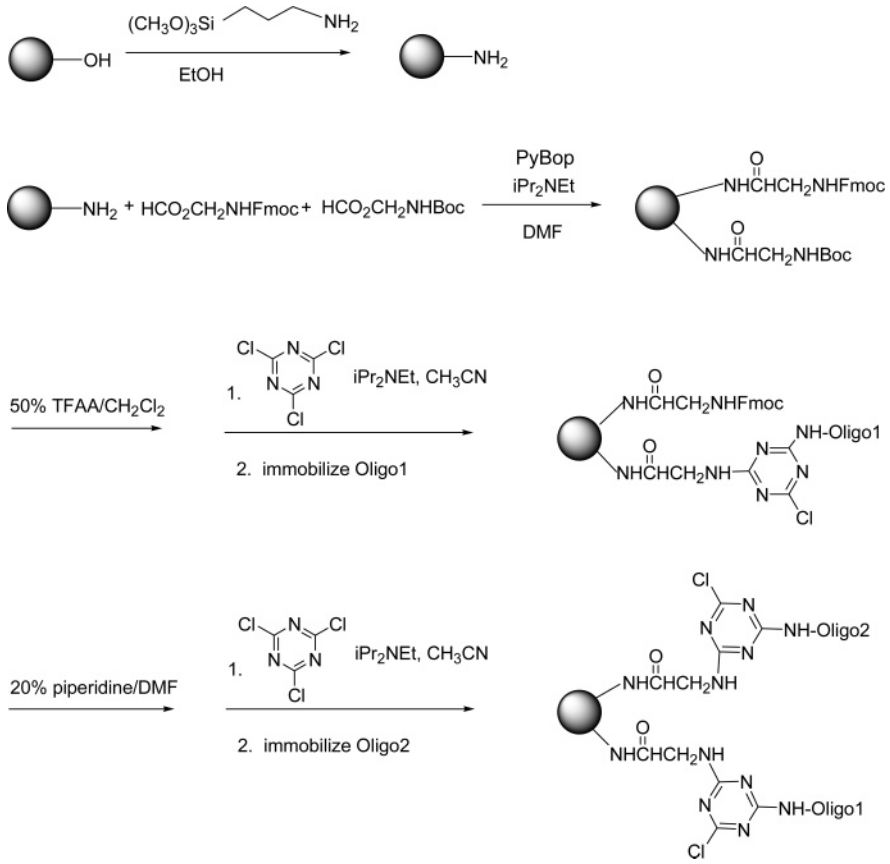

Figure 2. Detailed chemical modifications of hydroxyl beads leading to two oligonucleotide attachment, as depicted in Figure 1, group A.

(1 mL), followed by addition of 35 μL of *N*,*N*-diisopropylethylamine (DIEA) (0.2 mmol). The suspension was sonicated, and an equimolar (1:1) mixture of *N*-α-*t*-Boc-glycine (8.75 mg, 0.05 mmol) and *N*-α-Fmoc-glycine (14.85 mg, 0.05 mmol) was added. This was followed by the addition of 52 mg (0.1 mmol) of PyBOP (benzotriazole-1-yl-oxy-tris-pyrrolidinophosphoniumhexa fluoro phosphate). The beads were shaken overnight at room temperature. They were then washed 6 times with 1 mL of DMF and 3 times with methylene chloride.

Amine Deprotection (from t-Boc). Beads coupled to the modified lysine (100 mg) were suspended in a solution of 50% trifluoroacetic acid in methylene chloride (1 mL) and shaken for 30 min at room temperature. They were then washed 3 times with 1 mL of methylene chloride and 3 times with 1 mL of acetonitrile.

Cyanuric Chloride Activation. Amino beads (100 mg) were suspended in acetonitrile (1 mL), followed by addition of 20 μL (0.12 mmol) of DIEA. After a brief sonication, 10 mg (0.05 mmol) of cyanuric chloride was added and the reaction mixture was shaken for 2 h at room temperature. The beads were washed 3 times with 1 mL of acetonitrile and twice with 1 mL of 0.05 M sodium borate buffer (pH 8.5).

Amine Deprotection (from Fmoc). Beads coupled to the modified lysine (100 mg) were suspended in a solution of 20% piperidine in DMF (1 mL) and shaken for 30 min at room temperature. They were then washed 3 times with 1 mL of DMF and 3 times with 1 mL of acetonitrile.

Figure 3 shows the potential schemes of group B from Figure 1. Both address and assay oligonucleotide sequences that can be attached to beads in these schemes.

Figure 4 shows the synthetic approach to sequential oligonucleotide attachment, as demonstrated in the potential scheme in Figure 1 group B.

Coupling of Orthogonally Protected Lysine to Silanized Beads. Aminopropyl beads (100 mg) were suspended in DMF

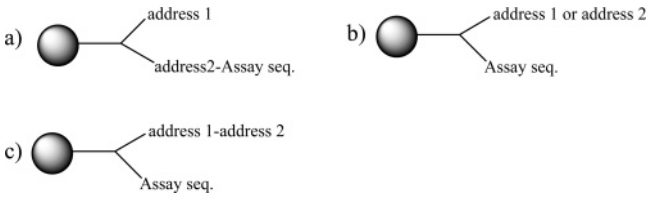

Figure 3. Detailed potential encoding schemes of group B from Figure 1.

(1 mL), followed by addition of 35 μL of DIEA (0.2 mmol). The suspension was sonicated and *N*-α-Fmoc-*N*-ϵ-1-(4,4-dimethyl-2,6-dioxocyclohex-1-ylidene)-3-methylbutyl-L-lysine (53 mg,0.1 mmol) was added followed by addition of 52 mg (0.1 mmol) of PyBOP (benzotriazole-1-yl-oxy-tris-pyrrolidinophosphoniumhexa fluoro phosphate). The beads were shaken overnight at room temperature. They were then washed 6 times with 1 mL of DMF.

Amine Deprotection (from Dde(iv), (4,4-Dimethyl-2,6-dioxocyclohexylidene)-3-methylbutyl). Beads coupled to the modified lysine (100 mg) were suspended in a solution of 2% hydrazine in DMF (1 mL) and shaken for 30 min at room temperature. They were then washed 6 times with 1 mL of DMF.

Figure 5 shows alternative approaches to the activation of the second amino group and immobilization of second oligonucleotide.

Coupling to Succinimidyl Hydraziniumnicotinate Hydrochloride (SHNH). Amino beads (100 mg) were suspended in DMF (1 mL), followed by addition of SHNH (28.6 mg, 1 mmol) and 48 μL of DMAP solution (dimethyl amino pyridine in DMF 0.5 M). The beads were shaken overnight at room temperature and then washed 3 times with DMF and 3 times with 0.1 M sodium citrate buffer, pH 5.0.

Coupling of amino beads to PDITC (1,4-phenylene diisothiocyanate), 4-nitrophenyl chloroformate, 4-carboxybenzaldehyde,

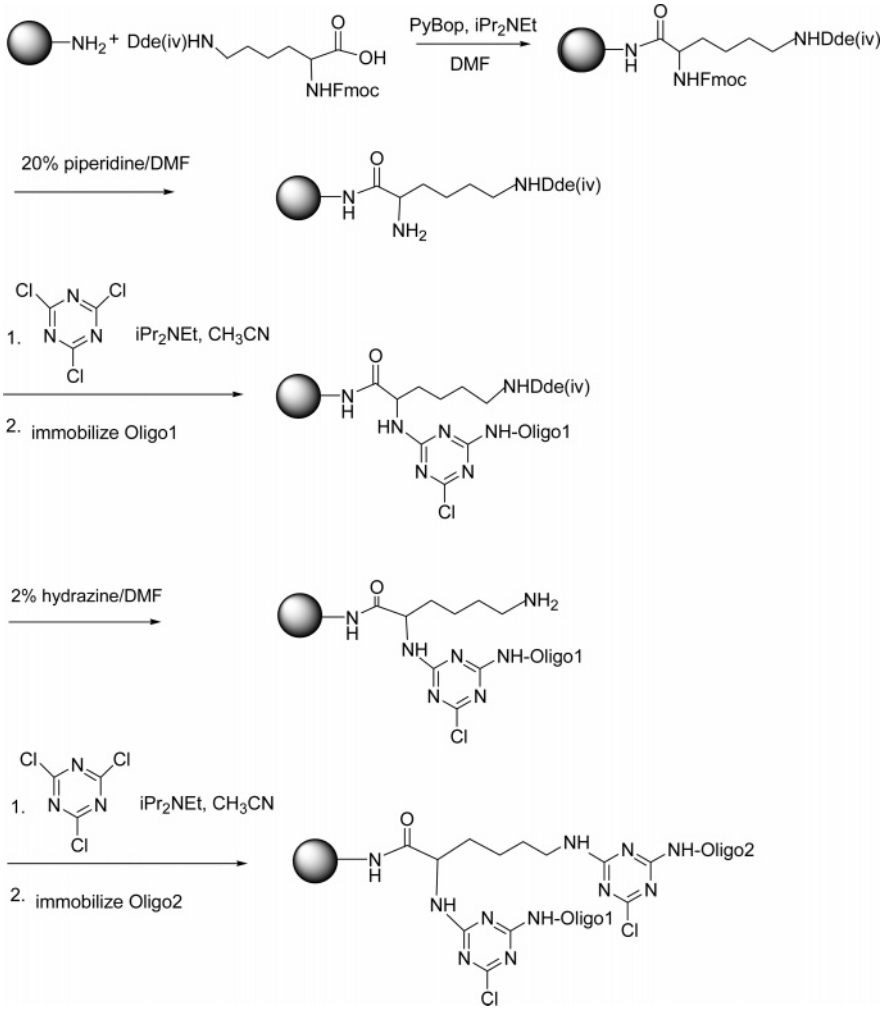

Figure 4. Detailed chemical modifications of amino silanized beads leading to two oligonucleotide attachment, as depicted in Figure 1, group B.

and succinimidyl 4-formylbenzoate (SFB) has been previously described **(*8*)**, see Figure 5A−D.

Oligo Immobilization. *Amino Oligonucleotide Immobilization.* A 5′-amino oligonucleotide (100 nmol in 0.05 M sodium borate buffer, pH 8.5) was added to 2 M sodium chloride solution (100 μL). The oligonucleotide solution was added to cyanuric chloride activated beads (25 mg beads in 100 μL of 0.05 M sodium borate buffer, pH 8.5). The beads were shaken overnight and then washed 3 times with OmniPur water.

5′-Amino oligonucleotides were synthesized in house using the standard coupling conditions and 5′-amino modifier phosphoramidite commercially available from Glen Research, Sterling, VA.

Aldehyde Oligonucleotide Immobilization. A 5′-aldehyde oligonucleotide (100 nmol in 0.1 M sodium citrate/citric acid, pH 5.0) was added to 2 M sodium chloride solution (100 μL). The oligonucleotide solution was added to hydrazine-activated beads (25 mg of beads in 100 μL of 0.1 M sodium citrate/citric acid, pH 5.0). The beads were shaken overnight and then washed 3 times with OmniPur water.

5′-Aldehyde oligonucleotides were synthesized in house using the standard coupling conditions and 5′-aldehyde phosphoramidite commercially available from Solulink, San Diego, CA.

Complementary Oligonucleotide (Target) Hybridization. Hybridization of complementary oligo (target) to beads containing immobilized probes was carried out in solution, and a fluorescence activated cell sorter (FACS) was used to measure hybridization intensity.

Hybridization was done in solution as follows. About 1 mg of probe-immobilized beads was suspended in 30 μL of hybe buffer (0.1 M potassium phosphate, 1 M sodium chloride, 0.1% Tween-20, and 5% ethanol, pH 7.6), followed by addition of 15−20 μL of ∼1 mM target (in 0.05 M borate buffer, pH 8.5) and then shaken for 2 h. The beads were washed 2 times with hybe buffer to remove excess target oligonucleotides. For the release of target from the beads, the beads were incubated with 50 μL of 0.1 M sodium hydroxide solution for 10 min.

Detection of Hybridization. Hybridization in solution was measured with FACS (Becton Dickinson Biosciences). We used constant laser power of 15 mW and a photomultiplier tube (PMT) gain of 659 for all measurements. Following hybridization in solution (described in the previous section), a small amount of beads was added to 0.2 mL of FACS flow buffer (in a FACS-compatible test tube), and average fluorescence intensity was recorded for at least 10 000 beads.

RESULTS AND DISCUSSION

Addressing Beads with Multiple Oligonucleotides. Various schemes, shown in Figure 1, were considered in an attempt to generate millions of bead types using a combinatorial approach. These schemes can be divided into 3 main groups: group A (where two orthogonally protected glycines are coupled to the beads followed by sequential oligonucleotide immobilization), group B (where one orthogonally protected lysine is coupled to the beads followed by sequential oligonucleotide immobilization), and group C (where one long oligonucleotide, which includes both address sequences, is immobilized).

The scalability of these schemes was evaluated based on the required number of oligonucleotides, the number of decoder

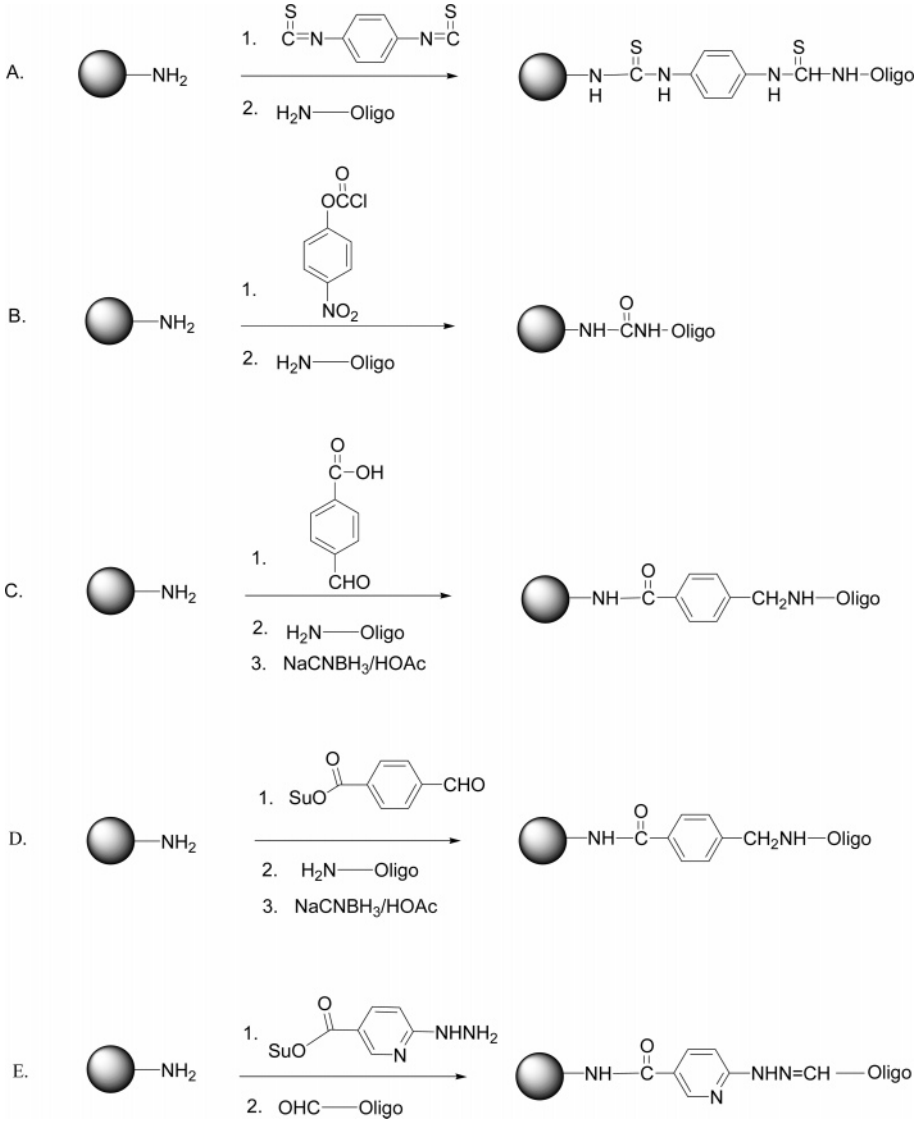

Figure 5. Alternative activation/immobilization schemes for second oligonucleotide attachment.

oligonucleotides, and the number of split and pool synthesis steps that would be necessary to implement a particular chemistry in an automated, high-throughput environment.

Group C schemes, while this study was carried out, involving one very long (100-mer) oligonucleotide, were not considered because low synthesis yields would be expected. Group A type schemes were evaluated first. The synthesis, shown in Figure 2, involved coupling of two orthogonally protected glycines to aminopropyl (silanized) beads as described in Experimental Procedures. The coupling was followed by deprotection of the *t*-Boc protected glycine and its activation with cyanuric chloride. The activation was followed by immobilization of an amino modified oligonucleo-tide. Following immobilization, the Fmoc protected glycine was deprotected with 20% piperidine solution, and the amine was activated with cyanuric chloride. Finally, another amino modified oligonucleotide (containing assay specific sequence) was immobilized as well.

Group A schemes, however, have an inherent problem. Since two orthogonally protected glycines are coupled to the beads simultaneously, it is hard to control the amount of each glycine that will couple to the amino beads. As a result, it is difficult to control the ratio of immobilized oligonucleotides, which can impact the decoding and/or assay robustness. In schemes from group B the aforementioned problem is avoided as only one orthogonally protected amino acid is coupled to the amino beads. The potential schemes for group B are shown in Figure 3.

The synthesis of group B schemes, shown in Figure 4, involved coupling of a lysine, with two orthogonally protected amino groups, to aminopropyl (silanized) beads as described in Experimental Procedures. The coupling was followed by the deprotection of the Fmoc protected amino group and its activation with cyanuric chloride. Immobilization of a single amino modified address oligonucleotide or an equimolar mix of two amino modified address oligonucleotides followed the activation. Then the second protecting group (Dde(iv)) was removed with 2% hydrazine in DMF solution and the second amine was again activated with cyanuric chloride. Finally amino modified oligonucleotide (containing assay specific sequence) was immobilized (as described in Experimental Procedures).

Variation in Signal Intensities of Oligonucleotides. After the first amino group was activated with cyanuric chloride (see Figure 4), an equimolar mix of oligonucleotide 1 and oligonucleotide 2 was immobilized onto the bead (Figure 3b). In spite of using only HPLC purified oligos, hybridization intensities for the various oligonucleotides varied sometimes by more than 10-fold. Even for the same oligonucleotides, signal intensity varied up to 2−3-fold depending on the neighboring sequence (i.e. the other oligonucleotide that was immobilized with it).

Although not as pronounced, these variations in hybridization signals were observed even on beads with a single oligonucleotide immobilized on them. To understand the reasons behind the variation in hybridization signals we first looked at beads

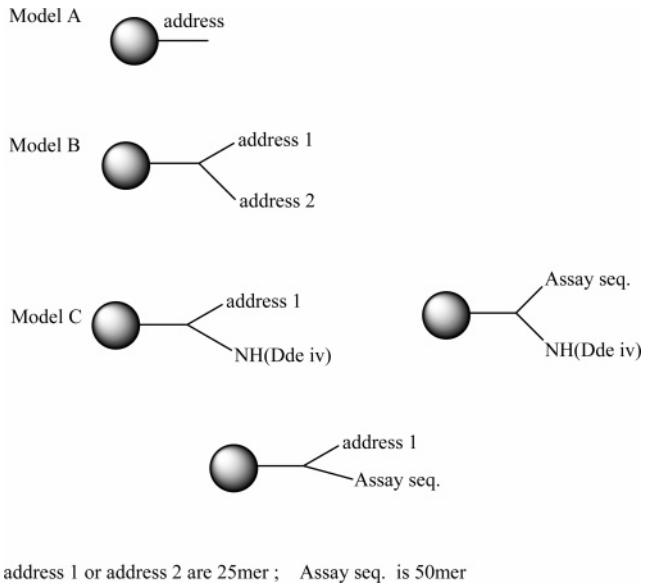

Figure 6. Bead models used for proof of various principles.

Chart 1. Effect of Titration of Oligonucleotide Amount on Beads for 5 Random Address Sequences (25mers)

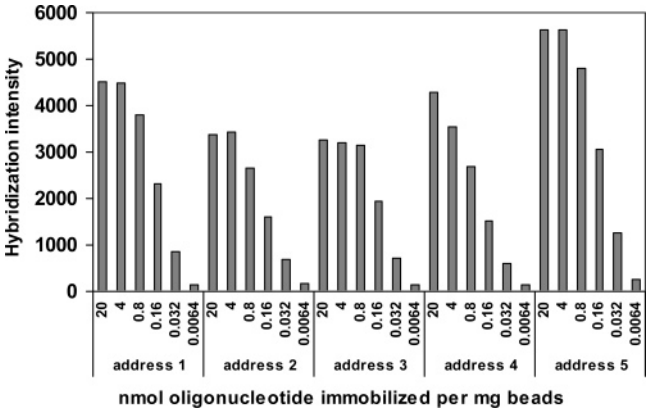

immobilized with only a single type of oligonucleotide (Figure 6, model A). Since we use excess oligo during the immobilization process (4 nmol of oligo per 1 mg of beads), we believe that the amount of oligo immobilized is consistent regardless of the sequence involved. To demonstrate the fact that a consistent amount of oligonucleotide is immobilized, the beads were immobilized at six different oligonucleotide concentrations ranging from 20 to 0.0064 nmol per mg of beads. These titration results for five address sequences are shown in Chart 1.

Another possible reason for variation in hybridization intensities could be variation in hybridization efficiency. This can be a result of sequence dependence or a result of variation in material quality.

To address variation in material quality, several oligonucleotides from different synthesis batches were immobilized on beads (single oligonucleotide immobilization) and then hybridized to the same target labeled oligos. The intensity of hybridization signals was measured using FACS.

Results show that there is similarity between hybridization intensities of the same sequences from different synthesis batches. This observation suggests that the major contribution to the variation in hybridization intensities comes from sequence variation, although material quality also contributes somewhat.

When two oligonucleotides are immobilized simultaneously (as in Figure 3b), the picture becomes even more complex, since oligonucleotide interactions can now come into play. Since immobilization kinetics can be different for different sequences,

Chart 2. Effect of Various Immobilization Conditions (Known To Disrupt Secondary Structure) on Hybridization Intensities of Two Oligonucleotides Immobilized Simultaneously[a]

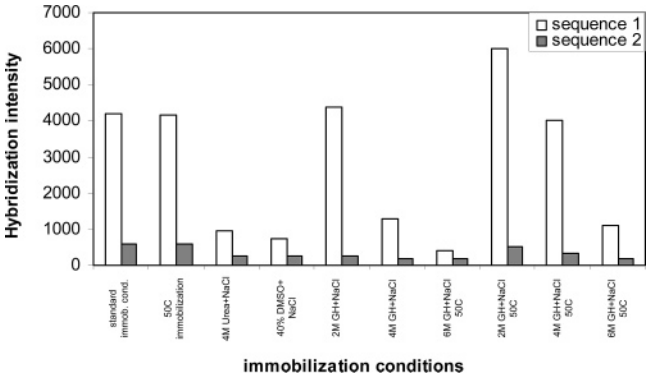

[a] Standard immobilization conditions (described in detail in Experimental Procedures) include 2 M NaCl and room temperature (a). To disrupt secondary structure immobilization was done at 50 °C (b), urea was added to a final concentration of 4 M (c), dimethyl sulfoxide (DMSO) was added to a final concentration of 40% (d), guanidinium hydrochloride (GH) was added to a final concentration of 2 M (e), 4 M (f), and 6 M (g). Also guanidinium hydrochloride was added to a final concentration of 2 M (h), 4 M (i), or 6 M (j) and immobilization was done at 50 °C.

we could have unequal amounts of the two oligonucleotides immobilized on the beads, which could result in very different hybridization intensities. To test whether the source of variation in the hybridization signals of oligonucleotides (immobilized simultaneously) is a result of unequal amounts of oligonucleotides immobilized on the beads, we attempted to equalize their immobilization kinetics by disrupting their secondary structure.

The immobilization procedure was carried out both under the usual conditions (see Experimental Procedures) and under conditions which are known to disrupt secondary structures, such as high temperatures (50 °C) and high concentrations of either urea (4 M) or guanidinium hydrochloride (6 M).

Chart 2 shows that, despite disruption of secondary structure, sequence 1 continues to yield much higher hybridization intensities than sequence 2. These observations suggest that, since equal amounts of the two oligonucleotides are immobilized, the variation in hybridization signals is a result of differences in hybridization efficiency for different sequences. It is still unclear why the variation in hybridization signals becomes more pronounced when two oligonucleotides are immobilized simultaneously on the bead.

We concluded that, if the scheme in Figure 3b were chosen, all oligonucleotides would have to be prescreened prior to use to select pairs with similar hybridization signals after immobilization. Since this problem is mainly sequence related, the screening would have to be done only once. Another way to avoid the problem would be to use the scheme in Figure 3a or the scheme in Figure 3c where immobilizations of the different oligonucleotides are done sequentially.

Immobilization of Second Oligonucleotide (Genespecific Assay Sequence). After either one or two oligonucleotides were immobilized on the first amino group (Figure 3a−c), the second amino group was then activated prior to the immobilization of the second oligonucleotide. As shown in Figure 4, the amine was deprotected with 2% hydrazine/DMF solution and then activated with cyanuric chloride. Following activation, a severe drop in the hybridization intensity of the first oligonucleotide(s) was observed. Apparently, cyanuric chloride damages the oligonucleotides already present on the beads and leaves them unable to hybridize well.

Table 1. Hybridization Intensities of First and Second Sequences Resulting from the Different Activation/Attachment Chemistries for the Second Sequence

1st Sequence: S9 5′ (NH_2) TTTGATGTCCCATTCCCCACGCGTT					
2nd Sequence: S13 5′ (NH_2 or CHO) TTTGATCGTAGCCGGTATGCGACGG					
immobilization chemistries for 2nd attachment	5A	5B	5C	5D	5E
hybridization intensity of the 1st sequence before the 2nd sequence was immobilized	4978	5100	5154	5120	4978
hybridization intensity of 1st sequence after the 2nd sequence was immobilized	3925	2640	2729	2852	2670
hybridization intensity of the 2nd sequence	808	205	457	430	2950
1st Sequence: S13 5′ (NH_2) TTTGATCGTAGCCGGTATGCGACGG					
2nd Sequence: S9 5′ (NH_2 or CHO) TTTGATGTCCCATTCCCCACGCGTT					
immobilization chemistries for 2nd attachment	5A	5B	5C	5D	5E
hybridization intensity of the 1st sequence before the 2nd sequence was immobilized	3095	2872	2950	2930	3093
hybridization intensity of 1st sequence after the 2nd sequence was immobilized	2488	1500	1580	1550	1650
hybridization intensity of the 2nd sequence	1400	108	800	820	4800

Chart 3. Effect of Cyanuric Chloride Concentration on the Ability of Capture Probes To Hybridize Their Complement (Target)[a]

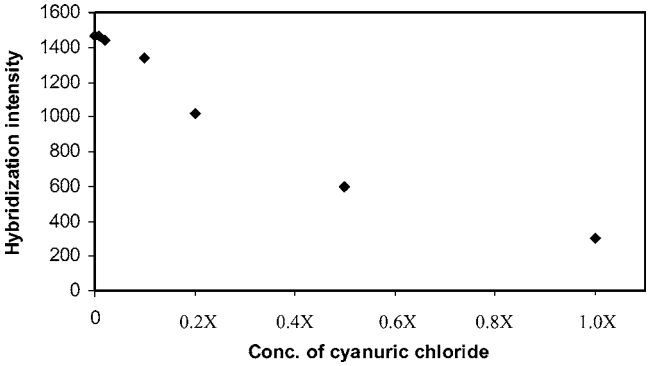

[a] During this experiment oligo-immobilized beads were shaken with cyanuric chloride for 2 h. 1X is the concentration normally used to activate our beads with cyanuric chloride, prior to oligonucleotide attachment.

The effect of cyanuric chloride concentration on the ability of capture probes to hybridize with their complement (target) was examined on a model bead (Figure 6, model A). The amount of cyanuric chloride that was added to oligo-immobilized beads was titrated as shown in Chart 3 (the beads were shaken with various amounts of cyanuric chloride for 2 h to emulate the conditions of an activation reaction).

Titration results show that, when the standard amount of cyanuric chloride (1X = 0.05 mmol) is shaken with oligonucleotide-immobilized beads for 2 h, up to a 5-fold drop in hybridization signal results (relative to beads that are not treated with cyanuric chloride). We then examined the effect of reducing cyanuric chloride concentration on the hybridization signal of oligonucleotides being immobilized. Chart 4 shows that reducing the amount of cyanuric chloride will decrease the hybridization signal of the oligonucleotide that is being immobilized.

This model study suggests that, if we use our standard cyanuric chloride concentration for the activation of the second amine group, up to 80% loss in hybridization intensity may be observed for the first oligonucleotides attached. If the amount of cyanuric chloride is reduced for the activation of the second amine group, there will be loss of hybridization intensity for the second oligonucleotide immobilized. Several attempts to optimize the amount of cyanuric chloride to be used during second amine activation proved unsuccessful. To prevent the drop in hybridization intensities of the first address oligos, new activation schemes were considered for the second amine. In all cases we examined the effect of a particular activation reaction on the hybridization intensities of the first oligonucleotide as well as the second oligonucleotide.

Based on results from our previous paper (*8*), where various amino group activation (and oligonucleotide immobilization) schemes were tested, the reaction schemes shown in Figure 5 were considered.

Chart 4. Effect of Cyanuric Chloride Concentration (during Activation of Amino Beads) on Oligonucleotide Immobilization and Consequently Hybridization Intensities of These Oligonucleotides

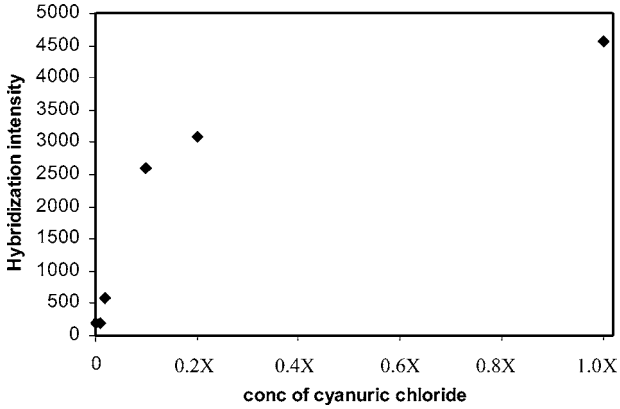

Model beads with two address sequences (Figure 6, model B) were synthesized, with the second amine group activated (and second oligonucleotide immobilized) according to the five different schemes shown in Figure 5. Table 1 summarizes hybridization intensities for both the first and second address sequences, for all of the schemes in Figure 5. The most promising scheme seems to be that in Figure 5E, where the amine was coupled to an activated ester hydrazine and a hydrazone bond was formed with the aldehyde-modified oligonucleotide. We observed very little signal loss for the first oligonucleotide and very good intensities for the second oligonucleotide.

Optimization of Capture Probe Loading. In our previous paper (*8*) we first optimized oligo loading (using 5′ amino labeled and 3′ Fmoc labeled oligos) and then measured the hybridization efficiency for single attachment beads. After coupling the beads to the modified lysine (see Figure 4) we have a different number of amino sites available for activation/immobilization and at a different proximity. As a result it is important to optimize the amount of oligo that we need to immobilize on these double-attachment beads in order to obtain the highest possible hybridization signals. In these experiments maximal hybridization efficiencies or oligo loading was not investigated; instead, when choosing the optimal oligo concentration for immobilization, we were more interested in hybridization intensities (functional results). Titration of oligonucleotide concentration during immobilization was done for several model beads. The titration was accomplished for beads with address oligonucleotides (25mers), beads with assay sequences (50mers), and beads with both oligonucleotides immobilized together on the two attachment beads (see Figure 6, model C). Chart 5 shows that maximal hybridization intensities were observed in the same range of oligonucleotide concentration (1−4 nmol of oligonucleotide per 1 mg of beads) regardless of oligonucleotide length. Similarly, maximal hybridization intensi-

Chart 5. Effect of Titration of Oligonucleotide Amount on Two Attachment Beads Shown in Figure 6 Model C, for 4 Random Address Sequences (25mers) and 4 Random Assay Sequences (50mers)

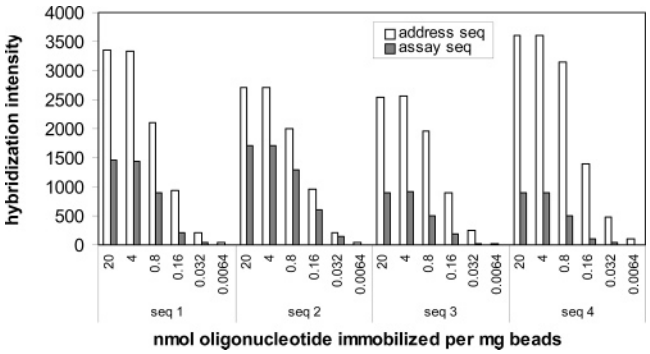

ties were observed in the same range of oligonucleotide concentration when both oligonucleotides were immobilized on the bead (results not shown).

Scale-Up to Over 1000 Bead Types. In order to test the scalability of our schemes (Figure 3a,b, group B), we prepared over 1000 bead types (using each scheme). In each of these schemes two address oligos were used, allowing us to create over 1000 bead types with a mere 60−70 address oligonucleotides.

Since the number of address oligonucleotides required is two times the square root of the number of unique beads, to create 1225 bead types requires only 70 address sequences. These address sequences were chosen out of 1100 random address sequences following a quick screening process where 4−5 address sequences were immobilized on a bead simultaneously, and 70 sequences that give the highest as well as similar hybridization intensities were then chosen. The address sequences were divided into two groups (address sequence 1 and address sequence 2) of 35 oligonucleotides each. Initially synthesis steps described in Figure 4 were followed; then after the first amine activation the beads were distributed into thirteen 96 well plates and to each well an equimolar mix of address sequence 1 and address sequence 2 (all possible combinations) was added creating 1225 unique bead types (immobilization is described in Experimental Procedures). The immobilization was followed by deprotection of the second amine (see Figure 4). The beads were then hybridized to the complementary FAM labeled targets one at a time (either complement to address sequence 1 or to address sequence 2), and hybridization intensities were measured on FACS. Distribution of the hybridization intensities is shown in Chart 6.

Chart 6 shows that hybridization intensities for the various bead types range from 400 to 2400 counts, and the ratio of hybridization intensities of address sequence 1 to address sequence 2 is around one. These hybridization intensities appear to be sufficient for a robust decoding. The main drawback of this model is the prescreening that must be done for the address oligonucleotides due to the interactions that were observed between oligonucleotides (causing extreme variations in hybridization intensities) when two or more were immobilized simultaneously.

Similarly, the scale-up for the scheme in Figure 3a was done using 64 address sequences creating 1024 unique bead types. The scale-up for the scheme in Figure 3a was done using a model for the scheme to demonstrate feasibility of scale-up (see Figure 6, model B). The address sequences were divided into two groups (address sequence 1 and address sequence 2) of 32 oligonucleotides each. Initially synthesis steps described in Figure 4 were followed; then after the first amine activation the beads were distributed into a 96 well plate, and one of the

Chart 6. Distribution of Hybridization Intensities for 1225 Two Attachment Beads Hybridized to Complement of Address 1

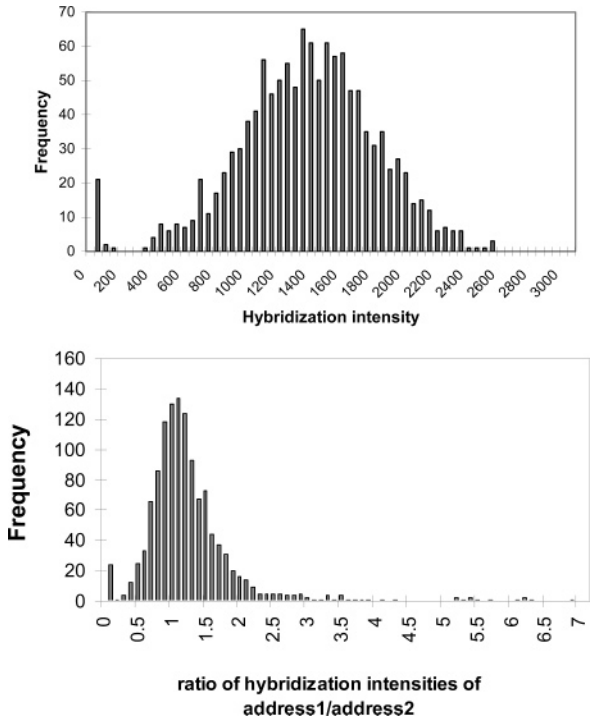

oligonucleotides from the first group (address sequence 1) was added to each well (immobilization is described in Experimental Procedures). The second amine was then deprotected and coupled to SHNH (see Figure 5 scheme E). Finally, beads from each well were distributed into 32 wells and immobilized with each of the 32 oligonucleotides from the second group (address sequence 2). The beads were then hybridized to the complementary FAM labeled targets one at a time (complement either to address sequence 1 or to address sequence 2), and hybridization intensities were measured on FACS. Distribution of the hybridization intensities is shown in Chart 7.

Chart 7 shows that hybridization intensities for the various bead types range from 1400 to 5000 counts, and the ratio of hybridization intensities of address sequence 1 to address sequence 2 is around one. The hybridization intensities are quite high and are more than sufficient for robust decoding. Even more importantly the address sequences were chosen completely at random yet hybridization intensities were fairly similar. We believe this is because the address sequences are immobilized separately and therefore there is no interaction between them during immobilization (see section about variation in signal intensities of oligonucleotides). One of our concerns was that there were reactive sites remaining after immobilization of oligo1; in such a case, oligo2 could immobilize on these reactive sites. However, the observation that the ratio of hybridization intensities of address sequence 1 to address sequence 2 is around one suggests that, if this type of immobilization is taking place, it is minimal; otherwise we would expect this ratio to be much less than one.

CONCLUSIONS

We evaluated several schemes for attaching two oligonucleotides on one bead. The schemes fall into 3 main groups. In the first group the oligonucleotides are sequentially immobilized following a simultaneous coupling (to the beads) of two orthogonally protected glycines. In the second group the oligonucleotides are sequentially immobilized following coupling of the beads to orthogonally protected lysine, and in the third group the oligonucleotides are synthesized in one long

Chart 7. Distribution of Hybridization Intensities for 1024 Two Attachment Beads Hybridized to Complement of Address 1

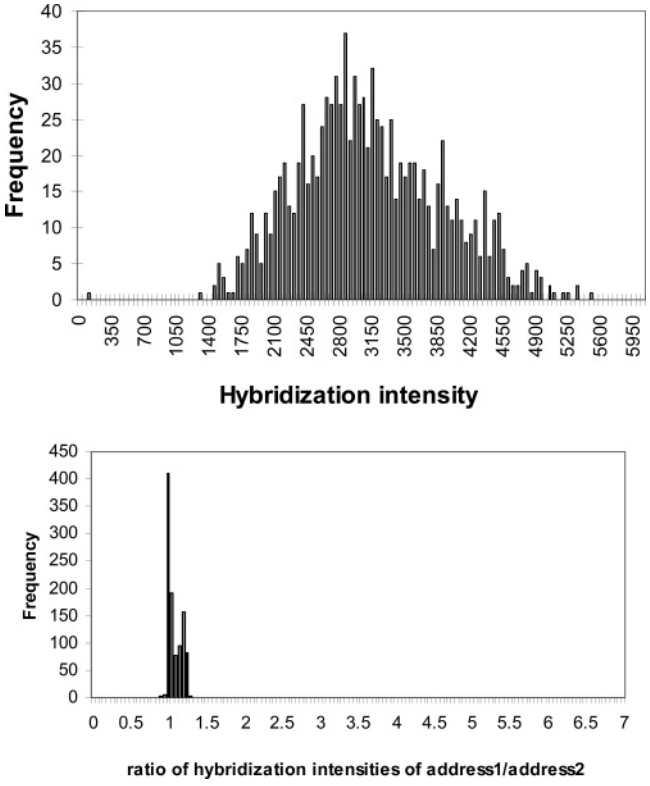

sequence and immobilized as one oligonucleotide. After schemes from group A and group C were rejected for various reasons (see Results and Discussion), we evaluated schemes from group B (shown in Figure 3). We found that, if two oligonucleotides are immobilized simultaneously (as in Figure 3b), they interact during immobilization and as a result their hybridization intensities can be vastly different. We also found that, in Figure 3a where the address sequences are immobilized sequentially, the differences in hybridization intensities are less pronounced, which allows us to avoid prescreening of the address sequences.

We also found that cyanuric chloride damages oligonucleotides and therefore activation of the second amine required a different chemistry. After testing five different approaches for amine activation and oligonucleotide immobilization, we showed that the best method involves amine coupling to an activated ester hydrazine and immobilization of an aldehyde-modified oligonucleotide.

Loading of oligonucleotides on beads was shown to be independent of oligonucleotide length and independent of whether one oligonucleotide or two (through lysine coupling) were immobilized.

Finally, in order to test the scalability of our schemes (Figure 3a,b) we prepared over 1000 bead types (using a model of each scheme). In each of these models two address oligos were used, allowing us to create over 1000 bead types with a mere 60−70 address oligonucleotides. We found that both approaches were successful. Hybridization intensities for all bead types were similar, and the ratio of hybridization intensities of address sequence 1 to address sequence 2 was around one. The hybridization intensities were quite high and were more than sufficient for robust decoding. The scheme in Figure 3a, however, has an advantage over the scheme in Figure 3b because the address sequences are immobilized separately and therefore there is no competition during immobilization so the address sequences can be chosen at random. In contrast, the scheme in Figure 3b requires prescreening of address sequences.

ACKNOWLEDGMENT

We would like to thank Dr. Semyon Kruglyak and Illumina's Bioinformatics group for all their help with image registration and analysis, and Dr. Igor Kozlov and the chemistry group for support and discussion.

LITERATURE CITED

(1) Ramsey, G. (1998) DNA chips: State-of-the art. *Nat. Biotechnol. 16*, 40−44.

(2) Freeman, W. M., Robertson, D. J., and Vrana, K. E. (2000) Fundamentals of DNA Hybridization Arrays for Gene Expression Analysis. *BioTechniques 29*, 1042−1055.

(3) Fodor, S. P. A., Read, J. L., Pirrung, M. C., Stryer, L., Lu, A. T., and Solas, D. (1991) Light-directed, spatially addressable parallel chemical synthesis. *Science 251*, 767−773.

(4) Schena, M., Shalon, D., Davis, R. W., and Brown, P. O. (1995) Quantitative monitoring of gene expression patterns with a complementary DNA microarray. *Science 270*, 467−470.

(5) Holloway, A. J., Van Laar, R. K., Tothill, R. W., and Bowtell, D. D. (2002) Options available—from start to finish—for obtaining data from DNA microarrays II. *Nat. Genet. 32* (Suppl.), 481−489.

(6) Gunderson, K. L., Kruglyak, S., Graige, M. S., Garcia, F., Kermani, B. G., Zhao, C., Che, D., Dickinson, T., Wickham, E., Bierle, J., Doucet, D., Milewski, M., Yang, R., Siegmund, C., Haas, J., Zhou, L., Oliphant, A., Fan, J. B., Barnard, S., and Chee, M. (2004) Decoding randomly ordered DNA arrays. *Genome Res. 14*, 870−877.

(7) Michael, K. L., Taylor, L. C., Schultz, S. L., and Walt, D. R. (1998) Randomly ordered addressable high-density optical sensor arrays. *Anal. Chem. 70*, 1242−1248.

(8) Steinberg, G., Stromsborg, K., Thomas, L., Barker, D., and Zhao, C. (2004) Strategies for covalent attachment of DNA to beads. *Biopolymers 73*, 597−604.

BC060012V

TECHNICAL NOTES

Targeted Liposomes: Convenient Coupling of Ligands to Preformed Vesicles Using "Click Chemistry"

Fatouma Said Hassane, Benoît Frisch, and Francis Schuber*

Institut Gilbert Laustriat, UMR 7175 CNRS/Université Louis Pasteur (Strasbourg I), Département de Chimie Bioorganique, Faculté de Pharmacie, 74 route du Rhin, 67400 Illkirch, France. Received October 24, 2005; Revised Manuscript Received February 28, 2006

An efficient and convenient chemoselective conjugation method based on "click chemistry" was developed for coupling ligands to the surface of preformed liposomes. It can be performed under mild conditions in aqueous buffers; the use of a water soluble Cu(I) chelator, such as bathophenanthrolinedisulfonate, was essential to obtain good yields in reasonable reaction times. A model reaction was achieved in which, in a single step, an unprotected α-D-mannosyl derivative carrying a spacer arm functionalized with an azide group was conjugated to the surface of vesicles presenting a synthetic lipid carrying a terminal alkyne function. When liposomes composed of saturated phospholipids were used, the reaction conditions developed in the present work did not damage the membranes as measured by the absence of leakage of entrapped 5,6-carboxyfluorescein. Moreover, as assessed by agglutination experiments using concanavalin A, the mannose residues were perfectly accessible on the surface of the targeted vesicles.

INTRODUCTION

Liposomes, which are self-closed vesicular structures composed of (phospho)lipid bilayers, have attracted considerable interest because of their potential applications in various fields such as membrane models, diagnostics, and drug/gene delivery (*1*). Several liposomal formulations have reached clinical application during this past decade especially for the treatment of cancer and opportunistic diseases (*2*). The discovery of "stealth liposomes"—liposomes coated with, e.g., poly(ethylene glycol) (PEG) chains characterized by much increased circulation times and modified biodistributions—provoked a new impetus for the design of targeted bioactive molecule delivery systems. Such liposomes carry ligands that provide specific interactions with receptors/antigens expressed at the surface of target cells. The design of targeted liposomes is heavily dependent on the development of well-controlled bioconjugation reactions (for reviews see refs *3*−*6*) which in most cases involve the coupling of ligands to the surface of preformed vesicles that carry functionalized (phospho)lipid anchors. Among the many conjugation methods available, the most popular ones involve the reaction of thiol-containing ligands with anchors carrying thiol-reactive functions such as maleimide, bromoacetyl, or 2-pyridyldithio linkages, generating thioether or disulfide bonds (*7*−*9*). More recently peptide ligands were also coupled to the surface of liposomes via hydrazone and α-oxo hydrazone linkages (*10*).

Chemically controlled conjugation between preformed liposomes and ligands should ideally combine several features such as mild reaction conditions in aqueous media, high yields, and chemoselectivity. In search of new coupling strategies we have explored the application of "click chemistry" (*11*, *12*) to this field; it involves a copper(I)-catalyzed Huisgen 1,3-dipolar cycloaddition reaction of azides and alkynes yielding 1,4-disubstituted 1,2,3-triazole linked conjugates (*13*, *14*). This reaction is particularly appealing because it is highly regiospecific, chemoselective, and tolerant to a wide variety of other functional groups. Moreover the click reaction, which can also be performed almost quantitatively under mild conditions in aqueous buffers, was recently extended to bioconjugation applications (see, e.g., refs *15*−*23*). Herein we report the successful application of click chemistry to the conjugation, in a single step, of an unprotected α-D-mannosyl derivative carrying a spacer arm functionalized with an azide group, to the surface of liposomes that incorporate a synthetic lipid carrying a terminal triple bond. Reaction conditions were optimized for this model reaction, and mannosylated vesicles were obtained in excellent yield. As assessed by agglutination experiments with the lectin concanavalin A (Con A), the mannose residues were perfectly accessible on the surface of the vesicles and could engage into multivalent interactions.

EXPERIMENTAL PROCEDURES

General. Reagent-grade solvents were used without further purification. The phospholipids 1,2-dipalmitoyl-*sn*-glycero-3-phosphocholine (DPPC) and 1,2-dipalmitoyl-*rac*-glycero-3-phospho-*rac*-(1-glycerol) sodium salt (DPPG) were purchased from Sigma-Aldrich (Saint-Quentin-Fallavier, France), and their purity (over 99%) was assessed by TLC. Cholesterol was recrystallized in methanol. The amine **5** (Scheme 2), that contains 12 ± 2 ethyloxide units, was a kind gift from Dr. L. Lebeau. The lectin concanavalin A, type VI (Jack Bean), was obtained from Sigma. L-Ascorbic acid sodium salt and bathophenanthrolinedisulfonic acid disodium salt are from Acros-Organics (Noisy-le-Grand, France) and Lancaster-Synthesis (Strasbourg-Bischheim, France), respectively. Silica gel 60 F

* To whom correspondence should be addressed. Phone: + 33 390 24 41 72. Fax: +33 390 24 43 06. E-mail: francis.schuber@pharma.u-strasbg.fr.

10.1021/bc050308l CCC: $33.50 © 2006 American Chemical Society
Published on Web 04/18/2006

Scheme 1. Model Reaction

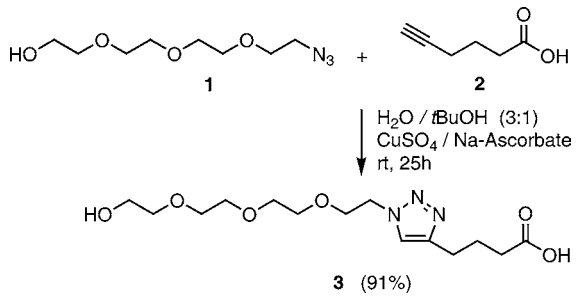

Scheme 2. Synthesis of the Functionalized Ligand Azidomannose, 7

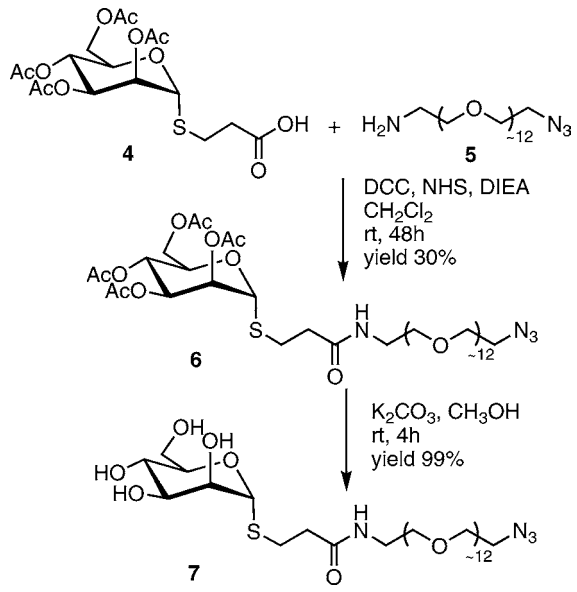

254 plates for thin-layer chromatography (TLC) were purchased from Merck (Darmstadt, Germany). Column chromatographic separations were carried out as flash chromatography using silica gel (Merck) with a particle size of 0.040−0.063 mm. ^{1}H and ^{13}C NMR were recorded on Bruker Avance 200 (200 MHz) and DPX-300 (300 MHz) spectrometers. Chemical shifts are expressed as parts per million using $CHCl_3$ ($\delta = 7.27$ ppm for ^{1}H and 77.7 ppm for ^{13}C) or CH_3OH ($\delta = 3.35$ ppm for ^{1}H and 49.0 ppm for ^{13}C) as the internal standard ($\delta = 0.0$ ppm). Mass spectra (ES-MS) were recorded on a ESI/TOF Mariner mass spectrometer by electrospray.

4-[1-(2-(2-(2-(2-Hydroxyethoxy)ethoxy)ethoxy)ethyl)-1*H*-1,2,3-triazol-4-yl]butanoic Acid (3). To 5-hexynoic acid (Lancaster-Synthesis) (21 mg, 0.187 mmol) in 200 μL of *t*-BuOH were added 200 μL of freshly prepared solutions of $CuSO_4 \cdot 5H_2O$ (1 mg, 4 μmol) and sodium ascorbate (3.6 mg, 18.2 μmol) in water. Compound **1** (*24*) (40 mg, 0.182 mmol) was then added dissolved in 200 μL of water. The reaction mixture was stirred under argon at room temperature for 25 h. The solvent was then evaporated to dryness, and the product **3** was obtained without any purification. The yield was estimated at 91% according to NMR analysis. R_f: 0.51 (CH_2Cl_2:MeOH 19:1). ^{1}H NMR (200 MHz, $CDCl_3$:CD_3OD, 1:2): δ 7.56 (s, 1H, C*H* triazole); 4.52−4.47 (t, $J = 4.9$ Hz, 2H, CH_2N); 3.85−3.80 (t, $J = 4.9$ Hz, 2H, CH_2CH$_2$N); 3.73−3.57 (m, 10H, CH_2OCH_2CH$_2$OCH_2CH$_2$OH); 3.40−3.06 (t, $J = 5.0$ Hz, 2H, CH_2OCH$_2$CH$_2$N); 2.81−2.74 (t, $J = 7.2$ Hz, 2H, CH_2CCH); 2.39−2.32 (t, $J = 7.1$ Hz, 2H, CH_2-COOH); 2.06−1.91 (m, 2H, CH_2CH$_2$COOH). ES-MS *m*/*z*: 332.2656 ([M + H]$^+$), calcd 331.1743 for $C_{14}H_{25}N_3O_6$.

N-[(2-(2-Azidoethoxy)ethoxy$_{10}$)ethyl-(1-deoxy-2,3,4,6-tetra-*O*-acetyl-thio-α-D-mannopyranosyl)]propionamide (6). To a solution of **4** (*25*) (149 mg, 0.342 mmol) in 3 mL of CH_2Cl_2 were added DCC (85 mg, 0.41 mmol) and NHS (47 mg, 0.41 mmol). After 45 min of stirring at room temperature under argon, the amine **5** (*26*) (210 mg, 0.342 mole) in 1 mL of CH_2Cl_2 containing DIEA (47.5 μL, 0.273 mol) was added to the reaction mixture. After 18 h, 20 μL of DIEA and 0.2 equiv of **5** were again added. The stirring was continued during 48 h. The precipitate was then removed by filtration, and the organic phase was washed with 2 × 10 mL of a citric acid solution (5%, w/v) followed by water. After passage over $MgSO_4$, the solvent was evaporated to dryness. The reaction product **6** (129 mg; yield 30%, yellow oil) was obtained after purification by chromatography on silica gel eluted with CH_2Cl_2:MeOH 30:1. R_f: 0.42 (CH_2Cl_2:MeOH 9:1). ^{1}H NMR (200 MHz, $CDCl_3$): δ 5.39−5.10 (m, 4H, 3 C*H* Man + 1 CHα); δ 5.39−5.10 (m, 4H, C*H* Man); 4.28−4.23 (m, 2H, CH_2 Man); 4.04−3.99 (m, 1H, C*H*-CH$_2$OH Man); 3.56−3.30 (m, 52H, CH_2NH, CH_2O−CH_2, CH_2CH$_2$NH, CH_2N$_3$); 2.88−2.81 (t, $J = 6.9$ Hz, 2H, CH_2S); 2.47−2.40 (t, $J = 7.04$ Hz, CH_2CH$_2$S); 2.08, 2.02, 1.97, 1.90 (s, 12H, CH_3CO). ^{13}C NMR (50 MHz, $CDCl_3$): δ 170.99 (*C*ONH); 170.13 (*C*OOCH$_3$); 83.03 (C_1); 71.37, 71.00, 70.68, 70.44 (CH$_2$O-*C*H$_2$, *C*H$_2$CH$_2$NH); 70.15 (C_2); 69.81 (C_5); 69.43 (C_3); 66.75 (C_4); 62.87 (C_6); 51.08 (*C*H$_2$N$_3$); 39.79 (*C*H$_2$NH); 36.56 (*C*H$_2$CO); 27.33 (*C*H$_2$S); 21.30 (*C*H$_3$OCO). ES-MS *m*/*z*: 1055.6430 ([M + Na$^+$]), calcd 1032,4672 for $C_{43}H_{76}N_4O_{22}S$.

***N*-[2-(2-Azidoethoxy)ethoxy$_{10}$)-ethyl(1-deoxy-1-thio-α-D-mannopyranosyl)]propionamide (7).** Compound **6** (100 mg, 0.097 mmol) was dissolved in 3 mL of MeOH, and K_2CO_3 (20 mg, 0.145 mmol) was then added with a few drops of water. The deprotection reaction was performed under argon at room temperature for 4 h. The reaction product **7** (84 mg, yield 100%) was obtained as a yellow oil after filtration to remove the salts and evaporation of the solvents. R_f: 0.30 (CH_2Cl_2:MeOH 8:2). ^{1}H NMR (200 MHz, CD_3OD): δ 5.26 (s, 1H, C*H*α); 3.92−3.87 (m, 2H, CH_2 Man); 3.67−3.32 (m, 55H, C*H* Man, CH_2-NH, CH_2OCH_2, CH_2CH$_2$NH, CH_2N$_3$); 3.02−2.86 (m, 2H, CH_2S); 2.64−2.48 (m, 2H, CH_2CH$_2$S). ^{13}C NMR (50 MHz, CD_3OD): δ 174.22 (*C*ONH); 87.48 (C_1); 75.04 (C_2); 73.63 (C_5); 73.21 (C_3); 70.79 (*C*H$_2$O-*C*H$_2$, *C*H$_2$CH$_2$NH,); 68.90 (C_4); 62.85 (C_6); 51.70 (*C*H$_2$N$_3$); 40.22 (*C*H$_2$NH); 37.34 (*C*H$_2$CH$_2$S); 28.82 (*C*H$_2$S). ES-MS *m*/*z*: 903.4658 ([M + K$^+$]), calcd 864.4249 for $C_{35}H_{68}N_4O_{18}S$.

***N*-[2-(2-(2-(2-(2,3-Bis(hexadecyloxy)propoxy)ethoxy)ethoxy)-ethoxy)ethyl]hex-5-ynamide (8).** DCC (52 mg, 0.25 mmol) and NHS (12 mg, 0.105 mmol) were added to a solution of 5-hexynoic acid (**2**) (23 mg, 0.21 mmol) in CH_2Cl_2 (4 mL). 2-(2-(2-(2,3-Bis(hexadecyloxy)propoxy)ethoxy)ethoxy)-ethoxyethanolamine (150 mg, 0.21 mmol), synthesized as outlined in ref *27*, and DIEA (43 μL, 0.25 mmol) were then added to the mixture. After 22 h of reaction with stirring at room temperature, and under argon, the formed precipitate was removed by filtration and the organic phase was washed with 2 × 10 mL of a solution of citric acid (5%, w/v) followed by 2 × 10 mL of brine. After passage over $MgSO_4$, the solvent was evaporated to dryness. The reaction product **8** (98 mg; yield 58%) was obtained after purification by chromatography on silica gel eluted with CH_2Cl_2:AcOEt 9:1 to 7:3. A white powder was obtained by recrystallization from CH_2Cl_2:MeOH (1:9, v/v). R_f: 0.54 (CH_2Cl_2:MeOH 19:1). ^{1}H NMR (300 MHz, $CDCl_3$): δ 3.65−3.39 (m, 25H, CH_2NH, CH_2O, *H*C(CH$_2$)$_2$O); 2.33−2.22 (m, 4H, NHCOCH_2, CH_2CCH); 1.98−1.96 (t, $J = 2.3$ Hz, 1H, CC*H*); 1.90−1.80 (m, 2H, CH$_2$CH_2CH$_2$); 1.56−1.51 (m, 4H, CH$_2$CH_2CH$_2$O); 1.24 (s, 52H, CH_2 alkyl chains); 0.89−0.84 (t, $J = 6.39$, 6H, CH_3). ^{13}C NMR (75 MHz, $CDCl_3$): δ 172.90 (*C*ONH); 84.26 (*C*CH); 78.54 (CH$_2$*C*HCH$_2$); 72.33, 72.10 (OCH$_2$C*H*CH$_2$O); 71.51 (CH$_2$CH$_2$*C*H$_2$O); 71.37, 71.25, 70.91, 70.54 (*C*H$_2$O); 69.77 (C*C*H); 39.84 (*C*H$_2$N); 35.65

(NHCO*C*H_2); 32.57 (*C*H_2*C*H_2*C*H_3); 30.76(*C*H_2*C*H_2*C*H_2O); 30.35, 30.17, 30.01 (alkyl chains); 26.76 (*C*H_2*C*H_2*C*H_2O); 24.86 (*C*H_2-*C*H_2CCH); 23.34 (*C*H_2*C*H_3); 18.54 (*C*H_2CCH); 14.76 (*C*H_3). ES-MS *m/z*: 832.8311 ([M + Na^+]), calcd 809.7109 for $C_{49}H_{95}NO_7$.

Liposome Preparation and Characterization. Small unilamellar vesicles (SUV) were prepared by sonication. Briefly, phospholipids (DPPC, DPPG) and cholesterol (70/20/50 molar ratio) dissolved in chloroform/methanol (9:1, v/v) were mixed in a round-bottom flask. For functionalized vesicles, the lipid anchor **8** dissolved in chloroform/methanol (9:1, v/v) was added at given concentrations (between 5 and 10 mol %). After solvent evaporation under high vacuum, the dried lipid film was hydrated by addition of 1 mL of HBS (10 mM HEPES, 145 mM NaCl, pH 6.5) to obtain a final concentration of 10 μmol of lipid/mL. The mixture was vortexed, and the resulting suspension was sonicated for 1 h at 60 °C, i.e., above the T_m of the lipids, using a 3 mm diameter probe sonicator (Vibra Cell, Sonics and Materials Inc., Danbury, CT). The liposome preparations were then centrifuged at 10000*g* during 10 min to remove the titanium particles originating from the probe. The size of the liposomes was determined by dynamic light scattering using a submicron particle analyzer (Coulter, Hialeah, FL) or a Zetamaster 3000 (Malvern Instrument, Orsay, France). The different vesicle preparations were homogeneous in size and exhibited an average diameter between 90 and 130 nm. The phospholipid content in liposomes was determined according to Rouser (*28*) with sodium phosphate as standard.

Azidomannose Coupling to Liposomes by Click Chemistry. Solutions containing 8 mM $CuSO_4 \cdot 5H_2O$ (solution A), 145 mM sodium ascorbate (solution B), and 28 mM bathophenanthrolinedisulfonic acid disodium salt (ligand **L**, Scheme 3) (solution C) were freshly prepared in 10 mM HEPES (pH 6.5) completed with NaCl to obtain an osmolarity of 300 mOsm. To a suspension of functionalized liposomes in 200 μL of HBS adjusted to a 1 mM concentration of anchor **8** (i.e., ~0.5 mM surface available alkyne group) were added solutions A and B (respectively 286 and 355 μL) followed by 164 μL of solution C. Following addition of 15 μL of a 13.9 mM solution of azidomannose **7** in water, the reaction mixture was gently stirred under argon at room temperature for 1−24 h. Alternatively, the ligand **L** was first added to the liposome suspensions, followed by the extratemporaneously made mixture of solution A and solution B and finally by azidomannose **7**. Control experiments were performed under the same conditions in the absence of the ligand **7**. After the conjugation step, the liposomes were purified by exclusion chromatography on a 1 × 18 cm Sephadex G-75 (Amersham Biosciences) column equilibrated in HBS.

Liposome Stability under Coupling Conditions. Liposomes were prepared as above in 10 mM Hepes buffer (pH 6.5) containing 100 mM NaCl and 40 mM 5,6-carboxyfluorescein. Nonencapsulated dye was eliminated by gel filtration (see above). The dye-loaded liposomal suspensions were treated as above for the click-chemistry coupling step. The leakage of 5,6-carboxyfluorescein was assessed by determining the fluorescence increase (λ_{ex} 490 nm; λ_{em} 520 nm) observed in the presence of excess detergent. To measure the total fluorescence intensity corresponding to 100% dye release, Triton X-100 (0.1% w/v final) was added to the vesicles. The percentage of dye release caused by the coupling conditions was calculated using the equation $(F - F_0) \times 100/(F_t - F_0)$, where F is the fluorescence intensity measured after exposing the vesicles to the coupling conditions and F_0 and F_t respectively are the intensities obtained before the coupling conditions and after Triton X-100 treatment (*29*). F_t values were corrected for dilutions caused by the Triton X-100 addition.

Lectin Binding Assay and Analytical Techniques. The lectin Con A (125 μg) was added to suspensions (1 mL final volume) of liposomes carrying mannose residues (60 nmol of lipids and ~3 nmol of surface coupled mannose residue) in HBS. The increase in turbidity was recorded at 360 nm at room temperature. Mannose coupled to the liposomes was quantified by the resorcinol−sulfuric acid method (*30*). The standard curve was established as follows: To a 12.2 × 100 mm glass tube containing 2−12 μg of reference mannose in 200 μL water were added successively 20 μL of 0.1% (w/v) Triton X-100, 200 μL of a 6 mg/mL aqueous solution of resorcinol, and 1 mL of 75% (v/v) H_2SO_4. The tubes were vortexed and covered with aluminum foil before heating in a boiling water bath for 12 min and then cooled to room temperature. The optical density was then recorded at 430 nm. Aliquots of conjugated liposomes (about 0.4 μmol of lipid) were first dried under vacuum using a Speed Vac (Savant Instrument Inc., Holbrook, NY). HBS (200 μL) was then added to the tubes and the mixtures, after vortex mixing, were treated as indicated above for the standards. Before optical density reading the samples were filtered through a 0.45 μm PTFE filter. The spectrophotometric determination of copper present in the final liposomal preparations was carried out using an atomic absorption spectrophotometer Varian SpectrAA 50B calibrated with a standard solution of $CuSO_4 \cdot 5H_2O$ (0.195−3.9 μg/mL). Samples (1 mL, about 0.65 μmol of phospholipids) were added to a solution of 5% nitric acid (5 mL) completed to 7 mL with water. The mixtures were vortexed and filtered on a 0.22-μm membrane (Millex, Millipore), and the copper content was determined.

RESULTS AND DISCUSSION

Chemistry. The synthesis of the azidomannose ligand **7** (Scheme 2), destined to be conjugated at the surface of preformed liposomes using a click reaction (Scheme 3), consisted in a coupling between the known mannosyl derivative **4** (*25*) and a PEG chain (n ~12) functionalized with amine and azide functions (compound **5**) synthesized as described previously (*26*). The carboxylic acid function of **7** was classically activated with dicyclohexylcarbodiimide and *N*-hydroxysuccinimide, at room temperature, in the presence of diisopropylethylamine. Compound **5** was then added, and the reaction was carried out for 48 h to give **6**, which, after quantitative deprotection of the acetyl groups with potassium carbonate in methanol, gave the ligand **7**. For the synthesis of the functionalized lipid anchor **8** (Scheme 3), 2-(2-(2-(2,3-bis(hexadecyloxy)propoxy)ethoxy)-ethoxy)ethoxyethanolamine was first synthesized in 7 steps starting from glycerol, triethylene glycol, and palmityl alcohol by an adaptation of a procedure we have described previously (*27*). The free amine of this compound was then reacted with the hydroxysuccinimide ester of 5-hexynoic acid, previously obtained by reaction of its acid function with *N*-hydroxysuccinimide in the presence of dicyclohexylcarbodiimide. The coupling reaction was carried out for 12 h, and the final product **8** was obtained with a satisfactory yield (58%).

Model Reaction. As a proof-of-concept we have explored the possibility to prepare mannosylated liposomes (Scheme 3) using click chemistry. Such liposomes, which have been prepared before (see, e.g., refs *27*, *31*−*34*), are easily characterized and serve as vehicles to target cells such as antigen presenting cells (*35*−*37*). For the conjugation step both alkyne and azide-terminated spacer arms between the mannose residue and the hydrophobic anchor associated with the liposomes can be envisaged. For that reason, in a first approach we have studied a model click reaction between a short PEG spacer functionalized with an azide (**1**, Scheme 1) and 5-hexynoic acid (**2**) catalyzed by copper(I) in solution. The reaction was performed in an aqueous solvent system with reagents that could be

Scheme 3. Coupling of the Ligand 7 to Preformed Liposomes That Incorporate the Alkyne Functionalized Anchor 8 by Click Chemistry in the Presence of the Cu(I) Ligand Bathophenanthrolinedisulfonate

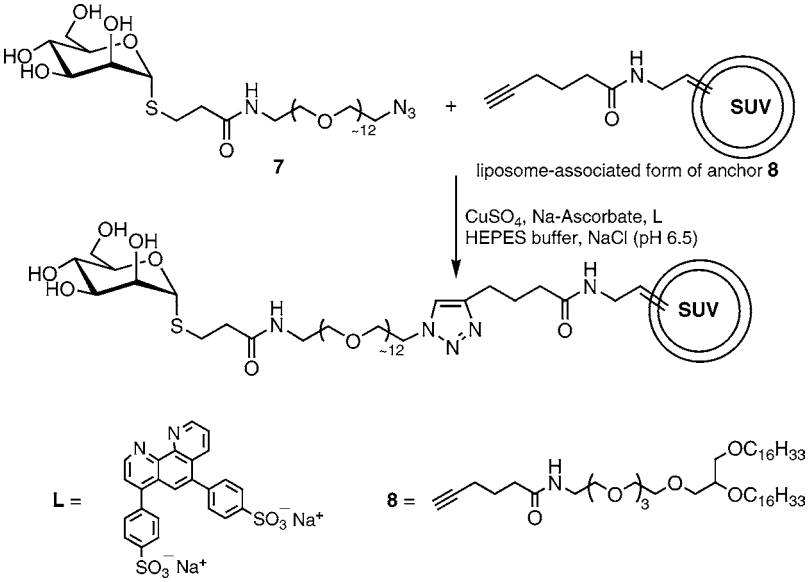

extended, in principle, to the coupling of ligands to the surface of preformed vesicles. The procedure involving in situ generation of active Cu(I) catalyst via reduction of $CuSO_4$ by sodium ascorbate (*13*) proved highly satisfactory and reliable. When starting with an equimolar mixture of **1** and **2** the expected product **3** was obtained over 90% yield after 1 day of reaction, at room temperature, using a copper(II) (2 mol % with respect to reactants)/Na ascorbate (10 mol %) system. In the absence of copper catalyst no reaction was observed. The reaction mechanism of this "ligand-free" Cu(I) catalyzed process (see below), which involves the formation Cu-acetylide, has been outlined recently (*38*, *39*).

Conjugation of Mannose Residues to the Surface of Preformed Liposomes. To perform the coupling of unprotected α-D-mannosyl residues to the surface of preformed liposomes with the click reaction we have first synthesized the ligand **7** that carries an azide function (Scheme 2). We have given a preference to an α-thiomannosyl derivative because this glycosidic bond is very resistant, in vivo, especially toward the action of glycosidases. The mannosyl derivative **4** (*25*) was reacted with a relatively long PEG spacer arm of defined length (*26*), the purpose being to provide an optimal accessibility of the liposomal mannose ligands to their receptors (*40*). Next we have synthesized the anchor **8** (Scheme 3) that carries the alkyne moiety. This function was selected for the anchor because of its chemical "inertness" in vivo and—considering that about 50% of the anchor is oriented toward the interior of the vesicles—its absence of reactivity with (bio)molecules that can be entrapped within the liposomes. The molecule **8** was quantitatively incorporated in the liposomes during their formation.

Small unilamellar vesicles composed of saturated phospholipids (DPPC, DPPG) and cholesterol (70/20/50 molar ratio) and containing 10 mol % of the anchor **8** were prepared (average size: 90−130 nm). For the conjugation of the mannose ligand **7** (Scheme 3) to the preformed liposomes several conditions were tested in an aqueous buffer (pH 6.5). We have first tried to adapt the conditions that gave excellent yields in the model reaction (Scheme 1): i.e., generation of the catalytic Cu(I) by reduction of Cu(II) by sodium ascorbate. Keeping constant the concentrations of liposome (0.1 mM surface accessible anchor **8**) and azidomannose **7** (0.2 mM), the reaction time (24 h), the temperature (25 °C), and the ascorbate/$CuSO_4$ ratio (=5), we have varied the concentration of $CuSO_4$ (1−10 μM). Under these conditions, compared to Scheme 1, covalent coupling of mannose to the liposomes in appreciable yields failed. In fact, much higher concentrations of the ascorbate/$CuSO_4$ couple were needed to observe a conjugation which nevertheless remained relatively modest, i.e., about 25% coupling was observed in the presence of 2.3 mM $CuSO_4$ and 51.5 mM sodium ascorbate. This observation is in agreement with other works which showed that, for bioconjugations involving for example large molecular complexes, catalytic quantities of the ascorbate/$CuSO_4$ system are not enough to drive click reactions to completion. To circumvent this limitation we have added a ligand of copper ions. Indeed, stabilization of the Cu(I) oxidation state by specific heterocyclic ligands was shown to largely accelerate the 1,3-dipolar cycloaddition reaction between azides and alkynes (*41*, *42*). In our case, bathophenanthrolinedisulfonate (**L**; Scheme 3) provided a water soluble (*41*) and potent chelate catalyst for the click reaction. It allowed—when used in a 2-fold excess over copper to reduce the agglutination of the vesicles—a large increase in the yield of mannosylation and a decrease in the reaction time. For example, under standard conditions (24 h) the coupling yield increased from 23%, in the absence of **L**, to nearly completion in its presence. Moreover reaction times could also be decreased because, within 1 h in the presence of **L**, the observed conjugation of **7** was already about 80%. Altogether, we have routinely conjugated, in high yield, ligands such as **7** (2-fold molar excess) to the surface of preformed liposomes carrying alkyne functions in the presence of $CuSO_4$/Na-ascorbate/**L** (2.3, 50, and 4.6 mM) in an aqueous buffer (pH 6.5) at room temperature for 6 h (standard conditions).

In the liposome field it is of importance to verify the integrity of the vesicles after the coupling steps. To that end, using a dynamic light scattering technique, we have first verified whether the reaction conditions described above altered the size of the vesicles. Some changes were noticeable using our standard conditions, i.e., about 50% diameter increases were noted even under control conditions in the absence of ligand **7**. However, we found that this effect could be efficiently limited just by changing the order of reactants added to the liposome suspensions. Thus, when ligand **L** was added before the $CuSO_4$/ascorbate mixture followed by the mannosyl ligand **7**, no significant increase in size of the vesicles could be observed and, importantly, an identical yield of conjugation was measured. Next, to test whether the experimental conditions used for the click reaction could provoke some leakage of the vesicles, we have exposed to our standard conditions the same type of

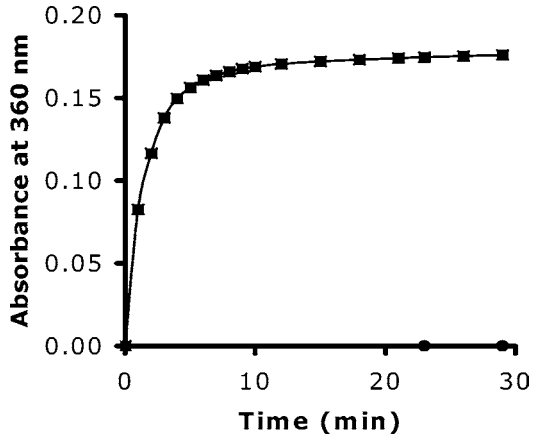

Figure 1. Turbidity changes of suspensions, in HBS (pH 6.5), of targeted liposomes composed of DPPC, DPPG, and Chol (70/20/50 molar ratio) after addition of Con A (125 μg/mL). The coupling time by click reaction (Scheme 3) for the targeted vesicles (−■−) that contained 10 mol % anchor **8** was 3 h; control liposomes (−●−). Liposome concentration = 60 μM lipids.

liposomes having encapsulated self-quenching concentrations of 5,6-carboxyfluorescein (*29*). Using a well-established method (*29*) based on fluorescence quenching determinations (see Experimental Procedures) we could demonstrate that, compared to vesicles incubated in the absence of the coupling reagents, essentially no leakage was triggered by the conjugation reaction. Importantly, these controls indicate that the standard conditions established here are harmless for liposomes made of saturated phospholipids.

Finally, residual copper in our targeted liposome preparations could be a potential concern. Determination by atomic absorption spectroscopy showed, that for our standard conditions, final copper concentrations in our constructs were in the low μM range, whereas using the modified protocol the presence of this ion was no more measurable (<0.03 μg/mL).

Determination of the Accessibility of the Mannose Residues at the Surface of the Liposomes. To determine whether the conjugated mannose residues were easily accessible at the surface of the liposomes we have incubated suspensions of targeted vesicles, that contained 10 mol % of α-thiomannosyl residues exposed at their surface, in the presence of concanavalin A. Addition of the lectin resulted in a gradual increase of turbidity, as assessed by an increase of OD at 360 nm which reached a plateau after about 15 min (Figure 1). In contrast, no absorbance change was observed with control liposomes. The subsequent addition of D-mannose (5.0 mM) to the aggregates triggered a prompt decrease in turbidity (not shown), confirming that the increase in turbidity was due to a specific recognition of the mannose residues on the surface of the vesicles by Con A that resulted in an aggregation due to multivalent interactions.

CONCLUSION

We have developed an efficient and convenient chemoselective conjugation method for coupling ligands onto the surface of preformed liposomes based on click chemistry (*13*). It can be performed under mild conditions in aqueous buffers; however, the use of Cu(I) chelators was essential to observe good yields under reasonable reaction times. Using liposomes composed of saturated phospholipids, the reaction conditions developed in the present work did not alter the integrity of the bilayers, in terms of leakiness, and provided perfectly functional targeted vesicles. This versatile approach, which is particularly suitable for the ligation of water soluble molecules and which can accommodate many chemical functions, is anticipated to be useful in the coupling of many other ligands. Nevertheless, it should be underlined that the mandatory use of copper catalysts in click chemistry could represent a limitation; indeed, vesicles made of unsaturated phospholipids are known to be readily (per)oxidized by copper ions in the presence of oxygen and become leaky (*43*, *44*). Alternative means of promoting catalyst-free ligation reactions between azides and alkynes have been described recently. They involve an activation of the alkyne partner either in strain-promoted activation of cycloalkynes in [3 + 2] cycloaddition reactions with azides (*45*) or 1,3-dipolar cycloadditions of azides with electron-deficient alkynes (*46*). These methods could constitute attractive extensions of the click reactions to biological systems that are sensitive to the action of copper ions.

ACKNOWLEDGMENT

This work was financially supported by the Centre National de la Recherche Scientifique and the Ministère de l'Enseignement Supérieur et de la Recherche (MESR). F.S.H. further acknowledges a graduate research scholarship from the MESR.

LITERATURE CITED

(1) Philippot, J., and Schuber, F. (1995) *Liposomes as Tools in Basic Research and Industry*, CRC Press, Boca Raton.
(2) Allen, T. M., and Cullis, P. R. (2004) Drug delivery systems: entering the mainstream. *Science 303*, 1818−1822.
(3) Schuber, F. (1995) Chemistry of ligand-coupling to liposomes, in *Liposomes as Tools in Basic Research and Industry* (Philippot, J. R., and Schuber, F., Eds.) pp 21−39, CRC Press, Boca Raton.
(4) Sapra, P., and Allen, T. M. (2003) Ligand-targeted liposomal anticancer drugs. *Prog. Lipid Res. 42*, 439−462.
(5) Nobs, L., Buchegger, F., Gurny, R., and Allemann, E. (2004) Current methods for attaching targeting ligands to liposomes and nanoparticles. *J. Pharm. Sci. 93*, 1980−1992.
(6) Torchilin, V. P. (2005) Recent advances with liposomes as pharmaceutical carriers. *Nat. Rev. Drug Discovery 4*, 145−160.
(7) Martin, F. J., and Papahadjopoulos, D. (1982) Irreversible coupling of immunoglobulin fragments to preformed vesicles. *J. Biol. Chem. 257*, 286−288.
(8) Schelté, P., Boeckler, C., Frisch, B., and Schuber, F. (2000) Differential reactivity of maleimide and bromoacetyl functions with thiols: application to the preparation of liposomal diepitope constructs. *Bioconjugate Chem. 11*, 118−128.
(9) Barbet, J., Machy, P., and Leserman, L. D. (1981) Monoclonal antibody covalently coupled to liposomes: specific targeting to cells. *J. Supramol. Struct. Cell Biochem. 16*, 243−258.
(10) Bourel-Bonnet, L., Pecheur, E. I., Grandjean, C., Blanpain, A., Baust, T., Melnyk, O., Hoflack, B., and Gras-Masse, H. (2005) Anchorage of synthetic peptides onto liposomes via hydrazone and alpha-oxo hydrazone bonds. Preliminary functional investigations. *Bioconjugate Chem. 16*, 450−457.
(11) Kolb, H. C., Finn, M. G., and Sharpless, K. B. (2001) Click chemistry: diverse chemical function from a few good reactions. *Angew. Chem., Int. Ed. 40*, 2004−2021.
(12) Kolb, H. C., and Sharpless, K. B. (2003) The growing impact of click chemistry on drug discovery. *Drug Discovery Today 8*, 1128−1137.
(13) Rostovtsev, V. V., Green, L. G., Fokin, V. V., and Sharpless, K. B. (2002) A stepwise huisgen cycloaddition process: copper(I)-catalyzed regioselective "ligation" of azides and terminal alkynes. *Angew. Chem., Int. Ed. 41*, 2596−2599.
(14) Tornoe, C. W., Christensen, C., and Meldal, M. (2002) Peptidotriazoles on solid phase: [1,2,3]-triazoles by regiospecific copper-(I)-catalyzed 1,3-dipolar cycloadditions of terminal alkynes to azides. *J. Org. Chem. 67*, 3057−3064.
(15) Wang, Q., Chan, T. R., Hilgraf, R., Fokin, V. V., Sharpless, K. B., and Finn, M. G. (2003) Bioconjugation by copper(I)-catalyzed azide-alkyne [3 + 2] cycloaddition. *J. Am. Chem. Soc. 125*, 3192−3193.
(16) Lee, L. V., Mitchell, M. L., Huang, S.-J., Fokin, V. V., Sharpless, K. B., and Wong, C.-H. (2003) A potent and highly selective

inhibitor of human alpha-1,3-fucosyltransferase via click chemistry. *J. Am. Chem. Soc. 125*, 9588−9589.
(17) Deiters, A., Cropp, T. A., Mukherji, M., Chin, J. W., Anderson, J. C., and Schultz, P. G. (2003) Adding amino acids with novel reactivity to the genetic code of *Saccharomyces cerevisiae*. *J. Am. Chem. Soc. 125*, 11782−11783.
(18) Breinbauer, R., and Kohn, M. (2003) Azide-alkyne coupling: a powerful reaction for bioconjugate chemistry. *ChemBioChem 4*, 1147−1149.
(19) Seo, T. S., Li, Z., Ruparel, H., and Ju, J. (2003) Click chemistry to construct fluorescent oligonucleotides for DNA sequencing. *J. Org. Chem. 68*, 609−612.
(20) Speers, A. E., and Cravatt, B. F. (2004) Profiling enzyme activities in vivo using click chemistry methods. *Chem. Biol. 11*, 535−546.
(21) Link, A. J., Vink, M. K., and Tirrell, D. A. (2004) Presentation and detection of azide functionality in bacterial cell surface proteins. *J. Am. Chem. Soc. 126*, 10598−10602.
(22) Chittaboina, S., Xie, F., and Wang, Q. (2005) One-pot synthesis of triazole-linked glycoconjugates. *Tetrahedron Lett. 46*, 2331−2336.
(23) Musiol, H. J., Dong, S., Kaiser, M., Bausinger, R., Zumbusch, A., Bertsch, U., and Moroder, L. (2005) Toward semisynthetic lipoproteins by convergent strategies based on click and ligation chemistry. *ChemBioChem 6*, 625−628.
(24) Frisch, B., Boeckler, C., and Schuber, F. (1996) Synthesis of short polyoxyethylene-based heterobifunctional cross-linking reagents. Application to the coupling of peptides to liposomes. *Bioconjugate Chem. 7*, 180−186.
(25) Ponpipom, M. M., Bugianesi, R. L., Robbins, J. C., Doebber, T. W., and Shen, T. Y. (1981) Cell-specific ligands for selective drug delivery to tissues and organs. *J. Med. Chem. 24*, 1388−1395.
(26) Iyer, S. S., Anderson, A. S., Reed, S., Swanson, B., and Schmidt, J. G. (2004) Synthesis of orthogonal end functionalized oligoethylene glycols of defined lengths. *Tetrahedron Lett. 45*, 4285−4288.
(27) Espuelas, S., Haller, P., Schuber, F., and Frisch, B. (2003) Synthesis of an amphiphilic tetraantennary mannosyl conjugate and incorporation into liposome carriers. *Bioorg. Med. Chem. Lett. 13*, 2557−2560.
(28) Rouser, G., Fleischer, J., and Yamamoto, A. (1970) Two-dimensional thin layer chromatographic separation of plant lipids and determination of phospholipids by phosphorus analysis of spots. *Lipids 5*, 494−496.
(29) Barbet, J., Machy, P., Truneh, A., and Leserman, L. D. (1984) Weak acid-induced release of liposome-encapsulated carboxyfluorescein. *Biochim. Biophys. Acta 772*, 347−356.
(30) Monsigny, M., Petit, C., and Roche, A. C. (1988) Colorimetric determination of neutral sugars by a resorcinol sulfuric acid micromethod. *Anal. Biochem. 175*, 525−530.
(31) Muller, C. D., and Schuber, F. (1989) Neo-mannosylated liposomes: synthesis and interaction with mouse Kupffer cells and resident peritoneal macrophages. *Biochim. Biophys. Acta 986*, 97−105.
(32) Sihorkar, V., and Vyas, S. P. (2001) Potential of polysaccharide anchored liposomes in drug delivery, targeting and immunization. *J. Pharm. Pharm. Sci. 4*, 138−158.
(33) Vyas, S. P., Singh, A., and Sihorkar, V. (2001) Ligand-receptor-mediated drug delivery: An emerging paradigm in cellular drug targeting. *Crit. Rev. Ther. Drug Carrier Syst. 18*, 1−76.
(34) Opanasopit, P., Hyoudou, K., Nishikawa, M., Yamashita, F., and Hashida, M. (2002) Serum mannan binding protein inhibits mannosylated liposome-mediated transfection to macrophages. *Biochim. Biophys. Acta 1570*, 203−209.
(35) Copland, M. J., Baird, M. A., Rades, T., McKenzie, J. L., Becker, B., Reck, F., Tyler, P. C., and Davies, N. M. (2003) Liposomal delivery of antigen to human dendritic cells. *Vaccine 21*, 883−890.
(36) Arigita, C., Bevaart, L., Everse, L. A., Koning, G. A., Hennink, W. E., Crommelin, D. J. A., van de Winkel, J. G. J., van Vugt, M. J., Kersten, G. F. A., and Jiskoot, W. (2003) Liposomal meningococcal B vaccination: role of dendritic cell targeting in the development of a protective immune response. *Infect. Immun. 71*, 5210−5218.
(37) Foged, C., Arigita, C., Sundblad, A., Jiskoot, W., Storm, G., and Frokjaer, S. (2004) Interaction of dendritic cells with antigen-containing liposomes: effect of bilayer composition. *Vaccine 22*, 1903−1913.
(38) Rodionov, V. O., Fokin, V. V., and Finn, M. G. (2005) Mechanism of the ligand-free Cu-I-catalyzed azide-alkyne cycloaddition reaction. *Angew. Chem., Int. Ed. 44*, 2210−2215.
(39) Himo, F., Lovell, T., Hilgraf, R., Rostovtsev, V. V., Noodleman, L., Sharpless, K. B., and Fokin, V. V. (2005) Copper(I)-catalyzed synthesis of azoles. DFT study predicts unprecedented reactivity and intermediates. *J. Am. Chem. Soc. 127*, 210−216.
(40) Engel, A., Chatterjee, S. K., Alarifi, A., Riemann, D., Langner, J., and Nuhn, P. (2003) Influence of spacer length on interaction of mannosylated liposomes with human phagocytic cells. *Pharm. Res. 20*, 51−57.
(41) Lewis, W. G., Magallon, F. G., Fokin, V. V., and Finn, M. G. (2004) Discovery and characterization of catalysts for azide-alkyne cycloaddition by fluorescence quenching. *J. Am. Chem. Soc. 126*, 9152−9153.
(42) Chan, T. R., Hilgraf, R., Sharpless, K. B., and Fokin, V. V. (2004) Polytriazoles as copper(I)-stabilizing ligands in catalysis. *Org. Lett. 6*, 2853−2855.
(43) Gal, S., Pinchuk, I., and Lichtenberg, D. (2003) Peroxidation of liposomal palmitoyllinoleoylphosphatidylcholine (PLPC), effects of surface charge on the oxidizability and on the potency of antioxidants. *Chem. Phys. Lipids 126*, 95−110.
(44) Lee, C., Barnett, J., and Reaven, P. D. (1998) Liposomes enriched in oleic acid are less susceptible to oxidation and have less proinflammatory activity when exposed to oxidizing conditions. *J. Lipid Res. 39*, 1239−1247.
(45) Agard, N. J., Prescher, J. A., and Bertozzi, C. R. (2004) A strain-promoted [3 + 2] azide-alkyne cycloaddition for covalent modification of biomolecules in living systems. *J. Am. Chem. Soc. 126*, 15046−15047.
(46) Li, Z., Seo, T. S., and Ju, J. (2004) 1,3-Dipolar cycloaddition of azides with electron-deficient alkynes under mild condition in water. *Tetrahedron Lett. 45*, 3143−3146.

BC050308L

Synthesis of Building Blocks for Solid-Phase Introduction of Diethylenetriaminepentaacetic Acid (DTPA) to Oligonucleotides and Oligopeptides

Jari Peuralahti, Lassi Jaakkola, Veli-Matti Mukkala, and Jari Hovinen*

PerkinElmer Life and Analytical Sciences, Turku Site, POB 10, FIN-20101 Turku, Finland. Received December 29, 2005; Revised Manuscript Received February 13, 2006

Synthesis of building blocks that allow site-specific incorporation of diethylenetriaminepentaacetic acid (DTPA) to oligonucleotides and oligopeptides using phosphoramidite and Fmoc chemistries, respectively, is described.

INTRODUCTION

Because of its excellent metal-chelating properties diethylenetriaminepentaacetic acid (DTPA) is one of the most widely used organic ligands in magnetic resonance imaging (MRI) and positron emission tomography (PET) (*1*−*3*). Indeed, the first FDA approved contrast agent in clinical use is the Gd^{3+} DTPA chelate (*4*). The corresponding ^{111}In and ^{68}Ga chelates are suitable for PET applications (*5*−*8*), while Eu^{3+}, Tb^{3+}, Sm^{3+}, and Dy^{3+} chelates can be used in dissociation enhanced lanthanide fluorescence immunoassay (DELFIA) based applications (*9*). ^{99m}Tc DTPA, in turn, has been applied for single positron emission computed tomography (SPECT) (*10*−*12*). Bioactive molecules labeled with ^{111}In or ^{117m}Sn DTPA may be used even as target-specific radiopharmaceuticals (*13*).

In several applications, covalent conjugation of DTPA to bioactive molecules is required. Accordingly, isothiocyanato, *N*-hydroxysuccinimide, or maleimide derivatives of the chelates are used in the labeling of the target molecules (*14*). Several bifunctional DTPA derivatives are currently commercially available. Because in all of these cases the labeling reaction is performed in the presence of an excess of an activated label, laborious purification procedures cannot be prevented. Especially when attachment of several label molecules is needed, purification and characterization of the desired biomolecule conjugate may be extremely difficult. The purification problems can be avoided by performing the labeling reaction on the solid phase. Hence, most of the impurities can be removed by washings when the biomolecule conjugate is still anchored to the solid support, and after release to the solution only one chromatographic purification is needed.

We have already developed a strategy for labeling of bioactive molecules with luminescent and nonluminescent lanthanide chelates on solid phase (*15*−*20*). The method involves synthesis of oligonucleotide and oligopeptide building blocks, which can be introduced to the biomolecule structure using commercial oligonucleotide and oligopeptide synthesizers by phosphoramidite and Fmoc chemistry, respectively. Upon completion of the chain assembly, the oligomer is deprotected and finally treated with the appropriate lanthanide(III) citrate to give rise to the desired biomolecule conjugate. Here our approach is used for the site-specific incorporation of diethylenetriaminepentaacetic acid (DTPA) to oligonucleotides and oligopeptides.

* To whom correspondence should be addressed. Tel + 358 2 2678 513; fax + 358 2 2678 380; e-mail: jari.hovinen@perkinelmer.com.

EXPERIMENTAL PROCEDURES

General Methods. Adsorption column chromatography was performed on columns packed with silica gel 60 (Merck). Reagents for oligonucleotide and oligopeptide synthesis were purchased from Proligo and Nova Biochem, respectively. Sodium sulfinate resin (200−400 mesh, 1% DVB, 1.3 mmol g^{-1}) was purchased from Tianjin Nankai Hecheng Science & Technology Company Limited (China). The oligopeptides and oligonucleotides were assembled on Applied Biosystems 433A and 3400 instruments, respectively, using recommended protocols. HPLC purifications were performed using a Shimadzu LC 10 AT instrument equipped with a diode array detector, a fraction collector, and a reversed phase column (LiChrocart 125−3 Purospher RP-18e 5 μm). Mobile phase: (buffer A): 0.02 M triethylammonium acetate (pH 7.0); (buffer B): A in 50% (v/v) acetonitrile. Gradient: from 0 to 1 min 95% A, from 1 to 21 min from 95% A to 100% B. Flow rate was 0.6 mL $min.^{-1}$ All dry solvents were from Merck, and they were used as received. NMR spectra were recorded on a Brucker 250 spectrometer operating at 250.13 MHz for ^1H and on a JEOL LA 400 spectrometer operating at 161.9 MHz for ^{31}P. The signal of TMS was used as an internal (^1H) and H_3PO_4 as an external (^{31}P) reference. ESI-TOF mass spectra and IR spectra were recorded on Applied Biosystems Mariner and PerkinElmer Spectrum One instruments, respectively.

4-Iodophenylalanine Methyl Ester, 1. Thionyl chloride (10 mL) was added dropwise to anhydrous methanol (40 mL) on an ice−water bath. The mixture was allowed to warm to RT, and it was stirred for 30 min. 4-Iodophenylalanine (4.90 g, 16.8 mmol) was added, and the mixture was heated overnight at reflux. All volatiles were removed in vacuo. The residue was triturated with diethyl ether, filtered, and dried in vacuo. Yield was 5.10 g (99%). ^1H NMR (DMSO-d_6): δ 8.15 (2H, br s); 7.70 (2H, d, *J* 8.2); 7.06 (2H, d, *J* 8.2); 4.30 (1H, t, *J* 6.6); 3.70 (3H, s); 3.07 (2H, d, *J* 6.6). IR (KBr) 1788 cm^{-1} (C═O). ESI-TOF-MS for $C_{10}H_{13}INO_2$ $(M+H)^+$: calcd, 306.04; found, 306.01.

2-Amino-*N*-(2-aminoethyl)-3-(4-iodophenyl)propanamide, 2. Compound **1** (5.10 g, 16.7 mmol) was added portionwise to ethylenediamine (35 mL) during 2 h. The mixture was stirred overnight at RT and concentrated. Aqueous ammonia (7 M; 30 mL) was added, and the product was extracted to dichloromethane (4 · 45 mL). The combined organic phases were dried over Na_2SO_4 and concentrated to give 5.57 g (93%) of compound **2**. ^1H NMR ($CDCl_3$): δ 7.64 (2H, d, *J* 8.2); 7.49 (1H, br t); 6.98 (2H, d, *J* 8.2); 3.59 (1H, dd, *J* 4.3 and 8.9); 3.30 (2H, q, *J* 6.1); 3.18 (1H, dd, *J* 4.3 and 13.8); 2.80 (2H, t,

10.1021/bc0503667 CCC: $33.50 © 2006 American Chemical Society
Published on Web 04/15/2006

J 6.4); 2.75 (1H, dd, *J* 8.9 and 13.1); 1.35 (4H, br s). IR (KBr) 1650 cm^{-1} (C═O). ESI-TOF-MS for $C_{11}H_{17}IN_3O$ $(M+H)^+$: calcd, 334.04; found, 334.04.

***N*¹-(2-Aminoethyl)-3-(4-iodophenyl)propane-1,2-diamine, 3.** Compound **2** (4.79 g, 14.4 mmol) was dissolved in dry THF (120 mL) and deaerated with argon. Borane-THF (1 M, 120 mL) was added dropwise during 30 min, and the mixture was heated overnight at reflux. The excess of borane was destroyed by cautious addition of water. All volatiles were removed in vacuo. The residue was dissolved in 6 M HCl and heated at reflux for 3 h and concentrated. The residue was suspended in concentrated ammonia (100 mL) and extracted with chloroform (5 ·75 mL). The combined organic layers were dried over Na_2SO_4, concentrated, and dried in vacuo. Yield was 2.9 g (63%). ^{1}H NMR ($CDCl_3$): δ 7.61 (2H, d, *J* 8.3); 6.95 (2H, d, *J* 8.3); 3.06 (1H, m); 2.79 (2H, m); 2.79 (4H, m); 2.51 (2H, m); 1.39 (5H, br s). ESI-TOF-MS for $C_{11}H_{19}IN_3$ $(M+H)^+$: calcd, 320.06; found, 320.06.

Pentamethyl 2-(4-Iodobenzyl)diethylenetriaminepenta-(acetate), 4. Compound **3** (2.7 g, 8.5 mmol) was suspended in dry DMF (80 mL), and the mixture was deaerated with argon. DIPEA (16.2 mL, 93 mmol), potassium iodide (1.54 g, 9.3 mmol), and methyl bromoacetate (7.2 mL, 75.8 mmol) were added, and the mixture was stirred overnight at RT. All volatiles were removed in vacuo. The residue was suspended on dichloromethane (140 mL), washed with sat. $NaHCO_3$ (3 ·55 mL), dried over Na_2SO_4, and concentrated. Purification on silica gel (eluent petroleum ether, bp 40−60 °C/ethyl acetate/ triethylamine 5:1:1, v/v/v) yielded 3.1 g (55%) of compound **4** as an oil. ^{1}H NMR ($CDCl_3$): δ 7.58 (2H, d, *J* 8.2); 6.97 (2H, d, *J* 8.2); 3.69 (6H, s); 3.66 (6H, s); 3.63 (3H, s); 3.57 (2H, s); 3.56 (2H, s); 3.54 (4H, s); 3.53 (2H, s); 3.10 (1H, p, *J* 6.6); 2.80 (1H, m) 2.74 (4H, m); 2.60 (1H, m); 2.47 (2H, m). ESI-TOF-MS for $C_{29}H_{39}IN_3O_{10}$ $(M + H)^+$: calcd, 680.17; found, 680.18. IR (film) 1747 cm^{-1} (C═O).

2′-Deoxy-5′-*O*-(4,4′-dimethoxytrityl)-3-(5-hexyn-1-yl)uridine, 5. 2′-Deoxy-5′-*O*-(4,4′-dimethoxy-trityl)uridine (5.0 g, 9.4 mmol), 5-hexyn-1-ol (1.25 mL, 11.3 mmol), and triphenylphosphine (3.0 g, 11.3 mmol) were dissolved in dry THF (50 mL). Diethylazodicarboxylate (1.80 mL, 11.3 mmol) was added dropwise during 30 min, and the reaction was allowed to proceed for 2 h at RT. All volatiles were removed in vacuo. Purification on silica gel using diethyl ether as the eluent gave 4.15 g (72%) of the title compound. ^{1}H NMR (DMSO-d_6): δ 7.70 (1H, d, *J* 8.1); 7.39 (2H, m); 7.31 (2H, m); 7.25 (5H, m); 6.90 (4H, d, *J* 8.0); 6.18 (1H, t, *J* 6.3); 5.49 (1H, *J* 8.1); 5.38 (1H, d, *J* 4.6; exch. with MeOD); 4.31 (1H, m); 3.90 (1H, m); 3.78 (2H, m); 3.74 (6H, s); 3.26 (1H, dd, *J* 5.4 and 10.7); 3.19 (1H, dd, *J* 2.9 and 10.7); 2.23 (3H, 3 · m); 1.63 (2H, p); 1.47 (1H, t); 1.43 (2H, m). ESI-TOF-MS for $C_{36}H_{39}N_2O_7$ $(M+H)^+$: calcd, 611.27; found, 611.29.

2′-Deoxy-5′-*O*-(4,4′-dimethoxytrityl)-3-{pentamethyl-2-[4-(5-hexyn-1-yl)benzyl]diethylene-triaminepentaacetato}-uridine, 6. Compounds **5** (1.15 g, 1.80 mmol) and **4** (1.00 g, 1.47 mmol) were dissolved in the mixture of dry THF (10 mL) and triethylamine (6 mL) under argon. $Pd(Ph_3P)_2Cl_2$ (22 mg, 0.03 mmol) and CuI (14 mg, 0.07 mmol) were added, and the mixture was stirred overnight at RT. The solid material was removed by filtration, and the filtrate was concentrated in vacuo. The residue was dissolved in dichloromethane (30 mL), washed with water (2 · 20 mL), and dried over Na_2SO_4. Purification on silica gel (eluent petroleum ether, bp 40−60 °C/ethyl acetate/ triethylamine 2:5:1, v/v/v) gave 1.30 g (74%) of compound **6**. ^{1}H NMR ($CDCl_3$): δ 7.74 (1H, d, *J* 8.2); 7.40−7.23 (11H, m); 7.11 (2H, d, *J* 8.2); 6.84 (4H, d, *J* 8.0); 6.32 (1H, t, *J* 6.4); 5.47 (1H, *J* 8.2); 4.55 (1H, m); 4.01 (1H, m); 3.97 (2H, m); 3.79 (6H, s); 3.68 (6H, s); 3.66 (6H, s); 3.62 (3H, s); 3.57 (2H, s); 3.55 (2H, s); 3.53 (4H, s); 3.47 (2H, m); 3.15 (1H, m); 2.85 (1H, m); 2.72 (2H, d, *J* 4.3); 2.58 (1H, m); 2.44 (2H, t, *J* 7.3); 1.82 (2H, m); 1.69 (2H, m). ESI-TOF-MS for $C_{62}H_{76}N_5O_{17}$ $(M+H)^+$: calcd, 1162.52; found, 1162.56.

2′-Deoxy-5′-*O*-(4,4′-dimethoxytrityl)-3-{pentamethyl-2-[4-(5-hexyn-1-yl)benzyl]diethylene-triaminepentaacetato}-uridine 3′-*O*-(2-cyanoethyl *N*,*N*-diisopropyl) Phosphoramidite, 7. Predried Compound **6** (1.43 g, 1.03 mmol) and 2-cyanoethyl *N*,*N*,*N*′,*N*′-tetraisopropylphosphordiamidite (0.47 g, 1.55 mmol) were dissolved in dry acetonitrile (10 mL). 1*H* tetrazole (2.3 mL; 0.45 M in acetonitrile) was added, and the mixture was stirred for 30 min at room temperature before being poured into 5% $NaHCO_3$, extracted with dichloromethane, and dried over Na_2SO_4. Purification on silica gel (eluent petroleum ether, bp 40−60 °C/ethyl acetate/triethylamine 5:5:1, v/v/v) gave 0.88 g (52%) of compound **7**. ^{31}P NMR ($CDCl_3$): δ 149.58 (0.5 P); 149.13 (0.5 P). ESI-TOF-MS for $C_{71}H_{93}N_7O_{18}P$ $(M+H)^+$: calcd, 1362.62; found, 1362.59.

Penta-*tert*-butyl 2-{4′-{2-[2-allyloxycarbonyl-2-(fluorenylmethyloxycarbonylamino)]-ethylcarboxamido}benzyl}-diethylenetriaminepentakis(acetate), 9. Fmoc-Glu-OAll (1.31 g, 3.21 mmol), HATU (1.22 g, 3.21 mmol), and DIPEA (0.57 mL, 3.21 mmol) were dissolved in dry DMF (5 mL), and the mixture was stirred for 15 min at RT. Compound **8** (*21*) (2.50 g, 3.21 mmol; predissolved in 2 mL of dry DMF) was added, and the mixture was stirred for an additional 2 h. The mixture was diluted with dichloromethane (50 mL), washed twice with 10% citric acid, and dried over Na_2SO_4. Purification on silica gel (eluent CH_2Cl_2/MeOH 9:1, v/v) gave 2.84 g (82%) of compound **9**. ^{1}H NMR ($CDCl_3$): δ 8.31 (2H, br s); 7.75 (2H, d, *J* 7.3); 7.61 (4H, m); 7.39 (2H, t, *J* 7.3); 7.30 (2H, m); 7.02 (2H, d, *J* 8.6); 5.96 (1H, m); 5.89 (1H, m); 5.26 (1H, m); 4.65 (2H, d, *J* 5.4); 4.41 (2H, m); 4.22 (1H, t, *J* 6.7); 3.40−2.38 (17 H); 1.48 (36H, s); 1.42 (9H, s). ESI-TOF-MS for $C_{64}H_{92}N_5O_{15}$ $(M+H)^+$: calcd, 1170.66; found, 1170.59.

Penta-*tert*-butyl-2-{4′-{2-[2-carboxy-2-(fluorenylmethyloxycarbonylamino)]-ethylcarboxamido}benzyl}diethylene-triaminepentakis(acetate), 10. Compound **9** (1.00 g, 0.90 mmol) was dissolved in dry THF (20 mL) and deaerated with argon. $Pd(Ph_3P)_4$ (63 mg, 55 μmol) and sodium sulfinate resin (1.0 g) were added, and the mixture was stirred for 2 h at RT. The resin was filtered off and washed with THF. The filtrate was concentrated. The residue was dissolved in methanolic dichloromethane (5:95, v/v; 20 mL), washed with 10% citric acid (10 mL), dried over 4 Å molecular sieves, and concentrated to give compound **10** (0.70 g, 69%) as a pale yellow solid. ESI-TOF-MS for $C_{61}H_{88}N_5O_{15}$ $(M+H)^+$: calcd, 1130.63; found, 1130.65.

Synthesis and Purification of the Oligonucleotide Conjugates. A model sequence d(TAA TGT AGC CCC TGA A) was assembled on a 1.0 μmol scale using phosphoramidite chemistry and recommended protocols (DMTr-Off synthesis). One or five phosphoramidites **7** were coupled to the 5′-terminus of the oligonucleotide (coupling time 10 min, concentration 0.2 M). As the chain assembly was completed, the oligonucleotides were deprotected and converted to the gadolinium(III) chelates as the following: (i) treatment with 0.1 M NaOH for 4 h at RT, (ii) concentration in vacuo in the presence of ammonium chloride, (iii) treatment with concentrated aqueous ammonia for 16 h at 55 °C, and (iv) treatment with gadolinium(III) citrate (5 equiv per ligand) for 90 min at RT. Desalting by gel filtration and denaturing PAGE yielded the oligonucleotide conjugates.

Synthesis and Purification of the Oligopeptide Conjugates. One or five blocks **10** were coupled to an amide resin followed by a model sequence (RKEAASIKVAVS) in 10 μmol scale using Fmoc chemistry and recommended protocols (coupling time 30 min for natural amino acid analogues, and 2 h for **10**).

Scheme 1

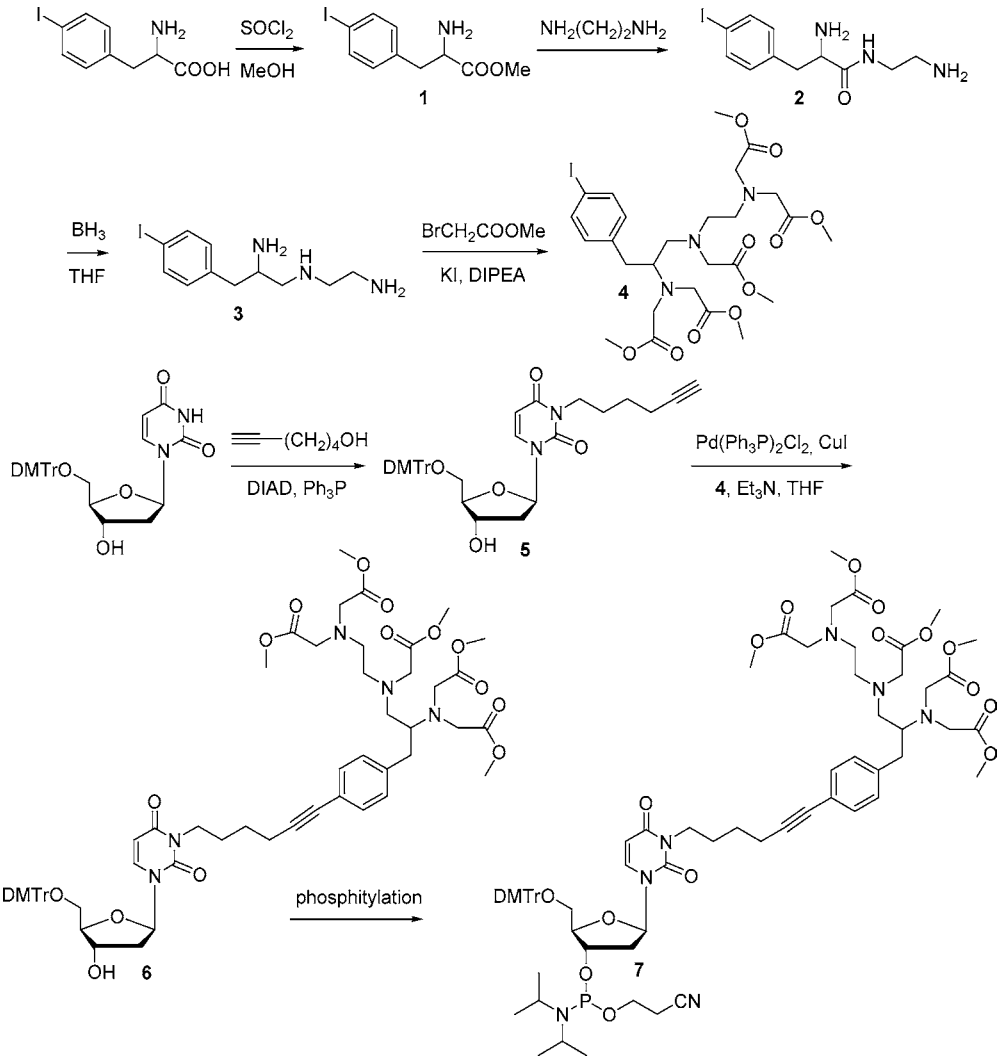

When the chain assembly was completed, the resin was treated with the mixture of crystalline phenol (75 mg), ethanedithiol (25 μL), thioanisole (50 μL), water (50 μL), and trifluoroacetic acid (1 mL) for 4 h. The resin was removed by filtration, and the solution was concentrated in vacuo. The crude oligopeptide was precipitated with diethyl ether. The precipitate was redissolved in water and treated with gadolinium(III) citrate (5 equiv per ligand). Purification was performed on HPLC.

RESULTS AND DISCUSSION

Although the DTPA molecule has been known for decades, no structures that allow its direct solid-phase conjugation to oligopeptides or oligonucleotides have been described. The only solid-phase methods published involve synthesis of oligopeptides where one ϵ-amino group of K can be selectively deprotected, while the oligomer is still anchored to the resin (*22*, *23*). Then, an activated DTPA molecule (as an anhydride or an HOBt-ester) is coupled to the primary amino function, the oligopeptide is deprotected and converted to the appropriate DTPA chelate. One should in theory be able to incorporate multiple lysine residues that could be orthogonally deprotected, and thus obtain oligopeptides labeled with several DTPA molecules. However, the applicability of this approach has not been demonstrated in practice. Furthermore, since one of the DTPA carboxylic acid groups is used for conjugation, the resulting chelate is less stable than the parent DTPA molecule (*24*, *25*). This may be a serious problem in in vivo applications especially in MRI due to the high toxicity of the free Gd(III) ion. Accordingly, an alternative synthetic strategy would be desirable.

Synthesis of the Oligonucleotide Labeling Reactant is shown in Scheme 1. Initially, 4-iodophenylalanine was esterified using thionyl chloride to give **1**. Substitution reaction with ethane-1,2-diamine yielded the amide, **2**, borane reduction of which gave the amine **3**. Alkylation of this with methyl bromoacetate using potassium iodide as the catalyst gave the corresponding iminoacetic acid derivative, **4**. Sonogashira reaction between the iodide **4** and the hexynyl tethered nucleoside **5** gave **6** in high yield. The nucleoside, **5**, in turn, was obtained from 2′-deoxy-5′-*O*-(4,4′-dimethoxytrityl)uridine by the reaction with 5-hexyn-1-ol in the presence of DIAD and triphenylphosphine (*17*). Finally, **6** was phosphitylated to **7** in conventional manner by treatment with 2-cyanoethyl *N*,*N*,*N*′,N′-tetraisopropylphosphordiamidite in anhydrous acetonitrile using 1*H* tetrazole as the catalyst.

Synthesis of the Oligopeptide Labeling Reactant is shown in Scheme 2. Reaction of Fmoc-glutamic acid allyl ester with the amine **8** in the presence of HATU and DIPEA gave the protected ligand **9** in high yield. Purification was easily performed using silica gel column chromatography. By contrast, palladium catalyzed cleavage of the allyl group (*26*, *27*) was challenging. Reaction of **9** with $(Ph_3P)_4Pd$ using phenylsilane as the allyl scavenger (*17*, *28*) was unexpectedly slow: an overnight reaction was required, and an extensive amount of dark impurities were formed. The use of a thiol scavenger was

Scheme 2

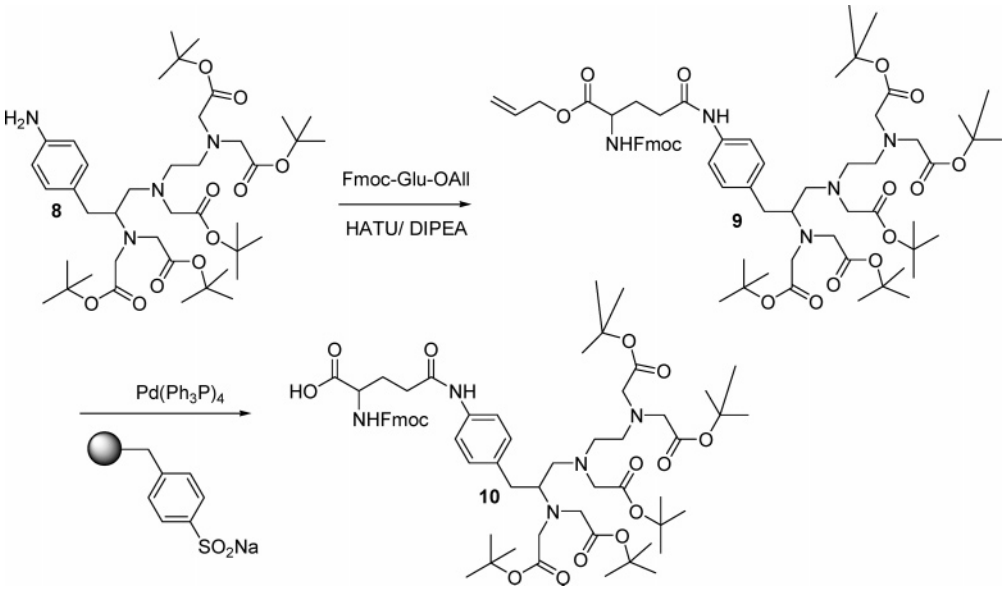

Chart 1

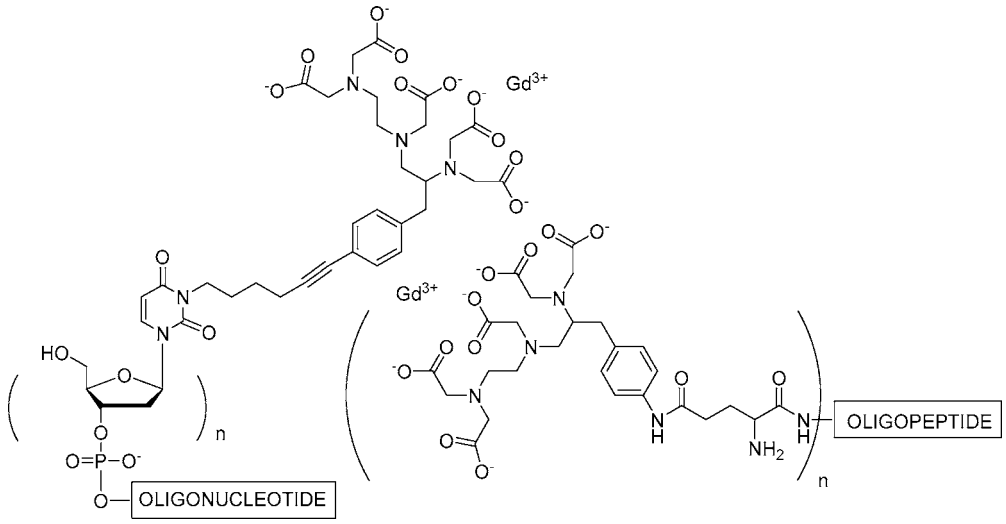

more successful: with sodium toluenesulfinate (*29*) the reaction was completed in 2 h at RT. However, removal of allyl-*p*-toluenesulfinate and some unidentified yellow impurities required silica gel column chromatography. Although these impurities could be removed with ease, the desired product, **10**, adsorbed tightly on silica gel. The product could not be completely eluted from the column even with highly polar solvent systems (up to 50% methanol in dichloromethane), which, in turn partially dissolved the matrix, causing additional problems. It is worth noting that all purification procedures involving extractions with strong aqueous bases and acids (*30*) had to be excluded due to the lability of the Fmoc and *t*-butyl groups of **10**, respectively. Fortunately, these problems could be solved using a commercially available scavenger resin. Accordingly, palladium-catalyzed allyl cleavage using resin-bound sodium *p*-toluenesulfinate produced **10** in 2 h at RT. The work up procedure was very simple, including removal of the resin by filtration, washing of the filtrate with 10% citric acid, and drying over 4 Å molecular sieves.

Synthesis of the Oligonucleotide and Oligopeptide Conjugates were performed on standard oligonucleotide and oligopeptide synthesizers using phosphoramidite and Fmoc chemistries, respectively. One or five building blocks (**7**, **10**) were coupled to the oligomers. Upon completion of the syntheses, the conjugates were deprotected and converted to the corresponding gadolinium(III) chelates by treatment with gadolinium(III) citrate. Finally, purification on gel electrophoresis (oligonucleotides) or reversed phase HPLC (oligopeptides) gave the desired bioconjugates (Chart 1). According to mass spectrometric analyses, the observed molecular weights were in accordance with the proposed structures.

As a summary, a simple method for the preparation of DTPA based labeling reactants is demonstrated. As shown here, the building blocks are suitable for site-specific introduction of MRI contrast agents to oligonucleotides and oligopeptides. Naturally, for PET and SPECT applications, the metal should be introduced as just prior to analysis.

LITERATURE CITED

(1) Aime, S., Botta, M., Fasano, M., and Terreno, E. (1998) Lanthanide(III) chelates for NMR biomedical applications. *Chem. Soc. Rev. 27*, 19−29.

(2) Caravan, P., Ellison, J. J., McMurry, T. J., and Lauffer, R. B. (1999) Gadolinium(III) chelates as MRI contrast agents: structure, dynamics, and applications. *Chem. Rev. 99*, 2293−2352.

(3) Woods, M., Kovacs, Z., and Sherry, A. D. (2002) Targeted complexes of lanthanide(III) ions as therapeutic and diagnostic pharmaceuticals. *J. Supramol. Chem. 2*, 1−15.
(4) Runge, V. M. (2000) Safety of approved MR contrast media for intravenous injection. *J. Magn. Reson. Imaging 12*, 205−213.
(5) Anderson, C. J., and Welch, M. J. (1999) Radiometal-labeled agents (non-technetium) for diagnostic imaging. *Chem. Rev. 99*, 2219−2234.
(6) Velikyan, I., Beyer, G. J., and Långström, B. (2004) Microwave-supported preparation of ^{68}Ga-bioconjugates with high specific radioactivity. *Bioconjugate Chem. 15*, 554−560.
(7) Velikyan, I., Lendvai, G., Välilä, M., Roivainen, A., Yngve, U., Bergström, M., and Långström, B. (2004) Microwave-accelerated ^{68}Ga-labelling of oligonucleotides. *J. Labeled Compd. Radiopharm. 47*, 79−89.
(8) Roivainen, A., Tolvanen, T., Salomäki, S., Lendvai, G., Velikyan, I., Numminen, P., Välilä, M., Sipilä, H., Bergström, M., Härkönen, P., Lönnberg, H., and Långström, B. (2004) ^{68}Ga-labelled oligonucleotides for in vivo imaging with PET. *J. Nucl. Med. 45*, 347−355.
(9) Hemmilä, I., Blomberg, K., Mukkala, V.-M., and Hakala, H. Dissociative fluoresence enhancement assay. PCT WO 03/076939.
(10) Lorberboym, M., Lampl, Y., and Sadeh, M. (2003) Correlation of ^{99m}Tc-DTPA SPECT of bood-brain barrier with neurologic outcome after acute stroke. *J. Nucl. Med. 44*, 1898−1904.
(11) Galuska, L., Leovey, A., Szucs-Farkas, Z., Garai, I., Szabo, J., Varga, J., and Nagy, E. V. (2002) *Nucl. Med. Commun. 23*, 1211−1216.
(12) Galuska, L., Varga, J., Szucs-Farkas, Z., Garai, I., Boda, J., Szabo, J., Leovey, A., and Nagy, E. V. (2003) Active retrobulbar inflammation in graves'ophthalmopathy visualized by Tc-99m DTPA SPECT. *Clin. Nucl. Med. 28*, 515−516.
(13) Volkert, W. A., and Hoffman, T. J. (1999) Therapeutic radiopharmaceuticals. *Chem. Rev. 99*, 2269−2292.
(14) Fichna, J., and Janecka, A. (2003) Synthesis of target-specific radiolabeled peptides for diagnostic imaging. *Bioconjugate Chem. 14*, 3−17.
(15) Peuralahti, J., Hakala, H., Mukkala, V.-M., Hurskainen, P., Mulari, O., and Hovinen, J. (2002) Introduction of lanthanide(III) chelates to oligopeptides on solid phase. *Bioconjugate Chem. 13*, 870−875.
(16) Hakala, H., and Hovinen, J. (2001) Versatile strategy for oligonucleotide derivatization. Introduction of lanthanide(III) chelates to oligonucleotides. *Org. Lett. 3*, 2473−2476.
(17) Hakala, H., Ollikka, P., Degerholm, J., and Hovinen, J. (2002) Oligonucletide conjugates based on acyclonucleotides and their use in DNA hybridization assays *Tetrahedron 58*, 8771−8777.
(18) Peuralahti, J., Suonpää, K., Blomberg, K., Mukkala, V.-M., and Hovinen, J. (2004) Labeling of steroids on solid phase. *Bioconjugate Chem. 15*, 927−930.
(19) Jaakkola, L., Peuralahti, J., Hakala, H., Kunttu, J., Tallqvist, P., Mukkala, V.-M., Ylikoski, A., and Hovinen, J. (2005) Solid-phase synthesis of oligonucleotides labeled with luminescent lanthanide(III) chelates. *Bioconjugate Chem. 16*, 700−709.
(20) Peuralahti, J., Jaakkola, L., Hakala, H., Mukkala, V.-M., Hurskainen, P., and Hovinen, J. Labeling of oligopeptides and proteins with luminescent lanthanide(III) chelates. *J. Peptide Sci. 12*, 199−205.
(21) Corson, D. T., and Meares, C. F. (2000) Efficient multigram synthesis of the bifunctional chelating agent (*S*)-1-*p*-isothiocyanatobenzyl-diethylenetriaminepentaacetic acid. *Bioconjugate Chem. 11*, 292−299.
(22) Nagy, I. B., Vagra, I., and Hudecz, F. (2000) Preparation of indium-115-labeled diethylenetriaminepentaacetic acid monoacetamide peptides purified by 8-hydroxyquinoline. *Anal. Biochem. 287*, 17−24.
(23) Handl, H. L., Vagner, J., Yamamura, H. I., Hruby, V. J., and Gilles, R. J. (2005) Development of lanthanide-based assay for detection of receptor−ligand interactions at the δ-opinoid receptor. *Anal. Biochem. 343*, 299−307.
(24) Paul-Roth, C., and Raymond, K. N. (1995) Amide functional group contribution to the stability of gadolinium(III) complexes: DTPA derivatives. *Inorg. Chem. 34*, 1408−1412.
(25) Li, W. P., Ma, D. S., Higginbotham, C., Hoffman, T., Ketring, A. R., Cutler, C. S., and Jurisson, S. S. (2001) Development of an in vitro model for assessing the in vivo stability of lanthanide chelates. *Nucl. Med. Biol.* 28, 145−154.
(26) Guibé, F. (1998) Allylic protecting groups and their use in a complex environment. Part II: allylic protecting groups and their removal through catalytic palladium π-allyl methodology. *Tetrahedron 54*, 2967−3042.
(27) Greene, T. W., and Wuts, P. G. M. *Protective Groups in Organic Synthesis*, 3rd ed., John Wiley & Sons, Inc., New York, 1999.
(28) Dessolin, M., Guillerez, M.-G., Thieriet, N., Guibé, F. and Loffet, A. (1995) New allyl group acceptors for palladium catalyzed removal of allylic protections and transacylation of allyl carbamates. *Tetrahedron Lett. 36*, 5741−5744.
(29) Honda, M., Morita, H., and Nagakura, I. (1997) Deprotection of allyl groups with sulfinic acids and palladium catalyst. *J. Org. Chem. 62*, 8932−8936.
(30) Genêt, J. P., Blart, E., Savignac, M., Lemeune, S., Lemaire-Audoire, S., and Bernard, J. M. (1993) A general and simple removal of the allyloxycarbonyl protection group by palladium-catalyzed reactions using nitrogen and sulfur nucleophiles. *Synlett* 680−682.

BC0503667

^{1}H NMR Spectroscopy as a Tool for Determining the Composition of Poly(hydroxyethyl-L-asparagine)-Coated Liposomes

Birgit Romberg,[†] J. Jantina Kettenes-van den Bosch,[§] Tom de Vringer,[‡] Gert Storm,[†] and Wim E. Hennink*,[†]

Departments of Pharmaceutics and Biomedical Analysis, Utrecht Institute for Pharmaceutical Sciences (UIPS), Utrecht University, Sorbonnelaan 16, 3584 CA Utrecht, The Netherlands, and Astellas Pharma Europe B.V., Leiderdorp, The Netherlands. Received February 22, 2006; Revised Manuscript Received April 11, 2006

Liposomes coated with the poly(amino acid) poly(hydroxyethyl-L-asparagine) (PHEA) show long-circulation properties comparable to the frequently used PEG-liposomes. The pharmacokinetic characteristics of long-circulating liposomes are dependent on the density of the shielding polymer on the liposome surface. Therefore, it is necessary to know the exact composition of the liposomes including the amount of coating polymer present on the liposome surface. In this study, a ^{1}H NMR method to establish the composition of liposomes coated with PHEA was developed and validated.

INTRODUCTION

The therapeutic use of nanoparticulate carriers for the targeted delivery of drugs, for example, liposomes and polymeric nanoparticles, can be significantly improved by coating them with sterically stabilizing polymers such as poly(ethylene glycol) (PEG) (*1*, *2*). Due to the hydrophilic PEG corona, these modified carriers display reduced recognition and uptake by cells of the mononuclear phagocyte system (MPS) and consequently show prolonged blood circulation times (*3*). Recently, we showed that liposome coatings based on poly(hydroxyethyl-L-asparagine) (PHEA) and poly(hydroxyethyl-L-glutamine) (PHEG) prolong liposome circulation to a similar extent as PEG (*4*). Such poly(amino acid) coatings are supposed to be biodegradable, as recently confirmed by the determination of the enzymatic degradation of PHEG (*5*).

In general, the pharmacokinetic characteristics of long-circulating colloidal drug carriers depend on the molecular weight of the stabilizing polymer and its density on the carrier surface (*6*). To address the latter aspect, it is necessary to quantify the amount of polymer that is grafted onto the carrier. For example, the composition of liposomes that are prepared by the film-hydration method is not exactly known since it is not ensured that all components are quantitatively incorporated into the liposome bilayer. Reliable methods to study the composition of liposomes are scarce. Proton nuclear magnetic resonance (^{1}H NMR) spectroscopy has been reported as an effective method for the quantitation and characterization of PEG−lipid conjugates in lipid mixtures (*7*), as well as on nanoparticle surfaces (*8*, *9*). The PEG−lipid is relatively easy to quantify because of its simple ^{1}H NMR spectrum. For the poly(amino acid) conjugates, however, quantitation is much more difficult because of strong peak overlap and partly broad signals of the polymer. In this study, a ^{1}H NMR method was developed and validated to accurately determine the composition of coated liposomes formed by the film-hydration method with emphasis on the new coating conjugate PHEA-DODASuc (Figure 1).

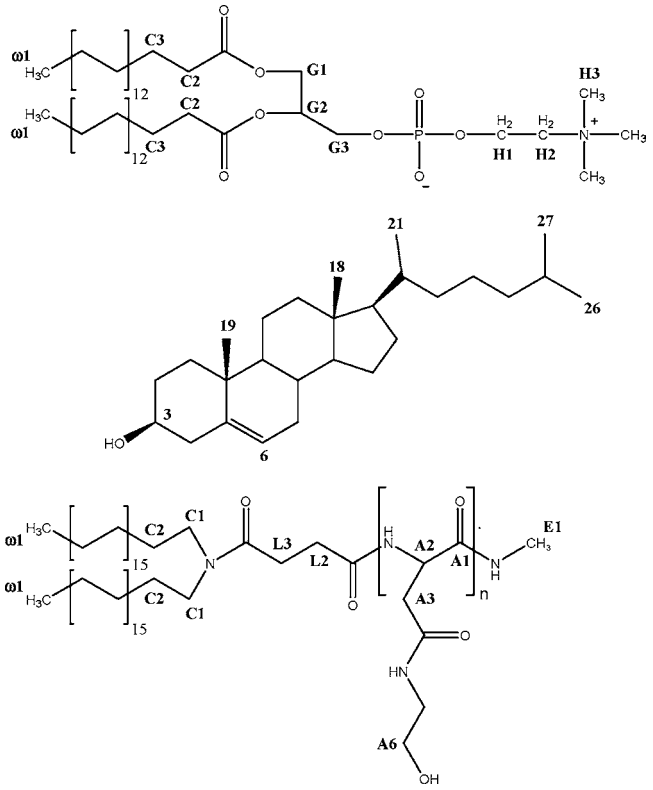

Figure 1. Molecular structure of DPPC, cholesterol, and PHEA-DODASuc ($n = 17$).

EXPERIMENTAL PROCEDURES

Materials. Poly(hydroxyethyl-L-asparagine)-*N*-succinyldioctadecylamine (PHEA-DODASuc) was synthesized as described previously (*4*). Dipalmitoylphosphatidylcholine (DPPC, Figure 1) was purchased from Lipoid GmbH, Ludwigshafen, Germany. α-Cyano-4-hydroxycinnaminic acid, cholesterol (Figure 1), deuteriochloroform (chloroform-*d*, 99.8 atom % D), and deuterated dimethyl sulfoxide (d_6-DMSO) were obtained from Sigma-Aldrich Chemie BV, Zwijndrecht, The Netherlands. All other reagents were of analytical grade.

MALDI-ToF Mass Spectrometry of PHEA-DODASuc. PHEA-DODASuc was dissolved in demineralized water to a

* To whom correspondence should be addressed. Tel: +31-(0)30-2536964. Fax: +31-(0)-2517839. E-mail: W. E.Hennink@pharm.uu.nl.
[†] Department of Pharmaceutics, Utrecht University.
[§] Department of Biomedical Analysis, Utrecht University.
[‡] Astellas Pharma Europe B.V.

10.1021/bc060045a CCC: $33.50 © 2006 American Chemical Society
Published on Web 04/28/2006

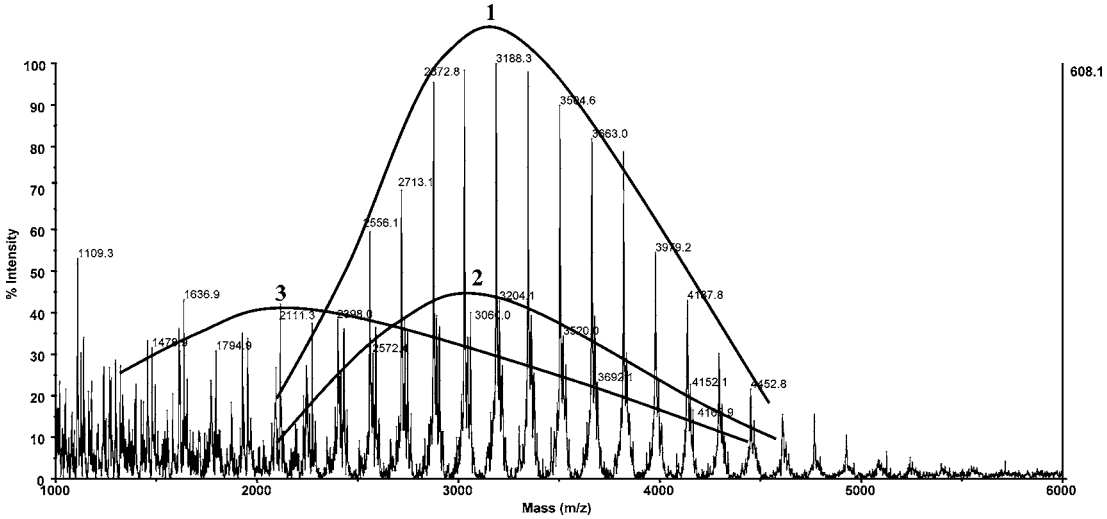

Figure 2. Mass spectrum of PHEA-DODASuc. The three major peak populations are indicated by approximated curves: population 1, Na^+ adduct of the conjugate; population 2, K^+ adduct of the conjugate; population 3, Na^+ adduct without the DODASuc anchor.

concentration of 1 mg/mL. The matrix compound α-cyano-4-hydroxycinnaminic acid was dissolved to a concentration of 10 mg/mL in acetonitrile/water (1:1) containing 0.1% trifluoroacetic acid and mixed in a ratio of 3:1 (v/v) with the conjugate solution. Three microliters of this mixture was put onto a sample deposition plate and left at room temperature to dry. The spectrum was acquired in the positive ion mode on a Voyager-DE STR MALDI-ToF mass spectrometer (Applied Biosystems, Foster City, CA). Ionization was initiated with a nitrogen laser operating at 337 nm with a repetition rate of 7.6 Hz. Delayed extraction linear mode with an accelerating voltage of 20 kV was used, and the acquisition mass range was 700−7000 Da. The spectrum was analyzed with the Applied Biosystems Data Explorer Software.

Sample Preparation for NMR Analysis. A mixture of $CDCl_3$ and d_6-DMSO in a ratio of 2:1 (v/v) was used for dissolving the samples containing DPPC, cholesterol, and PHEA-DODASuc. For signal assignment, DPPC and cholesterol were dissolved in $CDCl_3$, and PHEA-DODASuc was dissolved in d_6-DMSO (approximately 20 mg/mL). The lipid mixtures were prepared by mixing the required amounts of lipid stock solutions and adding $CDCl_3$ and d_6-DMSO to obtain the proper solvent ratio. For instance, for a lipid mixture of DPPC, cholesterol, and PHEA-DODASuc (molar ratio of 62:33:5), a stock solution of 81 μmol of DPPC and 43 μmol of cholesterol per milliliter was prepared in $CDCl_3$, and PHEA-DODASuc was dissolved to a concentration of 13 μmol/mL in d_6-DMSO. Two hundred microliters of the DPPC/cholesterol stock solution and 100 μL of the PHEA-DODASuc stock were mixed and further diluted with 200 μL of d_6-DMSO and 400 μL of $CDCl_3$. The total lipid concentration in the samples was approximately 20 mg/mL.

Liposome Preparation. Lipids (DPPC, cholesterol, PHEA-DODASuc, total lipid ≈ 75 mg) at different ratios were dissolved in about 2 mL of a mixture of chloroform and methanol (1:1 v/v). A film was obtained by evaporation of the solvents under reduced pressure at 50 °C in a 50 mL round-bottom flask. After flushing with nitrogen, the lipid film was hydrated in 5 mM NaCl solution (total lipid concentration 30 μmol/mL). Liposomes were sequentially extruded through two stacked polycarbonate filters (Poretics, 400, 200, 100, and 50 nm) with a high-pressure extrusion device to a final mean size of approximately 100 nm (confirmed by dynamic light scattering measurements). One milliliter of the liposome dispersion was freeze-dried overnight and dried further in a vacuum oven at room temperature for several hours. The dry cake was dissolved in a mixture of $CDCl_3$/d_6-DMSO (2:1) and subsequently analyzed by NMR.

Table 1. Peak Assignment in the Mass Spectrum of PHEA-DODASuc

population no.[a]	*m/z*	assignment of highest peak	repeating unit (r.u.)	range (r.u.)
1	3188.3	$[DODASuc\text{-}(PHEA)_{16} + Na]^+$	158	9−27
2	3204.1	$[DODASuc\text{-}(PHEA)_{16} + K]^+$	158	10−25
3	3060.0	$[(PHEA)_{19} + Na]^+$	158	7−27

[a] The peak population as depicted in Figure 2.

To separate liposomes from possible nonincorporated components, 1 mL of the liposome dispersion obtained after extrusion was subjected to ultracentrifugation at 200 000 g (30 min, 4 °C) using a Beckman LE-80K Ultracentrifuge. The supernatant was collected, freeze-dried, dissolved in d_6-DMSO, and analyzed by NMR. The pellet was dispersed in 1 mL of 5 mM NaCl solution and subsequently freeze-dried and vacuum-dried, dissolved in $CDCl_3$/d_6-DMSO (2:1), and analyzed by NMR.

NMR Analysis. Homonuclear correlation (COSY, TOCSY) and unidimensional analysis of DPPC, cholesterol, and PHEA-DODASuc for signal assignment were carried out with a Varian INOVA 500 spectrometer (Varian, Palo Alto, CA) at 500 MHz. Signals were assigned based on chemical shifts, peak intensities, and spin−spin coupling. Spectra of lipid and liposomal mixtures were recorded with a Varian G-300 spectrometer (Varian, Palo Alto, CA) at 300 MHz. The number of accumulated transients was set to 16−32, the pulse angle was 62.5°, and the relaxation delay D1 was set to 10 s.

RESULTS AND DISCUSSION

MALDI-ToF and NMR Analysis of PHEA-DODASuc. Figure 2 shows the mass spectrum of PHEA-DODASuc, and Table 1 gives the corresponding peak assignments. Three major peak populations are present in the spectrum. The most abundant population can be assigned to the Na^+ adduct of the conjugate (Figure 2, population 1). The two less abundant populations belong to the K^+ adduct of the conjugate (Figure 2, population 2) and the Na^+ adduct of PHEA without the DODASuc anchor (Figure 2, population 3). The presence of the latter compound is likely due to incomplete coupling during synthesis of the conjugate. Due to differences in ionization efficiency, no quantitative data can be obtained from this spectrum. The number-average molecular weight of PHEA-DODASuc based on the peak population of the Na^+ adduct of the conjugate was

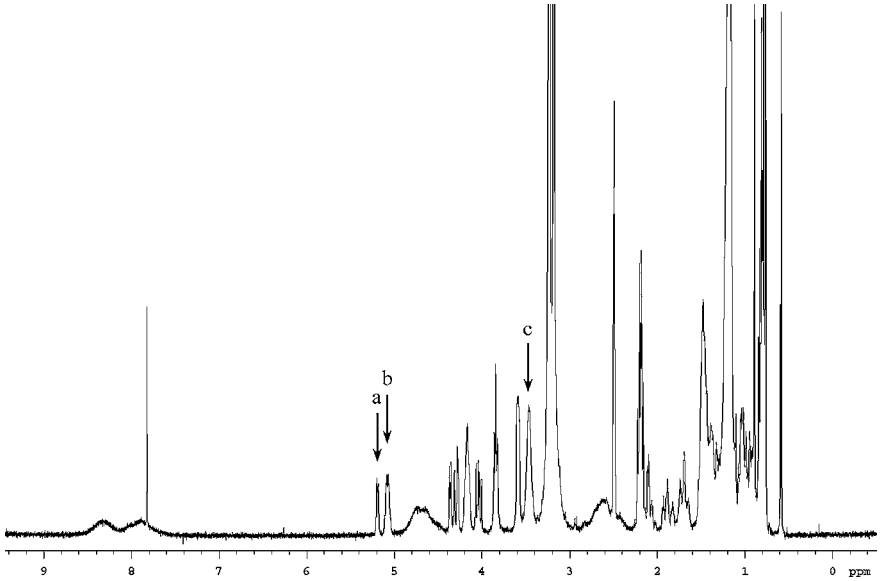

Figure 3. Typical ^{1}H NMR spectrum of a mixture of DPPC/cholesterol/PHEA-DODASuc (molar ratio 62:33:5). Arrows indicate the peaks chosen for evaluation: (a) cholesterol; (b) DPPC; (c) PHEA-DODASuc.

Table 2. Assignment of the Signals in the ^{1}H NMR Spectrum of a Mixture of DPPC/Cholesterol/PHEA-DODASuc

chemical shift (ppm)	assignment
0.6	18 cholesterol
0.8−2.3	ω1, methylene bulk acyl chain, C2+C3 DPPC
	1−2, 4, 7−17, 19−27 cholesterol
	ω1, methylene bulk acyl chain, C2 PHEA-DODASuc
2.4−2.8	A3, E1, L2+L3 PHEA-DODASuc
3.2	H3 DPPC, 3 cholesterol, A5, C1 PHEA-DODASuc
3.5	A6 PHEA-DODASuc
3.6	H2 DPPC
3.8	G3 DPPC
4.1 + 4.3	G1 DPPC
4.2	H1 DPPC
4.6	A2 PHEA-DODASuc
5.1	G2 DPPC
5.2	C6 cholesterol
7.8−8.2	N PHEA-DODASuc (peptide, side chain and end group)

3300 Da and corresponds to an average degree of polymerization of 17. This is in good agreement with the molecular weight (M_n) of 4000, which was calculated after NMR analysis.

NMR Signal Assignment. A typical spectrum of a mixture of DPPC, cholesterol, and PHEA-DODASuc is shown in Figure 3. Table 2 gives the peak assignments based on chemical shifts and intensities and comparison with literature (*10*−*12*). The cholesterol signal chosen for calculation of the ratio of the three compounds in the lipid mixture was at δ 5.2 (proton at C6 at the double bond); for DPPC the signal at δ 5.1 (proton at G2, the middle glycerol carbon atom) and for PHEA-DODASuc the signal at δ 3.5 (protons at C8, side chain-CH_2 next to OH, two protons, for $n = 17$, $2 \times 17 = 34$ protons) were used. The chosen peaks are relatively narrow and sufficiently resolved to make correction for overlap unnecessary.

NMR Analysis of Lipid Mixtures: Accuracy, Precision, and Linearity. Accuracy and precision of the NMR analysis was assessed by analyzing a single lipid mixture with a DPPC/cholesterol/PHEA-DODASuc molar ratio of 62:34:4 on five consecutive days. The method allows for a relative quantitation of the lipid mixtures or, more precisely, assessing their molar composition. The integral values of the proton signals of DPPC (δ 5.1) and PHEA-DODASuc (δ 3.5, corrected for the number of protons by division by 34) were compared with the value of the cholesterol integral (δ 5.2), which was set to one. Results were expressed as percentage of the feed fraction. The DPPC amount was determined to be 98% ± 5% of the feed fraction. In the case of PHEA-DODASuc 104% ± 5% of the feed fraction was found. Thus, these findings are in excellent agreement with the actual composition of the lipid mixture.

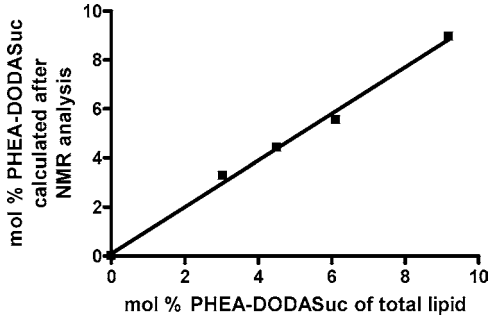

Figure 4. Correlation between the percentage of PHEA-DODASuc (mol % of total lipid) in the feed and the calculated percentage of PHEA-DODASuc after NMR analysis.

Additionally, the accuracy and precision of the sample preparation were investigated. Five lipid mixtures with the same composition (DPPC/cholesterol/PHEA-DODASuc, 62:34:4) were prepared and analyzed on five subsequent days. For DPPC 100% ± 6% of the feed fraction was found. The spectrum of PHEA-DODASuc revealed 101% ± 4% of the feed fraction. Again, these values are in excellent agreement with the actual composition of the lipid mixture. Hence, the sample preparation does not influence the accuracy of the method.

To study the linearity of the method, lipid mixtures with different amounts of PHEA-DODASuc were analyzed by NMR. Lipid ratios were chosen in a range relevant for liposome preparation (PHEA-DODASuc 3.0, 4.5, 6.1, and 9.2 mol % of total lipid). In Figure 4, the percentage of PHEA-DODASuc found after NMR analysis is plotted against the percentage of PHEA-DODASuc in the feed. This figure shows that the fraction of the coating conjugate in the mixture determined by NMR corresponds linearly with the feed fraction. The regression coefficient was >0.99. The NMR method is therefore suitable to accurately determine the composition of mixtures of DPPC, cholesterol, and PHEA-DODASuc.

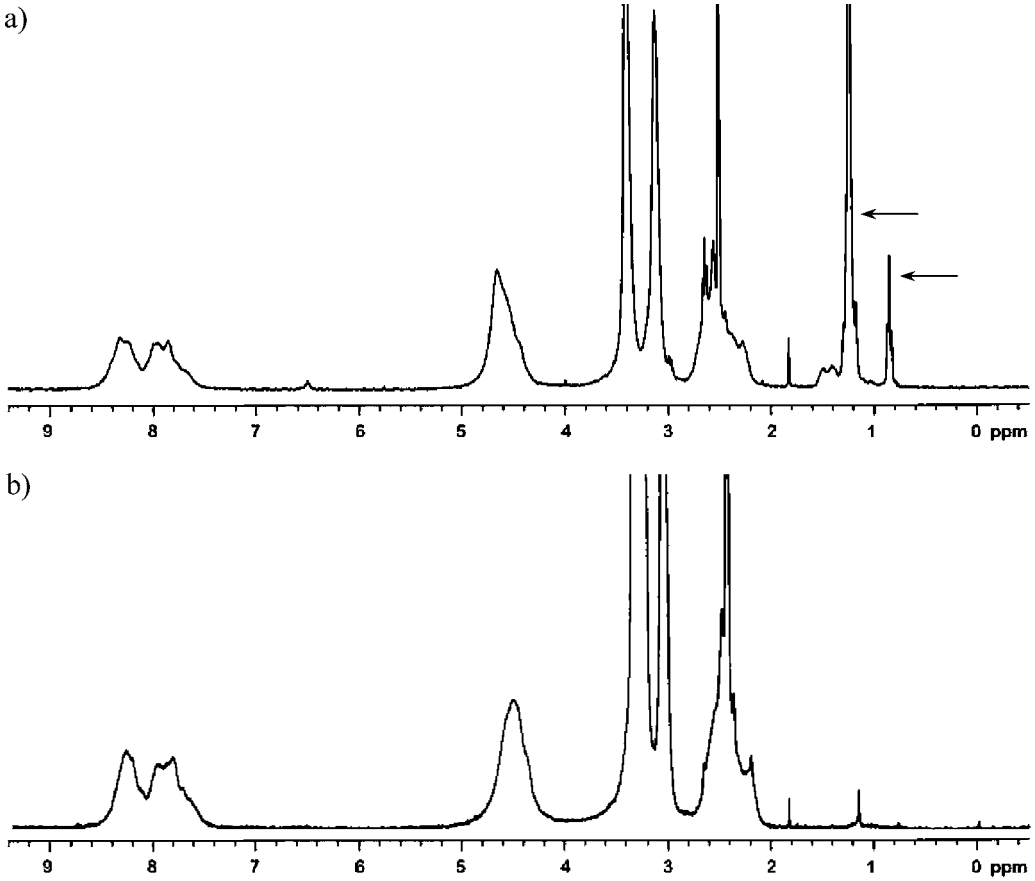

Figure 5. ^{1}H NMR spectrum of (a) native PHEA-DODASuc and (b) the freeze-dried supernatant of ultracentrifugation-treated liposomes, both in d_6-DMSO. The arrows indicate peaks of the DODASuc anchor.

Table 3. Amount of DPPC and PHEA-DODASuc Relative to Cholesterol in Two Liposomal Mixtures[a]

lipid composition DPPC/chol/ PHEA-DODASuc	DPPC % of feed		PHEA-DODASuc % of feed	
	before separation[b]	after separation[b]	before separation[b]	after separation[b]
65:33:2	96 ± 5	102 ± 5	98 ± 5	85 ± 5
62:33:5	100 ± 5	100 ± 5	107 ± 5	88 ± 5

[a] The results are expressed as the calculated value ± the error. [b] separation: removal of nongrafted conjugate from liposomes by ultracentrifugation (see Materials and Methods)

NMR Analysis of Liposomal Mixtures. Table 3 shows the results of the analysis of two freeze-dried liposomal dispersions. The compositions were determined before and after separation of nongrafted components from the liposomes by ultracentrifugation. The calculated fractions of DPPC, both before and after centrifugation, are in good agreement with the fraction in the feed. The fraction of PHEA-DODASuc in liposomes before ultracentrifugation is also in agreement with the feed fraction. This implies that the liposome preparation process does not alter the molar composition of the initial lipid mixture and the lipid film was fully converted into liposomes. After separation of nongrafted components by ultracentrifugation, however, the fractions of PHEA-DODASuc were 85% (17 nmol of PHEA/μmol of total lipid) and 88% (44 nmol of PHEA/μmol of total lipid) of the feed fractions, respectively. This indicates that not all of the PHEA molecules that are used for liposome preparation were attached to the liposome surface. It is likely that the nonincorporated fraction is the fraction of the added PHEA molecules that lack the lipid anchor (DODASuc) and therefore is not grafted onto the liposome bilayer. To evaluate this, an NMR spectrum of the supernatant of liposomes obtained after ultracentrifugation and freeze-drying was recorded. Figure 5b shows that the peaks that belong to the anchor part of the molecule at a chemical shift of δ 0.8−1.6 are absent in this spectrum (compare the spectrum of the native PHEA-DODASuc, Figure 5a). Whereas conjugate molecules with the anchor are likely quantitatively grafted onto the bilayers, the PHEA molecules without the anchor stay in solution. This means that approximately 85% of the PHEA molecules of the batch used in these experiments are attached to the DODASuc anchor and can be grafted onto the liposome bilayer. This is an important issue when studying the shielding properties of PHEA-DODASuc in relation to the grafting density.

In summary, this paper presents a fast, reproducible, and relatively sensitive NMR-based analysis method for the quantitation of PHEA-DODASuc in liposomes.

LITERATURE CITED

(1) Woodle, M. C., and Lasic, D. D. (1992) Sterically stabilized liposomes. *Biochim. Biophys. Acta 1113*, 171−199.

(2) Torchilin, V. P., and Trubetskoy, V. S. (1995) Which polymers can make nanoparticulate drug carriers long-circulating? *Adv. Drug Delivery Rev. 16*, 141−155.

(3) Storm, G., Belliot, S. O., Daemen, T., and Lasic, D. D. (1995) Surface modification of nanoparticles to oppose uptake by the mononuclear phagocyte system. *Adv. Drug Delivery Rev. 17*, 31−48.

(4) Metselaar, J. M., Bruin, P., de Boer, L. W., de Vringer, T., Snel, C., Oussoren, C., Wauben, M. H., Crommelin, D. J., Storm, G., and Hennink, W. E. (2003) A novel family of L-amino acid-based biodegradable polymer−lipid conjugates for the development of long-circulating liposomes with effective drug-targeting capacity. *Bioconjugate Chem. 14*, 1156−1164.

(5) Romberg, B., Metselaar, J. M., de Vringer, T., Motonaga, K., Kettenes-van den Bosch, J. J., Oussoren, C., Storm, G., and Hennink, W. E. (2005) Enzymatic Degradation of Liposome-Grafted Poly(hydroxyethyl L-glutamine). *Bioconjugate Chem. 16*, 767−774.

(6) Torchilin, V. P., Omelyanenko, V. G., Papisov, M. I., Bogdanov, A. A., Jr., Trubetskoy, V. S., Herron, J. N., and Gentry, C. A. (1994) Poly(ethylene glycol) on the liposome surface: on the mechanism of polymer-coated liposome longevity. *Biochim. Biophys. Acta 1195*, 11−20.

(7) Vernooij, E. A., Gentry, C. A., Herron, J. N., Crommelin, D. J., and Kettenes-van den Bosch, J. J. (1999) 1H NMR quantification of poly(ethylene glycol)-phosphatidylethanolamine in phospholipid mixtures. *Pharm. Res. 16*, 1658−1661.

(8) Boada, J., Gallardo, M., and Estelrich, J. (1997) Determination of poly(ethylene glycol) activated with cyanuric chloride in liposomes. *Anal. Biochem. 253*, 33−36.

(9) Garcia-Fuentes, M., Torres, D., Martin-Pastor, M., and Alonso, M. J. (2004) Application of NMR Spectroscopy to the Characterization of PEG-Stabilized Lipid Nanoparticles. *Langmuir 20*, 8839−8845.

(10) Han, X., Chen, X., and Gross, R. W. (1991) Chemical and magnetic inequivalence of glycerol protons in individual subclasses of choline glycerophospholipids: implications for subclass-specific changes in membrane conformational states. *J. Am. Chem. Soc. 113*, 7104−7109.

(11) Sparling, M. L., Zidovetzki, R., Muller, L., and Chan, S. I. (1989) Analysis of membrane lipids by 500 MHz 1H NMR. *Anal. Biochem. 178*, 67−76.

(12) Spectral Database for Organic Compounds SDBS, National Institute of Advances in Industrial Science and Technology, 887HSP-40-636 and 16108HSP-45-792.

BC060045A

JULY/AUGUST 2006
Volume 17, Number 4

© Copyright 2006 by the American Chemical Society

Bioconjugate Chemistry

COMMUNICATIONS

Annexin A5-Conjugated Quantum Dots with a Paramagnetic Lipidic Coating for the Multimodal Detection of Apoptotic Cells

Geralda A. F. van Tilborg,*[,†] Willem J. M. Mulder,[†] Patrick T. K. Chin,[‡] Gert Storm,[§] Chris P. Reutelingsperger,[||] Klaas Nicolay,[†] and Gustav J. Strijkers[†]

Biomedical NMR, Department of Biomedical Engineering, Eindhoven University of Technology, P.O. Box 513, 5600 MB Eindhoven, The Netherlands, Laboratory of Macromolecular and Organic Chemistry, Eindhoven University of Technology, P.O. Box 513, 5600 MB Eindhoven, The Netherlands, Department of Pharmaceutics, Utrecht Institute for Pharmaceutical Sciences (UIPS), 3508 TB, Utrecht, The Netherlands, and Department of Biochemistry, University of Maastricht, P.O. Box 616, 6200 MD Maastricht, The Netherlands. Received February 24, 2006; Revised Manuscript Received April 25, 2006

Apoptosis, or programmed cell death, plays an important role in the etiology of a variety of diseases, including cancer. Visualization of apoptosis would allow both early detection of therapy efficiency and evaluation of disease progression. To that aim we developed a novel annexin A5-conjugated bimodal nanoparticle. The nanoparticle is composed of a quantum dot that is encapsulated in a paramagnetic micelle to enable its use both for optical imaging and MRI. Multiple recombinant human annexin A5 protein molecules were covalently coupled to the nanoparticle for targeting. In this study the specificity of the annexin A5-conjugated nanoparticles for apoptotic cells was demonstrated both with fluorescence microscopy and MRI, which confirms its potential for the detection of apoptosis with both imaging modalities in vivo.

Apoptosis, or programmed cell death, is an essential biological process that both occurs in normal tissue homeostasis and in diseased tissue (*1*). In pathophysiological situations the measurement of apoptotic activity may greatly enhance possibilities for staging the disease, and, equally important, apoptosis may serve as an early indicator for the effect of therapeutic interventions. In antitumor therapies the induction of apoptosis by, for example, cytotoxic drugs leads to an arrest of tumor proliferation, since the unrestrained division of tumor cells is related to insufficient apoptosis (*2*). Other disorders, like reperfusion injury after myocardial infarction or stroke, are rather associated with excessive apoptosis. Several biochemical markers of apoptosis have been identified and could in principle be exploited for the detection of apoptosis. The exposure of the normally asymmetrically distributed phosphatidylserine (PS) at the outer monolayer of the cell membrane of apoptotic cells is an especially attractive hallmark of apoptosis, since the protein annexin A5 binds with high affinity to this negatively charged phospholipid (*3*). For the visualization of apoptosis, annexin A5 may be used as a targeting ligand, which requires the protein

* To whom correspondence should be addressed. Fax: +31 40 243 2598. E-mail: g.a.f.v.tilborg@tue.nl.
[†] Biomedical NMR, Department of Biomedical Engineering, Eindhoven University of Technology.
[‡] Laboratory of Macromolecular and Organic Chemistry, Eindhoven University of Technology.
[§] Utrecht Institute for Pharmaceutical Sciences.
[||] University of Maastricht.

10.1021/bc0600463 CCC: $33.50 © 2006 American Chemical Society
Published on Web 06/16/2006

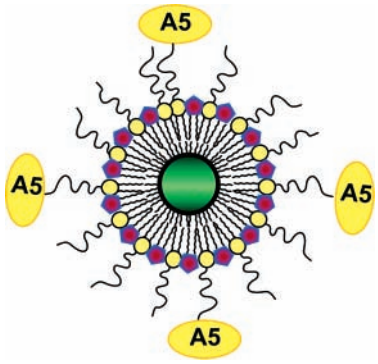

Figure 1. Schematic representation of a TOPO/HDA quantum dot with a paramagnetic lipid coating, to which multiple annexin A5 proteins are conjugated (A5-pQD). The lipids drawn with the yellow and red headgroups represent PEG-DSPE and Gd-DTPA-BSA, respectively. Annexin A5 (indicated with A5) is conjugated to the maleimide group of Mal-PEG-DSPE.

to be conjugated to a contrast agent for the imaging modality of choice. Fluorescently labeled annexin A5 for optical imaging and annexin A5 conjugated with a radioactive label for nuclear imaging have been used successfully to visualize apoptosis in animal models (*4*) and in patients (*5*), respectively. Recently, annexin A5 conjugated to a magnetic nanoparticle was used for the detection of apoptosis in tumors and after myocardial infarction in mice with magnetic resonance imaging (MRI) (*6*). Although MRI excels in depicting opaque soft tissue with higher spatial resolution and better contrast as compared to, for example, nuclear methods, it is a relatively insensitive technique and it lacks the microscopic resolution of the optical methods. The bimodal approach of using MRI in combination with optical imaging would therefore make it possible to visualize apoptosis at the microscopic and macroscopic level.

In this study we report on the development of a novel annexin A5-conjugated nanoparticle, which has excellent paramagnetic and fluorescent properties. The nanoparticle consists of a quantum dot (QD), which is encapsulated in a paramagnetic micelle. Quantum dots have received much attention lately as optical imaging agents because of their excellent photostability and sensitivity, and narrow and tunable emission wavelength (*7*). Because of the small size of this nanoparticle, less than 10 nm, compared to most other nanoparticulate MRI contrast agents, which are typically in the order of 50−250 nm (*8*, *9*), quantum dots may distribute more easily into diseased tissue. This improves the bioavailability and can be expected to enhance the binding to apoptotic cells.

CdSe/ZnS core/shell quantum dots were synthesized under a flow of argon by injection of the precursors into a hot coordinating solvent (*10*). The TOPO/HDA-capped quantum dots were coated with paramagnetic micelles according to an extended procedure described by Dubertret et al. (*11*). In short, TOPO/HDA-capped quantum dots were washed and suspended in chloroform. A mixture of 40 mol % 1,2-distearoyl-sn-glycero-3-phosphoethanolamine-*N*-[methoxy(poly(ethylene glycol))-2000] (PEG-DSPE), 10 mol % 1,2-distearoyl-sn-glycero-3-phosphoethanolamine-*N*-[maleimide(poly(ethylene glycol))2000] (Mal-PEG−DSPE), and 50 mol % of the paramagnetic lipid Gd-DTPA-bis(stearylamide) (Gd-DTPA−BSA) dissolved in chloroform/methanol (20/1) was added to the quantum dots. The solvent was gently evaporated, and a solution of HEPES buffer (pH 6.7) that had been heated to 70 °C was added to the obtained mixed film. This mixture was rigorously heated and vortexed until a clear suspension was obtained. Empty micelles and micelles containing a quantum dot were separated with ultracentrifugation (1 h, 500000*g*). Both the gadolinium and the cadmium content of the annexin A5−pQD preparations were determined with inductively coupled plasma atomic emission spectrometry (ICP-AES). Furthermore it was measured with thermogravimetric analysis (TGA) that 56 mass % of the quantum dots consists of CdSe/ZnS. From these values an average value of 150−200 Gd-DTPA−BSA lipid molecules per nanoparticle could be derived.

The ability of the annexin A5-conjugated nanoparticle (A5-pQD) to reduce the intrinsic T_1 and T_2 values of water are described by its molar relaxivities r_1 and r_2, which are expressed in $mM^{-1}\ s^{-1}$. The ionic relaxivities of this nanoparticle at 37 °C and 60 MHz, were measured to be $r_1 = 12.4 \pm 0.7\ mM^{-1}s^{-1}$ and $r_2 = 18.0 \pm 0.1\ mM^{-1}s^{-1}$, respectively. The relaxivity per mM particles therefore is at least 150 times higher than the ionic relaxivity. Next, recombinant human annexin A5, containing a single free cysteine, was covalently linked to the maleimide group of Mal-PEG-DSPE via the thiol of the cysteine as described previously (*12*). A schematic representation of the annexin A5-conjugated nanoparticle (A5-pQD) is shown in Figure 1.

The specificity of this contrast agent for apoptotic cells was obtained in vitro. For that purpose the T-lymphoma cell line Jurkat (ATCC) was grown in RPMI1640 medium (Gibco), which was supplemented with 10% fetal calf serum and a mixture of antibiotics (100 units ml^{-1} penicillin, 0.1 mg ml^{-1} streptomycin). Cells were grown at 37 °C in a humified atmosphere and 5% CO_2. Apoptosis is naturally occurring without exposing the cells to apoptotic stimuli, typically involving 5 to 10% of the cells within the culture. To induce an increased number of apoptotic cells, the cells were resuspended to 10^6 cells ml^{-1} medium and treated with 200 ng ml^{-1} anti-Fas (CD95 human monoclonal antibody, Beckman Coulter B.V.) for 3 h, which initiates approximately 40 to 50% apoptosis. To allow fluorescence imaging and MRI of cell pellets, 5 million cells were treated with anti-Fas and subsequently incubated for 15 min with the annexin A5-conjugated nanoparticles at a final

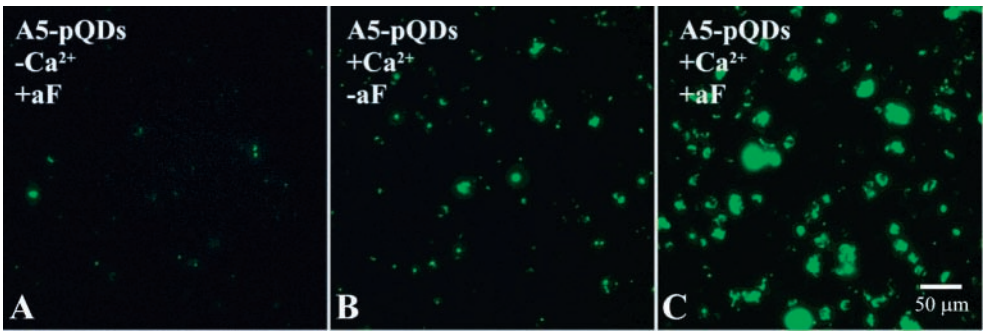

Figure 2. Fluorescence microscopy of Jurkat cells incubated with annexin A5-conjugated pQDs. (A) Apoptotic cells incubated in the presence of EDTA, (B) vital cells with a naturally occurring percentage of apoptotic cells, and (C) apoptotic cells. +aF denotes stimulation with anti-Fas, while −aF denotes no stimulation. $+Ca^{2+}$ indicates the presence of Ca^{2+}, while $-Ca^{2+}$ indicates incubation in the presence of EDTA to remove Ca^{2+}.

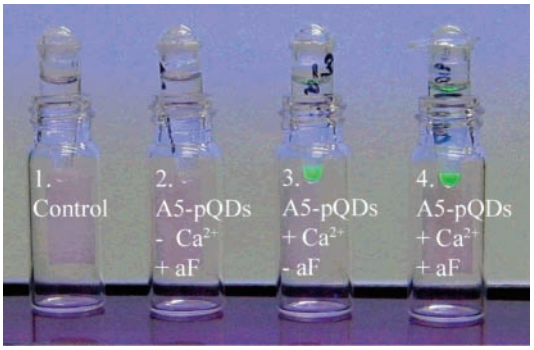

Figure 3. Cell pellets of the different incubations illuminated with 254 nm UV light. From left to right: Control cells (sample 1), apoptotic cells incubated with A5-pQDs in the presence of EDTA to remove Ca^{2+} (sample 2), vital cells incubated with A5-pQDs (sample 3), and apoptotic cells incubated with A5-pQDs (sample 4).

concentration of 392.4 μM quantum dots in Ca^{2+}-containing binding buffer (10 mM HEPES, 150 mM NaCl, 5 mM KCl, 1 mM $MgCl_2$, 2.5 mM $CaCl_2$, pH 7.4). To further assess the binding specificity 5×10^6 cells that were not treated with anti-Fas were also incubated with A5-pQDs. Since annexin A5 binds to phosphatidylserine in a Ca^{2+}-dependent manner, the removal of Ca^{2+} will prevent binding. Therefore, A5-pQDs that were incubated in HEPES-buffered saline that was supplemented with EDTA (25 mM HEPES, 140 mM NaCl and 5 mM EDTA, pH 7.4) were also used as control. Following the incubations, all cell samples were extensively washed in binding buffer or HEPES-buffered saline supplemented with EDTA, respectively.

For fluorescence imaging and MRI of cell pellets, the 5 million cells of the different incubations were collected, fixed in a 4% paraformaldehyde solution, and put in small cups. Cells were allowed to settle as loosely packed cell pellets overnight at 4 °C Fluorescence microscopy of the apoptotic cells that were incubated with A5-pQDs in binding buffer showed bright fluorescence indicative for a massive association of the contrast agent with the cells (Figure 2C). On the contrary, the cells that were not stimulated with anti-Fas showed much less fluorescence (Figure 2B), because of the lower percentage of apoptotic cells. In the cell pellet that was incubated with A5-pQDs in the presence of EDTA almost no fluorescence was observed (Figure 2A). The observed low fluorescent intensity in sample 2 could not be induced by fluorescent quenching due to EDTA since the emission spectrum of paramagnetic quantum dots in HEPES-buffered saline was measured to remain unchanged after addition of EDTA to a final concentration of 5 mM.

In Figure 3 the different cups with loosely packed cell pellets, illuminated with 254 nm UV light, are depicted. The green emitting cell pellet that originated from the incubation of annexin A5 nanoparticles with apoptotic cells (Figure 3, sample 4) can clearly be distinguished from the other incubations (Figure 3, samples 1−3).

Following the above optical analysis, the cell pellets were measured with MRI. T_1-weighted images (Figure 4A) revealed a strong signal enhancement of the apoptotic cells incubated with A5-pQDs in binding buffer (sample 4) as compared to the three control incubations (samples 1, 2, and 3). The cells that were not treated with anti-Fas (sample 3) also showed association of the contrast material. This accounts for the low level of apoptosis that is commonly seen in cell suspensions even in the absence of apoptotic stimuli. For absolute quantification of the T_1 and T_2 relaxation times an MRI inversion recovery experiment and a multi-echo experiment were performed, respectively. From these data the T_1 and T_2 relaxation times of the different cell pellets were calculated. Since the concentration of a paramagnetic agent is proportional with the relaxation rate R_1 ($1/T_1$) and R_2 ($1/T_2$), these values were calculated for the different cell pellets. In Figure 4B and 4C the R_1 and R_2 relaxation rates of the different cell pellets are depicted. Control cells that were not incubated with the contrast agent (sample 1) showed the lowest R_1 and R_2. Cell pellets of apoptotic cells incubated with A5-pQDs in binding buffer (sample 4) showed the highest R_1 and R_2 values. The cell pellet of anti-Fas treated cells that were incubated with A5-pQDs in the presence of EDTA (sample 2), as well as the untreated cell pellet incubated with A5-pQDs (sample 3), had much lower relaxation rates than the anti-Fas treated cells that were incubated with A5-pQDs in the presence of Ca^{2+} (sample 4).

The novel annexin A5-conjugated nanoparticle presented in this study may be of great use for successive MRI and intravital microscopy of apoptosis in animal models of cardiac dysfunction or in tumor models. This allows the detection of apoptosis both at the macroscopic and the microscopic level in vivo. Dumont et al. have demonstrated the feasibility to detect apoptosis in the beating murine heart, following the administration of fluorescently labeled annexin A5 (*4*). A comparable setup could be used for intravital microscopy of subcutaneously grown tumors in mice. Recently, Stroh et al. have demonstrated simultaneous detection of multiple quantum dot species (*13*). The application of near-infrared quantum dots would additionally increase the penetration depth, which allows the real time investigation of tissue as deep as 1 cm (*14*). The technology developed in this study may also be applied to quantum dots with a different size and consequently with a different emission wavelength. This allows optimization of the nanoparticle both for the tissue of interest and the additional fluorescent dyes to be imaged.

In conclusion, we have developed a novel nanoparticulate contrast agent for the detection of apoptosis, with excellent paramagnetic and fluorescent properties. The in vitro results demonstrated a high specificity of this contrast agent for apoptotic cells, suggesting its potential for the detection of apoptosis in different animal models with both intravital fluorescence microscopy and MRI in vivo. Because of the relatively small size of this QD-based contrast agent compared

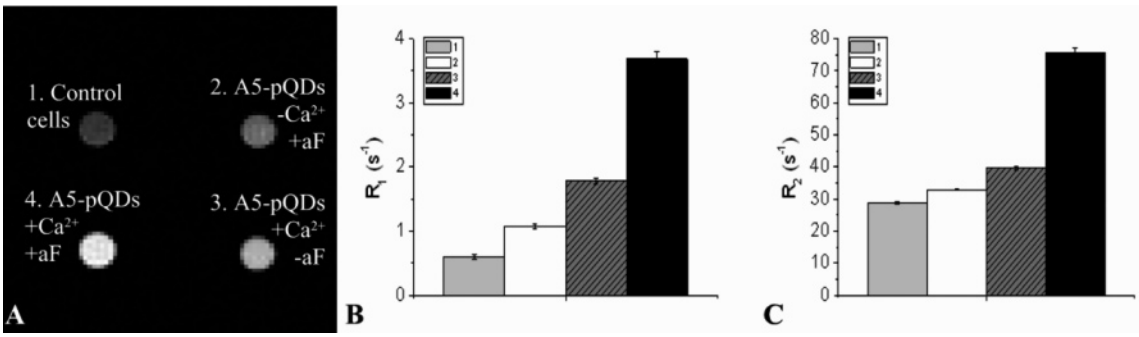

Figure 4. (A) T_1-weighted image of the different cell pellets. (B, C) The R_1 and R_2 relaxation rates of the different cell pellets with the highest values were measured for apoptotic cells incubated with A5-pQDs (black bar). The cells in sample 1 are untreated control cells. Sample 2, 3, and 4 are incubated with A5-pQDs.

to most other MRI detectable nanoparticles the availability of the present contrast agent for apoptotic cells in the extravascular space may be greatly enhanced. This technology opens exciting new opportunities for multimodality molecular imaging of apoptotic processes in animal models of human disease processes.

ACKNOWLEDGMENT

This study was funded in part by the EC − FP6-project DiMI, LSHB-CT-2005-512146-, and by the BSIK program entitled Molecular Imaging of Ischemic Heart Disease (project number BSIK03033). The authors thank Dr. Rolf Koole and Dr. Celso de Mello Donegá for reading the manuscript and useful discussions.

LITERATURE CITED

(1) Leist, M., and Jaattela, M. (2001) Four Deaths and a Funeral: From Caspases to Alternative Mechanisms. *Nat. Rev. Mol. Cell Biol. 2*, 589−598.

(2) Brown, J. M., and Attardi, L. D. (2005) The Role of Apoptosis in Cancer Development and Treatment Response. *Nat. Rev. Cancer 5*, 231−237.

(3) Koopman, G., Reutelingsperger, C. P., Kuijten, G. A., Keehnen, R. M., Pals, S. T., and van Oers, M. H. (1994) Annexin V for Flow Cytometric Detection of Phosphatidylserine Expression on B Cells Undergoing Apoptosis. *Blood 84*, 1415−1420.

(4) Dumont, E. A., Reutelingsperger, C. P., Smits, J. F., Daemen, M. J., Doevendans, P. A., Wellens, H. J., and Hofstra, L. (2001) Real-Time Imaging of Apoptotic Cell-Membrane Changes at the Single-Cell Level in the Beating Murine Heart. *Nat. Med. 7*, 1352−1355.

(5) Hofstra, L., Liem, I. H., Dumont, E. A., Boersma, H. H., van Heerde, W. L., Doevendans, P. A., De Muinck, E., Wellens, H. J., Kemerink, G. J., Reutelingsperger, C. P., and Heidendal, G. A. (2000) Visualisation of Cell Death in Vivo in Patients With Acute Myocardial Infarction. *Lancet 356*, 209−212.

(6) Sosnovik, D. E., Schellenberger, E. A., Nahrendorf, M., Novikov, M. S., Matsui, T., Dai, G., Reynolds, F., Grazette, L., Rosenzweig, A., Weissleder, R., and Josephson, L. (2005) Magnetic Resonance Imaging of Cardiomyocyte Apoptosis With a Novel Magneto-Optical Nanoparticle. *Magn Reson. Med. 54*, 718−724.

(7) Michalet, X., Pinaud, F. F., Bentolila, L. A., Tsay, J. M., Doose, S., Li, J. J., Sundaresan, G., Wu, A. M., Gambhir, S. S., and Weiss, S. (2005) Quantum Dots for Live Cells, in Vivo Imaging, and Diagnostics. *Science 307*, 538−544.

(8) Josephson, L., Tung, C. H., Moore, A., and Weissleder, R. (1999) High-Efficiency Intracellular Magnetic Labeling With Novel Superparamagnetic-Tat Peptide Conjugates. *Bioconjugate Chem. 10*, 186−191.

(9) Mulder, W. J., Strijkers, G. J., van Tilborg, G. A., Griffioen, A. W., and Nicolay, K. (2006) Lipid-Based Nanoparticles for Contrast-Enhanced MRI and Molecular Imaging. *NMR Biomed. 19*, 142−164.

(10) Mulder, W. J., Koole, R., Brandwijk, R. J., Storm, G., Chin, P. T., Strijkers, G. J., de Mello, D. C., Nicolay, K., and Griffioen, A. W. (2006) Quantum Dots With a Paramagnetic Coating As a Bimodal Molecular Imaging Probe. *Nano Lett. 6*, 1−6.

(11) Dubertret, B., Skourides, P., Norris, D. J., Noireaux, V., Brivanlou, A. H., and Libchaber, A. (2002) In Vivo Imaging of Quantum Dots Encapsulated in Phospholipid Micelles. *Science 298*, 1759−1762.

(12) Mulder, W. J., Strijkers, G. J., Griffioen, A. W., van Bloois, L., Molema, G., Storm, G., Koning, G. A., and Nicolay, K. (2004) A Liposomal System for Contrast-Enhanced Magnetic Resonance Imaging of Molecular Targets. *Bioconjugate Chem. 15*, 799−806.

(13) Stroh, M., Zimmer, J. P., Duda, D. G., Levchenko, T. S., Cohen, K. S., Brown, E. B., Scadden, D. T., Torchilin, V. P., Bawendi, M. G., Fukumura, D., and Jain, R. K. (2005) Quantum Dots Spectrally Distinguish Multiple Species Within the Tumor Milieu in Vivo. *Nat. Med. 11*, 678−682.

(14) Kim, S., Lim, Y. T., Soltesz, E. G., De Grand, A. M., Lee, J.; Nakayama, A., Parker, J. A., Mihaljevic, T., Laurence, R. G., Dor, D. M., Cohn, L. H., Bawendi, M. G., and Frangioni, J. V. (2004) Near-Infrared Fluorescent Type II Quantum Dots for Sentinel Lymph Node Mapping. *Nat. Biotechnol. 22*, 93−97.

BC0600463

An Affinity-Based Method for the Purification of Fluorescently-Labeled Biomolecules

Trung Nguyen, Neel S. Joshi, and Matthew B. Francis*

Department of Chemistry, University of California, Berkeley, California 94720-1460, and Materials Sciences Division, Lawrence Berkeley National Labs, Berkeley, California 94720. Received May 22, 2006; Revised Manuscript Received June 17, 2006

Due to the difficulty of separating mixtures of labeled and unlabeled biomolecules, a general new method for the affinity purification of modified proteins has been developed. A Sepharose-based solid support bearing β-cyclodextrin groups was used to capture chromophore-modified proteins selectively, while unmodified proteins remained in solution. After isolation of the resin, the modified proteins were released by treating the sample with a competitive cyclodextrin binder, such as adamantane carboxylic acid. This procedure was demonstrated for several dyes displaying a wide range of spectral characteristics and diverse chemical structures. Preliminary studies have shown that this method can also be used to enrich modified peptide fragments present in proteolytic digests. This technique is anticipated to accelerate the development of new protein modification reactions and could provide a useful tool for proteomics applications.

The attachment of chromophores to biomolecules is a common practice in chemical biology, affording fluorescent probes that can track protein localization (*1a*), detect the binding of substrates (*1b*), and measure distances through fluorescence resonance energy transfer (FRET) (*1c*,*d*). Typically these labels are introduced through the reaction of lysine residues with NHS-esters, isocyanates, or isothiocyanates, or through the modification of cysteine residues with maleimides or iodoacetamides (*2*). However, these reactions commonly do not reach full conversion, yielding inseparable mixtures of labeled and unlabeled proteins. Although this is acceptable in some instances, many applications (such as FRET studies) would benefit from the removal of unreacted proteins from the sample. Unfortunately, no general method exists to achieve this separation under conditions mild enough to maintain the folded, native structure of the protein targets. To address this, we report herein a general affinity-based method that can isolate biomolecules that are labeled with small organic chromophores.

Numerous strategies have emerged for the formation of host−guest complexes through molecular recognition events (*3*). Of these, complexes formed with cyclodextrins and their derivatives are arguably the most general (*4*). A wide range of organic molecules has been found to form complexes with cyclodextrins with binding constants that span 6 orders of magnitude (*5*), and, as a result, cyclodextrins have found use in applications ranging from the solubilization of pharmaceutical compounds (*6*) to chiral chromatography (*7*). Several studies have established the ability of cyclodextrins to form host−guest complexes with fluorescent chromophores (*7b*, *8*, *9*); in contrast, we have found that they have little-to-no affinity for most proteins. We envisioned using biocompatible resins functionalized with cyclodextrins to sequester labeled biomolecules selectively, while leaving unlabeled species in solution, Figure 1b. After isolation of the resin, it was anticipated that the captured proteins could be released through the addition of a competitive binder, such as **3**.

A solid support suitable for this purpose was prepared through the exposure of commercially available NHS-ester functionalized Sepharose resin to amine-functionalized β-cyclodextrin (*9*) (**1a**), yielding resin **2a**, Figure 1a. The efficiency of the coupling reaction was monitored by UV analysis of the released NHS, indicating that a loading of 8.7 μmol of β-cyclodextrin/mL of dry resin was obtained. Following hydrolysis of any remaining NHS-esters using ethanolamine, the resin was thoroughly rinsed with water and stored in solution at 4 °C until use (*10*).

In light of the high cost of **1a**, we have also developed a more practical route for the preparation of the resin. Activation of inexpensive β-cyclodextrin with carbonyl diimidazole followed by treatment with excess propylenediamine afforded carbamate **1b** with only minimal amounts of doubly coupled product. This mixture was used to prepare resin analogue **2b**, which performed equivalently in the studies described below.

The ability of the cyclodextrin resin to purify labeled biomolecules was evaluated in the context of a typical lysine modification experiment. After exposure of a solution of myoglobin to 1 equiv of Oregon Green NHS-ester (yielding conjugate **4**) and subsequent removal of the small molecules using gel filtration, 320 μL of the resulting 1 mg/mL solution was exposed to 37 mg of resin **2a** for 5 min. UV−vis analysis indicated the complete disappearance of the Oregon Green absorbance from the supernatant (λ_{max} = 495 nm), while unlabeled myoglobin (λ_{max} = 410 nm) remained in solution, Figure 2a. SDS−PAGE analysis of the supernatant indicated that no fluorescent protein remained (Figure 2b, lane 2), and ESI-MS confirmed that virtually all of the labeled protein had been captured (Figure 2c,d). After isolation via filtration, it was found that the resin could be washed with several portions of water without releasing the bound protein.

Several competitive binders have been used to liberate the modified protein from the resin. Adamantane carboxylic acid (**3**, 10 mM in 100 mM ammonium chloride, pH 7) has been particularly useful in this regard, resulting in nearly complete release in under 1 min, Figure 2a,b. ESI-MS analysis of the resulting solution confirmed that >90% of the eluted protein had been modified, Figure 2e (*11*). Under saturating conditions, UV−vis analysis indicated that 100 mg of resin was able to capture 40 nmol (0.67 mg, in this case) of labeled protein.

10.1021/bc060130i CCC: $33.50 © 2006 American Chemical Society
Published on Web 07/01/2006

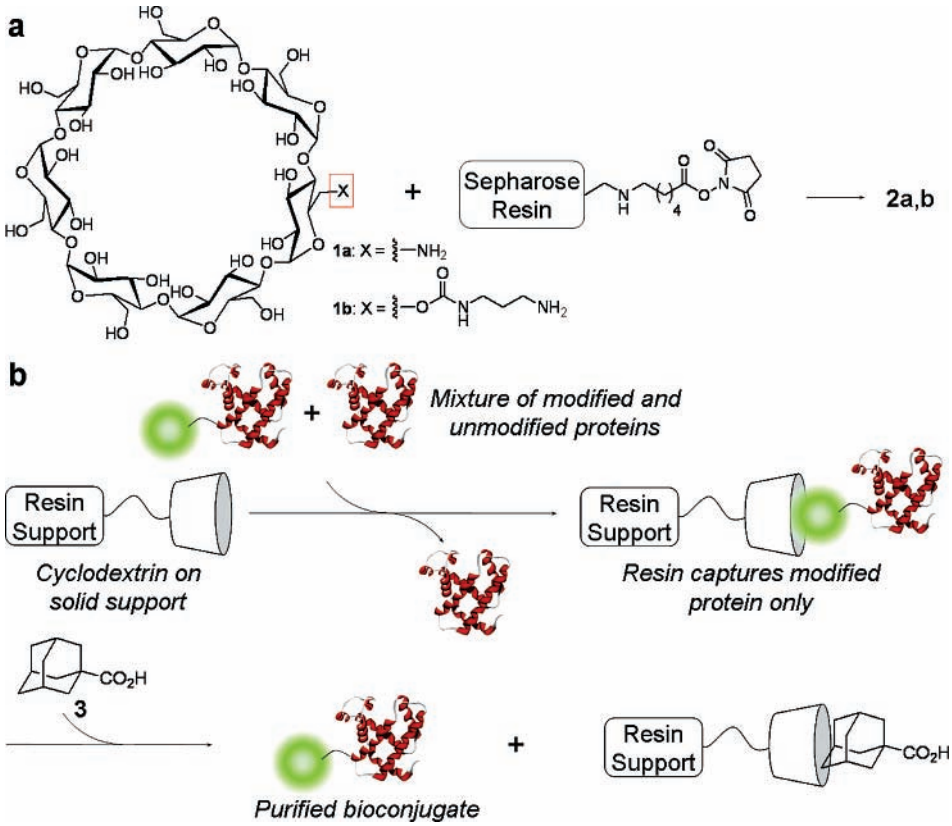

Figure 1. A general strategy for the purification of chromophore-labeled proteins. (a) The solid support used in this approach is prepared by reacting Sepharose-NHS resin with amino-substituted β-cyclodextrin **1a** or **1b**. (b) This resin can then be used to capture chromophore-labeled proteins selectively, allowing facile removal of unmodified protein via filtration. The captured proteins can be eluted from the resin using a competitive cyclodextrin binder, such as adamantane carboxylic acid (**3**).

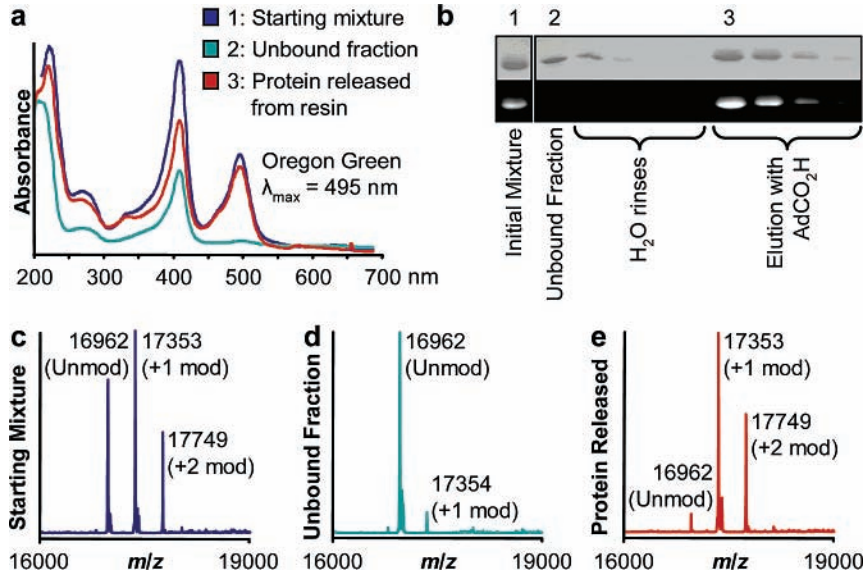

Figure 2. Purification of Oregon Green labeled myoglobin. (a) UV analysis of supernatants during the purification process. Blue = crude labeling solution. Cyan = supernatant after exposure to resin **2a**. Red = protein fraction released from isolated resin after treatment with **3**. The absorbance at 410 nm is due to the myoglobin heme group. The composition of each fraction was also verified using (b) SDS−PAGE and (c−e) ESI-MS analysis.

In terms of buffers, we have found that efficient capture of labeled proteins can be achieved in 50−100 mM HEPES (pH 7), although the use of increased amounts of resin was sometimes required to improve the amount of captured protein (Table 1, entries 2, 9). Other buffers, including phosphate, tris, and acetate, consistently afforded 60−90% yields of modified protein. The technique was also effective for chymotrypsinogen A labeled with FITC (**5**) in a variety of buffers (entries 8−12) and for subtilisin Carlsberg (entry 13). In all cases, MS analysis indicated that the fractions eluted with **3** contained only labeled proteins. Importantly, the chymotrypsinogen A was found to possess similar levels of proteolytic activity before and after the purification process (*12*). This technique has also been applied to the purification of TAMRA- (**6**), Cascade Blue- (**7**), and coumarin-labeled (**8**) proteins, Table 1, entries 15−17.

Consistent with cyclodextrin-dependent binding, resin prewashed with **3** was unable to capture either labeled or unlabeled protein. However, we have observed in several cases that

Table 1. Recovery of Modified Protein after Resin Pulldown[a]

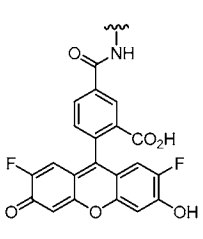

4: *Oregon Green*

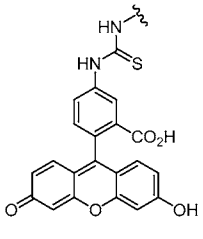

5: *Fluorescein*

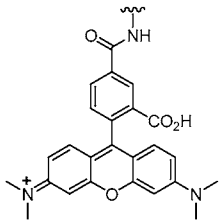

6: *TAMRA*

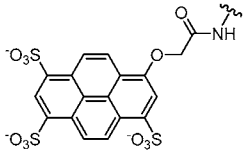

7: *Cascade Blue*

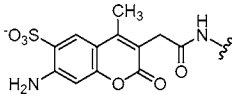

8: *Alexafluor 350*

entry	protein[b]	dye	buffer	mg of resin	% fluorescence[c]
1	myoglobin	**4**	none	15	85
2	myoglobin	**4**	100 mM HEPES	45	91
3	myoglobin	**4**	25 mM phosphate	45	72
4	myoglobin	**4**	50 mM phosphate	45	65
5	myoglobin	**4**	100 mM phosphate	45	69
6	myoglobin	**4**	100 mM Tris	45	70
7	myoglobin	**4**	100 mM acetate	45	67
8	chymotrypsinogen a	**5**	none	15	75
9	chymotrypsinogen a	**5**	50 mM HEPES	15	74
10	chymotrypsinogen a	**5**	50 mM phosphate	45	53
11	chymotrypsinogen a	**5**	50 mM Tris	45	72
12	chymotrypsinogen a	**5**	50 mM acetate	15	59
13	subtilisin Carlsberg	**4**	none	15	98[d]
14	myoglobin	**5**	none	15	75
15	myoglobin	**6**	none	15	95
16	myoglobin	**7**	none	15	97
17	myoglobin	**8**	none	15	98

[a] For detailed procedure see Supporting Information. [b] Each experiment was carried out with 100 μL of protein solution at 50 μM in the indicated buffer at pH 7. [c] Total fluorescence eluted from the resin with **3** as a percentage of all detected fluorescence in bound and unbound fractions (based on SDS−PAGE analysis). Mass spectrometry and UV−vis spectroscopy indicated that samples eluted with **3** possessed only modified protein. [d] Sample quantitation was carried out by UV analysis.

protein−chromophore conjugates bind the resin stronger than a single dye alone; thus, secondary interactions between the protein and the solid support are also functioning. This is advantageous, as modified proteins can be isolated from crude labeling reactions that still contain excess reagents.

In initial experiments, the ability of this method to collect labeled biomolecules from mixtures has also proven useful for the analysis of proteolytic digests. As an example, a sample of myoglobin modified with TAMRA-NHS (yielding **6**) was denatured before incubation with trypsin. The resulting peptide mixture was exposed to resin **2a**, and the solid support was isolated and rinsed. After elution of the peptides into a minimal volume of the solution of **3** described above, LC-ESI-MS indicated enrichment in the modified peptides relative to digested samples that had not been exposed to resin **2a** (See Figure S8 in Supporting Information). A particular advantage of this method is its ability to isolate the modified fragments from unmodified peptides, denaturants, and peptide contaminants arising from trypsin autoproteolysis. The design of specific digest "tags" with improved cyclodextrin binding affinity is in progress.

In conclusion, a new general procedure has been developed for the isolation of modified proteins and peptides. This technique features mild conditions for the capture and release of biomolecular targets, ease-of-use, and the potential to purify a large number of synthetic modification products. It is anticipated that this method will also find use as a tool for proteomic analysis and will facilitate the development of new protein modification reactions. Current efforts are exploring the use of this strategy to separate singly labeled proteins from multiply labeled proteins, as well as the adaptation of this technique to afford continuous flow LC-based methods.

ACKNOWLEDGMENT

We would like to thank the NIH for financial support (GM072700-01), as well as the University of California, Berkeley, Chemistry Department. N.S.J. acknowledges the Saegebarth family for generous fellowship support.

Supporting Information Available: Experimental details. This material is available free of charge via the Internet at http://pubs.acs.org.

LITERATURE CITED

(1) For examples using fluorescent bioconjugates, see: (a) Straight, A. F., Cheung, A., Limouze, J., Chen, I., Westwood, N. J., Sellers, J. R., and Mitchison, T. J. (2003) Dissecting Temporal and Spatial Control of Cytokinesis with a Myosin II Inhibitor. *Science*, *299*, 1743−1747. (b) Pickup, J. C., Hussain, F., Evans, N. D., Rolinski, O. J., and Birch, D. J. S. (2005) Fluorescence-based glucose sensors. *Biosensors Bioelectronics 20*, 2555−2565. (c) Borsch, M., Diez, M., Zimmermann, B., Reuter, R., and Graber, P. (2002) Stepwise rotation of the γ-subunit of EF_0F_1-ATP synthase observed by intramolecular single-molecule fluorescence resonance energy transfer. *FEBS Lett. 527*, 147−152. (d) Wallrabe, H., and Periasamy, A. (2005) Imaging protein molecules using FRET and FLIM microscopy. *Curr. Opin. Biotechnol. 16*, 19−27.

(2) For an excellent review of common bioonjugation techniques, see G. T. Hermanson, (1996) *Bioconjugate Techniques*, Academic Press, San Diego.

(3) An entire issue of *Chemical Reviews* has been devoted to this topic: (1997) *Chem. Rev. 97*, 1231−1734.

(4) Connors, K. A. (1997) The Stability of Cyclodextrin Complexes in Solution. *Chem. Rev. 97*, 1325−1358.

(5) Connors, K. A. (1995) Population characteristics of cyclodextrin complex stabilities in aqueous solution. *J. Pharm. Sci. 84*, 843−848.

(6) Del Valle, E. M. M. (2004) Cyclodextrins and their uses: a review. *Process Biochem. 39*, 1033−1046.
(7) For a recent review, see: (a) Ward, T. J. (2000) Chiral separations. *Analytical. Chem. 72*, 4521−4528. (b) Li, S., and Purdy, W. C. (1992) Cyclodextrins and their applications in analytical chemistry. *Chem. Rev. 92*, 1457−1470.
(8) (a) Politzer, I. R., Crago, K. T., Hampton, T., and Joseph, J. (1989) Effect of β-cyclodextrin on the fluorescence, absorption and lasing of rhodamine 6G, rhodamine B and fluorescein disodium salt in aqueous solutions. *Chem. Phys. Lett. 159*, 258−262. (b) Flamigni, L. (1993) Inclusion of fluorescein and halogenated derivatives in α-, β-, and γ-cyclodextrins: a steady-state and picosecond time-resolved study. *J. Phys. Chem. 97*, 9566−9572.
(9) Hamasaki, K., Ikeda, H., Nakamura, K., Ueno, A., Toda, F. Suzuki, I., and Osa, T. (1993) Fluorescent sensors of molecular recognition. Modified cyclodextrins capable of exhibiting guest-responsive twisted intramolecular charge-transfer fluorescence. *J. Am. Chem. Soc. 115*, 5035−5040. This compound is also commercially available.
(10) Resin samples have been stored at 4 °C for months with no loss in activity.
(11) Comparison of the heme absorbance at 409 nm to the Oregon Green absorbance at 495 nm was consistent with this observation. Control experiments have also confirmed that unlabeled protein has no affinity to resin **2a** or **2b** (see Supporting Information Figure S10).
(12) See Supporting Information for details.

BC060130I

An Affinity-Based Method for the Purification of Fluorescently-Labeled Biomolecules

Trung Nguyen, Neel S. Joshi and Matthew B. Francis*

Department of Chemistry, University of California, Berkeley, CA 94720-1460, and Materials Sciences Division, Lawrence Berkeley National Labs, Berkeley, CA 94720

Supporting Information

General Procedures. Unless otherwise noted, all chemicals were obtained from commercial sources and used without further purification. All small molecule reactions were carried out under a nitrogen atmosphere in oven dried glassware unless otherwise noted. All organic solvents were removed under reduced pressure using a rotary evaporator. Pyridine was distilled under an inert atmosphere from calcium hydride. Water (ddH_2O) used in biological procedures or as a reaction solvent was deionized using a NANOpure™ purification system (Barnstead, USA). Myoglobin (M 1882) from horse heart, Subtilisin Carlsberg protease (P5380) from Bacillus licheniformis, and α-chymotrypsinogen A (P 5380) from bovine pancreas were purchased from Sigma (St. Louis, USA) and used without further purification. Size exclusion chromatography was performed using NAP™ 5 columns from Amersham Biosciences. Microspin™ G-25 columns were purchased from Amersham Biosciences. The pre-packed Sephadex resin was discarded and the columns were thoroughly washed prior to use. Dyes used for protein labeling experiments were purchased from Invitrogen and used without further purification. Samples were mixed using a Barnstead Thermolyne Labquake® Shaker Rotisserie. NHS-activated Sepharose™ 4 Fast Flow resin (17-0906-01) was purchased from Amersham Biosciences. 6-monodeoxy-6-monoamino-β-cyclodextrin (M 2314) and β-cyclodextrin hydrate (856088) were obtained from Aldrich Chemical Company.

Instrumentation and Sample Analysis Preparations. UV-Vis spectroscopic measurements were conducted on a Tidas-II benchtop spectrophotometer (J & M, Germany).

Matrix assisted laser desorption-ionization time-of-flight mass spectrometry (MALDI-TOF MS) was performed on a Voyager-DE™ system (PerSeptive Biosystems, USA). All samples were co-crystallized using either an α-cyano-4-hydroxycinnamic acid or a sinapinic acid solution (10 mg/mL in 1:1 MeCN:ddH_2O with 0.1% TFA). Electrospray LC/MS analysis was performed using an API 150EX system (Applied Biosystems, USA) equipped with a Turbospray source and an Agilent 1100 series LC pump. Protein mass reconstruction was performed on the charge ladder with Analyst software (version 1.3.1, Applied Biosystems). Prior to MS analysis, biological samples were desalted and/or separated from small molecule contaminants using μC18 ZipTip® pipet tips (Millipore, USA), NAP-5™ columns (Amersham Biosciences, USA), Strata C-18E™ reversed-phase columns (Phenomenex, USA), or 3500 molecular weight cutoff Slide-A-Lyzer® Dialysis Cassettes (Pierce Biotechnology, Inc., USA) as indicated below. Intact protein chromatography was performed using a Jupiter 5u C5 300Å reversed phase column (2.0 mm x 150 mm) with a ddH_2O:MeCN gradient mobile phase containing 0.1% formic acid (250 μL/min). An Agilent Zorbax 3.5 μm 300SB-C8 reversed phase column (2.1 mm x 50 mm) was used for the analysis of trypsin digest fragments.

For protein analysis, sodium dodecyl sulfate-polyacrylamide gel electrophoresis (SDS-PAGE) was accomplished on a Mini-Protean apparatus (Bio-Rad, USA), following the general protocol of Laemmli.[1] Crude reaction mixtures were diluted by a factor of 5

(v/v) in ddH_2O and combined 1:1 (v/v) with gel loading buffer containing SDS, DTT, and bromophenol blue. Samples were then loaded onto the gel without heating. After removal of the completed gels from their cassettes, the bottom portions containing free dye were excised promptly, after which the gels were submerged in water for rinsing and imaging. Commercially available markers (Bio-Rad, USA) were applied to at least one lane of each gel for calculation of apparent molecular weights. Fluorescence visualization of gels was obtained by UV transillumination at 302 nm. Visualization of protein bands was accomplished by staining with Coomassie® Brilliant Blue R-250 (Bio-Rad, USA). Gel imaging was performed on an EpiChem3 Darkroom system (UVP, USA).

General procedure for fluorescent labeling of proteins. In a typical procedure, 3.5 mL of a 0.1 mM myoglobin solution in 0.1 M $NaHCO_3$ pH 8.3 aqueous buffer was transferred to a centrifuge tube. An amine reactive fluorophore (~1 mg) in 20-40 μL of DMF was then added. The solution was stirred on a laboratory mixer for 2.5 h and then quenched with 0.1 M H_2NOH pH 7.2 (80 μL, 8.0 μmol) aqueous solution. The reaction was then mixed overnight at room temperature. For specific examples of protein labeling reactions refer to Table 1. A portion of the crude reaction was purified by size exclusion chromatography. The purified solution was analyzed by UV-vis spectroscopy, MALDI-TOF-MS or ESI-MS, and SDS-PAGE. The sample used for many of the experiments presented in the supporting information will be referred to as **S1** (see Table S1)

Table S1. Fluorescent labeling of myoglobin with amine reactive dyes.

Dye/fluorophore	Conjugate #	Eq. of dye added	Conjugates detected[1]
Oregon Green 488 carboxylic acid SE	**4**	1.0	Unmod, +1, +2
TAMRA-NHS	**6**	5.0	+2, +3, +4, +5
Cascade Blue acetyl azide	**7**	5.0	Unmod, +1, +2
Alexa Fluor 350 carboxylic acid SE	**8**	5.0	+2, +3, +4, +5
Oregon Green 488-X-succinimidyl ester	**S1**	5.0	Unmod, +1, +2, +3

[1]Extent of labeling was determined by MALDI-TOF or ESI-LC MS. Only predominant species present in the spectra were reported.

Quantification of sepharose resin coupling reaction. In order to quantify the degree of modification to the NHS-activated sepharose resin the Amersham literature procedure was employed. To analyze the amount of NHS hydrolyzed during a coupling experiment, a calibration curve was formed by monitoring the absorbance at 260 nm for serial dilutions of a 30 mM NHS aqueous solution in 0.2 M $NaHCO_3$/0.5 M NaCl pH 8 buffer. For coupling reactions to the NHS-activated resin, Amersham Biosciences literature values predicted concentrations of released NHS to be from 16-23 μmol/mL of resin.

Synthesis of β-cyclodextrin modified sepharose resin (2a). NHS-activated resin was transferred to a fritted column as a slurry and filtered to dryness. The resin occupied a volume of 17.5 mL. A solution of 6-monodeoxy-6-monoamino-cyclodextrin (0.44 g) in 10 mL 0.2 M $NaHCO_3$/0.5 M NaCl pH 8 aqueous buffer was added to the resin. The column was then capped and agitated on a laboratory shaker for 2 h. The reaction tube was drained and the eluting solvent was collected for subsequent analysis. Afterwards, the resin was subjected to the following series of washes:

- 3 washes of 0.2 M $NaHCO_3$/0.5 M NaCl pH 8 aqueous buffer (10 mL portions)
- 3 washes of 0.5 M ethanolamine/0.5 M NaCl pH 8.3 aqueous buffer (10 mL portions)

- 3 washes of 0.1 M acetate/0.5 M NaCl pH 4 aqueous buffer (10 mL portions)
- 1 wash of H_2O (10 mL portions)
- 2 washes of 25 mM phosphate buffer pH 7 (10 mL portions)
- 3 washes of H_2O (200 mL portions)

The resin was then stored as a slurry in H_2O at 4 ^oC.

The eluting fraction from the coupling reaction was determined to contain 153 μmol of NHS. This corresponds to a cyclodextrin loading of 8.7 μmol/mL of dry resin. Expected values for NHS release during this reaction were 280-403 μmol according to Amersham loading values.

Synthesis of amino β-cyclodextrin derivative (1b). β-cyclodextrin monohydrate was placed in a flask as a solid and dried under vacuum at 50 ºC overnight. The dry cyclodextrin (1.0 g, 0.86 mmol) was transferred to a new flask and dissolved in freshly distilled pyridine (3.0 mL). A solution of carbonyldiimidazole (140 mg, 0.86 mmol) dissolved in 1 mL of freshly distilled pyridine was added to the reaction mixture dropwise over 2 minutes while stirring. The activation reaction was allowed to proceed at rt for 2 h. After this time, the activated cyclodextrin solution was added dropwise to a flask containing 1,3-diaminopropane (360 μL, 4.32 mmol) while stirring. After 1 h, the cyclodextrin mixture was precipitated by adding the reaction solution dropwise to a flask containing 500 mL of CH_2Cl_2 with vigorous stirring. The flaky white precipitate was isolated *via* suction filtration through filter paper, then placed under vacuum overnight. The cyclodextrin mixture was analyzed by MALDI-TOF mass spectrometry (Figure S1) and used without further purification.

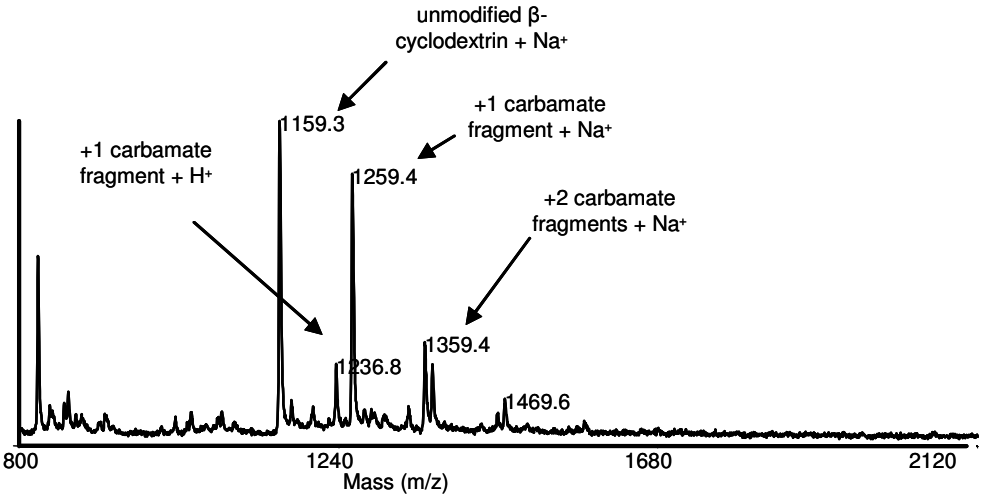

Figure S1. MALDI-TOF spectrum of **1b** using α-cyano-4-hydroxycinnamic acid matrix. Expected mass for β-cyclodextrin [M+Na]+ = 1158.0. Other peaks correspond to additions of the 100 Da carbamate fragment (see Figure 1 in main text).

Synthesis of β-cyclodextrin modified Sepharose resin (2b). Sepharose-NHS resin slurry (0.5 mL) was placed in a fritted tube and filtered. To the dry resin was added a solution of **1b** (75 mg in 1.5 mL of $NaHCO_3$ (0.1 M), NaCl (0.5 M), pH 8). The resulting slurry was agitated overnight. The resin was then subjected to the following rinses:

- 3x 1 mL of 0.5 M ethanolamine/0.5 M NaCl pH 8
- 3x 1 mL 0.1 M acetic acid/0.5 M NaCl pH 4
- 2x 20 mL H_2O

The resin was stored at 4 ^{o}C as a slurry in water.

General procedure for resin capture of proteins. First, the crude protein solution was purified by size-exclusion chromatography using a NAP^{TM} 5 column into pure H_2O or into the appropriate buffer solution. To a microcentrifuge tube containing 10-20 mg of dry CD modified sepharose resin, the

purified protein (100-200 μL of 60 μM solution) was added. Additional water was added to the heterogeneous solution to ensure proper mixing of the resin and protein solution. The solution was then agitated on a laboratory mixer for approximately 5 min. The heterogeneous solution was then transferred to a fritted microspin column and spun dry.

The eluting solvent was collected in microcentrifuge tubes. It was observed that the color of the protein solution had been transferred to the resin. Water (0.5 mL) was then added to the column and mixed by manual inversion for 1 min. The resin was rinsed with additional amounts of H_2O. To elute the protein, 0.5 mL of 10 mM adamantane carboxylic acid/100 mM NH_4Cl pH 7 was added to the resin and inverted by hand for 1 min. The color of the eluting solution resembled that of the beginning protein solution. Additional washes with the eluting solvent mixture were performed to achieve higher levels of protein recovery. The eluting fractions were analyzed by UV-vis spectroscopy (Figure S2), and SDS-PAGE (Figure S3).

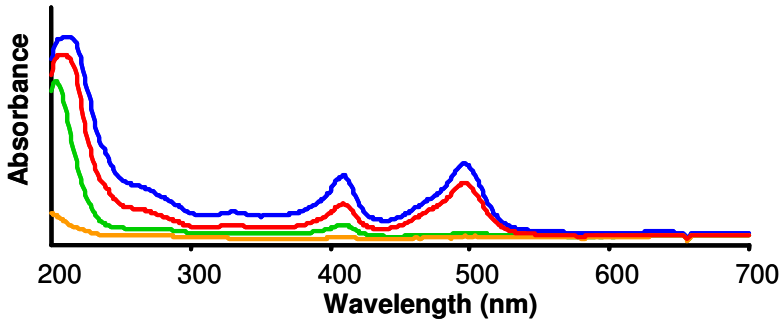

Figure S2. UV-vis spectrum of resin **2b** capture of **S1**: before exposure to resin (blue), flow through after resin exposure (green), H_2O washes of resin (orange), elution off of resin with 10 mM adamantane carboxylic acid, 100 mM NH_4Cl, pH 7 (red).

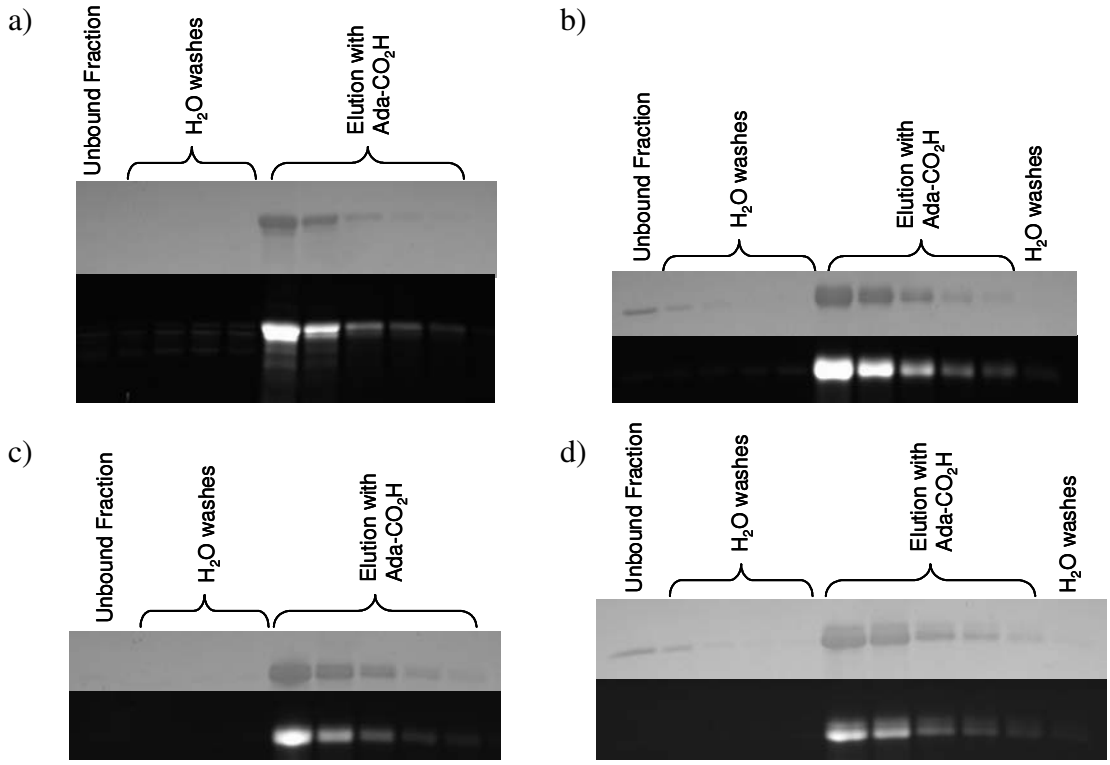

Figure S3. SDS PAGE analysis of eluting fractions for a) TAMRA labeled myoglobin b) Oregon Green labeled myoglobin c) Alexa Fluor 350 labeled myoglobin d) Cascade Blue labeled myoglobin.

SDS-PAGE quantification of modified protein recovery. SDS-PAGE analysis was used to quantify the amount of modified protein recovered by the resin. The values in the "% fluorescence" column of Table 1 were calculated in the following manner:

Using the fluorescent images of the gels in Figure S3 as an example,

% fluorescence = 100*(sum of fluorescence in elution lanes)/(sum of fluorescence in all lanes)

The fluorescence in each lane was quantified using ImageJ 1.34s, an image processing and analysis program available free from the NIH website (http://rsb.info.nih.gov/ij/download.html).

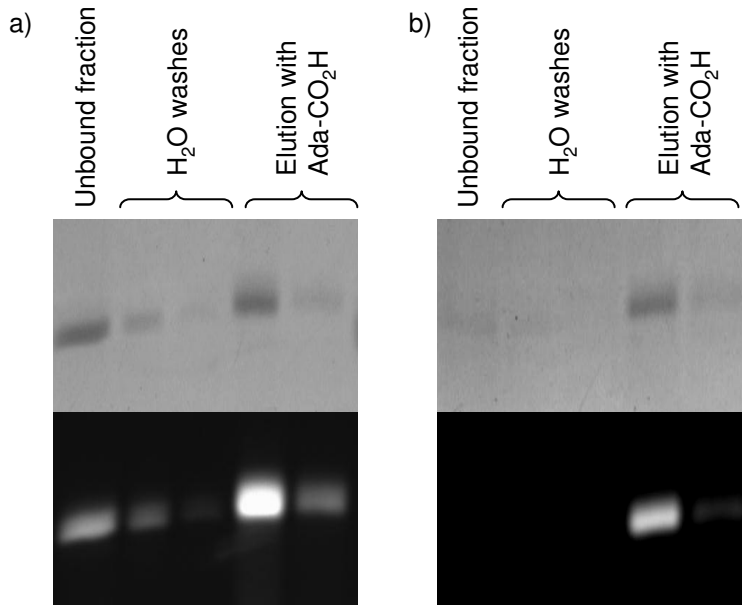

Figure S4. SDS-PAGE analysis of eluting fractions for Oregon Green-labeled myoglobin in the presence of a) 100 mM sodium phosphate buffer and b) 100 mM HEPES buffer. These samples correspond to entries 2 and 5 in Table S1.

Protein binding in commonly used buffer solutions. A solution of **S1** was diluted into 4 different buffers (Tris, HEPES, NH_4OAc, and phosphate) to a final buffer concentration of 0.1 M, pH 7. These solutions were then added to centrifuge tubes containing resin **2a**. The proteins were purified as described in the protein purification procedure. The eluting fractions were analyzed by SDS-PAGE and UV-vis spectroscopy (Figures S4 and S5).

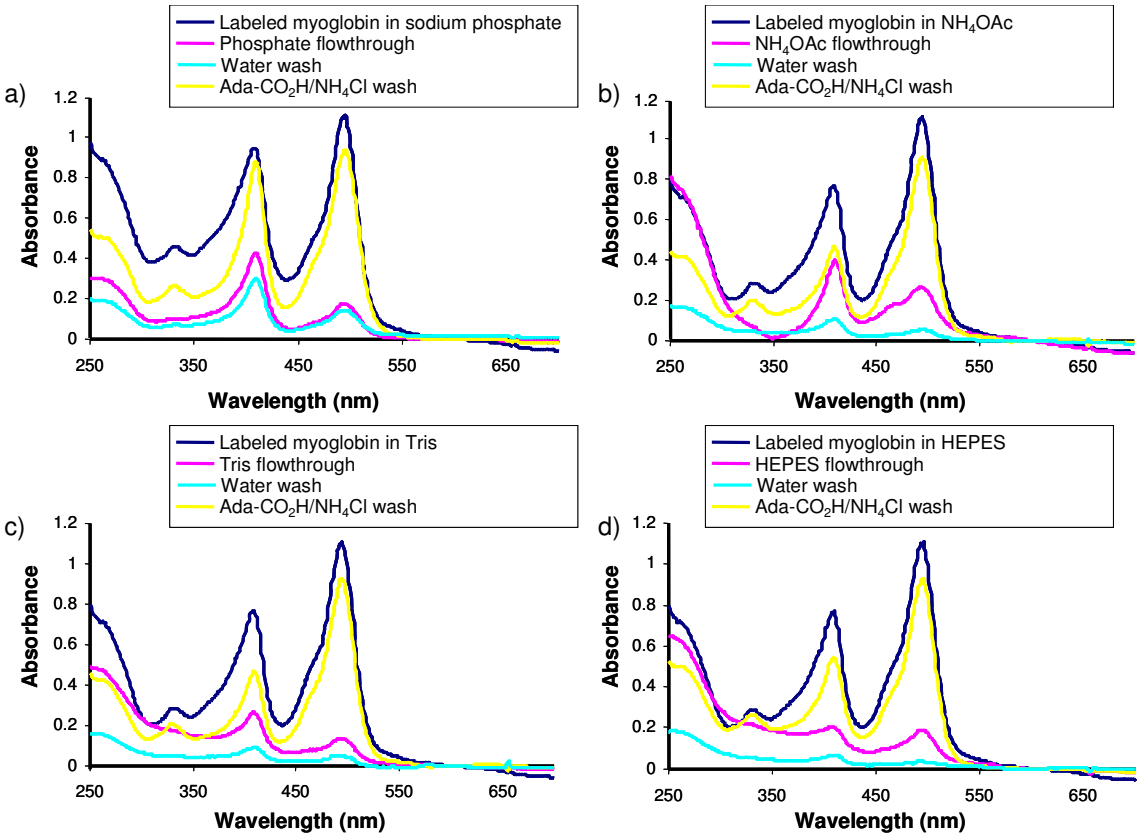

Figure S5. UV-vis spectra of Oregon Green-labeled myoglobin binding to resin **2a** in commonly used buffers (each 0.1 M, pH 7) a) sodium phosphate b) NH_4OAc c) Tris d) HEPES.

Adamantane effects on protein binding. Resin **2a** (71.4 mg) was suspended in 500 µL of 10 mM adamantane carboxylic acid/100 mM NH_4Cl pH 7 and then agitated for 15 min by a laboratory mixer. The solution was transferred to separate microspin columns and spun dry. A solution of **S1** (250 µL) was diluted to 1 mL and added to the respective resin in a centrifuge tube. The heterogeneous solution was mixed for 5 min. Afterwards, the solution was transferred to microspin column and spun dry. The eluent was analyzed by UV-vis spectroscopy. The resin was then washed with 500 µL H_2O (2x). The collected washes were analyzed by UV-vis spectroscopy. A final wash was performed with 500 µL 10 mM adamantane carboxylic acid/100 mM NH_4Cl (2x). The collected washes were also analyzed by UV-vis spectroscopy (Figure S6).

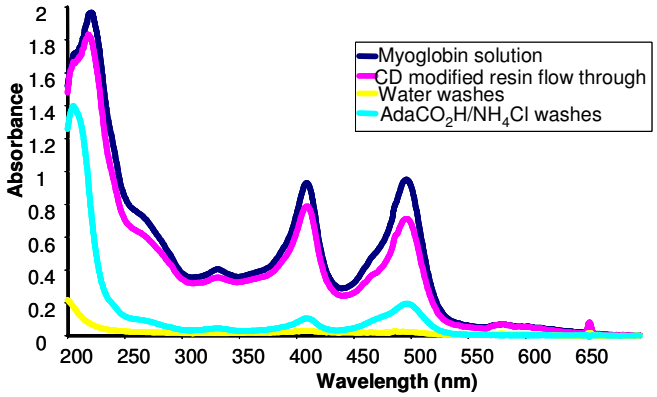

Figure S6. UV-vis spectra of **S1** exposed to resin **2a** pre-washed with 10 mM adamantane carboxylic acid/100 mM NH_4Cl pH 7 solution.

MALDI-TOF MS analysis of the resin. To resin **2a** (33.2 mg), 50 µL of myoglobin conjugate **4** and 250 µL of H_2O were added. After mixing for 5 min, the heterogeneous solution was spun dry in a microspin column. The resin was then washed with 500 µL of H_2O and a small portion of the dry resin was cocrystallized with sinapinic acid on a MALDI plate for analysis. The remaining resin was washed with 500 µL of 10 mM adamante carboxylic acid/100 mM NH_4Cl pH 7 buffer. The aqueous fractions were then analyzed by MALDI-TOF MS (Figure S7).

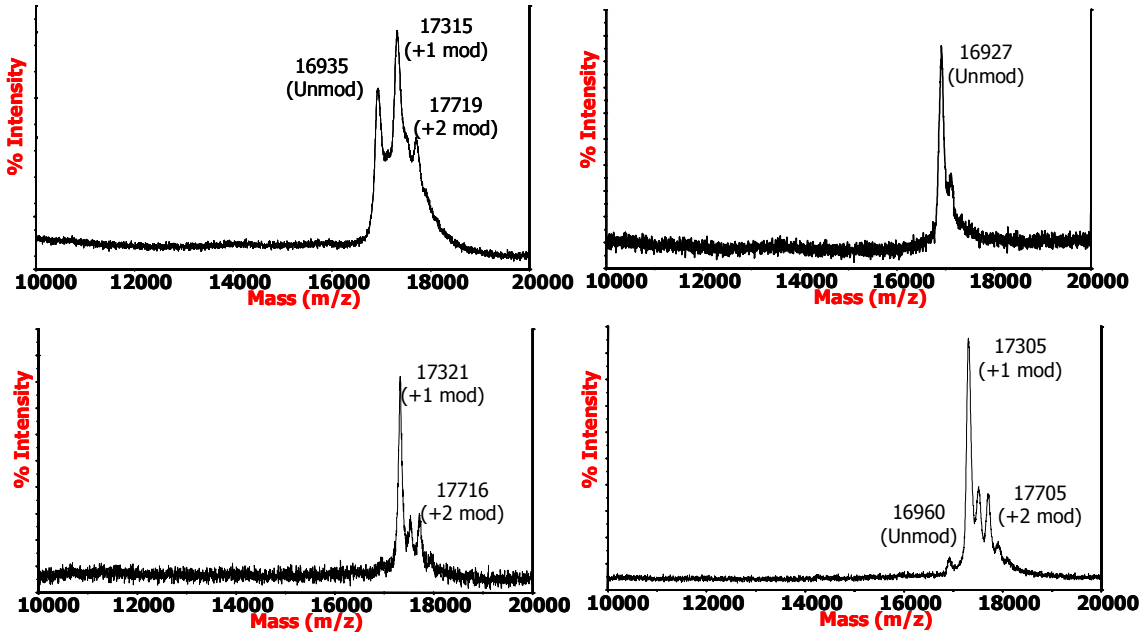

Figure S7. MALDI-TOF spectrum of a) Oregon Green labeled myoglobin b) aqueous flow through solution c) cyclodextrin modified sepharose resin after exposing to a solution of Oregon Green labeled myoglobin d) the eluting solution from the 10 mM adamantane carboxylic acid/100 mM NH_4Cl pH 7 wash

Procedure for enrichment of modified trypsin digest fragments. 50 mL of a solution of myoglobin conjugate **6** (1 mg/mL) was combined with 50 µL of acetonitrile. DTT was added to the resulting solution to a final concentration of 10 mM. The protein was denatured at 65 ºC for 1 h. The denatured protein solution was diluted by the addition of 0.45 mL of 50 mM NH_4HCO_3, pH 7.8. Trypsin (Promega Sequencing Grade) was then added to the myoglobin solution in a 1:100 (w/w) ratio. After 5 hours of incubation at 37 ºC, the proteolysis solution was lyophilized overnight. The peptide mixture was dissolved in 200 µL of water and divided into two 100 µL portions. To one portion was added 5 mg of dry resin **2a**. The heterogeneous mixture was agitated for 5 min before being transferred to an empty MicroSpinTM (Amersham) column and centrifuged at 14,500 rpm for 30 s. The dry resin, which appeared brown due to the capture of modified peptides, was washed twice with 200 µL aliquots of H_2O. The resin was then washed with one 100 µL aliquot of 10 mM adamantane carboxylic acid, 100 mM NH_4Cl, pH 7.

The brown color was transferred from the resin to the solution. Aliquots from before and after the resin capture procedure were both analyzed by LC-ESI MS (Figures S8).

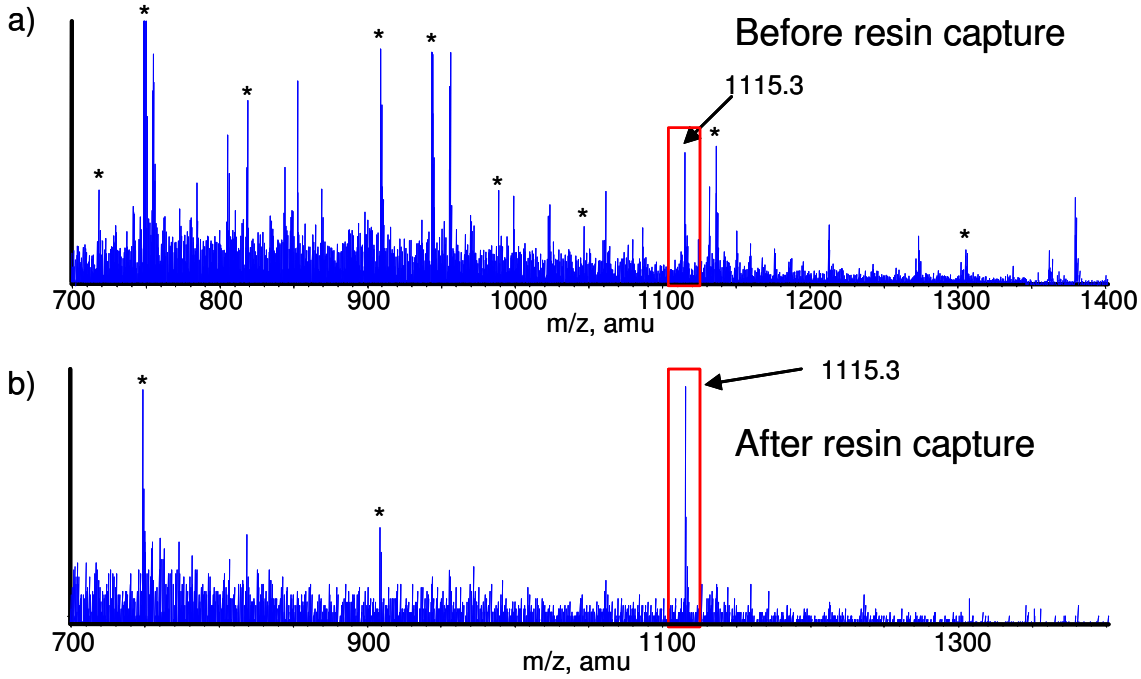

Figure S8. LC-MS analysis of modified trypsin fragments from digestion of TAMRA modified myoglobin: [a]mass spectrum of trypsin fragments before resin capture. Starred masses represent unmodifed trypsin digest fragments. [b]mass spectrum of trypsin fragments after elution from **2a** with adamantane-CO_2^- solution. Modified N-terminal fragment (GLSDGEWQQVLNVWGK) expected m/2 = 1115.5.

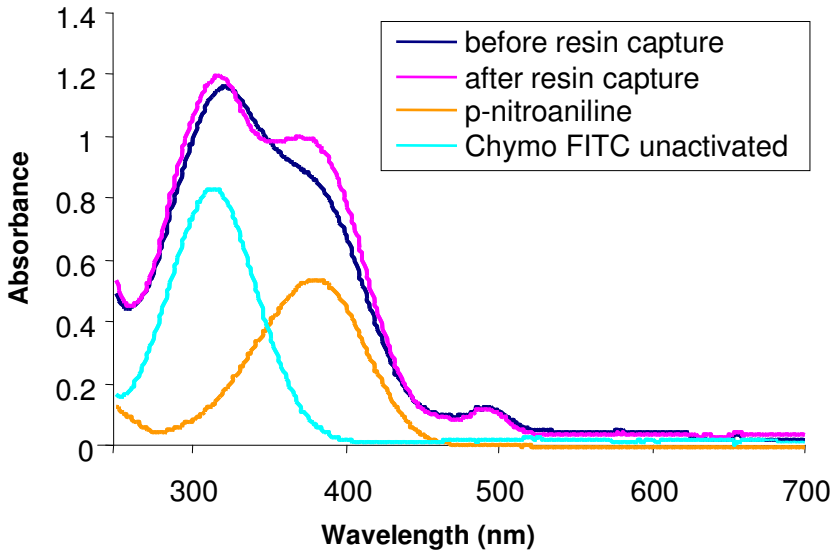

Figure S9. Normalized spectra for chymotrypsin activity assay. Absorbance at 380 nm indicates the hydrolysis of *p*-nitroaniline from the assay substrate. The intact assay substrate has an absorbance maximum at 305 nm. Chymotrypsin shows similar levels of activity before (blue) and after (pink) resin capture.

Activity assay of resin captured chymotrypsinogen. After a typical resin capture procedure was performed on chymotrypsinogen modified with **5**, the eluted fractions were assayed for chymotryptic activity. 20 uL of the released protein was treated with 2.9 uL of a 0.4 mg/mL trypsin solution in 50 mM acetic acid. The activation of the zymogen was allowed to proceed for 10 min at room temperature before the addition of 80 uL of 0.5 mM chymotrypsin substrate I, colorometric (Suc-GGF-pNA, Calbiochem 230912) in 50 mM Tris, 20 mM $CaCl_2$ buffer, pH 7.6. The hydrolysis of p-nitroaniline from the tripeptide substrate occurred at room temperature for 30 min. The progress of the hydrolysis reaction was followed by monitoring the absorbance at 390 nm (Figure S9).

Additional figures.

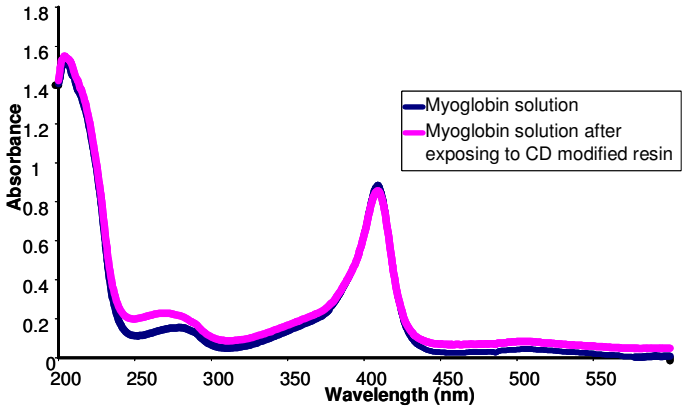

Figure S10. Complete recovery of unmodified myoglobin was obtained in the supernatant after exposure to resin **2a**, confirming that the protein does not bind in the absence of the fluorescent label.

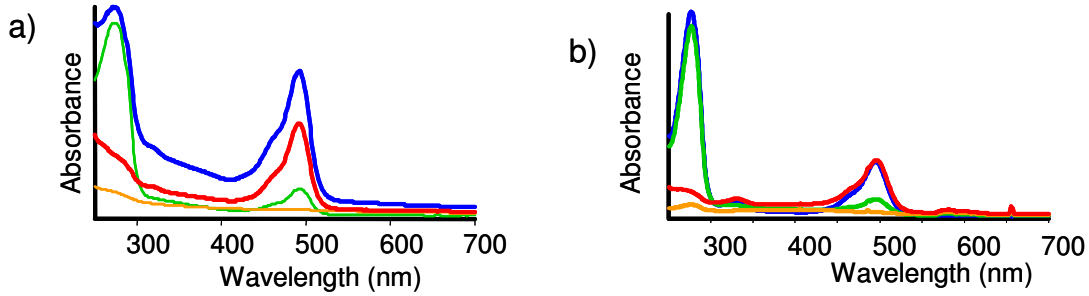

Figure S11. UV/vis spectra of modified protein resin capture: starting mixture (blue), flow through (green), water washes of resin (orange), elution with 10 mM adamantane carboxylic acid, 100 mM NH_4Cl, pH 7 (red). (a) Chymotrypsinogen modified with FITC. (b) Subtilisn Carlsberg modified with Oregon Green-succinimidyl ester.

---

[1] Laemmli, U. K. *Nature* **1970,** *227*, 680.

Hydrogels Formed by Multiple Peptide Ligation Reactions To Fasten Corneal Transplants

Michel Wathier,[†] C. Starck Johnson,[‡] Terry Kim,[‡] and Mark W. Grinstaff*[,†]

Departments of Biomedical Engineering and Chemistry, Metcalf Center for Science and Engineering, Boston University, Boston, Massachusetts 02215, and Department of Ophthalmology, Duke University Medical Center, Durham, North Carolina 27710. Received March 7, 2006; Revised Manuscript Received May 31, 2006

A stable cross-linked hydrogel was formed under mild aqueous conditions using pseudoproline peptide ligation chemistry. A cysteine-terminated lysine dendron containing four cysteines and a PEG macromolecule modified with terminal ester aldehydes were prepared. Upon mixing, the two macromers gave a stable hydrogel. This hydrogel along with sutures was used to successfully secure a corneal transplant in vitro.

Mild chemoselective reactions with biomacromolecules are of significant interest and of widespread use in chemistry, biology, and more recently in nano-biotechnology. Such reactions can afford bioconjugates for characterization of native functions (e.g., electron-transfer proteins) (*1*), attachment to solid substrates (e.g., chemiluminescence biosensor applications) (*2*), preparation of biohybrid structures (e.g., derivatized bacteriophage) (*3*), and introduction of new activity (e.g., photoresponsive membrane channels) (*4*). Of these reactions, chemical ligation is a particularly attractive approach to prepare large proteins that are otherwise unattainable using conventional solid-phase peptide synthesis (*5*−*8*). Moreover this mild coupling reaction can be performed in the presence of functional groups in aqueous solutions. Recently, we used multiple thiazolidines as the chemical ligation between macromolecules to render a cross-linked hydrogel for the repair of acute corneal wounds (*9*). For applications where a hydrogel adhesive is required for longer periods, such as in a corneal transplant, we are evaluating the use of pseudoproline ligations between a dendron and poly(ethyleneglycol) possessing N-terminal cysteines and aldehyde esters, respectively. Herein we report the synthesis, characterization, and capability of this in situ polymerizing hydrogel to fasten corneal transplants in vitro.

Pseudoproline formation is one type of chemoselective and orthogonal peptide ligation method that has been applied successfully to the synthesis of a variety of proteins (*5*, *6*, *10*, *11*). In this mild coupling strategy, a peptide possessing a C-terminal glycol aldehyde ester is reacted with another peptide possessing a N-terminal cysteine. The reaction occurs in a stepwise process with imine ligation and thiazolidine formation followed by an *O*,*N*-acyl migration to afford the pseudoproline linkage (Figure 1). For this approach to translate to a cross-linked network, two macromers are required where at least one possesses two and the other three or more reactive groups. Specifically, the dendron macromer (Figure 1) was prepared via successive amidations using the pentafluorophenyl activated esters of Lys (ZLys(Z)OPFP) and Cys (IsoCys(Boc)OPFP) (*9*). This macromer was selected because dendritic macromolecules provide a highly branched structure of defined composition with extensive surface functionalization capabilities (*12*−*17*), which facilitates subsequent intermolecular cross-linking to form a hydrogel. The two ester-aldehyde functionalities on the PEG macromer (MW 3400) were introduced as follows. The PEG diol was first reacted with succinic anhydride in pyridine to afford poly(ethylene glycol) disuccinic acid. Next, the cesium salt was prepared by neutralization of the acid with 1 M $CsCO_3$ until pH 8 followed by coupling bromoacetaldehyde dimethyl acetal in DMF to give the protected aldehyde. The acetal was deprotected using 10% TFA in DCM to afford the poly(ethylene glycol) diester-aldehyde (see Supporting Information for details).

Upon mixing an aqueous solution of the poly(ethylene glycol) diester-aldehyde and dendron macromers, a hydrogel (*18*, *19*) forms within about 30 s (20, 33, or 50 wt % polymer solutions). Cylindrical hydrogel samples of 8 mm diameter and 3 mm thickness were prepared in aqueous buffer pH = 7.4, and the mechanical properties were measured at a frequency of 1 Hz. The hydrogels exhibited viscoelastic properties. The compressive (*E*) and complex modulus (*G**) for the 20, 33, and 50 wt % hydrogels prepared were measured after 24 h of formation or after incubating for 24 h in an aqueous buffer solution at pH = 7.4 (Figure 2). As expected the mechanical properties increased with increasing macromer wt %. After swelling over 24 h, the moduli decrease relative to the unswollen hydrogels consistent with a more hydrated structure. The hydrogels are optically transparent with a UV cutoff of ≈300 nm (see Figure 4A).

The hydrogel formed between the dendron and poly(ethylene glycol) diester-aldehyde is stable and retains its shape and size over time. As shown in Figure 3, this pseudoproline-cross-linked hydrogel remains intact for more than 6 months with less than a 10% change in weight when placed in a humidity chamber. At six months the value for compressive modulus is ≈90% of the original value, indicating that an extensive network is still present. This result is in contrast to a hydrogel formed between the dendron and poly(ethylene glycol) dialdehyde (*9*). In this later reaction, a hydrogel is formed via formation of multiple thiazolidines. This reaction represents the first half of the reaction sequence shown in Figure 1. Given that thiazolidine formation is reversible, the hydrogel is intact for relatively short periods. When placed in a humidity chamber, the thiazolidine-cross-linked hydrogel loses its original cylindrical shape and is an unstructured gelatinous mass at approximately one week (see Figure 3). Confirmation of the thiazolidine and the pseudoproline

* To whom correspondence should be addressed. E-mail: mgrin@bu.edu.

[†] Boston University.

[‡] Duke University Medical Center.

10.1021/bc060060f CCC: $33.50 © 2006 American Chemical Society
Published on Web 06/28/2006

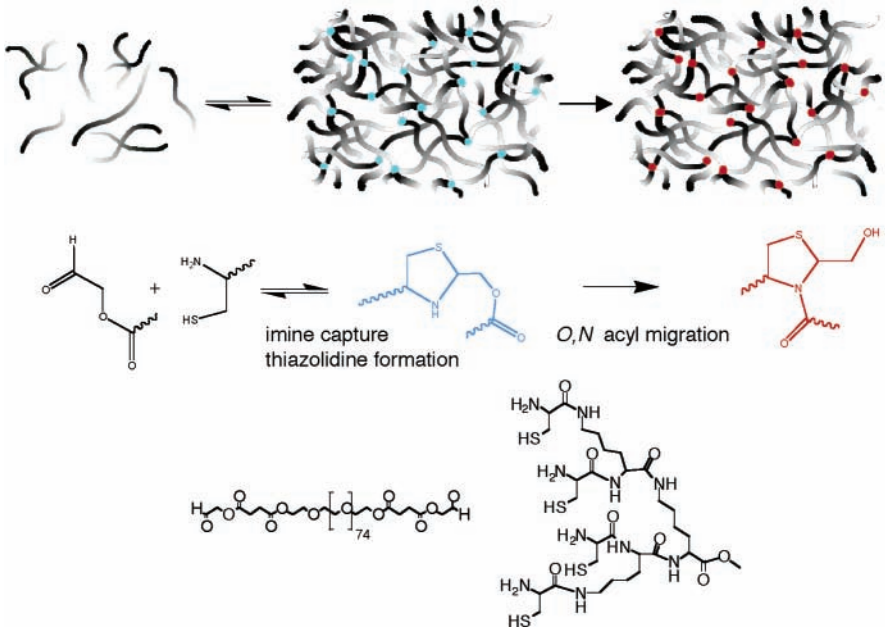

Figure 1. (top) Reaction scheme for pseudoproline ligation to form cross-linked hydrogel. (bottom) poly(ethylene glycol) diester-aldehyde and N-terminal cysteine lysine dendron macromers.

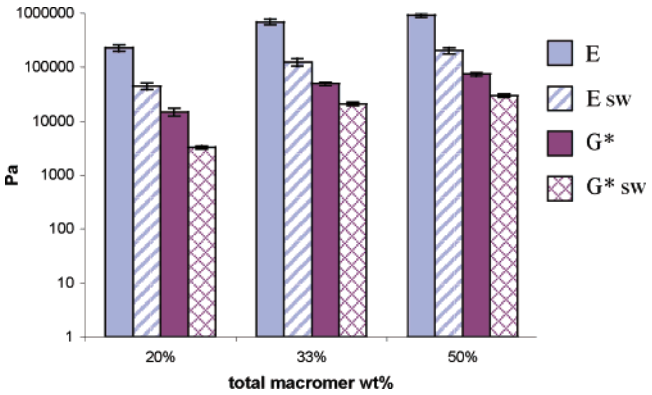

Figure 2. Compressive (*E*) and complex (*G**) moduli for the various wt % hydrogels before and after swelling (sw) in neutral aqueous solution.

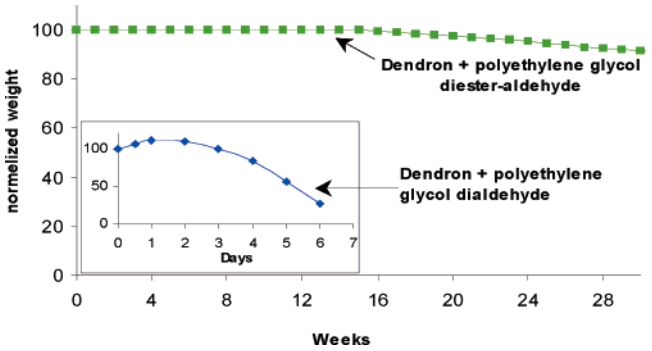

Figure 3. Hydrogel weight loss as a function of time at 25 °C when stored in a humidity chamber.

ligations was obtained using a model small molecular weight system in a manner analogous to that previously reported (see SI) (*20*).

We are interested in the design requirements and properties of hydrogels as sealants for the repair of ophthalmic wounds created as a result of injury, infection, or surgical procedure (*21*−*25*). For relatively small, acute wounds such as a cataract incision, the hydrogel adhesive formed via multiple thiazolidines (*9*) offers the advantages of securing the wound but not residing

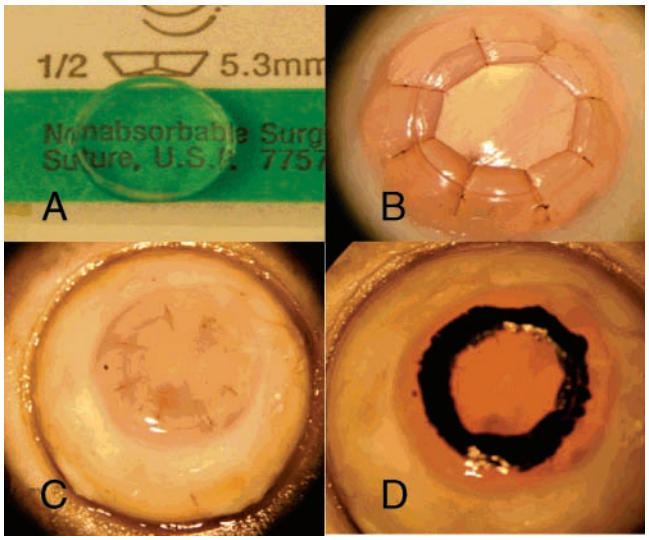

Figure 4. (A) Photograph of the hydrogel. (B) Photograph of a corneal autograft fastened with 8 interrupted 10-0 nylon sutures. (C) photograph of a corneal autograft fastened with 8 interrupted 10-0 nylon sutures and the hydrogel sealant. (D) photograph after application of indy ink applied to a corneal autograft shown in C.

long-term at the wound site. In fact corneal re-epithelization of a small wound in humans occurs within about 3 days (*26*). However, for the repair of large corneal wounds such as corneal transplants, a sealant is desired that can remain longer at the wound site.

Corneal transplantation or penetrating keratoplasty (PKP) is one of the most common and successful tissue transplants (*27*). In a corneal transplantation the recipient cornea undergoes a large circular full-thickness cutting, or trephination, to remove the diseased or damaged tissue and then a previously trephinated donor corneal button is manually sutured to the recipient corneal rim. The major disadvantages related to this procedure include delayed visual recovery, suprachoroidal hemorrhage, neovascularization, microbial keratitis, postoperative suture removal (typically nine-months after transplantation), and surgically induced astigmatism (*28*−*31*). Furthermore, these complications in PKP are often a result of the use of sutures. A sutureless corneal transplant procedure would significantly improve PKP

with regard to the multiple intraoperative and postoperative issues mentioned above. The idea of a sutureless keratoplasty is not new, but the development of a practical sutureless ophthalmic procedure has eluded the field since its original inception by Gradle in 1921, although there have been some encouraging results (*32*−*34*).

Toward this goal, we determined whether this in situ polymerizing hydrogel would reduce the number of sutures necessary to secure the incision between the host and graft corneal tissue. In this in vitro model, an 8 mm central corneal trephination was made in an enucleated eye and then this newly formed button was autografted back to the original eye. The host−graft tissue interface was secured using sutures, sutures plus the hydrogel sealant, or the hydrogel sealant alone (Figure 4). The leaking pressure for the autografted eyes was measured as we have done for corneal laceration studies to determine the extent to which the wound was sealed (*9*). The leaking pressure for autografts receiving 16 interrupted 10-0 nylon sutures was 13 ± 5 mmHg ($n = 4$). Today, this is a standard procedure for a PKP. Normal intraocular pressure (IOP) is ≈15 mmHg. When the hydrogel sealant was applied (33 wt %; 60 μL) to the sutured wound with 16 interrupted sutures, the leaking pressure increased to 63 ± 7 mmHg ($n = 4$). Increasing the macromer wt % to 50% (60 μL) with 16 interrupted sutures afforded a leaking pressure of 101 ± 5 mmHg ($n = 4$). Next, we evaluated if the hydrogel sealant in concert with 8 interrupted 10-0 nylon sutures would secure the wound. The autograft with 8 sutures had a leaking pressure of 5 mmHg or less ($n = 4$). When the hydrogel sealant at 33wt % % (60 μL) and 8 sutures were used to secure the autograft, the wound leaked at a pressure of 45 ± 6 mmHg ($n = 4$). This leaking pressure approaches the upper bounds of the physiologically relevant limit, and thus we decided to increase the wt % of the polymers to attain a stronger seal. Application of the 50 wt % formulation (60 μL) and 8 sutures afforded an autograft that leaked at a pressure of 77 ± 5 mmHg ($n = 4$). Application of the hydrogel sealant reduced the number of sutures required to secure the autograft. We were unable to secure the autograft to a safe high pressure when the hydrogel sealant was used alone, indicating that this hydrogel does not possess sufficient adhesivity by itself to secure a PKP. However, an additional benefit to this hydrogel sealant, beyond closing the wound with a reduced number of sutures, is the potential of the hydrogel barrier formed at the wound interface to protect the wound from postoperative infections. As a first indicator for the potential effectiveness of this hydrogel barrier, the transport of India ink across the hydrogel can be monitored as described by McDonnell (*35*). As shown in Figure 4D when India ink is applied to the wound, the dye does not penetrate into the anterior chamber, indicating that the wound interface is secured.

In summary, an in situ polymerizing hydrogel is described that forms in aqueous solution under mild conditions. This chemical-ligation strategy is attractive for hydrogel preparation since it allows synthetic flexibility in the use of a wide-range of macromer compositions, including potentially those with reactive groups, in a manner analogous to the reaction diversity obtained with previous bioconjugated proteins and enzymes. The hydrogel can be used in conjunction with a reduced number of sutures to successfully fasten a corneal transplant and secure the wound interface. The dendron macromer used in hydrogel formation belongs to a family of dendritic macromolecules composed of biocompatible building blocks (*21*, *22*). This macromer system enables efficient cross-linking, varied hydrogel properties, and aqueous polymer solutions for application to a wound site. Dendritic macromolecules, due to their unique properties, structure, and high degree of compositional preciseness, are finding ever-increasing uses in medicine, ranging from vehicles for drug delivery and imaging agents to biomaterials for wound management and tissue restoration.

ACKNOWLEDGMENT

This work was supported by the NIH.

Supporting Information Available: Experimental details. This material is available free of charge via the Internet at http://pubs.acs.org.

LITERATURE CITED

(1) Gray, H. B., and Winkler, J. R. (2003) Electron tunnelling through proteins. *Q. Rev. Biophys. 36*, 341−372.
(2) Pande, R., et al. (1996) A biotinylated undecylthiophene copolymer bioconjugate for surface immobilization: Creating an alkaline phosphatase chemiluminescence-based biosensor. *Bioconjugate Chem. 7*, 159−164.
(3) Hooker, J. M., Kovacs, E. W., and Francis, M. B. (2004) Interior surface modification of bacteriophage ms2. *J. Am. Chem. Soc. 126*, 3718−3719.
(4) Banghart, M., et al. (2004) Light activated ion channels for remote control of neuron firing. *Nat. Neurosci. 7*, 1381−1386.
(5) Liu, C. F., Rao, C., and Tam, J. A. (1996) Orthogonal ligation of unprotected peptide segments through pseudoproline formation for the synthesis of hiv-1 protease analogues. *J. Am. Chem. Soc. 118*, 307−312.
(6) Tam, J. P., Xu, J., and Eom, K. D. (2001) Methods and strategies of peptide ligation. *Biopolymers 60*, 194−205.
(7) Shao, J., and Tam, J. P. (1995) Unprotected peptides as building blocks for the synthesis of peptide dendrimers with oxime, hydrazone, and thiozolidine linkages. *J. Am. Chem. Soc. 117*, 3893−3899.
(8) Dawson, P. E., et al. (1994) Synthesis of proteins by native chemical ligation. *Science 266*, 766−778.
(9) Wathier, M., et al. (2004) Dendritic macromers as in situ polymerizing biomaterials for securing cataract incisions. *J. Am. Chem. Soc. 126*, 12744−12745.
(10) Liu, C. F., and Tam, J. P. (1994) Chemical ligation approach to from a peptide bond between unprotected peptide segments: Concepts and model study. *J. Am. Chem. Soc. 116*, 4149−4153.
(11) Tam, J. P., and Miao, Z. (1999) Stereospecific pseudoproline ligation of n-terminal serine and thereonine, or cysteine-containing unprotected peptides. *J. Am. Chem. Soc. 121*, 9013−9022.
(12) Fréchet, J. M. J. (2002) Dendrimers and supramolecular chemistry. *Proc. Natl. Acad. Sci. U.S.A. 99*, 4782−4787.
(13) Newkome, G. R., Moorefield, C. N., and Vögtle, F. (1996) Dendritic molecules: Concepts, syntheses, perspectives, VCH, New York.
(14) Bosman, A. W., Janssen, H. M., and Meijer, E. W. (1999) About dendrimers: Structure, physical properties, and applications. *Chem. Rev. 99*, 1665−1688.
(15) Mathews, O. A., Shipway, A. N., and Stoddart, J. F. (1998) Dendrimers-branching out from curiosities into new technologies. *Prog. Polym. Sci. 23*, 1−56.
(16) Zeng, F., and Zimmerman, S. C. (1997) Dendrimers in supramolecular chemistry: From molecular recognition to self-assembly. *Chem. Rev. 97*, 1681−1712.
(17) Tomalia, D. A., and Fréchet, J. M. J. (2001) *Dendrimers and other dendritic polymers*, Wiley and Sons Ltd., Chichester.
(18) Park, K., Shalaby, S. W. S., and Park, H. (1993) *Biodegradable hydrogels for drug delivery*, p 252, Technomic Publishing, Lancaster, PA.
(19) Hubbell, J. A. (1996) In situ material transformation in tissue engineering. *Mater. Res. Soc. Bull. 21*, 33−35.
(20) Liu, C. F., and Tam, J. P. (1994) Peptide segment ligation strategy without the use of protecting groups. *Proc. Natl. Acad. Sci. U.S.A. 91*, 6584−6588.
(21) Grinstaff, M. W. (2002) Biodendrimers: New polymeric materials for tissue engineering. *Chem. Eur. J. 8*, 2838−2846.
(22) Luman, N. R., Kim, T., and Grinstaff, M. W. (2004) Dendritic polymers composed of glycerol and succinic acid: Synthetic methodologies and medical applications. *Pure Appl. Chem. 76*, 1375−1385.

(23) Carnahan, M. A., et al. (2002) Hybrid dendritic-linear polyester-ethers for in situ photopolymerization. *J. Am. Chem. Soc. 124*, 5291−5293.
(24) Velazquez, A. J., et al. (2004) New dendritic adhesives for sutureless ophthalmic surgeries: In vitro studies of corneal laceration repair. *Arch Ophthalmol. 122*, 867−870.
(25) Kang, C., et al. (2005) Novel tissue adhesives to secure laser in situ keratomileusis flaps. *J. Cataract Refract. Surg. 31*, 1208−1212.
(26) Records, R. E. (1979) *Physiology of the human eye and visual system*, p 691, Harper & Row, Cambridge.
(27) NIH (2004) NIH Eye Institute. www.NIE.NIH.gov.
(28) Volker-Dieben, H. J. M., et al. (1982) Different influences on corneal graft survival in 539 transplants. *Acta Ophthalmol. 60*, 190−202.
(29) Paque, J., and Poirier, R. H. (1977) Corneal allograft reaction and its relationship to suture site neovascularization. *Ophthalmic Surg. 8*, 71−74.
(30) Wilson, S. E., and Kaufman, H. E. (1990) Graft failure after penetrating keratoplasty. *Surv. Ophthalmol. 34*, 325−356.
(31) Khodadoust, A. A. (1973) *The allgraft rejection reaction: The leading cause of late failure of clinical corneal grafts. Corneal graft failure*, pp 151−164, Elsevier Scientific, New York.
(32) Gradle, H. S. (1921) The present status of keratoplasty. *Am. J. Ophthalmol. 4*, 895−899.
(33) Katzin, H. M. (1945) Aqueous fibrin fixation of corneal tranplants in the rabbit. *Arch. Ophthalmol. 35*, 415−420.
(34) Goins, K. M., Khadem, J., and Majmudar, P. A. (1998) Relative strength of photodynamic biological tissue glue in penetrating keratoplasty in cadaver eyes. *J. Cataract Refract. Surg. 24*, 1566−1570.
(35) McDonnell, P. J., et al. (2003) Dynamic morphology of clear corneal cataract incisions. *Ophthalmology 110*, 2342−2348.

BC060060F

ARTICLES

Dendritic Cationic Lipids with Highly Charged Headgroups for Efficient Gene Delivery

Kai K. Ewert,* Heather M. Evans, Nathan F. Bouxsein, and Cyrus R. Safinya*

Department of Materials, Department of Physics, and Molecular, Chemical, and Developmental Biology Department, University of California, Santa Barbara, California 93106. Received October 24, 2005; Revised Manuscript Received April 10, 2006

Gene therapy is expected to lead to powerful new approaches for curing many diseases, a potential that is currently explored in worldwide clinical trials. Nonviral DNA delivery systems are desirable to overcome the inherent problems of viral vectors, but their current efficiency requires improvement and the understanding of their mechanism of action is incomplete. We have synthesized new multivalent cationic lipids with highly charged dendritic headgroups to probe the structure−transfection efficiency relationships of cationic liposome (CL)−DNA complexes, a prevalent nonviral vector. The lipid headgroups are constructed from ornithine cores and ornithine or carboxyspermine endgroups. The dendritic lipids were prepared on a gram scale, using a synthetic scheme that permits facile variation of the lipid building blocks headgroup, spacer, and hydrophobic moiety. They carry four to sixteen positive charges in their headgroups. Complexes of DNA with mixtures of the dendritic lipids and neutral 1,2-dioleoyl-*sn*-glycero phosphatidylcholine (DOPC) exhibit novel structures at high contents of the highly charged lipids, while the well-known lamellar phase is formed at high contents of DOPC. DNA complexes of the new dendritic lipids efficiently transfect mammalian cells in culture without cytotoxicity and, in contrast to lamellar complexes, maintain high transfection efficiency over a broad range of composition.

INTRODUCTION

Gene therapy is based on the use of DNA as a therapeutic agent. This novel medical approach is being investigated in numerous current clinical trials (*1*, *2*). Inherited diseases and cancers feature most prominently as targets, but cardiovascular and a large range of other diseases are amenable to gene therapeutic treatment as well (*3*). In addition, new therapeutic applications for the delivery of nucleic acids have been opening up (*4*) due to discoveries of novel pathways of gene expression and regulation, such as that of RNA interference (RNAi) (*5*−*8*).

Efficient and safe DNA carriers (vectors) are essential for the success of gene therapy. While engineered viruses are very efficient (*9*, *10*) both in vitro and in vivo, their carrying capacity is limited, their preparation is comparatively complex and concerns about their safety have recently been intensified by a few severe setbacks (*11*). Thus, there has been increasing interest in nonviral or synthetic vectors (*12*−*14*). Typically, these are complexes of DNA with cationic macroions, such as cationic liposomes (CLs) (*15*−*17*) or cationic polyelectrolytes (*18*, *19*). Synthetic vectors are facile to prepare and often allow a variation of the vector properties simply by modifying their composition; they lack immunogenic protein components and can transport DNA of unlimited length. However, their efficiency needs to be improved to render them viable for widespread therapeutic use (*20*).

Dendrimers are highly branched synthetic molecules typically based on AB_2 monomers. In contrast to branched polymers, however, dendrimers are monodisperse and typically assembled by adding generations of monomer to a core molecule (*21*−*23*). Some commercially available dendrimers with protonatable amino groups, such as poly(amidoamine) (PAMAM) and poly(propylenimine) (PPI) dendrimers, have been used as gene delivery vectors (*19*, *24*−*28*), and the structure of their DNA complexes has been investigated (*29*). Conjugates of dendritic molecules to PEG have also been used for gene delivery (*30*).

A large number of cationic and other lipids have been synthesized in efforts to improve the efficiency of CL−DNA complexes. Earlier work has been reviewed in detail (*31*−*33*), and several more recent reviews with a smaller scope have also appeared (*34*−*36*). Some lipid vectors have been commercialized, and many are able to efficiently transfect cultured mammalian cells. Nevertheless, establishing structure−efficiency relationships of CL−DNA complexes has turned out to be challenging. This is mainly due to the large number of relevant parameters, such as lipid structure, lipid composition, lipid/DNA charge ratio, and complex structure. To date, only a few unifying concepts regarding structure−efficiency relationships have emerged. For example, it has recently been shown that the transfection behavior of cationic lipids exhibits universal trends when properties of the self-assembled system as a whole, such as the membrane charge density σ_M, are used to plot the data from various lipids (*37*, *38*). The lipids described in this paper were designed to further explore this finding: their highly charged, dendritic headgroups allow for very high membrane charge densities.

The nanostructure of CL−DNA complexes has a significant impact on their mechanism and efficiency of transfection (*39*). Optimized complexes of either of the two well-known phases of CL−DNA complexes, the inverted hexagonal (H_{II}^C) (*40*), and the lamellar (L_α^C) (*41*) liquid crystal phase, show equally

* To whom correspondence should be addressed. K.K.E.: E-mail: ewert@mrl.ucsb.edu, Phone +1 805 893 7931, Fax +1 805 893 8502; C.R.S.: E-mail: safinya@mrl.ucsb.edu, Phone +1 805 893 8635, Fax +1 805 893 7221.

10.1021/bc050310c CCC: $33.50 © 2006 American Chemical Society
Published on Web 07/01/2006

high transfection efficiency. However, the transfection mechanisms of the two phases vary greatly as a consequence of their structures (*42*−*44*). A third, hexagonal phase of CL−DNA complexes (H_I^C), which also transfects cells efficiently, has recently been described (*45*). Which CL−DNA complex phase a particular mixture of lipids forms with DNA is governed by the composition and the rigidity of the membrane (*40*). Molecularly, the shape and corresponding preferred curvature of a lipid, encoded in the lipid structure, is a crucial parameter. DOPE with its cone-shaped structure, for example, favors formation of the H_{II}^C phase. Similarly, a complex structure with positive curvature should result from using lipids with large headgroups (corresponding to an inverted cone molecular shape). Multivalent lipids with 3 to 5 cationic charges in the headgroup, however, still form L_α^C complexes with DNA (*38*, *46*). Thus, we further increased the headgroup charge and size by synthesizing the lipids with dendritic headgroups described in this paper. Their headgroups have an ornithine-based core that is terminated by ornithine or carboxyspermine moieties, resulting in a maximum headgroup charge of +16 e at complete protonation. These lipids naturally extend the level of headgroup charge and, therefore, the accessible range of membrane charge density for multivalent lipids (*16*, *47*, *48*). They also bridge the gap to previously reported lipid−polymer and lipid−dendrimer hybrid materials (*49*−*53*).

The lipids have been prepared by an efficient synthetic scheme that permits their gram-scale synthesis. Modular assembly of the headgroup, spacer, and hydrophobic moieties allows facile variation of these components in the final lipid. Measurements of the headgroup charge of the lipids in complexes with DNA via an ethidium bromide displacement assay and their zeta potential show complete protonation of the headgroups. Mixtures of the dendritic lipids with DOPC at various ratios were used to prepare their DNA complexes. The structure of the complexes was investigated with X-ray diffraction, and their transfection efficiency was assessed using a luciferase reporter gene assay. X-ray diffraction shows formation of the L_α^C phase (*41*) for lipids with lower headgroup charge (4+) or lower contents of dendritic lipid in the membrane. For high contents of highly charged (8+, 16+) dendritic lipids, the observed scattering patterns are not consistent with any of the previously reported phases of CL−DNA complexes, except for a relatively narrow composition window that corresponds to the H_I^C phase (*45*). DNA complexes of the dendritic lipids efficiently transfect mammalian cells, at mol fractions of cationic lipid as low as 10%. For optimal transfection, a slightly higher lipid to DNA charge ratio than for the standard cationic lipid 2,3-dioleyloxy-propyl-trimethylammonium chloride (DOTAP) (*54*) is required. DNA complexes of the dendritic lipids are less cytotoxic than those of DOTAP, and no cytotoxicity is observed at the amounts required for transfection. In contrast to the lamellar complexes of less highly charged multivalent lipids, complexes of the dendritic lipids remain efficiently transfecting over a broad range of lipid composition, including high contents of cationic lipid (i.e. high membrane charge densities), pointing to differences in the transfection mechanism.

EXPERIMENTAL PROCEDURES

General Methods. NMR spectroscopy was carried out on a Bruker Avance 200 MHz spectrometer. MALDI-TOF mass spectrometry was performed on a Dynamo spectrometer from Thermal BioAnalysis Ltd. using 2,5-dihydroxybenzoic acid as the matrix and 30 vol.-% water in acetonitrile as the solvent. For thin-layer chromatography, silica covered plastic sheets with fluorescence indicator (Macherey-Nagel) were used. Detection of spots was achieved with UV light and ninhydrin reagent (300 mg in 95 mL of 2-propanol and 5 mL of acetic acid). By addition of methanol to a 4:2:1 (v/v/v) mixture of chloroform, methanol, and 25% ammonia until the mixture became homogeneous, solvent mixture A was obtained. Similarly, solvent mixture B was prepared starting with a 1:1:1 (v/v/v) mixture of the same solvents. Silica gel from Fisher Scientific with a mesh size of 200−425 was used for flash chromatography (*55*). Zeta potential measurements were performed as described (*56*).

Lipid Solutions. Stock solutions of the dendritic lipids were prepared in chloroform/methanol (9:1, v/v). DOPC and DOTAP were purchased as a solution in chloroform from Avanti Lipids. These lipid solutions were combined at the desired ratio of lipids and dried, first by a stream of nitrogen and subsequently in a vacuum for 8 to 12 h. To the residue, high conductivity (18.2 MΩ) water was added and the mixture was incubated at 37 °C for at least 12 h to give solutions of a final concentration of 30 mM for X-ray samples (15 mM for MVLBisG2). For transfection, aqueous lipid solutions were prepared at 0.6 mM. Lipid mixtures containing higher mol fractions of DOPC formed opaque suspensions, which were sonicated to clarity and filtered through 0.2 μm syringe filters. The lipid solutions were stored at 4 °C until use.

Ethidium Bromide (EtBr) Displacement Assay. Lipid−DNA complexes were prepared in duplicate in a 96 well plate. Each well contained 2.4 μg HPCT DNA, 0.28 μg EtBr, and the desired amount of lipid in a final volume of 250 μL. The emission at 605 nm was measured on a Cary Eclipse fluorescence spectrophotometer, following excitation at 519 nm.

Transfection. Mouse fibroblast L-cells were cultured at 37 °C in supplemented cell medium (Dulbecco's Modified Eagle's Medium (DMEM) with 1% penicillin−streptomycin and 5% fetal bovine serum, v/v; from Gibco BRL) in an atmosphere containing 5% CO_2 and were reseeded approximately every 72 h to maintain subconfluency. Measurements were performed in duplicate and are displayed as mean plus/minus standard deviation. The day before the transfection experiment, cells were seeded in 24-well plates. At the time of transfection, the cells were approximately 70% confluent. Luciferase plasmid DNA (pGL3 Control Vector, Promega) was prepared using a Qiagen Giga Kit. For each well, 0.4 μg of Luciferase plasmid DNA was used. Liposomes (0.6 mM) were added to the DNA, and the mixture was diluted to a final volume of 0.1 mL with nonsupplemented DMEM. The cells were incubated with this solution for 6 h, rinsed three times with phosphate-buffered saline (PBS, Invitrogen), and incubated with supplemented cell media for an additional 24 h. Luciferase gene expression was measured with the Luciferase Assay System (Promega), and light output readings were taken on a Berthold AutoLumat luminometer. Transfection efficiency, measured as relative light units (RLU), was normalized to the weight of total cellular protein determined using Bio-Rad Protein Assay Dye Reagent (Bio-Rad).

Cytotoxicity. Cytotoxicity was assayed by measuring extracellular levels of lactate dehydrogenase. At 18 h prior to treatment, cells were seeded in 96-well plates at 15 000 cells per well. Lipid−DNA complexes were prepared as above and added to the wells, adding a total of 0.08 μg DNA per well. After incubation for 6 h, 75 μL of CytoTox-ONE Homogeneous Membrane Integrity Assay (Promega) and 35 μL of culture medium were added to each well. Fluorescence was quantified on a Bio-Rad PharosFX Molecular Imager system and converted to percent cytotoxicity as described in the manufacturer's instructions.

Synthesis. Chemicals were from Fisher Scientific and at least of analytical grade unless otherwise indicated. They were used as received. Our syntheses of 3,4-dioleylbenzoic acid (DOB) (*59*) and of **MVLBG2** and the intermediates leading to it

(**Boc_2Orn**, **CbxSpr(Boc)$_4$**, **BocG2OMe**, **G2OMe**, **MVLBG2**, **BocBG2OMe**, **BocBG2En**) have been published previously (*45*).

General Procedure for TBTU-Mediated Coupling (dendron synthesis; amine compound with *n* amino groups). To a mixture of 1.1*n* mmol of acid component, 1.1*n* mmol of *O*-benzotriazol-1-yl-*N*,*N*,*N*′,*N*′-tetramethyluronium tetrafluoroborate (TBTU; Bachem), and 1.1*n* mmol of 1-hydroxybenzotriazole (HOBt) hydrate (Peptides International) in dimethylformamide (DMF) (peptide synthesis grade, Applied Biosystems) was added 2*n* mmol of *N*,*N*-diisopropylethylamine (DIEA; Aldrich). After 10 min, a mixture of 1 mmol of amine compound (hydrochloride or hydrotrifluoroacetate form) and *n* mmol of DIEA in DMF was added to the resulting solution with stirring. Stirring was continued at room temperature for 2 h, and chloroform and water were added with vigorous stirring after evaporation of most of the DMF (*57*). The phases were separated, and after extracting two more times with chloroform, the organic phases were combined and washed twice with 2 M HCl, twice with 2 M NaOH, and once with water. After drying (Na_2SO_4), the solvents were evaporated.

General Procedure for the Aminolysis of Methyl Esters with Diamines. The methyl ester was dissolved in methanol, if necessary, by addition of some chloroform. Twenty equivalents of diamine were added in one portion, and the mixture was stirred at room temperature until the reaction appeared complete by TLC. The solvent was evaporated, and water and chloroform were added. After agitation, the phases were separated, and the organic layer was washed two more times with water, dried (Na_2SO_4), and evaporated. The residue was then purified as required.

***N*1-(2-Aminoethyl)-(2*S*)-2,5-di[(1*S*)-1,4-di(*tert*-butyl-carbamoyl-amino)butyl]carboxamidopentanamide (BocG2En).** To a solution of 1.90 g (2.45 mmol) of **BocG2OMe** in 5 mL of methanol, 3.3 mL (2.96 g, 49.3 mmol) of ethylenediamine (Fluka) was added, and the mixture was stirred for 16 h at room temperature. After the addition of 100 mL water, the mixture was stirred vigorously at room temperature until the formed precipitate crystallized. Filtration and drying of the residue yielded 1.7 g (2.1 mmol, 86%) of **BocG2En** as colorless crystals: $R_f = 0.33$ ($CHCl_3$/MeOH 6:1, 1% concentrated NH_4OH); ^{1}H NMR ($CDCl_3$): $\delta = 0.8-2.1$ (m, C−CH_2−C), 1.35 (s, C(CH_3)$_3$), 2.34 (b, 2 H, NH_2) 2.76 (b, 2 H, CH_2−N), 2.9−3.5 (bm, 10 H, CH_2−N), 3.95−4.55 (2 bm, 3 H, C*H*), 4.9−5.7 (3 m, 2 H, C(O)N*H*), 5.7−6.3 (2 b, 2 H, C(O)N*H*), 7.2−7.7 (bm, 3 H, C(O)N*H*); ^{13}C NMR ($CDCl_3$): $\delta = 25.6$, 25.9 (CH$_2$−CH_2−CH$_2$), 28.3, 28.4 (C(**C**H$_3$)$_3$), 29.4, 29.9, 30.3 (CH$_2$−CH_2−CH), 38.4, 39.6, 39.8, 41.0, 41.8 (CH_2−N), 53.0, 53.6, 54.1 (**C**H), 78.9, 79.8, 79.9 (**C**(CH$_3$)$_3$), 156.1, 156.2 (O−*C*(O)−N), 171.9, 173.1, 173.2 (C−*C*(O)).

***N*1-2-[2-(2-Aminoethoxy)ethoxy]ethyl-(2*S*)-2,5-di[(1*S*)-1,4-di(*tert*-butyl-carbamoyl-amino)butyl]carboxamidopentanamide (BocG2NTEG).** As described in the general procedure for aminolysis, 2.00 g (2.58 mmol) of **BocG2OMe** was reacted with 2,2′-(Ethylenedioxy)diethylamine (NTEG, Aldrich) for 60 h. Extraction and evaporation yielded 1.89 g (2.13 mmol, 83%) of **BocG2NTEG** as a colorless solid: $R_f = 0.33$ ($CHCl_3$/MeOH 6:1, 1% concentrated NH_4OH); ^{1}H NMR ($CDCl_3$): $\delta = 0.8-2.0$ (m), 1.35 (s) (48 H, C−CH_2–C, C(CH_3)$_3$), 2.80 ("t", $J = 5.0$ Hz, 2 H, CH_2−NH$_2$), 2.9−3.2 (m, 4 H, CH_2−NBoc), 3.2−3.7 (m, 12 H, CH_2−N, CH_2−O), 4.0−4.5 (2 bm, 3 H, C*H*), 4.9−5.4 (2 m, 2 H, C(O)N*H*), 5.5−6.0 (2 b, 2 H, C(O)N*H*), 7.1−7.7 (m, 3 H, C(O)N*H*); ^{13}C NMR ($CDCl_3$): $\delta = 25.5$, 25.9, 26.0 (CH$_2$−CH_2−CH$_2$), 28.3, 28.4 (C(*C*H$_3$)$_3$), 29.3, 30.0, 30.2 (CH$_2$−CH_2−CH), 38.6, 39.1, 39.7, 39.8, 41.5 (*C*H$_2$−N), 52.6, 53.7, 53.9 (*C*H), 69.5, 70.0, 70.1, 73.0 (*C*H$_2$O), 78.9, 79.8 (*C*(CH$_3$)$_3$), 155.9, 156.1, 156.2 (O−*C*(O)−N), 171.5, 172.7, 173.1 (C−*C*(O)).

Methyl (2*S*)-2,5-Di[((1*S*)-1,4-di[(1*S*)-1,4-di(*tert*-butyl-carbamoyl-amino)butyl]carboxamidobutyl)carboxamido]-pentanoate (BocG3OMe). As described in the general procedure for dendron synthesis, 6.34 g (19.1 mmol) of **Boc_2Orn** was reacted for 3 h with 3.60 g (4.33 mmol) of **G2OMe**. For workup, the reaction mixture was evaporated and 600 mL of diethyl ether was added. The precipitate was isolated by filtration, and dichloromethane and 5% $NaHCO_3$ were added. The phases were separated, and the organic phase was washed once more with 5% $NaHCO_3$, twice with 5% citric acid, and once with water. It was then dried (Na_2SO_4) and evaporated to yield 5.51 g (3.38 mmol, 78%) of **BocG3OMe** as a colorless solid: $R_f = 0.72$ ($CHCl_3$/MeOH 6:1, 1% concentrated NH_4OH); ^{1}H NMR ($CDCl_3$): $\delta = 0.7-2.2$ (m), 1.37 (s) (100 H, C−CH_2−C, C(CH_3)$_3$), 2.9−3.4, 3.4−3.7 (2 m, 18 H, CH_2−N, OCH_3), 3.8−4.7 (bm, 7 H, C*H*), 4.7−6.2 (several bm, 6 H, N*H*), 7.0−8.0 (4 m, 8 H, N*H*); ^{13}C NMR ($CDCl_3$): $\delta = 25.2$, 25.8, 29.3, 30.0 (all b, C−CH_2−C), 28.1, 28.2 (C(*C*H$_3$)$_3$), 38.4, 39.6 (b, CH_2−N), 51.7, 52.2, 52.6, 53.7, 54.1 (O*C*H$_3$, *C*H), 78.8 (b, 4), 79.6 (b,4) (*C*(CH$_3$)$_3$),155.8, 156.2 (2 b, overlap, 6) (O−*C*-(O)−N), 171.9 (b, 2), 172.4, 172.9 (b,4) (C−*C*(O)).

***N*1-(2-Aminoethyl)−(2*S*)-2,5-di[((1*S*)-1,4-di[(1*S*)-1,4-di-(*tert*-butyl-carbamoyl-amino)butyl]carboxamidobutyl)carboxamido]pentanamide (BocG3En).** As described in the general procedure for aminolysis, 2.50 g (1.53 mmol) of **BocG3OMe** was reacted with ethylenediamine for 7 days. Extraction and evaporation yielded 1.58 g (0.95 mmol, 62%) of **BocG3En** as a colorless solid: $R_f = 0.40$ ($CHCl_3$/MeOH 6:1, 1% concentrated NH_4OH); ^{1}H NMR ($CDCl_3$/MeOH-d_4): $\delta = 0.7-1.9$ (m), 1.10 (s) (100 H, C−CH_2−C, C(CH_3)$_3$), 2.43 ("t", $J = 5.7$ Hz, 2 H), 2.55−3.1 (m, 16 H) (CH_2−N), 3.69, 3.99 (2 b, 7 H, C*H*); ^{13}C NMR ($CDCl_3$/MeOH-d_4,): $\delta = 25.0$, 25.5 (CH$_2$−CH_2−CH$_2$), 27.5, 27.6 (C(*C*H$_3$)$_3$), 28.4, 28.8, 29.3 (CH$_2$−CH_2−CH), 38.0, 39.2, 40.2, 41.5 (CH_2−N), 52.6, 53.0, 53.8, 54.4 (*C*H), 78.5, 79.3, 79.5 (*C*(CH$_3$)$_3$), 155.8, 156.2, 156.5 (O−*C*(O)−N), 171.8, 171.9, 172.2, 173.1 (C−*C*(O)).

***N*1-2-[2-(2-Aminoethoxy)ethoxy]ethyl-(2*S*)-2,5-di[((1*S*)-1,4-di[(1*S*)-1,4-di(*tert*-butyl-carbamoyl-amino)butyl]carboxamidobutyl)carboxamido]pentanamide (BocG3NTEG).** As described in the general procedure for aminolysis, 2.43 g (1.49 mmol) of **BocG3OMe** was reacted with NTEG for 11 days. Extraction and evaporation yielded 1.67 g (0.96 mmol, 64%) of **BocG3NTEG** as a colorless solid: $R_f = 0.40$ ($CHCl_3$/MeOH 6:1, 1% concentrated NH_4OH); ^{1}H NMR (MeOH-d_4): $\delta = 0.8-2.1$ (m), 1.44 (s) (100 H, C−CH_2−C, C(CH_3)$_3$), 2.7−2.9 (m, 2 H, CH_2−NH$_2$), 2.95−3.75 (several m, 24 H, CH_2−N, CH_2−O), 3.85−4.15 (b, 4 H), 4.2−4.5 (bm, 3 H) (C*H*); ^{13}C NMR (MeOH-d_4): $\delta = 26.8$, 27.1, 27.5, 27.6 (CH$_2$−CH_2−CH$_2$), 28.9 (C(*C*H$_3$)$_3$), 30.3, 30.7, 31.0 (CH$_2$−CH_2−CH), 39.8, 40.5, 41.0, 42.2 (*C*H$_2$−N), 54.3, 54.4, 54.5, 56.0 (*C*H), 70.6, 71.4 (2), 73.6 (*C*H$_2$O), 80.0, 80.7, 80.9 (*C*(CH$_3$)$_3$), 157.9, 158.0, 158.2, 158.6 (O−*C*(O)−N), 173.9, 174.0 (dbl peak), 175.2 (C−*C*(O)).

Methyl (2*S*)-2,5-Di[((1*S*)-1,4-di[(*tert*-butyl-carbamoyl)(3-[*tert*-butyl-carbamoyl-amino]propyl)] aminobutyl)carboxamido]pentanoate (BocBG1OMe). As described in the general procedure for dendron synthesis (but using diethyl ether in place of chloroform), 5.25 g (8.12 mmol) of **Bis(Boc)$_4$** was reacted with 870 mg (3.85 mmol) of ornithine methyl ester dihydrochloride to yield 4.97 g (3.54 mmol, 92%) of **BocBG1OMe** as a colorless solid: $R_f = 0.58$ ($CHCl_3$/MeOH 9:1, 1% concentrated NH_4OH); ^{1}H NMR ($CDCl_3$): $\delta = 0.8-2.2$ (m, 92 H, C−CH_2−C, C(CH_3)$_3$), 2.5−3.5 (m, 22 H, CH_2−N), 3.59 (s, 3 H, OCH_3), 3.9−4.6 (bm, 3 H, C*H*), 4.6−5.6 (bm, 3 H), 6.4−7.2 (2 b, 2 H), (N*H*); ^{13}C NMR ($CDCl_3$): $\delta = 24.8$, 25.2, 26.0, 27.9, 28.9, 29.8 (C−CH_2−C), 28.2 (C(CH_3)$_3$), 37.2 (2), 37.9 (2), 38.5, 42.8,

43.4, 44.2, 46.1, 46.3 (b, 2) (CH_2−N), 51.7, 52.2, 58.4 (b) (OCH_3, *C*H), 78.7, 79.4, 80.6, 80.7 (*C*(CH_3)$_3$), 155.4 (b), 155.9 (O−*C*(O) −N), 171.4 (b), 172.0 (C−*C*(O)); MALDI-MS: *m*/*z* = 1425.9 (M + Na^+).

***N*1-(2-Aminoethyl)-(2*S*)-2,5-di[((1*S*)-1,4-di[(*tert*-butyl-carbamoyl)(3-[*tert*-butyl-carbamoyl-amino]propyl)]aminobutyl-)carboxamido]pentanamide (BocBG1En).** As described in the general procedure for aminolysis, 1.51 g (1.07 mmol) of **BocBG1OMe** was reacted with ethylenediamine for 16 h. The residue was purified by flash chromatography on 120 g of silica gel using chloroform/methanol (11:1, changed to 6:1 once the product started to elute) as the eluent to yield 1.30 g (0.90 mmol, 84%) of **BocBG1En** as a colorless solid: R_f = 0.51 ($CHCl_3$/MeOH 6:1, 1% concentrated NH_4OH); ^{1}H NMR ($CDCl_3$): δ = 0.9−2.0 (m), 1.32, 1.34, 1.36 (3 s), (92 H, C−CH_2−C, C(CH_3)$_3$), 2.70 (("t", *J* = 5.3 Hz, 2 H, CH_2−NH_2), 2.8−3.45 (m, 26 H, CH_2−N), 3.95−4.45 (m, 3 H, C*H*), 5.42 (b, NH); ^{13}C NMR ($CDCl_3$): δ = 25.2, 25.9, 27.8, 29.6 (C−CH_2−C), 28.08, 28.16 (C(*C*H_3)$_3$), 37.3, 37.9, 40.6, 41.3, 43.2, 43.7, 44.3, 46.4 (*C*H_2−N), 52.3, 58.3, 59.2 (*C*H), 78.8, 79.6, 80.7, 80.8 (*C*(CH_3)$_3$), 155.8, 156.1 (O−*C*(O)−N), 171.4, 171.9 (C−*C*(O)); MALDI-MS: *m*/*z* = 1433.5 (M + H^+), 1455.3 (M + Na^+).

***N*1-2-[2-(2-Aminoethoxy)ethoxy]ethyl-(2*S*)-2,5-di[((1*S*)-1,4-di[(*tert*-butyl-carbamoyl)(3-[*tert*-butyl-carbamoyl-amino]propyl)]aminobutyl)carboxamido]pentanamide (BocBG1NTEG).** As described in the general procedure for aminolysis, 1.51 g (1.07 mmol) of **BocBG1OMe** was reacted with NTEG for 40 h. The residue was purified by flash chromatography on 120 g of silica gel using chloroform/methanol (11:1, changed to 6:1 once the product started to elute) as the eluent to yield 1.25 g (0.82 mmol, 77%) of **BocBG1NTEG** as a colorless solid: R_f = 0.51 ($CHCl_3$/MeOH 6:1, 1% concentrated NH_4OH); ^{1}H NMR (MeOH-d_4): δ = 0.9−2.1 (m), 1.44, 1.47, 1.49 (3 s) (92 H, C−CH_2−C, C(CH_3)$_3$), 2.84 ("t", *J* = 5.3 Hz, 2 H, CH_2−NH_2), 3.04 ("t", *J* = 6.5 Hz), 2.9−3.45 (m), 24 H, CH_2−N), 3.55 ("t", *J* = 5.3 Hz), 3.63 (s) (8 H, CH_2−O), 4.2−4.6 (bm, 3 H, C*H*); ^{13}C NMR (MeOH-d_4): δ = 26.3, 26.9, 27.8, 30.3, 30.9 (C−CH_2−C), 28.97, 29.02 (C(*C*H_3)$_3$), 39.0, 39.3, 40.0, 42.1, 44.8, 45.7, 46.2, 48.0 (*C*H_2−N), 54.3, 60.2 (b) (*C*H), 70.6, 71.4, 73.0 (*C*H_2O), 79.9, 81.1, 81.8, 82.0 (*C*(CH_3)$_3$), 157.4, 158.4 (O−*C*(O)−N), 173.4, 174.0 (C−*C*(O)); MALDI-MS: *m*/*z* = 1519.0 (M + H^+), 1541.4 (M + Na^+).

***N*1-2-[2-(2-Aminoethoxy)ethoxy]ethyl-(2*S*)-2,5-di((1*S*)-1,4-di[((1*S*)-1,4-di(*tert*-butyl-carbamoyl)(3-[*tert*-butyl-carbamoyl-amino]propyl)aminobutyl)carboxamido]butylcarboxamido)-pentanamide (BocBG2NTEG).** As described in the general procedure for aminolysis, 2.00 g (0.69 mmol) of **BocBG2OMe** was reacted with NTEG for 10 days. The residue was purified by flash chromatography on 120 g of silica gel using chloroform/methanol (15:1, changed to 6:1 once the product started to elute) as the eluent to yield 1.23 g (0.41 mmol, 59%) of **BocBG2NTEG** as a colorless solid: R_f = 0.57 ($CHCl_3$/MeOH 6:1, 1% concentrated NH_4OH);

General Procedure for the Synthesis of the Boc-Protected Lipids. A solution of 1.1 mmol of DOB (46,59) in dichloromethane was added to a mixture of 1.1 mmol of TBTU and 1.1 mmol of HOBt hydrate in DMF. Following the addition of 3 mmol of DIEA, the mixture was left to stand for 10 min and a solution of 1 mmol of amine compound in DMF was added. After standing for 4 h, the solvents were evaporated. Following the addition of chloroform and 5% citric acid and agitation, the phases were separated and the organic phase was washed one more time with 5% citric acid, twice with 10% $NaHCO_3$, and once with water. After drying (Na_2SO_4), the solvent was evaporated and the residue was purified as required.

***N*1-2-[((1*S*)-1,4-Di[(1*S*)-1,4-di(*tert*-butyl-carbamoyl-amino)-butyl]carboxamidobutyl)carboxamido]ethyl-3,4-di[(*Z*)-9-octadecenyloxy]benzamide (BocMVLG2).** As described in the general procedure, 1.01 g (1.25 mmol) of **BocG2En** was coupled with DOB. The product was purified by flash chromatography on 150 g of silica gel using chloroform/methanol (19:1) as the eluent (*58*) to yield 1.55 g (1.08 mmol, 86%) of **BocMVLG2** as a colorless solid: R_f = 0.28 ($CHCl_3$/MeOH 19:1); ^{1}H NMR ($CDCl_3$): δ = 0.79 ("t", 6 H, CH_2−CH_3), 0.9−2.2 (several m, lg. peaks @ 1.32, 1.23, 1.18, 104 H, C−CH_2−CH_2, C(CH_3)$_3$), 2.7−3.7 (m, 10 H, N−CH_2), 3.9−4.5 (m, 7 H, O−CH_2, C*H*), 5.0−5.75 (m, 8 H, =C*H*−, N*H*), 6.76 (d, ^3J = 8.3 Hz, 1 H, H_{ar} *m*-C(O)), 7.1−7.7 (m, 6 H, H_{ar}, N*H*); ^{13}C NMR ($CDCl_3$): δ = 14.0 (*C*H_3), 22.5 (*C*H_2−CH_3), 28.2, 28.2, 28.3 (C(*C*H_3)$_3$), 25.9, 25.9, 26.0, 27.1, 29.2, 29.3, 29.4, 29.6, 30.0, 31.8 (CH_2−*C*H_2−C), 38.3, 39.3, 39.8, 40.2, 40.9 (*C*H_2−N), 53.0, 53.8, 54.5 (*C*H), 68.9, 69.2 (*C*H_2−O), 78.9, 79.7, 79.9 (*C*(CH_3)$_3$), 112.1, 112.9, 120.1 (C_{ar}H), 126.6 (C_{ar}−C(O)N), 129.6, 129.8 (=*C*H−CH_2), 148.6, 151.7 (C_{ar}−O), 156.0, 156.2, 156.3 (O−*C*(O) −N), 167.6, 172.4, 172.9, 173.0 (C−*C*(O)).

***N*1-[2-((1*S*)-1,4-Di[((1*S*)-1,4-di[(1*S*)-1,4-di(*tert*-butyl-carbamoyl-amino)butyl]carboxamidobutyl)carboxamido]-butylcarboxamido)ethyl]-3,4-di[(*Z*)-9-octadecenyloxy]benzamide (BocMVLG3).** As described in the general procedure, 1.475 g (889 μmol) of **BocG3En** was coupled with DOB. The product was purified by flash chromatography on 150 g of silica gel using chloroform/methanol (15:1) as the eluent (58) to yield 1.85 g (806 μmol, 91%) of **BocMVLG3** as a colorless solid: R_f = 0.14 ($CHCl_3$/MeOH 19:1); ^{1}H NMR ($CDCl_3$/MeOH-d_4 = 9:1): δ = 0.70 ("t", 6 H, CH_2−CH_3), 0.7−2.1 (several m, lg. peaks @ 1.10, 1.15, 1.25, 1.35, 156 H, C−CH_2−C, C(CH_3)$_3$), 2.7−3.45 (m, 18 H, CH_2−N), 3.6−4.3 (m, 11 H, O−CH_2, C*H*), 5.05−5.35 (m, 4 H, =C*H*−), 6.70 (d, ^3J = 8.4 Hz, 1 H, H_{ar} *m*-C(O)), 7.1−7.3 (m, 2 H, H_{ar}); ^{13}C NMR ($CDCl_3$/MeOH-d_4 = 9:1): δ = 13.7 (*C*H_3), 22.3 (*C*H_2−CH_3), 27.9, 28.0 (C(*C*H_3)$_3$), 25.0, 25.2, 25.7, 26.9, 29.0, 29.2, 29.4, 29.5, 31.6 (CH_2−*C*H_2−C), 38.1, 38.3, 39.2, 39.5 (all b, CH_2−N), 52.8 (3), 53.9 (2), 54.4 (2) (*C*H), 68.9, 69.2 (*C*H_2−O), 78.9, 79.6, 79.8 (*C*(CH_3)$_3$), 112.1, 112.9, 120.2 (C_{ar}H), 126.3 (C_{ar}−C(O)N), 129.5, 129.6 (=*C*H−CH_2), 148.4, 151.7 (C_{ar}−O), 155.9, 156.1, 156.5 (O−*C*(O)−N), 168.1 (1), 171.9 (2), 172.5 (1), 173.2 (4, b) (C−*C*(O)).

***N*1-[2-((1*S*)-1,4-Di[((1*S*)-1,4-di[(*tert*-butyl-carbamoyl)(3-[*tert*-butyl-carbamoyl-amino]propyl)amino]butyl)carboxamido]butylcarboxamido)ethyl]-3,4-di[(*Z*)-9-octadecenyloxy]-benzamide (BocMVLBG1).** As described in the general procedure, 1.02 g (712 μmol) of **BocBG1En** was coupled with DOB. The product was purified by flash chromatography on 100 g of silica gel using chloroform/methanol (25:1) as the eluent (58) to yield 1.3 g (0.63 mmol, 88%) of **BocTMVLBG1** as a colorless solid: R_f = 0.38 ($CHCl_3$/MeOH 19:1); ^{1}H NMR ($CDCl_3$): δ = 0.76 ("t", 6 H, CH_2−CH_3), 0.9−2.3 (several m, lg. peaks @ 1.16, 1.21, 1.32, 1.33, 148 H, C−CH_2−C, C(CH_3)$_3$), 2.7−3.7 (m, 26 H, N−CH_2), 3.8−4.55 (m, 7 H, O−CH_2, C*H*), 4.75−5.7 (m, 8 H, =C*H*−, N*H*), 6.5−7.15 (m, 3 H), 7.15−7.7 (m, 4 H) (H_{ar}, N*H*); ^{13}C NMR ($CDCl_3$): δ = 13.9 (*C*H_3), 22.5 (*C*H_2−CH_3), 25.4, 25.8, 27.0, 29.1, 29.2, 29.3, 29.6, 31.7 (C−CH_2−C), 28.2, 28.3 (C(*C*H_3)$_3$), 37.4 (b), 37.9 (b), 39.5, 40.4, 43.2 (b), 43.5 (b), 44.2 (b), 46.4 (b) (*C*H_2−N), 52.1, 59.1 (very b, *C*H), 68.9, 69.1, (*C*H_2−O), 78.8, 79.5, 80.7, 80.8 (*C*(CH_3)$_3$), 112.1, 112.8, 119.8 (C_{ar}H), 126.5 (C_{ar}−C(O)N), 129.6, 129.7 (=*C*H−CH_2), 148.6, 151.7 (C_{ar}−O), 155.9, 156.0 (b, O−*C*(O)−N), 167.5, 171.3, 172.4 (C−*C*(O)).

***N*1-[2-(2−2-[((1*S*)-1,4-Di[(1*S*)-1,4-di(tert-butyl-carbamoyl-amino)butyl]carboxamidobutyl)carboxamido]ethoxyethoxy)-ethyl]-3,4-di[(*Z*)-9-octadecenyloxy]benzamide (BocTMV-LG2).** As described in the general procedure, 1.10 g (1.23 mmol) of **BocG2NTEG** was coupled with DOB. The product was purified by flash chromatography on 150 g of silica gel

using chloroform/methanol (19:1) as the eluent (58) to yield 1.63 g (1.07 mmol, 87%) of **BocTMVLG2** as a colorless solid: $R_f = 0.28$ ($CHCl_3$/MeOH 19:1); ^{1}H NMR ($CDCl_3$): $\delta = 0.77$ ("t", 6 H, CH_2–CH_3), 0.9−2.4 (104 H, C−CH_2−C, C(CH_3)$_3$), 2.8−3.7 (m, 18 H, N−CH_2, O−CH_2), 3.8−4.5 (m, 7 H, O−CH_2, C*H*), 4.9−6.1 (m, 8 H, =C*H*−, N*H*), 6.74 (d, $^3J = 8.3$ Hz, 1 H, H_{ar} *m*-C(O)), 7.1−7.8 (m, 6 H, H_{ar}, N*H*); ^{13}C NMR ($CDCl_3$): $\delta = 13.9$ (*C*H_3), 22.5 (*C*H_2−CH_3), 28.2, 28.3 (C(*C*H_3)$_3$), 25.9, 27.0, 29.1, 29.2, 29.3, 29.6, 29.9, 30.1, 31.7 (CH_2−*C*H_2−C), 38.6, 39.0, 39.7 (C*H*$_2$−N), 52.7, 53.7, 53.8 (*C*H), 68.9, 69.1, 69.4, 69.8, 69.9, 70.0 (*C*H_2−O), 78.8, 79.7, 79.8 (*C*(CH$_3$)$_3$), 112.1, 113.0, 119.6 (C_{ar}H), 126.8 (C_{ar}−C(O)N), 129.6, 129.7 (=*C*H−CH_2), 148.7, 151.7 (C_{ar}−O), 155.9, 156.1 (O−*C*(O)−N), 167.2, 171.4, 172.8, 173.2 (C−*C*(O)).

***N*1-(2−2-[2-((1*S*)-1,4-Di[((1*S*)-1,4-di[(1*S*)-1,4-di(*tert*-butylcarbamoyl-amino)butyl]carboxamidobutyl)carboxamido]butylcarboxamido)ethoxy]ethoxyethyl)-3,4-di[(*Z*)-9-octadecenyloxy]benzamide (BocTMVLG3).** As described in the general procedure, 1.565 g (895 μmol) of **BocG3NTEG** was coupled with DOB. The product was purified by flash chromatography on 150 g of silica gel using chloroform/methanol (15:1) as the eluent (58) to yield 1.73 g (716 μmol, 81%) of **BocTMVLG3** as a colorless solid: $R_f = 0.18$ ($CHCl_3$/MeOH 19:1); ^{1}H NMR ($CDCl_3$): $\delta = 0.78$ ("t", 6 H, CH_2–CH_3), 0.9−2.4 (several m, lg. peaks @ 1.17, 1.22, 1.32, 156 H, C−CH_2−C, C(CH_3)$_3$), 2.75−3.7 (m, 26 H, O−CH_2, CH_2−N), 3.8−4.5 (m, 11 H, O−CH_2, C*H*), 4.9−6.5 (m, 12 H, =C*H*−, N*H*), 6.76 (d, $^3J = 8.4$ Hz, 1 H, H_{ar} *m*-C(O)), 6.9−8.0 (m, 10 H, H_{ar}, N*H*); ^{13}C NMR ($CDCl_3$): $\delta = 13.9$ (*C*H_3), 22.5 (*C*H_2−CH_3), 28.3 (C(*C*H_3)$_3$), 25.3, 25.9, 27.0, 29.1, 29.2, 29.3, 29.6, 31.7 (CH_2−*C*H_2−C), 38.6, 39.1, 39.6 (all b, C*H*$_2$−N), 52.5, 53.8, 54.2 (*C*H), 68.9, 69.2, 69.4, 69.7, 70.0 (*C*H_2−O), 78.8, 79.7 (*C*(CH$_3$)$_3$), 112.1, 113.0, 119.6 (C_{ar}H), 126.7 (C_{ar}−C(O)N), 129.6, 129.7 (=*C*H−CH_2), 148.7, 151.7 (C_{ar}−O), 156.1 (O−*C*(O)−N), 167.2, 171.5, 171.7, 172.9, 173.1 (C−*C*(O)).

***N*1-(2−2-[2-((1*S*)-1,4-Di[((1*S*)-1,4-di[(*tert*-butyl-carbamoyl)-(3-[*tert*-butyl-carbamoyl-amino]propyl)amino]butyl)carboxamido]butylcarboxamido)ethoxy]ethoxyethyl)-3,4-di[(*Z*)-9-octadecenyloxy]benzamide (BocTMVLBG1).** As described in the general procedure, 1.10 g (723 μmol) of **BocBG1NTEG** was coupled with DOB. The product was purified by flash chromatography on 100 g of silica gel using chloroform/methanol (19:1) as the eluent (58) to yield 1.3 g (0.60 mmol, 83%) of **BocTMVLBG1** as a colorless solid: $R_f = 0.28$ ($CHCl_3$/MeOH 19:1); ^{1}H NMR ($CDCl_3$): $\delta = 0.75$ ("t", 6 H, CH_2−CH_3), 0.9−2.3 (several m, lg. peaks @ 1.14, 1.19, 1.31, 1.32, 148 H, C−C*H*$_2$−C, C(C*H*$_3$)$_3$), 2.7−3.7 (m, 34 H, O−C*H*$_2$, N−C*H*$_2$), 3.8−4.5 (m, 7 H, O−C*H*$_2$, C*H*), 4.75−5.7 (m, 8 H, =C*H*−, N*H*), 6.5−7.5 (several m, 7 H), H_{ar}, N*H*); ^{13}C NMR ($CDCl_3$): $\delta = 13.9$ (*C*H_3), 22.5 (*C*H_2−CH_3), 25.3, 25.8, 27.0, 29.1, 29.3, 29.6, 31.7 (C−C*H*$_2$−C), 28.1, 28.2 (C(*C*H_3)$_3$), 38.0 (b), 38.4 (b), 39.1, 39.6, 43.1 (b), 43.6 (b), 44.2 (b), 46.4 (b) (*C*H_2−N), 52.1, 58.6, 59.2 (all b, *C*H), 68.9, 69.1, 69.4, 69.8, 70.0 (*C*H_2−O), 78.7, 79.5, 80.6, 80.8 (*C*(CH$_3$)$_3$), 112.1, 112.9, 119.6 (C_{ar}H), 126.7 (C_{ar}−C(O)N), 129.6, 129.7 (=*C*H−CH_2), 148.7, 151.7 (C_{ar}−O), 155.9 (b) (O−*C*(O)−N), 167.1, 171.3, 171.7 (C−*C*(O)).

***N*1−2-[2-(2-[(1*S*)-1,4-Di((1*S*)-1,4-di[(*tert*-butyl-carbamoyl)-(3-[*tert*-butyl-carbamoyl-amino]propyl)amino]butyl)carboxamido]butylcarboxamido)butylcarboxamido]ethoxy)ethoxy]-ethyl-3,4-di[(*Z*)-9-octadecenyloxy]benzamide (BocTMVLBG2).** As described in the general procedure, 1.05 g (349 μmol) of **BocBG2NTEG** was coupled with DOB. The product was purified by flash chromatography on 100 g of silica gel using chloroform/methanol (19:1) as the eluent (58) to yield 1.06 g (0.29 mmol, 84%) of **BocTMVLBG2** as a colorless solid: $R_f = 0.24$ ($CHCl_3$/MeOH 19:1); ^{1}H NMR ($CDCl_3$): $\delta = 0.75$ (CH_2−C*H*$_3$), 0.85−2.3 (several m, lg. peaks @ 1.14, 1.19, 1.30, 1.32, 244 H, C−C*H*$_2$−C, C(C*H*$_3$)$_3$), 2.7−3.7 (m, 58 H, N−C*H*$_2$, O−C*H*$_2$), 3.89 (("t", 4 H, O−C*H*$_2$), 4.0−4.5 (bm, 7 H, C*H*), 4.7−5.7 (m, 12 H, =C*H*−, N*H*), 6.5−7.7 (several m and b, 11 H), H_{ar}, N*H*); ^{13}C NMR ($CDCl_3$): $\delta = 13.9$ (*C*H_3), 22.4 (*C*H_2−CH_3), 25.3 (very b), 25.8, 27.0, 29.1, 29.2, 29.3, 29.5, 31.7 (C−C*H*$_2$−C), 28.2 (C(*C*H_3)$_3$), 37.2, 38.0, 39.1, 39.6, 43.5, 44.1, 46.3 (*C*H_2−N), 52.4, 54.7, 58.6, 59.3 (very b, *C*H), 68.9, 69.1, 69.3, 69.7, 69.9, 70.0 (*C*H_2−O), 78.7, 79.4, 80.5, 80.7 (*C*(CH$_3$)$_3$), 112.1, 112.9, 119.6 (C_{ar}H), 126.7 (C_{ar}−C(O)N), 129.6, 129.7 (=*C*H−CH_2), 148.6, 151.7 (C_{ar}−O), 155.3, 155.4, 155.9 (O−*C*(O)−N), 167.1, 171.4, 171.7 (C−*C*(O)).

General Procedure for the Deprotection of Boc-Protected Lipids. The protected lipid (0.9−1.6 g) was dissolved in 10 mL of 95% TFA (5% water), which had been saturated with nitrogen and cooled on ice. The mixture was left to stand at room temperature for 25 min with occasional swirling, and most of the TFA was then evaporated in vacuo. A mixture of diethyl ether/pentane (1:1, 30 mL/g protected lipid) was added with stirring, and the precipitate isolated by decanting. This was repeated twice, and the precipitate was dried in vacuo.

***N*1−2-[((1*S*)-1,4-Di[(1*S*)-1,4-diaminobutyl]carboxamidobutyl)carboxamido]ethyl-3,4-di[(*Z*)-9-octadecenyloxy]benzamide (MVLG2).** Deprotecting 1.25 g (868 μmol) of **BocMVLG2** as described in the general procedure yielded 1.06 g (712 μmol, 82%) of **MVLG2** as a colorless solid: $R_f = 0.31$ (solvent mixture A); ^{1}H NMR (MeOH-d_4): $\delta = 0.88$ ("t", 6 H, C*H*$_3$), 1.0−2.2 (m, lg. peaks at 1.28, 1.35, 68 H, C−C*H*$_2$−C), 2.8−3.7 (m, 10 H, N−C*H*$_2$), 3.8−4.1 (m, 6 H, O−C*H*$_2$, C*H*), 4.25−4.5 (m, 1 H, C*H*), 5.2−5.45 (m, 4 H, =C*H*−), 6.96 (d, $^3J = 9.1$ Hz, 1 H, H_{ar} *m*-C(O)), 7.3−7.5 (m, 2 H, H_{ar}), 7.8−8.8 (m, N*H*); ^{13}C NMR (MeOH-d_4): $\delta = 14.7$ (*C*H$_3$), 23.9, 24.2, 26.7, 28.3, 29.5, 29.7, 30.5, 30.6, 30.8, 30.9, 31.0, 33.2 (C−C*H*$_2$−C), 39.7, 40.1, 40.5 (C*H*$_2$−N), 53.7, 54.1, 54.5 (*C*H), 70.2, 70.7 (*C*H$_2$–O), 113.8, 114.3, 122.3 (C_{ar}H), 118.2 (q, $J = 294$ Hz, *C*F), 127.7 (C_{ar}−C(O)N), 130.9, 131.0 (=*C*H−CH_2), 150.2, 153.9 (C_{ar}−O), 163.2 (q, $J = 35$ Hz, TFA *C*(O)), 170.0, 170.16, 170.24, 174.3 (*C*(O)); MALDI-MS: $m/z = 1039.6$ (M + H$^+$).

***N*1-[2-((1*S*)-1,4-Di[((1*S*)-1,4-di[(1*S*)-1,4-diaminobutyl]carboxamidobutyl)carboxamido]butylcarboxamido)ethyl]-3,4-di[(*Z*)-9-octadecenyloxy]benzamide (MVLG3).** Deprotecting 1.55 g (675 μmol) of **BocMVLG3** as described in the general procedure yielded 1.61 g (668 μmol, 99%) of **MVLG3** as a colorless solid: $R_f = 0.27$ (2:2:1 $CHCl_3$/ MeOH/ 25% NH_4-OH); ^{1}H NMR (MeOH-d_4): $\delta = 0.88$ ("t", C*H*$_3$), 0.75−2.3 (m, lg. peaks @ 1.28, 1.35, C−C*H*$_2$−C) (90 H), 2.8−3.7 (m, 18 H, N−C*H*$_2$), 3.85−4.25 (m, 8 H, O−C*H*$_2$, C*H*), 4.25−4.6 (2 m, 3 H, C*H*), 5.2−5.45 (m, 4 H, =C*H*−), 6.96 (d, $^3J = 8.6$ Hz, 1 H, H_{ar} *m*-C(O)), 7.4−7.55 (m, 2 H, H_{ar}), 7.9−8.9 (m, N*H*); ^{13}C NMR (MeOH-d_4): $\delta = 14.7$ (*C*H$_3$), 23.9, 24.2, 26.7, 27.5, 28.3, 29.6, 30.5, 30.6, 30.8, 30.9, 30.99, 31.04, 33.2 (C−C*H*$_2$−C), 39.8, 40.2 (C*H*$_2$−N), 53.7, 54.1, 54.6, 55.1 (*C*H), 70.2, 70.7 (*C*H$_2$−O), 113.8, 114.3, 122.3 (C_{ar}H), 118.1 (q, $J = 293$ Hz, *C*F), 127.6 (C_{ar}−C(O)N), 130.9, 131.0 (=*C*H−CH_2), 150.2, 153.9 (C_{ar}−O), 163.0 (q, $J = 35$ Hz, TFA *C*(O)), 170.08, 170.16, 170.25, 170.32 (*C*(O)); MALDI-MS: $m/z = 1494.8$ (M + H$^+$).

***N*1-(2-[(1*S*)-1,4-Di((1*S*)-1,4-di[(3-aminopropyl)amino]butylcarboxamido)butyl]carboxamidoethyl)-3,4-di[(*Z*)-9-octadecenyloxy]benzamide (MVLBG1).** Deprotecting 1.15 g (556 μmol) of **BocMVLBG1** as described in the general procedure yielded 1.02 g (468 μmol, 84%) of **MVLBG1** as a colorless solid: $R_f = 0.51$ (solvent mixture B); ^{1}H NMR (MeOH-d_4): $\delta = 0.88$ ("t", C*H*$_3$), 0.8−2.3 (several m, lg. peaks at 1.29, 1.35, C−C*H*$_2$−C) (82 H), 2.9−3.7 (m, 26 H, N−C*H*$_2$), 3.8−4.2 (m, 6 H, O−C*H*$_2$, C*H*), 4.3−4.55 (m, 1 H, C*H*), 5.2−5.45 (m, 4 H, =C*H*−), 6.96 (d, $^3J = 8.6$ Hz, 1 H, H_{ar} *m*-C(O)), 7.35−7.55

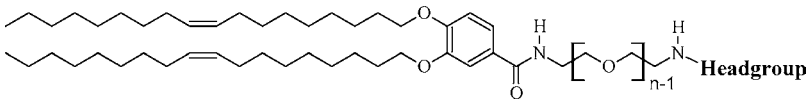

Figure 1. General structure of the new cationic lipids with dendritic headgroups; spacer lengths are $n = 1$ and $n = 3$. See Table 1 for headgroup structures and lipid names.

(m, 2 H, H_{ar}), 7.9−9.1 (m, N*H*); ^{13}C NMR (MeOH-d_4): δ = 14.7 (*C*H$_3$), 22.4, 22.9, 23.9, 25.4, 26.6, 27.5, 28.3, 30.5, 30.6, 30.8, 31.0, 33.2 (C−C*H*$_2$−C), 38.0, 38.5, 40.1, 40.5, 44.9, 45.8, 46.0, 48.0 (*C*H$_2$−N), 54.8, 61.0, 61.4 (*C*H), 70.2, 70.8, (*C*H$_2$–O), 113.9, 114.4, 122.4 (C_{ar}H), 118.2 (q, J = 294 Hz, *C*F), 127.7 (C_{ar}−C(O)N), 130.9, 131.0 (=*C*H−CH$_2$), 150.2, 154.0 (C_{ar}−O), 163.2 (q, J = 34 Hz, TFA *C*(O)), 168.66, 168.70, 170.2, 174.1 (*C*(O)); MALDI-MS: m/z = 1268.3 (M + H$^+$).

***N*1-[2-(2−2-[((1*S*)-1,4-Di[(1*S*)-1,4-diaminobutyl]carboxamidobutyl)carboxamido]ethoxyethoxy)ethyl]-3,4-di[(*Z*)-9-octadecenyloxy]benzamide (TMVLG2).** Deprotecting 1.48 g (967 μmol) of **BocTMVLG2** as described in the general procedure yielded 1.44 g (909 μmol, 94%) of **TMVLG2** as a colorless solid: R_f = 0.31 (solvent mixture A); ^{1}H NMR (MeOH-d_4): δ = 0.88 ("t", 6 H, C*H*$_3$), 1.0−2.2 (m, lg. peaks at 1.28, 1.34, 68 H, C−C*H*$_2$−C), 2.8−3.8 (3 m, 18 H, N−C*H*$_2$, O−C*H*$_2$), 3.8−4.1 (m, 6 H, C_{ar}-O−C*H*$_2$, C*H*), 4.25−4.5 (m, 1 H, C*H*), 5.2−5.45 (m, 4 H, =C*H*−), 6.95 (d, ^3J = 9.1 Hz, 1 H, H_{ar} *m*-C(O)), 7.3−7.5 (m, 2 H, H_{ar}), 7.8−8.8 (m, N*H*); ^{13}C NMR (MeOH-d_4): δ = 14.7 (*C*H$_3$), 23.9, 24.2, 26.7, 27.5, 28.4, 29.5, 29.6, 30.5, 30.6, 30.8, 30.9, 31.0, 31.1, 33.2 (C−*C*H$_2$−C), 40.1, 40.3, 40.9 (C*H*$_2$−N), 53.7, 54.0, 54.6 (*C*H), 70.2, 70.4, 70.6, 70.8, 71.2, 71.4 (*C*H$_2$−O), 113.8, 114.3, 122.2 (C_{ar}H), 118.2 (q, J = 293 Hz, *C*F), 127.8 (C_{ar}−C(O)N), 130.9, 131.0 (=*C*H−CH$_2$), 150.2, 153.8 (C_{ar}−O), 163.0 (q, J = 35 Hz, TFA *C*(O)), 169.9, 170.0, 170.1, 174.0 (*C*(O)); MALDI-MS: m/z = 1127.5 (M + H$^+$).

***N*1-(2−2-[2-((1*S*)-1,4-Di[((1*S*)-1,4-di[(1*S*)-1,4-diaminobutyl]carboxamidobutyl)carboxamido]butylcarboxamido)ethoxy]-ethoxyethyl)-3,4-di[(*Z*)-9-octadecenyloxy]benzamide (TMVLG3).** Deprotecting 1.55 g (650 μmol) of **BocTMVLG3** as described in the general procedure yielded 1.57 g (631 μmol, 97%) of **TMVLG3** as a colorless solid: R_f = 0.26 (2:2:1 CHCl$_3$/ MeOH/ 25% NH$_4$OH); ^{1}H NMR (MeOH-d_4): δ = 0.88 ("t", C*H*$_3$), 0.8−2.3 (m, lg. peaks @ 1.28, 1.35, C−C*H*$_2$−C) (90 H), 2.85−3.85 (m, 26 H, N−C*H*$_2$, O−C*H*$_2$), 3.85−4.25 (m, 8 H, C_{ar}-O−C*H*$_2$, C*H*), 4.25−4.6 (m, 3 H, C*H*), 5.2−5.45 (m, 4 H, =C*H*−), 6.96 (d, ^3J = 9.1 Hz, 1 H, H_{ar} *m*-C(O)), 7.4−7.55 (m, 2 H, H_{ar}), 7.9−8.9 (m, N*H*); ^{13}C NMR (MeOH-d_4): δ = 14.7 (*C*H$_3$), 23.9, 24.2, 26.7, 27.5, 28.3, 29.6, 30.5, 30.6, 30.8, 31.0, 33.2 (C−*C*H$_2$−C), 0.39.7, 40.1, 40.9 (C*H*$_2$−N), 53.7, 54.1, 54.5, 55.1 (*C*H), 70.2, 70.7, 70.8, 71.3 (*C*H$_2$−O), 113.8, 114.3, 122.2 (C_{ar}H), 118.1 (q, J = 292 Hz, *C*F), 127.7 (C_{ar}−C(O)N), 130.9, 131.0 (=*C*H−CH$_2$), 150.2, 153.9 (C_{ar}−O), 163.0 (q, J = 35 Hz, TFA *C*(O)), 170.06, 170.17, 170.21, 170.3, 173.9, 174.2 (*C*(O)); MALDI-MS: m/z = 1583.2 (M + H$^+$).

***N*1-2-[2-(2-[(1*S*)-1,4-Di((1*S*)-1,4-di[(3-aminopropyl)amino]-butylcarboxamido)butyl]carboxamidoethoxy)ethoxy]ethyl-3,4-di[(*Z*)-9-octadecenyloxy]benzamide (TMVLBG1).** Deprotecting 1.15 g (533 μmol) of **BocTMVLBG1** as described in the general procedure yielded 0.96 g (421 μmol, 79%) of **TMVLBG1** as a colorless solid: R_f = 0.49 (solvent mixture B); ^{1}H NMR (MeOH-d_4): δ = 0.88 ("t", C*H*$_3$), 0.7−2.5 (several m, lg. peaks at 1.28, 1.35, C−C*H*$_2$−C) (82 H), 2.85−3.8 (m, 34 H, N−C*H*$_2$, O−C*H*$_2$), 3.8−4.25 (m, 6 H, C_{ar}-O−C*H*$_2$, C*H*), 4.3−4.55 (m, 1 H, C*H*), 5.2−5.45 (m, 4 H, =C*H*−), 6.96 (d, ^3J = 8.6 Hz, 1 H, H_{ar} *m*-C(O)), 7.35−7.55 (m, 2 H, H_{ar}), 7.9−9.1 (m, N*H*); ^{13}C NMR (MeOH-d_4): δ = 14.7 (*C*H$_3$), 22.4, 22.9, 23.9, 25.5, 26.6, 27.5, 28.3, 30.5, 30.6, 30.76, 30.82, 30.97, 31.03, 33.2 (C−C*H*$_2$−C), 38.0, 38.5, 40.5, 40.9, 45.0, 45.8, 46.0, 48.1 (*C*H$_2$−N), 54.9, 61.0, 61.4 (*C*H), 70.2, 70.4, 70.7, 71.3, 71.4 (*C*H$_2$−O), 113.8, 114.3, 122.2 (C_{ar}H), 118.3 (q, J = 293 Hz, *C*F), 127.8 (C_{ar}−C(O)N), 130.9, 131.0 (=*C*H−CH$_2$), 150.2, 153.8 (C_{ar}−O), 163.2 (q, J = 35 Hz, TFA *C*(O)), 168.56, 168.64, 170.0, 173.9 (*C*(O)); MALDI-MS: m/z = 1355.7 (M + H$^+$).

***N*1-[2-(2−2-[((1*S*)-1,4-Di[(1*S*)-1,4-di((1*S*)-1,4-di[(3-aminopropyl)amino]butylcarboxamido)butyl]carboxamidobutyl)-carboxamido]ethoxyethoxy)ethyl]-3,4-di[(*Z*)-9-octadecenyloxy]-benzamide (TMVLBG2).** Deprotecting 910 mg (250 μmol) of **TMVLBG2** as described in the general procedure yielded 910 mg (235 μmol, 94%) of **TMVLBG2** as a colorless solid: R_f = 0.06 (solvent mixture B); ^{1}H NMR (MeOH-d_4): δ = 0.88 ("t", C*H*$_3$), 0.75−2.4 (several m, lg. peaks at 1.28, 1.35, C−C*H*$_2$−C) (106 H), 2.85−3.8 (m, 58 H, N−C*H*$_2$, O−C*H*$_2$), 3.8−4.2 (m, 8 H, C_{ar}-O−C*H*$_2$, C*H*), 4.25−4.6 (m, 3 H, C*H*), 5.2−5.45 (m, 4 H, =C*H*−), 6.97 (d, ^3J = 9.1 Hz, 1 H, H_{ar} *m*-C(O)), 7.35−7.55 (m, 2 H, H_{ar}), 8.0−9.2 (m, N*H*); ^{13}C NMR (MeOH-d_4): δ = 14.6 (*C*H$_3$), 22.5, 22.9, 23.8, 25.5, 26.7, 27.4, 28.3, 28.5, 30.5, 30.6, 30.7, 30.8, 30.95, 31.00, 33.2 (C−C*H*$_2$−C), 38.0, 38.5, 40.1, 40.4, 40.9, 45.0, 45.9, 46.0, 48.2 (*C*H$_2$−N), 54.7, 55.1, 61.0, 61.4 (*C*H), 70.2, 70.5, 70.7, 71.4 (*C*H$_2$−O), 113.9, 114.3, 122.3 (C_{ar}H), 118.2 (q, J = 293 Hz, *C*F), 127.8 (C_{ar}−C(O)N), 130.9, 131.0 (=*C*H−CH$_2$), 150.2, 153.9 (C_{ar}−O), 163.3 (q, J = 34 Hz, TFA *C*(O)), 168.6, 168.7, 168.8, 168.9, 170.1, 173.7, 173.8, 174.3 (*C*(O)); MALDI-MS: m/z = 2040.2 (M + H$^+$).

RESULTS AND DISCUSSION

Lipid Design and Synthesis. Figure 1 shows the general structure of the new dendritic lipids. Their names, headgroup structures, spacer lengths, and charges are compiled in Table 1. All lipids share a hydrophobic moiety based on 3,4-dioleyloxybenzoic acid (DOB) (*46*, *59*). The oleyl chains prevent chain crystallization in the bilayer and confer stable membrane anchoring and miscibility with DOPC and DOPE. The amino acid ornithine is used as an AB$_2$ branching building block in the core of the headgroups. Using a core made up of one or three (1+2) ornithine molecules, and ornithine or carboxyspermine (*45*, *60*, *61*) as end groups, lipids bearing four to 16 amino groups in the headgroup have been prepared. An ethylendiamine- or triethyleneglycol-based linker connects headgroup and DOB. Thus, the lipids enable investigations of the effect of spacer length, high charge density, and charge arrangement (two headgroups bear eight charges, but in different geometry) on complex structure and transfection efficiency.

The synthesis of the dendritic headgroup building blocks is shown in Figure 2. It proceeds similarly to that of multiple antigenic peptides (MAPs) (*62*, *63*) and poly(ethylene glycol)-dendritic oligo-lysine block copolymers (*64*), doubling the number of available amino groups for each generation of ornithine that is coupled onto itself. Ornithine methyl ester is first coupled with 2.2 equiv of Boc-protected ornithine. After deprotection of the amino groups, this process is repeated. Alternatively, the initial or second coupling was performed using Boc-protected carboxyspermine (*45*, *60*, *61*) to yield headgroups of higher charge.

The synthesis of the lipids is illustrated in Figure 3, using MVLG2 and TMVLG2 as examples. The methyl ester of the headgroup building block is subjected to aminolysis with an

Table 1. Abbreviated Names and Spacer Lengths of the Synthesized Lipids, Their Charge, and the Chemical Structures of Their Headgroups

Lipid name	Charge / e		Headgroup structure
	Z_{max} [a]	Z_{exp} [b]	
MVLG2 (n=1) TMVLG2 (n=3)	+ 4	3.98 ± 0.24	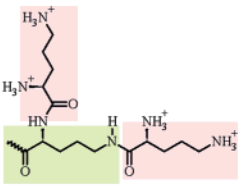
MVLBG1 (n=1) TMVLBG1 (n=3)	+ 8	8.00 ± 0.10	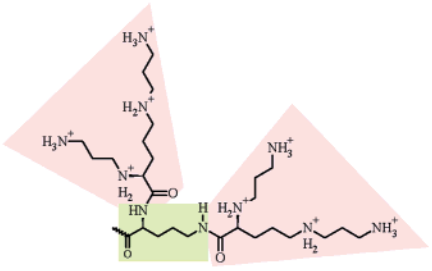
MVLG3 (n=1) TMVLG3 (n=3)	+ 8	7.93 ± 0.26	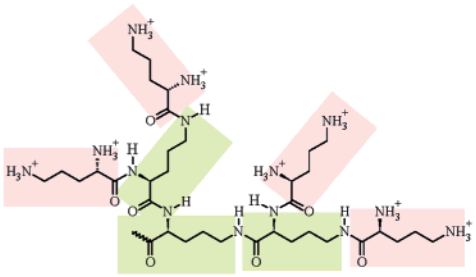
MVLBG2 (n=1) TMVLBG2 (n=3)	+ 16	15.9 ± 1.0	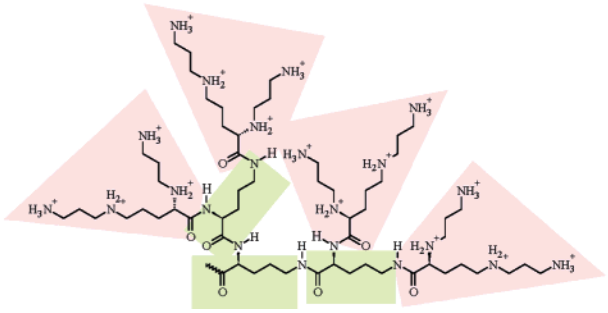

The lipids have the general structure shown in Figure 1. [a] Charge at full protonation. [b] Charge in complex determined by an ethidium bromide displacement assay: see text.

excess of ethylenediamine or 2-[2-(2-aminoethoxy)ethoxy]-ethanamine (α,ω-diaminotriethyleneglycol, NTEG) to yield an amine-functionalized spacer-headgroup building block. This was coupled with DOB (*46*, *59*), and the resulting Boc-protected lipids were purified by flash chromatography and deprotected with TFA. This synthetic route has been carried out on a gram scale and allows facile variation of the spacer length and the headgroup charge by employing other diamines and multivalent headgroup building blocks (*38*, *43*), respectively.

Determination of the Headgroup Charge. We determined the headgroup charge of the lipids effective in DNA complexation with an ethidium bromide (EtBr) displacement assay (*38*, *65*−*67*) and zeta potential measurements. Adding lipid to a mixture of DNA and EtBr reduces the measured fluorescence as EtBr is expelled from the DNA during complex formation and self-quenches in solution. Thus, increasing amounts of lipid were added to a constant amount of DNA and EtBr, recording the resulting fluorescence and normalizing it to the fluorescence without added lipid. The data from this assay is shown in Figure 4: initially, a steep drop in fluorescence with increasing amount of added lipid is observed. The fluorescence then reaches a baseline value. The isoelectric point is obtained from analysis of these data (*68*−*70*), yielding the lipid headgroup charges Z_{exp} documented in Table 1. These data show that the lipids essentially bear their maximal charge when incorporated in the complex. While the lipid charge is calculated from the onset of the baseline value, it is also evident from the data that this final value of the fluorescence varies with the headgroup charge: higher charge corresponds to a lower value for the final fluorescence intensity. Zeta potential measurements confirm the headgroup charges determined by the EtBr displacement assay. This is illustrated in Figure 5, which shows the zeta potential of MVLBG1−DNA complexes as a function of the lipid/DNA charge ratio ρ_{chg}. The zeta potential of the complexes changes sign when ρ_{chg}, calculated using Z_{exp} for the lipid, is unity. Similar results were obtained for lipids of different headgroup charge (MVLG2 and MVLBG2) and for mixtures of the cationic lipids with DOPC (data not shown).

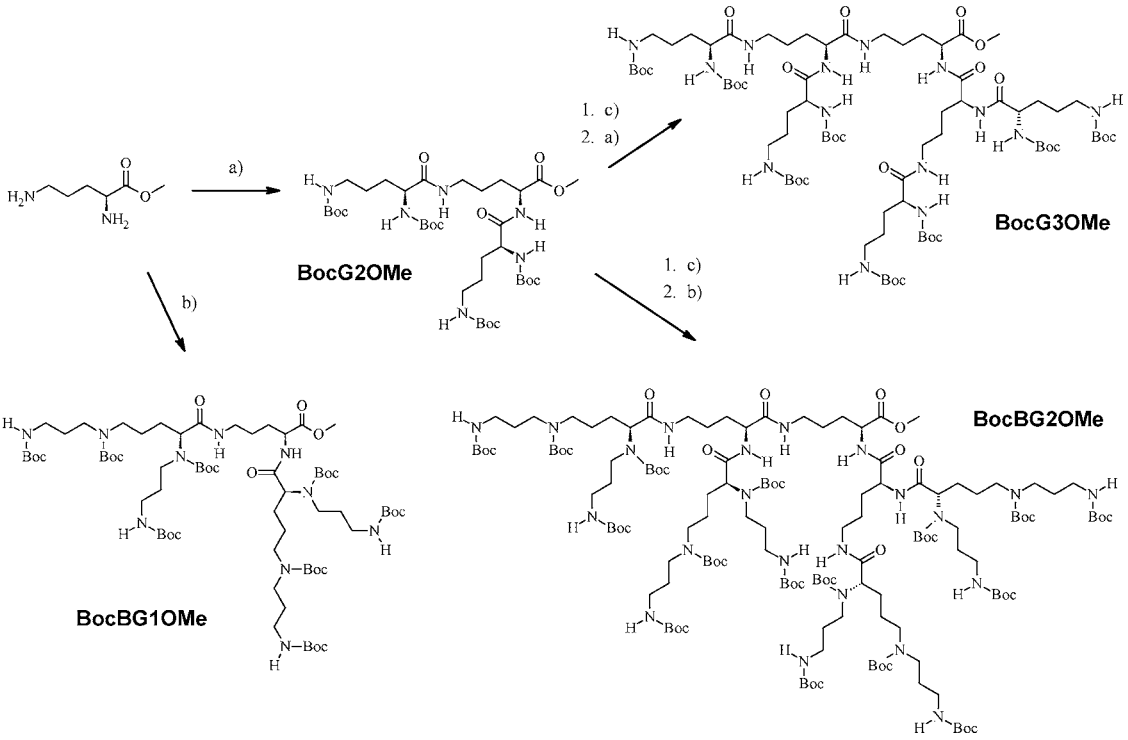

Figure 2. Synthesis of the dendritic headgroup building blocks, starting from ornithine methyl ester. Reaction conditions: (a) Boc-ornithine, TBTU, HOBt, DIEA; (b) Boc-carboxyspermine, TBTU, HOBt, DIEA; (c) TFA. HOBt: 1-hydroxybenzotriazole hydrate; DIEA: *N*,*N*-diisopropylethylamine; TBTU: *O*-benzotriazol-1-yl-*N*,*N*,*N*′,*N*′-tetramethyluronium tetrafluoroborate; TFA: trifluoroacetic acid.

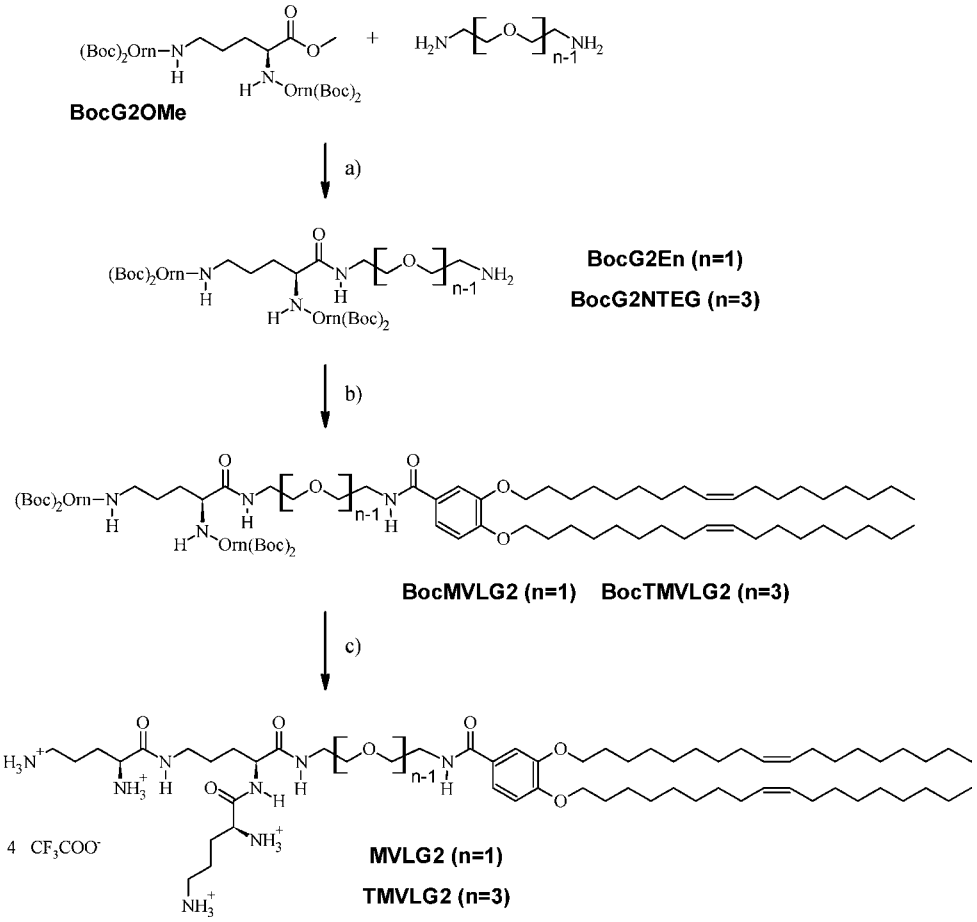

Figure 3. Synthesis of the dendritic cationic lipids **MVLG2** ($n = 1$) and **TMVLG2** ($n = 3$); $Orn(Boc)_2 = C(O)CH(NHBoc)(CH_2)_3NHBoc$. Reaction conditions: (a) excess diamine (20×) in MeOH; b) DOB, TBTU, HOBt, DIEA; (c) TFA. DOB: 3,4-dioleyloxybenzoic acid; HOBt: 1-hydroxybenzotriazole hydrate; DIEA: *N*,*N*-diisopropylethylamine; TBTU: *O*-benzotriazol-1-yl-*N*,*N*,*N*′,*N*′-tetramethyluronium tetrafluoroborate; TFA: trifluoroacetic acid.

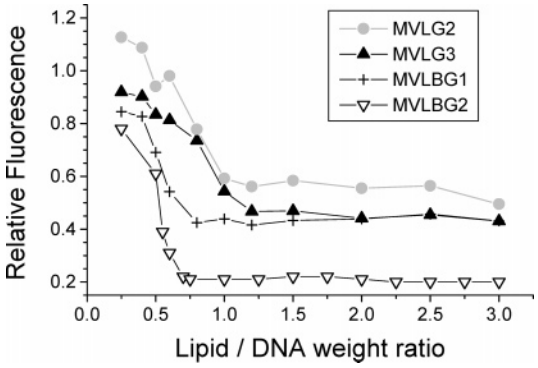

Figure 4. Data from an ethidium bromide (EtBr) displacement assay, used to measure the charge of the dendritic lipids in complexes with DNA. EtBr fluoresces when intercalated into DNA but is expelled by lipid−DNA complex formation, which results in reduced fluorescence intensity due to self-quenching of EtBr in solution. The fluorescence intensity is normalized to that of DNA with EtBr and no lipid.

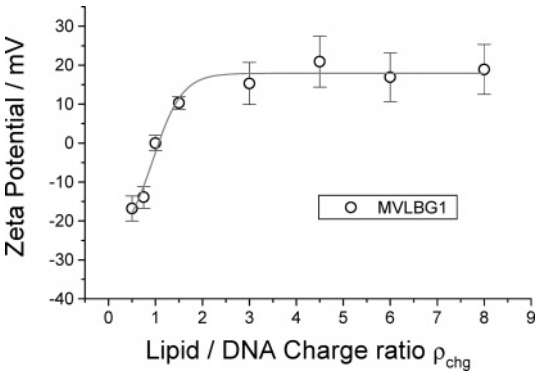

Figure 5. Zeta potential of MVLBG1-DNA complexes as a function of ρ_{chg}. The lipid/DNA charge ratio was calculated using Z_{exp} from the EtBr displacement assay. The line (sigmoidal fit) is a guide to the eye. Note that the zeta potential changes sign at approximately $\rho_{chg} = 1$.

Characterization of CL−DNA complexes. CL−DNA complexes were formed by combining DNA and aqueous lipid preparations consisting of mixtures of DOPC and a dendritic lipid or DOTAP. In addition to performing transfection experiments, we employed small-angle X-ray scattering (SAXS) to characterize the nanoscale internal structure of DNA complexes of the dendritic lipids. All SAXS experiments were performed in the presence of DMEM, the medium used in the transfection experiments. While their structure changes significantly with varying ratio of neutral to cationic lipid (see below), it is not affected by the lipid to DNA charge ratio (ρ_{chg}) above the isoelectric point (*71*). Lipids with identical headgroups but different spacer (MVLs vs TMVLs) and lipids of identical charge but different headgroup structure (G3 vs BG2) yield DNA complexes of similar structure (*71*). The characteristic scattering pattern of the lamellar phase is observed for all complexes of the least highly charged dendritic lipid MVLG2 (charge: 4+) as well as for complexes containing mol fractions below and including 50% and 15% of the lipids with G3/BisG1 (8+) and BisG2 (16+) headgroups, respectively (data not shown). Complexes at certain intermediate contents of highly charged dendritic lipids in the membrane exhibit SAXS patterns indicative of the H_I^C phase (*45*). However, the scattering patterns at the remaining compositions do not correspond to any previously described structure. A detailed investigation of the structures of these complexes is in progress and will be described elsewhere.

Under low ionic strength conditions, all lipid DNA complexes (at $\rho_{chg} \neq 1$) form particles of about 200 nm size. These aggregate in the higher salt conditions of, e.g., cell medium, resulting in μm-sized particles that vary in size over time (*56*).

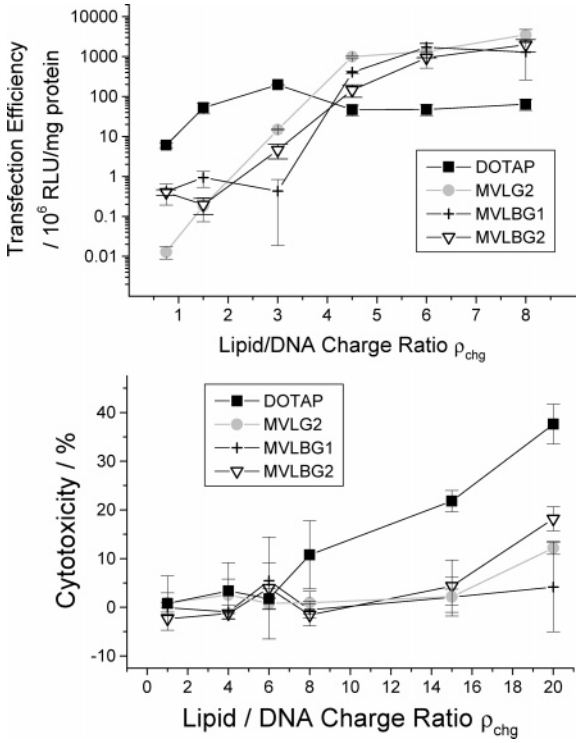

Figure 6. Transfection efficiency (top) and cytotoxicity (bottom) of DNA complexes containing 60 mol % cationic lipid at various lipid/DNA charge ratios. Note the difference in scale of the charge ratio axes. The amount of DNA is constant for all data points.

Consistent with this, fluorescence microscopy of dendriticlipid−DNA complexes shows colocalization of lipid and DNA and complex particles with dimensions on the μm scale, consisting of aggregates of globular submicron particles (*45*).

Cell Transfection and Cytotoxicity. We have measured the transfection efficiencies of DNA complexes of the dendritic lipids in mouse L cells using a luciferase reporter gene assay and compare them to the standard monovalent lipid DOTAP. The headgroup charge dominates the transfection behavior of the lipids, while neither the spacer length nor the headgroup architecture have a significant effect (*71*). Thus, in the following we show data for three lipids representing the three different headgroup charges, MVLG2 (4+), MVLBG1 (8+), and MVLBG2 (16+). In these experiments, both the lipid to DNA charge ratio ρ_{chg} and the ratio of cationic lipid and neutral DOPC in the membrane were varied.

For DOTAP, TE increases with ρ_{chg} up to a saturation value; this behavior is independent from the composition of the membrane (*72*). A similar trend is observed for the dendritic lipids, but with saturation occurring at a higher charge ratio: $\rho_{chg} = 3$ lies in the saturated regime for DOTAP, while all dendritic lipids require at least $\rho_{chg} = 4.5$ (*71*). This is illustrated in Figure 6 (top), which shows transfection efficiencies of complexes with 60 mol % cationic lipid for DOTAP, MVLG2, MVLBG1, and MVLBG2 at various values of ρ_{chg}. Cell toxicities of the complexes were measured using a commercially available assay that probes cell membrane integrity. Figure 6 (bottom) shows the cytotoxicity of CL−DNA complexes as a function of ρ_{chg}, at 60 mol % cationic lipid. Note the different scale of the ρ_{chg}-axis when comparing with the transfection efficiency plot. For all lipids, only charge ratios exceeding those required for efficient transfection produce any notable toxicity. Furthermore, the onset of the curve is much delayed for the dendritic lipids in comparison with DOTAP, demonstrating their reduced cytotoxicity.

In Figure 7 (top), TE of complexes at $\rho_{chg} = 6$ is plotted against the composition of the membrane. The plots for all lipids

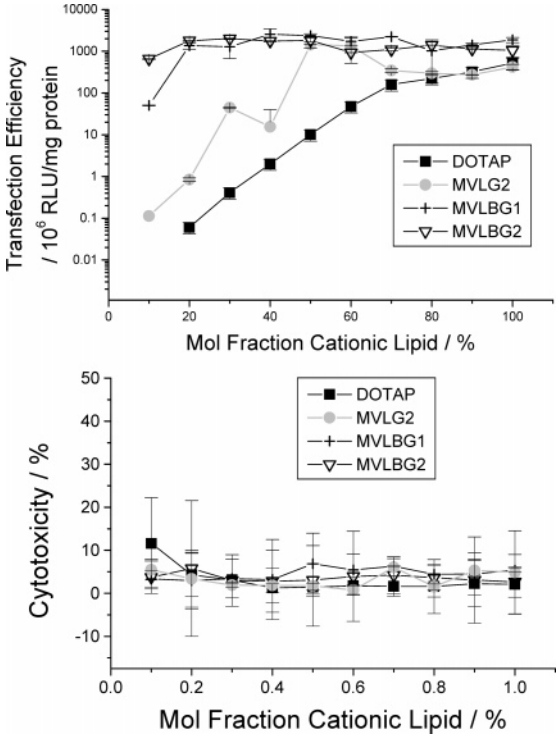

Figure 7. Transfection efficiency (top) and cytotoxicity (bottom) of DNA complexes of DOTAP, MVLG2, MVLBG1, and MVLBG2 plotted against the mol fraction of cationic lipid in mixtures with DOPC. All data points were taken at a lipid/DNA charge ratio of 6, using a constant amount of DNA.

show an initial, exponential rise with increasing mol fraction of cationic lipid. The higher the headgroup charge of the lipid, the lower the mol fraction of cationic lipid where this rise occurs, consistent with our previous findings on the relevance of membrane charge density (*37*, *38*). Thus, optimal transfection can be achieved with mol fractions as small as 10% (MVLBG2) or 20% (MVLBG1). Since the cationic lipid is the more expensive lipid component in CL−DNA complexes, this is advantageous for potential applications. Interestingly, the highly charged lipids MVLBG1 and MVLBG2 do not show the drop in TE at higher mol fractions (very high charge densities) that has been observed for multivalent lipids of charge 2+ to 5+ (*38*). This deviation coincides with a structural transition, away from the lamellar complex structure (*71*). As expected from the data shown in Figure 6, no significant cytotoxicity is observed for any of the complexes (Figure 7 (bottom)). This further confirms that the dendritic lipids are a safe and efficient DNA delivery vector. Of note, DNA complexes of MVLBG2 were shown to be much superior over those of DOTAP in a "hard to transfect" mouse embryonic fibroblast cell line (*45*).

Currently, we are conducting further experiments with the dendritic lipids. The high headgroup charge of multivalent lipids appears to be particularly advantageous for transfections with siRNA, which require very high lipid to DNA charge ratios.

ACKNOWLEDGMENT

This work was supported by NIH GM59288. Our NMR characterization work made use of MRL Central Facilities supported by the MRSEC Program of the National Science Foundation under award No. DMR00-80034.

LITERATURE CITED

(1) Extensive and current information on clinical trials in the field of gene therapy can be found on the Internet at http://www.wiley.co.uk/genetherapy/clinical/. See ref 32 for a compilation of open trials as of July 2004.

(2) Griesenbach, U., Geddes, D. M., and Alton, E. W. F. W. (1999) Cystic Fibrosis Gene Therapy. In ref 15, pp 337−356.

(3) Smyth-Templeton, N., and Lasic, D. D., Eds. (2000) *Gene Therapy. Therapeutic Mechanisms and* Strategies, Marcel Dekker Inc., New York.

(4) Mahato, R. I. and Kim, S. W., Eds. (2002) *Pharmaceutical Perspectives of Nucleic Acid-Based Therapeutics*, Taylor and Francis, London and New York.

(5) McManus, M. T., and Sharp, P. A. (2002) Gene Silencing in Mammals by Small Interfering RNAs. *Nature Rev. Genet. 3*, 737.

(6) Dorsett, Y., and Tuschl, T. (2004) siRNAs: Applications in Functional Genomics and Potential as Therapeutics. *Nature Rev. Drug Discovery 3*, 318.

(7) Caplen, N. J. (2004) Gene Therapy Progress and Prospects: Downregulating Gene Expression: the Impact of RNA interference. *Gene Ther. 11*, 1241.

(8) Sioud, M. (2004) Therapeutic siRNAs. *Trends Pharm. Sci. 25*, 22.

(9) Smith, A. E. (1995) Viral Vectors in Gene Therapy. *Annu. Rev. Microbiol. 49*, 807.

(10) Kay, M. A., Glorioso, J. C., and Naldini, L. (2001) Viral vectors for gene therapy: the art of turning infectious agents into vehicles of therapeutics. *Nature Med. 7*, 33.

(11) a) Marshall, E. (2000) Gene Therapy on Trial. *Science 288*, 951. (b) Marshall, E. (2002) What to Do When Clear Success Comes With an Unclear Risk? *Science 298*, 510.

(12) Huang, L., Hung, M.-C., and Wagner, E., Eds. (2005) *Advances in Genetics, Vol. 53: Non-Viral Vectors for Gene Therapy*, 2nd ed., Part I, Elsevier, San Diego.

(13) Huang, L., Hung, M.-C., and Wagner, E., Eds. (1999) *Nonviral Vectors for Gene Therapy*, Academic Press, San Diego.

(14) Felgner, P. L., Heller, M. J., Lehn, P., Behr, J.-P., and Szoka, F. C., Eds. (1996) *Artificial self-assembling systems for gene delivery*, American Chemical Society, Washington, DC.

(15) Felgner, P. L., Gader, T. R., Holm, M., Roman, R., Chan, H. W., Wenz, M., Northrop, J. P., Ringold, G. M., and Danielsen, M.(1987) Lipofection: A highly efficient, lipid-mediated DNA-transfection procedure. *Proc. Natl. Acad. Sci. U.S.A. 84*, 7413.

(16) Byk, G., Dubertret, C., Escriou, V., Frederic, M., Jaslin, G., Rangara, R., Pitard, B., Crouzet, J., Wils, P., Schartz, B., and Scherman, D. (1998) Synthesis, Activity, and Structure−Activity Relationship Studies of Novel Cationic Lipids for DNA Transfer. *J. Med. Chem. 41*, 224.

(17) Remy, J.-S., Sirlin, C., Vierling, P., and Behr, J.-P. (1994) Gene Transfer with a Series of Lipophilic DNA-Binding Molecules. *Bioconjugate Chem. 5*, 647.

(18) Boussif, O., Lezoualc′h, F., Zanta, M. A., Mergny, M. D., Scherman, D., Demeneix, B., and Behr, J.-P. (1995) A versatile vector for gene and oligonucleotide transfer into cells in culture and *in vivo*: Polyethylenimine. *Proc. Natl. Acad. Sci. U.S.A. 92*, 7297.

(19) Haensler, J., and Szoka, F. C. (1993) Polyamidoamine Cascade Polymers Mediate Efficient Transfection of Cells in Culture. *Bioconjugate Chem. 4*, 372.

(20) Miller, A. D. (2003) The Problem with Cationic Liposome/Micelle Based Non-Viral Vector Systems for Gene Therapy. *Curr. Med. Chem. 10*, 1195.

(21) Bosman, A. W., Janssen, H. M., and Meijer, E. W. (1999) About Dendrimers: Structure, Physical Properties, and Applications. *Chem. Rev. 99*, 1665.

(22) Fischer, M., and Vögtle, F. (1999) Dendrimers: From Design to Application − A Progress Report. *Angew. Chem., Int. Ed. 38*, 884.

(23) Frechet, J. M. J., and Tomalia, D. A., Eds. (2001) *Dendrimers and Other Dendritic Polymers*, Wiley, Chichester.

(24) Tang, M. X., Redemann, C. T., and Szoka, F. C. Jr. (1996) In Vitro Gene Delivery by Degraded Polyamidoamine Dendrimers. *Bioconjugate Chem. 7*, 703.

(25) Kukowska-Latallo, J. F., Bielinska, A. U., Johnson, J., Spindler, R., Tomalia, D. A., and Baker, J. R., Jr. (1996) Efficient transfer of genetic material into mammalian cells using Starburst polyamidoamine dendrimers. *Proc. Natl. Acad. Sci. U.S.A. 93*, 4897.

(26) Kukowska-Latallo, J. F., Raczka, E., Quintana, A., Chen, C. L., Rymaszewski, M., and Baker, J. R. Jr. (2000) Intravascular and endobronchial DNA delivery to murine lung tissue using a novel, nonviral vector. *Human Gene Ther. 11*, 1385.

(27) Rudolph, C., Lausier, J., Naundorf, S., Müller, R. H., and Rosenecker, J. (2000) *In vivo* gene delivery to the lung using polyethylenimine and fractured polyamidoamine dendrimers. *J. Gene Med. 2*, 269.
(28) Ohsaki, M., Okuda, T., Wada, A., Hirayama, T., Niidome, T., and Aoyagi, H. (2002) In Vitro Gene Transfection Using Dendritic Poly(L-lysine). *Bioconjugate Chem. 13*, 510.
(29) Evans, H. M., Ahmad, A., Ewert, K., Pfohl, T., Martin-Herranz, A., Bruinsma, R. F., and Safinya, C. R. (2003) Structural polymorphism of DNA-dendrimer complexes. *Phys. Rev. Lett. 91*, 075501.
(30) Kim, T. I., Seo, H. J., Choi, J. S., Jang, H. S., Baek, J. U., Kim, K., and Park, J. S. (2004) PAMAM-PEG-PAMAM: Novel Triblock Copolymer as a Biocompatible and Efficient Gene Delivery Carrier. *Biomacromolecules 5*, 2487.
(31) Miller, A. D. (1998) Cationic Liposomes for Gene Therapy. *Angew. Chem., Int. Ed. 37*, 1768.
(32) Zabner, J. (1997) Cationic lipids used in gene transfer. *Adv. Drug Delivery Rev. 27*, 17.
(33) Behr, J.-P. (1994) Gene Transfer with Synthetic Cationic Amphiphiles: Prospects for Gene Therapy. *Bioconjugate Chem. 5*, 382.
(34) Byk, G., and Scherman, D. (2000) Genetic Chemistry: Tools for Gene Therapy Coming From Unexpected Directions. *Drug Dev. Res. 50*, 566.
(35) Chesnoy, S., and Huang, L. (2000) Structure and Function of Lipid-DNA Complexes for Gene Delivery. *Annu. Rev. Biophys. Biomol. Struct. 29*, 27.
(36) de Lima, M. C. P., Simões, S., Pires, P., Faneca, H., and Düzgüneş, N. (2001) Cationic lipid-DNA complexes in gene delivery: from biophysics to biological applications. *Adv. Drug Delivery Rev. 47*, 277.
(37) Lin, A. J., Slack, N. L., George, C. X., Samuel, C. E., and Safinya, C. R. (2003) Three-Dimensional Imaging of Lipid Gene-Carriers: Membrane Charge Density Controls Universal Transfection Behavior in Lamellar Cationic Liposome-DNA Complexes. *Biophys. J. 84*, 3307.
(38) Ahmad, A., Evans, H. M., Ewert, K., George, C. X., Samuel, C. E., and Safinya, C. R. (2005) New multivalent lipids reveal bell curve for transfection efficiency versus membrane charge density: lipid-DNA complexes for gene delivery. *J. Gene Med. 7*, 739.
(39) Ewert, K., Evans, H. M., Ahmad, A., Slack, N. L., Lin, A. J., Martin-Herranz, A., and Safinya, C. R. (2005) Lipoplex Structures and Their Distinct Cellular Pathways. In ref 14, pp 119−155.
(40) Koltover, I., Salditt, T., Rädler, J. O., and Safinya, C. R. (1998) An Inverted Hexagonal Phase of Cationic Liposome-DNA Complexes Related to DNA Release and Delivery. *Science 281*, 78.
(41) Rädler, J. O., Koltover, I., Salditt, T., and Safinya, C. R. (1997) Structure of DNA-Cationic Liposome Complexes: DNA Intercalation in Multilamellar Membranes in Distinct Interhelical Packing Regimes. *Science 275*, 810.
(42) Lin, A. J., Slack, N. L., Ahmad, A., Koltover, I., George, C. X., Samuel, C. E., and Safinya, C. R. (2000) Structure and structure−function studies of lipid/plasmid DNA complexes. *J. Drug Targeting 8*, 13.
(43) Ewert, K., Slack, N. L., Ahmad, A., Evans, H. M., Lin, A. J., Samuel, C. E., and Safinya, C. R. (2004) Cationic lipid-DNA complexes for gene therapy: Understanding the relationship between complex structure and gene delivery pathways at the molecular level. *Curr. Med. Chem. 11*, 133.
(44) Ewert, K., Ahmad, A., Evans, H. M., and Safinya, C. R. (2005) Cationic lipid-DNA complexes for non-viral gene therapy: relating supramolecular structures to cellular pathways. *Expert Opin. Biol. Ther. 5*, 33.
(45) Ewert, K. K., Evans, H. M., Zidovska, A., Bouxsein, N. F., Ahmad, A., and Safinya, C. R. (2006) A Columnar Phase of Dendritic Lipid-Based Cationic Liposome-DNA Complexes for Gene Delivery: Hexagonally Ordered Cylindrical Micelles Embedded in a DNA Honeycomb Lattice. *J. Am. Chem. Soc. 128*, 3998.
(46) Ewert, K., Ahmad, A., Evans, H. M., Schmidt, H.-W., and Safinya, C. R. (2002) Efficient Synthesis and Cell-Transfection Properties of a New Multivalent Cationic Lipid for Nonviral Gene Delivery. *J. Med. Chem. 45*, 5023.
(47) Cooper, R. G., Etheridge, C. J., Stewart, L., Marshall, J., Rudginsky, S., Cheng, S. H., and Miller, A. D. (1998) Polyamine Analogues of DC−Chol as Agents for Gene Delivery. *Chem. Eur. J. 4*, 137.
(48) Behr, J.-P., Demeneix, B., Leffler, J.-P., and Perez-Mutul J. (1989) Efficient Gene Transfer into Mammalian Primary Endocrine Cells with Lipopolyamine-Coated DNA. *Proc. Natl. Acad. Sci. U.S.A. 86*, 6982.
(49) Dewa, T., Ieda, Y., Morita, K., Wang, L., MacDonald, R. C., Iida, K., Yamashita, K., Oku, N., and Nango, M. (2004) Novel Polyamine−Dialkyl Phosphate Conjugates for Gene Carriers. Facile Synthetic Route via an Unprecedented Dialkyl Phosphate. *Bioconjugate Chem. 15*, 824.
(50) Sugiyama, M., Matsuura, M., Takeuchi, Y., Kosaka, J., Nango, M., and Oku, N. (2004) Possible mechanism of polycation liposome (PCL)-mediated gene transfer. *Biochim. Biophys. Acta 1660*, 24.
(51) Usol'tseva, N., Bykova, V., Smirnova, A., Grusdev, M., Lattermann, G., and Facher, A. (2004) Induction of mesomorphic properties in poly(propylene imine) dendrimers and their model compounds. *Mol. Cryst. Liquid Cryst. 409*, 29.
(52) Grohn, F., Bauer, B. J., and Amis, E. J. (2001) Hydrophobically modified dendrimers as inverse micelles: Formation of cylindrical multidendrimer nanostructures. *Macromolecules 34*, 6701.
(53) Schenning, A. P. H. J., Elissenroman, C., Weener, J. W., Baars, M. W. P. L., Vandergaast, S. J., and Meijer, E. W. (1998) Amphiphilic Dendrimers as Building Blocks in Supramolecular Assemblies. *J. Am. Chem. Soc. 120*, 8199.
(54) Leventis, R., and Silvius, J. R. (1990) Interactions of mammalian cells with lipid dispersions containing novel metabolizable cationic amphiphiles. *Biochim. Biophys. Acta 1023*, 124.
(55) Still, W. C., Kahn, M., and Mitra, A. (1978) Rapid Chromatographic Technique for Preparative Separations with Moderate Resolution. *J. Org. Chem. 43*, 2923.
(56) Koltover, I., Salditt, T., and Safinya, C. R. (1999) Phase Diagram, Stability, and Overcharging of Lamellar Cationic Lipid-DNA Self-Assembled Complexes. *Biophys. J. 77*, 915.
(57) Due to the sensitivity of the methyl ester to hydrolysis, immediate workup of the reaction mixture is mandatory after the addition of water.
(58) This compound elutes faster than estimated by thin-layer chromatography, probably because its retention factor increases with its concentration.
(59) Schulze, U., Schmidt, H.-W., and Safinya, C. R. (1999) Synthesis of Novel Cationic Poly(ethylene glycol)-Containing Lipids. *Bioconjugate Chem. 10*, 548.
(60) Behr, J.-P. (1989) Photohydrolysis of DNA by polyaminobenzenediazonium salts. *J. Chem. Soc., Chem. Commun.* 101.
(61) Huber, M., Pelletier, J. G., Torossian, K., Dionne, P., Gamache, I., Charest-Gaudreault, R., Audette, M., and Poulin, R. (1996) 2,2-Dithiobis(N-ethyl-spermine-5-carboxamide) Is a High Affinity, Membrane-impermeant Antagonist of the Mammalian Polyamine Transport System. *J. Biol. Chem. 271*, 27556.
(62) Veprek, P., and Jezek, J. (1999) Peptide and Glycopeptide Dendrimers. Part I. *J. Pept. Sci. 5*, 5.
(63) Veprek, P., and Jezek, J.(1999) Peptide and Glycopeptide Dendrimers. Part II. *J. Pept. Sci. 5*, 203.
(64) Choi, J. S., Lee, E. J., Choi, Y. H., Jeong, Y. J., and Park, J. S. (1999) Poly(ethyleneglycol)-*block*-poly(L-lysine) Dendrimer: Novel Linear Polymer/Dendrimer Block Copolymer Forming a Spherical Water-Soluble Polyionic Complex with DNA. *Bioconjugate Chem. 10*, 62.
(65) Gershon, H., Ghirlando, R., Guttman, S. B., and Minsky, A. (1993) Mode of Formation and Structural Features of DNA-Cationic Liposome Complexes Used for Transfection. *Biochemistry 32*, 7143.
(66) Akao, T., Fukumoto, T., Ihara, H., and Ito, A. (1996) Conformational change in DNA induced by cationic bilayer membranes. *FEBS Lett. 391*, 215.
(67) Eastman, S. J., Siegel, C., Tousignant, J., Smith, A. E., Cheng, S. H., and Scheule, R. K. (1997) Biophysical characterization of cationic lipid: DNA complexes. *Biochim. Biophys. Acta-Biomembr. 1325*, 41.
(68) The data from the EtBr assay was fit to a sigmoidal curve to determine the isoelectric point. For MVLBisG2, the small number of data points at high fluorescence prevented accurate fitting, and the previously described procedure was used to analyze the data (see ref 43).
(69) Ham, Y. W., Tse, W. C., and Boger, D. L. (2003) High-resolution assessment of protein DNA binding affinity and selectivity utilizing

a fluorescent intercalator displacement (FID) assay. *Bioorg. Med. Chem. Lett. 13*, 3805.
(70) Boger, D. L., Fink, B. E., Brunette, S. R., Tse, W. C., and Hedrick, M. P. (2001) A simple, high-resolution method for establishing DNA binding affinity and sequence selectivity. *J. Am. Chem. Soc. 123*, 5878.
(71) Evans, H. M. Ph.D. Dissertation, University of California, Santa Barbara, California 2005.
(72) Slack, N. Ph.D. Dissertation, University of California, Santa Barbara, California 2000.

BC050310C

Synthesis and Characterization of Monomolecular DNA G-Quadruplexes Formed by Tetra-End-Linked Oligonucleotides

Giorgia Oliviero,[†] Jussara Amato,[†] Nicola Borbone,[†] Aldo Galeone,[†] Luigi Petraccone,[‡] Michela Varra,[†] Gennaro Piccialli,*[,†] and Luciano Mayol[†]

Dipartimento di Chimica delle Sostanze Naturali, Università degli Studi di Napoli "Federico II", Via D. Montesano 49, I-80131 Napoli, Italy, and Dipartimento di Chimica, Università degli Studi di Napoli "Federico II", Via Cintia, I-80126 Napoli, Italy. Received January 17, 2006; Revised Manuscript Received May 18, 2006

Guanine-rich DNA sequences are widely dispersed in the eukaryotic genome and are abundant in regions with relevant biological significance. They can form quadruplex structures stabilized by guanine quartets. These structures differ for number and strand polarity, loop composition, and conformation. We report here the syntheses and the structural studies of a set of interconnected d(TG_4T) fragments which are tethered, with different orientations, to a tetra-end-linker in an attempt to force the formation of specific four-stranded DNA quadruplex structures. Two synthetic strategies have been used to obtain oligodeoxyribonucleotide (ODN) strands linked with their 3′- or 5′-ends to each of the four arms of the linker. The first approach allowed the synthesis of tetra-end-linked ODN (TEL-ODN) containing the four ODN strands with a parallel orientation, while the latter synthetic pathway led to the synthesis of TEL-ODNs each containing antiparallel ODN pairs. The influence of the linker at 3′- or 5′-ODN, on the quadruplex typology and stability, in the presence of sodium or potassium ions, has been investigated by circular dichroism (CD), CD thermal denaturation, ^{1}H NMR experiments at variable temperature, and molecular modeling. All synthesized TEL-ODNs formed parallel G-quadruplex structures. Particularly, the TEL-ODN containing all parallel ODN tracts formed very stable parallel G-quadruplex complexes, whereas the TEL-ODNs containing antiparallel ODN pairs led to relatively less stable parallel G-quadruplexes. The molecular modeling data suggested that the above antiparallel TEL-ODNs can adopt parallel G-quadruplex structures thanks to a considerable folding of the tetra-end-linker around the whole quadruplex scaffold.

INTRODUCTION

DNA quadruple helices (quadruplexes) based on guanine (G)[1] quartets have recently emerged as biologically important structures (*1*−*4*). G-rich sequences, which are found primarily in telomeric region at 3′-end of chromosomes, are able to fold into G-quadruplex structures. It has been suggested that quadruplex formation could inhibit the telomere maintenance provided by telomerase activity thus affecting the lifespan of the cells of a number of cancer types characterized by a high level of telomerase expression (*5*−*8*). Furthermore, studies on the oncogene *c-MYC*, involved in a number of malignancies, have demonstrated the existence of G-quadruplex structures in vivo which can be considered useful targets to repress c-MYC transcription (*9*−*11*). G-quadruplex structures are present in the scaffold of several aptamers provided with useful biological properties (*12*−*16*), as well as within the insulin gene-linked polymorphic region of the human insulin gene, in vivo, where they may play a role in the expression of the insulin gene (*17*). G-quadruplexes, have been also put forth as DNA structures capable of transferring electrons through the G-quadruplex π-stack and forming nanowires for molecular nanoelectronics (*18*−*20*). Within this framework, a number of studies have been undertaken to investigate the DNA G-quadruplexes and, particularly, to define the factors that can stabilize them as well as proposing synthetic ODN analogues capable of forming novel quadruplex typologies.

G-quadruplexes can be classified based upon the number of strands involved in the structure, their relative orientation and the glycosidic conformation of guanosine residues (anti or syn). The stability of G-quadruplexes mainly depends on the number of G-tetrad planes, the molecularity of the complex, and the nature of cations which accommodate themselves in the central channel of the quadruplex lowering the energy of the complex (*1*−*3*). Normally, the molecularity of the complex induces well defined patterns in the relative ODN strand orientation. The monomolecular complexes largely involved in biomolecular events (*1*−*4*) are prevalently of antiparallel type even if examples of parallel monomolecular complexes have been discovered (*21*−*24*). Tetramolecular complexes, which have recently displayed interesting biological properties (*25*−*27*), always show the four strands in a parallel orientation. However, the development of therapeutic applications for such ODN complexes has been so far prevented by their unfavorable kinetic and thermodynamic parameters. It is a fact that the in vitro formation of a tetramolecular quadruplex is very slow and may require high ODN and salt concentrations (*28*). On the contrary, monomolecular quadruplexes are mostly characterized by high stability and fast kinetic formation (*1*−*3*). On these bases, the construction of new and stable monomolecular quadruplexes possessing unusual strand orientation could expand their employment in both the study and control of important biological processes as well as in DNA-based nanotechnologies. Several studies have investigated the effect of loops on quadruplex stability and typology (*29*−*35*). With regard to

* Corresponding author. E-mail: picciall@unina.it. Voice: +39-081-678541. Fax: +39-081-678552.

† Dipartimento di Chimica delle Sostanze Naturali.

‡ Dipartimento di Chimica.

[1] Abbreviations: ODN, oligodeoxyribonucleotide; TEL, tetra-end-linked; CD, circular dichroism; G, guanine; Fmoc, fluorenylmethoxycarbonyl; DMT, 4,4′-dimethoxytrityl; NMI, 1-methylimidazole; MSNT, 1-(2-mesitylenesulfonyl)-3-nitro-1*H*-1,2,4-triazole; DCA, dichloracetic acid; TEAB, triethylammonium bicarbonate; CPG, controlled pore glass; TBE, Tris-borate electrophoresis.

10.1021/bc060009b CCC: $33.50 © 2006 American Chemical Society
Published on Web 06/23/2006

Scheme 1. Synthetic Procedures for Quadruplexes I and II[a]

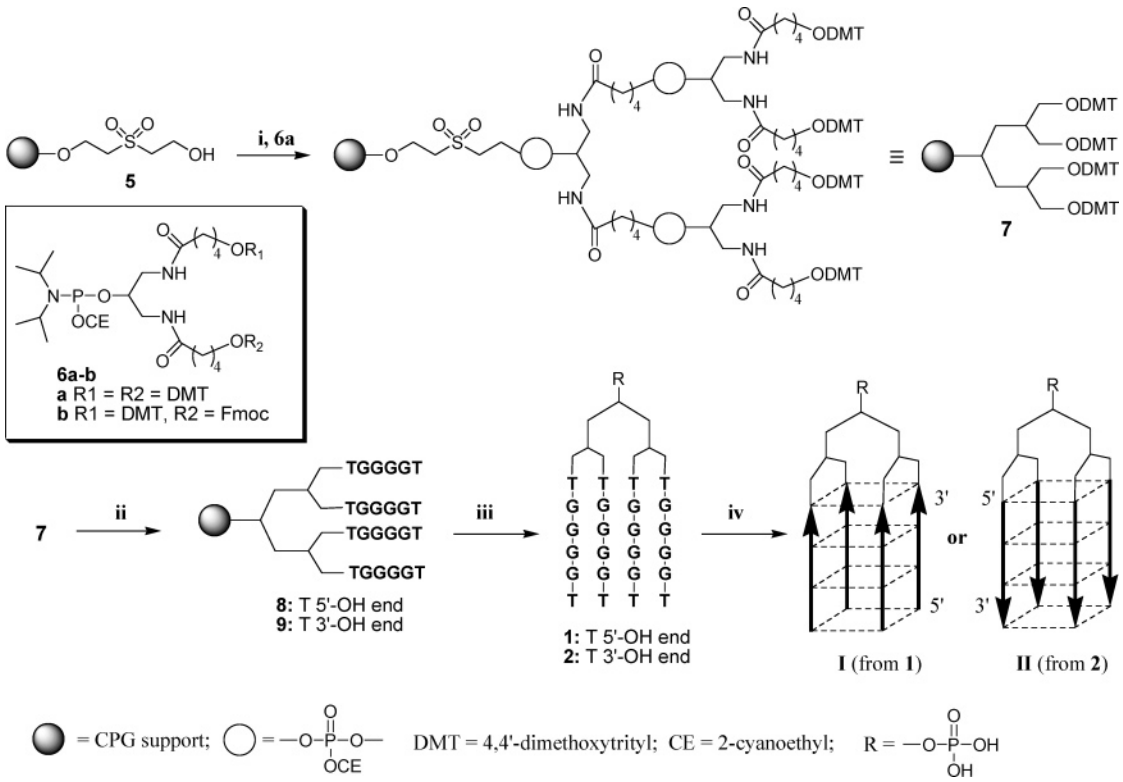

[a] i: two couplings with **6a**; ii: ODN synthesis with 3′ or 5′-phosphoramidites; iii: detachment and deprotection with NH_4OH concd 32% (7 h, 55 °C); iv: HPLC purification and annealing.

nucleotidic loops, the base composition, the length, and the orientation of the phosphodiester linkage have already been examined (*29*−*34*). In addition, mono- or bimolecular quadruplexes formed by circular ODNs have been shown to display noteworthy thermal and enzymatic degradation stability (*35*). In another reported approach aimed at studying the effect of the connecting loops on the stability and typology of the monomolecular quadruplexes, non nucleotidic linkers have been inserted between d(GGG) tracts into a single ODN strand (*30*). In this case both the kinetics of the quadruplex formation and the complex stabilities were found to be affected by the nature of the linker.

Starting from these observations, we recently proposed the synthesis of a new modified ODN (TEL-ODN, **1**, Scheme 1) capable of forming the monomolecular parallel G-quadruplex **I** (Scheme 1) whose thermal stability has been proved to be significantly higher than that observed for its tetramolecular counterpart $[d(TG_4T)]_4$ (*36*). The main structural feature of this molecule is the presence of four ODN strands whose 3′-ends are attached to a non nucleotidic tetra-end-linker. Furthermore, TEL-ODNs were also shown to be a useful tool to study quadruplexes containing less stable quartets such as T-tetrad (*37*).

We wish to report here our study on the influence of the tetra-end-linker placement on the typology and stability of this kind of quadruplexes. Two synthetic strategies have been used to obtain $d(TG_4T)$ ODN strands which were linked with their 3′ or 5′-ends to each of the four arms of the linker. The first approach allowed the synthesis of the TEL-ODNs containing the four ODN strands with a parallel orientation (**1**, **2**, Scheme 1) while the latter synthetic pathway led to the synthesis of TEL-ODNs each containing antiparallel ODN pairs (**3**, **4**, Scheme 2). CD, CD melting, NMR spectroscopy, and molecular modeling have been used to investigate the solution structures of the resulting TEL-quadruplexes **I**−**IV** (Schemes 1 and 3) formed in the presence of sodium or potassium ions.

EXPERIMENTAL PROCEDURES

Reagents and Equipment. Chemicals and solvents were purchased from Fluka-Sigma-Aldrich. Reagents and phosphoramidites for DNA syntheses were purchased from Glen Research. ODN syntheses were performed on a PerSeptive Biosystems Expedite. HPLC analyses and purifications were performed by a JASCO PU2089 pumps equipped with UV detector 2075 Plus using a Merck Hibar (5 μm, 250−10) column. CPG support **5** and linkers **6a**,**b** were purchased from Glen Research. Tentagel carboxy resin, used as starting material for preparation of solid support **10**, was purchased from Novabiochem. Preparation of **10** was carried out in a short column (10 cm length, 1 cm i.d.) equipped with a sintered glass filter, a stopcock and a cap. The ODNs were assembled by a PerSeptive Biosystems Expedite DNA synthesizer using phosphoramidite chemistry. UV spectra were run with a Jasco V 530 spectrophotometer. CD spectra and thermal denaturation experiments were obtained with a Jasco 715 circular dichroism spectrophotometer equipped with a JASCO 505T temperature controller unit. NMR spectra were recorded on a Varian Unity Inova 500 MHz spectrometer. MALDI-TOF mass spectrometric analyses were performed on a PerSeptive Biosystems voyager-De Pro MALDI mass spectrometer using a picolinic/3-hydroxypicolinic acids mixture as the matrix. The ODN concentration was determined spectrophotometrically at $\lambda = 260$ nm and 90 °C, using the molar extinction coefficient $\epsilon = 57800\ cm^{-1}\ M^{-1}$ calculated for the unstacked oligonucleotide by the nearest neighbor mode (*38*).

Synthesis and Purification of TEL-ODNs 1 and 2. 50 mg of support **5** (0.048 mequiv/g) was used for each synthesis in the automated DNA synthesizer following standard phosphoramidite chemistry, using 45 mg/mL of solution of phosphoramidite **6a** (two coupling cycles) and 3′- or 5′-phosphoramidite nucleotide building block (six cycles) in anhydrous CH_3CN, thus obtaining the polymer bound ODN **8** and **9**, respectively. The coupling efficiency with nucleotide units was consistently

Scheme 2. Synthetic Procedures for Quadruplexes III and IV[a]

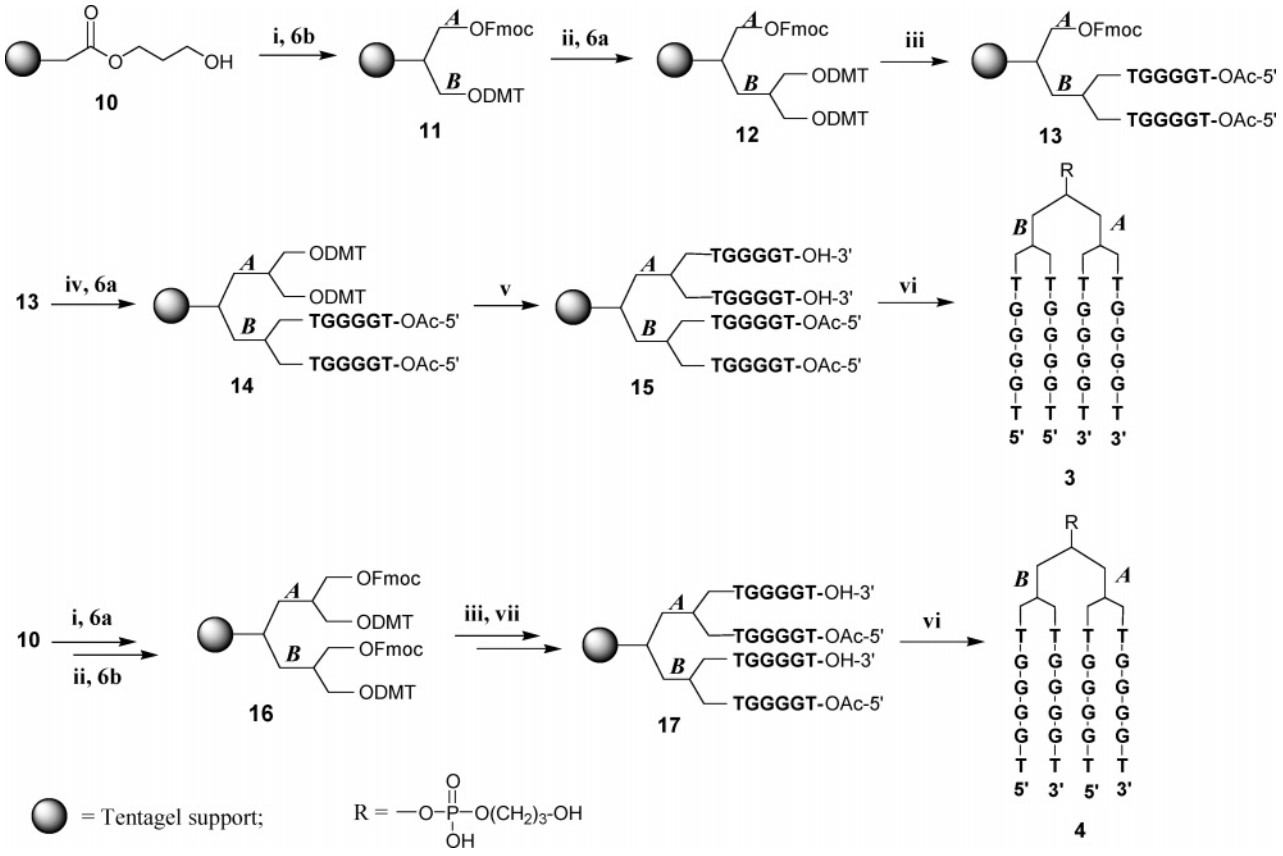

[a] i: coupling with linker **6**; ii: DMT removal and coupling with linker **6**; iii: ODN synthesis with 3′-phosphoramidites; iv: Fmoc removal and coupling with linker **6a**; v: ODN synthesis with 5′-phosphoramidites; vi: detachment and deprotection with NH_4OH concd 32% (7 h, 55 °C) and HPLC purification; vii: Fmoc removal and ODN synthesis with 5′-phosphoramidites;

Scheme 3. Quadruplexes III and IV from TEL-ODNs 3 and 4 after the Annealing Procedure in K^+ or Na^+ Buffer

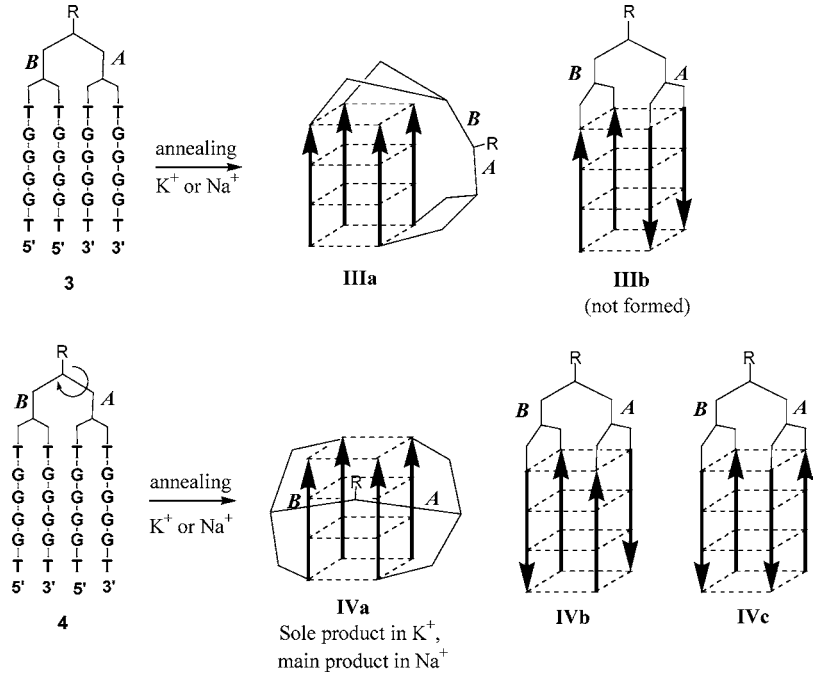

higher than 98% (by DMT spectrophotometric measurements). The solid support **8** (or **9**) was then treated with 25% aq ammonia solution for 7 h at 55 °C. The filtered solution and washings were concentrated under reduced pressure and purified by HPLC on a RP18 column eluted with a linear gradient CH_3CN in TEAB buffer (pH 7.0, from 0 to 100% in 60 min, flow 1.0 mL/min), retention time 26.1 and 27.0 min for **1** and **2**, respectively. The collected peaks furnished pure **1** and **2** (72 and 77 OD_{260} units, respectively) which, after lyophilization, were characterized by spectroscopic data.

TEL-ODN **2**: MALDI TOF-MS (negative mode): calculated mass (8763.7); found: 8762.6.

Preparation of Support 10. 500 mg of Tentagel carboxy resin (0.28 mequiv/g of COOH) suspended in CH_2Cl_2 were left

in contact with a CH_2Cl_2 solution (7.0 mL) containing 1,3-dihydroxypropane (0.56 mmol, 0.36 mL), NMI (0.56 mmol, 0.40 mL) and MSNT (0.056 mmol, 1.48 g) and the mixture was shaken for 36 h at room temperature. The obtained hydroxy-support **10** was exhaustively washed with CH_2Cl_2 and then dried under reduced pressure. The amount of hydroxyl groups, determined by DMT measurements after the successive coupling step with 3′-phosphoramidite nucleotide units, resulted to be in the range 0.18−0.20 mequiv/g.

Synthesis and Purification of TEL-ODNs 3 and 4. 50 mg of support **10** (0.18 mequiv/g) reacted, in the automated DNA synthesizer, with phosphoramidite **6b** (45 mg/mL in CH_3CN) following standard phosphoramidite chemistry at 15-μmol scale, yielded support **11** (0.17 mequiv/g of DMT groups). After removal of the DMT group by DCA/standard treatment, the second coupling cycle was performed in the same manner using phosphoramidite **6a**, thus obtaining support **12** (0.30 mequiv/g of DMT groups). **12** was then subjected to six coupling cycles using 3′-phosphoramidite nucleotide building blocks (45 mg/mL in CH_3CN, 15-μmol scale), followed by final DMT removal and 5′-OH capping with Ac_2O, to yield ODN-functionalized support **13**. The removal of Fmoc groups was achieved by treatment with piperidine/DMF solution (2:8 v/v, 30 min RT). The resulting support was then reacted with phosphoramidite **6a**, thus obtaining **14** (0.27 mequiv/g of DMT groups). On branches A of **14** the second ODN domain was assembled, performing six coupling cycles with the 5′-phosphoroamidite nucleotide building block as described for support **12**, yielding the polymer bound ODN **15**.

For the synthesis of **4**, support **10** (50 mg) was functionalized with **6a** and then **6b**, as described before, yielding the tetra-branched support **16** (0.28 mequiv/g of DMT groups). After removal of the DMT protecting groups, the first two ODN chains were assembled, using 3′-phosphoramidite nucleotide building blocks. After capping of the terminal 5′-OH functions by Ac_2O treatment, the Fmoc groups were removed as previously described, and the successive two ODN chains were assembled using 5′-phosphoroamidite nucleotide building blocks, thus obtaining the polymer bound ODN **17**.

TEL-ODNs were detached from the supports **15** and **17**, deprotected, and purified as described for **1** and **2**, thus obtaining **3** and **4** (retention time 25.8 and 25.2 min, respectively). After lyophilization, the final pure products **3** and **4** (68 and 62 OD_{260} units, respectively) were characterized by spectroscopic data.

TEL-ODN **3**: MALDI TOF-MS (negative mode): calculated mass (8821.7); found: 8820.5.

TEL-ODN **4**: MALDI TOF-MS (negative mode): calculated mass (8821.7); found: 8820.2

Preparation of Quadruple Helices (Annealing). Quadruplexes **I**−**IV** were formed by dissolving the TEL-ODNs **1**−**4**, in the appropriate buffer and annealed by heating to 90 °C for 20 min followed by slow cooling to room temperature. The solutions were equilibrated at 10 °C for 24 h before performing the experiments. The buffers used were 10 mM Na_2HPO_4, 70 mM NaCl, 0.2 mM EDTA (Na^+ buffer) or 10 mM K_2HPO_4 70 mM KCl, and 0.2 mM EDTA (K^+ buffer).

Native Gel Electrophoreses. Native gel electrophoreses were run on 20% nondenaturing polyacrylamide gels in 0.6x TBE buffer, pH 7.0, with 50 mM NaCl. ODN solutions, with a final concentration of 300 μM in quadruplex, were prepared in 50 mM Tris-borate pH 7.0, 80 mM NaCl, 1 mM spermine, and 3 mM $MgCl_2$ and annealed as above-described. At 2 μL of the ODN solution (300 μM in quadruplex) was then added 1 μL of 30% glycerol and the mixture charged on gel. The gels were run at room temperature at constant voltage (100 V) for 2.5 h. The bands were visualized by UV shadowing.

CD Experiments. CD spectra of the quadruplexes were registered on a Jasco 715 circular dichroism spectrophotometer in a 0.1 cm path length cuvette at 25 and 90 °C at 1.0×10^{-5} and 5.0×10^{-5} M quadruplex concentrations. The wavelength was varied from 220 to 320 nm at 5 nm min^{-1}. The spectra were recorded with a response of 16 s, at 2.0 nm bandwidth and normalized by subtraction of the background scan with buffer. CD thermal denaturation−renaturation experiments were performed monitoring the CD value (mdeg) at 264 nm in the range 25−90 °C with 1 °C/min heating rate.

^{1}H NMR Experiments. ^{1}H NMR data were collected on a Varian Unity INOVA 500 spectrometer equipped with a broad-band inverse probe with z-field gradient and processed using Varian VNMR software package. 1D NMR spectra were acquired as 16384 data points with a recycle delay of 1.0 s at temperatures in the range 25−85 °C. Data sets were zero filled to 32768 points prior to Fourier transformation and apodized with a shifted sinebell squared window function. Pulsed-field gradient WATERGATE (*39*) sequence was used for H_2O suppression. All NMR samples **I**−**IV** were prepared in H_2O/D_2O (9:1, v/v) at 0.5 mM of quadruplex concentration with a final salt concentration of 100 mM KCl and 10 mM K_2HPO_4 or 100 mM NaCl and 10 mM Na_2HPO_4 for K^+ or Na^+ buffer, respectively.

Molecular Modeling. The conformational features of the quadruplexes **III** and **IV** have been explored by means of molecular modeling study. All the calculations were performed on a personal computer running the HyperChem 7.5 suite of programs. The AMBER force field based on AMBER 99 parameter set was used (*40*). The initial coordinates for the starting model of $[d(TGGGGT)]_4$ quadruplex were taken from the NMR solution structure of the $[d(TTGGGGT)]_4$ quadruplex (Protein Data Bank entry number 139D), choosing randomly one of the four available structures. The initial $[d(TGGGGT)]_4$ quadruplex models were built by deletion of the 5′-end tymidine residue in each of the four TTGGGGT strands. The complete structures of **III** and **IV** were then built using the HyperChem 7.5 building tool. Partial charges for each of the tetra-end-linker atoms were assigned using the Gasteiger-Marsili algorithm (*41*) implemented in the QSAR module of HyperChem suite. The resulting coordinates of tetra-end-linker's atoms were energy-minimized in a vacuum, keeping all DNA coordinates frozen (500 cycles of the steepest descent method). Three sodium ions were manually positioned in the central channel, equidistant from adjacent G-tetrads to allow octahedral coordination with G carbonyl oxygen O6 atoms. The two complexes were neutralized by addition of further 26 sodium ions placed in the most negative positions of the systems. Each quadruplex was then solvated by a periodic TIP3P water box (5833 water molecules) (*42*), which extended to a distance of 10 Å from each atom. The minimal distance between water and system atoms was set to 2.3 Å. The whole systems were initially subjected to energy minimization followed by 50 ps of molecular dynamics at 300 K, and then the systems were slowly cooled at 10 K. The obtained structures were further minimized using 1000 cycles of the steepest descent method followed by conjugate gradient method until convergence to a rms gradient of 0.1 kcal mol^{-1} $Å^{-1}$.

RESULTS AND DISCUSSION

Synthesis and Purification of TEL-ODNs 1−4. In the synthesis of the TEL-ODNs **1**−**4** we used two hydroxy-functionalized solid supports (**5** and **10**) and the bifunctional linkers **6a,b**. Support **5** (0.048 mequiv/g), by way of two coupling cycles with **6a** by an automatic DNA synthesizer, was turned into support **7** bearing a symmetrical tetra-end-linker with four protected primary alcoholic functions prone to ODN-chain

assembly (0.085 mequiv/g of OH functions, by DMT spectrophotometric test). Support **7** was used to synthesize the TEL-ODNs **1** and **2** in which the four ODN strands were attached to the tetra-end-linker by the same end (3′- and 5′-end, respectively). ODN chains were assembled on **7** by using 3′- or 5′-phosphoramidite nucleotide building blocks, thus obtaining the polymer bound TEL-ODNs **8** and **9**, respectively. In both syntheses coupling yields were higher than 98% per cycle, thus reducing the amounts of TEL-ODNs having one or more truncated chains. The presence of a β-sulfone phosphodiester function connecting the linker to the solid support, allows the release of the TEL-ODN via a β-elimination under basic treatment. In this way supports **8** and **9**, treated with concentrated NH_4OH (7 h, 55 °C), afforded crude TEL-ODNs **1** and **2**, which after HPLC purification and the annealing procedure, furnished the quadruplex **I** and **II**, respectively.

As a further step of this work we synthesized the TEL-ODNs **3** and **4** (Scheme 2). In **3** a pair of strands was linked to the primary linker branch A through the 5′-ends whereas the second pair is linked to the primary branch B through the 3′-ends. Instead **4** is characterized by both branches (A and B) carrying two strands linked through opposite ends. For the preparation of **3** and **4**, we adopted two synthetic strategies both based upon bifunctional linker **6b** in which the two alcoholic functions, thanks to the orthogonal protection with Fmoc and DMT groups, allowed the sequential synthesis of the ODN chains with opposite polarity. **10** was used as solid support since, when **5** was used, we observed the release of ODN material from the support during the Fmoc deprotection step, due to the concomitant β-elimination at the sulfone group. Therefore, we prepared the hydroxy-functionalized support **10** bearing an ester function, stable under Fmoc deprotection conditions but cleavable by ammonia treatment, to release the assembled TEL-ODN. Support **10** (0.18−0.20 mequiv/g of OH groups), prepared by reacting a carboxy-functionalized Tentagel resin (0.28 mequiv/g of COOH groups) with 1,3-dihydroxypropane in the presence of MSNT and NMI (*43*), was used in two synthetic pathways leading to the TEL-ODNs **3** and **4**. Support **10**, by reaction with the phosphoramidite linker **6b** yielded the asymmetrical protected bifunctional support **11** (0.17 mequiv/g by DMT test) which, after removal of DMT protection from the branch B and successive reaction with linker **6a** furnished the three-functionalized support **12**. Six coupling cycles with 3′-phosphoramidite units, performed as described for **7**, and a final capping step of the 5′-OH ODN ends, gave **13**. Then the 5′-Fmoc group was removed from the branch A by piperidine treatment, and the successive coupling with **6a** yielded **14**. On **14** the second ODN domain was assembled using 5′-phosphoramidite units, thus obtaining polymer bound TEL-ODN **15**. The synthetic pathway to obtain **4** started with reaction of **10** with **6a** and subsequently **6b** as described above, thus obtaining the tetra-branched support **16** (0.28 mequiv/g by DMT). The removal of DMT groups, followed by ODN synthesis with 3′-phosphoramidite units, allowed the assembly of the first pair of ODN chains. After Fmoc deprotection, the remaining ODN pair having opposite polarity was then assembled using 5′-phosphoramidite units, thus obtaining **17**. Detachment from the solid support and complete deprotection of the TEL-ODNs **3** and **4** were achieved treating supports **15** and **17** with concentrated NH_4OH as described for **1** and **2**. Analyses and purifications of crude products **1**−**4** were carried out by HPLC using an RP18 column. The purity of the products was checked by PAGE, and the structures were confirmed by ^1H NMR and MALDI-MS data. The quadruple helices were obtained by dissolving the samples **1**−**4** in Na^+ or K^+ buffers and by the annealing procedure to ensure the correct formation of quadruplex structures.

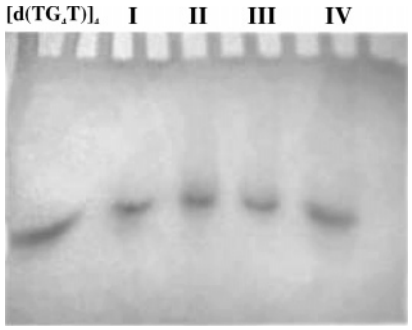

Figure 1. Nondenaturing gel analysis of **I**−**IV** and $[d(TG_4T)]_4$ (20% polyacrylamide), Tris-borate (TBE), pH 7.0. The samples were annealed in Na^+ buffer. The bands were visualized by UV shadowing.

Native Gel Electrophoresis. The purity of the products **1**−**4** and the molecularity of the complexes obtained were investigated by performing a nondenaturing polyacrylamide gel electrophoresis (Figure 1) in comparison to the tetramolecular quadruplex $[d(TG_4T)]_4$. The samples (300 μM quadruplex) were annealed in Na^+ buffer, and the electrophoretic analysis was carried out using a 20% polyacrylamide gel in TBE buffer. TEL-quadruplexes **I**−**IV** and $d[(TG_4T)]_4$ migrated as single bands demonstrating quite similar mobilities. This result, besides indicating the purities of **I**−**IV**, strongly suggests that they form monomeric species at this concentration.

CD and CD Thermal Analysis. To investigate whether TEL-ODNs **2**−**4** adopt quadruplex structures and, if such is the case, determine their nature and stability, we carried out CD studies, including CD thermal denaturation experiments, which were compared with those already reported for **1** (*36*) and their tetramolecular counterpart $[d(TG_4T)]_4$ (*27*, *38*). The ODN samples were analyzed in Na^+ or K^+ buffers after the annealing procedure. CD spectra (Figure 2) were performed at 25 and 90 °C at a quadruplex concentration of 1.0×10^{-5} and 5.0×10^{-5} M. TEL-ODNs **1**, **2** and $[d(TG_4T)]_4$ showed almost identical CD profiles in K^+ buffer at 25 °C, characterized by positive and negative bands centered around 264 and 244 nm, respectively, which are indicative of a parallel stranded G-quadruplex structure (*36*, *44*−*47*). Upon the basis of these findings, it is reasonable to hypothesize that the TEL-ODN **2**, bearing the tetra-end-linker at the 5′-end of quadruplex, adopts the parallel G-quadruplex structure **II**. The data also suggest that **3** and **4** adopt parallel G-quadruplex structures which, considering the mutual antiparallel orientation of the ODN pairs, can be explained only by hypothesizing that a considerable folding of the linker around the whole G-quadruplex takes place. The parallel structures adopted by **3** and **4** were substantiated by molecular modeling studies (see below) that clearly indicate that these conformations are obtainable and stable as a result of the linker arrangement as shown in Figure 4 and schematically depicted in **IIIa** and **IVa** (Scheme 3).

CD spectra of **1**−**3** and $[d(TG_4T)]_4$ in Na^+ buffer at 25 °C match those observed in K^+ showing positive and negative bands at 262 and 244 nm, respectively, whereas in the CD profile of **4** in Na^+ buffer a slight shift of the positive and negative bands at 259 and 239 nm, respectively, takes place. Furthermore, in the latter the presence of a new lower positive band centered at 289 nm is observable. These data indicate that even in Na^+ buffer, possessing a lower stabilizing effect on G-quadruplex structures when compared to K^+ buffer (*3*, *48*), the TEL-ODN **1**−**3** are structured in parallel quadruplexes. For **4** in Na^+ buffer we hypothesize the coexistence of two or more conformational species, among which the parallel (main) **IVa** and the antiparallel (minor) **IVb**,**c** structures are present, considering that most antiparallel G-quadruplexes are characterized by a positive band centered at 290−295 nm and a negative

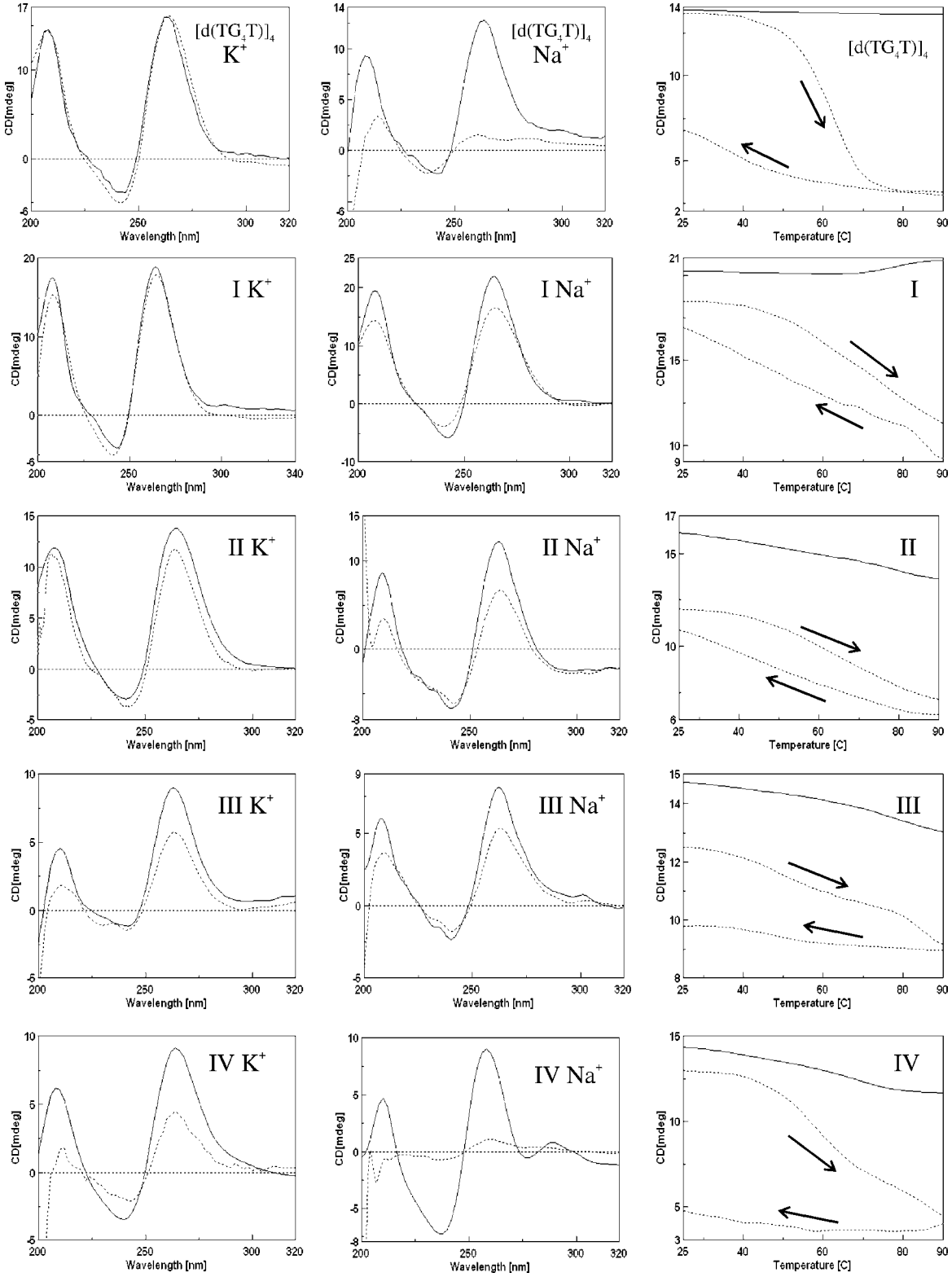

Figure 2. CD and CD melting spectra of **I**−**IV** and d[$(TG_4T)]_4$ in K^+ buffer (left column), in Na^+ buffer (middle column) at 25 °C (solid line) and 90 °C (dotted line). CD_{265} melting profiles (right column) in K^+ (solid line) and Na^+ (dotted line).

band centered around 265 nm (*44*−*47*). CD spectra of **1**−**4** and d[$(TG_4T)]_4$ at 90 °C for both buffers are reported in Figure 2. The data in K^+ buffer confirm that the parallel G-quadruplex structures are completely retained in the complexes **I** and **II** while a detectable destructuration can be observed for complexes **III** and **IV**. CD spectra in Na^+ at 90 °C suggest that complexes **I**−**III** retain, to some extent the characteristic parallel G-quadruplex profile, while complex **IV** and d[$(TG_4T)]_4$ are completely unstructured to random coils.

CD thermal denaturation−renaturation experiments were performed monitoring the CD value (mdeg) at 265 nm in the range 25−90 °C with 1 °C/min temperature scan rate. CD melting curves in K^+ buffer for quadruplexes **I**, **II** and d[$(TG_4T)]_4$ underwent irrelevant or low CD_{265} variations up to 90 °C while a relatively high CD_{265} variation was shown by the complexes **III** and **IV**. The melting profiles of the complexes **I**−**IV** and d[$(TG_4T)]_4$ in Na^+ showed higher CD_{265} variation with respect to the corresponding values registered in K^+;

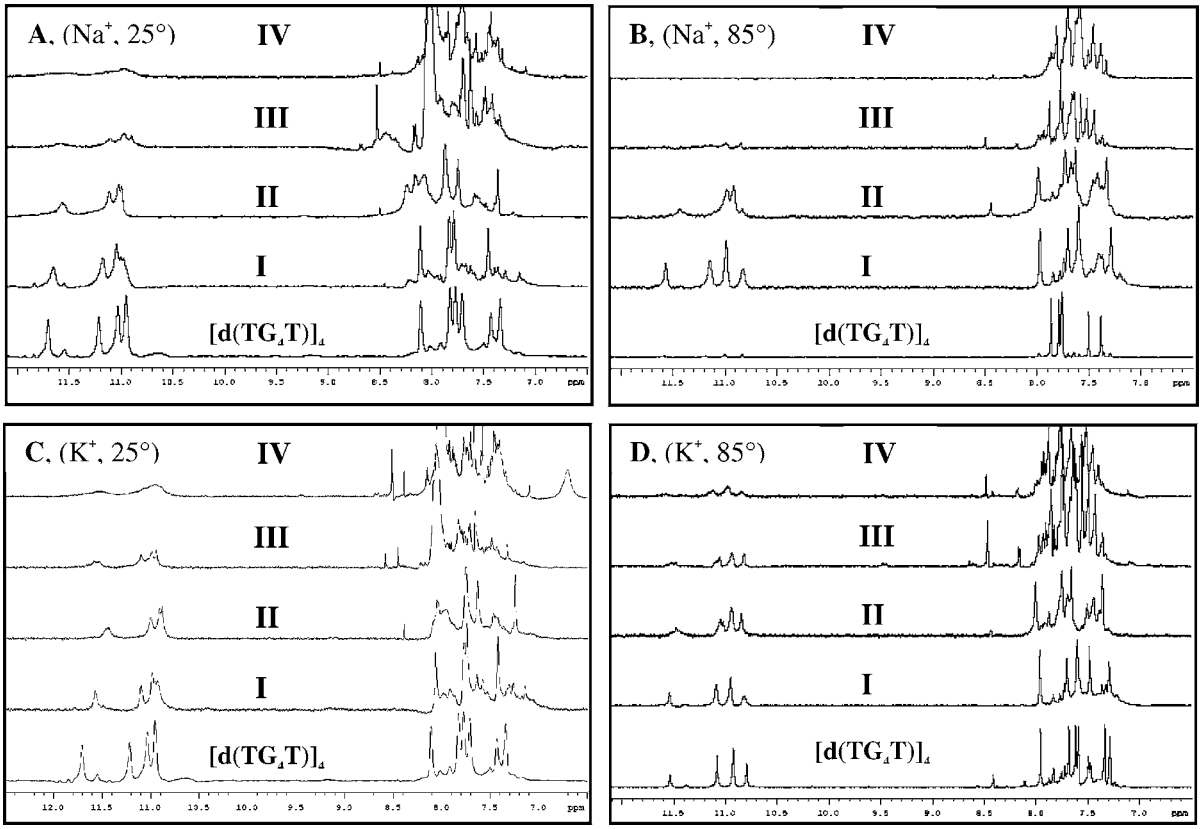

Figure 3. ^{1}H NMR (500 MHz) spectra of **I**−**IV** and $[d(TG_4T)]_4$ in Na^+ and K^+ buffers. The spectra were registered in H_2O/D_2O, (9:1, v/v) solution at 0.5 mM of quadruplex at 25 and 85 °C. The aromatic and imino proton regions of the spectra are reported.

however, only for the $[d(TG_4T)]_4$ complex was a typical and derivatizable sigmoidal curve (T_m = 59 °C) registered. These data indicate that the melting process for the complexes **I**−**III** in Na^+ is not complete at 90 °C, while a complete melting of **IV** can be observed in Na^+ at this temperature. However, considering the shape of the apparent sigmoidal curve and the possible polymorphism of **IV**, we could not determine its melting temperature in both buffers. We also registered the CD_{265} thermal renaturation curves for all complexes in the range 90−25 °C. For the tetramolecular $[d(TG_4T)]_4$ complex, as expected, a very slow renaturation process and a high hysteresis phenomenon was indicated by the profile of the renaturation curve at 1 °C/min scan rate. The renaturation curves of **I** and **II** showed relatively low hysteresis at the same temperature scan rate. The fast reformation of the complexes **I** and **II** was also confirmed by the CD spectrum profiles registered at the end of the renaturation processes (data not shown). In the case of complexes **III** and **IV** the renaturation curves showed high hysteresis associated with low restructuration levels.

^{1}H NMR Studies on Quadruplexes I−IV and $[d(TG_4T)]_4$. ^{1}H NMR studies on quadruplexes **I**−**IV** were performed, after annealing, in the same buffers used for CD measurements. The spectrum of **I** and **II**, recorded in Na^+ buffer at 25 °C (Figure 3A), showed the presence of four singlets in the range 10.9−11.8, two of them partially overlapped, attributable to exchange protected imino protons involved in Hoogsteen N(1)/O(6) hydrogen bonds of G-quartets (*45*, *48*, *49*). These signals were almost superimposable with those observed in the spectrum of the $[d(TG_4T)]_4$ complex already characterized by NMR data (*50*). The ^{1}H NMR spectra recorded in Na^+ buffer at 85 °C (Figure 3B) indicated that **I** is completely stable at least up to 85 °C. **II** is partially preserved (only two imino proton signals are still detectable at this temperature), whereas the tetramolecular complex $[d(TG_4T)]_4$ is completely unstructured as indicated by the disappearance of all the imino proton signals. Upon the basis of these data, it appears that quadruplex **II** in Na^+ buffer is more stable than the tetramolecular counterpart, yet it is less stable than quadruplex **I**. The ^{1}H NMR spectra of **I**, **II**, and $[d(TG_4T)]_4$ recorded in K^+ buffer displayed quite similar signal patterns; however, it was not possible to observe any quenching of the imino proton signals up to 85 °C (Figure 3D). This observation is in accordance with reported data about the capability of K^+ cations to form more stable quadruplex structures in comparison with those observed in Na^+ buffer (*51*). As expected, ^{1}H NMR spectra of **III** indicated that this compound is more structured in K^+ than in Na^+ buffer. In K^+ buffer it was possible to detect the four imino proton signals up to 85 °C (Figure 3C and 3D), whereas in Na^+ the spectrum showed large imino proton signals at 25 °C (Figure 3A) which almost disappeared at 85 °C (Figure 3B). The ^{1}H NMR spectra of **IV** at 25 °C showed very large and overlapped imino proton signals both in Na^+ (Figure 3A) and K^+ buffers (Figure 3C). The increase of temperature for ^{1}H NMR spectra of **IV** led to the sharpening of all imino proton signals both in Na^+ and K^+ buffers. In K^+ buffer at least three imino proton signals are clearly detectable even at 85 °C (Figure 3D), whereas in Na^+ buffer all imino proton signals are completely lost since 65 °C (data not shown). These data, which are consistent with UV and CD experiments, indicate that both complexes **III** and **IV** result in less stable quadruplex structures than **I** and **II**. Furthermore, **III** results more stable than **IV** especially in K^+ buffer.

Molecular Modeling. To explore the capability of TEL-ODNs **3** and **4** of adopting the parallel quadruplex structure **IIIa** and **IVa**, respectively, a modeling study was performed. The minimized structures obtained are shown in Figure 4. Inspection of these structures reveals that in both **IIIa** and **IVa**, the tetra-end-linker is able to span the distance between the 5′- and 3′-ends of the strands assembled in parallel quadruplex structure. It can be noted that the orientation of the linker with respect to the helical axis is different in **IIIa** and **IVa**

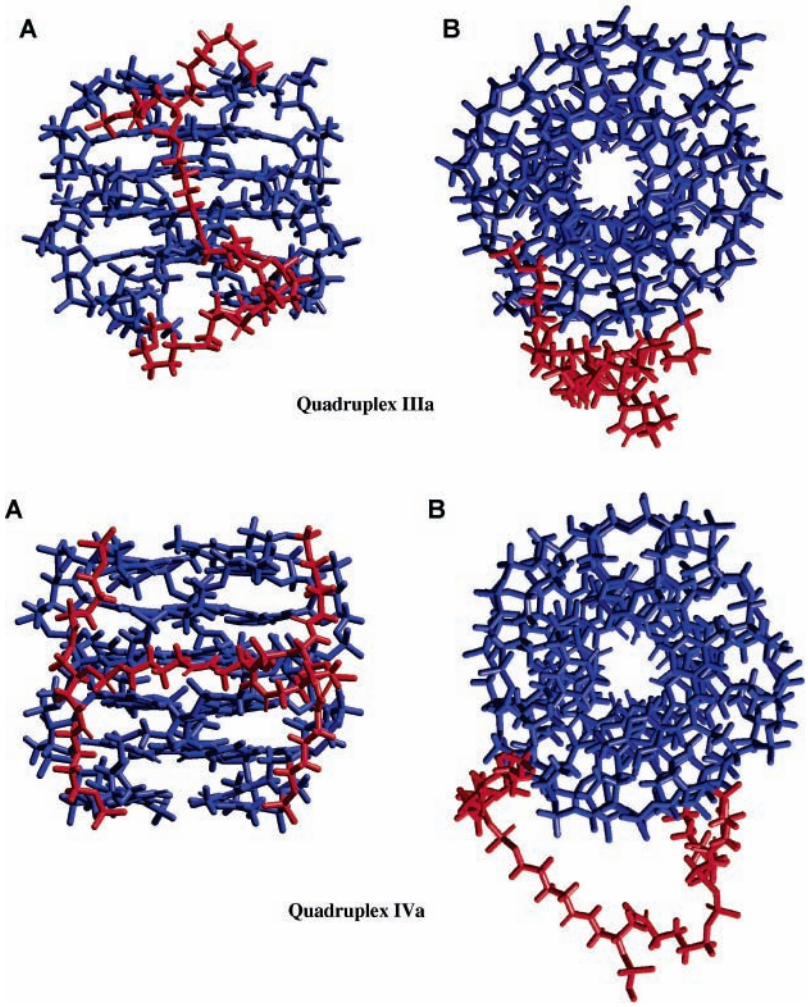

Figure 4. Molecular model pictures of quadruplex structures **IIIa** and **IVa**; A: front view; B: top view. The tetra-end-linker is in red.

quadruplexes. For both the complexes the interatomic distances between the linker atoms and the quadruplex groove hydrogen bonding sites suggest the possibility of favorable nonbonded interactions. Although the integrity of the G-tetrads is maintained after energy minimization for both complexes, a detailed analysis of the H-bonds scheme inside the G-tetrads reveals some differences between the quadruplexes. In particular, in **IIIa**, each G-tetrad shows the same hydrogen bond scheme with an optimum distance and angle between donor and acceptor atoms, resulting in strong hydrogen bonds. Indeed in **IVa** there is a change of hydrogen-bond distances and angles between adjacent quartets, and, on average, two hydrogen bonds for each G-tetrad are lost. Furthermore, the degree of coplanarity between the G residues in each G-tetrad is greater in **IIIa** than in **IVa**. It is important to point out that the perturbation of each G-tetrad directly affects the stacking energy of the neighboring G-tetrads. In summary, the TEL-ODN **3** can form a parallel quadruplex structure **IIIa** without causing any distortion in the G-tetrad region, whereas in the TEL-ODN **4**, which forms the quadruplex **IVa**, a major readjustment of the G-tetrads occurs. These findings appear consistent with the experimental CD and NMR data revealing the formation of a more stable quadruplex **III** in comparison to **IV**.

The results described in this paper confirm the potential of TEL-ODNs as a new class of ODN analogues prone to adopt stable intramolecular quadruplex structures. In each case the T_m values are higher in potassium- than in sodium-containing buffer. It is noteworthy that, irrespective of the ends by which the four strands are attached to the tetra-end-linker, the CD spectra of the obtained complexes are typical of parallel quadruplex structures, displaying positive maxima centered at 264 nm, in contrast to maxima at 295 nm observed for antiparallel structures. The only exception concerns the CD spectrum of **4** in Na^+ buffer, in which a positive shoulder at 295 nm is present, indicating that a mixture of parallel and antiparallel forms could exist (quadruplex **IVa**−**c**). The whole of data, including molecular modeling calculations, suggest that the tetra-end-linker used in the present study is long and flexible enough to allow the organization of the ODN strands into a parallel quadruplex structure and (ii) that, at least in the presence of potassium ions, this form is favored over the antiparallel one, even if it is at the cost of a major readjustment of G-tetrads, which is the case of **IVa**. We believe that TEL-quadruplexes with suitable sequences and predetermined strand orientations could be used as aptamers, decoy and molecular probes, when used in a labeled form. Furthermore, TEL-ODNs may prove to be important tools for structural studies of alternative less stable quartets such as A-tetrads (*52*, *53*), C-tetrads (*54*), T-tetrads (*55*), and mixed tetrads (*56*) as well as tetrads formed by modified nucleosides (*57*, *58*). To confirm these conclusions as well as to get hold of a suitable tool to prepare monomolecular quadruplex structures with a preordered strand orientation, the syntheses of several TEL-ODNs characterized by shorter branched spacers and/or longer DNA stretches are currently in progress in our laboratory.

ACKNOWLEDGMENT

The authors are grateful to "Centro di Servizi Interdipartimentale di Analisi Strumentale", C.S.I.A.S., for supplying NMR

facilities. This work is supported by Italian M.U.R.S.T. (P.R.I.N. 2003 and 2004) and Regione Campania (L.R. 5).

LITERATURE CITED

(1) Davis, J. T. (2004) G-quartets 40 years later: from 5′-GMP to molecular biology and supramolecular chemistry. *Angew. Chem., Int. Ed. 43*, 668−698.
(2) Keniry, M. A. (2001) Quadruplex structures in nucleic acids. *Biopolymers 56*, 123−146.
(3) Simonsson, T. (2001) G-Quadruplex DNA Structures Variations on a Theme. *Biol. Chem. 382*, 621−628.
(4) Arthanari, H., and Bolton, P. H. (2001) Functional and dysfunctional roles of quadruplex DNA in cells. *Chem. Biol. 8*, 221−238.
(5) Cuesta, J., Read, M. A., and Neidle, S. (2003) The Design of G-quadruplex ligands as telomerase inhibitors. *Mini Rev. Med. Chem. 3*, 11−21.
(6) Neidle, S., and Parkinson, G. (2002) Telomere maintenance as a target for anticancer drug discovery. *Nature Rev. Drug Discovery 1*, 383−393.
(7) Kerwin, S. M. (2000) G-Quadruplex DNA as a target for drug design. *Curr. Pharm. Des. 6*, 441−466.
(8) White, L. K., Wright, W. E., and Shay, J. W. (2001) Telomerase inhibitors. *Trends Biotechnol. 19*, 114−120.
(9) Ambrus, A., Chen, D., Dai, J., Jones, R. A., and Yang, D. (2005) Solution structure of the biologically relevant G-quadruplex element in the human c-MYC promoter. Implications for G-quadruplex stabilization. *Biochemistry 44*, 2048−2058.
(10) Seenisamy, J., Rezler, E. M., Powell, T. J., Tye, D., Gokhale, V., Joshi, C. S., Siddiqui-Jain, A., Hurley, L. H. (2004) The dynamic character of the G-quadruplex element in the c-MYC promoter and modification by TMPyP4. *J. Am Chem. Soc. 126*, 8702−8709.
(11) Simonsson, T., Pecinka, P., and Kubista, M. (1998) DNA tetraplex formation in the control region of c-myc. *Nucleic Acids Res. 26*, 1167−1172.
(12) Macaya, R. F., Schultze, P., Smith, F. W., Roe, J. A., and Feigon, J. (1993) Thrombin-binding DNA aptamer forms a unimolecular quadruplex structure in solution. *Proc. Natl Acad. Sci. U.S.A. 90*, 3745−3749.
(13) Jing, N., Marchand, C., Guan, Y., Liu, J., Pallansch, L., Lackman-Smith, C., De Clercq, E. and Pommier, Y. (2001) Structure−activity of inhibition of HIV-1 integrase and virus replication by G-quartet oligonucleotides. *DNA Cell Biol. 20*, 499−508.
(14) Smirnov, I., and Shafer, R. H. (2000) Effect of loop sequence and size on DNA aptamer stability. *Biochemistry 39*, 1462−1468.
(15) Pileur, F., Andreola, M. L., Dausse, E., Michel, J., Moreau, S., Yamada, H., Gaidamarov, S. A., Crouch, R. J., Toulmé, J. J., and Cazenave, C. (2003) Selective inhibitory DNA aptamers of the human RNase H1. *Nucleic Acids Res. 31*, 5776−5788.
(16) Chinnapen, D. J., and Sen, D. (2002) Hemin-stimulated docking of cytochrome *c* to a hemin-DNA aptamer complex. *Biochemistry 41*, 5202−5212.
(17) Hammond-Kosack, M. C., Kilpatrick, M. W., and Docherty, K. (1992) Analysis of DNA structure in the human insulin gene-linked polymorphic region *in vivo*. *J. Mol. Endocrinol. 9*, 221−225.
(18) Delaney, S., and Barton, J. K. (2003) Charge Transport in DNA Duplex/Quadruplex Conjugates. *Biochemistry 42*, 14159−14165.
(19) de Champdore, M., De Napoli, L., Montesarchio, D., Piccialli, G., Caminal, C., Mulazzani, Q. G., Navacchia, M. L., and Chatgilialoglu, C. (2004) Excess electron transfer in G-quadruplex. *Chem. Commun. 15*, 1756−1757.
(20) Calzolari, A., Di Felice, R., Molinari, E., and Garbesi, A. (2004) Electron Channels in Biomolecular Nanowires. *J. Phys. Chem. B 108*, 2509−2515.
(21) Parkinson, G. N., Lee, M. P. H., and Neidle, S. (2002) Crystal structure of parallel quadruplexes from human telomeric DNA. *Nature 417*, 876−880.
(22) Patel, D. J. (2002) A molecular propeller. *Nature 417*, 807−808.
(23) Phan, A. T., Modi, Y. S., and Patel, D. J. (2004) Propeller-type parallel-stranded G-quadruplexes in the human *c-myc* promoter. *J. Am. Chem. Soc. 126*, 8710−8716.
(24) Ambrus, A., Chen, D., Dai, J., Jones, R. A., and Yang, D. (2005) Solution structure of the biologically relevant G-quadruplex element in the human *c-myc* promoter. Implications for G-quadruplex stabilization. *Biochemistry 44*, 2048−2058.
(25) Chou, S.-H., Chin, K.-H., and Wang, A. H.-J. (2005) DNA aptamers as potential anti-HIV agents. *Trends Biochem. Sci. 30*, 231−234.
(26) Koizumi, M., Akahori, K., Ohmine, T., Tsutsumi, S., Sone, J., Kosaka, K., Kaneko, M., Kimura, S., and Shimada, K. (2000) Biologically active oligodeoxyribonucleotides. Part 12: N2-methylation of 2′-deoxyguanosines enhances stability of parallel G-quadruplex and anti-HIV-1 activity. *Biorg. Med. Chem. Lett. 10*, 2213−2216.
(27) Wyatt, J. R., Vickers, T. A., Roberson, J. L., Buckheit, R. W., Jr., Klimkait, T., DeBaets, E., Davis, P. D., Rayner, B., Imbach, J. L., and Ecker, D. J. (1994) Combinatorially selected guanosine-quartet structure is a potent inhibitor of human immunodeficiency virus envelope-mediated cell fusion. *Proc. Natl. Acad. Sci. U.S.A. 91*, 1356−1360.
(28) Wyatt, J. R., Davis, P. W., and Freier, S. M. (1996) Kinetics of G-quartet-mediated tetramer formation. *Biochemistry 35*, 8002−8008.
(29) Hazel, P., Huppert, J., Balasubramanian, S., and Neidle, S. (2004) Loop-length-dependent folding of G-quadruplexes. *J. Am. Chem. Soc. 126*, 16405−16415.
(30) Risitano, A., and Fox, K. R. (2004) Influence of loop size on the stability of intramolecular DNA quadruplexes. *Nucleic Acid Res. 32*, 2598−2606.
(31) Jing, N., Rando, R. F., Pommier, Y., and Hogan, M. E. (1997) Ion selective folding of loop domains in a potent anti-HIV oligonucleotides. *Biochemistry 36*, 12498−12505.
(32) Rujian, I. L., Meleney, J. C., and Bolton, P. H. (2005) Vertebrate telomere repeat DNAs favour external loop propeller quadruplex structures in the presence of high concentrations of potassium. *Nucleic Acid Res. 33*, 2022−2031.
(33) Risitano, A., and Fox, K. R. (2003) Stability of intramolecular DNA quadruplexes: comparison with DNA duplexes. *Biochemistry 42*, 6507−6513.
(34) Lu, M., Guo, Q., and Kallenbach, N. R. (1993) Thermodynamics of G-tetraplex formation by telomeric DNAs. *Biochemistry 32*, 598−601.
(35) Zhou, T., Chen, G., Wang, Y., Zhang, Q., Yang, M., and Li, T. (2004) Synthesis of unimolecular circular G-quadruplexes as prospective molecular probes. *Nucleic Acid Res. 32*, e173/1−e173/9.
(36) Oliviero, G., Borbone, N., Galeone, A., Varra, M., Piccialli, G., and Mayol, L. (2004) Synthesis and characterization of a bunchy oligonucleotide forming a monomolecular parallel quadruplex structure in solution. *Tetrahedron Lett. 45*, 4869−4872.
(37) Oliviero, G., Amato, J., Borbone, N., Galeone, A., Varra, M., Piccialli, G., Mayol, L. (2006) Synthesis and characterization of DNA quadruplexes containing T-tetrads formed by bunch-oligonucleotides. *Biopolymers 81*, 194−201.
(38) Breslauer, K. J., Frank, R., Blöcker, H., and Marky, L. A. (1986) Predicting DNA duplex stability from the base sequence. *Proc. Natl. Acad. Sci. U. S.A 83*, 3746−3750.
(39) Piotto, M., Saudek, V., and Sklenar, V. (1992) Gradient-tailored excitation for single-quantum NMR spectroscopy of aqueous solutions. *J. Biomol. NMR 2*, 661−665.
(40) Cornell, W. D., Cieplack, P., Bayly, C. I., Gould, I. R., Merz, K. M., Ferguson, D. M., Spellmeyer, D. C., Fox, T., Caldwell, J. W., and Kollman, P. A. (1995) A Second Generation Force Field for the Simulation of Proteins, Nucleic Acids, and Organic Molecules. *J. Am. Chem. Soc. 117*, 5179−5197.
(41) Gasteiger, J., and Marsili, M. (1980) Iterative partial equalization of orbital electronegativity: a rapid access to atomic charges. *Tetrahedron 36*, 3219−3228.
(42) Jorgensen, W. L., Chandrasekhar, J., Madura, J. D., Impey, R. W., and Klein, M. L. (1983) Comparison of Simple Potential Functions for Simulating Liquid Water. *J. Chem. Phys. 79*, 926−935.
(43) Nielsen, J., and Lyngsø, L. O. (1996) Combinatorial Solid-Phase Synthesis of Balanol Analogues. *Tetrahedron Lett. 37*, 8439−8442.
(44) Petraccone, L., Erra, E., Esposito, V., Randazzo, A., Mayol, L., Nasti, L., Barone, G., and Giancola, C. (2004) Stability and structure of telomeric DNA sequences forming quadruplexes containing four G-tetrads with different topological arrangements. *Biochemistry 43*, 4877−4884.
(45) Jin, R., Gaffney, B. L., Wang, C., Jones, R. A., and Breslauer, K. J. (1992) Thermodynamics and Structure of a DNA Tetraplex: A

Spectroscopic and Calorimetric Study of the Tetramolecular Complexes of d(TG_3T) and d($TG_3T_2G_3T$). *Proc. Natl. Acad. Sci. U. S.A 89*, 8832−8836.

(46) Dapić, V., Abdomerović, V., Marrington, R., Pederby, J., Rodger, A., Trent, J. O., and Bates, P. J. (2003) Biophysical and biological properties of quadruplex oligodeoxyribonucleotides. *Nucleic Acids Res. 31*, 2097−2170.

(47) Hardin, C. C., Perry, A. G., and White, K. (2001) Thermodynamic and kinetic characterization of the dissociation and assembly of quadruplex nucleic acids. *Biopolymers 56*, 147−194.

(48) Feigon, J., Koshlap, K. M., and Smith, F. W. (1995) ^{1}H NMR spectroscopy of DNA triplexes and quadruplexes. *Methods Enzymol. 261*, 225−255.

(49) Feigon, J. (1996) DNA Triplexes, Quadruplexes, and Aptamers. *Encycl. Nuclear Magn. Reson. 3*, 1726−1731.

(50) Aboul-ela, F., Murchie, A. I. H., Norman, D. G., and Lilley, D. M. J. (1994) Solution structure of a parallel-stranded tetraplex formed by d(TG_4T) in the presence of sodium ions by nuclear magnetic resonance spectroscopy. *J. Mol. Biol. 243*, 458−471.

(51) Hud, N. V., Smith, F. W., Anet, F. A., and Feigon, J. (1996) The selectivity for K^+ versus Na^+ in DNA quadruplexes is dominated by relative free energies of hydration: a thermodynamic analysis by ^{1}H NMR. *Biochemistry 35*, 15383−15390.

(52) Patel, P. K., Koti, A. S. R., and Hosur, R. V. (1999) NMR studies on truncated sequences of human telomeric DNA: observation of a novel A-tetrad. *Nucleic Acids Res. 27*, 3836−3843.

(53) Gavathiotis, E., and Searle, M. S. (2003) Structure of the parallel-stranded DNA quadruplex d($TTAGGGT)_4$ containing the human telomeric repeat: evidence for A-tetrad formation from NMR and molecular dynamics simulations. *Org. Biomol. Chem. 1*, 1650−1656.

(54) Patel, P. K., Bhavesh, N. S., and Hosur, R. V. (2000) NMR observation of a novel C-tetrad in the structure of the SV40 repeat sequence GGGCGG. *Biochem. Biophys. Res. Commun. 270*, 967−971.

(55) Patel, P. K., and Hosur, R. V. (1999) NMR observation of T-tetrads in a parallel stranded DNA quadruplex formed by Saccharomyces cerevisiae telomere repeats. *Nucleic Acids Res. 27*, 2457−2464.

(56) Meyer, M., Schneider, C., Brandl, M., and Suehnel, J. (2001) Cyclic Adenine-, Cytosine-, Thymine- and Mixed Guanine-Cytosine-Base-Tetrads in Nucleic Acids Viewed From a Quantum-Chemical and Force Field Perspective. *J. Phys. Chem. A 105*, 11560−11573.

(57) Esposito, V., Randazzo, A., Piccialli, G., Petraccone, L., Giancola, C., and Mayol, L. (2004) Effects of an 8-bromodeoxyguanosine incorporation on the parallel quadruplex structure [d($TGGGT)]_4$. *Org. Biomol. Chem. 2*, 313−318.

(58) Chen, J., Zhang, L. R., Min, J. M., and Zhang, L. H. (2002) Studies on the synthesis of a G-rich octaoligoisonucleotide $(isoT)_2(isoG)_4$-$(isoT)_2$ by the phosphotriester approach and its formation of G-quartet structure. *Nucleic Acids Res. 30*, 3005−3014.

BC060009B

Induction of Differential T-Cell Epitope by Plain- and Liposome-Coupled Antigen

Maiko Taneichi,[†] Yuriko Tanaka,[†] Michiyuki Kasai,[†] Masahito Mori,[‡] Mitsuhiro Nishida,[‡] Hiroyuki Yamamura,[‡] Junichiro Mizuguchi,[§] and Tetsuya Uchida[†,*]

Department of Safety Research on Blood and Biological Products, National Institute of Infectious Diseases, Tokyo 208-0011, Japan, Drug Delivery System Development Division, Nippon Oil and Fat Corporation, Tokyo 150-6019, Japan, and Department of Immunology, Tokyo Medical University, Tokyo 160-8402, Japan. Received January 31, 2006; Revised Manuscript Received April 30, 2006

The T-cell receptors of $CD4^+$ T lymphocytes recognize immunogenic peptide sequences bound within the groove of MHC class II molecules, and the peptides that bind to these molecules are known to share common structural motifs. For example, $OVA_{323-339}$, an I-A^d-binding peptide, involves a motif of the I-A^d peptide-binding groove. In the present study, OVA peptides of up to 26-mer were sequentially synthesized and screened, and two additional I-A^d binding OVA peptides, OVA_{20-43} and $OVA_{264-286}$, were found to stimulate $CD4^+$ T cells of OVA-immune BALB/c mice. OVA_{20-43} involved structural motifs of the I-A^d peptide-binding groove, while $OVA_{264-286}$ did not. The ability of these three I-A^d binding OVA peptides to induce antigen-specific cytokine production was compared among $CD4^+$ T cells of mice immunized either with alum-adsorbed OVA (OVA−alum) or OVA chemically coupled to the surface of liposome (OVA−liposome). $CD4^+$ T cells of mice immunized with OVA−alum produced more cytokines when stimulated with $OVA_{264-286}$ than with $OVA_{323-339}$, while $CD4^+$ T cells of mice immunized with OVA−liposome conjugates produced more cytokines when stimulated with $OVA_{323-339}$ than with $OVA_{264-286}$. OVA_{20-43} induced production of comparable levels of cytokines in mice immunized either with OVA−alum or OVA−liposome. Confocal laser scanning microscopic analysis demonstrated that chemically coupled OVA and liposomes were colocalized in APCs until OVA received processing. Three-dimensional structural analysis demonstrated that both $OVA_{264-286}$ and $OVA_{323-339}$ were present on the surface of OVA, but OVA_{20-43} was not. These results suggested that the chemical coupling of OVA to liposome affected antigen processing in APCs and thus resulted in the induction of differential T-cell epitopes as compared with those induced by plain OVA.

INTRODUCTION

In general, T-cell receptors (TCRs) of $CD4^+$ T cells do not recognize native protein antigens, but do recognize antigenic peptides displayed in association with major histocompatibility complex (MHC) class II molecules by antigen-presenting cells (APCs). TCRs occur as either of two distinct heterodimers, $\alpha\beta$ or $\gamma\delta$. The $\alpha\beta$ TCR heterodimer-expressing cells predominate in most lymphoid compartments (90% to 95%) of humans and mice and are responsible for the classical helper or cytotoxic T cell responses. In most cases, the $\alpha\beta$ TCR ligand is a peptide antigen bound to the class I and class II MHC molecule (*1*). Class I and II molecules encoded by genes within the MHC play a central role in regulating immune responses through their ability to bind and display small peptides derived from foreign antigens.

Grey and co-workers identified ovalbumin (OVA) peptide 323−339 as being immunodominant in H-2^d mice (*2*) and showed that this peptide binds to I-A^d, but not I-E^d, the latter of which is an Ia molecule that will not present this peptide (*3*). Ever since $OVA_{323-339}$ was identified, it has been used extensively to study the nature of class II MHC-peptide binding and T-cell activation (*4*−*9*). However, this peptide is responsible for 25−35% of the T-cell responses in BALB/c mice immunized with whole ovalbumin (*2*), suggesting the presence of other I-A^d binding OVA peptides with T-cell stimulatory activity while, at present, no other I-A^d binding OVA peptides have been reported.

We previously reported that OVA chemically coupled to the surface of liposomes via glutaraldehyde (OVA−liposome conjugates) induced IgE-selective unresponsiveness in mice (*10*). The IgE-selective unresponsiveness was induced by antigen−liposome conjugates, regardless of the coupling procedure of antigen and liposomes (*11*), using liposomes of different lipid formulations (*12*), or using different antigens such as tetanus toxin (*13*) or Shiga-like toxin (*14*). Thus, antigen−liposome conjugates are expected to be applicable as part of a novel protocol for the development of vaccines that would induce minimal IgE synthesis.

In the present study, sequentially synthesized OVA peptides were screened for the ability to stimulate OVA-specific $CD4^+$ T cells of BALB/c (H-2^d) mice and two additional I-A^d binding OVA peptides, OVA_{20-43} and $OVA_{264-286}$, were found. The ability of these three OVA peptides to stimulate $CD4^+$ T cells of OVA-immune BALB/c mice was compared among the $CD4^+$ T cells of mice immunized either with OVA−alum or with OVA−liposome conjugates. The aim of this study was to investigate the effect of antigen modification on the in vivo induction of T cell epitopes.

EXPERIMENTAL PROCEDURES

Mice. BALB/c mice (female, 8 weeks of age) were purchased from Charles River, Kanagawa, Japan. The mice were maintained in sterile cages under specific pathogen-free conditions at the Division of Experimental Animals Research (National Institute of Infectious Diseases, Tokyo, Japan).

* To whom correspondence should be addressed. Tel: +81-42-561-0771; Fax: +81-42-562-7892. E-mail: tuchida@nih.go.jp.

[†] National Institute of Infectious Diseases.

[‡] Nippon Oil and Fat Corporation.

[§] Tokyo Medical University.

10.1021/bc060024g CCC: $33.50 © 2006 American Chemical Society
Published on Web 06/21/2006

Antigens. Ovalbumin (OVA, Grade VII) was purchased from Sigma (St. Louis, MO). For analysis of the processing of liposome-coupled OVA by macrophages, DQ−OVA, which exhibits green fluorescence upon proteolytic degradation, was purchased from Molecular Probes, Inc. (Eugene, OR).

OVA Peptides. OVA peptides consisting of 20−26 amino residues were sequentially synthesized, and the ability of each peptide to induce cytokine production by $CD4^+$ T cells of BALB/c mice immunized with OVA was investigated. All OVA peptides used in the present study were synthesized and supplied by Operon Biotechnologies, K. K. (Tokyo, Japan). Precursor peptide material attached to polystyrene resin was synthesized by an automated peptide synthesizer (model 433A; Applied Biosystems, Foster City, CA) using Fmoc (9-fluorenylmethoxycarbonyl) chemistry. Then, the resins on the peptide C-terminus and the building blocks on the peptide side chain were removed by trifluoroacetic acid. The purification of the peptide was performed by high-performance liquid chromatography (HPLC) using an automated system (HPLC-10A; Shimazu Co., Kyoto, Japan) with a 35−55% acetonitrile gradient in the acidic aqueous phase. As a result, the highly purified material was obtained with a >95% area ratio on the HPLC elution chart and was determined by mass spectroscopic analysis with the matrix-assisted laser desorption/ionization time-of-flight method using Applied Biosystems Voyager DE. The peptide solution was lyophilized and used for the subsequent experiments.

Fluorescence Labeling of OVA. OVA were labeled with fluorescence using an Alexa Fluor 488 protein labeling kit (Molecular Probes, Inc.) following the manufacturer's protocol. The estimated F:P ratio of Alexa Fluor 488−OVA conjugate was 1.4:1.

Chemicals. All phospholipids were obtained from NOF Co., Tokyo, Japan. Reagent grades of cholesterol were purchased from Wako Pure Chemical Industries, Osaka, Japan.

Liposomes. The liposomes used in the present study consisted of dipalmitoyl phosphatidylcholine, dipalmitoyl phosphatidyl ethanolamine, cholesterol, and dimyristoyl phosphatidyl glycerol in 4:3:7:2 molar ratios. The crude liposome solution was passed through a membrane filter (Nucleopore polycarbonate filter, Coster, Cambridge, MA) with a pore size of 0.2 μm.

Red-Labeled liposome. Red-labeled liposomes were prepared by adding 1,2-dimyristoyl-sn-glycero-3-phosphoethanolamine-*N*-(lissamine rhodamine B sulfonyl) (Product Number: 810157, Avanti Polar Lipids Inc, Alabaster, AL) into the above lipid constituent of liposomes.

Coupling of OVA to Liposomes. Liposomal conjugates with plain OVA, Alexa−OVA, or DQ−OVA were prepared essentially in the same way as described previously (*15*) via glutaraldehyde. Briefly, to a mixture of 90 mg of liposomes and 6 mg of OVA in 2.5 mL of phosphate buffer (pH 7.2) was added 0.5 mL drops of 2.5% glutaraldehyde solution. The mixture was stirred gently for 1 h at 37 °C, and then 0.5 mL of 3 M glycine−NaOH (pH 7.2) was added to block excess aldehyde groups. This was followed by incubation overnight at 4 °C. The liposome-coupled OVA and uncoupled OVA in the resulting solution were separated using CL-4B column chromatography (Pharmacia Fine Chemical Co., Upsala, Sweden). The amount of lipid in the liposomal fraction was measured using a Phospholipid-Test-Wako phospholipid content assay kit (Wako Pure Chemical Industries). The OVA−liposome solution was adjusted to 10 mg lipid/mL in RPMI-1640, sterile-filtered using a Millex-HA syringe filter unit (0.45 μm, Millipore Corp., Bedford, MA), and kept at 4 °C until use.

Immunization. The mice were immunized intraperitoneally (ip) with 200 μL of 10 μg of OVA adsorbed with 100 μg of alum (Alhydrogel, Superfos Biosector, Vedbaek, Denmark) in PBS or with 200 μL of OVA−liposome conjugates, at 0 and 4 weeks.

Preparation of Splenic Adherent Cells. Splenic adherent cells (SACs) were used as antigen-presenting cells in the cultures of the $CD4^+$ T cells and OVA peptides. SACs were obtained from naive BALB/c mice as follows. Spleen cell suspensions were prepared in RPMI-1640 containing 10% fetal calf serum (FCS). Cells (5×10^7) in 5 mL of medium containing 10% FCS were plated into 50-mm plastic tissue culture dishes (No. 3002; Becton-Dickinson Labware, Franklin Lakes, NJ) and incubated at 37 °C in a humidified 5% CO_2 atmosphere for 2 h. After culture, nonadherent cells were removed by three vigorous washings in warm media, and adherent cells were then harvested with a cell scraper.

Preparation of $CD4^+$ T Cells. $CD4^+$ T-cell purification from spleen cells of mice immunized with OVA−alum was performed with the MACS magnetic cell sorter system (Miltenyi Biotec GmbH, Bergisch Gladbach, Germany) according to the manufacturer's protocol and using anti-CD4 antibody-coated microbeads (No. 492-01; Miltenyi Biotec). $CD4^+$ T cells were suspended in RPMI-1640 containing 10% FCS at a cell density of 2×10^6/mL. In the present study, OVA peptides at a final concentration of 10 μM with 1 and 5 d culture periods were employed for the production of the Th1 (IL-2, IFN-γ) and Th2 (IL-4, IL-5) cytokines, respectively. The $CD4^+$ T-cell suspension was plated at 250 μL per well onto 48-well culture plates (No. 3047; Becton-Dickinson Labware), and 500 μL of 20 μM OVA peptide solution and 250 μL of 8×10^5/mL SAC in the same medium were added to the plates. After incubation in a CO_2 incubator, the culture supernatants were collected and assayed to determine the concentrations of cytokines.

Cytokine Assays. IL-5 and IFN-γ in the culture supernatant were measured using the Biotrak mouse ELISA system (Amersham International, Buckinghamshire, UK). All test samples were assayed in duplicate, and the standard error in each test was always less than 5% of the mean value.

Cloned Macrophage Hybridoma. Macrophage hybridoma clone No. 39, obtained from the fusion of splenic adherent cells from CKB mice and $P388D_1$ (*16*), was maintained in RPMI-1640 (Gibco Laboratories, Grand Island, NY) supplemented with 10% heat-inactivated FCS (Hyclone Laboratories, Logan, UT), 100 U/mL of penicillin, and 100 μg/mL of streptomycin (Gibco Laboratories) in a 75 cm^2 flask (No. 3111; Becton Dickinson Labware, Franklin Lakes, NJ).

Flow Cytometry. To investigate the processing of OVA coupled to liposome by macrophages, #39 macrophage clone was incubated for 15 to 60 min at 37 °C in the presence of DQ−OVA−liposome conjugates that contained a final concentration of 4 μg/mL OVA. After incubation, the cells were washed with ice-cold PBS and then were analyzed on a FACS Calibur flow cytometer (BD Biosciences, Mountain View, CA). The histograms of fluorescence distribution were plotted as the number of cells versus fluorescence intensity on a logarithmic scale.

Confocal Laser Scanning Microscopy. To investigate the processing of liposome-coupled OVA by macrophages, macrophage clone No. 39 was cultured for 18 h at 37°C on 8-hole heavy Teflon-coated slides (Bokusui Brown, New York, NY) and then incubated with DQ−OVA−liposome conjugates for 2 h at 37 °C. The slides were washed with MEM and fixed with 4% paraformaldehyde in PBS for 10 min at room temperature. After fixation, they were incubated for 10 min in 0.1 M glycine-HCl, pH 7.0, to block the remaining ardehyde residue. They were then washed two times in PBS. After washing, the slides were sealed with PBS/glycerin (PBS:glycerin = 1:9). They were then analyzed under a confocal laser scanning

Table 1. OVA Peptides Investigated in the Present Study

OVA peptides	amino acid sequence
1−20	GSIGAASMEFCFDVFKELKV
20−43	VHHANENIFYCPIAIMSALAMVYL
53−78	INKVVRFDKLPGFGDSIEAQCGTSVN
61−85	KLPGFGDSIEAQCGTSVNVHSSLRD
164−181	SSVDSQTAMVLVNAIVFK
190−207	DEDTQAMPFRVTEQESKP
220−245	ASMASEKMKILELPFASGTMSMLVLL
264−286	LTEWTSSNVMEERKIKVYLPRMK
302−327	ITDVFSSSANLSGISSAESLKISQAV
323−339	ISQAVHAAHAEINEAGR

Table 2. Induction of Cytokine Production by OVA Peptides[a]

OVA peptides	IL-2	IL-4	IL-5	IFN-γ
1−20	ND	ND	ND	ND
20−43	278.3 ± 53.5	221.2 ± 78.1	1201.5 ± 58.3	1275.5 ± 507.9
53−78	ND	ND	ND	ND
61−85	ND	ND	ND	ND
164−181	ND	ND	ND	ND
190−207	ND	ND	ND	ND
220−245	ND	ND	ND	ND
264−286	511.7 ± 85.0	140.3 ± 28.3	1073.4 ± 156.3	1321.6 ± 260.7
302−327	ND	ND	ND	ND
323−339	215.6 ± 35.5	27.8 ± 15.1	560.1 ± 51.1	302.6 ± 72.6
OVA	856.7 ± 60.8	78.0 ± 30.1	1133.4 ± 39.1	2457.0 ± 667.3

[a] Each peptide was assessed for its ability to induce cytokine production by CD4 T cells of mice immunized with OVA−alum. CD4 T cells were cultured in the presence of OVA peptides as described in Experimental Procedures. Data represent mean cytokine concentration (pg/mL) and SE of triplicate cultures. ND, not detected.

microscope system, LSM410 (Carl Zeiss Co., Germany). Internalization of Alexa−OVA−red liposome conjugates in the macrophages was investigated in essentially the same manner as above.

Analysis of Three-Dimensional Structure of OVA. The three-dimensional structure of OVA reported by Stein et al. (*17*, *18*) was obtained from DBGET database links (http://www.genome.jp/dbget/), and the locations of the OVA peptides were displayed using ProteinAdviser (Fujitsu Kyusyu System Engineering Ltd., Fukuoka, Japan).

RESULTS

OVA Peptides Capable of Inducing Cytokine Production by OVA-Specific CD4$^+$ T Cells of BALB/c Mice. A series of sequentially synthesized OVA peptides shown in Table 1 were screened for the ability to induce cytokine production by CD4$^+$ T cells of BALB/c mice immunized with OVA−alum. Since, under the culture conditions described in Materials and Methods, no cytokine production was observed in the absence of OVA, nor by the use of CD4$^+$ T cells of naive BALB/c mice, the data shown in Table 2 were considered to represent antigen-specific cytokine production. In addition to well-known $OVA_{323-339}$, two OVA peptides, OVA_{20-43} and $OVA_{264-286}$, were found to induce significant production of all cytokines tested. The levels of cytokines induced by OVA_{20-43} and $OVA_{264-286}$ were even higher than those induced by $OVA_{323-339}$ in all cytokines tested. OVA_{20-43} involved the core motif of the I-A^d peptide-binding groove, OVA_{31-36}, but $OVA_{264-286}$ did not.

Cytokine Production by OVA-Specific CD4$^+$ T Cells Of Mice Immunized with OVA−Alum or OVA−Liposome, after Stimulation with OVA Peptides. The next attempt was performed using newly found OVA peptides, OVA_{20-43} and $OVA_{264-286}$, and a well-known OVA peptide, $OVA_{323-339}$. Splenic CD4$^+$ T cells were obtained from mice immunized either with OVA−liposome or OVA−alum and were cultured with OVA_{20-43}, $OVA_{264-286}$, or $OVA_{323-339}$ in the presence of APCs. As shown in Figure 1, the levels of cytokines produced by CD$^+$ T cells of mice immunized with OVA−liposome were significantly ($p < 0.01$) higher when the T cells were cultured either with OVA_{20-43} or $OVA_{323-339}$ than when they were cultured with $OVA_{264-286}$. On the other hand, in the culture of the CD4$^+$ T cells of mice immunized with OVA−alum, OVA_{20-43} and $OVA_{264-286}$ induced significantly higher levels of IL-5 and IFN-γ as compared to those induced by $OVA_{323-339}$, consistent with the results shown in Table 1. Similar results were obtained for the other cytokines, IL-2, IL-4, and IL-10 (data not shown).

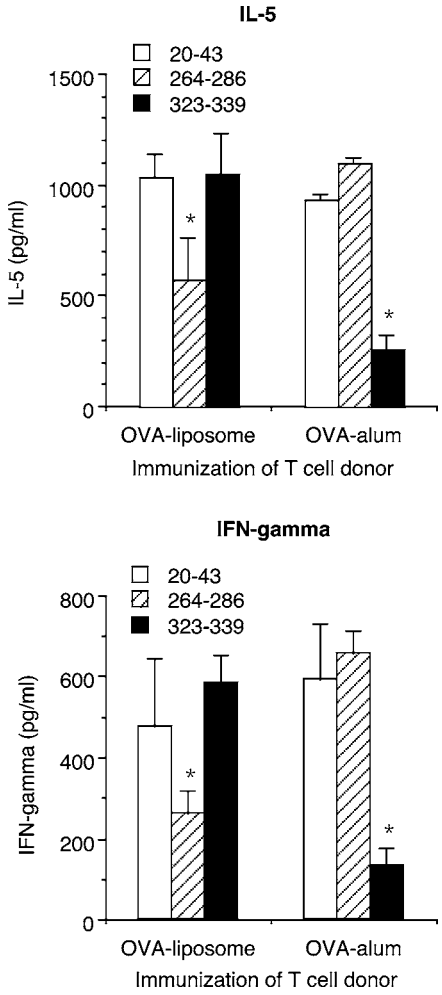

Figure 1. Cytokine production by CD4$^+$ T cells of mice immunized with OVA−liposome or OVA−alum, after in vitro stimulation with OVA peptides. CD4$^+$ T cells were taken from OVA-immune mice and cultured with OVA peptides as described in Materials and Methods. Data represent mean cytokine concentration (pg/mL) and SE of triplicate culture. Data are representative of three independent experiments.

Duration of Processing of Liposome-Coupled OVA in APCs. DQ−OVA coupled to liposome was cultured for 15 to 60 min with macrophage clone No. 39, and FACS analysis was performed. Figure 2a shows the fluorescence intensity of macrophages. A maximal processing of OVA was observed at 60 min. A consistent result was observed by confocal microscopic analysis (Figure 2b); the green fluorescence in the macrophages increased gradually within 60 min, suggesting that liposome-coupled OVA received processing significantly within 60 min after onset of the culture.

Internalization of Alexa−OVA−Red Liposome Conjugates in Macrophages. Alexa−OVA−red liposome conjugates, which appear yellow due to association with the green in Alexa−OVA and the red in the liposome, were cultured with macrophage clone No. 39 for 15 to 60 min, and confocal

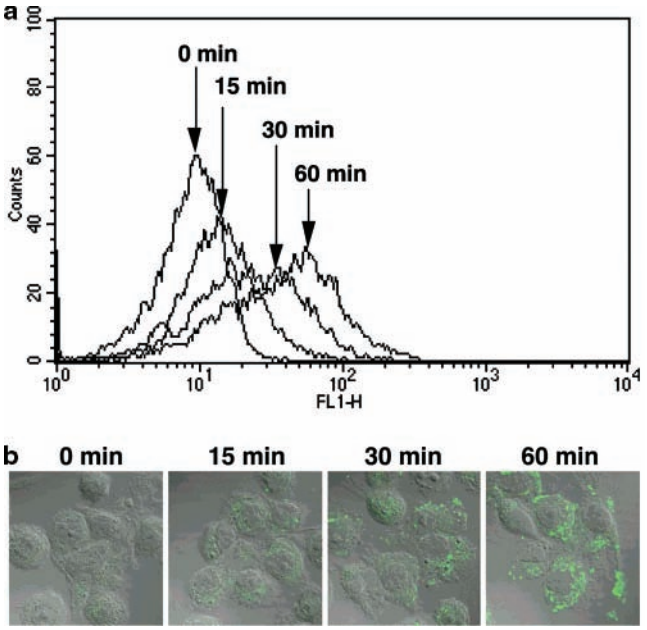

Figure 2. Digestion of liposome-coupled OVA by macrophages. DQ−OVA coupled to the surface of liposomes were added to the macrophage culture. Zero to 60 min after the onset of the culture, the macrophages were recovered and analyzed using flow cytometry (a) and confocal laser scanning microscopy (b).

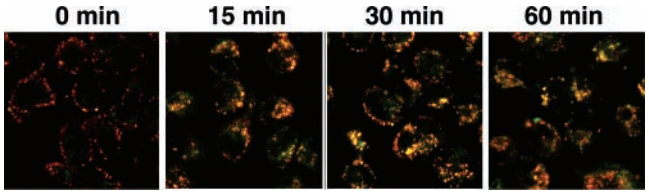

Figure 3. Association of OVA and liposomes in macrophages. Conjugates of Alexa488-labeled OVA and red-labeled liposomes were added to the macrophage culture. Zero to 60 min after the onset of the culture, the macrophages were recovered and analyzed using confocal laser scanning microscopy. The yellow spots observed in the macrophages are the result of the association with the Alexa488 (green) and red-labeled liposomes.

scanning microscopic analysis was performed. As shown in Figure 3, yellow spots were observed up to 60 min, suggesting that the OVA and liposomes were associated until liposome-coupled OVA received processing (Figure 2).

OVA Peptides in Three-Dimensional Structure of OVA. The locations of the three OVA peptides, OVA_{20-43}, $OVA_{264-286}$, and $OVA_{323-339}$, in the three-dimensional structure of OVA were analyzed. As shown in Figure 4, both $OVA_{264-286}$ and $OVA_{323-339}$ located on the surface of OVA in the three-dimensional structure, while OVA_{20-43} was situated inside the three-dimensional structure of OVA.

DISCUSSION

In the present study, OVA_{20-43} and $OVA_{264-286}$ were newly found among sequentially synthesized OVA peptides to stimulate $CD4^+$ T cells of OVA-immune BALB/c mice for cytokine production. A length of six residues has been proposed for core motifs of the I-A^d peptide-binding groove, with the first, third, and fourth residues being hydrophobic and the sixth generally being alanine or serine (*5*, *19*). OVA contains at least eight different epitopes with the I-A^d-binding motif, including $OVA_{327-332}$ which is involved in $OVA_{323-339}$. OVA_{20-43} involved core motifs of the I-A^d peptide binding groove, OVA_{31-36} and OVA_{32-37}, while $OVA_{264-286}$ did not. In addition, although OVA_{1-20}, OVA_{53-78}, $OVA_{220-245}$, and $OVA_{302-327}$ involved the core motifs OVA_{1-6}, OVA_{63-68}, $OVA_{230-235}$, and $OVA_{312-317}$, respectively, none of them induced OVA-specific cytokine production by $CD4^+$ T cells of OVA-immune BALB/c mice (Table 2). These results suggest that the involvement of structural motifs of the MHC class II peptide binding groove in an antigenic peptide is not an essential condition for the activation of antigen-specific $CD4^+$ T cells. Also, regarding class I, although OVA contains six potential epitopes with the H-$2K^b$-binding motif (*20*), the CTL response is dominated by just one, $OVA_{257-264}$ (*21*−*23*). Thus, immunodominance would be directed by more than just the presence of an appropriate class I- or class II-binding motif.

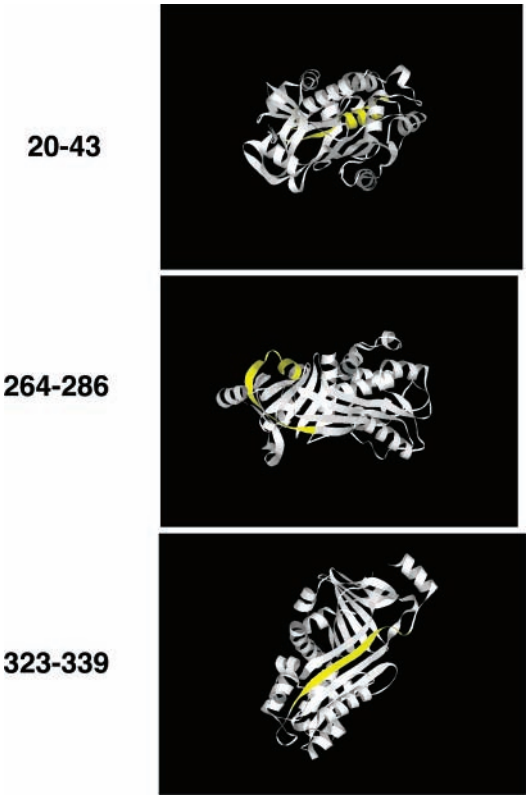

Figure 4. Location of OVA peptides in the three-dimensional structure of OVA. The OVA peptides in the three-dimensional structure of OVA are indicated as yellow strings.

The $\alpha\beta$ TCR comprises disulfide-linked α and β chains, each of which has a membrane-distal variable (Vα or Vβ) and membrane-proximal constant (Cα and Cβ) immunoglobulin superfamily (IgSF) domain, transmembrane regions, and short cytoplasmic segments (*24*). The peptide-MHC binding site is formed primarily from three complementary-determining regions (CDRs) or loops contributed by each Vα and Vβ domain. TCRs dock to the peptide-MHC in a topologically constrained manner, i.e., with the Vα domain of the TCR positioned over the N-terminal half of the peptide and the Vβ domain over the C-terminus (*25*, *26*). Thus, the shape of the TCR and/or peptide-MHC binding surfaces might limit the number of docking orientations (*24*). Therefore, the processing of both OVA_{20-43} and $OVA_{264-286}$ in APC to produce the "essential" length of the I-A^d-binding peptides sequence would be indispensable for the presentation of those peptides to $CD4^+$ T cells via the interaction between the peptide-MHC and TCRs.

Each Ia is considered to possess a single peptide binding site, based on the observation that unrelated peptides restricted by the same Ia molecule are capable of inhibiting the binding of one another to that particular Ia (*27*). This in turn supports the concept that a single site on Ia is capable of recognizing a structural motif common to many antigens (*5*). However, in the

present study, among two newly found I-A^d-binding OVA peptides, although each were found capable of stimulating antigen-specific $CD4^+$ T cells, one was demonstrated to involve a structural motif of the I-A^d peptide-binding groove but the other was not, suggesting the existence of another motif of the I-A^d peptide-binding groove.

$OVA_{323-339}$ induced a significantly higher level of cytokine production by $CD4^+$ T cells of mice immunized with OVA−liposome than that induced by $OVA_{264-286}$. However, in contrast, $OVA_{323-339}$ induced a significantly lower level of cytokine production by $CD4^+$ T cells of mice immunized with OVA−alum than that induced by $OVA_{264-286}$. These results suggest that the modification of OVA by the chemical coupling of OVA with liposomes may interrupt or alter antigen processing in APCs and result in the presentation of a differential set of peptides to T cells. In fact, the results of the present study demonstrated that the OVA and liposomes were associated until liposome-coupled OVA was processed (Figures 2 and 3). In the previous study (*13*), antigen−liposome conjugates were shown to be stable for at least 6 months if stored at 4 °C, and, if tetanus toxoid was coupled to liposomes and lyophilized, their efficacy was maintained for 6 months at 37 °C. The fact that both $OVA_{264-286}$ and $OVA_{323-339}$ were present on the surface of the three-dimensional structure of OVA made it reasonable to consider the effect of antigen-modification on the antigen processing in APCs. On the other hand, OVA_{20-43}, which induced a comparable level of cytokine production in both OVA−alum- and OVA−liposome-immune mice, was present inside the structure of OVA and likely not affected by the antigen-modification.

It is unlikely that the antigen-modification by the chemical coupling of antigen to liposomes detracts from the efficacy of vaccines when liposome-coupled antigen is applied to the vaccination protocol, since liposome-coupled toxins successfully induced protection against the tetanus toxin (*13*) or Shiga-like toxin (*14*, *28*, *29*) in mice (*13*, *14*) and also in monkeys (*28*). Nor it is unlikely that the difference between the two OVA peptides, $OVA_{264-286}$ and $OVA_{323-339}$, in the ability to induce cytokine production by $CD4^+$ T cells is reflected by the difference of immunodominance (i.e., affinity to bind I-A^d) in these two OVA peptides, since these peptides yielded opposite results in the stimulation of OVA-specific cytokine production by $CD4^+$ T cells of mice immunized by two different ways of immunization, i.e., OVA−alum and OVA−liposome. Thus, the results in the present study suggested that the modification of antigen affects antigen processing in APCs and results in the induction of differential T-cell epitopes as compared with those induced by plain antigen.

ACKNOWLEDGMENT

This work was supported in part by a grant from The Japan Health Sciences Foundation (Research on Health Sciences focusing on Drug Innovation).

LITERATURE CITED

(1) Chien, Y.-H., Jores, R., and Crowley, M. P. (1996) Recognition by γ/δ T cells. *Annu. Rev. Immunol. 14*, 511−532.

(2) Shimonkevitz, R., Colon, S., Kappler, J., Marrack, P. and Grey, H. M. (1984) Antigen recognition by H-2-restricted T cells. II. A tryptic ovalbumin peptide that substitutes for processed antigen. *J. Immunol.* 133, 2067−2074.

(3) Buus, S., Colon, S., Smith, C., Freed, J. H., Miles, C. and Grey, H. M. (1986) Interaction between a "processed" ovalbumin peptide and Ia molecules. *Proc. Natl. Acad. Sci. U.S.A. 83*, 3968−3971.

(4) Sette, A., Buus, S., Colon, S., Smith, J. A., Miles, C. and Grey, H. M. (1987) Structural characteristics of an antigen required for its interaction with Ia and recognition by T cells. *Nature 328*, 395−399.

(5) Sette, A., Buus, S., Colon, S., Miles, C. and Grey, H. M. (1988) I-A^d binding peptides derived from unrelated protein antigens share a common structural motif. *J. Immunol. 141*, 45−48.

(6) Sette, A., Buus, S., Appella, E., Smith, J. A., Chesnut, R., Miles, C., Colon, S. M., and Grey, H. M. (1989) Prediction of major histocompatibility complex binding regions of protein antigens by sequence pattern analysis. *Proc. Natl. Acad. Sci. U.S.A. 86*, 3296−3300.

(7) Sette, A., Buus, S., Colon, S., Miles, C. and Grey, H. M. (1989) Structural analysis of peptides capable of binding to more than one Ia antigen. *J. Immunol. 142*, 35−40.

(8) Sette, A., Lamont, A., Buus, S., Colon, S. M., Miles, C. and Grey, H. M. (1989) Effect of conformational propensity of peptide antigens in their interaction with MHC class II molecules: failure to document the importance of regular secondary structures. *J. Immunol. 143*, 1268−1273.

(9) Sette, A., Sidney, J., Albertson, M., Miles, C., Colon, S. M., Pedrazzini, T., Lamont, A. G. and Grey, H. M. (1990) A novel approach to the generation of high affinity class II-binding peptides. *J. Immunol. 145*, 1809−1813.

(10) Naito, S., Horino, A., Nakayama, M., Nakano, Y., Nagai, T., Mizuguchi, J., Komuro, K., and Uchida, T. (1996) Ovalbumin-liposome conjugate induces IgG but not IgE antibody production. *Int. Arch. Allergy Immunol. 109*, 223−228.

(11) Nakano, Y., Mori, M., Nishinohara, S., Takita, Y., Naito, S., Horino, A., Kato, H., Taneichi, M., Komuro, K., and Uchida, T. (1999) Antigen-specific, IgE-selective unresponsiveness induced by antigen-liposome conjugates: Comparison of four different conjugation methods. *Int. Arch. Allergy Immunol. 120*, 199−208.

(12) Nakano, Y., Mori, M., Nishinohara, S., Takita, Y., Naito, S., Kato, H., Taneichi, M., Komuro, K., and Uchida, T. (2001) Surface-linked liposomal antigen induces IgE-selective unresponsiveness regardless of the lipid components of liposomes. *Bioconjugate Chem. 12*, 391−395.

(13) Naito, S., Horino, A., Komiya, T., Fukuda, T., Takahashi, M., Ami, Y., Suzaki, Y., Oka, T., Okuma, K., Morokuma, M., Nakano, Y., Mori, M., Nishinohara, S., Komuro, K., and Uchida, T. (1998) Induction of protection against tetanus toxin in mice by tetanus toxoid-liposome conjugate. *Int. Arch. Allergy Immunol. 116*, 215−219.

(14) Fukuda, T., Komiya, T., Takahashi, M., Arakawa, Y., Ami, Y., Suzaki, Y., Naito, S., Horino, A., Nagata, N., Satoh, S., Gondaira, F., Sugiyama, J., Nakano, Y., Mori, M., Nishinohara, S., Komuro, K., and Uchida, T. (1998) Induction of protection against oral infection with cytotoxin-producing Escherichia coli O157: H7 in mice by Shiga-like toxin-liposome conjugate. *Int. Arch. Allergy Immunol. 116*, 313−317.

(15) Tanaka, Y., Kasai, M., Taneichi, M., Naito, S., Kato. H., Mori, M., Nishida, M., Maekawa, N., Yamamura, H., Komuro, K., and Uchida, T. (2004) Liposomes with differential lipid components exert differential adjuvanticity in antigen-liposome conjugates via differential recognition by macrophages. *Bioconjugate Chem. 15*, 35−40.

(16) Uchida, T., Ju, S. T., Fay, A., Liu, Y. N. and Dorf, M. E. (1985) Functional analysis of macrophage hybridomas. I. Production and initial characterization. *J. Immunol. 134*, 772−778.

(17) Stein, P. E., Leslie, A. G. W., Finch, J. T., Turnell, W. G., Mclaughlin, P. J., and Carrell, R. W. (1990) Crystal structure of ovalbumin as a model for the reactive centre of serpins. *Nature 347*, 99−102.

(18) Stein P. E., Leslie, A. G., Finch, J. T., and Carrel, R. W. (1991) Crystal structure of uncleaved ovalbumin at 1.95A resolution. *J. Mol. Biol. 221*, 941−959.

(19) Scott, C. A., Peterson, P. A., Teyton, L. and Wilson, I. A. (1998) Crystal structures of two I-A^d-peptide complexes reveal that high affinity can be achieved without large anchor residues. *Immunity 8*, 319−329.

(20) Jameson, S. C., and Bevan, M. J. (1988) Dissection of major histocompatibility complex (MHC) and T cell receptor contact residues in a K^b-restricted ovalbumin peptide and an assessment of the predictive power of MHC-binding motifs. *Eur. J. Immunol. 22*, 2663−2667.

(21) Moor, M. W., Carbone, F. R., and Bevan, M. J. (1988) Introduction of soluble protein into the class I pathway of antigen processing and presentation. *Cell 54*, 777−785.

(22) Rotzschke, O., Falk, K., Stevanovic, G., Walden, P., and Ramensee, H. G. (1991) Exact prediction of a natural T cell epitope. *Eur. J. Immunol*, *21*, 2891−2894.

(23) Kim, D. T., Mitchell, D. J., Brockstedt, D. G., Fong, L., Nolan, G. P., Fathman, C. G., Engleman, E. G., and Rothbard, J. B. (1997) Introduction of soluble proteins into the MHC class I pathway by conjugation to an HIV *tat* peptide. *J. Immunol*. *159*, 1666−1668.

(24) Anton van der Merwe, P., and Davis, S. J. (2003) Molecular interactions mediating T cell antigen recognition. *Annu. Rev. Immunol. 21*, 659−684.

(25) Hennecke, J., and Wiley, D. C. (2001) T cell receptor-MHC interactions up close. *Cell 104*, 1−4.

(26) Rudolph, M. G., and Wilson, I. A. (2002) The specificity of TCR/pMHC interaction. *Curr. Opin. Immunol. 14*, 52−65.

(27) Buus, S., Sette, A., Colon, S., Miles, C., and Grey, H. M. (1987) The relation between MHC restriction and the capacity of Ia to bind immunogenic peptides. *Science 235*, 1353−1357.

(28) Suzaki, Y., Ami, Y., Nagata, N., Naito, S., Kato, H., Taneichi, M., Takahashi, M., Komiya, T., Satoh, S., Gondaira, F., Sugiyama, J., Nakano, Y., Mori, M., Komuro, K., and Uchida, T. (2002) Protection of monkeys against Shiga toxin induced by Shiga toxin-liposome conjugates. *Int. Arch. Allergy Immunol. 127*, 294−298.

(29) Uchida, T. (2003) Stx-liposome conjugates as candidate vaccines. *Drugs Today 39*, 673−693.

BC060024G

Imaging Pancreatic Cancer with a Peptide−Nanoparticle Conjugate Targeted to Normal Pancreas

Xavier Montet, Ralph Weissleder, and Lee Josephson*

Center for Molecular Imaging Research, Massachusetts General Hospital, Harvard Medical School, Building 149, 13th Street, Charlestown, Massachusetts 02129. Received February 13, 2006; Revised Manuscript Received April 14, 2006

Designing molecules that bind to targets that become upregulated or overexpressed as normal cells become cancerous is an important strategy for both therapeutic and diagnostic drug design. We hypothesized that pancreatic ductal adenocarcinoma (PDAC) might be imaged with the inverse strategy, that is by the design of a nanoparticle−conjugate targeted to bombesin (BN) receptors present on normal acinar cells of the pancreas. Using the fluorescein hapten visualization method to assess the presence of bombesin (BN) receptors, we first demonstrated BN receptors in the normal mouse and human pancreas, but then the lack of BN binding receptors in 13 out of 13 specimens of PDAC. The BN peptide−nanoparticle conjugate, BN−CLIO(Cy5.5), was synthesized and accumulated in the mouse pancreas in receptor dependent fashion, but not in a receptor dependent fashion in other tissues, based on tissue fluorescence measurements. The BN−CLIO(Cy5.5) nanoparticle decreased the T2 of normal pancreas and enhanced the ability to visualize tumor in a model of pancreatic cancer by MRI. The use of BN−CLIO(Cy5.5) nanoparticle as a normal tissue-targeted, T2-reducing contrast agent offers a promising approach to imaging PDAC.

INTRODUCTION

Pancreatic ductal adenocarcinoma (PDAC) ranks as the fourth leading cause of cancer death in the US. In 2004, an estimated 32 000 cases will be matched with 31 500 deaths. The mean survival averages 6 months, and less than 5% of all patients survive beyond 5 years (http://seer.cancer.gov/). The dire situation in PDAC relates to the tumor's intense drug resistance and late diagnosis, among other factors. Late diagnosis is due to the lack of specific symptoms and limitations in diagnostics, allowing the disease to elude detection during its formative stages. Though improved imaging methods are needed to assist in the detection and treatment, few agents have been designed to image molecular targets expressed by PDAC. This is in part due to the fact that many molecularly targeted, radioactive peptides (somatostatin, secretin, bombesin, CCK, VIP) employed in tumor imaging in nonpancreatic organ settings have limited utility as pancreatic imaging agents because of the expression of these receptors on cells of the noncancerous pancreas (*1*−*6*).

The large number of receptors present on normal pancreatic stroma, however, suggests an alternative strategy for tumor visualization, one where agents target receptors expressed on normal cells. The strategy of targeting normal rather than tumor cells has worked well with magnetic nanoparticles which selectively decrease the T2 of the normal liver and lymph nodes by targeting macrophages in those tissues and enhance tumor visualization in those tissues by MRI (*7*, *8*). We refer to this approach as a normal tissue-targeted nanoparticle/T2 reduction strategy.

We therefore hypothesized that a peptide−nanoparticle conjugate targeted to the bombesin peptide binding receptors on normal pancreatic acinar cells might enhance the visualization of pancreatic tumors in an orthotopic animal model and, potentially, in human PDAC. We noted that the literature suggested a molecular target(s), bombesin peptide binding receptors, was present in the normal pancreas and not PDAC (*9*). The distribution of the bombesin binding receptors in PDAC and the normal pancreas is discussed below. Second, bombesin binding receptors internalize ligands, offering a potentially dynamic mechanism of nanoparticle accumulation and amplification (*10*−*12*). The broad goal of developing a nanoparticle targeted to normal pancreas for imaging PDAC by MRI included the following subaims: (i) to develop a nanoparticle targeted to bombesin peptide binding receptors in the normal pancreas, (ii) to demonstrate that the nanoparticle decreased the T2 of normal pancreas and, (iii) to demonstrate enhanced tumor/normal visualization on T2 weighted pancreatic images.

MATERIALS AND METHODS

Peptide−Nanoparticle Conjugate Synthesis. Peptides were synthesized by the Tufts Core Facility (Tufts University Core facility, Boston, MA) to obtain a bombesin-like peptide (FITC)-BCDDDGQRLGNQWAVGHLM or BN, as well as a scrambled version of the bombesin-like peptide, (FITC)BCDDDGQM-LGNHLAVGQWR or ScrBN. Peptides were C-terminal amides. B stands for betalanine and FITC for fluorescein isothiocyanate. The 13 C-terminal amino acids are found in bombesin. Three negatively charged aspartate residues (DDD) were employed as spacers and provide a negative charge bias on the nanoparticle; these increase nanoparticle solubility and decrease nonspecific interactions with negatively charged cells. The amino-CLIO nanoparticle, synthesized as described (*13*, *14*), was first reacted with the *N*-hydroxysuccinimde ester of Cy5.5 (Amersham Biosciences Corp, Piscataway, NJ) to obtain a ratio of 5.1 dyes per nanoparticle which is denoted CLIO(Cy5.5) (*15*). The majority of amines remained available for reaction with succinimidyl iodoacetic acid, which then reacted with the sulfhydryl group of the BN or ScrBN peptides (*15*, *16*). The resulting nanoparticles, BN−CLIO(Cy5.5) and ScrBN−CLIO(Cy5.5), were identical in composition, but because of the sequence difference, the ScrBN nanoparticle was unable to bind receptors for bombesin. Fluorescein, attached to peptides before conjugation to the nanoparticle, does not appear in this notation; it allows characterization of the peptide:iron ratio based on its absorption at 493 nm. The resulting nanoparticles, BN−

* Corresponding author. Fax: 617-726-5708. Phone: 617-726-5788. E-mail: ljosephson@partners.org.

10.1021/bc060035+ CCC: $33.50 © 2006 American Chemical Society
Published on Web 05/26/2006

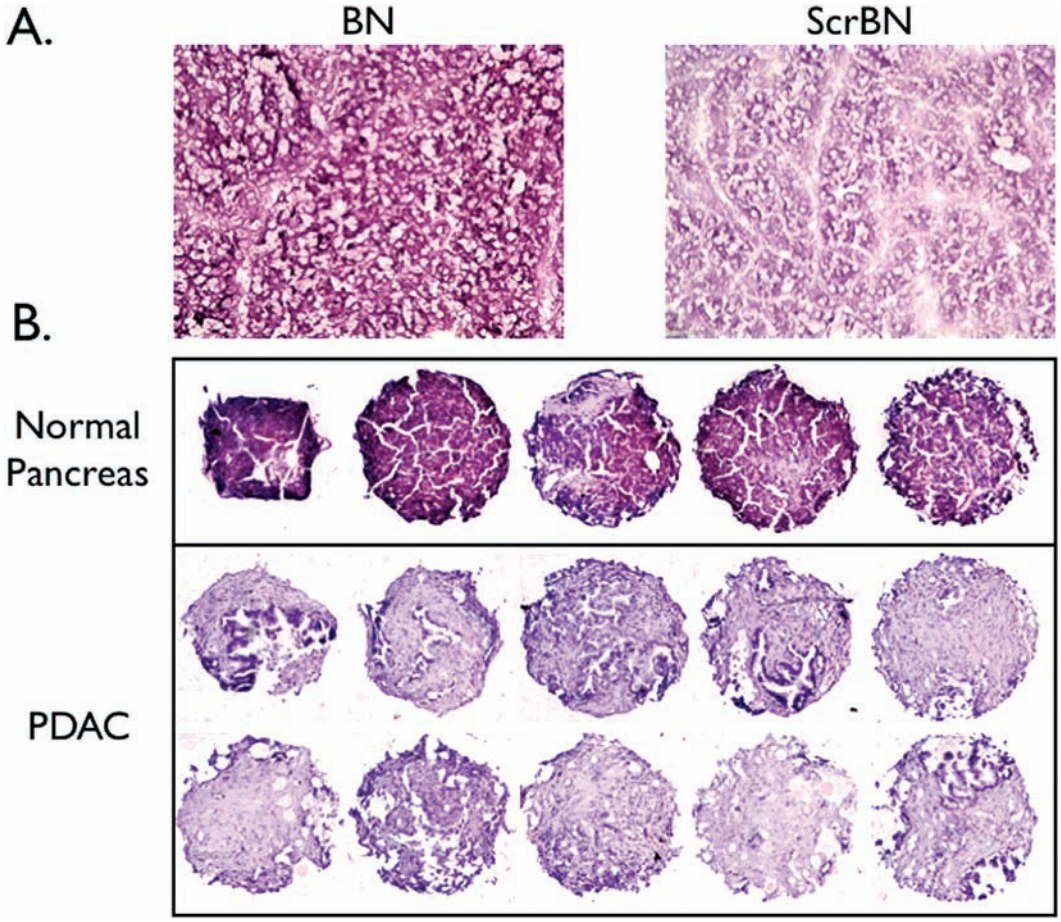

Figure 1. Binding of bombesin peptide to normal pancreas. (A) Bombesin peptide (BN) or scrambled version (ScrBN) were exposed to normal mouse pancreas. The fluorescein on the peptide is visualized by an anti-fluorescein horseradish peroxidase conjugate. Normal pancreas stained dark purple. BN stains more darkly than ScrBN, indicating specific binding. (B) BN was exposed to a human tissue microarray of normal human pancreas and pancreatic ductal adenocarcinomas. Normal tissue stained more darkly than pancreatic adenocarcinomas.

CLIO(Cy5.5) and ScrBN−CLIO(Cy5.5), had diameters of 35 and 41 nm by laser light scattering, relaxivities of 70 and 62 $mM^{-1}\ s^{-1}$, and 50 and 48 peptides per nanoparticle, respectively. The numbers of dyes or peptides per nanoparticle were based on 8000 iron atoms per amino-CLIO nanoparticle, obtained by the viscosity/light scattering method for estimating nanoparticle core weights (*17*). The design of the peptide−nanoparticles used here is shown schematically in Figure 1 of Koch (*15*), except (i) Cy5.5 replaced Cy3.5 as the fluorochrome attached to the dextran, and (ii) peptides coupled were the BN and ScrBN peptides rather than the tat peptide. In both conjugations succinimidyl iodoacetic acid was used to attach the thiol of a cysteine group to the amine of the nanoparticle, so the linker chemistry in the current study is that shown by Koch.

To determine the binding of the BN peptide and ScrBN peptides to the normal mouse pancreas, the fluorescein hapten visualization (FHV) and assay (FHA) methods were used, a more complete analysis of which has been published (*18*). Tissue sections of mouse pancreas, 7 μm thick, were snap frozen. To determine the binding of BN peptide to human tissue specimens, tissue microarrays of pancreatic tumor were obtained (Tristar Technology Group, LLC, Bethesda, MD), which contained 13 cancers and 5 normal pancreas specimens. Tissue microarrays or normal mouse pancreas specimens were incubated for 1 h at room temperature with either BN or ScrBN peptides at 1 μg/mL diluted in PBS containing 10% rabbit serum, 0.3% sodium azide w/v, and 0.5% H_2O_2 to block the endogenous peroxidases. Unbound peptide was removed by washing three times with the PBS. An anti-FITC horseradish peroxidase conjugate (Molecular Probes, Eugene OR), diluted into PBS containing 2% human serum to 5 μg/mL, was applied to the sample for 40 min. Unbound conjugate was removed by washing three times with the PBS. Enzyme activity was developed for 8 min using the Vectastain Elite ABC kit (Vector Laboratories, Burlingame, CA). For the fluorescein hapten assay, specimens were fixed as above, incubated with ligand, and washed free of unbound ligand as above for the fluorescein hapten receptor visualization method. The immunoassay for immunoreactive fluorescein was employed to quantitate bound fluorescein (*19*). To the slide chamber was added 500 μL of lysis buffer (PBS, 0.1% BSA, 0.1% Triton X-100, 1 mM 8-anilino-1-naphthalenesulfonic acid with 40 ng/mL of anti-fluorescein-HRP. Incubation was for 2 h at room temperature. Duplicate 200 μL volumes were then transferred to a 96-well plate (MaxiSorp, Nunc) coated with 12.5 ng/mL FITC-labeled BSA (Sigma-Aldrich, St, Louis, MO) and incubated for 1 h at room temperature. Plates were then washed three times (PBS, 0.1% BSA, 0.1% Tween) to remove unreacted anti-fluorescein-HRP, and bound peroxidase was quantitated by absorbance at 650 nm using 200 μL of 3,3′,5,5′-tetramethylbenzidine dihydrochloride after 30 min incubation at room temperature. The concentration of fluoresceinated ligand was determined from a standard curve of fluoresceinated ligand diluted in PBS, 0.1% BSA, 0.1% Tween.

To determine nanoparticle tissue distribution, normal athymic female nude mice (20−25 g) ($n = 13$) were divided in three groups. Group 1 ($n = 3$) was injected with PBS and was used to measure the intrinsic fluorescence of each organ. Groups 2 and 3 ($n = 5$) were injected with BN−CLIO(Cy5.5) or ScrBN−CLIO(Cy5.5) (10 mg Fe/kg), respectively, and sacrificed after 24 h. Tissue fluorescence was obtained using a commercially

available fluorescence reflectance imaging system (BonSAI system, Siemens, Malvern, PA). Slices of tissues (about 1 mm thick, roughly 5 mm in diameter) were placed on a dark plate. Fluorescence was determined using operator-defined regions-of-interest (ROI) on tissues from both injected and uninjected animals. Background fluorescence was subtracted and the values of BN−CLIO(Cy5.5) and ScrBN−CLIO dependent tissue fluorescence were obtained.

To examine whether the BN−CLIO(Cy5.5) could enhance visualization of pancreatic tumors by MRI an orthotopic tumor model was employed. The pancreatic tumor cell line, MIA-PaCa 2 from the American Tissue Culture Collection (ATCC, Manassas, VA), was cultured according to the manufacturer's instructions. Following anesthesia (Isofluorane, 2%), a paramedian laparotomy allowed access to the pancreas and two million MIA-PaCa2 cells in 10 μL were implanted directly in the pancreatic tail of athymic nude female mice. Histology indicated a single, well-defined tumor per pancreas in all animals with a lack of micrometastases ($n = 5$).

Mice were imaged on a 4.7T Bruker system (Pharmascan, Karlsruhe, Germany) 6 days after implantation, followed by BN−CLIO(Cy5.5) tail vein injection (10 mgFe/kg), with postcontrast images acquired 24 h later. Isofluorane 2% was used for anesthesia during imaging. Coronal T2* maps were generated using the parameters: TR = 2000 ms, 16 different TE values from 6.5 to 104 ms, flip angle = 90°, matrix size = 128 × 64, number of average = 4, field of view = 4.24 × 2.12 cm, slice thickness = 0.8 mm. Tumor to normal contrast (CNR) ratio was obtained at TR = 2000 ms, TE = 52 ms where CNR was taken as the difference in signal intensity of the tumor and normal pancreas divided by the standard deviation of the noise. Hand-drawn regions of interest of clearly hyperintense signal (1−3 mm) were taken as tumor, whose dimensions and position were verified by dissection and histology. After the second MR imaging session, tissues were removed, snap frozen, and cut into 7 μm sections (for hemotoxylin and eosin) or into 15 μm for direct fluorescence microscopy.

To characterize the presence of BN binding receptors, the pancreas from athymic female nude mice was removed and digested with collagenase/Dispase enzymes solution (Roche Diagnostics, Penzberg, Germany) for 1 h at 37 °C. Cell suspensions were filtered through strainers of 100 μm (BD Biosciences, Franklin Lakes, NJ) and centrifuged (1000 rpm for 5 min) to obtain disaggregated pancreatic cells. Cells were then incubated with either BN or ScrBN and an anti-acinar cell antibody, obtained from the Developmental Studies Hybridoma Bank developed under the auspice of the NICHD and maintained by the University of Iowa (Department of Biological Sciences, Iowa City, IA) (*20*). FACS analysis was performed on a FACScalibur (Becton Dickinson, Franklin Lakes, NJ). All animal studies were approved by the MGH animal care committee.

RESULTS

Tissue-based radioreceptor assays have found bombesin binding receptors to be absent in human pancreatic ductal adenocarcinomas (*9*), while studies of GRP receptor mRNA expression in different tissues found bombesin binding receptor mRNA to be abundant in the normal human pancreas (*21, 22*). (The presence of bombesin binding receptors in the pancreas is discussed more fully below.) To determine if the BN peptide had the desired interaction with normal pancreatic tissue, we used the recently developed fluorescein hapten visualization (FHV) and fluorescein hapten assay (FHA) methods for bound peptide. Here the binding of fluoresceinated peptides to receptors in tissues is visualized or assayed using an anti-fluorescein−horseradish peroxidase conjugate and horseradish peroxidase substrate (*18*). An FHV method with normal mouse pancreas is shown in Figure 1A, where the tissue was treated with the BN peptide or ScrBN peptides; the former produced a notably darker stain that appeared to be homogeneous. To verify the visual difference in stain intensity from the two peptides, tissues were exposed to either peptide, a volume of lysis buffer was added to dissolve the tissue, and the fluorescein in the lysate was quantified by the fluorescein immunoassay, a procedure we term an FHA method (*18*). There was 3.5 times more BN peptide than the ScrBN peptide on tissue specimens. The binding of the BN peptide to acinar cells in the mouse pancreas was also evident when disaggregated cells from the pancreas were exposed to the peptide and analyzed by FACS, see Figure 4D. We applied that FHV method to a tissue microarray consisting of 5 normal human pancreas specimens and 13 pancreatic ductal adenocarcinomas. The binding of the BN peptide was assessed using the anti-fluorescein−horseradish peroxidase conjugate. As shown in Figure 1B, the BN peptide produced a notably darker peroxidase stain with normal pancreatic specimens than ductal adenocarcinoma specimens. On the basis of a limited number of specimens, it appears that the BN peptide binds normal human pancreas and not pancreatic adenocarcinomas.

To determine the tissue specificity of the BN−CLIO(Cy5.5) nanoparticle, we compared the uptake of the nanoparticle in the pancreas with that of ScrBN−CLIO(Cy5.5), a nanoparticle which has identical physical properties to BN−CLIO(Cy5.5) but which is made with a peptide having a scrambled sequence (Figure 1). As shown in Figure 2A, the pancreas of animals injected with BN−CLIO(Cy5.5) was distinctly brighter than those injected with ScrBN−CLIO(Cy5.5). Organ fluorescence obtained with each nanoparticle, together with tissue autofluorescence, is shown in Figure 2B. The hepatic uptake reflects the fact that nanoparticles are too large for renal elimination, and both BN−CLIO(Cy5.5) and ScrBN−CLIO(Cy5.5) are withdrawn by Kupffer cells of the liver in a nonreceptor dependent fashion. The uptake of the two nanoparticles was similar ($p > 0.11-0.57$) for all tissues except the pancreas, which had a 3-fold higher fluorescence with BN−CLIO(Cy5.5) than ScrBN−CLIO(Cy5.5), ($p < 0.003$); see Figure 2C. On the basis of the ratio of fluorescence, receptor-mediated targeting of BN−CLIO(Cy5.5) occurred with the pancreas, with high nonpeptide dependent uptake by the liver and spleen. This method of demonstrating receptor specificity (receptor binding and nonreceptor binding nanoparticles) was employed because the BN peptide has a shorter blood half-life than the BN−CLIO(Cy5.5) nanoparticle and the peptide cannot block receptor-mediated interactions in vivo (Montet and Josephson, unpublished observations).

We next examined whether the injection BN−CLIO(Cy5.5) could improve the contrast between normal pancreas and tumor as shown in Figure 3. T2 weighted MR images (TR = 2000 ms, TE = 52 ms) before and after the injection of BN−CLIO(Cy5.5) of a mouse with a tumor-bearing pancreas are shown in Figure 3A and 3B, respectively. Tumor (arrow) is not visible or barely visible in the precontrast image but after the injection of BN−CLIO(Cy5.5), and darkening of normal pancreas, tumor mass became readily discernible, see Figure 3C (magnified version of 3B). A colorized map of pancreatic T2 values is shown in Figure 3D, superimposed on the T2 weighted image. Tumors were present as well-defined single masses (no micrometastases), whose location was confirmed on dissection, see Figure 3E. With a cutoff of 53 ms for tumor versus normal pancreas, T2 values were 62 ± 6 and 62 ± 5 ms ($n = 5$) for tumors, pre- and postinjection, respectively. The average T2 values of the normal pancreas decreased from 46 ± 5 to 39 ± 5 ms ($n = 8$) with BN−CLIO(Cy5.5) injection ($p = 0.036$). Thus BN−CLIO(Cy5.5) enhanced tumor visualization by selectively decreasing the T2 of the normal pancreas.

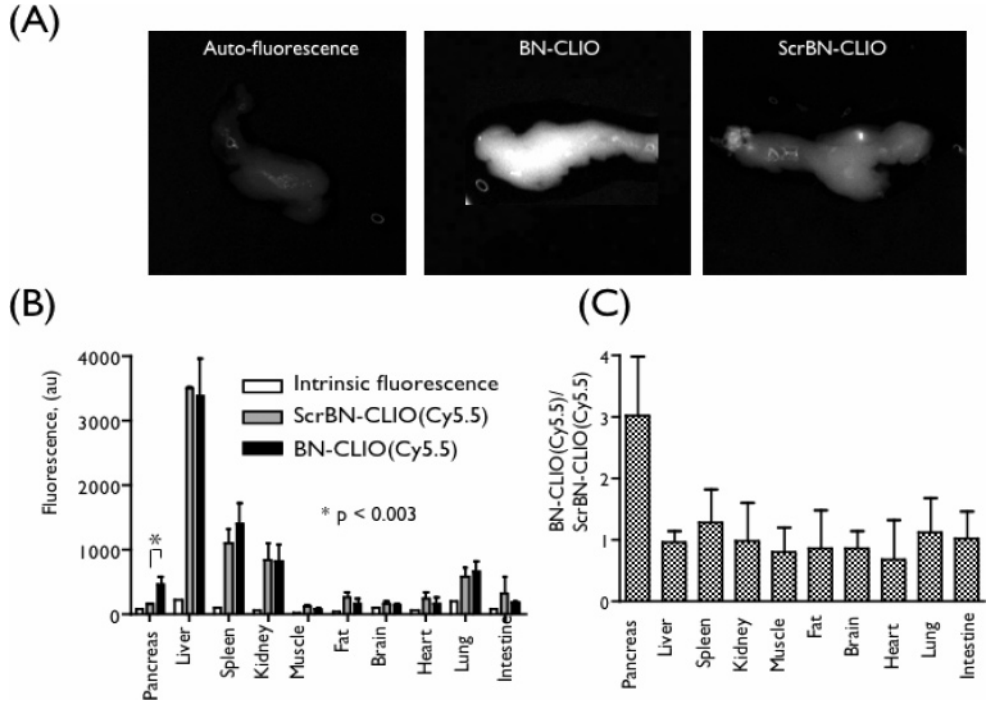

Figure 2. BN peptide targets the BN−CLIO(Cy5.5) nanoparticle to the normal mouse pancreas. (A) Tissue autofluorescence and tissue fluorescence postinjection of ScrBN−CLIO(Cy5.5) or BN−CLIO(Cy5.5) nanoparticle for a normal mouse pancreas. (B) Fluorescence of dissected tissues after injection with nanoparticles and from uninjected animals. (C) Ratio of tissue fluorescence for BN−CLIO(Cy5.5) and ScrBN−CLIO(Cy5.5), obtained after background subtraction. The pancreas was the only organ to preferentially accumulate the BN−CLIO(Cy5.5).

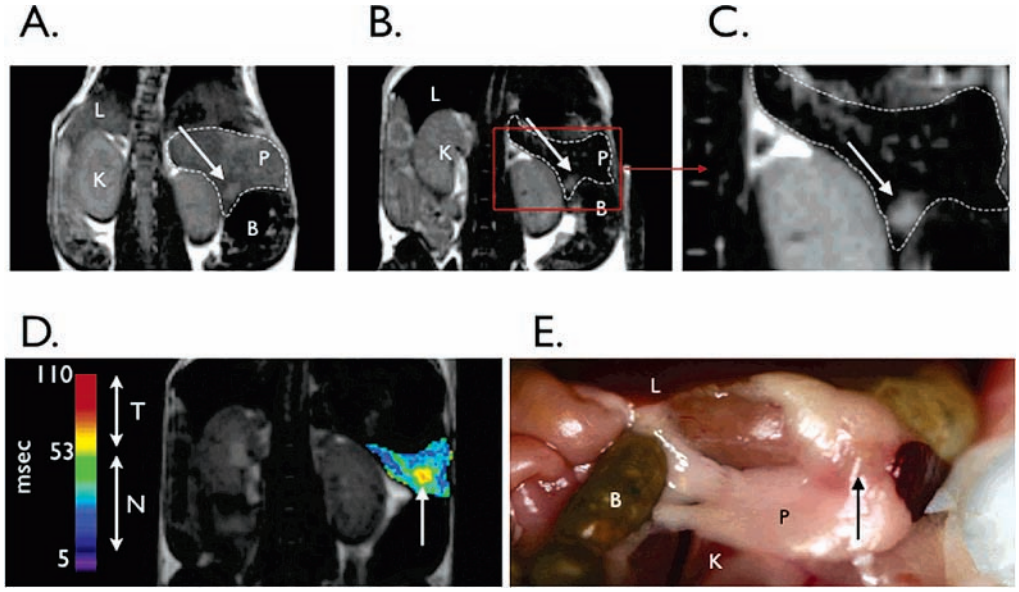

Figure 3. T2 weighted images of pancreas and tumor. Preinjection (A) and postinjection (B) of pancreas and tumor. (C) Image from B at higher magnification. BN−CLIO(Cy5.5) permits tumor (arrows) to be seen. Arrow indicates bulk tumor. (D) Postcontrast agent, colorized T2 map of a pancreas with implanted tumor. Tumor has higher T2s than normal pancreas. Abbreviations: L, liver; P, pancreas; K, kidney; B, bowel. (E) Photograph of partially dissected mouse with pancreas and tumor visible.

We next examined the distribution of BN−CLIO(Cy5.5) within the pancreas by fluorescence microscopy and FACS as shown in Figure 4. Figure 4A and 4B show the tumor margin with H and E stain or fluorescence microscopy, respectively. As shown in Figure 4B, the nanoparticle was preferentially accumulated at the border of the tumor, with substantial regions of low nanoparticle accumulation elsewhere in the micrograph. The BN−CLIO(Cy5.5) nanoparticle was visible in the fluorescein channel, due to fluorescein on the BN peptide or Cy5.5 channel, due to Cy5.5 attached directly to the nanoparticle. Background fluorescence in these channels was corrected using tissues from noninjected animals. We also injected a mouse, disaggregated the pancreas, and ran the disaggregated cells through a single channel FACS as shown in Figure 4C. Some 8% of the cells were labeled as a distinct population with a median fluorescence of 198 au compared to the median fluorescence of 21 au obtained for the unlabeled cell fraction from the injected animal. We characterized cells from the disaggregated pancreas using a specific anti-acinar cell antibody using dual wavelength FACS as shown in Figure 4D and 4E. Some 33−34% of the cells bound the anti-acinar antibody and these cells also bound the BN peptide and an anti-gastrin

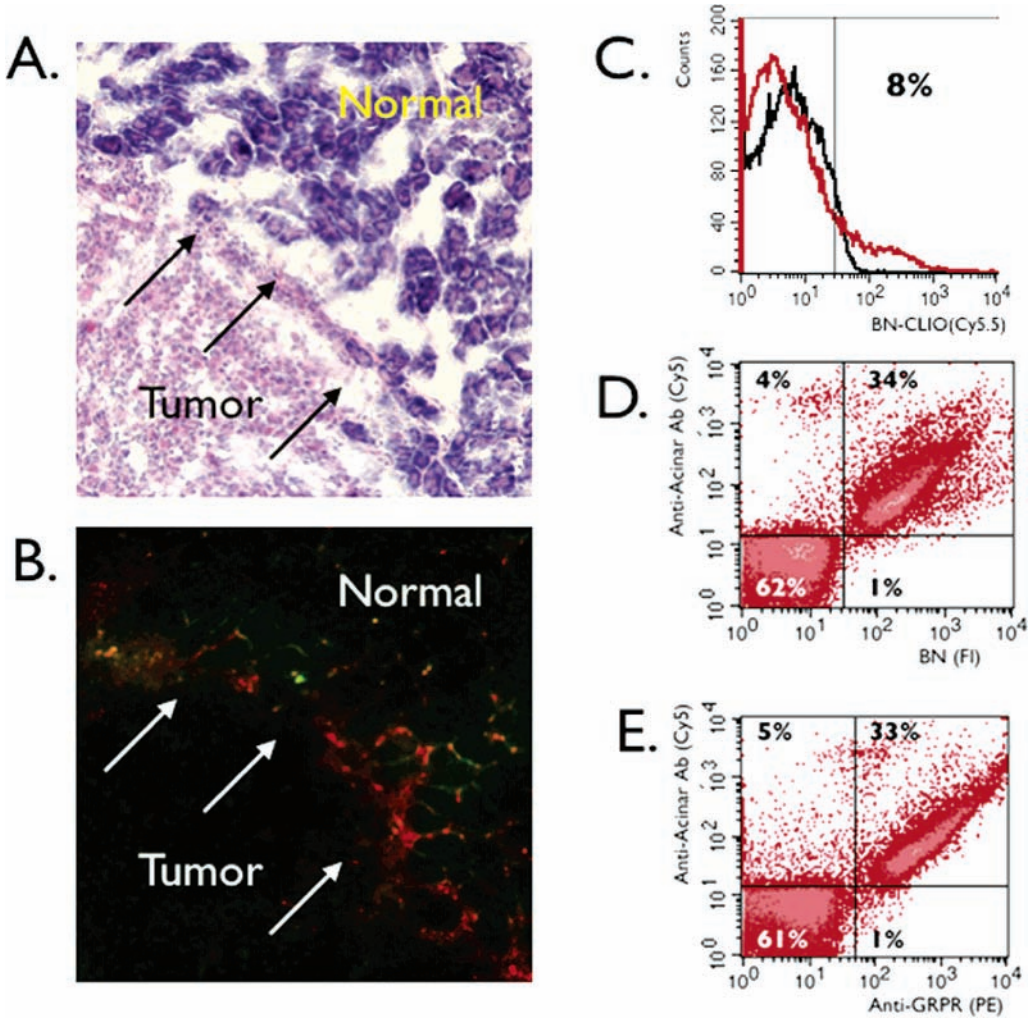

Figure 4. Accumulation of the BN−CLIO(Cy5.5) nanoparticle in the mouse pancreas. (A) Border (arrows) between tumor and normal pancreas with H and E stain. (B) Fluorescent microscopy of the adjacent tissue slice to that shown in (A). Cy5.5 fluorescence (red) and fluorescein fluorescence (green) are shown. Nanoparticle concentrates at tumor border (arrows). (C) Single channel FACS of disaggregated normal mouse pancreas after injection of BN−CLIO(Cy5.5). Some 8% of cells have Cy5.5 fluorescence. (D) Dual wavelength FACS of cells from disaggregated pancreas binding Cy5 labeled anti-acinar antibody and BN peptide (fluorescein labeled). (E) Cells from disaggregated pancreas binding anti-acinar antibody and anti-GRP. Acinar cells (34% of total pancreatic cells) express GRP receptor and bind BN peptide.

releasing peptide receptor antibody. Since only 8% of the cells were labeled, it appears that most acinar cells (34% of total) cells did not internalize BN−CLIO(Cy5.5).

DISCUSSION

A feature of the postinjection BN−CLIO(Cy5.5) images of the mouse pancreas was the heterogeneous signal intensity obtained (Figure 3C). Though we did not correlate local changes in pancreatic signal intensity with higher or lower concentrations of nanoparticles in specific regions of the pancreas, two lines of evidence indicate a generally heterogeneous particle distribution within the pancreas. First, fluorescence microscopy (Figure 4B) showed regions of higher and lower nanoparticle concentration in the nontumor bearing, normal pancreas. Second, FACS analysis of disaggregated acinar cells (Figure 4C, D, E) showed the nanoparticle concentrated in a small percentage of cells. In contrast to these results for the postinjection distribution of BN−CLIO(Cy5.5) nanoparticle in the pancreas, examination of dissected pancreatic tissue showed a uniform binding of the BN peptide. First, dual wavelength FACS of cells from the disaggregated pancreas indicated all acinar cells both expressed the GRP receptor (Figure 4E) and bound the BN peptide (Figure 4D). Second, by histochemistry the binding of the BN peptide to the normal mouse pancreas was uniform (Figure 1A). It seems likely that the heterogeneous change in signal intensity post BN−CLIO(Cy5.5) injection reflects selective regions within the exocrine pancreas which are permeable to BN−CLIO(Cy5.5) and that after extravasating the nanoparticle binds the GRP receptor and is internalized by acinar cells. This hypothesis is supported by the fact that the pancreatic exocrine vasculature is heterogeneous, consisting of both fenestrated and nonfenestrated capillaries (*23*).

We employed a peptide with the 13 C-terminal amino acids of bombesin, see above, which can bind to any of three receptors, the NMB receptor (BB1), the GRP receptor (BB2), or the orphan bombesin binding receptor BB3. These three receptors comprise the bombesin peptide binding receptors in mammals, though they are different gene products with somewhat different ligand specificities. We made no effort to determine whether the NMB, GRP, or BB3 receptors bound the BN peptide or the BN−CLIO(Cy5.5) nanoparticle, noting only that the binding of the BN peptide to pancreatic ductal adenocarcinoma was decreased relative to that seen with normal pancreas and providing a rationale for the development of a BN peptide−nanoparticle conjugate. The distribution of bombesin binding receptors is discussed further below.

For the approach we have taken to be useful clinically, receptors binding the BN−CLIO(Cy5.5) nanoparticle must be

(i) absent in PDAC and (ii) present in the normal pancreas. **Absence on PDAC (prior studies):** Bombesin binding receptors have been found on dissected cancers from the lung, prostate, and breast, and on many tumor cell lines (*5*, *24*). However, PDAC appears to be different from other cancers; bombesin binding was absent when 29 PDAC specimens were examined using a radiolabeled bombesin peptide (*9*). **Presence on normal pancreas (prior studies):** Though the same authors did not detect bombesin binding in the normal human pancreas (*9*), the mRNA for the GRP receptor is expressed at high levels in the pancreas of primates (*21*, *22*) and the expression of bombesin binding receptors in the rodent pancreas is observed with injected radiolabeled bombesin peptides (*4*, *12*, *25*). **Absence on PDAC and presence on normal pancreas (our studies):** To clarify this situation with respect to the presence of bombesin binding receptors in the normal human pancreas, and verify the observations of Fleischman (*9*) that receptors are missing in human PDAC, we examined the binding of the BN peptide, first to the normal mouse pancreas (Figure 1A) and then to normal human pancreatic tissue and PDAC specimens. In agreement with Fleischman et al., we could *not* detect bombesin binding in human PDAC specimens, but were able to detect the binding of our BN peptide in the normal human pancreas (Figure 1B). We therefore conclude that bombesin binding receptors are absent in PDAC and present in the both the normal rodent and normal human pancreas. Difference in results may be due to different detection limits of the methods used, different specificity of peptides or nucleic acid binding probes, or different definitions of what comprises a truly normal, noncancerous specimen of human pancreas.

A variety of radioactive bombesin-like peptides have been used to image the overexpression of bombesin binding receptors in animal tumor models (*4*, *12*, *25*−*28*) and clinically (*29*−*32*). We have taken the inverse targeting approach termed a "normal tissue targeted nanoparticle/T2 reduction strategy", designing a nanoparticle-based MR contrast agent image targeted to bombesin binding receptors of the normal pancreas. The approach of enhancing tumor visualization by targeting normal tissue takes advantage of the spatial localizing ability of MR, that is its ability to determine the signal from individual voxels, without interference from adjacent voxels. Thus a nanoparticle agent can enhance tumor/normal contrast if it decreases the T2 of normal tissue surrounding a tumor more than the T2 of tumor. Similarly, T2 reductions in other organs such as the liver do affect contrast enhancement in the pancreas. It should be noted that the condition for a normal tissue-targeted nanoparticle, T2 reducing contrast agent is not a complete loss of gene expression/activity in the cancerous state, but only relatively higher activity in a normal tissue than that of tumor. Obviously, the decrease of expression/activity of the marker responsible for selective nanoparticle accumulation in normal tissue should decrease in a highly uniform fashion for a significant class of cancers. Radiolabeled peptides are generally targeted to tumors, and uptake by normal tissue raises background and reduces tumor visualization.

In conclusion, we have designed a magneto/fluorescent nanoparticle conjugate that was successfully targeted to the bombesin binding receptors of the rodent pancreas and used it to enhance the visualization of a tumor with a normal tissue targeted nanoparticle/T2 reduction strategy. Heterogeneous changes in the T2 of the normal pancreas were inferred to be due to a heterogeneous vasculature limiting nanoparticle delivery to acinar cells. Preliminary experiments indicate that this heterogeneity can be overcome by using an intraperitoneal mode of administration for BN−CLIO(Cy5.5), which can increase pancreatic targeting of high molecular weight liposomes (*33*) or chemotherapeutic agents (*34*). However, even with relatively inefficient receptor specific targeting of the pancreas obtained with intravenous administration, the peptide was targeted to the pancreas by tissue fluorescence, reduced the T2 of the normal pancreas, and enhanced the visualization of an implanted tumor.

ACKNOWLEDGMENT

Work was supported in part by grants from the Department of Defense (DAMD-170210089) and from the NIH (R01 EB00662, P50 86355, R24 CA92782, and PO1 117969). X.M. was supported by a fellowship from the Swiss National Science foundation (PBGEB-104665).

LITERATURE CITED

(1) Korner, M., Hayes, G. M., Rehmann, R., Zimmermann, A., Friess, H., Miller, L. J., and Reubi, J. C. (2005) Secretin receptors in normal and diseased human pancreas: marked reduction of receptor binding in ductal neoplasia. *Am. J. Pathol. 167*, 959−68.

(2) Jensen, R. T., Wank, S. A., Rowley, W. H., Sato, S., and Gardner, J. D. (1989) Interaction of CCK with pancreatic acinar cells. *Trends Pharmacol. Sci. 10*, 418−23.

(3) Reubi, J. C. (2000) In vitro evaluation of VIP/PACAP receptors in healthy and diseased human tissues. Clinical implications. *Ann. N. Y. Acad. Sci. 921*, 1−25.

(4) Nock, B., Nikolopoulou, A., Chiotellis, E., Loudos, G., Maintas, D., Reubi, J. C., and Maina, T. (2003) [99mTc]Demobesin 1, a novel potent bombesin analogue for GRP receptor-targeted tumour imaging. *Eur. J. Nucl. Med. Mol. Imaging 30*, 247−58.

(5) Reubi, J. C. (2003) Peptide receptors as molecular targets for cancer diagnosis and therapy. *Endocr. Rev. 24*, 389−427.

(6) Reubi, J. C., and Waser, B. (2003) Concomitant expression of several peptide receptors in neuroendocrine tumours: molecular basis for in vivo multireceptor tumour targeting. *Eur. J. Nucl. Med. Mol. Imaging 30*, 781−93.

(7) Harisinghani, M. G., Barentsz, J., Hahn, P. F., Deserno, W. M., Tabatabaei, S., van de Kaa, C. H., de la Rosette, J., and Weissleder, R. (2003) Noninvasive detection of clinically occult lymph-node metastases in prostate cancer. *N. Engl. J. Med. 348*, 2491−9.

(8) Chachuat, A., and Bonnemain, B. (1995) European clinical experience with Endorem. A new contrast agent for liver MRI in 1000 patients. *Radiologe 35*, S274−6.

(9) Fleischmann, A., Laderach, U., Friess, H., Buechler, M. W., and Reubi, J. C. (2000) Bombesin receptors in distinct tissue compartments of human pancreatic diseases. *Lab. Invest. 80*, 1807−17.

(10) Zachary, I., and Rozengurt, E. (1987) Internalization and degradation of peptides of the bombesin family in Swiss 3T3 cells occurs without ligand-induced receptor down-regulation. *EMBO J. 6*, 2233−9.

(11) Zhu, W. Y., Goke, B., and Williams, J. A. (1991) Binding, internalization, and processing of bombesin by rat pancreatic acini. *Am. J. Physiol. 261*, G57−64.

(12) Breeman, W. A., De Jong, M., Bernard, B. F., Kwekkeboom, D. J., Srinivasan, A., van der Pluijm, M. E., Hofland, L. J., Visser, T. J., and Krenning, E. P. (1999) Pre-clinical evaluation of [(111)In-DTPA-Pro(1), Tyr(4)]bombesin, a new radioligand for bombesin-receptor scintigraphy. *Int. J. Cancer 83*, 657−63.

(13) Josephson, L., Tung, C. H., Moore, A., and Weissleder, R. (1999) High-efficiency intracellular magnetic labeling with novel superparamagnetic-Tat peptide conjugates. *Bioconjugate Chem. 10*, 186−91.

(14) Josephson, L., Perez, J. M., and Weissleder, R. (2001) Magnetic nanosensors for the detection of oligonucleotide sequences. *Angew. Chem., Int. Ed. 40*, 3204−3206.

(15) Koch, A. M., Reynolds, F., Kircher, M. F., Merkle, H. P., Weissleder, R., and Josephson, L. (2003) Uptake and metabolism of a dual fluorochrome Tat-nanoparticle in HeLa cells. *Bioconjugate Chem. 14*, 1115−21.

(16) Reynolds, F., Weissleder, R., and Josephson, L. (2005) Protamine as an efficient membrane-translocating peptide. *Bioconjugate Chem. 16*, 1240−5.

(17) Reynolds, F., O'Loughlin, T., Weissleder, R., and Josephson, L. (2005) Method of determining nanoparticle core weight. *Anal. Chem. 77*, 814−7.
(18) Montet, X., Yuan, H., Weissleder, R., and Josephson, L. (2006) Enzyme based visualization of receptor−ligand binding in tissues. *Lab. Invest. 86*, 517−525.
(19) Kelly, K. A., Reynolds, F., Weissleder, R., and Josephson, L. (2004) Fluorescein isothiocyanate-hapten immunoassay for determination of peptide-cell interactions. *Anal. Biochem. 330*, 181−5.
(20) De Lisle, R. C., Logsdon, C. D., Hootman, S. R., and Williams, J. A. (1988) Monoclonal antibodies as probes for plasma membrane domains in the exocrine pancreas. *J. Histochem. Cytochem. 36*, 1043−51.
(21) Sano, H., Feighner, S. D., Hreniuk, D. L., Iwaasa, H., Sailer, A. W., Pan, J., Reitman, M. L., Kanatani, A., Howard, A. D., and Tan, C. P. (2004) Characterization of the bombesin-like peptide receptor family in primates. *Genomics 84*, 139−46.
(22) Xiao, D., Wang, J., Hampton, L. L., and Weber, H. C. (2001) The human gastrin-releasing peptide receptor gene structure, its tissue expression and promoter. *Gene 264*, 95−103.
(23) Aharinejad, S., and Bock, P. (1994) Identification of fenestrated capillary segments in microvascular corrosion casts of the rat exocrine pancreas. *Scanning 16*, 209−14.
(24) Zhou, J., Chen, J., Mokotoff, M., and Ball, E. D. (2004) Targeting gastrin-releasing peptide receptors for cancer treatment. *Anticancer Drugs 15*, 921−7.
(25) Karra, S. R., Schibli, R., Gali, H., Katti, K. V., Hoffman, T. J., Higginbotham, C., Sieckman, G. L., and Volkert, W. A. (1999) 99mTc-labeling and in vivo studies of a bombesin analogue with a novel water-soluble dithiadiphosphine-based bifunctional chelating agent. *Bioconjugate Chem. 10*, 254−60.
(26) Smith, C. J., Volkert, W. A., and Hoffman, T. J. (2003) Gastrin releasing peptide (GRP) receptor targeted radiopharmaceuticals: a concise update. *Nucl. Med. Biol. 30*, 861−8.
(27) Rogers, B. E., Bigott, H. M., McCarthy, D. W., Della Manna, D., Kim, J., Sharp, T. L., and Welch, M. J. (2003) MicroPET imaging of a gastrin-releasing peptide receptor-positive tumor in a mouse model of human prostate cancer using a 64Cu-labeled bombesin analogue. *Bioconjugate Chem. 14*, 756−63.
(28) Lin, K. S., Luu, A., Baidoo, K. E., Hashemzadeh-Gargari, H., Chen, M. K., Brenneman, K., Pili, R., Pomper, M., Carducci, M. A., and Wagner, H. N., Jr. (2005) A new high affinity technetium-99m-bombesin analogue with low abdominal accumulation. *Bioconjugate Chem. 16*, 43−50.
(29) Van de Wiele, C., Dumont, F., Vanden Broecke, R., Oosterlinck, W., Cocquyt, V., Serreyn, R., Peers, S., Thornback, J., Slegers, G., and Dierckx, R. A. (2000) Technetium-99m RP527, a GRP analogue for visualisation of GRP receptor-expressing malignancies: a feasibility study. *Eur. J. Nucl. Med. 27*, 1694−9.
(30) Van de Wiele, C., Dumont, F., Dierckx, R. A., Peers, S. H., Thornback, J. R., Slegers, G., and Thierens, H. (2001) Biodistribution and dosimetry of (99m)Tc−RP527, a gastrin-releasing peptide (GRP) agonist for the visualization of GRP receptor-expressing malignancies. *J. Nucl. Med. 42*, 1722−7.
(31) De Vincentis, G., Remediani, S., Varvarigou, A. D., Di Santo, G., Iori, F., Laurenti, C., and Scopinaro, F. (2004) Role of 99mTc-bombesin scan in diagnosis and staging of prostate cancer. *Cancer Biother. Radiopharm. 19*, 81−4.
(32) Scopinaro, F., Varvarigou, A., Ussof, W., De Vincentis, G., Archimandritis, S., Evangelatos, G., Corleto, V., Pulcini, A., Capoccetti, F., Remediani, S., and Massa, R. (2002) Breast cancer takes up 99mTc bombesin. A preliminary report. *Tumori 88*, S25−8.
(33) Syrigos, K. N., Vile, R. G., Peters, A. M., and Harrington, K. J. (2003) Biodistribution and pharmacokinetics of 111In-dTPA-labeled pegylated liposomes after intraperitoneal injection. *Acta Oncol. 42*, 147−53.
(34) Armstrong, D. K., Bundy, B., Wenzel, L., Huang, H. Q., Baergen, R., Lele, S., Copeland, L. J., Walker, J. L., and Burger, R. A. (2006) Intraperitoneal cisplatin and paclitaxel in ovarian cancer. *N. Engl. J. Med. 354*, 34−43.

BC060035+

Self-Assembled "Dock and Lock" System for Linking Payloads to Targeting Proteins

Marina V. Backer,* Vimal Patel, Brian T. Jehning, and Joseph M. Backer

SibTech, Inc., Newington, Connecticut 06111. Received February 14, 2006

Random conjugation of therapeutic or diagnostic payloads to targeting proteins generates functionally heterogeneous products. Conjugation of payloads to an adapter that binds to a peptide tag engineered into a targeting protein provides an alternative strategy. To progress into clinical development, an adapter/docking tag system should include humanized components and be stable in circulation. We describe here an adapter/docking tag system based on mutated fragments of human RNase I that spontaneously bind to each other and form a conjugate with a disulfide bond between complimentary cysteine residues. This self-assembled "dock and lock" system utilizes the previously described fusion C-tag, a 1−15 aa fragment of human RNase I with the R4C amino acid substitution, and a newly engineered adapter protein (Ad-C), a 21−127-aa fragment of human RNase I with the V118C substitution. Two vastly different C-tagged recombinant proteins, human vascular endothelial growth factor (VEGF) and a 254-aa long N-terminal fragment of anthrax lethal factor (LFn), retain functional activities after spontaneous conjugation of Ad-C to N-terminal or C-terminal C-tag, respectively. Ad-C modified with pegylated phospolipid and inserted into the lipid membrane of drug-loaded liposomes (Doxil) retained the ability to conjugate C-tagged proteins, yielding targeted liposomes decorated with functionally active proteins. To further optimize the system, we engineered an adapter with an additional cysteine residue at position 88 for site-specific modification, conjugated it to C-tagged VEGF, and labeled with a near-infrared fluorescent dye Cy5.5, yielding a unique functionally active probe for in vivo molecular imaging. We expect that this self-assembled "dock and lock" system will provide new opportunities for using functionally active proteins for biomedical purposes.

INTRODUCTION

Conjugation of therapeutic or diagnostic "payloads" (e.g. drugs, radionuclides, nanoparticles, liposomes) to targeting proteins encounters a well-recognized problem of functional heterogeneity of the final products (*1*, *2*). The protein−payload conjugates are usually synthesized via random modification of available chemical groups, most often ϵ-amino groups of lysine residues, and are inevitably heterogeneous, both structurally and functionally. One approach to solving this problem is to engineer targeting proteins with an additional cysteine residue that does not interfere with protein folding and can be used for a site-specific conjugation (*3*−*7*). Alternatively, native cysteines dispensable for target recognition can be coupled to a payload, as it has been recently reported for cysteines involved in the interchain disulfide bonds in IgG molecules (*8*, *9*). Although these strategies eliminate or decrease heterogeneity of the conjugates, they do not solve sterical problems associated with coupling of either bulky or highly charged payloads, which might interfere with functional activity of the resulting conjugates. To minimize this interference, payloads can be linked to an adapter protein that can be docked to a "tag" engineered in targeting protein. Currently, streptavidin/biotin is the most popular adapter/docking tag system, although it is hardly suitable for clinical development (*10*−*13*). Another promising but highly specialized approach is the engineering of bispecific recombinant antibodies recognizing one epitope on the cell surface and the other one on a drug carrier (*14*, *15*).

We have recently developed and tested in vitro and in vivo a fully humanized adapter/docking tag system based on high affinity interactions between two fragments of human RNase I,

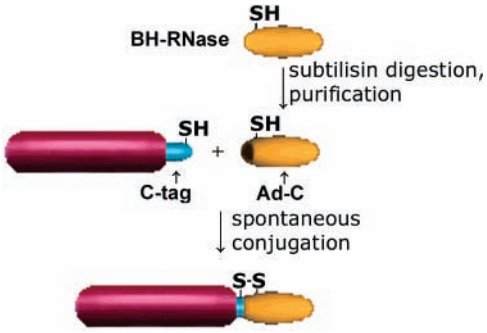

Figure 1. "Dock and lock" system.

a 1−15 aa fragment (Hu-tag) fused to a targeting protein as a docking tag, and a 21−127 aa fragment (HuS) as an adapter (*16*, *17*). However, the utility of this, as well as all other noncovalent adapter/docking tag systems, depends on their stability in a complex environment of the human bloodstream. We reasoned that "locking" of an adapter/docking tag complex with an intra-complex disulfide bond would eliminate a stability problem. We describe here such a "dock and lock" system, which is based on appropriately mutated fragments of human RNase I (Figure 1). Docking tag, named C-tag, contains a cysteine in position 4; it has been recently used for direct site-specific modification of C-tagged VEGF with derivatized dendrimers (*7*). An adapter, named Ad-C, contains cysteine in position 118 (positions are indicated for full-length human RNase I). This choice of cysteine positions was based on an observation that stability of human RNase I (R4C,V118C) double mutant is increased relative to wild-type molecule, suggesting possible formation of an intramolecular C4−C118 disulfide bond (*18*).

We hypothesized that C4 and C118 introduced in C-tag and Ad-C, respectively, would spontaneously form a disulfide bond

* To whom correspondence should be addressed, at SibTech, Inc., 705 North Mountain Road, Newington, CT 06111. Phone: (860) 953-1753; Fax: (860) 953-1317; E-mail: mbacker@sibtech.com.

10.1021/bc060037u CCC: $33.50 © 2006 American Chemical Society
Published on Web 05/25/2006

in the adapter/tag complex. To test this hypothesis, we used two proteins: a newly constructed LFn-C, a 254-aa long catalytically inactive N-terminal fragment of anthrax lethal factor with no native cysteines, fused to C-terminal C-tag, and previously described human C-tagged $VEGF_{121}$ (18 native cysteines per dimer), expressed with an N-terminal C-tag (*7*). Here we report that both C-tagged proteins covalently bind Ad-C without compromising their respective activities. We demonstrate that doxorubicin-loaded liposomes can be decorated with Ad-C and then coupled to either C-tagged protein, providing a simple and efficient method for molecular targeting of bulky payloads. Furthermore, an additional cysteine introduced in Ad-C in position 88 allowed for site-specific modification of VEGF-Ad conjugate with a charged near-infrared fluorescent dye, Cy5.5. This approach yielded a functionally active molecular probe for in vivo imaging, while direct conjugation of Cy5.5 resulted in a significant drop of VEGF functional activity.

MATERIALS AND METHODS

Construction and Purification of Chimeric BH-RNase-(V118C) Mutant. Chimeric $^{1-29}B/^{30-127}H$-RNase (BH-RNase) consisting of a 1−29-aa fragment of bovine RNase A and a 30−127-aa fragment of human RNase I has been constructed as described (*19*). The V118C mutation was introduced in the pET29/$^{1-29}B/^{30-127}H$-RNase plasmid DNA by site-directed mutagenesis (Gene-Tailor Site Directed mutagenesis kit, Invitrogen) using primers: 5′-AA GGC TCT CCG TAC GTT CCG TGT CAT TTC gac gcg (sense, the mutation underlined) and 5′-CGG AAC GTA CGG AGA GCC TTC GCA TGC AAC (antisense). BH-RNase(V118C) was used for construction of double mutant BH-RNase(N88C,V118C) by introducing the N88C amino acid substitution as described (*20*). The V118C substitution and double V118C, N88C mutations were confirmed by sequencing. BH-RNase(V118C) and BH-RNase(N88C,-V118C) were expressed in BL21(DE3) *E. coli* (Novagen, Madison WI), refolded from inclusion bodies, and purified by ion-exchange chromatography on HiTrap SP Sepharose Fast Flow (1-mL prepacked columns, Amersham Biosciences, Piscataway, NJ) as described for wild-type BH-RNase (*19*). The yield of BH-RNase(V118C) was 45−50 mg/L, while double mutant BH-RNase(N88C,V118C) yielded 20−25 mg/L. Free cysteines were tested by reaction with *N*-(1-pyrene)maleimide (Molecular Probes, Eugene, OR) followed by RP HPLC analysis as described (*21*) Briefly, *N*-(1-pyrene)maleimide dissolved in DMSO was added to protein at the molar ratio of 10:1, incubated for 1 h at RT, and analyzed by RP HPLC.

Purification of Mutant Adapter Ad-C. To release Ad-C, which is a 21−127-aa fragment of BH-RNase(V118C), BH-RNase(V118C) was digested with subtilisin (Sigma) at the protein to protease w/w ratio of 10:1 for 15−20 min at 4 °C. Subtilisin digestion was stopped by 1% ice-cold TFA. After a 5-min incubation on ice, the reaction mixture was purified by ion-exchange chromatography on SP Sepharose Fast Flow as described (*19*, *20*). Digested BH-RNase(V118C) was purified by affinity chromatography on a Hu-column carrying CA-extended Hu-peptide (CA-KESRAKKFQRQHMDS synthesized by Genemed Synthesis, Inc., South San Francisco, CA) as described (*16*). Protein eluted from Hu-column with 0.1 M citric acid was neutralized with 1 M Na_2HPO_4 and analyzed by RP HPLC on C18 Waters Nova-Pack 5 μm column (150 × 3.9 mm) with elution at 0.75 mL/min with 0.1% TFA (v/v) and a linear gradient of acetonitrile (5−50% over 20 min). The concentration of Ad-C was calculated using 216-nm integral absorption in HPLC profiles with bovine S-protein (Sigma) serving as a standard.

Construction of the pET/$(G_4S)_3$Hu-R4C Vector. The pET/Hu-R4C$(G_4S)_3$ vector for bacterial expression of recombinant proteins with N-terminal C-tag was constructed as described (*7*). To construct a vector for expression of proteins with C-terminal C-tag, a DNA fragment encoding Hu-tag (described in *16*) was cloned in *Nde-Kpn* sites of the pT7Blue vector (Novagen). Then a single-stranded DNA fragment encoding a $(G_4S)_3$ linker 5′- pTAT GGG TGG CGG TGG TAG TGG TGG TGG CGG TTC AGG CGG TGG TCA and a complimentary fragment 5′- pTAT GAC CAC CGC CTG AAC CGC CAC CAC CAC TAC CAC CGC CAC CCA (synthesized by GeneLink, Thornwood, NY) were annealed with reconstitution of *Nde*I sites on both termini and ligated immediately upstream of Hu-tag into *Nde* I site of the pT7Blue-Hu vector. Plasmid DNA with correct orientation of the cloned fragment was selected by sequencing, and the inner *Nde* I site was destroyed by site-directed mutagenesis (Gene-Tailor Site Directed mutagenesis kit, Invitrogen). A DNA fragment encoding $(G_4S)_3$-Hu-tag was amplified from pT7Blue$(G_4S)_3$Hu vector with primers introducing an *Nde*I site to the 5′-terminus, a stop codon and a *Kpn*I site to the 3′-terminus and cloned into *Nde-Kpn* of the pET29a(+) bacterial expression vector (Novagen). The R4C amino acid substitution was introduced in Hu-tag of the pET/$(G_4S)_3$Hu vector by site-directed mutagenesis and confirmed by sequencing. The resulting vector for bacterial expression of proteins fused to C-terminal C-tag via a $(G_4S)_3$ linker was designated pET/$(G_4S)_3$Hu-R4C.

Cloning and Expression of C-Tagged Proteins. Coding sequence for a 1−254-aa fragment of anthrax lethal factor (LFn) was amplified from the pGEX-KG LF254 plasmid (kindly provided by Dr. S. Leppla, National Institute of Allergy and Infectious Diseases, NIH, Bethesda, MD). For construction of LFn-C (C-terminally fused C-tag), primers introduced *Nde* I sits (italicized): 5′- CTACCT *CATATG* GCG GGC GGT CAT GGT GATG (sense) and 5′- CTACCT *CATATG* TAG ATT TAT TTC TTG TTC GTT AAA TTT ATC (antisense). For construction of C-LFn (N-terminally fused C-tag), primers introduced *Nco* I sits, and the fragment was cloned in *Nco* I site of the pET/Hu-R4C$(G_4S)_3$ vector downsream of the $(G_4S)_3$ linker. Clones with correct orientation of LFn fragment were selected by PCR using a T7-promoter-based sense primer and then confirmed by sequencing. Both C-tagged LFn fusion proteins were expressed in BL21(DE3). The expression was induced by 1 mM IPTG at the optical density of 0.5−0.7 unit at 600 nm. After induction, cultures were grown for 2.5−3 h at 37 °C with shaking at 300 rpm, harvested by centrifugation, and ruptured using EmulsiFlex-C5 (Avestin, Ottava, Canada). The soluble part of bacterial lysate was dialyzed against 200 volumes of 20 mM Tris-HCl pH 8.0 for 20 h at 4 °C, clarified by centrifugation (15 000*g* for 20 min), and passed through Sepharose Q FF column. C-LFn-containing fractions were pooled together, dialyzed against 100 volumes of 20 mM NaOAc pH 6.5 for 20 h at 4 °C, and further purified on Heparin HP Sepharose followed by hydrophobic interaction chromatography on Butyl FF Sepharose (1-ml prepacked columns, Amersham). The yield of Hu(R4C)-LFn was 8−10 mg/L, purity >98% by SDS−PAGE followed by SimplyBlue Safe Stain (Invitrogen). Human $VEGF_{121}$ was expressed with N-terminal C-tag and recovered from inclusion bodies as described (*7*). Hu-VEGF, human $VEGF_{121}$ fused to Hu-tag, was cloned and expressed as described (*16*).

Synthesis of VEGF/Ad-Cy5.5 Conjugate. BH-RNase(N88C,-V118C) was deprotected with DTT and digested with subtilisin as described for BH-RNase(V118C). Purified double mutant adapter was mixed with C-tagged VEGF at the molar ratio of 3:1 and incubated for 4 °C for 16 h. Cy5.5-maleimide (GE Healthcare) dissolved in dimethylformamide was added then to the reaction mixture to a final protein-to-Cy molar ratio of 1:10, incubated at RT for 1 h, and purified by RP-HPLC on a

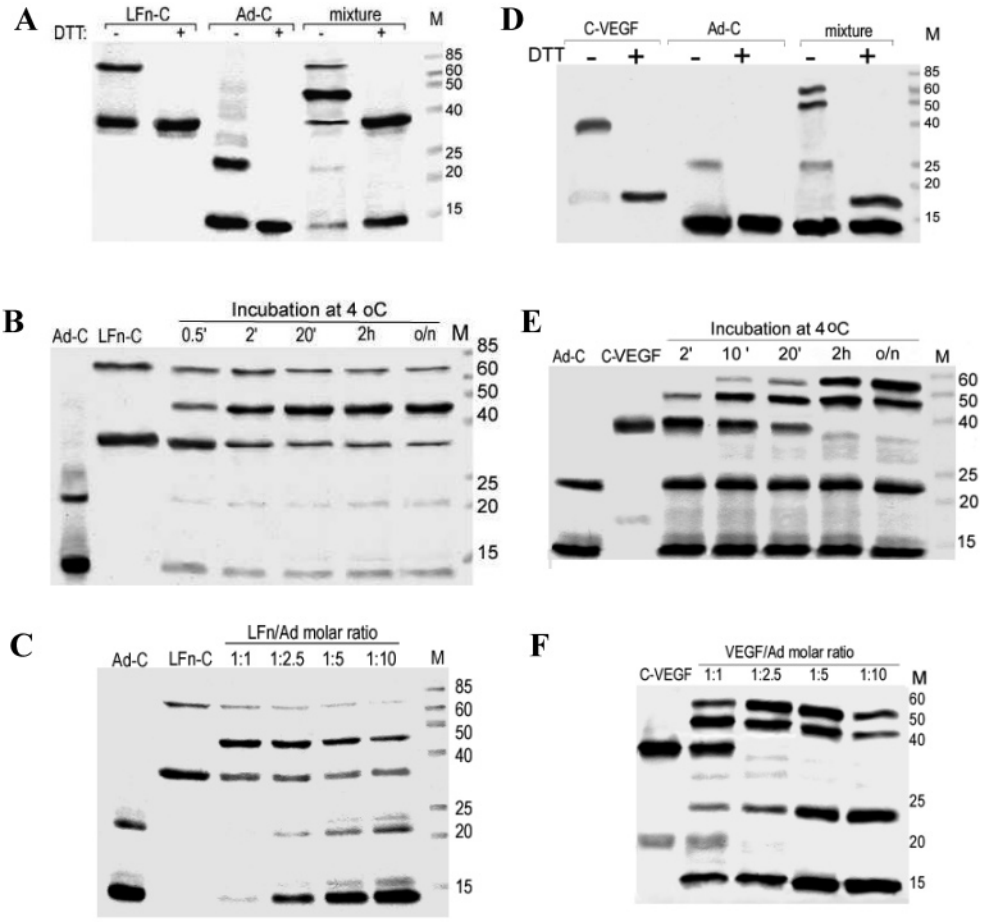

Figure 2. Self-assembly of Ad-C/C-tag conjugates. Ad-C was mixed with LFn-C (panel A) at a molar ratio of 1:1 or C-tagged VEGF (panel D) at a molar ratio of 3:1 and incubated for 16 h at 4 °C. Samples were analyzed by nonreducing (−DTT) and reducing (+DTT) SDS−PAGE on 17.5% gels followed by Bio-Safe Coomassie G-250 staining (Bio-Rad). In panels B and E, nonreducing SDS−PAGE analysis of kinetics of conjugation. Ad-C was mixed with LFn-C at a 1:1 molar ratio (B) or with C-VEGF at a 3:1 ratio (E) and incubated at 4 °C for indicated periods of time. In panels C and F, nonreducing SDS−PAGE analysis of conjugation dose-dependencies: varying amounts of Ad-C were mixed with LFn-C (C) or C-VEGF (F) and incubated at 4 °C for 2 h.

preparative C-4 column (GE Healthcare). The extent of modification was calculated as a ratio of integral peak intensities at 216 nm (for protein) and at 598 nm (for Cy5.5).

Cells. HEK293 human transformed embryonic kidney cells (CRL-1573) and RAW 264.7 mouse monocytes (TIB-71) were from American Type Culture Collection (Rockville, MD). 293/KDR cells expressing 2.5×10^6 VEGFR-2/cell have been developed in SibTech, Inc. (*22*). PAE/KDR porcine aortic endothelial cells expressing 2.5×10^5 VEGFR-2/cell were kindly provided by Dr. B. Terman (Albert Einstein School of Medicine, Bronx, NY). 4T1luc mouse breast carcinoma cells expressing firefly luciferase was developed as described (*23*). All cells were grown in DMEM with 10% FBS, 2 mM L-glutamine and antibiotics at 37 °C, 5% CO_2.

In Vivo Imaging. Female 5−6 weeks old BALB/c mice were from Charles River Laboratories (Wilmington, MA). 4T1luc cells were implanted subcutaneously in the backs (5−10,000 cells/mouse). For imaging, mice with 10−14 days old tumors received 5−7 μg of VEGF/Ad-Cy5.5 per mouse via the tail vein, 5 min later were injected intraperitoneally with aqueous luciferin (0.5 mg/mouse), and anesthetized 5 min later with ketamine/xylazine mixture as described (*7*). Images were obtained on Kodak Image Station 4000. The protocol for the animal studies was approved by the Institutional Animal Care and Use Committee at the University of Connecticut Health Center.

Insertion of Ad-C into Doxorubicin-Loaded Liposomes. Ad-C was modified with 2-fold molar excess Traut's reagent (Sigma) in a buffer containing 50 mM NaPi, 150 mM NaCl, 1 mM EDTA, pH 8.0 for 2 h. Ten-fold molar excess of mPEG-DSPE maleimide (FW 3400, Nectar Technologies) was added to the reaction mixture and incubation continued for 4 h. Equal volume of Doxil (pegylated liposomal doxorubicin, OrthoBiothech) was added to the reaction and incubated at 37 °C for 16 h followed by gel-filtration on Sephadex 4B as described (*20*). The efficiency of Ad-C/DSPE insertion into liposomes was analyzed by RP HPLC, as described elsewhere (*20*). C-Tagged proteins were mixed with Ad-C/Doxil at the C-tag to Ad-C molar ratio of 1:3 and incubated for 16 h at 4 °C followed by purification on Sepharose 4B. C-Tagged protein concentration in purified liposomes was determined by Western blotting.

RESULTS

Preparation Adapter Protein for "Dock and Lock". To obtain Ad-C, an adapter protein that binds to and forms a disulfide bond with C-tag, we engineered the V118C amino acid substitution in BH-RNase, a source of adapter protein (*19*). BH-RNase comprising a 1−29aa long fragment of bovine RNase A and a 30−127 aa long fragment of human RNase I carries a unique subtilisin cleavage site between S20 and A21, making it possible to release a 21−127aa fragment (adapter protein) after limited subtilisin digestion. Enzymatically active BH-RNase(V118C) was expressed, refolded in glutathione-containing Red-Ox buffer, and purified as described elsewhere (*20*). On the basis of our experience with another BH-RNase mutant containing the N88C amino acid substitution (*20*), we expected

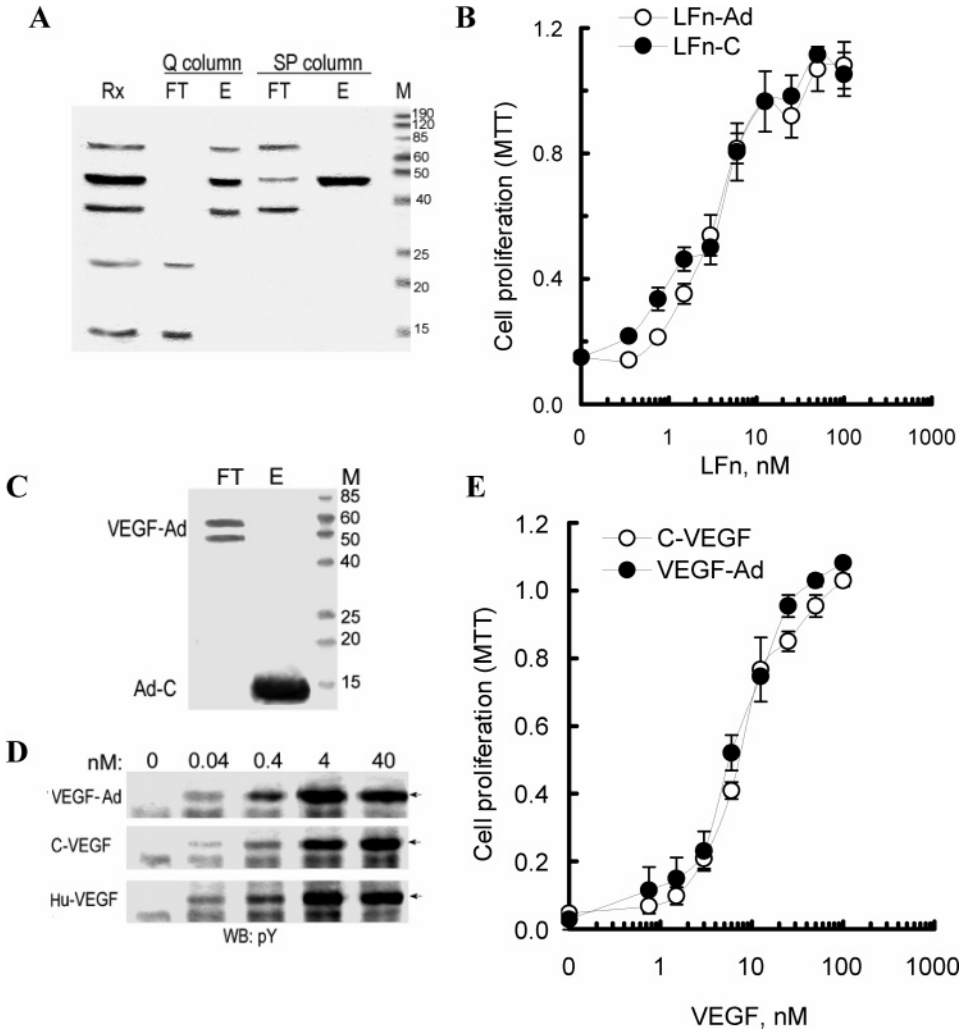

Figure 3. Conjugation to Ad-C does not affect functional activity of C-tagged proteins. In panel A, purification of LFn-Ad by ion-exchange chromatography on a Q-column followed by a SP-column. Rx, reaction mixture; FT, flow-through; E, elution. In panel B, competition of LFn-Ad with LF for binding to RAW cells in the presence of PA. Cells were plated on 96-well plates 15×10^3 cells/well 20 h before the experiment. Varying amounts of LFn-C or LFn-Ad were mixed with LF and PA (List Biological, Campbell, CA) in DMEM complete culture medium and added to cells in triplicate wells to final concentrations of 2 nM PA and 0.2 nM LF. After 2.5 h of incubation at 37 °C in 5% CO_2, viable cell numbers were determined by CellTiter 96 AQ_{ueous} One Solution Cell Proliferation Assay kit (Promega). In panel C, purification of VEGF-Ad conjugate by affinity chromatography on Hu-peptide column. FT, flow-through fraction; E, elution. In panel D, induction of VEGFR-2 tyrosine autophosphorylation in 293/KDR cells. After overnight starvation (DMEM/0.5% FBS), cells were shifted to serum-free DMEM with 0.5 mM sodium vanadate for 20 min at 37 °C and then stimulated for 10 min at 37 °C, lysed, and analyzed by Western blotting using anti-phosphotyrosine RC20:HRPO conjugate (BD Transduction Labs, San Diego, CA). C-VEGF, C-tagged $VEGF_{121}$; Hu-VEGF, Hu-tagged $VEGF_{121}$. Arrows indicate positions of VEGFR-2. In panel E, competition with SLT-VEGF chimeric toxin. 293/KDR cells were plated on 96-well plates 20 h before the experiment, 1000 cells/well. Varying amounts of VEGF-Ad or C-tagged $VEGF_{121}$ were mixed with SLT-VEGF in complete culture medium, and added to cells in triplicate wells to a final SLT-VEGF concentration of 1 nM. Viable cells were quantitated 96 h later by a CellTiter 96 AQ_{ueous} One Solution Cell Proliferation Assay kit (Promega, Madison, WI).

that unpaired C118 in BH-RNase(V118C) would be involved in a mixed disulfide with glutathione. Indeed, modification of BH-RNase(V118C) with a sulfhydryl-directed reagent *N*-(1-pyrene)maleimide varied between 0 and 0.3 mol/mol for different preparations. However, after a mild DTT treatment (1.5-fold molar excess DTT at 4 °C for 16 h), modification of BH-RNase(V118C) reached ~1 mol/mol, suggesting that a single thiol group per protein was "deprotected". BH-RNase-(V118C), with or without deprotection, was digested with subtilisin, and Ad-C was purified by affinity chromatography on Hu-peptide affinity column as described (*20*). The resulting protein was more than 98% pure by SDS−PAGE (Figure 2). Under nonreducing conditions, a part of Ad-C migrated as a dimer that was absent in the presence of DTT reflecting dimerization of Ad-C via unpaired C118 residues.

Self-Assembly of Conjugates between Ad-C and C-Tagged Proteins. We expected that the close proximity of C4 and C118 thiol groups in Ad-C/C-tag complex might lead to formation of a C4−C118 disulfide bond, even when one or both thiol groups were involved in mixed disulfides with glutathione. We first tested this hypothesis using Ad-C and LFn-C, a catalytically inactive fragment of anthrax lethal factor with C-terminal C-tag. LFn-C was bacterially expressed and purified from a soluble fraction through a process that did not require red-ox refolding, and therefore C4 thiol group was available for conjugation. LFn-C, Ad-C, and their 1:1 mixture were incubated at 4 °C for 16 h and then analyzed by SDS−PAGE. As expected, for both LFn-C and Ad-C incubated separately, part of each protein migrated in DTT-sensitive bands corresponding to homodimers of these proteins (Figure 2A). However, in the LFn-C/Ad-C mixture, the majority of protein was found in a DTT-sensitive band corresponding to ~46 kDa LFn-Ad conjugate (Figure 2A). Thus, this conjugation occurs even when the majority of C118 thiol groups in Ad-C were involved in mixed disulfide bonds with glutathione. Importantly, LFn-Ad conjugation was more efficient than homodimer formation, supporting the notion that

the process proceeded in the noncovalent complex between C-tag and Ad-C, rather than via random collisions. We found that conjugation was detectable after 30 s of incubation at 4 °C and reached a plateau by 20 min (Figure 2B). Interestingly, an increase of the Ad-C to LFn-C molar ratio did not enhance the yield of the conjugate (Figure 2C), suggesting that a fraction of LFn-C was proteolytically degraded and thus has a nonfunctional C-tag.

To test the ability of protected C4 thiol group to form a disulfide bond with Ad-C, we used recently described C-tagged human $VEGF_{121}$, a dimeric protein with C-tag fused to the N-terminus of each monomer (*7*). This protein was recovered from inclusion bodies and had both C4 thiol groups in the form of mixed disulfides due to refolding in a glutathione-containing red-ox buffer (*7*). C-Tagged $VEGF_{121}$, Ad-C, and their mixture at a molar ratio of 1:3 were incubated at 4 °C for 16 h and then analyzed by SDS−PAGE. As shown on Figure 2D, under nonreducing conditions, C-tagged $VEGF_{121}$ migrated in a DTT-sensitive band corresponding to a native dimer, while only a part of Ad-C (smaller in this Ad-C preparation, than in the one shown on Figure 2A) migrated as a dimer. However, in the protein mixture, virtually all C-tagged VEGF was found in DTT-sensitive bands corresponding to ~45 kDa and ~57 kDa VEGF-Ad conjugates with either one or two adapter molecules per VEGF dimer, respectively (Figure 2D). Thus, the presence of glutathione on both C4 and C118 did not prevent formation of VEGF-Ad conjugate.

Conjugation of C-tagged VEGF and Ad-C mixed at the molar ratio of 1:3 was detectable after a few minutes of incubation at 4 °C and reached a plateau by 2 h (Figure 2E). Free VEGF disappeared from the reaction mixture at 2.5-fold molar excess of Ad-C (Figure 2F), although complete VEGF modification, e.g. two Ad-C molecules per each VEGF dimer, was not achievable. As with LFn-Ad conjugate, we explain it by possible N-terminal proteolysis during protein purification. Deprotection of C4 and/or C118 by mild DTT treatment did not accelerate conjugate formation (data not shown), suggesting that freeing the thiol groups from the form of mixed disulfide was not a limiting step in this process.

Functional Activities of Adapter-Conjugated C-Tagged Proteins. LFn-Ad conjugate was purified from the reaction mixture by anion-exchange chromatography that removed unconjugated Ad-C, followed by cation-exchange chromatography to remove free LFn-C and its dimers (Figure 3A). Purified LFn-Ad was tested for its ability to rescue RAW 264.7 cells from cytotoxicity of anthrax lethal toxin, a combination of full-length lethal factor (LF) and protective antigen (PA). It was demonstrated previously that LFn completely retained the ability to bind to PA, while it displayed no toxicity for target RAW 264.7 cells (*24*). We found that in this assay, purified LFn-Ad conjugate competed with LF as effectively as free LFn-C, rescuing RAW 264.7 cells with IC_{50} of ~3 nM (Figure 3B), indicating that the conjugation did not affect the ability of LFn to interact with PA.

VEGF-Ad conjugate was purified from unreacted Ad-C by affinity chromatography on a Hu-peptide column that retained free Ad-C (Figure 3C). Purified VEGF-Ad conjugate was found to be as active as free $VEGF_{121}$ in a short-term 10-min assay, induction of VEGF receptor (VEGFR-2) tyrosine autophosphorylation (Figure 3D). In a long-term 3-day assay, VEGF-Ad was tested for the ability to rescue VEGFR-2-expressing cells from the cytotoxicity of SLT-VEGF chimeric toxin (*25*, *26*). In this assay VEGF-Ad was as effective as C-tagged $VEGF_{121}$, rescuing 293/KDR cells with the IC_{50} of ~8 nM (Figure 3E), which was also similar to previously reported IC_{50} value for Hu-$VEGF_{121}$ (*26*). Thus, both assays demonstrated that conjugation did not affect the ability of $VEGF_{121}$ to bind to VEGFR-2.

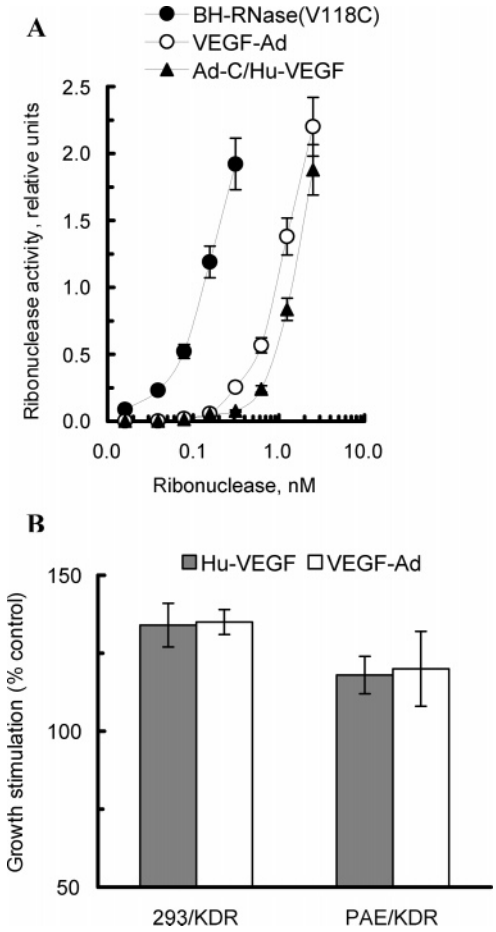

Figure 4. Reconstituted ribonuclease activity of VEGF-Ad conjugate is not cytotoxic. In panel A, BH-RNase(V118C), VEGF-Ad conjugate, or a equimolar mixture of Ad-C and Hu-VEGF was added, separately, to a buffer containing 20 mM Tris-HCl, 100 mM NaCl, pH 7.5, 0.1 mg/mL polyC and incubated for 5 min at RT. Ribonuclease activity was measured by 280-nm absorbance of the reaction mixtures cleared from TCA-precipitated material. One optical unit of TCA-soluble material released from polyC under these conditions was defined as one relative unit of ribonuclease activity (the method is described in details in 16). In panel B, VEGF induced growth stimulation of VEGFR-2 expressing cells. 293/KDR and PAE/KDR cells were plated on 96-well plates at densities of 500−1000 cell/well. Varying amounts of VEGF-Ad, or control Hu-VEGF, were added to cells in triplicate wells 20 h later. Cells were allowed to grow for 72−96 h and then quantitated by a CellTiter 96 AQ_{ueous} One Solution Cell Proliferation Assay kit (Promega).

Since ribonuclease activity is reconstituted in noncovalent complexes of Hu-tagged proteins with Ad (*16*), we tested whether introduction of C4 and C118 affected proper alignment of RNase fragments. We found that both VEGF-Ad and LF-Ad conjugates displayed similar ribonuclease activity (Figure 4A, for VEGF-Ad). Although VEGF-Ad activity was ~10-fold lower than that of BH-RNase(V118C), the conjugate was more active than noncovalent complexes between Ad-C and Hu-VEGF (Figure 4A). To address the issue of potential cytotoxicity of "dock and lock" complexes, we tested the effects of VEGF-Ad conjugate on cell growth. VEGFR-2-expressing cells of different tissue origin were plated at low densities and allowed to grow for 72−96 h in the presence of 10 nM VEGF-Ad conjugate. Both cell lines displayed low but significant growth stimulation in response to either VEGF-Ad or Hu-VEGF served as a control, indicating no toxic effects of VEGF-Ad (Figure 4B).

Self-Assembly of Conjugates between C-Tagged Proteins with Ad-C Decorated Liposomes. To assess self-assembly of "dock and lock" conjugates in the presence of bulky payloads,

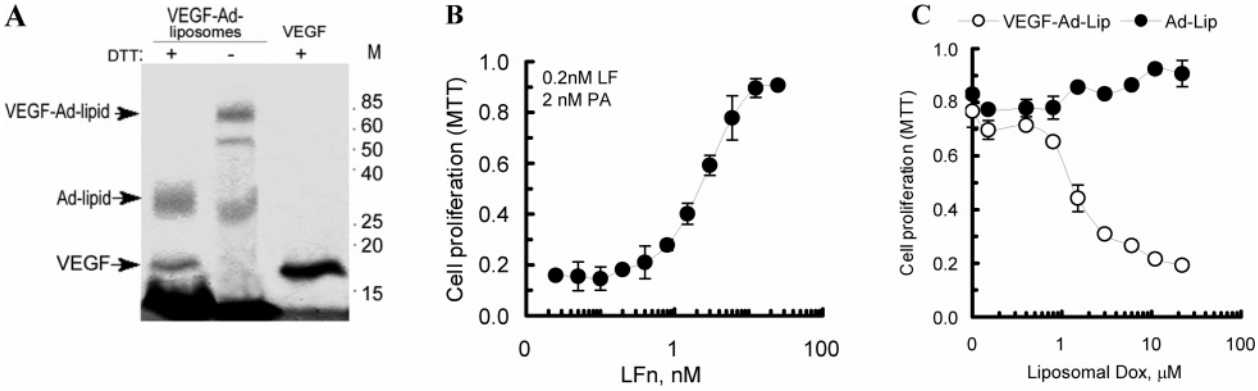

Figure 5. C-Tagged proteins conjugated to liposomes derivatized with Ad-C retain the functional activity. In panel A, VEGF-Ad-liposomes purified on Sepharose 4B were analyzed by SDS−PAGE as described in legend to Figure 2. In panel B, LF-Ad-liposome competition with the full length LF in the presence of PA on Raw cells was done as described in legend to Figure 4. In panel C, 293/KDR cells were plated on 96-well plates, 1000 cell/well. Twenty hours later, varying amounts of VEGF-Ad-liposomes or equivalent amounts of Ad-liposomes were added to cells in triplicate wells. After a 2-h incubation at 37 °C, liposome-containing media were removed, and cells were shifted to complete culture medium and allowed to grow for 96 h under normal culture conditions. Cells were quantitated by a CellTiter 96 AQ_{ueous} One Solution Cell Proliferation Assay kit (Promega).

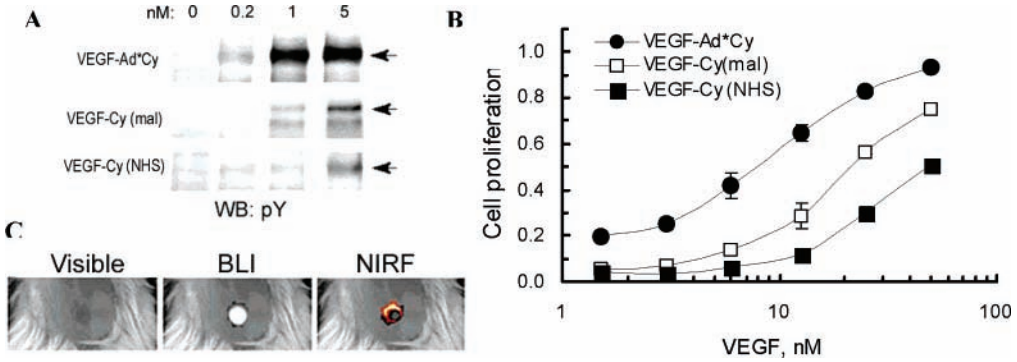

Figure 6. Functionally active Cy5.5-labeled VEGF-Ad* conjugate. VEGF modified with Cy5.5 directly using Cy5.5-maleimide (mal), or Cy5.5-NHS (NHS) or modified via adapter (VEGF-Ad*Cy) was purified and analyzed in VEGFR-2 tyrosine phosphorylation assay (panel A), or SLT-VEGF protection assay (panel B) as described in legend to Figure 3. In panel C, mice bearing 2-week old sc 4T1Luc tumors ($n = 5$) received ip injection of 0.5 mg luciferin and iv injection of 5 μg VEGF-Ad*Cy and were anesthetized and imaged. BLI, bioluminescent image; NIRF, pseudocolored in a "fire" range near-infrared image.

we used commercially available pegylated doxorubicin-loaded liposomes (Doxil). Ad-C with protected C118 was first modified with Trout's reagent to provide one free thiol group per Ad-C molecule and then modified with mPEG-DSPE maleimide, connecting a phospholipid moiety to Ad-C via 3.4 kDa poly-(ethylene glycol) linker. The lipidation mixture was then incubated with Doxil for 16 h at 37 °C and purified by gel-filtration on Sepharose 4B, as described elsewhere (*20*). Purified adapter-decorated liposomes were conjugated to either C-tagged $VEGF_{121}$ or LFn-C for 16 h at 4 °C and purified by gel filtration, and the resulting liposomes were analyzed by SDS−PAGE. We found that all liposome-associated C-tagged $VEGF_{121}$ and LFn were present in the DTT-sensitive bands corresponding to conjugates formed with lipidated adapter (Figure 5A, for C-tagged $VEGF_{121}$). Although a fraction of liposome-associated Ad-C remained free, the conjugation yielded ~25−50 molecules of C-tagged proteins per liposome and was sufficient for in vitro testing.

LFn-decorated liposomes were tested for their ability to protect RAW 264.7 cells from LF/PA toxicity and found to be as active as free LFn or LFn-Ad conjugate at the equal protein concentrations (Figure 5B, compare to Figure 3B). $VEGF_{121}$-decorated liposomes were tested for their ability to deliver cytotoxic doxorubicin into 293/KDR cells via receptor-mediated endocytosis. In these experiments, untargeted liposomes served as a control for nonspecific toxicity. We found that only $VEGF_{121}$-decorated liposomes were highly cytotoxic under selected conditions, indicating that the liposome payload did not prevent binding to VEGFR-2 and receptor-mediated endocytosis (Figure 5C).

Adapter for Covalent Self-Assembly and Site-Specific Labeling of Conjugates. To eliminate heterogeneity in Ad-C labeling, we have engineered Ad*-2C adapter by introducing the N88C substitution that provided a thiol group suitable for site-specific conjugation (*20*). We found that Ad*-2C can be recovered from the corresponding BH-RNase(N88C,V118C) mutant and self-assembled into functionally active conjugates with C-tagged $VEGF_{121}$ and LFn, as readily as Ad-C (data not shown). Ad*-2C was first deprotected by mild DTT treatment and then conjugated to C-tagged $VEGF_{121}$, and the conjugate was labeled with a near-infrared fluorescent dye Cy5.5 via maleimide chemistry to the molar ratio of one Cy5.5 per $VEGF_{121}$ monomer. The functional activities of Cy5.5-labeled VEGF-Ad* conjugate were close to that of C-tagged $VEGF_{121}$ in VEGFR-2 tyrosine phosphorylation assay (Figure 6A) and identical to that in protection from SLT-VEGF cytotoxicity (Figure 6B). In contrast, direct labeling of C-tagged $VEGF_{121}$ with either Cy5.5-maleimide or Cy5.5-NHS to the same ratio of one Cy5.5 per $VEGF_{121}$ monomer resulted in a significant decrease of functional activity, in both assays (Figure 6A,B). For in vivo testing, Cy5.5-labeled VEGF-Ad* conjugate was injected intravenously into mice bearing subcutaneous 4T1luc tumors. Since tumor cells were engineered to express luciferase, 4T1luc tumor could be visualized by bioluminescent imaging after intraperitoneal injection of luciferin (*23*). We found that Cy5.5-labeled VEGF-Ad* conjugate rapidly and selectively

accumulated in the tumor region visualized by bioluminescent imaging (Figure 6C). As expected, the strongest Cy5.5 fluorescence was observed at the growing edges of the tumor, which are enriched with VEGFR-2 overexpressing cells (Figure 6C).

DISCUSSION

We describe here self-assembled "dock and lock" conjugates between C-tagged targeting proteins and Ad-C adapter protein, which are based on a unique intermolecular disulfide bond. Since both C-tag and Ad-C are mutated fragments of human RNase I, reconstitution of ribonuclease activity in Ad-C/C-tag conjugate indicates their proper folding and alignment (*16*). Self-assembly proceeds remarkably rapidly, even when both complimentary cysteines are involved in mixed disulfides with glutathione, suggesting that C4−C118 bonding is facilitated by formation of Ad-C/C-tag complex.

The "dock and lock" system presents a flexible platform for linking payloads to targeting proteins. The human origin of both components makes it suitable for potential clinical development. Combined size of C-tag (15-aa) and adapter (105-aa) is significantly smaller than that of biotin/streptavidin complex and is comparable to that of the adapter arm of recombinant diabodies. Importantly, C-tag can be fused to either N- or C-terminus, making it compatible with various targeting proteins. The "dock and lock" self-assembly appears to be a robust process: two completely different C-tagged proteins readily formed functionally active conjugates with Ad-C even when it was associated with such a bulky payload such as a liposome.

On the basis of our previous work on site-specific modification of RNase I derived adapter (*20*), we further optimized "dock and lock" system by engineering an Ad*-2C adapter protein with the N88C substitution. Not only Ad*-2C allows for site-specific modification eliminating heterogeneity of randomly modified Ad-C, but it also positions a payload as far as possible from the tag, protecting C-tagged proteins from potential interactions with the payload (*20, 27*). By design, C88 and C118 are released from mixed disulfides first, and then deprotected Ad*-2C is conjugated to C-tagged protein, leaving the C88 thiol group available for site-specific modification. This procedure was used to prepare VEGF-Ad* conjugate carrying a near-infrared fluorescent dye Cy5.5 that appeared to be fully active in vitro and in vivo. In contrast, direct conjugation of Cy5.5 to thiol groups in deprotected C-tagged $VEGF_{121}$ results in significant loss of VEGF activity, most likely because of interactions between negatively charged Cy5.5 and VEGF lysine residues involved in receptor binding (*28*). These observations suggest that insertion of Ad*-2C between C-tagged $VEGF_{121}$ and Cy5.5 might prevent such interactions, allowing for full activity of the final conjugate. Indeed, we have recently described functional conjugates of C-tagged $VEGF_{121}$ with 5th generation PAMAM boronated dendrimers derivatized with Cy5.5, where dendrimer was functionally "inserted" between C-tagged $VEGF_{121}$ and Cy5.5 (*7*).

Although we describe here conjugates with adapter-carrying therapeutic or diagnostic payloads, a similar approach might be used for surfaces derivatized with functionally active proteins, which might be useful for various devices, tissue scaffolds, and biosensors. In this strategy, the surface is first derivatized with adapter protein, and then conjugates are formed with "working" C-tagged protein(s). Taken together, our results suggest that self-assembled "dock and lock" conjugates might provide a standardized and versatile approach to using recombinant proteins for biomedical purposes.

LITERATURE CITED

(1) Dubowchik, G. M., and Walker, M. A. (1999) Receptor-mediated and enzyme-dependent targeting of cytotoxic anticancer drugs. *Pharmacol. Ther. 83*, 67−123.

(2) Moghimi, S. M., Hunter, A. C., and Murray, J. C. (2005) Nanomedicine: current status and future prospects. *FASEB J. 19*, 311−330

(3) Durek, T., and Becker, C. F. (2005) Protein semi-synthesis: new proteins for functional and structural studies. *Biomol. Eng. 22*, 153−172.

(4) Wood, R. J., Pascoe, D. D., Brown, Z. K., Medlicott, E. M., Kriek, M., Neylon, C., and Roach, P. L. (2004) Optimized conjugation of a fluorescent label to proteins via intein-mediated activation and ligation. *Bioconjugate Chem. 15*, 366−372.

(5) Li, L., Olafsen, T., Anderson, A. L., Wu, A., Raubitschek, A. A., and Shively, J. E. (2002) Reduction of kidney uptake in radiometal-labeled peptide linkers conjugated to recombinant antibody fragments. Site-specific conjugation of DOTA-peptides to a Cys-diabody. *Bioconjugate Chem. 13*, 985−995.

(6) Albrecht, H., Burke, P. A., Natarajan, A., Xiong, C. Y., Kalicinsky, M., DeNardo, G. L., and DeNardo, S. J. (2004) Production of soluble ScFvs with C-terminal-free thiol for site-specific conjugation or stable dimeric ScFvs on demand. *Bioconjugate Chem. 15*, 16−26.

(7) Backer, M. V., Gaynutdinov, T. I., Patel V., Bandyopadhyaya A. K., Thirumamagal, B. T. S, Tjarks W., Barth, R., Claffey, K. P., and Backer, J. M. (2005) Vascular endothelial growth factor selectively targets boronated dendrimers to tumor vasculature. *Mol. Cancer Ther. 4*, 1423−1429

(8) Sun, M. M., Beam, K. S., Cerveny, C. G., Hamblett, K. J., Blackmore, R. S., Torgov, M. Y., Handley, F. G., Ihle, N. C., Senter, P. D., and Alley, S. C. (2005) Reduction-alkylation strategies for the modification of specific monoclonal antibody disulfides. *Bioconjugate Chem. 16*, 1282−1290.

(9) Hamblett, K. J., Senter, P. D., Chace, D. F., Sun, M. M., Lenox, J., Cerveny, C. G., Kissler, K. M., Bernhardt, S. X., Kopcha, A. K., Zabinski, R. F., Meyer, D. L., and Francisco, J. A. (2004) Effects of drug loading on the antitumor activity of a monoclonal antibody drug conjugate. *Clin. Cancer Res. 10*, 7063−7070

(10) Fahmy, T. M., Samstein, R. M., Harness, C. C., and Saltzman, M. W. (2005) Surface modification of biodegradable polyesters with fatty acid conjugates for improved drug targeting. *Biomaterials 26*, 5727−5736.

(11) Forero-Torres, A., Shen, S., Breitz, H., Sims, R. B., Axworthy, D. B., Khazaeli, M. B., Chen, K. H., Percent, I., Besh, S., LoBuglio, A. F., and Meredith, R. F. (2005) Pretargeted radioimmunotherapy (RIT) with a novel anti-TAG-72 fusion protein. *Cancer Biother Radiopharm. 20*, 379−390.

(12) Dinauer, N., Balthasar, S., Weber, C., Kreuter, J., Langer, K., and von Briesen, H. (2005) Selective targeting of antibody-conjugated nanoparticles to leukemic cells and primary T-lymphocytes. *Biomaterials 26*, 5898−5906.

(13) Medina, L. A., Calixto, S. M., Klipper, R., Phillips, W. T., and Goins, B. (2004) Avidin/biotin-liposome system injected in the pleural space for drug delivery to mediastinal lymph nodes. *J. Pharm. Sci. 93*, 2595−2608.

(14) Kriangkum, J., Xu, B., Nagata, L. P., Fulton, R. E., and Suresh, M. R. (2001) Bispecific and bifunctional single chain recombinant antibodies. *Biomolecul. Eng. 18*, 31−40.

(15) Zhu, H., Jain, R. K., and Baxter, L. T. (1998) Tumor pretargeting for radioimmunodetection and radioimmunotherapy. *J Nuclear Med 39*, 65−76.

(16) Backer, M. V., Gaynutdinov, T. I., Gorshkova, I. I., Crouch, R. J., Hu, T., Aloise, R., Arab, M., Przekop, K., and Backer, J. B. (2003) Humanized docking system for assembly of targeting drug delivery complexes. *J. Controlled Release 89*, 499−511.

(17) Blankenberg, F. G, Mandl, S., Cao, Y.-A., O'Connell-Rodwell, C., Contag, C., Mari, C., Gaynutdinov, T. I., Vanderheyden, J.-L., Backer, M. V., and Backer, J. M. (2004) Tumor imaging using a standardized radiolabeled adapter protein docked to vascular endothelial growth factor (VEGF). *J. Nuclear Med. 45*, 1373−1380.

(18) Futami, J., Tada, H., Seno, M., Ishikami, S., and Yamada H. (2000) Stabilization of Human RNase 1 by Introduction of a Disulfide Bond between Residues 4 and 118. *J. Biochem. 128*, 245−250.

(19) Gaynutdinov, T. I., Myshkin, E., Backer, J. M., and Backer, M. V. (2003) chimeric ribonuclease as a source of human adapter protein for targeted drug delivery. *Prot. Engineering 16*, 771−775.

(20) Backer, M. V., Gaynutdinov, T. I., Patel, V., Myshkin, E., and Backer, J. M. (2004) Adapter protein for site-specific conjugation of payloads for targeted drug delivery. *Bioconjugate Chem. 15*, 1021−1029.

(21) Backer, M. V., Gaynutdinov, T. I., Aloise, R., Przekop, K., and Backer, J. (2002) Engineering S-protein fragments of bovine ribonuclease A for targeted drug delivery. *Protein Exp. Purif. 26*, 455−461

(22) Backer, M. V., and Backer, J. M. (2001) Functionally active VEGF fusion proteins. *Protein. Exp. Purif. 23*, 1−7.

(23) Backer, M. V., Levashova, Z., Patel, V., Jehning, B. T., Claffey, K., Blankenberg, F. G., and Backer, J. M. Molecular imaging of VEGF receptors in angiogenic vasculature with single-chain VEGF driven probes. *Nat. Med.*, submitted.

(24) Tang, G., and Leppla, S. H. (1999) Proteasome activity is required for anthrax lethal toxin to kill macrophages. *Infect. Immun. 67*, 3055−3060

(25) Backer, M. V., and Backer, J. M (2001) Targeting endothelial cells overexpressing VEGFR-2: selective toxicity of Shiga-like toxin-VEGF fusion proteins. *Bioconjugate Chem. 12*, 1066−1073.

(26) Backer, M. V., Elliot, J., Gaynutdinov, T. I., and Backer, J. M. (2004) Assembly of targeting complexes driven by a single-chain antibody. *J. Immunol. Meth. 289*, 35−43.

(27) Pous, J., Mallorquí-Fernández, G., Peracaula, R., Terzyan, S. S., Futami, J., Tada, H., Yamada, H., Seno, M., de Llorens, R., Gomis-Rüth, F. X., and Coll, M. (2001) Three-dimensional structure of human RNase 1 delta N7 at 1.9 Å resolution. *Acta Crystallogr., Sect. D.: Biol. Crystallogr. 57*, 498−505.

(28) Keyt, B. A. et al. (1996) Identification of vascular endothelial growth factor determinants for binding KDR and FLT-1 receptors. Generation of receptor-selective VEGF variants by site-directed mutagenesis. *J. Biol. Chem. 271*, 5638−5646.

BC060037U

Self-Assembled Quantum Dot−Peptide Bioconjugates for Selective Intracellular Delivery

James B. Delehanty,[†,*] Igor L. Medintz,[†] Thomas Pons,[‡,||] Florence M. Brunel,[§] Philip E. Dawson,[§] and Hedi Mattoussi[‡,*]

Center for Bio/Molecular Science and Engineering, Code 6900, U.S. Naval Research Laboratory, Washington, D.C. 20375, Optical Sciences Division, Code 5611, U.S. Naval Research Laboratory, Washington, D.C. 20375, Departments of Cell Biology & Chemistry and the Skaggs Institute for Chemical Biology, The Scripps Research Institute, La Jolla, California 92037, and Chemical & Biomolecular Engineering Department, Johns Hopkins University, Baltimore, Maryland 21218. Received February 21, 2006; Revised Manuscript Received May 16, 2006

We demonstrate the use of self-assembled luminescent semiconductor quantum dot (QD)−peptide bioconjugates for the selective intracellular labeling of several eukaryotic cell lines. A bifunctional oligoarginine cell penetrating peptide (based on the HIV-1 Tat protein motif) bearing a terminal polyhistidine tract was synthesized and used to facilitate the transmembrane delivery of the QD bioconjugates. The polyhistidine sequence allows the peptide to self-assemble onto the QD surface via metal-affinity interactions while the oligoarginine sequence allows specific QD delivery across the cellular membrane and intracellular labeling as compared to nonconjugated QDs. This peptide-driven delivery is concentration-dependent and thus can be titrated. Upon internalization, QDs display a punctate-like staining pattern in which some, but not all, of the QD signal is colocalized within endosomes. The effects of constant versus limited exposure to QD−peptide conjugates on cellular viability are evaluated by a metabolic specific assay, and clear differences in cytotoxicity are observed. The efficacy of using peptides for selective intracellular delivery is highlighted by performing a multicolor QD labeling, where we found that the presence or absence of peptide on the QD surface controls cellular uptake.

INTRODUCTION

Luminescent semiconductor nanocrystals or quantum dots (QDs)[1] are a relatively new class of fluorescent probe whose unique optical properties suggest that they are superior to conventional organic dyes for many biological applications (*1*−*5*). QD properties include high quantum yield, broad absorption spectra, large achievable Stokes shifts, narrow symmetric, size-tunable emission spectra, and exceptional resistance to photo- and chemical degradation (*2*−*6*). These properties are particularly appealing for the visualization of cellular processes, as they can potentially facilitate long-term and multicolor labeling of both fixed and living cells. An intensive exploration is currently underway by several groups to optimize methods for the intracellular delivery of QDs and QD bioconjugates and to characterize their long-term in vivo photophysical properties.

Three important criteria must be met for the successful development of QDs and QD bioconjugates as reliable reagents for cellular labeling and in vivo imaging. First, hydrophilic QD probes must be prepared in a facile and controlled manner. Second, their intracellular uptake must exhibit an element of selective delivery, and the QD probes must be able to access various subcellular compartments. Third, the QD bioconjugates must elicit minimal or no cytotoxicity over the time course required for efficient cellular delivery, labeling, subsequent targeting, and sensing. Reports describing QD bioconjugates that meet all three of these criteria, however, remain limited.

A few strategies for developing QD−cell penetrating peptide (CPP) bioconjugates for cellular delivery have been attempted and mixed results have been demonstrated in terms of providing effective cellular transmembrane delivery and labeling. Silver and Ou used commercially available QDs functionalized with streptavidin/poly(ethylene glycol) and complexed to both biotinylated and nonbiotinylated peptides expressing a 9-mer poly-arginine sequence (*7*). These bioconjugates were delivered to lysosomes and formed aggregates in both HeLa and baby hamster kidney cells. Coating the same QDs with protein A and complexing them with poly-L-lysine also produced equally effective cellular delivery, suggesting that charge alone may be the dominant translocation mediator in these cells. Lagerholm attached 25- to 50-fold excess of a biotinylated 9-mer poly-arginine containing peptide to streptavidin QDs and found intracellular labeling in Swiss 3T3, HeLa, and MG63 cells with a brightness 2 orders of magnitude stronger than unconjugated QDs alone (*8*). Rozenzhak used a noncovalently complexed 21-residue peptide carrier for cellular delivery of QDs into HeLa cells (*9*). This peptide, which is believed to function independently of endocytosis, consists of a hydrophobic tryptophan-rich domain for efficient membrane translocation and a lysine-rich domain for solubility. Efficient intracellular delivery of QDs with punctate cytoplasmic staining was reported using this peptide carrier. Hoshino reported that 48-62 copies of an 11-mer poly-arginine-containing sequence covalently attached to QDs facilitated their rapid cellular uptake and localization to the nucleus in Vero cells (*10*). In contrast, Derfus reported that complexing QDs with a Chariot peptide actually decreased HeLa cell uptake to levels below those of uncomplexed QDs (*11*). A similar Tat protein-derived sequence has been shown to

* To whom correspondence should be addressed: Email: jdelehanty@cbmse.nrl.navy.mil. Phone: 202-767-0291. Fax: 202-767-9594; hedimat@ccs.nrl.navy.mil. Phone 202-767-9473. Fax: 202-404-8114.

[†] Center for Bio/Molecular Science and Engineering, Code 6900.

[‡] Optical Sciences Division, Code 5611.

[§] The Scripps Research Institute.

[||] Johns Hopkins University.

[1] Abbreviations used: AF546-transferrin, AlexaFluor 546-conjugated transferrin; CPP, cell penetrating peptide; DHLA, dihydrolipoic acid; QD, quantum dot; PBS, phosphate-buffered saline; PL, photoluminescence.

10.1021/bc060044i CCC: $33.50 © 2006 American Chemical Society
Published on Web 06/23/2006

efficiently mediate the nuclear translocation of gold nanoparticles that were less than 5 nm in diameter (*12*).

Strategies for the intracellular delivery of QDs have relied largely on the use of receptor-mediated or nonspecific endocytosis (*1*, *13*). In a detailed report, Jaiswal et al. demonstrated passive endocytotic uptake of hydrophilic QDs capped with dihydrolipoic acid (DHLA) by incubating HeLa cells with solutions containing QDs at concentrations of 400−600 nM QDs for 3−4 h (*1*). QDs entering cells by this pathway remained largely sequestered within endocytic vesicles for several hours (*1*, *11*). Other methods for the cellular uptake of QDs that have been reported include: electroporation (*14*), cationic transfection reagents (*11*, *15*), and microinjection (*11*). Each of these methods has certain drawbacks, however. For example, microinjection is a limited throughput process, as individual cells must be manipulated one at a time, while electroporation necessitates forming pores in the cellular membrane. Peptide-mediated delivery on the other hand remains one of the more attractive methods due to the ease of use. This involves complexing QDs with cell penetrating peptides (CPP) to facilitate their transmembrane delivery. These peptide motifs are most often based on the HIV-1 Tat peptide (*16*), antennapedia (*17*), and transportan sequences (*18*). The classical or core CPP motif is derived from the HIV-1 Tat peptide and usually consists of 7−11 consecutive repeats of positively charged arginine residues (*19*). While the mechanism of CPP-mediated membrane translocation remains under investigation, increasing evidence points to the involvement of several types of endocytosis (*20*−*25*).

In this report, we describe the development and characterization of self-assembled QD−peptide bioconjugates for the specific intracellular delivery into several eukaryotic cell lines. A poly-histidine-appended peptide expressing an 8-mer polyarginine sequence is first self-assembled onto DHLA-capped CdSe−ZnS QDs, then used to facilitate QD transmembrane delivery. We found that once internalized, some, but not all, of the QD staining colocalizes with endosomal compartments. We also found that peptide-mediated QD uptake is dependent on conjugate concentration while exposure of cells to nonconjugated QDs results in negligible intracellular labeling. Significant differences in cellular toxicity are also noted for chronic (long-term) versus acute (short-term) cell incubation with QD−peptide conjugates. Selective intracellular labeling is further highlighted by performing a multicolor QD labeling experiment, where the presence or absence of peptide on the QD surface was found to determine whether cellular uptake can occur or not.

MATERIALS AND METHODS

Quantum Dots. CdSe−ZnS core−shell QDs with emission maxima centered at 510 and 551 nm were synthesized and made hydrophilic by exchanging the native trioctylphosphine/trioctylphosphine oxide (TOP/TOPO) capping shell with DHLA ligands as described previously (*26*). The QDs are identified by their wavelength of maximum emission, e.g., a sample of 510 nm QDs designates a population of QDs which exhibits maximum photoluminescence centered at 510 nm (see Figure 1B).

Peptide Synthesis. The cell-penetrating peptide (CPP) used in this study is composed of the sequence $(His)_8$ -Trp-Gly-Leu-Ala-Aib-Ser-Gly-$(Arg)_8$-amide, where Aib is α-aminoisobutyric acid and the C-terminus is blocked with an amide. The N-terminal polyhistidine $(His)_8$ tract mediates self-assembly onto DHLA-capped CdSe−ZnS QDs (*27*−*34*). The peptide was synthesized manually using in-situ neutralization cycles for Boc-solid-phase peptide synthesis on 0.2 mmol MBHA resin (4-methylbenzhydrylamine, Peptides International, Louisville, KY) using 1.1 mmol amino acid, 1.0 mmol HCTU ([2-(1*H*-6-chlorobenzotriazol-1-yl)-1,1,3,3-tetramethyluronium hexafluorophosphate]), 2 mL of 0.5 M solution in DMF), and 0.5 mL DIEA

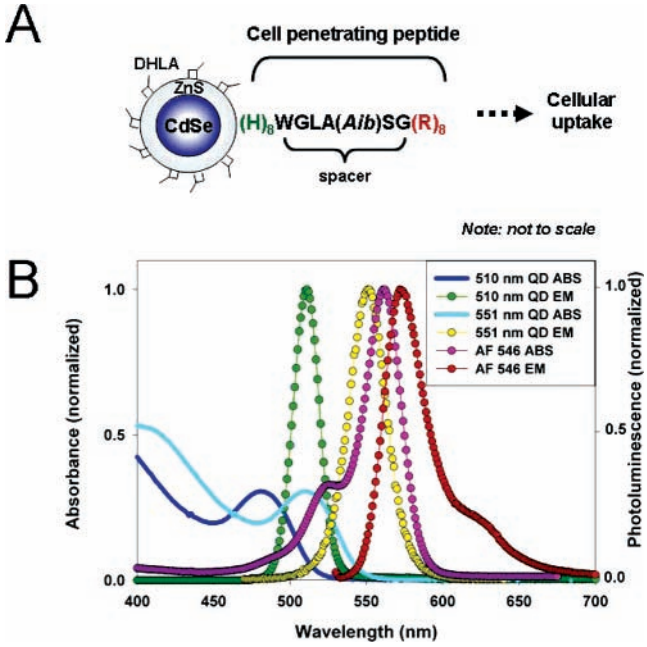

Figure 1. Schematic representation of a QD−peptide assembly and relevant absorbance/emission spectra for materials used in this study. (A) The peptide self-assembles onto the DHLA-capped CdSe/ZnS QD surface via $(His)_8$-Zn metal-affinity coordination. A short spacer separates the $(His)_8$ QD attachment domain from the HIV-1 Tat-derived $(Arg)_8$ cellular uptake sequence. Aib is α-aminoisobutyric. (B) Absorbance of 510 and 551 nm QDs are represented by the solid black and cyan lines, respectively. The fluorescence spectra of the QDs and AlexaFluor 546 are also shown.

(*N*,*N*-(diisopropyl)aminomethylpolystyrene) (*35*). Coupling times were typically 20 min. Following chain assembly, the peptide was cleaved from the resin with hydrofluoric acid and 10% anisole for 1 h at 0 °C, purified by HPLC, and characterized by electrospray ionization mass spectrometry using an API-III triple quadruple mass spectrometer (Sciex, Thornhill, CA). The peptide mass was calculated from the experimental mass to charge (*m*/*z*) ratios from all of the observed protonation states of the peptide using MacSpec software (Sciex). The observed peptide mass agreed with the calculated average mass within 0.5 Da.

Cell Culture. HEK 293T/17 and COS-1 cell lines (both from ATCC, Manassas, VA) were cultured as exponentially growing subconfluent monolayers in complete growth medium (Dulbecco's Modified Eagle's Medium (DMEM) supplemented with 4 mM L-glutamine, 1 mM sodium pyruvate, 1% (v/v) antibiotic/antimycotic, and 10% (v/v) heat-inactivated fetal bovine serum (FBS)). Cells were grown on 60-mm dishes and incubated at 37 °C under 5% CO_2 atmosphere. A subculture was performed every 3−4 days.

Assembly of Quantum Dot−Cell Penetrating Peptide Bioconjugates. Self-assembled QD−CPP bioconjugates were prepared by incubating stock solutions of 1 μM QD with appropriate ratios of desalted CPP in 10 mM sodium tetraborate buffer pH 9.6 for at least 1 h. QD−CPP assemblies were diluted into complete growth medium immediately prior to use. Once diluted into growth medium, QD−CPP assemblies typically remained in solution for >24 h. We have found that if the peptide was not desalted prior to use, there were instances where the QD−CPP conjugates precipitated.

Cellular Uptake of Quantum Dot−Peptide Assemblies. All cellular internalization experiments were performed on microscope slides fitted with multiwell forms as described previously (*36*). Aminopropylsilane-functionalized glass slides (GAPSII, Corning) were coated overnight with 50 μg/mL fibronectin (Sigma) in sodium bicarbonate buffer (pH 8.5). Slides were washed twice with distilled water and dried under a stream of

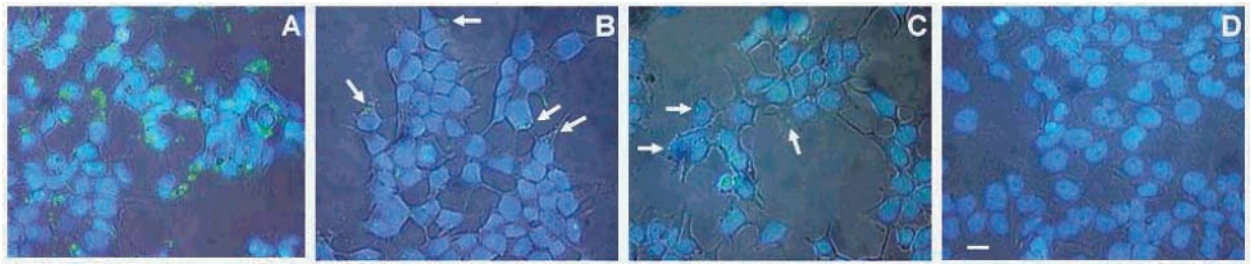

Figure 2. Dose-dependent cellular internalization of QD−CPP assemblies. HEK 293T/17 cells were incubated with 510-nm QD−CPP assemblies (QD:CPP ratio 1:50) at QD concentrations of 250 nM (A), 60 nM (B), 15 nM (C), or with 250 nM QDs without CPP (D); cells were also stained with DAPI. Overlay of phase contrast, QD fluorescence (green), and DAPI fluorescence (blue), show the dose-dependent nature of the QD−CPP delivery. Images also show that QD staining is nonnuclear, punctate fluorescence located in the cytoplasm. Negligible cell-surface associated fluorescence was observed. Arrows indicate regions of QD−CPP internalization at lower concentrations. Scale bar is 10 μm.

nitrogen, and an eight-well adhesive silicone form (Schleicher and Schuell) was affixed. Cells (2×10^4 cells/well) were seeded into the wells and cultured overnight. For delivery experiments, QDs or QD−CPP assemblies were diluted into complete culture medium and incubated with the cells at 37 °C for 1 h. For experiments aimed at assessing QD−CPP colocalization with endosomes, an Alexa Fluor 546-transferrin conjugate (AF546-transferrin, Molecular Probes) was included with the assemblies at a final concentration of 40 μg/mL. After incubation, excess unbound QDs were removed by washing three times with phosphate-buffered saline (PBS, pH 7.4). Cells were then fixed in 3.7% paraformaldehyde for 10 min at room temperature. The cells were washed twice with PBS and mounted in ProLong Antifade mounting media containing DAPI (Molecular Probes).

Fluorescence Microscopy and Image Analysis. Intracellular distribution of QD staining was analyzed by bright field and epifluorescence microscopy using a Nikon ES800 upright fluorescence microscope equipped with a 40× lens. Images were collected using standard Nikon filter sets for DAPI, FITC (for 510 QDs), and TRITC (for AF546−transferrin). Merged images were generated using Adobe PhotoShop. Images of cell cultures incubated with a mixture of two-color QDs were collected by scanning confocal fluorescence microscopy using a Zeiss LSM 510 inverted microscope equipped with a 60× oil immersion lens. Images were collected using the following excitation (ex) lines and emission (em) filters: 510 QDs, 488 nm (ex), 490−510 nm (em); 551 QDs, 488 nm (ex), 545−585 nm (em); AF546-transferrin, 546 nm (ex), 570 nm long-pass filter (em). Phase contrast images were collected using 633 nm laser illumination. Composite merged images were produced using the LSM Image Browser (Zeiss).

Cytotoxicity Assays. Cellular toxicity of the CPP, unconjugated QDs, and QD−CPP assemblies were assessed using the CellTiter 96 Cell Proliferation Assay (Promega, Madison WI) according to the manufacture's instructions. This assay is based upon the conversion of a tetrazolium substrate to a formazan product by viable cells at the assay end point (*37*). The formazan product absorbs at 570 nm. Cells (1×10^4 cells/well) were cultured in 96-well microtiter plates in complete growth medium in the presence of increasing concentrations of QDs, CPP, or QD−CPP assemblies. For the assessment of chronic toxicity, the QD materials were applied to cells and incubated for 24 h prior to assaying the number of viable cells. For acute toxicity studies, the materials were incubated with the cells for 1 h and removed, and the media was replaced with complete growth media. Cells were then cultured for 24 h prior to assaying for cell viability.

RESULTS AND DISCUSSION

Formation of Quantum Dot−CPP Assemblies. QD−peptide bioconjugates were formed by mixing the $(His)_8$-terminated CPP with DHLA-capped QDs for at least 30 min prior to use (Figure 1A). This allows the CPP to self-assemble onto the QD surface. We have previously shown that proteins and peptides expressing terminal polyhistidine sequences self-assemble onto DHLA-capped CdSe−ZnS QDs via metal-affinity coordination (*27*−*34*). Furthermore, this conjugation scheme allows control over the peptide-to-QD ratio in these conjugates. The dissociation constant of this interaction is estimated to be stronger than most antibody−antigen interactions ($K_d \geq 10^{-9}$ M) (*38*). We have found that upon addition of CPP to QD solutions a substantial increase in the solution photoluminescence (PL) intensity is measured; at a ratio of ∼10 peptides per QD−conjugate ∼100% enhancement in solution PL is measured in comparison to a control solution of unconjugated QDs. This observation is consistent with our previous results on self-assembled QD−protein-His and QD−peptide-His conjugates and we used it as an indicator of QD−CPP bioconjugate formation (*26*, *31*, *39*).

Cellular Uptake of Quantum Dot−CPP Assemblies. To determine the efficiency of CPP-mediated internalization, cells were incubated with either nonconjugated QDs or QD−CPPs assembled at QD:CPP ratios of 1:5, 1:25, or 1:50. Figure 2 shows epifluorescence/phase contrast image overlays of HEK 293T/17 cells that were incubated with nonconjugated 510 nm-emitting QDs or with a concentration series of QD−CPP assemblies (ratio of 1:50). The images clearly show that the presence of CPPs on the QD surface resulted in the concentration-dependent cellular uptake of the assemblies, with the highest intracellular QD fluorescence observed for cells incubated with solutions containing higher concentrations of QDs (Figure 2A). Punctate QD fluorescence was dispersed throughout the cytoplasm as well as in close proximity to the cell nuclei (perinuclear), but no nuclear staining was apparent. When the cells were incubated with lower concentrations of QD−CPP assemblies, the degree of cellular uptake was noticeably reduced (Figure 2B,C). In the absence of CPP, no intracellular QD fluorescence was observed (Figure 2D). Similarly, control experiments performed with a non-$(His)_8$-CPP peptide resulted in no noticeable cellular uptake. We also observed essentially no difference in the efficiency of uptake between QD−CPPs assembled at ratios of 1:50 and 1:25. However, a noticeable decrease in uptake occurred when the ratio was decreased to 1:5 (data not shown). Further, we observed no detectable fluorescence signal remaining on the plasma membrane, indicating a negligible degree of nonspecific binding of the QD−CPP assemblies to the cell surface after washing. These results provide strong evidence that complexing the CPPs with QDs allows for specific cellular internalization relative to the same concentration of nonconjugated QDs and also demonstrate the concentration-dependent nature of the peptide-facilitated uptake. We should emphasize that similar experiments performed with COS-1 cells resulted in an approximately 2- to 3-fold lower efficiency of QD−CPP conjugate uptake and likely point to

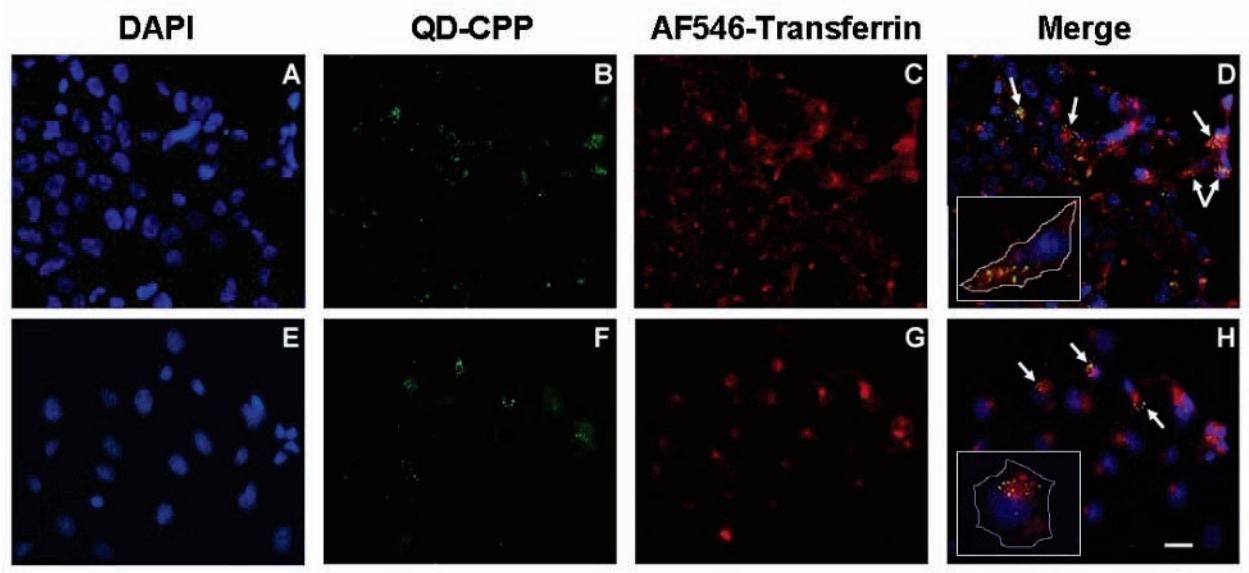

Figure 3. QD−CPP internalization and colocalization within endocytotic vesicles. HEK 293T/17 (A−D) and COS-1 (E−H) cells were coincubated with 510 nm QD−CPP assemblies (QD:CPP ratio 1:25) and 40 μg/mL AlexaFluor 546−transferrin for 1 h. Following washing and fixation, cells were imaged by epifluorescence. DAPI-stained nuclei are shown in panels A and E. QD fluorescence is shown in B and F and is largely perinuclear. Staining with AlexaFluor 546−transferrin, an endocytotic marker, is shown in C and G, and merged images appear in D and H. The insets in D and H show representative single cells with the cell membrane marked for clarity. Arrows indicate areas of colocalization. Scale bar is 10 μm.

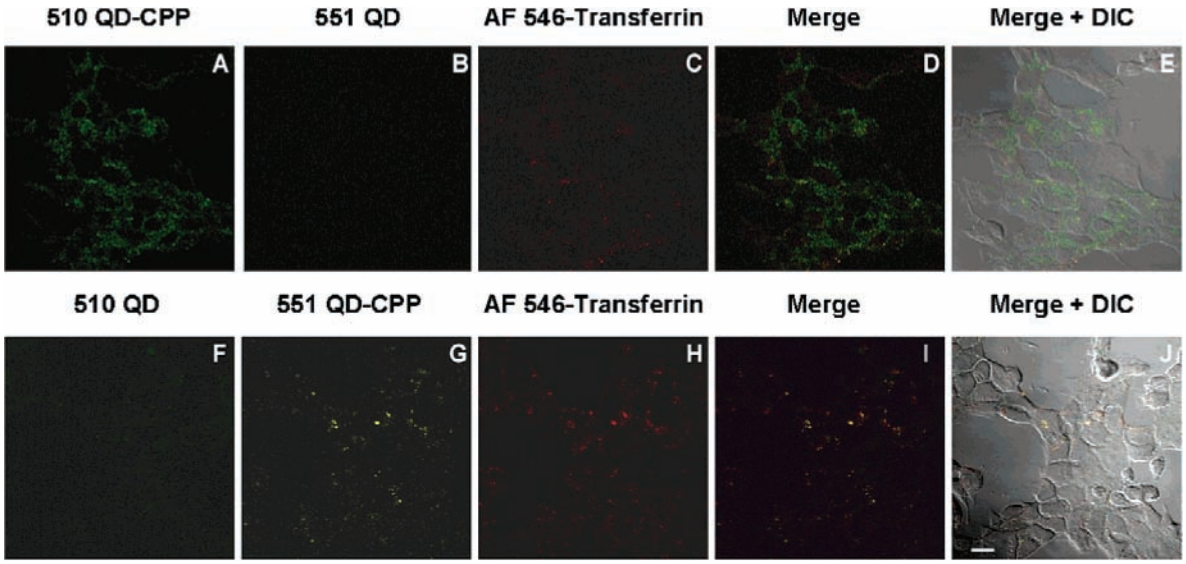

Figure 4. Selective cellular internalization of QD−CPP assemblies. HEK 293T/17 cells were incubated with mixtures of 510 nm QD−CPP (250 nM QD concentrated) and unconjugated 551 nm QDs (60 nM) (in A−E) or to unconjugated 510 nm QDs (60 nM in QDs) and 551 nm QD−CPP (250 nM QD concentrated) (in F−J). In both cases, cells were coincubated with 40 μg/mL AF546-transferrin. The merged/DIC images show that assemblies are excluded from the nucleus. Scale bar is 10 μm.

differences between the two cell lines used. Nonetheless, the amount of delivered QD cargos was large enough to produce a strong fluorescence signal and to carry out additional comparative experiments.

To monitor the fate of the internalized QD−CPP assemblies in HEK293T/17 and COS-1 cells, we examined the intracellular distribution of QD−CPP assemblies that were simultaneously delivered with AlexaFluor 546-conjugated transferrin (AF546−transferrin). Transferrin is an 80 kDa serum glycoprotein that mediates iron uptake in vertebrate cells via receptor-mediated endocytosis, and labeled transferrin is commonly used to monitor the endocytic pathway (*40*, *41*). To visualize the nuclei, the cells were also stained with DAPI (Figure 3, A and E). In both cell lines, a punctate and vesicular QD fluorescence pattern was observed within the cytoplasm and within perinuclear spaces (Figure 3, parts B and F). This punctate appearance is not unexpected for this type of DHLA-capped QD when present within the slightly acidic cellular environment and is consistent with previously published results (*1*, *11*). When the QD fluorescence pattern was merged with the vesicular staining pattern of AF546-transferrin (Figure 3, parts C and G), it was evident that at least a portion of the internalized QD−CPP assemblies were colocalized within endosomes (Figure 3, parts D and H). Simultaneous incubation with AF546-transferrin did not alter QD−CPP uptake or staining in any manner. Further, when cells were incubated with the QD−CPP assemblies at 4 °C, where endocytosis is inhibited, cellular uptake was completely eliminated (data not shown). These results strongly suggest a role for endocytosis in the uptake of the QD−CPP assemblies. Recent studies using live-cell imaging and FACS analysis have also established that arginine-rich CPPs and their conjugated cargos are internalized by endocytosis (*24*, *25*, *42*).

Selective Quantum Dot−CPP Cellular Uptake. To investigate the ability of cells to discriminate between two QD

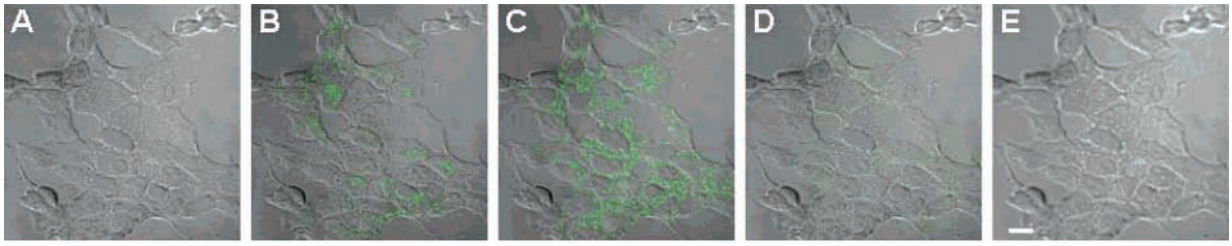

Figure 5. Laser scanning fluorescence images of cross-sectional slices along z-direction of internalized QD−CPP assemblies. HEK 293T/17 cells were incubated with a mixture of 510 nm QD−CPP conjugates (250 nM QD concentrated) and unconjugated 551 nm QDs (60 nM in QDs). Sequential images (~0.4 μm sections with ~0.25 μm overlap between adjoining sections) were acquired along the *z*-axis. Panel A is below the cells while panel E is above the cells. Images show that QD fluorescence is located exclusively in the cytoplasm and is nonnuclear. After washing, no nonspecifically bound QDs remaining on the cell surface were observed. Scale bar is 10 μm.

populations (colors) presenting distinct surface functionalities, HEK 293T/17 cells were incubated for 1 h with a mixture of 510 nm QD−CPP conjugates and unconjugated 551 nm QDs. The cells were then fixed and examined by scanning confocal fluorescence microscopy. As shown in Figure 4A, when cells were incubated with 510 nm QD−CPP assemblies (at a concentration of 250 nM QD) and unconjugated 551 nm QDs (at a concentration of 60 nM QD), internalization of only the 510 nm QDs was observed.[2] No intracellular QD fluorescence corresponding to the 551 nm QDs was observed (Figure 4B). Consistent with our previous experiments, the pattern of intracellular QD fluorescence was punctate in nature and was excluded from the nucleus. However, in contrast to our previous observations using epifluorescence microscopy, the more sensitive confocal analysis used here indicated a higher degree of intracellular QD fluorescence than what was previously measured above (see Figure 3) as demonstrated by the QD signal dispersed nearly homogeneously throughout the cytoplasm. When the pattern of QD fluorescence was compared to that of AF546-transferrin (Figure 4C), a modest degree of overlap was observed indicating partial colocalization of QDs within endosomes (Figure 4D). The majority of the QDs appeared to be excluded from endocytotic vesicles (Figure 4E). The presence of the QDs within the cytoplasm coupled with the lack of QD signal within the nucleus is notable in light of previous investigations which have shown that paraformaldehyde or methanol fixation protocols can cause an artificial redistribution of CPPs and CPP conjugates from the cytoplasm to the nucleus (*42*). The fact that we observed no nuclear translocation suggests that the radius of the QD (hydrodynamic radius ~5−6 nm) precluded the passive diffusion of the QD−CPP assembly through the nuclear pore complex whose hydrodynamic radius is approximately 5 nm (*43*).

In the converse experiment, HEK 293T/17 cells were incubated with mixtures of 551 nm QD−CPP assemblies (at a concentration of 250 nM QDs) and unconjugated 510 nm QDs (at a concentration of 60 nM QDs). Again, the cells internalized only QDs that were complexed with CPPs as only signal corresponding to the 551 nm QDs was apparent (Figure 4G). We did, however, note that the overall intracellular fluorescence of the internalized 551 nm QDs was lower than that previously observed for the CPP-mediated delivery of 510 nm QDs. This difference is attributable to the differential excitation efficiency of the two QD species with the 488 nm laser line, which corresponds to the first absorption peak of the 510 nm QDs while it coincides with the absorption "valley" of the 551 nm QDs (see Figure 1B). Also in contrast with the internalization of 510 nm QD−CPP assemblies, we found that the 551 nm QDs were almost exclusively colocalized with the transferrin conjugate, indicating the sequestration of the 551 QDs within endosomes (Figure 4, H and I). Minimal 551 nm QD fluorescence was dispersed within the cytoplasm (Figure 4J). While it is likely that the differential excitation efficiencies of the two QD species also contribute to these observed differences, it is worth noting that previous studies have demonstrated the ability of poly-L-histidine to increase the endosomal escape of plasmid DNA via the membrane destabilization of acidic endocytotic vesicles following protonation of the imidazole groups (*44*−*46*). It is possible that the CPP plays a contributing role in aiding the endosomal escape of the QD−CPP assemblies, as the CPP peptide contains a $(His)_8$ sequence.

Confocal analysis of these same samples also confirmed that the QD fluorescence was localized exclusively to the cell interior with no evidence of nonspecifically bound QDs on the cell membrane. Figure 5 (panels A−E) shows a sequential z-step analysis taken through HEK 293T/17 cells incubated with a mixture of 510 nm QD−CPP conjugates and unconjugated 551 nm QDs. Standard washing of the cells with PBS was sufficient to remove all loosely bound QDs from the cell surface. This is in contrast to other reports wherein trypsin digestion (*42*) or modification of the QD surface (e.g., with poly(ethylene glycol) ligands) (*47*) were required to remove nonspecific QD binding to the cell surface.

Cytotoxicity of Quantum Dot−CPP Assemblies. The cytotoxicity of the free CPP, unconjugated QDs, and QD−CPP assemblies was assessed by monitoring their ability to inhibit cellular proliferation. Using a colorimetric tetrazolium-based cell proliferation assay, we assessed the toxicity of both short-term (acute) and long-term (chronic) incubation of COS-1 cells and HEK 293T/17 cells to these materials. Under conditions of acute exposure, wherein cells were incubated with the materials for 1 h followed by rinsing and subsequent culture for 24 h, we observed no significant change in proliferation for the CPP (12.5 μM highest concentration tested), unconjugated QDs (250 nM QD highest concentration tested), or QD−CPP assemblies (CPP: QD ratio of 50:1, 12.5 μM CPP: 250 nM QD highest concentration tested) in either COS-1 or HEK 293T/17 cell lines relative to the untreated control (Figure 6 parts A and B, respectively). These exposure conditions are identical to those used to achieve the intracellular delivery of QD−CPP assemblies described in this report and illustrate that the acute exposure of either cell line to the QD−CPP assemblies does not result in any appreciable change in cell viability at the concentrations required for efficient cellular uptake. Under conditions of chronic exposure (incubation for 24 h or longer), however, a distinct dose-dependent cytotoxic effect of the materials was observed (Figure 6, parts C and D, respectively). For both cell lines, the QD−CPP assemblies had the greatest effect on cell proliferation, eliciting a slightly higher degree of toxicity in HEK 293T/17 cells than in COS-1 cells. This result is consistent with our observations of the slightly higher efficiency of QD−CPP

[2] For the unconjugated QDs, a concentration of 60 nM QD was used since our previous results demonstrated that no uptake of unconjugated QDs occurred when they were present at a concentration of 250 nM (see Figure 2).

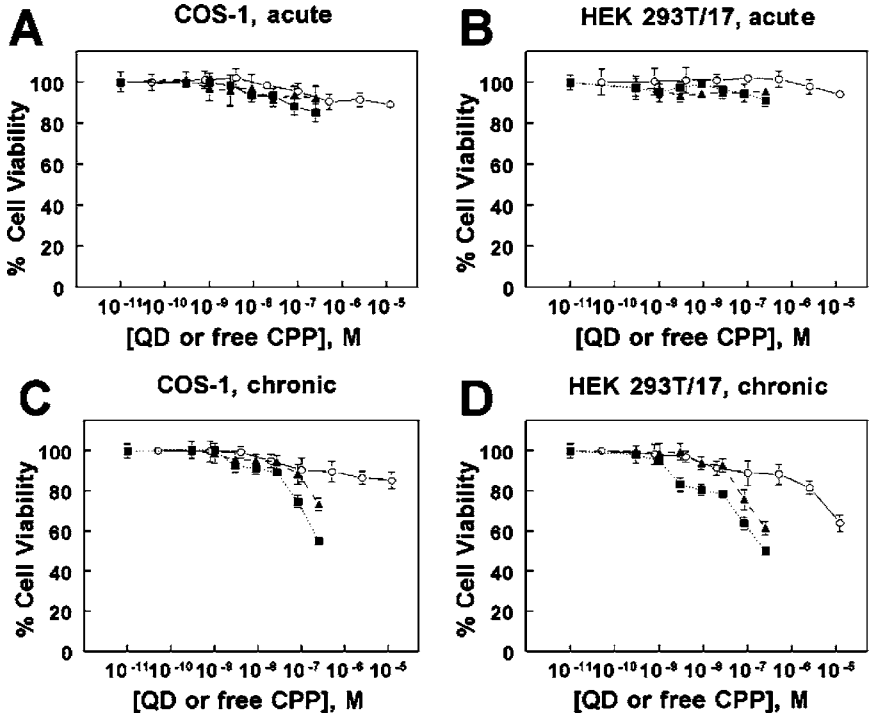

Figure 6. Differential cytotoxicity of QDs, CPP, or QD−CPP assemblies. The acute (short-term) and chronic (long-term) cytotoxicity of unconjugated QDs, free CPP, or QD−CPP assemblies (ratio QD:CPP = 1:25) was assessed using COS-1 and HEK 293T/17 cells. In the acute studies, COS-1 (panel A) and HEK 293T/17 (panel B) cells were incubated with the materials for 1 h, washed, and subsequently cultured for 24 h prior to viability assay. In the chronic studies, COS-1 (panel C) and HEK 293T/17 (panel D) cells were cultured for 24 h in the presence of the materials prior to viability assay. Symbols correspond to: QD−CPP (■), unconjugated QDs (▲), and free CPP (○). For QD−CPP or unconjugated QDs, the concentrations designate those of the QDs. Each data point represents the mean ± SD of triplicate measurements.

internalization by HEK 293T/17 cells. The unconjugated QDs were slightly less toxic than the QD−CPP assemblies. While the free CPP had only a slight effect on the proliferation of COS-1 cells, it was increasingly toxic to HEK 293T/17 cells at concentrations greater than ~750 nM.

While other studies have characterized the toxicity of unconjugated QDs (*48, 49*) and QD bioconjugates (*1*) or free CPPs (*50*) and their associated cargos (*51*), reports detailing the comparative effects of acute versus chronic incubation conditions across multiple cell lines remain limited. Importantly, our results demonstrate not only distinct differences between the two incubation conditions but may also point to cell type-dependent differences in the degree of toxicity.

CONCLUSIONS

We have demonstrated the effective use of cell penetrating peptides to drive the noninvasive intracellular delivery of hydrophilic QD cargos. The approach was applied to two different eukaryotic cell lines, HEK 293T/17 and COS-1. The QD−peptide bioconjugates described in this report are prepared by the facile self-assembly of a polyhistidine-appended cell penetrating peptide with DHLA-capped CdSe−ZnS core shell QDs. This assembly process may ultimately allow for the generation of mixed peptide surfaces, wherein each different peptide imparts a unique functionality to the resulting bioconjugate. A similar strategy has been suggested by Weiss (*52*).

We found that the level of intracellular uptake of the QD−CPP assemblies depends on the QD concentration, the number of QD-associated CPPs, and the cell type used. In the absence of CPP, the extent of QD internalization is essentially nonexistent. Our results show that QD fluorescence is localized to the cell interior with no nonspecific binding of QD−CPP to the cell surface. While other studies have detailed the use of covalent modification of the QD surface with poly(ethylene glycol) (*47*) ligands or trypsin digestion of cells (*42*) to reduce the non-specific binding of QDs, we found that the QD−CPP assemblies were easily removed from the cell surface by washing with PBS. Consistent with other reports that have established the role of endocytosis in the uptake of arginine-rich CPPs and their cargos (*24, 25, 42*), the partial colocalization of the internalized QD−CPPs within endosomes and the complete elimination of their uptake upon incubation at 4 °C provide strong evidence for the role of endocytosis in the uptake of our QD−CPP assemblies. Further, the use of QD−CPP conjugates allows for the intracellular delivery of QDs at lower concentrations and with shorter incubation times compared to other reports which have used nonspecific endocytosis of unconjugated QDs (*1*).

We also observed significant differences between acute and chronic exposure of cells to the QD−CPP complexes. While our chronic exposure results are consistent with those previously reported for unconjugated QDs (*49*), CPPs (*51*), and QD bioconjugates (*7*), the acute toxicity data presented here represents the first description of the minimal cytotoxicity associated with a delivery time course required for successful intracellular uptake. These results are very promising and indicate that cells can be exposed to these assemblies, effectively labeled, and used without significant alteration of their viability or function.

The fine degree of controlled QD−CPP delivery coupled with the minimal toxicity associated with that delivery now sets the stage for more elegant in vitro and in vivo labeling applications, such as the simultaneous delivery and tracking of multiple color QDs to different intracellular compartments (molecular "barcoding"). The use of multipeptide labeled QDs will likely facilitate these studies where each peptide contributes a different function such as cellular uptake, endosomal escape, and organelle targeting.

ACKNOWLEDGMENT

The authors acknowledge NRL and L. Chrisey at the Office of Naval Research (ONR grant no. N001404WX20270 to H.M.)

and NIH (NIH grant no. GM066119 to P.E.D.). T. Pons acknowledges support from the Foundation pour la Recherche Midicale. We are also grateful to Michelle Husain and the Integrated Imaging Center at Johns Hopkins University for their assistance with the confocal microscopy.

LITERATURE CITED

(1) Jaiswal, J. K., Mattoussi, H., Mauro, J. M., and Simon, S. M. (2003) Long-term multiple color imaging of live cells using quantum dot bioconjugates. *Nat. Biotechnol. 21*, 47−51.

(2) Alivisatos, A. P., Gu, W., and Larabell, C. A. (2005) Quantum dots as cellular probes. *Ann. Rev. Biomed. Eng. 7*, 55−76.

(3) Alivisatos, P. (2004) The use of nanocrystals in biological detection. *Nat. Biotechnol. 22*, 47−52.

(4) Medintz, I. L., Uyeda, H., Goldman, E. R., and Mattoussi, H. (2005) Quantum dot bioconjugates for imaging, labeling and sensing. *Nat. Mater. 4*, 435−446.

(5) Parak, W. J., Gerion, D., Pellegrino, T., Zanchet, D., Micheel, C., Williams, S. C., Boudreau, R., Le Gros, M. A., Larabell, C. A., and Alivisatos, A. P. (2003) Biological applications of colloidal nanocrystals. *Nanotechnology 14*, R15−R27.

(6) Parak, W., Pellegrino, T., and Plank, C. (2005) Labelling of cells with quantum dots. *Nanotechnology 16*, R9−R25.

(7) Silver, J., and Ou, W. (2005) Photoactivation of quantum dot fluorescence following endocytosis. *Nano Lett. 5*, 1445−1449.

(8) Lagerholm, B. C., Weinreb, G. E., Thompson, N. L., and Jacobson, K. (2004) Multicolor coding of quantum dots with cationic peptide coated quantum dots. *Nano Lett. 4*, 2019−2022.

(9) Rozenzhak, S. M., Kadakia, M. P., Caserta, T. M., Westbrook, T. R., Stone, M. O., and Naik, R. R. (2005) Cellular internalization and targeting of semiconductor quantum dots. *Chem. Commun. 17*, 2217−2219.

(10) Hoshino, A., Fujioka, K., Oku, T., Nakamura, S., Suga, M., Yamaguchi, Y., Suzuki, K., Yasuhara, M., and Yamamoto, K. (2004) Quantum dots targeted to the assigned organelle in living cells. *Microbiol. and Immunol. 48*, 985−994.

(11) Derfus, A. M., Chan, W. C. W., and Bhatia, S. N. (2004) Intracellular delivery of quantum dots for live cell labeling and organelle tracking. *Adv. Mater. 16*, 961−966.

(12) de la Fuente, J. M., and Berry, C. C. (2006) Tat peptide as an efficient molecule to translocate gold nanoparticles into the cell nucleus. *Bioconjugate Chem. 16*, 1176−1180.

(13) Chan, W. C., and Nie, S. (1998) Quantum dot bioconjugates for ultrasensitive nonisotopic detection. *Science 281*, 2016−2018.

(14) Chen, F. Q., and Gerion, D. (2004) Fluorescent CdSe/ZnS nanocrystal-peptide conjugates for long-term, nontoxic imaging and nuclear targeting in living cells. *Nano Lett. 4*, 1827−1832.

(15) Voura, E. B., Jaiswal, J. K., Mattoussi, H., and Simon, S. M. (2004) Tracking early metastatic progression with quantum dots nanocrystals and emission scanning microscopy. *Nat. Med. 10*, 993−998.

(16) Futaki, S. (2005) Membrane-permeable arginine-rich peptides and the translocation mechanisms. *Adv. Drug Delivery Rev. 57*, 547−548.

(17) Derossi, D., Joliot, A. H., Chassaing, G., and Prochiantz, A. (1994) The third helix of the Antennapedia homeodomain translocates through biological membranes. *J. Biol. Chem. 269*, 10444−10450.

(18) Pooga, M., Hallbrink, M., Zorko, M., and Langel, U. (1998) Cell penetration by transportan. *FASEB J. 12*, 67−77.

(19) Zhao, M., and Weissleder, R. (2004) Intracellular cargo delivery using tat peptide and derivatives. *Med. Res. Rev. 24*, 1−12.

(20) Richard, J. P., Melikov, K., Brooks, H., Prevot, P., Lebleu, B., and Chernomordik, L. V. (2005) Cellular uptake of unconjugated TAT peptide involves clathrin-dependent endocytosis and heparan sulfate receptors. *J. Biol. Chem. 280*, 15300−15306.

(21) Drin, G., Cottin, S., Blanc, E., Rees, A. R., and Temsamani, J. (2003) Studies on the internalization mechanism of cationic cell-penetrating peptides. *J. Biol. Chem. 278*, 31192−311201.

(22) Fittipaldi, A., Ferrari, A., Zoppe, M., Arcangeli, C., Pellegrini, V., Beltram, F., and Giacca, M. (2003) Cell membrane lipid rafts mediate caveolar endocytosis of HIV-1 Tat fusion proteins. *J. Biol. Chem. 278*, 34141−34149.

(23) Saalik, P., Elmquist, A., Hansen, M., Padari, K., Saar, K., Viht, K., Langel, U., and Pooga, M. (2004) Protein cargo delivery properties of cell-penetrating peptides. A comparative study. *Bioconjugate Chem. 15*, 1246−1253.

(24) Wadia, J. S., Stan, R. V., and Dowdy, S. F. (2004) Transducible TAT-HA fusogenic peptide enhances escape of TAT-fusion proteins after lipid raft macropinocytosis. *Nat. Med. 10*, 310−5.

(25) Kaplan, I. M., Wadia, J. S., and Dowdy, S. F. (2005) Cationic TAT peptide transduction domain enters cells by macropinocytosis. *J. Control Release 102*, 247−53.

(26) Mattoussi, H., Mauro, J. M., Goldman, E. R., Anderson, G. P., Sundar, V. C., Mikulec, F. V., and Bawendi, M. G. (2000) Self-Assembly of CdSe−ZnS Quantum Dot Bioconjugates Using an Engineered Recombinant Protein. *J. Am. Chem. Soc. 122*, 12142−12150.

(27) Goldman, E., Medintz, I. L., Whitley, J., Hayhurst, A., Clapp, A., Uyeda, H., Deschamps, J., Lassman, M., and Mattoussi, H. (2005) A hybrid quantum dot−antibody fragment fluorescence resonance energy transfer-based TNT sensor. *J. Am. Chem. Soc. 127*, 6744−6751.

(28) Clapp, A. R., Medintz, I. L., Fisher, B. R., Anderson, G. P., and Mattoussi, H. (2005) Can luminescent quantum dots be efficient energy acceptors with organic dye donors? *J. Am. Chem. Soc. 127*, 1242−1250.

(29) Clapp, A. R., Medintz, I. L., Mauro, J. M., Fisher, B. R., Bawendi, M. G., and Mattoussi, H. (2004) Fluorescence Resonance Energy Transfer Between Quantum Dot Donors and Dye-Labeled Protein Acceptors. *J. Am. Chem. Soc. 126*, 301−310.

(30) Medintz, I. L., Konnert, J. H., Clapp, A. R., Stanish, I., Twigg, M. E., Mattoussi, H., Mauro, J., Matthew, and Deschamps, J. R. (2004) A fluorescence resonance energy transfer derived structure of a quantum dot-protein bioconjugate nanoassembly. *Proc. Natl. Acad. Sci. U.S.A. 101*, 9612−9617.

(31) Medintz, I. L., Clapp, A. R., Mattoussi, H., Goldman, E. R., Fisher, B., and Mauro, J. M. (2003) Self-assembled nanoscale biosensors based on quantum dot FRET donors. *Nat. Mat. 2*, 630−638.

(32) Medintz, I. L., Trammell, S. A., Mattoussi, H., and Mauro, J. M. (2004) Reversible modulation of quantum dot photoluminescence using a protein-bound photochromic fluorescence resonance energy transfer acceptor. *J. Am. Chem. Soc. 126*, 30−31.

(33) Sapsford, K. E., Medintz, I. L., Golden, J. P., Deschamps, J. R., Uyeda, H. T., and Mattoussi, H. (2004) Surface-immobilized self-assembled protein-based quantum dot nanoassemblies. *Langmuir 20*, 7720−7728.

(34) Medintz, I. L., Clapp, A. R., Melinger, J. S., Deschamps, J. R., and Mattoussi, H. (2005) A reagentless quantum dot sensing assembly based on förster resonance energy transfer. *Adv. Mater. 17*, 2450−2455.

(35) Schnolzer, M., Alewood, P., Jones, A., Alewood, D., and Kent, S. B. (1992) *In situ* neutralization in Boc-chemistry solid phase peptide synthesis. Rapid, high yield assembly of difficult sequences. *Int. J. Pept. Prot. Res. 40*, 180−193.

(36) Delehanty, J. B., Shaffer, K. M., and Lin, B. (2004) Transfected cell microarrays for the expression of membrane-displayed single-chain antibodies. *Anal. Chem. 76*, 7323−7328.

(37) Mosmann, T. (1983) Rapid colorimetric assay for cellular growth and survival: application to proliferation and cytotoxicity assays. *J. Immunol. Methods 65*, 55−63.

(38) Hainfeld, J. F., Liu, W., Halsey, C. M. R., Freimuth, P., and Powell, R. D. (1999) Ni−NTA-Gold Clusters Target His-Tagged Proteins. *J. Struct. Biol. 127*, 185−198.

(39) Goldman, E. R., Medintz, I. L., Hayhurst, A., Anderson, G. P., Mauro, J. M., Iverson, B. L., Georgiou, G., and Mattoussi, H. (2005) Self-assembled luminescent CdSe−ZnS quantum dot bioconjugates prepared using engineered poly-histidine terminated proteins. *Anal. Chim. Acta. 534*, 63−67.

(40) Ponnambalam, S., Rabouille, C., Luzio, J. P., Nilsson, T., and Warren, G. (1994) The TGN38 glycoprotein contains two nonoverlapping signals that mediate localization to the trans-Golgi network. *J. Cell Biol. 125*, 253−268.

(41) Thorstensen, K., and Romslo, I. (1988) Uptake of iron from transferrin by isolated rat hepatocytes. A redox-mediated plasma membrane process? *J. Biol. Chem. 263*, 8844−8850.

(42) Richard, J. P., Melikov, K., Vives, E., Ramos, C., Verbeure, B., Gait, M. J., Chernomordik, L. V., and Lebleu, B. (2003) Cell-penetrating peptides. A reevaluation of the mechanism of cellular uptake. *J. Biol. Chem. 278*, 585−590.

(43) Keminer, O., and Peters, R. (1999) Permeability of single nuclear pores. *Biophys. J. 77*, 217−228.

(44) Midoux, P., and Monsigny, M. (1999) Efficient gene transfer by histidylated polylysine/pDNA complexes. *Bioconjugate Chem. 10*, 406−411.

(45) Singh, R. S., Goncalves, C., Sandrin, P., Pichon, C., Midoux, P., and Chaudhuri, A. (2004) On the gene delivery efficacies of pH-sensitive cationic lipids via endosomal protonation: a chemical biology investigation. *Chem. Biol. 11*, 713−723.

(46) Hatefi, A., Megeed, Z., and Ghandehari, H. (2006) Recombinant polymer-protein fusion: a promising approach towards efficient and targeted gene delivery. *J. Gene Med*., in press.

(47) Bentzen, E. L., Tomlinson, I. D., Mason, J., Gresch, P., Warnement, M. R., Wright, D., Sanders-Bush, E., Blakely, R., and Rosenthal, S. J. (2005) Surface modification to reduce nonspecific binding of quantum dots in live cell assays. *Bioconjugate Chem. 16*, 1488−1494.

(48) Lovric, J., Bazzi, H. S., Cuie, Y., Fortin, G. R., Winnik, F. M., and Maysinger, D. (2005) Differences in subcellular distribution and toxicity of green and red emitting CdTe quantum dots. *J. Mol. Med. 83*, 377−385.

(49) Shiohara, A., Hoshino, A., Hanaki, K., Suzuki, K., and Yamamoto, K. (2004) On the cyto-toxicity caused by quantum dots. *Microbiol. Immunol. 48*, 669−675.

(50) Saar, K., Lindgren, M., Hansen, M., Eiriksdottir, E., Jiang, Y., Rosenthal-Aizman, K., Sassian, M., and Langel, U. (2005) Cell-penetrating peptides: a comparative membrane toxicity study. *Anal. Biochem. 345*, 55−65.

(51) Futaki, S., Suzuki, T., Ohashi, W., Yagami, T., Tanaka, S., Ueda, K., and Sugiura, Y. (2001) Arginine-rich peptides. An abundant source of membrane-permeable peptides having potential as carriers for intracellular protein delivery. *J. Biol. Chem. 276*, 5836−40.

(52) Michalet, X., Pinaud, F. F., Bentolila, L. A., Tsay, J. M., Doose, S., Li, J. J., Sundaresan, G., Wu, A. M., Gambhir, S. S., and Weiss, S. (2005) Quantum dots for live cells, in vivo imaging, and diagnostics. *Science 307*, 538−544.

BC060044I

Enhanced Cellular Uptake with a Cobaltacarborane−Porphyrin−HIV-1 Tat 48−60 Conjugate

Martha Sibrian-Vazquez, Erhong Hao, Timothy J. Jensen, and M. Graça H. Vicente*

Department of Chemistry, Louisiana State University, Baton Rouge LA, 70803. Received February 24, 2006; Revised Manuscript Received April 24, 2006

A series of four porphyrin−cobaltacarborane conjugates have been synthesized, containing three or four cobaltabisdicarbollide anions linked by $O(CH_2CH_2O)_2$ groups to the porphyrin macrocycle and one of them containing a HIV-1 Tat 48−60 peptide sequence linked via a low molecular weight poly(ethylene glycol) (PEG) spacer. The cellular uptake, cytotoxicity, and preferential sites of intracellular localization of the conjugates were evaluated in human HEp2 cells. All conjugates are nontoxic in the dark at the concentrations studied. Upon exposure to low light dose (1 J cm^{-2}) only the porphyrin−cobaltacarborane−HIV-1 Tat 48−60 conjugate showed 30% inhibition of cell proliferation at a concentration of 10 μM. The cellular uptake was dependent on the number of carborane cages and was significantly enhanced by the presence of the cell penetrating peptide sequence HIV-1 Tat 48−60. All conjugates preferentially localized in the cell lysosomes.

INTRODUCTION

The efficient cellular delivery of porphyrin sensitizers for the boron neutron capture therapy (BNCT) and the photodynamic therapy (PDT) of tumors has been the subject of increasing interest in recent years (*1*−*3*). BNCT (*4*−*6*) and PDT (*7*, *8*) are binary therapies for cancer treatment that involve the activation of a tumor-localized sensitizer with low-energy neutrons (in BNCT) or with red light (in PDT), which generates highly cytotoxic species that cause tumor destruction. The main advantage of these localized therapeutic modalities is the selectivity of the treatment; upon activation of the sensitizing drug only those cells that incorporate it are killed. Both the amount and biodistribution of the porphyrin sensitizer within tumor tissue determine its biological effectiveness and, consequently, the outcome of the BNCT and PDT treatments (*9*, *10*). To date, two porphyrin-based drugs, Photofrin and Visudyne, have been approved by the Federal Drug Administration (FDA) for the PDT treatment of various cancers and the wet form of macular degeneration, respectively, but no porphyrin-based sensitizer has yet been approved for use in BNCT. One of the main challenges in BNCT is the discovery of boron-containing drugs capable of selectively delivering therapeutic amounts of boron-10, between 15 and 30 μg of boron/(g of tumor), depending on the exact location of the boron atoms, to target cells with minimum systemic toxicity (*11*, *12*). Porphyrin derivatives containing multiple boron clusters are particularly promising delivery vehicles for BNCT because of the usually low dark toxicity of this type of macrocycle, their ready detection by fluorescence, and their inherent ability to accumulate within tumors and to persist there during the entire radiation treatment (*1*, *13*, *14*). In addition, boronated porphyrin derivatives are being investigated as dual sensitizers for the BNCT and PDT of tumors (*15*−*17*).

Because of the high amount of boron needed for effective BNCT, the cellular uptake of boron-containing porphyrins is a crucial parameter in determining their biological effectiveness. Lipid vehicles such as Cremophor EL and liposomes have been used to enhance the solubility and tumor delivery of boronated porphyrin derivatives (*18*−*20*). The syntheses of carboranylporphyrins containing either a methoxy poly(ethylene glycol) (PEG) chain (*21*) or a positively charged peptide sequence (PKKKRKV) (*22*) have also been reported but their biological properties have not yet been studied. A particularly attractive strategy for increasing the cellular uptake of porphyrin macrocycles consists of their conjugation to a fusogenic or cell-penetrating peptide sequence, such as that found in the human immunodeficiency virus I transcriptional activator (HIV-1 Tat) (*23*). This short peptide sequence has been successfully used to enhance the cellular uptake of several drugs and macromolecules (*24*, *25*), and we have recently shown that it efficiently delivers a nonboronated porphyrin intracellularly (*26*). Although the porphyrin−HIV-1 Tat conjugate is expected to be taken up by both tumor and normal cells, a leaky tumor vasculature and poor lymphatic clearance might result in favorable differential boron concentrations between tumor and normal tissues and therefore selective tumor accumulation. Furthermore, the conjugation of a boronated porphyrin to the HIV-1 Tat peptide is expected to significantly enhance the delivery of boron to target tumors via convection enhanced delivery (*6*, *27*). Herein we report the synthesis of a new boronated porphyrin−HIV-1 Tat 48−60 conjugate containing PEG linkers between the macrocycle, the peptide sequence (GRKKRRQRRRPPQ), and the cobaltabisdicarbollide anions. We have previously shown that porphyrin−cobaltacarborane conjugates are efficiently prepared in high yields from reaction of a nucleophilic porphyrin with zwitterionic cobaltacarborane [3,3′-Co(8-$C_4H_8O_2$-1,2-$C_2B_9H_{10}$)(1′,2′-$C_2B_9H_{11}$)] (*28*). Furthermore we showed that the cellular uptake of a series of conjugates containing one to four cobaltabisdicarbollide anions increases with the number of carborane cages (*29*). In our continuing investigation of structure/activity relationships in carborane-containing porphyrins, we now report the synthesis and characterization of four new porphyrin−cobaltacarborane conjugates containing three or four cobaltabisdicarbollide anions and compare their cellular uptake, cytotoxicity, and intracellular localization in human HEp2 cells. We show that the presence of the HIV-1 Tat 48−60 peptide sequence significantly enhances the cellular uptake of porphyrin−cobaltacarborane conjugates while it does not alter the preferential sites of intracellular localization.

* Corresponding author. Phone: (225) 578 7405. Fax: (225) 578 3458. E-mail: vicente@lsu.edu.

10.1021/bc060047v CCC: $33.50 © 2006 American Chemical Society
Published on Web 06/29/2006

EXPERIMENTAL PROCEDURES

Syntheses. All commercially available starting materials were used directly without further purification, unless otherwise indicated. Reactions under anhydrous conditions were performed in dried and distilled solvents under an argon atmosphere. All reactions were monitored by thin-layer chromatography (TLC) using Sorbent Technologies 0.25 mm silica gel plates with UV indicator (60F-254). Silica gel Sorbent Technologies 32−63 μm was used for flash column chromatography. ^{1}H and ^{13}C NMR were obtained on either a DPX-250 or ARX-300 Bruker spectrometer. Chemical shifts (δ) are given in parts per million relative to acetone-d_6 (2.05 ppm, ^{1}H; 29.92 ppm, ^{13}C), unless otherwise indicated. Electronic absorption spectra were measured on a Perkin-Elmer Lambda 35 UV−vis spectrophotometer. Mass spectra were obtained on an Applied Biosystems QSTAR XL, a hybrid QqTOF mass spectrometer with a MALDI ionization source using either CCA or dithranol as the matrix. HPLC separation and analysis were carried out on a Dionex system equipped with P680 pump and a UVD340U detector. Semipreparative HPLC was carried out using a Luna C_{18} 100 Å, 5 μm, 10 × 250 mm (Phenomenex, USA) column and a stepwise gradient; analytical HPLC was carried out using a Delta Pak C_{18} 300 Å, 5 μm, 3.9 × 150 mm (Waters, USA) column and a stepwise gradient. 5,10,15,20-Tetra(4-hydroxyphenyl)-porphyrin (**1**) was purchased from Aldrich.

5,10,15-Tri(4-hydroxyphenyl)-20-(4-methoxyphenyl)porphyrin (2). To a solution of porphyrin **1** (170 mg, 0.250 mmol) in anhydrous dimethyl sulfoxide (DMSO; 40 mL) was added K_2CO_3 (280 mg, 2.03 mmol). After heating this mixture to 60 °C for 15 min under argon, iodomethane (0.016 mL, 0.26 mmol) was added in one portion and the final mixture was stirred at 60 °C overnight. The reaction mixture was cooled to room temperature, poured into 200 mL of brine, extracted with ethyl acetate until colorless, and dried over anhydrous sodium sulfate. The solvent was removed under vacuum, and the resulting purple residue was purified by flash column chromatography on silica gel using a gradient of chloroform/ethyl acetate (1:1 to 100% ethyl acetate) for elution. The title porphyrin was collected and further purified by recrystallization from ethyl acetate/hexanes to give 42.6 mg, 25% yield, of dark purple crystals. The ^{1}H NMR and UV−vis for the title porphyrin are in agreement with those reported in the literature (*30*). Mp > 300 °C; HRMS (MALDI-TOF) *m*/*z* 693.2468 $(M + H)^+$, calcd for $C_{45}H_{32}N_4O_4$ 693.2501.

5,10,15-Tri(4-hydroxyphenyl)-20-[4-(*tert*-butoxycarbonylmethyl)phenyl]porphyrin (3). To a solution of porphyrin **1** (500 mg, 0.737 mmol) in anhydrous DMSO (15 mL) was added Cs_2CO_3 (480 mg, 1.47 mmol). The mixture was heated at 50 °C for 1 h under argon before *tert*-butyl bromoacetate (287 mg, 1.473 mmol) was added in one portion and the final mixture heated at 60 °C for 2 h. After cooling to room temperature, ethyl acetate (100 mL) was added to the reaction mixture and the organic phase was washed with water (3 × 100 mL) and dried over anhydrous Na_2SO_4. The solvent was removed under vacuum, and the title porphyrin was purified by flash column chromatography on silica gel using chloroform/methanol 95/5 for elution to give 175 mg, 30% yield, of pure title porphyrin residue, mp > 300 °C. HPLC t_R = 5.90 min. UV−vis ($CHCl_3$) λ_{max} (ϵ/(M^{-1} cm^{-1})) 421 (401 690), 522 (28 400), 553 (21 950), 596 (10 500), 654 (11 000). ^{1}H NMR ($CDCl_3$, 300 MHz): δ 8.90−8.93 (m, 8H, β-H), 8.00−8.05 (m, 8H, PhH), 7.14−7.27 (m, 8H, PhH), 4.87 (s, 2H, CH_2), 1.56 (s, 9H, ^{t}Bu), −2.68 (s, 2H, NH). ^{13}C NMR ($CDCl_3$, 75 MHz): δ 168.80, 159.18, 158.45, 136.52, 136.24, 135.84, 134.08, 121.13, 120.34, 114.75, 113.90, 82.39, 66.54. 28.38. HRMS (MALDI-TOF) *m*/*z* 793.3048 ($M + H^+$), calcd for $C_{50}H_{41}N_4O_6$, 793.3026.

General Procedure for Conjugation of Cobaltacarborane to a 4-Hydroxyphenylporphyrin. To a solution of 4-hydroxyphenylporphyrin (0.1 mmol) in acetone (20 mL) was added K_2CO_3 (0.6 mmol), and the mixture was heated to reflux for 30 min under argon. After cooling to room temperature [3,3′-Co(8-$C_4H_8O_2$-1,2-$C_2B_9H_{10}$(1′,2′-$C_2B_9H_{10}$)] (0.3 mmol) was added and the final mixture was refluxed under argon overnight. A second portion of K_2CO_3 (0.3 mmol) and [3,3′-Co(8-$C_4H_8O_2$-1,2-$C_2B_9H_{10}$(1′,2′-$C_2B_9H_{10}$)] (0.15 mmol) were added to the reaction mixture, and reflux continued for 1 day. A third portion of [3,3′-Co(8-$C_4H_8O_2$-1,2-$C_2B_9H_{10}$(1′,2′-$C_2B_9H_{10}$)] (0.1 mmol) was added, and reflux continued for another day, while monitoring the reaction by HPLC. After 3 days the mixture was cooled to room temperature, the acetone removed under vacuum, and the residue dissolved in ethyl acetate. The organic phase was washed with water and dried over anhydrous Na_2SO_4 and the solvent removed under vacuum. The resulting solid residue was washed with ethyl ether (5 × 5 mL) to remove impurities, and the porphyrin−cobaltacarborane conjugate was dried under vacuum at 50 °C for 2 days.

Porphyrin Conjugate 4. This conjugate was prepared from porphyrin **2** and [3,3′-Co(8-$C_4H_8O_2$-1,2-$C_2B_9H_{10}$(1′,2′-$C_2B_9H_{10}$)] as described above and obtained in 93% (64.2 mg) yield, mp = 230 °C (dec). HPLC t_R = 11.04 min. UV−vis (acetone) λ_{max} (ϵ/(M^{-1} cm^{-1})) 419 (593 000), 516 (23 900), 553 (18 000), 593 (9 000), 651 (8 900). ^{1}H NMR (acetone-d_6): δ 8.91−8.94 (m, 8H, β-H), 8.14 (d, 8H, J = 7.9 Hz, *o*-PhH), 7.34−7.37 (m, 8H, *m*-PhH), 4.45−4.50 (m, 6H, OCH_2), 4.37 (br, 6H, OCH_2), 4.30 (br, 6H, OCH_2), 4.11 (s, 3H, OCH_3), 4.02−4.06 (m, 6H, OCH_2), 3.74 (br, 12H, carborane-H), 1.30−1.60 (br, 51H, BH), −2.68 (s, 2H, NH). ^{13}C NMR (acetone-d_6) 160.3, 136.6, 135.5, 121.1, 114.2, 113.5, 73.4, 70.8, 69.8, 69.0, 60.9, 55.5, 47.7. HRMS (MALDI-TOF) *m*/*z* 1992.1954 $(M - 3K^+ + 3Na^+ + H^+)^+$, calcd for $C_{69}H_{117}B_{54}N_4O_{10}Co_3Na_3$ 1992.1899.

Porphyrin Conjugate 5. This conjugate was prepared from porphyrin **3** and [3,3′-Co(8-$C_4H_8O_2$-1,2-$C_2B_9H_{10}$(1′,2′-$C_2B_9H_{10}$)] as described above, and the corresponding *tert*-butyl protected conjugate **5** was obtained in 91% yield, mp = 262−265 °C (dec). HPLC t_r = 12.52 min. UV−vis (acetone) λ_{max} (ϵ/(M^{-1} cm^{-1})) 419 (396 700), 516 (26 000), 552 (21 200), 593 (8 600), 650 (9 000). ^{1}H NMR (acetone-d_6, 250 MHz): δ 8.90−8.93 (m, 8H, β-H), 8.13 (d, 8H, J = 7.9 Hz, *o*-PhH), 7.36−7.43 (d, 8H, J = 8.5 Hz, *m*-PhH), 4.92 (s, 2H, CH_2), 4.50 (s, 6H, OCH_2), 4.33 (s, 6H, OCH_2), 4.28 (s, 6H, OCH_2), 4.04 (s, 6H, OCH_2), 3.75 (s, 12H, carborane-H), 1.6−3.0 (br, 51H, BH), 1.59 (s, 9H, CH_3), −2.70 (s, 2H, NH). ^{13}C NMR (acetone-d_6, 63 MHz): δ 168.5, 159.7, 158.9, 136.1, 135.5, 134.9, 131.8, 120.6, 120.2, 113.7, 82.1, 72.8, 70.2, 69.2, 68.5, 66.3, 65.8, 61.6, 54.8, 47.1, 28.1. LRMS (MALDI-TOF) *m*/*z* 2139.003 (M^+), calcd for $C_{74}H_{124}N_4O_{12}B_{54}Co_3K_3$ 2139.602. To a solution of this conjugate (100 mg, 0.0467 mmol) in chloroform (5 mL) was added TFA (5 mL) and the final mixture stirred at room temperature for 4 h. The solvent was removed under vacuum and the residue triturated with 5 mL of Et_2O. The resulting green precipitate was washed with Et_2O (6 × 10 mL) to remove residual TFA and dried under vacuum to give 93 mg, 95% yield, of pure conjugate **5**, mp = 283−285 °C (dec). HPLC t_r = 16.59 min. UV−vis (acetone) λ_{max} (ϵ/(M^{-1} cm^{-1})) 419 (408 000), 516 (17 800), 553 (14 250), 593 (8 300), 650 (8 800). ^{1}H NMR (acetone-d_6, TFA): δ 8.78 (br, 8H, β-H), 8.48 (br, 8H, *o*-PhH), 7.64 (br, 8H, *m*-PhH), 5.10 (s, 2H, CH_2), 4.53 (s, 6H, OCH_2), 4.36 (s, 6H, OCH_2), 4.29 (s, 6H, OCH_2), 4.05−4.06 (m, 6H, OCH_2), 3.73 (s, 12H, carborane-H), 0.77−2.43 (br, 51H, BH). LRMS (MALDI-TOF) *m*/*z* 2083.518 $(M + H)^+$, calcd for $C_{70}H_{116}N_4O_{12}B_{54}Co_3K_3$ 2083.498.

Porphyrin Conjugate 6. Peptidyl resin (0.02 mmol) was introduced into a glass synthesizer, swelled in dimethylforma-

mide (DMF) for 1 h, and then washed with DMF (2 × 5 mL). To the resin was added 500 μL of a solution containing 0.08 mmol of $FmocNH(CH_2CH_2O)_7CH_2CH_2NHCOCH_2OCH_2CO_2H$, 0.120 mmol of DIEA, 0.08 mmol of HOBt, and 0.08 mmol of TBTU. The reaction mixture was allowed to react until the Kaiser test was negative, and then the resin was washed with DMF (5 × 5 mL) to remove residual reactants. The Fmoc protecting group was removed by treatment with 20% piperidine/DMF, for 40 min at room temperature. The pegylated peptidyl resin was washed with DMF (5 × 5 mL) and then 500 μL of a solution containing 0.04 mmol of conjugate **5**, 0.120 mmol of DIEA, 0.04 mmol of HOBt, and 0.038 mmol of HATU was added. The reaction mixture was shaken 24 h at room temperature and then filtered to give a dark purple resin. This resin was washed to remove unreacted porphyrin, first with DMF until the filtrate was colorless, then with dichloromethane and methanol, before being dried under vacuum. Cleavage and deprotection was carried out by treatment of the dried resin with 3 mL of a mixture of TFA/phenol/TIS/H_2O, 88:5:2:5 at room temperature for 4 h. The resin was filtered and washed with TFA (3 × 2 mL), and the filtrates were combined and evaporated under vacuum to give a green residue. The conjugate was precipitated by addition of cold Et_2O, washed repeatedly with Et_2O, and dried under vacuum. The purification of the porphyrin conjugate was accomplished by reverse phase HPLC on a Luna C_{18} semipreparative column (10 × 250 mm, 5 μm) (Phenomenex, USA) using water/acetonitrile both containing 0.1% TFA as the mobile phase, with a stepwise gradient from 80 to 95%. The fraction containing the conjugate was collected and lyophilized to afford pure conjugate **6** (6.9 mg) in 8% yield, mp > 300 °C. The purity of conjugate **6** was > 98% as obtained by HPLC on an analytical Delta Pak C_{18} (3.9 × 150 mm, 5 μm) column. HPLC t_r = 7.29 min. UV−vis (methanol) λ_{max} (ϵ/(M^{-1} cm^{-1})) 421 (178 700), 559 (21 700), 553 (18 200), 593 (13 700), 654 (12 500). ^1H NMR (CD_3OH, 300 MHz): δ 7.66 (s, 8H, β-H), 7.50 (s, 8H, *o*-PhH), 7.33 (s, 8H, *m*-PhH), 3.92 (s, 6H, OCH_2) 3.89 (s, 6H, OCH_2), 3.63−3.77 (m, 32H, OCH_2, carborane-H and peptide-H), 0.99−2.64 (m, 84H, peptide-H and BH). LRMS (MALDI-TOF) *m/z* 4302.084 ($M - 3K^+ + 7Na^+)^+$, calcd for $C_{160}H_{283}N_{42}O_{26}B_{54}Co_3Na_7$ 4301.391.

Porphyrin Conjugate 7. This conjugate was prepared from porphyrin **1** and [3,3′-Co(8-$C_4H_8O_2$-1,2-$C_2B_9H_{10}$(1′,2′-$C_2B_9H_{10}$)] as described above and obtained in 85% (106.1 mg) yield, mp = 290−292 °C (dec). HPLC t_R = 13.93 min. UV−vis (acetone) λ_{max} (ϵ/(M^{-1} cm^{-1})) 419 (383 000), 516 (13 700), 552 (9 900), 595 (3 900), 651 (4 600). ^1H NMR (acetone-d_6, 300 MHz): δ 8.94 (s, 8H, β-H), 8.17 (d, 8H, *J* = 8.5 Hz, *o*-PhH), 7.43 (d, 8H, *J* = 8.5 Hz, *m*-PhH), 4.48 (s, 8H, OCH_2), 4.37 (s, 8H, OCH_2), 4.30 (s, 8H, OCH_2), 4.05 (s, 8H, OCH_2), 3.76 (s, 16H, carborane-H), 1.6−3.0 (br, 68H, BH), −2.70 (s, 2H, NH). ^{13}C NMR (acetone-d_6, 75 MHz): δ 160.5, 136.8, 135.7, 121.3, 114.4, 73.6, 71.0, 69.9, 69.3, 55.9, 47.9. HRMS (MALDI-TOF) *m/z* 2411.4881 ($M - 4K^+ + 4Na^+ + H^+$), calcd for $C_{76}H_{143}N_4O_{12}B_{72}Co_4Na_4$ 2411.4855.

Cell Culture. All tissue culture media and reagents were obtained from Invitrogen. Human HEp2 cells were obtained from ATCC and maintained in a 50:50 mixture of DMEM/Advanced MEM containing 5% FBS. The cells were subcultured biweekly to maintain subconfluent stocks.

Cellular Uptake. HEp2 cells were plated at 10 000/well in a Costar 96 well plate and allowed to grow overnight. Conjugate stocks were prepared in a mixture of 9:1 DMSO/cremophore at a concentration of 1 mM and then diluted into medium to final working concentrations maintaining DMSO at 1%. The cells were exposed to 10 μM of each conjugate for 0, 1, 2, 4, 8, and 24 h. At the end of the incubation time the loading medium was removed and the cells were washed with PBS pH = 7.4. The cells were solubilized upon addition of 100 μL of 0.25% Triton X-100 (Calbiochem) in PBS. To determine the conjugate concentration, fluorescence emission was read at 410:650 nm (excitation/emission) using a BMG FLUOstar plate reader. Then the cell numbers were quantified using the CyQuant reagent (Molecular Probes).

Cytotoxicity. The HEp2 cells were plated as described above and allowed 36 h to attach. The cells were exposed to increasing concentrations of conjugate up to 10 μM and incubated for 24 h in the dark. The loading medium was then removed, and the cells washed twice with 100 μL of growing medium containing 50 mM HEPES pH 7.4 and then fed with medium containing Cell Titer Blue (Promega) as per manufacturer's instructions. The cell toxicity was then measured by reading the fluorescence at 520:584 nm using a BMG FLUOstar plate reader. The signal was normalized to 100% viable (untreated) cells and 0% viable (treated with 0.2% saponin from Sigma) cells. For the phototoxicity experiments the HEp2 cells were prepared as described above. After conjugate loading, the medium was removed and replaced with medium containing 50 mM HEPES pH 7.4. The cells were then placed on ice and exposed to light from a 100 W halogen lamp filtered through a 610 nm long pass filter (Chroma) for 20 min; the total light dose was approximately 1 J cm^{-2}. An inverted plate lid filled with water to a depth of 5 mm acted as an IR filter. The cells were returned to the incubator for 24 h, and the cytotoxicity was assayed as described above.

Microscopy. HEp2 cells were plated on Lab Tek II chamber coverslips and incubated for 48 h prior to exposure to conjugate. The conjugates were diluted from 10 mM stocks to a working concentration of 10 μM in medium. The cells were then loaded with conjugate by incubating overnight. Organelle tracers were obtained from Molecular Probes and incubated concurrently with conjugate for 30 min prior to microscopy. Mitochondria were visualized using MitoTracker Green FM at 250 nM, lysosomes with LysoSensor Green DND-189 at 50 nM, Endoplasmic Reticulum (ER) with ER Tracker Blue-White DPX at 100 nM, and Golgi Complex with BODIPY FL C_5-ceramide at 50 nM. The cells were then washed three times with medium containing 50 mM HEPES pH 7.4. Microscopy was performed using a Zeiss Axiovert 200M inverted fluorescent microscope fitted with an AxioCam MRm CCD camera (Zeiss).

RESULTS

Synthesis and Characterization. Porphyrins **2** and **3** were prepared from commercially available porphyrin **1** in 25−30% yields, by Williamson etherification using CH_3I and *tert*-butyl bromoacetate, respectively. The zwitterionic cobaltacarborane [3,3′-Co(8-$C_4H_8O_2$-1,2-$C_2B_9H_{10}$(1′,2′-$C_2B_9H_{10}$)] was prepared from the reaction of cobaltabisdicarbollide anion $[Co(C_2B_9H_{11})_2]^-$ with 1,4-dioxane in the presence of BF_3**.**Et_2O, according to the literature (*31*). The nucleophilic ring opening reaction of the dioxane ring of cobaltacarborane [3,3′-Co(8-$C_4H_8O_2$-1,2-$C_2B_9H_{10}$-(1′,2′-$C_2B_9H_{10}$)] using hydroxyporphyrins **1**, **2**, and **3** afforded the corresponding porphyrin−cobaltacarborane conjugates in 85−93% yield (*28*). The free carboxylic acid group of compound **5** was converted into the corresponding hydroxybenzotriazole ester and coupled to a pegylated−peptide−PAL−PEG−PS resin containing the HIV-1 Tat 48−60 sequence. After cleavage and deprotection from the solid support using 88:2:5:5 TFA/TIS/phenol/H_2O, the porphyrin−peptide−cobaltacarborane conjugate **6** was isolated by reverse-phase HPLC in 8% yield. This low yield may be due to the following: (1) the weak electrophilic character of the free carboxylate, (2) steric effects imposed by the close proximity of the macrocycle to the carboxylic group during the coupling reaction, (3) the formation of aggregates in the solvent used, and/or (4) to the "PEG effect" which seems to cause several conventional reactions to go less

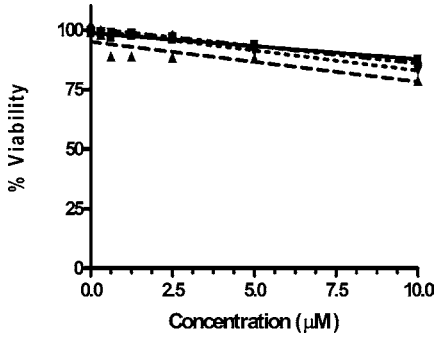

Figure 1. Dark toxicity of porphyrin conjugates **4** (—••—), **5** (— —), **6** (—), and **7** (--) toward HEp2 cells using the Cell Titer Blue assay.

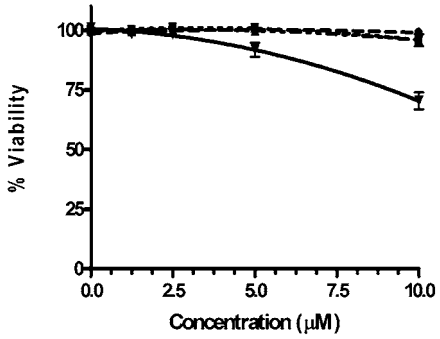

Figure 2. Phototoxicity of porphyrin conjugates **4** (—••—), **5** (— —), **6** (—), and **7** (--) toward HEp2 cells using 1 J cm^{-2} dose light.

effectively when there are $(CH_2CH_2O)_n$ motifs in the reactants. Conjugates **4** and **5** are soluble in polar organic solvents, such as acetonitrile, acetone, methanol, tetrahydrofuran (THF), and DMSO, but insoluble in water, while **6** and **7** are partially water-soluble and also show good solubility in polar organic solvents.

Cellular Studies. The dark and phototoxicity of conjugates **4**, **5**, **6**, and **7** were evaluated in human HEp2 cells, and the results obtained are shown in Figures 1 and 2, respectively. Due to their limited water solubility, both DMSO and Cremophor EL were used as delivery vehicles at low, nontoxic concentrations (0.9:0.1 DMSO/Cremophor EL) (*29*). At concentrations up to 10 μM (higher concentrations were not studied because of the low solubility of the conjugates in aqueous solution), all compounds are nontoxic to the cells in the dark, as determined using the Cell Titer Blue assay. Upon exposure to a low light dose (1 J cm^{-2}), only conjugate **6** shows mild cytotoxicity, with approximately 30% inhibition of cell proliferation at the highest concentration investigated in this study (10 μM). The cellular uptake of conjugates **4**−**7** depends significantly on the number of cobaltacarborane moieties linked to the porphyrin ring and on the presence of the HIV-1 Tat 48−60 peptide sequence. As shown in Figure 3, conjugate **7** containing four cobaltacarborane moieties is taken up to a larger extent at all time points studied than conjugates **4** and **5**, which contain only three cobaltacarborane units. The presence of an acetic acid group in place of a methyl does not have an effect on the cellular uptake nor on the dark toxicity and phototoxicity under the conditions studied. Conjugate **6** containing three cobaltacarborane moieties and the HIV-1 Tat 48−60 peptide sequence accumulated the most within cells of all conjugates at long time points (>2 h) (Figure 3). For example after 24 h, 11 times more conjugate **6** was found within cells than either **4** or **5** with the same number of cobaltacarboranes and three times more than **7**, which contains one more cobaltacarborane moiety. At short time points however, the uptake of **6** was similar to that of **7**, and always higher than that of conjugates **4** and **5**. Conjugates **6** and **7** were taken up rapidly in the first 2 h, after which the uptake of **7** reached a plateau, whereas that of **6** continued to steadily increase. The kinetics of uptake of conjugates **4** and **5** was similar to that of **7**, but the amount of conjugate taken up by cells was significantly lower than that of **7**.

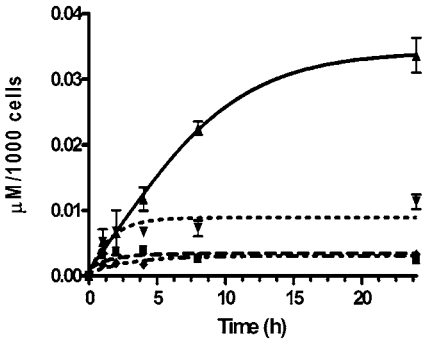

Figure 3. Time-dependent uptake of porphyrin conjugates **4** (—••—), **5** (— —), **6** (—), and **7** (--) at 10 μM by HEp2 cells.

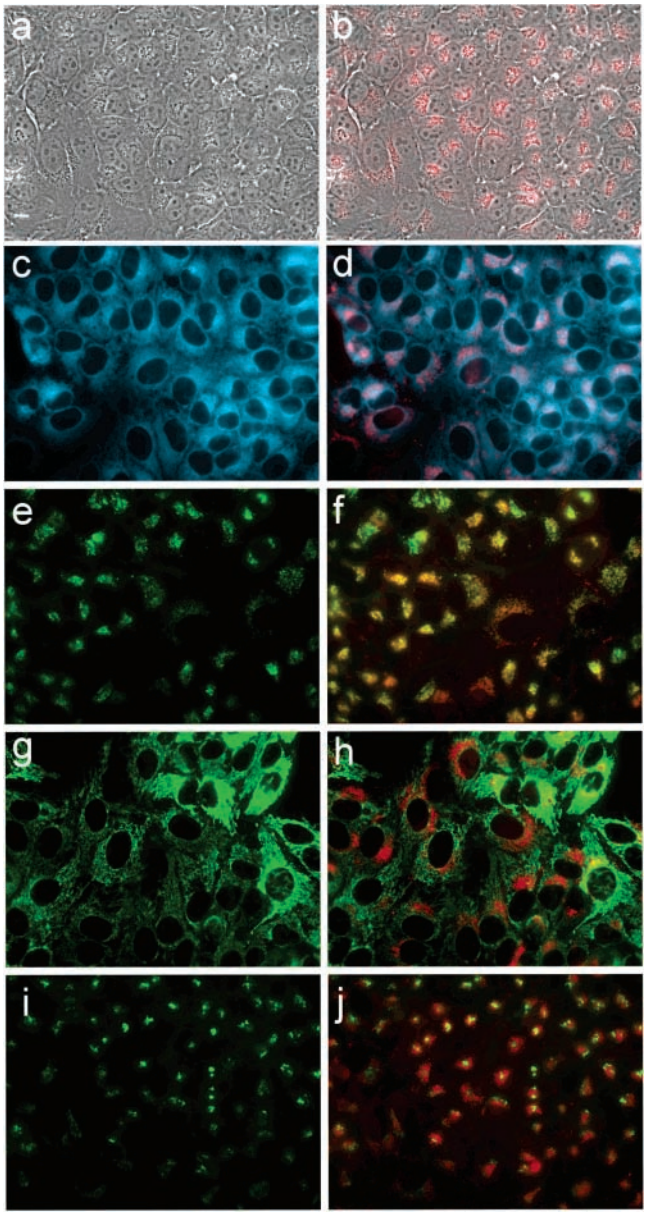

Figure 4. Subcellular localization of conjugate **6** in HEp2 cells at 10 μM for 18 h: (a) phase contrast, (b) overlay of **6** fluorescence and phase contrast, (c) ER Tracker Blue/White fluorescence, (e) LysoSensor Green fluorescence, (g) MitoTracker Green fluorescence, (i) BODIPY Ceramide, and (d, f, h, j) overlays of organelle tracers with **6** fluorescence. Scale bar: 10 μm.

Scheme 1 [a]

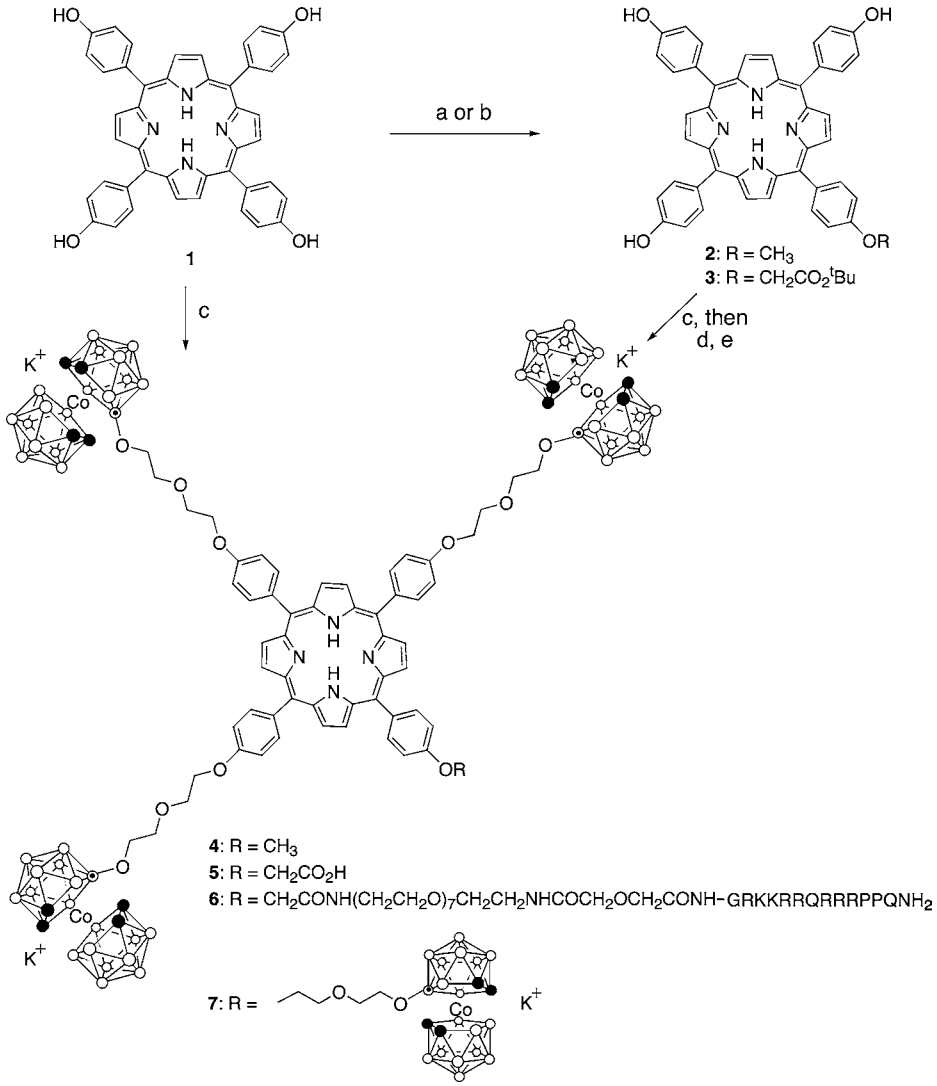

[a] Conditions: (a) CH_3I, K_2CO_3, DMSO, 60 °C, overnight (25%); (b) $BrCH_2COO^tBu$, Cs_2CO_3, DMSO, 60 °C, 2 h (30%); (c) [3,3′-Co(8-$C_4H_8O_2$-1,2-$C_2B_9H_{10}$)(1′,2′-$C_2B_9H_{11}$)], K_2CO_3, acetone, reflux, 72 h (85−93%); (d) TFA, CH_2Cl_2, rt, 4 h (95%); (e) HOBt, HATU, DIPEA, pegylated-peptidyl PAL−PEG-PS resin, DMF, rt, 24 h then TFA/TIS/H_2O/Phenol, 88:2:5:5 (8%).

The subcellular localization of conjugates **4**−**7** in HEp2 cells was evaluated by fluorescence microscopy, 24 h after exposure to the cells. Figure 4 shows the fluorescent patterns observed for the porphyrin−cobaltacarborane−HIV-1 Tat 48−60 conjugate **6**, and its overlay with the organelle specific fluorescent probes LysoSensor Green (lysosomes), Mitotracker Green (mitochondria), ER Tracker Blue-White (ER), and BODIPY Ceramide (Golgi). Similar figures were obtained for conjugates **4**, **5**, and **7** (see Supporting Information). The microscopy shows punctate, predominantly perinuclear staining that localized in vesicles for all compounds. These vesicles were quite large for conjugate **6** and are clearly visible in the phase contrast micrograph. All compounds showed clear co-localization with lysosomes as evidenced by a yellow to orange color in the fluorescence signal when the green organelle tracer signal is overlaid with the red conjugate signal.

DISCUSSION

Porphyrin−cobaltacarborane conjugates **4**−**7** were synthesized as shown in Scheme 1 from commercially available tetra-(hydroxyphenyl)porphyrin **1**. These conjugates were designed to have either three or four cobaltacarborane moieties linked to the porphyrin macrocycle via $O(CH_2CH_2O)_2$ chains, and, in the case of **6**, a HIV-1 Tat 48−60 peptide sequence attached via a low molecular weight PEG spacer. The PEG-based linkages were chosen because they tend to increase the water solubility of porphyrin macrocycles and to minimize their aggregation and intramolecular interactions in aqueous media (*26*). Furthermore, PEG-drug conjugates are known to exhibit enhanced serum life and tumor accumulation (*32*). Low molecular weight PEGs were preferred over high molecular weight PEGs because of the polydispersity of the latter.

The starting porphyrin **1** was monofunctionalized using the Williamson etherification reaction to produce porphyrins **2** and **3** in 25−30% yield (Scheme 1). The conjugation of porphyrins **1**−**3** with cobaltacarborane was performed in a single step in 85−93% yield, by the nucleophilic ring-opening of the dioxane ring of zwitterionic [3,3′-Co(8-$C_4H_8O_2$-1,2-$C_2B_9H_{10}$)(1′,2′-$C_2B_9H_{11}$)], as we have previously reported (*28*). The porphyrin−cobaltacarborane−peptide conjugate **6** was prepared by coupling conjugate **5** with the pegylated HIV-1 Tat 48−60 sequence on solid support, following our recently published procedure (*26*). All conjugates were isolated in >98% purity as determined by reverse phase HPLC and were characterized by MS, UV−vis, and NMR spectroscopy.

The achievement of therapeutic boron concentrations (15−30 μg/(g of tumor)) within tumors is still a major challenge in BNCT (*6*). Porphyrin−cobaltacarborane conjugates of high

boron content and with no dark cytotoxicity are potential promising boron delivery drugs for BNCT. We have previously reported that the cellular uptake of a series of zwitterionic porphyrin−cobaltacarborane conjugates increases with the number of cobaltacarborane moieties linked to the porphyrin macrocycle (*29*). To further increase the uptake of this type of compound, we designed and synthesized conjugate **6**, bearing a cell-penetrating peptide sequence. Indeed, conjugate **6** was taken up by cells to a significantly higher extent than conjugates **4** and **5**, containing the same number of cobaltacarborane moieties (Figure 3). At short time points (<2 h) conjugates **6** and **7** showed similar uptake into cells, indicating that both the number of cobaltacarborane residues and the presence of a fusogenic peptide increase cellular uptake. However at longer time points (>2 h), conjugate **6** was taken up to a much larger extent than **7**. These results are in agreement with previous reports by us (*26*) and others (*33*−*37*) showing that the Tat 48−60 peptide fragment from the HIV-1 Tat protein has the ability to efficiently translocate cellular membranes. Our results are also in agreement with our previous observation that the cellular uptake increases with the number of cobaltacarborane residues attached to the porphyrin macrocycle (*29*); at all time points studied the uptake of conjugate **7**, bearing four cobaltacarboranes, was always significantly higher than that of conjugates **4** and **5**, containing three cobaltacarboranes and therefore one less negative charge. On the other hand, the replacement of a methyl group (in **4**) for an acetic acid group (in **5**) had no effect on cellular uptake. All conjugates were found to be nontoxic in the dark at the concentrations studied (Figure 1) and only conjugate **6** showed mild phototoxicity at low light dose (1 J cm^{-2}) and concentrations > 5 μM (Figure 2), probably as a result of its large accumulation within cells.

Porphyrin−cobaltacarborane conjugates **4**−**7** preferentially localize within cells in vesicles and lysosomes, as evaluated by fluorescence microscopy (Figure 4), probably as a result of an endocytotic mechanism of uptake of all conjugates into cells. These results are in agreement with previous reports showing that negatively charged carboranyl-containing porphyrins localize mainly in the cell lysosomes (*38*−*41*). The presence of the HIV-1 Tat 48−60 peptide sequence in conjugate **6** significantly increased the cellular uptake of porphyrin−cobaltacarborane conjugates but did not alter their preferential sites of intracellular localization. Since the cytotoxic particles produced in BNCT, $^{4}He^{2+}$, and $^{7}Li^{3+}$ have average ranges in tissue of 9 and 5 μm, respectively, ^{10}B-loaded vesicles and lysosomes in the vicinity of tumor cell nuclei could potentially lead to effective tumor destruction upon activation with low-energy neutrons. The amount of boron needed for effective BNCT could be substantially lower than 30 μg/(g of tumor) if the boron-10 localizes within tumor cells rather than extracellularly, and further reduced if the boron-10 localizes inside or in the close proximity to the cell nucleus (*11*, *12*, *42*). Conjugates of boronated agents to the HIV-1 Tat peptide sequence could induce higher accumulation of boron within target tumors due to enhanced tumor retention compared with normal tissues, therefore resulting in a more efficient BNCT treatment.

ACKNOWLEDGMENT

The authors thank Martha Juban for HIV-1 Tat 48-60 peptide synthesis. This work was supported by the National Science Foundation, Grant No. CHE-304833, and the National Institutes of Health, Grant No. CA098902.

Supporting Information Available: Traces of HPLC analysis for porphyrins **3**−**7** and microscopy images for conjugates **4**, **5**, and **7**. This material is available free of charge via the Internet at http://pubs.acs.org.

LITERATURE CITED

(1) Vicente, M. G. H. (2001**)** Porphyrin-based sensitizers in the detection and treatment of cancer: Recent progress. *Curr. Med. Chem. Anti-Cancer Agents 1*, 175−194.

(2) Osterloh, J., and Vicente, M. G. H. (2002**)** Mechanisms of porphyrinoid localization in tumors. *J. Porphyrins Phthalocyanines 6*, 305−324.

(3) Hudson, R., and Boyle, R. W. (2004) Strategies for selective delivery of photodynamic sensitizers to biological targets. *J. Porphyrins Phthalocyanines 8*, 954−975.

(4) Soloway, A. H., Tjarks, W., Barnum, B. A., Rong, F. G., Barth, R. F., Codogni, I. M., and Wilson, J. G. (1998) The chemistry of neutron capture therapy. *Chem. Rev. 98*, 1515−1562.

(5) Hawthorne, M. F. (1993) The role of chemistry in the development of boron neutron-capture therapy of cancer. *Angew. Chem., Int. Ed. Engl. 32*, 950−984.

(6) Barth, R. F., Coderre, J. A., Vicente, M. G. H., and Blue, T. E. (2005) Boron neutron capture therapy of cancer: Current status and future prospects. *Clin. Cancer Res. 11*, 3987−4002.

(7) Dougherty, T. J., Gomer, C. J., Henderson, B. W., Jori, G., Kessel, D., Korbelik, M., Moan, J., and Peng, Q. (1998) Photodynamic therapy. *J. Natl. Cancer Inst. 90*, 889−905.

(8) Pandey, R. K., and Zheng, G. (2000). Porphyrins as photosensitizers in photodynamic therapy. *The Porphyrin Handbook*. Applications: Past, present and future (Kadish, K. M., Smith, K. M., Guilard, R., Eds.) Vol. 6, Chapt. 43, pp 157−230, Academic Press, New York.

(9) Kessel, D. (2004) Correlation between subcellular localization and photodynamic efficacy. *J. Porphyrins Phthalocyanines 8*, 1009−1014.

(10) Rosenkranz, A. A., Jans, D. A., and Sobolev, A. S. (2002) Targeted intracellular delivery of photosensitizers to enhance photodynamic efficiency. *Immunol. Cell Biol. 78*, 452−464.

(11) (a) Fairchild, R. G., and Bond, V. P. (1985) Current status of ^{10}B neutron capture therapy: Enhancement of tumor dose via beam filtration and dose rate, and the effects of these parameters on minimum boron content: a theoretical evaluation. *Int. J. Radiat. Oncol., Biol., Phys. 11*, 831−840. (b) Gabel, D., Foster, S., and Fairchild, R. G. (1987) The Monte Carlo simulation of the biological effect of the $^{10}B(n, a)^{7}Li$ reaction in cells and tissue and its implication for boron neutron capture therapy. *Radiat. Res. 111*, 14−25.

(12) (a) Hartman, T., and Carlsson, J. (1994) Radiation dose heterogeneity in receptor and antigen mediated boron neutron capture therapy. *Radiother. Oncol. 31*, 61−75. (b) Hartman, T., Lundqvist, H., Westlin, J.-E., and Carlsson, J. (2000) Radiation doses to the cell nucleus in single cells and cells in micrometastases in targeted therapy with I-131 labeled ligands or antibodies. *Int. J. Radiat. Oncol., Biol., Phys. 46*, 1025−1036.

(13) Bregadze, V. I., Sivaev, I. B., Gabel, D., and Wohrle, D. (2001) Polyhedral boron derivatives of porphyrins and phthalocyanines. *J. Porphyrins Phthalocyanines 5*, 767−781.

(14) Renner, M. W., Miura, M., Easson, M. W., and Vicente, M. G. H. (2006) Recent progress in the syntheses and biological evaluation of boronated porphyrins for boron neutron capture therapy. *Anti-Cancer Agents Med. Chem. 6*, 145−158.

(15) Rosenthal, M. A., Kavar, B., Hill, J. S., Morgan, D. J., Nation, R. L., Stylli, S. S., Basser, R. L., Uren, S., Geldard, H., Green, M. D., Kahl, S. B., and Kaye, A. H. (2001) Phase I and pharmacokinetic study of photodynamic therapy for high-grade gliomas using a novel boronated porphyrin. *J. Clin. Oncol. 19*, 519−524.

(16) Vicente, M. G. H., Nurco, D. J., Shetty, S. J., Osterloh, J., Ventre, E., Hegde, V., and Deutsch, W. A. (2002) Synthesis, dark toxicity and induction of in vitro DNA photodamage by a tetra(4-nidocarboranylphenyl)porphyrin. *J. Photochem. Photobiol. B: Biol. 68*, 123−132.

(17) (a) Fabris, C., Jori, G., Giuntini, F., and Roncucci, G. (2001) Photosensitizing properties of a boronated phthalocyanine: studies at the molecular and cellular level. *J. Photochem. Photobiol., B 64*, 1−7. (b) Giuntini, F., Raoul, Y., Dei, D., Municchi, M., Chiti, G., Fabris, C., Colautti, P., Jori, G., and Roncucci, G. (2005) Synthesis of tetrasubstituted Zn(II)-phthalocyanines carrying four carboranyl-units as potential BNCT and PDT agents. *Tetrahedron Lett. 46*, 2979−2982.

(18) Miura, M., Micca, P. L., Fisher, C. D., Gordon, C. R., Heinrichs, J. C., and Slatkin, D. N. (1998) Evaluation of carborane-containing porphyrins as tumour targeting agents for boron neutron capture therapy. *Br. J. Radiol. 71*, 773−781.

(19) Miura, M., Morris, G. M., Micca, P. L., Lombardo, D. T., Youngs, K. M., Kalef-Ezra, J. A., Hoch, D. A., Slatkin, D. N., Ma, R., and Coderre, J. A. (2001) Boron neutron capture therapy of a murine mammary carcinoma using a lipophilic carboranyltetraphenylporphyrin. *Radiat. Res. 155*, 603−610.

(20) Friso, E., Roncucci, G., Dei, D., Soncin, M., Fabris, C., Chiti, G., Colautti, P., Esposito, J., Nardo, L. D., Rossi, C. R., Nitti, D., Giuntini, F., Borsetto, L., and Jori, G. (2005) A novel ^{10}B-enriched carboranyl-containing phthalocyanine as a radio- and photo-sensitising agent for boron neutron capture therapy and photodynamic therapy of tumours: In vitro and in vivo studies. *Photochem. Photobiol. Sci. 1*, 39−50.

(21) Frixa, C., Mahon, M. F., Thompson, A. S., and Threadgill, M. D. (2003) Synthesis of meso-substituted porphyrins carrying carboranes and oligo(ethylene glycol) units for potential applications in boron neutron capture therapy. *Org. Biomol. Chem. 1*, 306−317.

(22) Dozzo, P., Koo, M.-S., Berger, S., Forte, T. M., and Kahl, S. B. (2005) Synthesis, characterization, and plasma lipoprotein association of a nucleus-targeted boronated porphyrin. *J. Med. Chem. 48*, 357−359.

(23) Vives, E. (2003) Cellular uptake of the Tat peptide: An endocytosis mechanism following ionic interactions. *J. Mol. Recognit. 16*, 265−271.

(24) (a) Futaki, S., Ohashi, W., Suzuki, T., Niwa, M., Tanaka, S., Ueda, K., Harashima, H., and Sugiura, Y. (2001) Stearylated arginine-rich peptides: A new class of transfection systems. *Bioconj. Chem. 12*, 1005−1011. (b) Rothbard, J. B., Garlington, S., Lin, Q., Kirschberg, T., Kreider, E., McGrane, P. L., Wender, P. A., and Khavari, P. A. (2000) Conjugation of arginine oligomers to cyclosporin A facilitates topical delivery and inhibition of inflammation. *Nat. Med. 6*, 1253−1257. (c) Kirschberg, T. A., VanDeusen, C. L., Rothbard, J. B., Yang, M., and Wender, P. A. (2003) Arginine-based molecular transporters: the synthesis and chemical evaluation of releasable taxol-transporter conjugates. *Org. Lett. 5*, 3459−3462. (d) Wadia, J. S., Stan, R. V., and Dowdy, S. F. (2004) Transductible TAT-HA fusogenic peptides enhances escape of TAT fusion proteins after lipid raft macropinocytosis. *Nat. Med. 10*, 310−315.

(25) (a) Efthymiadis, A., Briggs, L. J., and Jans, D. A. (1996) The HIV-1 Tat nuclear localization sequence confers novel nuclear import properties. *J. Biol. Chem. 273*, 1623−1628. (b) Vives, E. (2003) Cellular uptake of the Tat peptide: an endocytosis mechanism following ionic interactions. *J. Mol. Recognit. 16*, 265−271. (c) Dietz, G. P., and Bahr, M. (2004) Delivery of bioactive molecules into the cell: The Trojan horse approach. *Mol. Cell. Neurosci. 27*, 85−131. (d) Vives, E. (2005) Present and future of cell-penetrating peptide mediated delivery systems: "Is the Trojan horse to wild to go only to Troy?" *J. Controlled Release 109*, 77−85.

(26) Sibrian-Vazquez, M., Jensen, T. J., Hammer, R. P., and Vicente, M. G. H. (2006) Peptide-mediated cell transport of water soluble porphyrin conjugates. *J. Med. Chem. 49*, 1364−1372.

(27) Kawabata, S., Barth, R. F., Yang, W., Wu, G., Binns, P. J., Riley, K. J., Gottumukkala, V., and Vicente, M. G. H. (2005) Evaluation of the carboranylporphyrin H_2TCP as a delivery agent for boron neutron capture therapy (BNCT). *Proceedings of the 13th World Congress of Neurological Surgery*. (Khamlichi, A., Ed.) pp 975−979.

(28) Hao, E., and Vicente, M. G. H. (2005) Expeditious synthesis of porphyrin-cobaltacarborane conjugates. *Chem. Commun. (Cambridge)* 1306−1308.

(29) Hao, E., Jensen, T. J., Courtney, B. H., and Vicente, M. G. H. (2005) Synthesis and cellular studies of porphyrin−cobaltacarborane conjugates. *Bioconjugate Chem. 16*, 1495−1502.

(30) Weinkauf, J. R., Cooper, S. W., Schweiger, A., and Wamser, C. C. (2003) Substituent and solvent effects on the hyperporphyrin spectra of diprotonated tetraphenylporphyrins. *J. Phys. Chem. A 107*, 3486-3496.

(31) Teixidor, F., Pedrajas, J., Rojo, I., Vinas, C., Kivekas, R., Sillanpaa, R., Sivaev, I., Bregadze, V., and Sjoberg, S. (2003) Chameleonic capacity of [3,3′-Co(1,2-$C_2B_9H_{11}$)(2)](−) in coordination. Generation of the highly uncommon S(thioether)−Na bond. *Organometallics 22*, 3414−3423.

(32) (a) Greenwald, R. B. (2001) PEG drugs: An overview. *J. Controlled Release 74*, 159−171. (b) Greenwald, R. B., Choe, Y. H., McGuire, J., and Conover, C. D. (2003) Effective drug delivery by PEGylated drug conjugates. *Adv. Drug Delivery Rev. 55*, 217−250.

(33) Schwartz, J. J., and Zhang, S. (2000) Peptide-mediated cellular delivery. *Curr. Opin. Mol. Ther. 2*, 162−167.

(34) Lundberg, P., and Langel, U. (2003) A brief introduction to cell-penetrating peptides. *J. Mol. Recognit. 16*, 227−233.

(35) Richard, J. P., Melikov, K., Vives, E., Ramos, C., Verbeure, B., Gait, M. J., Chernomordik, L. V., and Lebleu, B. (2003) Cell-penetrating peptides: A reevaluation of the mechanism of cellular uptake. *J. Biol. Chem. 278*, 585−590.

(36) Futaki, S., Goto, S., Suzuki, T., Nakase, I., and Sugiura, Y. (2003) Structural variety of membrane permeable peptides. *Curr. Protein Pept. Sci. 4*, 87−96.

(37) Deshayes, S., Morris, M. C., Divita, G., and Heitz, F. (2005) Cell-penetrating peptides: Tools for intracellular delivery of therapeutics. *Cell. Mol. Life Sci*. 1839−1849.

(38) Nguyen, T., Brownell, G. L., Holden, S. A., Kahl, S., Miura, M., and Teicher, B. A. (1993) Subcellular distribution of various boron compounds and implications of their efficacy in boron neutron capture therapy by Monte Carlo simulations. *Radiat. Res. 133*, 33−40.

(39) Vicente, M. G. H., Edwards, B. F., Shetty, S. J., Hou, Y., and Boggan, J. E. (2002) Synthesis and preliminary biological studies of four tetra(*nido*-carboranylmethylphenyl)porphyrins. *Bioorg. Med. Chem. 10*, 481−492.

(40) Gottumukkala, V., Luguya, R., Fronczek, F. R., Vicente, M. G. H. (2005) Synthesis and cellular studies of an octa-anionic 5,10,-15,20-tetra[3,5-(*nido*-carboranylmethyl)phenyl]porphyrin (H_2OCP) for Application in BNCT. *Bioorg. Med. Chem. 13*, 1633−1640.

(41) Gottumukkala, V., Ongayi, O., Baker, D. G., Lomax, L. G., and Vicente, M. G. H. (2006) Synthesis, cellular uptake and animal toxicity of a tetra(carboranylphenyl)-tetrabenzoporphyrin. *Bioorg. Med. Chem. 14*, 1871−1879.

(42) Ye, S.-J. (1999) Monte Carlo based protocol for cell survival and tumor control probability in BNCT. *Phys. Med. Biol. 44*, 447−461.

BC060047V

Intracellular Delivery of Proteins in Complexes with Oligoarginine-Modified Liposomes and the Effect of Oligoarginine Length

Masahiko Furuhata,[†] Hiroko Kawakami,[‡] Kazunori Toma,[‡] Yoshiyuki Hattori,[†] and Yoshie Maitani*[,†]

Institute of Medicinal Chemistry, Hoshi University, Shinagawa-ku, Tokyo 142-8501, Japan, and The Noguchi Institute, Itabashi-ku, Tokyo 173-0003, Japan. Received February 13, 2006; Revised Manuscript Received June 5, 2006

The intracellular delivery of proteins using cell-penetrating peptides (CPPs) including oligoarginine (oligo-Arg) carriers raises the possibility of establishing novel therapeutic methods. We compared the effect of the length of oligo-Arg in modified liposomes ($(Arg)_n$-L; $n = 4, 6, 8, 10$) on the delivery of proteins by flow cytometry, fluorescence microscopy, and spectrofluorimetry. As a free liposome, Arg4-modified liposome Arg4-L was most efficiently internalized in cells. The efficiency decreased depending on the length of oligo-Arg. For the intracellular delivery of proteins, $(Arg)_n$-L was physically associated with proteins. Concerning the effect of oligo-Arg length, liposome/protein complexes showed a different behavior. Arg4-L carried bovine serum albumin (BSA, 66 kDa) and β-galactosidase (β-Gal, 120 kDa) 6-fold higher than free BSA and free β-Gal. Arg10-L showed similar performance for these two proteins to Arg4-L. The enzymatic activity of β-Gal in the cells showed that proteins were transported as a biologically active form. Arg10-L carried 100-fold more immunoglobulin G (IgG, 150 kDa) than free IgG, and 3-fold more than Arg4-L into cells. Shorter oligo-Arg chain on liposomes may be enough for liposomes alone to be taken up in cells, but more Arg residues may be needed to form a complex with high molecular weight proteins and deliver them into cells. This information will aid in the design of $(Arg)_n$-L as a carrier for delivering proteins into cells.

INTRODUCTION

The development of therapeutic peptides and proteins is hampered by their poor ability to penetrate the plasma membrane because of their high hydrophilicity and molecular weight. Therefore, it is necessary to construct an efficient protein delivery system. One approach to solve this problem is to incorporate short peptides derived from protein-transduction domains (PTDs) or cell-penetrating peptides (CPPs), such as HIV-1 Tat fragments, penetratin and VP22. PTDs or CPPs are less than 30 amino acid residues in length and have the capability of crossing the plasma membrane (*1*−*6*). Since the PTDs and CPPs can deliver conjugated molecules, such as proteins, into cells (*7*, *8*), they are usually used as conjugates with cargo molecules, as part of a very strong and specific complex with biotin (*9*). However, these CPP carriers require cross-linking to the target peptide or protein. The only exception is pep-1, which has been reported to deliver a variety of peptides and proteins into several cell lines by forming physical assemblies without covalent chemical coupling (*6*). Since CPP-modified nanoparticles (*10*) and liposomes (*11*) can be taken up into cells, liposomes modified with Tat and penetratin were utilized in the intracellular delivery of drugs by entrapping the drugs in the liposomes (*12*). However, in the case of proteins, it is hard for them to be released from the liposomes, even if the liposomes are internalized in cells.

We synthesized oligo-Arg conjugates with an artificial lipid, and they were incorporated in liposomes for a protein delivery study. In our system, the surface of liposomes were modified with oligo-Arg ($(Arg)_n$-L; $n = 4, 6, 8, 10$), and proteins were physically associated on the surface. Cargo proteins were not entrapped in the liposomes. Therefore, the preparation of the complex between proteins and $(Arg)_n$-L is simple. Although investigations delineating the influence of Arg length on the uptake of oligo-Args alone have been reported (*5*, *13*−*15*), to our knowledge there is no report on $(Arg)_n$-L as a protein delivery system. $(Arg)_n$-L provides two characteristic interactions; a hydrophobic one by liposome, and a positively charged and hydrophilic one by (Arg)n. These two kinds of interactions were expected to help forming complexes with proteins.

The aim of this study is first to show that our system can transport proteins into cells, and then to examine the effect of oligo-Arg length on the protein delivery in human cervical carcinoma HeLa cells. Cellular uptake efficacy was evaluated by flow cytometry, spectrofluorimetry, and fluorescence microscopic observation of the cells. We also analyzed the interaction of $(Arg)_n$-L with proteins by fluorescence intensity distribution analysis (FIDA).

Our studies showed that the effect of oligo-Arg length on the intracellular delivery of proteins by $(Arg)_n$-L/protein complexes was different from that of $(Arg)_n$-L alone. Short oligo-Arg was enough for liposomes to be taken up into the cells, but longer oligo-Arg may be needed to form a complex with large proteins and deliver them into the cells.

EXPERIMENTAL PROCEDURES

Materials. All amino acid derivatives and coupling reagents were obtained from Kokusan Chemical Co., Ltd. (Tokyo, Japan). Egg phosphatidylcholine (EPC) was purchased from Q. P. Co., Ltd. (Tokyo, Japan). Cholesterol (Chol) and bovine serum albumin (BSA) were purchased from Wako Pure Chemical Industries, Ltd. (Osaka, Japan). Calcein was obtained from Tokyo Kasei Kogyo Co., Ltd. (Tokyo, Japan). Fluorescein isothiocyanate-labeled BSA (FITC−BSA), stearylamine, 3β-[*N*-(dimethylaminoethane)carbamoyl]cholesterol (DC−Chol), 5-(*N*-ethyl-*N*-isopropyl)amiloride (EIPA), phorbol 12-myristate 13-acetate (PMA) were from Sigma Chemical Co. (St. Louis, MO). FITC-immunoglobulin G (FITC−IgG) was provided by

* Corresponding author. Fax/phone: +81-3-5498-5048; e-mail: yoshie@hoshi.ac.jp.

[†] Hoshi University.

[‡] The Noguchi Institute.

10.1021/bc060034h CCC: $33.50 © 2006 American Chemical Society
Published on Web 07/06/2006

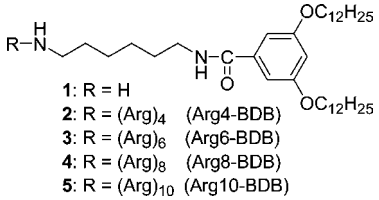

Figure 1. Chemical structures of $(Arg)_n$-BDBs.

MP Biomedicals Co. (Irvine, CA). IgG was obtained from Oriental Yeast Co., Ltd. (Tokyo, Japan). β-Galactosidase (β-Gal) and the β-Gal staining kit were purchased from Active Motif, Inc. (Carlsbad, CA). Lumi-Gal 530 (Reporter assay kit of β-Gal) was from Toyobo Co., Ltd. (Osaka, Japan). Bicinchonic acid (BCA) protein assay reagent was obtained from Pierce (Rockford, IL). Dulbecco's modified Eagle's medium (DMEM) was purchased from Invitrogen Co. (Carlsbad, CA). Fetal bovine serum (FBS) was provided by Life Technologies (Grand Island, NY). 1,1′-Dioctadecyl-3,3,3′,3′-tetramethylindocarbocyanine perchlorate (DiI) was obtained from Lambda Probes & Diagnostics (Graz, Austria). All other reagents were of analytical grade.

Synthesis of $(Arg)_n$-BDBs. $(Arg)_n$-BDBs (**2**, **3**, **4**, and **5**) were synthesized similarly to other peptide−lipid conjugates of different amino acid sequences (*16*) (Figure 1). The oligo-Arg portion was extended similarly to the compounds with a PEG linker between oligo-Arg and BDB (*17*). For example, N^{α}-9-fluorenylmethoxycarbonyl-N^{g}-2,2,5,7,8-pentamethylchroman-6-sulfonyl-L-arginine (Fmoc-Arg(Pmc)-OH) was condensed with *N*-(6-aminohexyl)-3,5-bis(dodecyloxy)benzamide (**1**) by 2-(1*H*-benzotriazol-1-yl)-1,1,3,3-tetramethyluronium hexafluorophosphate and 4-(dimethylamino)pyridine in *N*,*N*-dimethylformamide, and the Fmoc protecting group was removed by piperidine. This amide condensation and Fmoc deprotection cycle was repeated four times to give the side chain protected **2**. MALDI-TOFMS (α-CHCA): found, 2280.24; calculated for $[M + H]^+$, 2278.33. Final trifluoroacetic acid deprotection of Pmc gave **2**. MALDI-TOFMS (α-CHCA): found, 1214.99; calculated for $[M + H]^+$, 1213.94.

Cell Culture. HeLa cells were kindly provided by Toyobo Co., Ltd. (Osaka, Japan). HeLa cells were grown in DMEM supplemented with 10% FBS at 37 °C in a humidified 5% CO_2 atmosphere.

Preparation of Liposomes. Four liposomal formulas were used: EPC, Chol, and $(Arg)_n$-BDB in a molar ratio of 7:3:0.05 or 7:3:0.5 for the oligo-Arg-modified liposome ($(Arg)_n$-L); EPC and Chol in a molar ratio of 7:3 for the control liposome (Con-L); EPC, Chol, and stearylamine in a molar ratio of 7:3:2 for the stearylmaine modified liposome (SA-L); EPC, Chol, and DC−Chol in a molar ratio of 7:3:0.5 for the DC−Chol modified liposome (DC-L) for the control liposomes containing cationic lipids. Liposomes were prepared by a dry film method with water or 20 mM calcein. For $(Arg)_n$-L, $(Arg)_n$-BDB, Chol, and EPC were dissolved in an appropriate volume of chloroform, which was then removed. The particle size distributions and the zeta-potentials were measured by the dynamic and the electrophoresis light scattering method, respectively (ELS-800, Otsuka Electronics Co., Ltd., Osaka, Japan), at 25°C, after the dispersion was diluted to an appropriate volume with water. pH titration of the zeta-potential was measured by Automatic Titrator GT-06 (Mitsubishi Chemical Corporation, Tokyo, Japan). For liposomes with calcein entrapped, this was followed by chromatography on Sephadex G-50 columns, and fractions of liposomes were collected. DiI-labeled liposomes were prepared as described above but with post-addition of DiI at 0.04 mol % of total lipids.

Uptake Experiments Using Flow Cytometry. An aqueous solution of FITC−BSA, FITC−IgG, or β-Gal was added to the $(Arg)_n$-L suspension with gentle shaking to form $(Arg)_n$-L/protein complexes. Each complex was left at room temperature for 10−15 min. Cell cultures were prepared by plating cells in a 35-mm culture dish 24 h prior to each experiment. The cells were washed three times with 1 mL of serum-free DMEM. Calcein-entrapped $(Arg)_n$-L (100 μg) alone or each $(Arg)_n$-L/protein complex ($(Arg)_n$-BDB: 5 μg of protein, from 50:1 to 1000:1 molar ratio), was diluted with serum-free DMEM to 1 mL and then gently applied to the cells. In this study, all samples were incubated with cells for 3 h at 37 °C in serum-free DMEM. At the end of the incubation of $(Arg)_n$-L/protein complexes or calcein-entrapped $(Arg)_n$-L with cells, the cells were washed three times with 1 mL of PBS and detached by incubating with 0.05% trypsin and EDTA solution at 37 °C for 3 min. The cells were centrifuged at 1500*g*, and the supernatant was discarded. The cells were resuspended with PBS (pH 7.4) containing 0.1% BSA and 1 mM EDTA and directly introduced into a FACSCalibur flow cytometer (Becton Dickinson, San Jose, CA) equipped with a 488 nm argon ion laser. Data for 10000 fluorescent events were obtained by recording forward scatter (FSC) and side scatter (SSC) with green (for FITC and calcein; 530/30 nm) and red (for DiI; 585/42 nm) fluorescence. To investigate the cellular uptake mechanism, cells were washed with serum-free medium and preincubated for 30 min at 37 °C with EIPA (25 μM) or PMA (1 μM). Subsequent incubation of the complex was carried out in the presence of the respective pharmacological reagents.

Spectrofluorimetric Quantification of Internalized FITC−BSA and IgG. At the end of the incubation of $(Arg)_n$-L/FITC-protein complexes with cells as described above, the cells were washed three times with 1 mL of PBS and lysed by incubating with 0.2% Triton X-100/PBS at 37 °C for 5 min, followed by centrifugation at 15000 rpm for 15 min. The supernatants were measured with a chemoluminometer (Ex = 485, Em = 535 nm) (Wallac ARVO SX 1420 multilabel counter, Perkin-Elmer Life Science, Japan, Co. Ltd., Kanagawa, Japan).

Fluorescence Microscopy. At the end of the incubation of $(Arg)_n$-L/protein complexes with cells as described in Uptake Experiments using Flow Cytometry, the cells were washed five times with 1 mL of PBS. Unfixed cells were observed with an Eclipse TS100/100-F for epifluorescence observations (Nicon, Tokyo, Japan). The level of contrast and the brightness of the images were adjusted.

***β*-Galactosidase Assay.** For the β-galactosidase assay, we used X-Gal staining and chemiluminescence measurements. For X-Gal staining, at the end of the incubation of $(Arg)_n$-L/β-Gal complex with cells as described in Uptake Experiments using Flow Cytometry, the cells were stained with the β-Gal staining kit and then observed with an Eclipse TS100/100-F for epifluorescence observations. The level of contrast and the brightness of the images were adjusted. For chemiluminescence measurements, β-Gal activity was measured according to the instructions accompanying the β-Gal assay system. Incubation of $(Arg)_n$-L/β-Gal complex with cells was terminated by washing the plates three times with cold PBS (pH 7.4). Cell lysis solution (Reporter assay kit of β-Gal) was added to the cell monolayers and subjected to freezing at −80 °C and thawing at 37 °C, followed by centrifugation at 15000 rpm for 2 min. Aliquots of 20 μL of the supernatants were mixed with 180 μL of Lumi-Gal 530 and then incubated for 30 min at 37 °C, and counts per second (cps) were measured with a chemoluminometer (Wallac ARVO SX 1420 multilabel counter). The protein concentration of the supernatants was determined with BCA reagent using BSA as a standard, and cps/μg protein was calculated.

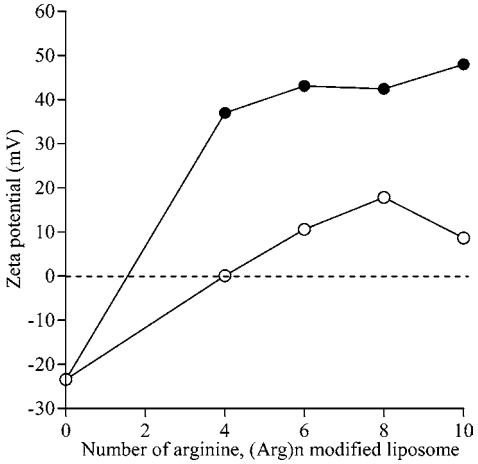

Figure 2. Effect of arginine number of $(Arg)_n$-L on the zeta potential. Open circle, liposome contained 0.5 mol % of oligo-Arg-BDB; Closed circle, liposome contained 5 mol % of oligo-Arg-BDB

Fluorescence Intensity Distribution Analysis (FIDA). FIDA was performed with a MF20 microplate reader (Olympus Corp. Tokyo, Japan) using the onboard 633-nm helium−neon laser at a power of 300 μW for excitation. Experiments were performed in 384-well glass-bottom plates using a sample volume of 50 μL. The FIDA data was analyzed with the MF20 software package. All single-molecule FIDAs were performed under identical conditions with respect to incubation (10 min) at room temperature. Protein-binding experiments were performed using the DiI-labeled Arg4-L and Arg10-L. The concentration of the labeled component was held constant whereas the concentration of BSA or IgG was varied in water.

Cytotoxicity. HeLa cells were seeded at a density of 1×10^4 cells per well in 96-well plates and maintained for 24 h before transfection in DMEM supplemented with 10% FBS. The cells were washed with PBS. The culture medium was replaced with serum-free DMEM (100 μL) including $(Arg)_n$-L/protein complex ($(Arg)_n$-BDB: 5 μg of protein = 50:1, molar ratio). After incubation for 3 h at 37 °C with serum-free DMEM (100 μL), the number of surviving cells was determined by a WST-8 assay (Dojindo Laboratories, Kumamoto, Japan). Cell viability was expressed as the ratio of the A_{450} of cells treated with the protein complex to that of the control samples.

Data Analysis. Significant differences in the mean values were evaluated using Student's unpaired *t*-test. A *p*-value of less than 0.05 was considered significant.

RESULTS

Characterization of $(Arg)_n$-L. We prepared five kinds of liposomes; a control liposome (Con-L) consisting of EPC and Chol at a molar ratio of 7:3, two positively charged control liposomes consisting of EPC, Chol, stearylamine or DC−Chol at a molar ratio of 7:3:2 or 0.5 (SA-L, DC-L, respectively), and two $(Arg)_n$-L (n = 4, 6, 8, 10) differing in $(Arg)_n$-BDB content, a molar ratio of EPC, Chol, and $(Arg)_n$-BDB at 7:3:0.05 and 7:3:0.5. Each particle size was adjusted to about 200 nm by sonication. To examine whether the liposomes were modified with Arg, we measured their zeta potential. Con-L was negatively charged, and the two $(Arg)_n$-L were positively charged (Figure 2). SA-L and DC-L were positively charged (over 50 mV in zeta potential, data not shown). The longer oligo-Arg had a higher zeta-potential, corresponding to the number of Arg residues. The zeta-potential of $(Arg)_n$-L containing 5 mol % of oligo-Arg lipid was higher than that of preparation containing 0.5 mol % (Figure 2). We used $(Arg)_n$-L containing 5 mol % of oligo-Arg lipid in the subsequent experiments, because we thought that highly positively charged carriers were desirable to form complexes with proteins and to deliver them into cells.

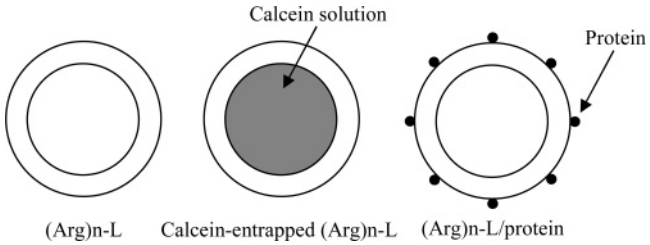

Figure 3. Schematic diagrams of the $(Arg)_n$-L, calcein-entrapped $(Arg)_n$-L and $(Arg)_n$-L/protein complex. ($(Arg)_n$-BDB in $(Arg)_n$-L): protein = 50:1, molar ratio.

Cellular Uptake of Calcein-Entrapped $(Arg)_n$-L, and $(Arg)_n$-L/FITC−BSA, and $(Arg)_n$-L/FITC−IgG Complexes. To examine the cellular uptake of $(Arg)_n$-L or the complex, cells were exposed to calcein-entrapped $(Arg)_n$-L alone, and $(Arg)_n$-L/FITC−BSA and $(Arg)_n$-L/FITC−IgG complexes for 3 h at 37 °C. Then, the cells were trypsinized and analyzed by flow cytometry. The cellular uptake of calcein-entrapped $(Arg)_n$-L decreased as the number of arginine residues increased (Figure 4A). The size of Arg4-L and Arg10-L was about 233 nm. The size of Arg4-L/FITC−BSA and FITC−IgG, and Arg10-L/FITC−BSA and FITC−IgG was about 289 nm, indicating that proteins were adhered to the surface of liposomes as schematically shown in Figure 3. The zeta potential of Arg10-L/BSA and Arg10-L/IgG was similar to that of Arg10-L at pH 3−11 when measured by the pH titration method (data not shown).

Free FITC−BSA, Con-L/FITC−BSA, SA-L/FITC−BSA, and DC-L/FITC−BSA were scarcely taken into the cell (Figure 4B). FITC−BSA in a complex with Arg4-L, Arg6-L, Arg8-L, and Arg10-L displayed a marked increase in fluorescence in the cells, showing about a 6-, 5-, 3-, and 6-fold higher intensity, respectively, than free FITC−BSA. Arg4-L and Arg10-L were most efficient at delivering FITC−BSA into the cells.

Free FITC−IgG (150 kDa), Con-L/FITC−IgG, SA-L/FITC−IgG, and DC-L/FITC−IgG complexes were scarcely taken up at all (Figure 4C). FITC−IgG in a complex with Arg4-L, Arg6-L, Arg8-L, and Arg10-L showed about 30-, 100-, 60-, and 100-fold greater cellular uptake, respectively, than free FITC−IgG. Arg6-L and Arg10-L showed the greatest efficiency in delivering FITC−IgG. However, FITC−IgG and Arg10-L without complex formation showed less cellular uptake of FITC−IgG than Arg4-L/FITC−IgG (data not shown).

We assayed the cellular internalization of the Arg4-L and Arg10-L/FITC−BSA or FITC−IgG complexes for a quantitative evaluation of the amount of internalized protein. Cells were exposed to the same conditions as for the flow cytometric analysis and lysed by 0.2% Triton X-100/PBS. FITC−BSA (5 μg/mL) was internalized in the cells at about 40% and 30% of the dose with Arg4-L and with Arg10-L, respectively. On the other hand, FITC−IgG was internalized at about 10% and 19% of the dose with Arg4-L and with Arg10-L, respectively.

Efficiency of the Cellular Uptake of Arg10-L/FITC−IgG Based on the Ratio of Arg10-L to IgG. We examined the optimal molar ratio of Arg10-BDB to IgG in the Arg10-L/FITC−IgG complex, assaying the cellular internalization of various Arg10-L/FITC−IgG complexes by flow cytometry (Figure 5). Here, the molar ratio of Arg10-L/FITC−IgG refers to the ratio of Arg10-BDB to FITC−IgG because the proportion of Arg10-BDB in liposomes was constant (5 mol %). Cells were exposed for 3 h to the Arg10-L/FITC−IgG complex and then trypsinized. The cellular uptake of FITC−IgG increased as the molar ratio of Arg10-L/FITC−IgG increased and seemed to reach a level of saturation above a molar ratio of 100. It could

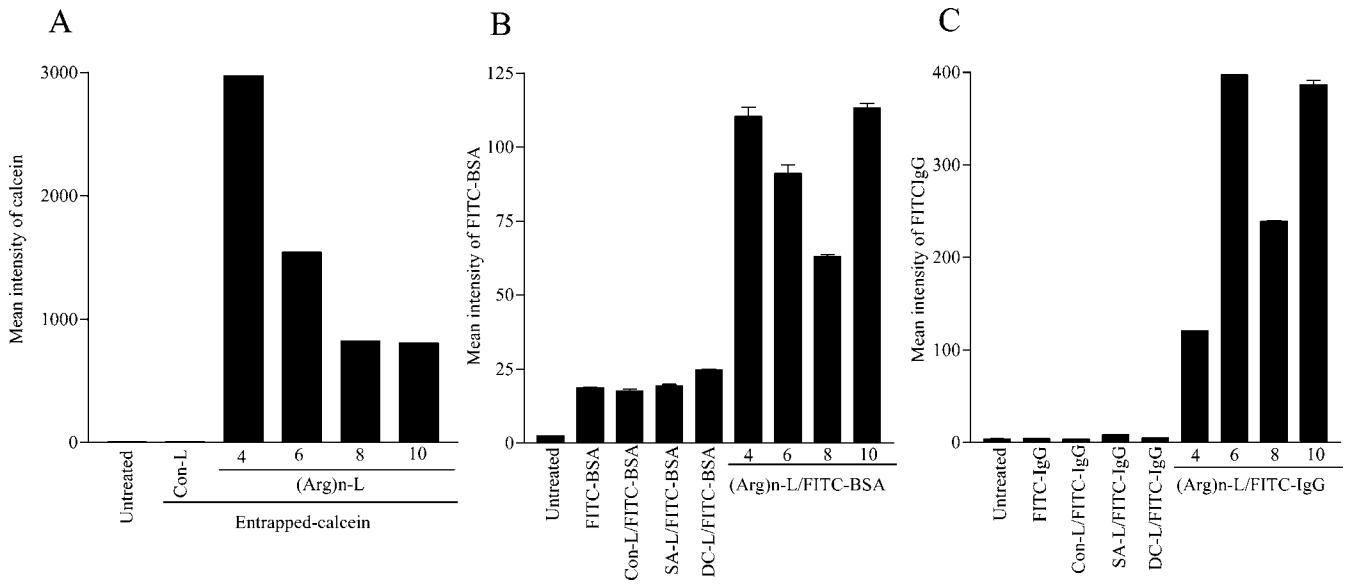

Figure 4. Cellular uptake of the calcein-entrapped $(Arg)_n$-L (A), and $(Arg)_n$-L in complexes with FITC−BSA (B) and FITC−IgG (C). Calcein-entrapped $(Arg)_n$-L (100 μg) alone or each $(Arg)_n$-L/protein complex (a variable $(Arg)_n$-BDB: 5 μg of FITC−BSA or FITC−IgG = 50:1, molar ratio) was diluted with serum-free DMEM to 1 mL and then gently applied to the cells, incubated with the cells for 3 h at 37 °C in serum-free DMEM, and treated with trypsin before FACS analysis. Con-L exhibits liposome without $(Arg)_n$-BDB. SA-L and DC-L exhibit liposome with stearylamine and DC−Chol, respectively. Each value is the mean ± SD of three separate determinations.

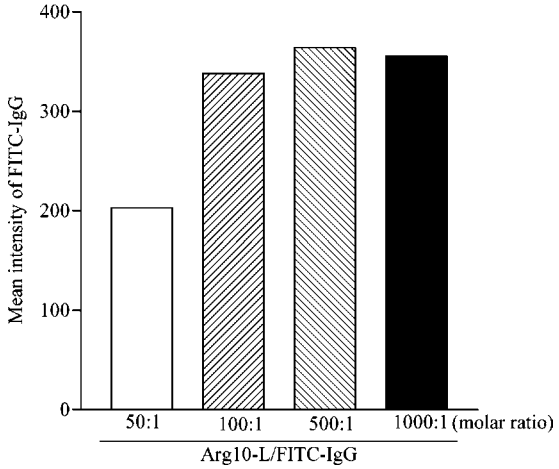

Figure 5. Cellular uptake of the Arg10-L/FITC−IgG complex as a function of the molar ratio between Arg10-BDB and FITC−IgG. Arg10-L/FITC−IgG (a variable Arg10-BDB: 5 μg of FITC−IgG, molar ratio from 50:1 to 1000:1) was diluted with serum-free DMEM to 1 mL and then gently applied to the cells and incubated with the cells at 37 °C for 3 h in serum-free DMEM and treated with trypsin before FACS analysis. Each value is the mean ± SD of three separate determinations.

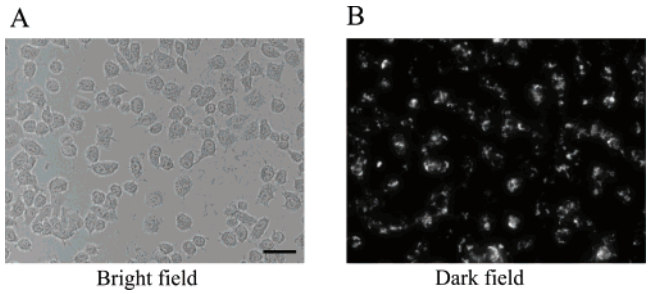

Figure 6. Analysis of FITC−IgG uptake by fluorescence microscopy. Arg10-L/FITC−IgG complex (Arg10:5 μg of FITC−IgG = 100:1, molar ratio) was diluted with serum-free DMEM to 1 mL, gently applied to the cells, and then incubated with the cells for 1 h at 37 °C in serum-free DMEM. The unfixed cells were observed with a fluorescence microscope (magnification × 200). Scale bar = 50 μm.

deliver about 1.5-fold more at a molar ratio of 100 than at 50 without change in the size of the complex.

To confirm the internalization and localization of FITC−IgG in the unfixed cells, we observed the cells by fluorescence microscopy after exposing them to the Arg10-L/FITC−IgG (100: 1) complex for 3 h and washing them five times (Figure 6A, B). FITC−IgG was observed to be taken into almost all cells.

Cellular Uptake of $(Arg)_n$-L/β-Gal Complexes. To examine whether the internalized protein is functional, we observed the enzymatic activity of β-Gal by microscopy. Cells were exposed to the Arg4-L and Arg10-L/β-Gal complexes for 3 h at 37 °C. Then, we observed the efficiency of protein delivery by monitoring the enzymatic activity of β-Gal using X-Gal staining (Figure 7). The cells treated with free β-Gal gave a similar image to untreated cells, suggesting that free β-Gal did not enter the cells (Figure 7A,B). About 70% and 50% of cells with Arg4-L and with Arg10-L, respectively, exhibited strong and uniform β-Gal activity (Figure 7C,D). At a higher magnification, we could confirm that β-Gal activity was present in the cytoplasm (Figure 7E,F). The β-Gal activity in the cells treated with Arg4-L and Arg10-L was about 5.9-fold and 4.4-fold stronger, respectively, than that of cells treated with free β-Gal, and β-Gal (5 μg/mL) was internalized in the cells at about 9.7% and 7.2% of the dose with Arg4-L and with Arg10-L, respectively in the chemiluminescence assay. Most notably, the presence of Arg4-L or Arg10-L did not alter the enzymatic activity of β-Gal upon delivery into cells. Arg4-L could deliver β-Gal (120 kDa) more efficiently than Arg10-L, similar to the transport of FITC−BSA. No cytotoxicity was observed for all $(Arg)_n$-L or $(Arg)_n$-L/protein complexes (data not shown).

FIDA Measurements. To examine whether there is a difference in the complex formation, we used FIDA to characterize the interaction of the $(Arg)_n$-L/protein complex. FIDA allows the characterization of fluorescently labeled molecules with respect to their molecular brightness and concentration at the single-molecule level (*18*). Briefly, the FIDA method is based on the collected photon numbers recorded in time intervals of fixed duration (time windows). Using this information, a count number histogram is built up. Then, a theoretical probability distribution of photon numbers is fitted against the obtained histogram, yielding specific brightness values (Q), corresponding to the concentrations (C), for all

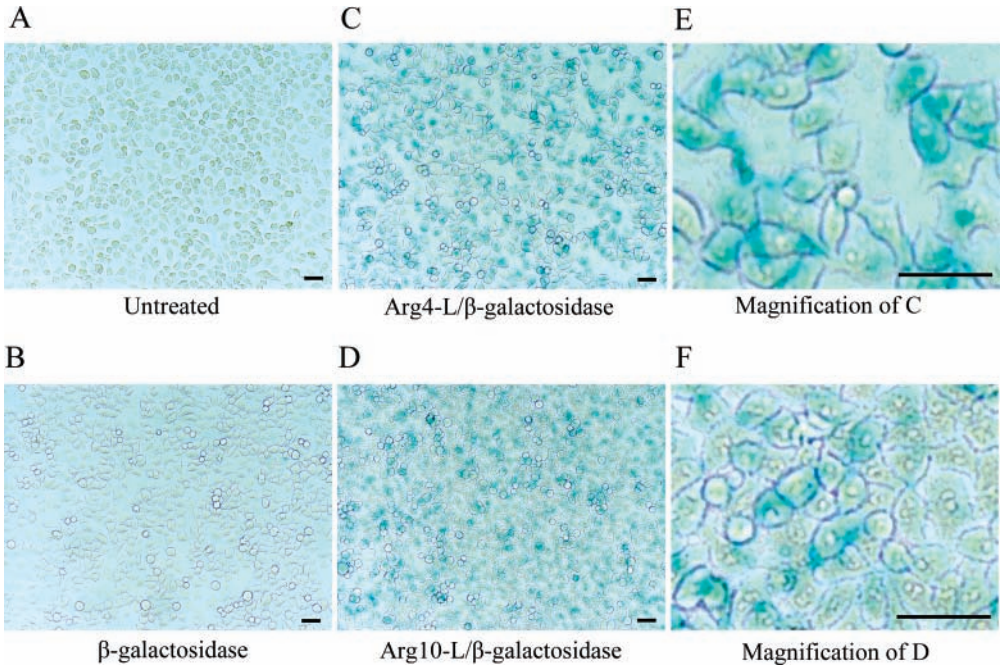

Figure 7. Analysis of β-galactosidase uptake by microscopy. Arg4-L, Arg10-L/β-galactosidase complex (Arg4-BDB or Arg10-BDB: 5 μg of β-galactosidase = 50:1, molar ratio), or 5 μg of β-galactosidase was diluted with serum-free DMEM to 1 mL and then gently applied to the cells and incubated with the cells for 1 h at 37 °C in serum-free DMEM. The cells were stained with a β-galactosidase staining kit and observed with a fluorescence microscope. Scale bar = 50 μm.

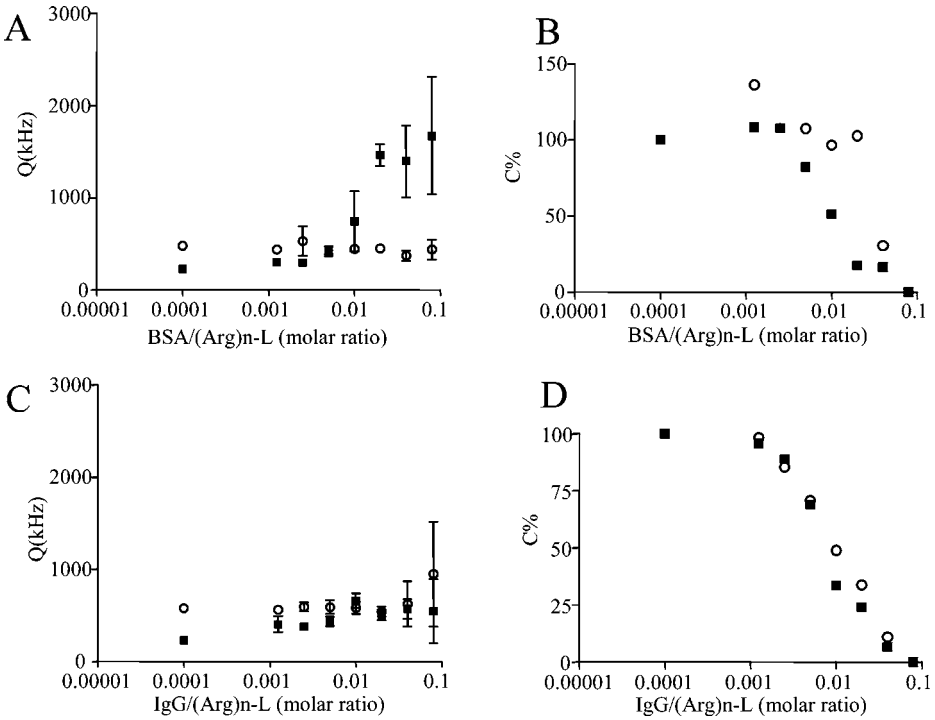

Figure 8. Fluorescence intensity distribution analysis (FIDA) of DiI-labeled Arg4- and Arg10-L/BSA or DiI-labeled Arg4-L and Arg10-L/IgG as a function of the molar ratio between Arg4- or Arg10-BDB and protein. Part A or C was the analytical result of the *Q* value. Part B or D was the analytical result of the ratio of the *C* value. Complex was diluted with water. Square, Arg4-L; Circle, Arg10-L. Each value is the mean ± SD of three separate determinations.

different species. To determine the interaction of the $(Arg)_n$-L with proteins, we measured fluorescence intensity distribution of lipid marker, DiI incorporated in the particle lipid layers as a function of the molar ratio between Arg4- or Arg10-L and protein. Here, the molar ratio of the Arg4-L or Arg10-L/protein complex refers to the ratio of Arg4- or Arg10-BDB to protein. *Q* value of Arg4-L increased at about 0.01 BSA/Arg4-L molar ratio, but that of Arg10-L did not (Figure 8A), corresponding to *C* value of Arg4-L decreased (Figure 8B). Increase of BSA might form complex with high molar ratio of Arg4-L, which increased brightness per complex (*Q* value) and decreased fluorescent Arg4-L number (*C* value). For Arg10-L, the ratio of Arg10-L/BSA in the complex was not changed in this range. Therefore, *Q* value of the complex was not changed. The interaction of IgG with Arg4-L and Arg10-L was similar (Figure 8C, D).

Mechanism of Cellular Uptake of Arg4-L, Arg10-L, and Complexes. To investigate the internalization mechanism of

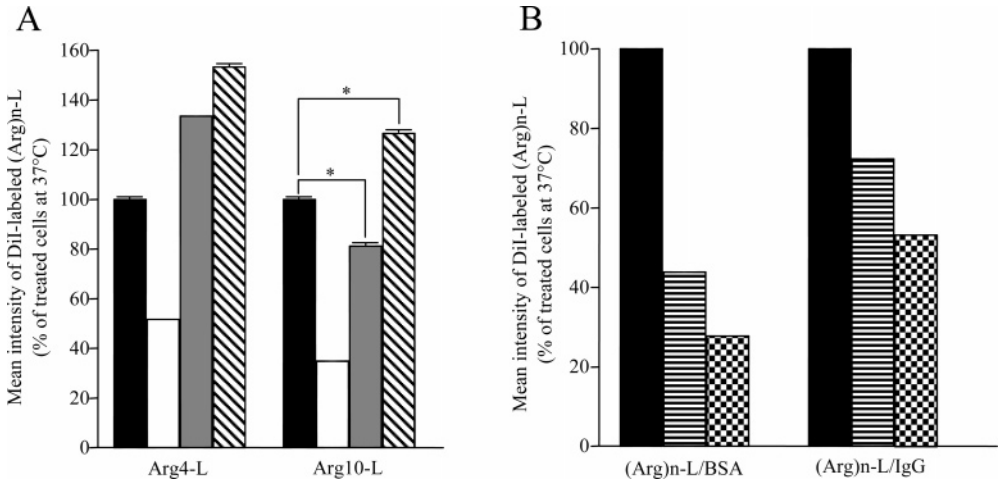

Figure 9. Effect of temperature and pharmacological reagents on the cellular uptake of DiI-labeled $(Arg)_n$-L (A) and $(Arg)_n$-L/protein complex (B). (A) HeLa cells were pretreated with EIPA (25 μM) or PMA (1 μM) at 37 °C for 30 min. The medium was replaced with fresh medium containing DiI-labeled Arg4-L or Arg10-L (100 μg/mL). The cells were incubated for 1 h at 37 °C in serum-free DMEM containing EIPA (25 μM) or PMA (1 μM) and then treated with trypsin before the flow cytometry. Dark bar, 37 °C or no pharmacological reagent; open bar, 4 °C; gray bar, EIPA; slashed bar, PMA. Each value is the mean ± SD of three separate determinations. (B) Effect of temperature on the cellular uptake of DiI-labeled Arg4-L and Arg10-L/protein complex. The experimental conditions were the same as in Figure 4B and C. Dark bar, 37 °C; sideline bar, Arg4-L at 4 °C; mosaic bar, Arg10-L at 4 °C. Each value is the mean ± SD of three independent experiments.

Arg4-L, Arg10-L and their complexes, we prepared DiI-labeled liposomes and examined the effect of temperature, a macropinocytosis inhibitor (EIPA) or an accelerator (PMA) on the cellular uptake of the liposomes. Cells were exposed to DiI-labeled Arg4-L or Arg10-L for 3 h at either 4 °C or 37 °C. Then, they were trypsinized and analyzed by flow cytometry. DiI-labeled Arg4-L and Arg10-L showed about a 50% and 65% lower internalization efficiency, respectively, at 4 °C than at 37 °C (Figure 9A). This finding suggests that the transport occurred through energy-dependent endocytosis. The cells were exposed to DiI-labeled Arg4-L or Arg10-L at 37 °C for 1 h in the absence or presence of EIPA or PMA (Figure 9A). The cellular uptake of Arg4-L increased about 34% in the presence of EIPA, and about 54% in the presence of PMA compared with untreated cells. The cellular uptake of Arg10-L significantly decreased about 20% in the presence of EIPA ($p < 0.05$), but significantly increased about 27% in the presence of PMA ($p < 0.05$) compared with untreated cells. The inhibition of cellular uptake at 4 °C for the Arg4-L/protein complex was lower than that for the Arg10-L/protein complex (Figure 9 B). This finding suggests that Arg4-L and Arg10-L/protein were taken up via an endocytotic pathway as well as Arg4-L or Arg10-L alone.

DISCUSSION

As a free liposome, Arg4-L was most efficiently internalized in the cells. The efficiency decreased depending on the length of oligo-Arg. To our knowledge, this may be the first experimental demonstration that the liposomes with shorter oligo-Arg-L alone were internalized more efficiently than those with longer ones. Besides the demonstration of the free $(Arg)_n$-L cellular uptake, our study reveals protein delivery by $(Arg)_n$-L. Concerning the effect of oligo-Arg length, liposome/protein complexes showed a different trend.

Generally, the cellular uptake of oligo-Arg increases in efficiency as the number of arginine residues increases (*5*). Both Tat and penetratin enhanced the efficiency of the uptake of liposomes in proportion to the number of peptides attached to the liposomal surface (*12*). In our experiments, the shorter oligo-Arg system, Arg4-L, penetrated the cells more efficiently than the longer one, Arg10-L, in the case of calcein-entrapped $(Arg)_n$-L.

To examine the internalization of liposomes, calcein, a water-soluble marker, was entrapped in $(Arg)_n$-L. Liposome−cell interaction on the surface might lead to the leakage of calcein due to liposome destabilization. However, the calcein leakage from $(Arg)_n$-L was small (data not shown). Uptake of DiI-labeled liposomes, which has label-lipid in the liposomes, also exhibited similar behavior to that of calcein-entapped liposomes (data not shown). These findings suggest that the calcein-entrapped $(Arg)_n$-L penetrated as liposomes, and that the difference in the cellular uptake of calcein corresponded to that of the liposomes.

FITC−BSA (66 kDa), β-Gal (120 kDa), and FITC−IgG (150 kDa) were used as model proteins. Cellular uptake of FITC−BSA was increased three to six times when it was in a complex with $(Arg)_n$-L. The highest level of cellular uptake of FITC−BSA was observed with Arg4-L and Arg10-L. For β-Gal, Arg4-L carried β-Gal 6-fold higher than free one. Arg4-L could deliver β-Gal more efficiently than Arg10-L. The enzymatic activity of β-Gal showed a protein to be transported as a biologically active protein. For FITC−IgG, Arg10-L gave the best result.

FIDA showed that the interaction of Arg4-L with BSA was stronger than that of Arg10-L with BSA, and the interaction of Arg4-L and Arg10-L with IgG was similar. At molar ratio of BSA/DiI labeled Arg4-L > 0.02, BSA associated on the surface of liposomes may interact with DiI or the complex may be aggregated. BSA may interact hydrophobic part of Arg4-L. The efficient cellular uptake of Arg4-L/BSA may reflect the strong interaction between Arg4-L and BSA. Also, DiI-labeled Arg4-L in a complex with proteins was taken up more efficiently than Arg10-L complex (data not shown). In the case of IgG, Arg10-L delivered about 3-fold more proteins than Arg4-L (Figure 4C). Because proteins formed complexes with $(Arg)_n$-L prior to the intracellular delivery, it can be postulated that the mode of interactions between proteins and $(Arg)_n$-L might be different depending on the protein.

The cellular uptake was also examined with the fluorescence microscope. To avoid artifacts caused by the fixation procedure, we observed live cells. Fixation was shown to cause significant artifacts regarding the cellular localization (*19*). From the microscopic observation, the fluorescence of FITC−IgG was observed in almost 100% of cells when transported as the Arg10-L complex (Figure 6). From the quantitative evaluation, Arg10-L delivered about 1.2-fold of IgG compared with Arg4-L, whereas FACS analysis indicated that Arg10-L delivered

almost 3-fold more than Arg4-L. The discrepancy could be explained by the sensitivity of fluorescein emission in the microenvironment and partial quenching in the endosomal structures of live cells used for the FACS analysis (*20*).

The cellular translocation by CPP was initially proposed to be an energy-independent process, because no difference was observed in cellular uptake between 37 °C and 4 °C (*2*, *5*). However, more recent papers suggest that the majority of the translocation occurs via an energy-dependent pathway, and that the translocation of CPP is reduced by endocytosis inhibitors (*21*−*23*). From the temperature-dependence, the internalization of Arg4-L and Arg10-L was shown to mainly involve endocytosis. Endocytosis represents a variety of mechanisms that fall into two broad categories, phagocytosis and pinocytosis. Phagocytosis is typically restricted to specialized mammalian cells, whereas pinocytosis occurs in most cells via at least four basic mechanisms: macropinocytosis, clathrin-mediated endocytosis, caveolae-mediated endocytosis, and clathrin- and caveolae-independent endocytosis (*24*). In the latest papers, the translocation of Tat peptide is suggested to occur through macropinocytosis which is dependent on lipidic microdomains (*25*), and that of octa-arginine (R8) peptide is also shown to involve macropinocytosis (*26*). EIPA inhibits the Na^+/H^+ exchange and has been shown to inhibit macropinocytosis (*25*). PMA is a protein kinase C activator and stimulates macropinocytosis by increasing membrane ruffles (*27*−*30*). The change in cellular uptake of Arg4-L and Arg10-L caused by a macropinocytosis inhibitor (EIPA) or an accelerator (PMA) suggests that the internalization of Arg10-L occurs mainly through macropinocytosis. Since the cellular translocation of Arg4-L did not decrease by EIPA, it might involve a different mechanism than macropinocytosis.

Pep-1 can efficiently deliver proteins into cells by forming physical assemblies with a variety of proteins at the optimal molar ratio of pep-1 and a protein (*6*, *31*). The internalization of pep-1 alone and pep-1/β-Gal complex is not dependent on the endocytotic pathway (*6*). The cellular uptake of the Arg10-L/FITC−IgG complex was greatly enhanced starting from a molar ratio of 50 up to 100 and reached a plateau thereafter. The difference in the behavior of pep-1 and Arg10-L concerning the molar ratio with a protein might also suggest differences in their uptake mechanism.

The most striking result of the present study is that the simple complex formation between oligo-Arg-modified liposomes and proteins, without the entrapment of proteins in the internalized space of liposomes, can produce a cellular transportable protein delivery system, which can deliver active proteins into cells. $(Arg)_n$-L will be useful to deliver macromolecules, which are difficult to entrap in liposomes, into cells. Furthermore, it could release proteins in the cytoplasm because proteins bind on the outer surface of the liposomes. A short oligo-Arg on $(Arg)_n$-L alone may be enough to be taken up in cells, but a longer Arg repeat might be needed to form a complex with large proteins and deliver them into cells. The most suitable (Arg)n-L for a protein delivery could be selected experimentally based on the results of $(Arg)_n$-L complexed with the protein. Such information will be helpful in the design of $(Arg)_n$-L as a carrier for delivering proteins into cells.

In summary, we synthesized $(Arg)_n$-BDB and prepared oligo-Arg modified liposomes as a novel carrier of proteins into cells. We found that the penetrating abilities of $(Arg)_n$-L alone and in complexes with proteins differed. The mechanism of cell membrane penetration of Arg4-L and Arg10-L, and their complexes with proteins, although not thoroughly understood, is probably different.

ACKNOWLEDGMENT

This project was supported in part by a grant from the Promotion and Mutual Aid Corporation for Private Schools of Japan and by a Grant-in-Aid for Scientific Research from the Ministry of Education, Culture, Sports, Science, and Technology of Japan.

LITERATURE CITED

(1) Derossi, D., Joliot, A. H., Chassaing, G., and Prochiantz, A. (1994) The third helix of the Antennapedia homeodomain translocates through biological membranes. *J. Biol. Chem. 269*, 10444−10450.

(2) Vives, E., Brodin, P., and Lebleu, B. (1997) A truncated HIV-1 Tat protein basic domain rapidly translocates through the plasma membrane and accumulates in the cell nucleus. *J. Biol. Chem. 272*, 16010−16017.

(3) Pooga, M., Hallbrink, M., Zorko, M., and Langel, U. (1998) Cell penetration by transportan. *FASEB J. 12*, 67−77.

(4) Oehlke, J., Scheller, A., Wiesner, B., Krause, E., Beyermann, M., Klauschenz, E., Melzig, M., and Bienert, M. (1998) Cellular uptake of an alpha-helical amphipathic model peptide with the potential to deliver polar compounds into the cell interior non-endocytically. *Biochim. Biophys. Acta 1414*, 127−139.

(5) Futaki, S., Suzuki, T., Ohashi, W., Yagami, T., Tanaka, S., Ueda, K., and Sugiura, Y. (2001) Arginine-rich peptides. An abundant source of membrane-permeable peptides having potential as carriers for intracellular protein delivery. *J. Biol. Chem. 276*, 5836−5840.

(6) Morris, M. C., Depollier, J., Mery, J., Heitz, F., and Divita, G. (2001) A peptide carrier for the delivery of biologically active proteins into mammalian cells. *Nat. Biotechnol. 19*, 1173−1176.

(7) Schwarze, S. R., Ho, A., Vocero-Akbani, A., and Dowdy, S. F. (1999) In vivo protein transduction: delivery of a biologically active protein into the mouse. *Science 285*, 1569−1572.

(8) Elliott, G., and O'Hare, P. (1997) Intercellular trafficking and protein delivery by a herpesvirus structural protein. *Cell 88*, 223−233.

(9) Saalik, P., Elmquist, A., Hansen, M., Padari, K., Saar, K., Viht, K., Langel, U., and Pooga, M. (2004) Protein cargo delivery properties of cell-penetrating peptides. A comparative study. *Bioconjugate Chem. 15*, 1246−1253.

(10) Lewin, M., Carlesso, N., Tung, C. H., Tang, X. W., Cory, D., Scadden, D. T., and Weissleder, R. (2000) Tat peptide-derivatized magnetic nanoparticles allow in vivo tracking and recovery of progenitor cells. *Nat. Biotechnol. 18*, 410−414.

(11) Torchilin, V. P., Rammohan, R., Weissig, V., and Levchenko, T. S. (2001) TAT peptide on the surface of liposomes affords their efficient intracellular delivery even at low temperature and in the presence of metabolic inhibitors. *Proc. Natl. Acad. Sci. U.S.A. 98*, 8786−8791.

(12) Tseng, Y. L., Liu, J. J., and Hong, R. L. (2002) Translocation of liposomes into cancer cells by cell-penetrating peptides penetratin and tat: a kinetic and efficacy study. *Mol. Pharmacol. 62*, 864−872.

(13) Mitchell, D. J., Kim, D. T., Steinman, L., Fathman, C. G., and Rothbard, J. B. (2000) Polyarginine enters cells more efficiently than other polycationic homopolymers. *J. Pept. Res. 56*, 318−325.

(14) Wender, P. A., Mitchell, D. J., Pattabiraman, K., Pelkey, E. T., Steinman, L., and Rothbard, J. B. (2000) The design, synthesis, and evaluation of molecules that enable or enhance cellular uptake: peptoid molecular transporters. *Proc. Natl. Acad. Sci. U.S.A. 97*, 13003−13008.

(15) Futaki, S., Ohashi, W., Suzuki, T., Niwa, M., Tanaka, S., Ueda, K., Harashima, H., and Sugiura, Y. (2001) Stearylated arginine-rich peptides: a new class of transfection systems. *Bioconjugate Chem. 12*, 1005−1011.

(16) Hara, M., Takanashi, Y., Tuzuki, N., Kawakami, H., Toma, K., and Higuchi, A. (2003) Production of interferon-β by NB1−RGB cells cultured on peptide-lipid membranes. *Cytotechnology 42*, 13−20.

(17) Furuhata, M., Kawakami, H., Toma, K., Hattori, Y., and Maitani, Y. (2006) Design, synthesis and gene delivery efficiency of novel oligo-arginine-linked PEG-lipids: Effect of oligo-arginine length. *Int. J. Pharm. 316*, 109−116.

(18) Kask, P., Palo, K., Ullmann, D., and Gall, K. (1999) Fluorescence-intensity distribution analysis and its application in biomolecular detection technology. *Proc. Natl. Acad. Sci. U.S.A. 96*, 13756−13761.

(19) Richard, J. P., Melikov, K., Vives, E., Ramos, C., Verbeure, B., Gait, M. J., Chernomordik, L. V., and Lebleu, B. (2003) Cell-penetrating peptides. A reevaluation of the mechanism of cellular uptake. *J. Biol. Chem. 278*, 585−590.

(20) Fischer, R., Kohler, K., Fotin-Mleczek, M., and Brock, R. (2004) A stepwise dissection of the intracellular fate of cationic cell-penetrating peptides. *J. Biol. Chem. 279*, 12625−12635.

(21) Vives, E. (2003) Cellular uptake of the Tat peptide: an endocytosis mechanism following ionic interactions. *J. Mol. Recognit. 16*, 265−271.

(22) Drin, G., Cottin, S., Blanc, E., Rees, A. R., and Temsamani, J. (2003) Studies on the internalization mechanism of cationic cell-penetrating peptides. *J. Biol. Chem. 278*, 31192−31201.

(23) Fischer, R., Waizenegger, T., Kohler, K., and Brock, R. (2002) A quantitative validation of fluorophore-labelled cell-permeable peptide conjugates: fluorophore and cargo dependence of import. *Biochim. Biophys. Acta 1564*, 365−374.

(24) Conner, S. D., and Schmid, S. L. (2003) Regulated portals of entry into the cell. *Nature 422*, 37−44.

(25) Wadia, J. S., Stan, R. V., and Dowdy, S. F. (2004) Transducible TAT-HA fusogenic peptide enhances escape of TAT-fusion proteins after lipid raft macropinocytosis. *Nat. Med. 10*, 310−315.

(26) Nakase, I., Niwa, M., Takeuchi, T., Sonomura, K., Kawabata, N., Koike, Y., Takehashi, M., Tanaka, S., Ueda, K., Simpson, J. C., Jones, A. T., Sugiura, Y., and Futaki, S. (2004) Cellular uptake of arginine-rich peptides: roles for macropinocytosis and actin rearrangement. *Mol. Ther. 10*, 1011−1022.

(27) Holm, P. K., Eker, P., Sandvig, K., and van Deurs, B. (1995) Phorbol myristate acetate selectively stimulates apical endocytosis via protein kinase C in polarized MDCK cells. *Exp. Cell Res. 217*, 157−168.

(28) Amyere, M., Payrastre, B., Krause, U., Van Der Smissen, P., Veithen, A., and Courtoy, P. J. (2000) Constitutive macropinocytosis in oncogene-transformed fibroblasts depends on sequential permanent activation of phosphoinositide 3-kinase and phospholipase C. *Mol. Biol. Cell. 11*, 3453−3467.

(29) Riezman, H., Woodman, P. G., van Meer, G., and Marsh, M. (1997) Molecular mechanisms of endocytosis. *Cell 91*, 731−738.

(30) Grimmer, S., van Deurs, B., and Sandvig, K. (2002) Membrane ruffling and macropinocytosis in A431 cells require cholesterol. *J. Cell Sci. 115*, 2953−2962.

(31) Henriques, S. T., Costa, J., and Castanho, M. A. (2005) Translocation of beta-Galactosidase Mediated by the Cell-Penetrating Peptide Pep-1 into Lipid Vesicles and Human HeLa Cells Is Driven by Membrane Electrostatic Potential. *Biochemistry 44*, 10189−10198.

BC060034H

"SMART" Drug Delivery Systems: Double-Targeted pH-Responsive Pharmaceutical Nanocarriers

R. M. Sawant, J. P. Hurley, S. Salmaso, A. Kale, E. Tolcheva, T. S. Levchenko, and V. P. Torchilin*

Department of Pharmaceutical Sciences, Northeastern University, Boston, Massachusetts 02115. Received March 30, 2006; Revised Manuscript Received May 13, 2006

To develop targeted pharmaceutical carriers additionally capable of responding to certain local stimuli, such as decreased pH values in tumors or infarcts, targeted long-circulating PEGylated liposomes and PEG-phosphatidylethanolamine (PEG-PE)-based micelles have been prepared with several functions. First, they are capable of targeting a specific cell or organ by attaching the monoclonal antimyosin antibody 2G4 to their surface via pNP-PEG-PE moieties. Second, these liposomes and micelles were additionally modified with biotin or TAT peptide (TATp) moieties attached to the surface of the nanocarrier by using biotin-PE or TATp-PE or TATp-short PEG-PE derivatives. PEG-PE used for liposome surface modification or for micelle preparation was made degradable by inserting the pH-sensitive hydrazone bond between PEG and PE (PEG-Hz-PE). Under normal pH values, biotin and TATp functions on the surface of nanocarriers were "shielded" by long protecting PEG chains (pH-degradable PEG_{2000}-PE or PEG_{5000}-PE) or by even longer pNP-PEG-PE moieties used to attach antibodies to the nanocarrier (non-pH-degradable PEG_{3400}-PE or PEG_{5000}-PE). At pH 7.4−8.0, both liposomes and micelles demonstrated high specific binding with 2G4 antibody substrate, myosin, but very limited binding on an avidin column (biotin-containing nanocarriers) or internalization by NIH/3T3 or U-87 cells (TATp-containing nanocarriers). However, upon brief incubation (15−30 min) at lower pH values (pH 5.0−6.0), nanocarriers lost their protective PEG shell because of acidic hydrolysis of PEG-Hz-PE and acquired the ability to become strongly retained on an avidin column (biotin-containing nanocarriers) or effectively internalized by cells via TATp moieties (TATp-containing nanocarriers). We consider this result as the first step in the development of multifunctional stimuli-sensitive pharmaceutical nanocarriers.

INTRODUCTION

Ideally, a nanoparticular drug delivery system (DDS) should be able (a) to specifically accumulate in the required organ or tissue and then (b) penetrate inside target cells, delivering its load (drug or DNA) intracellularly. Organ or tissue (tumor, infarct) accumulation could be achieved by the passive targeting via the enhanced permeability and retention (EPR) effect (*1*, *2*) or by antibody-mediated active targeting (*3*, *4*), while the intracellular delivery could be mediated by certain internalizable ligands (folate, transferrin) (*5*, *6*) or by cell-penetrating peptides (CPPs, such as TAT or polyArg) (*7*, *8*). Such a DDS should simultaneously carry on its surface various active moieties, i.e., be multifunctional and possess the ability to switch on and switch off certain functions when necessary, under the action of local stimuli characteristic of the target pathological zone (first of all, increased temperature or lowered pH values characteristic of inflamed, ischemic, and neoplastic tissues). Another important requirement is that different properties of the multifunctional DDS are coordinated in an optimal fashion. Thus, for example, if the system is to be constructed that can provide the combination of the longevity allowing for the target accumulation via the EPR effect and specific cell surface binding allowing for its internalization by target cells, two requirements have to be met. First, the half-life of the carrier in the circulation should be long enough to fit EPR effect requirements, and second, the internalization of the DDS by the target cells should proceed fast enough not to allow for the carrier degradation and drug loss in the interstitial space. However, development of systems such as this still represents a challenge.

* To whom correspondence should be addressed. E-mail: v.torchilin@neu.edu.

Intracellular transport of different biologically active molecules is one of the key problems in drug delivery in general. Nanoparticular DDS, such as liposomes and micelles, are frequently used to increase the efficacy of drug and DNA delivery and targeting (*9*, *10*). So far, multiple and not always successful attempts have been made to deliver various drug carriers directly into the cell cytoplasm, bypassing the endocytic pathway, to protect drugs and DNA from the lysosomal degradation, thus enhancing drug efficiency and DNA incorporation into the cell genome (*11*−*14*). Within the paradigm of multifunctional DDS, one can think about the development of a DDS built in such a way that during the first phase of delivery, a nonspecific cell-penetrating function is shielded by the function providing organ/tissue-specific delivery (sterically protecting polymer or antibody). Upon accumulating in the target, protecting polymer or antibody attached to the surface of the DDS via the stimuli-sensitive bond should detach under the action of local pathological conditions (abnormal pH or temperature) and expose the previously hidden second function allowing for the subsequent delivery of the carrier and its cargo inside cells. While such DDS should be stable in the blood for a long time (hours) to allow for an efficient target accumulation, it has to lose the protective coat inside the target almost instantly to allow for the fast internalization (minutes) to minimize the washing away of the released drug or DNA. The schematic pattern of such system is shown in Figure 1. Intracellular trafficking, distribution, and fate of the carrier and its cargo can be additionally controlled by its charge and composition, which can drive it to the nuclear compartment or toward other cell organelles.

Within the past few years, it has been demonstrated that certain proteins and peptides (CPPs, such as TAT peptide,

10.1021/bc060080h CCC: $33.50 © 2006 American Chemical Society
Published on Web 06/30/2006

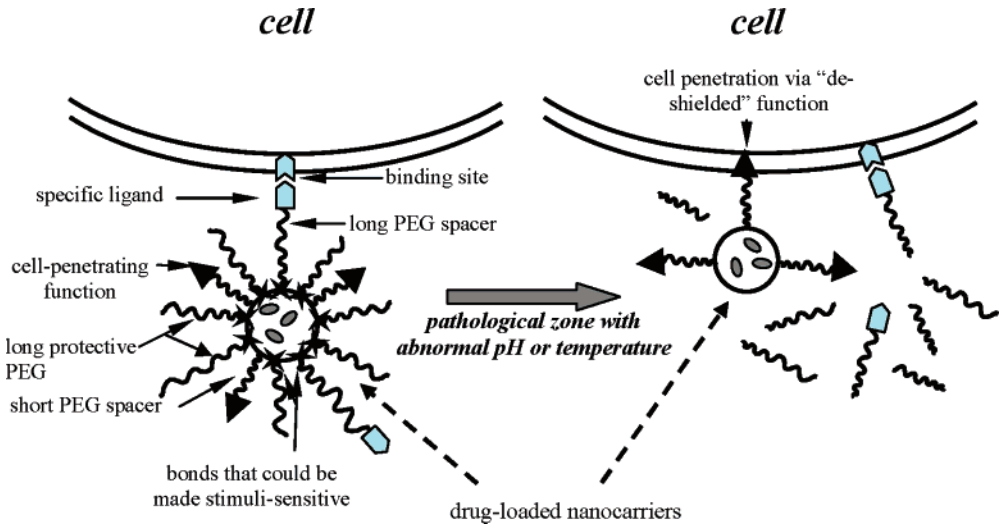

Figure 1. Interaction of the multifunctional pH-responsive pharmaceutical nanocarrier with the target cell. Local stimuli-dependent removal of protecting PEG chains or mAb-PEG moieties allows for the direct interaction of the CPP moiety with the cell membrane.

TATp) can enter cell cytoplasm directly and even target cell nuclei (*15*, *16*). CPPs have also been successfully used for the intracellular delivery of small drug molecules, large molecules (enzymes, DNA), and nanoparticulates (quantum dots, iron oxide nanoparticles, liposomes) (*13*, *17*−*22*). The mechanism of this phenomenon is still under investigation, although important progress has been already made, and it was shown that electrostatic interactions and hydrogen bonding lay behind the CPP-mediated direct transduction of small molecules (*23*, *24*), while the energy-dependent macropinocytosis is responsible for the CPP-mediated intracellular delivery of large molecules and nanoparticulates with their subsequent enhanced release from endosomes into the cell cytoplasm (*25*, *26*).

In this study, we have attempted to prepare and test in vitro stable targeted PEGylated DDS (liposomes and micelles) containing the second specific function (i.e. the intracellular internalization of the DDS), which, under normal conditions, is shielded by the protecting polymer or polymer−antibody conjugate, however can be "developed" upon brief incubation at lowered pH values characteristic of inflamed or neoplastic areas. As the first step on the way to multifunctional drug delivery systems, we have prepared liposomes and micelles sterically protected by the low pH-cleavable PEG chains and additionally containing a monoclonal antibody attached to the surface of the DDS via a noncleavable longer PEG spacer and an additional function (biotin or TATp) attached to the surface of the DDS via the noncleavable anchor shorter than the cleavable PEG chain.

MATERIALS AND METHODS

Materials. Cell lines, mouse fibroblast NIH 3T3 and human astrocytoma U-87 MG, were purchased from the American Type Culture Collection (Manassas, VA). All cell culture media, DMEM and RPMI 1640, heat-inactivated fetal bovine serum (FBS), and concentrated solutions of sodium pyruvate and penicillin/streptomycin stock solutions were purchased from Cellgro (Herndon, VA). TAT-peptide (11-mer: TyrGlyArgLys-LysArgArgGlnArgArgArg; molecular mass, 1560 Da; three reactive amino groups) was prepared by Research Genetics (Huntsville, AL). Monoclonal antibody (mAb) 2G4 was produced and purified in our laboratory. Also, pNP-PEG_{3400}-PE was synthesized and purified according to an established method in our laboratory (*27*). Egg phosphatidylcholine (PC), cholesterol, 1,2-distearoyl-*sn*-glycero-3-phosphoethanolamine-*N*-[methoxy(poly(ethylene glycol))-750] (ammonium salt) ($mPEG_{750}$-PE), 1,2-distearoyl-*sn*-glycero-3-phosphoethanolamine-*N*-[methoxy (poly(ethylene glycol))-2000] (ammonium salt) ($mPEG_{2000}$-PE), 1,2-dipalmitoyl-*sn*-glycero-3-phosphoethanolamine-*N*-(cap biotinyl) (sodium salt) (biotin-PE) 1,2-dipalmitoyl-*sn*-glycero-3-phosphothioethanol (sodium salt) (PE-SH), and 1,2-dioleoyl-*sn*-glycero-3-phosphoethanolamine-*N*-(lissamine rhodamine B sulfonyl) (ammonium salt) (Rh-PE) were obtained from Avanti Polar Lipids, Inc. (Alabaster, AL). $mPEG_{2000}$-butyraldehyde ($mPEG_{2000}$-CHO) and $mPEG_{5000}$-butyraldehyde ($mPEG_{5000}$-CHO) was obtained from Nektar (Huntsville, AL). Control bovine antibody IgG was obtained from Serologicals Proteins, Inc. (Kankakee, IL). 3-(2-Pyridyldithio) propionyl hydrazide (PDPH) and Immobilized NeutrAvidin protein was purchased from Pierce Biotechnology, Inc. (Rockford, IL). Bovine serum albumin and all other chemicals and buffer solution components were from Sigma (St. Louis, MO) and were of analytical grade.

Synthesis of pH-Cleavable $mPEG_{2000}$-Hydrazone-Phosphatidylethanolamine ($mPEG_{2000}$-Hz-PE). Developing the method of coupling oxidized antibody to the PEG terminus through a hydrazone bond as suggested by Hansen et al. (*28*), we devised our own scheme of conjugate reaction for synthesis of pH-cleavable PEG-PE. The reaction was performed in two steps: first, the activation of $mPEG_{2000}$-CHO with PDPH, and second, the conjugation of 1,2-dipalmitoyl-*sn*-glycero-3-phosphothioethanol (sodium salt) (PE-SH) to activated mPEG-CHO.

For step I of the synthesis, 150 mg (64 μmol) of $mPEG_{2000}$-CHO was dissolved in dry chloroform containing 3.5 molar excess of 3-(2-pyridyldithio) propionyl hydrazide (PDPH) to obtain 50 mg/mL solution of $mPEG_{2000}$-CHO. The mixture was incubated for 48 h at room temperature with stirring under argon. Thin-layer chromatography (TLC) ($CHCl_3$:CH_3OH:H_2O, 80:20:2) revealed that the reaction was complete. The starting material $mPEG_{2000}$-CHO did not absorb UV and was positive to Dragendorff spray, while PDPH absorbed UV and was negative for Dragendorff spray. The product, $mPEG_{2000}$-Hz-PDP, absorbed UV and was positive to Dragendorff spray. Organic solvents were then removed using a rotary evaporator. $mPEG_{2000}$-Hz-PDP was then dissolved in deionized water (adjusted to pH 10−11 using 1 M NaOH) and purified from unreacted PDPH using Sepharose G25 column and deionized water (adjusted to pH 10.5 using 1 M NaOH). Pooled fractions containing $mPEG_{2000}$-Hz-PDP (Dragendorff and UV positive) were freeze-dried.

For step II of the reaction, 20 mg (26 μmol) of 1,2-dipalmitoyl-*sn*-glycero-3-phosphothioethanol (sodium salt) (PE-SH) was dissolved in dry chloroform containing 1.5 molar excess of $mPEG_{2000}$-Hz-PDP, to get a 10 mg/mL solution of

PE-SH. The solution was supplemented with 15 μL (approximately 3-fold molar excess over PEG) of triethylamine (TEA). The sample was incubated overnight at room temperature with stirring under argon. TLC ($CHCl_3$:CH_3OH:H_2O, 80:20:2) revealed that the reaction was complete. The starting material $mPEG_{2000}$-Hz-PDP was positive to Dragendorff spray and negative for molybdenum blue, while PE-SH was positive to molybdenum blue and negative for Dragendorff spray. The product, $mPEG_{2000}$-Hz-PE, was positive to both Dragendorff spray and molybdenum blue. The organic solvents were then removed using a rotary evaporator. The $mPEG_{2000}$-Hz-PE micelles were formed in deionized water (adjusted to pH 10.5 using 1 M NaOH) by vortexing. The micelles were separated from the unbound PEG and released pyridine-2-thione on CL-4B column using deionized water (adjusted to pH 10.5 using 1 M NaOH) as an eluent. Pooled fractions containing $mPEG_{2000}$-Hz-PE were freeze-dried and extracted with chloroform. $mPEG_{2000}$-Hz-PE was stored as 10 mg/mL chloroform solution at −80 °C under argon until further use. $mPEG_{5000}$-Hz-PE used in some experiments was synthesized in the same way starting with $mPEG_{5000}$-CHO.

Acidic pH Cleavability of $mPEG_{2000}$-Hz-PE. *TLC Analysis.* TLC-verified degradation of the polymer conjugates after pH treatment and spots corresponding to plain PEG and plain PE were observed after incubation of the polymers at pH 5.0 for 15 min at 37 °C.

HPLC Analysis. Micelles of $mPEG_{2000}$-Hz-PE were prepared containing 1 mol % of rhodamine-PE as fluorescent marker as follows. Lipid film was prepared by mixing chloroform solutions of both the lipids in a round-bottom flask and then removing chloroform using rotary evaporator. To ensure complete removal of any traces of chloroform further drying was done using lyophilizer. Appropriate volume of pH 8.5 phosphate buffer (100 mM phosphate, 150 mM sodium chloride) was added and vortexed for 2 min to form 0.5 mM solution of $mPEG_{2000}$-Hz-PE micelles. Sample was then divided into equal volumes and treated for different pH incubation. For pH 7.4 treatment, a 50 μL aliquot of the first half of the micelle formulation was applied, as is, to a Shodex KW-804 size exclusion column at regular intervals using pH 7.4 Phosphate buffer (100 mM phosphate, 150 mM sodium sulfate) was used as the eluent and run at 1.0 mL/min. Both UV (from 200 to 400 nm) and fluorescence (550/590) was used to monitor the micelles. To the second half of the micelle formulation an appropriate volume of 1 N HCl was added to get a final pH of ~5.0, aliquots of which were then analyzed as above at different intervals. As a control, micelles of $mPEG_{2000}$-PE (non-pH-sensitive micelles) were prepared and analyzed after treatment at both the pH values as above.

Kinetics of the pH-Dependent Degradation of $mPEG_{2000}$-Hz-PE. The degradation of the micelles spontaneously formed by $mPEG_{2000}$-Hz-PE under the action of the acidic pH was studied by following the presence or absence of micelles over the period of time in buffer solutions of different pHs (i.e. pH values 6.0, 7.0, 8.0, and 10). Rh-PE-labeled micelles of $mPEG_{2000}$-Hz-PE conjugate were prepared in phosphate buffer (10 mM phosphate, 150 mM NaCl) solutions of different pH values. The pH of the solution was adjusted using appropriate amounts of either 1 N HCl or NaOH. 50 μL aliquots were sampled out at different time intervals for size exclusion chromatographic analysis in 100 mM phosphate buffer (pH 7.0) containing 150 mM sodium sulfate using a fluorescence detector (EX: 550 nm, EM: 590 nm). The area under the micelle peak (mean retention time: 9.35 min) was determined for each chromatogram.

Preparation of pH-sensitive DDS. *Micelles.* For micelle preparations, a mixture of $mPEG_{750}$-PE, pH-sensitive $mPEG_{2000}$-Hz-PE, biotin-PE (or TATp-PE), and Rh-PE at molar ratio of 40:54:5:1 was prepared in chloroform. Chloroform was removed on a rotary evaporator followed by freeze-drying on a Freezone 4.5 (Labconco, Kansas City, MO). The film was hydrated with PBS, pH 8.0 (10 mM phosphate, 150 mM sodium chloride), at room temperature and vortexed for 5 min. Micelle size was controlled by using a Coulter N4 Plus submicron particle analyzer.

Liposomes. For liposome preparations, a mixture of phosphatidylcholine and cholesterol in 6:3 molar ratio and with the addition of various quantities (up to 18% mol) of PEG_{5000}-Hz-PE or $mPEG_{5000}$-PE was prepared in chloroform. When required, the composition for liposome preparation was supplemented with 0.5 to 1% mol of TATp- PEG_{2000}-PE (prepared as described earlier in (*13*)) and with 0.5% mol of Rh-PE (for the fluorescent labeling). Chloroform was removed on a rotary evaporator followed by freeze-drying on a Freezone 4.5 (Labconco, Kansas City, MO). The film obtained was hydrated with HBS buffer (pH 8.0) at room temperature for 5 min. The lipid dispersion was extruded 20 times through polycarbonate filters (pore size 200 nm) by using a Micro extruder (Avanti). Vesicle size was controlled by using a Coulter N4 Plus submicron particle analyzer.

Preparation of Immunocarriers. First, mAb 2G4 or nonspecific control bovine IgG was conjugated to pNP-PEG_{3400}-PE as in (*27*) with some modifications. Briefly, pNP-PEG_{3400}-PE and $mPEG_{750}$-PE was dried in a rotary evaporator and freeze-dryer to form a thin film. The film was hydrated with 5mM citrate buffered saline, pH 5.0, and vortexed. Antibody solution was prepared in 50mM tris-buffered saline, pH 8.7 and incubated with a 10-fold molar excess of pNP-PEG_{3400}-PE for 24 h at 4 °C to allow the attachment of the antibody to the activated PEG terminus with the simultaneous hydrolysis of nonreacted pNP groups, thus forming the antibody−micelle solution. Then, the required aliquot of this solution was added to liposomes or micelles prepared as described above and incubated for about 1 h to allow for the quantitative incorporation of the modified antibody into the appropriate DDS (*29*).

ELISA. An ELISA assay (indirect, using an enzyme-tagged secondary Ab) was performed to show the ability of the pH-sensitive immunocarriers to recognize the target antigen at different pH values (pH 8.0 and 5.0).

First, ELISA plates were coated with 50 μL of 10 μg/mL cardiac myosin and incubated overnight at 4 °C. Then, each well was washed three times with 200 μL of TBST (TBS containing 0.05% w/v Tween-20), and incubated with 50 μL of serial dilutions of 2G4 antibody (or nonspecific IgG) in TBST-casein (TBST with 2 mg/mL casein) for 1 h at RT. After incubation, the wells were washed as before and incubated with 50 μL/well of 1:5000 dilution of goat anti-mouse IgG peroxidase conjugate (ICN Biomedicals, Inc., Aurora, OH) in TBST-Casein for 1 h at RT. The wells were again washed as before, and each well was incubated with 100 μL of enhanced Kblue TMB peroxidase substrate (Neogen Corporation, Lexington, KY) for 15 min. The microplate was read at a dual wavelength of 620 nm with the reference filter at 492 nm using a Labsystems Multiskan MCC/340 microplate reader installed with GENESIS-LITE windows based microplate software.

Biotin−Avidin Binding. To test the binding of biotin-bearing Rh-PE-labeled DDS before and after incubation at lowered pH values, the corresponding samples were kept for 15 min at pH 8.0 or pH 5.0 and then applied onto the Immobilized NeutrAvidin protein column. The degree of the retention of the corresponding preparation on the column was estimated following the decrease in the sample rhodamine fluorescence at 550/590 nm after passing through the NeutrAvidin column.

Interaction of TATp-Containing pH-Sensitive DDS with

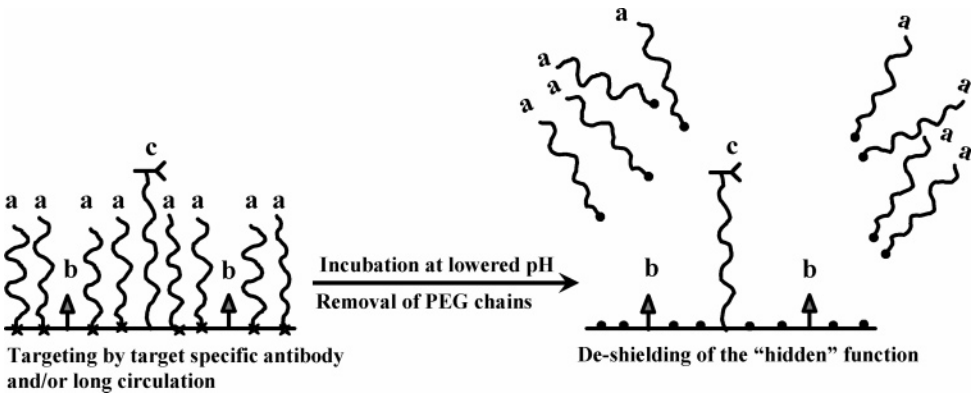

Figure 2. Schematic for the design of the multifunctional DDS used in this study that includes pH-cleavable PEG-Hz-PE (a), temporarily "shielded" biotin or TATp (b), and monoclonal antibody (c) attached to the surface of DDS via pH-noncleavable spacer.

Cells. For experiments with the micelles, NIH 3T3 cells (fibroblasts) have been chosen. After the initial passage in tissue culture flasks, NIH 3T3 cells were grown on coverslips in six-well tissue culture plates (100 000 cells per well) in DMEM with 10% BSA. After 48 h the plates were washed twice with PBS, pH 7.4 and then treated with various Rh-PE-labeled micelle samples (without and with preincubation for 15 min at pH 5.0) in serum-free medium (2 mL/well, 30 mg total PEG-PE/mL). After a 1 h incubation period, the media were removed and the plates washed with serum-free medium three times. Individual coverslips were mounted cell-side down onto fresh glass slides with PBS. Cells were viewed with a Nikon Eclipse E400 microscope under bright light or under epifluorescence with rhodamine/TRITC.

For experiments with the liposomes, U-87 MG cells (astrocytoma) have been chosen. After the initial passage in tissue culture flasks, U-87 MG cells were grown on coverslips in six-well tissue culture plates (20 000 cells per well) in DMEM with 10% BSA. After 48 h the plates were washed twice with PBS, pH 7.4, and then treated with various Rh-PE-labeled liposome samples (with and without preincubation for 20 min at pH 5.0) in serum-free medium (2 mL/well, 30 mg total lipid/mL). After a 1 h incubation period, the media were removed and the plates washed with serum-free medium three times. Individual coverslips were mounted cell-side down onto fresh glass slides with PBS. Cells were viewed with a Nikon Eclipse E400 microscope under bright light or under epifluorescence with rhodamine/TRITC.

RESULTS AND DISCUSSION

The particular design of the multifunctional DDS we have used in this study is presented in Figure 2. The suggested DDS (liposome or micelle) bears on its surface a "hidden" function (we have used biotin and TATp moieties for this purpose) inserted into the liposome membrane or micelle core via its modification with a PE moiety, protecting PEG chains (PEG_{2000}) attached to the surface via the pH-cleavable bond, and a specific antibody attached to the surface via a noncleavable long PEG spacer (PEG_{3400}). In some experiments with liposomes, cleavable PEG_{5000}-Hz-PE and noncleavable TATp-PEG_{2000}-PE conjugates have been used. Such DDS are expected to demonstrate specific targeted properties (via antibody-mediated recognition) at both normal (7.4−8.0) and acidic (5.0−6.0) pH values; however, the incubation of the DDS at lowered pH should eliminate (detach) protecting PEG chains and deshield the second function, i.e., after the exposure to the lowered pH, in addition to the immune recognition, such DDS should acquire the ability to bind with avidin column if the second, "hidden" function is biotin, or to demonstrate better internalization by cells if the second, "hidden" function is TATp. As an antibody, we have used the cardiac myosin-specific monoclonal 2G4 antibody (mAb 2G4) (*30*). The coupling of mAb 2G4 and biotin or TATp to the DDS surface was performed using the reactive derivative of poly(ethylene glycol)-phosphatidylethanolamine conjugate (PEG-PE) activated at free PEG terminus with a *p*-nitrophenylcarbonyl (pNP) group (pNP-PEG-PE) according to the protocol developed by us earlier (*27*).

Synthesis of pH-Cleavable PEG-PE Conjugate. The scheme of the synthesis of PEG-PE conjugated via the pH-cleavable hydrazone group (PEG-Hz-PE) is shown in the Figure 3. The synthesis was carried out in two steps. The first step involves the conjugation of 3-(2-pyridyldithio) propionyl hydrazide (PDPH) to $mPEG_{2000}$-CHO. The hydrazide group in PDPH reacts with the aldehyde group of $mPEG_{2000}$-CHO to form the acidic-pH-labile hydrazone bond. Since this bond is vulnerable to hydrolysis, efforts were taken to carry out the reaction in anhydrous conditions. Use of PDPH as the cross linker not only offers the advantage of forming the hydrazone bond but also introducing pyridyldisulfanyl groups for subsequent conjugation of PEG to the thiol component of 1,2-dipalmitoyl-*sn*-glycero-3-phosphothioethanol (PE-SH) in the second step of the synthesis. The PE-SH in the conjugate serves as a hydrophobic anchor to ensure its association with the lipid bilayer of the liposome or the hydrophobic core of micelles. All steps of the reaction were followed on TLC to confirm the progress of the reaction. The structure of the final conjugate, $mPEG_{2000}$-phospatidylethanolamine hydrazone ($mPEG_{2000}$-Hz-PE), was confirmed by the proton NMR characterization: ^{1}H NMR (500 MHz, $CDCl_3$) δ (ppm) for $mPEG_{2000}$-Hz-PE: 0.87 (t, CH_3 of lipid, 6H), 1.27 (b,s, CH_2, ≈ 56H), 2.29 (t, $OCOCH_2$, 4H), 2.40 (t, $COCH_2CH_2S$, 2H), 2.45 (t, SCH_2CH_2O, 2H), 2.5 (t, $COCH_2$-CH_2S, 2H), 2.59 (m, $CH_2CH{=}N$, 2H), 3.1 (t, CH_2CH, 2H), 3.39 (s, OCH_3 of PEG, 3H) and 3.5 (bm, PEG, ≈ 184H).

The stability of the conjugate and the kinetics of its degradation were analyzed by size-exclusion HPLC, following the area under the micelle peak on the chromatogram after conjugate incubation for different time intervals at different pH values (the conjugate spontaneously forms micelles in aqueous solutions similar to "normal" PEG-PE conjugate). Rhodamine-PE was incorporated into the micelles as a fluorescent tag, and the sample was monitored using a fluorescence detector with excitation at 550 nm and emission at 590 nm. As a typical example, HPLC for $mPEG_{2000}$-Hz-PE is shown in Figure 4; after appropriate pH treatment, the peak at retention time 9.7 min (peak for micelle) observed in case of intact micelle (pH 8.0) disappears after the incubation at pH 5.0. This disappearance of the peak is indicative of the destruction of the micelle structure due to the loss of PEG corona, while non-pH-sensitive micelles produce the peak at both pH values. Table 1 shows the representative data for the degradation kinetics of PEG_{2000}-

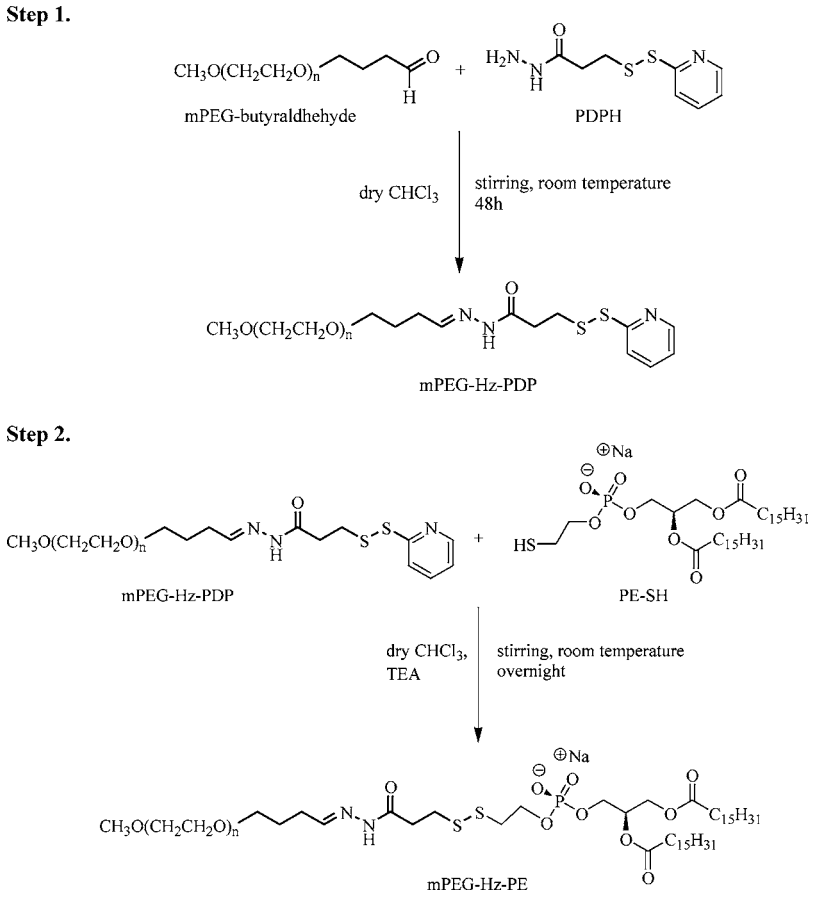

Figure 3. Schematic description of the conjugation reaction.

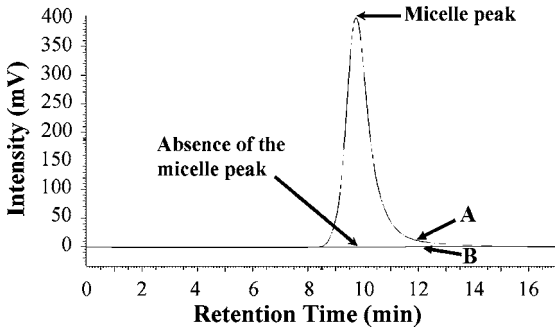

Figure 4. HPLC analysis of the pH-sensitive mPEG$_{2000}$-Hz-PE micelles after incubation in pH 8.0 (A) and after incubation in pH 5 (B) at room temperature.

Table 1. PEG$_{2000}$-Hz-PE Micelle Stability at Different pH Values (as percent of remaining micelles)

incubation tim, mine	pH 5.0	pH 7.0	pH 8.0	pH 10.0
20	3	56	94	99
40	2.5	28	62	99
60	2	10	53	99

Hz-DPPE micelles at different pH values. It is clearly seen from there that such micelles are quite stable at high pH value (8 and above), and they disintegrate within a few minutes at pH 5.0. This result was also confirmed by the TLC, when two different spots of PEG and PE were observed after a few minutes of incubation at pH 5.0 with no spot of PEG-PE seen after the incubation (data not shown).

Characterization of Liposomes and Micelles. According to the particle size analysis data, all prepared liposomes had the size within the 120-to-160 nm interval; micelle size was within the 7-to-15 nm interval. Critical micellation concentration (CMC) for both hydrolizable and nonhydrolyzable PEG-PE

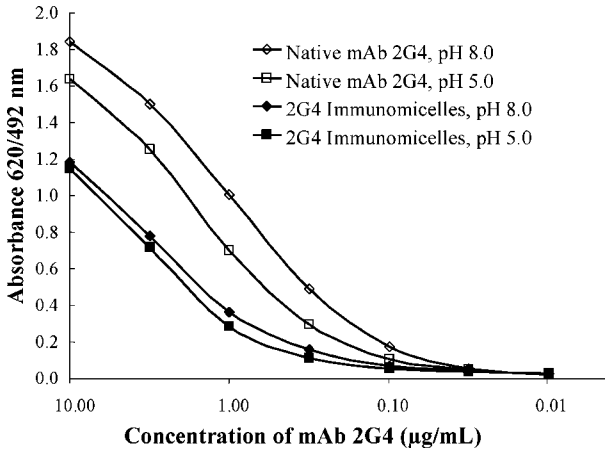

Figure 5. Binding of antimyosin mAb 2G4-PEG$_{2000}$-Hz-PE-immunomicelles to a monolayer of dog cardiac myosin in comparison to the native mAb 2G4 at corresponding pH values.

conjugates determined by the pyrene method as in ref 31 was around 1.1×10^{-5} M. The average number of antibody molecule per single 150 nm liposome determined as in ref 29 was between 60 and 80; the average number of antibody molecules per single 10 nm micelle was around 5.

Immunoreactivity of Multifunctional DDS. Fully assembled 2G4 antibody-bearing DDS demonstrated clear immunoreactivity toward the antigen. The monolayer of dog cardiac myosin in the standard ELISA test at both tested pH values, 8.0 and 5.0, are shown in Figure 5 (the results for PEG-PE-based 2G4-immunomicelles are shown). Although, one can observe some affinity decrease for the antibodies modified with the pNP-PEG-PE anchor and incorporated into the micelle structure (the same pattern is observed for immunoliposomes), this decrease is more

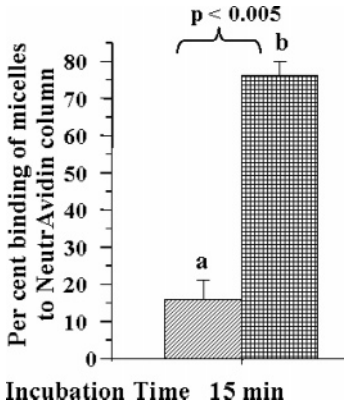

Figure 6. Binding of pH-sensitive biotin-micelles to NeutrAvidin columns after 15 min incubation at room temperature at pH 8.0 (a) and at pH 5.0 (b).

apparent than real, since not all DDS-attached antibodies, even if they remain active, can interact with the substrate because of their steric orientation on the DDS surface. In a previous study it was shown that this reduction of activity in some of the antibodies is well compensated by the multipoint interaction of the DDS with the target (*32*, *33*). Thus, the systems prepared are immunologically active at both chosen pH values. Control preparations bearing a nonspecific IgG exhibited no binding to myosin at any pH.

Avidin Binding of Multifunctional Biotin-Containing DDS. The avidin−biotin complexation was used initially as an easy-to-handle test system to follow the shielding and deshielding of the second hidden function in pH-sensitive DDS. Liposomes and micelles containing 5% mol of the biotin-PE in addition to 2G4-PEG_{3400}-PE and pH-sensitive PEG_{2000}-Hz-PE have been prepared and labeled with rhodamine-PE, and their ability to interact with avidin (NeutrAvidin affinity column) was investigated at pH 8.0 and after the brief (15 min) exposure at the lowered pH of 5.0. It was found that although biotin-containing 2G4-DDS have demonstrated identical immunoreactivity at both pH values, their ability to bind with avidin was dramatically different at pH 8.0 and after 15 min incubation at pH 5.0, which was expected to cleave away a substantial portion of the shielding PEG_{2000} micelle corona (or liposome coating). The data in Figure 6 (for micellar DDS) clearly show that while at pH 8.0 only about 15% of micelles were retained by the avidin column, after 15 min incubation at pH 5.0 about 75% of micelles were retained (the degree of the binding was estimated following the decrease in the sample rhodamine fluorescence at 550/590 nm after passing through the avidin column). This result clearly confirms that the elimination of the pH-cleavable PEG coat deshields the hidden biotin function and allows for more biotin moieties to interact with avidin on the column.

TATp-Mediated Interaction of Multifunctional DDS with Cells in Vitro. For cell culture experiments, we have used rhodamine-labeled DDS similar to those described above but containing TATp moieties attached to their surface instead of biotin groups. In this case, we have investigated DDS internalization by various cells (nontargets for the 2G4 antibody) at pH 8.0 and after the brief (20−30 min) exposure at the pH 5.0. It was found that TATp-containing DDS have also demonstrated a dramatically different ability to interact with cells at pH 8.0 and after the incubation at pH 5.0, which was expected to cleave away a substantial portion of the shielding PEG_{2000} micelle corona (or liposome coating). The data in Figure 7 clearly show that while cleavable PEG-PE-based TATp-containing micelles kept at pH 8.0 show only marginal association with NIH-3T3 murine fibroblasts, the same micelles preincubated for 30 min at pH 5.0 demonstrated dramatically enhanced association with the cells (higher fluorescence), i.e., better accessibility of TATp

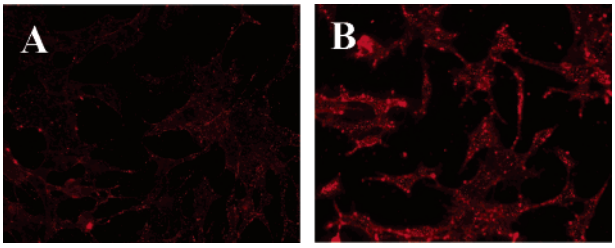

Figure 7. Fluorescence microscopy showing internalization of Rh-PE-labeled-TATp containing micelles by NIH 3T3 fibroblast cells after incubating micelles at pH 8.0 (A) and pH 5.0 (B) for 30 min.

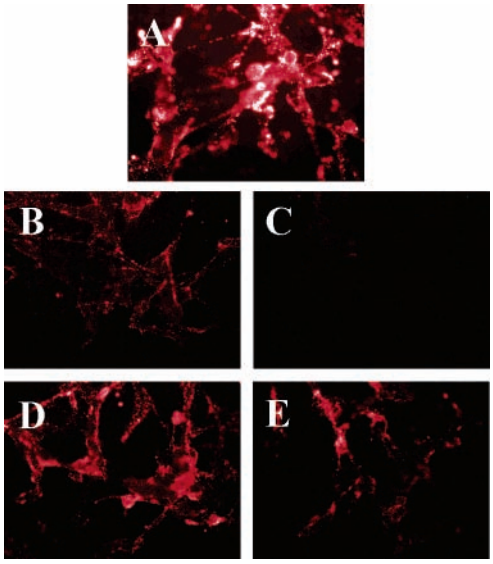

Figure 8. Fluorescence microscopy showing internalization of Rh-PE-labeled-TATp containing liposomes by U-87 MG astrocytoma cells using PEG-free TATp-liposomes (A), 9% mol pH-noncleavable PEG-PE at pH 7.4 (B), 18% mol pH-noncleavable PEG-PE at pH 7.4 (C), 9% mol pH-cleavable PEG-Hz-PE after incubation at pH 5.0 for 20 min (D)*, and 18% mol pH-cleavable PEG-Hz-PE after incubation at pH 5.0 for 20 min (E)*. *The pH of these formulations was raised back to pH 7.4 after their incubation at pH 5.0 and prior to incubation with cells.

moieties for cell interaction. In case of TAT-bearing liposomes (Figure 8), we have shown that the incorporation of 9% mol of PEG-PE strongly diminished TATp-uptake of liposomes (Figure 8B), and the incorporation of 18% mol of PEG-PE completely eliminated it (Figure 8C). However, when pH-degradable PEG-PE was used, 20 min preincubation of both preparations at pH 5.0 significantly increased the association of both preparations with cells, bringing the cell binding of the liposomes with 9% mol PEG (Figure 8D) almost back to the level of PEG-free TATp-liposomes (Figure 8A) and significantly improving the cell binding of the TATp-liposomes with 18% mol of the initial PEG (Figure 8E). These results clearly confirm that the elimination of the pH-cleavable PEG coat deshields the hidden TATp function and allows for better association of DDS with cells.

The development of the double-targeted drug carriers, which, in addition to prolonged circulation (via the attached PEG) and target recognition (via the attached antibody) carry the temporarily hidden function that can develop under the action of certain local stimuli (such as lowered pH), represent a significant step on the way toward "smart" multifunctional pharmaceutical nanocarriers capable of both target accumulation and intracellular penetration in a controlled fashion.

ACKNOWLEDGMENT

This work was supported by the NIH grants R01 HL55519 and R01 EB001961 to Vladimir P. Torchilin.

LITERATURE CITED

(1) Maeda, H., Wu, J., Sawa, T., Matsumura, Y., and Hori, K. (2000) Tumor vascular permeability and the EPR effect in macromolecular therapeutics: a review. *J. Controlled Release 65*, 271−84.

(2) Palmer, T. N., Caride, V. J., Caldecourt, M. A., Twickler, J., and Abdullah, V. (1984) The mechanism of liposome accumulation in infarction. *Biochim. Biophys. Acta 797*, 363−8.

(3) Jaracz, S., Chen, J., Kuznetsova, L. V., and Ojima, I. (2005) Recent advances in tumor-targeting anticancer drug conjugates. *Bioorg. Med. Chem. 13*, 5043−54.

(4) Torchilin, V. P. (2004) Targeted polymeric micelles for delivery of poorly soluble drugs. *Cell Mol. Life Sci. 61*, 2549−59.

(5) Gabizon, A., Shmeeda, H., Horowitz, A. T., and Zalipsky, S. (2004) Tumor cell targeting of liposome-entrapped drugs with phospholipid-anchored folic acid-PEG conjugates. *Adv. Drug Delivery Rev. 56*, 1177−92.

(6) Widera, A., Norouziyan, F., and Shen, W. C. (2003) Mechanisms of TfR-mediated transcytosis and sorting in epithelial cells and applications toward drug delivery. *Adv. Drug Delivery Rev. 55*, 1439−66.

(7) Gupta, B., Levchenko, T. S., and Torchilin, V. P. (2005) Intracellular delivery of large molecules and small particles by cell-penetrating proteins and peptides. *Adv. Drug Delivery Rev. 57*, 637−51.

(8) Lochmann, D., Jauk, E., and Zimmer, A. (2004) Drug delivery of oligonucleotides by peptides. *Eur. J. Pharm. Biopharm. 58*, 237−51.

(9) Torchilin, V. P. (2005) Lipid-core micelles for targeted drug delivery. *Curr. Drug Delivery 2*, 319−27.

(10) Torchilin, V. P. (2005) Recent advances with liposomes as pharmaceutical carriers. *Nat. Rev. Drug Discovery 4*, 145−60.

(11) Maheshwari, A., Mahato, R. I., McGregor, J., Han, S., Samlowski, W. E., Park, J. S., and Kim, S. W. (2000) Soluble biodegradable polymer-based cytokine gene delivery for cancer treatment. *Mol. Ther. 2*, 121−30.

(12) Tachibana, R., Harashima, H., Shono, M., Azumano, M., Niwa, M., Futaki, S., and Kiwada, H. (1998) Intracellular Regulation of Macromolecules Using pH-Sensitive Liposomes and Nuclear Localization Signal: Qualitative and Quantitative Evaluation of Intracellular Trafficking. *Biochem. Biophys. Res. Commun. 251*, 538−544.

(13) Torchilin, V. P., Rammohan, R., Weissig, V., and Levchenko, T. S. (2001) TAT peptide on the surface of liposomes affords their efficient intracellular delivery even at low temperature and in the presence of metabolic inhibitors. *Proc. Natl. Acad Sci. U.S.A. 98*, 8786−91.

(14) Wattiaux, R., Laurent, N., Wattiaux-De Coninck, S., and Jadot, M. (2000) Endosomes, lysosomes: their implication in gene transfer. *Adv. Drug Delivery Rev. 41*, 201−208.

(15) Caron, N. J., Torrente, Y., Camirand, G., Bujold, M., Chapdelaine, P., Leriche, K., Bresolin, N., and Tremblay, J. P. (2001) Intracellular delivery of a Tat-eGFP fusion protein into muscle cells. *Mol. Ther. 3*, 310−8.

(16) Vives, E., Brodin, P., and Lebleu, B. (1997) A truncated HIV-1 Tat protein basic domain rapidly translocates through the plasma membrane and accumulates in the cell nucleus. *J. Biol. Chem. 272*, 16010−7.

(17) Fawell, S., Seery, J., Daikh, Y., Moore, C., Chen, L. L., Pepinsky, B., and Barsoum, J. (1994) Tat-mediated delivery of heterologous proteins into cells. *Proc. Natl. Acad. Sci. U.S.A. 91*, 664−8.

(18) Rudolph, C., Plank, C., Lausier, J., Schillinger, U., Muller, R. H., and Rosenecker, J. (2003) Oligomers of the arginine-rich motif of the HIV-1 TAT protein are capable of transferring plasmid DNA into cells. *J. Biol. Chem. 278*, 11411−8.

(19) Santra, S., Yang, H., Holloway, P. H., Stanley, J. T., and Mericle, R. A. (2005) Synthesis of water-dispersible fluorescent, radio-opaque, and paramagnetic CdS: Mn/ZnS quantum dots: a multifunctional probe for bioimaging. *J. Am. Chem. Soc. 127*, 1656−7.

(20) Schwarze, S. R., Ho, A., Vocero-Akbani, A., and Dowdy, S. F. (1999) In vivo protein transduction: delivery of a biologically active protein into the mouse. *Science 285*, 1569−72.

(21) Torchilin, V. P., Levchenko, T. S., Rammohan, R., Volodina, N., Papahadjopoulos-Sternberg, B., and D'Souza, G. G. (2003) Cell transfection in vitro and in vivo with nontoxic TAT peptide-liposome-DNA complexes. *Proc. Natl. Acad. Sci. U.S.A. 100*, 1972−7.

(22) Zhao, M., Kircher, M. F., Josephson, L., and Weissleder, R. (2002) Differential conjugation of tat peptide to superparamagnetic nanoparticles and its effect on cellular uptake. *Bioconjugate Chem. 13*, 840−4.

(23) Mai, J. C., Shen, H., Watkins, S. C., Cheng, T., and Robbins, P. D. (2002) Efficiency of protein transduction is cell type-dependent and is enhanced by dextran sulfate. *J. Biol. Chem. 277*, 30208−18.

(24) Vives, E., Richard, J. P., Rispal, C., and Lebleu, B. (2003) TAT peptide internalization: seeking the mechanism of entry. *Curr. Protein Pept. Sci. 4*, 125−32.

(25) Snyder, E. L., and Dowdy, S. F. (2004) Cell penetrating peptides in drug delivery. *Pharm. Res. 21*, 389−93.

(26) Wadia, J. S., Stan, R. V., and Dowdy, S. F. (2004) Transducible TAT-HA fusogenic peptide enhances escape of TAT-fusion proteins after lipid raft macropinocytosis. *Nat. Med. 10*, 310−5.

(27) Torchilin, V. P., Levchenko, T. S., Lukyanov, A. N., Khaw, B. A., Klibanov, A. L., Rammohan, R., Samokhin, G. P., and Whiteman, K. R. (2001) *p*-Nitrophenylcarbonyl-PEG-PE-liposomes: fast and simple attachment of specific ligands, including monoclonal antibodies, to distal ends of PEG chains via *p*-nitrophenylcarbonyl groups. *Biochim. Biophys. Acta 1511*, 397−411.

(28) Hansen, C. B., Kao, G. Y., Moase, E. H., Zalipsky, S., and Allen, T. M. (1995) Attachment of antibodies to sterically stabilized liposomes: evaluation, comparison and optimization of coupling procedures. *Biochim. Biophys. Acta 1239*, 133−44.

(29) Torchilin, V. P., Lukyanov, A. N., Gao, Z., and Papahadjopoulos-Sternberg, B. (2003) Immunomicelles: targeted pharmaceutical carriers for poorly soluble drugs. *Proc. Natl. Acad. Sci. U.S.A. 100*, 6039−44.

(30) Liang, W., Levchenko, T., Khaw, B. A., and Torchilin, V. (2004) ATP-containing immunoliposomes specific for cardiac myosin. *Curr. Drug Delivery 1*, 1−7.

(31) Lukyanov, A. N., Gao, Z., Mazzola, L., and Torchilin, V. P. (2002) Polyethylene glycol-diacyllipid micelles demonstrate increased accumulation in subcutaneous tumors in mice. *Pharm. Res. 19*, 1424−9.

(32) Klibanov, A. L., Muzykantov, V. R., Ivanov, N. N., and Torchilin, V. P. (1985) Evaluation of quantitative parameters of the interaction of antibody-bearing liposomes with target antigens. *Anal. Biochem. 150*, 251−7.

(33) Lukyanov, A. N., Elbayoumi, T. A., Chakilam, A. R., and Torchilin, V. P. (2004) Tumor-targeted liposomes: doxorubicin-loaded long-circulating liposomes modified with anti-cancer antibody. *J Controlled Release 100*, 135−44.

BC060080H

Synthesis of Twisted Intercalating Nucleic Acids Possessing Acridine Derivatives. Thermal Stability Studies

Imrich Géci, Vyacheslav V. Filichev, and Erik B. Pedersen*

Nucleic Acid Center, Department of Chemistry, University of Southern Denmark, Campusvej 55, DK-5230, Odense M, Denmark. Received March 7, 2006; Revised Manuscript Received May 3, 2006

Twisted intercalating nucleic acids (TINA) possessing acridine derivatives have been synthesized via the postsynthetic modifications of oligonucleotides possessing insertions of (*R*)-1-*O*-(4-iodobenzyl)glycerol (**8**) or (*R*)-1-*O*-(4-ethynylbenzyl)glycerol (**9**) at the 5′-end or in the middle as a bulge. In the first postsynthetic step, oligonucleotides **8** and **9** on the CPG support were treated with a Sonogashira coupling reaction mixture containing 9-chloro-2-ethynylacridine or 9-chloro-2-iodoacridine, respectively. After the postsynthetic step, treatment of the oligonucleotides with 32% aq ammonia or 50% ethanolic solution of tris(2-aminoethyl)amine led to the substitution of chloride on acridine concurrent with deprotection of the bases and cleavage of the oligonucleotides from CPG. Molecular modeling of the parallel triplex with a bulged insertion of the monomer (*R*)-3-*O*-[4-(9-aminoacridin-2-ylethynyl)benzyl]glycerol in the triplex-forming oligonucleotide (TFO) showed that the acridine moiety was stacking between the bases of the duplex, while phenyl was placed between the bases of the TFO. Thermal denaturation studies and fluorescence properties of TINA-acridine oligonucleotide duplexes and triplexes are discussed.

INTRODUCTION

Although double-stranded DNA (dsDNA) has long been known to form a triple-helical structure, only recently, new strategies of using triplexes in molecular biology became largely investigated. The sequence-specific recognition of dsDNA by triplex-forming oligonucleotide (TFO) has led to the transcriptional control, sequence selective treatment of genomic DNA aiming for mutated or recombined genes (*1*). Because of low stability of triplexes at physiological pH, much effort has been devoted to modifying the TFO to achieve better triplex stability.

Derivatives of 9-aminoacridine are well-known due to their broad biological activities. They are ascribed to the ability of planar acridine to stack between the nucleic acids bases (*2*). Derivatives of 6-chloro-2-methoxy-acridin-9-ylamine have been used for triplex stabilization as oligonucleotide conjugates, when covalently linked to the TFO in the middle or at the end of the sequence (*3*−*8*). In the case of 3′−3′ alternate-strand triple helix complexes, the stabilization effect has been observed, when the acridine moiety was placed on the nucleotide base flanking the 3′−3′ junction (*9*). 9-Aminoacridine conjugates stabilized Hoogsteen type triplexes with a single base pair inversion, when inserted to the oligonucleotide via a hexyl linker as a bulge. On the other hand, the absence of base pair inversion, or introduction of double base pair inversion, led to destabilization (*10*, *11*).

Recently, we observed the extraordinary stable Hoogsteen type triplexes and duplexes, when the monomer (*R*)-1-*O*-[4-(1-pyrenylethynyl)benzyl]glycerol (**1**, Figure 1) was inserted as a bulge in the middle of the TFO (*12*). At the same time, Watson−Crick duplexes were destabilized. Moreover, TINA was able to discriminate between matched and mismatched sequences. It was supposed that twisting around the triple bond could help the intercalator to fit properly inside of the dsDNA part of the triplex. Because of this property, this type of oligonucleotide was called a twisted intercalating nucleic acid (TINA).

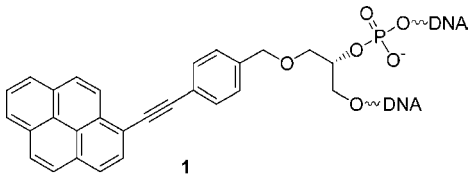

1

Figure 1. TINA monomer.

In our present study, we focused on the synthesis of TINA bearing acridine derivatives instead of a pyrene-1-yl moiety in the structure of **1**. We suppose that this replacement should also lead to a high thermal stability of Hoogsteen type triplexes, as we have already seen for the naphthalene and pyrene systems (*12*). Acridine is also an attractive substituent for the incorporation of functional groups in different positions of the aromatic ring. This can be further exploited in the construction of peptide−oligonucleotide conjugates for delivery of DNA into the cell nucleus (*13*).

Here, we report the postsynthetic synthesis of (*R*)-3-*O*-[4-(9-aminoacridin-2-ylethynyl)benzyl]glycerol (**X**) and (*R*)-3-*O*-[4-(9-{2-[bis-(2-aminoethyl)amino]ethylamino}acridin-2-ylethynyl)benzyl]glycerol (**Y**) for the synthesis of the oligonucleotides **11** and **12**, respectively. Such incorporations led to an increased stability of parallel triplexes in comparison with unmodified triplexes, which were also correlated with molecular modeling and fluorescence studies.

EXPERIMENTAL PROCEDURES

Materials. Solvents were purchased from Bie and Berenstein Co., and chemicals were purchased from Aldrich Chemical Co. Solvents were sufficiently dried before they were used, and chemicals were used as purchased. Thin-layer chromatography (TLC) analyses were carried out with use of TLC plates 60 F254 purchased from Merck and were visualized in an UV light (254 nm). The silica gel (0.040−0.063 mm) used for column chromatography was purchased from Merck. Solvents used for column chromatography were distilled prior to use.

* To whom correspondence should be addressed. Phone: (+45) 6550-2555; fax: (+45) 6615-8780; e-mail: ebp@chem.sdu.dk.

10.1021/bc060058o CCC: $33.50 © 2006 American Chemical Society
Published on Web 06/21/2006

Spectroscopy. NMR spectra were measured on a Varian Gemini 2000 spectrometer at 300 MHz for ^{1}H using TMS (δ: 0.00) as an internal standard and at 75 MHz for ^{13}C using $CDCl_3$ (δ: 77.0) as an internal standard. Mass spectra of the synthesized compounds were determined on the Ionspec 4.7 T HiResMALDI Ultima Fourier transform (FT) mass spectrometer (Ion Spec, Irvine, CA). The $[M + Na]^+$ ions were peak matched using ions derived from the 2,5-dihydroxybenzoic acid matrix. Electrospray ionization mass spectra (ESI-MS) were performed on 4.7 T HiResESI Ultima (FT) mass spectrometer. Both spectrometers are controlled by the OMEGA Data System. MALDI-TOF mass spectra of isolated oligodeoxynucleotides (ONs) were determined on a Voyager Elite biospectrometry research station (PerSeptive Biosystems).

Molecular Modeling. Molecular modeling experiments and the construction of the modified triplex were performed using the program MacroModel 8.0. 2-Phenylethynyl-9-aminoacridine was energy-minimized with MM3 method before being inserted to the triplex. The starting 14-mer parallel triplex was built via consecutive superimposition of triples (CGC) and (TAT), which were generated with Insight II v9.72 from MSI and transported to MacroModel.

The insertion of the acridine intercalator was done in several steps. TFO was disconnected by deletion of the phosphate group in place of the predicted bulged insertion. Afterward, 2-phenylethynyl-9-aminoacridine was placed between the bases of the triplex, and minimization was performed to extend the triplex and create enough space for the intercalator. The triplex was reconnected by addition of the two phosphate groups with an ethyleneglycol linker between, which were supposed to be a part of the linker. The structure was again minimized. The intercalator was connected to the TFO backbone by creating the site chain, taking into consideration the stereochemistry of the linker and the whole structure possessing (*R*)-3-*O*-[4-(9-aminoacridin-2-ylethynyl)benzyl]glycerol as a bulge was again energy-minimized.

All molecular dynamics simulations were achieved with the AMBER* force field. The stochastic dynamics calculation generating 250 structures was performed using a water solvent model and extended cutoff potential. The simulation temperature was 300 K, the simulation time was 400 ps, and the equilibration time was 100 ps. In the next step, all 250 structures were minimized at the same time by a multiple minimization method. For classification of founded conformations, the XCluster program was used, in which the lowest energy representative structure was selected.

Measurement of Melting Temperatures (T_m). Melting profiles were measured on a Perkin-Elmer UV/vis spectrometer Lambda 35 fitted with a PTP-6 temperature programmer. The parallel triplexes were formed by mixing the two strands of the Watson−Crick duplex each at a concentration of 1.0 μM and the TFO at a concentration of 1.5 μM in the corresponding buffer solution. The solution was heated to 80 °C for 5 min and afterward cooled to 15 °C for 30 min. The antiparallel duplexes were formed by mixing the two strands, each at a concentration of 1.0 μM in the corresponding buffer solution followed by heating to 70 °C for 5 min and then cooling to room temperature. The absorbance of both triplexes and duplexes was measured at 260 nm from 10 to 70 °C with a heating rate of 1.0 °C/min. The melting temperatures (T_m, °C) were determined as the maximum of the first derivative plots of the melting curves.

Fluorescence Measurements. Fluorescence measurements were carried out on a Perkin-Elmer luminescence spectrometer LS-55 fitted with a Julabo F25 temperature controller. The spectra were recorded at 10 °C in the same buffer solution as for T_m studies using a 1.0 μM concentration of each ON. The excitation slit was set to 4 nm, and the excitation wavelength was 322 nm. The emission slit for **ON11** and **ON12** was set to 2.5 nm and for **ON4** and **ON5** was set to 0 nm.

Synthesis of 9-Chloro-2-ethynylacridine (3). 9-Chloro-2-iodoacridine (**2**, ref *17*) (0.34 g, 1 mmol), $PdCl_2(PPh_3)_2$ (14 mg, 0.02 mmol), and CuI (8 mg, 0.04 mmol) were added to a round-bottomed flask flushed with Ar. The flask was again flushed for the next 5 min with Ar. Afterward, THF (3 mL) and Et_3N (1 mL) were added, and Ar was bubbled through the mixture for 10 min. Trimethylsilylacetylene (TMSA, 0.155 mL, 1.1 mmol) was added, and the reaction was completed after 30 min at room temperature under Ar. The solvent was evaporated in vacuo. The residue was dissolved in CH_2Cl_2 (15 mL) and washed with H_2O (3 × 20 mL). The organic layer was dried (Na_2SO_4), filtered, and evaporated in vacuo. The crude product was purified using silica gel dry column vacuum chromatography with cyclohexan/acetone (1%, v/v). 9-Chloro-2-trimethylsilylethynylacridine was obtained in 98% yield (0.15 g) as a yellow powder. ^{1}H NMR (DMSO-d_6) δ 0.36 (s, 9H, 3 × CH_3), 7.63 (m, 1H, Ar), 7.80 (m, 2H, Ar), 8.17 (m, 2H, Ar), 8.38 (d, 1H, J = 9.2 Hz, Ar), 8.56 (d, 1H, J = 2.4 Hz, Ar); ^{13}C NMR (DMSO-d_6) 0.2 (3 × CH_3), 97.4, 104.6 (*C*≡*C*), 121.7, 123.8, 124.7, 127.2, 128.5, 129.8, 130.6, 130.9, 133.1, 140.8, 148.1, 149.2 (Ar); HR-MALDI-MS: *m*/*z* calcd for $C_{18}H_{17}NClSi$ $[M + H]^+$ 310.0813, found 310.0809.

The trimethylsilyl compound (0.15 g, 0.48 mmol) was dissolved in THF (6 mL), and $Et_3N{\cdot}3HF$ (26 μL, 0.48 mmol) was added. The reaction mixture was stirred at room temperature overnight. The solvent was evaporated in vacuo, and acridine **3** was purified using silica gel dry column vacuum flash chromatography with acetone (1%, v/v)/cyclohexane in quantitative yield (0.115 g). ^{1}H NMR (DMSO-d_6) δ 2.21 (s, 1H, C≡CH), 7.24−7.86 (m, 5H, Ar), 8.32 (d, 1H, J = 8.7 Hz, Ar), 8.62 (d, 1H, J = 2.2 Hz, Ar); ^{13}C NMR (DMSO-d_6) 82.3 (C≡*C*H), 97.9 (*C*≡CH), 116.2, 118.4, 119.8, 125.0, 132.2, 131.1, 133.6, 138.9, 139.6, 143.4, 147.5, (Ar); HR-MALDI-MS: *m*/*z* calcd for $C_{15}H_9NCl$ $[M + H]^+$ 238.0418, found 238.0427.

(*S*)-1-*O*-(4,4′-Dimethoxytriphenylmethyl)-3-*O*-(4-ethynylbenzyl)glycerol (5). To the solution of (*R*)-3-*O*-(4-iodobenzyl)-glycerol (**4**, 1.18 g, 4.2 mmol) in DMF (40 mL) was added Et_3N (5.8 mL), and Ar was bubbled through the solution for 30 min. Afterward, TMSA (0.67 g, 4.62 mmol) was dissolved under Ar, and CuI (48 mg, 0.25 mmol) and $Pd(PPh_3)_4$ (96 mg, 0.08 mmol) were added to the mixture. This was stirred at room temperature under Ar overnight, followed by the addition of $Et_3N{\cdot}3HF$ (0.38 mL, 2.38 mmol). After 30 min, CH_2Cl_2 (100 mL) was added, and the mixture was extracted with a 0.3 M aq solution of ammonium salt of EDTA (2 × 75 mL). The organic layer was washed with H_2O (3 × 100 mL), dried (Na_2SO_4), filtered, and evaporated in vacuo to dryness. The residue was coevaporated twice with toluene/EtOH (50 mL, 3:1, v/v) affording (*R*)-1-*O*-(4-ethynylbenzyl)glycerol as an oil. The oil was coevaporated with pyridine (20 mL) and then dissolved in anhydrous pyridine (75 mL) and cooled by an ice water bath, and 4,4′-dimethoxytrityl chloride (1.45 g, 4.41 mmol) was added under Ar. The mixture was stirred at room temperature for 16 h, and then an extra portion of 4,4′-dimethoxytrityl chloride (0.7 g, 2.1 mmol) was added. After 24 h, TLC showed no more starting material, and the reaction mixture was quenched by MeOH (2 mL), diluted with EtOAc (150 mL), and extracted with saturated aq $NaHCO_3$ (2 × 100 mL). The water phase was extracted with EtOAc (2 × 50 mL). The combined organic layers were dried (Na_2SO_4), filtered, and evaporated under diminished pressure. The residue was coevaporated twice with toluene/EtOH (25 mL, 1:1, v/v). The residue was dissolved in EtOAc (50 mL) and adsorbed on silica gel (2.5 g) by evaporation in vacuo and subsequently purified using dry column vacuum

chromatography with Et_3N (0.5%, v/v)/EtOAc (0−50%)/cyclohexane to afford (*S*)-1-*O*-(4,4′-dimethoxytriphenylmethyl)-3-*O*-(4-ethynylbenzyl)glycerol (**5**, 58%, 1.23 g) as a yellow foam. ^{1}H NMR ($CDCl_3$) δ 2.48 (br. s, 1H, OH), 3.06 (s, 1H, C≡CH), 3.21 (dd, 2H, J = 5.1 and 7.7 Hz, CH(OH)CH_2OCH_2), 3.57 (m, 2H, CH_2ODMT), 3.78 (s, 6H, 2 × OCH_3), 3.95 (m, 1H, *CH*OH), 4.52 (s, 2H, CH_2Ph), 6.80 (d, 4H, J = 8.8 Hz, DMT), 7.20−7.50 (m, 13H, CH_2−Ph and DMT); ^{13}C NMR ($CDCl_3$), 55.2 (OCH_3), 64.3 (*C*HOH), 69.9 (CH(OH)CH_2OCH_2), 71.6 (CH_2ODMT), 72.8 (CH_2-phenyl), 76.5 (C≡*C*H), 83.4 (*C*≡CH), 86.1 [*C*(Ar)$_3$], 121.3, 128.8, 132.1, 138.9 (phenyl), 113.1, 126.7−129.9, 135.9, 144.8, 158.5 (DMT); HR-MALDI-MS: *m*/*z* calcd for $C_{33}H_{32}Na^+O_5$ $[M + Na]^+$ 531.2142, found 531.2143.

(*S*)-2-*O*-[2-Cyanoethoxy(diisopropylamino)phosphino]-1-*O*-(4,4′-dimethoxy triphenylmethyl)-3-*O*-(4-ethynylbenzyl)-glycerol (6). (*S*)-1-*O*-(4,4′-Dimethoxytriphenylmethyl)-3-*O*-(4-ethynylbenzyl)glycerol (**5**, 1.2 g, 2.4 mmol) was dissolved under nitrogen in anhydrous CH_2Cl_2 (50 mL). *N*,*N*-Diisopropylammonium tetrazolide (0.62 g, 3.6 mmol) was added followed by dropwise addition of 2-cyanoethyl *N*,*N*,*N*′,*N*′-tetraisopropylphosphordiamidite (0.95 g, 3.2 mmol) under external cooling with an ice water bath. After 24 h, analytical TLC showed no more starting material, and the reaction was quenched with H_2O (30 mL). Layers were separated, and the organic phase was washed with H_2O (30 mL). Combined water layers were washed with CH_2Cl_2 (25 mL). Combined organic phase was dried (Na_2SO_4) and filtered, and silica gel (1.5 g) and pyridine (0.5 mL) were added. The solvents were removed under reduced pressure. The residue was purified using silica gel dry column vacuum chromatography with Et_3N (0.5%, v/v)/EtOAc (0−25%)/cyclohexane. Combined UV-active fractions were evaporated in vacuo affording the final compound **6** (1.45 g, 85%) as a foam that was used in DNA synthesis. ^{31}P NMR ($CDCl_3$) δ 150.3, 150.4 in a ratio of 3:2; HR-MALDI-MS: *m*/*z* calcd for $C_{42}H_{49}N_2Na^+O_6P$ $[M + Na]^+$ 731.3220, found 731.3246.

Solid-Phase Synthesis of TINA-Acridine Oligonucleotides. DMT-on oligodeoxynucleotides were synthesized in a 0.2 μmol scale on CPG supports using Expedite Nucleic Acid Synthesis System Model 8909 (Applied Biosystems), using 4,5-dicyanoimidazole as an activator and a 0.075 M solution of the corresponding phosphoramidites **6** and **7** in a 1:1 mixture of dry MeCN/CH_2Cl_2. For insertion of the monomer **6** or (*S*)-2-*O*-[2-cyanoethoxy(diisopropylamino)phosphino]-1-*O*-(4,4′-dimethoxytriphen ylmethyl)-3-*O*-(4-iodobenzyl)glycerol (**7**, ref *12*), the increased coupling (2 min) and deprotection (100 s) time were used. DMT-on oligonucleotides **8** and **9** on a CPG supports were treated twice with a freshly prepared Sonogashira coupling reagent mixture consisting of $Pd(PPh_3)_4$ (8.7 mg, 0.08 mmol), CuI (1.4 mg, 0.25 mmol), DMF/Et_3N (3.5:1.5, 500 μL), and iodoacridine **2** (5.4 mg, 22.5 μmol) in the case of sequence **9** (Method B) or ethynylacridine **3** (7.6 mg, 22.5 μmol) in the case of sequence **8** (Method A, Scheme 3). The reaction mixture was prepared by weighing all the reagents in a 1 mL plastic syringe followed by flushing with Ar and the addition of DMF and Et_3N. The syringe was connected to the one side of the column with the oligonucleotide on a CPG support. This system was thoroughly shaken to dissolve reagents, and another syringe was connected to another end of the column. The reaction mixture was thoroughly flushed from one syringe to the other through the column several times, and this operation was repeated every 45 min for 3 h. Obtained DMT-on oligonucleotide **10** bound to CPG supports was treated with 32% aq ammonia (1 mL) or with a freshly prepared 50% ethanolic solution of tris(2-aminoethyl)amine (1 mL) at room temperature for 2 h and then at 55 °C overnight. Purification of 5′-*O*-DMT-on ONs was accomplished using a reverse-phase semipreparative HPLC on a Waters Xterra MS C_{18} column. DMT groups were cleaved with 80% AcOH (100 μL) for 20 min. Afterward, H_2O (100 μL) and 3 M aq AcONa (50 μL) were added, and ONs were precipitated from 99% EtOH (550 μL). Their purity was found to be over 80% by ion-exchange chromatography on a LaChrom system (Merck Hitachi) using a GenPak-Fax column (Waters).

Scheme 1. Synthesis of Ethynylacridine[a]

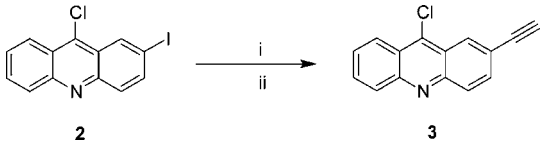

2 **3**

[a] (i) Trimethylsilylacetylene (TMSA), $Pd_2Cl_2(PPh_3)_2$, CuI, Et_3N/THF, room temperature, 99% and (ii) Et_3N·3HF, THF, room temperature, 98%.

RESULTS AND DISCUSSION

Synthesis of TINA-Acridine. We decided to use 9-chloro-2-ethynylacridine (**3**, Scheme 1), which can be coupled by a Sonogashira reaction to the ONs possessing an insertion of the previously described monomer **7** (*12*). Afterward, the chloride in the nine position of the acridine can be substituted by primary amines. Free amino groups can be protonated under physiological conditions and therefore reduce the electrostatic repulsion between the phosphates of the nucleic acid backbones. This may stabilize nucleic acid duplexes and triplexes. Oligonucleotides possessing 2-methoxy-2-oxoethyl (*14*), methoxyoxalamido (*15*), and benzyl thioester (*16*) precursor groups have been successfully derivatized using different primary amines in high yields. Simultaneously, the base and phosphate protective groups were removed, and the desired oligonucleotides were cleaved from the solid support. The use of secondary amines (40% aq dimethylamine) resulted in a considerably lower conversion of the oligonucleotides (*14*).

The starting 9-chloro-2-iodoacridine (**2**, ref *17*) was prepared by Ullmann condensation from *o*-chlorobenzoic acid and *p*-iodoaniline in the presence of Cu and K_2CO_3 in refluxing *i*-amyl alcohol in 20% yield followed by cyclization with $POCl_3$ in 75% yield. The yield of the Ullmann condensation was increased to 48%, when the reaction was done in refluxing 2-methoxyethanol (*18*). In the next step, the Sonogashira reaction with TMSA took place selectively on iodine. When $PdCl_2(PPh_3)_2$ instead of $Pd(PPh_3)_4$ was used as a catalyst (2 mol %), the reaction was finished in 30 min in 99% yield as compared to 24 h and 20% yield for $Pd(PPh_3)_4$. In the latter case, the addition of the fresh portion of the catalyst did not increase the yield. To obtain the high yield of the product, it was also necessary to remove the oxygen from the reaction environment with argon. The Sonogashira reaction has been demonstrated on 9-chloroacridine (*19*), but the substitution of the iodine atom in compound **2** by TMSA was confirmed by the characteristic signals in ^{13}C NMR and by mass spectrometry. Thus, the shift from 93.2 ppm (compound **2**) to 121.7 ppm (compound **3**) in ^{13}C NMR was observed for the C-2 atom of the acridine ring, which corresponded to the substitution of iodine. At the same time, the chemical shift in ^{13}C NMR of the C-9 atom of the acridine bearing chlorine remained in the same region: 130.0 and 130.6 ppm for compounds **2** and **3**, respectively. The mass spectra (HiResMALDI) of **3** confirmed the presence of the chlorine atom in the structure. The protective trimethylsilyl group was removed using Et_3N·3HF in THF at room temperature, and acridine **3** was obtained in quantitative yield. The required TINA precursor (*R*)-1-*O*-(4-iodobenzyl)-glycerol phosphoramidite **7** was synthesized in four steps as previously described (*12*), and it was used in the synthesis of ON **8** (Method A).

Scheme 2. Synthesis of (4-Ethynylbenzyl)glycerol Phosphoramidite[a]

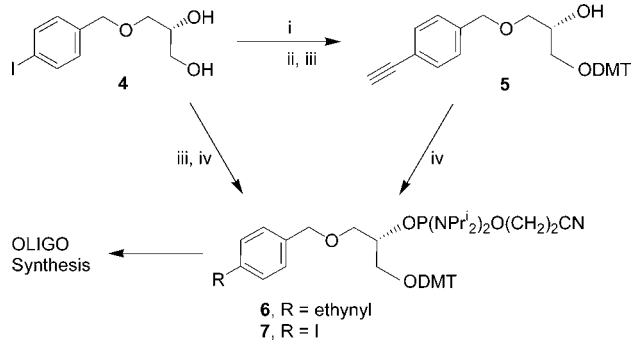

[a] (i) TMSA, CuI, $Pd(PPh_3)_4$, Et_3N/DMF, room temperature, Ar, overnight. (ii) $Et_3N{\cdot}3HF$, CH_2Cl_2. (iii) DMTCl, pyridine, 0 °C, Ar, 24 h. (iv) $NC(CH_2)_2OP(NPr^i_2)_2$, diisopropylammonium tetrazolide, CH_2Cl_2, 0 °C to room temperature, 24 h.

Because of the selectivity observed in the Sonogashira reaction between TMSA and acridine **2**, we decided to explore an alternative route using compound **2** for the conversion ONs into TINA-acridine oligonucleotides (Method B). For this purpose, the (*R*)-1-*O*-(4-ethynylbenzyl)glycerol phosphoramidite **6** was synthesized in four steps from (*R*)-3-*O*-(4-iodobenzyl)-glycerol (**4**) in 49% overall yield (Scheme 2). The latter compound was treated with the Sonogashira reaction mixture having TMSA followed by cleavage of the silyl protective group with $Et_3N{\cdot}3HF$, which was done in one pot affording (*R*)-3-*O*-(4-ethynylbenzyl)glycerol. This compound was used in the next step without chromatographic purification. Compound **5** was obtained in 56% overall yield from **4** after protection of the primary alcohol with DMTCl in dry pyridine. Treatment of compound **5** with 2-cyanoethyl-*N*,*N*,*N*′,*N*′-tetraisopropylphosphordiamidite in the presence of diisopropylammonium tetrazolide in dry CH_2Cl_2 overnight followed by silica gel purification gave the phosphoramidite **6**, which was used in DNA synthesis. Corresponding ONs **9** were prepared, applying the same conditions as for **8** (*12*). To avoid the transamination during the treatment with amines, dC^{Ac} phosphoramidite was used for the incorporation of 2′-deoxycytidine into ONs. Standard phosphoramidites for the incorporation of A, T, and G and commercial CPG solid supports were used.

For the postsynthetic Sonogashira type modification on a solid phase, ONs with an insertion of (*R*)-1-*O*-(4-iodobenzyl)glycerol (**8**) or (*R*)-1-*O*-(4-ethynylbenzyl)glycerol (**9**) in the middle and at the 5′-end were used. CPG supports with DMT-on ONs **8** or **9** were treated with a freshly prepared Sonogashira coupling reagent mixture possessing ethynylacridine **3** or iodoacridine **2**, respectively (Scheme 3). In both cases, the same product **10** on a solid support was obtained. However, we preferred to use Method B because the preparation of compound **9** is easy. In a previous study, it has been determined that double treatment of the CPG-bound oligonucleotides with a freshly prepared Sonogashira mixture increased the coupling efficiency (*12*). In our case, it was also obligatory due to the low solubility of acridines **2** and **3** in DMF/Et_3N at room temperature. We have now shown that the previously reported postsynthetic Sonogashira coupling on ONs can be extended to aromatic heterocyclic systems (*12*). Furthermore, this route was an advantage in our case because the required phosphoramidite for the synthesis of ONs **8** and **9** was readily available in our laboratory.

In the second postsynthetic step, the treatment of ONs **10** with 32% aq ammonia or a 50% ethanolic solution of tris(2-aminoethyl)amine at 55 °C overnight led to the substitution of the chlorine atom on acridine. The cleavage of ONs from the CPG support and deprotection of the bases and phosphates were performed in the same step. The reaction mixture was purified

Scheme 3. Postsynthetic Modification of Oligonucleotides[a]

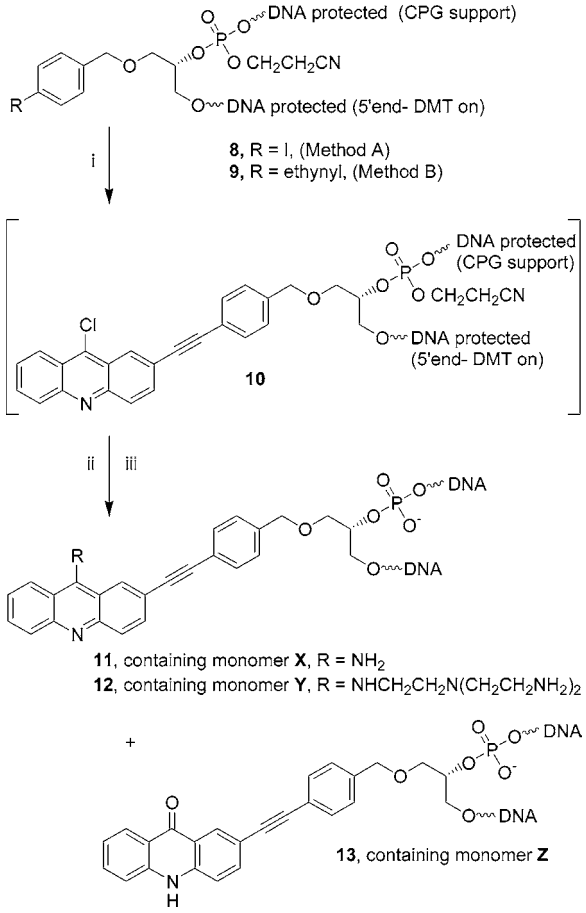

[a] (i) Reaction of **8** with **3** or reaction of **9** with **2** both using $Pd(PPh_3)_4$, CuI, DMF/Et_3N, Ar. (ii) 32% NH_4OH or 50% ethanolic solution of tris(2-aminoethyl)amine, room temperature for 2 h then 55 °C overnight. (iii) RP-HPLC; 80% aq AcOH, 3 M aq AcONa, 99% EtOH.

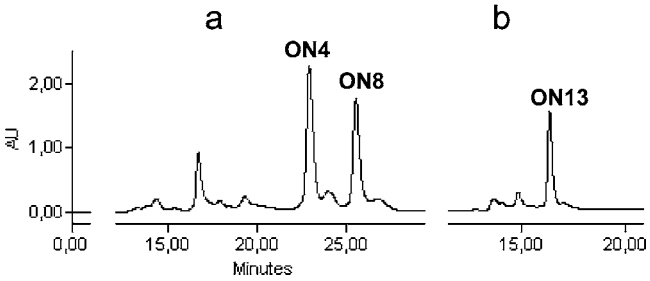

Figure 2. Reverse-phase HPLC profiles of oligonucleotides **11** (a) after treatment of ON **10** using 32% aq ammonia (isolated **ON4** at 22.4 min and **ON8** at 25.2 min). (b) After treatment of ON **10** using a 50% ethanolic solution of tris(2-aminoethyl)amine (isolated **ON13** at 16.4 min).

by semipreparative HPLC on a C_{18} column. UV-active fractions after evaporation of the solvent were treated with 80% aq AcOH to remove DMT protective groups followed by precipitation from EtOH. ONs were characterized by MALDI-TOF MS. Treatment of ONs **10** with secondary amines (*N*,*N*-dimethylethylenediamine or piperazin) gave no desired product after reaction at 55 °C for several days.

In the case of treatment of ON **10** with 32% aq ammonia, two peaks at 22.4 and 25.2 min were collected during HPLC purification (Figure 2a), which gave the same *m*/*z* values in MALDI-TOF. More accurate determination was performed using ESI mass spectrometry. For the fraction that appeared at 22.4 min, the *m*/*z* peak was detected at 4580.98 Da. For the second fraction, *m*/*z* was found to be 4581.99 Da. According

Table 1. T_m (°C) Data for Parallel Triplex1 Melting, Taken from UV-Melting Curves at 260 nm and Mass Spectra of Synthesized ONs[a]

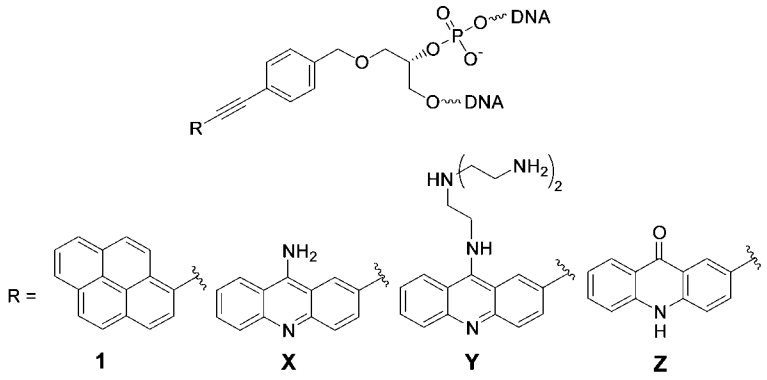

3′-CTGCCCCTTTCTTTTTT
5′-GACGGGGAAAGAAAAAA (**D1**) *m/z* (Da)

No.	TFO	pH = 5	pH = 6	pH = 7.2	calc.	found
ON1	5′-CCCCTTTCTTTTTT	55.0[3]	28.0	<5.0	-	-
ON2	5′-CCCCTT**1**TCTTTTTT[2]	59.0[3]	46.0	28.0	-	-
ON3	5′-**1**CCCCTTTCTTTTTT[2]	61.0[3]	44.5	20.5	-	-
ON4	5′-CCCCTT**X**TCTTTTTT	56.0[4]	36.0	17.5	4580.9	4580.98[5]
ON5	5′-**X**CCCCTTTCTTTTTT	59.5[3]	44.0	18.5	4582.5	4580.0[6]
ON6	5′-CCCCTT**Y**TCTTTTTT	-[4]	32.0	-[4]	4708.0	4704.0[6]
ON7	5′-**Y**CCCCTTTCTTTTTT	-[4]	30.0	-[4]	4708.0	4704.0[6]
ON8	5′-CCCCTT**Z**TCTTTTTT	-[4]	35.5	-[4]	4581.9	4581.99[5]

[a] [1]c = 1.5 μM TFO and 1.0 μM each strand of dsDNA in 20 mM sodium cacodylate, 100 mM NaCl, 10 mM $MgCl_2$, pH 5.0, 6.0, and 7.2; duplex T_m = 56.5 °C (pH 5.0), 58.5 °C (pH 6.0), and 57.0 °C (pH 7.2). [2]The T_m values for parallel triplex were taken from a previous study (*12*). [3]Third strand and duplex melting overlaid. [4]Not determined. [5]Measured by ESI-MS. [6]Measured by MALDI-TOF MS.

Table 2. T_m (°C) Data[a] for Antiparallel Duplex[1] Melting, Taken from UV-Melting Curves at 260 nm and Mass Spectra of Synthesized ONs

		DNA (**ON14**)	RNA (**ON15**)	*m/z* (Da)	
No.	TFO	5′-AGCTTGCTTGAG	5′-AGCUUGCUUGAG	calc.	found
ON9	3′-TCGAACGAACTC	47.5	40.5	-	-
ON10	3′-TCGAAC**1**GAACTC[2]	39.5	30.5	-	-
ON11	3′-TCGAAC**X**GAACTC	44.5	36.5	4072.0	4072.7[4]
ON12	3′-TCGAACGAACTC**X**	53.5	45.5	4072.0	4073.5[4]
ON13	3′-TCGAAC**Y**GAACTC	43.0	-[3]	4201.0	4208.0[4]

[a] [1] c = 1.0 μM each oligonucleotide in 140 mM NaCl, 10 mM sodium phosphate buffer, 1 mM EDTA, pH 7.0. [2]The T_m values were taken from a previous study (*12*). [3]Not determined. [4]Measured by MALDI-TOF MS.

to calculated mass, the fraction appearing at 22.4 min corresponded to **11** (**ON4**) containing the **X** monomer with 9-aminoacridine. One dalton difference *m/z* for the peak at 25.2 min means that the use of 32% aq ammonia for the modification of **10** resulted also in the formation of **13** (**ON8**) containing the **Z** monomer with 9-oxoacridine. It has been shown previously that in the reaction of 9-chloroacridine with amines, 9-oxoacridine also can be observed as a side product (*20*). From RP-HPLC profiles in Figure 2a,b, we observed a high conversion of ONs during the two postsynthetic steps. The lowest amounts of ONs were obtained in the case of treatment with a 50% ethanolic solution of tris(2-aminoethyl)amine.

Thermal Stability and Fluorescence Studies. Melting temperatures (T_m) of parallel triplexes and antiparallel duplexes consisting of **ON1**−**ON13** were estimated as the first derivative of melting curves and are shown in Tables 1 and 2. For comparison, previously published data for TINA possessing monomer **1** are also listed in Tables 1 and 2.

Stabilization of parallel triplexes was found in all cases when compared with the wild-type **ON1** at pH 5.0, 6.0, and 7.2 (Table 1). TINA-acridine intercalators **X**−**Z** gave less stable parallel triplexes, when inserted as a bulge in the middle of TFO as compared to **ON2** possessing a pyrene derivative **1** (*12*). In the case of **ON5** bearing 9-aminoacridine **X** at the 5′-end, the triplex stabilization was found to be similar as for TINA-pyrene (**ON3**). The similarity in T_m values for **ON4** and **ON8** means that the contribution of the amino group connected directly to the acridine ring (monomer **X**) into the triplex stabilization is negligible. The introduction of the 2-[bis-(2-aminoethyl)amino]-ethylamino group by reaction of **10** with tris(2-aminoethyl)-amine (monomer **Y**) in the middle of the TFO (**ON6**) led to lower triplex stabilization as compared with **ON4**. Moreover, the incorporation of the monomer **Y** at the 5′-end of the TFO (**ON7**) led to the least stabilized modified triplexes studied here. We suppose that the latter effect is due to electrostatic interactions between the positively charged cytosine of TFO and the protonated amino groups in the monomer **Y**.

When monomers **X** and **Y** were incorporated as a bulge in the middle of the oligodeoxynucleotides (**ON11** and **ON13**) (Table 2), destabilization of antiparallel DNA/DNA and DNA/RNA duplexes was observed when compared with the wild-type duplexes **ON9**/**ON14** and **ON9**/**ON15**. This destabilization effect was found to be smaller as compared with the TINA-containing pyrenyl moiety (**ON10**) ($T_{m\mathbf{ON11/ON14}} - T_{m\mathbf{ON10/ON14}}$ = 5.0 °C). Such a difference can be explained by a lower number of fused benzene rings in acridine than in pyrene and

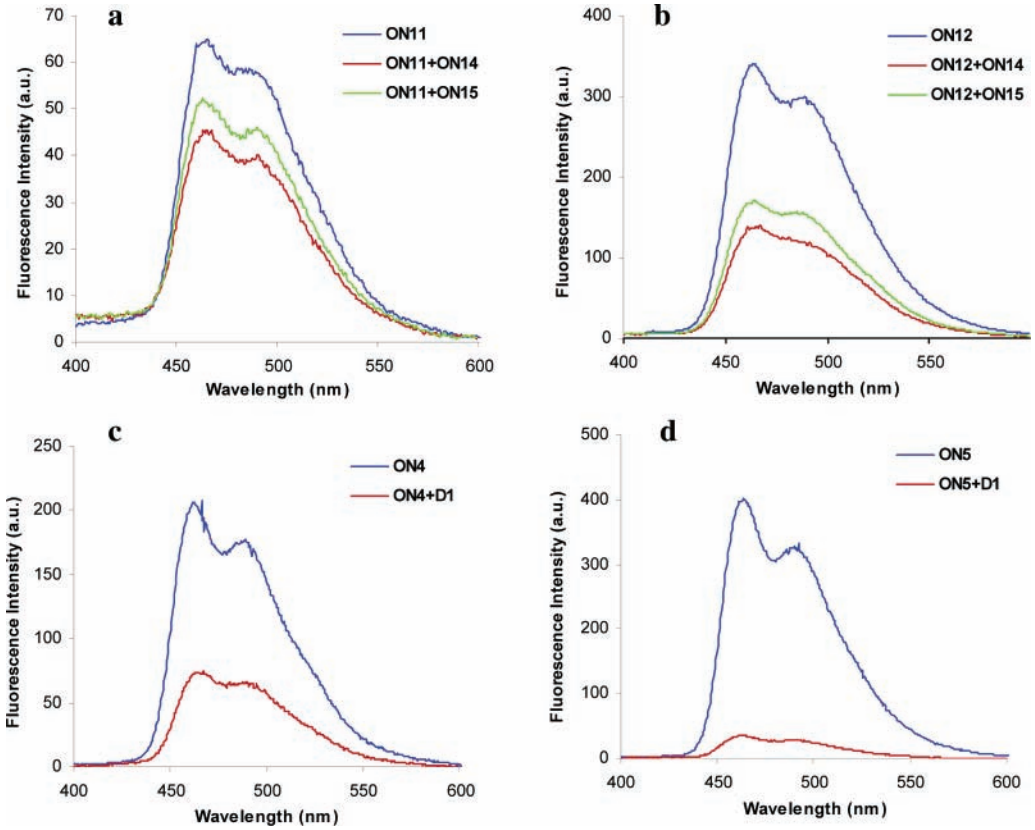

Figure 3. Fluorescence emission spectra of TINA bearing 9-aminoacridine inserted in the middle (a) and at the 5′-end (b) of the duplex and at the middle (c) and at the 5′-end (d) of the triplex.

by the presence of amino groups in **X** and **Y**. When the intercalator **X** was inserted at the 5′-end (**ON12**) as a dangling end, stabilization of the DNA/DNA ($\Delta T_m = +6.0$) and DNA/RNA ($\Delta T_m = +5.0$) duplexes was observed.

We studied fluorescence properties of TINA bearing 9-aminoacridine (**X**) in the middle and at the 5′-end of ONs in the structure of Hoogsteen type triplexes and Watson−Crick duplexes. When the modification was placed in the middle of the strand (**ON11**, Figure 3a), no quenching of the fluorescence intensity was observed for DNA/DNA and DNA/RNA duplexes, when compared with the single-strand **ON11**. However, the fluorescence intensity of **ON4** at the same excitation wavelength was quenched considerably, when a parallel triplex was formed (Figure 3c). Quenching was also observed upon both duplex and triplex formation with the oligonucleotides **ON12** and **ON5**, respectively, upon insertion of the acridine moiety at the 5′-end (Figure 3b,d). This can be explained by a partial quenching of the monomer fluorescence as a result of communication of the acridine with neighboring bases upon its insertion in the middle of the sequence. These results indicate that the acridine ring in the structure of TINA intercalates better, when inserted in the TFO strand of the parallel triplexes, than insertion of the TINA-acridine moiety in one of the strands of the antiparallel duplexes. This is also in agreement with the melting studies from the present work.

Molecular Modeling. Modeling studies were carried out to provide better structural understanding of binding of the acridine derivative in the parallel triplex mode used in triplex experiments (**ON4** + **D1**). Such a triplex structure was modified by the insertion of (*R*)-3-*O*-[4-(9-aminoacridin-2-ylethynyl)benzyl]-glycerol (**X**) as a bulge in the middle of the 14-mer sequence (Figure 4a,b).

According to the structure minimized by the AMBER* force field, 9-aminoacridine was stacked between the bases of the dsDNA, while the phenyl was placed in the TFO strand. Twisting around the triple bond of 19.3° was also observed for structure **X**, which is shown on the detailed view in Figure 4b. As it can be seen in Figure 4a, the amino group in the ninth position of the acridine was directed into the major groove of dsDNA. This can explain why the presence of both the amino group and the 2-[bis-(2-aminoethyl)amino]ethylamino group at position 9 of the acridine did not give a great contribution in thermal stabilization of the parallel triplex. With this orientation, these groups cannot reach the phosphates of the nucleic acid backbone and neutralize the negative charge. According to modeling, directing the amino group into the minor groove gave more energy-rich structures. It can be proposed that substitutions at positions 4 and 5 of the acridine ring or at position 10 of the acridone should direct aminoalkyl groups in the minor groove of dsDNA and point amines closer to phosphates by the appropriately chosen alkyl linker.

To elucidate the destabilization of duplexes, we simulated the intercalation of **X** in the modeling of the antiparallel duplex **ON11**/**ON14**. The amino group was directed into the minor or into the major groove, as is shown in Figure 4c,d, respectively. After the comparison of potential energies of the leading conformations obtained from AMBER* calculations, it was found that the preferable position of the acridine is when the amino group is directed into the minor groove. A twisting around the triple bond of 34.9° was observed. However, in both cases, the stacking of the intercalator between the bases was imperfect. These results are in agreement with the lower T_m values of the duplexes, and they explain also the negligible fluorescence quenching of the acridine upon duplex formation.

CONCLUSION

In this paper, we describe the postsynthetic synthesis of twisted intercalating nucleic acids possessing acridine derivatives. Using the Sonogashira reaction, 9-chloroacridine was

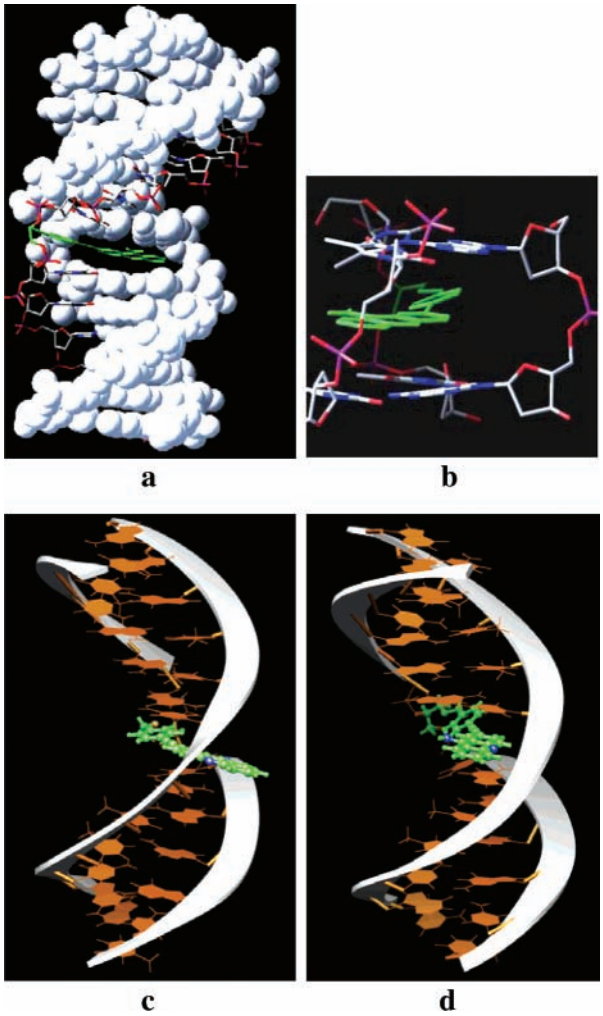

Figure 4. (a) Energy-minimized averaged AMBER* representative structure of the parallel triplex-containing (*R*)-3-*O*-[4-(9-aminoacridin-2-ylethynyl)benzyl]glycerol (**X**) (dsDNA displayed in CPK form in white, TFO in stick form as well as the TINA-acridine intercalator marked with green). (b) Detailed view of the monomer **X** placed between the two triples showing the torsion between the acridinyl and the phenyl ring connected via acetylene. (c) Representative structure of the antiparallel duplex-containing monomer **X** directed into the minor groove. (d) Representative structure of the antiparallel duplex-containing monomer **X** directed into the major groove.

introduced into ONs possessing TINA precursor monomers **8** and **9**. In the second postsynthetic step, treatment of ONs **10** with aq ammonia or ethanolic tris(2-aminoethyl)amine allowed substitution of the chlorine atom on acridine, cleavage from the CPG support, and deprotection of the bases in one pot.

Thermal denaturating studies showed that the introduction of acridine into TINA led to the stabilization of parallel triplexes. However, as compared with TINA possessing pyrene **1**, the stabilization effect of acridines **X**−**Z** was not as significant with the exception of the **ON5**-containing TINA-acridine monomer **X** at the 5′-end. It was supposed that the triplex thermal stability can be further increased by the introduction of primary amines into the acridine via an alkyl linker, which should reduce the electrostatic repulsion between phosphates. Nevertheless, the introduction of TINA-acridine **Y** possessing a tris(2-aminoethyl)amine moiety gave the least thermally stable parallel triplex. In the case of antiparallel duplexes, introduction of TINA acridines **X** and **Y** to the dsDNA structures resulted in less destabilized DNA/DNA and DNA/RNA Watson−Crick duplexes as compared with TINA **1**. The stabilization effect in the case of **ON12/ON14** and **ON12/ON15** was found when 9-aminoacridine **X** was inserted at the 5′-end of the ON.

Molecular modeling calculations showed that the triplex stabilization was due to the intercalation of the acridine moiety between the bases of the dsDNA and via the interaction of the phenyl ring with the bases of TFO. 9-Chloroacridine was found to be a good precursor for the incorporation of primary amines to the oligonucleotides. We believe that parallel triplex stabilization can be further improved by the appropriately chosen substitution on the acridine in the structure of TINA monomers.

ACKNOWLEDGMENT

This work was supported by the Sixth Framework Program Marie Curie Host Fellowships for Early Stage Research Training under Contract MEST-CT-2004-504018 and by the Nucleic Acid Center, which is funded by The Danish National Research Foundation for studies on nucleic acid chemical biology. Kim F. Haselmann is gratefully acknowledged for measuring the ESI-MS spectra. Molecular graphics images (Figure 4c,d) were produced using the UCSF Chimera package from the Resource for Biocomputing, Visualization, and Informatics at the University of California, San Francisco (supported by NIH P41 RR-01081).

LITERATURE CITED

(1) Gutanaka, R. V., Varma, B. R., and Weber, K. T. (2003) Review: Triplex-forming oligonucleotides as modulators of gene expression. *Int. J. Biochem. Cell Biol. 35*, 22−31.

(2) Roubaud, G., Billeau, S., Faure, R., Robin M., and Galy, J.-P. (2005) Synthesis of new 9-(N-substituted)-acridinamines bearing a pendant polymerizable side chain. *Synth. Commun. 35*, 683−692.

(3) Cassidy, S. A., Strekowski, L., and Fox, K. R. (1996) DNA sequence specificity of a naphthylquinoline triple helix-binding ligand. *Nucleic Acids Res. 24*, 4133−4138.

(4) Cassidy, S. A., Strekowski, L., Wilson, W. D., and Fox, K. R. (1994) Effect of a triplex-binding ligand on parallel and antiparallel DNA triple helices using short unmodified and acridine-linked oligonucleotides. *Biochemistry 33*, 15338−15347.

(5) Orson, F. M., Klysik, J., Bergstrom, D. E., Ward, B., Glass, G. A., Hua, P., and Kinsey, B. M. (1999) Triple helix formation: binding avidity of acridine-conjugated AG motif third strands containing natural, modified, and surrogate bases opposed to pyrimidine interruptions in a polypurine target. *Nucleic Acids Res. 27*, 810−816.

(6) Aubert, Y., Perrouault, L., Hélène, C., Giovannangeli, C., and Asseline, U. (2001) Synthesis and properties of triple helix-forming oligodeoxyribonucleotides containing 7-chloro-7-deaza-2′-deoxyguanosine. *Bioorg. Med. Chem. 9*, 1617−1624.

(7) Brunet, E., Corgnali, M., Perrouault, L., Roig, V., Asseline, U., Sørensen, M. D., Babu, B. R., Wengel, J., and Giovannangeli, C. (2005) Intercalator conjugates of pyrimidine locked nucleic acid-modified triplex-forming oligonucleotides: improving DNA binding properties and reaching cellular activities. *Nucleic Acids Res. 33*, 4223−4234.

(8) Helm, C. W., Shrestha, K., Thomas, S., Shingleton, H. M., and Miller, D. M. (1993) A unique c-myc-targeted triplex-forming oligonucleotide inhibits the growth of ovarian and cervical carcinomas in vitro. *Gynecol. Oncol. 49*, 339−343.

(9) Amato, J., Galeone, A, Oliviero, G., Mayol, L., Piccialli, G., and Varra, M. (2004) Synthesis of 3′−3′-linked pyrimidine oligonucleotides containing an acridine moiety for alternate strand triple helix formation. *Eur. J. Org. Chem.* 2331−2336.

(10) Kukreti, S., Sun, J.-S., Garestier, T., and Hélène, C. (1997) Extension of the range of DNA sequences available for triple helix formation: stabilization of mismatched triplexes by acridine-containing oligonucleotides. *Nucleic Acids Res. 25*, 4264−4270.

(11) Zhou, B.-W., Puga, E., Sun, J.-S., Garetier, T., and Hélène, C. (1995) Stable triple helices by acridine-containing oligonucleotides with oligopurine tracts of DNA interrupted by one or two pyrimidines. *J. Am. Chem. Soc. 117*, 10425−10428.

(12) Filichev, V. V., and Pedersen, E. B. (2005) Stable and selective formation of Hoogsteen type triplexes and duplexes using twisted intercalating nucleic acids (TINA) prepared via postsynthetic Sonogashira solid-phase coupling reactions. *J. Am. Chem. Soc. 127*, 14849−14858.

(13) Shiraishi, T., Hamzavi, R., and Nielsen, P. E. (2005) Targeted delivery of plasmid DNA into the nucleus of cells via nuclear localization signal peptide conjugated to DNA intercalating bis- and trisacridines. *Bioconjugate Chem. 16*, 1112−1116.

(14) Prakash, T. P., Kawasaki, A. M., Lesnik, E. A., Owens, S. R., and Manoharan, M. (2003) 2′-*O*-[2-(Amino)-2-oxoethyl]oligonucleotides. *Org. Lett. 5*, 403−406.

(15) Polushin, N. N. (2000) The precursor strategy: terminus methoxyoxalamido modifiers for single and multiple functionalization of oligodeoxyribonucleotides. *Nucleic Acids Res. 28*, 3125−3133.

(16) Hovinen, J., Guzaev, A., Azhayeva, E., Azhayev, A., and Lönnberg, H. (1995) Imidazole tethered oligodeoxyribonucleotides: synthesis and RNA cleaving activity. *J. Org. Chem. 60*, 2205−2209.

(17) Mietzsch, F., and Mauss, H. Basically substituted acridine compounds. U.S. Patent No. 24 774, 1937; pp 1−3.

(18) Wolf, C., and Mei, X. (2003) Synthesis of conformationally stable 1,8-diarylnaphthalenes: Development of new photoluminescent sensors for ion-selective recognition. *J. Am. Chem. Soc. 125*, 10651−10658.

(19) Elangovan, A., Chiu, H.-H., Yang, S.-W., and Ho, T.-I. (2004) Arylethynylacridines: electrochemiluminescence and photophysical properties. *Org. Biomol. Chem. 2*, 3113−3118.

(20) Gourdie, T. A., Prakash, A. S., Wakelin, L. P. G., Woodgate, P. D., and Denny, W. A. (1991) Synthesis and evaluation of DNA-targeted spatially separated bis(aniline mustards) as potential alkylating agents with enhanced DNA cross-linking capability. *J. Med. Chem. 34*, 240−248.

BC060058O

Carbohydrate-Functionalized Dendrimers To Investigate the Predictable Tunability of Multivalent Interactions

Mark L. Wolfenden and Mary J. Cloninger*

Department of Chemistry and Biochemistry and Center for Bioinspired Nanomaterials, Montana State University, 108 Gaines Hall, Bozeman, Montana 59717. Received April 24, 2006; Revised Manuscript Received May 10, 2006

Multivalent protein−carbohydrate interactions mediate a wide variety of intercellular recognition processes with high selectivity and specificity. Many synthetic multivalent molecules have been designed to mimic and to inhibit these processes. Using carbohydrate functionalized dendrimers, our goal is to devise a system where the binding activity and the degree of protein clustering induced by the glycopolymer can be readily attenuated. In this paper, dendrimers were functionalized with mixtures of mannose, glucose, and galactose. Their association with concanavalin A was studied using precipitation and hemagglutination assays. With less idealized systems where the association was not optimized, mixtures of low- and high-affinity ligands caused smaller than the theoretically determined differences in binding activity, although linear binding trends were observed. When systems were optimized so that high-affinity binding was achieved, then mixing low- and high-affinity ligands on the dendrimer's surface showed a predictable trend for lectin binding.

INTRODUCTION

Multivalent carbohydrate displays are involved in a myriad of biological recognition processes (*1*−*4*). A variety of glycopolymers have been developed to decipher the mechanistic details of binding processes with lectins (*5*). Glycoconjugates include many frameworks, varying from linear polymers to virus cages and proteins to dendrimers (*6*−*30*). Multivalent compounds are now being tested for biological activity. Noteworthy examples include carbohydrate functionalized gold nanoparticles whose antiadhesive properties involving cancer cell lines have been reported by Penades and co-workers (*31*). Also, Kihlberg and co-workers reported antiviral properties of a glycoprotein using human serum albumin as a scaffold with up to 19 sialyllactose motifs attached (*32*). The glycoproteins were designed to inhibit binding of an adenovirus involved in causing epidemic koratoconjunctivitus and were found to generate a 1000-fold potency increase in the IC_{50} value. In addition, Seeberger and co-workers have reported carbohydrate functionalized fluorescent poly(*p*-phenylene ethynylene) polymers that serve as a detection system for bacteria (*33*).

Synthetic multivalent molecules are generally optimized for their particular application in an empirical fashion. However, model systems have been used to more generally evaluate the parameters governing multivalent protein−carbohydrate interactions. Concanavalin A (Con A) is the lectin that is used most commonly in model studies with glycopolymers. Con A is a plant lectin isolated from the jackbean, which exists as a homotetramer at pH 7. Each monomer unit has one sugar binding site. Con A has specificity for the α-pyranose forms of D-mannose and D-glucose, and the four sugar binding sites are 65 Å apart (*34*). In work that inspired our choice of the Con A model system for this report, Kiessling and co-workers compared Con A binding by various scaffolds (*35*), compared Con A binding by linear polymers bearing various glucose and mannose derivatives (*36*), and compared Con A binding by glucose functionalized linear polymers of varying lengths (*37*). In work that inspired our choice of the dendrimer framework, Roy and co-workers studied the binding of lactose functionalized dendrimers to several lectins (*38*).

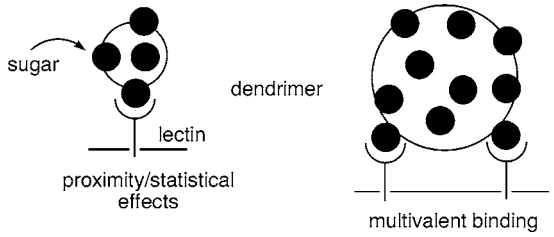

Figure 1. Proximity effects vs multivalent binding.

Nature augments weak monovalent protein carbohydrate interactions by using multivalency. Multivalency can be broadly described as many interactions that have a more than additive effect, making low-affinity interactions ($K_d \approx 10^{-3}$ M) into physiologically relevant affinities (*39*−*41*). Glycoside clustering has been previously defined as "affinity enhancement achieved by multivalent ligands over monovalent ones that is greater than would be expected from a simple effect of concentration increase" (*42*). For the discussion in this paper, we adopt this definition of glycoside clustering but apply it more specifically than it is sometimes used in the carbohydrate literature. Namely, we define multivalent binding (the ability of one dendrimer to bind to multiple lectin binding sites) and proximity/statistical effects (a ligand concentration effect) as two related but distinct terms. These definitions are shown pictorially in Figure 1.

Efforts to quantify the effects one would expect from the multivalent presentation of ligands have been reported. Page and Jencks' discussion of the chelate effect (*43*), and Jencks' presentation of a "connection Gibbs energy" (*44*) serve as an important introduction to this area. Jencks proposed that binding of a protein to a bivalent molecule could be described as the sum of the "intrinsic binding energies" of the component parts plus a "connection Gibbs energy" arising primarily from changes in the translational and rotational entropy upon bivalent binding (*44*). Two more recent examples of efforts to quantify components of multivalency have been presented by Lees et al. (*45*) and by Reinhoudt et al. (*46*) Lees and co-workers describe a binding enhancement value for divalent, pentameric, and linear

* To whom correspondence should be addressed. Phone: 406-994-3051. Fax: 406-994-5407. E-mail: mcloninger@chemistry.montana.edu.

10.1021/bc060107x CCC: $33.50 © 2006 American Chemical Society
Published on Web 06/23/2006

polymer systems (*45*), while Reinhoudt and co-workers relate the monovalent association constant to the multivalent association constant using an effective concentration value and a scaling factor (*46*). Both these methods progress the discussion of how monovalent association constants effect multivalent interactions, but both suffer from the difficulty of determining the appropriate value for the effective concentration.

In 1998, Whitesides et al. proposed a relationship between degree of multivalency and binding affinity with respect to the monomer (see eq 1 and Discussion below) (*39*). Recently, we published results that could be described well by this model; changes in activity could be predictably introduced into a multivalent dendritic system (*47*).

$$K_N^{poly} = (K^{mono})^{\alpha N} \quad (1)$$

Here, we describe our study in full detail, with a larger library of dendrimers bearing varying amounts of mannose, glucose, and galactose residues, and with additional assays to evaluate the protein−carbohydrate interaction. Binding trends are reported for dendrimers of different generations bearing presentations of ligands with varying affinities for Con A. Hemagglutination assay results to show changes in activity with Con A are presented, and precipitation assay results to show how protein activity and protein clustering can be independently attenuated are described.

EXPERIMENTAL PROCEDURES

Compounds 4a−n. Representative Procedure for the Synthesis of Heterogeneously Functionalized Generation 3.0 PAMAM-Based Thiourea-Linked 1-*O*-(6-Thiourea-4-thiohexyl)-2,3,4,6-tetra-*O*-acetyl-α-D-galactopyranoside, 1-*O*-(6-Thiourea-4-thiohexyl)-2,3,4,6-tetra-*O*-acetyl-α-D-glucopyranoside, and 1-*O*-(6-Thiourea-4-thiohexyl)-2,3,4,6-tetra-*O*-acetyl-α-D-mannopyranoside. An aqueous solution of amine terminated G(3)-PAMAM dendrimer (1.925 g of a 18% (w/w) solution in water, 346 mg, 51 μmol) was lyophilized to leave a foamy residue. A 5.8 mL aliquot of dimethyl sulfoxide (DMSO) was then added to this residue to give a 60 mg/mL solution. A 47 μL aliquot of a 300 mM solution of **2a** (14.1 μmol, 6.8 mg) in DMSO was added to 0.5 mL of a 60 mg/mL G(3) PAMAM dendrimer (30 mg, 4.4 μmol) solution. The reaction was stirred for 48 h, and a 75 μL aliquot was removed for MALDI-TOF analysis. After MALDI-TOF indicated reaction completion, 0.17 mL of a 300 mg/mL solution of **2b** (49.4 μmol, 20.1 mg) was added. The solution was stirred for 48 h. A 75 μL aliquot was removed for analysis. After MALDI-TOF indicated reaction completion, 0.19 mL of a 300 mg/mL solution of **2c** (58.3 μmol, 23.4 mg) was added and was stirred for 48 h, and a 75 μL aliquot was removed for analysis. According to MALDI-TOF analysis, the final addition did not fully functionalize the remaining amine groups, so an additional spacer was added. 47 mg (30 μmol) of **3** in DMSO was added and was stirred at room temperature for 2 days. Again MALDI-TOF analysis indicated no further addition. This step was repeated with mild warming (up to 40 °C) and vigorous stirring. MALDI-TOF analysis again indicated no addition. Amounts of reagents used for formation of **4a−n**, and characterization data for **4a−n** are provided in the Supporting Information.

Compounds 5a−n. Representative Procedure for the Synthesis of Heterogeneously Functionalized Generation 4.0 PAMAM-Based Thiourea-Linked 1-*O*-(6-Thiourea-4-thiohexyl)-2,3,4,6-tetra-*O*-acetyl-α-D-galactopyranoside, 1-*O*-(6-Thiourea-4-thiohexyl)-2,3,4,6-tetra-*O*-acetyl-α-D-glucopyranoside, and 1-*O*-(6-Thiourea-4-thiohexyl)-2,3,4,6-tetra-*O*-acetyl-α-D-mannopyranoside. An aqueous solution of amine terminated G(4) PAMAM dendrimer (2.48 g of a 17% (w/w) solution in water, 421 mg, 31 μmol) was lyophilized to leave a foamy residue. A 7.0 mL aliquot of DMSO was then added to this residue to give a 60 mg/mL solution. A 47 μL aliquot of a 300 mM solution of **2a** (14.1 μmol, 6.8 mg) in DMSO was added to 0.5 mL of a 60 mg/mL G(4) PAMAM dendrimer (30 mg, 4.4 μmol) solution. The reaction was stirred for 48 h, and a 75 μL aliquot was removed for MALDI-TOF analysis. After MALDI-TOF analysis indicated reaction completion, 0.17 mL of a 300 mM solution of **2b** (49 μmol, 25 mg) was added. The solution was stirred for 48 h. A 75 μL aliquot was removed for analysis. After MALDI-TOF analysis indicated reaction completion, 0.19 mL of a 300 mM solution of **2c** (57 μmol, 29 mg) was added and was stirred for 48 h, and a 75 μL aliquot was removed for analysis. According to MALDI-TOF analysis the final addition did not fully functionalize all remaining amine groups, so an additional spacer was added. 47 mg (30 μmol) of **3** in DMSO was added and was stirred at room temperature for 2 d. Again MALDI-TOF analysis indicated no further addition. This step was repeated with mild warming (up to 40 °C) and vigorous stirring. MALDI-TOF analysis again indicated no further addition. Amounts of reagents used for formation of **5a−n**, and characterization data for **5a−n** are provided in the Supporting Information.

Compounds 6a−l. Representative Procedure for the Synthesis of Heterogeneously Functionalized Generation 5.0 PAMAM-Based Thiourea-Linked 1-*O*-(6-Thiourea-4-thiohexyl)-2,3,4,6-tetra-*O*-acetyl-α-D-galactopyranoside, 1-*O*-(6-Thiourea-4-thiohexyl)-2,3,4,6-tetra-*O*-acetyl-α-D-glucopyranoside, and 1-*O*-(6-Thiourea-4-thiohexyl)-2,3,4,6-tetra-*O*-acetyl-α-D-mannopyranoside. An aqueous solution of amine terminated G(5) PAMAM dendrimer (1.938 g of a 23% (w/w) solution in water, 446 mg, 18 μmol) was lyophilized to leave a foamy residue. A 7.4 mL aliquot of DMSO was then added to this residue to give a 60 mg/mL solution. A 39 μL aliquot of a 300 mM solution of **2a** (12 μmol, 6.0 mg) in DMSO was added to 0.5 mL of a 60 mg/mL G(5) PAMAM dendrimer (30 mg, 1.2 μmol) solution. The reaction was stirred for 48 h, and a 75 μL aliquot was removed for MALDI-TOF analysis. After MALDI-TOF analysis indicated reaction completion, 0.14 mL of a 300 mM solution of **2b** (42.4 μmol, 22 mg) was added. The solution was then stirred for 48 h. A 75 μL aliquot was removed for analysis. After MALDI-TOF indicated reaction completion, 0.15 mL of a 300 mM solution of **2c** (45 μmol, 23 mg) was added and was stirred for 48 h, and a 75 μL aliquot was removed for analysis. According to MALDI-TOF analysis, the final addition did not fully functionalize the remaining amine groups, so an additional spacer was added. A 47 mg (30 μmol) amount of **3** in DMSO was added and was stirred at room temperature for 2 days. Again MALDI-TOF analysis indicated no further addition. This step was repeated with mild warming (up to 40 °C) and vigorous stirring. MALDI-TOF analysis again indicated no addition. Amounts of reagents used for formation of **6a−l**, and characterization data for **6a−l** are provided in the Supporting Information.

Compounds 7a−l. Representative Procedure for the Synthesis of Heterogeneously Functionalized Generation 6.0 PAMAM-Based Thiourea-Linked 1-*O*-(6-Thiourea-4-thiohexyl)-2,3,4,6-tetra-*O*-acetyl-α-D-galactopyranoside, 1-*O*-(6-Thiourea-4-thiohexyl)-2,3,4,6-tetra-*O*-acetyl-α-D-glucopyranoside, and 1-*O*-(6-Thiourea-4-thiohexyl)-2,3,4,6-tetra-*O*-acetyl-α-D-mannopyranoside. An aqueous solution of amine terminated Starburst G(6) PAMAM dendrimer (2.78 g of a 17% (w/w) solution in water, 472 mg, 9.3 μmol) was lyophilized to leave a foamy residue. A 7.9 mL aliquot of DMSO was added to this residue to give a 60 mg/mL solution. A 33 μL aliquot of a 300 mM solution of **2a** (9.9 μmol, 5.1 mg) in DMSO was added to 0.5 mL of a 60 mg/mL G(6) PAMAM dendrimer (30

mg, 4.4 μmol) solution. The reaction was stirred for 48 h, and a 75 μL aliquot was removed for MALDI-TOF analysis. After MALDI-TOF analysis indicated reaction completion, 120 μL of a 300 mM solution of **2b** (36 μmol, 18 mg) was added. The solution was stirred for 48 h. A 75 μL aliquot was removed for analysis. After MALDI-TOF analysis indicated reaction completion, 140 μL of a 300 mM solution of **2c** (42 μmol, 22 mg) was added and was stirred for 48 h, and a 75 μL aliquot was removed for analysis. According to MALDI-TOF analysis the final addition did not fully functionalize the remaining amine groups, so an additional spacer was added. A 47 mg (30 μmol) amount of **3** in DMSO was added and was stirred at room temperature for 2 days. Again MALDI-TOF analysis indicated no further addition. This step was repeated with mild warming (up to 40 °C) and vigorous stirring. MALDI-TOF analysis again indicated no addition. Amounts of reagents used for formation of **7a**−**l**, and characterization data for **7a**−**l** are provided in the Supporting Information.

General Procedure for Deacylation of Dendrimers 4a−**n, 5a**−**n, 6a**−**l, and 7a**−**l.** To the lyophilized solid compounds **4a**−**n**, **5a**−**n**, **6a**−**l**, and **7a**−**l**, 1 mL of 1:1 water:methanol was added, at which point the dendrimer became a white precipitate. To this mixture was added 0.2 equiv of NaOMe (0.8 M in MeOH) for each peripheral carbohydrate, and the mixture was stirred for 3 h. If the mixture had not become a clear solution after 3 h, then a further 0.2 equiv of NaOMe (0.8 M in MeOH) was added, and this step was repeated until the mixture became a clear and colorless solution. HCl(aq) (0.1 M) was added slowly until the pH was ∼7. This neutralized solution was placed in a centrifugal filter device, diluted with 3 mL of 1:1 H_2O:MeOH, and filtered at 3500 rpm for 30 min. The filtrate was removed, and 3 mL of H_2O was added and filtered for 30 min at 3500 rpm. This procedure was repeated 2 more times. The remaining residue was taken up in Millipore water and lyophilized to give a white fluffy solid. Characterization data for all deprotected compounds are provided in the Supporting Information.

RESULTS

Synthesis and Characterization of Carbohydrate Functionalized PAMAM Dendrimers. A general procedure for functionalization of the dendrimers with two or three carbohydrates is shown in Scheme 1. Mannose/glucose/galactose, mannose/glucose, glucose/galactose, and mannose/galactose functionalized dendrimers were synthesized as shown for mannose in Scheme 1b. To retain the α-anomeric integrity of the carbohydrates, we chose to allylate the anomeric position and perform a thiol addition to the olefin (*48*). The subsequently formed peracylated isothiocyanto sugars **2** were added sequentially to a solution of PAMAM dendrimer in DMSO (*49*). When adding more than one sugar to the PAMAM dendrimer, incomplete loading was observed. The addition of excess isothiocyanato sugar with mild warming did not induce further loading to any significant extent. A third isothiocyanato sugar or isothiocyanato alcohol **3** also failed to give full loading (steps 3 and 5 in Scheme 1b; step 3 was omitted when only two carbohydrates were added to the dendrimer), indicating that any remaining primary amines on the dendrimer were inaccessible for reaction with the desired isothiocyanates. Global deprotection via Zemplen conditions in 1:1 MeOH:H_2O and purification by centrifugal filtration in water and lyophilization afforded compounds **4a**−**n**, **5a**−**n**, **6a**−**l**, and **7a**−**l**. The compound numbers **4**−**7** indicate the generation of the dendrimer that was used (G(3) = **4**, G(4) = **5**, G(5) = **6**, G(6) = **7**), and the letters indicate the number and nature of the sugars that are added to the dendrimers. The sugar compositions of each dendrimer are given in Tables 1−4. Although not shown in Scheme 1, addition of **3** to protected carbohydrate functionalized dendrimers

Scheme 1. Synthesis of Mannose, Glucose, and Galactose Functionalized Dendrimers[a]

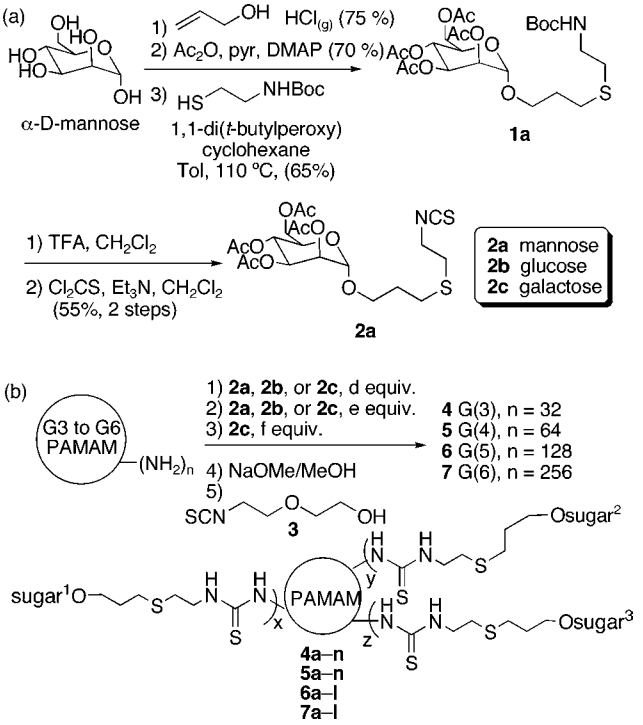

[a] Letters after 4−7 correlate the number of mannose, glucose, and galactose residues present on each dendrimer (see Tables 1−4). The amount of **2** added in each reaction is provided in the Supporting Information.

(reversal of steps 4 and 5 in Scheme 1b) also failed to increase the carbohydrate loadings of the dendrimers.

Because previous studies indicated that 50% dendrimer functionalization with the binding ligand (mannose) produced optimal results (*50*), we synthesized a series of dendrimers with 50% mannose + glucose (plus additional galactose residues for spacing, Table 1), and we compared these dendrimers to a series of dendrimers with higher loadings of mannose + glucose (Table 2).

MALDI-TOF MS was used to determine the number of carbohydrate residues of each type on the dendrimers. Both the change in M_W after each sequential addition and the change in M_W after deacylation were used. Details of the calculations are provided in the Supporting Information. The MALDI-TOF MS-derived number of sugars tethered to each dendrimer is shown in Tables 1−4. Data for man/glc/gal functionalized dendrimers (where the total amount of man/glc loading is kept constant at 50%) are reported in Table 1, data for man/glc functionalized dendrimers are reported in Table 2, data for glc/gal functionalized dendrimers are reported in Table 3, and data for man/gal functionalized dendrimers are reported in Table 4.

Although NMR spectra revealed that the carbohydrates had been successfully added to the dendrimers (downfield thiourea peaks appear in the ^{1}H NMR spectra, for example), the spectra were broadened and overlapped such that the integration ratios could not be used to quantify carbohydrate loadings. The ^{1}H NMR spectra did reveal the level of deprotection of the acetyl groups, since these methyl groups caused sharp distinctive peaks at ∼2 ppm.

Hemagglutination Inhibition Assays. Hemagglutination inhibition assays were performed by adding erythrocytes to preincubated solutions of Con A (∼1 μM) with varying concentrations of dendrimer (*51*). We previously reported the synthesis and analysis of G(4) to G(6) PAMAM dendrimers with 50% mannose and glucose incorporation (*47*). These

Table 1. Summary of Characterization Data for Dendrimers with 50% Man/Glc Functionalization

dendrimer generation	compd	mannose residues[a]	glucose residues[a]	galactose residues[a]	inhibiting sugar concn[b] (nmol)[b]	rel activity/ active sugar[c]	Con A/ dendrimer[d]
3	**4a**	15	0	11	1395	120	7
3	**4b**	10	4	9	1320	110	7
3	**4c**	6	7	8	1300	110	7
3	**4d**	3	12	7	1300	120	6
3	**4e**	0	14	7	2070	65	4
4	**5a**	30	0	10	17	3820	12
4	**5b**	24	7	7	22	2660	13
4	**5c**	18	13	9	28	2260	12
4	**5d**	10	26	5	51	1090	12
4	**5e**	0	29	16	270	260	8
5	**6a**	44	0	31	9	4830	15
5	**6b**	38	13	29	12	3040	14
5	**6c**	16	40	18	27	1270	14
5	**6d**	0	45	31	130	310	13
6	**7a**	53	0	73	7	5350	25
6	**7b**	34	35	55	8	3510	23
6	**7c**	16	50	55	13	2150	23
6	**7d**	0	77	51	27	470	18

[a] Average number of sugar residues was determined using MALDI-TOF MS data. See the Supporting Information for details. [b] Active sugar = man + glc. Standard deviation values ≤45%. All values represent at least three trials. [c] Relative activity of methyl mannose = 1 [d] All values represent at least three trials.

Table 2. Summary of Characterization Data for Man/Glc Functionalized Dendrimers

dendrimer generation	compd	mannose residues[a]	glucose residues[a]	galactose residues[a]	inhibiting sugar concn[b] (nmol)	rel activity/ active sugar[c]	Con A/ dendrimer[d]
3	**4f**	0	28	0	1190	60	5
3	**4g**	5	19	0	405	190	6
3	**4h**	13	11	0	290	480	ND[e]
3	**4i**	11	12	0	165	300	7
3	**4j**	28	0	0	230	280	7
4	**5f**	0	60	0	78	370	8
4	**5g**	4	45	0	140	280	12
4	**5h**	12	27	0	120	390	12
4	**5i**	19	21	0	55	830	12
4	**5j**	60	0	0	30	1030	13
5	**6e**	0	104	0	41	380	14
5	**6f**	13	57	0	36	760	17
5	**6g**	33	40	0	26	980	ND
5	**6h**	39	34	0	19	1350	16
5	**6i**	104	0	0	10	1780	17
6	**7e**	0	172	0	16	690	18
6	**7f**	33	72	0	18	960	25
6	**7g**	48	61	0	11	1540	26
6	**7h**	176	0	0	4	2460	25

[a] Average number of sugar residues was determined using MALDI-TOF MS data. See the Supporting Information for details. [b] Active sugar = man + glc. Standard deviation values ≤45%. All values represent at least three trials. [c] Relative activity of methyl mannose = 1. [d] All values represent at least three trials. [e] ND = not determined.

Table 3. Summary of Characterization Data for Glc/Gal Functionalized Dendrimers

dendrimer generation	compd	mannose residues[a]	glucose residues[a]	galactose residues[a]	inhibiting sugar concn[b] (nmol)	rel activity/ active sugar[c]	Con A/ dendrimer[d]
3	**4k**	0	10	10	NR[e]	NR	5
3	**4e**	0	14	11	2070	65	ND[f]
3	**4l**	0	18	6	1290	75	8
3	**4f**	0	28	0	1190	55	7
4	**5k**	0	20	17	8035	10	8
4	**5e**	0	29	15	270	240	8
4	**5l**	0	43	4	95	450	12
4	**5f**	0	60	0	78	370	13
5	**6j**	0	32	35	1520	40	14
5	**6d**	0	45	31	130	320	13
5	**6k**	0	62	14	52	580	15
5	**6e**	0	104	0	41	380	16
6	**7i**	0	47	79	470	80	20
6	**7d**	0	77	51	52	470	18
6	**7j**	0	80	38	27	860	21
6	**7e**	0	172	0	16	690	22

[a] Average number of sugar residues was determined using MALDI-TOF MS data. See the Supporting Information for details. [b] Active sugar = man + glc. Standard deviation values ≤45%. All values represent at least three trials. [c] Relative activity of methyl mannose = 1. [d] All values represent at least three trials. [e] NR = no detectable response [f] ND = not determined.

dendrimers showed a linear trend for relative activity in the hemagglutination assay (on a per active sugar basis) versus percent mannose of the mannose/glucose mixture and were consistent with a divalent interaction in the model set out by Whitesides et al. (see Discussion below for full details) (*39*). Here, we have added the G(3) series of 50% mannose/glucose functionalized dendrimers. Mannose/galactose, glucose/galactose, and mannose/glucose dendrimers with higher carbohydrate loadings in generations 3−6 are also reported. Results of the hemagglutination assays are shown in Tables 1−4. The relative activity numbers in the tables are on a per carbohydrate (glc + man) basis and are relative to methyl mannose.

Some of the compounds appear in multiple tables, since assays were performed simultaneously for compounds when

Table 4. Summary of Characterization Data for Man/Gal Functionalized Dendrimers

dendrimer generation	compd	mannose residues[a]	glucose residues[a]	galactose residues[a]	inhibiting sugar concn[b] (nmol)	rel activity/ ctive sugar[c]	Con A/ dendrimer[d]
3	**4m**	8	0	12	8795	30	6
3	**4a**	12	0	7	1395	120	7
3	**4n**	19	0	5	320	310	7
3	**4j**	28	0	0	230	280	7
4	**5m**	18	0	31	290	360	12
4	**5a**	30	0	10	55	1140	12
4	**5n**	38	0	9	42	1150	12
4	**5j**	60	0	0	30	1030	13
5	**6l**	26	0	43	97	750	17
5	**6a**	43	0	30	30	1440	15
5	**6i**	104	0	0	10	1780	16
6	**7k**	30	0	87	27	2300	17
6	**7a**	53	0	73	10	3370	25
6	**7l**	87	0	33	7	3170	26
6	**7h**	176	0	0	4	2460	25

[a] Average number of sugar residues was determined using MALDI-TOF MS data. See the Supporting Information for details. [b] Active sugar = man + glc. Standard deviation values ≤45%. All values represent at least three trials. [c] Relative activity of methyl mannose = 1. [d] All values represent at least three trials.

their results were to be compared. Different samples of rabbit erythrocytes, and even the relative freshness of erythrocytes from the same blood sample, can affect the absolute (but not the relative) values that are obtained from the hemagglutination assay. The hemagglutination assay affords activity trends that are clearly reproducible, although the absolute values for the assays are more variable.

Precipitation Assays. To determine the lectin clustering ability of these dendrimers, we performed precipitation assays. As described by Brewer et al., the dendrimer was incubated at varying concentrations with a constant concentration of Con A (*52*). When the Con A concentration is sufficiently high, the mannose functionalized dendrimer forms a precipitate with the Con A. The supernatant is removed, and the precipitate is washed with cold buffer and subsequently redissolved with a solution of 0.1 M methyl mannopyranoside solution. The Con A concentration in the remaining solution is then determined by measuring the UV absorbance at 280 nm. At the point that maximum precipitation of Con A is observed, the maximum Con A to dendrimer ratio can be determined. The precipitation assay results are provided in Tables 1−4. As with the hemagglutination assay results, some compounds are listed in more than one table so that trends across a series of carbohydrate loadings are easier to evaluate.

DISCUSSION

Synthesis and Characterization of Carbohydrate Functionalized Dendrimers. Dendrimers, macromolecules that are comprised of a series of branches emanating from a central core (*53*), are the ideal frameworks for the study of how systematic structural changes alter the way that a glycopolymer interacts with a protein. Higher generation dendrimers (PAMAM generations 4−6) are large enough to span multiple binding sites on a lectin (see Figure 1b), while lower generation dendrimers (generations 1−3) are too small to bind to multiple binding sites on Con A (see Figure 1a). In addition to changing the dendrimer generation, the degree of carbohydrate loading on a dendrimer can also be readily changed by controlling the number of equivalents of isothiocyanate that are added to the dendrimer solution. Because systematic changes can readily be made and because the three-dimensional (roughly spherical) structure of the dendrimer lends itself well to data interpretation, we chose dendrimers as the structural frameworks for our synthetic multivalent systems. We chose to use mannose, glucose, and galactose as ligands because of their known differences in affinity when binding to Con A. Mannose has a 4-fold higher affinity for Con A than glucose does, and galactose has no affinity for Con A (*54*). Because of the tetrahedral arrangements of the Con A binding sites, even the largest dendrimers used in this study (G(6)) cannot simultaneously bind to more than two of the four binding sites. Thus, for the dendrimer−Con A system, monovalent (as in Figure 1a) and divalent (as in Figure 1b) associations can be expected to occur.

Previously, we reported the binding by Con A of mannose/hydroxyl functionalized dendrimers. Optimal activity in the hemagglutination assay was observed when the dendrimers had 50% mannose incorporation. Dendrimers with higher mannose loadings had reduced activities with Con A (on a per sugar basis), suggesting that unfavorable steric interactions precluded optimal binding at high carbohydrate functionalization (*50*). For the research reported here, our goal was to quantify the effect that functionalization of the dendrimer with monomers of varying affinities would have on the multivalent activity of the dendrimer with lectins. Because of the previously optimized mannose/hydroxyl functionalized dendritic system, we first synthesized dendrimers with 50% functionalization by mannose and glucose. The preliminary results with these compounds were reported in a recent communication (*47*). Full studies with mannose/glucose functionalized dendrimers at 50% combined loading of mannose and glucose are reported here. In addition, complete studies with mannose/glucose, mannose/galactose, and glucose/galactose functionalized dendrimers are reported.

The synthesis scheme for dendrimer functionalization is shown in Scheme 1. When multiple sugars were added to the PAMAM dendrimers, incomplete addition of the final carbohydrate was observed. The excess isothiocyanate could be monitored by ^{1}H NMR, with the methylene group alpha to the isothiocyanato group giving rise to a triplet at 3.8 ppm. To cap any remaining accessible terminal amines, reactions with excess isothiocyanato sugars and with isothiocyanato ethoxyethanol **3** were heated to 40 °C. When neither of these additions was successful, we concluded that no primary amines were accessible on the periphery of the carbohydrate functionalized dendrimers. Unfunctionalized primary amines near the dendrimer surface could be protonated at physiological pH and could cause nonspecific interactions with Con A during assays. However, control hemagglutination assay and precipitation assay experiments with unfunctionalized PAMAMs and Con A indicated no interaction between the amine-functionalized PAMAM dendrimers and the protein. The degree of carbohydrate functionalization was in all cases determined by MALDI-TOF MS. Details of the MALDI-TOF MS characterization procedure are provided in the Experimental Section and in the Supporting Information, and the resultant number of sugars is reported in Tables 1−4.

Hemagglutination Inhibition Assays Using Dendrimers with 50% Mannose/Glucose Incorporation. In Figure 2, the activity with Con A of dendrimers with 50% combined

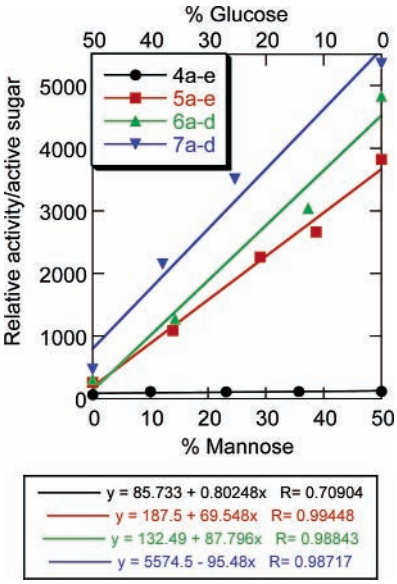

Figure 2. Relative activity per active sugar (man + glc) for dendrimers with 50% man/glc functionalization (see Table 1 for compound numbers and values).

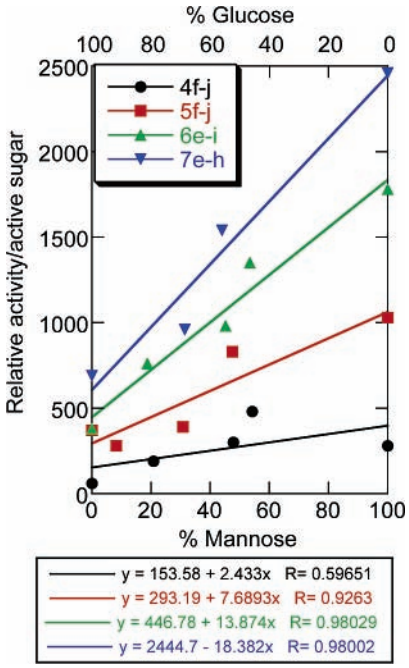

Figure 3. Relative activity per active sugar (man + glc) for man/glc functionalized dendrimers (see Table 2 for compound numbers and values).

functionalization by mannose and glucose (**4a**−**e**, **5a**−**e**, **6a**−**d**, **7a**−**d**) is shown. When dendrimers are 50% functionalized with man/glc mixtures, the relative amounts of glucose and mannose induce a linear change in the relative activity for generation 4, 5, and 6 dendrimers. The difference in relative activity between glucose functionalized and mannose functionalized dendrimers in the G(4) series (**5a** vs **5e**) is 14.7, the difference for G(5) dendrimers (**6a** vs **6d**) is 15.6, and the difference for G(6) dendrimers (**7a** vs **7d**) is 11.4. Dendrimers with partial mannose and partial glucose incorporation fall linearly between the all mannose and all glucose functionalized dendrimers. In the G(3) series, all of the dendrimers have comparable activities toward Con A. This is as expected, since carbohydrate functionalized G(3) PAMAMs are too small to bind divalently to Con A and only monovalent associations are likely.

Equation 1 was used to evaluate the hemagglutination assay data for compounds **5a**−**e**, **6a**−**d**, and **7a**−**d**. In eq 1, K^{mono} is the monovalent association constant, K_N^{poly} is the multivalent association constant, N is the number of receptor−ligand interactions, and α is the cooperativity factor. Here, a cooperativity constant α of 1 was used. Negatively cooperative, positively cooperative, and noncooperative systems are all theoretically possible. However, only one or two examples of protein−carbohydrate interactions with thermodynamic parameters suggestive of positive cooperativity have been reported (*39*). Negatively cooperative and noncooperative systems are much more common. We have chosen to leave $\alpha = 1$ because of the precedent where noncooperative associations were assumed for Con A (*55*) and because a Con A−dendrimer interaction where the first binding event at one binding site is thermodynamically significantly different from the second binding event at a second binding site is not expected. Although the appropriate value of N for this system cannot be assigned with absolute certainty (because precipitation occurs under conditions appropriate for ITC), N must surely be equal to 1 or 2. The shape of tetrameric Con A and the relative locations of the mannose binding sites on tetrameric Con A preclude trivalent or tetravalent binding by a roughly spherical, dendritic system. Although a value of $N = 1$ is possible, $N = 2$ is suggested for **5**−**7** by the results of precipitation assay experiments, transmission electron micrographs, and hemagglutination assays (*47*, *50*, *56*).

Using eq 1, and assuming $\alpha = 1$ and $N = 2$, one would predict that exchanging mannose for glucose would cause a 4^2 or 16-fold reduction in binding to Con A, since the relative activities of monomeric methyl mannose and methyl glucose vary by a factor of 4. This is very close to the values observed for G(4) (14.6), G(5) (15.6), and G(6) (11.4). Perhaps the larger deviation from 16 for G(6) is due to the larger size of G(6), which could allow for a compensatory effect due to increased sugar clustering around the binding sites (*40*). Alternatively, the curvature of the G(6) dendrimers may be different enough from G(4) and G(5) to change the shape complementarity between Con A and the dendrimer, which can significantly change the association motif (*57*).

Hemagglutination Inhibition Assays Using Mannose/Glucose Functionalized Dendrimers. The activity with Con A of man/glc functionalized dendrimers **4f**−**4j**, **5f**−**5j**, **6e**−**i**, and **7e**−**7h** is shown in Figure 3. Increasing the number of mannose residues while decreasing the number of glucose residues causes an increase in the relative activity with Con A. As with the dendrimers bearing 50% mannose/glucose loading, a linear relationship between man/glc loading and assay activity is observed for compounds in generations 4−6. However, the difference between fully mannose functionalized dendrimers and fully glucose functionalized dendrimers never approaches 16. For generation 3 compounds **4f**−**4j**, mannose functionalized compounds **4j** have a 5-fold higher relative activity with Con A than do the glucose functionalized compounds **4f**. For generations 4−6, the differences between mannose and glucose functionalized compounds are 2.8 (**5f** vs **5j**), 4.7 (**6e** vs **6i**), and 3.7 (**7e** vs **7h**), respectively. Also, having more than 50% loading by the active sugars decreases the assay activity (for example, **6b** is about twice as active as **6h**).

We previously attributed the lower affinity of dendrimers above 50% sugar loading to unfavorable steric interactions between the dendrimer and the protein (*50*). The deviation from the 16-fold affinity difference predicted by eq 1, and the reduced activity for compounds with higher than 50% loading suggest that the degree of clustering of the sugars may be more important for some compounds than for others. Dendrimers with higher glucose content have lower intrinsic binding affinities for Con

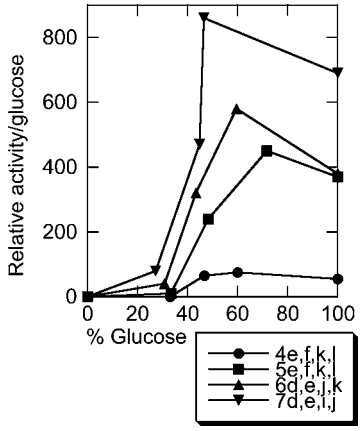

Figure 4. Relative activity per glucose for glc/gal functionalized dendrimers (see Table 3 for compound numbers and values).

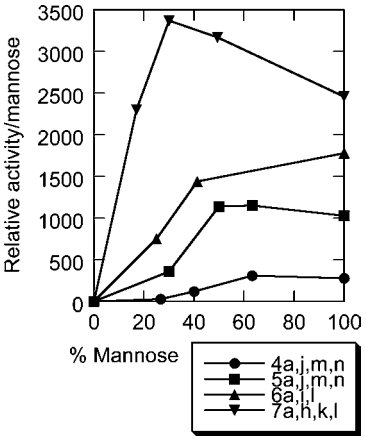

Figure 5. Relative activity per mannose for man/gal functionalized dendrimers (see Table 4 for compound numbers and values).

A (than highly mannose functionalized dendrimers) and may rely more on statistical binding effects (Figure 1a). Differences in how the dendrimers overcome unfavorable steric crowding coupled to differences in how important clustering of carbohydrates is could cause the cooperativity constant α to change from 1 and could account for the fact that the difference between mannose and glucose functionalized dendrimers is significantly lower than 16.

Hemagglutination Inhibition Assays with Mannose/Galactose and Glucose/Galactose Functionalized Dendrimers. The activities with Con A of glc/gal and man/gal functionalized dendrimers (**4e**,**f**,**k**−**n**, **5e**,**f**,**j**−**n**, **6d**−**f**,**j**−**l**, and **7d**,**e**,**i**−**l**) are shown in Figures 4 and 5. All of the glc/gal dendrimers have lower activities than their analogous man/gal dendrimers. In the G(3) series, the glc/gal dendrimers with the highest activity are four times less active than the highest activity man/gal dendrimers (**4j** vs **4l**). In generations 4−6, the glc/gal dendrimers with the highest activity are 2.6 times (**5n** vs **5l**), 2.5−3.1 times (**6a** or **6i** vs **6k**), and 3.7−3.9 times (**7a** or **7l** vs **7j**) less active. These differences are considerably lower than those observed for the 50% functionalized mannose/glucose series (Figure 2), where nearly 16-fold differences in activity were observed.

Following trends that were previously observed for mannose/hydroxyl functionalized dendrimers,[38] the fully carbohydrate functionalized dendrimers have lower relative activities (on a per sugar basis) than the partially carbohydrate functionalized dendrimers do. Man/gal functionalized dendrimers have optimum activity with Con A at 50−60% mannose incorporation (G(4)), 40−50% mannose incorporation (G(5)), and 30−40% mannose incorporation (G(6)). Higher glucose loadings are required to achieve optimal activity with glc/gal dendrimers; roughly 70, 60, and 50% glucose functionalization produced the highest activity with Con A for generations 4−6, respectively. This is of interest as it may indicate that, with a weaker interaction, proximity/statistical effects are more important to binding. Both the man/gal and the glc/gal G(3) dendrimers have relatively low activity toward Con A in the assay, as would be expected for small dendrimers where statistical enhancements on binding affinity (and not multivalency) are observed.

Hemagglutination Inhibition Assays in General. Hemagglutination assays display qualitative trends rather than absolute values. In our studies, performing the assay with different samples of erythrocytes changed the absolute values but never the relative trends for this assay. Taken together, the data from the four series of compounds above suggest that, for optimized systems, eq 1 works well to predict how monovalent ligands displayed on a multivalent framework attenuate binding activity. However, the system must be optimized, or affinity differences much lower than those predicted by eq 1 will be obtained. When low-affinity ligands (such as glucose) are present in significant quantities, proximity effects may become more important than they are when higher affinity ligands (such as mannose) are present as the major functionality.

Precipitation Assays. Graphs showing the maximum number of Con A lectins recruited by each dendrimer are shown in Figure 6. Figure 6a shows the Con A:dendrimer ratio for 50% mannose/glucose functionalized dendrimers, Figure 6b shows the Con A:dendrimer ratio for mannose/glucose functionalized dendrimers, Figure 6c shows the Con A:dendrimer ratio for mannose/galactose functionalized dendrimers, and Figure 6d shows the Con A:dendrimer ratio for glucose/galactose functionalized dendrimers. The maximum average number of Con A's that can fit around carbohydrate functionalized dendrimers

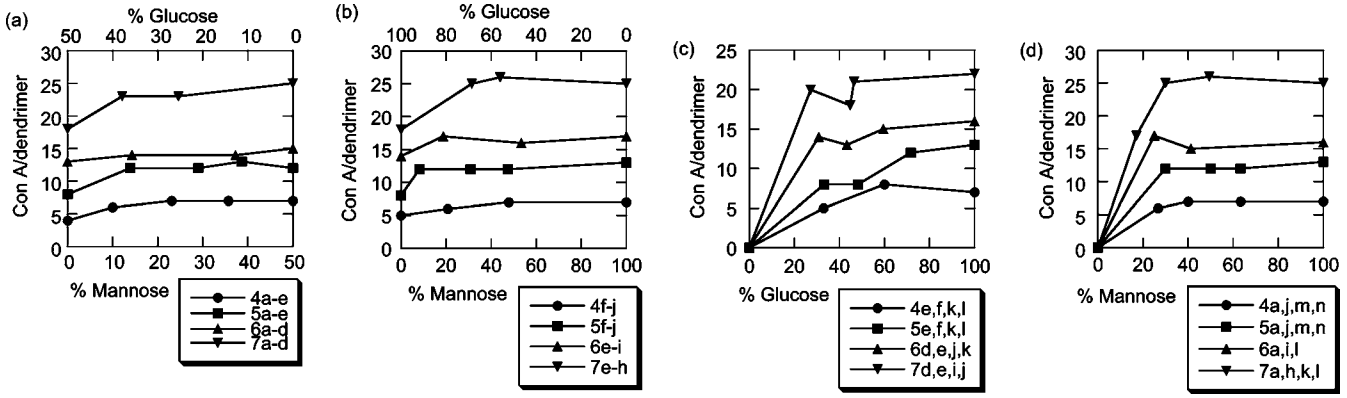

Figure 6. Number of Con A lectins per dendrimer (a) dendrimers with 50% man/glc functionalization, (b) man/glc functionalized dendrimers, (c) glc/gal functionalized dendrimers, and (d) man/gal functionalized dendrimers. Values are given in Tables 1−4.

was previously determined to be 9−10, 12−13, 15−16, and 22−23 for G(3) through G(6), respectively (*50*). For all of the series shown here, the G(3) dendrimers recruit less than the optimal number of Con A lectins. This suggests that Con A binds monovalently to all of the G(3) PAMAMs, reducing the strength of the association and causing unoptimized binding to occur (*58*). All carbohydrate functionalized G(4) and G(5) PAMAMs recruit the optimal number of Con A lectins, while the carbohydrate functionalized G(6) PAMAMs typically bind to slightly more than the theoretically determined number of proteins (*59*). The 50% man/glc functionalized compounds **5a**−**e, 6a**−**d**, and **7a**−**d** show no change in clustering until all the active sugar is glucose; then the ratios drop from 12−13 to 8, from 14−15 to 13, and from 23−25 to 18, respectively (Figure 6a). Comparable trends are observed for man/glc functionalized dendrimers with higher ligand loadings (Figure 6b). Similarly, in the man/gal series (Figure 6c) and the glc/gal series (Figure 6d), the maximum number of Con A lectins that can be recruited are clustered around the dendrimers when at least 25% of the carbohydrates are Con A binding ligands. Glc/gal dendrimers appear to show small increases in Con A recruitment with increased glucose functionalization, but man/gal dendrimers level off after 25% mannose incorporation. The number of Con A lectins recruited is the same for generations 3−5. For generation 6, man/gal functionalized dendrimers cluster consistently more Con A lectins (25−26 lectins) than glc/gal functionalized dendrimers do (18−22 lectins). Control dendrimers with only galactose functionalization fail to precipitate Con A. The precipitation assay results indicate that the number of Con A lectins that can be recruited by a dendrimer is not greatly affected when the relative activity (as determined in the hemagglutination assays) is altered by an order of magnitude.

CONCLUSION

Multivalent binding between proteins and carbohydrates mediates many biological events. The goal of the research reported here was to determine whether monovalent differences in affinity affect multivalent association constants in predictable ways. For optimized systems such as the dendrimers with 50% loading of mannose and glucose, the equation described by Whitesides and co-workers (eq 1) works well to predict how monovalent ligands displayed on a multivalent framework will attenuate binding activity. For more highly functionalized man/glc, man/gal, and glc/gal dendrimers, activity differences for hemagglutination assays with Con A that were much lower than those predicted by eq 1 were obtained. For this system, dendrimers with more glucose residues appear to compensate for the steric downfall of full functionalization by relying more on proximity enhancements than mannose functionalized dendrimers do. Although varying the ligands on the dendrimer can cause up to 16-fold differences in relative activity in the hemagglutination assay, only small differences in the maximum number of Con A lectins recruited by the dendrimers were observed.

The results reported here suggest that multivalency can be influenced in predictable—and therefore tunable—ways. Monovalent differences are amplified by multivalent associations, and mixtures of low- and high-affinity ligands can be used to attenuate multivalent binding activities. Attenuation of the binding activity (as studied in the hemagglutination assay) is largely independent of the degree of protein clustering (as measured in the precipitation assay). Natural systems likely use modulation of properties such as avidity and protein clustering to control physiological processes. Because of their ready tunability, the carbohydrate functionalized dendrimers described here should provide guidelines for the development of synthetic multivalent frameworks for many applications in chemical biology. Studies are currently underway to investigate how these results will transpose into more complex biological systems.

ACKNOWLEDGMENT

Funding of this work by the NIH (Grant NIGMS 62444) is gratefully acknowledged. M.L.W. gratefully acknowledges NSF EPSCoR for a predoctoral fellowship.

Supporting Information Available: Experimental procedures and characterization data for **4**−**7**. This material is available free of charge via the Internet at http://pubs.acs.org.

LITERATURE CITED

(1) Lis, H., and Sharon, N. (1998) Lectins: Carbohydrate-specific proteins that mediate cellular recognition. *Chem. Rev. 98*, 637−674.
(2) Dwek, R. A. (1996) Glycobiology: Toward understanding the function of sugars. *Chem. Rev. 96*, 683−720.
(3) Mann, D. A., and Kiessling, L. L. The chemistry and biology of multivalent saccharide displays. In (2001) *Glycochemistry: Principles, Synthesis, and Applications*, (Wang, G., Bertozzi, C. R., Eds.) pp 221−275, P. Marcel Dekker, New York.
(4) Gabius, H.-J., Siebert, H. C., Andre, S., Jimenez-Barbero, J., and Rudiger, H. (2004) Chemical biology of the sugar code. *ChemBioChem 5*, 740−764.
(5) Choi, S. K. (2004) *Synthetic Multivalent Molecules*, Wiley-VCH, New York.
(6) Mowery, P., Yang, Z.-Q., Gordon, E. J., Dwir, O., Spencer, A. G., Alon, R., and Kiessling, L. L. (2004) Synthetic glycoprotein mimics inhibit L-selectin-mediated rolling and promote L-selectin shedding. *Chem. Biol. 11*, 725−732.
(7) Sigal, G. B., Mammen, M., Dahmann, G., and Whitesides, G. M. (1996) Polyacrylamides bearing pendant α-sialoside groups strongly inhibit agglutination of erythrocytes by influenza virus: The strong inhibition reflects enhanced binding through cooperative polyvalent interactions *J. Am. Chem. Soc. 118*, 3789−3800.
(8) Gupta, S. S., Kuzelka, J., Singh, P., Lewis, W. G., Manchester, M., and Finn, M. G. (2005) Accelerated bioorthogonal conjugation: A practical method for the Ligation of diverse functional molecules to a polyvalent virus scaffold. *Bioconjugate Chem. 16*, 1572−1579.
(9) Svarovsky, S. A., Szekely, Z., and Barchi, J. J. (2005) Synthesis of gold nanoparticles bearing the Thomsen-Frienenreich disaccharide: A new multivalent presentation of an important tumor antigen. *Tetrahedron Asym. 16*, 587−598.
(10) Nelson, A., Belitsky, J. M., Vidal, S., Joiner, C. S., Baum, L. G., and Stoddart, J. F. (2004) A self-assembled multivalent pseudopolyrotaxane for binding galectin-1. *J. Am. Chem. Soc. 126*, 11914−11922.
(11) Andre, S., Kaltner, H., Furuike, T., Nishimura, S.-I., and Gabius, H.-J. (2004) Persubstituted cyclodextrin-based glycoclusters as inhibitors of protein-carbohydrate recognition using purified plant and mammalian lectins and wild-type and lectin-gene-transfected tumor cells as targets. *Bioconjugate Chem. 15*, 87−98.
(12) Dong, C.-M., and Chaikof, E. L. (2005) Self-assembled nanostructures of a biomimetic glycopolymer-polypeptide triblock copolymer. *Colloid Polym. Sci. 283*, 1366−1370.
(13) Buskas, T., Ingale, S., and Boons, G.-J. (2005) Towards a fully synthetic carbohydrate-based anticancer vaccine: Synthesis and immunological evaluation of a lipidated glycopeptide containing the tumor-associated Tn antigen. *Angew. Chem., Int. Ed. 44*, 5985−5988.
(14) Wang, Y., and Kiick, K. L. (2005) Monodisperse protein-based glycopolymers via a combined biosynthetic and chemical approach. *J. Am. Chem. Soc. 127*, 16392−16393.
(15) Thayer, D. A., Yu, H. N., Galan, M. C., and Wong, C.-H. (2005) A general strategy toward S-linked glycopeptides. *Angew. Chem., Int. Ed. 44*, 4596−4599.
(16) Kanda, V., Kitov, P., Bundle, D. R., and McDermott, M. T. (2005) Surface plasmon resonance imaging measurements of the inhibition of Shiga-like toxin by synthetic multivalent inhibitors. *Anal. Chem. 7*, 7497−7504.
(17) Thoma, G., Streiff, M. B., Katopodis, A. G., Duthaler, R. O., Voelcker, N. H, Ehrhardt, C., and Masson, C. (2006) Non-covalent

polyvalent ligands by self-assembly of small glycodendrimers: A novel concept for the inhibition of polyvalent carbohydrate-protein interactions in vitro and in vivo. *Chem. Eur. J. 12*, 99−117.
(18) Roy, R. (2003) A decade of glycodendrimer chemistry. *Trends Glycosci. Glycotech. 15*, 291−310.
(19) Pieters, R. J. (2004) Interference with lectin binding and bacterial adhesion by multivalent carbohydrates and peptidic carbohydrate mimics. *Trends Glycosci. Glycotechnol. 16*, 243−254.
(20) Benito, J. M., Gomez-Garcia, M., Ortiz Mellet, C., Baussanne, I., Defaye, J., and Garcia Fernandez, J. M. (2004) Optimizing saccharide-directed molecular delivery to biological receptors: Design, synthesis, and biological evaluation of glycodendrimer−cyclodextrin conjugates. *J. Am. Chem. Soc. 126*, 10355−10363.
(21) Kalovidouris, S. A., Blixt, O., Nelson, A., Vidal, S., Turnbull, W. B., Paulson, J. C., and Stoddart, J. F. (2003) Synthetic carbohydrate dendrimers, part 11. Chemically defined sialoside scaffolds for investigation of multivalent interactions with sialic acid binding proteins. *J. Org. Chem. 68*, 8485−8493.
(22) Vrasidas, I., Valentini, P., Bock, C., Lensch, M., Kaltner, H., Liskamp, R. M. J., Gabius, H.-J., and Pieters, R. J. (2003) Rigidified multivalent lactose molecules and their interactions with mammalian galectins; a route to selective inhibitors. *Org. Biomol. Chem. 1*, 803−810.
(23) Page, D., and Roy, R. (1997) Synthesis and biological properties of mannosylated starburst poly(amidoamine) dendrimers. *Bioconjugate Chem. 8*, 714−723.
(24) Hayes, W., Osborn, H. M. I., Osborne, S. D., Rastall, R. A., Romagnoli, B. (2003) One-pot synthesis of multivalent arrays of mannose mono- and disaccharides. *Tetrahedron 59*, 7983−7996.
(25) Dimick, S. M., Powell, S. C., McMahon, S. A., Moothoo, D. M., Naismith, J. H., and Toone, E. J. (1999) On the meaning of affinity: Cluster glycoside effects and concanavalin A. *J. Am. Chem. Soc. 121*, 10286−10296.
(26) Tsvetkov, D. E., Cheshev, P. E., Tuzikov, A. B., Chinarev, A. A., Pazynina, G. V., Sablina, M. A., Gambaryan, A. S., Bovin, N. V., Rieben, R., Shashkov, A. S., and Nifant'ev, N. E. (2002) Neoglycoconjugates based on dendrimer poly(aminoamides). *Russ. J. Bioorg. Chem. (Transl. Bioorg. Khim.) 28*, 470−486.
(27) Lee, N.-Y., Jang, W.-J., Yu, S.-H., Im, J., and Chung, S.-K. (2005) Syntheses of glycodendrimers having scyllo-inositol as the scaffold. *Tetrahedron Lett. 46*, 6063−6066.
(28) Srinivas, O., Radhika, S., Bandaru, N. M., Nadimpalli, S. K., and Jayaraman, N. (2005) Novel multivalent mannose compounds and their inhibition of the adhesion of type 1 fimbriated uropathogenic *E. coli*. *Org. Biomol. Chem. 3*, 4252−4257.
(29) Rele, S. M., Cui, W., Wang, L., Hou, S., Barr-Zarse, G., Tatton, D., Gnanou, Y., Esko, J. D., and Chaikof, E. L. (2005) Dendrimer-like PEO glycopolymers exhibit antiinflammatory properties. *J. Am. Chem. Soc. 127*, 10132−10133.
(30) Kensinger, R. D., Yowler, B. C., Benesi, A. J., and Schengrund, C.-L. (2004) Synthesis of novel, multivalent glycodendrimers as ligands for HIV-1 gp120. *Bioconjugate Chem. 15*, 349−358.
(31) Rojo, J., Diaz, V., de la Fuente, J. M., Segura, I., Barrientos, A. G., Riese, H. H., Bernad A., and Penades, S. (2004) Gold glyconanoparticles as new tools in antiadhesive therapy. *ChemBioChem 5*, 291−297.
(32) Johansson, S. M. C., Arnberg, N., Elofsson, M., Wadell, G., and Kihlberg, H. (2005) Multivalent HSA conjugates of 3′-siallyllactose are potent inhibitors of adenoviral cell attachment and infection. *ChemBioChem 6*, 358−364.
(33) Disney, M. D., Zheng, J., Swager, T. M., and Seeberger, P. H. (2004) Detection of bacteria with carbohydrate-functionalized fluorescent polymers. *J. Am. Chem. Soc. 126*, 13343−13346.
(34) Van Damme, E. J. M., Peumans, W. J., Barre, A., and Rouge, P. (1998) Plant lectins: A composite of several distinct families of structurally and evolutionary related proteins with diverse biological roles. *Crit. Rev. Plant Sci. 17*, 575−692.
(35) Gestwicki, J. E., Cairo, C. W., Strong, L. E., Oejten, K. A., and Kiessling, L. L. (2002) Influencing receptor−ligand binding mechanisms with multivalent ligand architecture. *J. Am. Chem. Soc. 124*, 14922−14933.
(36) Mortell, K. H., Weatherman, R. V., and Kiessling, L. L. (1996) Recognition specificity of neoglycopolymers prepared by ring-opening metathesis polymerization. *J. Am. Chem. Soc. 118*, 2297−2298.
(37) Kanai, M., Mortell, K. H., and Kiessling, L. L. (1997) Varying the size of multivalent ligands: The dependence of concanavalin A binding on neoglycopolymer length. *J. Am. Chem. Soc. 119*, 9931−9932.
(38) Andre, S. Ortega, P. J. C., Perez, M. A., Roy, R., and Gabius, H. J. (1999) Lactose-containing starburst dendrimers: Influence of dendrimer generation and binding-site orientation of receptors (plant/animal lectins and immunoglobulins) on binding properties. *Glycobiology 9*, 1253−1261.
(39) Mammen, M., Choi, S.-K., and Whitesides, G. M. (1998) Polyvalent interactions in biological systems: Implications for design and use of multivalent ligands and inhibitors. *Angew. Chem., Int. Ed. 37*, 2754−2794.
(40) Lee, R. T., and Lee, Y. C. (2000) Affinity enhancement by multivalent lectin-carbohydrate interaction. *Glycoconjugate J. 17*, 543−551.
(41) Lundquist, J. J., and Toone, E. J. (2002) The cluster glycoside effect. *Chem. Rev. 102*, 555−578.
(42) Quesenberry, M. S., Lee, R. T., and Lee, Y. C. (1997) Difference in the binding mode of two mannose-binding proteins: Demonstration of a selective minicluster effect. *Biochemistry 36*, 2724−2732.
(43) Page, M. I., and Jencks, W. P. (1971) Entropic contributions to rate accelerations in enzymatic and intramolecular reactions and chelate effect. *Proc. Natl. Acad. Sci. U.S.A. 68*, 1678−1683.
(44) Jencks, W. P. (1981) On the attribution and additivity of binding-energies. *Proc. Natl. Acad. Sci. U.S.A. 78*, 4046−4050.
(45) Gargano, J. M., Ngo, T., Kim, J. Y., Acheson, D. W. K., and Lees, W. J. (2001) Multivalent inhibition of AB(5) toxins. *J. Am. Chem. Soc. 123*, 12909−12910.
(46) Mulder, A., Huskens, J., and Reinhoudt, D. N. (2004) Multivalency in supramolecular chemistry and nanofabrication. *Org. Biomol. Chem. 2*, 3409−3424.
(47) Wolfenden, M. L., and Cloninger, M. J. (2005) Mannose/glucose-functionalized dendrimers to investigate the predictable tunability of multivalent interactions. *J. Am. Chem. Soc. 127*, 12168−12169.
(48) Lee, T. L., and Lee, Y. C. (1974) Synthesis of 3-(2-aminoethylthio)propyl glycosides. *Carbohydr. Res. 37*, 193−201.
(49) This method has been shown to give equal loading amounts. Newkome, G. R., Wies, C. D., Moorefield, C. N., Baker, G. R., Childs, B. J., and Epperson, J. (1998) Isocyanate-based dendritic building blocks: Combinatorial tier construction and macromolecular-property modification. *Angew. Chem., Int. Ed. 37*, 307−310.
(50) Woller, E. K., Walter, E. D., Morgan, J. R., Singel, D. J., and Cloninger, M. J. (2003) Altering the strength of lectin binding interactions and controlling the amount of lectin clustering using mannose/hydroxyl-functionalized dendrimers. *J. Am. Chem. Soc. 125*, 8820−8826.
(51) Osawa, T., and Matsumoto, I. (1972) Gorse (*Ulex europeus)* phytohemagglutinins. *Methods Enzymol. 28*, 323−327.
(52) Khan, M. I., Mandal, D. K., and Brewer C. F. (1991) Interactions of concanavalin A with glycoproteins-A quantitative precipitation study of concanavalin-A with the soybean agglutitnin *Carbohydr. Res. 213*, 69−77.
(53) Newkome, G. R., Moorefield, C. N., and Vögtle, F. (2001) Dendrimers and Dendrons: Concepts, Syntheses. *Applications*, Wiley-VCH, Weinheim, Germany.
(54) Mandal D. K., Kishore N., and Brewer C. F. (1994) Thermodynamics of lectin−carbohydrate interactions. Titration microcalorimetry measurements of the binding of N-linked carbohydrates and ovalbumin to concanavalin A. *Biochemistry 33*; 1149−56.
(55) Corbell, J. B., Lundquist, J. J., and Toone, E. J. (2000) A comparison of biological and calorimetric analyses of multivalent glycodendrimer ligands for concanavalin A. *Tetrahedron Asym. 11*, 95−111.
(56) Woller, E. K., and Cloninger, M. J. (2002) The lectin-binding properties of six generations of mannose-functionalized dendrimers. *Org. Lett. 4*, 7−10.
(57) Schlick, K. H., Udelhoven, R. A., Strohmeyer, G. A., and Cloninger, M. J. (2005) *Mol. Pharm. 2*, 295−301.
(58) See ref 44 for an example of precipitation assays where monovalent associations between dendrimers and lectins are occurring.
(59) See the Supporting Information for a more complete discussion on this point.

BC060107X

Site-Specific, Covalent Attachment of Proteins to a Solid Surface

Benjamin P. Duckworth,[†] Juhua Xu,[†] T. Andrew Taton,[†] Athena Guo,[‡] and Mark D. Distefano*,[†]

Department of Chemistry, University of Minnesota, Minneapolis, Minnesota 55455 and MicroSurfaces, Inc., 4001 Stinson Boulevard, Suite 430, Minneapolis, Minnesota 55421. Received May 16, 2006; Revised Manuscript Received June 6, 2006

Immobilized and site-specifically labeled proteins are becoming invaluable tools in proteomics. Here, we describe a strategy to attach a desired protein to a solid surface in a covalent, site-specific manner. This approach employs an enzymatic posttranslational modification method to site-specifically label a target protein with an azide; an alternative substrate for protein farnesyl transferase containing an azide group was developed for this purpose. A bio-orthogonal Cu(I)-catalyzed cycloaddition reaction is then used to covalently attach the protein to agarose beads bearing an alkyne functional group. We demonstrate that both the azide incorporation and the capture steps can be performed on either a purified protein target or on a protein present within a complex mixture. This approach involves the use of a four-residue tag which is significantly smaller than most other tags reported to date and results in covalent immobilization of the target protein. Hence it should have significant applicability in protein science.

INTRODUCTION

The attachment of proteins and other biomolecules to surfaces in a site-specific, covalent manner is becoming increasingly important in the field of biotechnology. Immobilized proteins are instrumental in identifying protein−protein (*1*), protein−DNA (*2*), and protein−small molecule (*3*) interactions; they can also be used for a variety of diagnostic purposes (*4*). Several approaches exist for linking proteins to surfaces including covalent and noncovalent strategies. Most methods that involve covalent attachment rely on nonselective reaction between a protein's surface lysine residues and a solid support (*5*, *6*); this results in a heterogeneous ensemble of immobilized molecules. While this problem can be circumvented through the introduction of unique cysteine residues, that approach becomes difficult with larger proteins where multiple cysteines are present (*7*). A different strategy for protein immobilization relies on the use of peptide tags (*8*) or protein fusions (*9*). While these methods result in homogeneous attachment of proteins to surfaces, they accomplish this via noncovalent protein−protein interactions or kinetically labile protein−metal interactions and are consequently intrinsically less stable. Another approach relies on active-site directed covalent attachment of fusion proteins to surfaces (*10*, *11*). Although this does yield a covalent, specific attachment, it requires the fusion of a large polypeptide segment (>22 kDa) to the target protein (*12*). Numerous researchers have commented that this is not always desirable (*13*−*16*). One recent solution to that problem was reported by Camarero and coworkers, who successfully immobilized proteins using a traceless, protein trans-splicing method (*17*).

Recently, several approaches using enzymatic methods have been developed that allow proteins to be modified for the purpose of site specific labeling (*18*−*21*). Such strategies capitalize on the high specificity of enzymes to modify a protein at a unique site in a manner that facilitates subsequent functionalization. Here we present a strategy that involves the labeling of a desired protein with an azide via an enzyme-catalyzed reaction. The recognition tag for the enzyme protein farnesyltransferase (PFTase) is only four amino acids in length and is recognized by the enzyme only when present at the C-terminus of a protein. The azide-labeled protein is then coupled to a surface bearing an alkyne group using a bio-orthogonal reaction (*22*−*26*). Thus, this new strategy provides a method for both site-specifically and covalently anchoring proteins to solid surfaces without the need for large fusion proteins. Additionally, this strategy can be applied to virtually any protein and any surface.

EXPERIMENTAL PROCEDURES

Materials and Methods. All synthetic reactions were conducted under air atmosphere and stirred magnetically, unless otherwise indicated. Analytical TLC was performed on precoated (250 μm) silica gel 60 F-254 plates from Merck. All plates were visualized by UV irradiation, staining with potassium permanganate ($KMnO_4$) or with phosphomolybdic acid (PMA). Flash chromatography (silica gel, 60−120 mesh) was obtained from Mallinckrodt Inc. CH_2Cl_2, THF, and CH_3CN were dried using a Mbraun solvent purification system. Deuterated NMR solvents were used as obtained from Cambridge Isotope Laboratories, Inc. ^{1}H NMR spectra were obtained at 300 or 500 MHz. ^{13}C NMR spectra were obtained at 75 MHz. All NMR spectra were obtained on Varian instruments at 25 °C. Chemical shifts are reported in ppm and *J* values are given in Hz. Preparative HPLC was carried out using a Beckman model 127/166 instrument equipped with a UV detector and a Phenomenex C_{18} column (Luna, 10 μM, 10.0 × 250 mm) equipped with a 5 cm guard column. Analytical HPLC was carried out using a Beckman model 125/168 instrument equipped with a UV detector, ABI Analytical Spectroflow 980 fluorescence detector, and a Varian C_{18} column (Microsorb-MV, 5 μm, 4.6 × 250 mm). $CuSO_4$ was purchased from Mallinckrodt while TCEP was purchased from Invitrogen. All other chemical agents were purchased from Aldrich Chemical Co. unless otherwise noted.

(*E*,*E*)-3,7,11-Trimethyl-1-*O*-THP-2,6,10-dodecatriene (1). A mixture of farnesol (8.9 g, 40 mmol), 3,4-dihydro-2*H*-pyran (DHP, 5.0 g, 60 mmol), and pyridium *p*-toluenesulfonate (PPTS, 1.0 g, 4.0 mmol) in dry CH_2Cl_2 was stirred at room temperature for 4 h. After concentration in vacuo, the crude mixture was redissolved in Et_2O and the organic layer was washed with saturated $NaHCO_3$ (50 mL) and dried using Na_2SO_4, yielding

* To whom correspondence should be addressed. Tel: (612) 624-0544; Fax (612) 626-7541; e-mail: distefan@chem.umn.edu.

[†] University of Minnesota.

[‡] MicroSurfaces, Inc..

10.1021/bc060125e CCC: $33.50 © 2006 American Chemical Society
Published on Web 06/28/2006

compound **1** (12 g, 98%). NMR assignments have previously been reported for compound **1** (*27*).

(*E*,*E*,*E*)-2,6,10-Trimethyl-12-*O*-THP-2,6,10-dodecatrienealdehyde (2). The allylic aldehyde **2** was prepared by a procedure based on several literature precedents. (*28*−*30*). Selenium dioxide (1.0 g, 9.0 mmol) and pyridine (3.0 mL) were added to a stirred solution of **1** (5.5 g, 18 mmol) in 50 mL of EtOH. The reaction mixture was heated to reflux for 4 h, after which the reaction was cooled to room temperature, filtered, and concentrated in vacuo. The residue was redissolved in Et_2O, washed with brine, and dried using Na_2SO_4. After removal of the solvent in vacuo, the crude product was dissolved in 50 mL of CH_2Cl_2, and to this solution was added 10 g (27 mmol) of pyridinium dichromate (PDC). The reaction mixture was stirred at room-temperature overnight and then filtered. Compound **2** was purified using column chromatography (flash silica) to yield 0.80 g (14%) of **2** as a colorless oil. (R_f = 0.63, hexanes:EtOAc = 3:1). ^{1}H NMR (300 MHz, $CDCl_3$) δ 1.55 (m, 5H), 1.63 (s, 3H), 1.67 (s, 3H), 1.74 (s, 3H), 1.82 (m, 1H), 2.0−2.25 (m, 6H), 2.46 (m, 2H), 3.51 (m, 1H), 3.89 (m, 1H), 4.02 (dd, J = 7.3 Hz, J = 12 Hz, 1H), 4.24 (dd, J = 6.3 Hz, J = 12 Hz, 1H), 4.62 (dd, J = 3.0 Hz, J = 4.5 Hz, 1H), 5.16 (t, J = 6.2 Hz, 3 H), 5.36 (dd, J = 6.3 Hz, J = 7.3 Hz, 1H), 6.46 (t, J = 7.2 Hz, 1H), 9.37 (s, 1H). ^{13}C NMR (75 MHz, $CDCl_3$) δ 195.38, 154.53, 139.95, 133.71, 125.33, 121.75, 120.86, 97.91, 63.70, 62.35, 39.51, 38.01, 30.77, 27.45, 26.25, 25.55, 19.69, 16.47, 15.97, 9.28. HR-ESI-MS calcd for $C_{20}H_{32}NaO_3$ [M + Na]$^+$ 343.2244, found 343.2234.

(*E*,*E*)-3,7,11-Trimethyl-1-*O*-THP-2,6-dodecadiene-12-ol (3). Compound **3** was prepared by a procedure developed by Moody and co-workers (*31*). To a solution of **2** (2.0 g, 6.0 mmol) in benzene (35 mL) and water (31 mL) were added $Na_2S_2O_4$ (85%, 3.2 g, 24 mmol), Aliquat 336 (0.48 g, 1.2 mmol), and $NaHCO_3$ (2.5 g, 30 mmol). The stirred reaction mixture was heated to 80 °C for 4 h. After being cooled to room temperature, the organic phase was concentrated in vacuo and diluted with 40 mL of Et_2O. The mixture was washed with brine (3 × 20 mL) and dried using Na_2SO_4. Compound **3** was purified using column chromatography (flash silica) to yield 0.95 g (50%) of **3**, a colorless oil. (R_f = 0.24, hexanes:EtOAc = 3:1). ^{1}H NMR (300 MHz, $CDCl_3$) δ 0.84 (d, J = 6.9, Hz, 3H), 1.34 (m, 6H), 1.50−1.66 (m, 7H), 1.69 (s, 3H), 1.80 (m, 1H), 1.86−2.18 (m, 6H), 3.38 (m, 1H), 3.48 (m, 2H), 3.87 (m, 1H), 4.01 (dd, J1 = 7.5 Hz, J2 = 11.7 Hz, 1H), 4.21 (dd, J = 6.6 Hz, J = 11.7 Hz, 1H), 4.60 (d, J = 3.9 Hz, 1H), 5.10 (t, J = 5.7 Hz, 1H), 5.33 (dd, J = 3.0 Hz, J = 6.9 Hz, 1H). ^{13}C NMR (75 MHz, $CDCl_3$) δ 140.26, 135.37, 123.94, 120.65, 97.80, 68.32, 63.70, 62.33, 39.88, 39.68, 35.71, 32.73, 30.74, 26.21, 25.53, 25.27, 19.64, 16.65, 16.44, 15.93. ^{13}C DEPT NMR (75 MHz, $CDCl_3$). δ 35.71 ($HOCH_2CHCH_3CH_2$). HR-ESI-MS calcd for $C_{20}H_{36}NaO_3$ [M + Na]$^+$ 347.2557, found 347.2540.

(*E*,*E*)-12-Azido-3,7,11-trimethyl-1-*O*-THP-2,6-dodecadiene (4). To a flame-dried flask under a nitrogen atmosphere containing 10 mL of CH_2Cl_2 were added *p*-toluenesulfonyl chloride (520 mg, 2.7 mmol) and 4-(*N*,*N*-dimethylamino)-pyridine (400 mg, 3.2 mmol). To this solution was added **3** (880 mg, 2.7 mmol) in 5.0 mL of CH_2Cl_2, and the reaction mixture was stirred at room-temperature overnight. After removing the CH_2Cl_2 in vacuo, the crude mixture was washed with Et_2O (2 × 100 mL). The Et_2O was removed in vacuo, and the residue was dissolved in DMF (10 mL). To this solution was added sodium azide (350 mg g, 5.4 mmol), and the mixture was heated to 80 °C and stirred for 8 h. After cooling, the reaction mixture was mixed with 100 mL of water and extracted using Et_2O (2 × 100 mL). The organic phases were combined and dried over Na_2SO_4. Compound **4** was purified using column chromatography (flash silica) to yield 710 mg (76%) of **4**, a colorless oil (R_f = 0.68, hexanes:EtOAc = 3:1). ^{1}H NMR (300 MHz, $CDCl_3$) δ 0.91 (d, J = 4.5 Hz, 3H), 1.38 (m, 6H), 1.52 (m, 4H), 1.60 (s, 3H), 1.68 (s, 3H), 1.82 (m, 1H), 1.99−2.12 (m, 6H), 3.09 (dd, J = 6.9 Hz, J = 12 Hz, 1H), 3.20 (dd, J = 6.0 Hz, J = 12 Hz, 1H), 3.51 (m, 1H), 3.88 (m, 1H), 4.02 (dd, J = 7.5 Hz, J = 12 Hz, 1H), 4.24 (dd, J = 6.5 Hz, J = 12 Hz, 1H), 4.62 (dd, J = 3.0 Hz, J = 4.5 Hz, 1H), 5.01 (t, J = 1.2 Hz, 1H), 5.33 (dd, J = 6.0 Hz, J = 6.5 Hz, 1H). ^{13}C NMR (75 MHz, $CDCl_3$) δ 140.23, 135.10, 124.17, 120.69, 97.83, 63.69, 62.32, 57.86, 39.74, 39.68, 33.68, 33.50, 30.78, 26.29, 25.57, 25.12, 19.69, 17.73, 16.46, 15.91. ^{13}C DEPT NMR (75 MHz, $CDCl_3$) δ 33.50 ($N_3CH_2CHCH_3CH_2$). IR 2096 cm^{-1} (N_3). HR-ESI-MS calcd for $C_{20}H_{35}N_3NaO_2$ [M + Na]$^+$ 372.2621, found: 372.2616.

(*E*,*E*)-12-Azido-3,7,11-trimethyl-2,6-dodecadienol (5). PPTS (51 mg, 200 μmol) was added to a solution of **4** (710 mg, 2.0 mmol) in 10 mL of absolute EtOH, and the reaction was stirred at 55 °C for 6 h. After being cooled to room temperature, the solvent was removed in vacuo and **5** was purified using column chromatography (flash silica) to yield 530 mg (98%) of **5**, a colorless oil (R_f = 0.3, hexanes:EtOAc = 3:1). ^{1}H NMR (300 MHz, $CDCl_3$) δ 0.94 (d, J = 6.9 Hz, 3H), 1.10 (m, 4H), 1.58 (s, 3H), 1.68 (s, 3H), 1.71 (m, 1H), 1.99−2.16 (m, 6H), 3.11 (dd, J = 6.9 Hz, J = 12 Hz, 1H), 3.21 (dd, J = 6.0 Hz, J = 12 Hz, 1H), 4.16 (d, J = 6.9 Hz, 2H), 5.10 (t, J = 7.2 Hz, 1H), 5.42 (t, J = 6.9 Hz, 1H). ^{13}C NMR (75 MHz, $CDCl_3$) δ 139.81, 135.27, 124.07, 123.43, 59.49, 57.89, 39.74, 39.59, 33.66, 33.52, 26.29, 25.12, 17.75, 16.35, 15.94. ^{13}C DEPT NMR (75 MHz, $CDCl_3$) δ 33.52 ($N_3CH_2CHCH_3CH_2$). IR 3376 cm^{-1} (OH), 2096 cm^{-1} (N_3). HR-ESI-MS calcd for $C_{15}H_{27}N_3NaO$ [M + Na]$^+$ 288.2046, found 288.2035.

Diethyl-[(*E*,*E*)-12-azido-3,7,11-trimethyl-2,6-dodecadiene]-phosphate (6). To a stirred solution of **5** (130 mg, 500 μmol) in 4.0 mL of CH_2Cl_2 was added pyridine (60 mg, 700 μmol). After cooling to 0 °C, diethyl chlorophosphate (100 mg, 600 μmol) was added. After 3 h of stirring at 0 °C, Et_2O (60 mL) was added and the crude mixture was filtered. The solution was washed with dilute HCl (2 × 10 mL), saturated $NaHCO_3$ (2 × 10 mL), and saturated NaCl (1 × 20 mL). The organic layer was dried over Na_2SO_4 and concentrated in vacuo to give a colorless oil. Purification of **6** by column chromatography (flash silica) yielded 160 mg (82%) of **6**, a colorless oil (R_f = 0.14, hexanes:EtOAc = 3:2). Slow decomposition of the phosphate was observed by silica gel TLC during fraction analysis. ^{1}H NMR (300 MHz, $CDCl_3$) δ 0.94 (d, J = 6.9 Hz, 3H), 1.31 (m, 10 H), 1.56 (s, 3H), 1.69 (s, 3H), 1.95−2.10 (m, 6H), 3.09 (dd, J1 = 6.9 Hz, J2 = 12 Hz, 1H), 3.19 (dd, J1 = 6.0 Hz, J2 = 12 Hz, 1H), 4.12 (m, 4H), 4.56 (t, J = 7.5 Hz, 2H), 5.06 (t, J = 6.0 Hz, 1H), 5.38 (t, J = 4.2 Hz, 1H). ^{13}C NMR (75 MHz, $CDCl_3$) δ 142.59, 135.42, 123.81, 119.03 (d, J = 6.8 Hz), 64.11 (d, J = 5.3 Hz), 63.65 (d, J = 5.8 Hz), 57.86, 39.72, 39.54, 33.67, 33.49, 26.18, 25.10, 17.72, 16.52, 16.27 (d, J = 6.8 Hz), 15.90. ^{13}C DEPT NMR (75 MHz, $CDCl_3$) δ 33.49 (N_3-$CH_2CHCH_3CH_2$). ^{31}P NMR (121 MHz, $CDCl_3$) δ −0.017 (s). FT-IR 2098 cm^{-1} (N_3).

(*E*,*E*)-12-Azido-3,7,11-trimethyl-2,6-dodecadiene-1-diphosphate (7). The following procedure was adapted from Coates's method for the synthesis of isoprenoid diphosphates (*32*). To a stirred solution of **6** (16 mg, 410 μmol) in dry CH_3CN (2.0 mL) was added $[(n\text{-}Bu)_4N]_3HO_7P_2$ (650 mg, 700 μmol). After dissolution, 4-Å molecular sieves were added and the flask was sealed and stirred at room temperature for 4 days. The solution was then filtered, and the filtrate was concentrated in vacuo. The crude mixture was resuspended in water (6.0 mL), and the suspension was applied to an ion exchange column (Dowex 50 W-X8, NH_4^+ form). The crude product was eluted with 25 mM NH_4HCO_3 with 2% 2-propanol, and the clear colorless eluent was lyophilized to dryness to yield a white solid, followed by

purification by reversed-phase HPLC using the following conditions: detection: 220 nm; flow rate: 5.0 mL/min; 5 mL injection loop; gradient: 0−60% solvent B in 60 min; solvent A: 25 mM NH_4HCO_3; solvent B: CH_3CN. Compound **7** eluted from 25% to 30% solvent B. Fractions containing pure **7** were pooled and lyophilized, yielding 54 mg (31%) of a fluffy white solid. ^{1}H NMR (D_2O and ND_4OD, 300 MHz) δ 0.76 (d, J = 6.9 Hz, 3H), 1.21 (m, 4H), 1.46 (s, 3H), 1.56 (s, 3H), 1. 61 (m, 1H), 1.84−2.02 (m, 6H), 3.10 (dd, J = 6.9 Hz, J = 12 Hz, 1H), 3.20 (dd, J = 6.0 Hz, J = 12 Hz, 1H), 4.31(t, J = 6.6 Hz, 2H), 5.08 (t, J = 6.6 Hz, 1H), 5.31 (t, J = 6.0 Hz, 1H).^{31}P NMR (D_2O and ND_4OD) δ −0.61 (d, J = 19 Hz, 1P) and −9.94 (d, J = 19 Hz, 1P). HR-ESI-MS calcd for $C_{15}H_{26}N_3O_7P_2$ [M − H]$^-$ 424.1408, found 424.1395.

Prenylation of *N*-Dansyl-GCVIA. To monitor the enzymatic incorporation of **7** by fluorescence spectroscopy, enzymatic reactions (500 μL) contained 50 mM Tris-HCl, pH 7.0, 10 mM $MgCl_2$, 10 μM $ZnCl_2$, 5.0 mM DTT, 2.4 μM *N*-dansyl-GCVIA, 10 μM **7**, 50 nM yeast PFTase, and *n*-dodecyl β-D-maltoside (0.04%, w/v). Reactions were equilibrated to 30 °C, initiated by the addition of yeast PFTase, and allowed to react for up to 5 min while the fluorescence (340 nm excitation, 505 nm emission) was monitored. Similar reactions containing FPP (10 μM) were run to compare the rate of **7** versus FPP incorporation. For HPLC analysis, enzymatic reactions (25 mL) contained 50 mM Tris-HCl, pH 7.0, 10 mM $MgCl_2$, 10 μM $ZnCl_2$, 5.0 mM DTT, 2.0 μM *N*-dansyl-GCVIA, 100 μM **7**, and 10 nM yeast PFTase. After the addition of the enzyme, the reaction was allowed to proceed for 1 h at 30 °C. The reaction progress was monitored by UV/Vis and fluorescence detection using analytical reversed-phase HPLC. The following conditions were employed: flow rate: 1.0 mL/min; 100 μL injection loop; gradient: 0−100% solvent B in 40 min; solvent A: 0.1% TFA in H_2O; solvent B: 0.1% TFA in CH_3CN.

Mutagenesis, Expression, and Purification of eGFP−CVIA. The cDNA of the coding region of eGFP with a CVIA-tag at the C-terminus was obtained by PCR using designed primers (5′-CCGTACCTGCTCGACATGTTCACG CAGTAG-CGTACTTTCGAACCC-3′) and then subcloned into the pET 23c vector (Novagen). The resulting construct was transformed into BL21(DE3) pLysS supercompetent cells (Novagen). The procedure for the expression and purification of eGFP−CVIA (**8**) was adapted from Yakhnin's procedure for the purification of a GFP mutant (*33*). LB media (250 mL), supplemented with ampicilin (0.15 mg/mL), was inoculated with a single colony of cells containing the eGFP−CVIA plasmid and grown with shaking overnight at 37 °C. The overnight culture (10 mL) was added to four 4 L flasks, each containing 1 L of LB and ampicilin (0.15 mg/mL). The OD_{600} of the cells was brought to 0.7 with shaking at 37 °C for 2 h, and induction was initiated by the addition of IPTG to a final concentration of 0.5 mM. The cells were grown with shaking for 14 h at 28 °C after induction. The cells were recovered by centrifugation (24 g). Wet cells were resuspended in 150 mL of Buffer A (20 mM Tris-HCl, pH 8.0; 150 mM NaCl; 1.0 mM PMSF). The cells were lysed by sonication using 30 s pulses for 8 total minutes. The lysis extract was centrifuged (20 400g × 30 min) after which the soluble extract appeared bright green, indicating that **8** was soluble. Triethylamine and ammonium sulfate were added to the supernatant to a final concentration of 100 mM and 1.6 M, respectively. After the suspension was stirred at 4 °C for 1 h, the precipitated proteins were removed by centrifugation (5500g × 20 min) at 4 °C. Additional ammonium sulfate was added to afford 167 mL of a solution that was 70% saturated. A one-fourth volume of EtOH (42 mL) was added to the suspension followed by vigorous shaking. The organic and aqueous phases were separated by centrifugation (4000g × 5 min). In this biphasic mixture, **8** was clearly seen in the organic phase. A one-fourth volume of *n*-butanol (40 mL) was added to the organic phase and, after shaking, the phases were separated by centrifugation (4000g × 5 min). **8** partitioned completely into the lower aqueous phase in this step. An equal volume of chloroform (135 mL) was added to the aqueous phase, and the two phases were separated as described above. **8** was present predominantly in the aqueous phase, which was then set aside. To recover **8** present in the chloroform phase, the lower organic phase was extracted with an equal volume of 30% saturated $(NH_4)_2SO_4$ in water (120 mL) and combined with the aqueous phase mentioned above. Both aqueous phases were combined and loaded directly onto 40 mL of wet phenyl-Sepharose (Amersham, column size: 2.75 × 21 cm), equilibrated with 20% saturated $(NH_4)_2SO_4$ in Buffer B (20mM Tris-HCl, pH 8.0). The column was washed with 100 mL of a $(NH_4)_2SO_4$ linear gradient from 20 to 0% saturation in Buffer B. **8** was eluted from the column with 30 mL of H_2O. The concentration of **8** was determined by UV/Vis spectrophotometry using the extinction coefficient at 488 nm (55 000 L mol^{-1} cm^{-1}) (*34*).

Prenylation of eGFP−CVIA. Enzymatic reactions (40 mL) contained 50 mM Tris-HCl, pH 7.0, 10 mM $MgCl_2$, 10 μM $ZnCl_2$, 5.0 mM DTT, 2 μM **8**, 10 μM **7**, and 10 nM yeast PFTase. Reactions were allowed to proceed for 2 h at 30 °C. The reaction was then concentrated to 500 μL using Amicon Centriprep centrifugation devices, and excess azide was removed using a NAP-5 column (Amersham). For prenylation in crude cell lysate, **8** was first overexpressed, and its concentration was determined by UV/Vis as described above. Large scale enzymatic prenylation reactions (40 mL) containing 2 μM of **8** in crude cell lysate were carried out as described above.

Synthesis of Alkyne-Functionalized Agarose. 10 mL of drained, NHS-activated agarose resin (Amersham) was washed four times with 20 mL of cold 1 mM HCl. 140 μL of propargylamine was added to 4.9 mL of Buffer C (50 mM HEPES, pH 7.2). This 5 mL solution was added to the 10 mL of drained resin, giving a coupling solution:resin ratio of 0.5:1 (v/v). This suspension was mixed on a rotary shaker at room temp for 4.5 h. Unreacted NHS groups were capped by mixing the resin in 10 mL of ethanolamine overnight at 4 °C. The resin was washed with 20 mL of 50 mM Tris-HCl, pH 8.5, followed by 20 mL of 50 mM NaOAc, pH 3.5. This two step washing sequence was repeated twice to remove unbound ligand.

Cycloaddition Reaction on Agarose Beads. The agarose-alkyne suspension was washed (at least 3×) to remove storage EtOH. To the washed beads was added 6.8 μL of 50 mM NaH_2PO_4, pH 7.3, 1.2 μL of $CuSO_4$ (25 mM stock in water), 1.2 μL of TCEP, (25 mM stock in water), 1.8 μL of ligand (1.67 mM stock in DMSO:*t*-BuOH 1:4), and 19 μL of eGFP-N_3 (160 μM stock in 50 mM NaH_2PO_4, pH 7.3). The reactions were mixed using a rotary shaker at room temperature. After allowing the reaction to proceed for 15 h (or 1 h for the quantitative experiments), the beads were washed three times with 50 mM phosphate buffer, pH 7.3, containing 1 M NaCl. For the immobilization of eGFP-N_3 which had been prenylated in crude cell lysate, 33 μL of impure eGFP-N_3 (150 μM stock in 50 mM NaH_2PO_4, pH 7.3) was reacted with the click conditions described above. For studies containing 3% eGFP-N_3, 30 μg of pure GFP-N_3 was diluted with 1 mg of uninduced crude cell lysate. To produce solutions containing lower percentages of eGFP-N_3, 30 μg of pure azide-labeled protein was diluted with increasing amounts of crude cell lysate to yield the desired percentage. These samples were then subjected to the click reaction described above. Fluorescent microscope images were obtained by placing 10 μL of the bead suspension on a microscope slide. The slides were imaged using a Zeiss Atto

Scheme 1. Synthesis of 10,11-Dihydrofarnesyl Azide Diphosphate

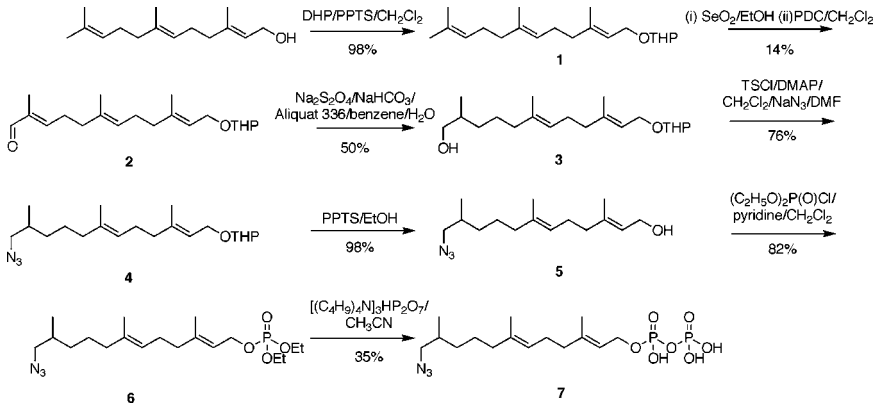

Arc HBO 110W Upright Microscope with 20× magnification. FITC filters were used with $\lambda_{ex} = 480$ nm and $\lambda_{em} = 535$ nm. For fluorescence microtiter plate images, the bead suspension was placed in a black-walled, clear-bottom 96-well plate and imaged using a BioRad Gel Doc GS700.

Mass Spectrometry Studies of eGFP Immobilization. After covalent attachment of eGFP-N_3 to the alkyne-functionalized agarose beads, the beads were washed two times each with 400 μL of PBS containing 2.0% SDS, 400 μL of 6.0 M guanidine, and 400 μL of 50 mM NH_4CO_3, pH 8.0 to remove noncovalently bound proteins. The proteins attached to the beads were digested in 50 mM NH_4CO_3, pH 8.0, containing 5.0 mM $CaCl_2$ and 2.6 μg (260 μL) of modified, sequence grade trypsin (Promega) overnight at 37 °C. Beads were then washed sequentially with 50% and 75% CH_3CN in H_2O and lyophilized to dryness. Peptides were redissolved in 400 μL of CH_3CN containing 0.1% TFA. 0.7 μL of this mixture was spotted on a MALDI target along with 0.7 μL of cyano-4-hydroxycinnamic acid (CCA) matrix. A Bruker Reflex III MALDI time-of-flight system (Bremen/Leipzig, Germany) was used to obtain the mass spectral data from this peptide mixture.

RESULTS

The enzyme catalyzed reaction exploited in this study is a posttranslational modification known as protein prenylation. The enzyme, protein farnesyl transferase (PFTase), transfers a 15-carbon isoprenoid to substrate proteins which contain the C-terminal tetrapeptide, CVIA, and related sequences (*35*). Previous studies have shown that peptides containing CVIA at their C-terminus can be prenylated by PFTase with modified isoprenoid diphosphates (*21*, *36*−*38*). In particular, PFTase can prenylate a pentapeptide with a farnesyl diphosphate molecule bearing an azide moiety (*27*). On the basis of these precedents, we reasoned that if a CVIA tag was genetically fused to the C-terminus of a target protein, an azide could be site-specifically incorporated into that protein. To accomplish this, we synthesized 10,11-dihydrofarnesyl azide diphosphate (**7**, Scheme 1), to avoid the isomerism problems resulting from sigmatropic interconversion that occur with analogues containing an alkene at C-10 (*27*). To evaluate **7** as a substrate for PFTase, a continuous spectrofluorometric assay was employed. This assay measures the time-dependent increase in dansyl group fluorescence that occurs as the peptide *N*-dansyl-GCVIA, is prenylated. Incubation of **7** with *N*-dansyl-GCVIA in the presence of PFTase results in a 6-fold increase in fluorescence that is similar to what is observed when the natural substrate, FPP, is used. As shown in Figure 1, at saturating concentrations of **7** (10 μM), the rate of enzymatic prenylation is approximately 2.7-fold slower than the corresponding rate when FPP is used. Thus, it appears that the absence of the alkene in the third isoprene unit of FPP and the presence of the azide group have minimal effect on the reactivity of **7** in the reaction catalyzed by PFTase. The enzymatic incorporation of **7** into *N*-dansyl-GCVIA was also monitored by HPLC (Figure 2). The starting peptide is shown in the lower chromatogram at 21 min; after 1 h of reaction at 30 °C, complete conversion to the prenylated peptide is observed (peak at 34 min, upper chromatogram).

To allow rapid visualization of an immobilized protein, the enhanced Green Fluorescent Protein (eGFP) was used as the model protein for these studies (*39*). The tetrapeptide CVIA was appended onto the C-terminus of eGFP using site-directed mutagenesis, and eGFP−CVIA was overexpressed and purified. Substrate **7** was enzymatically linked to the cysteine of the CVIA tag using PFTase (Scheme 2) to produce eGFP-N_3 (**9**) using the conditions previously established with the peptide substrate to achieve efficient incorporation (100 μM, 10 nM

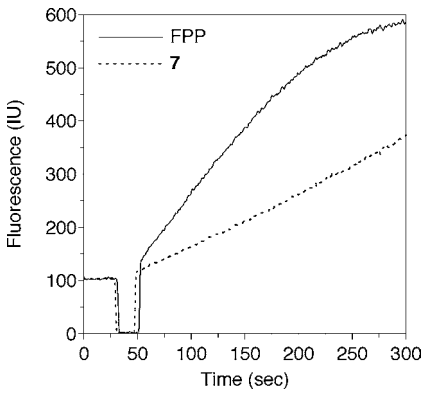

Figure 1. Spectrofluorometric enzyme assay for PFTase-catalyzed prenylation of *N*-dansyl-GCVIA with FPP or **7**. Reactions contained equal concentrations of enzyme (50 nM) and diphosphate substrate (10 μM).

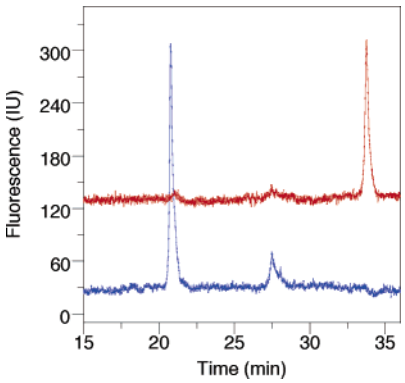

Figure 2. HPLC analysis of PFTase-catalyzed prenylation of *N*-dansyl-GCVIA with **7**. Reactions contained 10 nM enzyme and 100 μM **7**. Lower chromatogram: reaction prior to addition of **7**. Upper chromatogram: reaction after 1 h.

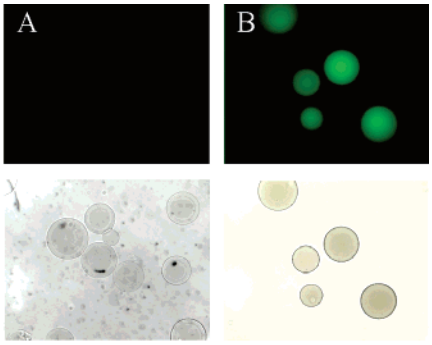

GFP-N_3	+	+
$CuSO_4$	-	+
TCEP	+	+
Ligand	+	+

Figure 3. Fluorescence microscope image (top) and bright-field microscope image (bottom) of the capture of pure eGFP-N_3. (A) Reaction of eGFP-N_3 with alkyne-functionalized agarose (**10**) in the absence of $CuSO_4$. (B) Reaction of eGFP-N_3 with **10** in the presence of $CuSO_4$. Beads were incubated with eGFP-N_3 (100 μM), TCEP (1 mM), and ligand (100 μM) in NaH_2PO_4 (50 mM, pH 7.3) with or without $CuSO_4$ (1 mM). After 15 h, beads were washed with buffer containing 1 M NaCl followed by buffer containing 5 mM EDTA.

Scheme 2. Prenylation of a Protein with an Azide and Subsequent Ligation to Alkyne-Functionalized Agarose Beads

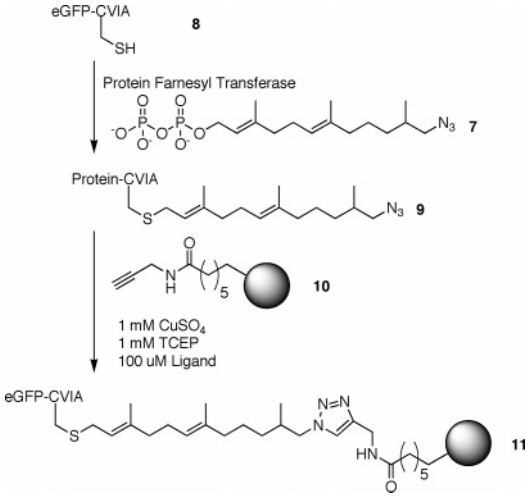

PFTase, 30 °C, 1 h); unreacted azide was removed by gel filtration chromatography. Alkyne-functionalized agarose beads (**10**), prepared by reacting NHS-functionalized agarose with propargylamine, were treated with eGFP-N_3, $CuSO_4$, TCEP, and ligand in NaH_2PO_4 buffer (click conditions) (*40*). The cycloaddition reaction was allowed to proceed for 15 h at 25 °C with mild shaking. Beads were then washed extensively with phosphate buffer containing 1 M NaCl to remove nonspecifically bound proteins.

Fluorescence labeling of the agarose beads was observed following reaction with eGFP-N_3 (Figure 3, Panel B). When $CuSO_4$ was omitted, no fluorescence was observed after extensive washing of the beads, indicating that no reaction had occurred between azide and alkyne (Figure 3, Panel A). If $CuSO_4$ is included in the reaction, however, the protein is covalently attached to **10** as indicated by the strong fluorescence of the beads. Fluorescence remained after washing with 1 M NaCl and 100 mM EDTA, consistent with the idea that the protein is covalently bound to the bead.

To confirm that the protein was covalently immobilized, agarose beads that had been reacted with eGFP-N_3 in the presence of the click conditions were washed extensively with

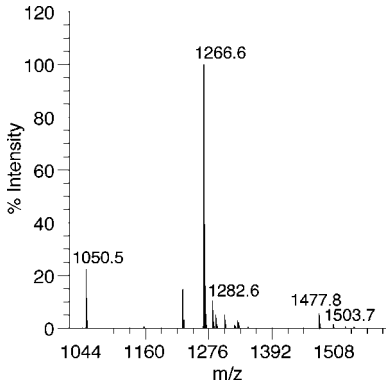

Figure 4. Mass spectrum (MALDI-TOF) of tryptic digest of eGFP immobilized on agarose beads. eGFP-N_3 was immobilized onto **10** using the click conditions described in the legend to Figure 3.

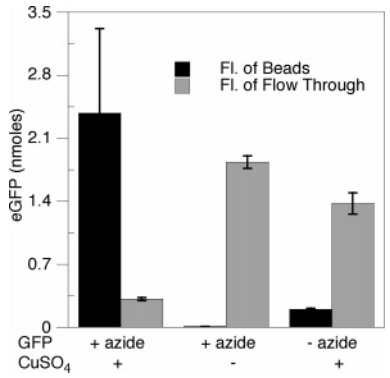

Figure 5. Quantitative analysis of eGFP immobilization. eGFP-N_3 was immobilized onto **10** using click conditions and the amount of eGFP on the beads and in the wash solution was quantified by fluorescence.

buffer containing 2% SDS and 6 M guanidine. This step was performed to ensure that any noncovalently bound species were removed from the beads prior to analysis. The eGFP-functionalized beads were then digested with trypsin overnight at 37 °C, and the eluted peptides were analyzed by MALDI-TOF-MS (Figure 4). Peptide fragments of *m*/*z* 1050.5, 1266.6 1282.6, 1477.8, and 1503.7 were observed, which correlate with tryptic peptide fragments of eGFP. It should be noted that the samples were not purified by ZipTip prior to spotting on the MALDI target, which might explain why only 5 out of roughly 40 tryptic peptides of eGFP were observed.

To determine the extent of the Cu(I)-catalyzed cycloaddition reaction, eGFP-N_3 was reacted with **10** under the click conditions for 1 h. Beads were then washed and resuspended in phosphate buffer, and the fluorescence intensity present in the suspended beads was measured. The moles of eGFP were directly calculated from the fluorescence intensity using a standard calibration curve. When azide-functionalized eGFP (2.5 nmol) was reacted with **10** under the click conditions, 2.4 nmol of eGFP (96%) was covalently immobilized onto the beads (Figure 5). However, when eGFP-N_3 was incubated with **10** in absence of $CuSO_4$, only 0.01 nmol of eGFP was covalently bound. Interestingly, 0.20 nmol of protein (8%) was immobilized when eGFP, which had not been prenylated with the azide, was incubated with **10** under the click conditions. This background labeling might be caused by the Cu(I)-induced activation of the alkyne-agarose, which can then react nonspecifically with proteins. Cravatt and co-workers have reported similar findings in their activity profiling experiments (*41*). The fluorescence of the flow through from the first washing of the beads after the cycloaddition reaction was also measured. When copper was omitted, approximately 83% of the eGFP was observed in the eluent. Alternatively, 18% of the fluorescent protein eluted after

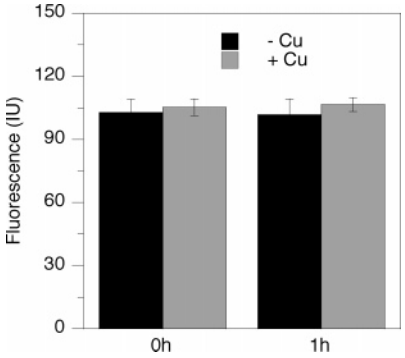

Figure 6. Effects of click conditions on eGFP fluorescence. 50 μM eGFP was incubated with 1 mM $CuSO_4$, 1 mM TCEP, 100 μM ligand in NaH_2PO_4 (50 mM, pH 7.3) for 1 h. The fluorescence intensity was measured ($\lambda_{ex} = 488$ nm; $\lambda_{em} = 508$ nm) and [eGFP] was determined using a standard calibration curve.

having been incubated with the click conditions for 1 h. These values are in general agreement with the moles of eGFP immobilized. Taken together, these two independent measurements suggest that when eGFP-N_3 is incubated with **10** under the click conditions for 1 h, more than 80% of the protein is covalently immobilized onto the beads.

We next tested whether the click conditions, specifically Cu(I), had deleterious effects on eGFP and its native fluorescence. The eGFP protein was incubated both in the presence and absence of $CuSO_4$, TCEP, and ligand for 1 h and the protein's fluorescence was measured (Figure 6). After incubation at room temperature for 1 h in the absence of the click conditions (protein + buffer), a 1% loss in the fluorescence of eGFP was observed. When the protein was incubated in the presence of the click conditions, no loss in the fluorescence of eGFP was observed. This indicates that the click conditions do not affect eGFP's native fluorescence.

In proteomic analysis, the desired target to be captured is not always pure or in high abundance, thus necessitating the need for specific modification strategies that function in a crude mixture. To test the ability of the above labeling and capture technique to target low abundance proteins, eGFP−CVIA was overexpressed and prenylated in the presence of crude cell lysate. The eGFP-N_3 concentration in that unpurified sample which was found to be 12% of the total protein content, was immobilized onto **10** only when copper was included in the reaction (data not shown). If copper is omitted, no cycloaddition reaction occurs between protein and bead. We next tested whether a sample containing a lower percentage of eGFP-N_3 could be immobilized. To accomplish this, uninduced, crude cell lysate was added to eGFP-N_3 (25 μM), so that the final amount of protein-azide was 3% of the total protein mixture. A sample of that protein mixture fractionated by SDS−PAGE is shown in Figure 7A; while eGFP-N_3 is still a major component in the mixture, it is clear many other proteins are present. The low abundance eGFP-N_3 sample was then subjected to the cycloaddition reaction in the presence and absence of $CuSO_4$ (Figure 7B). When copper was included in the reaction, the beads remained fluorescent even after extensive washing indicating the cycloaddition reaction occurred, while omission of copper resulted in no fluorescence. Lower percentages of eGFP-N_3 were also tested for their ability to be captured by **10** (Figure 7C). Pure eGFP-N_3 (25 μM) was diluted with varying amounts of crude cell lysate and reacted with **10** under the click conditions. Remarkably, protein mixtures containing as low as 1% eGFP-N_3 can be successfully ligated to the alkyne-functionalized agarose beads. Actually, this lower limit is probably dictated by the somewhat weak fluorescence of GFP and not the efficiency of the linking reaction.

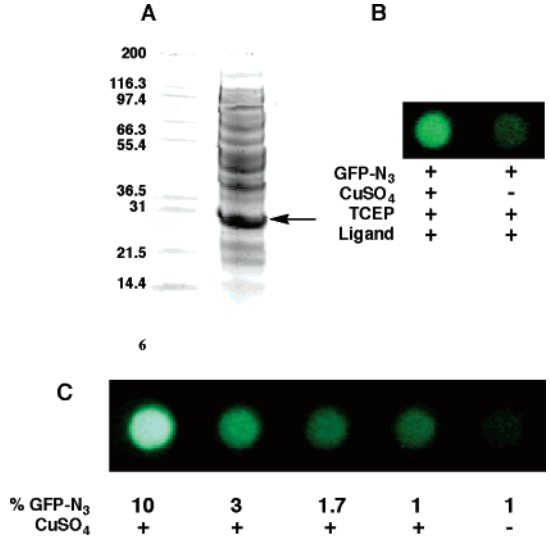

Figure 7. Capture of varying percentages of eGFP-N_3 in crude cell lysate. (A) SDS−PAGE analysis of 3% eGFP-N_3 in crude cell lysate. Lane 1: molecular weight standard; Lane 2: 3% eGFP-N_3; eGFP-N_3 is marked by the arrow. (B) Reaction of 3% GFP-N_3 with **10** in the presence and absence of $CuSO_4$. Uninduced crude cell lysate (1 mg, determined using the BioRad assay) was added to 30 μg of eGFP-N_3 to yield 3% GFP-N_3. (C) Labeling of agarose with varying percentages of eGFP-N_3. **10** was treated overnight with varying percentages of eGFP-N_3 in crude cell lysate in the presence of the click conditions described in the legend to Figure 3.

DISCUSSION

This work highlights the development of a method to covalently attach proteins to surfaces in a site-specific manner. This strategy offers several key advantages over other immobilization techniques. To date, most site-specific immobilization strategies have relied on the use of large (>20 kDa) protein fusions (*13*−*16*). While such systems have already proven to be useful for a variety of applications, there are some limitations to such approaches. The fusion protein strategy requires that the fusion protein be efficiently expressed and that the resulting chimeric molecule be soluble and free from problems of aggregation (*42-44*). Fusion proteins are also not always posttranslationally processed and/or localized in the same fashion as their parental progenitors (*45-47*). Finally, fusion domains may interfere with the function of the desired protein or enzyme (*48*). Recently, Camarero has introduced a method for proteins that uses a split-intein ligation method to achieve traceless immobilization (*17*). While that method has significant potential, it still requires the desired target protein to be initially expressed as a fusion prior to intein- mediated immobilization. It also requires chemical synthesis of a 39 residue C-terminal intein fragment and its linkage to a solid support for capture of the expressed target protein−intein fusion.

In the method described here, a small fusion (four residues) is used, and hence it is unlikely to impact the physical properties or the target protein. The specificity of PFTase ensures that the protein of interest is only modified on its C-terminus, which in most cases should not affect its function once attached to the surface. Additionally, the azide functional group can be coupled to a specific site within the protein even in the presence of multiple cysteines. A search of the Swiss-Prot Protein Database revealed 64 *E. coli* proteins with a cysteine located at the fourth residue from the C-terminus. However, none of these proteins have aliphatic residues at the two "X" positions within the CAAX box motif and a C-terminal residue (Ser, Met, Ala, Cys) that is recognized by PFTase. Therefore, only the protein of interest will be modified by **7** when using *E. coli* as the overexpression host. This method is also a procedure amenable

to large scale immobilization. The precursor for azide **7** is farnesol (**1**), a relatively inexpensive starting material; PFTase, used to incorporate the azide, is used in catalytic amounts. Additionally, the linkage is covalent and thus stable to a variety of conditions. Importantly, neither the enzymatic azide incorporation nor the subsequent immobilization chemistry require the target protein to be pure. Finally, it should be noted that the approach reported here is not limited only to the immobilization of target proteins. In principle, it can also be used to link a broad range of reporter groups ranging from low molecular weight fluorophores to proteins and nanoparticles to the C-termini of many proteins. Consequently, this chemoenzymatic approach should be broadly applicable for a variety of studies in proteomics and protein chemistry.

ACKNOWLEDGMENT

The authors thank the Cravatt and Sharpless labs for the gift of the ligand, and Byeong-Su Kim, Jin-Hwa Chung, and the University of Minnesota Biomedical Image Processing Lab for technical assistance. This work was supported by the National Institutes of Health (Grant No. GM008700 and GM58442).

Supporting Information Available: NMR spectra related to the synthesis of C_{15}-dihydrofarnesyl azide diphosphate. This material is available free of charge via the Internet at http://pubs.acs.org.

LITERATURE CITED

(1) Kim, S. H., Tamrazi, A., Carlson, K. E., and Katzenellenbogen, J. A. (2005) A proteomic microarray approach for exploring ligand-initiated nuclear hormone receptor pharmacology, receptor selectivity, and heterodimer functionality. *Mol. Cell Prot. 4*, 267−277.

(2) Hall, D. A., Zhu, H., Zhu, X., Royce, T., Gerstein, M., and Snyder, M. (2004) Screening yeast proteins for DNA binding identified a biosynthetic enzyme for the amino acid arginine that also unexpectedly binds to DNA and regulates genes directly. *Science 306*, 482−484.

(3) Huang, J., Zhu, H., Haggarty, S. J., Spring, D. R., Hwang, H., Jin, F., Snyder, M., and Schreiber, S. L. (2004) Finding new components of the target of rapamycin (TOR) signaling network through chemical genetics and proteome chips. *Proc. Natl. Acad. Sci. U.S.A. 101*, 16594−16599.

(4) Joos, T. O., Schrenk, M., Höpfl, P., Kröger, K., Chowdhurg, U., Stoll, D., Schorner, D., Durr, M., Herick, K., Rupp, S., Sohn, K., and Hämmerle, H. (2000) A microarray enzyme-linked immunosorbent assay for autoimmune diagnostics. *Electrophoresis 21*, 2641−2650.

(5) MacBeath, G. and Schreiber, S. L. (2000) Printing proteins as microarrays for high-throughput function determination. *Science 289*, 1760−1763.

(6) Zhu, H., Klemic, J. F., Chang, S., Bertone, P., Casamayor, A., Klemic, K. G., Smith, D., Gerstein, M., Reed, M. A., and Snyder, M. (2000) Analysis of yeast protein kinases using protein chips. *Nat. Genet. 26*, 283−289.

(7) Persson, M., Bulow, L., and Mosbach, K. (1990) Purification and site-specific immobilization of genetically engineered glucose dehydrogenase on thiopropyl-sepharose. *FEBS Lett. 270*, 41−44.

(8) Cha, T., Guo, A., Jun, Y., Pei, D., and Zhu, X.-Y. (2004) Immobilization of oriented protein molecules on poly(ethylene glycol)-coated Si(111). *Proteomics 4*, 1965−1976.

(9) Ramachandran, N., Hainsworth, E., Bhullar, B., Eisenstein, S., Rosen, B., Lau, A. Y., Walter, J. C., and LaBaer, J. (2004) Self-assembling protein microarrays. *Science 305*, 86−90.

(10) Hodneland, C. D., Lee, S.-L., Min, D.-H., and Mrksich, M. (2002) Supramolecular chemistry and self-assembly special feature: selective immobilization of proteins to self-assembled monolayers presenting active site-directed capture ligands. *Proc. Natl. Acad. Sci. U.S.A. 99*, 5048−5052.

(11) Kindermann, M., Gerogre, N., Johnsson, N., and Johnsson, K. (2003) Covalent and selective immobilization of fusion proteins. *J. Am. Chem. Soc. 125*, 7810−7811.

(12) Chmura, A. J., Orton, M. S., and Meares, C. F. (2001) Antibodies with infinite affinity. *Proc. Natl. Acad. Sci. U.S.A. 98*, 8480−8484.

(13) Camarero, J. A., Kwon, Y., and Coleman, M. A. (2004) Chemoselective attachment of biologically active proteins to surfaces by expressed protein ligation and its application for "protein chip" fabrication. *J. Am. Chem. Soc. 126*, 14730−14731.

(14) Zhu, H. and Snyder, M. (2001) Protein arrays and microarrays. *Curr. Op. in Chem. Biol. 5*, 40−45.

(15) Lue, R. Y. P., Chen, G. Y. J., Hu, Y., Zhu, Q., Yao, S. Q. (2004) Versatile protein biotinylation strategies for potential high-throughput proteomics. *J. Am. Chem. Soc. 126*, 1055−1062.

(16) Yin, J., Liu, F., Li, X., and Walsh, C. T. (2004) Labeling proteins with small molecules by site-specific posttranslational modification. *J. Am. Chem. Soc. 126*, 7754−7755.

(17) Kwon, Y., Coleman, M. A., and Camarero, J. A. (2006) Selective immobilization of proteins onto solid supports through split-intein-mediated protein trans-splicing. *Angew. Chem., Int. Ed. 45*, 1726−1729.

(18) Yin, J., Straight, P. D., McLoughlin, S. M., Zhou, Z., Lin, A. J., Golan, D. E., Kelleher, N. L., Kolter, R., and Walsh, C. T. (2005) Genetically encoded short peptide tag for versatile protein labeling by Sfp phosphopantetheinyl transferase. *Proc. Natl. Acad. Sci. U.S.A. 102*, 15815−15820.

(19) Saxon, E. and Bertozzi, C. R. (2000) Cell surface engineering by a modified Staudinger reaction. *Science 287*, 2007−2010.

(20) Howarth, M., Takao, K., Hayashi, Y., and Ting, A. Y. (2005) Targeting quantum dots to surface proteins in living cells with biotin ligase. *Proc. Natl. Acad. Sci. U.S.A. 102*, 7583−7588.

(21) Kho, Y., Kim, S. C., Jiang, C., Barma, D., Kwon, S. W., Cheng, J., Jaunbergs, J., Weinbaum, C., Tamanoi, F., Falck, J., and Zhao, Y. (2004) A tagging-via-substrate technology for detection and proteomics of farnesylated proteins. *Proc. Natl. Acad. Sci. U.S.A. 101*, 12479−12484.

(22) Kolb, H. C., Finn, M. G., and Sharpless, K. B. (2001) Click chemistry: diverse chemical function from a few good reactions. *Angew. Chem., Int. Ed. 40*, 2004−2021.

(23) Wang, Q., Chan, T. R., Hilgraf, R., Fokin, V. V., Sharpless, K. B., and Finn, M. G. (2003) Bioconjugation by copper(I)-catalyzed azide-alkyne [3 + 2] cycloaddition. *J. Am. Chem. Soc. 125*, 3192−3193.

(24) Speers, A. E., Adam, G. C., and Cravatt, B. F. (2003) Activity-based protein profiling in vivo using a copper(I)-catalyzed azide-alkyne [3 + 2] cycloaddition. *J. Am. Chem. Soc. 125*, 4686−4687.

(25) Kiick, K. L., Saxon, E., Tirrell, D. A., and Bertozzi, C. R. (2002) Incorporation of azides into recombinant proteins for chemoselective modification by the Staudinger ligation. *Proc. Natl. Acad. Sci. U.S.A. 99*, 19−24.

(26) Soellner, M. B., Dickson, K. A., Nilsson, B. L., and Raines, R. T. (2003) Site-specific protein immobilization by Staudinger ligation. *J. Am. Chem. Soc. 125*, 11790−11791.

(27) Rose, M. W., Rose, N. D., Boggs, J., Lenevich, S., Xu, J., Barany, G., and Distefano, M. D. (2005) Evaluation of geranylazide and farnesylazide diphosphate for incorporation of prenylazides into a CAAX box-containing peptide using protein farnesyltransferase. *J. Pept. Res. 65*, 529−537.

(28) Di Guardia, S., Valls, R., Mesguiche, V., Brunel, J.-M., and Culioli, G. (1999) Enantioselective synthesis of (−)-Bifurcadiol: a natural antitumor marine product. *Tetrahedron Lett. 40*, 8359−8360.

(29) Camps, F., Coll, J., and Parente, A. (1978) Selenium dioxide oxidation of substrates with acid labile groups. *Synthesis 3*, 215−216.

(30) Corey, E. J. and Schmidt, G. (1979) Useful procedures for the oxidation of alcohols involving pyridinium dichromate in approtic media. *Tetrahedron Lett. 20*, 399−402.

(31) Davies, M. J., Heslin, J. C., and Moody, C. J. (1989) Rhodium carbenoid mediated cyclisations. Part 4. Synthetic approaches to oxepanes related to zoapatanol. *J. Chem. Soc., Perkin Trans. 1 12*, 2473−2484.

(32) Ravn, M. M., Jin, Q., and Coates, R. M. (2000) Synthesis of allylic isoprenoid diphosphates by SN2 displacement of diethyl phosphate. *Eur. J. Org. Chem. 2000*, 1401−1410.

(33) Yakhnin, A. V., Vinokurov, L. M., Surin, A. K., and Alakhov, Y. B. (1998) Green fluorescent protein purification by organic extraction. *Prot. Expr. Purif. 14*, 382−386.

(34) Schmid, J. A. and Neumeier, H. (2005) Evolutions in science triggered by green fluorescent protein (GFP). *ChemBioChem. 6*, 1149−1156.
(35) Reid, T. S., Terry, K. L., Casey, P. J., and Beese, L. S. (2004) Crystallographic analysis of CaaX prenyltransferases complexed with substrates defines rules of protein substrate selectivity. *J. Mol. Biol.* 343, 417−433.
(36) Edelstein, R. L. and Distefano, M. D. (1997) Photoaffinity labeling of yeast farnesyl protein transferase and enzymatic synthesis of a Ras protein incorporating a photoactive isoprenoid. *Biochem. Biophys. Res. Commun. 235*, 377−382.
(37) Turek, T. C., Gaon, I., Distefano, M. D., and Strickland, C. L. (2001) Synthesis of farnesyl diphosphate analogues containing ether-linked photoactive benzophenones and their application in studies of protein prenyltransferases. *J. Org. Chem. 66*, 3253−3264.
(38) Chehade, K. A. H., Andres, D. A., Morimoto, H., and Spielmann, H. P. (2000) Design and synthesis of a transferable farnesyl pyrophosphate analogue to Ras by protein farnesyltransferase. *J. Org. Chem. 65*, 3027−3033.
(39) Tsien, R. Y. (1998) The green fluorescent protein. *Annu. Rev. Biochem. 67*, 509−544.
(40) Chan, T. R., Hilgraf, R., Sharpless, K. B., and Fokin, V. V. (2004) Polytriazoles as copper(I)-stabilizing ligands in catalysis. *Org. Lett. 6*, 2853−2855.
(41) Speers, A. E. and Cravatt, B. F. (2004) Profiling enzyme activities in vivo using click chemistry methods. *Chem. Biol. 11*, 535−546.
(42) Vasina, J. A. and Baneyx, F. (1997) Expression of aggregation-prone recombinant proteins at low temperatures: a comparative study of the *Escherichia coli* cspA and tac promoter systems. *Prot. Expr. Purif. 9*, 211−218.
(43) Routzahn, K. M. and Waugh, D. S. (2002) Differential effects of supplementary affinity tags on the solubility of MBP fusion proteins. *J. Struct. Funct. Gen. 2*, 83−92.
(44) Spiegel, H., Schillberg, S., Sack, M., Holzem, A., Nahring, J., Monecke, M., Liao, Y.-C., and Fischer, R. (1999) Accumulation of antibody fusion proteins in the cytoplasm and ER of plant cells. *Plant Sci. 149*, 63−71.
(45) Hackeng, T. M., Rosing, J., Spronk, H. M., and Vermeer, C. (2001) Total chemical synthesis of human matrix Gla protein. *Protein Sci. 10*, 864−870.
(46) Sokal, I., Alekseev, A., Baehr, W., Haeseleer, F., and Palczewski, K. (2002) Soluble Fusion Proteins between single transmembrane photoreceptor guanylyl cyclases and their activators. *Biochemistry 41*, 251−257.
(47) Claros, M. G., Perea, J., Shu, Y., Samatey, F. A., Popot, J.-L., and Jacq, C. (1995) Limitations to in vivo import of hydrophobic proteins into yeast mitochondria. The case of a cytoplasmically synthesized apocytochrome b. *Eur. J. Biochem. 228*, 762−771.
(48) Thomas, C. L. and Maule, A. J. (2000) Limitations on the use of fused green fluorescent protein to investigate structure−function relationships for the cauliflower mosaic virus movement protein. *J. Gen. Virol. 81*, 1851−1855.

BC060125E

PAMAM Dendrimeric Conjugates with a Gd−DOTA Phosphinate Derivative and Their Adducts with Polyaminoacids: The Interplay of Global Motion, Internal Rotation, and Fast Water Exchange

Jakub Rudovský,[†] Mauro Botta,*[,‡] Petr Hermann,*[,†] Kenneth I. Hardcastle,[§] Ivan Lukeš,[†] and Silvio Aime[||]

Department of Inorganic Chemistry, Charles University in Prague, Hlavova 2030, 128 40 Prague 2, Czech Republic, Department of Environmental and Life Sciences, University of Eastern Piedmont, "A. Avogadro", Via Bellini 25/G, I-15100 Alessandria, Italy, Department of Chemistry, Emory University, 1515 Dickey Drive, Atlanta, Georgia 30322, and Department of Chemistry I. F. M., University of Turin, Via P. Giuria 7, I-10125 Torino, Italy. Received June 1, 2006; Revised Manuscript Received June 14, 2006

A series of dendrimeric conjugates based on a PAMAM (polyamidoamine) backbone with macrocyclic Gd−DO3A-P^{ABn} complexes (monophosphinated analogue of DOTA) was prepared. The chelates were covalently attached to the G1-, G2-, and G4-PAMAM dendrimers through a thiourea linker in high loads (>90%). The prepared conjugates G1−(Gd−DO3A-P$^{BnN\{CS\}}$)$_8$, G2−(Gd−DO3A-P$^{BnN\{CS\}}$)$_{16}$, and G4−(Gd−DO3A-P$^{BnN\{CS\}}$)$_{59}$ showed relaxivities of 10.1, 14.1, and 18.6 s^{-1} mM^{-1} at 20 MHz and 37 °C and pH = 7.5, respectively. A variable-pH study (range 2−12) revealed up to 30% increase in the relaxivity at low pH for the G2−(Gd−DO3A-P$^{BnN\{CS\}}$)$_{16}$ conjugate. As confirmed by ^{1}H NMR titration of the unmodified G2 dendrimer, this is due to protonation of core tertiary amines leading to a more open and rigid structure. The variable-temperature ^{17}O NMR and ^{1}H NMRD relaxometric studies confirmed that the relaxivity is not controlled by water exchange but by rotational dynamics. A multiparametrical data evaluation using the Lipari−Szabo approach revealed that the water residence lifetime, $^{298}\tau_M$, for the conjugates studied was ca. 45−70 ns, which is longer than the value found for the monomeric model compound Gd−DO3A-P^{ABn} (16 ns) but short enough so as not to limit the relaxivity. The global rotational correlation time, $^{298}\tau_{Rg}$, varied from 1.5 to 3.1 ns and seemed to indicate a sufficiently slow molecular tumbling to achieve the high relaxivities measured; however, the rigidity factor S^2 (∼0.26), describing the internal flexibility, was far from optimum. The overall relaxivity was significantly increased (e.g. by a factor of 1.8 for the G1−(Gd−DO3A-P$^{BnN\{CS\}}$)$_8$ conjugate) when a positively charged polyaminoacid like poly(Arg) or poly(Lys) was added to the conjugate solutions. The electrostatic interactions partially "freeze" the internal mobility of the conjugate and also slow down global motion. This assumption was confirmed by an evaluation of ^{1}H relaxometric data obtained for the G2−(Gd−DO3A-P$^{BnN\{CS\}}$)$_{16}$−poly(Lys)$_{59}$ adduct. Importantly, it was proved that the adduct formation did not hamper the water exchange process.

INTRODUCTION

The family of polyamidoamine (PAMAM) starburst dendrimers has been the first class of dendrimers well characterized and commercialized (*1*). They are based primarily on an aliphatic di- or multiamine core, which is surrounded by a shell synthesized in a successive addition reaction of methyl acrylate with ethylenediamine (*1*). By an iterative application of this step, the dendrimeric architecture grows and one concentric shell (generation) is covered by another. PAMAM dendrimers are highly water-soluble globular molecules with primary amino groups exposed on their surface (Chart 1).

The number of amino groups on the surface grows exponentially with the dendrimer generation: i.e. there are 8 amino groups on the dendrimer of a generation one (G1), 16 on G2, 32 on G3, 64 on G4, etc. (*2*). These dendritic structures are characterized by an extremely low polydispersity, nontoxicity, and an ease of chemical modification, and they have been exploited in a wide range of biomedical applications such as drug delivery, gene therapy, micelle mimics, decontamining agents, immunodiagnostics, and/or in vitro gene expression (*1*). For their broadly favorable properties, PAMAM dendrimers have been used also in the preparation of contrast agents (CA) for magnetic resonance imaging (MRI) (*3*), specifically as carriers able to covalently bind molecules responsible for the contrast enhancement effect.

MRI has become one of the most powerful and fastest developing diagnostic methods in medicine. In particular it has proved to be very effective in visualizing soft tissues with excellent spatial resolution. The principle of this method lies in a "mapping" of concentration and magnetic properties of tissue water by measuring signal intensity and magnetic relaxation times of protons in 3D space. These characteristics may vary significantly not only between different tissues but also within one type of a tissue resulting in a significant gain in image contrast. This contrast can be enhanced further by application of MRI CAs, which are routinely administered in more than 45% of MRI investigations. A molecule of CA catalyzes the magnetic relaxation of water protons in its vicinity and can increase further the contrast between healthy and pathological tissue. In the past two decades, chemists have made significant progress in the design and application of such compounds and have clarified the relationship between a CA's structure and its efficacy. The efficacy is measured by the

* Authors to whom correspondence should be addressed. E-mail: petrh@natur.cuni.cz; mauro.botta@mfn.unipmn.it.

[†] Charles University in Prague. Tel: (+420) 22195-1263. Fax: (+420) 22195-1253.

[‡] University of Eastern Piedmont, "A. Avogadro". Tel: (+39) 0131-360253. Fax: (+39) 0131-360250.

[§] Emory University.

[||] University of Turin.

10.1021/bc060149l CCC: $33.50 © 2006 American Chemical Society
Published on Web 07/06/2006

Chart 1. Sketches of the Free G2-PAMAM Dendrimer and Its G2-16 Conjugate with the Gadolinium(III) Complex

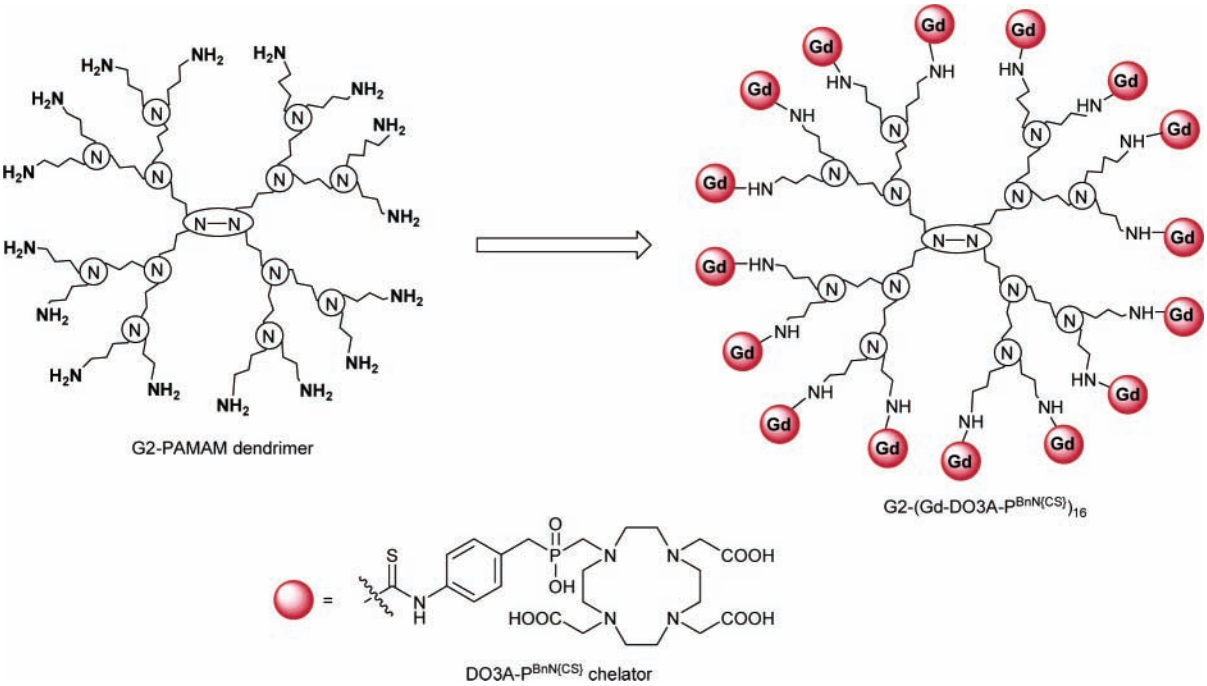

Chart 2. Ligands Discussed in the Paper

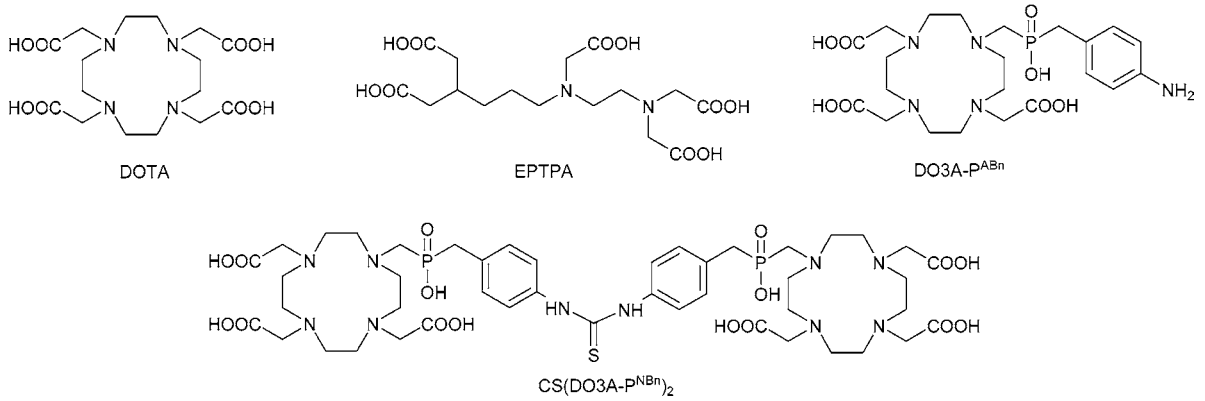

increase in the longitudinal relaxation rate of the water protons in a 1 mM solution of the CA; this parameter is known as *relaxivity*, r_1 (*4*−*7*). Among the most commonly used CAs affecting the longitudinal relaxation time T_1 are complexes of the highly paramagnetic Gd^{3+} ion. As this ion is highly toxic in a "free" state, it has to be bound as a thermodynamically stable and kinetically inert complex but should still allow for exchange of magnetic information between the metal center and bulk water. Linear polyamine (e.g. DTPA = diethylenetriamine-pentaacetic acid) or polyazamacrocycle (e.g. DOTA = 1,4,7,-10-tetraazacyclododecane-1,4,7,10-tetraacetic acid) derivatives with coordinating acetate arms have been commercially employed as they form sufficiently stable Gd(III) complexes and leave one or two coordination sites available for water molecule(s) (Chart 2). Unfortunately, the typical relaxivities of these compounds are about 4−5 s^{-1} mM^{-1} (at 20 MHz and 298 K) whereas according to the theoretical model these values could be increased to more than 100 s^{-1} mM^{-1} for an ideal CA (*8*). In order to attain theoretical relaxivities and challenge the new emerging applications of MRI, e.g. in molecular imaging (*9*), the structure of the Gd(III) chelates must be optimized.

According to the Bloembergen−Solomon−Morgan (BSM) theory, which connects the macroscopic relaxivity with intrinsic structural parameters of Gd(III) complexes, the residence lifetime of the coordinated water molecules, τ_M, and the rotational correlation time, τ_R, are the most crucial factors. Optimal values of τ_M lie in the range 10−50 ns, but most commercial CAs show values that are approximately 1 order of magnitude higher. In the past few years, several systems endowed with a sufficiently fast water exchange have been developed. The rate of water exchange was shown to be dependent on the overall charge (*10*), coordination geometry (*11*), flexibility of the coordination polyhedron (*11*), and/or steric interaction with proximate groups of the ligand (*12*−*17*). For instance, when one acetate arm in DOTA (i.e. DO3A-P^{ABn}) is replaced by a bulky phosphinate group, the water residence lifetime for the corresponding Gd(III) complex (at 298 K) was found to change from 243 ns (*18*) to 16 ns (*16*).

For complexes with an optimized water exchange rate, the relaxivity is controlled primarily by the rotational correlation time: if the molecular tumbling is too fast, the relaxivity enhancement is limited. In order to increase the size of the molecule, the small Gd(III) complexes could be covalently conjugated to macromolecular carriers like PAMAM dendrimers. The conjugation may not only increase the rotational correlation time but also significantly improve the biochemical properties of the CA (*3*); however, most of the dendrimeric systems investigated in the past suffered from the same two primary limitations: (i) the slow water exchange process (*19*) and (ii) the high degree of an internal mobility which super-

imposes the global motion of the whole dendrimer (*20*). A few covalent conjugates with gadolinium(III) complexes, characterized by a rather fast water exchange, have been studied (*21*−*23*), but in all cases the relaxivity was limited by the internal mobility of the system.

To reduce this undesired effect, we explored systems where the fast-water-exchanging Gd−DO3A-P^{ABn} complex was covalently attached to PAMAM dendrimers and then the whole negatively charged structure made rigid by addition of cationic polyaminoacids such as poly(Arg) or poly(Lys). Recently, we published a brief account where it was shown that the adduct of G2−(Gd−DO3A-$P^{BnN\{CS\}}$)$_{16}$ dendrimer with poly(Arg)$_{56}$ afforded relaxivity enhancement by a factor of 1.6 in comparison with the pure conjugate (*24*).

In this research four low- and middle-generation PAMAM-based gadolinum(III) complexes were studied: G1−(Gd−DO3A-$P^{BnN\{CS\}}$)$_8$, G2−(Gd−DO3A-$P^{BnN\{CS\}}$)$_9$, G2−(Gd−DO3A-$P^{BnN\{CS\}}$)$_{16}$, and G4−(Gd−DO3A-$P^{BnN\{CS\}}$)$_{59}$. The influence of a possible, undesired electronic Gd^{3+}−Gd^{3+} interaction was evaluated by comparison of the properties of the G2-Gd(III)/Gd(III) and mixed -Y(III)/Gd(III) complexes, and in addition to the routine solution characterization measurements such as variable-temperature ^{17}O NMR, ^{1}H NMRD, and pH-dependent relaxivity studies, relaxometric titrations with several polyaminoacids, poly(Arg)$_{56}$, poly(Arg)$_{320}$, poly(Lys)$_{56}$, and poly(Lys)$_{17}$, were also measured. For selected adducts, ^{1}H NMRD profiles and variable-temperature relaxivity measurements were performed to quantify the change of structural parameters during adduct formation.

EXPERIMENTAL SECTION

Materials. All reagents and solvents commercially available were used as received. DO3A-P^{NCS} and CS(DO3A-P^{NBn})$_2$ were prepared according to the procedure described in the literature (*25*). The starburst PAMAM dendrimers (producer, Dendritech Inc., Midland, MI) of generation 1 (G1), 2 (G2), and 4 (G4) with 8, 16 and 64 terminal primary amino groups were purchased as methanolic solutions from Aldrich, respectively. The lanthanide(III) chloride salts were obtained from Strem or Aldrich. Commercially available polyaminoacids were purchased from Sigma. Ultrafiltration equipment (UF-cell 8050 and 800 mL storage) including membranes YM3 and YM10 (Amicon, Bedford, MA) were purchased from Millipore. Analytical ^{1}H and ^{31}P spectra were recorded on a Varian ^{UNITY}-INOVA-400 spectrometer. All NMR samples were measured in D_2O (99.98%, Chemtrade, Germany) if not otherwise stated. Elemental analysis was performed by Redox S.n.c. (Monza, Italy). ICP-MS spectra were measured on an Element-2, Thermo-Finnigan spectrometer (Rodano, Italy). MS spectra of synthesized poly(Lys)$_{17}$ were acquired on a MALDI spectrometer in a positive reflection ion mode with delayed extraction on a Reflex III TOF instrument (Bruker Daltonics, Bremen, Germany) equipped with a 337 nm nitrogen laser. This instrument was located in the Laboratorio Integrato di Metodologie Avanzate (LIMA), Bioindustry Park of Canavese, Colleretto Giacosa, Ivrea, Italy.

Synthesis of PAMAM-DO3A-$P^{BnN\{CS\}}$ Conjugates. General Procedure. The synthesis of G1−(DO3A-$P^{BnN\{CS\}}$)$_8$, G2−(DO3A-$P^{BnN\{CS\}}$)$_9$, G2−(DO3A-$P^{BnN\{CS\}}$)$_{16}$, and G4−(DO3A-$P^{BnN\{CS\}}$)$_{59}$ followed the same protocol. For preparation of about 200 mg of conjugate, equimolar amounts of DO3A-P^{NCS} (per number of primary amino groups on PAMAM) and PAMAM were mixed in a small volume of H_2O (typically 5 mL), pH was adjusted to 9 with 1.5 M KOH, and the solution was stirred for 12 h at 40 °C. Then, an additional portion (0.5 molar equiv) of DO3A-P^{NCS} was added, the pH was readjusted to 9, and the mixture was stirred at 40 °C for an additional 12 h. Subsequently, the pH was adjusted to 7 by addition of concentrated HCl and the solution filtered through Millipore Millex 5 μm and 0.22 μm syringe filters into the ultrafiltration cell. The solutions were ultrafiltered in two cycles at 3 atm (i.e. concentrated from 50 mL to 10 mL and diluted again). For G1 and G2 conjugates, membranes YM3 (with cutoff at 3 kDa) were used, whereas the G4 conjugate was filtered through YM10 membrane (with cutoff at 10 kDa). The solutions were diafiltered at 4 atm until ca. 800 mL of elution water was collected. The resulting conjugate solution was evaporated to dryness, yielding a solidified, glassy product. The number of chelates attached to the dendrimer was determined by ^{1}H NMR spectrum integration (aromatic vs alkyl region) and by calculation of the nitrogen/sulfur ratio obtained from elemental analysis (*3*). The loadings indicated in this work are the averages from both methods; the observed loadings were quite similar with maximum differences of 0.5 chelate unit for the G1 and G2 conjugates and 1 chelate unit for the G4 conjugate.

Synthesis of Gd(III) and Gd(III)/Y(III) Complexes. For preparation of the full-loaded Gd(III) complexes, the conjugate (typically 200 mg) was dissolved in H_2O (8 mL) and 2 equiv of $GdCl_3$ (per one chelate unit attached to the dendrimer) was added. A small amount of bromothymol blue indicator was added and the pH adjusted to about 6.5−7.0 (green color of the solution) by addition of 1.5 M KOH, and the excess Gd(III) salt precipitated. The mixture was stirred overnight at 50 °C and 1.5 equiv of Na_2H_2EDTA (per total Gd(III) amount) added, the pH value readjusted, and the solution stirred for an additional 6 h at RT. Almost immediately after addition of Na_2H_2EDTA, the Gd(III) salt precipitate was complexed by EDTA and dissolved. The resulting clear green solution was filtered through Millipore Millex 5 μm and 0.22 μm syringe filters into the ultrafiltration cell, and the solution was concentrated twice and then diafiltrated until about 500 mL of water was collected. The slightly yellow solution of the complex was evaporated to obtain a glassy, solid product. The procedure for preparation of the mixed Gd(III)/Y(III) complex of G2−(DO3A-$P^{BnN\{CS\}}$)$_{16}$ was similar except that in the first step only 0.5 equiv of $GdCl_3$ (per number of chelates on the dendrimer) was added. After 12 h at 50 °C, 1.5 equiv of YCl_3 was added and the following workup was the same as in the previous case. Typical yields obtained from this procedure were about 80% calculated on the empirical formula obtained from elemental analysis. The exact Gd(III) loads were obtained from a comparison of the sulfur and the gadolinium contents determined by ICP-MS measurement. For G1−(DO3A-$P^{BnN\{CS\}}$)$_8$, G2−(DO3A-$P^{BnN\{CS\}}$)$_9$, G2−(DO3A-$P^{BnN\{CS\}}$)$_{16}$, and G4−(DO3A-$P^{BnN\{CS\}}$)$_{59}$ conjugates, 7.5, 8.5, 15.2, and 58.3 gadolinium ions per conjugate were found, respectively. In the case of G2−(Gd−DO3A-$P^{BnN\{CS\}}$)$_{16}$ and G4−(Gd−DO3A-$P^{BnN\{CS\}}$)$_{59}$ complexes, the results from ICP-MS were compared with ^{1}H NMR relaxometric titrations and were in good agreement (see below). Unfortunately, we were not able to obtain any mass spectrometric data (ESI with ion-trap detector or MALDI-TOF) from the pure conjugates or their gadolinium(III) complexes. Most likely the procedure failed because of the polyanionic and complexing nature of the compounds responsible for the unavoidable capture of a large number of H^+, Na^+, and/or K^+ cations during the measurements.

Gd(III) Loads Determination by Relaxometric Titration. Diluted 1 mM and 0.2 mM solutions, respectively, were prepared from the conjugates G2−(DO3A-$P^{BnN\{CS\}}$)$_{16}$ and G4−(DO3A-$P^{BnN\{CS\}}$)$_{59}$. Solutions for the relaxometric titrations for both conjugates were divided into 13 vials (0.6 mL each) into which the $GdCl_3$ was added so as to vary the molar ratio of Gd per chelate from 0 to 2. The Gd(III) complex formed during stirring overnight at pH 7 and 50 °C; each solution was

subsequently passed through a syringe filter (5 μm) into an NMR tube. The relaxivities were measured and plotted against exact Gd^{3+} concentrations as determined by the bulk magnetic susceptibility shift (BMS) measurement (*26*). The sample without Gd^{3+} was used as a reference. In both cases, the relaxivity increased linearly with Gd^{3+} concentration up to the point where the theoretical equivalence was reached, and then the data deviated indicating an "overtitrated" solution wherein hydrolysis of the "free" Gd^{3+} occurred. This nonlinearity was ascribed to the presence of nonstoichiometric Gd-conjugate phase, wherein the Gd^{3+} was nonspecifically sorbed.

Synthesis of Poly(Lys)$_{17}$ Peptide. The peptide was prepared on an automatic robotic synthesizer Syro II (Multisintech GmbH, Germany) located at LIMA laboratories, Bioindustry Park of Canavese, Colleretto Giacosa, Ivrea, Italy. The Fmoc-protected amino acids were purchased from Advance Biotech srl (Italy), and the coupling reaction was carried out on Fmoc-PAL-PEG-PS resin (Applied Biosystem). The poly(lysine) chain was doped by three proline residues to avoid an aggregation. The sequence was $(Lys)_5$-Pro-$(Lys)_5$-Pro-$(Lys)_5$-Pro-$(Lys)_2$.

^{17}O NMR Measurements. Variable-temperature ^{17}O NMR relaxation measurements were performed on a JEOL EX-90 spectrometer (2.1 T, 12.2 MHz) with external locking system (D_2O). Experimental settings were as follows: spectral width 10 000 Hz, pulse width 7 μs (90°), acquisition time 10 ms, 2048 scans, and no sample spinning. The complex solutions were enriched by addition of $H_2{}^{17}O$ (6%, Yeda, Israel) to an overall ca. 0.2% ^{17}O concentration. Transversal ^{17}O NMR relaxation rates were calculated from the line widths of the ^{17}O signals at half-heights. The ^{17}O profiles were measured from 0 to 90 °C at 10 °C increments. All the samples were conditioned for 10 min at each temperature prior to the measurement to ensure the full temperature equilibrium. The temperature was calibrated using a thermocouple probe and is correct within ±0.5 °C. The time necessary for temperature stabilization has been established from a number of similar measurements made with this instrument. The exact concentrations of Gd^{3+} were determined by BMS measurements. As references, the samples of Gd-free conjugates at the same pH were used.

^{1}H NMRD (Nuclear Magnetic Relaxation Dispersion) Profiles. ^{1}H NMRD profiles were measured on a Stelar Spinmaster FFC-2000 fast-field cycling relaxometer (Mede, Italy) in a magnetic field range from 2.4×10^{-4} to 1.6 T (corresponding to 0.01−70 MHz of proton Larmor frequencies). For all measurements, the samples contained about 1 mM concentration of Gd^{3+} in nondeuterated water, but the exact concentrations of Gd^{3+} were determined by measurement of BMS. The ^{1}H T_1 relaxation times were acquired by the standard inversion recovery method with typical 90° pulse width of 3.5 μs, 16 experiments of 4 scans. The reproducibility of the T_1 data was ±5%. The temperature was controlled with a Stelar VTC-91 airflow heater equipped with a calibrated copper−constantan thermocouple (precision of ±0.1 °C). The NMRD profiles were measured at 25 and 37 °C.

pH and Temperature Dependence of Proton Relaxivity. The pH and VT studies of proton T_1 relaxation times were carried out on an FFC relaxometer at the fixed field of 0.45 T (corresponding to 20 MHz of proton Larmor frequency) and 25 °C. For the pH dependence measurements, 1 mL samples of 0.5−1 mM solutions of the conjugate (calculated per gadolinium) were prepared and about 100 μL was placed in a 5 mm NMR tube. The pH was adjusted by addition of 1 M KOH or concentrated hydrochloric acid to cover the range from 2 to 12. Some values were measured repeatedly to exclude any influence from increasing ionic strength or a changing concentration; the reproducibility of the values was good within the experimental error (±2%). The VT-^{1}H r_1 dependence was measured for the G2−(Gd−DO3A-P$^{BnN\{CS\}}$)$_{16}$−poly(Lys)$_{61}$ adduct at a molar ratio of poly(Lys)$_{56}$/conjugate of 10:1 and pH 7.5. The temperature was controlled by a Stelar VTC-91 airflow unit equipped with a calibrated copper−constantan thermocouple (precision of ±0.1 °C). The desired temperature was set up either by the internal heater or by an attached liquid nitrogen evaporator.

Interaction with Polyaminoacids. Relaxometric Study. The titrations were carried out at fixed concentrations of the dendrimer and variable concentrations of the polyaminoacid. For each study, 5 mL of the 0.5 mM batch solution (calculated per gadolinium) of the dendrimeric complex was prepared and this solution divided into 11−15 samples containing 300 μL each. In the second step, the polyaminoacids were dissolved in water to obtain solutions of about 1 mM concentration each. The titration sample for ^{1}H T_1 measurement was obtained by adding 50 μL of the polyaminoacid solution into the vial containing the dendrimeric complex and about 100 μL of the resulting solution transferred into a 5 mm NMR tube. In the next step, the batch solution of the polyaminoacid was diluted twice and the procedure repeated. In this way the dendrimer/aminoacid ratio changed during the titration by 3.5−4 orders of magnitude. The pH values of the samples were randomly checked and found to be about 7.5.

Data Processing, Evaluation, and Molecular Modeling. The simultaneous least-squares fitting of the ^{1}H NMRD and ^{17}O NMR T_2 data was performed with Micromath Scientist (*27*) fitting routines based on the Bloembergen−Solomon−Morgan (BSM) equations or the Lipari−Szabo modification (see Supporting Information). All data and charts were preprocessed and exported in Microcal Origin (*28*) or MSI WebLab Viewer (*29*). Molecular modeling was performed in Hypercube Hyperchem 7.5 (*30*). Acidity constants of the pure G2-PAMAM were obtained using the OPIUM package (*31*).

RESULTS AND DISCUSSION

Synthesis of Conjugates and Their Lanthanide(III) Complexes. All "full-loaded" conjugates were prepared by the same general procedure. The isothiocyanate derivative DO3A-P^{NCS} was prepared in advance according to the published procedure (*25*) and then added in two portions (50% overall excess) to the methanol/water solution of the corresponding free dendrimer. This approach leads to the higher loads because part of the isothiocyanate is wasted when it is added in one step due to the formation of the ditopic compound CS(DO3A-P^{NBn})$_2$ (Chart 2) arising from the reaction between the hydrolyzed isothiocyanate (i.e. the amine) and the other isothiocyanate molecule. The pure conjugates were obtained by ultrafiltration through a membrane with an appropriate cutoff. The "half-loaded" G2 conjugate was prepared by addition of 9 equiv of DO3A-P^{NCS} to a solution of the free G2 dendrimer. The subsequent workup of the reaction mixture followed the same procedure as described above. The loads of the chelate were determined by ^{1}H NMR signal integration and by elemental analysis using the N/S ratio. With both methods very similar results were obtained; since the isothiocyanate group is highly reactive under these conditions, full saturation was realized in G1 and G2 conjugates and 92% saturation for the G4 conjugate. For the "half-saturated conjugate", a 56% load was obtained, as expected, because the low-generation dendrimers adopt a flexible conformation in solution in contrast to that expected for the higher generations that tend to form internal cavities preventing the penetration of the reactant to the interior (*2*). The N/S ratio does not depend on water content, and, therefore, it was possible to calculate the amount of the pure conjugate in the solid samples; on average, all conjugates in solid form contained about 10% water. Characterization of the prepared conjugates by various mass

spectrometric techniques (MALDI or ESI) was attempted; however, it was not possible to observe any resolved signals as a consequence of a formation of multiply charged species containing a high number of H^+, K^+, and/or Na^+ counterions.

The Gd(III) complexes were prepared by mixing a solution of the appropriate conjugate with a 50% excess of $GdCl_3$. The noncomplexed Gd^{3+} ion was scavenged by addition of excess Na_2H_2EDTA, and all low-molecular-weight impurities were removed by ultrafiltration. A check for the presence of "free" Gd^{3+} ions in the gadolinium-loaded conjugates by the standard Xylenol Orange test was proved unreliable as the negatively charged conjugates may coordinate some number of Gd^{3+} ions in a nonspecific way. In order to determine the degree of loading of Gd^{3+}, relaxometric titrations and ICP-MS measurements were performed to get the exact number of gadolinium(III) per chelate. Both methods were in agreement and indicated that there were approximately 0.9 gadolinium atom per chelate in all conjugated complexes. Additionally, the value of relaxivity obtained by relaxometric titration indicated that the conjugates have one water molecule coordinated to the Gd^{3+} ion (Figure S1, Supporting Information).

The mixed Gd(III)/Y(III) G2 conjugate was prepared sequentially as follows: the free conjugate was mixed with 0.5 equiv of $GdCl_3$ per chelate and the solution heated (50 °C) and stirred overnight; 1 equiv of YCl_3 per chelate was added, and after incubation under the same conditions as before, Na_2H_2EDTA was added to scavenge any remaining lanthanide(III) salts and the resulting solution was ultrafiltrated. The amount of conjugate-bound gadolinium was determined by ICP/MS to be 44%.

The molecular structure of the complex should be the same as that observed for lanthanide(III) complexes of DOTA and the parent ligands, DO3A-P^{ABn} and CS(DO3A-P^{NBn})$_2$. As shown previously, in the solid state (*15*, *32*) as well as in the solution (*15*, *16*, *25*) the central ions are sandwiched between N4 (ring amine nitrogen atoms) and O4 (three acetate and one phosphinic acid oxygen atoms) coordination planes with one water molecule capping the O4 plane. As in other lanthanide(III) complexes with DOTA-like ligands, equilibrium between two distereoisomeric forms, SA (square-antiprism) and TSA (twisted square-antiprism), was observed in solutions of the complexes with the parent ligands (*15*, *16*, *25*).

Studies on pH-Responsive Structural Changes. It is well-known that PAMAM dendrimers as a class of polyelectrolytes can adopt a wide range of conformations in solution depending on the stage of protonation since, as the outer-shell and inner-shell amines are being protonated, the electrostatic repulsion results in a more expanded and more hydrated structure (*33*). This issue has been the subject of many physicochemical studies on pure PAMAMs; however, it was discovered quite recently by Merbach et al. (*22*) and us (*24*) that this phenomenon could have an impact on PAMAM-conjugated MRI CAs. It was demonstrated that the rotational correlation time increases by passing from an alkaline to an acidic environment (as a consequence of more expanded structure and higher hydration of the dendrimer core) and the relaxivity of a conjugated Gd(III) complex increases as well.

In order to gain insight into these protonation phenomena a ^1H NMR titration of the free G2 dendrimer was carried out. The spectra of such polyamines are rather complex, but it was possible to track reliably five signals of methylene protons in the pH range from 11 to 2 and record their chemical shifts (Figure S2, Supporting Information). Each profile is characterized by the position of an inflection point on the pH scale and by the differences in the chemical shift ($\Delta\delta_H$) between the protonated and deprotonated forms. There are two kinds of amino groups in the PAMAM structure that can be protonated: (i) the terminal primary amino groups (those are rather basic and converted to thioamides after a conjugation) and (ii) the tertiary branching amines including the core ethylenediamine moiety, which are neutral or slightly acidic (*2*). As a rough approximation we can assume that the protonation of any amino group is independent of the others so we can consider an equilibrium existing between three possibilities: (i) totally deprotonated species in very alkaline solutions, (ii) the species occurring in neutral solutions having all primary amines protonated, and (iii) totally protonated species in acidic solutions. Using this very simple model, a parallel fitting (*31*) of all measured chemical shifts was performed resulting in "average" pK_a values (assigned hereinafter as $\langle pK \rangle$) (*34*) for both protonation equilibria with a good precision: $\langle pK_1 \rangle = 5.76(3)$ (corresponding to protonation of the tertiary amines) and $\langle pK_2 \rangle = 9.12(3)$ (corresponding to the protonation of the primary amines). The pK values correspond well with those obtained from potentiometric titration data for the free G0-PAMAM dendrimer having four primary amino groups with pK_a 8.3−9.8, and for the tertiary amino groups of the ethylenediamine core with pK_a 6.6 and 2.8 (*35*).

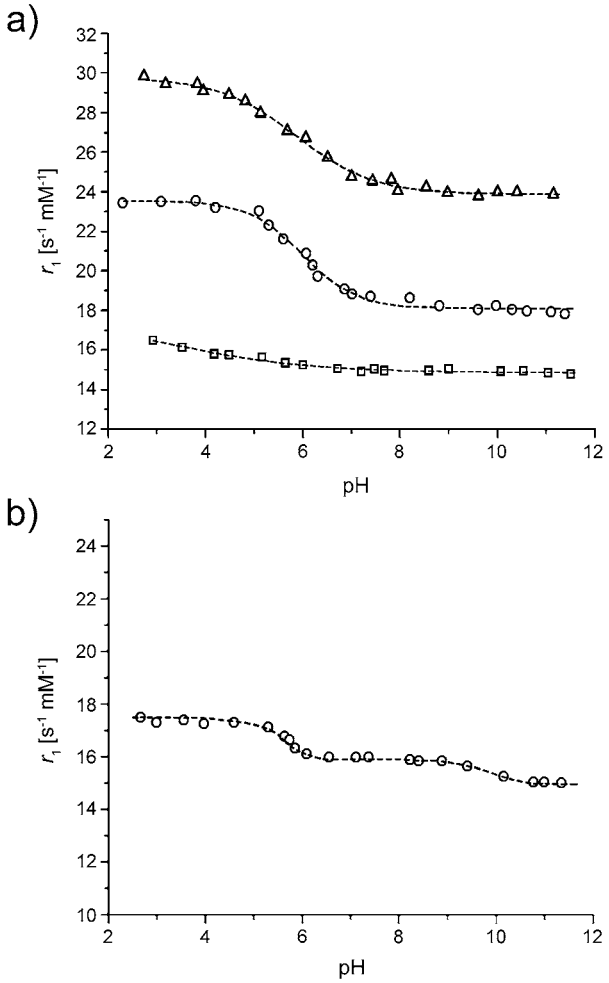

Figure 1. (a) r_1 vs pH profiles (20 MHz, 25 °C) for the G1−(Gd−DO3A-$P^{BnN\{CS\}}$)$_8$ (□), G2−(Gd−DO3A-$P^{BnN\{CS\}}$)$_{16}$ (○), and G4−(Gd−DO3A-$P^{BnN\{CS\}}$)$_{59}$ (△) conjugates. The dashed lines are the result of a sigmoidal least-squares fitting of the data. (b) r_{1p} vs pH profile (20 MHz, 25 °C) for the G2−(Gd−DO3A-$P^{BnN\{CS\}}$)$_9$ conjugate. The dashed line here is only a polynomial fit to guide the eyes.

Subsequently, the pH dependence of the relaxivity was measured for the "full-loaded" dendrimeric conjugates: G1−(Gd−DO3A-$P^{BnN\{CS\}}$)$_8$, G2−(Gd−DO3A-$P^{BnN\{CS\}}$)$_{16}$, and G4−(Gd−DO3A-$P^{BnN\{CS\}}$)$_{59}$ (Figure 1a). All profiles show inflection points at pH values corresponding to the $\langle pK_1 \rangle$ values assigned to the protonation of the tertiary branching amines inside the

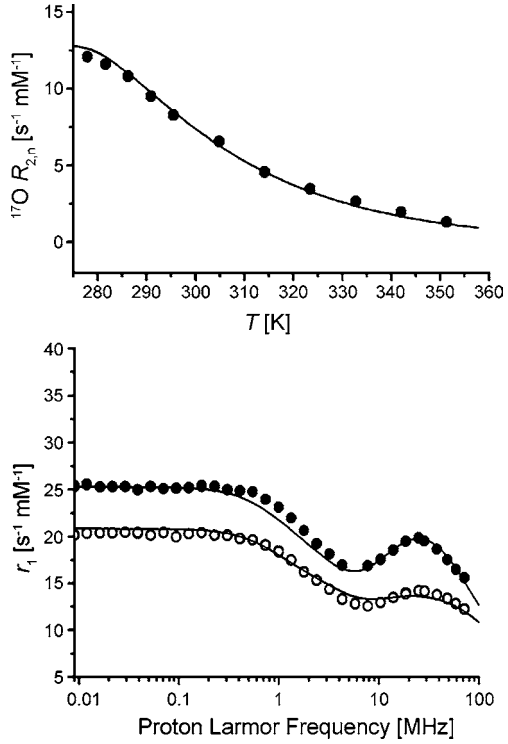

Figure 2. ^{17}O $R_{2,n}$ (top) and ^{1}H NMRD relaxation profiles (bottom; full circles 25 °C (●), open circles 37 °C (○)) for the G2−(Gd−DO3A-$P^{BnN\{CS\}}$)$_{16}$ conjugate. Transverse relaxation rates ($R_{2,n}$) were normalized to 1 mM concentration of gadolinium. The solid lines represent the best results of the simultaneous fitting to the experimental data (vide infra).

free G2-PAMAM dendrimer confirming that the relaxivity enhancement in acidic solutions is a direct consequence of the protonation of the PAMAM inner-shell amines. The relaxivity increase at low pH reflects the larger rotational correlation times of the Gd(III) complexes due to the more expanded structures of the dendrimers. Interestingly, a calculation of the relaxivities at pH 8 and at pH 3 for the given conjugates showed a 10% increase for G1−(Gd−DO3A-$P^{BnN\{CS\}}$)$_8$, 30% for G2−(Gd−DO3A-$P^{BnN\{CS\}}$)$_{16}$ (ref *24*), and 20% for G4−(Gd−DO3A-$P^{BnN\{CS\}}$)$_{59}$. To explain the highest enhancement of the G2−(Gd−DO3A-$P^{BnN\{CS\}}$)$_{16}$ conjugate, the overall size and the flexibility of the internal structure of the conjugate must be considered. For the G1 conjugate, the size is rather small and the structure is dictated primarily by a repulsion of the negatively charged complexes on its surface thus limiting the effect of protonation; multiple protonation of the core amines also is more difficult so the inflection points are likely characterized by pK_a values covering a broader range. This latter effect may account for the lack of a well-defined inflection in the profile. For the G4 conjugate, the smaller inflection is probably due to the leveling off of the relaxivity with longer τ_R (vide infra, Figure 4).

Investigation of the influence of different loading of the G2 dendrimer on the pH-dependent relaxivity might be a potentially important issue especially in high-molecular-weight conjugates where loads are typically between 50% and 80% (*20*, *22*, *23*). The "half-loaded" conjugate (G2−(Gd−DO3A-$P^{BnN\{CS\}}$)$_9$) was synthesized and the dependence of its relaxivity on pH (Figure 1b) measured.

Overall this profile is significantly lower than for its "full-loaded" analogue (Figure 1a) and the relaxivity enhancement at low pH is much less pronounced. This could be the result of the much higher flexibility of the "half-loaded" structure. In addition to the inflection point at pH ∼5.5 observed for all other conjugates there is a minor step at pH ∼10 that clearly corresponds to the protonation of the primary amines. This small

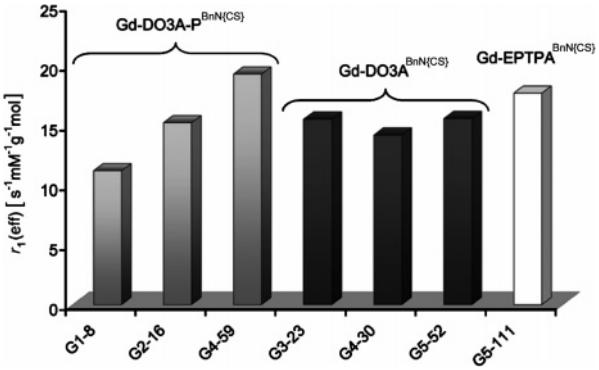

Figure 3. The comparison of effective relaxivities (20 MHz, 37 °C) for some PAMAM conjugates; Gd−DO3A$^{BnN\{CS\}}$ (ref *20*), Gd−EPTPA$^{BnN\{CS\}}$ (ref *22*).

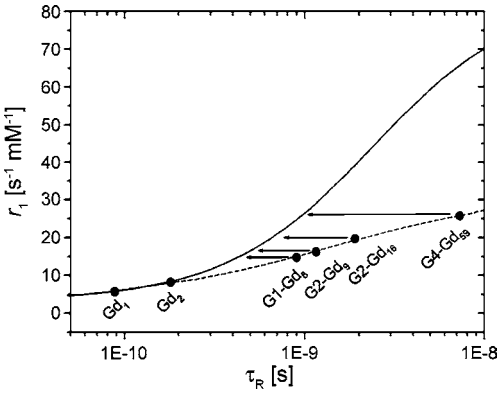

Figure 4. Experimental relaxivities (20 MHz, 25 °C) as a function of theoretical τ_R for our G*n*−(Gd−DO3A-$P^{BnN\{CS\}}$) conjugates together with parent Gd−DO3A-P^{ABn} and ditopic Gd$_2$−CS(DO3A-P^{NBn})$_2$ complexes. The dashed line is just to guide the eyes. The solid line is the simulation of relaxivity vs τ_R assuming $\tau_M = 50$ ns, $\tau_v = 30$ ps, $\Delta^2 = 0.1 \times 10^{20}$ s^{-2}, $q = 1$, $R_{GdH} = 3.1$ Å, $a = 3.5$ Å, $D = 2.24 \times 10^{-5}$ cm^2 s^{-1} (*37*).

relaxivity increase may arise from a more open structure due to the electrostatic repulsion between the charged amine groups and/or the result of more rigidity in the surface caused by hydrogen bonding between these protonated amines and the proximate (negatively charged) phosphinate groups of the chelate.

^{17}O and ^{1}H NMR Relaxometry. Relaxometry is a technique in which the solvent nuclei are investigated in order to obtain information on the solute molecules. It represents a fundamental tool for the study of the structural and dynamic properties of paramagnetic molecules in aqueous solutions. Measurements of the water ^{17}O NMR transverse relaxation rates R_2 at variable temperatures (12.1 MHz ≡ 2.1 T) and ^{1}H nuclear magnetic relaxation dispersion, NMRD, profiles (frequency dependence of r_1) at 25 and 37 °C were carried out at pH 7.5 on G1−(Gd−DO3A-$P^{BnN\{CS\}}$)$_8$, G2−(Gd−DO3A-$P^{BnN\{CS\}}$)$_{16}$, and G4−(Gd−DO3A-$P^{BnN\{CS\}}$)$_{59}$ conjugates (Figure 2 and Figure S3, Supporting Information).

Without any numerical evaluation, it is apparent from a simple inspection of the ^{17}O R_2 temperature profiles that relaxivity is not limited by a slow water exchange as the maxima for all systems are in the low-temperature region (*36*). This is also confirmed by the dependence of ^{1}H relaxivity vs temperature; as apparent from the NMRD profiles, the relaxivity in all cases is decreased with increasing temperature suggesting that, in terms of Bloembergen−Solomon−Morgan theory (BSM), the relaxivity is controlled primarily by the molecular tumbling rate (*37*). It is worth noting that this is an important difference from most of the dendrimeric conjugates of DOTA and DTPA reported previously (*19*, *20*, *38*). All NMRD profiles show

Table 1. Parameters Obtained from Simultaneous Fitting of ^{17}O NMR and ^{1}H NMRD Data Based on the Lipari−Szabo Approach[a]

	gadolinium(III) complex				
parameter	G1-8	G2-16	G4-59	CS(DO3A-P^{NBn})$_2$ [b]	DO3A-P^{ABn} [c]
r_1 [s^{-1} mM^{-1}][d]	10.1/14.8	14.1/19.7	18.6/25.8	6.1/8.2	4.2/5.7
$^{298}\tau_M$ [ns]	48 ± 5	66 ± 4	68 ± 7	53	16
$\Delta H_M^{\#}$ [kJ mol^{-1}]	55 ± 5	50 ± 4	51 ± 5	39	20.6
$^{298}\tau_{Rg}$ [ps]	1560 ± 280	2690 ± 270	3140 ± 210	183	88
E_{rg} [kJ]	44 ± 4	43 ± 4	35 ± 3	37	29
$^{298}\tau_{Rl}$ [ps]	115 ± 4	100 ± 3	133 ± 4		
E_{rl} [kJ]	27 ± 2	20 ± 1	28 ± 1		
S^2	0.25 ± 0.02	0.24 ± 0.01	0.29 ± 0.01		
q	1	1	1	1	1
q_{ss}	2	2	2	1	1

[a] The conjugates are labeled in a shortcut form. [b] Reference *25*. [c] Reference *16*. [d] The relaxivity values were measured at 37/25 °C, 20 MHz; all solutions of the conjugates were measured at pH = 7.5; the underlined values were fixed during the fitting process.

shapes typical for high-molecular-weight systems with high-field peaks centered at ca. 20−30 MHz and roughly proportional to the molecular size (overall mobility) of the systems.

Recently, the use of the effective relaxivities per unit of mass has been suggested for comparing the efficacy of different multimeric paramagnetic complexes (*39*). We have calculated these values, at 37 °C and 20 MHz, which are plotted in Figure 3 and compared with those from similar systems reported in the literature.

Surprisingly, the effective relaxivities for different G2- and G5-dendrimeric conjugates are rather similar; apparently there is no additional benefit in loading more gadolinium(III) complexes on a larger PAMAM backbone. This saturation effect of r_{1p} in a series of macromolecular systems of increasing size has been observed previously, and often it has been attributed to the limiting effect of the slow rate of water exchange that becomes more important for longer values of τ_R. However, this is not the case for the present series of conjugates and for the G5 dendrimer conjugated to Gd−EPTPA$^{BnN\{CS\}}$ (Figure 3) (*22*) that are characterized by a sufficiently fast rate of water exchange. The second important factor that needs to be taken into account is the effective rotational correlation time, i.e. the presence of internal degree of rotation of the complexes superimposed to the global motion of the dendrimer.

As a result, the effective τ_R may be significantly shorter than that expected on the basis of the molecular weight of the system. This was observed previously on related DOTA, DTPA, or EPTPA conjugates (*19*, *22*). The importance of this effect is graphically represented in Figure 4 for the present series of conjugates. We plotted the relaxivities for the G*n*−(Gd−DO3A-P$^{BnN\{CS\}}$) conjugates together with the values obtained for the parent monomeric Gd−DO3A-P^{ABn} complex (*16*) and the ditopic Gd−CS(DO3A-P^{NBn})$_2$ complex (*25*) (Chart 2) as a function of the rotational correlation time. The τ_R values for the G1, G2, and G4 conjugates were calculated on the basis of the assumption of a linear correlation between τ_R and the molecular weight that is roughly valid for spheroidal molecules. For comparison, we also simulated the theoretical profile of relaxivity vs τ_R calculated on the basis of the BSM (*37*) and Freed's equations (*40*) for the inner-sphere and the outer-sphere contributions, respectively. In the simulation the water residence lifetime was adjusted to 50 ns (vide infra) and all the other parameters were set to their standard values (see the caption of Figure 4). It can be seen that the experimental points are below the theoretical values indicating that the effective rotational correlation times are much lower than expected on the basis of the molecular weight. This effect increases in importance with increasing size of the conjugate. These observations highlight the current limitation of the dendrimeric concept: for systems with an optimized rate of water exchange the relaxivity appears to be damped by lack of sufficient rigidity of the conjugated systems.

A comparison of the ^{1}H NMRD profiles for the G2−(Gd−DO3A-P$^{BnN\{CS\}}$)$_{16}$ conjugate at pH 7.5 and pH 4 (Figure S4, Supporting Information) indicates that τ_R increases with decreasing pH as can be seen by the higher relaxivity peak in the region 10−30 MHz. This observation corresponds well to the proposed (vide supra) change of structure toward a more expanded configuration; a similar effect has been observed in the case of Gd−EPTPA−PAMAM conjugates (*22*).

To obtain quantitative information about the solution dynamics (e.g. molecular tumbling rate, degree of internal motion, and/or water exchange rate), the ^{17}O and ^{1}H relaxation data were fitted simultaneously according to the established model of paramagnetic relaxation. It is well-known that the nuclear magnetic relaxation in the presence of multi-paramagnetic systems of this size and complexity cannot be described solely by the BSM set of spectral density functions (*41*) because the internal motion is, to some extent, always superimposed on the overall molecular tumbling. In order to solve this problem it is preferable the use of the Lipari−Szabo (LS) approach (*42*) that introduces an independent set of parameters for the local and global motions; this method has been successfully applied in the past (*19*, *22*, *23*). In addition, due to a slow overall motion of macromolecules, the interpretation of the electronic relaxation parameter values (τ_v and Δ^2) is quite difficult because the time evolution of the electronic correlation functions cannot be described within the Redfield theory (*41*). It should be emphasized, however, that the other parameters influencing relaxivity remain physically meaningful and significant insight can be realized by the parameters fitting. Selected results of simultaneous fitting of ^{1}H and ^{17}O NMR relaxation data at pH 7.5 for the present PAMAM conjugates based on the Lipari−Szabo approach are listed in Table 1 (see full set of equations and Table S1 in Supporting Information). The values obtained for G1−(Gd−DO3A-P$^{BnN\{CS\}}$)$_8$, G2−(Gd−DO3A-P$^{BnN\{CS\}}$)$_{16}$, and G4−(Gd−DO3A-P$^{BnN\{CS\}}$)$_{59}$ are compared with those found for the parent Gd-CS(DO3A-P^{NBn})$_2$ and Gd−(DO3A-P^{ABn}) complexes.

Since the model uses a large set of parameters, some constraints needed to be applied to obtain a reasonable fit; for example, the value of the hyperfine coupling constant, $A/\hbar$, was set to -2.89×10^6 rad s^{-1}, the value found for the parent monomeric Gd−DO3A-P^{ABn} complex. Also, the number of water molecules directly coordinated to the Gd^{3+} ion, q, was set to 1. The distances between Gd^{3+} and the oxygen and hydrogen atoms of the inner-sphere water molecule, R_{GdO} and R_{GdH}, were fixed to standard values of 2.6 and 3.1 Å, respectively. The value of the free energy of the electronic relaxation, E_v, was set to 1 kJ, that found for the Gd−DOTA complex (*18*). Unfortunately, the use of only inner-sphere and outer-sphere contributions did not yield any meaningful results. The fit of the ^{1}H NMRD profiles showed an unacceptable deviation from the experimental points even in the high-field

region (>10 MHz), a region not usually affected by any inadequacy in the theory (*41*). A second-sphere contribution to relaxivity was then introduced into the model on the basis of the well-known property of phosphorus-containing pendants to provide an extra hydration by a hydrogen-bonding network, particularly in neutral and acidic solutions (*43*).

It is also quite reasonable that the PAMAM core itself could hold additional water molecules within its structure due to the rather hydrophilic amino-amide moieties. The best results were found by fixing the number of second-sphere water molecules q_{ss} to 2 (per Gd^{3+} ion). The complementary parameters, namely, the second-sphere water residence lifetime τ_{Mss}, the free exchange energy $\Delta H_{Mss}^{\#}$, and the average distance between the metal ion and the second-sphere water molecules R_{ss}, were constrained to those values used for the ditopic CS(Gd−DO3A-P^{NBn})$_2$ complex. The simulation of the observed relaxivity (at 20 MHz and 37 °C) showed that the second-sphere contribution represented on average about 10% of the overall value.

Comparison of the water residence lifetimes $^{298}\tau_M$ for the present series of conjugates indicated that there is a slight decrease in the water exchange rate by going from the smallest dendrimer ($^{298}\tau_M$ ∼50 ns) to the largest one ($^{298}\tau_M$ ∼70 ns); this could be ascribed to an increasing structural complexity of the conjugates as previously demonstrated for DOTA−PAMAM conjugates (*38*). Despite this, the water residence lifetimes for all our conjugates are rather close to the value found for the ditopic Gd_2−CS(DO3A-P^{NBn})$_2$ complex ($^{298}\tau_M$ = 53 ns) (*25*), indicating that the accessibility of the water binding site is not significantly affected by the conjugation itself. The global rotational correlation time $^{298}\tau_{Rg}$ smoothly increases with increasing molecular size of the conjugate up to 3.1 ns for the G4−(Gd−DO3A-$P^{BnN\{CS\}}$)$_{59}$ complex, a value typical for molecules of this size (*22*). On the other hand, the local rotational correlation time $^{298}\tau_{Rl}$ remains at around 115 ps, a value just between that for the parent monomeric (88 ps) and dimeric (183 ps) complexes. Therefore, the linking arm is not completely flexible but far from rigid, probably due to the rather free rotation around all CH_2 single bonds in the phosphinate pendant arm and/or in the PAMAM structure. The crucial parameter for assessment of the internal flexibility of the system is the S^2 term, the Lipari−Szabo factor of internal rigidity: its value is 1 for totally rigid structures and 0 if totally flexible. The value for the present conjugates of DO3A-P^{ABn} is about 0.26 indicating, unfortunately, a high degree of internal mobility, also indicated above (Figure 4). Comparison of the rigidity of our conjugates with other published systems indicates that it is lower than that of EPTPA−PAMAM conjugates (∼0.36) (*22*) or DTPA conjugated to linear polymers (∼0.35) (*44*) but slightly higher than the DOTA micelle systems (∼0.2) (*45a,b*).

Finally, we explored the possible influence of an electronic dipole−dipole interaction between Gd^{3+} ions on the surface of the conjugates. It was suggested by Merbach et al. that if two neighboring Gd^{3+} ions can have a mutual magnetic contact, their electronic relaxation rate is increased and the overall relaxivity of the multimeric complex is damped (*22*, *46*). This could be an important issue in low-generation dendrimeric conjugates as their surfaces are magnetically rather dense. The mixed G2−(Gd/Y−DO3A-$P^{BnN\{CS\}}$)$_{16}$ conjugate was prepared in order to test this interaction; the Gd^{3+} was "diluted" by Y^{3+} in a ratio of about 1:1, but the overall charge was maintained in order to minimize any perturbation of the structure. The ^{1}H NMRD profiles were measured and compared with those obtained for the full-Gd^{3+} analogue (Figure S5, Supporting Information). Both profiles differed less than 5% over the whole field range and thus exclude any negative influence of dipole−dipole interaction on the observed relaxivity. In addition, studies of CS(Gd−DO3A-P^{NBn})$_2$ and CS(Gd−DO3A-P^{NBn})(Y−DO3A-P^{NBn}) ditopic complexes have unambiguously proved there is no effect of the dipole−dipole interaction between two gadolinium(III) ions on the overall relaxivity even if the lanthanide atoms are separated only by 6.3 Å (*25*).

Interaction with Polyaminoacids. The conjugates prepared in this research are all polyanions (each complex moiety bears one negative charge), and, in addition, the phosphinate groups are able to set up strong hydrogen bonds with hydrogen atom donors (e.g. protonated amino groups); therefore, an investigation exploiting the electrostatic and hydrogen-bonding interactions between these conjugates and polycationic amines was carried out. In a preliminary communication, it was observed that the titration of the G2−(Gd−DO3A-$P^{BnN\{CS\}}$)$_{16}$ conjugate with poly(Arg) or poly(Lys) at pH 7.5 resulted in up to ∼60% enhancement of the relaxivity (*24*). To explore this effect in more detail, various titration experiments to determine (i) the extent of the enhancement factor ϵ* (defined in eq 1) as a function of length of the polyaminoacid chain and (ii) the dependence of maximum relaxivity enhancement ϵ^b for a given polyaminoacid on the size of the conjugate were initiated. In eq 1, the observed longitudinal relaxation rates refer to solutions

$$\epsilon^* = (R_{1,obs}^{Gd-Sub} - R_{1,obs}^{Sub})/(R_{1,obs}^{Gd} - R_{1,obs}^{water}) \qquad (1)$$

containing the conjugate complex and the polyaminoacid (Gd−Sub), the polyaminoacid (Sub), the conjugate complex (Gd), and the pure solvent (water), respectively. The limiting value of ϵ*, corresponding to the fully bound conjugate complex, is denoted with ϵ^b. All "full-loaded" conjugates, i.e. G1−(Gd−DO3A-$P^{BnN\{CS\}}$)$_8$, G2−(Gd−DO3A-$P^{BnN\{CS\}}$)$_{16}$, and G4−(Gd−DO3A-$P^{BnN\{CS\}}$)$_{59}$, were titrated with a solution of poly(Arg)$_{320}$ (M_W ∼ 60000).

For comparison, the same experiment with the ditopic Gd_2−CS(DO3A-$P^{BnN\{CS\}}$)$_2$ complex was carried out. The results are plotted in the form of a relaxivity enhancement factor ϵ* as a function of the polyaminoacid concentration on a logarithmic scale (Figure 5) (*47*).

Whereas ϵ^b ∼2.2 was found for the ditopic complex, the values for the conjugates vary from 1.8 for the smallest G1 conjugate (i.e. relaxivity varies from 14.5 to 26.0 s^{-1} mM^{-1} at 25 °C and 20 MHz) to 1.4 for the largest G4 conjugate. It is important to note that when the theoretical charge equilibria were reached in the titration, there was precipitation. Additionally, in all cases the plateau was reached when the theoretical concentration of a positive charge was in 30% excess; both observations clearly prove a pure electrostatic basis for the interaction. To verify our findings, the G2−(Gd−DO3A-$P^{BnN\{CS\}}$)$_{16}$ conjugate with the small poly(Lys_{17}−Pro_3) peptide (further denoted as poly(Lys)$_{17}$) was titrated and the result (Figure S6, Supporting Information) compared with those previously obtained from the titration of this conjugate with poly(Arg)$_{56}$, poly(Arg)$_{320}$, and poly(Lys)$_{61}$ (*24*). The values of ϵ^b for all the titration experiments are summarized in Table 2.

In order to understand the rules governing adduct formation, one must consider that the molecular weight ratio (conjugate/amino acid) changes dramatically with different combinations of the conjugate−polyaminoacid. For example, in the G2−(Gd−DO3A-$P^{BnN\{CS\}}$)$_{16}$−polyaminoacid system this ratio varies from 3:1 for poly(Lys)$_{17}$ to 1:4 for poly(Arg)$_{320}$ and the enhancement factor ϵ^b changes from 1.2 to 1.6 (Table 2), indicating that the effect involves an increase in the global rotational correlation time τ_{Rg}. Since an approximately 6-fold increase in length of the poly(Arg) chain brings no further relaxivity enhancement, one can assume that the multimeric adducts are formed so that one polyaminoacid chain partially wraps around several molecules of the conjugate; and since the strand of the polyaminoacid is highly flexible, the interacting sites are essentially

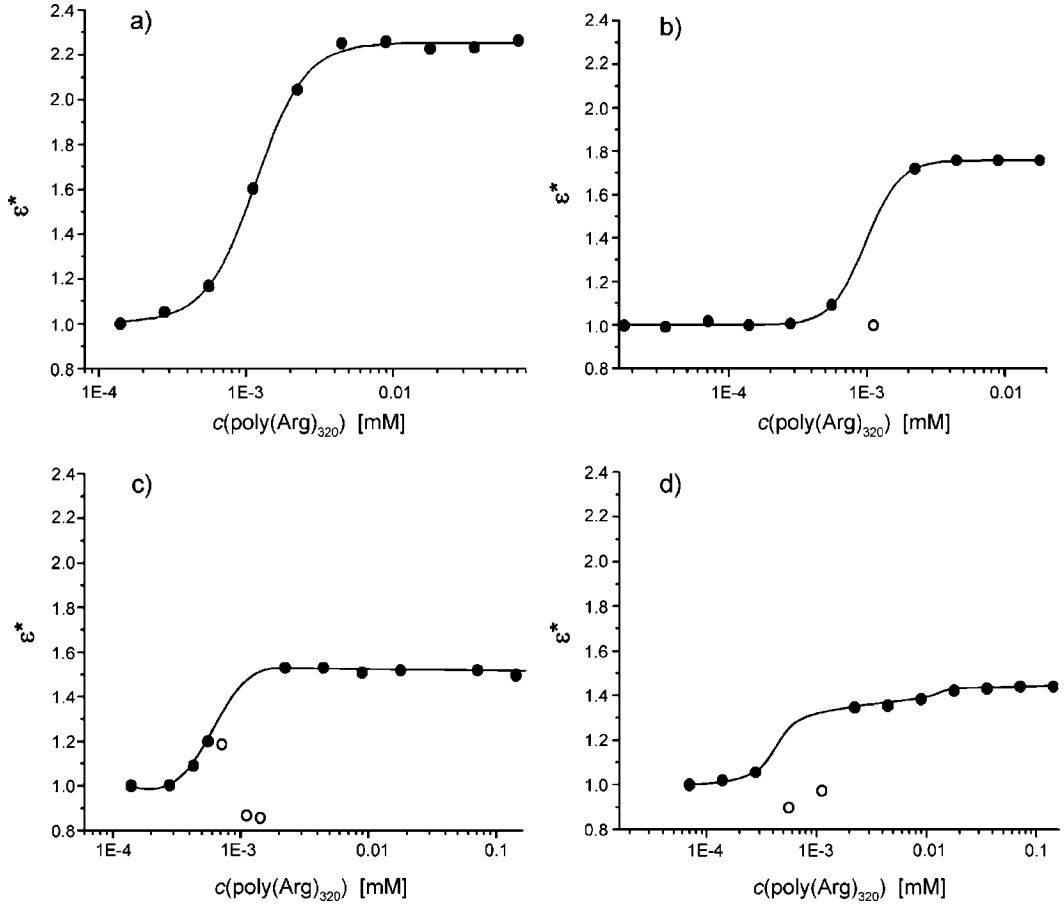

Figure 5. Results of the titration experiments with poly(Arg)$_{320}$: (a) Gd$_2$−CS(DO3A-P^{NBn})$_2$; (b) G1−(Gd−DO3A-P$^{BnN\{CS\}}$)$_8$; (c) G2−(Gd−DO3A-P$^{BnN\{CS\}}$)$_{16}$; (d) G4−(Gd−DO3A-P$^{BnN\{CS\}}$)$_{59}$. The results are expressed as the relaxivity enhancement factor ϵ* as a function of poly(Arg)$_{320}$ concentration (in log scale). The solid lines are only to guide the eyes. The open points correspond to the solutions where precipitation occurred. All the experiments were performed at 20 MHz, 25 °C, and pH 7.5. The concentrations of the conjugates are not the same: the experiments were set up in a way to maintain the analytical concentration of gadolinium in each sample at ca. 0.5 mM.

Table 2. Summary of Maximal Relaxivity Enhancement Factors ϵ^b for All Studied Systems at pH 7.5[a]

	ϵ^b			
	Gd$_2$−CS(DO3A-P^{NBn})$_2$	G1-8	G2-16	G4-59
poly(Lys)$_{17}$	1.4	n/a	1.2	n/a
poly(Lys)$_{61}$	n/a	n/a	1.4[b]	n/a
poly(Arg)$_{56}$	2.1	1.8	1.6[b]	n/a
poly(Arg)$_{320}$	2.2	1.8	1.6[b]	1.4

[a] The Gd(III) conjugates are labeled in a shortcut form. [b] Reference *24*.

independent and the global τ_R is not increased further. The higher value of ϵ^b for the G2−(Gd−DO3A-P$^{BnN\{CS\}}$)$_{16}$−poly-(Arg)$_{56}$ adduct over the adduct of G2−(Gd−DO3A-P$^{BnN\{CS\}}$)$_{16}$−poly(Lys)$_{61}$ could be accounted for by a significantly higher pK_a of arginine moieties in comparison to those of lysine resulting in a higher positive charge density and, in turn, stronger electrostatic interaction. As mentioned above, for a given polyaminoacid, the enhancement for the different conjugates decreases as the size of the conjugate increases. To explain that, it is assumed that a molecule of a polyaminoacid serves as a "molecular glue" that reduces the internal mobility of the conjugate so that a strand of a particular polyaminoacid may wrap only around a certain part of the conjugate surface independent of conjugate size and charge density. A demonstration of the size ratios for the "full-loaded" conjugates and poly-(Arg)$_{56}$ studied in this research is shown in Figure 6.

As the size of the conjugate increases, a smaller fraction of its surface interacts with a particular chain of the polyaminoacid and the internal mobility is reduced. From this point of view, the enhancement factor for the ditopic compound ($\epsilon^b \sim 2.2$) can be considered as the maximum achievable effect because this molecule was shown to be quite rigid (*25*) and, moreover, wrapped by a polyaminoacid the most easily.

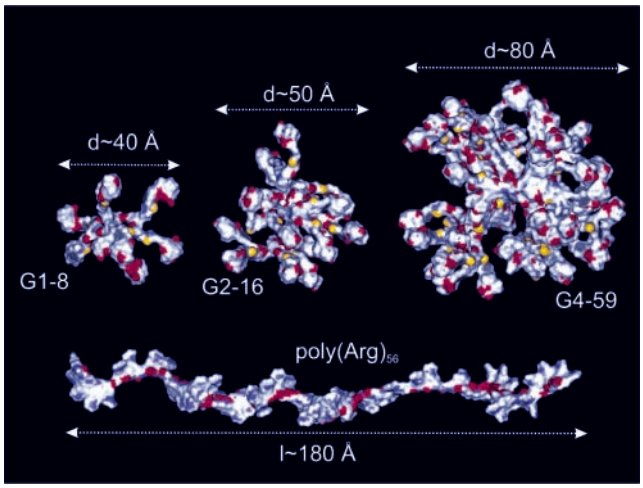

Figure 6. The demonstration of the size ratios for the G1-8, G2-16, and G4-59 conjugates and poly(Arg)$_{56}$. The sizes and the conformations of all species are the results from a molecular modeling. The surfaces represent the solvent accessibility areas (1.4 Å probe) in the following element color scheme: H, white; N, blue; O, red; S, yellow.

Additional support for our model was sought by measuring the relaxivity as a function of temperature for a particular system, G2−(Gd−DO3A-P$^{BnN\{CS\}}$)$_{16}$−poly(Arg)$_{56}$, in a molar ratio polyaminoacid/conjugate of ca. 10:1 (Figure 7a). The data

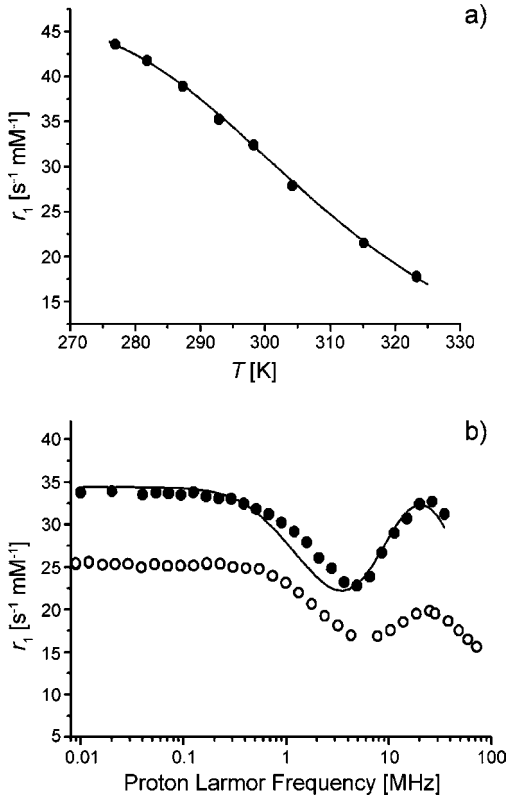

Figure 7. Relaxometric characterization of the G2−(Gd−DO3A-$P^{BnN\{CS\}}$)$_{16}$−poly(Arg)$_{56}$ adduct: (a) proton relaxivity at variable temperature and 20 MHz; (b) ^{1}H NMRD profile at 25 °C for the adduct (●) and the free conjugate (○). The solid lines are the best simultaneous fits to the experimental points. Both measurements were done at pH 7.5 and at a poly(Arg)$_{56}$/conjugate molar ratio 10:1.

Table 3. Comparison of the Parameter Values Obtained from Simultaneous Fitting of Relaxometric Data for G2−(Gd−DO3A-$P^{BnN\{CS\}}$)$_{16}$−poly(Arg)$_{56}$ Adduct and G2−(Gd−DO3A-$P^{BnN\{CS\}}$)$_{16}$ Conjugate

	gadolinium(III) complex	
parameter	G2-16−poly(Arg)$_{56}$	G2-16
$^{298}r_1$ [s^{-1} mM^{-1}][a]	30.8	19.5
$^{298}\tau_M$ [ns]	97 ± 9	66 ± 4
$\Delta H_M^{\#}$ [kJ mol^{-1}]	33 ± 2	50 ± 4
$^{298}\tau_{Rg}$ [ps]	3890 ± 100	2690 ± 270
E_{rg} [kJ]	23 ± 6	43 ± 4
$^{298}\tau_{Rl}$ [ps]	172 ± 14	100 ± 3
E_{rl} [kJ]	38 ± 16	20 ± 1
S^2	0.35 ± 0.03	0.24 ± 0.01
q	1	1
q_{ss}	2	2

[a] The relaxivity values were measured at 25 °C and 20 MHz; molar ratio of poly(Arg)$_{56}$/conjugate 10:1; the pH values of all samples were 7.5; the underlined values were fixed during the fitting process.

were subsequently analyzed by means of the multiparametrical Lipari−Szabo fitting along with the ^{1}H NMRD profile at 25 °C (Figure 7b); the results are shown in Table 3.

Unfortunately, we were not able to measure any ^{17}O NMR data as it was not possible to obtain a sample with sufficient concentration. In particular, despite rather low statistical errors, the lack of longitudinal ^{17}O T_1 relaxation times significantly lowers the precision of the fitting results, which should consequently be taken just as rather rough estimations (but still fully relevant for the following discussion). During the fitting procedure, several parameters were fixed to be those of the pure conjugate (for full results see Table S2, Supporting Information). The decrease in relaxivity with increasing temperature indicates that the water access is not significantly blocked by interaction

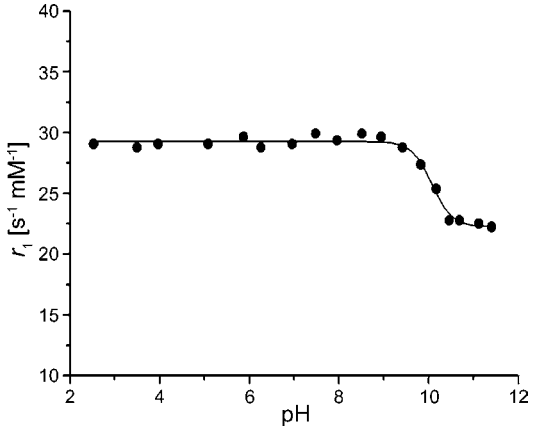

Figure 8. The dependence of relaxivity for the system G2−(Gd−DO3A-$P^{BnN\{CS\}}$)$_{16}$−poly(Lys)$_{61}$ on solution pH. The solid line is the best sigmoidal fit to the experimental points. The molar ratio poly(Lys)$_{61}$/conjugate was about 10:1.

with the polyaminoacid. The mean water residence lifetime of the adduct ($^{298}\tau_M$ ∼100 ns) is not much longer than that of the pure conjugate (∼70 ns); the global rotational correlation time τ_{Rg} increased by about 45% and the local rotational correlation time τ_{Rl} by about 70% in comparison to the free conjugate.

As the relaxivity is flattened with increasing τ_R (see Figure 4), it is noted that the most important factor for the enhancement is the reduction in the internal mobility indicated also by an increase in the S^2 factor. This is an important result since, for the first time, it was experimentally shown that a decrease of the rotational dynamics of the complex linked to a macromolecular substrate can result in a more than 40% increase of relaxivity. It was stated that, even in the noncovalent conjugate of MS-325 and human serum albumin (HSA) endowed with a very high relaxivity, the complex moiety exhibits almost free isotropic movement, which somewhat limits a maximum attainable relaxivity (*48*).

In addition to the response of the adduct structure to the pH of the solution, the dependence of the relaxivity on the pH value for the two adducts, G2−(Gd−DO3A-$P^{BnN\{CS\}}$)$_{16}$−poly(Lys)$_{61}$ (Figure 8) and G2−(Gd−DO3A-$P^{BnN\{CS\}}$)$_{16}$−poly(Arg)$_{320}$ (Figure S7, Supporting Information), was investigated.

Whereas, in the case of the poly(Arg)$_{320}$ adduct, the profile is almost flat, there is a significant change in the profile of the poly(Lys)$_{61}$ adduct at pH 10.06 ± 0.05 due to the different basicity of the amino and the guanidine groups. The guanidinium moieties of poly(Arg)$_{320}$ are rather basic and remain protonated even at high pH, whereas the primary amino groups of lysine have a pK_a around 10 (the pK_a's of lysine amino groups are 9.15 and 10.66) (*49*). Therefore, once the poly(Lys) chain is deprotonated in alkaline solution, the interaction with negatively charged molecules of the conjugate is almost "switched off" and the relaxivity sharply decreases. In fact, upon increase of pH up to 12, the relaxivity of the unbound dendrimeric complex is not fully restored likely due to a partial binding. This behavior is opposite to that observed for the Gd−(DO3A-squaric acid)−poly(Orn) covalent conjugate wherein the protonation increases the mobility of the whole molecule leading to a lowering of the overall relaxivity (*50*).

CONCLUSIONS

The macrocyclic DO3A-P^{ABn} ligand was attached to PAMAM dendrimers of generations 1, 2, and 4 by an effective benzylisothiocyanate linking strategy that allowed high loading yields to be achieved resulting in G1−(Gd−DO3A-$P^{BnN\{CS\}}$)$_8$ (100% theoretical loading), G2−(Gd−DO3A-$P^{BnN\{CS\}}$)$_{16}$ (100% theoretical loading), and G4−(Gd−DO3A-$P^{BnN\{CS\}}$)$_{59}$ (92% theo-

retical loading) conjugates. The relaxivities measured under standard conditions (20 MHz and 37 °C) were 10.1, 14.1, and 18.6 s^{-1} mM^{-1}, respectively, and measurement of the relaxivity dependence on solution pH showed that the relaxivity values could be increased by a factor of 1.3 when the core amino groups of the conjugates became protonated. This was verified by the complementary ^{1}H NMR titration of the free G2 dendrimer. In addition it was shown that the "unused" primary amines on the dendrimer surface may contribute as well since, in the case of the "half-loaded" G2−(Gd−DO3A-$P^{BnN\{CS\}}$)$_9$ conjugate, a small relaxivity response at pH 8−11 was indicated. The relaxometric characterization of all "full-loaded" conjugates was carried out by means of VT-^{17}O NMR and ^{1}H NMRD measurements, and according to the numerical evaluation of the relaxometric data based on the Lipari−Szabo approach, the relaxivity is controlled by an insufficient rigidity of the structure, e.g. the S^2 factor indicating inner flexibility was approximately 0.26. The water residence lifetime $^{298}\tau_M$ increases from 48 to 68 ns as the molecular size of the conjugates increases; however, in comparison with the model ditopic Gd_2−CS(DO3A-P^{NBn})$_2$ complex's value of $^{298}\tau_M$ 53 ns, it appears that the conjugation to PAMAMs does not disturb the water binding site and all values are not far from the optimal values (10−50 ns). An attempt to partially "freeze" all types of molecular tumbling was carried out, and it was shown that the relaxivity was significantly increased by addition of a positively charged polyaminoacid, namely, poly(Arg) or poly(Lys) species; the highest enhancement factor $\epsilon^b = 1.8$ was found for the G1−(Gd−DO3A-$P^{BnN\{CS\}}$)$_8$−poly(Arg)$_{320}$ adduct. From a comparative study of adducts of the different conjugates with various poly(Arg)s and poly(Lys)s the data suggested that the interaction is based purely on an electrostatic effect and the structure of the adduct depends primarily on the size ratio of both components. A strand of a polyaminoacid partly wraps around the negatively charged surface of the conjugate, and the internal mobility of the complex moiety is reduced. As the effective molecular weight of the whole system increases, the global motion is slowed down, resulting in an additional increase in the relaxivity. This model is also supported by ^{1}H NMRD characterization of the G2−(Gd−DO3A-$P^{BnN\{CS\}}$)$_{16}$−poly(Arg)$_{56}$ adduct wherein the molecular tumbling modes were reduced. In addition, it was shown that the relaxivity of the system with poly(Arg) remains constant up to pH 12 whereas the adduct with poly(Lys) dissociates when lysine primary amines become deprotonated (relaxivity steeply decreases at pH >9.5).

The new supramolecular approach presented here opens new possibilities as to how one might reduce the internal motion of polymeric MRI CAs in order to increase the overall relaxivity. The dependence of adduct formation on solution pH offers the possibility to prepare, if properly designed, a new family of pH-responsive MRI CAs for applications in the physiological pH range.

ACKNOWLEDGMENT

The authors are thankful to Dr. Jan Kotek for help with the determination of dissociation constants. The authors also want to thank to Dr. Alessandro Barge for crucial help with the synthesis of the poly(Lys) peptide. We are grateful to the GAČR (Grants 203/03/0168 and 203/06/0467), GAUK (423/2004/B-CH/PrF), AV ČR (KAN 201110651), and MIUR (FIRB). M.B., P.H., K.I.H. and J.R. gratefully acknowledge the support of a NATO travel grant (No. PST.CLG 980045). The work was carried out in frame of COST D18 and the EU-supported NoE projects EMIL (No. LSHC-2004-503569) and DiMI (No. LSHB-2005-512146).

Supporting Information Available: Figure S1, relaxometric titration of G2−(DO3A-$P^{BnN\{CS\}}$)$_{16}$ conjugate with $GdCl_3$; Figure S2, NMR titration of G2-PAMAM dendrimer; Figure S3, VT-^{17}O ^{1}H NMRD profiles for all conjugated Gd(III) complexes; Figure S4, comparison of the ^{1}H NMRD profiles for the G2−(Gd−DO3A-$P^{BnN\{CS\}}$)$_{16}$ at variable pH; Figure S5, comparison of ^{1}H NMRD profiles of G2−(Gd−DO3A-$P^{BnN\{CS\}}$)$_{16}$ and G2-(Gd/Y−DO3A-$P^{BnN\{CS\}}$)$_{16}$; Figure S6, relaxometric titration of the G2−(Gd−DO3A-$P^{BnN\{CS\}}$)$_{16}$ conjugate solution with poly(Lys)$_{17}$; Figure S7, dependence of proton relaxivity on pH for the G2−(Gd−DO3A-$P^{BnN\{CS\}}$)$_{16}$−poly(Arg)$_{56}$ system; Table S1, full relaxometric results for present PAMAM conjugates; Table S2, full relaxometric results for the G2−(Gd−DO3A-$P^{BnN\{CS\}}$)$_{16}$−poly(Arg)$_{56}$ adduct; full set of BSM+LS equations in a Scientist script. This material is available free of charge via the Internet at http://pubs.acs.org.

LITERATURE CITED

(1) Esfand, R., and Tomalia, D. A. (2001) Poly(amidoamine) (PAMAM) dendrimers: from biomimicry to drug delivery and biomedical applications. *Drug Discovery Today 6*, 427−436.

(2) Maiti, P. K., Çagin, T., Wang, G., and Goddard, W. A., III (2004) Structure of PAMAM dendrimers: Generations 1 through 11. *Macromolecules 37*, 6236−6254.

(3) (a) Wiener, E. C., Brechbiel, M. W., Brothers, H., Magin, R. L., Gansow, A., Tomalia, D. A., and Lauterbur, P. C. (1994) Dendrimer-based metal-chelates—a new class of magnetic-resonance-imaging contrast agents. *Magn. Reson. Med. 31*, 1−8. (b) Venditto, V. J., Regino, C. A. S., and Brechbiel, M. W. (2005) PAMAM dendrimer based macromolecules as improved contrast agents *Mol. Pharm. 2*, 302−311. (c) Kobayashi, H., and Brechbiel, M. W. (2004) Dendrimer-based nanosized MRI contrast agents. *Curr. Pharm. Biotechnol. 5*, 539−549.

(4) (2001) *The Chemistry of Contrast Agents in Medical Magnetic Resonance Imaging* (Merbach, A. E., and Tóth, É., Eds.) Wiley, Chichester, U.K.

(5) (2002) *Topics in Current Chemistry*, Vol. 221, Springer-Verlag, Heidelberg, Germany.

(6) Caravan, P., Ellison, J. J., McMurry, T. J., and Laufer, R. B. (1999) Gadolinium(III) chelates as MRI contrast agents: Structure, dynamics, and applications. *Chem. Rev. 99*, 2293−2352.

(7) Aime, S., Botta, M., and Terreno, E. (2005) Gd(III)-based contrast agents for MRI. *Adv. Inorg. Chem. 57*, 173−237.

(8) Aime, S., Botta, M., Fasano, and M., Terreno, E. (1999) Gd(III)-based contrast agents for MRI. Prototropic and water-exchange processes in aqueous solutions of Gd(III) chelates. *Acc. Chem. Res. 32*, 941−949.

(9) (a) Lowe, M. P. (2004) Activated MR contrast agents *Curr. Pharm. Biotechnol. 5*, 519−528. (b) Aime, S., Cabella, C., Colombatto, S., Crich, S. G., Gianolio, E., and Maggioni, F. (2002) Insights into the use of paramagnetic Gd(III) complexes in MR-molecular imaging investigations. *J. Magn. Reson. Imag. 16*, 394−406. (c) Woods, M.; Kovacs, Z.; and Sherry, A. D. (2002) Targeted complexes of lanthanide(III) ions as therapeutic and diagnostic pharmaceuticals *J. Supramol. Chem. 2*, 1−15.

(10) Szilágyi, E., Tóth, É., Brücher E., and Merbach, A. E. (1999) Lanthanide(III)-1,4,7,10-tetraazacyclododecane-1,4,7,10-tetraacetic acid complexes in acidic medium: significant decrease in water exchange rate. *J. Chem. Soc., Dalton Trans.* 2481−2486.

(11) (a) Woods, M., Kovacs, Z., Zhang, S., and Sherry, A. D. (2003) Towards the rational design of magnetic resonance imaging contrast agents: Isolation of the two coordination isomers of lanthanide DOTA-type complexes. *Angew. Chem., Int. Ed. 42*, 5889−5892. (b) Woods, M.; Botta, M., Avedano, S., Wang, J., and Sherry, A. D. (2005) Towards the rational design of MRI contrast agents: a practical approach to the synthesis of gadolinium complexes that exhibit optimal water exchange. *Dalton Trans.* 3829−3837.

(12) (a) Laus, S., Ruloff, R., Tóth, É., and Merbach, A. E. (2003) Gd^{III} complexes with fast water exchange and high thermodynamic stability: Potential building blocks for high-relaxivity MRI contrast agents. *Chem. Eur. J. 9*, 3555−3566. (b) Ruloff, R., Tóth, É., Scopelliti, R., Tripier, R., Handel, H., and Merbach, A. E. (2002)

Accelerating water exchange for Gd^{III} chelates by steric compression around the water binding site. *Chem. Commun.* 2630−2631.
(13) Polášek, M., Rudovský, J., Hermann, P., Lukeš, I., Vander Elst, L., and Muller, R. N. (2004) Lanthanide(III) complexes of a pyridine *N*-oxide analogue of DOTA: exclusive *M* isomer formation induced by a six-membered chelate ring. *Chem. Commun.* 2602−2603.
(14) Jászberényi, Z., Sour, A., Tóth, É., Benmelouka, M., and Merbach, A. E. (2005) Fine-tuning water exchange on Gd^{III} poly(amino carboxylates) by modulation of steric crowding. *Dalton Trans.* 2713−2719.
(15) Rudovský, J., Cígler, P., Kotek, J., Hermann, P., Vojtíšek, P., Lukeš, I., Peters, J. A., Vander Elst, L, and Muller, R. N. (2005) Lanthanide(III) complexes of a mono (methylphosphonate) analogue of H_4dota: The influence of protonation of the phosphonate moiety on the TSAP/SAP isomer ratio and the water exchange rate. *Chem. Eur. J. 11*, 2373−2384.
(16) Rudovský, J., Kotek, J., Hermann, P., Lukeš, I., Mainero, and V., Aime, S. (2005) Synthesis of a bifunctional monophosphinic acid DOTA analogue ligand and its lanthanide(III) complexes. A gadolinium(III) complex endowed with an optimal water exchange rate for MRI applications. *Org. Biomol. Chem. 3*, 112−117.
(17) Kotek, J., Lebdušková, P., Hermann, P., Vander Elst, L., Muller, R. N., Maschmeyer, T., Lukeš, I., and Peters, J. A. (2003) Lanthanide(III) complexes of novel mixed carboxylic-phosphorus acid derivatives of diethylenetriamine: A step towards more efficient MRI contrast agents. *Chem. Eur. J. 9*, 5899−5915.
(18) Powell, D. H., Dhubhghaill, O. M. N., Pubanz, D., Helm, L., Lebedev, Y. S., Schlaepfer, W., and Merbach, A. E. (1996) Structural and dynamic parameters obtained from ^{17}O NMR, EPR, and NMRD studies of monomeric and dimeric Gd^{3+} complexes of interest in magnetic resonance imaging: An integrated and theoretically self-consistent approach. *J. Am. Chem. Soc. 118*, 9333−9346.
(19) Nicolle, G. M., Tóth, E., Schmitt-Willich, H., Radüchel, B., and Merbach, A. E. (2002) The impact of rigidity and water exchange on the relaxivity of a dendritic MRI contrast agent. *Chem. Eur. J. 8*, 1040−1048.
(20) Tóth, É., Pubanz, D., Vauthey, S., Helm, L., and Merbach, A. E. (1996) The role of water exchange in attaining maximum relaxivities for dendrimeric MRI contrast agents. *Chem. Eur. J. 2*, 1607−1615.
(21) Lebdušková, P., Kotek, J., Hermann, P., Vander Elst, L., Muller, R. N., Lukeš, I., and Peters, J. A. (2004) A gadolinium(III) complex of a carboxylic-phosphorus acid derivative of diethylenetriamine covalently bound to inulin, a potential macromolecular MRI contrast agent. *Bioconjugate Chem. 15*, 881−889.
(22) Laus, S., Sour, A., Ruloff, R., Tóth, E., and Merbach, A. E. (2005) Rotational dynamics account for pH-dependent relaxivities of PAMAM dendrimeric, Gd-based potential MRI contrast agents. *Chem. Eur. J. 11*, 3064−3076.
(23) Lebdušková, P., Sour, A., Helm, L., Tóth, É., Kotek, J., Lukeš, I., and Merbach, A. E. (2006) Phosphinic derivative of DTPA conjugated to a G5 PAMAM dendrimer: an ^{17}O and ^{1}H relaxation study of its Gd(III) complex. *Dalton Trans.* DOI: 10.1039/b517847a.
(24) Rudovský, J., Hermann, P., Botta, M., Aime, S., and Lukeš, I. (2005) Dendrimeric Gd(III) complex of a monophosphinated DOTA analogue: optimizing relaxivity by reducing internal motion. *Chem. Commun*. 2390−2392.
(25) Rudovský, J., Botta, M., Hermann, P., Koridze, A., and Aime, S. (2006) Relaxometric and solution NMR structural studies on ditopic lanthanide(III) complexes of a phosphinate analogue of DOTA with a fast rate of water exchange. *Dalton Trans.* 2323−2333.
(26) Corsi, D. M, Platas-Iglesias, C., van Bekkum, H., and Peters, J. A. (2001) Determination of paramagnetic lanthanide(III) concentrations from bulk magnetic susceptibility shifts in NMR spectra. *Magn. Reson. Chem. 39*, 723−726.
(27) Scientist for Windows version 2.01, Micromath Inc., Salt Lake City, UT, 1995.
(28) Origin version 6.0, MicroCal Software Inc., Northampton, MA. 1999.
(29) MSI WebLabViewerPro 4.0 Preview, http://www.msi.com 2000.
(30) HyperChemRelease 7.5 for Windows, Molecular Modeling System, Hypercube Inc., 2002.
(31) (a) Kývala, M., and Lukeš, I. (1995) *International Conference Chemometrics '95*, p 63. Pardubice, Czech Republic, full version of *"OPIUM"* is available on http://www.natur.cuni.cz/~kyvala/opium.html. (b) Kývala M., Lubal P., and Lukeš I. (1998) *IX. Spanish-Italian and Mediterranean Congress on Thermodynamics of Metal Complexes*. Girona, Spain.
(32) Kotek, J., Rudovský, J., Hermann, P., and Lukeš, I. (2006) Three in one: TSA, TSA′, and SA units in one crystal structure of a yttrium(III) complex with a monophosphinated H_4dota analogue. *Inorg. Chem. 45*, 3097−3102.
(33) Chen, W., Tomalia, D. A., and Thomas, J. L. (2000) Unusual pH-dependent polarity changes in PAMAM dendrimers: Evidence for pH-responsive conformational changes. *Macromolecules 33*, 9169−9172.
(34) By an average p*K* value $\equiv \langle pK_a \rangle$ we mean the average of all p*K* values of all amino groups of the same type in the PAMAM molecule.
(35) Krot, K. A., de Namor, A. F. D., Aguilar-Cornejo, A., and Nolan, K. B. (2005) Speciation, stability constants and structures of complexes of copper(II), nickel(II), silver(I) and mercury(II) with PAMAM dendrimer and related tetraamide ligands. *Inorg. Chim. Acta 358*, 3497−3505.
(36) Swift, T. J., and Connick, R. E. (1962) NMR-relaxation mechanisms of ^{17}O in aqueous solutions of paramagnetic cations and the lifetime of water molecules in the first coordination sphere. *J. Chem. Phys. 37*, 307−320.
(37) Peters, J. A.; Huskens J.; and Raber, D. J. (1996) Lanthanide induced shifts and relaxation rate enhancements. *Prog. NMR Spectrosc. 32*, 283−350.
(38) Bryant, L. H., Jr., Brechbiel, M. W., Wu, C., Bulte, J. W. M., Herynek, V., and Frank, J. A. (1999) Synthesis and relaxometry of high-generation (G = 5, 7, 9, and 10) PAMAM dendrimer-DOTA-gadolinium chelates. *J. Magn. Reson. Imag. 9*, 348−352.
(39) Livramento, J. B., Tóth, É., Sour, A., Borel, A., Merbach, A. E., and Ruloff, R. (2005) High relaxivity confined to a small molecular space: A metallostar-based, potential MRI contrast agent. *Angew. Chem., Int. Ed. 44*, 1480−1484.
(40) Freed, J. H. (1978) Dynamic effects of pair correlation functions on spin relaxation by translational diffusion in liquids. II. Finite jumps and independent T_1 processes. *J. Chem. Phys. 68*, 4034−4037.
(41) Zhou, X., Caravan, P., Clarkson, R. B., and Westlund, P.-O. (2004) On the philosophy of optimizing contrast agents. An analysis of ^{1}H NMRD profiles and ESR lineshapes of the Gd(III)complex MS-325 + HSA *J. Magn. Reson. 167*, 147−160.
(42) (a) Lipari, G., and Szabo,S. (1982) Model-free approach to the interpretation of nuclear magnetic-resonance relaxation in macromolecules. 1. Theory and range of validity. *J. Am. Chem. Soc. 104*, 4546−4559. (b) Lipari, G., and Szabo, S. (1982) Model-free approach to the interpretation of nuclear magnetic-resonance relaxation in macromolecules. 2. analysis of experimental results. *J. Am. Chem. Soc. 104*, 4559−4570.
(43) (a) Zhang, S., Wu, K., and Sherry, A. D. (1999) A novel pH-sensitive MRI contrast agent. *Angew. Chem., Int. Ed. 38*, 3192−3194. (b) Botta, M. (2000) Second coordination sphere water molecules and relaxivity of gadolinium(III) complexes: Implications for MRI contrast agents. *Eur. J. Inorg. Chem.* 399−407. (c) Caravan, P., Greenfield, M. T., Li, X., and Sherry, A. D. (2001) The Gd^{3+} complex of a fatty acid analogue of DOTP binds to multiple albumin sites with variable water relaxivities. *Inorg. Chem. 40*, 6580−6587.
(44) Tóth, É., Helm, L., Kellar, K. E., and Merbach, A. E. (1999) Gd-(DTPA-bisamide)alkyl copolymers: A hint for the formation of MRI contrast agents with very high relaxivity. *Chem. Eur. J. 5*, 1202−1211.
(45) (a) Nicolle, G. M., Tóth, É., Eisenwiener, K. P., Mäcke, H. R., and Merbach, A. E. (2002) From monomers to micelles: investigation of the parameters influencing proton relaxivity. *J. Biol. Inorg. Chem. 7*, 757−769. (b) André, J. P., Tóth, É., Fischer, H., Seelig, A., Mäcke, H. R., and Merbach, A. E. (1999) High relaxivity for monomeric Gd(DOTA)-based MRI contrast agents, thanks to micellar self-organization. *Chem. Eur. J. 5*, 2977−2983. (c) Lattuada, L., and Lux, G. (2003) Synthesis of Gd-DTPA-cholesterol: a new lipophilic gadolinium complex as a potential MRI contrast agent. *Tetrahedron Lett. 44*, 3893−3895. (d) Parac-Vogt, T. N., Kimpe, K., Laurent, S., Piérart, C., Vander Elst, L., Muller, R. N., and Binnemans, K. (2004) Gadolinium DTPA-monoamide complexes incorporated into mixed micelles as possible MRI contrast agents. *Eur. J. Inorg. Chem.* 3538−3543.
(46) Nicolle, G. M., Yerly, F., Imbert, D., Böttger, U., Bünzli, J.-C., and Merbach, A. E. (2003) Towards binuclear polyaminocarboxylate

MRI contrast agents? Spectroscopic and MD study of the peculiar aqueous behavior of the Ln(III) chelates of OHEC (Ln = Eu, Gd, and Tb): Implications for relaxivity. *Chem. Eur. J. 9*, 5453−5467.

(47) Aime, S., Botta, M., Fasano, M., and Terreno, E. (2001) *The Chemistry of Contrast Agents in Medical Magnetic Resonance Imaging* (Merbach, A. E., and Tóth, É., Eds.) Chapter 5, John Wiley & Sons, Chichester, U.K.

(48) Caravan, P., Cloutier, N. J., Greenfield, M. T., McDermid, S A., Dunham, S. U., Bulte, J. W. M., Amedio, J. C. Jr., Looby R. J., Supkowski R. M., Horrocks, W. DeW., Jr., McMurry T. J., and Lauffer, R. B. (2002) The interaction of MS-325 with human serum albumin and its effect on proton relaxation rates *J. Am. Chem. Soc. 124*, 3152−3162.

(49) *NIST Standard Reference Database 46 (Critically Selected Stability Constants of Metal Complexes)*, Version 7.0, 2003.

(50) Aime, S., Botta, M., Crich, S. G., Giovenzana, G., Palmisano, and G., Sisti, M. (1999) A macromolecular Gd(III) complex as pH-responsive relaxometric probe for MRI applications. *Chem. Commun.* 1577−1578.

BC060149L

Self-Assembly of Natural Light-Harvesting Bacteriochlorophylls of Green Sulfur Photosynthetic Bacteria in Silicate Capsules as Stable Models of Chlorosomes

Yoshitaka Saga,[†,§] Sho Akai,[†] Tomohiro Miyatake,[‡] and Hitoshi Tamiaki[†,*]

Department of Bioscience and Biotechnology, Faculty of Science and Engineering, Ritsumeikan University, Kusatsu, Shiga 525-8577, Japan, and Department of Materials Chemistry, Faculty of Science and Technology, Ryukoku University, Otsu, Shiga 520-2194, Japan. Received November 26, 2005; Revised Manuscript Received May 17, 2006

Naturally occurring bacteriochlorophyll(BChl)s-*c*, -*d*, and -*e* from green sulfur photosynthetic bacteria were self-assembled in an aqueous solution in the presence of octadecyltriethoxysilane and tetraethoxysilane, followed by polycondensation of the alkoxysilanes by incubation for 50 h at 25 °C. The resulting BChl self-assemblies in silicate capsules exhibited visible absorption and circular dichroism spectra similar to the corresponding natural light-harvesting systems (chlorosomes) of green sulfur bacteria. Dynamic light scattering measurements indicated that the silicate capsules had an average hydrodynamic diameter of several hundred nanometers. BChl self-aggregates in silicate capsules were significantly stable to a nonionic surfactant Triton X-100, which was apt to decompose the BChl aggregates to their monomeric form, compared with conventional micelle systems. BChls in silicate capsules were more tolerant to demetalation of the central magnesium under acidic conditions than the natural systems.

INTRODUCTION

Photosynthesis is an excellent light-energy conversion system in nature, where sunlight energy is captured and is converted into chemical energy with high efficiency. In photosynthetic supramolecular systems, the photofunctional molecules chlorophyll(Chl)s and bacteriochlorophyll(BChl)s are highly organized by pigment−protein interaction and pigment−pitment interaction.

In a broad variation of photosynthetic supramolecules, extramembranous light-harvesting complexes, chlorosomes, of green photosynthetic bacteria are unique in terms of their supramolecular structures. Chlorosomes from green sulfur bacteria are ellipsoidal particles with 150-nm length, 50-nm width, and 25-nm height.[1,2] In chlorosomes, BChl-*c*, -*d*, and -*e* molecules (the molecular structures are shown in Figure 1) form self-aggregates only through pigment−pigment interaction, where the central magnesium of one BChl molecule is coordinated by the 3^1-hydroxy group of another BChl molecule and a hydrogen bond is formed between the 3^1-hydroxy group and 13-keto group of the third BChl molecule.[3−6] These BChl self-aggregates are surrounded by a lipid monolayer.

Green sulfur photosynthetic bacteria have BChl homologues that vary in the alkyl groups at the 8- and 12-positions (R_8 and R_{12} in Figure 1, respectively). Methyl, ethyl, *n*-propyl, and isobutyl groups at the 8- and 12-positions of chlorosomal BChls are denoted as M, E, Pr, and I. Such a diversity of molecular structures of BChl homologues affects supramolecular structures, spectral properties, and excited states of chlorosomal BChl self-aggregates.[1,3,7,8] However, precise effects of R_8 and R_{12} groups of BChl homologues on chlorosomal supramolecular structures and biological meaning of the homologue diversity of green sulfur photosynthetic bacteria have been ambiguous.

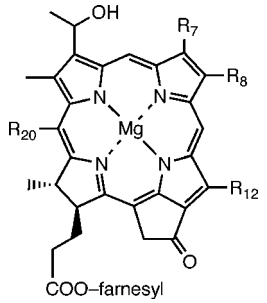

Figure 1. Molecular structures of light-harvesting [R_8,R_{12}]BChls-*c*, -*d*, and -*e* in green sulfur photosynthetic bacteria. BChl-*c*: $R_7 = CH_3$, $R_{20} = CH_3$, BChl-*d*: $R_7 = CH_3$, $R_{20} = H$, BChl-*e*: $R_7 = CHO$, $R_{20} = CH_3$. $R_8 = C_2H_5$ (E), *n*-C_3H_7 (Pr), *iso*-C_4H_9 (I). $R_{12} = CH_3$ (M), C_2H_5 (E).

The architecture of chlorosomal self-aggregates is in sharp contrast to other photosynthetic apparatus, where photofunctional pigments are embedded in proteins. Such supramolecular structures of chlorosomal self-aggregates can be appropriate for the construction of artificial photofunctional nanodevices. Self-aggregates of natural BChls[8,9] and their model compounds[10,11] have been extensively studied in aqueous micelles as structural and functional models of chlorosomes. These chlorophyllous pigments could be assembled in the envelope of lipids and surfactants by the same pigment−pigment interaction as that in natural chlorosomes. The chlorosomal self-aggregates in microheterogeneous media, however, did not have mechanical strength or stability to external perturbation.

Sol−gel methods[12−14] have recently been used for encapsulation of biomaterials such as enzymes,[15−17] heme proteins,[18−21] and photoactive proteins.[22,23] In porous sol−gel matrixes, many kinds of proteins achieve stability without loss of their functionality. The sol−gel process requires little or no heating for hydrolysis and polycondensation of alkoxides. Such mild reaction conditions are suitable for hybridization of biomaterials with inorganic materials toward bioactive devices. Additionally, sol−gel matrix is an attractive candidate to support photofunctional biomaterials because of optical transparency of the matrix.

* Corresponding author. Fax: +81-77-561-2659; E-mail: tamiaki@se.ritsumei.ac.jp.

[†] Ritsumeikan University.

[‡] Ryukoku University.

[§] Present address: Department of Chemistry, Faculty of Science and Engineering, Kinki University, Higashi-Osaka 577-8502, Japan.

10.1021/bc050343s CCC: $33.50 © 2006 American Chemical Society
Published on Web 06/28/2006

We preliminarily reported the preparation of self-aggregates of synthetic zinc chlorins, which were model compounds of chlorosomal BChls, in a silicate micelle using the sol−gel process,[24] and demonstrated the excitation energy transfer from self-aggregates of zinc chlorins to bacteriochlorins in the silicate micelle.[25] These works indicated that alkoxysilane molecules possessing a long alkyl chain provided an appropriate hydrophobic microenvironment for self-assembly of zinc chlorins.

Here we report the preparation and characterization of stable self-assemblies of natural BChls-*c*, -*d*, and -*e* in silicate capsules by sol−gel processes. In the present sol−gel condition, natural BChls, which were more easily denatured than synthetic zinc chlorins, formed self-aggregates possessing similar spectral properties and particle sizes to natural chlorosomes. The resulting BChl self-assemblies could be hardly deaggregated by addition of a nonionic surfactant Triton X-100. Natural BChls in the present silicate capsule also had significant tolerance to the demetalation by addition of an aqueous acid.

MATERIALS AND METHODS

Apparatus. Visible absorption and fluorescence spectra were measured with Hitachi U-3500 and F-4500 spectrophotometers, respectively. CD spectra were measured with a JASCO J-720W spectropolarimeter. Dynamic light scattering measurements were performed with a Marvern Nano ZS particle size analyzer. HPLC was carried out with a Shimadzu LC-20AT pump and an SPD-M20A photodiode array detector.

Pigment Preparation. BChls-*c*, -*d*, and -*e* were extracted from harvested cells of green sulfur photosynthetic bacteria *Chlorobium* (*Chl.*) *tepidum* ATCC49652, *Chl. vibrioforme* NCIB8327 substrain containing BChl-*d*, and *Chl. phaeobacteroides* 1549, respectively, according to the procedures described previously.[26−28] Extracted BChls were purified by reverse-phase HPLC.[28,29] The homologue compositions of purified BChls were as follows: 8-ethyl-12-methyl([E,M])-: 8-ethyl-12-ethyl([E,E])-: 8-propyl-12-ethyl([Pr,E])-: 8-isobuthyl-12-ethyl([I,E])-BChl-*c* = 1:63:31:5, [E,M]-: [E,E]-: 8-propyl-12-methyl([Pr,M])-: ([Pr,E]+8-isobuthyl-12-methyl([I,M]))-: [I,E]-BChl-*d* = 7:18:11:48:16, and [E,E]-: [Pr,E]-: [I,E]-BChl-*e* = 46:41:13.

Preparation of Silicate Capsules. Octadecyltriethoxysilane (ODTES) and tetraethoxysilane (TEOS) were purchased from Shin-etsu Chemical Co., Ltd. and Nacalai Tesque, respectively, and were used without further purification. ODTES (200 μL) and TEOS (200 μL) were dissolved in 1.6 mL of ethanol, and 30 μL of 1 M HCl was added to the ethanol solution. After stirring for 30 min, 30 μL of 1 M NaOH was added to the mixture to neutralize pH of the solution. The resulting solution containing alkoxysilanes (10 μL) was mixed with 30 μL of an ethanol solution of chlorophyllous pigments (pigment concentration, ca. 0.9 mM), and the mixed solution was dispersed in distilled water (4 mL) at 50 °C. The prepared aqueous suspension was then incubated at 25 °C for 50 h.

Deaggregation by Triton X-100. A small aliquot of aqueous Triton X-100 solution was added in an aqueous suspension of BChl self-aggregates in silicate capsules, and the solution was rigorously mixed. After incubation in the dark for 4 min, the visible absorption spectra were measured.

Demetalation under Acidic Conditions. BChl self-aggregates in silicate capsules were incubated in 50 mM HCl solution, and changes of their visible absorption spectra were measured as a function of incubation time in the dark.

RESULTS

Preparation of Silicate Capsules. Three types of natural BChls were dispersed with prehydrolyzed alkoxysilanes (ODTES and TEOS) in aqueous media and incubated at 25 °C for 50 h.

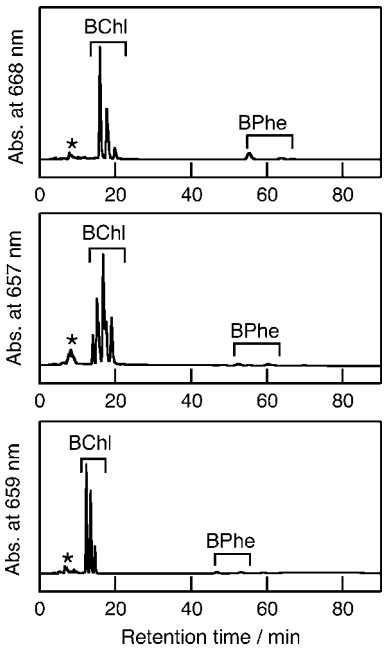

Figure 2. HPLC elution patterns of BChls extracted from silicate capsules after incubation at 25 °C for 50 h (Cosmosil 5C18-AR−II, 6 mmϕ × 250 mm, methanol/water = 96/4(v/v) as the eluent, 1.0 mL/min). Top, BChl-*c*; middle, BChl-*d*; bottom, BChl-*e*.

BChl molecules self-assembled to give visible absorption and CD spectra similar to the corresponding chlorosomes mentioned in the following section. DLS measurements showed that the average hydrodynamic diameter of silicate capsules containing self-aggregates of BChl-*c*, -*d*, and -*e* were 3.6×10^2, 4.6×10^2, and 2.7×10^2 nm, respectively. These values were comparable to the long axis (ca. 150 nm) of chlorosomes from green sulfur photosynthetic bacteria.

BChls in the prepared silicate capsules were extracted with ethanol and analyzed by reverse-phase HPLC. As shown in Figure 2, large amounts of natural BChls (denoted as BChl in the figure) remained intact. The denatured fractions around 50−70 min (denoted as BPhe) exhibited visible absorption spectra of bacteriopheophytin(BPhe)s, which were demetalated forms of natural BChls. Therefore, a little pheophytinization inevitably occurred during the preparation of silicate capsules containing natural BChls. In our preliminary procedure, where synthetic zinc chlorins were incubated overnight at a higher temperature (50 °C) with ODTES and TEOS, large amounts of natural BChls were denatured (data not shown). Small amounts of other fractions (denoted as * in Figure 2), which exhibited the same visible absorption spectra as those of BChls, appeared at around 10 min. These fractions might be ascribable to BChls whose ester groups at the 17-position were varied during the preparation. In the present procedure, we successfully prepared silicate capsules containing natural chlorosomal BChls, which tended to be decomposed easily, with slight denaturation.

Visible Absorption and CD Spectra. Figure 3 depicts visible absorption spectra of aqueous suspensions of natural BChl-*c*, -*d*, and -*e* in silicate capsules after incubation at 25 °C for 50 h, and these spectra are compared with those of the corresponding chlorosomes and monomeric pigments. The Soret and Q_y bands of chlorosomal BChls in silicate capsules in an aqueous solution were shifted to a longer wavelength relative to the monomeric bands in a polar organic solvent. BChl-*c* in silicate capsules had the Soret and Q_y bands at 460 and 752 nm, respectively (solid curve in Figure 3 top), whereas the peak positions of monomeric BChl-*c* were 436 and 667 nm (broken curve in Figure 3 top). The Q_y peak position of BChl-*c* self-aggregates in silicate capsules was shifted to a slightly longer

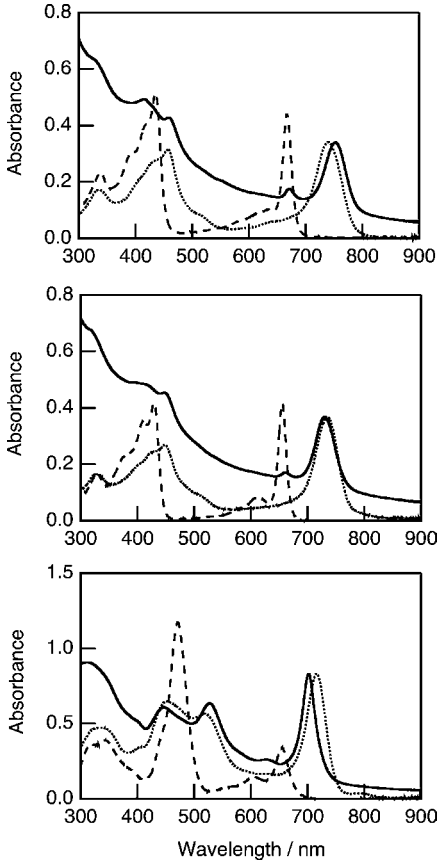

Figure 3. Visible absorption spectra of BChl self-aggregates in silicate capsules in aqueous solution (solid curve), chlorosomes in 50 mM Tris buffer, pH 8.0 (dotted curve), and BChl monomers in an ethanol solution (broken curve). Top, BChl-*c*; middle, BChl-*d*; bottom, BChl-*e*. BChls, ODTES, and TEOS concentrations were ca. 7 μM, 2.4×10^{-4}% (v/v), and 2.4×10^{-4}% (v/v), respectively. The spectra of chlorosomes were normalized with those of the silicate capsules at the Q_y peaks.

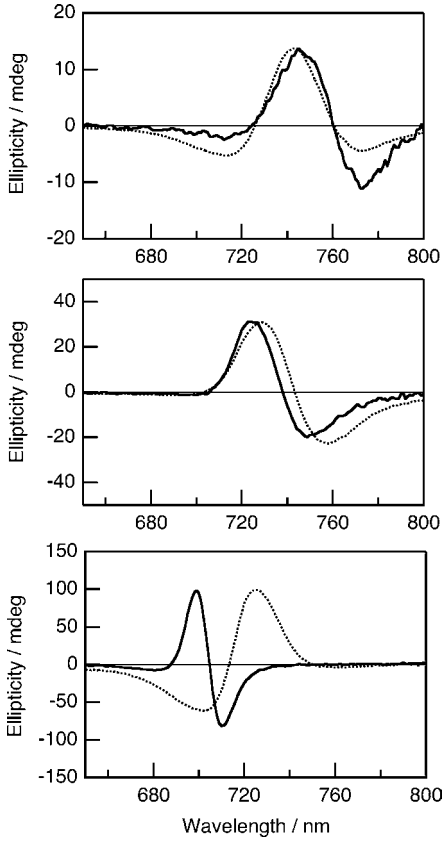

Figure 4. CD spectra of BChl self-aggregates in silicate capsules in aqueous solution (solid curve) and chlorosomes in 50 mM Tris buffer, pH 8.0 (dotted curve). Top, BChl-*c*; middle, BChl-*d*; bottom, BChl-*e*. The spectra of chlorosomes were normalized with those of the silicate capsules at the positive CD signals.

wavelength than natural chlorosomes from *Chl. tepidum* (dotted curve in Figure 3 top), and its bandwidth was very similar to the chlorosomal. These spectral properties indicate the chlorosome-like self-aggregation of BChl-*c* in silicate capsules formed by alkoxysilane molecules. BChl-*d* with alkoxysilanes in aqueous media exhibited a visible absorption spectrum with peak positions at 449 and 730 nm, which were also red-shifted relative to the monomeric (Figure 3 middle). The Q_y peak position and bandwidth of BChl-*d* aggregates in silicate capsules were almost the same as natural chlorosomes containing BChl-*d* from *Chl. vibrioforme*. A visible absorption spectrum of BChl-*e* in the presence of alkoxysilanes had two peaks at 446 and 527 nm in the Soret region, which were characteristic of chlorosomes containing BChl-*e* (Figure 3 bottom). The Q_y absorption band of BChl-*e* aggregates in silicate capsules was shifted to a longer wavelength compared with the monomeric band, and the spectral shape was close to that of natural chlorosomes from *Chl. phaeobacteroides*. In the cases of BChls-*c* and -*d* in silicate capsules, small monomeric absorption bands were observed around 670 and 660 nm, respectively.

CD spectra of natural BChls in silicate capsules are shown in Figure 4. Self-aggregates of three kinds of BChls exhibited intense inverse S-shaped CD signals in the Q_y region. Such intense CD signals in the Q_y region were characteristic of chlorosomal self-aggregates, since monomeric BChls hardly showed CD signals in an organic solution. The CD spectrum of BChl-*c* self-aggregates in silicate capsules resembled that of chlorosomes containing BChl-*c*, although the signals around 775 and 715 nm were intense and weak, respectively, compared with natural chlorosomes (Figure 4 top). CD signals of BChl-*d* self-aggregates in silicate capsules were similar to natural chlorosomes containing BChl-*d* (Figure 4 middle). BChl-*e* self-aggregates in silicate capsules also exhibited intense CD signals at almost the same position as natural chlorosomes containing BChl-*e*, although the polarity was the reverse of that of natural chlorosomes (Figure 4 bottom). It was reported that the polarity of in vivo CD signals in the Q_y region was changeable,[30] and in vitro BChl-*e* self-aggregates in a nonpolar organic solvent actually showed CD signals in the Q_y region that were the reverse of those of in vivo aggregates.[28]

Visible absorption and CD spectra of BChl self-aggregates in silicate capsules, which were similar to the natural corresponding chlorosomes, indicate that hydrophobic microenvironments formed by prehydrolyzed alkoxysilanes possessing a C18 alkyl chain are suitable for chlorosomal self-assemblies of these BChls.

Deaggregation by Triton X-100. Addition of a surfactant Triton X-100 transforms chlorosomal BChl self-aggregates into monomers. The deaggregation process can be easily monitored by visible absorption spectroscopy, where Soret and Q_y absorption bands of BChl self-aggregates around 450−520 and 720−750 nm, respectively, decrease accompanied by the increase of absorption bands of BChl monomers around 420−450 and 650−670 nm, respectively. Spectral changes of BChl-*c* self-aggregates with alkoxysilanes before and after incubation are shown in Figure 5. Most BChl-*c* aggregates before incubation changed to their monomeric form by addition of 0.3% (w/v) of Triton X-100 (see top of the left column in Figure 5). BChl-*c* aggregates with alkoxysilanes after incubation at 25 °C for 50 h, on the other hand, were significantly tolerant of Triton X-100. The ratio of Q_y absorbance of BChl-*c* self-aggregates in silicate capsules after incubation in 0.3% Triton X-100 solution to that

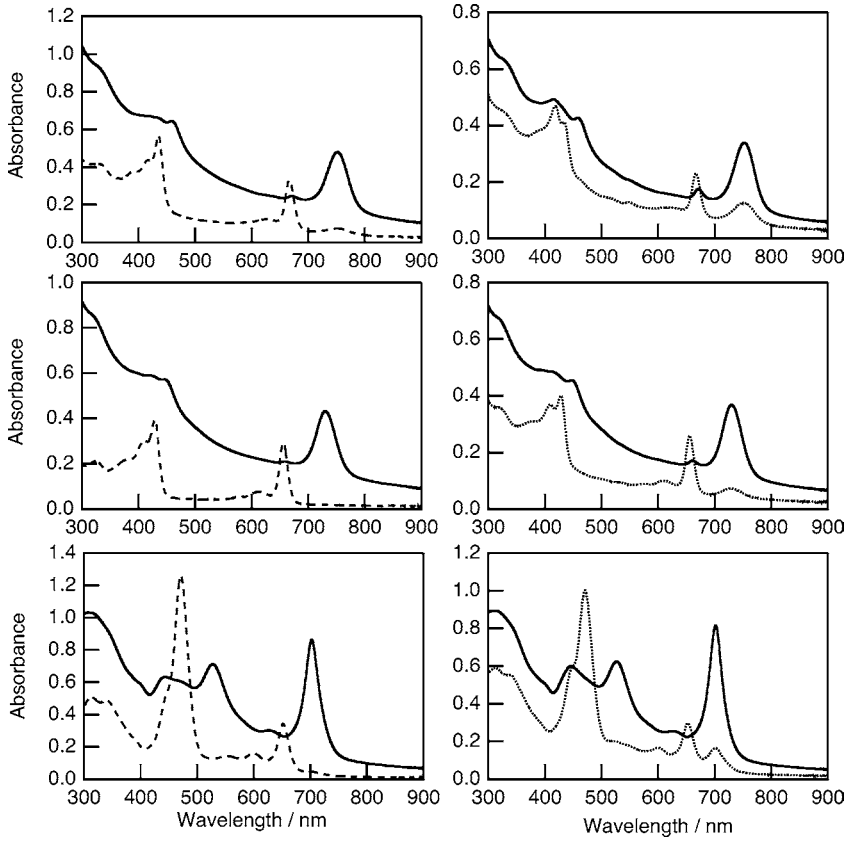

Figure 5. Spectral changes of BChl self-aggregates with alkoxysilanes in aqueous solution by addition of Triton X-100. Top, BChl-*c*; middle, BChl-*d*; bottom, BChl-*e*. Left column, before polycondensation; right column, after polycondensation at 25 °C for 50 h. Spectra at 0, 0.3, and 0.5% Triton X-100 are shown by solid, broken, and dotted curves, respectively.

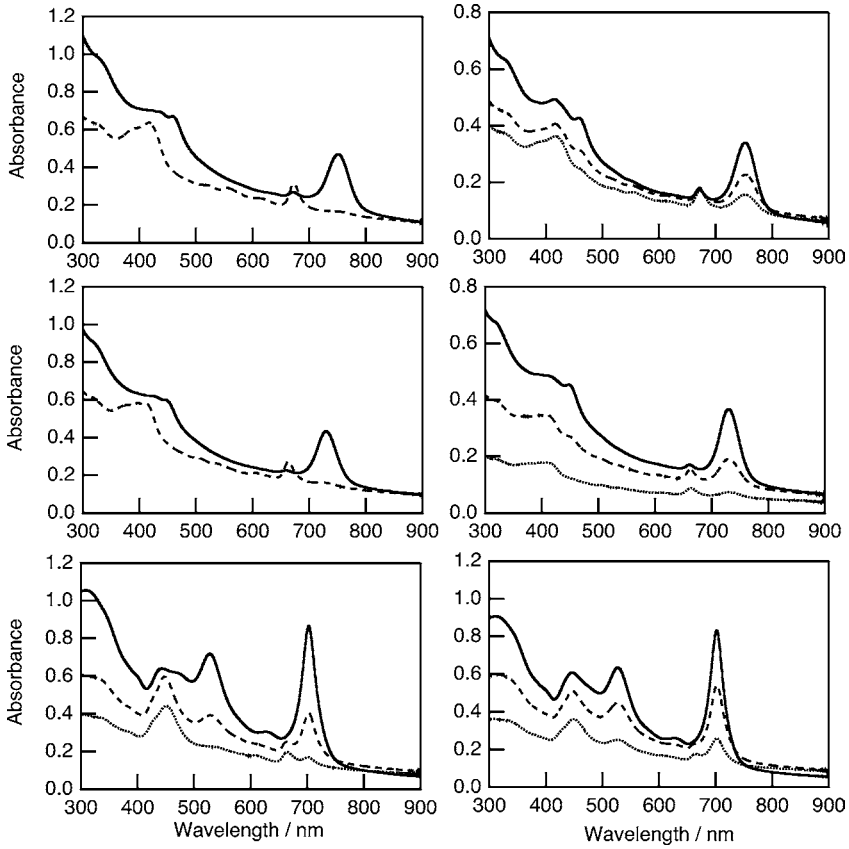

Figure 6. Spectral changes of BChl-*c* self-aggregates with alkoxysilanes in 50 mM HCl solution. Top, BChl-*c*; middle, BChl-*d*; bottom, BChl-*e*. Left column, before polycondensation; right column, after polycondensation at 25 °C for 50 h. Spectra at 0, 20, and 120 min after incubation in 50 mM HCl solution are shown by solid, broken, and dotted curves, respectively.

in distilled water (0% Triton X-100) was 0.36. The Q_y absorption band of BChl-*c* aggregates in silicate capsules after incubation around 750 nm remained even in 0.5% Triton X-100 solution (see top of the right column in Figure 5). This indicates that BChl-*c* self-aggregates were stabilized to a decomposer Triton X-100 by sol−gel polycondensation on the surface of chlorosomal capsules.

Similar tendency was observed in the cases of BChl-*d* and -*e* in silicate capsules, as shown in Figure 5. Most BChl-*d* and -*e* self-aggregates with alkoxysilanes before incubation were converted into their monomers by addition of 0.3% of Triton X-100, whereas 14% and 18% of Q_y absorbance of BChl-*d* and -*e* self-aggregates, respectively, remained in silicate capsules, which were prepared after incubation at 25 °C for 50 h, by addition of 0.3% (w/v) of Triton X-100. In 0.5% Triton X-100 solution, BChl-*d* and -*e* aggregates in silicate capsules after incubation still existed as shown in middle and bottom of the right column in Figure 5, respectively. These results indicate that polycondensation of alkoxysilanes makes natural BChl self-aggregates stable.

Demetalation under Acidic Conditions. Natural chlorophylls possessing magnesium as a central metal are easily demetalated under acidic conditions. This phenomenon is called pheophytinization. Pheophytinization of chlorosomal BChls in silicate capsules by an acid was examined to learn the stability of natural BChls in the present capsules. Figure 6 depicts the pheophytinization of BChls in silicate capsules with alkoxysilanes before and after incubation. BChl-*c* and -*d* self-aggregates before polycondensation of alkoxysilanes (before incubation) lost their Q_y absorption bands around 750 and 730 nm, respectively, by incubation in the acidic solution for 20 min, and new absorption bands appeared around 670 and 660 nm, which were ascribable to monomeric BPhes-*c*/*d*. BChl-*c* and -*d* self-aggregates after polycondensation of alkoxysilanes (after incubation at 25 °C for 50 h) were thereafter pheophytinized very slowly, and Q_y absorption bands of BChl self-aggregates remained even after 120 min under the acidic conditions.

In the case of BChl-*e*, self-aggregates both before and after polycondensation of alkoxysilanes were tolerant to the acid, compared with BChl-*c* and -*d* self-aggregates. This might be an inherent property of BChl-*e* molecules, since Chl-*b* possessing a formyl group at the 7-position is pheophytinized more slowly than Chl-*a* possessing a methyl group at the 7-position.[31] However, the pheophytinization process of BChl-*e* self-aggregates in silicate capsules after polycondensation was clearly different from that in micelles of alkoxysilanes before polycondensation; that is, these self-aggregates in silicate capsules after polycondensation had more resistance to the demetalation than those before polycondensation of alkoxysilanes. After 120 min incubation in 50 mM HCl solution, the absorbance ratio of BChl-*e* self-aggregates in silicate capsules (after polycondensation) was ca. 3-times larger than that before polycondensation of alkoxysilanes.

Figure 7 depicts time courses of the ratio of Q_y absorbance of BChl self-aggregates with alkoxysilanes incubated in 50 mM HCl solution to that in distilled water. In all cases, the absorbance ratio of the self-aggregates was gradually decreased with incubation time under the acidic conditions. In early phases of the pheophytinization processes, reaction rate constants, *k*, could be obtained by fitting the time courses of the Q_y absorbance ratio of BChl self-aggregates to the following kinetic formula:

$$\ln (A - A_\infty)/(A_0 - A_\infty) = -kt$$

where A_0, A, and A_∞ are Q_y absorbances of BChl self-aggregates with alkoxysilanes in distilled water, in 50 mM HCl solution at time *t*, and at the complete pheophytinization, respectively. The

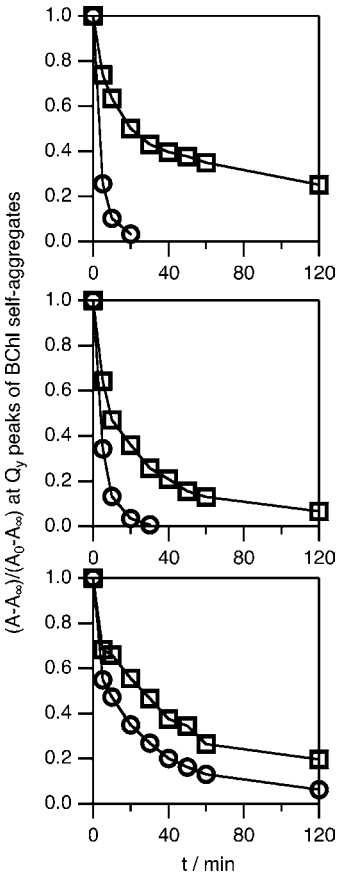

Figure 7. Time courses of the ratio of Q_y absorbance of BChl self-aggregates with alkoxysilanes in 50 mM HCl solution to that in distilled water. Open circles, before polycondensation; open squares, after polycondensation. Top, BChl-*c*; middle, BChl-*d*; bottom, BChl-*e*. A_0, A, and A_∞ are Q_y absorbances of BChl self-aggregates with alkoxysilanes in distilled water, in 50 mM HCl solution at time *t*, and at the complete pheophytinization, respectively.

Table 1. The Estimated Reaction Rate Constants *k* (min^{-1}) of Pheophytinization Processes of BChl Self-Aggregates with Alkoxysilanes Incubated in 50 mM HCl Solution

	k in micelles (before polycondensation)	*k* in capsules (after polycondensation)
BChl-*c*	0.23	0.022
BChl-*d*	0.20	0.035
BChl-*e*	0.029	0.016

estimated reaction rate constants are summarized in Table 1. The rate constants of the pheophytinization processes of BChl-*c* and -*d* self-aggregates before polycondensation of alkoxysilanes were 10.5- and 5.7-times larger than those in silicate capsules (after polycondensation), respectively. In the case of BChl-*e* self-aggregates, the rate constants were clearly different between the capsules after polycondensation of alkoxysilanes and the micelles before polycondensation. Therefore, the pheophytinization processes of three types of chlorosomal BChl self-aggregates indicate that the siloxane network on the surface made them significantly stable under the acidic conditions.

DISCUSSION

Natural light-harvesting BChls of green sulfur photosynthetic bacteria, which are well-known to be more unstable pigments than synthetic zinc chlorins in terms of pheophytinization, were successfully self-assembled in silicate capsules by the present sol−gel procedure to give similar supramolecular structures to those of chlorosomes. The BChl self-aggregates had enhanced stability to external perturbation such as addition of a surfactant and an acid.

It was reported that chlorophyll-*a* molecules in mesoporous silica enhanced their photostability.[32] Other reports of the inclusion of chlorophyllous pigments into mesoporous silica are available.[33,34] In these works, chlorophyllous pigments would be monomeric[33,34] or dimeric forms.[32] On the contrary, chlorosomal self-assemblies of light-harvesting BChls could be stabilized by encapsulation in sol−gel matrixes in this study. Such an encapsulation of photosynthetic supramolecules in sol−gel matrixes will provide a clue to constructing organic−inorganic hybrid supramolecules based on photosynthetic apparatus.[35,36]

The comparison between spectral changes of BChl self-aggregates before polycondensation and those after polycondensation clearly indicates that their stabilization in silicate capsules originates from the siloxane network on the surface of the aggregates. The rigid inorganic network would prevent the access of decomposers in solutions. Additionally, the rigidity of silicate cages might not allow BChl molecules to move for deaggregation in the capsules, as proposed in the case of proteins in sol−gel matrixes.[13,17]

BChl-*c* molecules in intact chlorosomes from *Chl. tepidum* were completely demetalated at pH 3.0 for 140 min at 40 °C, and monomeric BChl-*c* molecules in aqueous methanol (buffer (pH 4.0)/methanol = 1/9) were demetalated for 2 min.[37] BChls in silicate capsules thereafter possessed Q_y absorption bands of their self-aggregates even at pH = ca. 1.5 at ca. 25 °C for 120 min. Therefore, the present chlorosome-mimicking silicate capsules would become stable under acidic conditions compared with natural systems. The increase of stability of alkaline phosphatase in sol−gel matrixes to acidic conditions has recently been reported,[17] where sol−gel matrixes kept alkaline phosphatase active under highly acidic conditions (pH > 0.9). The extreme stability of these biomolecules in sol−gel matrixes under acidic conditions would be ascribable to hydrophobic microenvironments in the matrixes where little proton and few water molecules were present as well as a rigid siloxane network around the biomolecules. The present capsules including BChl self-aggregates will be useful for elucidation of precise supramolecular structures and functions of chlorosomes because of their high stability and will lead to artificial photosynthetic devices operating under non-native conditions.

ACKNOWLEDGMENT

This work was partially supported by Grants-in-Aid for Scientific Research (No. 17029065) on Priority Areas (417) from the Ministry of Education, Culture, Sports, Science and Technology (MEXT) of the Japanese Government, and for Scientific Research (B) (No. 15350107) from the Japan Society for the Promotion of Science (JSPS), by the "Academic Frontier" Project for Private Universities: matching fund subsidy from MEXT, 2003-2007, and by the Nissan Science Foundation. Y. S. is grateful for a JSPS Fellowship for Young Scientists.

LITERATURE CITED

(1) Olson, J. M. (1998) Chlorophyll organization and function in green photosynthetic bacteria. *Photochem. Photobiol. 67*, 61−75.

(2) Staehelin, L. A., Golecki, J. R., and Drews, G. (1980) Supramolecular organization of chlorosomes (Chlorobium vesicles) and of their membrane attachment sites in *Chlorobium limicola*. *Biochim. Biophys. Acta 589*, 30−45.

(3) Blankenship, R. E., Olson, J. M., and Miller, M. (1995) Antenna complexes from green photosynthetic bacteria. *Anoxygenic Photosynthetic Bacteria* (Blankenship, R. E., Madigan, M. T., and Bauer, C. E., Eds.) pp 399−435, Kluwer Academic Publishing, Dordrecht.

(4) Tamiaki, H. (1996) Supramolecular structure in extramembraneous antennae of green photosynthetic bacteria. *Coord. Chem. Rev. 148*, 183−197.

(5) Miyatake, T., and Tamiaki, H. (2005) Self-aggregates of bacteriochlorophylls-*c*, *d* and *e* in a light-harvesting antenna system of green photosynthetic bacteria: effect of stereochemistry at the chiral 3-(1-hydroxyethyl) group on the supramolecular arrangement of chlorophyllous pigments. *J. Photochem. Photobiol. C: Photochem. Rev. 6*, 89−107.

(6) Balaban, T. S., Tamiaki, H., and Holzwarth, A. R. (2005) Chlorins programmed for self-assembly. *Topics Curr. Chem. 258*, 1−38.

(7) Tamiaki, H. (2005) Self-aggregates of natural and modified chlorophylls as photosynthetic light-harvesting antenna systems: substituent effect on the B-ring. *Photochem. Photobiol. Sci. 4*, 675−680.

(8) Uehara, K., Mimuro, M., Ozaki, Y., and Olson, J. M. (1994) The formation and characterization of the in vitro polymeric aggregates of bacteriochlorophyll *c* homologs from *Chlorobium limicola* in aqueous suspension in the presence of monogalactosyl diglyceride. *Photosynth. Res. 41*, 235−243.

(9) Hirota, M., Moriyama, T., Shimada, K., Miller, M., Olson, J. M., and Matsuura, K. (1992) High degree of organization of bacteriochlorophyll *c* in chlorosome-like aggregates spontaneously assembled in aqueous solution. *Biochim. Biophys. Acta 1099*, 271−274.

(10) Miyatake, T., Tamiaki, H., Holzwarth, A. R., and Schaffner, K. (1999) Self-assembly of synthetic zinc chlorins in aqueous microheterogeneous media to an artificial supramolecular light-harvesting device. *Helv. Chim. Acta 82*, 797−810.

(11) Prokhorenko, V. I., Holzwarth, A. R., Müller, M. G., Schaffner, K., Miyatake, T., and Tamiaki H. (2002) Energy transfer in supramolecular artificial antennae units of synthetic zinc chlorins and co-aggregated energy traps. A time-resolved fluorescence study. *J. Phys. Chem. B 106*, 5761−5768.

(12) Schmidt, H. (1994) Inorganic−organic composites by sol−gel techniques. *J. Sol-Gel Sci. Technol. 1*, 217−231.

(13) Jin, W., and Brennan, J. D. (2002) Properties and applications of proteins encapsulated within sol−gel derived materials. *Anal. Chim. Acta 461*, 1−36.

(14) Katagiri, K., Hamasaki, R., Ariga, K., and Kikuchi, J. (2002) Layerd paving of vesicular nanoparticles formed with cerasome as a bioinspired organic−inorganic hybrid. *J. Am. Chem. Soc. 124*, 7892−7893.

(15) Narang, U., Prasad, P. N., and Bright, F. V. (1994) Glucose biosensor based on a sol−gel-derived platform. *Anal. Chem. 66*, 3139−3144.

(16) Smith, K., Silvernail, N. J., Rodgers, K. R., Elgren, T. E., Castro, M., and Parker, R. M. (2002) Sol−gel encapsulated horseradish peroxidase: a catalytic material for peroxidation. *J. Am. Chem. Soc. 124*, 4247−4252.

(17) Frenkel-Mullerad, H., and Avnir, D. (2005) Sol−gel materials as efficient enzyme protectors: preserving the activity of phosphatases under extreme pH conditions. *J. Am. Chem. Soc. 127*, 8077−8081.

(18) Ellerby, L. M., Nishida, C. R., Nishida, F., Yamanaka, S. A., Dunn, B., Valentine, S., and Zink, J. I. (1992) Encapsulation of proteins in transparent porous silicate glasses prepared by the sol−gel method. *Science 255*, 1113−1115.

(19) Shibayama, N., and Saigo, S. (1995) Fixation of the quaternary structures of human adult haemoglobin by encapsulation in transparent porous silica gels. *J. Mol. Biol. 251*, 203−209.

(20) Shen, C., and Kostic, N. M. (1997) Kinetics of photoinduced electron-transfer reactions within sol−gel silica glass doped with zinc cytochrome *c*. Study of electrostatic effects in confined liquids. *J. Am. Chem. Soc. 119*, 1304−1312.

(21) Khan, I., Shannon, C. F., Dantsker, D., Friedman, A. J., Perez-Gonzalez-de-Apodaca, J., and Friedman, J. M. (2000) Sol−gel trapping of functional intermediates of hemoglobin: geminate and bimolecular recombination studies. *Biochemistry, 39*, 16099−16109.

(22) Weetall, H. H., Robertson, B., Cullin, D., Brown, J., and Walch, M. (1993) Bacteriorhodopsin immobilized in sol−gel glass. *Biochim. Biophys. Acta 1142*, 211−213.

(23) Shamansky, L. M., Luong, K. M., Han, D., and Chronister, E. L. (2002) Photoinduced kinetics of bacteriorhodopsin in a dried xerogel glass. *Biosens. Bioelectron. 17*, 227−231.

(24) Saga, Y., Miyatake, T., and Tamiaki, H. (2002) Self-assembly of synthetic zinc chlorins in a silicate micelle prepared by sol−gel process. *Bioorg. Med. Chem. Lett. 12*, 1229−1231.

(25) Saga, Y., Akai, S., Miyatake, T., and Tamiaki, H. (2004) Excitation energy transfer from self-aggregates of zinc chlorins to a bacteriochlorin in a silicate nanocapsule. *Chem. Lett. 33*, 544−545.

(26) Saga, Y., Wazawa, T., Mizoguchi, T., Ishii, Y., Yanagida, T., and Tamiaki, H. (2002) Spectral heterogeneity in single light-harvesting chlorosomes from green sulfur photosynthetic bacterium *Chlorobium tepidum*. *Photochem. Photobiol. 75*, 433−436.

(27) Saga, Y., Oh-oka, H., Hayashi, T., and Tamiaki, H. (2003) Presence of exclusively bacteriochlorophyll-*c* containing substrain in the culture of green sulfur photosynthetic bacterium *Chlorobium vibrioforme* strain NCIB 8327 producing bacteriochlorophyll-*d*. *Anal. Sci. 19*, 1575−1579.

(28) Saga, Y., Matsuura, K., and Tamiaki, H. (2001) Spectroscopic studies on self-aggregation of bacteriochlorophyll-*e* in nonpolar organic solvents: effects of stereoisomeric configuration at the 3^1-position and alkyl substituents at the 8^1-position. *Photochem. Photobiol. 74*, 72−80.

(29) Saga, Y., and Tamiaki, H. (2004) Comparison between chlorosomes containing bacteriochlorophyll-*c* and chlorosomes containing bacteriochlorophyll-*d* isolated from two substrains of green sulfur photosynthetic bacterium *Chlorobium vibrioforme* NCIB 8327. *J. Photochem. Photobiol. B: Biol. 75*, 89−97.

(30) Griebenow, K., Holzwarth, A. R., van Mourik, F., and van Grondelle, R. (1991) Pigment organization and energy transfer in green bacteria 2. Circular and linear dichroism spectra of protein-containing and protein-free chlorosomes isolated from *Chloroflexus aurantiacus*. *Biochim. Biophys. Acta 1058*, 194−202.

(31) Mazaki, H., Watanabe, T., Takahashi, T., Struck, A., and Scheer, H. (1992) Pheophytinization of eight chlorophyll derivatives in aqueous acetone. *Bull. Chem. Soc. Jpn. 65*, 3212−3214.

(32) Itoh, T., Yano, K., Inada, Y., and Fukushima, Y. (2002) Photostabilized chlorophyll *a* in mesoporous silica: adsorption properties and photoreduction activity of chlorophyll *a*. *J. Am. Chem. Soc. 124*, 13437−13441.

(33) Furukawa, H., Watanabe, T., and Kuroda, K. (2001) Immobilization of chlorophyll derivatives into mesoporous silica and energy transfer between the chromophores in mesopores. *Chem. Commun.*, 2002−2003.

(34) Murata, S., Furukawa, H., and Kuroda, K. (2001) Effective inclusion of chlorophyllous pigments into mesoporous silica modified with α,ω-diols. *Chem. Mater. 13*, 2722−2729.

(35) Chen, Z. P., Samuelson, L. A., Akkara, J., Kaplan, D. L., Gao, H., Kumar, J., Marx, K. A., and Tripathy, S. K. (1995) Sol−gel encapsulated light-transducing protein phycoerythrin: a new biomaterial. *Chem. Mater. 7*, 1779−1783.

(36) O'Neill, H., and Greenbaum, E (2005) Spectroscopy and photochemistry of spinach Photosystem I entrapped and stabilized in a hybrid organosilicate glass. *Chem. Mater. 17*, 2654−2661.

(37) Steensgaard, D. B., Matsuura, K., Cox, R. P., and Miller, M. (1997) Changes in bacteriochlorophyll *c* organization during acid treatment of chlorosomes from *Chlorobium tepidum*. *Photochem. Photobiol. 65*, 129−134.

BC050343S

Preparation and Stability of N-Terminal Mono-PEGylated Recombinant Human Endostatin

Yongjun Nie, Xin Zhang, Xinchang Wang, and Junhui Chen*

State Key Laboratory of Pharmaceutical Biotechnology, Department of Biochemistry, Nanjing University, Nanjing 210093, P.R. China. Received December 14, 2005; Revised Manuscript Received May 27, 2006

Endostatin can specifically inhibit endothelial proliferation and potently inhibit angiogenesis and tumor growth. N-Terminal site-specific mono-PEGylation of recombinant human endostatin (mPEG-rhES) was accomplished by using methoxy poly-ethylene glycol (mPEG) propionaldehyde with an average molecular weight of 5000 Da through a reactive terminal aldehyde group. The site-specific mPEG conjugation was conducted under optimal conditions, which were identified through a statistical $L_9(3^4)$ orthogonal test. In this study, we have investigated the stability and antitumor activity of mPEG-rhES. SDS−PAGE, RP-HPLC, and UV spectrophotometric analysis were used to identify the purity and stability of mPEG-rhES. When incubated with protease or placed in an extreme environment, mPEG-rhES was more stable than rhES. The unmodified and PEGylated rhES were tested for their ability to inhibit the tumor growth of mouse H22 liver cancer in male mice. In a multiple versus single doses comparison study, daily administration of 0.25, 0.50, and 1.00 μmol/kg of unmodified rhES for 7 days resulted in 26.9%, 43.0%, and 64.9% reductions in tumor weight, respectively, while single doses of 0.13, 0.25, and 0.50 μmol/kg of the PEGylated protein per day resulted in 24.8%, 38.0%, and 64.5% reductions, respectively. Both treatments resulted in statistically significant reductions in mean tumor weight as compared to the physiological saline solution (control)-treated mice, with the dose of mPEG-rhES being a half of rhES, respectively, while the tumor inhibition rates were similar. Therefore, it is suggested that PEGylation enhances the stability of rhES and improves its antitumor activity.

INTRODUCTION

Protein and peptide drugs have great potential as therapeutic agents. However, many of them are degraded by proteolytic enzymes in vivo, and they are rapidly cleared by the kidneys. In addition, B cells can generate neutralizing antibodies against these proteins and peptides. Therefore, these drugs usually have a short circulating half-life (*1*). Poly(ethylene glycol) (PEG) is a widely investigated polymer used for the covalent modification of biological macromolecules for many pharmaceutical and biotechnical applications, especially of peptides and proteins (*2*). By increasing the molecular mass of proteins and peptides and shielding them from proteolytic enzymes, PEGylation improves pharmacokinetics (*1*). A wide range of therapeutic proteins, including human growth hormone, interferon, insulin, granulocyte-colony stimulating factor (G-CSF), and interleukin II, have been PEGylated (*3*). The first few PEG−protein products, now on the market (Adagen, Oncospar, and PEG-Intron), were developed using first generation of PEG chemistry. The second generation of PEGylation was designed to avoid the problems of first generation chemistry, notably diactivated PEG impurities, restriction to low molecular weight mPEG, unstable linkages, and lack of selectivity in modification (*1*). Recently, site-specific PEGylation of proteins has been attempted using a special class of functionalized PEG derivatives under specific conjugation conditions. For example, N-terminal specific PEGylation of G-CSF was obtained by conjugating methoxy-PEG derivatives at acidic pH conditions (*4*). This strategy was based on the fact that primary amine residues in protein have different pK_a values: pK_a 7.8 for the N-terminal α-amino group and 10.1 for the ϵ-amino group in lysine residues (*5*). When the propionaldehyde or *N*-hydroxysuccinimide PEG was conjugated at lower pH conditions, PEGylation at the N-terminus site occurred preferentially due to the different pK_a values between the two kinds of ϵ and α primary amines (*6*).

Endostatin, a 20 kDa carboxy-terminal fragment of collagen XVIII, was isolated from the conditioned media of hemangioendothelioma (EOMA) cells. It specifically inhibits endothelial proliferation and potently inhibits angiogenesis and tumor growth (*7*). Endostatin is derived from elastase-mediated cleavage (*8*). Ongoing angiogenesis is essential for the rapid growth of solid tumors, and it appears that successful tumors actively influence the 'angiogenic switch' to sustain continuous cell proliferation (*9*). Interestingly, endostatin does not seem to induce drug resistance. Furthermore, repeated cycles of systemic endostatin administration in tumor-bearing mice caused sustained tumor dormancy in the absence of further treatment (*10*). Therefore, endostatin will become the new and important antitumor agent.

In this study, we PEGylated the N-terminus of rhES in a site-specific manner with PEG-propionaldehyde derivative (*4, 6*). Various characterization methods, such as fast protein liquid chromatography (FPLC) and reversed phase high-performance liquid chromatography (RP-HPLC) techniques were used to reveal that the mono-PEGylation reaction occurred site-specifically at the N-terminal α-amine group. In vitro stability experiments such as incubating with trypsin or chymotrypsin and being kept at an extreme pH or temperature and in vivo antitumor activity experiments investigated in mice with H22 liver cancer were performed to examine the therapeutic potential of mono-PEGylated endostatin.

EXPERIMENTAL PROCEDURES

Materials. Recombinant human endostatin (rhES) was donated by ZhongKai Bio-pharma (Suzhou, Jiangsu, China). The 5 kDa mPEG-propionaldehyde was purchased from SunBio

* To whom correspondence should be addressed. Phone: 086-25-83592331. Fax: 086-25-83592331. E-mail: jhchen@nju.edu.cn.

10.1021/bc050355d CCC: $33.50 © 2006 American Chemical Society
Published on Web 06/23/2006

Table 1. Factors and Levels of the Orthogonal Tests

	factor			
level	pH	molar ratio mPEG/rhES	temperature (°C)	time (h)
1	5.0	2	4	10
2	5.5	5	20	16
3	6.0	10	30	24

(Anyang city, Seoul, Korea); trypsin, chymotrypsin, sodium cyanoborohydride, and dialysis membranes (MW cutoff 1000) were from Sigma (St. Louis, MO); CM Sepharose FF was form Amersham Pharmacia Biotech (Buckinghamshire, UK); 5 μm pore size BDS C_{18} reversed phase column (150 × 4.6 mm) was from Hypersil (Shandon HPLC, Runcorn, Cheshire, UK); and mouse H22 liver cancer cells and KunMing mice were form SIPI (Shanghai, CN).

PEGylation of rhES with PEG-Propionaldehyde Derivatives. The optimal condition of the reaction was achieved through a statistical $L_9(3^4)$ orthogonal test. The four factors were pH, molar ratio of mPEG propionaldehyde to rhES, temperature, and time. Table 1 reports the three levels of each factor. The reactions were terminated by adjusting pH to 3.5 with 1 M HCl, and samples were analyzed by SDS−PAGE and Gelworks 1D intermediate software system.

Separation and Purification by ÄCTA FPLC. The reaction mixture was loaded onto a CM Sepharose FF cation exchange column (1.0 cm × 20 cm) preequilibrated with 20 mM sodium acetate, pH 4.5 (buffer A), at a flow rate of 1.0 mL/min using a Pharmacia LCC 501 Plus FPLC system. The column was washed with 300 mL of buffer A before a ladder gradient to 20%, 40%, and 60% buffer B (buffer A + 1 M NaCl) was applied about 5 column volumes per gradient. The fractions were analyzed by nonreducing SDS−PAGE and Gelworks 1D intermediate software system. The samples containing mono-PEGylated and unmodified rhES were collected sequentially. Samples were stored at −20 °C after dialysis and lyophilization.

UV Spectrophotometry. The protein content of PEGylated rhES can be determined by comparing the UV absorbance of pure rhES and mPEG-rhES at 280 nm. The purity and PEG-residue count of PEGylated rhES can be identified by the protein content.

Reversed Phase HPLC (RP-HPLC). PEGylated rhES or rhES was analyzed on a Hypersil BDS C_{18} column equilibrated with buffer C (H_2O containing 0.1% TFA) with a flow rate of 1.0 mL/min and monitored at 280 nm, and eluted with a linear gradient to 60% buffer D (CH_3CN containing 0.1% TFA) over 20 min.

In Vitro Proteolysis. 400 μL of mPEG-rhES (1.25 mg/mL, pH 7.4 phosphate buffer (PBS)) was incubated with 4 μL trypsin (1.0 mg/mL) or 20 μL chymotrypsin (2.0 mg/mL) at 37 °C. 20 μL of each sample was loaded onto a C_{18} column at different intermediate incubation time and identified by RP-HPLC. The peak area with mPEG-rhES characteristic retention time indicated the remaining mPEG-rhES. Meanwhile the rhES was taken as compared with mPEG-rhES.

Stability of mPEG-rhES at Extreme pH or Temperature. To obtain the effects of temperature on rhES and mPEG-rhES, the mPEG-rhES (1.25 mg/mL, pH 7.4 PBS, 400 μL) or rhES (1.0 mg/mL, pH 7.4 PBS, 400 μL) was incubated at 4, 25, 37, 45, 50, 55, 60, 65 °C, respectively. After 24 h of incubation, all samples were centrifuged at 15000 rpm for 10 min. The absorbance of supernatant was measured at 280 nm to determine the remaining protein.

Similarly, to obtain the effects of acid or alkali, the pH of mPEG-rhES (1.25 mg/mL, pH 7.4 PBS, 400 μL) or rhES (1.0 mg/mL, pH 7.4 PBS, 400 μL) was adjusted to 2, 3, 4, 5, 6 using acetic solution and 8, 9, 10, 11 using sodium hydroxide solution. The samples were incubated at 37 °C for 24 h and collected by centrifugation. The remaining protein in supernatant was measured by UV spectrophotometry.

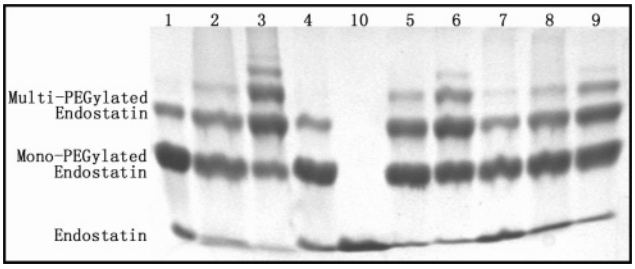

Figure 1. SDS−PAGE analysis of the orthogonal samples stained with Coomassie Blue. Lane 1−9: nine samples in the orthogonal tests corresponding to the test number. Lane 10: the original unmodified rhES solution.

Antitumor Activity of mPEG-rhES in Mouse H22 Liver Cancer Allografts. Well-growth ascites of mouse H22 liver cancer, obtained from SIPI (Shanghai Institute of Pharmaceutical Industry, Shanghai, CN), were aspirated and diluted with 4-fold volumes physiological saline solution. 0.2 mL of the diluted ascites was subcutaneously inoculated with a trocar needle into the axillary flank of each male KunMing mouse (age 4 weeks; weight 19−21 g). The next day after inoculation, the mice were randomly allocated to drug groups of 10 animals each and 0.2 mL drug injections were administered, respectively. The rhES was administered intravenously (i.v.) to the tail at doses of 0.25, 0.50, and 1.00 μmol/kg, respectively, once a day for 7 consecutive days, and mPEG-rhES at doses of 0.13, 0.25, and 0.50 μmol/kg, and physiological saline solution at a dose of 12.5 mL/kg in the control group. After 10 days, the mice were sacrificed, and tumors were harvested for weight-measuring. The following formula was used to calculate the antitumor effect: tumor inhibition rate (TIR%) = (1 − mean tumor weight of treatment group/mean tumor weight of untreated group) × 100. All animal experiments were carried out in accordance with the Guidelines for the Welfare of Animals in Experimental Neoplasia.

RESULTS

PEGylation of rhES. The statistical $L_9(3^4)$ orthogonal test analyzed by SDS−PAGE indicated mono-PEGylation was better in Lane 1 or 4 (Figure 1). The ratios of mono-PEGylated rhES were 66.80% and 63.08% in Lane 1 and 4, respectively. The higher PEG concentration led to a higher ratio of multi-PEGylated rhES (Lane 3, 6, 9 in Figure 1). After orthogonal analysis on the four factors, we found the factor which played the most important role in the reaction was the molar ratio of mPEG to rhES, followed by temperature, time, and pH (Table 2).

The mono-PEGylated rhES produced in the PEGylation acylation reaction was separated from multi-PEGylated rhES and the unreacted rhES molecules by cation exchange chromatography (Figure 2). After dialysis and lyophilization, the purity of the mono-PEGylated rhES was measured by SDS−PAGE (Figure 3), UV spectrophotometry, and RP-HPLC (Figure 4). The results of SDS−PAGE and PR−HPLC chromatography indicated that the mPEG-rhES were pure. The experimental protein content of PEGylated rhES was 80.21%, and its PEG-residue count was 1. This result not only indicated that mPEG-rhES was pure, but also exactly showed that the product was unitarily PEGylated.

Stability of mPEG-rhES. Quantitations of percent remaining rhES following incubation with trypsin or chymotrypsin, by C_{18} column RP-HPLC, showed that the PEGylated rhES was more

Table 2. Results of Orthogonal Tests[a]

test no.	pH	molar ratio mPEG/rhES	temperature (°C)	time (h)	RMPES%[b]
1	1	1	1	1	66.80
2	1	2	2	2	47.54
3	1	3	3	3	21.78
4	2	1	2	3	63.08
5	2	2	3	1	47.79
6	2	3	1	2	39.61
7	3	1	3	2	49.36
8	3	2	1	3	48.85
9	3	3	2	1	41.35
K_1[c]	136.11	179.23	155.26	155.94	
K_2	150.48	144.18	151.97	136.50	
K_3	139.56	102.74	118.92	133.71	
$K_1/3$[d]	45.37	59.74	51.75	51.98	
$K_2/3$	50.16	48.06	50.66	45.50	
$K_3/3$	46.52	34.25	39.64	44.57	
R[e]	4.79	25.50	12.11	7.41	

[a] The factor which played the most important role in the reaction was found out by the statistical orthogonal test. [b] The ratios of mono-PEGylated rhES (RMPES%) were worked out from the gel by Gelwoks 1D intermediate software system. [c] K value was the sum of the RMPES% of a certain factor with the same level. [d] $K_1/3$ meant that K_1 value was divided by 3. [e] To a certain factor, the minimal $K_x/3$ ($x = 1$, 2, or 3) subtracted from the maximal one gave the R value. The larger the R value, the more important the factor's role in the reaction. In a degressive order, the most important factor was the molar ratio of mPEG to rhES, followed by temperature, time, and pH.

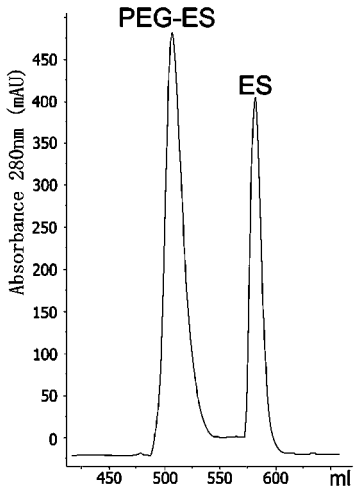

Figure 2. The profile of cation exchange fast protein liquid chromatogram (ÄCTA FPLC) of the PEGylated rhES.

resistant to trypsin or chymotrypsin proteolysis than rhES. After 40 min of incubation with trypsin, only 4% mono-PEGylated rhES in contrast to 90% of rhES was degraded (Figure 5). When mPEG-rhES and rhES were incubated with chymotrypsin, the results showed that the half-life of mPEG-rhES was about 60 min while that of rhES was about 24 min (Figure 6). Therefore, PEGylation distinctly increased the antiproteolytic stability of rhES.

Recombinant hES was stable during 4 °C to 40 °C just like mPEG-rhES. However when the temperature was increased to 50 °C, there was only 20% rhES remaining while almost 100% mPEG-rhES remaining. When the denaturalization ratio of rhES was 50% the temperature was about 47.6 °C, whereas the corresponding temperature of mPEG-rhES was about 62.6 °C (Figure 7). Therefore, PEGylation significantly increased the heat stability of endostatin.

Recombinant hES was stable during pH 2 to pH 7 as well as mPEG-rhES. When the pH exceeded 9, mPEG-rhES was significantly more stable than rhES. Even the pH rose to 10, mPEG-rhES was still stable while the denaturalization ratio of

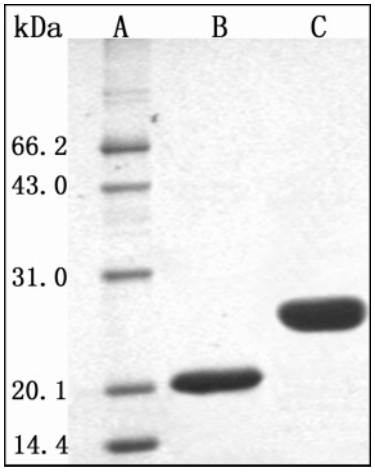

Figure 3. SDS−PAGE analysis of the two purified fractions on a nonreducing 17% gel and stained with Coomassie brilliant Blue. Lane A, molecular weight markers; Lane B, unmodified rhES (Peak 2 in Figure 2); Lane C, mono-PEGylated rhES (Peak 1 in Figure 2).

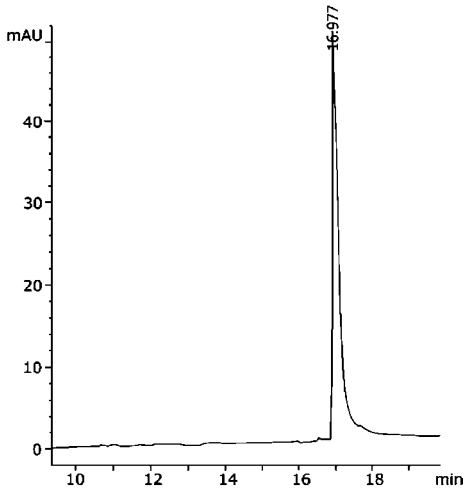

Figure 4. The HPLC profile of mono-PEGylated rhES after purification.

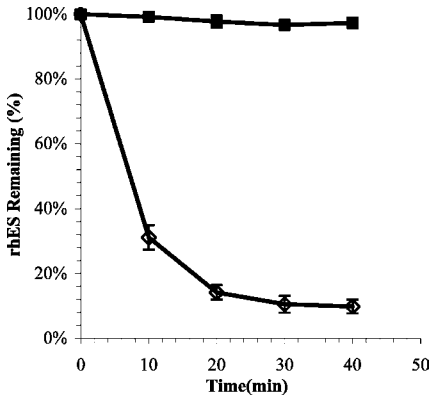

Figure 5. The relative resistance of PEG-rhES (■) and rhES (◇) to trypsin proteolysis. Each data value represents means ± SD ($n = 3$).

rhES reached at 84.4% (Figure 8). Therefore, the N-terminus site-specific PEGylation also enhanced the acid−base stability of rhES significantly.

In Vivo Activity of Unmodified and PEGylated rhES. In a multiple versus single doses comparison study, daily administration of 0.25, 0.50, and 1.0 μmol/kg of unmodified rhES for 7 days resulted in 26.9%, 43.0%, and 64.9% reductions in tumor weight respectively, while single doses of 0.13, 0.25, and 0.50 μmol/kg of the PEGylated protein per day resulted in

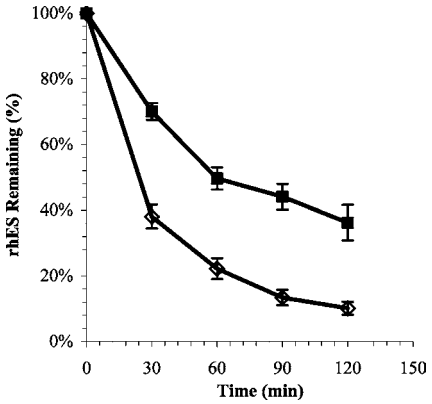

Figure 6. The relative resistance of PEG-rhES (■) and rhES (◇) to chymotrypsin proteolysis. Each data value represents means ± SD (n = 3).

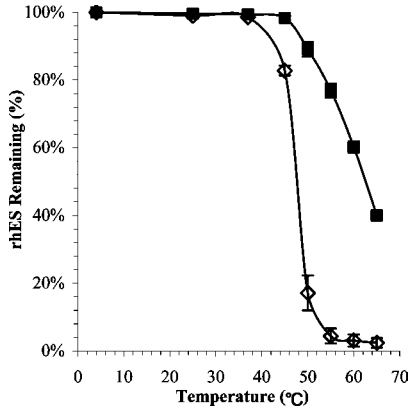

Figure 7. The effect of PEGylation on the relative susceptibility of PEG-rhES (■) and rhES (◇) to temperature. Each data value represents means ± SD (n = 3).

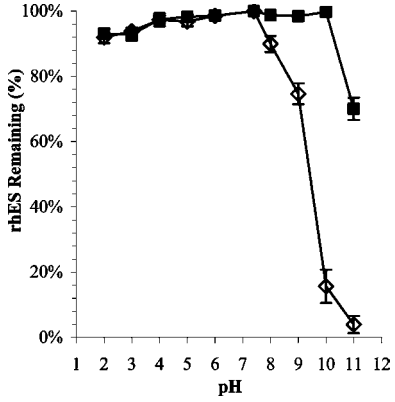

Figure 8. The effect of PEGylation on the relative susceptibility of PEG-rhES (■) and rhES (◇) to pH. Each data value represents means ± SD (n = 3).

24.8%, 38.0%, and 64.5% reductions respectively (Table 3). Both treatments resulted in statistically significant reductions in mean tumor weight as compared to the physiological saline solution (control)-treated mice at P-value < 0.001. The dose of mPEG-rhES was a half of rhES, repectively, while the tumor inhibition rate (TIR%) was rather closer.

DISCUSSION

The conjugation of PEG derivative to primary amine groups of endostatin takes place primarily via a nucleophilic substitution reaction: the attack of unprotonated amine group to the carbonyl groups of aldehyde. This indicated that all the primary amines

Table 3. Antitumor Activities of RhES and MPEG-rhES against Mouse H22 Liver Cancer Allografts

drug	dose (μmol/kg)	administration	tumor weight (g)[a]	TIR%[b]
PSS	12.5 mL/kg	iv × 7	2.42 ± 0.28	−
rhES	0.25	iv × 7	1.77 ± 0.32[c]	26.9 ± 13.2
	0.50	iv × 7	1.38 ± 0.14[c]	43.0 ± 5.8
	1.00	iv × 7	0.85 ± 0.30[c]	64.9 ± 12.4
mPEG-rhES	0.13	iv × 7	1.82 ± 0.29[c]	24.8 ± 12.0
	0.25	iv × 7	1.50 ± 0.17[c]	38.0 ± 7.0
	0.50	iv × 7	0.86 ± 0.22[c]	64.5 ± 9.1

[a] After 10 days, the mice were sacrificed, and the tumors were harvested for weight-measuring. Values represent the means and standard deviations of results from 10 tumors. [b] Tumor inhibition rate (TIR%) = (1 − mean tumor weight of treatment group/mean tumor weight of untreated group) × 100. [c] Significantly different from the PSS control group at P < 0.001.

(α and ϵ) were equally reactive to PEGylation in basic conditions, so a heterogeneous mixture of multi-PEGylated species may be produced. In contrast, in the acidic condition, selective unprotonation of the N-terminal α-amine group could occur, making it more reactive than the ϵ-amine groups in lysine residues because of the difference of the pK_a values: 7−8 for α-amine, and 10−11 for ϵ-amine (*5*). This reductive amination reaction with the N-terminal α-amine group, in the presence of sodium cyanoborohydride as a reducing agent, possibly resulted in the site-specific mono-PEGylated CSF and EGF (*4*, *6*). Mono-PEGylated protein conjugates, such as endostatin, were similarly obtained through a selective conjugation at the N-terminal α-amine residue by a statistical orthogonal test.

After the simple purification steps of cation exchange chromatography and dialysis, the pure mono-PEGylated rhES conjugate could be obtained in the absence of rhES as evidenced by the SDS−PAGE and RP-HPLC analysis. The content of rhES protein in the mono-PEGylated rhES was measured by UV 280 nm. Through calculation, the protein content of mPEG-rhES was 80.21% and the PEG-residue count (n) was 1. This result not only indicated that mPEG-rhES was pure, but also adequately revealed that the molecular weights were in good agreement with the endostatin conjugate containing a single 5000 Da PEG derivative.

In the United States, phase I clinical trials of rhES therapy were performed with doses ranging from 15 to 600 mg/m^2, and the doses were generally well tolerated (*11*, *12*). In October 2002, rhES entered phase II clinical trials for neuroendocrine tumors and metastatic melanoma (*13*). Recently rhES therapy passed Phase III clinical trials in non small cell lung cancer in China (*14*), and rhES developed by Shandong Yantai Medgenn Co., Ltd., was approved by China State Food and Drug Administration in March 2005.

The dosage of rhES is 7.5−60 mg/m^2 per day (*14*, *15*). Such a dosage is a huge challenge to a recombinant gene product. However, the results of this study indicate that PEGylated rhES develops significant resistance to proteolysis and exhibits high stability to changes of temperature or pH. On the other hand, when we tested a 1 μmol/kg (20 mg/kg) dosage of rhES against mouse H22 liver cancer, the tumor inhibition rate (TIR%) was 64.9%. While the TIR% of mPEG-rhES was equivalent to rhES (64.5%), the dose of mPEG-rhES was just a half of rhES. Therefore, the PEGylation did not diminish the antitumor efficacy of rhES and also showed the possibility of reducing the administerial dosage in tumor treatments. In summary, it is suggested that PEGylation enhances the stability of rhES and improves its antitumor activity. Our data reveal the possibility to use a lower dosage of rhES in the clinic by the use of mono-PEGylation.

CONCLUSIONS

In this study, we showed that mPEG-propionaldehyde was specifically conjugated at the N-terminal α-amine group of rhES in a weak acidic pH environment. The stability of mono-PEGylated rhES, analyzed by protease degradation and an extreme environment in vitro, was enhanced significantly. Moreover, endostatin's antitumor activity, investigated in mice with H22 liver cancer, was also improved by PEGylation.

ACKNOWLEDGMENT

The authors thank Suzhou ZhongKai Bio-Pharma. Co., Ltd. for the generous donation of recombinant human endostatin.

LITERATURE CITED

(1) Harris, J. M., and Chess, R. B. (2003) Effect of pegylation on pharmaceuticals. *Nat. Rev. Drug Discovery 2*, 214−221.

(2) Roberts, M. J., Bentley, M. D., and Harris. J. M. (2002) Chemistry for peptide and protein PEGylation. *Adv. Drug Delivery Rev. 54*, 459−476.

(3) Harris, J. M., and Zilpsky, S. (1997) Poly(ethylene glycol): Chemistry and Biological Applications. *ACS Symposium Series 680*, American Chemical Society, Washington, DC.

(4) Kinstler, O. B., Brems, D. N., Lauren, S. L., Paige, A. G., Hamburger, J. B., and Treuheit, M. J. (1996) Characterization and stability of N-terminally PEGylated rhG-CSF. *Pharm. Res. 13*, 996−1002.

(5) Wong, S. S. (1991) *Chemistry of protein conjugation and cross-linking.* CRC Press, Boca Raton, FL.

(6) Lee, H., Jang, I. H., Ryu, S. H., and Park, T. G. (2003) N-terminal site-specific mono-PEGylation of epidermal growth factor. *Pharm. Res. 20*, 818−825.

(7) O'Reilly, M. S., Boehm, T., Shing, Y., Fukai, N., Vasios, G., Lane, W. S., Flynn, E., Birkhead, J. R., Olsen, B. R., and Folkman, J. (1997) Endostatin: an endogenous inhibitor of angiogenesis and tumor growth. *Cell 88*, 277−285.

(8) Wen, W., Moses, M. A., Wiederschain, D., Arbiser, J. L., and Folkman, J. (1999) The generation of endostatin in mediated by elastase. *Cancer Res. 59*, 6052−6056.

(9) Hanahan, D., and Folkman, J. (1996) Patterns and emerging mechanisms of the angiogenic switch during tumorigenesis. *Cell 86*, 353−364.

(10) Boehm, T., Folkman, J., Browder, T., and O'Reilly, M. S. (1997) Antiangiogenic therapy of experimental cancer does not induce acquired drug resistance. *Nature 390*, 404−407.

(11) Herbst, R. S., Hess, K. R., Tran, H. T., Tseng, J. E., Mullani, N. A., Charnsangavej, C., Madden, T., Davis, D. W., McConkey, D. J., O'Reilly, M. S., Ellis, L. M., Pluda, J., Hong, W. K., and Abbruzzese, J. L. (2002) Phase I study of recombinant human endostatin in patients with advanced solid tumors. *J. Clin. Oncol. 20*, 3792−3803.

(12) Eder, J. P., Jr., Supko, J. G., Clark, J. W., Puchalski, T. A., Carbonero, R. G., Ryan, D. P., Shulman, L. N., Proper, J., Kirvan, M., Rattner, B., Connors, S., Keogan, M. T., Janicek, M. J., Fogler, W. E., Schnipper, L., Kinchla, N., Sidor, C., Phillips, E., Folkman, J., and Kufe, D. W. (2002) Phase I clinical trial of recombinant human endostatin administered as a short intravenous infusion repeated daily. *J. Clin. Oncol. 20*, 3772−3784.

(13) Rehman, S., and Jayson, G. C. (2005) Molecular imaging of antiangiogenic agents. *Oncologist 10*, 92−103.

(14) Sun, Y., Wang, J., Liu, Y., Song, X., Zhang, Y., Li, K., Zhu, Y., Zhou, Q., You, L., and Yao, C. (2005) Results of Phase III trial of EndostarTM (rh-endostatin, YH-16) in advanced nonsmall cell lung cancer (NSCLC) patients. *ASCO Annual Meeting Summaries*, No. 7138.

(15) Kulke, M., Bergsland, E., Ryan, D. P., Clark, J. W., Enzinger, P. C., Michelini, A., Kinsella, K., Fogler, W., Venook, A., and Fuchs, C. (2003) A phase II, open-label, safety, pharmacokinetic, and efficacy study of recombinant human endostatin in patients with advanced neuroendocrine tumors. *ASCO Annual Meeting Summaries*, No. 958.

BC050355D

Chitosan−Pentaglycine−Phenylboronic Acid Conjugate: A Potential Colon-Specific Platform for Calcitonin

Reem Smoum,[†,§] Abraham Rubinstein,*[,‡] and Morris Srebnik*[,†]

Department of Medicinal Chemistry and Natural Products, School of Pharmacy, Faculty of Medicine, The Hebrew University of Jerusalem, and Department of Pharmaceutics, School of Pharmacy, Faculty of Medicine, The Hebrew University of Jerusalem, Jerusalem, Israel. Received December 19, 2005; Revised Manuscript Received June 7, 2006

Novel drug delivery vehicles based on the biodegradable, mucoadhesive polysaccharide chitosan covalently linked to a boronic acid protease inhibitor have been prepared and characterized. It was anticipated that these conjugates could protect a proteinaceous drug, such as salmon calcitonin, against proteolysis by serine proteases, an obstacle that prevents its oral administration. Specifically, 4-formylphenylboronic acid was linked to chitosan. Three types of conjugates were prepared. In the first, 4-formylphenylboronic acid was directly linked to chitosan. The other two conjugates employed glycylglycine and pentaglycine spacers. Enzyme-inhibition assays toward trypsin and elastase, in the presence of the enzyme chitosanase, demonstrated a strong inhibitory effect for the chitosan−pentaglycine−phenylboronic acid conjugates, while no inhibitory effect could be detected without chitosanase. The chitosan−pentaglycine−phenylboronic acid conjugate with the highest degree of substitution of 4-formylphenylboronic acid was able to decrease the salmon calcitonin degradation rate by trypsin. It is concluded that chitosan−pentaglycine−phenylboronic acid conjugates are a potential multifunctional, colon-specific vehicle for orally administered salmon calcitonin.

INTRODUCTION

Oral administration of peptide and protein drugs is a challenge because of their large size, their susceptibility to luminal and brush border proteolysis, and their limited stability (*1*). Consequently, protein drugs exhibit poor oral bioavailability (*2*). To increase their availability into the body after oral administration, proteinaceous drugs require absorption enhancers, protease inhibitors, or both (*3*). In this context, the colon is an interesting organ in the gastrointestinal (GI) tract. In addition to its improved ability to respond to absorption enhancers (*4*), reports in the literature indicate that proteolysis occurs into a lesser extent in the human colon compared with the small intestine (*5*). It was, therefore, suggested that colon-specific drug carriers could facilitate the oral absorption of proteinaceous drugs. Still, even the relatively lower proteolytic activity of the colon requires that protein drugs should be protected due to the longer residence time in the this organ (*6*). If protection is successful, the prolonged residence time could turn out to be advantageous because the drug would be exposed for extended periods of time to the absorptive epithelium. An efficient drug carrier would be the one that would provide ongoing protection over time. One possible solution is the development of synchronous release polymeric drug platforms, which would release drugs and enzyme inhibitors in a concomitant manner (*7*). An attractive alternative to the synchronous release formulations is the one in which the protease inhibitor is covalently bound to the drug carrier. In a recent study, antipain, chymostatin, elastatinal, and Bowman−Birk inhibitors were each covalently attached, together with ethylenediamine tetraacetic acid (EDTA), to chitosan to guarantee the inactivation of the pancreatic serine proteases, membrane-bound Zn-dependent peptidases, and carboxypeptidase A and B (*8*).

Boronic acids form reversible covalent adducts with the active site of serine proteases. The tetrahedral geometry of boron coordination mimics the high-energy tetrahedral geometry on the reaction center carbon during the hydrolysis reaction (*9*). For this reason, boronic acid inhibitors are often considered to be transition state analogue inhibitors. Peptide boronic acid inhibitors are usually tri- or tetrapeptides with a boronic acid group in place of the C-terminal carboxylate (*10*). When the peptide composition is based on the substrate specificity of a particular protease, the inhibitor combines the favorable geometry of the adduct formed by the boron atom in the active site with the enzyme−substrate interactions of the peptide chain. In this context, we propose to design new drug delivery vehicles based on a biodegradable polysaccharide linked to a peptide boronic acid. It is anticipated that such compounds could avoid protein hydrolysis by serine proteases such as trypsin and chymotrypsin.

A variety of vehicles have been developed to allow colon-specific delivery of drugs (*11*). Special efforts have been dedicated in our group to fermentable polysaccharides (*12*). Chitosan, a natural polysaccharide, is made of *N*-acetyl-D-glucoamine and D-glucosamine and the *N*-acetyl-2-amino-2-deoxy-D-glucopyranose units linked by (1 → 4)-β-glycosidic bonds. In the past decade, it became popular as a drug delivery vehicle due to its biocompatibility, degradation properties, and ability to be conjugated with a variety of substrates via its amine groups (*13*). Tozaki and co-workers have identified its ability to degrade in the human colon and suggested it as a colon-specific vehicle (*14*).

We, therefore, hypothesized that if a protease inhibitor was conjugated to chitosan, a novel colon-specific platform could be produced for protein drugs. In this study, 4-formylphenylboronic acid was found to inhibit the α-chymotrypsin, trypsin, elastase, and leucine aminopeptidase, and thus was selected as

* To whom correspondence may be addressed. Morris Srebnik: mailng address POB 12065, 91120, Jerusalem, Israel; fax +972-2-675-8201; tel +972-2-675-7301; e-mail msrebni@md.huji.ac.il. Abraham Rubinstein: mailing address POB 12065, 91120, Jerusalem, Israel; fax +972-2-675-8201; tel +972-2-675-7301; e-mail avri@cc.huji.ac.il.

[†] Department of Medicinal Chemistry and Natural Products.

[§] E-mail: reems@md.huji.ac.il.

[‡] Department of Pharmaceutics.

10.1021/bc050357y CCC: $33.50 © 2006 American Chemical Society
Published on Web 06/29/2006

the protease inhibitor that could be covalently attached to chitosan. The protein drug chosen was salmon calcitonin (sCT). Calcitonin is a 32 amino acid polypeptide used in the treatment of postmenopausal osteoporosis and Paget's disease and in the management of hypercalcemia (*15*). The current mode of administration of commercial sCT is intranasally, a route that suffers from large variability in bioavailability (0.3−30%) (*16*). For this reason, it is appealing to administer it orally if the barrier of serine proteases is overcome.

The specific goals of the present study were to (a) conjugate phenylboronic acid to chitosan with and without spacers, (b) study, in vitro, the inhibition properties of the polysaccharide conjugates, and (c) assess the possible protective effect of the optimal polysaccharide inhibitor conjugate(s) toward a model protein drug, sCT.

EXPERIMENTAL PROCEDURES

Chitosan [DS = 85% glucosamine (GlcN), 15% *N*-acetylglucosamine (GlcNAc)], trypsin, α-chymotrypsin, elastase, *N*-benzoyl-arginine-*p*-nitroanilide, *N*-benzoyl-tyrosine-*p*-nitroanilide, *N*-succinyl-$(Ala)_3$-*p*-nitroanilide, L-leucine-*p*-nitroanilide, 1-ethyl-3,3-dimethylaminopropyl carbodimide (EDAC), and sodium borohydride ($NaBH_4$) were all purchased from Sigma-Aldrich. Salmon calcitonin (sCT) was obtained from CALBIOCHEM. Solvents from Biolab were purchased as analytical grade. HPLC-grade trifluoroacetic acid (TFA) and acetonitrile were obtained from Biolab. All solutions and buffers were prepared with deionized water. All other materials were of reagent grade. ^1H, ^{13}C, and ^{11}B NMR was recorded on a Varian 300 MHz instrument at frequencies of 300, 75.9, and 96.29 MHz, respectively. Shift values were reported with respect to TMS (^1H, ^{13}C) and $BF_3{\cdot}OEt_2$ (^{11}B). Infrared spectra were run for samples as KBr disks on a Bruker Vector 22 FT-IR spectrophotometer. Biological assays were performed on a $UVIKON_{xs}$-BIO-TEK instrument.

Synthesis and Purification of Chitosan−Phenylboronic Acid Conjugates. Chitosan (50 mg, 0.3 mmol of NH_2) was dissolved in 5 mL of 1% acetic acid, and the mixture was stirred for 1 h to obtain a 1% (m/v) solution. Various amounts of 4-formylphenylboronic acid (Table 1) dissolved in 3 mL of methanol were added to the solution, which was stirred at room temperature. After 1 h, sodium borohydride ($NaBH_4$) (1.5%) in 2 mL of methanol was added. The reaction mixture was then incubated for 24 h at room temperature under continuous stirring. The precipitate formed was filtered and washed with water and methanol thoroughly.

Selected data for **3** are as follows: ^1H NMR (1% CD_3COOD in D_2O) δ 1.899 (s, NHAc), 3.012 (br m, H-2 of GlcN), 3.591−3.748 (br m, H-2,3,4,5,6 of β-D-glucose (Glc)), 4.577 (br, $-NHCH_2Ph$), 4.726 (br, H-1 of β-D-Glc), 7.36 (br, H-2,6 of Ar), 7.705 (br, H-3,5 of Ar). FT-IR (KBr, cm^{-1}) 3359, 2876, 1654.95, 1610.48, 1560.75, 1411.74, 1376.74, 1261.59, 1070.44, 65.17.

N-Succinylation of the Chitosan−Phenylboronic Acid Conjugates. Chitosan−boronic acid conjugate (20 mg) was dissolved in 2 mL of 1% acetic acid, and then the solution was diluted with 2 mL of methanol. Succinic anhydride (6 equiv = 72 mg) was added to the diluted solution and stirred at room temperature (rt). After the mixture was stirred for 24 h, the pH of the mixture was adjusted to 5.0 with 5% w/v aq NaOH to give a precipitate. The precipitate was collected by filtration and dispersed in water. The pH of the dispersion was adjusted to 10−12 with 5% w/v aq NaOH to give a solution. The solution was dialyzed using dialysis membrane (molecular weight cut off, 12 000−14 000) at room temperature for 2−3 days and lyophilized.

Table 1. Preparation of Conjugates 3 with Aldehyde 2

entry	**2** (equiv)	DS[a]	recovery[b] (wt %, g/g)	solubility in H_2O	elemental analysis C	H	N
1	0.4	46.9	46.9	no	42.03	6.97	6.12
2	0.8	51.2	51.9	no	42.19	6.91	5.61
3	1.0	53.0	53.0	no	44.11	6.90	5.41
4	2.0	56.0	78.2	no	45.34	6.71	5.14
5	3.0	58.0	79.9	moderate	46.02	6.60	4.94

[a] DS (degree of substitution) was determined from the peak area of phenyl protons (δ 7.0−7.4) and H-2 of GlcN and N-alkylated GlcN residues (δ 3.2) and from elemental analysis. [b] Recovery (%) was obtained by dividing the obtained product weight by the weight of the chitosan: Recovery (%) = [wt of product (g)/wt of DAC 85%] × 100.

N-Succinyl-conjugated chitosan (DS = 32.5%). ^1H NMR (D_2O) δ 2.085 (s, $-NH(CO)CH_2$), 2.3 (br s, $-NH(CO)CH_2$ and $-CH_2COONa$), 3.602 (br m, H-2,3,4,5,6 of GlcN), 7.259 (br, H2,6 of Ar), 7.620 (br, H3,5) of Ar.

Synthesis of Glycylglycine−Phenylboronic Acid Conjugates. To a 10 mL solution of glycylglycine (2.645 g, 20 mmol) in water containing NaOH (0.405 g, 10 mmol), ethanol (10 mL) was added. Then, 4-formylphenylboronic acid (1.5 g, 10 mmol) dissolved in 2 mL of ethanol was added. The resulting solution was stirred at room temperature for 30 min and then cooled to ca. 2 °C. Sodium borohydride (0.460 g, 12 mmol) in ethanol (5 mL), containing a few drops of a 2 M NaOH solution was then slowly added, a colorless solution being obtained. A few drops of 3 M HCl were added till pH 4−5 was reached, and the mixture was left overnight with stirring. A white precipitate formed, was collected by filtration, and was washed with cold water and diethyl ether. To this white solid, water at ca. 40 °C was added; the mixture was stirred for a few minutes and left at ca. 4 °C for several hours. The solid was filtered, washed with water and diethyl ether, and dried. Yield: 52.60%. ^1H NMR (CD_3OD): δ 3.723 (2H, s, CH_2COOH), 3.796 (2H, s, CH_2NH), 4.172 (2H, s, CH_2-phenol), 7.448 (2H, d, CH aromatic), 7.758 (2H, d, CH aromatic). ^{13}C NMR (CD_3OD) 42.775, 51.110, 128.761, 132.240, 133.642, 134.341, 166.028, 174.462. ^{11}B NMR 30.791. Anal. ($C_{11}H_{15}BN_2O_5$) C, H, N.

Synthesis of Pentaglycine−Phenylboronic Acid Conjugates. The procedure was similar to that of glycylglycine−phenylboronic acid. Yield: 64.46%. ^1H NMR (DMSO): δ 3.099 (2H, s, CH_2COOH), 3.674 (2H, s, CH_2NH), 3.713 (2H, s, CH_2NH), 3.750 (2H, s, CH_2NH), 3.768 (2H, s, CH_2NH), 4.439 (2H, s, CH_2-phenol), 7.284 (2H, d, CH aromatic), 7.707 (2H, d, CH aromatic). ^{13}C NMR (DMSO) 41.894, 42.509, 42.737, 45.010, 51.717, 53.144, 127.892, 134.746, 142.037, 166.795, 169.501, 169.790, 169.968, 171.733, 172.044. ^{11}B NMR 30.791. Anal. ($C_{17}H_{24}BN_5O_8$) C, H, N.

Synthesis and Purification of Chitosan−Spacer−Phenylboronic Acid Conjugates (Spacer = Glycylglycine or Pentaglycine). The covalent attachment of the spacer−phenylboronic acid conjugates to chitosan was achieved by the formation of amide bonds between amino groups of the polymer and the terminally located carboxylic acid group of the spacer−phenylboronic acid inhibitor. The general procedure was as follows: Chitosan (50 mg, 0.3 mmol NH_2) was dissolved in 5 mL of 1% acetic acid solution, and the mixture was stirred for 1 h to obtain a 1% (m/v) solution. Increasing amounts of spacer−phenylboronic acid conjugate (glycylglycine−phenylboronic acid in 3 mL of methanol or pentaglycine−phenylboronic acid in 2 mL of H_2O) were added to the solution, which was stirred at room temperature. After 1 h, 1-ethyl-3,3-dimethylaminopropyl carbodimide (EDAC) (1:1 mole ratio of EDAC/glycylglycine−phenylboronic acid; 2:1 mole ratio of EDAC/pentaglycine−phenylboronic acid) in 2 mL of methanol was added to mediate the formation of amide bonds between the amino groups of chitosan and the carboxyl groups of the

spacer−phenylboronic acid conjugate. The reaction mixture was then incubated for 24 h at room temperature under continuous stirring. The resulting polymer conjugate was isolated by exhaustive dialysis against deionized water for 2 days. Then the methanol was evaporated, and the purified product was lyophilized. The yellow solid (film) obtained was stored at room temperature until use. ^{1}H NMR (D_2O) for chitosan−glycyl-glycine−phenylboronic acid conjugates δ 2.924 (H, br m, H_2 of GlcN), 3.587 (10H, br m, H-2,3,4,5,6 of β-D-glucose (Glc), CH_2COOH and CH_2NH), 4.172 (2H, s, CH_2-phenol), 7.104 (2H, br m, CH-aromatic), 7.546 (2H, br m, CH-aromatic). FT-IR (KBr, cm^{-1}) 3421.15, 2926.78, 1653.77, 1637.15, 1560.03, 1409.70, 1377.45, 1316.99, 1259.65, 1154.28, 1073.13, 898.09, 653.53).

Synthesis and Purification of Chitosan−Pentaglycine−Phenylboronic Acid Conjugates. The procedure for the synthesis and purification of chitosan−pentaglycine−phenylboronic acid conjugates is similar to that of the chitosan−spacer−phenylboronic acid conjugates. ^{1}H NMR (D_2O) for chitosan−pentaglycine−phenylboronic acid conjugates δ 1.877 (s, NHAc), 2.669 (H, br m, H_2 of GlcN), 3.324 (6H, br m, H-2,3,4,5,6 of β-D-glucose (Glc)), 3.481 (H, s, CH_2CONH), 3.594 (2H, s, CH_2NH), 3.953 (2H, s, CH_2NH), 4.058 (2H, s, CH_2-phenol), 7.163 (2H, br s, CH-aromatic), 7.595 (2H, br s, CH-aromatic).

Determination of the Degree of Modification. ^{1}H NMR spectroscopy and elemental analysis were used to quantify the amount of phenylboronic acids, glycylglycine−phenylboronic acids and pentaglycine−phenylboronic acids conjugated to chitosan.

In Vitro Evaluation of the Protective Effect of 4-Formylphenylboronic Acid, Glycylglycine−Phenylboronic Acid, and Pentaglycine−Phenylboronic Acid Conjugates toward Serine Proteases and Leucine Aminopeptidase. α-Chymotrypsin, type II (EC 3.4.21.1) from bovine pancreas, was purchased from Sigma (MW 25 000). The inhibitors were tested by competitive assay against benzoyl-tyrosine-*p*-nitroanilide as a substrate. The hydrolytic reaction was carried out at 37 °C at pH = 7.00 with 50 mM Tris buffer and 0.02 M $CaCl_2$. Inhibitor stock solutions in DMSO/H_2O (1:10) were prepared with concentrations ranging from 6.02 to 0.0602 mM. A stock enzyme solution of 0.2 mg/mL was made in 1 mM HCl solution. A series of substrate concentrations (dissolved in 36.6% DMSO and 63.4% methanol) ranging from 0.043 to 0.43 mM was prepared. The assay was performed by adding 700 μL of Tris buffer to a 1.5 mL Epindorph tube followed by 100 μL of inhibitor and 100 μL of enzyme, and these were incubated for 10 min at 37 °C. Then 100 μL of substrate was added to the reaction followed by incubation for 20 min at 37 °C. The reaction was stopped by adding 200 μL of 30% acetic acid solution. The progress of the reaction was followed by monitoring the appearance of the absorption band of *p*-nitroaniline at 410 nm. K_i values for reversible competitive inhibitors were estimated by the method of Lineweaver and Burk. Data were fitted to the best straight line by the least-squares procedure.

Trypsin, type II-S (EC 3.4.21.4) from porcine pancreas, was purchased from Sigma. The inhibition constants were determined exactly as was done for chymotrypsin except that the substrate was benzoyl-arginine-*p*-nitroanilide dissolved in DMF.

Elastase, type II-A (EC 3.4.21.36) from porcine pancreas, was purchased from Sigma. The hydrolytic reaction was carried out at 37 °C, standard pH 7.5, with 50 mM phosphate buffer, 0.2 M NaCl, and the progress of the reaction was followed by monitoring the appearance of the absorption band of *p*-nitroaniline at 410 nm (substrate = *N*-succinyl-$(Ala)_3$-*p*-nitroanilide).

Leucine aminopeptidase, type VI (EC 3.4.11.2) from porcine kidney microsomes, was purchased from Sigma. The hydrolytic reaction was carried out at 37 °C, standard pH 7.5, with 50 mM phosphate buffer, 0.02 M $CaCl_2$, 10 vol % DMF, and the progress of the reaction was followed by monitoring the appearance of the absorption band of *p*-nitroaniline at 410 nm (substrate = L-leucine-*p*-nitroanilide).

In Vitro Evaluation of the Protective Effect of the Succinylated Chitosan−Phenylboronic Acid, Chitosan−Glycylglycine−Phenylboronic Acid, and Chitosan−Pentaglycine−Phenylboronic Acid Conjugates toward Serine Proteases and Leucine Aminopeptidase. One to ten milligrams of the polymer−inhibitor conjugates was hydrated in 1 mL of 80 mM TBS buffer (Tris-HCl buffered saline), pH 6.8. Thereafter, trypsin (28.4 units), chymotrypsin (1 unit), elastase (0.4 units/mL), or leucine aminopeptidase (0.12 units/mL) dissolved in 100 μL of 80 mM TBS, pH 6.8, was added, and the mixture incubated for 1 h at room temperature. After addition of the corresponding substrates, each dissolved in a certain solvent as mentioned above, the reaction mixture was incubated for 20 min. The reaction mixture was stopped by adding 200 μL of 30% acetic acid solution. The absorbance (410 nM) caused by the formation of *p*-nitroanilide was recorded.

In Vitro Evaluation of the Protective Effect of the Succinylated Chitosan−Phenylboronic Acid, Chitosan−Glycylglycine−Phenylboronic Acid, and Chitosan−Pentaglycine−Phenylboronic Acid Conjugates toward Trypsin, Elastase, and Chymotrypsin in the presence of Chitosanase. The inhibitory activity of succinylated chitosan−phenylboronic acid, chitosan−glycylglycine−phenylboronic acid, and chitosan−pentaglycine−phenylboronic acid conjugates toward trypsin, elastase, and chymotrypsin was determined by the following enzyme assays. One milligram of the polymer conjugate was hydrated in 975 μL of 50 mM acetate buffer (pH 5.5). The solution was incubated for 5 min at 37 °C. Then, 50 μL of a chitosanase solution (chitosan *N*-acetylglucosaminohydrolase; EC 3.2.1.132 from *Streptomyces* species, 0.1 units dissolved in 55 mM acetate buffer, pH 5.5) was added, and the mixture was incubated for 1 h at 37 °C. Thereafter, 100 μL of the enzyme solution (trypsin (8.88 units/mL), elastase (0.4 units/mL), or chymotrypsin (156 units/mL)) in 50 mM acetate buffer, pH 5.5, was added, and the mixture was incubated at room temperature for 30 min. Following incubation, 100 μL (0.1 M solution) of the substrate (benzoyl-arginine-*p*-nitroanilide in DMF for trypsin, *N*-succinyl-Ala-Ala-Ala-*p*-nitroanilide in 20% DMF/H_2O for elastase, or benzoyl-tyrosin-*p*-nitroanilide in methanol/DMSO for chymotrypsin) was added, and the enzymatic reaction was allowed to proceed at room temperature for 40 min for trypsin and 20 min for both elastase and chymotrypsin. The enzymatic activity was stopped by adding 200 μL of 30% acetic acid solution. The progress of the reaction was followed by monitoring the appearance of the absorption band of *p*-nitroaniline at 405 nm. The controls used were the buffer and the unmodified chitosan.

Evaluation of the Protective Effect for Calcitonin. Salmon calcitonin solutions were freshly prepared prior to experiments conducted at a concentration of 1 mg/mL.

Three milligrams of succinylated chitosan−phenylboronic acid, chitosan−glycylglycine−phenylboronic acid, and chitosan−pentaglycine−phenylboronic acid conjugates were each dissolved in 950 μL of 50 mM acetate buffer, pH 5.5. Each solution was incubated for 5 min at 37 °C. Then, 50 μL of a chitosanase solution was added, and the solution was incubated for 1 h at 37 °C. Thereafter, 100 μL of a calcitonin solution (2 mg of salmon calcitonin dissolved in 100 μL of 50 mM acetate buffer, pH 5.5) was added, and the solution was incubated at room temperature for 20 min. Following this, 100 μL of the same buffer but containing trypsin (8.88 mg/mL) was added. Immediately after the addition of the enzyme solution, aliquots

Scheme 1[a]

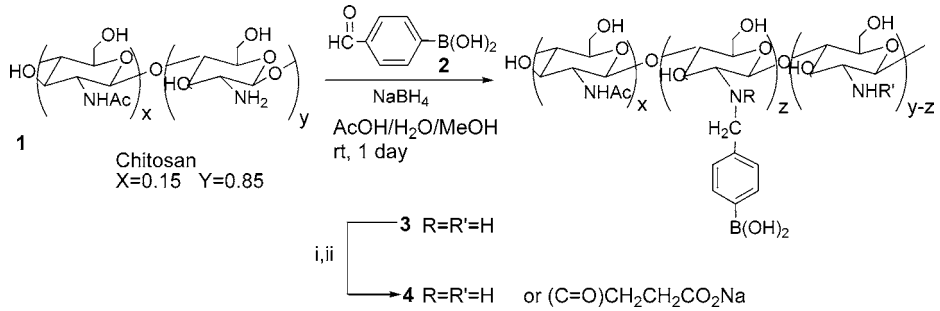

[a] Reagents and conditions: (i) succinic anhydride, AcOH, H_2O, MeOH; (ii) 1% aq NaOH, room temp, 2 h.

of 60 μL were withdrawn and diluted with the same volume of 1% trifluoroacetic acid (TFA) used as stop solution to avoid any enzymatic degradation of the peptide. These first samples were used as reference values (time point zero). After that, aliquots of 60 μL were withdrawn at 1, 5, 10, 20, 30, and 60 min, and the enzymatic degradation was terminated as described above. All samples were centrifuged to remove any remaining polymer contents. For determining the remaining undigested calcitonin, 20 μL of the supernatant fluid was directly injected for HPLC analysis. Samples prepared in the same way but without adding chitosanase were used as controls. In addition, samples prepared in the same way but containing 3 mg of unmodified chitosan instead of chitosan−inhibitor conjugates served as controls.

HPLC Analytical Method. Salmon calcitonin (sCT) was analyzed by means of a validated HPLC method. HPLC Computer Controlled Waters Chromatography workstation with the following components was used: control 600, water pump 600, detector 996 photodiode array, and Millenium[32] chromatography software. Room temperature was maintained for the column, and chromatographic separations were performed on a Waters RP Symmetry C18 4.6 mm × 250 mm column. Twenty microliters of sample was injected into the column, and samples were analyzed by a reversed phase HPLC method. The mobile phase consisted of 0.1% v/v TFA/water (A) and 0.1% v/v TFA/acetonitrile (B). The gradient conditions were 20−35% B for 10 min, 35−37% B from 10 to 20 min, and 37−20% B from 20 to 25 min at a flow rate of 1 mL/min. The detection was achieved at a wavelength of 210 nm. Concentrations of sCT were quantified from integrated peak areas and calculated by interpolation from the standard curve.

RESULTS

Synthesis and Structural Analysis of Succinylated Chitosan−Phenylboronic Acid Conjugates. New chitosan derivatives were synthesized by direct reductive N-alkylation of chitosan with 4-formylphenylboronic acid, **2**. Scheme 1 shows the preparation of chitosan−phenylboronic acid conjugates **3** by reductive N-alkylation using sodium borohydride ($NaBH_4$). The degree of N-substitution could be controlled by increasing the amount of the aldehyde **2** in the reaction mixture (Table 1). The reactivity of **2** was found to vary in the range of 47−80%, which was caused by the simultaneous reduction of some of the aldehyde groups of **2** under the acidic conditions. The degree of N-substitution was calculated from the ratio of C% to N% in elemental analysis (*17*). In the FTIR spectra of chitosan and chitosan derivatives, the characteristic peaks of the amine NH vibration deformation appeared at 1595 cm^{-1} for chitosan, whereas it disappears in chitosan derivatives caused by the formation of $NH-CH_2$ band at C-2 in chitosan and a new peak at a higher wavelength (1611.31 cm^{-1}) due to C−C stretches in the aromatic ring. Characteristic absorption bands of para-substituted benzene appeared at 650.47, 816.05, 1515.33, 1560.80, and 1611.31.

Table 2. Chemical Structures of the Succinylated Conjugates 4

	functional group (DS)			
conjugates	−boronic compd[a]	−Suc[b]	$-NH_2$[c]	−NHAc[d]
1	0.469	0.34	0.041	0.15
2	0.512	0.32	0.018	0.15
3	0.530	0.32	0.000	0.15
4	0.560	0.32	0.000	0.15
5	0.580	0.32	0.000	0.15

[a] DS (degree of substitution) of phenylboronic acid residues. [b] DS of succinate residues. [c] Free amine residues. [d] Free acetylated amine residues.

Water-soluble material was only obtained moderately at high degree of substitution (DS = 79.9%). However, the other chitosan−boronic acid conjugates **3** were insoluble in neutral water and thus would not be useful for biological evaluation. To improve the solubility, the remaining amino groups of the conjugates **3** were transformed by succinylation with succinic anhydride to give conjugates **4** in 90−100% yields. The chemical structures of the succinylated conjugates **4** are summarized in Table 2. The degree of substitution for most compounds was between 32% and 34%. Despite using a large excess of succinic anhydride, some unreactive amino groups still remained in several conjugates. High-field ^1H NMR spectra also indicated that no succinylation had occurred at the N-glycosylation sites (δ H-1 of GclN−Neu5Ac). All succinylated products **4** were soluble in water.

Synthesis and Structural Analysis of the Chitosan−Spacer−Phenylboronic Acid Conjugates (Spacer = Glycylglycine or Pentaglycine). As shown in Scheme 2, 4-formylphenylboronic acid was attached to the spacer, glycylglycine or pentaglycine, by reductive N-alkylation using sodium borohydride ($NaBH_4$). The resulting spacer−phenylboronic acid conjugates were covalently coupled to the amino group of chitosan using EDAC, a water-soluble carbodiimide, Scheme 3. Two sets of conjugates were prepared (Figures 1 and 2); each consisted of different amounts of conjugated glycylglycine/pentaglycine−phenylboronic acids (Tables 3 and 4). The degree of N-substitution was determined by ^1H NMR and elemental analysis. As can be seen, there was a good correlation between the data obtained by the two methods. Conjugation was confirmed by the existence of an amide band at 1653.77 cm^{-1} from the FTIR spectrum of chitosan derivatives. The characteristic peaks of amine NH vibration deformation at 1595 cm^{-1} found in chitosan disappeared in the chitosan derivatives. Characteristic absorption bands of para-substituted benzene ring appeared at 653.53, 898.09, and 1560.03. All the conjugates prepared were soluble in water.

The inhibitory efficacy of the 4-formylphenylboronic acid, glycylglycine−phenylboronic acid, and pentaglycine−phenylboronic acid as well as their corresponding chitosan conjugates (succinylated chitosan−phenylboronic acid, chitosan−glycyl-

Scheme 2. Preparation of the Spacer−Boronic Acid Conjugates

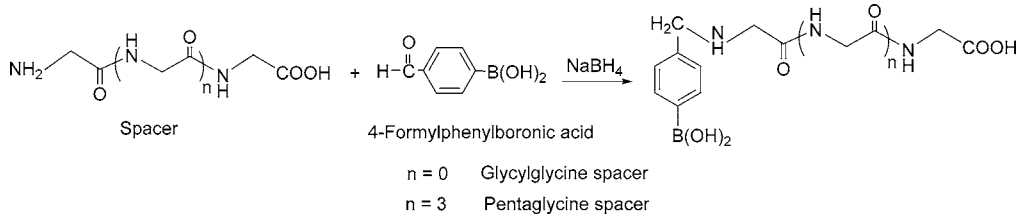

Scheme 3. Preparation of the Chitosan−Spacer−Boronic Acid Conjugates

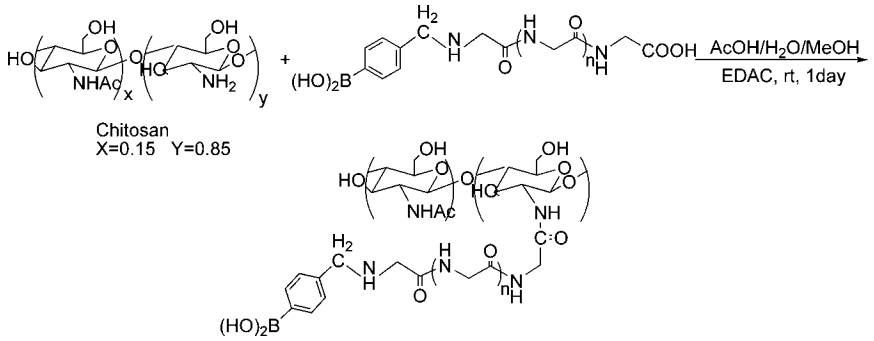

Table 3. Preparation of Chitosan−Glycylglycine−Phenylboronic Acid Conjugates

entry	conjugate	DS[a]	recovery[b] (wt %, g/g)	solubility in H_2O	elemental analysis C	H	N
1	0.2	23.18	80.8	moderate	40.61	6.63	6.75
2	0.4	25.70	78.6	yes	39.24	6.69	6.61
3	0.6	28.17	79.3	yes	40.14	6.76	6.48
4	0.8	29.73	76.2	yes	40.03	6.73	6.40
5	1.0	30.50	76.5	yes	39.29	6.71	6.36

[a] DS was determined from the peak area of phenyl protons (δ 7.0−7.4) and H-2 of GlcN and N-alkylated GlcN residues (δ 3.2) and from elemental analysis. [b] Recovery (%) was obtained by dividing the obtained product weight by the weight of the chitosan: Recovery (%) = [wt of product (g)/ wt of DAC 85%] × 100.

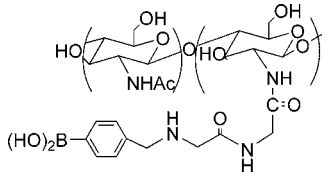

Figure 1. Structure of chitosan−glycylglycine−phenylboronic acid conjugate.

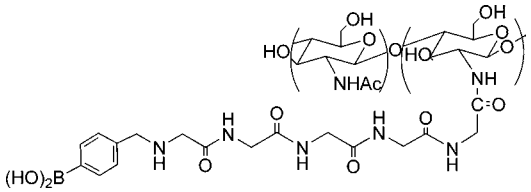

Figure 2. Structure of chitosan−pentaglycine−phenylboronic acid conjugate.

glycine−phenylboronic acid, and chitosan−pentaglycine−phenylboronic acid) toward serine proteases and leucine aminopeptidase was determined. In addition, the protective effect of these conjugates for salmon calcitonin toward the luminally secreted serine protease trypsin was evaluated.

Enzyme Inhibition Studies. Enzyme inhibition studies were carried out with trypsin, α-chymotrypsin, elastase, and leucine aminopeptidase N.

Inhibitory Efficacy of 4-Formylphenylboronic Acid, Glycylglycine−Phenylboronic Acid, and Pentaglycine−Phenylboronic Acid Conjugates. 4-Formylphenylboronic acid was chosen to be conjugated to chitosan because it is a simple molecule with an aldehyde group that can be conjugated to the amino group of the chitosan by reductive N-alkylation. This compound was checked for its ability to inhibit the serine proteases and leucine aminopeptidase. It was found that 4-formylphenylboronic acid is capable of inhibiting trypsin, chymotrypsin, elastase, and leucine aminopeptidase in a moderate range (Table 5).

Table 4. Preparation of Chitosan−Pentaglycine−Phenylboronic Acid Conjugate

entry	conjugate	DS[a]	recovery[b] (wt %, g/g)	solubility in H_2O	elemental analysis C	H	N
1	0.4	26.06	72.8%	yes	40.53	6.64	9.42
2	0.6	28.20	76.4%	yes	40.58	6.52	9.43
3	0.8	29.00	72.7%	yes	40.38	6.48	9.48
4	1.0	43.75	78.6%	yes	40.69	6.33	10.46

[a] DS was determined from the peak area of phenyl protons (δ 7.0−7.4) and H-2 of GlcN and N-alkylated GlcN residues (δ 3.2) and from elemental analysis. [b] Recovery (%) was obtained by dividing the obtained product weight by the weight of the chitosan: Recovery (%) = [wt of product (g)/ wt of DAC 85%] × 100.

Table 5. Inhibition Constants (K_i in mM) for the 4-Formylphenylboronic Acid, Glycylglycine−Phenylboronic Acid, and Pentaglycine−Phenylboronic Acid as Measured with Chymotrypsin, Trypsin, Elastase, and Leucine Aminopeptidase

compound	chymotrypsin	trypsin	elastase	leucine aminopeptidase
4-formylphenylboronic acid	0.4	0.8	0.6	4
glycylglycine−phenylboronic acid	6	3	2	>10
pentaglycine−phenylboronic acid	5	3	3	8

4-Formylphenylboronic acid was then attached to two spacers, glycylglycine and pentaglycine. The influence of the spacers on the inhibition ability of 4-formylphenylboronic acid was checked. It was found that both the glycylglycine−phenylboronic acid and pentaglycine−phenylboronic acid were still able to inhibit trypsin, chymotrypsin, elastase, and leucine aminopeptidase (Table 5). However, the activities of these conjugates were an order of magnitude less than the original 4-formylphenylboronic acid.

Inhibitory Efficacy of Chitosan−Phenylboronic Acid Conjugates with and without Spacers. The chitosan−phenylboronic acid conjugates without any spacer were not soluble in water, DMSO, or methanol; however, they were soluble in 1% acetic

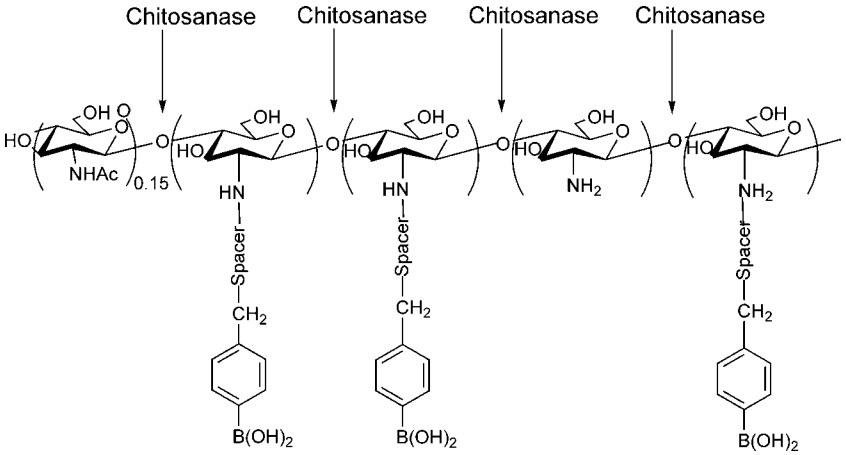

Figure 3. The assumed cleavage of chitosan−spacer−phenylboronic acid conjugate by the chitosanase enzyme (spacer = none, glycylglycine, or pentaglycine).

acid/H_2O. On the other hand, their succinylated derivatives were soluble in water, and therefore, they were used for biological evaluation. All the succinylated conjugates with different degrees of substitutions (Table 2) were checked for protease inhibition against the serine proteases trypsin, chymotrypsin, and elastase at concentrations up to 10 mg/mL. All conjugates with different degrees of substitution did not inhibit the serine proteases at any concentration.

In addition, the chitosan−glycylglycine−phenylboronic acid and the chitosan−pentaglycine−phenylboronic acid conjugates at all degrees of substitutions and at concentrations up to 10 mg/mL were tested for their ability to inhibit serine proteases. In the same manner, all these conjugates were not capable of inhibiting the enzymes.

Inhibitory Efficacy of Chitosan Conjugates with and without Spacers in the Presence of Chitosanase: A Proof of Concept. All the chitosan conjugates that contained phenylboronic acid without and with spacers did not inhibit the serine proteases. This may be because the conjugates were so bulky that the phenylboronic acid compound was not accessible to the active site of the enzyme even with the use of short and long spacers.

As mentioned before, chitosan is hydrolyzed by bacterial glycosidases in the colon (*14*). For the conjugated polymers prepared in this paper, this hydrolysis would allow the release of monomers, dimers, and oligomers of chitosan that are conjugated to 4-formylphenylboronic acid with or without spacers. These smaller conjugates may inhibit in turn the serine proteases and leucine aminopeptidase.

Therefore, this led to the idea of using an enzyme that would be able to hydrolyze the polymer conjugate into monomers, dimers, and oligomers similarly as would the bacterial enzymes in the colon. In this context, the enzyme chitosanase was chosen. Chitosanase is responsible for the endohydrolysis of β-1,4-linkages between GlcNAc−GlcN and GlcN−GlcN bonds in a partly acetylated chitosan (*18*) (Figure 3). Chitosanase is used as a model for glycosidases that can hydrolyze chitosan in the colon. The polymers were incubated with chitosanase for 1 h, a time that was calibrated for the complete hydrolysis of chitosan into monomers, dimers, and oligomers. This was followed by the addition of the required enzyme (trypsin, chymotrypsin, elastase, or leucine aminopeptidase) and incubation of the mixture for another 1 h, after which the substrate was added.

The results showed that only the conjugates with the pentaglycine spacer were able to inhibit trypsin and elastase, Figure 4. In these experiments, the buffer and the unmodified chitosan were used as controls. The inhibition increases with increasing the degree of substitution of the polymer conjugate. The polymer conjugate with the highest degree of substitution

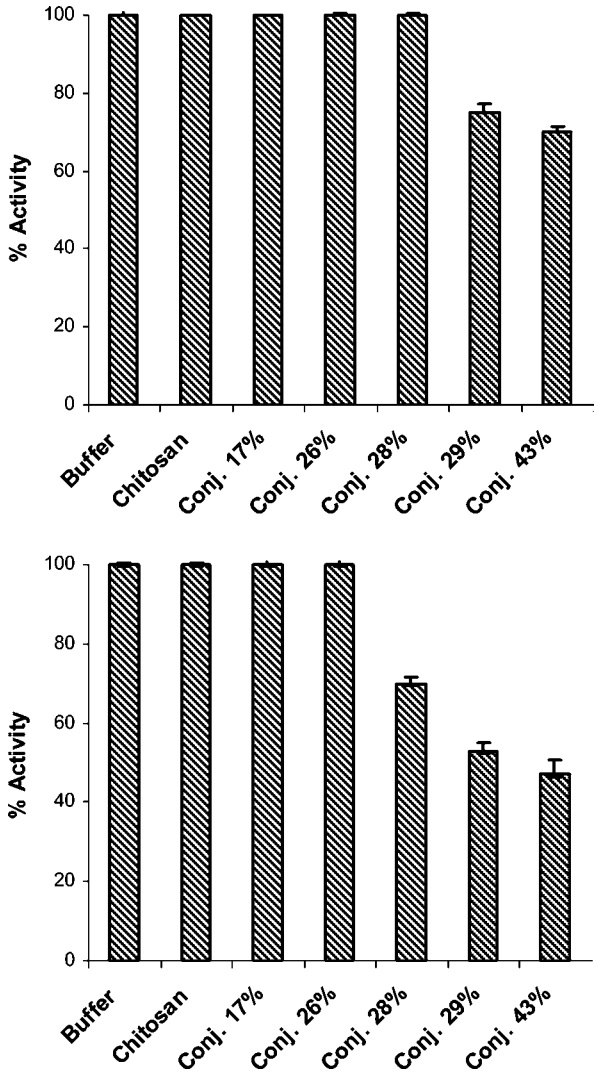

Figure 4. Effect of the buffer, chitosan, and the chitosan−pentaglycine−boronic acid conjugates with different degrees of substitutions on the relative activity of elastase (top) and trypsin (bottom).

(43%) demonstrated a strong inhibitory activity toward trypsin resulting in a significant decrease in the degradation of the trypsin substrate *N*-α-benzoyl-L-arginine-*p*-nitroanilide. After 40 min of enzymatic reaction, only 50% of the substrate was digested in the presence of 1 mg of chitosan conjugate, whereas at this reference point, 100% of the substrate was degraded in the presence of the same concentration of unmodified chitosan.

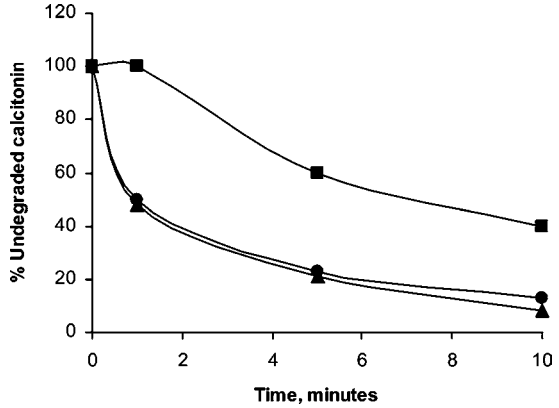

Figure 5. The degradation of sCT in the presence of chitosanase and (▲) 1 mg of chitosan$(Gly)_5B(OH)_2$ or (■) 3 mg of chitosan$(Gly)_5B(OH)_2$ or (●) 3 mg of chitosan$(Gly)_5B(OH)_2$ without chitosanase (control). Shown are the mean of 2 different measurements.

Also, elastase was inhibited by the same conjugate, but the effect displayed by the decrease in the degradation of the substrate succinyl-$(alanyl)_3$-*p*-nitroanalide was not as pronounced as in the case of trypsin.

The chitosan−spacer−phenylboronic acid conjugates were also evaluated with regard to their inhibitory activity toward α-chymotrypsin and leucine aminopeptidase in the presence of chitosanase, but no significant inhibition of the enzymes was observed.

Protective Effect toward Calcitonin. The chitosan−pentaglycine−phenylboronic acid conjugate with the highest degree of substitution (DS = 43%), which inhibited 50% of trypsin and 30% of elastase at 1 mg/ml concentration, was evaluated for a protective effect on the enzymatic degradation of calcitonin. After 10 min incubation with the proteases, only 8.4% of undegraded salmon calcitonin remained in a solution of chitosan−pentaglycine−boronic acid conjugate without the use of the chitosanase. With the use of chitosanase, only 13% undegraded salmon calcitonin remained in the presence of 1 mg of chitosan−pentaglycine−boronic acid. But by increasing the amount of the conjugate to 3 mg in the presence of chitosanase, 40% of undegraded calcitonin remained (Figure 5).

DISCUSSION

In the present study, novel boronated chitosan conjugates were prepared and tested for their ability to potentially serve as oral delivery systems of calcitonin.

Chitosan was selected due to its mucoadhesive properties (*19*), as well as strong permeation enhancing capabilities for protein drugs (*20*). It was shown that its mucoadhessiveness was maintained even after conjugation with enzyme inhibitors (*21*), allowing it to function in close proximity to the intestinal wall, while providing a continuous protection to its protein drug cargo. The combined use of mucoadhesive polymers and enzyme inhibitors could be interesting (*22*). However, there is always a risk of losing the protease inhibitor along the journey in the lumen of the gut. This can be resolved by their covalent attachment to polymeric drug carrier matrices, allowing them safety as long as the platform retains its integrity. Chitosan derivatives exhibiting a better solubility, stronger mucoadhesive capabilities, and enzyme inhibitory properties toward luminal secreted proteases and brush border membrane bound peptidases could be generated. These unique features make chitosan and in particular its derivatives an interesting excipient for the preoral administration of peptide drug (*23*).

4-Formylphenylboronic acid was found to be a moderate inhibitor of serine proteases. It was conjugated through its aldehydic group to chitosan by reductive N-alkylation. N-Succinylation of the prepared conjugates gave water-soluble succinylated chitosan−phenylboronic acid conjugates. In our study, succinylated conjugates were unable to inhibit serine proteases and leucine peptidase, probably due to the bulkiness of the polymer conjugate, so the inhibitor 4-formylphenylboronic acid was not accessible enough to the protease to inhibit it, even with the high degree of N-substitution. However, Bernkop-Schnürch and co-workers synthesized a series of mucoadhesive polymers that displayed strong protective effects toward all pancreatic proteases (*24*). In their study, the serine protease inhibitors antipain, chymostatin, and elastatinal were covalently linked to chitosan together with EDTA. These polymer conjugates showed a strong inhibitory activity toward trypsin, chymotrypsin, elastase, carboxypeptidases A and B, and aminopeptidase N.

To increase the accessibility of the 4-formylphenylboronic acid to the enzyme, we suggested using spacers. Two kinds of spacers were chosen, glycylglycine and pentaglycine spacers. The 4-formylphenylboronic acid−spacer conjugates inhibited serine proteases and leucine aminopeptidase moderately. However, after conjugating the spacer−phenylboronic acids to chitosan, no inhibition for the resulting polymer conjugates could be detected. The use of the longer pentaglycine spacer was thought to improve the inhibitory effect. Yet, inhibition studies revealed opposite results. Indeed, the inhibitory activity of chitosan−EDTA−ACE (ACE = antipain, chymostatin, elastatinal) conjugate toward elastase was markedly weaker than that of poly(acrylate) derivative−elastatinal conjugates and carboxymethylcellulose−elastatinal conjugates (*25*). A reason for the comparably stronger inhibitory effect of these already established polymer conjugates can be seen in the additional use of a spacer, providing an easy accessibility of the immobilized inhibitor for the corresponding protease. Moreover, Marschütz and co-workers reported recently that the use of a small rigid C4 spacer was highly advantageous compared to a long and more flexible poly(ethylene glycol) spacer (*26*). In our study, neither the short nor the long spacers had any effect on increasing the accessibility of the boronic acid to the active site of the protease.

To mimic the colonic enzyme cleavage of chitosan, chitosanase was used in our study. This enzyme is responsible for the endohydrolysis of β-1,4-linkages between GlcNAc−GlcN and GlcN−GlcN bonds in a partly acetylated chitosan (*18*). Surprisingly, it was observed in our study that only in the presence of chitosanase were the pentaglycine derivatives of the conjugates active in a ratio-dependent manner. At a concentration of 1 mg/mL of the chitosan−pentaglycine−phenylboronic acid conjugate with a 43% degree of substitution, 50% inhibition for trypsin and 30% inhibition for elastase were observed. We concluded that the chitosanase used in our study hydrolyzed the chitosan conjugates into monomers, dimers, and oligomers containing conjugated pentaglycine−phenylboronic acids. The higher the relative amount of pentaglycine−phenylboronic acid in the polymer, the more the degradation products, the monomers, dimers, and oligomers, were obtained. This observation supports the assumption that the polymer bulkiness was the reason for the interference with its enzyme inhibition capability.

The luminally secreted serine proteases seem to be the major cause for the digestion of salmon calcitonin (sCT). It has been shown that sCT is degraded by trypsin, α-chymotrypsin (*27*), and elastase (*28*). Although many attempts have been undertaken, the development of a commercially applicable oral delivery system for this peptide has failed so far (*3*). The use of mucoadhesive polymers is believed to provide a prolonged residence time of the drug at the absorption site, leading to an

improved bioavailability (*29*). To ascertain a protection within the polymeric carrier matrix (*28*), chitosan−enzyme inhibitor conjugates were added. Similar to the results obtained with thiolated polymers (*30*), our study showed that the conjugate with the highest degree of substitution (43%) was able to reduce the digestion of sCT by trypsin only in the presence of the chitosanase enzyme. Therefore, these conjugates seem to be promising agents in protecting sCT from intestinal pancreatic serine proteases. This study provides a proof of concept for further research aimed at identifying potent boron-based protease inhibitors.

ACKNOWLEDGMENT

The study was supported by a research grant from the Israeli Science Foundation, Grant 663/ 99-2, and a Scholarship grant (R.S.) from the Ministry of Science and Technology. Morris Srebnik and Abraham Rubinstein are affiliated with the David R. Bloom Center of Pharmacy.

LITERATURE CITED

(1) Bai, J. P., Chang, L. L., and Guo, J. H. (1995) Targeting of peptide and protein drugs to specific sites in the oral route. *Crit. Rev. Ther. Drug Carrier Syst. 12*, 339−371.

(2) Lee, H. J. (2002) Protein drug oral delivery: the recent progress. *Arch. Pharm. Res. 25*, 572−584.

(3) Shah, R. B., Ahsan, F., and Khan, M. A. (2002) Oral delivery of proteins: progress and prognostication. *Crit. Rev. Ther. Drug Carrier Syst. 19*, 135−169.

(4) Sintov, A., Simberg, M., and Rubinstein, A. (1996) Absorption enhancement of captopril in the rat colon as a putative method for captopril delivery by extended release formulations. *Int. J. Pharm. 143*, 101−106.

(5) Haupt, S., and Rubinstein A. (2002) The colon as a possible target for orally administered peptide and protein drugs. *Crit. Rev. Ther. Drug Carrier Syst. 19*, 499−545.

(6) Phillips, S. F., Pemberton, J. H., and Shorter, R. G. (1991) *The Large Intestine: Physiology, Pathophysiology, and Disease*, Raven Press, New York.

(7) Baluom, M., Friedman, M., and Rubinstein, A. (1998) The importance of intestinal residence time of absorption enhancer on drug absorption and implication on formulative considerations. *Int. J. Pharm. 176*, 21−30.

(8) Bernkop-Schnürch, A., and Kast, C. E. (2001) Chemically modified chitosans as enzyme inhibitors. *Adv. Drug Delivery Rev. 52*, 127−137.

(9) Matthews, D. A., Alden, R. A., Birktoft, J. J, Freer, S. T., and Kraut, J. (1975) X-ray crystallographic study of boronic acid adducts with subtilisin BPN′ (Novo). A model for the catalytic transition state. *J. Biol. Chem. 250*, 7120−7126.

(10) Kettner, C. A., and Shenvi, A. B. (1984) Inhibition of the serine proteases leukocyte elastase, pancreatic elastase, cathepsin G, and chymotrypsin by peptide boronic acids. *J. Biol. Chem. 259*, 15106−15114.

(11) Rubinstein, A. (2005) Colonic drug delivery. *Drug Discovery Today Technol. 2*, 33−37.

(12) Rubinstein, A. (2000) Natural polysaccharides as targeting tools of drugs to the human colon. *Drug Dev. Res. 50*, 435−439.

(13) Ravi Kumar, M. N. V., Muzzarelli, R. A. A., Muzzarelli, C., Sashiwa, H., and Domb, A. J. (2004) Chitosan chemistry and pharmaceutical perspectives. *Chem. Rev. 104*, 6017−6084.

(14) Tozaki, H., Odoriba, T., Okada, N., Fujita, T., Terabe, A., Suzuki, T., Okabe, S., Muranishi, S., and Yamamoto, A. (2002) Chitosan capsules for colon-specific drug delivery: enhanced localization of 5-aminosalicylic acid in the large intestine accelerates healing of TNBS-induced colitis in rats. *J. Controlled Release 82*, 51−61.

(15) Azria, M. (1989) in *The Calcitonins: Physiology and Pharmacology* (Azria, M., Ed.), Karger, Basel, Switzerland.

(16) Morimoto, K., Katsumata, H., Yabuta, T., Iwanaga, K., Kakemi, M., Tabata, Y., and Ikada, Y. (2001) Evaluation of gelatin microspheres for nasal and intramuscular administrations of salmon calcitonin. *Eur. J. Pharm. Sci. 13*, 179−185.

(17) Omura, Y., Renbutsu E., Morimoto M., Saimoto H., and Shigemasa Y. (2003) Synthesis of new chitosan derivatives and combination with biodegradable polymer. *Polym. Adv. Technol. 14*, 35−39.

(18) Fukamizo, T., Honda, Y., Goto, S., Boucher, I., and Brzezinski, R. (1995) Reaction mechanism of chitosanase from *Streptomyces* sp. N174. *Biochem. J. 311*, 377−383.

(19) Lehr, C.-M., Bouwstra, J. A., Schacht, E. H., and Junginger, H. E. (1992) In vitro evaluation of mucoadhesive properties of chitosan and some other natural polymers. *Int. J. Pharm. 78*, 43−48.

(20) Ranaldi, G., Marigliano, I., Vespignani, I., Perozzi, G., and Sambuy, Y. (2002) The effect of chitosan and other polycations on tight junction permeability in the human intestinal Caco-2 cell line. *J. Nutr. Biochem. 13*, 157−167.

(21) Bernkop-Schnürch, A., Bratengeyer, I., and Valenta, C. (1997) Development and in vitro evaluation of a drug delivery system protecting from trypsinic degradation. *Int. J. Pharm. 157*, 17−25.

(22) Lehr, C.-M. (1994) Bioadhesion Technologies for the delivery of peptide and protein drugs to the gastrointestinal tract. *Crit. Rev. Ther. Drug 11*, 119−160.

(23) Bernkop-Schnürch, A. (2000) Chitosan and its derivatives: potential excipients for peroral peptide delivery systems. *Int. J. Pharm. 194*, 1−13.

(24) Bernkop-Schnürch, A., and Scerbe-Saiko, A. (1998) Synthesis and in vitro evaluation of chitosan−EDTA-Protease-Inhibitor conjugates which might be useful in oral delivery of peptides and proteins. *Pharm. Res. 15*, 263−269.

(25) Bernkop-Schnürch, A., Schwarz, G. H., and Kratzel, M. (1997) Modified mucoadhesive polymers for the peroral administration of mainly elastase degradable therapeutic (poly)peptides. *J. Controlled Release 47*, 113−121.

(26) Marschütz, M. K., Veronese, F. M., and Bernkop-Schnürch, A. (2001) Influence of the spacer on the inhibitory effect of different polycarbophil-protease inhibitor conjugates. *Eur. J. Pharm. Biopharm. 52*, 137−144.

(27) Sakuma, S. Ishida, Y., Sudo, R., Suzuki, N., Kikuchi, H., Hitawari, K., Kishida, A., Akashi, M., and Hayashi, M. (1997) Stabilization of salmon calcitonin by poly(styrene) nanoparticles having surface hydrophilic polymeric chains against enzymatic degradation. *Int. J. Pharm. 159*, 181−189.

(28) Guggi, D., and Bernkop-Schnürch A. (2003) In vitro evaluation of polymeric excipients protecting calcitonin against degradation by intestinal serine proteases. *Int. J. Pharm. 252*, 187−196.

(29) Takeuchi, H., Yamamoto, H., and Kawashima, Y. (2001) Mucoadhesive nanoparticulate systems for peptide drug delivery. *Adv. Drug Delivery Rev. 47*, 39−54.

(30) Marschütz, M. A., Caliceti, P., and Bernkop-Schnürch, A. (2000) Design and in vivo evaluation of the oral delivery system of an oral delivery system for insulin. *Pharm. Res. 17*, 1468−1474.

BC050357Y

Synthesis and Active Oxygen Generation by New Emodin Derivatives and Their Gonadotropin-Releasing Hormone Conjugates

Vered Lev-Goldman,[‡] Brenda Mester,[‡] Nurit Ben-Aroya,[†] Yitzhak Koch,[†] Lev Weiner,[§] and Mati Fridkin*[,‡]

Departments of Organic Chemistry, Neurobiology, and Chemical Research Support, The Weizmann Institute of Science, Rehovot 76100, Israel. Received October 6, 2005; Revised Manuscript Received May 1, 2006

In an attempt to develop efficient chemotherapeutic agents targeted at malignant cells that express receptors, we synthesized five new emodin derivatives and their gonadotropin-releasing hormone (GnRH) conjugates to be used as potential photoactive conjugates. Emodin was modified at its hydroxy groups and included different spacers for conjugation of the peptide. We used electron spin resonance (ESR) and spin trapping techniques to study the light-stimulated redox properties of the emodin derivatives and their GnRH conjugates. Upon irradiation, all new emodin derivatives and their conjugates stimulated the formation of singlet oxygen, that is, $^1O_2$, and oxygen radicals, that is, $O_2^{-\bullet}$ and $OH^\bullet$. However, substantial differences were found between the tested derivatives as to the efficacy of reactive oxygen species (ROS) production. Because of its superior ROS production properties, [D-Lys^6(MeoEmo)]GnRH was selected as a leading conjugate. En-route to evaluate its targeting capacity, this potentially cytotoxic conjugate was tested in vitro to determine its hormonal activity and binding affinity to GnRH receptors.

INTRODUCTION

Targeted chemotherapy has been conceived as a means to differentiate between healthy and cancer cells, by minimizing undesired toxicity and affording high drug concentrations at selected loci. These properties can be potentially achieved by conjugation of drugs to vectors that have unique affinities toward a variety of binding sites, such as monoclonal antibodies (*1*), proteins (*2*), peptides (*3*), or oligonucleotides (*4*). Since receptors to the gonadotropin-releasing hormone (GnRH) are overexpressed in gynecological cancer cells such as breast, prostate, ovarian, and endometrial (*5*−*9*) cancers, covalent conjugation of chemotherapeutic agents to GnRH analogues may improve the selectivity of these drugs toward tumor cells that overexpress GnRH receptors. Targeted chemotherapy with [D-Lys^6]GnRH employed as a vector has recently gained considerable attention (*10*−*13*). However, because healthy pituitary gonadotropes also express GnRH receptors, [D-Lys^6]GnRH may reach and damage these cells (*14*). Such undesirable side effects can potentially be overcome by the use of targeted photodynamic therapy (PDT).

PDT is a promising cancer treatment that involves the combination of light and a photosensitizer (PS). While each of these factors by itself is harmless, in the presence of oxygen they produce lethal reactive oxygen species (ROS) that can kill tumor cells. The phototoxicity of the PSs occurs most likely through two major reaction pathways—type I, involving radical cascade, and type II, involving singlet oxygen pathway (*15*). An ideal PS should preferentially accumulate in tumor tissues. However, most PSs are distributed in healthy cells too, causing direct damage as well as post-therapeutic complications, such as skin cytotoxicity following exposure to sunlight (*16*). Therefore, target-specific PSs are highly advantageous.

Hydroxylated 9,10-anthraquinones are natural compounds that display marked pharmacological activities and are used as anticancer and antimicrobial drugs (*17*). Due to their suitable reduction potential, these quinones could undergo enzymatic reduction leading to the generation of ROS and consequent degradation of proteins and nucleic acids (*4*, *18*−*20*). In addition to their redox activity, hydroxylated anthraquinones are also known as PSs (*21*, *22*). Emodin (1,3,8-trihydroxy-6-methyl-9,10-anthraquinone, Scheme 1) is a naturally occurring poly-hydroxylated anthraquinone and a well-known PS with broad anticancer and antiviral activities (*23*, *24*). In preliminary experiments carried out in our lab, emodic acid (Emo, Scheme 1) was found to produce high ROS production and elicit significant phototoxicity toward αT3-1 cells at a concentration of 10 μM. In an attempt to produce a model for an effective targeted PS against cancerous cells, this PS was conjugated to [D-Lys^6]GnRH. However, the thus produced conjugate, [D-Lys^6(Emo)]GnRH, exhibited poor ROS production and no cell toxicity (*25*, *26*).

In an attempt to improve the photodynamic properties of the conjugates, we derivatized the emodin moiety and attached different spacers between the resulting derivatives and the peptide carrier. Thus, new methoxylated derivatives of emodin were prepared and conjugated with [D-Lys^6]GnRH and [D-Glu^6]GnRH peptide analogues. We used electron spin resonance (ESR) and spin trapping techniques to study the light-stimulated redox properties of the emodin derivatives and their conjugates with peptides. Based on results presented here, [D-Lys^6(MeoEmo)]-GnRH was selected as the leading conjugate toward its targeting mission. This conjugate was tested in vitro to determine its hormonal activity and binding affinity to GnRH receptors.

EXPERIMENTAL PROCEDURES

Chemicals. 6-Methyl-1,3,8-trihydroxyanthraquinone (emodin) was obtained from Extrasynthese (La Rechassiere Genay, France). 2,2,6,6-Tetramethyl piperidine (TEMP), 5,5′-dimethylpyrroline *N*-oxide (DMPO), and nicotinamide adenine dinucleotide (NADH) were obtained from Sigma Chemical Co. (St. Louis, MO). The colored impurity present in the commercial DMPO was removed by treatment with neutral decolorizing charcoal (*27*).

Identification of Emodin Derivatives and Their Conjugates. Nuclear magnetic resonance (NMR) spectra were recorded at 25 °C on Brucker spectrometers (250 and 400 MHz,

* Corresponding author. Tel: 972-8-9342505. Fax: 972-8-9344142. E-mail: mati.fridkin@weizmann.ac.il.

[‡] Department of Organic Chemistry.

[†] Department of Neurobiology.

[§] Department of Chemical Research Support.

10.1021/bc050293r CCC: $33.50 © 2006 American Chemical Society
Published on Web 07/06/2006

Scheme 1. Chemical Structure of Anthraquinonic Moieties[a]

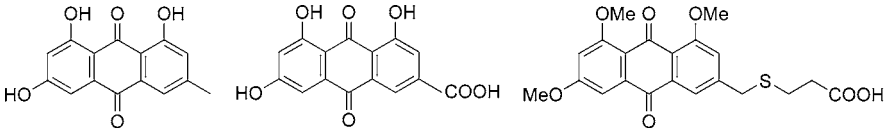

[a] The chemical names are (1) 1,3,8-trihydroxy-6-methyl-9,10-anthraquinone (emodin), (2) 1,3,8-trihydroxy-6-oxy-9,10-anthraquinone (emodic acid), (3) 1,3,8-trimethoxy-9,10-anthraquinone mercaptopropanoic acid (MeoEmo).

Karlsruhe, Germany). Mass spectrometry was performed on a Micromass platform LCZ 4000 (Manchester, U.K.) utilizing the electron spray ionization (ESI) method. Reversed-phase high-performance liquid chromatography (HPLC) was performed on a Spectra-Physics SP-8800 liquid chromatography system equipped with an Applied Biosystems 757 variable wavelength absorbance detector at 220 nm. HPLC prepacked columns used were VYDAC RP-18 column (250 mm × 22 mm; Hesperia, CA; 10 mL/min) for semipreparative purification and Chromolith RP-18e column (4.6 mm × 100 mm; Merck, Darmstadt, Germany) for analytical purposes. HPLC purifications and analyses were achieved by using the following eluents: 0.1% trifluoroacetic acid (TFA) in water as solvent A and 0.1% TFA in 75% aqueous acetonitrile as solvent B. The purity of all synthetic peptides and conjugates was screened by analytical HPLC eluent composition of 10−100% B in 10 min, 3 mL/min. The crude synthetic peptides were purified using binary A/B gradients. Chromatograms were recorded on a Chrom-Jey SP-4270 electronic integrator. For amino acid composition analysis, peptides were hydrolyzed in 6 N HCl at 110 °C for 22 h under vacuum, and the hydrolyzates were analyzed with a Dionex automatic amino acid analyzer.

Synthesis. [D-Lys^6]GnRH and [D-Glu^6]GnRH were synthesized on an automatic multiple peptide synthesizer (AMS-422, Abimed-Technik GnbH, Langenfeld, Germany) with Rink amide resin as a polymeric support following the company's protocol for Fmoc strategy as described (*28*, *29*).

*1,3,8-Trimethoxy-9,10-anthraquinone (**2**).* A mixture of emodin, **1** (3.8 g, 18.5 mmol), K_2CO_3 (7.1 g, 50 mmol), and Me_2SO_4 (7.1 mL, 75 mmol) in Me_2CO (190 mL) was stirred under reflux for 19 h, cooled to room temperature, and concentrated under reduced pressure. The residue was well triturated with water (150 mL), and the product was filtered. Recrystallization from EtOH (400 mL) gave yellow-orange crystalline needles (2.71 g, 47% yield) that were collected by filtration and air-dried. Melting point: 238 °C. ^{1}H NMR ($CDCl_3$, δ, 250 MHz): 7.61(s, ar-H5), 7.30(d, J = 2.14 Hz, ar-H4), 7.07(s, ar-H7), 6.74-(d, J = 2.34 Hz, ar-H2), 3.96(s, OCH_3), 3.93(s, OCH_3), 3.92(s, OCH_3), 2.44(s, CH_3). MS (m/z): experimental [M + H$^+$] = 313.59; calcd m/z for $C_{18}H_{17}O_5$ [M + H$^+$] = 313.32.

*6-Bromomethyl-1,3,8-trimethoxy-9,10-anthraquinone (**3**).* To a solution of **2** (2.71 g, 8.65 mmol) and NBS (*N*-bromosuccinimide) (1.94 g, 10 mmol) in CCl_4 (250 mL), a catalytic amount of benzoyl peroxide was added, and the mixture was heated under reflux for 3 h. After cooling to room temperature, the mixture was concentrated under reduced pressure. Water (120 mL) was added, and the suspension was stirred for 1 h in an ice water bath. The yellow precipitate was filtered, washed with cold water and hexane, and recrystallized from toluene to give 2.67 g of product (79% yield). The precipitate contained also the 6-dibromomethyl-1,3,8-trimethoxy-9,10-anthraquinone product as an impurity (16% of the product), but the crude precipitate was used without further purification. Melting point: 230 °C. ^{1}H NMR ($CDCl_3$, δ, 250 MHz): 7.81(d, J = 1.67 Hz, ar-H5), 7.29(m, ar-H4,7), 6.75(m, ar-H2), 4.50(s, CH_2−Br), 3.99(m, OCH_3 1,3 and 8). MS (m/z): experimental [M + H$^+$]= 391.59 calcd m/z for $C_{18}H_{17}BrO_5$ [M + H$^+$] = 392.21.

*3-(4,5,7-Trimethoxy-9,10-dioxo-9,10-dihydro-anthracen-2-yl-methylsulfanyl)-propionic Acid, MeoEmo (**4**).* NaH (408 mg, 60% oil dispersion containing 10 mmol) was added gradually to a cooled solution (ice water bath) of 3-mercaptopropanoic acid (490 μL, 5.6 mmol) in DMF (5 mL) under argon. The suspension was stirred for 30 min in ice water bath and warmed to room temperature, and then compound **3** (2 g, 5.1 mmol) in DMF (35 mL) was added. The yellow suspension was stirred overnight at room temperature. The suspension was acidified with 5 N HCl solution and extracted with dichloromethane. The organic solvent was washed with brine and then dried over Na_2SO_4. The solvent was removed under reduced pressure to give a yellow-gray oil. After addition of ethyl acetate, the product solidified to give 1.07 g (50.5% yield). Melting point: 180 °C. ^{1}H NMR ($CDCl_3$, δ, 250 MHz): 7.71(d, J = 1.21 Hz, ar-H5), 7.29(d, J = 1.98 Hz, ar-H4,7), 6.75(d, J = 2.31 Hz, ar-H2), 3.98(s, OCH_3), 3.94(s, OCH_3), 3.93(s, OCH_3), 3.79(s, ar-CH_2S), 2.68(d, J = 6.13 Hz, CH_2S), 2.62(d, J = 5.79 Hz, CH_2COOH). MS (m/z): experimental [M − H$^+$] = 415.09; calcd m/z for $C_{21}H_{19}O_7S$ [M − H$^+$] = 415.45.

*3-(4,5-Dihydroxy-7-methoxy-9,10-dioxo-9,10-dihydro-anthracen-2-ylmethylsulfanyl)-propionic Acid, DihydroxyEmo (**5**).* A mixture of **4** (20 mg, 0.05 mmol), AcOH (5 mL), and 49% HBr/AcOH (0.5 mL) (a small amount of phenol had been added to the HBr to remove traces of Br_2) was heated at 100 °C for 4 h. The mixture was then cooled, and the solvent was removed under reduced pressure. The crude mixture was purified by preparative HPLC (10% B for 10 min and then increased linearly to 100% B in 60 min) to give 6 mg of pure product (30% yield). ^{1}H NMR (d^6-DMSO, δ, 400 MHz): 12.17 and 12.03(2s, ar-OH1 and ar-OH8), 7.70(d, J = 1.2 Hz, ar-H5), 7.33(d, J = 1.2 Hz, ar-H4), 7.21(d, J = 2.0 Hz, ar-H7), 6.90(d, J = 2.4 Hz, ar-H2), 3.94(s, OCH_3), 3.89(s, ar-CH_2S), 2.59(m, CH_2S), 2.52(m, CH_2COOH). MS (m/z): experimental [M − H$^+$] = 387.28; calcd m/z for $C_{19}H_{15}O_7S$ [M − H$^+$] = 387.39. The position of the methoxy group was determined by 1D NOE difference. By irradiation of the methoxy group at δ = 3.94 ppm, a response at the adjacent protons H2 and H4 confirmed the methoxy position at C3.

*3-(4,5,7-Trihydroxy-9,10-dioxo-9,10-dihydro-anthracen-2-yl-methylsulfanyl)-propionic Acid, TrihydroxyEmo (**6**).* A mixture of **4** (20 mg, 0.05 mmol), AcOH (5 mL), and 49% HBr/AcOH (0.8 mL) (a small amount of phenol was previously added to the HBr to remove traces of Br_2) was heated at 100 °C overnight. The mixture was then cooled, and the solvent was removed under reduced pressure. The crude mixture was purified by preparative HPLC (10% B for 10 min and then increased linearly to 100% B in 60 min) to give 5 mg of pure product (26% yield). ^{1}H NMR (CD_3OD, δ, 250 MHz): 7.76(d, J = 1.731 Hz, ar-H5), 7.26(d, J = 1.77 Hz, ar-H4), 7.21(d, J = 2.43 Hz, ar-H7), 6.58(d, J = 2.42 Hz, ar-H2), 3.84(s, ar-CH_2S), 2.70(m, CH_2S), 2.56(m, CH_2COOH). MS (m/z): M = 388 g/mol, 387 (M − 1), 412 (M + Na$^+$). MS (m/z): experimental [M − H$^+$] = 372.99; calcd m/z for $C_{18}H_{13}O_7S$ [M − H$^+$] = 373.37.

*3-Aminomethyl-1,6,8-trimethoxy-anthraquinone, MeoEmo-NH_2 (**7**).* 6-Bromomethyl-1,3,8-trimethoxy-9,10-anthraquinone (**3**) (100 mg, 0.3 mmol) was dissolved in 20 mL of dry THF. Ammonia gas (dried over sodium hydroxide) was bubbled for 3 h through the solution, and the reaction mixture was left

overnight in a closed round-bottom flask with stirring. The reaction was checked for completion by analytical HPLC. The reaction mixture was evaporated, and the crude product was used without further purification. A small portion of the crude product (5 mg) was purified by preparative HPLC, and the pure compound was characterized by MS and NMR. NMR (d^6-acetone/$CDCl_3$, δ, 250 MHz): 7.98(m, ar-H5), 7.79(m, ar-H4), 7.24(d, $J = 2.46$ Hz, ar-H7), 6.96(d, $J = 2.53$ Hz, ar-H2), 5.06-(s, ar-CH_2N), 3.98(s, OCH_3), 3.97(s, OCH_3), 3.96(s, OCH_3). MS (*m*/*z*): experimental [M − H^+] = 326.24; calcd *m*/*z* for $C_{18}H_{16}NO_5$ [M − H^+] = 326.33.

*N-(4,5,7-Trimethoxy-9,10-dioxo-9,10-dihydro-anthracen-2-yl-methyl)-succinic Acid, MeoEmo-N-Succinyl (**8**).* A mixture of MeoEmo-NH_2 (**7**) (32.7 mg, 0.1 mmol), succinic anhydride (20 mg, 0.2 mmol), and triethylamine (41 μL, 0.3 mmol) in 1 mL of DMF was stirred for 4 h at room temperature. Reaction progress was followed by analytical HPLC, and the crude mixture was purified by preparative HPLC (solvent gradient 10% B for 10 min and then increased linearly to 80% B in 70 min) to give 8 mg of pure product (19% yield). ^{1}H NMR (DMSO-d^6, δ, 250 MHz): 8.65(m, NH), 7.58(m, ar-H5), 7.39-(m, ar-H,7), 7.16(d, $J = 2.39$ Hz, ar-H,4), 6.98(d, $J = 2.39$ Hz, ar-H2), 4.37(d, $J = 5.69$ Hz, ar-CH_2−N), 4.01(s, 3H, OCH_3), 3.99(s, 6H, OCH_3), 3.79(s, ar-CH_2S), 2.42(m, CH_2CH_2COOH), MS (*m*/*z*): experimental [M − H^+] = 426.39; calcd *m*/*z* for $C_{22}H_{20}NO_8$ [M − H^+] = 426.40.

[D-Lys^6]GnRH Conjugates. [D-Lys^6]GnRH (10 mg, 8 μmol) was dissolved in *N*,*N*′-dimethylformamide (DMF, 500 μL). The emodin derivative (24 μmol), 4-methylmorpholine (NMM) (40 μL, 36 μmol), and benzotriazole-1-yl-oxy-tris-pyrrolino-phosphonium hexafluoro-phosphate (PyBOP) (18.8 mg, 40 μmol) were added. The mixture was stirred for 4 h at room temperature. The progress of the reaction was followed by the disappearance of [D-Lys^6]GnRH as revealed by analytical HPLC (see Scheme 3). Upon completion of the reaction, the crude peptide was precipitated with ice-cold *tert*-butyl methyl ether (3 mL), collected by centrifugation, and dried. The peptide was then purified by preparative HPLC (eluent composition was 10% B for the first 10 min and increased linearly to 100% B after 60 min, 10 mL/min). In this manner [D-Lys^6(MeoEmo)]GnRH, [D-Lys^6(DihydroxyEmo)]GnRH, [D-Lys^6(TrihydroxyEmo)]GnRH, and [D-Lys^6(MeoEmo-N-Succinyl)]GnRH were synthesized in solution and analyzed by HPLC, MS, amino acid analysis, and UV/visible spectra (data in Tables 2 and 3).

[D-Glu^6]GnRH Conjugate. A solution of [D-Glu^6]GnRH (1.5 mg, 2,4 μmol) and MeoEmo-NH_2 (1 mg, 4.8 μmol) in 1 mL of DMF was added with PyBOP (1.2 mg, 5 μmol) and *N*,*N*′-diisopropylethylamine (DIPEA, 2 μL, 10 μmol), and the mixture was stirred for 2 h at room temperature. Reaction progress was followed by analytical HPLC, and the crude product was purified by semipreparative HPLC (solvent gradient 10% B to 70% B in 60 min, semi-prep column Vydac 10 mm × 25 mm C18) to give 1 mg of pure product (26% yield).

ESR Studies. *Photoexcitation of Emodin Derivatives and Their Peptide Conjugates.* All spin trapping studies were performed with a Bruker electron paramagnetic resonance ER200D-SRC spectrometer at 25 °C. For ESR studies, the irradiation source was a KL 1500 electronic projector lamp (Schott, Germany). Irradiations were carried out with appropriate filters according UV/visible spectra (Figure 1) at band-pass of 320−510 nm with $\lambda_{max} = 400$ nm or cutoff filters of 355 nm. Samples were irradiated directly inside the ESR cavity with an optical fiber while the ESR spectra was recorded. For spin trapping studies, a mixture of DMPO (0.1 M) or TEMP (0.1 M) and emodin derivative/conjugate (1−2 mM) was irradiated in a 70 or 200 μL ESR flat cell. NADH was used as potential donor in phosphate buffered saline (PBS) solutions. For *g* factor

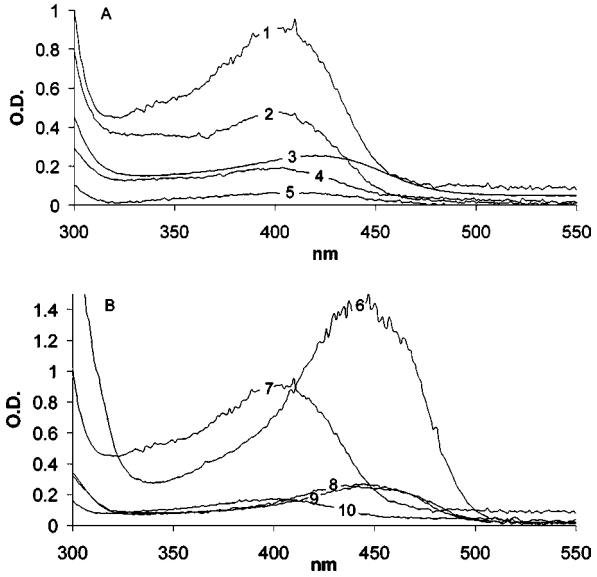

Figure 1. Relative absorption spectra (UV/vis): (A) emodin derivatives vs their conjugates in 0.1 mM DMSO/PBS (1 = MeoEmo(DMSO), 2 = MeoEmo-conj(DMSO), 3 = MeoEmo-conj(PBS), 4 = MeoEmo-N-Succinyl(DMSO), 5 = MeoEmo-N-Succinyl-conj(DMSO)); (B) emodin derivatives in 0.1 mM DMSO (6 = emodin, 7 = MeoEmo, 8 = DihydroxyEmo, 9 = TrihydroxyEmo, 10 = MeoEmo-NH_2).

measurements, we used 2,2-diphenyl-1-picrylhydrazyl (DPPH) as reference ($g = 2.0023$).

Receptor Binding Assay. [D-Lys^6]GnRH was iodinated by the chloroamine T method and purified by analytical HPLC. The binding affinities of the [D-Lys^6]GnRH analogues to preparations of rat pituitary receptors were obtained by competitive binding experiment (*30*). Briefly, crude preparation of rat pituitary membranes (about 25 μg of protein/tube, prepared from pro-estrous rats) in 0.4 mL of assay buffer (0.1% BSA in 10 mM Tris-HCl, pH 7.4) were incubated in duplicate with ^{125}I-[D-Lys^6]GnRH (40 000−50 000 cpm, 23.5 pM, 50 μL) in the presence (10^{-7}−10^{-10} M) or absence of [D-Lys^6]GnRH conjugate (50 μL) in a total volume of 500 μL of assay buffer for 90 min at 4 °C. The reaction was terminated by rapid filtration through Whatman GF/C filters presoaked in 2−3% polyethylenimine solution in 10 mM Tris-HCl to minimize filter absorption. The filters were washed three times with cold 10 mM Tris-HCl (3 mL each) and were counted in a Packard Auto-Gamma Counting System (Packard, Meriden, CT). Nonspecific binding was defined as the residual radioactivity in the presence of excess (1 μM) [D-Lys^6]GnRH. Specific binding was calculated by subtracting the nonspecific binding from the maximal binding, determined in the absence of any competing peptide.

Effect of [D-Lys^6(MeoEmo)]GnRH on Luteinizing Hormone (LH) Release. The LH-releasing potencies of the GnRH conjugate and its precursor peptide were evaluated in primary pituitary cell cultures prepared from 21-day-old Wistar female rats as described earlier (*31*). The cultures were maintained in M-199 medium supplemented with 10% horse serum and antibiotics and were plated (50 000 cells/well) in 96-multiwell tissue culture dishes. After 48 h, the medium was replaced by phenol red- and serum-free M-199 containing the desired concentration of the peptides (three wells per experimental group) and incubated in the dark at 37 °C for 4 h. The experiments were carried out in the dark to avoid photoactivation of the emodin derivative moiety. At the end of the incubation period, supernatants (0.1 mL) were diluted with 1% BSA/PBS (0.9 mL) and analyzed for LH content by double-antibody radioimmunoassay (RIA) (*32*, *33*) using kits kindly supplied by the National Institute of Arthritis, Metabolism and Digestive Diseases (NIMDD).

Table 1. Characterization of the Emodin Derivatives

product no.	name	$[M - H^+]$ (calcd)[a] (g/mol)	λ_{max} (nm) 0.1 mM in DMSO
4	MeoEmo	415.09 (415.45)	404
5	DihydroxyEmo	387.28 (387.39)	445
6	TrihydroxyEmo	372.99 (373.37)	445
7	MeoEmo-NH_2	326.24 (326.33)	400
8	MeoEmo-N-Succinyl	426.39 (426.40)	404

[a] Calculated *m*/*z* values of $[M - H^+]$ are in parentheses.

Scheme 2. Synthetic Pathways towards Emodin Derivatives[a]

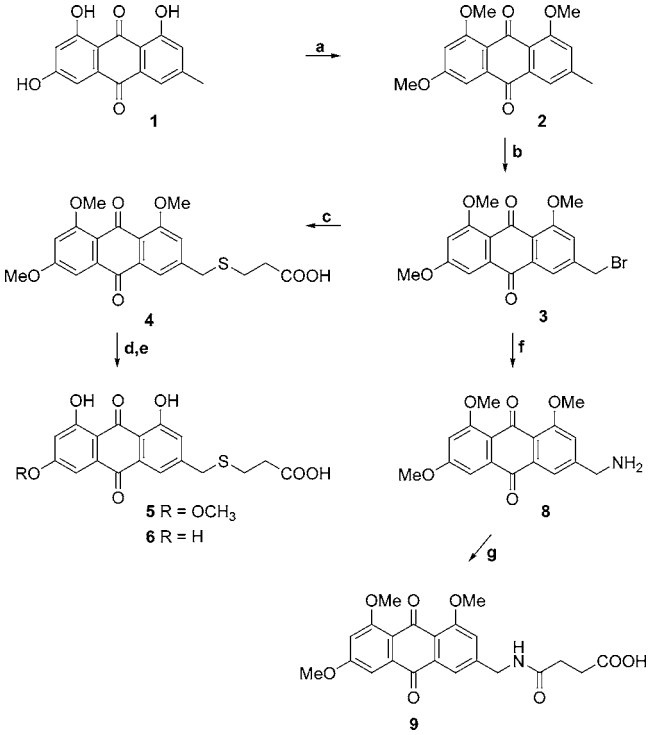

[a] Reagents and conditions: (a) K_2CO_3, Me_2SO_4, acetone, reflux for 19 h; (b) NBS, peroxide (catalytic), CCl_4, reflux for 3 h; (c) 3-mercaptopropanoic acid, NaH, DMF, rt, overnight; (d) HBr 49% in AcOH, 4 h at 130 °C; (e) HBr 49% in AcOH, overnight at 130 °C; (f) NH_3 in dry THF for 3 h; (g) succinic anhydride/Et_3N in DMF.

RESULTS

Synthesis. Emodin (1,3,8-trihydroxy-6-methyl-9,10-anthraquinone), a poly-hydroxylated, redox-active anthraquinone, was employed as a lead compound. Novel emodin derivatives and their conjugates with [D-Lys^6]GnRH and [D-Glu^6]GnRH were synthesized and characterized. The method of preparation of MeoEmo, **4**, was based on nucleophilic attack of 3-bromomethyl-1,6,8-trimethoxy-anthraquinone, **3**, by 3-mercapto-propanoic acid. The nucleophilic substitution of **3** led to the production of desired compound **4** (50% yield). DihydroxyEmo and TrihydroxyEmo, **5** and **6**, were synthesized from the MeoEmo by an acidolytic deprotection step in a yield of 30% and 26%, respectively. Amination of the brominated emodin, **3**, led to compound MeoEmo-NH_2, **7**, which was used directly for the next synthetic step. Addition of succinic anhydride as a spacer to the amino side group gave MeoEmo-N-Succinyl, **8** (19% yield) (Table 1, Scheme 2).

Synthesis of GnRH Analogs. [D-Lys^6]GnRH and [D-Glu^6]-GnRH were synthesized as described in the Experimental Procedures section. The synthesis of the corresponding emodin−peptide conjugates was carried out in solution according to Scheme 3. In the conjugation of [D-Lys^6]GnRH, the carboxylic moiety of the corresponding emodin derivative was activated, using benzotriazole-1-yl-oxy-tris-pyrrolidinophosphonium-hexafluorophosphate (PyBOP), and reacted with the free ϵ-amino group of [D-Lys^6]GnRH in the presence of 4-methylmorpholine (NMM) in DMF. The crude [D-Lys^6]GnRH conjugate was then purified by preparative HPLC. In this manner, [D-Lys^6(MeoEmo)]-GnRH, [D-Lys^6(DihydroxyEmo)]GnRH, [D-Lys^6(TrihydroxyEmo)]GnRH, and [D-Lys^6(MeoEmo-N-Succinyl)]GnRH were synthesized (Scheme 3). [D-Glu^6]GnRH was reacted with MeoEmo-NH_2, **7**, for rendering [D-Glu^6(MeoEmo-NH_2)]GnRH. The peptide was conjugated by activating the γ-carboxylic moiety of the peptide with PyBOP and diisopropylamine (DIPEA) as a base. The conjugates were analyzed by HPLC, MS, and amino acid analysis and tested for their λ_{max} (Tables 2 and 3).

ESR Studies. Filters for the ESR experiments were chosen according to the obtained visible−UV spectra in Figure 1A,B.

Singlet Oxygen ($^1O_2$) Photogeneration by Emodin Derivatives. Since the efficiency of quinones for inhibiting cancer cell growth is believed to be related, among other factors, to their capacity to produce ROS, the ability of the various potentially cytotoxic emodin derivatives to generate ROS was compared. For testing singlet oxygen, $^1O_2$, we used the spin trap TEMP, which produces a stable nitroxyl radical, TEMPO, having a triplet ESR signal ($a_N = 14.8-15$ G) as a result of a chemical reaction with a singlet oxygen (*34*). The kinetics of singlet oxygen formation was evaluated by measuring the initial rate of ESR signal of the central component of the TEMPO triplet.

As shown in Figure 2A,B, all emodin derivatives can generate singlet oxygen. We examined the influence of the different spacers (Figure 2A) and the influence of the methoxylated substitution (Figure 2B) on the emodin ROS production. The largest initial rate of the ESR signal was observed for MeoEmo and for MeoEmo-N-Succinyl, as compared with DihydroxyEmo,

Scheme 3. Synthesis of the [D-Lys^6]GnRH Conjugates with the Emodin Derivatives[a]

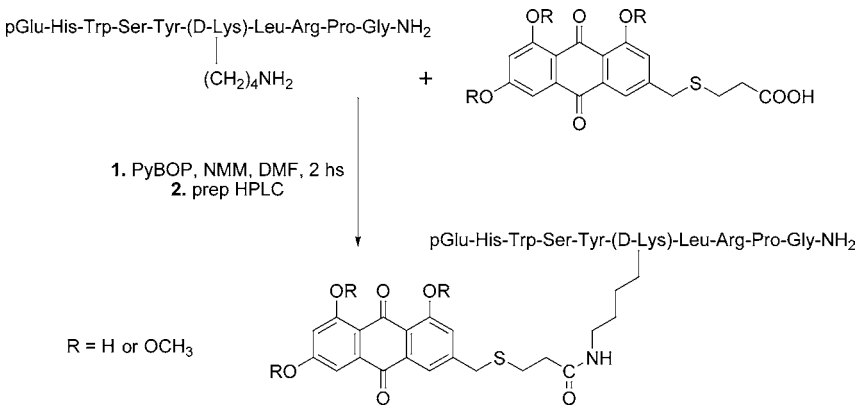

[a] See Experimental Procedures section for details.

Table 2. Characterization of the GnRH Conjugates of Emodin Derivatives

peptide conjugate	retention time (min) (HPLC)[a]	yield (%)	[M + H$^+$] (calcd)[b] (g/mol)	λ_{max} (nm) 0.1 mM in DMSO
[D-Lys^6(MeoEmo)]GnRH	7.74	38	1653.21 (1652.85)	403
[D-Lys^6(MeoEmo-N-Succinyl)]GnRH	7.19	85	1663.51 (1663.80)	410
[D-Lys^6(DihydroxyEmo)]GnRH	8.51	31	1625.05 (1624.79)	441
[D-Lys^6(TriydroxyEmo)]GnRH	8.67	75	1610.41 (1610.76)	*c*
[D-Glu^6(MeoEmo-NH$_2$)]GnRH	7.22	26	1565.30 (1564.67)	401

[a] Analytical HPLC. Eluent composition: from 0 to 100% B in 10 min, then 100% B for 4 min more. Solvent A was 0.1% trifluoroacetic acid (TFA) in water. Solvent B was 0.1% TFA in 75% aqueous acetonitrile. [b] Calculated (calcd) *m*/*z* values of [M − H$^+$] are in parentheses. [c] Not determined.

Table 3. Amino Acid Analysis of the Peptidic Conjugate after Acidic Hydrolysis[a]

	Glu	His	Ser	Tyr	Lys	Leu	Arg	Pro	Gly
[D-Lys^6]GnRH theoretical	1.00	1.00	1.00	1.00	1.00	1.00	1.00	1.00	1.00
MeoEmo[b]	1.00	1.00	0.90	0.98	1.06	1.05	1.16	0.95	1.03
MeoEmo-N-Succinyl[b]	1.00	1.02	0.89	0.98	1.02	1.03	1.17	1.00	1.01
DihydroxyEmo[b]	1.00	0.99	0.90	0.98	1.01	1.02	1.12	1.00	1.10
TriydroxyEmo[b]	1.00	0.94	0.89	0.98	1.02	1.08	1.13	0.96	1.00
MeoEmo-NH$_2$[c]	2.04	1.00	0.89	1.00		1.09	1.18	0.94	1.00

[a] Tryptophan could not be detected due to its destruction under the acidic conditions of hydrolysis. [b] Conjugate of [D-Lys^6]GnRH. [c] Conjugate of [D-Glu^6]GnRH. Theoretical composition: Glu 2.00; His 1.00; Ser 1.00; Tyr 1.00; Leu 1.00; Arg 1.00; Pro 1.00; Gly 1.00.

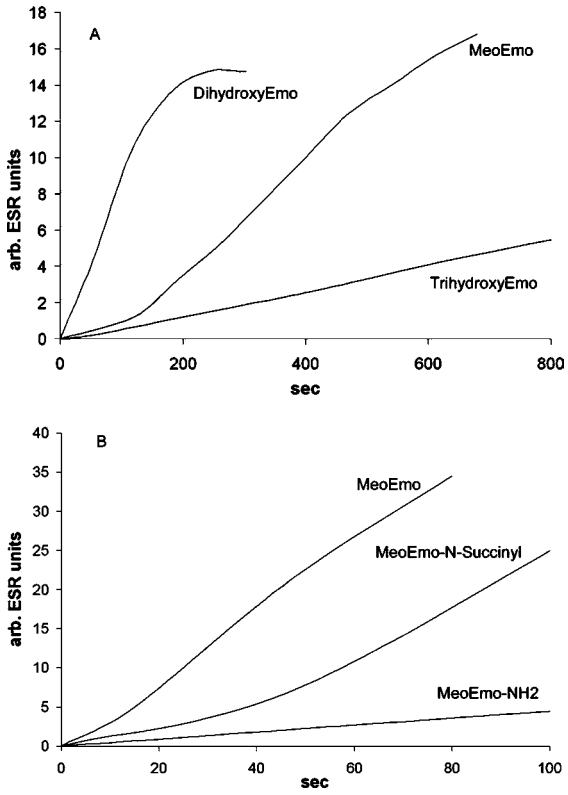

Figure 2. Effect of light on generation of TEMPO ESR signal in the presence of emodin derivatives: (A) 355 nm cutoff; (B) blue filter, λ_{max} = 400 nm. ESR conditions: microwave power 31 mW; TC 1.25 s; MA 1.1 G; temp 25 °C; solvent DMSO; components TEMP (0.1 M); quinones concentration, 1 mM.

TrihydroxyEmo, and MeoEmo-NH$_2$. TrihydroxyEmo showed much less reactivity compared with the other derivatives.

Singlet Oxygen ($^1O_2$) Photogeneration by the Conjugates [D-Lys^6(MeoEmo)]GnRH and [D-Lys^6(MeoEmo-N-Succinyl)]-GnRH. To study the influence of the peptide carrier on singlet oxygen production, the kinetics of TEMPO adduct formation of MeoEmo and [D-Lys^6(MeoEmo)]GnRH were compared. We found that incorporation of MeoEmo into the [D-Lys^6]GnRH peptide carrier significantly decreased the rate of TEMPO formation, though it still remained active. The same pattern, even more pronounced, was repeated when we tested MeoEmo-N-Succinyl and its GnRH conjugate under the same experimental conditions. Clearly, the peptide markedly decreases the singlet oxygen production of the quinone moiety (Figure 3).

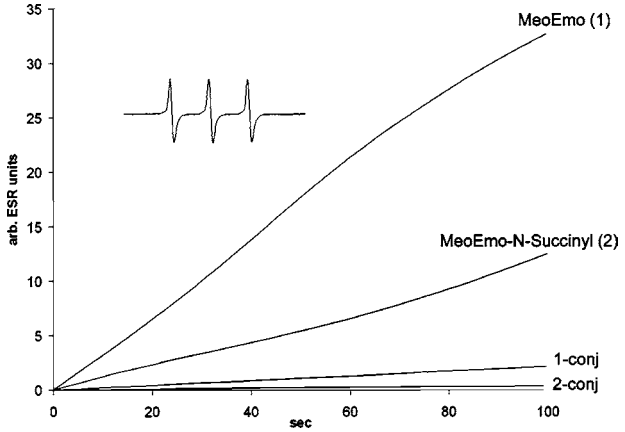

Figure 3. Influence of the [D-Lys^6]GnRH carrier on TEMPO formation (blue filter, λ_{max} = 400 nm). ESR conditions: microwave power 31 mW; MA 1.1 G; TC 1.1 s; temp 25 °C; solvent DMSO; components TEMP (0.1 M); quinones and conjugates concentration, 1 mM.

Oxygen Radicals Photogeneration by Emodin Derivatives. In an excited state, quinones produce ROS by energy transfer (reaction 2) and electron transfer (reaction 3−6). The ability to generate oxygen radicals was detected by the spin trap 5,5′-dimethyl-1-pyrroline *N*-oxide (DMPO), which reacts with short-lived radicals, for example, $O_2^{-\bullet}$, HO$^\bullet$, and $CH_3^\bullet$, to produce long-lived spin adducts, each of which possess a characteristic ESR spectrum.

$$Q \xrightarrow{h\nu} Q^* \quad (1)$$

$$Q^* + O_2 \rightarrow Q + {}^1O_2 \quad (2)$$

$$Q^* + D \rightarrow Q^{-\bullet} + D^{+\bullet} \quad (3)$$

$$Q^{-\bullet} + O_2 \leftrightarrow O_2^{-\bullet} + Q \quad (4)$$

$$O_2^{-\bullet} + O_2^{-\bullet} \xrightarrow{2H^+} H_2O_2 + O_2 \quad (5)$$

$$O_2^{-\bullet} + H_2O_2 \xrightarrow{\text{Fe (cat.)}} O_2 + HO^\bullet + OH^- \quad (6)$$

$$H_2O_2 + Fe(II) \rightarrow HO^\bullet + OH^- + Fe(III) \quad (7)$$

$$Q^{-\bullet} + Fe(III) \rightarrow Q + Fe(II) \quad (8)$$

where Q* represents quinone in an excited state, D is electron donor, and $Q^{-\bullet}$ is semiquinone.

Figure 4A shows the effect of light on MeoEmo in the presence of DMPO and demonstrates the influence of an additional physiological electron donor like NADH. The ESR signal found was a quartet ($a_N = a_H$ = 14.8 G and 1:2:2:1 ratio), typical for hydroxyl-DMPO spin adduct in water; a weak signal

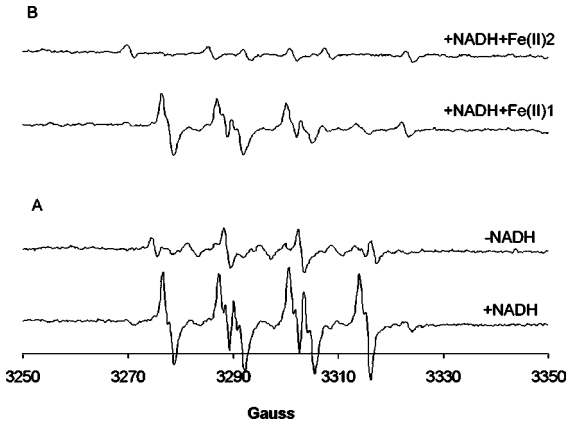

Figure 4. (A) Effect of NADH on ESR signal of MeoEmo in the presence of DMPO upon irradiation (blue filter, $\lambda_{max} = 400$ nm). ESR conditions: microwave power 31 mW, modulation amplitude 890 MG; time constant 640 MS; temp 25 °C; solvent 10% DMSO/90% PBS; components MeoEmo (1 mM), DMPO (0.1 M) with and without NADH (1 mM). (B) Effect of $FeSO_4$ on ESR signal of MeoEmo in the presence of DMPO (cutoff filter, 355 nm). ESR conditions: microwave power 31 mW, modulation amplitude 1.1 G, time constant 1.25 s; temp 25 °C; solvent 10% DMSO/90% PBS; components MeoEmo (1 mM), DMPO (0.1 M), NADH (1 mM), and $FeSO_4$ (0.01 mM)).

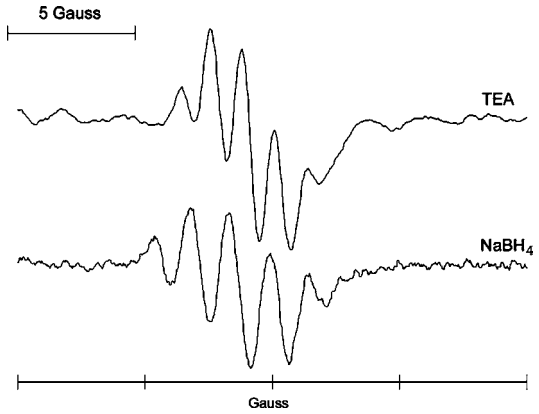

Figure 5. Effect of light on MeoEmo with electron donors produced semiquinone-like signal (blue filter, $\lambda_{max} = 400$ nm): (TEA) MeoEmo (1 mM), DMPO (1 mM), TEA (0.04 M) in 50% DMSO/50% PBS solution (ESR conditions: microwave power 31 mW; modulation amplitude 1.0 G; RG = 2×10^5; temp 25 °C); ($NaBH_4$) MeoEmo (1 mM), $NaBH_4$ (pH = 9) in 50% DMSO/50% H_2O solution (ESR conditions: microwave power 31 mW; modulation amplitude 630 MG; RG = 8×10^5; temp 25 °C.

of superoxide−DMPO spin adduct was also observed (a_N = 14.2 G, $a_H^\beta = 11.3$ G, $a_H^\gamma = 1.25$ G, 12 lines). Adding NADH to the MeoEmo−DMPO solution stimulated stronger superoxide DMPO ESR signal. Figure 4B shows changes in the ESR signal when Fe(II) was added. DMPO−superoxide spin adduct was converted with time (in the first 200 s of the experiment) to the sextet spectrum, typical for DMPO−CH_3 spin adduct ($a_N = 15$ G, $a_H = 22.2$ G).

The involvement of the semiquinone radical in the ROS mechanism was also assessed when triethylamine (TEA) was used as an electron donor. TEA (1 mM) acted as an enhancer of superoxide ESR signal, as predicted (data not shown). Moreover, when TEA (10% v/v) was used with MeoEmo in DMSO, a semiquinone-like signal appeared. The same ESR signal was observed by reduction of MeoEmo with $NaBH_4$ (Figure 5, $g = 2.0051$).

Figure 6A,B compares the effects of the emodin derivatives on photogeneration of ROS in the presence of NADH. As shown, MeoEmo and MeoEmo-N-Succinyl produced more intense ESR superoxide signal than the other derivatives tested.

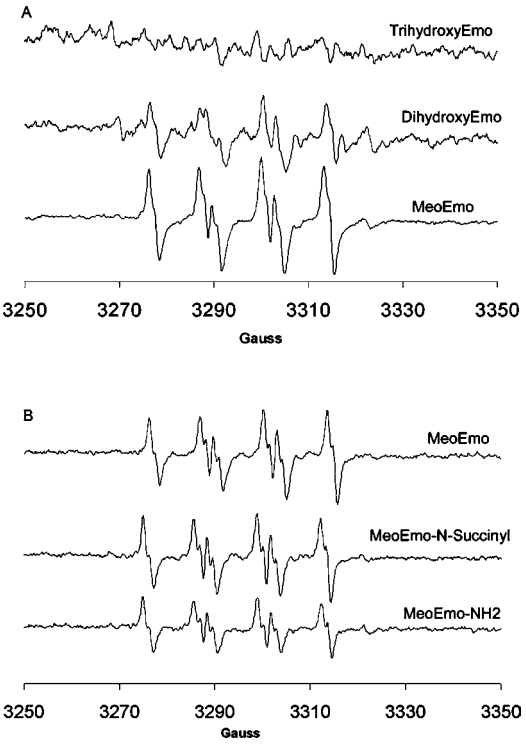

Figure 6. The ESR spectra of the DMPO−superoxide radical adduct produced upon irradiation of the emodin derivatives in 10% DMSO/90% PBS (components: quinones (1 mM), DMPO (1 mM), NADH (1 mM)): (A) cutoff filter 355 nm (ESR conditions: microwave power 31 mW; modulation amplitude 1.1 G; time constant 1.25 s; temp 25 °C; with different receiver gain (RG), for MeoEmo RG = 2.5×10^5, for DihydroxyEmo RG = 6.3×10^5, for TrihydroxyEmo RG = 8×10^5); (B) blue filter, $\lambda_{max} = 400$ nm (ESR conditions: microwave power 31 mW; modulation amplitude 890 MG; time constant 640 ms; temp 25 °C; RG = 2.5×10^5).

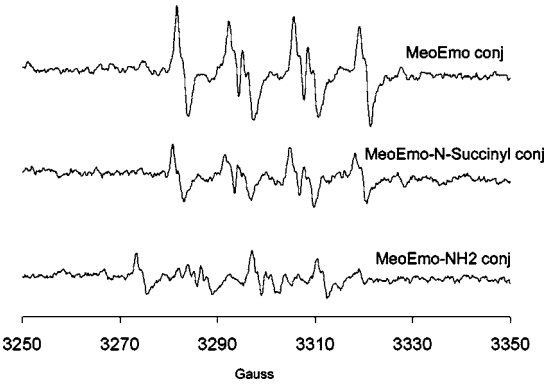

Figure 7. Effect of light on [D-Lys^6]GnRH and [D-Glu^6]GnRH conjugates upon irradiation. The ESR signals represent superoxide−DMPO spin adduct, 12 lines, $a_N = 14.2$ G, $a_H^\beta = 11.3$ G, $a_H^\gamma = 1.25$ G. PBS system containing 10% DMSO; components: DMPO (0.1 M), GnRH conjugates (1 mM), NADH (1 mM). ESR conditions: microwave power 31 mW; modulation amplitude 630 MG; RG = 1×10^6; time constant 1.25 s; temp 25 °C.

Oxygen Radical Photogeneration by Emodin Conjugates. In the case of the peptide conjugate, the ESR signal observed is typical for superoxide−DMPO spin adduct (Figure 7). Comparison of the emodin conjugates shows that MeoEmo conjugate gave the stronger peak compared with MeoEmo-N-Succinyl and MeoEmo-NH_2 conjugates.

Stability of the Conjugate toward ROS Generation. Generation of ROS by compounds under study can destroy, in principle, the peptide carriers. Stability of [D-Lys^6(MeoEmo)]GnRH toward the ROS produced by its own irradiation is a prerequisite for specific and efficient targeting. This aspect was evaluated

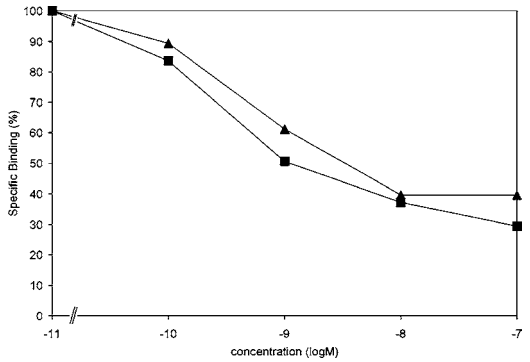

Figure 8. Displacement (%) of specific binding of ^{125}I[D-Lys^6]GnRH from pituitary membranes of pro-estrous rats by increasing concentrations of unlabeled GnRH analogues [D-Lys^6(MeoEmo)]GnRH (■) and [D-Lys^6]GnRH (▲). Membranes were incubated for 90 min at 4 °C with ^{125}I[D-Lys^6]GnRH and with unlabeled peptides. Nonspecific binding was defined as binding of the labeled ligand in the presence of 1 μM [D-Lys^6]GnRH and was extracted from the total binding for the calculation of specific maximal binding (MB). Results are the mean of an experiment carried out in duplicate.

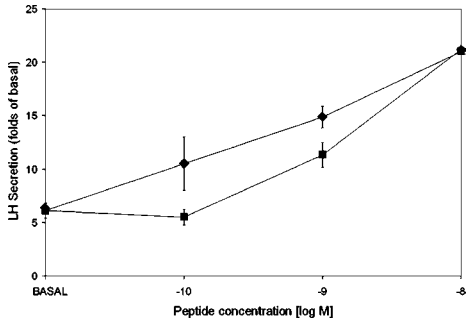

Figure 9. Effect of [D-Lys^6(MeoEmo)]GnRH on the secretion of LH from primary cultures of rat pituitary cells. Primary cultures of rat pituitary cells were incubated in M-199 medium containing the indicated concentrations of [D-Lys^6]GnRH (●) and [D-Lys^6(MeoEmo)]GnRH (■) for 4 h at 37 °C. The media were then collected, and LH concentration was determined by RIA. Results are the means ± SD of LH concentration of an experiment with 3 wells/experimental group. The basal release after 4 h of incubation in M-199 was 6.08 ± 0.52 ng/mL.

by an HPLC study. According to the ESR measurements, ROS were efficiently formed when the mixture of [D-Lys^6(MeoEmo)]-GnRH in phosphate buffer containing 10% DMSO was irradiated for 40 min. The mixture was then analyzed by analytical HPLC. Results showed that less than 3% of [D-Lys^6(MeoEmo)]-GnRH was degraded by the generated ROS, similar to other cytotoxic derivatives of [D-Lys^6]GnRH (*25*).

Biological Assays. *Evaluation of Binding Affinity and Bioactivity*. Introduction of a large/bulky quinone moiety to a peptide can perturb its binding properties. The ability of the [D-Lys^6(MeoEmo)]GnRH to bind to rat pituitary GnRH receptors was evaluated in vitro by displacement assays, using ^{125}I-[D-Lys^6]GnRH as a radioligand. As shown in Figure 8, the agonist-based conjugate, [D-Lys^6(MeoEmo)]GnRH, bound specifically to the GnRH receptor, although its binding affinity was slightly lower than that of the parent agonist (IC_{50} = 5 and 1.1 nM, respectively). For evaluating the LH-releasing potencies of the [D-Lys^6]GnRH conjugate, rat pituitary cells were incubated in M-199 containing the desired concentrations of the tested peptide in the dark at 37 °C for 4 h as described (*30*). The bioactivity of [D-Lys^6(MeoEmo)]GnRH and of the parent peptide [D-Lys^6]GnRH (Figure 9) demonstrated that the agonist conjugate exhibited lower LH-releasing activity than its parent peptide. This result followed the same pattern that we found with respect to binding affinity.

DISCUSSION

A large number of quinones have been tested for antitumor activity and presently form one of the largest classes of antitumor agents approved for clinical use (*17*, *35*). Among them, 9,10-anthraquinone derivatives are also known as PSs. Upon irradiation in the presence of molecular oxygen, these compounds are able to generate ROS (*21*). We chose the anthraquinone-derivatized emodin as a lead molecule to develop new derivatives that can be used as potentially phototoxic drugs for conjugation with a carrier. Five new derivatives of emodin and their GnRH conjugates were synthesized (Schemes 2 and 3). Two main modifications were done on the emodin molecule: (i) the hydroxy groups in positions 4, 5, and 7 were partly or fully substituted by methoxy groups to study their influence on the ROS production potential, and (ii) the methyl group in position 6 was functionalized with different spacers to develop new synthetic methods to attach the cytotoxic molecule to the carrier, for example, peptide.

One of the new spacers is based on mercapto-propanoic acid, which was attached to the aromatic ring through the methyl in position 6. Its carboxylic group was conjugated to Lys6 in the agonist GnRH analogue. Alternatively, the methyl group of the emodin aromatic ring was converted into methylene amine (MeoEmo-NH_2). The amine moiety was then attached to the D-Glu6 of the GnRH analogue to give [D-Glu^6(MeoEmo-NH_2)]-GnRH. Also, the methylene amine was reacted with succinic anhydride and the resulting compound (MeoEmo-N-Succinyl) was conjugated to [D-Lys^6]GnRH. Thus, both amino and carboxylic "handles" can be used for the appropriate conjugation.

All new emodin derivatives under study stimulated the formation of singlet oxygen, $^1O_2$ (Figure 2), and oxygen radicals (Figure 6) when irradiated. However, there were substantial differences in the ROS production efficacy by these derivatives. MeoEmo and MeoEmo-N-Succinyl, which contain a methoxy group, produced the strongest ESR signals of detected spin adducts, indicating that they might be the better candidates for further conjugation with peptides. Apparently, the methoxy substitution elevates the ROS production. This was also shown previously for cynodontin (6-methyl-1,4,5,8-tetrahydroxyanthraquinone) and its methoxylated derivative (1,4-dimethoxy-5,8-dihydroxyanthraquinone). It was suggested that this effect may be attributed to the electron-donating (methoxy) groups directly attached to the quinone ring system (*36*). This view is in accordance with the report that electron-donating functional groups such as amino and alkoxy groups enhance the photodynamic efficiency (*37*).

Quinones are known to participate in both type I and type II photochemical reactions (*38*, *39*). The photoexcited states of quinones are known to be quenched by molecular oxygen to generate ROS. The involvement of $^1O_2$ in the production of the ESR signal was assessed by irradiation of the MeoEmo in d^6- or H^6-DMSO. We found (see Supporting Information) a stronger TEMPO ESR signal in deuterated solvent in accordance with a previous study showing that the lifetime of $^1O_2$ is longer in deuterated solvent (*40*).

We next compared the effect of emodin derivatives on the stimulation of superoxide radicals. The enhancement of the superoxide ESR signal by NADH can be explained according to reactions 3−6, showing that an electron donor can enhance semiquinone production. The photoreduced quinone anion may be the precursor for the formation of oxygen radicals such as the superoxide radical.

It is well established that iron ions and their complexes, known to be present in most biological systems, play an important role in the generation of ROS (*41*). As the result of dismutation of superoxide radical (spontaneous or superoxide

dismutase stimulated), hydrogen peroxide (H_2O_2, reaction 5) is formed. Hydrogen peroxide reacts either with superoxide anion radical in the presence of trace amounts of transition metal ion like Fe(II) ion (Haber−Weiss reaction, reaction 6), or directly with Fe(II) ion to produce hydroxyl radical by the Fenton reaction (reaction 7). The product of their reaction, hydroxyl radical ($HO^{\bullet}$), is a very strong oxidant mediating most quinones cytotoxicity. Adding Fe(II) to the MeoEmo solution resulted in the appearance of first superoxide ESR signal and fast generation of the DMPO−CH_3 adduct (Figure 4B). The observed transformation can be explained by stimulation of hydroxyl radical ($OH^{\bullet}$) produced by Fe(II) and hydrogen peroxide (H_2O_2) interaction (reactions 6 and 7). DMSO is known to react with hydroxyl radical at a high rate to generate methyl radical ($CH_3^{\bullet}$), which can be trapped by a DMPO and identified by its characteristic hyperfine pattern (*4*).

The generation of semiquinone radicals is a precondition for the formation of ROS (*42*, *43*). The similarity between ESR spectra of semiquinone generated by photoreduction and those obtained by chemical reduction (Figure 5) strongly suggests generation of MeoEmo semiquinone following irradiation, according to reactions 3 and 4.

The peptide carrier can decrease ROS production ability by the emodin derivative moiety. However, unlike the poor ROS photogeneration efficacy obtained with the emodic acid conjugate (*25*, *26*), our new conjugates with both peptides, [D-Lys^6]-GnRH and [D-Glu^6]GnRH, showed relatively high ROS production (Figures 3 and 7). The conjugates of MeoEmo and MeoEmo-N-Succinyl were found most active in generation of ROS through type I and type II reactions. The stability of the [D-Lys^6(MeoEmo)]GnRH conjugate was tested under irradiation conditions, and less than 3% degradation was found after 40 min under the same irradiation conditions.

We hypothesized that the conjugation of quinones as PSs to GnRH analogues may be a selective way of destroying cancerous cells through selective illumination of the tumor site. Breast, prostate, and other types of cancers were shown to express GnRH receptors, and GnRH analogues have been found to exhibit direct antiproliferative effect on related cancer cells (*5-9*, *44*, *45*). Indeed, GnRH analogues carrying cytotoxic drugs bind with high affinity to GnRH receptors and are subsequently internalized (*10*, *13*, *46*). We have used two analogues of GnRH as carriers for the emodin derivatives. The agonist [D-Lys^6]-GnRH was chosen because it can be conjugated selectively to the emodin derivatives MeoEmo, DihydroxyEmo, TrihydroxyEmo, and MeoEmo-N-Succinyl via the only free amino group in position 6. In previous works, this GnRH analogue was successfully conjugated with several quinonic and photoporphyrin derivatives and found stable upon irradiation (*25*, *29*, *47*). Another GnRH analogue, [D-Glu^6]GnRH, was chosen based on previous studies showing that the incorporation of a D-amino acid substituting for glycine in position 6 enhances the bioactive β-turn conformation of GnRH at the Gly^6−Leu^7 bond and decreases the susceptibility of the peptide to proteolytic degradation (*48*, *49*). The GnRH analogue [D-Glu^6]GnRH was selectively conjugated to the MeoEmo-NH_2 via the only free carboxylic group in position 6.

The MeoEmo conjugate was chosen as the lead conjugate since it showed the best ROS production. We therefore studied its binding and bioactivity properties compared to the parent peptide, [D-Lys^6]GnRH. The capability of [D-Lys^6(MeoEmo)]-GnRH to bind to rat pituitary GnRH receptors was determined by competitive binding assay using ^{125}I[D-Lys^6]GnRH as a tracer (Figure 8). The results demonstrated that the binding affinity of this conjugate is similar to that of the parent peptide. Investigation of the in vitro LH-releasing potencies, carried out in the dark, demonstrated a correlation between binding affinity to GnRH receptors and bioactivity (Figure 9). Based on previous studies (*26*) and on the results presented here, it is expected that this potential cytotoxic conjugate would bind specifically to cells that express GnRH receptors.

ACKNOWLEDGMENT

We thank Mrs. Sara Rubinraut and Mrs. Aviva Kapitovsky for the synthesis of [D-Lys^6]GnRH and [D-Glu^6]GnRH peptides. M.F. is the Lester Pearson Professor of Protein Chemistry. Y.K. is the Adlai E. Stevenson III Professor of Endocrinology and Reproductive Biology. This work was supported by a grant of the Israel Science Foundation (No. 703939).

Supporting Information Available: Effect of deuterated solvent on generation of ESR TEMPO signal by MeoEmo. This material is available free of charge via the Internet at http://pubs.acs.org.

LITERATURE CITED

(1) FitzGerald, D., and Pastan, I. (1989) Targeted toxin therapy for the treatment of cancer. *J. Natl. Cancer Inst. 81* (19), 1455−1463.

(2) Varga, J. M. (1985) Hormone-drug conjugates. *Methods Enzymol. 112*, 259−269.

(3) Kreitman, R. J., FitzGerald, D., and Pastan, I. (1992) Targeting growth factor receptors with fusion toxins. *Int. J. Immunopharmacol. 14* (3), 465−472.

(4) Weiner, L. M. (1994) Oxygen radicals generation and DNA scission by anticancer and synthetic quinones. *Methods Enzymol. 233*, 92−105.

(5) Kakar, S. S., Grizzle, W. E., and Neil, J. D. (1994) The nucleotide sequences of human GnRH receptors in breast and ovarian tumors are identical with that found in pituitary. *Mol. Cell. Endocrinol. 106*, 145−149.

(6) Eidne, K. A., Flanagan, C. A., Harris, N. S., and Millar, R. P. (1987) Gonadotropin-releasing hormone (GnRH)-binding sites human breast cancer cell lines and inhibitory effects of GnRH antagonists. *J. Clin. Endocr. Metab. 64*, 425−432.

(7) Quayum, A., Gullick, W., Clayton, R. C., Sikora, K., and Waxman, J. (1990) The effects of gonadotrophin hormone analogs in prostate cancer are mediated through specific tumor receptors. *Br. J. Cancer 62*, 96−99.

(8) Grundker, A. R., Gunthert, C., Millar, R. P., and Emons, G. (2002) Expression of gonaditropin-releasing hormone II (GnRH−II) receptor in human endometrial and ovarian cancer cells and effects of GnRH−II on tumor cell proliferation. *J. Clin. Endocrinol. Metab. 87* (3), 1427−1430.

(9) Volker, P., Grundker, C., Schmidt, O., Schulz, K. D., and Emons, G. (2002) Expression of receptors for luteinizing hormone-releasing hormone in human ovarian and endometrial cancers: frequency, autoregulation, and correlation with direct antiproliferative activity of luteinizing hormone-releasing hormone analogs. *Am. J. Obstet. Gynecol. 186*, 171−179.

(10) Hazum, E., Meidan, R., Liscovitch, M., Keinan, D., Linder, H. R., and Koch, Y. (1983) Receptor-mediated internalization of LHRH antagonists by pituitary cells. *Mol. Cell. Endocrinol. 30*, 291−301.

(11) Bajusz, S., Janaky, T., Csemus, V. J., Bokser, L., Fekete, M., Srkalovic, G., Redding, T. W., and Schally, A. V. (1989) Highly potent analogs of luteinizing hormone-releasing hormone containing D-phenylalanine nitrogen mustard in position 6. *Proc. Natl. Acad. Sci. U.S.A. 86*, 6318−6322.

(12) Janaky, T., Juhasz, A., Bajusz, S., Csernus, V., Srkalovic, G., Bokser, L., Milovanovic, S., Redding, T. W., Rekasi, Z., Nagy, A., and Schally, A. V. (1992) Analogs of luteinzing hormone-releasing hormone containing cytotoxic groups. *Proc. Natl. Acad. Sci. U.S.A. 89*, 972−976.

(13) Nagy, A., Schally, A. V., Armatis, P., Szepeshazi, K., Halmos, G., Kovacs, M., Zarandi, M., Groot, K., Miyazaki, M., Jungwirth, A., and Horvath, J. (1996) Cytotoxic analogs of luteinizing hormone-releasing hormone containing doxorubicin or 2-pyrrolinodoxorubicin, a derivative 500−1000 times more potent. *Proc. Natl. Acad. Sci. U.S.A. 93*, 7269−7273.

(14) Kovacs, M., Schally, A. V., Nagy, A., Koppan, M., and Groot, K. (1997) Recovery of pituitary function after treatment with a targeted cytotoxic analog of luteinizing hormone-releasing hormone. *Proc. Natl. Acad. Sci. U.S.A. 94*, 1420−1425.
(15) Foote, C. S. (1991) Definition of type I and type II photosensitized oxidation. *Photochem. Photobiol. 54* (5), 659.
(16) (a) Dougherty, T. J., Gomer, C. J., Henderson, B. W., Jori, G., Kessel, D., Korbelik, M., Moan, J., and Peng, Q. (1998) Photodynamic therapy. *J. Natl. Cancer Inst. 90* (12), 889−905. (b) Pass, H. I. (1993) Photodynamic therapy in oncology: mechanisms and clinical use. *J. Natl. Cancer Inst. 85* (6), 443−456.
(17) Powis, G. (1989) Free radical formation by antitumor quinones. *Free Radical Biol. Med. 6* (1), 63−101.
(18) Burkitt, M. J., Fitchett, M., and Gilbert, B. C. (1989) Free-radical damage to nucleic acid components initiated by the Fenton reaction: an ESR study, in *Medical, biochemical and chemical aspects of free radicals* (Hayaishi, O., Niki, E., Kondo, M., and Yoshikawa, T., Eds.) pp 63−70, Proceedings of the 4th Biennial General Meeting of the Society for Free Radical Research, Kyoto, Japan, 9−13 April 1988, Elsevier Science Publishers, B. V., Amsterdam.
(19) Pacifici, R. E., and Davies, K. J. (1990) Protein degradation as an index of oxidative stress. *Methods Enzymol. 186*, 485−502.
(20) Stadtman, E. R. (1993) Oxidation of free amino acids and amino acid residues in proteins by radiolysis and by metal-catalyzed reaction. *Annu. Rev. Biochem. 62*, 797−821.
(21) Gollinick, K., Held S., Martire, D. O., and Braslavsky, S. E. (1992) Hydroxyanthraquinones as sensitizers of singlet oxygen reactions: quantum yields of triplet formation and singlet oxygen generation in acetonitrile. *J. Photochem. Photobiol. A: Chem. 69*, 155−165.
(22) Dabestani, R., Hall, R. D., Sik, R. H., and Chignell, C. F. (1990) Spectroscopic studies of cutaneous photosensitizing agents−XV. Anthralin and its oxidation product 1,8-dihydroxyanthraquinone. *Photochem. Photobiol. 52* (5), 961−971.
(23) Thomas, C., and Pardini, R. S. (1992) Oxygen dependence of Hypericin-induced phototoxicity to EMT6 mouse mammary carcinoma cells. *Photochem. Photobiol. 55* (6), 831−837.
(24) Lavie, G., Valentine, F., Levin, B., Mazur, Y., Gallo, G., Lavie, D., Weiner, D., and Meruelo, D. (1989) Studies of the mechanisms of action of the antiretroviral agents hypericin and pseudohypericin. *Proc. Natl. Acad. Sci. U.S.A. 86* (15), 5963−5967.
(25) Rahimipour. S., Bilkis, I., Peron, V., Gescheidt, G., Barbosa, F., Mazur, Y., Koch, Y., Weiner, L., and Fridkin, M. (2001) Generation of free radicals by emodic acid and its [D-Lys^6]GnRH-conjugate. *Photochem. Photobiol. 74* (2), 226−236.
(26) Rahimipour. S., Ben-Aroya, N., Koch, Y., and Fridkin, M. (2001) Design, synthesis and evaluation of long-acting, potent analogue of gonadotropin-releasing hormone. *J. Med. Chem. 44* (22), 3645−3652.
(27) Buettner, G. R., and Oberley, L. W. (1978) Considerations in the spin trapping of superoxide and hydroxyl radical in aqueous systems using 5,5-dimethyl-1-pyrroline-1-oxide. *Biochem. Biophys. Res. Commun. 83* (1), 69−74.
(28) Atherton, E., and Sheppard, R. C. (1989) *Solid-phase peptide synthesis - A practical approach*, IRL Press, Oxford.
(29) Rahimipour, S., Weiner, L., Shrestha-Dawadi, P. B., Bittner, S., Koch Y., and Fridkin M. (1998) Cytotoxic peptides: naphthoquinonyl derivatives of luteinizing-hormone-releasing hormone. *Lett. Pept. Sci. 5*, 421−427.
(30) Yahalom, D., Koch, Y., Ben-Aroya, N., and Fridkin, M. (1999) Synthesis and bioactivity of fatty acid conjugated GnRH derivatives. *Life Sci. 64* (17), 1543−1552.
(31) Yahalom, D., Rahimipour, S., Koch, Y., Ben-Aroya, N., and Fridkin, M. (2000) Structure−activity studies of reduced-size gonadotropin-releasing hormone agonists derived from the sequence of an endothelin antagonist. *J. Med. Chem. 43* (15), 2824−2830.
(32) Daane, T. A., and Parlow, A. F. (1971) Periovulatory patterns of rat serum follicle stimulating hormone and luteinizing hormone during the normal estrous cycle as revealed by radioimmunoassys: effects of pentobarbital. *Endocrinology 88* (3), 653−663.
(33) Desbuquois, B., and Aurbach, G. D. (1971) Use of poly(ethylene glycol) to separate free and antibody-bound peptide hormones in radioimmunoassays. *J. Clin. Endocrinol. Metab. 33* (5), 732−738.
(34) Buettner, G. R. (1987) Spin trapping: ESR parameters of spin adducts. *Free Radical Biol. Med. 3*, 259−303.
(35) Moore, H. W., Czerniak, R., and Hamdan, A. (1986) Natural quinones as quinonemethide precursors−ideas in rational drug design. *Drugs Exp. Clin. Res. 12* (6−7), 475−494.
(36) Rajendran, M., Ramasamy, S., Rajamanickam, C., Gandhidasan R., and Murugesan, R. (2003) Photodynamic effects of two hydroxyanthraquinones. *Biochim. Biophys. Acta 1622* (2), 65−72.
(37) Driscoll, J. S., Hazard G. F. Jr., Wood H. B. Jr., and Goldin, A. (1974) Structure-antitumor activity relationships among quinone derivatives. *Cancer Chemother. Rep. 24* (2), 1−362.
(38) Wu, T., Shen, J., Song, A., Chen, S., Zhang, M., and Shen, T. (2000) Photodynamic action of amino substituted hypocrellins: EPR studies on the photogenerations of active oxygen and free radical species. *J. Photochem. Photobiol. B 57* (1), 14−21.
(39) Zhenjun D., and Lown, J. W. (1990) Hypocrellins and their use in photosensitization. *Photochem. Photobiol. 52* (3), 609−616.
(40) Zang, L. Y., Zhang, Z. Y., and Misra, H. P. (1990) EPR studies of trapped singlet oxygen ($^1O_2$) generated during photoirradiation of hypocrellin A. *Photochem. Photobiol. 52* (4), 677−83.
(41) Lauffer, R. B., Ed. (1992) *Iron and human disease*, CRC Press, Boca Raton, FL.
(42) Svingen, B. A., and Powis G. (1981) Pulse radiolysis studies of antitumor quinones: radical lifetimes, reactivity with oxygen, and one-electron reduction potentials. *Arch. Biochem. Biophys. 209* (1), 119−126.
(43) Li, A. S., and Chignell, C. F. (1987) Spectroscopic studies of cutaneous photosensitizing agents-X. A spin-trapping and direct electron spin resonance study of the photochemical pathways of daunomycin and adriamycin. *Photochem. Photobiol. 45* (4), 565−570.
(44) Limonta, P., Dondi, D., Moretti, R. M., Maggi, R., and Motta, M. (1992) Antiproliferative effects of luteinizing hormone-releasing hormone agonists on the human prostatic cancer cell line LNCaP. *J. Clin. Endocrinol. Metab. 75* (1), 207−212.
(45) Eidne, K. A., Flanagan, C. A., Harris, N. S., and Millar, R. P. (1987) Gonadotropin-releasing hormone (GnRH)-binding sites in human breast cancer cell lines and inhibitory effects of GnRH antagonists. *J. Clin. Endocrinol. Metab. 64* (3), 425−432.
(46) Szoke, B., Horvath, J., Halmos, G., Rekasi, Z., Groot, K., Nagy, A., and Schally, A. V. (1994) LH−RH analogue carrying a cytotoxic radical is internalized by rat pituitary cells in vitro. *Peptides 15* (2), 359−366.
(47) Rahimipour, S., Ben-Aroya, N., Ziv, K., Chen, A., Fridkin, M., and Koch, Y. (2003) Receptor-mediated targeting of a photosensitizer by its conjugation to gonadotropin-releasing hormone analogues. *J. Med. Chem. 46* (19), 3965−3974.
(48) Karten, M. J., and Rivier, J. E. (1986) Gonadotropin-releasing hormone analog design. Structure−function studies toward the development of agonists and antagonists: rationale and perspective. *Endocr. Rev. 7* (1), 44−66.
(49) Koch, Y., Baram, T., Hazum, E., and Fridkin, M. (1977) Resistance to enzymic degradation of LH−RH analogues possessing increased biological activity. *Biochem. Biophys. Res. Commun. 74* (2), 488−491.

BC050293R

Solid-Phase Synthesis of 2-[^{18}F]Fluoropropionyl Peptides

Jan Marik, Sven H. Hausner, Lauren A. Fix, M. Karen J. Gagnon, and Julie L. Sutcliffe*

Department of Biomedical Engineering, University of California, Davis, California 95616. Received March 6, 2006; Revised Manuscript Received June 9, 2006

The 2-[^{18}F]fluoropropionic (2-[^{18}F]FPA) acid is used as a prosthetic group for radiolabeling proteins and peptides for targeted imaging using positron emission tomography (PET). Radiolabeling of compounds with more than one acylable functional group can lead to complex mixtures of products; however, peptides can be labeled regioselectively on the solid phase. We investigated the use of a solid-phase approach for the preparation of 2-[^{18}F]fluoropropionyl peptides. [^{18}F]FPA was prepared and conjugated to the peptides attached to the solid phase support. The ^{18}F-labeled peptides were obtained in 175 min with decay corrected yields of 10% (related to [^{18}F]-fluoride) and with a purity of 76−99% prior HPLC purification. The suitability of various coupling reagents and solid supports were tested for radiolabeling of several peptides of various lengths.

INTRODUCTION

Radiotracers labeled with fluorine-18 (^{18}F, β^+ $t_{1/2}$ = 109.7min) are extensively used for positron emission tomography (PET) imaging of various physiological and pathological processes (*1*). The use of biomolecules such as peptides, proteins, or nucleic acids labeled with ^{18}F as agents for PET is a rapidly growing field (*2*). Examples of labeled peptides include octreotide (*3*), vasoactive intestinal peptide (*4*, *5*), integrin specific peptides (*6*−*10*), N^{ϵ}-(γ-glutamyl)lysine (*11*), neurotensin analogues (*12*), human C-peptide (*13*), and insulin (*14*). Incorporation of ^{18}F into biomolecules, including peptides, is exclusively carried out by employing various prosthetic groups. A large number of prosthetic groups bearing ^{18}F have been developed. These include acylation agents (*3*, *15*−*20*), amidation agents (*14*), imidation agents (*21*−*23*), alkylation agents (*21*), and species for photochemical conjugation (*20*). Undoubtedly, 4-[^{18}F]-fluorobenzoic acid ([^{18}F]FBA) is the most common prosthetic group used for labeling peptides since it can be relatively easily prepared, activated as succinimidyl fluorobenzoate ([^{18}F]SFB), and subsequently conjugated to the purified peptide in aqueous media. The synthesis of [^{18}F]SFB has been automated using the GE TracerLab synthesizer (*24*). However, the in-solution conjugation of [^{18}F]SFB to the peptide is limited to sequences bearing only one acylation-prone nucleophilic group; otherwise a complex mixture of nonselectively radiolabeled products is obtained (*5*). The slight difference between the pK_a of a backbone N^{α} amino group and a N^{ϵ} of lysine can be utilized, to some extent, to control the selectivity of the acylation process (*25*). To overcome this drawback, we previously developed a solid-phase approach for the incorporation of [^{18}F]FBA into the protected peptide sequence attached to the solid support, followed by removal of the protecting groups and cleavage from the solid phase (*8*, *26*). Our approach brings into the radiochemistry field all the advantages of solid-phase organic chemistry which has been extensively developed in the last 20 years. Particularly, it significantly simplifies the handling and purification of the desired product.

In 1996, Wester et al. reported a study comparing various prosthetic groups for incorporation of ^{18}F into proteins (*20*). Among these reagents 2-[^{18}F]fluoropropionc acid ([^{18}F]FPA) (*3*, *18*) offers an interesting alternative to the widely used [^{18}F]FBA. Compared to the [^{18}F]FBA, it was suggested that the [^{18}F]FPA would not significantly alter the properties of the peptide required for the biological activity such as size and lipophilicity which may result, for example, in reduction of hepatobiliary excretion of the radiolabeled species (*20*). Previously, [^{18}F]FPA was successfully attached to D-Phe^1-octreotide and used for imaging of the somatostatin receptor (*3*) and was also used to radiolabel an RGD-containing glycopeptide (*9*, *10*, *27*, *28*). The radiolabeled glycopeptide showed specificity for the $\alpha_v\beta_3$ integrin during in vitro binding assays and for the $\alpha_v\beta_3$ integrin expressing tumors in vivo. In both cases, the [^{18}F]FPA was activated as a 4-nitrophenyl ester and conjugated to the peptide precursor in solution. The glycopeptide contained only one amino group; hence, the labeling using 4-nitrophenyl 2-[^{18}F]-fluoropropionate was accomplished in a single step. However, D-Phe^1-octreotide contains Lys in position 5 and the acylation of the amino group in its side chain would result in loss of the high affinity to the somatostatin receptor. Therefore, the prosthetic group was attached to the N-terminal amino group of the ϵ-Boc-Lys^5 protected octreotide followed by removal of the Boc protecting group using trifluoroacetic acid.

In this paper, we extend our previously published procedure for radiolabeling of peptides on the solid-phase support, and the method for radiolabeling of peptides with [^{18}F]FPA is described. Various coupling conditions and solid supports were investigated for the conjugation of the [^{18}F]FPA to the peptides assembled on solid support.

EXPERIMENTAL PROCEDURES

Materials. Solvents and chemicals were purchased from Aldrich (Milwaukee, WI) if not stated otherwise. Racemic (±)-2-fluoropropionic acid was obtained from Matrix Scientific (Columbia, SC). The protected amino acids and coupling reagents were purchased from NovaBiochem (San Diego, CA) or GL Biochem (Shanghai, China). Resins for solid-phase peptide synthesis were obtained from the following vendors: NovaGel HL (A) and Amino PEGA (F) from NovaBiochem (San Diego, CA), TentaGel S (G) from Rapp Polymere GmbH (Tubingen, Germany), PL-PEGA (E) from Polymer Laboratories (Amherst, MA), CLEAR Amide (C) from Peptides International, Inc. (Louisville, KY), Rink Amide-MBHA (B) from Tianjin Nankai Hecheng Sci. and Tech. Co. Ltd. (Tianjin, China), and

* Corresponding author: Julie Sutcliffe, Ph.D., Department of Biomedical Engineering, 451 East Health Sciences Dr., University of California, Davis, Davis, CA 95616-5294. Tel: 530 754−7107. Fax: 530 754 5739. e-mail: jlsutcliffegoulden@ucdavis.edu.

10.1021/bc0600564 CCC: $33.50 © 2006 American Chemical Society
Published on Web 07/06/2006

Table 1. Decay Corrected Yields of [^{18}F]FPA Coupling to the Different Peptides on NovaGel HL Resin and Yields of the Product Cleavage[a]

compd	sequence	coupling	cleavage	total	purity
1	[^{18}F]FPA-YGGFL	16	36	6	90
2	[^{18}F]FPA-NAVPNLRGDLQVLAQKVART	6	43	3	76
3	[^{18}F]FPA-AGDLHVLR	10	40	4	99
4	AGDLHVLR-Ebes-Lys([^{18}F]FPA)	14	44	6	98

[a] Yields and purity are given in %.

PAL-PEG-PS (D) from Applied Biosystems (Warrington, UK). Protected hydrophilic ethylene glycol-based linker 2,2′-(ethylenedioxy)bis(ethylamine)monosuccinamide (Fmoc-Ebes-OH) was synthesized according to the previously published procedure (*29*), and 9-methylanthranyl 2-bromopropionate was prepared according to the published procedure (*18*). Mass spectrometry analysis was performed using a Finnigan LCQ instrument. RP-HPLC was used to analyze and purify the products. Analytical reverse-phase HPLC system A: Phenomenex Jupiter 4 μm Proteo 90A (250 × 4.6 mm, 4 μm), linear gradient 0.05% TFA−acetonitrile 10−90% in 30 min, flow rate 1 mL/min. Semi-preparative reverse-phase HPLC system B: Phenomenex Jupiter 10 μm Proteo 90A (250 × 10 mm, 10 μm), linear gradient 0.05% TFA−90% acetonitrile 10−90% in 30 min, flow rate 3 mL/min; system C: Phenomenex Jupiter 10 μm C18 300A (250 × 10 mm, 10μm), isocratic 60% acetonitrile − 0.05% TFA, flow rate 3 mL/min. ^{18}F was produced from the ^{18}O(p,n)^{18}F nuclear reaction on [^{18}O]H_2O (Marshall Isotopes Ltd. (Tel Aviv, Israel)) using the CTI RDS 111 negative ion cyclotron. Sep-Pak SPE cartridges were obtained from Waters (Milford, MA).

Peptide Synthesis. The peptides **1**−**4** (Table 1) were synthesized on resin A. The synthesis was performed using a Pioneer continuous flow synthesizer ABI (Foster City, CA) using 4-fold excess of amino acid and DIC/HOBt activation and a 2 h coupling cycle followed by a 10 min Fmoc deprotection with 20% piperidine in DMF. Peptide **1** synthesized on resins **B**−**G** was prepared manually using 3-fold excess of amino acid and using HATU/DIEA activation for 30 min followed by Fmoc deprotection with 20% piperidine−DMF (2 × 10 min). The hydrophilic linker was incorporated into the peptide chain using a Fmoc-protected analogue (Fmoc-Ebes-OH) and HATU/DIEA activation. The N-terminal amino group in peptide **4** was protected by incubation of the resin with 3-fold excess of di-*tert.*-butyl dicarbonate and DIEA for 30 min to yield N-Boc-protected peptide. The allyloxycarbonyl (Alloc) protecting group in peptide **4** was removed using 0.2 equiv of Pd[PPh_3]$_4$ and 20 equiv of phenylsilane 2 × 30 min (*30*). The peptide resins were washed with DMF and methanol and dried in vacuo.

Synthesis of (±)-2-Fluoropropionyl Peptides. 2-Fluoropropionic acid ([^{19}F]FPA) was coupled to the peptide using 3-fold excess of [^{19}F]FPA and DIC/HOBt activation for 30 min. The progress of the reaction was monitored by ninhydrin-based Kaiser test (*31*). The [^{19}F]FPA-peptides **1**−**4** were cleaved from the solid support using trifluoroacetic acid/triisopropylsilane/water 95:2.5:2.5 v/v/v. The crude peptides were precipitated from the cleavage mixture by the addition of an excess of chilled diethyl ether. The solvent was then removed, and the solid product was triturated three times with diethyl ether. The peptides were purified on semipreparative HPLC (system B) and characterized using mass spectrometry. Analytical data for peptides **1**−**4**: **1** HPLC (system A) retention times 15.5, 15.6 min; MS ESI *m*/*z* 629.5 $[M + H]^+$; **2** HPLC (system A) retention time 14.6 min; MS ESI *m*/*z* 2236.8 $[M + H]^+$; **3** HPLC (system A) retention times 10.7, 11.0 min; MS ESI *m*/*z* 953.7 $[M + H]^+$; **4** HPLC (system A) retention time 9.4 min; MS ESI *m*/*z* 1311.8 $[M + H]^+$.

Radiochemical Synthesis of (±)-2-[^{18}F]Fluoropropionic Acid. The fluoride anion was captured on a QMA Sep-Pak cartridge and eluted with 1 mL of 4,7,13,16,21,24-hexaoxa-1,-10-diazabicyclo[8.8.8]hexacosane (K222) and potassium carbonate solution (10 mg of K222, 2 mg of K_2CO_3) in acetonitrile containing 6% water. The acetonitrile was evaporated at 100 °C under a gentle stream of nitrogen and dried by azeotropic distillation with 3 × 1 mL of acetonitrile. The solution of 9-methylanthranyl 2-bromopropionate in acetonitrile (2 mL) was added, and the mixture was heated in sealed vial to 100 °C for 15 min. The product was isolated on semipreparative HPLC (system C) retention time 18−20 min. The fraction containing the product was diluted with water to 10 mL, and the product was captured on a C-18 Sep-Pak cartridge. The cartridge was washed with 5 mL of water and dried with a stream of nitrogen. The 9-methylanthranyl 2-[^{18}F]fluoropropionate was eluted with 3 mL of dichloromethane, and the solvent was evaporated under a stream of nitrogen. The methylanthranyl ester was hydrolyzed using 200 μL of the hydrolysis mixture (9.5 mL water, 0.5 mL triethylamine) and 300 μL of DMF in a closed vial at 100 °C for 10 min. The solvent was evaporated at 100 °C under a stream of nitrogen, and the product was dried using azeotropic distillation with acetonitrile (3 × 1 mL). The product was obtained with a decay corrected yield of 63% and a synthesis time of 82 min (Scheme 1).

Scheme 1. Labeling of Peptides with 2-[^{18}F]fluoropropionic Acid ([^{18}F]FPA) on Solid Phase

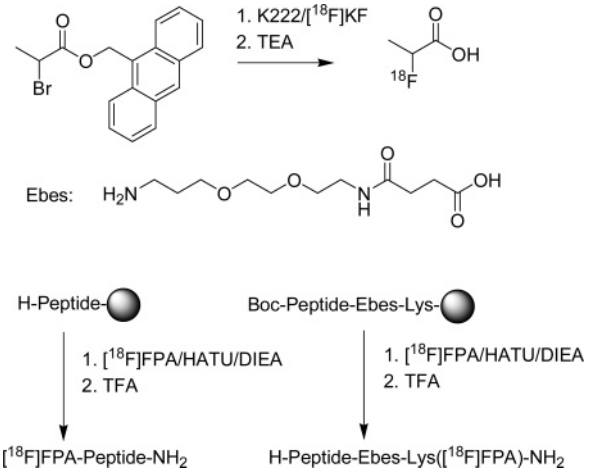

Radiochemical Synthesis of (±)-2-[^{18}F]Fluoropropionyl Peptides (1−4). The coupling of [^{18}F]FPA to the peptide and the cleavage from the resin were carried out in a 1 mL syringe equipped with a frit at the bottom of the cylinder. The reagents and washing solvents were withdrawn and dispensed using the plunger. This procedure can be easily performed using robotic manipulators. The [^{18}F]FPA in 50 μL of DMF was added to 1−2 mg of the peptide resin swollen in DMF, followed with HATU (5 mg) in 50 μL of DMF, and DIEA (10 μL) in 50 μL of DMF. The reaction mixture was incubated with shaking at 30 °C for 30 min. The solvent was removed, and the solid support was washed with DMF (3 × 0.5 mL) and methanol (3 × 0.5 mL). The TFA-based cleavage mixture (0.7 mL of trifluoroacetic acid/triisopropylsilane/water 95:2.5:2.5 v/v/v) was withdrawn into the syringe, and the reaction mixture was incubated at 30 °C for (3 × 10 min). The product was collected, and the resin was washed with dichloromethane (0.5 mL). The

cleavage solution was evaporated under a stream of nitrogen, and the crude product was analyzed on radio-HPLC (system A). Analytical data for peptides **1**−**4** (the radiochemical yields were decay corrected to the end of [18F]FPA preparation): **1** HPLC (system A) retention time 15.7 min; yield 6%; **2** HPLC (system A) retention time 14.7 min; yield 3%; **3** HPLC (system A) retention times 11.0, 11.2 min; yield 4%; **4** HPLC (system A) retention time 9.6 min; yield 6%. The synthesis time from EOB was 175 min.

RESULTS AND DISCUSSION

The procedure for the preparation of [18F]FPA from racemic 9-methylanthranyl 2-bromopropionate provides both enantiomers; thus, two diastereoisomers of the final labeled peptide are obtained. The function of the prosthetic group is to introduce the radionuclide into the target molecule without changing its biological properties; therefore, the presence of two diastereoisomers of the product is not expected to have any effect on its pharmacological properties. To address this problem and the effect of the prosthetic group in general, two approaches for the introduction of the prosthetic group are presented (Scheme 1). In the first approach the prosthetic group was attached to the amino terminus of the peptide sequence (Table 1, compounds **1**−**3**) as previously reported (*8*, *26*). This strategy is the most straightforward method to introduce the prosthetic group into the molecule and does not significantly change its final size. However, when the prosthetic group is attached directly to the peptide, it can potentially have a deteriorating effect on the biological properties of the peptide, especially in the case where a free amino terminus is required for receptor binding. In the latter approach, the prosthetic group was attached to the C-terminal part of the molecule via the N^{ϵ} amino group of lysine. The ethylene glycol-based hydrophilic linker Ebes was inserted between the lysine bearing the prosthetic group and the peptide (Table 1, compound **4**) (*29*). The suitability of the first or second labeling strategy should be investigated for each particular application.

We slightly modified the previously published procedure for the preparation of [18F]FPA and its use for protein radiolabeling (*18*). The methylanthranyl 2-[18F]fluoropropionate was obtained from the 2-bromo precursor and purified on semipreparative HPLC followed by the hydrolysis of the 9-methylanthranyl ester using 5% aqueous triethylamine and DMF as a cosolvent. The obtained [18F]FPA was dried using azeotropic distillation with acetonitrile in the presence of DMF. We found that DMF prevented the undesired evaporation of the volatile product, and it did not have any significant effect on the subsequent coupling reaction as DMF is the reaction solvent.

Three different carboxylic acid activating reagents were used in this study: *N*,*N*′-diisopropylcarbodiimide (DIC), 2-(7-aza-1*H*-benzotriazol-1-yl)-1,1,3,3-tetramethyluronium hexafluorophosphate (HATU), and diethyl cyanophosphonate (DECP). DIC activates the acid as the *O*-acyl diisopropyl urea derivative which reacts subsequently with the primary or secondary amine. HATU is a superior reagent used for coupling of "difficult" sequences in the peptide synthesis. The 7-aza-1-hydroxybenzotriazolyl ester is formed in the presence of base, and it reacts readily with nucleophiles such as a primary or secondary amine. DECP forms a mixed anhydride of 2-fluoropropionic acid and diethyl phosphonate which subsequently reacts with a primary or secondary amine in the presence of base (*32*). We found that HATU-mediated activation provided comparable results to the DECP activation for coupling [18F]FPA to the peptide **1**; however, the DIC activation did not provide satisfactory results. The yield of the coupling reaction using HATU was 16%, and the purity of the crude product was 90%. In the case of DECP activation the yield of the conjugation was 9% and the purity of the final product was 93%. The only radioactive material isolated from the activation mixture was unreacted [18F]FPA.

[18F]FPA was conjugated to various peptides listed in Table 1. The products were obtained in yields ranging from 6 to 16%, and only a slight dependency of the yield on the size and complexity of the peptide was observed. The radiochemical purity was confirmed by coinjection of the corresponding [19F]-FPA-labeled peptides. The standards were prepared by DIC mediated coupling of [19F]FPA to the N-terminus or NH^{ϵ} of lysine and analyzed using HPLC and mass spectrometry. The cleavage was performed at 30 °C, and the purity of the crude material was in the range of 90−99% in most cases. In solid-phase peptide synthesis, the purity of the crude products decreases with increasing length of the peptide chain; this accounts for the lower purity of the 20 amino acid long peptide **2**. The "no-carrier-added" (n.c.a) radiolabeled peptides were obtained with a specific activity greater than 37 GBq/μmol.

In the standard peptide synthesis strategy, 3-fold excess of the amino acid and coupling reagent and 6-fold excess of the base are used to accomplish the successful attachment of the amino acid to the free amino terminus of the peptide chain attached to the resin (*33*). Such conditions cannot be satisfied in the case of coupling of the n.c.a. prosthetic groups such as [18F]FPA, and as a result, the amount of the coupling reagent is in huge excess if compared to the amount of the acid. The excess of the uronium salt-based coupling reagents such as HATU could lead to the guanidylation of the N-terminus of the peptide (*33*). We investigated the effect of the amount of the HATU/DIEA in the reaction mixture, and we found that the yields of the coupling reaction were not changed when 1−10 mg of HATU was used together with 10 μL of DIEA in 200 μL of DMF. Lower amounts of HATU led to lower yields, and a lower amount of the base (DIEA) was not sufficient to adjust pH to the desired range 8−9. Unfortunately, the yield of the conjugation remained between 10 and 20%. Since the yield of the [18F]FPA coupling was comparable with that of DECP, which uses the mixed anhydride activation method, and the N-terminal guanidylation is not possible, the formation of the N-terminal guanidylation byproducts is therefore not a yield-limiting effect.

The presence of an auxiliary base required to prevent undesired evaporation of the [18F]FPA during azeotropic removal of the water from the mixture used for the hydrolysis of the precursor could affect the yield of the conjugation. The commonly used bases are tetralkylammonium hydroxides (*20*) or potassium carbonate K222 mixture (*34*). As mentioned above, we found that the high boiling point aprotic solvent DMF minimized the loss of the hydrolyzed acid during the azeotropic distillation. The presence of potassium carbonate K222 complex led to lower yields of the conjugation; however, the use of DMF provided the product with yields and purity identical to the previously reported tetramethylammonium hydroxide.

To further investigate the factors limiting the coupling of the prosthetic groups to the resin-bound peptides, we compared various commercially available solid-phase peptide synthesis (SPPS) resins. The common SPPS resins are polymer beads with a diameter of 100−300 μm. The linker allows selective detachment of the product from the solid support and is covalently attached to the polymer matrix. There are two factors which affect the behavior of the solid support: the composition of the polymer matrix and the nature of the linker. The polymer matrix used for SPPS is based on various cross-linked polystyrene (PS), poly(ethylene glycol) (PEG), polyamide or polyacrylamide copolymers, or grafted polymers. The amount of the linker attached to the beads determines the loading of the particular resin. The nature of the linker determines the nature of the C-terminus of the final product as well as the procedure

Table 2. Decay Corrected Yields of [^{18}F]FPA Coupling to the Peptide 1 Attached to the Different Solid Supports and Yields of the Product Cleavage[a]

resin	resin	coupling	cleavage	total	purity
A	NovaGel HL	16	36	6	90
B	Rink Amide-MBHA	15	76	11	99
C	CLEAR Amide	9	75	7	98
D	PAL-PEG-PS	13	89	11	100
E	PL-PEGA	9	70	7	92
F	Amino-PEGA	14	71	10	95
G	TentaGel S	14	81	11	92

[a] Yields and purity are given in %.

required for cleavage. In this study, we focused on the preparation of the peptide amides; thus, the acid-sensitive linkers Rink and PAL were used. The results are summarized in Table 2. We did not find any significant effect of the resin nature on the coupling step, and the best obtained yields remained below 20% for all resins evaluated. However, we found some resins more suitable for this radiochemical application due to better yields obtained during the cleavage step. The cleavage of the product from the solid support and simultaneous side chain protecting group removal were accomplished using a mixture of trifluoroacetic acid and appropriate scavengers. We found that the incubation of the resin with the cleavage mixture for 30 min provided 75% of the product from the Rink linker decorated resins, except the high loading NovaGel resin where the cleavage yields were below 50%. The resin containing the PAL linker provided 89% of the product in 20 min incubation. The use of very acid-labile linkers such as XAL has been previously reported to provide similar cleavage reaction yields (*8*, *26*). However, the stability of side chain protecting groups has to be considered in this case; when the cleavage time is short, some of them may not be fully removed.

In conclusion, [^{18}F]FPA was conjugated with various peptides. The ^{18}F-labeled peptides were obtained in 175 min with decay corrected yields around 10% (related to [^{18}F]fluoride) and with a purity of 76−99%. Several solid-phase synthesis supports were found suitable for this application.

ACKNOWLEDGMENT

We would like to thank Salma Jivan (radiochemist, Center for Molecular and Genomic Imaging) and Dave Kukis (Cyclotron Facilities Manager, Center for Molecular and Genomic Imaging) for radionuclide production.

Supporting Information Available: RP-HPLC chromatographs for compounds **1**−**4**. The material is available free of charge via the Internet at http://pubs.acs.org.

LITERATURE CITED

(1) Glaser, M., Luthra, S. K., and Brady, F. (2003) Applications of positron-emitting halogens in PET oncology (Review). *Int. J. Oncol. 22*, 253−267.

(2) Okarvi, S. M. (2001) Recent progress in fluorine-18 labelled peptide radiopharmaceuticals. *Eur. J. Nucl. Med. 28*, 929−938.

(3) Guhlke, S., Wester, H. J., Bruns, C., and Stocklin, G. (1994) (2-[^{18}F]fluoropropionyl-(D)phe1)-octreotide, a potential radiopharmaceutical for quantitative somatostatin receptor imaging with PET: synthesis, radiolabeling, in vitro validation and biodistribution in mice. *Nucl. Med. Biol. 21*, 819−825.

(4) Jagoda, E. M., Aloj, L., Seidel, J., Lang, L., Moody, T. W., Green, S., Caraco, C., Daube-Witherspoon, M., Green, M. V., and Eckelman, W. C. (2002) Comparison of an ^{18}F labeled derivative of vasoactive intestinal peptide and 2-deoxy-2-[^{18}F]fluoro-D-glucose in nude mice bearing breast cancer xenografts. *Mol. Imaging Biol. 4*, 369−379.

(5) Moody, T. V., Leyton, J., Unsworth, E., John, C., Lang, L., and Eckelman, W. C. (1998) (Arg15, Arg21) VIP: Evaluation of biological activity of localization to breast cancer tumors. *Peptides 19*, 585−592.

(6) Chen, X., Tohme, M., Park, R., Hou, Y., Bading, J. R., and Conti, P. S. (2004) Micro-PET imaging of alphavbeta3-integrin expression with ^{18}F-labeled dimeric RGD peptide. *Mol. Imaging 3*, 96−104.

(7) Chen, X., Park, R., Shahinian, A. H., Tohme, M., Khankaldyyan, V., Bozorgzadeh, M. H., Bading, J. R., Moats, R., Laug, W. E., and Conti, P. S. (2004) ^{18}F-labeled RGD peptide: initial evaluation for imaging brain tumor angiogenesis. *Nucl. Med. Biol. 31*, 179−189.

(8) Sutcliffe-Goulden, J. L., O'Doherty, M. J., Marsden, P. K., Hart, I. R., Marshall, J. F., and Bansal, S. S. (2002) Rapid solid-phase synthesis and biodistribution of ^{18}F-labelled linear peptides. *Eur. J. Nucl. Med. Mol. Imaging 29*, 754−759.

(9) Haubner, R., Wester, H. J., Weber, W. A., Mang, C., Ziegler, S. I., Goodman, S. L., Senekowitsch-Schmidtke, R., Kessler, H., and Schwaiger, M. (2001) Noninvasive imaging of alpha(v)beta3 integrin expression using ^{18}F-labeled RGD-containing glycopeptide and positron emission tomography. *Cancer Res. 61*, 1781−1785.

(10) Haubner, R., Kuhnast, B., Mang, C., Weber, W. A., Kessler, H., Wester, H. J., and Schwaiger, M. (2004) [^{18}F]Galacto-RGD: synthesis, radiolabeling, metabolic stability, and radiation dose estimates. *Bioconjugate Chem. 15*, 61−69.

(11) Wust, F., Hultsch, C., Bergmann, R., Johannsen, B., and Henle, T. (2003) Radiolabeling of isopeptide N^{ϵ}-(γ-glutamyl)-L-lysine by conjugation with *N*-succinimidyl-4-[^{18}F]fluorobenzoate. *Appl. Radiat. Isot. 59*, 43−48.

(12) Bergmann, R., Scheunemann, M., Heichert, C., Mading, P., Wittrisch, H., Kretzschmar, M., Rodig, H., Tourwe, D., Iterbeke, K., Chavatte, K., Zips, D., Reubi, J. C., and Johannsen, B. (2002) Biodistribution and catabolism of ^{18}F-labeled neurotensin(8−13) analogs. *Nucl. Med. Biol. 29*, 61−72.

(13) Fredrickson, A., Johnstrom, P., Stone-Elander, S., Jonasson, P., Nygren, P. A., Ekberg, K., Johansson, B. L., and Wahren, J. (2001) Labeling of human C-peptide by conjugation with N-succinimidyl-4-[^{18}F]fluorobenzoate. *J. Labelled Compd. Radiopharm. 44*, 509−519.

(14) Shai, Y., Kirk, K. L., Channing, M. A., Dunn, B. B., Lesniak, M. A., Eastman, R. C., Finn, R. D., Roth, J., and Jacobson, K. A. (1989) ^{18}F-labeled insulin: a prosthetic group methodology for incorporation of a positron emitter into peptides and proteins. *Biochemistry 28*, 4801−4806.

(15) Block, D., Coenen, H. H., and Stocklin, G. (1988) ^{18}F-fluoroacylation via fluorocarboxylic acid esters. *J. Labelled Compd. Radiopharm. 25*, 185−200.

(16) Herman, L. W., Fischman, A. J., Tompkins, R. G., Hanson, R. N., Byon, C., Strauss, H. W., and Elmaleh, D. R. (1994) The use of pentafluorophenyl derivatives for the ^{18}F labeling of proteins. *Nucl. Med. Biol. 21*, 1005−1010.

(17) Lang, L., and Eckelman, W. C. (1994) One-step synthesis of ^{18}F labeled [^{18}F]-*N*-succinimidyl 4-(fluoromethyl)benzoate for protein labeling. *Appl. Radiat. Isot. 45*, 1155−1163.

(18) Guhlke, S., Coenen, H. H., and Stocklin, G. (1994) Fluoroacylation Agents Based on Small n.c.a. [^{18}F]Fluorocarboxylic Acids. *Appl. Radiat. Isot. 45*, 715−727.

(19) Vaidyanathan, G., and Zalutsky, M. R. (1994) Improved synthesis of *N*-succinimidyl 4-[^{18}F]fluorobenzoate and its application to the labeling of a monoclonal antibody fragment. *Bioconjug. Chem. 5*, 352−356.

(20) Wester, H. J., Hamacher, K., and Stocklin, G. (1996) A comparative study of n.c.a. fluorine-18 labeling of proteins via acylation and photochemical conjugation. *Nucl. Med. Biol. 23*, 365−372.

(21) Kilbourn, M. R., Dence, C. S., Welch, M. J., and Mathias, C. J. (1987) Fluorine-18 labeling of proteins. *J. Nucl. Med. 28*, 462−470.

(22) Poethko, T., Schottelius, M., Thumshirn, G., Hersel, U., Herz, M., Henriksen, G., Kessler, H., Schwaiger, M., and Wester, H. J. (2004) Two-step methodology for high-yield routine radiohalogenation of peptides: ^{18}F-labeled RGD and octreotide analogs. *J. Nucl. Med. 45*, 892−902.

(23) Poethko, T., Schottelius, M., Thumshirn, G., Herz, M., Haubner, R., Henriksen, G., Kessler, H., Schwaiger, M., and Wester, H. J. (2004) Chemoselective pre-conjugate radiohalogenation of unprotected mono- and multimeric peptides via oxime formation. *Radiochim. Acta 92*, 317−327.

(24) Mading, P., Fuchtner, F., and Wust, F. (2005) Module-assisted synthesis of the bifunctional labeling agent *N*-succinimidyl 4-[18F]-fluorobenzoate ([18F]SFB). *Appl Radiat Isot. 63*, 329−332.

(25) Wester, H. J., Krommeich, C. H., Fixmann, A., Former, W., Muller-Gartner, H. W., and Stocklin, G. (1995) *J. Labelled Compd. Radiopharm. 37*, 513.

(26) Sutcliffe-Goulden, J. L., O'Doherty, M. J., and Bansal, S. S. (2000) Solid-phase synthesis of [18F]labelled peptides for positron emission tomography. *Bioorg. Med. Chem. Lett. 10*, 1501−1503.

(27) Haubner, R., Weber, W. A., Beer, A. J., Vabuliene, E., Reim, D., Sarbia, M., Becker, K. F., Goebel, M., Hein, R., Wester, H. J., Kessler, H., and Schwaiger, M. (2005) Noninvasive visualization of the activated $\alpha v\beta 3$ integrin in cancer patients by positron emission tomography and [18F]Galacto-RGD. *PLoS Med. 2*, e70.

(28) Beer, A. J., Haubner, R., Goebel, M., Luderschmidt, S., Spilker, M. E., Wester, H. J., Weber, W. A., and Schwaiger, M. (2005) Biodistribution and pharmacokinetics of the $\alpha v\beta 3$-selective tracer 18F-galacto-RGD in cancer patients. *J. Nucl. Med. 46*, 1333−1341.

(29) Song, A., Wang, X., Zhang, J., Marik, J., Lebrilla, C. B., and Lam, K. S. (2004) Synthesis of hydrophilic and flexible linkers for peptide derivatization in solid phase. *Bioorg. Med. Chem. Lett. 14*, 161−165.

(30) Grieco, P., Gitu, P. M., and Hruby, V. J. (2001) Preparation of 'side-chain-to-side-chain' cyclic peptides by Allyl and Alloc strategy: potential for library synthesis. *J. Pept. Res. 57*, 250−256.

(31) Kaiser, E., Colescott, R. L., Bossinger, C. D., and Cook, P. I. (1970) Color test for detection of free terminal amino groups in the solid-phase synthesis of peptides. *Anal. Biochem. 34*, 595−598.

(32) Ninomiya, K., Shioiri, T., and Yamada, S. (1976) Phosphorus in organic synthesis. XII. Amino acids and peptides. XXII. Reaction of penicillin sulfoxides with diethyl phosphorocyanidate (DEPC). *Chem Pharm Bull (Tokyo), 24*, 2711−2715.

(33) Albericio, F., Bofill, J. M., El-Faham, A., and Kates, S. (1998) Use of Uronium Salt-Based Coupling Reagents in Peptide Synthesis. *J. Org. Chem. 63*, 9678−9683.

(34) Zijlstra, S., Gunawan, J., and Burchert, W. (2003) Synthesis and evaluation of a 18F-labelled recombinant annexin-V derivative, for identification and quantification of apoptotic cells with PET. *Appl Radiat Isot. 58*, 201−207.

BC0600564

Synthesis of Very Short Chain Lysophosphatidyloligodeoxynucleotides†

Rosa Chillemi, Danilo Aleo, Giuseppe Granata, and Sebastiano Sciuto*

Dipartimento di Scienze Chimiche, Università di Catania, viale A. Doria 6, 95125, Catania, Italy. Received December 28, 2005; Revised Manuscript Received May 19, 2006

Very short chain 5′-*O*-lysophosphatidyloligonucleotides [5′-*O*-(1-*O*-palmitoyl-*sn*-glycero-3-phosphoryl)oligodeoxynucleotides, (5′-LyPOdNs)] were synthesized following a two-step chemoenzymatic synthesis. 5′-*O*-(*sn*-Glycero-3-phosphoryl)oligodeoxynucleotides (5′-GPOdNs) were first prepared by simply using a phosphoramidite of [(4*S*)-2,2-dimethyl-1,3-dioxolan-4-yl]methanol (**1**) in a further coupling step after the solid-phase elongation of each desired oligodeoxynucleotide. Next, the regioselective palmitoylation at the C-1 hydroxyl of the glycerol moiety of 5′-GPOdNs was achieved by a lipase-catalyzed transacylation with trifluoroethyl palmitate in organic solvent. Despite of the molecular bulkiness of 5′-GPOdNs, 2-, 3-, and 4-mer 5′-LyPOdNs were prepared by this procedure. Although in very low yield, 5- and 6-mer 5′-LyPOdNs were also obtained by this way.

INTRODUCTION

In the continuous searching for antiviral drugs with different structures and unique mechanisms of action, other than those conferred by conventional nucleoside analogues (*1*), a number of small oligonucleotides and oligonucleotide analogues have been shown to be of great pharmacological interest. Some natural dinucleotides and dinucleotide analogues have been discovered as inhibitors of HIV integrase (*2*), while short oligonucleotide analogues have been reported as novel inhibitors of RNA-dependent RNA polymerase of HCV (*3*). More recently, some di- and trinucleotide analogues have been identified as potent inhibitors of HBV replication (*4*). So, the use of very short chain oligonucleotide analogues as inhibitor molecules to target viral replication represents a promising novel approach to antiviral interference. However, one of the recurring problems encountered for in vivo application of oligonucleotides is the low permeability of cell membranes to these large polyionic molecules (*5*, *6*). Nevertheless, the transport of these molecules into cells has been shown to be facilitate by linking them to lipophilic carriers (*7*, *8*); so, pharmacologically active oligonucleotides bearing a terminal biodegradable lipophilic group attached through a phosphoester bond could be useful pro-drugs with improved cellular uptake.

In this regard, the phosphatidyl group seems to be one of the most suitable lipophilic groups, on account of its widespread occurrence in the molecular structure of many lipid constituents of cell membranes. But, to our knowledge, neither this group nor the structurally related lysophosphatidyl one have been utilized as the lipophilic moiety of lipo-oligonucleotides.

This is probably due to an actual difficulty encountered in a direct chemical attachment of these groups to oligonucleotides elongated on the solid phase by standard phosphoramidite chemistry procedures; such a way, in fact, suffers from the lability of the carboester bond in these groups under the strongly basic conditions routinely used to remove classical amino protecting groups of nucleotides.

In our previous work (*9*, *10*) we developed a general synthetic preparation of 5′(3′ or 2′)-*O*-lysophosphatidyl conjugates of deoxyribo- and ribonucleosides as well. Following a two-step chemoenzymatic strategy, mono[(2*R*)-2,3-dihydroxypropyl] esters of the pertinent 5′(3′ or 2′)-mononucleotides (glycerophosphorylnucleosides, GPNs) were first prepared by opportunely applying the phosphoramidite chemistry on solid phase or in solution. In a subsequent step, selective acylation at 1-OH of the glycerol moiety of GPNs was achieved by a lipase-catalyzed (Lipozyme) transacylation with activated fatty acid esters in organic solvent. By this procedure, lysophosphatidyl derivatives of pharmacologically active nucleoside analogues were also prepared, which showed a clearly enhanced ability to penetrate model lipid monolayers over that of free nucleoside counterparts (*10*).

So, in light of these findings and aiming to overcome the above drawbacks, we considered the possibility of preparing lysophosphatidyl conjugates of short chain oligodeoxynucleotides by exploiting once again the chemoenzymatic strategy previously followed for the preparation of lysophosphatidylnucleosides. This work reports usefulness and limits of such a procedure for the preparation of this kind of lipoconjugates.

EXPERIMENTAL PROCEDURES

General Methods. ^{1}H and ^{13}C NMR spectra were recorded on a Varian Unity Inova spectrometer at 500 and 125.7 MHz, respectively. The chemical shifts are reported as δ (ppm) referenced to the following: (a) TMS as internal standard for the experiments in $CDCl_3$, C_6D_6, and CD_3OD; (b) the resonance of the residual HOD ($\delta = 4.82$ ppm) for ^{1}H experiments in D_2O; (c) the signal of appropriately added CD_3OD ($\delta = 49.0$ ppm) for ^{13}C experiments in D_2O. Unequivocal assignments of ^{1}H and ^{13}C resonances were supported by 1D (spin decouplings, NOEDS, DEPT, or APT) and 2D (^{1}H−^{1}H COSY, HSQC, ROESY) experiments. FAB-MS spectra were recorded with a Fisons ZAB 2SE spectrometer with glycerol as matrix (unless otherwise specified). ESI-MS spectra were recorded with a Finnigan LCQ Deca instrument. MALDI-MS spectra were recorded with a Voyager-DE PRO time-of-flight (Applied Biosystems) using 3-hydroxypicolinic acid as matrix. The solid-phase oligonucleotide syntheses were carried out on the Cyclone Plus 8400 DNA synthesizer. Aminopropyl-CPG (500 Å pore size) was purchased from CPG Inc. PLC were performed on silica gel (40−63 μm, Merck). HPLC was performed on a Hewlett-Packard 1050 chromatograph equipped with UV detector set at 260 nm, using LiChrospher-100 ODS (5 μm; 4 × 250

† Dedicated to Professor Mario Piattelli on the occasion of his 80th birthday.

* To whom correspondence should be addressed. Tel: +39-095-738-5208. Fax: +39-095-58-0138. E-mail: ssciuto@dipchi.unict.it.

10.1021/bc050365e CCC: $33.50 © 2006 American Chemical Society
Published on Web 06/20/2006

mm) and Zorbax SB-C18 (5 μm; 9.4 × 250 mm) columns for analytical and semipreparative runs, respectively. Modified oligodeoxynucleotides dissolved in water were spectroscopically quantified (A_{260}) by attributing to them the extinction coefficient values reported elsewhere (*11*). Commercially purchased solvents and reagents were all of reagent quality. Diethyl ether, petroleum ether, CH_2Cl_2, triethylamine, and *t*BuOH were freshly dried and stored under argon as previously reported (*9*). Trifluoroethyl palmitate (TFEP) was synthesized by standard procedure, using trifluoroethanol and palmitic anhydride in pyridine and DMAP as catalyst; its purity was checked on the basis of its chromatographic and spectroscopic properties. Lipases from *Rhizomucor miehei* (immobilized, Lipozyme), *Rhizomucor miehei* (not immobilized), *Candida antarctica*, *Candida cylindracea*, *Pseudomonas cepacea*, *Pseudomonas fluorescens*, hog pancreas, and *Rhizopus niveus* were purchased from Fluka. Before use all the enzymes were allowed to stand in dried *t*BuOH for 45 min.

2-Cyanoethyl [(4*R*)-2,2-Dimethyl-1,3-dioxolan-4-yl]methyl Diisopropylamidophosphite (1). The synthesis and the purification of compound **1** were performed by using a previously reported procedure (*9*). Its purity was checked on the basis of its chromatographic and spectroscopic properties.

General Procedure for the Synthesis of 5′-GPOdNs (2−8). Compounds **2**−**8** were synthesized according to solid-phase cyanoethyl phosphoramidite chemistry by using a DNA synthesizer (15 μmol scale) with two or more coupling cycles between the appropriate 3′-CPG-linked protected nucleoside [5′-*O*-(4,4′-dimethoxytrityl)-*N*^{6}-benzoyl-2′-deoxyadenosine or 5′-*O*-(4,4′-dimethoxytrityl)-2′-deoxythymidine] and 2-cyanoethyl-*N*,*N*-diisopropylphosphoramidite of 5′-*O*-(4,4′-dimethoxytrityl)-*N*^{6}-benzoyl-2′-deoxyadenosine, 5′-*O*-(4,4′-dimethoxytrityl)-*N*^{2}-isobutyryl-2′-deoxyguanosine, or 5′-*O*-(4,4′-dimethoxytrityl)-2′-deoxythymidine, ending each synthetic run by a coupling cycle with the phosphoramidite **1**. After detachment of the condensation product from the CPG column by treatment with concd ammonia at room temperature for 1 h, the ammonia solution was kept at 55 °C for 6 h and then taken to dryness in vacuo. The residue was dissolved in 30% aqueous AcOH and allowed to stand at room temperature for 5 h. The mixture was then taken to dryness in vacuo and the totally deprotected product was purified by semipreparative RP-HPLC, eluting with a gradient of CH_3CN in 0.1 M triethylammonium acetate (TEAA; pH 7.0) from 4 to 15% in 40 min, at a flow rate of 3.5 mL min^{-1}.

The above mild acid treatment had been set up in our previous work (*9*, *10*) to remove the isopropylidene ketal protecting group from the glycerol moiety of various glycerophosphorylnucleosides. The removal of this protecting group is commonly accomplished by using 80% AcOH at room-temperature overnight, but depurination may occur under these conditions. For this reason, benzylidene acetals have been proposed by Edupuganti et al. (*12*) as alternative protecting groups for vic-diols which may be removed by 80% AcOH at room temperature for 1 h, without significant depurination.

To this regard, the purine rich 5′-GPd(GpA) was in parallel checked for its stability in 80% AcOH at room temperature for 1 h, and in 30% AcOH at room temperature for 5 h. HPLC analysis of the reaction mixtures obtained after the two different acidic treatments gave quite similar results in both the cases, thus indicating that removal of isopropylidene ketal protecting group by the mild acidic treatment we used did not produce significant depurination of 5′-GPOdNs.

5′-GPd(ApA) (2). (74% isolated yield). ^{1}H NMR (D_2O): δ 2.55 and 2.58 (partially overlapped multiplets, 2 H altogether, 2″-H A2 and 2′-H A1 respectively), 2.73 (ddd, $J_{2'',2'} = -14.3$, $J_{2'',1'} = 5.8$, $J_{2'',3'} = 1.5$ Hz, 1 H, 2″-H A1), 2.79 (ddd, $J_{2',2''} = -13.8$, $J_{2',1'} = 7.3$, $J_{2',3'} = 6.7$ Hz, 1 H, 2′-H A2), 3.47 (dd, $J_{1a,1b} = -11.6$, $J_{1a,2} = 6.0$ Hz, 1 H, 1a-H of glycerol), 3.56 (dd, $J_{1b,1a} = -11.6$, $J_{1b,2} = 4.0$ Hz, 1 H, 1b-H of glycerol), 3.68 (m, 1 H, 3a-H of glycerol), 3.77−3.82 (overlapped multiplets, 2 H, 2-H and 3b-H of glycerol), 3.98 (ddd, $J_{5',5''} = -11.5$, $J_{5',4'} = 2.8$, $J_{5',P} = 4.7$ Hz, 1 H, 5′-H A1), 4.06 (ddd, $J_{5'',5'} = -11.5$, $J_{5'',4'} = 3.6$, $J_{5'',P} = 4.5$ Hz, 1 H, 5″-H A1), 4.20 (ddd, $J_{5'',5'} = -11.5$, $J_{5'',4'} = 2.8$, $J_{5'',P} = 3.0$ Hz, 1 H, 5"-H A2), 4.26 (ddd partially overlapping with next signal, $J_{5',5''} = -11.5$, $J_{5',4'} = 2.0$, $J_{5',P} = 3.8$ Hz, 1 H, 5′-H A2), 4.29 (m partially overlapping with previous signal, 1 H, 4′-H A2), 4.39 (dddd, $J_{4',5'} = 2.8$, $J_{4',5''} = 3.6$, $J_{4',3'} = 2.0$, $J_{4',P} = 2.1$ Hz, 1 H, 4′-H A1), 4.99 (dddd, $J_{3',2'} = 5.6$, $J_{3',2''} = 1.5$, $J_{3',4'} = 2.0$, $J_{3',P} = 4.3$ Hz, 1 H, 3′-H A1), 6.19 (dd, $J_{1',2'} = 8.8$, $J_{1',2''} = 5.8$ Hz, 1 H, 1′-H A1), 6.33 (dd, $J_{1',2'} = 7.3$, $J_{1',2''} = 6.7$ Hz, 1 H, 1′-H A2), 7.98 (s, 1 H, 2-H A1), 8.11 (s, 1 H, 2-H A2), 8.24 (s, 1 H, 8-H A1), 8.37 (s, 1 H, 8-H A2) ppm. The 3′-H A2 resonance is obscured by the residual HOD signal. ^{13}C NMR (D_2O): δ 39.9 (C-2′ A1), 41.8 (C-2′ A2), 64.7 (C-1 of glycerol), 67.3 (d, $J_{COP} = 4.6$ Hz, C-5′ A2), 67.9 (d, $J_{COP} = 5.4$ Hz, C-5′ A1), 69.1 (d, $J_{COP} = 6.0$ Hz, C-3 of glycerol), 72.7 (C-3′ A2), 73.4 (d, $J_{CCOP} = 8.4$ Hz, C-2 of glycerol), 79.5 (d, $J_{COP} = 5.4$ Hz, C-3′ A1), 85.4 (C-1′ A2), 86.3 (C-1′ A1), 87.8 (t, $J_{CCOP} = 9.8$ Hz, C-4′ A1), 87.9 (d, $J_{CCOP} = 9.9$ Hz, C-4′ A2), 120.4 and 121.0 (C-5 A1 and A2), 142.6 (C-8 A2), 142.7 (C-8 A1), 150.8 and 150.9 (C-4 A1 and A2), 153.8 (C-2 A1 and A2), 156.7 and 156.9 (C-6 A1 and A2) ppm. HRFAB-MS(−) calcd for $C_{23}H_{31}N_{10}O_{13}P_2$ $(M - H)^-$ 717.1547, found 717.1539.

5′-GPd(ApApT) (3). (72% isolated yield). ^{1}H NMR (D_2O): δ 1.75 (d, $J = 1.1$ Hz, 3 H, CH_3 T3), 2.27 (dt partially overlapping with next signal, $J_{2',2''} = -14.1$, $J_{2',1'} = 6.9$, $J_{2',3'} = 6.9$ Hz, 1 H, 2′-H T3), 2.31 (ddd partially obscured by previous signal, $J_{2'',2'} = -14.1$, $J_{2'',1'} = 6.9$, $J_{2'',3'} = 4.5$ Hz, 1 H, 2″-H T3), 2.64 (ddd, $J_{2',2''} = -14.0$, $J_{2',1'} = 9.2$, $J_{2',3'} = 5.3$ Hz, 1 H, 2′-H A1), 2.77−2.83 (overlapped multiplets, 3 H, 2′-H and 2″-H A2, 2″-H A1), 3.47 (dd, $J_{1a,1b} = -11.7$, $J_{1a,2} = 6.1$ Hz, 1 H, 1a-H of glycerol), 3.56 (dd, $J_{1b,1a} = -11.7$, $J_{1b,2} = 4.2$ Hz, 1 H, 1b-H of glycerol), 3.69 (m, 1 H, 3a-H of glycerol), 3.78−3.83 (overlapped multiplets, 2 H, 2-H and 3b-H of glycerol), 3.99 (ddd, $J_{5',5''} = -11.5$, $J_{5',4'} = 2.6$, $J_{5',P} = 4.8$ Hz, 1 H, 5′-H A1), 4.08 (ddd, $J_{5'',5'} = -11.5$, $J_{5'',4'} = 3.6$, $J_{5'',P} = 4.4$ Hz, 1 H, 5"-H A1), 4.12−4.16 (partially overlapped multiplets, 2 H, 5″-H and 4′-H T3), 4.22−4.30 (partially overlapped multiplets, 3 H, 5′-H and 5″-H A2, 5′-H T3), 4.42 (m, 1 H, 4′-H A1), 4.49 (m, 1 H, 4′-H A2), 4.59 (ddd, $J_{3',2'} = 6.9$, $J_{3',2''} = 4.5$, $J_{3',4'} = 4.1$ Hz, 1 H, 3′-H T3), 5.02 (m, 1 H, 3′-H A1), 5.08 (m, 1 H, 3′-H A2), 6.14 (t, $J = 6.9$ Hz, 1 H, 1′-H T3), 6.19 (dd, $J_{1',2'} = 9.2$, $J_{1',2''} = 5.7$ Hz, 1 H, 1′-H A1), 6.29 (dd, $J_{1',2'} = 8.0$, $J_{1',2''} = 6.3$ Hz, 1 H, 1′-H A2), 7.46 (q, $J = 1.1$ Hz, 1 H, 6-H T3), 7.98 (s, 1 H, 2-H A), 8.09 (s, 1 H, 2-H A), 8.26 (s, 1 H, 8-H A1), 8.41 (s, 1 H, 8-H A2) ppm. ^{13}C NMR (D_2O): δ 14.4 (CH_3 T3), 39.9 (C-2′ A1), 40.6 (C-2′ A2), 41.6 (C-2′ T3), 64.9 (C-1 of glycerol), 67.3 (d, $J_{COP} = 4.6$ Hz, C-5′ T3), 67.7 (d, $J_{COP} = 4.6$ Hz, C-5′ A2), 68.2 (d, $J_{COP} = 4.2$ Hz, C-5′ A1), 69.2 (d, $J_{COP} = 5.0$ Hz, C-3 of glycerol), 72.5 (C-3′ T3), 73.5 (d, $J_{CCOP} = 7.6$ Hz, C-2 of glycerol), 78.2 (d, $J_{COP} = 4.6$ Hz, C-3′ A2), 79.9 (d, $J_{COP} = 5.0$ Hz, C-3′ A1), 85.3 (C-1′ A2), 86.3 (C-1′ A1), 87.0 (C-1′ T3), 87.3 (t, $J_{CCOP} = 9.2$ Hz, C-4′ A2), 87.4 (d, $J_{CCOP} = 8.8$ Hz, C-4′ T3), 88.0 (t, $J_{CCOP} = 8.9$ Hz, C-4′ A1), 114.1 (C-5 T3), 120.7 and 121.2 (C-5 A1 and A2), 139.6 (C-6 T3), 142.3 (C-8 A2), 142.5 (C-8 A1), 150.9 and 151.2 (C-4 A), 153.9 (C-2 T3), 154.7 and 154.9 (C-2 A1 and A2), 157.4 and 157.7 (C-6 A1 and A2), 168.5 (C-4 T3) ppm. HRFAB-MS(−) calcd for $C_{33}H_{44}N_{12}O_{20}P_3$ $(M - H)^-$ 1021.2008, found 1021.2020.

5′-GPd(ApApApT) (4). (68% isolated yield). HRFAB-MS(−) calcd for $C_{43}H_{56}N_{17}O_{25}P_4$ $(M - H)^-$ 1334.2584, found 1334.2561.

5′-GPd(ApApApApT) (5). (65% isolated yield). MALDI-MS(−) calcd for $C_{53}H_{68}N_{22}O_{30}P_5$ $(M - H)^-$ 1647.32, found 1648.10 $(M - H)^-$, 1669.93 $(M - 2\,H + Na)^-$.

5′-GPd(ApTpApTpTpA) (6). (64% isolated yield). MALDI-MS(−) calcd for $C_{63}H_{82}N_{21}O_{39}P_6$ $(M - H)^-$ 1942.35, found 1942.74 $(M - H)^-$, 1964.63 $(M - 2\,H + Na)^-$.

5′-GPd(GpA) (7). (73% isolated yield). HRFAB-MS(−) calcd for $C_{23}H_{31}N_{10}O_{14}P_2$ $(M - H)^-$ 733.1496, found 733.1490.

5′-GPd(TpA) (8). (76% isolated yield). HRFAB-MS(−) calcd for $C_{23}H_{32}N_7O_{15}P_2$ $(M - H)^-$ 708.1432, found 708.1428.

Synthesis of 3′-GPd(ApA) (19). *Synthesis of 1-O-Benzoyl-3-O-(4,4′-dimethoxytrityl)-sn-glycerol (**16**).* To a solution of [(*R*)-2,2-dimethyl-1,3-dioxolan-4-yl]methanol (49 μL, 0.39 mmol) in anhydrous pyridine (800 μL) was added benzoyl chloride (45 μL, 0.39 mmol), and the stirred mixture was kept at room temperature for 1 h. Then, more benzoyl chloride (45 μL, 0.39 mmol) was added, and the mixture was allowed to react at 55 °C for 4 h. The reaction mixture was dissolved in EtOAc (15 mL) and the solution washed with H_2O (3 × 10 mL). The organic layer was dried (Na_2SO_4) and taken to dryness in vacuo. The residual oil was taken up in 50% aqueous AcOH (10 mL) and the mixture stirred at room temperature for 5 h. After evaporation of the solvents in vacuo, the residue was chromatographed on silica gel eluting with petroleum ether/EtOAc/*i*PrOH (70:20:10), and fractions containing pure 1-*O*-benzoyl-*sn*-glycerol were taken to dryness. The residue (0.29 mmol) was dissolved in anhydrous pyridine (2 mL) and the stirred solution added with 4,4′-dimethoxytrityl chloride (0.35 mmol). The reaction mixture was kept at room temperature for 3 h, quenched with CH_3OH (1 mL), and taken to dryness in vacuo. The residue was dissolved in CH_2Cl_2 (15 mL) and the solution washed with H_2O (3 × 10 mL), dried on Na_2SO_4 and evaporated in vacuo. The product was purified by PLC on silica gel (preeluted with anhydrous triethylamine) eluting with petroleum ether/*n*BuOH/triethylamine (97:3:1). Pure compound **16** (119 mg, 61% overall yield) was then obtained and analyzed for its spectroscopic (NMR) properties.

*Synthesis of Succinic Acid [(2S)-1-O-Benzoyl-3-O-(4,4′-dimethoxytrityl)trihydroxypropyl] Hemiester (**17**).* To a stirred solution of **16** (100 mg, 0.20 mmol) in anhydrous pyridine (2 mL) containing DMAP (18 mg, 0.15 mmol) was added succinic anhydride (26 mg, 0.26 mmol). The reaction mixture was left at 60 °C for 18 h and then added to CH_2Cl_2 (15 mL) and washed with H_2O (3 × 10 mL). The organic layer was dried on Na_2SO_4 and evaporated in vacuo. The residue was chromatographed on silica gel, preeluted with anhydrous triethylamine, eluting with EtOAc/CH_3OH/triethylamine (80:20:1), giving pure compound **17** (103 mg, 87% yield). Selected NMR data referring to the succinyl group: ^{1}H NMR ($CDCl_3$): δ 2.57 (t, $J = 6.5$ Hz, 2 H, C*H*$_2$COOH), 2.64 (t, $J = 6.5$ Hz, 2 H, C*H*$_2$COOR) ppm. ^{13}C NMR ($CDCl_3$): δ 30.8 (*CH*$_2$COOH), 31.1 (*CH*$_2$-COOR), 173.0 (COOR), 177.0 (COOH) ppm. FABMS(−) (3-nitrobenzyl alcohol as matrix): *m/z* 597 $(M - H)^-$.

Coupling of Succinic Acid [(2S)-1-O-Benzoyl-3-O-(4,4′-dimethoxytrityl)trihydroxypropyl] Hemiester to CPG Support. To carry out the title coupling, a procedure commonly used in solid-phase peptide synthesis (*13*) was adapted as follows. To a solution of compound **17** (84 mg, 0.14 mmol) and *O*-(7-azabenzotriazol-1-yl)-1,1,3,3-tetramethyluronium hexafluorophosphate (HATU, 49 mg, 0.13 mmol) in DMF (1.5 mL) was added diisopropylethylamine (DIEA, 24 μL, 0.14 mmol), and the mixture was shaken for 5 min. After more DIEA (24 μL, 0.14 mmol) was added, the solution was poured onto the aminopropyl-CPG support (0.65 g, capacity: 85.3 μmol g^{-1}). The slurry was kept for 1 h with occasional swirling, and then the solution was filtered off and the CPG was washed with DMF (3 × 5 mL) and CH_3CN (3 × 5 mL). The functionalized CPG was suspended in anhydrous THF (4 mL) and added to capping solutions (Cap A: 10% acetic anhydride in THF, 2.2 mL; Cap B: 10% 1-methylimidazole in THF/pyridine 8:1, 2.2 mL). The mixture was shaken for 2.5 h, and then the CPG was filtered, washed successively with THF (5 × 5 mL), CH_2Cl_2 (5 × 5 mL), and diethyl ether (5 × 5 mL), and finally dried in vacuo. A total yield of 0.63 g of functionalized CPG (**18**) was obtained with a capacity of 81.0 μmol g^{-1}, as estimated on the basis of DMT group determination.

3′-GPd(ApA) (19). The prepared solid phase **18** (3 × 15 μmol scale columns) was then utilized to accomplish on a DNA synthesizer two coupling cycles with the 2-cyanoethyl-*N*,*N*-diisopropylphosphoramidite of 5′-*O*-(4,4′-dimethoxytrityl)-N^6-benzoyl-2′-deoxyadenosine. After detachment of the condensation product from the CPG column by treatment with concd ammonia at room temperature for 1 h, the ammonia solution was kept at 55 °C for 6 h and then taken to dryness in vacuo. The totally deprotected product was purified by semipreparative HPLC as above-described for 5′-GPOdNs (76% isolated yield). ^{1}H NMR (D_2O): δ 2.25 (ddd, $J_{2',2''} = -13.7$, $J_{2',1'} = 9.1$, $J_{2',3'} = 5.6$ Hz, 1 H, 2′-H A1), 2.57 (dd, $J_{2'',2'} = -13.7$, $J_{2'',1'} = 5.6$, $J_{2'',3'} = 0$ Hz, 1 H, 2′′-H A1), 2.75 (ddd, $J_{2'',2'} = -14.0$, $J_{2'',1'} = 6.1$, $J_{2'',3'} = 3.2$ Hz, 1 H, 2′′-H A2), 2.94 (ddd, $J_{2',2''} = -14.0$, $J_{2',1'} = 8.1$, $J_{2',3'} = 6.5$ Hz, 1 H, 2′-H A2), 3.67 (dd, $J_{1a,1b} = -11.8$, $J_{1a,2} = 5.9$ Hz, 1 H, 1a-H of glycerol), 3.75 (dd, $J_{1b,1a} = -11.8$, $J_{1b,2} = 4.2$ Hz, 1 H, 1b-H of glycerol), 3.78 (d, $J_{5',4'} = 3.3$ Hz, 2 H, 5′-H A1), 3.93−4.05 (partially overlapped multiplets, 3 H, 2-H and 3-H of glycerol), 4.23 (m, 2 H, 5′-H A2), 4.29 (dt, $J_{4',3'} = 1.1$, $J_{4',5'} = 3.3$ Hz, 1 H, 4′-H A1), 4.51 (m, 1 H, 4′-H A2), 4.87 (ddd, $J_{3',2'} = 5.6$, $J_{3',4'} = 1.1$, $J_{3',P} = 4.5$, $J_{3',2''} = 0$ Hz, 1 H, 3′-H A1), 5.13 (dddd, $J_{3',2'} = 6.5$, $J_{3',2''} = 3.2$, $J_{3',4'} = 3.1$, $J_{3',P} = 6.0$ Hz, 1 H, 3′-H A2), 6.17 (dd, $J_{1',2'} = 9.1$, $J_{1',2''} = 5.6$ Hz, 1 H, 1′-H A1), 6.38 (dd, $J_{1',2'} = 8.1$, $J_{1',2''} = 6.1$ Hz, 1 H, 1′-H A2), 7.99 (s, 1 H, 2-H A1), 8.08 (s, 1 H, 8-H A1), 8.14 (s, 1 H, 2-H A2), 8.43 (s, 1 H, 8-H A2) ppm. ^{13}C NMR (D_2O): δ 39.9 (C-2′ A1), 40.8 (C-2′ A2), 64.6 (C-5′ A1), 65.0 (C-1 of glycerol), 67.5 (C-5′ A2), 69.3 (C-3 of glycerol), 73.6 (C-2 of glycerol), 77.7 (C-3′ A2), 79.7 (C-3′ A-1), 85.5 (C-1′ A2), 87.4 (C-4′ A2), 87.8 (C-1′ A1), 89.7 (C-4′ A1), 120.7 and 121.8 (C-5), 142.5 (C-8 A2), 143.2 (C-8 A1), 150.5 and 151.3 (C-4), 154.6 (C-2 A2), 154.8 (C-2 A1), 157.3 and 157.9 (C-6) ppm. HRFAB-MS(−) calcd for $C_{23}H_{31}N_{10}O_{13}P_2$ $(M - H)^-$ 717.1547, found 717.1539.

General Procedure for the Enzymatic Synthesis of 5′(3′)-O-(1-*O*-Palmitoyl-sn-glycero-3-phosphoryl)oligodeoxynucleotides 9−15 and 20 [5′(3′)-LyPOdNs]. The enzymatic synthesis and the purification of the title compounds were accomplished following the optimized experimental conditions reported in our previous work (*10*). Each 5′-GPOdN (25 μmol) was first converted into the relevant TBA salt by passing it through a column of Dowex-50 W (TBA^+ form). The aqueous eluate was taken to dryness in vacuo, and the residue was allowed to stand under reduced pressure over P_2O_5 overnight. The residue was then dissolved in dried *t*BuOH (40 mL), and the solution added with TFEP (1.0 mmol) and Lipozyme (220 mg). The suspension was shaken at 240 rpm at 38 °C. Each reaction course was followed by HPLC monitoring of the rising amount of the relevant 5′(3′)-LyPOdN, prolonging the reaction time until it was of practical convenience. HPLC analyses were carried out using a linear gradient of CH_3CN in 0.1 M TEAA (pH 7) from 0 to 70% in 30 min at a flow rate of 1.0 mL min^{-1}. The enzyme was then filtered off and the solvent evaporated in vacuo. The residue was taken up and partitioned in a heptane/CH_3OH (3:1) mixture, and the CH_3OH layer was concentrated in vacuo.

The residue containing the acylated product was then purified by semipreparative HPLC eluting with a linear gradient of CH_3CN in 0.1 M TEAA (pH 7) from 0 to 70% in 30 min and a flow rate of 3.5 mL min^{-1}. Fractions containing the desired compound were pooled, evaporated in vacuo to remove CH_3CN and then freeze-dried. A minimum amount of each of compounds **9**, **10**, and **20** was dissolved in CH_3OH and passed through a column of Dowex-50 W (NH_4^+ form), while the remainder was passed through a column of Dowex-50 W (Na^+ form) to optimize the relevant MS and NMR analyses, respectively. The freeze-dried residues of compounds **11**−**15**, dissolved in CH_3OH, were passed through a micro-column of Dowex-50 W (NH_4^+ form) and then analyzed by MS.

5′-LyPd(ApA) (9). 10.4 μmol (reaction time 52 days, 41.4% isolated yield from **2**). ^{1}H NMR (CD_3OD): δ 0.90 (t, J = 7.0 Hz, 3 H, CH_3 of palmitoyl), 1.25 and 1.28 (br. singlets, 24 H altogether, from γ- to ξ-CH_2 of palmitoyl), 1.54 (m, 2 H, β-CH_2 of palmitoyl), 2.27 (t, J = 7.5 Hz, 2 H, α-CH_2 of palmitoyl), 2.45 (ddd, $J_{2'',2'} = -13.4$, $J_{2'',1'} = 6.2$, $J_{2'',3'} = 2.8$ Hz, 1 H, 2′′-H A2), 2.73 (ddd, $J_{2'',2'} = -13.7$, $J_{2'',1'} = 5.5$, $J_{2'',3'} = 1.4$ Hz, 1 H, 2′′-H A1), 2.80 (ddd, $J_{2',2''} = -13.4$, $J_{2',1'} = 8.0$, $J_{2',3'} = 5.9$ Hz, 1 H, 2′-H A2), 2.86 (ddd, $J_{2',2''} = -13.7$, $J_{2',1'} = 8.7$, $J_{2',3'} = 5.2$ Hz, 1 H, 2′-H A1), 3.89 (m, 2 H, 3-H_2 of glycerol), 3.95 (m, 1 H, 2-H of glycerol), 4.05−4.15 (partially overlapped multiplets, 6 H, 1-H_2 of glycerol, 5′-H_2 A1 and A2; on the basis of the 1a-H/2-H and 1b-H/2-H cross-peaks showed in the COSY spectrum it was possible to assign the resonances of 1a-H and 1b-H of glycerol at δ = 4.07 and 4.14, respectively), 4.18 (m, 1 H, 4′-H A2), 4.39 (m, 1 H, 4′-H A1), 4.72 (ddd, $J_{3',2'} = 5.9$, $J_{3',2''} = 2.8$, $J_{3',4'} = 2.5$ Hz, 1 H, 3′-H A2), 5.06 (m, 1 H, 3′-H A1), 6.49 (overlapped multiplets, 2 H, 1′-H A1 and A2), 8.16 and 8.17 (singlets, 2 H altogether, 2-H A1 and A2), 8.47 (s, 1 H, 8-H A1), 8.52 (s, 1 H, 8-H A2) ppm. ^{13}C NMR (CD_3OD): δ 14.4 (CH_3 of palmitoyl), 23.7 (ξ-CH_2 of palmitoyl), 26.0 (β-CH_2 of palmitoyl), 30.2, 30.4, 30.5, 30.6, 30.8 (from γ- to μ-CH_2 of palmitoyl), 33.1 (ν-CH_2 of palmitoyl), 34.9 (α-CH_2 of palmitoyl), 40.1 and 40.2 (C-2′ A1 and A2), 66.0 (d, J_{COP} = 4.6 Hz, C-5′ A1), 66.2 (C-1 of glycerol), 66.5 (d, J_{COP} = 6.6 Hz, C-5′ A2), 67.7 (d, J_{COP} = 5.0 Hz, C-3 of glycerol), 69.6 (d, J_{CCOP} = 7.2 Hz, C-2 of glycerol), 72.8 (C-3′ A2), 77.6 (d, J_{COP} = 4.8 Hz, C-3′ A1), 85.2 and 85.4 (C-1′ A1 and A2), 86.6 (br. dd, C-4′ A1), 87.5 (d, J_{CCOP} = 8.5 Hz, C-4′ A2), 141.4 (C-8 A2), 142.5 (C-8 A1), 150.2 (C-4 A1 and A2), 153.5 (C-2 A1 and A2), 157.2 and 157.4 (C-6 A1 and A2), 175.4 (COO) ppm; C-5 not detectable. ESI-MS(−) calcd for $C_{39}H_{61}N_{10}O_{14}P_2$ $(M - H)^-$ 955.38, found 477.3 $(M - 2\ H)^{2-}$, 955.4 $(M - H)^-$, 977.6 $(M - 2\ H + Na)^-$.

5′-LyPd(ApApT) (10). 3.1 μmol (reaction time 60 days, 12.3% isolated yield from **3**). ^{1}H NMR (CD_3OD): δ 0.89 (t, J = 7.0 Hz, 3 H, CH_3 of palmitoyl), 1.26 and 1.27 (br. singlets, 24 H altogether, from γ- to ξ-CH_2 of palmitoyl), 1.54 (m, 2 H, β-CH_2 of palmitoyl), 1.92 (d, J = 1.1 Hz, 3 H, CH_3 T3), 2.23 (ddd, $J_{2'',2'} = -13.5$, $J_{2'',1'} = 6.3$, $J_{2'',3'} = 2.9$ Hz, 1 H, 2′′-H T3), 2.28 (t overlapping with next signal, J = 7.5 Hz, 2 H, α-CH_2 of palmitoyl), 2.30 (ddd partially obscured by previous signal, $J_{2',2''} = -13.5$, $J_{2',1'} = 7.8$, $J_{2',3'} = 6.2$ Hz, 1 H, 2′-H T3), 2.66 (ddd, $J_{2'',2'} = -13.9$, $J_{2'',1'} = 5.6$, $J_{2'',3'} = 1.4$ Hz, 1 H, 2′′-H A1), 2.74 (ddd partially overlapping with next signal, $J_{2',2''} = -13.9$, $J_{2',1'} = 8.4$, $J_{2',3'} = 5.5$ Hz, 1 H, 2′-H A1), 2.76 (ddd partially overlapping with previous signal, $J_{2'',2'} = -13.8$, $J_{2'',1'} = 5.8$, $J_{2'',3'} = 2.3$ Hz, 1 H, 2′′-H A2), 2.94 (ddd, $J_{2',2''} = -13.8$, $J_{2',1'} = 8.2$, $J_{2',3'} = 5.6$ Hz,1 H, 2′-H A2), 3.88 (m, 2 H, 3-H_2 of glycerol), 3.94 (m, 1 H, 2-H of glycerol), 4.04−4.15 (partially overlapped multiplets, 7 H altogether; 1-H_2 of glycerol, 4′-H T3, 5′-H_2 A1 and T3; on the basis of the 1a-H/2-H and 1b-H/2-H cross-peaks shown in the COSY spectrum, it was possible to assign the resonances of 1a-H and 1b-H of glycerol at δ = 4.08 and 4.13, respectively), 4.17 (dd, $J_{5',4'} = 3.5$, $J_{5',P} = 4.8$ Hz, 2 H, 5′-H_2 A2), 4.37 (m, 1 H, 4′-H A1), 4.42 (m, 1 H, 4′-H A2), 4.57 (ddd, $J_{3',2'} = 6.2$, $J_{3',2''} = 2.9$, $J_{3',4'} = 2.4$ Hz, 1 H, 3′-H T3), 5.04 and 5.07 (partially overlapped multiplets, 2 H, 3′-H A1 and A2, respectively), 6.32 (dd, $J_{1',2'} = 7.8$, $J_{1',2''} = 6.3$ Hz, 1 H, 1′-H T3), 6.47 (dd partially overlapping with next signal, $J_{1',2'} = 8.4$, $J_{1',2''} = 5.6$ Hz, 1 H, 1′-H A1), 6.49 (dd partially overlapping with previous signal, $J_{1',2'} = 8.2$, $J_{1',2''} = 5.8$ Hz, 1 H, 1′-H A2), 7.80 (q, J = 1.1 Hz, 1 H, 6-H T3), 8.14 and 8.15 (singlets, 2 H altogether, 2-H A1 and A2), 8.43 (s, 1 H, 8-H A1), 8.49 (s, 1 H, 8-H A2) ppm. ^{13}C NMR (CD_3OD): δ 12.7 (CH_3 T3), 14.4 (CH_3 of palmitoyl), 23.7 (ξ-CH_2 of palmitoyl), 25.9 (β-CH_2 of palmitoyl), 30.2, 30.4, 30.5, 30.6, 30.8 (from γ- to μ-CH_2 of palmitoyl), 33.1 (ν-CH_2 of palmitoyl), 34.9 (α-CH_2 of palmitoyl), 40.1 and 40.2 (C-2′ A1 and A2), 40.9 (C-2′ T3), 66.2 (C-1 of glycerol), 66.5 (C-5′ A1 and T3), 66.7 (d, J_{COP} = 6.9 Hz, C-5′ A2), 67.7 (d, J_{COP} = 5.2 Hz, C-3 of glycerol), 69.9 (d, J_{CCOP} = 7.2 Hz, C-2 of glycerol), 72.5 (C-3′ T3), 77.4 (d, J_{COP} = 4.3 Hz, C-3′ A2), 77.9 (d, J_{COP} = 4.7 Hz, C-3′ A1), 85.3 (C-1′ A2), 85.5 (C-1′ A1), 86.2 (C-1′ T3), 86.7 (br. dd, C-4′ A2), 87.0 (br. dd, C-4′ A1), 87.5 (d, J_{CCOP} = 8.8 Hz, C-4′ T3), 112.1 (C-5 T3), 120.2 and 120.6 (C-5 A1 and A2), 138.1 (C-6 T3), 141.1 (C-8 A1 and A2), 150.6 (C-4 A1 and A2), 152.5 (C-2 T3), 153.9 (C-2 A1 and A2), 157.20 and 157.23 (C-6 A1 and A2), 166.5 (C-4 T3), 175.5 (COO) ppm. ESI-MS(−) calcd for $C_{49}H_{74}N_{12}O_{21}P_3$ $(M - H)^-$ 1259.43, found 629.3 $(M - 2\ H)^{2-}$, 1259.3 $(M - H)^-$, 1281.3 $(M - 2\ H + Na)^-$.

5′-LyPd(ApApApT) (11). 1.1 μmol (reaction time 70 days, 4.4% isolated yield from **4**). ESI-MS(−) calcd for $C_{59}H_{86}N_{17}O_{26}P_4$ $(M - H)^-$ 1572.49, found 786.2 $(M - 2\ H)^{2-}$, 1572.8 $(M - H)^-$, 1594.4 $(M - 2\ H + Na)^-$.

5′-LyPd(ApApApApT) (12). 0.46 μmol (reaction time 70 days, 1.8% isolated yield from **5**). MALDI-MS(−) calcd for $C_{69}H_{98}N_{22}O_{31}P_5$ $(M - H)^-$ 1885.55, found 1885.58 $(M - H)^-$, 1908.14 $(M - 2\ H + Na)^-$.

5′-LyPd(ApTpApTpTpA) (13). 0.22 μmol (reaction time 70 days, 0.88% isolated yield from **6**). MALDI-MS(−) calcd for $C_{79}H_{112}N_{21}O_{40}P_6$ $(M - H)^-$ 2180.58, found 2180.96 $(M - H)^-$, 2202.37 $(M - 2\ H + Na)^-$.

5′-LyPd(GpA) (14). 10.1 μmol (reaction time 50 days, 40.5% isolated yield from **7**). HRFAB-MS(−) calcd for $C_{39}H_{61}N_{10}O_{15}P_2$ $(M - H)^-$ 971.3793, found 971.3801 $(M - H)^-$.

5′-LyPd(TpA) (15). 10.7 μmol (reaction time 50 days, 42.9% isolated yield from **8**). HRFAB-MS(−) calcd for $C_{39}H_{62}N_7O_{16}P_2$ $(M - H)^-$ 946.3728, found 946.3725 $(M - H)^-$.

3′-LyPd(ApA) (20). 10.8 μmol (reaction time 52 days, 43.0% isolated yield from **19**). ^{1}H NMR (CD_3OD): δ 0.89 (t, J = 6.9 Hz, 3 H, CH_3 of palmitoyl), 1.25 and 1.28 (br. singlets, 24 H altogether, from γ- to ξ-CH2 of palmitoyl), 1.56 (m, 2 H, β-CH_2 of palmitoyl), 2.30 (t, J = 7.5 Hz, 2 H, α-CH_2 of palmitoyl), 2.64 (ddd, $J_{2'',2'} = -13.9$, $J_{2'',1'} = 5.8$, $J_{2'',3'} = 1.6$ Hz, 1 H, 2′′-H A1), 2.72 (ddd, $J_{2'',2'} = -14.0$, $J_{2'',1'} = 5.7$, $J_{2'',3'} = 1.7$ Hz, 1 H, 2′′-H A2), 2.79 (ddd, $J_{2',2''} = -13.9$, $J_{2',1'} = 8.6$, $J_{2',3'} = 5.5$ Hz, 1 H, 2′-H A1), 2.94 (ddd, $J_{2',2''} = -14.0$, $J_{2',1'} = 8.4$, $J_{2',3'} = 5.6$ Hz, 1 H, 2′-H A2), 3.78 (d, $J_{5',4'} = 2.7$ Hz, 2 H, 5′-H_2 A1), 3.91−4.02 (partially overlapped multiplets, 3 H, 2-H and 3-H_2 of glycerol), 4.12 (dd, $J_{1a,1b} = -11.3$, $J_{1a,2} = 5.9$ Hz, 1 H, 1a-H of glycerol), 4.18 (dd partially overlapping with next signal, $J_{1b,1a} = -11.3$, $J_{1b,2} = 4.4$ Hz, 1 H, 1b-H of glycerol), 4.19 (m partially obscured by previous signal, 2 H, 5′-H_2 A2), 4.27 (dt, $J_{4',5'} = 2.7$, $J_{4',3'} = 1.4$ Hz, 1 H, 4′-H A1), 4.45 (m, 1 H, 4′-H A2), 5.01 (dddd, $J_{3',2'} = 5.5$, $J_{3',2''} = 1.6$, $J_{3',4'} = 1.4$, $J_{3',P} = 6.9$ Hz, 1 H, 3′-H A1), 5.11 (dddd, $J_{3',2'} = 5.6$, $J_{3',2''} = 1.7$, $J_{3',4'} = 1.8$, $J_{3',P} = 6.0$ Hz, 1 H, 3′-H A2), 6.40 (dd, $J_{1',2'} = 8.6$, $J_{1',2''} = 5.8$ Hz, 1 H, 1′-H A1), 6.52 ((dd, $J_{1',2'} = 8.4$, $J_{1',2''} = 5.7$ Hz, 1 H, 1′-H A2), 8.15 (s, 1 H, 2-H A1), 8.16 (s, 1 H,

Scheme 1. Synthesis of 5′-Glycerophosphoryloligodeoxynucleotides

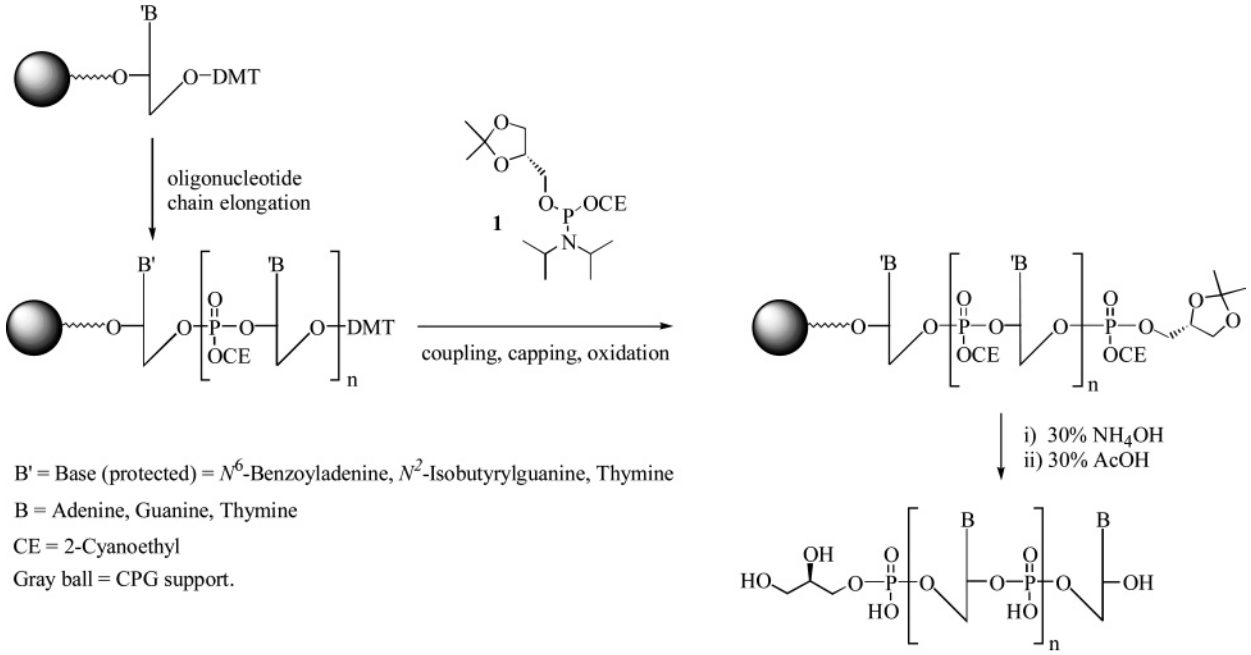

	n	5'-GPOdN
2	1	5'-GPd(ApA)
3	2	5'-GPd(ApApT)
4	3	5'-GPd(ApApApT)
5	4	5'-GPd(ApApApApT)
6	5	5'-GPd(ApTpApTpTpA)
7	1	5'-GPd(GpA)
8	1	5'-GPd(TpA)

2-H A2), 8.29 (s, 1 H, 8-H A1), 8.54 (s, 1 H, 8-H A2) ppm. ^{13}C NMR (CD_3OD): δ 14.2 (CH_3 of palmitoyl), 23.5 (ξ-CH_2 of palmitoyl), 25.9 (β-CH_2 of palmitoyl), 30.2, 30.3, 30.4, 30.5, 30.6, 30.7 (from γ- to μ-CH_2 of palmitoyl), 33.0 (ν-CH_2 of palmitoyl), 34.7 (α-CH_2 of palmitoyl), 39.8 (C-2′ A1), 39.9 (C-2′ A2), 63.2 (C-5′ A1), 66.0 (C-1 of glycerol), 66.5 (d, J_{COP} = 4.1 Hz, C-5′ A2), 67.7 (d, J_{COP} = 5.2 Hz, C-3 of glycerol), 69.7 (d, J_{CCOP} = 7.5 Hz, C-2 of glycerol), 76.9 (d, J_{COP} = 4.9 Hz, C-3′ A2), 77.4 (d, J_{COP} = 4.5 Hz, C-3′ A1), 85.1 (C-1′ A2), 86.4 (br. dd, C-4′ A2), 87.3 (C-1′ A1), 88.8 (d, J_{CCOP} = 6.0 Hz, C-4′ A1), 141.4 (C-8 A2), 142.5 (C-8 A1), 149.4 and 150.0 (C-4 A1 and A2), 153.6 (C-2 A1 and A2), 157.2 and 157.6 (C-6 A1 and A2), 175.3 (COO) ppm. HRFAB-MS(−) calcd for $C_{39}H_{61}N_{10}O_{14}P_2$ $(M - H)^-$ 955.3844, found 955.3836.

RESULTS AND DISCUSSION

Bearing in mind that mono[(2*R*)-2,3-dihydroxypropyl] esters of 5′-nucleotides (5′-GPNs) had been prepared from a phosphoramidite of [(4*S*)-2,2-dimethyl-1,3-dioxolan-4-yl]methanol (**1**) and the appropriately protected CPG-anchored nucleosides (*9*), we hypothesized that, in a similar way, a glycerophosphoryl residue could be joined to whichever oligodeoxynucleotide by simply using phosphoramidite **1** in a last coupling step after the solid-phase elongation of that given oligodeoxynucleotide. After detaching from CPG and removing of all protective groups, 5′-*O*-glycerophosphoryloligodeoxynucleotide (5′-GPOdN) would subsequently be acylated by Lipozyme (or other lipases) in organic solvent in the presence of suitable acyl donors. This idea was of course based on the assumption that substrates as large as 5′-GPOdNs could be recognized by the enzyme.

Synthesis of the Oligomeric Substrates. In accordance with the planned way, various 5′-GPOdNs were synthesized by automated DNA synthesizer, following the path reported in Scheme 1. First, adenine and thymine nucleotides only were employed to build up the 5′-GPOdNs, these being selected as a model of purine and pyrimidine nucleotide, respectively. While the nucleotide sequence of each oligomer was chosen regardless of any specific sense, all of them contained the adenine nucleotide at the 5′-end involved in the formation of the phosphodiester bond with the glycerol moiety. Thus, that molecular side of 5′-GPOdNs which would undergo enzyme recognition showed in any case a common structural motif. Taking into account that bulky substrates are not easily accommodated inside the active site of most enzymes, 5′-GPOdNs no longer than 6-mer were prepared as starting material.

After purification by HPLC, the synthesized 5′-GPOdNs (**2**−**6**) were characterized on the basis of their spectroscopic (NMR and HRMS) properties. The correct sequence of each of them was ascertained by ROESY or NOEDS experiments.

Later on, to give additional evidence of the method generality, 5′-GPd(GpA) (**7**) and 5′-GPd(TpA) (**8**) were also synthesized by the same route and successively underwent enzymatic acylation.

Enzymatic Acylation of 5′-GPOdNs. Enzymatic acylation of each 5′-GPOdN [as tetrabutylammonium (TBA) salt] was then carried out by use of *Rhizomucor miehei* lipase (immobilized, Lipozyme) in *tert*-butyl alcohol and in the presence of trifluoroethyl palmitate (TFEP), following the same experimental procedure previously reported for the acylation of glycerophosphoryl derivatives of nucleoside analogues (Scheme 2) (*10*).

Scheme 2. Synthesis of 5′-Glycerophosphoryloligodeoxynucleotides

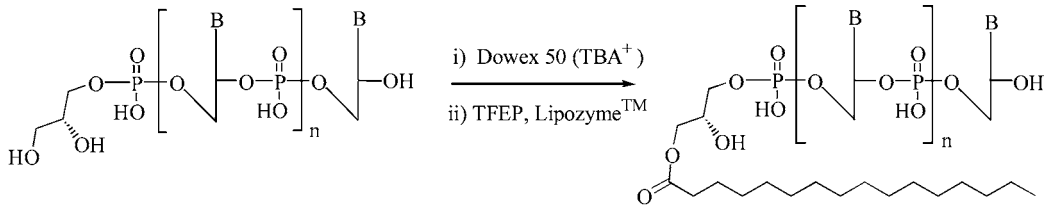

2 - 8 **9 - 15**

B = Adenine, Guanine, Thymine

	n	5'-LyPOdN
9	1	5'-LyPd(ApA)
10	2	5'-LyPd(ApApT)
11	3	5'-LyPd(ApApApT)
12	4	5'-LyPd(ApApApApT)
13	5	5'-LyPd(ApTpApTpTpA)
14	1	5'-LyPd(GpA)
15	1	5'-LyPd(TpA)

At the end of the synthetic run, HPLC analyses of the crude reaction mixtures in each case revealed the presence of only one acylation product which was next isolated by semipreparative HPLC and characterized on the basis of its spectroscopic features. It is worth noting that, when parallel experiments were carried out under the same experimental conditions but in the absence of the enzyme, no acylation took place.

The NMR spectral data obtained for compounds **9** and **10** are reported in detail in Experimental Procedures. Unequivocal assignments of ^{1}H and ^{13}C resonances were supported by 1D (spin decouplings, NOEDS, DEPT or APT) and 2D ($^{1}H-^{1}H$ COSY, HSQC, ROESY) experiments, and by the analysis of $^{13}C-^{31}P$ coupling constants.

The NMR spectra showed the presence in both compounds of one palmitoyl residue and indicated its location. In particular, in the ^{13}C NMR spectra of **9** and **10** the C-1 and C-2 resonances of the glycerol moiety, compared with those of the pertinent 5′-GPOdNs, were downfield ($\Delta\delta = 1.4 \pm 0.1$ ppm) and upfield ($\Delta\delta = -3.7 \pm 0.1$ ppm) shifted, respectively. On account of the α and β effect of acylation, these data indicated that both the relevant 5′-GPOdNs **2** and **3** had undergone regioselective acylation at the primary hydroxyl group of their glycerol residue. In accordance, in the ^{1}H NMR spectra of **9** and **10**, 1-H_2 resonances of the glycerol residue were downfield ($\Delta\delta = 0.59 \pm 0.02$ ppm) shifted, in comparison with the relevant ones in the spectra of **2** and **3**. From these results, the structures of 5′-*O*-(1-*O*-palmitoyl-*sn*-glycero-3-phosphoryl)d(ApA) [5′-LyPd-(ApA)] and 5′-*O*-(1-*O*-palmitoyl-*sn*-glycero-3-phosphoryl)d-(ApApT) [5′-LyPd(ApApT)] were assigned to **9** and **10**, respectively. ESI-MS(−) spectra of these two 5′-*O*-lysophosphatidyloligodeoxynucleotides were in agreement with the proposed structures as well (see Experimental Procedures).

Once the structural features of the previous two acylated products had been outlined, the identification of 5′-LyPd-(ApApApT) (**11**), 5′-LyPd(ApApApApT) (**12**) and 5′-LyPd-(ApTpApTpTpA) (**13**), 5′-LyPd(GpA) (**14**) and 5′-LyPd(TpA) (**15**), was achieved by MS analysis only. On the other hand, this way was unavoidable for compound **13,** whose available amount was so small to make difficult NMR spectroscopic analysis.

ESI-MS(−) spectrum of **11** showed diagnostically important peaks at *m*/*z* 1572.8 $(M - H)^-$ and 786.2 $(M - 2H)^{2-}$. MALDI-MS(−) spectra of **12** and **13** gave peaks of diagnostic value at *m*/*z* 1885.58 $(M - H)^-$ and 1908.14 $(M - 2H + Na)^-$ for compound **12,** and at *m*/*z* 2180.96 $(M - H)^-$ and 2202.37 $(M - 2H + Na)^-$ for compound **13**. FAB-MS(−) spectra of **14** and **15** gave the relevant $(M - H)^-$ peaks at *m*/*z* 971.38 and 946.37.

Table 1. Lipase-Catalyzed Palmitoylation of Glycerophosphoryloligodeoxynucleotides

substrate	product	conversion[a] (%)
5′-GPdA	5′-LyPdA	98.0
5′-GPd(ApA)	9	31.3
5′-GPd(ApApT)	10	7.8
5′-GPd(ApApApT)	11	4.6
5′-GPd(ApApApApT)	12	1.7
5′-GPd(ApTpApTpTpA)	13	0.95
5′-GPd(GpA)	14	31.2
5′-GPd(TpA)	15	32.1
3′-GPd(ApA)	20	32.5

[a] After 26 days incubation in the experimental conditions reported under Experimental Procedures for the synthesis of 5′(3′)-LyPOdNs.

Table 1 reports the conversion values obtained after 26 days enzymatic palmitoylation of seven 5′-GPOdNs, in comparison with that found, under the same experimental conditions, for the palmitoylation of the mononucleotide 5′-GPdA.

These values were derived from HPLC analyses of single crude reaction mixtures at the fixed incubation time, assuming that the new formed 5′-LyPOdN had the same molar extinction coefficient of the relevant 5′-GPOdN.

The results, as a whole, indicated that in each case the enzymatic step had actually yielded the desired LyPOdN, but showed also that the ability of Lipozyme to acylate 5′-GPOdNs had been dramatically affected by the molecular size of the utilized substrate. Suffice it to observe that the conversion value for enzymatic acylation of the dinucleotide 5′-GPd(ApA) was near one-third of that found for 5′-GPdA.

Aiming to understand if the position of the glycerol residue on the sugar moiety of GPOdNs could anyhow influence the enzymatic acylation behavior, 3′-GPd(ApA) (**19**) was synthesized, to subject it to subsequent palmitoylation by Lipozyme, in comparison with the relevant 5′-GPOdN (**2**).

To this purpose, the synthesis of **19** was achieved by carrying out two successive coupling steps of appropriately protected adenosine 3′-*O*-phosphoramidite, on a solid support consisting of a protected glycerol residue anchored to aminoalchil-CPG (**18**, Scheme 3).

Such a solid phase was prepared by coupling the succinic acid hemiester of a suitably protected glycerol (**17**) to aminoalchil-CPG, by applying the efficient HATU-DIEA in situ activation protocol commonly used (*13*) in solid-phase peptide

Scheme 3. Synthesis of 3′-Glycerophosphoryl- and 3′-Lysophosphatidyld(ApA)

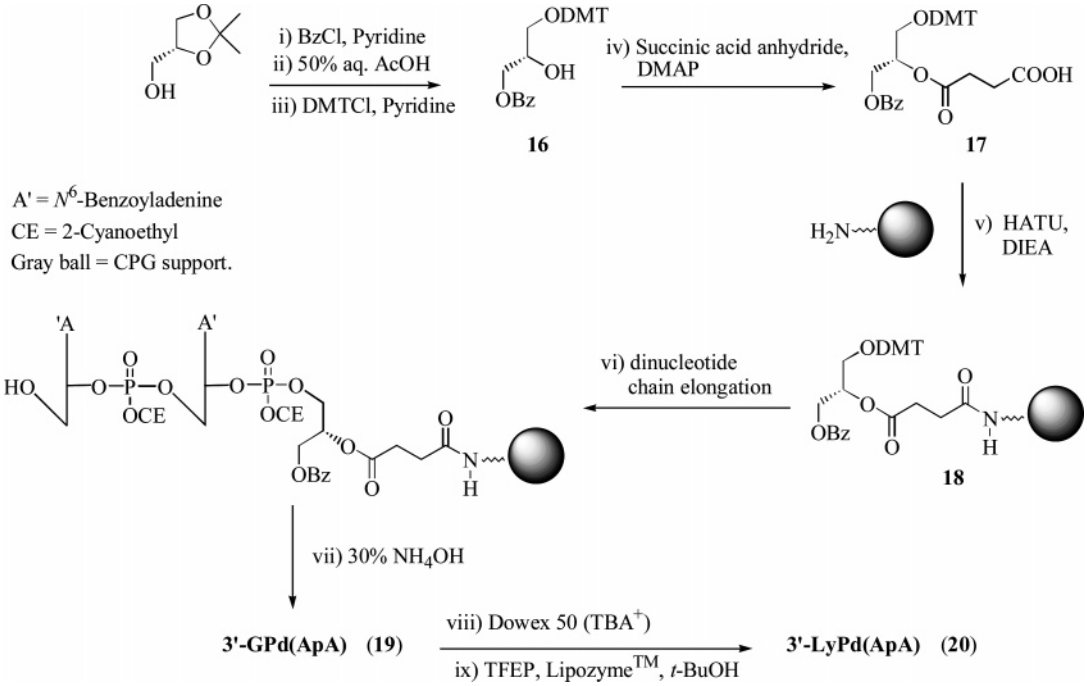

synthesis. The primary alcoholic function of glycerol, involved in the subsequent formation of phosphodiester bond, was protected with the dimethoxytrityl group, which was removed following the first deblocking step of the solid-phase elongation of the dinucleotide.

Next treatment of **19** with Lipozyme and TFEP afforded the expected 3′-LyPd(ApA) (**20**), with a conversion value near to that observed following enzymatic palmitoylation of the 5′-counterpart (see Table 1), thus indicating that the position of the glycerol unit on the sugar moiety does not play a crucial role in determining the extent of the enzymatic acylation of GPOdNs.

It should be noted that oligonucleotides containing 3′-(*RS*)-glycerol moiety were previously synthesized by other authors *(14)* by a different route. Then, the synthesis of 3′-*O*-[(2*RS*)-glycerophosphoryl]d(ApA) followed by enantioselective enzymatic acylation of the *R*-isomer would be an elegant way to prepare 3′-LyPd(ApA) with the natural *R* configuration at the chiral center of the glycerol moiety. However, a preliminary attempt to enzymatically palmitoylate the test compound 3′-*O*-[(2*RS*)-glycerophosphoryl]dA gave a near equimolar mixture of two diastereomeric 3′-LyPdA. So, as Lypozyme does not show the desired selectivity, the synthetic run reported in Scheme 3 appears to be more appropriate.

To evaluate the possibility that lipases different from Lipozyme could be used to acylate 5′-GPOdNs, the enzymes reported in Table 2 were tested, in parallel experiments, for their ability to palmitoylate 5′-GPd(ApApApApT) (**5**).

Apart from Lipozyme, the tested lipases were nonimmobilized enzymes and a constant (total enzyme activity)/(substrate amount) ratio (E/S) was used in all the experiments. The parallel reference experiment with Lipozyme (*Rhizomucor miehei* lipase, immobilized on an ion-exchange resin) was carried out following the same experimental conditions previously set up for the preparation of LyPOdNs (see Experimental Procedures). Under these conditions, the E/S ratio was near 100 times lower than that fixed for the remaining part of experiments. Indeed, considering that the specific activity of Lipozyme was 2 or 3 orders of magnitude lower than that of the nonimmobilized enzymes, a considerable amount of this enzyme should have been used to reach the fixed E/S ratio. We abandoned this approach to avoid an undesired marked absorption of the substrate on the polymeric support of the enzyme.

Table 2. Acylation of 5′-GPd(ApApApApT) by Various Lipases

lipase source	specific enzyme activity (U/mg)	enzyme amount (mg)	conversion[a] (%)
Candida antarctica	3	10	0.5
Candida cylindracea	2	15	-
Pseudomonas cepacea	50	0.7	-
Pseudomonas fluorescens	40	0.8	1.5
hog pancreas	30	1	-
Rhizopus niveus	1.5	20	-
Rhizomucor miehei	1	30	-
Rhizomucor miehei immobilized, Lipozyme	3×10^{-2}	11	1.7

[a] Determined by HPLC, after 26 days incubation of single aliquots of 5′-GPd(ApApApApT) (TBA^+ form, 1.25 μmol) in the presence of TFEP (50 μmol) and the selected enzyme, in dried *t*BuOH (2 mL).

The above experiments showed that only lipases from *Pseudomonas fluorescens* and *Candida antarctica* were capable of acylating the pentameric substrate. The former giving better results than the latter, but both working at a lower extent than Lipozyme. Of course, the different behavior of the tested lipases with respect to Lipozyme comes out more stressed when considering that the latter worked with an activity/substrate ratio much lower than that fixed for the other enzymes.

From these results it was evident that the attempt to use some enzymes different from Lipozyme did not allow an effective improvement of the enzymatic step. Nevertheless, since a check of Lipozyme activity before and after a single reaction cycle did not show any significant variation, in those cases in which conversion values of the enzymatic step were low, it was possible to increase the target compound yield by properly recycling the enzyme and the unreacted substrate.

CONCLUSIONS

In this report the chemoenzymatic synthesis of lysophosphatidyl conjugates of short chain oligonucleotides, ranging from 2- to 4-mer, has been described. The same synthetic strategy has allowed us to obtain also, but in very small yield, lysophosphatidyl derivatives of 5- and 6-mer oligonucleotides.

It is worthy of note that, in the chemical step of the reported synthesis, the desired GPOdN is prepared making use of the phosphoramidite chemistry protocol commonly employed on DNA synthesizers. This, when required, would allow easy preparation of glycerophosphoryl derivatives of those oligonucleotide analogues cited in the literature for their antiviral properties. These could subsequently undergo enzymatic palmitoylation to give the relevant LyPOdN analogues.

Also, the newly synthesized LyPOdNs could be useful building blocks for the preparation of lipoconjugates of higher-mer oligonucleotides, possibly by chemical ligation. In fact, considering that all the LyPOdNs we prepared are water-soluble compounds, their template-directed chemical ligation (*15*, *16*) to selected 5′-P-oligonucleotide donors appears to be an interesting route for the preparation of lysophosphatidyl antisense oligonucleotides. Further work is in progress in this regard.

ACKNOWLEDGMENT

This work was supported by Ministero dell'Istruzione, dell'Università e della Ricerca, Italy (PRIN), and by University of Catania, Italy (Progetti di Ricerca d'Ateneo).

Supporting Information Available: ^{1}H and ^{13}C NMR spectra of compounds **4**, **5**, and **16** , and ^{1}H NMR spectra of compounds **6**−**8**. This material is available free of charge via the Internet at http://pubs.acs.org/BC.

LITERATURE CITED

(1) Balfour, H. H., Jr. (1999). Antiviral drugs. *N. Engl. J. Med. 340*, 1255−1268.

(2) Nair, V. (2002). HIV integrase as a target for antiviral chemotherapy. *Rev. Med. Virol. 12*, 179−193.

(3) Zhong, W., An, H., Barawkar, D., and Hong, Z. (2003). Dinucleotide analogues as novel inhibitors of RNA-dependent RNA polymerase of hepatitis C virus. *Antimicrob. Agents Chemother. 47*, 2674−2681.

(4) Iyer, R. P., Jin, Y., Roland, A., Morrey, J. D., Mounir, S., and Korba, B. (2004). Phosphorothioate di- and trinucleotides as novel class of anti-hepatitis B virus agents. *Antimicrob. Agents Chemother. 48*, 2199−2205.

(5) Crooke, S. T. (1995) Delivery of oligonucleotides and polinucleotides. *J. Drug Target. 3*, 185−190.

(6) Stein, C. A., and Narayan, R. (1996) Antisense oligodeoxynucleotides: internalization, compartmentalization and nonsequence specificity. *Perspect. Drug Discovery Des. 4*, 41−50.

(7) Beaucage, S. L., and Iyer, R. P. (1993) The synthesis of modified oligonucleotides by the phosphoramidite approach and their applications. *Tetrahedron 49*, 6123−6194.

(8) Bologna, J. C., Vives, E., Imbach, J. L., and Morvan, F. (2002) Uptake and quantification of intracellular concentration of lipophilic pro-oligonucleotides in HeLa cells. *Antisense Nucleic Acid Drug Dev. 12*, 33 − 41.

(9) Chillemi, R., Russo, D., and Sciuto, S. (1998) Chemoenzymatic synthesis of lysophosphatidylnucleosides. *J. Org. Chem. 63*, 3224−3229.

(10) Chillemi, R., Aleo, D., Granata, G., and Sciuto, S. (2002) Synthesis of 3′(2′)-*O*-lysophosphatidylnucleosides − a further application of a chemoenzymatic strategy. *Eur. J. Org. Chem.* 3622−3631.

(11) Gray, D. M., Hung, S.-H., and Johnson, K. H. (1995) Absorption and circular dichroism spectroscopy of nucleic acid duplexes and triplexes. *Methods Enzymol. 246*, 19−34.

(12) Edupuganti, O. P., Singh, Y., Defrancq, E., and Dumy, P. (2004) New strategy for the synthesis of 3′,5′-bifunctionalized oligonucleotide conjugates through sequential formation of chemoselective oxime bonds. *Chem. Eur. J. 10*, 5988−5995.

(13) Chan, W. C., and White, P. D. (2000) *Fmoc Solid-Phase Peptide Synthesis: A Practical Approach*, Oxford University Press, Oxford.

(14) Urata, H., and Akagi, M. (1993) A convenient synthesis of oligonucleotides with a 3′-phospho-glycolate and 3′-phosphoglycaldehyde terminus. *Tetrahedron Lett. 34*, 4015−4018.

(15) Fedorova, O. A., Gottikh, M. B., Oretskaya, T. S., and Shabarova, Z. A. (1996) Cyanogen bromide-induced chemical ligation: mechanism and optimization of the reaction conditions. *Nucleosides Nucleotides 15*, 1137−1147.

(16) Selvasekaran, J., and Turnbull, K. D. (1999) Chemical ligation of oligodeoxyribonucleotides on circular DNA templates. *Nucl. Acids Res. 27*, 624−627.

BC050365E

Syntheses of Functionalized Biotin N-1′ Derivatives: New Tools for the Control of Gene Expression with Small Molecules

Cyril Inard,[†,§] Emmanuelle Fourcade,[†,§] Rudi Baron,[†] Daniel Tovar,[†] Laurent Chaisemartin,[†,‡] Casimir Blonski,[‡] and Jean-Charles Faye[†,*]

INSERM U563, C. P. T. P., Département Innovation Thérapeutique et Oncologie Moléculaire, Institut Claudius Regaud, 20-24 rue du pont Saint Pierre, 31052 Toulouse Cédex, France, Groupe de Chimie Organique Biologique, Laboratoire de Synthèse et Physicochimie de Molécules d'Intérêt Biologique (LSPCMIB), ESA 5068, Université Paul Sabatier, Bât IIR1, 118 Rte de Narbonne, 31062 Toulouse Cedex 4, France, and MilleGen, Prologue Biotech, rue Pierre et Marie Curie, BP 700, 31319 Labège Cédex, France. Received January 19, 2006; Revised Manuscript Received April 25, 2006

The exceptionally high affinity of biotin toward avidin and streptavidin is at the basis of (strept)avidin−biotin biotechnology, which has numerous applications in life sciences. Recent biotin developments for in vivo and in vitro acylation of selective targeted protein and intein-mediated site specific protein biotinylation require the free biotin carboxyl function to covalently bind with the targeted protein. However, recently this carboxylic function has been used to substitute biotin with numerous ligands and flags. In the present work, we propose the N-1′ labeling possibilities of biotin, keeping the valeric chain free. We describe liquid and solid-phase syntheses of functionalized biotin N-1′ derivatives. Although the N-1′ modification involves a two-log decrease in affinity, in vitro these molecules kept their high avidin affinity (around 10^{-12} M) and the in vivo acylation ability of new biotin derivatives.

INTRODUCTION

Biotin has been extensively used in the life sciences for many years, and renewed interest in this molecule has recurred with recent biological developments (*1*−*4*). In numerous applications, the carboxyl function of biotin has been chemically linked to the desired oligonucleotide, peptide, or fluorochrome, etc., and complexed with avidin and streptavidin for recognition. However, not all of these biotins modified on the carboxyl function at the end of its valeric chain allow covalent linkage with peptides. The initial challenge of the present work was to obtain a labeled biotin that could target a fusion between the desired protein with either the biotin carboxy carrier protein (BCCP) or the biotin linker peptide (BLP). However, nearly all of the chemical modifications of labeled biotin have involved this carboxyl function, which results in molecules that are not usable for our purposes. There are few reports of chemical modifications of commercial biotin on the N-1′ position (*5*, *6*). Using these studies as a reference, we developed derivatives of biotin that have been modified at N-1′ and bear active functions at the extremity of the N-1′ arm while keeping the carboxyl function at the end of its valeric chain free. A series of syntheses were first conducted in solution, using classical reaction procedures (Scheme 1). The last methyl deprotection of biotin appeared to be the rate-limiting step of the synthesis; moreover, in numerous cases this deprotection was not able to give the desired final product. To ensure good recovery, facile synthesis, and gentle deprotection of the product, in a second series of experiments biotin was linked to a solid phase (Scheme 2) to generate the bifunctional biotin derivatives.

Because lipid−protein interactions are of great interest for our group (*7*, *8*) the ligands chosen to make biotin derivatives were *cis*-9-octadecanoic acid (oleic acid), geranyl geraniol, and estradiol. Their in vitro affinities for avidin were evaluated and then the ability of the radioactive conjugated molecule oleic acid−biotin to penetrate into *Escherichia coli* and to link BCCP, and the fusion protein $LexA_{DB}$-BCCP, were assessed.

EXPERIMENTAL PROCEDURES

Materials and Methods. All chemical and biochemical reagents were purchased either from Sigma-Aldrich or Prolabo except for (9,10(n)-^{3}H) oleic acid (10 Ci/mmol), which was purchased from ICN. All reactions using nonaqueous solvents were carried out under a dry argon atmosphere. The progress of the reactions was monitored by analytical thin-layer chromatography on silica gel Merck 60F254. The TLC visualization was done by iodine, ninhydrin, or ammonium-cerium(IV) nitrate. Flash chromatography was performed on a Merck Kieselgel 60 device (230−400 mesh). Preparative TLC was carried out on silica gel Merck 60F254. Radioactive compounds were revealed by a Berthold ^{3}H radioactivity detector. ^{1}H NMR spectra were recorded on a Brucker AC-200 at 200 MHz or on a Brucker AC-400 at 400 MHz, and ^{13}C NMR spectra were recorded on a Brucker AC-200 at 50 MHz or on a Brucker AC-400 at 100 MHz, using tetramethylsilane as an internal standard. DCI and FAB mass spectra were obtained on a Nermag R10-10 machine. High-resolution FAB mass spectra were obtained by the Mass Spectrometry Service, CESAMO, Bordeaux. Elemental analyses were performed on a Carlo Erba 1106. The radioactivity in the solutions was counted with a Packard 2000CA scintillation counter in ReadySafe scintillation liquid (Beckman). A protein assay was done with a Biorad kit, using bovine serum albumin (BSA) as a standard. For bacterial culture, Luria broth (LB) was purchased from Gibco-BRL. Luminescence enhancement of the nitrocellulose filters (Protran BA83 0.25 mM; Schleicher & Schuell) was accomplished with an ECL kit (Amersham). Autoradiography was performed on Kodak XLS films developed on an Amersham Hyperprocessor.

* Corresponding author: Fax: 33 (0)5 61 42 46 31. E-mail: faye@icr.fnclcc.fr.
† Institut Claudius Regaud.
‡ Université Paul Sabatier.
§ MilleGen.

10.1021/bc060010a CCC: $33.50 © 2006 American Chemical Society
Published on Web 05/26/2006

Scheme 1. Synthesis of *N*-1′-(4-Oleylamido-1-butoxycarbonyl)-D-biotin[a]

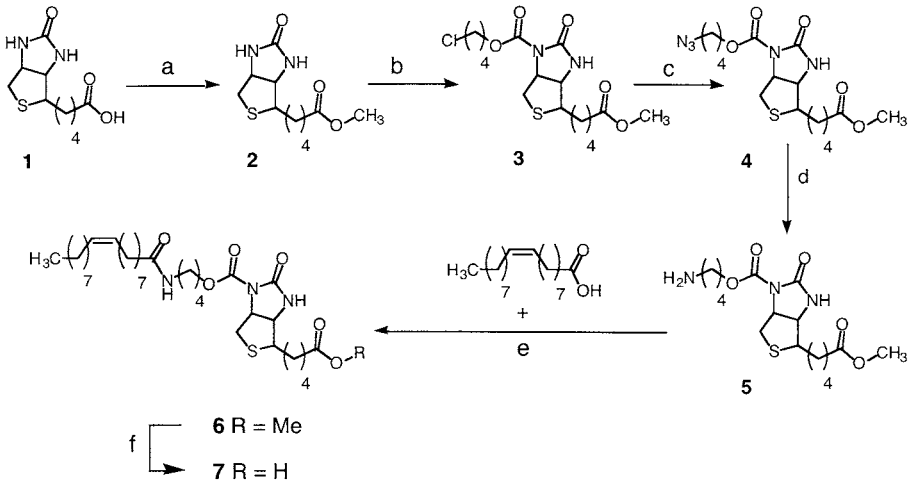

[a] Reaction conditions: (a) Amberlite IR120, MeOH, reflux, 79.5%; (b) 4-chlorobutyl chloroformate, $CHCl_3$, reflux, 89.5%; (c) NaN_3, NaI, acetone: H_2O, reflux, 95%; (d) H_2, Pd/C, EtOH, 75%. (e) *N*-methylmorpholine, BOP, *N*-hydroxybenzotriazole, Et_3N, DMF, 54%; (f) H^+/H_2O, acetonitrile, 70 °C.

Scheme 2. Solid-Phase Synthesis of *N*-1′-(4-(Geranylgeranyl-*N*-acetyl cysteine)-1-butoxycarbonyl)-D-biotin[a]

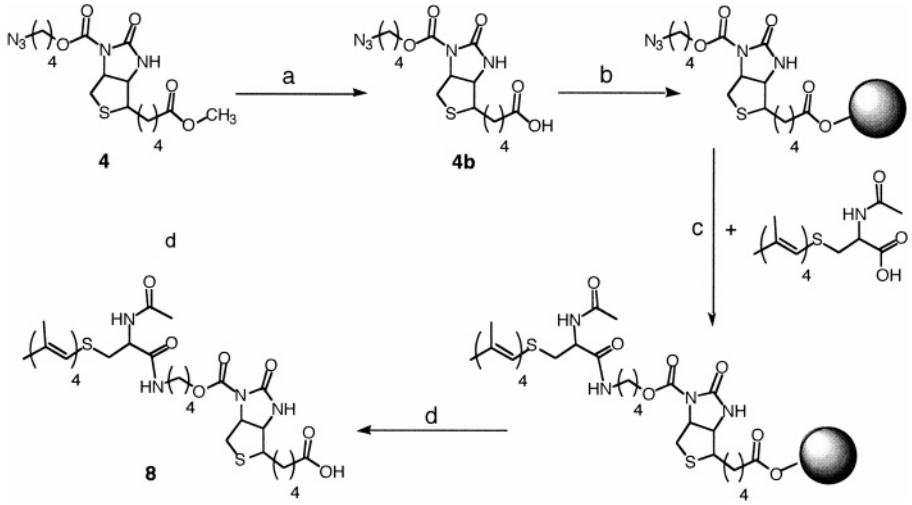

[a] Reaction conditions: (a) HCl (3 M), acetone, reflux; (b) 2-chlorotrityl chloride resin, DIEA, and DMF at RT; (c) geranylgeranyl-*N*-acetyl cysteine plus HOAt, DIC, tributylphosphine, THF anhydrous at RT; (d) acetic acid, trifluoroethanol, CH_2Cl_2 at RT.

Chemicals. D-Biotin Methyl Ester (2). A mixture of D-biotin (**1**) (2.44 g, 10 mmol) and hydrochloric Amberlite resin (IR120, 2.6 g) in anhydrous methanol (75 mL) was heated to reflux for 7 h. The resin was filtered and washed with methanol. The combined organic solutions were concentrated under reduced pressure to obtain D-biotin methyl ester **2** as a white solid (2.05 g, 7.95 mmol, 79.5%). $R_f = 0.41$ (MeOH:$CHCl_3$ 5:95). ^{1}H NMR (200 MHz, DMSO, 25 °C, TMS) $\delta = 6.37$ (d, *J* (H, H) = 13.8 Hz, 2H; >NH), 4.31 (m, 1H; >CH−NH-), 4.14 (m, 1H; >CH−NH-), 3.59 (s, 3H; $COOCH_3$), 3.12 (m, 1H; >CH−S-), 2.63 (dd, *J* (H, H) = 5.0 Hz, 12.4 Hz, 1H; $-CH_2-$S), 2.58 (d, *J* (H, H) = 12.4 Hz, 1H; $-CH_2-$S), 2.30 (t, *J* (H, H) = 7.3 Hz, 2H; $-CH_2-COOCH_3$), 1.7−1.4 (m, 6H; -$(CH_2)_3-CH_2-COOCH_3$); ^{13}C NMR (50 MHz, DMSO, 25 °C) $\delta = 173.22$ ($-COOCH_3$), 162.66 (−HN−CO−NH-), 60.96 (>CH−NH-), 59.11 (>CH−NH-), 55.26 (>CH−S-), 51.11 ($-COOCH_3$), 39.43 ($-CH_2-$S-, $-CH_2-COOCH_3$), 33.01, 27.91, 24.40 (-$(CH_2)_3-CH_2-COOCH_3$).

***N*-1′-(4-Chloro-1-butoxycarbonyl)-D-biotin Methyl Ester (3).** A solution of (258 mg, 1 mmol) and 4-chlorobutyl chloroformate (2.46 mL, 18 mmol) in anhydrous chloroform (5 mL) was heated to reflux for 4 days. The chloroform was evaporated under reduced pressure, and the solution was diluted in a large volume of petroleum ether at 4 °C. The resulting precipitate was filtered and purified by flash chromatography (methanol:dichloromethane, 3: 97) to yield **3** as a yellow solid (351 mg, 0.895 mmol, 89.5%). $R_f = 0.33$ (MeOH:CH_2Cl_2 3:97). ^{1}H NMR (200 MHz, $CDCl_3$, 25 °C, TMS) δ = 6.7 (s, 1H; >NH), 4.7 (m, 1H; >CH−N<), 4.24 (m, 3H; >CH−NH-, $-CH_2-O-CO-$), 3.63 (s, 3H; $-COOCH_3$), 3.57 (t, *J* (H, H) = 2.4 Hz, 2H; $-CH_2-$Cl), 3.3 (m, 1H; >CH−S-), 3.03 (m, 2H; $-CH_2-$S-), 2.31 (t, *J* (H, H) = 7.3 Hz, 2H; $-CH_2-COOCH_3$), 1.8−1.4 (m, 10H; -$(CH_2)_3-CH_2-COOCH_3$, Cl−CH_2-$(CH_2)_2-CH_2-O-CO-$); ^{13}C NMR (50 MHz, $CDCl_3$, 25 °C) $\delta = 173.98$ ($-COOCH_3$), 155.93 (>N−CO−NH-), 151.75 (−O−CO−N<), 65.77 ($-CH_2-O-CO-$), 62.75 (>CH−N<), 57.80 (>CH−NH-), 55.26 (>CH−S-), 51.11 ($-COOCH_3$), 44.52 ($-CH_2-$Cl), 38.74 ($-CH_2-$S-), 33.57 ($-CH_2-COOCH_3$), 29.14, 28.29, 28.05, 26.10, 24.63 (-$(CH_2)_3-CH_2-COOCH_3$, Cl−CH_2-$(CH_2)_2-CH_2-O-CO-$); MS (DCI/NH_3, CH_2Cl_2): *m*/*z*: 393 [$M^+ - H$]; 410 [$M^+ - NH_4$]; $C_{16}H_{25}ClN_2O_5S$ (392.9): calculated C 48.91, H 6.41, N 7.13, O 20.36; found C 48.97, H 6.46, N 7.12, O 20.36.

***N*-1′-(4-Azido-1-butoxycarbonyl)-D-biotin Methyl Ester (4).** A solution of (392 mg, 1 mmol), sodium iodide (17 mg, 0.1 mmol), and sodium azide (325 mg, 5 mmol) in acetone:

water (4:1; 10 mL) was heated to reflux for 4 days. The acetone was evaporated under reduced pressure, and the resulting aqueous solution extracted three times with dichloromethane. The organic phase was dried (Na_2SO_4) and concentrated under reduced pressure. Purification by flash chromatography (methanol:dichloromethane, 4:96) yielded a yellow solid (379 mg, 0.95 mmol, 95%). R_f = 0.33 (MeOH:CH_2Cl_2 3:97). ^{1}H NMR (200 MHz, $CDCl_3$, 25 °C, TMS) δ = 7.26 (s, 1H; >NH), 4.80 (m, 1H; >CH−N<), 4.24 (m, 3H; >CH−NH-, $-CH_2-O-CO$-), 3.63 (s, 3H; $-COOCH_3$), 3.32 (t, *J* (H, H) = 6.4 Hz, 2H; $-CH_2-N_3$), 3.32 (m, 1H; >CH−S-), 3.02 (m, 2H; $-CH_2-S$-), 2.31 (t, *J* (H, H) = 7.3 Hz, 2H; $-CH_2-COOCH_3$), 1.8−1.4 (m, 10H; -$(CH_2)_3-CH_2-COOCH_3$, $N_3-CH_2-(CH_2)_2-CH_2-O-CO$-); ^{13}C NMR (50 MHz, CD_3OD, 25 °C) δ = 175.81 ($-COOCH_3$), 157.96 (>N−CO−NH-), 153.10 ($-O-CO-N<$), 66.98 ($-CH_2-O-CO$-), 64.20 (>CH−N<), 59.36 (>CH−NH-), 56.67 (>CH−S-), 52.21 ($-COOCH_3$), 52.14 ($-CH_2-N_3$), 39.71 ($-CH_2-S$-), 34.63 ($-CH_2-COOCH_3$), 27.14, 29.76, 29.45, 26.65, 25.95 (-$(CH_2)_3-CH_2-COOCH_3$, $N_3-CH_2-(CH_2)_2-CH_2-O-CO$-); MS (DCI/$NH_3$, CH_2Cl_2) *m*/*z* 400 [M^+ − H], 417 [M^+ − NH_4]; $C_{16}H_{25}N_5O_5S$ (399.5): calculated C 48.11, H 6.31, N 17.53, O 20.03; found C 48.03, H 6.49, N, 17.29, O 20.02.

***N*-1′-(4-Amino-1-butoxycarbonyl)-D-biotin Methyl Ester (5).** The catalytic hydrogenation of (**4**) (300 mg, 0.75 mmol) was performed in ethanol (10 mL), in the presence of Pd/C (150 mg). After 4 h under an H_2 atmosphere, the solution was filtered, and the Pd/C was washed with methanol. The filtrate was concentrated under reduced pressure to yield **5** as a yellow oil (210 mg, 0.56 mmol, 75%). ^{1}H NMR (400 MHz, CD_3OD, 25 °C, TMS) δ = 4.88 (m, 1H; >CH−N<), 4.26 (m, 3H; >CH−NH-, $-CH_2-O-CO$-), 3.66 (s, 3H; $-COOCH_3$), 3.30 (m, 1H; >CH−S-), 3.05 (m, 4H; $-CH_2-S$-, $-CH_2-NH_2$), 2.36 (t, *J* (H, H) = 7.4 Hz, 2H; $-CH_2-COOCH_3$), 1.8−1.4 (m, 10H; -$(CH_2)_3-CH_2-COOCH_3$, $NH_2-CH_2-(CH_2)_2-CH_2-O-CO$-); ^{13}C NMR (400 MHz, CD_3OD, 25 °C) δ = 175.83 ($-COOCH_3$), 158.05 (>N−CO−NH-), 153.13 ($-O-CO-N<$), 66.95 ($-CH_2-O-CO$-), 64.28 (>CH−N<), 61.69 (>CH−NH-), 56.67 (>CH−S-), 52.11 ($-COOCH_3$), 41.11 ($-CH_2-NH_2$), 40.33 ($-CH_2-S$-), 34.57 ($-CH_2-COOCH_3$), 29.74, 29.44, 26.50, 25.89, 25.63 (-$(CH_2)_3-CH_2-COOCH_3$, $NH_2-CH_2-(CH_2)_2-CH_2-O-CO$-); MS (FAB, Gly/Thio, MeOH) *m*/*z* 374 [M^+ − H].

***N*-1′-(4-Oleylamido-1-butoxycarbonyl)-D-biotin Methyl Ester (6).** A solution of **5** (38 mg, 0.1 mmol) and triethylamine (28 μL, 0.2 mmol) dissolved in anhydrous dimethylformamide (4 mL) was added to a stirred mixture of oleic acid (28.3 mg, 0.1 mmol), *N*-methylmorpholine (0.15 mmol), BOP reagent (44 mg, 0.1 mmol), and *N*-hydroxybenzotriazole (14 mg, 0.1 mmol) dissolved in anhydrous dimethylformamide (5 mL). The solution was stirred at room temperature for 4 days. The solution became dark yellow. The dimethylformamide was evaporated under reduced pressure, and the residue was dissolved in dichloromethane (10 mL). The solution was extracted four times with water and washed once with brine. The organic phase was dried (Na_2SO_4), and the dichloromethane was evaporated under reduced pressure. The residue was added to diethyl ether to form a white precipitate, which was separated from the solution by filtration. The filtrate was concentrated under reduced pressure and the residue purified by flash chromatography (methanol: dichloromethane, 3:97), to yield **6** as a yellow oil (35 mg, 0.055 mmol, 55%). R_f = 0.55 (MeOH:CH_2Cl_2 8:92). ^{1}H NMR (200 MHz, $CDCl_3$, 25 °C, TMS) δ = 6.5 (s, 1H; >NH), 5.9 (s, 1H; −NH-), 5.32 (m, 2H; −CH=CH-), 4.8 (m, 1H; >CH−N<), 4.25 (m, 3H; >CH−NH-, $-CH_2-O-CO$-), 3.66 (s, 3H; $-COOCH_3$), 3.4−3.1 (m, 5H; >CH−S-, $-CH_2-S$-, $-CH_2-NH-CO$-), 2.33 (t, *J* (H, H) = 7.2 Hz, 2H; $-CH_2-COOCH_3$), 2.15 (t, *J* (H, H) = 8.0 Hz, 2H; $-CH_2-CO-NH$-), 1.99 (m, 4H; $-CH_2-CH=CH-CH_2$-), 1.7−1.6 (m, 12H; -$(CH_2)_3-CH_2-COOCH_3$, $-NH-CH_2-(CH_2)_2-CH_2-O-CO$-, $-CH_2-CH_2-CO-NH$-), 1.3−1.2 (m, 20H; $CH_3-(CH_2)_6-CH_2-CH=CH-CH_2-(CH_2)_4$-), 0.86 (t, *J* (H, H) = 6.5 Hz, 3H; $-CH_3$); ^{13}C NMR (50 MHz, $CDCl_3$, 25 °C) δ = 173.58 ($-COOCH_3$, −CO−NH-), 155.38 (>N−CO−NH-), 152.02 ($-O-CO-N<$), 130.01 (−CH=), 129.82 (=CH-), 67.08 ($-CH_2-O-CO$-), 62.91 (>CH−N<), 57.59 (>CH−NH-), 55.14 (>CH−S-), 51.65 ($-COOCH_3$), 38.73 ($-CH_2-S$-), 38.55 ($-CH_2-NH-CO$-), 36.69 ($-CH_2-CO-NH$-), 33.47 ($-CH_2-COOCH_3$), 31.94 ($-CH_2-CH=CH-CH_2$-), 29.80 ($-CH_2-CH_2-CO-NH$-), 29.55, 29.36, 29.24, 28.18, 28.03, 27.25, 26.32, 25.92, 25.38, 24.63, 22.71 (-$(CH_2)_3-CH_2-COOCH_3$, $-NH-CH_2-(CH_2)_2-CH_2-O-CO$-, $CH_3-(CH_2)_6-CH_2-CH=CH-CH_2-(CH_2)_4$-), 14.14 ($-CH_3$); HRMS (FAB+, MeOH) *m*/*z* 638.41958 (638.42028 calculated for $C_{34}H_{59}N_3O_6S$, [M^+ − H]).

***N*-1′-(4-Oleylamido-1-butoxycarbonyl)-D-biotin (7).** Acidic Hydrolysis**.** To a solution of **6** (80 mg, 0.13 mmol) in a mixture of acetonitrile (30 mL) and water (10 mL) was added 1 M H_2SO_4 (400 μL). The resulting solution was stirred at 70 °C for 48 h. The acetonitrile was evaporated, and the aqueous phase was extracted three times with dichloromethane (3 times, 10 mL). The combined organic phases were washed once with brine, dried (Na_2SO_4), and concentrated under reduced pressure, to yield **7** as a yellow oil (39 mg, 0.063 mmol, 48%). R_f = 0.25 (MeOH:CH_2Cl_2 8:92). ^{1}H NMR (200 MHz, CD_3OD, 25 °C, TMS) δ = 5.34 (m, 2H; −CH=CH-), 4.86 (m, 1H; >CH−N<), 4.23 (m, 3H; >CH−NH-, $-CH_2-O-CO$-), 3.3−3.05 (m, 5H; >CH−S-, $-CH_2-S$-, $-CH_2-NH-CO$-), 2.32 (t, *J* (H, H) = 8.1 Hz, 2H; $-CH_2-COOH$), 2.16 (t, *J* (H, H) = 7. 7 Hz, 2H; $-CH_2-CO-NH$-), 2.03 (m, 4H; $-CH_2-CH=CH-CH_2$-), 1.7−1.5 (m, 12H; -$(CH_2)_3-CH_2-COOH$, $-NH-CH_2-(CH_2)_2-CH_2-O-CO$-, $-CH_2-CH_2-CO-NH$-), 1.4−1.2 (m, 20H; $CH_3-(CH_2)_6-CH_2-CH=CH-CH_2-(CH_2)_4$-), 0.90 (t, *J* (H, H) = 6.5 Hz, 3H; $-CH_3$); ^{13}C NMR (50 MHz, CD_3OD, 25 °C) δ = 177.52 (−COOH), 176.35 (−CO−NH-), 158.05 (>N−CO−NH-), 153.14 ($-O-CO-N<$), 130.92 (−CH=), 130.83 (=CH-), 67.20 ($-CH_2-O-CO$-), 64.18 (>CH−N<), 59.33 (>CH−NH-), 56.61 (>CH−S-), 39.81 ($-CH_2-S$-), 39.65 ($-CH_2-NH-CO$-), 37.19 ($-CH_2-CO-NH$-), 35.00 ($-CH_2-COOH$), 34.70 ($-CH_2-CH=CH-CH_2$-), 33.11 ($-CH_2-CH_2-CO-NH$-), 30.88, 30.65, 30.49, 30.37, 30.28, 29.75, 29.44, 28.17, 27.60, 27.14, 27.00, 26.14, 25.93, 23.78 (-$(CH_2)_3-CH_2-COOH$, $-NH-CH_2-(CH_2)_2-CH_2-O-CO$-, $CH_3-(CH_2)_6-CH_2-CH=CH-CH_2-(CH_2)_4$-), 14.50 ($-CH_3$); HRMS (FAB+, MeOH) *m*/*z* 646.38715 (646.38658 calcd for $C_{33}H_{57}N_3O_6S$, [M^+ − Na]).

***N*-1′-(4-(9,10(n)-^{3}H)-Oleylamido-1-butoxycarbonyl)-D-biotin Methyl Ester (^{3}H6).** A solution of **5** (0.2 mg, 0.5 μmol) and triethylamine (0.14 μL, 1 μmol), dissolved in anhydrous dimethylformamide (30 μL), was added to a stirred mixture of (9,10(n)-^{3}H) oleic acid (140 μg, 0.5 μmol, 5 mCi), *N*-methylmorpholine (0.1 μL, 0.5 μmol), BOP reagent (220 μg, 0.5 μmol), and *N*-hydroxybenzotriazole (70 μg, 0.5 μmol) dissolved in anhydrous dimethylformamide (50 μL). Anhydrous dimethylformamide (920 μL) was added, and the mixture was stirred at room temperature for 5 days. The dimethylformamide was evaporated under reduced pressure, and the residue was dissolved in dichloromethane (100 μL). The solution was purified by two successive preparative TLC runs (methanol 5%, dichloromethane 95%), to yield **^{3}H6** (34.8 μCi). The identity of the compound was checked by comigration with **6** on TLC. R_f = 0.55 (MeOH:CH_2Cl_2 8:92, ^{3}H radioactivity detection).

***N*-1′-(4-(9,10(n)-^{3}H)-Oleylamido-1-butoxycarbonyl)-D-biotin (^{3}H7).** Acidic hydrolysis. We assumed that the tritiated product had the same specific activity as the initial tritiated oleic acid (10 Ci/mmol).

Solid-Phase Synthesis. *N*-1′-(4-Azido-1-butoxycarbonyl)-D-biotin (4b). To a solution of **4** (399 mg, 1 mmol) dissolved in acetone (4 mL) was added 2 mL of HCl (3 M), and the solution was stirred for 7 h at reflux. The acetone was evaporated off and the resulting powder dissolved and purified by a preparative TLC run (MeOH:CH_2Cl_2, 5:95); 270 mg of pure product was obtained (recovery = 70%). R_f = 0.39 (MeOH: CH_2Cl_2, 5: 95). ^{1}H NMR (200 MHz, CD_3OD, 25 °C, TMS) δ = 4.90 (m, 1H; >CH−N<), 4.25 (m, 3H; >CH−NH-, $-CH_2-$O−CO-), 3.36(t, *J* (H−H) = 7.3 Hz, 2H; $-CH_2-$COOH), 3.36 (m, 1H; >CH−S-), 3.05 (m, 2H; $-CH_2-$S-), 2.32 (t, J (H, H) =7.3 Hz, 2H; $-CH_2-$COOH), 1.72−1.47 (m, 10H; -$(CH2)_3-$ CH_2-COOH, $N_3-CH_2-(CH_2)_2-CH_2-$O−CO-).

Anchorage of 4b on Styrene-DVB Resin (S-DVB). A solution of **4b** (1.2 equiv/ S-DVB) in 2.5 mL of DMF was added, with diisopropylethylamine (DIEA) (4 equiv/**4b**), to S-DVP (261 mg: 0.261 mmol, in 2 mL of CH_2Cl_2), and the mixture was stirred for 18 h. The polymer was then filtered and washed three times with a solution of CH_2Cl_2:MeOH:DIEA (17:2:1) and then twice with 2.5 mL of DMF and twice with 2.5 mL of CH_2Cl_2. The polymer was then dried overnight under vacuum in the presence of P_2O_5.

Coupling of Geranyl-geranyl *N*-Acetylcysteine to *N*-1′-(4-Azido-1-butoxycarbonyl)-D-biotin−S-DVB (N3−S-DVB). N3−S-DVB (62.1 mg, 0.56 mmol/g) was incubated in anhydrous CH_2Cl_2 for 15 min and then washed three times with 1 mL of anhydrous THF and filtered before being evaporated to dryness. The carboxyl function of geranyl-geranyl *N*-acetylcysteine (4 equiv/N3−S-DVB) was activated at 0 °C in the presence of 1-hydroxy-7azabenzotriazole (HOAt) (4 equiv/N3−S-DVB) in anhydrous THF (1 mL); 4 equiv of diisopropylcarbodiimine (DIC) was added, and the mixture was stirred at 0 °C for 30 min. At that time, the mixture was added to N3−S-DVB, 3 equiv/N3−S-DVB of tributylphosphine was added, and the mixture was stirred at room temperature for 18 h. The polymer was washed with DMF and with 3 × 1 mL of CH_2Cl_2 and then dried under vacuum in the presence of P_2O_5.

***N*-1′-(4-(Geranyl-geranyl-*N*-acetylcysteine)-1-butoxycarbonyl)-D-biotin (8).** Acidic cleavage of the polymer was performed in CH_2Cl_2 by addition of acetic acid and trifluoroethanol (6:2:2) stirred at room temperature for 7 h. The polymer was filtered and washed three times with 1 mL of the cleavage solution. The flow through was mixed with 80 mL of hexane and evaporated. TLC purification yielded a yellow oil with a 54% recovery MM = 777.092 g·mol^{-1}. ^{1}H NMR (400 MHz, $CDCl_3$, 25 °C, TMS) δ = 4.65 (m, 1H; >CH−N<), 4.23 (m, 3H; >CH−NH-, $-CH_2-$O−CO-), 3.15 (m, 1H; >CH−S-), 2.95 (m, 4H; $-CH_2-$S-, $-CH_2-$NH), 2.16 (t, *J* (H, H) = 7.4 Hz, 2H; $-CH_2-$COOH), 1.70−1.55 (m, 10H; -$(CH_2)_3-CH_2-$ $COOCH_3$, $-NH-CH_2-(CH_2)_2-CH_2-$O−CO-), 3.03 (m, 1H; >CH−NH−$COOCH_3$), 1.98 (s, 3H; $-CH_3-$CO−NH-), 2.80 (m, 2H; >CH−CH_2-CO-), 3.15 (d, 2H; >CH−CH_2-S-), 5.10 (m, 4H; >CH−C-), 1.59 (s, 15H; CH_3-C<), 2.05 (m, 12H; >C−$(CH_2)_2-$CH<); ^{13}C NMR (400 MHz, $CDCl_3$, 25 °C) δ = 171.541 (−COOH), 174.157 (>N−CO−NH-), 170.256 (CH3−CO−NH-), 169.590 (−NH−CO−CH<), 139.568, 135.456, 134.257, 132.894 (>C<), 151.236 (−O−CO−N<), 119.568 (>CH−C<), 67.125 ($-CH_2-$O−CO-), 53.546 (>CH−N<), 51.699 (>CH−NH-), 52.527 (>CH−S-), 52.807 (−$COOCH_3$), 39.624 ($-CH_2-$NH), 38.709 ($-CH_2-$S-), 35.535 ($-CH_2-$ $COOCH_3$), 20−40 (-$(CH_2)_3-CH_2-COOCH_3$, NH_2-CH_2- $(CH_2)_2-CH_2-$O−CO-, >C−$(CH_2)_2-$CH<, >C−CH_2-S-, >C− CH_2-S−CH_2-), 10−25 (CH_3-C<, CH_3-CO−NH-); MS (DCI/NH_3) *m*/*z* 777 [M^+ − H].

Biochemicals. *Strains*. The bacterial strains used were *E. coli* DH5α for subcloning and SU 202 (9) for lexA-BCCP expression study.

Plasmids. All the biological tools were described previously by Dmitrova et al. (*9*). pMS604 and pDP804 were generous gifts of Schnarr group (Strasbourg, France) and were used for *E. coli* studies. pMS604-$LexA_{DB}$-BCCP was constructed by insertion of the BCCP gene, generated from PCR fragments of *E. coli* genomic DNA, into BstEII-XhoI restriction sites of pMS604 (*9*). The oligonucleotides used for PCR were 5′AAA-CGGGTGACCGCGCGCGATATTCGTAAGATTAAAAA-AC3′ and 3′GACCAGCAGT AGCTCATTGAGCTCTAGAAG AAA 5′.

Fluorescence in Vitro Binding Studies to Avidin. Avidin (Sigma; A9275) was coated on C8 White Maxisorp Fluoro-NUNC plates (NUNC; 437591) at 5 μg/mL at RT for 18 h. The plates were then washed and saturated with PBS in the presence of 0.5% BSA and stored at 4 °C for less than 1 week before use. Fluorescent biotin, 50 nM (biotin-4-fluorescein; Sigma B-9431), was loaded into the plates in the presence or absence of increasing concentrations of various N1′ biotin derivatives (10^{-8}−10^{-4} M). After 3 h incubation at RT, the plates were washed three times with PBS, and the remaining fluorescence was determined with a fluorometer (Wallac; Flite Fluorometer at excitation 485 nm and emission 535 nm).

In Vivo Binding of the Oleic Acid−Biotin Molecule to BCCP. Transformed bacteria were grown overnight at 37 °C in LB (3 mL) that contained tetracyclin (50 μg/mL). The solution was diluted to $OD_{600\ nm}$ = 0.05 and grown at 37 °C in the same culture medium until $OD_{600\ nm}$ = 0.4 (start of exponential growth). Synthesis of the $LexA_{DLA}$-BCCP fusion protein was then induced by the addition of 1 mM IPTG until the OD reached approximately 0.8 (end of exponential growth). At the same time as IPTG, 0.1 nM of [^{3}H]-oleic acid−biotin (10 Ci/mmol) was added.

Extraction of Proteins. *E. coli*. The bacterial solution (10 mL) ($OD_{600\ nm}$ = 0.7 to 1) was centrifuged for 10 min at 4000*g*. The supernatant was eliminated, and the bacterial pellet was washed twice with PBS (1 mL each). The pellet was then resuspended in Tris-HCl buffer (pH 7.8), 2% SDS, and 0.1 M DTT (100 μL). The solution was incubated for 10 min at 100 °C and then sonicated four times for 30 s each. The solution was centrifuged (16000*g*) at 4 °C for 15 min. The supernatant contained the extracted proteins.

Electrophoresis and Immunodetection. The proteins were separated on a 12.5% acrylamide/bisacrylamide gel, and 100 μg amounts of proteins were run on the gel. The proteins were transferred onto a nitrocellulose filter, and immunodetection was achieved using the monoclonal anti-biotin antibody. Visualization was enabled by an enhanced chemiluminescence kit (Amersham).

Radioactivity Distribution in the Cells. The nitrocellulose filter lanes corresponding to the [^{3}H]-oleic acid−biotin conditions (Figure 2) were cut into 4-mm strips. The radioactivity present on each strip was quantified with a scintillation counter Packard 2000CA in ReadySafe scintillation liquid (Beckman).

RESULTS

Synthesis of N1′-Biotin Derivatives (Scheme 1). Our objective was to modify biotin on its N-1′ end with an arm that would facilitate subsequent coupling of a large variety of molecules.The different steps of the synthesis are shown in Scheme 1. Protection of the carboxyl group of biotin was carried out by the usual methods (*6*). From the biotin methyl ester (**2**), the N-1′ modification was adapted to our purposes: 4-chlorobutyl chloroformate was condensed on N-1′, to give *N*-1′-(4-chloro-1-butoxycarbonyl)-D-biotin methyl ester (**3**) with a yield close to 90%. The drastic reaction conditions (4 days at reflux with 18 equiv of 4-chlorobutyl chloroformate) are required because of the lack of reactivity of the N-1′ function of biotin.

Formation of an azido group from the chlorides (**3**) was carried out with sodium azide in the presence of potassium iodide. This step was performed by maintaining in reflux a solution of **3** and sodium azide in DMF. *N*-1′-(4-Azido-1-butoxycarbonyl)-D-biotin methyl ester (**4**) was obtained with a yield of 90%. This azide can be kept in the dark and −20 °C for several months without any degradation.

Catalytic hydrogenation of **4** was carried out in ethanol, in the presence of Pd/C. After 4 h under a H_2 atmosphere, the solution was filtered and the Pd/C washed with ethanol. The filtrate was concentrated under reduce pressure to afford **5** as yellow oil (yield = 75%).

Coupling of Oleic Acid to Biotin. As we have reported elsewhere (*7*), oleic acid could be involved in the mechanism of action of antiestrogen; it has been implicated in various diseases, and a commercially radioactive form is available. Oleic acid was therefore chosen to improve our biological system. The coupling reaction was achieved using a classical method of carboxylic acid activation using the BOP reagent (benzotriazolyl-*N*-oxytris(dimethylamino)phosphonium hexafluorophosphate). *N*-1′-(4-Oleylamido-1-butoxycarbonyl)-D-biotin methyl ester (**6**) was then obtained with a yield of 54%.

The final step of the synthesis consisted of the deprotection of the methyl ester of **6** (R = Me), to regenerate the free carboxyl group of biotin (R = OH). This involved acid hydrolysis, in which a solution of **6** and H_2SO_4 in acetonitrile/water was heated for 48 h, to produce *N*-1′-(4-oleylamido-1-butoxycarbonyl)-D-biotin (oleic acid−biotin **7**) with a yield of 47%. It should be noted that basic hydrolysis of **6** was not considered because of the degradation of the carbamate group that would result. The same procedure was done with tritiated oleic acid; however, our tools were not suited to working with very small quantities of product, and losses were high, leading to a final recovery of around 1%.

Although this methodology worked with oleic acid, it did not work in numerous other syntheses namely estradiol and geranyl-geraniol. It appeared that the difficulty in acheiving the last methyl deprotection was a limiting step.

Solid-Phase Synthesis (Scheme 2). To circumvent these problems, methylbiotin was hydrolyzed with 3 M HCl at the N-1′-(4-azido-1-butoxycarbonyl)-D-biotin methyl ester (**4**) step. Then, the biotin carboxyl group (1.2eq/Sresin) was linked to a styrene-DVB resin (2-chlorotrityl chloride resin) in methyldichloride in the presence of diisopropylethylamine (4 eq). After 18 h of shaking, 70% of the **4b** was bound to the resin.

Coupling of Geranyl-geranyl-*N*-acetylcysteine to Biotin. Geranyl-geranyl-*N*-acetylcysteine was synthesized as described elsewhere (*8*). A modified Staudinger (*10*) reaction allowed, in the presence of 1-hydroxy-7-azabenzotriazole plus diisopropylcarbodiimine and tributylphosphine, a direct linkage of the carboxyl function of cysteine, giving an amide link between biotin and the geranyl-geranyl-*N*-acetylcysteine. *N*-1′-(4-(Geranyl-geranyl-*N*-acetylcysteine)-1-butoxycarbonyl)-D-biotin (**8**) was then obtained after cleavage from the resin in acetic acid, trifluorethanol, and methylene dichloride; the global recovery was 54%.

The solid-phase synthesis strategy allowed the obtention of *N*-1′-(4-(17β-estradiol-6-one 6-(*O*-amidomethyloxime))-1-butoxycarbonyl)-D-biotin which, in our hands, could not be obtained with other methodologies (data not shown).

Avidin Affinities. The affinities of N-1′ biotin derivatives were determined by competition with fluorescent biotin on coated avidin plates. If biotin appeared, as shown in Figure 1, the most efficient ligand to compete with fluorescent biotin on avidin binding, N-1′-(4-azido-1-butoxycarbonyl)-D-biotin (N3-biotin), competes with fluorescent biotin at a 1.5-log difference with regard to biotin. *N*-1′-(4-Oleylamido-1-butoxycarbonyl)-D-biotin (oleic-biotin, **7**) and *N*-1′-(4-(Geranyl-geranyl-*N*-acetyl cystein)-1-butoxycarbonyl)-D-biotin (GG-biotin, **8**) displaced fluorescent biotin with a 2-log difference with regard to biotin. Although a strong loss of affinity for avidin is induced by the N-1′ modification of biotin, and assuming that biotin's avidin affinity is around 10^{-14} M, the newly synthesized derivatives would keep sufficient affinities (around 10^{-12} M) to be recognized by avidin. The same results were obtained with streptavidin (data not shown).

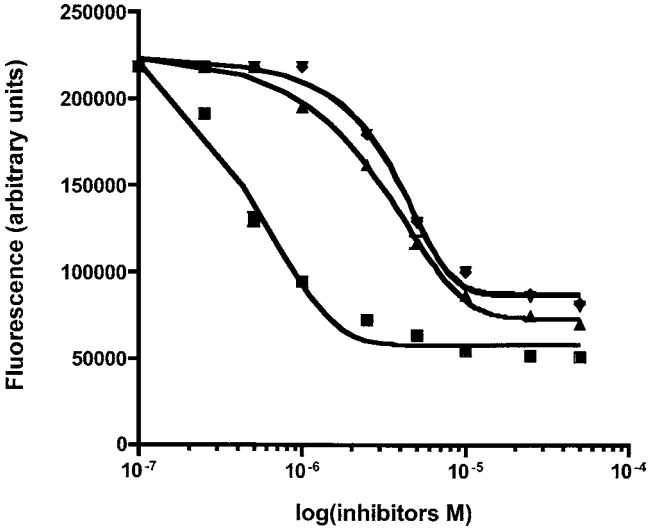

Figure 1. Relative binding affinity to avidin. Competition of biotin derivatives with fluorescent biotin (FB) on avidin-coated 96-well plate. Fluorescent binding saturation was obtained with FB = 0.2 μM. Competition was performed with a constant concentration of 50 nM of FB (100% relative fluorescence) in the presence of increasing concentrations of biotin (■), N3-B (▲), oleic-B (◆), GG-B (▼).

Study of BCCP Labeling by Oleic Acid−Biotin Molecules. Oleic Acid−Biotin and [^{3}H]-Oleic Acid−Biotin Were Used for the Studies of Binding to BCCP in *E. coli*. The system of in vivo detection of small molecule−protein interactions which used the LexA-based genetic system for monitoring protein−protein interaction has been described by Dmitrova (*9*). The gene coding $LexA_{DB}$-BCCP was under the control of an IPTG (isopropyl D-thiogalactopyranoside)-inducible promoter, allowing its overexpression with a theoretical 26-kDa molecular mass, whereas endogenous BCCP is a 16.7-kDa protein. The construction was used to check the ability of the biotin derivatives to penetrate and to bind in vivo to the $LexA_{DB}$-BCCP fused protein.

The proteins were extracted from the cells, and the results of immunoelectrophoresis with an anti-biotin antibody revealed, as expected, two biotinylated proteins (Figure 2, left, lanes 1 and 2). The first, present both with and without IPTG, exhibited a molecular mass of about 22 kDa. This corresponds to endogenous BCCP, which has been reported to possess atypical migration properties on SDS−PAGE: although its gene codes a 16.7-kDa protein, it behaves like a 22.5-kDa protein (*11*). The second protein detected with the anti-biotin antibody, which was weakly visible without treatment with IPTG, was clearly detected after treatment with IPTG and had an apparent molecular mass of 31 kDa. It was identified as the fusion protein $LexA_{DB}$-BCCP. Given that this protein exhibits the same atypical migration properties as BCCP, the chimeric protein $LexA_{DB}$-BCCP is biotinylated in vivo. Moreover, the mutated (−35 lys/gly) $LexA_{DB}$-BCCP protein, which was unable to link biotin, was not revealed by anti-biotin antibody (data not shown). The presence of a weak band at the $LexA_{DB}$-BCCP position, without induction with IPTG, is probably due to a slight leak of promoter. The addition of the oleic acid−biotin derivative to the culture medium gave an unchanged Western blot pattern

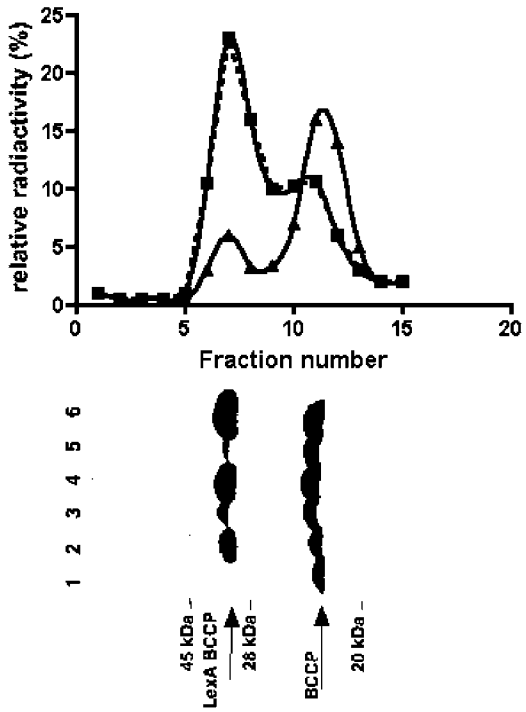

Figure 2. Western blots and radioactivity pattern in *E. coli*. Transformed bacteria were grown in selective medium (containing tetracyclin 50 μg/mL). When their concentrations reached OD = 0.4, they were divided in two parts, one grown in the initial conditions (lanes 1, 3, and 5) and the second submitted to IPTG 1 mM (lanes 2, 4, and 6) until OD = 0.8. Proteins were extracted and submitted to immunoelectrophoresis. Western blots used anti-biotin antibody: culture medium did not contain (lanes 1, 3, and 5) or did contain IPTG (lanes 2, 4, and 6). Oleic-biotin (10 μM) was added in lanes 3 and 4, and [^{3}H]-oleic-biotin (0.1 nM) was added in lanes 5 and 6. After Western blots, lanes 5 and 6 of the nitrocellulose filter were cut into 4-mm strips and counted for tritium activity. The percentage of radioactivity measured for each strip of nitrocellulose versus total radioactivity present in the lane is shown in Figure 2B, lane 5 (solid line) and lane 6 (dotted line).

(Figure 2, left, lane 3 in the absence and lane 4 in the presence of IPTG). When we incubated cells overexpressing $LexA_{DB}$-BCCP with [^{3}H]-oleic acid−biotin, two bands corresponding to endogenous BCCP and $LexA_{DB}$-BCCP were revealed by the anti-biotin antibody (Figure 2, left, lanes 5 and 6), and they fixed the radioactivity (Figure 2, Right). This observation indicates that the compound is able to penetrate *E. coli* and to be covalently linked to BCCP and chimeric lexA-BCCP.

CONCLUSION

Although the avidin−biotin interaction has numerous life-science applications, in recent years, various reports have increased its sphere of operations in cell biology. However, these new biotechnologies need the carboxyl function of biotin to be free, impairing the use of commercially available labeled biotin derivatives. The aim of the present work was, first, to synthesize a labeled biotin that would be able to be used in the new developments of the (strept)avidin−biotin interaction (*1*−*3*), keeping the carboxyl function of biotin free. We have described the synthesis of biotin N-1′ derivatives that allow the coupling of most molecules of interest. Compound **4**, a derivative of biotin bearing an azide group, is stable for several months at −20 °C. It was linked to a styrene-DVB polymer, allowing, with a modified Staudinger reaction, the solid-phase coupling of numerous molecules such as geranyl-geranyl-*N*-acetylcysteine. Estradiol and fluorescein have also been successfully linked (data not shown). Although these derivatives have lost a 2-log affinity for (strept)avidin, they are still able to be used in biotin−avidin life-science applications. We show that, when linked to the N-1′ of biotin, lipids such as oleic acid or geranyl-geranyl-*N*-acetylcysteine can be carried into bacteria; moreover, they are able to covalently bind BCCP chimeras in vivo. This work is the first step toward the use of bifunctional biotin as a small molecule able to tag protein or to control gene expression.

ACKNOWLEDGMENT

This work was supported by INSERM and Millegen. We thank the team of M. Schnarr for the generous gifts of plasmids and strains. We thank P. Chinestra and C. Giammarchi for their technical contributions.

LITERATURE CITED

(1) Beckett, D., Kovaleva, E., and Schatz, P. J. (1999) A minimal peptide substrate in biotin holoenzyme synthetase-catalyzed biotinylation. *Protein Sci. 8*, 921−919.

(2) Lue, R. Y., Chen, G. Y., Hu, Y., Zhu, Q., and Yao, S. Q. (2004) Versatile protein biotinylation strategies for potential high-throughput proteomics. *J. Am. Chem. Soc. 126*, 1055−1062.

(3) Ashraf, S. S., Benson, R. E., Payne, E. S., Halbleib, C. M., and Gron, H. (2004) A novel multi-affinity tag system to produce high levels of soluble and biotinylated proteins in Escherichia coli. *Protein Expr. Purif. 33*, 238−245.

(4) Chen, I., Howarth, M., Lin, W., and Ting, A. Y. (2005) Site-specific labeling of cell surface proteins with biophysical probes using biotin ligase. *Nat. Methods 2*, 99−104.

(5) Knappe, J., Ringelman, E., and Lynen, F. (1961) Zur biochemischenfunktion des biotins. *Biochem. Z. 335*, 168−176.

(6) Sundberg, S. A., Barrett, R. W., Pirrung, M., Lu, A. L., Kiangsoontra, B., and Holmes, C. P. (1995) Spatially addressable immobilization of macromolecules on solid supports. *J. Am. Chem. Soc. 117*, 12050−12057.

(7) Mesange, F., Sebbar, M., Capdevielle, J., Guillemot, J. C., Ferrara, P., Bayard, F., Poirot, M., and Faye, J. C. (2002) Identification of two tamoxifen target proteins by photolabeling with 4-(2-morpholinoethoxy)benzophenone. *Bioconjugate Chem. 13*, 766−772.

(8) Baron, R., Fourcade, E., Lajoie-Mazenc, I., Allal, C., Couderc, B., Barbaras, R., Favre, G., Faye, J. C., and Pradines, A. (2000) RhoB prenylation is driven by the three carboxyl-terminal amino acids of the protein: evidenced in vivo by an anti-farnesyl cysteine antibody. *Proc. Natl. Acad. Sci. U.S.A. 97*, 11626−11631.

(9) Dmitrova, M., Younes-Cauet, G., Oertel-Buchheit, P., Porte, D., Schnarr, M., and Granger-Schnarr, M. (1998) A new LexA-based genetic system for monitoring and analyzing protein heterodimerization in Escherichia coli. *Mol. Gen. Genet. 257*, 205−212.

(10) Malkinson, J. P., Falconer, R. A., and Toth, I. (2000) Synthesis of C-terminal glycopeptides from resin-bound glycosyl azides via a modified Staudinger reaction. *J. Org. Chem. 65*, 5249−5252.

(11) Li, Q. T., and Das, N. P. (1994) Comparison of the effects of cholesterol and oxysterols on phospholipid bilayer microheterogeneity: a study of fluorescence lifetime distributions. *Arch. Biochem. Biophys. 315*, 473−478.

BC060010A

Synthesis of Immunoisolation Barriers That Provide Localized Immunosuppression for Encapsulated Pancreatic Islets

Charles Y. Cheung and Kristi S. Anseth*

Department of Chemical and Biological Engineering and the Howard Hughes Medical Institute, University of Colorado, Campus Box 424, Boulder, Colorado 80309-0424. Received January 31, 2006; Revised Manuscript Received April 14, 2006

Pancreatic islet encapsulation into synthetic, passive material matrixes can provide protection for transplanted islets from destruction via cell-contacted mediated interactions with autoreactive immune cells for treatment of Type I diabetes mellitus. However, one of the fundamental deficiencies with current encapsulation technology is that passive material barriers cannot protect islets from exposure to cytokines and other small, diffusible cytotoxic molecules produced by activated immune cells, subsequently leading to β-cell destruction. Preparation of material matrixes that can actively provide localized immunosuppression of autoreactive immune cells may prolong the viability, and hence function, of encapsulated islet grafts. We have demonstrated the ability to conjugate apoptosis-inducing anti-Fas monoclonal antibodies (MAbs) to the surfaces of poly(ethylene glycol)-modified hydrogels, providing a surface that actively attempts to locally down-regulate the autoimmune response by destroying autoreactive T cells against pancreatic islet cells. We have conjugated anti-Fas MAbs to a high degree to the surface of these hydrogels, with retention of anti-Fas recognition of the Fas antigen as shown by ELISA testing. Apoptosis induction of Fas-sensitive Jurkat T cells was enhanced in the presence of anti-Fas conjugated hydrogels. In addition, this apoptosis induction was specific to anti-Fas MAbs, with no apoptosis induction with control antibodies or with Fas-insensitive T cells. These experiments promote the concept that surface-conjugated hydrogel constructs can provide localized immunosuppression for encapsulated grafted tissue.

INTRODUCTION

Pancreatic islet transplantation represents an attractive treatment option for Type I diabetes mellitus but requires lifelong systemic immunosuppressive therapies to be successful. Encapsulation of islets within a cell impermeant polymer matrix provides a passive physical barrier that allows for small molecule diffusion through the barrier but prevents T-cell infiltration and cell contact-mediated destruction of grafted islets. Most of the current research has focused on forming polyionic complexes using sodium alginate mixed with different polycationic compounds to form polymeric barriers for immunoisolation of islets (*1*). The first and most extensively investigated microencapsulation system of individual islets was with a polyelectrolyte complex of alginate and polylysine (*2*). Over the past 20 years, this system has been continually optimized and has seen limited success in a number of animal models. Islets encapsulated in alginate matrixes have survived in vivo for a significant duration of time while maintaining euglycemia, up to 6 months (*3*), but biocompatibility issues with these types of matrixes still persist, especially with the choice of polycation used to form these membrane barriers (*4*).

Poly(ethylene glycol) (PEG) represents an alternative biomaterial that holds potential promise for encapsulation of pancreatic islets. PEG is a biocompatible polymer that has gained FDA approved when incorporated into different drug formulations (*5*). Cruise et al. microencapsulated islets by photopolymerizing PEG diacrylate (PEGDA) to form their passive membrane barriers (*6*). Islets encapsulated in PEGDA were able to maintain normoglycemia in streptozotocin-induced mice for up to 4 months (*7*). Investigations into the biocompatibility of PEG has shown that in vitro PEG itself does not activate immune cells, such as splenetic lymphocytes and macrophages; however, PEG cannot actively protect islets from cytotoxic molecules produced by preactivated immune cells (*8*). This example illustrates one of the fundamental deficiencies with current encapsulation technology, that cytokines and other effector molecules produced by immune cells can still diffuse through these passive barrier matrixes to inactivate or destroy transplanted β-cells within these islets (*9*−*11*).

Encapsulation of grafted islets with passive materials may prevent destruction of β-cells initiated by cell−cell contact with autoreactive T cells; however, such passive barriers cannot protect islets from exposure to cytokines and other effector molecules, such as IL-1, produced by activated immune cells that can subsequently lead to β-cell destruction (*9, 12*). Preparing encapsulation matrixes that can actively suppress the autoimmune response will therefore be beneficial in prolonging the survivability and function of islet grafts. One method of activating these polymeric barriers is to conjugate monoclonal antibodies to the surface of these hydrogel constructs that can actively induce destruction of T cells, thereby providing localized immunosuppression for transplanted tissue grafts.

EXPERIMENTAL PROCEDURES

Preparation and Characterization of Mouse Anti-Human IgG Conjugated Hydrogels. Poly(ethylene glycol diacrylate) (PEGDA, MW = 4600 g/mol) was polymerized with *N*-hydroxysuccinimide-PEG-acrylate (NPA, MW = 3400 g/mol) by UV-initiated photopolymerization to form PEGDA-*co*-NPA hydrogels with PEGDA-to-NPA ratios ranging from 95/5 to 50/50 (wt) using a 0.05% (wt) UV photoinitiator, 1-[4-(2-hydroxyethoxy)phenyl]-2-hydroxy-2-methyl-1-propan-1-one (I2959, Ciba Geigy, Newport, DE). Hydrogel constituents were dissolved in 0.15 M sodium phosphate buffer, pH 6.5, and hydrogels were prepared by photopolymerization for 15 min at 365 nm. Mouse anti-human IgG (MAH IgG, Fitzgerald Industries International, Concord, MA) was then conjugated to these

* Corresponding author. Tel: (303) 492-7471, Fax: (303) 492-4341, E-mail: kristi.anseth@colorado.edu.

10.1021/bc060023o CCC: $33.50 © 2006 American Chemical Society
Published on Web 07/01/2006

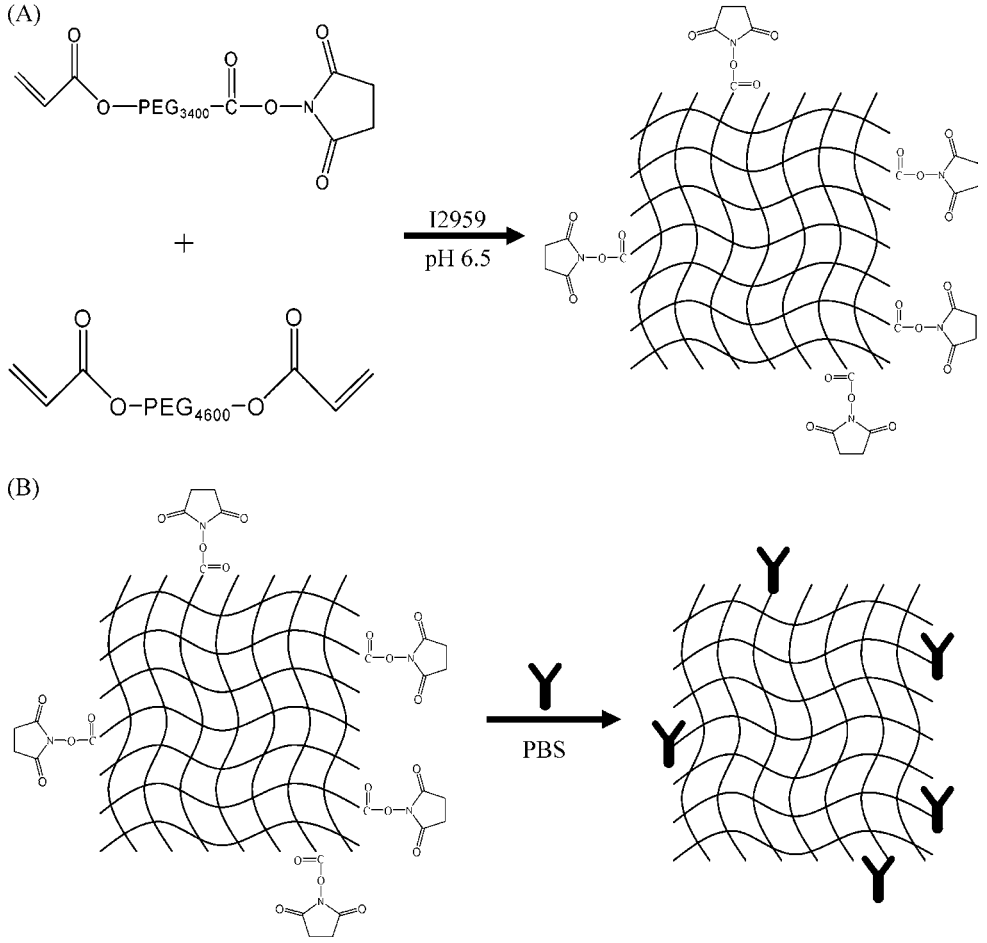

Figure 1. (A) Schematic representation of photopolymerization of PEG_{4600} diacrylate and NPA, forming hydrogel networks with pendant NHS moieties on the hydrogel surface, and (B) conjugation of MAH IgG MAbs to the surface of these hydrogels.

hydrogels at concentrations ranging from 0.05 to 1 mg/mL for 1 h in PBS. Hydrogels were then incubated with 50 mM glycine in PBS to quench the reactivity of any unreacted NHS groups remaining in the gels.

The level of MAH IgG conjugated to the surface of the hydrogels was assessed by a modified indirect ELISA using goat anti-mouse horseradish peroxidase (GAM HRP) (Jackson Immunoresearch, West Grove, PA) to detect surface-conjugated MAH IgG. A modified sandwich ELISA was prepared to determine the extent to which MAH IgG retained the ability to recognize its antigen, human IgG, after conjugation. 75/25 or 50/50 PEGDA-*co*-NPA hydrogels conjugated with MAH IgG were exposed to human IgG at concentrations ranging from 0 to 50ng/mL, followed by incubation with goat anti-human HRP. Hydrogels in both assays were incubated with Ultra-TMB (Pierce Biotechnology, Rockford, IL), and quantitative absorbance measurements were taken at 450 nm.

Immunostaining and Cryosectioning of Hydrogels. 75/25 PEGDA-*co*-NPA hydrogels were polymerized and conjugated with 0−0.5 mg/mL MAH IgG, as described in the previous section. Hydrogels were then soaked in Cryo-Gel (Instrumedics, Hackensack, NJ), snap-frozen in liquid N_2, and sectioned into 50 μm sections with a Leica CM 1850 cryostat (Leica, Bannockburn, IL) and placed onto glass slides. The sections were then soaked three times in PBS for 5 min and blocked with 1% BSA in PBS for 1 h. After an additional PBS wash, the sections were then immunostained with Alexa 488-conjugated goat anti-mouse $F(ab')^2$ antibody fragments for 1 h. The sections were washed three times with PBS and then mounted with Biomeda Gel/Mount (Biomeda, Foster City, CA) supplemented with 1,4-diazabicyclo[2.2.2]octane and coverslipped. Fluorescence images were taken with a Zeiss Axioplan 2 confocal microscope (Zeiss, Thornwood, NY).

Preparation and Characterization of Anti-Fas MAb Conjugated Hydrogels. PEGDA-*co*-NPA hydrogels were prepared at 100/0 to 50/50 PEGDA/NPA ratios as described in the previous section. These hydrogels were then conjugated with 0−0.25 mg/mL of anti-Fas MAbs (DX2 clone, R&D Systems, Minneapolis, MN) using the same reaction conditions as described previously for MAH IgG. Following conjugation to DX2 antibodies, 50 mM glycine methyl ester (Sigma-Aldrich, St. Louis, MO) was then added to the gels to quench any unreacted NHS groups within the gels. Both modified indirect and sandwich ELISAs were performed as described previously. The degree of DX2 conjugation was assessed by indirect ELISAs using goat anti-mouse HRP. Sandwich ELISAs to verify DX2 recognition and binding of recombinant human Fas (Peprotech, Rocky Hill, NJ) was performed utilizing goat anti-Fas PAb (R&D Systems) for the sandwich antibody and donkey anti-goat HRP for secondary detection (Jackson Immunoresearch).

Apoptosis Assessment by Annexin V Assay. Jurkat T cell lymphoma cells were a kind gift from Dr. Peter Mariner (Department of Chemistry & Biochemistry, University of Colorado). Jurkat cells were cultured with RPMI 1640 supplemented with 100 units/mL penicillin/streptomycin and fungizone and 10% fetal bovine serum (FBS). For apoptosis induction experiments, 75/25 PEGDA/NPA hydrogels were polymerized in 96-well TCPS under aseptic conditions. These gels were soaked in sterile-PBS for 5 min and then conjugated to 0.25 mg/mL MAH IgG, or 0.25 mg/mL DX2 anti-Fas MAbs in PBS. After washing and blocking remaining reactive sites on hydro-

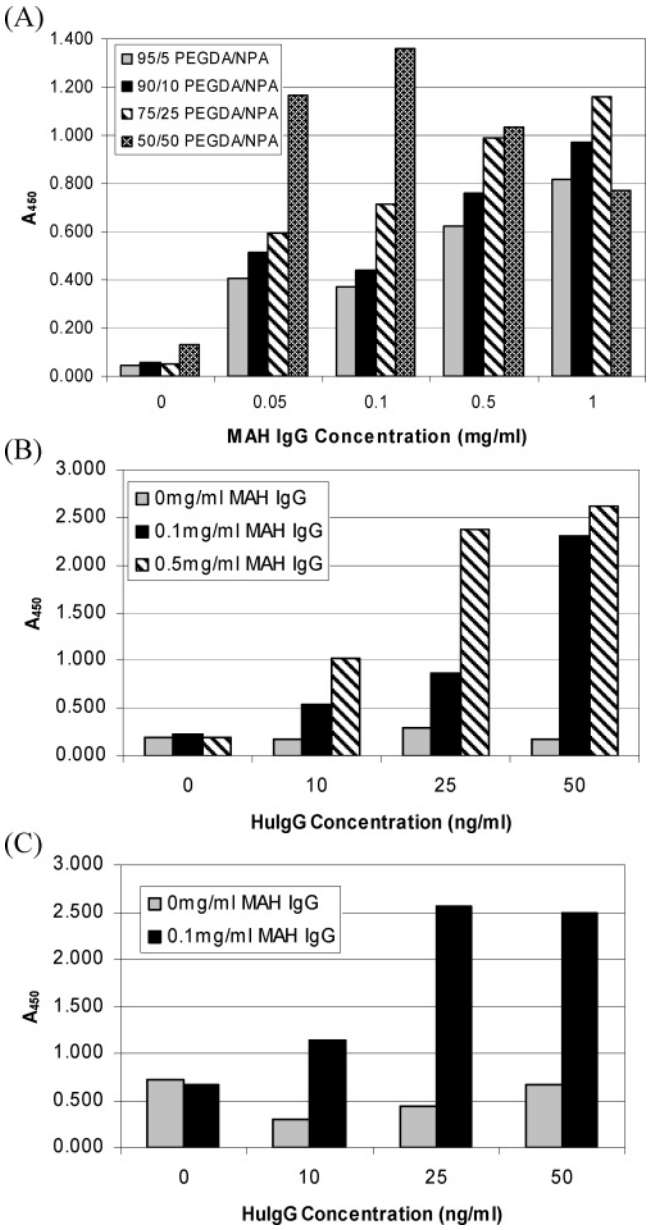

Figure 2. (A) Indirect ELISA for detection of MAH IgG conjugated to PEGDA-*co*-NPA hydrogels. PEGDA-*co*-NPA hydrogels were photopolymerized at 100/0, 90/10, 75/25, and 50/50 (wt) ratios of PEGDA to NPA. Hydrogels were conjugated to MAH IgG at concentrations ranging from 0 to 1 mg/mL antibody. MAH IgG conjugated to the surface of hydrogels was detected using GAM HRP. Sandwich ELISAs were formed for (B) 75/25 and (C) 50/50 PEGDA-*co*-NPA hydrogels conjugated with MAH IgG. Hydrogels were conjugated with 0−0.5 mg/mL MAH IgG and then exposed to Human IgG antigen. Sandwiches were completed using goat anti-human HRP.

gels using 50 mM glycine methyl ester, 5000 or 10000 Jurkat cells were added to the gels and the cells were allowed to incubate suspended atop these hydrogels for 2 days at 37 °C. Jurkat cells were then removed and placed into fresh wells following the incubation period. The Annexin Apoptosis Assay (Invitrogen, Carlsbad, CA) was then used to determine the extent of apoptosis. Cells were stained with annexin V-FITC conjugate and then counterstained with propidium iodide (PI), which allows for the differentiation between necrotic and apoptotic cells. The cells were resuspended in RPMI without phenol red and supplemented with 10% FBS, and images were taken with a Nikon Eclipse TE300 fluorescent microscope (Nikon, Lewisville, TX). The fraction of apoptotic and necrotic cells within each condition tested was quantitated by counting cells within four random fields of view. Approximately 150−400 cells were counted per field of view.

Additional apoptosis studies compared the ability of DX2-conjugated hydrogels to induce apoptosis within Fas-sensitive (Jurkat) and Fas-insensitive (I9.2) T cell lines. 75/25 PEGDA/NPA hydrogels were conjugated with either no DX2 or 0.25 mg/mL DX2 in the same manner as stated above. 10000 cells/well of either Jurkat cells or I9.2 cells (ATCC, Manassas, VA), a caspase-8 mutant Jurkat cell line that is Fas-insensitive, were then added to these hydrogels. Annexin V-FITC binding studies were then performed following 2 days incubation. Quantitation of the fraction of apoptotic cells with all samples was calculated using the same techniques as described above.

RESULTS

PEGDA-*co*-NPA hydrogels were photopolymerized prior to conjugation to MAH IgG (Figure 1A). NHS moieties were utilized to react to amine groups in the antibodies (Figure 1B). Preliminary results showed that a high level of MAH IgG was conjugated to the surface of prepolymerized PEGDA-*co*-NPA hydrogels. Indirect ELISA assays showed higher levels of MAH IgG conjugated to these hydrogels upon both increasing MAH IgG solution concentration (0−1 mg/mL) and fraction of NPA (5−50 mol %) comprising the hydrogels (Figure 2A). The highest degree of conjugation was observed with 50/50 PEGDA-*co*-NPA gels; however, these gels were less mechanically robust due to the lower quantity of cross-linking PEGDA monomer present within these gels. In addition, minimal color formation was evident when 100/0 PEGDA/NPA control gels were reacted with MAH IgG antibodies, indicating that the presence of antibody was due to conjugation to NPA groups and not due to physical adsorption of the antibodies to the hydrogel matrix (data not shown). Sandwich ELISA assays performed on 75/25 and 50/50 PEGDA-*co*-NPA hydrogels showed that conjugated MAH IgG retained the ability to recognize human IgG antigen, with greater detection sensitivity with gels that contain higher quantities of conjugated MAH IgG (Figure 2B, 75/25 gels). High nonspecific background absorbance was observed with 50/50 gels in the absence of human IgG (Figure 2C, 50/50 gels). Detection levels for human IgG become saturated at 25ng/mL with both gel compositions. These ELISA results indicate that monoclonal antibodies can be conjugated to a high degree to preformed PEGDA-*co*-NPA hydrogels without significantly compromising the abilities of the antibodies to recognize their antigens.

Cryosectioning and immunostaining of MAH-conjugated hydrogels showed that MAH IgG conjugation was limited to the hydrogel surface, as indicated by the lack of fluorescence observed within the interior of the gels (Figure 3). No fluorescence was observed with hydrogels not exposed to MAH (Figure 3A). In addition, a thicker band of fluorescence on the hydrogel surfaces was evident with higher concentrations of MAH used for conjugation, which may be indicative of greater degrees of surface conjugation (Figure 3B,C).

Conjugation of DX2 anti-Fas MAbs to PEGDA-*co*-NPA hydrogels was performed using the methodology and conditions developed for MAH IgG discussed in the above section. Indirect and sandwich ELISAs were performed with PEGDA-*co*-NPA hydrogels prepared at varying ratios (100:0 to 50:50 PEGDA:NPA). These assays show similar trends for detection of protein conjugation and antigen recognition by DX2, respectively, as seen with ELISAs with model MAH IgG antibodies (Figure 4). A higher degree of DX2 conjugation was observed with higher concentrations of antibody added for conjugation (Figure 4A). However, minimal differences in conjugation efficiency were observed with gels polymerized with different concentrations of NPA, which is in contrast to MAH IgG results. Greater

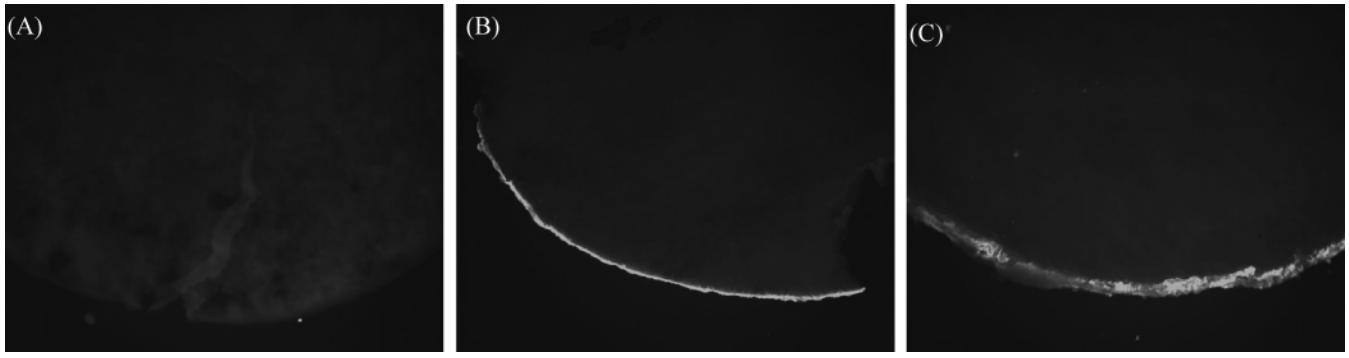

Figure 3. Immunological staining of MAH IgG-conjugated PEG-*co*-NPA hydrogel cryosections. Hydrogels were conjugated with (A) 0 mg/mL, (B) 0.1 mg/mL, and (C) 0.5 mg/mL MAH IgG. Conjugated hydrogels were then frozen and cryosectioned at 50 μm thickness. Section were then stained with goat anti-mouse (H+L) $F(ab')_2$ Alexa 488 conjugate. Images were taken at 4× (objective) magnification. Fluorescently stained sections were then observed by fluorescence microscopy.

sensitivity of rFas detection was evident with higher concentrations of DX2 conjugated to both 75/25 and 50/50 PEGDA/NPA hydrogels; however, significant background was evident with 50/50 hydrogels, most likely due to rFas entrapment within these gels (due to greater pore sizes) (Figure 4B,C).

The ability of DX2-conjugated hydrogels to induce apoptosis within Jurkat cells, a model T cell line, was assessed by monitoring Annexin V binding. Annexin V binds to phosphatidylserine, which is usually located on the inner leaflet of the phospholipids bilayer of the cell membrane, but becomes translocated to the outer leaflet in dying cells. Binding of Annexin-FITC conjugates to apoptotic Jurkat cells can be visualized by fluorescence microscopy. Counterstaining of cells with propidium iodide can differentiate between apoptotic and necrotic cells, as PI can diffuse into and bind with the DNA only within necrotic cells. In our experiments, relatively few cells (less than 1%) were observed to be necrotic throughout all conditions tested, and therefore only apoptosis results are shown and discussed.

Experiments were performed to compare the ability of DX2-conjugated hydrogels to induce apoptosis within Jurkat cells compared to control hydrogels. Control hydrogels were either unconjugated or were conjugated with MAH IgG control antibodies that are not apoptosis-inducing. Fluorescence images screening for Annexin V fluorescence showed that while similar fractions of cells appear to induce apoptosis in the presence of both control hydrogel formulations, a significant increase in apoptotic cells was observed with hydrogels conjugated with DX2 (Compare fluorescence images from Figure 5A and 5B with 5C). These cell images were also used for quantitation of the fraction of apoptotic cells within each condition tested. Quantitative results confirm that an enhancement in apoptosis induction was observed with Jurkat cells exposed to DX2-conjugated gels. Only 5−7.5% of Jurkat cells were apoptotic in the presence of control gels, whereas approximately 20% of Jurkats appeared apoptotic with DX2-conjugated gels (Figure 6). Statistical analysis by student's *t*-test showed that all *p*-values were lower than 0.05, indicating statistical significance of the data. Other tests were performed to test the specificity of apoptosis induction by DX2 antibodies. I9.2 Fas-insensitive T cells were exposed to DX2-conjugated hydrogels to determine whether apoptosis induction occurred due to the specific action of the Fas/anti-Fas interaction or whether apoptosis induction was a nonspecific occurrence. Results from this study show that no enhancement in apoptosis was observed with I9.2 cells exposed to 0.25 mg/mL DX2 over levels induces with control gels lacking conjugated antibodies, whereas higher levels of apoptosis were observed within Jurkat cells as expected (Figure 7).

DISCUSSION

Passive encapsulation technology has made great strides in providing protection for islets against cell−cell-mediated immunity by presenting a physical barrier between islet cells and activated $CD4^+$ and $CD8^+$ T cells. However, inflammatory cytokines produced by these activated cells, such as TNFα, IL-1, and IFNγ, can elicit a toxic response within islets, leading to β-cell destruction (*13*). PEG represents a functionally versatile inert polymer material that can be modified to attach biological moieties to actively promote and assist the long-term survival of islet grafts by down-regulating the immune response around encapsulated tissue. In addition, PEGylation has improved the serum half-life and stability of proteins. The studies discussed in this work describe the application of PEGylated antibodies into hydrogel network for the treatment of autoimmune diabetes, assessing the potency of antibodies conjugated to hydrogel surfaces to act in a therapeutic manner. Investigators have previously incorporated polymerizable antibodies and antibody fragments into hydrogels by free radical polymerization, but with the sole purpose for the diagnostic detection of antigens and biosensor applications (*14*, *15*).

Studies have shown that conjugation of apoptosis-inducing anti-Fas IgG MAbs to PEGDA hydrogels provides a matrix that can actively work to suppress T cell mediated immunity. Fas is a 45kD is a cell surface protein belonging to the TNF receptor family of proteins that can induce apoptosis when engaged with Fas Ligand (FasL). Fas-mediated apoptosis is normally involved in clonal deletion of autoreactive T cells by negative selection (*16*). The Fas pathway is also responsible for the elimination of activated T cells following the completion of the immune response to infection. Many tissues and cell lines weakly express Fas, but Fas is highly expressed in activated, mature lymphocytes, making lymphocytes highly susceptible to Fas-mediated apoptosis (*17*, *18*). FasL is the natural homotrimeric protein binding ligand for Fas, binding to three Fas receptor molecules to induce apoptosis (*18*). FasL expression is induced upon activation of cytotoxic T lymphocytes, which can then destroy Fas-expressing activated lymphocytes (*17*). Fas activation requires FasL multimerization or cross-linking of Fas receptors to initiate the signal transduction cascade for apoptosis (*19*). Binding of MAbs to Fas receptors can also induce apoptosis. The multimeric nature of Anti-Fas IgM antibodies effectively induce apoptosis by allowing for multiple cooperative binding events to cross-link several Fas receptors simultaneously on cell surfaces (*20*, *21*). Monomeric IgG subclass anti-Fas antibodies do not induce apoptosis as effectively as the IgM subclass due to their inability to simultaneously cross-linking multiple Fas receptors in the absence of exogenously added cross-linking molecules (*22*). DX2 is an anti-Fas monoclonal antibody (IgG1

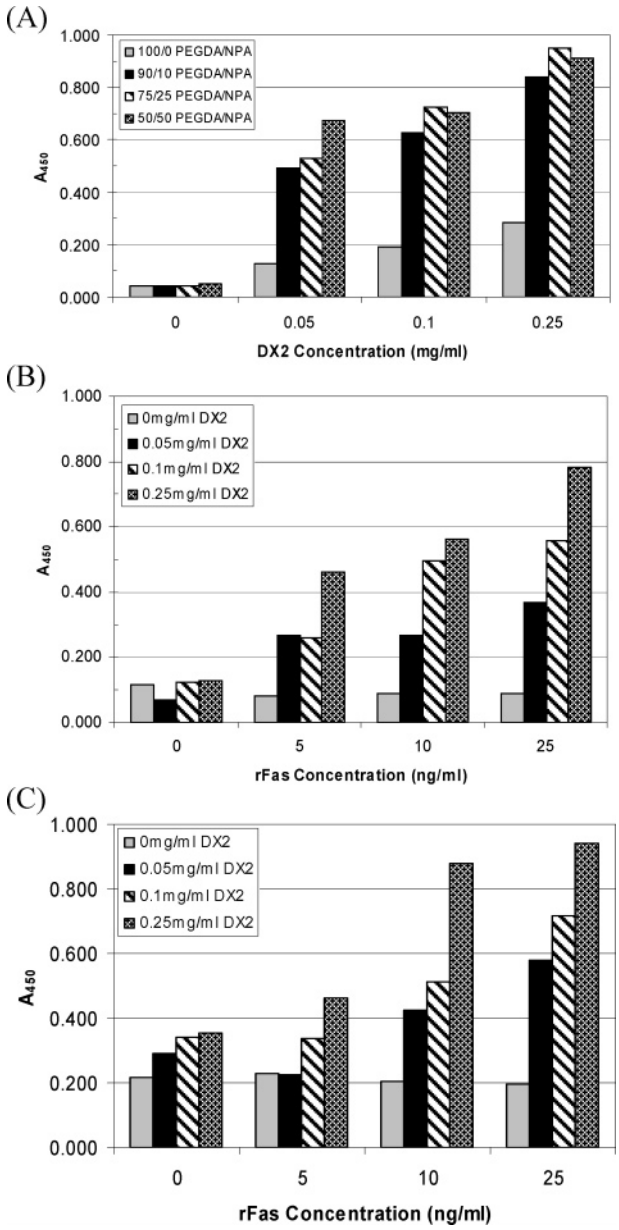

Figure 4. (A) Indirect ELISA for detection of DX2 anti-Fas MAb conjugated to PEGDA-*co*-NPA hydrogels. PEGDA-*co*-NPA hydrogels were photopolymerized at 100/0, 90/10, 75/25, and 50/50 (wt) ratios of PEGDA to NPA. Hydrogels were conjugated to DX2 at concentrations ranging from 0 to 0.25 mg/mL antibody. DX2 conjugated to the surface of hydrogels was detected using GAM HRP. Sandwich ELISAs were formed for (B) 75/25 and (C) 50/50 PEGDA-*co*-NPA hydrogels conjugated with DX2. Hydrogels were conjugated with 0−0.25 mg/mL DX2 and then exposed to rFas antigen. Sandwiches were completed using goat anti-Fas PAb, followed by detection with donkey anti-goat HRP secondary antibodies.

subclone) that can induce apoptosis in human T cells lines in solution upon antibody cross-linking (*21, 23*).

Antibody immobilization can induce cellular activation more effectively than soluble antibodies due to the ability to provide high local concentrations of antibodies for binding and receptor clustering that leads to enhanced transcriptional signal strength of activation signals or secondary messengers (*24*). Immobilization of anti-CD3 antibodies on solid surfaces has been shown to both enhance stimulation and activation of T cells and induce anergy within T cells in the presence and absence of co-stimulatory factors, respectively (*21, 24−26*). Surface immobilization techniques were modified in our studies to account for the future presence of live islets to be encapsulated within

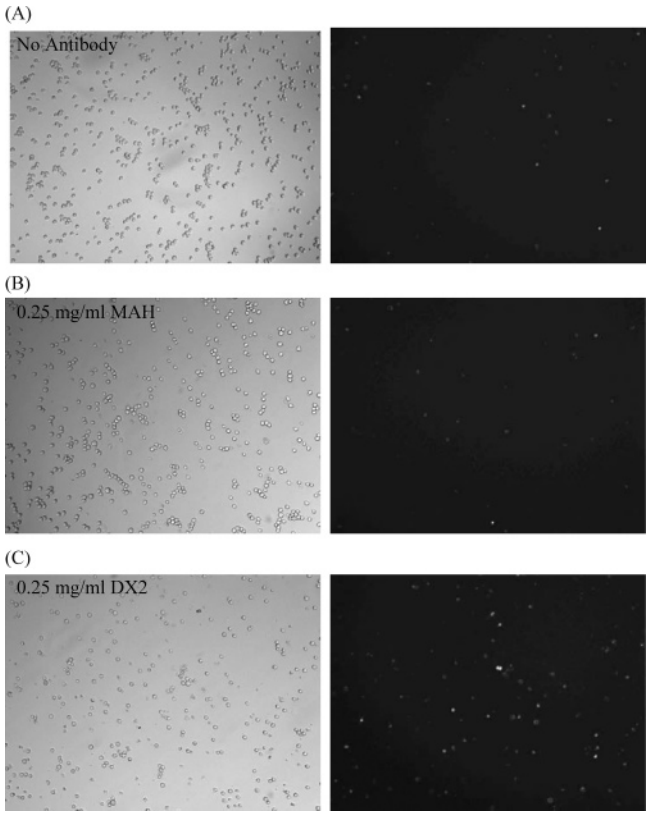

Figure 5. Brightfield and fluorescent images of Jurkat T cells exposed to hydrogels conjugated with various antibodies. Jurkat T cells were cultured for 2 days in 96-well tissue culture plates in the presence of PEG-*co*-NPA hydrogels conjugated with (A) no antibody, (B) 0.25 mg/mL MAH IgG control MAb, or (C) 0.25 mg/mL DX2 anti-Fas MAb. Following the culture period, Jurkat cells were removed from wells containing hydrogels and then assayed for the presence of phosphatidylserine using annexin V-FITC conjugates. Images were taken at 10× (objective) magnification. Brightfield images show Jurkat cell density for each condition tested, whereas green fluorescence observed in fluorescent images (shown in grayscale) are indicative of annexin V-FITC conjugation to phosphatidylserine, which is indicative of apoptotic cells.

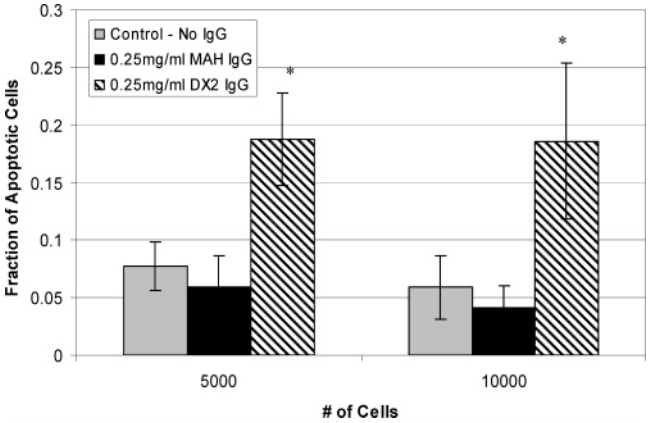

Figure 6. Quantitative evaluation of annexin V binding to Jurkat cells. The fraction of apoptotic cells was calculated by counting both apoptotic and total cell numbers from four random fields of view. Data were generated from both 5000 and 10000 Jurkat cells exposed to hydrogels prepared at the various experimental conditions described in Figure 4. * denotes $p \leq 0.04$ when results are compared to controls lacking conjugated antibody.

our hydrogel devices, which precluded the use of organic solvents for surface conjugation. Therefore, aqueous conjugation conditions at physiological salt concentrations were required. Copolymerization of PEGDA with NPA allowed for incorpora-

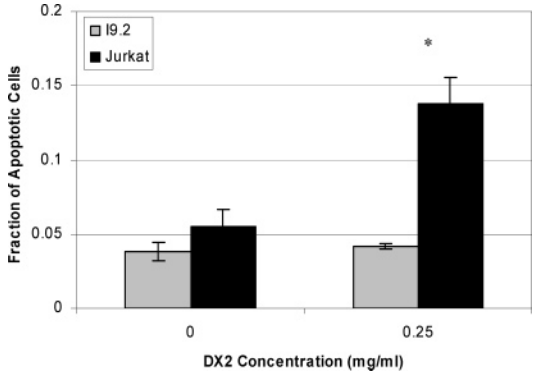

Figure 7. Quantitative evaluation of annexin V binding to both Fas-insensitive I9.2 and Fas-sensitive Jurkat T cells. 10000 I9.2 or Jurkat cells were exposed to hydrogels conjugated with either no antibody or 0.25 mg/mL DX2 anti-Fas MAb. * denotes $p \leq 0.001$ when results are compared to controls for the same cell line exposed to hydrogels lacking conjugated antibody.

tion of aqueous-reactive NHS groups prevalent both within the hydrogel as well as on the surface of hydrogels. Initial studies with MAH IgG model antibodies confirmed the ability to conjugate antibodies to the surfaces of NHS-reactive hydrogels, as well as demonstrated the ability of these antibodies to retain antigen recognition after conjugation. Surface conjugation was verified by cryosectioning and immunostaining of MAH IgG-conjugated hydrogels. These studies with MAH IgG also provided framework conditions to conjugate DX2 anti-Fas MAb to hydrogel surfaces at varying surface densities. Preliminary data indicated that DX2 antibodies adsorbed onto TCPS surfaces induced higher levels of Jurkat cell apoptosis compared to DX2 antibodies added in solution, suggesting that higher localized concentrations of DX2 promoted apoptosis induction (data not shown). In accordance with these results, immobilization of DX2 antibodies onto the surface of PEGDA-*co*-NPA hydrogels also enhanced apoptosis of Jurkat cells over passive, unconjugated hydrogel controls. These studies also showed that apoptosis induction was a unique quality observed solely with DX2 antibodies and demonstrated the specificity of apoptosis induction with DX2, as only Fas-sensitive cells underwent apoptosis in the presence of DX2.

The results presented in this study demonstrate the utility of surface conjugation of immunosuppressive moieties into encapsulation matrixes to down-regulate the immune response to transplanted tissues. Although the degree of T cell apoptosis with current systems may not be high enough to fully down-regulate immune responses to grafted tissue, this work demonstrates the potential that activation of passive barrier holds, whereby biological processes may be altered by the addition of biological moieties, favoring enhanced survival and function of encapsulated grafted tissue. Modifications to improve current systems, such as developing systems with higher degrees of grafting/clustering of immunosuppressive proteins on hydrogel surfaces, may lead to adequate and sustainable immunosuppression and allow for long-term graft survival. Research into active barrier systems will hopefully change traditional views and begin addressing the different shortcomings associated with current encapsulation systems pursued for treating diabetes mellitus.

ACKNOWLEDGMENT

The authors would like to thank the National Science Foundation (Grant No. EEC0444771) and the Howard Hughes Medical Institute for financial support for this project.

LITERATURE CITED

(1) Orive, G., Hernandez, R. M., Rodriguez Gascon, A., Calafiore, R., Chang, T. M., de Vos, P., Hortelano, G., Hunkeler, D., Lacik, I., and Pedraz, J. L. (2004) History, challenges and perspectives of cell microencapsulation. *Trends Biotechnol. 22*, 87−92.

(2) Lim, F., and Sun, A. M. (1980) Microencapsulated islets as bioartificial endocrine pancreas. *Science 210*, 908−10.

(3) de Vos, P., van Hoogmoed, C. G., van Zanten, J., Netter, S., Strubbe, J. H., and Busscher, H. J. (2003) Long-term biocompatibility, chemistry, and function of microencapsulated pancreatic islets. *Biomaterials 24*, 305−12.

(4) Strand, B. L., Ryan, T. L., In't Veld, P., Kulseng, B., Rokstad, A. M., Skjak-Brek, G., and Espevik, T. (2001) Poly-L-Lysine induces fibrosis on alginate microcapsules via the induction of cytokines. *Cell Transplant 10*, 263−75.

(5) http://www.nektar.com/content/pipeline_2.

(6) Cruise, G. M., Hegre, O. D., Scharp, D. S., and Hubbell, J. A. (1998) A sensitivity study of the key parameters in the interfacial photopolymerization of poly(ethylene glycol) diacrylate upon porcine islets. *Biotechnol. Bioeng. 57*, 655−65.

(7) Cruise, G. M., Hegre, O. D., Lamberti, F. V., Hager, S. R., Hill, R., Scharp, D. S., and Hubbell, J. A. (1999) In vitro and in vivo performance of porcine islets encapsulated in interfacially photopolymerized poly(ethylene glycol) diacrylate membranes. *Cell Transplant 8*, 293−306.

(8) Jang, J. Y., Lee, D. Y., Park, S. J., and Byun, Y. (2004) Immune reactions of lymphocytes and macrophages against PEG-grafted pancreatic islets. *Biomaterials 25*, 3663−9.

(9) Bottino, R., Lemarchand, P., Trucco, M., and Giannoukakis, N. (2003) Gene- and cell-based therapeutics for type I diabetes mellitus. *Gene Ther. 10*, 875−89.

(10) de Vos, P., and Marchetti, P. (2002) Encapsulation of pancreatic islets for transplantation in diabetes: the untouchable islets. *Trends Mol. Med. 8*, 363−6.

(11) Gray, D. W. (2001) An overview of the immune system with specific reference to membrane encapsulation and islet transplantation. *Ann. N. Y. Acad. Sci. 944*, 226−39.

(12) Mandrup-Poulsen, T., Zumsteg, U., Reimers, J., Pociot, F., Morch, L., Helqvist, S., Dinarello, C. A., and Nerup, J. (1993) Involvement of interleukin 1 and interleukin 1 antagonist in pancreatic beta-cell destruction in insulin-dependent diabetes mellitus. *Cytokine 5*, 185−91.

(13) Piro, S., Lupi, R., Dotta, F., Patane, G., Rabuazzo, M. A., Marselli, L., Santangelo, C., Realacci, M., Del Guerra, S., Purrello, F., and Marchetti, P. (2001) Bovine islets are less susceptible than human islets to damage by human cytokines. *Transplantation 71*, 21−6.

(14) Lu, Z., Kopeckova, P., and Kopecek, J. (2003) Antigen responsive hydrogels based on polymerizable antibody Fab′ fragment. *Macromol. Biosci. 3*, 296−300.

(15) Miyata, T., Asami, N., and Uragami, T. (1999) A reversibly antigen-responsive hydrogel. *Nature 399*, 766−9.

(16) Palmer, E. (2003) Negative selection−clearing out the bad apples from the T-cell repertoire. *Nat. Rev. Immunol. 3*, 383−91.

(17) Nagata, S., and Golstein, P. (1995) The Fas death factor. *Science* 267, 1449−56.

(18) Timmer, T., de Vries, E. G., and de Jong, S. (2002) Fas receptor-mediated apoptosis: a clinical application? *J. Pathol. 196*, 125−34.

(19) Holler, N., Tardivel, A., Kovacsovics-Bankowski, M., Hertig, S., Gaide, O., Martinon, F., Tinel, A., Deperthes, D., Calderara, S., Schulthess, T., Engel, J., Schneider, P., and Tschopp, J. (2003) Two adjacent trimeric Fas ligands are required for Fas signaling and formation of a death-inducing signaling complex. *Mol. Cell Biol. 23*, 1428−40.

(20) Fadeel, B., Thorpe, C. J., Yonehara, S., and Chiodi, F. (1997) Anti-Fas IgG1 antibodies recognizing the same epitope of Fas/APO-1 mediate different biological effects in vitro. *Int. Immunol. 9*, 201−9.

(21) Komada, Y., Inaba, H., Li, Q. S., Azuma, E., Zhou, Y. W., Yamamoto, H., and Sakurai, M. (1999) Epitopes and functional responses defined by a panel of anti-Fas (CD95) monoclonal antibodies. *Hybridoma 18*, 391−8.

(22) Dhein, J., Daniel, P. T., Trauth, B. C., Oehm, A., Moller, P., and Krammer, P. H. (1992) Induction of apoptosis by monoclonal

antibody anti-APO-1 class switch variants is dependent on cross-linking of APO-1 cell surface antigens. *J. Immunol*. *149*, 3166−73.
(23) Cifone, M. G., De Maria, R., Roncaioli, P., Rippo, M. R., Azuma, M., Lanier, L. L., Santoni, A., and Testi, R. (1994) Apoptotic signaling through CD95 (Fas/Apo-1) activates an acidic sphingomyelinase. *J. Exp. Med*. *180*, 1547−52.
(24) Geppert, T. D., and Lipsky, P. E. (1987) Accessory cell independent proliferation of human T4 cells stimulated by immobilized monoclonal antibodies to CD3. *J. Immunol*. *138*, 1660−6.
(25) van Lier, R. A., Brouwer, M., Rebel, V. I., van Noesel, C. J., and Aarden, L. A. (1989) Immobilized anti-CD3 monoclonal antibodies induce accessory cell-independent lymphokine production, proliferation and helper activity in human T lymphocytes. *Immunology 68*, 45−50.
(26) Wolf, H., Muller, Y., Salmen, S., Wilmanns, W., and Jung, G. (1994) Induction of anergy in resting human T lymphocytes by immobilized anti-CD3 antibodies. *Eur. J. Immunol*. *24*, 1410−7.

BC060023O

Dendritic Iodinated Contrast Agents with PEG-Cores for CT Imaging: Synthesis and Preliminary Characterization

Yanjun Fu,[§] Danute E. Nitecki,[§] David Maltby,[‡] Gerhard H. Simon,[§] Kirill Berejnoi,[§] Hans-Juergen Raatschen,[§] Benjamin M. Yeh,[§] David M. Shames,[§] and Robert C. Brasch[§,*]

Center for Pharmaceutical and Molecular Imaging, Department of Radiology, and Mass Spectra Facility, Department of Pharmaceutical Chemistry, University of California—San Francisco (UCSF), San Francisco, California 94143-0628. Received January 26, 2006; Revised Manuscript Received April 20, 2006

The purpose of this study was to design, synthesize, and initially characterize a representative set of novel constructs for large-molecular radiographic/computed tomography (CT) contrast agents, intended for a primarily intravascular distribution. A new assembly of well-known and biocompatible components consists of paired, symmetrical dendritic polylysines initiated from both ends of a poly(ethylene glycol) (PEG) core, yielding an array of multiple free amino groups to which were conjugated highly soluble and stable triiodophthalamide ("triiodo") moieties. An array of six dendritic contrast agents was synthesized originally, using three different PEG cores (3, 6, 12 kDa) with t-Boc lysine-generated dendrimer "amplifiers" (from three to five generations) containing 16 to 64 amino groups for conjugation with reactive triiodo moieties. A clinically used, nonionic, small molecular CT contrast agent, iobitridol, was derivatized via a hydroxyl protection/deprotection strategy, introducing a new carboxyl group available for conjugation to the lysine amino groups of dendrimers. Final products were purified by size exclusion chromatography and characterized by NMR, UV, HPLC, and elemental analysis. Preliminary evaluations were conducted for physicochemical characterization and in vivo CT contrast enhancement in a rat model. All six iodinated PEG-core dendrimer conjugates were synthesized in good yields, with a high degree of size monodispersity, large apparent molecular weight, favored physicochemical properties. A representative compound, PEG12000-carbamate-Gen4-IOB conjugate, 27% (w%) rich in iodine, demonstrated a desirable strong and persistent intravascular enhancement with a monoexponential blood half-life of approximately 35 min assayed by dynamic CT imaging and also showed high water solubility (>550 mg/mL at 25 °C), large apparent molecular size (comparable to a 143-kDa protein), high hydrophilicity (butanol−water partition coefficient 0.015), and stability to autoclaving conditions. This study showed the synthetic feasibility, desired basic characteristics, and potential utility for CT contrast enhancement achieved with a new type of iodinated, large-molecular PEG-core dendritic construct. Further development of this class of macromolecular contrast agents will be required to define the optimal formulation, pharmacology, safety profile, and the full range of diagnostic applications including tumor microvascular quantitative characterization by CT imaging.

INTRODUCTION

New water-soluble radio-dense iodinated pharmaceuticals administered intravenously in conjunction with diagnostic X-ray and computed tomography (CT) have the potential to improve the quality, nature, and yield of resulting diagnostic information. So-called iodinated "contrast media" were first considered in the same year as Wilhelm Roentgen's discovery of the X-ray and have evolved over the past century to the current state of well tolerated and highly efficacious drugs used in the vast majority of patient CT examinations. Without exception, the CT contrast media currently given parenterally, either intravenously or intra-arterially, belong to a class of relatively small molecular compounds, less than 2000 Da, which quickly equilibrate between the intravascular and extracellular fluid compartments of the body. However, another class of compounds, namely macromolecular contrast media (MMCM), has been described, both for CT and magnetic resonance imaging (MRI) tomography, as being potentially better suited for quantitative characterization of tissues and blood vessels and certain types of pathologic abnormalities as found in cancer, ischemic injury, and altered states of angiogenesis (*1*−*4*). These MMCM, sometimes referred to as "blood pool" contrast media, have in common a prolonged intravascular half-life, an initial volume of distribution approximating the plasma volume, and molecular weights generally greater than 30 kDa.

Properties considered desirable for candidate macromolecular CT contrast media, in addition to an intravascular distribution, include relatively high content of iodine or other radiodense atoms, high stability, near or complete monodispersity, low osmolality, high water solubility, limited viscosity, high in vivo tolerance, and complete elimination from the body.

Toward these goals, a new group of iodinated MMCM, intended for use as blood pool CT contrast enhancing agents, has been designed, synthesized, and preliminarily tested. This class of agents consists of paired, symmetrical dendritic polylysines in a cascade arrangement initiated from both ends of a poly(ethylene glycol) (PEG) core, yielding an array of multiple (16 to 64) free amino groups for conjugation with tri-iodinated ring intermediates. Six of these tri-iodo PEG dendrimer conjugates with varying sizes of the PEG core (3, 6, and 12 kDa) and varying dendritic generations (3, 4, and 5) were synthesized as examples of the class and compared for physicochemical properties. One selected compound was further

* Corresponding author. Phone: (415) 476-2275. Fax: (415) 476-0616. E-mail: robert.brasch@radiology.ucsf.edu, yanjun.fu@radiology.ucsf.edu.

[§] Center for Pharmaceutical and Molecular Imaging, Department of Radiology.

[‡] Mass Spectra Facility, Department of Pharmaceutical Chemistry.

10.1021/bc060019c CCC: $33.50 © 2006 American Chemical Society
Published on Web 07/01/2006

evaluated by in vivo CT imaging in an experimental animal subject for angiographic contrast enhancement.

EXPERIMENTAL PROCEDURES

Materials and Apparatus. Poly(ethylene glycol) (PEG) 6000 (M_n 6470, M_w 6517, polydispersity index 1.01, measured by MALDI-TOF mass spectroscopy) was purchased from Fluka. PEG12000 (M_n 12163, M_w 12650, polydispersity index 1.04 according to the manufacturer's data) was purchased from Polymer Labs. These PEGs were dried by azeotropical distillation with anhydrous benzene. Poly(ethylene glycol) bisamine 3400 (M_n 3290, M_w 3321, polydispersity index 1.01) was purchased from Shearwater Polymers Inc., N^2,N^6-di-*tert*-butyloxycarbonyl-L-lysine dicyclohexylamine salt (N^2,N^6-di-t-Boc-L-Lys·DCHA) was from Advanced ChemTech, dicyclohexyl carbodiimide (DCC), *N*-hydroxysuccinimide (HONSu), *p*-nitrophenyl chloroformate, *N*,*N*-dimethylaminopyridine (DMAP), diisopropylethylamine (DIPEA), trifluoroacetic acid (TFA), *N*,*N*-dimethylformamide (DMF, dried with 4−8 mesh 4 Å molecular sieves), 1,3,5-trinitrobenzenesulfonic acid (TNBS), and other reagents were purchased from Aldrich, Sigma, or Fischer Scientific. All these reagents are of analytical grade or superior. Conventional iodinated contrast agents Iohexol, Iobitridol, and Iodixanol were commercially available, and Iobitridol solution was lyophilized to give a white powder of 99.9% purity (by reversed phase HPLC).

H-1 and C-13 NMR spectra were recorded on a Varian 400 NMR spectrometer. Analytical SE-HPLC was performed on a Superdex 200 10/300 GL column (10 mm × 300 mm) using a Rainin HPXL solvent delivery system and a Rainin pressure module (Rainin Instrument Inc., Emeryville, CA) with a Knauer diode array UV detector and a Shimadzu RID-6A as the refractive index detector. A solution of 0.1% TFA and 0.3 M Na_2SO_4 (pH 2.7) was used as the mobile phase at 0.80 mL/min and 23 °C for purity test of PEG-core dendritic polylysines (UV detection at 210 nm), while a solution of 0.05 M phosphate and 0.15 M NaCl (pH 7.0) was used as the mobile phase at 0.80 mL/min and 23 °C for the purity test of iodinated contrast agents (245 nm). Preparative size exclusion chromatography (SEC) was run on a Sephadex G-100 (or G-75) column (5 cm I. D. × 50 cm) with UV detection. TLC with detection by UV or iodine vapor, or a ninhydrin spray test, was conducted on precoated Merck TLC plates with silica gel G25 UV_{254} (5 × 20 cm, 250 μm). UV spectra were recorded on a Shimadzu UV-260 spectrophotometer. ESI mass spectra were recorded on a Perkin-Elmer SCIEXAPI300 LC/MS mass spectrometer. MALDI-TOF mass spectra were obtained on a Perkin-Elmer Voyger DESTR mass spectrometer. Melting points were determined on an electrothermal melting point apparatus (uncorrected). Dialysis was carried out using the regenerated cellulose Spectra/Por tubing (cutoff M_w 3500 Da).

The CT experiment was performed at 80 kVp and 130 mA on an eight-slice clinical GE LightSpeed QX/I CT Scanner (GE Medical Systems, Milwaukee, WI). One seven-week-old healthy Sprague Dawley rat (180 g, female, Charles River Laboratories, Wilmington, MA) was used for CT imaging.

Activation of N^2,N^6-Di-*tert*-butyloxycarbonyl-L-lysine. *Preparation of Free N^2,N^6-Di-t-Boc-L-lysine*. According to a standard procedure, dicyclohexylamine (DCHA) was removed from N^2,N^6-di-t-Boc-L-Lys·DCHA by thoroughly washing its CH_2Cl_2 solution with 0.5 M citrate buffer (pH 3.5). Yield 92%. TLC: R_f = 0.70 ($CHCl_3$:CH_3OH: HAc = 90:8:2). ^1H NMR (400 MHz, $CDCl_3$): δ (ppm) 1.22−1.28 (t, 4H, CH_2CH_2), 1.44 (s, 18H, *tert*-butyl), 1.68 (m, 2H, C*H*$_2$CH), 3.10 (t, 2H, CH_2N), 4.21 (t, 1H, NCHCO), 4.90 (br, 1H, N^6-H), 5.42 (d, 1H, N^2-H, J = 7.2 Hz), 10.39 (br, 1H, COOH).

Carboxy Activation of N^2,N^6-Di-t-Boc-L-lysine. DCC (2.06 g, 10 mmol) was dissolved in 10 mL of CH_2Cl_2 and cooled to −15 °C. With stirring, to this cold solution was dropwise added a solution of N^2,N^6-di-t-Boc-L-Lys (3.47 g, 10 mmol) in CH_2Cl_2 (20 mL). The reaction temperature was kept below −10 °C. Several minutes later, the reaction mixture turned turbid and then was continued to stir for 3−4 min. The resulting solution containing DCC-activated di-t-Boc-lysine should be used immediately in the subsequent coupling reaction with the amines.

For comparison, two types of active esters of di-t-Boc-lysine, namely 4-nitrophenyl ester or *N*-hydoxysuccinimide ester, were also prepared by the reaction of this t-Boc amino acid with 4-nitrophenol (or *N*-hydroxysuccinimide) and DCC in an equivalent mole ratio in anhydrous chloroform.

Synthesis of PEG-Core Dendrimers (with PEG6000 as an example). *Preparation of PEG6000 Bis(4-nitrophenyl carbonate (**5a**).* Dried PEG6000 (M_n 6470, 4.0 g, 0.62 mmol) was dissolved in anhydrous CH_2Cl_2 (15 mL) and dry pyridine (15 mL) and then cooled to 0 °C. To it was added 1.0 g of 4-nitrophenyl chloroformate (4.96 mmol) and 80 mg of DMAP. At 0 °C this mixture was stirred for 8 h. The reaction mixture was evaporated and precipitated by 80 mL of ether. After standing 0.5 h, the syrupy precipitate solidified and was filtered and washed by ether. The crude product was dissolved in 1−2 mL of CH_2Cl_2 and precipitated in 40 mL of anhydrous ether; this procedure was repeated twice. A white powder (**5a**, 4.06 g) was finally obtained (97% yield). ^1H NMR ($CDCl_3$), δ 3.61 (s, CH_2CH_2O), 7.3 (d, aromatic H), 8.2 (d, aromatic H). In ^{13}C NMR ($CDCl_3$), δ 155.2 (OCO_2). UV spectrophotometry at 400 nm showed, after complete hydrolysis of this carbonate at pH 12, each mole of the carbonate contained 2.05 mol of 4-nitrophenyl group.

α,ω-Bis(N-t-Boc-ethylcarbamoyl)-PEG6000. A solution of **5a** (2.58 g, 0.38 mmol) in 15 mL of $CHCl_3$ was added dropwise to a solution of 1-*N*-*t*-Boc-ethylenediamine (493 mg, 3.08 mmol, prepared according to the literature method) (*5*) and DIPEA (0.6 g, 4.64 mmol) in 10 mL of $CHCl_3$ at 0 °C. This reaction continued for 24 h at room temperature. The resulting mixture was evaporated and precipitated by 50 mL of ether and purified by three cycles of dissolution-precipitation using $CHCl_3$ and ether. A slightly yellow powder **6** (2.50 g) was obtained in a yield of 97%. ^1H NMR ($CDCl_3$), δ 1.41 (s, *tert*-butyl), 2.92, 3.13 (2 m, CH_2N), 3.62 (s, CH_2CH_2O).

PEG6000 Bisamine. Boc-protected biscarbamate **6** (3.02 g, 0.446 mmol) obtained above was dissolved in 8 mL of CH_2Cl_2 and cooled to 0 °C, to which was added 8 mL of TFA. This mixture was stirred at 0 °C for 30 min and room temperature for another 2 h. Evaporation of the solution under 60 °C gave an oil after adding 50 mL of anhydrous ether. Dissolution/precipitation of the crude product was performed twice with CH_2Cl_2/ether. The precipitate solidified while standing at room temperature for several hours, further purified by dialysis (cutoff M_w 3500 Da), and then lyophilized to give 2.93 g of a white powder (yield 97.5%). ^1H NMR ($CDCl_3$), δ 1.42 (s, *tert*-butyl), 2.90, 3.11 (2 m, NCH_2), 3.61 (s, CH_2CH_2O). This PEG bisamine was thus used as an initiator core molecule for subsequent dendrimer synthesis. PEG6000 bisamine can be also regarded as "PEG6000-carbamate-Gen0.0" dendrimer, while "Gen" stands for "generation" and "carbamate" is the chemical linkage between the PEG core and lysine dendrimer component.

Dendrimer Propagation (two-step cycle to reach a higher generation). *Typical Coupling Step (PEG6000-Gen0.5 preparation).* Immediately after the DCC-activated di-t-Boc-lysine was formed as described above, a cooled solution of PEG6000 bisamine (2.07 g, 0.608 mmol NH_2) and DIPEA (0.39 g, 3 mmol) in 10 mL of CH_2Cl_2 was added with stirring at −5 °C. This coupling reaction (COOH/NH_2 mole ratio = 4.0) was

Table 1. Synthetic Yields and Structure Data of Six PEG-Core Dendrimeric Polyamines

code	yield, % (based on PEG)	molecular weight [a] M_n	molecular weight [a] M_w	polydispersity (M_w/M_n)	NH_2 number[b] measured (theoretical)	-CH_2CH_2O-/lysyl ratio NMR-measured (theoretical)
8a	50	8462	8532	1.012	15.3 (16)	11.03 (10.47)
8b	41	13871	13942	1.005	15.6 (16)	19.93 (19.72)
9a	45	10262	10321	1.006	30.8 (32)[c]	5.16 (4.89)
9b	45	16785	17260	1.028	31.6 (32)	9.05 (9.20)
11a	39	7270	7288	1.002	31.8 (32)[c]	2.29 (2.48)
11b	32	11328	11339	1.001	62.9 (64)[c]	1.25 (1.20)

[a] Measured by MALDI-TOF mass spectrometry. [b] Determined by a classic TNBS method (*6*). [c] Determined by a modified TNBS method.

continued at −5 °C for 0.5 h and room temperature for 20 h. A white precipitate was filtered and washed by CH_2Cl_2, and the combined filtrate was evaporated under reduced pressure to give a thick syrup. After the dissolution of the syrup in 3 mL of CH_2Cl_2, 120 mL of anhydrous ether was added. Standing 0.5 h, a white precipitate separated and gradually solidified. This procedure was repeated twice so as to remove DIPEA and excess di-t-Boc-lysine from the crude product. The compound was washed profusely by ether and dried in a vacuum. A white, loose solid was afforded in a yield of 87% (1.93 g). Ninhydrin test: negative.

Typical Deprotection Step (PEG6000-Gen1.0 preparation). PEG6000-Gen0.5 (1.8 g, 0.247 mmol) was dissolved in 15 mL of CH_2Cl_2 and cooled to 0−5 °C. With stirring, 15 mL of TFA was added slowly while the reaction temperature was kept below 20 °C. After the TFA addition, the reaction was continued at room temperature for 2−3 h. An anhydrous $MgSO_4$ drying tube was connected to the reaction flask since gaseous byproducts such as CO_2 and isobutene were emitted in this deprotection. After the reaction went to completion, the mixture was evaporated under reduced pressure below 40 °C, giving a slightly yellow syrup. Anhydrous ether was added. After standing 1−2 h at room temperature, the syrup solidified. The dissolution/precipitation procedure was repeated twice. A white precipitate was collected, washed with ether, and dried in a vacuum to give 1.78 g of a white powder (yield 98%, positive for ninhydrin test).

Following procedures from Gen1.0 through Gen5.0 are similar. Yields of coupling steps ranged from 85 to 92%, while the yields of deprotection steps varied from 90 to 98%. Every reaction was monitored by ninhydrin test. Of important note, one repeated coupling was conducted in the preparation of Gen4 and Gen5 dendrimers to guarantee a complete capping of those amino groups. Preparative SEC (Sephadex-75 gel, mobile phase 0.1 M trifluoroacetate buffer with pH 3.0, flow rate 14 $mL\cdot min^{-1}\cdot cm^{-2}$) and subsequent dialysis were employed for purification of these full-generation dendrimers (**8a** through **11b**). NMR, MALDI-TOF MS, and UV (for amino quantification using TNBS method) (*6*) were used for characterization of main intermediates and undecorated dendrimers (data shown in Table 1).

For t-Boc-protected half-generation dendrimers including Gen0.5, Gen1.5, Gen2.5, Gen3.5, and Gen4.5, ^1H NMR spectra ($CDCl_3$) were given: δ 1.3−1.6 (br, $(CH_2)_3$ in lysine), 1.42 (s, *tert*-butyl), 3.1(br, NCH_2), 3.61 (s, CH_2CH_2O), 4.2 (br, NCH-CO). For deprotected full-generation dendrimers including Gen1.0, Gen 2.0, Gen3.0, Gen4.0, and Gen5.0 (TFA salts), ^1H NMR spectra (D_2O): δ 1.3−1.8 (br, $(CH_2)_3$ in lysine), 2.9−3.2 (br, NCH_2), 3.62 (s, CH_2CH_2O), 4.1−4.3 (d, br, NCHCO). The integration ratio of characteristic peaks (PEG and CH_2-CH_2CH_2 in lysine) obtained in ^1H NMR confirmed that the t-Boc-protected and deprotected dendrimers had the expected structure. Six synthesized dendrimers for subsequent decoration include PEG6000-carbamate-Gen3.0 (**1a**), PEG12000-carbamate-Gen3.0 (**1b**), PEG6000-carbamate-Gen4.0 (**2a**), PEG12000-carbamate-Gen4.0 (**2b**), PEG3400-amide-Gen4.0 (**3a**), and PEG3400-amide-Gen5.0 (**3b-I**).

For two representative dendrimers, ^{13}C NMR data were given. For PEG3400-carbamate-Gen5.0: δ (ppm) 22.7, 26.5, 28.0, 30.9 ($CH_2CH_2CH_2CH$), 39.4 (CH_2N), 53.4, 54.6 (CH), 69.7 (PEG), 112.2, 115.1, 118.0, 120.9 (CF_3), 162.7, 163.1 (CF_3COO^-), 174.7, 179.0 (N^6-CO and N^2-CO); for PEG6000-carbamate-Gen4.0, δ (ppm) 25.7, 26.5, 28.1 ($CH_2CH_2CH_2$), 39.1, 39.5 (CH_2N), 53.2, 53.8 (CH), 69.7 (PEG), 112.2, 115.0, 117.9, 120.7 (CF_3), 162.5, 163.0 (CF_3COO^-), 174.4, 178.7 (N^6-CO and N^2-CO in dendritic lysine).

Quantification of Periphery Amino Groups in the "PEG Amplifiers". The NH_2 analysis was conducted according to a typical TNBS method (*6*). To 1 mL of a standard solution (a series of L-lysine mono hydrochloride solution with known concentration, 20−100 μg/mL) or 1 mL of a dendrimer sample solution (0.2−1.5 mg/mL) were added 1.0 mL of 4% sodium bicarbonate solution (pH 8.5) and 1.0 mL of 0.1% freshly prepared TNBS solution. The reaction was continued at 40 °C for 4 h, and 1.0 mL of 10% sodium dodecylsulfonate (SDS) solution and then 0.5 mL of 1 N HCl were added, consecutively. Against a blank control solution the absorbance at 335 nm of standard or sample solutions were recorded. Amino concentration in solutions and hence amino contents in dendrimers were determined (results shown in Table 1). For **9a**, **11a**, and **11b**, their trinitrophenyl conjugates obtained above were redissolved in 1,4-dioxane for UV quantification at 415 nm.

Synthesis of an Amino-Reactive "Triiodo" Derivative. *Hydroxyl Protection of Iobitridol by Ketalization (compound **13** synthesis). Method A.* A powder of Iobitridol **12** (16.70 g, 20 mmol) was added in 50 mL of DMF. With stirring, 10.4 g of 2,2′-dimethoxylpropane (DMP, 100 mmol) and 100 mg of *p*-toluenesulfonic acid monohydrate were then added. The resulting solution was brought up to 90 °C and stirred at this temperature for 1 h in which the acetalization reaction was shown complete by TLC ($CHCl_3/CH_3OH$ 15:1, material R_f = 0, product R_f = 0.64, 0.50, isomers). DMF and excess DMP were removed by vacuum distillation. A crude product was obtained as a yellow syrup. Further purification was conducted by silica gel chromatography using $CHCl_3$ and then $CHCl_3/CH_3OH$ 8:1 as the eluting solvent, 18.7 g of slightly yellow crystalline **13** was obtained (yield 98%). M.p. 88−90 °C. ESI-MS: m/z = 956.0 $(M + H)^+$, 978.0 $(M + Na)^+$, 898.0 $(M - CH_3COCH_3 + H)^+$ for $C_{29}H_{40}O_9I_3N_3$. ^1H NMR (400 MHz, $CDCl_3$): δ (ppm) 1.35, 1.40, 1.46 (3s, 18H, 3 isopropylidene groups), 2.96, 2.97 (2 s, 6H, 2 N-CH_3), 3.22 (m, 1H, CHC═O), 3.36, 4.03 (2 br, 4 H, 1:1, $CH(CH_2O)_2$), 3.85, 4.17 (2m, 4H, 1:1, 2 NCH_2), 4.25, 4.29 (2 m, 4 H, 1:1, 2 OCH_2CHO), 4.53 (m, 2 H, 2 OCH_2CHO), 8.52, 9.45 (2 br, 1 H, 0.45:0.55, PhNHC═O). ^{13}C NMR (75 MHz, $CDCl_3$): δ (ppm) 21.0, 25.7, 27.2, 31.7, 36.7, 37.9, 38.2, 41.9, 42.2, 50.3, 61.0, 61.3, 67.2, 67.8, 68.0, 74.2, 74.5, 98.3, 98.8, 109.6, 143.6, 149.0, 162.8, 169.9, 170.6.

Method B. A powder of Iobitridol **12** (2.64 g, 3.16 mmol) was suspended in 60 mL of dry acetone. With vigorous stirring, 3 g of freshly fused zinc chloride (finely ground) was added, the resulting mixture was allowed to react for 24 h at room temperature. During this period, Iobitridol was converted to a new derivative, which was monitored by TLC ($CHCl_3/CH_3OH$

= 15:1). Sodium carbonate (5 g) in 25 mL of water was added to the reaction mixture. Vigorous stirring was continued for 1−2 h to completely precipitate the zinc catalyst. After filtering the white precipitate, the filtrate was evaporated to remove acetone. The residue was neutralized to pH 7 and extracted with 3 × 25 mL of $CHCl_3$, the organic phase was then dried overnight (anhydrous $MgSO_4$) and evaporated. Following chromatographic purification was similar to Method A above. Slightly yellow product **13** was obtained in a yield of 83% (2.56 g).

*Subsequent N-Alkylation by Ethyl Bromoacetate (compound **14** synthesis).* Sodium methoxide solution was freshly prepared from sodium and methanol, with a concentration of 1.90 M titrated by potassium hydrogen phthalate. This $NaOCH_3/CH_3OH$ solution (8.27 mL, 15.72 mmol) was added to a 150-mL anhydrous THF solution of **13** (10.00 g, 10.47 mmol). Upon addition, the clear yellow solution turned orange. Ten minutes after $NaOCH_3$ addition, ethyl bromoacetate (2.85 g, 15.70 mmol) was added. White precipitate appeared in minutes, and the reaction mixture was stirred at room temperature for 1 h as shown to be complete by TLC ($CHCl_3/CH_3OH$ 15:1). In this procedure, compound **13** (R_f = 0.64 and 0.50) was completely converted into **14** (R_f = 0.96 and 0.85, isomers), and the color of solution turned back to yellow. After filtration, the tetrahydrofuran solution was washed to neutral by water and dried over anhydrous $MgSO_4$. The solution was evaporated to give a yellow oil as crude product. Purification was conducted by silica gel chromatography, eluting first with $CHCl_3$ to remove excess ethyl bromoacetate, and then with $CHCl_3/CH_3OH$ (10:1, v/v) to give the pure product **14** as slightly yellow crystals. The yield was 95% (10.30 g). M.p. 112−4 °C. ESI-MS: m/z = 1042.0 $(M + H)^+$, 1064.0 $(M + Na)^+$, 983.9 $(M - CH_3COCH_3 + H)^+$ for $C_{33}H_{46}O_{11}I_3N_3$. ^{1}H NMR (400 MHz, $CDCl_3$): δ (ppm) 1.28 (t, J = 5.2 Hz, 3 H, CH_2CH_3), 1.35, 1.40, 1.46 (3s, 18H, three isopropylidene groups), 2.63 (m, 2 H, CH_2CH_3), 2.95, 3.03 (2 s, 6H, 2 N−CH_3), 3.25 (m, 1 H, CHC=O), 3.36 (m, 2 H, O=CCHCH_2O), 3.83 (m, 2 H, CH_3NCH_2), 3.98−4.42 (m, 10 H, NCH_2C=O, CH_3NCH_2, O=CCHCH_2O and 2 OCH_2CHO), 4.54 (m, 2 H, 2 OCH_2CHO). ^{13}C NMR (75 MHz, $CDCl_3$): δ (ppm) 19.5, 20.3, 25.6, 27.2, 28.7, 31.5, 35.4, 36.9, 37.8, 41.6, 50.3, 62.0, 62.4, 67.8, 74.3, 74.6, 98.3, 98.7, 109.6, 150.5, 151.4, 162.9, 168.5, 170.0, 170.6.

*Hydrolysis of Ethyl Ester (compound **15** synthesis).* A 2 N NaOH solution (18 mL) was added slowly to a 20-mL solution of ester **14** (10.50 g, 10.09 mmol). After the addition, the reaction was continued for 2.5 h at room temperature. The solution was neutralized to pH 7 and evaporated to remove most methanol under 40 °C. The residue was dissolved in 80 mL of water, and the solution pH was adjusted to 3.5 by 2 N HCl at which time an abundant white precipitate appeared. Saturated NaCl solution (80 mL) was added, and then 3 × 100 mL of chloroform was used to extract the carboxylic acid. The extracts were dried over anhydrous $MgSO_4$ overnight and evaporated to give 9.37 g of yellowish crystalline **15** (yield 91.7%). TLC ($CHCl_3/CH_3OH$ 15:1): R_f = 0.33 and 0.20 (isomers). M.p. 118−120 °C. ESI-MS: m/z = 1014.0 $(M + H)^+$, 1036.0 $(M + Na)^+$ and 956.0 $(M - CH_3COCH_3 + H)^+$ for $C_{31}H_{42}O_{11}I_3N_3$. ^{1}H NMR (400 MHz, $CDCl_3$): δ (ppm) 1.34, 1.40, 1.46 (3s, 18H, 3 isopropylidene groups), 2.95, 3.03 (2 m, 6H, 2 N−CH_3), 3.21 (m, 1H, CHC=O), 3.35 (m, 2 H, O=CCHCH_2O), 3.82 (m, 2 H, CH_3NCH_2), 4.02 (s, 2 H, NCH_2C=O), 4.1−4.4 (m, 8 H, CH_3NCH_2, O=CCHCH_2O and 2 OCH_2CHO), 4.52 (m, 2 H, 2 OCH_2CHO). ^{13}C NMR (75 MHz, $CDCl_3$): δ (ppm) 18.9, 19.4, 25.7, 27.2, 28.4, 28.9, 31.1, 37.1, 37.6, 41.2, 50.4, 62.2, 62.5, 67.8, 74.4, 74.6, 98.3, 98.6, 109.7, 150.8, 151.3, 162.9, 168.2, 170.2, 170.9.

*Preparation of N-Hydroxysuccinimde Ester (compound **16** synthesis).* Carboxylic acid **15** (9.12 g, 9.0 mmol) and *N*-hydroxysuccinimide (1.04 g, 9.0 mmol) were dissolved in 40 mL of chloroform. After cooling to −5−0 °C, dicyclohexylcarbodiimide (1.85 g, 9.0 mmol) in 5 mL of chloroform was added. The reaction continued for 0.5 h at 0 °C and r.t. for 24 h. The white precipitate was filtered, and the filtrate was evaporated to give 9.89 g of active ester **16** (99%). TLC ($CHCl_3/CH_3OH$ 15:1): R_f = 0.93 and 0.80 (isomers). M.p. 116−118 °C. ESI-MS: m/z = 1111.0 $(M + H)^+$, 1133.0 $(M + Na)^+$ and 1053.0 $(M - CH_3COCH_3 + H)^+$ for $C_{35}H_{45}O_{13}I_3N_4$. ^{1}H NMR (400 MHz, $CDCl_3$), δ (ppm) 1.35, 1.40, 1.47 (3 s, 18H, three isopropylidene groups), 2.84 (m, 4 H, CH_2CH_2), 2.98, 3.04 (2 m, 6 H, 2 N-CH_3), 3.21 (m, 1 H, CHC=O), 3.37 (m, 2H, O=CCHCH_2O), 3.83 (m, 2 H, CH_3NCH_2), 3.90−4.45 (m, 10 H, NCH_2C=O, CH_3NCH_2, O=CCHCH_2O and 2 OCH_2CHO), 4.53 (m, 2 H, 2 × OCH_2CHO). ^{13}C NMR (75 MHz, $CDCl_3$): δ (ppm) 18.1, 23.9, 24.2, 24.9, 25.1, 26.6, 28.4, 29.0, 34.1, 40.9, 41.0, 47.2, 49.8, 53.8, 61.7, 67.2, 73.9, 97.7, 109.2, 110.0, 148.1, 150.4, 162.2, 168.1, 168.3, 168.5, 169.8, 172.2.

Synthesis of Dendritic Iodinated Contrast Agents. A general procedure is described here with PEG6000-carbamate-Gen4-triiodo as an example.

PEG6000-carbamate-Gen4.0 dendrimer **9a** (0.76 g, 1.72 mmol NH_2 groups) and DIPEA (0.66 g, 5.13 mmol) were dissolved in 20 mL of DMF. Active ester **16** (8.59 g, 7.74 mmol) was added in two portions 24 h apart (2/3 was added initially and 1/3 added later). The reaction lasted for 96 h at room temperature at which time the reaction was shown to be complete by a negative ninhydrin test. A small amount of 2-aminoethanol (6 mmol) was added to destroy the excess unreacted ester. The solvent was removed by distillation in a vacuum, and the residue obtained was dissolved in 10 mL of chloroform and precipitated by 180 mL of anhydrous ether. A yellowish solid was obtained and subsequently treated by 40 mL of 60% (v/v) aqueous TFA at room temperature for 6 h. After the deprotection, the solution pH was brought to 7 by 2 N NaOH and then dialyzed against 2 × 2 L of deionized water (cutoff M_w of 3500 Da). The dialysate was concentrated and then purified by SEC on a Sephadex G-100 column (mobile phase 0.05 M phosphate and 0.15 M NaCl, pH 7.0, flow rate 12 mL·min^{-1}·cm^{-2}). Chromatographically pure macromolecular fractions were combined, dialyzed (to remove buffer salts), and lyophilized to give a white material, PEG6000-carbamate-Gen4.0-IOB, namely **2a** (1.84 g, 90% yield, "IOB" stands for Iobitridol moiety). UV (λ_{max}, water): 245 nm. Iodine analysis by UV: 31.88%. Elemental analysis measured for I, C, H, and N. ^{1}H NMR (400 MHz, D_2O): δ (ppm) 1.20−1.80 (m, $CH_2CH_2CH_2CH$), 2.39 (br, NCH_2), 3.02, 3.16 (2 s, 2 N-CH_3), 3.2−3.6 (m, CH_2 and CH groups of IOB), 3.62 (s, PEG), 4.0−4.4 (br, other CH groups of IOB, NCHCO of lysine residue). ^{13}C NMR (75 MHz, D_2O): δ (ppm) 22.9, 25.7, 28.2, 31.0, 37.9, 39.4, 43.6, 47.7, 48.0, 50.6, 52.3, 54.4, 59.9, 60.6, 63.6, 64.2, 69.3, 69.8,71.0, 71.8, 90.7, 98.0, 99.6, 148.2, 150.4, 168.9, 171.6, 172.0, 174.2, 175.1. SE-HPLC: retention time 18.41 min.

Similarly, other conjugates including PEG6000-carbamate-Gen3-IOB (**1a**), PEG12000-carbamate-Gen3-IOB (**1b**), PEG-12000-carbamate-Gen4-IOB (**2b**), PEG3400-amide-Gen4-IOB (**3a**), and PEG3400-amide-Gen5-IOB (**3b-I**) were synthesized and purified. Of note, the feeding [IOB]/[NH_2] ratio was 3, 4.5, and 6, respectively, for Gen3, Gen4, and Gen5 dendrimers. The conjugation reaction time was 72, 96, and 120 h for Gen3, Gen4, and Gen5 dendrimers, respectively. Their structures were similarly characterized by ^{1}H (and ^{13}C) NMR. Synthetic yields, iodine analysis, and SE-HPLC results were also given. (Table 2).

Table 2. Synthetic Yields and Structure Characterization of Dendritic Iodinated Contrast Agents

code	yield (%)[a]	iodine % (w/w) measured by UV (or microanalysis)	no. of IOB[b] measured (theoretical)	molecular weight (M_n)[c]	polydispersity (M_w/M_n)[d]	retention time (min) in SE-HPLC
1a	82	26.67 (26.31)	15.2 (16)	21700	1.012	19.30
1b	90	21.67 (nd)	15.5 (16)	27500	1.014	17.52
2a	78	31.88 (31.24)	30.3 (32)	36800	1.010	18.41
2b	87	27.28 (27.05)	30.5 (32)	42500	1.033	16.08
3a	80	33.48 (nd)	29.1 (32)	32900	1.008	19.84
3b-I	84	32.14 (31.86)	39.4 (64)	46700	1.023	19.07
3b-II	86	35.64 (nd)	57.5 (64)	66400	1.017	18.35

[a] Yield based on the PEG dendrimer. [b] Measured by ^{1}H NMR (IOB stands for iobitridol). [c] Calculated by microanalysis data (iodine %). [d] Determined by size exclusion HPLC.

UV Quantification of the "Triiodo" Group in Iodinated Dendrimers. A series of dilute Iobitridol (IOB) solutions in distilled water, with known concentrations ranging from 1.0 to 50 μg /mL, was prepared. Their absorption at 245 nm was measured; thus, the standard absorbance versus concentration curve was set up. Data points for this curve followed Beer's law in the range of 0−30 μg IOB/mL ($r = 0.9995$). UV absorption data of dilute sample solutions (**1a** to **3b**) at 245 nm were measured, yielding the IOB contents; hence, iodine percentages were obtained for these iodinated dendrimers (Table 2).

Measurement of Apparent Molecular Weight and Size Distribution by SE-HPLC. Analytical SE-HPLC, performed on a Superdex 200 10/300 GL column (10 mm × 300 mm, Amersham Biosciences, Uppsala, Sweden), was utilized for molecular weight/size characterization of synthesized polymers in this work (see conditions in Apparatus). A molecular weight calibration curve was set up based on the SE-HPLC measurements of five protein standards (cytochrome C, carbonic anhydrase, bovine serum albumin, alcohol dehydrogenase, and amylase) with a molecular weight range of 13 to 200 kDa. Size distribution of each iodinated dendrimer, represented by the polydispersity index (PDI), was calculated by the equation: PDI $= M_w/M_n = (\Sigma N_i M_i^2/\Sigma N_i M_i)/(\Sigma N_i M_i/\Sigma N_i)$, M_w and M_n are weight- and number-average molecular weights, respectively, while N_i and M_i stand for the molecular number and molecular weight respectively of the i-th fraction of a polymer sample.

Basic Physicochemical Characterization. A specific amount of a test iodinated dendrimer containing 300 mg iodine was added to 2 mL of distilled water and allowed to stand overnight with gentle stirring, to observe if the test conjugate was completely dissolved at this concentration (150 mg iodine/mL). The unit, mg iodine/mL, was then converted to "mg contrast agent /mL" since the iodine% was known for each compound.

Through the flask-shaking method, the butanol−water partition equilibrium of each iodinated contrast agent was measured. Tris buffer (50 mM, pH 7.4) and 1-butanol were chosen as two immiscible solvents. The contrast agent was dissolved in Tris buffer at a concentration of 10 μg iodine/mL. Eight milliliters of a contrast agent solution was mixed with 8 mL of butanol and shook for 0.5 h in a separation funnel (30 mL). After centrifugation, the water phase was separated and its IOB concentration was determined by UV spectrophotometry at 245 nm. The partition coefficient thus was calculated by $(C_0 - C)/C$, where C_0 and C represent the IOB concentration of the contrast agent prior to and after the partition in aqueous phase. In addition, Iobitridol and Iodixilan were tested as standard controls. For each contrast agent, this measurement was conducted in triplicate.

Osmolality of the solutions containing synthesized CT MMCM was measured using a conventional freezing point depression method on a wide range osmometer (Model 3W, Advanced Instruments, Needham Heights, MA), expressed with a unit of "mOsm/kg water". The osmometer was calibrated with standard NaCl solutions (100 and 900 mOsm/Kg water) before sample measurements. Viscosity of certain contrast agent solutions (Iohexol at 300 mgI/mL, **2b** at 75 mgI/mL) were measured by a standard Ubbelohde viscometer (capillary diameter 0.4 mm) in a water bath (37.0 ± 0.3 °C). Each sample was measured in triplicate.

Formulation of Contrast Agents. Prior to CT experiments, lyophilized macromolecular contrast agents were dissolved in distilled water in the presence of a trace amount of stabilizer, i.e. 0.40 mg of tris(hydroxymethyl)methylamine (*7*) per 100 mg of iodine, followed by sterile filtration twice with Acrodisk 25 mm syringe filters (membrane pore size 0.2 μm, Gelman Laboratory). They were finally formulated as 75 mg iodine/mL solutions with pH of 6.8−7.4.

The formulated contrast media were autoclaved for 30 min at 120 °C, followed by a series of tests including SE-HPLC, inorganic iodide detection, and free iodine detection, respectively, to see if any decomposition occurred in this procedure.

Preliminary CT Imaging in a Rat Model. The CT scan was performed using an eight-detector-row clinical CT scanner (Lightspeed QX/I, GE Healthcare, Milwaukee, WI). One anesthetized Sprague Dawley rat was placed supine in the CT scanner. Immediately before, and 2, 10, 22, 32 min after, tail-vein intravenous contrast injection (dose 450 mg iodine/kg body weight), CT images of the entire animal were acquired using the following imaging parameters: 80 kVp, 130 mA, 0.5 s/gantry rotation, 1.25 mm slice thickness, 2.5 mm/s table speed (pitch 0.625), and 10 cm field of view. Images were transferred to a picture archiving and communications workstation (Impax, AGFA, Mortsel, Belgium). Representative axial images at the level of liver were chosen for comparison of intravascular CT enhancement over the time.

RESULTS AND DISCUSSION

Concept and Molecular Design (Scheme 1). Poly(ethylene glycol) (PEG) was selected as the backbone of the iodinated blood pool contrast agents due to its unique properties. PEG's each repeating units CH_2CH_2O has the ability to bind several water molecules. Compared to other water-soluble polymers (either naturally occurring or synthetic) with the same molecular weight, PEG has an extremely simple chemical structure but with an extremely high exclusion volume in water. In aqueous solution, PEG physically repulses all other surrounding macromolecules and is well-known for its nonimmunogenicity and good biocompatibility. Attachment of PEG to biomacromolecules can dramatically increase their blood half-life while markedly reduce the immunogenicity. As early as in 1991, the first PEG−protein conjugate (Adagen) for intravenous use was approved by FDA. Extremely narrow size distribution is another advantage of PEG, which makes it possible to synthesize nearly monodisperse PEG conjugates. In addition, PEG has good solubility not only in water but also in organic solvents including methylene chloride, a useful characteristic in practical synthesis (*8*−*10*).

For CT contrast media development, radiopaque atoms (e.g. iodine, barium) are necessary due to their outstanding X-ray

attenuation ability under clinical CT conditions. Comparing various elements with relatively high atomic number (39−82) comprehensively in their radio-opacity effectiveness, biocompatibility, and synthetic availability, the iodine atom (atomic number 53) now still remains our first choice as the radiopaque atom. (*11*−*13*)

In the subsequent screening of iodinated building blocks, tolerability is considered as the criterion with the highest priority. Thus, abandoning the ionic or incompletely substituted triiodobenzene derivatives, we selected a type of nonionic, highly soluble and stable structure containing *N*,*N*′-bis(polyhydroxyalkyl)-5-(*N*-acylamino)-2,4,6-triiodo-1,3-phthalamide moiety for signal enhancement. Specifically, Iobitridol, a new nonionic clinically used contrast agent, was chosen as the initial ''triiodo'' building block in our syntheses.

PEG has only two termini available for derivatization; thus, an appropriate amplifying method needs to be adopted to produce sufficient reactive termini (such as NH_2 groups) for following chemical decoration.

To carry out this method, dendritic polylysines as "amplifiers" with the varying generations are introduced to two ends of PEG diol (or PEG bisamine) via carbamate (or amide) linkages (see Scheme 2). Different from commonly used pegylation strategies in syntheses of PEG-based macromolecular pharmaceuticals (*8*, *14*, *15*), in this design we use the PEG as a macro core to initiate the total synthesis of dendrimeric contrast agents, instead of conjugating PEG to either a synthetic or a naturally occurring macromolecule. Thus, both the number of conjugated PEG (only one here) and conjugation site could be exactly controlled.

Rational derivatization of Iobitridol molecules and subsequent conjugation to PEG-core dendrimers were originally designed (see Schemes 3 and 4). The overall molecular size and terminal group number may be precisely controlled by adjusting PEG size and number of generation during the synthesis. On the basis of PEG-core dendrimer structure, we synthesized and preliminarily characterized six macromolecular iodinated contrast agents for CT imaging in this study.

Synthesis and Chemical Characterization of PEG-Core Dendritic Polylysines. To synthesize the dendritic polylysine part, t-Boc chemistry was chosen due to the substantially lower cost of the monomer di-t-Boc-L-lysine compared with di-Fmoc-L-lysine. PEG3400 bisamine was used directly as the core molecule due to the high reactivity of terminal NH_2 groups. PEG6000 and PEG12000 bisamines were not commercially available and were thus prepared from their corresponding PEG diols. PEG diol was first converted to its bis(4-nitrophenyl) biscarbonate, subsequently reacted with 1-*N*-t-Boc-ethylenediamine, and then deprotected by TFA, yielding PEG bisamines containing stable linkages (NHCOO) in the backbone.

The synthesis of each dendrimeric generation includes two steps: the coupling step and the deprotection step. Coupling reaction between an amino-terminated lower generation dendrimer Gen *n* ($n = 0, 1, 2, 3$ ...) and excess COOH-activated di-t-Boc-lysine gives a t-Boc-protected dendrimer, defined as Gen ($n + 0.5$), namely the half generation. To prevent the formation of a defected structure, such as missing lysine sequences or coexistence of different generations, we must ensure that every coupling step is complete, or else the defective structure would arise and exponentially accumulate with the increase of generation. To address this extremely important issue, several factors including reactant feeding ratio, reaction time, and reaction solvent need to be considered carefully.

The equivalent ratio of activated di-t-Boc-lysine to the dendrimer amino group, namely the [COOH]/[NH_2] ratio, needs to be at least 3, and up to 6 in our synthesis. The ratio of <3 may lead to incomplete capping of NH_2, but the ratio of >6 did not give further benefits in the reaction completeness. For

Scheme 1. Synthesized PEG-Core Dendrimer Conjugates with Multiple Triiodophthalamide Moieties as Macromolecular Contrast Agents for Computed Tomography (CT)[a]

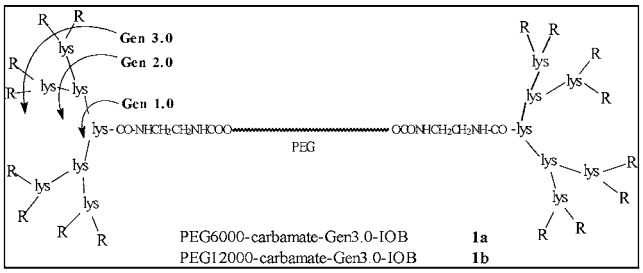

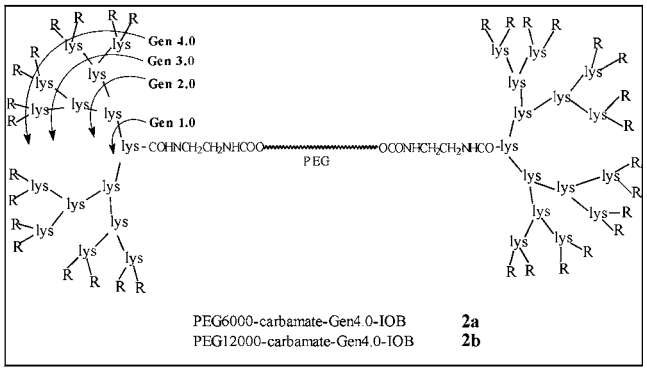

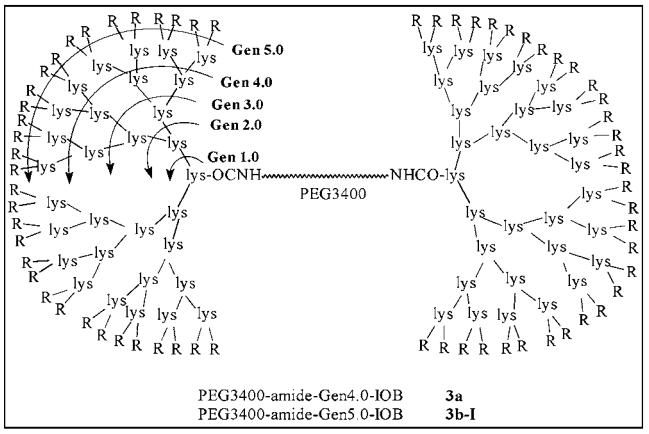

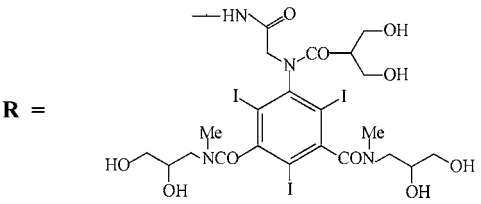

[a] Note: As a typical example, the abbreviation "PEG6000-carbamate-Gen4-IOB" stands for a macromolecular conjugate of generation-4 (Gen4) dendritic polylysine initiated with a PEG3400 core via carbamate linkages, having iobitridol (IOB) moieties as terminal decorating groups.

lower generations (<Gen3), the feeding ratio [COOH]/[NH_2] is chosen to be between 3 and 4, while for relatively higher generations (≥ Gen3), the feeding ratio is chosen to be between 4 and 6. The coupling reaction needs 24−48 h to the completion for lower-generation (<Gen3) dendrimers, and 48−120 h for higher generations. The obvious incompletion is detectable by ninhydrin test. Double coupling with t-Boc lysine is recommended to minimize the defects of synthesized dendrimer especially of those with Gen3 or higher.

The reaction solvent needs to be carefully chosen, too. In the preparation of dendrimers of ≥3 generations, after the failure of methylene chloride, chloroform, CH_3CN, tetrahydrofuran, and

Scheme 2. Synthetic Route to the PEG-Core Dendrimers with 3.4-kDa, 6-kDa, or 12-kDa PEG Cores, Varying Generations from 3 to 5, and Varying Amino Numbers from 16 to 64

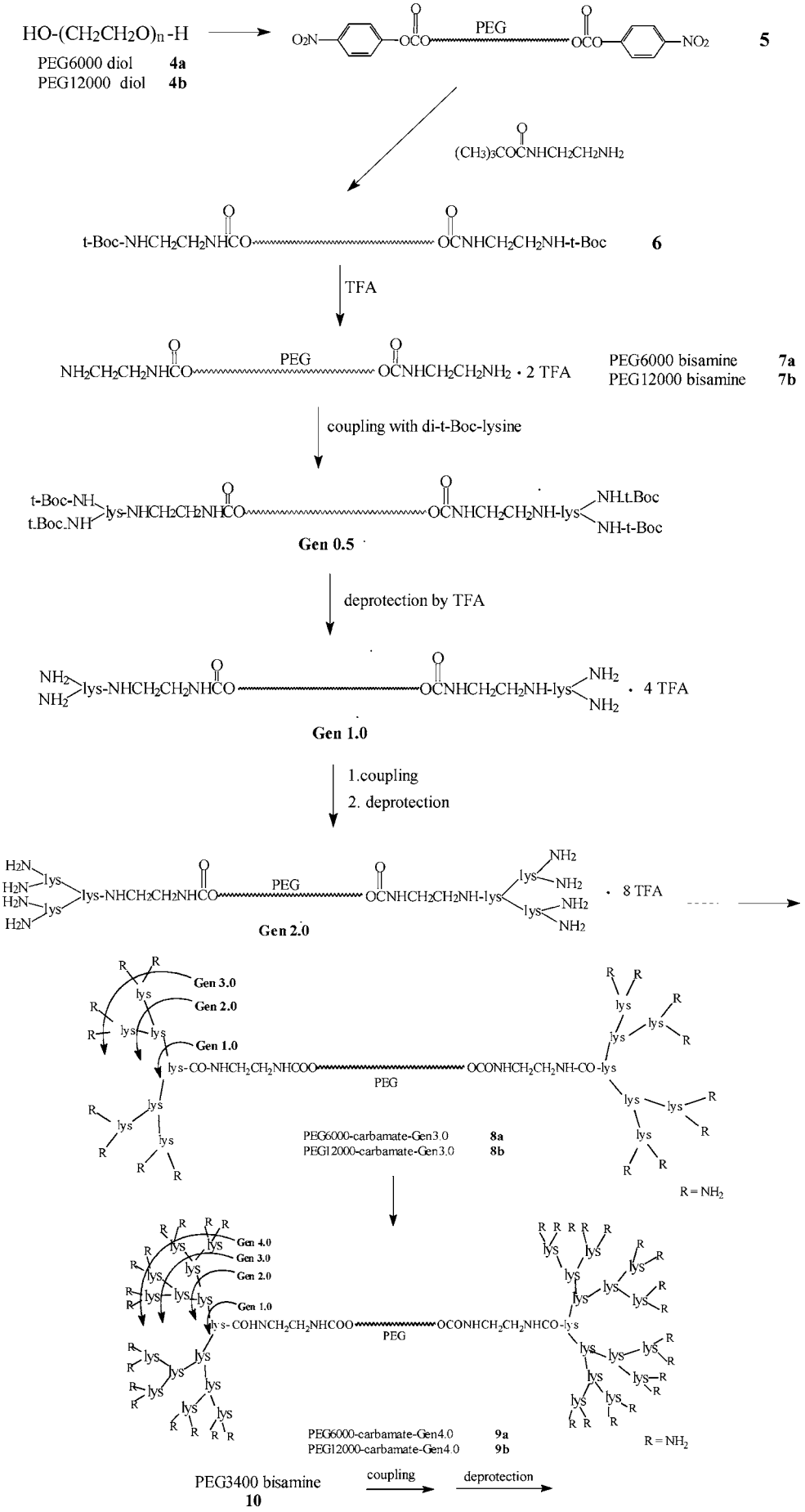

Scheme 2. (Continued)

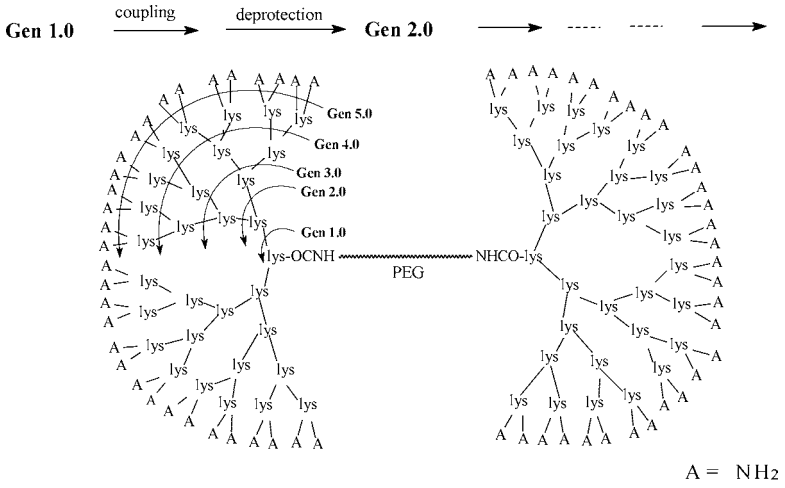

PEG3400-amide-Gen4.0 **11a**
PEG3400-amide-Gen5.0 **11b**

Scheme 3. Synthesis of a Nonionic Reactive Triiodophthalamide Derivative from Iobitridol

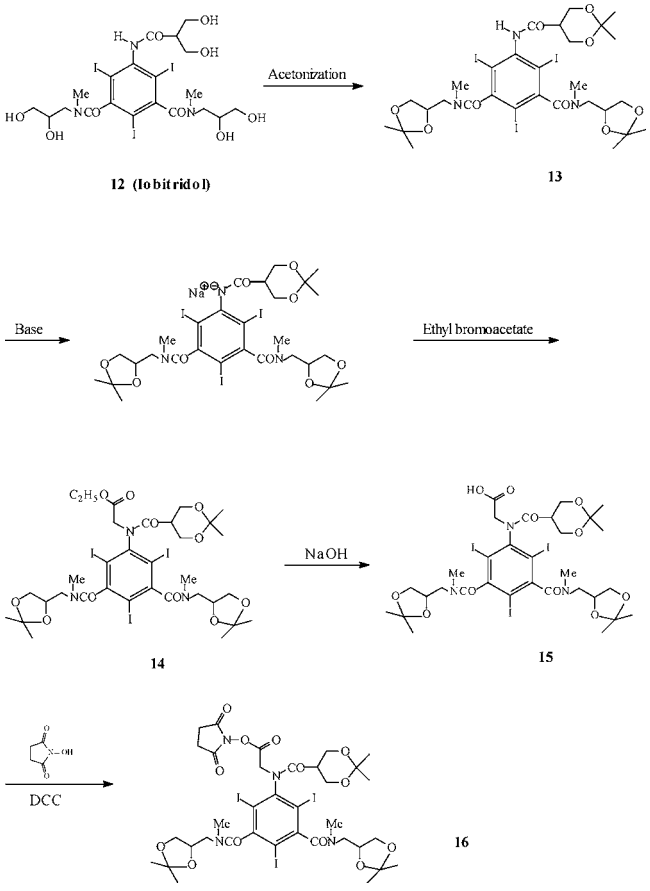

1,4-dioxane, DMF was eventually chosen as the reaction solvent to well dissolve both reactants and products. For the deprotection step, CH_2Cl_2/TFA (1:1) was always used as the reaction medium without problems. In the synthesis of PEG3400-amide-Gen4, three activated species of di-t-Boc lysine, including DCC-activated t-Boc lysine, 4-nitrophenyl ester, and *N*-hydoxysuccinimide ester, were employed for the coupling reaction, respectively. Each approach yielded the similar dendrimer eventually under similar conditions. The first approach was generally used for dendrimer synthesis in this work.

The PEG-core polylysine dendrimers were nicely purified by preparative SEC on a Sephadex G-75 column. Dendrimer

Scheme 4. Synthesis of Iodinated Macromolecular Contrast Agents from PEG-Core Dendritic Polylysines

8a		**1a**
8b		**1b**
9a	1. Acylation with **16** 2. Deprotection by TFA-H_2O	**2a**
9b		**2b**
11a		**3a**
11b		**3b-I**

fractions could be readily detected by UV or a ninhydrin test. Small molecular byproducts, such as lysine or its oligomers, were completely removed.

MALDI-TOF mass spectra gave expected results of their molecular weights (Figure 1). Characteristically, the regular mass interval of 44 (CH_2CH_2O unit) between adjacent MALDI peaks demonstrated the existence of PEG, while we could not find a typical mass interval of 128 (lysine residue) which indicated the absence of defected polylysine dendrons with a missing lysine sequence (see Figure 1). The PDI values derived from these spectra were highly close to 1.00, less than 1.05, and even less than the PDI values of their precursor PEGs, proving that these synthesized dendrimers have a high degree of size homogeneity. $^1H/^{13}C$ NMR spectra confirmed the expected structure of the synthesized new dendrimers. (Figures 4a and 5a, Table 1) Interestingly, in the ^1H NMR spectra of PEG12000-carbamate-Gen4 as an example, two well-resolved peaks (1.38, 1.70 ppm) were found in the range of 1.2−1.8 ppm characteristic for a lysine trimethylene group, and also two smaller peaks (2.95, 3.15 ppm) found in the range of 2.9−3.2 ppm for another CH_2 adjacent to α-C. This implied that all dendritic lysine residues were likely divided into one exterior population with unconjugated NH_2 termini, and another interior population. This was supported by the fact that after conjugation with IOB groups, only one broad peak containing three poorly resolved subpeaks was found in 1.2−1.8 ppm region, corresponding to three adjacent methylene groups.

In a recent work a Gen-3.5 dendritic polylysine with 16 hydrophobic t-Boc termini and one ester-bonded monomethoxy PEG tail (only 5 kDa PEG tested) was synthesized for testing as a surfactant (*16*). In another work an ABA triblock copolymer with a PEG core (3.4 kDa) and generation-4 dendritic polylysines at each end was synthesized via Fmoc chemistry for the use as a nonviral plasmid DNA vector (*17*). By contrast,

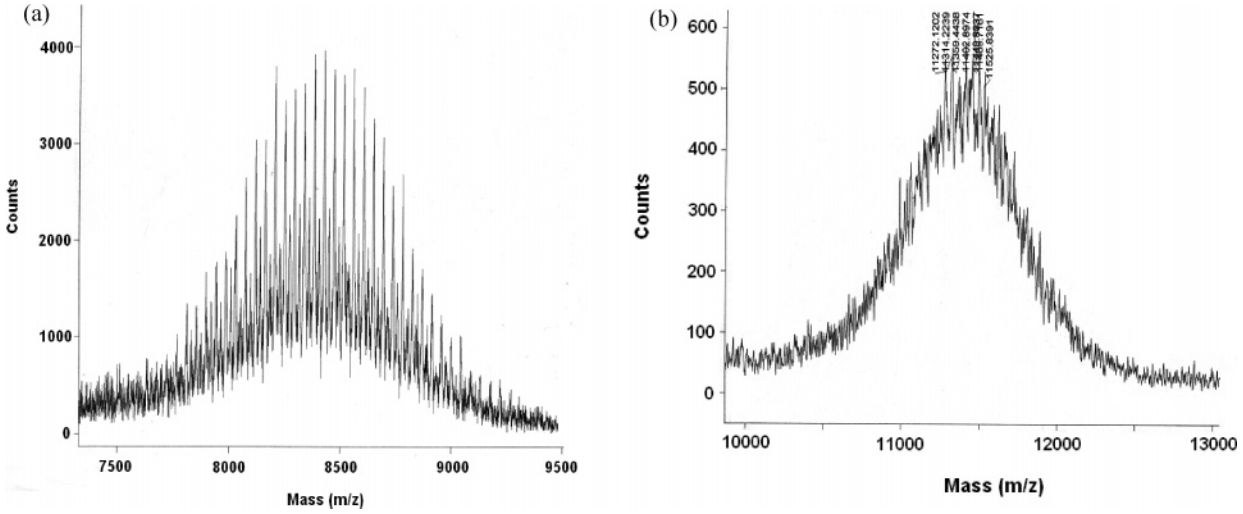

Figure 1. MALDI-TOF mass spectra of two representative PEG-core dendrimers: (a) PEG6000-carbamate-Gen3 (**8a**) and (b) PEG3400-amide-Gen5 (**11b**).

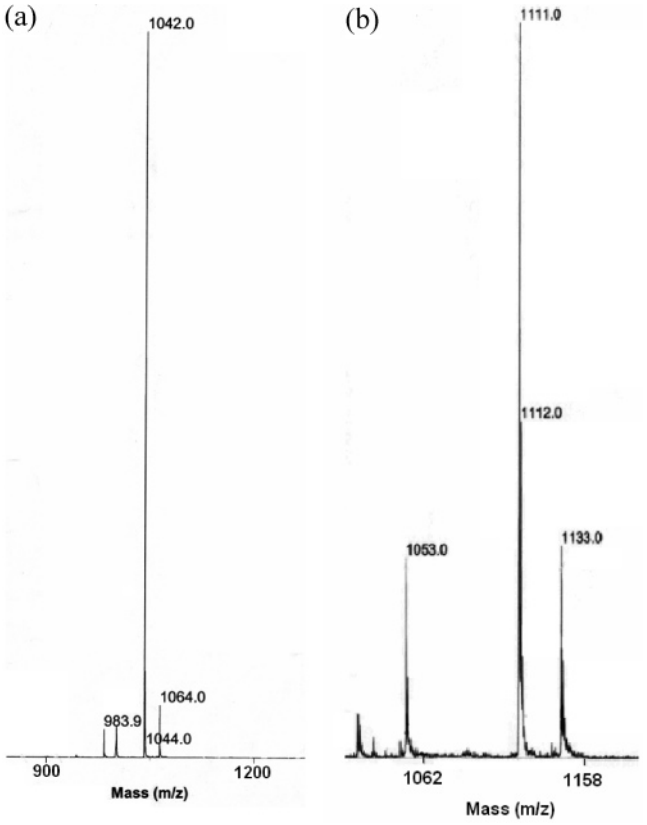

Figure 2. ESI mass spectra of triiodophthalamide derivatives, ethyl ester **14** (a) and *N*-hydroxysuccinimidyl ester **16** (b).

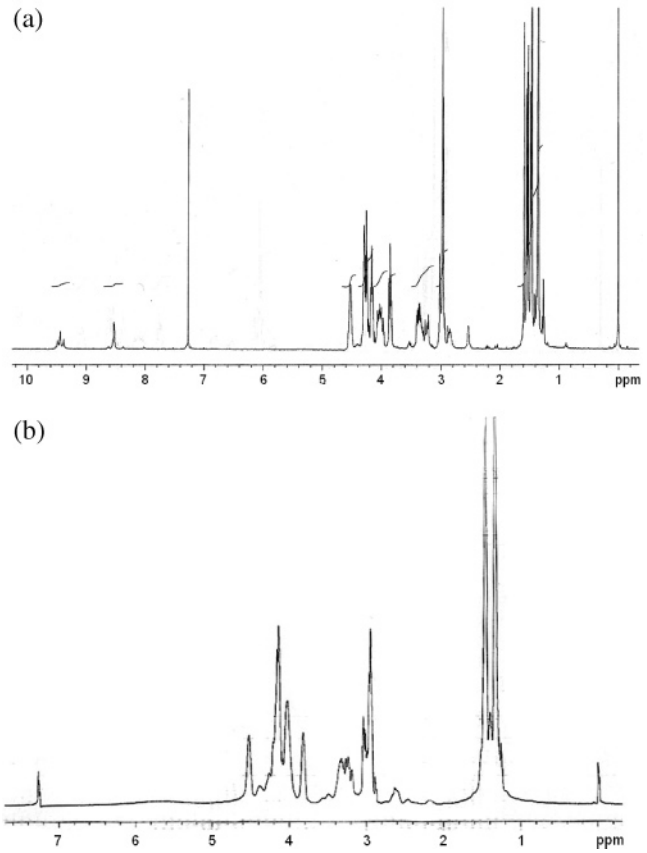

Figure 3. ^{1}H NMR of triiodophthalamide derivatives, ketal **13** (a) and carboxylic acid **15** (b) in $CDCl_3$.

our synthesis of PEG-core polylysine dendrimers featured larger PEGs (up to 12 kDa), higher generation (up to 5), comprehensive structure characterization (SE-HPLC besides MALDI-MS and NMR), relatively inexpensive t-Boc chemistry, and subsequent chemical decoration by triiodophthalamides.

"Triiodo" Derivatives Synthesis and Characterization. In the development of clinically approved iodinated contrast media, tolerability has been an extremely important issue. Nonionic contrast media were proven better tolerated than their ionic counterparts due to their lower osmotic pressure, close to that of plasma (*18*−*20*). A recent study showed that a nonionic iodinated contrast agent with molecular weight of 13 kDa was highly tolerated with an acute toxicity dose of >8900 mg iodine/kg in rodents (*21*). In our work, a nonionic, well-tolerated clinically approved contrast agent Iobitridol was thus selected as the precursor "triiodo" molecule for subsequent derivatization. Of additional note, by choosing this approach, a lengthy and time-consuming de novo synthetic route generally starting from triiodination of 5-amino-1,3-phthalic acid could be avoided and be replaced by a substantially shorter and more economical synthetic route. Iobitridol was preferably chosen due to its higher hydroxyl number compared with Iopamidol and Ioxilan (six vs five OH), also due to its possession of only one remained modifiable CONH group compared with Iohexol, allowing a possible regioselective derivatization.

Somewhat similar to monosaccharides, Iobitridol has six hydroxyl groups including two 1,3-diol and one 1,2-diol

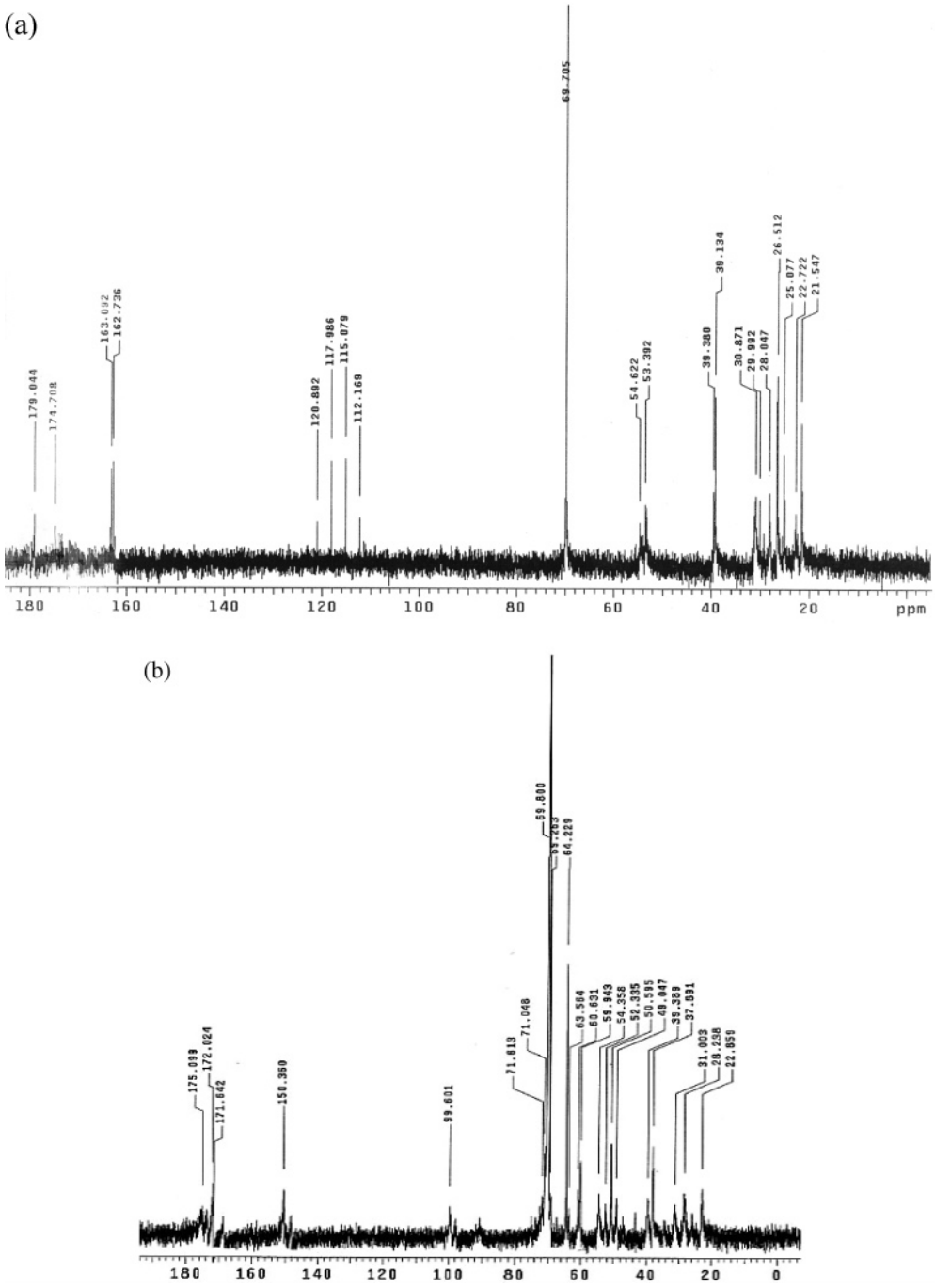

Figure 4. ^{13}C NMR spectra of PEG3400-amide-Gen5 dendrimer **11b** (a, TFA salt) and PEG6000-carbamate-Gen3-IOB conjugate **1a** (b) in D_2O.

structure. It is natural to think of using ketal chemistry to block all hydroxyl groups, leaving the only CONH group exposed for selective modification. Two ketalization approaches, the acetone/$ZnCl_2$ method and the 2,2-dimethoxypropane/*p*-toluenesulfonic acid (DMP/TsOH) method, were compared. The conventional $ZnCl_2$ method requires the use of a large amount of fused zinc chloride (irritant!), a $CHCl_3$ extraction step, and a relatively long time (24 h) since the reaction proceeds in a heterogeneous phase. By contrast, the less common DMP/TsOH method gave a facile and clean ketalization in DMF with a trace amount of TsOH as the catalyst and was also fast (1 h reaction in homogeneous phase) in a superior and near quantitative yield (98% vs 83% after chromatography). Silica gel chromatography was used to remove a minor unknown byproduct ($R_f = 0.90$). The DMP/TsOH ketalization was found complete at 90 °C with a mole ratio of [DMP]/[IOB] = 5. It was found that either a reduction of [DMP]/[IOB] ratio to 3 or a temperature decline to 25 °C led to an incomplete ketalization, yielding an Iobitridol di-isopropylidenyl byproduct identified by ^1H NMR. This byproduct has a lower $R_f = 0.20$ and 0.14, compared to the desired product ($R_f = 0.64$, 0.50). Both compounds showed two highly close spots in TLC essentially due to the well-known aromatic amide isomerism (*22*).

A subsequent amide N-alkylation of **13** is a key step to introduce a spacer between a "triiodo" group and a dendrimer. Various halides were tested as the electrophiles. First, $ClCH_2$-$CH_2OCH_2CO_2Me$ as a flexible spacer molecule was synthesized according to the literature (*23*) and reacted with **13** in the presence of anhydrous K_2CO_3 in DMF, which however did not give a significant amount of alkylation product (yield < 5%) at various temperatures up to 120 °C for a reaction time up to 24 h. Further, TLC showed no significant change even after

addition of potassium iodide as a catalyst. Alternatively, $ICH_2CH_2OCH_2CO_2Me$ was prepared (*24*) and used for the alkylation with **13** under similar conditions. TLC showed that no reaction virtually occurred. The likely reasons for these failed N-alkylations are that, on one hand, the chloride $ClCH_2CH_2OCH_2CO_2Me$ is not electrophilic enough toward the anion of **13**, and on the other hand, the iodine atom in $ICH_2CH_2OCH_2CO_2Me$ is too bulky and may exert a high steric hindrance effect on the alkylation. Their bromide analogue might be a suitable electrophile here. However, $BrCH_2CH_2OCH_2CO_2Me$ could not be prepared easily by refluxing its chloride analogue with NaBr or KBr. This bromide could be prepared by the reflux of 4-dioxan-2-one with HBr/methanol solution via a ring-opening transesterification, but the method was momentarily abandoned since the highly reactive cyclic ester is difficult to obtain. Alternatively, another simple bromide, $BrCH_2CO_2Et$, was used instead, even though it is not a long spacer molecule, but its N-alkylation with the anion of **13** was proven straightforward and highly efficient. Additionally, $BrCH_2CH_2CO_2Et$ was also tried as an electrophile in the alkylation of **13**, but it was proven unsuccessful probably because a severe β-elimination of the bromide happened under basic conditions, yielding the unwanted ethyl acrylate.

In the N-alkylation using ethyl bromoacetate, other condition variables including the solvent, base, temperature and reaction time were also investigated. Certainly, DMF can be used since it can dissolve both reactants and products. Other aprotic polar solvents with lower boiling points are also tried. For example, acetone/1,4-dioxane (1:1, v/v) or tetrahydrofuran alone worked fairly well. Tetrahydrofuran is preferred due to its easy removal and chemical inertness. The base used in this alkylation is $NaOCH_3$ in methanol. Use of anhydrous K_2CO_3 in DMF as a reaction system also worked well for this alkylation. $NaOCH_3$ method was carried out in the homogeneous phase at room temperature while the K_2CO_3 method conducted in the heterogeneous phase required a higher reaction temperature ($\geq$60 °C). Reaction time is much less for the $NaOCH_3$ method (0.5−1 h) compared to the K_2CO_3 method (16−20 h). Of note, an initial addition of 50% excess of both sodium methoxide and the bromide was helpful for the full conversion of **13**.

The ester **14** obtained above was hydrolyzed in 2.5 h in 1 N NaOH solution (1:1 methanol/water). As expected, the isopropylidene ketal groups were stable at this condition. Subsequent acidification of the hydrolysis product in pH 3.5 citrate buffer produced acid **15** which could be extracted by chloroform. In chloroform the acid **15** was then converted to its *N*-hydroxysuccinimidyl ester which, instead of 4-nitrophenyl ester, is chosen due to its higher reactivity toward the amine.

"Triiodo" derivatives **13**−**16** were characterized by TLC, ESI mass spectra, and ^1H and ^{13}C NMR. As examples, the mass spectra of compound **14** and **16** were given in Figure 2. For each, the molecular ion $(M + H)^+$ peak is the base peak; other characteristic peaks include the $(M + Na)^+$ peak, and the $(M - CH_3COCH_3 + H)^+$ peak, which corresponds to a likely 1,2-epoxy structure produced in ESI process. In ^1H NMR spectra of all these derivatives (see examples in Figure 3), several singlet peaks at 1.3−1.5 ppm indicated the presence of isopropylidene groups (18 H). Peaks at 1.28 and 2.63 ppm belong to the ethyl group in **14**. The peak at ~1.28 ppm disappeared after the hydrolysis of **14**. For compound **16**, the succinimidyl group was indicated by the existence of a peak at ~2.86 ppm (4 H). From **13** through **16**, ^{13}C NMR spectra showed small but consistent changes (position of peaks, number of peaks) with their structure variation in two regions, 20−50 ppm (aliphatic C) and 160−175 nm (carbonyl) (see details in Experimental Section). TLC showed that R_f values were significantly affected by the side chain attached to the aromatic amino N atom. Compared to ketal **13** (0.64, 0.50), esters **14** (0.96, 0.85) and **16** (0.93, 0.80) gave higher R_f values while acid **15** (0.33, 0.20) had a lower R_f value, which agrees well with the polarity change of this N-alkylated side chain. All these "triiodo" derivatives gave two close spots in TLC because isomers exist in each of them owing to restricted rotation along the aromatic amide bond, which is a well-known phenomenon for iodinated CT contrast media (*25*).

Scheme 5. Insertion of a β-Alanine Spacer, between Dendrimer NH_2 and the Triiodo Group, Resulted in Higher Efficiency of Triiodo Conjugation for a Generation-5 Dendrimer (e.g., use of PEG3400-amide-Gen5 dendrimer to synthesize iodinated conjugate 3b-II)

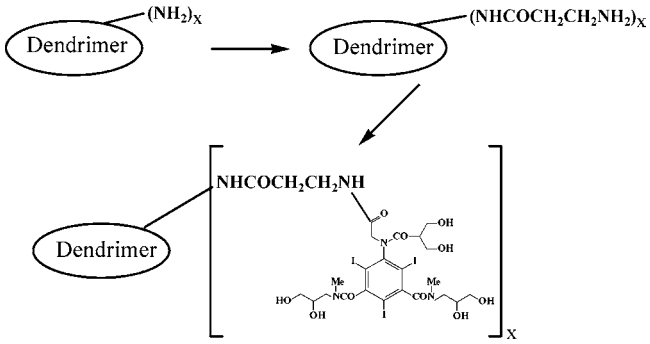

Synthesis and Chemical Characterization of Dendritic Contrast Agents. In the triiodo conjugation step, we added the active ester **16** to the dendrimer solution in two portions with a 24-h interval, which worked better than single addition since a higher degree of IOB-substitution was obtained (in the case of **1a**, 99% vs 92%). The feeding equivalent ratio of [IOB]/[NH_2] has to be sufficient. In the case of PEG6000-Gen4 dendrimer, when this ratio increased from 3 to 4.5, the percentage of amino substitution increased from 87% to nearly 100%. The 72-h coupling reaction was required for Gen3 dendrimer synthesis, while 96-h and 120-h were needed for preparation of Gen4 and Gen5 dendrimers due to increasing steric hindrance effect.

For dendrimers with generation-4 or less, single coupling often gave a high substitution degree close to 100% under specific conditions, while in some other batches incomplete coupling was still found (substitution degree lower than 92%). In the latter cases, a second coupling was recommended and proven useful to minimize the defects of decorated dendrimers to less than 5%. However, Gen5 dendrimer has such high steric hindrance that unsatisfactory amino-substitution degrees (40% and 63%) were obtained after a single coupling, and even a second coupling with IOB (see **3b-I** in Table 2). Thus a spacer arm β-alanyl group was covalently attached to each amino terminus of PEG3400-amide-Gen5 by reacting with the *N*-hydroxysuccinimide ester of t-Boc alanine. After t-Boc deprotection, the resulting β-alanyl-terminated Gen5 dendrimer was subsequently conjugated with the "triiodo" active ester **16** for a single coupling under standard conditions, yielding an iodinated Gen5-dendrimer **3b-II** with a remarkedly higher degree of amino substitution (91.4%) (see Scheme 5 and Table 2).

DMF, a good solvent for both the dendrimers and their iodinated conjugates, was selected as the conjugation reaction medium. Room temperature was adopted and recommended because higher temperatures (>50 °C) caused formation of minor byproducts with higher molecular weights, likely due to intermolecular cross-linking of unreacted lysine chains.

In contrast agent synthesis, the final step, namely the hydroxyl deprotection, was completed in 60% (v%) aqueous TFA solution at room temperature. Other acids such as 2 N HCl in 1:1 methanol/water also worked well.

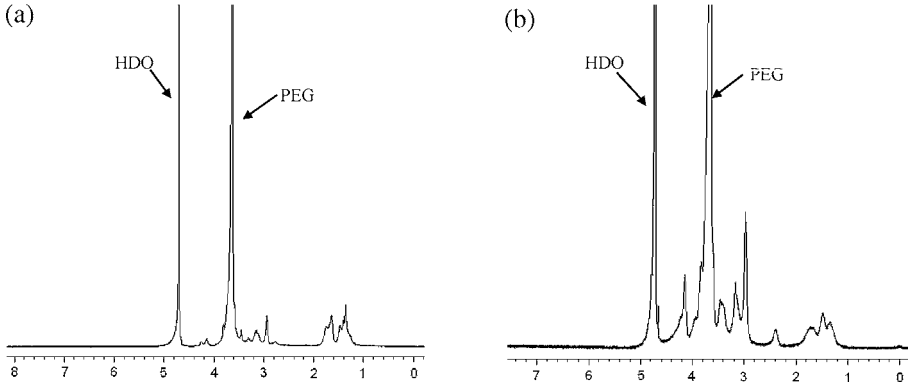

Figure 5. ^{1}H NMR spectra of PEG12000-carbamate-Gen4 **9b** (a, TFA salt) and PEG12000-carbamate-Gen4-IOB **2b** (b) in D_2O.

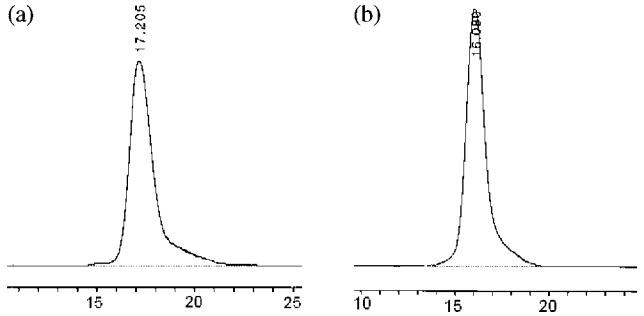

Figure 6. SE-HPLC traces of PEG12000-carbamate-Gen4 polyamine **9b** (a, TFA salt) and PEG12000-carbamate-Gen4-IOB conjugate **2b** (b) on a Superdex 200 column, with flow rate of 0.8 mL/min and each run time of 30 min. Other HPLC conditions: (a) mobile phase 0.1% trifluoroacetic acid and 0.3 M Na_2SO_4 (pH 2.7), UV detection at 210 nm; (b) 0.05 M phosphate and 0.15 M NaCl (pH 7.0), 245 nm.

All synthesized iodinated dendrimers were first dialyzed and then purified by a Sephadex G-100 column eluted with phosphate buffer at pH 7. An alternative mobile phase includes 0.1 M ammonium acetate (pH 7). Excess small molecular iodinated derivatives and seldom found large-molecular cross-linked byproducts were removed efficiently and completely. Analytical SE-HPLC (Figure 6) showed that PEG12000-carbamate-Gen4-IOB gave considerably narrow and symmetric peaks in size exclusion chromatography, indicating a high degree of monodispersity in molecular size. Iodine quantitative analysis (both by UV and elemental analysis), ^{1}H/^{13}C NMR, and UV confirmed that synthesized contrast agents have the expected structure. Both PEG (3.62 ppm in ^{1}H NMR, ~69.7 ppm in ^{13}C NMR) and the iobitridol derivative (NCH_3 at 3.0−3.2 ppm, in ^{1}H NMR, aromatic C in regions of 90−100 ppm and 145−150 ppm in ^{13}C NMR, λ_{max} 245 nm in UV) were present in the final products (Figures 4b and 5b). Due to overlapping of the PEG peak (3.62 ppm) with most IOB side chain peaks (3.2−4.5 ppm), the degree of dendrimer amino substitution could not be determined using the PEG peak. However, the ratio of IOB/lysine can be obtained by comparing the integrals of lysine trimethylene group (1.2−1.8 ppm) and characteristic NCH_3 groups (3.0−3.2 ppm) in IOB. Thus, the degree of dendrimer amino substitution can be calculated; for example, the conjugation degree was 96% in the case of PEG12000-carbamate-Gen4 dendrimer (Table 2). Iodine percentages (w%) measured by UV or elemental analysis agree with these NMR-measured amino substitution results. These data were used to calculate the actual molecular weights of iodinated dendrimer products (Table 2).

To directly measure the absolute molecular weights, MALDI-TOF mass spectrometry of these iodinated dendrimers were tried but failed under varying conditions (different ratios of matrix/sample, different spectrometers in different MS labs). Additionally, two derivatives of PEG12000-carbamate-Gen4-IOB, including its ketal precursor (i.e. the intermediate compound prior to hydroxyl deprotection) and its fully acetylated derivative, were isolated or prepared and then underwent MALDI mass spectral analysis; unfortunately there still were no peaks observed because their protonated ions could not fly under test conditions. Compared with our successful MALDI analyses of the undecorated PEG-core dendrimers, this unexpected difficulty must be due to the existence of a large number of heavy iodine atoms in their structure.

Preliminary Data of Physicochemical Characteristics of Iodinated PEG-Core Dendrimers. The ideal macromolecular CT contrast agent could be defined as being (a) highly efficient in X-ray attenuation, (b) primarily intravascular in distribution, (c) well-tolerated and nonimmunogenic, (d) monodisperse or near-monodisperse in size, (e) eliminated completely in a timely manner, and (f) with certain desired physicochemical properties including high water solubility, low osmolality, limited viscosity, and good stability to autoclave conditions.

The new structures described in this work virtually demonstrated most of these desired features, at least all of those tested in this preliminary study (Table 3). Apparent molecular weight based on protein standards ranged from 35 kDa (PEG3400-amide-Gen4-IOB) to 143 kDa (PEG12000-carbamate-Gen4-IOB) with a high degree of molecular monodispersity (Table 2, polydispersity index $M_w/M_n < 1.04$ for all six compounds), and the ratios between apparent and actual molecular weights were as large as 3.4, indicating that the choice of PEG as the macromolecular backbone substantially increased the molecular hydrodynamic size. The largest one of this series, PEG12000-carbamate-Gen4-IOB, had a CT-assayed blood half-life ($t_{1/2}$) of approximately 35 min (monoexponential kinetics) and an estimated volume of distribution (V_d) of 13%, intermediate between the accepted normal intravascular volume (~5%) and the normal extracellular fluid volume (~25% of the body weight), as reported somewhere else (*11*). Of note, both blood $t_{1/2}$ and V_d might be underestimated due to relatively short time course (~30 min) at dynamic CT. The same compound was tested by SE-HPLC prior to and after heat sterilization, showing identical HPLC traces, and neither inorganic iodide nor iodine was detected in autoclaved solutions. This contrast agent was proven to be highly stable to autoclaving conditions for 30 min at 120 °C. The six synthesized iodinated dendrimers were effective for producing strong X-ray attenuation due to generally high iodine contents (21−36%, w/w). (Table 2).

Water solubility for each of the four compounds tested for this characteristic was >440 mg/mL. These new compounds also showed high levels of hydrophilicity. Butanol−water partition coefficients of the four test compounds were between 0.015 and 0.064, similar to or more hydrophilic than clinically used CT contrast media (Iobitridol, 0.070; Iodixanol, 0.046;

Table 3. Physicochemical Properties of Iodinated Dendritic Contrast Agents with PEG Cores

contrast agent	PEG size (kDa)	gen. no.	theor. no. of dendrimer termini	no. of "triiodo" attached	MW (kDa) actual	MW (kDa) apparent	solubility (mg/mL, 25 °C)	hydrophilicity[a]	viscosity (cP, 37 °C)	osmolality (mOsm/kg water)
1a	6	3	16	15.2	21.7	43.7	nd[d]	nd	nd	nd
1b	12	3	16	15.5	27.5	84.0	nd	nd	nd	nd
2a	6	4	32	30.3	36.8	60.6	>470	0.034	nd	306[b]
2b	12	4	32	30.5	42.5	142.7	>550	0.015	11.4[b]	253[b]
3a	3.4	4	32	29.1	32.9	35.8	>440	0.042	nd	268[b]
3b-II	3.4	5	64	57.5	66.4	61.9	>460	0.064	nd	237[b]
iohexol	na[e]	na	na	1	0.82	na	>750	0.055	6.1[c]	684[c]

[a] Partition coefficient between 1-butanol and 50 mM Tris buffer (pH 7). [b] 75 mgI/mL. [c] 300 mgI/mL. [d] Not determined. [e] Not applicable.

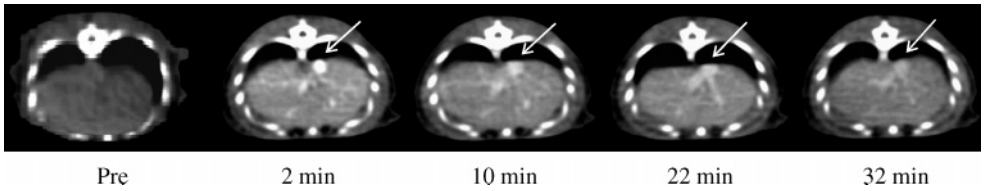

Figure 7. Serial axial CT images of a normal Sprague−Dawley rat at the level of liver prior to, 2, 10, 22, and 32 min after intravenous injection of PEG12000-carbamate-Gen4-IOB as a CT contrast agent at a dose of 450 mg iodine/Kg body weight. Note the strong and persistent enhancement of the inferior vena cava (see the arrows) and other vessels (hepatic veins) within the liver.

Iohexol, 0.055), likely due to the presence of the PEG core. Of note, taking advantage of the so-called "hydrophilic sphere stabilization" effect (*26*), Iobitridol molecules were carefully derivatized, chemically activated, and conjugated to the dendrimer with such a strategy that did not sacrifice any of its six hydroxyl groups upon conjugation. This strategy enabled all attached IOB moieties to remain highly soluble and hydrophilic after conjugation. Our initial attempts to conjugate Ioxilan to the same dendrimers via exploitation of one of its five hydroxyl groups yielded poorly water-soluble iodinated dendrimers, indicating that it is mandatory to keep a sufficient number of hydroxyl groups surrounding the hydrophobic triiodobenzene core so as to retain the required hydrophilicity and solubility of attached "triiodo" moieties (*11*).

The optimal concentration chosen for intravenous use will depend not only on water solubility but also on the viscosity and osmolality of the contrast agent. The viscosity of PEG12000-carbamate-Gen4-IOB was measured to be 11.4 cP (75 mg I/mL, 37 °C), a value considered acceptable for a macromolecular formulation, but higher than viscosity values obtained for conventional small molecular (<2 kDa) contrast agents (6.1 cP for 300 mgI/mL Iohexol; 6.5 cP for 270 mg I/mL Iodixilan) at the same temperature. Osmolality of four tested formulations at 75 mgI/mL concentation ranged from 230 to 310 mOsm/kg water, comparable or superior to certain clinically used formulations (684 mOsm/Kg for Iohexol at 300 mgI/mL, 295 mOsm/Kg for Iodixanol at 270 mgI/mL).

The presence of PEG cores makes the PEG-core dendrimers appear larger than their actual molecular weights, with only one exception of **3b-II** (one with the smallest PEG and highest triiodo content). The apparent molecular weights measured by SE-HPLC at physiological pH were consistent with our prediction: the bigger the PEG core, the larger the apparent molecular weight (or hydrodynamic size) for same-generation iodinated dendrimers, i.e. **3a** < **2a** < **2b**. Also the measured hydrophilicity did increase with the same order when the size of PEG increases. Interestingly, properties of PEG12000-based dendrimers are basically different from those based on PEG6000 and PEG3400; so are Gen4 and Gen5 dendrimers compared with Gen3 dendrimers. Looking at different generations, Gen3, Gen4, and Gen5 dendrimers gave the iodine percentage as high as 27%, 33%, and 36%, respectively; in general, generation-4 seemed the best generation choice for this type of dendrimers.

The PEG-core iodinated dendrimers described in this study are distinctly different from agents now available for clinical use in CT imaging. Iodinated contrast agents currently used and approved are quite similar to each other in design and characteristics. All are small-molecular ones, less than 2 kDa, and all distribute throughout the extracellular fluid (ECF) space, not primarily the intravascular compartment. These ECF agents can be divided into monomeric (e.g., Iohexol, Iopamidol, Iobitridol) or dimeric species (e.g., Iotrolan, Iodixilan). Dissociating "ionic" agents containing carboxylates have generally fallen from favor and are now rarely used clinically. Compared to ECF agents, the macromolecular CT contrast agents for intravascular distribution have been less explored with the exception of emulsion-type contrast agents, represented by perfluorooctyl bromide (PFOB) (*27*). PFOB has been extensively evaluated in preclinical and clinical CT studies, but for unclear reasons its development has been discontinued.

Other efforts to develop water-soluble macromolecular contrast agents (>30 kDa) for CT enhancement have not advanced to the point of warranting clinical trials. Previously reported macromolecular formulations include iodinated hydroxyethyl starch (*28*), carboxymethyl dextran derivatives with triiodobenzoic acid (*29*), and vinyl copolymers from acrylamide and hydrophilic "triiodo" monomer (*30*). Different designs revealed different shortcomings: some were highly heterogeneous in molecular size. For others, radioopacity was low, and some were too viscose, not sufficiently stable, or poorly tolerated. Of note, there were other efforts reported to achieve pegylated long-circulating vesicles including Iopromide-encapsulated liposome (*31*), iodinated triglyceride emulsion (*32*), and iodinated micelles (*33*).

Experimental CT Imaging. As shown in Figure 7, the intravascular CT enhancement in the normal rat through 32 min postinjection of PEG12000-Gen4-IOB (450 mg I/kg dose) was considerably intensive and persistent. Although not shown, it is well-known that for CT imaging obtained after administration of conventional small-molecular contrast media there is exhaustion of the vascular enhancement in less than 5 min. The iodinated PEG-core dendrimers by virtue of their large size remain much longer in the blood pool. The details of the considerable advantages of prolonged intravascular enhancement in CT go beyond the scope of this chemistry-focused report.

For the in vivo CT image enhancement available with iodinated PEG-core dendrimers, only one compound was evaluated in this study as an example. Further characterization studies of this new class of CT contrast agents including pharmacology, metabolism, and the safety profile are ongoing.

CONCLUSION

To summarize, a new design for macromolecular contrast enhancing agents with potential applications in angiographic and dynamic CT imaging has been developed by the synthesis and preliminary testing of six representative compounds. The basic construct consists of a poly(ethylene glycol) core with two dendritic polylysine amplifiers (dendrons) at both PEG termini, to which amplifiers are conjugated multiple "triiodo" moieties. Basically, the desirable characteristics for such a macromolecular contrast agent could be approximated by one or more of these PEG-core dendrimer conjugates. Demonstrated favorable characteristics include prolonged intravascular enhancement in an animal model, adjustable and large apparent molecular weights (35 to 143 kDa), near monodispersity in size, high X-ray attenuation, high water-solubility and hydrophilicity, low osmolality, and good chemical stability. This new class of iodinated dendrimers has good potential in angiography and, more importantly, in quantitative microvascular characterization of a wide variety of diseases and abnormalities including cancer, ischemic injury, inflammation, and altered states of angiogenesis.

ACKNOWLEDGMENT

This work was supported in part by NIH grants CA103850 and CA82923 and by Lucile-Packard Foundation. MALDI-TOF MS and ESI-MS measurements were conducted by the UCSF Mass Spectrometry Facility (Director Dr. A. L. Burlingame) supported by NIH NCRR RR01614. ^{1}H NMR and ^{13}C NMR spectra were recorded on a Varian 400 NMR spectrometer in the NMR Lab, School of Pharmacy at UCSF. Drs. Karl Turetschek and Vincenzo Lucidi are thanked for their generous gifts of Iobitridol. Mr. Jason Kipke, Ms. Christina Hampton, and Ms. Jessica Pfannenstiel are acknowledged for their great assistance in the CT scans.

LITERATURE CITED

(1) Su, M. Y., Najafi, A. A., and Nalcioglu, O. (1995) Regional comparison of tumor vascularity and permeability parameters measured by albumin-Gd-DTPA and Gd-DTPA. *Magn. Reson. Med. 34*, 402−411.

(2) Brasch, R. C. (1991) Rationale and applications of macromolecular Gd-based contrast agents. *Magn. Reson. Med. 22*, 282−287.

(3) Daldrup-Link, H. E., and Brasch, R. C. (2003) Macromolecular contrast agents for MR mammography: current status. *Eur. Radiol. 13*, 354−65.

(4) Schwitter, J., Saeed, M., Wendland, M. F., Derugin, N., Canet, E., Brasch, R. C., and Higgins, C. B. (1997) Influence of severity of myocardial injury on distribution of macromolecules: extravascular versus intravascular gadolinium-based magnetic resonance contrast agents. *J. Am. Coll. Cardiol. 30*, 1086−94.

(5) Krapcho, A. P., and Kuell, C. S. (1990) Monoprotected diamines. N-tert-Butoxycarbonyl-α,ω−alkanediamines from alkanediamines. *Synth. Commun. 20*, 2559−2564.

(6) Habeeb, A. F. S. A. (1966) Determination of free amino groups in proteins by trinitro-benzenesulfonic acid. *Anal. Biochem. 14*, 328−336.

(7) Morris, T. W. (1989) *Intravascular contrast media and their properties*, Aspen Publishers, Frederick, MD.

(8) Zalipsky, S. (1995) Chemistry of polyethylene glycol conjugates with biologically active molecules. *Adv. Drug Delivery Rev. 16*, 157−182.

(9) Harris, J. M. (1992) *Poly(ethylene glycol) Chemistry: Biotechnical and Biomedical Applications*, Plenum Press, New York.

(10) Delgado, C., Francis, G., and Fisher, D. (1992) The uses and properties of PEG-linked proteins. *Crit. Rev. Ther. Drug Carrier Syst. 9*, 249−304.

(11) Fu, Y., Nitecki, D. E., and Brasch, R. C. (2005) *Proceedings of PACIFICHEM 2005*, Honolulu, HI, American Chemical Society, Washington, DC.

(12) Seltzer, S. E. (1981) Rare earth contrast agents in hepatic computed tomography. In *Contrast Media in Computed Tomography* (Felix, R., Kazner, E., *and* Wegener, O. H., Eds.) Excerpta Medica, Princeton, NJ.

(13) Yu, S. B., and Watson, A. D. (1999) Metal-based X-ray contrast media. *Chem. Rev. 99*, 2353−2377.

(14) Okuhata, Y. (1999) Delivery of diagnostic agents for magnetic resonance imaging. *Adv. Drug Delivery Rev. 37*, 121−137.

(15) Wang, Y. S., Youngster, S., Grace, M., Bausch, J., Bordens, R., and Wyss, D. F. (2002) Structural and biological characterization of pegylated recombinant interferon alpha-2b and its therapeutic implications. *Adv. Drug Delivery Rev. 54*, 547−570.

(16) Chapman, T. M., Hillyer, G. L., NMahan, E. J., and Shaffer, K. A. (1994) Hydraamphiphiles: novel linear dendritic block copolymer surfactants. *J. Am. Chem. Soc. 116*, 11195−11196.

(17) Choi, J. S., Joo, D. K., Kim, C. H., Kim, K., and Park, J. S. (2000) Synthesis of a barbell-like triblock copolymer, poly(L-lysine) dendrimer-*block*-poly(ethyleneglycol)-*block*-poly(L-lysine) dendrimer, and its self-assembly with plasmid DNA. *J. Am. Chem. Soc. 122*, 474−480.

(18) Almen, T., and Wiedeman, M. P. (1968) Application of contrast media to the external surface of the vasculature. Effects on microcirculation in the bat wing. *Invest. Radiol. 3*, 151−158.

(19) Almen, T. (1985) Development of nonionic contrast media. *Invest. Radiol. 20*, S2−S9.

(20) Sovak, M. (1984) *Radiocontrast agents*, Springer-Verlag, Berlin.

(21) Idee, J. M., Port, M., Robert, P., Raynal, I., Prigent, P., Dencausse, A., Le Greneur, S., Tichkowsky, I., Le Lem, G., Bourrinet, P., Mugel, T., Benderbous, S., Devoldere, L., Bourbouze, R., Meyer, D., Bonnemain, B., and Corot, C. (2001) Preclinical profile of the monodisperse iodinated macromolecular blood pool agent P743. *Invest. Radiol. 36*, 41−49.

(22) Krause, W. (1999) Delivery of diagnostic agents in computed tomography. *Adv. Drug Delivery Rev. 37*, 159−173.

(23) Hiroshi, F. (1991) Novel tetracyclic compounds having anti-allergic and anti-asthmatic activities, their preparation and use. Eur. Pat. Appl. 421823 A2.

(24) Frederik, L. A., Fyles, T. M., Gurprasad, N. P., and Whitfield, D. M. (1981) Membrane transport systems. I. Synthesis and characterization of carriers for a proton driven alkali metal cation pump. *Can. J. Chem. 59*, 1724−1731.

(25) Krause, W., and Schneider, P. W. (2002) Chemistry of X-ray contrast agents. *Topics Curr. Chem. 222*, 107−150.

(26) Violon, D. (2001) Stabilization of the hydrophilic sphere of non-ionic monomers: are all protected in a similar way? *Br. J. Radiol. 74*, 1097−1102.

(27) Mattrey, R. F. (1989) A new contrast agent for CT, sonography, and MR imaging. *Am. J. Roentgenol. 152*, 247−252.

(28) Sako, M., Watanabe, H., Okuda, K., Shimuzu, T., Hase, M., Hirota, S., Kono, M., and Sakamoto, K. (1987) Studies of water-soluble iodinated starch as a new potential contrast material. *Nippon Igaku Hoshasen Gakkai Zasshi 47*, 1472−1477.

(29) Doucet, D., Chambon, M. C., and Bonnemain, B. (1991) Blood-pool X-ray contrast agents. *Invest. Radiol. 26*, S53− S54.

(30) Sovak, M., Douglass, J. G., Terry, R. C., Brown, J. W., Bakir, F., and Wasden, T. S. (1994) Blood pool radiopaque polymers: design considerations. *Invest. Radiol. 29*, S271−S274.

(31) Sachse, A., Leike, J. U., Schneider, T., Wagner, S. E., Rossling, G. L., Krause, W., and Brandl, M. (1997) Biodistribution and computed tomography blood-pool imaging properties of polyethylene glycol-coated iopromide-carrying liposomes. *Invest. Radiol. 32*, 44−50.

(32) Weichert, J. P., Lee, F. T., Longino, M. A., Chosy, S. G., and Counsell, R. E. (1998) Lipid-based blood-pool CT imaging of the liver. *Acad. Radiol. 5*, S16−S19.

(33) Trubetskoy, V. S., Gerald, G. S., and Torchilin, V. P. (1997) Block-copolymer of polyethylene Glycol and polylysine as a carrier of organic iodine: design of long-circulating particulate contrast medium for X-ray computed tomography. *J. Drug Targeting 4*, 381−388.

BC060019C

Gene Transfer with Poly-Melittin Peptides

Chang-Po Chen, Ji-seon Kim, Erin Steenblock, Dijie Liu, and Kevin G. Rice*

Division of Medicinal and Natural Products Chemistry, College of Pharmacy, University of Iowa, Iowa City, Iowa 52242.
Received February 3, 2006; Revised Manuscript Received May 15, 2006

The 26 amino acid hemolytic melittin peptide was converted into a gene transfer peptide that binds to DNA and polymerized through disulfide bond formation. Melittin analogues were synthesized by the addition of one to four Lys repeats at either the C- or the N-subterminal end along with terminal Cys residues. Melittin analogues were able to bind and polymerize on plasmids resulting in the formation of DNA condensates. In the absence of DNA, melittin analogues retained their red blood cell hemolytic potency but were inactive when bound to plasmid DNA. The in vitro gene transfer efficiency mediated by poly-melittin analogues was equivalent to PEI in HepG2 cells. Attempts to truncate portions of either of the two melittin α-helices resulted in concurrent loss of hemolytic potency and gene transfer efficiency. The results demonstrate the ability to transform melittin into a gene transfer peptide by transiently masking its membrane lytic activity by the addition of Lys and Cys residues to promote DNA binding and polymerization.

INTRODUCTION

Nonviral gene delivery systems depend on endosomal lysis to allow DNA to enter the cytosol (*1*−*3*). Two main strategies have emerged to achieve endosomal lysis. The first relies upon endosomal lytic peptides that respond to a lowering of the pH, leading to fusion with the endosomal membrane and lysis (*3*−*7*). The most widely used fusogenic peptides used to enhance gene delivery include the hemolytic peptide (HA2), GALA, and melittin. The second strategy to achieve endosomal lysis relies upon the use of endosomal buffering agents that resist changes in pH leading to osmotic lysis. This is the reported mechanism by which chloroquine, PEI, and polyhistidine achieve enhanced gene delivery (*8*−*10*).

Naturally occurring melittin from bee venom is a 26 amino acid peptide composed of two α-helices joined by an interrupting proline (*11*−*13*). A number of prior studies have examined melittin and its analogues to elucidate the amino acid sequences that are essential to its potent hemolytic and antimicrobial activity (*14*−*16*). Likewise, one prior study examined the hemolytic activity of dimeric melittin formed by disulfide bond formation between terminal Cys residues (*17*). Unlike HA2, which is primarily hemolytic at pH 4 but not 7, the hemolytic activity of melittin is not pH dependent. Consequently, because melittin remains hemolytic at pH 7, its utility for enhancing gene delivery necessitates masking to avoid unintended cell lysis.

Despite this potential limitation, melittin has been examined as an in vitro gene transfer agent to increase endosomal escape of DNA (*3*, *5*, *18*, *19*). Several groups have incorporated a Cys containing melittin into either a lipid or a PEI resulting in a significant improvement in the gene transfer efficiency while simultaneously diminishing melittin's toxicity (*3*, *5*, *19*). An alternate strategy involved masking the hemolytic activity of melittin by reversible derivatization of Lys residues (*18*).

We previously reported that the gene transfer efficiency of short polylysine peptides can be dramatically increased by installing terminal Cys residues resulting in peptide polymerization (*20*, *21*). The multiplication of cationic residues in sulfhydryl polymerized peptides relative to a monomeric peptide results in much greater DNA binding affinity. Likewise, sulfhydryl polymerized peptides are postulated to undergo intracellular reduction to trigger the release of DNA (*22*).

In the present study, we have transformed melittin into a sulfhydryl polymerized peptide and investigated its in vitro gene transfer activity. One of the goals of this study was to investigate how structural modifications in the melittin sequence influence its hemolysis of red blood cells and gene transfer efficiency. The results establish a relationship between melittin hemolytic activity and gene transfer efficiency and provide a means to transiently mask the membrane lytic activity of melittin to enhance gene transfer.

EXPERIMENTAL PROCEDURES

Substituted Wang resin for peptide synthesis, N-terminal Fmoc protected amino acids, 9-hydroxybenzotriazole, diisopropylcarbodiimide, and diisopropylethylamine were obtained from Advanced ChemTech (Lexington, KY). *N*,*N*-Dimethylformamide, trifluoroacetic acid (TFA), acetic anhydride, acetonitrile, and piperidine were purchased from Fisher Scientific (Pittsburgh, PA). Tris(2-carboxyethyl)-phosphine hydrochloride (TCEP) and thiazole orange were obtained from Sigma Chemical Co. (St. Louis, MO). Polyethylene amine (PEI) of 25 KDa was purchased from Aldrich (Milwaukee, WI). D-Luciferin and luciferase from *Photinus pyralis* (EC 1.13.12.7) were obtained from Roche Applied Science (Indianapolis, IN). HepG2, CHO, and COS-7 cells were acquired from the American Type Culture Collection (Manassas, VA). Inactivated qualified fetal bovine serum (FBS) was from Life Technologies, Inc. (Carlsbad, CA). BCA reagent was purchased from Pierce (Rockford, IL).

Peptide synthesis was carried out on an Apex 396 Advanced ChemTech solid-phase peptide synthesizer. Peptidepurification was performed using a semipreparative (10 μm) C_{18} RP-HPLC column from Vydac (Hesperia, CA). Preparative HPLC was performed using a computer-interfaced HPLC and fraction collector from ISCO (Lincoln, NE). Electrospray ionization mass spectrometry (ESI-MS) was performed using an Agilent 1100 Ion Trap LC-MS system.

* To whom correspondence should be addressed. Tel: 1-319-335-9903; fax: 1-319-335-8766; e-mail: Kevin-rice@uiowa.edu.

10.1021/bc060028l CCC: $33.50 © 2006 American Chemical Society
Published on Web 06/16/2006

Synthesis and Characterization of Melittin Analogues. Melittin and its analogues were synthesized using standard Fmoc procedures with 9-hydroxybenzotriazole and diisopropylcarbodiimide double couplings on a 30 μmol scale. Peptides were cleaved from the resin, and side chain protecting groups were removed by reaction with TFA/ethane dithiol/water (95:2.5:2.5 v/v/v) for 3 h. Cleaved peptides were precipitated with cold ether. The precipitate was washed twice with cold ether and dissolved in 0.1% TFA for purification. Peptides were purified to homogeneity on RP-HPLC by injecting 2 μmol onto a Vydac C_{18} semipreparative column (2 × 25 cm) eluted at 10 mL/min with 0.1 v/v % TFA and a gradient of acetonitrile of 20−55 v/v % over 30 min while monitoring tryptophan absorbance at 280 nm. The major peak was collected and pooled from multiple runs, concentrated by rotary evaporation, lyophilized, and stored dry at −20 °C. Purified peptides were reconstituted in 0.1 v/v % TFA (degassed with argon) and quantified by tryptophan absorbance ($\epsilon_{280} = 5600\ M^{-1}\ cm^{-1}$) to determine the isolated yield, which was typically 10−25%.

Purified peptides were characterized by LC-MS by injecting 1 nmol onto a Vydac C_{18} analytical column (0.47 × 25 cm) eluted at 0.7 mL/min with 0.1 v/v % TFA and an acetonitrile gradient of 5−65 v/v % over 30 min. The mass spectral data were obtained in the positive mode.

Circular Dichroism (CD) Spectrometry Melittin Analogues. CD spectra were recorded on a JASCO-J-715 spectra polarimeter in 1 cm path length cells under nitrogen at 25 °C. The spectra were recorded between 200 and 240 nm at a peptide concentration of 10 μM in either 10 mM Na_2HPO_4 pH 7.4 or 40 v/v % TFE (trifluoroethanol) in 10 mM Na_2HPO_4 pH 7.4. The percentage of α-helix structure was calculated as follows: α-helix (%) = $([\theta]_{222} - [\theta]^0_{222})/[\theta]^{100}_{222}$, where $[\theta]_{222}$ is the experimentally observed absolute mean residue ellipticity at 222 nm. Values for $[\theta]^0_{222}$ and $[\theta]^{100}_{222}$, corresponding to 0 and 100% helix content at 222 nm, were estimated to be −2000 and −28 400 deg cm^2/dmol, respectively (*16*). The absolute mean residue ellipticity at 222 nm was calculated using the formula $[\theta]_{222} = 100\ (\theta)/(lcN)$, where (θ) is the observed ellipticity in degrees, l is the optical path length in centimeters, c is the molar concentration of the peptide, and N is the number of residues in the peptide.

RBC Hemolysis by Melittin Analogues. Whole blood samples were obtained from male ICR mice by heart puncture with heparinized 22G needles and collected in conical tubes containing 10 mL of 0.15 M PBS (pH 7.4) prewarmed to 37 °C. The erythrocytes were immediately separated from plasma by centrifugation at 2000 rpm for 2 min, washed three times with 10 mL of PBS, and then diluted to 1.5 × 10^8 cells/mL.

Peptide stock solutions of 15 μM were prepared and serially diluted in a total volume of 100 μL in a MultiScreenHTS BV 96 well plate. Erythrocytes (50 μL, 7.5 × 10^6 cells) were added to the peptide and incubated at 37 °C for 1 h followed by filtration on a Multiscreen vacuum manifold (Millipore Corporation, Billerica, MA). The filtrate was measured for Abs_{415nm} on a plate reader, and the percent hemolysis was calculated relative to complete hemolysis caused by replacing PBS with water. Peptide DNA condensates (5 μg of DNA, 1 nmol of peptide in 100 μL of PBS) were also assayed for hemolysis as described previously.

Formulation of Melittin DNA Condensates. Peptide DNA condensates were prepared by combining 50 μg of DNA in 500 μL of Hepes-buffered mannitol (HBM) (0.27 M mannitol, 5 mM Hepes, pH 7.5) with 5−75 nmol of peptide in 500 μL of HBM while vortexing to create DNA condensates possessing a calculated charge ratio (NH_4^+/PO_{4-}) ranging from 0.1 to 2.4. Peptide DNA condensates were incubated for 1 h at room temperature to allow peptide polymerization.

The particle size of each peptide DNA condensate was determined by quasi-elastic light scattering at a scatter angle of 90° on a Brookhaven ZetaPlus particle sizer. Condensates were analyzed at a DNA concentration of 50 μg/mL in HBM at a stoichiometry of 0.3−0.8 nmol of peptide/μg of DNA corresponding to a charge ratio of approximately 1.5:1 for each. The mean diameter was computed from the diffusion coefficient using a unimodal cumulate analysis supplied by the manufacturer.

Stability of Poly-Melittin DNA Condensates. DNA condensates (50 μL of 50 μg/mL) were formed at 0.9 nmol peptide per μg of pCMVL and incubated at RT for 30 min and then combined with 0−50 μL of 4 M sodium chloride and normalized to 100 μL with HBM to achieve a final sodium chloride concentration of 0, 0.2, 0.4, 0.8, 1.0, and 2.0 M. Each sample was sonicated for 30 s with a 100 W Microson XL-2000 ultrasonic probe homogenizer (Kontes, Vineland, NJ) with a vibrational amplitude of 6 to fragment uncondensed DNA (*23*). DNA condensates were digested with 2.5 μg of proteinase K for 18 h at 37 °C and then electrophoresed on a 1% agarose gel and visualized by ethidium bromide staining.

In Vitro Gene Transfer Using Poly-Melittin DNA Condensates. HepG2 cells (5 × 10^5) were plated on 6 × 35 mm wells and grown to ca. 50% confluency. Transfections were performed in MEM (2 mL/35 mm well) supplemented with 2% FBS, sodium pyruvate (1 mM), and penicillin/streptomycin (100 U and 100 μg/mL). Melittin analogues were combined with pCMVL in HBM to form condensates at a 1.5:1 (N:P) charge ratio. Peptide−DNA condensates (10 μg of DNA in 0.2 mL of HBM) were added dropwise to wells in triplicate. After 6 h incubation at 37 °C, the transfection media were replaced with 10% FBS supplemented culture media.

After 24 h, cells were washed twice with 2 mL of ice-cold phosphate-buffered saline (Ca^{2+}- and Mg^{2+}-free) and then treated with 0.5 mL of lysis buffer (25 mM Tris chloride, pH 7.8, 1 mM EDTA, 8 mM magnesium chloride, 1% Triton X-100) for 10 min at 4 °C. The cell lysates were scraped, transferred to 1.5 mL microcentrifuge tubes, and centrifuged for 7 min at 13 000*g* at 4 °C to pellet cell debris. Luciferase relative light units were measured by a Lumat LB 9501 (Berthold Systems, Germany) with 10 s integration after automatic injection of 100 μL of 0.5 mM D-luciferin. The relative light units were converted to fmol using a standard curve generated by adding a known amount of luciferase to 35 mm wells containing 50% confluent HepG2 cells. The resulting standard curve had an average slope of 8.4 × 10^4 relative light units/fmol of enzyme. Protein concentrations were measured by a BCA assay using bovine serum albumin as a standard (*24*). The amount of luciferase recovered in each sample was normalized to milligrams of protein and reported as the mean and standard deviation obtained from triplicate transfections.

PEI pCMVL complexes were prepared by mixing 50 μg of DNA in 500 μL of HBM with 60 μg of PEI in 500 μL of HBM while vortexing to create DNA complexes possessing a charge ratio (NH_4^+/PO_4^-) of 9:1. HepG2 cells were transfected with 10 μg of PEI-DNA condensates as described previously. COS-7 and CHO cells (1 × 10^5) were plated on 6 × 35 mm wells and grown to ca. 50% confluency and then transfected as described previously.

The toxicity of melittin analogues was evaluated by MTT assay (*25*). Briefly, HepG2, COS-7, and CHO cells were plated on 6 × 35 mm wells at 3 × 10^5 cells/well and grown to 40−70% confluency. The culture media were replaced with 2 mL of fresh MEM supplemented with 2% FBS and 3 μM melittin analogues. After 6 h of incubation, the media was replaced with fresh culture media and grown for an additional 18 h. The media was replaced with 2 mL of fresh media and 500 μL of 0.5%

Table 1. Structure and Properties of Melittin Analogues and DNA Condensates

	Amino Acid Sequence of Synthetic Melittin Analogues	Mass[a]	HL_{50} (μM)[b] pH 7.4 : 4.5	NaCl[c] (M)	Particle Size[d] (μm)	Zeta Potential[e] (+ mV)
M0	GIGA VLKV LTTG LPAL ISWI KRKR QQ	2847.5 / 2850.0	1.5 : 6	0.1	>1	5.8
M1	C IGA VLKV LTTG LPAL ISWI KRKR QQ C	2996.7 / 2998.8	3.0 : 1.5	0.4	>1	5.0
M2	CK IGA VLKV LTTG LPAL ISWI KRKR QQ C	3124.9 / 3126.9	3.5 : >10	0.4	>1	5.0
M3	CKK IGA VLKV LTTG LPAL ISWI KRKR QQ C	3253.0 / 3255.4	5.0 : >10	0.4	>1	5.0
M4	CKKK IGA VLKV LTTG LPAL ISWI KRKR QQ C	3381.2 / 3383.7	7.5 : >10	0.4	>1	5.0
M5	CKKKK IGA VLKV LTTG LPAL ISWI KRKR QQ C	3509.4 / 3509.7	7.5 : >10	0.4	>1	5.5
M6	CKK IGA VLKV LTTG LPAL ISWI KRKR QQ KKC	3509.4 / 3509.7	2.5 : >10	0.4	>1	17.2
M7	CKKK IGA VLKV LTTG LPAL ISWI KRKR QQ KKKC	3765.3 / 3765.9	2.5 : >10	0.4	>1	22.3
M8	CKKKK IGA VLKV LTTG LPAL ISWI KRKR QQ KKKKC	4022.1 / 4022.4	2.5 : >10	0.8	0.326	32.0
M9	CKKKK A VLKV LTTG LPAL ISWI KRKR QQ KKKKC	3851.9 / 3852.3	2.5 : >10	0.8	0.233	24.2
M10	CKKKK LKV LTTG LPAL ISWI KRKR QQ KKKKC	3681.7 / 3682.3	5.0 : >10	0.8	0.341	22.4
M11	CKKKK V LTTG LPAL ISWI KRKR QQ KKKKC	3440.3 / 3440.9	>10: >10	0.8	0.275	27.6
M12	CKKKK TTG LPAL ISWI KRKR QQ KKKKC	3228.0 / 3228.3	>10: >10	0.8	0.229	32.2
M13	CKKKK G LPAL ISWI KRKR QQ KKKKC	3025.8 / 3026.0	>10: >10	0.8	0.206	20.5
M14	CKKKK IGA VLKV LTTG LPAL ISWI KKKKC	3197.1 / 3198.4	8: >10	0.8	0.253	29.6
M15	CKKKK IGA VLKV LTTG LPAL ISW KKKKC	3083.9 / 3086.4	>10: >10	0.8	0.332	12.9
M16	CKKKK IGA VLKV LTTG LPAL W KKKKC	2883.7 / 2885.7	>10: >10	0.8	0.145	15.4
M17	CKKKK IGA VLKV LTTG LP W KKKKC	2699.5 / 2700.4	>10: >10	0.4	0.252	5.9
M18	CKKKK IGA VLKV LTTG W KKKKC	2489.2 / 2490.6	>10: >10	0.4	0.159	6.5

[a] Calculated and observed mass. [b] RBC hemolytic activity at pH 7.4 and 4.5. [c] Salt concentration above which the peptide dissociates from DNA determined by gel electrophoresis as illustrated in Figure 2. [d] Mean particle size of peptide DNA condensates as determined by QELS. [e] Mean zeta potential determined in 5 mM Hepes, pH 7.4.

(w/v) 3-(4,5-dimethylthiazole-2-yl)-2,5-diphenyl tetrazolium bromide (MTT) in PBS solution and then incubated for 2 h to let formazan crystals form. The crystals were dissolved by adding 2 mL of dimethyl sulfoxide (DMSO) and then measured spectrophotometrically at 595 nm on a microplate reader (Bio-Rad, Bethesda, MD). The percent viability was determined relative to untreated cells.

RESULTS

Melittin is a well-characterized α-helical membrane disrupting peptide derived from bee venom. Its utility in enhancing PEI mediated gene transfer has been previously established (*3*, *19*). To investigate its potential utility for gene transfer, the hemolytic activity of melittin has been transiently masked by reversible N-acetylation (*18*). On the basis of these results, we proposed the transient masking of melittin's hemolytic activity by controlling its reversible binding to plasmid DNA. This would potentially mask the hemolytic activity of melittin until released intracellularly following disulfide bond reduction.

Natural melittin possesses six positively charged amino groups that are insufficient to mediate strong binding to DNA to form stable condensates. Therefore, we prepared a series of melittin analogues supplemented with additional Lys residues to endow it with the ability to bind and condense plasmid DNA. To facilitate DNA binding, one to four Lys residues were added to the N-terminus or C-terminus of melittin (Table 1). In addition, each melittin analogue was equipped with N- and C-terminal Cys residues to encourage melittin disulfide polymerization on DNA. We anticipated that polymeric melittin should possess a higher DNA binding affinity due to the larger number of amines per molecule.

The hemolytic activity of melittin analogues was evaluated using mouse blood cells as a primary screen. Dose−response curves revealed that natural melittin (M0) possessed an HL_{50} (hemolytic activity of 50%) of approximately 1.5 μM at pH 7.4 (Figure 1), whereas M0 was 4-fold less active at pH 4.5. Importantly, the combination of M0 and DNA resulted in hemolytic activity at pH 7.4 that was indistinguishable from M0 alone (Figure 1), suggesting that M0 failed to bind to DNA.

Comparison of the results of M0 with a melittin peptide endowed with C- and N-terminal Cys residues (M1) established an $HL_{50} = 3$ μM at pH 7.4 and 1 μM at pH 4.5. In contrast to M0, there was nearly a complete loss of hemolytic activity in the presence of DNA up to 5 μM peptide, followed by a recovery of activity at higher concentrations of peptide (Figure 1). This result suggested that M1 was able to weakly bind and polymerize on DNA, resulting in its lack of hemolytic activity below 5 μM.

To enhance the ability of melittin to bind DNA, analogues were prepared by adding additional Lys residues to the N-terminal side of the peptide, considering that the endogenous KRKR sequence in melittin would likely be sufficient to promote DNA binding near the C-terminal and encourage disulfide bond formation with a neighboring peptide. The addition of one to four N-terminal Lys residues (Table 1, M2−M5) resulted in up to a 5-fold decrease in hemolytic activity relative to M0 but simultaneously afforded increased DNA binding affinity as determined by gel electrophoresis as described next.

Melittin analogues were also prepared with two to four Lys residues added to both the N- and the C-subterminal end of melittin, along with terminal Cys residues. Comparison of the hemolytic activity for melittin analogues possessing two, three, or four N- and C-subterminal Lys residues (M6, M7, and M8) established that each was slightly less potent than M0 (Table 1).

Comparison of the hemolytic activity of peptides M0−M8 at pH 4.5 revealed that only M0 and M1 possessed significant activity at low pH, whereas M2−M8 were inactive. Interestingly, M1, which possessed terminal Cys residues, was more potent in hemolysis at pH 4.5 as compared to native melittin (M0) (Table 1).

The hemolytic activity of M2−M8 at pH 7.4 was masked when the peptides were combined with DNA as illustrated for M6 (Figure 1). This result can be rationalized by considering the binding properties of M0−M8 with DNA using a gel based assay as illustrated in Figure 2 (*20*, *21*). Agarose gel electrophoresis revealed peptide protection of the DNA from sonication until a critical salt concentration, at which the peptide dissociates and DNA is fragmented. The results established that M0 dissociates from DNA between 0 and 0.2 M sodium chloride (Figure 2A, lane 2), whereas M6 binds and polymerizes on DNA, resulting in condensates that are stable up to 0.4 M sodium chloride (Figure 2B, lane 6). A similar result was

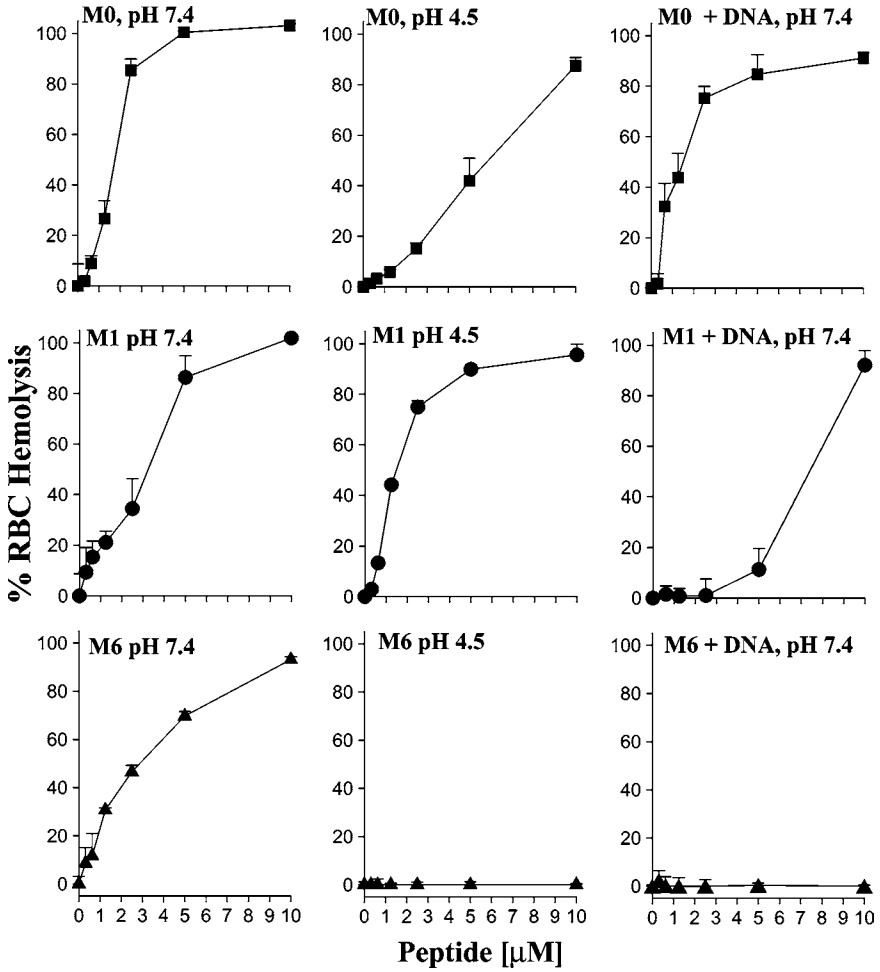

Figure 1. Hemolysis activity of melittin analogues and melittin DNA condensates. The RBC hemolytic activity of melittin (M0) and melittin analogues (M1 and M6) are compared at pH 7.4 and 4.5 and when bound to DNA at pH 7.4. The results illustrated in the left panels indicate that M0 is able to lyse RBCs with HL_{50} of 1.5 μM at pH 7.4, as compared to M1 and M6 with HL_{50} of 3.0 and 2.5 μM. At pH 4.5 (middle panels), M0 is less potent (HL_{50} of 6 μM), whereas M1 has an HL_{50} of 1 μM and M6 is inactive. When combined with plasmid DNA at pH 7.4 (right panels), M0 retains its hemolytic activity, M1 is reduced to HL_{50} of 8 μM, and M6 is completely inactivated.

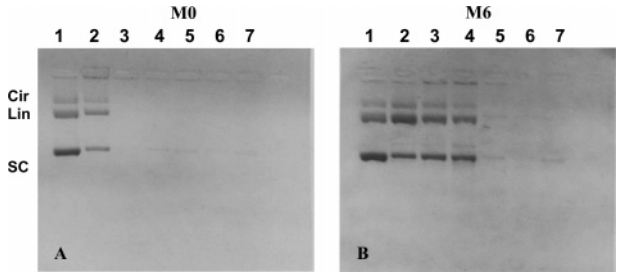

Figure 2. Stability of melittin DNA condensates. The stability of melittin DNA condensates was analyzed by gel electrophoresis following 30 s sonication in the presence of increasing concentrations of sodium chloride. Lanes 1−7 represent DNA standard (1) and peptide−DNA in 0 (2), 0.2 (3), 0.4 (4), 0.8 (5), 1.0 (6), and 2.0 M (7) sodium chloride, respectively. In panel A, M0 was only able to protect DNA during sonication at 0 M sodium chloride (lane 2) but not at 0.2 M (lane 3), whereas in panel B, M6 was able to polymerize on DNA and stabilized condensates up to 0.4 M sodium chloride (lane 4).

observed for peptides M2−M8, all of which demonstrated the ability to bind and polymerize on DNA and thereby protect it from sonication in 0.4 M sodium chloride or higher (Table 1). These data establish that melittin analogues with four or more additional Lys and terminal Cys residues bind and polymerize on DNA, thereby masking their hemolytic activity.

A second series of shorter melittin analogues was prepared in an attempt to truncate either the C- or the N-terminal α-helix while retaining hemolytic activity. To evaluate which of the two α-helices was most active, analogues were prepared that eliminated either two, four, six, eight, or 10 amino acids from the N-terminal α-helix of M8. The hemolytic potency of M9 and M10 established that most of the activity could be retained after deletion of four residues but that further deletion of six, eight, or 10 N-terminal melittin residues (M 11, M12, and M13) abolished hemolytic activity (Table 1).

A melittin analogue (M14) possessing a full-length N-terminal α-helix sequence with a deletion of six amino acids from the C-terminal α-helix retained modest hemolytic activity (Table 1). However, deletion of seven, eight, nine, or 10 amino acids from the C-terminal α-helix (M15, M16, M17, and M18) resulted in complete loss of hemolytic activity (Table 1). In addition, the hemolytic activity of melittin analogues was not influenced by the addition of 1 mM DTT, suggesting that the monomeric peptides were the primary form active in hemolysis.

The conformation of melittin peptides was examined by CD spectroscopy acquired in 10 mM sodium phosphate, pH 7.4, containing 40% TFE in an attempt to mimic a membrane environment (*16*). Representative hemolytic peptides M0, M6, and M14 each produced coincident CD spectra calculated to be 80% α-helical (Figure 3). In contrast, M11, which was devoid of hemolytic activity, produced a CD spectrum consistent with a random coil (Figure 3). These results are representative of the data obtained in each of the peptides in the series.

The particle size of each poly-melittin DNA condensate was evaluated using quasi-elastic light scattering at a constant charge

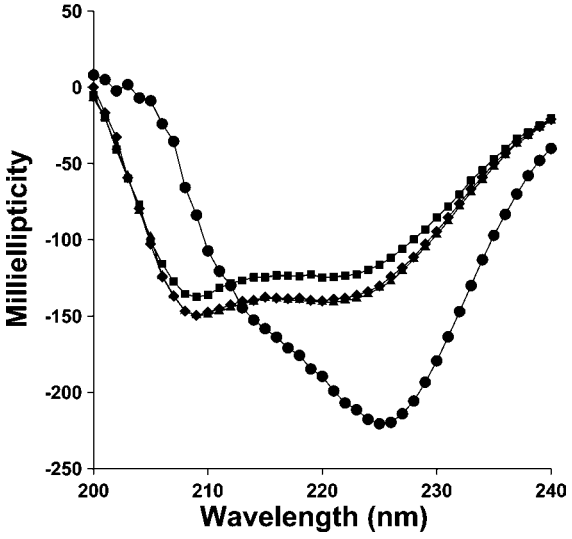

Figure 3. Circular dichroism of melittin analogues. The CD spectra of M0 (▲), M6 (◆), M11 (●), and M14 (■) acquired in 40% trifluoroethanol (v/v) in 10 mM pH 7.4 phosphate buffer at 25 °C are compared. The results establish that M11 was unable to form an α-helix, thereby accounting for its lack of hemolytic activity and gene transfer efficiency.

ratio of 1.5:1 (N:P). M0−M7 formed large DNA condensates >1 μm in mean diameter (Table 1). Alternatively, M8−M18 condensed DNA to form smaller condensates of a mean diameter of approximately 200−300 nm.

Poly-melittin DNA condensates were evaluated for their in vitro transfection activity in HepG2, COS-7, and CHO cells using PEI and $CWK_{17}C$ (*20*) to bracket the level of gene expression with (PEI) and without ($CWK_{17}C$) endosomal escape. In all three cell lines, M0 DNA failed to produce measurable luciferase expression, which was due to its cellular toxicity as demonstrated by MTT assay. In contrast, M1 mediated equivalent gene expression as $CWK_{17}C$ in CHO and COS 7 and was 10-fold more efficient in mediating gene expression in HepG2 (Figure 4). The cellular toxicity of M0 DNA (<20% cell viability) by MTT assay, in comparison to that determined for M1−M18 DNA (>70% cell viability), supports the hypothesis that DNA binding transiently masks the membrane lytic activity of melittin analogues.

Comparison of the relative luciferase gene expression mediated by M1−M8 in all three cell lines established a general trend in which melittin analogues were either equivalent or 10-fold more potent than $CWK_{17}C$. Within the series, M3 and M6 demonstrated the most potent activity in HepG2 cells, which was equivalent to the gene transfer mediated by PEI (Figure 4).

Comparison of the gene transfer efficiency of M1−M8 with deletion peptides M9−M13 established a loss of activity for M9−M13 in all three cell lines that was coincident with the loss of hemolytic potency (Figure 4). The partial recovery of gene transfer activity for M14 was coincident with its ability to produce hemolysis (Figure 4 and Table 1). Likewise, the decreased gene transfer activity for deletion peptides M15−M18 was coincident with the lack of hemolytic activity for these truncated melittin peptides (Figure 4 and Table 1).

DISCUSSION

One of the rate-limiting steps in gene delivery is the efficient escape of DNA from targeting lysosomes. To facilitate this process, fusogenic peptides have been incorporated into gene delivery carriers in an attempt to mimic the process used by viruses. A recent example emphasizes an important directionality

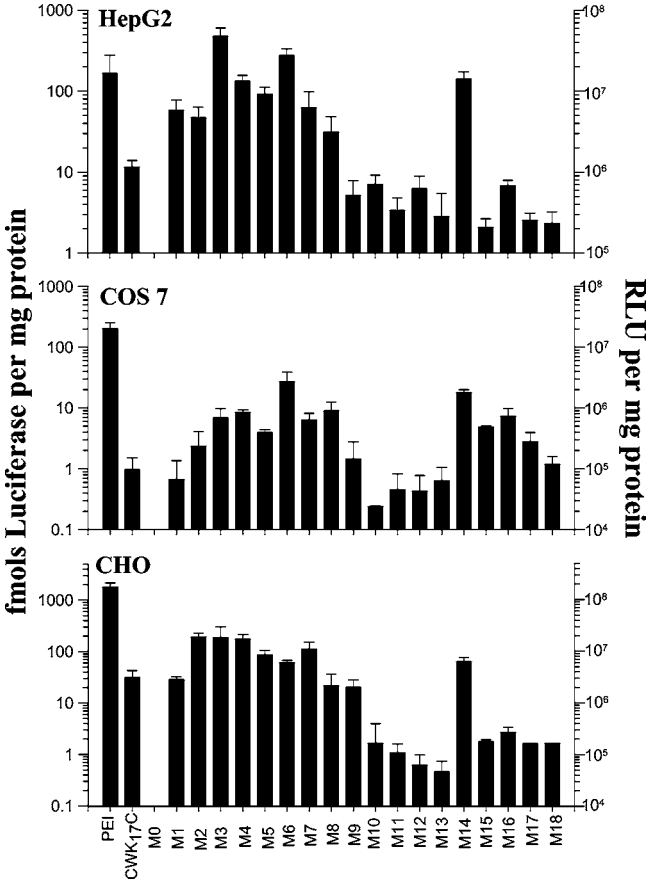

Figure 4. In vitro gene transfer of melittin analogue DNA condensates. Transfections were performed with a peptide DNA charge ratio of 1.5:1. The luciferase reporter gene expression was measured in HepG2 (A), COS-7 (B), and CHO (C) cells at 24 h. PEI and $CWK_{17}C$ mediated gene delivery were used as positive controls. The results represent the mean and standard deviation for three independent transfections.

in linking melittin into a gene delivery system. In this study, it was found that linking melittin to PEI through its C-terminus improves its activity relative to linking through the N-terminus (*19*).

In the present study, we attempted to evolve melittin into a sulfhydryl polymerized peptide, considering that its potent membrane lytic properties could potentially be transient while bound to DNA. We further considered that a sulfhydryl polymerized melittin analogue could potentially be adapted for in vivo use by incorporating it into a nonviral gene delivery system through copolymerization with Cys containing peptides (*26*). One potential difficulty in using melittin for this purpose would be its cytotoxicity, since unlike HA2, it is highly hemolytic at pH 7.

In order for a peptide to be active in nonviral gene delivery, it must bind and condense DNA, usually through cationic interactions. Although melittin has six cationic residues, we have previously shown that polycations of a minimum of 13−18 are usually necessary to fully condense DNA and mediate gene transfer in vitro (*27*). Fewer cationic groups result in DNA condensates that are large (>1 μm) and dissociate at physiological salt concentrations (0.15 M) (*23*). The results of the gel electrophoresis assay (Figure 3) demonstrate this effect for M0 binding to DNA to form large condensates that dissociate between 0 and 0.2 M sodium chloride. Dissociation at this salt concentration would release M0 from ionic binding to DNA and explains why M0 DNA results in red blood cell lysis (Figure 1). These results also explain the lack of gene transfer activity and the cytotoxicity observed by M0 DNA in three cell lines (Figure 4).

It was possible to decrease the cellular toxicity of M0 by the addition of C- and N-terminal Cys residues resulting in M1. This modification leads to the improved salt stability of M1 DNA condensates (Table 1), indicating that the peptide is able to polymerize on DNA. Polymeric M1 displays weaker hemolysis activity when bound to DNA and an increase in gene transfer potency. The further addition of one to four Lys residues on the N-terminal side of melittin (M2−M5) or two to three Lys residues on both the C- and the N-terminal (M6 and M7) did not increase polymerization as measured by gel electrophoresis (Table 1). DNA condensates prepared with M1−M7 were large (>1 μm) and possessed a relatively low zeta potential (+5 mV). The large particle size was most likely the result of particle coalescences initiated through interaction of hydrophobic domains on melittin peptides. Nonetheless, M1−M7 possessed significant hemolytic activity, and M3 proved to be one of the most potent gene transfer peptides in the series. The addition of four Lys residues to the C- and N-subterminal to form M8 led to a more complete polymerization on DNA as revealed by dissociation above 0.8 M sodium chloride (Table 1). Despite a decrease in particle size for M8 DNA to approximately 0.3 μm (Table 1), the gene transfer efficiency was not increased (Figure 4).

Attempts to truncate a portion of either the N- or the C-terminal α-helix revealed a relationship between hemolytic activity and gene transfer activity. Only M14, in which KRKR QQ was deleted and replaced with a tetra Lys and terminal Cys, was able to mediate gene transfer activity comparable to full-length melittin analogues. This was likely because the QQ was unnecessary, and the KRKR substituted for KKKK.

The results of this study demonstrate the conversion of a hemolytic peptide into a DNA condensing peptide. We hypothesize that melittin analogues function by depolymerizing in the reducing environment inside the cell, resulting in the release of DNA. The neutralization of hemolytic activity when melittin analogues bind and polymerize on DNA appears to protect cells from cytotoxicity and facilitate gene transfer. This strategy should be useful to evolve many different fusogenic peptides into sulfhydryl polymerized peptides to positively influence nonviral gene delivery.

ACKNOWLEDGMENT

The authors gratefully acknowledge support for this paper from NIDDK 063196.

LITERATURE CITED

(1) Plank, C., Oberhauser, B., Mechtler, K., Koch, C., and Wagner, E. (1994) The Influence of Endosome-disruptive Peptides on Gene Transfer Using Synthetics. *J. Biol. Chem. 269*, 12918−12924.

(2) Van Dyke, R. W. (1996) Acidification of lysosomes and endosomes. *Subcell. Biochem. 27*, 331−360.

(3) Ogris, M., Carlisle, R. C., Bettinger, T., and Seymour, L. W. (2001) Melittin Enables Efficient Vesicular Escape and Enhanced Nuclear Access of Nonviral Gene Delivery Vectors. *J. Biol. Chem. 276*, 47550−47555.

(4) Wagner, E., Plank, C., Zatloukal, K., Cotten, M., and Birnstiel, M. L. (1992) Influenza virus hemagglutinin HA-2 N-terminal fusogenic peptides augment gene transfer by transferring polylysine−DNA complexes: Toward a synthetic virus-like gene transfer vehicle. *Proc. Natl. Acad. Sci. U.S.A. 89*, 7934−7938.

(5) Legendre, J. Y., Bohrmann, T. B., Deuschle, U., Kitas, E., and Supersaxo, A. (1997) Dioleoymelittin as a Novel Serum-Insensitive Reagent for Efficient Transfections of Mammalian Cells. *Bioconjugate Chem. 8*, 57−63.

(6) Li, W., Nicol, F., and Szoka, F. C., Jr. (2004) GALA: a designed synthetic pH-responsive amphipathic peptide with applications in drug and gene delivery. *Adv. Drug Delivery Rev. 56*, 967−985.

(7) Balicki, D., Putnam, C. D., Scaria, P. V., and Beutler, E. (2002) Structure and function correlation in histone H2A peptide mediated gene transfer. *Proc. Natl. Acad. Sci. U.S.A. 99*, 7467−7471.

(8) Midoux, P., and Monsigny, M. (1999) Efficient gene transfer by histidylated polylysine/pDNA complexes. *Bioconjate Chem. 10*, 406−411.

(9) Wolfert, M. A., and Seymour, L. W. (1998) Chloroquine and amphipathic peptide helices show synergistic transfection in vitro. *Gene Ther. 5*, 409−414.

(10) Godbey, W. T., Wu, K. K., and Mikos, A. G. (1999) Poly-(ethylenimine) and its role in gene delivery. *J. Controlled Release 60*, 149−160.

(11) Goto, Y., and Hagihara, Y. (1992) Mechanism of the conformational transition of melittin. *Biochemistry 31*, 732−738.

(12) Subbalakshmi, C., Nagaraj, R., and Sitaram, N. (1999) Biological activities of a C-terminal 15-residue synthetic fragment of melittin: design of an analogue with improved antibacterial activity. *FEBS Lett. 448*, 62−66.

(13) Terwilliger, T. C., and Eisenberg, D. (1982) The structure of melittin. II. Interpretation of the structure. *J. Biol. Chem. 257*, 6016−6022.

(14) Blondelle, S. E., and Houghten, R. A. (1991) Hemolytic and Antimicrobial Activities of the Twenty-Four Individual Omission Analogues of Melittin. *Biochemistry 30*, 4671−4678.

(15) Juvvadi, P., Vunnam, S., and Merrifield, R. B. (1996) Synthetic Melittin, Its Enantio, Retro, and Retroenantio Isomers, and Selected Chimeric Analogues: Their Antibacterial, Hemolytic, and Lipid Bilayer Action. *J. Am. Chem. Soc. 118*, 8989−8997.

(16) Yan, H., Li, S., Sun, X., Mi, H., and He, B. (2003) Individual substitution analogues of Mel(12−26), melittin's C-terminal 15-residue peptide: their antimicrobial and hemolytic actions. *FEBS Lett. 554*, 100−104.

(17) Takei, J., Remenyi, A., Clarke, A. R., and Dempsey, C. E. (1998) Self-association of disulfide-dimerized melittin analogues. *Biochemistry 37*, 5699−5708.

(18) Rozema, D. B., Ekena, K., Lewis, D. L., Loomis, A. G., and Wolff, J. A. (2003) Endosomolysis by masking of a membrane-active agent (EMMA) for cytoplasmic release of macromolecules. *Bioconjugate Chem. 14*, 51−57.

(19) Boeckel, S., Wagner, E., and Ogris, M. (2005) C- versus N-terminally Linked Melittin−Polyethylenimine Conjugates: The Site of Linkage Strongly Influences Activity of DNA Polyplexes. *J. Gene Med. 7*, 1335−1347.

(20) McKenzie, D. L., Kwok, K. Y., and Rice, K. G. (2000) A potent new class of reductively activated peptide gene delivery agents. *J. Biol. Chem. 275*, 9970−9977.

(21) McKenzie, D., Smiley, B., Kwok, K. Y., and Rice, K. G. (2000) Low molecular weight disulfide cross-linking peptides as nonviral gene delivery carriers. *Bioconjugate Chem. 11*, 901−911.

(22) Oupicky, D., Carlisle, R. C., and Seymour, L. W. (2001) Triggered intracellular activation of disulfide cross-linked polyelectrolyte gene delivery complexes with extended systemic circulation in vivo. *Gene Ther. 8*, 713−724.

(23) Adami, R. C., and Rice, K. G. (1999) Metabolic stability of glutaraldehyde cross-linked peptide DNA condensates. *J. Pharm. Sci. 88*, 739−746.

(24) Smith, P. K., Krohn, R. I., Hermanson, G. T., Mallia, A. K., Gartner, F. H., Provenzano, M. D., Fujumoto, E. K., Goeke, N. M., Olson, B. J., and Klenk, D. C. (1985) Measurement of protein using bicinchoninic acid. *Anal. Biochem. 150*, 76−85.

(25) Mosmann, T. (1983) Rapid colorimetric assay for cellular growth and survival: application to proliferation and cytotoxicity assays. *J. Immunol. Methods 65*, 55−63.

(26) Kwok, K. Y., Park, Y., Yongsheng, Y., McKenzie, D. L., and Rice, K. G. (2003) In Vivo Gene Transfer using Sulfhydryl Cross-linked PEG-peptide/Glycopeptide DNA Co-Condensates. *J. Pharm. Sci. 92*, 1174−1185.

(27) Wadhwa, M. S., Collard, W. T., Adami, R. C., McKenzie, D. L., and Rice, K. G. (1997) Peptide mediated gene delivery: influence of peptide structure on gene expression. *Bioconjugate Chem. 8*, 81−88.

BC060028L

A Mixed-Phase Immunoassay Based on Simultaneous Binding of Fluorescently Tagged and PNA-Conjugated Peptide Epitopes on Antibodies: Quantification on PNA-Coated Microparticles

Kaisa Ketomäki* and Harri Lönnberg

Department of Chemistry, University of Turku, FIN-20014 Turku, Finland. Received February 7, 2006; Revised Manuscript Received June 9, 2006

A mixed-phase immunoassay based on simultaneous binding of an antibody to its fluorescently tagged peptide epitope and a PNA conjugate of the same peptide has been developed. As a fluorescent marker, a europium(III) chelate allowing time-resolved measurement from a single particle has been employed. The ternary complex formed in solution is immobilized by Watson−Crick base-pairing to a microparticle bearing a PNA sequence complementary to that present in the complex. The concentration of the antibody in the sample may then be determined by a single particle measurement. Accordingly, different antibodies may in principle be addressed by sequence-specific hybridization to different categorized microparticles.

INTRODUCTION

High density peptide microarrays have received increasing interest as a highly potent analytical construct for high-throughput screening of peptide−protein interactions (*1*−*4*). Such arrays, obtained by parallel light-directed assembly of peptide chains on a glass surface (*4*−*9*) or by covalent immobilization of prefabricated peptides to an appropriately activated support (*1*, *10*−*16*), have been applied to detection of antibodies from biological samples (*1*, *14*, *15*), epitope screening of antibodies (*8*), determination of enzyme activitities (*1*, *11*, *12*, *16*−*19*), and studies on adhesion of cells to peptides (*1*, *20*). While the efficiency of high density microarrays in high-throughput screening undoubtedly is unbeatable, their superiority in assays where accurate quantification of a limited number of antibodies plays a key role is not as self-evident. For the latter purpose, categorized microparticles as a solid phase and lanthanide chelates as photoluminescent labels offer a competitive alternative (*21*). The applicability of this methodology to both immunoassays (*22*−*24*) and oligonucleotide hybridization (*25*−*29*) has been previously established. Lanthanide chelates as markers allow application of a time-resolved mode in the measurement of the fluorescence emission, and hence the prompt background fluorescence may be effectively eliminated. Of even greater importance is that these markers do not suffer from concentration quenching, owing to large difference between the wavelength of excitation and emission. For this reason, the linear dynamic range of emission is over 6 orders of magnitude. On using a microfluorometer equipped with a microscope, the fluorescence emission can be measured from a single microparticle in a reproducible manner. This allows a multiplexed assay based on a suspension array of categorized microparticles (*30*). We now report on a novel assay format for quantification of antibodies, the principle of which is depicted in Scheme 1. Antibody **A** is allowed to form in solution a ternary complex **D** with its fluorescently tagged epitopic peptide **B** and a PNA-conjugate **C** of the same peptide. This ternary complex may then be immobilized by hybridization to a microparticle coated with a PNA[1] sequence complementary to that in conjugate **C** and the intensity of the fluorescence emission is determined by time-resolved fluorometry. A related approach has previously been applied to conversion of an oligonucleotide microarray to spatially addressable arrays of small molecules and used for functional proteomic profiling (*31*). The advantage of the assay described in Scheme 1 is that covalent labeling of the antibodies is avoided. In case a large number of samples are analyzed, the same prefabricated peptide conjugates may be used for quantification of each sample. The present study is aimed at demonstrating the feasibility of such an approach. Three cardiac antibodies, generally used for detection of peptides as markers for cardiac diseases, are now employed as analysts (**A**) and their epitopic peptides as fluorescently tagged (**B**) and PNA conjugates (**C**) for detection and capture probes, respectively.

Scheme 1

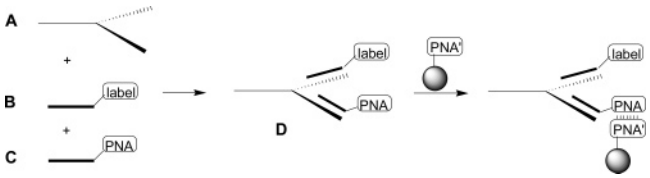

EXPERIMENTAL PROCEDURES

Peptide Synthesis. Peptides were assembled by the Fmoc/^{t}Bu chemistry on a Rink Amide Resin (Novabiochem) using a 431A peptide synthesizer (Applied Biosystems). For the C-terminal cysteine, *S*-trityl protection was used. All couplings

* To whom correspondence should be addressed. Tel: +358-2-3337-631. Fax: +358-2-3337-631. e-mail: kaisa.ketomaki@utu.fi.

[1] Abbreviations: Ac_2O, acetic anhydride; anti-cTnI, troponin I specific antibody; $BM[PEO]_3$, 1,8-bis(maleimido)triethylene glycol; DELFIA, Dissociation-Enhanced Lanthanide FluoroImmunoAssay; DIC, diisopropylcarbodiimide; DMF, dimethylformamide; ESI-TOF-MS, electronspray ionization time-of-flight mass spectrometry; TEAA, triethylammonium acetate; TFA, trifluoroacetic acid; Fmoc, 9-fluorenylmethoxycarbonyl; HOBt, 1-hydroxybenzotriazole; NaN_3, sodium azide; NMI, 1-methylimidazole; NMP, *N*-methylpyrrolidone; NT-proBNP, human N-terminal proBNP antibody; PNA, peptide nucleic acid; sulfo-SMCC, sulfosuccinimidyl 4-(*N*-maleimidomethyl)cyclohexane-1-carboxylate; Tris HCl, tris(hydroxymethyl)aminomethane hydrochloride.

10.1021/bc0600315 CCC: $33.50 © 2006 American Chemical Society
Published on Web 07/01/2006

Scheme 2

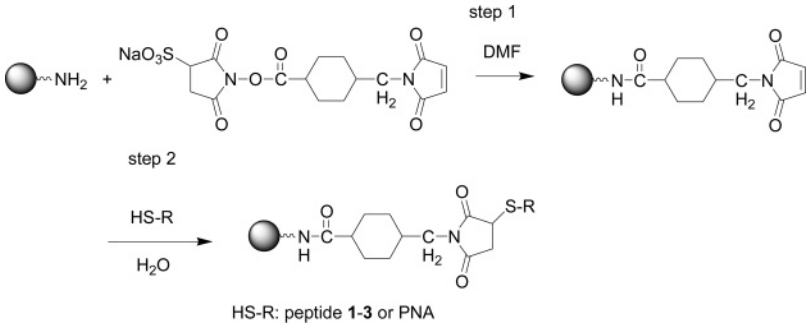

Table 1. Sequences, Observed and Calculated Average Molecular Masses, and HPLC Retention Times for the Peptides and Their Eu Chelates and PNA Conjugates Prepared

compound	observed[d]	calculated	difference, %	retention time/min[e]
KISASRKLQLKTC[a] (**1**)	1474.27	1474.83	0.03	16.3
GSPGSASDLEC[a] (**2**)	1020.94	1021.07	0.01	15.2
RGHRKMVLYTLC[a] (**3**)	1474.85	1476.83	0.13	20.3
KISASRKLQLKTC-⟨Eu⟩[b] (**4**)	2278.47	2278.95	0.02	24.0
GSPGSASDLEC-⟨Eu⟩[b] (**5**)	1824.41	1825.19	0.04	17.6
RGHRKMVLYTLC-⟨Eu⟩[b](**6**)	2278.66	2280.94	0.1	28.0
KISASRKLQLKTC−PNA[c] (**7**)	4613.91	4612.20	0.03	18.0
GSPGSASDLEC−PNA[c] (**8**)	4305.56	4304.10	0.03	16.0
RGHRKMVLYTLC−PNA[c] (**9**)	4760.57	4759.95	0.01	19.3
CTHQDIDFLIEEIERLGQDL (**10**)	2499.08	2499.66	0.02	21.9

[a] The sequences are given from the amino terminus (left) to the carboxamide terminus (right). [b] ⟨Eu⟩ stands for the photoluminescent europium(III) chelate attached to the mercapto group of the C-terminal cysteine residue. For the structure, see Scheme 4. [c] PNA stands for the sequence H-AGTGATCTAC-Cys-NH_2, given from the amino terminus (left) to the carboxamide terminus (right). For the structure, see Scheme 5. [d] By ESI-TOF mass spectrometry. [e] For **1**−**3** and **7**−**10**, buffer A: 0.1% TFA/H_2O, buffer B: 0.1% TFA/MeCN; linear gradient 0−70% B in 30 min; ThermoHypersil HyPURITY C-18 column (4.6 mm × 150 mm, 5 μm). For **4**−**6**: buffer A: 20 mmol L^{-1} TEAA; buffer B: 20 mmol L^{-1} TEAA + 65% MeCN; linear gradient 5−100% B in 30 min; ThermoHypersil C-18 column (4.6 mm × 250 mm, 5 μm).

were conducted by HOBt/DIC activation in NMP. The crude products were purified by RP HPLC on a ThermoHypersil HyPURITY C-18 column (4.6 mm × 150 mm, 5 μm). A linear gradient from 0.1% TFA in water to 0.1% TFA in 70% aq MeCN in 30 min was applied. The peptides were characterized by ESI-TOF mass spectrometry. Table 1 lists the sequences, observed and calculated molecular masses, and the HPLC retention times for the peptides (**1**−**3**, **10**) prepared.

Preparation of Peptide- and PNA-Coated Microparticles. The beads employed as a solid-phase in the mixed-phase assays were uniformly sized (59 μm) polymer particles of SINTEF (Norway). They were made of a copolymer of glycidyl methacrylate (40%) and ethylene dimethylacrylate (60%) and were functionalized with primary amino groups (1 mmol g^{-1}). The particles were modified for attachment of peptides or PNA probes by acylating the amino groups with sulfosuccinimidyl 4-(*N*-maleimidomethyl)cyclohexane-1-carboxylate (sulfo-SMCC; Pierce) (step 1 in Scheme 2). This was achieved by incubating the particles with a 5-fold molar excess of sulfo-SMCC in DMF at room-temperature overnight. After repeated washings, the unreacted amino functions were capped with Ac_2O in pyridine using NMI as a catalyst. Peptides **1**−**3** and **10** (20 nmol), containing an C-terminal Cys residue, were incubated with the maleimido-functionalized particles (2 mg) in water at room-temperature overnight (step 2 Scheme 2). After repeated washings, the unreacted maleimido groups were capped with hexanethiol in 1,4-dioxane (45 min) and the particles were washed. The PNA probe, H-GTAGATCACT-Cys-NH_2 (MedProbe, Norway), was immobilized similarly through the C-terminal cysteine residue.

Antibody Labeling. Monoclonal mouse anti-cardiac troponin I (anti-cTnI) clone 19C7, monoclonal mouse anti-NT-proBNP clone 29D12 and monoclonal mouse anti-NT-proBNP clone 15-C4 (products of HyTest, Finland) were labeled with {2,2′,2″,2‴-{[4′-(4‴-isothiocyanatophenyl)-2,2′:6,2″-terpyridine-6,6″-diyl]bis(methylenenitrilo)}tetrakis(acetato)}europium(III) (*32*) (Scheme 3). For this purpose, the antibody was incubated with

Scheme 3

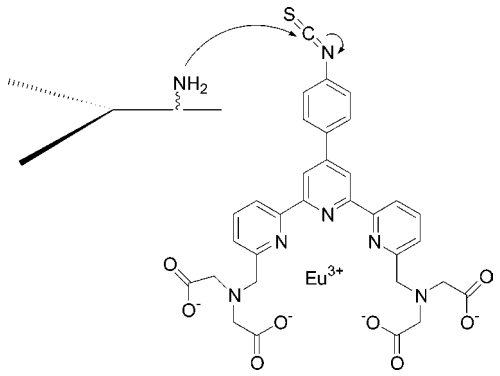

a 30-fold molar excess of the chelate in a 50 mmol L^{-1} HCO_3^-/CO_3^{2-}-buffer (pH 9.8) at room-temperature overnight (in dark). The labeled antibody was purified from the excess of the chelate by gel filtration on a Superdex75 column (Pharmacia Biotech). A Tris-HCl buffer (50 mmol L^{-1}, pH 7.5) containing NaCl (0.39 mol L^{-1}) and NaN_3 (7.7 mmol L^{-1}) was used as an eluent. The labeling degree of the antibody varied from 2.1 to 4.4 Eu^{3+} ions per antibody molecule, when assayed according to the DELFIA protocol (*33*) against a Eu^{3+} calibration solution.

Peptide Labeling. The antibody specific peptides (**1**−**3**) were labeled to the C-terminal Cys residue with {2,2′,2″,2‴-{[4′-(4‴-iodoacetamido)-2,2′:6,2″-terpyridine-6,6″-diyl]bis(methylenenitrilo)}tetrakis(acetato)}europium(III). The peptide was incubated with a 3.5-fold molar excess of the chelate in a 50 mmol L^{-1} HCO_3^-/CO_3^{2-}-buffer (pH 8.5) at room-temperature overnight in dark (Scheme 4). The crude product was purified on an RP HPLC ThermoHypersil C-18 column (4.6 mm × 250 mm) eluting with a TEAA buffer: buffer A 20 mmol L^{-1} aq TEAA, buffer B 20 mmol L^{-1} aq TEAA containing 65% MeCN (*v*/*v*), a linear gradient from 5% to 100% B in 30 min. The conjugates obtained (**4**−**6**) were characterized by ESI-TOF mass

Scheme 4

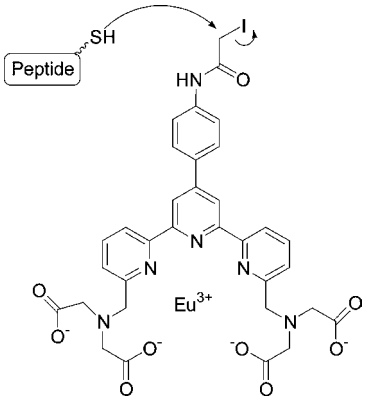

spectrometry. The observed and calculated molecular masses and the HPLC retention times are given in Table 1.

Preparation of Peptide−PNA Conjugates. A PNA probe complementary to that immobilized in particles, i.e. H-AGT-GATCTAC−Cys-NH_2 (MedProbe, Norway), was converted to a maleimido conjugate with 1,8-bis(maleimido)triethyleneglycol ($BM[PEO]_3$, Pierce) (Scheme 5). 15 nmol (40 μg) of PNA and 1.6 μmol (0.5 mg) of $BM[PEO]_3$ were incubated in 10 mmol L^{-1} phosphate-buffer (pH 6.7) at 37 °C for 2 h. The conjugate was purified on a RP HPLC ThermoHypersil HyPURITY C-18 column (4.6 mm × 150 mm, 5 μm) eluting with 0.1% TFA: buffer A 0.1% aq TFA, buffer B 0.1% TFA in MeCN, linear gradient from 0 to 70% B (*v*/*v*) in 30 min. The purified PNA−maleimido conjugate was incubated with the peptide (67 nmol; 0.1 mg) in 10 mmol L^{-1} phosphate buffer (pH 6.7) at 37 °C for 2 h. The PNA−peptide conjugate obtained was purified as described above for the PNA-maleimido conjugate. The identity of the conjugates (**7**−**9**) was verified by ESI-TOF mass spectrometry. The mass spectrometric and chromatographic data is given in Table 1.

Assays with Peptide-Coated Particles. Immunoassays with peptide-coated particles were carried out in Tris-HCl-buffer (50 mmol L^{-1}, pH 7.5) containing 0.5 mol L^{-1} NaCl and 0.01% Tween 20. Labeled antibody was shaken with 50 particles (Rotamix, 15 rpm) in 50 μL of the buffer room-temperature overnight and washed with a DELFIA-wash buffer (8 × 200 μL). A single particle was subjected to a time-resolved fluorescence measurement (*21*). The time-resolved channel was adjusted to count the emission over a time window of 300 μs after a delay of 600 μs from the beginning of the excitation pulse and 1000 excitations were integrated in one measurement. Each measurement was repeated with 10 particles to eliminate the influence of random variation. The measurements with a mixture of an unlabeled antibody and fluorescently labeled peptide (**4**−**6**) were carried out similarly.

Assays with Peptide−PNA Conjugates. Immunoassays with PNA−peptide conjugates (**7**−**9**) were carried out in Tris-HCl-buffer (10 mmol L^{-1}, pH 7.5) containing 0.01% Tween 20, the total volume being 10 μL. The PNA−peptide conjugate, unlabeled monoclonal antibody, and fluorescently labeled peptide (**4**−**6**) were shaken (Rotamix, 15 rpm) at room-temperature overnight. Fifty particles coated with a PNA probe complementary to the sequence of the PNA−peptide conjugate were added, and the shaking was continued overnight. The particles were washed with Tris-HCl-buffer (10 mmol L^{-1}, pH 7.5, 4 × 200 μL) and subjected to a single particle time-resolved fluorescence measurement described above.

RESULTS AND DISCUSSION

PNA− and Peptide-Coated Microparticles. To construct a mixed-phase assay setup depicted in Scheme 1, PNA-coated microparticles were prepared. Uniformly sized (59 μm) amino-functionalized (1 mmol g^{-1}) porous particles that were made of a copolymer of glycidyl methacrylate (40%) and ethylene dimethylacrylate (60%) and had an average pore size of 50 nm and a surface area of 92 m^2 g^{-1} were used for the purpose. The amino groups were acylated with sulfosuccinimidyl 4-(*N*-maleimidomethyl)cyclohexane-1-carboxylate, as depicted in Scheme 2, and the unreacted amino groups were carefully capped by acetylation. A mercapto-functionalized PNA bearing a C-terminal cysteine residue, H-GTAGATCACT-Cys-NH_2, was then immobilized to the particles by allowing the mercapto function to react with the support-bound maleimido groups. The remaining maleimido groups were capped with hexanethiol. Particles bearing antibody-specific peptides instead of PNA probes were prepared for comparative purposes. They were obtained as the PNA-coated particles using Cys-derivatized epitopic peptides (**1**−**3**).

Binding of Antibodies to Particle-Bound Peptides. To verify that peptides **1**−**3** exhibited sufficiently high affinity to the respective antibodies, viz. monoclonal mouse anti-cardiac troponin I clone 19C7, monoclonal mouse anti-NT-proBNP clone 29D12 and monoclonal mouse anti-NT-proBNP clone 15C4 (HyTest, Finland), the binding of photoluminescently labeled antibodies (Scheme 3) to the support-bound peptides was quantified. The peptide-coated particles were incubated with the labeled antibodies at different concentrations falling in the range 0.05−3 μg mL^{-1}, and the intensity of the fluorescence emission was measured directly from a single particle. Unspecific binding of anti-cardiac troponin I was determined with the aid of particles bearing a sequence H-CTHQDIDFLIEE-IERLGQDL-NH_2 (**10**). The specific signal was at least 100-fold compared to the unspecific one. The unspecific binding of anti-NT-proBNP clones 29D12 and 15C4, when determined with H−RGHRKMVLYTLC−NH_2 and H-GSPGSASDLEC−NH_2, respectively, was considerably higher, ≤10% of the specific signal. As seen from Figures 1−3, the fluorescence intensity measured from a single particle was with each peptide−antibody pair proportional to the concentration of the antibody in solution.

Binding of Peptide−Antibody Complexes to Particle-Bound Peptides. The next experiments were aimed at clarifying whether a complex of an unlabeled antibody and a labeled epitopic peptide could be captured by the same epitopic peptide covalently immobilized to a microparticle. In other words, could unlabeled antibodies be quantified by a mixed-phase assay by using their epitopic peptide both as a fluorescent label and as a catcher probe.

Scheme 5

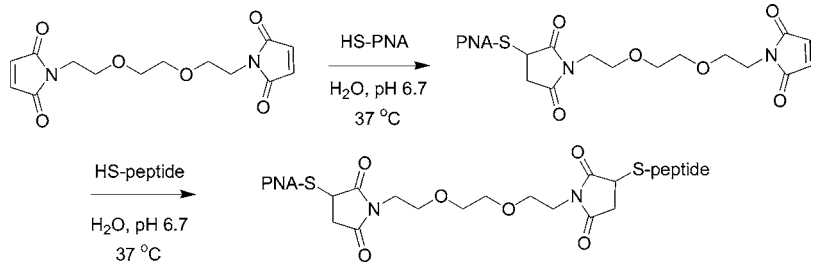

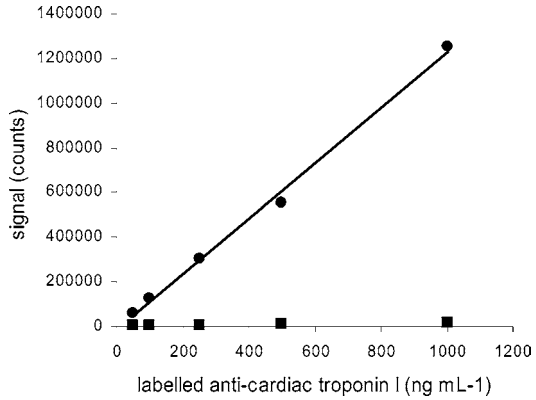

Figure 1. Binding of fluorescently labeled anti-cardiac troponin I antibody (clone 19C7) to microparticles coated with its epitopic peptide **1** (●): intensity of the fluorescence emission of a single particle plotted against the concentration of the antibody in solution ($R^2 = 0.996$). The loading of peptide **1** on particles was ≤ 2 μmol g^{-1}. Unspecific binding (■) was determined on particles coated with peptide **10**.

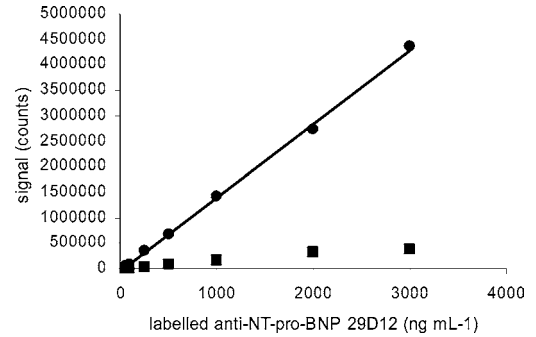

Figure 2. Binding of fluorescently labeled anti-NT-proBNP antibody (clone 29D12) to microparticles coated with its epitopic peptide **2** (●): intensity of the fluorescence emission of a single particle plotted against the concentration of the antibody in solution ($R^2 = 0.999$). The loading of peptide **2** on particles was ≤ 10 μmol g^{-1}. Unspecific binding (■) was determined on particles coated with peptide **3**.

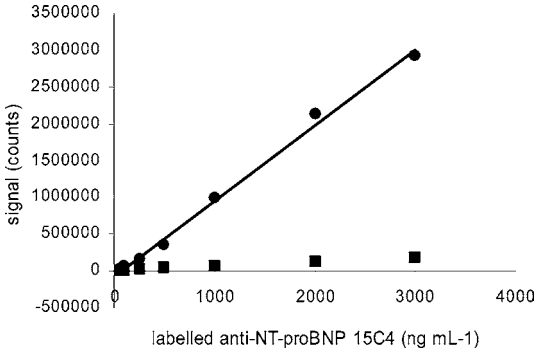

Figure 3. Binding of fluorescently labeled anti-NT-proBNP antibody (clone 15D4) to microparticles coated with its epitopic peptide **3** (●): intensity of the fluorescence emission of a single particle plotted against the concentration of the antibody in solution ($R^2 = 0.994$). The loading of peptide **3** on particles was ≤ 10 μmol g^{-1}. Unspecific binding (■) was determined on particles coated with peptide **2**.

The assay was first performed in two steps. Anti-cardiac troponin I antibody was first incubated (24 h) with the particles coated with peptide **1**. The particles were washed and then incubated (24 h) with the labeled peptide (**4**). When the concentration of the antibody was varied from 1 to 10 μg mL^{-1} and the concentration of labeled peptide was kept constant, the intensity of the fluorescence emission was proportional to the antibody concentration. Figure 4 shows the results obtained when the concentration of the labeled peptide was 22 nmol L^{-1}. The experiments were then repeated by adding all three components, viz. the antibody, labeled peptide and peptide-coated particles, at the same time and incubating them for 24 h. The results obtained were virtually identical with those obtained on using the stepwise addition format described above (Figure 4). The unspecific binding was measured by carrying out the assay as described above but in the absence of the antibody.

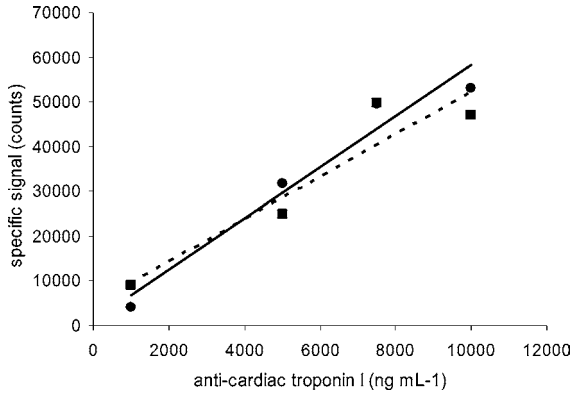

Figure 4. Binding of a complex of anti-cardiac troponin I antibody (clone 19C7) and its fluorescently tagged epitopic peptide (**4**) to microparticles coated with the same peptide (**1**): intensity of the fluorescence emission of a single particle plotted against the concentration of the antibody in solution. The loading of peptide **1** on particles was ≤ 10 μmol g^{-1}. Notation: binding of the antibody and the fluorescently tagged peptide in a stepwise manner (●, $R^2 = 0.88$), binding of the antibody and the fluorescently tagged peptide in a single step (■, $R^2 = 0.95$). The concentration of the fluorescently tagged peptide (**4**) was 22 nmol L^{-1}. At this concentration, the unspecific signal obtained in the absence of the antibody was 17000 counts on applying a stepwise mode and 18000 counts on applying a single step mode for the quantification.

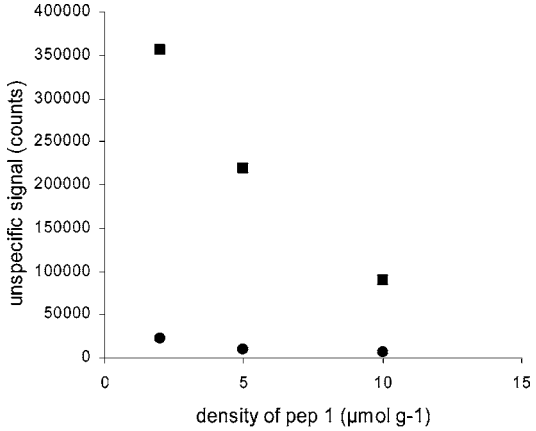

Figure 5. Unspecific binding of fluorescently tagged peptide **4** to microparticles coated with the same peptide (**1**): signal vs loading of peptide **1** on microparticles at two concentrations of the labeled peptide (**4**): 22 nmol L^{-1} (●) and 658 nmol L^{-1} (■).

To optimize the assay conditions, the effects of the peptide-loading on the particles and the concentration of labeled peptide on the signal intensity were studied. The concentration of labeled peptide (**4**) was varied from 22 nmol L^{-1} to 8.8 μmol L^{-1}. The signal intensities expectedly increased with the increasing concentration of **4**, but at the same time the proportion of unspecific binding was continuously increased, reducing the reproducibility of measurements (Figure 5). This was especially the case when a single-step format was applied, i.e. when all the components were added at the same time. For this reason, a relatively low concentration of labeled peptide (44 nmol L^{-1}) turned out to be optimal for detection. Particles having three different loadings of peptide **1**, viz. 2, 5, and 10 μmol g^{-1}, were then tested as a solid phase for detection of anti-cardiac Troponin

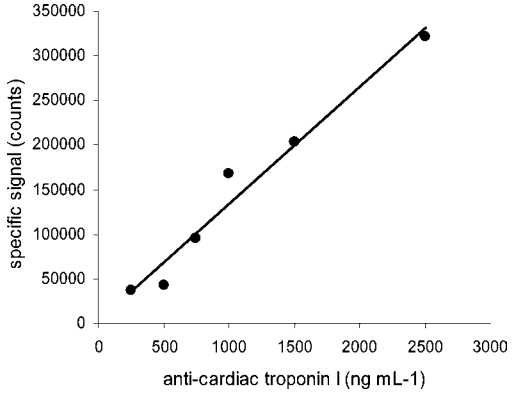

Figure 6. Binding of a ternary complex of anti-cardiac troponin I antibody (clone 19C7), its fluorescently tagged epitopic peptide (**4**), and a PNA conjugate (**7**) of the same peptide to microparticles coated with a PNA sequence complementary to that in conjugate **7**: intensity of the fluorescence emission of a single particle plotted against the concentration of the antibody in solution ($R^2 = 0.96$). The loading of PNA ≤ 10 μmol g^{-1}. The concentrations of peptide-conjugates **4** and **7** were 32 nmol L^{-1} and 1.67 nmol L^{-1}, respectively. At these concentrations, the unspecific signal obtained in the absence of the antibody was 21000 counts.

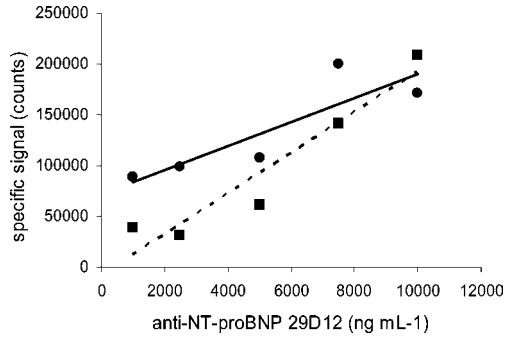

Figure 7. Binding of a ternary complex of anti-NT-proBNP antibody (clone 29D12), its fluorescently tagged epitopic peptide (**5**) and a PNA conjugate (**8**) of the same peptide to microparticles coated with a PNA sequence complementary to that in conjugate **8**: intensity of the fluorescence emission of a single particle plotted against the concentration of the antibody in solution. Notation: measurement in the absence (●, 0.74) and in the presence (■, 0.91) of anti-cardiac troponin I antibody (1000 ng mL^{-1}). The concentrations of peptide-conjugates **5** and **8** were 0.82 μmol L^{-1} and 0.53 nmol L^{-1}, respectively. At these concentrations, the unspecific signal obtained in the absence of both anti-NT-proBNP and anti-cardiac troponin I was 20000 counts and that obtained in the absence of anti-NT-proBNP but in the presence of anti-cardiac troponin I 19900 counts.

I. Interestingly, the signal intensity exhibited inverse dependence on the peptide-loading. Evidently, the antibody tends to bind to two solid-supported peptides when the peptide-loading is sufficiently high. In other words, the labeled peptide is not any more able to compete with the support-bound peptides. Unfortunately, low peptide-loading also increased the proportion of unspecific binding of the labeled peptide.

Binding of Ternary Complexes of Antibody, Labeled Peptide, and Peptide−PNA Conjugate to PNA-Coated Particles. Encouraged by the preliminary experiments described above, implementation of the assay format depicted in Scheme 1 was tried. In other words, a fluorescently tagged epitopic peptide and a PNA conjugate of the same peptide compete for the antibody, and the ternary complexes consisting of the antibody, labeled peptide, and PNA−peptide conjugate is immobilized by Watson−Crick base-pairing to a particle bearing a complementary PNA sequence. On using categorized microparticles, each antibody present in a multiplexed assay may, hence, in principle be immobilized to a different PNA-coated

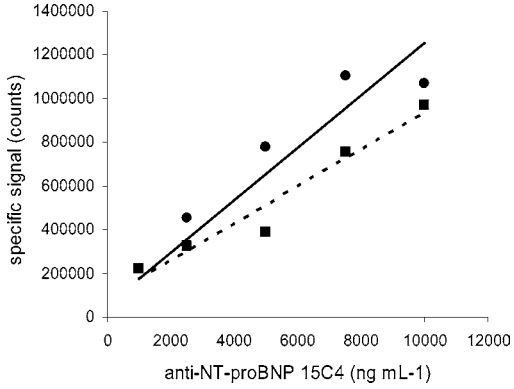

Figure 8. Binding of a ternary complex of anti-NT-proBNP antibody (clone 15C4), its fluorescently tagged epitopic peptide (**6**) and a PNA conjugate (**9**) of the same peptide to microparticles coated with a PNA sequence complementary to that in conjugate **9**: intensity of the fluorescence emission of a single particle plotted against the concentration of the antibody in solution. Notation: measurement in the absence (●, 0.86) and in the presence (■, 0.95) of anti-cardiac troponin I antibody (1000 ng mL^{-1}). The concentrations of peptide-conjugates **6** and **9** were 0.66 μmol L^{-1} and 0.48 nmol L^{-1}, respectively. At these concentrations, the unspecific signal obtained in the absence of both anti-NT-proBNP and anti-cardiac troponin I was 236000 counts and that obtained in the absence of anti-NT-proBNP but in the presence of anti-cardiac troponin I 227000.

microparticle or a PNA chip could be used for spatially addressable detection.

For this purpose, the epitopic peptides **1**−**3** were converted to their PNA conjugates **7**−**9** as follows. A Cys-derivatized PNA 10-mer, H-AGTGATCTAC-Cys-NH_2, was first reacted with 1,8-bis(maleimido)triethyleneglycol to obtain a maleimido-conjugate, with which the Cys-containing peptides were then allowed to react (Scheme 5). The PNA−peptide conjugates obtained were used in a mixed-phase immunoassay together with microparticles bearing a PNA sequence, H-GTAGATCACT-Cys-NH_2, attached to the particle through the cysteine residue. The PNA−peptide conjugate (**7**−**9**), the fluorescently tagged peptide component (**4**−**6**) of the conjugate, and the antibody were incubated overnight to form the desired ternary complex (**D** in Scheme 1). PNA-coated microparticles were then added, and another overnight incubation was performed to collect the ternary complex on the particles. Individual particles were finally subjected to measurement of fluorescence emission by time-resolved fluorometry.

Measurements were carried out at various concentrations of the PNA−peptide conjugate (0.48−166 nmol L^{-1}) and labeled peptide (22 nmol L^{-1} − 2.2 μmol L^{-1}). The optimal concentration for detection of the three antibodies studied varied somewhat from one antibody to another. With anti-cardiac troponin I, the best results were obtained on using a low concentration of the PNA−peptide conjugate **7** (1.67 nmol L^{-1}) and approximately a 1 order of magnitude higher concentration of the labeled peptide **4** (32 nmol L^{-1}). As seen from Figure 6, the assay showed a good linear dependence of the fluorometric signal intensity on the concentration of the antibody. The two other antibodies could only be detected by using the labeled peptides in larger excess compared to the PNA−peptide conjugates (**5** 0.82 μmol L^{-1}, **6** 0.66 μmol L^{-1} vs **8** 0.53 nmol L^{-1}, **9** 0.48 nmol L^{-1}). For this reason, the unspecific binding varied from 10 to 40% of the observed signal, making the plots of signal intensity vs antibody concentration rather scattered, as seen from Figures 7 and 8. The presence of another antibody does not seem to disturb the detection. As seen from Figures 7 and 8, addition of anti-cardiac troponin I antibody to give a concentration of 1000 ng mL^{-1} only moderately reduced the observed signals.

In summary, the assay depicted in Scheme 1 appears to be a viable method for quantification of a limited number of antibodies from a single sample. The applicability of the method is, however, limited by the fact that the relative affinities of the fluorescently labeled epitopic peptide and the PNA conjugate of the same peptide for the antibody appear to differ from one antibody to another. Accordingly, approximate information on the variation of the relative binding affinities is desirable for proper planning of the assay conditions. It is also worth noting that PNA rather than oligonucleotides should be used as a catcher probe. The reason is that the negatively charged sugar−phosphate backbone of oligonucleotides tends to bind electrostatically positively charged peptides. The sensitivity of detection is somewhat lower than the detection of covalently labeled antibodies, but labeling of the antibody is avoided.

ACKNOWLEDGMENT

Financial aid from the Technology Development Agency of Finland is gratefully acknowledged. The authors wish to thank Dr. Harri Hakala for performing the ESI-MS analyses. HyTest Ltd is acknowledged for providing antibodies for experiments.

LITERATURE CITED

(1) Falsey, J. R., Renil, M., Park, S., Li, S., and Lam, K. S. (2001) Peptide and small molecule microarray for high throughput cell adhesion and functional assays. *Bioconjugate Chem. 12*, 346−353.

(2) Reimer, U., Reineke, U., and Schneider-Mergerer, J. (2002) Peptide arrays: from macro to micro. *Curr. Opin. Biotechnol. 13*, 315−320.

(3) MacBeath, G. (2002) Protein microarrays and proteomics. *Nature Genet. Suppl. 32*, 526−532.

(4) Gao, X., Pellois, J. P., Na, Y., Kim, Y., Gulari, E., and Zhou, X. (2004) High-density peptide microarrays. In situ synthesis and applications. *Mol. Diversity 8*, 177−187.

(5) Fodor, S. P. A., Read, J. L., Pirrung, L. C., Stryer, L., Lu, A. T., and Solas, D. (1991) Light-directed, spatially addressable parallel chemical synthesis. *Science 251*, 767−773.

(6) Pellois, J. P., Wang, W., and Gao, X. (2000) Peptide synthesis based on t-Boc chemistry and solution photogenerated acids. *J. Comb. Chem. 2*, 355−360.

(7) LeProust, E., Pellois, J. P., Yu, P., Zhang, H., Gao, X., Srivannavit, O., Gulari, E., and Zhou, X. (2000) Digital light-directed synthesis. A microarray platform that permits rapid reaction optimization on a combinatorial basis. *J. Comb. Chem. 2*, 349−354.

(8) Pellois, J. P., Zhou, X., Srivannavit, O., Zhou, T., Gulari, E., and Gao, X. (2002) Individually addressable parallel peptide synthesis on microchips. *Nature Biotechnol. 20*, 922−926.

(9) Komolpis, K., Srivannavit, O., and Gulari, E. (2002) Light-directed simultaneous synthesis of oligopeptides on microarray substrate using a photogenerated acid. *Biotechnol. Prog. 18*, 641−646.

(10) MacBeath, G., Koehler, A. N., and Schreiber, S. L. (1999) Printing small molecules as microarrays and detecting protein−ligand interactions *en masse*. *J. Am. Chem. Soc. 121*, 7967−7968.

(11) MacBeath, G., and Schreiber, S. L. (2000) Printing proteins as microarrays for high-throughput function determination. *Science 289*, 1760−1763.

(12) Houseman, B. T., Huh, J. H., Kron, S. J., and Mrksich, M. (2002) Peptide chips for the quantitative evaluation of protein kinase activity. *Nat. Biotechnol. 20*, 270−274.

(13) Lesaicherre, M.-L., Uttamchandani, M., Chen, G. Y. J., and Yao, S. Q. (2002) Developing site-specific immobilization strategies of peptides in a microarray. *Bioorg. Med. Chem. Lett. 12*, 2085−2088.

(14) Melnyk, O., Duburcq, X., Olivier, C., Urbes, F., Auriault, C., and Gras-Masse, H. (2002) Peptide arrays for highly sensitive and specific antibody-binding fluorescence assays. *Bioconjugate Chem. 13*, 713−720.

(15) Duburcq, X., Olivier, C., Malingue, F., Desmet, R., Bouzidi, A., Zhou, F., Auriaul, C., Gras-Masse, H., and Melnyk, O. (2004) Peptide−protein microarrays for the simultaneous detection of phatogen infections. *Bioconjugate Chem. 15*, 307−316.

(16) Salisbury, C. M., Maly, D. J., and Ellman, J. A. (2002) Peptide microarrays for the determination of protease substrate specificity. *J. Am. Chem. Soc. 124*, 14868−14870.

(17) Kreegipuu, A., Blom, N., and Brunak, S. (1999) PhosphoBase, a database of phosphorylation sites: release 2.0. *Nucleic Acids Res. 27*, 237−239.

(18) Bairoch, A., and Apweiler, R. (2000) The SWISS−PROT protein sequence database and its supplement TrEMBL in 2000. *Nucleic Acids Res. 28*, 45−48.

(19) Lizcano, J. M., Deak, M., Morrice, N., Kieloch, A., Hastie, C. J., Dong, L., Schutkowski, M., Reimer, U., and Alessi, D. R. (2002) Molecular basis for the substrate specificity of NEK6: evidence that it does not phosphorylate the hydrophobic motif of S6K and SGK *in vivo*. *J. Biol. Chem. 277*, 27839−27849.

(20) Xu, Q., Miyamoto, S., and Lam, K. S. (2004) A novel approach to chemical microarray using ketone-modified macromolecular scaffolds: application in micro cell-adhesion assay. *Mol. Diversity 8*, 301−310.

(21) Lövgren, T., Heinonen, P., Hakala, H., Heinola, J., Harju, R., Takalo, H., Mukkala, V.-M., Schmid, R., Lönnberg, H., Pettersson, K., and Iitiä, A. (1997) Sensitive Bioaffinity Assays on Individual Microparticles Using Time-resolved Fluorometry. *Clin. Chem. 43*, 1937−1943.

(22) Härmä, H., Lehtinen, P., Takalo, H., and Lövgren, T. (1999) Immunoassay on a single microparticle: the effect of particle size and number on a miniaturized time-resolved fluorometric assay of free prostate-specific antigen. *Anal. Chim. Acta 387*, 11−19.

(23) Härmä, H., Tarkkinen, P., Soukka, T., and Lövgren, T. (2000) Miniature single-particle immunoassay for prostate-specific antigen in serum using recombinant Fab fragments. *Clin. Chem. 46*, 1755−1761.

(24) Härmä, H., Aronkytö, P., and Lövgren, T. (2000) Multiplex immunoassays on size-categorized individual beads using time-resolved fluorescence. *Anal. Chim. Acta 410*, 85−96.

(25) Hakala, H., Heinonen, P., Iitiä, A., and Lönnberg, H. (1997) Detection of oligonucleotide hybridization on a single microparticle by time-resolved fluorometry: hybridization assays on polymer particles obtained by direct solid phase assembly of the oligonucleotide probes. *Bioconjugate Chem. 8*, 378−384.

(26) Hakala, H., and Lönnberg, H. (1997) Time-resolved fluorescence detection of oligonucleotide hybridization on a single microparticle: covalent immobilization of oligonucleotides and quantitation of a model system. *Bioconjugate Chem. 8*, 232−237.

(27) Hakala, H., Mäki, E., and Lönnberg, H. (1998) Detection of oligonucleotide hybridization on a single microparticle by time-resolved fluorometry: quantitation and optimization of a sandwich type assay. *Bioconjugate Chem. 9*, 316−321.

(28) Hakala, H., Virta, P., Salo, H., and Lönnberg, H. (1998) Simultaneous detection of several oligonucleotides by time-resolved fluorometry: the use of a mixture of categorized microparticles in a sandwich type mixed-phase hybridization assay. *Nucleic Acids Res. 26*, 5581−5588.

(29) Ketomäki, K., Hakala, H., and Lönnberg, H. (2002) Mixed-phase hybridization of short oligodeoxyribonucleotides on microscopic polymer particles: Effect of one base mismatches on duplex stability. *Bioconjugate Chem. 13*, 542−547.

(30) Fulton, R. J., McDade, R. L., Smith, P. L., Kienker, L. J., and Kettman, J. R., Jr. (1997) Advanced multiplexed analysis with the FlowMetrix system. *Clin. Chem. 43*, 1749−1756.

(31) Wissinger, N., Harris, J. L., Backes, B. J., and Schultz, P. G. (2001) From split-pool libraries to spatially addressable microarrays and its application to functional proteomic profiling. *Angew. Chem., Int. Ed. 40*, 3152−3155.

(32) Mukkala, V.-M., Helenius, M., Hemmilä, I., Kankare, J., and Takalo, H. (1993) Development of luminescent europium(III) and terbium(III) chelates of 2,2′:6′,2″-terpyridine derivatives for protein labeling. *Helv. Chim. Acta 76*, 1361−1378.

(33) Hemmilä, I., Dakubu, S., Mukkala, V.-M., Siitari, H., and Lövgren, T. (1984) Europium as a label in time-resolved immunofluorometric assays. *Anal. Biochem. 137*, 335−343.

BC0600315

^{99m}Tc-Labeled Cyclic RGDfK Dimer: Initial Evaluation for SPECT Imaging of Glioma Integrin $\alpha_v\beta_3$ Expression

Bing Jia,[†,||] Jiyun Shi,[†,||] Zhi Yang,[§] Bing Xu,[§] Zhaofei Liu,[†] Huiyun Zhao,[†] Shuang Liu,[‡,*] and Fan Wang[†,*]

Medical Isotopes Research Center, Peking University, Beijing 100083, China, Department of Isotopes, China Institute of Atomic Energy, Beijing 102413, China, School of Health Sciences, Purdue University, Indiana 47907, and Department of Nuclear Medicine, Peking University Oncology School, Beijing 100036, China Received March 5, 2006; Revised Manuscript Received April 24, 2006

This report describes the evaluation of biodistribution properties of three radiotracers, [^{99m}Tc(SQ168)(EDDA)], [^{99m}Tc(SQ168)(tricine)(PDA)], and [^{99m}Tc(SQ168)(tricine)(TPPTS)] (SQ168 = [2-[[[5-[carboonyl]-2-pyridinyl]-hydrazono]methyl]benzenesulfonic acid]-Glu(cyclo{Lys-Arg-Gly-Asp-D-Phe})-cyclo{Lys-Arg-Gly-Asp-D-Phe}; EDDA = ethylenediamine-*N*,*N*′-diacetic acid; PDA = 2,5-pyridinedicarboxylic acid; TPPTS = trisodium triphenylphosphine-3,3′,3″-trisulfonate), and their potential to image the glioma integrin $\alpha_v\beta_3$ expression in BALB/c nude mice bearing the U87MG human glioma xenografts. It was found that all three radiotracers were able to localize in glioma tumors with a relatively high tumor uptake and long tumor retention time by binding to the integrin $\alpha_v\beta_3$ expressed on both tumor cells and endothelial cells of tumor neovasculature. It seems that the coligand has minimal effect on integrin $\alpha_v\beta_3$ targeting capability of the ^{99m}Tc-labeled RGDfK dimer, but it has a significant impact on their biodistribution properties. For example, the complex [^{99m}Tc(SQ168)(tricine)(TPPTS)] has the lowest liver uptake and the highest metabolic stability in normal BALB/c nude mice. Results from SPECT imaging studies show that the glioma tumors can be clearly visualized with all three radiotracers at 4 h postinjection. Among the three radiotracers evaluated in this study, [^{99m}Tc(SQ168)(tricine)(TPPTS)] has the best imaging quality and is a promising candidate for more preclinical evaluations in the future.

INTRODUCTION

Gliomas or tumors derived from glial cells of the central nerve system are the most frequent primary intracranial neoplasma in adults. Malignant gliomas are the second leading cause of cancer death in children under age 15 and also in young adults up to age 34 (*1*, *2*). With a high proliferation rate, marked neovascularization, and extensive local invasion of tumor cells into the normal brain parenchyma, gliomas are resistant to conventional treatment, such as surgery, chemotherapy, and radiation therapy. The median survival of aggressively treated patients with glioblastoma is about 12 months (*3*). Therefore, early detection of brain tumors such as glioma is highly desirable so that various therapeutic regimens can be given before the primary tumors become widely spread. Since gliomas are extremely invasive with a high level of integrin $\alpha_v\beta_3$ overexpression (*4*−*6*), which also correlates with metastatic disease human neuroblastomas (*7*), it would be of great clinical benefit to develop a radiotracer that can be used not only to noninvasively visualize and quantify integrin $\alpha_v\beta_3$ expression but also to select patients under consideration for anti-integrin treatment and monitor treatment efficacy in integrin $\alpha_v\beta_3$-positive patients.

For the last several years, many high affinity integrin $\alpha_v\beta_3$ antagonists (RGD-containing cyclic peptides and nonpeptide RGD mimetics) have been proposed as targeting biomolecules to carry the diagnostic "probes" into the integrin $\alpha_v\beta_3$-positive tumors (*8*−*13*). Several molecular probes have been developed for magnetic resonance imaging (*14*), ultrasound (*15*), optical imaging (*16*), positron emission tomography (PET) (*17*−*23*), and single-photon emission computed tomography (SPECT) imaging (*24*−*28*). Although most of "molecular" probes containing a monomeric RGD-tripeptide sequence are able to target tumors by binding to the integrin $\alpha_v\beta_3$ overexpressed on tumor cells and endothelial cells of the tumor neovasculature, they suffer from several shortcomings, such as low tumor uptake, which limit their application as tumor imaging agents in clinics.

We and others have been using cyclic RGD peptide dimers, such as E[c(RGDfK)]$_2$, for development of the integrin $\alpha_v\beta_3$-targeted diagnostic (^{64}Cu, ^{99m}Tc, and ^{111}In) radiotracers (*29*−*35*). Recently, we reported evaluation of complexes [^{99m}Tc(SQ168)(tricine)(L)] (Figure 1: SQ168 = [2-[[[5-[carboonyl]-2-pyridinyl]hydrazono]methyl]benzenesulfonic acid]-Glu(cyclo{Lys-Arg-Gly-Asp-D-Phe})-cyclo{Lys-Arg-Gly-Asp-D-Phe}; L = ISONIC (isonicotinic acid), TPPTS (trisodium triphenylphosphine-3,3′,3″-trisulfonate), and PDA (2,5-pyridinedicarboxylic acid)) as radiotracers for imaging the integrin $\alpha_v\beta_3$ expression in nude mice bearing the MDA-MB-435 human breast cancer xenografts (*29*, *31*). It was found that coligands have minimal effect on tumor targeting capability, but it has a significant impact on excretion kinetics of the ^{99m}Tc-labeled cyclic RGDfK dimer. Results from the blocking experiment suggest that the tumor localization of the ^{99m}Tc-labeled cyclic RGDfK dimer is indeed integrin $\alpha_v\beta_3$-mediated (*31*).

As continuation of our interest in the integrin $\alpha_v\beta_3$-targeted radiotracers for imaging solid tumors of different origin, we have evaluated the biodistribution characteristics of ternary ligand complexes [^{99m}Tc(SQ168)(tricine)(PDA)] and [^{99m}Tc(SQ168)(tricine)(TPPTS)] in the female BALB/c nude mice bearing the U87MG human glioma xenografts. The main objective is to assess their potential as SPECT radiotracers for imaging the integrin $\alpha_v\beta_3$-expression in gliomas. For comparison

* To whom correspondence should be addressed. Dr. Shuang Liu, School of Health Sciences, Purdue University, 550 Stadium Mall Drive, West Lafayette, IN 47907. Phone: 765-494-0236, Fax: 765-496-3367, E-mail: lius@pharmacy.purdue.edu; or Dr. Fan Wang, Medical Isotopes Research Center, Peking University, 38# Xueyuan Road, Beijing 100083, China. Phone and Fax: 86-10-82801145, E-mail: wangfan@bjmu.edu.cn.

† Peking University.

‡ Purdue University.

§ Peking University Oncology School.

|| China Institute of Atomic Energy.

10.1021/bc060055b CCC: $33.50 © 2006 American Chemical Society
Published on Web 06/29/2006

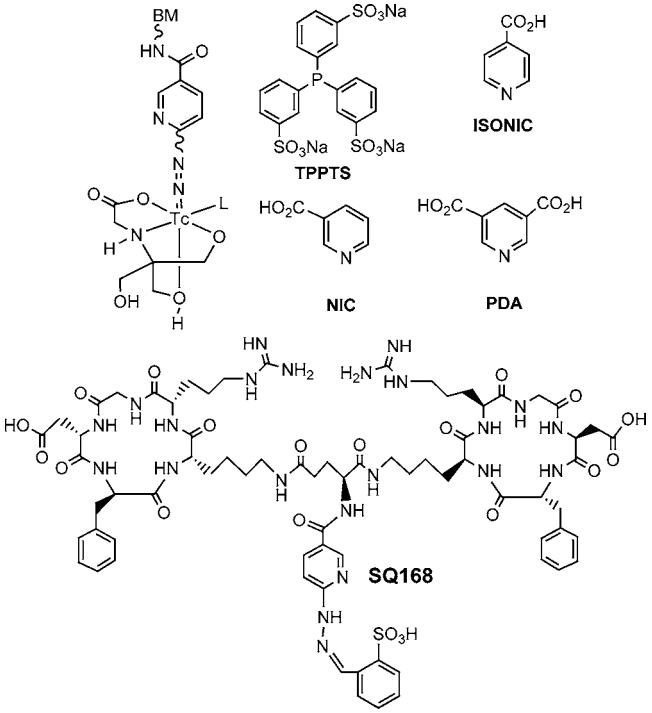

Figure 1. Structures of the HYNIC-conjugated cyclic RGDfK dimer (SQ168), coligands, and their ternary ligand complexes [^{99m}Tc(SQ168)-(tricine)(L)] (SQ168 = HYNIC-E[c(RGDfK)]$_2$; L = TPPTS, ISONIC, NIC, and PDA).

purposes, we also evaluated the complex [^{99m}Tc(SQ168)-(EDDA)] (EDDA = ethylenediamine-*N*,*N*′-diacetic acid) in the same tumor animal model. EDDA has been used as a coligand for preparation of ^{99m}Tc-labeled somatostatin analogues, which are under investigation as new radiotracers for imaging somatostatin receptor-positive tumors in humans (*36*−*38*).

EXPERIMENTAL SECTION

Materials and Methods. All chemicals were purchased from Aldrich Chemical Co., unless specified. Synthesis of SQ168 (HYNIC-E[c(RGDfK)]$_2$) was described in our previous communication (*31*). Na^{99m}TcO$_4$ was obtained from a commercial ^{99}Mo/^{99m}Tc generator (Beijing Atom High Tech Co., Ltd.). The radio-HPLC method used a HP Hewlett Packard Series 1100 HPLC system equipped with Radioflow Detector LB509 and Agilent Zorbax SB-C18 column (4.6 mm × 250 mm, 5 μm). The flow rate was 1.0 mL/min. The mobile phase was isocratic with 90% solvent A (25 mM NaOAc buffer, pH = 5.0) and 10% solvent B (acetonitrile) at 0−2 min, followed by a gradient mobile phase going from 10% solvent B at 2 min to 15% solvent B at 5 min and to 20% solvent B at 20 min, then to 10% solvent B at 25 min.

Synthesis of [^{99m}Tc(SQ168)(EDDA)]. To a clean vial were added 100 μL of SQ168 solution (100 μg/mL in H_2O), 100 μL of tricine solution (100 mg/mL in 25 mM succinate buffer, pH 5.0), 20 μL of $SnCl_2$ solution (3.0 mg/mL in 0.1 N HCl), and 100 μL of Na^{99m}TcO$_4$ solution (∼10 mCi). The reaction mixture was kept at room temperature for 10 min. To the solution was added 200 μL of EDDA (30 mg/mL in 1 M NaOH, pH 7.0). The mixture was heated at 100 °C for 30 min. After radiolabeling, a sample of the resulting solution was analyzed by radio-HPLC.

Synthesis of [^{99m}Tc(SQ168)(tricine)(L)] (L = PDA and TPPTS). To a clean vial were added 100 μL of SQ168 solution (100 μg/mL in H_2O), 100 μL of tricine solution (100 mg/mL in 25 mM succinate buffer, pH 5.0), 20 μL of $SnCl_2$ solution (3.0 mg/mL in 0.1 N HCl), and 100 μL of Na^{99m}TcO$_4$ (∼10 mCi). The reaction mixture was kept at room temperature for 10 min. To the solution above was added 120 μL of TPPTS or PDA solution (50 mg/mL in 25 mM succinate buffer, pH 5.0), and the mixture was heated at 100 °C for 30 min. After radiolabeling, a sample of the resulting solution was analyzed by radio-HPLC.

Doses Preparation for Animal Studies. All three ^{99m}Tc radiotracers were purified using Sep-Pak C-18 cartridge (Waters, Milford MA) before animal studies. The Sep-Pak C-18 cartridge was activated with 10 mL of ethanol followed by washing with 10 mL of water. The radiotracer was passed through a Sep-Pak C-18 cartridge to filter out the [^{99m}Tc]-colloid. The Sep-Pak C-18 cartridge was then washed with 10 mL of saline to remove unlabeled SQ168 and excess coligand. The ^{99m}Tc radiotracer was eluted with 0.4 mL of 80% ethanol. Doses for animal studies were prepared by dissolving the purified radiotracer in saline to give a concentration of 150 μCi/mL for biodistribution studies, 4.0 mCi/mL for metabolism, and 2.0 mCi/mL for imaging studies. For the blocking experiment, E[c(RGDfK)]$_2$ was used as the blocking agent. Doses were prepared by dissolving E[c(RGDfK)]$_2$ in saline to give a final concentration of 3.0 mg/mL. Each tumor-bearing mouse was injected with 0.1 mL of E[c(RGDfK)]$_2$ solution, which corresponds to a dose of 15 mg/kg.

Animal Studies. Both biodistribution and imaging studies were performed by Dr. Wang's group at the Peking University Medical Isotopes Research Center, according to the literature (*21*, *23*, *39*). All animal experiments were performed in accordance with guidelines of Peking University Health Science Center Animal Care and Use Committee.

Tumor-Bearing Mice. The human U87MG glioma tumor cells from Professor Jingde Zhu (Shanghai Cancer Research Institute) were maintained at 37 °C and 5% CO_2 in Dulbecco's modified Eagle's medium (DMEM) containing 10% fetal bovine serum (FBS). Female BALB/c nude mice (4−5 weeks of age) were purchased from Department of Animal Experiment, Peking University Health Science Center. The U87MG cells (5×10^6) were implanted subcutaneously into the right upper flanks of mice. When tumors reached ∼0.8 cm in mean diameter, the tumor-bearing mice were used to biodistribution and imaging studies.

Biodistribution. Sixteen tumor-bearing mice were randomly divided into four groups, each of which had four animals. Animals were anesthetized with an intraperitoneal injection of sodium pentobarbital at a dose of 45.0 mg/kg. The ^{99m}Tc radiotracer (∼15 μCi in 0.1 mL saline) was administered intravenously to each tumor-bearing mouse. Animals were sacrificed by cervical dislocation at 0.5, 1, 2, and 4 h postinjection. Blood, heart, liver, spleen, kidney, stomach, intestine, muscle, and tumor were harvested, weighed, and measured for radioactivity in a γ-counter (Wallac 1470−002, Perkin-Elmer, Finland). The organ uptake was calculated as a percentage of the injected dose per gram of wet tissue mass (%ID/g). For the blocking experiment, each animal was administered with 300 μg of E[c(RGDfK)]$_2$ (0.1 mL in saline) 30 min prior to the injection of [^{99m}Tc(SQ168)(tricine)(PDA)]. At 1 h postinjection, all four animals were sacrificed for biodistribution using the same procedure above. The results were compared to those obtained in animals without the injection of E[c(RGDfK)]$_2$.

Metabolism. The metabolic stability of ^{99m}Tc radiotracers was evaluated in normal BALB/c nude mice. Animals were anesthetized with intraperitoneal injection of sodium pentobarbital (45.0 mg/kg). Each mouse was administered with the radiotracer at a dose of 800 μCi in 0.2 mL saline via intravenous injection. The mice were sacrificed by cervical dislocation at 2 h postinjection, and livers were removed and homogenized. The homogenate was extracted with 500 μL of 50% acetonitrile aqueous solution. The extract was centrifuged at 1500 rpm for

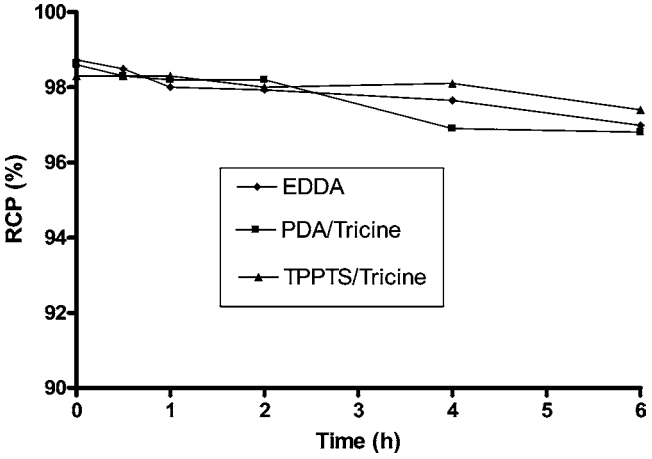

Figure 2. Solution stability data for [^{99m}Tc(SQ168)(EDDA)], [^{99m}Tc-(SQ168)(tricine)(PDA)], and [^{99m}Tc(SQ168)(tricine)(TPPTS)] in the presence of cysteine (1.0 mg/mL).

15 min, and the supernatant was filtered through a 0.22 μ Millex-LG syringe driven filter unit. The filtrate was analyzed by radio-HPLC. Urine samples were collected at 2 h postinjection and were mixed with equal volume of acetonitrile. The mixtures were centrifuged at 1500 rpm for 15 min. The supernatants were collected and filtered through a 0.22 μ Millex-LG syringe driven filter unit. The filtrates were analyzed by radio-HPLC.

SPECT Imaging. SPECT imaging was performed on nine tumor-bearing mice (three groups). Animals were anesthetized with an intraperitoneal injection of sodium pentobarbital at a dose of 45.0 mg/kg. Each animal was administered with 400 μCi of the ^{99m}Tc radiotracer in 0.2 mL of saline. Animals were placed supine on a two-head γ-camera (SIEMENS, E. CAM) equipped with a parallel-hole, low-energy, and high-resolution collimator. Anterior images were acquired 4 h postinjection and stored digitally in a 128 $\times$ 128 matrix. The acquisition count limits were set at 1000 K. After completion of imaging, animals were sacrificed by cervical dislocation.

Statistical Analysis. The biodistribution data and T/B ratios are reported as an average plus the standard variation. Comparison between two different radiotracers was also made using the one-way ANOVA test. The level of significance was set at $p = 0.05$.

RESULTS

Radiochemistry. Complexes [^{99m}Tc(SQ168)(EDDA)], [^{99m}Tc-(SQ168)(tricine)(PDA)], and [^{99m}Tc(SQ168)(tricine)(TPPTS)] were prepared using a two-step radiolabeling procedure. First, HYNIC-E[c(RGDfK)]$_2$ (SQ168) was allowed to react with Na^{99m}TcO$_4$ in the presence of excess tricine and stannous chloride to form the [^{99m}Tc(SQ168)(tricine)$_n$] intermediate, which underwent ligand exchange with EDDA to give the complex [^{99m}Tc(SQ168)(EDDA)], or reacted with PDA or TPPTS to form ternary ligand complexes [^{99m}Tc(SQ168)-(tricine)(L)] (L = PDA and TPPTS). The radiochemistry purity (RCP) for all three ^{99m}Tc radiotracers was >95% after purification with the Sep-Pak C-18 cartridge before animal studies.

Solution Stability. The solution stability of complexes [^{99m}Tc(SQ168)(EDDA)], [^{99m}Tc(SQ168)(tricine)(PDA)], and [^{99m}Tc(SQ168)(tricine)(TPPTS)] was monitored by radio-HPLC after addition of cysteine. Figure 2 shows their solution stability data. It is quite clear that all three radiotracers remain stable over 6 h in the presence of cysteine (1.0 mg/mL).

Biodistribution. Biodistribution studies were performed using female BALB/c nude mice bearing the U87MG human glioma xenografts. This animal model has been used to evaluate radiolabeled RGD peptides as potential radiotracers for imaging gliomas (*21*, *23*, *39*). The selected biodistribution data for [^{99m}Tc(SQ168)(EDDA)], [^{99m}Tc(SQ168)(tricine)(PDA)], and [^{99m}Tc(SQ168)(tricine)(TPPTS)] with/without the presence of excess E[c(RGDfK)]$_2$ are summarized in Figure 3. Figure 4 illustrates their tumor-to-background (T/B) ratios in several selected organs. Figure 5 shows the direct comparison of their organ uptake at 0.5, 1, 2, and 4 h postinjection and excretion kinetics from the blood, liver, and kidneys.

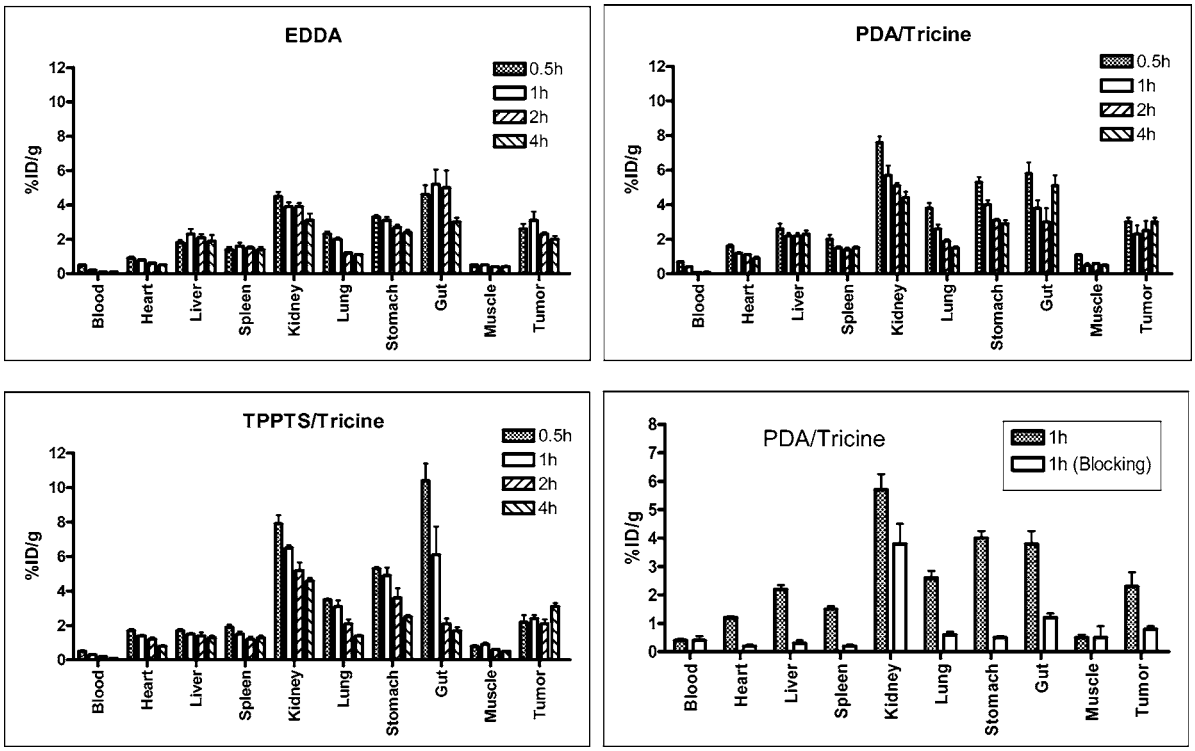

Figure 3. Comparison of the organ uptake (%ID/g) between [^{99m}Tc(SQ168)(EDDA)], [^{99m}Tc(SQ168)(tricine)(PDA)], and [^{99m}Tc(SQ168)(tricine)-(TPPTS)] in BALB/c nude mice bearing the U87MG human glioma xenografts. Each data point represents an average of biodistribution data in four animals.

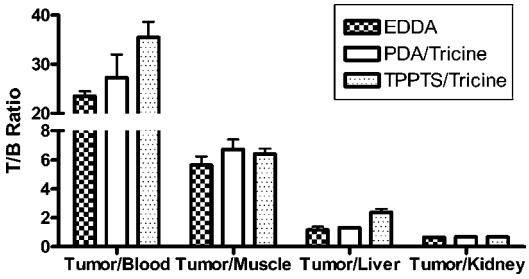

Figure 4. Tumor/background ratios for [^{99m}Tc(SQ168)(EDDA)], [^{99m}Tc(SQ168)(tricine)(PDA)], and [^{99m}Tc(SQ168)(tricine)(TPPTS)] in BALB/c nude mice bearing the U87MG human glioma xenografts at 4 h postinjection.

In general, all three complexes, [^{99m}Tc(SQ168)(EDDA)], [^{99m}Tc(SQ168)(tricine)(PDA)], and [^{99m}Tc(SQ168)(tricine)-(TPPTS)], displayed a rapid clearance from the blood via renal and hepatobiliary routes. Their blood clearance curves were almost identical (Figure 5), suggesting that coligands have little impact on their protein binding. Their tumor uptake remained relatively unchanged over 2 h within the experimental error (Figure 5). However, the tumor uptake of [^{99m}Tc(SQ168)-(tricine)(PDA)] (3.01 ± 0.47%ID/g) and [^{99m}Tc(SQ168)(tricine)-(TPPTS)] (3.10±0.35%ID/g) was significantly ($p < 0.01$) higher than that of [^{99m}Tc(SQ168)(EDDA)] (1.99 ± 0.44%ID/g) at 4 h postinjection. The kidney uptake of [^{99m}Tc(SQ168)(tricine)-(PDA)] and [^{99m}Tc(SQ168)(tricine)(TPPTS)] was higher than that of [^{99m}Tc(SQ168)(EDDA)]. The liver uptake of [^{99m}Tc-(SQ168)(tricine)(TPPTS)] was lower than that of [^{99m}Tc-(SQ168)(EDDA)] and [^{99m}Tc(SQ168)(tricine)(PDA)] at >1 h postinjection (Figure 5). As a result, it has the best tumor-to-liver ratio (2.39 ± 0.46) at 4 h postinjection (Figure 4).

The blocking experiment was performed by preinjecting or coinjecting a known receptor ligand to demonstrate the tumor-specificity of target-specific radiotracers. In this study, we used E[c(RGDfK)]$_2$ (15 mg/kg or 300 μg/mouse), the IC_{50} of which was 32.1 ± 2.1 nM against ^{125}I-echistatin binding to integrin $\alpha_v\beta_3$ on U87MG tumor cells (*39*), as the blocking agent. Figure 3 shows the comparison of uptake (%ID/g) for [^{99m}Tc(SQ168))-(tricine)(PDA)] at 1 h postinjection with/without E[c(RGDfK)]$_2$. Obviously, excess E[c(RGDfK)]$_2$ resulted in a significant reduction in the uptake of [^{99m}Tc(SQ168))(tricine)(PDA)] in the tumor, lungs, liver, spleen, stomach, and guts. The kidney uptake was also inhibited (to a lesser degree) by excess E[c(RGDfK)]$_2$ (Figure 3). Similar results were obtained for [^{99m}Tc(SQ168)-(tricine)(TPPTS)] and ^{111}In-DOTA-E[c(RGDfK)]$_2$ in the BALB/c mice bearing ovarian carcinoma (*33*−*35*) and for [^{99m}Tc-(SQ168)(tricine)(ISONIC)] and ^{64}Cu-DOTA-E[c(RGDfK)]$_2$ in the nude mice bearing the MDA-MB-435 human breast cancer xenografts (*31*, *32*). However, there is no significant difference in the blood activity with/without excess E[c(RGDfK)]$_2$ (Figure 3).

Imaging Studies. We performed imaging studies on all three radiotracers in the BALB/c nude mice bearing the U87MG human glioma xenografts. Figure 6 illustrates representative SPECT images of tumor-bearing mice administered with ∼400 μCi of [^{99m}Tc(SQ168)(EDDA)] (left), [^{99m}Tc(SQ168)(tricine)-(TPPTS)] (middle), and [^{99m}Tc(SQ168)(tricine)(PDA)] (right). In general, tumors in all three SPECT images are clearly visualized at 4 h postinjection. The complex [^{99m}Tc(SQ168)-(tricine)(TPPTS)] has the least activity accumulation in the abdominal region while [^{99m}Tc(SQ168)(EDDA)] has relatively low kidney uptake (Figure 6), which is completely consistent with the ex vivo biodistribution data at the same time point (Figure 3). Among three radiotracers evaluated in this study, [^{99m}Tc(SQ168)(tricine)(TPPTS)] has the best imaging quality at 4 h postinjection due to its rapid clearance from liver and lungs in BALB/c nude mice bearing the U87 human glioma xenografts.

Metabolic Properties. We performed metabolism studies on all three radiotracers using normal BALB/c nude mice. Since they are excreted from both renal and hepatobiliary routes, we analyzed the samples from both liver and urine to determine if these radiotracers retain their chemical integrity at 2 h postinjection. Figure 7 illustrates the radio-HPLC chromatograms of [^{99m}Tc(SQ168)(tricine)(PDA)] (left) and [^{99m}Tc(SQ168)(tricine)-(TPPTS)] (right) in the kit matrix before injection (A), in the liver (B), and in the urine (C). It is quite clear that [^{99m}Tc-(SQ168)(tricine)(TPPTS)] retained its integrity while [^{99m}Tc-(SQ168)(tricine)(PDA)] showed a certain degree of metabolism (10−15%) in both urine and liver samples at 2 h postinjection.

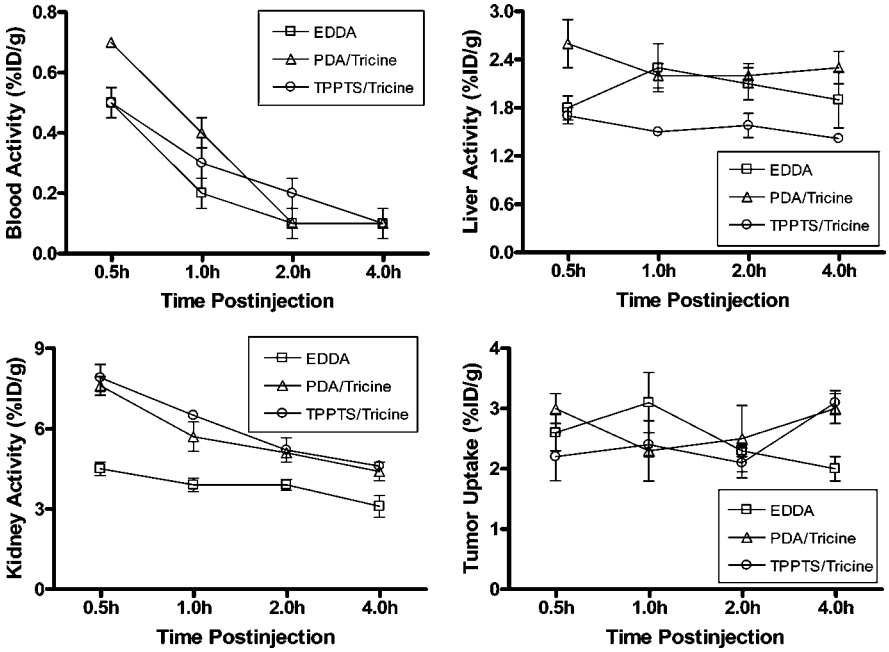

Figure 5. Direct comparison of excretion kinetics between [^{99m}Tc(SQ168)(EDDA)], [^{99m}Tc(SQ168)(tricine)(PDA)], and [^{99m}Tc(SQ168)(tricine)-(TPPTS)] in BALB/c nude mice bearing the U87MG human glioma xenografts.

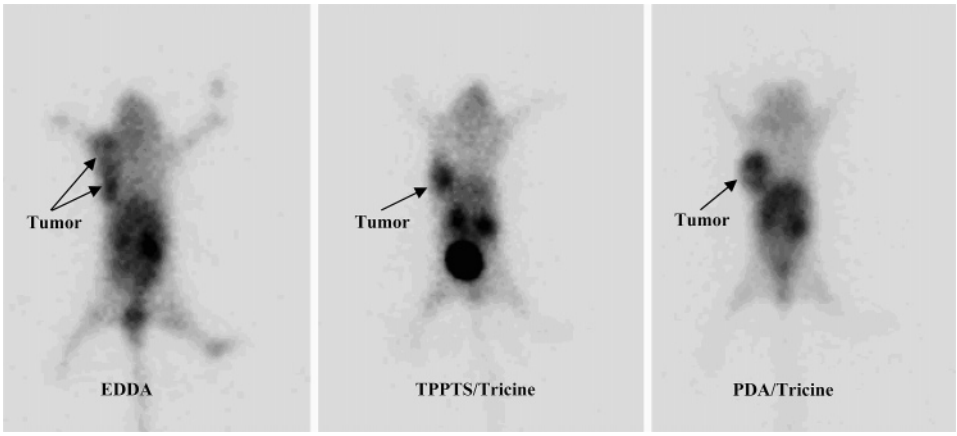

Figure 6. SPECT images of BALB/c nude mice bearing the U87MG human glioma xenografts administered with ~400 μCi of [^{99m}Tc(SQ168)-(EDDA)] (left), [^{99m}Tc(SQ168)(tricine)(TPPTS)] (middle) and [^{99m}Tc(SQ168)(tricine)(PDA)] (right) at 4 h postinjection. Arrows indicate the location of glioma tumors.

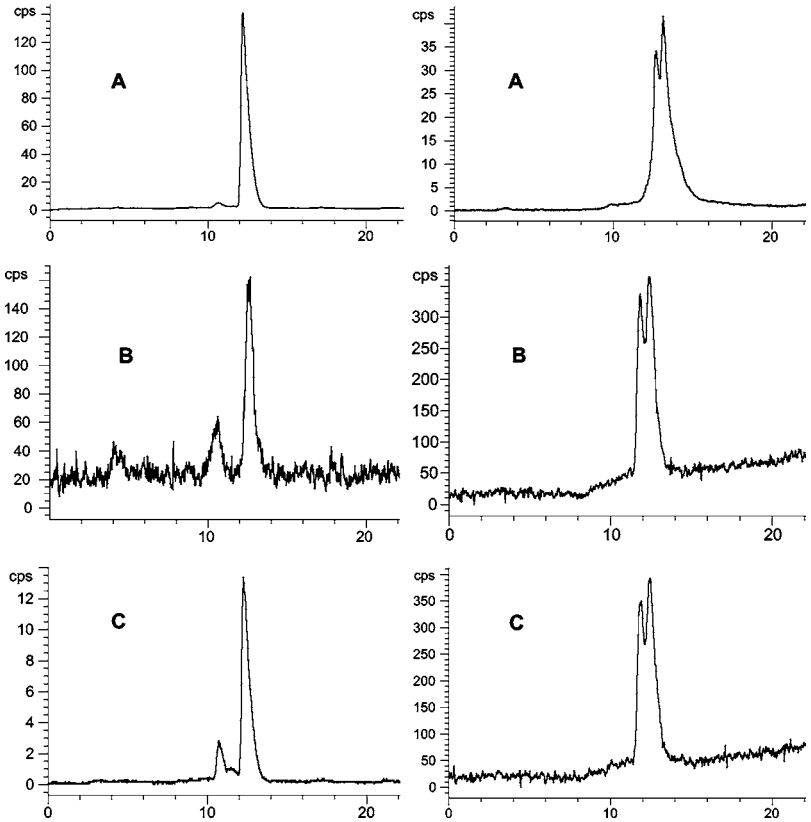

Figure 7. Radio-HPLC chromatograms of [^{99m}Tc(SQ168)(tricine)(PDA)] (left) and [^{99m}Tc(SQ168)(tricine)(TPPTS)] (right) in the kit matrix before injection (A), in the liver (B), and in the urine (C) at 2 h postinjection.

The metabolic patterns of [^{99m}Tc(SQ168)(EDDA)] are very similar to those of [^{99m}Tc(SQ168)(tricine)(PDA)] (Figure SI).

DISCUSSION

It is well established that the integrin $\alpha_v\beta_3$ overexpressed on the neovasculature of many solid tumors, including neuroblastomas, glioblastomas, melanomas, lung carcinomas, and breast, prostate, and bladder cancers (*6*, *40*−*50*). The integrin $\alpha_v\beta_3$ expression level also correlates well with tumor progression in melanoma, glioma, and ovarian and breast cancers (*7*, *40*−*47*). For the past decade, many cyclic RGD peptides and nonpeptide RGD mimetics have been labeled with different radioisotopes to develop the angiogenesis-targeting radiotracers for both diagnosis (^{125}I, ^{99m}Tc, ^{111}In, ^{18}F, and ^{64}Cu) and tumor-specific radiotherapy (^{90}Y and ^{177}Lu) (*17*−*35*). Since integrin $\alpha_v\beta_3$ is overexpressed on the surface of the "activated" endothelial cells of tumor neovasculature, the integrin $\alpha_v\beta_3$-targeted radiotracers would be specific for rapidly growing and metastatic tumors.

In general, the radiolabeled RGD peptide radiotracer of clinical importance should have high affinity and specificity for integrin $\alpha_v\beta_3$. In the last several years, we and others have been using the "multivalency" concept to improve $\alpha_v\beta_3$ binding affinity and the tumor targeting of the radiolabeled RGD peptides (*11*, *13*, *29*−*35*, *51*−*55*). It is found that the use of a multimeric cyclic RGD peptide could significantly increase the affinity of radiotracers for integrin $\alpha_v\beta_3$ through either simultaneous receptor binding or reduction of dissociation from the integrin $\alpha_v\beta_3$ binding sites. For example, the integrin $\alpha_v\beta_3$ binding affinity of E[c(RGDfK)]$_2$ (a cyclic RGDfK dimer) is 10-fold higher than that of its monomeric analogue c(RGDfK) (*33*). In athymic female BALB/c nude mice with subcutaneous OVCAR-3 ovarian cancer xenografts, the ^{99m}Tc-labeled RGDfK

dimer had significantly higher tumor retention than its monomeric counterpart (*33*). Similar results were also obtained with ^{64}Cu- and ^{90}Y-labeled cyclic RGD dimer conjugates: DOTA-E[c(RGDfK)]$_2$ and DOTA-E[c(RGDyK)]$_2$ (*27*, *32*, *34*, *35*).

For the radiolabeled RGD peptide radiotracer to be clinically useful, it is necessary to demonstrate its capability to image the integrin $\alpha_v\beta_3$ expression in animal models bearing solid tumors of different origin. Janssen and co-workers evaluated the biodistribution characteristics of [^{99m}Tc(SQ168)(tricine)(TPPTS)] in BALB/c nude mice with subcutaneous OVCAR-3 ovarian cancer xenografts (*33*). Recently, we reported the evaluation of [^{99m}Tc(SQ168)(tricine)(L)] (L = TPPTS, ISONIC, and PDA) in nude mice bearing the MDA-MB-435 human breast cancer xenografts (*31*). In this study, we use the BALB/c nude mice bearing the U87MG human glioma xenografts to examine biodistribution properties of three radiotracers, [^{99m}Tc(SQ168)(EDDA)], [^{99m}Tc(SQ168)(tricine)(PDA)], and [^{99m}Tc(SQ168)(tricine)(TPPTS)], and their capability to image the glioma integrin $\alpha_v\beta_3$ expression. On the basis of biodistribution data, it is clear that all three radiotracers are able to localize in glioma tumors with moderately high tumor uptake (>2% ID/g over 4 h study period) and long tumor retention time. Results from the blocking experiment suggest that their tumor localization is integrin $\alpha_v\beta_3$-mediated. SPECT imaging studies have demonstrated that the glioma tumors can be clearly visualized with all three radiotracers at 4 h postinjection. On the basis of their clearance patterns from blood, muscle, liver, and lungs, it seems that [^{99m}Tc(SQ168)(tricine)(TPPTS)] has the best imaging quality (Figure 6).

Several approaches have been used to modify pharmacokinetics of the radiolabeled cyclic RGD peptides. For example, a sugar moiety has been used to improve the hepatobiliary clearance of ^{18}F-labeled cyclic RGD peptides (*17*−*19*). The poly(ethylene glycol) linking groups are also useful for improving both tumor uptake and liver clearance of radiolabeled cyclic RGD peptides (*23*, *24*, *27*, *52*−*54*). A number of coligands have been used to modify biological properties of the ^{99m}Tc-labeled HYNIC-biomolecule conjugates (*29*, *31*, *36*−*38*, *56*−*60*). For example, it was found that the coligands had significant impact on biodistribution properties of complexes [^{99m}Tc(fMLFK−HYNIC)(L)$_2$] (L = glucoheptonate, mannitol, glucamine, and tricine) (*57*). [^{99m}Tc(HYNIC-TOC)(tricine)$_2$] (TOC = Tyr^3-octreotide) was found to have higher protein binding than [^{99m}Tc(HYNIC-TOC)(EDDA)] and [^{99m}Tc(HYNIC-TOC)(tricine)(NA)] (*58*, 59). It was reported that the best coligand combinations are tricine/NIC and tricine/ISONIC for the ^{99m}Tc-lablled HYNIC−CCK8 (CCK8 = cholecystokinin peptides) conjugates (*60*). In our previous study, we also found that [^{99m}Tc(SQ168)(tricine)(PDA)] had lower liver uptake in the athymic nude mice bearing the MDA-MB-435 human breast cancer xenografts over 2 h study period, and better tumor/liver ratios than [^{99m}Tc(SQ168)(tricine)(TPPTS)] at >60 min postinjection (*31*). In this study, [^{99m}Tc(SQ168)(tricine)(TPPTS)] was found to have the lowest liver uptake (Figure 5) and the best imaging quality (Figure 6) in BALB/c nude mice bearing U87MG human glioma xenografts. It also has the highest metabolic stability (Figure 7) in normal BALB/c nude mice. We believe that this discrepancy is most likely caused by the animal species. Therefore, caution must be taken when comparing biodistribution and excretion characteristics of radiotracers in different animals.

The choice of coligand for routine preparation of complexes [^{99m}Tc(SQ168)(tricine)(L)] (L = TPPTS, NIC, ISONIC, and PDA) depends on several factors. For example, the radiotracer must demonstrate its capability to image the tumor integrin $\alpha_v\beta_3$ expression in various animal models. It must be excreted via the renal route to minimize the unwanted radioactivity accumulation in the abdominal region. It should have a high metabolic stability. In addition, a kit formulation is needed for routine preparation of the radiotracer. From the formulation development point of view, TPPTS has the obvious advantage over ISONIC and PDA since it is a strong reducing agent, and stannous chloride is not needed for successful preparation of [^{99m}Tc(SQ168)(tricine)(TPPTS)]. A non-$SnCl_2$ formulation has been developed for routine ^{99m}Tc-labeling of the HYNIC-conjugated cyclic RGD peptides (*61*). Since TPPTS is able to "extract" the oxygen from [^{99m}Tc]pertechnetate, there is virtually no [^{99m}Tc]colloid formation if the non-$SnCl_2$ formulation is used for ^{99m}Tc-labeling.

On the basis of the results from this and our previous studies, it is concluded that coligands in ternary ligand ^{99m}Tc complexes [^{99m}Tc(SQ168)(tricine)(L)] (L = TPPTS, NIC, ISONIC, and PDA) have minimal effect on their tumor-targeting capability. The coligand effect on excretion kinetics and metabolic fate of the radiotracer is not completely consistent in two animal species. Therefore, their biodistribution patterns and metabolic stability must be verified in larger rodents or mammals, which are more indicative of those in humans.

CONCLUSION

The key finding of this study is that all three radiotracers, [^{99m}Tc(SQ168)(EDDA)], [^{99m}Tc(SQ168)(tricine)(PDA)], and [^{99m}Tc(SQ168)(tricine)(TPPTS)], are able to localize in glioma tumors via integrin $\alpha_v\beta_3$-binding. The coligand has minimal effect on the integrin $\alpha_v\beta_3$-targeting capability of radiotracers, but it has a significant impact on their biodistribution properties. Results from the SPECT imaging studies show that glioma tumors can be clearly visualized with all three radiotracers at 4 h postinjection. On the basis of their clearance patterns from blood, muscle, liver, and lungs, it seems that [^{99m}Tc(SQ168)(tricine)(TPPTS)] has the best imaging quality and is a promising candidate for more preclinical evaluations in the future.

ACKNOWLEDGMENT

Authors would thank Professor Jingde Zhu, Shanghai Cancer Research Institute, for providing the U87MG human glioma cells. This work is supported, in part, by Peking University Health Science Center (F.W.) and research grants: Z00004105040311 (F.W.) from Beijing Science and Technology Program and BCTR0503947 (S.L.) from Susan G. Komen Breast Cancer Foundation.

Supporting Information Available: Biodistribution data (%ID/g) for [^{99m}Tc(SQ168)(EDDA)], [^{99m}Tc(SQ168)(tricine)(PDA)], and [^{99m}Tc(SQ168)(tricine)(TPPTS)] are listed in Tables S1−S3. Figure SI shows the radio-HPLC chromatograms of [^{99m}Tc(SQ168)(EDDA)] in kit matrix, urine, and feces at 2 h postinjection. These materials are available free of charge at http://pubs.acs.org.

LITERATURE CITED

(1) Davis, F. G., Freels, S., Grutsch, J., Barlas, S., and Brem, S. (1998) Survival rates in patients with primary malignant brain tumors stratified by patient age and tumor histological type: an analysis based on Surveillance, Epidemiology, and End Results (SEER) data, 1973−1991. *J. Neurosurg. 88*, 1−10.

(2) Black, P. M. (1991) Brain Tumor. Part 2. N. *Engl. J. Med. 324*, 1555−1564.

(3) Grossman, S. A., and Batara, J. F. (2004) Current management of glioblastoma multiforme. *Semin. Oncol. 31*, 635−644.
(4) Puduvali, V. K., and Sawaya, R. (2000) Antiangiogenesis-therapeutic strategies and clinical implications for brain tumors. *J. Neuro-Oncol. 50*, 189−200.
(5) Bögler, O., and Mikkelsen, T. (2003) Angiogenesis in Glioma: molecular mechanisms and roadblocks to translation. *Cancer J. 9*, 205−213.
(6) Bello, L., Francolini, M., Marthyn, P., Zhang, J., Carroll, R. S., Nikas, D. C., Strasser, J. F., Villani, R., Cheresh, D. A., and Black, P. M. (2001) Alpha(v)beta3 and alpha(v)beta5 integrin expression in glioma periphery integrin expression in glioma periphery. *Neurosurgery 49*, 380−390.
(7) Meitar, D., Crawford, S. E., Rademaker, A. W., and Cohn, S. L. (1996) Tumor angiogenesis correlates with metastatic disease, N-*myc*-amplification, and poor outcome in human neuroblastoma. *J. Clin. Oncol. 14*, 405−414.
(8) Weber, W. A., Haubner, R., Vabuliene, E., Kuhnast, B., Webster, H. J., and Schwaiger, M. (2001) Tumor angiogenesis targeting using imaging agents. *Q. J. Nucl. Med. 45*, 179−182.
(9) Costouros, N. G., Diehn, F. E., and Libutti, S. K. (2002) Molecular imaging of tumor angiogenesis. *J. Cell Biol. Suppl. 39*, 72−78.
(10) van de Wiele, C., Oltenfreiter, R., De Winter, O., Signore, A., Slegers, G., and Dieckx, R. A. (2002) Tumor angiogenesis pathways: related clinical issues and implications for nuclear medicine imaging. *Eur. J. Nucl. Med. 29*, 699−709.
(11) Liu, S., Robinson, S. P., and Edwards, D. S. (2003) Integrin $\alpha_v\beta_3$ directed radiopharmaceuticals for tumor imaging. *Drugs Future 28*, 551−564.
(12) McDonald, D. M., and Choyke, P. (2003) Imaging Angiogenesis: from microscope to clinic. *Nat. Med. 9*, 713−725.
(13) Haubner, R., and Wester, H. J. (2004) Radiolabeled tracers for imaging of tumor angiogenesis and evaluation of anti-angiogenic therapies. *Curr. Pharm. Des. 10*, 1439−1455.
(14) Sipkins, D. A., Cheresh, D. A., Kazemi, M. R., Nevin, L. M., Bednarski, M. D., Li, K. C. (1998) Detection of tumor angiogenesis *in vivo* by $\alpha_v\beta_3$-targeted magnetic resonance imaging. *Nat. Med. 4*, 623−626.
(15) Ellegala, D. B., Leong-Poi, H., Carpenter, J. E., Klibanov, A. L., Kaul, S., Shaffrey, M. E., Sklenar J., and Lindner, J. R. (2003) Imaging tumor angiogenesis with contrast ultrasound and microbubbles targeted to $\alpha_v\beta_3$. *Circulation 108*, 336−341.
(16) Chen, X., Conti, P. S., and Moats, R. A. (2004) In vivo near-infrared fluorescence imaging of integrin $\alpha_v\beta_3$ in brain tumor xenografts. *Cancer Res. 64*, 8009−8014.
(17) Haubner, R., Wester, H. J., Weber, W. A., Mang, C., Ziegler, S. I., Goodman, S. L., Senekowisch-Schmidtke, R., Kessler, H., and Schwaiger, M. (2001) Noninvasive imaging of $\alpha v\beta 3$ integrin expression using ^{18}F-labeled RGD-containing glycopeptide and positron emission tomography. *Cancer Res. 61*, 1781−1785.
(18) Beer, A. J., Haubner, R., Goebel, M., Luderschmidt, S., Spilker, M. E., Webster, H.-J., Weber, W. A., and Schwaiger, M. (2005) Biodistribution and pharmacokineticss of the $\alpha_v\beta_3$-selective tracer ^{18}F−Galacto-RGD in cancer patients. *J. Nucl. Med. 46*, 1333−1341.
(19) Haubner, R., Weber, W. A., Beer, A. J., Vabulience, E., Reim, D., Sarbia, M., Becker, K.-F., Goebel, M., Hein, R., Wester, H.-J., Kessler, H., and Schwaiger, M. (2005) Noninvasive visuallization of the activiated $\alpha_v\beta_3$ integrin in cancer patients by positron emission tomography and [^{18}F]Galacto-RGD. *PLOS Med.* 2: e70.
(20) Chen, X., Shahinian, A., Park, R., Bozorgzadeh, M. H., Bading, J. R., and Conti, P. S. (2003) ^{18}F-labeled cyclic RGD peptide for PET imaging of tumor angiogenesis. *J. Nucl. Med. 55 (5 Suppl)*, 271−272P.
(21) Chen, X., Park, R., Shahinian, A. H., Tohme, M., Khankaldyyan, V., Bozorgzadeh, M. H., Bading, J. R., Moats, R., Laug, W. E., and Conti, P. S. ^{18}F-labeled RGD peptide: initial evaluation for imaging brain tumor Angiogenesis. *Nucl. Med. Biol.* **2004**, *31*, 179−189.
(22) Chen, X.-Y., Park, R., Tohme, M., Shahinian, A. H., Bading, J. R., and Conti, P. S. (2004) MicroPET and autoradiographic imaging of breast cancer α_v-integrin expression using ^{18}F- and ^{64}Cu-labeled RGD peptide. *Bioconjugate Chem. 15*, 41−49.
(23) Chen, X., Park, R., Shahinian, A. H., Tohme, M., Khankaldyyan, V., Bozorgzadeh, M. H., Bading, J. R., Moats, R., Laug, W. E., and Conti, P. S. (2004) ^{18}F-labeled RGD peptide: initial evaluation for imaging brain tumor Angiogenesis. *Nucl. Med. Biol. 31*, 179−189.
(24) Chen, X., Park, R., Shahinian, A. H., Bading, J. R., and Conti, P. S. (2004) Pharmacokinetics and tumor retention of ^{125}I-labeled RGD peptide are improved by PEGylation. *Nucl. Med. Biol. 31*, 11−19.
(25) Haubner, R., Wester, H.-J., Reuning, U., Senekowisch-Schmidtke, R., Diefenbach, B., Kessler, H., Stöcklin, G., and Schaiger, M. (1999) Radiolabeled $\alpha_v\beta_3$ integrin antagonists: a new class of tracers for tumor imaging. *J. Nucl. Med. 40*, 1061−1071.
(26) Haubner, R., Wester, H. J., Burkhart, F., Senekowisch-Schmidtke, R., Weber, W., Goodman, S. L., Kessler, H., and Schwaiger, M. (2001) Glycolated RGD-containing peptides: tracer for tumor targeting and angiogenesis imaging with improved biokinetics. *J. Nucl. Med. 42*, 326−336.
(27) Chen, X., Sievers, E., Hou, Y., Park, R., Tohme, M., Bart, R., Bremner, R., Bading, J. R., and Conti, P. S. (2005) Integrin $\alpha_v\beta_3$-targeted imaging of lung cancer. *Neoplasia 7*, 271−279.
(28) Haubner, R., Bruchertseifer, F., Bock, M., Schwaiger, M., Wester, H.-J. (2004) Synthesis and biological evaluation of ^{99m}Tc-labeled cyclic RGD peptide for imaging integrin $\alpha_v\beta_3$ expression. *Nuklearmedizin 43*, 26−32.
(29) Liu, S., Edwards, D. S., Ziegler, M. C., Harris, A. R., Hemingway, S. J., and Barrett, J. A. (2001) ^{99m}Tc-Labeling of a hydrazinonicotinamide-conjugated vitronectin receptor antagonist. *Bioconjugate Chem. 12*, 624−629.
(30) Liu, S., Cheung, E., Rajopadyhe, M., Ziegler, M. C., and Edwards, D. S. (2001) ^{90}Y- and ^{177}Lu-labeling of a DOTA-conjugated vitronectin receptor antagonist for tumor therapy. *Bioconjugate Chem. 12*, 559−568.
(31) Liu, S., Hsieh, W. Y., Kim, Y. S., and Mohammed, S. I. (2005) Effect of coligands on biodistribution characteristics of ternary ligand ^{99m}Tc complexes of a HYNIC-conjugated cyclic RGDfK dimer. *Bioconjugate Chem. 16*, 1580−1588.
(32) Chen, X. Y., Liu, S., Hou, Y., Tohme, M., Park, R., Bading, J. R., and Conti, P. S. (2004) MicroPET imaging of breast cancer integrin $\alpha_v\beta_3$ expression with ^{64}Cu-labeled dimeric RGD-containing cyclic peptides. *Mol. Imag. Biol.* 350−359.
(33) Janssen, M., Oyen, W. J. G., Massuger, L. F. A. G., Frielink, C., Dijkgraaf, I., Edwards, D. S., Rajopadyhe, M., Corsten, F. H. M., and Boerman, O. C. (2002) Comparison of a monomeric and dimeric radiolabeled RGD-peptide for tumor targeting. *Cancer Biother. Radiopharm. 17*, 641−646.
(34) Janssen, M., Oyen, W. J. G., Dijkgraaf, I., Massuger, L. F. A. G., Frielink, C., Edwards, D. S., Rajopadyhe, M., Boonstra, H., Corsten, F. H., and Boerman, O. C. (2002) Tumor targeting with radiolabeled integrin $\alpha_v\beta_3$ binding peptides in a nude mice model. *Cancer Res. 62*, 6146−6151.
(35) Janssen, M. L., Frielink, C., Dijkgraaf, I., Oyen, W. J., Edwards, D. S., Liu, S., Rajopadhye, M., Massuger, L. F., Corstens, F. H., and Boerman O. C. (2004) Improved tumor targeting of radiolabeled RGD-peptides using rapid dose fractionation. *Cancer Biother. Radiopharm. 19*, 399−404.
(36) Bangard, M., Béhé, M., Guhlke, S., Otte, R., Bender, H., Maecke, H. R., and Biersack, H. J. (2000) Detection of somatostatin receptor-positive tumors using the new ^{99m}Tc-tricine-HYNIC-D-Phe^1-Tyr^3-octreotide: first results in patients and comparison with ^{111}In-DTPA-D-Phe^1-octreotide. *Eur. J. Nucl. Med. 27*, 628−637.
(37) Decristoforo, C., Melendez-Alafort, L., Sosabowski, J. K., and Mather, S. J. (2000) ^{99m}Tc−HYNIC-[Tyr^3]-octreotide for imaging somatostatin-receptor-positive tumors: preclinical evaluation and comparison with ^{111}In-Octreotide. *J. Nucl. Med. 41*, 1114−119.
(38) Decristoforo, C., Mather, S. J., Cholewinski, W., Donnemiller, E., Riccabona, G., and Moncayo, R. (2000) ^{99m}Tc-EDDA/HYNIC-TOC: a new ^{99m}Tc-labeled radiopharmaceutical for imaging somatostatin receptor-positive tumors: first clinical results and intrapatient comparison with ^{111}In-labeled octreotide derivatives. *Eur. J. Nucl. Med. 27*, 1318−1325.
(39) Wu, Y., Zhang, X. Z., Xiong, Z. M., Cheng, Z., Fisher, D. R., Liu, S., and Chen, X. Y. (2005) MicroPET imaging of glioma α_v-integrin expression using ^{64}Cu-labeled tetrameric RGD peptide. *J. Nucl. Med. 46*, 1707−1718.
(40) Folkman, J. (2002) Role of angiogenesis in tumor growth and metastasis. *Semin. Oncol. 29*, 15−18.
(41) Brook, P. C., Clark, R. A. F., and Cheresh, D. A. (1994) Requirement of vascular integrin $\alpha_v\beta_3$ for angiogenesis. *Science 264*, 569−571.

(42) Friedlander, M., Brooks, P. C., Shiller, R. W., Kincaid, C. H., Varner, J. A., and Cheresh, D. A. (1995) Definition of two angiogenic pathways by distinct α_v integrin. *Science 270*, 1500−1502.

(43) Horton, M. A. (1997) The $\alpha_v\beta_3$ integrin "vitronectin receptor". *Int. J. Biochem. Cell Biol. 29*, 721−725.

(44) Carmeliet, P. (2000) Mechanism of angiogenesis and atherogenesis. *Nat. Med. 6*, 389−395.

(45) Gasparini, G., Brooks, P. C., Biganzoli, E., Vermeulen, P. B., Bonoldi, E., Dirix, L. Y., Ranieri, G., Miceli, R., and Cheresh, D. A. (1998) Vascular integrin $\alpha_v\beta_3$: a new prognostic indicator in breast cancer. *Clin. Cancer Res. 4*, 2625−2634.

(46) Sengupla, S., Chattopadhyay, N., Mitra, A., Ray, S., Dasgupta, S., and Chatterjee, A. (2001) Role of $\alpha_v\beta_3$ integrin receptors in breast tumor. *J. Exp. Clin. Cancer Res. 20*, 585−590.

(47) Zitzmann, S., Ethemann, V., and Schwab, M. (2002) Arginine-Glycine-Aspartic acid (RGD)-peptide binds to both tumor and tumor endothelial cells in vivo. *Cancer Res. 62*, 5139−5143.

(48) Hwang, R., and Varner, J. V. (2004) The role of integrins in tumor angiogenesis. *Hematol. Oncol. Clin. North. Am. 18*, 991−1006.

(49) Jin, H., and Varner, J. (2004) Integrins: roles in cancer development and as treatment targets. *Br. J. Cancer 90*, 561−565.

(50) Kumar, C. C. (2003) Integrin $\alpha_v\beta_3$ as a therapeutic target for blocking tumor-induced angiogenesis. *Curr. Drug Targets 4*, 123−131.

(51) Poethko, T., Schottelius, M., Thumshirn, G., Hersel, U., Herz, M., Henriksen, G., Kessler, H., Schaiger, M., and Wester, H. J. (2004) Two-step methodology for high yield routine radiohaligenation of peptides: ^{18}F-labeled RGD and octreotide analogs. *J. Nucl. Med. 45*, 892−902.

(52) Thumshirn, G., Hersel, U., Goodman, S. L., and Kessler, H. (2003) Multimeric cyclic RGD peptides as potential tools for tumor targeting: solid-phase peptide synthesis and chemoselective oxime ligation. *Chem. Eur. J. 9*, 2717−2725.

(53) Poethko, T., Schottelius, M., Thumshirn, G., Hersel, U., Herz, M., Henriksen, G., Kessler, H., Schaiger, M., and Wester, H. J. (2004) Two-step methodology for high yield routine radiohaligenation of peptides: ^{18}F-labeled RGD and octreotide analogs. *J. Nucl. Med. 45*, 892−902.

(54) Poethko, T., Schottelius, M., Thumshirn, G., Herz, M., Haubner, R., Henriksen, G., Kessler, H., Schwaiger, M., and Wester, H.-J. Chemoselective pre-conjugate radiohalogenation of unprotected mono- and multimeric peptides via oxime formation. *Radiochim. Acta* **2004**, *92*, 317−327.

(55) Dijkgraaf, I., John, A. W., Kruijtzer, J. A. W., Liu, S., Soede, A., Oyen, W. J. G., Corstens, F. H. M., Liskamp, R. M. J., and Boerman, O. C. Improved Targeting of $\alpha_v\beta_3$ by Multimerization of RGD Peptides. *Eur. J. Nucl. Med.* Submitted.

(56) Barrett, J. A., Crocker, A. C., Damphousse, D. J., Heminway, S. J., Liu, S., Edwards, D. S., Lazewatsky, J. L., Kagan, M., Mazaika, T. J., and Carroll, T. R. (1997) Biological evaluation of thrombus imaging agents utilizing water soluble phosphines and tricine as coligands when used to label a hydrazinonicotinamide-modified cyclic glycoprotein IIb/IIIa receptor antagonist with ^{99m}Tc. *Bioconjugate Chem. 8*, 155−160.

(57) Babich, J. W., and Fischman, A. J. (1995) Effect of "co-ligand" on the biodistribution of ^{99m}Tc-labeled hydrazino nicotinic acid derivatized chemotactic peptides. *Nucl. Med. Biol. 22*, 25−30.

(58) Decristoforo, C., and Mather, S. J. (1999) Preparation, ^{99m}Tc-labeling, and in vitro characterization of HYNIC and N_3S modified RC-160 and [Tyr^3]octreotide. *Bioconjugate Chem. 10*, 431−438.

(59) Decristoforo, C., and Mather, S. J. (1999) Technetium-99m somatostatin analogues: effect of labelling methods and peptide sequence. *Eur. J. Nucl. Med. 26*, 869−876.

(60) Laverman, P., Béhé, M., Oyen, W. J. G., Willems, P. H. G. M., Corstens, F. H. M., Behr, T. M., and Boerman, O. C. (2004) Two technetium-99m-labeled cholecystokinin-8 (CCK8) peptides for scintigraphic imaging of CCK receptors. *Bioconjugate Chem. 15*, 561−568.

(61) Liu, S., Edwards, D. S., Harris, A. R., Ziegler, M. C., Poirier, M. J., Ewels, B. A., DiLuzio, W. R., and Hui, P. (2001) Towards developing a non-$SnCl_2$ formulation for RP444: a new radiopharmaceutical for thrombus imaging. *J. Pharm. Sci. 90*, 114−123.

BC060055B

Methacrylamide Polymers with Hydrolysis-Sensitive Cationic Side Groups as Degradable Gene Carriers

Jordy Luten, Niels Akeroyd, Arjen Funhoff, Martin C. Lok, Herre Talsma, and Wim E. Hennink*

Department of Pharmaceutics, Utrecht Institute for Pharmaceutical Sciences (UIPS), Faculty of Pharmaceutical Sciences, Utrecht University, P.O. Box 80.082, 3508 TB Utrecht, The Netherlands. Received March 17, 2006; Revised Manuscript Received June 8, 2006

Water-soluble polymers with hydrolyzable cationic side groups (structure of the monomers are shown in Figure 1) were synthesized and evaluated as DNA delivery systems. The polymers, except for pHPMA−NHEM, were able to condense plasmid DNA into positively charged nanosized particles. The rate of hydrolysis at 37 °C and pH 7.4 of the side groups differed widely; the fastest rate of hydrolysis was observed for HPMA−DEAE (half-life of 2 h), while HPMA−DMAPr had the lowest rate of hydrolysis (half-life of 70 h). In line with this, pHPMA−DEAE-based polyplexes showed the fastest destabilization of the polyplexes at 37 °C and pH 7.4. Polyplexes based on pHPMA−DEAE, pHPMA−DMAE, and pHPMA−MPPM showed release of intact DNA within 24, 48, and 48 h, respectively, after incubation at 37 °C and pH 7.4. PHPMA−DEAE and pHPMA−MPPM based polyplexes showed the highest transfection activity (almost twice as active as pEI). Importantly, the pHPMA−DEAE, pHPMA−MPPM, and pHPMA−BDMPAP polyplexes preserved their transfection activity in the presence of serum proteins. All polymers investigated showed a substantial lower in vitro cytotoxicity than pEI. In conclusion, pHPMA-based polyplexes are an attractive class of biodegradable vectors for nonviral gene delivery.

INTRODUCTION

Gene therapy aims to treat various forms of diseases with a genetic origin including cystic fibrosis, different forms of cancer, and cardiovascular disorders (*1*−*3*). For the treatment of patients using gene therapy protocols, safe and efficient DNA delivery vehicles are needed. The gene delivery vehicles under investigation at present can be divided into viral and nonviral systems. The majority of gene therapy protocols clinically used in the past decade employs viral delivery systems, such as retroviruses, adenoviruses, and adeno-associated viruses (*4*). However, severe drawbacks are associated with the use of viral vectors, like the induction of an immune response against the viral proteins, possible recombination with wild-type viruses, limitations in the size of inserted DNA, and difficult large-scale pharmaceutical grade production (*5*, *6*).

As an alternative for the viral vectors, cationic lipids and polymers have been developed as nonviral carrier systems. Examples of frequently studied cationic gene delivery polymers are polyethylenimine (pEI), poly(2-dimethylaminoethyl methacrylate) (pDMAEMA), and poly-L-lysine (pLL) (*7*−*10*). However, these polymers either are nonbiodegradable (pEI and pDMAEMA) or show low transfection activity (pLL). Therefore, in recent years, biodegradable polycations are designed as DNA delivery vehicles. The potential advantage of biodegradable carriers is their reduced toxicity. Moreover, the degradation of the polymer can be used as a tool to release the plasmid DNA into the cytosol. It has been reported that biodegradable polymers, like poly[α-(4-aminobutyl)-L-glycolic acid] (pAGA), poly(2-aminoethylpropylene phosphate), and more recently polyphosphazenes and poly(ester amine)s, mediate gene transfection (*11*−*16*). Generally speaking, these polymers indeed have a lower toxicity than their nondegradable counterparts. However, the degradation of these polymers depends on the degradation of the polymer backbone and is rather slow (from days to months). Since the cellular uptake and endosomal escape of polyplexes take place within hours (*17*), the design of polymers with more rapid degradation kinetics is a logical step. Pack et al. (*18*) reported on degradable pEI derivatives, which had half-lives between 4 and 30 h. However, the degradation rate of the polymers was the same under conditions mimicking cytoplasmic and endosomal conditions. Recently, Funhoff et al. (*19*) reported on a novel polymer, poly(carbonic acid 2-dimethylamino-ethyl ester 1-methyl-2-(2-methacryloylamino)-ethyl ester) (pHPMA−DMAE), that has degradable cationic side groups with a half-life of around 10 h at pH 7.4 at 37 °C. Moreover, this polymer is rather stable at pH 5, therefore protecting the plasmid DNA in the endosomal compartment of the cell against DNAase induced degradation. A limitation of pHPMA−DMAE is that it only shows significant transfection in the absence of serum.

The aim of this study is to investigate whether a polymer with hydrolysis-sensitive cationic side groups could be developed that shows significant transfection in the presence of serum. It has been reported that structural variations in gene delivery polymers can have a significant impact on their transfection efficacy (*9*, *20*, *21*). Therefore, polymers with structures related to that of pHPMA−DMAE were synthesized and characterized. The corresponding polyplexes were studied for their destabilization behavior and evaluated in vitro for their transfection activities and cytotoxicity properties.

MATERIALS AND METHODS

Materials. The following materials were used as received: D,L-1-amino-2-propanol 99+%,1-methyl-2-piperidine methanol (MPPM), *N*-(2-hydroxyethyl)morpholine (NHEM), *N*,*N*-diethylaminoethanol (DEAE), 1,1′-carbonyldiimidazole (CDI) (all purchased from Acros, Geel, Belgium), *N*,*N*-dimethylaminoethanol (DMAE), 1-[bis[3-(dimethylamino)propyl]amino]-2-propanol (BDMPAP), and *N*,*N*-dimethylaminopropanol (DMAPr) (all purchased from Aldrich, Zwijndrecht, The Netherlands). Hydroquinone monomethyl ether and poly(L-aspartic acid),

* To whom correspondence should be addressed. Phone: +31-30-2536964. Fax: +31-30-2517839. E-mail: W.E.Hennink@pharm.uu.nl.

10.1021/bc060068p CCC: $33.50 © 2006 American Chemical Society
Published on Web 06/27/2006

Table 1. Overview of Results of the Synthesis and Polymerization of the Monomers, the Molecular Mass of the Synthesized Polymers, and pK_a Values of the Monomers and Polymers

monomer	amount of alcohol (mL)[a]	yield of monomer over two steps	pK_a monomer in NaCl[b]	M_w of polymer (kDa)	M_n of polymer (kDa)	average pK_a of polymer in NaCl[b]	yield of polymer
HPMA−DMAE	2.50	2.70 g (42%)	9.9	100	50	9.5	600 mg (72%)
HPMA−DEAE	3.50	2.86 g (40%)	9.8	40	20	8.7	605 mg (66%)
HPMA−DMAPr	3.00	3.75 g (55%)	8.1	60	15	7.1	655 mg (75%)
HPMA−MPPM	3.50	3.73 g (50%)	9.7	25	10	9.3	649 mg (68%)
HPMA−BDMPAP	7.00	3.11 g (30%)	5.8, 8.1, 8.9	70	25	7.0	796 mg (60%)
HPMA−NHEM	3.00	3.90 g (52%)	9.3	90	40	9.1	673 mg (70%)

[a] 25 mmol of alcohol used in the first step of the monomer synthesis. [b] $\mu = 0.15$ M.

p(Asp) (p5387), were purchased from Sigma (Zwijndrecht, The Netherlands). Methacryloyl chloride (97%, Fluka, Zwijndrecht, The Netherlands) was freshly distilled before use. The plasmid pCMVLacZ, containing a bacterial LacZ gene preceded by a nuclear localization signal under control of a CMV promoter, was purchased from Sanvertech (Heerhugowaard, The Netherlands). INF-7, a 24 amino acid containing peptide with fusogenic activity derived from the influenza virus, was synthesized via standard Fmoc solid-phase synthesis (*22*). Poly((dimethylamino)ethyl methacrylate) (pDMAEMA, $M_n = 92$ kg/mol) was synthesized via radical polymerization (*23*), and PEI (branched, 25 kDa) was purchased from Sigma. *N*-(2-Hydroxypropyl)-methacrylamide (HPMA) was synthesized according to Oupicky et al. (*24*).

Monomer Synthesis. A dry round-bottom flask was filled with 1,1′-carbonyldiimidazole (CDI) (6.84 g, 45.0 mmol) and 40 mL of dichloromethane. The different alcohols (25.0 mmol) (Table 1) were added dropwise over a period of 15 min to the suspension of CDI in dichloromethane. During the addition of the alcohol a clear solution was obtained, which was stirred for 2 h at room temperature. Next, the reaction mixture was washed with water (70 mL), dried over $MgSO_4$, and filtered, and the solvent was removed under reduced pressure, yielding the corresponding carbamates as colorless oils. The ^{1}H NMR data of the carbamates are given below.

DMAE−CI: ^{1}H NMR ($CDCl_3$, δ in ppm) 8.12 (s, 1H, NC*H*N), 7.40 (s, 1H, NCHCHN), 7.04 (s, 1H, NCHC*H*N), 4,48 (t, 2H, OCH_2), 2,68 (t, 2H, CH_2N), 2.29 (s 6H, N(CH_3)$_2$).

DEAE−CI: ^{1}H NMR ($CDCl_3$, δ in ppm) 8.14 (s, 1H, NC*H*N), 7.43 (s, 1H, NCHCHN), 7.06 (s, 1H, NCHC*H*N), 4.48 (t, 2H, OCH_2), 2.82 (t, 2H, CH_2N), 2.62 (dq, 4H, N(CH_2)$_2$), 1.04 (dt, 6H, N(CH_2CH_3)$_2$).

MPPM−CI: ^{1}H NMR ($CDCl_3$, δ in ppm) 8.13 (s, 1H, NC*H*N), 7.41 (s, 1H, NCHCHN), 7.04 (s, 1H, NCHC*H*N), 4.48 (t, 2H, OCH_2), 2.80 (m, 1H, OCH$_2$C*H*N), 2.37 (s, 3H, CH_3N), 2.23 (m, 2H, CH_2-ring), 1.65 (m, 6H, CH_2-ring).

DMAPr−CI: ^{1}H NMR ($CDCl_3$, δ in ppm) 8.14 (s, 1H, NC*H*N), 7.42 (s, 1H, NCHCHN), 7.08 (s, 1H, NCHC*H*N), 4.49 (t, 2H, OCH_2), 2.45 (t, 2H, CH_2N), 2.29 (s 6H, N(CH_3)$_2$), 2.01 (quintet, 2H, (CH_2CH_2CH$_2$).

BDMPAP−CI: ^{1}H NMR ($CDCl_3$, δ in ppm) 8.13 (s, 1H, NC*H*N), 7.43 (s, 1H, NCHCHN), 7.06 (s, 1H, NCHC*H*N), 5.21 (m, 1H, OC*H*CH$_3$), 2.71 (bs, 2H, OCH(CH$_3$)CH_2N), 2.52 (m 4H, CH_2N((CH$_2$)$_3$N(CH$_3$)$_2$)$_2$), 2.43 (m, 4H, CH_2CH_2CH_2N-(CH$_3$)$_2$)$_2$), 2.24 (bs 12H, N((CH$_2$)$_3$N(CH_3)$_2$)$_2$), 1.57 (m, 4H, CH$_2$N(CH_2CH_2CH_2N(CH$_3$)$_2$)$_2$), 1.37 (d, 3H, OCHCH_3).

NHEM−CI: ^{1}H NMR ($CDCl_3$, δ in ppm) 8.15 (s, 1H, NC*H*N), 7.44 (s, 1H, NCHCHN), 7.09 (s, 1H, NCHC*H*N), 4.58 (t, 2H, OCH_2), 3.74 (bs, 4H, (CH_2)$_2$O), 2.81 (t, 2H, CH_2N), 260 (bs, 4H, N(CH_2)$_2$).

In the next step the carbamate was dissolved in toluene (10 mL) and *p*-methoxyphenol (10 mg) was added as an inhibitor to prevent premature polymerization. HPMA (1.1 equiv) in toluene (10 mL) was added. The reaction mixture was stirred overnight at 80 °C, and subsequently the solvent was removed under reduced pressure. The product was purified using silica flash column chromatography (eluent 1 (EtOAc) used to remove the inhibitor ($R_f = 0.9$) and free HPMA ($R_f = 0.4$), followed by eluent 2 (MeOH/CH_2Cl_2 (1/9 v/v) used to elute the product from the column). The ^{1}H NMR data of the monomers are given below.

HPMA−DMAE: ^{1}H NMR ($CDCl_3$, δ in ppm) 6.40 (bs, 1H, CON*H*CH$_2$), 5.73 (s 1H, H_2C═C), 5.34 (s 1H, H_2C═C), 4.86 (m, 1H, CH$_2$C*H*(CH$_3$)O), 4.20 (m, 2H, s OCH_2CH$_2$), 3.60 (m, 2H, CH_2CH(CH$_3$)O), 2.74 (t, 2H, OCH$_2$CH_2N), 2.40 (s, 6H, N(CH_3)$_2$), 1.97 (s, 3H, CH_2═CCH_3), 1.30 (d, 3H, CH_2CH-(CH_3)O).

HPMA−DEAE: ^{1}H NMR ($CDCl_3$, δ in ppm) 6.60 (bs, 1H, CON*H*CH$_2$), 5.73 (s 1H, H_2C═C), 5.34 (s 1H, H_2C═C), 4.86 (m, 1H, CH$_2$C*H*(CH$_3$)O), 4.30 (m, 2H, s OCH_2CH$_2$), 3.60 (m, 2H, CH_2CH(CH$_3$)O), 2.92 (t, 2H, OCH$_2$CH_2N), 2.78 (q, 2H, N(CH_2)$_2$), 2.57 (q, 2H, N(CH_2)$_2$), 1.97 (s, 3H, CH_2═CCH_3), 1.27 (d, 3H, CH_2CH(CH_3)O), 1.18 (t, 3H, N(CH_2CH_3)$_2$), 1.04 (t, 3H, N(CH_2CH_3)$_2$).

HPMA−MPPM: ^{1}H NMR ($CDCl_3$, δ in ppm) 6.40 (bs, 1H, CON*H*CH$_2$), 5.70 (s 1H, H_2C═C), 5.34 (s 1H, H_2C═C), 4.86 (m, 1H, CH$_2$C*H*(CH$_3$)O), 4.20 (m, 2H, s OCH_2CH$_2$), 3.60 (m, 2H, CH_2CH(CH$_3$)O), 2.86 (m, 1H, OCH$_2$C*H*N), 2.40 (s, 3H, NCH_3), 2.20 (m, 2H, CH_2-ring), 1.96 (s, 3H, CH_2═CCH_3), 1.60 (m, 6H, CH_2-ring) 1.30 (d, 3H, CH_2CH(CH_3)O).

HPMA−DMAPr: ^{1}H NMR ($CDCl_3$, δ in ppm) 6.50 (bs, 1H, CON*H*CH$_2$), 5.70 (s 1H, H_2C═C), 5.36 (s 1H, H_2C═C), 4.88 (m, 1H, CH$_2$C*H*(CH$_3$)O), 4.10 (m, 2H, s OCH_2CH$_2$), 3.60 (m, 2H, CH_2CH(CH$_3$)O), 2.48 (t, 2H, OCH$_2$CH$_2$CH_2N), 2.35 (s, 6H, N(CH_3)$_2$), 1.97 (s, 3H, CH_2═CCH_3), 1.80 (m, 2H, (CH_2CH_2-CH$_2$), 1.27 (d, 3H, CH_2CH(CH_3)O).

HPMA−BDMPAP: ^{1}H NMR ($CDCl_3$, δ in ppm) 6.60 (bs, 1H, CON*H*CH$_2$), 5.73 (s 1H, H_2C═C), 5.47 (s 1H, H_2C═C), 4.85 (m, 3H, CH$_2$C*H*(CH$_3$)O, OC*H*CH$_3$), 3.60 (m, 2H, NCH_2-CH(CH$_3$)O), 2.50 (m, 10H, CH_2N((CH$_2$)$_3$N(CH$_3$)$_2$)$_2$, CH$_2$N(CH_2-CH$_2$CH_2N(CH$_3$)$_2$)$_2$), 2.25 (m, 12H, N((CH$_2$)$_3$N(CH_3)$_2$)$_2$), 1.95 (s, 3H, CH_2═CCH_3), 1.65 (m, 4H, CH$_2$N(CH_2CH_2CH_2N-(CH$_3$)$_2$)$_2$), 1.26 (m, 6H, CH$_2$CH(CH_3)O, OCHCH_3).

HPMA−NHEM: ^{1}H NMR ($CDCl_3$, δ in ppm) 6.80 (bs, 1H, CON*H*CH$_2$), 5.58 (s 1H, H_2C═C), 5.23 (s 1H, H_2C═C), 4.80 (m, 1H, CH$_2$C*H*(CH$_3$)O), 4.14 (m, 2H, CH_2CH$_2$), 3.74 (bs, 4H, (CH_2)$_2$O), 3.60 (m, 2H, CH_2CH(CH$_3$)O), 2.81 (m, 2H, CH_2N), 260 (bs, 4H, N(CH_2)$_2$), 1.95 (s, 3H, CH_2═CCH_3), 1.27 (d, 3H, CH$_2$CH(CH_3)O).

Polymer Synthesis. The different monomers (3.2 mmol) were dissolved in dry dioxane (total volume of 2 mL) in a glass vial. Then 2,2′-azo-bis(isobutyronitrile) (AIBN) (1.2 mg, M/I = 400 (mol/mol) was added and the vial was capped, degassed, and extensively flushed with nitrogen. The reaction mixture was heated to 70 °C and stirred at this temperature for 16 h. Next, the reaction mixture was diluted with 20 mM ammonium acetate buffer, pH 5, and dialyzed with a Spectra/Por membrane MWCO 3500 (SPECTRUM, Breda, The Netherlands) against the same buffer for 3 days. After dialysis the solution was freeze-dried, and the polymer was obtained as a white fluffy material.

pK_a Measurements. The pK_a values of monomers and polymers were determined by titration with a Mettler Toledo DL21 titrator (Mettler Toledo, Tiel, The Netherlands). The compounds were dissolved in 0.9 w/v % NaCl solutions (concentration of 0.2−0.3 w/v %), acidified with 0.1 M HCl, and titrated with 0.25 M NaOH.

Hydrolysis of the Monomers. The different monomers (100 mg) were dissolved in 100 mM 4-(2-hydroxyethyl)-1-piperazine-ethanesulfonic acid (HEPES), adjusted to 150 mM with NaCl, pH 7.4, or in 100 mM sodium acetate, adjusted to 150 mM with NaCl, pH 5.0. The solutions were incubated at 37 °C, and samples were withdrawn at regular time intervals and immediately measured using RP-HPLC. The RP-HPLC system consisted of a Waters pump model 515 (Waters Associates, Milford, MA), Spark Marathon Basic+ injector (Spark, Emmen, The Netherlands), and a LKB 2151 UV detector (LKB, Roosendaal, The Netherlands) set at 210 nm. The columns used were a Merck LiChrosphere 100 (Merck, Darmstadt, Germany) RP-18 column (5 μm, 125 mm × 4 mm i.d.) and a RP-18 guard column (4 mm × 4 mm). The mobile phase consisted of a water−acetonitrile 95/5 (w/w) solution completed with 10 mM triethylamine and brought to pH 2 with TFA. The flow rate was 1 mL/min; the injection volume was 20 μL.

GPC Measurements. Weight average molecular weight (M_w) and number average molecular weight (M_n) of the synthesized polymers were determined by gel permeation chromatography (GPC), performed with three thermostated (35 °C) columns in series (Shodex OHpak SB-G and two SB-806M HQ, Showa Denko, Kawasaki, Japan) on a Waters HPLC system consisting of a controller (type 600), autosampler (type 717plus), tunable absorbance detector (type 486), and a differential refractometer (type 410) (Waters, Milford MA). Data were analyzed with Empower Pro software (Waters, Milford MA). The eluent was an aqueous solution of 0.3 m NaAc, pH 4.4, at a flow rate of 0.5 mL/min (*25*). The columns were calibrated with PEG standards (Fluka).

Size and Charge Measurements of the Polyplexes. The *Z*-average diameter of the polymer/plasmid DNA complexes were measured by dynamic light scattering (DLS) using a Malvern ALV CGS-3 system equipped with an argon-ion laser (488 nm, 10.4 mW) (uniphase). The ALV correlator software in combination with DTS(Nano) and ALVFilereader software was used. The instrument was calibrated with 100 nm poly(styrene) particles dispersed in water. In a typical experiment, 200 μL of HEPES buffer (5.0 mM, pH 7.4, adjusted to 150 mM with NaCl), containing 15 μg of plasmid DNA, was added to 800 μL of HEPES buffer (5.0 mM, pH 7.4, adjusted to 150 mM with NaCl) with various amounts of polymer. The resulting solution was vortexed for 5 s, and after 30 min of incubation time at room temperature the size of the polyplexes was determined using DLS at 25 °C.

The ζ-potential of the polyplexes was measured at 25 °C using a Zetasizer 2000 unit (Malvern) equipped with a DTS5001 cell. The instrument was calibrated using a poly(styrene) dispersion with a known ζ-potential. In a typical experiment, 200 μL of HEPES buffer (5.0 mM, pH 7.4), containing 15 μg of plasmid DNA was added to 800 μL of HEPES buffer (5.0 mM, pH 7.4) with various amounts of polymer. The resulting solution was vortexed for 5 s, and after 30 min of incubation time at room temperature the surface charge properties of the polyplexes was determined.

Polyplex Destabilization Studied with DLS. Polyplexes of the polymers and plasmid DNA were made at a polymer/DNA (w/w) ratio of 12 (corresponding to a N/P ratio of 14 and in the case of pHPMA−BDMPAP to a ratio of 28), either in 10 mM HEPES, pH 7.4, or in 10 mM acetate buffer, pH 5, ionic strength adjusted to 150 mM with NaCl. The size of the polyplexes at 37 °C was monitored in time using DLS.

Polyplex Destabilization Studied with Agarose Gel Electrophoresis. Polyplexes were made by mixing 10 μL of plasmid solution, 200 μg/mL, with 40 μL of polymer solution, 200 μg/mL, corresponding to a polymer/DNA (w/w) ratio of 12, and incubated for 30 min at room temperature. The buffers used were 10 mM HEPES, pH 7.4, and 10 mM sodium acetate, pH 5; ionic strength was adjusted to 150 mM with NaCl. The polyplex dispersions were subsequently incubated at 37 °C for 0, 2, 4, 7, 24, or 48 h. After the mixture was cooled to room temperature, 10 μL of the corresponding buffer and 3 μL of sample buffer (0.4% w/v bromophenol blue, 10 mM EDTA, 50% v/v glycerol in water) were added to 20 μL of each polyplex dispersion. An amount of 30 μL of these solutions was applied onto a 0.7% agarose gel containing 0.5 μg/mL ethidium bromide, and the gels were run at 100 V (*26*).

Transfection Studies. Transfection studies were done in COS-7 cells as described previously using pCMVLacZ as reporter gene (*23*). In brief, 96-well plates were seeded with cells at a density of 3×10^4 cm^{-2} 24 h before transfection. Polyplexes were prepared as follows: 150 μL of polymer solution (various concentrations) was added to 50 μL of plasmid solution (50 μg/mL), and after incubation for 30 min at room temperature, 50 μL of either buffer or INF-7 solution (150 μg/mL) was added, and the polyplexes were incubated for another 15 min before addition to the cells. After the cells were rinsed with HBS, 100 μL of polyplex dispersion and 100 μL of culture medium (with or without 10% serum) were incubated with the cells for 1 h. After removal of the polyplex dispersion, fresh culture medium was added, and the cells were incubated for another 48 h. All transfection experiments were performed in two identical series in separate 96-well plates. One series was tested for reporter gene expression (β- galactosidase) by ONPG colorimetric assay. The other series was used to determine the number of viable cells using an XTT colorimetric assay. Transfection efficiencies were normalized to that of pDMAEMA polyplexes (polymer/DNA ratio of 3/1) in the presence of serum. For comparison, the transfection activity of polyplexes of PEI (branched, 25 kDa) in the presence of 5% serum was also measured.

Fluorescence Measurements. The binding of the cationic polymers to DNA was examined by the fluorescence quenching of ethidium bromide (*27*). Ethidium bromide was added at a 1:10 molar ratio to DNA phosphates in 20 mM HBS (20 mM HEPES buffer (pH 7.4) containing 150 mM NaCl). Polyplexes were formed at different polymer/DNA ratios by vortexing solutions of known concentration of DNA/ethidium bromide and polymer in 20 mM HBS (final concentration of DNA, 2.5 μg/mL), followed by incubation at room temperature for 30 min. The fluorescence was measured using a Spex Fluorolog III spectrofluorimeter (Spex, Edison). The excitation and emission wavelengths were 520 and 600 nm, respectively. The excitation and emission slit widths were set at 1.26 and 4.52 nm, respectively. The relative fluorescence (F_r) values were calculated as

$$F_r = \frac{F_{obs} - F_e}{F_0 - F_e}$$

where F_{obs} is the measured fluorescence, F_e is the fluorescence of ethidium bromide in the absence of DNA, and F_0 is the initial fluorescence of DNA/ethidium bromide in the absence of a cationic polymer. Dissociation of polyplexes was studied by measuring the fluorescence 30 min after addition of p(Asp) (final concentration is 100 μg/mL) (*26*).

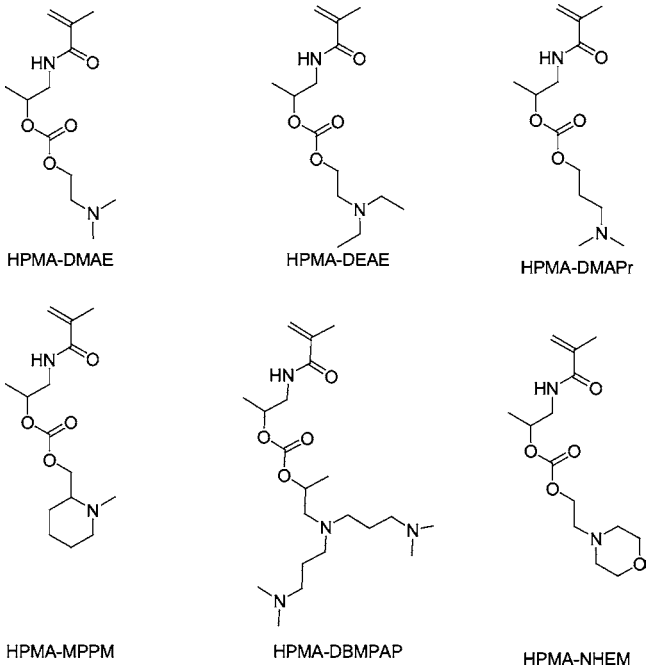

Figure 1. Chemical structures of the synthesized monomers.

RESULTS AND DISCUSSION

Synthesis and Characterization of the Different Monomers and Polymers. The synthesis of the monomers was performed in two steps. In the first step, the amino alcohols DMAE, DEAE, DMAPr, MPPM, BDMPAP, and NHEM were activated with 1,1′-carbonyldiimidazole. The corresponding carbamates were obtained in a good yield (70−90%) and good purity (>97% by NMR). Funhoff et al. (*19*) reported the synthesis of HPMA−DMAE with 5 days of reaction time at room temperature for the second step. However, this method was not successful for some of the monomers, e.g., HPMA−BDMPAP and HPMA−NHEM. Therefore, the second reaction (coupling of HPMA and CI-activated alcohol) was done in toluene overnight at 80 °C instead of in dichloromethane at room temperature for 5 days. Under these conditions all monomers were successfully synthesized (Figure 1, Table 1).

Radical polymerization of the monomers was performed in freshly distilled dioxane using AIBN as initiator, and the resulting polymers were obtained in good yields (60−75%). The weight-average molecular weight (M_w) and the number-average molecular weight (M_n) of the polymers are given in Table 1. The M_w of the polymers was between 25 and 100 kDa, and the M_n of the polymers was between 10 and 50 kDa. Furthermore, Table 1 shows the pK_a values of the monomers and the average pK_a values of the polymers (which is defined as the pH at which 50% of the amine groups of the polymers is protonated). Since the pK_a of PHPMA−DBMPAP and pHPMA−DMAPr is around 7.0, these polymers, in contrast to the other synthesized polymers (pK_a values ranging from 8.7 to 9.5), have higher buffer capacities in the endosomal vesicles.

Hydrolysis of the Monomers. The hydrolysis kinetics of the monomers at 37 °C were studied with RP-HPLC. The k_{obs} for the hydrolysis of the monomer was calculated by plotting the natural logarithm of the peak areas of the monomer divided by the peak area at time zero of the monomer versus the time using a linear fit. Table 2 gives the results. By far the fastest hydrolysis is observed for HPMA−DEAE (half-life 2 h). HPMA−DMAE and HPMA−MPPM are more stable with a half-life of around 10 h. As expected, the half-live of HPMA−BDMPAP is much longer (40 h) because the carbonate function originates from two secondary alcohols instead of one as in the case of the other monomers. The long half-lives of HPMA−DMAPr (79 h) and HPMA−NHEM (40 h) are not fully understood at this moment and needs further investigation.

Table 2. Monomer Hydrolysis at 37 °C and pH 7.4

monomer	k_{obs} (h^{-1})	$t_{1/2}$ (h)
HPMA−DMAE	$6.2 \times 10^{-2} \pm 5.6 \times 10^{-4}$	11 ± 0.1
HPMA−DEAE	$3.0 \times 10^{-1} \pm 2.1 \times 10^{-2}$	2.3 ± 0.2
HPMA−DMAPr	$8.8 \times 10^{-3} \pm 1.4 \times 10^{-4}$	79 ± 1.2
HPMA−MPPM	$7.0 \times 10^{-2} \pm 9.1 \times 10^{-4}$	10 ± 0.1
HPMA−NHEM	$2.4 \times 10^{-2} \pm 9.2 \times 10^{-5}$	29 ± 0.1
HPMA−BDMPAP	$1.6 \times 10^{-2} \pm 1.4 \times 10^{-4}$	43 ± 0.4

Table 3. Particle Size (Diameter) and ζ-Potential of the Polyplexes at a Polymer/DNA Ratio of 12 (w/w) in HBS Buffer (5.0 mM, pH 7.4, Adjusted to 150 mM with NaCl) and in HEPES Buffer (5.0 mM, pH 7.4), Respectively

polymer	*Z*-average (nm)	ζ-potential (mV)
PHPMA−DMAE	169 ± 3	30 ± 2
PHPMA−DEAE	200 ± 2	35 ± 2
PHPMA−DMAPr	142 ± 3	25 ± 4
PHPMA−MPPM	117 ± 2	20 ± 2
PHPMA−BDMPAP	136 ± 3	35 ± 3
PHPMA−NHEM	aggregates	-17 ± 1

Particle Size and ζ-Potential Measurements. pHPMA−DMAE, pHPMA−DEAE, pHPMA−MPPM, pHPMA−DMAPr, and pHPMA−BDMPAP were capable of condensing DNA into positively charged nanoparticles at N/P ratios greater than 4 (size between 120 and 150 nm). In buffer with physiological ionic strength (5 mM hepes, 150 mM NaCl) the size of the polyplexes slightly increased (120−200 nm, Table 3). Independent of the ionic strength, DNA/polymer aggregates were observed at lower N/P ratios of <4. The ζ-potentials of these polyplexes were all between 20 and 30 mV (Table 3). Although ^{1}H NMR showed no degradation of the polymer, pHPMA−NHEM was unable to condense DNA; the addition of pHPMA−NHEM to plasmid DNA resulted in the formation of large aggregates.

Polyplex Destabilization Studied with DLS. The (in)stability of the polyplexes was investigated by dynamic light scattering at 37 °C at both pH 7.4 and pH 5.0 (parts A and B of Figure 2, respectively). At pH 5.0 the size of the polyplexes remained constant for at least 16 h. The polyplexes based on pHPMA−DMAE, pHPMA−MPPM, and pHPMA−DEAE increased in size at pH 7.4 and 37 °C (Figure 2A) in time. This can be explained by hydrolysis of the side chains. Because of this hydrolysis, the charge density of the polymer decreased, leading to a decreased binding and condensing capacity of the polymer which results in swelling and aggregation of the polyplexes. The results are consistent with those of the monomer hydrolysis. HPMA−DEAE, the monomer with shortest hydrolysis half-life at pH 7.4, gave the fastest polyplex destabilization (Figure 2A). The monomers with long hydrolysis half-lives, e.g., pHPMA−BDMPAP and pHPMA−DMAPr, lead to polyplexes that were stable at pH 7.4 for more than 16 h. Beyond 13 h and at pH 7.4, complex aggregation and precipitation made accurate DLS measurements impossible for pHPMA−DMAE and pHPMA−MPPM based polyplexes.

Polyplex Destabilization Studied with Agarose Gel Electrophoresis. To investigate whether plasmid DNA can be released from the polyplexes by side chain hydrolysis of the polymers, polyplexes were incubated at 37 °C at pH 7.4 up to 48 h (Figure 3A). This figure shows that after 7 h of incubation and independent of the polyplex formulation all the plasmid DNA remained in the starting slots, indicating that the polymers are still complexed with DNA. After 24 h, pHPMA−DEAE showed release of intact DNA. After 48 h, pHPMA−DMAE and pHPMA−MPPM also showed release of DNA. PHPMA−BDMPAP and pHPMA−DMAPr showed no release of DNA

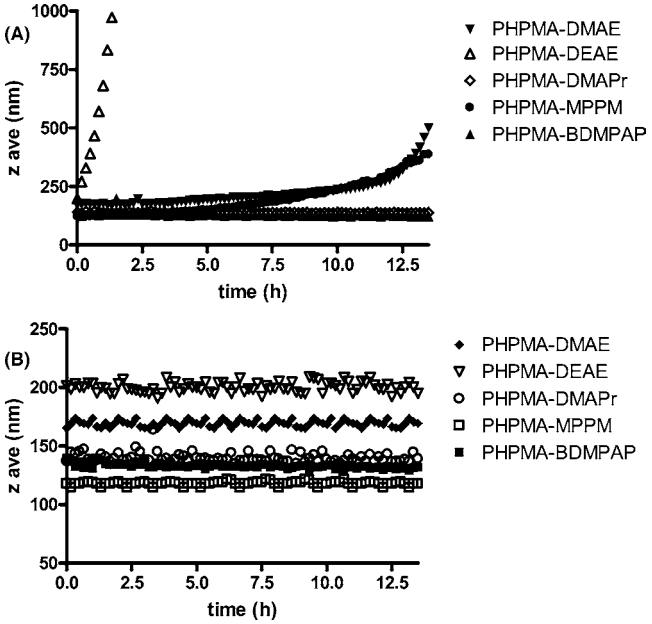

Figure 2. (A) Destabilization of polyplexes studied with DLS at 37 °C, adjusted to 150 mM with NaCl at pH 7.4. The polymer/DNA ratio is 12 (w/w). (B) Destabilization of polyplexes studied with DLS at 37 °C, adjusted to 150 mM with NaCl at pH 5.0. The polymer/DNA ratio is 12 (w/w).

in the time frame studied. As a control, polyplexes were incubated at 37 °C at pH 5.0 up to 48 h (Figure 3B). Under these conditions no release of DNA was observed from the polyplexes. The results obtained in the agarose gel study are in line with the results obtained with the destabilization of the polyplexes as studied with DLS. The polymer with the fastest destabilization at pH 7.4 and 37 °C, pHPMA−DEAE, also shows the fastest release of DNA (Figure 3). PHPMA−DMAE and pHPMA−MPPM both show similar release of plasmid DNA and also have similar destabilization curves and hydrolysis rates. Polyplexes of the polymers with long half-lives, e.g., pHPMA−BDMPAP and pHPMA−DMAPr, did not release plasmid DNA within the time frame studied. The results further suggest that partial degraded polymers are still capable of complexing DNA because the hydrolysis rate of the polymer is much faster than the DNA release.

Fluorescence Measurements. The binding of the polymers to plasmid DNA was studied using ethidium bromide fluorescence measurements (Table 4). This table shows that all the polymers quenched the plasmid DNA/ethidium bromide fluorescence except for pHPMA−NHEM. This result is in line with the DLS data where we also found that pHPMA−NHEM did not complex the DNA. PDMAEMA and pLL showed more quenching than the HPMA polymers, indicating a stronger binding of former mentioned polymers to the plasmid DNA. Of the different HPMA polymers, pHPMA−DMAE, pHPMA−DMAPr, and pHPMA−BDMPAP showed the strongest quenching, suggesting the strongest binding of the polymer to the plasmid DNA. The addition of p(Asp) to the polyplexes caused little effect on the DNA/ethidium bromide fluorescence intensity of pHPMA−DEAE and pHPMA−MPPM. In contrast, for the other polymers p(Asp) caused a substantial increase in the DNA/ethidium bromide fluorescence intensity. This indicates that the polyplexes based on pHPMA−DEAE and pHPMA−MPPM are more resistant toward destabilization by anionic macromolecules than the polyplexes based on the other polymers.

Transfection Activity and Cell viability Studies. The in vitro transfection properties of the polyplexes were studied with the COS-7 cell line (Figures 4 and 5). As a representative example, Figure 4 shows the transfection activity of pHPMA−

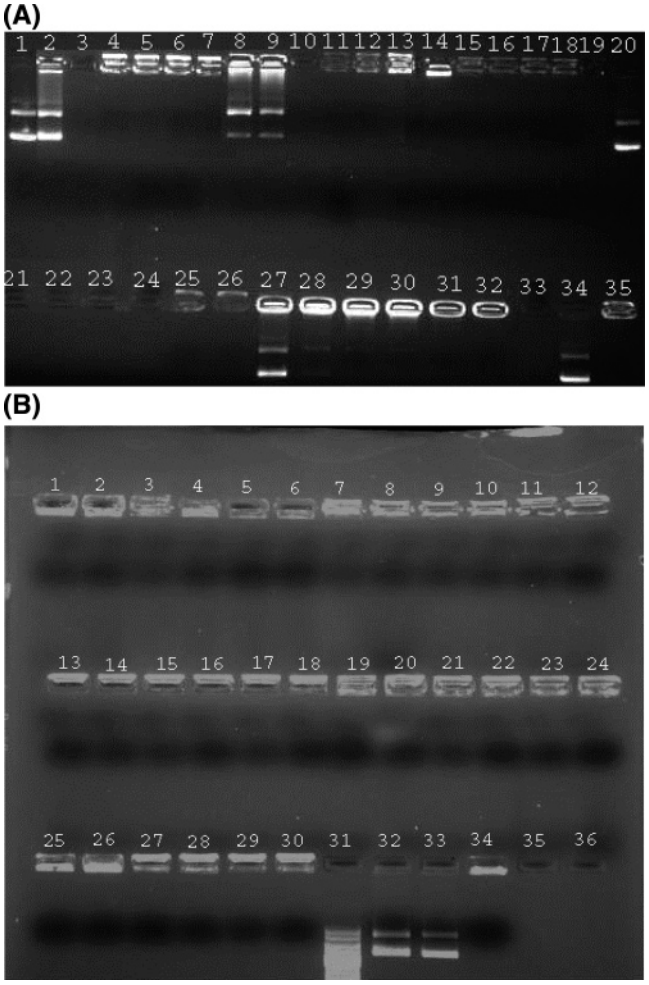

Figure 3. (A) Agarose gel electrophoresis of polyplexes incubated at 37 °C at different time intervals at pH 7.4: (lanes 1, 20, 34) free DNA; (lanes 2−7) pHPMA−DMAE based polyplexes for 48, 24, 7, 4, 2, 0 h; (lanes 8−13) pHPMA−DEAE based polyplexes for 48, 24, 7, 4, 2, 0 h; (lanes 14−19) pHPMA−DMAPr based polyplexes for 48, 24, 7, 4, 2, 0 h; (lanes 21−26) pHPMA−BDMPAP based polyplexes for 48, 24, 7, 4, 2, 0 h; (lanes 27−32) pHPMA−MPPM based polyplexes for 48, 24, 7, 4, 2, 0 h; (lane 33) empty; (lane 35) pDMAEMA based polyplexes (3/1) as control. (B) Gel electrophoresis of polyplexes incubated at 37 °C at different time intervals at pH 5.0: (lanes 32, 33) free DNA; (lanes 1−6) pHPMA−DMAE based polyplexes for 48, 24, 7, 4, 2, 0 h; (lanes 7−12) pHPMA−DEAE based polyplexes for 48, 24, 7, 4, 2, 0 h; (lanes 13−18) pHPMA−DMAPr based polyplexes for 48, 24, 7, 4, 2, 0 h; (lanes 19−24) pHPMA−BDMPAP based polyplexes for 48, 24, 7, 4, 2, 0 h; (lanes 25−30) pHPMA−MPPM based polyplexes for 48, 24, 7, 4, 2, 0 h; (lane 31: marker; (lane 34) pDMAEMA based polyplexes (3/1) as control; (lanes 35, 36) empty.

MPPM based polyplexes in the presence and the absence of INF-7 peptide. Without the addition of the endosomal membrane disrupting INF-7 peptide to the polyplex dispersion, low transfection activity was observed. However, when INF-7 peptide was added to the polyplex dispersion, high levels of transfection were observed, as reported previously for pHPMA−DMAE (*19*). The low transfection activity of the polyplexes in the absence of INF indicates that the polyplexes are unable to destabilize endosomal vesicles. PHPMA−BDMPAP, despite its buffering capacity, also needed the addition of INF-7 peptide to escape from the endosome. This has been observed previously by Funhoff et al. (*28*) for pDAMA polymers and leads to further indications that the proton sponge hypothesis (*29*) is not generally valid.

Figure 5 shows the transfection activity and cytotoxicity of the different polyplexes in the presence of INF-7 peptide and in the presence and the absence of serum. PHPMA−DMAPr

Table 4. Fluorescence of Ethidium Bromide/Plasmid[a] Incubated with Different Cationic Polymers

polymer	relative fluorescence before the addition of p(Asp)[b]	relative fluorescence after the addition of p(Asp)[b,c]
PHPMA−DMAE	0.64 ± 0.03	0.84 ± 0.04
PHPMA−DEAE	0.77 ± 0.03	0.80 ± 0.03
PHPMA−DMAPr	0.63 ± 0.05	0.88 ± 0.05
PHPMA−MPPM	0.74 ± 0.03	0.81 ± 0.02
PHPMA−BDMPAP	0.61 ± 0.06	0.96 ± 0.05
PHPMA−NHEM	0.98 ± 0.14	1.00 ± 0.10
PDMAEMA[d]	0.42 ± 0.02	0.81 ± 0.03
PLL[d]	0.08 ± 0.02	0.27 ± 0.09

[a] Concentration of plasmid, 2.5 μg/mL; ethidium bromide/DNA phosphate, 1:10 (mol/mol). [b] Relative fluorescence measured at a polymer/DNA ratio of 12. [c] Final concentration of p(Asp), 100 μg/mL. [d] Reference 14.

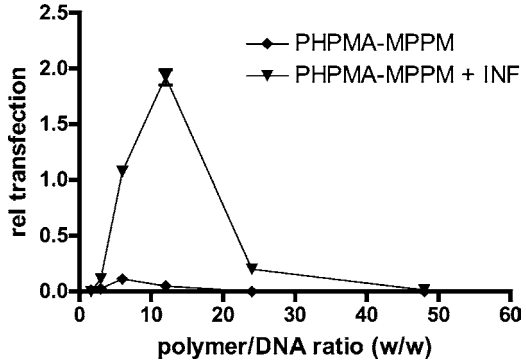

Figure 4. Transfection activity of pHPMA−MPPM based polyplexes with and without INF-7 peptide and in the presence of serum. Values are relative to pDMAEMA/plasmid DNA 3:1 (w/w). β-Galactosidase activity was determined using OPNG as substrate (*27*).

based polyplexes, like pHPMA−DMAE based polyplexes, only show efficient gene expression in the absence of serum. PHPMA−DEAE and pHPMA−MPPM polyplexes were twice as active as pHPMA−DMAE polyplexes in the absence of serum. PHPMA−DEAE, pHPMA−MPPM, and pHPMA−BDMPAP based polyplexes showed similar transfection levels in the presence and absence of serum and suggest that these polyplexes, in contrast to pHPMA−DMAE based polyplexes (*19*), are stable toward serum. The presence of serum proteins can lead to a decrease in transfection activity due to destabilization and/or aggregation of the polyplexes (*19*, *30*, *31*). The pHPMA−DEAE and pHPMA−MPPM polyplexes were also twice as active as the well-known transfectants pDMAEMA and pEI in the presence of serum proteins (Figure 5A).

The IC_{50} (defined as the concentration resulting in 50% inhibitory activity (cell death)) for the pHPMA-based polyplexes was between 12 and 96 μg/mL in the presence of serum (Figure 5A), whereas the IC_{50} for the polyplexes with nondegradable polymers, like pDMAEMA and pEI, was around 5 μg/mL (*14*, *32*). The toxicity of the polyplexes was lower in the presence of serum than in the absence of serum (Figure 5B). The serum proteins likely mask cationic surfaces of the polyplexes, thereby reducing the toxicity (*14*). The maximum transfection efficiency of the different polyplexes was observed at 50−80% cell viability as described before for other polymeric carrier systems (*14*, *22*).

Potentially limiting barriers to efficient gene transfer include endocytosis, escape from endosome into the cytoplasm, cytoplasmic mobility, transport across the nuclear membrane, and release of the plasmid DNA (*33*, *34*). Successful polymeric transfectants have to overcome all these different barriers in the different stages of transfection pathway. The polymer with the highest overall transfection activity is the polymer with the best average over all these barriers. Therefore, polymers with

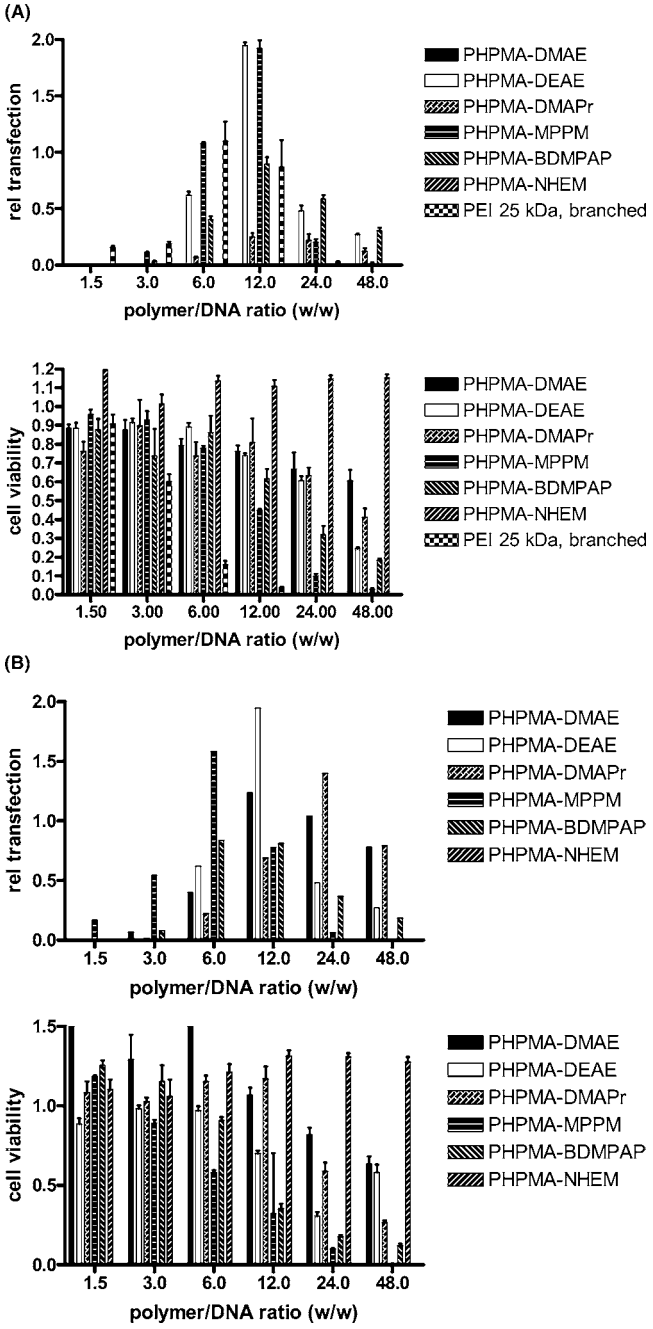

Figure 5. (A) Transfection activity and cell viability of the polyplexes in the presence of serum (5%) and in the presence of INF-7 peptide. Values are relative to pDMAEMA/plasmid DNA 3:1 (w/w). β-Galactosidase activity was determined using OPNG as substrate (*26*). The transfection activity and cell viability of 25 kDa branched pEI-based polyplexes in the presence of serum (5%) are also shown. (B) Transfection activity and cell viability of the polyplexes in the absence of serum and in the presence of INF-7 peptide. Values are relative to pDMAEMA/plasmid DNA 3:1 (w/w). β-Galactosidase activity was determined using OPNG as substrate (*26*).

different physical properties such as pHPMA−DMAE, pHPMA−BDMPAP, and pHPMA−DMAPr can have similar transfection properties, and polymers with similar physical properties can have different transfection properties. For example, pHPMA−DMAE and pHPMA−MPPM have similar pK_a values, similar half-lives, and similar polyplex destabilization characteristics; however, their transfection and cell viability properties differed widely, indicating that a small structural change of the side group can have a drastic effect on the transfection activity. This has also been observed for other structurally related polymers (*35*, *36*).

CONCLUSION

We have synthesized a series of new gene delivery polymers with hydrolyzable cationic side groups. It was shown that polyplexes based on these polymers were stable at pH 5.0. Some of these polymers showed release of intact DNA within 24 h (pHPMA−DEAE) or 48 h (pHPMA−DMAE and pHPMA−MPPM) after incubation at 37 °C and pH 7.4. Polyplexes based on these polymers showed a lower cytotoxicity than well-known polymeric transfectants such as pEI and pDMAEMA. The transfection activities of PHPMA−DEAE, pHPMA−MPPM, and pHPMA−BDMPAP were also serum-independent. The transfection activities of PHPMA−DEAE and pHPMA−MPPM are even superior to the transfection activity of pEI. Future work will focus on in vivo application of the new polymers.

ACKNOWLEDGMENT

This study was supported by a grant from NDRF/STIGO, Project Number 014-80-01.

LITERATURE CITED

(1) Dif, F., Djediat, C., Alegria, O., Demeneix, B., and Levi. G. (2006) Transfection of multiple pulmonary cell types following intravenous injection of PEI-DNA in normal and CFTR mutant mice. *J. Gene Med. 8*, 82−89.

(2) Wang, Y., Liu, S., Li, C. Y., and Yuan, F. (2005) A novel method for viral gene delivery in solid tumors. *Cancer Res. 65*, 7541−7545.

(3) Shah, P. B., and Losordo, D. W. (2005) Non-viral vectors for gene therapy: clinical trials in cardiovascular disease. *Adv. Genet. 54*, 339−361.

(4) Connolly, J. B. (2002) Lentiviruses in gene therapy clinical research. *Gene Ther. 9* 1730−1734.

(5) McTaggart, S., and Al-Rubeai, M. (2002) Retroviral vectors for human gene delivery. *Biotechnol. Adv. 20*, 1−31.

(6) Gorecki, D. C. (2001) Prospects and problems of gene therapy: an update. *Expert Opin. Emerging Drugs 6*, 187−198.

(7) Boussif, O., Lezoualch, F., Zanta, M. A., Mergny, M. D., Scherman, D., Demeneix, B., and Behr, J.-P. (1995) A versatile vector for gene and oligonucleotide transfer into cells in culture and in vivo: polyethylenimine. *Proc. Nat. Acad. Sci. U.S.A. 92*, 7297−7301.

(8) Cherng, J. Y., van de Wetering, P., Talsma, H., Crommelin, D. J. A., and Hennink, W. E. (1996) Effect of size and serum proteins on transfection efficiency of poly((2-dimethylamino)-ethyl methacrylate)-plasmid nanoparticles. *Pharm. Res. 13*, 1038−1042.

(9) Eldred, S. E., Pancost, M. R., Otte, K. M., Rozema, D., Stahl, S. S., and Gellman, S. H. (2005) Effects of side-chain configuration and backbone spacing on the gene delivery properties of lysine-derived cationic polymers. *Bioconjugate Chem. 16*, 694−699.

(10) De Smedt, S. C., DeMeester, J., and Hennink, W. E. (2000) Cationic polymer based gene delivery systems. *Pharm. Res. 17*, 113−125.

(11) Lim, Y.-B., Kim, C.-H., Kim, K., Kim, S. W., and Park J.-S. (2000) Development of a safe gene delivery system using biodegradable polymer, poly[α-(4-aminobutyl)-L-glycolic acid]. *J. Am. Chem. Soc. 122*, 6524−6525.

(12) Wang, J., Zhang, P. C., Mao, H. Q., and Leong, K. W. (2002) Enhanced gene expression in mouse muscle by sustained release of plasmid DNA using PPE-EA as a carrier. *Gene Ther. 9*, 1254−1261.

(13) De Wolf, H. K., Luten, J., Snel, C. J., Ousorren, C., Hennink, W. E., and Storm, G. (2005) In vivo tumor transfection mediated by polyplexes based on biodegradable poly(DMAEA)-phosphazene. *J. Controlled Release 109*, 275−287.

(14) Luten, J., van Steenis, J. H., van Someren, R., Kemmink, J., Schuurmans-Nieuwenbroek, N. M. E., Koning, G. A., Crommelin, D. J. A., van Nostrum, C. F., and Hennink, W. E. (2003) Polyphosphazenes as biodegradable nonviral vector systems. *J. Controlled Release 89*, 483−497.

(15) Lynn, D. M., and Langer, R. (2000) Degradable poly(β-amino esters): synthesis, characterization, and self-assembly with plasmid DNA. *J. Am. Chem. Soc. 122*, 10761−10768.

(16) Zhong, Z., Song, Y., Engbersen, J. F. J., Lok, M. C., Hennink, W. E., and Feijen, J. (2005) A versatile family of degradable non-viral gene carriers based on hyperbranched poly(ester amine)s. *J. Controlled Release 109*, 317−329.

(17) Varga, C. M., Hong, K., and Lauffenburger, D. A. (2001) Quantitative analysis of synthetic gene delivery vector design properties. *Mol. Ther. 4*, 438−446.

(18) Forrest, M. L., Koerber, J. T., and Pack, D. W. (2003) A degradable polyethylenimine derivative with low toxicity for highly efficient gene delivery. *Bioconjugate Chem. 14*, 934−940.

(19) Funhoff, A. M., van Nostrum, C. F., Janssen, A. P. C. A., Fens, M. H. A. M., Crommelin, D. J. A., and Hennink, W. E. (2004) Polymer side-chain degradation as a tool to control the destabilization of polyplexes. *Pharm. Res. 21*, 170−176.

(20) van de Wetering, P., Moret, E. E., Schuurmans-Nieuwenbroek, N. M. E., van Steenbergen, M. J., and Hennink, W. E. (1999) Structure−activity relationships of water-soluble cationic methacrylate/methacrylamide polymers for nonviral gene delivery. *Bioconjugate Chem. 10*, 589−597.

(21) Akinc, A., Lynn, D. M., Anderson, D. G., and Langer, R. (2003) Parallel synthesis and biophysical characterization of a degradable polymer library for gene delivery. *J. Am. Chem. Soc 125*, 5316−5323.

(22) Plank, C., Oberhauser, B., Mechtler, K., Koch, C., and Wagner, E. (1994) The influence of endosome-disruptive peptides on gene-transfer using synthetic virus-like genetransfer systems. *J. Biol. Chem. 269*, 12918−12924.

(23) van de Wetering, P., Cherng, J. Y., Talsma, H., and Hennink, W. E. (1997) Relation between transfection efficiency and cytotoxicity of poly(2-(dimethylamino)ethyl methacrylate/plasmid complexes. *J. Controlled Release 49*, 59−69.

(24) Oupicky, D., Konak, C., and Ulbrich, K. (1999) DNA complexes with block and graft copolymers of *N*-(2-hydroxypropyl) methacrylamide and 2-(trimethylammonio)ethyl methacrylate. *J. Biomater. Sci., Polym. Ed. 10*, 573−590.

(25) Jiang, X., van der Horst, A., van Steenbergen, M. J., Akeroyd, N., van Nostrum, C. F., Schoenmakers, P. J., and Hennink, W. E. (2006) Molar-mass characterization of cationic polymers for gene delivery by aquaous size-exclusion chromatography. *Pharm. Res. 23*, 595−603.

(26) Arigita, C., Zuidam, N. J., Crommelin, D. J. A., and Hennink, W. E. (1999) Association and dissociation characterics of polymer/DNA complexes used for gene delivery. *Pharm. Res. 16*, 1534−1541.

(27) Tang, M. X., and Szoka, F. C. (1997) The influence of polymer structure on the interactions of cationic polymers with DNA and morphology of the resulting complexes. *Gene Ther. 4*, 823−832.

(28) Funhoff, A. M., van Nostrum, C. F., Koning, G. A., Schuurmans-Nieuwenbroek, N. M. E., Crommelin, D. J. A., and Hennink, W. E. (2004) Endosomal escape of polymeric gene delivery complexes is not always enhanced by polymers buffering at low pH. *Biomacromolecules 5*, 32−39.

(29) Cho, Y. W., Kim, J. D., and Park, K. (2003) Polycation gene delivery systems: escape from endosomes to cytosol. *J. Pharm. Pharmacol. 55*, 721−734.

(30) Audouy, S., Molema, G., de Leij, L., and Hoekstra, D. (2000) Serum as modulator of lipoplex-mediated gene transfection: dependence of amphiphile, cell type and complex stability. *J. Gene Med. 2*, 465−476.

(31) Yang, J.-P., and Huang, L. (1998) Time-dependent maturation of cationic liposome−DNA complex for serum resistance. *Gene Ther. 5*, 380−387.

(32) Verbaan, F. J., Bos, G. W., Snel, C., Oussoren, C., Woodle, M. C., Hennink, W. E., and Storm, G. A (2004) A comparative study of different cationic transfection agents for in vivo gene delivery after intravenous administration. *J. Drug Delivery Technol. 14*, 105−111.

(33) Hwang, S. J., and Davis, M. E. (2001) Cationic polymers for gene delivery: Designs for overcoming barriers to systemic administration. *Curr. Opin. Biotechnol. 3*, 183−191.
(34) Zabner, J., Fasbender, A. J., Moninger, T., Poellinger, K. A., and Welsh, M. J. (1995) Cellular and molecular barriers to gene transfer by a cationic lipid. *J. Biol. Chem. 270*, 18997−19007.
(35) Anderson, D. G., Lynn, D. M., and Langer R. (2003) Semi-automated synthesis and screening of a large library of degradable cationic polymers for gene delivery. *Angew. Chem., Int. Ed. 42*, 3153−3158.
(36) Chen, D. J., Majors, B. S., Zelikin, A., and Putnam, D. (2005) Structure−function relationships of gene delivery vectors in a limited polycation library. *J. Controlled Release 103*, 273−283.

BC060068P

N^{ϵ}-(3-[*I]Iodobenzoyl)-Lys^5-N^{α}-maleimido-Gly^1-GEEEK ([*I]IB-Mal-D-GEEEK): A Radioiodinated Prosthetic Group Containing Negatively Charged D-Glutamates for Labeling Internalizing Monoclonal Antibodies

Ganesan Vaidyanathan,*[,†] Kevin L. Alston,[†] Darrel D. Bigner,[‡] and Michael R. Zalutsky[†,‡]

Departments of Radiology and Pathology, Duke University Medical Center, Durham, North Carolina 27710.
Received March 27, 2006; Revised Manuscript Received May 18, 2006

Novel methods are needed for the radiohalogenation of cell-internalizing proteins and peptides because rapid loss of label occurs after lysosomal processing when these molecules are labeled using conventional radioiodination methodologies. We have developed a radiolabeled prosthetic group that contains multiple negatively charged D-amino acids to facilitate trapping of the radioactivity in the cell after proteolysis of the labeled protein. N^{ϵ}-(3-[^{125}I]iodobenzoyl)-Lys^5-N^{α}-maleimido-Gly^1-GEEEK ([^{125}I]IB-Mal-D-GEEEK) was synthesized via iododestannylation in 90.3 ± 3.9% radiochemical yields. This radioiodinated agent was conjugated to iminothiolane-treated L8A4, an anti-epidermal growth factor receptor variant III (EGFRvIII) specific monoclonal antibody (mAb) in 54.3 ± 17.7% conjugation yields. In vitro assays with the EGFRvIII-expressing U87MGΔEGFR glioma cell line demonstrated that the internalized radioactivity for the [^{125}I]IB-Mal-D-GEEEK-L8A4 conjugate increased from 14.1% at 1 h to 44.7% at 24 h and was about 15-fold higher than that of directly radioiodinated L8A4 at 24 h. A commensurately increased tumor uptake in vivo in athymic mice bearing subcutaneous U87MGΔEGFR xenografts (52.6 ± 14.3% injected dose per gram versus 17.4 ± 3.5% ID/g at 72 h) also was observed. These results suggest that [^{125}I]IB-Mal-D-GEEEK is a promising reagent for the radioiodination of internalizing mAbs.

INTRODUCTION

Targeted radionuclide therapy is an attractive alternative cancer treatment to conventional external beam radiation, particularly when the molecule being targeted is truly tumor specific. An example of such a target is the epidermal growth factor receptor variant III (EGFRvIII), a mutant receptor found on glioma, and breast, lung, and ovarian carcinomas, and characterized by a deletion in the extracellular domain of EGFR (*1*). EGFRvIII-specific monoclonal antibodies (mAbs) have been generated and, as is generally the case with anti-receptor mAbs, undergo rapid internalization and extensive lysosomal degradation after cell surface receptor binding (*2*).

Internalization is a necessary prelude for cytotoxic potency with immunotoxins (*3*). On the other hand, internalization creates a serious problem for radioimmunotherapy because of the rapid loss of radioactivity after tumor cell processing of mAbs radioiodinated by the direct electrophilic route (*4*, *5*). This has provided motivation for the development of "residualizing" labeling methods which seek to overcome the rapid egress of radioiodine from tumor by labeling the mAb via a labeled prosthetic group that will remain trapped inside the cell after mAb degradation (*6*−*9*). The approach taken by our group for labeling internalizing mAbs has been to exploit the limited diffusion of charged species across cell and lysosomal membranes. We have evaluated a series of aromatic acylation agents bearing positively (*4*, 10) or negatively charged (*11*) substituents for this purpose. Indeed, in preclinical studies, substantially higher retention of radioiodine in tumor cells and human tumor xenografts have been achieved for anti-EGFRvIII mAbs radioiodinated using such templates compared to the same mAbs radioiodinated by the direct method (*12*−*14*).

In an extension of this general strategy, the anti-EGFRvIII mAb L8A4 was radioiodinated using D-N^{α}-Ac-KRYRR, a peptide containing three arginines to impart positive charge and composed of D-amino acids to inhibit proteolysis (*15*). The procedure involved three steps: peptide radioiodination, reaction with the bifunctional agent sSMCC, and finally, conjugation to mAb derivatized by reaction with iminothiolane. Tumor retentions of radioiodine, both in cells and xenografts, for L8A4 mAb labeled by this method compared favorably with those observed using other labeling approaches; however, kidney uptake was also higher, presumably due to the cationic nature of the D-amino acid peptide. In addition, the procedure involves radioiodination of the D-tyrosine, rendering the labeled mAb susceptible, albeit to a lesser degree (*16*), to in vivo deiodination. Furthermore, extension of this method for use with the heavier halogen ^{211}At, of interest for α-particle radioimmunotherapy (*17*), would be problematic because introduction of ^{211}At onto tyrosine residues has not been successful (*18*, *19*).

The objective of the current study was to refine our D-amino acid peptide prosthetic group strategy by developing a labeling reagent with the following properties: (1) simpler chemistry, (2) potential applicability for both radioiodination and astatination, (3) structural dissimilarity to thyroid hormones, and (4) D-peptide sequence with net negative charge. To accomplish this, a pentapeptide consisting of a maleimidoglycine, three D-glutamines, and a D-lysine was synthesized, and the lysine ϵ-amino group was derivatized with a 3-(tri-*n*-butylstannyl)benzoyl moiety. Herein we present the results of synthesis of this precursor and its radioiodination to N^{ϵ}-(3-[*I]iodobenzoyl)-Lys^5-N^{α}-maleimido-Gly^1-GEEEK ([*I]IB-Mal-D-GEEEK) and evaluation of the potential utility of this reagent for labeling the anti-EGFRvIII mAb L8A4.

* Correspondence to Ganesan Vaidyanathan, Box 3808, Radiology, Duke University Medical Center, Durham, NC 27710. Phone: (919) 684-7811. Fax: (919) 684-7122. e-mail: ganesan.v@duke.edu.

† Department of Radiology.

‡ Department of Pathology.

10.1021/bc0600766 CCC: $33.50 © 2006 American Chemical Society
Published on Web 06/24/2006

EXPERIMENTAL SECTION

General. All chemicals were purchased from Sigma-Aldrich unless otherwise noted. Sodium [^{125}I]iodide and sodium [^{131}I]iodide with specific activities of 2200 Ci/mmol and 1200 Ci/mmol, respectively, were obtained from Perkin-Elmer Life and Analytical Sciences (Boston, MA). Fmoc-D-Lys(Boc) attached to Wang resin and Fmoc-D-Glu-(O-*t*Bu) were obtained from Novabiochem (West Chester, PA). *N*-Succinimidyl 3-iodobenzoate (SIB) and *N*-succinimidyl 3-(tri-*n*-butyl)stannylbenzoate (STB) were prepared as reported (*20*). D-Amino acid peptides N^{α}-Ac-KRYRR and KEYEE were obtained from Peptide Technologies Corp. (Gaithersburg, MD) and LSU Health Sciences Center Core Laboratories (New Orleans, LA), respectively.

Solid-phase peptide synthesis was carried out on a Perkin-Elmer Applied Biosystems (Foster City, CA) Model 433A automated peptide synthesizer employing their Fast-Moc chemistry with HBTU activation of carboxyl groups. FAB mass spectra were obtained on a JEOL SX-102 high-resolution mass spectrometer. Two HPLC systems were used. For radiochemistry, a Beckman System Gold HPLC equipped with a Model 126 programmable solvent module, a Model 166 NM variable wavelength detector, a Model 170 radioisotope detector, and a Beckman System Gold remote interface module SS420X was employed; data were acquired in this system using 32 Karat software. For nonradioactive and preparative work, a Waters Model Delta 600 semiprep system with a Model 600 controller and a Model 2487 dual wavelength absorbance detector was used; data were acquired using Millenium software. A Waters XTerra C18 HPLC column (4.6 × 250 mm, 5 μm), which was eluted at a flow rate of 1 mL/min was used for analytical chromatography and a Waters XTerra C18 column (19 × 150 mm, 7 μm), which was eluted at 10 mL/min was used for semipreparative chromatography. In some cases, a YMC-basic column (S-5 micron, 4.6 × 250 mm; YMC Inc., Wilmington, NC) was used. For size-exclusion HPLC, a 7.5 × 600-mm TSK gel G3000 SW 113 (10 μm) gel filtration column (Tosohaas; Montgomeryville, PA) was used. The following different HPLC solvents and gradient conditions were employed: (I) XTerra analytical column; A = 0.1% TFA/Water, B = 0.1% TFA/CH_3CN; 90:10 (A/B) for 10 min and then to 10:90 over next 10 min; (II) XTerra analytical column; A = 0.1% HOAc in water, B = 0.1% HOAc in CH_3CN; 96:4 (A/B) for 10 min and then to 0:100 over 30 min; (III) Semipreparative column; same solvents and gradient as in II; (IV) XTerra analytical column; same solvents as in II; 96:4 (A/B) for 10 min and then to 0:100 over 15 min and held at this composition for additional 15 min; (V) semipreparative column; same solvents and gradient as in IV; (VI) XTerra analytical column; same solvents as in IV; 96:4 (A/B) for 10 min, then to 0:100 over 5 min and held at this composition for additional 15 min; (VII) YMC column was eluted at a flow rate of 1 mL/min; same solvents as in I; 99:1 (A/B) for 1 min, to 35:65 in 25 min; and (VIII) Size-exclusion column; phosphate-buffered slaine (PBS) at 1 mL/min.

Cells, mAb, and Culture Conditions. Murine IgG1 L8A4 is a mAb which reacts specifically with the 145 kDa deletion mutant EGFRvIII molecule found on multiple human malignancies including gliomas and breast carcinomas (*21*). The EGFRvIII-expressing cell line used for these studies was U87MGΔEGFR which was established from U87 MG human glioma cell line by transfection with EGFRvIII cDNA (*22*). In cell culture, this line expresses an average of $4-13 \times 10^5$ EGFRvIII molecules per cell (*12*). Cells were grown in Zinc Option media (Life Technologies, Inc., Grand Island, NY) containing 10% fetal calf serum and Geneticin sulfate (600 mg/mL).

Synthesis. *Mal-D-GEEEK.* Maleimido glycine (maleimido acetic acid) was synthesized following a literature procedure (*23*). Three D-glutamic acids (*O-t*Bu) and the above glycine derivative were sequentially attached to D-lysine (Boc) supported on Wang resin (0.1 mmol) using the automated synthesizer. Cleavage from the resin and simultaneous removal of side-chain protecting groups were achieved by treatment with 100:95:2.5:2.5 (v/v/v/v/) DCM:TFA:water:triisopropylsilane. The resin was filtered, and the peptide was precipitated from the concentrated filtrate with diethyl ether to yield 40 mg (60%) of N^{α}-maleimido-Gly^1-GEEEK (Mal-D-GEEEK). HPLC conditions I: t_R = 5.4 min. MS (*m*/*z*) Calcd. for: $C_{27}H_{38}N_6O_{14}$ 670.6. Found: 671.1 (MH^+); 693.1 $(M + Na)^+$.

*N^{ϵ}-(3-Iodobenzoyl)-Lys^5-N^{α}-maleimido-Gly^1-GEEEK (IB-Mal-D-GEEEK) (**5**).* This compound was synthesized for use as an HPLC standard. A solution of Mal-GEEEK (1.2 mg; 1.8 μmol) in 30 μL DMF was added to a solution of SIB (7.2 mg; 21 μmol) in 70 μL of 1% (v/v) triethylamine in DMF over a period of 15 min, and the homogeneous mixture was stirred at room-temperature overnight. The peptide was precipitated with excess ether, pelleted, washed twice with ether, and purified by preparative HPLC using conditions III to obtain **5** (yield not determined). HPLC conditions II: t_R = 26.8 min. MS (*m*/*z*) Calcd. for: $C_{34}H_{41}IN_6O_{15}$ 900.6. Found: 901.1 (MH^+).

*N^{ϵ}-(3-(Tri-n-butyl)benzoyl)-Lys^5-N^{α}-maleimido-Gly^1-GEEEK (TB-Mal-D-GEEEK) (**6**).* A solution of Mal-D-GEEEK (8 mg; 12 μmol) in 75 μL DMF was added over a period of 15 min to a solution of STB (24.4 mg; 48.75 μmol) in 125 μL of 1% triethylamine in DMF. The homogeneous mixture was stirred at room-temperature overnight, and the peptide was isolated as above and purified using HPLC conditions V to get 3 mg (23%). HPLC conditions IV: t_R = 30.2 min. MS (*m*/*z*) Calcd. for: $C_{46}H_{68}N_6O_{15}Sn$ 1063.8. Found: cluster peaks around 1087.4 $(M + Na)^+$; 1109.3 $(M + 2Na - H)^+$; 1131.3 $(M + 3Na - 2H)^+$; 1153.3 $(M + 4Na - 3H)^+$.

Radiochemistry. *N^{ϵ}-(3-[^{125}I]Iodobenzoyl)-Lys^5-N^{α}-maleimido-Gly^1-GEEEK ([^{125}I]IB-Mal-D-GEEEK) (**5a**).* Acetic acid (20 μL) was added to a vial containing [^{125}I]sodium iodide (0.5 mCi in 1 μL 0.1 N NaOH) followed by **6** (25 μg; 1 μg /μL AcOH) and NCS (0.4 mg/20μL AcOH). The mixture was incubated for 5 min, and the labeled peptide was isolated by reversed-phase HPLC (conditions VI; t_R = 19.7 min). The HPLC fractions containing the product was pooled and evaporated to dryness using an argon stream.

D-N^{α}-Ac−KR[^{125}I]YRR and D-*KE[^{131}I]YEE.* These peptides were prepared by electrophilic substitution of their tyrosine residues using the Iodogen method. For this, peptide in PBS (480 μg/160 μL and 400 μg/200 μL, respectively, for the positively and negatively charged peptides), was added to $^1/_2$-dram vials coated with Iodogen (10 μg) and containing 558 μCi of ^{125}I and 457 μCi of ^{131}I, respectively. The mixtures were incubated at room temperature for 40 min, and the labeled peptides were isolated by reversed-phase HPLC using conditions VII. The retention times for D-N^{α}-Ac-KR[^{125}I]YRR and D-KE[^{131}I]YEE were 10.3 and 7.5 min, respectively. The pooled HPLC fractions containing the peptide were concentrated by solid-phase extraction using a Sep-pak plus tC18 cartridge (Waters, Milford, MA). After the HPLC fractions were loaded on the cartridge, it was washed sequentially with 5 mL each of water and 5 mM hexanesulfonic acid. The peptides were eluted with 1% HOAc in methanol (4 × 1 mL). The solvents were evaporated with a stream of argon, and the residual radioactivity was reconstituted in PBS prior to use in the animal experiment.

mAb Labeling. *Direct.* A solution of mAb L8A4 (250 μg; 2.5 mg/mL) in phosphate buffer, pH 7.4, was added to a $^1/_2$-dram vial coated with Iodogen (10 μg) followed by a solution

of [^{131}I]sodium iodide (0.5 mCi) in PBS (40 μL). The mixture was incubated for 10 min with occasional shaking, and the labeled mAb was isolated by gel filtration on a PD-10 column (GE Healthcare, Piscataway, NJ) eluted with PBS.

*[^{125}I]IB-Mal-*D*-GEEEK.* L8A4 was dialyzed overnight against PBS, pH 7.4, containing 1 mM EDTA. The above solution of L8A4 (95 μL; 2.6 mg/mL) was treated with a solution of 2-iminothiolane in 1 mM EDTA in PBS (1.5 mL; 2 mg/mL), and the mixture was incubated for 90 min at room temperature. The thiol-derivatized mAb was isolated using a Microspin G-25 column (GE Healthcare, Piscataway, NJ) and added to [^{125}I]IB-Mal-D-GEEEK (0.4 mCi). The mixture was incubated at room temperature for 70 min with occasional mixing. Iodoacetamide (10 μL; 100 mg/mL PBS/EDTA) was added to quench the reaction. After a further incubation for 10 min, the labeled mAb was purified on a PD-10 column eluted with PBS.

Characterization of Labeled mAbs. Protein-associated radioactivity was determined by coprecipitating the labeled mAbs with BSA in a paired-label format with cold methanol. The fraction of radioiodine activity with a retention time corresponding to IgG was measured by size-exclusion HPLC (conditions VIII). The immunoreactive fraction of the labeled mAbs was determined in a paired-label format using magnetic beads coated with EGFRvIII and analyzed according to the Lindmo method as described before (*11*).

Internalization Assay. The retention of radioiodine activity inside the cell and on the cell surface for the L8A4 labeled by the two methods was determined as a function of time. The in vitro assay was performed in a paired-label format using the EGFRvIII-expressing U87MGΔEGFR cell line following previously described procedures (*10*). Briefly, cells at a density of 5 $\times$ 10^5 cells per well were incubated with 1 μCi (0.5−1.0 μg of each mAb) of the labeled mAbs for 1 h at 4 °C. The cells were washed and brought to 37 °C and then processed in triplicate at 0, 1, 2, 4, 8−10, 16, and 24 h as follows: The cell culture supernatant was withdrawn, and surface-bound radioactivity was removed by washing the cells with pH 2 Zinc Option medium. Finally, the cells were solubilized in 0.5 mL of 0.5 N NaOH to determine internalized radioactivity. The cell culture supernatants, acid washes (cell surface-bound), and the cell lysates (internalized) were counted and the results expressed as the percentage of radioactivity initially bound to the cells after the 1 h incubation at 4 °C. The experiment was performed twice.

Biodistribution Measurements. Animal studies were performed under the guidelines established by the Duke University Institutional Animal Care and Use Committee. In these experiments, labeled compounds were injected intravenously via the tail vein, and groups of five animals were evaluated at each time point. Mice were killed by an overdose of halothane and dissected, and tissues of interest were harvested. Blood samples were obtained by retro-orbital bleeding. Tissues were blot-dried, weighed, and counted along with input standards for both ^{125}I and ^{131}I using a dual-channel automated gamma counter that applied corrections for radioactive decay and crossover. Results were expressed as the percent of injected dose per gram of tissue (% ID/g). The difference in the tissue radioactivity levels of the two compounds administered in each experiment was analyzed for statistical significance with a paired *t*-test using the Microsoft Excel program, with $p < 0.05$ considered to represent a significant difference.

D-N$^\alpha$-Ac−KR[^{125}I]YRR versus D-KE[^{131}I]YEE. The experiment was performed to evaluate the effect of charge (three negatively charged glutamates versus three positively charged arginine residues) on the tissue distribution of D-amino acid pentapeptides. Normal mice weighing approximately 25 g were obtained from Charles River Laboratories International Inc. (Wilmington, MA). Animals were injected with 5 μCi of each peptide, and groups of five mice were killed at 0.5, 1, 2, and 4 h postinjection.

Paired-Label Biodistribution of L8A4 Labeled with [^{125}I]IB-Mal-D-GEEEK and with ^{131}I Using Iodogen. BALB/c *nu*/*nu* mice were obtained from a closed breeding colony at the Duke University Cancer Center Isolation Facility. Xenografts were established from the U87MGΔEGFR cell line (*22*). On the basis of the flow cytometry data, disaggregated U87MGΔEGFR xenografts express a mean of 2.5 $\times$ 10^5 EGFRvIII receptors per cell (*12*). The xenografts were generated by injecting the mice subcutaneously in the flank with 50 μL of U87MGΔEGFR tumor homogenate through a 16-gauge needle. Biodistribution measurements were initiated when the xenograft volume reached 200−400 mm^3. Mice were injected with 5 μCi (18.5 μg) and 1.5 μCi (1.6 μg) of ^{125}I- and ^{131}I-labeled L8A4, respectively. Necropsy was performed at 12, 24, 48, 72, and 144 h postinjection.

RESULTS AND DISCUSSSION

Receptor-mediated internalization of radioligands generally results in their translocation to lysosomes where they are subject to degradation by proteases. A consequence of these processes for mAbs labeled by direct methods is the rapid loss of radioiodine from the cell in the form of mono-iodotyrosine (*4*). Because D-amino acids are poor substrates for endogenous proteases, prosthetic groups containing a D-peptide core are a "natural" choice for labeling internalizing mAbs. In this way, different modifications can be made at multiple positions along the peptide with the expectation that the molecule will remain intact in vivo.

A series of D-peptides bearing one or two diethylenetriaminepentaacetic acid (DTPA) substituents have been evaluated for use in labeling internalizing mAbs (*8*, *24*). The rationale for this particular approach is based on the fact that when radiometals are administered as DTPA−mAb conjugates, they are retained inside cells in the form of radiometal-DTPA-lysine. All D-peptide−DTPA reagents provided similar advantages in tumor retention of radioiodine activity for an internalizing mAb compared with directly labeled mAb. In contrast, considerable differences in normal tissue retention were observed, with less accumulation achieved when the hydrophilicity of the peptide was maximized by appending two DTPA moieties.

We have been pursuing an alternative strategy in which the characteristics of the D-amino acid peptide itself are modulated in order to achieve trapping of the radionuclide inside the cell after mAb internalization. The feasibility of this approach was demonstrated in studies utilizing D-N$^\alpha$-Ac-KRYRR (*15*), a peptide with three positively charged arginine residues included in the sequence in order to inhibit egress of labeled catabolites across lysosome and cell membranes. Considerably higher tumor levels were observed for an internalizing mAb labeled with ^{125}I-labeled D-N$^\alpha$-Ac-KRYRR compared with ^{131}I-labeled L-N$^\alpha$-Ac-KRYRR, confirming the role of D-amino acids in achieving these favorable results. One of the motivations for the current study was to determine whether similar results could be obtained with other D-amino acid peptides, in this case, bearing three negatively charged glutamic acids.

In our D-N$^\alpha$-Ac-KRYRR-based conjugation labeling method (*15*), the radiolabeled peptide was conjugated first to iminothiolane-treated mAb via a bifunctional reagent containing a maleimido moiety. To avoid this extra step, we have included a maleimido-glycine at the N-terminus of the peptide. This was built-in during the solid-phase synthesis of the peptide (Scheme 1). The stability of maleimido moiety to coupling and cleavage conditions (peptide synthesis) was evaluated by thin-layer chromatography, and the maleimido glycine was shown to be inert under these conditions (data not shown). Other investigators

Scheme 1. Syntheses of IB-Mal-D-GEEEK and Its Tin Precursor[a]

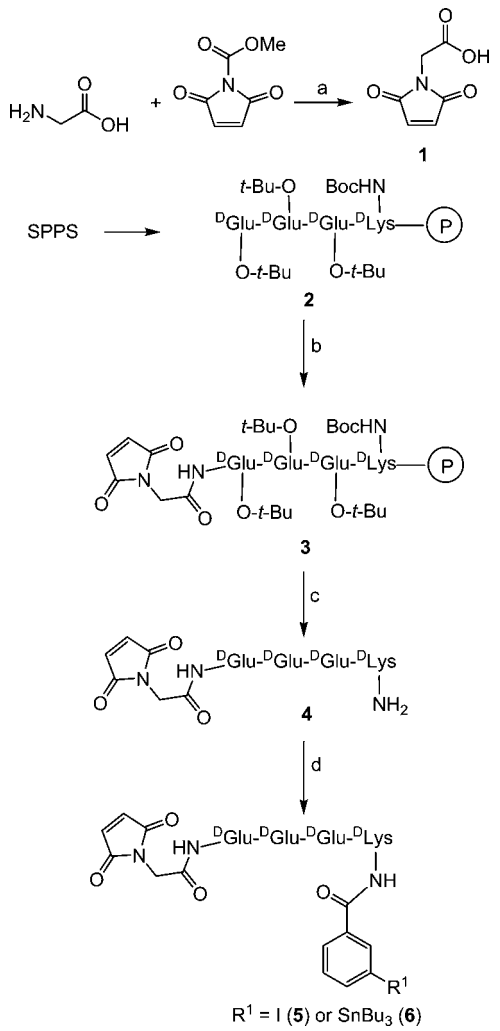

[a] (a) $NaHCO_3$; (b) **1**; solid-phase peptide synthesis (SPPS); (c) TFA cocktail; (d) *N*-succinimidyl 3-iodo- or 3-(tri-*n*-butylstannyl)benzoate.

Scheme 2. Synthesis of [*I]IB-Mal-D-GEEEK[a]

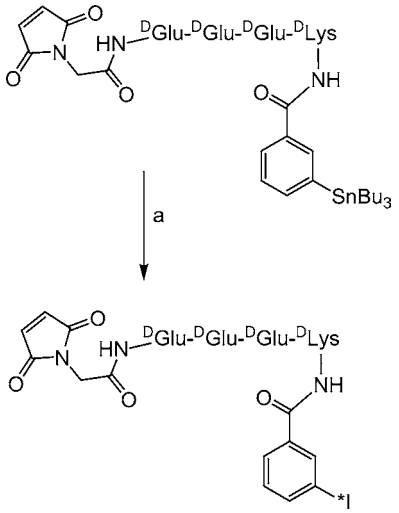

[a] (a) Radioiodine, NCS, acetic acid.

also have synthesized peptides with built-in maelimido functionalities (*25*). The molecular weights observed for the backbone peptide, as well as the SIB- and STB-derivatized peptides, were consistent with the theoretically calculated values.

The tin precursor was radioiodinated to [^{125}I]IB-Mal-D-GEEEK (Scheme 2) in 90.3 ± 3.9% radiochemical yield and in more than 99% radiochemical purity. [^{125}I]IB-Mal-D-GEEEK was coupled to thiolated mAb L8A4 in conjugation efficiencies of 54.3 ± 17.7%. Conjugation efficiencies were similar to those observed previously for D-*N*$^{\alpha}$-Ac-KRYRR to this same mAb (*15*) and comparable to those reported by Stein et al. (*24*) for D-peptides with one maleimido functionality. Although these investigators were able to increase coupling yield by inclusion of a second maleimido group, we chose not to pursue this tactic because of the potential for forming multimeric mAb species.

Coprecipitation of the labeled protein with BSA using methanol indicated that 94 ± 6% of the radioactivity was protein-associated. This was corroborated by size-exclusion HPLC of the preparation, which showed a single radioactivity peak eluting with a retention time corresponding to monomeric IgG with minimal aggregation of the protein (data not shown). The immunoreactive fraction as determined by the Lindmo method was 83 ± 2% compared to 70% obtained for L8A4 labeled with Iodogen.

The primary hypothesis of this work is that incorporation of multiple negatively charged amino acids in the D-peptide prosthetic group for mAb radiohalogenation would provide labeled catabolites that will be trapped inside cells after mAb internalization. The labeled reagent that was developed, [*I]IB-Mal-D-GEEEK, has three glutamic acid residues with carboxylate side chains (p*K* 4.25) that should be predominantly anionic at lysosomal pH. To determine whether labeling the anti-EGFRvIII mAb L8A4 with [*I]IB-Mal-D-GEEEK increased cellular retention of radioactivity compared with direct iodination, a paired-label internalization experiment was performed in vitro using the U87MGΔEGFR cell line. As shown in Figure 1A, the percent of initially bound radioactivity that internalized increased with time throughout the 24 h observation period for L8A4 labeled with [^{125}I]IB-Mal-D-GEEEK; on the other hand, not only was this amount considerably lower for L8A4 labeled by the direct method but intracellular activity decreased with the time. For example, internalized radioactivity for L8A4 labeled with [^{125}I]IB-Mal-D-GEEEK at 24 h (44.7 ± 3.1%) was about 15-fold higher than that from directly labeled L8A4 (3.0 ± 0.3%). The surface-bound radioactivity (Figure 1B) was higher for L8A4 labeled with [^{125}I]IB-Mal-D-GEEEK at each time point compared to the directly labeled mAb. As a result, the total cell-associated radioactivity was substantially higher for the mAb labeled using this novel method. The radioactivity pattern seen in cell culture supernatants (Figure 1C) was complementary to the above.

The degree of enhancement in cell-associated radioactivity obtained with [*I]IB-Mal-D-GEEEK at 24 h was even more favorable than that obtained with D-*N*$^{\alpha}$-Ac-KRYRR (5-fold; same mAb and cell line) (*15*). The tumor delivery advantage obtained using the IB-Mal-GEEEK template also is higher than that obtained with other residualizing labels (*10, 11*). Although comparison to other mAbs and cell lines must be done with caution, it is worth noting that the increase in intracellular and total cell associated radioactivity seen with [*I]IB-Mal-D-GEEEK was substantially higher than that reported for other D-amino acid peptide prosthetic groups (*24*). In addition, [*I]IB-Mal-D-GEEEK was the only reagent that resulted in an increase in intracellular activity with time. The reason for these differences is not known at this time. We speculate that a probable factor is the fact that the site of [*I]IB-Mal-D-GEEEK radioiodination is less susceptible to deiodination, with the result that a greater fraction of the label is still associated with the mAb at later time points.

A drawback of the KRYRR method, which provided one of the motivations for the current study, was that the use of this reagent for labeling L8A4 increased renal uptake considerably

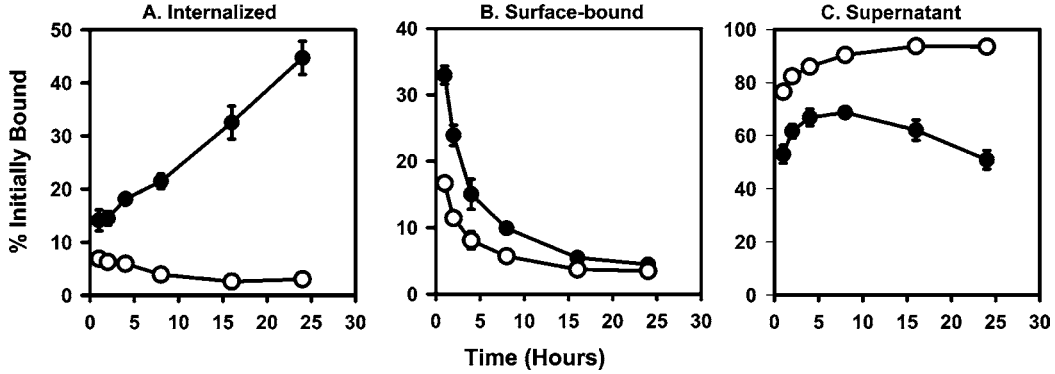

Figure 1. Paired-label internalization by U87MGΔEGFR cells of L8A4 directly radioiodinated with ^{131}I using Iodogen (open circles) and that labeled with [^{125}I]IB-Mal-GEEEK (filled circles). Cells were allowed to take the tracers by incubating them together for 1 h at 4 °C. Medium containing unbound radioactivity was removed, and the cells were supplemented with fresh medium, brought up to 37 °C and processed as described under Experimental Section.

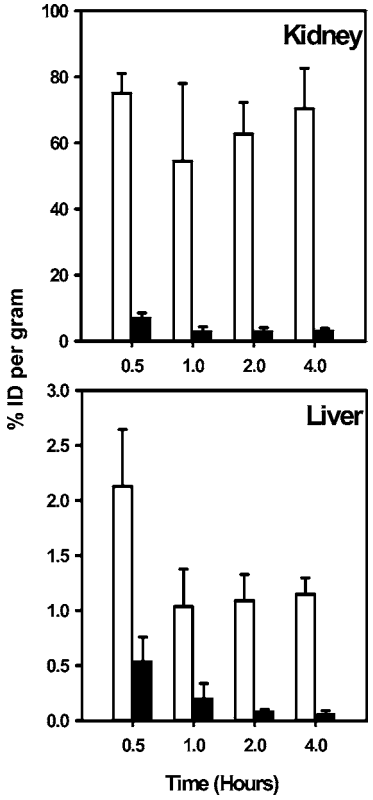

Figure 2. Paired-label uptake of D-N^{α}-Ac-KR[^{125}I]YRR (open bars) and D-KE[^{131}I]YEE (closed bars) in kidneys and liver of normal mice.

(*15*). It is well-known that positively charged molecules are retained to a greater degree by the kidneys because they are more likely to undergo tubular absorption due to the negative charge of the luminal membranes of kidney (*26*). In fact, lysine is often pre-administered to obviate the high renal accumulation of several radiopharmaceuticals (*27*). On the basis of this, we hypothesized that utilization of a peptide with multiple D-glutamates instead of D-lysines should allow enhancement of tumor retention of radioactivity without increasing uptake in kidneys.

To determine whether a decrease in kidney uptake, and possibly other normal organ accumulation, could be achieved by substitution of negatively charged for positively charged amino acids, a tissue distribution experiment was performed in normal mice comparing the organ uptake of radioactivity from D-N^{α}-Ac-KR[^{125}I]YRR and D-KE[^{131}I]YEE. The latter peptide was derived by substituting D-glutamates for D-lysines in D-N^{α}-Ac-KRYRR; in addition, the N-terminus was not acetylated.

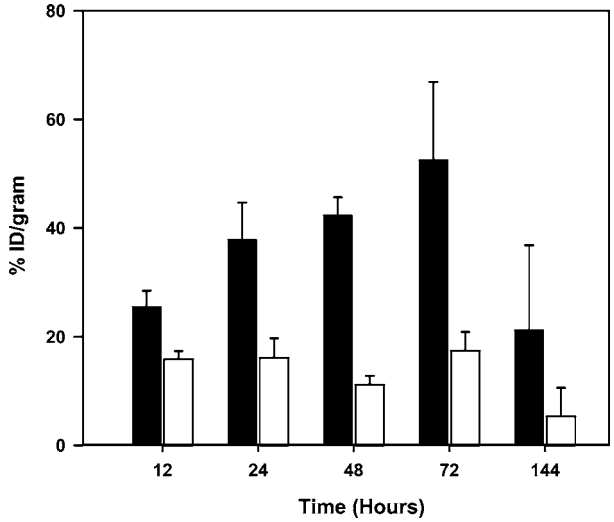

Figure 3. Paired-label tumor uptake of L8A4 directly radioiodinated with ^{131}I using Iodogen (open bars) and that labeled with [^{125}I]IB-Mal-GEEEK (filled bars) in athymic mice bearing U87MGΔEGFR xenografts.

As shown in Figure 2, over a period of 4 h, the uptake of radioactivity in kidneys from D-KE[^{131}I]YEE was more than 10-fold lower than that from the coadministered D-N^{α}-Ac-KR[^{125}I]YRR ($p < 0.01$). Accumulation of radioiodine in the liver with D-KE[^{131}I]YEE also was at least four times less than observed for co-administered D-N^{α}-Ac-KR[^{125}I]YRR ($p < 0.01$). The substantial reduction in the renal uptake is consistent with the net negative charge of the KEYEE construct. In addition to negative charge, the lower lipophilicity of KEYEE might have been a contributory factor to lowering liver uptake. One would expect the cationic peptide to be more lipophilic due to capping of its N-terminus with an acetyl group, and indeed, under identical conditions, it had a retention time of 10.3 min in reversed-phase HPLC compared with 7.5 min for KEYEE. On the basis of these results, we embarked on the design and evaluation of IB-Mal-GEEEK as a reagent for labeling internalizing mAbs.

The biodistribution of L8A4 labeled with [^{125}I]IB-Mal-GEEEK and mAb labeled with ^{131}I using Iodogen method were compared in a paired-label format in athymic mice bearing subcutaneous U87MGΔEGFR human glioma xenografts. In concert with the in vitro internalization data, the tumor uptake in vivo of [^{125}I]IB-Mal-GEEEK-labeled L8A4 was substantially higher ($p < 0.05$ except at 144 h) than that of the directly labeled mAb (Figure 3). The tumor uptake of [^{125}I]IB-Mal-GEEEK-labeled L8A4 increased with time, reaching a maximum of 52.6 ± 14.3% ID/g at 72 h. A 1.6, 2.3, 3.8, 3.0, and 4.0-fold higher

Table 1. Paired-Label Biodistribution of L8A4 Labeled with [^{125}I]IB-Mal-GEEEK and with ^{131}I Using Iodogen in Athymic Mice Bearing U87MGΔEGFR Xenografts

	%ID/gram[a]				
tissue	12 h	24 h	48 h	72 h	144 h
			Iodine-125		
liver	4.84 ± 1.10	4.20 ± 0.98	2.94 ± 0.46[b]	4.52 ± 0.76[b]	1.08 ± 0.62[b]
spleen	3.34 ± 2.80	2.80 ± 0.36	2.73 ± 0.42	4.07 ± 0.87	1.33 ± 0.70
lungs	4.43 ± 0.64	3.69 ± 0.66	2.89 ± 0.63	5.11 ± 1.25	0.94 ± 0.84
heart	3.49 ± 0.64	2.95 ± 0.74	2.61 ± 0.45	4.11 ± 0.46	0.82 ± 0.72
kidneys	10.75 ± 1.27	9.75 ± 1.16	7.40 ± 0.75	8.68 ± 0.73	3.74 ± 0.69
stomach	0.54 ± 0.18	0.64 ± 0.17	0.56 ± 0.07	0.67 ± 0.18	0.15 ± 0.10
small intestine	0.75 ± 0.17	0.75 ± 0.21	0.64 ± 0.14	1.04 ± 0.15	0.21 ± 0.15
large intestine	0.66 ± 0.14[b]	0.56 ± 0.14[b]	0.55 ± 0.11	0.73 ± 0.10	0.26 ± 0.11
muscle	0.61 ± 0.13	0.63 ± 0.17	0.56 ± 0.11	0.87 ± 0.18	0.21 ± 0.11
blood	12.58 ± 2.16	10.57 ± 2.59	8.39 ± 1.55	14.07 ± 2.27	2.65 ± 2.13
brain	0.34 ± 0.12	0.24 ± 0.05	0.23 ± 0.09	0.36 ± 0.10	0.07 ± 0.06
			Iodine-131		
liver	4.23 ± 1.17	3.60 ± 0.71	2.84 ± 0.47	4.35 ± 0.94	1.03 ± 0.66
spleen	2.73 ± 0.73	2.06 ± 0.40	1.90 ± 0.38	3.03 ± 0.75	0.66 ± 0.45
lungs	4.90 ± 0.54	4.27 ± 0.69	3.36 ± 0.67	5.73 ± 1.41	1.28 ± 1.04
heart	3.94 ± 0.71	3.45 ± 0.77	3.09 ± 0.37	4.57 ± 0.43	1.20 ± 0.92
kidneys	4.26 ± 0.66	3.80 ± 0.76	2.92 ± 0.47	4.66 ± 0.82	1.30 ± 0.79
stomach	2.05 ± 0.70	2.55 ± 0.98	1.87 ± 0.83	1.13 ± 0.34	0.56 ±0.22
small intestine	0.90 ± 0.16	0.91 ± 0.19	0.72 ± 0.14	1.10 ± 0.15	0.28 ± 0.17
large intestine	0.59 ± 0.09	0.58 ± 0.11	0.42 ± 0.08	0.57 ± 0.07	0.19 ± 0.08
muscle	0.73 ± 0.12	0.77 ± 0.18	0.72 ± 0.15	1.01 ± 0.19	0.36 ± 0.15
blood	14.32 ± 2.54	12.50 ± 2.73	10.04 ± 1.47	16.06 ± 2.41	4.04 ± 2.76
brain	0.39 ± 0.13	0.29 ± 0.06	0.27 ± 0.10	0.41 ± 0.11	0.10 ± 0.07

[a] Mean ± S.D ($n = 5$; for 144 h, $n = 4$) of %ID/gram. [b] The difference in uptake between the two methods not statistically significant ($p > 0.05$).

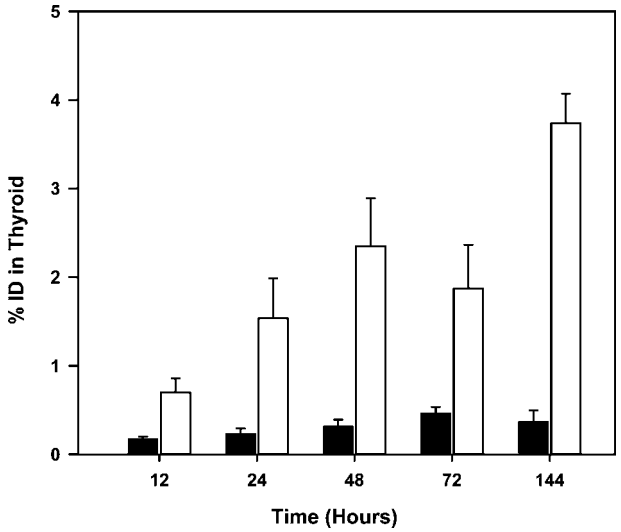

Figure 4. Uptake of radioiodine activity in mouse thyroid after administration of L8A4 labeled with ^{125}I using [^{125}I]IB-Mal-GEEEK (filled bars) and with ^{131}I using the Iodogen method (open bars).

tumor uptake was observed for mAb labeled with [^{125}I]IB-Mal-GEEEK compared with that labeled using Iodogen at 12, 24, 48, 72, and 144 h, respectively. The tumor delivery advantage using [^{125}I]IB-Mal-GEEEK was about the same as observed previously with D-N^{α}-Ac-KR[^{125}I]YRR; however, the maximum tumor uptake was seen at 3 days rather than 1 day after injection (*15*). This suggests that [*I]IB-Mal-GEEEK may be a useful radiohalogenation method for increasing the tumor radiation dose achievable in radioimmunotherapy with internalizing mAbs such as L8A4 labeled with 8.1-day half-life ^{131}I.

Thyroid uptake is frequently used as an indicator of degree of in vivo deiodination of radioiodinated compounds. In Figure 4, the thyroid accumulation of ^{125}I and ^{131}I activity following injection of [^{125}I]IB-Mal-GEEEK-labeled L8A4 and L8A4 labeled with ^{131}I using Iodogen are compared. The % ID recovered from the thyroid for L8A4 labeled with [^{125}I]IB-Mal-GEEEK ranged from 0.18 ± 0.02% at 12 h to 0.47 ± 0.07% at 72 h and were 4- to 10-fold lower than that seen for mAb labeled using Iodogen, but not significantly different from those observed for L8A4 labeled with D-N^{α}-Ac-KR[^{125}I]YRR (*15*). Thus, labeling on an iodobenzoyl moiety offered no advantage compared with a D-tyrosine site in minimizing the deiodination in vivo of this internalizing mAb.

These results are consistent with the stability of D-tyrosine toward deiodination (*16*) but also may reflect other factors as well. Thyroid accumulation of a mAb that does not undergo internalization, 81C6, labeled by coupling to SIB was about an order of magnitude lower than that seen in the current study (*28*). Interestingly, the thyroid uptake observed after injection of this mAb labeled with using *N*-succinimidyl iodobenzoates bearing positively (*10*) or negatively (*11*) charged polar substituents was somewhat lower than that seen with the two D-amino acid peptide reagents. In addition differences related to the processing of the two mAbs and the nature of the linkage between the prosthetic group and the mAb also may play a role.

The tissue distribution of radioiodine labels in other normal tissues was similar for L8A4 mAb labeled by the two methods with two notable exceptions (Table 1). Uptake of ^{131}I was higher at all time points in the stomach, another tissue known to take up free iodide avidly, and this is consistent with the observed higher thyroid uptake of ^{131}I. Contrary to the expectations, however, the accumulation of radioactivity in the kidneys for L8A4 labeled with [^{125}I]IB-Mal-GEEEK was about 2- to 3-fold higher than that for directly labeled mAb. In fact, the renal uptake of [^{125}I]IB-Mal-GEEEK-labeled L8A4 was similar to that seen for the same mAb labeled with the cationic D-peptide reagent (*15*), suggesting that changing the net charge of the D-peptide from positive to negative was not an effective strategy for reducing kidney uptake of intact mAbs labeled using this type of prosthetic group. On the other hand, the uptake in liver for L8A4 labeled with [^{125}I]IB-Mal-GEEEK was quite similar to that for coadministered mAb labeled using Iodogen and about 3-fold lower compared to L8A4 labeled with D-N^{α}-Ac-KR[^{125}I]YRR (*15*). Increased kidney and liver retention of radioiodine has been observed, compared with direct labeling,

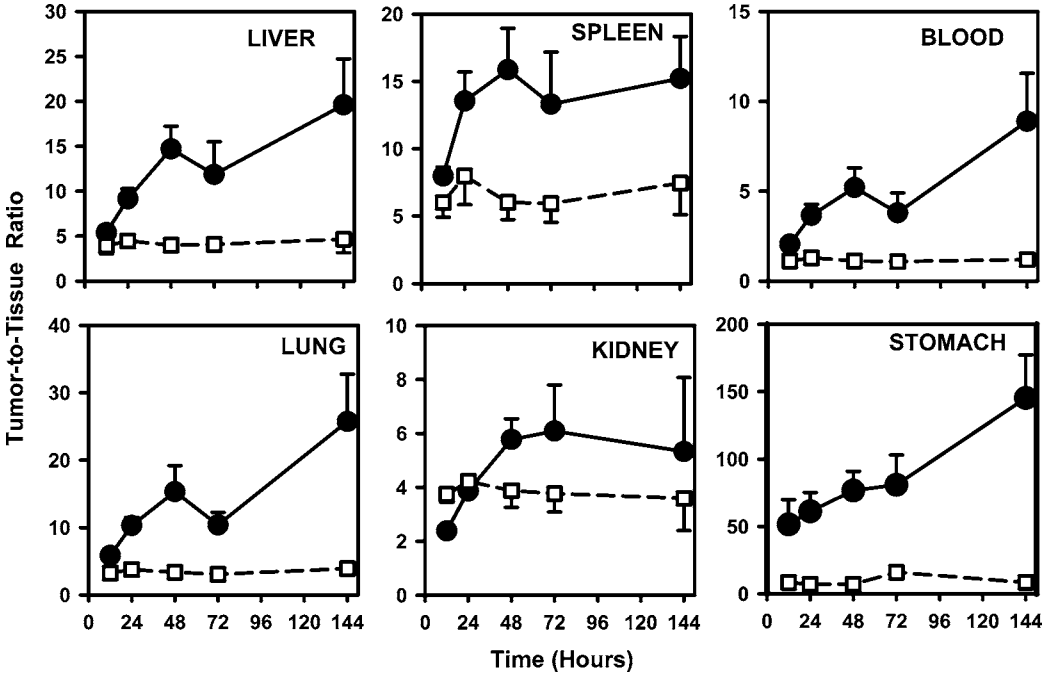

Figure 5. Tumor-to-normal tissue ratios of ^{125}I (filled circles) and ^{131}I (open circles) in athymic mice after paired injection of L8A4 labeled with [^{125}I]IB-Mal-GEEEK and with ^{131}I using the Iodogen method.

for mAb RS7 after labeling with six different D-peptide labeling reagents, with the effect most prominent for the IMP−R2 peptide bearing four tyrosine residues, a DTPA, and two maleimido moieties (*24*). Taken together, these results suggest that decreasing the hydrophobicity of the D-peptide results in decreased liver accumulation; however, it is difficult to ascertain the best strategy for minimizing renal accumulation with this class of radiohalogenation agents.

Tumor:normal tissue ratios for L8A4 labeled with [^{125}I]IB-Mal-GEEEK and with ^{131}I using Iodogen are shown in Figure 5. Except for the kidney at some time points, significantly higher tumor:normal tissue ratios were observed for the D-peptide conjugate. With the exception of the kidney, selectivity of radioiodine increased with time as did the selectivity advantage for mAb labeled using the D-peptide reagent. At 6 days after injection, tumor:normal tissue ratios for L8A4 labeled with [^{125}I]IB-Mal-GEEEK reached 5.3 ± 2.7, 8.9 ± 2.7, 15.2 ± 3.1, 19.6 ± 5.1, 25.7 ± 7.0, and 145 ± 32 in kidney, blood, spleen, liver, lung and stomach, respectively. These values were 1.5- to 17-fold higher than those for coadministered L8A4 labeled using Iodogen and reported previously for this mAb labeled with D-N^{α}-Ac-KR[^{125}I]YRR (*15*).

In summary, a new prosthetic group, [*I]IB-Mal-GEEEK, consisting of three D-glutamates, a D-lysine carrying an [*I]iodobenzoyl moiety, and a maleimide function was synthesized from a tin precursor and conjugated to an internalizing anti-EGFRvIII mAb with preservation of immunoreactivity. Compared with mAb labeled using Iodogen, labeling L8A4 using [*I]IB-Mal-GEEEK enhanced intracellular retention of radioiodine in EGFRvIII-expressing tumor cells in vitro and in tumor xenografts and resulted in significantly higher tumor:normal organ uptake ratios. We conclude that [*I]IB-Mal-GEEEK is a promising reagent for the radioiodination of mAbs that undergo internalization. Further work is in progress to evaluate the potential of this approach for labeling mAbs with the α-emitter astatine-211.

ACKNOWLEDGMENT

This work was supported by Grants CA42324, NS20003, and CA93371 from National Institutes of Health. The authors want thank Philip Welsh, Katia Peixoto, and Susan Slade for excellent technical assistance.

LITERATURE CITED

(1) Wikstrand, C. J., McLendon, R. E., Friedman, A. H., and Bigner, D. D. (1997) Cell surface localization and density of the tumor-associated variant of the epidermal growth factor receptor, EGFRvIII. *Cancer Res. 57*, 4130−4140.

(2) Press, O. W., DeSantes, K., Anderson, S. K., and Geissler, F. (1990) Inhibition of catabolism of radiolabeled antibodies by tumor cells using lysosomotropic amines and carboxylic ionophores. *Cancer Res. 50*, 1243−1250.

(3) Wargalla, U. C., and Reisfeld, R. A. (1989) Rate of internalization of an immunotoxin correlates with cytotoxic activity against human tumor cells. *Proc. Natl. Acad. Sci. U.S.A. 86*, 5146−5150.

(4) Reist, C. J., Garg, P. K., Alston, K. L., Bigner, D. D., and Zalutsky, M. R. (1996) Radioiodination of internalizing monoclonal antibodies using *N*-succinimidyl 5-iodo-3-pyridinecarboxylate. *Cancer Res. 56*, 4970−4977.

(5) Geissler, F., Anderson, S. K., and Press, O. (1991) Intracellular catabolism of radiolabeled anti-CD3 antibodies by leukemic T cells. *Cell Immunol. 137*, 96−110.

(6) Ali, S. A., Eary, J. F., Warren, S. D., Badger, C. C., and Krohn, K. A. (1988) Synthesis and radioiodination of tyramine cellobiose for labeling monoclonal antibodies. *Int. J. Rad. Appl. Instrum. B 15*, 557−561.

(7) Ali, S. A., Warren, S. D., Richter, K. Y., Badger, C. C., Eary, J. F., Press, O. W., Krohn, K. A., Bernstein, I. D., and Nelp, W. B. (1990) Improving the tumor retention of radioiodinated antibody: aryl carbohydrate adducts. *Cancer Res. 50*, 783s−788s.

(8) Govindan, S. V., Mattes, M. J., Stein, R., McBride, B. J., Karacay, H., Goldenberg, D. M., Hansen, H. J., and Griffiths, G. L. (1999) Labeling of monoclonal antibodies with diethylenetriaminepenta-acetic acid-appended radioiodinated peptides containing D-amino acids. *Bioconjugate Chem. 10*, 231−240.

(9) Kobayashi, H., Kao, C. H., Kreitman, R. J., Le, N., Kim, M. K., Brechbiel, M. W., Paik, C. H., Pastan, I., and Carrasquillo, J. A. (2000) Pharmacokinetics of ^{111}In- and ^{125}I-labeled antiTac single-chain Fv recombinant immunotoxin. *J. Nucl. Med. 41*, 755−762.

(10) Vaidyanathan, G., Affleck, D. J., Li, J., Welsh, P., and Zalutsky, M. R. (2001) A polar substituent-containing acylation agent for the radioiodination of internalizing monoclonal antibodies: *N*-succin-

imidyl 4-guanidinomethyl-3-[^{131}I]iodobenzoate ([^{131}I]SGMIB). *Bioconjugate Chem. 12*, 428−438.

(11) Shankar, S., Vaidyanathan, G., Affleck, D., Welsh, P. C., and Zalutsky, M. R. (2003) *N*-succinimidyl 3-[(^{131})I]iodo-4-phosphonomethylbenzoate ([(^{131})I]SIPMB), a negatively charged substituent-bearing acylation agent for the radioiodination of peptides and mAbs. *Bioconjugate Chem. 14*, 331−341.

(12) Reist, C. J., Archer, G. E., Wikstrand, C. J., Bigner, D. D., and Zalutsky, M. R. (1997) Improved targeting of an anti-epidermal growth factor receptor variant III monoclonal antibody in tumor xenografts after labeling using *N*-succinimidyl 5-iodo-3-pyridinecarboxylate. *Cancer Res. 57*, 1510−1515.

(13) Vaidyanathan, G., Affleck, D. J., Bigner, D. D., and Zalutsky, M. R. (2002) Improved xenograft targeting of tumor-specific anti-epidermal growth factor receptor variant III antibody labeled using *N*-succinimidyl 4-guanidinomethyl-3-iodobenzoate. *Nucl. Med. Biol. 29*, 1−11.

(14) Shankar, S., Vaidyanathan, G., Affleck, D. J., Peixoto, K., Bigner, D. D., and Zalutsky, M. R. (2004) Evaluation of an internalizing monoclonal antibody labeled using *N*-succinimidyl 3-[^{131}I]iodo-4-phosphonomethylbenzoate ([^{131}I]SIPMB), a negatively charged substituent bearing acylation agent. *Nucl. Med. Biol. 31*, 909−919.

(15) Foulon, C. F., Reist, C. J., Bigner, D. D., and Zalutsky, M. R. (2000) Radioiodination via D-amino acid peptide enhances cellular retention and tumor xenograft targeting of an internalizing anti-epidermal growth factor receptor variant III monoclonal antibody. *Cancer Res. 60*, 4453−4460.

(16) Dumas, P., Maziere, B., Autissier, N., and Michel, R. (1973) Specificity of thyroidal and hepatic microsomal iodotyrosine deiodinase. *Biochim. Biophys. Acta 293*, 36−47.

(17) Zalutsky, M. R., and Vaidyanathan, G. (2000) Astatine-211-labeled radiotherapeutics: an emerging approach to targeted alpha-particle radiotherapy. *Curr. Pharm. Des. 6*, 1433−1455.

(18) Aaij, C., Tschroots, W., Lindner, L., and Feltkamp, T. E. (1975) The preparation of astatine labelled proteins. *Int. J. Appl. Radiat. Isot. 26*, 25−30.

(19) Vaughan, A. T., and Fremlin, J. H. (1978) The preparation of astatine labelled proteins using an electrophilic reaction. *Int. J. Nucl. Med. Biol. 5*, 229−230.

(20) Zalutsky, M. R., and Narula, A. S. (1987) A method for the radiohalogenation of proteins resulting in decreased thyroid uptake of radioiodine. *Appl. Radiat. Isot. 38*, 1051−1055.

(21) Wikstrand, C. J., Hale, L. P., Batra, S. K., Hill, M. L., Humphrey, P. A., Kurpad, S. N., McLendon, R. E., Moscatello, D., Pegram, C. N., and Reist, C. J. (1995) Monoclonal antibodies against EGFRvIII are tumor specific and react with breast and lung carcinomas and malignant gliomas. *Cancer Res. 55*, 3140−3148.

(22) Nishikawa, R., Ji, X. D., Harmon, R. C., Lazar, C. S., Gill, G. N., Cavenee, W. K., and Huang, H. J. (1994) A mutant epidermal growth factor receptor common in human glioma confers enhanced tumorigenicity. *Proc. Natl. Acad. Sci. U.S.A. 91*, 7727−7731.

(23) Keller, O., Rudinger, J. (1975) Preparation and some properties of maleimido acids and maleoyl derivatives of peptides. *Helv. Chim. Acta 58*, 531−541.

(24) Stein, R., Govindan, S. V., Mattes, M. J., Chen, S., Reed, L., Newsome, G., McBride, B. J., Griffiths, G. L., Hansen, H. J., and Goldenberg, D. M. (2003) Improved iodine radiolabels for monoclonal antibody therapy. *Cancer Res. 63*, 111−118.

(25) Mier, W., Eritja, R., Mohammed, A., Haberkorn, U., and Eisenhut, M. (2000) Preparation and evaluation of tumor-targeting peptide−oligonucleotide conjugates. *Bioconjugate Chem. 11*, 855−860.

(26) Maack, T., Park, C. H., and Camargo, M. J. (1992) Filtration, transport, and metabolism of proteins. *The Kidney: Physiology and Pathophysiology* (Seldin, D. W., and Giebisch, G., Eds.) pp 3005−3038, Raven Press, New York.

(27) Behr, T. M., Goldenberg, D. M., and Becker, W. (1998) Reducing the renal uptake of radiolabeled antibody fragments and peptides for diagnosis and therapy: present status, future prospects and limitations. *Eur. J. Nucl. Med. 25*, 201−212.

(28) Zalutsky, M. R., Noska, M. A., Colapinto, E. V., Garg, P. K., and Bigner, D. D. (1989) Enhanced tumor localization and in vivo stability of a monoclonal antibody radioiodinated using *N*-succinimidyl 3-(tri-*n*-butylstannyl)benzoate. *Cancer Res. 49*, 5543−5549.

BC0600766

TECHNICAL NOTES

Thermostability of Native and Pegylated *Myceliophthora thermophila* Laccase in Aqueous and Mixed Solvents

J. I. López-Cruz,[†] G. Viniegra-González,*[,†] and A. Hernández-Arana[‡]

Laboratorio de Biología Molecular y Enzimología de Hongos Filamentosos, Departamento de Biotecnología, and Laboratorio de Biofisicoquímica, Departamento de Química, Universidad Autónoma Metropolitana Iztapalapa, CP. 09340, Avenida San Rafael Atlixco, 186, México D.F. . Received December 5, 2005; Revised Manuscript Received April 17, 2006

A commercial preparation of laccase (EC 1.10.3.2), cloned from *Myceliophthora thermophila* and expressed in *Aspergillus oryzae* (MtL), was purified and modified by conjugation with poly(ethylene glycol) ($M_r = 5000$) and is labeled PEG−MtL. Native enzyme was found to have a molecular mass of 80 kDa, as determined by gel filtration, and 110 kDa, by SDS−PAGE. The oxidative dimerization of 2,6-dimethoxyphenol (DMP) to produce the corresponding dibenzoquinone was catalyzed by MtL in a manner comparable to that for a diffusion-controlled reaction ($k_{cat}/K_M \cong 10^8$ M^{-1} s^{-1} and $E_a \cong 18$ kJ M^{-1}). PEG−MtL was found, by TNBS titration, to have blocked 54% of lysine groups; its hydrodynamic and charge properties were different from those of MtL. Catalytic efficiency (k_{cat}/K_M) of PEG−MtL was similar to that of MtL with DMP as substrate; however, k_{cat}/K_M was 2-fold reduced for the reaction in which 2′,2-azinobis(3-ethylbenzothiazoline-6-sulfonic acid) (ABTS) is oxidized to form a radical cation. E_a values were similar in both enzyme preparations when assayed in buffered solutions. Far-UV CD spectra were similar for MtL and PEG−MtL and consistent with a protein rich in β-sheet structure with negligible content of α-helices. A blue shift of near-UV CD spectrum for PEG−MtL as compared to MtL was consistent with the decreased polarity of the tyrosyl side chains upon PEG conjugation. Also the blue band of the copper active site was shifted from $\lambda \sim 610$ nm (MtL) to $\lambda \sim 575$ nm (PEG−MtL). Scanning microcalorimetry showed small denaturation enthalpies (6.3 and 7.5 J g^{-1} for MtL and PEG−MtL, respectively), indicating the high stability of the β-sheet folding pattern of laccases. However, PEG−MtL proved to be more stable, its half-denaturation temperature being 2 °C higher than that of MtL. In 30% alcohol, pegylated laccase showed slower enzyme-activity decay rates than the unmodified enzyme; this behavior was caused by a decrease in the activation entropy of the denaturation reaction. Results can be explained by entropic stabilization by PEG conjugation because of the restricted motion of some surface amino acid side chains, which results in a more stable active site.

INTRODUCTION

Laccase is an enzyme (*p*-diphenol: dioxygen oxido-reductase, EC 1.10.3.2) that catalyzes the oxidation of a large variety of phenolic and polyaromatic compounds (*1*). It has been proposed as a potential bleaching agent of cellulose pulp and organic dyes (*2*, *3*) and also as a catalyst for the oxidation of polluting polycyclic aromatic hydrocarbons (*4*, 5). This enzyme has four copper atoms in its active site that reduce O_2 to water using an appropriate electron donor as substrate (*6*, *7*). One of those copper atoms (T_1) absorbs light near 620 nm due to a highly covalent bond between cysteine and Cu (*8*, *9*). Another copper (T_2) does not show strong absorption of light, and two other copper atoms (T_3) are coupled through a hydroxide and shuttle electrons from substrate to the trinuclear T_2/T_3 cluster (*11*, *12*).

Among the future applications of laccase, the oxidation of dibenzothiophene derivatives in diesel fuel has been mentioned (*13*, *14*), but the rates of oxidation of this compound were found too slow, perhaps because the substrate is sparsely soluble in water and the enzyme is inactivated by the presence of organic solvents (*13*). García-Arellano et al. (*15*) showed that the conjugation of cytochrome *c* with poly(ethylene glycol) (PEG) improved the thermal stability of the catalytic site. Furthermore, Vandertol-Varnier et al. (*16*) showed that laccase from *Coriolopsis gallica* conjugated with PEG had a higher catalytic activity on syringaldazine than the native enzyme.

In this work the thermal stability of laccase from *Myceliophthora thermophila* (*17*) conjugated with PEG was studied in relation to the presence of alcohols of different polarity using spectropolarimetric, calorimetric, and enzymological techniques as compared with the native preparation. The hypothesis of this work was that the thermal stability of PEG−laccase would be better than that of native laccase.

EXPERIMENTAL PROCEDURES

Chemicals. The enzyme MtL was obtained from the company Novo Nordisk, in the form of a commercial preparation called Deni Lite IIs. Bovine serum albumin (BSA), cyanuric chloride-activated monomethoxy poly(ethylene glycol) ($M_r = 5$ kDa), 2′,2-azinobis(3-ethylbenzothiazoline-6-sulfonic acid) (ABTS), 2,6-dimethoxyphenol (DMP), and trinitrobenzenesulfonic acid (TNBS) were from Sigma (St. Louis, MO).

Extraction and Purification of Laccase. Fifty grams of Deni Lite IIs was suspended in 200 mL of 50 mM potassium

* Corresponding author. Tel. +52-5804-4719. Fax: +52-5804-6407. E-mail: vini@xanum.uam.mx.

[†] Departamento de Biotecnología.

[‡] Departamento de Química.

10.1021/bc0503465 CCC: $33.50 © 2006 American Chemical Society
Published on Web 06/20/2006

phosphate buffer, pH 6.0, and shaken for 24 h at 4 °C. Solids were removed by centrifugation at 10 000 rpm for 30 min. The supernatant was concentrated nearly 40-fold and dialyzed against the phosphate buffer using an ultrafiltration stirred system (Millipore) with a 10 kDa cutoff cellulose membrane pressurized at 5.95 bar with N_2, on ice. The concentrate was applied to an anion exchange Q-Sepharose column (Hi-Prep 16/10 QFF, Bio-Rad, 120 mg HSA/mL gel) preequilibrated with two column volumes of 50 mM Tris-HCl, pH 7.3, and eluted with a linear gradient from 0.0 to 0.5 M NaCl in the Tris-HCl buffer. Fractions with laccase activity were pooled and concentrated, dialyzed, and stored at −5 °C in phosphate buffer. This preparation was labeled as MtL (native enzyme). To determine the molecular weight of the enzyme a sample was dialyzed against 0.5 mM acetate buffer solution (pH 5.0) and applied to a Superdex 200 HR 10/30 column (Amersham Pharmacia); protein was eluted with buffer containing 0.5 M NaCl (0.5 mL min^{-1}).

Determination of Enzymatic Activity. Laccase activity was routinely assayed by measuring the rate of ABTS oxidation at room temperature. The reaction mixture contained 1.0 mL of 5 mM ABTS dissolved in 50 mM potassium phosphate buffer (pH 6.0) and 100 μL of appropriately diluted enzyme. ABTS oxidation was followed by an increase of absorbance at 420 nm ($\epsilon_{420} = 36\,000\ M^{-1}\ cm^{-1}$). One unit of activity was defined as the amount of laccase that oxidized 1 μmol of substrate per minute. In assays carried out at other pH values, reaction solutions were buffered with citrate (pH 3.0 and 4.0), acetate (pH 5.0), and phosphate (pH 6.0, 7.0, and 8.0) solutions at 50 mM. For determination of catalytic constants, ABTS solutions were prepared in the phosphate buffer (pH 6.0) at concentrations varying from 0.01 to 5.0 mM. When DMP was the substrate, it was dissolved in a mixture of 10% propanol in the same buffer to a final concentration from 0.01 to 0.50 mM. Oxidation of DMP was followed by the absorption increment at 469 nm ($\epsilon_{469} = 49\,600\ M^{-1}\ cm^{-1}$).

Protein Concentration. The protein was assayed by the Bradford method (*18*) using the Bio-Rad protein reagent with bovine serum albumin as standard.

Chemical Modification of Laccase. Chemical modification of the exposed lysine amino groups of laccase was carried out with 50-fold excess of monomethoxy poly(ethylene glycol) activated with cyanuric chloride (Sigma) in 40 mM borate buffer, pH 10.0. The reaction was allowed to proceed for 2.5 h at 25 °C (*16*). The resulting solution was dialyzed and concentrated 20-fold with 50 mM phosphate buffer, pH 6.0, by using the same procedure as for the native enzyme. This preparation was labeled as PEG−MtL.

Determination of Modified Amino Groups. The degree of protein modification was estimated by titration of the residual free amino groups using the reagent TNBS in order to obtain the corresponding trinitrophenyl derivatives, according to the Habeeb method (*19*). The reaction was carried out at pH 8.5. Absorbance was measured at 335 nm against the appropriate blank. The molar extinction coefficient was taken to be $\epsilon_{335} = (1.09 \pm 0.01) \times 10^4\ M^{-1}\ cm^{-1}$.

Gel Electrophoresis. Polyacrylamide gel electrophoresis with sodium dodecyl sulfate (SDS−PAGE) was performed in a Mini-Protean II Cell (Bio-Rad), using a 10.0% gel containing 0.1% SDS according to the methodology of Laemmli (*20*). Protein bands were revealed with Coomassie Blue G-250 or the silver staining kit (Amersham Biosciences, Uppsala, Sweden). The samples were compared to high-range molecular weight markers of Sigma (St. Louis, MO). Other experiments were carried out using a 10.0% polyacrylamide gel, without SDS and mercaptoethanol.

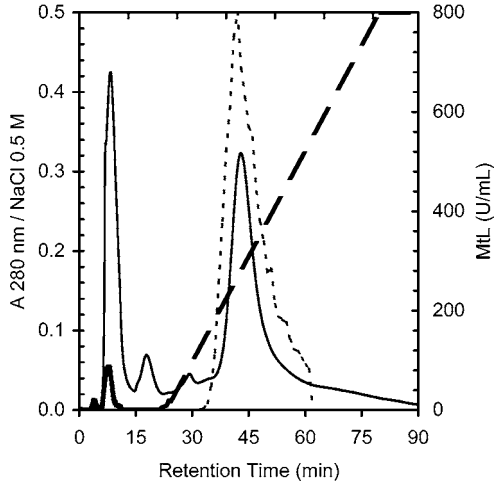

Figure 1. Purification of commercial laccase by ion-exchange chromatography. Six milliliters of mediator-free Deni Lite IIs solution was applied to a Q-Sepharose column and eluted with a NaCl gradient (0−0.50 M). —, absorbance at 280 nm; - - -, laccase activity; − − −, concentration of NaCl in the eluent.

Stability Assays. The stabilities of MtL and PEG−MtL preparations were compared by measuring the decay of enzyme activities (assayed by ABTS oxidation at room temperature) when incubated at various temperatures (40−80 °C) in the presence of 0, 10.0, or 30.0% (v/v) of methanol, ethanol, propanol, or acetonitrile. Decay rate constants, k_i, were estimated by fitting the first-order equation, $A = A_o \exp(-k_i t)$, to the experimental data.

Circular Dichroism (CD) Measurements. CD measurements were performed in a Jasco J-715 spectropolarimeter (Jasco Inc, Easton, MD) equipped with a PTC-348WI Peltier-type cell holder for temperature control. MtL or PEG−MtL samples (0.2 mg mL^{-1}) were dissolved in 50 mM phosphate buffer (pH 6.0) and placed in a 0.10 cm cell. CD scans were run at 25 °C in the range from 190 to 250 nm. For the aromatic absorption region (above 250 nm) protein concentration was increased to 1.0 mg mL^{-1} and a 1.00 cm cell was used.

Differential Scanning Calorimetry (DSC). Calorimetric endotherms were obtained with a Microcal MC2 differential scanning calorimeter (MicroCal Inc, Northampton, MA). Measurements were carried out with a degassed enzyme solution (2.0 mg mL^{-1}, prepared in 5 mM citrate buffer, pH 5.0) in the sample cell. The reference cell was filled with the buffer alone. Both cells were pressurized to nearly 2.0 atm with N_2 gas and heated from 25 to 109 °C at a rate of 1.0 °C min^{-1}. The adiabatic jacket was kept at a partial vacuum of 0.0106 atm. Buffer (blank) tracings were recorded under the same conditions. The Origin software package (MicroCal) was used for data analysis including baseline subtraction and the calculation of specific enthalpies (ΔH_{cal}).

RESULTS AND DISCUSSION

Purification and Catalytic Properties of *M. thermophyla* Laccase (MtL). The reddish color of Deni Lite IIs, which is due to the presence of the redox mediator 10-phenotyazinpropionic acid (*21*), was completely eliminated by extensive dialysis through a 10 kDa cellulose membrane. This operation produced an apparent decrease of approximately 10.0% in the total laccase activity of the material. The elution profile from the ion-exchange column (Figure 1) showed four peaks with absorbance at 280 nm, but all the laccase activity was contained in the peak that eluted last; fractions with enzyme activity were pooled and further submitted to PAGE, where a single major protein band was observed (Figure 2).

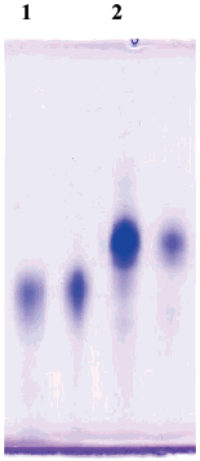

Figure 2. Native PAGE of *M. thermophila* laccase (MtL) and its PEG derivative at pH 6.8. Lane 1, MtL; lane 2, PEG−MtL. The anode is on top.

Table 1. Catalytic Constants for MtL and PEG−MtL[a]

	MtL			PEG_{5000}-MtL		
substrate	k_{cat} (s^{-1})	K_M (μM)	k_{cat}/K_M ($s^{-1}\,M^{-1}$)	k_{cat} (s^{-1})	K_M (μM)	k_{cat}/K_M ($s^{-1}\,M^{-1}$)
ABTS	6.01×10^2	49.5	1.21×10^7	3.76×10^2	71.2	5.29×10^6
DMP	3.48×10^2	5.02	6.93×10^7	8.73×10^2	9.06	9.63×10^7

[a] Michaelis−Menten constants (k_{cat}, K_M) were determined from activity assays in 50 mM phosphate buffer (pH 6.0) at 25 °C.

After ion-exchange chromatography the specific activity was 29 U mg^{-1}, approximately twice the value shown by the original, mediator-free Deni Lite IIs; the yield was about 60%, based on the amount of protein recovered. All further studies were performed with the enzyme obtained from the Q-Sepharose column. The molecular mass of MtL, as determined by SDS−PAGE (data not shown), was 110 kDa, whereas gel filtration chromatography gave a M_r of 80 kDa. Such a difference in M_r determinations probably arises from differences in the glycosylated nature of MtL (*17*), because it is well-known that the presence of covalently attached carbohydrates often results in incorrect M_r values when using SDS or gel filtration techniques (*15*). It should be mentioned that the protein moiety of this enzyme has a mass of 61 781 kDa, according to its amino acid sequence (*22*). The isoelectric point of the laccase was 3.8, in agreement with previous determinations (*17*).

MtL displayed good activity toward ABTS in the 3.0−7.0 pH range; however, the enzyme was more stable between pH 6.0 and 8.0. Determination of kinetic constants was carried out at pH 6.0. With either ABTS or DMP as substrate, MtL showed typical Michaelis−Menten kinetics (results not shown). The values obtained for k_{cat} and K_M (Table 1) indicate that the catalytic efficiency (k_{cat}/K_M) of the enzyme is comparable to that of diffusion-controlled enzyme reactions (i.e., about 1×10^8 M^{-1} s^{-1}; *23*) when the substrate is the relatively small DMP molecule. With ABTS as substrate, the value found for k_{cat}/K_M is about 5-fold smaller, but still close to that for diffusion-controlled reactions, and 2 orders of magnitude larger than the value reported by Li et al (*3*).

The apparent activation energy, E_a, for the MtL-catalyzed oxidation of ABTS was determined from activity assays in the 25−70 °C temperature range; at temperatures higher than 70 °C, thermal denaturation of the enzyme led to notable loss of activity (Figure 3). From the Arrhenius plot on the low-temperature arm of Figure 3, E_a was determined as 18.0 kJ mol^{-1}, in agreement with the low value observed for diffusion-controlled reactions, which have E_as between 10 and 30 kJ mol^{-1} (*23*).

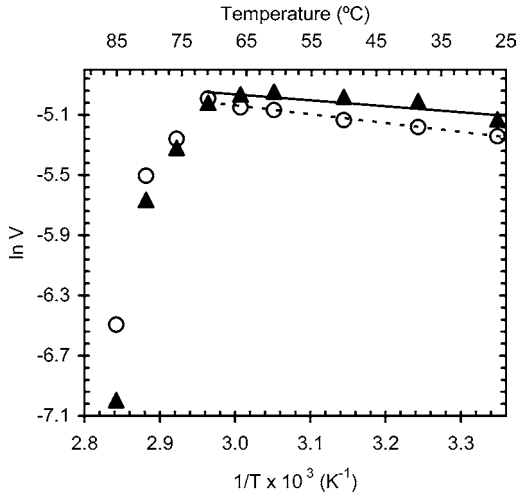

Figure 3. Arrhenius plots for the ABTS-oxidation reaction (pH 6.0) with MtL (▲) and PEG−MtL (○) as catalysts.

Catalytic Properties of Chemically Modified MtL. Under the conditions described in the Experimental Procedures, chemical modification of MtL resulted in a protein material with 54% of its amino groups linked to PEG chains. As a consequence of the reduction in the number of free amino groups, the enzyme derivative (PEG−MtL) showed a smaller electrophoretic mobility toward the cathode than the unmodified laccase (Figure 2). Similarly, attachment of PEG chains notably affected the hydrodynamic properties of MtL, leading to a large reduction of its elution volume in the gel filtration column; the apparent M_r of PEG−MtL determined by this method was larger than 300 kDa, although the expected increase in molecular mass, as computed from the number of modified amino groups, amounts to only 40 kDa.

Determination of the catalytic constants for PEG−MtL gave the results listed in Table 1. It can be seen that the kinetic constants k_{cat} and K_M of the enzyme suffered only minor changes after chemical modification. This is an important result, because with other enzymes the use of cyanuryl chloride−PEG has led sometimes to substantial loss of enzymatic activity due to the low selectivity of this reagent as a protein modifier (*24*, *25*). In the case of MtL, PEG modification slightly affected the affinity of the enzyme (i.e., K_M increased less than 2-fold) for both of the substrates tested. In contrast, PEG−MtL showed a value of k_{cat} that was twice that for the unmodified laccase when DMP was the substrate; with ABTS as substrate, however, k_{cat} was about 2-fold reduced. As a result of these changes in the individual kinetic constants, the catalytic efficiency (k_{cat}/K_M) of the laccase, with the substrate DMP, was practically unaltered by chemical modification; with ABTS, on the contrary, k_{cat}/K_M was more than 2-fold diminished. These findings indicate that the presence of PEG chains on the macromolecular surface somewhat reduces the binding rate of the larger, more hydrophilic ABTS molecule but not that of the small hydrophobic DMP molecule. In other words, PEG modification apparently increased the relative selectivity of the enzyme toward two of its substrates. On the other hand, the apparent activation energy (E_a) for the oxidation of ABTS, whose value is also shown in Table 1, keeps the characteristic small magnitude of diffusion-controlled enzymatic reactions (see Figure 3).

Conformational Characteristics of the Laccase Forms. At 20 °C, the far-UV CD spectrum of MtL (Figure 4) shows a negative band around 216 nm and a positive one at 194−195 nm, both of which are typical of proteins rich in β-strands and with poor helix content (*26*). This observation was expected, given the high sequence identity between MtL and the laccase from *Melanocarpus albomyces* (*27*), whose secondary structure

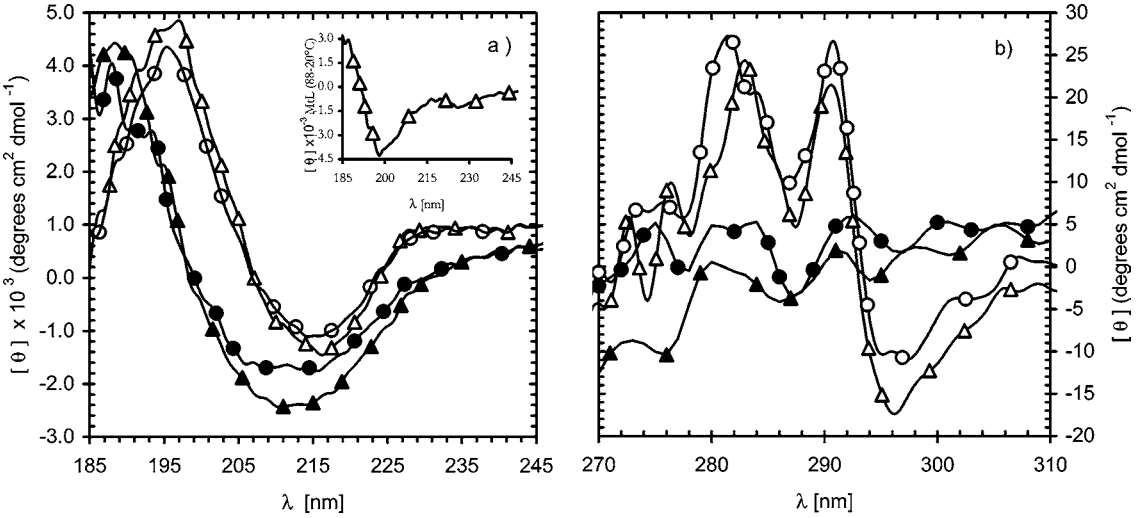

Figure 4. Circular dichroism (CD) spectra of MtL and PEG−MtL at low and high temperature (pH 6.0). Far- and near-UV regions are shown in the left and right panel, respectively. Spectra of MtL (triangles) and PEG−MtL (circles) were recorded at low temperature (25 °C; open symbols) and at high temperature (recorded at 88 °C, after thermal denaturation; closed symbols). Shown in the inset is the difference spectrum obtained by subtracting the low-temperature CD curve of MtL from that of the heat-denatured enzyme.

contains about 33% β-sheet and only 8% helices. As seen in Figure 4, the spectrum of PEG−MtL looks similar to that of its parent enzyme, indicating that chemical modification introduced no major structural changes in the secondary structure of the protein. On the other hand, in the near-UV spectra it is seen that the band envelope at 276−282 nm, a region where tyrosine residues display intense CD bands, is blue-shifted in the modified enzyme; this spectral shift might be caused by a less polar environment for the tyrosine side chains (*28*) in PEG−MtL owing to the presence of the hydrocarbon chains of PEG. Similar polarity changes seem to take place around the active site, as inferred from absorption spectra (results not shown): the absorption maximum in the visible region, characteristic of type 1 copper atoms present in laccase enzymes (*29*, *30*), was shifted from 610 to 575 nm as a result of chemical modification.

Thermal Denaturation. When MtL was heated to 88 °C until the enzyme activity was reduced to only 5% of the original value measured at room temperature, its far-UV CD bands were shifted toward shorter wavelengths (Figure 4). The spectrum of denatured MtL, however, differs from those observed in other heat-denatured proteins such as lysozyme and trypsin (*31*). Thus, although some structural changes occurred at high temperature, the laccase molecule likely possesses residual native secondary structure (*31*). That some protein segments became unstructured at high temperature is clearly discerned from the difference spectrum of heat-denatured versus native MtL, which shows the negative peak around 198−201 nm (inset to Figure 4) characteristic of irregular polypeptide structures (*28*). Heating had more drastic effects on the local environment of aromatic residues, as judged from the abatement of the near-UV bands (Figure 4). Regarding PEG−MtL, its thermal denaturation was accompanied by conformational changes resembling those observed with the unmodified enzyme, as judged by the CD spectra at high temperature.

Thermal scannings of MtL and its PEG derivative were carried out to determine the heat absorbed upon denaturation, as well as the changes in stability introduced by PEG modification. Both laccase preparations denatured irreversibly, with small denaturation enthalpies of only 6.3−7.5 g^{-1} (1.5−1.8 cal g^{-1}), but the modified enzyme proved to be more stable, its temperature of half-denaturation being approximately 2 °C higher than that of MtL (Figure 5). For comparative purposes, the scanning thermogram of hen's egg lysozyme, recorded in the same instrument, is also shown in Figure 5. The specific

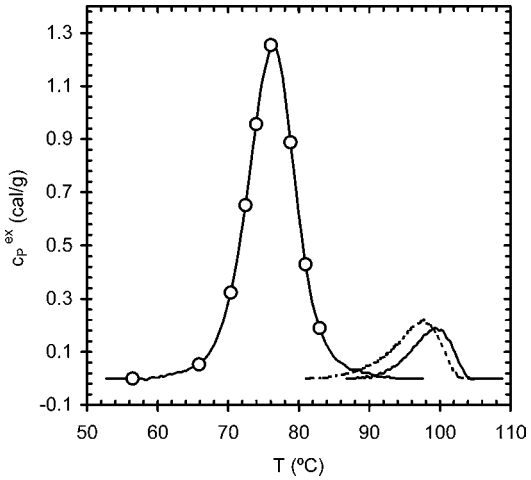

Figure 5. DSC profiles for the denaturation of the laccase enzymes at pH 5.0. Dashed line, MtL; solid line, PEG−MtL. For comparison, the scanning profile of hen's egg lysozyme, at pH 3.0, is also shown (−○−). Curves represent the excess heat capacity function, C_P^{ex}, obtained by subtracting buffer−buffer tracings and neglecting any change in heat capacity that takes place after denaturation. The area under a C_P^{ex} curve is the denaturation enthalpy. The protein concentration was ca. 2.0 mg mL^{-1}; the scanning rate was 1.0 °C min^{-1}.

heat of denaturation of this protein, which is representative of values found with other small proteins, was determined as 10.8 cal g^{-1}, in accord with previously reported determinations (*32*). It is clear then that thermal unfolding of the laccase enzymes is much less extensive than those of other typical proteins. This result is in keeping with the aforementioned characteristics of the CD spectra at high temperature and suggests that the β-structure scaffolding of the laccase family is notably resistant to high temperatures. Additional stability for the protein molecule may come from disulfide bonds; indeed, three of these bonds are known to be present in the structure of *M. albomyces* laccase (*27*), and the six Cys residues involved in those S−S bonds are all conserved in the sequence of MtL.

Inactivation of the Laccases in Mixed Solvents. The kinetics of inactivation of MtL and its PEG derivative in mixed aqueous−organic solvents was studied at several temperatures. The loss of enzyme activity followed first-order kinetics, with an apparent rate constant, k_i, that increased with the amount of organic cosolvent. We also made some measurements of the time course of ellipticity changes, at 202 nm, under the same

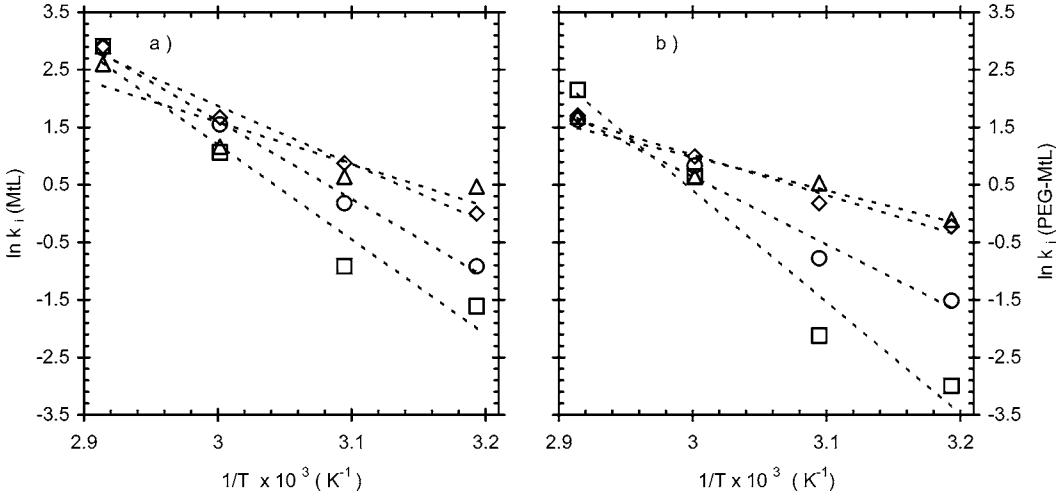

Figure 6. Arrhenius plots for denaturation of MtL (a) and PEG−MtL (b) in mixed solvents. Values of the rate constant (k_i) were determined by measuring the loss of laccase activity upon incubation in aqueous−organic solutions containing 30% v/v of the following organic solvents: methanol (□), ethanol (○), propanol (△), acetonitrile (◇). k_i is in min^{-1}.

Table 2. Activation Energies (E_a^i) and Preexponential Factors (A) for the Inactivation of MtL and PEG−MtL in Mixed Solvents[a]

	MtL		PEG−MtL	
solvent	E_a^i (kJ/mol)	ln A	E_a^i (kJ/mol)	ln A
methanol	33.0 ± 4.9	51.0	38.8 ± 5.6	59.0
ethanol	27.2 ± 1.4	42.7	23.6 ± 2.6	36.2
propanol	14.6 ± 4.6	23.6	11.7 ± 2.7	18.6
acetonitrile	20.2 ± 1.8	32.4	14.0 ± 1.5	22.2

[a] Values were determined from the linear fits shown in Figure 6. Solvents contained 30% (v/v) of the organic component in 50 mM phosphate buffer. [b] E_a^i and A represent the activation energy and the preexponential factor, respectively, in the Arrhenius equation (see the text).

solvent composition and temperature as those used to follow enzyme inactivation. Rate constants determined by both methods were nearly identical within experimental error, indicating that the loss of activity is accompanied by the appearance of disordered regions in the enzyme molecules. In solutions containing 30% of the organic component, the effect of temperature on k_i showed a clearly distinct trend depending on the nature of the cosolvent being present. Results obtained are plotted in Figure 6 according to the Arrhenius equation: $\ln k_i = \ln A - (E_a^i/R)(1/T)$. Values of the preexponential term (A) and the activation energy (E_a^i) for the inactivation reaction are given in Table 2. It is seen in Figure 6 that at temperatures below 70 °C the denaturing efficiency of linear alcohols increases with the length of the alkyl chain. The denaturing effect of *n*-alcohols is well-documented in the literature (*33*), where it has been attributed mainly to a decrease in the strength of "hydrophobic interactions" in water−alcohol solutions. The contribution of alcohols to protein denaturation has both enthalpic and entropic terms that compensate with each other in a rather complex way (*34*, *35*), depending on the concentration and type of the organic cosolvent. With 30% alcohol−water mixtures, Velicelebi and Sturtevant (*35*) found that the greater denaturing action of 1-propanol, with respect to ethanol and methanol, on hen lysozyme is due to a smaller enthalpy of denaturation. A similar situation is observed for the inactivation of both laccase forms: the activation energy suffers a large drop in *n*-propanol (Table 2) that results in the largest kinetic destabilization of the enzymes. When acetonitrile was the cosolvent, the temperature dependence of k_i was similar to that observed in the presence of *n*-propanol. In this case, however, it is difficult to rationalize the effect of the cosolvent on the basis of the hydrophobic effect alone. Other mechanisms, such as the influence of acetonitrile on hydrogen bonding and electrostatic interactions, may also play relevant roles.

It should be noted that, despite the similar inactivation behavior of both laccase samples in different solvents, the value of k_i for the modified enzyme was 2−3-fold smaller than that for the unmodified enzyme. An inspection of data in Table 2 shows that the extra stability of PEG−MtL can be attributed to its smaller activation entropy, because the A term is proportional to the entropy difference between the transition and native states of a reaction (*23*). This entropic stabilization may have its origin in the restricted motion of some amino acid groups on the protein surface due to the shell-like structure formed by coiled PEG chains (*36*).

CONCLUSIONS

Chemical modification of *M. thermophila* laccase (MtL) with PEG_{5000} yielded an enzyme derivative showing only minor changes in both secondary structure and enzyme activity, in comparison with the parent enzyme. Besides, pegylation led to a modest increase in the enzyme thermostability and to a decrease in the rate of inactivation in aqueous−organic solvents. To enhance these effects, an issue that would be of importance for the industrial applications of MtL, it would be interesting to carry out studies with bigger PEG molecules. Furthermore, it should be noticed that only eight out of the 16 lysine residues of MtL seemed to have been linked to PEG. A more extensive modification could be attempted by increasing the number of solvent-exposed lysines using directed mutagenesis of cloned and expressed versions of the corresponding gene.

ACKNOWLEDGMENT

This work was supported in part by CONACyT (convenio SEP-2003-CO2-44681). We thank the Novo Co., for providing the sample of Deni Lite IIs. Also Dr. Rafael Vazquez Duhalt (Instituto de Biotecnología, UNAM) helped us to do the pegylation reaction. L.-C.J.I. had a doctoral fellowship from Consejo Nacional de Ciencia y Tecnología (CONACYT).

LITERATURE CITED

(1) Ryan, S., Schnitzhofer, W., Tzanov, T., Cavaco-Paulo, A., Gübitz, M. (2003) An acid-stable laccase from *Sclerotium rolfsii* with potential for wool dye decolourization. *Enzyme Microb. Technol. 33*, 766−774.

(2) Bourbonnais, R., Leech, D., and Paicez, M. G. (1998) Electrochemical analysis of the interactions of laccase mediators with lignin model compounds. *Biochim. Biophys. Acta 1379*, 381−390.

(3) Li, K., Xu, F., and Karl-Erick, L. E. (1999) Comparison of fungal laccases and redox mediators in oxidation of a nonphenolic lignin model compound. *Appl. Environ. Microbiol. 65*, 2654−2660.

(4) Collins, P. J., Kotterman, M. J. J., Field, J. A., and Dobson, A. D. W. (1996) Oxidation of anthracene and benzo[*a*]pyrene by laccases from *Trametes versicolor*. *Appl. Environ. Microbiol. 62*, 4563−4567.
(5) Johannes, C., Majcherczyk, A., and Huttermann, A. (1996) Degradation of anthracene by laccase of *Trametes versicolor* in the presence of different mediator compounds. *Appl. Environ. Microbiol. 46*, 313−317.
(6) Cole, J. L., Yang, E. K., Sandusky, P. O., and Solomon, E. I. (1989) Spectroscopic characterization of the trinuclear copper active site in laccase. *J. Inorg. Biochem. 36*, 245.
(7) Szilagyi, R. K., and Solomon, E. I. (2002) Electronic structure and its relation to function in copper proteins. *Curr. Opin. Chem. Biol. 6*, 250−258.
(8) Giardina, P., Palmieri, G., Scaloni, A., Fontanella, B., Faraco, V., Cenamo, G., and Sannia, G. (1999) Protein and gene structure of a blue laccase from *Pleurotus ostreatus*. *Biochem. J. 34*, 655−663.
(9) Huang, H., Zoppellaro, G., and Sakurai, T. (1999) Spectroscopic and kinetics studies on the oxygen-centred radical formed during the four-electron reduction process of dioxygen by *Rhus vernicifera* laccase. *J. Biol. Chem. 274*, 32718−32724.
(10) Sundaram, U. M., Zhang, H. H., Hedman, B., Hodgson, K. O., and Solomon, E. I. (1997) Spectroscopic investigation of peroxide binding to the trinuclear copper cluster site in laccase: Correlation with the peroxy-level intermediate and relevance to catalysis. *J. Am. Chem. Soc. 119*, 12525−12540.
(11) Randall, D. W., DeBeer, S. G., Holland, P. L., Hedman, B., Hodgson, K. O., Tolman, W. B., and Solomon, E. I. (2000) Spectroscopic and electronic structural studies of blue copper model complex 2. Comparison of three and four coordinate Cu(II)−thiolate complex and fungal laccase. *J. Am. Chem. Soc. 122*, 11632−11648.
(12) Solomon, E. I., Sundaram, U. M., and Machonkin, T. E. (1996) Multicopper oxidases and oxygenases. *Chem. Rev. 96*, 2563−2605.
(13) Villaseñor, F., Loera, O., Campero, A., and Viniegra-González, G. (2004) Oxidation of dibenzothiophene by laccase or hydrogen peroxide and deep desulfurization of diesel fuel by the latter. *Fuel Process. Technol. 86*, 49−59.
(14) Bressler, D. C., Fedorak, P. M., and Pickard, M. A. (2000) Oxidation of carbazole, *N*-ethylcarbazole, fluorene, and dibenzothiophene by the laccase of *Coriolopsis gallica*. *Biotechnol. Lett. 22*, 1119−1125.
(15) García-Arellano, H., Valderrama, B., Saab-Rincón, G., and Vazquez-Duhalt, R. (2002) High temperature biocatalysis by chemically modified cytochrome *c*. *Bioconjugate Chem. 13*, 1336−1344.
(16) Vandertol-Varnier, H. A., Vazquez-Duhalt, R., Tinoco, R., and Pickard, M. A. (2002) Enhanced activity by poly(ethylene glycol) modification of *Coriolopsis gallica* laccase. *J. Ind. Microbiol. Biotechnol. 29*, 214−220.
(17) Berka, R. M., Schneider, P., Golightly, E. J., Brown, S. H., Madden, M., Brown, K. M., Halkier, T., Mondorf, K., and Xu, F. (1997) Characterization of the gene encoding an extracellular laccase of *Myceliophthora thermophila* and analysis of the recombinant enzyme expressed in *Aspergillus oryzae*. *Appl. Environ. Microbiol. 63*, 3151−3157.
(18) Bradford, M. M. (1976) A rapid and sensitive method for the quantitation of microgram quantities of protein utilizing the principle of protein-dye binding. *Anal. Biochem. 72*, 248−254.
(19) Habeeb, A. (1966) Determination of free amino groups in proteins by trinitrobenzenesulfonic acid. *Anal. Biochem. 14*, 328−336.
(20) Laemmli, U. K. (1970) Cleavage of structural proteins during the assembly of head of bacteriophage T4. *Nature. 227*, 680.
(21) Soares, M. B. G., Amorim, M. T. P., Hrdina, R., and Costa-Ferreira, M. (2002) Studies on the bio transformation of novel disazo dyes by laccase. *Proc. Biochem. 37*, 581−587.
(22) Berka, R. M., Stephen, H. B., Xu, F., Schneider, P., Oxenbøll, K. M., and Aaslyng D. A. (1997) Purified *Myceliophthora thermophila* laccases and nucleic acids encoding same. Patent 5795760, 1−22.
(23) Gutfreund H. (1998) *Kinetics for the life sciences*: *Receptors transmitters and catalysts*. pp 237−245, Cambridge University Press, New York.
(24) Ashihara, Y., Kono, T., Yamazaki, S., and Inada Y. (1978) Modification of *E. coli* L-asparaginase with poly(ethyleneglycol): Disappearance of binding ability to anti-asparaginase serum. *Biochem. Biophys. Res. Commun. 83*, 385−391.
(25) Wieder, K. J., Palczuk, N. C., Van Es, T., and Davis, F. F. (1979) Some properties of poly(ethyleneglycol): Phenylalanine ammonia−lyase adducts. *J. Biol. Chem. 254*, 12579−12587.
(26) Van Holde, K. E. (1971) *Physical Biochemistry*. pp 201−245, Prentice Hall, New York.
(27) Hakulinen, N., Kiiskinen, L. L., Kruus, K., Saloheimo, M., Paananen, A., Koivula, A., and Rouvinen, J. (2002) Crystal structure of a laccase from *Melanocarpus albomyces* with an intact trinuclear copper site. *Nat. Struct. Biol. 9*, 601−605.
(28) Fasman, D. G. (1996) *Circular dichroism and the conformational analysis of biomolecules*. pp 125−350, Plenum, New York.
(29) Palmer, A. E., Szilagyi, R. K., Cherry, J. R., Jones, A., Xu, F., and Solomon, E. I. (2003) Spectroscopic characterization of the Leu513His variant of fungal laccase: Effect on increased axial ligand interaction on the geometric and electronic structure of the type 1 Cu site. *Inorg. Chem. 42*, 4006−4017.
(30) Reinhammar, B. (2002) *Laccase*. *In Copper Proteins and Copper Enzymes*. Vol III, pp 1−35, CRC Press, Boca Raton, FL.
(31) Benitez-Cardoza, C. G., Rojo-Domínguez, A., and Hernández-Arana, A. (2001) Temperature-induced denaturation and renaturation of triosephosphate isomerase from *Saccharomyces cerevisiae*: Evidence of dimerization coupled to refolding of the thermally unfolded protein. *Biochemistry. 40*, 9049−9058.
(32) Privalov, P. L. (1979) Stability of proteins: Small globular proteins. *Adv. Protein Chem. 33*, 167−241.
(33) Mozhaev, V. V., Khmelnitsky, Y. L., Sergeeva, M. V., Belova, A. B., Klyachko, N., Levashov, A. V., and Martinek, K. (1989) Catalytic activity and denaturation of enzymes in water/organic cosolvent mixtures. α-Chymotrypsin and laccase in mixed water/alcohol, water/glycol and water/formamide solvents. *Eur. J. Biochem. 184*, 597−602.
(34) Khmelnitsky, Y. L., Mozhaev, V. V., Belova, A. B., Sergeeva, M. V., and Martinek, K. (1991) Denaturation capacity: A new quantitative criterion for selection of organic solvents as reaction media in biocatalysis. *Eur. J. Biochem. 198*, 31−41.
(35) Velicelebi, G., and Sturtevant, J. M. (1979) Thermodynamics of the denaturation of lysozyme in alcohol−water mixtures. *Biochemistry. 18*, 1180−1186.
(36) Gaertner, H. F., and Puigserver, A. J. (1992) Increased activity and stability of poly (ethylene glycol)-modified trypsin. *Enzyme Microb. Technol. 14*, 150−155.

BC0503465

Facile Functionalization of Lipid Bilayer Vesicles by Titania: The Use of Cerasome-Forming Lipids for Surface and Core Modification

Mineo Hashizume, Maki Yamada, Kiyofumi Katagiri,† Masahiko Tsuji, and Jun-ichi Kikuchi*

Graduate School of Materials Science, Nara Institute of Science and Technology, 8916-5 Takayama, Ikoma, Nara 630-0192, Japan. Received January 11, 2006; Revised Manuscript Received April 10, 2006

Two kinds of functionalization of a lipid bilayer vesicle by titania were achieved by utilizing a cerasome-forming lipid, which is the starting material to prepare a cerasome, a morphologically stable lipid bilayer vesicle having an atomic layer of siloxane networks on its surface. One system is the preparation of the titania-coated cerasomes by immobilizing nanaometer-sizes of titania onto the surface siloxane network of cerasomes. The other is the creation of an asymmetric lipid bilayer structure on the surface of the colloidal titania particles. The characteristics of these surface- and core-functionalized vesicles were investigated, and it was found that these conjugates showed photocatalytic activity as evaluated by photolysis experiments of the cationic dye methylene blue.

INTRODUCTION

Lipid bilayer vesicles prepared from natural and synthetic lipids are well-known biomembrane models and have been widely investigated for the last 40 years (*1*, *2*). There has been interest in the functionalization of vesicles not only for use in the reconstruction of biological systems but also in the creation of supramolecular systems (*3*, *4*). To add specific functions to a vesicle, incorporation of functional components, for example membrane proteins or glycosphingolipids, into the vesicle is a commonly used approach. Not only naturally occurring components but also synthetic and semisynthetic compounds are useful for this purpose. One method for the functionalization is the incorporation of synthetic lipids having specific hydrophilic headgroups, such as receptor molecules (*5*, *6*), antibodies and their subunits (*7*, *8*), poly(ethylene glycol)s (*9*), etc., into the lipid bilayer. Another method is the coating of polymers with anchoring parts that can be inserted into the lipid bilayer (*10*). The polymer coating is also simply achieved by covalent boning or electrostatic adsorption to the vesicle surface (*11*). These modifying compounds are usually biomimetic organic molecules. Although there are many examples of the preparation of inorganic nanocomposites templated by supramolecular assemblies (*12*, *13*), coating them on a vesicle surface has not been very widely investigated (*14*−*16*), probably due to the structural instability of vesicles when interacting with inorganic precursors compared to other assembled structures. Metal or semiconductor (metal oxide) materials having a size of several nanometers or less in at least one dimension, for example, ultrathin films, nanowires, and nanoparticles, have unique physicochemical properties expressed by the term "quantum size effect". The conjugates of these materials and biomolecules have recently been paid much more attention, especially in applications for sensing devices (*17*). Nanomaterials of metals and metal oxides can be expected to bring new functionality when they are coupled to the surface of the vesicles. However, there are few studies focusing on this point.

Recently, we have developed a novel vesicular system, named "cerasome", which is a lipid bilayer vesicle having an atomic layer of siloxane networks on its surface (*18*, *19*). The cerasomes are prepared from organoalkoxysilane lipids that have an organic dialkyl chain and an inorganic triethoxysilyl headgroup connected to each other in one molecule. The surface siloxane networks of the cerasome bring remarkably high morphological stability compared to that of conventional vesicles. For example, the cerasome can maintain its vesicular structure even in the presence of an excessive amount of a surfactant, whereas the reference vesicle is completely dissolved (*20*, *21*). Also the cerasome can be integrated onto a solid substrate to form a multicellular structure (*22*, *23*), which is triggered by electrostatic interaction. Under the same conditions, conventional vesicles collapse to form a supported bilayer on the substrate. Furthermore, the cerasome still possesses the features intrinsic to conventional vesicles, such as gel-to-liquid crystalline phase transition behavior.

Another advantage of the surface siloxane network of the cerasome is its high chemical reactivity. We have successfully functionalized the cerasome surface by introducing alkoxide compounds such as tetraethoxysilane (TEOS) or (3-aminopropyl)triethoxysilane (APS) during the preparative process of the cerasome (*24*). These alkoxides were incorporated into the siloxane network of the cerasome surface through the siloxane bonding. The resultant surface-modified cerasomes represented the surface characteristics coming from the added alkoxide compounds.

The other system that highlights the advantages of the cerasome is an asymmetric bilayer coating of monodispersed colloidal silica particles (*25*). The particles were first coated with a cerasome-forming lipid and then coated with a bilayer-forming lipid to form an asymmetric lipid bilayer structure, which is usually seen in nature and difficult to reconstitute by conventional techniques, on the particle surface.

In this study, on the basis of studies noted above, two systems for the functionalization of the cerasome by metal oxides were investigated (Figure 1). To show the possibility of these resultant conjugates as novel functional materials, we chose titania as the metal oxide component because it is known as a functional metal oxide which, for example, exhibits photocatalytic activity (*26*, *27*). One of the two systems investigated in this study is the surface coating of the cerasome by titania. The other is the asymmetric bilayer coating of colloidal titania particles. The

* To whom correspondence should be addressed. E-mail: jkikuchi@ms.naist.jp. Fax: +81-743-72-6099.

† Present address: Department of Applied Chemistry, Graduate School of Engineering, Nagoya University, Furo-cho, Chikusa, Nagoya 464-8603, Japan.

10.1021/bc060004e CCC: $33.50 © 2006 American Chemical Society
Published on Web 06/21/2006

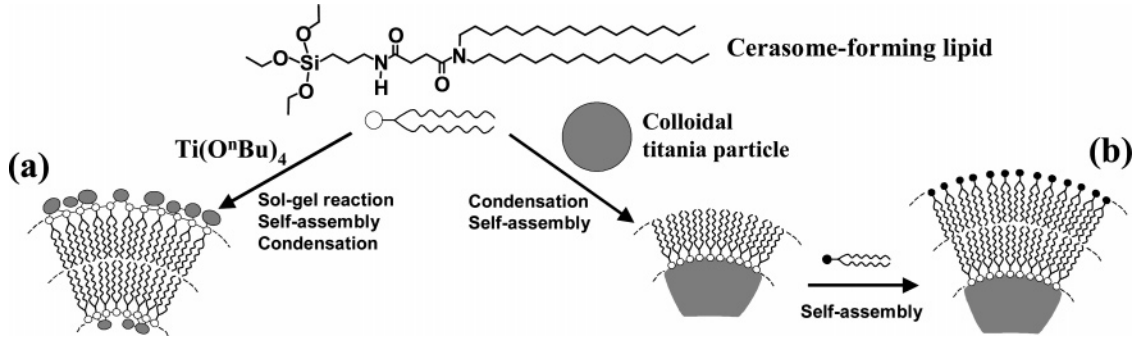

Figure 1. A cerasome-forming lipid and the schematic illustration of the titania-coated cerasome (a) and the asymmetric bilayer-coated colloidal titania particles (b).

characteristics of these two kinds of conjugates were investigated and their photocatalytic activities were evaluated.

EXPERIMENTAL PROCEDURES

Materials. Unless otherwise stated, all reagents and chemicals were obtained commercially and used without further purification. Titanium tetrabutoxide ($Ti(O^nBu)_4$), hydroxypropylcellulose (HPC), and acetylacetone (AcAc) were purchased from Wako Pure Chemical Industries. Colloidal titania particles were prepared by the procedure described in ref 28, with the exception that the particles were not submitted to hydrothermal treatments. Methylene blue (MB) was purchased from Nacalai Tesque, Inc. Titania sol TKS-203 was kindly donated by Tayca Corporation, Japan. The cerasome-forming lipids, *N*-[*N*-(3-triethoxysilyl)propylsuccinamoyl]dihexadecylamine (**1**) and *N*,*N*-dihexadecyl-*N*$^{\alpha}$-[6-[(3-triethoxysilyl)propyldimethylammonio]hexanoyl]glycinamide bromide (**2**) (*18*, *22*), and bilayer-forming peptide lipids, *N*,*N*-dihexadecyl-*N*$^{\alpha}$-[6-(trimethylammonio)hexanoyl]alaninamide bromide (**3**) (*29*), and sodium *N*,*N*-dihexadecyl-*N*$^{\alpha}$-(6-sulfohexanoyl)alaninamide (**4**) (*30*), were synthesized in our laboratory as described in previous reports. Dimyristoylphosphatidylcholine (DMPC; **5**) was obtained from Funakoshi Co., Ltd. These chemical structures are shown in Chart 1. Solvents used for the synthesis and coating were purified by distillation. Water used for the particle preparation and coating was distilled and deionized using an Autostill WS33 (Yamato Scientific) and Milli-Q Labo (Nihon Millipore), respectively.

Preparation of Titania-Coated Cerasomes. The surface coating of the cerasome by titania was performed by a similar procedure as that for the preparation of tetraethoxysilane (TEOS) or (3-aminopropyl)triethoxysilane (APS)-coated cerasomes (*24*). First, because of its high reactivity compared to that of ethoxysilane compounds, $Ti(O^nBu)_4$ was capped by 1 equiv of AcAc in ethanol, followed by the addition of deionized water. The mixture was stirred for 6 h to form a complex named $Ti(O^nBu)_3(AcAc)$. The ratio of ethanol:$Ti(O^nBu)_4$:AcAc:H_2O was 200:1:1:10. In the case of the lipid **1**, an ethanol sol of **1** with the ratio of **1**:ethanol:H_2O:HCl = 1:200:19:0.03 was stirred for 8 h using a vortex mixer. This ethanol sol was mixed with the $Ti(O^nBu)_3(AcAc)$ solution in the molar ratio of **1** and Ti to be 1:1, and further stirred for 30 min. The resultant sol was then injected into H_2O of appropriate pH. After the incubation of the solution at room temperature for more than 24 h, the AcAc group was finally photocleaved by xenon lamp irradiation without an optical filter, to obtain the titania-coated cerasome **1**. Lipid **2** was directly mixed with the $Ti(O^nBu)_3(AcAc)$ solution in the molar ratio of **2**:Ti to be 1:1. The mixture was stirred for 4 h and then injected into H_2O, followed by the photocleavage process.

Asymmetric Bilayer Coating on Colloidal Titania Particles. The procedure for the asymmetric bilayer coating on the surface of colloidal titania particles was basically same as that for coating on colloidal silica particles (*25*). The first (inner) layer was created from the lipid **1** by condensation of triethoxysilyl group of **1** with the surface hydroxyl group of titania in toluene while refluxing. The second (outer) layer was created from the lipids **3**−**5**. First a thin film of the lipid was prepared in the presence of the particle on the wall of a vial. After the addition of water, the film was detached and dispersed by a vortex mixer, followed by ultrasonication. The particles were collected by centrifugation and well washed with H_2O to remove excess lipids.

Chart 1. Chemical Structures of the Lipids and Methylene Blue (MB) Employed in This Study.

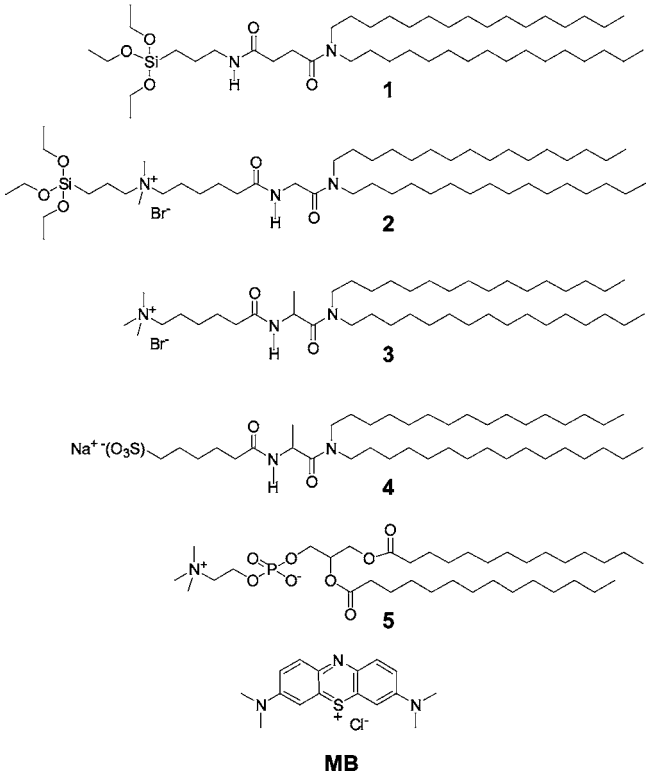

Characterization. The titania-coated cerasomes and the bilayer-coated colloidal titania particles were evaluated by the following conventional physical measurements. Hydrodynamic diameters of the cerasomes and titania particles were obtained by dynamic light scattering (DLS) measurements (DLS-6000HL, Otsuka Electronics). Scanning electron microscopy (SEM) was performed using a Hitachi S-5000 with an acceleration voltage of 25 kV, and the samples were coated by Pt. Transmission electron microscopy (TEM) was performed using a Hitachi H-7100 with an acceleration voltage of 100 kV. To see the distribution of titania components on cerasome surface, some of the samples were observed without using staining agents such

as uranyl acetate. Zeta-potential of the samples were obtained using an ELS-6000 (Otsuka Electronics) in an aqueous NaCl (10 mM). Inductively coupled plasma atomic emission spectroscopy (ICP-AES) was performed using an Optima 2000 DV Instruments (Perkin-Elmer). Standard Si and Ti solutions were used for calibration. X-ray diffraction (XRD) patterns of the titania-coated cerasomes and colloidal titania particles were obtained by a RINT-2200VL (Rigaku). The sample dispersions were cast on amorphous Si plates for measurements.

Photocatalysis Measurements. Photocatalytic activity of the titania-coated cerasomes and the bilayer-coated colloidal titania particles were evaluated as the photolysis of methylene blue (MB). The sample solution was irradiated by a xenon light source system (SX-UID500XAMQ, USHIO Inc, Japan). The light was passed through the UV-D35 filter to cut the light below 300 nm and over 600 nm. The power of the light was around 10 mW cm^{-2} at 400 nm. The titania-coated cerasome solution was mixed with the stock solution of MB. The final concentration of the lipid and MB were 0.1 mM and 0.01 mM, respectively. In the case of the bilayer-coated colloidal titania particles, the concentration of the particle was adjusted to 0.1 mM as Ti, and that of MB was adjusted to 0.01 mM. In the first 30 min the sample was placed in the dark and not irradiated, to observe the spontaneous degradation of MB. The sample was then irradiated and the photolysis of MB was monitored as the change of the UV−vis spectra. To obtain the rate constant (k) corresponding to a first-order reaction, the decomposition amount of MB by photolysis was obtained by subtracting the amount of spontaneous decomposition of MB from the total decrease of MB.

RESULTS AND DISCUSSION

Titania-Coated Cerasomes. Compared to the surface modification of the cerasome by TEOS or APS, titanium alkoxides have higher reactivity than ethoxysilyl compounds, so that we modified the procedure for the preparation of the titania-coated cerasome. $Ti(O^nBu)_4$ was partly capped with AcAc, and the vesicle was prepared by the ethanol sol injection method in the presence of $Ti(O^nBu)_3(AcAc)$ followed by the photocleavage of the AcAc group. The cleavage of AcAc group was confirmed by the spectral change of the solution, which showed a decrease of the peak corresponding to $\pi-\pi^*$ transition ($\lambda_{max} = 270$ nm). The optimal timing to mix the lipid and $Ti(O^nBu)_3(AcAc)$ was different between the cerasome-forming lipid **1** and **2**, which seems to reflect the difference in hydrolysis activity of the triethoxysilyl groups in each lipid (*19*). The hydrodynamic diameter of the titania-coated cerasome **1** was 144 nm both before and after the photoclevage of AcAc group, which indicated that the vesicular morphology was not affected by this irradiation. We previously reported that the diameter of the cerasome **1** without titania components prepared by the ethanol sol injection method was around 300 nm (*24*). The smaller diameter of the titania-coated cerasome might be due to the coupling of the titania component to the lipid headgroup. That is, the lipid having a larger headgroup tends to form a smaller vesicle based on the concept of the critical packing parameter (*31*). The formation of vesicular structure was also confirmed by the results of SEM measurements (Figure 2a). The nonstaining TEM images of the titania-coated cerasome **1** indicate that the titania components of titania-coated cerasome **1** had nanoparticle-like shapes and scattered on the bilayer surface (Figure 2b). This is different from the cases of other inorganic coating system reported by other groups, which form continuous inorganic layers on the vesicular surfaces (*14*−*16*). Such a difference is probably attributed to the difference in their preparative methods. In the current system, the ratio of lipid/Ti was 1 and Ti source was first mixed with the lipids in the ethanol sols before forming the vesicular structures in water, whereas inorganic sources were excess to the lipid and added after the vesicles were formed in other groups' systems. In our system, the lipid bilayer surface can be exposed to water even after the coupling of titania components. This is an additional useful functionality to titania-coated cerasomes. For example, ligand−receptor interactions on the vesicular surface can be achieved by incorporating other kinds of lipids having a ligand headgroup into the bilayer part of titania-coated cerasomes. The hydrodynamic diameter of the titania-coated cerasome **2** was 140 nm. There is no large difference in size before and after titania coating, because the existence of the quaternary ammonium group of lipid **2** makes the vesicular size of the cerasome **2** smaller compared to the case of the cerasome **1** (*19*). The SEM image of the titania-coated cerasome **2** shows similar morphology to that of the titania-coated cerasome **1** (Figure 2c).

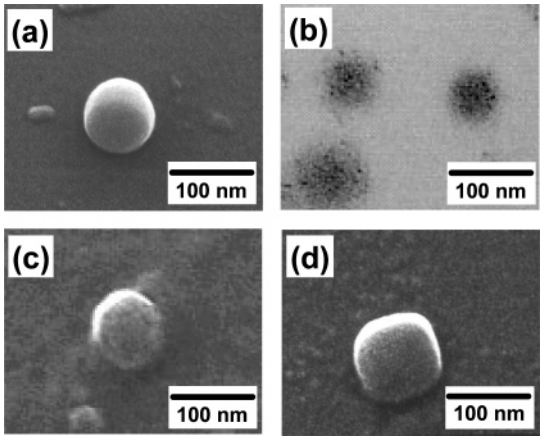

Figure 2. SEM (a) and TEM (b) images of the titania-coated cerasome **1**. (c) A SEM image of the titania-coated cerasome **2**. (d) A SEM image of the titania-coated cerasome **1** after the photolysis experiment.

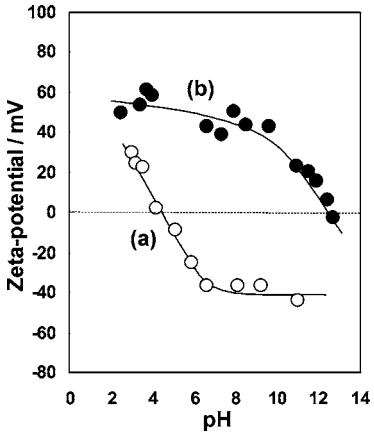

Figure 3. pH dependences of the zeta-potentials of the titania-coated cerasomes **1** (open circle) and the titania-coated cerasome **2** (closed circles).

Figure 3 shows pH dependences of zeta-potentials of the titania-coated cerasomes. The zeta-potential of the titania-coated cerasome **1** changed from +30 to −40 mV depending on the media pH, whereas that of cerasome **2** was positive in a wide pH range, which is largely due to its quaternary ammonium group. The isoelectric point (IEP) of the titania-coated cerasome **1** and the titania-coated cerasome **2** was obtained as 4.8 and 12.7, respectively. The IEP values of the cerasome **1** and the cerasome **2** are 4.3 and 11.5, and that of colloidal titania are 5−7 (*32*), respectively. So these results also support the maintenance of the surface nature of the cerasomes even after the titania coating. In addition, it was found that we can prepare both positively and negatively charged titania-coated cerasomes

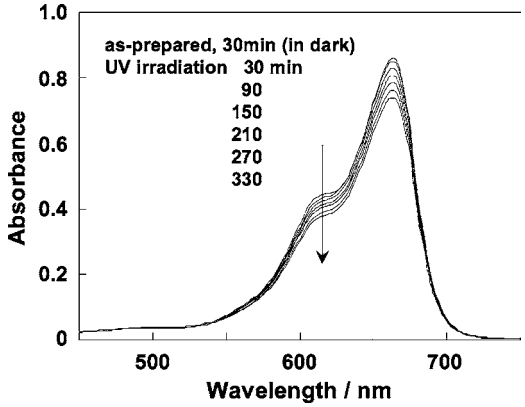

Figure 4. Time course of the UV−vis spectra of the MB solution in the presence of the titania-coated cerasome **1** upon the light irradiation.

in physiological pH at will. It is also possible to prepare the titania-coated cerasome having the desired IEP by mixing these two lipids at the proper ratio.

Asymmetric Bilayer-Coated Colloidal Titania Particles. The cerasome-forming lipid can covalently bond to a surface having hydroxyl groups. The formation of the first layer by the lipid **1** on the titania particle surface was confirmed by FT-IR spectroscopy as the appearance of the peak corresponding to the stretching vibrations of methylene part. Drastic decrease of dispersibility of the particle in water also strongly indicates the existence of the monolayer of lipid **1**. The following coating of the second layer by bilayer-forming lipids resulted in the recovery of the dispersibility of the particles in water. The hydrodynamic diameter and the zeta-potential in aqueous NaCl of the unmodified titania particle were 274 nm and −7.9 mV, respectively. Those parameters for asymmetric bilayer-coated particles for the lipid **3** (cationic), **4** (nonionic), and **5** (zwitterionic) as the second layer were (289 nm, 23.3 mV) for **3**, (284 nm, −38.0 mV) for **4**, and (288 nm, −0.2 mV) for **5**, respectively. The increases of hydrodynamic diameters for bilayer-coated particles were reasonable when thinking about the thickness of a lipid bilayer. TEM images of negatively stained samples showed the existence of such ultrathin organic layers (data not shown), similar to the case of colloidal silica particles (*25*). Also, zeta-potentials of the samples were well reflected in the nature of the coating lipids. These results showed that the asymmetric bilayer coating on the surface of the colloidal titania particles was successfully achieved.

Photocatalytic Activity. To show the usefulness of the titania-coated cerasomes, the photocatalytic activity of the titania-coated cerasome was evaluated by photolysis experiments of a commercial cationic dye, methylene blue (MB). The conditions for the light irradiations were adjusted to prevent self-decomposition of MB. The mixed solution of the titania-coated cerasomes with MB did not show decomposition of MB, which can be monitored by UV−vis spectroscopy, when placed in the dark. On the other hand, the light irradiation of the sample solution preceded decomposition of MB (Figure 4). This indicates that the decomposition of MB was the result of photolysis by the titania-coated cerasome. Figure 2d shows the SEM image of the titania-coated cerasome **1** after photolysis measurements, which confirms the maintenance of its vesicular morphology. The photocatalytic activity of the titania-coated cerasome was normalized as the rate constant assuming a first-order reaction, and the results were summarized in Table 1. Both of the titania-coated cerasomes prepared from the lipid **1** and **2** showed photocatalytic activity; however, there was a difference in the effect of the media pH. At pH 3, the rate constant was similar between **1** and **2**, whereas the value for **1** was larger than that of **2** at pH 8. The results seem to be due to the effect

Table 1. Rate Constants (k)[a] of the Photolysis of MB for the Titania-Coated Cerasomes[b]

catalyst	k/h^{-1} at pH 3	k/h^{-1} at pH 8
titania-coated cerasome **1**	0.022	0.056
titania-coated cerasome **2**	0.021	0.027

[a] The rate constant assuming a first-order reaction. [b] [Ti] = [lipid] = 0.1 mM, [MB] = 0.01 mM.

Table 2. Rate Constants (k)[a] of the Photolysis of MB for the Asymmetric Bilayer-Coated Colloidal Titania Particles[b]

catalyst	k/h^{-1}
unmodified colloidal titania	0.025
lipid **3** in the second layer	0.019
lipid **4** in the second layer	0.017
lipid **5** in the second layer	0.020

[a] The rate constant assuming a first-order reaction. [b] [Ti] = 0.1 mM, [MB] = 0.01 mM, at pH 3.

of the surface charge of the titania-coated cerasomes; both are positively charged at pH 3, and **1** is negative and **2** is still positive at pH 8 according to the results seen in Figure 3. At pH 8, positively charged MB should be more accessible to the titania-coated cerasome **1** than that prepared from **2**. These phenomena are welcomed for designing substrate-selective catalyst systems. However, the photocatalytic activities were relatively small compared with that of commercial anatase titania sol TKS-203 (0.19 h^{-1}), normalized as the same titania amount. The main difference is that the present titania-coated cerasome was not intended to make titania to form its specific crystal structure like anatase, which shows high catalytic activity. According to previous reports for the effect of photoirradiation on anatase formation by sol−gel processes (*33*, *34*), there is a possibility that the formation of anatase structure proceeds when the sample is irradiated by whole xenon light to cleave AcAc group. However, XRD patterns of the titania-coated cerasome **1** did not show significant peak patterns assignable to those of anatase, nor rutile and brookite, which indicates that the majority of the titania components on the cerasome surface were amorphous. In addition, not all of the titania components seemed to couple to the cerasome surface under current condition. When the titania-coated cerasome **1** was purified by conventional gel permeation chromatography and analyzed by ICP-AES, the ratio of Ti:Si was obtained as 1:2.7, which is ideally 1:1. The rest of the titania probably existed as sols similar to the photocleaved products of Ti(O^{n}Bu)$_3$(AcAc) which were prepared in the absence of the cerasome-forming lipid. The photocatalytic activity of such a sol was, however, significantly small (k = 0.0055 h^{-1}) compared to that of the titania-coated cerasomes. The pH dependence of the photocatalytic activity also strongly suggests that the activity mainly comes from the titania-coated cerasome. The procedure without purification is quite powerful for practical application, so we are currently improving the preparative condition to minimize the amount of titania components which do not couple to the cerasome surface.

Table 2 shows the rate constant of MB decomposition in the presence of the asymmetric bilayer-coated colloidal titania particles. These values were in the range of 10^{-2} h^{-1} as were those of the template titania colloidal particle and also the titania-coated cerasomes, and approximately ten-times smaller than that of TKS-203. The template colloidal titania particles were not calcinated or hydrothermally treated, because such treatment diminishes surface hydroxyl groups of the particles. The XRD patterns of the particles show that these particles were amorphous, which is in good agreement with the literature (*28*). Different from the case of the titania-coated cerasome, there was not good correlation between the surface charges of the asymmetric bilayer-coated colloidal titania particles and their photocatalytic activities in this case. Since photocatalytic

reactions have distance dependencies, the existence of a lipid bilayer between MB and the titania surface may largely affect the photocatalytic activity. In such cases, the difference in accessibility of the substrate to the particle surface may not appear significant to the photocatalytic activity. However, the important point of the results in Table 2 is that these colloidal titania particles covered by ultrathin organic layers still retain their photocatalytic activities. The bilayer structure on the titania surface could donate a molecular recognition site for substrate-specific catalysis, similar to the case for the monolayer-coated systems developed by Ohno et al. (*35*, *36*), which show substrate-selective photocatalytic reactions based on the interactions between the substrate and the organic layer.

The photocatalytic activities of both the titania-coated cerasomes and the bilayer-coated colloidal titania particles should be able to be improved. Hydrothermal treatment (*28*) of these conjugates is one of the possible techniques for this purpose since it can form the anatase structure of titania without burning out the organic components in the conjugates. In the case of titania-coated cerasomes, increase of the relative amount of titania in the conjugates is another considerable factor to increase the photocatalytic activity. We are continuing systematic investigations of these points to find out general rules for precise control of these conjugates' photocatalytic activities.

In summary, we showed that the surface and the core modifications of lipid bilayer vesicles by titania were successfully achieved by employing cerasome-forming lipids. The resultant conjugates have unique organic−inorganic hybrid structures and show photocatalytic activities owing to their titania components. One important advantage of these conjugates is that they can maintain and utilize the nature of the lipid bilayer surface even after the titania modification. Not only for the control of surface charges, the bilayer parts of these conjugates can be used for selective incorporation of hydrophobic substrates, realizing ligand−receptor interactions on membrane surfaces, immobilization of membrane proteins, etc. Such conjugates are expected to be useful as substrate-specific catalysts, sensing systems for events which occur on and in the membranes, carriers for drug delivery systems, scaffolds for artificial signal transduction systems (*4*, *37*, *38*) combining photochemical processes, etc. The current two methods are simple and applicable to various metal oxide species, which could open a new field of biomembrane models.

ACKNOWLEDGMENT

The authors greatly thank Mr. K. Hayashi (NAIST) for SEM and TEM observations and Prof. M. Tanihara and Dr. M. Kamitakahara (NAIST) for the use of ICA-AES apparatus and XRD analyses. This study was partly supported by the Japan Society for the Promotion of Science, Grant-in-Aid for Scientific Research (A), 15205022, and by the Ministry of Education, Culture, Sports, Science and Technology, Grant-in-Aid for Scientific Research on Priority Areas (432), 17034043.

LITERATURE CITED

(1) Torchilin, V., and Weissig, V. (2003) *Liposomes, Second Edition: A Practical Approach*, Oxford University Press, Oxford.

(2) Kunitake, T. (1996) Synthetic Bilayer Membranes: Molecular Design and Molecular Organization. *Comprehensive Supramolecular Chemistry. Vol. 9.* (Atwood, J. L., Davies, J. E. D., MacNicol, D. D., Vögtle, F., Lehn, J.-M., Eds.) pp 351−406, Pergamon, Oxford.

(3) Murakami, Y. and Kikuchi, J. (1991) Supramolecular Assemblies Formed with Synthetic Peptide Lipids. Functional Models of Biomembranes and Enzymes. *Bioorganic Chemistry Frontiers. Vol. 2.* (Dugas, H., Ed.) pp 73−113, Springer-Verlag, Berlin.

(4) Kikuchi, J. Ariga, K., and Sasaki, Y. (2002) Molecular Recognition and Functional Connection in Lipid Membranes. *Advances in Supramolecular Chemistry* (Gokel, G. W., Ed.) pp 131−173, Cerberus Press, South Miami.

(5) Wang, S., Lee, R. J., Cauchon, G., Gorenstein, G., and Low, P. S. (1995) Delivery of antisense oligodeoxyribonucleotides against the human epidermal growth factor receptor into cultured KB cells with liposomes conjugated to folate via polyethylene glycol. *Proc. Natl. Acad. Sci., USA 92*, 3318−3322.

(6) Iwamoto, S., Otsuki, M., Sasaki, Y., Ikeda, A., and Kikuchi, J. (2004) Gemini peptide lipids with ditopic ion-recognition site. Preparation and functions as an inducer for assembling of liposomal membranes. *Tetrahedron 60*, 9841−9847.

(7) Egger, M., Heyn, S. P., and Gaub, H. E. (1992) Synthetic lipid-anchored receptors based on the binding site of a monoclonal antibody. *Biochim. Biophys. Acta 1104*, 45−54.

(8) Ho, J. A. and Hsu, H.-W. (2003) Procedures for Preparing Escherichia coli O157: H7 Immunoliposome and Its Application in Liposome Immunoassay. *Anal. Chem. 75*, 4330−4334.

(9) Woodle, M. C. (1997) Poly(ethylene glycol)-grafted liposome therapeutics. *ACS Symposium Series 680* (Poly(ethylene glycol)) pp 60−81, American Chemical Society, Washington, DC.

(10) Sato, T. and Sunamoto, J. Site-specific liposomes coated with polysaccharides. (1993) *Liposome Technology* (Gregoriadis, G., Ed.) pp 179−198, 2nd ed., Vol. 3. CRC, London.

(11) Ringsdorf, H., Schlarb, B., and Venzmer, J. (1988) Molecular architecture and function of polymeric oriented systems: Models for the study of organization, surface recognition, and dynamics of biomembranes. *Angew. Chem., Int. Ed. Engl. 27*, 113−158.

(12) Cölfen, H. and Mann, S. (2003) Higher-Ordered Organization by Mesoscale Self-Assembly and Transformation of Hybrid Nanostructures. *Angew. Chem., Int. Ed. 42*, 2350−2365.

(13) van Bommel, K. J. C., Friggeri, A., and Shinkai, S. (2003) Organic Templates for the Generation of Inorganic Materials. *Angew. Chem., Int. Ed. 42*, 980−999.

(14) Hubert, D. H. W., Jung, M. Frederik, P. M., Bomans, P. H. H., Meuldijk, J., and German, A. L. (2000) Vesicle-Directed Growth of Silica. *Adv. Mater. 12*, 1286−1290.

(15) Bégu, S., Girod, S., Lerner, D. A., Jardiller, N., Tourné-Péteilh, C., and Devoisselle, J.-M. (2004) Characterization of a phospholipid bilayer entrapped into non-porous silica nanospheres. *J. Mater. Chem. 14*, 1316−1320.

(16) Schmidt, H. T. and Ostafin, A. E. (2002) Liposome Directed Growth of Calcium Phosphate Nanoshells. *Adv. Mater. 14*, 532−535.

(17) Mirkin, C. A. (2000) Programming the Assembly of Two- and Three-Dimensional Architectures with DNA and Nanoscale Inorganic Building Blocks. *Inorg. Chem. 39*, 2258−2272.

(18) Katagiri, K., Ariga, K., and Kikuchi, J. (1999) Preparation of Organic−Inorganic Hybrid Vesicle "Cerasome" Derived from Artificial Lipid with Alkoxysilyl Head. *Chem. Lett.* 661−662.

(19) Katagiri, K., Ariga, K., and Kikuchi, J. (2001) Novel class of organic−inorganic hybrid vesicle "Cerasome" derived from various amphiphiles with alkoxysilyl head. *Studies Surf. Sci. Catal. 132*, 599−602.

(20) Hashizume, M., Kawanami, S., Iwamoto, S., Isomoto, T., and Kikuchi, J. (2003) Stable vesicular nanoparticle 'Cerasome' as an organic−inorganic hybrid formed with organoalkoxysilane lipids having a hydrogen-bonding unit. *Thin Solid Films 438−439*, 20−26.

(21) Hashizume, M., Inoue, H., Katagiri, K., Ikeda, A., and Kikuchi, J. (2004) Cerasome as an Organic−Inorganic Vesicular Nanohybrid: Characterization of cerasome-forming Lipids having a Single or a Dual Trialkoxysilyl Head. *J. Sol-Gel Sci. Technol. 31*, 99−102.

(22) Katagiri, K., Hamasaki, R., Ariga, K., and Kikuchi, J. (2002) Layered Paving of Vesicular Nanoparticles Formed with Cerasome as a Bioinspired Organic−Inorganic Nanohybrid. *J. Am. Chem. Soc. 124*, 7892−7893.

(23) Katagiri, K., Hamasaki, R., Ariga, K., and Kikuchi, J. (2002) Layer-by-Layer Self-Assembling of Liposomal Nanohybrid "Cerasome" on Substrates. *Langmuir 18*, 6709−6711.

(24) Katagiri, K., Hamasaki, R., Ariga, K., and Kikuchi, J. (2003) Preparation and Surface Modification of Novel Vesicular Nano-Particle "Cerasome" with Liposomal Bilayer and Silicate Surface. *J. Sol−Gel Sci. Technol. 26*, 393−396.

(25) Katagiri, K., Hashizume, M., Kikuchi, J., Tatetani, Y., and Murakami, M. (2004) Creation of asymmetric bilayer membrane on monodispersed colloidal silica particles. *Colloids Surf. B: Biointerfaces 38*, 149−153.

(26) Linsebigler, A. L., Lu, G., and Yates, J. T., Jr. (1995) Photocatalysis on TiO_2 Surfaces: Principles, Mechanisms, and Selected Results. *Chem. Rev. 95*, 735−758.

(27) Rao, T. N., Tryk, D. A., and Fujishima, A. (2003) Applications of TiO_2 photocatalysis. *Encyclopedia of Electrochemistry* (Bard, A. J., and Startmann, M., Eds.) pp 536−561, Vol. 6, Wiley-VCH Verlag GmbH & Co. KGaA, Weinheim.

(28) Sakamoto, R., Nishimori, H., Tatsumisago, M., and Minami, T. (1998) Preparation of Titania Thick Films by Electrophoretic Sol−Gel Deposition Using Hydrothermally Treated Particles. *J. Ceram. Soc. Jpn. 106*, 1034−1036.

(29) Murakami, Y., Nakano, A., and Ikeda, H. (1982) Preparation of Stable Single-Compartment Vesicles with Cationic and Zwitterionic Amphiphiles Involving Amino Acid Residues. *J. Org. Chem. 47*, 2137−2144.

(30) Murakami, Y., Kikuchi, J., Takaki, T., Katsuya, T., Uchimura, K., and Nakano, A. (1985) Aggregate Morphology and Intermembrane Interaction of Synthetic Peptide Lipid Bearing Various Head Group. *J. Am. Chem. Soc. 107*, 2161−2167.

(31) Israelachvili, J. N., Mitchell, D. J., and Ninham, B. W. (1976) Theory of Self-Assembly of Hydrocarbon Amphiphiles into Micelles and Bilayers. *J. Chem. Soc., Faraday Trans. 2 72*, 1525−1568.

(32) Parks, G. A. (1965) The Isoelectric Points of Solid Oxides, Solid Hydroxysides, and Aqueous Hydroxo Coplex Systems. *Chem. Rev. 65*, 177−197.

(33) Guan, Z., Zhang, X., Ma, Y., Cao, Y., and Yao, J. (2001) Photocatalytic activity of TiO_2 prepared at low temperature by a photo-assisted sol−gel method. *J. Mater. Res. 16*, 907−909.

(34) Imai, H., Hirashima, H., and Awazu, K. (1999) Alternative modification methods for sol−gel coatings of silica, titania, and silica−titania using ultraviolet irradiation and water vapor. *Thin Solid Films 351*, 91−94.

(35) Ohno, T., Tsubota, T., Kakiuchi, K., and Sayama, K. (2004) Oxidation of Aldehydes on TiO_2 Photocatalysts Modified with Alkylsilyl Group. *Chem. Lett. 33*, 1610−1611.

(36) Ohno, T., Tsubota, T., Miyayama, S., and Sayama, K. (2005) Selective oxidation of benzaldehyde derivatives on TiO_2 photocatalysts modified with fluorocarbon group. *Catal. Lett. 102*, 207−210.

(37) Kikuchi, J., Ariga, K., Sasaki, Y., and Ikeda, K. (2001) Control of Enzymatic Activity by Artificial Cell-Surface Receptors. *J. Mol. Catal. B 11*, 977−984.

(38) Tian, W.-J., Sasaki, Y., Fan, S.-D., and Kikuchi, J. (2005) Switching of Enzymatic Activity through Functional Connection of Molecular Recognition on Lipid Bilayer Membranes. *Supramol. Chem. 17*, 113−119.

BC060004E

Simple Synthesis of a Building Block for Solid-Phase Labeling of Oligonucleotides with 1,4,7,10-Tetraazacyclododecane-1,4,7,10-tetraacetic Acid (DOTA)

Lassi Jaakkola, Alice Ylikoski, and Jari Hovinen*

PerkinElmer Life and Analytical Sciences, Turku Site, POB 10, FIN-20101 Turku, Finland. Received February 14, 2006; Revised Manuscript Received April 20, 2006

Synthesis of a nucleosidic phosphoramidite building block which allows solid-phase introduction of 1,4,7,10-tetraazacyclododecane-1,4,7,10-tetraacetic acid (DOTA) to synthetic oligonucleotides using a standard oligonucleotide synthesizer is described.

INTRODUCTION

Because of its excellent metal chelating properties and high in vivo and in vitro stability, 1,4,7,10-tetraazacyclododecane-1,4,7,10-tetraacetic acid (DOTA) is widely used as an organic ligand in magnetic resonance imaging (MRI) and positron emission tomography (PET) (*1*−*3*). Indeed, Gd^{3+}-DOTA is one of the most commonly used clinical MRI contrast agents (*4*, *5*). Bioactive molecules labeled with DOTA, in turn, have found applications as target-specific radiopharmaceuticals (*6*).

In several applications, covalent conjugation of DOTA to bioactive molecules is required. Most commonly, isothiocyanato, *N*-hydroxysuccinimide, or maleimide derivatives of the chelates are used in the labeling of amino and mercapto functions of the target molecules (*7*). Because the labeling reaction is performed in the presence of an excess of an activated label, laborious purification procedures cannot be prevented. Especially, when attachment of several label molecules is needed, purification and characterization of the desired biomolecule conjugate may be extremely difficult. These problems can be avoided by performing the labeling reaction on solid phase. Indeed, derivatives of DOTA for the solid-phase oligopeptide derivatization using standard oligopeptide synthesizers have been reported (*8*, *9*). Surprisingly, no methods for the attachment of DOTA to synthetic oligonucleotides have been available: oligonucleotide labeling is still a multistep procedure including synthesis of an oligonucleotide bearing a tether with a nucleophilic ω-function followed by its reaction with an activated chelate derivative (*10*, *11*). Here is presented a simple method for the preparation of a nucleosidic DOTA derivative which allows solid-phase oligonucleotide conjugation.

EXPERIMENTAL PROCEDURES

General Methods. Adsorption column chromatography was performed on columns packed with silica gel 60 (Merck). Reagents for oligonucleotide syntheses were from Proligo. The oligonucleotides were assembled on an Applied Biosystems 3400 instrument using recommended protocols. All dry solvents were from Merck, and they were used as received. NMR spectra were recorded on a Brucker 250 spectrometer operating at 250.13 MHz for ^{1}H and on and on a JEOL LA 400 spectrometer operating at 161.9 MHz for ^{31}P. The signal of TMS was used as an internal (^{1}H) and H_3PO_4 as an external (^{31}P) reference. ESI-TOF mass spectra were recorded on an Applied Biosystems Mariner instrument.

* To whom correspondence should be addressed. Tel + 358 2 2678 513; fax + 358 2 2678 380; e-mail jari.hovinen@perkinelmer.com.

1,4,7,10-Tetraazacyclododecane-4,7,10-tricarboxymethyl Methyl Ester 1-Carboxymethyl-benzyl Ester, 2. To a stirred mixture of 1,4,7,10-tetraazacyclododecane-1-carboxymethyl-benzyl ester, **1** (*8*) (0.45 g, 1.4 mmol), and potassium carbonate (0.79 g, 5.7 mmol) in anhydrous acetonitrile (8 mL) was added methyl bromoacetate (0.54 mL, 5.7 mmol; predissolved in 2 mL of MeCN) dropwise during 0.5 h. The reaction was allowed to proceed for additional 2 h before being filtered. The filtrate was concentrated in vacuo. Purification was performed on silica gel (eluent MeOH:CH_2Cl_2, 1:9, v/v). Yield was 0.45 g (60%). ^{1}H NMR ($CDCl_3$): δ 7.35 (5H, m); 5.20 (2H, s); 3.76 (6H, s); 3.74 (3H, s); 3.49−2.35 (24 H). ESI-TOF-MS for $C_{26}H_{41}N_4NaO_8^+$ $(M + Na)^+$: calcd, 559.27; found, 559.27.

1,4,7,10-Tetraazacyclododecane-1,4,7,10-tetraacetic Acid Tris-methyl Ester, 3. Compound **2** (0.35 g, 0.64 mmol) was dissolved in methanol (50 mL). Pd/C (10%, 55 mg) was added, and the mixture was hydrogenated at atmospheric pressure overnight. The mixture was filtered through Celite and concentrated. It was used for the next step without further derivatization. ESI-TOF-MS for $C_{19}H_{34}N_4NaO_8^+$ $(M + Na)^+$: calcd, 469.23; found, 469.22.

2′-Deoxy-5′-*O*-(4,4′-dimethoxytrityl)-3-(6-aminohexyl)uridine, 4. 2′-Deoxy-5′-*O*-(4,4′-dimethoxytrityl)-3-(6-trifluoroacetamidohexyl)uridine (*12*) (1.41 g, 1.95 mmol) was suspended in the mixture of concentrated aqueous ammonia and methanol (100 mL; 1:1, v/v) and heated overnight at reflux. All volatiles were removed in vacuo. The residue was partitioned between water and dichloromethane. The organic layer was dried over Na_2SO_4 and concentrated. Yield was quantitative. ^{1}H NMR ($CDCl_3$): δ 7.75 (1H, d, *J* 8.3, H-6); 7.40−7.23 (9H, DMTr); 6.84 (4H, d, *J* 8.9, DMTr); 6.31 (1H, t, *J* 6.2, H-1′); 5.45 (1H, d, *J* 8.3, H-5); 4.53 (1H, m, H-3′); 4.00 (1H, m, H-4′); 3.89 (2H, m); 3.78 (6H, s, 2 · OMe); 3.49 (1H, dd, *J* 3.0 and 10.6, H-5′); 3.41 (1H, dd, *J* 3.3 and 10.6, H-5″); 2.64 (2H, t, *J* 6.5); 2.42 (1H, m, H-2″); 2.24 (1H, m, H-2′); 2.19 (3H, br); 1.62 (2H, p, *J* 6.4); 1.40 (2H, p, *J* 6.7); 1.34 (4H, m). ESI-TOF-MS for $C_{36}H_{44}N_3O_7^+$ $(M + H)^+$: calcd, 630.31; found, 630.34.

The DOTA Nucleoside, 5. Compound **3** (0.26 g, 0.58 mmol) and DIPEA (100 μL) were dissolved in dry DMF (9 mL). HATU (220 mg, 0.58 mmol) was added, and the mixture was stirred for 30 min at RT. Compound **4** (0.37 g, 0.58 mmol) was added, and the mixture was stirred for 4 h at RT and concentrated. The residue was dissolved in dichloromethane, washed twice with sat. $NaHCO_3$, and dried. Purification on silica gel (eluent, MeOH:CH_2Cl_2 1:9, v/v) gave 0.43 g (82%) of the title compound. ^{1}H NMR ($CDCl_3$) δ 7.75 (1H, d, *J* 8.3, H-6); 7.40−7.22 (9H, DMTr); 6.84 (4H, d, *J* 8.8); 6.47 (1H, br t, *J*

10.1021/bc0600362 CCC: $33.50 © 2006 American Chemical Society
Published on Web 06/22/2006

Scheme 1

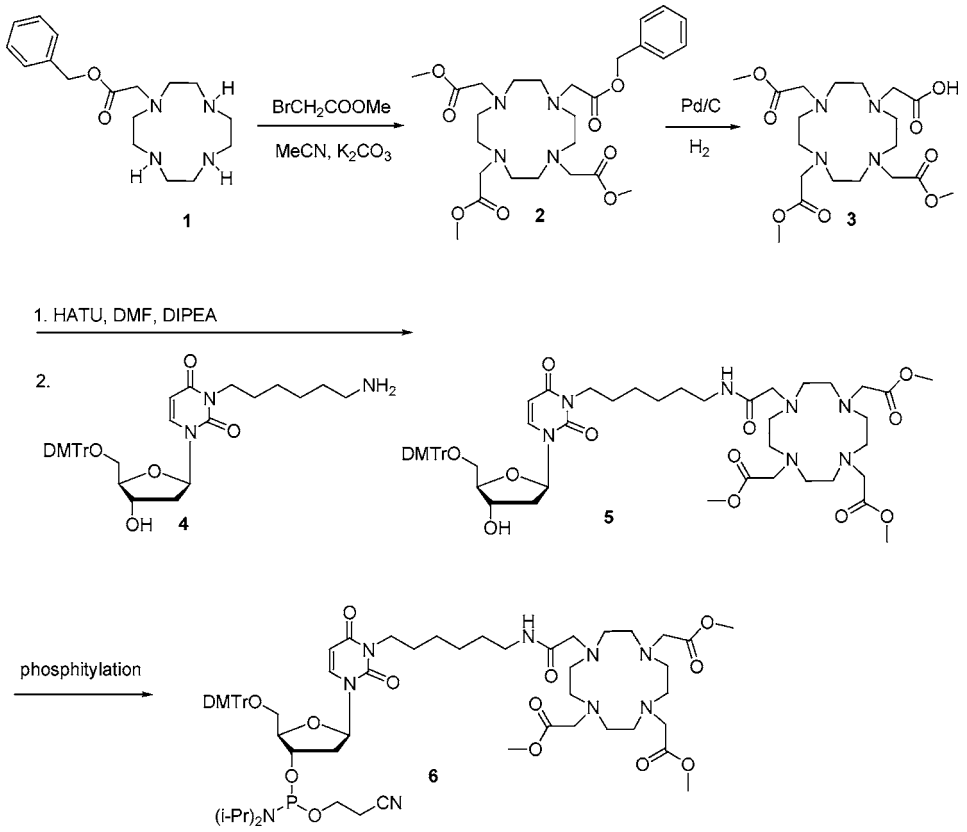

4.7, NH); 6.32 (1H, t, *J* 6.3, H-1′); 5.43 (1H, d, *J* 8.0, H-5); 4.59 (1H, m, H-3′); 4.05 (1H, m, H-4′); 3.89 (2H, m); 3.79 (6H, s, 2 · OMe); 3.74 (6H, s); 3.73 (3H, s); 3.42 (2H, d, *J* 2.9, H-5′ and H-5″); 3.20 (8H); 2.60 (16H); 2.46 (1H, m, H-2″); 2.27 (1H, m, H-2′); 1.70 (1H, br); 1.62 (2H, m); 1.50 (2H, m); 1.35 (4H, m). ESI-TOF-MS for $C_{55}H_{76}N_7O_{14}^+$ $(M + H)^+$: calcd, 1058.54; found, 1058.54.

Synthesis of the Phosphoramidite, 6. Predried compound **5** (0.30 g, 0.28 mmol) and 2-cyanoethyl *N,N,N*′,N′-tetraisopropylphosphordiamidite (1.5 equiv) were dissolved in dry acetonitrile. 1*H*-Tetrazole (1 equiv; 0.45 M in acetonitrile) was added, and the mixture was stirred for 30 min at room temperature before being poured into 5% $NaHCO_3$, extracted with dichloromethane, and dried over Na_2SO_4. Purification on silica gel (eluent: MeOH:CH_2Cl_2:TEA, 5:95:1, v/v/v) yielded the desired phosphoramidite. ^{31}P NMR ($CDCl_3$): δ 149.60 (0.5 P); 149.20 (0.5 P). ESI-TOF-MS for $C_{64}H_{93}N_9O_{15}P^+$ $(M + H)^+$: calcd, 1258.65; found, 1258.66.

Synthesis and Purification of the Oligonucleotide Conjugate. A sequence 5′-TAATGTAGCCCCTGAA-3′ was assembled on 1.0 μmol scale using phosphoramidite chemistry and recommended protocols (DMTr-Off synthesis). The block **6** was coupled to its 5′-terminus (coupling time 10 min, concentration 0.2 M). As the chain assembly was completed, the oligonucleotide was deprotected and converted to the gadolinium(III) chelate as follows: (i) treatment with 0.1 M NaOH for 4 h at RT; (ii) concentration in vacuo in the presence of ammonium chloride; (iii) treatment with concentrated aqueous ammonia for 16 h at 55 °C; (iv) treatment with gadolinium(III) citrate (15 equiv per ligand) overnight at RT; (v) desalting by gel filtration (NAP 5); (vi) denaturing 20% PAGE; (vii) passive elution from the gel to aqueous solution (Na_2CO_3 buffer, pH 9.8); (viii) butanol concentration; (ix) desalting by gel filtration (NAP 5). Yield was 2.02 OD (ca 100 μg, 19%). ESI-TOF MS *m*/*z*: 566.55 $[M - 10H]^{10-}$, 629.96 $[M - 9H]^{9-}$, 708.71 $[M - 8H]^{8-}$, 810.22 $[M - 7H]^{7-}$, 945.28 $[M - 6H]^{6-}$, 1134.32 $[M - 5H]^{5-}$, 1418.64 $[M - 4H]^{4-}$. Reconstitution of the data gives M = 5674.05, which is in accordance with the proposed structure.

RESULTS AND DISCUSSION

Synthesis of the nucleosidic phosphoramidite building block is shown in Scheme 1. Accordingly, treatment of 1,4,7,10-tetraazacyclododecane-1-carboxymethyl-benzyl ester (*8*), **1**, with bromomethyl acetate yielded the tetraester, **2**. Removal of the benzyl group by hydrogenolysis gave the corresponding carboxylic acid derivative, **3**. Reaction of **3** with the nucleoside **4**, in the presence of HATU [*O*-(7-azabenzotriazol-1-yl)-1,1,3,3-tetramethyluronium hexafluorophosphate] and DIPEA (*N,N*-diisopropylethylamine) gave the nucleoside derivative, **5**. Finally, conventional phosphitylation yielded the phosphoramidite **6**.

To demonstrate the applicability of the phosphoramidite **6** for the preparation of oligonucleotide conjugates, an oligonucleotide was synthesized using standard instrument-assisted chemistry. The block **6** was coupled to the 5′-terminus of the coding sequence using 10 min coupling time and 0.2 M concentration. No differences in coupling efficiency between **6** and commercial nucleoside analogues were detected as judged on DMTr-cation assay. Upon completion of the syntheses, the conjugate was deprotected (*13*) and converted to the corresponding gadolinium(III) chelate by treatment with gadolinium(III) citrate (Scheme 2). It is worth noting that a prolonged reaction time (overnight at RT) and an excess of gadolinium(III) citrate was required to ensure complete chelate formation. According to gel electrophoresis, the crude oligomer containing the tethered DOTA survived completely the reaction conditions required for deprotection and chelate formation. The desired oligonucleotide conjugate (over 95% of the crude reaction mixture) was easily isolated from the gel and characterized by mass spectrometry. The observed molecular weight was in accordance with the proposed structure.

Scheme 2

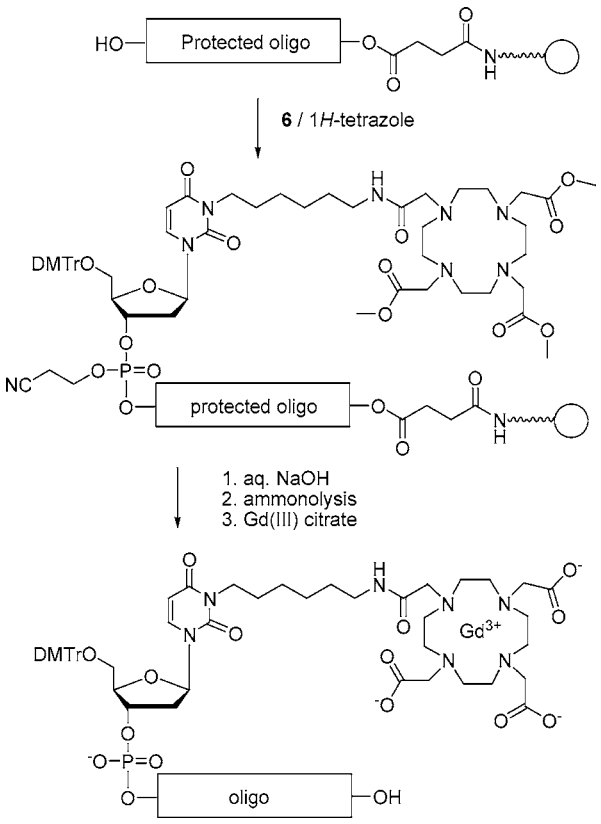

The major advantages of the present method are as follows: (i) The block can be introduced to the biomolecule structure with a standard oligonucleotide synthesizer in high efficiency using normal procedures. (ii) The position of the label in the oligonucleotide chain is not restricted. (iii) The method allows multilabeling. This is very advantageous in applications where high detection sensitivity is required. (iv) Since the metal is introduced after the chain assembly is completed, the molecule synthesized can be used in various applications simply by changing the metal. (v) Because of the synthetic strategy, the oligonucleotide conjugate is always free from unconjugated chelate. This is extremely important for in vivo applications.

In summary, a simple method for the preparation of a DOTA-based oligonucleotide labeling reactant is demonstrated. As shown here, the building block is suitable for site specific introduction of MRI contrast agents to oligonucleotides. Naturally, for PET and SPECT applications, the metal should be introduced just prior to analysis. Since the formation of the chelate is rather slow, the complexation can be accelerated using microwaves (*10*). It is worth noting that the labels attached at the N3 position of uracil residues naturally weaken hydrogen bonds in the duplex. Thus, these labels should be used only up- or downstream of the coding sequence.

LITERATURE CITED

(1) Aime, S., Botta, M., Fasano, M., and Terreno, E. (1998) Lanthanide(III) chelates for NMR biomedical applications. *Chem. Soc. Rev. 27*, 19−29.

(2) Caravan, P., Ellison, J. J., McMurry, T. J., and Lauffer, R. B. (1999) Gadolinium(III) chelates as MRI contrast agents: structure, dynamics, and applications. *Chem. Rev. 99*, 2293−2352.

(3) Woods, M., Kovacs, Z., and Sherry, A. D. (2002) Targeted complexes of lanthanide(III) ions as therapeutic and diagnostic pharmaceuticals. *J. Supramol. Chem. 2*, 1−15.

(4) Runge, V. M. (2000) Safety of approved MR contrast media for intravenous injection. *J. Magn. Reson Imaging 12*, 205−213.

(5) Anderson, C. J., and Welch, M. J. (1999) Radiometal-labeled agents (non-technetium) for diagnostic imaging. *Chem. Rev. 99*, 2219−2234.

(6) Volkert, W. A., and Hoffman, T. J. (1999) Therapeutic radiopharmaceuticals. *Chem. Rev. 99*, 2269−2292.

(7) Fichna, J., and Janecka, A. (2003) Synthesis of target-specific radiolabeled peptides for diagnostic imaging. *Bioconjugate Chem. 14*, 3−17.

(8) Heppeler, A., Froilevaux, S., Mäcke, H. R., Jermann, H. E., Béhé, M., Powell, P., and Hennig, M. (1999) Radiometal-labeled macrocyclic chelator-derivatised somatostatin analogue with superb tumor-targeting properties and potential for receptor-mediated tumor therapy. *Chem. Eur. J. 1*, 1974−1981.

(9) De Leon-Rodriguez, Kovacs, Z., Dieckmann, G. R., Sherry, A. D. (2004) Solid-phase synthesis of DOTA-peptides. *Chem. Eur. J. 10*, 1149−1155.

(10) Velikyan, I., Lendvai, G., Välilä, M., Roivainen, A., Yngve, U., Bergström, M., and Långström, B. (2004) Microwave-accelerated ^{68}Ga-labelling of oligonucleotides. *J. Labelled Compd. Radiopharm. 47*, 79−89.

(11) Roivainen, A., Tolvanen, T., Salomäki, S., Lendvai, G., Velikyan, I., Numminen, P., Välilä, M., Sipilä, H., Berström, M., Härkönen, P., Lönnberg, H., and Långström, B. (2004) ^{68}Ga-labelled oligonucleotides for in vivo imaging with PET. *J. Nucl. Med. 45*, 347−355.

(12) Hakala, H., and Hovinen, J. (2001) Versatile strategy for oligonucleotide derivatization. Introduction of lanthanide(III) chelates to oligonucleotides. *Org. Lett. 3*, 2473−2476.

BC0600362

SEPTEMBER/OCTOBER 2006
Volume 17, Number 5

© *Copyright 2006 by the American Chemical Society*

Bioconjugate Chemistry

ARTICLES

HER2 Specific Tumor Targeting with Dendrimer Conjugated Anti-HER2 mAb

Rameshwer Shukla, Thommey P. Thomas, Jennifer L. Peters, Ankur M. Desai, Jolanta Kukowska-Latallo, Anil K. Patri, Alina Kotlyar, and James R. Baker, Jr.*

Michigan Nanotechnology Institute for Medicine and Biological Sciences, Department of Internal Medicine, Division of Allergy, University of Michigan, 9220 MSRB III, Box 0648, Ann Arbor, Michigan 48109. Received December 6, 2005; Revised Manuscript Received July 12, 2006

In the present study, we report the synthesis and human growth factor receptor-2 (HER2) specific tumor targeting properties of a dendrimer conjugated to anti-HER2 mAb (monoclonal antibody) conjugate. The polyamidoamine (PAMAM) dendrimer generation five (G5) was labeled with alexaFluor 488 and conjugated to anti-HER2 mAb. The binding and internalization of the antibody-conjugated dendrimer to HER2-expressing cells was evaluated by flow cytometry and confocal microscopy. Uniquely, the conjugate demonstrated cellular uptake and internalization in HER2-expressing cells as compared to free antibody. The time course of internalization and blocking experiments with free antibody suggest that the rapid and efficient cellular internalization of the dendrimer−antibody conjugate was achieved without alterations in specificity of targeting. Animal studies demonstrated that the conjugate targets HER2-expressing tumors.

INTRODUCTION

Tumor-targeted drug delivery can enhance the effectiveness of chemotherapeutics while decreasing the systemic toxicity of these drugs. The use of monoclonal antibodies (mAbs) with specificity toward tumor markers is a well-established immunological strategy in cancer therapy. Monoclonal antibodies against various antigens have been used to deliver chemotherapeutic drugs (*1*, *2*), potent plant and bacterial toxins (*3*), and radionuclides (*4*) to tumors. The carrier capacity of antibodies can be increased significantly by attaching drug reservoirs such as nanoparticles, liposomes, and polymers. This approach potentially allows the delivery of a higher payload of drugs in a cell-specific manner.

Human epidermal growth factor receptor-2 (HER2) is one of the most promising targets in immunotherapy. The expression of the HER2 protein has been observed in a variety of tumors, in particular, breast and ovarian cancers (*5*), and has been associated with poor clinical outcomes (*6*). The overexpression of HER2 receptors in tumor cells provides an opportunity for development of HER2-targeted drug delivery systems. In addition, the presence of an extracellular domain makes the HER2 receptor an ideal target for receptor-mediated drug delivery in tumors. Monoclonal antibodies directed against HER2 offer a potential strategy for HER2-targeted delivery. Trastuzumab (Herceptin), a recombinant humanized monoclonal anti-HER2 antibody which has been approved for clinical use is reported to bind the HER2 receptor (*7*) with nanomolar affinity (*8*, *9*) and inhibits the growth of HER2-expressing breast cancer cells (*10*, *11*). The main objective of the present study was to investigate the utility of anti-HER2 mAb−PAMAM dendrimer conjugates as targeted drug delivery vectors. Antibody−dendrimer conjugates have been utilized in targeting prostate-specific membrane antigen (PSMA) (*12*) and CD14 antigen (*13*), delivery of boron (*14*), and tumor imaging applications (*15*). There has been growing interest in the synthesis of anti-HER2 mAb conjugates for gene delivery (*16*), tumor targeting (*17*), and imaging applications (*18*).

* jbakerjr@umich.edu.

10.1021/bc050348p CCC: $33.50 © 2006 American Chemical Society
Published on Web 08/15/2006

PAMAM dendrimers are biocompatible (*19*), nonimmunogenic (*20*), and water soluble and have been attached to many biological molecules such as proteins, synthetic drugs, and small molecules (*21*, *22*). In this study, we synthesized anti-HER2−mAb−dendrimer conjugate and studied its binding and internalization in HER2-overexpressing tumor cells. The specific targeting was clearly demonstrated in cell lines overexpressing HER2 by flow cytometry analysis. In addition, preincubation of HER2-overexpressing cells with free antibody prevented binding and uptake of antibody-conjugated dendrimers. This observation suggested that binding of the conjugate is mediated by HER2 on the surface of the analyzed cells. The cellular uptake of the conjugate as well as cellular distribution pattern was studied by confocal laser scanning microscopy. The antibody conjugated to dendrimer was shown to internalize in the cells faster and more efficiently than the antibody alone.

EXPERIMENTAL PROCEDURES

General. G5−PAMAM dendrimer was prepared at the Michigan Nanotechnology Institute for Medicine and Biological sciences, University of Michigan, and analyzed extensively by ^{1}H and ^{13}C NMR, matrix-assisted laser desorption ionization time-of-flight (MALDI-TOF) mass spectrometry, high-performance liquid chromatography (HPLC), gel-permeation chromatography (GPC), and polyacrylamide gel electrophoresis (PAGE). The molecular weight of synthesized dendrimer was found to be 26 530 g/mol by GPC, and the average number of primary amino groups was estimated to be 108 by potentiometric titration (*23*). The heterobifunctional cross-linkers sulfosuccinimidyl 3-(2-pyridyldithio)propionate (sulfo-LC-SPDP) and sulfosuccinimidyl-4-(*N*-maleimidomethyl)cyclohexane-1-carboxylate (sulfo-SMCC) were obtained from Pierce (Rockford, IL). Prepacked Sephadex G-25 PD-10 columns were purchased from Amersham Pharmacia Biotech (Piscataway, NJ) and equilibrated with degassed eluting buffer before sample introduction.

Synthesis of G5−Ac, 1. G5 amine dendrimer (0.265 g, 0.0099 mmol) and triethyl amine (0.088 g, 0.8635 mmol) were dissolved in 30 mL anhydrous MeOH and allowed to stir for 30 min. To this solution, acetic anhydride (0.076 g, 0.744 mmol) in anhydrous MeOH (15 mL) was added dropwise while stirring. The reaction mixture was allowed to stir overnight at room temperature. After evaporation of the solvent, the residue was dissolved in H_2O and dialyzed in 10 000 MWCO regenerated cellulose dialysis bags initially against PBS buffer followed by water. The partially acetylated dendrimer was lyophilized to give a colorless powder (0.270 g, 91.2%). The average number of acetyl groups (*80*) was determined on the basis of a ^{1}H NMR calibration curve drawn by plotting a ratio of acetyl protons and the sum of all methylene protons vs degree of actetylation (*24*).

Synthesis of G5−Ac−SPDP, 2. To a solution of G5−Ac, **1**, (0.042 g, 0.0014 mmol) in PBS buffer (pH 7.4, 10 mL), Sulfo-LC-SPDP (0.0052 g, 0.0098 mmol) dissolved in 2 mL PBS buffer was added dropwise, and the reaction mixture was allowed to stir for 3 h. The unreacted reagents and byproducts were separated by ultrafiltration using a 10K MWCO Pelicon device washing initially with PBS and then with DI water. The conjugate was lyophilized to give 0.036 g, 85.7% of conjugate as a white powder. The compound was characterized by HPLC and ^{1}H NMR spectroscopy. The number of SPDP linker was determined by pyridine-2-thione assay as described in the manufacturer's protocol. Briefly, conjugate **2** was dissolved in PBS/EDTA buffer (pH 7.4, 1 mg/mL), and the absorbance was recorded at 343 nm in comparison to a PBS−EDTA blank. To this solution, 10 μL of 15 mg/mL DTT was added and stirred for 15 min. After exactly 15 min, the absorbance at 343 nm of the reduced sample was recorded. The experiment was carried out in triplicate. On the basis of the change in absorbance, a molar ratio of 3.6 SPDP linkers per mole of dendrimer was calculated.

Scheme 1. Synthesis of Dendrimer Thiol, 4

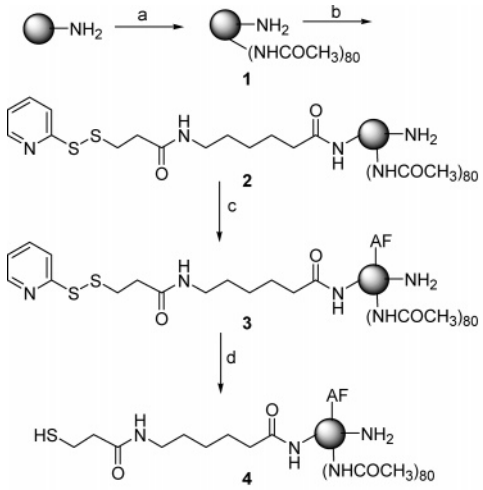

(a) Ac_2O, Et_3N, MeOH, rt, 24 h; (b) Sulfo-LC-SPDP, PBS, rt, 3 h; (c) AF-NHS ester, DMSO/PBS, 24 h; (d) DTT, PBS-EDTA, 2h

Scheme 2. Conjugation of Dendrimer Thiol with Anti-HER2 mAb

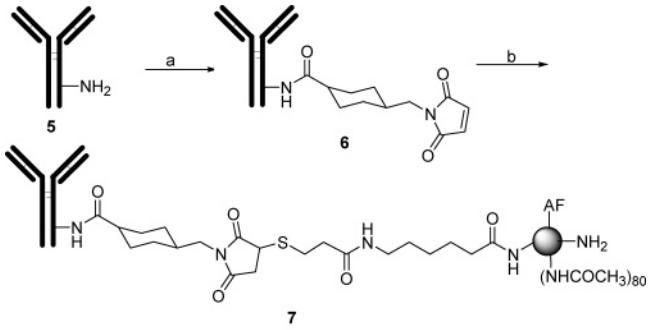

a) Sulfo-SMCC, PBS, rt, 2h b) **4**, PBS EDTA, rt, 2h, N-ethylmaleimide

Synthesis of G5−Ac−SPDP−AF, 3. AlexaFluor-NHS ester (0.003 g, 0.0046 mmol) dissolved in DMSO was added to a solution of dendrimer disulfide conjugate, **2** (0.030 g, 0.00096 mmol) in PBS buffer (pH 7.4) while stirring. The solution was allowed to stir for 18 h at room temperature. Concentration of the reaction mixture by membrane filtration and further purification on a G-25 Sephadex column gave the dendrimer conjugate, which was further purified by membrane filtration and lyophilized to give an orange powder (0.027 g, 90.0%). The purified conjugate was characterized by ^{1}H NMR and UV−vis spectroscopy and HPLC.

Synthesis of G5−AF−HN, 7. The disulfide bond on dendrimer conjugate **3** was reduced with 10 mM DTT solution in degassed PBS−EDTA buffer (pH 7.4) at room temperature (RT) under nitrogen to provide dendrimer−thiol, **4**. This conjugate was purified by gel filtration eluting with PBS−EDTA buffer (pH 7.4) under nitrogen on a PD-10 column to remove excess reagents and byproducts and was used immediately for antibody conjugation. A thiol-reactive maleimide group was introduced in anti-HER2 mAb, **5** (0.002 g, 0.00013 mmol), by reacting with sulfo-SMCC (0.0006 g, 0.00136 mmol) at room temperature for 2 h to give modified antibody **6**. The excess reagent was removed by gel filtration on a Sephadex G-25 column. Conjugate **6** was then concentrated on a microcon YM100 and immediately reacted with dendrimer thiolate (0.004 g, 0.00013 mmol) for 2 h at room temperature in PBS−EDTA buffer. After 2 h, *N*-ethylmaleimide (0.003 g, 0.024 mmol) was added to the

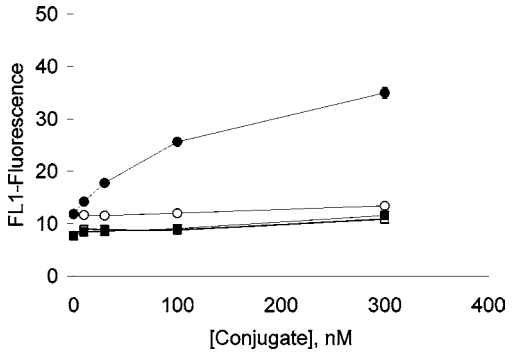

Figure 1. In vitro binding of the control conjugate G5−AF (open symbols) and the targeted conjugate G5−AF−HN (filled symbols) in control MCA207 cells (square symbols) and HER2-expressing (circle symbols) MCA207 cells. The cells were exposed to different concentrations of the conjugates for 1 h at 37 °C, rinsed, and the fluorescence measured by flow cytometry. Shown is the mean ± SE of three cell samples from an experiment. Similar results were obtained in an independent experiment.

reaction mixture. The final conjugate (G5−Ac−AF−HN, **7**) was purified by ultrafiltration (MWCO 100 000). The dendrimer−antibody conjugate was analyzed by HPLC, PAGE, and UV−vis spectroscopy.

Cell Culture and in Vitro Microscopy Experiments. MCA 207 control and −HER2 cells were a generous gift from Dr. Kevin McDonagh (University of Kentucky). SK-BR-3 cells were obtained from American Type Tissue Collection (Manasass, VA) and were grown as a monolayer at 37 °C and 5% CO_2 in McCoy's 5A medium supplemented with 15% fetal bovine serum, penicillin (100 units/mL), and streptomycin (100 μg/mL). The standard fluorescence of the dendrimer solutions was quantified using a Beckman spectrofluorimeter. For flow cytometric analysis of the uptake of the targeted polymer, cells were trypsinized and suspended in PBS containing 0.1% bovine serum albumin (PBSB) and analyzed using a Becton Dickinson FACScan analyzer. The FL1 fluorescence of 10 000 cells was measured, and the mean fluorescence of gated viable cells was quantified. For confocal experiments, cells were seeded at a density of 5×10^5 cells/plate on glass-bottom culture dishes (Mattek, Ashland, MA) 2 days prior to the experiment. Before each experiment, cells were washed three times in Dubelco's phosphate buffered saline (pH = 7.4) and incubated with 30 nM G5−HN−AF 488 or HN−AF 488 for 60 min at 37 °C except where noted. Preincubation experiments were carried with 3 μM HER2−mAb solution. For quenching experiments, anti-Alexa 488 (Molecular Probes, Eugene, OR) 600 nM was applied. The cells were fixed with 2% *p*-formaldehyde for 15 min at room temperature, washed, and mounted with a coverslip using Prolong Gold (Molecular Probes, Eugene, OR). In some cases, Prolong gold with DAPI was used to counterstain the nuclei of the cells. Cells were imaged on an Olympus FluoView

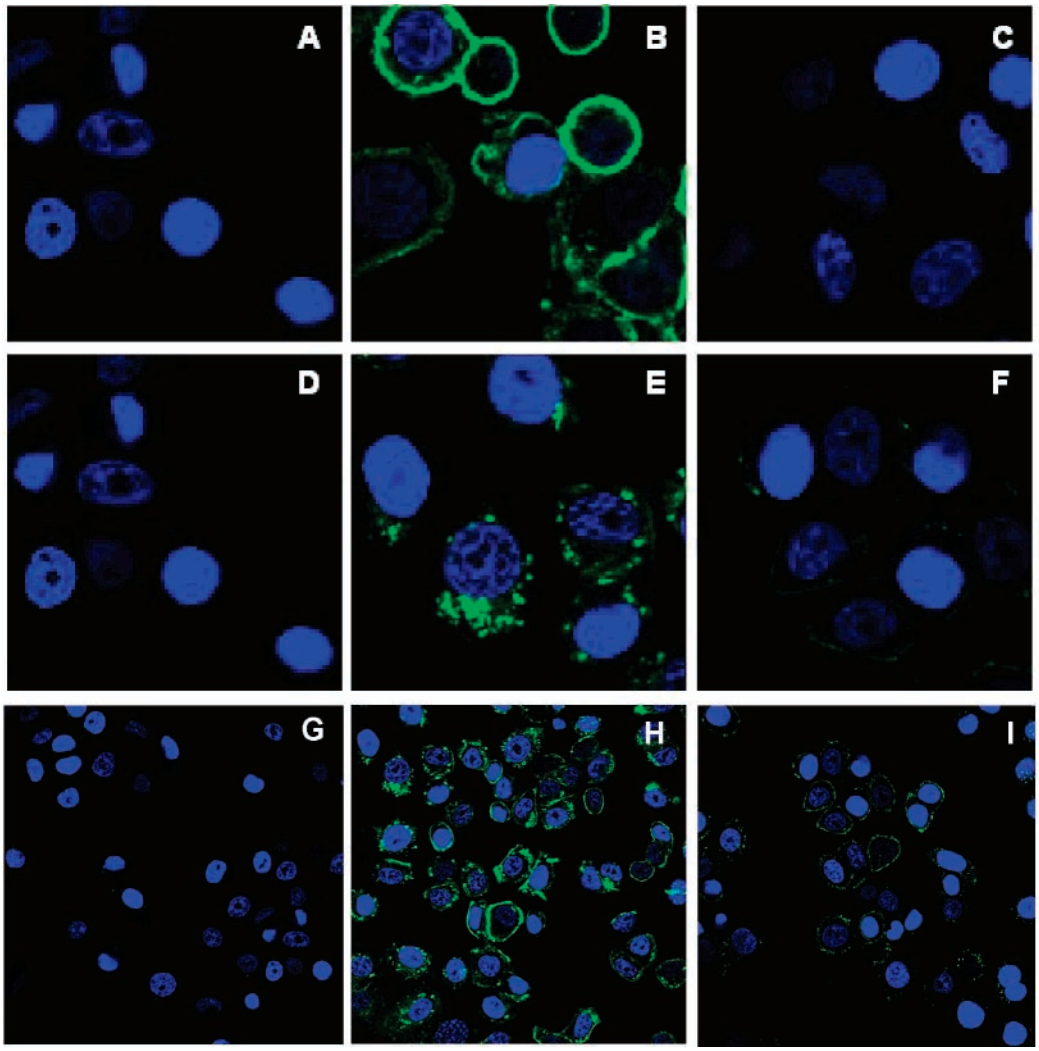

Figure 2. The blocking of HN−AF (A−C) and G5−HN−AF (D−F) by free anti-HER2 mAb in SKBR-3 cells. (A,D) Unstained cells. (B,E) Cells stained with 30 nM compound. (C,F) Cells blocked with 3 μM free anti-HER2 mAb before the addition of 30 nM compound. Panels G, H, and I show the lower-magnification images of D, E, and F, respectively.

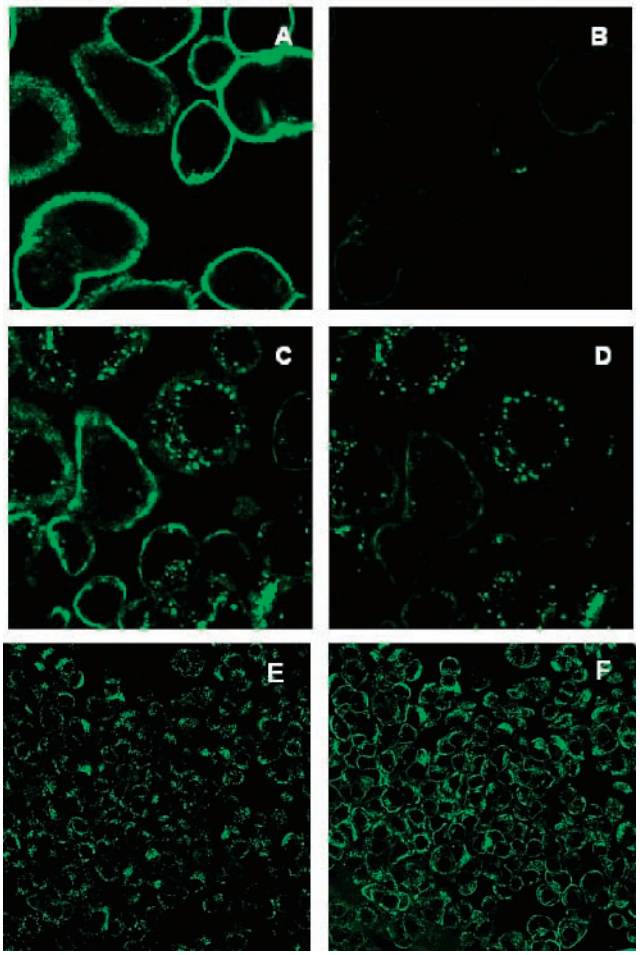

Figure 3. The quenching of surface-bound AlexaFluor with anti-Alexa 488 in SKBR-3 cells. (A,B) Cells stained with 30 nM HN−AF 488. The same field of view is shown before (A) and 10 min after (B) the addition of 600 nM anti-Alexa. (C,D) The same experiment using G5−HN−AF. (E,F) Lower-magnification images of C and D, respectively.

500 laser scanning confocal microscope with a 60×, 1.4 NA objective and pinhole settings resulting in an optical section thickness of 0.5 μm.

Animal Model. MCA207 control and −HER2 xenograft tumors were developed in 7-week-old female SCID mice by subcutaneous inoculation of 50 000 cells in the left and right flank areas. The cells were rinsed and injected as a 0.1 mL suspension using sterile PBS. Mice were housed under sterile conditions, and the tumors were allowed to reach 0.7−0.8 cm in diameter before analysis. A solution of 2.4 nmol of the conjugate in 0.1 mL of PBS or a control solution of PBS alone was administered through the tail vein. Fifteen hours later, at the end of the study, the mice were anesthetized with isoflurane, and the tumors were excised and frozen in Optimum Cutting Temperature solution (Sakura Finetechnical, Tokyo, Japan) by immersing in methylbutane/dry ice, as we have described before (*25*). The tumors were subsequently sectioned on a cryostat into 10 μm sections which were thawed, rinsed three times with DPBS, and fixed in 2% *p*-formaldehyde for 15 min at 4 °C. The sections were then rinsed and mounted with coverslips using Prolong gold with DAPI. Images were taken on an Olympus FluoView 500 laser scanning confocal microscope using a 20×, 0.7 NA objective and an optical section thickness of 1.0 μm, unless otherwise indicated.

RESULTS

Conjugate Synthesis and Characterization. The dendrimer terminal group modification was done as shown in Scheme 1. In order to improve targeting efficacy and reduce the nonspecific interactions, amine-terminated G5 dendrimers were partially surface modified with acetic anhydride (75 mol equiv) in the presence of triethylamine as base. The surface modification leaves some unreacted amines on the surface while considerably reducing the nonspecific binding to cells. The partially acetylated G5 dendrimer (G5−Ac, **1**) was purified by repeated dialysis initially using pH 7.4 PBS and subsequently using water. The purity of compound **1** and the extent of acetylation were measured and monitored by ^{1}H NMR, which shows a distinct signal for the terminal $NHCOCH_3$ protons of the dendrimer at δ1.85. ^{13}C NMR spectrum also showed a new peak at δ174.4 for the carbonyl carbon of the acetyl group. The degree of acetylation was measured by comparing the ratio of $NHCOCH_3$ protons with the sum of all methylene protons in the dendrimer to a calibration curve as described previously (*24*). In order to introduce a disulfide group on the dendrimer, heterobifunctional cross-linking agent sulfo-SPDP was conjugated to the partially acetylated dendrimer (G5−Ac, **1**) to provide a protected thiol in the form of a disulfide (G5−Ac−SPDP, **2**) as described previously (*13*). The extent of disulfide modification was monitored by UV spectroscopy, using the pyridine-2-thione assay as described in the manufacturer's protocol. Briefly, DTT was added to a measured quantity of dendrimer, and absorbance of the released 2-thiopyridine at 343 nm was recorded. On the basis of this measurement, an average of three disulfide groups per dendrimer in **2** were calculated, which is in agreement with values obtained by ^{1}H NMR by comparing the integral values of the heteroaromatic signals of the pyridine and the aliphatic signals of the dendrimer.

Compound **2** was reacted with alexaFluor NHS ester (5 molar excess) to give alexaFluor-labeled conjugate **3**. The ^{1}H NMR spectrum of the conjugate shows overlapping signals in the aromatic region for both the alexaFluor and the pyridine ring from the disulfide linker apart from the expected aliphatic signals for the dendrimer. The number of dye molecules was calculated to be ∼3 based on UV−vis spectroscopy. The reduction of disulfide bonds on dendrimer conjugate **3** was carried out using dithiothreatol, DTT, in PBS−EDTA buffer. The resultant dendrimer thiol, **4**, was carefully purified under an inert atmosphere in degassed PBS−EDTA buffer.

A thiol-reactive maleimide group was introduced on the antibody, **5**, with water-soluble sulfo-SMCC using standard protocols (*13*), and the resultant conjugate, **6**, was purified by gel filtration. To minimize the free antibody, a tenfold molar excess of dendrimer conjugate was used in the antibody−dendrimer coupling reaction; the unreacted thiols were quenched with *N*-ethylmaleimide to minimize the dimer formation due to cross-linking of dendrimer to antibodies. Free unreacted dendrimer was removed by filtration with a 100K MWCO microcon. The resultant conjugate, **7** (Scheme 2), was analyzed using PAGE, which shows a band above the antibody band that confirms the conjugation and an absence of a band for the free dendrimer. The fluorescence of the conjugates gives indirect proof of conjugation, as the fluorescent label was attached to the dendrimer.

In Vitro Targeting Studies. The cellular uptake of dendrimer−anti-HER2−mAb conjugates was measured in MCA207 control and MCA207−HER2 cells by flow cytometry (*25*). As shown in Figure 1, the conjugate G5−AF−HN bound the HER2-expressing cells but not MCA 207 control cells that do not express the receptor. The receptor specificity of the conjugates was further tested in SKBR-3 cells, which have been shown to express the HER2 receptor by confocal microscopy (*17*). SKBR-3 cells stained with HN−AF or G5−AF−HN (30 nM) were washed and fixed with *p*-formaldehyde; the nuclei were counterstained with DAPI. It is evident from the appear-

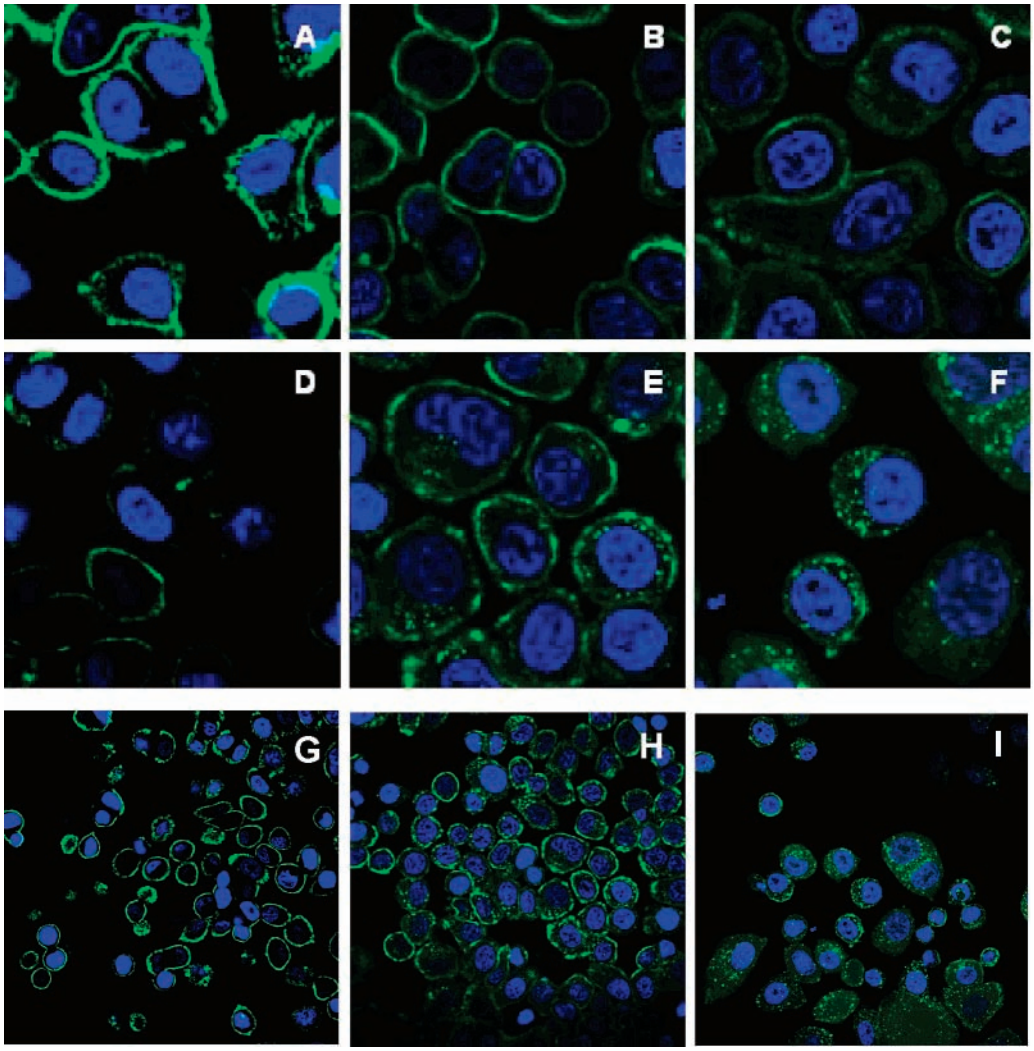

Figure 4. The time course of the internalization of HN−AF (A−C) and G5−HN−AF (D−F) in SKBR-3 cells. Cells were stained with 30 nM compound according to the following conditions: (A,D) 30 min at 4 °C; (B,E) 1 h at 37 °C; (C,F) 6 h at 37 °C; (G,H,I) lower-magnification images of D, E, and F, respectively.

ance of fluorescence in Figure 2B,E that conjugate **7** binds to the cell surface receptors and internalizes, whereas HN−AF reveals a different pattern with a higher signal on the cell surface and more uniform distribution of staining, suggesting a different internalization pattern. The images of cells stained only with DAPI (A,D) did not show autofluorescence within the instrumental parameters used. As shown in Figure 2C,F, pretreatment of cells with a 100-fold excess of free anti-HER2−mAb completely blocked fluorescence. The flow cytometry and confocal microscopic analysis suggest that anti-HER2−mAb dendrimer conjugate not only binds the cell surface HER2 receptor but is also internalized in the cells overexpressing the HER2 receptor.

In Vitro Internalization. AlexaFluor 488 serves as a hapten that is recognized by specific rabbit, anti-Alexa 488 antibodies. Upon binding, anti-Alexa 488 effectively quenches the fluorescence of AlexaFluor 488. Since anti-Alexa 488 does not cross cellular membranes, it quenches the fluorescence of surface-bound AlexaFluor-labeled conjugates, leaving aside the conjugates internalized within cells. Therefore, the decrease in fluorescence upon binding of anti-Alexa 488 to cells pretreated with HN−AF 488 or G5−AF−HN provides a useful index of the degree of internalization of these compounds. Figure 3A shows cells that were incubated with HN−AF for 1 h at 37 °C. In Figure 3B, after the addition of anti-Alexa 488, nearly all of the fluorescence was quenched, confirming that this compound is mainly surface-bound. In contrast, when the same experiment is performed with G5−AF−HN, a much smaller decrease in fluorescence is observed, indicating that antibody−dendrimer conjugate is largely internalized.

Comparison of the time course of the internalization of HN−AF and G5−AF−HN in SKBR-3 cells reveals that the antibody−dendrimer conjugate was rapidly internalized in HER2-expressing cells in comparison with antibody alone. As shown in Figure 4A,D, after 30 min at 4 °C, both conjugates were mainly localized in the cellular membrane. After 1 h incubation at 37 °C (panels B and E), HN−AF was still present in the plasma membrane, whereas a significant internalization was observed in the cells incubated with G5−AF−HN. After 6 h incubation at 37 °C (panels C and F), G5−AF−HN internalization was significantly higher as compared to HN−AF.

In Vivo Studies. Tumors were developed in SCID mice by subcutaneous injection of the control and HER2-expressing MCA 207 cells, on left and right flank areas of the mice. The tumor uptake of G5−AF−HN or its vehicle was tested by injecting the conjugates into the bloodstream from the tail vein. As shown in Figure 5, the conjugate showed an increased binding to HER2-expressing tumor when compared with control tumor, whereas both PBS and control compound (G5−AF) did not show any preferential binding by flow cytometry.

We also analyzed the in vivo binding by confocal microscopy. Internalized fluorescence due to uptake of the conjugate can be clearly seen in HER2-expressing tumor cells (Figure 6A), whereas no fluorescence was observed in any of the control

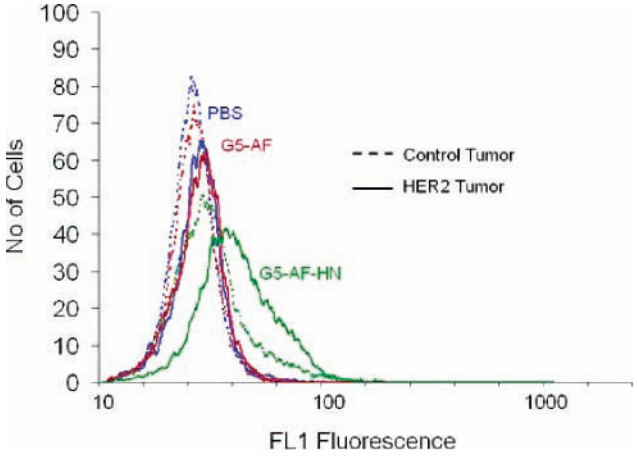

Figure 5. Binding of G5−AF−HN in MCA 207 control and HER2-expressing mice xenograft tumors in vivo. Tumors were developed in SCID mice by subcutaneous injection of the two cell lines on left and right flank areas, respectively, of the mice. When the tumors were about 0.7 cm in diameter, 2.4 nmols G5−AF−HN or its vehicle were injected intravenously. The tumors were isolated after 15 h, and the cells were separated by collagenase digestion and analyzed by flow cytometry.

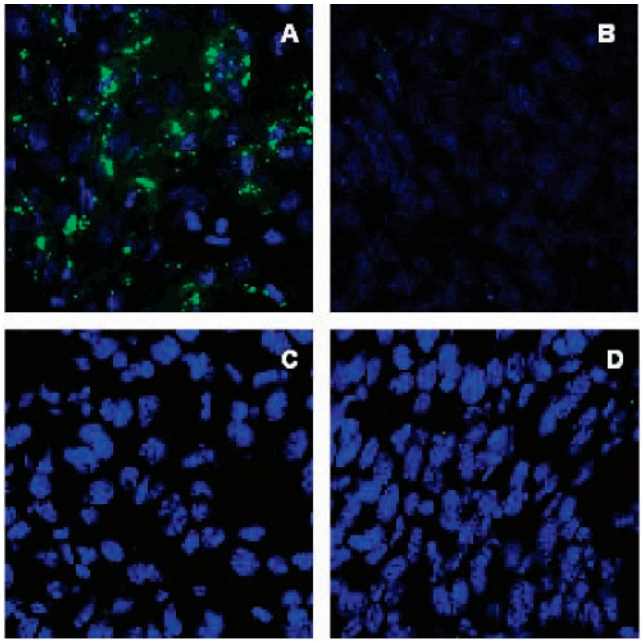

Figure 6. Images of tumor sections. (A,B) HER2+ (A) and HER2− (B) tumors from an animal injected with G5−HN−AF. (C,D) HER2+ tumors from an animal injected with PBS (C) or G5−AF (D).

cells, including an HER2-negative tumor from the same animal (B) and HER2-positive tumors in animals where PBS (C) or the control conjugate G5−AF (D) was given.

DISCUSSION

The major disadvantage of most antitumor drugs is their high toxicity, which leads to toxic side effects. Targeted cancer therapy aims to reduce or eliminate side effects by specifically delivering a cytotoxic pharmaceutical agent to tumor cells. Successful drug targeting can also result in a lower dosage required to obtain a therapeutic response, thus improving antitumor effects and again limiting systemic toxicity. Antibodies themselves can be used as drug carrier systems, but attaching drugs to an immunoglobulin may result in the loss of binding efficacy and decrease the solubility of the immunoconjugates. These problems can be overcome by attaching a water-soluble drug reservoir to the antibodies. The G5−PAMAM dendrimer is stable and nonimmunogenic and contains, on average, 110−128 primary amines on the surface. This provides an ample number of reactive sites for the construction of complex drug delivery systems by attaching multiple chemical moieties, such as radiopharmaceuticals, drugs, dyes, and contrast agents (*26*). The overexpression of HER2 protein in a high percentage of epithelial tumors and substantially greater expression of HER2 protein on cancerous cells will permit the selective targeting of malignant cells using anti-HER2−mAb. Therefore, in the present study, we synthesized a conjugate of HER2−mAb with PAMAM dendrimer as the drug carrier. Amine-terminated PAMAM dendrimers are reported to bind to the cells in a nonspecific manner owing to the positive charge on the surface and were also shown to be comparatively more toxic than charge neutral surfaces. The amine-terminated G5 dendrimer was partially surface modified with acetic anhydride in presence of triethylamine as base. The partial modification of the surface also improves the aqueous solubility and minimizes aggregate formation. The partially acetylated dendrimer was reacted with a heterobifunctional linker, sulfo-LC-SPDP to provide a 2-pyridylthiol group on the surface, which upon reduction with DTT gives a reactive thiol group. For detection of conjugates by flow cytometry or confocal microscopy, a detectable fluorescent probe is needed. We used AlexaFluor 488 (AF) as the fluorescent label, because it is significantly brighter than fluorescein conjugates (*27*) and is also much more photostable. The reduction of the 2-pyridylthiol group and conjugation to anti-HER2−mAb which was modified with maleimide linker gave the final dendrimer−mAB conjugate. The remaining thiol groups were capped with *N*-ethylmaleimide to prevent cross-linking. The HPLC analysis of the final conjugate shows a homogeneous peak, which indicates that under the present reaction conditions there was minimal cross-linking, possibly because of the steric hindrance posed by the relatively larger size of the antibody.

The dendrimer−anti-HER2−mAb bound HER2-expressing MCA 207 to the cell in a dose-dependent manner as shown by flow cytometery. As flow cytometry cannot distinguish between conjugate uptake and cell surface binding, confocal laser scanning microscopy was used to evaluate the cellular uptake of the synthesized dendrimer conjugate. By confocal microscopic analysis, it was shown that the dendrimer−HER2−mAb conjugate not only bound to the outer surface of the HER2-expressing cells but was also internalized. The conjugate uptake was further confirmed by quenching experiments carried out using anti-Alexa 488. The anti-Alexa is a noninternalizing antibody that interacts with surface-bound AlexaFluor and quenches its fluorescence. This experiment indicates that dendrimer−HER2−mAb conjugate was predominantly internalized into HER2-expressing tumor cells. A time course study of internalization demonstrated that the antibody-conjugated dendrimer internalized in the HER2-expressing cells more efficiently and rapidly. The in vivo experiments indicate that this conjugate may be capable of targeting imaging agents and/or chemotherapeutics to HER2-overexpressing tumors. In conclusion, we have synthesized anti-HER2−dendrimer conjugate that efficiently binds to HER2-overexpressing cells. From flow cytometery and confocal microscopic analysis, it was demonstrated that the anti-HER2−mAb−dendrimer conjugates not only bound the HER2-overexpressing cells but was also internalized in the cells. Preincubation experiments with unlabeled antibody, a lack of binding and uptake in control cells, and insignificant binding of control antibody−dendrimer conjugates all suggest that the conjugates internalize in HER2-overexpressing cells. The time course of internalization reveals a faster and more efficient internalization of the conjugate than anti-HER2 antibody alone. In vivo experiments indicate that

this conjugate may be capable of targeting imaging agents and/or chemotherapeutics to HER2-overexpressing tumors.

ACKNOWLEDGMENT

The authors gratefully acknowledge financial support of the National Cancer Institute through contract N01-CM-97065−32.

Supporting Information Available: Potentiometric titration, pyridine-2-thione assay, and HPLC analysis data. This material is available free of charge via the Internet at http://pubs.acs.org.

LITERATURE CITED

(1) Guillemard, V., and Saragovi, H. U. (2001) Taxane-Antibody Conjugates Afford Potent Cytotoxicity, Enhanced Solubility and Tumor Target Selectivity. *Cancer Res. 61*, 694−699.

(2) Baloglu, E., Miller, M. L., Roller, E. E., Cavanagh, E. E., Leece, B. A., Goldmacher, V. S., and Chari, R. V. J. (2004) Synthesis and biological evaluation of novel taxoids designed for targeted delivery to tumors. *Bioorg. Med. Chem. Lett. 14*, 5885−5888.

(3) Smallshaw, J. E., Ghetie, V., Rizo, J., Fulmer, J. R., Trahan, L. L., Ghetie, M. A., and Vitetta, E. S. (2003) Genetic engineering of an immunotoxin to eliminate pulmonary vascular leak in mice. *Nat. Biotechnol. 21*, 387−389.

(4) Seidl, C., Schrock, H., Seidenschwang, S., Beck, R., Schmid, E., Abend, M., Becker, K. F., Apostolidis, C., Nikula, T., Kremmer, E., Schwaiger, M., and Senekowitsch-Schmidtke, R. (2005) Cell death triggered by alpha-emitting Bi-213-immunoconjugates in HSC45-M2 gastric cancer cells is different from apoptotic cell death. *Eur. J. Nucl. Med. Mol. Imaging 32*, 274−285.

(5) Slamon, D. J., Godolphin, W., Jones, L. A., Holt, J. A., Wong, S. G., Keith, D. E., Levin, W. J., Stuart, S. G., Udove, J., Ullrich. A., and Press, M. F. (1989) Studies of the HER-2/neu proto-oncogene in human breast and ovarian cancer. *Science 244*, 707−712.

(6) Olayioye, M. A., Neve, R. M., Lane, H. A., and Hynes, N. E. (2000) The ErbB signaling network: receptor heterodimerization in development and cancer. *EMBO J. 19*, 3159−3167.

(7) Cho, H.-S., Mason, K., Ramyar, K. X., Stanley, A. M., Gabelli, S. B., Denney, D. W. J., and Leahy, D. J. (2003) Structure of the extracellular region of Her2 alone and in complex with the herceptin Fab. *Nature (London) 421*, 756−760.

(8) Park, J. W., Hong, K., Carter, P., Asgari, H., Guo, L. Y., Keller, G. A., Wirth, C., Shalaby, R., Kotts, C., and Wood, W. I. (1995) Development of anti-p185her2 immunoliposomes for cancer therapy. *Proc. Natl. Acad. Sci. U.S.A.* 92, 1327−1331.

(9) Carter, P., Presta, L., Gorman, C. M., Ridgway, J. B. B., Henner, D., Wong, W. L. T., Rowland, A. M., Kotts, C., Carver, M. E., and Shepard, H. M. (1992) Humanization of an anti-p185her2 antibody for human cancer therapy. *Proc. Natl. Acad. Sci. U.S.A. 89*, 4285−4289.

(10) Baselga, J., Tripathy, D., Mendelsohn, J., Baughman, S., Benz, C. C., Dantis, L., Sklarin, N. T., Seidman, A. D., Hudis, C. A., Moore, J., Rosen, P. P., Twaddell, T., Henderson, I. C., and Norton, L. (1999) Phase II study of weekly intravenous trastuzumab (herceptin) in patients with her2/neu-overexpressing metastatic breast cancer. *Semin. Oncol. 26*, 78−83.

(11) Vogel, C., Cobleigh, M. A., Tripathy, D., Gutheil, J. C., Harris, L. N., Fehrenbacher, L., Slamon, D. J., Murphy, M., Novotny, W. F., Burchmore, M., Shak, S., and Stewart, S. J. (2001) First-line, single-agent herceptin (trastuzumab) in metastatic breast cancer: a preliminary report. *Eur. J. Cancer 37*, 25−29.

(12) Patri, A. K., Myc, A., Beals, J., Thomas, T. P., Bander, N. H., and Baker, J. R. (2004) Synthesis and in vitro testing of J591 antibody−dendrimer conjugates for targeted prostate cancer therapy. *Bioconjugate Chem. 15*, 1174−1181.

(13) Thomas, T. P., Patri, A. K., Myc, A., Myaing, M. T., Ye, J. Y., Norris, T. B., and Baker, J. R. (2004) In vitro targeting of synthesized antibody-conjugated dendrimer nanoparticles. *Biomacromolecules 5*, 2269−2274.

(14) Wu, G., Barth, R. F., Yang, W. L., Chatterjee, M., Tjarks, W., Ciesielski, M. J., and Fenstermaker, R. A. (2004) Site-specific conjugation of boron-containing dendrimers to anti-EGF receptor monoclonal antibody cetuximab (IMC-C225) and its evaluation as a potential delivery agent for neutron capture therapy. *Bioconjugate Chem. 15*, 185−194.

(15) Kobayashi, H., Reijnders, K., English, S., Yordanov, A. T., Milenic, D. E., Sowers, A. L., Citrin, D., Krishna, M. C., Waldmann, T. A., Mitchell, J. B., and Brechbiel, M. W. (2004) Application of a macromolecular contrast agent for detection of alterations of tumor vessel permeability induced by radiation. *Clin. Cancer Res. 10*, 7712−7720.

(16) Chiu, S. H., Ueno, N. T., and Lee, R. J. (2004) Tumor-targeted gene delivery via anti-HER2 antibody (trastuzumab, Herceptin (R)) conjugated polyethylemmine. *J. Controlled Release 97*, 357−369.

(17) Wartlick, H., Michaelis, K., Balthasar, S., Strebhardt, K., Kreuter, J., and Langer, K. (2004) Highly specific HER2-mediated cellular uptake of antibody-modified nanoparticles in tumour cells. *J. Drug Targeting 12*, 461−471.

(18) Copland, J. A., Eghtedari, M., Popov, V. L., Kotov, N., Mamedova, N., Motamedi, M., and Oraevsky, A. A. (2004) Bioconjugated gold nanoparticles as a molecular based contrast agent: Implications for imaging of deep tumors using optoacoustic tomography. *Mol. Imaging Biol. 6*, 341−349.

(19) Duncan, R., and Izzo, L. (2005) Dendrimer biocompatibility and toxicity. *Adv. Drug Delivery Rev. 57*, 2215−2237.

(20) Roberts, J. C., Bhalgat, M. K., and Zera, R. T. (1996) Preliminary biological evaluation of polyamidoamine (PAMAM) starburst dendrimers. *J. Biomed. Mater. Res. 30*, 53−65.

(21) Patri, A. K., Majoros, I. J., and Baker, J. R. (2002) Dendritic polymer macromolecular carriers for drug delivery. *Curr. Opin. Chem. Biol. 6*, 466−471.

(22) Boas, U., and Heegaard, P. M. H. (2004) Dendrimers in drug research. *Chem. Soc. Rev. 33*, 43−63.

(23) Majoros, I. J., Thomas, T. P., Mehta, C. B., and Baker, J. R. (2005) Poly(amidoamine) dendrimer-based multifunctional engineered nanodevice for cancer therapy. *J. Med. Chem. 48*, 5892−5899.

(24) Majoros, I. J., Keszler, B., Woehler, S., Bull, T., and Baker, J. R. (2003) Acetylation of poly(amidoamine) dendrimers. *Macromolecules 36*, 5526−5529.

(25) Thomas, T. P., Myaing, M. T., Ye, J. Y., Candido, K., Kotlyar, A., Beals, J., Cao, P., Keszler, B., Patri, A. K., Norris, T. B., and Baker, J. R. (2004) *Biophys. J. 86*, 3959−3965.

(26) Kukowska-Latallo, J. F., Candido, K. A., Cao, Z. Y., Nigavekar, S. S., Majoros, I. J., Thomas, T. P., Balogh, L. P., Khan, M. K., and Baker, J. R. (2005) Nanoparticle targeting of anticancer drug improves therapeutic response in animal model of human epithelial cancer. *Cancer Res. 65*, 5317−5324.

(27) Shukla, R., Thomas, T. P., Peters, J., Kotlyar, A., Myc, A., Baker, J. R. (2005) Tumor angiogenic vasculature targeting with PAMAM dendrimer−RGD conjugates. *Chem. Commun. 46*, 5739−5741.

BC050348P

Amino-Terminal Dimerization of Peptides on the Solid Support. Synthesis and Biological Activity of the Immunosuppressive HLA−DR Fragments Linked by Poly(ethylene glycol)s

Monika Biernat,[†] Piotr Stefanowicz,[†] Michał Zimecki,[‡] and Zbigniew Szewczuk*,[†]

Faculty of Chemistry, University of Wrocław, Wrocław, Poland, and Institute of Immunology and Experimental Therapy, PAN, Wrocław, Poland. Received December 22, 2005; Revised Manuscript Received July 27, 2006

The nonapeptide fragment of the HLA−DR molecule, located in the exposed loop of the β chain (164−172) and having the sequence VPRSGEVYT, suppresses the immune response. On the basis of the three-dimensional structure of the HLA−DR superdimer, we designed new dimeric analogs in which the VPRSGEVYT peptides are linked through their N-termini by poly(ethylene glycol) linkers of different lengths and are able to mimic the dimeric nature of the immunosuppressive fragments of HLA class II molecules. The analogs were synthesized using standard solid-phase peptide synthesis protocols. The dimerization was achieved by cross-linking the N-terminal positions of the peptides, attached to an MBHA resin, with α,ω-bis(acetic acid) poly(ethylene glycol), activated by esterification with pentafluorophenol. Our results demonstrate that the amino-terminal dimerization of the peptide results in enhanced immunosuppressive activity and that the potency of the conjugates depends on the length of the poly(ethylene glycol) linker. MS/MS analysis of the obtained dimeric peptides is also presented.

INTRODUCTION

MHC[1] class II molecules present antigenic peptides to helper T cells and thereby alert the immune system to infectious attack (reviewed by Pieters (*1*), Hiltbold and Roche (*2*)). MHC class II molecules are heterodimers with a molecular mass of 60 kDa consisting of noncovalently associated polymorphic α and β subunits. The class II molecules are highly polymorphic proteins. The presence of several isotypes (DP, DQ, and DR) of human MHC (HLA) class II molecules further increases their diversity.

Our previous studies showed that fragments located in the β164−172 loop of HLA−DQ suppress the humoral and cellular immune responses (*3, 4*) and inhibit some integrins (*5*). The fragments contain the RGD sequence, known to be important in several proteins in mediating cell adhesion interactions. The sequence is located in an exposed loop of the HLA−DQ molecule and may therefore be involved in interactions with other proteins. The immunosuppressive region is situated in close spatial proximity to the site identified as interacting with the T-cell coreceptor CD4 (*6*). The pentateptide fragment of the loop, Arg-Gly-Asp-Val-Tyr-NH_2, is the shortest immunosuppressive sequence found, although its potency is relatively low (*7*). The corresponding fragments of HLA−DP and HLA−DR show immunological properties similar to the HLA−DQ fragment (*8*). Particularly, the nonapeptide fragment of HLA−DR (Val-Pro-Arg-Ser-Gly-Glu-Val-Tyr-Thr) is a strong suppressor of the immune response, although the fragment does not contain the RGD sequence. We also designed and synthesized constrained (by cyclization) analogs of the fragment to mimic the immunosuppressive loop of HLA class II molecules and found that some of the investigated peptides suppress immune responses more strongly than their linear counterparts (*9, 10*). On the basis of our results, we suggested that the loop may serve as a functional epitope on the HLA class II surface for intermolecular binding and that a possible mechanism of biological action of the synthesized peptides is connected with specific interference with the adhesion of HLA class II molecules to their coreceptors, e.g., some specific integrins and/or the T-cell coreceptor CD4 (*11*). Recently, we pointed out some topological correspondence between the β-164−172 loop of HLA−DQ and the 50−59 loop of ubiquitin, suggesting that the proteins may interact with similar proteins, although the ubiquitin fragment contains the retro-RGD sequence. We showed that the linear and cyclic fragments of ubiquitin, designed to mimic the loop, may significantly inhibit both humoral and cellular immune responses (*12*). The low toxicity of such compounds compared with classic suppressors such as cyclosporine A (CsA) may lead to potential application of the peptides in therapy. A combined use of these peptides with conventional immunosuppressors may have even better therapeutic perspectives.

The three-dimensional structure of the HLA class II molecule has been determined by X-ray crystallography (*13*). The crystal structure shows that the $\alpha\beta$ heterodimer can itself dimerize to form a four-chain $(\alpha\beta)_2$ superdimer of 120 kDa. There is also evidence for the existence of the 120 kDa $(\alpha\beta)_2$ complex of the class II molecules in animal B cells (*14*). It has been suggested that MHC class II molecules may interact with the T-cell receptor (TCR) and $CD4^+$ as an $(\alpha\beta)_2$ superdimer, potentially ensuring more stable and stimulatory interactions than can be provided by the simple $\alpha\beta$ heterodimer alone (*15, 16*). Evidence has also been presented that the formation or rearrangement of a T-cell receptor dimer is necessary and sufficient for initiation of T-cell signaling (*17*). Self-association of the CD4 coreceptor may also affect T-cell activation (*18*). Therefore, substances that are able to modulate the receptors'

* Correspondence to Z. Szewczuk, Wydział Chemii, Uniwersytet Wrocławski, ul. F. Joliot-Curie 14, 50-383 Wrocław, Poland. Fax: +48-71-3282348. Tel.: +48-71-3757212. E-mail: szewczuk@wchuwr.chem.uni.wroc.pl.

[†] University of Wrocław.

[‡] Institute of Immunology and Experimental Therapy.

[1] Abbreviations and symbols are in accordance with recommendations of the European Peptide Society (*J. Peptide Sci. 5*, 465−471, 1999). AFC, antibody-forming cells; HLA, human leukocyte antigen; MHC, major histocompatibility complex; PEG-Pfp_2, poly(ethyleneglycol)bis(carboxymethyl)ether activated by esterification with pentafluorophenol; SRBC, sheep red blood cells.

10.1021/bc050360h CCC: $33.50 © 2006 American Chemical Society
Published on Web 08/22/2006

dimerization may control such a process and are potential immunomodulators. Dimeric ligands are known candidates for mediating dimerization of these types of receptors (*19, 20*). It was previously found (*21*) that peptides that consist of two tandemly repeated epitopes joined by a flexible linker have an increased affinity for class II molecules and are more potent in inducing proliferation of T-cell clones than monomeric epitopes. These results support a role of the MHC class II dimer of heterodimers in amplifying the proliferative response of T cells to antigen by dint of the superdimers having a higher affinity for CD4 than the nominal class II $\alpha\beta$ heterodimers. Recently, we synthesized a series of dimeric analogs of the immunosuppressive fragments of HLA class II molecules. The dimeric analogs consist of two VPRSGEVYT sequences joined through their C-termini by oligoglycine spacers of different length connected to the lysine residue $(VPRSGEVYTG_n)_2K\text{-}NH_2$ ($n = 4$, 5, and 6). Our results demonstrate that the immunosuppressive activities of the resulting dimeric analogs are significantly higher than those of their monomeric counterparts and their potencies depend on the length of their linker (*22*). However, employment of the oligoglycine sequences in the dimers significantly decreased their solubility in aqueous media. This problem might be solved by replacing the linker by a more soluble one, for example, poly(ethylene glycol).

Conjugation of poly(ethylene glycol) with bioactive proteins or peptides (PEGylation) increases their solubility in physiological fluids as well as their plasma half-life and resistance to proteolytic cleavage (*23*). In addition, the conjugate's immunogenicity may also be decreased (*24, 25*). It has also been shown that the length of the PEG chains that are attached to the protein affects the protein's biological activities (*26*).

In this paper, we report the synthesis of dimeric peptides linked through their N-termini by poly(ethylene glycol) spacers of different length. On the basis of the three-dimensional structure of the HLA−DR superdimer, we designed new dimeric analogs able to mimic the dimeric nature of the immunosuppressive fragments of HLA class II molecules by which the VPRSGEVYT peptides were linked with a commercially available mixture of α,ω-bis(acetic acid) poly(ethylene glycol) (PEG−diacid) activated by esterification with pentafluorophenol. The dimeric peptides (peptides **1** and **2**), in which the sequences VPRSGEVYT were linked with polyether linkers of defined length, were also obtained. The synthesized dimers were analyzed by ESI-MS/MS spectrometry, and their immunomodulatory properties were also tested.

MATERIALS AND METHODS

Peptide Synthesis. *Materials.* The derivatives of amino acids for peptide synthesis and the coupling reagent (TBTU) were purchased from NovaBiochem. The side-chain-protecting groups for Fmoc−amino acids were *t*-butyl for Thr, Tyr, Glu, and Ser, and Pmc for Arg. The MBHA-Rink amide resin (0.55 mmol/g) was purchased from NovaBiochem. Poly(ethylene glycol) 600 diacid and poly(ethylene glycol) 250 diacid α,ω-bis(acetic acid) poly(ethylene glycol) were purchased from Aldrich. The poly(ethylene glycol) 250 diacid used for the synthesis of dimeric peptide **2** contains α,ω-bis(acetic acid) tri(ethylene glycol) as a main component. The homogeneous α,ω-bis(propionic acid) dodecae(ethylene glycol) used for the synthesis of dimeric peptide **1** was purchased from Iris Biotech GmbH (Germany). The solvents for peptide synthesis were obtained from Riedel de Haën (DMF) and J.T. Baker (methanol).

Preparation of Peptides. Peptides were prepared by manual solid-phase techniques using the standard Fmoc synthesis procedure. The first amino acid attached to the MBHA-Rink amide resin was Thr(Bu^t). Fmoc-protecting groups were removed in the presence of 25% piperidine in dimethylformamide (DMF). Single coupling by TBTU was performed in DMF followed by acetylation with acetic anhydride at the end of each cycle.

Preparation of Pentafluorophenol−PEG Diesters (PEG-Pfp_2). The poly(ethylene glycol) 600 diacid (90 mg, 0.15 mmol (according to the average molecular weight)) and pentafluorophenol (55 mg, 0.3 mmol) components were dissolved in 20 mL of ethyl acetate at 0 °C, and DCC (62 mg, 0.3 mmol) was added. The reaction mixture was stirred for 1.5 h at 0 °C. Dicyclohexylurea was filtered off, and the filtrate was evaporated in vacuo. The resulting PEG-Pfp_2 product was used for the following synthesis without further purification. Syntheses of the pentafluorophenol diesters of the individual PEG−diacids (α,ω-bis(propionic acid) dodecae(ethylene glycol) and α,ω-bis(acetic acid) tri(ethylene glycol)) were carried out with an identical procedure.

Dimerization. The peptide on the resin was linked by forming an amide bond between the N-terminal amino acid residues and PEG-Pfp_2 in DMF at room temperature in the presence of 1-hydroxybenzotriazol. The peptidyl resin (120 mg, 0.7 mmol) was mixed in DMF in the reaction vessel. The PEG diester (34 mg, 0.35 mmol) and HOBT (50 mg, 1.75 mmol) were added to the reaction mixture in five equal portions (one portion per day). The peptide was cleaved from the resin using Reagent K (TFA/thioanisole/water/phenol/TIS 33:2:2:2:1, v/v) at room temperature for 4 h and extracted with trifluoroacetic acid, followed by precipitation with cold diethyl ether.

Purification and Characterization of the Product. The crude product was characterized by HPLC on a 5-μm C-18 column (ODS 4.6 mm × 250 mm). Solvent systems were S1, 0.1% aqueous trifluoroacetic acid (TFA); S2, 80% acetonitrile + 0.1% TFA, linear gradient from 0−100% of S2 for 60 min, flow rate 1.0 mL/min, determined at 220 nm. The main heterogeneous reaction product was further purified and fractionated to three approximately equal fractions by preparative reversed-phase HPLC on a Vydac C-18 column (22 mm × 250 mm) using the solvent systems S1, 0.1% aqueous TFA; S2, 40% acetonitrile + 0.1% TFA, linear gradient from 50−100% of S2 for 60 min, flow rate 7.0 mL/min, determined at 220 nm. The fractions were collected, transformed into acetate forms, and lyophilized. The homogenic peptides **1** and **2** were purified by the same method. Their purity was over 98% measured by reversed-phase HPLC analyses. The obtained products possessed the correct amino acid composition (measured on a DIONEX-AAA Direct System). Their molecular weights were checked on a Finnigan MAT TSQ 700 mass spectrometer equipped with a Finnigan electrospray ionization source and Q-TOF instrument (Micromass, Manchester, U.K.). The identity of peptides **1** and **2** was confirmed using a micrOTOF-Q (Bruker, Germany) electrospray mass spectrometer on the basis of high-resolution mass measurement.

Structural Analysis. *MS/MS Spectra.* Mass spectrometric measurements were performed on a quadruple time-of-flight instrument (Q-TOF Micromass, Manchester, U.K.) equipped with an electrospray source. Spectra were recorded using aqueous solutions of acetonitrile (50%) and formic acid (1%) at a peptide concentration of typically 5 μM (according to the average molecular weight). The potential between the spray needle and the orifice was set to 2.5 kV, and the cone voltage was 35 V. In MS/MS mode, the quadrupole was used to select the precursor ions, which were fragmented in the hexapole collision cell, generating product ions that were subsequently mass analyzed by the orthogonal reflectron TOF mass analyzer. For CID MS/MS measurements, the voltage over the hexapole collision cell varied from 25 to 70 V, and argon was used as the collision gas at a pressure of 11 kPa. MS/MS data were processed by a maximum entropy data enhancement program,

Table 1. Effect of the Peptides on the Secondary Humoral Immune Response of Splenocytes from CBA Mice to SRBC

peptide	dose (μg/mL)	AFC/ 10^6 splenocytes	$\pm$SE[a]	*P* (Student's *t*-test)	suppression (%)
control[b]		2169	120		
fraction A	1	2085	201	NS	(4)
	10	566	102	<0.001	74
	100	1518	107	<0.05	30
fraction C	1	1908	164	NS	(12)
	10	1396	80	<0.01	36
	100	686	85	<0.001	68
control		1040	41		
peptide 1	1	910	37	<0.05	12
	10	625	61	<0.01	39
	100	550	33	<0.001	47
control		912	45		
peptide 2	1	682	76	<0.05	25
	10	337	72	<0.001	63
	100	283	13	<0.001	69
control		1382	11		
VPRSGEVYT[c]	1	1253	9	<0.001	9
	10	956	14	<0.001	31
	100	813	14	<0.001	41

[a] The results are presented as a mean from four determinations $\pm$ standard error. [b] Control - 0.9% NaCl solution. [c] Results for nonapeptide VPRSGEVYT were published previously (*8*).

MaxEnt 3 (Micromass, U.K.), to deconvolute spectra where peaks in a variety of charge states are present. The simplified spectra, consisting of mono-isotopic peaks in only a single charge state are presented.

Immunological Tests. *Animals.* Twelve-week-old female BALB/c mice were used for the experiments. The mice were kept at the Animal Facility of the Institute of Immunology and Experimental Therapy, Wroclaw, and fed commercial granulated food and water ad libitum.

Reagents. Sheep red blood cells (SRBCs) were provided by the Wroclaw Agriculture Academy. The SRBCs were kept in Alsever's solution until use.

Priming of Mice with Antigen. Mice were sensitized with 0.2 mL of a 1% SRBC suspension in 0.09% NaCl intraperitoneally (i.p.). Four days later, the spleens were used for generating the secondary immune response in vitro.

Determination of the Antibody-Forming Cell (AFC) Numbers in the Cell Culture. The spleens were isolated aseptically and pressed through a plastic screen into Hank's medium. The cells were then centrifuged and treated for 5 min at room temperature with 0.83% ammonium chloride to lyze erythrocytes. Subsequently, the cells were washed twice with Hank's medium and passed through cotton wool columns to remove cell debris. Finally, the splenocytes were resuspended in culture medium (RPMI 1640, supplemented with 10% fetal calf serum, glutamine, sodium pyruvate, 2-mercaptoethanol, and antibiotics) and distributed to 24-well culture plates (5×10^6/well). The cell cultures were immunized with 50 μL of 0.001% SRBC, and the peptides were added at the dose range of 1−100 μg/mL. To control cultures, 0.1 mL of the culture medium was added. After 4 days of incubation in a cell culture incubator, the AFC numbers were determined using the Mishell and Dutton assay (*27*). The results are presented as mean AFC numbers from 4 wells, calculated per 1 million viable splenocytes plus/minus standard error (SE). The Student's *t*-test was applied in evaluating the data. The results are presented as mean AFC numbers from quadriplicate wells (determinations) plus/minus SE. The results are regarded as significant when $p < 0.05$. To make comparison of the data easier, we included the percentage values of the inhibition of the immune responses. The values were calculated according to the equation

$$\%\ \text{of immunosuppression} = 100\left(1 - \frac{\text{experimental value}}{\text{control}}\right)$$

The values are shown in brackets in the case of statistically nonsignificant (NS) results. The results of the immunological tests are summarized in Table 1.

RESULTS

Peptide Synthesis. We synthesized a series of dimeric compounds consisting of two VPRSGEVYT sequences linked through their N-termini by flexible PEG spacers of different length. The dimerization was achieved directly on a solid support by cross-linking the N-terminal amino groups of the peptides attached to an MBHA resin with α,ω-bis(acetic acid) poly(ethylene glycol) activated by esterification with pentafluorophenol (PEG-Pfp_2) (Scheme 1). Previously, a similar reagent was successfully used for peptide cyclization via connecting lysine side chains by the PEG linker (*28*). The progress of the reaction was monitored by HPLC and ESI-MS. The synthesis parameters (resin loading, coupling reagent, temperature, incubation time, number of portions of PEG-Pfp_2 added to the reaction mixture) were optimized to obtain the best yield of the dimers. The optimized parameters are given in the experimental part. Our experiments showed that shortening the incubation time or adding a greater excess of PEG-Pfp_2 at once gave significant amounts of monomeric PEGylated peptide. The solubility of the obtained dimers in water was very good (more than 10 mg in 1 mL).

The presented data show that under the described experimental conditions the peptide dimer was formed with a relatively high yield. The HPLC profile and ESI-MS spectrum of the crude peptide dimer are shown in Figures 1 and 2, respectively. The ESI-MS spectrum of the synthetic dimeric peptide PEG−(VPRSGEVYT-NH_2)$_2$ revealed a very characteristic pattern, typical of heterogeneous polymeric material (*29*). There were two groups of peaks in the spectrum. The first group, at lower *m*/*z* values, corresponded to $[MH_3]^{+3}$ ions, while the second, at higher *m*/*z* values, corresponded to $[MH_2]^{+2}$ ions (confirmed by the pattern of isotopic peaks). $[MH]^{+1}$ ions were not observed, probably because each dimeric molecule contained two cationic arginine residues. Experimental *m*/*z* values are in excellent agreement with *m*/*z* calculated theoretically on the basis of the formulas of the synthesized compounds. The maximal abundance corresponds to the linker containing ten ethylene ether units.

The analysis of the HPLC profile (Figure 1) showed the same number of molecular species observed in the ESI-MS spectrum.

Scheme 1. Cross-linking of N-terminal Position of the Immunosuppressive Nonapeptide Fragment of HLA−DR Molecules, Attached to an MBHA Resin, with Poly(ethylene glycol)bis(carboxymethyl)ether Activated by Esterification with Pentafluorophenol

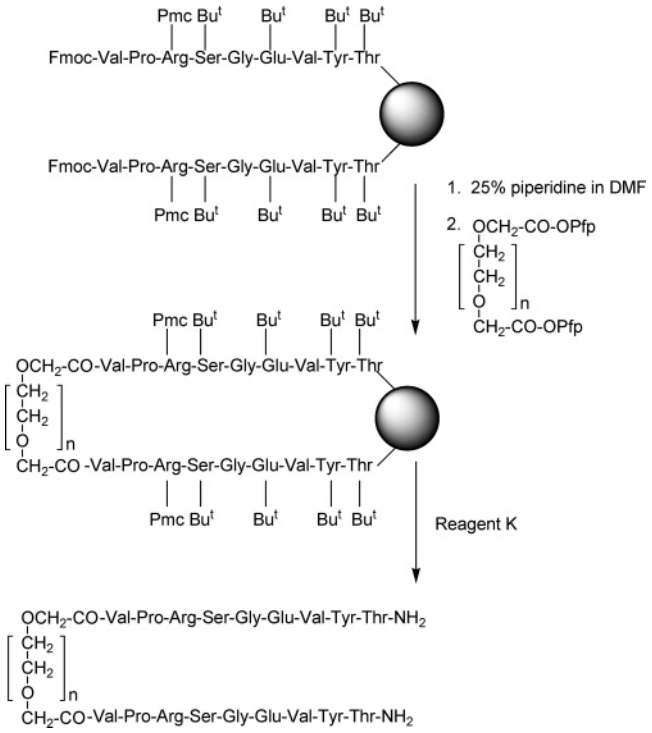

The distribution of the molecular masses of the PEG−diacids used in the synthesis (Figure 3) and in the obtained dimers (Figure 4A) was evaluated on the basis of ESI-MS spectra. The most populated PEG−diacid contained twelve ethylene ether units, which corresponded to $[MNa]^+$ 685.9 (the value corresponds well to the average value of molecular weight provided by manufacturer (655) and estimated acidimetrically by us (647)), while in the peptide dimer, the most populated linker contained ten ethylene ether units ($[MH_2]^{2+}$ 1276.4).

To answer the question whether this synthesis approach is of general value, we additionally performed the synthesis of other model peptide dimers. Dimerization of hexapeptide RGDVYT-NH_2, containing the RGD sequence, produced essentially the same results. Surprisingly, even the application of a significantly shorter, commercially available PEG−diacid with a molecular weight of 250 (purchased from Aldrich) as well as other non-poly(ethylene glycol) diacids (including glutaric, adipic, suberic, and sebacic acids) gave similarly satisfactory results (not shown in the experimental part).

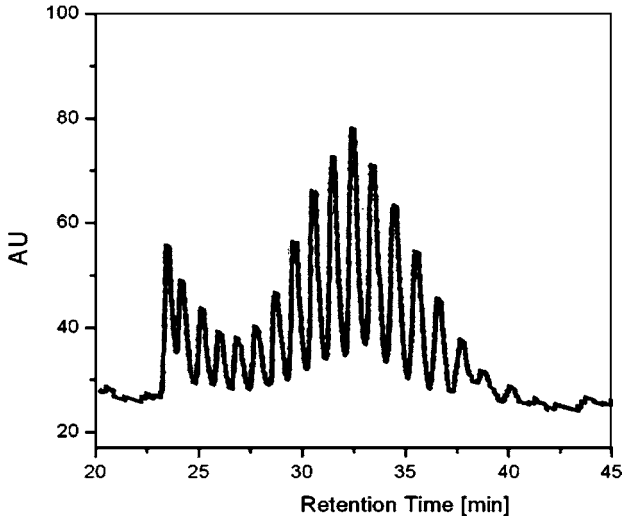

Figure 1. HPLC profile of the crude product of the solid-phase dimerization of VPRSGEVYT-NH_2 peptide.

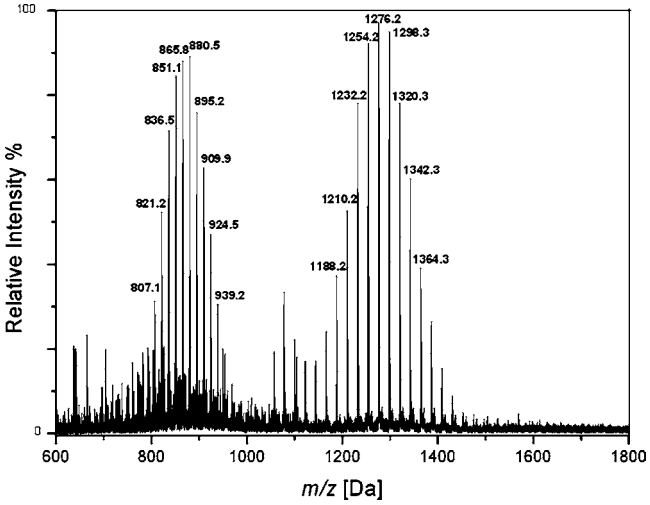

Figure 2. ESI-MS spectrum of the crude product of the solid-phase dimerization of VPRSGEVYT-NH_2.

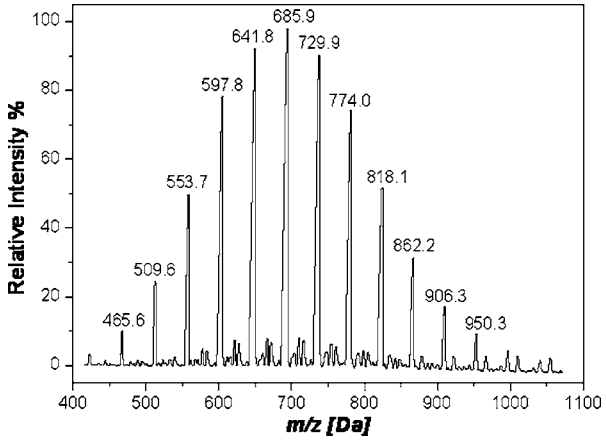

Figure 3. ESI-MS spectrum of PEG−diacid (average molecular mass approximately 600 Da) used in the syntheses of dimers. Spectrum obtained by cationization with a 10^{-4} M solution of NaCl in methanol. The most populated PEG−diacid contains 12 ethylene ether units, which corresponds to $[MNa]^+$ 685.9.

A partial separation of the dimers according to linker length by analytical HPLC encouraged us to attempt fractionation of the dimeric peptides on the preparative scale. We did not obtain homogeneous samples of defined linker length; however, fractions separated in preparative HPLC showed a relatively narrow distribution of molecular masses (Figure 4). Fraction A, which contained a set of dimeric peptides with the linker consisting of 35 or fewer atoms in their backbone chain, and fraction C, mostly populated by molecules with longer linkers (41−50 atoms), were tested for their immunological properties. Fraction C contained only a small amount (less than 20%) of shorter linker molecules. The structures of the fractionated peptides were further confirmed by amino acid analysis and mass spectrometry.

Although we were able to separate and purify small amounts of the individual PEG dimer peptides on reverse-phase HPLC, this separation is impractical because only very small amounts of purified material were obtained, too little to perform the biological test. On the other hand, the inhomogeneity of the synthesized peptide library with PEG linkers might be beneficial.

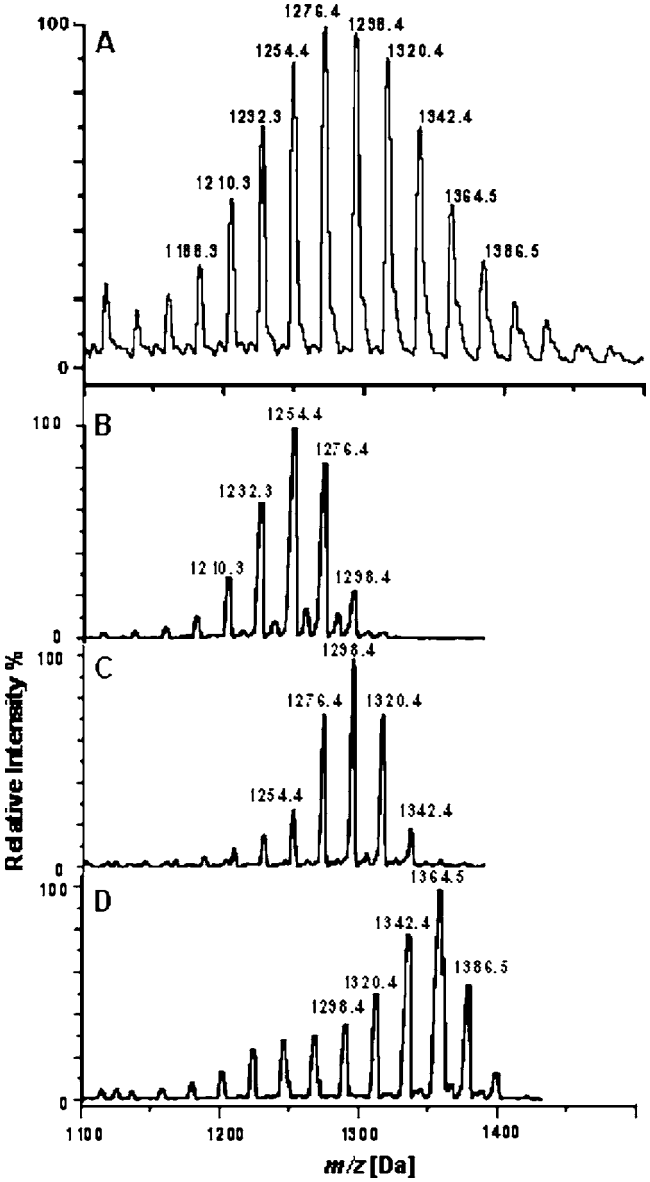

Figure 4. ESI-MS spectra (measured on Finnigan TSQ 700) of PEG−$(VPRSGEVYT\text{-}NH_2)_2$ conjugate. Presented are the double-charged set of peaks only. (A) Crude product of reaction dimerization. (B) Fraction A with the highest *m/z* peak of 1254.4, corresponding to a linker length of 32 atoms. (C) Fraction B mostly populated by molecules with a 38-atom linker (*m/z* 1298.4). (D) Fraction C, containing dimeric peptides mostly populated by molecules with linkers containing 41−50 atoms (*m/z* 1320.4−1386.5).

Such a peptide library is more likely to span two receptor molecules when the distance and orientation between them are not certain.

We also attempted to obtain peptide dimers linked by a polyether bridge of defined length. We synthesized two new compounds (peptides **1** and **2**) starting from commercially available α,ω-bis(propionic acid) dodecae(ethylene glycol) and PEG−diacid 250 (composed mainly of α,ω-bis(acetic acid) tri-(ethylene glycol)), respectively. The synthesis protocols were essentially identical to the dimerization procedure described above (Scheme 1). The reaction products were easily purified by the HPLC method, and their identities were confirmed by high-resolution mass spectrometry. The high yields of the synthesis of these dimers suggest that the method we proposed is appropriate for the synthesis of both individual PEG−peptides and their libraries with various linker lengths.

ESI-MS/MS Studies of Peptide Dimers Linked by PEG−Diacid. The MS/MS experiments were performed on $[MH_2]^{+2}$ ions of the dimeric peptides PEG−$(VPRSGEVYT\text{-}NH_2)_2$ and PEG−$(RGDVYT\text{-}NH_2)_2$. The representative MS/MS spectrum of the parent ion 1276 ($[MH_2]^{2+}$) for PEG−$(VPRSGEVYT\text{-}NH_2)_2$ is given in Figure 5. The analysis of the spectrum showed mainly a, b, and y ion types, according to the Roepstorf and Fohlmann nomenclature (*30*). Series b ions, ranging from b_1 to b_7, were accompanied by corresponding ions of type a. Ions belonging to the y series (y_2, y_3, y_4, y_7, y_8, and y_9) did not contain a PEG linker and therefore were located at lower *m/z*. The fragments of PEG linker were not found in the fragmentation spectrum. Similarly, fragmentation of PEG−$(RGDVYT\text{-}NH_2)_2$ (2+ ion) revealed a series of b ions, ranging from b_1 to b_5 (Figure 6). Ions of the b type were accompanied by ions of type a. The abundance of type y ions was low, with only the fragment y_2 being well-pronounced. In contrast to the dimeric peptide PEG−$(VPRSGEVYT\text{-}NH_2)_2$, internal fragments were relatively abundant, and the series (b_3b_3) and (b_3b_4) were observed. This particular type of internal fragment ions was observed only in dimeric peptides connected by the N-termini or side chains. Fragmentation of the PEG linker was not observed in PEG−$(RGDVYT\text{-}NH_2)_2$ either. Comparison of the fragmentations of molecules differing by the length of the linker did not reveal any essential differences.

Biological Properties. The effects of the peptides on humoral, secondary immune response to SRBC were tested in vitro. The results (Table 1) show that the peptides added to the cultures of SRBC-primed splenocytes suppressed the number of AFCs in the cell cultures in different ways. Fraction A exhibited a strong inhibitory effect at the concentration of 10 μg/mL; however, its inhibitory action at the 100 μg/mL dose was much smaller. On the other hand, Fraction C clearly exhibited a dose-dependent inhibition of the immune response. Similar dose-dependent immunosuppressive effects were observed for the homogenic dimeric peptides **1** and **2**.

DISCUSSION

Receptor dimerization is an essential part of cellular signal transduction. Molecules that induce or stabilize the association of receptor macromolecules hold tremendous promise as biological effectors. Ligands having two pharmacophores connected by a spacer (bivalent ligands) have a potential for bridging vicinal receptors. Such a bridging should be manifested by a modulation of biological responses (*31*). Indeed, homodimeric analogs of biologically active peptides with a specific spacer length have been reported to possess enhanced agonistic or antagonistic potencies compared with their monomeric counterparts (*32*−*38*). The increase in potency of these analogs may also be due to the high local concentration of the free pharmacophore in the vicinity of the proximal recognition site when the dimeric peptide ligand is bound in a monovalent mode.

The relatively easy synthesis of new dimeric analogs of biologically active peptides has attracted a great deal of attention. The rotationally symmetric homodimeric peptide analogs can be synthesized by covalent linkage through either side chains (for example, by disulfide bridge) or the N- or C-termini of the two-monomer backbone. So far, direct synthesis of dimeric peptides in the solid phase utilized simultaneous synthesis of two identical peptide chains on lysine (or other diamino acid) attached to the resin (*22*). This method allowed the formation of antiparallel dimeric peptides where monomer residues were covalently linked through their C-termini, whereas dimeric constructs linked through their N-termini were synthesized utilizing tedious methods "in solution" only.

The idea of dimerization of the molecules directly on a solid support has been described as a tool for the synthesis of natural

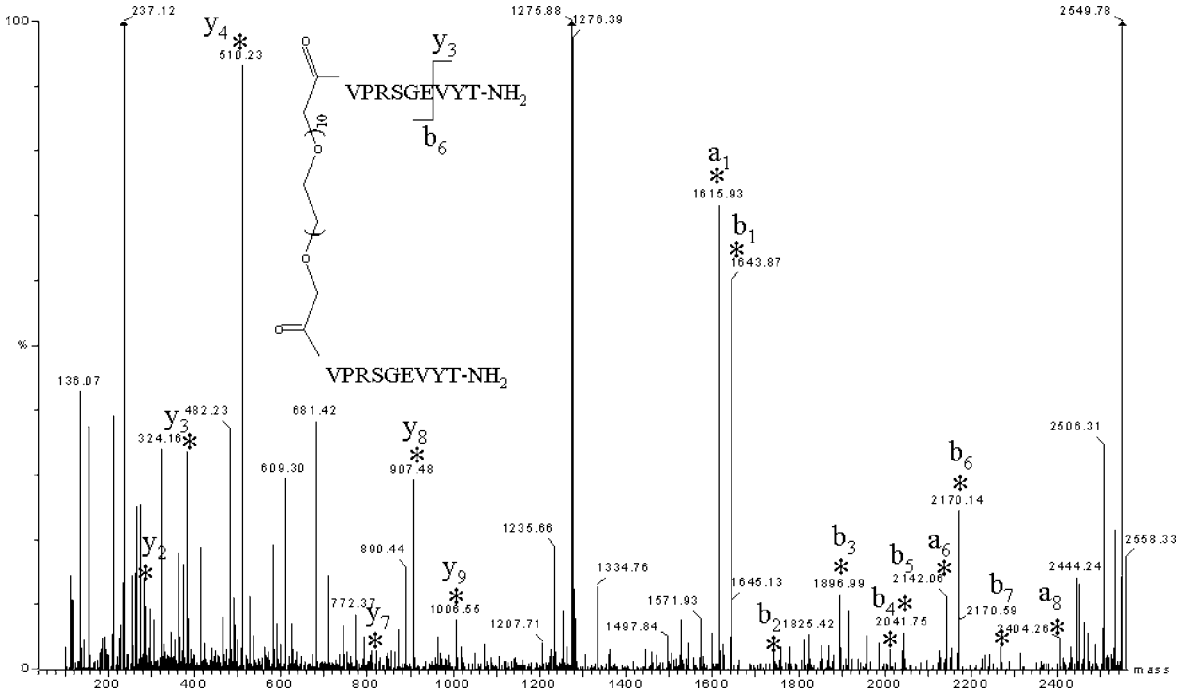

Figure 5. Fragmentation spectrum of $[MH_2]^{2+}$ ion of dimeric peptide PEG−(VPRSGEVYT-NH_2)$_2$. The parent ion is at *m*/*z* 1276. Spectrum was deconvoluted using the Maxent program.

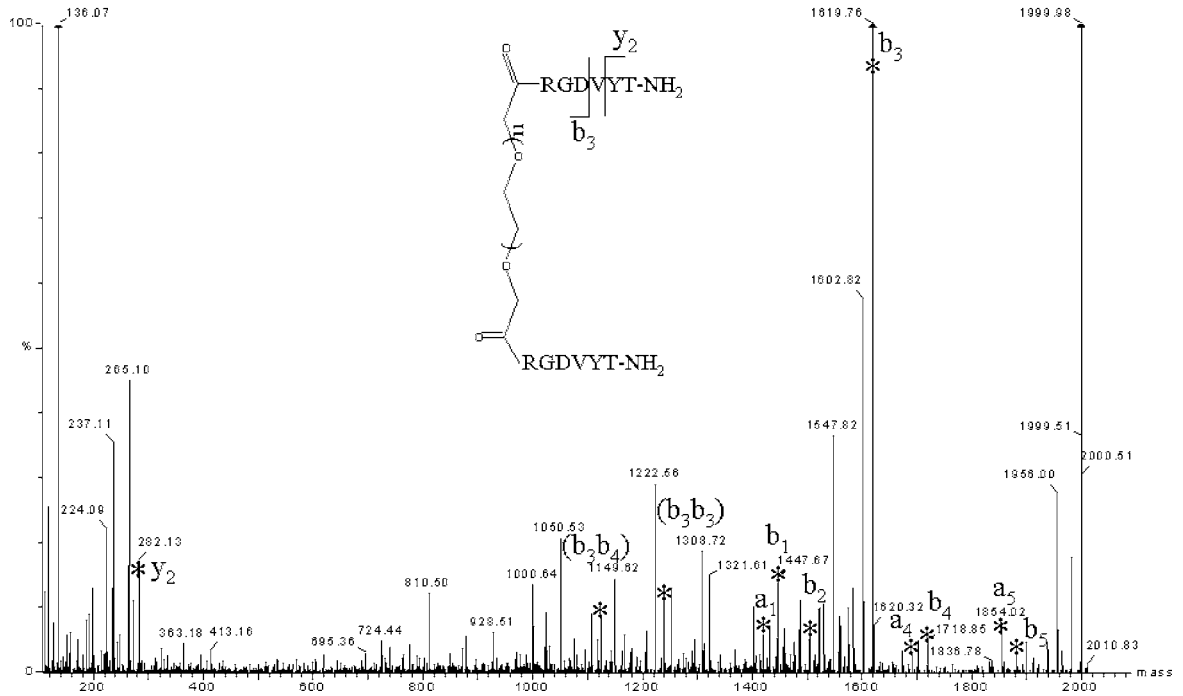

Figure 6. Fragmentation spectrum of $[MH_2]^{2+}$ ion of dimeric peptide PEG−(RGDVYT-NH_2)$_2$. The parent ion is at *m*/*z* 1001. Spectrum was deconvoluted using the Maxent program.

product-like molecules (*39, 40*). Peptide dimerizations on solid support were observed previously as a side reaction during peptide cyclization on a resin (*41, 42*) and by linkage through lysine side chains (*43*). To the best of our knowledge, this paper describes the first cross-linking reaction between two N-terminal amino groups of peptide chains attached to a resin to produce the desired products. Our results suggest that this method is general and may be applied to various peptide sequences. The basic restriction of this method is that only symmetrical dimers containing two identical sequences can be obtained. The dimers can be synthesized rapidly in a relatively small number of synthesis steps, because the strategy of synthesis is convergent.

The bivalent analog of the immunosuppressive fragment of the HLA−DR molecule (VPRSGEVYT) should consist of two monomers covalently linked by a spacer with sufficient length to be able to position them in the same manner as in the HLA−DR superdimers. We began the design by examining the three-dimensional structure of the superdimers (*13*) (Figure 7A). The distance between the N-terminal groups of Val$^{\beta 164}$ is significantly shorter (37 Å) than that of the carbonyl groups of C-terminal Thr$^{\beta 172}$ (47 Å) in the nonapeptide immunosuppressive fragment, suggesting that the amino-terminal dimerization may be more efficient than that obtained by C-terminal linkage. The molecular modeling study (results not shown) suggested

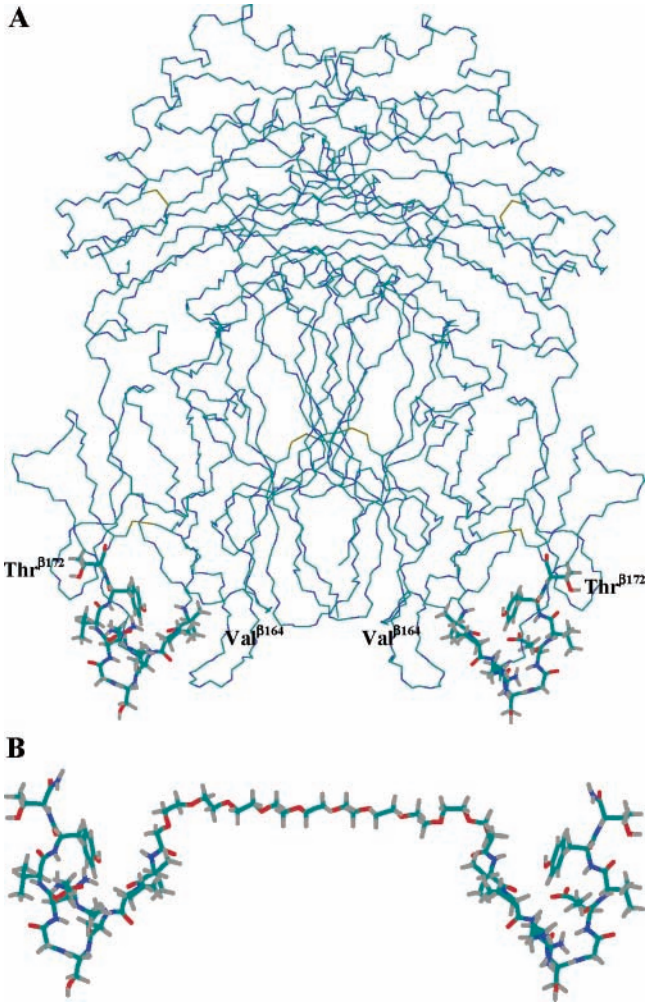

Figure 7. (A) View of the superdimer of human class II histocompatibility antigen HLA−DR1. The β164−172 loops with the immunosuppressive sequences (VPRSGEVYT) are boldface. (B) The β164−172 loops connected with a 35-atom linker to span the distance between the carbonyl groups of Val$^{\beta164}$. The linker structure is stretched and may produce distortions on the peptide fragments if oriented as in the superdimer structure. Therefore, the linker should be longer than the 35-atom one.

that a linker consisting of 35 atoms in the main chain may be too short to span the N-terminal groups of Val$^{\beta164}$ without distortions (Figure 7B).

It was previously shown that the linker length may dramatically affect the biological potencies of bivalent bioligands (*44*). We synthesized a library of dimeric analogs containing linkers of various lengths using a commercially available mixture of PEG−diacids. The distribution of the molecular masses in the mixture can be calculated from the spectrum in Figure 4. A comparison of the spectra presented in Figures 4A and 3 suggests that the dimerization yield does not depend dramatically on the length of the linker.

Although we were unable to separate a practical amount of each dimer molecule with a particular linker length, we succeeded in fractionating the library according to the molecules' ability to span the gap between the N-terminal groups of Val$^{\beta164}$ residues in the crystal structure (Figure 7A). Fraction A comprises mostly molecules with a linker not longer than the 35-atom one. The linkers may be too short to locate the suppressors in the same position as in the crystal structure. In contrast to this, fraction C contains dimeric peptides mostly populated by molecules with linkers of sufficient length. The structures of the fractionated peptides were further confirmed by amino acid analysis and mass spectrometry.

The heterogeneous peptides obtained by our method are difficult to characterize by the routine methods used to confirm the structures of organic compounds. Therefore, tandem mass spectrometry must be the method of choice. Direct ESI measurement provides information concerning the distribution of the linker length. This information may also be applied to verify the purity of the obtained set of compounds. MS/MS experiments were performed to confirm the primary structures of the obtained dimeric analogs. Mass spectrometry fragmentation of conjugates composed of dimeric peptide sequences N-terminally linked with PEG−dicarboxylic acid has not been reported in the literature. However, MS/MS analysis of peptides containing a PEG amino acid was described by Catalina et al. (*45*). The authors established that fragmentation of these conjugates produced not only ions of the b, y, and d types and the internal ions (y_nb_m) (y_nb_m) but also fragmentation of the PEG amino acid. The dimeric compounds described in this paper produced a set of ions generated in collision-induced dissociation belonging to the b and a series. Some ions of the y series and internal ions (b_nb_m) were also observed. However, we did not observe any fragmentation of the PEG linker, which suggests that the PEG−diacid linker does not decompose as easily as the amino acid PEG one or that its fragmentation pathway is different. As can be expected, introducing the PEG bridge shifted the series of b and a peaks toward a higher *m/z*, which facilitated the MS/MS analysis. The information provided by the fragmentation spectra is sufficient to confirm the sequences unambiguously.

With the potential therapeutic value of the studied peptides taken into consideration, it seems that application of the dimeric peptides may be beneficial in preventing rejection of allotransplants, since it significantly suppressed, at a low dose, the magnitude of the secondary immune response, which is dependent on the presence of memory T cells. Other studies showed that memory T cells are resistant to apoptosis during chemotherapy (*46*), so our finding that the peptide**s** are effective in the suppression of immunological memory suggests that this new approach to preventing allogeneic organ rejection by the immune system is plausible to implement.

The enhancement of the immunosuppressive activity of our dimeric analogs could be explained by a microaggregation of the receptors at the cell surface induced by the dimeric antagonists, which would prevent access of the agonist to the receptors. Nevertheless, the increased affinity of dimeric analogs of the ligands may also be independent of receptor density (*47*). Their potencies may be attributed to a higher concentration of pharmacophores in the proximity of their recognition sites by a simple statistical advantage. Bivalent ligands are known to produce thermodynamically more favorable binding interactions with their receptors than monovalent ones (*48*). Our results are in agreement with those reported previously by Cochran et al. (*49*). The authors studied the influence of intermolecular orientation within the activating T-cell receptor dimer on T-cell activation. Dimers of class II MHC proteins coupled in a variety of orientations and topologies were able to activate $CD4^+$ T cells, although the triggering was affected by the intermolecular distance between the MHC molecules. Interestingly (Table 1), the A mixture was less suppressive at higher (100 μg/mL) concentration. However, lack of a direct dose-dependent effect of a given immunosuppressive compound is not a rare phenomenon in immunological processes. We observed a similar phenomenon in our previous investigation with one of the dimeric, immunosuppressive peptides (peptide **4**), which was less suppressive of both the humoral and cellular immune response (*22*). A much smaller suppressive activity at very high doses, in contrast to cyclosporine A, was also observed for cyclolinopeptide A, a natural nonapeptide from linseed oil (*50*).

Methotrexate (MTX) could serve as another example of a lack of correlation between dose and cytotoxic effect. In the model of mitogen-activated human peripheral blood mononuclear cells (*51*), MTX caused a progressive decrease in viable cell counts in the concentration range 0.1−10 μM, whereas at low (0.01 μM) and high (100 μM) concentrations, MTX inhibited cell proliferation but induced only a moderate loss of viable cells. The reason for these observations remains largely unexplained, although even such a basic immunological phenomenon as specific antigen tolerance occurs at very low or high, but not at moderate, doses of antigen (*52*).

In summary, we presented a new and straightforward procedure for the direct amino-terminal dimerization of peptides on a solid support by a poly(ethylene glycol) spacer which is compatible with solid-phase peptide synthesis protocols. The amino-terminal dimerization of the nonapeptide fragment of HLA−DR results in enhanced immunosuppressive properties. The dimerization may also serve as a new derivatization method to facilitate MS/MS peptide analysis by shifting the series of b and a peaks toward higher *m/z*.

ACKNOWLEDGMENT

This work was supported by the Ministry of Scientific Research and Information Technology grant no. 3 T09A 082 27. We thank Professor Michał Dadlez for the use of his Micromass Q-TOF mass spectrometer and Dr. Andreas Jakob from Bruker Daltonik GmbH for the high-resolution mass analysis. We also thank Ms. Marzena Cydzik for technical assistance. This work is part of a doctoral thesis (M.B.).

LITERATURE CITED

(1) Pieters, J. (2000) MHC class II-restricted antigen processing and presentation. *Adv. Immunol. 75*, 159−208.

(2) Hiltbold, E. M., and Roche, P. A. (2002) Trafficking of MHC class II molecules in the late secretory pathway. *Curr. Opin. Immunol. 14*, 30−35.

(3) Szewczuk, Z., Siemion, I. Z., and Wieczorek, Z. (1996) Immunological properties of the thymopentin-like fragments of HLA-DQ. *Mol. Immunol. 33*, 903−908.

(4) Szewczuk, Z., Wieczorek, Z., Stefanowicz, P., Wilczyñski, A., and Siemion, I. Z. (1997) Further investigations on thymopentin-like fragments of HLA-DQ and their analogues. *Arch. Immunol. Exp. Ther. 45*, 335−341.

(5) Szewczuk, Z., Stefanowicz, P., Wilczyñski, A., Siemion, I. Z., Cierniewski, C. S., Kralisz, U., and Wieczorek, Z. (1996) The immunosuppressory and adhesive mini-region of the human major histocompatibility protein, HLA-DQ. *Biopolymers 40*, 571−583.

(6) Brogdon, J., Eckels, D. D., Davies, C., White, S., and Doyle, C. (1998) A site for CD4 binding in the beta 1 domain of the MHC class II protein HLA-DR1. *J. Immunol. 161*, 5472−5480.

(7) Stefanowicz, P., Boratyñski, P. J., Staszewska, A., Wilczyñski, A., Zimecki, M., and Szewczuk, Z. (2004) Threonine at position 6 is not essential for the immunosuppressive activity of HLA-DQ(b164-172)-hexapeptide. *Mol. Immunol. 41*, 911−917.

(8) Szewczuk, Z., Wilczyñski, A., Stefanowicz, P., Fedorowicz, W., Siemion, I. Z., and Wieczorek, Z. (1999) Immunosuppressory mini-regions of HLA-DP and HLA-DR. *Mol. Immunol. 36*, 525−533.

(9) Szewczuk, Z., Buczek, P., Stefanowicz, P., Krajewski, K., Siemion, I. Z., and Wieczorek, Z. (2001) Immunosuppressory activity of the cyclodimeric peptide with RGD-sequences. *Acta Biochim. Pol. 48*, 121−130.

(10) Szewczuk, Z., Wilczyñski, A., Dyba, M., Petry, I., Siemion, I. Z., and Wieczorek, Z. (2000) New conformationally restricted analog of the immunosuppressory mini-domain of HLA-DQ and its biological properties. *Peptides 21*, 1849−1858.

(11) Szewczuk, Z., Wilczyñski, A., Petry, I., Siemion, I. Z., and Wieczorek, Z. (2001) Design, synthesis and biological evaluation of a new bridged immunosuppressor. *Acta Biochim. Pol. 48*, 1147−1150.

(12) Szewczuk, Z., Stefanowicz, P., Wilczyñski, A., Staszewska, A., Siemion, I. Z., Zimecki, M., and Wieczorek, Z. (2004) Immunosuppressory activity of ubiquitin fragments containing retro-RGD sequence. *Biopolymers 74*, 352−362.

(13) Brown, J. H., Jardetzky, T. S., Gorga, J. C., Stern, L. J., Urban, R. G., Strominger, J. L., and Wiley, D. C. (1993) Three-dimensional structure of the human class II histocompatibility antigen HLA-DR1. *Nature (London) 364*, 33−39.

(14) Schafer, P. H., and Pierce, S. K. (1994) Evidence for dimers of MHC Class II molecules in B lymphocytes and their role in low affinity T cell responses. *Immunity 1*, 699−707.

(15) Schafer, P. H., Malapati, S., Hanfelt, K. K., and Pierce, S. K. (1998) The assembly and stability of MHC class II-(alpha beta)$_2$ superdimers. *J. Immunol. 7*, 389−398.

(16) Bakker, A. H., and Schumacher, T. N. (2005) MHC multimer technology: current status and future prospects. *Curr. Opin. Immunol. 17*, 428−233.

(17) Cochran, J. R., Cameron, T. O., and Stern, L. J. (2000) The relationship of MHC-peptide binding and T cell activation probed using chemically defined MHC class II oligomers. *Immunity 12*, 241−250.

(18) Moldovan, M. C., Yachou, A., Levesque, K., Wu, H., Hendrickson, W. A., Cohen, E. A., and Sekaly, R. P. (2002) CD4 dimers constitute the functional component required for T cell activation. *J. Immunol. 169*, 6261−6268.

(19) Clemons, P. A. (1999) Design and discovery of protein dimerizers. *Curr. Opin. Chem. Biol. 3*, 112−115.

(20) Cochran, J. R., Aivazian, D. A., Cameron, T. O., and Stern, L. J. (2001) Receptor clustering and transmembrane signaling in T cells. *Trends Biochem. Sci. 26*, 304−310.

(21) Hayball, J. D., Fidler, S. J., Palliser, D., Rees, A. D., Lamb. J. R., and Lake, R. A. (1997) Tandem peptide epitopes facilitate CD4-dependent activation of T cell clones. *Immunol. Cell Biol. 75*, 148−153.

(22) Szewczuk, Z., Biernat, M., Dyba, M., and Zimecki, M. (2004) Dimerization of the immunosuppressive peptide fragment of HLA-DR molecule enhances its potency. *Peptides 25*, 207−215.

(23) Lee, S. H., Lee, S., Youn, Y. S., Na, D. H., Chae, S. Y., Byun, Y., and Lee, K. C. (2002) Synthesis, characterization, and pharmacokinetic studies of PEGylated glucagon-like peptide-1. *Bioconjugate Chem. 13*, 1238−1243.

(24) Veronese, F. M. (2001) Peptide and protein PEGylation: A review of problems and solutions. *Biomaterials 22*, 405−417.

(25) Roberts, M. J., Bentley, M. D., and Harris, J. M. (2002) Chemistry for peptide and protein PEGylation. *Adv. Drug Delivery Rev. 54*, 459−476.

(26) Francis, G. E., Fisher, D., Delgado, C., Malik, F., Gardiner, A., and Neale, D. (1998) PEGylation of cytokines and other therapeutic proteins and peptides: the importance of biological optimisation of coupling techniques. *Int. J. Hematol. 68*, 1−18.

(27) Mishell, R. I., and Dutton, R. W. (1967) Immunization of dissociated spleen cell cultures from normal mice. *J. Exp. Med. 126*, 423−428.

(28) Bouvier, M., and Wiley, D. C. (1996) Antigenic peptides containing large PEG loops designed to extend out of the HLA-A2 binding site form stable complexes with class I major histocompatibility complex molecules. *Proc. Natl. Acad. Sci. U.S.A. 93*, 4583−4588.

(29) Jedliñski, Z., Adamus, G., Kowalczuk, M., Schubert, R., Szewczuk, Z., and Stefanowicz, P. (1998) Electrospray tandem mass spectrometry of poly(3-hydroxybutanoic acid) end groups analysis and fragmentation mechanism. *Rapid Commun. Mass Spectrom. 12*, 357-360.

(30) Roepstorf, P., and Fohlmann, J. (1984) Proposal for a common nomenclature for sequence ions in mass spectra of peptides. *J. Biomed. Mass Spectrom. 11*, 601.

(31) Clemons, P. A. (1999) Design and discovery of protein dimerizers. *Curr. Opin. Chem. Biol. 3*, 112−115.

(32) Romanowski, M., Zhu, X., Ramaswami, V., Misicka, A., Lipkowski, A. W., Hruby, V. J., and O'Brien, D. F. (1997) Interaction of a highly potent dimeric enkephalin analog, biphalin, with model membranes. *Biochim. Biophys. Acta 1329*, 245−258.

(33) Lin, C., Sarath, G., Frank, J. A., and Krueger, R. J. (1991) Bivalent ACTH antagonists: influence of peptide and r components on potency enhancement. *Biochem. Pharmacol. 41*, 789−795.

(34) Kitajima, Y., Catt, K. J., and Chen, H. C. (1989) Enhanced biological activity of dimeric gonadotropin releasing hormone. *Biochem. Biophys. Res. Commun. 159*, 893−898.

(35) Higuchi, Y., Takano, Y., Shimazaki, H., Shimohigashi, Y., Kodama, H., Matsumoto, H., Sakaguchi, K., Nonaka, S., Saito, R., and Waki, M. (1989) Dimeric substance P analogue shows a highly potent activity of the in vivo salivary secretion in the rat. *Eur. J. Pharmacol. 160*, 413−416.

(36) Lazarus, L. H., Guglietta, A., Wilson, W. E., Irons, B. J., and de Castiglione, R. (1989) Dimeric dermorphin analogues as mu-receptor probes on rat brain membranes. Correlation between central mu-receptor potency and suppression of gastric acid secretion. *J. Biol. Chem. 264*, 354−362.

(37) Kodama, H., Shimohigashi, Y., Sakaguchi, K., Waki, M., Takano, Y., Yamada, A., Hatae, Y., and Kamiya, H. (1988) Dimerization of neurokinin A and B COOH-terminal heptapeptide fragments enhanced the selectivity for tachykinin receptor subtypes. *Eur. J. Pharmacol. 151*, 317−320.

(38) Wagner, J., Handl, H. L., Gillies, R. J., and Hruby, V. J. (2004) Novel targeting strategy based on multimeric ligands for drug delivery and molecular imaging: homooligomers of alpha-MSH. *Bioorg. Med. Chem. Lett. 14*, 211−215.

(39) Liao, Y., Fathi, R., and Yang, Z. (2003) Convergent solid-phase synthesis of symmetrical benzo[b]furan's dimerizers. *J. Comb. Chem. 5*, 79−81.

(40) Blackwell, H. E., Clemons, P. A., and Schreiber, S. L. (2001) Exploiting site-site interactions on solid support to generate dimeric molecules. *Org. Lett. 3*, 1185−1188.

(41) Schiller, P. W., Nguyen, T. M. D., Lemieux, C., and Maziak, L. (1985) Synthesis and activity profiles of novel cyclic opioid peptide monomers and dimers. *J. Med. Chem. 28*, 1766−1771.

(42) Szewczuk, Z., Gibbs, B. F., Yue, S-Y., Purisima, E. O., and Konishi, Y. (1992) Conformationally restricted thrombin inhibitors resistant to proteolytic digestion. *Biochemistry 31*, 9132−9140.

(43) Ashraf, M. A., Notta, J. K., and Snaith, J. S. (2003) Solid phase synthesis of peptide dimers and trimers linked through an N-terminal lysine residue. *Tetrahedron Lett. 44*, 9115−9119.

(44) Szewczuk, Z., Gibbs, B. F., Yue, S. Y., Purisima, E., Zdanov, A., Cygler, M., and Konishi, Y. (1993) Design of a linker for trivalent thrombin inhibitors: Interaction of the main chain of the linker with thrombin. *Biochemistry 32*, 3396−3404.

(45) Catalina, M. I., Dekker, F. J., Liskamp, R. M. J., Versluis, C., Maier, C. S., and Heck, A. J. R. (2003) Structural analysis of high affinity divalent phosphopeptide hybrids of spleen tyrosine kinase. *Int. J. Mass Spectrom. 228*, 879−890.

(46) Zielinsky, C. C., Stuller, I., Dorner, F., Potzi, P., Muller, C., and Eibl, M. M. (1986) Impaired primary, but not secondary, immune response in breast cancer patients under adjuvant chemotherapy. *Cancer 58*, 1648−1652.

(47) Lutz, R. A., Costa, T., Cruciani, R. A., Jacobson, A. E., Rice, K. C., Burke, T. R., Jr., Krumins, S. A., and Rodbard, D. (1985) Increased affinity of dimeric enkephalins is not dependent on receptor density. *Neuropeptides 6*, 167−174.

(48) Hopfner, K. P., Ayala, Y., Szewczuk, Z., Konishi, Y., and DiCera, E. (1993) Chemical compensation in macromolecular bridge-binding to thrombin. *Biochemistry 32*, 2947−2953.

(49) Cochran, J. R., Cameron, T. O., Stone, J. D., Lubetsky, J. B., and Stern, L. J. (2001) Receptor proximity, not intermolecular orientation, is critical for triggering T-cell activation. *J. Biol. Chem. 276*, 28068−28074.

(50) Wieczorek, Z., Bengtsson, B., Trojnar, J., and Siemion, I. Z. (1991) Immunosuppressive activity of cyclolinopeptide A. *Peptide Res. 4*, 275−283.

(51) Genestier, L., Paillot, R., Fournel, S., Ferraro, C., Miossec, P., and Revillard, J. P. (1998) Immunosuppressive properties of methotrexate: apoptosis and clonal deletion of activated peripheral T cells. *J. Clin. Invest. 102*, 322−328.

(52) Koh, D. R. (1998) Oral tolerance: mechanisms and therapy of autoimmune diseases. *Ann. Acad. Med. Singapore 27*, 47−53.

BC050360H

Immobilization and Clustering of Structurally Defined Oligosaccharides for Sugar Chips: An Improved Method for Surface Plasmon Resonance Analysis of Protein−Carbohydrate Interactions

Yasuo Suda,*[,†,‡] Akio Arano,[‡] Yasuhiro Fukui,[§] Shuhei Koshida,[§] Masahiro Wakao,[†] Tomoaki Nishimura,[†,‡] Shoichi Kusumoto,[§,▽] and Michael Sobel[⊥]

Department of Nanostructure and Advanced Materials, Graduate School of Science and Engineering and Venture Business Laboratory, Kagoshima University, Kohrimoto, Kagoshima 890-0065, Japan, Japan Science and Technology Agency (JST), 5-3-4 Bancho, Chiyoda-ku, Tokyo 102-8666, Japan, Department of Chemistry, Graduate School of Science, Osaka University, Toyonaka, Osaka 560-0043, Japan, and Department of Surgery, University of Washington and VA Puget Sound Health Care System, Seattle, Washington 98108. Received March 11, 2006; Revised Manuscript Received July 7, 2006

Oligosaccharides are increasingly being recognized as important partners in receptor−ligand binding and cellular signaling. Surface plasmon resonance (SPR) is a very powerful tool for the real-time study of the specific interactions between biological molecules. We report here an advanced method for the immobilization of oligosaccharides in clustered structures for SPR and their application to the analysis of heparin−protein interactions. Reductive amination reactions and linker molecules were designed and optimized. Using mono-, tri-, or tetravalent linker compounds, we incorporated synthetic structurally defined disaccharide units of heparin and immobilized them as ligands for SPR. Their binding to an important hemostatic protein, von Willebrand factor (vWf), and its known heparin-binding domain was quantitatively analyzed. These multivalent ligand conjugates exhibited reproducible binding behavior, with consistency of the surface conditions of the SPR chip. This novel technique for oligosaccharide immobilization in SPR studies is accurate, specific, and easily applicable to both synthetic and naturally derived oligosaccharides.

INTRODUCTION

Oligosaccharides of two to ten sugar moieties are responsible for many important biological functions (*1*). Both the specific structural attributes of the minimum oligosaccharide unit and the spacing and distribution of these key binding units determine the ultimate biological function of heparins and heparin-like glycosaminoglycans (*2*). Often, the minimal oligosaccharide unit with a structurally specific interaction may be as small as a di- or trisaccharide (*3*, *4*). However, for full biological activity, these key binding units must often be presented in repeating units or clusters, appropriately spaced to interact with the heparin-binding sites of the cognate protein. Two major problems arise in the study of these structure−function relations. First, it is not easy to obtain large quantities of a homogeneous, structurally defined oligosaccharide. They cannot be expressed recombinantly, like proteins, and therefore, long and tedious chemical processes are necessary to synthesize or derive them from natural sources. The second problem is that an individual oligosaccharide motif may have low affinity but in biological systems they are often presented in clustered or repeating forms, which contribute significantly to their potency and affinity. We hypothesized that a chip or an array technology, in which structurally defined key oligosaccharide binding units are two-dimensionally immobilized on a surface, would be an effective method to solve these problems and could be used as a high-throughput screening method.

A number of investigators have tackled the challenges of oligosaccharide immobilization. Techniques for self-assembled monolayers have been described by Horan et al. (*5*), Mrksich and co-workers (*6*, *7*), and others. However, no method has so far been devised that both is procedurally simple and does not significantly modify or potentially interfere with the biological activity of the oligosaccharide. Most of these techniques require significant chemical modifications of the glycans, potentially obscuring the interpretation of structure−function relations. For example, conventional methods have involved chemical modifications at the 1-position of the carbohydrate, such as amination or allylation (*8*, *9*). But these approaches invariably put functional sulfate or phosphate groups at risk. Finally, currently established methods do not afford the opportunity to control the clustering or multimerization of oligosaccharide functional domains. To this end, we pursued novel immobilization strategies for oligosaccharides, which would be technically simpler and less destructive, making them useful to a wider group of investigators. For detection, we chose surface plasmon resonance (SPR) technology, which permits the real-time analysis of molecular binding using microgram quantities of analyzing materials, without further labeling (*10*−*14*). It can measure the binding affinity and on (association) and off (dissociation) rates and is useful for high-throughput screening of new drug targets.

In previous work, we had shown that a specific disaccharide unit in heparin, *O*-(2-deoxy-2-sulfamido-6-*O*-sulfo-α-D-glucopyranosyl)-(1−4)-2-*O*-sulfo-α-L-idopyranosyluronic acid (abbreviated as GlcNS6S-IdoA2S), was a key unit responsible for heparin binding to human platelets (*15*) and von Willebrand factor (vWf) (*16*). We also found that the clustering of these disaccharides significantly enhanced the interaction (*17*, *18*). To systematically investigate heparin's binding interactions, we

* Corresponding author. Tel: +81-99-285-8369 or +81-99-285-8598. Fax: +81-99-285-3630. E-mail: ysuda@eng.kagoshima-u.ac.jp.
† Kagoshima University.
‡ Japan Science and Technology Agency.
§ Osaka University.
▽ Present address: Suntory Institute for Bioorganic Research, Shimamoto-cho, Mishima-gun, Osaka 618-8503, Japan.
⊥ University of Washington and VA Puget Sound Health Care System.

10.1021/bc0600620 CCC: $33.50 © 2006 American Chemical Society
Published on Web 08/31/2006

have developed a novel method for the immobilization of sulfated oligosaccharide onto a gold-coated SPR chip to prepare a "sugar chip" and devised an analytical system that can be applied to the binding interactions of a variety of structurally defined oligosaccharides in clustered structures that mimic nature.

In this paper, mono-, tri-, and tetravalent types of linker compounds containing one, three, or four aromatic amines and thioctic acid moieties were designed. The ligand moiety, a GlcNS6S-IdoA2S unit, was conjugated with these novel linker compounds to prepare a ligand conjugate using an optimized reductive amination reaction. The ligand conjugates were immobilized on a gold SPR sensor chip through an improved gold−sulfur (Au−S) permanent bond. By this approach, we were able to accurately measure the specific interactions of the GlcNS6S-IdoA2S structure in heparin with native human vWf protein and with the recombinant fragment of its A1 domain. To compare our method with conventional immobilization techniques, the GlcNS6S-IdoA2S unit was conjugated with a hydrophobic aromatic amine by a similar reductive amination reaction and immobilized through hydrophobic interactions with a hydrophobic 1-octanethiol-coated chip surface.

The goal of this current work was to refine the methods for immobilizing clustered oligosaccharides using these new techniques, to measure their uniformity and distribution on the SPR chip, and to measure the relative impact of ligand clustering on the binding of well-known heparin-binding proteins. Our long-term goal is to provide a simple, versatile, and reproducible method for studying glycosaminoglycan−protein interactions, which can be implemented by a wide range of investigators beyond the specialized laboratories that pioneered these approaches.

EXPERIMENTAL PROCEDURES

General Procedure. All reactions in organic media were carried out with freshly distilled solvents or with commercially available extra grade solvents purchased from Kanto Chem. Co. (Tokyo, Japan), Nacalai Tesque (Kyoto, Japan), or Wako Chem. Co. (Osaka, Japan). Silica gel column chromatography was performed using silica gel 60 (no. 9386, Merck & Co. Inc., Whitehouse Station, NJ). Spectral data were obtained as follows. Electrospray ionization time-of-flight mass (ESI-TOF/MS) spectra were obtained by Mariner (Applied Biosystems, Framingham, MA). ^{1}H NMR measurements were performed with JEOL (Tokyo, Japan) Lambda-500, GSX-400, and ECA-600. The chemical shifts are expressed in δ-values using tetramethylsilane (δ 0) or HDO (δ 4.65) as an internal standard.

SPR Experiments. SPR experiments were perfomed with SPR-670 (Nippon Laser and Electric Lab., Nagoya, Japan) under the recommended manufacture's guideline with a slight modification. Sensor chips used for SPR experiments were prepared as follows. The gold-coated chip was purchased from Nippon Laser and Electronics Lab. For ligand conjugates containing the thioctic acid moiety, the gold-coated chip was soaked in a 100 μM solution (methanol/water = 1/1, v/v) of the appropriate ligand conjugate at room temperature for 2 h or overnight, followed by subsequent washing with methanol/water containing 0.05% Tween-20, phosphate-buffered saline (PBS) at pH 7.4 containing 0.05% Tween-20, and PBS (pH 7.4). All washings were done with microwave irradiation for 5−30 min. The solvent for the binding experiment was PBS at pH 7.4 and run at a flow rate of 15 μL/min at 25 °C.

For ligand conjugates containing an octyl group, the gold chip was first soaked in 1 mM methanol solution of octanethiol at room temperature overnight, followed by washing with methanol, methanol/water (1/1, v/v), and PBS (pH 7.4) containing 10% 2-propanol. The octanethiol immobilized chip (self-assembled monolayer (SAM) chip) was set in the SPR-670; then the solution of ligand conjugate containing the octyl group in PBS (pH 7.4) containing 10% 2-propanol was loaded and run at a flow rate of 15 μL/min at 25 °C. The ligand conjugate became immobilized through a hydrophobic interaction between the SAM on the chip and the octyl group of the conjugate. This was monitored by SPR-670. The subsequent saccharide−protein binding experiments were done using PBS (pH 7.4) containing 10% 2-propanol. Bovine serum albumin (BSA) was employed as the control, nonspecific protein of study. It is ubiquitous in biological systems and is known to have low nonspecific interactions with sulfated polysaccharides.

Synthesis of Compounds. Details of compound syntheses can be found in Supporting Information.

RESULTS

Preparation of Oligosaccharide-Linker Conjugates (Abbreviated as "Ligand Conjugates"). Mono-, tri-, and tetravalent linker molecules and ligand conjugates were prepared as illustrated in Schemes 1−5. The linker compounds possessed one, three, or four incorporating points, and the ligand conjugates were composed of the linker attached to a structurally defined, biologically active sulfated disaccharide unit (GlcNS6S-IdoA2S) or D-glucose as a control. All the structures of the compounds were confirmed by ESI-TOF/MS and NMR.

Monovalent Linkers and Ligand Conjugates (Schemes 1 and 2). The reaction of *m*-phenylenediamine **1** with di-*t*-butyl dicarbonate in methanol solution yielded 3-(*t*-butoxycarbonylamino)phenylamine **2**. The compound **2** was then reacted with thioctic acid **3** in dichloromethane to give the thioctamide derivative **4**, followed by treatment with trifluoroacetic acid to yield the linker compound **5**. A reductive amination reaction with a sulfated trisaccharide **6** (synthesized as previously reported (*18*)) was employed to incorporate the disaccharide unit into a novel ligand conjugate **7** (Mono-GlcNS6S-IdoA2S-Glc). By a similar reductive amination reaction using D-glucose, a control ligand conjugate **8** (Mono-Glc) was also prepared.

For the hydrophobic immobilization strategy (Scheme 2), a hydrophobized ligand conjugate **13** containing the GlcNS6S-IdoA2S unit was prepared. The reaction of 4-aminobenzoic acid **9** with di-*t*-butyl dicarbonate in methanol solution yielded 4-(*t*-butoxycarbonylamino)benzoic acid **10**. Further reaction with *n*-octylamine in dichloromethane gave benzamide **11**, which was then treated with trifluoroacetic acid to yield the hydrophobic linker *N*-octyl-4-aminobenzamide **12**. The linker **12** was coupled with the trisaccharide **6** using a reductive amination reaction to give the hydrophobized compound **13** (Hydro-mono-GlcNS6S-IdoA2S-Glc). A similar reductive amination was performed with D-maltose to give D-glucopyranoside-containing ligand conjugate **14** (Hydro-mono-Glc-Glc), which was used for the control experiments.

Trivalent Linker and Ligand Conjugate (Scheme 3). For the trivalent type linker compound **24**, the Michael addition reaction followed by reduction with Raney nickel was applied to nitromethane **15** to give tribranching amine **18** according to Weis and Newkome (*19*) with a slight modification. The production of a side product, di-*t*-butyl 4-[(2-*t*-butoxycarbonyl)ethyl]-4-aminoheptanedicarboxylate, was less than 5% in this case. To the amine moiety **18**, a *Z*-glycine unit was incorporated, which served as a spacer between the branching part and the further incorporating thioctic acid moiety. The coupling reductive amination reaction was performed as above with a slight modification, in which dimethylacetoamide was used to dissolve the tribranched linker compound **24** instead of methanol. The reaction was monitored with thin-layer chromatography (TLC) and ESI-TOF/MS. After confirmation of the formation of the Shiff base, the ratio of the mixed solvent was changed to promote a more efficient reduction reaction. We found that it

Scheme 1. Synthesis of Monovalent Linker and Ligand Conjugates

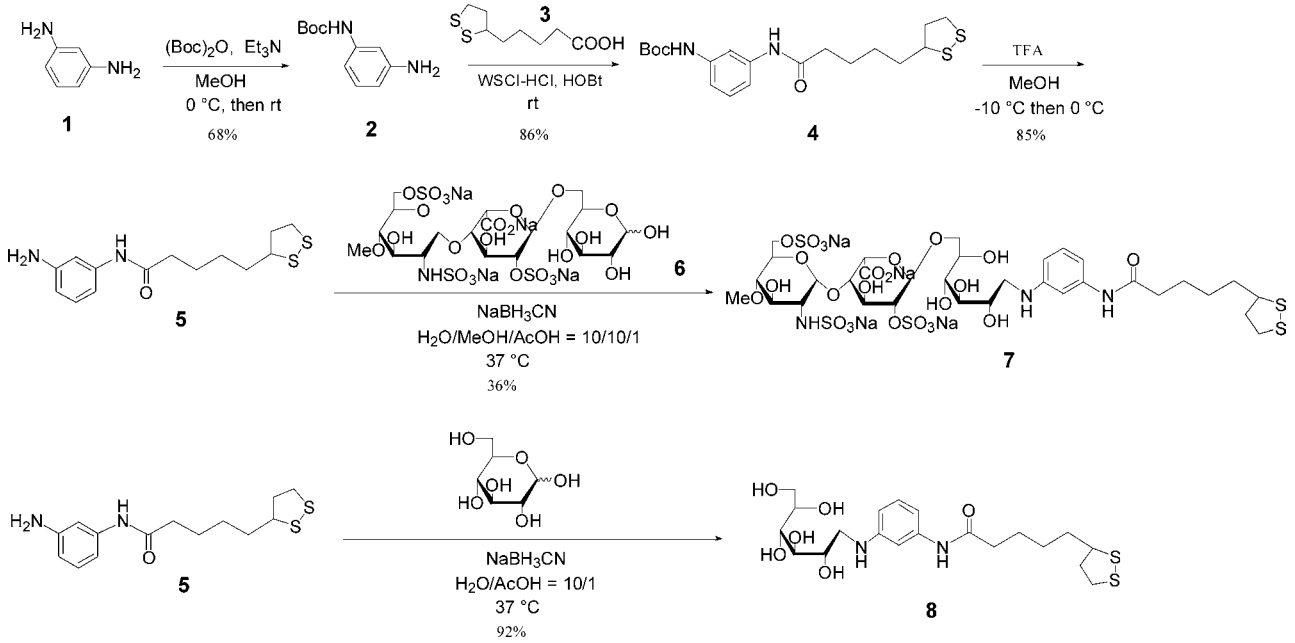

Scheme 2. Synthesis of Hydrophobized Monovalent Linker and Ligand

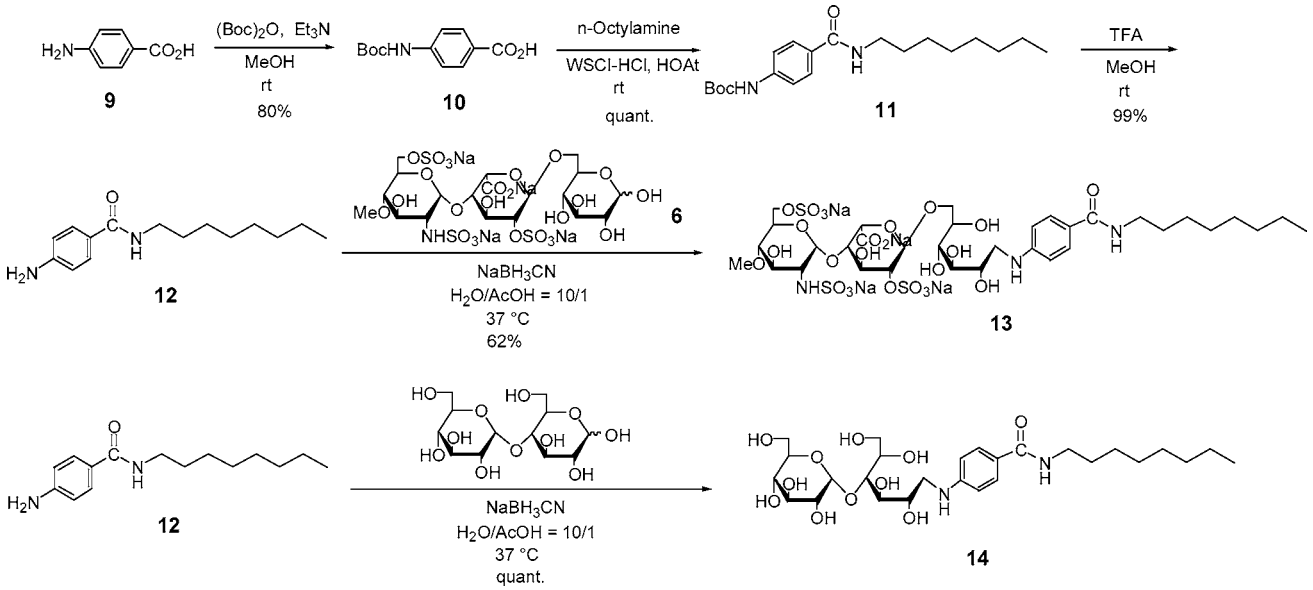

was important to maintain the pH of the solvent between 3 and 4 to increase the conversion of the reaction. A 5-fold ratio of sulfated trisaccharide **6** to the linker **24** was necessary to incorporate all three of the aromatic amine moieties in **24** to produce **25** (Tri-GlcNS6S-IdoA2S-Glc). The lower than expected yield (66%) was due to losses during purification.

Tetravalent Linker and Ligand Conjugate (Scheme 4). The tetravalent linker compound **34** was prepared according to Ashton et al. (*20*) with modifications. In brief, two units of aminobenzoic acid moieties were incorporated into the two primary amines in diethylenetriamine with a relatively good yield by precisely controlling their molar ratio. For the spacer between the thioctic acid moiety and the branching part, *Z*-glycine was incorporated to give compound **30**. The condensation of **27** and **31** needed a stronger condensation reagent, pentafluorophenyl diphenylphosphinate (FDDP), to give the tetravalent linker unit containing four units of aromatic amine derivative **35**. The incorporation of sulfated disaccharide units to yield **35** was performed by similar reaction conditions as applied to **24**. A 5-fold ratio of sulfated trisaccharide **6** to the linker **35** was also necessary to incorporate all four of the aromatic amine moieties in **35** to produce **36** (Tetra-GlcNS6S-IdoA2S-Glc-short). Diminished yield (40%) was again due to losses during purification.

Tetravalent Linker and Ligand Conjugate with Longer Spacer Arm (Scheme 5). In order to create an immobilized oligosaccharide cluster with a longer leash, or spacer arm, we created tetravalent linker **48** and ligand conjugate **49** by modifying **35** and **36**, respectively (Scheme 5). An oligo(ethylene glycol) unit was incorporated between the branched part and the thioctic acid moiety. The oligo(ethylene glycol) unit was derivatized according to Houseman and Mrksich (*6*) to afford the *O*-toluenesulfonyl compound **40**. By the S_N2 reaction with sodium azide, an azide unit was incorporated. After hydrolysis, we obtained **42**, which was then used for the spacer unit instead of *Z*-glycine in the preparation of **30**. The azide moiety was converted to amine by mild reduction, and the thioctic acid moiety was condensed to the amino group, followed by deblocking of the aromatic amine by trifluroacetic acid to yield the tetravalent linker **48** containing an oligo(ethylene glycol)

Scheme 3. Synthesis of Trivalent Linker and Ligand Conjugate

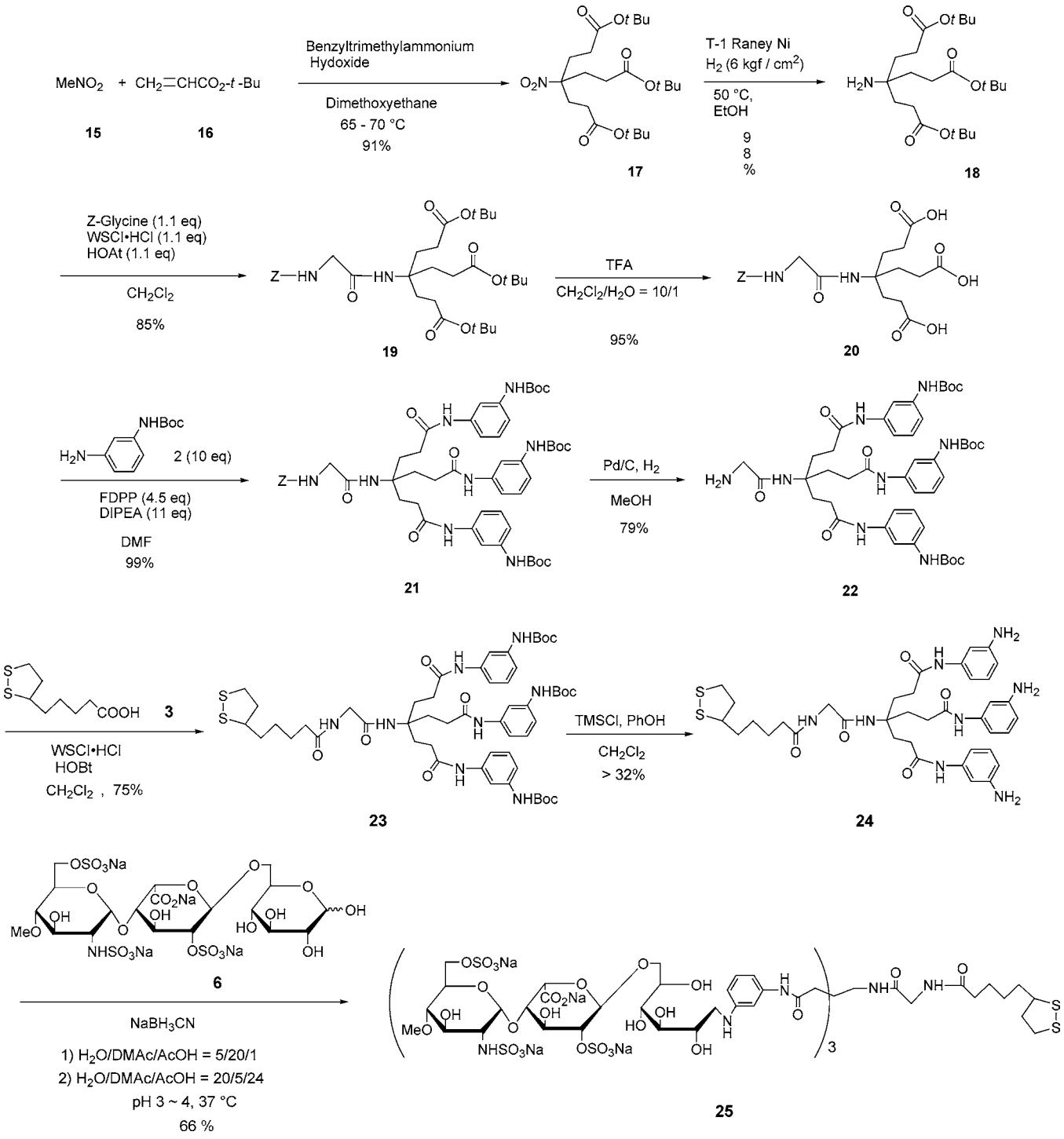

unit. The incorporation of sulfated disaccharide units into **48** was performed by the same reaction as applied to **25**. A 7-fold ratio of sulfated trisaccharide **6** to the linker **48** was necessary to incorporate the four aromatic amine moieties in **48** to prepare **49** (Tetra-GlcNS6S-IdoA2S-Glc-long). Yield (22%) was again diminished primarily due to purification. All the structures of the compounds were confirmed by ESI-TOF/MS and ^{1}H NMR.

Comparison of Immobilization Methods. The monovalent ligand conjugates **7** (Mono-GlcNS6S-IdoA2S-Glc) and **8** (Mono-Glc) were first immobilized on the gold chip by soaking the chip in the 100 μM 50% aqueous methanol solution of the ligand conjugate for 2 h or overnight at room temperature with gentle agitation. It was predicted that the ligand conjugates would be immobilized on the gold-coated chip through direct Au−S bonding. With use of an SPR670 apparatus (Nippon Laser and Electronics Lab, Nagoya, Japan), a binding interaction to the ligand moiety on the chip was confirmed when 2 μM of the synthetic peptide KDRKRSELRRIASQVK (a discrete heparin-binding domain of human vWf (*21*), abbreviated as vWf-peptide) was injected over the surface of the chip in the apparatus (Figure 1a). Because minimal binding was observed with 1.5 μM of BSA, it was not even necessary to subtract a nonspecific binding value.

When the control Mono-Glc was immobilized using the same method, no significant increase in resonance units was observed even though a high concentration of synthetic vWf-peptide was used (Figure 1b). In contrast, a typically positive binding saturation curve was seen with the Mono-GlcNS6S-IdoA2S-

Scheme 4. Synthesis of Tetravalent Linker Containing Short Spacer Arm and Ligand Conjugate

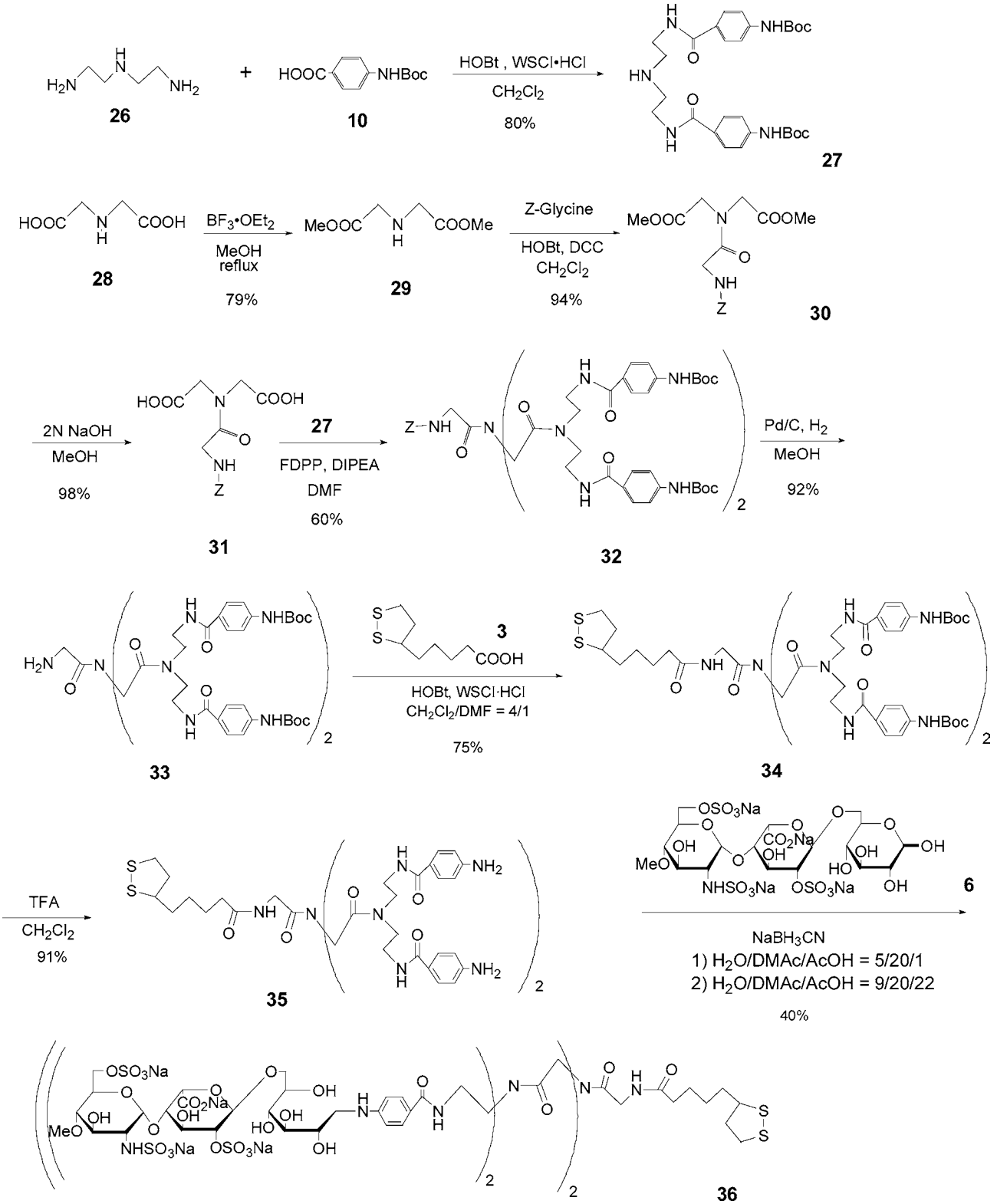

Glc immobilized chip. The K_D, dissociation constant, was estimated to be 220 nM, very close to that reported previously (370 ± 100 nM) for unfractionated heparin and vWf using a conventional radioligand binding assay (*21*).

This direct, covalent immobilization method was then compared to a conventional hydrophobic method of immobilization. A self-assembled monolayer (SAM) of octanethiol was first prepared on the chip as previously reported (*10*, *11*). The SAM chip was set in the SPR670 apparatus and a solution of **13** or **14** was loaded on the chip in phosphate-buffered saline. The total amount of **13** or **14** that was immobilized on the sensor chip is indicated by the differences in resonance units (ΔRU^1) at equilibrium shown in Figure 2a. Then, the binding of synthetic vWf-peptide was evaluated. Figure 2b shows that the vWf-peptide bound to both the sulfated oligosaccharide SAM chip (using **13**, Hydro-mono-GlcNS6S-IdoA2S-Glc) and the control SAM chip (using **14,** Hydro-mono-Glc-Glc). These nonspecific interactions were confirmed when BSA was tested on the same SAM sensor chip; strong binding of BSA to both chips was observed (data not shown).

Scheme 5. Synthesis of Tetravalent Linker Containing Long Spacer Arm and Ligand Conjugate

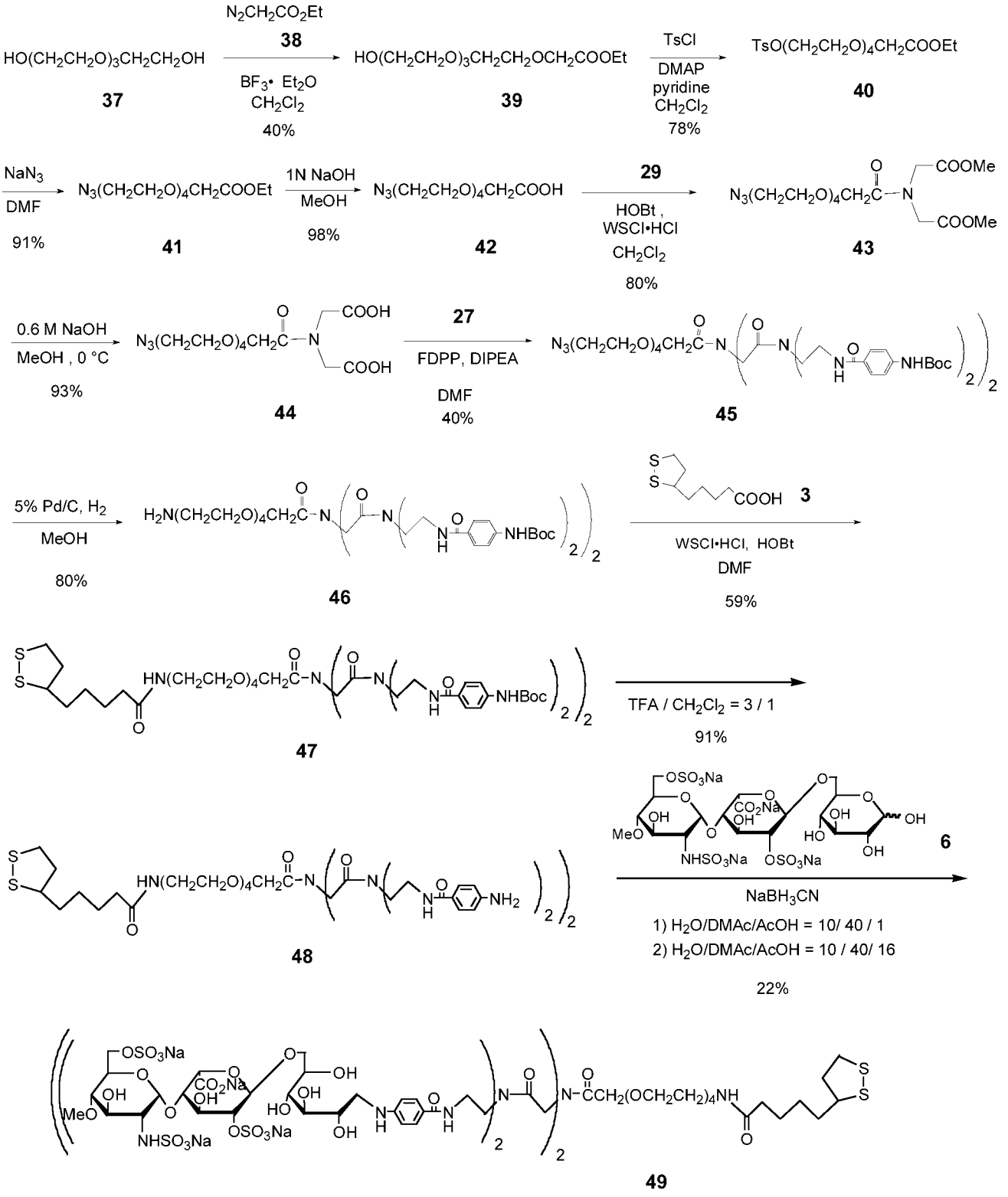

Evaluation of Immobilization of the Ligand Conjugates via the Covalent Attachment Method. The tri- and tetravalent ligand conjugates containing the sulfated disaccharide units were immobilized on gold chips as described above, and nonspecific binding to 1.5 μM BSA was measured. Experience showed that the chips prepared in this manner were quite stable, retaining full binding potency when stored dry at room temperature for 6 months (data not shown). Figure 3 shows that chips immobilized with conjugates **25** (Tri-GlcNS6S-IdoA2S-Glc) and **49** (Tetra-GlcNS6S-IdoA2S-Glc-long) showed very little nonspecific binding, just as was observed in Figure 1a with the Mono-GlcNS6S-IdoA2S-Glc (conjugate **7**). The tetravalent conjugate with the short linker arm (conjugate **36**) exhibited high nonspecific binding (Figure 3) that is typical of a BSA interaction with a bare, unmodified gold chip. Hence, we concluded that conjugate **36** did not achieve optimal immobilization to the gold chip. Its more flexible linkage chemistry, combined with a short spacer arm, may have obscured the accessibility of the S−S portion of the linker for effective immobilization. In subsequent experiments, trivalent

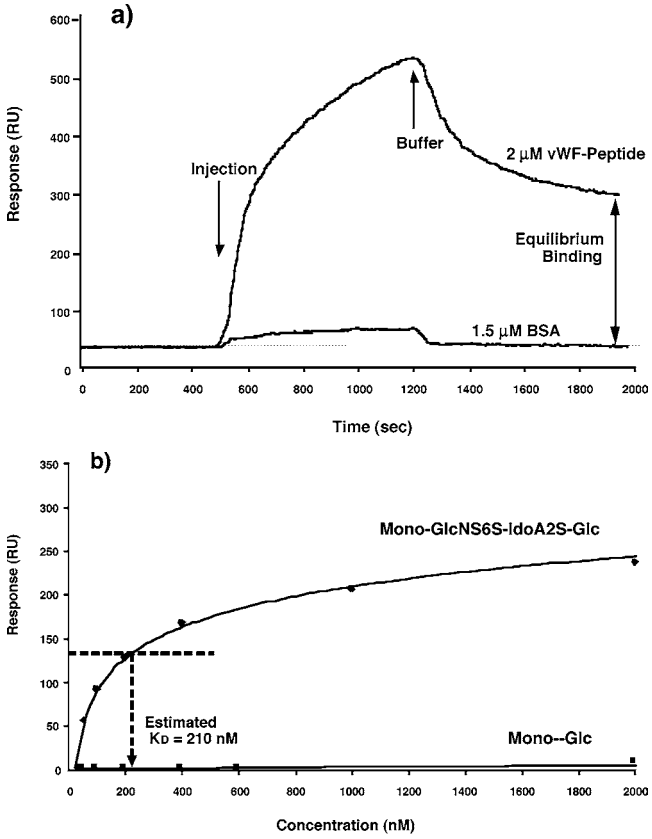

Figure 1. (a) Binding of vWf-peptide and BSA to Mono-GlcNS6S-IdoA2S-Glc (ligand conjugate **7**) on the chip was observed (flow rate = 5 μL/min, temp = 25 °C, pH 7.4, PBS); (b) the equilibrium binding data were used to generate a saturation curve for vWf-peptide binding to Mono-GlcNS6S-IdoA2S-Glc and to the control ligand conjugate **8** (Mono-Glc).

ligand conjugate **25** (Tri-GlcNS6S-IdoA2S-Glc) and ligand conjugate **49** (Tetra-GlcNS6S-IdoA2S-Glc-long) were used in addition to Mono-GlcNS6S-IdoA2S-Glc (compound **7**).

Density and Homogeneity of Immobilization. We wished to determine how the density of immobilization of different conjugates on the chip would influence binding activity. Accordingly, different percentages of biologically active ligand conjugates were individually diluted with the control glucose monovalent conjugate **8** (Mono-Glc) and immobilized as above. The relative concentration of the immobilized sulfated disaccharide was determined by attenuated total reflection (ATR) FT-IR spectra with IRPrestige-21 equipped with MIRacle (Shimdzu Co., Kyoto, Japan). Figure 4a shows parts of the ATR-FT-IR spectra for the region of sulfate groups (1200 and 1303 cm^{-1}) on the gold surface, where Mono-GlcNS6S-IdoA2S-Glc was immobilized over a range of relative densities. The intensity of absorbance increased as the chip was coated with an increasing percentage of Mono-GlcNS6S-IdoA2S-Glc in the ligand conjugate mixture. The absorbance between 1200 and 1303 cm^{-1} was integrated and plotted against the relative concentration of ligand conjugate including the sulfated disaccharide units. As shown in Figure 4b−d, there were linear relationships between the integral of absorbance for sulfate groups on the chip and the relative concentration of the active ligand conjugate in the mixture, suggesting that the sulfated disaccharide units were homogeneously immobilized on the gold surface. In other words, the relative density of ligand oligosaccharides on the chip surface can be controlled by admixing the Mono-Glc ligand conjugate, since the efficiency of S−Au bonding does not appear to be altered between Mono-GlcNS6S-IdoA2S-Glc and Mono-Glc.

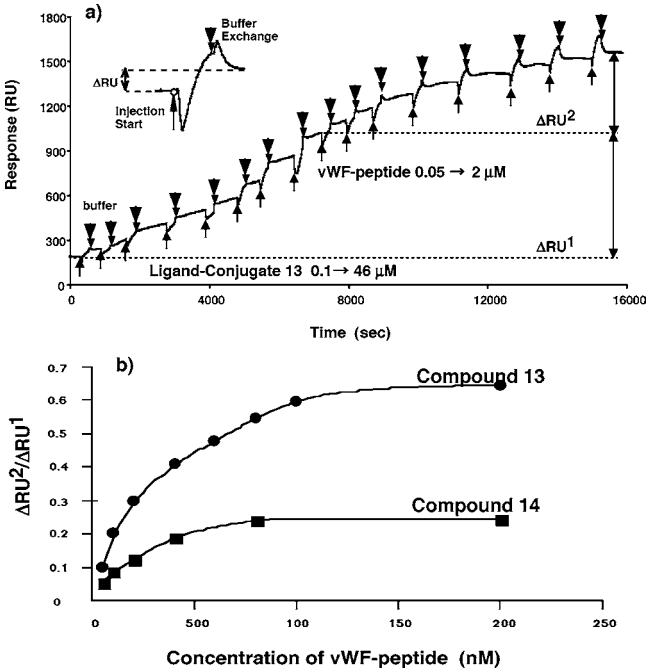

Figure 2. (a) Immobilization of ligand conjugate **13** (Hydro-mono-GlcNS6S-IdoA2S-Glc) containing GlcNS6S-IdoA2S on the SAM chip and the binding of vWf-peptide were observed (flow rate = 15 μL/min, temp = 25 °C, pH 7.4, PBS containing 10% 2-propanol); (b) the equilibrium binding data were used to generate saturation curves for the binding of vWf-peptide to the ligand conjugate **13** and to the control **14** (Hydro-mono-Glc-Glc).

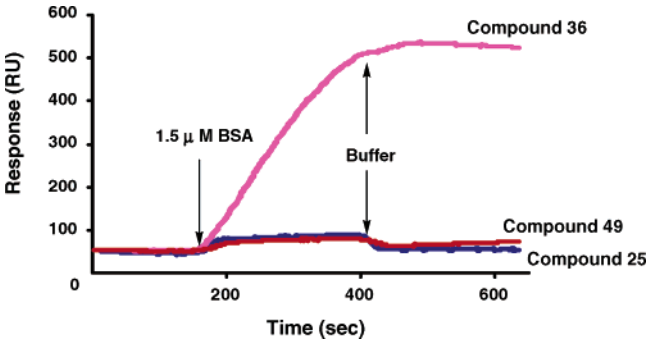

Figure 3. Binding of BSA to the sulfated disaccharide, GlcNS6S-IdoA2S, immobilized chips by ligand conjugates **25** (Tri-GlcNS6S-IdoA2S-Glc), **36** (Tetra-GlcNS6S-IdoA2S-Glc-short), and **49** (Tetra-GlcNS6S-IdoA2S-Glc-long). The immobilization and SPR experiment were done as described in the Experimental Procedures.

Measurement of Binding Affinities for Model Heparin-Binding Proteins. To evaluate the influence of oligosaccharide immobilization density on protein binding, 2 μM vWf-peptide was injected over chips immobilized with different percentages of Mono-GlcNS6S-IdoA2S-Glc to Mono-Glc immobilized chip (Figure 5). The binding affinity decreased as the relative density of the surface-immobilized sulfated disaccharide units diminished. When the biologically active disaccharide comprised less than 40% of the immobilized ligand, binding was minimal.

We also studied the binding of the recombinant human vWf-A1 domain (rhvWf-A1) (*22*). This protein contains the same heparin-binding domain studied in Figure 5 (vWf-peptide) but also includes a secondary or cooperative heparin binding site (*23*). The three ligand conjugates, Mono-GlcNS6S-IdoA2S-Glc, Tri-GlcNS6S-IdoA2S-Glc, and Tetra-GlcNS6S-IdoA2S-Glc-long, were immobilized at 100% and 50% density (mixed 1:1 with Mono-Glc). Table 1 compares the effects of clustering (valency) and immobilization density on the binding parameters

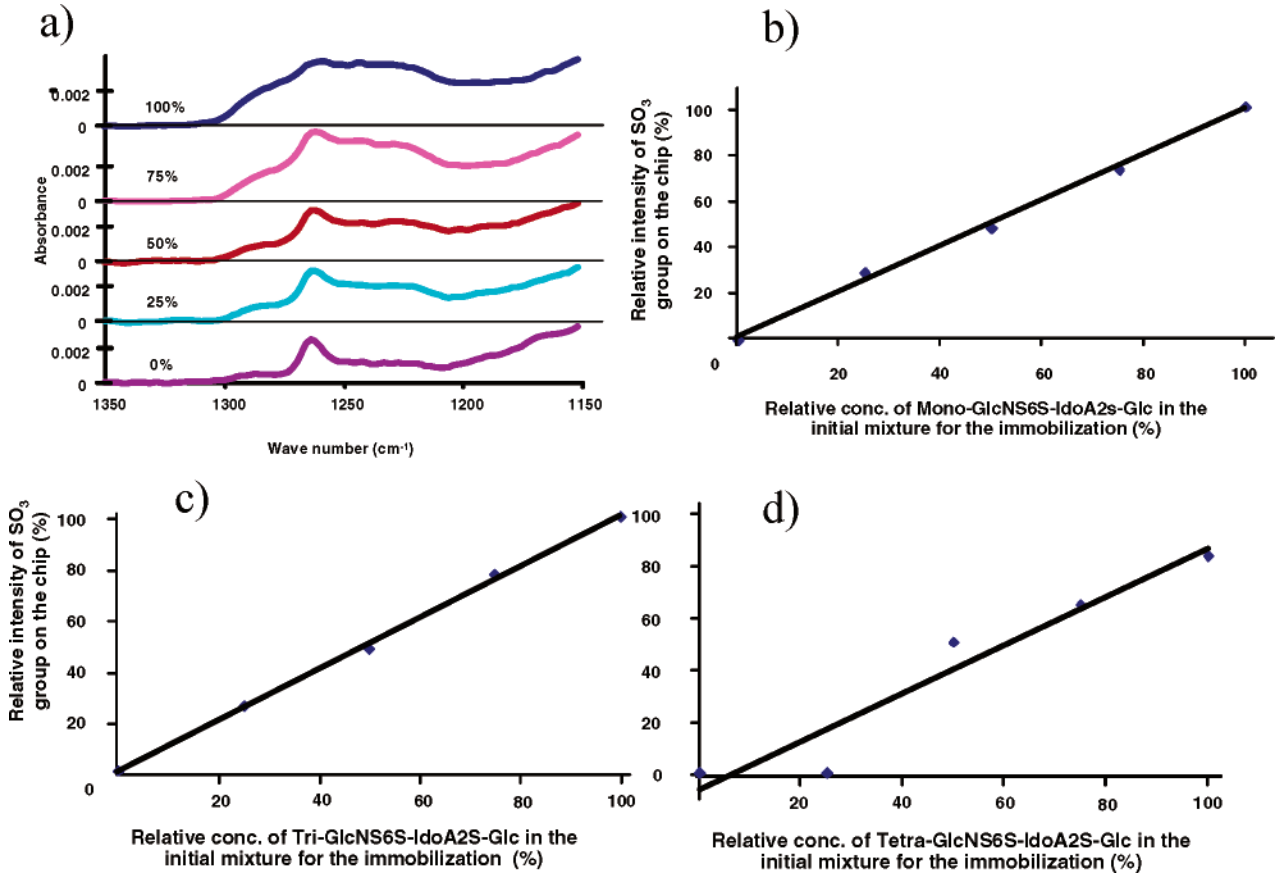

Figure 4. (a) ATR-FT-IR spectra of Mono-GlcNS6S-IdoA2S-Glc immobilized chip. The immobilization was done by adding Mono-GlcNS6S-IdoA2S-Glc to the control ligand conjugate (Mono-Glc) with changing concentration (0 to 100%). Intensity of ATR-FT-IR was plotted against the initial concentration of (b) Mono-GlcNS6S-IdoA2S-Glc ($R^2 = 0.9984$), (c) Tri-GlcNS6S-IdoA2S-Glc (compound **25**; $R^2 = 0.9993$), and (d) Tetra-GlcNS6S-IdoA2S-Glc-long (compound **49**; $R^2 = 0.9610$) in the ligand conjugate mixture.

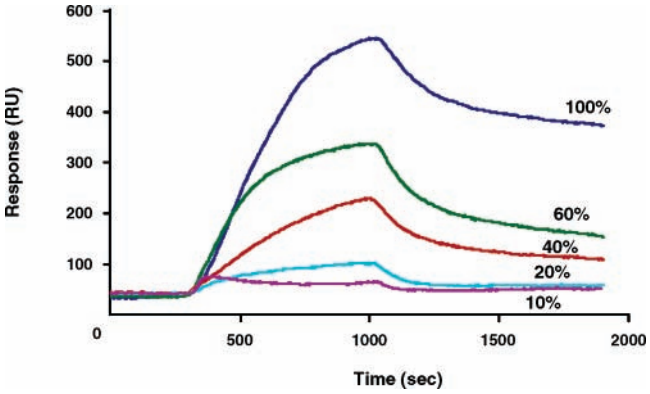

Figure 5. SPR sensorgram of vWf-peptide binding. Chips were immobilized with increasing proportions of Mono-GlcNS6S-IdoA2S-Glc, with the total concentration ([Mono-GlcNS6S-IdoA2S-Glc] + [Mono-Glc]) fixed at 100 μM. vWf-peptide was 2 μM.

(calculated from kinetic data using the analytical software of the SPR670).

The increased clustering of oligosaccharides provided by the tri- and tetravalent conjugates uniformly yielded lower dissociation constants K_D and lower dissociation rates k_d. The monovalent conjugate had an ~2.5−3-fold higher K_D and k_d. A 50% decrease in the density of immobilization hardly changed the binding parameters of the tri- and tetravalent ligand conjugates, while the same decrease in density of the monovalent ligand raised the K_D by 1.5-fold and doubled the k_d.

We then measured oligosaccharide binding of an even more complex version of this heparin-binding protein, the whole human vWf protein. A single vWf monomer protein is 270 kDa

Table 1. Binding of rhvWf-A1: Clustering Effect of Sulfated Oligosaccharide on the Chip

ligand conjugates	ratio	K_D [a] (μM)	k_a [b] ($M^{-1}\,s^{-1} \times 10^3$)	k_d [c] ($s^{-1} \times 10^{-3}$)
Mono-GlcNS6S-IdoA2S-Glc	100/0	2.60	8.38	21.9
Mono-GlcNS6S-IdoA2S-Glc/Mono-Glc	50/50	3.79	14.6	55.2
Tri-GlcNS6S-IdoA2S-Glc	100/0	1.20	6.60	8.05
Tri-GlcNS6S-IdoA2S-Glc/Mono-Glc	50/50	1.50	4.52	6.83
Tetra-GlcNS6S-IdoA2S-Glc	100/0	0.99	6.50	6.44
Tetra-GlcNS6S-IdoA2S-Glc/Mono-Glc	50/50	1.00	5.24	5.26

[a] k_d/k_a (dissociation constant). [b] Association rate. [c] Dissociation rate.

Table 2. Binding of Whole rhvWf: Lack of Clustering Effect of Sulfated Oligosaccharide on the Chip

ligand conjugates	ratio	estimated K_D (nM)
Mono-GlcNS6S-IdoA2A-Glc	100/0	35
Mono-GlcNS6S-IdoA2A-Glc/Mono-Glc	20/80	41
Tri-GlcNS6S-IdoA2A-Glc	100/0	24
Tri-GlcNS6S-IdoA2A-Glc/Mono-Glc	20/80	27
Tetra-GlcNS6S-IdoA2A-Glc	100/0	35
Tetra-GlcNS6S-IdoA2A-Glc/Mono-Glc	20/80	32

molecular mass, but it forms large multimers reaching several million daltons, displaying multiple heparin-binding sites. Experiments were performed using mono-, tri-, and tetravalent (long) ligand conjugates immobilized at 100% and 20% relative concentrations. Table 2 summarizes the estimated binding constants derived from the data illustrated in Figure 6a−c. The estimated K_D values were all very similar and did not depend

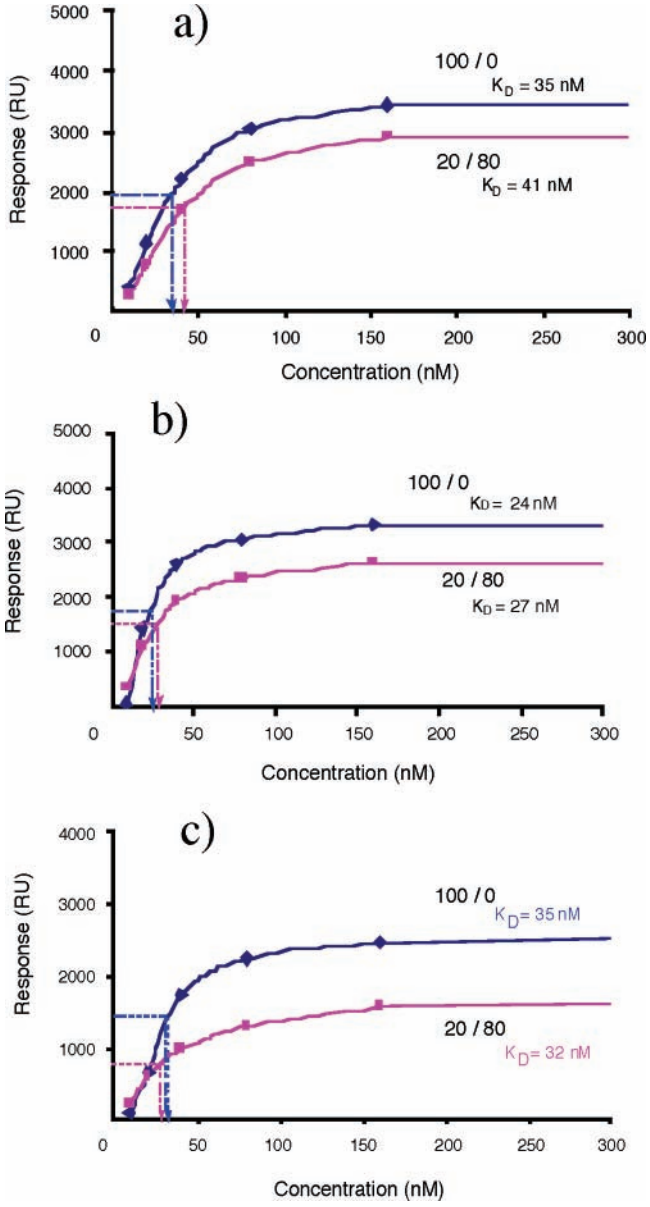

Figure 6. Equilibrium binding of whole hvWf protein to chips immobilized with Mono-GlcNS6S-IdoA2S-Glc/Mono-Glc (a), Tri-GlcNS6S-IdoA2S-Glc/Mono-Glc (b), and Tetra-GlcNS6S-IdoA2S-Glc-long/Mono-Glc (c). The ratios of Mono-GlcNS6S-IdoA2S-Glc, Tri-GlcNS6S-IdoA2S-Glc, or Tetra-GlcNS6S-IdoA2S-Glc-long/Mono-Glc were 100/0 and 20/80.

on the relative density of the immobilization of the ligand conjugates nor the multivalency of the ligand conjugate.

Finally, we studied the binding affinity for a completely different heparin-binding protein, human basic fibroblast growth factor (bFGF). Here we performed competitive binding studies with immobilized Tri-GlcNS6S-IdoA2S-Glc (compound **25**) and bFGF (200 nM) in solution phase admixed with increasing concentrations of unfractionated pharmaceutical grade heparin (Nacalai Tesque, from porcine intestine, average MW = 15000). Figure 7a shows that with increasing concentrations of soluble heparin, the binding of 200 nM of bFGF decreased. Figure 7b shows the estimated IC_{50} of heparin to be 50−100 nM, which is close to the reported K_D of bFGF for heparan sulfate proteoglycan (*24*).

DISCUSSION

The first goal of this work was to devise and refine a simpler and nondestructive strategy for immobilizing structurally defined

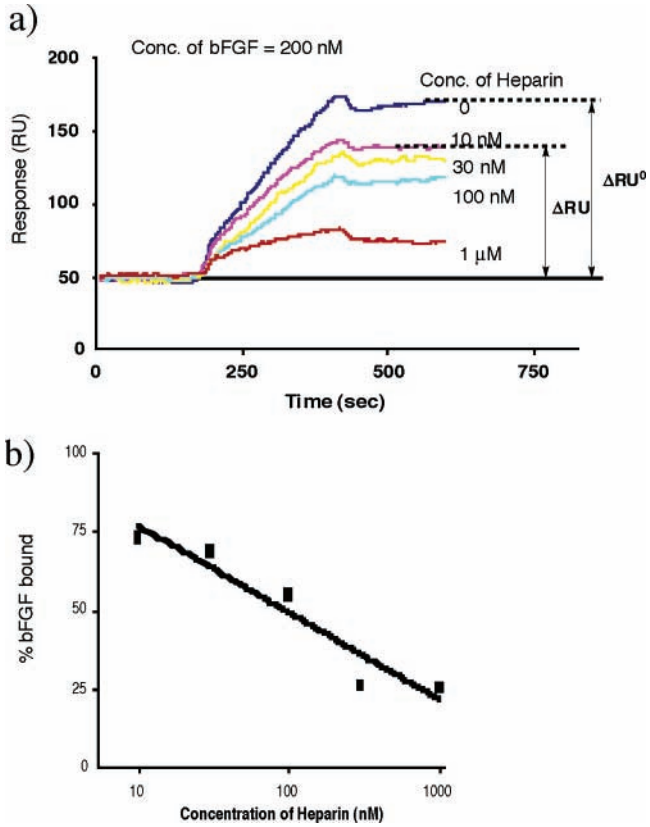

Figure 7. (a) SPR sensorgram of competitive heparin binding to bFGF. Mixtures of bFGF (200 nM) with or without soluble commercial heparin (Nacalai Tesque, from porcine intestine, average MW = 15000) were run on the chip of Tri-GlcNS6S-IdoA2S-Glc. (b) Relationship between the concentration of heparin and ΔRU at equilibrium.

oligosaccharides on a chip for SPR. When ligand immobilization methods were compared, the direct, covalent immobilization to the gold surface via Au−S bonds yielded minimal nonspecific binding interactions, as examplified by the negligible binding of BSA, and minimal protein binding to the control glucose ligand. In contrast, BSA bound to the self-assembled monolayer of octanethiol through nonspecific hydrophobic interactions, and the vWf-peptide bound with some measurable affinity even to the negative control glucose ligand.

We also sought to develop a linkage method that was simple, nondestructive, and applicable to a wider range of naturally occurring oligosaccharides. The reductive amination coupling to linker compounds containing aromatic amines offered more precise, quantitative control over the linkage process, especially when compared with techniques of mass immobilization using the lysine groups of albumin or other proteins. The reductive amination reaction is certainly a well-established method. It is typically used for the labeling of oligosaccharides, such as in the pyridyl amination reaction. In that case, excess amounts of pyridylamine are used, and the labeled compounds have been used primarily for the analysis of the structure of oligosaccharides. With use of this known pyridyl amination reaction, ligand conjugates for the immobilization of oligosaccharides onto the gold surface cannot be obtained.

Other methods have used the amino groups in a carrier protein, like bovine serum albumin, to form multivalent ligand oligosaccharides with dramatic increases in binding affinity. We previously examined the reductive amination strategy in detail and found the optimized conditions (*25*). In brief, the reaction should be done at around pH 4 to get a high yield. Therefore, regular alkyl amines gave lower yields because of the protonation of the amino group. If the pH is increased to over seven to have more free amino groups, the simple reduction at the

reducing end of oligosaccharide predominated. Thus, we found that aromatic amines had the optimal properties. Using those linker compounds described here, many other oligo- and polysaccharides including sialic containing ones, unfractionated high molecular weight heparin, low molecular weight heparins (LMWHs) prepared by several different methods, or amyloses, were also successfully conjugated. Those results will be reported soon.

Gold−sulfur immobilization schemes have also been used by Ratner et al. (*26*) and Horan et al. (*5*), but the regular thiol-containing compounds they used for self-assembling monolayers can form both S−S and S−H bonds, depending on the concentration. Therefore, purification of these oligosaccharide−thiol conjugates may be challenging, with low yields. Our current approach using a linker compound containing a thioctic acid with intramolecular S−S bonds avoids these significant challenges in purification during the synthesis. The advantages of using thioctic acid have been recognized in our patent (*27*) and in a recent publication (*28*).

The second purpose was to precisely quantify the nanostructural contributions of clustering, or valency, on the affinity of oligosaccharide ligands for increasingly complex heparin-binding proteins by varying spacer-arm length, immobilization density, and valency. Here, the distinction should be made between the minimal oligosaccharide binding unit and the minimal functional oligosaccharide necessary for biological activity. Often, a di- or trisaccharide of specific structure can be identified as the key binding unit (as we have done previously (*17*)). However, an isolated disaccharide often has low affinity and biological activity for the target protein. When multiple copies of this minimal binding unit are spaced appropriately (either within a single heparin chain or by adjacent chains), then the ligand protein may engage in higher affinity equilibrium binding that results in biological effects. Thus, overall the tri- or tetravalent compounds had higher affinities than the monovalent type, and the affinity was less dependent on their relative density on the surface of the SPR gold chip (Table 1). That is, when multivalency was incorporated as an intrinsic property of the ligand, variations in the density of immobilization had significantly less effect on the observed affinities. In contrast, the affinities of the monovalent ligand conjugates dropped dramatically when their relative density fell to 50%. Even though the changes shown in Table 1 were small, we observed a larger increase of K_D (lower affinity) of rhvWf-A1 when the relative density was decreased to 20% (data not shown). A larger k_d rate constant (Table 1) was observed compared to 100% density, suggesting that the observed binding of rhvWf-A1 occurred via equilibrium binding. These results support the concept that oligosaccharide ligand valency and density are important determinants for protein affinity. In biological systems, the key minimal oligosaccharide structure may either be spaced appropriately as a repeating unit within the same polymer chain or be displayed by clusters of neighboring polymers.

In addition to intrinsic ligand valency and density, it was interesting to find that a third factor also influenced equilibrium binding, the complexity of the heparin-binding protein. In the case of the simplest monovalent disaccharide ligand conjugate, its binding to a single, linear heparin-binding domain peptide (vWf-peptide) was highly dependent on the density of immobilized ligand (Figure 5). The monovalent ligand's interaction with a more complex heparin-binding protein (rhvWf-A1 containing major and minor heparin-binding domains) was still dependent on immobilization density, but slightly less so (Table 1). Finally, the monovalent ligand's interaction with the native multimeric vWf protein (containing multiple heparin-binding sites) showed the least dependency on immobilization density (Table 2). The binding of multivalent oligosaccharide ligands to increasingly complex heparin-binding proteins was much less sensitive to immobilization density. The trivalent and tetravalent constructs with the long spacer arm exhibited no significant change in K_D with reduced density.

Microarrays of synthetic heparin oligosaccharides have been reported very recently (*29*). But from these "sugar chips", the influence of the heparin-binding protein lends insights into the nature of protein−glycosaminoglycan binding mechanisms. It suggests that as the protein presents a multiplicity of heparin-binding sites, the interactions with the sulfated disaccharide units change from static multipoint binding to kinetic equilibrium binding. Neither ligand clustering nor density seemed to play as important a role in binding native multimeric hvWf, most likely because of the many widely spaced ligand binding sites presented by the protein itself. These results point to one unexpected advantage of this current technology: by altering the relative density and valency of the ligand on the surface, one can easily distinguish between single-site and multisite binding interactions between proteins and oligosaccharides. Thus, the heparin-binding properties of an unknown protein can be deduced.

Another utility of this approach is illustrated by the competitive binding assay using the trivalent ligand conjugate and human bFGF. We measured similar competition curves by soluble heparin against the monovalent or tetravalent ligand conjugates (data not shown). This technique can be easily applied, for example, to the screening of inhibitors or competitors of growth factors.

In previous work, we have found that the surface of the commercial gold-coated chip, at nanometer scale, is not perfectly flat. It varies in vertical elevation by as much as 10 nm up and down (detected by atomic force microscopy (AFM), data not shown). Thus, it was not surprising that the immobilization of ligands less than 2 nm in size might be affected by surface conditions, producing less consistent two-dimensional clustering of ligand on the surface. However, in the tri- or tetravalent type ligand conjugates, the biologically active oligosaccharides were dispersed within 2−3 nm, making a nanometer-sized cluster, which is independent of the surface irregularities of the gold-coated chip. Up to a point, a clustering-type effect can be achieved by immobilizing monovalent ligands at a higher density, but the nanostructural properties of the surface may interfere with the consistency and reproducibility of this effect. One explanation may be that the multivalent linkers are less affected by these surface conditions and thus show comparable affinities at lower density. Among them, the trivalent type may have some advantages. The trivalent linker contains an sp^3 carbon at the branching point. This branching makes a rigid structure and therefore gives an open space for the thioctic acid moiety (intramolecular S−S part) to immobilize the ligand conjugate to the gold surface. In contrast, the tetravalent type linker's branching parts are flexible enough to allow the large oligosaccharides to move apart and potentially mask the thioctic acid moiety. The ligand conjugate **36** (short spacer, tetravalent) was not able to be effectively immobilized. When a longer spacer arm was inserted (four units of ethylene glycol between the branching part and the thioctic acid moiety), compound **49** could then be successfully immobilized.

CONCLUSION

We have studied the binding of mono- and multivalent oligosaccharide ligands to increasingly complex heparin-binding protein structures. We have devised relatively simple and novel nondestructive methods of conjugation and immobilization that are applicable to a wide range of synthetic or naturally occurring oligosaccharides. The data show that clustering of the biologically active oligosaccharides enhances their affinity for simple

heparin-binding motifs and reduces the impact of surface irregularities or variations in the density of immobilization. For more complex heparin-binding proteins, the density of immobilization and the degree of ligand valency play less of a role. This relative dependence on density can thus be used as one rapid method to characterize the nature of the glycosaminoglycan−protein interaction.

Several technical advantages are conferred by these approaches. The reductive amination technique using an aromatic amino moiety offers a simpler, more quantitatively precise method of conjugation than that reported by Feizi and Chai (*30*). It is suitable for any oligosaccharide with a reducing end and does not require significant modification of their functional sulfate groups. The sulfur−gold immobilization using a thioctic acid moiety permits tighter control of the sulfur reactions, and easier purification of the conjugate. With tri- or tetravalent linkers, the oligosaccharides can easily be incorporated as a clustered form that mimics nature. These novel applications of SPR offer the potential to elucidate a range of fundamental structure−function relations of oligosaccharide−protein interactions at the molecular level and hold promise as a novel approach to rapid throughput screening of new bioactive molecules.

ACKNOWLEDGMENT

We wish to thank Mr. Y. Murakami (Shimazu Co., Kyoto Customer Support Center) for his great support for the measurement of ATR-FT-IR. This work was supported in parts by grants from Japan Science and Technology Agency (YS), the National Institutes of Health (Grants RO1HL39903 and HL079182 to M.S.) and the Department of Veterans Affairs Research Service (to M.S.).

Supporting Information Available: Details of compound syntheses. This material is available free of charge via the Internet at http://pubs.acs.org.

LITERATURE CITED

(1) Varki, A. (1999) In *Essentials of Glycobiology* (Varki, A., Cummings, R., Esko, J., Freeze, H., Hart, G., and Marth, J., Eds.), Cold Spring Harbor Laboratory Press, Cold Spring Harbor, New York, pp 57−68 and references therein.

(2) Gallagher, J. (2001) Heparan sulfate: growth control with a restricted sequence menu. *J. Clin. Invest. 108*, 357−361.

(3) Ostrovsky, O., Berman, B., Gallagher, J., Mulloy, B., Fernig, D. G., Delehedde, M., and Ron, D. (2001) Differential effects of heparin saccharides on the formation of specific fibroblast growth factor (FGF) and FGF receptor complexes. *J. Biol. Chem. 277*, 2444−2453.

(4) Faham, S., Hileman, R. E., Fromm, J. R., Linhardt, R. J., and Rees, D. C. (1996) Heparin structure and interactions with basic fibroblast growth factor. *Science 271*, 1116−1120.

(5) Horan, N., Yan, L., Isobe, H., Whitesides, G. M., and Kahne, D. (1999) Nonstatistical binding of a protein to clustered carbohydrates. *Proc. Natl. Acad. Sci. U.S.A. 96*, 11782−11786.

(6) Houseman, B. T., and Mrksich, M. (2002) Carbohydrate arrays for the evaluation of protein binding and enzymatic modification. *Chem. Biol. 9*, 443−454.

(7) Kato, M., and Mrksich, M. (2004) Using model substrates to study the dependence of focal adhesion formation on the affinity of integrin−ligand complexes. *Biochemistry 43*, 2699−2707.

(8) Fazio, F., Bryan, M. C., Blixt, O., Paulson, J. C., and Wong, C.-H. (2002) Synthesis of sugar arrays in microtiter plate. *J. Am. Chem. Soc. 124*, 14397−14402.

(9) Park, S., Lee, M.-R., Pyo, S.-J., and Shin, I. (2004) Carbohydrate chips for studying high-throughput carbohydrate-protein interactions. *J. Am. Chem. Soc. 126*, 4812−4819.

(10) Plant, A. L., Brigham-Burke, M., Petrella, E. C., and O'Shannessy, D. J. (1995) Phospholipid/alkanethiol bilayers for cell-surface receptor studies by surface plasmon resonance. *Anal. Biochem. 226*, 342−348.

(11) Peterlinz, K. A., and Georgiadis, R. (1996) In situ kinetics of self-assembly by surface plasmon resonance spectroscopy. *Langmuir 12*, 4731−4740.

(12) Liedberg, B., Nylander, C., and Lundström, I. (1983) Surface plasmon resonance for gas detection and biosensing. *Sens. Actuators 4*, 299−304.

(13) Flanagan, M. T., and Pantell, R. H. (1984) Surface plasmon resonance and immunosensors. *Electron. Lett. 20*, 968−970.

(14) Matsubara, K., Kawata, S., and Minami, S. (1988) Optical chemical sensor based on surface plasmon measurement. *Appl. Opt. 27*, 1160−1163.

(15) Suda, Y., Marques, D., Kermode, J. C., Kusumoto, S., and Sobel, M. (1993) Structural characterization of heparins binding domain for human platelets. *Thromb. Res. 69*, 501−508.

(16) Poletti, L. F., Bird, K. E., Marques, D., Harris, R. B., Suda, Y., and Sobel, M. (1997) Structural aspects of heparin responsible for interactions with von Willebrand factor. *Arterioscler., Thromb., Vasc. Biol. 17*, 925−931.

(17) Koshida, S., Suda, Y., Fukui, Y., Ormsby, J., Sobel, M., and Kusumoto, S. (1999) Synthesis of heparin partial structures and their binding activities to platelets. *Tetrahedron Lett. 40*, 5725−5728.

(18) Koshida, S., Suda, Y., Sobel, M., and Kusumoto, S. (2001) Synthesis of oligomeric assemblies of a platelet-binding key disaccharide in heparin and their biological activities. *Tetrahedron Lett. 42*, 1289−1292.

(19) Weis, C. D., and Newkome, G. R. (1990) Building-blocks for cascade polymers. 3. Facile elimination of nitrous-acid form quaternary nitroalkanes. *J. Org. Chem. 55*, 5801−5802.

(20) Ashton, P. R., Boyd, S. E., Brown, C. L., Nepogodiev, S. A., Meijer, E. W., Peerlings, H. W. I., and Stoddart, J. E. (1997) Synthesis of glycodendrimers by modification of poly(propylene imine) dendrimers. *Chem.—Eur. J. 3*, 974−984.

(21) Sobel, M., Soler, D. F., Kermode, J. C., and Harris, R. B. (1992) Localization and characterization of a heparin binding domain peptide of human von Willebrand factor. *J. Biol. Chem. 267*, 8857−886.

(22) Cruz, M. A., Handin, R. I., and Wise, R. J. (1993) The interaction of the von Willebrand factor A1 domain with platelet glycoprotein Ib Ix−The role of glycosylation and disulfide bonding in a monomeric recombinant A1 domain protein. *J. Biol. Chem. 268*, 21238−21245.

(23) Rastegar-Lari, G., Villoutreix, B. O., Ribba, A. S., Legendre, P., Meyer, D., and Baruch, D. (2002) Two clusters of charged residues located in the electropositive face of the von Willebrand factor A1 domain are essential for heparin binding. *Biochemistry 41*, 6668−6678.

(24) Presta, M., Maier, J. A., Rusnati, M., and Ragnotti, G. (1989) Basic fibroblast growth factor is released from endothelial extracellular matrix in a biologically active form. *J. Cell. Physiol. 140*, 68−74.

(25) Koshida, S., Suda, Y., Arano, A., Sobel, M., and Kusumoto, S. (2001) An efficient method for the assembly of sulfated oligosaccharides using reductive animation. *Tetrahedron Lett. 42*, 1293−1296.

(26) Ratner, D. M., Adams, E. W., Su, J., O'Keefe, B. R., Mrksich, M., and Seeberger, P. H. (2004) Probing protein−carbohydrate interactions with microarrays of synthetic oligosaccharides. *ChemBioChem 5*, 379−383.

(27) Suda, Y., Kusumoto, S., and Arano, A. (2003) Japan Patent P2003-83969A.

(28) Karamanska, R., Mukhopadyay, B., Russell, D. A., and Field, R.A. (2005) Thioctic acid amides: convenient tethers for achieving low nonspecific protein binding to carbohydrates presented on gold surfaces. *Chem. Commun.* 3334−3336.

(29) de Paz, J. L., Noti, C., and Seeberger, P. H. (2006) Microarrays of synthetic heparin oligosaccharides. *J. Am. Chem. Soc. 128*, 2766−2767.

(30) Feizi, T., and Chai, W. (2004) Oligosaccharide microarrays to decipher the glyco code. *Nat. Rev. 5*, 582−588.

BC0600620

Synthesis and *in Vitro* Characterization of Antigen-Conjugated Polysaccharide as a CpG DNA Carrier

Naohiko Shimada,[†] Ken J. Ishii,[§,⊥] Yoichi Takeda,[†] Cevayir Coban,[§,∥] Yuichi Torii,[⊥] Seiji Shinkai,[‡,#] Shizuo Akira,[§,⊥,∥] and Kazuo Sakurai*,[†]

Department of Chemical Processes & Environments, The University of Kitakyushu, 1-1, Hibikino, Wakamatu-ku, Kitakyushu, Fukuoka 808-0135, Japan, Department of Chemistry & Biochemistry, Graduate School of Engineering, and Center for Future Chemistry, Kyushu University, Motooka 744, Nishi-ku, Fukuoka 819-0395, Japan, and Exploratory Research for Advanced Technology (ERATO), Japan Science and Technology Agency (JST), and Department of Host Defense and The 21st Century COE, Combined Program on Microbiology and Immunology, Research Institute for Microbial Diseases, Osaka University, Osaka 565-0871, Japan. Received March 20, 2006; Revised Manuscript Received July 4, 2006

Oligodeoxynucleotides containing unmethylated CpG sequences (CpG DNAs) are known as an immune adjuvant. CpG DNAs coupled with a particular antigen enabling both CpG DNA and antigen delivery to the same antigen-presenting cell have been shown to be more effective. Based on our previous finding that β-(1→3)-D-glucan schizophyllan (SPG) can be used as a CpG DNA carrier, here we present the synthesis of an antigen-conjugated SPG and the characterization of the conjugate. Ovalbumin (OVA, 43 kDa) was used as a model antigen, and two OVA were conjugated to one SPG molecule (M_w = 150 000), denoted by OVA−SPG. Circular dichroism and gel electrophoresis showed that OVA−SPG could form a complex with a $(dA)_{40}$-tailed CpG DNA at the 3′ end (1668-$(dA)_{40}$). When OVA−SPG was added to macrophages (J774.A1), the amount of the ingested OVA−SPG was increased compared with that of OVA itself, suggesting that Dectin-1 (proinflammatory nonopsonic receptor for β-glucans) is involved to ingest OVA−SPG. Furthermore, the complex of the conjugate and DNA was co-localized in the same vesicles, implying that OVA (antigen) and CpG DNA (adjuvant) were ingested into the cell at the same time. This paper shows that OVA−SPG can be used as a CpG DNA carrier to induce antigen-specific immune responses.

INTRODUCTION

Antigen-presenting cells (APCs), particularly dendritic cells, macrophages, and B-cells, play a crucial role in initiating immune responses. Generally, the immune responses are outcomes of the following events: foreign proteins are engulfed by APCs with phagocytosis and the fragments of the protein are presented on the surface of APCs as a major histocompatibility complex (MHC). Naïve T cells bind MHC through T cell receptors, eventually, to induce differentiation of T cells into two cell subsets: T helper 1 (Th1) and T helper 2 (Th2) cells, depending on what cytokines are induced.

Oligodeoxynucleotides containing unmethylated CpG sequences (CpG DNAs) are known as an immune adjuvant to effectively induce Th1 response (*1*−*4*). After CpG DNAs are engulfed by APCs, they are recognized by toll-like receptor 9 (TLR-9) in phagosome-like vesicles to produce cytokines (*5*, *6*). Among pro-inflammatory cytokines induced by CpG DNAs, interleukin (IL)-12 facilitates development of Th1 cells, and thus Th1 cells produce interferon γ (IFN-γ), which can suppress the differentiation of Th2 cells (*7*). Consequently, CpG DNAs can decrease Th2-mediated IgE production, which is a major cause of allergy if excessively secreted. Taking advantage of this response of CpG DNAs, they can be used as an antiallergy adjuvant. Especially, when phagocytosis-mediated antigen presentation is coupled with TLR-9-triggered events in the same cell, the resultant cytokines and co-stimulatory molecules should develop antigen-specific Th1 immunity. Therefore, to effectively induce this type of immunity, it is essentially important that CpG DNA and antigen are co-delivered to the same APC. The importance of the co-delivery has been proved by several groups using alum (*8*), cationic liposome (*9*), or bifunctional cross-linker (*10*, *11*). However, there are some drawbacks in those methods. The most serious one is that CpG DNA is quickly degraded by nuclease under biological conditions. To protect CpG DNA, the terminal nucleotides are converted to phosphorothioate (*12*); however, phosphorothioate creates cytotoxicity and undesirable side effects (*13*, *14*). Furthermore, cytotoxicity of cationic liposomes sometimes leads to serious side effects (*15*−*17*).

We found that a natural polysaccharide called schizophyllan (SPG)[1] forms a complex with single-stranded homo-polynucleotides (*18*). SPG is composed of a β-(1→3)-D-glucan main chain, and one β-(1→6)-D-glycosyl side chain links to the main chain every three glucose residues (Figure 1) (*19*). The complex can protect the bound DNA against nuclease-mediated hydrolysis or nonspecific binding to serum proteins. We have showed that these characteristics make it possible to use native phos-

* Corresponding author. Tel: +81-93-695-3294. Fax: +81-93-695-3368. E-mail: sakurai@env.kitakyu-u.ac.jp.

[†] The University of Kitakyushu.

[§] Japan Science and Technology Agency (JST).

[⊥] Department of Host Defense, Research Institute for Microbial Diseases, Osaka University.

[∥] The 21st Century COE, Combined Program on Microbiology and Immunology, Research Institute for Microbial Diseases, Osaka University.

[‡] Graduate School of Engineering, Kyushu University.

[#] Center for Future Chemistry, Kyushu University.

[1] Abbreviations: FITC, fluorescein isothiocyanate; FACS, fluorescence activated cell sorting; OVA, ovalbumin; F−OVA, FITC-labeled OVA; F−OVA−SPG, FITC-labeled OVA−SPG; CLSM, confocal laser scanning microscopy; ROX, rhodamine X; ROX-$(dA)_{40}$, rhodamine X-labeled $(dA)_{40}$; 1668-$(dA)_{40}$, 5′-TCC ATG ACG TTC CTG ATG-$(dA)_{40}$-3′; SPG, schizophyllan.

10.1021/bc060070g CCC: $33.50 © 2006 American Chemical Society
Published on Web 08/30/2006

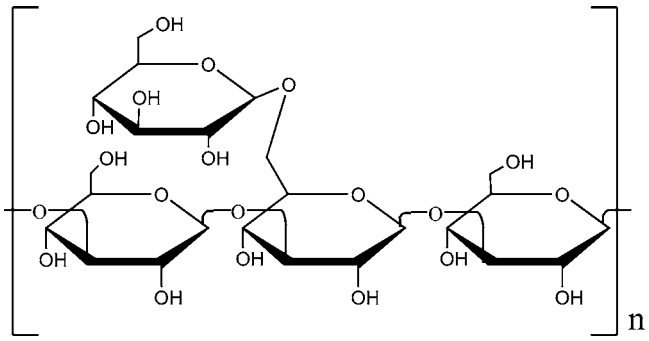

Figure 1. Repeating unit of schizophyllan.

phodiester DNAs for antisense therapy (*20*−*22*). Furthermore, SPG was selectively distributed in reticuloendothelial tissues such as liver, spleen lymph node, and bone marrow (*23*). On the basis of these findings, we have applied the SPG/DNA complex to a CpG DNA carrier. When the complex was added to macrophages or spleen cells, the secretion of IL-12 was enhanced over that with the naked dose. Moreover, when CpG DNA was complexed with SPG and intraperitoneally injected into mouse, the maximum secretion of IFN-γ was found to be twice as large as that invoked by the naked doses, and the secretion period was prolonged dramatically (*24*, *25*). These excellent performances should be ascribed to both the stability of the SPG composite and the reticuloendothelial localization of SPG itself. In this paper, we synthesized an antigen-conjugated SPG and examined the performance of the conjugate as a CpG DNA carrier using circular dichroism (CD), fluorescence activated cell sorting (FACS) analysis, and confocal laser scanning microscopy (CLSM).

EXPERIMENTAL PROCEDURES

Materials. Mitsui Sugar Co., Ltd. (Japan) kindly supplied the SPG sample. The weight-average molecular weight (M_w) and the number of repeating units were found to be 1.5×10^5 and 231, respectively. Ovalbumin (OVA, a model antigen) was purchased from Sigma-Aldrich. As a CpG DNA, we adopted the sequence of 5′-TCC ATG ACG TTC CTG ATG-3′. To combine these sequences with SPG, we attached a $(dA)_{40}$ tail at the 3′ end (*26*). Hereinafter, we denote this phosphodiester 5′-TCC ATG ACG TTC CTG ATG-$(dA)_{40}$-3′ as 1668-$(dA)_{40}$. For CD and CLSM, we used $(dA)_{40}$ and rhodamine X-labeled $(dA)_{40}$ (ROX-$(dA)_{40}$), respectively. All DNA samples were synthesized at Hokkaido System Science (Hokkaido, Japan) and purified with high-pressure liquid chromatography. The lengths of the synthesized DNAs were confirmed with denatured PAGE. The fetal bovine serum (FBS), and penicillin/streptomycin were purchased from Gibco/BRL. Dulbecco's modified Eagle's medium (DMEM) was obtained from Nissui Pharmaceutical Co., Ltd.

Preparation of OVA-Conjugated SPG. We already established a method to introduce functional groups only to the side chain of SPG (*26*, *27*). SPG (100 mg) was dissolved in water, sodium periodate (27 mg) was added to the solution, and the solution was stirred at 5 °C for 2 days to obtain an oxidized SPG bearing aldehyde groups. The oxidized SPG (1.25 mg/mL), OVA (2.5 mg/mL), and sodium cyanoborohydride (100 mg) were dissolved into 0.1 M sodium bicarbonate, and the mixture was stirred at room temperature for 14 h. The OVA-conjugated SPG (OVA−SPG) was purified by gel filtration (Sephacryl S200, Amersham), and the purity was examined with SDS−PAGE. The amount of OVA introduced to SPG was determined with a protein quantification kit (DOJINDO).

Analysis of Gel Electrophoresis. OVA−SPG (or unmodified SPG) was dissolved in 97% DMSO and 3% H_2O. The OVA−SPG solution (final concentration 0.67 mg/mL) was added to 1668-$(dA)_{40}$ (final concentration 0.01 mg/mL) in a 30 mM Tris-HCl (pH = 7.0) buffer containing 0.15 M NaCl. The mixture was incubated at 5 °C for 2 days, and the formation of the complex was examined with agarose gel (2%) electrophoresis. The bands were visualized with GelStar (Amersham).

Measurement of CD Spectra. OVA−SPG (or unmodified SPG) was dissolved in 97% DMSO and 3% H_2O. The OVA−SPG solution (final concentration 0.67 mg/mL) was added to $(dA)_{40}$ (final concentration 0.175 mg/mL) in a 30 mM Tris-HCl (pH = 7.0) buffer containing 0.15 M NaCl. The mixture was incubated at 5 °C for 2 days. CD was measured at 5 °C on a JASCO J-720WI spectrometer with a 1 mm cell.

Cell Culture. Murine macrophage-like cells (J774.A1) were obtained from the American Type Culture Collection (ATCC, Rockville, MD). The J774.A1 cells were maintained in DMEM supplemented with 10% FBS, containing a 1 wt % penicillin/streptomycin mixture. The cell incubation was always carried out at 37 °C in fully humidified air containing 5 wt % CO_2.

Fluorescence Activated Cell Sorting (FACS) Analysis and Confocal Laser Scanning Microscopy (CLSM). FITC-labeled OVA−SPG was prepared for FACS and CLSM. FITC (72 μL of a 5 mg/mL solution) was added to 1 mL of OVA−SPG (4.4 mg/mL) in 0.1 M sodium bicarbonate (pH = 9.0), and the mixture was stirred at 4 °C for 15 h. The mixture was purified with dialysis and gel filtration. FITC-labeled OVA was prepared by the same method. The amounts of OVA and FITC were determined with a protein quantification kit and the UV absorbance of FITC, respectively. The FITC/protein (F/P) molar ratios were 1.5 and 1.6 for F−OVA−SPG and F−OVA, respectively.

For FACS, J774.A1 cells were plated in a 48-well dish (2×10^6 cells/mL; 200 μL/well) and allowed to attach to the wells at 37 °C for 24 h. The cells were washed twice with DMEM without FBS, and then 25 μg/mL (200 μL) OVA in F−OVA−SPG or F−OVA was added to the cells. The cells were incubated at 37 °C for 2 h, washed twice with PBS, harvested with a scraper, and fixed with 5% HCHO at 4 °C for 20 min. The number of the cells that had FITC was counted with an EPICS XL (BECKMAN COULTER). For CLSM, J774.A1 cells were plated in a glass-bottom dish (ϕ = 12 mm) and allowed to attach to the dish at 37 °C for 24 h. The cells were washed twice with DMEM without FBS, and 200 μL of F−OVA−SPG/ROX-$(dA)_{40}$ complex or F−OVA was added to the cells at the concentration of 25 μg/mL OVA in F−OVA−SPG or F−OVA and 37.5 μg/mL ROX-$(dA)_{40}$ in the complex. The cells were incubated at 37 °C for 2 h and washed twice with PBS and fixed with 5% HCHO containing 4′,6-diamidino-2-phenylindole (DAPI) at 4 °C for 20 min. The cells were observed with a Nikon fluorescence microscope (ECLIPS TE2000-U) with a Radiance2100 BioRad confocal scan unit attached.

RESULTS AND DISCUSSION

Preparation of OVA-Conjugated SPG. OVA−SPG was synthesized as described in the Experimental Procedures section. Figure 2A shows the gel filtration chromatograms of a crude OVA−SPG (before purification, including a large amount of unconjugated OVA) and OVA itself. OVA has a large peak around 40−45 mL, and the crude OVA−SPG peak is overlaid with that of OVA. It can be seen that OVA−SPG conjugate was eluted at 25−30 mL as a shoulder. We carefully collected the shoulder ranging 25−28 mL. Figure 2B compares SDS−PAGE patterns for OVA−SPG before and after the purification, as well as free OVA. Before the purification, two bands were observed (lane 4), corresponding the migrated and unmigrated bands to free OVA and OVA−SPG, respectively. After the purification, there was no appreciable band of free OVA,

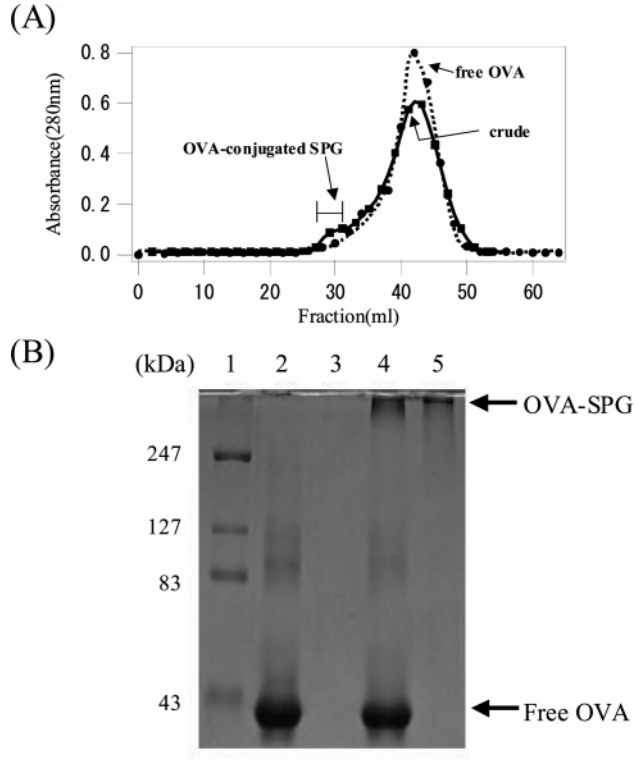

Figure 2
Shimada et al

Figure 2. (A) Gel filtration chromatograms of OVA−SPG and OVA. The shoulder ranging 25−28 mL was collected. (B) Analysis of OVA−SPG by 8% SDS−PAGE: lane 1, a molecular weight marker; lane 2, OVA only; lane 3, SPG only; lane 4, the crude sample examined in the gel filtration; lane 5, the purified sample obtained from the shoulder.

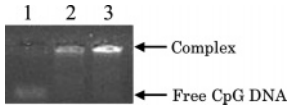

Figure 3. Confirmation of complex formation between OVA−SPG and 1668-$(dA)_{40}$ by 2% agarose gel electrophoresis stained with GelStar: lane 1, 1668-$(dA)_{40}$ only; lane 2, mixture of unmodified SPG and 1668-$(dA)_{40}$; lane 3, mixture of OVA−SPG and 1668-$(dA)_{40}$; [unmodified SPG] = 0.42 mg/mL, [OVA−SPG] = 0.67 mg/mL, and [1668-$(dA)_{40}$] = 0.01 mg/mL.

indicating that the purification removed all free OVA. We determined that 0.4 mg of OVA per 1 mg of OVA−SPG was introduced, meaning that two OVA (43 kDa) molecules were attached to one SPG (M_w = 150 000) molecule.

DNA Binding Ability of OVA-SPG. Figure 3 shows agarose gel electrophoresis when 1668-$(dA)_{40}$ only, SPG/1668-$(dA)_{40}$, and OVA−SPG/1668-$(dA)_{40}$ were applied. The 1668-$(dA)_{40}$ migrated into the gel. On the other hand, the complexed 1668-$(dA)_{40}$ with unmodified SPG stayed at the well and never moved to show a retarded band, which is evidence of the complex formation (lane 2) (*28*). The retarded band at the well was observed in lane 3 in the same way as in lane 2, indicating that OVA−SPG formed a complex with 1668-$(dA)_{40}$. To confirm the complexation, CD spectra were measured (Figure 4A). In this case, for convenience, we used $(dA)_{40}$ instead of 1668-$(dA)_{40}$. OVA−SPG itself and SPG itself were not CD-active, showing no spectrum at 240−320 nm. When OVA−SPG was added to $(dA)_{40}$, a negative band at 250 nm disappeared, and a new negative band at 275 nm appeared. The band at 280 nm in $(dA)_{40}$ itself seemed to red-shift and increase in intensity upon complexation with OVA−SPG. These spectral changes completely agree with those of the SPG/$(dA)_{40}$ complex (*29*),

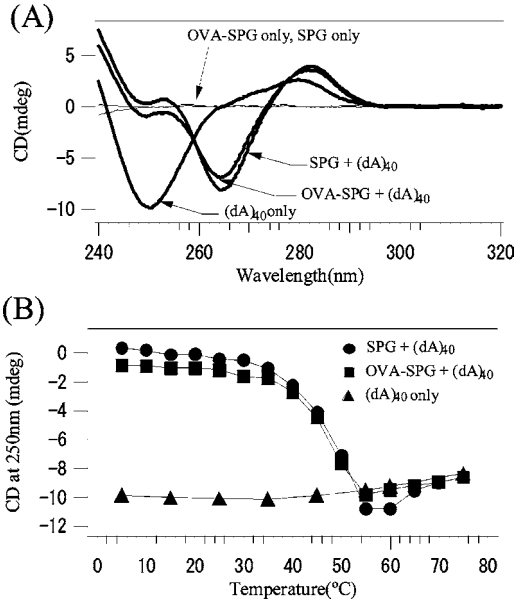

Figure 4. (A) Comparison of CD spectra for the mixture of OVA−SPG + $(dA)_{40}$, unmodified SPG + $(dA)_{40}$, SPG only, OVA−SPG only, and $(dA)_{40}$ only measured at 5 °C in 30 mM Tris-HCl (pH = 7.0) containing 0.15 M NaCl and 8.3% DMSO. (B) Temperature dependence of the CD intensity at 250 nm of the complexes and $(dA)_{40}$ only. [unmodified SPG] = 0.42 mg/mL, [OVA−SPG] = 0.67 mg/mL, and [$(dA)_{40}$] = 0.175 mg/mL.

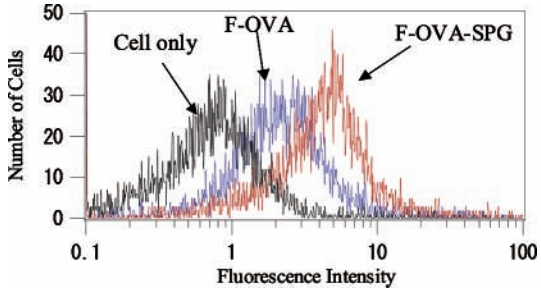

Figure 5. FACS profiles of F−OVA or F−OVA−SPG-treated macrophage-like cells (J774.A1). OVA (25 μg/mL) in F−OVA or F−OVA−SPG was added to the cells in DMEM without FBS at 37 °C for 2 h. Black line, blue line, and red line indicate untreated cells, F−OVA-treated cells, and F−OVA−SPG-treated cells, respectively.

indicating that the attachment of two OVA molecules to SPG does not interfere in the complexation ability at all.

Figure 4B plots the CD intensity at 250 nm of OVA−SPG/$(dA)_{40}$ complex against temperature, compared with SPG/$(dA)_{40}$ and $(dA)_{40}$. Owing to the presence of the complexes, 250 nm CD intensities for OVA−SPG/$(dA)_{40}$ and SPG/$(dA)_{40}$ are larger than that of $(dA)_{40}$ at low temperatures. They merge into that of $(dA)_{40}$ above 55 °C, indicating that the dissociation of the complex takes place at this temperature. The melting (or dissociation) curves are almost the same between the two complexes. These results indicate that OVA−SPG can form a thermally stable complex with DNA in the same manner as SPG/DNA complexes. The morphological (*30*) and fundamental thermodynamic properties (*18*, *28*) of SPG/nucleic acid complexes have been well studied, and the similarity in CD spectrum between SPG/DNA and OVA−SPG/DNA complexes implies that the basic properties of the complex are not changed after conjugation of OVA.

Ingestion and Distribution of OVA−SPG and Complexed DNA. Figure 5 compares the FACS profiles between F−OVA and F−OVA−SPG when these were added to J774.A1. The number of cells that had ingested FITC was increased when F−OVA−SPG was added, compared with F−OVA. This result

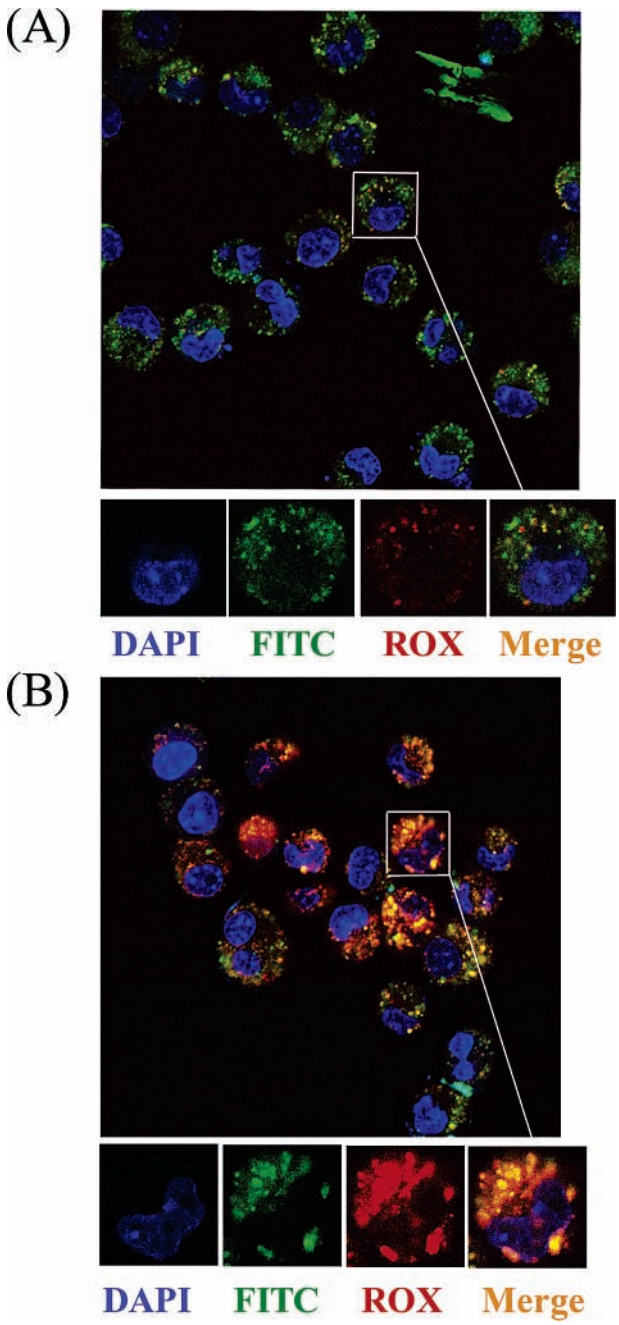

Figure 6. Intracellular localization of (A) a mixture of unmodified SPG/ROX-$(dA)_{40}$ and F−OVA and (B) the complex made from F−OVA−SPG and ROX-$(dA)_{40}$ in J774.A1 cells. The blue, green, and red colors correspond to DAPI (nucleus), FITC (OVA), and ROX (DNA), respectively. The yellow color is the outcome of the merge between FITC and ROX, which is only observed for the complex.

indicates that the presence of SPG enhanced the cellular ingestion. It has been reported that β-1,3-glucans, especially for zymosan and other cell-wall glucans, are recognized by a receptor called Dectin-1 (*31*) and are internalized by phagocytosis (*32*). Increased uptake of OVA−SPG might be ascribed to the receptor-mediated uptake for SPG.

By use of CLSM, we examined the intracellular distribution for the OVA−SPG/ROX-$(dA)_{40}$ complex compared with a mixture of F−OVA and SPG/ROX-$(dA)_{40}$. Figure 6A shows the CLSM image when a mixture of F−OVA and the unmodified SPG/ROX-$(dA)_{40}$ complex were added to the J774.A1 cells, where F−OVA and the SPG/ROX-$(dA)_{40}$ complex do not form a complex. The image A shows that F−OVA and ROX-$(dA)_{40}$ are distributed heterogeneously within the cytosol. However, most of F−OVA and ROX-$(dA)_{40}$ seem not to localize at the same vesicles, indicating that both objects were ingested independently. Figure 6B is the CLSM image when the F−OVA−SPG/ROX-$(dA)_{40}$ complex was added. F−OVA−SPG and ROX-$(dA)_{40}$ are distributed heterogeneously within cytosol in the same manner as Figure 6A. In contrast to the previous image, most images are yellow, indicating that a large number of F−OVA−SPG and ROX-$(dA)_{40}$ are colocalized in the same vesicles. In addition, there seemed to be a quantitative difference in the ingested CpG DNA between photos A and B in Figure 6. OVA−SPG induces more uptake of CpG DNA than SPG itself. Presumably, an unknown uptake mechanism for OVA as an antigen might be responsible for this increment.

The present results imply that OVA (antigen) and CpG DNA (adjuvant) were ingested at the same time and delivered to the same vesicles when CpG DNA and OVA−SPG were complexed. Therefore, we can speculate that the present complex can antigen-specifically induce a TLR-9-dependent Th1 immune response.

CONCLUSIONS

An OVA-conjugated SPG was synthesized, and the characterization of the conjugate was carried out. Composition analysis showed that two OVA molecules are attached to one SPG molecule, and agarose gel electrophoresis and CD proved that the conjugate can form a complex with 1668-$(dA)_{40}$. When the FITC-labeled conjugate was added to J774.A1 cells, the number of cells that had ingested FITC was increased compared with OVA itself, suggesting that the cells ingested the conjugate by SPG/Dectin-1 recognition. CLSM showed that the ingested OVA and DNA were in the same vesicles. We believe that antigen-conjugated SPG is applicable as a carrier to induce an antigen-specific and TLR-9-dependent Th1 immune response.

ACKNOWLEDGMENT

This work is financially supported by JST SORST and ERATO programs and Grant-in-Aid for Scientific Research (16350068 and 16655048).

LITERATURE CITED

(1) Klinman, D. M., Yi, A. K., Beaucage, S. L., Conover, J., and Krieg, A. M. (1996) CpG motifs present in bacteria DNA rapidly induce lymphocytes to secrete interleukin 6, interleukin 12, and interferon gamma. *Proc. Natl. Acad. Sci. U.S.A. 93*, 2879−2883.

(2) Krieg, A. M., Yi, A. K., Matson, S., Waldschmidt, T. J., Bishop, G. A., Teasdale, R., Koretzky, G. A., and Klinman, D. M. (1995) CpG motifs in bacterial DNA trigger direct B-cell activation. *Nature 374*, 546−549.

(3) Roman, M., Martin-Orozco, E., Goodman, J. S., Nguyen, M. D., Sato, Y., Ronaghy, A., Kornbluth, R. S., Richman, D. D., Carson, D. A., and Raz, E. (1997) Immunostimulatory DNA sequences function as T helper-1-promoting adjuvants. *Nat. Med. 3*, 849−854.

(4) Sparwasser, T., Miethke, T., Lipford, G., Erdmann, A., Hacker, H., Heeg, K., and Wagner, H. (1997) Macrophages sense pathogens via DNA motifs: induction of tumor necrosis factor-alpha-mediated shock. *Eur. J. Immunol. 27*, 1671−1679.

(5) Latz, E., Schoenemeyer, A., Visintin, A., Fitzgerald, K. A., Monks, B. G., Knetter, C. F., Lien, E., Nilsen, N. J., Espevik, T., and Golenbock, D. T. (2004) TLR9 signals after translocating from the ER to CpG DNA in the lysosome. *Nat. Immunol. 5*, 190−198.

(6) Hemmi, H., Kaisho, T., Takeda, K., and Akira, S. (2003) The roles of Toll-like receptor 9, MyD88, and DNA-dependent protein kinase catalytic subunit in the effects of two distinct CpG DNAs on dendritic cell subsets. *J. Immunol. 170*, 3059−3064.

(7) Mosmann, T. R., Schumacher, J. H., Street, N. F., Budd, R., O'Garra, A., Fong, T. A., Bond, M. W., Moore, K. W., Sher, A., and Fiorentino, D. F. (1991) Diversity of cytokine synthesis and function of mouse CD4+ T cells. *Immunol. Rev. 123*, 209−229.

(8) Shirota, H., Sano, K., Kikuchi, T., Tamura, G., and Shirato, K. (2000) Regulation of T-helper type 2 cell and airway eosinophilia by transmucosal coadministration of antigen and oligodeoxynucleotides containing CpG motifs. *Am. J. Respir. Cell Mol. Biol. 22*, 176−182.

(9) Gursel, I., Gursel, M., Ishii, K. J., and Klinman, D. M. (2001) Sterically stabilized cationic liposomes improve the uptake and immunostimulatory activity of CpG oligonucleotides. *J. Immunol. 167*, 3324−3328.

(10) Shirota, H., Sano, K., Hirasawa, N., Terui, T., Ohuchi, K., Hattori, T., Shirato, K., and Tamura, G. (2001) Novel roles of CpG oligodeoxynucleotides as a leader for the sampling and presentation of CpG-tagged antigen by dendritic cells. *J. Immunol. 167*, 66−74.

(11) Heit, A., Maurer, T., Hochrein, H., Bauer, S., Huster, K. M., Busch, D. H., and Wagner, H. (2003) Cutting edge: Toll-like receptor 9 expression is not required for CpG DNA-aided cross-presentation of DNA-conjugated antigens but essential for cross-priming of CD8 T cells. *J. Immunol. 170*, 2802−2805.

(12) Krieg, A. M., Matson, S., and Fisher, E. (1996) Oligodeoxynucleotide modifications determine the magnitude of B cell stimulation by CpG motifs. *Antisense Nucleic Acid Drug Dev. 6*, 133−139.

(13) Stein, C. A., and Krieg, A. M. (1994) Problems in interpretation of data derived from in vitro and in vivo use of antisense oligodeoxynucleotides. *Antisense Res. Dev. 4*, 67−69.

(14) Stein, C. A., and Cheng, Y. C. (1993) Antisense oligonucleotides as therapeutic agents is the bullet really magical. *Science 261*, 1004−1012.

(15) Lappalainen, K., Jaaskelainen, I., Syrjanen, K., Urtti, A., and Syrjanen, S. (1994) Comparison of cell proliferation and toxicity assays using two cationic liposomes. *Pharm. Res. 11*, 1127−1131.

(16) Dokka, S., Toledo, D., Shi, X., Castranova, V., and Rojanasakul, Y. (2000) Oxygen radical-mediated pulmonary toxicity induced by some cationic liposomes. *Pharm. Res. 17*, 521−525.

(17) Filion, M. C., and Phillips, N. C. (1997) Toxicity and immunomodulatory activity of liposomal vectors formulated with cationic lipids toward immune effector cells. *Biochim. Biophys. Acta 1329*, 345−356.

(18) Sakurai, K., and Shinkai, S. (2000) Molecular Recognition of Adenine, Cytosine, and Uracil in a Single-Stranded RNA by a Natural Polysaccharide: Schizophyllan. *J. Am. Chem. Soc. 122*, 4520−4521.

(19) Tabata, K., Ito, W., Kojima, T., Kawabata, S., and Misaki, A. (1981) Ultrasonic degradation of schizophyllan, an antitumor polysaccharide produced by *Schizophyllum commune* Fries. *Carbohydr. Res. 89*, 121−135.

(20) Mizu, M., Koumoto, K., Kimura, T., Sakurai, K., and Shinkai, S. (2004) Protection of polynucleotides against nuclease-mediated hydrolysis by complexation with schizophyllan. *Biomaterials 25*, 3109−3116.

(21) Mizu, M., Koumoto, K., Anada, T., Sakurai, K., and Shinkai, S. (2004) Antisense oligonucleotides bound in the polysaccharide complex and the enhanced antisense effect due to the low hydrolysis. *Biomaterials 25*, 3117−3123.

(22) Mizu, M., Koumoto, K., Anada, T., Karinaga, R., Kimura, T., Nagasaki, T., Shinkai, S., and Sakurai, K. (2004) Enhancement of the antisense effect of polysaccharide−polynucleotide complexes by preventing the antisense oligonucleotide from binding to proteins in the culture medium. *Bull. Chem. Soc. Jpn. 77*, 1101−1110.

(23) Horiba, M., Akima, K., Hase, T., Arika, T., Amemiya, K., Munechika, K., Tabata, K., and Aimoto, T. (1988) [Studies on metabolism and disposition of sizofiran (SPG), an anti-tumor polysaccharide. I. Excretion and tissue distribution of 14C-SPG]. *Yakugaku Zasshi 108*, 763−771.

(24) Mizu, M., Koumoto, K., Anada, T., Matsumoto, T., Numata, M., Shinkai, S., Nagasaki, T., and Sakurai, K. (2004) A polysaccharide carrier for immunostimulatory CpG DNAs to enhance cytokine secretion. *J. Am. Chem. Soc. 126*, 8372−8873.

(25) Shimada, N., Ishii, K., Takeda, Y., Mizu, M., Anada, T., Minari, J., Coban, C., Shinkai, S., Akira, S., and Sakurai, K. A Polysaccharide carrier for CpG DNAs to effectively deliver native phosphodiester DNAs. *Biomacromolecules*, submitted for publication.

(26) Matsumoto, T., Numata, M., Anada, T., Mizu, M., Koumoto, K., Sakurai, K., Nagasaki, T., and Shinkai, S. (2004) Chemically modified polysaccharide schizophyllan for antisense oligonucleotides delivery to enhance the cellular uptake efficiency. *Biochim. Biophys. Acta 1670*, 91−104.

(27) Koumoto, K., Kimura, T., Mizu, M., Sakurai, K., and Shinkai, S. (2001) Chemical modification of schizophyllan by introduction of a cationic charge into the side chain which enhances the thermal stability of schizophyllan-poly(C) complexes. *Chem. Commun. (Cambridge*), 1962−1963.

(28) Sakurai, K., Mizu, M., and Shinkai, S. (2001) Polysaccharide−polynucleotide complexes. 2. Complementary polynucleotide mimic behavior of the natural polysaccharide schizophyllan in the macromolecular complex with single-stranded RNA and DNA. *Biomacromolecules 2*, 641−650.

(29) Mizu, M., Koumoto, K., Kimura, T., Sakurai, K., and Shinkai, S. (2003) Polysaccharide-polynucleotide complexes Part 17. Solvent effects on conformational-transition of polydeoxyadenylic acid in the complex with schizophyllan. *Polym. J. 35*, 714−720.

(30) Bae, A. H., Lee, S. W., Ikeda, M., Sano, M., Shinkai, S., and Sakurai, K. (2004) Rod-like architecture and helicity of the poly(C)/schizophyllan complex observed by AFM and SEM. *Carbohydr. Res. 339*, 251−258.

(31) Brown, G. D., Herre, J., Williams, D. L., Willment, J. A., Marshall, A. S., and Gordon, S. (2003) Dectin-1 mediates the biological effects of beta-glucans. *J. Exp. Med. 197*, 1119−1124.

(32) Herre, J., Marshall, A. S., Caron, E., Edwards, A. D., Williams, D. L., Schweighoffer, E., Tybulewicz, V., Reis e Sousa, C., Gordon, S., and Brown, G. D. (2004) Dectin-1 uses novel mechanisms for yeast phagocytosis in macrophages. *Blood 104*, 4038−4045.

BC060070G

Receptor-Targeted Liposomal Delivery of Boron-Containing Cholesterol Mimics for Boron Neutron Capture Therapy (BNCT)

B.T.S. Thirumamagal,[†,‡] Xiaobin B. Zhao,[†,§] Achintya K. Bandyopadhyaya,[‡] Sureshbabu Narayanasamy,[‡] Jayaseharan Johnsamuel,[‡] Rohit Tiwari,[‡] Danold W. Golightly,[∥] Vimalkumar Patel,[○] Brian T. Jehning,[○] Marina V. Backer,[○] Rolf F. Barth,[⊥,#] Robert J. Lee,[§,#,▽] Joseph M. Backer,[○] and Werner Tjarks*[,‡,#]

Division of Medicinal Chemistry & Pharmacognosy, Division of Pharmaceutics, Department of Civil and Environmental Engineering, Department of Pathology, Comprehensive Cancer Center, and Nanoscale Science and Engineering Center of The Ohio State University, Columbus, Ohio 43210, and SibTech, Inc., Newington, Connecticut 06111. Received March 26, 2006; Revised Manuscript Received June 16, 2006

Liposomes have been a main focus of tumor-selective boron delivery strategies in boron neutron capture therapy (BNCT), a binary method for the treatment of cancer that is based on the nuclear reaction between boron atoms and low-energy thermal neutrons. Three novel carboranyl cholesterol derivatives were prepared as lipid bilayer components for the construction of nontargeted and receptor-targeted boronated liposomes for BNCT. A major structural feature of these novel boronated cholesterol mimics is the replacement of the B and the C ring of cholesterol with a carborane cluster. Computational analyses indicated that all three boronated compounds have structural features and physicochemical properties that are very similar to those of cholesterol. One of the synthesized boronated cholesterol mimics was stably incorporated into non-, folate receptor (FR)-, and vascular endothelial growth factor receptor-2 (VEGFR-2)-targeted liposomes. No major differences were found in appearance, size distribution, and lamellarity between conventional dipalmitoylphosphatidylcholine (DPPC)/cholesterol liposomes, nontargeted, and FR-targeted liposomal formulations of this carboranyl cholesterol derivative. FR-targeted boronated liposomes were taken up extensively in FR overexpressing KB cells in vitro, and the uptake was effectively blocked in the presence of free folate. In contrast, a boronated cholesterol mimic incorporated into nontargeted liposomes showed significantly lower cellular uptake. There was no apparent in vitro cytotoxicity in FR overexpressing KB cells and VEGFR-2 overexpressing 293/KDR cells when these were incubated with boronated FR- and (VEGFR-2)-targeted liposomes, respectively, although the former accumulated extensively in KB cells and the latter effectively interacted with VEGFR-2 by causing autophosphorylation and protecting 293/KDR cells from SLT (Shiga-like toxin)−VEGF cytotoxicity.

INTRODUCTION

Boron neutron capture therapy (BNCT) is a binary method for the treatment of cancer (*1*), which is based on the nuclear reaction between boron atoms and low-energy thermal neutrons. Naturally occurring elemental boron has two stable isotopes, namely, boron-10 (^{10}B) and boron-11 (^{11}B). The abundant isotope is ^{11}B (around 80%); however, the most distinguishing property of ^{10}B is its high neutron capture cross section for thermal (slow) neutrons. Hence, the reaction of a neutron with ^{10}B yields two charged particles, a ^{4}He nucleus and a ^{7}Li nucleus, each of which are able to kill tumor cells due to their high linear energy transfer. For successful BNCT, a minimum of 20−30 μg of nonradioactive ^{10}B per gram of tumor tissue is required. Another key requirement for the success of BNCT is the selective delivery of high amounts of boronated compounds to tumor cells, while at the same time, the boron concentration in the cells of surrounding normal tissue should be kept low to minimize the damage to normal tissue.

Liposomes have been a main focus of tumor selective boron delivery strategies in BNCT since research activities in this area were initiated by Hawthorne (*2*) and Yanagie (*3*) in the early 1990s. Design strategies for boron-containing liposomes for BNCT centered on both nontargeted (*4*, *5*), and tumor-targeted formulations. The latter included liposomes conjugated to transferrin (*6*), the epidermal growth factor (EGF) (*7*), antibodies (*8*), α (v)-integrin specific arginine−glycine−aspartate (RGD) peptides (*9*), and folic acid (*10*, *11*). Most liposomes designed for BNCT contained hydrophilic low molecular weight boron agents, which presumably localized in the aqueous core of the liposomes during preparation. These boron agents include sodium borocaptate (BSH) (*12*, *13*) and boronophenylalanine (BPA) (*14*), both of which have been used in clinical BNCT (*1*), negatively charged boron clusters with or without simple substitution patterns (*2*, *15*), as well as carborane cage-substituted polyamines (*11*), acridines (*7*, *8*), porphyrins (*16*), carbohydrates (*17*), and nucleosides (*18*).

Phospholipids are common lipid bilayer components of liposomes and have proven to be effective anchors for boron entities in the form of dual- (*19*, *20*) or single- (*10*, *21*) chain *nido*-carboranyl phospholipid mimics. Cholesterol is another major component of the mammalian cell membrane and most liposomal formulations. It is transported in the blood stream by low-density lipoprotein (LDL). Owing to its natural carrier capability and receptor-targeting specificity, LDL has been

* Corresponding author. Werner Tjarks, The Ohio State University, College of Pharmacy, 500 West 12th Avenue, Columbus, OH 43210; phone (614) 292 7624, fax (614) 292 2435, e-mail: tjarks.1@osu.edu.
† B.T.S.T. and X.B.Z made equal contributions to this manuscript.
‡ Division of Medicinal Chemistry & Pharmacognosy.
§ Division of Pharmaceutics.
∥ Department of Civil and Environmental Engineering.
⊥ Department of Pathology.
Comprehensive Cancer Center.
▽ Nanoscale Science and Engineering Center.
○ SibTech, Inc.

10.1021/bc060075d CCC: $33.50 © 2006 American Chemical Society
Published on Web 08/15/2006

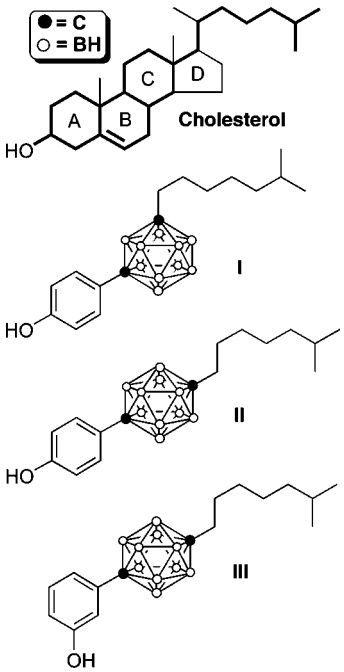

Figure 1. Structures of cholesterol and boronated cholesterol mimics **I**−**III.**

extensively studied as a drug carrier (*22*). Therefore, the development of boron-containing compounds that mimic physiological cholesterol and cholesterol esters is potentially an effective approach for boron delivery to cancer cells via both liposomes and LDL, and thus, extensive efforts in BNCT drug development have focused on such structures (*23*−*30*).

To the best of our knowledge, all synthetic approaches directed toward boron-containing cholesterol derivatives have focused on the attachment of carboranyl moieties to the hydroxyl group of cholesterol via ether or ester linkages. In the present manuscript, we report a novel strategy for the design and synthesis of carboranyl cholesterol mimics. This design strategy is based on a groundbreaking concept developed by Endo et al. for the synthesis of a carboranyl analogues of estradiol (*31*, *32*). Analogous to Endo's carboranyl estradiols, both the B and the C ring of cholesterol were replaced with a carborane cluster in the boronated cholesterol mimics described in this paper (Figure 1). The design and synthesis of these structures, their incorporation into liposomes, and the evaluation of the capacity of these liposomes for efficient boron delivery are the subjects of this paper. Both the folate receptor (FR) (*33*, *34*) and the vascular endothelial growth factor receptor-2 (VEGFR-2) (*35*, *36*) have been identified as important molecular targets for cancer therapy in recent years. The capacity of the designed boronated liposomes for incorporation of receptor-targeting ligands such as folate and VEGF (vascular endothelial growth factor) and the results of in vitro uptake and cytotoxicity studies with the resulting constructs are discussed.

EXPERIMENTAL PROCEDURES

General Chemical Procedures. Proton and carbon-13 NMR spectra were obtained on Bruker (250 MHz or 400 MHz) NMR instruments at The Ohio State University College of Pharmacy. Chemical shifts are reported in parts per million (ppm) from an internal tetramethylsilane standard. The coupling constants are reported in hertz (Hz). High resolution electron impact mass spectrometry (HR-EIMS) was carried out with a Kratos MS-25 instrument with typical ionization conditions of 70 eV electron impact ionization at the Department of Chemistry of The Ohio State University by Dr. Christopher M. Hadad and Ms. Susan Hatcher. Compound visualization on silica gel 60 F_{254} precoated TLC plates (0.25 mm layer thickness) (Merck, Darmstadt, Germany) was attained by UV light. Carborane-containing compounds were selectively visualized by spraying a solution of 0.06% $PdCl_2$/1% aqueous HCl on TLC plates and subsequent heating to ∼120 °C, which caused the slow formation (15−45 s) of gray spots due to the reduction of Pd^{2+} to Pd^0. Reagent-grade solvents were used for column chromatography using silica gel 60, particle size 0.040−0.063 mm (Merck, New Jersey). Standard chemicals were purchased from various vendors. *Para*- and *meta*-carborane were purchased from Katchem, Prague, Czech Republic. All chemicals were used as purchased without further purification. Anhydrous benzene, anhydrous dichloromethane, and anhydrous tetrahydrofurane (THF) were purchased from VWR Scientific Products. THF was additionally dried over sodium metal before use. All chemical syntheses were carried out under argon atmosphere to maintain inert reaction condition unless mentioned otherwise.

1-(4-Methoxyphenyl)-7-(6-methylheptyl)-1,7-dicarba-*closo*-dodecaborane (2). To a solution of 1-(4-methoxyphenyl)-1,7-dicarba-*closo*-dodecaborane (*31*) (**1**) (125 mg, 0.5 mmol) in THF (20 mL) at 0 °C was added *n*-BuLi (2.5 M in hexane, 0.2 mL, 0.51 mmol). The mixture was first stirred at 0 °C for 45 min and then for 1 h at room temperature. Toluene-4-sulfonic acid 6-methylheptyl ester (*37*) (142 mg, 0.5 mmol) in 5 mL THF was added and the resulting mixture stirred for 12 h at room temperature, poured into ice−water (50 mL), extracted with ether (3 × 50 mL), washed with brine, and dried over $MgSO_4$. The solvent was evaporated under vacuum, and the residue was purified by silica gel flash column chromatography using hexanes/ethylacetate (9:1) as the eluent (TLC R_f: 0.5) to give **2** in 61% yield. ^{1}H NMR ($CDCl_3$): δ 0.83−0.85 (d, 6H, J = 6.5 Hz) 1.15−1.38 (m, 9H, CH_2), 2.16 (2H, t, J = 6 Hz), 3.75 (s, 3H), 6.64−6.67 (2H, d, J = 8.6 Hz), 7.51−7.55 (2H, d, J = 8.6 Hz). ^{13}C NMR ($CDCl_3$): δ 19.59, 23.01, 27.40, 28.31, 29.86, 30.12, 30.45, 37.59, 39.20, 54.89, 55.72, 72.23, 113.89, 128.19, 129.39, 160.14. HR-EIMS calcd for $C_{17}H_{34}B_{10}O$ (M^+): 362.3607. Found 362.3585.

1-(4-Methoxyphenyl)-12-(6-methylheptyl)-1,12-dicarba-*closo*-dodecaborane, an intermediate in the synthesis of compound **II**, was obtained by adapting the procedure described for compound **2** using 1-(4-methoxyphenyl)-1,12-dicarba-*closo*-dodecaborane (*31*) as the starting material. Purification by silica gel flash chromatography using hexanes/ethylacetate (9:1) as the eluent (TLC R_f: 0.5) gave 1-(4-methoxyphenyl)-12-(6-methylheptyl)-1,12-dicarba-*closo*-dodecaborane in 52% yield. ^{1}H NMR ($CDCl_3$): δ 0.82−0.84 (d, 6H, J = 6.6 Hz) 1.20−1.39 (m, 9H, CH_2), 2.15 (t, 2H, J = 6.5 Hz), 3.75 (s, 3H), 6.75−6.72 (d, 2H, J = 7.5 Hz), 7.32−7.29 (d, 2H, J = 7.5 Hz). ^{13}C NMR ($CDCl_3$): δ 23.01, 27.40, 28.31, 29.86, 30.12, 30.45, 37.60, 39.20, 55.72, 72.25, 113.64, 113.90, 116.75, 128.58, 129.39, 129.73, 138.59, 159.95. HR-EIMS calcd for $C_{17}H_{34}B_{10}O$ (M^+): 362.3607. Found: 362.3585.

1-(3-Methoxyphenyl)-12-(6-methylheptyl)-1,12-dicarba-*closo*-dodecaborane, an intermediate in the synthesis of compound **III**, was obtained by adapting the procedure described for compound **2** using 1-(3-methoxyphenyl)-1,12-dicarba-*closo*-dodecaborane (*31*) as the starting material. Purification by silica gel flash chromatography using hexanes/ethylacetate (9:1) as the eluent (TLC R_f: 0.5) gave the 1-(3-methoxyphenyl)-12-(6-methylheptyl)-1,12-dicarba-*closo*-dodecaborane in 55% yield. ^{1}H NMR ($CDCl_3$): δ 0.82−0.84 (d, 6H, J = 6.6 Hz) 1.11−1.39 (9H, m, CH_2), 1.97 (t, 2H, J = 8.3 Hz), 3.64 (3H, s), 6.71−6.75 (dd, 2H, J = 10 Hz), 7.29 (s, 1H), 7.32−7.31(d, 1H, J = 2.2 Hz). ^{13}C NMR ($CDCl_3$): δ 24.3, 28.10, 29.20, 30.02, 31.03, 32.24, 40.12, 50.10, 115.20, 113.89, 128.20, 129.25, 129.39,

160.15. HR-EIMS calcd for $C_{17}H_{34}B_{10}O$ (M^+): 362.3607. Found: 362.3585.

1-(4-Hydroxyphenyl)-7-(6-methylheptyl)-1,7-dicarba-*closo*-dodecaborane (I). To a solution of 1-(4-methoxyphenyl)-7-(6-methylheptyl)-1,7-dicarba-*closo*-dodecaborane (**2**) (90.5 mg, 0.25 mmol) in CH_2Cl_2 (5 mL) was added dropwise a 1 M solution of BBr_3 in CH_2Cl_2 (0.48 mL) at −78 °C. The mixture was stirred at room temperature for 2 h, then poured into ice water and extracted with CH_2Cl_2. The organic layer was washed with brine, dried over Na_2SO_4, and concentrated under vacuum. Purification by silica gel flash chromatography (hexanes/ethylacetate 8:2; R_f: 0.4) gave **I** in 56% yield. ^{1}H NMR ($CDCl_3$): δ 0.87−0.85 (d, 6H, J = 7.9 Hz), 1.10−1.64 (m, 9H, CH_2), 1.98 (t, 2H, J = 8.2 Hz), 6.68−6.70 (d, 2H, J = 8.6 Hz), 7.78−7.80 (d, 2H, J = 8.0 Hz). ^{13}C NMR ($CDCl_3$): δ 23.01, 27.40, 28.316, 29.86, 30.12, 30.45, 37.59, 39.20, 81.12, 86.41, 115.38, 128.50, 129.65, 156.181. HR-EIMS calcd for $C_{16}H_{32}B_{10}O$ (M^+): 348.3450. Found: 348.3453.

1-(4-Hydroxyphenyl)-12-(6-methylheptyl)-1,12-dicarba-*closo*-dodecaborane (II) was obtained by adapting the procedure described for compound **I** using 1-(4-methoxyphenyl)-12-(6-methylheptyl)-1,12-dicarba-*closo*-dodecaborane as the starting material. Purification by silica gel flash chromatography (hexanes/ethylacetate 8:2; R_f: 0.4) gave **II** in 50% yield. ^{1}H NMR ($CDCl_3$): δ 0.82−0.85 (d, 6H, J = 6.5 Hz), 1.09−1.36 (m, 9H, CH_2), 1.97 (2H, t, J = 8.0 Hz), 6.65−6.68 (d, 2H, J = 8.7 Hz), 7.24−7.28 (d, 2H, J = 8.7 Hz), ^{13}C NMR: δ 23.01, 26.37, 27.40, 28.31, 28.62, 29.86, 30.12, 30.54, 32.34, 34.09, 66.64 72.26, 128.29, 128.50, 129.65, 156.17. HR-EIMS calcd for $C_{16}H_{32}B_{10}O$ (M^+): 348.3450. Found: 348.3454.

1-(3-Hydroxyphenyl)-12-(6-methylheptyl)-1,12-dicarba-*closo*-dodecaborane (III) was obtained by adapting the procedure described for compound **I** using 1-(3-methoxyphenyl)-12-(6-methylheptyl)-1,12-dicarba-*closo*-dodecaborane as the starting material. Purification by silica gel flash chromatography (hexanes/ethylacetate 8:2; R_f: 0.4) gave **III** in 46% yield. ^{1}H NMR ($CDCl_3$): δ 0.82−0.84 (d, 6H, J = 6.6 Hz) 1.11−1.39 (m, 9H, CH_2), 1.99 (t, 2H, J = 8.3 Hz), 6.70−6.74 (dd, 2H, J = 10 Hz), 7.29 (s, 1H), 7.30−7.31 (d, 1H, J = 2.2 Hz). ^{13}C NMR ($CDCl_3$): δ 22.59, 26.97, 27.90, 29.45, 30.03, 37.20, 38.80, 68.54, 77.87, 114.98, 129.24, 134.07, 135.21, 145.10, 165.02. HR-EIMS calcd for $C_{16}H_{32}B_{10}O$ (M^+): 348.3450. Found: 348.3453.

RMS Fit of Cholesterol with Compounds I−III (Figure 2). *Hyperchem 7.51* (Hypercube, Inc., Gainsville, FL) was used on a Dell Inspiron 4100 to produce the rms fit of cholesterol with the carboranyl cholesterol mimics **I−III**. Carboranyl cholesterols **I−III** were energy-minimized with the HyperMMplus module, using the Polak−Ribiere conjugate gradient method and an energy gradient of 0.03 kcal mol^{-1} Å^{-1}. The minimized structures of **I−III** were then used for the rms fit with the energy-minimized structure of cholesterol. Appropriate side-chain carbons were used to obtain the optimal fit.

Polar and Apolar Surface Areas (PSAs/APSAs) of Cholesterol and Compounds I−III (Table 1). Parameters for minimized structures, generated as described in the previous section, were transferred to the *VEGA ZZ 2.0.4* software package (*38*) for the calculation of PSAs and APSAs. Analogous to previous theoretical studies involving carborane-containing compounds (*39*, *40*), boron atom types in the carborane clusters of compounds **I−III** were replaced with carbon atom types using *Hyperchem 7.51* before data transfer to *VEGA ZZ 2.0.4*.

Calculated LogP Values of Cholesterol and Compounds I−III (Table 1). LogP calculations were carried out using the *ChemDraw 7.0.1* version (CambridgeSoft Corporation, Cambridge, MA). This software package does not allow LogP calculations with compounds containing hexavalent boron and/or carbon atoms, as they can be found in the carborane cluster. Therefore, the carborane clusters in compounds **I−III** (Figure 1) were replaced with adamantane, because both cage structures are comparable in lipophilicity and dimensions (*41*). In order to mimic para and meta substitution patterns in compounds **I−III**, the 1,4(6,10)-position and 1,3(5,7)-position of the adamantane moiety were substituted appropriately. For validation, experimental LogP values of a series of twelve previously described carboranyl compounds (*42*) and the calculated LogP values of their virtual adamantane counterparts were fitted on a straight line to obtain the R^2 value. The obtained R^2 value of 0.92 indicated that the approximation of using adamantane instead of the carborane moiety for the theoretical calculation of the LogP values of carboranyl compounds with *ChemDraw* is acceptable.

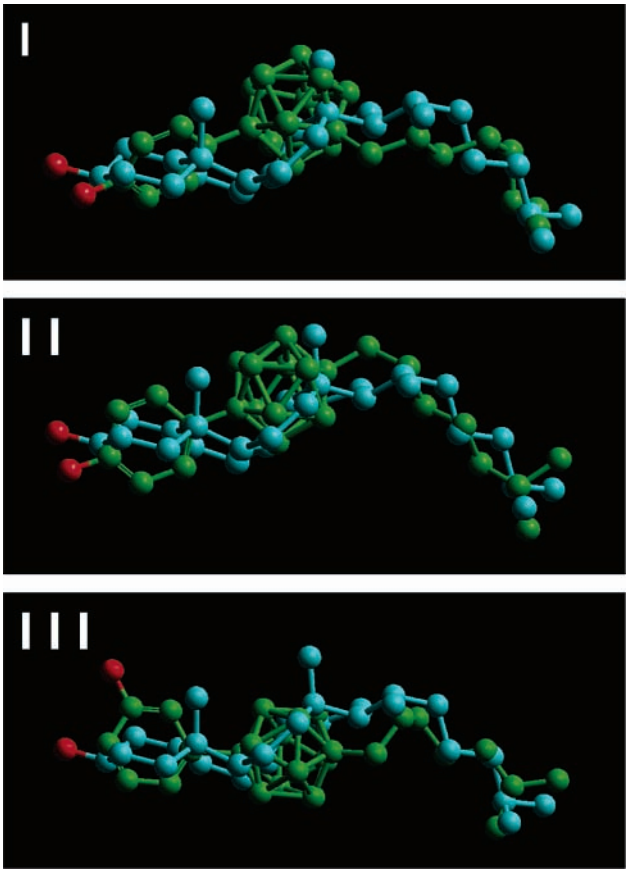

Figure 2. RMS fit of cholesterol with compounds **I−III**. Hydrogen atoms were omitted for the clarity. Cholesterol is shown in cyan and compounds **I−III** in green. For better orientation, oxygen atoms of all molecules are shown in red.

Table 1. Calculated LogPs,[a] Apolar Surface Areas (APSAs),[a] Polar Surface Areas (PSAs),[a] and APSA/PSA Ratios of Cholesterol and Compounds I−III

Compd.	LogP	APSA (Å^2)	PSA (Å^2)	Ratio APSA/PSA
Chol[b]	7.35	504.4	29.0	17.4
I	7.12	492.4	33.2	14.8
II	7.26	468.8	32.8	14.3
III	7.26	467.0	29.2	15.9

[a] See Experimental Procedures ("Calculated LogP Values of Cholesterol and Compounds I-III" and "Polar and Apolar Surface Areas (PSAs/APSAs) of Cholesterol and Compounds I-III") for detailed descriptions. [b] Cholesterol [experimental LogP: 7.445 (http://redpoll.pharmacy.ualberta.ca/drugbank)].

Materials for Biological Studies. Dipalmitoylphosphatidylcholine (DPPC) was purchased from Genzyme (Boston, MA). Monomethoxypolyethylene glycol(2000)−distearoylphosphati-

dylethanolamine (mPEG−DSPE) was purchased from Lipoid (Newark, NJ). Distearoylphosphatidylethanolamine−polyethylene glycol(2000)−maleimide (DSPE−PEG(2000)−maleimide) was purchased from Avanti Polar Lipids, Inc. (Alabaster, AL). Cholesterol, calcein, and Sepharose CL-4B were purchased from Sigma (St. Louis, MO). Folate−polyethylene glycol-(2000)−cholesterol (folate−PEG−cholesterol) was synthesized as described previously (*43*). Spectra/Por DispoDialyzer dialysis tubes (1 mL, molecular weight cutoff [MWCO] 10 000) were purchased from Spectrum Lab (Rancho Dominguez, CA). Tissue culture media RPMI 1640 without folic acid, fetal bovine serum (FBS), and antibiotics were purchased from Life Technologies (Rockville, MD). The KB HeLa variant cell line (ATCC # CCL-17) was gift from Dr. Philip Low, Purdue University (West Lafayette, IN). The 293/KDR cell line, expressing 2.5×10^6 VEGFR-2/cell, has been described in detail previously by us (*44*). Nitric acid (trace metal quality) was purchased from Fisher Scientific (Pittsburgh, PA) and 18.2 MΩ−cm water was obtained from a Milli-Q laboratory purification unit (Millipore, Billerica, MA). Other materials and vendors are listed in the following: Mouse antihuman VEGF monoclonal antibody (Pharmingen, San Diego, CA); Anti-mouse IgG: horseradish peroxidase (HRP) conjugate (GE Healthcare, Piscataway, NJ), Enhanced Chemiluminescent (ECL) Plus kit (GE Healthcare, Piscataway, NJ), Anti-phosphotyrosine RC20 antibody conjugated to horseradish peroxidase (BD Transduction Labs, San Diego, CA), SLT (Shiga-like toxin)−VEGF (SibTech, Newington, CT), CellTiter 96 AQ_{ueous} One Solution Cell Proliferation Assay kit (Promega, Madison, WI).

Preparation of Liposomes. Nontargeted liposomes, control liposomes, and FR-targeted liposomes were prepared using the thin-layer evaporation method (*45*). The particle size was reduced by ultrasonication and extrusion. The compositions for each liposomal formulation were as follows: Nontargeted liposome (DPPC/compound **I**/mPEG−DSPE, 55:40:5 mol %), control liposome (DPPC/cholesterol, 55:45 mol %), and FR-targeted liposome (DPPC/compound **I**/mPEG−DSPE/folate−PEG−cholesterol, 55:40:4.5:0.5 mol %). Lipids were first dissolved in chloroform, dried to a thin film in a round-bottom flask under nitrogen, and then further dried using vacuum for 4 h. The dried lipid was then resuspended using 10 mM calcein solution and pulse-sonicated for 5 min. The resulting liposomal suspension was passed through a 100 nm polycarbonate membrane for five cycles using a high-pressure extruder (Northern Lipid, Vancouver, British Columbia, Cannada). A 10 mL Sepharose CL-4B column equilibrated with pH 7.4 phosphate buffered saline (PBS) was applied to separate the liposomal portions from low molecular weight components. Elutions were collected in 1 mL quantities and subjected to the determination of boron concentrations by inductively coupled plasma atomic emission spectroscopy (ICP-AES) as described in a following section on boron measurements.

(VEGFR-2)-targeted liposomes were prepared as follows: Cys-tagged single-chain VEGF (scVEGF) was constructed and expressed, as described previously (*46*). Briefly, two 3−112 aa long fragments of human $VEGF_{121}$ were fused head-to-tail and expressed with a N-terminal Cys-tag, a novel cysteine-containing 15-aa peptide tag for site-specific modification of recombinant proteins (*47*). scVEGF was site-specifically lipidated with DSPE−PEG(2000)−maleimide and incorporated into liposomes as follows: scVEGF was incubated with DSPE−PEG(2000)−maleimide at a molar protein to lipid ratio of 1:10 at ambient temperature for 2 h, then mixed with an equal volume of the nontargeted liposomal formulation of compound **I** described above and incubated at 37 °C for 16 h. Non-incorporated scVEGF was removed by chromatography on Sepharose CL-4B. Purified VEGF/liposomes were analyzed by Western blotting using mouse antihuman VEGF monoclonal antibody diluted 1:2000 followed by anti-mouse IgG−HRP conjugate diluted 1:10 000. The anti-VEGF antibody was visualized on the blots by the ECL Plus kit.

In Vitro Release Analysis of Liposomes. The in vitro release profiles of nontargeted liposomes, control liposomes, and FR-targeted liposomes were measured by both calcein release and determination of boron concentrations via ICP-AES. Briefly, 1 mL of Sepharose CL-4B column-purified liposome samples were added to 1 mL dialysis tubes (MWCO 10 000) and incubated in 500 mL PBS at 37 °C. Constant magnetic stirring (100 rpm) was applied to the dialysis beaker. At 24, 48, 72, and 96 h, 1 mL samples were taken from the beaker, and the released calcein was measured using a Perkin-Elmer spectrofluorometer (Wellesley, MA) with excitation and emission at 485 and 520 nm, respectively. Excitation and emission slits were set to 5 nm. The boron concentrations of liposomal suspensions before and after the dialysis were also measured by ICP-AES. The percentage of retention was calculated on the basis of normalization using the original concentration before dialysis.

Boron Uptake Study of Liposomes in FR-Positive KB Cells. KB cells were cultured as a monolayer in folate-free Roswell Park Memorial Institute (RPMI) 1640 media supplemented with penicillin, streptomycin, and 10% FBS in a humidified atmosphere containing 5% CO_2 at 37 °C. After reaching confluence, KB cells were collected with trypsin/ethylenediaminetetraacetic acid (EDTA), washed with PBS, and suspended in folate-free RPMI media at a density of 2×10^7 cells/mL. Boronated FR-targeted or nontargeted liposomes (40 μg/mL boron) were added to the media, and cells were incubated under CO_2 atmosphere at 37 °C for 2 h. Subsequently, cells were centrifuged at 400 g for 10 min, and the media was removed. Cells were washed twice with cold PBS by resuspension and centrifugation at 400 g. Cell pellets were then collected, and boron concentrations were determined by direct current plasma-atomic emission spectroscopy (DCP-AES) (*48*). All treatments and measurements were triplicated.

Functional Activity of (VEGFR-2)-Targeted Liposomal Formulations of Compound I. The functional activity of VEGF inserted into nontargeted liposomal formulations of compound **I** (see Preparation of Liposomes section) was evaluated in tissue culture using 293/KDR cells expressing 2.5×10^6 VEGFR-2/cell. Two functional assays, VEGFR-2 tyrosine autophosphorylation and protection of 293/KDR cells from VEGFR-2 mediated toxicity of the SLT−VEGF chimeric toxin, were carried out as described previously by us (*49*). Briefly, for VEGFR-2 autophosphorylation, 7.5×10^4 293/KDR cells were plated into 24-well plates. After 6 h, complete medium (Dulbecco's Modified Eagle Medium [DMEM]/10% FBS) was replaced with starvation medium (DMEM/0.5% FBS) and the cells were incubated for 16 h at 37 °C in 5% CO_2. Subsequently, the starvation medium was replaced with serum-free DMEM containing 0.5 mM sodium vanadate for 20 min at 37 °C; the cells were incubated with VEGF-2 or (VEGFR-2)-targeted liposomes for 10 min at 37 °C, lysed, and analyzed by Western blotting using anti-phosphotyrosine RC20 antibody conjugated to horseradish peroxidase. For the SLT−VEGF protection assay, 10^3 293/KDR cells were plated on 96-well plates. Varying amounts of (VEGF-2)-targeted liposomes were mixed with SLT−VEGF in complete medium (DMEM/10% FBS) and added to cells in triplicate wells to a final SLT−VEGF concentration of 1 nM. Cells were quantitated after 96 h incubation using a CellTiter 96 AQ_{ueous} One Solution Cell Proliferation Assay kit.

Transmission Electron Microscope (TEM) and Photon Correlation Spectroscopy (PCS) Analysis. The consistencies of nontargeted liposomes, control liposomes, and FR-targeted

liposomes constructed with compound **I** were investigated with TEM after negative staining with uranyl acetate (UA) as described previously (*50*). Briefly, the liposomal samples were placed onto 100-mesh grids. After 3 min, excess solution was wiped off with filter paper, and the grid was immersed in 2% UA. The UA solution was removed after 1 min, and the grids were washed twice with 200 μL of distilled water. The grids were then imaged on a Philips CM 12 transmission electron microscope (Campus Microscopy and Imaging Facility, OSU, Columbus, OH). Photos were taken at 55 000-fold magnification from the suspended liposomal particles. The mean particle diameter and distribution were measured by PCS on a NICOMP particle sizer model 370 (Santa Barbara, CA), and the normalized Gaussian-distributed volume-weighted particle size was collected after 3 runs.

Boron Determinations. Boron concentrations of samples obtained from boron uptake studies with KB cells were obtained by DCP-AES, as described previously (*48*). Boron concentrations for all other samples were obtained by ICP-AES with a Varian VISTA AX ICP spectrometer system. The Varian argon-purged echelle spectrometer, which has a bandpass of $\leq$10 pm at wavelengths below 260 nm, enabled intensity measurements free of spectral interferences for the four neutral-atom boron lines used in this study: 208.889 nm, 208.956 nm, 249.678 nm, and 249.772 nm. All relative intensities for boron spectral lines were based on background-corrected peak heights. A charge-coupled device (CCD) detector, maintained at -34 °C by a Peltier cooler, generated all spectrum-based electronic signals processed by the spectrometer system. The central axial region of a 1.3 kW, 40 MHz ICP was aligned optically with the axis of the acceptance angle of the Echelle spectrometer. Sample solutions were injected into the high-temperature plasma as aerosols produced by a perfluoroalkoxy (PFA) nebulizer. The aerosols first passed through a 50 mL Polycon cyclone spray chamber from which fine aerosol particles were swept by an argon stream through a polytetrafluoroethylene (PTFE) tube and alumina injector tube into the plasma. In the plasma, free atoms and ions were produced and excited to emit quantized radiation. Calibration was achieved with one blank and four accurately diluted aliquots of a single-element standard solution. The boron concentration in the original standard was certified traceable to the National Institute of Standards and Technology (NIST) by the supplier, Inorganic Ventures (Lakewood, NJ). All dilutions, including those for samples, were accomplished in polyethylene tubes on a mass basis enabled by an analytical balance capable of measurements to 0.1 mg. The diluent was 0.5 M nitric acid in 18.2 M$\Omega-$cm water. Samples (1 mL) were diluted by factors that ranged from 3 to 15 to provide the 3 mL solution volume needed for nebulization into the ICP. Calibration functions were second-degree polynomial least-square regression fits with correlation coefficients greater than 0.995. Concentration values obtained by this approach generally are within 10% of actual concentrations. Certified reference materials were not available for further corroboration of accuracy.

RESULTS AND DISCUSSION

Design of Carboranyl Cholesterol Mimics. As already discussed in the Introduction, the design strategy for carboranyl cholesterol mimics described in this paper is based on the a replacement of the B and C rings of cholesterol with highly lipophilic *meta*- and *para*-carborane clusters (*31*, *32*). The dimensions of these clusters are approximately 50% larger than the space occupied by the three-dimensional sweep of a phenyl group (*51*). Figure 1 shows the structural resemblance of cholesterol and the carboranyl cholesterols mimics **I**−**III**. In order to further validate our design strategy, we calculated apolar and polar surface areas (APSAs, PSAs) as well as the LogP values of all compounds shown in Figure 1 prior to embarking on the synthesis of compounds **I**−**III**. Using *HyperChem 7.51* software, we also produced an overlay of energy-minimized structures of compounds **I**−**III** with that of cholesterol. The data are summarized in Figure 2 and Table 1. In particular, the structures of compounds **I** and **II** showed very good structural overlap with the structure of cholesterol, and APSAs, PSAs, and LogP values of all compounds were similar.

Scheme 1. Representative Synthesis of Carboranyl Cholesterol Mimics Using Compound I as the Example[a]

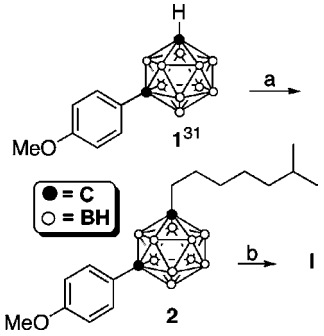

[a] Key: a, *n*-BuLi/toluene-4-sulfonic acid 6-methylheptyl ester/benzene/room temperature; b, BBr_3/CH_2Cl_2, room temperature.

Synthesis of Carboranyl Cholesterol Mimics. Encouraged by our computational studies, we carried out the syntheses of compounds **I**−**III** as shown in Scheme 1 by the example of compound **I**. Starting material for the synthesis of compound **I** was 1-(4-methoxyphenyl)-1,7-dicarba-*closo*-dodecaborane (Scheme 1, compound **1**), which was previously described by Endo et al. (*31*). For the syntheses of compounds **II** and **III**, 1-(4-methoxyphenyl)- (*31*) and 1-(3-methoxyphenyl)-substituted *para*-carborane (*31*), respectively, were used as starting materials. Compound **1** was reacted with toluene-4-sulfonic acid 6-methylheptyl ester (*37*) to afford compound **2**. The yields for compound **2** and its derivatives used in the syntheses of **II** and **III** ranged from 52% to 61%. The methoxy group in **2** was removed using boron tribromide in dichoromethane to afford target compound **I**. Target compounds **II** and **III** were obtained in a similar fashion, and yields for all three target compounds ranged from 46% to 56%. All intermediates and target compounds were purified effectively by silica gel column chromatography and characterized by ^{1}H NMR, ^{13}C NMR, and HR-EIMS. An important criterion for the synthesis of compounds **I**−**III** was practicability. All target compounds were synthesized from readily available starting materials. However, structural resemblance of carboranyl cholesterol mimics with cholesterol probably could be further improved by substituting the A ring of cholesterol with nonaromatic ring systems instead of using the phenyl group (*52*), methyl substitution at boron atoms of the carborane clusters (*53*), and insertion of a 2,6-dimethylheptane (*54*) rather than a 6-methylheptane side chain. However, such a structure would require multiple laborious reaction steps. It should be noted that, due to the high lipophilicity of all carboranyl compounds described in this paper, standard ESI-MS (electrospray ionization mass spectrometry) was unsuccessful, and EIMS had to be used.

Incorporation of Carboranyl Cholesterol Mimics into Liposomes. Compounds **I**−**III** were formulated into nontargeted liposomes using the thin-layer evaporation method (*10*), and the particle sizes and lamellarities were further defined using ultrasonication followed by extrusion. We characterized the incorporation efficiency using size-exclusion chromatography. Liposomal and free compound fractions were separated at different elution volumes, and the boron concentrations were measured by ICP-AES. The results, shown in Figure 3, indicated

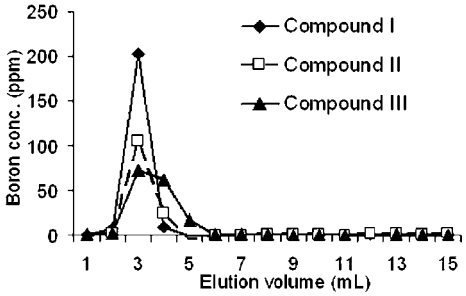

Figure 3. Incorporation of compounds **I**−**III** into liposomes. The preparation for the liposomes are described in Experimental Procedures (composition = DPPC/compound **I**−**III**/PEG−DSPE, 55:40:5 mol %). Encapsulation of boron compounds was determined by eluting 0.5 mL liposomal samples through a 10 mL Sepharose CL-4B column with pH 7.4 PBS. Fractions were collected for determination of boron concentrations by ICP-AES. The encapsulation efficiencies were 99.7% for compound **I**, 94.3% for compound **II**, and 96.8% for compound **III**.

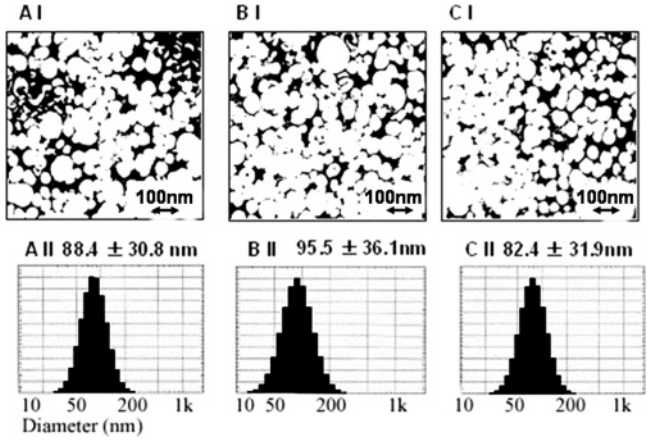

Figure 4. Characterization of size distribution and lamellarity of liposomal formulations of compound **I**. (A) nontargeted boronated liposome; (B) non-boronated control liposome (DPPC/cholesterol); (C) FR-targeted boronated liposome. (I) Morphology of the liposomes visualized by transmission electronic microscopy (TEM). Negative staining was applied to observe the particle size and lamellarity of liposomes. Formation of small unilamellar vesicle (SUV) was confirmed for all three formulations of compound **I**. (II) Particle sizes measured by photon correlation method. Numbers shown are the mean particle size ± standard deviation (volume-weighted) of the individual samples.

that all three compounds had >90% incorporation efficiency (**I** = 99.7%, **II** = 94.3%, and **III** = 96.8%). For all liposomal formulations prepared subsequently from compound **I** for in vitro release and cell uptake studies, >90% incorporation efficiency was confirmed with the same method (data not shown). Samples for in vitro release and cell uptake studies were all purified using the Sepharose CL-4B column to eliminate free compound. Compound **I** was selected for all further studies because of its good structural overlap with cholesterol (Figure 2) and its high incorporation efficiency.

Size and Lamellarity Characterization of Liposomal Formulations of Compound I. For liposomal delivery of BNCT agents, as well as other anticancer therapeutics, the size distribution and lamellarity of liposomes are of great importance for parameters such as stability, drug release profile, in vivo half-life, and tissue distribution. Small, homogeneous, and unilamellar particles are preferred for optimal delivery to malignant tissues, as they are able to escape reticular endothelial system (RES) uptake (*55*). We applied TEM and PCS for the analysis of the physical properties of conventional, nontargeted, and FR-targeted liposomes. After negative staining, both FR-targeted and nontargeted liposomal formulation of compound **I** were inspected with TEM (Figure 4AI,CI) for particle size distribution and lamellarity observation. As a control, conventional liposomes (DPPC/cholesterol [55:45 mol %]) were also constructed under identical conditions and analyzed accordingly (Figure 4BI). Since the TEM method does not allow the particle size quantification, the same samples were also analyzed for mean particle size and distribution using a laser particle sizer in parallel (Figure 4AII,CII). Data presented in Figure 4 demonstrate that homogeneous small unilamellar vesicles (SUVs) were formed by using compound **I** both for nontargeted and FR-targeted liposomal formulations. The mean particle sizes for all three formulations ranged from 82.4 to 95.5 nm with size distributions around 30−40 nm. No major differences were found in appearance, size distribution, and lamellarity between conventional DPPC/cholesterol liposomes, nontargeted, and FR-targeted liposomal formulations of compound **I**.

In Vitro Release of Liposomal Formulations of Compound I. The performance of boron-containing liposomes in vivo is highly affected by the stability of incorporation of the boron entities. Therefore, a standard in vitro release experiment (*56*) was conducted using PBS as the media at 37 °C, and the stability of incorporation of compound **I** in both FR-targeted and nontargeted liposomal formulation was evaluated. Control liposomes were constructed with cholesterol instead of compound **I**, and thus, calcein, a green fluorescent dye, was encapsulated into the liposomal hydrophilic compartment of all liposomal formulations to analyze stability via fluorescence measurements of calcein release. Samples were taken at different time points beginning at 0.5 h after the initiation of incubation, and calcein release was measured by absorbance (Figure 5A). Boron concentrations of samples obtained at 0 and 96 h were determined by ICP-AES (Figure 5B). Overall, both data sets indicate that a 45% molar ratio of compound **I** was stably incorporated into the vesicles and that the release of calcein followed a pattern similar to that of conventional DPPC−cholesterol liposomes. For both the nontargeted and FR-targeted formulation, the calcein release was less than 30% at 24 h, which was not significantly different from the control liposome. At later time points, however, the targeted formulation appeared to release calcein, and presumably also boron, at an increased rate. This could be due to insufficient anchoring of folate−PEG−cholesterol to the lipid bilayer or even the degradation of this receptor-targeting ligand. We have made similar observations previously in studies using doxorubicin as the incorporated compound (X.B. Zhao, unpublished results). Nevertheless, nontargeted liposomal formulations showed a release profile comparable to that of the control liposomes, with more than 50% calcein and boron remaining unreleased at 96 h. The release rate of FR-targeted liposomes at least until 48 h should be sufficient for selective receptor-mediated boron delivery to tumor cells for BNCT.

In Vitro Uptake of FR-Targeted Liposomal Formulations of Compound I. We determined the in vitro delivery of compound **I** to KB cells, an established FR-expressing cell line (*57*), in the form of nontargeted liposomal formulations as well as in FR-targeted liposomal formulations in the presence and absence of free 5 mM free folate. No significant cytotoxicity was noted during the 4 h incubation time based on a microscopic inspection of the cells. Cellular uptake of the liposomes was determined by measuring cell-associated boron concentrations with DCP-AES (*48*). The obtained data are summarized in Figure 6. The nontargeted liposomal formulation of compound **I** appeared to bind in a nonspecific way to KB cells (30 μg boron/g cells), which have a very low background level of boron (<1 μg boron/g cells; data not shown) in cell culture environment. Specific targeting to FR was demonstrated by increased boron levels for FR-targeted liposomal formulation of compound

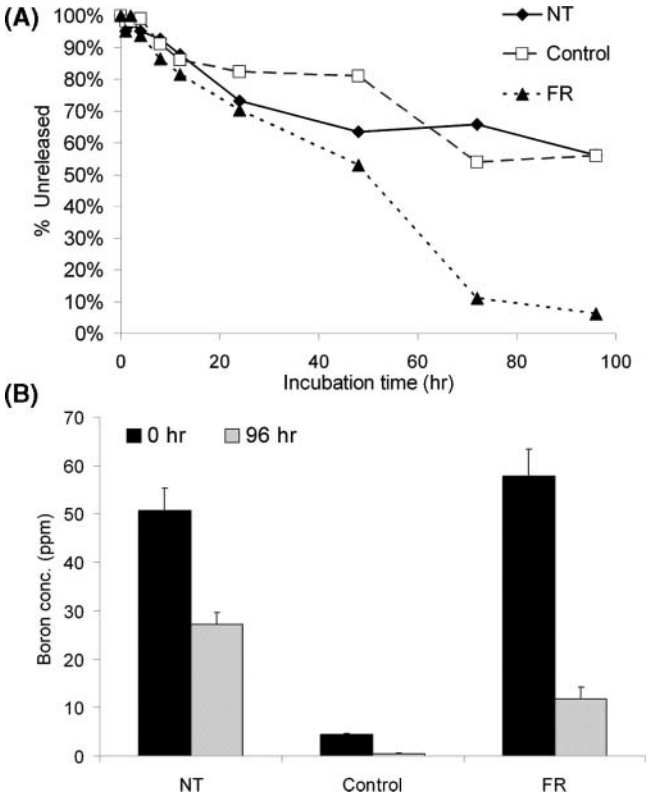

Figure 5. In vitro release profile of liposomal formulations of compound **I** in pH 7.4 PBS at 37 °C. (A) Compound **I** was formulated into liposomes with different compositions as described in Experimental Procedures. In parallel, DPPC/cholesterol control liposomes without boron components were prepared using the same protocol. All liposomal formulations contain a 10 mM solution of calcein. The percentage of calcein release was determined by fluorescence and absorbance measurements. (B) Boron concentrations of the liposomal suspensions were measured at 0 and 96 h by ICP-AES. NT: boronated liposomes (nontargeted). Control: control liposomes (no boron). FR: FR-targeted boronated liposomes. Error bars shown in Figure 5B are based on standard deviations calculated from three measurements.

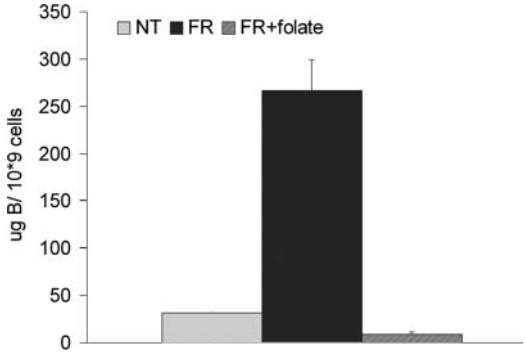

Figure 6. Cellular uptake of liposomal formulations of compound **I**. NT: Nontargeted boronated liposomes. FR: FR-targeted boronated liposomes. FR + folate: FR-targeted boron-containing liposomes were coincubated with 5 mM free folate. 2×10^7 cells in 1 mL media were incubated with liposomes containing 40 μg/mL boron. Each data point represents the mean of boron amount in the cell lysates normalized to 1×10^9 cells (equivalent to 1 g tissue). Error bars stand for standard deviations of the normalized boron amount in triplicates.

I (267 μg/g cells). FR specificity was further demonstrated by the reduction of the boron concentration of FR-targeted boronated liposomes that were incubated with KB cells in the presence of 5 mM free folate (9 μg/g cells). All three liposomal formulations were colabeled with calcein, and specific binding was also confirmed by the increased fluorescence intensity in KB cells treated with FR-targeted boronated

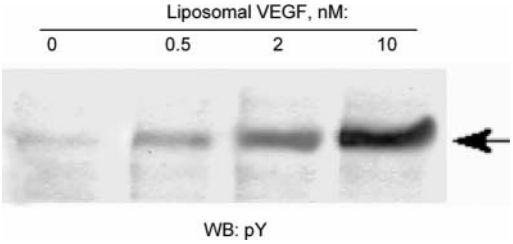

Figure 7. (VEGFR-2)-targeted liposomes induce VEGFR-2 autophosphorylation in a dose-dependent manner. 293/KDR cells were stimulated with the indicated concentrations of liposomal scVEGF, and tyrosine phosphorylation of VEGFR-2 was determined by Western blotting with an anti-phosphotyrosine RC20−HRP conjugate. The arrow indicates the position of VEGFR-2.

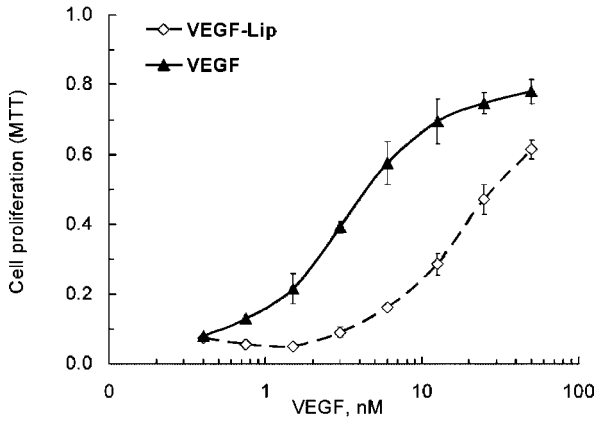

Figure 8. Boronated (VEGFR-2)-targeted liposomes protect VEGFR-2 expressing 293/KDR cells from SLT−VEGF-induced cell death. 293/KDR cells were exposed to boronated (VEGFR-2)-targeted liposomes (VEGF-Lip) or scVEGF (VEGF) that was serially diluted in a complete culture medium containing 1 nM SLT−VEGF.

liposomes, as demonstrated by fluorescence microscopy (data not shown).

(VEGFR-2)-Targeted Liposomal Formulations of Compound I. The purpose of these studies was to establish that liposomal formulations of compound **I** are also effective in targeting cell receptors other than FR. For this purpose, nontargeted liposomal formulations of compound **I** were decorated with a novel single-chain VEGF (scVEGF) that comprises two 3−112-aa-long fragments of human $VEGF_{121}$ fused head-to-tail (*46*) and expressed with a N-terminal 15-aa Cys tag, a novel cysteine-containing peptide tag for site-specific modification of recombinant proteins (*47*). Cys-tagged scVEGF was site-specifically lipidated with DSPE−PEG(2000)−maleimide at the molar lipid/protein ratio 10:1, and the reaction mixture was added to a nontargeted liposomal formulations of compound **I** for a so-called postinsertion of lipidated scVEGF into the liposomal membrane, as described in Experimental Procedures.

After purification on Sepharose CL-4B, the concentration of scVEGF in the liposomal formulations of compound **I** was determined by Western blot analysis, and the functional activities of the VEGF moiety were tested in two different tissue culture assays. In a short-term (10 min) assay, we tested the ability to induce VEGFR-2 tyrosine autophosphorylation in 293/KDR cells (*44*, *47*, *49*), and in a long-term (72−96 h) assay, we tested the ability to protect 293/KDR cells from VEGFR-2 mediated toxicity of the chimeric toxin SLT−VEGF, comprising a catalytic subunit of Shiga-like toxin and $VEGF_{121}$ (*47*, *49*). As shown in Figures 7 and 8, liposomal (VEGFR-2)-targeted formulations of compound **I** effectively activated VEGFR-2 autophosphorylationin 293/KDR in a nanomolar range typical for these cells (*44*) and protected 293/KDR cells from SLT−

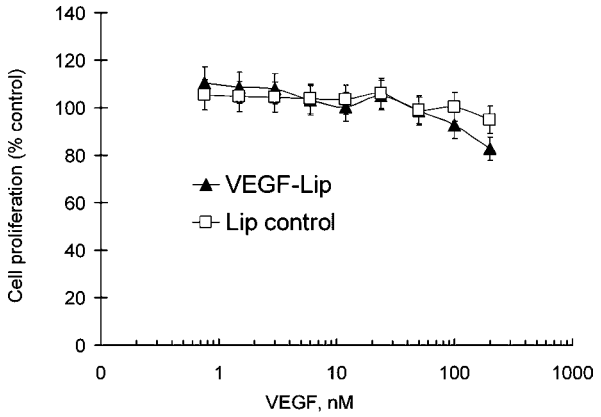

Figure 9. (VEGFR-2)-targeted boronated liposomes are not toxic to VEGFR-2 expressing cells. 293/KDR cells were exposed to indicated amounts of (VEGFR-2)-targeted boronated liposome (VEGF-Lip) or volume equivalents of nontargeted boronated liposomal formulation of compound **I** (Lip control).

VEGF cytotoxicity, although not to the same extent as parental scVEGF. When taken together, these data indicate that boronated (VEGFR-2)-targeted liposomes are indeed effective in targeting VEGFR-2 expressing cells. Furthermore, the data suggest that these liposomes most likely will be internalized via VEGFR-2-mediated endocytosis, as has been demonstrated by us for (VEGFR-2)-targeted liposomes loaded with doxorubicin (*58*).

The cytotoxicity of the (VEGFR-2)-targeted liposomal formulation of compound **I** was evaluated in 293/KDR cells. The cells were plated at low density (1000 cells/well) and allowed to grow for 96 h in the presence of different amounts of either (VEGFR-2)-targeted or nontargeted liposomal formulations of **I**. The obtained results (Figure 9) indicate that neither liposomal formulation affected significantly the growth of 293/KDR cells. Given the recently reported rapid receptor-mediated internalization of VEGF-targeted therapeutic liposomes by 293/KDR cells (*59*), one can expect that these cells also internalize the (VEGFR-2)-targeted liposomal formulations of **I** and that the internalized liposomes are not toxic in the absence of neutron irradiation.

SUMMARY AND CONCLUSIONS

Three carboranyl cholesterol derivatives were synthesized and analyzed applying novel molecular design concepts. All three compounds have structural features and physicochemical properties that are very similar to those of cholesterol. One of the synthesized boronated cholesterol mimics (compound **I**) was stably incorporated into non-, FR-, and (VEGFR-2)-targeted liposomes. No major differences were found in appearance, size distribution, and lamellarity between conventional DPPC/cholesterol liposomes, nontargeted, and FR-targeted liposomal formulations of compound **I**. The calcein release properties of conventional DPPC/cholesterol liposomes and nontargeted boronated liposomes were comparable and were reflected by the boron release rate of the latter. The calcein and boron release rates of FR-targeted boronated liposomes were higher than those of nontargeted boronated liposomes, but the overall stability of the latter was acceptable for the purpose of tumor-selective boron delivery for BNCT. There was no apparent in vitro cytotoxicity to FR overexpressing KB cells and VEGF overexpressing 293/KDR cells when these were incubated with boronated FR- and (VEGFR-2)-targeted liposomal formulations, respectively, although the former accumulated extensively in KB cells, and the latter effectively interacted with VEGFR-2 by causing autophosphorylation and protecting 293/KDR cells from SLT−VEGF cytotoxicity. These results convincingly demonstrate that the novel carboranyl cholesterol mimics are excellent lipid bilayer components for the construction of nontargeted and receptor-targeted boronated liposomes for BNCT of cancer.

ACKNOWLEDGMENT

This work was supported by the U.S. Department of Energy grant DE-FG-2-02ER83520 (J.M.B.) and, in part, by the National Institutes of Health grant R01 CA098945 (R.F.B.). The authors thank Ms. Michele Swindall for technical assistance.

LITERATURE CITED

(1) Barth, R. F., Coderre, J. A., Vicente, M. G. H., and Blue, T. E. (2005) Boron neutron capture therapy of cancer: Current status and future prospects. *Clin. Cancer Res. 11*, 3987−4002.

(2) Shelly, K., Feakes, D. A., Hawthorne, M. F., Schmidt, P. G., Krisch, T. A., and Bauer, W. F. (1992) Model studies directed toward the boron neutron-capture therapy of cancer: boron delivery to murine tumors with liposomes. *Proc. Natl. Acad. Sci. U.S.A. 89*, 9039−9043.

(3) Yanagie, H., Fujii, Y., Tomita, T., Nariuchi, H., Sekiguchi, M., and Kobayashi, H. (1992) Application of boronated anti-CEA immunoliposome to boron neutron capture therapy. In *Progress in Neutron Capture Therapy for Cancer* (Allen, B. J., Moore, D. E., and Harrington, B. V., Eds.) pp 273−275, Plenum Press, New York.

(4) Hawthorne, M. F., and Shelly, K. (1997) Liposomes as drug delivery vehicles for boron agents. *J. Neurooncol. 33*, 53−58.

(5) Yanagie, H., Maruyama, K., Takizawa, T., Ishida, O., Ogura, K., Matsumoto, T., Sakurai, Y., Kobayashi, T., Shinohara, A., Rant, J., Skvarc, J., Ilic, R., Kuhne, G., Chiba, M., Furuya, Y., Sugiyama, H., Hisa, T., Ono, K., Kobayashi, H., and Eriguchi, M. (2006) Application of boron-entrapped stealth liposomes to inhibition of growth of tumour cells in the in vivo boron neutron-capture therapy model. *Biomed. Pharmacother. 60*, 43−50.

(6) Maruyama, K. (2005) Intracellular targeting by transferrin-PEG pendant type liposomes, for boron neutron-capture therapy (BNCT). *Drug Delivery Syst. 20*, 35−41.

(7) Kullberg, E., Wei, Q., Capala, J., Giusti, V., Malmstroem, P.-U., and Gedda, L. (2005) EGF-receptor targeted liposomes with boronated acridine: Growth inhibition of cultured glioma cells after neutron irradiation. *Int. J. Radiat. Biol. 81*, 621−629.

(8) Wei, Q., Kullberg, E. B., and Gedda, L. (2003) Trastuzumab-conjugated boron-containing liposomes for tumor-cell targeting; development and cellular studies. *Int. J. Oncol. 23*, 1159−1165.

(9) Krijger, G. C., Fretz, M. M., Woroniecka, U. D., Steinebach, O. M., Jiskoot, W., Storm, G., and Koning, G. A. (2005) Tumor cell and tumor vasculature targeted liposomes for neutron capture therapy. *Radiochim. Acta 93*, 589−593.

(10) Sudimack, J. J., Adams, D., Rotaru, J., Shukla, S., Yan, J., Sekido, M., Barth, R. F., Tjarks, W., and Lee, R. J. (2002) Folate receptor-mediated liposomal delivery of a lipophilic boron agent to tumor cells in vitro for neutron capture therapy. *Pharm. Res. 19*, 1502−1508.

(11) Pan, X. Q., Wang, H., Shukla, S., Sekido, M., Adams, D. M., Tjarks, W., Barth, R. F., and Lee, R. J. (2002) Boron-containing folate receptor-targeted liposomes as potential delivery agents for neutron capture therapy. *Bioconjugate Chem. 13*, 435−442.

(12) Awad, D., Tabod, I., Lutz, S., Wessolowski, H., and Gabel, D. (2005) Interaction of $Na_2B_{12}H_{11}SH$ with liposomes: Influence on zeta potential and particle size. *J. Organomet. Chem. 690*, 2732−2735.

(13) Mehta, S. C., Lai, J. C. K., and Lu, D. R. (1996) Liposomal formulations containing sodium mercaptoundecahydrododecaborate (BSH) for boron neutron capture therapy. *J. Microencapsulation 13*, 269−279.

(14) Martini, S., Ristori, S., Pucci, A., Bonechi, C., Becciolini, A., Martini, G., and Rossi, C. (2004) Boronphenylalanine insertion in cationic liposomes for boron neutron capture therapy. *Biophys. Chem. 111*, 27−34.

(15) Feakes, D. A., Shelly, K., Knobler, C. B., and Hawthorne, M. F. (1994) $Na_3[B_{20}H_{17}NH_3]$: Synthesis and liposomal delivery to murine tumors. *Proc. Natl. Acad. Sci. U.S.A. 91*, 3029−3033.

(16) Zhou, R., Balasubramanian, S. V., Kahl, S. B., and Straubinger, R. M. (1999) Biopharmaceutics of boronated radiosensitizers: Liposomal formulation of MnBOPP (manganese chelate of 2,4-(α,β-dihydroxyethyl) deuterioporphyrin IX) and comparative toxicity in mice. *J. Pharm. Sci. 88*, 912−917.
(17) Ristori, S., Oberdisse, J., Grillo, I., Donati, A., and Spalla, O. (2005) Structural characterization of cationic liposomes loaded with sugar-based carboranes. *Biophys. J. 88*, 535−547.
(18) Rossi, S., Schinazi, R. F., and Martini, G. (2005) ESR as a valuable tool for the investigation of the dynamics of EPC and EPC/cholesterol liposomes containing a carboranyl-nucleoside intended for BNCT. *Biochim. Biophys. Acta 1712*, 81−91.
(19) Li, T., Hamdi, J., and Hawthorne, M. F. (2006) Unilamellar liposomes with enhanced boron content. *Bioconjugate Chem. 17*, 15−20.
(20) Nakamura, H., Miyajima, Y., Takei, T., Kasaoka, S., and Maruyama, K. (2004) Synthesis and vesicle formation of a *nido*-carborane cluster lipid for boron neutron capture therapy. *Chem. Commun. (Cambridge, U.K.)* 1910−1911.
(21) Feakes, D. A., Shelly, K., and Hawthorne, M. F. (1995) Selective boron delivery to murine tumors by lipophilic species incorporated in the membranes of unilamellar liposomes. *Proc. Natl. Acad. Sci. U.S.A. 92*, 1367−1370.
(22) Firestone, R. A. (1994) Low-density lipoprotein as a vehicle for targeting antitumor compounds to cancer cells. *Bioconjugate Chem. 5*, 105−113.
(23) Ji, B., Peacock, G., and Lu, D. R. (2002) Synthesis of cholesterol-carborane conjugate for targeted drug delivery. *Bioorg. Med. Chem. Lett. 12*, 2455−2458.
(24) Pan, G., Oie, S., and Lu, D. R. (2005) Uptake of the carborane derivative of cholesteryl ester by glioma cancer cells is mediated through LDL receptors. *Pharm. Res. 21*, 1257−1262.
(25) Peacock, G., Sidwell, R., Pan, G., Oie, S., and Lu, D. R. (2004) In vitro uptake of a new cholesteryl carborane ester compound by human glioma cell lines. *J. Pharm. Sci. 93*, 13−19.
(26) Alanazi, F., Halpern, D. S., and Lu, D. R. (2004) Intracerebral diffusion of new cholesterol-based anticancer conjugate in tumor-bearing rat model. *J. Appl. Res. 4*, 127−134.
(27) Feakes, D. A., Spinler, J. K., and Harris, F. R. (1999) Synthesis of boron-containing cholesterol derivatives for incorporation into unilamellar liposomes and evaluation as potential agents for BNCT. *Tetrahedron 55*, 11177−11186.
(28) Setiawan, Y., Moore, D. E., and Allen, B. J. (1996) Selective uptake of boronated low-density lipoprotein in melanoma xenografts achieved by diet supplementation. *Br. J. Cancer 74*, 1705−1708.
(29) Laster, B. H., Kahl, S. B., Popenoe, E. A., Pate, D. W., and Fairchild, R. G. (1991) Biological efficacy of boronated low-density lipoprotein for boron neutron capture therapy as measured in cell culture. *Cancer Res. 51*, 4588−4593.
(30) Leppala, J., Kallio, M., Nikula, T., Nikkinen, P., Liewendahl, K., Jaaskelainen, J., Savolainen, S., Gylling, H., Hiltunen, J., and Callaway, J. (1995) Accumulation of ^{99m}Tc-low-density lipoprotein in human malignant glioma. *Br. J. Cancer 71*, 383−387.
(31) Endo, Y., Iijima, T., Yamakoshi, Y., Fukasawa, H., Miyaura, C., Inada, M., Kubo, A., and Itai, A. (2001) Potent estrogen agonists based on carborane as a hydrophobic skeletal structure: a new medicinal application of boron clusters. *Chem. Biol. 8*, 341−355.
(32) Endo, Y., Iijima, T., Yamakoshi, Y., Yamaguchi, M., Fukasawa, H., and Shudo, K. (1999) Potent estrogenic agonists bearing dicarba-*closo*-dodecaborane as a hydrophobic pharmacophore. *J. Med. Chem. 42*, 1501−1504.
(33) Stephenson, S. M., Low, P. S., and Lee, R. J. (2004) Folate receptor-mediated targeting of liposomal drugs to cancer cells. *Methods Enzymol. 387*, 33−50.
(34) Gosselin, M. A., and Lee, R. J. (2002) Folate receptor-targeted liposomes as vectors for therapeutic agents. *Biotechnol. Annu. Rev. 8*, 103−131.
(35) Cardones, A. R., and Banez, L. L. (2006) VEGF inhibitors in cancer therapy. *Curr. Pharm. Des. 12*, 387−394.
(36) Bergsland, E. K. (2004) Update on clinical trials targeting vascular endothelial growth factor in cancer. *Am. J. Health Syst. Pharm. 61*, S12−S20.
(37) Tai, A., Syouno, E., Tanaka, K., Fujita, M., Sugimura, T., Higashiura, Y., Kakizaki, M., Hara, H., and Naito, T. (2002) Regio- and stereochemical study of sex pheromone of pine sawfly; Diprion nipponica. *Bull. Chem. Soc. Jpn. 75*, 111−121.
(38) Pedretti, A., Villa, L., and Vistoli, G. (2004) VEGA - An open platform to develop chemo-bio-informatics applications, using plug-in architecture and script programming. *J. Comput.-Aided Mol. Des. 18*, 167−173.
(39) Johnsamuel, J., Byun, Y., Jones, T. P., Endo, Y., and Tjarks, W. (2003) A new strategy for molecular modeling and receptor-based design of carborane containing compounds. *J. Organomet. Chem. 680*, 223−231.
(40) Johnsamuel, J., Byun, Y., Jones, T. P., Endo, Y., and Tjarks, W. (2003) A convenient method for the computer-aided molecular design of carborane containing compounds. *Bioorg. Med. Chem. Lett. 13*, 3213−3216.
(41) Fauchere, J. L., Kim Quang, D., Jow, P. Y. C., and Hansch, C. (1980) Unusually strong lipophilicity of 'fat' or 'super' amino acids, including a new reference value for glycine. *Experientia 36*, 1203−1204.
(42) Al-Madhoun, A. S., Johnsamuel, J., Barth, R. F., Tjarks, W., and Eriksson, S. (2004) Evaluation of human thymidine kinase 1 substrates as new candidates for boron neutron capture therapy. *Cancer Res. 64*, 6280−6286.
(43) Guo, W., Lee, T., Sudimack, J., and Lee, R. J. (2000) Receptor-specific delivery of liposomes via folate-PEG-Chol. *J. Liposome Res. 10*, 179−195.
(44) Backer, M. V., and Backer, J. M. (2001) Functionally active VEGF fusion proteins. *Protein Expression Purif. 23*, 1−7.
(45) Lee, R. J., and Low, P. S. (1994) Delivery of liposomes into cultured KB cells via folate receptor-mediated endocytosis. *J. Biol. Chem. 269*, 3198−204.
(46) Backer, M. V., Patel, V., Jehning, B. T., Claffey, K. P., and Backer, J. M. (2006) Surface immobilization of active vascular endothelial growth factor via a cysteine-containing tag. *Biomaterials 27*, 5452−5458.
(47) Backer, M. V., Gaynutdinov, T. I., Patel, V., Bandyopadhyaya, A. K., Thirumamagal, B. T. S., Tjarks, W., Barth, R. F., Claffey, K., and Backer, J. M. (2005) Vascular endothelial growth factor selectively targets boronated dendrimers to tumor vasculature. *Mol. Cancer Ther. 4*, 1423−1429.
(48) Barth, R. F., Adams, D. M., Soloway, A. H., Mechetner, E. B., Alam, F., and Anisuzzaman, A. K. M. (1991) Determination of boron in tissues and cells using direct-current plasma atomic emission spectroscopy. *Anal. Chem. 63*, 890−893.
(49) Backer, M. V., and Backer, J. M. (2001) Targeting endothelial cells overexpressing VEGFR-2: selective toxicity of Shiga-like toxin-VEGF fusion proteins. *Bioconjugate Chem. 12*, 1066−1073.
(50) Goncalves, E., Debs, R. J., and Heath, T. D. (2004) The effect of liposome size on the final lipid/DNA ratio of cationic lipoplexes. *Biophys. J. 86*, 1554−1563.
(51) Lunato, A. J., Wang, J., Woollard, J. E., Anisuzzaman, A. K. M., Ji, W., Rong, F.-G., Ikeda, S., Soloway, A. H., Eriksson, S., Ives, D. H., Blue, T. E., and Tjarks, W. (1999) Synthesis of 5-(carboranylalkylmercapto)-2′-deoxyuridines and 3-(carboranylalkyl)thymidines and their evaluation as substrates for human thymidine kinases 1 and 2. *J. Med. Chem. 42*, 3378−3389.
(52) Fujii, S., Hashimoto, Y., Suzuki, T., Ohta, S., and Endo, Y. (2005) A new class of androgen receptor antagonists bearing carborane in place of a steroidal skeleton. *Bioorg. Med. Chem. Lett. 15*, 227−230.
(53) Eriksson, L., Winberg, K. J., Claro, R. T., and Sjoeberg, S. (2003) Palladium-catalyzed heck reactions of styrene derivatives and 2-iodo-*p*-carborane. *J. Org. Chem. 68*, 3569−3573.
(54) Cohen, N., Scott, C. G., Neukom, C., Lopresti, R. J., Weber, G., and Saucy, G. (1981) Total synthesis of all eight stereoisomers of α-tocopheryl acetate. Determination of their diastereoisomeric and enantiomeric purity by gas chromatography. *Helv. Chim. Acta 64*, 1158−1173.
(55) Gabizon, A., and Papahadjopoulos, D. (1988) Liposome formulations with prolonged circulation time in blood and enhanced uptake by tumors. *Proc. Natl. Acad. Sci. U.S.A. 85*, 6949−6953.
(56) Cirli, O. O., and Hasirci, V. (2004) UV-induced drug release from photoactive REV sensitized by suprofen. *J. Controlled Release 96*, 85−96.
(57) Elwood, P. C., Kane, M. A., Portillo, R. M., and Kolhouse, J. F. (1986) The isolation, characterization, and comparison of the

membrane-associated and soluble folate-binding proteins from human KB cells. *J. Biol. Chem. 261*, 15416−15123.

(58) Backer, M. V., Gaynutdinov, T. I., Patel, V., Myshkin, E., and Backer, J. M. (2004) Adapter protein for site-specific conjugation of payloads for targeted drug delivery. *Bioconjugate Chem. 15*, 1021−1029.

(59) Backer, M. V., Patel, V., Jehning, B. T., and Backer, J. M. (2006) Self-assembled "dock and lock" system for linking payloads to targeting proteins. *Bioconjugate Chem. 4*, 912−919.

BC060075D

Cholesterol-Linked Fluorescent Molecular Beacons with Enhanced Cell Permeability

Young Jun Seo,[†] Hyun Seok Jeong,[†] Eun-Kyoung Bang,[†] Gil Tae Hwang,[†] Jong Ha Jung,[‡] Sung Key Jang,[‡] and Byeang Hyean Kim*,[†]

National Research Laboratory, Department of Chemistry, and Department of Life Science, Division of Molecular and Life Sciences, Pohang University of Science and Technology, San 31 Hyoja Dong, Pohang 790-784, Korea. Received March 29, 2006; Revised Manuscript Received July 29, 2006

We appended pyrene units covalently onto adenosine (forming A^P units) and then incorporated them into oligonucleotides such that they were positioned in complementary locations in opposite strands in the middle positions of hairpin stems. System **1** (A^PA^P) behaves as an effective molecular beacon (MB) that changes color from green to blue upon duplex formation. In addition, we attached a cholesterol unit to a free terminus of one of these hairpins; this approach enhanced the cellular delivery of the modified MB relative to those encountered when using conventional transfection methods. These structurally simple cholesterol-based MB systems, which can be synthesized very efficiently, have good potential for opening up new and exciting opportunities in the field of in vivo biosensors.

INTRODUCTION

The detection of the molecular dynamics of DNA and RNA in living cells is becoming one of the most rapidly growing areas of research among all of the comprehensive investigations into the genomic information provided by nature (*1*). Such studies are aimed at providing information regarding the biological functions of DNA and RNA, the roles they play in disease, and their uses as (or interactions with) novel types of drugs. Fluorescence biosensors are powerful tools for probing the structures and interactions of biomolecules, but a strong demand exists for increasingly more advanced biomolecular recognition probes (*2*). We are interested in preparing chemically modified fluorescence biosensors, especially those exploiting $\pi-\pi$ stacking interactions, that can also be used to investigate nucleic acid interactions and structures (*3*−*5*). One of the most useful aromatic planar dyes is pyrene, and its fluorescence has been utilized widely for detecting the DNA and RNA structures (*6*−*8*).

Among the most useful probe systems for detecting molecular dynamics are the molecular beacons (MBs) (*9*−*11*). Unfortunately, these systems are somewhat limited for use as oligonucleotide probes in vivo, because they are difficult to transfect into cells due to their polar anionic backbones and bulky structures. Even though there is much demand for materials that enhance the transfection efficiencies of materials suitable for studying the dynamics of mRNA and DNA, the only means possible at present are the use of transfection agent, microinjection and electroporation techniques. General transfection techniques, such as those employing liposomes or dendrimers, often result in false positive signals and significantly increase the aggregation signal in the endosomes (*12*−*14*); microinjection (*15*) and electroporation (*16*) are invasive and may cause severe damage to cells.

To overcome these difficulties, we have developed novel cholesterol-linked MBs. The cholesterol unit positioned at the 5′ terminus of the hairpin MB allows these systems to enter into living cells efficiently without the need for any other transfection agent. Although there have been many research reports published in this area (*17*−*22*), to the best of our knowledge there are no papers describing cholesterol-containing MBs whose signal formation occurs through aromatic stacking within the stem of a hairpin. In this paper, we report such a system and demonstrate how it can be utilized effectively in vivo.

EXPERIMENTAL PROCEDURES

Synthesis of Cholesterol Monomer Cholesterol-3-(2-cyanoethyl)-*N*,*N*-diisopropylphosphoramidite. Chloro-(2-cyanoethoxy)-*N*,*N*-diisopropylaminophosphine (225 mg, 0.95 mmol) was added to a solution of cholesterol (261 mg, 0.67 mmol) and 4-methylmorpholine (223 mg, 2.20 mmol) in CH_2Cl_2 (7 mL). After stirring the reaction mixture at room temperature for 5 min, the solution was washed with 5% aqueous $NaHCO_3$. The organic layer was dried (Na_2SO_4) and concentrated under reduced pressure. Purification by flash chromatography (ethylacetate/hexane 1:7) provided the product as a white solid (277 mg, 70%). ^{1}H NMR (300 MHz, $CDCl_3$) δ = 5.31 (m, 1H), 3.77 (m, 2H), 3.58 (m, 3H), 2.60 (t, J = 6.3 Hz, 2H), 2.34 (m, 2H), 2.00−1.79 (m, 6H), 1.65−1.05 (m, 32H), 0.98 (s, 6H), 0.89 (d, J = 6.3 Hz, 6H), 0.84 (d, J = 6.5 Hz, 6H), 0.65 (s, 3H); ^{13}C NMR (75.5 MHz, $CDCl_3$) δ = 140.8, 140.6, 121.8, 121.7, 117.6, 74.1, 74.1, 73.9, 73.8, 58.4, 58.2, 56.8, 56.2, 50.1, 43.1, 42.9, 42.3, 39.8, 39.6, 36.2, 35.8, 31.9, 28.3, 28.0, 24.8, 24.7, 24.5, 24.4, 24.3, 23.9, 22.9, 22.6, 21.1, 19.4, 18.8, 11.9; ^{31}P NMR (121 MHz, $CDCl_3$) δ = 148.3, 148.2; IR (neat) υ = 3749.8, 3734.4, 2964.7, 2962.3, 2902.5, 2867.4, 2252.8, 1465.0, 1457.6, 1363.7, 798.8, 731.1, 1183.0, 1060.1, 1031.4, 975.4, 798.8, 731.1 cm^{-1}; HRMS (FAB) calcd for $C_{36}H_{63}N_2O_2P$ 586.4627 $[M + Na]^+$; found 609.4525.

Synthesis of Oligonucleotides. The phosphoramidite A^P and cholesterol were introduced as building blocks to produce fluorescent oligodeoxynucleotides (ODNs) on a controlled-pore glass (CPG) solid support by using the phosphoramidite approach and an automated DNA synthesizer (Perceptive Biosystems 8909 Expedite Nucleic Acid Synthesis System). For comparison, the unmodified ODNs were also prepared. The synthesized oligonucleotides were cleaved from the solid support upon treatment with 30% aqueous NH_4OH (1.0 mL) for 10 h

* Corresponding author. National Research Laboratory, Department of Chemistry, Pohang University of Science and Technology, San 31 Hyoja Dong, Pohang 790-784, Korea. Fax: (82) 54-279-3399. Tel: (82) 54-279-2115. E-mail: bhkim@postech.ac.kr.

[†] National Research Laboratory, Department of Chemistry.

[‡] Department of Life Science, Division of Molecular and Life Sciences.

10.1021/bc060078q CCC: $33.50 © 2006 American Chemical Society
Published on Web 08/22/2006

at 55 °C. The crude products from the automated ODN synthesis were lyophilized and diluted with distilled water (1 mL). The ODNs were purified by HPLC (Merck LichoCART C18 column; 10 × 250 mm; 10 μm; pore size: 100 Å). The HPLC mobile phase was held isocratically for 10 min with 5% acetonitrile/0.1 M triethylammonium acetate (TEAA) (pH 7.0) at a flow rate of 2.5 mL/min. The gradient was then increased linearly over 10 min from 5% to 50% acetonitrile/0.1 M TEAA at the same flow rate. The fractions containing the purified ODN were cooled and lyophilized. 80% aqueous AcOH was added to the ODN. After 30 min at ambient temperature, the AcOH was evaporated under reduced pressure. The residue was diluted with water (1 mL), and this solution was then purified by HPLC using the same conditions as those described above. The ODNs were analyzed by HPLC (Hewlett−Packard, ODS Hypersil; 4.6 × 200 mm; 5 m; 79916OD-574) using almost the same eluent system. For characterization, matrix-assisted laser desorption ionization time-of-flight (MALDI-TOF) mass spectrometric data of the fluorescent ODNs were collected using a PE Biosystems Voyager System 4095 instrument operated in the positive-ion mode and a 1:1 mixture of 3-hydroxypicolinic acid (0.35 M) and ammonium citrate (0.1 M) as the matrix; the accelerating voltage was 25 kV.

Steady-State Fluorescence Measurements. Steady-state fluorescence (FL) spectra were recorded using an MD-5020 PTI model microscope photometer operating at a bandwidth of 15 nm and quartz cuvettes (0.5 × 2 cm) having a light pass length of 1 cm. The cell holder was thermostatted with circulating water that was controlled using a PolyScience digital temperature controller 9110. An excitation wavelength of 386 nm was used; all excitation and emission slits were set to 1 nm. All hybridizations and fluorescence experiments were performed in 1 mM $MgCl_2$/100 mM Tris−HCl buffer (pH 8) containing a one-to-one ratio of complementary ODNs at a duplex concentration of 1.5 μM.

Cell Culture and Transfection. Monolayers of human hepatoma cell line Huh7 were grown in Dulbecco's Modified Eagle's Medium (DMEM; Gibco-BRL), 10% FBS (Hyclone), penicillin, and streptomycin. For fluorescence microscopy imaging, the coverslips were washed with HCl and rinsed with distilled water. 0.5% gelatin-coated coverslips were placed in 6-well dishes; culture cells were grown directly on the coverslips, with up to 80% confluence. Each ODN was diluted in serum-free DMEM to a final concentration of 40 nM. The cells were washed with phosphate-buffered saline (PBS); serum-free media containing each ODN (2 mL) were added to the cells grown on the coverslips. The lipofectamine 2000 reagent (Invitrogen) was used to compare the transfection efficiencies of the different delivery methods. Transfection assays were performed according to the manufacturer's instructions.

Image Acquisition and Processing. After incubation with an MB for the indicated time, the cells were washed three times with PBS and then fixed with 3.5% (w/v) paraformaldehyde (Sigma) at room temperature (RT) for 12 min. After being washed three times with PBS, the coverslips were placed on a glass slide and then sealed with transparent nail polish. The fluorescence images were captured using a cooled charge-coupled device camera and a Zeiss Axioplan microscope (Jena, Germany). Data were processed using *Adobe Photoshop* software (Mountain View, CA).

Cellular Uptake of the Cholesterol-Bearing MB. The amount of ODN present within the transfected cells was quantified using a SPECTRAmax GEMINI microplate spectrofluorometer (Molecular Device). Huh7 cells were seeded onto 48-well culture dishes before transfection. 40 nM ODN solutions in serum-free DMEM were used in the transfection analyses. Cell extracts were collected after lysis of the cells (the cell lysis had been performed through the addition of lysis buffer). The fluorescence intensity was recorded with the excitation wavelength set at 386 nm and the emission wavelengths set at 450 and 510 nm. Concurrently, the total cell mass was determined using the BCA method (Pierce, Rockford, IL).

A

1 5'd- GC**A**^{P} GAG AAG TTA GAA CCT ATG CTC **A**^{P}GC
2 3'd- TTC AAT CTT GGA TAC
3 5'd- **C**$^{\#}$GC**A**^{P}GAG GTG CAC GGT CTA CGA GAC C CTC **A**^{P}GC
4 5'd- GC**A**^{P}GAG GTG CAC GGT CTA CGA GAC C CTC **A**^{P}GC
5 3'd- CAC GTG CCA GAT GCT CTG G

B

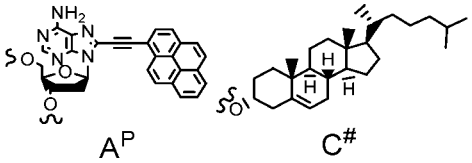

Figure 1. Molecular beacons and their target DNA sequences. The underlined nucleotides are present in the loop regions for hybridizing with their complementary sequences.

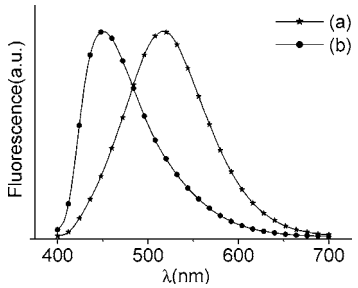

Figure 2. Fluorescence spectra of **1** in their different states. (a) Emission of hairpin state **1**; (b) emission of the duplex state **1·2**; All spectra were recorded using 1.5 μM solutions in buffer (100 mM trizma HCl/1 mM $MgCl_2$; pH 8) at 25 °C; 386 nm.

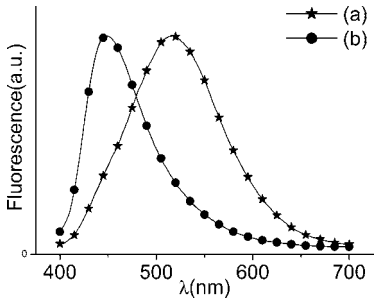

Figure 3. Fluorescence spectra of (a) ODN **3** (λ_{max} = 509 nm) and (b) the perfectly matched duplex **3·5** (445 nm). The conditions were the same as those described in Figure 2.

RESULTS AND DISCUSSION

Design of Functional Oligonucleotides. We synthesized pyrene-modified nucleoside building blocks through Sonogashira coupling of pyrene units to the 8-position of a 2′-deoxyadenosine base (i.e., to form 8-(1-ethynylpyrenyl)-2′-deoxyadenosine; A^{P}) (*23*). The quantum yields of A^{P} are very high: 81% and 89% in $CHCl_3$ and MeOH (*23*), respectively. We incorporated A^{P} into oligodeoxynucleotides (ODNs) by using the phosphoramidite method and the aid of a DNA synthesizer. We constructed modified single-stranded ODN **1** in which the two fluorophores were positioned in opposite strands of the stem of each hairpin. We also synthesized a perfectly matched sequence **2** for hybridizing to the loop regions of ODN **1**. We synthesized a cholesterol-bearing MB system (ODN **3**) that is complementary to ODN **5**. We also synthesized the corresponding unmodified ODN **4** to compare the transfection properties between two systems (Figure 1).

Cholesterol-Bearing MB. *In Vitro Fluorescence Changes.* Figure 2 displays the fluorescence spectra of A^{P}A^{P}. Interestingly, **1** (existing in its hairpin state) emits a strongly red-shifted band

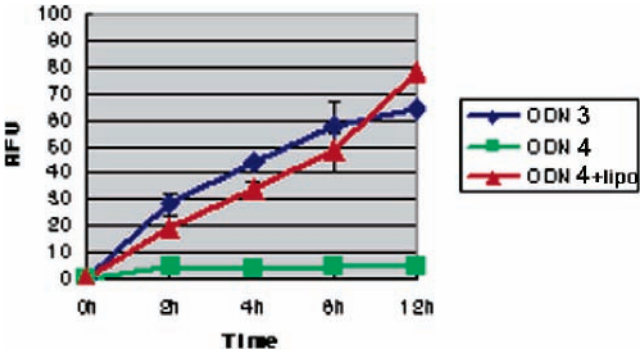

Figure 4. Time-dependent cellular uptake of ODNs **3** and **4** in the absence and presence of lipofectamine ("lipo"). The fluorescence intensities were recorded with the excitation wavelength set at 386 nm and the emission wavelengths set at 510 nm. Concurrently, the total cell mass was determined using the BCA method (Pierce, Rockford, IL).

(λ_{max} = 521 nm; Figure 2a); in comparison, the value of λ_{max} of the duplex **1·2** is 450 nm (Figure 2b).

On the basis of the results presented above, we prepared a cholesterol-bearing ODN incorporating a cholesterol unit at the 5′ end of the hairpin; because the 5′ and 3′ termini of ODN **1** are unsubstituted, it is very easy to use an ODN synthesizer to modify them with functional molecules. Thus, we synthesized a cholesterol-bearing MB system (ODN **3**) that is complementary to the ODN **5**. We also synthesized the corresponding unmodified ODN **4** to compare the two systems' transfection properties. Figure 3 displays the change in the appearance of the fluorescence spectrum of ODN **3** after the addition of its target sequence, ODN **5**. The spectra suggest that, even though we had attached a cholesterol moiety at the 5′ end of the MB, the photophysical signals of the MB system remained unaffected. We believe that the strongly red-shifted band at 509 nm must arise from stacking interactions between the two pyrene units of A^P. In our fluorescence experiments. specific origin of this red-shifted band comes from an exiplex or merely that of a dimer of the two pyrene units. Fluorescence wavelengths are very close to that of a typical pyrene excimer (*24*), suggesting that the excited complex of each fluorophore was formed in the hairpin state.

In Vivo Fluorometry. Our cholesterol-bearing MBs can enter into living cells efficiently without the need for any transfection agent (Figure 4). The transfection efficiency of the MB conjugated with cholesterol (ODN **3**, blue curve) during the first 12 h in Huh7 cells was much higher than that of the unmodified MB (ODN **4**, green curve); we observed essentially no signal for the latter, even after 12 h. For the sake of comparison, the unmodified ODN **4** was transfected with a commercial transfection reagent, lipofectamine ("ODN **4** + lipo," red curve). The fluorescence obtained when using the transfection reagent (lipofectamine) was similar to that of the cholesterol-linked MB.

In Vivo Fluorescence Microscopy. We performed a fluorescence microscopy experiment to observe the transfection pattern of the cholesterol-bearing MB in Huh7 cells. Figure 5 displays

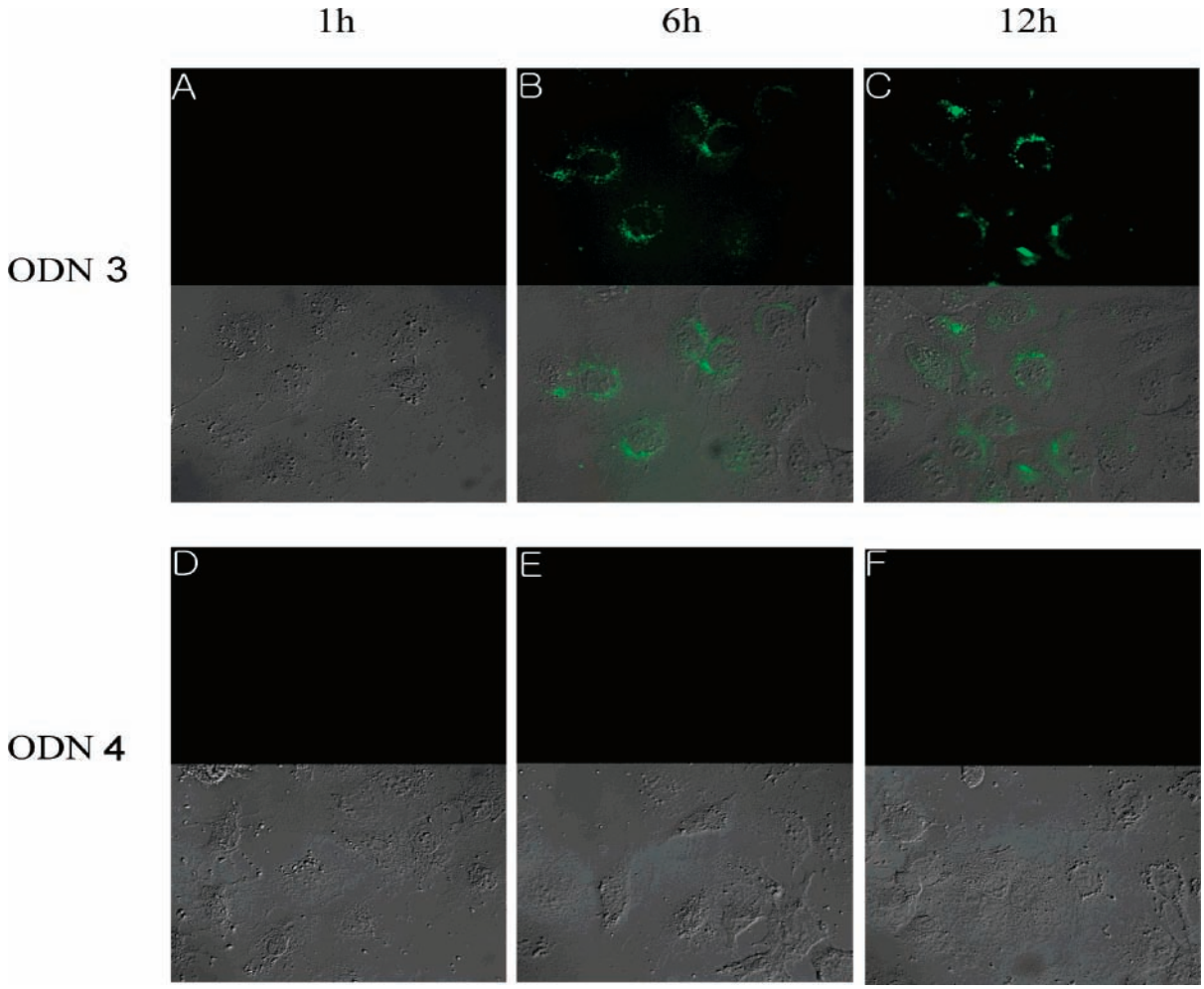

Figure 5. Cellular delivery of MBs in Huh7 cells. (A−C) Fluorescence signals of cholesterol-conjugated ODN **3** transfected into Huh7 cells at different times (p.t.). Fluorescence signals of ODN **3** were not observed at 1 h p.t., but were detected in the cytoplasm around the nucleus at 6 and 12 h p.t. (D−F) Fluorescence of the unmodified ODN **4** after the indicated times (p.t.). The upper panels present the fluorescence signals of the MBs; the lower panels represent a combination of the images in the upper panels and the phase-contrast images of the cells.

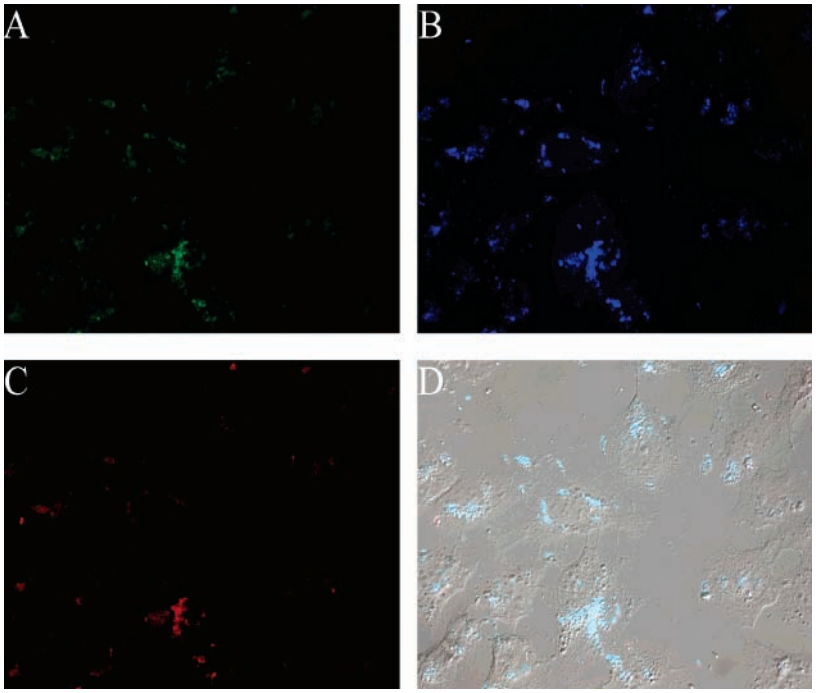

Figure 6. Cellular delivery of ODN **4** when using the lipofectamine reagent. (A−C) Fluorescence signals in Huh7 cells after transfection of the unmodified MB with lipofectamine for 12 h. Each emission filter accepted a different range of wavelengths: (A) 410−490 nm; (B) 508−523 nm; (C) >570 nm. (D) The three separate images from A−C (coded blue, green, and red, respectively) merged into a single image.

the cellular transfection property as imaged directly in vivo. Consistent with our fluorometry experiments, these images clearly demonstrate that the cellular transfection of the ODN **3** (bearing the cholesterol unit) is far better than that of ODN **4** (without cholesterol) and that obtained by using the conventional transfection agent (Figure 6). Indeed, in the case of ODN **4**, we observed no signal, as expected, whereas ODN **3** displayed extremely strong signals in the cytoplasm. To demonstrate whether the ODN **3** reached the cytoplasm of cells, double-fluorescence staining experiments were carried out with Lysotracker (see Supporting Information). In the presence of the transfection reagent (lipofectamin), ODN **4** displayed different characteristics than did the cholesterol-linked ODN **3**. Specially, the fluorescence signals obtained by using lipofectamin were concentrated in random "bright spots" in both the cytoplasm and the nucleus, indicating the aggregation pattern (Figure 6). We observed a similar trend after we transfected other oligonucleotides with lipofectamin in Huh7 cells (data not shown). However, we did not observe any cross-signal or nonspecific aggregated bright spots (compare Figure 5 to Figure 6) in our MB system. Therefore, our MB system is more efficient than one using the transfection agent. We are now investigating the ability of using such MB systems to fluorescently detect the dynamic pathway of hepatitis C virus in living cells.

CONCLUSION

Systems **1** (A^PA^P) individually exhibit aromatic stacking between the opposing pyrene units in the stems of their hairpins; their spectra display the characteristics of π-stacked pyrene units. Systems **1** (A^PA^P) can be used as effective MBs that change color from green to blue upon duplex formation. These novel types of MBs are relatively simple to synthesize, and their termini remain free for the introduction of other useful functionalities. We introduced a cholesterol unit into one terminus of an MB and demonstrated clearly that the cellular delivery of this modified MB was enhanced significantly relative to those obtained by using the corresponding unmodified MB or by using conventional transfection agent-based methods. Cholesterol-based transfection has the potential to avoid the endocentric pathway and, therefore, to reduce the number of false positive signals arising from nuclease degradation. The cholesterol-bearing, pyrene-π-stacking-based MB system represents a new type of MB whose high cellular uptake efficiency makes such probes unique and novel; we believe that this one holds great promise for studying the dynamics of biomolecular systems in living cells and that its use will open up other new and exciting opportunities for applications in vivo.

ACKNOWLEDGMENT

We are grateful to KOSEF for financial support through the National Research Laboratory Program (Laboratory for Modified Nucleic Acid Systems), Gene Therapy R&D program (M10534-000011-05N3400-01110) and KNRRC program. BHK and SKJ are grateful to the National Core Research Center for Systems Bio-Dynamics.

Supporting Information Available: MALDI-TOF mass spectra and confocal microscopy of synthesized compounds. This material is available free of charge via the Internet at http://pubs.acs.org.

LITERATURE CITED

(1) Dirks, R. W., Molenaar, C., and Tanke, H. J. (2001) Methods for visualizing RNA processing and transport pathways in living cells. *Histochem. Cell Biol. 115*, 3−11.

(2) Mcdonald, D., Vodicka, M. A., Lucero, G., Svitkins, T. M., Borisy, G. G., Emerman, M., and Hope, T. J. (2002) Visualization of the intracellular behavior of HIV in living cells. *J. Cell Biol. 159*, 441−452.

(3) Guckian, K. M., Schweitzer, B. A., Ren, R. X.-F., Sheils, C. J., Paris, P. L., Tahmassebi, D. C., and Kool, E. T. (1996) Experimental measurement of aromatic stacking affinities in the context of duplex DNA. *J. Am. Chem. Soc. 118*, 8182−8183.

(4) Paris, P. L., Langenhan, J. M., and Kool, E. T. (1998) Probing DNA sequences in solution with a monomer-excimer fluorescence color change. *Nucleic Acids Res. 26*, 3789−3793.

(5) Matray, T. J., and Kool, E. T. (1998) Selective and stable DNA base pairing without hydrogen bonds. *J. Am. Chem. Soc. 120*, 6191−6192.
(6) Kierzek, R., Li, Y., Turner, D. H., and Bevilacqua, P. C. (1993) 5′-Amino pyrene provides a sensitive, nonperturbing fluorescent probe of RNA secondary and tertiary structure formation. *J. Am. Chem. Soc. 115*, 4985−4993.
(7) Caldwell, R. A., Creed, D., DeMarco, D. C., Melton, L. A., Ohta, H., and Wine, P. H. (1980) Charge-transfer quenching of singlet excited complexes. *J. Am. Chem. Soc. 102*, 2369−2377.
(8) Shafirovich, V. Y., Courtney, S. H., Ya, N., and Geacintov, N. E. (1995) Proton-coupled photoinduced electron transfer, deuterium isotope effects, and fluorescence quenching in noncovalent benzo-[a]pyrenetetraol-nucleoside complexes in aqueous solutions. *J. Am. Chem. Soc. 117*, 4920−4929.
(9) Tyagi, S., Bratu. D., and Kramer, F. R. (1998) Multicolor molecular beacons for allele discrimination. *Nat. Biotechnol. 16*, 49−53.
(10) Steemers, F. J., Ferguson, J. A., and Walt, D. R. (2000) Screening unlabeled DNA targets with randomly ordered fiber-optic gene arrays. *Nat. Biotechnol. 18*, 91−94.
(11) Li, J. J., Geyer, R., and Tan, W. (2000) Using molecular beacons as a sensitive fluorescence assay for enzymatic cleavage of single-stranded DNA. *Nucleic Acids Res. 28.* 11, e52.
(12) Barton, G. M., and Medzhitov, R. (2002) Retroviral delivery of small interfering RNA into primary cells. *Proc. Natl. Acad. Sci. U.S.A. 99*, 14943−14945.
(13) Cheung, C. Y., Murthy, N., Stayton, P. S., and Hoffman, A. S. (2001) A pH-sensitive polymer that enhances cationic lipid-mediated gene transfer. *Bioconjugate Chem. 12*, 906−910.
(14) Mitchell, P. (2001) Turning the spotlight on cellular imaging. *Nat. Biotechnol. 19*, 1013−1017.
(15) Sokol, D. L., Zhang, X., Lu, P., and Gewirtz, A. M. (1998) Real time detection of DNA·RNA hybridization in living cells. *Proc. Natl. Acad. Sci. U.S.A. 95*, 11538−11543.
(16) Yin, D., and Tang, J. G. (2001) Gene therapy for streptozotocin-induced diabetic mice by electroporational transfer of naked human insulin precursor DNA into skeletal muscle in vivo. *FEBS Lett. 495*, 16−20.
(17) Nakano, S., Uotani, Y., Nakashima, S., Anno, Y., Fujii, M., and Sugimoto, N. (2003) Large stabilization of a DNA duplex by the deoxyadenosine derivatives tethering an aromatic hydrocarbon group. *J. Am. Chem. Soc. 125*, 8086−8087.
(18) Seo, Y. J., Ryu, J. H., and Kim, B. H. (2005) Quencher-free, end-stacking oligonucleotides for probing single-base mismatches in DNA. *Org. Lett. 7*, 4931−4933.
(19) Lewis, F. D., Zhang, Y., and Lestinger, R. L. (1997) Bispyrenyl excimer fluorescence: a sensitive oligonucleotide probe. *J. Am. Chem. Soc. 119*, 5451−5452.
(20) Okamoto, A., Kanatani, K., and Saito, I. (2004) Pyrene-labeled base-discriminating fluorescent DNA probes for homogeneous SNP typing. *J. Am. Chem. Soc. 126*, 4820−4827.
(21) Wagner, C., Rist, M., Elke, M. E., and Wagenknecht, H. A. (2005) 1-Ethynylpyrene-modified guanine and cytosine as optical labels for DNA hybridization. *Org. Biomol. Chem. 3*, 2062−2063.
(22) Fujimoto, K., Shimizu, H., and Inouye, M. (2004) Unambiguous detection of target DNAs by excimer-monomer switching molecular beacons. *J. Org. Chem. 69*, 3271−3275.
(23) Hwang, G. T., Seo, Y. J., and Kim, B. H. (2005) Pyrene-labeled deoxyuridine and deoxyadenosine: fluorescent discriminating phenomena in their oligonucleotides. *Tetrahedron Lett. 46*, 1475−1477.
(24) Förster, Th. (1969) Excimers. *Angew. Chem., Int. Ed. 8*, 333−343.

BC060078Q

DNA Binding to Protein−Gold Nanocrystal Conjugates

Michelle K. Calabretta,[§,*] Kathleen S. Matthews,[†] and Vicki L. Colvin[§]

Department of Chemistry and Department of Biochemistry and Cell Biology, Rice University, 6100 Main Street, Houston, Texas 77005. Received April 9, 2006; Revised Manuscript Received June 1, 2006

The *E. coli* DNA binding protein *lac* repressor (LacI) and a derivative with a designed thiol (T334C) were developed as gold nanocrystal conjugates to assess the effects of conjugation on DNA binding function. The designed derivative was engineered with a solvent-accessible thiol to promote oriented conjugation, avoiding obstruction of the DNA-binding domain by the nanocrystal. Analytical ultracentrifugation (AU) and electrophoretic mobility shift assays (EMSA) were used to evaluate the ability of conjugated repressors to bind the natural operator DNA sequence O^1. The results show that LacI does not retain significant DNA binding function when conjugated to gold nanocrystals, presumably because the basic DNA-binding domain is the site for nonspecific conjugation. T334C, with the potential for both directed and nonspecific conjugation, shows enhanced interaction with O^1 when conjugated. Interestingly, the order of component addition is a key factor in producing functional *lac* repressor conjugates.

INTRODUCTION

DNA recognition proteins have recently been the subject of interest in nanoscience (*1*−*5*). Yun and co-workers (2002) tested the ability of DNA binding proteins to interact with DNA oligonucleotides tethered on both ends to small (1.4 nm) gold nanocrystals. Interparticle distances obtained from TEM demonstrate that EcoRI can cause topological changes, such as bending, in conjugated DNA. This type of manipulation generates the potential for design of nanoarchitectures for electronics and sensors (*5*). Protein−DNA complexes have also been used as functional scaffolds for the fabrication of nanoelectronics. For example, Keren and co-workers used the structural and functional properties of the RecA nucleoprotein filament to produce gold nanowires with branched architectures and other structural characteristics (*1*). Another nanoarchitecture, using protruding biotinylated thymine loops on DNA oligonucleotides, produced uniformly spaced streptavidin-coated gold nanocrystals. The researchers propose that regularly spaced arrays of gold nanocrystals could interconnect nanoelectric components and aid in the development of logical nanoelectronic devices (*2*).

The *lac* repressor (LacI), an *E. coli* DNA binding protein, is attractive for use as a structural and functional nano building block because of the large amount of genetic and biochemical information available for this protein (for review see ref 6). LacI is structurally well characterized, with several crystallographic and solution structures available. This protein binds two types of ligand: DNA (operator) and small sugar molecules (inducer). The binding of an inducer sugar reduces the ability of LacI to bind DNA, effectively making LacI a logic switch, where "on" is the high DNA affinity state and "off" is in the presence of inducer when DNA affinity is low. One approach to the assembly of nanoelectronic components onto DNA nanostructures could utilize the specificity of DNA binding proteins, like LacI, for their DNA substrates. For example, DNA sequences created with natural operator sequence O^1 at regular intervals could be mixed with LacI-bound gold nanocrystals, resulting in uniformly spaced gold nanocrystal architectures. This type of application requires oriented protein conjugation and would be sensitive to the ability of the conjugated repressor to interact with DNA, which is in turn modulated by inducer binding.

There is substantial evidence that nonspecific protein−gold nanocrystal interactions are largely electrostatic, occurring through basic surface residues and the negatively charged nanocrystal surface (*7*, *8*). The DNA-binding domain is logically the most probable region for gold nanocrystal conjugation to LacI because it is highly basic, having a theoretical pI ∼9.3, and lacks well-defined structure in the absence of operator DNA, providing easy accessibility (*9*). If the DNA-binding domain is the site of interaction, then LacI−gold nanocrystal conjugates would be sterically prevented from binding operator DNA. The purpose for creating T344C, with its solvent accessible cysteines, was to provide a means for thiol-directed conjugation to gold through the C-terminal region of LacI, thereby precluding nanocrystal interference with the DNA-binding domain. Here, we assess the operator DNA binding affinity of LacI and T334C gold nanocrystal conjugates. This work develops the understanding of how conjugation can be manipulated to optimize the function of protein-nanocrystal materials.

EXPERIMENTAL PROCEDURES

Materials. All materials were purchased from Sigma unless specified otherwise.

Protein Mutation, Purification, and Conjugation. The T334C mutation was produced on plasmid pLS1 (*10*) with the QuikChange PCR site-directed mutagenesis kit (Stratagene) using the provided protocol. Mutant plasmids were transformed into supercompetent GC5 cells (Gene Choice) for growth and purification. Mutant plasmids were sequenced (SeqWright) to verify that no other mutations were present. Purification of wild type LacI was carried out as described previously (*11*−*14*). Briefly, expression occurred in *E. coli* strain BLIM (Novagen), which was cured of the LacI episome (*15*). After centrifugation, cell culture pellets were resuspended and lysed, and the lysis supernatant was precipitated in 37% ammonium sulfate. The resuspended precipitate was dialyzed overnight and loaded onto phosphocellulose. LacI was eluted with a gradient of 0.12−0.3 M potassium phosphate buffer, pH 7.5. The concentration of LacI-containing fractions was determined by absorbance at 280 nm (extinction coefficient = 1.6 mL mg^{-1} cm^{-1}). The T334C

* Corresponding author. Phone: (713) 348-4936; E-mail: mcal@rice.edu.
§ Department of Chemistry.
† Department of Biochemistry and Cell Biology.

10.1021/bc0600867 CCC: $33.50 © 2006 American Chemical Society
Published on Web 08/04/2006

mutant was purified similarly to wild type protein, with the following exceptions: Protease inhibitor tabs (Roche) were added to inhibit degradation of the protein. Dialysis time of the resuspended ammonium sulfate pellet is reduced to three 20-min steps. All buffers contained 10 mM DTT to prevent aggregation via the solvent-exposed cysteine residues. Last, T334C was eluted stepwise (0.12 M KP to 0.3 M KP) instead of with a gradient to minimize time of purification. Proteins were stored at −20 °C for up to 6 months with 10 mM DTT.

Conjugates were formed as follows: The LacI potassium phosphate storage buffer was exchanged for conjugation buffer (50 mM Tris, pH 9.2, 5% (w/v) glucose) by centrifugation in Amicon Ultra-15 (MWCO 30000) centrifugal filters (Millipore). LacI or T334C (250 μL) was diluted into 15 mL of conjugation buffer and centrifuged at 2500*g* for 15 min. The process was repeated twice more to ensure complete exchange. A gold nanocrystal suspension, prepared by citrate reduction and characterized as described previously (*14*), was added to specified repressor concentrations diluted in conjugation buffer so that the final concentration of gold nanocrystal was one-fourth the initial concentration. This dilution factor was necessary to decrease the nanocrystal absorbance in the UV−visible region to below 1 absorbance unit and sufficiently dilutes the nanocrystals so that concentration-dependent nonideality in sedimentation is minimized. Samples were allowed to conjugate for approximately 30 min at room temperature unless specified otherwise.

[^{35}S]-Methionine-labeled LacI and T334C were generated as described previously (*14*) with the TNT T7 Quick for PCR DNA transcription/translation kit (Promega). Briefly, the LacI gene (with and without the T334C mutation) under the T7 promoter was cloned into pGEM-T (Promega). Following translation, unincorporated [^{35}S]-methionine (ICON Isotopes) was removed with protein desalting spin columns (Pierce). [^{35}S]-repressors were further purified on a small phosphocellulose column and diluted with unlabeled repressor to determine protein concentration (μg/μL) by absorbance at 280 nm. The amount of radioactive isotope in counts per minute (cpm) was measured for an aliquot of the repressor mixture to produce a specific activity (cpm/g) for the sample. For [^{35}S]-repressor−gold nanocrystal conjugates, free protein was removed by centrifugation at 14000 rpm for 30 min in a desktop centrifuge. The conjugated repressor concentration was determined based on the amount of radioactive isotope present using the specific activity of the initial protein sample.

Operator DNA Radiolabeling. Operator affinities of conjugated proteins were measured with double-stranded natural operator O^1 (5′-TGTTGTGTGGAATTGTGAGCGGATAACAATTTCACACAGG-3′). Complementary strands (BioSource) were hybridized in annealing buffer (8 mM Tris-HCl, pH 7.5, 4 mM $MgCl_2$, 10 mM NaCl) and labeled with [^{32}P] by polynucleotide kinase (NEB) and γ-[^{32}P]-ATP (MP Biomedicals) in a final volume of 15 μL. The labeling reaction was terminated with 2 μL of 0.5 M EDTA and diluted to 50 μL with Tris-EDTA, pH 8. Labeled operator was purified from unincorporated γ-[^{32}P]-ATP on NICK columns (Amersham Biosciences) and eluted with Tris-EDTA, pH 8.0. DNA was aliquoted and stored at −20 °C for up to 1 month.

Analytical Ultracentrifugation (AU). AU data were collected using the vendor's software on a Beckman XL-A analytical ultracentrifuge. Sedimentation velocity experiments were performed at 20 °C at 3100 rpm. A total of 80 scans were taken at 10 scans per hour for each sample. Raw data were processed with the enhanced van Holde−Weischet and second moment utilities in Ultrascan version 7.2 (*16*).

NaCl Flocculation Assays. Conjugates, prepared as described above, were mixed with NaCl to a final concentration of 1%. Flocculation proceeded for 10 min before recording the UV−visible spectra (200−800 nm) on a Varian Cary 50 UV−visible spectrophotometer. A minimum of three spectra for each protein concentration were recorded.

Electrophoretic Mobility Shift Assay (EMSA). Nondenaturing 4% polyacrylamide (37.5:1 acrylamide:bisacrylamide) gels containing 2% glycerol were preelectrophoresed in 0.5× TBE (0.045 M Tris-borate, pH 8.0, 1.0 mM EDTA) at 100 V, constant current, for 1 h prior to loading the samples. Conjugate-[^{32}P]-O^1 interactions were measured in conjugation buffer at pH 8 (50 mM Tris-HCl, pH 8, 5% glucose w/v), with BSA added to a final concentration of 1 mg/mL just prior to loading to aid in entry of the sample into the gel. Samples were loaded onto gels at 250 V until separation of loading dye occurred. The voltage was reduced to 150 V, and gels were run for approximately 1.5 h or until the loading dye reached a distance of 6 cm into the gel. Gels were dried with a vacuum gel dryer and exposed overnight to a Fuji phosphorimaging plate. Binding data were visualized and quantified with MultiGauge software (Fuji).

RESULTS

The DNA recognition capability of LacI requires contact between operator DNA (^{1}O) and the charged binding domain of LacI. Negatively charged gold nanocrystals could in principle interact with this important region and render the protein inactive. With that possibility in mind, we developed a mutant of LacI, T334C, to direct nanocrystal attachment to another region of the protein. This system contains a solvent-exposed cysteine residue in the C-terminus, on the opposite end of the protein from the N-terminal DNA-binding domain. Figure 1 shows the crystal structure of tetrameric LacI and the position of the basic DNA-binding domain and threonine 334 on each monomer. The cysteine mutation provides potential for site-directed conjugation via a gold−sulfur bond, and its location would orient the DNA-binding domain away from the nanocrystal. Additionally, nanocrystal attachment to the cysteines of T334C would require a stronger, more stable gold−sulfur bond than the nonspecific and reversible electrostatic interactions expected for binding between gold nanocrystals and the native LacI repressor (*17*).

Central to any comparison of function between nanoparticle-bound and free proteins is accurate evaluation of the stoichiometry of the nanobionconjugates; in particular, it is important that nanobioconjugates are produced with saturation coverage of proteins and that free protein is removed from the suspensions. Here, these issues were addressed for gold nanocrystal−repressor conjugates using three methods: NaCl-induced flocculation, [^{35}S]-repressor association, and analytical ultracentrifugation. Taken together these techniques provide both a measure of the success of conjugation strategies, and also a determination of the stoichometry of the resulting complexes. The results from all methods are summarized in Table 1.

In NaCl-induced flocculation assays, gold nanocrystals become aggregated because of the reduced electrostatic repulsion at higher ionic strengths. This aggregation is signaled by a pronounced shift in the peak position of their absorbance. If nanocrystals are bound to proteins, the aggregation is modified significantly and can in fact be avoided when nanocrystals are fully coated by proteins. Thus, an examination of the gold nanocrystal−repressor solutions as a function of [gold nanocrystal]/[repressor] ratio provides a verification of the successful conjugation of LacI and T334C to nanocrystals. Figure 2 shows that ∼12 LacI repressors are needed to prevent flocculation, whereas a smaller number of repressors produce the same outcome for T334C (Table 1). These data suggest that reversible electrostatic interactions are important in the conjugation of gold nanocrystals to the native LacI repressor. Compared to a stronger

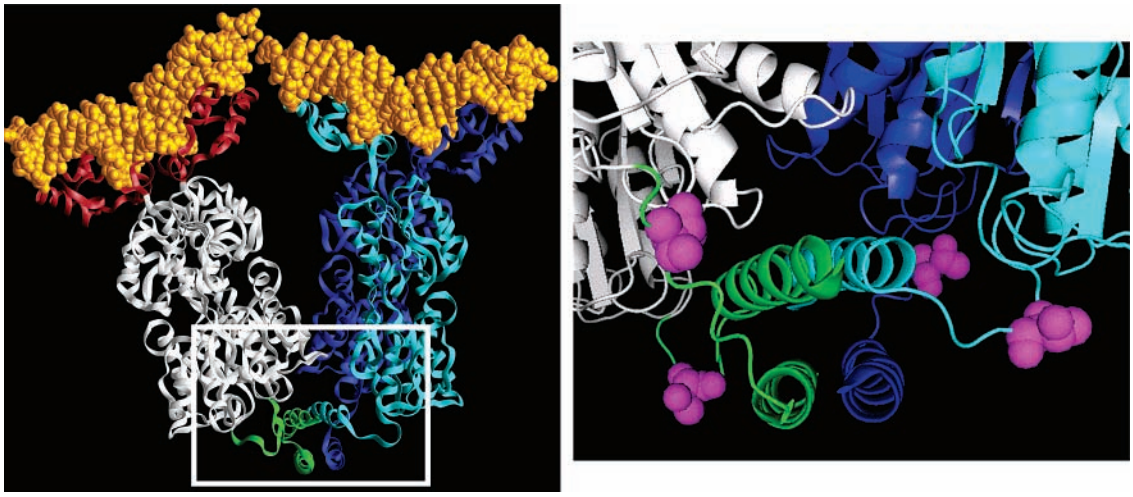

Figure 1. Crystal structure of LacI and placement of the T334C mutation. LacI is a dimer of dimers. In the right dimer, one monomer of LacI is shown in light blue and the other in dark blue. In the left dimer, the DNA-binding domain is colored red, the core domain (that binds sugar inducer) of the protein white, and the tetramerization domain in green. Operator DNA is shown as the yellow space-filled molecule. The white box indicates the region for enlargement to show the position of threonine 334. Threonine 334, shown in magenta in the enlargement, was chosen for cysteine mutation because it is solvent accessible and should orient the protein so that neither the DNA-binding domain nor the inducer sugar pocket are obstructed when the protein is bound to gold nanocrystals. Figure generated from pdb files 1LBG and 1LBI (*9*).

Table 1. Repressor−Gold Nanocrystal Ratios (13.2 nm Gold Nanocrystals)[a]

	repressors per nanocrystal		
protein	NaCl flocculation	[^{35}S]-labeling	AU S_{max}
LacI	~12	7.1 ± 0.7	10.8 ± 0.7
T334C	~8	9.6 ± 0.2	10.4 ± 1.0.

[a] For comparison, a theoretical prediction of 11 repressors per nanocrystal is based on the average diameter of the gold core from TEM data and dimensions from the LacI crystal structure 1LBI (*9*).

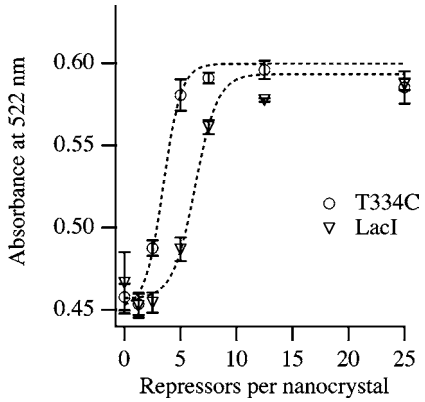

Figure 2. NaCl-induced flocculation of repressor conjugates. The absorbance of the gold nanocrystal plasmon peak was measured after NaCl was added to samples with a range of repressor concentrations. T334C (circles) prevents flocculation at lower concentration than LacI (triangles). Lines are shown for guidance only. Data are from three separate experiments.

gold−sulfur bond such as that engineered in T334C, native LacI repressors would require higher protein concentrations for stabilization.

The relative amount of gold nanocrystal and protein in these conjugates can also be found using radiolabeled [^{35}S]-repressor conjugates (Table 1). Here, [^{35}S]-repressors were conjugated to gold nanocrystals using our standard methods, and free protein was separated from conjugates by multiple rounds of centrifugation. The results show that LacI−gold nanocrystal conjugates have on average three fewer proteins per nanocrystal than conjugates produced using T334C mutants, a result that contradicts the trend found in the NaCl flocculation assay. In this analysis, bionanoconjugates were separated from proteins using a strong centrifugal force (14000 rpm for 30 min) to rapidly pellet the sample; subsequent washes, and recovery, could result in the removal of weakly bound LacI repressor proteins from gold nanocrystal surfaces and subsequently lower [protein]/[nanocrystal] ratios. This effect would be less substantial for T334C−gold nanocrystal conjugates since conjugation in that case relies on the stronger gold−sulfur bond.

Bioconjugate structure can also be evaluated by shifts in the *S* value obtained from AU sedimentation velocity experiments (*14*). Sedimentation velocity, unlike repeated centrifugation and separation of pellet and supernatant, occurs at much lower centrifugal forces and in equilibrium (i.e., the components are not separated during the measurement). Therefore, the [gold nanocrystal]/[protein] values calculated using this technique should reflect both those protein molecules that are weakly and strongly bound to the nanocrystal surfaces. The ratios for both LacI and T334C proteins are ~10 repressors per nanocrystal. This result is consistent with the fact that, despite the mutation, LacI and T334C have the same physical dimensions. Given the average diameter of the gold nanocrystals used in these experiments (13.2 ± 1.5 nm) and the approximate dimensions of an unliganded LacI tetramer (7.8 × 7.9 × 7.7 nm) (*9*), we estimate 11 repressors as the maximum number that the surface of a gold nanocrystal could accommodate, in good agreement with our ratios as measured both by flocculation assays and in ultracentrifugation (Figure 3).

Of great interest in this work is how the conjugation process affects protein function, in this case the binding of operator DNA. To examine this, we used analytical ultracentrifugation to measure the sedimentation characteristics of conjugates mixed with operator DNA. When conjugated repressors interact with operator DNA, substantial changes in the hydrodynamic properties should be signaled by a change in the *S* values measured by AU. Figure 4 compares the *S* values of repressor conjugates with O^1 and an inducer sugar, IPTG. We first considered the properties of the native LacI conjugates. When the LacI conjugate is formed before O^1 is added, the nanocrystals have *S* values comparable to the LacI conjugate without O^1 (Figure 4A). This result suggests that O^1 is not binding to the conjugated LacI, as predicted if the nanocrystals are blocking the DNA recognition domain. We confirmed this by reversing the order of addition, and generated LacI-O^1 complexes that were then exposed to gold nanocrystals. These samples have higher *S*

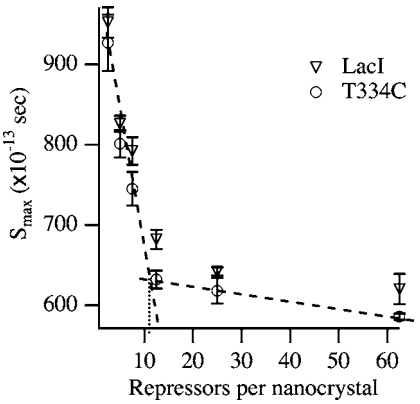

Figure 3. Repressor−gold nanocrystal stoichiometries using S_{max} as an observable. The stoichiometric ratio corresponds to the point where the line fit at lower protein concentrations intersects the line extending the saturation plateau. For simplicity only the lines for LacI are shown. Both LacI (triangles) and T334C (circles) have similar ratios of ~10 repressors per nanocrystal (D = 13.2 nm) at the stoichiometric breakpoint. Data are from three separate experiments.

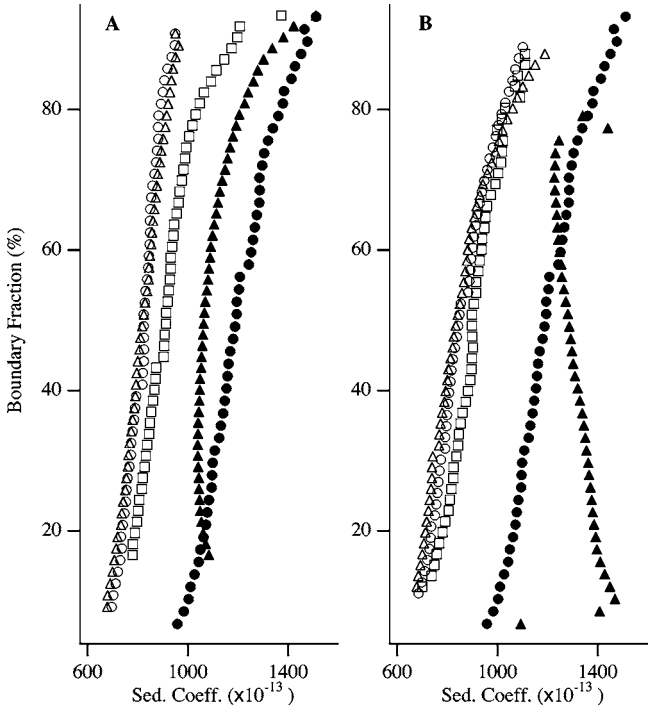

Figure 4. Comparison of S for repressor conjugates with O^1 and inducer IPTG. Integral plots from raw data analyzed in the Enhanced van Holde−Weischet utility in Ultrascan are shown. A, Samples containing LacI and B, samples containing T334C. ●, Gold nanocrystals (4 nM). △, Repressor (30 nM) gold nanocrystal (4 nM) conjugate. ○, Gold nanocrystal conjugated first, then operator (90 nM). ▲, Operator complexed first, then gold nanocrystals. □, Operator complexed first, then gold nanocrystals, then 1 mM IPTG. Data from three separate T334C-operator first experiments displayed a negative slope, indicative of strong repulsive interactions.

values comparable to gold nanocrystals alone, indicating no substantial conjugation occurs (Table 2). These data suggest that LacI interacts with either O^1 or gold nanocrystals, but does not significantly interact with both at the same time. In other words, the gold nanocrystals and operator DNA compete for the same binding site on the native LacI repressor.

The behavior of the mutant T334C repressor conjugates with operator DNA is quite different than that found for native LacI (Figure 4B). When the T334C conjugate is formed prior to O^1 addition, there is a small but significant increase in S (Table 2, $p < 0.2$). This change is larger than that for LacI under similar

Table 2. Average *S* Values of Repressor Conjugates with O^1 and IPTG

protein	AuNC	AuNC, then O^1	O^1, then AuNC	O^1, AuNC, then IPTG
LacI	838 ± 9	855 ± 21	1169 ± 19	947 ± 45
T334C	889 ± 10	906 ± 17	1242 ± 69[a]	952 ± 56
no protein	1114 ± 19	1147 ± 11		1107 ± 137

[a] This value is not accurate due to the strong concentration-dependent nonideality in this sample (see Figure 4).

conditions. What remains uncertain is whether this change arises from conjugate-operator binding, or is the result of reduced nanocrystal coverage when T334C associates with O^1 instead of nonspecifically with the nanocrystal. Interestingly, when the T334C-O^1 complex is formed prior to conjugation, the data are poorly behaved in the van Holde−Weischet analysis and yield an S value distribution with a negative slope, indicative of repulsive interactions in the sample (Figure 4B). Second moment analysis of the data sets in Ultrascan reveal that there is a large concentration-dependent nonideality in these samples (not shown). One possible explanation for the concentration-dependent nonideality is that gold nanocrystals with a primary layer of T334C attached through the engineered cysteine and a secondary layer of O^1 bound to T334C have an exceptionally large hydrodynamic radius. If correct, these conjugates would also possess a strong negative charge on the surface. DNA and large particles like viral capsids are well-known for concentration-dependent nonideality, especially in the low salt conditions found in these experiments. The proposed O^1-T334C−gold nanocrystal complex thus contains all of the elements that cause concentration-dependent nonideality in other systems. Interestingly, when IPTG is added to the T334C O^1-first conjugates, the anomalous behavior is alleviated and the slope of the distribution becomes positive like the other samples. This result indirectly demonstrates that the nonideality is due to T334C-O^1 interactions, although confirmation of the assembly of the O^1-T334C−gold nanocrystal complex cannot be unambiguously deduced from the sedimentation velocity experiments.

Although analytical ultracentrifugation indicates distinctive differences between how T334C and native LacI repressor conjugates recognize DNA, another method is required to confirm the relative ability of each system to interact with operator DNA. Electrophoretic mobility shift assays (EMSA) are readily adapted to this conjugate system. Indeed, agarose gel electrophoresis has been used previously to separate (*18*, *19*), characterize the structure (*20*, *21*), and quantify the binding (*22*) of gold nanocrystal−DNA conjugates. The assembly of albumin and antibody−quantum dot conjugates has also been assessed with polyacrylamide gel electrophoresis (*23*, *24*). Here we use the EMSA to provide information about the operator DNA−repressor complexes.

An EMSA gel of repressor conjugates with [^{32}P]-O^1 is shown in Figure 5. The first four lanes establish the necessary controls. The faster migrating band present in the operator only control is attributed to single stranded DNA (lane 3). When O^1 is bound to unconjugated repressor, the free O^1 band is shifted due to a reduction in electrophoretic mobility (lanes 1 and 2), whereas gold nanocrystals alone do not cause a shift, establishing that there is no significant interaction between the operator and the nanocrystals (lane 4).

When the repressor−operator complex is formed before gold nanocrystals are added, native LacI retains significant O^1 binding affinity as an unconjugated protein, demonstrated by the band with similar mobility to the LacI-operator control (lanes 5−7). Here, the presence of operator appears to compete with conjugate formation, as observed in the AU experiments. Additional bands in these samples as compared to the control lanes are also apparent. First, the supershifted band (lowest mobility

	1	2	3	4	5-7	8-10	11-13	14-16
AuNC	--	--	--	_	2	2	1	1
repressor	L	T	--	--	LacI	T334C	LacI	T334C
O^1	_	_	_	_	1	1	2	2

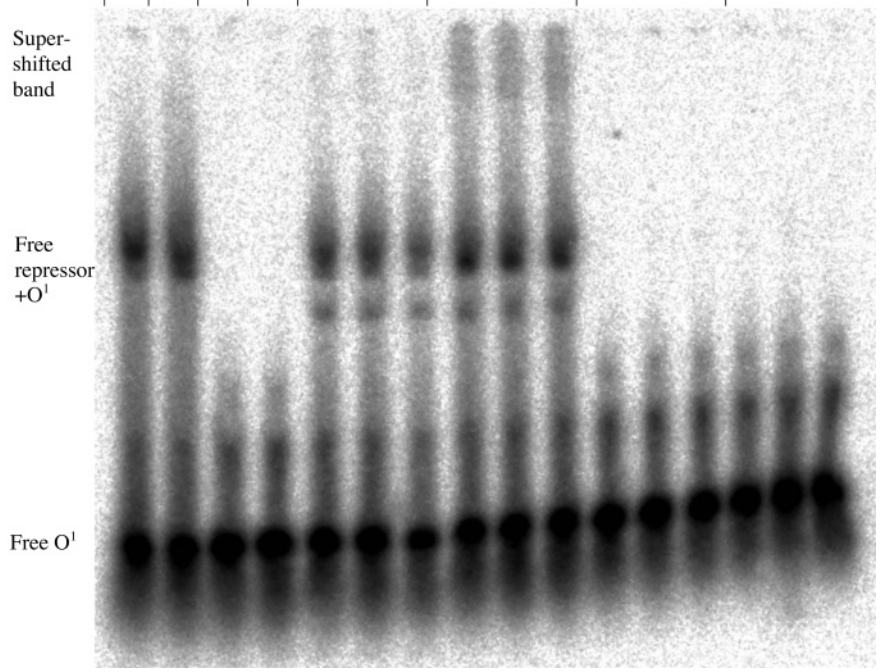

Figure 5. EMSA of 30 nM repressor conjugates with operator DNA O^1. [^{32}P]-O^1 (90 nM) is shown with 30 nM LacI (L) or T334C (T) and 4 nM gold nanocrystals. This protein concentration was chosen because it is slightly below the stoichiometric concentration for repressor−gold nanocrystal conjugation, so all of the protein should be conjugated in the gold nanocrystal-first conditions. The order of reaction components was varied and is denoted 1 or 2. Three predominant bands were observed corresponding to free O^1, unconjugated repressor−O^1 complex, and a super-shifted band representing O^1 bound to conjugate. Lanes 1−3, no nanocrystal added; 4, O^1 and nanocrystal; 5−7, LacI, O^1 added first; 8−10, T334C, O^1 first; 11−13, LacI, nanocrystal first; 14−16, T334C, nanocrystal first.

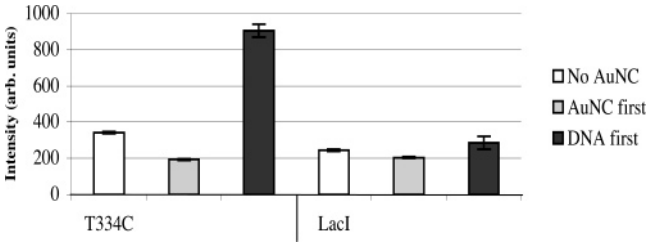

Figure 6. Quantification of the intensities of the supershifted bands in the EMSA. Intensities are measured in the region of the gel corresponding to the supershifted band. All areas used were identical, and data from three separate experiments were averaged. The T334C-O^1 first sample is the only one with significant intensity over background, demonstrating that T334C can interact with both O^1 and gold nanocrystal.

band), which we assign to O^1 bound to gold nanocrystal−protein conjugates (O^1•AuNC•protein) is more significant in the T334C sample (lanes 8−10) than for the native repressor, as predicted from the previous experiments. Visual inspection of the gel shows that, in addition to radiolabeled O^1, this region contains gold nanocrystal-based pink color (data not shown). Quantification of the [^{32}P]-O^1 signal from this band in Figure 6 shows that the T334C super-shifted band is ∼3−4-fold more intense than the analogous LacI band, corresponding to enhanced DNA binding capacity of the T334C conjugate. This difference presumably arises from the ability of O^1-bound T334C to orient conjugation through the engineered cysteine sulfhydryl. The other observed band in lanes 5−10 not present in the control lanes is faster migrating and weaker in intensity than the unconjugated repressor-operator band; this band is assigned to two operators binding to a single tetramer. As expected, no difference in the intensity of this band is observed between LacI and T334C.

In contrast, when LacI or T334C are conjugated to gold nanocrystals prior to the addition of O^1, signals are not observed at the positions corresponding to unconjugated repressor-O^1 complex nor the gold-nanocrystal-conjugated repressor-O^1 complex (lanes 11−16). At these repressor concentrations, little free protein appears to be present to form the unconjugated repressor-O^1 complex, and assembly of O^1-repressor−gold nanocrystal is precluded, presumably by gold nanocrystal binding blocking the basic DNA-binding domain. Note that conjugation prior to O^1 addition interferes with both LacI and T334C binding, suggesting that oriented binding by T334C does not preclude interaction of the basic N-terminal DNA binding domain with gold nanocrystals in the absence of operator DNA sequences.

Similar to AU, the EMSA data demonstrate that the order of addition of reactants is critical for the maintenance of DNA binding function, presumably due to an electrostatic interaction with the DNA-binding domain despite the strong nature of the possible T334C gold−sulfur bond. However, with addition of DNA first, T334C is able to conjugate to the gold nanocrystals through the engineered cysteine and retain significant interaction with O^1 as a conjugate.

DISCUSSION

We developed a LacI mutant designed with a solvent-exposed cysteine residue to facilitate directed conjugation through a gold−sulfur bond, alleviating the functionally deleterious consequences of nonspecific conjugation through the DNA-binding domain. This mutant, T334C, prevents NaCl-induced

flocculation at lower concentrations than native LacI. This observation suggests that LacI conjugates through a weaker, reversible electrostatic interaction, making it less efficient at preventing flocculation compared to T334C, which has the ability to conjugate through a gold−sulfur bond. Furthermore, more radiolabeled repressor is present in the T334C conjugate than the LacI conjugate after removal of free repressor via repeated centrifugation, indicating again that T334C has a stronger, more robust interaction with gold nanocrystals than LacI. Precise ratios of protein to nanocrystal were obtained under equilibrium conditions by the sedimentation velocity of conjugates. With this equilibrium technique, both LacI and T334C exhibit ratios of approximately 10 repressors per nanocrystal, in good agreement with calculations based on the nanocrystal and repressor dimensions.

Analytical ultracentrifugation and EMSA allow characterization of the interaction of conjugated LacI and T334C with the operator DNA sequence O^1. LacI conjugates do not interact strongly with O^1 in either assay. In contrast, T334C conjugates associate with O^1 depending on the order in which the operator-T334C−nanocrystal complex is formed. These data establish that T334C is capable of oriented conjugation to maintain DNA binding function, whereas LacI appears to conjugate primarily through its basic DNA-binding domain, thereby blocking the interaction with O^1 when conjugated. Nonspecific electrostatic protein−gold nanocrystal interactions, while easy to implement, may result in a loss of function for proteins with basic functional regions. If the biological function of the final hybrid material is to be maintained, the possibility of nonspecific interactions between functional regions and the nanostructure must be considered. We have shown that these complications can be avoided at least in part by directing conjugation using thiols placed in regions of the biomolecule that direct orientation to minimize inhibition of function.

ACKNOWLEDGMENT

The authors thank Jennifer Jamison for preparation of the gold nanocrystals used in this work and Joshua Falkner for TEM characterization of the nanocrystals. This work is supported in part by the Nanoscale Science and Engineering Initiative of the National Science Foundation under NSF Award Number EEC-0118007, The National Institutes of Health (GM22441), and the Robert A. Welch Foundation (C-576).

LITERATURE CITED

(1) Keren, K., Krueger, M., Gilad, R., Ben-Yoseph, G., Sivan, U., and Braun, E. (2002) Sequence-specific molecular lithography on single DNA molecules. *Science 297*, 72−75.

(2) Li, H., Park, S. H., Reif, J. H., LaBean, T. H., and Yan, H. (2004) DNA-templated self-assembly of protein and nanoparticle linear arrays. *J. Am. Chem. Soc. 126*, 418−419.

(3) Pena, S. R. N., Raina, S., Goodrich, G. P., Fedoroff, N. V., and Keating, C. D. (2002) Hybridization and enzymatic extension of Au nanoparticle-bound oligonucleotides. *J. Am. Chem. Soc. 124*, 7314−7323.

(4) Tsai, C.-Y., Shiau, A.-L., Cheng, P.-C., Shieh, D.-B., Chen, D.-H., Chou, C.-H., Yeh, C.-S., and Wu, C.-L. (2004) A Biological Strategy for Fabrication of Au/EGFP Nanoparticle Conjugates Retaining Bioactivity. *Nano Lett. 4*, 1209−1212.

(5) Yun, C. S., Khitrov, G. A., Vergona, D. E., Reich, N. O., and Strouse, G. F. (2002) Enzymatic manipulation of DNA-nanomaterial constructs. *J. Am. Chem. Soc. 124*, 7644−7645.

(6) Matthews, K. S., and Nichols, J. C. (1998) Lactose repressor protein: functional properties and structure. *Prog. Nuc. Acid Res. Mol. Biol. 58*, 127−164.

(7) Zhou, D., Wang, X., Birch, L., Rayment, T., and Abell, C. (2003) AFM study on protein immobilization on charged surfaces at the nanoscale: Toward the fabrication of three-dimensional protein nanostructures. *Langmuir 19*, 10557−10562.

(8) Brewer, S. H., Glomm, W. R., Johnson, M. C., Knag, M. K., and Franzen, S. (2005) Probing BSA binding to citrate-coated gold nanoparticles and surfaces. *Langmuir 21*, 9303−9307.

(9) Lewis, M., Chang, G., Horton, N. C., Kercher, M. A., Pace, H. C., Schumacher, M. A., Brennan, R. G., and Lu, P. (1996) Crystal structure of the lactose operon repressor and its complexes with DNA and inducer. *Science 271*, 1247−1254.

(10) Swint-Kruse, L., Elam, C. R., Lin, J. W., Wycuff, D. R., and Matthews, K. S. (2001) Plasticity of quaternary structure: Twenty-two ways to form a LacI dimer. *Protein Sci. 10*, 262−276.

(11) Falcon, C. M., Swint-Kruse, L., and Matthews, K. S. (1997) Designed disulfide between N-terminal domains of lactose repressor disrupts allosteric linkage. *J. Biol. Chem. 272*, 26818−26821.

(12) Falcon, C. M., and Matthews, K. S. (1999) Glycine insertion in the hinge region of lactose repressor protein alters DNA binding. *J. Biol. Chem. 274*, 30849−30857.

(13) Chen, J., and Matthews, K. S. (1992) Deletion of lactose repressor carboxyl-terminal domain affects tetramer formation. *J. Biol. Chem. 267*, 13843−13850.

(14) Calabretta, M., Jamison, J. A., Falkner, J. C., Liu, Y., Yuhas, B. D., Matthews, K. S., and Colvin, V. L. (2005) Analytical ultracentrifugation for characterizing nanocrystals and their bioconjugates. *Nano Lett. 5*, 963−967.

(15) Wycuff, D. R., and Matthews, K. S. (2000) Generation of an AraC-araBAD promoter-regulated T7 expression system. *Anal. Biochem. 277*, 67−73.

(16) Demeler, B. (2005) UltraScan 7.2. http://www.ultrascan.uthscsa.edu/.

(17) Nakata, S., Kido, N., Hayashi, M., Hara, M., Sasabe, H., Sugawara, T., and Matsuda, T. (1996) Chemisorption of proteins and their thiol derivatives onto gold surfaces: Characterization based on electrochemical nonlinearity. *Biophys. Chem. 62*, 63−72.

(18) Zanchet, D., Micheel, C. M., Parak, W. J., Gerion, D., and Alivisatos, A. P. (2001) Electrophoretic isolation of discrete Au nanocrystal/DNA conjugates. *Nano. Lett. 1*, 32−35.

(19) Arnaud, I., Abid, J.-P., Roussel, C., and Girault, H. H. (2005) Size-selective separation of gold nanoparticles using isoelectric focusing electrophoresis (IEF). *Chem. Commun. 6*, 787−788.

(20) Parak, W. J., Pellegrino, T., Micheel, C. M., Gerion, D., Williams, S. C., and Alivisatos, A. P. (2003) Conformation of oligonucleotides attached to gold nanocrystals probed by gel electrophoresis. *Nano Lett. 3*, 33−36.

(21) Zanchet, D., Micheel, C. M., Parak, W. J., Gerion, D., Williams, S. C., and Alivisatos, A. P. (2002) Electrophoretic and structural studies of DNA-directed Au nanoparticle groupings. *J. Phys. Chem. B 106*, 11758−11763.

(22) Sandström, P., Boncheva, M., and Åkerman, B. (2003) Nonspecific and Thiol-Specific Binding of DNA to Gold Nanoparticles. *Langmuir 19*, 7537−7543.

(23) Mamedova, N. N., Kotov, N. A., Rogach, A. L., and Studer, J. (2001) Albumin-CdTe nanoparticle bioconjugates: preparation, structure and interunit energy transfer with antenna effect. *Nano Lett. 1*, 281−286.

(24) Wang, S., Mamedova, N., Kotov, N. A., Chen, W., and Studer, J. (2002) Antigen/antibody immunocomplex from CdTe nanoparticle bioconjugates. *Nano Lett. 2*, 817−822.

BC0600867

Biodegradable Polymeric Vectors for Gene Delivery to Human Endothelial Cells

Jordan J. Green,[†] Julie Shi,[‡] Eugene Chiu,[§] Elizaveta S. Leshchiner,[‡] Robert Langer,[†,‡,§,⊥] and Daniel G. Anderson*[,⊥]

Division of Biological Engineering, Department of Chemical Engineering, Division of Health Sciences and Technology, and Center for Cancer Research, Massachusetts Institute of Technology, Cambridge, Massachusetts 02139. Received April 18, 2006; Revised Manuscript Received July 10, 2006

Endothelial cells are an important cell type to both cardiovascular disease and cancer, as they play critical roles in vascular function and angiogenesis. However, effective and safe gene delivery to primary endothelial cells in the presence of serum proteins is known to be particularly challenging. A library of biodegradable poly(β-amino esters) was synthesized for use as potential vectors. Promising vectors were optimized for high efficacy and low cytotoxicity to human umbilical vein endothelial cells (HUVECs) in serum. Vector parameters including polymer type, polymer weight, and DNA loading were varied, and biophysical properties including particle size, ζ potential, and particle stability over time were studied. While many of the poly(β-amino ester) vectors have similar biophysical properties in the presence of buffer, their biophysical properties changed differentially in the presence of serum proteins, and the properties of these serum-interacting particles correlated to transfection efficacy. Leading poly(β-amino ester) vectors were found to transfect HUVECs in the presence of serum significantly higher ($47 \pm 9\%$ positive, $n = 10$) than the best commercially available transfection reagents including jetPEI ($p < 0.001$) and Lipofectamine 2000 ($p < 0.01$). These results demonstrate the potential of a new class of biomaterials, poly(β-amino esters), for effective human endothelial cell gene therapy.

INTRODUCTION

Cardiovascular disease and cancer are the leading causes of death in the United States. Gene therapy has the potential to treat many cardiovascular conditions including peripheral arterial disease, restenosis, and myocardial ischemia, as gene delivery enables long-term expression of target genes useful for treatments such as therapeutic angiogenesis and inhibition of cell proliferation (*1*−*3*). Endothelial cells are a significant cell target in cardiovascular disease, as they control vascular function. Endothelial cells are also an important cell type for cancer treatments that target against vasculogenesis and angiogenesis (*4*, *5*). In these experiments, we use human umbilical vein endothelial cells (HUVECs) as a model primary cell system to test the efficacy of gene delivery vectors. This is a challenge, as primary endothelial cells have higher intrinsic resistance to gene delivery than other cell lines (*6*).

There are two main approaches to gene delivery: viral and nonviral. The primary advantages of viral delivery are efficient infection of cells and long-term gene expression (*7*, *8*). However, problems with viral vectors as compared to nonviral vectors include limited cargo capacity, resistance to repeated infection, production and quality control issues, and safety (*7*, *9*). Specific safety concerns include acute toxicity, cellular immune response, and oncogenicity due to insertional mutagenesis (*7*). Nonviral vectors are attractive for gene delivery, as they do not have these viral vector limitations.

To improve stability and uptake of DNA, numerous biomaterials have been used to create synthetic gene delivery vectors. The main biomaterials that have been studied include cationic polymers, cationic lipids, liposomes, chitosans, inorganic nanoparticles, and dendrimers (*8*−*10*). Though these biomaterials improve transfection in comparison to naked DNA, they still have relatively low transfection efficacy, and many of these materials are cytotoxic.

Recently, a large library of 2350 structurally unique poly(β-amino esters) was developed using high-throughput combinatorial chemistry (*11*). Poly(β-amino esters) are promising for nonviral gene delivery due to their (1) ability to condense DNA into nanoparticles, (2) ability to buffer the endosome, (3) ability to promote endosomal escape, (4) low cytotoxicity compared to other cationic polymers, (5) biodegradability via hydrolytic cleavage of ester groups, and (6) large potential for structural diversity (*12*−*16*).

Previously, we have shown that top-performing poly(β-amino ester) vectors have particle sizes smaller than 150 nm, positive ζ potentials, polymer weight to DNA weight ratios greater than or equal to 40, molecular weights above 10 000, amine-terminated chains, and other structural similarities (*11*, *13*, *17*, *18*). However, all of these assays and measurements were conducted in serum-free conditions, and the role of serum interactions on biophysical properties and transfection efficacy of poly(β-amino ester) vectors has not previously been studied. Important particle properties such as size, ζ potential, and particle stability are dependent on the local aqueous environment, and gene delivery particles demonstrated to have certain biophysical characteristics in a buffer may not have the same characteristics in the presence of serum or in vivo (*19*, *20*).

Here, we demonstrate that poly(β-amino esters) as a class, and C32 in particular, transfect human primary endothelial cells better than several top commercially available reagents. Analysis of the biophysical properties of poly(β-amino ester)/DNA complexes as a function of media and over time provide insight into serum stability and efficacy of these complexes.

EXPERIMENTAL PROCEDURES

Cell Culture. Human umbilical vein endothelial cells (HUVECs) (Cambrex, Walkersville, MD) were cultured in

* Corresponding author. Massachusetts Institute of Technology, Room E25-342, 77 Massachusetts Avenue, Cambridge, MA 02139. E-mail: dgander@mit.edu. Phone: (617) 258-6843. FAX: (617) 258-8827.

[†] Division of Biological Engineering.

[‡] Department of Chemical Engineering.

[§] Division of Health Sciences and Technology.

[⊥] Center for Cancer Research.

10.1021/bc0600968 CCC: $33.50 © 2006 American Chemical Society
Published on Web 08/16/2006

EGM-2 media supplemented with SingleQuot Kits (Cambrex). HUVEC cells were used by passage five and in accordance with the manufacturer's instructions. Cells were grown at 37 °C in a humid 5% CO_2 atmosphere.

Polymer Synthesis. Monomers were purchased from Aldrich (Milwaukee, WI), TCI (Portland, OR), Pfaltz and Bauer (Waterbury, CT), Matrix Scientific (Columbia, SC), Scientific Polymer (Ontario, NY), and Dajac Monomer−Polymer (Feasterville, PA). Optimal amine/diacrylate stoichiometric ratios for each polymer were determined from previous work (*13*). To synthesize each polymer, 400 mg of amino monomer was weighed into a 1-mL sample vial with a Teflon-lined screw cap. Next, the appropriate amount of diacrylate was added to the vial, and a small Teflon-coated stir bar was then put in each vial. Polymers were then synthesized on a multiposition magnetic stir-plate residing in an oven at either 95 °C (solvent-free) or 60 °C (with 2 mL DMSO added). High-temperature synthesis was performed for approximately 12 h, and low-temperature synthesis was performed for 2 days. After completion of reaction, all vials were removed from the oven and stored at 4 °C. All polymers were analyzed by gel-permeation chromatography (GPC) as previously discussed (*13*).

Polymeric Vectors. The nonviral vectors are formed through electrostatic interactions between poly(β-amino esters) and plasmid DNA. Depending on transfection experiments, plasmid DNA encoding either pEGFP-enhanced green fluorescent protein (ElimBiopharmaceuticals, South San Francisco, CA) or pCMV-Luc firefly luciferase (ElimBiopharmaceuticals, South San Francisco, CA) was used. By varying the amount of DNA used in preparation, the amount of DNA loading per cellular well was varied. At a fixed DNA basis, by varying the weight of polymer, the charge ratio (N/P) of polymer nitrogen (N) to DNA phosphate (P) was varied. To ease handling, polymer stock solutions (100 mg/mL) were prepared in DMSO solvent prior to use. Working dilutions of each polymer were prepared in 25 mM sodium acetate buffer (pH 5). For 96-well plate experiments, 25 μL of the diluted polymer was added to 25 μL of DNA and mixed well. The mixtures were then incubated at room temperature for 10 min to allow for complex formation. For 24-well experiments and for biophysical characterization experiments, the same steps were followed, but all volumes were scaled up appropriately.

Biophysical Characterization. Particle size and ζ potential measurements were measured by using a ZetaPALS dynamic light scattering detector (Brookhaven Instruments Corp., Holtsville, NY, 15-mW laser, incident beam 676 nm). Samples were prepared for biophysical characterization in the same manner and at the same concentrations as they were for transfections, but the media/polymer/DNA solution was scaled up to a final volume of 1.6 mL. Generally, particles were first sized in 25 mM NaAc buffer while initial polymer/DNA complexation occurred and then added to 12% serum EGM-2 media and sized dynamically in time for up to 8 days. Particle stability was determined by changes to particle size over time. Polymer/DNA ratios shown are those determined to have the highest transfection efficacy unless otherwise stated. Correlation functions were collected at a scattering angle of 90°, and particle sizes were calculated using the MAS option of BICTs particle-sizing software (version 2.30) using the viscosity and refractive index of water at 25 °C. Particle sizes are expressed as effective diameters assuming a log-normal distribution. Average electrophoretic mobilities were measured at 25 °C using BIC PALS ζ potential analysis software, and ζ potentials were calculated using the Smoluchowsky model for aqueous suspensions.

Luciferase Transfections. Nonviral vector transfections were performed on HUVECs with and without the presence of serum. HUVECs were seeded (15 000 cells/well) into each well of an opaque white 96-well plate (Corning-Costar, Kennebunk, ME) 24 h prior to transfection to allow for growth to confluence. Vectors were constructed as previously mentioned, and then, 30 L of each polymer/DNA solution was added to either 200 μL of Opti-MEM with sodium bicarbonate (Invitrogen), EGM-2 media (2% serum), or FBS supplemented EGM-2 media (12% serum) in 96-well polystyrene plates. The growth medium was removed from the cells using a 12-channel aspirating wand (V&P Scientific, San Diego, CA) after which 150 μL of the media/polymer/DNA solution was immediately added. Complexes were incubated with the cells for 1−4 h and then removed using the 12-channel wand and replaced with 100 μL of warm EGM-2 media. Final DNA loading was 0.3 or 0.6 μg per well depending on the experiment. Cells were then allowed to grow for 48 h and then analyzed for luciferase expression. Control experiments were also performed with PEI (MW 25 000; Sigma−Aldrich), jetPEI (Qbiogene, Irvine, CA), jetPEI−HUVEC (Bridge Bioscience Corporation, Portsmouth, NH), and Lipofectamine 2000 (Invitrogen). PEI transfections were performed as described above using a polymer/DNA weight ratio of 1/1. Jet PEI, jetPEI−HUVEC, and Lipofectamine 2000 transfections were performed as described by their vendors. The same quantity of DNA per well and incubation time was used with the control vectors as with the poly(β-amino ester) vectors. Luciferase expression was analyzed using Bright-Glo assay kits (Promega, Madison, WI). Briefly, 100 μL of Bright-Glo solution was added to each well of the 96-well plate containing cell medium and cells. Luminescence was measured using a Mithras luminometer (Berthold, Oak Ridge, TN).

GFP Transfections. GFP transfections paralleled the luciferase transfections except that all volumes were scaled up fivefold and the experiments were conducted in clear 24-well plates (Becton Dickinson, Franklin Lakes, NJ) with 3 ug GFP DNA per well. Cells were seeded at 75 000 per well, 24 h prior to transfection, and cells were transfected with 750 μL of media/polymer/DNA solution. Cells were aspirated prior to transfection using a 6-channel aspirating wand (V&P Scientific, San Diego, CA). After a 1−4 h incubation, the nonviral vector solution was aspirated off and replaced with 500 μL of warm EGM-2 media. After 48 h, transfected and untransfected control cells were washed, removed from the 24-well plates by trypsinization, microcentrifuged, and resuspended in 1 mL of FACS running buffer (98% PBS/2% FBS/1:200 propidium iodide solution (Invitrogen)) for FACS analysis.

Flow Cytometry. GFP expression was measured using fluorescence activated cell sorting (FACS) on a FACSCalibur (Becton Dickinson, San Jose, CA). Propidium iodide staining was used to exclude dead cells from the analysis, and 20 000 live cells per sample were acquired. Two-dimensional gating was used to separate increased autofluorescence signal from increased GFP signal to more accurately count positively expressing cells. Gating and analysis was performed using *FlowJo 6.3* software (TreeStar, Ashland, OR).

Cell Viability Measurements. To measure cytotoxicity and cell viability, cellular metabolic activity was measured using the Cell Titer 96 Aqueous One Solution assay kit (Promega, Madison, WI). Metabolic activity was measured using optical absorbance on a Victor3 Multilabel plate counter (Perkin-Elmer Life Sciences, Boston, MA). Measurements of treated cells were converted to percent viability by comparison to untreated controls.

Statistics. Statistical calculations were carried out using *GraphPad Prism 4.0* for Windows. Results are reported as mean ± standard deviation. For comparison of gene delivery vectors, statistical significance was obtained by using unpaired, two-tailed, Student's *t*-tests with 99% confidence.

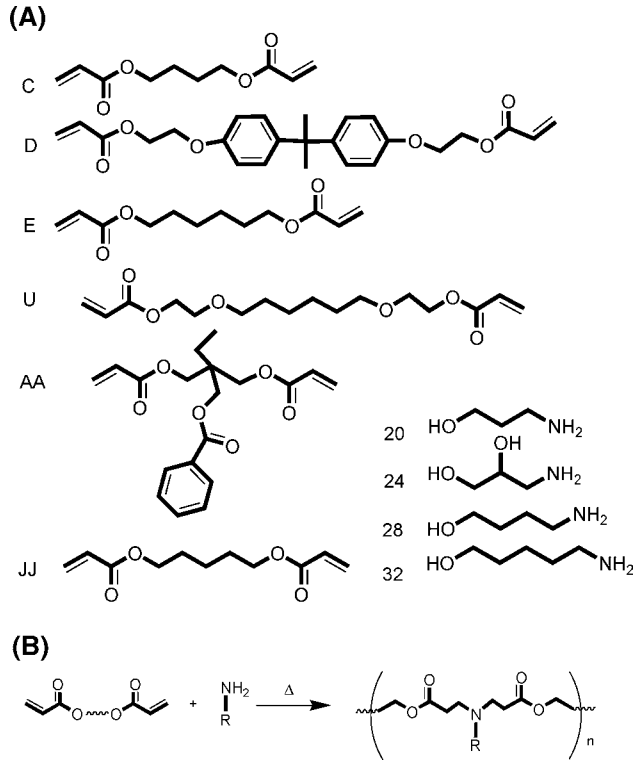

Figure 1. (A) Diacrylate esters and amine monomers. (B) Synthesis of poly(*β*-amino esters).

RESULTS AND DISCUSSION

Polymer Synthesis and Gene Delivery Vector Formulation. Poly(*β*-amino esters) are synthesized by the conjugate addition of amine monomers to acrylate esters. The acrylate and amine monomers used in this experiment and their synthesis scheme can be seen in Figure 1. High-throughput screening and synthesis of a large library of over 2000 poly(*β*-amino esters) was conducted (*11*). The top 486 polymers were then resynthesized on a larger scale at a range of molecular weights (*13*). On the basis of transfection efficacy to COS-7 cells in serum-free conditions, 11 of the best-performing polymers were then selected for further analysis and optimization for transfection to human primary cells in the presence of serum.

Cationic polymeric gene delivery vectors were formed in sodium acetate buffer solution. It was determined that particles quickly self-assemble and that a 10-min complexation time is optimal for transfection efficacy. Adding poly(*β*-amino esters) to DNA was found to create vectors that were significantly more effective than those vectors formed by adding DNA to the polymers. These results parallel earlier results found with PEI (*21*) and suggest that this mixing order may be a general rule for all cationic polymers used to condense DNA.

Biophysical Characterization. Previously, nanoparticle size and *ζ* potential of poly(*β*-amino ester) vectors in PBS buffer were reported. For the top-performing vectors, particle sizes were smaller than 150 nm and *ζ* potentials were positive (*13*). We hypothesized that these biophysical properties change during actual transfections when the complexes are added either to serum-free OptiMem or cell culture media with differential levels of serum. As it has been reported that nonviral vector formulations have low efficacy in the presence of serum (*19, 20*), we wanted to determine how media and serum might change the biophysical properties of these vectors and if serum proteins inhibited poly(*β*-amino ester) vector transfection.

Figure 2 shows the effect of media type on poly(*β*-amino ester) vector particle size and stability over time. In this figure, gene delivery particles are prepared at the same concentrations as they are for typical in vitro bioassays. This figure demonstrates that C32/DNA particles delivered in OptiMem are significantly larger than those delivered in cell culture media with serum. This figure also demonstrates that in OptiMem, these particles are unstable and the biophysical properties of the particles change over time. This is important, as during transfection, the population of functional gene delivery nanoparticles can be dynamically changing in time. In contrast, serum proteins are shown to differentially reduce particle size and instability, presumably, from negative electrostatic repulsions.

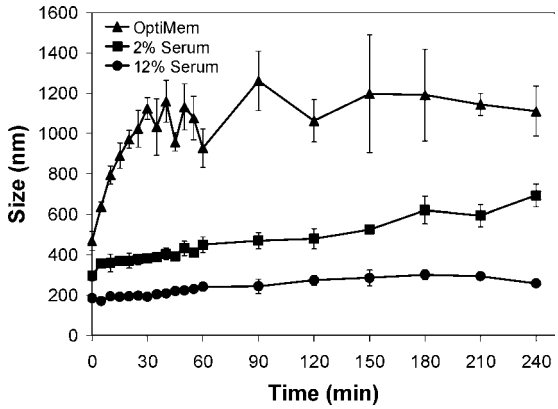

Figure 2. C32/DNA (50 w/w) particle size and stability is dependent on media type and serum concentration and can change dynamically in time. Error bars are the standard deviations of triplicate samples.

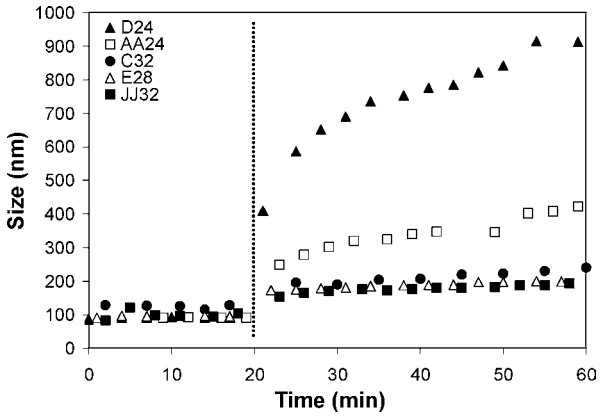

Figure 3. Particle size and stability is dependent on polymer type. All particles have a similar <150-nm size in NaAc buffer but grow disparately in size when added to 12% serum-containing media (indicated by the vertical line). Size in serum-containing media correlated to transfection efficacy.

The size of a polymeric gene delivery complex is known to dramatically affect transfection efficacy (*13, 19, 22*). However, there is some controversy in the literature about what size is optimal for delivery. Some researchers have found that, for in vitro experiments, large aggregated particles transfect better than small particles (*19, 23, 24*). This is believed to be from a sedimentation effect of large particles. Interestingly, the reverse has also been reported (*13, 22*). In either case, for an in vivo application, larger particles could cause problems due to physical size exclusions in capillaries and tissues. Small particles that are stable in serum are typically preferred.

Figure 3 demonstrates that the choice of aqueous solution used during bioassays can result in dramatic differences in the biophysical characteristics of closely related biomaterials. In this figure, poly(*β*-amino ester) vectors are first sized in sodium acetate buffer and then sized in high-serum-containing media. Whereas all vectors condensed DNA into small nanoparticles below 150 nm while in buffer, particle size dramatically changed

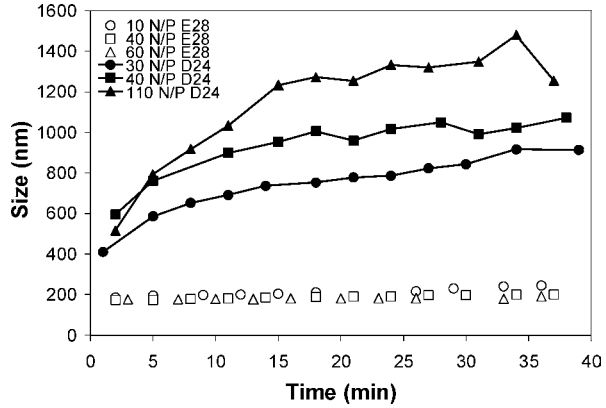

Figure 4. Particle size and stability in 12% serum is dependent on polymer type and the N/P (and w/w) ratios of polymer to DNA. E28/DNA particles show stability over a range of N/P ratios, whereas D24/DNA complexes grow increasingly larger based on their N/P ratio. E28/DNA particles were found to transfect well, whereas D24/DNA particles were found to transfect poorly.

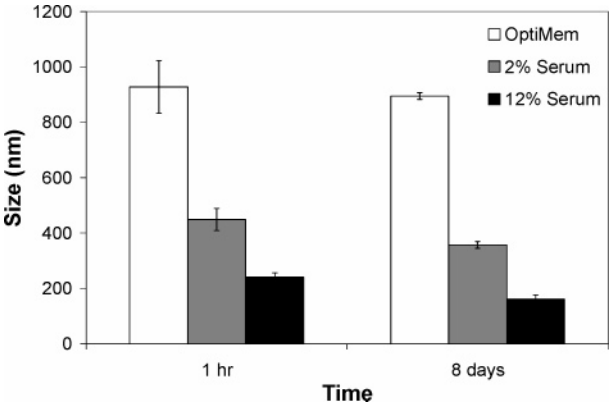

Figure 5. C32/DNA (50 w/w) particles are stable over a long time period while in various media conditions. Error bars are the standard deviations of triplicate samples.

when these particles were sized in serum. Some vectors such as C32, JJ32, and E28 formed small, stable particles in the 200-nm range, whereas other vectors such as D24 aggregated in serum to large particles in the 1-μm range. The biophysical characteristics of a gene delivery vector in a high-serum environment are likely one important indicator in predicting effectiveness for in vivo cardiovascular gene delivery.

Figure 4 shows how particle size depends on poly(β-amino ester) to DNA N/P ratio (and weight ratio) for top-performing and poor-performing vectors in the poly(β-amino ester) library. This figure shows that E28, a representative top-performing vector, forms uniformly sized small nanoparticles over a range of weight ratios, whereas a poor-performing vector, such as D24, forms large, aggregating particles that are differentially sized according to N/P ratio.

Figure 5 shows the long-term stability of C32/DNA gene delivery vectors. C32/DNA vectors were found to stay stable for at least 8 days in OptiMem, 2% low-serum enhanced media, and 12% high-serum enhanced media. For all the poly(β-amino ester) vectors tested, particles that aggregated tended to do so within the first hour of formation and then remained relatively stable for subsequent time points. Nonaggregating particles were stable for all time points tested. Particle stability is advantageous for effective delivery by circulating nanoparticles, consistent transfections, and for storage.

Table 1 shows the optimized polymer weight ratios (w/w), nitrogen to phosphate charge ratios (N/P), and biophysical parameters for the poly(β-amino ester) vectors in 12% serum-containing media. This table demonstrates that, for efficient transfection of HUVECs in serum, a higher w/w ratio and N/P ratio were generally required as compared to our previous work in COS-7 cells without the presence of serum (*13*). As previously mentioned, gene delivery particle sizes in PBS were all sub-150 nm, but in serum varied greatly from 200 nm to 1 μm. ζ potential was found to go from positive in PBS to negative in serum. This is likely due to negatively charged serum proteins adsorbing to the positively charged nanoparticles and coating them to have an overall net negative surface charge. Among the different types of polymers, ζ potential was found to vary depending on polymer type from nearly neutral to strongly negative. Interestingly, the difference in ζ potential and size between similar vectors in serum seems to correlate to single atom changes to their constitutive monomers. For example, at the same fixed N/P ratio of 60, JJ32 vectors have nearly neutral ζ potential and small size (−6 mV and 193 nm), JJ28, which has one less carbon on its amine monomer, forms larger, more negatively charged vectors (−14 mV and 226 nm), and JJ20, which is missing yet another carbon on its amine monomer forms vectors still more negative in charge and larger in size (−22 mV and 251 nm). JJ32, with the longest amine monomer chain and forming the most neutral and smallest JJ-based particle overall, transfected best in serum, followed next by JJ28, and last JJ20. This analysis highlights the use of a large polymeric library in elucidating structure/function relationships.

Luciferase Transfections. Transfection experiments are commonly performed in vitro on immortal cancerous cell lines under serum-free conditions. Immortal cancerous cell lines are frequently chosen, as they are easier to propagate and manipulate than primary cells, and are often easier to transfect. Primary endothelial cells in particular have been shown to have an intrinsic resistance to the uptake of exogenous genes compared to other cell lines (*6*). Serum-free conditions are routinely employed to prevent unwanted electrostatic interactions between positively charged nanoparticles and negatively charged serum proteins. Though these conditions are known to maximize in vitro transfection, they do not closely correspond to the conditions likely to be found in vivo.

Poly(β-amino ester)/DNA vector transfections to confluent HUVECs in 12% serum containing media were initially found to be relatively poor when using particle formulations optimized for serum-free media conditions. The differences in transfection performance among several poly(β-amino ester)/DNA vectors in different media conditions as a function of polymer type, polymer to DNA w/w ratio, and DNA loading can be seen in Figure 6A,B. In this figure, optimal transfection of HUVECs in high-serum-containing media occurs at much higher w/w ratios (and higher N/P ratios) than in non-serum-containing media (polymers C32 and AA24). Other polymers like C28 are unable to transfect well in serum-containing media at any weight ratio tested even though they are quite efficacious in non-serum-containing media. In non-serum conditions, peak transfection is relatively insensitive to DNA loading (200 ng vs 600 ng per well), whereas the higher DNA loading is needed for effective transfection in serum-containing media.

These results highlight the differences in polymer vector design depending on the application conditions. Given the previous biophysical characterization results, it appears that particle size, stability, and surface charge changes are likely factors that are in part responsible for these differences in efficacy.

GFP Transfections. While high-throughput screening gives a measurement of the total gene expression per microtiter plate well, this is an aggregate measurement without any information on individual cells. To learn the transfection efficacy to

Table 1. Optimized Polymer Weight Ratios (w/w), Nitrogen to Phosphate Charge Ratios (N/P), Biophysical Parameters, and Efficacy for Poly(β-amino ester) Vectors in 12% Serum-Containing Media

acrylate	amine	MW	w/w	N/P	% positive	size (nm)	ζ potential (mV)	HUVEC rank	COS-7 rank
C	32	25101	100	110	46.9	236	−13	1	1
JJ	32	19400	57	60	29.7	193	−6.0	2	9
E	28	14300	38	40	25.8	199	−14	3	11
AA	28	20900	40	30	13.8	206	−4.9	4	7
JJ	28	16800	55	60	13.5	226	−14	5	2
AA	24	5304	53	40	12.8	422	−12	6	8
AA	20	16200	29	24	6.3	208	−13	7	5
U	28	15600	147	120	2.9	327	−10	8	4
C	28	27900	122	140	2.7	309	−12	9	3
D	24	9542	47	30	0.3	913	−12	10	10
JJ	20	20200	52	60	0.2	251	−22	11	6

individual cells, we used fluorescent activated cell sorting (FACS) and enhanced green fluorescent protein (GFP) DNA.

FACS data was interpreted by using a two-dimensional density plot that compares the ratio of GFP channel fluorescence (*x*-axis) to yellow channel autofluorescence (*y*-axis). This method was chosen as it separates changes in autofluorescence from changes in actual GFP signal and divides the cells into two distinct populations, thereby reducing the overcounting of falsely positive cells. For example, Figure 7B shows the two-dimensional density plot of a C32/DNA transfection as 60% positive, whereas Figure 7C, which shows a one-dimensional histogram of the same experiment, would count the cells to be 76% positive. All FACS results of poly(β-amino ester) vectors and control vectors were calculated using this more conservative two-dimensional analysis.

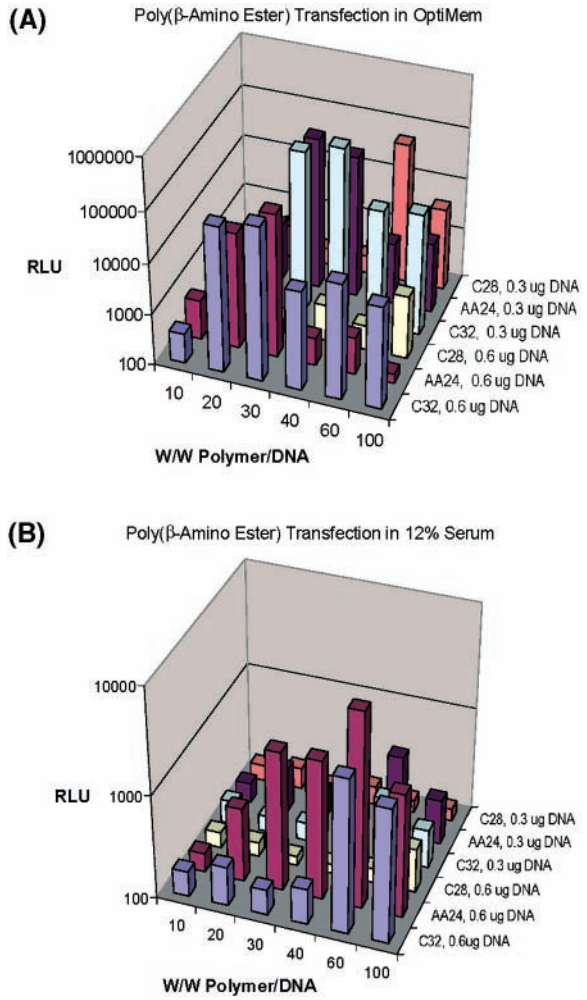

Figure 6. High-throughput screening of vectors. Optimal transfection is dependent on DNA loading, polymer weight ratio (N/P ratio), type of polymer, and presence of serum.

The best previously known transfecting polymers from the poly(β-amino ester) library (*13*) were reoptimized for transfecting HUVECs in high serum levels, and the results are shown in Figure 8. This figure demonstrates that high transfection to COS-7 cells in the absence of serum is not a guarantee of efficacy to primary human endothelial cells in serum. However, Figure 8 also demonstrates that several poly(β-amino ester) vectors were indeed found to transfect HUVECs at high levels, particularly polymers C32, JJ32, and E28.

Interestingly, the best-performing polymers all share a nearly identical structure, and single molecular differences in the polymers' structure were found to correlate to transfection efficacy. For example, polymers formed with C, JJ, and E differ by only the length of their acrylate monomer carbon chain (4, 5, and 6 carbons, respectively). Similarly, polymers formed with 20, 28, and 32 differ by only the length of their amine monomer carbon chain (3, 4, and 5 carbons, respectively). Yet, these small changes to molecular structure lead to dramatic differences in transfection efficacy. For example, increasing the length of the number of carbons in the constituent amine monomer was found to correlate to increased transfection efficacy. Polymers formed with the same acrylate monomer but different-length amine monomers transfected differentially according to length: 32 (5 carbons) > 28 (4 carbons) > 24 (3 carbons + hydroxyl group) > 20 (3 carbons). It has been reported that amine groups on a polymer are functionally responsible for the ability of a gene delivery vector to bind and unpack DNA (*25*) and to buffer the endosome to promote osmotic swelling and rupture (*26*). We hypothesize that that the seemingly small changes to constituent amine monomer length may play a role in at least one of these gene delivery bottlenecks. This analysis highlights the utility of a combinatorial library approach to designing a nonviral gene delivery vector, as similarly structured but functionally different vectors can be obtained and analyzed.

The ranked order of efficacy of these polymers shows similarities and differences between the two cell systems tested. Table 1 shows relative effectiveness of poly(β-amino ester) vector transfections to HUVECs in high-serum media versus transfections to COS-7 cells in OptiMem based on our previous work (*13*). Generally, higher w/w ratios of polymer to DNA (and correspondingly higher N/P ratios) were needed for effective delivery in high-serum-containing media. Polymer C32 was reinforced as the lead poly(β-amino ester) vector, but interestingly, other vectors performed differentially between these two cells types. C28 and U28 were previously found to be in the top 5 transfecting vectors of the whole class, but were found to transfect HUVECs in serum rather poorly. In contrast, JJ32 and E28, which were previously seen as mediocre vectors, were found to transfect HUVECs in serum with high efficacy. These findings demonstrate that a vector able to transfect well

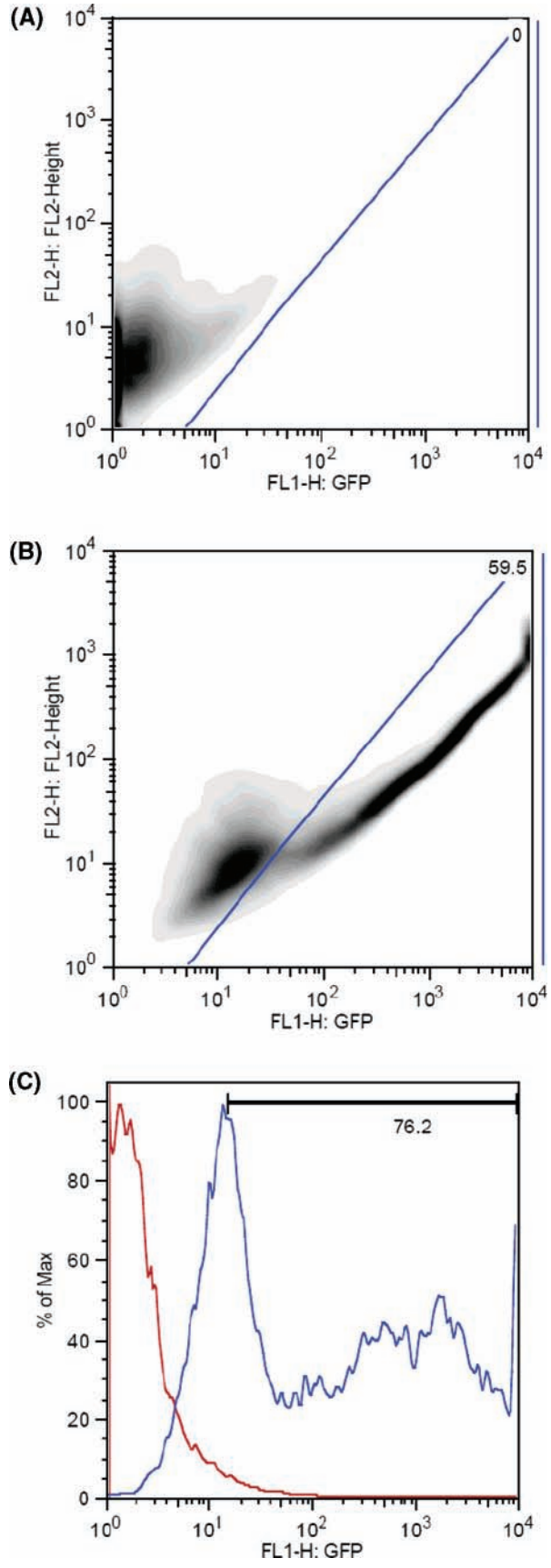

Figure 7. (A) FACS density plot and gating for negative control (0% positive) and comparison to (B) C32/DNA vector transfection (59.5% positive). Ratio of GFP fluorescence (*x*-axis) to background fluorescence (*y*-axis) was used to accurately gate positive cells. (C) The same FACS data shown in a one-dimensional histogram plot. C32/DNA transfected cells (76.2% positive) include some falsely positive cells that are excluded during the two-dimensional analysis used in part B.

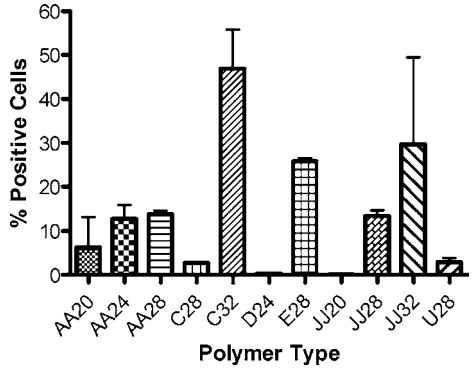

Figure 8. HUVEC FACS transfection results in 12% serum media. Each polymer type is shown at its optimal polymer weight to DNA weight (w/w) ratio. Error bars are standard deviations ($n \geq 2$).

in serum-free conditions may not necessarily transfect human primary cells well in high-serum conditions.

High transfection in serum-free OptiMem with poly(β-amino ester) vectors may be due in part to large particle size and positive surface charge, both promoting physical interaction of the gene delivery complexes with cells through sedimentation and attractive electrostatic forces respectively. However, in serum-containing media, ζ potential of these particles is neutral to negative, and particle size changes according to weight ratio and polymer material properties as previously indicated in the biophysical characterization section. Thus, serum interactions are potentially responsible for poorer transfection by reducing particle uptake. This hypothesis was furthered by experiments that varied particle incubation time and found that, in OptiMem or serum-free media, a 1 h incubation is sufficient for high expression, whereas in serum-containing media, a 4 h incubation is necessary (but not sufficient) to achieve high expression.

Biophysical properties of the particles in serum were found to correlate to HUVEC transfection in serum, whereas biophysical properties in buffer were unable to give the same predictive information. For example, as mentioned above, all poly(β-amino ester) vectors tested were able to condense DNA into small nanoparticles below 150 nm while in buffer, but some vectors such as C32, JJ32, and E28 formed small, stable particles while in high-serum containing media, whereas other vectors such as D24, aggregated in serum to form large particles in the micron range. C32, JJ32, and E28 were found to be the highest transfecting vectors for HUVECs in serum, whereas D24 and other aggregating polymers were found to transfect much more poorly. The top five performing polymeric vectors in serum formed particles in the 193−236-nm range, whereas the bottom performing polymers tended to form particles larger than 250 nm in the presence of high-serum-containing media. Thus, the formation of small, stable gene delivery particles in serum was found to be predictive for high efficacy in serum-containing media, and the formation of large and/or aggregating particles in serum was found to correlate to poor efficacy. On the other hand, particle size of these polymers in buffer was found not to be predictive of transfection performance in serum.

As compared to other top commercially available nonviral transfection vectors, poly(β-amino ester) vectors as a class, and C32, in particular, were found to be very efficacious. Figure 9 compares the best-performing poly(β-amino ester), C32, to other commonly used nonviral vectors. Polymeric vector C32 averages 47 ± 9% positively transfected HUVECs, which is statistically significant versus the control vectors 25K PEI (2 ± 1%, $p < 0.001$), jetPEI (11 ± 2%, $p < 0.001$), jetPEI−HUVEC (6 ± 5%, $p < 0.001$), and Lipofectamine 2000 (29 ± 1%, $p < 0.01$).

Other researchers have recently shown that tetraglucose-grafted L-PEI (jetPEI−HUVEC) is a top-performing nonviral transfection agent for transfection of HUVECs as compared

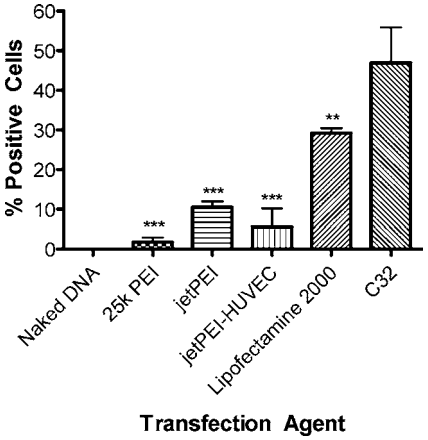

Figure 9. Comparison of vectors for HUVEC transfection in 12% serum-containing media. Each vector is shown at its optimal formulation. Error bars are standard deviations ($n \geq 4$). As compared to C32, (**) and (***) indicate statistical significance of $p < 0.01$ and $p < 0.001$ respectively.

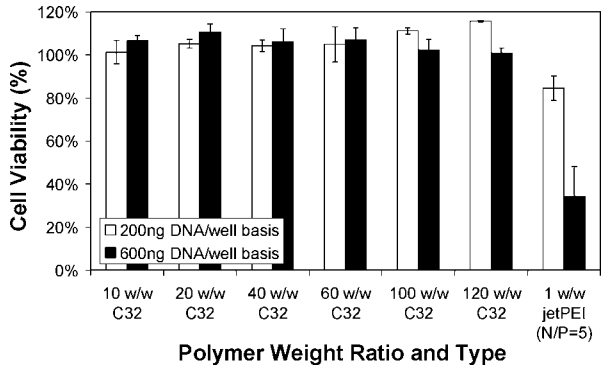

Figure 10. Poly(β-amino ester) C32 is non-cytotoxic to HUVECs in contrast to the premiere commercially available polymeric vector jetPEI. Error bars are the standard deviations of quadruplicate samples.

to other commercially available reagents (*27*). To our knowledge, C32 and other poly(β-amino ester) vectors can transfect HUVECs significantly higher than any reported nonviral vector system. It is important to note that this high transfection took place under conditions generally seen as difficult for in vitro transfection but important for an in vivo cardiovascular application: fully confluent primary cells in the presence of a high concentration of serum proteins. The percentage of HUVECs positively transfected by C32 approach those achieved with viral systems. Recently, 70% in vitro transfection of HUVECs was reported by using an engineered vesicular stomatis virus G-protein (VSV-G)-pseudotyped lentiviral vector and a nuclear localizing signal (NLS)-tagged lacZ gene (*28*). Improvements to C32 to allow for cellular targeting and nuclear targeting are hypothesized to further narrow this gap between viral and nonviral vectors.

Cell Viability. We have previously shown that poly(β-amino ester) vectors are biodegradable and generally non-cytotoxic (*16, 18*). In this study, C32 was non-cytotoxic to HUVECs. Figure 10 shows the cell viability of HUVECS transfected with C32 gene delivery particles as compared to non-transfected controls. Over a range of polymer to DNA w/w ratios and DNA loadings, C32/DNA vectors were determined to be non-cytotoxic. In comparison, jetPEI particles are found to be cytotoxic, particularly at high concentrations of gene delivery particles and higher DNA loading. It is also interesting to note that the C32/DNA particles are non-cytotoxic at polymer concentrations as high as ~500 ug/mL (600 ng DNA, 120 w/w C32) over 2 orders of magnitude more concentrated than when jetPEI shows cytotoxicity, indicating the relative safety of poly(β-amino esters). Of note, C32 has been shown to have good in vivo biocompatibility (*12*), in contrast to certain viral systems (*29*).

CONCLUSIONS

We have demonstrated that poly(β-amino esters) as a class, and C32 specifically, transfect human primary endothelial cells better than several leading commercially available reagents. We have determined that these particles have high efficacy, are stable in the presence of serum proteins, and are non-cytotoxic. It was also demonstrated that analyzing biophysical properties of poly(β-amino ester)/DNA complexes including size, stability, and ζ potential in the proper media conditions and dynamically over time provides good correlation to transfection efficacy and can pick up phenomena missed when biophysical particle properties are only tested in buffer. We optimized vector parameters including DNA loading and polymer-to-DNA weight ratio and determined efficacy with and without serum-containing media. As biodegradable polymers have certain safety advantages over viruses, poly(β-amino ester) gene delivery vectors may prove useful in various clinical applications.

ACKNOWLEDGMENT

The authors would like to thank Naushad Hossain and Gregory Zugates for helpful discussions. J.G. wishes to thank the Whitaker Foundation and the NSF for fellowship support. This work was supported by NIH grant EB 00244.

LITERATURE CITED

(1) Nabel, E. G. (1999) Gene therapy for cardiovascular diseases. *J. Nucl. Cardiol. 6*, 69−75.
(2) Shah, P. B., and Losordo, D. W. (2005) Non-viral vectors for gene therapy: clinical trials in cardiovascular disease. *Adv. Genet. 54*, 339−361.
(3) Jones, J. M., and Koch, W. J. (2005) Gene therapy approaches to cardiovascular disease. *Methods Mol. Med. 112*, 15−35.
(4) Segura, I., Serrano, A., De Buitrago, G. G., Gonzalez, M. A., Abad, J. L., Claveria, C., Gomez, L., Bernad, A., Martinez, A. C., and Riese, H. H. (2002) Inhibition of programmed cell death impairs in vitro vascular-like structure formation and reduces in vivo angiogenesis. *FASEB J. 16*, 833−841.
(5) Muller, K., Nahde, T., Fahr, A., Muller, R., and Brusselbach, S. (2001) Highly efficient transduction of endothelial cells by targeted artificial virus-like particles. *Cancer Gene Ther. 8*, 107−117.
(6) Suh, W., Han, S. O., Yu, L., and Kim, S. W. (2002) An angiogenic, endothelial-cell-targeted polymeric gene carrier. *Mol. Ther. 6*, 664−672.
(7) Kay, M. A., Glorioso, J. C., and Naldini, L. (2001) Viral vectors for gene therapy: the art of turning infectious agents into vehicles of therapeutics. *Nat. Med. 7*, 33−40.
(8) Partridge, K. A., and Oreffo, R. O. C. (2004) Gene delivery in bone tissue engineering: Progress and prospects using viral and nonviral strategies. *Tissue Eng. 10*, 295−307.
(9) Merdan, T., Kopecek, J., and Kissel, T. (2002) Prospects for cationic polymers in gene and oligonucleotide therapy against cancer. *Adv. Drug Delivery Rev. 54*, 715−758.
(10) Wagner, E., Kircheis, R., and Walker, G. F. (2004) Targeted nucleic acid deliver into tumors: new avenues for cancer therapy. *Biomed. Pharmacother. 58*, 152−161.
(11) Anderson, D. G., Lynn, D. M., and Langer, R. (2003) Semi-automated synthesis and screening of a large library of degradable cationic polymers for gene delivery. *Angew. Chem., Int. Ed. 42*, 3153−3158.
(12) Anderson, D. G., Peng, W. D., Akinc, A., Hossain, N., Kohn, A., Padera, R., Langer, R., and Sawicki, J. A. (2004) A polymer library approach to suicide gene therapy for cancer. *Proc. Natl. Acad. Sci. U.S.A. 101*, 16028−16033.
(13) Anderson, D. G., Akinc, A., Hossain, N., and Langer, R. (2005) Structure/property studies of polymeric gene delivery using a library of poly(beta-amino esters). *Mol. Ther. 11*, 426−434.

(14) Akinc, A., and Langer, R. (2002) Measuring the pH environment of DNA delivered using nonviral vectors: Implications for lysosomal trafficking. *Biotechnol. Bioeng. 78*, 503−508.

(15) Lynn, D. M., Anderson, D. G., Putnam, D., and Langer, R. (2001) Accelerated discovery of synthetic transfection vectors: parallel synthesis and screening of a degradable polymer library. *J. Am. Chem. Soc. 123*, 8155−8156.

(16) Lynn, D. M., and Langer, R. (2000) Degradable poly(beta-amino esters): Synthesis, characterization, and self-assembly with plasmid DNA. *J. Am. Chem. Soc. 122*, 10761−10768.

(17) Akinc, A., Anderson, D. G., Lynn, D. M., and Langer, R. (2003) Synthesis of poly(beta-amino ester)s optimized for highly effective gene delivery. *Bioconjugate Chem. 14*, 979−988.

(18) Akinc, A., Lynn, D. M., Anderson, D. G., and Langer, R. (2003) Parallel synthesis and biophysical characterization of a degradable polymer library for gene delivery. *J. Am. Chem. Soc. 125*, 5316−5323.

(19) Ogris, M., Steinlein, P., Kursa, M., Mechtler, K., Kircheis, R., and Wagner, E. (1998) The size of DNA/transferrin-PEI complexes is an important factor for gene expression in cultured cells. *Gene Ther. 5*, 1425−1433.

(20) Guo, W., and Lee, R. J. (2001) Efficient gene delivery via non-covalent complexes of folic acid and polyethylenimine. *J. Controlled Release 77*, 131−138.

(21) Boussif, O., Lezoualc'h, F., Zanta, M. A., Mergny, M. D., Scherman, D., Demeneix, B., and Behr, J. P. (1995) A versatile vector for gene and oligonucleotide transfer into cells in culture and in vivo: polyethylenimine. *Proc. Natl. Acad. Sci. U.S.A. 92*, 7297−7301.

(22) Thomas, M., and Klibanov, A. M. (2003) Non-viral gene therapy: polycation-mediated DNA delivery. *Appl. Microbiol. Biotechnol. 62*, 27−34.

(23) Zuber, G., Dauty, E., Nothisen, M., Belguise, P., and Behr, J. P. (2001) Towards synthetic viruses. *Adv. Drug Delivery Rev. 52*, 245−253.

(24) Ogris, M., Steinlein, P., Carotta, S., Brunner, S., and Wagner, E. (2001) DNA/polyethylenimine transfection particles: Influence of ligands, polymer size, and PEGylation on internalization and gene expression. *AAPS PharmSci. 3*, article no. 21.

(25) Schaffer, D. V., Fidelman, N. A., Dan, N., and Lauffenburger, D. A. (2000) Vector unpacking as a potential barrier for receptor-mediated polyplex gene delivery. *Biotechnol. Bioeng. 67*, 598−606.

(26) Akinc, A., Thomas, M., Klibanov, A. M., and Langer, R. (2005) Exploring polyethylenimine-mediated DNA transfection and the proton sponge hypothesis. *J. Gene Med. 7*, 657−663.

(27) Zaric, V., Weltin, D., Erbacher, P., Remy, J. S., Behr, J. P., and Stephan, D. (2004) Effective polyethylenimine-mediated gene transfer into human endothelial cells. *J. Gene Med. 6*, 176−184.

(28) Totsugawa, T., Kobayashi, N., Maruyama, M., Okitsu, T., Noguchi, H., Watanabe, T., Matsumura, T., Fujiwara, T., and Tanaka, N. (2003) Successful lentivirus-based delivery of a LacZ gene into human endothelial cells. *Transplant. Proc. 35*, 499−500.

(29) Thomas, C. E., Ehrhardt, A., and Kay, M. A. (2003) Progress and problems with the use of viral vectors for gene therapy. *Nat. Rev. Genet. 4*, 346−358.

BC0600968

Preparation of Bioactive and Surface Functional Oligomannosyl Neoglycoprotein Using Extracellular pH-Sensitive Glycosylation of Mutant Lysozyme Having N-Linked Signal Sequence in Yeast

Soichiro Nakamura,*,† Masanori Ban,# and Akio Kato#

Department of Biosciences and Biotechnology, Shinshu University, Nagano 399-4598, Japan, and Department of Biochemistry, Yamaguchi University, Yamaguchi 753, Japan. Received April 19, 2006; Revised Manuscript Received July 21, 2006

Bioactive oligomannosyl lysozyme with improved surface functionalities was successfully prepared by using an extracellular pH-sensitive glycosylation system for heterogeneous protein in yeast cell. A recombinant *Saccharomyces cerevisiae* carrying a mutant lysozyme gene encoding the signal sequence of an N-linked glycosylation site at position 49 was cultivated in various pH conditions to investigate the effects of extracellular pH on the glycosylation patterns and the expression of the protein. A large polymannose ($Man_{310}GlcNAc_2$) chain-linked lysozyme was predominantly expressed accompanied by small amounts of a core-type oligomannose chain ($Man_{14}GlcNAc_2$)-linked lysozyme in the yeast medium where the extracellular pH was kept at 3.5 or above, while an oligomannose chain lysozyme was preferentially expressed in the yeast medium where the pH was less than 3. The lytic activities of the oligomannosyl and the polymannosyl lysozymes were found to be 70.4 and 5.1%, respectively, of the wild-type lysozyme when *Micrococcus lysodeikticus* cells were used as the substrate. The enzymatic activity of the oligomannosyl lysozyme was totally conserved for the glycolysis assay with a soluble substrate, glycol chitin, whereas that of the polymannosyl lysozyme was not. After heating the sample up to 95 °C at pH 7.0 where no visible protein coagulation was observed, thermostability of the enzymatic activity of the oligomannosyl lysozyme was drastically improved with more than 60% of residual lytic activity. Emulsifying properties of the protein also were highly improved by the oligomannosylation, in which the emulsifying activity was 3.2 times higher than that of the wild-type protein. Corresponding to the increase of the surface functionalities, the surface tension of the oligomannosyl protein exhibited a significantly ($p < 0.05$) lower value compared to that of the wild-type. By using the lower pH medium at 3.0, it was revealed that a substantial amount (0.31 mg/L) of the oligomannosyl lysozyme was successfully obtained in the culture medium. Therefore, the extracellular pH-sensitive glycosylation system can be used to obtain bioactive and surface functional neoglycoproteins.

INTRODUCTION

Yeasts are considered cost-effective host organisms for producing high titers of recombinant heterologous proteins (*1*). The yeast *Saccharomyces cerevisiae* has been expected to be a promising candidate to produce therapeutic human glycoproteins (*2*). Yeasts and mammalian cells share the features of asparagine-linked (N-linked) oligosaccharide processing in the endoplasmic reticulum (ER), including the attachment of the common dolichol-linked precursor oligosaccharide (Dol-PP-$GlcNAc_2$-Man_9-Glc_3) and subsequent truncation to $GlcNAc_2$-Man_8. However, the oligosaccharide processed in the ER is subsequently modified in the Golgi apparatus in different glycosylation systems when comparing mammalian cells and yeasts. In *S. cerevisiae*, the core oligosaccharide is elongated in the Golgi cisternae through stepwise addition of mannose residues catalyzed by several mannosyltransferases, leading to highly branched outer chains consisting of 50−150 mannose residues (*3*, *4*). Although the yeast expression system can be used to increase the stability during heating or protease attack, hyperglycosylation in *S. cerevisiae* is a problem for therapeutic glycoprotein production. Indeed, the large molecular size of N-glycosylated lysozyme with a few hundred mannose residues was expressed in the yeast carrying the mutant lysozyme expression plasmid (*5*). The unusual polymerization of mannose outer chains in mutant lysozyme may be due to the time interval during which the protein molecule is present in Golgi cisternae. There is little information on the effects of culture condition on the expression and glycosylation patterns of heterologous proteins in yeast cells, while much work has been accomplished on the production of human therapeutics requiring glycosylation using mammalian cells (*6*−*14*). Mammalian expression studies revealed that culture pH, ammonia concentration, temperature, and carbon source influenced the glycosylation level and yield of recombinant glycoproteins (*13*−*16*). The existence of extracellular ammonia has been shown to decrease the amount of glycosylation and degree of sialylation in the mammalian expression system, indicating that this is due to local intracellular pH alterations as a result of importing ammonia into the cell (*13*, *15*, *16*). An extracellular ammonia concentration of 10−15 mM can increase the trans-Golgi pH to 7.0−7.2, while β-1,4-galactosyltransferase has been identified as having optimum activity at pH 6.5 (*15*). The shift in culture pH can alter the enzymatic activity of the transferase involved in protein processing, resulting in changes in glycosylation of the protein (*14*). It has been postulated that the extracellular pH of yeast transformants indirectly affects glycosylation during processing. In the present study, we assumed that the glycosylation pattern of mutant lysozyme could be affected by the culture condition, especially by the culture pH.

Although it has been anticipated that the attachment of carbohydrate chains to protein brings about its stability and surface functionalities, polyglycosylation appears to be inappropriate to use for the production of biologically active proteins

* To whom correspondence should be addressed. Tel & Fax: +81-265-77-1609. E-mail: snakamu@shinshu-u.ac.jp.

† Shinshu University.

Yamaguchi University.

10.1021/bc0600970 CCC: $33.50 © 2006 American Chemical Society
Published on Web 08/17/2006

because of the steric hindrance of excessively long chains. The lytic activity of lysozyme was drastically diminished by the polyglycosylation with dextran through Maillard-type glycosylation (*17*), while the conjugation with small carbohydrate molecules such as glucose or lactose caused insoluble aggregates with poor surface properties (*18*). Accordingly, if a conjugation with oligosaccharide were to be applied, then a desirable active neoglycoprotein with improved surface functionalities could be created. The objective of this study was to synthesize bioactive and surface functional oligomannosyl lysozyme using an extracellular pH-sensitive glycosylation system of heterogeneous protein in yeast cells.

EXPERIMENTAL PROCEDURES

Materials. The yeast expression plasmid pYG-100 was supplied from Dr. K. Matsubara, Osaka University. The recombinant plasmid pKK-1, which contains a full-length hen egg-white lysozyme cDNA (*19*), was from Dr. I. Kumagai, University of Tokyo. T4 DNA ligase, alkaline phosphatase, and restriction enzymes were purchased from Takara Shuzo (Kyoto). The 7-DEAZA sequence kit for sequencing and the kit for blunting were also purchased from Takara Shuzo. The oligonucleotide-directed in vitro mutagenesis system (version 2) for site-directed mutagenesis and [α-^{32}P] dCTP (800 Ci/mmol) were purchased from Amersham Pharmacia Biotech. CM-Toyopearl 650M resin was from Tosoh (Tokyo). Concanavalin A-Sepharose and α-methylmannoside were from Amersham Pharmacia Biotech and Wako Pure Chemical Industries Ltd. (Tokyo), respectively. Sephadex G-50 was from Amersham Pharmacia Biotech. *Micrococcus lysodeikticus* dried cells and ethylene glycol chitin for lysozyme assay were from Sigma and Nacalai Tesque Inc. (Kyoto), respectively. Endo-β-*N*-acetylglucosaminidase (endo-H) was from Genzyme. All other chemicals were of analytical grade for biochemical use.

Construction of Yeast Expression Plasmid Carrying a Mutation of the Lysozyme Gene. A mutant lysozyme cDNA was constructed to introduce the potential asparagine-linked (N-linked) glycosylation sites (Asn-Ser-Thr) on the molecular surface at position 49, as described before (*5*). The conversion of Gly^{49} codon to Asn was carried out by site-specific mutagenesis using the bacteriophage vector M13mp19. The *Eco*RI/*Hind*III fragment of pKK-1 plasmid was subcloned into the *Eco*RI/*Hind*III site of the bacteriophage vector M13mp19. The mutant hen egg-white lysozyme cDNA was constructed in the M13mp19 vector by the Amersham oligonucleotide-directed mutagenesis system (version 2). A mutagenic oligonucleotide primer, 5′-AACACCGATAACAGTACCGA-3′, which was synthesized by the phosphoamidate method using a Pharmacia DNA synthesizer, was used to convert the Gly^{49} (GGG) codon to Asn (AAC). The presence of the mutation was confirmed by dideoxy DNA sequencing analysis (*20*). For construction of the vector, the mutant lysozyme cDNA was inserted into *Sal*I site of a yeast expression plasmid pYG-100, as previously described (*19*, *21*).

Yeast Transformation and Cultivation. The expression vector carrying a mutant lysozyme gene was introduced into *S. cerevisiae* AH22 (*MAT*a, *Leu*2, *His*4, Cir$^{\pm}$) according to the lithium acetate procedure (*22*). Leu^{+} transformants were screened by subculturing in the modified Burkholder minimum medium (*23*) plates supplemented with histidine (20 μg/mL) at 30 °C. After cultivation, well-growing colonies were then replica-cultivated in the yeast medium on a small scale (5 mL), and the overexpression subclones with the highest levels of lysozyme activity were screened and propagated from single colonies. The overexpression colonies were directly subcultured on a large scale (6 L) at 30 °C in the yeast minimum medium, in which ammonium sulfate or L-asparagine was used as a nitrogen source. Extracellular pH of the culture was controlled at the given pHs by addition of 1 N sodium hydroxide solution. Duplicate 10 mL samples were removed for monitoring pH and measuring turbidity of the culture mediums. The culture pH for all experiments was controlled within $\pm$0.1 pH units.

Isolation and Purification of the Mutant Lysozyme from Yeast Culture Medium. The supernatant of yeast culture medium was directly applied to a CM-Toyopearl 650M opened column (1.8 $\times$ 5 cm) equilibrated with 50 mM Tris-HCl buffer (pH 7.5), and the column was washed with the same buffer until the washing solution was free from proteins. The adsorbed lysozyme was eluted with 0.5 M NaCl in 50 mM Tris-HCl buffer (pH 7.5). The protein solution was diluted with deionized water at least five times and again applied to the regenerated CM-Toyopearl 650M column. The eluted lysozyme was collected and then lyophilized to measure the secretion amount and to analyze SDS−polyacrylamide gel electrophoresis. For the chemical analysis and assay of enzymatic activity, further purification was carried out using the gel filtration on a Sephadex G-50 equilibrated and eluted with 50 mM Tris-HCl buffer, pH 7.5. The protein content in each fraction was detected by measuring the absorbance at 280 nm, and the carbohydrate content was determined by measuring the absorbance at 490 nm after color development with the phenol−sulfuric acid reaction. All fractions containing glycoprotein were collected and concentrated using a regenerated cation-exchange column. The glycoprotein samples were further applied to a concanavalin A-Sepharose column (0.9 $\times$ 3 cm), which was prewashed with 10 bed volumes of 20 mM Tris-HCl buffer (pH 7.5) containing 0.5 M NaCl and then washed with the same buffer until the washing solution was free from proteins. The adsorbed glycoprotein was subsequently eluted with 100 mM α-methylmannoside in the 20 mM Tris-HCl buffer containing 0.5 M NaCl. The glycoprotein solution was diluted with deionized water at least five times and again applied to the regenerated CM-Toyopearl 650M opened column (1.8 $\times$ 2 cm).

SDS−Polyacrylamide Gel Electrophoresis. SDS−polyacrylamide gel electrophoresis (SDS−PAGE) was conducted according to the method of Laemmli (*24*) using a 15% (w/v) acrylamide separating gel and a 5% (w/v) stacking gel containing 1% (w/v) SDS. Samples were heated at 100 °C for 5 min in Tris-glycine buffer (pH 8.8) containing 1% SDS and 1% (v/v) 2-mercaptoethanol. Electrophoresis was carried out at a constant current of 10 mA for 5 h using an electrophoretic buffer of Tris-glycine containing 0.1% (w/v) SDS. After electrophoresis, the gels were stained for protein and carbohydrate with 0.025% (w/v) Coomassie Brilliant Blue R-250 solution and 0.5% (w/v) periodic acid-Fuchsin solution (*25*), respectively.

Endo-H Treatment. The digestion of the glycosylated lysozymes with endo-H was carried out according to the slightly modified method of Tarentino and Maley (*26*). The glycosylated lysozymes (0.1 mg/mL) were boiled in 50 mM sodium citrate buffer (pH 5.5) containing 1% (w/v) SDS and 200 μg/mL of phenylmethylsulfonyl fluoride for 5 min. After cooling, samples were supplemented with an equal volume of either 0.02 unit of endo-H in 50 mM sodium citrate buffer (pH 5.5) or the same buffer without the enzyme and were subsequently incubated at 37 °C for 20 h. After incubation, the samples were analyzed by SDS−PAGE.

Analysis of the N-Linked Oligosaccharide Length of Mutant Lysozyme. The total sugar content of the glycosylated lysozymes was estimated using the phenol−sulfuric acid reaction employing mannose as a standard. HPLC analysis serves as a method of identification of the hexose liberated from glycosylated lysozymes by hydrolysis with 2 N HCl at 100 °C for 3 h in a sealed glass ample. The hydrolysates were dried, dissolved in water, and chromatographed on an Asahipak NH2P-

50 column (Asahi Chemical, Tokyo) in 75% acetonitrile using the Hitachi HPLC system equipped with an RI detector. For the analysis of hexosamine, the hydrolysates with 3 N HCl at 100 °C for 4 h were dried and then analyzed using an amino acid analyzer (Tosoh, HLC 805).

Enzymatic Assay. Lysozyme activity was measured by a lysis and glycolysis assays using *M. lysodeikticus* cells and ethylene glycol chitin as substrates, respectively. Bacteriolytic activity of lysozyme was assayed by the method of Parry et al. (*27*) with a slight modification. The suspensions of *M. lysodeikticus* cells ($OD_{450} = 0.7$) were prepared in 100 mM acetic acid-sodium acetate buffer at pH 6.0. After its absorbance at 280 nm was first adjusted to 0.050, the assay lysozyme solution (0.1 mL) was added to 2.4 mL of the cell suspension in sodium acetate buffer (pH 6.0). The initial decrease in the absorbance at 450 nm of the mixture caused by lysis of *M. lysodeikticus* cells was measured at 20 °C for 1 min with a Hitachi U-2000 spectrophotometer. Hydrolytic activity with glycolysis was measured by following the reducing procedure (*28*). 0.5 mL of the lysozyme solution in 10 mM acetate buffer (pH 4.5) was added into a 1.0 mL of 0.05% (w/v) solution of ethylene glycol chitin. The mixture was incubated at 40 °C for 30 min. After the reaction, 2.0 mL of the color reagent (made by dissolving 0.5 g of potassium ferricyanide in 1 L of 0.5 M sodium carbonate) was added, and the mixture was immediately boiled for 15 min to estimate the reducing power resulting from hydrolysis of ethylene glycol chitin.

Emulsifying Properties and Surface Tension. Emulsifying activity and emulsion stability were estimated according to the modified method of Pearce and Kinsella (*29*). An emulsion was prepared by homogenizing the mixture of 1.0 mL of corn oil and 3.0 mL of a 0.1% (w/v) protein solution in a Polytron homogenizer PT 10-35 (Kinematica Co., Switzerland) at 12 000 rpm for 1 min at 20 °C. A total of 100 μL of emulsion was taken from the bottom of the test tube after the sample stood for 0, 1, 2, 3, 5 and 10 min and was diluted with 5.0 mL of 0.1% (w/v) SDS solution. The absorbance of the diluted emulsion was then measured at 500 nm. The relative emulsifying activity was represented as the absorbance at 500 nm measured immediately after emulsion formation (0 min). The emulsion stability was estimated by measuring the half-life of the turbidity detected immediately after the emulsion had formed. Surface tension was measured by an interfacial tensiometer (Kyowa Kagaku Co., Tokyo), a duNouy tensiometer, which is essentially a torsion balance with platinum ring (2 cm diameter) suspended from the beam. The platinum ring was put into 2 mL of a 0.05% (w/v) protein solution, and then the force required to release the ring from the surface was measured using the apparatus. The exhibitions of the steady surface tension required 5 min after preparation of the interface. Therefore, the measurement was carried out at 5 min intervals.

Thermal Denaturation. The apparent heat stability was estimated by measuring the developed turbidity when 0.1% (w/v) protein concentration of native and glycosylated lysozymes were heated to 95 °C from 30 °C at a heating rate of 1 °C/min in 1/15 M sodium phosphate buffer (pH7.0). After a given temperature, the heated sample was immediately replaced into a cuvette and the turbidity was measured at 500 nm. The residual lytic activity of the heated samples was determined by using *M. lysodeikticus* cells as substrate.

RESULTS

Effect of Extracellular pH on the Glycosylation and Secretion of Mutant Lysozyme. Ammonium sulfate as a nitrogen source is not used for the yeast minimum medium because the pH of the medium is lowered by the increases in sulfate during the growth of yeast. However, the nitrogen source was very useful for investigating the effect of pH on the glycosylation and expression of the heterologous lysozyme. When ammonium sulfate was used as a nitrogen source, the extracellular pH during yeast growth was reduced to 2.0, as shown in Figure 1A, whereas the pH in a culture of *S. cerevisiae* AH22 was kept at 4.6−4.7 in the yeast minimum medium in which L-asparagine was used as a nitrogen source. Although the growth of yeast was slightly suppressed in the medium containing ammonium sulfate, compared to that in the medium containing L-asparagine, almost the same order (10^8 cells/mL) of cell growth was kept in the stationary phase despite the extreme lowering of the extracellular pH. To investigate the effect of the extracellular pH on the expression of mutant lysozyme, the pH regulation of yeast culture was carried out as follows. After the cultivation of the recombinant yeast in the medium of ammonium sulfate for 4 days at 30 °C, the pH of the medium was raised to 4.0 by addition of 1 N NaOH and then kept to the same pH for another 4 days. As shown in Figure 1B, the secreted amount of lysozyme was greatly increased with the recovery of pH to 4.0. The SDS−polyacrylamide gel electrophoretic patterns of mutant lysozyme at each culture stage are shown in Figure 2. After incubation in the culture medium

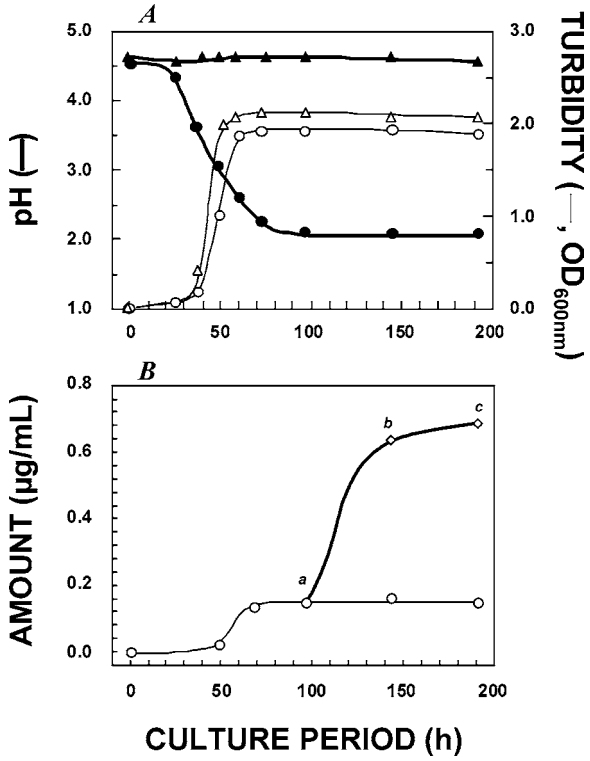

Figure 1. Effects of extracellular pH on expression of mutant lysozyme in the recombinant yeast *S. cerevisiae* AH22. (A) pH profiles and growth curves when the recombinant yeast cells carrying mutant lysozyme gene were cultured at 30 °C for 8 days in Burkholder's yeast minimum medium with L-asparagine (△, ▲) or ammonium sulfate (○, ●) as sole nitrogen sources. The solid and open symbols indicate pH and the turbidity of culture, respectively. Duplicate 10 mL samples were removed and used for monitoring pH and turbidity of the culture mediums. (B) Time course of secretion amount of the mutant lysozyme. The yeast cells were grown in Burkholder's yeast minimum medium with ammonium sulfate as a sole nitrogen source at 30 °C for 4 days (at final pH 2.0) and then incubated continuously at 30 °C for 4 days in the pH-controlled medium at pH 4.0 by the addition of NaOH. The secretion amounts of the mutant lysozyme at pH 2.0 (○) and pH 4.0 (◇) were determined by measuring the dry weight of the mutant proteins purified by two steps of cation-exchange chromatography with CM-Toyopearl from the cultivation medium. The small letters a, b, and c in the panel indicate the position and the secreted amount of mutant lysozymes obtained 0, 2, and 4 days after raising the pH to 4.0, respectively.

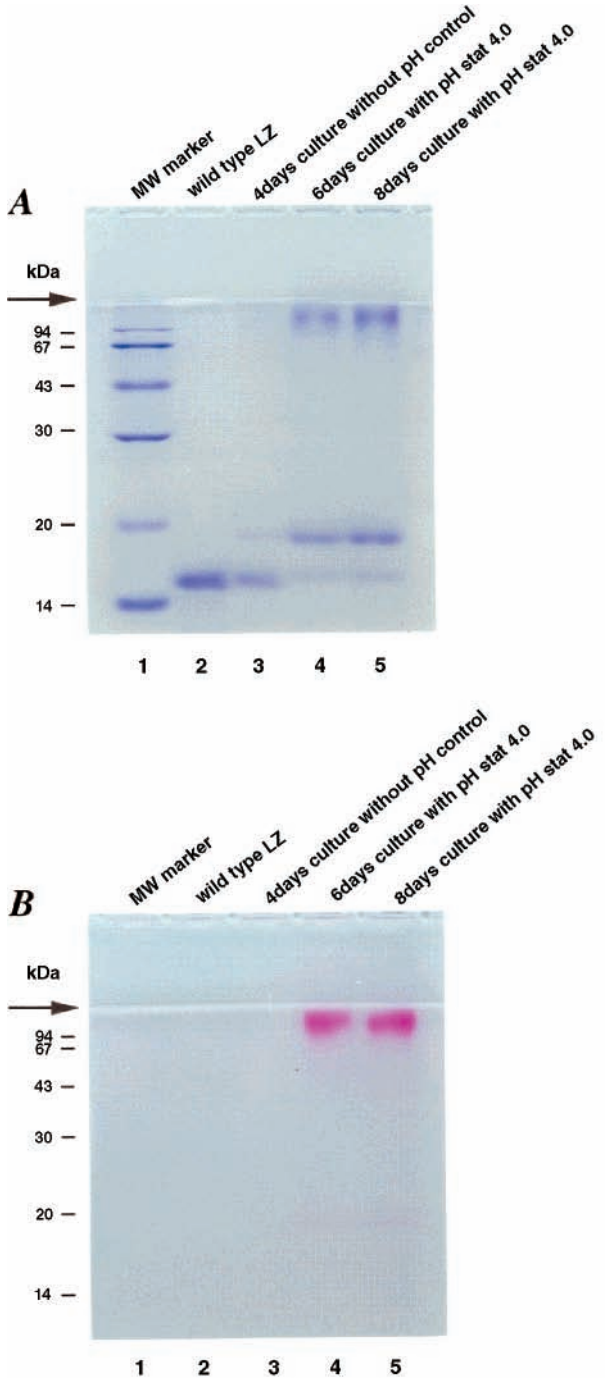

Figure 2. Changes in the SDS−polyacrylamide gel electrophoretic patterns of mutant lysozymes secreted from the recombinant yeast *S. cerevisiae* AH22 in the pH-controlled condition. The yeast cells were cultured in the yeast minimum medium with ammonium sulfate as a sole nitrogen source at 30 °C for 4 days and then incubated continuously at 30 °C for 4 days in the controlled medium at pH 4.0. The secreted lysozyme in the culture supernatant after 4 (lane 3), 6 (lane 4), and 8 days (lane 5) of incubation were purified by cation-exchange chromatography with CM-Toyopearl and subjected directly to SDS−PAGE. Electrophoresis was carried out at a constant current of 10 mA for 5 h in an electrophoresis of Tris-glycine buffer (pH 8.8) containing 0.1% SDS. The gels were stained for proteins and carbohydrates with Coomassie Brilliant Blue (A) and periodic acid-Fuchsin (B), respectively. Arrows indicate the position of the boundary between the stacking (upper) and separating (lower) gels. Lane 1, molecular weight markers (94 000, phosphorylase *b*; 67 000, bovine serum albumin; 43 000, ovalbumin; 30 000, carbonic anhydrase; 20 100, trypsin inhibitor; 14 300, α-lactalbumin); lane 2, wild-type lysozyme; lane 3, 4-day culture product shown in Figure 1B, a; lane 4, 6-day culture product shown in Figure 1B, b; lane 5, 8-day culture product shown in Figure 1B, c.

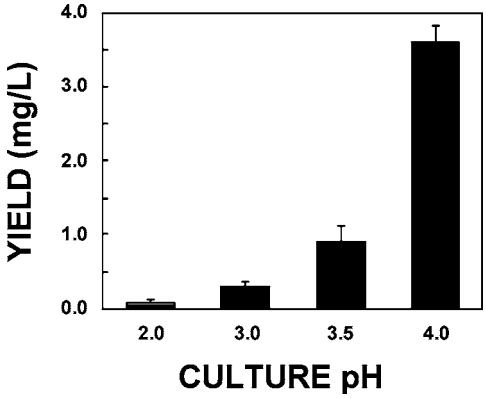

Figure 3. Effect of extracellular pH on the expression rates of mutant lysozyme. The yeast cells were cultured in the yeast minimum medium with ammonium sulfate as a sole nitrogen source at 30 °C for 4 days. To maintain pH conditions at 4.0, 3.5, and 3.0, 1 N NaOH was added in constantly maintaining by pH controller. The final pH became 2.0 without pH control. The secreted lysozymes were purified by cation-exchange chromatography with CM-Toyopearl, and the concentration was determined based on the absorbance at 280 nm. Represented values are means of three independent experiments, and the bars indicate the standard deviation.

for 4 days at 30 °C (pH 2.0), most lysozymes were not glycosylated, but a small amount of oligomannosyl protein was observed (Figure 2, lane 3). The subsequent incubation at pH 4.0 resulted in dramatic increases in the expression of polymannosyl and oligomannosyl lysozymes (Figure 2, lanes 4 and 5), although cell growth was not observed during incubation at pH 4.0. This result suggests that the glycosylation of the mutant lysozyme in yeast was regulated by the extracellular pH.

To confirm the above result, the effects of the extracellular pH in the yeast culture medium on the glycosylation of the mutant lysozyme were further examined. In the medium containing ammonium sulfate as a nitrogen source, the extracellular pHs were constantly adjusted to 4.0, 3.5, and 3.0 using 1 N NaOH, and yeast cell growth was monitored by the measurement of the culture turbidity. The cell growth increased in proportion to the incubation time at each pH and attained stationary phase after a 60 h incubation. No significant differences in the cellular growth were observed at each pH. On the other hand, remarkable increases in the secretion amounts of the lysozyme were observed with the increase in extracellular pH (Figure 3). The secretion amounts from the cultured yeast cells incubated at pH 2.0, 3.0, 3.5, and 4.0 were 0.10, 0.31, 0.91, and 3.6 mg/L of medium, respectively. When the extracellular pH was maintained at 4.0, the yield of the mutant lysozyme was 36% of that in the medium (pH 4.6−4.7) using L-asparagine as a nitrogen source (*5*). Figure 4 shows the SDS−PAGE patterns of the secreted lysozymes in the supernatant of the pH-controlled media at 4.0, 3.5, and 3.0. Polymannosyl lysozyme was secreted in proportion to increases in extracellular pH. It is interesting that pH regulation of the yeast medium greatly affected the glycosylation patterns of the mutant lysozyme. The first step in glycosylation (oligomannosylation) of the mutant lysozyme was greatly suppressed at pH 2.0 (lane 3), although protein synthesis proceeded normally. On the other hand, the mutant lysozyme was predominantly oligomannosylated at pH 3.0 (lane 4) and mostly polymannosylated at pH 3.5 (lane 5) or above (lane 6). These observations suggest that the glycosylation of proteins in yeast is affected by the extracellular pH. These data indicate that a substantial amount (0.31 mg/L) of the oligomannosyl lysozyme could be obtained in the culture medium by using the lower pH medium, i.e., at 3.0.

The glycosylated lysozymes were treated with endo-H which cleaves the high mannose-type asparagine-linked oligosaccharide

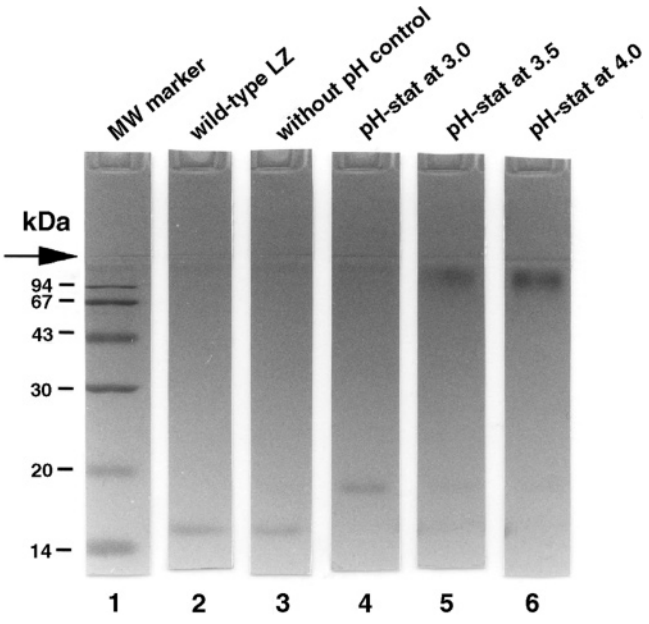

Figure 4. Electrophoretic patterns of mutant lysozymes secreted from the recombinant yeast *S. cerevisiae* AH22 cultured at various pH. The secreted lysozymes in the various pH-controlled conditions were purified by cation-exchange chromatography with CM-Toyopearl and treated with endo-H as described in Experimental Procedures and then subjected to SDS−PAGE. The gels were stained with Coomassie Brilliant Blue. Arrow indicates the position of the boundary between the stacking (upper) and separating (lower) gels. Lane 1, molecular weight markers; lane 2, wild-type lysozyme; lane 3, product obtained from the medium without pH control (final pH 2.0); lane 4, product obtained from the medium controlled at pH 3.0; lane 5, product obtained from the medium controlled at pH 3.5; lane 6, product obtained from the medium controlled at pH 4.0.

(*30*). Oligomannosyl and polymannosyl lysozyme were completely digested by endo-H, suggesting that these glycosyl lysozymes are a type of N-linked glycosylation (data not shown). The cell growth of the yeast may affect the glycosylation pattern of mutant lysozyme. To elucidate this point, the glycosylation pattern of the mutant lysozyme in various growth stages was investigated. The polymannosylation occurred in the early or mid-log phase, and no differences in the polymannosylation of mutant lysozymes were observed in each growth stage. On the other hand, as shown in Figures 2 and 4, the polymannosylation in extremely acidic medium (less than pH 3.0) did not occur in the stationary phase where the yeast growth was almost the same as that in normal medium. These results suggest that the polymannosylation was affected only by extracellular pH, independent of the yeast cell growth. The extracellular pH may affect the sorting and secretion of the foreign lysozyme in yeast cells. The polymannosyl lysozyme may remain in the cytosol or cell membrane at extremely low pH. Therefore, the presence of polymannosyl lysozyme in the yeast cell membrane and the cytosol was investigated. No polymannosyl lysozyme was observed in the cytosol or cell membrane at pH 2.0, although considerable amounts of glycosylated lysozymes were obtained at pH 4.0 or 4.6. Except for the presence of mutant lysozymes, there are no differences in the SDS−PAGE patterns of membrane proteins under various medium conditions (data not shown). Thus, it was confirmed that the glycosylated lysozyme did not remain in the yeast cell membrane or cytosol at low pH 2.0.

Chemical and Enzymatic Analysis of Glycosylated Lysozymes. The chemical composition analysis revealed that the polysaccharide chain of the polymannosyl lysozyme consisted of 310 mol of mannose and 2 mol of *N*-acetylglucosamine, while that of oligomannosyl one consisted of 14 and 2 mol, respectively (Table 1). The composition indicates that poly- and oligomannosyl lysozymes carry $Man_{310}GlcNA_2$-linked and $Man_{14}GlcNAc_2$-linked forms, respectively. This result corresponds to an increase in apparent molecular mass in SDS−PAGE (Figure 2). The carbohydrate composition of oligomannosyl lysozyme secreted at acidic pH 3.0 is almost the same as that of the core type N-linked oligosaccharide, $Man_8GlcNAc_2$, while the length of the polymannosyl chains secreted at pH 4.0 was almost the same as that secreted in normal medium (*5*). These results suggest that the acidic extracellular pH 3.0 did not affect the processing in the ER membrane but affected the subsequent elongation of the outer chains in the Golgi cisternae. Thus, it was confirmed that the lysozyme glycosylated with N-linked oligosaccharide and polysaccharide chains were separately secreted in the recombinant yeast and controlled by the extracellular pH. A similar dependency of the glycosylation of the mutant lysozyme on the extracellular pH was also observed in the medium in which asparagine was used as a nitrogen source.

Table 1. Carbohydrate Analysis of Glycosylated Lysozymes

	contents (mol/mol lysozyme) of	
lysozyme	*N*-acetylglucosamine[a]	mannose[b]
polymannosyl[c]	2	310 ± 7.5
oligomannosyl[d]	2	14 ± 0.4

[a] Determined with an amino acid analyzer using the hydrolysates with 3 N HCl at 100 °C for 4 h. [b] Determined by HPLC analysis using an NH2P-50 column and by the phenol−sulfuric acid method. Each value is the means ± standard deviation of three replications. [c] Obtained from the medium at pH 4.0. [d] Obtained from the medium at pH 3.0.

Table 2. Enzymatic Activity of Oligomannosyl and Polymannosyl Lysozymes

	enzymatic activity (%)[a] determined by	
types of protein	*M. lysodeikticus*[b]	glycol chitin[c]
wild-type lysozyme	100	100
oligomannosyl lysozyme	70.4 ± 2.7	100 ± 1.5
polymannosyl lysozyme	5.1 ± 2.8	88.7 ± 3.1

[a] Enzymatic activity was represented as the percentages of wild-type lysozyme. Each value is the means ± SD of independent experiences performed in triplicate. [b] The lytic activity was measured in 0.1 M acetate buffer (pH 6.0) with *M. lysodeikticus* as substrate. [c] The glycosis activity was measured in 0.01 M acetate buffer (pH 4.5) with glycol chitin as substrate.

The lysozyme activities were measured by lysis and glycolysis assays for oligomannosyl lysozyme and polymannosyl lysozyme secreted in the medium at pH3.0. The enzymatic activities of oligomannosyl and polymannosyl lysozymes were, respectively, 70.1 and 5.1% of the wild-type protein when *M. lysodeikticus* cells were used as substrate; therefore, long-chain glycosylation may be unsuitable for producing biologically active proteins (Table 2). These lysozyme activities were recovered by treating with endo-H. On the other hand, when glycol chitin was used as the substrate, the enzymatic activity of the oligomannosyl lysozyme was almost the same as that of unglycosylated (wild-type) lysozyme, while that of the polymannosyl lysozyme was 88.7% (Table 2). These results indicate that mature oligomannosyl lysozyme was correctly processed during the secretion in the recombinant yeast at lower pH (3.0), suggesting the inhibition of oligomannosylation was not caused by the structural changes in protein structure under the acidic condition. The biological activity of lysozyme was not appreciably deteriorated by oligomannosylation in the yeast expression system. The inhibitory activity was highly conserved in the oligomannosylated lysozyme, whereas it was significantly decreased in the fully polymannosylated lysozyme. This result indicates that the long polymannosyl chain may interfere with

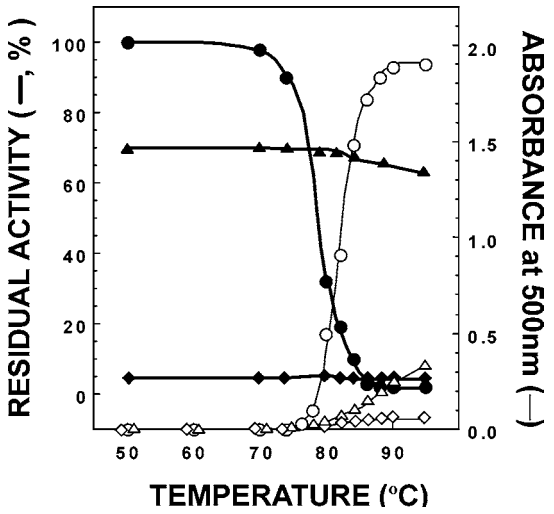

Figure 5. Thermal stability of oligomannosyl lysozyme. The thermal stability was determined by measuring the turbidity and residual activity. Samples were heated to 95 °C from 30 °C at a rate of 1 °C/min in 1/15 M sodium phosphate buffer, pH 7.0. After a given temperature, the heated sample was immediately replaced into a cuvette, and the residual activity was determined based on the lytic activity using *M. lysodeikticus* as substrate (solid symbols). The turbidity of the sample solution was measured at the absorbance of 500 nm (open symbols). Data shown are from a representative experiment repeated three times with similar results. ●○, wild-type lysozyme; ▲△, oligomannosyl lysozyme; ◇◆, polymannosyl lysozyme.

effective interaction between enzymatic pockets of the protein moiety and the substrate.

Heat Stability of Recombinant Lysozymes. Figure 5 shows the heat stability of oligomannosyl lysozyme, which was assessed by monitoring its thermal denaturation when a 0.1% protein solution was heated to 95 °C at a rate of 1 °C/min. As a result, the heating assay revealed that polymannosylation greatly improved the heat stability of the protein to an extent that no coagulation was observed. Under the same conditions, unglycosylated protein had coagulated. Almost the same phenomenon was observed in the heating system coexisting with oligomannosyl lysozyme. During heating, the protein molecules are partially unfolded, resulting in aggregation due to the heat-induced disruption of a delicate balance of various noncovalent interactions. This process was reversible in the glycosylated cystatins because of the inhibition of aggregation by poly and oligomannosyl chains through interaction of unfolded proteins, whereas that of wild-type lysozyme was irreversible. In addition, as shown in Figure 5, considerably high residual lytic activity of lysozyme toward *M. lysodeikticus* cells was kept in the oligomannosyl lysozyme after heating to 95 °C. After heating of the sample to 95 °C, the lytic activity of the polymannosyl lysozyme was 4.5% that of the native wild-type lysozyme, whereas that of oligomannosyl lysozyme was 63.3%. Thus, we have succeeded in obtaining a bioactive and stable lysozyme with an oligomannose chain. The oligomannosyl lysozyme was used for further investigation.

Improved Surface Functionalities of Oligomannosyl Lysozyme. The emulsifying properties of the oligomannosyl lysozyme constructed by genetic modification were measured under various solution systems (Figure 6). The turbidity of emulsion is plotted as the ordinate, and standing time after emulsion formation is plotted as the abscissa. The value of the ordinate at zero time is relative emulsifying activity, and the half-life of initial turbidity reflects the stability of the emulsion. Better emulsifying properties were observed in the emulsion of the oligomannosyl lysozyme. Emulsifying activity was 3.2 times higher than that of wild-type lysozyme in the neutral pH system (Figure 6A). The emulsifying properties of the oligo-

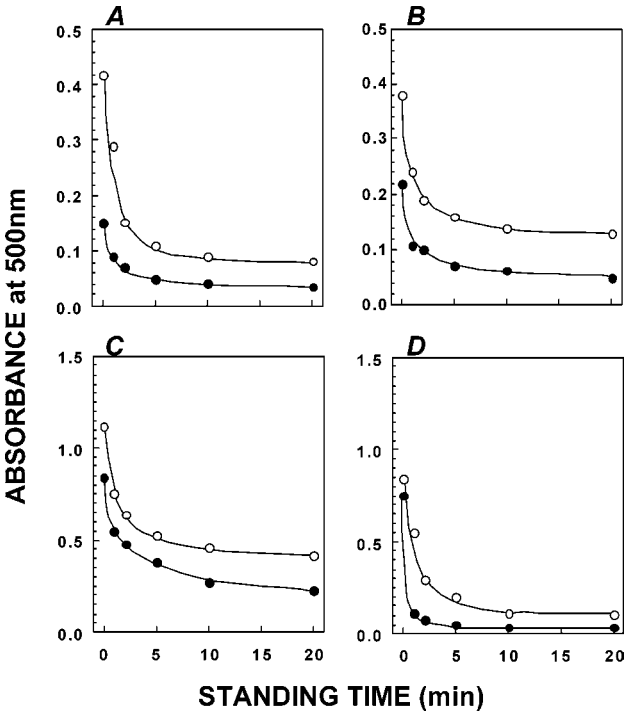

Figure 6. Emulsifying properties of oligomannosyl lysozyme under a neutral pH (1/15 M sodium phosphate buffer, pH 7.0) condition (A), an acidic pH (1/15 M sodium citrate buffer, pH 3.0) condition (B), a high-salt concentration (1/15 M sodium phosphate buffer, pH 7.0, containing 0.2 M NaCl) condition (C), and in a heating (at 65 °C for 30 min in the above neutral pH solution) condition (D). Representative data are obtained from three independent experiments with similar results. ○, oligomannosyl lysozyme; ●, wild-type lysozyme.

mannosyl lysozyme were still excellent in the high-salt condition containing 0.2 M NaCl compared to those of wild-type. The emulsifying activity and the emulsion stability of the oligomannosyl lysozyme were respectively 1.8- and 3.1-fold higher in the wild-type lysozyme (Figure 6B). The emulsifying properties of lysozymes were substantially improved in the acidic (1/15 M acetate buffer, pH 3.0) system. In particular, further improvement was demonstrated in the oligomannosyl lysozyme (Figure 6C). The emulsifying activity of the oligomannosyl lysozyme was increased 1.1 times that of the native form by preheating to 95 °C from 30 °C at a rate to 1 °C/min in the neutral pH system (Figure 6D). As shown in Figure 5, the oligomannosyl lysozyme was heat-stable, and no coagulate was observed during heat treatment at 95 °C. The resulting unfolded form of the oligomannosyl lysozyme was kept by the attached oligomannosyl outer chains without coagulation of the protein portion. The amphiphilic balance between the protein and the carbohydrate chain may play an important role for better emulsifying properties of glycoproteins. It is assumed that the hydrophobic residues of the protein moiety partially denaturated during emulsion formation at the oil−water interface may be anchored to the surface of oil droplets in emulsion, where the hydrophilic residues of the extended branched oligomannosyl chains oriented to water may cover oil droplets to inhibit the coalescence of oil droplets, resulting in higher emulsion formation. Indeed, the emulsifying properties of the oligomannosyl lysozyme were deteriorated compared to those of wild-type lysozyme after deglycosylation with endo-H (data not shown). The measurement of surface tension supplied us reasonable data to elucidate the mechanisms of the improved surface functional properties of the oligomannosyl lysozyme. As shown in Table 3, the surface tension of a 0.05% protein concentration of lysozyme solution was significantly ($p < 0.05$) reduced by the oligomannosylation compared to that of wild-

Table 3. Surface Tension of Oligomannosyl and Polymannosyl Lysozymes[a]

types of protein	surface tension (dynes/cm)
wild-type lysozyme	71.5 ± 1.7^{a}
oligomannosyl lysozyme	65.5 ± 1.5^{b}
polymannosyl lysozyme	60.1 ± 1.3^{c}

[a] The surface tension was determined in room temperature (20 °C) where the value of distilled water without any protein was 75.6 ± 0.9. Values are the means ± SD of ten times replications, and values with different letters are significantly different ($P < 0.05$).

type lysozyme. The oligomannosylation allows lysozyme to convert to a surface-active protein without a fatalloss of the biological activity.

DISCUSSION

We have shown that the polymannosyl lysozyme was preferentially secreted in the medium when the mutant lysozyme gene encoding the N-linked signal sequence at the position 49 was expressed in the yeast *S. cerevisiae* AH22 (*5*). The length of the mannose chain was found to be widely distributed from 200 to 350 residues per mole of protein, as reported in the previous paper (*5*). The length of the mannose residues of the polymannosyl lysozyme was above twice that of the general mannoproteins in yeast. This observation suggests that extensive glycosylation of the outer chain occurs in the secretion system of the heterogeneous lysozyme in yeast, probably due to its specific structural factors. In the yeast *S. cerevisiae* cells, the polymannose chain can be elongated by a highly branched outer chain that has an α-1,6-linked backbone attached to numerous side chains with one to two α-1,2-mannoses and terminal residues in an α-1,3 linkage (*31*). In addition, the mannose outer chains are extended by the different elongation specific α-1,6-mannosyltransferases (*31*). The chain length of the carbohydrate is reported to be strain specific for glycoproteins in yeast (*32*). The presence of various sizes of mannose outer chains in the yeast seems to be dependent on the characteristic of the protein structure, the degree of phosphorylation of the side chains, and the action of mannosyl transferase, etc. In addition, the size of the outer chains may also be determined by the time interval in which the corresponding proteins are present in the Golgi cisternae. Therefore, the unusual polymannosylation of lysozyme may arise from the activation of these factors to secrete harmful heterogeneous protein into the exterior of the yeast cell. However, the secretion amounts of the polymannosyl lysozyme were greatly dependent on the conditions used in the yeast culture as described in this paper. The results in Figure 1 demonstrate that the glycosylation and expression of the recombinant N-glycosylated lysozyme are reversibly recovered by raising the extracellular pH after the suppression of the glycosylation at pH 2.0. When the cultured medium pH was raised from 2.0 (extremely acidic condition) to 4.0, the yeast cells began to produce significant quantities of oligomannosyl or polymannosyl lysozyme, indicating that the recovery of the culture environment to normal pH caused the activation of the glycosylation events in the ER membrane and Golgi cisternae. This suggests that the glycosylation of protein in the ER membrane is inhibited, and further modification in the Golgi apparatus is suppressed by pH stress (the extremely low pH). No polymannosyl lysozyme was secreted; only a core-type oligomannosyl protein was secreted in a yeast culture medium at pH 3.0.

A core-type oligosaccharide ($Man_{14}GlcNAc_2$) is formed in the initial steps in the elongation pathway in the Golgi. The selective secretion of core-type oligomannosyl lysozyme at pH 3.0 is important for elucidating the mechanism of the polymannosylation of lysozyme. The possible explanations are due to inhibition of the subsequent elongation events of enzymes, alteration of the steric accessibility in the core oligosaccharide, and/or shortened period of time in the Golgi in the low pH (3.0) condition. The internal pH in yeast cells may be lowered to less than 6.0 when the extracellular pH is less than 3.0, although it is well-known that yeasts are able to maintain their internal pH between 6 and 7.5 when the extracellular pH varies from 3.5 to 9.0 (*33*). The decrease in the internal pH of yeast cells may affect the various events in the elongation of mannose outer chains in the Golgi cisternae. It is most likely that the enzymes involved in the elongation of polymannosyl residues may be inhibited at an extremely low pH. The results obtained in this study also suggest that the glycosylated lysozymes could be subjected to the transport and sorting mechanisms, which regulate their direction into regulated or constitutive secretion pathways even at an extracellular pH of less than 3.0. Defects in the polymerization of the outer chains lead to a clumped morphology, reduced viability, and distortion of the yeast cell wall (*34*), although a functional explanation is not possible at the moment. The secretion of polymannosyl lysozyme was observed at the normal extracellular pH but not at lower pH. However, the membrane proteins were secreted at lower pH as well as at the normal pH. It seems that the elongation of the outer chains in the heterologous lysozymes is sensitive to pH stress and is uniquely inhibited in the yeast culture at the low pH. Hence, the heterologous lysozyme gene could be used as a reporter in studies of the intracellular traffic of proteins through the ER and Golgi apparatus. It was also revealed that the processing of the N-linked glycosylation of heterologous proteins in yeast is greatly affected by the extracellular pH.

In this paper, we demonstrated that oligomannosylation in yeast using lower extracellular pH is able to carry an excellent emulsifying properties to lysozyme without serious loss of biological activity. The mechanism was supported by the measurement of surface tension of the oligoglycosyl lysozyme solution. It has been confirmed that the reduction of surface tension of protein solution induces excellent surfactant activity (*35*). The excellent emulsifying properties of the oligoglycosyl lysozyme were not reduced even in a high-salt solution system (1/15 M phosphate buffer, pH 7.4, containing 0.2 M NaCl) nor in an acidic (1/15 M sodium citrate buffer, pH 3.0) system and in a heating (at 65 °C for 30 min in the above neutral pH solution) system. Since high-salt, acidic pH, and heating conditions are commonly used in industrial applications, the oligomannosyl lysozyme constructed by the genetic modification could be a suitable ingredient for food agents. The oligomannosyl lysozyme revealed much better emulsifying properties, especially emulsion stability, than those of the wild-type protein, suggesting the special role of the carbohydrate chain in emulsion stability. It is well-known that amphiphilic proteins such as casein, serum albumin, and β-lactoglobulin show good emulsifying properties (*36*). By the natural attachment of the carbohydrate chain, the amphiphilicity of the protein increased in the oligomannosyl lysozyme. The enzymatic activity of lysozyme was highly conserved in the oligomannosylation in the yeast expression system; therefore, the novel oligomannosyl lysozyme with improved emulsifying properties suggests the direction of the design of new functional proteins. There is accumulating evidence that the N-linked oligosaccharide serves to improve the folding and function of bioactive proteins including *Erthrina corallodendron* lectin, soybean agglutinin, RNase B, protein aquaporin 2, and so on (*37*). We previously demonstrated that anti-rotavirus activity of human cystatin C was substantially enhanced by site-directed oligomannosylation using the yeast expression system. The highly efficient action of oligomannosyl cystatin was interpreted as a binding effect of the oligomannosyl chain to rotavirus (*38*). With the improved

surface functionalities by oligomannosylation, proteins are capable of acquiring extended biological activities. The characteristics can be exploited for various health benefits, for example, in pharmaceuticals, nutraceuticals, and food ingredients. Thus, the present study will be further appreciated from many fields.

ACKNOWLEDGMENT

This work was supported by a Grant-in-Aid for Scientific Research from the Minister of Education, Science and Culture of Japan (No. 02660143).

LITERATURE CITED

(1) Bergquist, P. L., Te'o, V. S., Gibbs, M. D., Cziferszky, A. C., De Faria, F. P., Azevedo, M. O., and Nevalainen, K. M. (2002) Production of recombinant bleaching enzymes from thermophilic microorganisms in fungal hosts. *Appl. Biochem. Biotechnol. 98*−*100*, 165−176.

(2) Chiba, Y., Sakuraba, H., Kotani, M., Kase, R., Kobayashi, K., Takeuchi, M., Ogasawara, S., Maruyama, Y., Nakajima, T., Takaoka, Y., and Jigami, Y. (2002) Production in yeast of alpha-galactosidase A, a lysosomal enzyme applicable to enzyme replacement therapy for Fabry disease. *Glycobiology 12*, 821−828.

(3) Kukuruzinska, M. A., Bergh, M. L., and Jackson, B. J. (1987) Protein glycosylation in yeast. *Annu. Rev. Biochem. 56*, 915−944.

(4) Tanner, W., and Lehle, L. (1987) Protein glycosylation in yeast. *Biochim. Biophys. Acta 906*, 81−99.

(5) Nakamura, S., Takasaki, H., Kobayashi, K., and Kato, A. (1993) Hyperglycosylation of hen egg white lysozyme in yeast. *J. Biol. Chem. 268*, 12706−12712.

(6) Rademacher, T. W., Parekh, R. B., and Dwek, R. A. (1988) Glycobiology. *Annu. Rev. Biochem. 57*, 785−838.

(7) Miller, W. M., Blanch, H. W., and Wilke, C. R. (1988) A kinetic analysis of hybridoma growth and metabolism in batch and continuous suspension culture: effect of nutrient concentration, dilution rate, and pH. *Biotechnol. Bioeng. 32*, 947−965.

(8) Rothman, R. J., Warren, L., Vliegenthart, J. F., and Hard, K. J. (1989) Clonal analysis of the glycosylation of immunoglobulin G secreted by murine hybridomas. *Biochemistry 28*, 1377−1384.

(9) Ozturk, S. S., and Palsson, B. O. (1991) Growth, metabolic, and antibody production kinetics of hybridoma cell culture. 2. Effects of serum concentration, dissolved oxygen concentration, and medium pH in a batch reactor. *Biotechnol. Prog. 7*, 481−494.

(10) Doyle, C., and Butler, M. (1990) The effect of pH on the toxicity of ammonia to a murine hybridoma. *J. Biotechnol. 15*, 91−100.

(11) Goochee, C. F., and Monica, T. (1990) Environmental effects on protein glycosylation. *Biotechnology (N Y). 8*, 421−427.

(12) Wang, X. B., Sato, N., Greer, M. A., Greer, S. E., and McAdams, S. (1990) Role of extracellular calcium and calmodulin in prolactin secretion induced by hyposmolarity, thyrotropin-releasing hormone, and high K+ in GH4C1 cells. *Acta Endocrinol. (Copenh*). *123*, 218−224.

(13) Goochee, C. F., Gramer, M. J., Andersen, D. C., Bahr, J. B., and Rasmussen, J. R. (1991) The oligosaccharides of glycoproteins: bioprocess factors affecting oligosaccharide structure and their effect on glycoprotein properties. *Biotechnology (N Y) 9*, 1347−1355.

(14) Borys, M. C., Linzer, D. I., and Papoutsakis, E. T. (1993) Culture pH affects expression rates and glycosylation of recombinant mouse placental lactogen proteins by Chinese hamster ovary (CHO) cells. *Biotechnology (N.Y.*) *11*, 720−724.

(15) Gawlitzek, M., Ryll, T., Lofgren, J., and Sliwkowski, M. B. (2000) Ammonium alters N-glycan structures of recombinant TNFR-IgG: degradative versus biosynthetic mechanisms. *Biotechnol. Bioeng. 68*, 637−646.

(16) Yang, M., and Butler, M. (2000) Effects of ammonia on CHO cell growth, erythropoietin production, and glycosylation. *Biotechnol. Bioeng. 68*, 370−380.

(17) Nakamura, S., Kato, A., and Kobayashi, K. (1991) New antimicrobial characeteristics of lysozyme-dextra conjugate. *J. Agric. Food Chem. 39*, 647−650.

(18) Kato, A., Sasaki, Y., Furuta, R., and Kobayashi, K. (1990) Functional protein-polysaccharide conjugate prepared by controlled dry-heating of ovalbumin-dextran mixture. *Agric. Biol. Chem. 54*, 107−12.

(19) Kumagai, I., and Miura, K. (1989) Enhanced bacteriolytic activity of hen egg-white lysozyme due to conversion of Trp62 to other aromatic amino acid residues. *J. Biochem. (Tokyo) 105*, 946−948.

(20) Sanger, F., Nicklen, S., and Coulson, A. R. (1977) DNA sequencing with chain-terminating inhibitors. *Proc. Natl. Acad. Sci. U.S.A. 74*, 5463−5467.

(21) Kato, A., Tanimoto, S., Muraki, Y., Kobayashi, K., and Kumagai, I. (1992) Structural and functional properties of hen egg-white lysozyme deamidated by protein engineering. *Biosci. Biotechnol. Biochem. 56*, 1424−1428.

(22) Ito, H., Fukuda, Y., Murata, K., and Kimura, A. (1983) Transformation of intact yeast cells treated with alkali cations. *J. Bacteriol. 153*, 163−168.

(23) Toh-e, A., and Wickner, R. B. (1981) Curing of the 2 mu DNA plasmid from *Saccharomyces cerevisiae*. *J. Bacteriol. 145*, 1421−1424.

(24) Laemmli, U. K. (1970) Cleavage of structural proteins during the assembly of the head of bacteriophage T4. *Nature 227*, 680−685.

(25) Zacharius, R. M., Zell, T. E., Morrison, J. H., and Woodlock, J. J. (1969) Glycoprotein staining following electrophoresis on acrylamide gels. *Anal. Biochem. 30*, 148−152.

(26) Tarentino, A. L., and Maley, F. (1974) Purification and properties of an endo-beta-N-acetylglucosaminidase from *Streptomyces griseus*. *J. Biol. Chem. 249*, 811−817.

(27) Parry, R. M., Jr., Chandan, R. C., and Shahani, K. M. (1965) A Rapid and Sensitive Assay of Muramidase. *Proc. Soc. Exp. Biol. Med. 119*, 384−386.

(28) Imoto, T., and Yagishita, K. (1971) A simple activity measurement of lysozyme. *Agric. Biol. Chem. 35*, 1154−1156.

(29) Pearce, K., and Kinsella, J. (1978) Emulsifying properties of protein:Evaluation of a turbidimetric technique. *J. Agric. Food Chem. 26*, 716−723.

(30) Kobata, A. (1979) Use of endo- and exoglycosidases for structural studies of glycoconjugates. *Anal. Biochem. 100*, 1−14.

(31) Ballou, L., Hernandez, L. M., Alvarado, E., and Ballou, C. E. (1990) Revision of the oligosaccharide structures of yeast carboxypeptidase Y. *Proc. Natl. Acad. Sci. U.S.A. 87*, 3368−3372.

(32) Ballou, C. E., and Raschke, W. C. (1974) Polymorphism of the somatic antigen of yeast. *Science 184*, 127−134.

(33) Eraso, P., and Gancedo, C. (1987) Activation of yeast plasma membrane ATPase by acid pH during growth. *FEBS Lett. 224*, 187−192.

(34) Ballou, L., Cohen, R. E., and Ballou, C. E. (1980) *Saccharomyces cerevisiae* mutants that make mannoproteins with a truncated carbohydrate outer chain. *J. Biol. Chem. 255*, 5986−5991.

(35) Kato, A., and Yutani, K. (1988) Correlation of surface properties with conformational stabilities of wild-type and six mutant tryptophan synthase alpha-subunits substituted at the same position. *Protein Eng. 2*, 153−156.

(36) Kato, A., and Nakai, S. (1980) Hydrophobicity determined by a fluorescence probe method and its correlation with surface properties of proteins. *Biochim. Biophys. Acta. 624*, 13−20.

(37) Mitra, N., Sinha, S., Ramya, T. N., and Surolia, A. (2006) N-linked oligosaccharides as outfitters for glycoprotein folding, form and function. *Trends Biochem. Sci. 31*, 156−163.

(38) Nakamura, S., Hata, J., Kawamukai, M., Matsuda, H., Ogawa, M., Nakamura, K., Jing, H., Kitts, D. D., and Nakai, S. (2004) Enhanced anti-rotavirus action of human cystatin C by site-specific glycosylation in yeast. *Bioconjugate Chem. 15*, 1289−1296.

BC0600970

Transcription Inhibition Using Oligonucleotide-Modified Gold Nanoparticles

Chiamaka Agbasi-Porter, Jessica Ryman-Rasmussen,† Stefan Franzen,* and Daniel Feldheim*

Department of Chemistry, North Carolina State University, Raleigh, North Carolina 27695. Received April 21, 2006; Revised Manuscript Received June 16, 2006

The capture of T7 RNA polymerase using double-stranded promoter DNA on the surface of gold nanoparticles has been demonstrated. The competitive binding and inhibition of T7 RNA polymerase due to specific interactions on the nanoparticle surface represents a transcription factor decoy approach in a model system. The efficiency of inhibition was determined for various nanoparticle sizes, surface coverage, and linker length for double-stranded promoter DNA on gold nanoparticles. The experiments provide a basis for determining the accessibility of binding sites on nanoparticle surfaces for applications involving cell targeting or the use of nanoparticles as binding agents in solution.

INTRODUCTION

Methods for interrupting genetic transcription and translation have become invaluable in studying the molecular biology of cells and have shown promise as in vivo therapeutic reagents (*1*−*10*). Several strategies are available to manipulate gene expression at the DNA or RNA stages. By introducing whole genes into cells, gene therapy (*2*) works at the DNA level, effectively replacing aberrant mRNA with mRNA that codes for functional protein. In contrast, antisense oligonucleotides hybridize to mRNA to alter gene splicing or prevent translation (*11*−*14*). Yet another strategy for manipulating gene expression is to prevent transcription altogether by interfering with transcription factors (*15*−*18*). This can be accomplished by introducing a competitive binding agent into the cell, for example a DNA duplex sequence that mimics a transcription factor binding site on the gene of interest. The DNA duplex acts as a "decoy", competitively binding to a transcription factor so that it is not available to perform its normal role in DNA transcription.

A critical limitation in the implementation of nearly all oligonucleotide therapeutic strategies remains the translocation of the active agent across cell and nuclear membranes. Oligonucleotides do not readily diffuse across cell membranes, and many transport vectors have been studied to aid in their cellular uptake. Nanoparticles with multiple targeting peptides have been observed to transit to both the cytoplasm and the nucleus of HepG2 and HeLa cell lines (*19*, *20*). These observations of intracellular internalization of gold nanoparticles (5 nm to 20 nm in diameter) modified with cell and nuclear targeting peptides provides the impetus to study nucleotide interactions on nanoparticle surfaces. The present study focuses on the interaction of the dsDNA promoter sequence for T7 RNA polymerase (RNAP) attached to gold nanoparticles with RNAP in solution. We show that the promoter-modified particles can effectively compete with a template DNA sequence for RNAP. This study also addresses the ability of gold particles in the 5−15 nm size range to interact with a large protein.

* Address correspondence to Stefan_Franzen@NCSU.edu and Dan_Feldheim@NCSU.edu.

† Current address: Center for Chemical Toxicology Research and Pharmacokinetics, College of Veterinary Medicine, North Carolina State University, Raleigh, NC 27695.

EXPERIMENTAL PROCEDURES

Reagents. Citrate-coated gold nanoparticles (10 and 15 nm) were purchased from Ted Pella. NAP-10 columns were purchased from Pharmacia Biotech. In vitro transcription assay kit and RNAP were obtained from Promega. Freeze & Squeeze gel extraction kit, 40% Acrylamide/Bis solution 19:1, TEMED, and ammonium persulfate were purchased from Bio-Rad. Dithiothreitol (DTT) was obtained from Pierce Chem.

The oligonucleotide sequences used in this study are listed in Table 1. Oligonucleotides were purchased from MWG Biotech Inc or IDT. The bold sections of the oligonucleotide sequence indicate the promoter region for RNAP binding. The control strand was a sequence that lacks the promoter region for RNA polymerase.

Preparation of Decoy Oligonucleotide−Gold Conjugates. Thiolated oligonucleotides were received as disulfides. The disulfide was cleaved using a 100 mM solution of dithiothreotol (DTT) in 0.1 M sodium phosphate, pH 8.3 buffer. The reaction was allowed to proceed for 30 min at room temperature, after which the oligonucleotide was desalted and separated from DTT on a NAP-10 column. The purified solution of the DNA was quantified using the absorbance at 260 nm and the extinction coefficient for each specific sequence.

Decoy oligonucleotide−Au conjugates were prepared as described in the literature with few modifications (*21*). Briefly, 20 μL or 7 μL of a 200 μM solution of the oligonucleotide were added to 500 μL of 10 nm diameter or 15 nm diameter colloidal gold solution, respectively. The final concentrations of decoy oligonucleotide and gold particles were 8 μM and 9.5 nM for 10 nm diameter particles, and 3 μM and 2.3 nM for 15 nm diameter particles, respectively. The samples were placed in a water bath at 37 °C for 4 h, after which the solution was diluted with 0.1 M NaCl/10 mM Na phosphate pH 7 to a total volume of 800 μL. The samples were incubated in the solution for at least 16 h at 37 °C. Following this, samples were centrifuged at 14 000*g* for 30 min and rinsed with 500 μL of 0.1 M NaCl/10 mM Na phosphate. After this procedure was repeated three times, the samples were resuspended in 0.3 M NaCl/10 mM Na phosphate to a final volume of 200 μL.

Mixed monolayers of decoy oligonucleotide/mercaptohexanol (MCH) were prepared by simultaneous addition of decoy oligonucleotide and MCH to gold nanoparticles. This was accomplished by adding 60 μL of 200 μM oligonucleotide solution, and 2.5 μL or 1 μL of 500 μM MCH to 2.5 mL of 10

10.1021/bc060100f CCC: $33.50 © 2006 American Chemical Society
Published on Web 07/12/2006

Table 1. Sequences of Modified Double-Stranded Oligonucleotides Used in This Work

name	sequence
template	HS-$(CH_2)_6$-**TAATACGACTCACTATA**GGGGGATCGAAGTTAGTAGGCCCC **ATTATGCTGAGTGATAT**CCCCCTAGCTTCAATCATCCGGGG
decoy	HS-$(CH_2)_6$-5′-**TAATACGACTCACTATA**GGGG-3′ 3′-**ATTATGCTGAGTGATAT**CCCC-5′
Rd-DNA	5′-**ATTATGCTGAGTGATAT**CCCC-3′-rhodamine
control	HS-$(CH_2)_6$-5′-AACCAGGATTATCCGCTCAC-3′ 3′-TTGGTCCTAATAGGCGAGTG-3′

Table 2. Number of Single-Stranded Oligonucleotides per Nanoparticle

	10 nm diameter particles: mole fraction of ssDNA during preparation			15 nm diameter particles: mole fraction of ssDNA during preparation		
linker[a]	1	0.9	0.75	1	0.9	0.75
C_6	148 ± 2	131 ± 2	122 ± 5	220 ± 6	207 ± 4	194 ± 2
C_6-A_6	133 ± 1	127 ± 4	112 ± 2	214 ± 2	197 ± 5	188 ± 1
C_6-EG_3	124 ± 2	117 ± 6	105 ± 3	204 ± 5	190 ± 4	184 ± 2
C_6-EG_6	111 ± 3	93 ± 5	81 ± 1	180 ± 1	175 ± 3	167 ± 2

[a] C_6 denotes six methylene units in the linker, A_6 denotes six adenine units, and EG_n denotes the number of ethylene glycol units.

Table 3. Number of Double-Stranded Oligonucleotides per Nanoparticle

	10 nm diameter particles: mole fraction of ssDNA during preparation			15 nm diameter particles: mole fraction of ssDNA during preparation		
linker	1	0.9	0.75	1	0.9	0.75
C_6	39 ± 6	47 ± 5	50 ± 7	94 ± 2	100 ± 4	130 ± 3
C_6-A_6	54 ± 3	60 ± 5	75 ± 2	122 ± 1	138 ± 2	151 ± 3
C_6-EG_3	61 ± 5	77 ± 4	98 ± 2	142 ± 5	155 ± 2	179 ± 3
C_6-EG_6	38 ± 7	46 ± 3	62 ± 1	132 ± 3	143 ± 2	159 ± 5

Table 4. Percentage of ssDNA per Particle That Hybridized To Form dsDNA

	10 nm diameter particles: mole fraction of ssDNA during preparation			15 nm diameter particles: mole fraction of ssDNA during preparation		
linker	1	0.9	0.75	1	0.9	0.75
C_6	26%	36%	41%	43%	48%	67%
C_6-A_6	40%	47%	67%	57%	70%	80%
C_6-EG_3	49%	66%	93%	70%	82%	97%
C_6-EG_6	34%	49%	77%	73%	82%	95%

nm diameter or 5 mL of 15 nm diameter gold nanoparticles, respectively, and allowing the reaction to proceed for 8 h. The reaction mixture was subsequently diluted with 0.1 M NaCl/10 mM Na phosphate pH 7 to a total volume of 4 mL and 9.5 mL for 10 and 15 nm gold nanoparticles, respectively. The samples were incubated in the solution for at least 16 h. The resulting nanoparticles were centrifuged three times at 14 000*g* for 30 min and washed with 500 μL of 0.1 M NaCl/10 mM Na phosphate between centrifugations. The samples were resuspended in 0.3 M NaCl/10 mM Na phosphate to a final volume of 1.5 mL.

To quantify surface-bound oligonucleotides, the nanoparticles were oxidatively etched with 0.1 M KCN. The freed oligonucleotides in solution were then quantified using OliGreen ssDNA Quantitation Kit (Molecular Probes) according to manufacturer's directions. The fluorescence was analyzed by a BioTek FL-600 plate reader.

To determine the number of oligonucleotides hybridized per nanoparticle, fluorophore-labeled oligonucleotides, which were complementary to the surface-bound oligonucleotides, were allowed to hybridize to the gold nanoparticles. Oligonucleotide−gold conjugates were prepared as described above and resuspended into a final volume of 300 μL of 0.1 M NaCl/10 mM sodium phosphate at pH 7.0. 20 μL of 100 μM fluorophore-labeled complement was added to the decoy oligonucleotide−gold conjugates. The samples were heated to 35 °C for 1 h and then allowed to anneal while cooling to room-temperature overnight in a water bath. After hybridization, the conjugates were centrifuged three times at 14 000 rpm for 30 min, washing with 200 μL of 0.3 M NaCl/10 mM sodium phosphate pH 7 buffer between centrifugations. Conjugates were resuspended into a final volume of 200 μL. The fluorophore-labeled oligonucleotides were denatured by addition of NaOH (final concentrated ∼50 mM, pH 11). After 2 h, the conjugates were centrifuged again at 14 000 rpm for 30 min. The pH of the supernatant was adjusted to 9 with 1.0 M HCl, and the fluorescence was analyzed by a BioTek FL-600 plate reader.

Transcription Assay. A competitive in vitro runoff transcription assay was performed utilizing a modification of the manufacturer's (Promega) instructions. Five micrograms (194 pmol) of the T7 DNA template was mixed with 80 units of RNAP, 33.3 mM nucleotide triphosphates (NTPs), and increasing concentrations of 10 and 15 nm decoy modified gold nanoparticles in a final reaction volume of 100 μL. The reaction was allowed to proceed for 16 h at 37 °C. The reaction mixture was spun at 14 000*g* for 30 min to pellet the gold nanoparticles, and 10 μL of the supernatants was run on a native 6% polyacrylamide gel in glycine-HCl buffer at 100 V for 90 min. The mRNA product was revealed by staining the gel with 0.45 μg/mL ethidium bromide. mRNA bands were excised, and the RNA was extracted with the Freeze & Squeeze Gel Extraction kit (Bio-Rad) according to instructions. The mRNA content of the excised bands was quantified by measuring the absorbance at 260 nm in a Hewlett-Packard 8453 Chemstation photodiode array spectrophotometer. All transcriptions were done in triplicate.

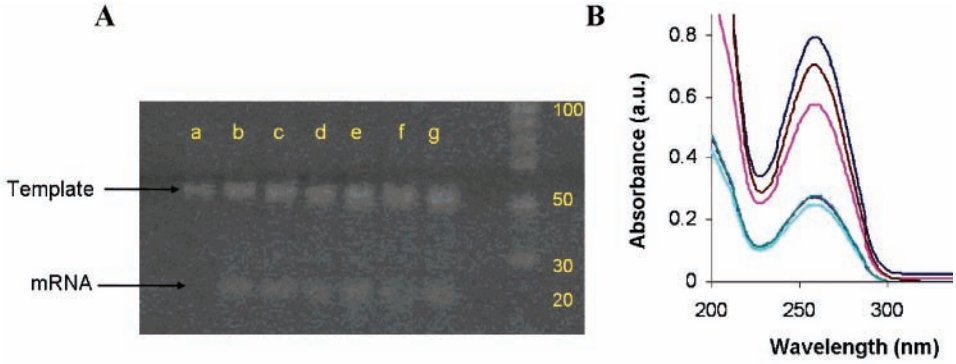

Figure 1. (A) 6% PAGE gel of transcripts after transcription assay. Lanes a) DNA template, b) no gold nanoparticles, c−g) 0.80 nM, 2.3 nM, 7.8 nM, and 11 nM, respectively, of 10 nm gold nanoparticles at 39 decoys/particle. (B) UV−visible spectra of mRNA following gel purification. Spectra correspond to material extracted from lanes b to g going from highest to lowest absorbance peak.

RESULTS

The effects of decoy surface density on RNAP binding were first studied by assembling mixed monolayers of the hexanethiol-terminated ssDNA decoy sequence (HS-$(CH_2)_6$-Decoy) and mercaptohexanol (MCH) on gold nanoparticles and then hybridizing the complement to form the fully double-stranded decoy sequence. Within the mole fractions studied (solution oligonucleotide mole fractions of 0.9, 0.75, and pure DNA), it was found that lowering the surface density of ssDNA increased the yield of duplex formation on the particle surface for both 10 and 15 nm diameter gold nanoparticles (Tables 2−4). A maximum of 50 ± 7 and 130 ± 3 duplexes per particle was found for 10 and 15 nm diameter particles, respectively, using a mole fraction of 0.75. Smaller mole fractions of DNA were investigated; however, particle aggregation was observed during preparation.

A transcription competition assay was used to compare in vitro inhibition of transcription by gold nanoparticles carrying the T7 transcription factor decoy as a function of particle diameter and number of dsDNA transcription factor decoys per particle. In a typical assay, the dsDNA template was incubated in solution with increasing concentrations of 10 or 15 nm diameter decoy-capped gold nanoparticles in the presence of NTPs and RNAP. After the transcription reaction was completed, the reaction mixture was centrifuged to separate the nanoparticles from the template and mRNA transcript (supernatants). The supernatants were eluted on a 6% PAGE gel, and the transcript bands were removed and purified by freeze and squeeze extraction. Figure 1A shows a representative PAGE gel. Lane a in Figure 1A is a sample containing only the dsDNA template, while lane b contains the template that had been transcribed with T7 polymerase in the absence of nanoparticles carrying the decoy. Lanes c−g are samples in which the transcription was performed in the presence of increasing concentrations of 10 nm diameter gold nanoparticles modified with 39 ± 6 decoy oligocnucleotides per particle. The top band in each lane corresponds to the dsDNA template, and the second band contains mRNA transcript. To quantify the amount of mRNA produced in each transcription, the second band from each lane was excised, and the mRNA was purified and analyzed by UV−visible spectroscopy.

The spectra presented in Figure 1B show that the T7 promoter-modified nanoparticles inhibited transcription of the template DNA. At the highest nanoparticle concentration, transcription was inhibited by approximately 80%. To determine if the inhibition of mRNA observed during the transcription assay was due to the oligonucleotide-capped gold nanoparticle decoy, controls were performed in which unmodified nanoparticles and nanoparticles modified with duplex DNA lacking the T7 promoter region were added to the transcription assay.

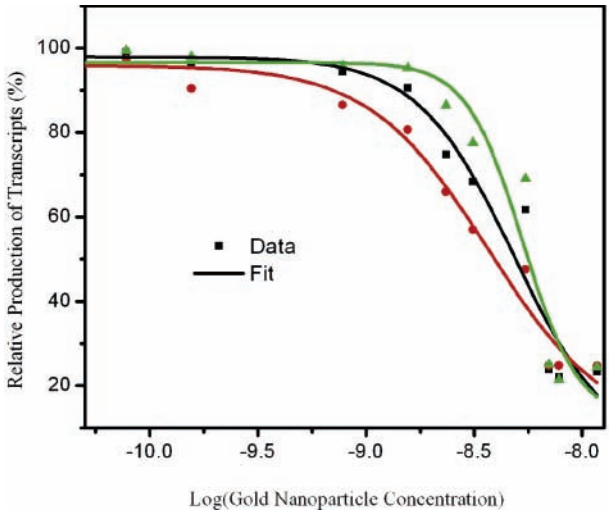

Figure 2. Dose−response curves used in the determination of IC_{50} values for decoy- modified 10 nm gold nanoparticles. The curves are (black) 1.2×10^{13} decoy/cm^2, (green) 1.5×10^{13} decoy/cm^2, (red) 1.6×10^{13} dsDNA decoy was bound to particles via a hexanethiol linker.

Transcription of the template was not inhibited in either experiment. This suggests that the oligonucleotide-capped gold nanoparticle decoy does play a specific role in the down regulation of RNA transcription by RNAP. It was then of interest to quantitatively assess transcription inhibition by nanoparticles of different sizes and decoy coverages.

To make quantitative comparisons between different nanoparticle decoys, the IC_{50} was determined. The IC_{50}, or 50% inhibition concentration values, were determined by plotting relative production of mRNA vs log nanoparticle concentration (dose−response curves, Figure 2). The dose−response curves showed, for a given particle size, only a modest change in IC_{50} as a function of decoy density (Table 5). The lowest density particles displayed an approximately 50% greater inhibition than the particles that were fully covered with the T7 promoter sequence. A much more important parameter appears to be particle size. Increasing particle size from 10 to 15 nm in diameter decreased IC_{50} by a factor of roughly 5 (Table 5). This is not solely a surface area effect since the surface area of 15 nm diameter particles is only a factor of 2 larger than that of 10 nm particles.

Another potential method for minimizing the effects of sterics on T7 polymerase binding to decoy-modified nanoparticles is to add a longer spacer between the promoter sequence and the particle surface. Three spacers were chosen to test this hypothesis, HS-$(CH_2)_6$-Adenine$_6$-Decoy (C_6-A_6), HS-$(CH_2)_6$-[OCH_2-CH_2O]$_3$-Decoy (C_6-EG_3), and HS-$(CH_2)_6$-[OCH_2CH_2O]$_6$-Decoy

Table 5. Coverages and IC_{50} Values of Oligonucleotide-Capped Gold Nanoparticles with Different Linkers

mole fraction of ssDNA during preparation	dsDecoys/cm^2 (10 nm dia.) $\times 10^{13}$	IC_{50}, 10 nm dia. (nM)	dsDecoys/cm^2 (15 nm dia.) $\times 10^{13}$	IC_{50}, 15 nm dia. (nM)
		C_6		
1	1.2 ± 0.1	5.3 ± 0.9	1.3 ± 0.1	1.4 ± 0.6
0.9	1.5 ± 0.2	4.8 ± 0.7	1.5 ± 0.1	0.93 ± 0.4
0.75	1.6 ± 0.2	3.2 ± 0.4	1.8 ± 0.1	0.85 ± 0.4
		C_6-A_6		
1	1.7 ± 0.1	5.1 ± 0.2	1.7 ± 0.1	0.94 ± 0.2
0.9	1.9 ± 0.2	4.6 ± 0.8	2.0 ± 0.1	0.89 ± 0.1
0.75	2.4 ± 0.1	3.8 ± 0.6	2.1 ± 0.1	0.85 ± 0.5
		C_6-EG_3		
1	1.9 ± 0.1	4.8 ± 0.5	2.0 ± 0.1	0.90 ± 0.3
0.9	2.4 ± 0.1	4.1 ± 0.8	2.2 ± 0.1	0.85 ± 0.2
0.75	3.1 ± 0.2	3.5 ± 0.6	2.5 ± 0.1	0.79 ± 0.4
		C_6 -EG_6		
1	1.2 ± 0.1	4.3 ± 0.8	1.9 ± 0.1	0.85 ± 0.5
0.9	1.5 ± 0.1	3.7 ± 0.9	2.0 ± 0.1	0.81 ± 0.3
0.75	2.0 ± 0.1	3.3 ± 0.4	2.2 ± 0.1	0.72 ± 0.2

(C_6-EG_6). Again, it was found that lowering the surface density of ssDNA increased the yield of duplex formation on the particle surface (Tables 3 and 4). A maximum of 77 ± 4 and 155 ± 2 duplexes per particle were found for 10 and 15 nm diameter particles, respectively, for the C_6-EG_3 linker at a mole fraction of 0.75. Surprisingly, the longer chain, C_6-EG_6, yielded less total hybridized dsDNA per particle than the shorter linkers, and a lower or comparable percentage of hybridized DNA than all but the C_6 linker. A comparison of IC_{50} values between linkers at constant particle size and mole fraction revealed a slight decrease in IC_{50} with increasing linker length in all but two cases. It is noteworthy that despite the relatively low coverage of dsDNA for particles modified with C_6-EG_6 (Table 3), IC_{50} values were lowest for this linker (Table 5).

DISCUSSION

The present study addresses the effects of steric crowding on the ability of proteins to recognize DNA-modified gold nanoparticles. One advantage of using gold nanoparticles in biological assays is that cooperative effects may enhance the binding of target molecules with biomolecules attached to the particles surface. This has been shown to improve internalization efficiencies of nanoparticles into cells (*19*−*22*) and greatly improve DNA hybridization assays (*23*, *24*). Indeed, dsDNA has been reported to be more stable when hybridized on the surface of a gold nanoparticle, yielding binding constants that are enhanced by two orders-of-magnitude compared to the identical sequences hybridized in solution (*25*). However, when a larger biomolecule such as T7 polymerase interacts with a dsDNA promoter sequence attached to a gold nanoparticle, one might expect that steric hindrance could negate any advantage afforded by the high density of DNA decoy strands on the nanoparticle. Thus, our main objective was to assess the role of steric interactions in a nanoparticle-based transcription factor decoy approach.

The role of oligonucleotides conjugated to nanoparticle surfaces in promoting nanoparticle interactions with proteins and complementary oligonucleotides has been probed in the present experiments using both differing surface concentrations of oligonucleotides and tether lengths. The congestion at the surface of a colloidal gold particle could affect the binding of proteins and the ability of DNA or RNA to hybridize. Such congestion will have functional consequences for cell targeting experiments. For this reason it is of interest to understand whether nanoparticles prepared with a high concentration of surface-bound species are able to interact with biological macromolecules.

The yield of DNA hybridization for three different surface concentrations of ssDNA was considered first. The surface concentration of ssDNA was diluted by mercaptohexanol (MCH), a passivating molecule that competes effectively with thiol-labeled ssDNA molecules for the gold surface. The importance of dilution in permitting sufficient freedom of the surface-attached ssDNA chains for hybridization was clearly demonstrated on both 10 and 15 nm particles. The implication from Tables 2−4 is that the hybridization increases as the surface density of oligonucleotides decreases. Similar observations have been made on gold nanoparticles, where hybridization efficiencies approaching 98% were also reported (*21*), and on planar gold surfaces where the maximum hybridization efficiency was observed for approximately 40% coverage by ssDNA (*26*). We would expect that the maximum hybridization yield would occur when the ssDNA chains are behaving as free nonentangled Gaussian chains. For Gaussian chain behavior the average diameter of the ssDNA would be $d = L\sqrt{N}$, where L is the distance between each successive monomer and N is the number of monomers. For ssDNA there are six single bonds separating each base (C5′-O−P−O−C3′−C4′−C5′). For the 21-mer sequence with a C_6 spacer (six carbon spacer) used in the transcription factor decoy experiments there are $N = 6 \times 22 = 132$ bonds (including the spacer) with an average bond length of $L = 1.55$ Å, we can estimate the Gaussian chain length to be $d = 1.8$ nm. We assume that the projection of the Gaussian chain length d on the surface gives the radius of gyration $r = d \cos \theta$. This simple model neglects the radius of curvature of the gold nanoparticle surface. Given this value, the area swept out by a tethered rotating ssDNA on the surface is approximately $\pi d^2 \cos \theta^2 = 4.2$ nm^2, if the projection angle θ on the surface is 50° as shown in Figure 3. The surface area of 10 and 15 nm nanoparticles are 314 nm^2 and 707 nm^2, respectively. Dividing the total surface area by the surface projection per free rotating ssDNA monomer gives an estimated maximum surface coverage of 74 and 168 ssDNA for 10 and 15 nm gold particles, respectively. If we assume that the requirement for efficient hybridization is that the ssDNA chains are free to rotate so that they can adopt a full range of conformations, and then maximum dsDNA coverage should correspond approximately to these values. These numbers compare reasonably well to the maximum values of 75 and 150 given in Table 2. If the ssDNA concentration is higher, then there is entanglement and restriction of motion leading to reduced hybridization yield.

The effect of spacer length can be to increase the freedom of the chains; however, this effect competes with an increase in the radius of gyration on the surface. The C_6-EG_3 and C_6-EG_6 chains have an increase of 9 and 18 bonds, respectively, compared to C_6. These linkers increase the Gaussian chain length by approximately 0.5 nm per EG_3 unit (i.e. 0.5 nm for EG_3 and 1.0 nm for EG_6). The longer chain and higher radius of gyration

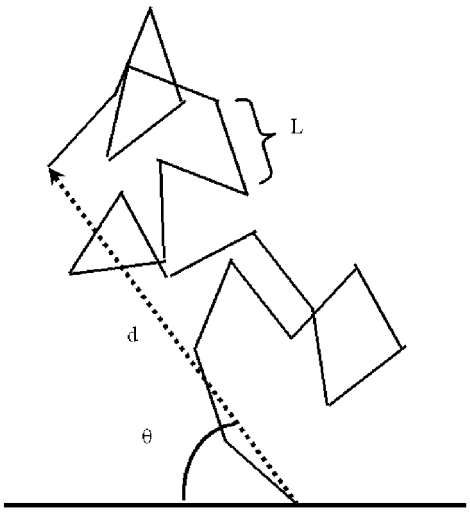

Figure 3. Illustration of the Gaussian chain length model for surface-attached oligonucleotides. The bond length is *L*. The angle of vector *d* with respect to the surface is θ.

tends to decrease the surface coverage at which maximum free rotation occurs (if the angle remains the same). For example, this model predicts that the coverage will decrease from 75 (C_6) to 67 (C_6-EG_6) for 10 nm particles and from 168 (C_6) to 151 (C_6-EG_6) for 15 nm particles due to the longer Gaussian chain length. To quantitatively explain the coverages given in Table 2 using the tethered Gaussian chain in Figure 3. Specifically, if the angle θ increases to 55° for the C_6-EG_3 linker, the predicted optimal surface coverage is 90 and 200 ssDNAs on 10 and 15 nm gold nanoparticles, respectively, which is in reasonable agreement with the data in Tables 2-4.

The binding of RNAP to the transcription factor decoy on the surface was probed by determining the IC_{50} value for inhibition of transcription in solution. The ability of RNAP to bind to dsDNA on nanoparticles with high surface densities is clearly hindered when compared to the binding to the same sequence in solution. The IC_{50} value for transcription inhibition using free decoy was found to be 1.1 pM. However, given its molar mass of 98 kDa, the fact that RNAP binds to decoy modified nanoparticles to the extent observed in this study indicates that there is a some free volume in these bioconjugates. Despite the lower surface coverage measured for decoys bound to nanoparticles through the C_6-EG_6 linker, this linker provided the optimum chain length for transcription inhibition. The results presented here thus serve to illustrate the importance of sterics in the design of nanoparticle bioconjugates for protein recognition. Short linkers or densely packed ssDNA monolayers can hinder both dsDNA formation and protein binding. The coverage of dsDNA, on the other hand, is actually highest for the C_6-EG_3 linker and decreases slightly for the longer the C_6-EG_6 linker. This effect may be due to greater entanglement of the complementary ssDNA strand if the nanoparticle-surface-bound ssDNA strand has many degrees of freedom.

One result from the current work appears to be that there is a confinement effect that hinders surface binding on small nanoparticles. We can use the transcription factor decoy assay to compare the functional binding of RNAP to oligonucleotides in solution and on nanoparticle surfaces. The binding of RNAP to oligonucleotides free in solution is ~2.5 orders-of-magnitude more favorable than binding to the same oligonucleotide on a 15 nm nanoparticle. The binding of RNAP to a tethered oligonucleotide (as represented by the IC_{50} value) is a factor of 5 stronger on a 15 nm nanoparticle than on a 10 nm nanoparticle that has the same coverage in terms of oligonucleotides/cm^2. This result is somewhat surprising since the radius of curvature is larger for the small particle, and this may be interpreted as providing greater access to the surface-attached promoter sequence for RNAP. This effect is counterbalanced by the avidity of the larger nanoparticle. On a per nanoparticle basis, a 15 nm particle has roughly twice the number of binding sites per particle.

CONCLUSIONS

The availability of surface-attached ssDNA and dsDNA on the surface of nanoparticles for binding has been probed both in terms of surface density and chain length of the linker between the oligonucleotide and the gold surface. The key results are that the optimum surface coverage for ssDNA requires a mole fraction of 0.25 for a relatively short surface passivation molecule such as MCH, and that the optimum chain length for both DNA hybridization and RNAP binding includes an EG_3 spacer adding nine bonds to the linker and greater conformational freedom of ether (CH_2OCH_2) bonding compared to aliphatic ($CH_2CH_2CH_2$) bonding. However, the enhancement of DNA hybridization promoted by the EG_3 spacer is a modest effect overall of ~10% on 15 nm particles and at most 60% on 10 nm particles. The inhibition of transcription has been demonstrated and while the binding of T7 to a surface-attached promoter sequence is clearly reduced significantly compared to a free oligonucleotide, the ability of nanoparticles to interact with DNA-binding proteins has been quantitatively demonstrated.

ACKNOWLEDGMENT

This work was supported by NIH grant CA098194.

LITERATURE CITED

(1) Jia, F. Y., Shimomura, T., Niyibizi, C., and Woo, S. L. Y. (2005) Downregulation of human type III collagen gene expression by antisense oligodeoxynucleotide. *Tissue Eng. 11*, 1429−1435.

(2) Yamanaka, K., Rocchi, P., Miyake, H., Fazli, L., Vessella, B., Zangemeister-Wittke, U., and Gleave, M. E. (2005) A novel antisense oligonucleotide inhibiting several antiapoptotic Bcl-2 family members induces apoptosis and enhances chemosensitivity in androgen-independent human prostate cancer PC3 cells. *Mol. Cancer Ther. 4*, 1689−1698.

(3) Tai, C. K., Wang, W. J., Logg, C. R., Solly, S., Frisen, C., Eiden, M. V., Klatzmann, D., Chen, T. C., and Kasahara, N. (2004) Replicative viral vectors for cancer: Quo vadis? *Cancer Gene Ther. 11*, 853−853.

(4) Correnti, J. M. and Pearce, E. J. (2004) Transgene expression in *Schistosoma mansoni*: introduction of RNA into schistosomula by electroporation. *Mol. Biochem. Parasitol. 137*, 75−79.

(5) Krull, C. (2004) Manipulating gene expression in chick. *FASEB J. 18*, A762-A763.

(6) Higashi, K., Inagaki, Y., Fujimori, K., Nakao, A., Kaneko, H., and Nakatsuka, I. (2003) Interferon-gamma interferes with transforming growth factor-beta signaling through direct interaction of YB-1 with Smad3. *J. Biol. Chem. 278*, 43470−43479.

(7) Segal, G., Song, R. T., and Messing, J. (2003) A new opaque variant of maize by a single dominant RNA-interference-inducing transgene. *Genetics 165*, 387−397.

(8) Stier, S., Cheng, T., Forkert, R., Lutz, C., Dombrowski, D. M., Zhang, J. L., and Scadden, D. T. (2003) Ex vivo targeting of p21-(Cip1/Waf1) permits relative expansion of human hematopoietic stem cells. *Blood 102*, 1260−1266.

(9) Beeri, R., Guerrero, J. L., Supple, G., Sullivan, S., Levine, R. A., and Hajjar, R. J. (2002) New efficient catheter-based system for myocardial gene delivery. *Circulation 106*, 1756−1759.

(10) Lessard, P. A., Kulaveerasingam, H., York, G. M., Strong, A., and Sinskey, A. J. (2002) Manipulating gene expression for the metabolic engineering of plants. *Metab. Eng. 4*, 67−79.

(11) Sierakowska, H., Sambade, M. J., Agrawal, S., and Kole, R. (1996) Repair of thalassemic human beta-globin mRNA in mammalian cells

by antisense oligonucleotides. *Proc. Natl. Acad. Sci. U.S.A. 93*, 12840−12844.
(12) Sazani, P., Gemignai, F., Kang, S. H., Maier, M., Manoharan, M., Persmark, M., Bortner, D., and Kole, R. (2002) Systemically delivered antisense oligomers upregulate gene expression in mouse tissues. *Nat. Biotechnol. 20*, 1228−1233.
(13) Tomita, N. and Morishita, R. (2004) Antisense oligonucleotides as a powerful molecular strategy for gene therapy in cardiovascular diseases. *Curr. Pharm. Des. 10*, 797−803.
(14) Cho-Chung, Y. S. (2000) Antisense and therapeutic oligonucleotides: toward a gene-targeting cancer clinic. *Expert Opin. Ther. Pat. 10*, 1711−1724.
(15) Xi, S. C., Gooding, W. E., and Grandis, J. R. (2005) In vivo antitumor efficacy of STAT3 blockade using a transcription factor decoy approach: implications for cancer therapy. *Oncogene 24*, 970−979.
(16) Martin, J. I., Broaddus, W. C., and Fillmore, H. I. (2004) A transcription factor decoy oligonucleotide that mimics the MMP-1 functional single nuclear polymorphism: A novel therapeutic for the inhibition of MMP-1 expression. *Neuro-Oncology 6*, 333−333.
(17) Ahn, J. D., Kim, C. H., Magae, J., Kim, Y. H., Kim, H. J., Park, K. K., Hong, S. H., Park, K. G., Lee, I. K., and Chang, Y. C. (2003) E2F decoy oligodeoxynucleotides effectively inhibit growth of human tumor cells. *Biochem. Biophys. Res. Commun. 310*, 1048−1053.
(18) Mann, M. J. and Dzau, V. J. (2000) Therapeutic applications of transcription factor decoy oligonucleotides. *J. Clin. Invest. 106*, 1071−1075.
(19) Tkachenko, A. G., Xie, H., Coleman, D., Glomm, W., Ryan, J., Anderson, M. F., Franzen, S., and Feldheim, D. L. (2003) Multifunctional gold nanoparticle-peptide complexes for nuclear targeting. *J. Am. Chem. Soc. 125*, 4700−4701.
(20) Tkachenko, A. G., Xie, H., Liu, Y. L., Coleman, D., Ryan, J., Glomm, W. R., Shipton, M. K., Franzen, S., and Feldheim, D. L. (2004) Cellular trajectories of peptide-modified gold particle complexes: Comparison of nuclear localization signals and peptide transduction domains. *Bioconjugate Chem. 15*, 482−490.
(21) Pena, S. R. N., Raina, S., Goodrich, G. P., Fedoroff, N. V., and Keating, C. D. (2002) Hybridization and enzymatic extension of Au nanoparticle-bound oligonucleotides. *J. Am. Chem. Soc. 124*, 7314−7323.
(22) Xie, H., Tkachenko, A. G., Glomm, W. R., Ryan, J. A., Brennaman, M. K., Papanikolas, J. M., Franzen, S., and Feldheim, D. L. (2003) Critical flocculation concentrations, binding isotherms, and ligand exchange properties of peptide-modified gold nanoparticles studied by UV−visible, fluorescence, and time-correlated single photon counting spectroscopies. *Anal. Chem. 75*, 5797−5805.
(23) Storhoff, J. J., Elghanian, R., Mucic, R. C., Mirkin, C. A., and Letsinger, R. L. (1998) One-pot colorimetric differentiation of polynucleotides with single base imperfections using gold nanoparticle probes. *J. Am. Chem. Soc. 120*, 1959−1964.
(24) Cao, Y. C., Jin, R. C., Thaxton, S., and Mirkin, C. A. (2005) A two-color-change, nanoparticle-based method for DNA detection. *Talanta 67*, 449−455.
(25) Lytton-Jean, A. K. R., and Mirkin, C. A. (2005) A thermodynamic investigation into the binding properties of DNA functionalized gold nanoparticle probes and molecular fluorophore probes. *J. Am. Chem. Soc. 127*, 12754−12755.
(26) Steel, A. B., Herne, T. M., and Tarlov M. J. (1998) Electrochemical quantitation of DNA immobilized on gold. *Anal. Chem. 70*, 4670−4677.

BC060100F

Oligonucleotide Microarrays: Immobilization of Phosphorylated Oligonucleotides on Epoxylated Surface

S. Mahajan, P. Kumar, and K. C. Gupta*

Nucleic Acids Research Laboratory, Institute of Genomics and Integrative Biology, Mall Road, Delhi University Campus, Delhi-110 007, India. Received April 24, 2006; Revised Manuscript Received July 19, 2006

A facile and efficient method for direct immobilization of phosphorylated oligonucleotides on an epoxy-activated glass surface is described. The new immobilization strategy has been analyzed for its performance in DNA microarray under both microwave and thermal conditions. It reflects high immobilization efficiency (~23%), and signal-to-noise ratio (~98) and resulted in high hybridization efficiency (~36%) in comparison to those obtained with standard methods, viz., NTMTA (~9.76%) and epoxide−amine (~9.82%). The probes immobilized through the new strategy were found to be heat-stable, since the performance of microarray decreased by only ~7% after subjecting it to 20 PCR-like heat cycles, suggesting that the chemistry could be used in integrated PCR/microarray devices. The immobilization of probes following the proposed chemistry resulted in spots of superior quality in terms of spot morphology, spot homogeneity, and signal reproducibility. The constructed microarrays have been successfully used for the discrimination of nucleotide mismatches. In conclusion, these features make the new immobilization strategy ideal for facile, efficient, and cost-effective manufacturing of DNA microarrays.

INTRODUCTION

DNA microarrays have rapidly evolved to become one of the essential tools to study expression or mutation of thousands of genes simultaneously (*1*−*4*). DNA microarrays are mostly based on hybridization of targets with double-stranded PCR amplicons or single-stranded oligonucleotides (probes) immobilized on a polymer surface (biochip), followed by detection via an imaging or a scanning process. These biochips are replacing labor-intensive and reagent-consuming conventional gel-based methods. Basically, oligonucleotide microarrays can be fabricated in two different ways, viz., (i) by *in situ* synthesis following conventional and photolithographic techniques (*5*−*8*) and (ii) by deposition method, i.e., immobilization of presynthesized oligonucleotides on selected polymer surfaces (*9*−*16*). The deposition method, where prefabricated oligonucleotides are immobilized either covalently or noncovalently onto various solid surfaces (organic or inorganic), offers flexibility insofar as a variety of ligands can be fixed after purification (*17*−*24*). In this approach, reactive groups are generated on the chip surface, which can form covalent bonds with the reactive functionalities available in presynthesized oligonucleotide sequence in the presence of an activator or condensing agent (*25*−*28*). The methodology allows the attachment of probes in a regioselective manner with a good surface coverage as well as retention of the full activity of probes.

In the present report, we describe a novel approach to synthesize oligonucleotide arrays that employs immobilization of 3′-phosphorylated oligonucleotides onto epoxy-functionalized glass microslides (Scheme 1) under microwave irradiation, where the reaction completes in just 10 min with remarkably high immobilization efficiency (~23% at 0.2 μM probe concentration). The uniqueness of the proposed strategy lies in opening of the epoxy ring anchored on the polymer support by the phosphate group of the 3′-phosphate oligomers, which can be synthesized simply by employing a commercially available aminoalkylated polymer support (universal support) instead of conventional nucleoside-loaded polymer supports and hence eliminates the use of engineered polymer supports. Even the larger fragments of DNA as well as PCR amplicons can be immobilized after incorporating phosphate groups by enzymatic phosphorylation.

* Tel. +91 11 27662491; Fax +91 11 27667471; Email: kcgupta@igib.res.in.

EXPERIMENTAL PROCEDURES

Glass Silanization. The glass slides (75 × 22 mm^2) were first cleaned according to published protocol (*29*). The silanization was accomplished using GOPTS (2%, v/v) in toluene (75 mL) for 4−5 h at 50 °C (*30*). After washing and drying, the slides were stored under an inert atmosphere.

Oligonucleotide Synthesis and Purification. Oligonucleotides were synthesized at 0.2 μmol scale on a Pharmacia Gene Assembler Plus (see Supporting Information) using the standard phosphoramidite approach following the manufacturer's protocol (Gene Assembler Plus Manual, Uppsala, Sweden, 1988) (*31*).

Determination of Optimal pH Required for Immobilization of Phosphorylated Oligomers on Epoxy-Activated Glass Surface. In order to study the effect of pH on immobilization of phosphorylated oligonucleotides on epoxylated glass slide, the attachment of the probe was carried out at different pHs (6−12). Briefly, a labeled oligomer, viz., TET-d (TCT TGT ACG TCC GTC AAC GT)-OPO_3^{2-} (3 μM) dissolved in reaction buffer (*N*-methylimidazole (0.1 M) containing 10% dimethylsulfoxide (DMSO) (v/v)) of different pHs 6, 8, 10, and 12, was spotted by a pipetteman (0.5 μL) on a functionalized glass microslide and incubated in a humid chamber for 12 h, followed by capping of the residual epoxy functionalities with a capping buffer (0.1 M Tris containing 50 mM ethanolamine, pH 9.0) for 15 min at 50 °C. The slide was then subjected to washings with 1× SSC buffer (4 × 50 mL), pH 7.0, for 20 min and Milli Q water (2 × 50 mL), followed by drying under vacuum. Finally, the slide was scanned under a laser scanner.

Immobilization Kinetics. The result obtained from the model experiment was used to study the immobilization kinetics of phosphorylated oligonucleotide onto the epoxy-functionalized glass surface under microwaves (see Supporting Information).

10.1021/bc0601065 CCC: $33.50 © 2006 American Chemical Society
Published on Web 08/30/2006

Scheme 1. Strategy for the Immobilization of Phosphorylated Oligonucleotides on Epoxy-Functionalized Glass Surface.

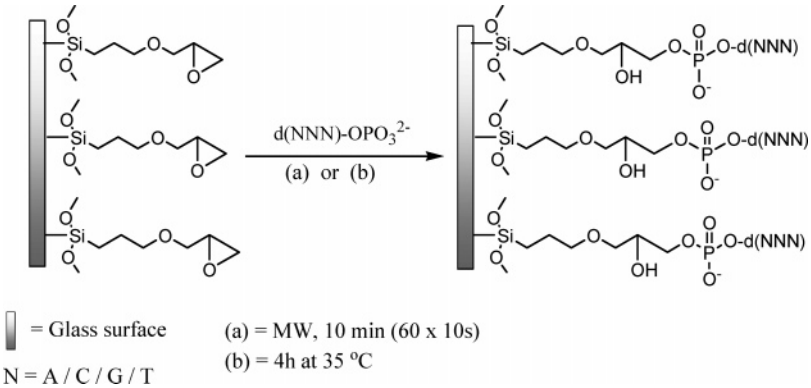

In order to determine the optimal time required for immobilization of 3′-phosphorylated oligonucleotide, TET-d (TCT TGT ACG TCC GTC AAC GT)-OPO_3^{2-} was diluted in reaction buffer (pH 10) to concentrations of 5, 10, and 20 μM and spotted onto epoxy-functionalized glass microslides in duplicates and subjected to microwave (MW) irradiation (with no exposure longer than 10 s in a humid chamber) in a MW oven operating at 800 W. Slides were withdrawn at regular time intervals (2, 4, 6, 8, 10, and 12 min) and subjected to capping and washings as described above. After drying under vacuum, the spots were visualized under a laser scanner and quantified.

Spotting and DNA Immobilization. In order to look into the effect of oligonucleotide concentration to achieve highest density of oligonucleotide attachment on the surface, the kinetics of the probe immobilization at various concentrations under microwave irradiation was investigated. The reactions were carried out by spotting a labeled probe, TET-d (TCT TGT ACG TCC GTC AAC GT)-OPO_3^{2-}, in a dilution series ranging from 0.2 to 40 μM concentrations for 10 min (60 $\times$ 10 s) under microwaves (as mentioned above). After treatment with capping buffer and usual washings, the slide was visualized under a laser scanner and quantified.

PCR Heat Cycling. To evaluate the thermal stability of the linkage formed by probe immobilization, a microarray was prepared by immobilizing labeled 3′-phosphorylated oligonucleotide TET-d (TCT TGT ACG TCC GTC AAC GT)-OPO_3^{2-} (5 μM) under microwave irradiation for 10 min. The constructed microarray was subjected to PCR-like conditions for 0, 5, 10, 15, and 20 cycles in 2$\times$ SSC buffer (pH 7). PCR parameters were as follows: 94 °C for 30 s (denaturing step), 54 °C for 30 s (annealing step), and 72 °C for 30 s (extension step). After thermocycling, the slide was washed, dried, and visualized under a laser scanner.

Similarly, the pH stability of the projected chemistry was evaluated by subjecting the constructed microarray to washings (4 $\times$ 15 min) with buffers of different pHs, ranging from 7 to 9.

Specificity of Immobilization Chemistry. In order to investigate the specificity of the system, four oligonucleotides, viz., d (ACG GTA ACA GGA AAA AGA AG)-OPO_3^{2-}, d (ACG GTA ACA GGA AAA AGC AG)-OPO_3^{2-}, d (ACG GTA ACA CGA AAA AGC AG)-OPO_3^{2-}, and d (TTT TTT TTT TTT TTT TTT TT)-OPO_3^{2-} (5 μM) having zero, one, and two mismatches and noncomplementary probe, were spotted on an epoxylated glass slide (under microwave irradiation) followed by capping and usual washings. Subsequently, the spots on the microslide were hybridized with a complementary labeled TET-d (CTT CTT TTT CCT GTT ACC GT) and kept at 45 °C for 1 h and then at room temperature for 12 h. After washings with hybridization buffer, 2$\times$ SSC buffer (pH 7) (5 $\times$ 5 min), the microslide was subjected to laser scanning followed by quantification.

For each experimental condition tested on the microarrays, the experiment was repeated 2−3 times. The immobilization and hybridization data presented are the average of these repetitions, and the error bars represent the percentage error ($\pm$2−4%) observed on this average. In order to determine the immobilization and hybridization efficiencies, a calibration curve was constructed using a labeled oligomer (see Supporting Information).

RESULTS AND DISCUSSION

Oligonucleotide probes bearing a 3′-phosphate group bind covalently to the epoxy-functionalized glass slide under the influence of microwaves (MW), a nonconventional energy source, which has significantly reduced the chemical reaction time from hours to minutes with increased yields (immobilization efficiency) and improved reproducibility (*32*−*34*). Though a large number of articles describe rate enhancement of reactions by microwaves, in contrast to thermal/photochemical reactions, the use of microwaves to construct oligonucleotide arrays has largely remained unexplored. We have constructed oligonucleotide arrays following the proposed chemistry and evaluated them for parameters like thermal stability, specificity, sensitivity for detection of targets, and reproducibility of attachment chemistry. The proposed strategy has been compared with the standard methods, viz., NTMTA and epoxide−amine, to highlight its advantages over them.

With the aim to determine the optimal time required to complete the reaction between 3′-phosphorylated oligomers and the epoxy-functionalized glass surface, a model experiment was designed for which a compound, 2-(4,4-dimethoxytrityloxy)-ethyl phosphate {$DMTrO(CH_2)_2OPO_3^{2-}$}, was synthesized and reacted with the epoxy-functionalized control pore glass (CPG 500 Å) under microwaves and thermal condition (see Supporting Information). The results with the model compound indicate that the reaction between phosphate and epoxy group essentially completes in 10 min under microwaves, while it takes ~4 h at 35 °C under thermal conditions.

The optimal pH required for effective immobilization of phosphorylated oligonucleotides on the epoxy-activated glass surface was determined by spotting a labeled probe (at 3.0 μM) at different pHs. The results show that maximum immobilization was achieved at pH 10.0 (Figures 1A,B); therefore, immobilization of modified probes was carried out at pH 10.0 for the rest of the experiments. Similarly, optimal time required for the immobilization process under microwaves was evaluated by constructing a microarray as mentioned in the Experimental Procedures. The results confirmed that attachment density reaches a maximum between 8 and 10 min under microwaves (Figure 2A). The immobilization of probes reaches saturation level above 20 μM as shown by the fluorescence intensity of

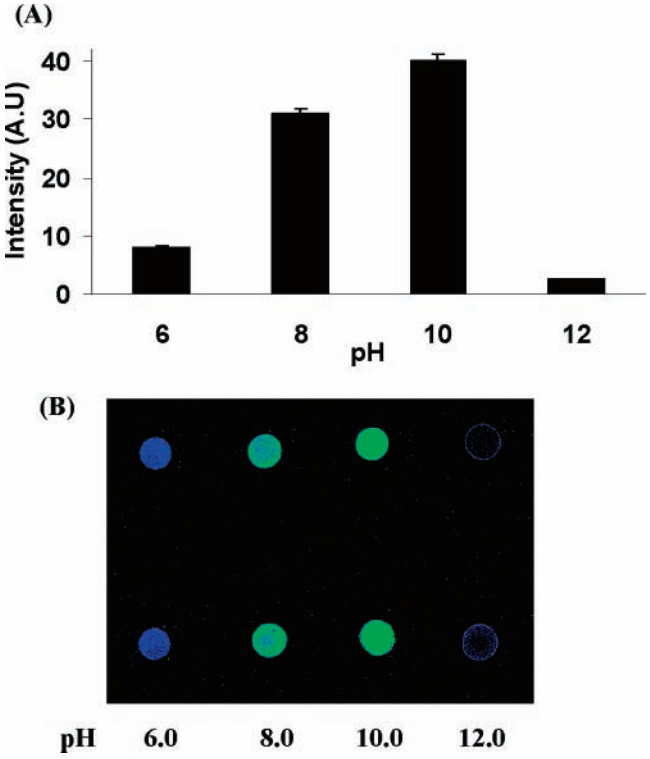

Figure 1. (A) A graph representing influence of pH on immobilization reaction of phosphorylated probe with epoxy-activated surface. (B) Fluorescence map obtained by immobilization of 5′-labeled, 3′-phosphorylated probe, TET-d (TCT TGT ACG TCC GTC AAC GT)-OPO_3^{2-}, at different pHs (6−12). Slide was scanned at 75% of laser power and 70% of photomultiplier gain.

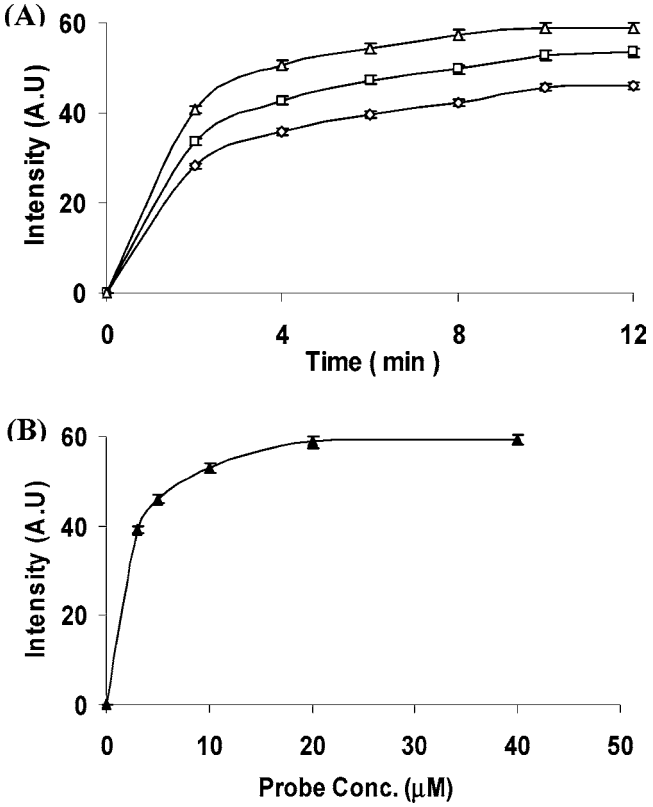

Figure 2. Graphs depicting (A) time kinetics to determine the optimal time required for immobilization of phosphorylated oligonucleotide on epoxy−glass slide under microwaves; ○, 5 μM; □, 10 μM; △, 20 μM; (B) Immobilization kinetics using different oligonucleotide concentrations under microwaves (10 min).

the spots (Figure 2B). The pictorial image showing the detection limit of 0.2 μM achieved with a 20-mer oligonucleotide is shown in Figure 3.

The extent of involvement of internucleotidic phosphodiester groups and amines of heterocyclic bases to the immobilization reaction was determined by taking 5′-labeled nonphosphorylated oligomer and 4,5,6,7-tetrachlorofluorescein (TET dye) as controls of the experiment. The 5′-labeled-3′-phosphorylated, 5′-labeled nonphosphorylated oligonucleotides, and 4,5,6,7-tetrachlorofluorescein were spotted at 0.5 μM concentration on the same slide and exposed to microwaves for 10 min followed by usual washings (Figure 4A). Fluorescence intensity of spots of the nonphosphorylated oligonucleotide was found to be ∼12% of the probe with the 3′-phosphate modification, whereas no signal was observed at the place where only TET dye was spotted, implying selective binding of the terminal phosphate to the epoxy-activated surface (Figure 4B). The low but noticeable amount of immobilization of unmodified oligonucleotide could have arisen from weaker binding of phosphodiester groups of the probe to the surface. This was significantly reduced by treating the slides with capping buffer.

The thermal stability of the constructed microarray was evaluated by subjecting it to 0, 5, 10, 15, and 20 cycles of PCR-like conditions. The fluorescent signal of the heat-treated microarrays was found to decrease by only ∼3% after 10 cycles and ∼7% after 20 cycles. The fluorescent signals of heat-treated and untreated microarrays (Figure 5A) show that the oligonucleotides immobilized on an epoxy−glass slide following the proposed strategy are sufficiently stable to be used in biological research.

In an analogous way, the vulnerability of the constructed microarray toward different pHs was evaluated. The quantification results revealed that fluorescence intensity decreases by ∼4.5% at pH 8, whereas it became slightly unstable with ∼15.3% of reduction at pH 9.0 as compared to the intensity obtained at pH 7 (Figure 5B).

The dynamics of microarray hybridization was demonstrated by performing the kinetics of the hybridization reaction for different target oligonucleotide concentrations. The results depict that, in the initial stage of increasing target concentration, the hybridization signal increases and then reaches a steady state between 40 and 80 μM (Figure 6A). The kinetics of hybridization efficiency (defined as the percent of covalently attached oligonucleotides that participated in duplex formation) for different probe concentration were realized by plotting the hybridization efficiency for different amounts of immobilized probes. The hybridization efficiency reaches a maximum (∼36%) for an optimal immobilized probe concentration of 5 μM; above this concentration, the efficiency did not increase even if the concentration of immobilized probes was increased (Figure 6B). This could be explained on the basis that overloading the surface with probes might cause a crowding effect that could lower the accessibility of the surface-bound probes. In addition, the efficiency of hybridization depends on many factors like the number of accessible epoxy groups to the 3′-phosphorylated oligonucleotides on the surface, the attachment efficiency of oligonucleotides to the epoxy-functionalized surface, and the efficiency in the reaction of hybrid formation between immobilized and target oligonucleotide concentration.

However, by using a more sensitive label in the target oligonucleotide, viz., Cy 3, immobilized probes can be recognized even at low concentration (1 nM) of the target (see Supporting Information).

In order to demonstrate the specificity of the system, four oligonucleotides were immobilized onto an epoxy-functionalized glass microslide, each at 5 μM concentration. After treatment with capping buffer, the microslide was subjected to a hybrid-

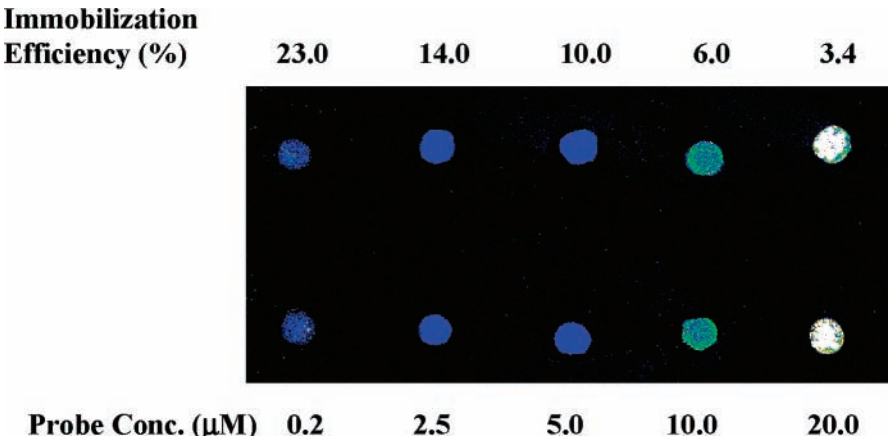

Figure 3. Fluorescence map of epoxy−glass slide spotted with TET-d (TCT TGT ACG TCC GTC AAC GT)-OPO_3^{2-} in a concentration dependent manner in duplicates. Slide was scanned at 75% of laser power and 70% of photomultiplier gain.

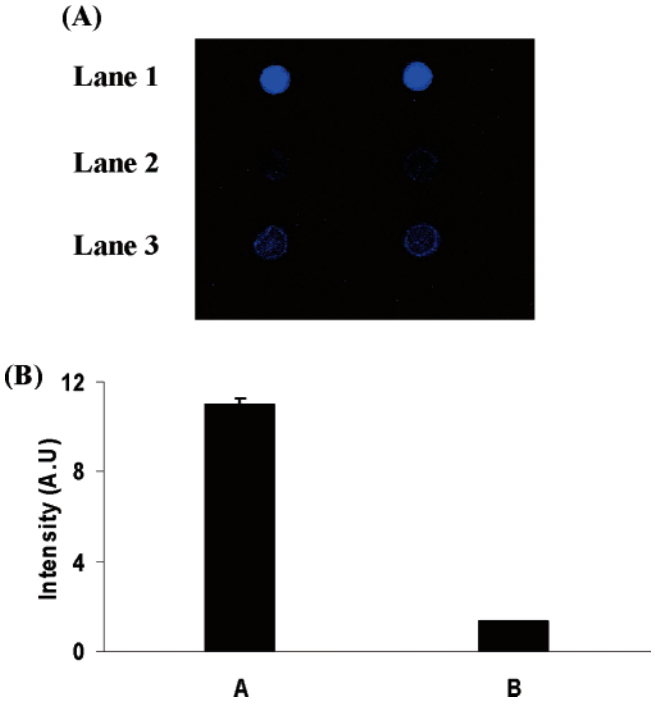

Figure 4. (A) Fluorescence map of epoxy−glass slide spotted with TET-d (TCT TGT ACG TCC GTC AAC GT) (lane 3), 4,5,6,7-tetrachlorofluorescein (TET) (lane 2), and TET-d (TCT TGT ACG TCC GTC AAC GT)-OPO_3^{2-} (lane 1), each one spotted at 0.5 μM; (B) Comparison of fluorescence intensity obtained by spotting 3′-phosphorylated A and unmodified oligomer B on epoxy−glass slide. Slide was scanned at 75% of laser power and 70% of photomultiplier gain.

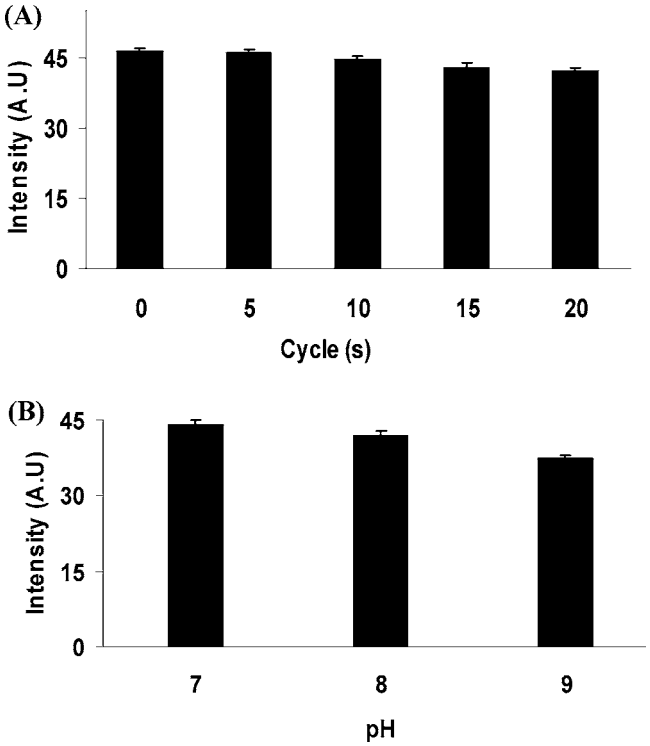

Figure 5. (A) Thermal stability of oligonucleotide probe attached to epoxy−glass slide and comparison of fluorescence signal obtained after 0, 5, 10, 15, and 20 cycles of PCR-like conditions. (B) pH stability of the constructed microarray.

ization step with a labeled oligomer (complementary to zero mismatch sequence). Fluorescence was only detected at spots exposed to the appropriate complement. Figure 7A clearly shows the base mismatches; the perfectly matched sequence gave the maximum intensity (lane 1), while spots having one (lane 2) and two (lane 3) mismatches showed fluorescence intensity in decreasing order. No measurable nonspecific hybridization signal from the noncomplementary control (lane 4) was detected, demonstrating that nonspecific hybridization did not occur. The signal-to-noise ratio was, on an average, >98 as calculated from the signals obtained from complementary hybridized spots and noncomplementary hybridized spots. The quantitative result of the scanned image is depicted in Figure 7B. The applicability of the projected strategy to recognize the target even at low concentration of spotted probe solution (0.2−1 μM) was determined by performing the hybridization experiment (see Supporting Information).

The proposed strategy for oligonucleotide microarray preparation was compared with the two existing standard methods, viz., NTMTA (*20*) and epoxide−amine (*21*). For comparison purposes, an equal concentration of the appropriate oligonucleotide (each at 5 μM) was used. However, different reaction times, as reported therein, were employed in all three methods. After immobilization, the slides were subjected to usual washings and drying. The spots were then scanned under a laser scanner for quantification, and the immobilization efficiencies for each method were calculated using the calibration curve (see Supporting Information). Similarly, to confirm the superiority of the proposed strategy, hybridization experiments were also performed at the same spotting concentration (5 μM), and the results obtained were quantified. The immobilization and hybridization efficiencies of the proposed method (∼10% and 36%) were found to be significantly higher than the method employing NTMTA reagent (∼4.5% and 9.76%) and epoxide−

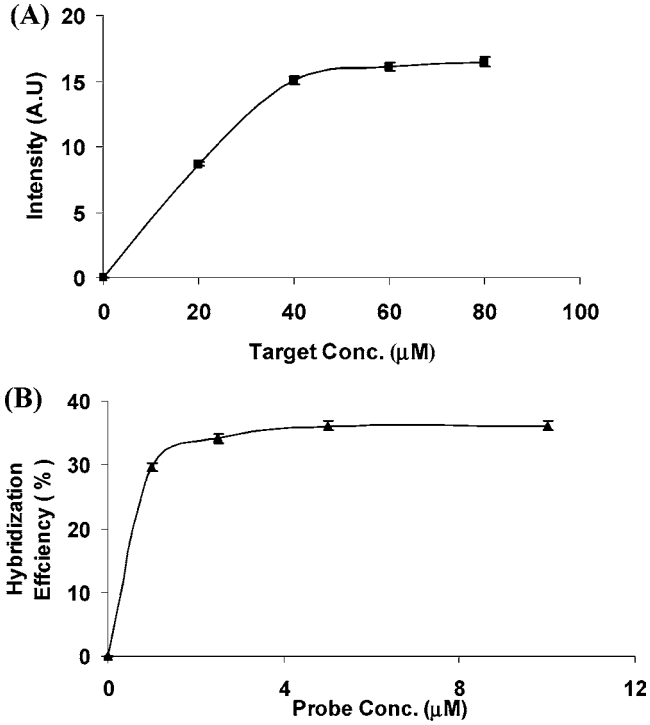

Figure 6. (A) Measurement of steady state hybridization by exposing immobilized probe (5 μM) to different target concentrations (20, 40, 60, and 80 μM). (B) Hybridization efficiency obtained by hybridization of phosphorylated oligonucleotide immobilized on to epoxy−glass slide, varying the amount of covalently immobilized probes (1, 3, 5, and 10 μM), with a complementary labeled target.

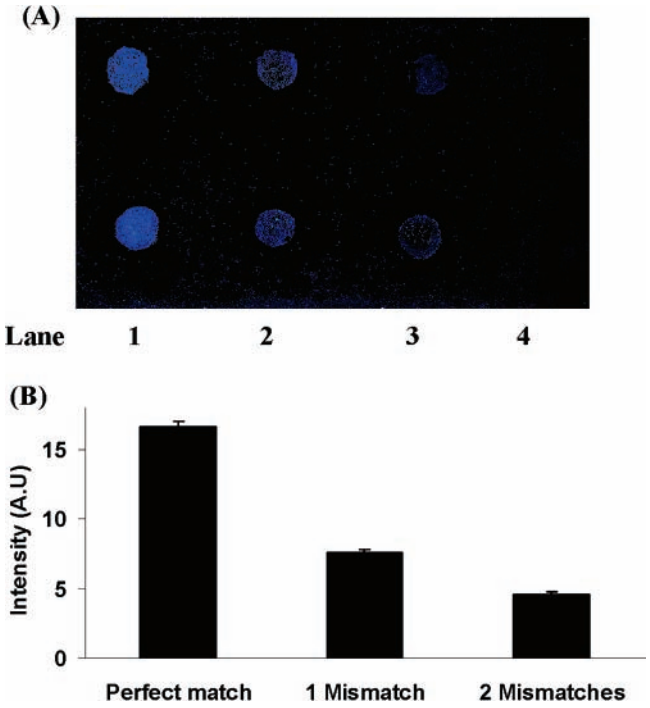

Figure 7. (A) Fluorescence map showing the detection of nucleotide mismatches and specificity of immobilization via hybridization with TET-d (CTT CTT TTT CCT GTT ACC GT) (40 μM): lane 1, d(ACG GTA ACA GGA AAA AGA AG)-OPO_3^{2-}; lane 2, d(ACG GTA ACA GGA AAA AGC AG)-OPO_3^{2-}; lane 3, d(ACG GTA ACA CGA AAA AGC AG)-OPO_3^{2-}; lane 4, d(TTT TTT TTT TTT TTT TT)-OPO_3^{2-}, each spotted at 5 μM. Slide was scanned at 70% of laser power and 65% of photomultiplier gain. (B) Comparison of fluorescence intensity observed with perfect, single, and double mismatch in probe after hybridization with target (complementary to zero mismatch).

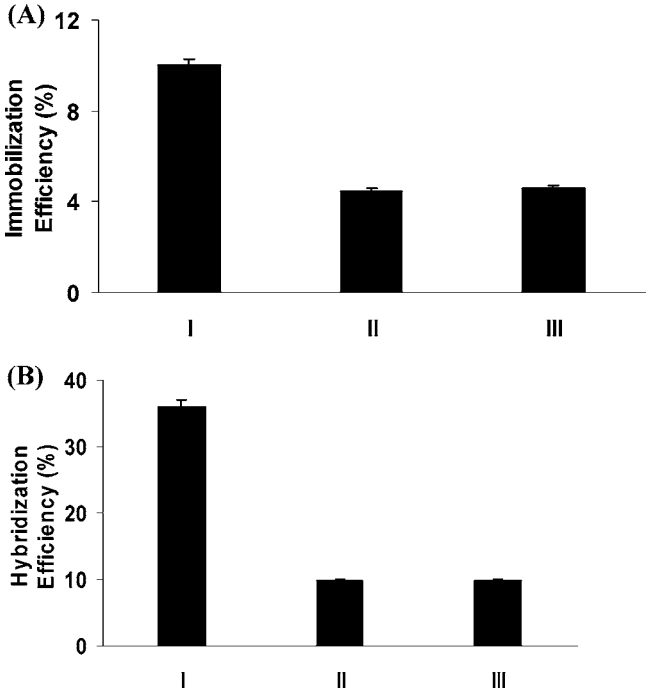

Figure 8. Comparison of immobilization (A) and hybridization efficiencies (B) of proposed strategy (I) with standard ones, viz., (II) = NTMTA and (III) = epoxide−amine.

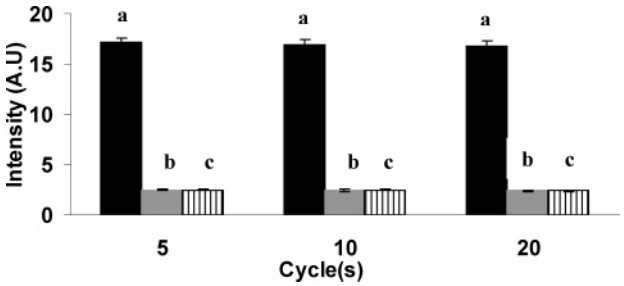

Figure 9. A histogram plotted between the number of washing cycles and fluorescence intensity obtained after hybridization: a, proposed strategy; b, NTMTA; and c, epoxide−amine.

amine immobilization chemistry (~4.62% and 9.82%), as shown in Figures 8A,B.

The effect of time of washing on fluorescence intensity for the above-discussed three approaches was also evaluated. Briefly, the microslides obtained after performing hybridization assay for the three methods, viz., the proposed, NTMTA, and epoxide−amine, were subjected to 5, 10, and 20 cycles of washing with 2× SSC buffer, pH 7 (each cycle of 5 min duration). The quantification results (Figure 9) reveal that the fluorescence intensities decrease by ~1.28% and 1.75% (proposed method), ~1.22% and 1.62% (NTMTA), and ~0.81% and 2.42% (epoxide−amine method) after 10 and 20 cycles, respectively.

CONCLUSIONS

We have demonstrated a new, efficient, and fast method for fabrication of oligonucleotide arrays under microwaves. The technique relies on modification of oligonucleotide at the 3′-end with a free phosphate group, an easy modification that can be performed by using commercially available aminoalkylated support, followed by reaction with epoxy-activated surface. The utility of the method is demonstrated by probing the chemical and thermal stability as well as the reproducibility of the constructed microarray. The highlighting feature of the proposed strategy is that DNA sequences as well as PCR amplicons can

also be immobilized on an epoxylated glass surface after enzymatic phosphorylation. We hope that the projected attachment chemistry involved in this effort will enable a nonchemist, the actual user, to construct oligonucleotide microarrays for routine applications.

ACKNOWLEDGMENT

Financial support for this work was provided by CSIR Task Force Project, NNIOSB. S.M. thanks the Council of Scientific and Industrial Research (CSIR), New Delhi, India, for the award of a Senior Research Fellowship.

Supporting Information Available: Additional experimental data. This material is available free of charge via the Internet at http://pubs.acs.org.

LITERATURE CITED

(1) Schena, M., Shalon, D., Davis, R. W., and Brown, P. O. (1995) Quantitative monitoring of gene expression patterns with a complementary DNA microarray. *Science 270*, 467−470.

(2) Brazma, A., and Vilo, D. (2000) Gene expression data analysis. *FEBS Lett. 480*, 17−24.

(3) Duggan, D. J., Bittner, M., Chen, Y., Meltzer, P., and Trent, J. M. (1999) Expression profiling using cDNA microarrays. *Nat. Genet. 21*, 10−14.

(4) Drobyshev, A. N., Mologina, N., Shick, V., Pobedimskaya, D., Yershov, G., and Mirzabekov, A. D. (1997) Sequence analysis by hybridization with oligonucleotide microchip: Identification of β-thalassemia mutations. *Gene 188*, 45−52.

(5) Pease, A. C., Solas, D., Sullivan, E. J., Cronin, M. T., Holmes, C. P., and Fodor, S. P. (1994) Light- generated oligonucleotide arrays for rapid DNA sequence analysis. *Proc. Natl. Acad. Sci. U.S.A. 91*, 5022−5026.

(6) Southern, E. M., Case-Green, S. C., Elder, J. K., Johnson, M., Mir, K. U., Wang, J., and Williams, J. C. (1994) Arrays of complementary oligonucleotides for analysing the hybridisation behaviour of nucleic acids. *Nucleic Acids Res. 22*, 1368−1373.

(7) Lipshutz, R. J., Fodor, S. P. A., Gingeras, T. R., and Lockhart, D. J. (1999) High density synthetic oligonucleotide arrays. *Nat. Genet. 21*, 20−24.

(8) Blanchard, A. P., Kaiser, R. J., and Hood, L. E. (1996) High-density oligonucleotide arrays. *Biosens. Bioelectron. 11*, 687−690.

(9) Seliger, H., Hinz, M., and Happ, E. (2003) Arrays of immobilized oligonucleotides − Contributions to nucleic acids technology. *Curr. Pharm. Biotechnol. 4*, 379−395.

(10) Hong, B. J., Sunkara, V., and Park, J. W. (2005) DNA microarrays on nanoscale-controlled surface. *Nucleic Acids Res. 33*, e106.

(11) Pirrung, M. C. (2002) How to make a DNA chip. *Angew. Chem., Int. Ed. 41*, 1276−1289.

(12) Beaucage, S. L. (2001) Strategies in the preparation of DNA oligonucleotide arrays for diagnostic applications. *Curr. Med. Chem. 8*, 1213−1244.

(13) Burns, N. L., Vanalstine, J. M., and Harris, J. M. (1995) Poly(ethylene glycol) grafted to quartz: Analysis in terms of a site dissociation model of electro-osmostic fluid flow. *Langmuir 11*, 2768−2776.

(14) Kimura, N., Oda, R., Inaki, Y., and Suzuki, O. (2004) Attachment of oligonucleotide probes to polycarbodiimide-coated glass for microarray applications. *Nucleic Acids Res. 32*, e68.

(15) Song, J. Y., Park, H. G., Jung, S., and Park, J. C. (2005) Diagnosis of HNF-1{α} mutations on a PNA zip-code microarray by single base extension. *Nucleic Acids Res. 33*, e19.

(16) Demers, L. M., Park, S. J., Taton, T. A., Li, Z., and Mirkin, C. A. (2001) Orthogonal assembly of nanoparticle building blocks on Dip-Pen nanolithographically-generated templates of DNA. *Angew. Chem., Int. Ed. 40*, 3071−3073.

(17) Osborne, M. A., Barnes, C. L., Balasubramanian, S., and Klenerman, D. (2001) Probing DNA surface attachment and local environment using single molecule spectroscopy. *J. Phys. Chem. B 105*, 3120−3126.

(18) Wennmalm, S., and Rigler, R. (1999) On death numbers and survival times of single dye molecules. *J. Phys. Chem. B 103*, 2516−2519.

(19) Dombi, K. L., Griesang, N., and Richert, C. (2002) Oligonucleotide arrays from aldehyde-bearing glass with coated background. *Synthesis* 816−824.

(20) Kumar, P., Choithani, J., and Gupta, K. C. (2004) Construction of oligonucleotide arrays on a glass surface using a heterobifunctional reagent, *N*-(2-trifluoroethanesulfonatoethyl)-*N*-(methyl)- triethoxysilylpropyl-3-amine (NTMTA). *Nucleic Acids Res. 32*, e80.

(21) Lamture, J. B., Beattie, K. L., Burke, B. E., Eggers, M. D., Ehrlich, D. J., Fowler, R., Hollis, M. A., Kosicki, B. B., Reich, R. K., and Smith, S. R. (1994) Direct detection of nucleic acid hybridization on the surface of a charge coupled device. *Nucleic Acids Res. 22*, 2121−2125.

(22) Kumar, P., and Gupta, K. C. (2003) A rapid method for construction of oligonucleotide microarrays. *Bioconjugate Chem. 14*, 507−512.

(23) Raddatz, S., Mueller-Ibeler, J., Kluge, J., Wab, L., Burdinski, G., Havens, J. R., Onofrey, T. J., Wang, D., and Schweitzer, M. (2002) Hydrazide oligonucleotides: new chemical modification for chip array attachment and conjugation. *Nucleic Acids Res. 30*, 4793−4802.

(24) Herne, T. M., and Tarlov, M. J. (1997) Characterization of DNA probes immobilized on gold surfaces. *J. Am. Chem. Soc. 119*, 8916−8920.

(25) Levicky, R., Herne, T. M., Tarlov, M. J., and Satija, S. K. (1998) Using self-assembly to control the structure of DNA monolayers on gold: A neutron reflectivity study. *J. Am. Chem. Soc. 120*, 9787−9792.

(26) Brockman, J. M., Frutos, A. G., and Corn, R. M. (1999) A multistep chemical modification procedure to create DNA arrays on gold surfaces for the study of protein−DNA interactions with surface plasmon resonance imaging. *J. Am. Chem. Soc. 121*, 8044−8051.

(27) Georgiadis, R., Peterlinz, K. P., and Peterson, A. W. (2000) Quantitative measurements and modeling of kinetics in nucleic acid monolayer films using SPR spectroscopy. *J. Am. Chem. Soc. 122*, 3166−3173.

(28) Nonglaton, G., Benitez, I. O., Guisle, I., Pipelier, M., Leger, J., Dubreuil, D., Telliar, C., Talham, D. R., and Bujoli, B. (2004) New approach to oligonucleotide microarrays using zirconium phosphonate-modified surfaces. *J. Am. Chem. Soc. 126*, 1497−1502.

(29) Wang, Y., Prokein, T., Hinz, M., Seliger, H., and Goedel, W. A. (2005) Immobilization and hybridization of oligonucleotides on maleimido-terminated self-assembled monolayers. *Anal. Biochem. 344*, 216−223.

(30) Consolandi, C., Castiglioni, B., Bordoni, R., Busti, E., Battaglia, C., Bernardi, L. R., and De Bellis, G. (2002) Two efficient polymeric chemical platforms for oligonucleotide microarray preparation. *Nucleosides, Nucleotides Nucleic Acids 21*, 561−580.

(31) Gait, M. J. (1984) *Oligonucleotide synthesis: A practical approach.* IRL Press, Oxford.

(32) Lidstrom, P., Tierney, J., Wathey, B., and Westman, J. (2001) Microwave assisted organic synthesis - a review. *Tetrahedron 57*, 9225−9283.

(33) Kappe, C. O. (2004) Controlled microwave heating in modern organic synthesis. *Angew. Chem., Int. Ed. 43*, 6250−6284.

(34) Kumar, P., and Gupta, K. C. (1996) Microwave assisted synthesis of *S*-trityl and *S*-acylmercaptoalkanols, nucleosides and their deprotection. *Chem. Lett. 8*, 635−63.

BC0601065

Trastuzumab−Polyethylenimine−Polyethylene Glycol Conjugates for Targeting Her2-Expressing Tumors

Oliver Germershaus,[†] Thomas Merdan,[†] Udo Bakowsky,[†] Martin Behe,[‡] and Thomas Kissel*[,†]

Department of Pharmaceutics and Biopharmacy, Philipps University Marburg, Ketzerbach 63, 35032 Marburg, Germany and Department of Nuclear Medicine, Philipps University Marburg, Baldingerstrasse, 35043 Marburg, Germany. Received April 27, 2006; Revised Manuscript Received July 20, 2006

In this study, we describe the synthesis and characterization of a conjugate consisting of poly(ethylene glycol 2000 Da)$_{10}$-*graft*-poly(ethylene imine 25 kDa) (PEG−PEI) covalently coupled to Trastuzumab (Herceptin) via *N*-succinimidyl-3-(2-pyridyldithio)propionate (SPDP) for specific gene delivery to Her2-expressing cell lines. The efficiency of DNA condensation was studied using an ethidium bromide exclusion assay and demonstrated negligible differences compared to PEG−PEI. Conjugate complex sizes were determined by dynamic light scattering to be in the range 130−180 nm. ζ potentials at different N/P ratios were close to neutral. Flow cytometry and confocal microscopy revealed efficient binding and uptake of Trastuzumab−PEI−PEG complexes using Her2-positive SK-BR-3 cells. In contrast, binding and uptake into Her2-negative OVCAR-3 cells was negligible. In good correlation with these findings, reporter gene expression using targeted complexes in SK-BR-3 cells was up to sevenfold higher than that of unmodified PEG−PEI complexes. With the use OVCAR-3 cells, no significant difference in expression efficiencies could be observed between conjugate and PEG−PEI complexes. Inhibition experiments with free Trastuzumab showed a significant decrease in reporter gene expression using SK-BR-3 cells but no decrease using OVCAR-3 cells, strongly supporting a specific Her2-receptor-mediated uptake mechanism. Our results suggest that Trastuzumab−PEI−PEG might be a promising new bioconjugate for targeted gene transfer to Her2-positive tumor cells in vivo.

INTRODUCTION

An ideal vector system for gene delivery under in vivo conditions needs to meet certain requirements: it should *efficiently* deliver genes to *specific target tissues* with *minimal toxicity* and *immunogenicity*.

Viral vectors are still the most efficient gene delivery systems, but some serious drawbacks such as immune and/or toxic reactions, oncogeniticity, and potential virus recombination limit their application (*1*, *2*).

Therefore, nonviral vectors may become a promising alternative. Among a multitude of nonviral vectors, poly(ethylene imine) (PEI) gained specific attraction, since it facilitates endosomal release and mediates efficient transfection without the use of endosomolytic reagents by the so-called proton-sponge effect (*3*−*5*). A major disadvantage of PEI−DNA polyplexes is their positive surface charge, leading to undesired interactions with nontargeted cells, blood components, or vessel endothelia (*6*, *7*). These interactions not only decrease polyplex blood half-life by fast opsonization and entrapment in fine capillaries, but they also decrease tumor specificity by accumulation of polyplexes in liver, lung, and spleen. Furthermore, biocompatibility and toxicity are major problems strongly related to these polyplex characteristics. Therefore, an important goal in developing polycation-based nonviral vectors is the design of polyplexes with decreased tendencies toward aggregation and unspecific adhesion under in vivo conditions.

To improve the aforementioned characteristics, our group (*7*, *8*) and others (*9*, *10*) have synthesized different poly(ethylene glycol)-grafted PEIs (PEG−PEI) and studied the biophysical and biological properties of the resulting complexes with DNA. Great emphasis was put on defining structure−function relationships between PEI chain length, the degree of substitution, and the MW of PEG chains for optimal complexation and shielding capacities. This research resulted in PEG-*graft*-bPEI copolymers, which showed good transfection results combined with low cytotoxicity (*7*). Furthermore, some of the resulting polyplexes showed encouraging results in pharmacokinetic studies in mice (*8*). Nevertheless, polymer composition, DNA dose, and experimental design strongly influence the outcome of such pharmacokinetic studies as shown by Merdan and co-workers (*11*), and more detailed studies will be needed.

Especially for tumor gene therapy, vectors are desired that show a high specificity for tumor cells while leaving normal cells unaffected. This would offer the possibility of applying high doses of gene constructs with minimal side effects. Several studies described specific ligand-mediated gene transfer using nonviral vectors, e.g., by transferrin (*12*, *13*), folate (*14*, *15*), or saccharides (*9*, *16*, *17*), or by antibodies or antibody fragments such as anti-CD3 (*13*, *18*), anti-PECAM (*19*), anti-OA3 (*20*), anti-GAD (*21*), or anti-PSMA antibodies (*22*). The coupling of antibodies is an advantageous strategy for targeted delivery due to their versatility, the highly specific binding to target cells, and, if an appropriate target was chosen, subsequent uptake by receptor-mediated endocytosis.

Trastuzumab, a monoclonal antibody directed against the Her2 epitope, offers the possibility of specific targeting of various cancers, such as breast, lung, ovarian, and prostate cancers (*23*−*26*). In normal tissues, Her2 is only expressed in low levels and only in certain epithelial cell types (*27*). Upon ligand binding, it is fully internalized, which is mimicked by Trastuzumab (*28*). Anti-Her2 antibodies were already successfully used for targeted drug delivery employing immunolipo-

* Address for correspondence: Thomas Kissel, Department of Pharmaceutics and Biopharmacy, Philipps Universität Marburg, Ketzerbach 63, 35032 Marburg, Germany. Tel: +49-6421-282-5881. Fax: +49-6421-282-7016. E-mail: kissel@staff.uni-marburg.de.

[†] Department of Pharmaceutics and Biopharmacy.

[‡] Department of Nuclear Medicine.

10.1021/bc0601119 CCC: $33.50 © 2006 American Chemical Society
Published on Web 08/15/2006

somes (*29*) or immunoconjugates with different chemo- or radiotherapeutics (*26, 30*−*32*), in virus-like particles for gene delivery (*33*), and, most recently, as targeting moieties coupled to linear (*34*) and branched PEI (*35*).

In these studies, Trastuzumab was coupled with different linkers to unmodified PEI and revealed varying specificity and efficiency depending on the linker chemistry used, the degree of substitution, and the N/P ratio. One major drawback in both studies was the use of unmodified linear or branched PEI with the aforementioned disadvantages.

Our aim in this study was the design of a Her2-targeted nonviral vector potentially applicable for in vivo gene therapy. As described above, unmodified branched as well as linear PEIs are not suitable due to their tendency toward aggregation, unspecificity, and toxicity. We therefore used PEG-grafted branched PEI and modified this copolymer with Trastuzumab, using SPDP as a linker. Complexes were characterized by photon correlation spectroscopy (PCS), laser doppler anemometry (LDA), ethidium bromide exclusion, and atomic force microscopy (AFM). We studied Her2 expression levels of SK-BR-3 and OVCAR-3 cells using flow cytometry and correlated the findings to the binding, uptake, and reporter gene expression of targeted and nontargeted complexes in vitro. Results were verified by competitive inhibition with free Trastuzumab, underlining the receptor-dependent manner of uptake and gene expression.

EXPERIMENTAL PROCEDURES

Chemicals and Plasmid. Branched PEI 25 kDa (Polymin, 99% water free) was a kind gift of BASF AG, Ludwigshafen, Germany. Salmon testes DNA and *N*-succinimidyl-3-(2-pyridyldithio)propionate (SPDP) were purchased from Sigma-Aldrich, Taufkirchen, Germany. Luciferase plasmid (pCMV-Luc) was purchased from the Plasmid Factory, Bielefeld, Germany. Trastuzumab (Herceptin) was purchased from Roche, Basel, Switzerland. All other chemicals were obtained from Merck, Darmstadt, Germany, if not otherwise indicated.

Cell Culture. SK-BR-3 and OVCAR-3 cells were purchased from ATCC, Teddington, U.K., and maintained in RPMI 1640 (PAA Laboratories, Cölbe, Germany) supplemented with 10% and 20% fetal calf serum (Cytogen, Sinn, Germany), respectively, in humidified atmosphere with 5% CO_2 at 37 °C.

Synthesis of PEG−PEI and Trastuzumab−PEG−PEI Conjugates. Poly(ethylene glycol 2000 Da)$_{10}$-*graft*-poly(ethylene imine 25 kDa) (abbreviated as PEG−PEI) was synthesized and characterized as described previously (*7*). For the synthesis of conjugates, 5 mg of PEG−PEI (equivalent to 2.8 mg of PEI) was dissolved in 1 mL reaction buffer (150 mM sodium chloride; 20 mM 4-(2-hydroxyethyl)-1-piperazine ethane sulfonic acid (HEPES); pH 7.5). 20 μL of a 10 mM solution of SPDP in 100% ethanol was added while stirring and allowed to react for 60 min at room temperature. Purification of the product was performed by gel filtration on a PD-10 column (Amersham Pharmacia Biotech, Freiburg, Germany) in reaction buffer. SPDP-activated PEG−PEI was reduced using 13 μmol dithiothreitol (DTT) in 500 μL reaction buffer for 1 h at 37 °C.

Twenty milligrams Trastuzumab in reaction buffer were allowed to react with 24 μL of SPDP solution (10 mM in pure ethanol) under stirring at room temperature and were purified according to the procedure described above. SPDP-activated Trastuzumab was added to PEG−PEI−thiopropionate and allowed to react for 24 h at room temperature. Purification of the conjugate was performed by a modified ion exchange chromatography method described by Kircheis et al. (*18*). Briefly, the solvent of the reaction solution was exchanged with 150 mM NaCl and 10 mM HEPES pH 7.4 (buffer A), and the solution was applied on two serial HiTrap SP Sepharose HP columns (1 mL column volume, flow rate 1 mL/min, ÄKTAprime System, Amersham Pharmacia Biotech, Freiburg, Germany). After elution of unbound antibody with buffer A, the solvent was changed to 3 M NaCl and 10 mM HEPES pH 7.4 (buffer B) stepwise, and the conjugate was eluted. The solvent was changed to 150 mM NaCl solution pH 7.4 in a further gel filtration step, and PEI was quantified by copper complexation (*36*). The amount of antibody was determined by UV spectrometry with background correction using a solution of PEG−PEI of equal concentration with Warburg's formula

$$c\ (\mathrm{mg/mL}) = 1.55 \times (A_{280} - A_{320}) - 0.76 \times (A_{260} - A_{320})$$

where c is protein concentration in milligrams per milliliter calculated with the absorbance at the wavelengths indicated.

Preparation of Polyplexes. Luciferase plasmid and the appropriate amount of polymer were prepared in equal volumes of 150 mM NaCl, pH 7.4. Complexes were formed by adding pCMV−Luc solution to polymer solution followed by intensive mixing. Complexes were allowed to incubate at room temperature for 10 min before use.

Ethidium Bromide Exclusion Assay. DNA condensation was measured by quenching of ethidium bromide as described earlier (*37*). Briefly, 8 μg of salmon testes DNA dissolved in 79 μL water and 50 μL of 60 mM Tris buffer pH 7.4 were added to each well of a 96-well plate. Water was added to give a final volume of 300 μL per well. Subsequently, appropriate volumes of 0.05 mg/mL polymer solutions were added to produce N/P ratios between 0.2 and 4. After a 10 min incubation, 20 μL of a 0.1 mg/mL ethidium bromide solution were added. Solutions were mixed intensively, and fluorescence was measured using a fluorescence plate reader (LS 50 B, Perkin-Elmer, Rodgau-Jügesheim, Germany) at 518 nm excitation and 605 nm emission wavelengths. Results are given as the mean of triplicate measurements plus or minus standard deviation and as relative fluorescence values, where 100 is the fluorescence of DNA without polycation and 0 is the remaining fluorescence of non-intercalating ethidium bromide.

Photon Correlation Spectroscopy and ζ Potential Measurements. Hydrodynamic diameters and ζ potentials were determined in a 150 mM NaCl solution employing a Zetasizer 3000 HS (Malvern Instruments, Herrenberg, Germany; 10 mW HeNe laser, 633 nm) as described previously (*17*). In the PCS measurements, scattered light was detected at a 90° angle through a 400 μm pinhole at a temperature of 25 °C. The viscosity (0.88 mPa s) and refractive index (1.33) of distilled water at 25 °C were used for data analysis. The accuracy of size measurements was routinely checked using reference polymer particles (Nanosphere Size Standards; 50, 100, and 200 nm; Duke Scientific Corp., Palo Alto, CA). Data were analyzed using the CONTIN algorithm. Determination of the ζ potential of complexes was carried out using the standard electrophoresis cell of the Zetasizer 3000 HS at position 17.0 at 25 °C. Sampling time was set to automatic. 4 μg of luciferase plasmid in 200 μL 150 mM NaCl, pH 7.4, was complexed with the appropriate amount of polymer in the same volume. The accuracy of the instrument was checked with ζ potential transfer standard (Malvern Instruments, Herrenberg, Germany). Values given are the mean of five measurements of the same sample plus or minus the standard deviation.

Atomic Force Microscopy. Size and surface morphology of polyplexes was analyzed by atomic force microscopy. Complexes of pCMV−Luc and PEG−PEI or conjugate were prepared as described above immediately after synthesis at an N/P ratio of 3.5. Silicon chips were used as sample support. The chips were incubated with complex suspension for 10 min before drying in a stream of dry nitrogen gas. Samples were

investigated within 2 h of preparation. Microscopy was performed on a vibration- and acoustic-damped Nanoscope IV Bioscope (Veeco Instruments, Santa Barbara, CA). Commercial pyramidal Si3N4 tips (NCH-W, Veeco Instruments, Santa Barbara, CA) on an I-type cantilever with a length of 125 μm, a resonance frequency of about 220 kHz, and a nominal force constant of 36 N/m were used. All measurements were performed in tapping mode to avoid damage to the sample surface. The scan speed was proportional to the scan size. The scan frequency was between 0.5 and 1.5 Hz. Heights and phase images were recorded simultaneously.

Flow Cytometry. For flow cytometry experiments, cells were seeded in 6-well plates at a density of 400 000 cells per well and grown for 24 h. For Her2 expression experiments, cells were detached with trypsin and washed twice with 500 mL PBS at 4 °C, and cell density was adjusted to 600 000 cells/mL. Cell suspensions were mixed with Trastuzumab solution to give concentrations of 500 μg/mL and 1000 μg/mL Trastuzumab, respectively, and incubated for 15 min at 4 °C. After three washings with cold PBS, cells were incubated with 5 μg/mL FITC−goat antihuman antibody (Sigma-Aldrich, Steinheim, Germany) at 4 °C for 15 min. After three washings with cold PBS, cells were suspended in 1 mL FACS Flow (BD Biosciences, San Jose, CA) containing 4% paraformaldehyde and stored on ice until analysis.

For polyplex binding experiments, pCMV−Luc was labeled with YOYO-1 (Molecular Probes, Eugene, OR) as described elsewhere (*38*). Cells were incubated for 15 min at 4 °C with polyplexes prepared with 10 μg of YOYO-1-labeled pCMV−Luc and the appropriate amount of either PEG−PEI−Trastuzumab or PEG−PEI to obtain an N/P ratio of 3.5. Cells were subsequently washed three times with ice cold PBS, suspended in 1 mL FACS Flow containing 4% paraformaldehyde, and stored on ice until analysis.

Flow cytometry was performed using a FACScan (BD Biosciences, San Jose, CA) equipped with a 488 nm argon-ion laser. The emission filter setting was 530/30 bandpass (FL1). First, forward and sideward scatter sensitivity was adjusted so that all signals were within detection limits. The amplification of fluorescence signals was set to mean fluorescence values of approximately 0.5×10^1 for untreated cells, and settings were kept constant throughout the measurement. 10 000 events were measured in each sample. Viable cells were gated according to untreated cell samples, and only cells within this gate were subjected to further analysis. Data thus obtained were then normalized to the untreated cells. *CellQuest 3.3* software (BD Biosciences, San Jose, CA) was used for data acquisition. Data analysis was performed with *FCS Express V3* (De Novo Software, Thornhill, Canada).

Confocal Laser Scanning Microscopy. Cells were incubated with either conjugate or PEG−PEI complexes prepared with 1.66 μg YOYO-1-labeled DNA (see flow cytometry) and the appropriate amount of polymer to obtain N/P 3.5 for 20 min at 4 °C and for 2 h at 37 °C, respectively. Afterward, cells were washed three times with PBS, fixed with 4% paraformaldehyde in PBS for 20 min, and subsequently incubated for 20 min with DAPI solution (0.18 μg/mL in PBS) at room temperature. Cells were washed again three times, embedded with FluorSave Reagent (Calbiochem, San Diego, CA), and kept on ice until analysis.

A Zeiss Axiovert 100 M microscope coupled to a Zeiss LSM 510 scanning device (Zeiss, Oberkochen, Germany) was used for confocal microscopy. For excitation of YOYO-1 fluorescence, an argon laser with an excitation wavelength of 488 nm was used. Fluorescence emission was detected using a 505 nm long-pass filter. Transmission images were obtained in the same scan. In a second scan, DAPI was detected using a Coherent Enterprise II 653 laser (Coherent, Inc., Santa Clara, CA) with an excitation wavelength of 351 nm and a 385−470 nm bandpass emission filter.

Transfection Experiments. Complexes for transfection experiments were prepared using 4 μg of luciferase plasmid per well in 100 μL 150 mM NaCl pH 7.4 and the appropriate amount of polymer in 100 μL of the same solution. Transfection experiments were carried out using PEI, PEG−PEI, and conjugated PEG−PEI at N/P ratios of 2.5, 3.5, 7, and 10. SK-BR-3 and OVCAR-3 cells were seeded in 12-well plates at a density of 80 000 cells per well. After 24 h of growth, medium was removed, and complexes were added to 1.5 mL fresh medium. For inhibition experiments, 1, 10, or 100 μg/mL of free Trastuzumab was added to fresh media 20 min before addition of the complexes. Medium was changed again after 4 h, and the cells were incubated for an additional 44 h.

Luciferase gene expression was quantified using a commercial kit (Promega, Mannheim, Germany) and photon counting on a luminometer (Sirius, Berthold, Pforzheim, Germany). Results were measured in relative light units per second (RLU/s) and afterward converted to nanograms of luciferase using a standard curve of recombinant luciferase (Promega, Mannheim, Germany). Protein concentration was determined using a modified BCA assay (Perbio Science, Bonn, Germany) with bovine serum albumin as a standard (*39*). All experiments were performed in triplicate, and results are expressed as nanograms of luciferase per milligrams of protein.

Statistical Analysis. Statistical significance of differences was evaluated by either two-tailed unpaired Student's *t*-test or one-way ANOVA with Dunnett's post test. The level of significance is indicated with a single asterisk if $p \leq 0.05$, two asterisks if $p \leq 0.01$, and three asterisks if $p \leq 0.001$.

RESULTS

Synthesis of PEG−PEI and PEG−PEI−Trastuzumab. Synthesis resulted in a copolymer consisting of 10 PEG chains of 2 kDa grafted onto a chain of branched PEI with a molecular weight of 25 kDa. Copolymer composition was determined by ^{1}H NMR and FT-IR spectroscopy (*7*).

Purification of PEG−PEI−Trastuzumab by ion exchange chromatography displayed one peak of free unconjugated antibody at low ionic strength conditions. When low-ionic buffer A was stepwise substituted with high-ionic buffer B, a second peak was found containing the conjugate. The elution volumes of free antibody and PEG−PEI−Trastuzumab were comparable to those of a blend of Trastuzumab and PEG−PEI. Under the chosen experimental conditions, the SPDP linker strategy led to conjugation of Trastuzumab to PEG−PEI with a PEI to antibody ratio of 1:0.2. Variations of Trastuzumab and PEG−PEI amounts as well as SPDP concentrations and reaction times did not increase the conjugation degree.

Ethidium Bromide Exclusion Assay. To probe whether DNA condensation properties were altered by antibody conjugation, we performed an ethidium bromide exclusion assay.

Free ethidium bromide shows only weak fluorescence, but its fluorescence is strongly increased when it intercalates into DNA. Condensation of DNA by PEI and other cationic polymers decreases fluorescence by inhibiting this intercalation.

The ethidium bromide exclusion assay with PEG−PEI−Trastuzumab showed only minor differences in shape and position of the curve compared to unmodified PEG−PEI (Figure 1), suggesting no inhibitory effect of antibody-modification to DNA condensation capacity. We assume that PEI and some PEG chains form a core, which is responsible for efficient complexation of DNA, while most of the hydrophilic PEG chains as well as coupled antibody form a shell structure. This accounts for efficient shielding and presentation of the targeting moiety

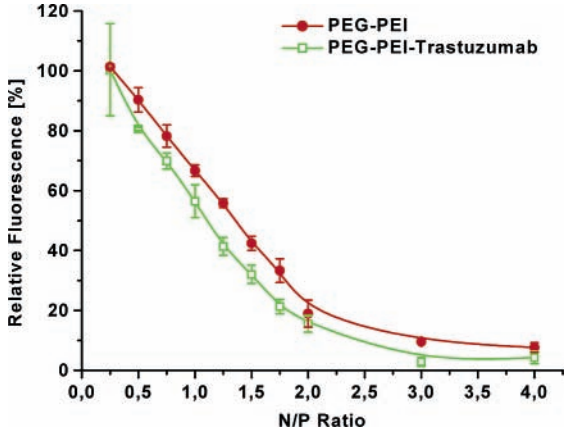

Figure 1. Ethidium bromide exclusion assay comparing unmodified PEG−PEI and PEG−PEI−Trastuzumab. Only minor differences in complexation efficiency were found after conjugation of Trastuzumab.

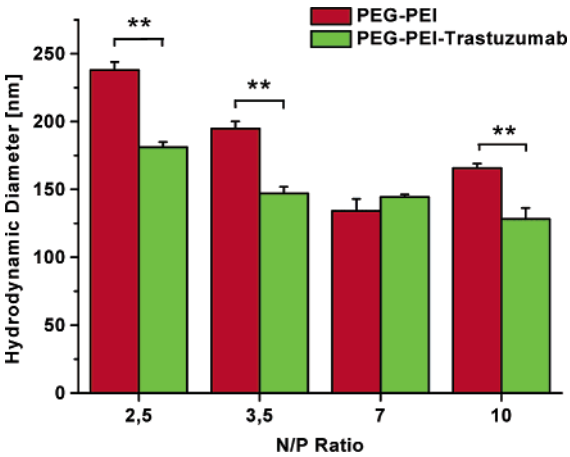

Figure 2. Comparison of hydrodynamic diameters of complexes of PEG−PEI and PEG−PEI−Trastuzumab at different N/P ratios. The PEG−PEI−Trastuzumab complexes are significantly smaller (except N/P 7) than the unmodified PEG−PEI complexes.

combined with effective complexation of DNA. These findings are in line with results obtained with Fab′−PEI−PEG conjugates (*20*). N/P ratios higher than 4 were not investigated, since DNA condensation was almost complete at this point.

Hydrodynamic Diameter and ζ Potential. Hydrodynamic diameters of PEG−PEI−Trastuzumab and PEG−PEI complexes were determined at different N/P ratios using photon correlation spectroscopy (Figure 2). The hydrodynamic diameter decreased with increasing N/P ratio for both targeted and nontargeted complexes. Complex sizes were 237.8 ± 6.1 nm or 181.0 ± 3.8 nm at N/P 2.5 and 165.7 ± 3.2 nm or 128.1 ± 8.2 nm at N/P 10 for PEG−PEI and PEG−PEI−Trastuzumab complexes, respectively. Conjugate complex sizes were significantly smaller than those of PEG−PEI complexes (except at an N/P ratio of 7). Complex sizes of 200 nm and less are favorable for endocytosis (*40*), the proposed route of cell entry for PEI/pDNA complexes (*41, 42*). Therefore, all complexes at N/P 3.5 and higher may be taken up via endocytosis.

ζ potential measurements revealed nearly neutral complex charges for PEG−PEI−Trastuzumab (maximum of +5 mV at N/P 3.5) and for PEG−PEI (maximum of +5 mV at N/P 3.5 and 10) complexes (Figure 3), which are in good correlation with earlier observations with this type of PEG−PEI copolymer (*7, 8, 20*).

Atomic Force Microscopy. Complexes were imaged using atomic force microscopy with the aim of visualizing fine structural differences in PEG−PEI−Trastuzumab vs PEG−PEI complexes. The extraordinarily high resolution of atomic force

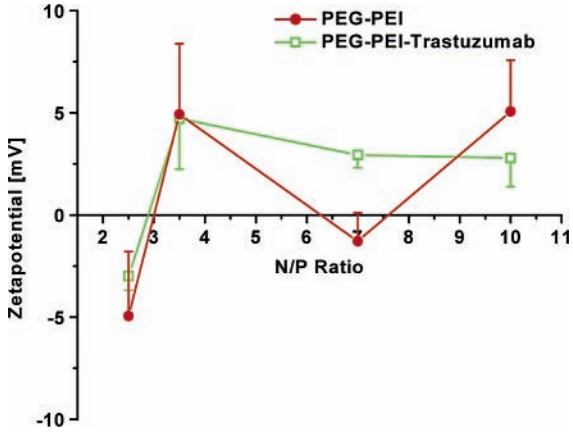

Figure 3. ζ potential values of PEG−PEI and PEG−PEI−Trastuzumab complexes at different N/P ratios. Slightly negative ζ potential values at N/P 2.5 are due to inefficient complexation of DNA. Overall ζ potential range is −5 to +5 mV, indicating nearly neutral surface charges for all complexes at each N/P ratio tested.

microscopy enables the visualization of structures down to the level of antibodies or even DNA strands. In these experiments, an N/P ratio of 3.5 was chosen to represent characteristics of complexes used for flow cytometry, confocal microscopy, and transfection studies.

PEG−PEI/pDNA complexes depicted in Figure 4A were of spherical shape with smooth surfaces and nearly homogeneous but with fairly soft material characteristics. Mean particles sizes were determined to be 152.2 ± 5.8 nm. The decrease in particle sizes compared to PCS measurements can be explained by sample preparation: Samples were measured in a semidry state in the case of AFM measurements and dispersed in sodium chloride solution in the case of PCS measurements.

In contrast, complexes of PEG−PEI−Trastuzumab were significantly smaller (Figure 4B). The mean diameter was determined to be 85.2 ± 4.2 nm. Again, complex size was significantly decreased compared to PCS measurements due to different experimental conditions. The complex surface was not as smooth as and even softer than that of PEG−PEI complexes. A small fraction of particles with sizes of about 10−20 nm was seen on and in the proximity of the complexes in the case of PEG−PEI−Trastuzumab (see arrows in 4B). The mean diameter of these particles was determined to be 18.6 nm. In a second experiment, the size of free Trastuzumab antibodies was determined under the same experimental conditions to be between 10 and 20 nm (Figure 4C). A recently published study by Thomson supports our results on sizes of IgG molecules (*43*). In this study, measurements of IgG molecules under comparable experimental conditions revealed diameters of approximately 9 nm for molecules in the "angled" position and approximately 20 nm for the "flat" orientation. We therefore conclude that the small particles found exclusively in PEG−PEI−Trastuzumab samples represent successfully coupled Trastuzumab antibodies. Hence, the presentation of targeting moieties on the complex surface can be directly verified by this method.

Flow Cytometry. Cell membrane adhesion of complexes at 4 °C was tested using flow cytometry. These data were then correlated to the binding of pure Trastuzumab to the corresponding cell line. For complex adhesion experiments, plasmid DNA was labeled using the intercalating dye YOYO-1. Unconjugated and Trastuzumab-conjugated PEG−PEI was then used to prepare complexes with labeled DNA at an N/P ratio of 3.5. After incubation at 4 °C, cell-associated fluorescence was quantified.

In the case of Trastuzumab binding studies, Trastuzumab was incubated with the cells and subsequently labeled using a

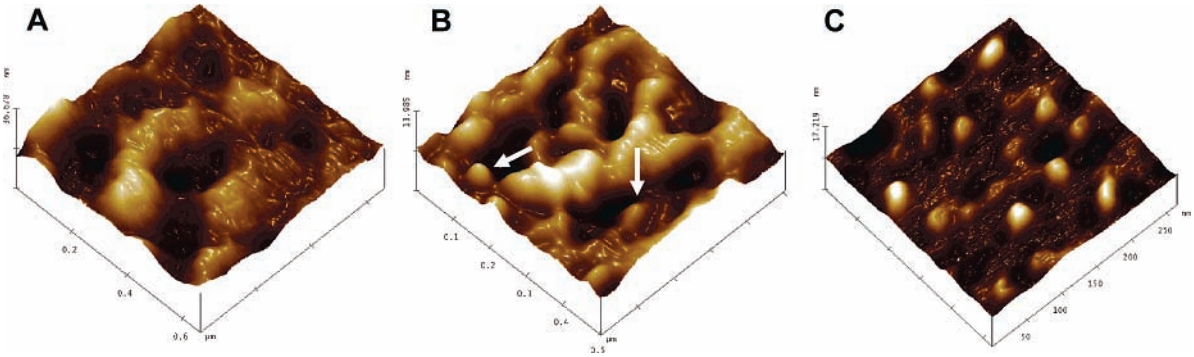

Figure 4. Atomic force micrographs of PEG−PEI/pDNA (A) and PEG−PEI−Trastuzumab/pDNA complexes (B) at N/P 3.5. Free antibody was visualized under the same experimental conditions (C). Arrows in B depict coupled Trastuzumab antibodies.

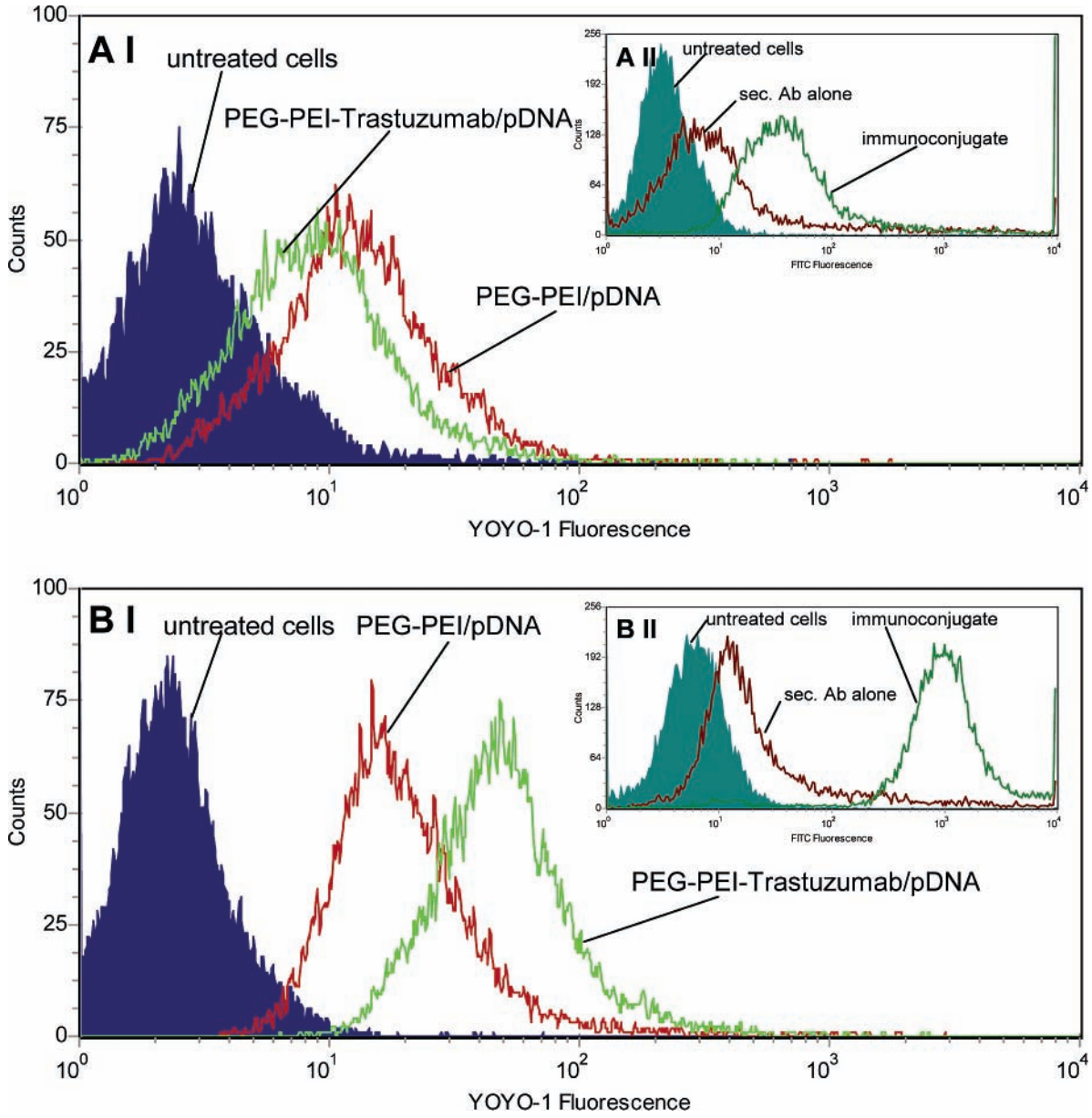

Figure 5. Flow cytometry using OVCAR-3 (A) and SK-BR-3 (B) cells. Cell surface adhesion of targeted and nontargeted PEG−PEI/YOYO-1-pDNA complexes at 4 °C were compared in OVCAR-3 and SK-BR-3 cells (A I and B I). These data can be correlated to Her2 expression levels in these cell lines tested by incubation with Trastuzumab at 4 °C and subsequent labeling with FITC−antihuman antibody (A II and B II).

secondary FITC−antihuman antibody. Cell-associated FITC fluorescence was then measured by flow cytometry as well.

OVCAR-3 cells were used as a negative control. Her2 expression was found to be very low using the immunoconjugate of Trastuzumab and FITC−antihuman antibody (Figure 5A II). When the immunoconjugate was used, the mean fluorescence increased only 4.7-fold compared to unspecific binding of FITC secondary antibody alone. With increasing amounts of Trastuzumab, the mean fluorescence showed no further increase, indicating saturation of receptors at the lowest concentration

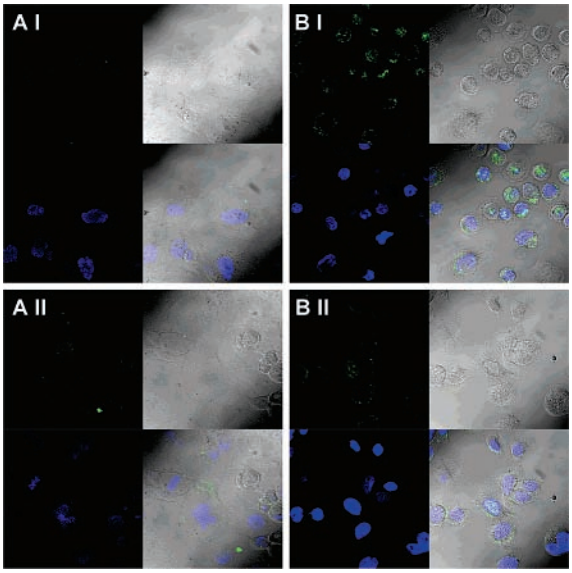

Figure 6. Confocal microscopy images of OVCAR-3 (A) and SK-BR-3 (B) cells. Cells were incubated with PEG−PEI−Trastuzumab/YOYO-1-pDNA (I) or PEG−PEI/YOYO-1-pDNA (II) complexes for 2 h at 37 °C. Upper left: YOYO-1 fluorescence (complexes). Upper right: phase contrast transmitted light image. Lower left: DAPI fluorescence (cell nuclei). Lower right: merge of all channels.

used (data not shown). These findings are consistent with low receptor expression levels in OVCAR-3 cells determined by Western blotting (*44*).

SK-BR-3 cells are reported to overexpress the Her2 antigen (*45*). Fluorescence increased 36-fold using 0.5 mg/mL Trastuzumab subsequently labeled with FITC secondary antibody compared to FITC labeled secondary antibody alone (Figure 5B II). A twofold increase of Trastuzumab concentration resulted in a 1.6-fold increase of relative fluorescence, indicating that, in the case of the lower Trastuzumab concentration, a certain number of Her2 receptors were still unsaturated (data not shown).

Unconjugated complexes showed moderate binding to OVCAR-3 cells with a mean fluorescence intensity of 13.28. By using PEG−PEI−Trastuzumab/pDNA complexes, cell adhesion decreased remarkably. The mean fluorescence value was only 8.82 in this case (Figure 5A I).

Unspecific binding of unconjugated PEG−PEI to Her2-positive SK-BR-3 cells produced a mean fluorescence intensity of 20.25. In contrast, cell-associated fluorescence increased 2.4-fold using PEG−PEI−Trastuzumab (mean fluorescence 49.58, Figure 5B I).

Confocal Laser Scanning Microscopy. Uptake of the complexes was studied by confocal microscopy. SK-BR-3 and OVCAR-3 cells were incubated for 20 min or 2 h at 37 °C with complexes composed of either unconjugated or Trastuzumab-conjugated PEG−PEI and YOYO-1-labeled plasmid DNA.

After incubating for 20 min, binding to the cell membrane occurred in both cell lines for unconjugated PEG−PEI, while a specific binding was observed only with SK-BR-3 cells if PEG−PEI−Trastuzumab was used (Data not shown).

A similar phenomenon was found when polyplexes were incubated with the cells for 2 h at 37 °C. Comparable cell uptake occurred within this time frame for both OVCAR-3 and SK-BR-3 cells using PEG−PEI/pDNA complexes (Figure 6A II and B II). With PEG−PEI−Trastuzumab/pDNA, only very little intracellular fluorescence was found for OVCAR-3 cells (Figure 6A I). In contrast, PEG−PEI−Trastuzumab complexes were readily taken up into SK-BR-3 cells (Figure 6B I).

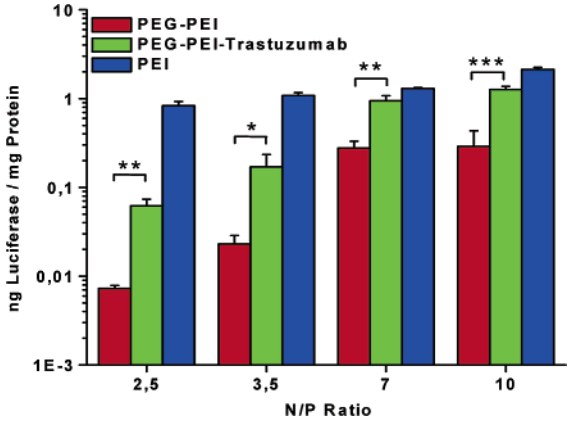

Figure 7. Transfection results using PEG−PEI/pDNA vs PEG−PEI−Trastuzumab/pDNA complexes at different N/P ratios with SK-BR-3 cells. With increasing N/P ratio, transfection efficiency of unconjugated and Trastuzumab-conjugated PEG−PEI complexes increases while differences between transfection efficiency of both complexes decrease. Transfection efficiencies of unmodified PEI 25 kDa are shown for comparison.

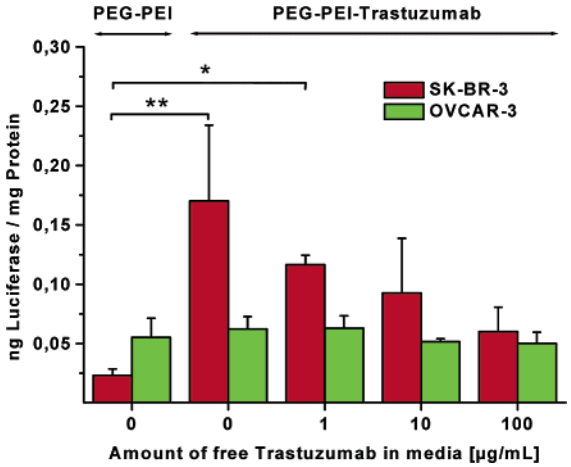

Figure 8. Reporter gene expression using PEG−PEI/pDNA vs PEG−PEI−Trastuzumab/pDNA complexes at N/P 3.5 in SK-BR-3 and OVCAR-3 cells. In the presence of free Trastuzumab in culture media, transfection efficiency is significantly decreased using SK-BR-3 cells but not in the case of OVCAR-3 cells.

Transfection Experiments. The aim of these experiments was to correlate receptor expression levels, binding, and internalization properties with transfection efficiency in vitro and to verify the receptor-dependent manner of uptake by competitive inhibition with free Trastuzumab in culture media. As a control, pure plasmid DNA was used for transfection in both cell lines. Luciferase expression levels were not significantly different from untreated cells in this case. Unmodified PEI 25 kDa, an efficient transfection reagent under in vitro conditions, was used as a positive control in these experiments. As anticipated, complexes of unmodified PEI 25 kDa and pDNA at a N/P ratio of 3.5 showed comparably high transfection efficiencies of 1.1 and 7.0 ng luciferase per milligram of protein in SK-BR-3 and OVCAR-3 cells, respectively. However, unmodified PEI is not suitable for in vivo gene delivery due to the earlier mentioned disadvantages and serves as a point of reference.

Transfection efficiencies in SK-BR-3 were determined at four different N/P ratios (Figure 7), showing decreasing differences between conjugate and unmodified PEG−PEI with increasing N/P ratio. The overall transfection efficiency increased for both polymers with increasing N/P ratio. For transfection experiments, an N/P ratio of 3.5 was favorable due to the ap-

Scheme 1. Synthesis of PEG−PEI−Trastuzumab Conjugate

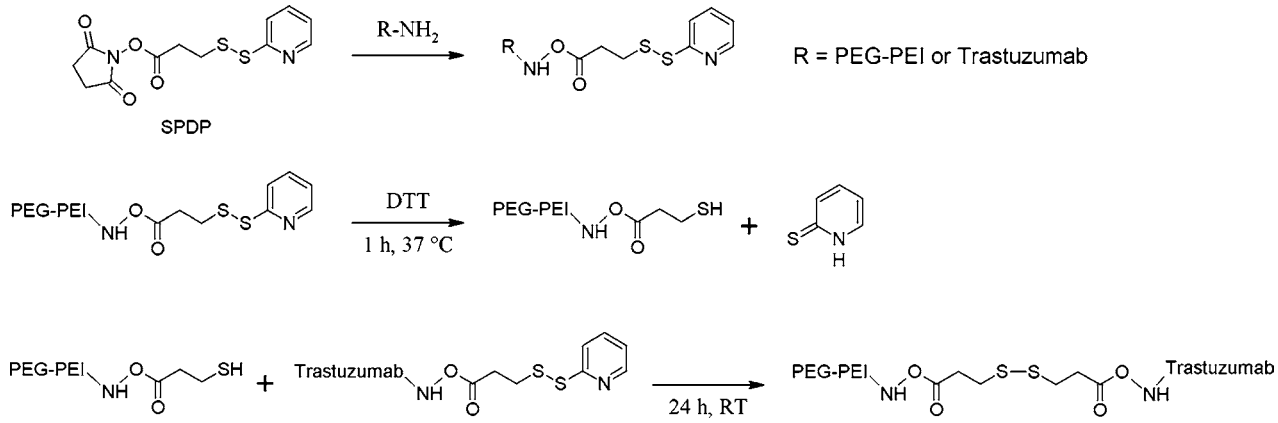

proximately neutral complex charges and appropriate complex sizes for both polymers at this point.

With OVCAR-3 cells, no significant increase in transfection efficiency could be detected with Trastuzumab conjugate compared to unmodified PEG−PEI, and no significant inhibition with free Trastuzumab was possible (Figure 8), which is in excellent agreement with the flow cytometry and confocal microscopy results.

Transfection experiments using SK-BR-3 showed up to sevenfold higher luciferase expression with Trastuzumab−PEG−PEI compared to PEG−PEI at N/P 3.5. Reporter gene expression was in this case significantly inhibited by increasing Trastuzumab concentrations. At 10 and 100 μg/mL Trastuzumab, transfection efficiencies decreased to values that were not significantly different from those of the nontargeted complexes (Figure 8).

DISCUSSION

The aim of this study was a detailed physicochemical and biological in vitro characterization of an antibody-targeted, surface-shielded, PEI-based nonviral vector system for potential in vivo application. Previous investigations with PEGylated PEIs showed efficient complexation of plasmid DNA combined with suitable complex sizes and a neutral ζ potential (*7*). If these copolymers are modified with targeting moieties such as antibodies, nonspecific interactions are minimized and transfection efficiencies in target cells are increased due to specific recognition and subsequent uptake of complexes (*46*). Therefore, PEG−PEIs are favorable for targeted gene delivery in vivo.

Recently, Chiu et al. (*34*) studied conjugates of Trastuzumab with linear PEI (22 kDa). Linear PEI is known to show a high selectivity for the lung if administered systemically (*6*, *47*). From this point of view, linear PEI is not the ideal vector system for targeted gene therapy of distant tumors in vivo. Chiu et al. used the homo-bifunctional linker dithio-bis(succinimidyl propionate) (DSP) to prepare Trastuzumab-conjugated PEI. It was reported that DSP can be used as a cross-linking reagent for branched PEI under comparable conditions (*48*). Even by using linear PEI and thereby reducing the amount of reactive amine groups per PEI molecule, intra- and intermolecular cross-linking of PEI cannot be completely ruled out. This may result in an ill-defined complex composition which would not be comparable to linear PEI itself and may lead to significantly altered physicochemical and biological complex properties. Furthermore, the reaction mixture was purified by dialysis, which does not allow separation of conjugate and free antibody. Therefore, in all probability, a mixture of L-PEI−Trastuzumab conjugate and free antibody was used by Chiu et al.

Strehblow et al. synthesized conjugates of Trastuzumab and PEI (branched, 25 kDa) using different linker chemistries (*35*). Conjugation of Trastuzumab to PEI via the hetero-bifunctional linker *N*-succinimidyl-3-(2-pyridyldithio)propionate (SPDP) resulted in nonspecific gene expression. The authors suspected that this is due to the blocking of critical amino groups either by the linker or by PEI itself. When Trastuzumab was coupled to PEI by sulfosuccinimidyl 4-(*N*-maleimidomethyl)cyclohexane-1-carboxylate (SMCC) or 3-(2-(2-(vinylsulfonyl)ethylthio)-ethyl)quinazoline-2,4(1*H*,3*H*)-dione (IBFB 110001), an effective and specific transfection was reported.

In contrast to the results of Strehblow et al., Kircheis et al. reported successful conjugation of an anti-CD3 antibody to PEI (800 kDa) via SPDP. By using this conjugate, transfection efficiency in CD3-positive Jurkat cells was increased 30-fold, whereas CD3-negative K562 cells showed no increase in transfection efficiency (*18*).

In our study, Trastuzumab was successfully coupled to PEG−PEI via SPDP, enabling specific conjugation without the risk of changing polymer properties by cross-linking. Trastuzumab and PEG−PEI were both activated with SPDP and were then coupled to form PEG−PEI−S−S−Trastuzumab (see Scheme 1).

Apart from a chemically defined polymer composition, our system offers several additional advantages over the Trastuzumab−PEI derivatives mentioned above. Tendency toward aggregation, toxicity, and electrostatic interaction with nontargeted cells are decreased, while biocompatibility is increased due to pegylation. On the other hand, endosomal escape and intracellular trafficking of complexes is improved due to potential intracellular cleavability of the disulfide bond between the targeting moiety and the polymer (*48*).

With this conjugation technique, every fifth PEI chain was modified with one Trastuzumab antibody. In contrast, Kircheis et al. report a coupling ratio of about 1:2.8 (PEI/Ab) with PEI 800 kDa (*18*). Coupling efficiencies comparable to PEG−PEI−Trastuzumab conjugates were obtained in a previous study in our laboratory, where conjugation of OV-TL 16 Fab′ to PEG−PEI via SPDP resulted in a PEI/Fab′ ratio of 1:0.5 (*20*).

Since 31% of the amino groups of PEI are primary amines (*49*), there is an upper limit for modification with PEG or antibody depending on the molecular weight of PEI, which accounts for reduced degree of antibody modification in our case. Attachment of PEG chains also increases steric hindrance, so that substitution is also hampered by this effect. Due to the decreased molecular weight of OV-TL 16 Fab′ (approximately 50 kDa) compared to Trastuzumab (approximately 150 kDa), reduced steric hindrance may explain the slightly higher conjugation degree in the former case.

Physicochemical properties of the complexes were not significantly influenced by the coupling of Trastuzumab. Complexation efficiencies as well as ζ potential values of the PEG−

PEI−Trastuzumab complexes were comparable to PEG−PEI complexes at all N/P ratios tested. Neutral surface charge of complexes is a main prerequisite for in vivo applicability. Opsonization, aggregation, and nonspecific interactions with blood components, vessel endothelia, and nontargeted cells will be minimized with neutral complexes; therefore, systemic circulation will be prolonged (*8*, *12*, *50*, *51*).

For both PEG−PEI and PEG−PEI−Trastuzumab complexes, the size decreases with increasing N/P ratio due to enhanced complexation of DNA, which was shown by the ethidium bromide exclusion experiments. Measurements of hydrodynamic diameters revealed significantly decreased complex sizes of Trastuzumab conjugate compared to unconjugated complexes (except at N/P ratio 7). This effect may be explained by an increased hydrophilicity of targeted complexes and a decreased interaction between particles due to additional steric shielding by coupled antibody. However, the proposed route of cell entry for these complexes is mainly by clathrin-mediated endocytosis, and uptake efficiency may not be significantly affected by particle size as long as complex diameters are within the range 100−200 nm (*41*, *42*).

Detailed analysis of complex shape and surface hardness was performed by atomic force microscopy. AFM measurements of complexes composed of PEI, PEG−PEI, or PEG−PEI conjugates and plasmid DNA or oligonucleotides were previously published by several authors (*7*, *20*, *52*, *53*). In all cases, complexes of more or less spherical shape with smooth surfaces were observed. These findings were confirmed for PEG−PEI and PEG−PEI−Trastuzumab complexes in our study. Visualization of coupled antibodies was to the best of our knowledge not previously reported for this type of bioconjugate. Small particles found only in the case of Trastuzumab−PEI−PEG complexes were identified as coupled antibodies by comparing the size and shape of particles to a control sample with pure antibody. A comparable approach was reported by Anabousi et al., who visualized the surface modification of liposomes with transferrin molecules by AFM (*54*). Due to the more rigid and defined shape of liposomes compared to polyplexes, targeting moieties could be visualized more easily in this case. Surface-bound water, softness of complexes, and possible interactions of antibodies with the polymer impaired a detailed visualization of antibody subdomains as reported in (*43*, *55*). However, AFM measurements verify the presentation of Trastuzumab on the complex surface, which is essential for targeted transfection.

In the next step, specific binding of Trastuzumab−PEI−PEG conjugates was proven by flow cytometry. Receptor expression levels could be directly correlated to the binding of targeted and nontargeted complexes. Even the effect of additional steric shielding by coupled Trastuzumab and therefore decreased binding compared to unmodified complexes was shown in the case of Her2-negative cells. These results are perfectly in line with previously performed flow cytometry experiments with OV-TL 16 Fab′−PEI−PEG conjugates (*20*). Furthermore, confocal laser scanning microscopy showed that the internalization of targeted complexes occurs exclusively in Her2-positive cells. In contrast, uptake of unconjugated complexes was negligible in both Her2-negative and Her2-positive cell lines.

Finally, transfection efficiencies in Her2-positive SK-BR-3 were determined at four different N/P ratios, showing overall increases in transfection efficiencies and decreasing differences between targeted and nontargeted PEG−PEI complexes with increasing N/P ratio. To explain these observations, we assume that the conjugate binds to the cell 1) via nonspecific interaction of cationic PEI with the cell surface and 2) via specific receptor-mediated interaction. With increasing N/P ratio, the effect of charge-mediated binding more and more outweighs the effect of specific binding via antibody−receptor interactions. A comparable effect was observed in different studies in the literature. Conjugation of PEI with anti-PECAM antibody led to efficient transfection of mouse lung endothelial cells, especially at lower N/P ratios (*19*). Targeting of HepG2 cells with galactosylated PEI complexes only showed improved transfection efficiencies for N/P ratios of 3 or lower (*16*, *17*). In contrast, no significant difference was found in transfection efficiencies of targeted and nontargeted complexes in Her2-negative cells. Ultimately, inhibition with increasing amounts of free Trastuzumab verified receptor-dependent uptake, which matches previous results obtained with different antibodies and antibody fragments (*18*, *20*, *21*, *34*, *38*).

Physicochemical and biological properties found in this study give rise to the assumption that this system may be applicable for in vivo use. In the next step, the balance between PEG and Trastuzumab substitution will be optimized to further enhance the targeting effect. Pharmacokinetic, organ distribution, and toxicity studies will then be performed to proceed toward the goal of targeted transfection of tumor tissues in vivo.

CONCLUSION

We have developed a targeted gene delivery system for highly specific in vitro transfection of Her2-positive cell lines, which may potentially be applicable for targeted transfection of tumor cells in vivo.

Polyplex surface charge was efficiently shielded by modification with PEG and targeting moieties, while efficient pDNA complexation was maintained. Hydrodynamic diameters of polyplexes are suitable for possible extravasation and efficient endocytosis. Trastuzumab was shown to be presented on the complex surface by AFM, and accessibility of antigen-binding domains was verified by flow cytometry and confocal microscopy experiments. Confocal microscopy was also used to demonstrate specific and efficient cellular uptake of targeted complexes. Finally, transfection experiments showed efficient and specific reporter gene expression in Her2-positive cells using targeted complexes. By inhibition with free Trastuzumab, Her2-receptor dependency of reporter gene expression was verified.

ACKNOWLEDGMENT

We are grateful to Eva Mohr and Nicole Bamberger (Department of Pharmaceutics and Biopharmacy) for their excellent support in cell culture experiments and Dr. Cornelia Brendel (FACS laboratory, Department of Hematology, Oncology and Immunology, University Hospital Marburg) for the generous use of equipment and facilities. We thank Erik Rytting for helpful discussions.

LITERATURE CITED

(1) Byrnes, A. P., Rusby, J. E., Wood, M. J., and Charlton, H. M. (1995) Adenovirus gene transfer causes inflammation in the brain. *Neuroscience 66*, 1015−24.

(2) Schreier, H. (1994) The new frontier: gene and oligonucleotide therapy. *Pharm. Acta Helv. 68*, 145−59.

(3) Behr, J. P. (1997) The proton sponge: A trick to enter cells the viruses did not exploit. *Chimia 51*, 34−36.

(4) Merdan, T., Kunath, K., Fischer, D., Kopecek, J., and Kissel, T. (2002) Intracellular processing of poly(ethylene imine)/ribozyme complexes can be observed in living cells by using confocal laser scanning microscopy and inhibitor experiments. *Pharm. Res. 19*, 140−6.

(5) Akinc, A., Thomas, M., Klibanov, A. M., and Langer, R. (2005) Exploring polyethylenimine-mediated DNA transfection and the proton sponge hypothesis. *J. Gene Med. 7*, 657−63.

(6) Chollet, P., Favrot, M. C., Hurbin, A., and Coll, J. L. (2002) Side-effects of a systemic injection of linear polyethylenimine-DNA complexes. *J. Gene Med. 4*, 84−91.

(7) Petersen, H., Fechner, P. M., Martin, A. L., Kunath, K., Stolnik, S., Roberts, C. J., Fischer, D., Davies, M. C., and Kissel, T. (2002) Polyethylenimine-*graft*-poly(ethylene glycol) copolymers: influence of copolymer block structure on DNA complexation and biological activities as gene delivery system. *Bioconjugate Chem. 13*, 845−54.

(8) Kunath, K., von Harpe, A., Petersen, H., Fischer, D., Voigt, K., Kissel, T., and Bickel, U. (2002) The structure of PEG-modified poly(ethylene imines) influences biodistribution and pharmacokinetics of their complexes with NF-kappaB decoy in mice. *Pharm. Res. 19*, 810−7.

(9) Erbacher, P., Bettinger, T., Belguise-Valladier, P., Zou, S., Coll, J. L., Behr, J. P., and Remy, J. S. (1999) Transfection and physical properties of various saccharide, poly(ethylene glycol), and antibody-derivatized polyethylenimines (PEI). *J. Gene Med. 1*, 210−22.

(10) Nguyen, H.-K., Lemieux, P., Vinogradov, S. V., Gebhart, C. L., Guérin, N., Paradis, G., Bronich, T. K., Alakhov, V. Y., and Kabanov, A. V. (2000) Evaluation of polyether-polyethyleneimine graft copolymers as gene transfer agents. *Gene Ther. 7*, 126−138.

(11) Merdan, T., Kunath, K., Petersen, H., Bakowsky, U., Voigt, K. H., Kopecek, J., and Kissel, T. (2005) PEGylation of poly(ethylene imine) affects stability of complexes with plasmid DNA under in vivo conditions in a dose-dependent manner after intravenous injection into mice. *Bioconjugate Chem. 16*, 785−92.

(12) Kircheis, R., Wightman, L., Schreiber, A., Robitza, B., Rossler, V., Kursa, M., and Wagner, E. (2001) Polyethylenimine/DNA complexes shielded by transferrin target gene expression to tumors after systemic application. *Gene Ther. 8*, 28−40.

(13) Buschle, M., Cotten, M., Kirlappos, H., Mechtler, K., Schaffner, G., Zauner, W., Birnstiel, M. L., and Wagner, E. (1995) Receptor-mediated gene transfer into human T lymphocytes via binding of DNA/CD3 antibody particles to the CD3 T cell receptor complex. *Hum. Gene Ther. 6*, 753−61.

(14) Dauty, E., Remy, J. S., Zuber, G., and Behr, J. P. (2002) Intracellular delivery of nanometric DNA particles via the folate receptor. *Bioconjugate Chem. 13*, 831−9.

(15) Leamon, C. P., Weigl, D., and Hendren, R. W. (1999) Folate copolymer-mediated transfection of cultured cells. *Bioconjugate Chem. 10*, 947−57.

(16) Zanta, M. A., Boussif, O., Adib, A., and Behr, J. P. (1997) In vitro gene delivery to hepatocytes with galactosylated polyethylenimine. *Bioconjugate Chem. 8*, 839−44.

(17) Kunath, K., von Harpe, A., Fischer, D., and Kissel, T. (2003) Galactose-PEI-DNA complexes for targeted gene delivery: degree of substitution affects complex size and transfection efficiency. *J. Controlled Release 88*, 159−72.

(18) Kircheis, R., Kichler, A., Wallner, G., Kursa, M., Ogris, M., Felzmann, T., Buchberger, M., and Wagner, E. (1997) Coupling of cell-binding ligands to polyethylenimine for targeted gene delivery. *Gene Ther. 4*, 409−18.

(19) Li, S., Tan, Y., Viroonchatapan, E., Pitt, B. R., and Huang, L. (2000) Targeted gene delivery to pulmonary endothelium by anti-PECAM antibody. *Am. J. Physiol. Lung Cell Mol. Physiol. 278*, L504−11.

(20) Merdan, T., Callahan, J., Petersen, H., Kunath, K., Bakowsky, U., Kopeckova, P., Kissel, T., and Kopecek, J. (2003) Pegylated polyethylenimine−Fab′ antibody fragment conjugates for targeted gene delivery to human ovarian carcinoma cells. *Bioconjugate Chem. 14*, 989−96.

(21) Jeong, J. H., Lee, M., Kim, W. J., Yockman, J. W., Park, T. G., Kim, Y. H., and Kim, S. W. (2005) Anti-GAD antibody targeted non-viral gene delivery to islet beta cells. *J. Controlled Release 107*, 562−570.

(22) Moffatt, S., Papasakelariou, C., Wiehle, S., and Cristiano, R. (2006) Successful in vivo tumor targeting of prostate-specific membrane antigen with a highly efficient J591/PEI/DNA molecular conjugate. *Gene Ther. 13*, 761−772.

(23) Slamon, D. J., Godolphin, W., Jones, L. A., Holt, J. A., Wong, S. G., Keith, D. E., Levin, W. J., Stuart, S. G., Udove, J., and Ullrich, A. (1989) Studies of the HER-2/neu proto-oncogene in human breast and ovarian cancer. *Science 244*, 707−12.

(24) Tripathy, D., and Benz, C. C. (1992) Activated oncogenes and putative tumor suppressor genes involved in human breast cancers. *Cancer Treat. Res. 63*, 15−60.

(25) Molland, J. G., Barraclough, B. H., Gebski, V., Milliken, J., and Bilous, M. (1996) Prognostic significance of c-erbB-2 oncogene in axillary node-negative breast cancer. *Aust. N. Z. J. Surg. 66*, 64−70.

(26) Li, Y., Cozzi, P. J., Qu, C. F., Zhang, D. Y., Abbas-Rizvi, S. M., Raja, C., and Allen, B. J. (2004) Cytotoxicity of human prostate cancer cell lines in vitro and induction of apoptosis using 213Bi-Herceptin alpha-conjugate. *Cancer Lett. 205*, 161−71.

(27) Press, M. F., Cordon-Cardo, C., and Slamon, D. J. (1990) Expression of the HER-2/neu proto-oncogene in normal human adult and fetal tissues. *Oncogene 5*, 953−62.

(28) Harries, M., and Smith, I. (2002) The development and clinical use of trastuzumab (Herceptin). *Endocr. Relat. Cancer 9*, 75−85.

(29) Park, J. W., Kirpotin, D. B., Hong, K., Shalaby, R., Shao, Y., Nielsen, U. B., Marks, J. D., Papahadjopoulos, D., and Benz, C. C. (2001) Tumor targeting using anti-her2 immunoliposomes. *J. Controlled Release 74*, 95−113.

(30) Gilbert, C. W., McGowan, E. B., Seery, G. B., Black, K. S., and Pegram, M. D. (2003) Targeted prodrug treatment of HER-2-positive breast tumor cells using trastuzumab and paclitaxel linked by A-Z-CINN Linker. *J. Exp. Ther. Oncol. 3*, 27−35.

(31) Mandler, R., Wu, C., Sausville, E. A., Roettinger, A. J., Newman, D. J., Ho, D. K., King, C. R., Yang, D., Lippman, M. E., Landolfi, N. F., Dadachova, E., Brechbiel, M. W., and Waldmann, T. A. (2000) Immunoconjugates of geldanamycin and anti-HER2 monoclonal antibodies: antiproliferative activity on human breast carcinoma cell lines. *J. Natl. Cancer Inst. 92*, 1573−81.

(32) Behr, T. M., Behe, M., and Wormann, B. (2001) Trastuzumab and breast cancer. *N. Engl. J. Med. 345*, 995−6.

(33) Gleiter, S., and Lilie, H. (2003) Cell-type specific targeting and gene expression using a variant of polyoma VP1 virus-like particles. *Biol. Chem. 384*, 247−55.

(34) Chiu, S. J., Ueno, N. T., and Lee, R. J. (2004) Tumor-targeted gene delivery via anti-HER2 antibody (trastuzumab, Herceptin(R)) conjugated polyethylenimine. *J. Controlled Release 97*, 357−69.

(35) Strehblow, C., Schuster, M., Moritz, T., Kirch, H. C., Opalka, B., and Petri, J. B. (2005) Monoclonal antibody-polyethyleneimine conjugates targeting Her-2/neu or CD90 allow cell type-specific nonviral gene delivery. *J. Controlled Release 102*, 737−47.

(36) von Harpe, A. (2000) Thesis. Department of Pharmaceutics and Biopharmacy, Philipps-University, Marburg, Germany.

(37) Petersen, H., Kunath, K., Martin, A. L., Stolnik, S., Roberts, C. J., Davies, M. C., and Kissel, T. (2002) Star-shaped poly(ethylene glycol)-*block*-polyethylenimine copolymers enhance DNA condensation of low molecular weight polyethylenimines. *Biomacromolecules 3*, 926−36.

(38) Ogris, M., Steinlein, P., Carotta, S., Brunner, S., and Wagner, E. (2001) DNA/polyethylenimine transfection particles: influence of ligands, polymer size, and PEGylation on internalization and gene expression. *AAPS PharmSci. 3*, E21.

(39) Hill, H. D., and Straka, J. G. (1988) Protein determination using bicinchonic acid in the presence of sulfhydryl reagents. *Anal. Biochem. 170*, 203−208.

(40) Mellman, I. (1996) Endocytosis and molecular sorting. *Annu. Rev. Cell Dev. Biol. 12*, 575−625.

(41) Grosse, S., Aron, Y., Thevenot, G., Francois, D., Monsigny, M., and Fajac, I. (2005) Potocytosis and cellular exit of complexes as cellular pathways for gene delivery by polycations. *J. Gene Med. 7*, 1275−86.

(42) Rejman, J., Oberle, V., Zuhorn, I. S., and Hoekstra, D. (2004) Size-dependent internalization of particles via the pathways of clathrin- and caveolae-mediated endocytosis. *Biochem. J. 377*, 159−69.

(43) Thomson, N. H. (2005) The substructure of immunoglobulin G resolved to 25 kDa using amplitude modulation AFM in air. *Ultramicroscopy 105*, 103−10.

(44) Campiglio, M., Ali, S., Knyazev, P. G., and Ullrich, A. (1999) Characteristics of EGFR family-mediated HRG signals in human ovarian cancer. *J. Cell. Biochem. 73*, 522−32.

(45) Lewis, G. D., Figari, I., Fendly, B., Wong, W. L., Carter, P., Gorman, C., and Shepard, H. M. (1993) Differential responses of human tumor cell lines to anti-p185HER2 monoclonal antibodies. *Cancer Immunol. Immunother. 37*, 255−63.

(46) Merdan, T., Kopecek, J., and Kissel, T. (2002) Prospects for cationic polymers in gene and oligonucleotide therapy against cancer. *Adv. Drug Delivery Rev. 54*, 715−58.

(47) Goula, D., Benoist, C., Mantero, S., Merlo, G., Levi, G., and Demeneix, B. A. (1998) Polyethylenimine-based intravenous delivery of transgenes to mouse lung. *Gene Ther. 5*, 1291−5.

(48) Gosselin, M. A., Guo, W., and Lee, R. J. (2002) Incorporation of reversibly cross-linked polyplexes into LPDII vectors for gene delivery. *Bioconjugate Chem. 13*, 1044−53.

(49) von Harpe, A., Petersen, H., Li, Y., and Kissel, T. (2000) Characterization of commercially available and synthesized polyethylenimines for gene delivery. *J. Controlled Release 69*, 309−22.

(50) Ogris, M., Brunner, S., Schuller, S., Kircheis, R., and Wagner, E. (1999) PEGylated DNA/transferrin-PEI complexes: reduced interaction with blood components, extended circulation in blood and potential for systemic gene delivery. *Gene Ther. 6*, 595−605.

(51) Kircheis, R., Blessing, T., Brunner, S., Wightman, L., and Wagner, E. (2001) Tumor targeting with surface-shielded ligand−polycation DNA complexes. *J. Controlled Release 72*, 165−70.

(52) Brus, C., Kleemann, E., Aigner, A., Czubayko, F., and Kissel, T. (2004) Stabilization of oligonucleotide-polyethylenimine complexes by freeze-drying: physicochemical and biological characterization. *J. Controlled Release 95*, 119−31.

(53) Kleemann, E., Dailey, L. A., Abdelhady, H. G., Gessler, T., Schmehl, T., Roberts, C. J., Davies, M. C., Seeger, W., and Kissel, T. (2004) Modified polyethylenimines as non-viral gene delivery systems for aerosol gene therapy: investigations of the complex structure and stability during air-jet and ultrasonic nebulization. *J. Controlled Release 100*, 437−50.

(54) Anabousi, S., Laue, M., Lehr, C. M., Bakowsky, U., and Ehrhardt, C. (2005) Assessing transferrin modification of liposomes by atomic force microscopy and transmission electron microscopy. *Eur. J. Pharm. Biopharm. 60*, 295−303.

(55) Thomson, N. H. (2005) Imaging the substructure of antibodies with tapping-mode AFM in air: the importance of a water layer on mica. *J. Microsc. 217*, 193−9.

BC0601119

Design, Synthesis, and Evaluation of Enhanced DNA Binding New Lipopolythioureas

Jeanne Leblond, Nathalie Mignet, Lucie Leseurre, Céline Largeau, Michel Bessodes, Daniel Scherman, and Jean Herscovici*

Inserm, U640, Paris, F-75006 France, CNRS, UMR8151, Paris, F-75006 France, Ecole Nationale Supérieure de Chimie de Paris, Paris, F-75005, Unité de Pharmacologie Chimique et Génétique, France, Université Paris Descartes, Faculté de Pharmacie Paris, F-75270 France, and Institut de Chimie Moléculaire de Paris Centre, CNRS FR 2769, F-75005. Received April 27, 2006; Revised Manuscript Received July 6, 2006

Nonviral gene delivery is limited to a large extent by the cationic nature of most of the chemical vector. We have shown that lipopolythioureas interact with DNA. However, lipopolythioureas were not very efficient at transfecting cells, probably due to reduced interaction between the noncationic synthetic lipid and the cell membrane. Here, we report that liposomes made from a new thiourea lipid, DPPC, and a lipid bearing an RGD ligand allowed very efficient entry of the lipopolythioureas into integrin $\alpha_v\beta_3$ expressing cells. In addition, we show that a stable interaction between DNA and lipopolythiourea could be obtain with two thiourea groups. Moreover, the addition of a hydrophilic terminus improves the formulation of these new DNA binding agents.

INTRODUCTION

Gene therapy considers the use of nucleic acid as a drug to treat or cure acquired or innate diseases. In most cases, the genetic material must be packed in a delivery system to be protected from nucleases and to cross physiological barriers and/or cell membranes (*1*). During the past years, efforts have been undertaken to develop physical (*2*), viral (*3, 4*), or synthetic DNA delivery processes (*5, 6*). Because of the polyanionic nature of DNA and the overall negative charge of cell membranes, nonviral vectors are mostly cationic. They have been proven to efficiently transfect cells in culture. However, most of them are ineffective for in vivo DNA delivery, due to interaction with serum, opsonins, or other physiological components (*7*). To improve synthetic vector efficiency, several attempts have been made to mask (*8*) or suppress cationic charges (*9, 10*).

Thiourea derivatives have been intensively investigated in the area of molecular recognition due to their strong hydrogen-bonding activity (*11*). Moreover, bis-thiourea moieties selectively bind to dihydrogenphosphate via multitopic hydrogen bonding, giving stronger complexes with $H_2PO_4^-$ than any synthetic neutral receptor known so far (*12*).

On the basis of these data, which suggested that stable lipoplexes could be made from the interaction between thiourea and nucleic acid, we reported that *N*-(2-{3-[2-(2-{3-[2-(3-methylthioureido)ethyl]thioureido}ethylamino)ethyl]thioureido}ethyl)-*N*′,*N*′-ditetradecylsuccinamide (DTTU, Figure 1) formulated with DPPC were able to interact with DNA and formed nanometric particles (*13*). This new lipopolythiourea lipid (LPT) was composed of a hydrophobic anchor connected to a linear trithiourea. Lipopolythiourea lipoplexes made from DTTU exhibited a longer circulation time in the blood than cationic lipid RPR209120 (*14*) taken as a reference compound. However, this particular lipopolythiourea was difficult to formulate as liposome because of its highly hydrophobic nature and presented very poor transfecting properties. These primary results clearly indicated that the LPT physicochemical properties and perhaps their interaction with cell membranes have to be improved.

A recent study using density functional theory (DFT) calculation (*15*) predicts that DTTU binds to DNA by six hydrogen bonds with a major contribution of thioureas **II** and **III** that form four of the six bonds (Figure 1). This interaction induces a conformational change with the three thiourea groups, normally in trans from one another in the bare molecule, which moves into the cis position. From these predictions, it could be expected that a headgroup containing two thioureas will lead to a stable complex with nucleic acid. On the other hand, it has been reported that a T-shaped branched structure improved the transfecting properties of cationic polyamine (*16*). Moreover, such a structure will probably avoid the constraints due to the cis conformation of DTTU.

So, we designed new noncationic lipids with a T-shaped bis-thiourea headgroup. We introduced also hydroxyl and diol termini, which have been proven to have a positive effect on transfection efficiency (*17*). Finally, we chose two different linkers composed of a benzyl group or a 3-motives-PEG to connect the hydrophobic anchor to the headgroup. These new lipopolythioureas (LPT) have been synthesized and evaluated in terms of DNA compaction and transfection efficiency. As a final point, we investigated RGD-mediated internalization of endothelial cells expressing integrin $\alpha_V\beta_3$.

MATERIALS AND METHODS

All solvents were purchased from Carlo Erba-SDS (Peypin France). Dichloromethane was distilled from P_2O_5. DMF was dried over 3 Å molecular sieves and pyridine over KOH. All chemicals were purchased from Sigma-Aldrich-Fluka or Lancaster. Tosyl chloride (petroleum ether) and cholesteryl chloroformate (acetone) were recrystallized, and diglycolic anhydride was dehydrated (P_2O_5) prior to use. Other solvents and products were used without further purification. Reactions were monitored by thin-layer chromatography using Merck precoated 60 F254 silica gel plates. Column chromatography was performed over SDS (Peypin France) 35−70 m silicagel according to the method of Still, Khan, and Mitra (*18*) or using small-column flash chromatography (SFC) according to the following procedure. A plastic syringe was filled with silicagel (product/silicagel 1/5) and connected to vacuum (12 mmHg). The column was

* Email: jean-herscovici@enscp.fr.

10.1021/bc060110g CCC: $33.50 © 2006 American Chemical Society
Published on Web 08/29/2006

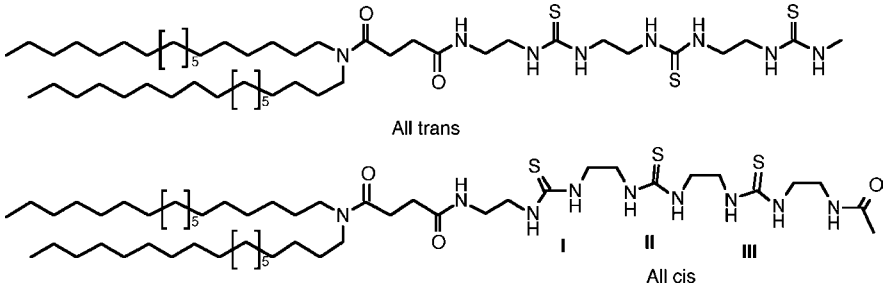

Figure 1. Structures of the linear trithiourea DTTU.

equilibrated with heptane, then the sample dissolved in a minimum of dichloromethane was added to the top. The column was eluted by ten fractions of a heptane/ethyl acetate mixture. The volume was equal to the silicagel volume. For each fraction, the amount of ethyl acetate was increased (10% (v/v) to 100% ethyl acetate in heptane). Inverse-phase solid-phase extraction (SPE) was performed on a Supelco Superclean C8 cartridge using water/acetonitrile/methanol mixture. ^{1}H and ^{13}C NMR spectra were recorded on a Bruker Advance DRX-300 spectrometer at 300.13 MHz for ^{1}H and 75.47 MHz for ^{13}C. NMR spectra were processed using XwinNmr (Bruker) or SwaN-MR (*19*). Mass spectra were carried out on a Shimazu 2010A LC-MS on ESI mode. High-resolution mass spectra and elemental analysis were carried out by the "Service Central de Micro-analyse du CNRS" Vernaison France. Dipalmytoylphosphatidylcholine (DPPC) and phosphatidylethanolamine lissamine rhodamine were purchased from Aventi Polar Lipids (Alabaster, Alabama).

Synthesis of Lipopolythioureas. *2,3-Dihydroxy-1,4-di-para-toluenesulfonyloxy butane (2).* A dichloromethane solution (60 mL) of tosyl chloride (15.6 g, 82 mmol) was added dropwise for 5 h to a cooled (−20 °C) pyridine solution (16.6 mL, 0.21 mole) of D,L-threitol (5.0 g, 41 mmol). The reaction mixture was stirred overnight at 0 °C, then the solvent was evaporated. 1 N HCl (100 mL) was added to the residual oil that was extracted six times with dichloromethane. The combined organic layers were washed with brine, dried ($MgSO_4$), and then evaporated under reduced pressure. The residual oil was purified by chromatography (heptane/ethyl acetate 6:4) to yield 9.1 g of **2** as a white solid (52%). mp 83 °C. ^{1}H NMR ($CDCl_3$) δ (ppm) 2.44 (s, 6H, CH_3), 2.95 (m, 2H, OH), 3.88 (m, 2H, CHOH), 4.05 (d, 4H, J = 5 Hz, CH_2O), 7.35 (d, 4H, J = 8.1 Hz, H_{arom}), 7.88 (d, 4H, J = 8.1 Hz, H_{arom}). ^{13}C NMR ($CDCl_3$) δ (ppm) 21.80 (s, CH_3), 68.62 (s, CHOH), 71.05 (s, CH_2O), 128.96 (s, CH_{arom}), 130.21 (CH_{arom}), 132.68 (s, C_{arom}), 145.81 (s, C_{arom}). MS (ESI, *m/z*) 431 $(M + H)^+$, HPLC purity 96% by ELSD. Anal. Calcd for $C_{18}H_{22}O_8S_2$ C, 50.22; H, 5.15; N, 14.90. Found: C, 50.21; H, 5.35; N, 14.64.

4-[4,5-Bis-(toluene-4-sulfonyloxymethyl)-1,3-dioxolan-2-yl]-benzoic Acid Methyl Ester (4). A solution of diol **2** (1.07 g, 2.5 mmol), *para*-toluene sulfonic acid monohydrate (48 mg, 0.25 mmol), and 4-dimethoxymethylbenzoic acid methyl ester **3** (0.58 g, 2.75 mmol) in dry benzene (30 mL) was heated under reflux with a Dean−Stark trap during 5 h. Then, pyridine was added (0.5 mL), and the reaction mixture was concentrated under reduced pressure. The resulting solid was purified by flash chromatography (heptane/ethyl acetate/CH_2Cl_2 4:1:1, then 4:4:1) to afford 1.1 g of dioxolane **4** as a white solid (75%). mp 130° C. ^{1}H NMR ($CDCl_3$) δ (ppm) 2.45 (s, 6H, CH_3), 3.96 (s, 3H, OCH_3), 4.14 (m, 2H, CHO), 4.22 (m, 4H, CH_2O), 5.82 (s, 1H, CHO_2), 7.28−7.37 (m, 6H, H_{arom}), 7.71−7.77 (m, 4H, H_{arom}), 7.97 (d, 2H, J = 7.5 Hz, H_{arom}). ^{13}C NMR ($CDCl_3$) δ (ppm) 21.80 (s, CH_3), 52.36 (s, OCH_3), 68.51 (d, CH_2O), 75.68 (d, CHO), 103.98 (s, CHO_2), 126.59 (s, CH_{arom}), 128.10 (s, CH_{arom}), 129.74 (s, CH_{arom}), 130.17 (s, CH_{arom}), 131.23 (s, C_{arom}),132.14 (s, C_{arom}), 141.12 (s, C_{arom}), 145.61 (s, C_{arom}), 166.71 (s, C═O). MS (ESI) *m/z* 577 $(M + H)^+$, HPLC purity 100% by ELSD. Anal. Calcd for $C_{27}H_{28}O_{10}S_2$: C, 56.24; H, 4.89; S, 11.12. Found: C, 55.65; H, 5.01; S, 11.44.

4-(4,5-Bis-azidomethyl-1,3-dioxolan-2-yl)benzoic Acid Methyl Ester (5). A solution of ditosyl **4** (1.48 g, 2.5 mmol) and sodium azide (0.97 g, 15.0 mmol) in DMF (25 mL) was heated overnight under reflux. The reaction mixture was evaporated under reduced pressure, then the residual solution was coevaporated several times with toluene. The resulting oil was treated with brine (30 mL) and extracted with ethyl acetate (3 × 20 mL). The combined organic extracts were dried ($MgSO_4$) and evaporated under reduced pressure to yield a yellow oil (0.75 g, 94%) that was used without further purification. ^{1}H NMR ($CDCl_3$) δ (ppm) 3.49 and 3.60 (m, 4H, CH_2), 3.90 (s, 3H, OCH_3), 4.20 (m, 2H, CHO), 6.03 (s, 1H, CHO_2), 7.57 (d, 2H, J = 8.1 Hz, H_{arom}), 8.06 (d, 2H, J = 8.1 Hz, H_{arom}). ^{13}C NMR ($CDCl_3$) δ (ppm) 51.88 (s, CH_2), 52.24 (s, CH_3), 77.54 and 78.36 (2s, CHO), 103.58 (s, CHO_2), 126.56 (s, CH_{arom}), 129.83 (s, CH_{arom}), 131.32 (s, C_{arom}), 141.57 (s, C_{arom}), 166.72 (s, C═O). MS (ESI, *m/z*) 378 $(M + H)^+$, HPLC purity 82% by ELSD.

4-(4,5-Bis-azidomethyl-1,3-dioxolan-2-yl)benzoic Acid (6). Ester **5** was treated with a solution of sodium hydroxide (0.64 g, 16.0 mmol) in a mixture of $H_2O/CH_3OH/THF$ (1:1:1 v/v/v, 45 mL). When all the starting material had disappeared, iced 2 N HCl was added to reach pH 3. Then, the reaction mixture was extracted with ethyl acetate (3 × 20 mL). The combined organic extracts were washed with brine, dried ($MgSO_4$), and evaporated under reduced pressure to give a yellow oil (0.75 g, 94%) that was used without further purification. ^{1}H NMR ($CDCl_3$) δ (ppm) 3.44−3.67 (m, 4H, CH_2), 4.23 (m, 2H, CHO), 6.07 (s, 1H, CHO_2), 7.61 (d, 2H, J = 8.1 Hz, H_{arom}), 8.15 (d, 2H, J = 8.1 Hz, H_{arom}). ^{13}C NMR ($CDCl_3$) δ (ppm) 51.80 (s, CH_2), 77.54 and 78.36 (s, CHO), 103.48 (s, CHO_2), 126.71 (s, CH_{arom}), 130.50 (s, CH_{arom}), 131.31 (s, C_{arom}), 142.39 (s, C_{arom}), 171.85 (s, C═O). MS (ESI, *m/z*) 302 $(M + HCOO)^-$. HPLC purity 98% by ELSD.

4-(4,5-Bis-azidomethyl-1,3-dioxolan-2-yl)-N,N-ditetradecyl-benzamide (7). *N*-methylmorpholin (0.20 mL, 1.8 mmol) was added to a THF solution (30 mL) of **6** (0.54 g, 1.8 mmol) cooled to −40 °C. Then, a THF solution (3 mL) of isobutyl chloroformate (0.23 mL, 1.8 mmol) was added slowly. The reaction mixture was stirred for 1 h at −40 °C, then a THF solution (5 mL) of ditetradecylamine (0.68 g, 1.8 mmol) and *N*-methylmorpholin (0.20 mL, 1.8 mmol) was added slowly. The resulting mixture was stirred vigorously for 20 h at RT. Then, ethyl acetate (150 mL) and water (150 mL) were added. The water layer was extracted twice with ethyl acetate; then, the combined organic layers were successively washed twice with 1 N HCl, twice with a saturated solution of $NaHCO_3$, twice with brine, and then dried ($MgSO_4$). The solvent was removed under reduced pressure, then the resulting oil was purified by chromatography (heptane/ethyl acetate 1:4, then 3:7) to yield **7** as a clear oil (0.55 g, 46%). ^{1}H NMR ($CDCl_3$) δ (ppm) 0.87 (t,

6H, $J = 6.9$ Hz, CH_3), 1.21−1.46 (m, 44H, $-CH_2-$), 1.63 (m, 4H, CH_2), 3.14 (t, 2H, $J = 7.2$ Hz, CH_2N), 3.38−3.63 (m, 6H, CH_2N, CH_2N_3), 4.20 (m, 2H, CHO), 6.01 (s, 1H, CHO_2), 7.37 (d, 2H, $J = 7.1$ Hz, CH_{arom}), 7.52 (d, 2H, $J = 7.1$ Hz, CH_{arom}). ^{13}C NMR ($CDCl_3$) δ (ppm) 14.20 (s, CH_3), 22.78 (s, $-CH_2-$), 27.17 (s, $-CH_2-$), 28.77 (s, $-CH_2-$), 29.73 (m, $-CH_2-$), 32.01 (s, $-CH_2-$), 44.76 and 49.04 (2s, CH_2N), 51.85 (s, CH_2N_3), 77.80 (d, CHO), 103.82 (s, CHO_2), 126.69 (s, CH_{arom}), 137.57 (s, C_{arom}), 138.76 (s, C_{arom}), 171.09 (s, C═O). MS (ESI, *m/z*) 697 $(M + H)^+$, HPLC purity 99% by ELSD.

*4-(4,5-Bis-aminomethyl-1,3-dioxolan-2-yl)-N,N-ditetradecylbenzamide (**8**).* A 25 mL round-bottom flask equipped with a magnetic stirring bar was filled successively with diazide **7** (0.35 g, 0.5 mmol), ethanol (10 mL), Pd/C (50 mg), and hydrogen. The suspension was stirred for 19 h at RT, then the mixture was filtered through celite to yield after evaporation the diamine **8** (0.31 g, 96%), which was used without further purification. ^1H NMR ($CDCl_3$) δ (ppm) 0.84 (t, 6H, $J = 6.9$ Hz, CH_3), 1.04−1.46 (m, 44H, $-CH_2-$), 1.56 (m, 4H, $-CH_2-$), 2.99−3.40 (m, 8H, CH_2N, CH_2NH_2), 4.24 (m, 2H, CHO), 5.97 (s, 1H, CHO_2), 6.40 (m, 4H, NH_2), 7.28 (d, 2H, $J = 7.1$ Hz, CH_{arom}), 7.55 (d, 2H, $J = 7.1$ Hz, CH_{arom}). ^{13}C NMR ($CDCl_3$) δ (ppm) 14.12 (s, CH_3), 22.71 (s, $-CH_2-$), 27.25 (s, $-CH_2-$), 28.82 (s, $-CH_2-$), 29.73 (m, $-CH_2-$), 31.97 (s, $-CH_2-$), 41.73 (d, CH_2NH_2), 45.02 and 49.24 (2s, CH_2-N), 78.15 (d, CHO), 102.87 (s, CHO_2), 126.51 (s, CH_{arom}), 127.31 (s, CH_{arom}), 138.16 (s, C_{arom}), 171.29 (s, C═O). MS (ESI, *m/z*) 645 $(M + H)^+$. HPLC purity 92% by ELSD.

*4-(4,5-Bis-isothiocyanatomethyl-1,3-dioxolan-2-yl)-N,N-ditetradecylbenzamide (**9**).* Diisopropylethylamine (0.26 mL, 1.5 mmol) and carbon disulfide (0.12 mL, 2 mmol) were successively added to a solution of diamine **8** (0.32 g, 0.5 mmol) in dichloromethane (5 mL). The solution was stirred for 90 min, then a solution of tosyl chloride (0.19 g, 1 mmol) in dichloromethane was added dropwise. The mixture was stirred for 20 h at room temperature, diluted with dichloromethane, and washed three times with brine. The organic solution was dried ($MgSO_4$) and evaporated under vacuum. The crude was purified by chromatography (heptane/ethyl acetate 8:2, 7:3, and 6:4) to yield **9** as a colorless oil (0.24 g, 66%). ^1H NMR ($CDCl_3$) δ (ppm) 0.84 (t, 6H, $J = 6.9$ Hz, CH_3), 1.04−1.30 (m, 44H, $-CH_2-$), 1.46 (m, 4H, $-CH_2-$), 3.15 and 3.46 (m, 4H, CH_2N), 3.80 and 3.90 (m, 4H, CH_2NCS), 4.28 (m, 2H, CHO), 6.06 (s, 1H, CHO_2), 7.39 (d, 2H, $J = 6.5$ Hz, CH_{arom}), 7.53 (d, 2H, $J = 6.5$ Hz, CH_{arom}). ^{13}C NMR ($CDCl_3$) δ (ppm) 14.07 (s, CH_3), 22.71 (s, $-CH_2-$), 27.17 (s, $-CH_2-$), 29.04 (s, $-CH_2-$), 29.73 (m, $-CH_2-$), 31.93 (s, $-CH_2-$), 44.97 and 49.19 (s, $-CH_2N$), 46.59 (CH_2NCS), 77.1 (d, CHO), 104.40 (s, CHO_2), 126.74 (s, CH_{arom}), 132.02 (s, C═S), 138.58 (s, C_{arom}), 138.83 (s, C_{arom}), 171.17 (s, C═O). IR (NaCl): σ (cm^{-1}) 1086 (ν_{C-O-C}), 1465 (δ_{CH_2}), 1629 ($\nu_{C=O}$), 2048 ($\nu_{N=C=S}$), 2842 ($\nu_{=C-H_2}$), 2934 (ν_{CH_2}), 3196 ($\nu_{=C-H_{arom}}$).

*4-{4,5-Bis-[3-(2-hydroxyethyl)thioureidomethyl]-1,3-dioxolan-2-yl}-N,N-ditetradecylbenzamide (**10**).* Ethanolamine (0.026 mL, 0.4 mmol) was added to a solution of diisothiocyanate **9** (62 mg, 0.09 mmol) in THF (1 mL), then the mixture was stirred for 22 h at room temperature. The solution was concentrated under reduced pressure. The resulting oil was purified by SPE (C-8 100% acetonitrile to 100% methanol) to afford the dithiourea **10** (29.8 mg, 39%) as a colorless oil. ^1H NMR ($CDCl_3$) δ (ppm) 0.87 (m, 6H, CH_3), 1.25 (m, 44H, $-CH_2-$), 1.62 (m, 4H, $-CH_2-$), 3.14 (m, 2H, $-CH_2NCO$), 3.44−3.78 (m, 14H, $-CH_2NCO$, CH_2NCS, CH_2OH), 4.16 (m, 2H, CHO), 5.94 (s, 1H, CHO_2), 7.25 (m, 4H, NH), 7.33 (m, 2H, CH_{arom}), 7.52 (m, 2H, CH_{arom}). ^{13}C NMR ($CDCl_3$) δ (ppm) 14.09 (s, CH_3), 22.71 (s, $-CH_2-$), 27.22 (s, $-CH_2-$), 28.83 (s, $-CH_2-$), 29.73 (m, $-CH_2-$), 31.97 (s, $-CH_2-$), 45.30 (s, CH_2NCS), 45.80 (s, CH_2NCS), 46.97 and 49.45 (s, CH_2NCO), 61.42 (s, CH_2OH), 78.23 (d, CHO), 102.83 (s, CHO_2), 126.48 (s, CH_{arom}), 127.05 (s, CH_{arom}) 138.14 (s, C_{arom}), 138.80 (s, C_{arom}), 171.71 (s, C═O), 183.35 (s, C═S).

*N,N-ditetradecyl-4-(4,5-bis-azidomethyl-1,3-dioxolan-2-yl)-benzamide (**11**).* 3-Amino-1,2-propanediol (22 mg, 0.24 mmol) was added to a solution of **9** (41 mg, 0.056 mmol) in dry DMF. The solution was stirred at RT for 20 h then concentrated to dryness. The crude was dissolved in ethyl acetate and washed three times with brine. The organic layer was dried ($MgSO_4$) and evaporated to dryness. Purification as for **10** gave **11** as a colorless oil (20 mg, 38%). ^1H NMR ($CDCl_3$) δ (ppm) 0.88 (m, 6H, CH_3), 1.27 (m, 44H, $-CH_2-$), 1.65 (m, 4H, $-CH_2-$), 3.16 (m, 2H, $-CH_2NCO$), 3.35−3.48 (m, 6H, $-CH_2NCO$, CH_2-NCS), 3.47−3.68 (m, 8H, CH_2NCS, CH_2OH), 3.97 (m, 2H, CHOH), 4.16 (m, 2H, CHO), 5.97 (s, 1H, CHO_2), 7.35 (m, 2H, CH_{arom}), 7.55 (m, 2H, CH_{arom}). ^{13}C NMR ($CDCl_3$) δ (ppm) 13.96 (s, CH_3), 22.64 (s, $-CH_2-$), 27.11 (s, $-CH_2-$), 28.78 (s, $-CH_2-$), 29.73 (m, $-CH_2-$), 31.91 (s, $-CH_2-$), 45.27 (s, $-CH_2NCS$), 45.83 (s, $-CH_2NCS$), 46.91 and 49.44 (s, $-CH_2NCO$), 63.65 (s, CH_2OH), 70.99 (s, CHOH), 78.33 (d, CHO), 102.88 (s, CHO_2), 126.42 (s, CH_{arom}), 126.86 (s, CH_{arom}), 138.02 (s, C_{arom}), 138.72 (s, C_{arom}), 171.87 (s, C═O), 183.49 (s, C═S). ES-HRMS Calcd. for $C_{48}H_{87}N_5O_7NaS_2$: 932.5945. Found: 932.5965.

*2-(2-{2-[2-(2,2-Diethoxyethoxy)ethoxy]ethoxy}ethoxy)-tetrahydropyran (**13**).* Sodium hydride (1.7 g, 43 mmol) was added portionwise to an iced cooled solution of **12** (previously dried by codistillation with THF) in THF (50 mL). The suspension was stirred for 30 min, then bromoacetaldehyde diethylacetal (2.3 mL, 17 mmol) was added dropwise. The mixture was stirred for 3 h at RT, then heated overnight at 60 °C. The reaction mixture was cooled with an ice bath, then the reaction was stopped by the addition of water (2 mL). Most of the solvent was removed by evaporation under reduced pressure, then water and dichloromethane were added. The water layer was extracted three times with dichloromethane, then the combined organic layer was washed with brine, dried ($MgSO_4$), and concentrated under reduced pressure. The residual oil was purified by chromatography (heptane/ethyl acetate 1:1) to afford **13** (3 g, 100%), which was used without further purification. ^1H NMR ($CDCl_3$) δ (ppm) 1.11 (t, 6H, $J = 6.9$ Hz, CH_3), 1.41−1.72 (m, 6H, $-CH_2-$ring), 3.43 (m, 4H, OCH_2-CH_3), 3.48 (m, 2H, CH_2O-ring), 3.53−3.59 (m, 12H, $-CH_2O-$), 3.75 (m, 2H, CH_2-CH), 4.53 (m, 2H, CHO_2). ^{13}C NMR ($CDCl_3$) δ (ppm) 15.32 (s, CH_3), 19.45 (s, CH_2-ring), 25.46 (s, CH_2-ring), 30.58 (s, CH_2-ring), 62.21 ($-CH_2O-$), 66.64 (CH_2O-ring), 70.62 (s, $-CH_2O-$), 70.91 (s, $-CH_2O-$), 71.95 (s, $-CH_2O-$), 98.86 (s, CHO_2), 101.22 (s, CHO_2). MS (ESI, *m/z*) 373 $(M + H)^+$. Anal. Calcd for $C_{17}H_{34}O_7$: C, 58.26; H, 97.8; Found: C, 57.79; H, 9.90.

*2-{2-[2-(4,5-Bis-(toluene-4-sulfonyloxymethyl)-[1,3]-dioxolan-2-ylmethoxy)ethoxy]ethoxy}ethanol (**14**).* Ditosyl **2** (0.28 g, 0.65 mmol) and *para*-toluenesulfonic acid (0.022 g, 0.13 mmol) was added to a solution of **13** (0.23 g, 0.65 mmol) in benzene (10 mL), then the solution was heated to reflux for 22 h. Pyridine (0.1 mL) was added at RT, then the solvent was removed under reduced pressure, and the residual oil was purified to yield a mixture of the acetals protected by THP (0.14 g, 31%) or with free hydroxyl terminus **14** (0.096 g, 24%). After dissolution of the THP-protected compound in methanol (2 mL), *para*-toluenesulfonic acid was added to the solution, and the reaction mixture was stirred for 6 h, then poured in an Erlenmeyer flask filled with solid potassium carbonate. The solution was filtered, and the filtrate was concentrated under reduced pressure. The residual oil was dissolved in dichloromethane and washed three times with a saturated $NaHCO_3$ solution and brine successively.

Then, the solvent was removed under reduced pressure to afford the alcohol **14**. The total yield for the reaction was 52% (65 mg). ^{1}H NMR ($CDCl_3$) δ (ppm) 2.46 (s, 6H, CH_3), 2.85 (m, 1H, OH), 3.47 (d, 2H, $J = 4.6$ Hz, CH_2O), 3.60−3.65 (m, 10H, $-CH_2O-$), 3.71 (m, 2H, $-CH_2OH$), 4.07−4.13 (m, 6H, CHO, CH_2OS), 5.11 (t, 1H, $J = 3.3$ Hz, CHO_2), 7.36 (d, 2H, $J = 8.1$ Hz, CH_{arom}), 7.78 (d, 2H, $J = 8.1$ Hz, CH_{arom}). ^{13}C NMR ($CDCl_3$) δ (ppm) 21.67 (s, CH_3), 61.84 (s, CH_2OH), 66.33 (d, CH_2OS), 70.56 (s, $-CH_2O-$), 70.69 (s, $-CH_2O-$), 71.26 (s, $-CH_2O-$), 71.88 (s, $-CH_2O-$), 72.54 (s, $-CH_2O-$), 75.67 (s, CHO), 104.16 (s, CHO_2), 128.05 (s, CH_{arom}), 130.06 (s, CH_{arom}), 132.71 (s, C_{arom}), 145.28 (s, C_{arom}). MS (ESI, *m/z*) 605 $(M + H)^+$.

*{2-[2-(4,5-Bis(toluene-4-sulfonyloxymethyl)-[1,3]-dioxolan-2-ylmethoxy)ethoxy]ethoxy}acetic acid (**15**).* Alcohol **14** (0.145 g, 0.24 mmol) was dissolved in acetone (2.5 mL). A solution of $NaHCO_3$ (15% in water, 0.75 mL) was added, and the reaction mixture was cooled to 0 °C. Then, sodium bromide (5 mg, 0.05 mmol), TEMPO (4 mg, 0.024 mmol), and trichloroisocyanuric acid (0.11 g, 0.48 mmol) were successively added. The reaction mixture was stirred vigorously for 14 h, and isopropanol (0.14 mL) was added to stop the reaction. After filtration, the solvent was evaporated under reduced pressure to yield a solid that was dissolved in a saturated solution of Na_2CO_3. The solution was extracted three times with ethyl acetate, dried ($MgSO_4$), and evaporated under reduced pressure to give the acid **15** as a yellow oil (0.106 g, 71%). ^{1}H NMR ($CDCl_3$) δ (ppm) 2.40 (s, 6H, CH_3), 3.41 (d, 2H, $J = 4.6$ Hz, $-CH_2O-$), 3.57−3.68 (m, 8H, $-CH_2O-$), 4.05 (m, 6H, CHO, CH_2OS), 4.10 (s, 2H, CH_2CO), 5.05 (t, 1H, $J = 3.3$ Hz, CHO_2), 7.31 (d, 2H, $J = 8.1$ Hz, CH_{arom}), 7.72 (d, 2H, $J = 8.1$ Hz, CH_{arom}). ^{13}C NMR ($CDCl_3$) δ (ppm) 21.65 (s, CH_3), 61.42 (d, CH_2OS), 70.35 (s, $-CH_2O-$), 70.50 (s, $-CH_2O-$), 71.08 (s, $-CH_2O-$), 71.67 (s, $-CH_2O-$), 75.61 (m, CHO, CH_2CO), 104.01 (s, CHO_2), 128.00 (s, CH_{arom}), 132.37 (s, CH_{arom}), 133.87 (s, C_{arom}), 145.28 (s, C_{arom}), 173.01 (s, C═O). MS (ESI, *m/z*) 619 $(M + H)^+$.

*2-{2-[2-(4,5-Bis(toluene-4-sulfonyloxymethyl)-[1,3]-dioxolan-2-ylmethoxy)ethoxy]ethoxy}-N,N-ditetradecylacetamide (**16**).* *N*-methylmorpholin (0.21 μL, 0.19 mmol) was added to a THF solution (4 mL) of **15** (0.54 g, 1.8 mmol) cooled to −40 °C. Then, a THF solution (0.5 mL) of isobutyl chloroformate (0.24 μL, 0.19 mmol) was added slowly. The reaction mixture was stirred for 1 h at −40 °C, then a THF solution (0.5 mL) of ditetradecylamine (0.07 g, 0.17 mmol) and *N*-methylmorpholin (0.21 μL, 0.19 mmol) was added slowly. The resulting mixture was stirred vigorously at RT for 20 h. Then, ethyl acetate (10 mL) and water (10 mL) were added. The water layer was extracted twice with ethyl acetate, then the combined organic solutions were successively washed twice with 1 N HCl, twice with a saturated solution of $NaHCO_3$, twice with brine, and then dried ($MgSO_4$). The solvent was removed under reduced pressure, then the resulting oil was purified by SFC to yield **16** as a clear oil (0.072 g, 42%). ^{1}H NMR ($CDCl_3$) δ (ppm) 0.86 (t, 6H, $J = 6.6$ Hz, $-CH_3$), 1.20−1.32 (m, 44H, $-CH_2-$), 1.49 (m, 4H, $-CH_2-$), 2.44 (s, 6H, CH_3), 3.15 and 3.26 (t, 4H, $J = 7.5$ Hz, $-CH_2N$), 3.42 (d, 2H, $J = 4.6$ Hz, $-CH_2O$), 3.58−3.68 (m, 8H, $-CH_2O-$), 4.01−4.09 (m, 6H, CHO, CH_2OS), 4.16 (s, 2H, CH_2CO), 5.07 (t, 1H, $J = 3.6$ Hz, CHO_2), 7.35 (d, $J = 8.1$ Hz, CH_{arom}), 7.75 (d, $J = 8.1$ Hz, CH_{arom}). ^{13}C NMR ($CDCl_3$) δ (ppm) 14.14 (s, $-CH_3$), 21.69 (s, CH_3), 22.72 (s, $-CH_2-$), 27.11 (s, $-CH_2-$), 29.03 (s, $-CH_2-$), 29.69 (m, $-CH_2-$), 31.97 (s, $-CH_2-$), 45.86 and 47.03 (s, $-CH_2N$), 68.25 (d, s, CH_2OS), 70.07 (s, $-CH_2O-$), 70.58 (m, $-CH_2O-$), 71.27 (s, $-CH_2O-$), 71.88 (s, $-CH_2O-$), 75.60 (s, CHO), 104.16 (s, CHO_2), 128.06 (s, CH_{arom}), 130.09 (s, CH_{arom}), 133.66 (s, C_{arom}), 145.31 (s, C_{arom}), 168.69 (s, C═O). MS (ESI, *m/z*) 1011 $(M + H)^+$.

*2-{2-[2-(4,5-Bis-azidomethyl-[1,3]-dioxolan-2-ylmethoxy)-ethoxy]ethoxy}-N,N-ditetradecylacetamide (**17**).* A solution of ditosyl **16** (0.36 g, 0.36 mmol) and sodium azide (0.23 g, 3.60 mmol) in DMF (10 mL) was heated overnight under reflux. The reaction mixture was evaporated under reduced pressure, then the residual solution was coevaporated several times with toluene. The resulting oil was treated with brine (30 mL) and extracted with ethyl acetate (3 × 20 mL). The combined organic extracts were dried ($MgSO_4$) and evaporated under reduced pressure to yield a yellow oil (0.28 g, 100%) that was used without further purification. ^{1}H NMR ($CDCl_3$) δ (ppm) 0.86 (t, 6H, $J = 6.6$ Hz, CH_3), 1.20−1.32 (m, 44H, $-CH_2-$), 1.52 (m, 4H, $-CH_2-$), 3.16 and 3.27 (t, 4H, $J = 7.5$ Hz, $-CH_2N$), 3.38−3.55 (m, 4H, CH_2N_3), 3.61 (d, 2H, $J = 4.6$ Hz, $-CH_2O$), 3.68 (m, 8H, $-CH_2O-$), 4.05 (m, 2H, CHO), 4.17 (s, 2H, $-CH_2CO$), 5.26 (t,1H, $J = 3.6$ Hz, CHO_2). ^{13}C NMR ($CDCl_3$) δ (ppm) 14.05 (s, CH_3), 22.65 (s, $-CH_2-$), 26.90 (s, $-CH_2-$), 28.07 (s, $-CH_2-$), 29.69 (m, $-CH_2-$), 31.90 (s, $-CH_2-$), 45.79 and 46.99 (2s, $-CH_2N$), 49.96 (s, $-CH_2N_3$), 70.13 (s, $-CH_2O-$), 70.56 (m, $-CH_2O-$), 71.24 (s, $-CH_2O-$), 72.07 (s, $-CH_2O-$), 77.12 (d, CHO), 103.66 (s, CHO_2), 162.49 (s, C═O).

*2-{2-[2-(4,5-Bis-aminomethyl-[1,3]-dioxolan-2-ylmethoxy)-ethoxy]ethoxy}-N,N-ditetradecylacetamide (**18**).* A 25 mL round-bottom flask equipped with a magnetic stirring bar was filled successively with diazide **17** (0.30 g, 0.4 mmol), ethanol (10 mL), Pd/C (50 mg), and hydrogen. The suspension was stirred for 19 h at RT, then the mixture was filtered through celite to yield after evaporation the diamine **18** (0.304 g, 100%), which was used without further purification. ^{1}H NMR ($CDCl_3$) δ (ppm) 0.80 (t, 6H, $J = 6.6$ Hz, CH_3), 1.20−1.32 (m, 44H, $-CH_2-$), 1.45 (m, 4H, $-CH_2-$), 2.50 (m, 4H, NH), 2.78−2.93 (m, 4H, CH_2NH_2), 3.09 and 3.20 (t, 4H, $J = 7.5$ Hz, $-CH_2N$), 3.53 (d, 2H, $J = 4.6$ Hz, $-CH_2O$), 3.59−3.63 (m, 8H, $-CH_2O-$), 4.09 (m, 2H, CHO), 4.12 (s, 2H, CH_2CO), 5.14 (t, 1H, $J = 3.6$ Hz, CHO_2). ^{13}C NMR ($CDCl_3$) δ (ppm) 14.11 (s, CH_3), 22.69 (s, $-CH_2-$), 27.05 (s, $-CH_2-$), 28.06 (s, $-CH_2-$), 29.69 (m, $-CH_2-$), 31.93 (s, $-CH_2-$), 43.66 (s, CH_2NH_2), 45.87 and 46.98 (s, $-CH_2N$), 69.88 (s, $-CH_2O-$), 70.55 (m, $-CH_2O-$), 71.17 (s, CH_2CO), 72.44 (s, $-CH_2O-$), 80.50 (d, CHO), 102.33 (s, CHO_2), 168.69 (s, C═O).

*2-{2-[2-(4,5-Bis-isothiocyanatomethyl-[1,3]-dioxolan-2-ylmethoxy)ethoxy]ethoxy}-N,N-ditetradecylacetamide (**19**).* Diisopropylethylamine (0.18 mL, 1 mmol) and carbon disulfide (0.084 mL, 1.4 mmol) were successively added to a solution of diamine **18** (0.26 g, 0.35 mmol) in dichloromethane (5 mL). The solution was stirred for 90 min, then a solution of tosyl chloride (0.13 g, 0.7 mmol) in dichloromethane (3 mL) was added dropwise. The mixture was stirred for 20 h, then evaporated under reduced pressure. The crude was purified by SFC to yield **19** as a colorless oil (0.096 g, 35%). ^{1}H NMR ($CDCl_3$) δ (ppm) 0.87 (t, 6H, $J = 6.6$ Hz, CH_3), 1.22−1.29 (m, 44H, $-CH_2-$), 1.51 (m, 4H, $-CH_2-$), 3.13 and 3.28 (t, 4H, $J = 7.5$ Hz, $-CH_2N$), 3.62 (d, 2H, $J = 4.3$ Hz, $-CH_2O-$), 3.65−3.73 (m, 8H, $-CH_2O-$), 3.79−3.84 (m, 4H, $-CH_2NCS$), 4.16 (m, 2H, CHO), 4.18 (s, 2H, −CH2CO−), 5.34 (t, 1H, $J = 3.6$ Hz, CHO_2). ^{13}C NMR ($CDCl_3$) δ (ppm) 14.14 (s, CH_3), 22.70 (s, $-CH_2-$), 27.07 (s, $-CH_2-$), 28.96 (s, $-CH_2-$), 29.67 (m, $-CH_2-$), 31.93 (s, $-CH_2-$), 45.87 and 46.44 (s, $-CH_2N$), 46.94 (s, $-CH_2NCS$), 69.88 (s, $-CH_2O-$), 70.51 (m, $-CH_2O-$), 71.32 (s, CH_2CO), 71.83 (s, $-CH_2O-$), 77.03 (d, CHO), 104.43 (s, CHO_2), 132.03 (s, C═S), 168.54 (C═O). MS (ESI, *m/z*) 785 $(M + H)^+$.

2-[2-(4-{4,5-Bis-[3-(2,3-dihydroxypropyl)thioureidomethyl]-[1,3]-dioxolan-2-ylmethoxy}ethoxy)ethoxy]-N,N-ditetradecyl-

Scheme 1. (i) TsCl, Pyridine, CH_2Cl_2, −20 °C, 52%; (ii) APTS, 3, Benzene, Reflux, 75%; (iii) NaN_3, DMF, Reflux, 94%; (iv) NaOH, MeOH/H_2O/THF, RT, 97%; (v) Isobutyl Chloroformate, *N*-Methylmorpholin, Ditetradecylamine, THF, −40 °C, 46%; (vi) Pd/C, H_2, Ethanol, RT, 96%; (vii) CS_2, TsCl, DIPEA, CH_2Cl_2, RT, 66%; (viii) Ethanolamine, THF, RT, 39%; (ix) 3-Aminopropane-1,2-diol, DMF, RT, 38%

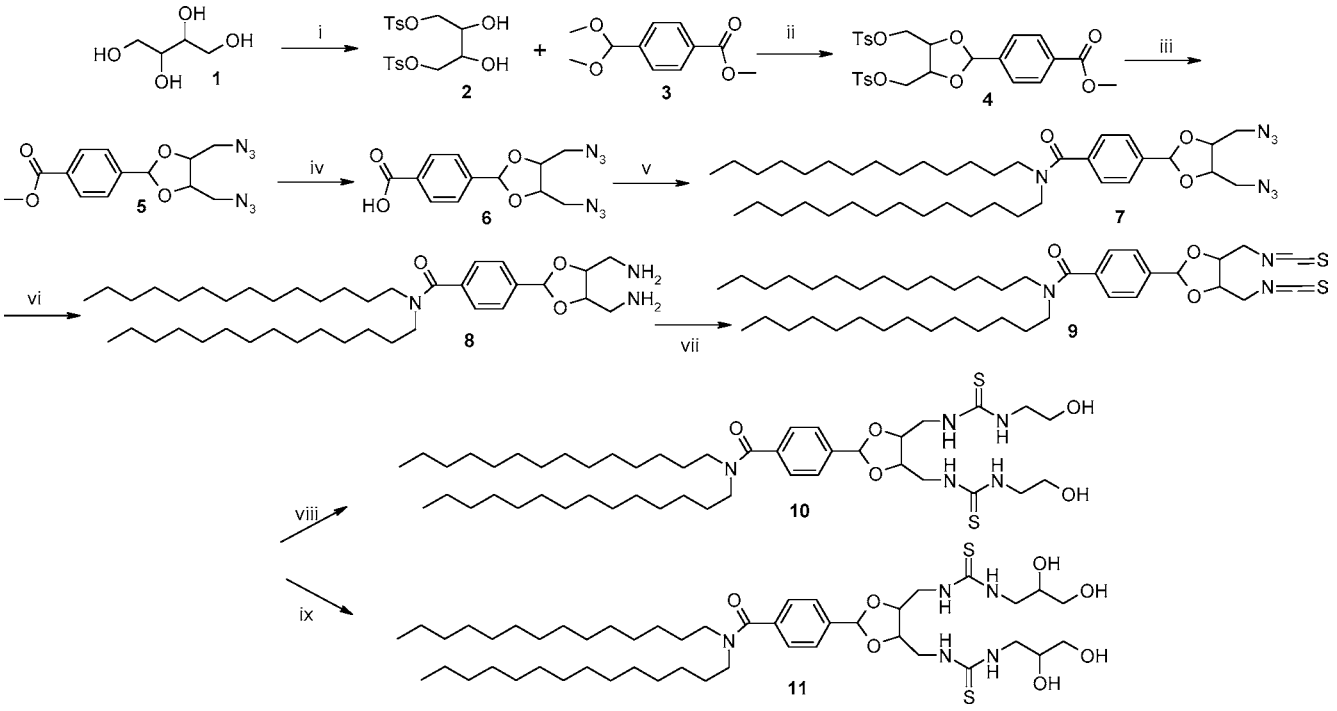

acetamide (20). 3-Amino-1,2-propanediol (0.008 g, 0.092 mmol) in DMF (0.1 mL) was added to a solution of **19** (41 mg, 0.056 mmol) in dry DMF (0.2 mL). The solution was stirred at RT for 20 h, then concentrated to dryness. The crude was dissolved in ethyl acetate and washed three times with brine. The organic layer was dried ($MgSO_4$) and evaporated to dryness. SFC purification yield **20** as a colorless oil (0.016 g, 72%). ^{1}H NMR ($CDCl_3$) δ (ppm) 0.88 (t, 6H, J = 6.6 Hz, CH_3), 1.22−1.29 (m, 44H, $-CH_2-$), 1.52 (m, 4H, $-CH_2-$), 3.11 and 3.28 (t, 4H, J = 7.5 Hz, $-CH_2N$), 3.50−3.75 (m, 22H, $-CH_2O-$, $-CH_2NCS$, CH_2OH), 4.13−4.34 (m, 6H, $-CH_2CO$, CHO, CHOH), 5.25 (t, 1H, J = 3.6 Hz, CHO_2). ^{13}C NMR ($CDCl_3$) δ (ppm) 14.13 (s, CH_3), 22.72 (s, $-CH_2-$), 27.16 (s, $-CH_2-$), 28.94 (s, $-CH_2-$), 29.67 (m, $-CH_2-$), 31.98 (s, $-CH_2-$), 45.44 (s, $-CH_2NCS$), 46.48 and 47.14 (s, $-CH_2NCO$), 63.74 (s, CH_2OH), 68.98 (s, CHOH), 69.84 (s, $-CH_2O-$), 70.28 (m, $-CH_2O-$), 70.59 (s, $-CH_2CO$), 71.39 (s, $-CH_2O-$), 78.35 (d, CHO), 101.93 (s, CHO_2), 169.06 (s, C═O), 183.55 (s, C═S). ES-HRMS Calcd for $C_{48}H_{95}N_5O_{10}NaS_2$: 988.6418. Found: 988.6389.

Lipopolythiourea Formulation. ARTUtetraol (2.27 mg, 2.5 μmol) and DPPC (3.66 mg, 5.0 μmol) were dissolved in a chloroform/acetone/ethanol mixture (1/5/4 v/v/v, 500 μL). This mixture was then added dropwise to 5 mL of stirred H_2O and vigorously stirred overnight. Most of the solvents were removed under vacuum to obtain a fairly concentrated suspension of liposomes (concentration of ARTUdiol = 8.5 mM). Similar procedures were used for the other LPT.

Complex Size. The complex diameter was determined by dynamic light scattering on a Zetasizer Nano Series Malvern. 10 μL of ARTUdiol/DPPC 1/2 (C = 8.5 mM) was added to 800 μL of H_2O; mean value of three runs is given (1 min equilibration, 3 min run).

Preparation of the Complexes LPT/DPPC/DNA. Plasmid DNA (pVax2luc) (100 μL, 0.02 g/L in H_2O) was added dropwise with constant vortexing to various amounts of ARTUdiol/DPPC 1/2 particles (for a ratio value of thiourea function over DNA phosphate of 20: 100 μL, 1.2 mM) at RT. The samples were left to incubate at RT overnight before size measurements, which were performed on a Zetasizer Nano Series Malvern.

Agarose Gel Electrophoresis. Samples were prepared as described above (20 μL), and 5 μL of bromophenol blue was added. The mixtures were loaded into 0.8% agarose gel in TBE buffer (1 M Tris, 0.9 M boric acid, 0.01 M EDTA) at 80 V/cm. DNA was revealed with ethidium bromide and visualized under UV light.

Luciferase Measurement. The NIH3T3, mice fibroblasts cells, were grown in DMEM medium, supplemented with 10% fetal bovine serum, 1% antibiotics (penicillin and streptomycin), and 1% glutamine. HUVEC cells, primocultures of human unbilical vein endothelial cels, were grown into endothelial cell growth medium kit (Promo Cell) medium. One day before transfection, the cells were treated with trypsin, deposed into 24-well plates (3T3, 50 000 cells/well; HUVEC, 70 000 cells/well) and incubated 24 h at 37 °C. A volume of 200 μL of LPT/DNA (corresponding to 0.5 μg DNA) complexes was loaded on each well, and the plates are incubated at 37 °C for 48 h. Then, the cells were washed twice with PBS and lysed with 200 μL of a passive lysis buffer (Promega) containing SDS (2.5%) and TRIS (50 mM) at pH 7.5. After 15 min, the cells were centrifuged for 5 min at 12 000 rpm. 10 μL of supernatant and 10 μL iodoacetamide were deposited onto a 96-well plate, which was incubated at 37 °C for 1 h. Protein quantification was performed with the BCA protein assay kit (Pierce) and reported to the BSA taken as a reference curve. Luciferase activity was quantified using a commercial kit Luciferase assay system (Promega). On 10 μL of the lysed cells, 50 μL of the luciferin substrate was injected via an injector, and the absorbance was read immediately at 563 nm on a Wallac Victor2 1420 Multilabel Counter (Perkin-Elmer).

RGD-Mediated Lipopolythiourea Liposomes Delivery to HUVEC and NIH3T3 Fibroblast Cells. One day before transfection, HUVEC or NIH3T3 cells were deposed into 12-well plates with glass lamellae (3T3, 70 000 cells/well; HUVEC, 150 000 cells/well) and incubated at 37 °C for 24 h in MEM

Scheme 2. (i) NaH, Bromoacetaldehyde Diethyl Acetal, THF, 60 °C, 100%; (ii) APTS, 2, Benzene, Reflux; (iii) APTS, Methanol, RT, 52% Two Steps; (iv) TEMPO, Trichloroisocyanuric Acid, NaBr, Acetone, RT, 71%; (v) Isobutyl Chloroformate, *N*-Methylmorpholin, Ditretradecylamine, THF, −40 °C, 42%; (vi) NaN_3, DMF, Reflux, 100%; (vii) H_2, Pd/C, Ethanol, RT, 100%; (viii) CS_2, TsCl, DIPEA, CH_2Cl_2, RT, 35%; (ix) 3-Amino-1,2-propanediol, DMF, RT, 72%

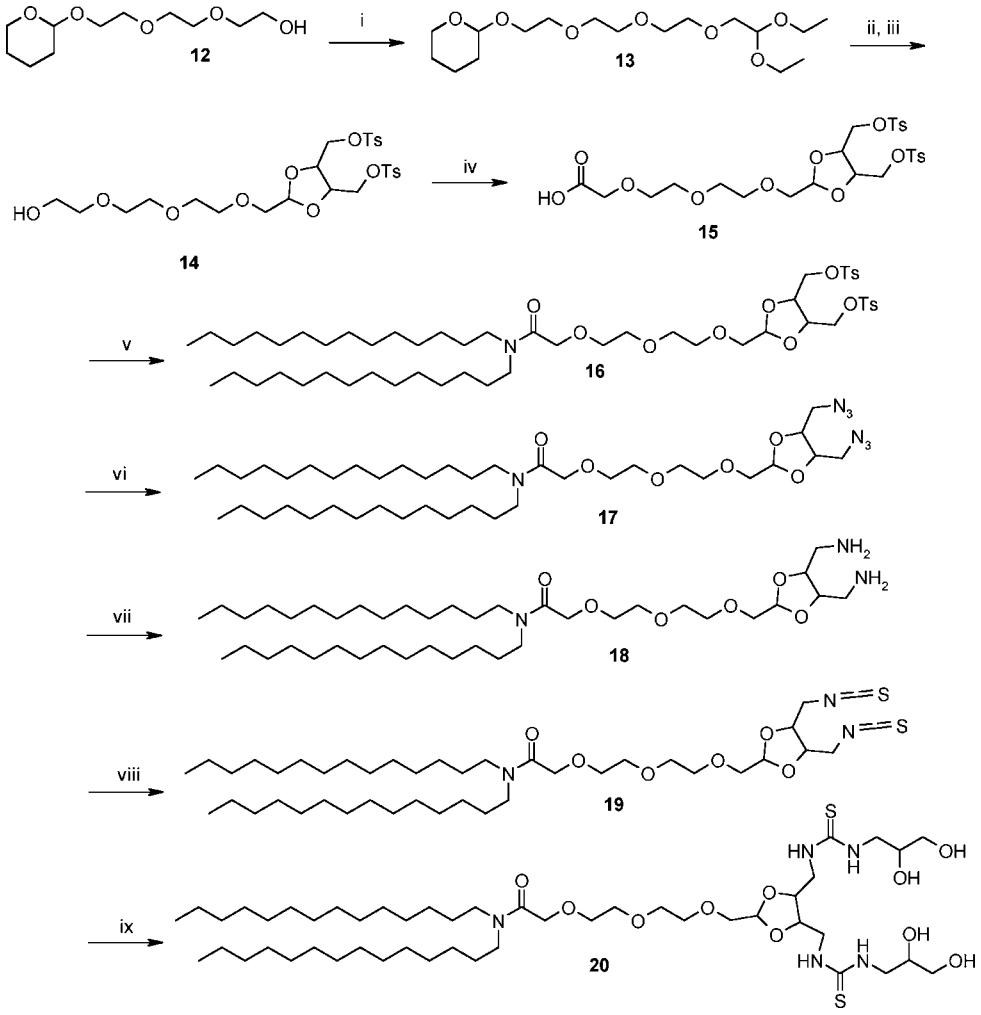

Table 1. Size (nm) of LPT/Colipid Particles Measured in H_2O on a Malvern Instrument Zetasizer NanoSeries

formulation	ARTUdiol	ARTUtetraol	PEG_3TUtetraol
LPT/DPPC (1:1)	no particles	79 ± 20	no particles
LPT/DPPC (1:2)	107 ± 26	122 ± 28	142 ± 49
LPT/Chol-PEG_{45} (10:1)	264	130	ND

medium. Lipopolythiourea/DNA complexes (200 μL, 0.5 μg DNA) were loaded in each well. After 7 h at 37 °C, the wells were washed twice with PBS, and 500 μL of PFA (3% in PBS) was added. The plates were left 30 min in the dark at RT before being washed twice with PBS. DAPI (0.05 μg in 500 μL PBS) was then added. The plates were left 30 min in the dark, washed with PBS, and treated with mowiol. Fluorescence was observed on a ZEISS Axiophot noninversed microscope.

RESULTS

Synthesis. Three myristyl compounds were chosen as models to evaluate the impact of LPT structural modifications to DNA compaction and to transfection efficacy. First, the synthesis of compounds **10** and **11**, bearing an aromatic linker, is described in Scheme 1.

Considering the structure of **10** and **11,** we chose to investigate a strategy starting from the readily available D,L-threitol (**1**). Tosylation of **1** with two tosyl chloride equivalents proceeded selectively (6:1) to give **2** in 52% yield with the tritosyl derivative as a minor product (8%) (*20*). Attempts to increase the selectivity using the more bulky trisyl chloride provided no improvement (*21*). Transacetalation with methyl 4-(dihydroxymethyl)cyclohexa-1,3-diene-1-carboxylate **3** (*22*) in the presence of a catalytic amount of APTS and using a Dean−Stark trap afforded the five-membered-ring acetal **4** in 75% yield (*23*). Azidation of **4** afforded the diazide **5** (94%), then saponification of the methyl ester gave the carboxylic acid **6** (97%).

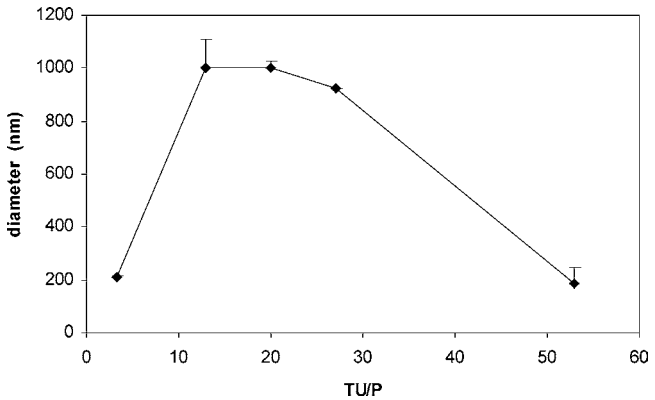

Figure 2. Diameter of particles PEG_3TUtetraol/DPPC (1:2) with increasing amounts of DNA measured in H_2O on a Malvern Instrument Zetasizer NanoSeries (ratio TU/P = mol thiourea functions/mol DNA phosphate groups).

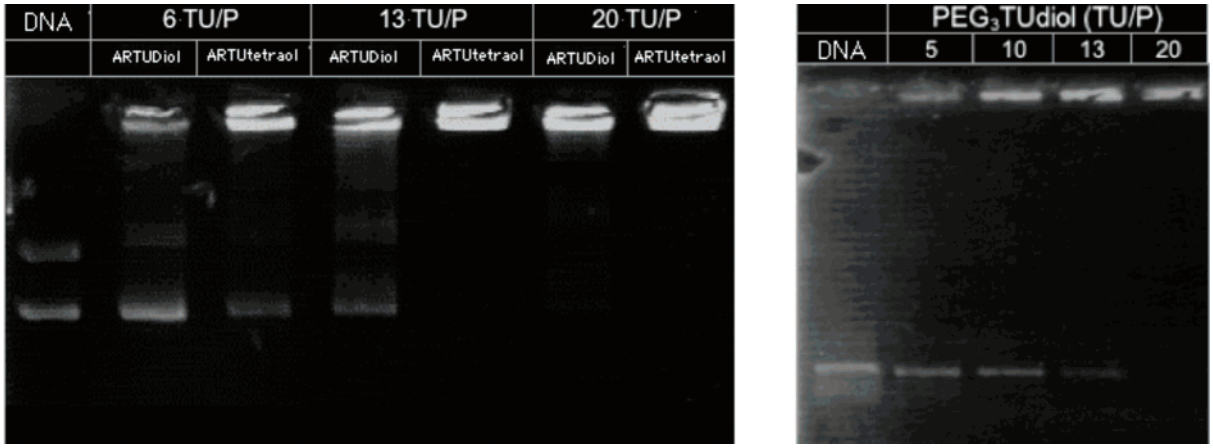

Figure 3. Migration of the ARTUdiol/DPPC(1:2)/DNA and ARTUtetraol/DPPC(1:2)/DNA complexes (left) and PEG_3TUtetraol/DPPC(1:2)/DNA complexes (right) on a 0.8% agarose gel in TBE (1×). DNA was revealed with ethidium bromide and visualized under UV light.

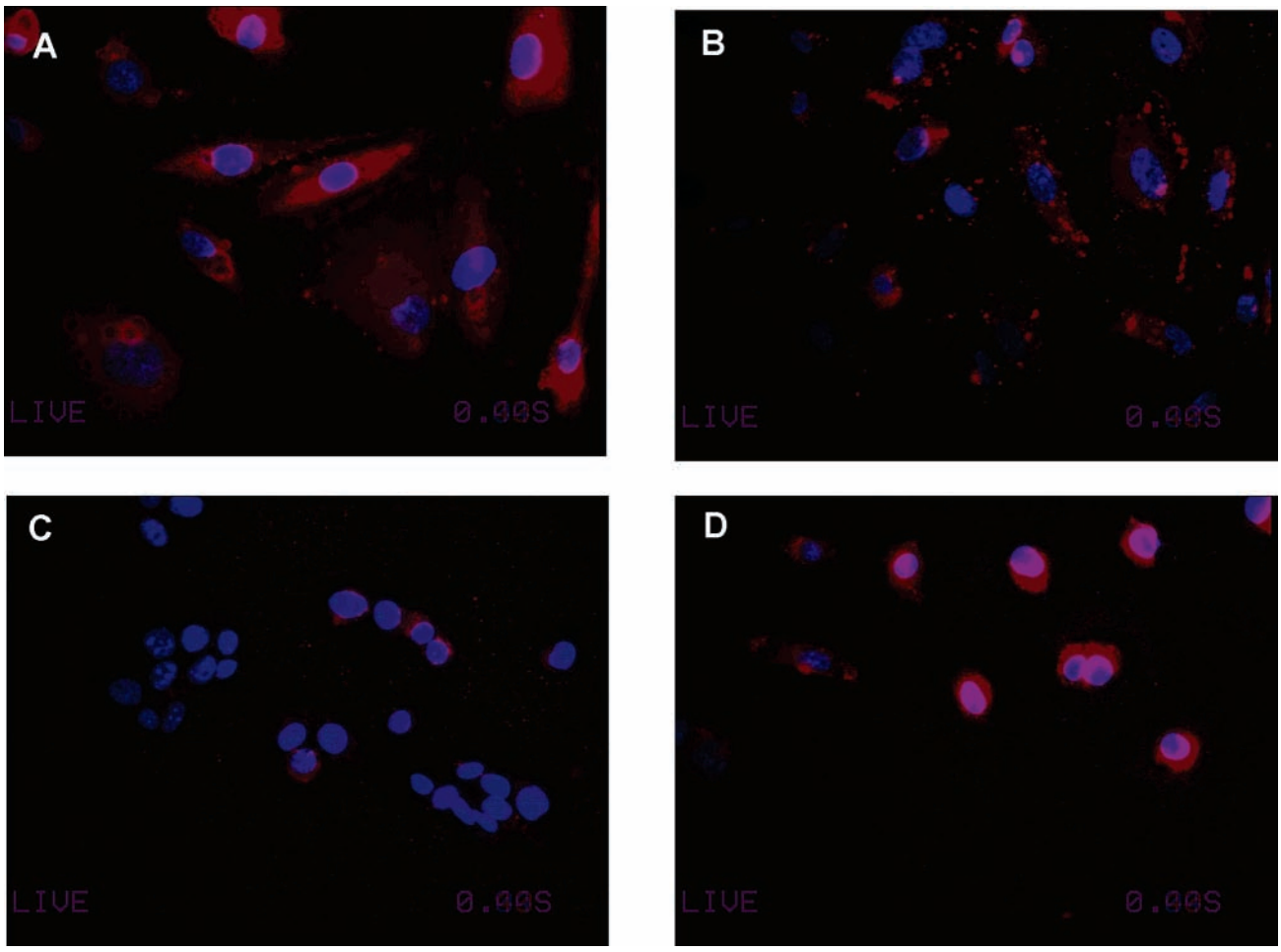

Figure 4. Fluorescence microscopy of ARTUtetraol particles. ARTUtetraol/DPPC/ $CholPEG_{45}$/DOPE−Rhodamine (10:10:0.20:0.1) ± Chol−PEG_{75}−RGD−4C (0.2) complexes were incubated for 7 h on HUVEC cells (A and B) in the absence (A) or presence (B) of RGD ligand, and on NIH3T3 cells (C and D) in the absence (C) or presence (D) of RGD ligand. Nuclei are stained with DAPI .

Subjecting **6** to amidation with ditetracedylamine using a mixed-anhydride procedure (*24*) provided good access to compound **7**. Catalytic reduction of the diazide **7** effected the conversion to the diamine **8** in high yield. The bis-isothiocyanate **9** was obtained in good yield by the reaction of **8** with CS_2 in the presence of tosyl chloride (*25*). The desired lipopolythioureas **10** and **11** were ultimately prepared by condensation of **9** with ethanolamine and 3-aminopropane-1,2-diol, respectively.

The synthesis of the lipopolythiourea bearing a short PEG linker is described in Scheme 2. It started with the synthesis of 2-{2-[2-(tetrahydropyranyl-2-yloxy)ethoxy]ethoxy}ethanol (**12**) as described in the literature (*26*).

Then, substitution of the hydroxyl terminus with bromoacetaldehyde diethyl acetal (*27*) led to the diethoxy acetal **13** that was converted to the 1,3-dioxolane **14** through treatment with diol **2** in the presence of APTS. Oxidation of **14** was performed using TEMPO and trichloroisocyanuric acid (*28*). The resulting acid **15** was treated with isobutyl chloroformate and ditetradecylamine to afford the amide **16**. Substitution of the tosyl group of **16** with sodium azide followed by palladium

reduction of the azido group gave the diamine **18** quantitatively. Elaboration of the diisothiocyanate **19** from the diamine **18** proved to be difficult and led to a modest 35% yield. Addition of 3-amino-1,2-propanediol to **19** completed the synthesis of the lipopolythiourea **20**.

Formulation Study. Compounds **10** (ARTUdiol) and **11** (ARTUtetraol) bear the same aromatic linker and differ only by the number of hydroxyl groups attached to the thiourea functionalities. Compound **20** is similar to compound **11** (PEG_3TUtetraol) considering the thiourea part, but differs by its linker. In terms of the hydrophilic/hydrophobic balance, we expected ARTUdiol < ARTUtetraol < PEG_3tetraol.

The ability of these 3 LPTs to form micellar or liposomal particles was evaluated. Similarly to the previously studied linear LPT (*13*), we chose DPPC or PEG_{45} lipid as co-lipids because of the hydrophobic behavior of the LPT. Several formulations were evaluated (Table 1). ARTUdiol/DPPC (1:2), ARTUtetraol/DPPC (1:1 and 1:2), ARTUdiol/Chol−PEG_{45} (10:1), ARTUtetraol/Chol−PEG_{45} (10:1), and PEG_3TUtetraol/DPPC (1:2) led to small particles whose diameters ranged from 100 to 250 nm, depending on the co-lipid. It is noteworthy that only ARTUtetraol could be formulated with 1 equiv of DPPC. Comparison among the aromatic lipids indicated that a tetraol terminus eased the formulation, since ARTUtetraol required a lower amount of DPPC than ARTUdiol, with the tetraol moiety probably increasing the hydrophilicity. Comparison of the two tetraol lipids showed that the lipid bearing an aromatic linker had a better capacity to form particles, possibly due to aromatic $\pi-\pi$ stacking within the lipid bilayer (*29*).

Interaction of LPT/DPPC with DNA. The capacity of LPT/DPPC (1:2) particles to associate to plasmid DNA was then studied. Setting a fixed DNA amount, we added on the DNA solution an increasing amount of lipids. After one night of incubation, we measured the size of the complexes by dynamic light scattering. The results are reported for PEG_3TUtetraol (Figure 2), but similar data have been obtained for ARTUdiol and ARTUtetraol. In the presence of DNA, we observed a size increase from 200 nm to the micrometer range, proving an interaction between lipopolythiourea particles and plasmid DNA. Adding an excess of lipids (30 equiv thiourea functions/DNA phosphate groups) let the system return to a colloidal stability.

Gel retardation experiments of LPT/DPPC/DNA complexes were performed to evaluate DNA association to particles ARTUdiol/DPPC (1:2), ARTUtetraol/DPPC (1:2), and PEGTUtetraol/DPPC (1:2). Partial retardation was observed above 6 thiourea functions/DNA phosphate groups (TU/P), and complete retardation was observed for ratios of 13 TU/P for ARTUtetraol and 20 TU/P for ARTUdiol and PEG_3TUtetraol (Figure 3). In our previous study (*13*), complete retardation was obtained for a ratio equal to 20 thiourea functions/DNA phosphate groups (TU/P). Thus, we observed that, using branched lipids bearing only two thiourea functions, we could obtain an interaction with DNA at lower or identical ratio TU/P, as compared to the DTTU lipid bearing three linear functions. These data indicated that a stable interaction between LPT and DNA could be established with only two thiourea groups.

Transfection Activity and RGD-Mediated Delivery into Endothelial Cells. DNA transfection mediated by ARTUdiol, ARTUtetraol, and PEGTUtetraol led to disappointing results, since no significative luciferase activity could be measured on the treated B16 cell. This lack of transfection activity may be explained by the noncationic nature of the LPT, causing poor contact with cell membranes. To improve these interactions, RGD-mediated internalization of endothelial cells expressing integrin $\alpha_V\beta_3$ was investigated. Thus, we added a PEG_{75}−lipid bearing a RGD peptide (*14*) to the formulation, and a rhodamine-labeled lipid/DNA complex were prepared. Their intracellular fate was investigated using fluorescence microscopy. These experiments were carried out on two cell types: human umbilical vein endothelial cells (HUVEC), which express integrin $\alpha_V\beta_3$, and NIH3T3 fibroblasts, taken as a negative control. Only the results with ARTUtetraol are shown in Figure 4. In the absence of Chol−PEG−RGD, we only observed extracellular binding of lipoplexes to the cell membrane. Such a result has also been reported for PEGylated lipoplexes (*30*). However, in its presence, we clearly saw intracellular punctuations, which indicated particle internalization. In opposition, no internalization was observed in NIH3T3 cell fibroblasts, although the extracellular binding to cell membranes seemed to be stronger with the RGD group. Thus, addition of Chol−PEG−RGD allowed a specific uptake of the LPT/DNA complexes into the cells. These results are in agreement with the specific capture previously reported on RGD-functionalized spherulites (*31*). However, this has been found to lead to neither HUVEC nor NIH3T3 transfection. This might result from a lack of DNA release from the LPT/DNA complex, possibly due to the PEG−lipid, that was shown to stabilize lipoplexes and reduce transfection efficiency (*32*).

CONCLUSION

These results present new lipopolythioureas able to associate DNA. Adding a diol or a tetraol terminus to the thiourea part improved the hydrophilicity and eased the DNA formulation. Use of Chol−PEG−RGD allowed observation of a specific internalization of the complexes in HUVEC cells as shown earlier with other particle types, such as spherulite. On the other hand, these particles were unable to transfect DNA, an effect which might be related to the presence of a PEG moiety in the formulation, thus inducing a shielding effect, which has been shown to affect transfection. Work is in progress to obtain more hydrophilic thiourea compounds and to study the internalization using an RGD derivative without any PEG moiety.

ACKNOWLEDGMENT

This work was financially supported by INSERM, CNRS, MNERT, and the Région Ile de France (SESAME, CPER). JL thanks the MNERT for a doctoral fellowship.

LITERATURE CITED

(1) Ruponen, M., Honkaski, P., Rönkkö, S., Tammi, M., and Urtti, A. (2003) Extracellular and intracellular barriers in non-viral gene delivery. *J. Controlled Release 93*, 213−217.
(2) Wells, D. J. (2004) Gene therapy progress and prospects: electroporation and other physical methods. *Gene Ther. 11*, 1363−136.
(3) Verma, I. M., and Weitzman, M. D. (2005) Gene therapy: twenty-first century medicine. *Annu. Rev. Biochem. 74*, 711−738.
(4) Thomas, A. E., Ehrhardt, A., and Kay, M. A. (2003) Progress and problems with the use of viral vectors for gene therapy. *Nat. Rev. Genet. 4*, 346−358.
(5) Nicolazzi, C., Garinot, M., Mignet, N., Scherman, D., and Bessodes, M. (2003) Cationic lipids for transfection. *Curr. Med. Chem. 10*, 1263−1277.
(6) Pack, D. W., Hoffman, A. S., Pun, S., and Stayton, P. S. (2005) Design and development of polymers for gene delivery. *Nat. Rev. Drug Discovery 4*, 581−593.
(7) Dass, C. R. (2004) Lipoplex-mediated delivery of nucleic acids: factors affecting in vivo transfection. *J. Mol. Med. 82*, 579−591.
(8) Nicolazzi, C., Mignet, N., de la Figuera, N., Cadet, M., Ibad, R. T., Seguin, J., Scherman, D., and Bessodes, M. (2003) Anionic polyethyleneglycol lipids added to cationic lipoplexes increase their plasmatic circulation time. *J. Controlled Release 88*, 429−43.
(9) Arigon, J., Prata, C. A. H., Grinstaff, M. W., and Barthélémy, P. (2005) Nucleic acid complexing glycosyl nucleoside-based amphiphile. *Bioconjugate Chem. 16*, 864−872.
(10) Thompson, B., Mignet, N., Hofland, H., Lamons, D., Seguin, J., Nicolazzi, C., de la Figuera, N., Kuen, R. L., Meng, X. Y., Scherman,

D., and Bessodes, M. (2005) Neutral postgrafted colloidal particles for gene delivery. *Bioconjugate Chem. 16*, 608−614.
(11) Takemoto, Y. (2005) Recognition and activation by ureas and thioureas: stereoselective reactions using ureas and thioureas as hydrogen-bonding donors. *Org. Biomol. Chem. 3*, 4299−4306.
(12) Buhlmann, P., Nishizawa, S., Xiao, K. P., and Umezawa, Y. (1997) Strong hydrogen bond-mediated complexation of $H_2PO_4^-$ by neutral bis-thiourea hosts. *Tetrahedron 53*, 1647−1654.
(13) Tranchant, I., Mignet, N., Crozat, E., Leblond, J., Girard, C., Scherman, D., and Herscovici, J. (2004) DNA complexing lipopolythiourea. *Bioconjugate Chem. 15*, 1342−1348.
(14) Tranchant, I., Thompson, B., Nicolazzi, C., Mignet, N., and Scherman, D. (2004) Physicochemical optimisation of plasmid delivery by cationic lipids. *J. Gene Med. 6*, Suppl. 1, S24−S35.
(15) Petit, L., Joubert, L., Tranchant, I., Herscovici, J., and Adamo, C. submitted.
(16) Byk, G., Dubertret, C., Escriou, V., Jaslin, G., Rangara, R., Pitard, B., Crouzet, J., Wils, P., Schwartz, B., and Scherman, D. (1998) Synthesis, activity and structure-activity relationship studies of novel cationic lipids for DNA transfer. *J. Med. Chem. 41*, 224−235.
(17) Majeti, B. K., Karmali, P. P., Reddy, B. S., and Chaudhuri, A. (2005) In vitro gene transfer efficacies of *N*,*N*-dialkylpyrrolidinium chlorides: a structure-activity investigation. *J. Med. Chem. 48*, 3784−3795.
(18) Still, W. C., Kahn, M. and Mitra, A. (1978) Rapid chromatographic technique for preparative separations with moderate resolution *J. Org. Chem. 43*, 2923−2926.
(19) Balacco, G. (1994) SwaN-MR: A Complete and Expansible NMR Software for the Macintosh. *J. Chem. Inf. Comput. Sci. 34*, 1235−124.
(20) Sommerdijk, N. A., Hoeks, T. H., Synak, M., Feiters, M. C., Nolte, R. J., and Zwanenborg, B. (1997) Stereodependent fusion of vesicles: calcium binding of synthetic gemini phospholipids containing two phosphate groups. *J. Am. Chem. Soc. 119*, 4338−4344.
(21) White, J. D., Bolton, G. L., Dantanarayana, A. P., Fox, C. M., Hiner, R. N., Jackson, R. W., Sakuma, K., and Warrier, U. S. (1995) Total synthesis of the antiparastic agent avermectin B1a. *J. Am. Chem. Soc. 117*, 1908−1939.
(22) Methyl 4-(dihydroxymethyl)cyclohexa-1,3-diene-1-carboxylate **3** was prepared in one step by the reaction of 4-formylcyclohexa-1, 3-diene-1-carboxylic acid with thionyl chloride in methanol.
(23) Harada, T., Nakamura, T., Kinusaga, M., and Oku, A. (1999) Mechanism of chiral Lewis acid mediated enantiotopic group-selective ring cleavage of cyclic acetals derived from meso-1,2-diols. *J. Org. Chem. 64*, 7594−7600.
(24) Wender, P. A., Jessop, T. C., Pattabiraman, K., Pelkey, E. T., and VanDeusen, C. L. (2001) Efficient, scalable synthesis of the novel molecular transporter Octa-Arginine. *Org. Lett. 3*, 3229−3232.
(25) Stephensen, H., and Zaragoza, F. (1997) Resin-bound isothiocyanates and their synthetic equivalents as intermediates for the solid-phase synthesis of substituted thiophenes. *J. Org. Chem. 62*, 6096−6097.
(26) Loiseau, F., Hii, K., and Hill, A. (2004) Multigram synthesis of well-defined extended bifunctional polyethylene glycol (PEG) chains. *J. Org. Chem. 69*, 639−647.
(27) Keane, J. F., Cuomo, J., Lex, L., and Seyedrezai, S. E. (1983) Azoethoxy nitroxide spin-labeled crown ethers and cryptands with the N−O group positioned near the cavity. *J. Org. Chem. 48*, 2647−2654.
(28) De Luca, L., Giacomelli, G., Masala, S., and Porcheddu, A. (2001) A very mild and chemoselective oxidation of alcohols to carbonyl compound. *Org. Lett. 3*, 3041−3043.
(29) Bhattacharya, S., Subramanian, M., and Hiremath, U. S. (1995) Surfactant lipids containing aromatic units produce vesicular membranes with high thermal stability. *Chem. Phys. Lipids 78*, 177−188.
(30) Shi, F., Wasingu, L., Nomoden, A., Stuart, M. C., Polushkin, E., Engberts, J. B., and Hoekstra, D. (2002) Interference of poly(ethylene glycol)−lipid analogues with cationic-lipid-mediated delivery of nucleotides; role of lipid exchangeability and non-lamellar transitions, *Biochem. J. 366*, 333−341.
(31) Chenevier, P., Delord, B., Amedee, J., Bareille, R., Ichas, F., and Roux, D. (2002) RGD-functionalized spherulites as targeted vectors captured by adherent cultured cells. *Biochim. Biophys. Acta 1593*, 17−27.
(32) Song, L. Y., Ahkong, Q. F., Rong, Q., Wang, Z., Ansell, S., Hope, M. J., and Mui, B. (2002) Characterization of the inhibitory effect of PEG−lipid conjugates on intracellular delivery of plasmid and antisense DNA mediated by cationic liposomes. *Biochim. Biophys. Acta 1558*, 1−13.

BC060110G

Influence of Polyethylene Glycol Chain Length on the Physicochemical and Biological Properties of Poly(ethylene imine)-*graft*-Poly(ethylene glycol) Block Copolymer/SiRNA Polyplexes

Shirui Mao,[†,‡] Michael Neu,[†] Oliver Germershaus,[†] Olivia Merkel,[†] Johannes Sitterberg,[†] Udo Bakowsky,[†] and Thomas Kissel*[,†]

Department of Pharmaceutics and Biopharmacy, Philipps Universität Marburg, Ketzerbach 63, 35032 Marburg, Germany, and School of Pharmacy, Shenyang Pharmaceutical University, 103 Wenhua Road, Shenyang, China. Received May 19, 2006; Revised Manuscript Received August 7, 2006

Polyplexes between siRNA and poly(ethylene imine) (PEI) derivatives are promising nonviral carriers for siRNA. The polyplex stability is of critical importance for efficient siRNA delivery to the cytoplasm. Here, we investigate the effect of PEGylation at a constant ratio (∼50%) on the biophysical properties of the polyplexes. Particle size, ζ potential, and stability against heparin as well as RNase digestion and reporter gene knockdown under in vitro conditions of different siRNA polyplexes were characterized. Stability and size of siRNA polyplexes were clearly influenced by PEI−PEG structure, and high degrees of substitution such as PEI(25k)-*g*-PEG(550)$_{30}$ resulted in large (300−400 nm), diffuse complexes (AFM) which showed condensation behavior only at high N/P ratios. All other polyplexes and the PEI control showed similar sizes (150 nm) and compact structures in AFM, with complete condensation reached at N/P ratio of 3. Stability of siRNA polyplexes against heparin displacement and RNase digestion could be modified by PEGylation. Protection against RNase digestion was highest for PEI(25k)-*g*-PEG(5k)$_4$ and PEI(25k)-*g*-PEG(20k)$_1$, while siRNA/PEI provided insufficient protection. In knockdown experiments using NIH/3T3 fibroblasts stably expressing *β*-galactosidase, it was shown that PEG chain length had a significant influence on biological activity of siRNA. Polyplexes with siRNA containing PEI(25k)-*g*-PEG(5k)$_4$ and PEI-(25k)-*g*-PEG(20k)$_1$ yielded similar efficiencies of ca. 70% knockdown as lipofectamine controls. Confocal microscopy demonstrated enhanced cellular uptake of siRNA into cytosol by polyplexes formation with PEI copolymers. In conclusion, both the chain length and graft density of PEG were found to strongly influence siRNA condensation and stability and hence affect the knockdown efficiency of PEI−PEG/siRNA polyplexes.

INTRODUCTION

RNA interference (RNAi) using small interfering RNA (siRNA, a double-stranded RNA with 21−23 bp) has recently emerged as a powerful tool for silencing target genes and holds great possibility for therapeutic application (*1*). The first clinical data on RNAi have been published recently (*2*). However, to achieve efficient gene knockdown under in vivo conditions, siRNA degradation in the physiological milieu, poor cellular uptake, and inefficient translocation into the cytoplasm need to be improved. Macromolecules like siRNA are typically internalized by endocytosis followed by lysosomal fusion causing siRNA degradation. Endosomal escape is a prerequisite for efficient delivery of intact siRNA to the cytosol, its site of biological action (*3*). Moreover, the polyanionic nature of siRNA impairs diffusion through cell membranes and cellular uptake. Therefore, delivery systems for siRNA are of particular importance to exploit their therapeutic potential (*4*). A promising approach could be siRNA delivery through complexation of siRNA using biodegradable and biocompatible polycations (*5*).

Poly(ethylene imine) (PEI) is well-known as an efficient nonviral nucleic acid vector demonstrating high transfection rates under in vitro and in vivo conditions (*6*). PEI forms polyplexes with anionic nucleotides by electrostatic interactions. The strong buffer capacity, designated as the proton sponge hypothesis, could be responsible for the fact that PEI-based delivery systems do not require endosome disruptive agents for lysosomal escape (*7*). Once released from endosomes, the siRNA may enter the cytosol, where it associates with its complementary siRNA strand and, depending on its complementarity, results in either targeting cleavage of the mRNA or translational arrest. However, intact PEI/plasmid complexes were found in the cell nucleus (*8*, *9*), implying that PEI/siRNA polyplexes might be too stable to be released in the cytosol and will be transported into the nucleus, as in the case of plasmid/PEI complexes (*8*); therefore, no knockdown will be observed. To guarantee the biological activity of siRNA, this point needs to be clarified, and stability of the PEI/siRNA polyplexes needs to be further modified. The polyplexes should be sufficiently stable during the endocytosis process to ensure sufficient intracellular uptake of siRNA, but thereafter, siRNA should be released into the cytosol. While it was noticed that a significant decrease in transfection activity for the PEI−PEG/DNA polyplexes was found (*10*, *11*), it is reasonable to assume that PEGylation might be able to destabilize PEI/siRNA polyplexes, leading to increased siRNA release in the cytoplasm and therefore efficient knockdown. This hypothesis was investigated in this study.

Recently, application of linear PEI or low molecular PEI as an siRNA delivery vector has been reported (*12*−*15*). In agreement with our hypothesis, linear PEI was efficient for delivering nucleic acids to cells but did not lead to siRNA activity within the applied dose of <0.5 pmol (*12*). Direct intratumor injection of a siRNA-encoding plasmid complexed

* To whom correspondence should be addressed. Department of Pharmaceutics and Biopharmacy, Phillips-Universität Marburg, Ketzerbach 63, D-35032 Marburg, Germany, Tel +49-6421-282-5881, FAX +49-6421-282-7016, E-mail: kissel@staff.uni-marburg.de.

[†] Philipps Universität Marburg.

[‡] Shenyang Pharmaceutical University.

10.1021/bc060129j CCC: $33.50 © 2006 American Chemical Society
Published on Web 09/01/2006

Table 1. Schematic Structure and Properties of the PEI-*g*-PEG Copolymers Investigated in This Study[a]

Compound	PEI	PEI (25k)-g -PEG(550)$_{30}$	PEI(25k)-g -PEG(2k)$_{10}$	PEI(25k)-g -PEG(5k)$_4$	PEI(25k)-g -PEG(20k)$_1$
PEI content	100%	60%	55%	55%	55%
Mw PEI	25000	25000	25000	25000	25000
Mw PEG		550	2000	5000	20000
Mw	25000	41500	45000	45000	45000
Structure	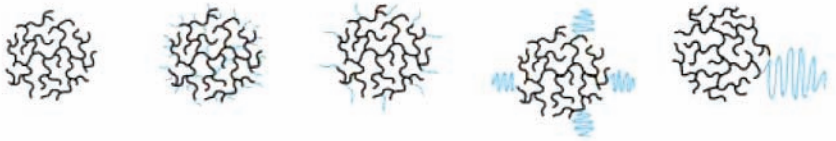				

[a] The black part of the structure represents the branched PEI 25 kDa, and the blue part represents the nonionic linear PEG segments.

with linear PEI efficiently reduced the vascularization of treated tumors but was not able to reduce tumor growth (*13*). The low activity of siRNA might be attributed to insufficient release in the cytosol.

PEGylated PEI was synthesized in our group to decrease the cytotoxicity of branched PEI and was extensively studied as vectors for DNA delivery (*16*). Moreover, strong evidence was provided that PEGylated PEI could be adapted to function as an effective carrier for cellular delivery of small oligonucleotides. Recent reports have characterized the properties and transfection capacity of PEGylated PEI25k complexed with oligonucleotides (*17*, *18*). Similarly, branched PEI-*graft*-poly(ethylene glycol) has been recently reported as a carrier of siRNA with different targeting ligands, and the results are promising (*19*−*21*).

Regarding PEGylation, both PEG chain length and graft density clearly affect pharmacokinetic properties of polyplexes containing nucleic acids, although in vivo results are discussed controversially. While some authors suggest that low graft densities with high molecular weight PEG are more effective in reducing protein adsorption than the higher surface density of low molecular weight polymers (*22*), others found that density of PEG grafting on the surface of polyplexes had a more pronounced effect on protein adsorption than PEG chain length on steric repulsion and van der Waals attraction (*23*). For DNA polyplexes, a sufficiently high graft density with PEG molecules seems to be necessary to prevent opsonization and avoid rapid clearance from the blood stream (*17*). However, little information is available regarding the influence of PEG chain length on the physicochemical and biological properties of nucleic nanoparticles (*17*).

Therefore, the objective of this study was to evaluate the stability of PEI and PEI−PEG polyplexes with siRNA using biophysical methods and to elucidate the influence of PEG chain length and graft density. Our hypothesis was tested with a panel of PEI−PEGs having similar composition (50% PEG content) but vastly different structures. Here, PEI(25k)-*g*-PEG copolymers with PEGylation degree in the range 40−60% and different PEG chain lengths (550, 2k, 5k, 20k, respectively) were selected and compared with that of the homopolymer PEI(25k). This selection is based on the fact that the molecular weights of linear PEGs used in biomedical applications usually range between a few hundred to 20 000 Da. The relationship between polymer structure and stability of the polyplexes was investigated. Furthermore, the knockdown efficiency of the selected polyplexes was studied in cell culture to find the correlation between in vitro stability and biological effect. Uptake and distribution of the polyplexes in cells were visualized by confocal laser scanning microscopy. Due to the different properties of siRNA compared to DNA (*24*), this study should provide a basis for the design of siRNA delivery systems.

MATERIALS AND METHODS

Materials. Branched poly(ethylene imine), PEI, with a molecular weight of 25 kDa was purchased from Sigma-Aldrich (Seelze, Germany). The poly(ethylene imine)-*graft*-poly(ethylene glycol) (PEI−PEG) with a PEG content of approximately 50% (w/w) was synthesized as previously described (*16*) by grafting linear PEG of 550 Da and 2, 5, and 20 kDa, respectively, onto branched PEI 25 kDa. Polymers were stored as sterile filtered, aqueous stock solutions (5 mg/mL) at pH 7.4. These graft copolymers were designated using the following nomenclature: PEI(25k)-*g*-PEG(x)$_n$. The number in brackets (25k or x, where x = 550, 2k, 5k, or 20k) represents the MW of PEI or PEG block in daltons, and the index n is the average number of PEG blocks per PEI molecule. This number was calculated on the basis of ^{1}H NMR spectra as described previously (*16*). The schematic structure and properties of the copolymers investigated in this paper are shown in Table 1. siGL3 (luciferase GL3 Duplex) was purchased from Dharmacon (Lafayette, CO) and used for physicochemical studies. The sequence is as follows: 5′-CUU ACG CUG AGU ACU UCG A dTdT/ dTdT GAA UGC GAC UCA UGA AGC U-5′. For the knockdown experiment in cell culture, an anti β-Gal siRNA duplex was purchased from Dharmacon with the following sequence: 5′-CUA CAC AAA UCA GCG AUU U UU /UU GAU GUG UUU AGU CGC UAA A P-5′. Cyanine 3 (Cy3)-labeled siRNA was from Dharmacon (Lafayette, CO). RNase A for the RNase digestion study was purchased from Roche Diagnostics GmbH, Mannheim, Germany. All other materials were obtained in analytical quality.

Preparation and Characterization of Polymer/siRNA Polyplexes. All polyplexes consisting of siRNA and PEI derivatives were prepared in isotonic glucose solution at pH 7 unless otherwise mentioned. The polymer/siRNA ratio was expressed as the nitrogen/phosphate (N/P) ratio, where N represents moles of amine on PEI and P represents moles of phosphate on siRNA. On the basis of the N/P ratio, the appropriate amount of polymer was added to the siRNA solution, mixed by vigorous pipetting, and incubated for 10 min at room temperature.

The hydrodynamic diameter of freshly prepared polyplexes was measured using a Zetasizer Nano ZS from Malvern Instruments (Herrenberg, Germany) equipped with a 10 mW HeNe laser at a wavelength of 633 nm. Measurements were

performed at 25 °C and analyzed in CONTIN mode. The instrument was checked periodically with nanospheres size standards (polymer microspheres in water, 199 nm ± 6 nm) from Duke Scientific (Palo Alto, CA). For data analysis, the viscosity and refractive index of water at 25 °C (0.89 mPa·s and 1.333, respectively) were used. The measurements were performed in triplicate. The ζ potentials (surface charge) of freshly prepared polyplexes were determined using the standard capillary electrophoresis cell of Zetasizer Nano ZS from Malvern Instrument at 25 °C. Measurements were performed in glucose 5%, pH 7.4. Average values were calculated with the data of 10 runs with standard deviation.

Atomic Force Microscopy (AFM). The polyplexes were prepared as described above and diluted in milliQ water. AFM images were obtained on a NanoWizard (JPK instruments, Berlin, Germany). The microscope was vibration-damped. Commercial pyramidal tips (Micromash, Estonia) on an I-tape cantilever with a length of about 230 μm, a resonance frequency of about 160 kHz, and a nominal force constant of 40 N/m were used. All measurements were performed in intermittent-contact mode at a scan speed of approximately 1 Hz to avoid damage of the sample surface. The acquired pictures had a resolution of 512 × 512 pixels. Polyplexes were directly transferred onto a prewashed silicon chip by dipping the chip into the polyplex solution for 10 min, rinsing it with MilliQ water, and allowing it to dry in air.

SiRNA Condensation. To study siRNA condensation as a function of N/P ratio, polyacrylamide gel (20%) electrophoresis (PAGE) retardation assays were performed (*18*). Briefly, polyplexes preparation was carried out in 5% glucose solution at pH 7.0. Increasing amounts of PEI were added to 6 pmol siRNA to reach final N/P ratios of 0.5, 0.7, 1, 1.5, 2, 3, and 5 for PEI 25k and 2, 3, 5, 7, 10, 15, and 20 for other copolymers. The resulting polyplexes were incubated for 10 min prior to loading to the gel. Then, the gel electrophoresis was run in TBE buffer pH 8 at a constant current of 15 mA. To visualize siRNA, the gel was immersed in 0.0017% ethidium bromide solution for 5 min. Thereafter, fluorescence of intercalated ethidium bromide was detected using a transilluminator (BioDoc Analyze, Biometra, Goettingen, Germany).

Polyanion Competition Assay. The relative stability of polyplexes was tested by measuring siRNA release from polyplexes in the presence of a competing polyanion heparin (*25*). All polyplexes were formed at N/P of 10. Polyplex solutions were incubated in the presence of 0.01, 0.02, 0.03, 0.04, 0.05, 0.1, and 0.15 IU of heparin/μg siRNA, respectively. These solutions were mixed well and incubated for 10 min before being applied to a 20% PAGE. In each gel, free siRNA was applied as a reference. Gels were run for 2 h at 15 mA and then scanned using a Biometra gel analyzing system. The experiments were performed in triplicate.

RNase Digestion. Stability of siRNA polyplexes against RNase digestion was investigated according to a method described previously (*26*) with little modification. The protection effect of different siRNA/PEI derivative polyplexes against series RNase digestion was investigated. Briefly, polyplexes were prepared at N/P of 10 in glucose 5%. Aliquots of 12.5 μL polyplexes corresponding to 0.17 μg of siRNA were incubated with 0.05, 0.10, 0.20, 0.50, 0.70, 1.0, and 1.2 mIU of RNase in phosphate buffer at pH 7.0 for 30 min at 37 °C. Afterward, samples were incubated for a further 30 min at 70 °C to inactivate RNase and divided into two equal fractions. The first fraction was used for determination of integrity of the polyplexes and the second fraction with 2 μL of a heparin solution containing 1000 IU per mL to release of the amount of siRNA remaining intact. Resulting mixtures were applied to a 20% PAGE gel, and electrophoresis was carried out at 15 mA for 2 h. A positive control containing free siRNA was tested under the same conditions. The resulting gel was imaged on a Biometra transilluminator. The intensity of the "free siRNA" band was quantified by densitometry using the software program *Scion Image 4.0.2. beta* (Scion Corporation, Frederick, MD). At a given RNase concentration, the percentage of siRNA dissociated from the polyplexes was obtained by normalizing against the siRNA band measured from a sample containing siRNA only on the same gel. All experiments were performed in triplicate.

Knockdown Experiments in NIH 3T3 Fibroblasts under in Vitro Conditions. The knockdown experiment was performed as described in the literature (*27*). Briefly, 24 h before transfection, NIH/3T3 cells stably expressing β-galactosidase (Orbigen, San Diego, CA) were seeded in 24-well plates at a density of 3×10^4 per well in 500 μL Dulbecco's modified Eagle's medium (DMEM) supplemented with 10% fetal bovine serum (FBS) at 37 °C and 5% CO_2 (v/v). Cells were at 50−80% confluence before experiment. siRNA polyplexes with different polymers were prepared at N/P of 10 and incubated for 10 min at room temperature. The total volume of the polyplexes was 100 μL, and the polyplexes were added to the cells in 400 μL DMEM/10% FBS (50 pmol siRNA per well). For lipofectamine 2000, the method was similar except that the lipofectamine 2000/siRNA ratio was 2:1. After 4 h incubation, the medium was changed, and cells were further incubated for 20 h. Thereafter, the cells were washed with PBS and then were lysed with 100 μL of lysis buffer (Galacto-Star System, Applied Biosystems, Bedford, MA). Protein concentration was measured by using the BCA assay kit. β-Galactosidase activity was measured with a luminometer. Relative light units were converted to picograms of β-galactosidase by using β-galactosidase as a standard. The experiments were performed in triplicate.

Preparation of FITC-Labeled Copolymer. Copolymer PEI(25k)-*g*-PEG(5k)$_4$ was labeled with fluorescein isothiocyanate (FITC) for cellular trafficking studies. Briefly, 10 mg PEI(25k)-*g*-PEG(5k)$_4$ was dissolved in 2 mL of 0.1 M sodium hydrogen carbonate (pH 8.2). FITC (1 mg in 200 μL water-free DMSO) was added to the solution dropwise under stirring, and the mixture was stirred at room temperature for 4 h under light exclusion. Purification was performed on a PD-10 column (Amersham Pharmacia Biotech, Freiburg, Germany).

Confocal Laser Scanning Microscopy (CLSM). Confocal laser scanning microscopy was utilized to visualize the internalization of siRNA polyplexes. NIH/3T3 cells stably expressing β-galactosidase were seeded at a density of 12 000 cells per well in 8-well chamber slides (LabTek, Nunc, Wiesbaden, Germany). After 24 h, medium was removed and polyplexes containing FITC-labeled PEI(25k)-*g*-PEG(5k)$_4$, and Cyanine 3 labeled siRNA, free Cyanine 3 labeled siRNA, and free FITC-labeled polymer were added in fresh media. After 2 h incubation, cells were washed three times with phosphate buffered saline (PBS). Fixation of cells was done by incubation with 4% paraformaldehyde solution in PBS pH 7.4 at room temperature for 30 min and counterstaining with DAPI (4,6-diamidino-2-phenylindole, 0.2 μg/mL) for 20 min, both under light exclusion. Cells were embedded in FluorSave Reagent (Calbiochem, San Diego, CA). A Zeiss Axiovert 100 M microscope coupled to a Zeiss LSM 510 scanning device (Zeiss, Oberkochen, Germany) was used for confocal microscopy. For excitation of Cy3 fluorescence, a helium−neon laser with an excitation wavelength of 543 nm was used. Fluorescence emission was detected using a 560−615 nm band-pass filter. In a second scan, FITC was detected using an argon laser with an excitation wavelength of 488 nm and a 505−550 nm band-pass emission filter. Simultaneously, transmitted light images were obtained in this scan. In a third scan, DAPI was excited at 364 nm using an Enterprise

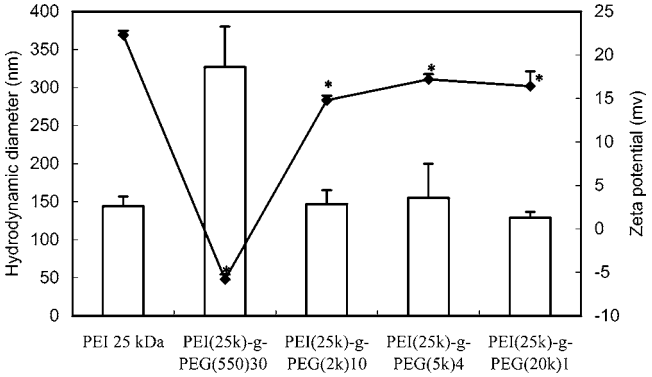

Figure 1. Physicochemical properties of PEI−PEG/siRNA (siGL3) polyplexes in 5% glucose at N/P ratio of 10. (◆) ζ potential; (bar) particle size. *$P < 0.05$.

II 653 laser (Coherent Inc., Santa Clara, CA), and fluorescence was detected using a 385−470 nm band-pass filter.

Statistics. The results are reported as mean ± standard deviation (SD) of at least three experiments. Significance between the mean values was calculated using one-way ANOVA analysis (*Origin 7.0 SRO*, Northampton, MA). Probability values $P < 0.05$ were considered to be significant.

RESULTS AND DISCUSSION

With PEG weight ratio (∼50%) kept constant, branched PEI 25 kDa was grafted with PEG 0.55k, 2k, 5k, and 20k, respectively, and the influence of PEG chain length on the stability and biological activity of the resulting siRNA polyplexes was studied. We hypothesized that PEGylation might modify the stability of the polyplexes and therefore affect the knockdown efficiency of siRNA by increasing the proportion of siRNA released in the cytoplasm avoiding uptake into the nucleus.

Characterization of the Polyplexes. The hydrodynamic diameters of PEI−PEG/siGL3 polyplexes were determined at nitrogen-to-phosphate (N/P) ratio of 10. In preliminary experiments with the copolymer PEI(25k)-*g*-PEG$(2k)_{10}$, it was shown that polyplex sizes decreased with increasing N/P ratios from 5 to 10 and remained constant up to N/P of 50. Therefore, N/P of 10 was adopted for size measurements. Properties of PEI−PEG/siGL3 polyplexes in 5% glucose are shown in Figure 1. The influence of PEG chain length could be seen in the way that the copolymer with fewer PEG blocks formed smaller polyplexes than copolymers with more PEG blocks. The homopolymer PEI exhibited a particle size of 144 nm. In contrast, copolymer PEI(25k)-*g*-PEG$(550)_{30}$ formed large polyplexes of 300−400 nm even at N/P ratio of 20, probably due to a decreased condensation efficiency of this highly grafted derivative, as indicated in the siRNA retardation assay. The copolymers with PEG chains 2k and 5k formed polyplexes of appropriately 150 nm, and slightly decreased particles size was found with copolymer PEI(25k)-*g*-PEG$(20k)_1$, with particles size around 130 nm.

The enhanced siRNA complexation might be attributed to the special copolymer structure. With only one PEG block on average, this is a diblock-like copolymer, and there might be a PEI domain and a PEG domain clearly separated from each other. Thus, the siRNA seems to interact with the PEI domain without interference from PEG. However, no statistical difference was found among the particle sizes of polyplexes prepared with copolymers of PEG chains 2k, 5k, and 20k. A similar trend was reported for NF-kB decoy and DNA PEI−PEG complexes (*17*, *28*). Moreover, the stability of the polyplexes was investigated for 20 min. It is very important to note that all the siRNA/copolymer polyplexes remained stable after 20 min incubation (data not shown). In comparison, the size of PEI(25k)/siRNA polyplexes increased approximately 35%. This can be explained by the steric shielding effect of PEG, thereby abolishing aggregation. This effect has been demonstrated for PEGylated PEIs in other studies (*28*). In addition, PEG might additionally participate in the siRNA condensation process in a synergistic manner (*29*). In contrast, particle size of PEI-*g*-PEG/oligonucleotides was reported to be less than 100 nm in 150 mM sodium chloride (*18*), and this was attributed to differing sequences of the nucleic acid and different media used in this study. To clarify this point, hydrodynamic diameters of PEI−PEG/siGL3 polyplexes were also investigated in 150 mM sodium chloride solution. Aggregation appeared immediately after preparation of polyplexes with particle sizes between 500 and 1000 nm. These data confirm that properties of the polyplexes were siRNA sequence- and medium-dependent. Similarly, particle size of β-Gal siRNA polyplexes of 400−900 nm was reported recently, which was measured in 20 mM HEPES buffer after incubating in OptiMEM medium for 30 min (*30*).

Interactions between polymer/siRNA polyplexes and cell surfaces are dependent upon the charge of the particles. The surface charges of PEI−PEG/siRNA polyplexes are described in Figure 1. PEI 25 kDa polyplexes revealed high positive surface charge of +22.3 mV. All copolymers showed a significantly reduced ζ potential compared to PEI. Full shielding was observed with copolymer PEI(25k)-*g*-PEG$(550)_{30}$. No statistically significant difference was found for the copolymers with PEG$(2k)_{10}$, PEG$(5k)_4$, and PEG$(20k)_1$, implying that at least part of the PEG blocks of the copolymers orientate toward the surface while PEI and siRNA are located in the inner part of the polyplexes. Therefore, it is reasonable to conclude that the PEG protective effect is caused by a combination of PEG chain length and density; a threshold PEG length is needed for higher efficiency.

Atomic Force Microscopy. Atomic force microscopy (AFM) was used to study the morphology of polymer/siRNA polyplexes and compared with that of free siRNA, as shown in Figure 2. Polyplexes were imaged at an N/P ratio of 10 except PEI−PEG(550) (N/P 20). As anticipated, a double-stranded structure was found for free siRNA duplex (Figure 2a). After complexation with the polymers, the double-stranded structure disappeared, and all the polyplexes were spherical or subspherical with smooth surfaces (Figure 2). The homopolymer PEI 25 kDa showed images of compact homogeneously distributed polyplexes, with some large particles. PEGylation affected the properties of the polyplexes considerably. Particle aggregation was quite serious in the case of PEI−PEG(550) (Figure 2c), and this is in agreement with the results from dynamic light scattering (DLS) measurement. The phenomenon of aggregation decreased with increasing PEG chain length to 2k and 5k (Figure 2d,e). For the PEI−PEG(20k) polyplexes, the majority of the particles was separated from each other (Figure 2f), suggesting that these polyplexes were better stabilized against agglomeration. This is in agreement with the decreased particle size measurement. Similarly, it was also reported that PEG chain length was a main determinant of polyplex aggregation (*31*).

SiRNA Condensation. To quantify siRNA condensation as a function of N/P ratio, we utilized the ability of PEI to quench siRNA/ethidium bromide fluorescence by immersing the gel in ethidium bromide solution for 5 min before imaging. If siRNA is condensed by cationic polymers, ethidium bromide can no longer intercalate, and fluorescence intensity decreases measurably. First of all, with PEI(25k)-*g*-PEG$(2k)_{10}$ copolymer taken as an example, the effect of ionic strength in the medium on the electrostatic interaction between polymer and siRNA was investigated. Complete siRNA condensation was found at N/P ratio of 5 in 150 mM NaCl solution, compared to N/P ratio of

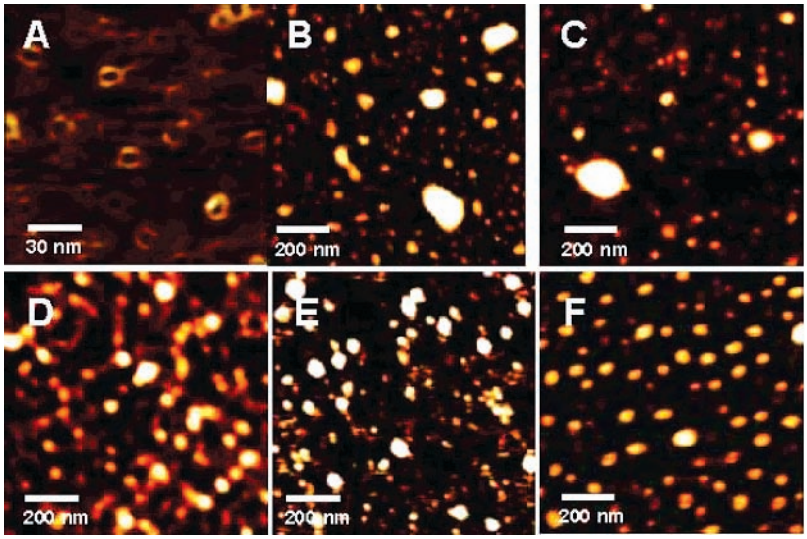

Figure 2. AFM images of different siRNA polyplexes. (a) free siRNA, (b) PEI 25kDa, (c) PEI(25k)-*g*-PEG(550)$_{30}$, (d) PEI(25k)-*g*-PEG(2k)$_{10}$, (e) PEI(25k)-*g*-PEG(5k)$_4$, (f) PEI(25k)-*g*-PEG(20k)$_1$.

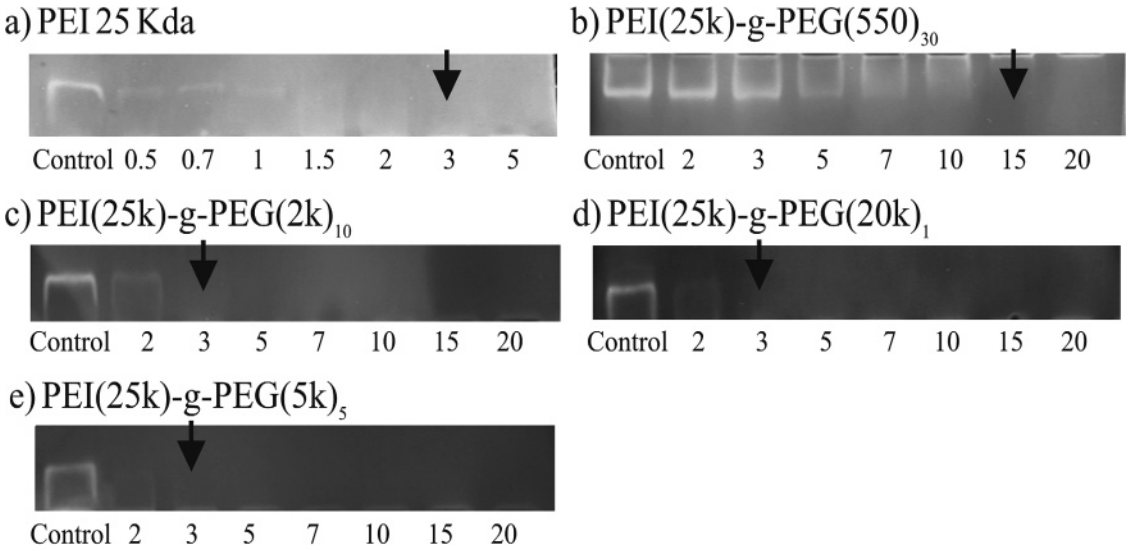

Figure 3. siRNA condensation of PEI and PEI−PEG by increasing the N/P ratio measured by polyacrylamide gel electrophoresis. Lane 1, N/P 0 (siRNA only as control); completed siRNA condensation ratio was indicated by arrows.

3 in 5% glucose solution, indicating that higher N/P is essential for complete siRNA complexation at higher ionic strength. Therefore, 5% glucose was used to prepare the polyplexes in the following studies.

As shown in Figure 3, unmodified PEI condenses siRNA even at N/P ratio as low as 0.5, and complete condensation was found at N/P ratio of 3, suggesting that all negatively charged siRNA phosphate residues are saturated with PEI. Similarly, it was reported that at N/P ratios of >2.5 plasmid DNA was fully retarded in agarose gel electrophoresis with PEI (*32*). When PEI was grafted with short PEG blocks as in the case of copolymer PEI(25k)-*g*-PEG(550)$_{30}$, the complexation was hindered slightly at N/P of 5.0 but complete condensation was realized at N/P ratio 15, probably due to the decreased charge density of the copolymer at a relatively high PEG density. In contrast, with the same copolymer, only slight hindrance for DNA complexation was found (*28*), emphasizing different properties between DNA and siRNA (*24*). No difference was found for copolymers PEI(25k)-*g*-PEG(2k)$_{10}$, PEI(25k)-*g*-PEG-(5k)$_5$, and PEI(25k)-*g*-PEG(20k)$_1$, and complete retardation of siRNA was achieved at N/P of 3, which is comparable to homopolymer PEI 25k, the same trend found in the size measurement. This implies that at similar PEG content PEG chain length plays a critical role for nucleic acid condensation. Anyway, no difference was found at PEG 2k, 5k, and 20k. In contrast, slightly increased DNA condensation was reported with increasing PEG MW from 550 to 20 kDa in the same copolymer (*28*).

Heparin Displacement. In this study, except for copolymer PEI(25k)-*g*-PEG(550)$_{30}$ (N/P 20), all the other polyplexes were prepared at N/P of 10, at which complete siRNA condensation was demonstrated in previous studies. The stability of different polymer/siRNA polyplexes against heparin displacement is shown in Figure 4. PEI/siRNA polyplexes were the most stable, and dissociation occurred at heparin 0.31 IU/μg siRNA; complete dissociation was found at heparin 0.42 IU/μg siRNA, suggesting a strong interaction of PEI with siRNA. In contrast, the stability of the polyplexes decreased after PEGylation. This observation is in agreement with our hypothesis and can probably be explained by the weakened interaction of siRNA with polymer as a result of decreased charge density. Interestingly, the protection efficiency increased with increasing PEG chain length at similar PEG content. PEI(25k)-*g*-PEG(550)$_{30}$/siRNA polyplexes were extremely unstable, and 81% siRNA dissociation was observed even at heparin of 0.10 IU/μg siRNA, which created doubt as to its capacity to bring a sufficient

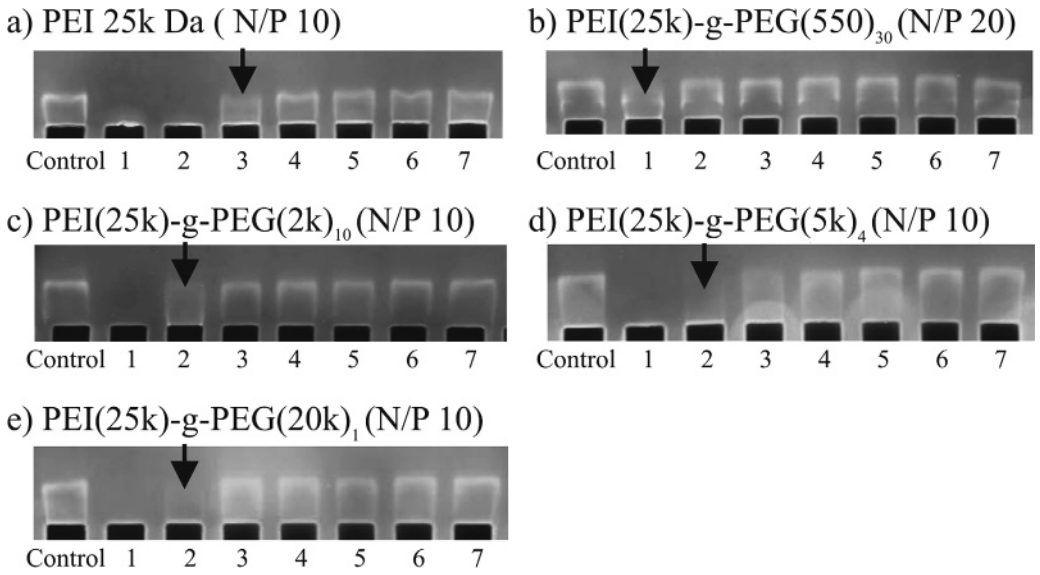

Figure 4. siRNA polyplexes stability against heparin displacement. Control: free siRNA. Lanes 1−7: heparin 0.10, 0.21, 0.31, 0.42, 0.52, 1.04, 1.57 IU/μg siRNA, respectively.

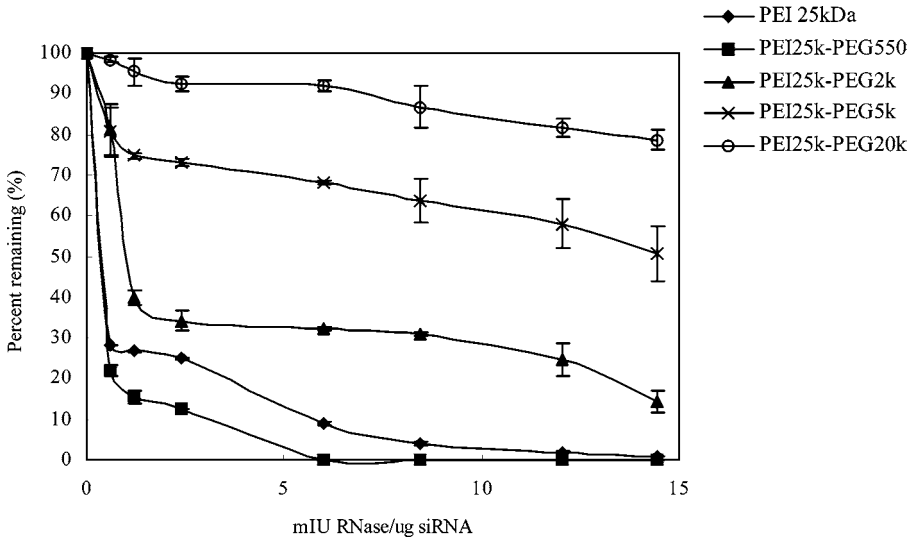

Figure 5. Incubation of PEI and PEG−PEI/siRNA polyplexes with RNase A at an N/P ratio of 10 over 0.5 h. The percentage recovery of intact siRNA is shown in reference to the intact amount of noncomplexed control siRNA.

amount of siRNA into cells. In contrast, for copolymers PEI(25k)-*g*-PEG(2k)$_{10}$, PEI(25k)-*g*-PEG(5k)$_4$, and PEI(25k)-*g*-PEG(20k)$_1$, dissociation of polyplexes occurred at heparin of 0.21 IU/μg siRNA, and 24%, 6.8%, and 5.9% of siRNA was released, respectively, indicating that PEG chain length instead of surface density played a critical role in protection of the polyplexes, and a better steric effect was found at PEG chain length of >2k. With the same copolymer PEI(25k)-*g*-PEG(2k)$_{10}$, previous study demonstrated that DNA polyplexes started to dissociate at heparin of 0.2 IU/μg DNA (*25*), which is comparable to our results. However, PEI(25k)/DNA polyplexes were less stable against heparin displacement (*25*) compared to PEG(25k)/siRNA polyplexes (0.2 IU/μg DNA vs 0.3 IU/μg DNA). This can probably be explained by the smaller MW of siRNA, which can be compacted more efficiently by the polymer. No statistically significant difference was found for the polyplexes prepared with the copolymer containing PEG 5k and 20k (P > 0.05), implying that PEG 5k might be sufficient for effective PEGylation.

Stability against RNase Digestion. The enzymatic degradation of siRNA is accompanied by a rapid decline in biological activity and therapeutic efficiency. The ability of the gene carrier to protect siRNA against enzymatic degradation by RNase, which is located in the cytoplasm, can be demonstrated by RNase digestion studies. First of all, stability of free siRNA against RNase was studied. It was found that free siRNA was degraded completely even at RNase of 0.01 mIU (0.12 mIU/μg). Thereafter, the protection effect of different PEI copolymer/siRNA polyplexes against RNase digestion was investigated. The PEG shell was expected to play an important role not only in sterically stabilizing the structure of the complex, but also in protecting the siRNA vector from being attacked by nucleases (*33*). The quantification of the siRNA displaced from the polyplexes is shown in Figure 5. At RNase of 6.0 mIU/μg siRNA, almost all the siRNA was degraded in PEI−PEG(550)/siRNA polyplexes, whereas 9% was left in PEI(25k)/siRNA polyplexes despite the strong interaction as indicated in the heparin displacement assay. In contrast, by sterically shielding the siRNA domains susceptible to proteolytic attack, the PEG layer can decrease the amount of siRNA degraded, and the effect is PEG chain-length-dependent. It showed that 32%, 68%, and 92% of siRNA was protected from degradation in PEI(25k)-*g*-PEG(2k)$_{10}$, PEI(25k)-*g*-PEG(5k)$_4$, and PEI(25k)-*g*-PEG(20k)$_1$ polyplexes, respectively. The super protection effect of PEG 5k and PEG 20k against RNase digestion suggest their promising application in vivo. The increased stability of the polyplexes

Table 2. Particle Size of Polymer/β-Gal siRNA Polyplexes in Different Media

		5% glucose		0.9% NaCl	
polymer	N/P	size	PI	size	PI
PEI 25 kDa	10	482 ± 28	0.38 ± 0.02	144 ± 12.2	0.078 ± 0.029
PEI(25k)-*g*-PEG(550)$_{30}$	20	1320 ± 4.6	0.28 ± 0.31	434 ± 55.5	0.524 ± 0.045
PEI(25k)-*g*-PEG(2k)$_{10}$	10	650 ± 65	0.46 ± 0.01	102 ± 4.96	0.273 ± 0.049
PEI(25k)-*g*-PEG(5k)$_4$	10	642 ± 24	0.47 ± 0.01	118 ± 24.1	0.320 ± 0.108
PEI(25k)-*g*-PEG(20k)$_1$	10	490 ± 85	0.45 ± 0.06	109 ± 3.86	0.270 ± 0.010

and enhanced enzymatic resistance support the hypothetical core−shell structure of these self-assembling polyplexes; that is, the siRNA is trapped within a cationic core surrounded by a hydrophilic PEG shell. The strength of the PEG shell is its chain length dependency. It is well-known that, in aqueous solutions, PEG is a highly hydrated polymer and has a high degree of segmental flexibility. It is thought to be capable of influencing the structure of several molecular layers of water, leading to its pronounced conformational entropy and large exclusion volume (*34*). The influence of molecular weight, surface density, and conformation of PEG affect dramatically the enzyme adsorption pattern. The brush conformation is presented as the highest steric protection against protein adsorption due to the steric hindrance of heavily hydrated chains of PEG molecules and their flexibility in terms of free rotation of individual polymer units around interunit linkage (*35*). The polymer chain flexibility correlates with its ability to squeeze nonlinked water molecules out of the molecular dynamic "cloud" formed over the surface (*36*). When PEG chains are short, like PEG 550, flexibility is insufficient, structured water can be "squeezed out" due to entropic instability, and RNase can adsorb on the surface of the polyplex, leading to siRNA degradation. As the molecular weight of a PEG molecule rises, the cloud temperature, which is the temperature at which the polymer separates from the water solution, also increases, suggesting an increased amount of structured water and, therefore, increased stability with increasing PEG molecular weight (*37*). As shown in our results, flexibility and high hydration of long chains like PEG 5000 and 20 000 Da allow the repulsion of RNase to a higher extent despite its low density. Similarly, computer simulations suggest that a relatively small number of molecules of a hydrophilic flexible polymer are sufficient to decrease the number of direct collisions of colloid surface with opsonizing proteins by creating a dense protective conformational cloud over the liposome surface (*38*). Oily core nanoparticles made of PLA or PEG−PLA were studied for complement consumption, and the testing of longer PEG chains (20 kDa) showed them to be more effective, even at lower surface density (*39*).

In addition, integrity of the siRNA polyplexes in the presence of RNase was investigated. No dissociation of polyplexes was found for siRNA polyplexes with PEI homopolymer and the copolymers with PEG chain lengths 2k, 5k, and 20k at N/P ratio of 10 even when the RNase amount was as high as 6 mIU/μg siRNA. In contrast, even at N/P ratio of 20, PEI(25k)-*g*-PEG(550)$_{30}$ could not inhibit siRNA release from the polyplexes even when the RNase amount was as low as 0.6 mIU/g (data not shown), implying that PEG 550 is too short to protect siRNA efficiently. Moreover, most of the PEG-modified proteins currently approved for human use by the FDA rely on PEG with MW 5000 Da or higher (*40*, *41*).

Knockdown Experiment in Cell Culture. On the basis of the in vitro properties of different polyplexes, the knockdown efficiency of siRNA polyplexes with the following copolymers, PEI(25k)-*g*-PEG(2k)$_{10}$, PEI(25k)-*g*-PEG(5k)$_4$, and PEI(25k)-*g*-PEG(20k)$_1$, were studied in cell culture and compared with that of the homopolymer PEI(25k)−siRNA polyplexes. The polyplexes were prepared in 150 mM sodium chloride solution based on the particle size data in Table 2. Lipofectamine 2000 was used as a positive control (*27*). The biological results are shown in Figure 6. All the polymers investigated could down-regulate gene expression significantly compared to the control ($P < 0.05$). Since it was reported that no difference between the use of small siRNA particles (50−100 nm) and large aggregates (200−600 nm) for gene knockdown was observed (*24*), it is reasonable to assume that the knockdown difference caused by particle size difference of the polyplexes was marginal. It was noticed that the knockdown efficiency increased with increasing PEG chain length up to PEG MW 5 k. Beyond this point, further increasing PEG MW to 20k led to no apparent change in knockdown efficiency, a similar trend observed in RNase digestion assay. The low knockdown efficiency of PEI can probably be explained by the fact that the high siRNA condensation of PEI might prevent siRNA release in the cytosol, in agreement with its high stability against heparin displacement. In contrast, for PEI−PEG polyplexes, heparin can reach siRNA in the condensed form even at quite a low concentration, implying that siRNA complexed with PEI−PEG was accessible to the targeting mRNA, in line with the enhanced knockdown efficiency. Therefore, in agreement with our hypothesis, PEGylation of PEI appears to enhance siRNA release in the cytoplasm, leading to enhanced biological activity. On the other hand, it should be mentioned that several important factors are likely to be synergistically involved in the pronounced siRNA activity of PEI−PEG(>2kDa) polyplexes, such as the improvement of the stability against enzymatic degradation, minimal interaction with serum proteins, and the effective transport of free siRNA from endosome into cytoplasm.

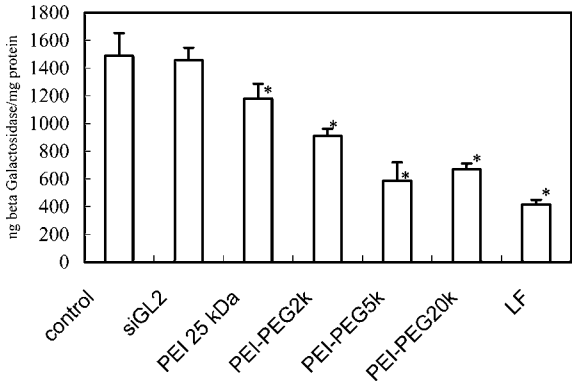

Figure 6. Biological activity of different polymer/siRNA polyplexes in NIH/3T3 fibroblasts stably expressing β-galactosidase. All polyplexes were prepared at N/P of 10. *$P < 0.05$.

Interestingly, an extremely good correlation between RNase digestion and knockdown efficiency data in cell culture was established. Figure 7 exemplifies the logarithmic relationship between stability of the polyplexes at RNase of 6 mIU and knockdown efficiency. The insert shows a linear correlation when remaining siRNA was less than 70%. It implies that RNase digestion stability could be employed as a potential tool to predict the biological activity of siRNA delivery systems.

In addition, our RNase digestion and cell culture data did indicate that stability and biological activity of siRNA polyplexes was significantly improved for the copolymer with PEG chain length of >5 kDa. This information provides further

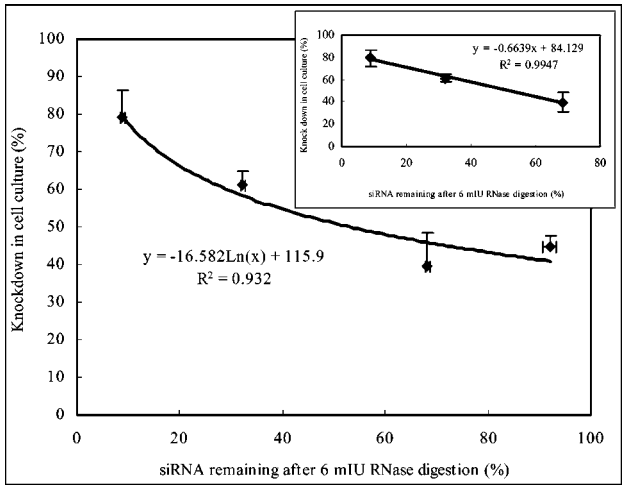

Figure 7. Correlation between RNase digestion stability and biological activity in cell culture. Insert shows a linear correlation when remaining siRNA was less than 70%.

rationale for using PEG with MW of >5 kDa in the FDA-approved protein products.

Subcellular Localization of the siRNA Polyplexes. On the basis of the results from cell culture, copolymer PEI(25k)-*g*-PEG(5k)$_4$ was selected for cellular trafficking of siRNA polyplexes. Confocal microscopy was employed to provide direct evidence for localization of polyplexes. To investigate the uptake and intracellular localization of the polyplexes, both siRNA and the copolymer were fluorescently labeled. With regard to free siRNA, rarely any red fluorescence was observed (Figure 8B). In contrast, a significantly higher internalization of siRNA was found for the copolymer/siRNA polyplexes (Figure 8A). As shown in Figure 8A, a large amount of yellow color, resulting from the colocalization of green and red, was distributed within the cytoplasm in a punctuated pattern, in small, round vesicles localized in the perinuclear area, implying that at least part of the polyplexes are being taken up by endocytosis without dissociation. The red spots in the image (Figure 8A(e)) indicated intracellular siRNA release in the cytosol after 2 h incubation. No fluorescence signal was found in the nuclear area, in this special image areas in white represent colocalization of green and red, as shown in Figure 8A(f). It shows that the polyplexes were mainly distributed in the cytosol, its site of action, instead of entering the nucleus. This is in agreement with our hypothesis. Distribution of polymer in the cells was investigated as well. Figure 8C showed that the polymer itself was dispersed throughout the cytoplasm, being taken up by the cells in an unspecific manner. This point has been mentioned in the former studies (*42*).

CONCLUSIONS

With the PEG ratio in the copolymer kept constant (~50%), influence of the polymer structure on the stability and biophysical properties of the polyplexes was studied. Interestingly, the stability and size of siRNA polyplexes were clearly influenced by PEI−PEG structure, and high degrees of substitution such as PEI(25k)-*g*-PEG(550)$_{30}$ resulted in large (300−400 nm), diffuse complexes (AFM) which showed condensation behavior only at N/P ratio of 15. All other polyplexes and the PEI control showed similar sizes (150 nm) and compact structures in AFM. Complete condensation was reached at N/P ratio of 3. Displacement of siRNA from polyplexes using heparin and stability against RNase digestion confirmed this observation. Surprisingly, protection against RNase digestion was highest for PEI(25k)-*g*-PEG(5k)$_4$ and PEI(25k)-*g*-PEG(20k)$_1$, while siRNA/PEI provided insufficient protection. In knockdown experiments

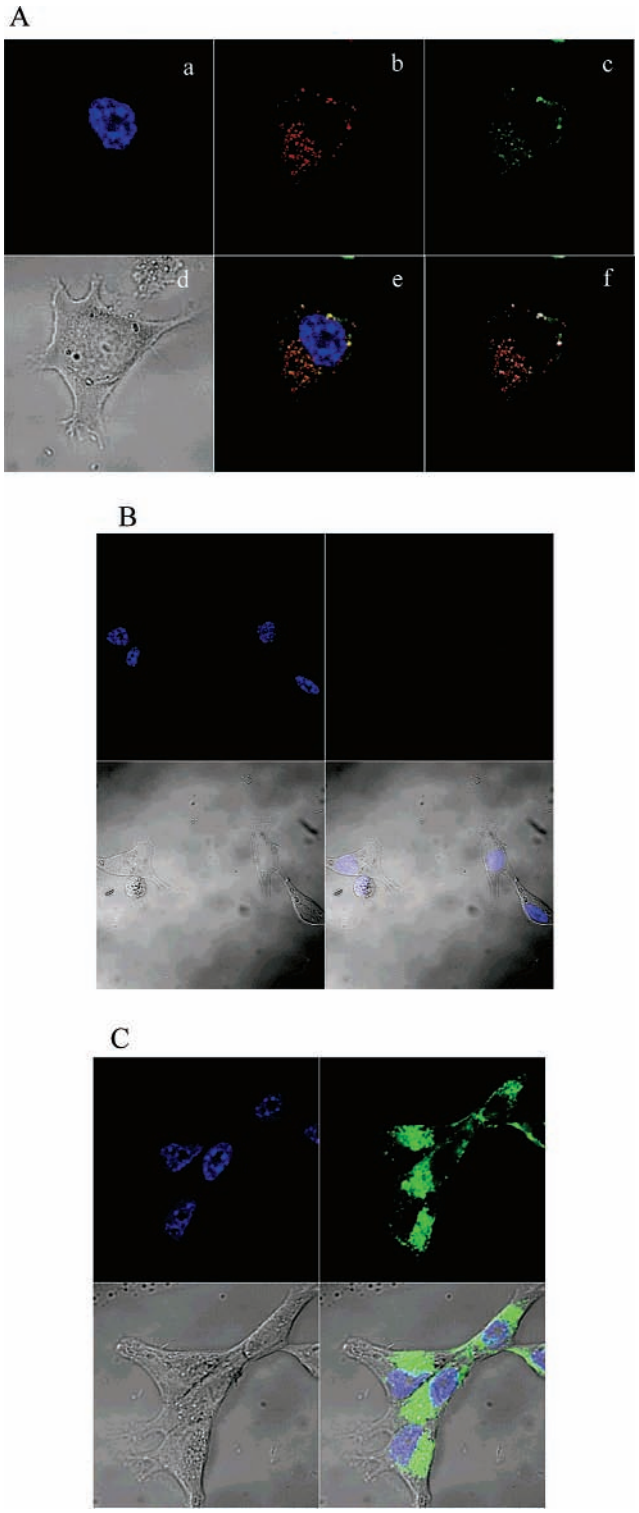

Figure 8. Confocal micrograph images of NIH/3T3 cells incubated with polyplexes, copolymer, and siRNA. Copolymer PEI(25k)-*g*-PEG(5k)$_4$ was labeled with FITC; siRNA was labeled with Cyanine 3. (A) Incubated with PEI(25k)-*g*-PEG(5k)$_4$ copolymer/siRNA polyplexes: (a) blue filter, (b) red filter, (c) green filter, (d) cell morphology, (e) overlay of a−c, and (f) overlay of b and c, indicating that the polyplexes were distributed in the cytosol instead of entering nucleus. Areas in white represent colocalization. (B) Incubated with free siRNA. (C) Incubated with free PEI(25k)-*g*-PEG(5k)$_4$ copolymer.

using NIH/3T3 fibroblasts stably expressing β-galactosidase, it was shown that PEG chain length had a significant influence on biological activity of siRNA. Polyplexes with siRNA containing PEI(25k)-*g*-PEG(5k)$_4$ and PEI(25k)-*g*-PEG(20k)$_1$ yielded similar efficiencies of ca. 70% knockdown as lipo-

fectamine controls. In conclusion, in agreement with our hypothesis, PEGylation can modify the stability of PEI/siRNA polyplexes. Release of siRNA in the cytosol depends on polyplex stability and protection against RNase digestion. A good correlation between RNase stability and knockdown efficiency in cell culture was found for the polyplexes studied. The in vivo behavior of the polyplexes is ongoing. Further optimizations are promising to develop biodegradable PEI−PEG as siRNA carriers.

ACKNOWLEDGMENT

Financial support of Deutsche Forschungsgemeinschaft DFG, Forschergruppe 627, is gratefully acknowledged.

LITERATURE CITED

(1) Aigner, A. (2006) Gene silencing through RNA interference (RNAi) in vivo: Strategies based on the direct application of siRNAs. *J. Biotechnol.* Jan 10, (Epub ahead of print).

(2) Whelan, J. (2005) First clinical data on RNAi. *Drug Discovery Today 10* (15), 1014−1015.

(3) Zeng, Y., and Cullen, B. R. (2002) RNA interference in human cells is restricted to the cytoplasm. *RNA 8*, 855−860.

(4) Oishi, M., Nagasaki, Y., Itaka, K., Nishiyama, N., and Kataoka, K. (2005) Lactosylated poly(ethylene glycol)−siRNA conjugate through acid-labile β-thiopropionate linkage to construct pH-sensitive polyion complex micelles achieving enhanced gene silencing in Hepatoma cells. *J. Am. Chem. Soc. 127*, 1624−1625.

(5) Merdan, T., Kopecek, J., and Kissel, T. (2002) Prospects for cationic polymers in gene and oligonucleotide therapy against cancer. *Adv. Drug Delivery Rev. 54*, 715−758.

(6) Boussif, O., Lezoualc'h, F., Zanta, M. A., Mergny, M. D., Scherman, D., Demeneix, B., and Behr, J. P. (1995) A versatile vector for gene and oligonucleotide transfer into cells in culture and in vivo: Polyethylenimine, *Proc. Natl. Acad. Sci. U.S.A. 92* (16), 7297−7301.

(7) Akinc, A., Thomas, M., Klibanov, A. M., and Langer, R. (2005) Exploring polyethylenimine-mediated DNA transfection and the proton sponge hypothesis. *J. Gene Med. 7* (5), 657−663.

(8) Honore, I., Grosse, S., Frison, N., Favatier, F., Monsigny, M., and Fajac, I. (2005) Transcription of plasmid DNA: Influence of plasmid DNA/polyethylenimine complex formation. *J. Controlled Release 107*, 537−546.

(9) Godbey, W. T., Wu, K. K., and Mikos, A. G. (1999) Tracking the intracellular path of poly(ethylenimine)/DNA complexes for gene delivery. *Proc. Natl. Acad. Sci. U.S.A. 96* (9), 5177−5181.

(10) Erbacher, P., Bettinger, T., Belguise-Valladier, P., Zou, S., Coll, J. L., Behr, J. P., and Remy, J. S. (1999) Transfection and physical properties of various saccharide, poly(ethylene glycol), and antibody-derivatized polyethylenimines (PEI). *J. Gene Med. 1*, 210−222.

(11) Ngyugen, H. K., Lemieux, P., Vinogradov, S. V., Gebhart, C. L., Guerin, N., Paradis, G., Bronich, T. K., Alakhov, V. Y., and Kabanov, A. V. (2000) Evaluation of polyether−polyethylenimine graft copolymers as gene transfer agents. *Gene Ther. 7*, 126−138.

(12) Hassani, Z., Lemkine, G. F., Erbacher, P., Palmier, K., Alfama, G., Giovannangeli, C., Behr, J. P., and Demeneix, B. A. (2005) Lipid-mediated siRNA delivery down-regulates exogenous gene expression in the mouse brain at picomolar levels. *J. Gene Med. 7* (2), 198−207.

(13) Niola, F., Evangelisti, C., Campagnolo, L., Massalini, S., Bue, M. C., Mangiola, A., Masotti, A., Maira, G., Farace, M. G., and Ciafre, S. A. (2006) A plasmid-encoded VEGF siRNA reduces glioblastoma angiogenesis and its combination with interleukin-4 blocks tumor growth in a xenograft mouse model. *Cancer. Biol. Ther. 5* (2), Feb 10 (Epub ahead of print).

(14) Thomas, M., Lu, J. J., Ge, Q., Zhang, C., Chen, J., and Klibanov, A. M. (2005) Full deacylation of polyethylenimine dramatically boosts its gene delivery efficiency and specificity to mouse lung. *Proc. Natl. Acad. Sci. U.S.A. 102* (16), 5679−5684.

(15) Urban-Klein, B., Werth, S., Abuharbeid, S., Czubayko, F., and Aigner, A. (2005) RNAi-mediated gene-targeting through systemic application of polyethylenimine (PEI)-complexed siRNA in vivo. *Gene Ther. 12* (5), 461−466.

(16) Petersen, H., Fechner, P., Fischer, D., and Kissel, T. (2002) Synthesis, characterization, and biocompatibility of polyethylenimine-*graft*-poly(ethylene glycol) block copolymers. *Macromolecules 35* (18), 6867−6874.

(17) Kunath, K., von Harpe, A., Petersen, H., Fischer, D., Voigt, K., Kissel, T., and Bickel, U. (2002) The structure of PEG-modified poly(ethylene imines) influences biodistribution and pharmacokinetics of their complexes with NF-kappa B decoy in mice. *Pharm. Res. 19* (6), 810−817.

(18) Brus, C., Petersen, H., Aigner, A., Czubayko, F., and Kissel, T. (2004) Physicochemical and biological characterization of polyethylenimine-*graft*-poly(ethylene glycol) block copolymers as a delivery system for oligonucleotides and ribozymes. *Bioconjugate Chem. 15* (4), 677−684.

(19) Kim, S. H., Mok, H., Jeong, J. H., Kim, S. W., and Park, T. G. (2006) Comparative evaluation of target-specific GFP gene silencing efficiencies for antisense ODN, synthetic siRNA, and siRNA plasmid complexed with PEI−PEG−FOL(PEG MW3400) conjugate. *Bioconjugate Chem. 17* (1), 241−244.

(20) Kim, S. H., Jeong, J. H., Cho, C. K., Kim, S. W., and Park, T. G. (2005) Target-specific gene silencing by siRNA plasmid DNA complexed with folate-modified poly(ethyleneimine). *Bioconjugate Chem. 104* (1), 223−232.

(21) Schiffelers, R. M., Ansari, A., Xu, J., Zhou, Q., Tang, Q., Storm, G., Molema, G., Lu, P. Y., Scaria, P. V., and Woodle, M. C. (2004) Cancer siRNA therapy by tumor selective delivery with ligand-targeted sterically stabilized nanoparticle. *Nucleic Acids Res. 32* (19), e149.

(22) Gombotz, W. R., Wang, G. H., Horbett, T. A., and Hoffman, A. S. (1991) Protein adsorption to poly(ethylene oxide) surfaces. *J. Biomed. Mater. Res. 25*, 1547−1562.

(23) Jean, S. I., Lee, J. H., Andrade, J. D., and De Gennes, P. G. (1991) Protein-surface interactions in the presence of polyethylene oxide I. Simplified theory. *J. Colloid Interface Sci. 142*, 149−158.

(24) Spagnou, S., Miller, A. D., and Keller, M. (2004) Lipidic carriers of siRNA: differences in the formulation, cellular uptake, and delivery with plasmid DNA. *Biochemistry 43* (42), 13348−56.

(25) Merdan, T., Callahan, J., Petersen, H., Kunath, K., Bakowsky, U., Kopeckova, P., Kissel, T., and Kopecek, J. (2003) Pegylated polyethylenimine−Fab′ antibody fragment conjugates for targeted gene delivery to human ovarian carcinoma cells. *Bioconjugate Chem. 14* (5), 989−996.

(26) Brus, C., Petersen, H., Aigner, A., Czubayko, F., and Kissel, T. (2004) Efficiency of polyethylenimines and polyethylenimine-*graft*-poly(ethylene glycol) block copolymers to protect oligonucleotides against enzymatic degradation. *Eur. J. Pharm. Biopharm. 57* (3), 427−430.

(27) Leng, Q., Scaria, P., Zhu, J., Ambulos, N., Campbell, P., and Mixson, A. J. (2005) Highly branched HK peptides are effective carriers of siRNA. *J. Gene Med. 7* (7), 977−986.

(28) Petersen, H., Fechner, P. M., Martin, A. L., Kunath, K., Stolnik, S., Roberts, C. J., Fischer, D., Davies, M. C., and Kissel, T. (2002) Polyethylenimine-*graft*-poly(ethylene glycol) copolymers: influence of copolymer block structure on DNA complexation and biological activities as gene delivery system. *Bioconjugate Chem. 13* (4), 845−854.

(29) Kleideiter, G., and Nordmeier, E. (1999) Poly(ethylene glycol)-induced DNA condensation in aqueous/methanol containing low-molecular-weight electrolytes solutions. Part II. Comparison between experiment and theory. *Polymer 40*, 4025−4033.

(30) Leng, Q., Scaria, P., Zhu, J., Ambulos, N., Campbell, P., and Mixson, A. J. (2005) Highly branched HK peptides are effective carriers of siRNA. *J. Gene Med. 7*, 977−986.

(31) Glodde, M., Sirsi, S. R., and Lutz, G. J. (2006) Physiochemical properties of low and high molecular weight poly(ethylene glycol)-grafted poly(ethylene imine) copolymers and their complexes with oligonucleotides. *Biomacromolecules 7* (1), 347−356.

(32) Boeckle, S., Wagner, E., and Ogris, M. (2005) C- versus N-terminally linked melittin-polyethylenimine conjugates: the site of linkage strongly influences activity of DNA polyplexes. *J. Gene Med. 7*, 1335−1347.

(33) Harada, A., Togawa, H., and Kataoka, K. (2001) Physicochemical properties and nuclease resistance of antisense-oligonucleotides entrapped in the core of polyion complex micelles composed of poly(ethylene glycol)-poly(L-lysine) block copolymers. *Eur. J. Pharm. Sci. 13*, 35−42.

(34) Zalipsky, S., and Lee, C. (1992) Use of functionalized polyethylene glycols for modification of polypeptides. In *Poly(ethylene glycol) Chemistry: Biotechnical and Biomedical Applications* (Harris, J. M., Ed.) Plenum Press, New York.

(35) Torchilin, V., and Trubetskoy, V. (1995) Which polymers can make nanoparticulate drug carriers long-circulating? *Adv. Drug Delivery Rev. 16*, 141−155.

(36) Torchilin, V. P. (1998) Polymer-coated long-circulating microparticulate pharmaceuticals. *J. Microencapsul. 15*, 1−19.

(37) Stolnik, S., Illum, L., and Davis, S. (1995) Long-circulating microparticulate drug carriers. *Adv. Drug Delivery Rev. 16*, 195−214.

(38) Torchilin, V. P., Omelyanenko, V. G., Papisov, M. I., Bogdanov, A. A., Jr., Trubetskov, V. S., Herron, J. N., and Gentry, C. A. (1994) Poly(ethylene glycol) on the liposome surface: on the mechanism of polymer-coated liposome longevity. *Biochim. Biophys. Acta. 1195*, 11−20.

(39) Mosqueira, V. C., Legrand, P., Gulik, A., Bourdon, O., Gref, R., Labarre, D., and Barratt, G. (2001) Relationship between complement activation, cellular uptake and surface physicochemical aspects of novel PEG-modified nanocapsules. *Biomaterials 22*, 2967−2979.

(40) Nucci, M. L., and Abuchowski, A. (1991) The therapeutic value of poly(ethylene glycol)-modified proteins. *Adv. Drug Delivery Rev. 6*, 133−151.

(41) Mahato, R. I. (2005) Biomaterials for delivery and targeting of proteins and nucleic acids. In *Protein conjugation, cross-linking, and PEGylation* (Hinds, K. D., Ed.) pp 168−171, CRC Press, New York.

(42) Ranaldi, G., Marigliano, I., Vespignani, I., Perozzi, G., and Sambuy, Y. (2002) The effect of chitosan and other polycations on tight junction permeability in the human intestinal Caco-2 cell line-(1). *J. Nutr. Biochem. 13* (3), 157−167.

BC060129J

Synthesis of a New Water-Soluble Rhodamine Derivative and Application to Protein Labeling and Intracellular Imaging

Rakeshwar Bandichhor,[†] Anca D. Petrescu,[‡] Aude Vespa,[‡] Ann B. Kier,[‡] Friedhelm Schroeder,[‡] and Kevin Burgess*[,†]

Department of Chemistry, Texas A & M University, Box 30012, College Station, Texas 77842-3012, and Departments of Physiology, Pharmacology, and Pathobiology, Texas A & M University, TVMC, College Station, Texas 77881.
Received May 30, 2006; Revised Manuscript Received July 27, 2006

Synthesis of a new fluorescent rhodamine derivative, dye **1**, is reported. This probe is different from other rhodamines insofar as it has several (four) carboxylic acid functionalities to promote water solubility and facilitate conjugation to proteins. It also has an aryl bromide functionality that could, in principle, be used to further functionalize the system for specialized applications. Dye **1** was conjugated to a model protein called ACBP (acyl-CoA binding protein). The properties of this conjugate were tested to establish that the label does not significantly perturb the binding function of the protein to its natural ligand in vitro and to confirm that its secondary structure was not significantly perturbed (circular dichroism). Experiments were performed to test if the labeled protein could be imported into *living* COS-7 cells (using the Chariot-peptide delivery system) and, if so, to observe, via fluorescence microscopy, which of the labeled protein was able to migrate to the nucleus, as expected for ACBP in cells. In the event, all these postulates were confirmed.

INTRODUCTION

Intracellular imaging (*1*) requires a selection of water-soluble, fluorescent dyes that absorb and emit at wavelengths longer than those commonly associated with autofluorescence in cells (*2*), i.e., above around 550 nm. Some rhodamine dyes with these characteristics are commercially available, but specialized situations call for "tailor-made" probes that can be modified with other functionalities via organic transformations. Preparation and manipulation of water-soluble fluorescent dyes is challenging, because separation of gram amounts of material tends to be more difficult for polar, water-soluble materials relative to others that are soluble, and chromatographically separable, using organic solvents. Furthermore, even recrystallization of highly colored, fluorescent dyes is experimentally difficult, simply because it is difficult to see when crystals are forming.

Our collaborative project on intracellular imaging of proteins involved in nuclear localization called for a special type of rhodamine dye. Specifically, the probe should (i) be water soluble; (ii) absorb and fluoresce above 550 nm; (iii) have functional groups that allow attachment to proteins; (iv) have another functional group that would allow attachment of other organic fragments to the dye via organometallic reactions involving conditions that would not perturb other functional groups in the dye; and (v) be synthetically accessible. Rhodamine derivative **1** was conceived on the basis of these considerations (Figure 1; "rosamine" is informal nomenclature introduced by Molecular Probes to denote rhodamine without a carboxylic acid on the peripheral benzene ring). This probe has four carboxylic acid groups to promote water solubility (at least above pH levels of approximately 4.5) and to provide points of attachment to proteins. Use of carboxylic acids means that most of the synthetic steps could be performed on tetraesters, and these compounds tend to be hydrophobic and more easily chromatographed on a gram scale. Finally, the aryl bromide functionality was included in the design to allow fusion of other entities to the fluorescent dye via palladium-catalyzed reactions (e.g., Suzuki (*3*) and Sonogashira (*4*) couplings). Our particular need was to attach other dye fragments to this site, to form "through-bond energy transfer cassettes" (*5*, *6*). That particular goal is beyond the scope of this paper, but what is important here is simply the concept that this functional group could be used to attach other groups to create dual-purpose probes. We propose that the second site could be modified to include useful entities such as EPR spin-labels, chelating groups to facilitate MRI imaging, or radioactive reporter functionalities.

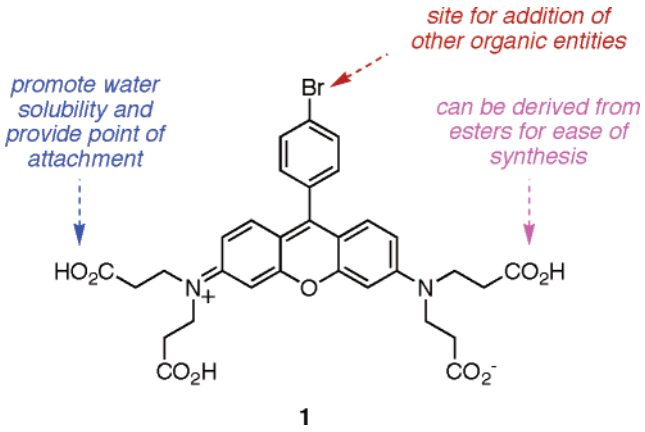

1

Figure 1. The target probe **1**.

EXPERIMENTAL PROCEDURES

Chemicals and Reagents. Unless otherwise noted, all nonaqueous reactions were carried out under an atmosphere of dry N_2 in dried glassware. When necessary, solvents and

* burgess@tamu.edu. Ph: (979)845-4345. Fax: (979)845-8839.
[†] Department of Chemistry.
[‡] Departments of Physiology, Pharmacology, and Pathobiology.

10.1021/bc0601424 CCC: $33.50 © 2006 American Chemical Society
Published on Web 08/23/2006

reagents were dried prior to use. Diethyl ether and dichloromethane were deoxygenated by purging with N_2 and then dried by passing through activated alumina. Tetrahydrofuran and toluene were distilled from sodium and hexanes from calcium hydride. DMF was distilled from CaH_2 under reduced pressure. K_2CO_3 was used as received from EMD ACS grade. 3-Aminophenol and acrylic acid from Across Organics were used as received, and 4-bromobenzaldehyde, *N*-hydroxysuccinimide, and DIC (diisopropylcarbodiimide) were purchased from Aldrich. Buffer ingredients and solutions for liquid chromatography, gel electrophoresis, and cell culture were purchased from Gibco BRL (Invitrogen, Carlsbad, CA) and Sigma-Aldrich (St. Louis, MO). Bio-Gel P-4 for gel filtration chromatography was from Bio-Rad (Hercules, CA).

Instruments. Analytical thin layer chromatography (TLC) was performed on EM Reagents 0.25 mm silica gel 60-F plates. Visualization was accomplished with UV light. Chromatography on silica gel was performed using a forced flow of the indicated solvent system on EM Reagents Silica Gel 60 (230−400 mesh). ^{1}H NMR spectra were recorded (VXR-300 and Inova 500 MHz spectrometer) at room temperature, and chemical shifts are reported in parts per million (ppm) from the solvent resonance ($CDCl_3$ 7.26 ppm, CD_2Cl_2 5.30 ppm, DMSO-d_6 2.49 ppm, D_2O 4.80 ppm). Data are reported as follows: chemical shift, multiplicity (s = singlet, d = doublet, t = triplet, q = quartet, br = broad, m = multiplet), coupling constants, and number of protons. Proton decoupled ^{13}C NMR spectra were also recorded (VXR and Inova spectrometers) at room temperature. Chemical shifts are reported in parts per million from tetramethylsilane resonance ($CDCl_3$ 77.36 ppm). MS were measured (Thermofinnigan LC-Q Deca spectrometer) under ESI, MALDI, or APCI conditions. IR spectra were recorded on a Bruker (Tensor 27), UV on an HP (Diode Array Spectrophotometer), and fluorescence spectra were recorded on a Fluorolog spectrometer.

Preparation of the Diester 2. A solution of 3-aminophenol (1.00 mol, 109 g) in acrylic acid (3.00 mol, 185 mL) and water (93 mL) was heated to 70 °C. After stirring for 3 h, the reaction mixture was cooled, ethanol (180 mL) was added and the solution kept at 5° C. After 12 h, precipitate appeared and was filtered, washed with ethanol (50 mL), and dried under vacuum to afford the intermediate diacid as a solid (200 g, 80%). Mp = 153−154 °C (lit (*7*) 149−150 °C); ^{1}H NMR (300 MHz, acetone−d_6) δ 7.02−6.98 (m, 1H), 6.28−6.24 (m, 2H), 6.19−6.17 (m, 1H), 3.65 (t, 4H, J = 4.5 Hz), 2.60 (t, 4H, J = 4.5 Hz); ^{13}C NMR (75 MHz, acetone−d_6) δ 172.6, 158.6, 148.6, 130.0, 104.0, 104.2, 99.6, 46.8, 31.7; MS (ESI) calcd for $C_{12}H_{15}NO_5$ 253.0950, found 253.0400.

A solution of the diacid prepared above (39.5 mmol, 10.0 g) in methanol (500 mL) and HCl (10 M, 1 mL) was refluxed for 12 h, then cooled to room temperature, and MeOH evaporated under reduced pressure. The residue was dissolved in EtOAc (100 mL), and the organic layer was washed with water (5 × 20 mL). The organic layer was evaporated under reduced pressure to yield **2** (*8*) as a yellow semisolid (7.0 g, 63%). R_f = 0.7 (50% EtOAc/hexane). ^{1}H NMR (300 MHz, CD_3OD) δ 7.05−6.95 (m, 1H), 6.25−6.15 (m, 3H), 3.65 (s, 6H), 3.60 (t, 4H, J = 7.2 Hz), 2.58 (t, 4H, J = 7.2 Hz); ^{13}C NMR (75 MHz, CD_3OD) δ 173.3, 158.36, 148.5, 130.1, 104.6, 104.2, 99.9, 51.1, 46.9, 32.1; MS (ESI) calcd for $C_{14}H_{19}NO_5$ 281.1263, found 281.3614.

Bromorosamine Tetraacid 1. 4-Bromobenzaldehyde (3.6 mmol, 0.66 g) was added to a solution of dimethyl ester **2** (7.2 mmol, 2.0 g) in ether (5 mL). After stirring for 15 min, the ether was evaporated. The neat mixture was subjected to microwave irradiation (300 W, 150−155 °C, 20 min). Chloranil (4.1 mmol, 1.0 g) in 1:1 (CH_2Cl_2/MeOH) (10 mL) was then added, and the reaction was stirred for 1 h. The solvents were removed, and residue was chromatographed (SiO_2; 20% MeOH/CH_2Cl_2) to afford **3** (0.5 g) in 20% yield (80−85% purity) as a sticky solid. R_f = 0.30 (10% MeOH/CH_2Cl_2); ^{1}H NMR (500 MHz, CD_3OD/$CDCl_3$) δ 7.89 (d, 2H, J = 8.5 Hz), 7.49 (d, 2H, J = 9.5 Hz), 7.46 (d, 2H, J = 8.5 Hz), 7.21 (dd, 2H, J = 2.5 Hz, 2.5 Hz), 7.13 (d, 2H, J = 2.5 Hz), 4.03 (t, 8H, J = 7.0 Hz), 3.72 (s, 12H), 2.81 (t, 8H, J = 7.5 Hz); MS (ESI) calcd for $C_{35}H_{38}BrN_2O_9^+$ 709.1755, found 709.1904, 711.1924.

Solid K_2CO_3 (1.4 mmol, 193 mg) was added to a solution of compound **3** (0.07 mmol, 50 mg) in 1:1:1 (H_2O/MeOH/THF) (10 mL). After stirring for 12 h at 40 °C, the MeOH and THF were removed, and the aqueous layer was extracted with EtOAc (3 × 50 mL). The aqueous layer was further acidified with conc HCl to attain pH = 2−3, then extracted with 1:2 (^{i}PrOH/CH_2Cl_2) and concentrated to afford crude compound **1** (30 mg). Crude compound **1** (30 mg) was dissolved in 1:1 (CH_3CN/H_2O) (30 mL) and subjected to reverse-phase preparative HPLC (C18, 5:95 (CH_3CN/H_2O), t_R = 12.0 min) to afford pure compound **1** (10 mg) in 22% yield as a solid: R_f = 0.10 (10% MeOH/CH_2Cl_2); ^{1}H NMR (500 MHz, CD_3OD/$CDCl_3$) δ 7.84 (d, 2H, J = 10 Hz), 7.48 (d, 2H, J = 10 Hz), 7.35 (d, 2H, J = 10 Hz), 7.12 (dd, 2H, J = 2.5 Hz, 2.0 Hz), 7.02 (d, 2H, J = 5.0 Hz), 4.00 (t, 8H, J = 5.0 Hz), 2.75 (t, 8H, J = 5.0 Hz); ^{13}C NMR (125 MHz, CD_3OD/$CDCl_3$) δ 173.1, 158.4, 158.0, 156.3, 132.6, 132.3, 131.2, 130.6, 125.5, 115.2, 114.1, 97.5, 77.8, 32.1; IR (neat) ν (cm^{-1}) 1644; MS (ESI) calcd for $C_{31}H_{30}BrN_2O_9^+$ 653.1129, found 653.1062, 655.1052.

Activation of Bromorosamine 4. *N*-Hydroxysuccinimide (0.003 mmol, 0.36 mg) and DIC (0.004 mmol, 0.47 mg) were added to a solution of **1** (0.003 mmol, 2.0 mg) in dry DMF (0.5 mL) under N_2. After stirring for 24 h at 25 °C, the solvent was removed, and the residue was dried under high vacuum. This sample, without purification, was used to label the protein.

Labeling of Recombinant Mouse Acyl-CoA Binding Protein (ACBP). A recombinant mouse ACBP as described before (*9*) was tagged with five histidine (His) residues at its C-terminus, expressed in *E. coli*, and purified by affinity chromatography on Ni-CAM-Sepharose. Newly synthesized water-soluble rhodamine-based dye **1** was coupled to ACBP by using multiple dye-to-protein molar ratios, and the optimal ratios were 5:1 and 10:1, so that in the end a molecule of protein would be labeled with 0.5−5 dye molecules. Typically, 50 nmoles of ACBP were incubated with 250−500 nmoles of rhodamine derivative **1** in PBS, pH 8.5. Incubation of protein with dye was allowed at room temperature for 1 h, in the dark with gentle stirring. ACBP/dye reaction mixtures were then centrifuged at 13 000 rpm for 20 s in an Eppendorf centrifuge 5415 D to remove possible large particles and aggregates resulting from the coupling reaction. The supernatant containing soluble dye-labeled protein and unbound dye was collected and loaded onto a 20 mL Bio-Gel P-4 (fine, 45−90 μm, wet gel particles) column which had been equilibrated in PBS, pH 7.4, in order to separate the colored protein from unbound dye. The column separated two bands: the first one contained labeled ACBP, while the slower band consisted of unbound dye; this separation was confirmed by reading protein absorbance at 280 nm in all collected fractions. The dye-labeled ACBP was characterized in terms of protein and dye concentrations, as well as dye-to-protein molar ratio. Protein concentration was determined by Bio-Rad protein assay as recommended by the manufacturer. The molecular size of ACBP protein after labeling with **1** was checked by SDS-PAGE in 14% polyacrylamide electrophoresis gel following a Bio-Rad procedure based on Laemmli's method (*10*).

Absorbance and Fluorescence Spectroscopy of Rhodamine-Dye-labeled ACBP. The absorbance properties of rhodamine dye after coupling to ACBP protein were measured by using a Carry 100 Scan UV−visible spectrophotometer from Varian (website at www.varianinc.com), while its fluorescence emission spectra were recorded with a PC1 photon-counting fluorometer from ISS (ISS, Inc., Urbana, IL).

Fluorescence Binding Assays. *cis*-Parinaroyl-CoA, a long acyl-CoA with an 18-carbon chain and 4 conjugated double bonds, that emits with a maximum at 410 nm when it is excited at 320 nm, was used for titration of 0.02−0.2 μM unlabeled and dye-labeled ACBP, as described before (*9, 11*). Increasing concentrations of *cis*-parinaroyl-CoA from 2.5 to 500 nM were added to a constant amount of ACBP, and fluorescence emission spectra were recorded at each titration point from 350 to 500 nm, with excitation of *cis*-parinaroyl-CoA at 320 nm. Controls for unbound ligand (identical concentrations of *cis*-parinaroyl-CoA but in the absence of protein) and for protein-interfering emission were measured and subtracted. The maximum fluorescence intensities from recorded spectra were then plotted against total concentration of *cis*-parinaroyl-CoA at each titration point. Further analysis of these binding curves by nonlinear regression and fitting to ligand binding to one site equations was performed with *Sigma Plot 8.0* software, and the values of K_d, i.e., dissociation constant, and B_{max}, i.e., maximum binding fluorescence intensity, were then obtained.

Circular Dichroism (CD) Analysis of ACBP Before and After Labeling with Dye 1. Far-UV CD spectra of unlabeled and **1**-ACBP at a concentration of 4 μM in 20 mM potassium phosphate buffer, pH 7.4, were recorded by the use of a J-710 spectropolarimeter (Jasco, Baltimore, MD). Measurements were done in a 1 mm cuvette, and spectra were recorded from 260 to 190 nm at 50 nm/min with a time constant of 1 s and a bandwidth of 2 nm. For each CD profile, an average of 10 scans was obtained. Percentages of secondary structures in ACBP when unlabeled or **1**-labeled were calculated from CD spectra by using the *CD-PRO* software (*12*).

Cell Culture and Delivery of Dye-1 Labeled ACBP into Cells for Intracellular Imaging. COS-7 cells were purchased from the American Type Culture Collection (ATCC, Manassas, VA) and grown in DMEM with 10% fetal bovine serum (FBS), in 2-well chamber glasses (LabTek from VWR, Suwanee, GA) at 37 °C and 5% CO_2. A sample of **1**-ACBP was delivered to cells grown to about 80% confluence, according to a modified procedure recommended by Active Motif (Carlsbad, CA) for the use of Chariot transfection reagent. Briefly, dye-labeled ACBP from 500 ng to 2 μg were preincubated with Chariot (from Active Motif, Carlsbad, CA) in protein-to-peptide ratio of 1:20 (w/w) for 30 min at room temperature and then added to COS-7 cells in the presence of serum-free DMEM. After 30 min incubation, the protein−Chariot mixes were washed off cells with PBS, and cells were incubated with 10% FBS/DMEM at 37 °C, 5% CO_2 for 2 h before confocal microscopy. Cell nuclei were counterstained by adding 1 μg/mL Hoechst 33342 nuclear marker solution (from Molecular Probes, Eugene, OR) about 30 min before confocal microscopy observation.

Intracellular Imaging of Labeled ACBP By Laser Scanning Confocal Microscopy (LSCM). An MRC1024 confocal imaging system (from Bio-Rad) consisting of an Axiovert 135 microscope (Zeiss, New York) equipped with three independent low-noise photomultiplier tube channels was used for LSCM. The excitation light (λ = 488 and 568 nm) from a 15 mW krypton−argon laser was delivered to sample through a 63× Zeiss Plan-Fluor oil immersion objective, numerical aperture 1.45. Emission filters 540/30 (allowing emission light of 520−530 nm wavelengths) and HQ598/40 (allowing emission light of 580−660 nm wavelengths) were employed to detect fluorescence images in the green (PMT2) and red (PMT1) channels, respectively. Hoechst 33342 nuclear marker was excited at 408 nm by using a solid-state laser (from Power Technology, Little Rock, AR) and detected in the green channel with a 540/30 emission filter in PMT2. Colocalization analysis was achieved by using the *LaserSharp* v 3.0 software from Bio-Rad, and colocalization coefficients were calculated as described (*13*). Additional processing of images was performed by using MetaMorph Image Analysis from Advanced Scientific Imaging (Meraux, LA).

Scheme 1. Synthesis of Dye 1

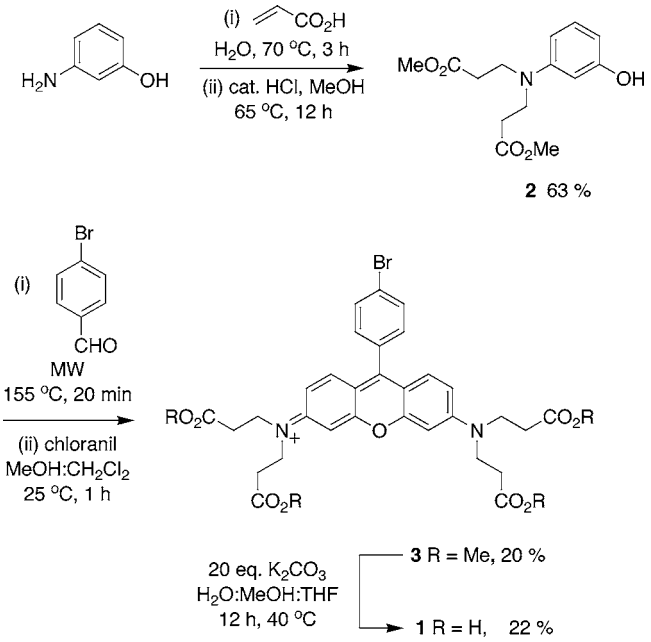

Electronic Spectra. Figure 3 shows the UV and fluorescence spectra of dye **1** in PBS at pH 7.4. For this solution, the molar extinction coefficient, ϵ, was measured to be 91 000 and $\lambda_{max\ abs}$ = 556 nm. It fluoresced at 579 nm with a quantum yield of 0.76. Fluorescence quantum yield measurements were measured on a photon counting spectrofluorometer PC1 SSI instrument equipped with an R928P photomultiplier tube which is sensitive up to ~850−900 nm. The slit width was 0.5 nm for both excitation and emission. Relative quantum efficiencies of fluorescence of dye **1** were obtained by comparing the areas under the corrected emission spectrum of the test sample in PBS buffer (pH = 7.4) with that of a solution of rhodamine B, which has a quantum efficiency of 0.97 according to the literature (*14*). DI water for the PBS buffer and a 10 mm quartz cuvette were used. Dilute solutions ($0.01 < A < 0.05$) were used to minimize reabsorption effects. The excitation wavelength was 556 nm for both compound **1** and the reference.

Quantum yields were determined using eq 1 (*15*)

$$\Phi_X = \Phi_{st}(I_X/I_{st})(A_{st}/A_X)(\eta_X^2/\eta_{st}^2) \quad (1)$$

where Φ_{st} is the reported quantum yield of the standard, I is the integrated emission spectra, A is the absorbance at the excitation wavelength, and η is the refractive index of the solvent used (η = 1 if same solvent). The X subscript denotes unknown, and "st" denotes standard.

RESULTS

Synthesis. Scheme 1 summarizes the synthesis of compound **1**. Double Michael addition of acrylic acid to 3-aminophenol

via a literature procedure (*7*) gave the diacid as a precipitate. This material, without purification, was esterified to give the diester **2** which could be isolated on a multigram scale via extraction with ethyl acetate. The next step in the synthesis was to condense the phenol **2** with an aldehyde to give the rosamine framework. Such syntheses usually feature protic acid media (*16*); however, we found that the reaction proceeds without solvent or added catalysts. We were unable to identify reaction conditions for this condensation that featured heating under conventional conditions. However, in a microwave reactor specifically designed for holding reactions at a set temperature (Discover, CEM Corporation), the reaction was found to proceed with good conversion in only 20 min. Chloranil was added to oxidize the initial condensation product to the rosamine tetraester **3**, which was then isolated by column chromatography. This tetraester was then hydrolyzed to the desired product **1**. Crude samples of the rosamine **1** with quite good purity could be isolated via an acid−base extraction procedure. Pure material was isolated via preparative RP-HPLC to give a 22% yield of the product. Selected data for compounds **1** and **3** are shown in Figure 2. The dye is highly soluble in aqueous buffer at pH 7.4.

Electronic spectra of compound **1** showed several desirable characteristics. The dye absorbs strongly at 556 nm and emits with a high quantum yield at 579 nm in aqueous buffer. Variation of the concentration of the dye in the buffer showed that the emission maxima wavelength did not shift; this indicates that the dye is not aggregated in this media (Figure 3).

Monoactivation of tetraacid **1** to give the reactive ester **4** was performed by employing DIC and *N*-hydroxysuccinimide in DMF (Scheme 2). Compound **4** was used, without purification, to tag with an illustrative protein, as described below. The unimolecular binding of dye **1** to protein is confirmed by MALDI-TOF (Figure 3).

Spectral Properties of Dye 1 After Conjugation to the Illustrative Protein: Acyl-CoA Binding Protein (ACBP). ACBP was chosen to test the possibility of using the newly synthesized water-soluble rhodamine derivative for intracellular imaging by laser scanning confocal microscopy. A recombinant mouse ACBP was purified and conjugated to dye **1** as described under Experimental Procedures. Tests to ensure that the basic physical and functional properties of fluorescent dyes were maintained after conjugation to the protein included absorbance and fluorescence spectra on the labeled protein and compared with dye **1**. Figure 4 shows the absorbance spectra of **1**−ACBP and the dye only, in PBS pH 7.4. The wavelength corresponding to maximum absorbance for the conjugate was slightly shifted from 553 nm for the dye only, to 560 nm for **1**−ACBP conjugate. The fluorescence emission spectra of **1** either free in PBS or conjugated to ACBP protein demonstrated that the maximum fluorescence wavelength exhibited a small red shift from 574 nm for free dye **1** to 583 nm for ACBP-coupled dye **1** when excitation was at 568 nm.

Physical and Functional Properties of Acyl-CoA Binding Protein (ACBP) After Conjugation to Dye 1. The structural and functional properties of the protein were also tested after conjugation to dye **1**. Thus, SDS-polyacrylamide gel electrophoresis, fluorescence binding assays, and circular dichroism were performed on the **1**−ACBP product and compared to unlabeled ACBP.

An SDS-PAGE test demonstrated that the molecular size of **1**−ACBP was very similar to that of ACBP (not shown). The small increase in molecular weight of ACBP after labeling was due to the additional weight of dye molecules that had been covalently attached to the protein by conjugation. Most importantly, the SDS-PAGE assay demonstrated that no intermolecular cross-linking occurred as a negative side effect during protein−

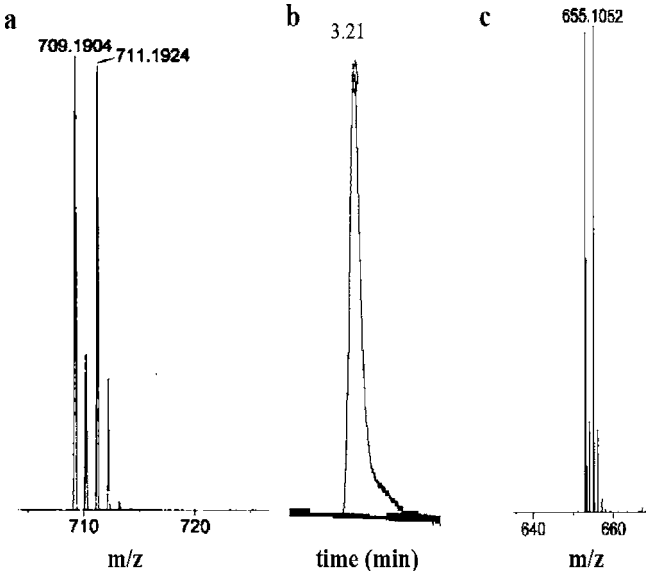

Figure 2. Data for **1** and **3**. (a) Electrospray MS showing molecular ion peak for **3**; (b) analytical RP-HPLC (C18, 5% CH_3CN in H_2O and 0.1% TFA, $t_R = 3.21$ min) for **1**; (c) electrospray MS showing molecular ion peak for **1**.

Scheme 2. Monoactivation of Dye 1

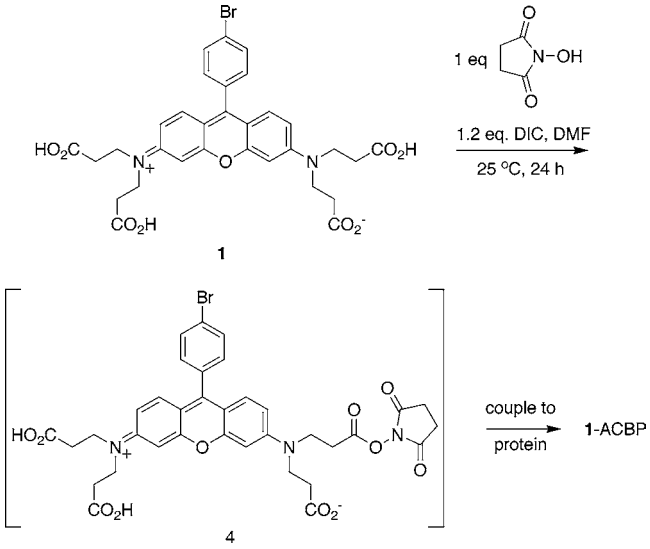

dye reaction. This result was possible by purposely activating dye **1** once to contain a single reactive group available for conjugation to amino groups on the surface of ACBP protein.

One of the most important functions of ACBP is to bind medium- and long-chain fatty acyl-CoA thioesters with high affinity (i.e., low-range nanomolar dissociation constant, K_d). To check if this property was maintained after labeling, the recombinant ACBP was assayed by titration with a fluorescent ligand, namely, *cis*-parinaroyl-CoA up to saturation of binding, as described under Experimental Procedures. The binding curves as shown in Figure 5a,b were obtained by plotting fluorescence intensities versus total concentration of ligand (*cis*-parinaroyl-CoA) at each titration point, followed by nonlinear regression analysis and calculation of K_d and B_{max} (maximum fluorescence intensity at binding saturation). The labeled **1**−ACBP exhibited *cis*-parinaroyl-CoA binding to saturation, just as the unlabeled ACBP did, with a K_d of 6.3 ± 2.7 nM; this was a slightly higher affinity for *cis*-parinaroyl-CoA than unlabeled ACBP (K_d of 11.3 ± 2.8 nM).

Circular dichroism (CD) spectra in the far UV were recorded to get more information about the structural and conformational

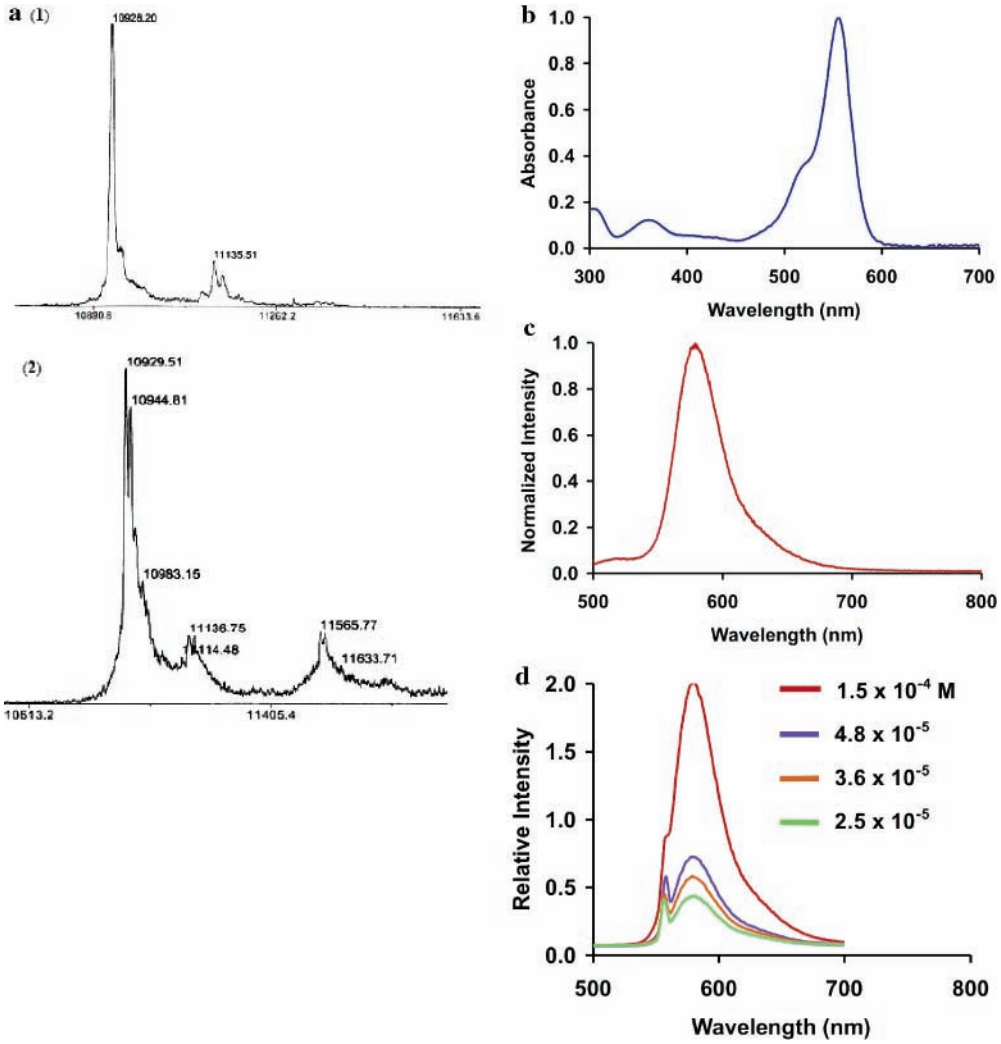

Figure 3. Mass spectra of free and labeled His−ACBP−**1** and electronic spectra of **1** in PBS buffer (pH = 7.4). (a) (1) MALDI-TOF of free His−ACBP [$M^+ + X.K^+/Na^+$(10 928.20)]; (2) MALDI-TOF for His−ACBP−**1** [$MH^+ + X.K^+/Na^+$ (11 565.77) (before conjugate purification)]; (b) normalized UV spectrum at concentration 10^{-4} M, ϵ 91 000, $\lambda_{max\ abs}$ = 556 nm; (c) fluorescence spectrum at 10^{-5} M, $\lambda_{max\ emis}$ = 579 nm, using 556 nm excitation wavelength; (d) the fluorescence emission wavelength of compound **1** does not vary with concentration.

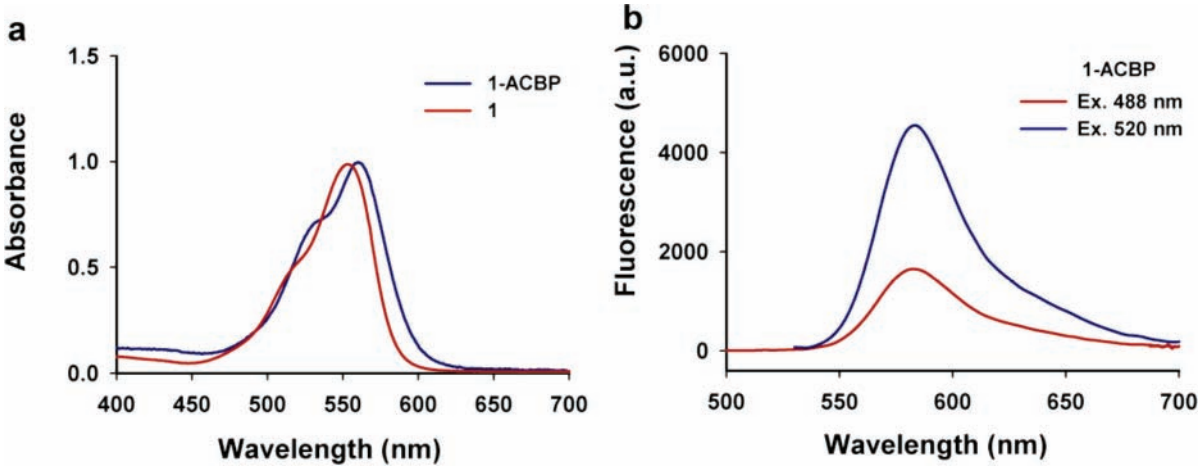

Figure 4. Absorbance and fluorescence spectra of free and **1**−ACBP-bound in PBS at pH 7.4. (a) UV−vis spectra of free dye is shown in red line and that of ACBP-bound dye in black line; (b) emission spectra of **1**−ACBP.

changes caused by dye **1** on ACBP. Figure 5c shows the CD spectra of ACBP and **1**−ACBP. The two spectra are similar, suggesting that only small changes in the secondary structure of ACBP were introduced by coupling it to dye **1**.

Intracellular Imaging of 1−ACBP. COS-7 cells were incubated with **1**−ACBP that had been labeled with dye **1** in the presence of the Chariot system (*17*) to test whether the labeled protein could be imported into cells in this way. If free **1**−ACBP is internalized in the cells, and functions in the same way as the unlabeled protein, then some of it should localize in the nucleus (*18*). The cell nuclei were counterstained with Hoechst 33342 dye to test for this. Figure 6a shows fluorescence

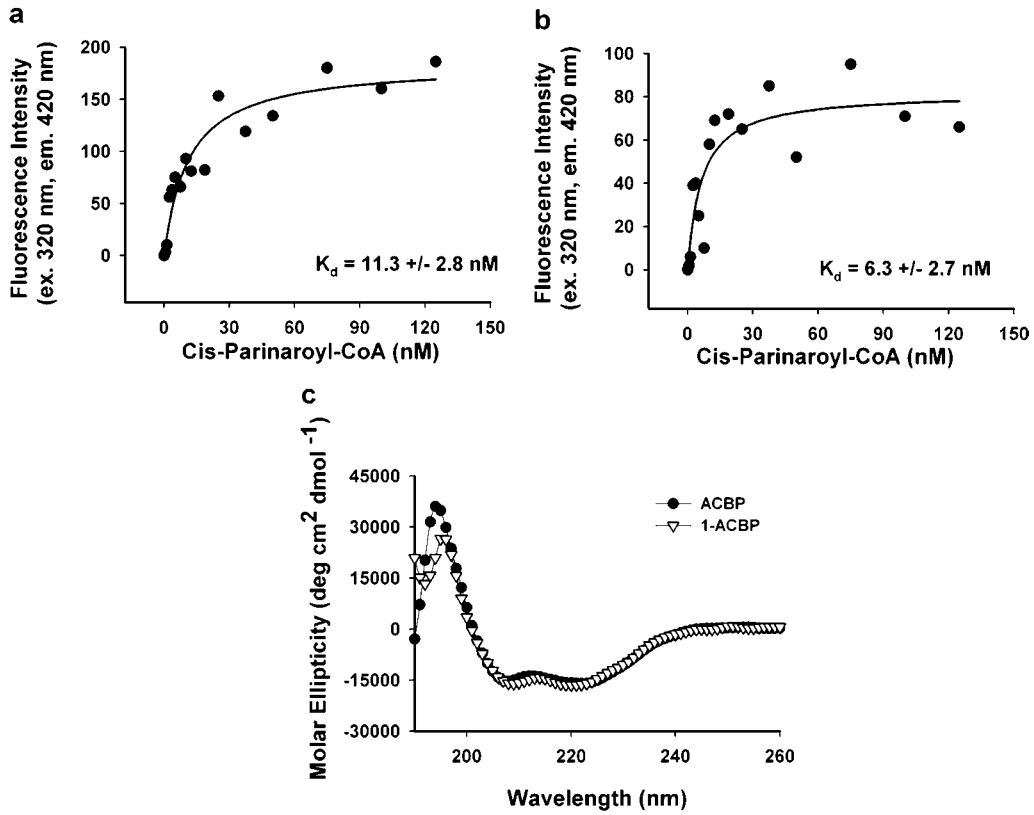

Figure 5. (a) Binding curve for ACBP; (b) binding curve for **1**−ACBP; (c) circular dichroic (CD) spectra of unlabeled ACBP (black circles) and **1**−ACBP (white triangles).

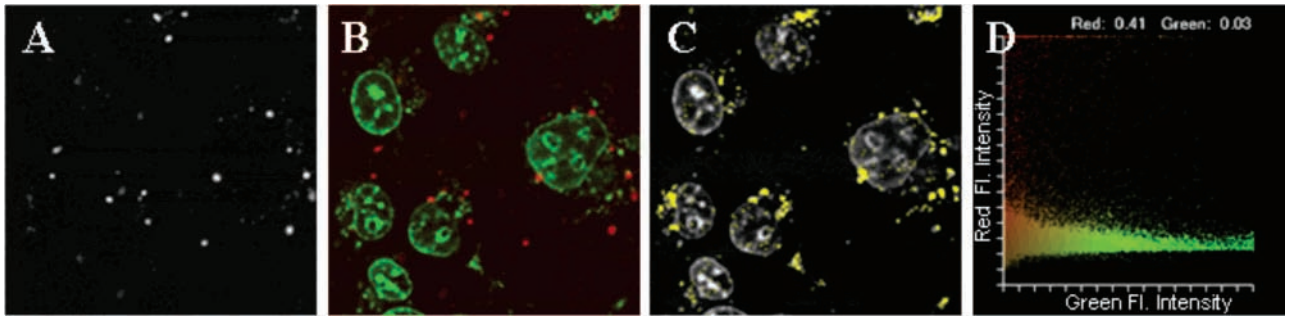

Figure 6. Intracellular imaging of **1**−ACBP labeled COS-7 cells by confocal microscopy. (A) **1**−ACBP with excitation at 568 nm, and emission filter HQ 598/40; (B) overlay of **1**−ACBP image (red) with nuclei image (green, given by the nuclear marker Hoechst 33342 that emits at 530 nm with excitation at 408 nm); (C) colocalized pixels (yellow) from **1**−ACBP and the nuclear marker; and (D) fluorograph indicating the extent of colocalization.

images of **1**−ACBP in cells (detected in the red channel, with an emission filter at 598 nm, excitation at 568 nm). In Figure 6b, fluorescence signals from **1**−ACBP (in red) and Hoechst-stained nuclei (in green) are shown to demonstrate the distribution of ACBP molecules inside cells relative to nuclei. Most of the fluorescently labeled ACBP molecules appeared in the cytoplasm, around nuclei, but a fraction of the **1**−ACBP molecules were observed inside nuclei. This demonstrates that the Chariot-mediated import of **1**−ACBP was successful and that some of the labeled protein is gravitating to the region of the cell (the nucleus) that is expected from its postulated function (*18*). Yellow pixels in Figure 6c represent the colocalization of **1**−ACBP with the nuclear marker. The fluorogram in Figure 6d shows a more quantitative colocalization analysis for the relative distribution and fluorescence intensities of the two signals (green and red).

DISCUSSION

This paper reports the synthesis of a new water-soluble dye, **1**. This compound has four carboxylic acid groups to increase water solubility and to facilitate coupling to proteins. It can be selectively coupled to just one protein molecule without significant cross-linking to a second one. In the particular case of the protein ACBP, the data presented here show that conjugation of this model probe does not significantly perturb the secondary structure or the natural binding function of the protein in vitro. Moreover, **1**−ACBP can be imported into *living* cells using the novel Chariot−peptide carrier system wherein it accumulates, at least partially, in the nucleus as expected.

Though the work presented here does not actually demonstrate this, it is clear that organometallic coupling reactions could be used to add different molecular entities to the aryl bromide functionality of compound **1**. If this were done, a variety of "bifunctional" labels might be prepared. They too might be imported into living cells via the Chariot system, then studied in vivo.

ACKNOWLEDGMENT

We thank Mr. Jiney Jose for developing a procedure to prepare compound **2**, CEM for support with the Discover unit

used in this research, and the TAMU/LBMS-Applications Laboratory directed by Dr. Shane Tichy for assistance with mass spectrometry. Support for this work was provided by The NIH (GM72041) and by The Robert A. Welch Foundation A-1121.

LITERATURE CITED

(1) Weissleder, R., and Ntziachristos, V. (2003) Shedding light onto live molecular targets. *Nat. Med. 9*, 123−8.

(2) Benson, R. C., Meyer, R. A., Zaruba, M. E., and McKhann, G. M. (1979) Cellular autofluorescence - is it due to flavins? *J. Histochem. Cytochem. 27*, 44−8.

(3) Miyaura, N., and Suzuki, A. (1995) Palladium-catalyzed cross-coupling reactions of organoboron compounds. *Chem. Rev. 95*, 2457−83.

(4) Sonogashira, K., Tohda, Y., and Hagihara, N. (1975) A convenient synthesis of acetylenes: catalytic substitutions of acetylenic hydrogen with bromoalkenes, iodoarenes, and bromopyridines. *Tetrahedron Lett. 16*, 4467−70.

(5) Burghart, A., Thoresen, L. H., Chen, J., Burgess, K., Bergström, F., and Johansson, L. B.-A. (2000) Energy transfer cassettes based on BODIPY dyes. *Chem. Commun.* 2203−4.

(6) Jiao, G.-S., Thoresen, L. H., and Burgess, K. (2003) Fluorescent, through-bond energy transfer cassettes for labeling multiple biological molecules in one experiment. *J. Am. Chem. Soc. 125*, 14668−9.

(7) Mitskyavichyus, V. Y., and Bilinskaite, I. (1996) Alkyl derivatives of 1-aryldihydro-4(1H,3H)-pyrimidinone-2-thiones and their structure. *Khim. Geterotsikl. Soedin.* 1255−60.

(8) Jose, J., and Burgess, K. (2006) Syntheses and Properties of Water-soluble nile red derivatives. *J. Org. Chem.* in press.

(9) Chao, H., Martin, G., Russell, W. K., Waghela, S. D., Russell, D. H., Schroeder, F., and Kier, A. B. (2002) Membrane charge and curvature determine interaction with acyl CoA binding protein (ACBP) and fatty acyl CoA targeting. *Biochemistry 41*, 10540−53.

(10) Laemmli, U. K. (1970) Cleavage of structural proteins during the assembly of the head of bacteriophage T4. *Nature (London) 227*, 680−685.

(11) Frolov, A. A., and Schroeder, F. (1998) Acyl coenzyme A binding protein: conformational sensitivity to long chain fatty acyl-CoA. *J. Biol. Chem. 273*, 11049−55.

(12) Sreerama, N., and Woody, R. W. (2000) Estimation of protein secondary structure from circular dichroism spectra: comparison of CONTIN, SELCON, and CDSSTR methods with an expanded reference set. *Anal. Biochem. 287*, 252−60.

(13) Manders, E. M. M., Verbeek, F. J., and Aten, J. A. (1993) Measurement of colocalization of objects in dual-colour confocal images. *J. Microsc. 169*, 375−82.

(14) Vincett, P. S., Voigt, E. M., and Rieckhoff, K. E. (1971) Phosphorescence and fluorescence of phthalocyanines. *J. Chem. Phys. 55*, 4131−40.

(15) Williams, A. T. R., Winfield, S. A., and Miller, J. N. (1983) Relative fluorescence quantum yields using a computer-controlled luminescence spectrometer. *Analyst (Cambridge, U.K.) 108*, 1067−71.

(16) Jiao, G.-S., Castro, J. C., Thoresen, L. H., and Burgess, K. (2003) Microwave-assisted syntheses of regioisomerically pure bromo-rhodamin derivatives. *Org. Lett. 5*, 3675−7.

(17) Morris, M. C., Depollier, J., Mery, J., Heitz, F., and Divita, G. (2001) A peptide carrier for the delivery of biologically active proteins into mammalian cells. *Nat. Biotechnol. 19*, 1173−6.

(18) Petrescu, A. D., Payne, H. R., Boedeker, A. L., Chao, H., Hertz, R., Bar-Tana, J., Schroeder, F., and Kier, A. B. (2003) Physical and functional interaction of acyl CoA binding protein (ACBP) with hepatocyte nuclear factor-4α (HNF4α). *J. Biol. Chem. 278*, 51813.

BC0601424

Synthesis and Biological Evaluation of EC140: A Novel Folate-Targeted Vinca Alkaloid Conjugate

Christopher P. Leamon,* Joseph A. Reddy, Iontcho R. Vlahov, Paul J. Kleindl, Marilynn Vetzel, and Elaine Westrick

Endocyte, Inc., 3000 Kent Ave., West Lafayette, Indiana 47906. Received May 31, 2006; Revised Manuscript Received August 1, 2006

A novel folate conjugate of desacetylvinblastine monohydrazide (DAVLBH), herein referred to as EC140, was designed and evaluated for biological activity against folate receptor (FR)-positive cells and tumors. EC140 was produced by coupling a peptidic analogue of the vitamin folic acid to DAVLBH via an acylhydrazone bond. This water-soluble conjugate was found to retain high affinity for FR-positive cells, and it produced specific, dose-responsive activity in vitro. Initial in vivo tests confirmed EC140's activity in both syngeneic and xenograft models. Hence, enduring complete responses were observed in animals bearing established, subcutaneous tumors prior to therapy using regimens that produced minor toxicity. In contrast, treatment with the unconjugated DAVLBH drug produced nominal efficacy when dosed at its MTD. Overall, EC140's performance *i*n vitro and in vivo warrants further preclinical study before this novel targeted chemotherapeutic is considered for clinical investigation.

INTRODUCTION

Chemotherapy is the principal method of treatment for patients with metastatic or disseminated cancers, and common regimens are designed to administer a drug in an intermittent fashion (e.g., once every 3 to 6 weeks) at its maximum tolerated dose (MTD) followed by a recovery period. Such regimens have been used for over 50 years, but very few agents produce adequate clinical improvements when administered this way. One cause for disappointing outcomes is that this method of treatment is plagued by toxicity resulting from the indiscriminate uptake of these poisons into proliferating cells of both normal and neoplastic tissue. Yet, because tumor tissue recovers from chemotherapy so much faster than normal tissue, tumor elimination is rare following infrequent drug administration.

Theoretically, the toxicity of a chemotherapeutic drug should be decreased or eliminated if the pharmacophore were specifically targeted to the cancer cells. This alternative approach has certainly been exemplified recently by the apparent clinical successes of tumor-targeted/tumor-specific agents like Herceptin and Gleevec (*1*). However, alternative methods for targeting drugs to cancer cells are also being explored. One such technique is to exploit the receptor-mediated uptake pathway for folic acid.

The vitamin folic acid is a ligand capable of targeting covalently attached bioactive agents quite specifically to folate receptor (FR)-positive cells (*2*). The FR, which is a tumor-associated protein, can actively internalize bound folates via endocytosis (*2*, *3*). It has been detected at very high levels in >90% of ovarian and other gynecological cancers, as well as at high to moderate levels in kidney, brain, lung, and breast carcinomas (*4*−*14*). The concept of "folate-drug targeting" has been effectively exemplified using payloads as diverse as small radiopharmaceutical agents to large DNA-containing formulations (see ref 15 for a comprehensive overview of this technology). Importantly, there are a few examples of folate-targeted chemotherapy applications; however, most of these investigations were limited to in vitro evaluations (*16*).

We recently published on the synthesis and in vitro/in vivo activity of a novel folate−mitomycin C conjugate, called EC72 (*17*, *18*). This agent was shown to produce targeted activity against FR cells and tumor xenografts; however, EC72 had difficultly eradicating established subcutaneous (s.c.) tumors as a stand-alone agent (*18*). Our laboratory's latest efforts, however, have led to the creation of a folate−vinca alkaloid conjugate. This novel FR-targetable chemotherapeutic, named EC140, was constructed using acyl hydrazone coupling technology to afford molecular separation of the vinca alkaloid from folate once this conjugate enters the acidic endosomes of FR-positive cancer cells. As reported below, EC140 was found to produce encouraging therapeutic activity in multiple FR-positive, established tumor models.

EXPERIMENTAL PROCEDURES

Materials. Pteroic acid (Pte) and N^{10}-trifluoroacetylpteroic acid were prepared according to Vlahov et al. (*19*). Peptide synthesis reagents were purchased from NovaBiochem (La Jolla, CA) and Bachem (San Carlos, CA). Folate-free RPMI media (FFRPMI) and PBS were obtained from Gibco, Grand Island, NY. *N*-(4-Acetylphenyl)maleimide was purchased from Avocado Research Chemicals (Ward Hill, MA). ^{3}H-thymidine was purchased from Moravek Biochemicals, Brea, CA. Vinblastine sulfate and all other common reagents were purchased from Sigma (St. Louis. MO).

Synthesis, Purification, and Analytical Characterization of EC140. The folate-containing spacer unit Pte-γGlu-Asp-Arg-Asp−Asp-Cys-OH[1] (herein referred to as EC119) was synthesized using standard fluorenylmethyloxycarbonyl-based solid-phase peptide synthesis (Fmoc SPPS) on a Wang resin polymeric support. It was purified by preparative HPLC (Waters NovaPak C_{18} 19 × 300 mm) with 10 mM NH_4OAc, pH 5 (solvent A) and acetonitrile (solvent B) using a gradient consisting of 1% B to 20% B over 40 min at a flow rate of 15 mL/min. The structure of EC119 was confirmed by ^{1}H NMR (300 MHz, D_2O): δ 8.68 (s, 1H, FA H-7), 7.57 (d, 2H, J =

* Corresponding author. Endocyte, Inc., 3000 Kent Ave., West Lafayette, IN 47906. Phone (765) 463-7175; Fax (765) 463-9271; E-mail chrisleamon@endocyte.com.

[1] Pte together with the adjacent γGlu residue of the peptide produces the folic acid (FA) moiety of EC140.

10.1021/bc060145g CCC: $33.50 © 2006 American Chemical Society
Published on Web 08/19/2006

8.4 Hz, FA H-12 and 16), 6.67 (d, 2H, $J = 9$ Hz, FA H-13 and 15), 4.40−4.75 (series of m, 5H), 4.35 (m, 2H), 4.16 (m, 1H), 3.02 (m, 2H), 2.55−2.95 (series of m, 8H), 2.42 (m, 2H), 2.00−2.30 (m, 2H), 1.55−1.90 (m, 2H), 1.48 (m, 2H) ppm); and ESI-MS ($(M + H)^+ = 1046$) analysis.

DAVLBH was prepared from commercially available vinblastine (VLB) following a literature procedure (*20*). The hydrazide was purified by preparative HPLC (Waters NovaPak C_{18} 19 × 300 mm) with 0.1% trifluoroacetic acid, pH 2.0 (solvent A) and acetonitrile (solvent B) using a gradient consisting of 5% B to 80% B over 30 min at a flow rate of 15 mL/min. Treatment of a tetrahydrofuran solution (350 μL) of this acylhydrazide (26 mg, 33 mol) with an equimolar amount of *N*-(4-acetylphenyl)maleimide (8.4 mg) for 1.5 h at room temperature resulted in the desired vinblastenyl hydrazone **B**. The tetrahydrofuran was removed in vacuo, and the pale white residue was used for the following reaction without any further manipulations.

The free acid form of EC119 (34 mg, 33 μmol) was dissolved in DMSO (150 μL) and treated under argon with an excess of triethylamine (75 μL, 538 μmol) and then reacted at room temperature for 2 h with the Michael acceptor **B** (dissolved in 300 μL DMSO and added with the help of microsyringe). The formation of the conjugate, EC140, was monitored by analytical HPLC (Waters NovaPak C_{18} 3.9 × 150 mm). This product was purified by preparative HPLC (Waters NovaPak C_{18} 19 × 300 mm) with 1 mM phosphate buffer, pH 7.0 (solvent A) and acetonitrile (solvent B) using a gradient consisting of 10% B to 50% B over 30 min at a flow rate of 15 mL/min. Acetonitrile was removed from the collected fractions in vacuo and the residue subjected to freeze-drying to give 62 mg (91% yield) of EC140 (Na form) as a yellow amorphous solid containing 15 mg phosphate salts (derived from the buffer used in the prep HPLC). LC-MS [ESI: $(M + H)^+ = 2013$; $(M - H)^+ = 2011$)] and ^{1}H NMR signals were in agreement with the expected structure. Selected ^{1}H NMR data for EC140 (D_2O, 300 MHz): δ 8.47 (s, 1H, FA H-7), 7.62−7.6 (m, 2H, VLB H-11′ and VLB H-14′), 7.50−7.35 (m, 3H, FA H-12 and H-16 and VLB H14′), 7.25 (m, 1H, VLB H-13′), 7.05−6.95 (m, 5H, VLB H-12′ and 4H from the linker), 6.51 (d, 2H, FA H-13 and 15), 6.4 (s, 2H, VLB H-14 and 17), 5.65 (m, 1H, VLB H-7), 5.5 (m, 1H, VLB H-6), 4.05(m,1H, VLB H-8′), 3.90 (s, 3H, $-CO_2CH_3$), 3.69 (s, 3H, VLB C_{16} $-OCH_3$), 2.8 (s, 3H, VLB N$-CH_3$), 1.35 (br s, 1H, VLB H-3′), 1.15 (m, 1H, VLB H-2′), 0.9 (t, 3H, $J = 7$ Hz, VLB H-21′), 0.55 (t, 3H, $J = 6.9$ Hz, VLB H-21) ppm.

The release of the free desacetylvinblastine monohydrazide moiety from EC140 was also studied by dissolving 1 mg of EC140 in isotonic buffer, pH 5.0, at 37 °C. The HPLC profile (UV detection at 280 nm) showed complete cleavage of the hydrazone bond with concomitant release of the *N*-succinimidyl acetophenone derivative of EC119 within 16 h ($t_{1/2} \approx 5.5$ h). The free DAVLBH unit was not observed as the result of its low solubility in this aqueous buffer; however, its formation was confirmed by LC-MS. The stability of the conjugate was also investigated as a 20 μM solution in PBS buffer, pH 7.4, at 37 °C. In this case, the $t_{1/2}$ of EC140 was ∼22 h.

Cell Culture. The cell lines used for these studies (KB, M109, and 4T1) have been previously described (*18*). Cells were grown continuously as a monolayer using folate-free RPMI medium (FFRPMI) containing 10% heat-inactivated fetal calf serum (HIFCS) at 37 °C in a 5% CO_2/95% air-humidified atmosphere with no antibiotics. The HIFCS contained its normal complement of endogenous folates which enabled the cells to sustain growth in this more physiologically relevant medium (*2*). All cell experiments were performed using FFRPMI containing 10% HIFCS (FFRPMI/HIFCS) as the growth medium.

Relative Affinity Assay. The relative affinity of EC140 was determined according to the method described by Westerhoff et al. (*21*) with slight modification. Briefly, FR-positive KB cells were seeded in 24-well Falcon plates and allowed to form adherent monolayers (∼80% confluent) overnight in FFRPMI/HIFCS. Spent incubation media was replaced with FFRPMI supplemented with 10% HIFCS and containing 100 nM of ^{3}H-folic acid in the absence and presence of increasing concentrations of unlabeled folic acid or EC140. Cells were incubated for 1 h at 37 °C and then rinsed three times with 0.5 mL of PBS. Five hundred microliters of 1% sodium dodecylsulfate in PBS were added to each well; after 5 min, cell lysates were collected, transferred to individual vials containing 5 mL of scintillation cocktail, and then counted for radioactivity. Cells exposed to only the ^{3}H-folic acid in FFRPMI (no competitor) were designated as negative controls, whereas cells exposed to the ^{3}H-folic acid plus 1 mM unlabeled folic acid served as positive controls; disintegrations per minute (DPMs) measured in the latter samples (representing nonspecific binding of label) were subtracted from the DPM values from all samples. Notably, relative affinities were defined as the inverse molar ratio of compound required to displace 50% of ^{3}H-folic acid bound to FR on KB cells, and the relative affinity of folic acid for the FR was set to 1.

Dose-Dependent Activity. Cells were heavily seeded in 24-well Falcon plates and allowed to form nearly confluent monolayers overnight in FFRPMI/HIFCS. Thirty minutes prior to the addition of EC140, spent medium was aspirated from all wells and replaced with fresh FFRPMI. Note, designated wells received media containing 100 μM folic acid, and cells within the latter wells were used to determine the targeting specificity, since cytotoxic activity produced in the presence of excess folic acid (enables competition for FR binding) would signify the portion of the total activity that was unrelated to FR-specific delivery. Following one rinse with 1 mL of fresh FFRPMI/HIFCS, each well received 1 mL of media containing increasing concentrations of test article (four wells per sample). EC140-treated cells were pulsed for 1 h at 37 °C, rinsed four times with 0.5 mL of media, and then chased in 1 mL of fresh media up to 70 h. VLB- and DAVLBH-treated cells were incubated continuously for 46 h at 37 °C. Spent media was aspirated from all wells and replaced with fresh media containing 5 μCi/mL ^{3}H-thymidine. Following a further 2 h 37 °C incubation, cells were washed three times with 0.5 mL of PBS and then treated with 0.5 mL of ice-cold 5% trichloroacetic acid per well. After 15 min, the trichloroacetic acid was aspirated and the cells solubilized by the addition of 0.5 mL of 0.25 N sodium hydroxide for 15 min. Four hundred and fifty microliters of each solubilized sample were transferred to scintillation vials containing 3 mL of Ecolume scintillation cocktail and then counted in a liquid scintillation counter. Final tabulated results were expressed as the percentage of ^{3}H-thymidine incorporation relative to untreated controls.

Tumor Models and Therapy. Four- to seven-week-old mice (*Balb*/*c* or *nu*/*nu* strains) were purchased from Harlan Sprague Dawley, Inc. (Indianapolis, IN). Since normal rodent chow contains a high concentration of folic acid (6 mg/kg chow), mice used in these studies were maintained on the folate-free diet (Harlan diet #TD00434) for 1 week before tumor implantation to achieve serum folate concentrations close to the range of normal human serum (*22*). For tumor cell inoculation, 1×10^6 M109 cells, 2×10^5 4T1 cells, or 1×10^6 KB cells in 100 μL were injected in the subcutis of the dorsal medial area. Tumors were measured in two perpendicular directions every 2−3 days using a caliper and their volumes calculated as $0.5 \times L \times W^2$, where L = measurement of longest axis in millimeters and W = measurement of axis perpendicular to L in millimeters. Dosing

A.

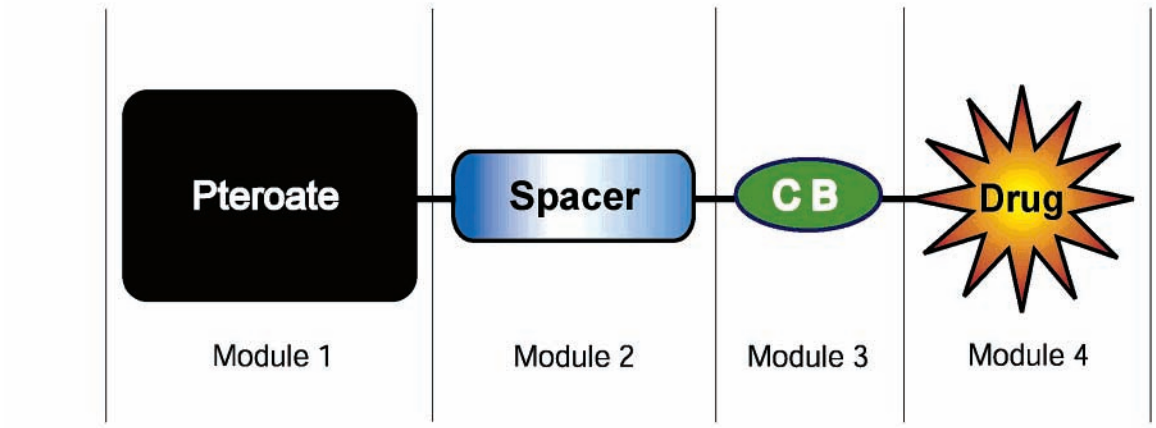

B.

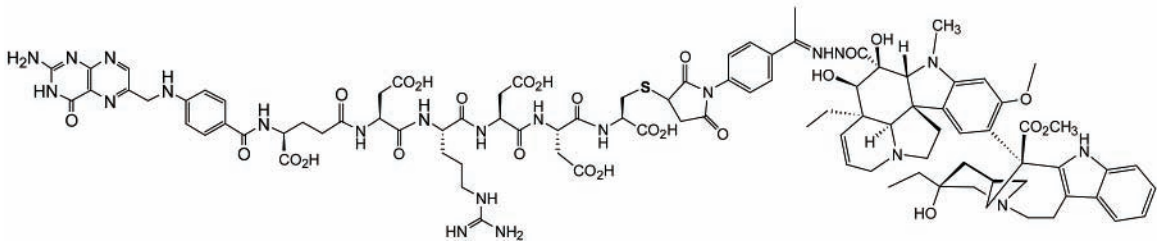

Figure 1. Modular design of folate−drug conjugates. Part A. A folate−drug conjugate consists of four basic modules: (1) a pteroate ligand, (2) a hydrophilic spacer, (3) a biologically cleavable bond, and (4) a potent drug moiety. Part B. Structure of EC140.

solutions for EC140 were prepared in PBS and administered through the lateral tail vein of the mice. Importantly, dosing was typically initiated when the s.c. tumors were between 50−100 mm^3 in volume.

Drug toxicity was assessed by collecting blood via cardiac puncture and submitting the serum for independent analysis of blood urea nitrogen (BUN), creatinine, AST-SGOT, and ALT-SGPT at Ani-Lytics, Inc. (Gaithersburg, MD). In addition, histopathologic evaluation of formalin-fixed heart, lungs, liver, spleen, kidney, intestine, skeletal muscle, and bone (tibia/fibula) were done at Animal Reference Pathology Laboratories (ARUP; Salt Lake City, Utah).

RESULTS

Folate-Targeted Chemotherapy. As shown in Figure 1A, a folate−drug conjugate consists of four basic modules: (1) a pteroate ligand such as Pte, (2) a hydrophilic spacer, (3) a biologically cleavable bond, and (4) a potent drug moiety. EC140 specifically consists of the vitamin folic acid covalently extended by the peptide Asp-Arg-Asp-Asp-Cys, which, in turn, is coupled to DAVLBH via an acylhydrazone linker (Figure 1B).

The mechanism of folate-targeted drug delivery has been previously described (*16*). Briefly, cells expressing the FR protein can bind folate−drug conjugates very tightly and endocytose them into acidic compartments. For EC140, it has been found that separation of the folate−peptide and DAVLBH moieties can occur within these vesicular structures; thus, it is possible that the released drug molecules are permitted to diffuse across these compartmentalized membranes to exert activity against microtubules (i.e., the biological target for vinca alkaloids).

EC140 Synthesis. The synthesis of EC140 is schematically shown in Scheme 1. A thiol containing folate−peptide spacer, EC119, was coupled in near-quantitative yield to DAVLBH to produce EC140. It was purified by preparative reverse-phase HPLC and stored as a lyophilized powder. The structure of EC140 was confirmed by ^{1}H NMR spectroscopy and electrospray ionization mass spectroscopy.

Drug release studies were performed in pH 5.0 buffer, since the milieu within a cancer cell's endosome (i.e., the compartment that EC140 will enter following endocytosis) is believed to be ∼pH 5 (*23*). Under these conditions, the hydrazone bond within EC140 was found to be labile, with an estimated $t_{1/2}$ of ∼5.5 h. In contrast, the $t_{1/2}$ of EC140 was found to be ∼22 h at pH 7.4.

Relative Affinity Assay. EC140 was first evaluated biologically using an in vitro relative affinity assay that measures a ligand's ability to directly compete with folic acid for binding to cell surface FRs. Importantly, a relative affinity value of 1.0 implies that the test article ligand has an affinity equal to that of folic acid for the FR. Likewise, values lower than unity reflect weaker affinity, and values higher than unity reflect stronger affinity.

Monolayer KB cells were incubated with 100 nM ^{3}H-folic acid in the presence of increasing concentrations of non-radioactive folic acid or EC140. Following a 1 h incubation at 37 °C, cells were rinsed free of unbound material and counted for residual cell-associated radioactivity. The quantity of bound radioactivity was plotted against the concentration of unlabeled ligand, and the IC_{50} value (concentration of ligand required to block 50% of ^{3}H-folic acid binding) was estimated. As shown in Figure 2, EC140 was experimentally determined to have an affinity of 0.35 relative to that of folic acid for human FRs. Thus, chemical modification of folate with the DAVLBH drug motif only minimally altered the vitamin's intrinsic affinity for the FR.

Dose-Dependent Activity. DAVLBH was chosen as the drug moiety for EC140 because it contains a modifiable hydrazide

Scheme 1. Synthetic Route for EC140.

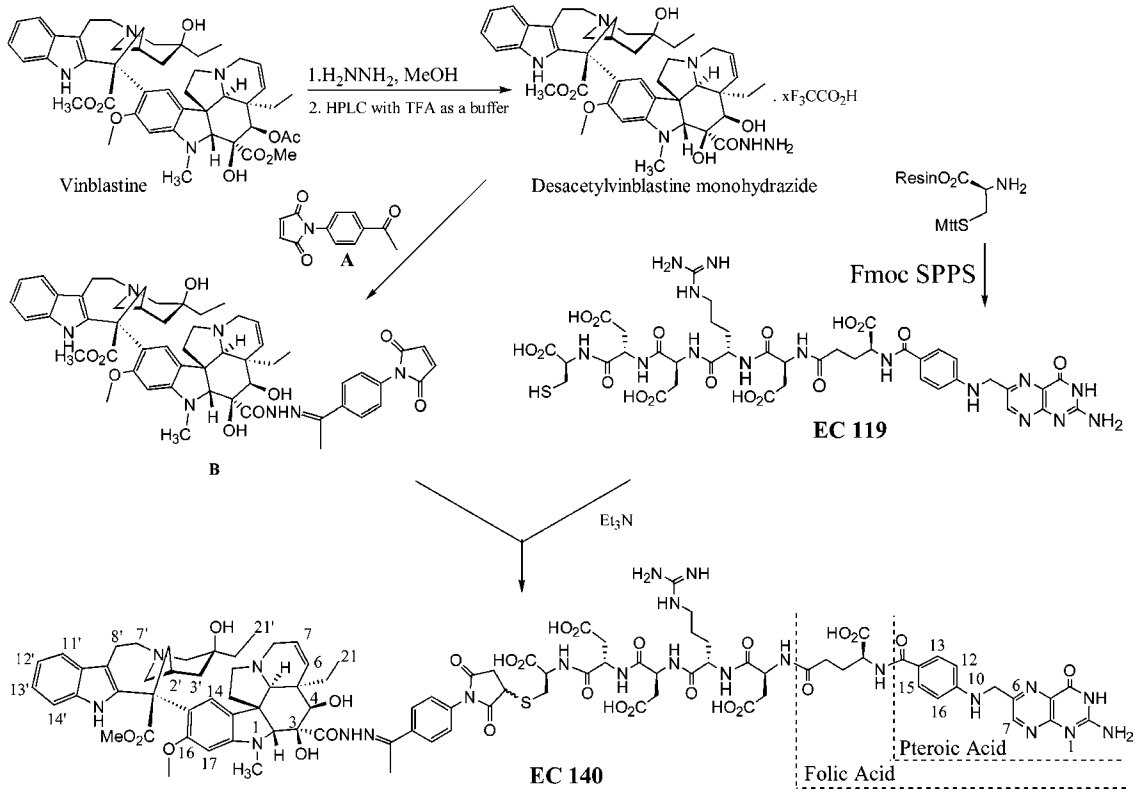

functional group to which we could attach our folate−spacer group. DAVLBH is a potent vinca alkaloid analog (*24*), and as shown in Figure 3, this agent displays high, dose-dependent activity against FR-positive KB cells. In fact, the IC_{50} of DAVLBH was determined to be nearly equivalent to the IC_{50} of VLB.

The activity of EC140 was also evaluated to determine its dose responsive properties. As shown in Figure 4, the activity of EC140 was found to be concentration dependent with an IC_{50} of ∼11 nM when cells were pulsed for only a 1 h period at 37 °C. The activity of EC140 was also effectively blocked in the presence of excess free folic acid, indicating that the observed activity was folate-mediated. The latter result is significant, for it suggests that normal tissues that express little to no FR may not be affected by EC140 (see discussion).

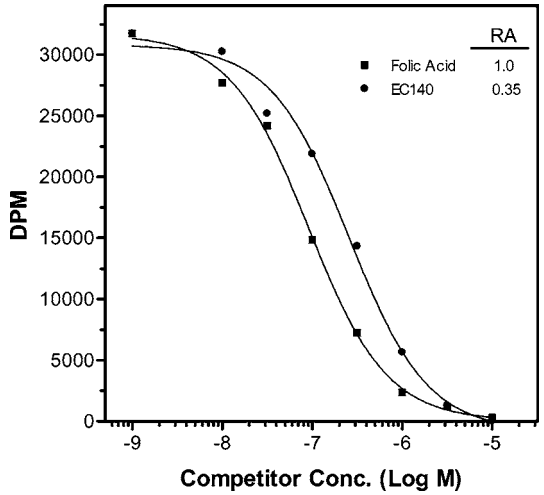

Figure 2. Relative folate receptor binding affinity of EC140. KB cells were incubated for 1 h at 37 °C with 100 nM ^{3}H-folic acid in the presence and absence of increasing competitor concentrations. (■) folic acid; (●) EC140. Error bars represent 1 standard deviation ($n = 3$). RA, relative affinity.

In Vivo Activity. *a. Syngeneic Model.* The activity of EC140 was next evaluated in vivo. Eleven days after receiving a subcutaneous (s.c.) inoculation of syngeneic, FR-positive M109 tumor cells, animals received i.v. injections of 10 μmol/kg EC140 given on days 11, 13, 15, and 18. As shown in Figure 5, tumors in the untreated animals reached ∼1000 mm^3 by day 29. In contrast, animals briefly treated with EC140 experienced a significant response; thus, tumors in 3 of 5 animals disappeared and did not recur during the study period, while the remaining 2 of the 5 animals in that cohort had a partial response (2.7 log cell kill, LCK; 175% *T/C*). Importantly, maximum weight loss during this therapy ranged from 3% to 16%, and no other gross toxicities or abnormalities were observed.

b. Activity against the KB Xenograft Model. The encouraging activity results obtained from our pilot in vivo study prompted us to test EC140 against a human tumor xenograft. Here, EC140 was evaluated against established s.c. KB tumor-bearing animals using a variety of different dose levels and schedules. Furthermore, the performance of EC140 was also compared to that of

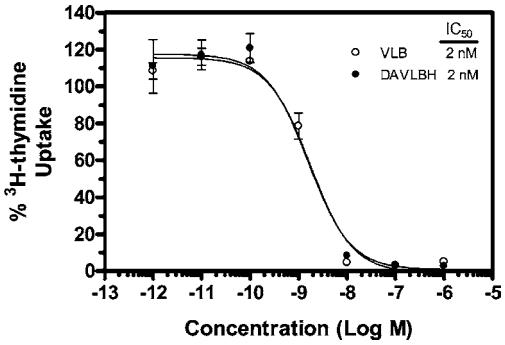

Figure 3. Activity of DAVLBH and VLB against KB cells. Adherent KB cells were incubated for 46 h at 37 °C with increasing concentrations of test article. Cells were then incubated for 2 h with ^{3}H-thymidine and then counted for radiolabel incorporation into newly synthesized DNA, as described in the Experimental Procedures. (●) DAVLBH; (○) VLB. Data represent the average ± 1 SD ($n = 4$).

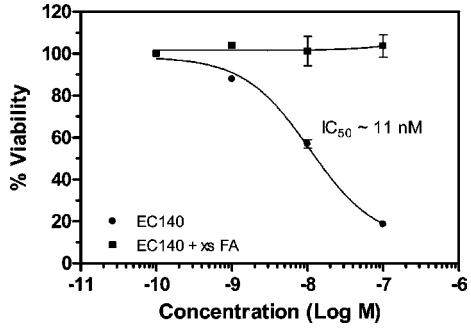

Figure 4. EC140 dose response. KB cells were pulsed for 1 h with increasing concentrations of EC140 in the presence or absence of 0.1 mM folic acid (as a competitor). Following a 70 h chase in fresh media, cells were incubated with ^{3}H-thymidine for 2 h and then counted for radiolabel incorporation into newly synthesized DNA, as described in the Experimental Procedures. (●), EC140; (■), EC140 plus 0.1 mM folic acid. Data represent the average ± 1 SD (n = 4).

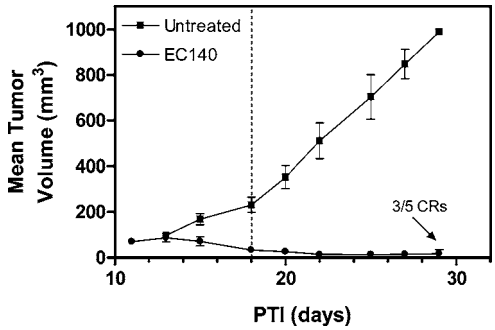

Figure 5. Antitumor activity of EC140 in a syngeneic model. 1 × 10^6 M109 cells were inoculated s.c. into each *Balb/c* mouse. Eleven days later, animals were treated intravenously with (●) 10 μmol/kg of EC140 on days 11, 13, 15, and 18. A control cohort (■) was not treated. Tumor volume was assessed every 2 to 3 days. The dotted vertical line represents the day of final dosing. Data represent the average ± 1 SD (n = 5 animals per cohort).

the free drug, DAVLBH, administered to *nu*/*nu* mice at its MTD. As shown in Table 1, EC140 therapy was found to be dose-dependent, and all animals in each cohort seemingly responded to this therapy. Dose levels of ≥5 μmol/kg consistently produced CRs in many of the treated mice. In fact, we observed 5 of 5 CRs in the cohort that received 10 μmol/kg of EC140 following a brief BIW, 2 week regimen. Interestingly, animals treated with DAVLBH at its MTD (TIW, 2 week schedule) did respond, but only partial responses were observed (i.e., no CRs). Taken together, EC140 has proven to be active against both murine and human FR-positive tumor models, and its overall response appears to be greater than the free DAVLBH drug when dosed at its MTD.

c. Activity against an FR-Negative Tumor Model. To gain insight on in vivo specificity, EC140 was next evaluated for activity against the recognized FR-negative 4T1 tumor model

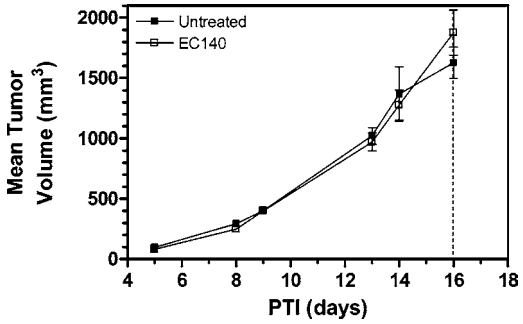

Figure 6. Antitumor activity of EC140 in a FR-negative model. 2 × 10^5 FR-negative 4T1 cells were inoculated s.c. into each *Balb/c* mouse. Five days later, animals were treated intravenously with (□) 3 μmol/kg of EC140 on days 11, 13, 15, 18, 20, and 22. A control cohort (■) was not treated. Tumor volume was assessed every 2 to 3 days. The dotted vertical line represents the day of final dosing. Data represent the average ± 1 SD (n = 5 animals per cohort).

(*14*, *17*, *18*). Thus, animals bearing established s.c. 4T1 tumors were treated intravenously TIW for two consecutive weeks with 3 μmol/kg EC140. Note, the 3 μmol/kg dose level was chosen for this study because (i) it is near the single-dose, receptor-saturable level (*25*), and (ii) as little as 1 μmol/kg doses were previously found to be active against an FR-positive tumor (see Table 1). As shown in Figure 6, 4T1 tumors grew at the same rate in both the untreated and EC140-treated animals. Taken together with the aforementioned data, these results suggest that EC140 activity could be specific for FR-expressing cells.

d. Toxicity. Aside from minimal to manageable weight loss during EC140 therapy, no other obvious gross toxicities or abnormal behavior were observed. If an EC140-treated animal were euthanized, it was principally due to the tumors reaching 1500 mm^3. However, preliminary toxicity assessments were made using the KB tumor-bearing *nu*/*nu* animals that completely responded to EC140 therapy. Thus, collected sera were analyzed for lasting adverse effects on kidney and liver function. When possible, hematology and tissue pathology assessments were also conducted. The following toxicity data correlates with the cohort information supplied in Table 1.

For mice treated with the 5 μmol/kg, TIW, 2 week regimen (a total dose of 30 μmol/kg; maximum weight loss of 5%), 3 of 5 were tumor-free 12 days after dosing began, and they remained tumor-free for 24 days thereafter (i.e., at the end of the study). At that time, animals were sacrificed, and biological samples were analyzed. In sera, AST-SGOT, BUN, creatinine, and total protein were all found to be within normal levels; however, ALT-SGPT levels were found to be lower (range: 17−22 U/L) than reference values (24−140 U/L). Tissue pathology indicated that heart, lung, spleen, bone, kidney, muscle, intestine, and brain of treated mice were all normal; occasional degeneration was, however, observed in some livers.

All 5 of the mice treated with the 10 μmol/kg, BIW, 2 week regimen (a total dose of 40 μmol/kg; maximum weight loss of

Table 1. Activity of EC140 and Free DAVLBH against FR-positive Human KB Tumor Xenografts[a]

formulation cohort					response					
					complete responses	partial responses			gross toxicity	
test article	dose level (μmol/kg)	dose schedule	total doses	total # animals	# animals	# animals	% *T*/*C*	LCK	deaths	weight loss
EC140	1	TIW, 3 wk	9	5	0	5	125	0.4	0	0−4%
	5	TIW, 2 wk	6	5	3	2	182	1.4	0	0−5%
	10	days 11, 13, 15, and 18	4	5	3	2	208	2.7	0	0−11%
	10	BIW, 2 wk	4	5	5	0	n/a	n/a	0	8−16%
DAVLBH	1	TIW, 2 wk	6	5	0	5	246	1.8	0	11−19%[b]

[a] 1 × 10^6 KB cells were inoculated s.c. into each *nu*/*nu* mouse. Eleven days later, animals were treated intravenously with various dose levels and schedules of EC140 or DAVLBH. Tumor volume was assessed every 2 to 3 days. Data represent the average ± 1 SD (n = 5 animals per cohort). LCK, log cell kill; % *T*/*C*, percent increase in lifespan of treated versus control animals; TIW, three times per week; BIW, two times per week. [b] MTD regimen.

16%), were tumor-free 12 days after dosing began, and they remained tumor-free for 24 days thereafter (end of study). At that time, animals were sacrificed, and biological samples were analyzed. In sera, creatinine and total protein were found to be within normal levels. AST-SGOT levels were occasionally found to be higher (range: 142−820 U/L) than reference values (72−288 U/L). ALT-SGPT levels (10−181 U/L) were also sometimes out of the reference range (24−140 U/L). BUN levels were found to be occasionally higher (range 14−37 mg/dL) than reference values (9−28 mg/dL). Whole blood analysis was essentially normal with the exception of an occasional high red blood cell count of $(8.1-10.3) \times 10^6/\mu$L (reference range: $(6.4-9.4) \times 10^6$/L), higher segmented neutrophil count of $(3.17-3.92) \times 10^3/\mu$L (reference range: $(0.13-2.57) \times 10^3/\mu$L) and a detectable basophil count of 10−20 cells/μL (basophils are normally not detectable). Tissue pathology indicated that liver, lung, spleen, bone, kidney,[2] muscle, intestine, and brain of treated *nu*/*nu* mice were all normal. Occasional to mild degeneration was observed in the hearts of some treated mice; however, such observations were also noted in untreated animals; therefore, heart toxicity was not considered to be EC140-related.

DISCUSSION

The objectives of this investigation were to design and test a novel folate−vinca alkaloid conjugate for activity against FR-positive cells and tumors. One drug candidate, named EC140, was created whereby a peptide derivative of the vitamin folic acid was coupled to DAVLBH via an acyl hydrazone linker. Notably, the inclusion of the acyl hydrazone bond is believed to be important for efficient release of the DAVLBH moiety within the acid endosomal milieu (*26*).

EC140 was found to retain high affinity for FR-positive cells, and it produced dose responsive activity in vitro against FR-positive cells via an endocytic mechanism. EC140 also proved to be active against syngeneic and xenograft in vivo models, and possible curative activity resulted with minimal to moderate toxicity. EC140 was also shown to be more effective and less toxic than its free drug counterpart (DAVLBH) when dosed at MTD.

Despite the ability of EC140 to cause complete regression of established s.c. tumors, animals periodically experienced weight loss; furthermore, this effect was not surprisingly found to be more pronounced with increasing dose. Whether the weight loss resulted from gastrointestinal toxicity could not be verified, because tissue samples were only analyzed by a pathologist after a modest recovery period (24 days post final dose). Regardless, future studies will be aimed at understanding whether acute toxicity of EC140 manifests during and/or immediately following therapy. Interestingly, we have confirmed that murine liver does not express the FR (*14*). Thus, if gastrointestinal toxicity is confirmed, it should prompt further studies to understand the full mechanism of EC140 clearance. Regardless, pharmacokinetic studies are warranted to better understand the disposition of EC140 and to also determine the extent of release of the DAVLBH moiety, because it is possible that the toxicities observed in mice treated with high EC140 dose levels were actually manifested by the release of free drug.

Importantly, EC140 represents a folate-targeted chemotherapeutic that can produce potent activity against established s.c. tumors. In recent publications, we demonstrated activity of a folate−mitomycin C conjugate (called EC72) against similar tumors; however, the extent of the maximal activity of EC72 is lower than that of EC140. For example, EC72 was found to be active as a single agent primarily when the tumors were young (i.e., not well-established), whereas the therapeutic benefit was reduced when EC72 was administered to animals bearing s.c. tumors of ≥ 30 mm^3 (i.e., 7 days post-inoculation) (*18*). In contrast, EC140 was found to cause complete tumor responses, even in animals originally bearing up to 100 mm^3 xenografts at the onset of therapy (vide supra). Interestingly, both agents are similar in that neither produced significant kidney toxicity despite the fact that murine kidney expresses very high levels of the FR (*14*). However, as previously stated in Reddy et al. (2005), these observations do support the hypothesis that the FRs in the kidney proximal tubules function primarily to shuttle scavenged folates (or small folate−drug conjugates) back into systemic circulation rather than to consume them for localized biological functions (*18*, *27*, *28*).

Additional animal studies with EC140 are planned to better understand the effects of dose level and dose schedule. We also plan to study the effects of tumor growth rate and FR content (i.e., different tumor models) on the overall observed antitumor response manifested by EC140 therapy. We feel that it is equally important to study the effect of replacing the acyl hydrazone bond with a biologically cleavable disulfide linker (*16*) or perhaps even a biologically cleavable peptide linker, such as that utilized successfully in various antibody−drug conjugates (*29*, *30*). Interestingly, the latter approach would most likely require the exploitation of an endosome-resident peptidase, since folate conjugates are known to largely avoid the more degradative lysosomal compartments during intracellular trafficking (*2*, *31*). Clearly, structure−activity studies for folate−vinca alkaloid conjugates are warranted to maximize the efficacy of this novel therapeutic approach.

[2] Normal kidney expresses high levels of the FR; see discussion.

ACKNOWLEDGMENT

The authors wish to thank Dr. Philip S. Low for his valuable comments.

Supporting Information Available: Spectra of EC140. This material is available free of charge via the Internet at http://pubs.acs.org.

LITERATURE CITED

(1) Brenner, D. E. (2002) New paradigms in oncological therapeutics: redefining combination chemotherapy. *Ann. Oncol. 13*, 1697−8.

(2) Leamon, C. P., and Low, P. S. (1991) Delivery of macromolecules into living cells: a method that exploits folate receptor endocytosis. *Proc. Natl. Acad. Sci. U.S.A. 88*, 5572−5576.

(3) Kamen, B. A., and Capdevila, A. (1986) Receptor-mediated folate accumulation is regulated by the cellular folate content. *Proc. Natl. Acad. Sci. U.S.A. 83*, 5983−5987.

(4) Boerman, O. C., van Niekerk, C. C., Makkink, K., Hanselaar, T. G., Kenemans, P., and Poels, L. G. (1991) Comparative immunohistochemical study of four monoclonal antibodies directed against ovarian carcinoma-associated antigens. *Int. J. Gynecol. Pathol. 10*, 15−25.

(5) Garin-Chesa, P., Campbell, I., Saigo, P. E., Lewis, J. L., Old, L. J., and Rettig, W. J. (1993) Trophoblast and ovarian cancer antigen LK26. *Am. J. Pathol. 142*, 557−567.

(6) Weitman, S. D., Lark, R. H., Coney, L. R., Fort, D. W., Frasca, V., Zurawski, V. R., and Kamen, B. A. (1992) Distribution of the folate receptor GP38 in normal and malignant cell lines and tissues. *Cancer Res. 52*, 3396−3401.

(7) Mattes, M. J., Major, P. P., Goldenberg, D. M., Dion, A. S., Hutter, R. V. P., and Klein, K. M. (1990) Patterns of antigen distribution in human carcinomas. *Cancer Res. Suppl.* 50, 880S.

(8) Coney, L. R., Tomassetti, A., Carayannopoulos, L., Frasca, V., Kamen, B. A., Colnaghi, M. I., and Zurawski, V. R. J. (1991) Cloning of a tumor-associated antigen: MOv18 and MOv19 antibodies recognize a folate-binding protein. *Cancer Res. 51*, 6125−6132.

(9) Ross, J. F., Chaudhuri, P. K., and Ratnam, M. (1994) Differential regulation of folate receptor isoforms in normal and malignant tissues in vivo and in established cell lines. Physiologic and clinical implications. *Cancer 73*, 2432−43.
(10) Weitman, S. D., Frazier, K. M., and Kamen, B. A. (1994) The folate receptor in central nervous system malignancies of childhood. *J. Neurol. Oncol. 21*, 107.
(11) Weitman, S. D., Weiberg, A. G., Coney, L. R., Zurawski, V. R., Jennings, D. S., and Kamen, B. A. (1992) Cellular localization of the folate receptor: potential role in drug toxicity and folate homeostasis. *Cancer Res. 52*, 6708−6711.
(12) Toffoli, G., Cernigoi, C., Russo, A., Gallo, A., Bagnoli, M., and Boiocchi, M. (1997) Overexpression of folate binding protein in ovarian cancers. *Int. J. Cancer 74*, 193−198.
(13) Holm, J., Hansen, S. I., Hoier-Madsen, M., and Bostad, L. (1991) High-affinity folate binding in human choroid plexus. Characterization of radioligand binding, immunoreactivity, molecular heterogeneity and hydrophobic domain of the binding protein. *Biochem. J. 280* (Pt 1), 267−71.
(14) Parker, N., Turk, M. J., Westrick, E., Lewis, J. D., Low, P. S., and Leamon, C. P. (2005) Folate receptor expression in carcinomas and normal tissues determined by a quantitative radioligand binding assay. *Anal. Biochem. 338*, 284−93.
(15) Low, P. S., and Antony, A. C. (2004) Folate receptor-targeted drugs for cancer and inflammatory diseases. *Adv. Drug Delivery Rev. 56*, 1055−1238.
(16) Leamon, C. P., and Reddy, J. A. (2004) Folate-targeted chemotherapy. *Adv. Drug Delivery Rev. 56*, 1127−1141.
(17) Leamon, C. P., Reddy, J. A., Vlahov, I. R., Vetzel, M., Parker, N., Nicoson, J. S., Xu, L. C., and Westrick, E. (2005) Synthesis and biological evaluation of EC72: a new folate-targeted chemotherapeutic. *Bioconjugate Chem. 16*, 803−11.
(18) Reddy, J. A., Westrick, E., Vlahov, I., Howard, S. J., Santhapuram, H. K., and Leamon, C. P. (2006) Folate receptor specific anti-tumor activity of folate-mitomycin conjugates. *Cancer Chemother. Pharmacol. 58*, 229−36.
(19) Xu, L., Vlahov, I. R., Leamon, C. P., Santhapuram, H. K. R., and Li, C. H. Synthesis, Purification, and Uses of Pterioc Acid and Derivatives and Conjugates Thereof, patent application number PCT/US2006/009153, filed March 14, 2006.
(20) Barnett, C. J., Cullinan, G. J., Gerzon, K., Hoying, R. C., Jones, W. E., Newlon, W. M., Poore, G. A., Robison, R. L., Sweeney, M. J., Todd, G. C., Dyke, R. W., and Nelson, R. L. (1978) Structure−activity relationships of dimeric Catharanthus alkaloids. 1. Deacetylvinblastine amide (vindesine) sulfate. *J. Med. Chem. 21*, 88−96.
(21) Westerhof, G. R., Schornagel, J. H., Kathmann, I., Jackman, A. L., Rosowsky, A., Forsch, R. A., Hynes, J. B., Boyle, F. T., Peters, G. J., Pinedo, H. M., and Jansen, G. (1995) Carrier- and receptor-mediated transport of folate antagonists targeting folate-dependent enzymes: Correlates of molecular structure and biological activity. *Mol. Pharm. 48*, 459−471.
(22) Mathias, C. J., Wang, S., Lee, R. J., Waters, D. J., Low, P. S., and Green, M. A. (1996) Tumor-selective radiopharmaceutical targeting via receptor-mediated endocytosis of gallium-67-deferoxamine-folate. *J. Nucl. Med. 37*, 1003−1008.
(23) Lee, R. J., Wang, S., and Low, P. S. (1996) Measurement of endosome pH following folate receptor-mediated endocytosis. *Biochim. Biophys. Acta 1312*, 237−42.
(24) Laguzza, B. C., Nichols, C. L., Briggs, S. L., Cullinan, G. J., Johnson, D. A., Starling, J. J., Baker, A. L., Bumol, T. F., and Corvalan, J. R. (1989) New antitumor monoclonal antibody−vinca conjugates LY203725 and related compounds: design, preparation, and representative in vivo activity. *J. Med. Chem. 32*, 548−55.
(25) Paulos, C. M., Reddy, J. A., Leamon, C. P., Turk, M. J., and Low, P. S. (2004) Ligand binding and kinetics of folate receptor recycling in vivo: impact on receptor-mediated drug delivery. *Mol. Pharm. 66*, 1406−14.
(26) Bae, Y., Nishiyama, N., Fukushima, S., Koyama, H., Yasuhiro, M., and Kataoka, K. (2005) Preparation and biological characterization of polymeric micelle drug carriers with intracellular pH-triggered drug release property: tumor permeability, controlled subcellular drug distribution, and enhanced in vivo antitumor efficacy. *Bioconjugate Chem. 16*, 122−30.
(27) Birn, H., Selhub, J., and Christensen, E. I. (1993) Internalization and intracellular transport of folate-binding protein in rat kidney proximal tubule. *Am. J. Physiol. 264*, C302−10.
(28) Birn, H., Nielsen, S., and Christensen, E. I. (1997) Internalization and apical-to-basolateral transport of folate in rat kidney proximal tubule. *Am. J. Physiol. 272*, F70−8.
(29) Francisco, J. A., Cerveny, C. G., Meyer, D. L., Mixan, B. J., Klussman, K., Chace, D. F., Rejniak, S. X., Gordon, K. A., DeBlanc, R., Toki, B. E., Law, C. L., Doronina, S. O., Siegall, C. B., Senter, P. D., and Wahl, A. F. (2003) cAC10-vcMMAE, an anti-CD30-monomethyl auristatin E conjugate with potent and selective antitumor activity. *Blood 102*, 1458−65.
(30) Walker, M. A., King, H. D., Dalterio, R. A., Trail, P., Firestone, R., and Dubowchik, G. M. (2004) Monoclonal antibody mediated intracellular targeting of tallysomycin S(10b). *Bioorg. Med. Chem. Lett. 14*, 4323−7.
(31) Turek, J. J., Leamon, C. P., and Low, P. S. (1993) Endocytosis of folate-protein conjugates: ultrastructural localization in KB cells. *J. Cell Sci. 106*, 423−430.

BC060145G

Reducible Poly(amido ethylenimine)s Designed for Triggered Intracellular Gene Delivery

Lane V. Christensen, Chien-Wen Chang, Won Jong Kim, and Sung Wan Kim*

Department of Pharmaceutics and Pharmaceutical Chemistry, University of Utah, Salt Lake City, Utah 84112-5820

Zhiyuan Zhong,† Chao Lin, Johan F. J. Engbersen,† and Jan Feijen

Department of Polymer Chemistry and Biomaterials, and Institute for Biomedical Technology (BMTI), Faculty of Science and Technology, University of Twente, P.O. Box 217, 7500 AE Enschede, The Netherlands. Received July 7, 2006; Revised Manuscript Received August 1, 2006

Poly(amido ethylenimine) polymers, a new type of peptidomimetic polymer, containing multiple disulfide bonds (SS-PAEIs) designed to degrade after delivery of plasmid DNA (pDNA) into the cell were synthesized and investigated as new carriers for triggered intracellular gene delivery. More specifically, three SS-PAEIs were synthesized from Michael addition reactions between cystamine bisacrylamide (CBA) and three different ethylene amine monomers, i.e., ethylenediamine (EDA), diethylenetriamine (DETA), or triethylenetetramine (TETA). Complete addition reactions were confirmed by ^{1}H NMR. The molecular weight, buffer capacity, and relative degree of branching for each SS-PAEI was determined by gel permeation chromatography (GPC), acid−base titration, and liquid chromatography−mass spectroscopy (LC-MS), respectively. Physicochemical characteristics of polymer/pDNA complexes (polyplexes) were analyzed by gel electrophoresis, particle size, and ζ-potential measurements. All three SS-PAEIs effectively complex pDNA to form nanoparticles with diameters less than 200 nm and positive surface charges of ~32 mV. The in vitro gene transfer properties of SS-PAEIs were evaluated using mouse embryonic fibroblast cell (NIH3T3), primary bovine aortic endothelial cell (BAEC), and rat aortic smooth muscle cell (A7R5) lines. Interestingly, polyplexes based on all three SS-PAEIs exhibited remarkably high levels of reporter gene expression with nearly 20× higher transfection efficiency than polyethylenimine 25k. The high transfection efficiency was maintained in the presence of 10% serum in the transfection medium. Furthermore, confocal microscopy experiments using labeled pDNA indicated that polyplexes of SS-PAEI displayed greater intracellular distribution of pDNA as compared to PEI, most likely due to environmentally triggered release. Therefore, SS-PAEIs are a new class of transfection agents that facilitate high gene expression while maintaining a low level of toxicity.

1. INTRODUCTION

Nucleic acid-based therapeutics for the treatment of genetic and acquired diseases has developed rapidly over the past decade as a direct result of the advances in molecular biology and biotechnology. Such progress has enabled the use of plasmid DNA (pDNA), antisense oligonucleotides, ribozymes, peptide nucleic acids, and silencing RNAs for gene therapy (*1*). Viral carriers in gene therapy has shown promising results; however, issues with potential immunogenicity and host chromosomal integration still remain (*2*, *3*). Nonviral carrier approaches are seen as the answer to the safety concerns introduced by viral vectors in addition to being relatively simple to prepare and having an unlimited cargo space (*4*).

Discovery and use of potent but nontoxic carriers is the key to unlocking the potential of nonviral gene delivery. Carriers such as polyethylenimine (PEI) (*5*, *6*), poly(L-lysine) (PLL) (*7*, *8*), cationic lipids (*9*), and polyamidoamine starburst dendrimers (PAMAM) (*10*) have all produced moderate gene expression but have also, to varied degrees, induced carrier associated toxicity to in vitro and/or in vivo (*11*, *12*).

Poly(amidoamine)s (PAAs) are water-soluble, peptidomimetic polymers obtained by polyaddition of primary or secondary aliphatic amines to bisacrylamide monomers (*13*). Their water-soluble nature makes PAAs ideal candidates in various drug delivery applications in pharmaceutics. Examples of these applications include tissue engineering, nucleic acid delivery, attachment of proteins and hydrophobic drugs, incorporation of stealth characteristics such as PEG to avoid uptake by the reticuloendothelial system, and passive targeting to tumors (*14*−*16*). Reinke and co-workers showed by synthesizing a new group of PAA-derived gene carrier, known as poly(glycoamidoamine)s, that significant gene expression could be achieved in different types of mammalian cells (*17*, *18*).

Davis and co-workers have shown that cellular toxicity increases as the molecular weight increases for cationic polymers such as PAAs (*19*). The use of reducible polymer systems provides a way to maintain polymer stability and achieve efficient gene expression in vivo while limiting effects of toxicity. The difference in redox potential (100-fold) between the oxidizing extracellular space and the reducing intracellular space makes disulfide bonds unique in cellular biology and may be utilized in therapeutic delivery systems (*20*). Reduction of PLL and polyrotaxane polymer-based nonviral systems containing disulfide bonds is thought to facilitate uncoupling of polymer/pDNA complexes to further increase gene expression (*21*−*23*). Moreover, recent studies of Lin et al. on various

* Phone: (801) 581-6654. Fax: (801) 581-7848; Email: rburns@deans.pharm.utah.edu.

† Phone: (+31) 53-489-2926. Fax: (+31) 53-489-2479. Email: z.zhong@tnw.utwente.nl (Z.Y. Zhong); j.f.j.engbersen@utwente.nl (J.F.J. Engbersen).

10.1021/bc0602026 CCC: $33.50 © 2006 American Chemical Society
Published on Web 08/24/2006

substituted linear poly(amidoamine)s as nonviral gene delivery systems, using COS-7 cells, have shown that the introduction of disulfide linkages in the polymer chains results in significantly increased transfection efficiency and cell viability (*24*). In this way, reduced polymer carriers may avoid issues of long-term toxicity and organ accumulation that have hampered in vivo applications of nondegradable, high molecular weight carriers.

In this paper, we report a new form of PAA, disulfide-containing poly(amido ethylenimine)s (SS-PAEIs), as potential carriers for gene delivery. We hypothesize that the combination of polyamines with multiple reducible disulfide bonds through amide bond formation will (1) introduce a new kind of nonviral carrier containing minimal toxicity while utilizing the effective nonviral characteristics of PEI-based systems such as pDNA condensation and buffer capacity, (2) produce polymers that form small, stable nanoparticles in an aqueous environment when combined with pDNA, and (3) protect against nucleic acid degradation until successfully triggered delivery in the intracellular cytoplasmic compartment by glutathione reduction. Polymers were synthesized from Michael addition reactions of different amine donors to a reducible cystamine bisacrylamide linker. Polymers were characterized by ^{1}H NMR, GPC, and acid−base titration and LC-MS measurements. Further characterization was done using reduction/protection of free sulfhydryls to look at the relative degree of branching for each polymer. Complex formation with pDNA was studied via gel electrophoresis and dynamic light scattering. In vitro transfection activity and cellular toxicity of SS-PAEIs complexed with pDNA was evaluated using mouse embryonic fibroblasts (NIH3T3), primary bovine aortic endothelial cells (BAEC), and/or rat aortic smooth muscle cells (A7R5). Finally, confocal miscroscopy was used to look at the intracellular distribution of labeled pDNA.

2. MATERIALS AND METHODS

2.1. Materials. Triethylenetetramine (TETA), diethylenetriamine (DETA), ethylenediamine (EDA), and hyperbranched polyethylenimine (bPEI, M_w = 25 000) were purchased from Aldrich (St. Louis, MO). Linear polyethylenimine (LPEI, M_w = 25 000) and cystamine bisacrylamide (CBA) were purchased from Polysciences, Inc. (Warrington, PA). The plasmid pCMV−Luc was made by insertion of luciferase cDNA into a pCI (Promega, Madison, WI) plasmid driven by the CMV promoter and was purified using standard Maxiprep (Invitrogen, Carlsbad, CA) protocols. Dubelcco's Modified Eagle's Medium (DMEM), penicillin−streptomycin, trypsin-like enzyme (TrypLE Express), and Dubelcco's phosphate buffered saline were purchased from Gibco BRL (Carlsbad, CA). Fetal bovine serum (FBS) was purchased from Hyclone Laboratories (Logan, UT). Other commercially available reagents were used as received.

2.2. Polymer Synthesis. Reducible PAA polymers were synthesized by a Michael's-type addition (Scheme 1) polymerization between ethylene amine monomer (TETA, DETA, or EDA) and CBA. Polymerizations were conducted in brown flasks using 10% aqueous MeOH as a solvent at 50 °C for a period of 18 h to 2 days under an argon atmosphere. In a typical experiment, a brown reaction vessel equipped with a stir bar was charged with TETA (449 mg, 3.07 mmol), solvent (2.8 mL), and CBA (0.8 g, 3.07 mmol). The vessel was closed and placed in an oil bath set at 50 °C. The polymerization was allowed to proceed until stirring of the magnetic bar became difficult due to the high viscosity of the reaction mixture (16 h). Excess TETA (~50 mg) in MeOH was then added to consume any remaining acrylamide functional groups and allowed to stir for an additional 2 h. Polymer product was isolated by ultrafiltration (MWCO 1000) by first diluting the reaction mixture with ultrapure deionized water (ddH_2O) to 10 mL and adjusting to pH 5. Purification was allowed to go overnight at 4 Barr followed by concentration and freeze-drying. Conditions for polymerizations using EDA and DETA with CBA were conducted in an identical fashion with the exception that the duration of the polymerization step prior to addition of excess amine was 18 h for DETA and 2 days for EDA. Composition of each polymer product was established by ^{1}H NMR (300 MHz, D_2O); poly(EDA/CBA) δ 2.48 (COCH_2CH$_2$NH, 4H), 2.72 (NHCH$_2$CH_2S-S, 4H), 3.01 (COCH$_2$CH_2NHCH_2-CH_2NH, 8H), 3.40 (NHCH_2CH$_2$S-S, 4H); poly(DETA/CBA) δ 2.61 (COCH_2CH$_2$NH, 4H), 2.72 (NHCH$_2$CH_2S-S, 4H), 2.84−3.21 (COCH2CH_2NHCH_2CH_2, 12H), 3.41 (NHCH_2CH$_2$S-S, 4H); poly(TETA/CBA) δ 2.61 (COCH_2CH$_2$NH, 4H), 2.72 (NHCH$_2$CH_2S-S, 4H), 2.90−3.21 (COCH2CH_2NHCH_2CH_2, 16H), 3.41 (NHCH_2CH$_2$S-S, 4H).

Scheme 1. Synthesis of SS-PAEIs[a]

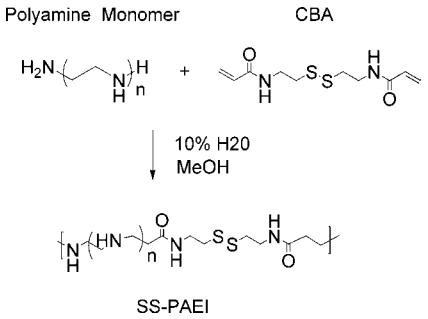

[a] Amino groups reacting with cystamine bisacrylamide (CBA) where the *n* values of 1, 2, and 3 represent the initial ethylene amine monomers of ethylenediamine (EDA), diethylenetriamine (DETA), and triethylenetetramine (TETA).

2.3. Polymer Characterization. *2.3.1. Gel Permeation Chromatography (GPC).* GPC experiments were conducted as previously reported (*25*). A Waters (Milford, MA) 2695 Alliance liquid chromatography system was used to perform the size exclusion chromatography (SEC) experiments. The instrument contained a built-in auto-injector and a Waters 2414 refractive index detector. A set of two PL aquagel−OH 30 columns (8 mm, 300 × 7.5 mm, Polymer Labs) were thermostated at 30 °C. The eluent was sodium acetate buffer (0.3 M NaAc, pH 4.4) with 30% (v/v) methanol. The eluent was filtered through a 0.2 μm HPLC filter (Nylon, Alltech) and degassed prior to use by simultaneous application of ultrasound and vacuum. The flow rate was 0.5 mL/min. The calibration curve was prepared with poly(ethylene glycol) (PEG) standards. The data collection and data analysis were done with Waters *Empower* software.

2.3.2. Acid−Base Titration. The buffering capacity of the SS-PAEIs between pH 10 and 3 was followed as previously described (*26*). Briefly, 6 mg of polymer was dissolved in 30 mL of 0.1 M NaCl (0.2 mg/mL polymer). Polymer solutions were titrated to an initial pH 10 with NaOH followed by subsequent additions of 0.1 M HCl.

2.3.3. Degree of Branching. Relative degree of branching was determined by reduction and protection of disulfide bonds followed by LC-MS analysis. Polymers were dissolved (2 mg/mL) in sodium phosphate buffer (20 mM, pH 7.2). Complete reduction of each disulfide bond was done in the presence of tris(2-carboxyethyl)phosphine (TCEP, 15 mM) stirring at room temperature in a sealed tube for 1 h. Protection of free sulfhydryls was immediately done by adding at least a twofold molar excess of *N*-ethylmaleimide (NEM) and stirring for 2 h at room temperature. The resulting fragments were subjected to positive-ion ESI LC-MS/MS analysis on a Finnigan LCQ Deca ion trap mass spectrometer (Thermo Finnigan, San Jose, CA) equipped with a Picoview Nanospray source. Chromatographic separation was accomplished using an HPLC system consisting of an Eksigent NanoLC-1D binary pump with a self-

packed column (100 um × 100 mm, 3 m particle size; Waters Atlantis dC18). A gradient of 5% acetonitrile (ACN), 95% water (solvent A), and 80% ACN and (solvent B) was operated at 400 nL/min, at 5% B for the first 3 min, followed by a linear increase to 50% B in 50 min, a linear increase to 80% B in 1 min, maintenance at 80% B for 14 min, and finally maintainence at 85% B for 5 min. Spectra were acquired in automated triple-play mode for recording of full-scan MS, zoom scan, and MS/MS data. The scan range for MS mode was set at *m*/*z* 300−1500.

2.4. Characterization of Polymer/pDNA Complexes. *2.4.1. Gel Retardation Assay.* Polymer/pDNA complexes were prepared at varying weight ratios (w/w) ranging from 0.75:1 to 48:1 in a buffered solution (20 mM HEPES, pH 7.4, 5% glucose) with or without 2.5 mM DTT. Polyplexes were incubated at room temperature for 30 min, then loaded (1 μg pDNA/well) onto a 1% agarose gel stained with ethidium bromide (EtBr, 5 μg/mL) at 96 V for 30 min in TAE (40 mM Tris-acetate, 1 mM EDTA) buffer.

2.4.2. DNase Protection Assay. The serum protection assay used was modified from a previously reported method (*27*). Each group contained 3 μg pCMV-Luc (in 30 μL) complexed with 29 μL of polymer at 6:1 w/w in 1 RQ1 DNase I buffer (Promega). After 30 min incubation at room temperature, 1 μL RQ1 RNase-free DNase I (10 mU/μL) was added, and each sample was incubated at 37 °C, taking 10 μL aliquots at 0, 30, 60, 90, and 120 min time points. At each time point, aliquots were added to 8 μL stop buffer (250 mM NaCl, 25 mM EDTA, 2% SDS) and incubated on ice for the remaining duration of the experiment. Samples were incubated overnight at 60 °C to completely dissociate polymer/pDNA complexes. Samples were then loaded onto a 1% agarose gel stained with EtBr and subjected to electrophoresis as explained above.

2.4.3. Light Scattering and ζ-Potential Measurements. The particle diameters and ζ-potentials of each polymer complexed with pDNA in HEPES buffer (20 mM, pH 7.4, 5% glucose) at 25 °C was determined using a Zetasizer 2000 instrument equipped with a DTS5001 cell and dynamic light scattering (DLS) on a Malvern 4700 system. The polymer/pDNA complexes were prepared by adding polymer with a desired concentration in 800 μL HEPES (14.1−900 μg/mL) to a buffered solution (200 μL) of pDNA (75 μg/mL) resulting in polymer/pDNA ratios ranging from 0.75:1 to 48:1 w/w. Complexes were vortexed, then allowed to incubate for 30 min at room temperature prior to analysis.

2.5. In Vitro Transfection and Cellular Toxicity. *2.5.1. Reporter Gene Expression.* In vitro characterization of the SS-PAEIs was carried out on mouse embryonic fibroblasts (NIH3T3, ATCC), primary bovine aortic endothelial (BAEC, Cambrex), and murine aortic smooth muscle (A7R5, ATCC) cell lines between passages 3 and 9 using a pCMV-Luc reporter plasmid. Cells were cultured according to specifications recommended by the provider in DMEM containing 10% FBS and 1% antibiotics (penicillin−streptomycin, 10 000 U/mL) at 37 °C in a humidified atmosphere containing 5% CO_2. Cells were plated in 6-well plates at 2.0×10^5, 2.5×10^5, and 1.2×10^5 cells/well for NIH3T3, BAEC, and A7R5 cells, respectively. Polyplexes were prepared using polymer/pDNA ratios ranging from 3:1 to 24:1 w/w in a buffered solution (20 mM HEPES, pH 7.4, 5% glucose) at a total pDNA concentration of 50 μg/mL. Cells were cultured in 2 mL media containing 10% serum until ∼70% confluency was reached, at which time cells were washed with 1 × PBS. Media with or without serum was then added, followed by addition of polymer/pDNA complexes, and the cells were allowed to incubate for 4 h. Media was replaced with fresh media containing serum, and cells were allowed to incubate further for a total of 48 h. Cells were washed with 1 × PBS and treated with cell culture lysis buffer (Promega). Luciferase quantification was performed using a luciferase assay system (Promega) on a Luminometer from Dynex Technologies, Inc. (Chantilly, VA). The amount of protein in the cell lysate was determined using a standard curve of bovine serum albumin (Sigma) and a BCA protein assay kit (Pierce).

2.5.2. Cell Viability Assay. For viability assays, BAEC cells were plated in 24-well plates at 4×10^4 cells/well, and transfections were carried out when cellular confluency reached ∼70%. Polyplexes were prepared using different polymer/pDNA ratios from 0.75:1 to 24:1 w/w in buffered solution as mentioned above. Briefly, media was replaced with fresh serum-free media followed by addition of complexes (0.5 μg pDNA/well). Media was again replaced with fresh serum (10% v/v) containing media after 4 h, and cells were left to incubate for a total of 24 h before analyzing cell viability using an MTT assay (Sigma). Cellular toxicity was determined relative to untreated cells. Experiments were performed in duplicate.

2.5.3. Confocal Microscopy Studies. Confocal microscopy was used to study pDNA release from polyplexes of poly(EDA/CBA). Fluorescently labeled pCMV-Luc using ethidium monoazide bromide (EMA, Invitrogen) was prepared as previously described (*28*). NIH3T3 cells were plated on 35 mm glass-bottom plates (MatTek Corp, Ashland, MA) at 2.5×10^5 cells/plate 24 h prior to and were ∼85% confluent at the time of transfections. Polymer/EMA−pDNA complexes were prepared at a polymer/pDNA ratio of 6:1 and added in a similar manner to those steps mentioned above using 2 μg EMA−pDNA/well. At specific time points, cells were washed with 1 × PBS and incubated with 1% *para*-formaldehyde at 4 °C until image analysis. Images were taken using a FluoView FV-300 Olympus microscope (Hauppauge, NY). As a control, bPEI/EMA−pDNA complexes at 0.75:1 and free EMA−pDNA were used.

3. RESULTS AND DISCUSSION

3.1. Synthesis and Characterization of Disulfide-Containing Poly(amido ethylenimine) (SS-PAEI). SS-PAEIs were synthesized by Michael addition reactions between three different amine monomers, i.e., ethylenediamine (EDA), diethylenetriamine (DETA), or triethylenetetramine (TETA) with cystamine bisacrylamide (CBA) (Scheme 1).

Polymerizations were carried out in 10% (v/v) aqueous MeOH at 50 °C under argon. In each case, during the course of the reaction, an increase of viscosity was observed. Reactions were terminated with 10% excess corresponding amine monomer prior to gelation. The ^{1}H NMR (D_2O) of the purified products showed that the characteristic acrylamide peaks between δ 5.8 and 6.5 were no longer present (data not shown), suggesting a complete consumption of the acrylamide functional group. The molecular weights of the SS-PAEIs were determined by gel permeation chromatography (GPC). As shown in Table 1, these polymers have M_w values in the range $(2.0-5.0) \times 10^3$. Commercial 25k branched and linear PEIs, as external controls, were also analyzed, producing values of 9.5 and 13.1 $\times 10^3$, respectively. This clearly indicates that the M_w values are underestimated. It should be noted that these SS-PAEIs have a rather low polydispersity ($M_w/M_n = 1.26-1.47$).

The buffering capacity of gene carriers is an important factor, since it may have direct impact on their ability to effectively condense, protect, and deliver pDNA into the cell for expression (*26*). The buffering capacity of SS-PAEIs was determined by acid−base titration in 0.1 M NaCl. Buffering capacity is defined as the percentage of amine groups becoming protonated from pH 7.4 to 5.1 as previously described (*29*). The results in Table 1 revealed that these polymers exhibit a higher buffering capacity as compared to LPEI and bPEI 25k controls (poly-

Table 1. Synthesis and characteristics of SS-PAEIs

polymer	reaction time	M_n[a] (kDa)	M_w[a] (kDa)	M_w/M_n[a]	titration[b] (μmol HCl)	% protonated nitrogens	degree of branching[c]
poly(EDA/CBA)	48 h	1.6	2.0	1.26	8.2	21.9	0.37
poly(DETA/CBA)	18 h	3.3	4.8	1.47	5.0	10.1	0.72
poly(TETA/CBA)	16 h	2.3	3.4	1.45	8.5	14.4	0.64
bPEI25k		6.5	9.5	1.47	18.8	13.5	
LPEI25k		7.2	13.1	1.82	16.0	11.5	

[a] Number average molecular weight (M_n), weight average molecular weight (M_w), and polydispersity (M_w/M_n) as determined by GPC. [b] Titration values determined by the volume of 0.1 M HCl required to shift pH from 7.4 to 5.1 in 0.1 M aqueous NaCl after adding 6 mg of polymer. [c] Relative degree of branching determined by reduction of disulfide bonds with TCEP, then protection of free sulfhydryls with NEM followed by LC-MS analysis.

(DETA/CBA) < LPEI < bPEI, < poly(TETA/CBA), poly(EDA/CBA)).

It has been reported that polymerization generally occurs predominantly through primary amines with a low degree of branching found through secondary amines (*17*). It was realized that, under the conditions set for SS-PAEI polymer synthesis, branching could occur depending on the relative reactivity of amines in each polyamine monomer. To test the relative degree of branching for each SS-PAEI polymer, each disulfide bond was cleaved using a thiol-free reducing agent, TCEP, followed by the formation of a stable thioether bond using NEM. Reduced fragments were then analyzed by liquid chromatography−mass spectroscopy (LC-MS). For example, poly(EDA/CBA) was completely reduced, then protected using conditions as described above (Figure 1). An LC-MS spectrum within the range *m*/*z* 400−1500 showed two distinct ions with $m/z = 573.3$ and 829.4 representing both a linear and a single-branched population of fragments. The relative degree of branching (DB) was determined by the following general equation:

$$\mathrm{DB} = \frac{\mathrm{BSeg}}{\mathrm{BSeg} + \mathrm{LSeg}} \quad (1)$$

where BSeg is the total number of branched segments and LSeg is the total number of linear segments. It should be noted that, for poly(EDA/CBA), there should also be an ion peak at *m*/*z* 316.24 representing the terminal fragments of the polymer. Analyzing the LC-MS spectrum within the range *m*/*z* 300−1500 produced such a peak at intensity ~10. We decided not to include the terminal fragments in the calculations for each polymer due to the minor contributions made and since we were mainly interested in comparison of the linear and branched portions in each polymer. On the basis of relative intensities for all three SS-PAEIs in this semiquantitative analysis, it was estimated that the degree of branching was the least for poly(EDA/CBA) followed by poly(TETA/CBA) and poly(DETA/CBA) as reported in Table 1.

3.2. Characterization of Polymer/pDNA Complexes. The ability of these SS-PAEIs to condense pDNA was investigated by particle size and ζ-potential measurements (Figure 2). Dynamic light scattering (DLS) studies using different polymer/pDNA (w/w) ratios showed that small particle sizes with diameters less than 200 nm are obtained when polymer/pDNA ratios are at or above 1.5:1 for poly(TETA/CBA), 3:1 for poly(DETA/CBA), and 6:1 for poly(EDA/CBA).

The ζ-potential profile showed a similar trend as the w/w ratio increased, but at and above 6:1 w/w, all three polymers exhibited a charge of +32 mV. These values were slightly lower than that obtained for bPEI 25k at and above 0.75:1 w/w (+36 mV). When poly(TETA/CBA) was complexed with pDNA in solution containing 2.5 mM DTT, there was no apparent shift in ζ-potential at any of the weight ratios, indicating the inability of the reduced polymer to actively interact with the pDNA by affecting its overall surface charge potential in solution. The lack of such interactions may suggest that pDNA would be fully

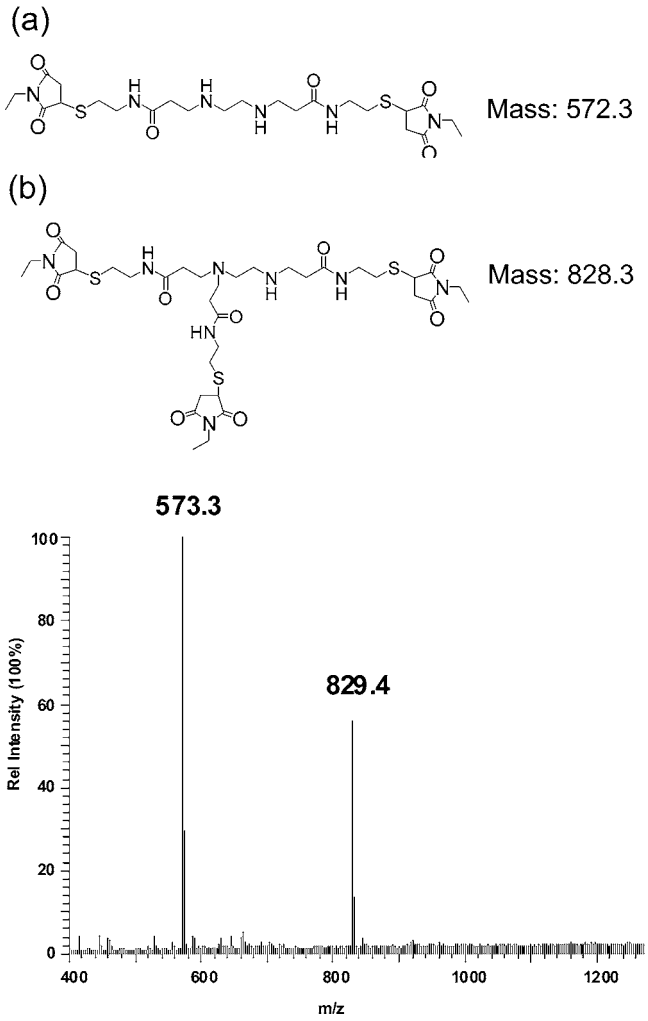

Figure 1. LC-MS spectrum of the reduced products for poly(EDA/CBA).

dissociated in the cytoplasm upon complete reduction of the SS-PAEI polymer/pDNA complexes.

Results from physicochemical characterizations were further verified by agarose gel electrophoresis stained with EtBr. Figure 3 shows gel electrophoresis results for poly(EDA/CBA). Poly(EDA/CBA) was capable of effectively condensing pDNA at w/w 0.75:1 and excluding EtBr intercalation with pDNA at and above 6:1 w/w. Poly(TETA/CBA) formed condensed, EtBr-excluding complexes sooner (1.5 w/w), followed by poly(DETA/CBA) at 3:1 w/w in agreement with DLS results (Figure 2a).

Polyplex formation can be better understood when the w/w ratios of each corresponding polymer/pDNA polyplex are converted into nitrogen/phosphate (N/P) ratios, where positively charged nitrogen atoms on the polymer backbone interact electrostatically with negatively charged phosphate residues on

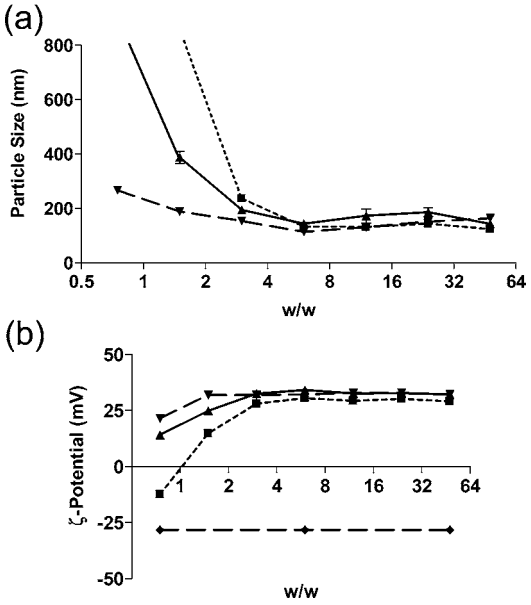

Figure 2. Physicochemical characterizations of polymer/pDNA complexes where (a) particle size and (b) ζ-potential ($n = 5 \pm$ SEM) are measured at varying w/w ratios with and without the presence of 2.5 mM DTT ($n = 3 \pm$ SEM). (■) poly(EDA/CBA); (▲) poly(DETA/CBA); (▼) poly(TETA/CBA); and (◆) poly(TETA/CBA) in the presence of 2.5 mM DTT.

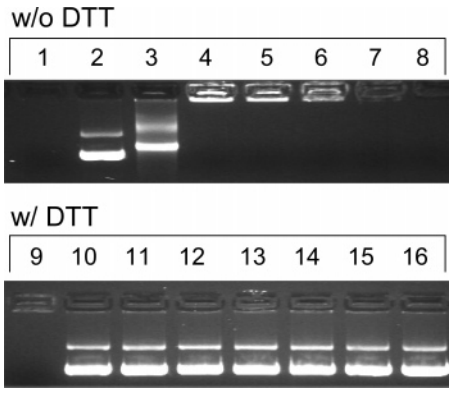

Figure 3. Gel electrophoresis of poly(EDA/CBA) complexed with pDNA at different polymer/plasmid ratios. Lanes 1 and 9, bPEI 25k at 0.75:1 w/w; lanes 2 and 10, free pDNA; lanes 3−8, poly(EDA/CBA) complexed with polymer/DNA ratios (w/w) of 0.25, 0.75, 1.5, 3, 6, and 12; and lanes 11−16, same conditions as lanes 3−8 except for the final concentration of 2.5 mM DTT. Polymers poly(DETA/CBA) and poly(TETA/CBA) were subjected to the same conditions producing complete condensation of pDNA and exclusion of EtBr at and above 6:1 w/w (data not shown).

pDNA to form compact structures as described previously (*30*). Weighted ratios used for SS-PAEIs at 6:1 convert into 12:1, 16:1, and 19:1 N/P ratios for poly(EDA/CBA), poly(DETA/CBA), and poly(TETA/CBA), respectively, where 0.75:1 w/w is 5:1 N/P for bPEI. The higher nitrogen content for poly(TETA/CBA) explains why pDNA condensation occurs sooner in contrast to poly(DETA/CBA) and poly(EDA/CBA).

When complexes were incubated with 2.5 mM DTT, unlike the bPEI control, all SS-PAEIs were unable to condense pDNA, producing results similar to those for the free pDNA control. Again, this complements results shown in Figure 2b where completely reduced SS-PAEI polymers are unable to interact with pDNA. The control polymer, bPEI, is not affected by DTT content and therefore sustains complete complexation of pDNA in both conditions. It is therefore likely that, upon reduction in the cytoplasm, SS-PAEIs will completely release pDNA, allowing for an increase in DNA uptake and gene expression

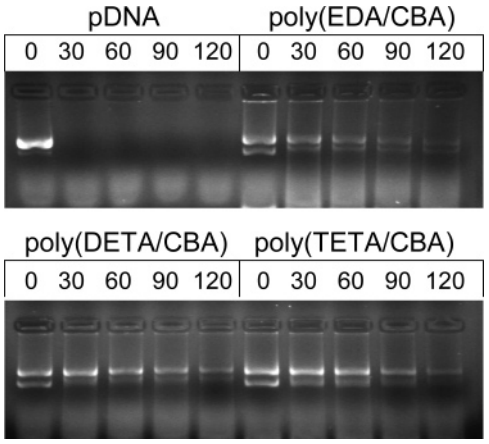

Figure 4. DNase I protection assay. SS-PAEI/pDNA complexes were prepared at 6:1 w/w and tested for their ability to protect pDNA against degradation. 10 μL aliquots containing 0.5 μg pDNA was taken at each time point (0, 30, 60, 90, 120 min).

inside the nucleus. Such mechanisms have already been proposed in the literature (*31*−*34*). It has been suggested that one limitation of bPEI 25k mediated nucleic acid delivery is the inability to completely release pDNA inside the cell, which would limit the accessibility of transcription machinery in the nucleus and therefore limit gene expression (*35*).

Last, to determine how effective these polymers are at protecting pDNA from DNase degradation, a DNase assay was conducted (Figure 4). All three polymers showed effective protection against DNase degradation up to 2 h incubation without any apparent difference between each polymer/pDNA complex analyzed. Under the same conditions, free pDNA was readily degraded by 15 min (data not shown).

3.3. In Vitro Transfection and Toxicity. Transfection experiments were conducted using SS-PAEIs at different polymer/pDNA ratios ranging from 0.75 to 24:1 on three different cell lines in the absence of serum. Optimized bPEI was used as a positive control showing the greatest gene expression while maintaining at least 80% cell viability. Figure 5 shows that poly(EDA/CBA) gives a significantly higher level of gene expression than the bPEI in all three cell lines. Specifically, poly(EDA/CBA) showed nearly a 20-fold increase in expression compared to bPEI in BAECs at 24:1 w/w. Other polymers showed an overall lower reporter expression compared to poly(EDA/CBA) where poly(DETA/CBA) appeared to decrease as w/w ratios increased, suggesting polymer carrier induced cellular toxicity. Poly(TETA/CBA), however, showed a w/w ratio dependence on gene expression producing luciferase higher than other polymer carriers in A7R5 cells only at 6:1 and 12:1 w/w. These results are especially interesting, since they show that SS-PAEIs produce significant gene expression not only in cells generally hard to transfect (NIH3T3), but also in a primary endothelial cell line (BAEC) and aortic smooth muscle cells (A7R5).

Kataoka and co-workers showed, after effective intracellular delivery of disulfide crosslinked complexes, that complete reduction leads to a substantial decrease in polymer/pDNA association and therefore higher gene expression (*21*). Gene expression results mediated by SS-PAEIs are supportive of these results. Of the three polymers, poly(EDA/CBA) has the lowest charge density of amines and therefore the lowest attraction to pDNA when reduced in the intracellular compartment but produces an overall higher gene expression.

Relative cellular viability was evaluated on the basis of an MTT assay against cells not receiving any formulated pDNA treatment on BAEC cells. Reduced toxicity was seen for SS-PAEIs compared to bPEI. The overall profile in Figure 6 showed

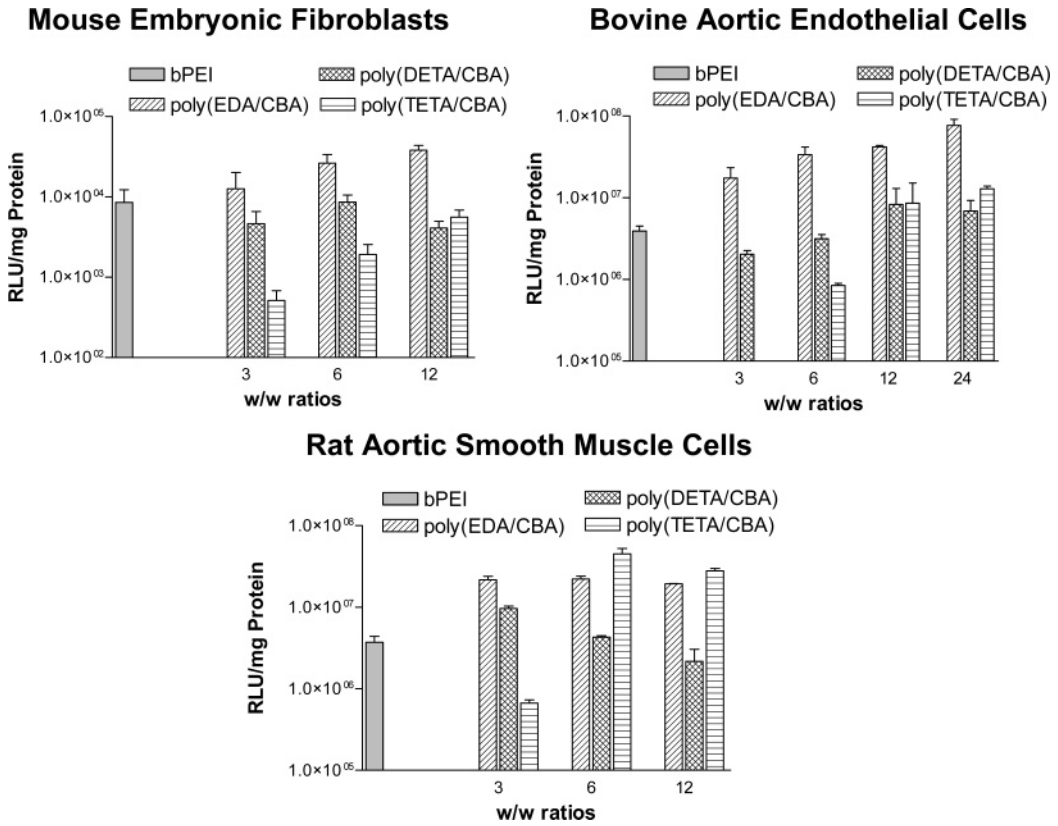

Figure 5. Transfection efficiencies for SS-PAEI/pDNA complexes in three different cell lines compared to a bPEI control at 0.75:1 w/w (2 μg pDNA/well). Results are expressed as the amount of reporter luciferase expressed normalized by the amount of protein in each well ($n = 3 \pm$ SEM).

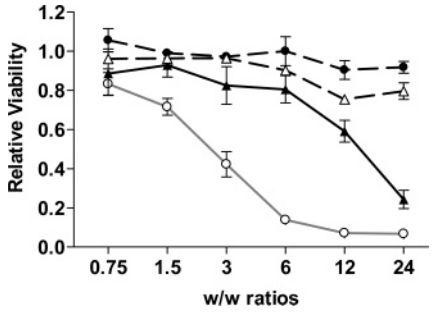

Figure 6. SS-PAEI/pDNA complex toxicity compared to a bPEI control: (Δ) poly(EDA/CBA), (▲) poly(DETA/CBA), (●) poly(TETA/CBA), and (○) bPEI. Relative cellular viability was determined using a MTT assay where results were compared to an untreated control ($n = 4 \pm$ SEM).

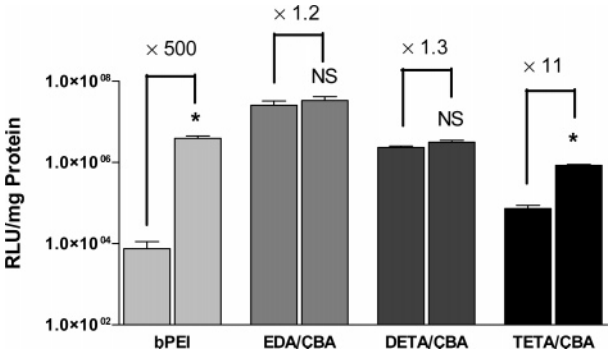

Figure 7. Effect of serum on SS-PAEI transfections. BAEC cells were used to look at the difference in gene expression with serum (left column) and without serum (right column) when polymers were complexed with pCMV-Luc reporter plasmid at 6:1 w/w and 0.75:1 for bPEI. Similar results were obtained at higher w/w ratios for SS-PAEIs (data not shown). Statistical significance was determined by a Student's *t*-test where $n = 3 \pm$ SEM, $^*p < 0.05$; NS—not significant.

an unexpected trend where poly(TETA/CBA) complexed with pDNA was less toxic than poly(EDA/CBA) followed by poly(DETA/CBA) and bPEI. Both poly(EDA/CBA) and poly(TETA/CBA) show a relative cellular viability of ≥80% at all polymer/pDNA ratios where poly(DETA/CBA) and bPEI produced similar viability up to 6:1 and 0.75:1, respectively. Higher toxicity would help explain the decrease in gene expression for poly(DETA/CBA) in Figure 5 using increasing w/w ratios on all three cell lines. In vitro results for this polymer may also directly correlate with the higher degree of branching and lower buffering capacity (Table 1) compared to the other SS-PAEIs where poly(EDA/CBA) produced the lowest degree of branching but the highest buffering capacity and overall gene expression.

Furthermore, transfections were conducted in the presence of 10% serum on BAEC cells in order to see the effect serum has on the gene expression of the SS-PAEI polymer/pDNA complexes. Interestingly, polyplexes containing reducible PAEIs did not show a large difference in gene expression between groups with and without serum, which contrasts significantly with the bPEI control, where there was a calculated 500× difference between gene expression in serum versus non-serum-containing groups (Figure 7). This might be explained by the difference in charge density of the overall polymer/pDNA complexes where a more densely charged colloid is likely to interact with serum proteins, leading to aggregation and therefore decreasing transfection efficiency (*12*).

Intracellular release of pDNA from polymer-labeled pDNA complexes was studied using confocal microscopy on NIH3T3 cells. Figure 8 shows the difference in intracellular distribution after 6 h as a result of delivery by poly(EDA/CBA) or bPEI. As a control, 2 μg free EMA−pDNA showed significantly less fluorescence after 90 min (data not shown). Cells receiving poly(EDA/CBA)/EMA−pDNA or bPEI/EMA−pDNA complexes

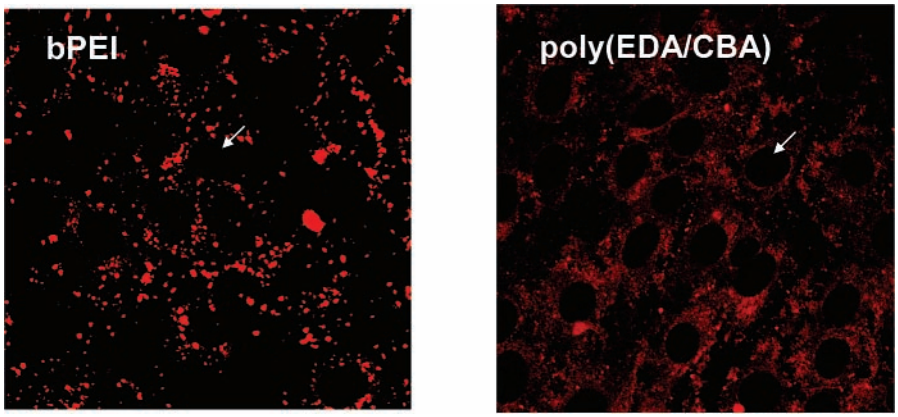

Figure 8. Confocal microscopy. Images show the difference in distribution of EMA-labeled pDNA on NIH 3T3 cells using poly(EDA/CBA) (6:1 w/w) and bPEI (0.75:1 w/w). Results show the distribution 6 h after transfection of polymer/EMA−pDNA complexes. Arrows point out the nucleus in each image. As a negative control, carrier free EMA−pDNA produced considerably less fluorescence after 90 min (data not shown).

did not produce any significant difference in intracellular images after 90 min incubation (data not shown). Both groups displayed a globular morphology suggesting that the complexes were still intact inside the cell (data not shown). Images taken after 6 h, however, show a distinct difference between the two polymer carriers. Delivery using poly(EDA/CBA) shows a more dispersed fluorescence inside the cell, suggesting that the polymer has been reduced, therefore releases the EMA−pDNA, where bPEI-mediated delivery still shows a globular fluorescence similar to both polymers after 90 min. This would suggest that both bPEI- and poly(EDA/CBA)-mediated delivery occur through similar pathways where both are endocytosed and subsequently released from the endosome by the "proton sponge effect" (*5*). Upon endosomal release, poly(EDA/CBA) polymer is reduced, therefore releases pDNA in the cytoplasm. A similar mechanism was proposed by Gosselin et al. using reversibly crosslinked low molecular weight PEI (*33*).

It was suggested previously that the reduction of disulfide-containing polymer/pDNA complexes in the intracellular compartment by glutathione reduces the cationic affinity to bind pDNA and therefore leads to enhanced gene expression (*33*, *34*). At the same time, Read et al. showed that increasing intracellular levels of GSH decreased gene expression of reducible gene carriers where a PEI control was not significantly affected (*36*). This suggests a time dependence of pDNA release inside the cell in order to obtain effective expression. Early reduction in the endo-lysosomal compartment could occur, as a result of higher glutathione levels inside the cell, that would lead to deprotection and early degradation of pDNA before it can be released into the cytoplasm.

Physicochemical characterization of our reducible PAEIs using ζ-potential and gel electrophoresis helps to confirm the effect that a completely reduced polymer has on pDNA. Results on confocal microscopy showed more dispersed pDNA using reducible poly(EDA/CBA) when compared to the bPEI control. A complete reduction of poly(EDA/CBA) in vitro is indicative of the dispersed fluorescence and would suggest a reason that higher gene expression is produced in cultured cells as shown in Figure 5.

4. CONCLUSIONS

We have shown that reducible SS-PAEIs are indeed a new class of peptidomimetic nonviral gene carrier designed for triggered intracellular nucleic acid delivery. Polymerization using Michael addition was used to produce three reducible poly(amido ethylenimine)s containing low polydispersity. These polymers were stable in aqueous solution allowing for possible facile vector modification. Polymers were further characterized with pDNA forming polyplexes exhibiting the ability to form stable nanoparticles and pDNA protection against degradation. SS-PAEIs also mediated significant gene expression in cell culture without showing inhibition by the presence of serum proteins. In the future, different forms of nucleic acid delivery will be evaluated in order to more fully characterize the potential of these polymers in established in vitro and in vivo models.

ACKNOWLEDGMENT

This work was supported by NIH grant HL 65477. We express our thanks to Xulin Jiang and Wim E. Hennink (Department of Pharmaceutics, Utrecht Institute for Pharmaceutical Sciences, Utrecht University) for help with the GPC measurements. Thanks also to Krishna Parsawar (Mass Spectroscopy and Proteomics Core Facility, University of Utah) for assistance with LC-MS experiments.

LITERATURE CITED

(1) Mahato, R. I., and Kim, S. W. (2002) *Pharmaceutical Perspectives of Nucleic Acid-Based Therapeutics*, Taylor and Francis, London and New York.

(2) Baum, C., Kustikova, O., Modlich, U., Li, Z., and Fehse, B. (2006) Mutagenesis and oncogenesis by chromosomal insertion of gene transfer vectors. *Hum. Gene Ther. 17*, 253−63.

(3) European Society of Gene Therapy (2003) French gene therapy group reports on the adverse event in a clinical trial of gene therapy for X-linked severe combined immune deficiency (X-SCID). Position statement from the European Society of Gene Therapy. *J. Gene Med. 5*, 82−4.

(4) Huang, L., Hung, M.-C., Wagner, E. (1999) *Nonviral Vectors for Gene Therapy*, Academic Press, San Diego.

(5) Boussif, O., Lezoualc'h, F., Zanta, M. A., Mergny, M. D., Scherman, D., Demeneix, B., and Behr, J. P. (1995) A versatile vector for gene and oligonucleotide transfer into cells in culture and in vivo: polyethylenimine. *Proc. Natl. Acad. Sci. U.S.A. 92*, 7297−301.

(6) Abdallah, B., Hassan, A., Benoist, C., Goula, D., Behr, J. P., and Demeneix, B. A. (1996) A powerful nonviral vector for in vivo gene transfer into the adult mammalian brain: polyethylenimine. *Hum. Gene Ther. 7*, 1947−54.

(7) Benns, J. M., and Kim, S. W. (2000) Tailoring new gene delivery designs for specific targets. *J. Drug Target. 8*, 1−12.

(8) Midoux, P., and Monsigny, M. (1999) Efficient gene transfer by histidylated polylysine/pDNA complexes. *Bioconjugate Chem. 10*, 406−11.

(9) Felgner, P. L., Tsai, Y. J., Sukhu, L., Wheeler, C. J., Manthorpe, M., Marshall, J., and Cheng, S. H. (1995) Improved cationic lipid formulations for in vivo gene therapy. *Ann. N. Y. Acad. Sci. 772*, 126−39.

(10) Tang, M. X., Redemann, C. T., and Szoka, F. C., Jr. (1996) In vitro gene delivery by degraded polyamidoamine dendrimers. *Bioconjugate Chem. 7*, 703−14.
(11) Eliyahu, H., Barenholz, Y., and Domb, A. J. (2005) Polymers for DNA delivery. *Molecules 10*, 34−64.
(12) Lungwitz, U., Breunig, M., Blunk, T., and Gopferich, A. (2005) Polyethylenimine-based non-viral gene delivery systems. *Eur. J. Pharm. Biopharm. 60*, 247−66.
(13) Emilitri, E., Ranucci, E., and Ferruti, P. (2005) New poly(amidoamine)s containing disulfide linkages in their main chain. *J. Polym. Sci., Part A: Polym. Chem. 43*, 1404−16.
(14) Ferruti, P., Marchisio, M. A., and Duncan, R. (2002) Poly(amidoamine)s: Biomedical Applications. *Macromol. Rapid Commun. 23*, 332−55.
(15) Caldwell, G., Neuse, E. W., and Stephanou, A. (1993) Synthesis of water-soluble polyamidoamines for biomedical applications. II. Polymers possessing intrachain-type secondary amino groups suitable for side-chain attachment. *J. Appl. Polym. Sci. 50*, 393−401.
(16) Hartmann, L., Krause, E., Antonietti, M., and Borner, H. G. (2006) Solid-Phase supported polymer synthesis of sequence-defined, multifunctional poly(amidoamines). *Biomacromolecules 7*, 1239−44.
(17) Liu, Y., Wenning, L., Lynch, M., and Reineke, T. M. (2004) New Poly(glucaramidoamine)s induce DNA nanoparticle formation and efficient gene delivery into mammalian cells. *J. Am. Chem. Soc. 126*, 7422−23.
(18) Liu, Y., and Reineke, T. M. (2006) Poly(glycoamidoamine)s for gene delivery: stability of polyplexes and efficacy with cardiomyoblast cells. *Bioconjugate Chem. 17*, 101−8.
(19) Hill, I. R., Garnett, M. C., Bignotti, F., and Davis, S. S. (1999) In vitro cytotoxicity of poly(amidoamine)s: relevance to DNA delivery. *Biochim. Biophys. Acta 1427*, 161−74.
(20) Saito, G., Swanson, J. A., and Lee, K. D. (2003) Drug delivery strategy utilizing conjugation via reversible disulfide linkages: role and site of cellular reducing activities. *Adv. Drug Delivery Rev. 55*, 199−215.
(21) Miyata, K., Kakizawa, Y., Nishiyama, N., Harada, A., Yamasaki, Y., Koyama, H., and Kataoka, K. (2004) Block catiomer polyplexes with regulated densities of charge and disulfide cross-linking directed to enhance gene expression. *J. Am. Chem. Soc. 126*, 2355−61.
(22) Ooya, T., Choi, H. S., Yamashita, A., Yui, N., Sugaya, Y., Kano, A., Maruyama, A., Akita, H., Ito, R., Kogure, K., and Harashima, H. (2006) Biocleavable polyrotaxane-plasmid DNA polyplex for enhanced gene delivery. *J. Am. Chem. Soc. 128*, 3852−3.
(23) Read, M. L., Bremner, K. H., Oupicky, D., Green, N. K., Searle, P. F., and Seymour, L. W. (2003) Vectors based on reducible polycations facilitate intracellular release of nucleic acids. *J. Gene Med. 5*, 232−45.
(24) Lin, C., Zhong, Z., Lok, M. C., Jiang, X., Hennink, W. E., Feijen, J., and Engbersen, J. F. J. Novel bioreducible poly(amido amine)s for highly efficient gene delivery. *Bioconjugate Chem.*, Submitted, 2006.
(25) Jiang, X., van der Horst, A., van Steenbergen, M. J., Akeroyd, N., van Nostrum, C. F., Schoenmakers, P. J., and Hennink, W. E. (2006) Molar-mass characterization of cationic polymers for gene delivery by aqueous size-exclusion chromatography. *Pharm. Res. 23*, 595−603.
(26) Benns, J. M., Mohato, R. I., and Kim, S. W. (2002) Optimization of factors influencing the transfection efficiency of folate-PEG-folate-*graft*-polyethylenimine. *J. Controlled Release 79*, 255−69.
(27) Lee, M., Nah, J. W., Kwon, Y., Koh, J. J., Ko, K. S., and Kim, S. W. (2001) Water-soluble and low molecular weight chitosan-based plasmid DNA delivery. *Pharm. Res. 18*, 427−31.
(28) Furgeson, D. Y., Yockman, J. W., Janat, M. M., and Kim, S. W. (2004) Tumor efficacy and biodistribution of linear polyethylenimine-cholesterol/DNA complexes. *Mol. Ther. 9*, 837−45.
(29) Zhong, Z., Feijen, J., Lok, M. C., Hennink, W. E., Christensen, L. V., Yockman, J. W., Kim, Y. H., and Kim, S. W. (2005) Low molecular weight linear polyethylenimine-*b*-poly(ethylene glycol)-*b*-polyethylenimine triblock copolymers: synthesis, characterization, and in vitro gene transfer properties. *Biomacromolecules 6*, 3440−8.
(30) Bloomfield, V. A. (1996) DNA condensation. *Curr. Opin. Struct. Biol. 6*, 334−41.
(31) McKenzie, D. L., Kwok, K. Y., and Rice, K. G. (2000) A potent new class of reductively activated peptide gene delivery agents. *J. Biol. Chem. 275*, 9970−7.
(32) Byk, G., Wetzer, B., Frederic, M., Dubertret, C., Pitard, B., Jaslin, G., and Scherman, D. (2000) Reduction-sensitive lipopolyamines as a novel nonviral gene delivery system for modulated release of DNA with improved transgene expression. *J. Med. Chem. 43*, 4377−87.
(33) Gosselin, M. A., Guo, W., and Lee, R. J. (2001) Efficient gene transfer using reversibly cross-linked low molecular weight polyethylenimine. *Bioconjugate Chem. 12*, 989−94.
(34) Oupicky, D., Carlisle, R. C., and Seymour, L. W. (2001) Triggered intracellular activation of disulfide crosslinked polyelectrolyte gene delivery complexes with extended systemic circulation in vivo. *Gene Ther. 8*, 713−24.
(35) Godbey, W. T., Wu, K. K., and Mikos, A. G. (1999) Tracking the intracellular path of poly(ethylenimine)/DNA complexes for gene delivery. *Proc. Natl. Acad. Sci. U.S.A. 96*, 5177−81.
(36) Read, M. L., Singh, S., Ahmed, Z., Stevenson, M., Briggs, S. S., Oupicky, D., Barrett, L. B., Spice, R., Kendall, M., Berry, M., Preece, J. A., Logan, A., and Seymour, L. W. (2005) A versatile reducible polycation-based system for efficient delivery of a broad range of nucleic acids. *Nucl. Acids Res. 33*, e86.

BC0602026

Hemoglobin Vesicles Containing Methemoglobin and L-Tyrosine to Suppress Methemoglobin Formation in Vitro and in Vivo

Tomoyasu Atoji,[†] Motonari Aihara,[†] Hiromi Sakai,[‡] Eishun Tsuchida,[‡] and Shinji Takeoka*[,†]

Department of Applied Chemistry, Graduate School of Science and Engineering, and Advanced Research Institute for Science and Engineering, Waseda University, Tokyo, 169-8555, Japan. Received December 8, 2005; Revised Manuscript Received July 20, 2006

Hemoglobin (Hb) vesicles have been developed as cellular-type Hb-based O_2 carriers in which a purified and concentrated Hb solution is encapsulated with a phospholipid bilayer membrane. Ferrous Hb molecules within an Hb vesicle were converted to ferric metHb by reacting with reactive oxygen species such as hydrogen peroxide (H_2O_2) generated in the living body or during the autoxidation of oxyHb in the Hb vesicle, and this leads to the loss of O_2 binding ability. The prevention of metHb formation by H_2O_2 in the Hb vesicle is required to prolong the in vivo O_2 carrying ability. We found that a mixed solution of metHb and L-tyrosine (L-Tyr) showed an effective H_2O_2 elimination ability by utilizing the reverse peroxidase activity of metHb with L-Tyr as an electron donor. The time taken for the conversion of half of oxyHb to metHb (T_{50}) was 420 min for the Hb vesicles containing 4 g/dL (620 μM) metHb and 8.5 mM L-Tyr ((metHb/L-Tyr) Hb vesicles), whereas the time of conversion for the conventional Hb vesicles was 25 min by stepwise injection of H_2O_2 (310 μM) in 10 min intervals. Furthermore, in the (metHb/L-Tyr) Hb vesicles, the metHb percentage did not reach 50% even after 48 h under a pO_2 of 40 Torr at 37 °C, whereas T_{50} of the conventional Hb vesicles was 13 h under the same conditions. Moreover, the T_{50} values of the conventional Hb vesicles and the (metHb/L-Tyr) Hb vesicles were 14 and 44 h, respectively, after injection into rats (20 mL/kg), confirming the remarkable inhibitory effect of metHb formation in vivo in the (metHb/L-Tyr) Hb vesicles.

INTRODUCTION

Hemoglobin (Hb)-based O_2 carriers (HBOCs) as red blood cell substitutes have been developed for clinical application in recent years (*1*−*3*). Their safety and usefulness have been demonstrated by many researchers in various fields such as physiology, toxicology, and biochemistry (*4*−*6*). The demand for HBOCs has been increasing year by year due to limitations of donated blood, such as infectious agents, shortage, and storage issues.

HBOCs are generally classified into two types: One is the acellular type, which comprises directly modified Hb molecules such as cross-linked Hb (*7*), polymerized Hb (*8*), and polymer-conjugated Hb (*9*). Some of the acellular-type HBOCs have advanced to phase III clinical trials (*10, 11*). Another kind is the cellular-type Hb systems such as Hb vesicles (*12*) or liposome-encapsulated Hb (*13*), in which Hb molecules are encapsulated with a phospholipid bilayer membrane. Although they are not yet in clinical trials, they have been shown to have excellent O_2 carrying ability and good safety profiles in vivo (*10, 14*−*18*).

Ferrous Hb (Hb(Fe^{2+})) molecules of HBOCs gradually lose their O_2 binding ability, because they react with reactive oxygen species (ROS) such as hydrogen peroxide (H_2O_2) (*19, 20*) or nitrogen monoxide (NO*) (*21*) to become nonfunctional ferric Hb (Hb(Fe^{3+}), metHb), in addition to the autoxidation of oxyHb molecules themselves. In humans, the concentration of metHb molecules in the red blood cells is usually kept below 1% by reduction systems such as NADH-cytochrome b_5, NADPH-flavin, glutathione, and ascorbic acid. Furthermore, ROS are eliminated by several mechanisms such as superoxide dismutase (SOD), catalase, and peroxidase that help to prevent the metHb formation (*23*, *24*). In contrast, metHb generated in the Hb vesicle are not reduced to the ferrous state due to the absence of the reduction systems, because constitutive enzymes and reductants necessary for metHb reduction are removed during the Hb purification process (*25*). The half-life of oxyHb of the Hb vesicles was 14 h in vivo, and more than 90% of oxyHb was converted to metHb within 48 h in the case of 20 vol % top loading to rats (*20*). In human plasma, the concentration of H_2O_2 is reported to be 4−5 μM (*26*) and to elevate to as much as 100−600 μM under inflammatory (*27*) or ischemia-reperfusion conditions (*28*). Therefore, Hb vesicles are required to have an H_2O_2 elimination system for effective prolongation of their O_2 carrying ability. We previously reported that H_2O_2 generated in the living body was the main reason for metHb formation of the Hb vesicles, and the O_2 carrying ability of the Hb vesicles in which catalase was coencapsulated was vastly prolonged in vivo by elimination of H_2O_2 (*20*). Regarding the catalase-coencapsulated vesicles, it is somewhat difficult to obtain a sufficient amount of human catalase from human donated blood. Furthermore, the catalase activity is gradually lost due to denaturation during storage at 25 °C.

Horseradish peroxidase (HRP), which also eliminates H_2O_2 in its enzymatic reaction, is converted to a ferrylHb radical Hb(Fe^{4+}═O*) state after reaction with H_2O_2, and the radical state is returned to the ferric state by acceptance of two electrons from substrates such as *p*-hydroxyphenylacetic acid (HPA) (*29, 30*). This is a well-known reaction in an H_2O_2 assay method. L-Tyrosine (L-Tyr) dimer or polymer can also be synthesized by an HRP-catalyzed oxidation (*31, 32*). We considered from the above mechanism that if metHb, which has ferric heme like HRP does, could also function as an H_2O_2 elimination enzyme in the presence of L-Tyr as a substrate, then metHb can easily

* Corresponding author. E-mail: takeoka@waseda.jp. Tel: +813-5286-3217. Fax: +813-5286-3217.

[†] Graduate School of Science and Engineering.

[‡] Advanced Research Institute for Science and Engineering.

10.1021/bc050349h CCC: $33.50 © 2006 American Chemical Society
Published on Web 09/02/2006

be prepared from purified Hb for the preparation of vesicles. Moreover, L-Tyr itself is an amino acid with high stability and good cost performance. In this study, we prepared Hb vesicles coencapsulating metHb and L-Tyr, thereby incorporating the metHb elimination system into the Hb vesicles themselves. We then evaluated the effect of this coencapsulation on the suppression of metHb formation. Furthermore, we evaluated the safety of the vesicles in vivo.

EXPERIMENTAL PROCEDURES

Purification of Hb from Red Blood Cells (*19, 33*). Hb was purified from outdated human red blood cells provided by the Japanese Red Cross. The red blood cells were washed three times with saline by centrifugation (2000*g*, 10 min) and concentrated by the removal of the supernatant. They were hemolyzed by the addition of an equal volume of water for injection, and then the stroma were removed by ultrafiltration (cutoff M_w 1000 kDa, Biomax-1000V, Millipore Co., Ltd., Bedford). The ligand exchange from O_2 to CO was carried out for the stroma-free Hb solution by CO gas flowing over the stirred solution. The proteins other than HbCO were denatured by heat treatment at 60 °C for 12 h and removed as precipitates. The HbCO solution was fractionated using ultrafiltration filters with a cutoff molecular weight between 1000 kDa and 8 kDa (Biomax-8V, Millipore), followed by concentration with an 8 kDa ultrafilter.

Reaction of Hb Samples with H_2O_2. HbCO was decarbonylated to HbO_2 by the irradiation of visible light to a liquid film of the Hb solution under O_2 atmosphere; potassium ferricyanide was added to the oxyHb solution to convert the oxyHb to metHb (*34*). The conversion of oxyHb to metHb was 99.9% as measured by the modified Evelyn−Malloy method (*35*). After the mixed solution was stirred at 25 °C for 2 h, the potassium ferricyanide was removed from the resulting metHb solution by gel filtration chromatography on Sephadex G-25 (Pharmacia AB, Uppsala). Deferoxamine mesylate (1.6 mM; DFO, Sigma, St. Louis) and L-Tyr (0 or 1 mM; free base, ICN Biomedicals, Inc., Aurora) were added to the oxyHb or metHb solutions, and these solutions were used as Hb samples. Hb samples ([heme] = 20 μM) were reacted with 200 μM H_2O_2 ([heme]/[H_2O_2] = 1/10 molar ratio) in phosphate buffered saline (PBS, pH 7.4 at 37 °C), and the reaction was monitored by the repetitive scanning of a visible region from 300 to 700 nm at 2 min interval by using a UV−vis spectrometer (V-570, Jasco, Tokyo).

For the measurement of H_2O_2 concentrations, samples were reacted with H_2O_2 under the same conditions and were periodically sampled, and the concentration of H_2O_2 was determined spectrofluorometrically by measuring the amount of 6,6′-dihydroxy-[1,1′-biophenyl]-3,3′-diacetic acid (DBDA; Ex, 317 nm; Em, 405 nm), generated by the HRP-catalyzed reaction of HPA with H_2O_2. The final concentrations of HRP and HPA were 4 μM and 6 mM, respectively, and the DBDA concentration was calculated after separating the Hb samples by centrifugal filtration (cutoff 5 kDa, Ultrafree-MC, Millipore, Bedford) (*19, 29*).

Preparation of the Hb Vesicles Containing metHb and L-Tyr ((metHb/L-Tyr) Hb Vesicles) (*36*). MetHb was prepared by the reaction of HbCO (10 g/dL) with an excess amount of potassium ferricyanide. The unreacted potassium ferricyanide and ferrocyanide were removed by ultrafiltration (cutoff M_w 50 kDa, ADVANTEC, Tokyo) until the concentration of potassium ferricyanide was less than 1 μM by monitoring the absorbance with the UV−vis spectrometer. The metHb solution was concentrated to 40 g/dL using a 50 kDa cutoff filter as noted above. HbCO solutions containing 5 or 10 mol % metHb were prepared by mixing the concentrated metHb solution with a 40 g/dL HbCO solution. Pyridoxal 5′-phosphate (PLP, Sigma, St. Louis, MO) was added to the Hb solution as an allosteric effector at a 2.5 equimolar ratio of PLP to HbCO. The L-Tyr solution prepared previously was added to 0.2 N NaOH, and the resulting solution was added to the HbCO/metHb solution. The final concentrations of Hb and L-Tyr in the HbCO/metHb solution were adjusted to 40 g/dL and 1.0 and 8.5 mM, respectively. To prepare the Hb vesicles, powders of 1,2-dipalmitoyl-*sn*-glycero-3-phosphatidylchorine (DPPC), cholesterol, 1,5-bis-*O*-hexadecyl-*N*-succinyl-L-glutaminate (DHSG) (Nippon Fine Chemical Co., Osaka), and 1,2-distearoyl-*sn*-glycero-3-phosphatidylethanolamine-*N*-PEG_{5000} (PEG-DSPE, NOF Co., Tokyo) were mixed at a molar ratio of 5:5:1:0.033 and added to the HbCO/metHb solution, and the mixture was stirred at 25 °C for 12 h. The resulting dispersion of the multilamellar vesicles was subsequently extruded through the nitrocellulose membrane filters with a pore size of 0.22 μm (Fuji Film Co., Tokyo) to prepare the Hb vesicles with an average diameter of 261 ± 30 nm. After the separation of unencapsulated Hb by ultracentrifugation (10000*g*, 60 min), the precipitate of the Hb vesicles was redispersed into saline in order to adjust the Hb concentration of the Hb vesicle dispersion to 10 g/dL. HbCO within the vesicles was decarbonized and oxygenated to HbO_2 by irradiation of visible light onto a liquid film under O_2 atmosphere.

Stepwise Injection of H_2O_2 to a Dispersion of (metHb/L-Tyr) Hb Vesicles. A dispersion of (metHb/L-Tyr) Hb vesicles in PBS (pH 7.4) coencapsulating metHb and L-Tyr (metHb/L-Tyr = 2 g/dL:1 mM, 4 g/dL:1 mM, or 4 g/dL:8.5 mM) was incubated with stirring, and H_2O_2 (310 μM, Ultra Pure Grade, Kanto Chemical Co., Tokyo) was injected in stepwise fashion into the solutions at 10 min intervals. Just before each injection, 20 μL of the dispersion of the (metHb/L-Tyr) Hb vesicles was sampled out, and 20 μL of a catalase solution (50 000 unit) was immediately added for the elimination of the remaining H_2O_2. The percentage of metHb in the (metHb/L-Tyr) Hb vesicles was periodically calculated by the ratio of absorbance at 405 nm (metHb) and 430 nm (deoxyHb) in the Soret band using a UV−vis spectrometer without destruction of the Hb vesicles.

Autoxidation of (metHb/L-Tyr) Hb Vesicles. A dispersion of (metHb/L-Tyr) Hb vesicles was incubated and shaken (120 times/min) under pO_2 of 40 Torr at 37 °C. The percentage of metHb in the vesicles was periodically measured with a UV−vis spectrometer.

Measurement of metHb Formation in the Hb Vesicles in Vivo. Wistar rats (body weight: 240−260 g) were anesthetized with diethyl ether, and a preparation of (metHb/L-Tyr) Hb vesicles containing 4 g/dL of metHb and 8.5 mM of L-Tyr was injected into the tail vein (20 mL/kg, n = 6). Blood was withdrawn from the tail vein and centrifuged (12000*g*, 5 min) to collect the vesicle fraction in the supernatant. The percentage of metHb within the vesicles was measured with a UV−vis spectrometer. The number of blood cells was measured with a blood cell counter (Sysmex, KX-21, Kobe).

RESULTS AND DISCUSSION

Reaction of the L-Tyr Containing metHb Solution with H_2O_2. We added H_2O_2 to the metHb solution (5 μM) with or without 1 mM L-Tyr. Figure 1 shows the changes of the H_2O_2 concentration in the metHb solutions with and without L-Tyr. The initial elimination rates of H_2O_2 in the metHb solutions were calculated on the basis of a pseudo-first-order rate law. The elimination rates with and without L-Tyr at 37 °C were 3.0×10^3 and 3.2×10^4 M^{-1} s^{-1}, respectively. The apparent rate constant of the metHb solution containing L-Tyr was about 10 times larger than that with the metHb solution alone, and this

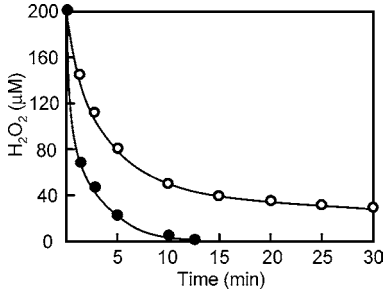

Figure 1. Time course of H_2O_2 elimination by (○) metHb (5 μM) (●) metHb (5 μM) + L-Tyr (1 mM) during the reaction with 200 μM of H_2O_2 at 37 °C.

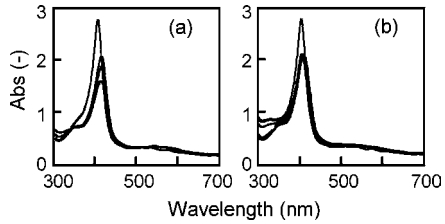

Figure 2. UV−vis spectral changes of (a) a metHb (5 μM) solution and (b) a metHb (5 μM) solution containing L-Tyr (1 mM) during the reaction with 200 μM H_2O_2 ([heme]:[H_2O_2] = = 1/10) at 37 °C. The scanning was performed at 4 min intervals, immediately after the addition of H_2O_2 solution to each Hb solution.

value was estimated to be approximately equal to the 150 units of catalase. Moreover, around 40 μM H_2O_2 remained after a 30 min reaction of 200 μM H_2O_2 in the metHb solution alone, whereas H_2O_2 was completely eliminated within 15 min in the metHb solution containing L-Tyr.

The UV−vis spectral changes during the reaction of H_2O_2 in the metHb solution (5 μM) and the metHb solution containing L-Tyr (1 mM) are shown in Figure 2a and b, respectively. In the case of metHb alone, there was a shift in the spectrum of metHb, namely, the Soret band of metHb (405 nm) was shifted to 417 nm, and the typical metHb peak at 630 nm was completely abolished, which indicated a change to a different form of metHb. There was a time-dependent decrease in peak intensities, indicating the degradation of this intermediate form of Hb during the reaction of H_2O_2. We speculated that this intermediate form of Hb was ferrylHb radical. It has been reported that the ferrylHb radical is formed by the reaction of metHb with H_2O_2 (*37*). Furthermore, the stoichiometry of metHb (5 μM) and the reacted H_2O_2 (200 μM) suggests that the metHb worked as an enzyme such as catalase, although the stability of the enzyme was low and it was degraded. Because the Fenton reaction can be prevented by the addition of DFO, which is a chelator of Fe^{3+}, this enzymatic H_2O_2 elimination was considered to be a pseudo-catalase-like reaction of metHb. Conversely, the metHb solution with L-Tyr showed a fast spectral change and then stayed constant during the reaction, as shown in Figure 2b. Also, the small spectral shift of the metHb solution with L-Tyr suggested that the metHb reacted with H_2O_2 was converted to the ferrylHb radical. The ratio of metHb to ferrylHb should be constant during reaction with H_2O_2. Comparing with the reaction mechanism of peroxidase, where the ferric state is converted to the ferrylHb radical state by the reaction of H_2O_2 to produce H_2O, and then the ferryl radical state is recovered to the ferric state by one-electron oxidation of two substrate molecules to generate another molecule of H_2O, we could compare, in this case, the peroxidase and the substrate to metHb and L-Tyr, respectively. More precisely, we could describe the enzymatic reaction as reverse peroxidation, and the substrate as H_2O_2 where L-Tyr works as an electron donor. Furthermore, we detected L-Tyr dimer (L-Tyr-L-Tyr (diTyr)), which was

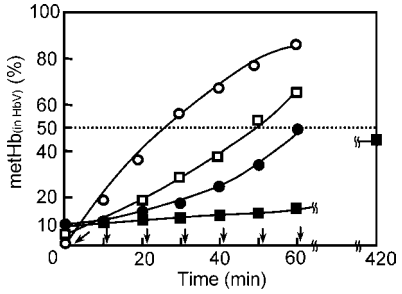

Figure 3. Time course of metHb formation in Hb vesicles at 37 °C during the stepwise addition of H_2O_2 (310 μM) to 5 g/dL Hb vesicle dispersions coencapsulating (●) 4 g/dL metHb and 1 mM L-Tyr, (□) 2 g/dL metHb and 1 mM L-Tyr, (■) 4 g/dL metHb and 8.5 mM L-Tyr, and (○) no metHb and L-Tyr.

produced from the coupling of the two L-Tyr radicals in their ortho position. Such a stable reaction of the unstable ferrylHb radical to metHb by L-Tyr would help the stable elimination reaction of H_2O_2. Therefore, we aimed to construct this system in the Hb vesicles.

H_2O_2 Stepwise Addition to the (metHb/L-Tyr) Hb Vesicles. Figure 3 shows the time course of metHb formation in the conventional Hb vesicles or the (metHb/L-Tyr) Hb vesicles by stepwise injection of H_2O_2 (310 μM) in 10 min intervals. H_2O_2 (310 M) injection to a 5 g/dL conventional Hb vesicle dispersion ([heme] = 3.1 mM) showed an elevation in the metHb percentage with increasing injections of H_2O_2, and the percentage of metHb reached 85% after 60 min (6 injections). However, the (metHb/L-Tyr) Hb vesicles (metHb/L-Tyr = 2 g/dL:1 mM, 4 g/dL:1 mM) showed a significant suppression of metHb formation in the vesicles. The metHb percentages of these Hb vesicles were 67% and 50% after 60 min (6 injections), respectively. Furthermore, by increasing the amount of L-Tyr to 8.5 mM (metHb: 4 g/dL), metHb formation was dramatically suppressed; the percentages were 17% and 45% after 60 and 420 min, respectively (6 and 42 injections, respectively).

From these results, it was confirmed that the formation of metHb from oxyHb by reaction with H_2O_2 was suppressed by the H_2O_2 elimination system of metHb and L-Tyr. Moreover, the persistence of the metHb suppression effect depends on the amount of metHb as an enzyme and L-Tyr as a substrate. The solubility of L-Tyr in pure water is 1.2 mM; however, we succeeded in preparation of an Hb solution containing 8.5 mM L-Tyr by using an alkali solution (NaOH) and the interaction of L-Tyr with highly concentrated Hb molecule (40 g/dL). We succeeded in the construction of Hb vesicles having an H_2O_2 elimination system using Hb only as protein or enzyme.

Autoxidation of the (metHb/L-Tyr) Hb Vesicles. Besides the formation of metHb by H_2O_2, oxyHb is automatically oxidized to metHb, initiated by one-electron reduction of a coordinated dioxygen molecule to generate superoxide anion radical (O_2^{-}*). MetHb formation in vesicles by such autoxidation was measured under the condition of the pO_2 of 40 Torr at 37 °C, because at this pO_2 value, the rate of metHb formation is maximal (*38*). In the conventional Hb vesicles, the percentage of metHb periodically increased by autoxidation of oxyHb in the vesicles. The T_{50} was 13 h, and the metHb percentage reached 90% after 24 h incubation (Figure 4). On the other hand, the metHb formation of the Hb vesicles containing 4 g/dL metHb and 1 mM L-Tyr was effectively suppressed; the T_{50} was 24 h. Furthermore, in the Hb vesicles containing 4 g/dL metHb and 8.5 mM L-Tyr, the percentage of metHb formed was 20% and 43% after 24 and 48 h, respectively, and did not reach 50% when the measurement ended (48 h).

Autoxidation of oxyHb is also an important factor of metHb formation. The autoxidation rate of oxyHb depends on many factors such as the O_2 affinity, P_{50}, the pO_2, temperature, and

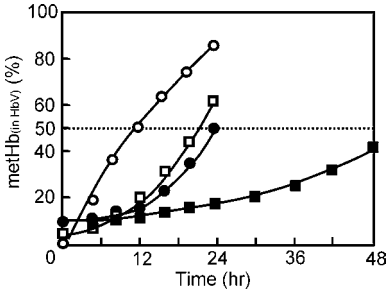

Figure 4. Time course of metHb formation in Hb vesicles under pO_2 of 40 Torr at 37 °C during autoxidation of 5 g/dL Hb vesicle dispersion coencapsulating (●) 4 g/dL metHb and 1 mM L-Tyr, (□) 2 g/dL metHb and 1 mM L-Tyr, (■) 4 g/dL metHb and 8.5 mM L-Tyr, and (○) no metHb and L-Tyr.

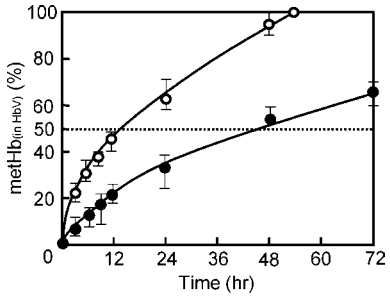

Figure 5. Time course of metHb formation in Hb vesicles injected into Wistar rats (20 mL/kg). Hb vesicles were encapsulating (●) 4 g/dL metHb and 8.5 mM L-Tyr, and (○) no metHb and L-Tyr.

pH. OxyHb molecules in the Hb vesicles are also influenced by these same factors, though the rates could be different from that of the oxyHb solution. The half-life of oxyHb to metHb (T_{50}) in the conventional Hb vesicles (P_{50} = 33 Torr) at 37 °C was about 12 h, shorter than that of the oxyHb solution (T_{50} = 24 h, PBS, pH 7.4). The autoxidation rate of the Hb vesicles containing metHb and L-Tyr was also effectively reduced in a similar way to that observed in the above experiment of H_2O_2 stepwise addition. The reason could be that the autoxidation of oxyHb is additionally influenced by H_2O_2. A superoxide anion radical (O_2^{-}*) generated by the oxyHb autoxidation is spontaneously converted to H_2O_2 in the presence of H^+. This H_2O_2 attacks the other oxyHb molecules. Therefore, the elimination of the H_2O_2 would result in the suppression of the autoxidation rate of oxyHb in the Hb vesicles.

Measurement of metHb Formation in (metHb/L-Tyr) Hb Vesicles in Vivo. Figure 5 shows the percentage of generated metHb after the intravenous injection (20 mL/kg) of the conventional Hb vesicles or the (metHb/L-Tyr) Hb vesicles into the tail vein of Wistar rats (n = 6). The metHb percentages of the conventional Hb vesicles and the (metHb/L-Tyr) Hb vesicles after 4 h were 22% and 18%, respectively, and the T_{50} values were 14 and 44 h, respectively. Furthermore, the Wistar rats were all alive for 72 h after the measurement, at which time they were sacrificed, indicating the safety of this system in vivo. These results confirmed the suppressive effect of metHb formation in vivo using the (metHb/L-Tyr) Hb vesicles.

In a previous study, we coencapsulated catalase to eliminate H_2O_2 generated in vivo, thus suppressing the formation of metHb within Hb vesicles, and we confirmed the suppression of metHb formation (*20*). The T_{50} of the catalase-coencapsulated Hb vesicles was 37 h with a catalase concentration of 4.2×10^4 unit/mL (0.5 g/dL catalase as a protein concentration). We estimated that the concentration of catalase was the amount at the saturation point of T_{50} prolongation, because the same T_{50} was obtained when 5.6×10^4 unit/mL catalase was used for coencapsulation. In comparison with these results, the (metHb/L-Tyr) system was more effective in the suppression of metHb formation by elimination of H_2O_2. It is thought that catalase activity is gradually lost at 37 °C in vivo (*20*), whereas the activity of the (metHb/L-Tyr) system should be very stable at 37 °C, and the amount of L-Tyr (8.5 mM within the Hb vesicle) was sufficient to eliminate H_2O_2 in the Hb vesicles. From these results, the increase of the metHb percentage of the (metHb/L-Tyr) Hb vesicles is likely due to the autoxidation of Hb, which is impossible to suppress in this system.

ACKNOWLEDGMENT

The authors thank Dr. K. Ohta at Oxygenix Co., Ltd., for technical advice about in vivo measurement of (metHb/L-Tyr) Hb vesicles. This work was supported in part by Health and Labor Science Research Grant, Ministry of Health, Labor and Welfare, Japan, Grant-in-Scientific Research (18500368), and 21COE "Practical Nano-Chemistry" and "Consolidated Research Institute for Advanced Science and Medical Care" from MEXT, Japan.

LITERATURE CITED

(1) Tsuchida, E. (1995) *Artificial Red Cells*, John Wiley and Sons, New York.
(2) Winslow, R. M. (1997) Progress on blood substitutes. *Nat. Med. 3*, 474−474.
(3) Chang, T. M. S. (1997) *Blood Substitutes: Principles, Methods, Products and Clinical Trials*, S. Karger AG, Switzerland.
(4) Tsuchida, E., Ed. (1998) *Blood Substitutes: present and future perspectives*, Elsevier Science, Amsterdam.
(5) Reiss, J. G. (2001) Oxygen carriers ("blood substitutes")-raison d'etre, chemistry, and some physiology. *Chem. Rev. 101*, 2797−2920.
(6) D'Agnillo, F., and Alayash, A. I. (2001) Redox cycling of diaspirin cross-liked hemoglobin induced G2/M arrest and apoptosis in cultured endothelial cells. *Blood 98*, 3315−3323.
(7) Przybelski, R. J., Dairy, E. K., and Birnbaum, M. L. (1997) The pressor of effect of hemoglobin − good or bad? In *Advances in Blood Substitutes: Industrial Opportunities and Medical Challenges* (Winslow, R. M., Vandegriff, K. D., and Intaglietta, M., Eds.) Birkhauser, Boston.
(8) Gould, S. A., Moore, E. E., Hoyt, D. B., Burch, J. M., Haenel, J. B., Garcia, J., DeWoskin, R., and Moss, G. S. (1998) The first randomized trial of human polymerized hemoglobin as a blood substitute in acute trauma and emergency surgery. *J. Am. Coll. Surg. 187*, 113−122.
(9) McCarthy, M. R., Vandegriff, K. D., and Winslow, R. M. (2001) The role of facilitated diffusion in oxygen transport by cell-free hemoglobins: implications for the design of hemoglobin-based oxygen carriers. *Biophys. Chem. 92*, 103−117.
(10) Mullon, J., Giacoppe, G., Clagett, C., McCune, D., and Dillard, T. (2000) Transfusions of polymerized bovine hemoglobin in a patient with severe sutoimmune hemolytic anemia. *N. Engl. J. Med. 342*, 1638−1643.
(11) Sloan, E. P., Koenigsberg, M., Gens, D., Cipolle, M., Runge, J., Mallory, M. N., and Rodman, G., Jr. (1999) Diaspirin cross-linked hemoglobin (DCLHb) in the treatment of severe traumatic hemorrhagic shock: a randomized controlled efficacy. *JAMA 282*, 1857−1864.
(12) Sakai, H., Horinouchi, H., Tomiyama, K., Ikeda, E., Takeoka, S., Kobayashi, K., and Tsuchida, E. (2001) Hemoglobin-vesicles as oxygen carriers. Influence on phagocytic activity and histopathological changes in reticuloendothelial system. *Am. J. Pathol. 159*, 1079−1088.
(13) Rudolph, A. S., Sulpizio, A., Hieble, P., MacDonald, V., Chavez, M., and Feuerstein, G. (1997) Liposome encapsulating attenuates hemoglobin-induced vasoconstriction inrabbit arterial segment. *J. Appl. Physiol. 82*, 1826−1835.
(14) Sakai, H., Cabrales, P., Tsai, A. G., Tsuchida, E., and Intaglietta, M. (2005) Oxygen release from low and normal P_{50} Hb vesicles in transiently occluded arterioles of the hamster window model. *Am. J. Physiol. 288*, H2897−H2903.

(15) Cabrales, P., Sakai, H., Tsai, A. G., Takeoka, S., Tsuchida, E., and Intaglietta, M. (2005) Oxygen transport by low and normal oxygen affinity hemoglobin vesicles in extreme hemodilution. *Am. J. Physiol. 288*, H1885−H1892.

(16) Sakai, H., Masada, Y., Horinouchi, H., Ikeda, E., Sou, K., Takeoka, S., Suematsu, M., Takaori, M., Kobayashi, K., and Tsuchida, E. (2004) Physiological capacity of the reticuloendothelial system for the degradation of hemoglobin vesicles (artificial oxygen carriers) after massive intravenous doses by daily repeated infusions for 14 days. *J. Pharmacol. Exp. Ther. 311*, 874−884.

(17) Yoshizu, A., Izumi, Y., Park, S., Sakai, H., Takeoka, S., Horinouchi, H., Ikeda, E., Tsuchida, E., and Kobayashi, K. (2004) Hemorrhagic shock resuscitation with an artificial oxygen carrier, hemoglobin vesicle, maintains intestinal perfusion and suppresses the increase in plasma tumor necrosis factor-α. *ASAIO J. 50*, 458−463.

(18) Sakai, H., Takeoka, S., Park, S. I., Kose, T., Hamada, K., Izumi, Y., Yoshizu, A., Nishide, H., Kobayashi, K., and Tsuchida, E. (1997) Surface modification of hemoglobin vesicles with poly(ethylene glycol) and effects on aggregation, viscosity, and blood flow during 90% exchange transfusion in anesthetized rats. *Bioconjugate Chem. 8*, 23−30.

(19) Takeoka, S., Teramura, Y., Atoji, T., and Tsuchida, E. (2002) Effect of Hb-encapsulation with vesicles on H_2O_2 reaction and lipid peroxidation. *Bioconjugate Chem. 13*, 1302−1308.

(20) Teramura, Y., Kanazawa, H., Sakai, H., Takeoka, S., and Tsuchida, E. (2003) Prolonged oxygen-carrying ability of hemoglobin vesicles by coencapsulation of catalase in vivo. *Bioconjugate Chem. 14*, 1171−1176.

(21) Herold, S., and Rock, G. (2003) Reactions of deoxy-, oxy-, and methemoglobin with nitrogen monoxide. *J. Biol. Chem. 278*, 6623−6634.

(22) Shikama, K. (1998) The molecular mechanism of autoxidation for myoglobin and hemoglobin: A venerable puzzle. *Chem. Rev. 98*, 1357−1373.

(23) Shikama, K. (1984) A controversy on the mechanism of autoxidation of oxymyoglobin and oxyhemoglobin: oxidation, dissociation, or displacement? *Biochem. J. 223*, 279−280.

(24) Tomoda, A., Yoneyama, T., and Tsuji, A. (1981) Changes in intermediate hemoglobins during autoxidation of hemoglobin. *Biochem. J. 195*, 485−492.

(25) Naito, Y., Fukutomi, I., Masada, Y., Sakai, H., Takeoka, S., Tsuchida, E., Abe, H., Hirayama, J., Ikebuchi, K., and Ikeda, H. (2002) Virus removal from hemoglobin solution using Planova membrane. *J. Artif. Organs 5*, 141−145.

(26) Nagababu, E., and Rifkind, J. M. (2000) Reaction of hydrogen peroxide with ferrylhemoglobin: superoxide production and heme degradation. *Biochemistry 39*, 12503−12511.

(27) Gunther, M. R., Sampath, V., and Caughey, W. S. (1999) Potential roles of myoglobin autoxidation in myocardial ischemia-reperfusion injury. *Free Radical Biol. Med. 26*, 1388−1395.

(28) Svistunenko, D. A., Patel, R. P., Voloshchenko, S. V., and Wilson, M. T. (1997) The globin-based free radical of ferryl hemoglobin is detected in normal human blood. *J. Biol. Chem. 272*, 7114−7121.

(29) Hofmann, F., Hofmann, L., Hubl, W., and Meissner, D. (1984) Determination of horseradish peroxidase (HRP) with the substrates H_2O_2 and *p*-hydroxyphenylacetic acid (HPA) in the fluorescence enzyme immunoassay. *Z. Med. Laboratoriumsdiagn. 25*, 14−21.

(30) Yusa, K., and Shikama, K. (1987) Oxidation of oxymyoglobin to metmyoglobin with hydrogen peroxide: involvement of ferryl intermediate. *Biochemistry 26*, 6684−6688.

(31) Fukuoka, T., Tachibana, Y., Tonami, H., Uyama, H., and Kobayashi, S. (2002) Enzymatic polymerization of tyrosine derivatives. peroxidase- and protease-catalyzed synthesis of poly(tyrosine)s with different structures. *Biomacromolecules 3*, 768−774.

(32) Malencik, D. A., Sprouse, J. F., Swanson, C. A., and Anderson, S. R. (1996) Dityrosine: preparation, isolation, and analysis. *Anal. Biochem. 242*, 202−213.

(33) Hinsberg, W. D., Milby, K. H., and Zare, R. N. (1981) Determination of insulin in serum by enzyme immunoassay with fluorimetric detection. *Anal. Chem. 53*, 1509−1512.

(34) Sakai, H., Onuma, H., Umeyama, M., Takeoka, S., and Tsuchida, E. (2000) Photoreduction of methemoglobin by irradiation in the near-ultraviolet region. *Biochemistry 39*, 14595−14602.

(35) Van Assendelft, O. W. (1970) *Spectrophotometer of hemoglobin derivatives*, Royal Vangorcum Ltd., Assen, The Netherlands.

(36) Sakai, H., Hamada, K., Takaoka, S., Nishide, H., and Tsuchida, E. (1996) Physical properties of hemoglobin vesicles as red cell substitutes. *Biotechnol. Prog. 12*, 119−125.

(37) Cashon, R. E., and Alayash, A. I. (1995) Reaction of human hemoglobin HbA_0 and two cross-linked derivatives with hydrogen peroxide: differential behavior of the ferryl intermediate. *Arch. Biochem. Biophys. 316*, 461−469.

(38) Takeoka, S., Sakai, H., Kose, T., Mano, Y., Seino, Y., Nishide, H., and Tsuchida, E. (1997) Methemoglobin formation in hemoglobin vesicles and reduction by encapsulated thiols. *Bioconjugate Chem. 8*, 539−544.

BC050349H

Delivery of the p38 MAPkinase Inhibitor SB202190 to Angiogenic Endothelial Cells: Development of Novel RGD-Equipped and PEGylated Drug−Albumin Conjugates Using Platinum(II)-Based Drug Linker Technology

Kai Temming,*[,†,‡] Marie Lacombe,[†] Paul van der Hoeven,[†] Jai Prakash,[‡] Teresa Gonzalo,[‡] Eli C. F. Dijkers,[∥] László Orfi,[⊥] Gyorgy Kéri,[#] Klaas Poelstra,[‡] Grietje Molema,[§] and Robbert J. Kok[‡,▽]

KREATECH Biotechnology B.V., Amsterdam, The Netherlands, Department of Pharmacokinetics and Drug Delivery, Groningen University Institute of Drug Exploration, Groningen, The Netherlands, Medical Biology Section, Department of Pathology and Laboratory Medicine, University Medical Center Groningen, University of Groningen, The Netherlands, Department of Nuclear Medicine and Molecular Imaging, University Medical Center Groningen, Groningen, The Netherlands, Department of Pharmaceutical Chemistry, Semmelweis University, Budapest, Hungary, and Department of Medical Chemistry, Peptide Biochemistry Research Group of the Hungarian Academy of Sciences, Semmelweis University, Budapest, Hungary.
Received January 23, 2006; Revised Manuscript Received June 14, 2006

Endothelial cells play an important role in inflammatory disorders, as they control the recruitment of leukocytes into inflamed tissue and the formation of new blood vessels. Activation of p38MAP kinase results in the production of proinflammatory cytokines and the expression of adhesion molecules. P38MAP kinase inhibitors are therefore considered important candidates for the treatment of inflammatory disorders. In the present study, we propose a novel strategy to counteract these processes by delivery of the p38MAP kinase inhibitor SB202190 into angiogenic endothelial cells. A drug-targeting conjugate was developed by conjugation of SB202190 to human serum albumin (HSA) using a novel platinum-based linker. Specificity for angiogenic endothelial cells was introduced by conjugation of cyclic RGD-peptides via bifunctional polyethylene glycol linkers. The final products contained an average of nine SB202190 and six RGDPEG groups per albumin. The platinum-based linker displayed high stability in buffers and culture medium, but released SB202190 slowly upon competition with sulfur-containing ligands like glutathione. RGDPEG−SB−HSA bound to α_{v3}-integrin expressing endothelial cells (human umbilical cord vein endothelial cells) with low nanomolar affinity and was subsequently internalized. When HUVEC were treated with TNF to induce inflammatory events, pretreatment with RGDPEG−SB−HSA partially inhibited proinflammatory gene expression (IL-8, E-selectin; 30% inhibition) and secretion of cytokines (IL-8, 34% inhibition). We conclude that the developed RGDPEG−SB−HSA conjugates provide a novel means to counteract inflammation disorders such as rheumatoid arthritis.

INTRODUCTION

In chronic inflammatory diseases, endothelial cells are a key player in induction and progression of the disease. Proinflammatory proteins like TNFα and IL-1β induce signaling via p38MAP kinase and NFκB to activate endothelial cells (*1*). The activated endothelial cell excrete cytokines and chemokines (IL-8, IL-6), which in concert with cellular adhesion molecules (P-selectin, E-selectin, VCAM, ICAM) promote leukocyte recruitment and infiltration, and mediate vascular remodeling (*2*, *3*). Signal transduction inhibitors have been developed to interfere with these processes (*4*−*6*), and especially, inhibitors of the p38MAP kinase are considered promising candidates for treatment of chronic inflammation (*7*, *8*). Despite promising results in preclinical inflammation models, most of the p38MAP kinase inhibitors have failed in phase II clinical studies due to unacceptable side effects. Local delivery of the inhibitor to endothelial cells may overcome this problem. Previously, we developed RGD-equipped conjugates that bind to $\alpha_v\beta_3$-integrin and are internalized by endothelial cells (*9*−*11*).

In the present paper, we investigate how activation of endothelial cells can be inhibited by a drug delivery approach, in which the p38MAP kinase inhibitor SB202190 is delivered to angiogenic endothelium. For the purpose of intracellular delivery of SB202190, we designed a macromolecular conjugate of drug, carrier backbone, and homing device (Figure 1). In the past, we succesfully applied the carrier protein human serum albumin (HSA) for drug delivery to the liver (*12*). HSA functions as a natural polymer featuring long circulation times, high biocompatibility, and excellent biodegradability that can be readily modified with drugs and targeting ligands. A novel type of platinum-based linker chemistry was applied to conjugate SB202190 to HSA. This linker, which has been named universal linkage system (ULS), binds SB202190 via a coordination linkage at the pyridyl nitrogen of SB202190 (Figure 2), and another coordination bond is formed with methionine or histidine

* Corresponding author. Kai Temming, Department of Pharmacokinetics and Drug Delivery, Groningen University Institute of Drug Exploration, Antonius Deusinglaan 1, 9813 AV, Groningen, The Netherlands. Email: k.temming@rug.nl. Tel: +31 50 363 7627. Fax: +31 50 363 3247.

[†] KREATECH Biotechnology B.V.

[‡] Department of Pharmacokinetics and Drug Delivery, Groningen University Institute of Drug Exploration.

[§] Department of Pathology and Laboratory Medicine, University Medical Center Groningen.

[∥] Department of Nuclear Medicine and Molecular Imaging, University Medical Center Groningen.

[⊥] Department of Pharmaceutical Chemistry, Semmelweis University.

[#] Peptide Biochemistry Research Group of the Hungarian Academy of Sciences, Semmelweis University.

[▽] Present affiliation: Department of Pharmaceutics, Utrecht University, The Netherlands.

10.1021/bc0600158 CCC: $33.50 © 2006 American Chemical Society
Published on Web 08/10/2006

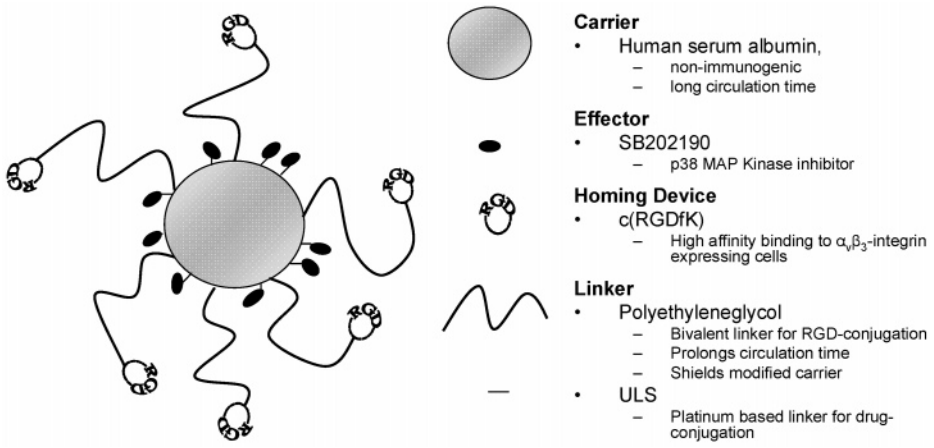

Figure 1. Schematic presentation of drug-targeting construct.

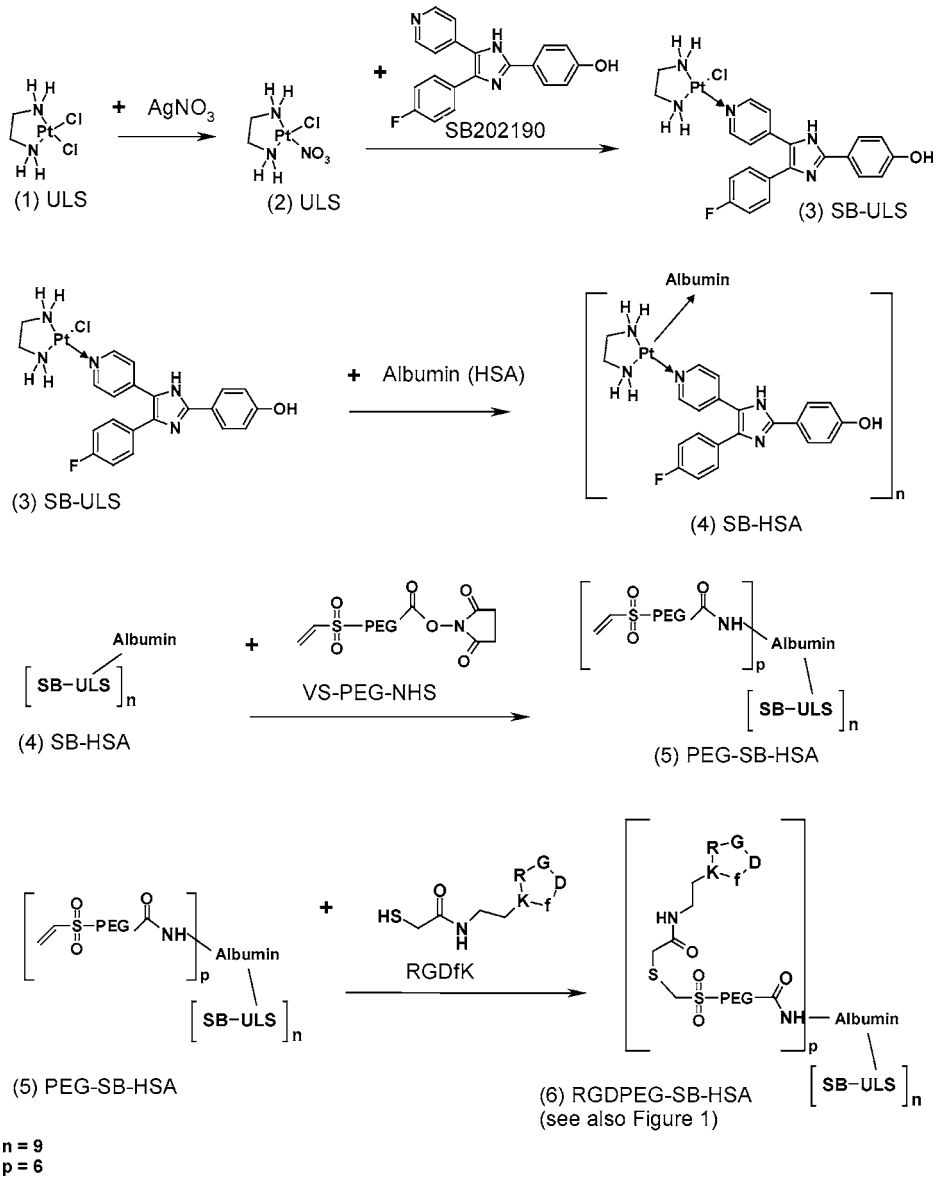

Figure 2. Reaction scheme for synthesis of RGDPEG−SB−HSA.

residues of the carrier (*13*). The stability and release properties of SB−ULS−HSA are reported in this study.

To infer specificity for angiogenic endothelial cells, we attached RGD-peptide targeting ligands to SB−HSA via bivalent 3.5 kDa PEG linkers. These PEG linkers will shield the modifications in the albumin, and thereby will prevent nonspecific uptake, prolong circulation times, and even might lead to passive retention in the leaky vasculature in inflamed tissue (*14*). The appended targeting ligand, cyclic RGDfK pentapeptide, is known to bind with high affinity and specificity to $\alpha_v\beta_3$-integrin, which is expressed in high amounts on angiogenic endothelium (*15*, *16*). Excessive angiogenesis is part of the pathology of

chronic inflammatory disease like rheumatoid arthritis or Crohn's disease. Expression of $\alpha_v\beta_3$-integrin is minimal on resting endothelial cells and highly limited in other healthy tissue. Significant amounts of $\alpha_v\beta_3$-integrin have only been found in osteoclasts (*17*). The restricted expression profile of endothelial cells makes it an ideal target for drug delivery purposes. Moreover, the endothelium is in direct contact with the systemic circulation, which renders these target cells easily accessible for macromolecules and particulate delivery systems. Vascular targeting strategies are therefore an exciting option for therapeutic intervention in chronic inflammation (*18*).

We now report on the synthesis and characterization of the RGDPEG−SB−HSA conjugate. The targeting potential of the product was evaluated on human umbilical cord vein endothelial cells (HUVEC), and pharmacological effects of the delivered drug were studied by its effects on the expression of TNFα-induced gene expression and cytokine secretion.

MATERIALS AND METHODS

Synthesis and Purification of RGDPEG−SB−HSA Conjugate. *Synthesis of SB−ULS. Cis*-[Pt(ethylenediamine)nitrate-chloride] (referred to as ULS, KREATECH Biotechnology, Amsterdam, The Netherlands) was synthesized by reacting *cis*-[Pt(ethylenediamine)dichloride] in *N*,*N*′-dimethylformamide (5 mg/mL) with 1 molar equiv of $AgNO_3$ (51 mM in *N*,*N*′-dimethylformamide (DMF)). Precipitated silver chloride was removed by centrifugation. SB202190 ((4-(fluorophenyl)-2-(4-hydroxyphenyl)-5-(4-pyridyl)-1*H*-imidazole, obtained from L.C. Laboratories, Woburn, MA) was dissolved in DMF at a concentration of 10 mg/mL. Then, 440 μL of the ULS solution (5.18 μmol) was added to 180 μL of the SB202190 solution (5.43 μmol). The resulting solution was heated at 37 °C for 3 h, and the reaction was followed by analytical HPLC using a Luna2 C18 column that was maintained at 40 °C. The mobile phase consisted of a binary solvent system of triethylammonium acetate (100 mM pH 5.0)/acetonitrile 90:10 (solvent A) and triethylammonium acetate (100 mM pH 5.0)/acetonitrile 70:30 (solvent B). The column was eluted at a flow rate of 1.1 mL/min. Compounds were eluted at a stepwise gradient (0% B from 0−4 min; 0−46% B from 4−17 min; 46−100% B from 17−19 min; 100% B from 19−25 min; 100−0% B from 25−27 min; 0% B from 27−34 min). SB202190 eluted at 14.7 min (33.6% B) and SB−ULS eluted earlier (21.8% B). After the reaction was completed, the mixture was evaporated to dryness under reduced pressure, affording a pale yellow solid (yield 92%). SB202190−ULS was analyzed by HPLC ^{1}H NMR and electronspray mass spectrometry.

^{1}H NMR of free SB202190 (CD_3OD): δ_H 6.88 (d, $J = 8.74$ Hz, 2H, $F(CHCH)_2$), 7.17 (m, 2H, $N(CHCH)_2$), 7.50 (m, 4H, $(CHCH)_2OH$), 7.82 (d, $J = 8.68$ Hz, 2H, $F(CHCH)_2$), 8.41 (m, 2H, $N(CHCH)_2$) ppm.

^{1}H NMR of SB202190−ULS (CD_3OD): δ_H 2.59 (m, 4H, $H_2N(CH_2)_2NH_2$), 5.58 (s, 2H, NH_2), 5.91 (s, 2H, NH_2), 6.89 (d, $J = 8.75$ Hz, 2H, $F(CHCH)_2$), 7.22 (m, 2H, $N(CHCH)_2$), 7.53 (m, 4H, $(CHCH)_2OH$), 7.82 (d, $J = 8.73$ Hz, 2H, $F(CHCH)_2$), 8.52 (m, 2H, $N(CHCH)_2$) ppm.

Mass spectrometry of SB202190−ULS (ESI^+): Theoretical mass *m*/*z* of SB−ULS: 620.97 [M]. Detected masses *m*/*z*: 622 $[M + H]^+$, 585 $[M - Cl^- - H^+]^+$.

Starting material of ULS was consumed completely, and formation of a new compound was observed by HPLC analysis. This new peak was SB−ULS as confirmed by LC-MS. SB−ULS was used without further purification in the next reaction step.

Synthesis of SB−ULS−HSA. HSA (22 mg, 325 nmol) was dissolved in 1 mL of 20 mM tricine−NaOH/$NaNO_3$ buffer pH 8.5. SB202190−ULS (3250 nmol) was added in tenfold molar excess, and the mixture was reacted for 24 h at 37 °C, after which nonreacted SB−ULS was removed by dialysis against PBS at 4° C using Slide-A-Lyzer dialysis cassettes (MWCO 10 000 Da, Pierce). The product was sterilized by filtration via a 0.2 μm filter and stored at −20 °C. Conjugation of SB−ULS to the protein was verified by UV analysis at 364 nm. SB−ULS−HSA displayed a specific absorbance at this wavelength ($\epsilon = 13\,955\ M^{-1}\ cm^{-1}$), not found in HSA. SB−ULS−HSA was furthermore characterized for protein content, drug content, and platinum linker content as described below.

Synthesis of RGDPEG−SB−HSA. In the final reaction step, SB−ULS−HSA was modified with PEG and RGD−peptide. SB−ULS−HSA (147 nmol) dissolved in PBS was incubated with a 50-fold molar excess of vinylsulfone−polyethylene glycol−*N*-hydroxysuccinimide ester (VNS−PEG−NHS; Nektar, Alabama; 3.5 kDa, 20 mg/mL in water, 7.39 μmol), which was added dropwise. The mixture was protected from light with aluminum foil and incubated for 1 h at room temperature while gently shaking on a spiramix. Meanwhile, the RGD-peptide c(RGDf(ϵ-*S*-acetylthioacetyl)K) (Ansynth Service, Roosendaal, The Netherlands) was dissolved at 10 mg/mL in a 1:4 acetonitrile/water mixture. The peptide (8.085 μmol) was added dropwise to the reaction mixture in a 55-fold molar excess, after which hydroxylamine was added to a final concentration of 50 mM. Reactions were carried out overnight at room temperature while protecting from light. Remaining VNS groups were quenched by addition of cysteine (8.085 μmol; equivalent to the amount of RGD-peptide), after which the product was dialyzed against PBS, and finally purified by size exclusion chromatography (SEC) on a Superdex200 column on an Äkta System (GE Healthcare, Uppsala, Sweden) using PBS at 0.5 mL/min as the mobile phase. Eluting peaks were monitored simultaneously at 214, 280, and 364 nm. The final products RGDPEG−SB−HSA and RADPEG−SB−HSA were stored at −20 °C. The control conjugate RADPEG−SB−HSA was prepared according to the same protocol with a c(RADf(ϵ-*S*-acetylthioacetyl)K) peptide.

Characterization of RGDPEG−SB−HSA. Protein content was evaluated using BCA protein assay kit (Pierce). Free drug and conjugated drug content were analyzed by isocratic HPLC using a Waters system (Massachusetts) with a C18 μBondapak column and a UV detector operating at 254 nm. SB202190 was eluted with a mixture of water/acetonitrile/trifluoroacetic acid 20/80/0.1 at 1 mL/min. The absence of free SB202190 and SB−ULS in the drug-targeting preparation was determined by analysis of PBS diluted samples (retention times: SB202190, 8.7 min; SB-ULS, 11 min). The amount of SB202190 conjugated to the carrier was determined after release of the drug by overnight incubation with 0.5 M KSCN in PBS at 80 °C. The cooled samples were injected into the HPLC without further sample pretreatment or stored at −20 °C for later HPLC analysis.

The ULS-linker content was evaluated by inductive coupled plasma atomic emission spectroscopy (ICP-AES) at the specific wavelengths of platinum (214.424 and 265.945 nm) on a VISTA AX CCD Simultaneous ICP-AES (Varian, Palo Alto, CA). Standard solutions were made with cisplatin, and yttrium was used as internal standard (360.074 nm).

Intermediate and final products were subjected to analytical SEC to reveal increases in size, purity, and grade of aggregation.

SDS-PAGE (12% ready gels in a mini-Protean II system; Bio-Rad, Veenendaal, The Netherlands) followed by Western blot detection with an in-house-prepared anti-RGD antiserum was performed to detect the presence of RGD-peptide conjugated to the PEGylated albumins (*9*). Duplicate gels were either stained for protein (Coomassie Brilliant Blue staining) or blotted on a PVDF membrane (Roche, Mannheim, Germany). The

membrane was blocked with bovine serum albumin (BSA) and subsequently incubated with rabbit anti-RGD antiserum. The signal was amplified with a polyclonal goat anti-rabbit IgG conjugated with horseradish peroxidase (GARPO, DAKO). Peroxidase was visualized by incubation with 3-amino-9-ethylcarbazole (AEC, Sigma).

The grade of PEGylation was accurately determined by MALDI-TOF analysis using a Voyager-DE PRO workstation (Applied Biosystems). HSA, SB−HSA, and RGDPEG−SB−HSA were dissolved at a concentration of 1 mg/mL in 50:50:0.1 methanol/water/acetic acid. A 1 μL aliquot was mixed with 1 μL of matrix (20 mg/mL sinapinic acid in 60:40:0.1 water/acetonitrile/trifluoroacetic acid), transferred onto a stainless steel sample holder, and dried before being introduced into the mass spectrometer. Mass spectra were obtained by averaging the signals from 100 laser shots. Spectra were calibrated using BSA as a control. MALDI-TOF analysis of BSA provided, among others, signals of single-charged monomeric BSA and of the single-charged dimer of BSA. Our products displayed masses that were inbetween these two calibration peaks. The number of RGDPEG groups bound per albumin was calculated from the averaged masses of the products.

Stability and Drug Release Properties of the SB−ULS Linkage. Appropriately diluted aliquots of SB−ULS−HSA (40 μM) were incubated for 24 h at 37 °C with different matrices to investigate the stability of the conjugate and its drug-releasing properties. Studied matrices were PBS (pH 7.4), 0.1 M sodium acetate buffer (pH 5.0), PBS or acetate buffer spiked with either 5 mM glutathione (GSH) or with 5 mM dithiothreitol (DTT), and endothelial cell (EC) medium containing 20% FCS. Complete release of SB202190 was effected by overnight incubation with 500 mM KSCN at 80 °C. 35 μL of the resulting solutions and standard solutions were treated with 100 μL of acetonitrile (3:1 v/v), vortexed, and centrifuged for 10 min to precipitate proteins. The clear supernatant was subjected to isocratic HPLC analysis as described above.

Cells. HUVEC were obtained from the UMCG Endothelial Cell Facility (*19*). Primary isolates were cultured in 1% gelatin-coated tissue culture flasks or culture wells (Corning, Costar, The Netherlands) at 37 °C under 5% CO_2/95% air. The culture medium, hereafter referred to as EC medium, consisted of RPMI 1640 (BioWittaker, Verviers, Belgium) supplemented with 20% heat-inactivated fetal calf serum (Integro, Zaandam, The Netherlands), 2 mM L-glutamine (Invitrogen, Breda, The Netherlands), 5 U/mL heparin (Leo Pharmaceutical Products, Weesp, The Netherlands), 100 U/mL penicillin (Yamanouchi Pharma, Leiderdorp, The Netherlands), 100 g/mL streptomycin (Radiumfarma-Fisiopharma, Italy), and 50 μg/mL endothelial cell growth factor supplement extracted from bovine brain. After attaining confluence, cells were detached from the surface by trypsin/EDTA (0.5/0.2 mg/mL in PBS) treatment and split into 1:3 ratio. Cells were used up to passage four.

Binding and Uptake of RGDPEG−SB−HSA to HUVEC. Binding affinity of RGDPEG−SB−HSA for target cells was determined by competitive binding studies with ^{125}I-labeled echistatin as $\alpha_v\beta_3$-integrin specific radioligand (*20*). Echistatin was radiolabeled using the chloramine T method (*21*). On the day of the experiment, ^{125}I-echistatin was purified using a PD-10 column (GE Healthcare). Confluent monolayers of HUVEC in 24-well plates (Costar) were incubated with 100 000 cpm ^{125}I-echistatin in the presence of serial dilutions of RGDPEG−SB−HSA in binding buffer (50 mM Tris−HCl, pH 7.4, 150 mM NaCl, 1 mM $CaCl_2$, 1 mM $MgCl_2$, 1 mM $MnCl_2$, and 1% BSA) at 4 °C for 4 h (*10*). Subsequently, the supernatant was harvested, and cells were washed three times with binding buffer and lysed with 1 M NaOH. Radioactivity was counted in a Packard RIASTAR multiwell gamma counter (GMI, Minnesota). Data were analyzed by nonlinear regression using the GraphPad Prism program (GraphPad Software).

To determine the specificity of RGDPEG−SB−HSA binding and its uptake by target cells, HUVEC were incubated with ^{89}Zr-radiolabeled RGDPEG−SB−HSA. For radiolabeling, 3.73 nmol RGDPEG−SB−HSA was mixed with 18.6 nmol of the chelator TFP−*N*-succinyldesferal−Fe(III) (desferal) (*22*) in 0.1 M $NaHCO_3$, pH 8.5. After an incubation period of 30 min, the reaction mixture was purified on a Hitrap desalting column (GE Healthcare). The conjugation of desferal to the product was confirmed by measurement of its UV absorbance at 430 nm. Fe(III) was replaced with radioactive ^{89}Zr (supplied by Cyclotron BV, Amsterdam) as described (*22*), but the incorporation of zirconium was performed at pH 6.8 and the product was purified using a centricon column (Millipore, Billerica, MA). Radiochemical purity was 96% as determined by trichloroacetic acid precipitation, and specific activity was 740 000 cpm/μg. Specificity of binding was studied by incubating confluent HUVEC layers (24 well plates) with 70 000 cpm ^{89}Zr−RGDPEG−SB−HSA in the presence of an excess of different competitors at 4 °C for 4 h, while uptake was studied by incubating the cells with 70 000 cpm ^{89}Zr−RGDPEG−SB−HSA at 37 °C for 4 h and 8 h. Supernatant and cell-associated radioactivity was harvested as described above, and radioactivity was counted on a 1282 COMPUGAMMA CS (Perkin-Elmer, Boston, MA).

Effect of RGDPEG−SB−HSA on Cell Viability. Platinum-related toxicity of RGDPEG−SB−HSA and ULS-containing intermediate products was evaluated by incubating HUVEC cells for 3 days with EC medium spiked with RGDPEG−SB−HSA (100 μg/mL), SB−ULS (100 μM), ULS (100 μM), or cisplatin (100 μM). The effect on cell proliferation and viability was detected by MTS assay (Promega) according to the manufacturer's protocol.

Effect of RGDPEG−SB−HSA on Inflammatory Events. Effect of targeted SB202190 on transcription and translation of inflammatory genes and proteins was evaluated using quantitative real time PCR (rtPCR) and enzyme-linked immunosorbent assay (ELISA) as described (*23*). In short, confluent monolayers of HUVEC in 12-well plates were incubated with EC medium spiked with RGDPEG−SB−HSA conjugate, RAD-containing control conjugate, free drug, RGDPEG−HSA without drug or an equivalent volume of PBS. After 24 h, the cells were activated by the addition of 5 ng TNFα. After an additional 24 h, medium was harvested, and cells were lysed for RNA isolation (Absolutely RNA Microprep Kit, Stratagene, CA). The amount of isolated RNA was quantified by NanoDrop according to the manufacturer's protocol. Equal amounts of RNA were translated to cDNA by SuperScript III First-Strand Synthesis System (Invitrogen). cDNA was diluted to 10 ng/μL concentration after RT reaction. Exons overlapping primers and Minor Groove Binder (MGB) probes used for RT-PCR were purchased as Assay-on-Demand from Applied Biosystems (Niewekerk a/d IJssel, The Netherlands). Expression levels of human IL-8, E-selectin, and GAPDH were evaluated by RT-PCR on an ABI Prism 7900HT sequence detection system (Applied Biosystems).

Harvested HUVEC supernatants were analyzed for IL-8 production by ELISA using a MoAb.anti-IL-8 (R&D Systems, Minneapolis, MN). The signal was amplified by a biotinylated secondary antibody (polyclonal swine anti-human IL-8; R&D) followed by streptavidin-E+ (CLB, Amsterdam, The Netherlands). Color development was performed using tetramethylbenzidine (Roth, Karlsruhe, Germany) as substrate for the peroxidase.

Statistical Analysis. Statistical analysis was performed using Student's two-tailed *t*-test, assuming equal variances. Difference were considered to be significant when $p < 0.05$ unless otherwise stated.

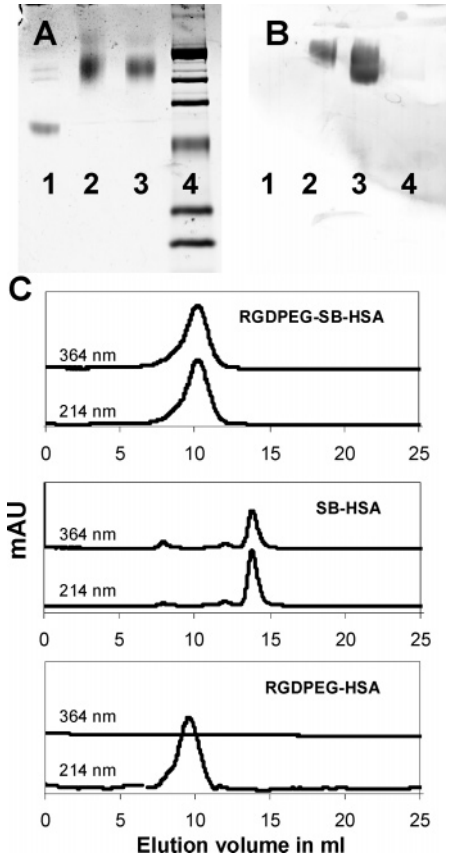

Figure 3. Characterization of RGDPEG−SB−HSA demonstrated successful introduction of SB202190, PEG, and RGD peptide. SDS-PAGE stained for protein with CBB (A) and Western blot with anti RGD antibody (B) of the same gel give proof of RGD-conjugation. The gel shows SB−HSA (1), RGDPEG−SB−HSA (2), RGDPEG−HSA (3), and molecular size marker (4). Size exclusion chromatography (C) demonstrated an increase in size of RGDPEG−SB−HSA compared to SB−HSA detected at 214 nm (bottom line of each graph) due to introduced PEG. SB−ULS absorbed also at 364 nm (upper line of each graph), which is indicative of conjugated SB202190. This peak was detected for RGDPEG−SB−HSA and SB−HSA but not for RGD-PEG−HSA.

RESULTS

Preparation and Characterization of RGDPEG−SB−HSA. We applied a novel type of drug linker to couple SB202190 to our albumin carrier (Figure 2). The ULS linker provided a rapid and straightforward alternative to conventional linkers for conjugation of SB202190. The synthesis of SB−ULS−HSA proceeded at an overall yield of 80% over the combined synthesis steps. In contrast, we also studied the conjugation of SB202190 via ester or carbamate linkages at the hydroxyl group of the drug, which eventually led to products at low yield and undesired fast drug release rates in serum (Prakash et al., submitted).

The first synthesis step between SB202190 and the linker yielded the desired 1:1 SB−ULS species as confirmed by mass spectrometry analysis. ^{1}H NMR studies indicated that binding of SB202190 took place via coordination of the N-donor of the pyridine ring, because only the protons of the pyridyl ring were shifted with the more prominent shift for the protons closest to the nitrogen (8.41 ppm to 8.52 ppm). Additionally, peak splitting was observed for these protons typical for an extra paramagnetic group like platinum. Conjugation of SB−ULS to HSA was confirmed by several techniques. First, the absorbance of SB−ULS at 364 nm was detectable in the SB−HSA product peak, while unmodified albumin had no UV absorption at this wavelength. Monitoring of the 364 nm absorbance also confirmed that SB−ULS remained attached to the carrier during subsequent PEGylation and purification procedures (Figure 3). Second, the drug load of SB−HSA was determined by release of the drug and subsequent HPLC detection (Table 1), and the number of ULS groups attached to the protein was determined by ICP-AES Pt analysis. Both analyses yielded similar numbers of conjugated SB/HSA and ULS/HSA, illustrating that SB202190 was bound to HSA via ULS. Free SB or SB−ULS levels in the conjugate were below the detection limit of the HPLC method (>0.3%).

The SB−HSA product was modified with RGD peptides via a 3.5 kDa PEG linker. Successful PEGylation and purity of the product was shown by size exclusion chromatography (SEC, Figure 3). SEC also revealed the absence of aggregates. Final proof of binding of the RGD peptide to the distal end of the PEG-linker was given by SDS-PAGE and Western blot with an anti-RGD antibody (Figure 3). The molecular weight (MW) of the products was determined by MALDI-TOF analysis, and differences in MW were used to calculate the number of RGDPEG bound per albumin (Table 1). On average, SB−ULS−HSA was modified with 6.3 RGDPEG/HSA, while 7.1 RGD-PEG/HSA were bound to parental HSA.

SB202190 is Released via Competition with Sulfur Donors. We studied the stability and release properties of the novel SB−ULS−HSA conjugate in different conditions. All incubations were performed at 37 °C for 24 h (Figure 4). Only minimal drug release was observed in buffers or culture medium containing 20% serum, indicating the high stability of the SB202190−ULS linkage. However, addition of thiols like GSH and DTT accelerated the release of the drug. Complete release of the drug could be effected by incubating the conjugate at 80° C with a large excess of the thiocyanate (data not shown). Since thiols are preferred ligands for platinum, competitive displacement seems a likely release mechanism. These results are in good agreement with prior studies in our group with other drug−ULS−albumin (*24*). Changing the pH from 7.4 (cytosolic) to pH 5.0 (lysosomal) gave a reduction in drug release by DTT, while GSH-induced release was not affected.

RGDPEG−SB−HSA Binds via $\alpha_v\beta_3$-Integrin to Target Cells and Is Internalized. Binding constants of RGDPEG−SB−HSA for target cells have been evaluated in competition experiments with the known $\alpha_v\beta_3$-integrin ligand ^{125}I-echistatin as shown in Figure 5A. The RGDPEG−SB−HSA conjugate demonstrated a higher affinity for $\alpha_v\beta_3$-integrin (IC_{50} = 71.4 nM; Table 2) compared to the single peptide (IC_{50} = 383 nM), but a lower affinity than RGDPEG−HSA (IC_{50} = 11.7 nM), which had been equipped with a higher amount of RGD groups.

Table 1. Characterization of Drug Targeting Conjugates (n.a., not applicable; n.d. not determined; −, negative; +, positive)

	number of SB bound per HSA[a]	number of ULS bound per HSA[a]	number of RGDPEG bound per HSA[b]	MW in kDa[b]	Western blot for RGD[b]
SB−HSA	9.1	7.8	n.a.	69.2	−
RGDPEG−SB−HSA	9.6	8.0	6.3	95.2	+
RADPEG−SB−HSA	7.6	6.1	n.d.	n.d	n.a.
RGDPEG−HSA	n.a.	n.a.	7.1	96.1	+

[a] average of duplicate analysis. [b] single analysis.

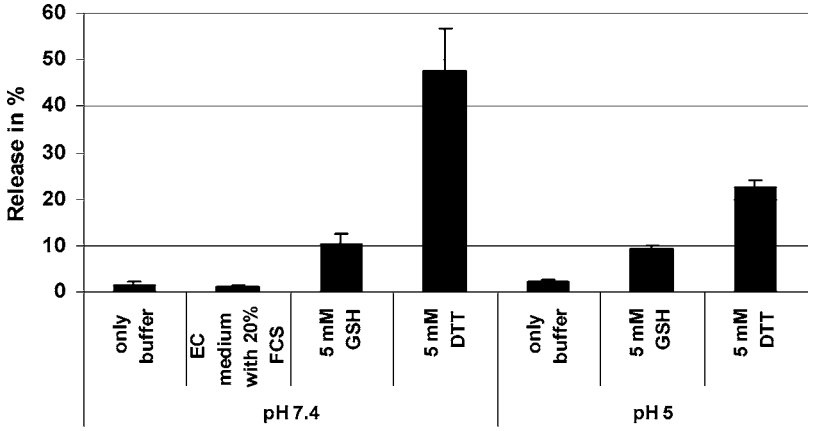

Figure 4. Release of SB202190. SB−ULS−HSA was incubated for 24 h at 37 °C with 5 mM GSH or DTT at pH 5 in acetic acid buffer or at pH 7.4 in PBS and in endothelial cell medium with 20% FCS. Released drug was determined by HPLC.

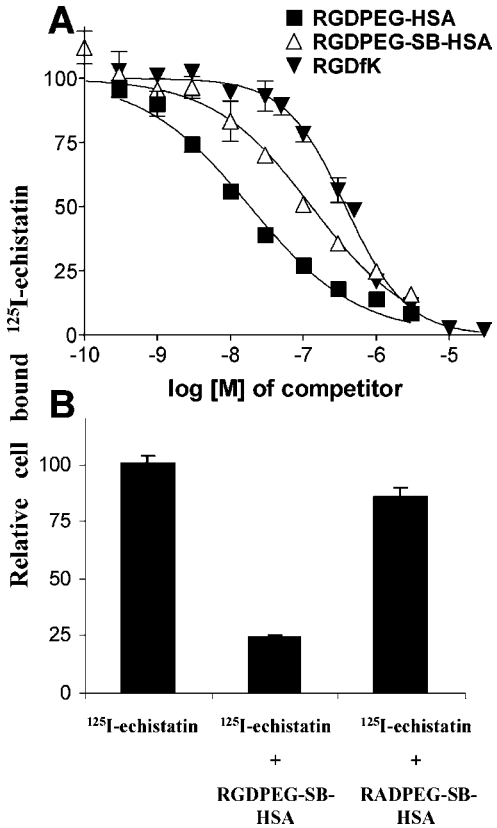

Figure 5. Binding properties of RGDPEG−SB−HSA. (A) shows competitive displacement of ^{125}I-echistatin with RGDPEG−HSA (squares), RGDPEG−SB−HSA (open triangles), and RGDfK (closed triangles). (B) demonstrates displacement of ^{125}I-echistatin by RGD-PEG−SB−HSA but not by control conjugate RADPEG−SB−HSA, both at 1 μM.

Table 2. IC_{50} of Binding to $\alpha_v\beta_3$-Integrin and the Fold Increase in Affinity Compared to the Single Peptide

	IC_{50} in nM	fold increase in affinity
RADfK	>10 000	−
RADPEG−SB−HSA	>3000	−
RGDfK	383	1
RGDPEG−SB−HSA	71.4	5.4
RGDPEG−HSA	11.7	33

RADPEG−SB−HSA could not displace ^{125}I-echistatin at any of the concentrations tested (Figure 5B).

We also studied binding and uptake of ^{89}Zr−RGDPEG−SB−HSA by endothelial cells. ^{89}Zr, captured by the chelator desferal, is highly stable, and its hydrophilicity will entrap it inside cells after degradation of the carrier (*25*, *26*). Since this will prevent redistribution of the radiolabel, Zr−desferal is an ideal label for uptake studies. We attached an average of 1.7 desferal groups/HSA, which were subsequently loaded with ^{89}Zr. Such a relatively minor modification will not affect the binding of RGDPEG−SB−HSA to target cells, as was also demonstrated by comparing the binding of ^{125}I and ^{89}Zr-labeled RGDPEG−SB−HSA (data not shown). Furthermore, the extended nature of the RGDPEG ligand will prevent steric interactions between radiotracer and RGD groups.

^{89}Zr−RGDPEG−SB−HSA was incubated at 4 °C and 37 °C with HUVEC. ^{89}Zr−RGDPEG−SB−HSA binding to $\alpha_v\beta_3$-expression HUVEC could only be blocked by excess of RGD peptide but not by excess of SB−HSA (Figure 6A). This proved that binding was solely mediated by the introduced RGD peptide. Cell-associated activity was increased when incubation were carried out at 37 °C and could be further increased with prolonged incubation times (Figure 6B). This indicated active uptake of RGDPEG−SB−HSA into endothelial cells.

RGDPEG−SB−HSA Is Not Toxic to Endothelial Cells. RGDPEG−SB−HSA, SB−ULS, and free ULS tested at 100 μM did not influence the proliferation and viability of HUVEC (Figure 7). In the same concentration, cisplatin eradicated all cells, suggesting that both monofunctional ULS derivatives as well as bifunctional ULS mononitratemonochloride are not toxic, whereas cisplatin (bifunctional) is.

Effect of RGDPEG−SB−HSA on Activated HUVEC. The anti-inflammatory effects of the conjugate were investigated in TNF-activated HUVEC. TNFα induced a 20-fold upregulation in gene expression of hIL-8 and 200-fold upregulation of hE-selectin (Figure 8). Free SB202190 inhibited this upregulation up to 50%, which is in agreement with previous studies (*23*). RGDPEG−SB−HSA was tested at 21 μg/mL and 70 μg/mL, which corresponds to a drug concentration of 3 μM and 10 μM, respectively. Significant down-regulation of the studied genes was observed in all conditions, except for hE-selectin when cells were incubated with a low concentration of RGDPEG−SB−HSA. Expression of both genes was reduced for approximately 30% compared to the TNF-activated control cells ($p < 0.01$). RGDPEG−HSA, i.e., carrier without drug, and nontargeted conjugate RADPEG−SB−HSA demonstrated no inhibitory effect. RGDPEG−HSA showed even a slight upregulation of the tested genes, especially when given in the higher dose.

Similar inhibitory effects of the delivered drug were observed when IL-8 secretion in the culture medium was analyzed (Figure 9). RGDPEG−SB−HSA at both concentrations reduced the IL-8 secretion by 18% and 34% as compared to untreated cells

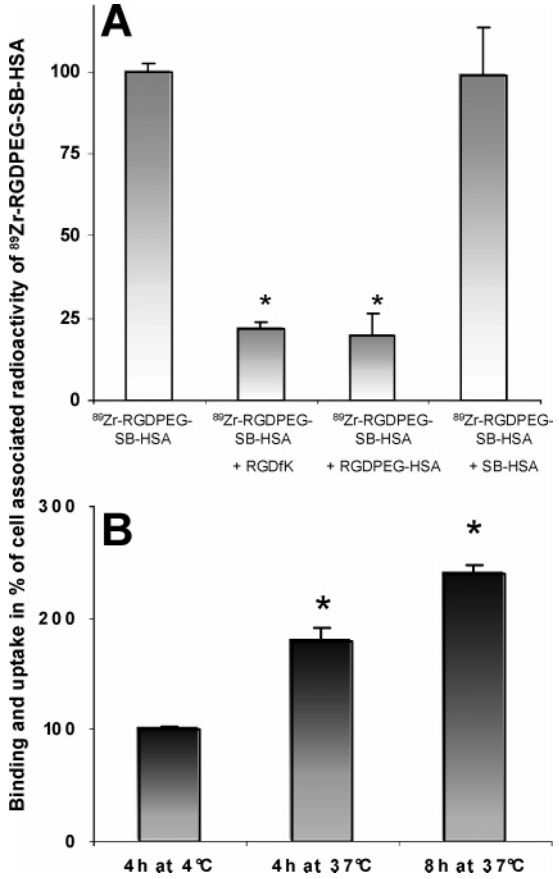

Figure 6. RGDPEG−SB−HSA binds via the introduced RGD moiety to target cells and is internalized. (A) ^{89}Zr−RGDPEG−SB−HSA was incubated with a confluent HUVEC monolayer. The addition of high excess of different competitors (RGDfK, 20 μM; RGDPEG−HSA, 1 μM; SB−HSA, 1 μM) demonstrated that RGDPEG−SB−HSA only bound via the RGD-peptide. (B) HUVEC were incubated with ^{89}Zr−RGDPEG−SB−HSA at 4 and 37 °C for 4 and 8 h to determine uptake of the drug-targeting conjugate. *$p < 0.01$ compared to no competitor in (A) and to 4 °C in (B).

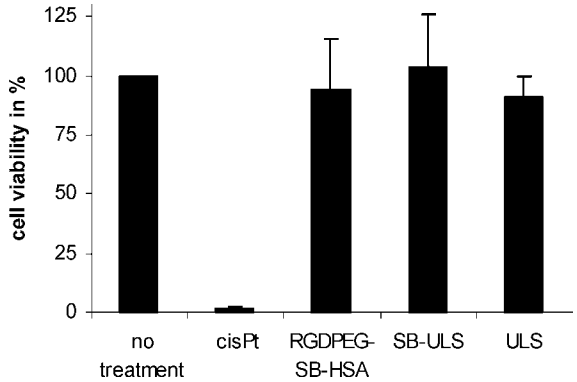

Figure 7. RGDPEG−SB−HSA and ULS containing conjugates displayed no toxicity for endothelial cells. RGDPEG−SB−HSA (100μg/mL), SB−ULS, ULS, or cisplatin (all at 100 μM) were added to EC medium and incubated for 3 days. Cell viability was assessed in comparison to nontreated control cells (=100% viability) using MTS assay.

($p < 0.01$). Control conjugates did not decrease levels of IL-8 in the medium.

DISCUSSION

In the present study, we developed an endothelial-directed conjugate for cell-specific intracellular delivery of SB202190, a potent p38MAPK inhibitor (Figure 1). We applied a novel

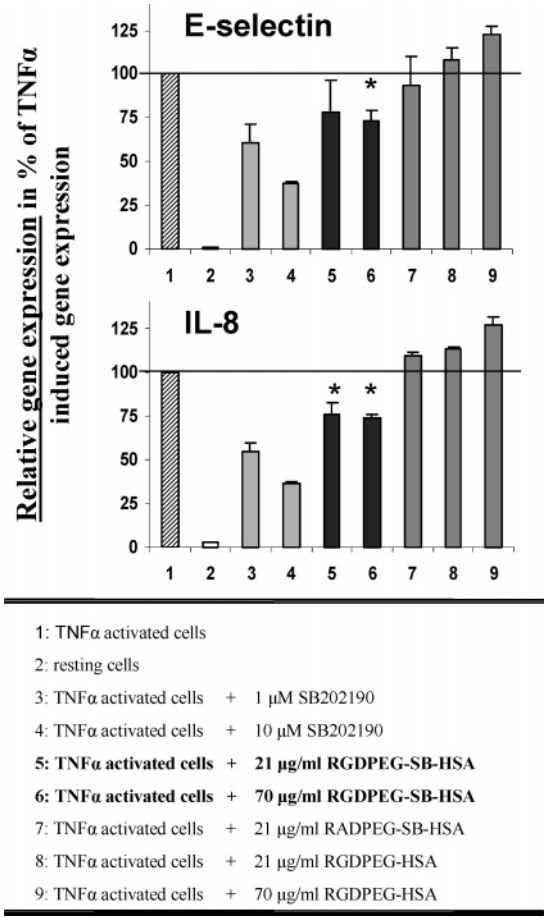

Figure 8. RGDPEG−SB−HSA delivered active SB202190 into target cells. HUVEC were preincubated with drug, drug-targeting conjugate, and control conjugates for and 24 h, after which TNFα was added. RNA was harvested after an additional 24 h of incubation. Gene expression levels of hE-selectin and hIL-8 as determined by qRT-PCR are shown. Light gray bars represent free drug, black bars represent drug-targeting conjugate, and dark gray bars represent different control conjugates. 21 μg/mL of RGDPEG−SB−HSA equals 3 μM SB202190 and 70 μg/mL equals 10 μM drug. $p < 0.01$ compared to respective control conjugates and to TNFα-treated control.

type of platinum linker for coupling of SB202190 to albumin, which provided a straightforward and robust coupling method (Figure 2). The conjugation of ULS with SB202190 took place by formation of a coordinative bond between the nitrogen of the pyridine and the Pt atom. Since aromatic nitrogens are present in many drug structures, our approach is applicable to many other drugs besides SB202190. We have recently reported on a similar linkage approach for the delivery of pentoxifyllin to hepatic stellate cells (*24*), and several other conjugates are under investigation.

We assume that the drug−ULS adduct binds to HSA by coordination to sulfur-containing residues, mostly methionine, but also with histidine residues as demonstrated earlier for other Pt(II) compounds (*27*, *28*). Our hypothesis that SB−ULS preferably binds to sulfur groups in the carrier is supported by the finding that pentoxifyllin−ULS/albumin conjugation ratios increased when HSA was first modified with a thiocarbonyl-containing targeting ligand (*24*). Similarly, elevated drug−ULS/carrier ratios were found when the kidney-selective carrier lysozyme was modified with extra methionine groups (J. Prakash et al., submitted). HSA contains only six methionine residues, which are not exposed at the protein surface. The hydrophobic character of SB−ULS will allow its binding to methionines in the core of HSA. As the number of SB−ULS per HSA exceeded

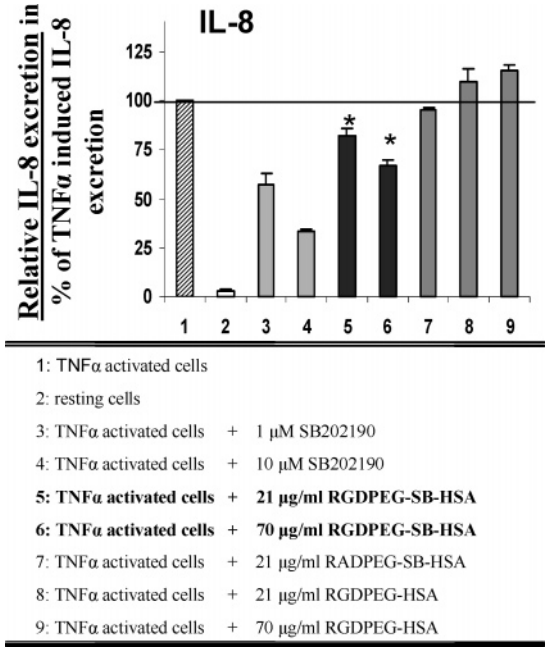

Figure 9. RGDPEG−SB−HSA treatment reduced the excretion of IL-8. HUVEC were preincubated with drug, drug-targeting conjugate, and control conjugates, and 24 h later, TNF was added. Medium was harvested after an additional 24 h of incubation. Relative levels of hIL-8 as determined by ELISA are depicted in the graph. Light gray bars represent free drug, black bars represent drug-targeting conjugate, and dark gray bars represent different control conjugates. 21 μg/mL of RGDPEG−SB−HSA equals 3 μM SB202190 and 70 μg/mL equals 10 μM SB202190. $p < 0.01$ compared to respective control conjugates and to TNFα-treated control.

the number of available methionines, it seems likely that SB−ULS is also bound to histidine or cysteine residues.

We assume that SB202190 needs to be released from the linker to exert therapeutic effects, since the pyridyl ring of SB202190 to which ULS is bound is also interacting with the ATP pocket of the p38 MAP kinase. Release of SB202190 was triggered by competition with sulfur ligands like glutathione at intracellular concentration. We have found the same release mechanism for other drug−ULS conjugates (Prakash et al., submitted) (*24*).

Conjugation of PEG and RGD peptide to SB−HSA resulted in a macromolecular conjugate that was characterized by several techniques. MALDI-TOF analysis illustrated that further modification of SB−HSA is not hampered by already bound SB202190−ULS. This was expected, given that ULS binds best to methionine residues, but also to cysteine and histidine residues, while the PEG linker reacted with amino groups of, e.g., lysine residues. The kind of RGD peptide (c(RGDfK)) used in this study binds specifically and with a high affinity to $\alpha_v\beta_3$-integrin due to the special constrained conformation. We now show that these properties are transferred to SB−HSA upon conjugation of RGD peptides. The 5.4-fold improvement in binding affinity as compared to the single peptide indicates multivalent binding of the conjugate. This is in line with earlier observations of Kok et al. (*9*) and is also relevant for receptor-mediated uptake of the conjugate, since multivalency is known to facilitate internalization and routing to lysosomes (*11*, *29*).

Platinum is an intrinsic component of ULS, and this prompted us to evaluate potential toxicity of the drug-targeting conjugate, and of ULS in particular. It is generally accepted that cisplatin toxicity involves cross-linking of DNA (*30*). The availability of a reactive ligand site at the platinum atom is essential for the toxicity of platinum(II) compounds. However, the platinum atom in RGDPEG−SB−HSA is fully coordinated, which prevents its binding with endogenous compounds. ULS can therefore only react with DNA after release of the drug or carrier. In view of the slow drug release from the construct, we expect only a slow formation of reactive platinum species in the target cells that will readily detoxified, as described for cisplatin and other platinum compounds (*31*, *32*). The absence of toxicity on HUVEC viability of ULS-containing compounds was clearly demonstrated even at high concentrations (Figure 7). Likely, glutathione adducts will be the major metabolite. We concluded that drug−ULS conjugates have no apparent toxicity despite their similarity to cisplatin. The same conclusion has been drawn for other ULS-containing drug-targeting conjugates that have been developed in our lab for the targeting to hepatic stellate cells (*24*) or kidney tubular cells (Prakash et al., submitted).

RGDPEG−SB−HSA partially inhibited the TNFα-induced activation of HUVEC, both at gene expression levels and when considering the secretion of proinflammatory cytokines (Figures 8 and 9). Since premature drug release in endothelial cell medium can be excluded on the basis of the drug release studies, we concluded that SB202190 was released after internalization of RGDPEG−SB−HSA. Although RGDPEG−SB−HSA demonstrated the anticipated effects, the observed inhibitions were lower than those of free SB202190. Several considerations may explain these differences. First, the different uptake mechanisms of conjugate and free drug will affect intracellular drug levels. The passive diffusion of a small molecule drug will be faster than the active uptake process and subsequent lysosomal degradation of a high molecular weight drug-targeting conjugate. Typically, inhibiting drugs are preincubated with the cells for about 1 h. Since such a short period would allow only limited uptake of the conjugate, we have preincubated the cells for 24 h with the compounds. Apparently, this had not resulted in extensive accumulation of active drug in the cells. Another explanation may be that intracellularly released SB202190 diffused out of the target cells. Such a redistribution of the compound by diffusion or active transport might limit the applicability of such conjugates in vivo. It therefore seems interesting to study the intracellular drug levels of free and conjugate-bound drug. This, however, proved to be impossible with the available HPLC techniques, as these have a relatively low sensitivity. Alternatively, one might prevent redistribution by delivering charged or hydrophilic drug molecules.

When considering the in vivo applicability of our approach, several studies support our strategy. The feasibility of RGD-mediated targeting for chronic inflammatory disorders has been demonstrated by RGD-peptide imaging agents that specifically accumulate in chronically inflamed tissue but not in acutely inflamed tissue (*33*, *34*). Furthermore, Gerlag et al. have treated mice suffering from collagen-induced arthritis with an RGD-targeted proapoptotic peptide (*35*). Their approach induced apoptosis of synovial blood vessels and significantly decreased clinical arthritis. We, however, aimed for the development of a therapeutic agent that can block inflammatory signaling pathways without compromising the viability of the vasculature. We furthermore expect improved pharmacokinetics of our macromolecular product as compared to smaller peptides or free SB202190. Free SB202190 is rapidly cleared from the circulation with a $t_{1/2}\alpha$ of 4.3 min in rats and has no affinity for inflamed tissue (*36*). In contrast, RGDPEG−SB−HSA can accumulate in inflamed endothelium in analogy to the RGD-peptide-based imaging agents. The long PEG linker will shield the modified albumin to prevent unspecific uptake and can increase the circulation time (*37*). Passive retention of the PEGylated drug carrier might also occur due to enhanced permeability of endothelium in inflamed tissues (*14*). In principle, RGDPEG−SB−HSA will be administered intravenously rather than by local injection in the joints. Since the

endothelium is in direct contact with the systemic circulation, these target cells can be reached from within the circulation. Thus, painful injections into inflamed joints would not be necessary.

In conclusion, we have prepared a novel drug-targeting conjugate in which we linked the drug via platinum coordination chemistry to the carrier. This RGDPEG−SB−HSA bound with high affinity and specificity to $\alpha_v\beta_3$-integrin and was subsequently internalized. The delivered drug was furthermore capable of interfering in inflammatory signaling cascades. These results show the potential of MAPkinase inhibitor delivery as a new strategy to counteract chronic inflammatory disorders.

ACKNOWLEDGMENT

J. H. Pol from the Department of Nuclear Medicine is kindly acknowledged for radiolabeling of echistatin, H. E. Moorlag from the Endothelial Cell Facility UMCG for skillful isolation and culturing of HUVEC, B. Doornbos-van der Meer for assistance with ELISA, and J. Ijmker for platinum detection using ICP-AES. We also acknowledge Prof. G. A. M. S. van Dongen and Ir. L. R. Perk of the VUmc for providing the desferal labeling technology. Our colleagues from KREATECH are acknowledged for critical review of the manuscript. This work was made possible by grants from Marie Curie (HPMI-CT-2002-00218), SenterNovem (TSGE1083), and Hungarian Scientific Research Fund OTKA (T-049478).

LITERATURE CITED

(1) Schett, G., Tohidast-Akrad, M., Smolen, J. S., Schmid, B. J., Steiner, C. W., Bitzan, P., Zenz, P., Redlich, K., Xu, Q., and Steiner, G. (2000) Activation, differential localization, and regulation of the stress-activated protein kinases, extracellular signal-regulated kinase, c-JUN N-terminal kinase, and p38 mitogen-activated protein kinase, in synovial tissue and cells in rheumatoid arthritis. *Arthritis Rheum. 43*, 2501−2512.

(2) Griffioen, A. W., and Molema, G. (2000) Angiogenesis: potentials for pharmacologic intervention in the treatment of cancer, cardiovascular diseases, and chronic inflammation. *Pharmacol. Rev. 52*, 237−268.

(3) Szekanecz, Z., and Koch, A. E. (2004) Vascular endothelium and immune responses: implications for inflammation and angiogenesis. *Rheum. Dis. Clin. North Am. 30*, 97−114.

(4) Kuldo, J. M., Ogawara, K. I., Werner, N., Asgeirsdottir, S. A., Kamps, J. A., Kok, R. J., and Molema, G. (2005) Molecular pathways of endothelial cell activation for (targeted) pharmacological intervention of chronic inflammatory diseases. *Curr. Vasc. Pharmacol. 3*, 11−39.

(5) Karin, M. (2005) Inflammation-activated protein kinases as targets for drug development. *Proc. Am. Thorac. Soc. 2*, 386−390.

(6) Schieven, G. L. (2005) The biology of p38 kinase: a central role in inflammation. *Curr. Top. Med. Chem. 5*, 921−928.

(7) Smolen, J. S., and Steiner, G. (2003) Therapeutic strategies for rheumatoid arthritis. *Nat. Rev. Drug Discovery 2*, 473−488.

(8) Kumar, S., Boehm, J., and Lee, J. C. (2003) p38 MAP kinases: key signalling molecules as therapeutic targets for inflammatory diseases. *Nat. Rev. Drug Discovery 2*, 717−726.

(9) Kok, R. J., Schraa, A. J., Bos, E. J., Moorlag, H. E., Asgeirsdottir, S. A., Everts, M., Meijer, D. K., and Molema, G. (2002) Preparation and functional evaluation of RGD-modified proteins as alpha(v) beta-(3) integrin directed therapeutics. *Bioconjugate Chem. 13*, 128−135.

(10) Schraa, A. J., Kok, R. J., Berendsen, A. D., Moorlag, H. E., Bos, E. J., Meijer, D. K., de Leij, L. F., and Molema, G. (2002) Endothelial cells internalize and degrade RGD-modified proteins developed for tumor vasculature targeting. *J. Controlled Release 83*, 241−251.

(11) Schraa, A. J., Kok, R. J., Moorlag, H. E., Bos, E. J., Proost, J. H., Meijer, D. K., de Leij, L. F., and Molema, G. (2002) Targeting of RGD-modified proteins to tumor vasculature: a pharmacokinetic and cellular distribution study. *Int. J. Cancer 102*, 469−475.

(12) Beljaars, L., Poelstra, K., Molema, G., and Meijer, D. K. (1998) Targeting of sugar- and charge-modified albumins to fibrotic rat livers: the accessibility of hepatic cells after chronic bile duct ligation. *J. Hepatol. 29*, 579−588.

(13) van Gijlswijk, R. P., Talman, E. G., Janssen, P. J., Snoeijers, S. S., Killian, J., Tanke, H. J., and Heetebrij, R. J. (2001) Universal Linkage System: versatile nucleic acid labeling technique. *Expert Rev. Mol. Diagn. 1*, 81−91.

(14) Maeda, H., Fang, J., Inutsuka, T., and Kitamoto, Y. (2003) Vascular permeability enhancement in solid tumor: various factors, mechanisms involved and its implications. *Int. Immunopharmacol. 3*, 319−328.

(15) Pablos, J. L., Santiago, B., Galindo, M., Torres, C., Brehmer, M. T., Blanco, F. J., and Garcia-Lazaro, F. J. (2003) Synoviocyte-derived CXCL12 is displayed on endothelium and induces angiogenesis in rheumatoid arthritis. *J. Immunol. 170*, 2147−2152.

(16) Creamer, D., Allen, M., Sousa, A., Poston, R., and Barker, J. (1995) Altered vascular endothelium integrin expression in psoriasis. *Am. J. Pathol. 147*, 1661−1667.

(17) Eliceiri, B. P., and Cheresh, D. A. (1999) The role of alphav integrins during angiogenesis: insights into potential mechanisms of action and clinical development. *J. Clin. Invest. 103*, 1227−1230.

(18) Schraa, A. J., Everts, M., Kok, R. J., Asgeirsdottir, S. A., Meijer, D. K., de Leij, L. F., and Molema, G. (2002) Development of vasculature targeting strategies for the treatment of cancer and chronic inflammatory diseases. *Biotechnol. Annu. Rev. 8*, 133−165.

(19) Mulder, A. B., Blom, N. R., Smit, J. W., Ruiters, M. H., van der, M. J., Halie, M. R., and Bom, V. J. (1995) Basal tissue factor expression in endothelial cell cultures is caused by contaminating smooth muscle cells. Reduction by using chymotrypsin instead of collagenase. *Thromb. Res. 80*, 399−411.

(20) Kumar, C. C., Nie, H., Rogers, C. P., Malkowski, M., Maxwell, E., Catino, J. J., and Armstrong, L. (1997) Biochemical characterization of the binding of echistatin to integrin alphavbeta3 receptor, *J. Pharmacol. Exp. Ther. 283*, 843−853.

(21) Hunter, W. M., and Greenwood, F. C. (1962) Preparation of iodine-131 labelled human growth hormone of high specific activity. *Nature (London) 194*, 495−496.

(22) Verel, I., Visser, G. W., Boellaard, R., Stigter-van, W. M., Snow, G. B., and van Dongen, G. A. (2003) 89Zr immuno-PET: comprehensive procedures for the production of 89Zr-labeled monoclonal antibodies. *J. Nucl. Med. 44*, 1271−1281.

(23) Kuldo, J. M., Westra, J., Asgeirsdottir, S. A., Kok, R. J., Oosterhuis, K., Rots, M. G., Schouten, J. P., Limburg, P. C., and Molema, G. (2005) Differential effects of NF-{kappa}B and p38 MAPK inhibitors and combinations thereof on TNF-{alpha}- and IL-1{beta}-induced proinflammatory status of endothelial cells in vitro. *Am. J. Physiol. Cell Physiol. 289*, C1229−C1239.

(24) Gonzalo, T., Talman, E. G., van, d., V, Temming, K., Greupink, R., Beljaars, L., Reker-Smit, C., Meijer, D. K., Molema, G., Poelstra, K., and Kok, R. J. (2006) Selective targeting of pentoxifylline to hepatic stellate cells using a novel platinum-based linker technology. *J. Controlled Release 111*, 193−203.

(25) Verel, I., Visser, G. W., Boerman, O. C., van Eerd, J. E., Finn, R., Boellaard, R., Vosjan, M. J., Stigter-van Walsum, M., Snow, G. B., and van Dongen, G. A. (2003) Long-lived positron emitters zirconium-89 and iodine-124 for scouting of therapeutic radioimmunoconjugates with PET. *Cancer Biother. Radiopharm. 18*, 655−661.

(26) Perk, L. R., Visser, G. W., Vosjan, M. J., Stigter-van, W. M., Tijink, B. M., Leemans, C. R., and van Dongen, G. A. (2005) (89)-Zr as a PET surrogate radioisotope for scouting biodistribution of the therapeutic radiometals (90)Y and (177)Lu in tumor-bearing nude mice after coupling to the internalizing antibody cetuximab. *J. Nucl. Med. 46*, 1898−1906.

(27) Cox, M. C., Barnham, K. J., Frenkiel, T. A., Hoeschele, J. D., Mason, A. B., He, Q. Y., Woodworth, R. C., and Sadler, P. J. (1999) Identification of platination sites on human serum transferrin using (13)C and (15)N NMR spectroscopy. *J. Biol. Inorg. Chem. 4*, 621−631.

(28) Trynda-Lemiesz, L., Kozlowski, H., and Keppler, B. K. (1999) Effect of cis-, trans-diamminedichloroplatinum(II) and DBP on human serum albumin. *J. Inorg. Biochem. 77*, 141−146.

(29) Boturyn, D., Coll, J. L., Garanger, E., Favrot, M. C., and Dumy, P. (2004) Template assembled cyclopeptides as multimeric system for integrin targeting and endocytosis. *J. Am. Chem. Soc. 126*, 5730−5739.

(30) Fuertes, M. A., Castilla, J., Alonso, C., and Perez, J. M. (2002) Novel concepts in the development of platinum antitumor drugs, *Curr. Med. Chem.: Anti-Cancer Agents 2*, 539−551.

(31) Sadowitz, P. D., Hubbard, B. A., Dabrowiak, J. C., Goodisman, J., Tacka, K. A., Aktas, M. K., Cunningham, M. J., Dubowy, R. L., and Souid, A. K. (2002) Kinetics of cisplatin binding to cellular DNA and modulations by thiol-blocking agents and thiol drugs. *Drug Metab. Dispos. 30*, 183−190.

(32) Volckova, E., Dudones, L. P., and Bose, R. N. (2002) HPLC determination of binding of cisplatin to DNA in the presence of biological thiols: implications of dominant platinum-thiol binding to its anticancer action. *Pharm. Res. 19*, 124−131.

(33) Pichler, B. J., Kneilling, M., Haubner, R., Braumuller, H., Schwaiger, M., Rocken, M., and Weber, W. A. (2005) Imaging of Delayed-Type Hypersensitivity Reaction by PET and 18F-Galacto-RGD. *J. Nucl. Med. 46*, 184−189.

(34) Lewis, M. R. (2005) Radiolabeled RGD Peptides Move Beyond Cancer: PET Imaging of Delayed-Type Hypersensitivity Reaction. *J. Nucl. Med. 46*, 2−4.

(35) Gerlag, D. M., Borges, E., Tak, P. P., Ellerby, H. M., Bredesen, D. E., Pasqualini, R., Ruoslahti, E., and Firestein, G. S. (2001) Suppression of murine collagen-induced arthritis by targeted apoptosis of synovial neovasculature. *Arthritis Res. 3*, 357−361.

(36) Prakash, J., Saluja, V., Visser, J., Moolenaar, F., Meijer, D. K., Poelstra, K., and Kok, R. J. (2005) Bioanalysis and pharmacokinetics of the p38 MAPkinase inhibitor SB202190 in rats. *J. Chromatogr., B 826*, 220−225.

(37) Caliceti, P., and Veronese, F. M. (2003) Pharmacokinetic and biodistribution properties of poly(ethylene glycol)−protein conjugates. *Adv. Drug Delivery Rev. 55*, 1261−1277.

BC0600158

Design and Synthesis Of Ferrocene Probe Molecules for Detection by Electrochemical Methods

Isabelle Tranchant,[‡] Anne-Cécile Hervé,[†,§] Stephen Carlisle,[†] Phillip Lowe,[†,||] Christopher J. Slevin,[‡,||] Camilla Forssten,[†] John Dilleen,[†,||] David E. Williams,[†,⊥] Alethea B. Tabor, and Helen C. Hailes*

Department of Chemistry, University College London, 20 Gordon Street, London WC1H 0AJ, U.K., and Unipath Ltd, Priory Business Park, Bedford, MK44 3UP, U.K. Received February 17, 2006; Revised Manuscript Received July 17, 2006

A series of ferrocenyl conjugates to fatty acids have been designed and synthesized to establish the key properties required for use in biomolecular binding studies. Amperometric detection of the ferrocene conjugates was sought in the region of 0.3 V (vs Ag/AgCl) for use in protein/blood solutions. Different linkers and solubilizing moieties were incorporated to produce a conjugate with optimal electrochemical properties. In electrochemical studies, the linker directly attached to the ferrocene was found to affect significantly the $E_{1/2}$ value and the stability of the ferrocenium cation. Ester-linked ferrocene conjugates had $E_{1/2}$ ranging from +400 to +410 mV, while amide-linked compounds ranged from +350 to +370 mV and the amines +260 to +270 mV. Folding of long-chain substituents around the ferrocene, also significantly affected by the choice of linker, was inferred as a secondary effect that increased $E_{1/2}$. The stability of the ferrocenium cation decreased systematically as $E_{1/2}$ increased. Disubstituted ferrocene ester and amide conjugates, with oxidation potentials of +640 and +570 mV, respectively, showed only a barely discernible reduction wave in cyclic voltammetry at 50 mV/s. Electrochemical measurements identified two lead compounds with the common structural characteristics of an amide and carbamate linker (compounds **17** and **21**) with a C_{11} fatty acid chain attached. It is envisaged that such molecules can be used to mimic and study the biomolecular binding interaction between fatty acids and molecules such as human serum albumin.

INTRODUCTION

Molecular interactions in biological systems have been studied using many different techniques such as surface plasmon resonance and fluorescence-based methodologies. There are, however, few reports in the literature utilizing electrochemical labels to study such interactions, with the exception of antibody−antigen interactions, where historically ferrocene-labeled molecules have been used. Metalloimmunoassays were first described in the 1970s when ferrocene was used to label steroid antigens with detection using flameless atomic absorption spectroscopy (*1*). Subsequently, an immunoassay incorporating a ferrocene electrochemical label was reported using a ferrocene−morphine conjugate whose electrochemistry was perturbed on binding to an antibody, resulting in a homogeneous competitive assay not requiring the separation of a free and antibody-bound label (*2*). Since then, a range of carbonylmetalloimmunoassays (CMIA) have been developed using metal−carbonyl-labeled molecules, in particular, incorporating ferrocene, which has been used as an electrochemical tracer and signaling molecule (*3*). The range of ferrocene derivatives available, ease of conjugation to a range of functionalities, reversible electrochemistry, and ability to synthetically tailor redox properties for a particular application makes it ideally placed for use in electrochemical sensing systems. More recent applications include the utilization of ferrocene as an oligonucleotide label in DNA probes (*4*−*6*) and as an electrochemical sensor for the detection of proteins (*7*). Ferrocene immunoassays with reduced glucose oxidase incorporating enzyme amplification (*8*), an amperometric immunoassay for lidocaine (*9*), and a homogeneous ferrocene−theophylline conjugate electrochemical assay (*10*) have also been reported.

Our aim was to demonstrate the utility of ferrocene for the study of biomolecular interactions and its potential in such applications. Interactions between fatty acids and their naturally occurring ligands have been intensively studied and thus provide a well-characterized system in which to study rationally designed synthetic electrochemical probe molecules; to our knowledge, no such probes have been reported in the literature. Fatty acid−human serum albumin (HSA) binding interactions are particularly important due to the effect on the transport of therapeutic drugs, for example, the reduced capacity of HSA to bind warfarin in the presence of bound fatty acids (*11*). Therefore, the synthesis of a series of ferrocene-labeled fatty acids would be a suitable model system for study but could also provide a greater understanding of the interactions between fatty acids and HSA. Conventionally such fatty acid ligand interactions have been studied by a number of techniques. Bhattacharya et al. have studied complexes of medium- and long-chain fatty acids and HSA using X-ray crystallography, identifying medium- and long-chain fatty acid binding sites (*12*). X-ray crystallography has also been used to study the complex of intestinal fatty acid binding protein and palmitate (*13*). Acrylodan-modified HSA has been used to study, using fluorescent techniques, the effect of oleic acid binding to the microenvironment around residue cysteine-34 in HSA (*14*). The binding characteristics of the fluorescently labeled fatty acid probe 11-(dansylamino)undecanoic acid with HSA (*15*) and a *Fascilo*

* Corresponding author. E-mail: h.c.hailes@ucl.ac.uk. Fax: +44 (0)20 7679 7463.

† Unipath Ltd.

‡ Current address: Diatos SA, Therapeutic Chemistry Department, 3-5 Impasse Reille, 75014 Paris, France.

§ Current address: Diatos NV, Brusselsestraat 69, B-3000 Leuven, Belgium.

|| Current address: Sterling Medical Innovations, Unit 10, Scion House, Stirling University Innovation Park, Stirling, FK9 4NF.

⊥ Current address: Department of Chemistry, University of Auckland, Private Bag, Auckland, New Zealand.

10.1021/bc060038m CCC: $33.50 © 2006 American Chemical Society
Published on Web 08/30/2006

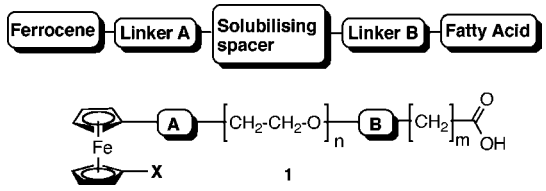

Figure 1. Ferrocene multifunctional conjugates.

hepatica fatty acid binding protein have also been studied (*16*). In addition, acrylodan-modified intestinal FABP (ADIFAB) has been used to investigate the binding of a range of fatty acids, allowing measurement of K_d values by fluorescent measurement (*17*). However, such measurements can only normally be performed in protein solution or plasma, while electrochemical measurements can potentially be performed in whole blood.

In the present study, we have designed and synthesized a range of electrochemically labeled molecules to establish the key properties required for use in binding studies in the presence of serum, such as $E_{1/2}$, reversibility, and aqueous compound solubility. The final component in the molecular design was the introduction of a moiety for recognition or binding purposes. In our studies, we conjugated a fatty acid as the specific biorecognition for potential applications in fatty acid binding studies. However, alternative functionalities can be introduced depending on the molecular interaction being investigated.

The molecular conjugates were designed as shown in Figure 1, incorporating ferrocene as the electrochemical detection method and a solubilizing spacer group together with the binding moiety, in these studies a fatty acid. Poly(ethylene glycol) (PEG)-modified ferrocenes have previously been reported incorporating long polymeric PEG units and have exhibited enhanced aqueous solubilities for use in homogeneous redox membrane biosensors (*18*, *19*). Commercially available PEG spacers were therefore incorporated as solubilizing moieties. However, short, defined PEG units were used to ensure that the spacer group did not interfere with any binding or recognition properties. Also, two linkers, **A** and **B**, were introduced to enable the rapid synthesis of a range of analogues that could be modified to alter molecular properties and stabilities. The ferrocene conjugate selected (**1**) is shown in Figure 1 with linkers **A** and **B**, PEG repeat unit *n*, the option of a second functionality on ferrocene (**X**), and fatty acid pendant group containing a methylene chain of length *m*.

EXPERIMENTAL PROCEDURES

Materials. Unless otherwise noted, solvents and reagents were reagent grade from commercial suppliers and used without further purification. THF was dried by distillation from a sodium/benzophenone suspension under a dry N_2 atmosphere. CH_2Cl_2 was dried by distillation from CaH_2 under a dry N_2 atmosphere. All moisture-sensitive reactions were performed under a nitrogen atmosphere using oven-dried glassware. Reactions were monitored by TLC on Kieselgel 60 F_{254} plates with detection by UV or permanganate, ninhydrin (for ureas), and phosphomolybdic acid stains. Flash column chromatography was carried out using silica gel (particle size 40−63 μm). Melting points are uncorrected. ^{1}H NMR and ^{13}C NMR spectra were recorded in $CDCl_3$ at the field indicated. 1-*t*Butyloxycarbonyl-1,8-diamino-3,6-dioxaoctane **7** (*20*), methyl 16-hydroxyhexadecanoate (*21*), and methyl 11-aminoundecanoate (*22*) were prepared as previously reported.

Ferrocenoyl-8-hydroxy-3,6-dioxaoctanoate (3). The reaction was carried out under anhydrous conditions. To a solution of tri(ethylene glycol) (3.26 g, 21.7 mmol) in CH_2Cl_2 (50 mL) was added a solution of ferrocenecarboxylic acid **2** (0.500 g, 2.17 mmol) in CH_2Cl_2 (10 mL). After 15 min, DCC (0.525 g, 2.30 mmol) and DMAP (0.03 g, 0.02 mmol) were added. The solution was stirred at room temperature for 18 h, then the solution was concentrated and purified by flash silica chromatography (EtOAc/hexane, 1:1) to afford **3** (0.55 g, 70%) as an orange oil. ^{1}H NMR (300 MHz; $CDCl_3$) 3.40 (br s, 1H, OH), 3.55 (t, J = 4.5 Hz, 2H), 3.58 (m, 6H), 3.72 (t, J = 4.8 Hz, 2H), 4.14 (s, 5H, C_5H_5), 4.28 (m, 2H, C_5H_2), 4.32 (m, 2H, CO_2CH_2), 4.75 (m, 2H, C_5H_2); ^{13}C NMR (75 MHz; $CDCl_3$) 61.8, 63.1, 69.5, 69.8, 70.2, 70.4, 70.7, 70.8, 71.4, 72.6, 171.7 (C═O); *m*/*z* HRMS calculated for $C_{17}H_{22}O_5FeNa$ $(MNa)^+$ 385.07089, found (ES+) 385.07110.

Ferrocenoyl-(8-ethanoate)-3,6-dioxaoctanoate (4). The reaction was carried out under anhydrous conditions. To compound **2** (100 mg, 0.27 mmol) in CH_2Cl_2 (5 mL) was added pyridine (0.25 mL) and DMAP (3 mg, 0.03 mmol). The solution was cooled to 0 °C and acetic anhydride (0.032 mL, 0.66 mmol) added dropwise. After 30 min, the solution was warmed to room temperature (rt) and stirred for 2 h. The solvents were evaporated and the resulting oil purified by flash silica chromatography (EtOAc/hexane, 7:3) to afford compound **4** (88 mg, 80%) as an orange oil. ^{1}H NMR (300 MHz; $CDCl_3$) 2.03 (s, 3H, $COCH_3$), 3.69 (m, 6H), 3.76 (t, J = 4.8 Hz, 2H), 4.17 (s, 5H, C_5H_5), 4.18 (m, 2H), 4.34 (m, 2H), 4.36 (m, 2H, C_5H_2), 4.79 (m, 2H, C_5H_2); ^{13}C NMR (75 MHz; $CDCl_3$) 20.8 ($COCH_3$), 63.1, 63.5, 69.1, 69.4, 69.7, 70.1, 70.5, 70.9, 71.2, 170.8 (C═O), 171.5 (C═O); *m*/*z* HRMS calculated for $C_{19}H_{25}O_6Fe$ $(MH)^+$ 404.09168, found (CI+) 404.09263.

***N*-(5-Hydroxy-3-oxapentanyl)ferrocenoylamide (5).** The reaction was carried out under anhydrous conditions. Ferrocene carboxylic acid **2** (3.00 g, 13.0 mmol) and HOBt (1.94 g, 14.3 mmol) were dissolved in CH_2Cl_2 (200 mL), and the reaction was stirred at rt for 10 min. EDCI (2.85 g, 13.0 mmol) and triethylamine (3.60 mL, 26.0 mmol) were then added, and after 30 min, 2-(2-aminoethoxy)ethanol (1.37 g, 13.0 mmoles) was added and the solution stirred at rt for 4 h. The solution was concentrated and purified by flash silica chromatography (gradient: 100% EtOAc to 15% methanol in EtOAc) to afford the title compound (3.47 g, 84%) as an orange oil. ^{1}H NMR (300 MHz; $CDCl_3$) 2.90 (br, 1H, OH), 3.44 (td, J = 5.2 and 5.2 Hz, 2H), 3.51 (m, 4H), 3.64 (t, J = 4.5 Hz, 2H), 4.07 (s, 5H, C_5H_5), 4.17 (m, 2H, C_5H_2), 4.63 (m, 2H, C_5H_2), 6.58 (br s, 1H, NH); ^{13}C NMR (75 MHz; $CDCl_3$) 39.2 (CH_2N), 61.3, 68.0, 69.4, 69.9−70.0 (signals superimposed), 72.2, 170.6 (C═O); *m*/*z* HRMS calculated for $C_{15}H_{19}NO_3FeNa$ $(MNa)^+$ 340.06066, found (ES+) 340.06126.

***N*-(8-Amino-3,6-dioxaoctanyl)ferrocenoylamide (8).** The reaction was carried out under anhydrous conditions. DCC (88 mg, 0.43 mmol) was added to compound **7** (95 mg, 0.39 mmol) and ferrocene carboxylic acid (80 mg, 0.35 mmol) in CH_2Cl_2 (20 mL), and the reaction was stirred for 18 h at rt. The solvent was evaporated in vacuo and the resulting oil purified by flash silica chromatography (100% EtOAc) to afford the Boc-protected intermediate (82 mg, 46%) as an orange oil. ^{1}H NMR (300 MHz; $CDCl_3$) 1.36 (s, 9H, 3 × CH_3), 3.24 (td, J = 5.2 and 5.1 Hz, 2H), 3.47 (m, 4H), 3.51 (m, 6H), 4.11 (s, 5H, C_5H_5), 4.24 (m, 2H, C_5H_2), 4.62 (m, 2H, C_5H_2), 4.98 (br s, 1H, NH), 6.24 (br s, 1H, NH); ^{13}C NMR (75 MHz; $CDCl_3$) 28.4 (Boc-*C*H_3), 39.3 (CH_2N), 40.3 (CH_2N), 68.2, 69.8, 70.2−70.4 (signals superimposed), 79.3 (Boc-*C*), 156.0 (C═O Boc), 170.4 (C═O amide).

The protected amine (82 mg, 0.18 mmol) was dissolved in a mixture of CH_2Cl_2/TFA (4 mL/4 mL), and the solution was stirred at rt for 2 h. The solvents were evaporated and the resulting oil purified by flash silica chromatography (CH_2Cl_2/MeOH/NEt_3; 85/10/5) to afford **8** (45 mg, 70%) as an orange oil. ^{1}H NMR (300 MHz; $CDCl_3$/CD_3OD) 3.09 (m, 2H), 3.28 (td, J = 5.3 and 5.3 Hz, 2H), 3.43 (m, 8H), 3.95 (s, 5H, C_5H_5),

4.14 (m, 2H, C_5H_2), 4.56 (m, 2H, C_5H_2), 6.70 (br s, 1H, NH); ^{13}C NMR (75 MHz; $CDCl_3$) 39.5 (CH_2N), 39.8 (CH_2N), 68.4, 69.9, 70.1−70.9 (signals superimposed), 75.5, 172.5 (C═O); *m/z* HRMS calculated for $C_{17}H_{25}N_2O_3Fe$ $(MH)^+$ 361.12091, found (ES+) 361.12111; *m/z* (ES+) 383 (MNa^+, 41%), 361 (MH^+, 100).

Ferrocenylmethylamine *N*-(5-hydroxy-3-oxapentanyl) (10). The reaction was carried out under anhydrous conditions. Ferrocene carboxaldehyde **9** (150 mg, 0.70 mmol) and 2-(2-aminoethoxy)ethanol (147 mg, 1.40 mmol) in toluene (30 mL) were heated at reflux for 18 h. After cooling to rt, sodium borohydride (79.8 mg, 2.10 mmol) was added, and the reaction was stirred at rt for 6 h. Water (5 mL) was added, the solvent removed in vacuo, and the residue suspended in CH_2Cl_2. The organic phase was washed with water (10 mL), dried (sodium sulfate), and evaporated. The residue was purified by flash silica chromatography (gradient: 100% EtOAc to 20% methanol in EtOAc) to give **10** (74 mg, 35%) as a dark orange oil. ^{1}H NMR (300 MHz; $CDCl_3$) 2.83 (t, J = 5.3 Hz, 2H, CH_2CH_2N), 3.53 (s, 2H, CH_2-ferrocenyl), 3.57−3.64 (m, 4H), 3.70 (t, J = 4.4 Hz, 2H), 4.10 (m, 2H, C_5H_2), 4.12 (s, 5H, C_5H_5), 4.18 (m, 2H, C_5H_2); ^{13}C NMR (75 MHz; $CDCl_3$) 48.9 (C-1), 61.9 (C-5), 67.9, 68.4, 68.5, 70.1, 72.4, 86.3; *m/z* (ES+) 326 (MNa^+, 91%), 304 (MH^+, 100).

Ferrocenylmethylamine *N*-methyl-*N*-(5-hydroxy-3-oxapentanyl) (11). The reaction was carried out under anhydrous conditions. To a solution of **10** (70 mg, 0.23 mmol) in CH_3CN (30 mL) was added formaldehyde (37%, 38 μL, 0.46 mmol). After stirring for 10 min, sodium borohydride (26 mg, 0.69 mmol) was added in portions, and the mixture was stirred for 5 h. Water (5 mL) was added, the solvent removed in vacuo, and the residue was suspended in CH_2Cl_2. The organic layer was washed with water (10 mL), dried (sodium sulfate), and evaporated, and the residue was purified by flash silica chromatography (gradient: 100% EtOAc to 20% methanol in EtOAc) to give **11** (26 mg, 35%) as an orange oil. ^{1}H NMR (300 MHz; $CDCl_3$) 2.21 (s, 3H, Me), 2.55 (t, J = 5.6 Hz, 2H, CH_2CH_2N), 3.47 (s, 2H, CH_2-ferrocenyl), 3.58 (m, 4H), 3.68 (t, J = 4.5 Hz, 2H), 4.11 (m, 7H, C_5H_5, C_5H_2), 4.18 (m, 2H, C_5H_2); ^{13}C NMR (75 MHz; $CDCl_3$) 41.2 (NMe), 55.6, 57.2, 62.0, 67.8, 68.3, 68.5, 70.4, 72.6; *m/z* (ES+) 340 (MNa^+, 100%), 318 (MH^+, 18).

1,1′-Ferrocenoyl-(8-ethoxy-3,6-dioxaoctanoate) (13). The reaction was carried out under anhydrous conditions. DCC (1.19 mmol, 245 mg) and DMAP (5 mg), were added to a solution of 1,1′-ferrocenedicarboxylic acid **12** (0.54 mmol, 150 mg) and tri(ethylene glycol) monoethyl ether (2.16 mmol, 385 mg) in CH_2Cl_2 (30 mL). The reaction was stirred at rt for 18 h. After filtration, the filtrate was concentrated in vacuo, dissolved in Et_2O, and urea was removed by filtration. The solvent was removed under reduced pressure and the residue purified by flash silica chromatography (EtOAc/hexane: 60/40) to give **13** (96 mg, 30%) as an orange oil. ^{1}H NMR (300 MHz; $CDCl_3$) 1.22 (t, J = 6.9 Hz, 6H, 2 × CH_3), 3.54 (q, J = 6.9 Hz, 4H, 2 × CH_2CH_3), 3.55−3.70 (m, 16H), 3.79 (m, 4H), 4.38 (m, 4H, CH_2OCO), 4.42 (m, 4H, 2 × C_5H_2), 4.86 (m, 4H, 2 × C_5H_2); ^{13}C NMR (75 MHz; $CDCl_3$) 15.2 (CH_3), 63.5, 66.7, 69.4, 69.9, 70.7, 70.8, 71.7, 72.6, 73.1, 170.4, 212.1 (C═O); *m/z* (ES+) 617 (MNa^+, 100%), 433 (28).

***N*-(5-Hydroxy-3-oxapentanyl)-1,1′-ferrocenoylamide (14).** The reaction was carried out under anhydrous conditions. 1-Ethyl-3-(3-dimethylaminopropyl)carbodiimide (2.20 mmol, 420 mg) (which had been previously neutralized with 2.20 mmol Et_3N) and HOBt (2.20 mmol, 295 mg) were added to a solution of 1,1′-ferrocenedicarboxylic acid **12** (0.54 mmol, 150 mg) in CH_2Cl_2 (20 mL), and the mixture was stirred for 30 min. A solution of aminoethoxyethanol (2.16 mmol, 227 mg) in CH_2Cl_2 (5 mL) was then added and the reaction stirred for 18 h at rt. The organic phase was washed with water (5 mL), dried (sodium sulfate), and the solvent removed under reduced pressure. The residue was purified by flash silica chromatography (gradient: 100% hexane to 100% EtOAc, then CH_2Cl_2/MeOH 95/5) to give **14** (107 mg, 50%) as an orange oil. ^{1}H NMR (300 MHz; $CDCl_3$) 3.62−3.75 (m, 16H), 4.35 (m, 4H, 2 × C_5H_2), 4.57 (m, 4H, 2 × C_5H_2), 7.32 (br, 2H, N*H*); ^{13}C NMR (75 MHz; $CDCl_3$) 39.8, 61.6, 69.9, 70.9, 71.3, 72.5, 78.0, 170.9, 212.0 (C═O); *m/z* (ES+) 471 (MNa^+, 100%), 449 (MH^+, 25).

11-(Ferrocenoyl-3,6-dioxaoctanyloxycarbonylamino)-undecanoic acid (15). The reaction was carried out under anhydrous conditions. To compound **3** (680 mg, 1.87 mmol) in acetonitrile (20 mL) at 0 °C was added *N*,*N*-disuccinimidyl carbonate (574 mg, 2.24 mmol). The solution was stirred at 0 °C for 30 min and at rt for 18 h. The solvent was then evaporated and the resulting oil purified by flash silica chromatography (hexane/EtOAc, 1:4) to afford the succinimidyl carbonate activated **3** (254 mg, 27%) as an orange oil. ^{1}H NMR (300 MHz; $CDCl_3$) 2.83 (s, 4H, CH_2 succinimidyl), 3.69 (m, 4H), 3.78 (m, 4H), 4.22 (s, 5H, C_5H_5), 4.40 (m, 4H), 4.45 (m, 2H), 4.82 (s, 2H, C_5H_2); ^{13}C NMR (75 MHz; $CDCl_3$) 25.4 (CH_2-succinimidyl), 63.2, 68.4, 69.5, 69.8, 70.1, 70.6−70.9 (signals superimposed), 71.3, 152.3, 162.4, 168.9 (C═O ester); *m/z* (ES+) 526 (MNa^+, 46%), 429 (100).

To 11-aminoundecanoic acid (12 mg, 0.06 mmol) in THF/H_2O (0.5 mL/1 mL) was added the succinimidyl carbonate activated **3** (15 mg, 0.03 mmol) in THF (0.5 mL). The reaction was stirred at rt for 18 h, then the solvents were evaporated under reduced pressure. The remaining oil was purified by flash silica chromatography (MeOH/CH_2Cl_2, 5/95) in to afford **15** (13 mg, 74%) as an orange oil. ^{1}H NMR (300 MHz; $CDCl_3$) 1.27 (m, 12H), 1.46 (quint, J = 6.8 Hz, 2H), 1.62 (quint, 2H, J = 6.8 Hz), 2.33 (t, J = 7.2 Hz, 2H, CH_2CO_2H), 3.13 (dt, J = 6.6 and 6.6 Hz, 2H, CH_2N), 3.68 (m, 6H), 3.79 (t, J = 4.8 Hz, 2H), 4.19 (m, 2H), 4.20 (s, 5H, C_5H_5), 4.38 (m, 2H, C_5H_2), 4.39 (m, 2H), 4.79 (m, 2H, C_5H_2), 4.81 (br, 1H, NH); ^{13}C NMR (75 MHz; $CDCl_3$/CD_3OD) 24.8, 26.6, 28.9, 29.1−29.7 (signals superimposed), 34.2, 40.8, 63.7, 68.1, 69.3−70.6 (signals superimposed), 75.4, 156.8 (C═O carbamate), 171.7, 177.9; *m/z* HRMS calculated for $C_{29}H_{43}NO_8FeNa$ $(MNa)^+$ 612.22303, found (ES+) 612.22331.

16-(Ferrocenoyl-3,6-dioxaoctanoyl)hexadecanoic acid (16). The reaction was carried out under anhydrous conditions. DCC (89 mg, 0.435 mmol) was added to a stirred solution of hexadecanedioic acid (230 mg, 0.829 mmol) in CH_2Cl_2 (20 mL), and the reaction was stirred at rt for 2 h. To this was added **3** (150 mg, 0.414 mmol), and DMAP (50 mg, 0.041 mol), and the reaction was stirred at rt overnight. Insoluble urea was filtered from the reaction and washed with CH_2Cl_2 (10 mL), and the combined organic extracts were removed under reduced pressure, leaving a brown viscous oil. The remaining oil was purified by flash silica chromatography (100% EtOAc) to afford the title compound (20 mg, 4%) as an orange oil. ^{1}H NMR (300 MHz; $CDCl_3$) 1.25 (m, 20H), 1.59 (m, 4H), 2.27 (m, 4H), 3.68 (m, 6H), 3.77 (t, J = 4.8 Hz, 2H), 4.22 (m, 7H), 4.38 (m, 4H), 4.81 (m, 2H, C_5H_2); ^{13}C NMR (75 MHz; $CDCl_3$) 24.7, 29.2, 29.3, 29.5, 29.6, 29.8, 30.0−30.1 (signals superimposed), 34.2, 34.6, 63.2, 63.3, 69.3, 69.5, 69.8, 70.2, 70.5−70.6 (signals superimposed), 71.4, 170.5, 172.2, 174.2; *m/z* HRMS calculated for $C_{33}H_{50}O_8FeNa$ $(MNa)^+$ 653.27473, found (ES+) 653.27595.

11-(Ferrocenoylamide-3-oxapentanyloxycarbonylamino)-undecanoic acid (17). The reaction was carried out under anhydrous conditions. Compound **5** (50 mg, 0.16 mmol) was dissolved in acetonitrile (10 mL), and triethylamine (45 μL, 0.32 mmol) was added. The solution was cooled to 0 °C, and *N*,*N*-disuccinimidyl carbonate (49 mg, 0.19 mmol) was added. The

solution was stirred at 0 °C for 30 min and at rt for 18 h. The solvent was then evaporated in vacuo and the resulting oil purified by flash silica chromatography (20% hexane in EtOAc) to afford the activated intermediate (64 mg, 87%) as an oil. ^{1}H NMR (300 MHz; $CDCl_3$) 2.76 (s, 4H, succinimide), 3.49 (m, 2H, C*H*$_2$NH), 3.62−3.74 (m, 4H), 4.11 (s, 5H, C_5H_5), 4.16 (m, 2H, C_5H_2), 4.45 (m, 2H, CH_2OCO), 4.68 (m, 2H, C_5H_2), 6.35 (br s, 1H, NH); ^{13}C NMR ($CDCl_3$; 75 MHz) 25.5, 39.4 (CH_2N), 68.1, 68.2, 69.7, 69.8, 69.9, 70.2, 70.5, 151.6 (C═O), 168.8 (C═O), 172.5 (C═O amide); *m*/*z* (ES+) 481 (MNa^+, 100%), 439 (48).

The intermediate (50 mg, 0.11mmol) was dissolved in DMF (0.7 mL), and triethylamine (18 μL, 0.13 mmol) was added. To this was added 11-aminoundecanoic acid (22 mg, 0.11 mmol) dissolved in a mixture of water/DMF (1.1 mL/0.4 mL). The reaction was stirred at rt for 18 h, and the solvents then evaporated in vacuo. The resulting oil was purified by flash silica chromatography (5% methanol in CH_2Cl_2) to afford **17** (54 mg, 90%) as an orange oil. ^{1}H NMR (300 MHz; $CDCl_3$) 1.23 (m, 12H), 1.41 (m, 2H), 1.59 (m, 2H), 2.32 (t, J = 7.5 Hz, 2H, C*H*$_2$CO$_2$H), 3.10 (dt, J = 4.8 and 4.6 Hz, 2H, $(CH_2)_9$C*H*$_2$-NH), 3.56−3.66 (m, 6H), 4.18 (s, 5H, C_5H_5), 4.21 (m, 2H, CH_2O), 4.31 (m, 2H, C_5H_2), 4.72 (m, 2H, C_5H_2), 4.90 (br, 1H, NH carbamate), 6.47 (br, 1H, NH amide); ^{13}C NMR (75 MHz; $CDCl_3$) 24.7, 26.6, 28.9, 29.0 (2 signals), 29.1, 29.2, 29.6, 34.0, 39.4, 41.0, 63.6, 68.2, 69.6, 69.7, 69.9, 70.5, 75.5, 156.4 (C═O carbamate), 171.2 (C═O amide), 177.9 (C═O acid); *m*/*z* HRMS calculated for $C_{27}H_{40}N_2O_6Fe$ M^+ 544.22356, found (FAB+) 544.22408.

2-(8-Hydroxy-3,6-dioxaoctanyl)isoindole-1,3-dione (19). The reaction was carried out under anhydrous conditions. 1-Chloro-3,6-dioxaoctan-1-ol **18** (5.00 g, 29.7 mmol) and potassium phthalimide (7.14 g, 28.6 mmol) were dissolved in DMF (20 mL) and heated at 40 °C for 4 h. The mixture was extracted with water and CH_2Cl_2. The organic phase was dried (magnesium sulfate) and evaporated to afford **19** (5.76 g, 70%) as a yellow oil, which was used without further purification. ^{1}H NMR (300 MHz; $CDCl_3$) 3.57 (m, 4H), 3.62 (m, 6H), 3.71 (m, 2H), 7.77 (m, 4H, H-phthalimide); ^{13}C NMR ($CDCl_3$; 75 MHz) 37.1, 62.3 (C-8), 68.9, 71.2, 71.5, 73.7, 124.2, 133.0, 135.4, 169.7 (C═O); *m*/*z* HRMS calculated for $C_{14}H_{17}NO_5Na$ $(MNa)^+$ 302.09989, found (ES+) 302.09998.

11-(8-[1,3-Dioxo-1,3-dihydroisoindol-2-yl]-3,6-dioxaoctanyloxycarbonylamino)undecanoic acid methyl ester (20). The reaction was carried out under anhydrous conditions. Compound **19** (1.00 g, 3.57 mmol) in acetonitrile (35 mL) was cooled to 0 °C, and *N*,*N*-disuccinimidyl carbonate (1.48 g, 4.28 mmol) was added. The solution was stirred at 0 °C for 30 min and at rt for 18 h. The solvent was evaporated in vacuo and the resulting oil purified by flash silica chromatography (20% hexane in EtOAc) to afford NHS activated **19** (910 mg, 61%) as a white solid. ^{1}H NMR (300 MHz; $CDCl_3$) 2.80 (s, 4H, H succinimidyl), 3.59 (m, 4H), 3.67 (m, 4H), 3.85 (t, J = 5.6 Hz, 2H), 4.32 (m, 2H), 7.67 (m, 2H, H-phthalimide), 7.80 (m, 2H, H-phthalimide); ^{13}C NMR ($CDCl_3$; 75 MHz) 25.3 (CH_2 succinimidyl), 37.0 (CH_2N), 67.6, 68.0, 69.8, 70.4, 71.1, 122.9, 132.5, 133.6 (C aromatic), 151.4 (C═O carbonate), 167.9 (C═O succinimidyl), 168.8 (C═O phthalimide); *m*/*z* (ES+) 443 (MNa^+, 18%).

The subsequent reaction was carried out under anhydrous conditions. 11-Aminoundecanoic acid methyl ester (285 mg, 1.32 mmol) was added to the NHS activated intermediate (556 mg, 1.32 mmol) in CH_2Cl_2 (30 mL), and the reaction was stirred at rt for 18 h. The solvent was evaporated and the resulting oil purified by flash silica chromatography (6:4 hexane/EtOAc) to afford **20** (228 mg, 34%). ^{1}H NMR (300 MHz; $CDCl_3$) 1.24 (m, 12H), 1.45 (m, 2H), 1.58 (m, 2H), 2.27 (t, J = 7.5 Hz, 2H, C*H*$_2$CO$_2$Me), 3.12 (q, J = 6.7 Hz, 2H, CH_2N), 3.59 (m, 6H), 3.63 (s, 3H, O-Me), 3.71 (t, J = 5.3 Hz, 2H), 3.87 (t, J = 6.0 Hz, 2H), 4.08 (m, 2H), 7.69 (m, 2H, H-phthalimide), 7.70 (m, 2H, H-phthalimide); ^{13}C NMR ($CDCl_3$; 75 MHz) 24.8, 25.4, 26.5, 26.6, 29.0−29.6 (signals superimposed), 33.8, 36.7, 37.1, 39.4, 40.8, 51.2 (O-Me), 63.4, 67.7, 69.4, 69.8, 70.4, 123.0 (CH-Ar), 131.8, 133.7 (CH-Ar), 156.2 (C═O carbamate), 168.0 (C═O phthalimide), 174.0 (C═O ester); *m*/*z* (ES+) 543 (MNa^+, 40%).

11-(Ferrocenoylamide-3,6-dioxaoctanyloxycarbonylamino)-undecanoic acid (21). A solution of **20** (228 mg, 0.44 mmol) and hydrazine hydrate (110 mg, 2.2 mmol) in ethanol (3 mL) was heated at reflux for 2 h. The solvent was evaporated and the resulting product dissolved in CH_2Cl_2. The precipitate was removed by filtration and the solvent evaporated to afford the amine intermediate as an oil (167 mg, 93%), which was used without further purification. ^{1}H NMR (300 MHz; $CDCl_3$) 1.26 (m, 12H), 1.38 (m, 2H), 1.54 (m, 2H), 2.27 (t, J = 7.5 Hz, 2H, C*H*$_2$CO$_2$Me), 3.12 (q, J = 5.5 Hz, 2H, CH_2N), 3.53 (m, 6H), 3.61 (s, 3H, OMe), 3.66 (t, J = 5.6 Hz, 2H), 3.83 (t, J = 5.6 Hz, 2H), 4.05 (m, 2H); ^{13}C NMR ($CDCl_3$; 75 MHz) 25.8, 26.9, 29.1−29.9 (signals superimposed), 31.2, 34.1, 38.1, 41.0, 51.5 (OMe), 63.7, 67.9, 69.6, 69.9, 70.5, 156.4 (C═O carbamate), 174.2 (C═O ester); *m*/*z* HRMS calculated for $C_{19}H_{39}N_2O_6$ $(MH)^+$ 391.28026, found (ES+) 391.28031.

The subsequent reaction was carried out under anhydrous conditions. To the amine intermediate (167 mg, 0.41 mmol) and ferrocenecarboxylic acid **2** (190 mg, 0.82 mmol) in CH_2Cl_2 (20 mL) was added EDCI (85 mg, 0.43 mmol), and the reaction was stirred for 18 h at rt. The solvent was evaporated and the resulting oil purified by flash silica chromatography (20% hexane in EtOAc) to afford the ferrocene-coupled methyl ester (35 mg, 15%) as an orange oil. ^{1}H NMR (300 MHz; $CDCl_3$) 1.25 (m, 12H), 1.39 (m, 2H), 1.49 (m, 2H), 2.28 (t, J = 7.5 Hz, 2H, C*H*$_2$CO$_2$Me), 3.14 (q, J = 5.5 Hz, 2H, CH_2N), 3.61 (m, 6H), 3.63 (s, 3H, O-Me), 3.68 (m, 2H), 3.75 (m, 2H), 4.06 (s, 5H, C_5H_5), 4.14 (m, 2H), 4.22 (m, 2H, C_5H_2), 4.61 (m, 2H, C_5H_2), 4.80 (br s, 1H, NH), 6.44 (br s, 1H, NH); ^{13}C NMR ($CDCl_3$; 75 MHz) 24.8, 26.9, 29.2−29.9 (signals superimposed), 30.2, 34.1, 38.1, 40.9, 51.53 (OMe), 63.7, 68.1, 69.7, 67.9, 69.6−70.5, 156.4 (C═O carbamate), 171.4 (C═O amide), 174.2 (C═O ester).

The ester (35 mg, 0.06 mmol) was dissolved in dioxane (3 mL), and to the solution was added lithium hydroxide (5 mg, 0.12 mmol) in water (2 mL). The reaction was stirred at rt for 3 h, and the dioxane removed in vacuo. The crude product was dissolved in CH_2Cl_2 (20 mL), the aqueous layer neutralized, and the organic layer was separated, dried ($MgSO_4$), and concentrated. The resulting oil was purified by flash silica chromatography (100% ethyl acetate to 5% MeOH in EtOAc) to afford **21** (20 mg, 60%) as an orange oil. ^{1}H NMR (300 MHz; $CDCl_3$) 1.29 (m, 12H), 1.41 (m, 2H), 1.54 (m, 2H), 2.22 (t, J = 7.5 Hz, 2H, CH_2CO_2H), 3.15 (q, J = 5.5 Hz, 2H, CH_2N), 3.64 (m, 6H), 3.69 (m, 2H), 3.77 (m, 2H), 4.09 (s, 5H, C_5H_5), 4.16 (m, 2H), 4.28 (m, 2H, C_5H_2), 4.64 (m, 2H, C_5H_2), 4.85 (br s, 1H, NH), 6.45 (br s, 1H, NH); ^{13}C NMR ($CDCl_3$; 75 MHz) 24.8, 26.9, 29.1−29.9 (signals superimposed), 30.3, 34.1, 39.1, 41.9, 64.4, 68.1, 69.8−70.2 (signals superimposed), 70.6, 156.9 (C═O carbamate), 171.9 (C═O amide), 174.2 (C═O acid); *m*/*z* HRMS calculated for $C_{29}H_{44}N_2O_7Fe$ M^+ 588.24977, found (CI+) 588.25104.

16-(2,5-Dioxopyrrolidin-1-yloxycarbonyloxy)hexadecanoic acid methyl ester (23). The reaction was carried out under anhydrous conditions. To methyl 16-hydroxyhexadecanoate (450 mg, 1.60 mmol) and triethylamine (0.240 mL) and acetonitrile (30 mL) at 0 °C was added *N*,*N*-disuccinimidyl carbonate (487 mg, 1.88 mmol). The reaction was stirred at 0 °C for 30 min and at rt for 18 h. The solvent was evaporated and the resulting

oil purified by flash silica chromatography (20% hexane in EtOAc) to afford **23** (590 mg, 85%) as an oil. ^{1}H NMR (300 MHz; $CDCl_3$) 1.19 (m, 22H), 1.71 (m, 2H), 1.68 (m, 2H), 2.23 (t, $J = 7.5$ Hz, 2H, CH_2CO$_2$Me), 2.77 (s, 4H, CH_2 succinimidyl), 3.59 (s, 3H, OMe), 4.25 (t, $J = 6.7$ Hz, 2H, CH_2O); ^{13}C NMR (75 MHz; $CDCl_3$) 25.4, 25.7, 26.2, 29.5, 29.6−30.1 (signals superimposed), 30.3, 34.0, 34.5, 51.5 (OMe), 68.4, 151.7, 168.4, 175.3 (C═O ester).

16-[8-(2-tert-Butoxycarbonylamino)-3,6-dioxaoctanylaminocarbamoyloxy]hexadecanoic acid methyl ester (24). The reaction was carried out under anhydrous conditions. Compound **7** (415 mg, 1.68 mmol) was added to **23** (590 mg, 1.4 mmol) in CH_2Cl_2 (30 mL), and the reaction was stirred at rt for 18 h. The solvent was evaporated and the resulting oil purified by flash silica chromatography (6:4, hexane/EtOAc) to afford **24** (311 mg, 42%). ^{1}H NMR (300 MHz; $CDCl_3$) 1.25 (m, 22H), 1.35 (m, 9H, CH_3-Boc), 1.58 (m, 4H), 2.26 (t, $J = 7.5$ Hz, 2H, CH_2CO$_2$Me), 3.28 (m, 2H), 3.33 (m, 2H), 3.57 (m, 8H), 3.62 (s, 3H, O-Me), 4.00 (m, 2H); ^{13}C NMR ($CDCl_3$, 75 MHz) 24.5, 25.5, 28.0, 28.7−29.2 (signals superimposed) 33.6, 40.0, 40.4, 51.0 (OMe), 64.4, 70.1 (signals superimposed), 78.6, 155.6 (C═O carbamate), 156.4 (C═O carbamate), 173.7 (C═O ester); *m*/*z* (ES+) 460 ([MH − Boc]$^+$, 100%).

16-(Ferrocenylamide-3,6-dioxactanylaminocarbamoyloxy-)hexadecanoic acid (25). The protected amine **24** (310 mg, 0.58 mmol) in a mixture of CH_2Cl_2/TFA (3 mL/3 mL) was stirred at rt for 2 h. The solvents were removed in vacuo, and the resulting oil was evaporated several times with methanol and CH_2Cl_2 to give the amine (250 mg, 99%) as a yellow oil. ^{1}H NMR (300 MHz; $CDCl_3$) 1.27 (m, 22H), 1.59 (m, 4H), 2.35 (t, $J = 7.5$ Hz, 2H, CH_2CO$_2$Me), 3.21−3.39 (m, 4H), 3.59 (m, 2H), 3.64 (m, 7H), 3.67 (m, 2H), 4.03 (m, 2H); ^{13}C NMR ($CDCl_3$, 75 MHz) 25.1, 25.8, 28.4 , 28.9−29.5 (signals superimposed), 31.7, 34.2, 34.5, 40.1, 51.9 (OMe), 65.3, 66.1, 69.7−69.7 (signals superimposed), 157.8 (C═O carbamate), 174.5 (C═O ester); *m*/*z* (ES+) 461 (MH$^+$, 100%), 449 (95).

The reaction was carried out under anhydrous conditions. To the amine intermediate (250 mg, 0.54 mmol) and triethylamine (0.113 mL) in CH_2Cl_2 (10 mL) was added ferrocenecarboxylic acid **2** (186 mg, 0.81 mmol) and DCC (165 mg, 0.81 mmol), and the reaction was stirred for 18 h. After removal of the solvents in vacuo, the resulting oil was purified by flash silica chromatography (100% EtOAc) to afford the ferrocenyl methyl ester intermediate (167 mg, 46%). ^{1}H NMR (300 MHz; $CDCl_3$) 1.20 (m, 22H), 1.53 (m, 4H), 2.32 (t, $J = 7.5$ Hz, 2H), 3.33 (m, 2H), 3.63 (m, 10H), 3.65 (s, 3H, OMe), 3.99 (m, 2H), 4.13 (s, 5H, C_5H_5), 4.26 (m, 2H, C_5H_2), 4.65 (m, 2H, C_5H_2), 5.24 (br s, 1H, NH), 6.13 (br s, 1H, NH); ^{13}C NMR ($CDCl_3$, 75 MHz) 24.9, 25.8, 29.0−29.6 (signals superimposed), 34.1, 39.3, 40.7, 51.9 (OMe), 65.1, 68.2, 69.7−70.3 (signals superimposed), 76.1, 156.9 (C═O carbamate), 170.3 (C═O amide), 174.3 (C═O ester).

The ferrocene conjugate (167 mg, 0.25 mmol) was dissolved in dioxane (3 mL), and sodium hydroxide (15 mg, 0.38 mmol) in water (2 mL) was added. The reaction was stirred at rt for 3 h, the dioxane was removed in vacuo, and then CH_2Cl_2 (10 mL) was added. The aqueous layer was neutralized and the organic layer separated, dried ($MgSO_4$), and concentrated. The resulting oil was purified by flash silica chromatography (100% EtOAc to 5% MeOH in EtOAc) to afford **25** (50 mg, 32%) as an orange oil. ^{1}H NMR (300 MHz; $CDCl_3$) 1.23 (m, 22H), 1.55 (m, 4H), 2.22 (t, $J = 7.5$ Hz, 2H, CH_2CO_2H), 3.37 (m, 2H), 3.51−3.65 (m, 10H), 4.01 (m, 2H), 4.17 (s, 5H, C_5H_5), 4.29 (m, 2H, C_5H_2), 4.67 (m, 2H, C_5H_2), 5.31 (br s, 1H, NH), 6.23 (br s, 1H, NH); ^{13}C NMR ($CDCl_3$, 75 MHz) 24.9, 25.9, 29.1−29.6 (signals superimposed), 34.1, 39.3, 40.8, 65.1, 68.2, 69.7−70.3 (signals superimposed), 71.5, 156.9 (C═O carbamate), 170.4 (C═O amide), 177.3 (C═O acid); *m*/*z* HRMS calculated for $C_{34}H_{54}N_2O_7FeNa$ (MNa)$^+$ 681.31727, found (ES+) 681.31763.

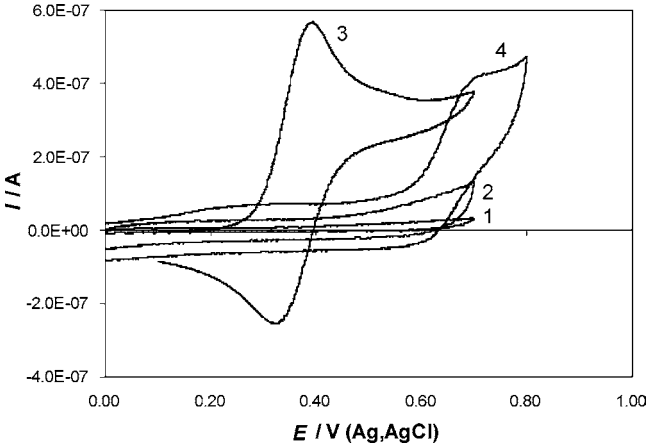

Figure 2. Cyclic voltammetry of substituted ferrocenes (~100 μM in PBS). Curves 1,2, background, illustrating the variability between different screen-printed carbon electrodes; 3, compound **17**; 4, compound **13**.

Electrochemical Methods. All measurements were performed with screen-printed electrodes consisting of carbon working (area 0.03 cm^2) and counter electrodes and a silver/silver chloride reference electrode. All electrochemical measurements were performed with an Autolab General Purpose Electrochemical System (Eco Chemie B.V. Netherlands).

All signal molecule stock solutions (approximately 100 μM) were dissolved in methanol due to poor solubility at high concentrations in phosphate-buffered saline (PBS: 0.137 M NaCl, 0.0027 M KCl, 0.01 M phosphate buffer pH 7.4). Subsequent dilutions were made with PBS, and the final concentration of methanol was never more than 5% v/v, which was found to have no effect on experiments. All solutions were filtered using a 0.2 μm cutoff filter.

20 μL of solution was applied to the sample/working area of the electrode ensuring complete coverage of the working, counter, and reference electrodes. All samples were premixed before being applied to the electrode, and a new electrode was used for each measurement. Cyclic voltammetry measurements were made immediately. The potential ramp was digitally generated and therefore in the form of a staircase, with a small step height. Cyclic voltammogram scan parameters were as follows: pretreatment of 0 V potential for 5 s, start potential 0 V, second vertex potential 0.7 V, step potential 0.00198 V, and scan rate 0.05 V/s. All potentials are quoted with respect to Ag/AgCl in PBS. Carbon electrodes prepared by screen printing have a small inherent variability associated with some porosity of the electrodes, that gives rise to a variable background and has some effect upon peak shape in cyclic voltammetry. Typical variability of background caused by electrode variability is illustrated in Figure 2.

RESULTS

The nature of linker **A** was initially explored with a range of spacers (together with either no group or a small group at position **B**), since this was likely to significantly affect the electrochemical properties of the ferrocene due to their close proximity and potential shielding properties. Three types of linker were synthesized: ester, amide, and amine. The synthesis of ferrocenyl esters has been reported using DCC as a coupling reagent, which was found to be effective unless the alcohol had poor solubility when rearrangement of the *O*-acyl urea occurred (*23*, *24*). This was not the case with tri(ethylene glycol), which readily reacted with ferrocenecarboxylic acid **2**, DCC, and

Scheme 1. Synthesis of Ferrocene Conjugates with Different Linkers at A[a]

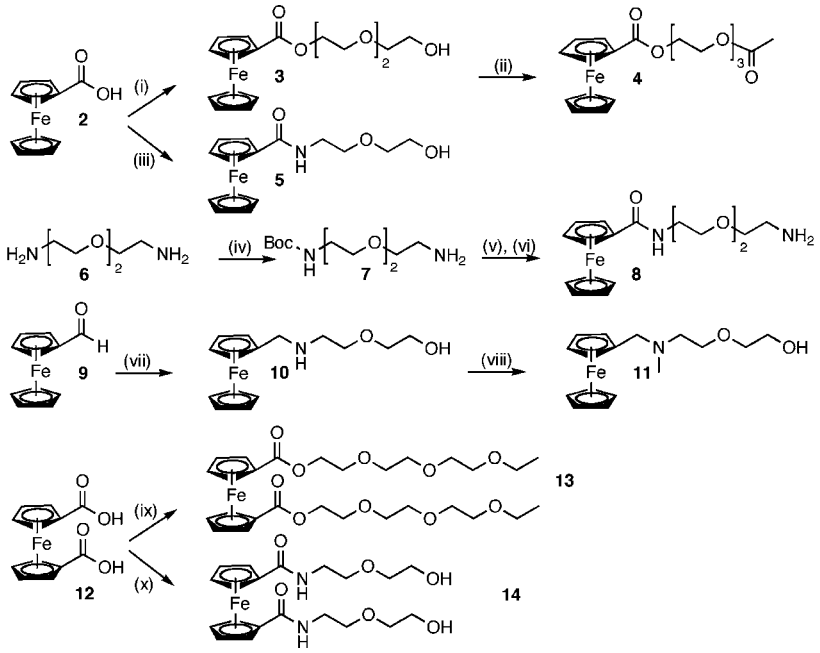

[a] (i) Tri(ethylene glycol), DCC, DMAP, CH_2Cl_2, 70%; (ii) $(CH_3CO)_2O$, pyridine, DMAP, 80%; (iii) 2-(2-aminoethoxy)ethanol, EDCI, HOBt, CH_2Cl_2, Et_3N, 84%; (iv) Boc_2O, CH_2Cl_2, 30%; (v) **2**, EDCI, HOBt, CH_2Cl_2, Et_3N, 46%; (vi) TFA, CH_2Cl_2, 70%; (vii) 2-(2-aminoethoxy)ethanol, $NaBH_4$, 35%; (viii) CH_2O, $NaBH_4$, 35%; (ix) tri(ethylene glycol), DCC, DMAP, CH_2Cl_2, 30%; (x) 2-(2-aminoethoxy)ethanol, EDCI, HOBt, CH_2Cl_2, Et_3N, 50%.

DMAP to give the ester **3** in 70% yield (Scheme 1). As a control, the ferrocene alcohol **3** was converted into the corresponding acetate **4**, to assess electrochemical properties compared to other analogues.

For the synthesis of the ferrocene amide, commercially available 2-(2-aminoethoxy)ethanol was reacted with ferrocenecarboxylic acid **2** and *N*-(3-dimethylaminopropyl)-*N*′-ethylcarbodiimide hydrochloride (EDCI), that has been used in ferrocenecarboxamide synthesis (*24*), together with HOBt to give **5** in 84% isolated yield. The synthesis of a second amide linker with an alternative spacer possessing a terminal amine group was also investigated. The monoprotection of *N*,*N*′-bis-(2-hydroxylethyl)ethylenediamine **6** was achieved using Boc anhydride to give **7** (*20*), which was coupled to ferrocenecarboxylic acid **2** again using EDCI (Scheme 1) in 46% yield. Removal of the Boc group using 50% TFA in CH_2Cl_2 generated **8** in 70% yield.

To synthesize amine-linked conjugates, ferrocenecarboxaldehyde **9** was used. This was coupled to 2-(2-aminoethoxy)-ethanol to afford the corresponding imine, which was then reduced in situ using sodium borohydride to the amine **10**. The amine **10** was also methylated to give the tertiary amine **11**, since this derivative could potentially be used in further coupling reactions to avoid a competing reaction at the nitrogen center. 1,1′-Ferrocenedicarboxylic acid **12** (**X** = CO_2H, Figure 1) was used to prepare disubstituted ferrocenes to assess the effect of difunctionalization on the electrochemical properties: the diester **13** from tri(ethylene glycol), and DCC and DMAP, and diamide **14** from 2-(2-aminoethoxy)ethanol, EDCI, and HOBt (Scheme 1).

From the initial electrochemical data (see below), the ester-linked compound **3**, amides **5** and **8**, and amine **11** were the most suitable ferrocenyl scaffolds. However, as the amine was generated in generally low yields, only the ester and amides were carried through for further structural elaboration. The nature of the solubilizing spacer together with the linker **B** were then explored to assess the influence of the spacer and second linker on electrochemical properties. Depending on the types of spacer and linker incorporated, three different functionalized acids were attached, either 11-aminoundecanoic acid, hexadecanedioic acid, or 16-hydroxyhexadecanoic acid.

Initially, a carbamate linkage was synthesized using the ferrocenyl ester with a PEG-3 spacer. Accordingly, alcohol **3** was activated using *N*,*N*′-disuccinimidyl carbonate (DSC) to give the corresponding *N*-hydroxysuccinimidyl ester which was converted into **15** via coupling with 11-aminoundecanoic acid in THF/H_2O in 74% isolated yield (Scheme 2).

The diester-linked analogue **16** was also prepared from **3** and hexadecanedioic acid using DCC and DMAP in low yield, due to isolation problems and side-product formation; however, sufficient material was prepared for electrochemical analysis. The synthesis of an amide analogue of **15** to establish any benefits of a longer PEG spacer was carried out using an identical method. Compound **5** was activated as the *N*-hydroxysuccinimidyl ester, which was isolated and coupled with 11-aminoundecanoic acid to afford **17** in 78% yield over the two steps.

To evaluate the potential benefits of a longer PEG spacer, compound **21** (an analogue of **17**) was also prepared. Synthesis of the spacer with a terminal amine and alcohol was required, and accordingly, 2-[2-(2-chloroethoxy)ethoxy]ethanol **18** was reacted with potassium phthalimide to give **19** in 70% yield. The hydroxyl group was then activated as before using DSC, and the isolated intermediate was coupled with methyl 11-aminoundecanoate to generate **20**. Removal of the phthalimide group was achieved by treatment with hydrazine in 93% yield, and ferrocenecarboxylic acid **2** was attached to the resulting free amino group using EDCI. Finally, hydrolysis of the methyl ester afforded compound **21**.

Finally, an analogue of **21** with the carbamate reversed was synthesized. To do this, initially methyl 16-hydroxyhexadecanoate **22** was activated and isolated as the *N*-hydroxysuccinimidyl ester **23** in 85% yield. The activated alcohol was coupled with the mono-Boc-protected diamine, **7**, to give compound **24**. The Boc group was removed in quantitative yield using TFA and the resulting amine coupled to ferrocenecarboxylic acid **2**, using DCC and triethylamine. Finally, hydrolysis of the methyl ester revealed the reverse carbamate analogue **25** (Scheme 2).

Scheme 2. Synthesis of Ferrocene Conjugates with a Range of Spacers and Linkers at B[a]

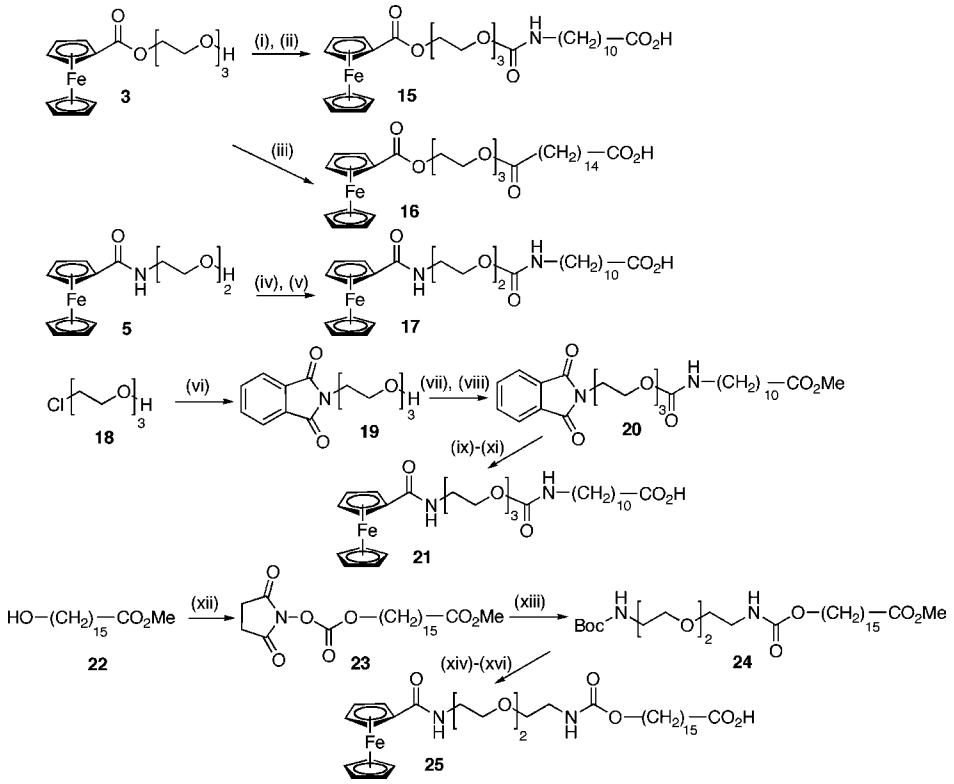

[a] (i) DSC, CH_3CN, 27%; (ii) 11-aminoundecanoic acid, THF/H_2O, 74%; (iii) hexadecanedioic acid, DCC, DMAP, CH_2Cl_2, 4%; (iv) DSC, CH_3CN, 87%; (v) 11-aminoundecanoic acid, DMF/H_2O, 90%; (vi) potassium phthalimide, DMF, 70%; (vii) DSC, CH_3CN, 61%; (viii) methyl 11-aminoundecanoate, THF/H_2O, 34%; (ix) N_2H_4, EtOH, reflux, 2 h, 93%; (x) **2**, EDCI, CH_2Cl_2, 15%; (xi) LiOH, dioxane/H_2O, 60%; (xii) **22**, DSC, CH_3CN, 85%; (xiii) **7**, CH_2Cl_2, 42%; (xiv) TFA, CH_2Cl_2, 50:50, 99%; (xv) **2**, Et_3N, DCC, CH_2Cl_2, 46%; (xvi) NaOH, dioxane/H_2O, 32%.

Table 1. Electrochemical Properties Measured for Ferrocene Compounds[a]

compound	A linker	B linker	*n*	*m*	X	$E_{1/2}$/ mV Ag,AgCl (PBS)	$I_{p,c}/I_{p,a}$	$E_{p,a} - E_{p,c}$/ mV	$E_{p,a} - E_{p,a/2}$/ mV
3	ester	H	3		H	402	0.68	81	59
4	ester	COMe	3		H	402	0.71	81	61
15	ester	H	2	10	H	408	0.55	77	58
16	ester	ester O(CO)	3	14	H	560	nd	nd	nd
5	amide	H	2		H	349	0.94	82	63
8	amide	$(CH_2)_2NH_2$	2		H	365	0.80	80	65
17	amide	carbamate O(CO)NH	2	10	H	357	0.76	76	58
21	amide	carbamate O(CO)NH	3	10	H	370	0.67[b]	98	64
25	amide	carbamate O(CO)NH	2	15	H	449	0.53	68	66
10	*sec*-amine	H	2		H	266	0.89	80	66
11	*tert*-amine	H	2		H	258	0.80	100	86
13	ester	Et	3		$CO_2(CH_2CH_2O)_3Et$	638	0		77
14	amide	Et	2		$CONH(CH_2CH_2O)_2H$	568	0.28	96	66

[a] Electrochemical data were obtained in PBS on printed carbon electrodes with scan rate 50 mV/s. $E_{1/2}$ was taken as the mean of the peak potentials for anodic and cathodic peaks or as the half-wave potential where there was no cathodic peak (compound **13**). The peak current ratio was determined by the extrapolation method illustrated in ref 29. nd: not determined. [b] Shoulder at $E_{1/2} = 250$ mV.

The properties of the ferrocene conjugates were then studied using cyclic voltammetry. In blood samples, electrochemical measurements are complicated due to the presence of several electrochemically active compounds including uric acid, glycine, ascorbic acid, and urea (*25*). These compounds have an oxidation potential of approximately +350 to +550 mV (vs Ag/AgCl reference). The various components of the blood including proteins such as HSA produce a significant electrochemical background signal at approximately +550 mV. For use in binding studies, compounds with reversible voltammograms and an $E_{1/2}$ of approximately +350 mV are preferred to limit the interference from such an electrochemical background.

The range of electrochemical behavior observed is given in Table 1 and illustrated in Figure 2. For some compounds (the esters and the disubstituted compounds), a second process appearing as a shoulder at lower $E_{a,p}$ was occasionally observed. The probable explanation, since the appearance of the effect correlated with the time between synthesis and electrochemical measurement (up to several weeks in some cases) is that it was due to ferrocene carboxylic acid formed by hydrolysis of the compound. For comparison, the cyclic voltammetry curve for ferrocenecarboxylic acid (FcCOOH) has a half-wave potential $E_{1/2}$ of approximately +300 mV (vs Ag/AgCl) (*26*). A one-electron reversible electrochemical process would have peak to half-peak and anodic peak to cathodic peak potential differences ($E_{p,a} - E_{p,a/2}$ and $E_{p,a} - E_{p,c}$) of approximately 60 mV, in the absence of effects due to ohmic drop between working and reference electrodes, and would have the peak current ratio $I_{p,a}/I_{p,c} = 1$. The compounds all essentially satisfied

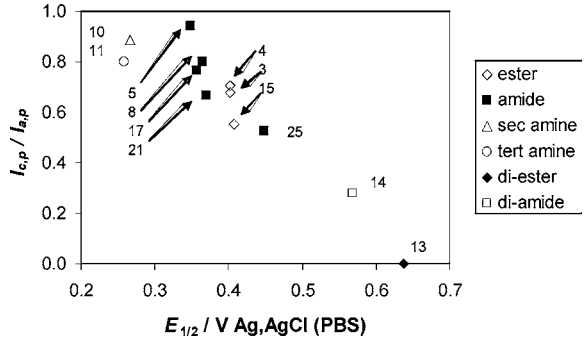

Figure 3. Variation with half-wave potential, $E_{1/2}$, of ratio of cathodic to anodic peak current in cyclic voltammetry, $I_{c,p}/I_{a,p}$ The points are labeled with the compound number.

the criteria for the peak potential differences, but not for the peak current ratio. A satisfactory interpretation is that the oxidized product of the anodic reaction (ferrocenium) decomposes to an electroinactive species at a rate dependent upon the substituents. There was a systematic trend with the nature of linker **A** and the length of the substituent chain, shown in Figure 3: as $E_{1/2}$ increased, indicating relative destabilization of the ferrocenium cation, the decomposition rate of ferrocenium, measured by $I_{p,c}/I_{p,a}$, also increased.

DISCUSSION

Since the carboxylate anion can stabilize ferrocenium more than an amide group, conversion of ferrocene carboxylic acid to an amide or ester should cause a shift to a higher redox potential, as observed. The shift in $E_{1/2}$ caused by substitution onto the ferrocene correlates with the expected relative ability of the substituent groups to disperse the charge on the ferrocenium cation: amine > amide > ester > diamide > diester. The amide **8**, possessing a slightly longer PEG unit than the amide conjugate **5** and a terminal amine group, had a similar $E_{1/2}$ value, indicating that further substitution should not affect the electrochemical properties significantly. Indeed, previous studies on ferrocenoyl peptides have indicated that the electrochemical behavior was relatively insensitive to the amino acid R group (*27*). However, there was a discernible effect in each group of compounds of the length of the alkyl chain—the longer the chain, the lower the ratio $I_{c,p}/I_{a,p}$ and, to a degree perhaps dependent on the nature of the second linker, the greater $E_{1/2}$.

These results indicated that when the ferrocenyl esters were linked through either a carbamate or an ester to a fatty moiety, $E_{1/2}$ increased such that compounds **15** and **16** were unsuitable for application in an electrochemistry in protein solutions, plasma, and blood. In contrast, ferrocenyl amides linked to a fatty moiety through a carbamate unit, compounds **17** and **21**, showed $E_{1/2}$ values close to that observed without the linked fatty acid chain. Interestingly, however, the reverse carbamate **25** had significantly increased $E_{1/2}$, possibly due to hydrogen-bonding effects and folding of the molecule. The best properties were displayed by compounds **17** and **21**, but **17** was more synthetically accessible. This was therefore selected as our model compound for further synthetic and electrochemical studies.

In summary, two structural characteristics can be identified that determine the reversibility and half-wave potential for oxidation. The first is stabilization of ferrocenium (Fc^+) by electron donation from ring substituents. Thus, the lowest $E_{1/2}$ is found for ferrocene carboxylic acid (stabilization of Fc^+ by carboxylate attached directly to the ring) and for amines **10** and **11** where the nitrogen is separated from the ring by a methylene group: ferrocene methanol has a similar $E_{1/2}$ value (*28*). If the carboxylic acid is derivatized as the corresponding amide or ester, then $E_{1/2}$ increases, with the amide being more effective at stabilizing Fc^+ than the ester. The disubstituted ferrocenes are most likely distorted: this was supported by the ^{13}C NMR spectroscopic data with the two carbonyl signals separated by more than 30 ppm. The second effect relates to the way in which long-chain substituents can potentially fold around the ferrocene (*5*, *6*). The effect seems to be determined by the length of the chain and functional group at the linker. Thus, we have identified that, to enable electrochemical measurements to be made in protein solutions, plasma, and blood, an amide at linker **A**, carbamate at linker **B**, short PEG unit, and fatty acid moiety are required for use in biomolecular binding studies, to mimic fatty acid binding. Applications of the model compound **17** and analogues as an electrochemical probe of biochemical interaction will be described in a future paper (*30*).

ACKNOWLEDGMENT

We thank Unipath for funding (IT) and for permission to publish this article.

Supporting Information Available: NMR spectra of synthesized compounds. This material is available free of charge via the Internet at http://pubs.acs.org.

LITERATURE CITED

(1) Cais, M., Slovin, E., and Snarsky, L. (1978) Metalloimmunoassay II. Iron-metallohaptens from estrogen steroids. *J. Organomet. Chem. 160*, 223−230.
(2) Weber, S. G., and Purdy, W. C. (1979) Homogeneous voltammetric immunoassay: a preliminary study. *Anal. Lett. 12*, 1−19.
(3) Tiefenauer, L. X., Kossek, S., Padeste, C., Thiebaud, P. (1997) Towards Amperometric Immunosensor Devices. *Biosens. Bioelectron. 12*, 213−223.
(4) Yu, C. J., Wang, H., Wan, Y., Yowanto, H., Lie, J., Tao, C., James, M. D., Tan, C. L., Blackburn, G. F., and Meade, T. J. (2001) 2-Ribose-ferrocene oligonucleotides for electronic detection of nucleic acids. *J. Am. Chem. Soc. 123*, 11155−11161.
(5) Hillier, S. C., Flower, S. E., Frost, C. G., Jenkins, A. T. A., Keay, R., Braven, H., Clarkson, J. (2004) An electrochemical gene detection assay utilizing T7 exonuclease activity on complementary probe-target oligonucleotide sequences. *Electrochem. Commun. 6*, 1227−1232.
(6) Hillier, S. C., Frost, C. G., Jenkins, A. T. A., Braven, H., Keay, R. W., Flower, S. E., Clarkson, J. M. (2004) An electrochemical study of enzymatic oligonucleotide digestion. *Bioelectrochemistry 63*, 307−310.
(7) Plumb, K., and Kraatz, H.-B. (2003) Interaction of a ferrocenyl-modified peptide with papain: toward protein-sensitive electrochemical probes. *Bioconjugate Chem. 14*, 601−606.
(8) Forrow, N. J., Sanghera, G. S., and Walters, S. J. (2002) The influence of structure in the reaction of electrochemically generated ferrocenium derivatives with reduced glucose oxidase. *J. Chem. Soc., Dalton Trans.* 3187−3194.
(9) Di Gleria, K., Hill, H. A. O., McNeil, C. J., and Green, M. J. (1988) Homogeneous ferrocene-mediated amperometric immunoassay. *Anal. Chem. 58*, 1203−1205.
(10) Forrow, N. J., Foulds, N. C., Frew, J. E., and Law, J. T. (2004) Synthesis, characterization, and evaluation of ferrocene−theophylline conjugates for use in electrochemical enzyme immunoassay. *Bioconjugate Chem. 15*, 137−144.
(11) Zatón, A. M. L., Ferrer, J. M., Ruizde Gorda, J. C., and Marquín, M. A. (1995) Binding of coumarins to site I of human serum albumin. Effects of fatty acids. *Chem.-Biol. Interact. 97*, 169−174.
(12) Bhattacharya, A. A., Grüne, T., and Curry, S. (2000) Crystallographic analysis reveals common modes of binding medium and long chain fatty acids to human serum albumin. *J. Mol. Biol. 303*, 721−732.
(13) Sacchettini, J. C., Gordon, J. I., and Banaszak, L. J. (1989) Crystal structure of rat intestinal fatty acid binding protein. Refinment and analysis of the *Escherichia coli*-derived protein with bound palmitate. *J. Mol. Biol. 208*, 327−339.

(14) Narazaki, R., Maruyama, T., and Otagiri, M. (1997) Probing the cysteine 34 residue in human serum albumin using fluorescence techniques. *Biochem. Biophys. Acta 1338*, 275−281.

(15) Wilton, D. C. (1990) The fatty acid analogue 11-(dansylamino)-undecanoic acid is a fluorescent probe for the bilirubin-binding sites of albumin and not for the high-affinity fatty acid-binding sites. *Biochem. J. 270* (1), 163−166.

(16) Timanova-Atanasova, A., Jordanova, R., Radoslavov, G., Deevska, G., Bankov, I., and Barrett, J. (2004) A native 13 kDa fatty acid binding protein from the liver fluke *Fasciola hepatica*. *Biochim. Biophys. Acta 1674*, 200−204.

(17) Richieri, G. V., Ogata, R. T., and Kleinfeld, A. M. (1992) A fluorescently labeled intestinal fatty acid binding protein. Interactions with fatty acids and its use in monitoring free fatty acids. *J. Biol. Chem. 33*, 23495−23501.

(18) Anne, A. (1998) Novel monolabeled redox biomaterials: Amino-ended poly(ethylene oxide) ferrocenes and their biotin-conjugates. *Tetrahedron Lett. 39*, 561−564.

(19) Anne, A., and Moiroux, J. (1999) Quantitative characterization of the flexibility of poly(ethylene glycol) chains attached to a glassy carbon electrode. *Macromolecules 32*, 5829−5835.

(20) Khersonsky, S. M., Jung, D. W., Kang, T. W., Walsh, D. P., Moon, H. S., Jo, H., Jacobson, E. M., Shetty, V., Neubert, T. A., and Chang, Y. T. (2003) A cross-linking method to study protein interactions. *J. Am. Chem. Soc. 125*, 2416−2425.

(21) Rees, G. D., Robinson, B. H., and Stephenson, G. R. (1995) Macrocyclic lactone synthesis by lipases in water-in-oil microemulsions. *Biochim. Biophys. Acta 1257*, 239−248.

(22) Ross, W. C. J. (1962) Some surface active alkylating agents. *J. Chem. Soc.* 4739−4740.

(23) Cooke, G., Radhi, A., Boden, N., Bushby, R. J., Lu, Z., Brown, S., and Heath, S. L. (2000) Synthesis and characterisation of tetrathiafulvalenyl- and ferrocenyl-triphenylenes. *Tetrahedron 56*, 3385−3390.

(24) Schetter, B., and Speiser, B. (2004) Reaction of ferrocenecarboxylic acid with *N*,*N*-disubstituted carbodiimides: synthesis, spectroscopic and X-ray crystallographic analysis of *N*,*N*′-disubstituted *N*-ferrocenoylureas and identification of a one-pot coupling reagent for the formation of ferrocenecarboxamides in a non-aqueous solvent. *J. Organomet. Chem. 689*, 1472−1480.

(25) Pravda, M., Junjar, C. M., Iwuoha, E. I., Smyth, M. R., Vytras, K., and Ivaska, A. (1995) Evaluation of amperometeric glucose biosensors based on co-immobilisation of glucose oxidase with an osmium redox polymer in electrochemically generated polyphenol films. *Anal. Chim. Acta 304*, 127−138.

(26) Rossier, J. S., Roberts, M. A., Ferringo, R., and Girault, H. H. (1999) Electrochemical detection in polymer microchannels. *Anal. Chem. 71*, 4294−4299.

(27) Sheehy, M. J., Gallagher, J. F., Yamashita, M., Ida, Y., White-Colangelo, J., Johnson, J., Orlando, R., and Kenny, P. T. M. (2004) Synthesis and structural characterization of redox-responsive N-ferrocenoyl amino acid esters; the X-ray crystal structure of N-ferrocenoyl alanine methyl ester; electrochemical anion recognition and 1H NMR complexation studies. *J. Organomet. Chem. 689*, 1511−1520.

(28) Yoon, H. C., Yang, H., and Byun, S. Y. (2004) Ferritin immunosensing on microfabricated electrodes based on the integration of immunoprecipitation and electrochemical signaling reactions. *Anal. Sci. 20*, 1249−1253.

(29) Southampton Electrochemistry Group (1990) *Instrumental methods in electrochemistry*, p 182, Ellis Horwood, Chichester, U.K.

(30) Tranchant, I., Hervé, A.-C., Carlisle, S., Lowe, P., Slevin, C. J., Forssten, C., Dilleen, J., Tabor, A. B., Williams, D. E., and Hailes, H. C., manuscript in preparation.

BC060038M

Synthesis of Potent Inhibitors of Anthrax Toxin Based on Poly-L-Glutamic Acid

Amit Joshi,[†] Arundhati Saraph,[†] Vincent Poon,[‡] Jeremy Mogridge,*[,‡] and Ravi S. Kane*[,†]

The Howard P. Isermann Department of Chemical and Biological Engineering, Rensselaer Polytechnic Institute, Troy, New York 12180, and Department of Laboratory Medicine and Pathobiology, University of Toronto, 1 King's College Circle, Toronto, Ontario M5S1A8, Canada. Received February 21, 2006; Revised Manuscript Received June 18, 2006

We report the synthesis of biodegradable polyvalent inhibitors of anthrax toxin based on poly-L-glutamic acid (PLGA). These biocompatible polyvalent inhibitors are at least 4 orders of magnitude more potent than the corresponding monovalent peptides in vitro and are comparable in potency to polyacrylamide-based inhibitors of anthrax toxin assembly. We have elucidated the influence of peptide density on inhibitory potency and demonstrated that these inhibitory potencies are limited by kinetics, with even higher activities seen when the inhibitors are preincubated with the heptameric receptor-binding subunit of anthrax toxin prior to exposure to cells. These polyvalent inhibitors are also effective at neutralizing anthrax toxin in vivo and represent attractive leads for designing biocompatible anthrax therapeutics.

INTRODUCTION

Polyvalency refers to the simultaneous attachment of multiple ligands to multiple complementary receptors (*1*, *2*). Nature uses polyvalency in a variety of biological contexts, including interactions between bacterial toxins and cell surface receptors (*1*, *3*−*6*). Polyvalent interactions can collectively be much stronger than the corresponding monovalent interactions, and several groups have successfully used this concept to enhance the potency of synthetic ligands (*1*, *2*, *7*−*15*). Linear polymers present an attractive scaffold for the polyvalent display of ligands, because they are easily synthesized and their structure and the composition of ligands can be modulated (*7*, *8*, *11*, *16*−*18*). Poly-L-glutamic acid (PLGA) represents a particularly attractive scaffold for designing polymeric therapeutics because of its high water solubility, biodegradability, and low toxicity (*19*−*21*). Consequently, researchers have conjugated PLGA with drugs such as camptothecin, paclitaxel, doxorubicin or antibodies for drug delivery (*21*−*26*), with DNA for gene delivery (*27*−*29*), and with other ligands for synthesizing inhibitors of the influenza virus (*20*, *30*, *31*).

We report the design of potent polyvalent inhibitors of anthrax toxin based on PLGA. Anthrax toxin—responsible for the major symptoms and death in anthrax—is composed of three proteins: two enzymes, lethal factor (LF) and edema factor (EF), and a cell-binding protein, protective antigen (PA). PA is cleaved into a 63 kDa fragment that forms heptamers, $[PA_{63}]_7$, on the surface of target cells and translocates LF and/or EF into the cytosol wherein they exhibit their toxic effects (*3*). The biocompatible inhibitors reported in this work prevent the binding of LF to $[PA_{63}]_7$ and neutralize anthrax toxin both in vitro and in vivo.

EXPERIMENTAL PROCEDURES

Materials and Methods. Poly-L-glutamic acid sodium salt (M_w = 7.5, 17.6, 41.4 kDa) and 1-hydroxybenzotriazole (HOBt), was purchased from Sigma (St. Louis, MO). 1-[3-(Dimethylamino)propyl]-3-ethylcarbodiimide (EDC) was purchased from Acros Chemicals (Somerville, NJ). Solvents were purchased from Acros Chemicals (Somerville, NJ) and were anhydrous unless stated otherwise. Peptide Ac-HTSTYWWLDGAPK-Am was purchased from Genemed Synthesis, Inc. (South San Francisco, CA). Spectra/Por4 (MWCO = 12 000−14 000) dialysis membranes were purchased from Spectrum Laboratories (Rancho Dominguez, CA). ^{1}H and ^{13}C NMR spectra were recorded on a Varian 500 MHz spectrometer. Chemical shifts are reported in parts per million (ppm) relative to trimethylsilane (TMS) for the ^{1}H NMR spectra and relative to DMSO-d_6 at 39.5 ppm for the ^{13}C spectra. Gel permeation chromatography (GPC) was carried out using a ViscoGEL column (GMPWXL, Mixed Bed, dimensions: 7.8 mm × 30 cm) using phosphate-buffered saline as the eluent (pH 7.5, 20 mM NaH_2PO_4, 130 mM NaCl, flow rate = 1 mL/min, dn/dc = 0.190 mL/g). Molecular weight was estimated using a light scattering instrument (Viscotek 270 Trisec Dual Detector; OmniSEC software, λ = 670 nm). Infrared measurements were made on an FT-IR spectrophotometer (Biorad FTS-3000 MX). CD spectra were recorded on a J-715 instrument (Jasco, Easton, MD) (Xe lamp, cell length 0.2 mm) using the Spectra Manager software.

Synthesis of Activated PLGA. EDC (140 mg, 0.662 mmol) and a solution of HOBt (111 mg, 0.728 mmol) in *N*,*N*-dimethylformamide (DMF) (1 mL) were added to a solution of PLGA sodium salt (50 mg, 0.331 mmol) in water (1 mL) at room temperature (*31*). The reaction mixture was stirred at room temperature for 1 h. The resulting precipitate was washed with water and dried under vacuum. The residue was dissolved in DMF (2 mL) along with HOBt (111 mg), and a solution of EDC (280 mg) in water (1 mL) was added. The reaction mixture was stirred at room temperature for 1 h. The resultant precipitate was washed with water, followed by 2-propanol and dried under vacuum to give activated PLGA (60% yield, complete conversion of carboxylic acid groups to activated esters). ^{1}H NMR (DMSO-d_6): δ 1.6−2.0 (br, 2H), 2.0−2.4 (br, 2H), 3.8−4.3 (br, 1H), 7.2−8.4 (br, m, 4H). ^{13}C NMR (DMSO-d_6): δ 27.2, 30.2, 52.0, 109.9, 119.1, 124.4, 126.8, 127.9. IR (KBr): 3295, 3073, 1717, 1655, 1549, 1388, 1297, 1263, 1105, 777, 742 cm^{-1}. Elemental analysis was carried out after reaction of the activated PLGA with aqueous ammonium hydroxide. Calcd. (%) for 0.7-($C_5H_7NO_3$)·0.3($C_5H_8N_2O_2$)·1H_2O: C, 40.89; H, 6.34; N, 12.41; O, 40.31. Found: C, 39.60; H, 5.84; N, 12.68; O, 38.46.

* Corresponding author. R.S.K.: tel (518) 276 2536; fax (518) 276 4030; e-mail kaner@rpi.edu. J.M.: tel (416) 946 8095; fax (416) 978 5959; e-mail jeremy.mogridge@utoronto.ca.

[†] Rensselaer Polytechnic Institute.

[‡] University of Toronto.

10.1021/bc060042y CCC: $33.50 © 2006 American Chemical Society
Published on Web 08/10/2006

Synthesis of Polyvalent Inhibitors of Anthrax Toxin. Activated PLGA was dissolved in DMF (5 mg/mL, 30 mM of repeat unit). Peptide, Ac-HTSTYWWLDGAPK-Am, dissolved in DMF, was then added to the polymer solution followed by triethylamine (twofold excess based on repeat unit). The mixture was allowed to react overnight at room temperature, following which the unreacted active ester groups in the polymer backbone were quenched using ammonium hydroxide (fivefold excess based on repeat unit). The polymer was dialyzed extensively using MilliQ water for 2 days and lyophilized to yield a white powder. ^{1}H NMR (DMSO-d_6): δ 0.6−0.86 (br), 0.88−1.06 (br), 1.1−1.4 (br), 1.4−1.6 (br), 1.6−2.0 (br), 2.0−2.3 (br), 2.7−3.0 (br), 3.8−3.95 (br), 3.95−4.2 (br), 4.2−4.4 (br), 4.4−4.6 (br), 6.4−6.6 (br), 6.7−6.8 (br), 6.8−7.2 (br), 7.2−7.4 (br), 7.4−7.6 (br), 7.6−8.4 (br).

Estimation of Molecular Weight. Polymers obtained by hydrolysis of activated PLGA with 0.1 N NaOH were characterized using aqueous GPC with a ViscoGEL column (GMPWXL, Mix Bed, dimensions: 7.8 mm × 30 cm) using phosphate-buffered saline as the eluent. The molecular weight was estimated using a laser light scattering instrument (Viscotek 270 Trisec Dual Detector; OmniSEC 4.0 software, λ = 670 nm) inline with the column. A decrease in molecular weight was observed after activation, as reported earlier by Paterson and Leach (*32*); the polydispersity of the polymers was ca. 1.3. The average number of peptides per polymer chain was calculated using the number average molecular weight (M_n) and the peptide density (estimated by ^{1}H NMR spectroscopy), accounting for the error due to the polydispersity of the polymer and the error in estimating the peptide density by NMR spectroscopy.

Circular Dichroism Measurements. Circular dichroism (CD) measurements were carried out at room temperature (23 °C) on a JASCO J-715 spectropolarimeter. The spectra were scanned in a quartz optical cell with a path length of 0.2 mm. All spectra were recorded in 0.2 nm wavelength increments with a 4 s response and a bandwidth of 1 nm and at a scanning speed of 100 nm/min. For observing the secondary structure of the polymers, the samples were dissolved in 20 mM sodium phosphate buffer (pH 7.5), and the spectra were scanned from 180 to 250 nm. Each spectrum is the average of five scans with a full scale sensitivity of 100 mdeg. All spectra were corrected for background.

Cytotoxicity Assay. RAW264.7 cells were grown in RPMI medium supplemented with 5% fetal calf serum (Hyclone). The cells were plated on a 96-well plate and either left untreated or treated with PA (10^{-9} M), LF (3×10^{-10} M), and various concentrations of the inhibitors and incubated for 4 h at 37 °C in 5% CO_2. For the preincubation experiments, $[PA_{63}]_7$ (3×10^{-9} M) was incubated with various concentrations of inhibitors for 0, 1, or 2 h, before adding LF (10^{-9} M) and incubating the mixture with cells for 4 h at 37 °C in 5% CO_2. Cell viability was assessed by adding 20 μL of a mixture of MTS (3-(4, 5-dimethylthiazol-2-yl)-5-(3-carboxymethoxyphenyl)-2-(4-sulfophenyl)-2*H*-tetrazolium) and phenazine methosulfate (PMS) to each well and incubating for 1 h, according to manufacturer's instructions (Promega). The amount of soluble formazan product generated from the reduction of MTS by living cells was determined by measuring the absorbance at 490 nm. The IC_{50} of each inhibitor was determined using the software program *Prism* (GraphPad Software).

Rat Intoxication. Purified PA (40 μg) and LF (8 μg) diluted in PBS were mixed with PBS, the monovalent peptide (300 nmol) in PBS, or the polyvalent inhibitor (300 nmol on a per-peptide basis) in PBS. Fisher 344 rats (Charles River Laboratories) were injected intravenously in the tail vein. The rats were injected with the different mixtures, and the appearance of symptoms of intoxication was monitored. When the symptoms were obvious, the rats were euthanized to avoid unnecessary distress.

Scheme 1. Synthesis of PLGA-based Polyvalent Inhibitor[a]

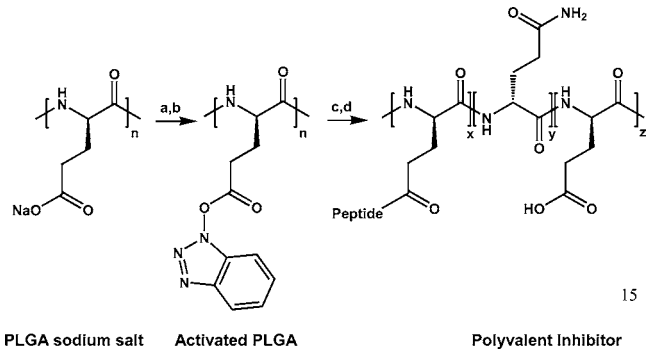

[a] (a) EDC, H_2O; (b) HOBt, DMF; (c) peptide, DMF, TEA (d) NH_4OH, dialysis. The polyvalent inhibitor is a random copolymer composed of peptide conjugates (*x* repeat units), glutamine (*y* repeat units), and glutamic acid (*z* repeat units).

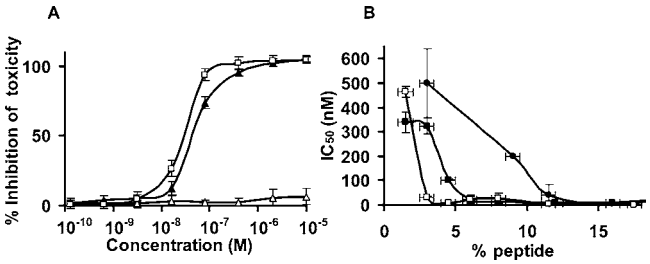

Figure 1. (A) Inhibition of cytotoxicity in cell culture by PLGA-based polyvalent inhibitor (□), polyacrylamide-based polyvalent inhibitor (▲), and control polymer (ammonium hydroxide quenched activated PLGA) (△). (B) Influence of peptide density on the potency of polyvalent inhibitors with different molecular weights M_w = 4.5 kDa (●), 12 kDa (■), and 29 kDa (□); average number of repeat units ca. 27, 70, 170, respectively.

RESULTS AND DISCUSSION

Synthesis and Characterization of PLGA-Based Polyvalent Inhibitors. To synthesize a PLGA-based polyvalent inhibitor, we activated the carboxylic acid groups of PLGA using 1-[3-(dimethylamino)propyl]-3-ethylcarbodiimide (EDC) and 1-hydroxybenzotriazole (HOBt) (see Experimental Procedures). The activated polymer was allowed to react with the peptide Ac-HTSTYWWLDGAPK-Am, a peptide that binds $[PA_{63}]_7$ and inhibits the binding of LF (*7*). The remaining active ester groups were quenched by a reaction with aqueous ammonium hydroxide (Scheme 1). We also synthesized unfunctionalized (control) polymers by reacting the activated polymers with aqueous ammonium hydroxide. Elemental analysis suggested that the polymer backbone of the control polymer was composed of a mixture of glutamine and glutamic acid units (3:7). This polymer had an aqueous solubility in excess of 30 mg/mL.

In Vitro Activity of Polyvalent Inhibitors. To test the ability of the PLGA-based polyvalent inhibitors to neutralize anthrax toxin in vitro, we incubated RAW264.7 cells with a mixture of PA and LF in the presence or absence of inhibitors. While the monovalent peptide had no activity at concentrations as high as 250 μM (data not shown), the polyvalent inhibitor could inhibit toxin activity with a half-maximal inhibitory concentration (IC_{50}) of 20 nM on a per-peptide basis (Figure 1A). Polyvalency therefore enabled an enhancement in the potency of the peptide by over 4 orders of magnitude. Unfunctionalized polymers showed no appreciable activity (Figure 1A). Furthermore, the potency of the inhibitor based on the biocompatible

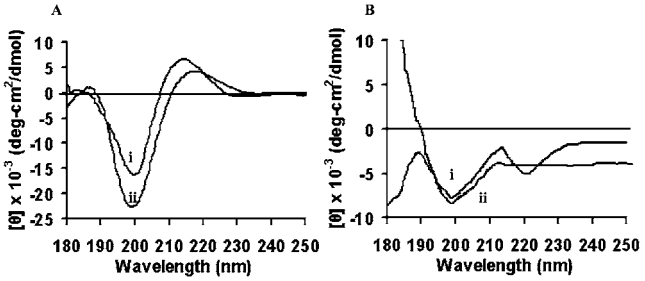

Figure 2. (A) CD spectrum of (i) ammonia hydrolyzed activated PLGA, (ii) NBS-treated PLGA-based polyvalent inhibitor. (B) CD spectrum of (i) monovalent peptide, (ii) NBS-treated monovalent peptide. [θ] is the mean residue molar ellipticity.

polymer, PLGA, was comparable to that of a previously reported inhibitor based on a polyacrylamide backbone (IC_{50} = 50 nM) (Figure 1A) (*33*).

Influence of Peptide Density on the Potency of the Polyvalent Inhibitors. To elucidate the influence of peptide density on inhibitory potency, we synthesized a series of polyvalent molecules based on PLGA backbones of three different molecular weights, with peptide densities varying between 0% and 18%. For each backbone, we observed an initial sharp increase in potency (decrease in IC_{50}) with increasing peptide density, followed by a transition to a plateau, where the potency is independent of peptide density (Figure 1B). While the polydispersity of the backbone prevents a precise estimation of the number of peptide units per chain near the transition, the number was small (less than ten) for each backbone and was also close to the number of peptide-binding sites on the heptameric target (seven).

Characterization of PLGA-Based Polyvalent Inhibitors by Circular Dichroism Spectroscopy. To further characterize these polyvalent molecules, we used circular dichroism (CD) spectroscopy. Characterization by CD spectroscopy revealed that the unfunctionalized (control) polymer obtained by the reaction of activated PLGA with aqueous ammonium hydroxide exists in an unordered (random coil) structure as seen from the strong negative band near 200 nm (Figure 2A) (*34*). A similar spectrum was previously reported for PLGA (*35*, *36*). The CD spectrum of the monovalent peptide shows two minima, one near 222 nm, which is characteristic of tryptophans (*37*), and the other near 200 nm (Figure 2B). In order to resolve the spectrum, we treated the monovalent peptide and the PLGA-based polyvalent inhibitor with *N*-bromosuccinimide (NBS), which is known to oxidize the indole of tryptophan to oxindole, resulting in the disappearance of the peak near 222 nm (*38*). The resulting spectra show that the monovalent peptide and the polyvalent inhibitor exist as unordered (random coil) structures (Figure 2A,B). The CD spectrum of the NBS-treated peptide is similar near 200 nm to that of the unmodified peptide, indicating that there is no significant change in the secondary structure of the peptide on modification.

Influence of Kinetics on the Potency of the Polyvalent Inhibitors. We hypothesized that the enhancement in potency obtained through polyvalency might be limited by kinetics, since equilibrium between the polyvalent inhibitor and $[PA_{63}]_7$ might not be reached before the toxin is endocytosed. To determine if kinetics limit the potency of the polyvalent inhibitor, we preincubated the inhibitor with $[PA_{63}]_7$ for different amounts of time before adding LF and exposing cells to this mixture. If kinetics play a role in influencing the potency of the inhibitor, then one would expect the IC_{50} to decrease with increasing preincubation time. We observed an order of magnitude decrease in the IC_{50} of the inhibitors following preincubation with $[PA_{63}]_7$ for 2 h (Figure 3), confirming that the enhancement in inhibitory potency is limited by kinetics.

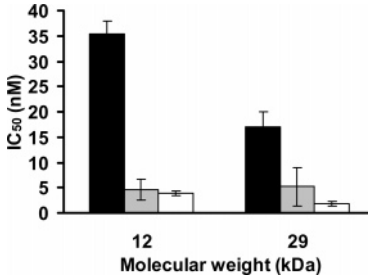

Figure 3. Preincubation of $[PA_{63}]_7$ with a polyvalent inhibitor decreases the measured IC_{50}. $[PA_{63}]_7$ was incubated with various concentrations of two different molecular weight inhibitors for 0 h (■), 1 h (grey shaded column), and 2 h (□). Following the preincubation period, the inhibitor−$[PA_{63}]_7$ mixtures were tested in cytotoxicity assays.

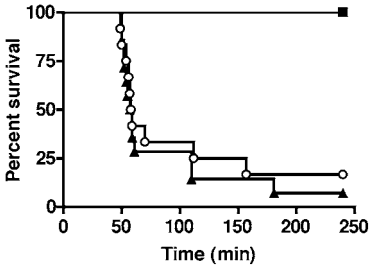

Figure 4. PLGA-based inhibitor protects rats from lethal toxin challenge. Rats were injected with lethal toxin alone (▲, n = 14), lethal toxin plus Ac-HTSTYWWLDGAPK-Am peptide (○, n = 12), or lethal toxin plus PLGA-based inhibitor (■, n = 7). The log-rank test indicates a statistically significant difference between the group that received lethal toxin alone and the group that received the toxin plus the PLGA-based inhibitor (P = 0.0002), but no significant difference between the group that received lethal toxin alone and the group that received the toxin along with peptide (P = 0.54).

In Vivo Activity of PLGA-Based Polyvalent Inhibitors. Biocompatible and biodegradable polymer scaffolds are particularly suitable for the synthesis of anthrax toxin inhibitors that can be used in vivo. We therefore tested the ability of PLGA-based inhibitors to neutralize anthrax toxin in Fischer rats. Although the inhibitor was coinjected with the toxin, neutralization could occur only in vivo, since the inhibitor binds to $[PA_{63}]_7$ and not to PA. As seen in Figure 4, 13 of 14 rats injected with toxin alone (40 μg of PA and 8 μg of LF) became moribund, while none of the rats that received the polyvalent inhibitor along with the toxin became moribund. The log-rank test indicates that the difference between these two groups is statistically significant (P = 0.0002). In contrast, the log-rank test does not indicate a significant difference between the group that received lethal toxin alone and the group that received the toxin along with the monovalent peptide (P = 0.54; see Figure 4).

CONCLUSION

In summary, we have designed inhibitors of anthrax toxin that are more than 4 orders of magnitude more potent than the corresponding monovalent inhibitors. This study shows that even a small number of pendant ligands, which is close to the number of binding sites on the target, may be sufficient to synthesize a potent polyvalent inhibitor. The enhancements in potency obtained from polyvalent systems may not be governed solely by thermodynamics, as is often assumed, but also by the kinetics of binding, suggesting that the intrinsic enhancements in affinity may be even greater than the already impressive numbers reported. These PLGA-based inhibitors are comparable in potency to the best polyvalent inhibitors of anthrax toxin assembly, and the biocompatibility of their scaffolds makes them attractive for in vivo use.

ACKNOWLEDGMENT

This research was supported by NIH grant U01 AI056546. We thank the Biochemistry Core Facility at the Wadsworth Center for use of the circular dichroism and chromatography instrumentation.

LITERATURE CITED

(1) Mammen, M., Choi, S.-K., and Whitesides, G. M. (1998) Polyvalent interactions in biological systems: Implications for design and use of multivalent ligands and inhibitors. *Angew. Chem., Int. Ed. 37*, 2754−2794.

(2) Kiessling, L. L., Strong, L. E., and Gestwicki, J. E. (2000) Principles for multivalent ligand design. *Annu. Rep. Med. Chem. 35*, 321−330.

(3) Bradley, K. A., Mogridge, J., Mourez, M., Collier, R. J., and Young, J. A. T. (2001) Identification of the cellular receptor for anthrax toxin. *Nature (London) 414*, 225−229.

(4) Scobie, H. M., Rainey, G. J. A., Bradley, K. A., and Young, J. A. T. (2003) Human capillary morphogenesis protein 2 functions as an anthrax toxin receptor. *Proc. Natl. Acad. Sci. U.S.A. 100*, 5170−5174.

(5) Holmgren, J., Lönnroth, I., Mansson, J.-E., and Svennerholm, L. (1975) Interaction of cholera toxin and membrane GM1 ganglioside of small intestine. *Proc. Natl. Acad. Sci. U.S.A. 72*, 2520−2524.

(6) Ling, H., Boodhoo, A., Hazes, B., Cummings, M. D., Armstrong, G. D., Brunton, J. L., and Read, R. J. (1998) Structure of the shiga-like toxin I B-pentamer complexed with an analogue of its receptor Gb3. *Biochemistry 37*, 1777−1788.

(7) Mourez, M., Kane, R. S., Mogridge, J., Metallo, S., Deschatelets, P., Sellman, B. R., Whitesides, G. M., and Collier, R. J. (2001) Designing a polyvalent inhibitor of anthrax toxin. *Nat. Biotechnol. 19*, 958−961.

(8) Sigal, G. B., Mammen, M., Dahmann, G., and Whitesides, G. M. (1996) Polyacrylamides bearing pendent α-sialoside groups strongly inhibit agglutination of erythrocytes by influenza virus: The strong inhibition reflects enhanced binding through cooperative polyvalent interactions. *J. Am. Chem. Soc. 118*, 3789−3800.

(9) Kitov, P. I., Sadowski, J. M., Mulvey, G., Armstrong, G. D., Ling, H., Pannu, N. S., Read, R. J., and Bundle, D. R. (2000) Shiga-like toxins are neutralized by tailored multivalent carbohydrate ligands. *Nature (London) 403*, 669−672.

(10) Fan, E., Zhang, Z., Minke, W. E., Hou, Z., Verlinde, C. L. M. J., and Hol, W. G. J. (2000) High-affinity pentavalent ligands of *Escherichia coli* heat-labile enterotoxin by modular structure-based design. *J. Am. Chem. Soc. 122*, 2663−2664.

(11) David, A., Kopeckova, P., Rubinstein, A., and Kopecek, J. (2001) Enhanced biorecognition and internalization of HPMA copolymers containing multiple or multivalent carbohydrate side-chains by human hepatocarcinoma cells. *Bioconjugate Chem. 12*, 890−899.

(12) Zhang, Z., Merritt, E. A., Ahn, M., Roach, C., Hou, Z., Verlinde, C. L., Hol, W. G., and Fan, E. (2002) Solution and crystallographic studies of branched multivalent ligands that inhibit the receptor-binding of cholera toxin. *J. Am. Chem. Soc. 124*, 12991−12998.

(13) Metallo, S. J., Kane, R. S., Holmlin, R. E., and Whitesides, G. M. (2003) Using bifunctional polymers presenting vancomycin and fluorescein groups to direct anti-fluorescein antibodies to self-assembled monolayers presenting D-alanine-D-alanine groups *J. Am. Chem. Soc. 123*, 4534−4540.

(14) Zhang, G., Leibowitz, M. J., Sinko, P. J., and Stein, S. (2003) Multiple-peptide conjugates for binding β-amyloid plaques of Alzheimer's disease. *Bioconjugate Chem. 14*, 86−92.

(15) Gujraty, K., Sadacharan, S., Frost, M., Poon, V., Kane, R. S., and Mogridge, J. (2005) Functional characterization of peptide-based anthrax toxin inhibitors. *Mol. Pharm. 2*, 367−372.

(16) Lees, W. J., Spaltenstein, A., Kingery-Wood, J. E., and Whitesides, G. M. (1994) Polyacrylamides bearing pendant α-sialoside groups strongly inhibit agglutination of erythrocytes by influenza A virus: Multivalency and steric stabilization of particulate biological systems. *J. Med. Chem. 37*, 3419−3433.

(17) Mammen, M., Dahmann, G., and Whitesides, G. M. (1995) Effective inhibitors of hemagglutination by influenza virus synthesized from polymers having active ester groups. Insight into mechanism of inhibition. *J. Med. Chem. 38*, 4170−4190.

(18) Carrillo, A., Gujraty, K. V., Rai, P. R., and Kane, R. S. (2005) Design of water-soluble, thiol-reactive polymers of controlled molecular weight: a novel multivalent scaffold. *Nanotechnology 16*, S416−421.

(19) Li, C. (2002) Poly(L-glutamic acid)-anticancer drug conjugates. *Adv. Drug Delivery Rev. 54*, 695−713.

(20) Kamitakahara, H., Suzuki, T., Nishigori, N., Suzuki, Y., Kanie, O., and Wong, C. H. (1998) A lysoganglioside poly-L-glutamic acid conjugate as a picomolar inhibitor of influenza hemagglutinin. *Angew. Chem., Int. Ed. 37*, 1524−1528.

(21) Hirabayashi, H., Nishikawa, M., Takakura, Y., and Hashida, M. (1996) Development and pharmacokinetics of galactosylated poly-L-glutamic acid as a biodegradable carrier for liver-specific drug delivery. *Pharm. Res. 13*, 880−884.

(22) Vega, J., Ke, S., Fan, Z., Wallace, S., Charsangavej, C., and Li, C. (2003) Targeting doxorubicin to epidermal growth factor receptors by site-specific conjugation of C225 to poly(L-glutamic acid) through a polyethylene glycol spacer. *Pharm. Res. 20*, 826−832.

(23) Li, C., Yu, D. F., Newman, R. A., Cabral, F., Stephens, L. C., Hunter, N., Milas, L., and Wallace, S. (1998) Complete regression of well-established tumors using a novel water-soluble poly(L-glutamic acid)−paclitaxel conjugate. *Cancer Res. 58*, 2404−2409.

(24) Singer, J. W., Bhatt, R., Tulinsky, J., Buhler, K. R., Heasley, E., Klein, P., and De Vries, P. (2001) Water-soluble poly(L-glutamic acid)−Gly−camptothecin conjugates enhance camptothecin stability and efficacy in vivo. *J. Controlled Release 74*, 243−247.

(25) Singer, J. W., De Vries, P., Bhatt, R., Tulinsky, J., Klein, P., Li, C., Milas, L., Lewis, R. A., and Wallace, S. (2000) Conjugation of camptothecins to poly(L-glutamic acid). *Ann. N. Y. Acad. Sci. 922*, 136−150.

(26) Bhatt, R., de Vries, P., Tulinsky, J., Bellamy, G., Baker, B., Singer, J. W., and Klein, P. (2003) Synthesis and in vivo antitumor activity of poly(L-glutamic acid) conjugates of 20S-camptothecin. *J. Med. Chem. 46*, 190−193.

(27) Dekie, L., Toncheva, V., Dubruel, P., Schacht, E. H., Barrett, L., and Seymour, L. W. (2000) Poly-L-glutamic acid derivatives as vectors for gene therapy. *J. Controlled Release 65*, 187−202.

(28) Dubruel, P., Dekie, L., and Schacht, E. (2003) Poly-L-glutamic acid derivatives as multifunctional vectors for gene delivery. Part A. Synthesis and physicochemical evaluation. *Biomacromolecules 4*, 1168−1176.

(29) Dubruel, P., Dekie, L., Christiaens, B., Vanloo, B., Rosseneu, M., Van De Kerckhove, J., Mannisto, M., Urtti, A., and Schacht, E. (2003) Poly-L-glutamic acid derivatives as multifunctional vectors for gene delivery. Part B. Biological evaluation. *Biomacromolecules 4*, 1177−1183.

(30) Totani, K., Kubota, T., Kuroda, T., Murata, T., Hidari, K. I., Suzuki, T., Suzuki, Y., Kobayashi, K., Ashida, H., Yamamoto, K., and Usui, T. (2003) Chemoenzymatic synthesis and application of glycopolymers containing multivalent sialyloligosaccharides with a poly(L-glutamic acid) backbone for inhibition of infection by influenza viruses. *Glycobiology 13*, 315−326.

(31) Honda, T., Yoshida, S., Arai, M., Masuda, T., and Yamashita, M. (2002) Synthesis and anti-influenza evaluation of polyvalent sialidase inhibitors bearing 4-guanidino-Neu5Ac2en derivatives. *Bioorg. Med. Chem. Lett. 12*, 1929−1932.

(32) Paterson, Y., and Leach, S. J. (1980) Chain fission of poly-L-glutamic acid by a water-soluble carbodiimide. *Biochem. Biophys. Res. Commun. 95*, 1722−1729.

(33) Gujraty, K. V., Joshi, A., Saraph, A., Poon, V., Mogridge, J., and Kane, R. S. (2006) Synthesis of Polyvalent Inhibitors of Controlled Molecular Weight: Structure−Activity Relationship for Inhibitors of Anthrax Toxin. *Biomacromolecules*, *7*, 2082−2085.

(34) Yang, J. T., Wu, C.-S. C., and Martinez, H. M. (1986) Calculation of protein conformation from circular dichroism. *Methods Enzymol. 130*, 208−269.

(35) Adler, A. J., Hoving, R., Potter, J., Wells, M., and Fasman, G. D. (1968) Circular dichroism of polypeptides. Poly(hydroxyethyl-L-glutamine) compared to poly(L-glutamic acid). *J. Am. Chem. Soc. 90*, 4736−4738.

(36) Kimura, T., Takahashi, S., Akiyama, S., Uzawa, T., Ishimori, K., and Morishima, I. (2002) Direct observation of the multistep helix formation of poly-L-glutamic acid. *J. Am. Chem. Soc. 124*, 11596−11597.

(37) Woody, R. W. (1994) Contributions of tryptophan side chains to the far-ultraviolet circular dichroism of proteins. *Eur. Biophys. J. 23*, 253−262.

(38) Arnold, G. E., Day, L. A., and Dunker, A. K. (1992) Tryptophan contributions to the unusual circular dichroism of fd bacteriophage. *Biochemistry 31*, 7948−7956.

BC060042Y

Synthesis and Characterization of AP5346, a Novel Polymer-Linked Diaminocyclohexyl Platinum Chemotherapeutic Agent

Paul Sood,* K. Bruce Thurmond, II, Jeremy E. Jacob, Lynda K. Waller, George O. Silva, Donald R. Stewart, and David P. Nowotnik

Access Pharmaceuticals, Inc., 2600 Stemmons Freeway, Suite 176, Dallas, Texas 75207. Received March 1, 2006; Revised Manuscript Received June 28, 2006

Syntheses of the novel polymer-bound platinum-based chemotherapeutic agent poly(HPMA)-GGG-Ama=Pt=(1*R*,2*R*)-DACH, AP5346, and its precursors are reported. The method utilized in preclinical development of AP5346 is described herein. Additionally, an improved synthesis, which has shown that ion exchange resins can be removed, significantly less platinum can be used when the reaction mixture is pH-stated, and the synthesis can be performed at a higher concentration, is reported. These combined improvements result in a more cost-effective, scaleable procedure. Various methods of analysis of the drug substance are also discussed. Specifically, ^{1}H NMR spectroscopy is used for identity and can also distinguish small molecule impurities to below 0.1%. ^{195}Pt NMR determines the coordination environment of the platinum and also identity and purity in relation to platinum chelation of the construct. Size exclusion chromatography is used to establish the molecular weight of AP5346 while ICP-AES determines platinum content and platinum release rates in phosphate-buffered saline. The cumulative results of this work have yielded an efficient syntheses of a polymer-based chemotherapeutic agent with subsequent detailed characterization methods.

INTRODUCTION

Since the serendipitous discovery of the anticancer properties of cisplatin by Rosenberg (*1*), platinum-containing drugs have been extensively used in the treatment of solid tumors (*2*). When administered with other agents, cisplatin has exhibited remarkable activity against refractive disease states. In combination chemotherapy with paclitaxel survival rates of patients with advanced ovarian cancer are significantly improved, while co-administering the drug with vinblastine and bleomycin is extremely effective against testicular cancer (*3*). This effectiveness has resulted in cisplatin now being one of the three most utilized chemotherapeutics in the world. However, clinical use of cisplatin has been limited by the severe side effects which accompany its use, the most prominent being nephrotoxicity, neurotoxicity, nausea, and vomiting (*4*−*7*). Additionally, intrinsic or acquired tumor resistance is a major issue.

Such limitations, coupled with a narrow therapeutic index and poor solubility, have been the driving force behind a sustained research effort into the discovery of novel platinum agents or novel formulations and delivery methods of existing platinum agents. The resulting compounds would preferably have better toxicity profiles, improved efficacies, and a broader spectrum of activity. Many new platinum molecules have undergone preclinical and clinical testing; however, only carboplatin and oxaliplatin (Figure 1) have been approved worldwide for routine use in the clinic. Additionally, nedaplatin has been approved for use against ovarian and cervical cancers in Japan (*8*). The *cis*-NH_3 ligands in cisplatin are also present in both carboplatin and nedaplatin, whereas the two chlorides have been replaced by the more stable cyclobutanedicarboxylate and glycolate ligands, respectively. In oxaliplatin the *cis*-NH_3 groups have been replaced by a diaminocyclohexyl (DACH) chelate ligand and the chlorides by an oxalato chelate. The influence of structure on the activity and toxicity of Pt anti-cancer drugs has been comprehensively described by Hambley (*9*). Carboplatin has been shown to less toxic than cisplatin and therefore can be administered at much higher doses (*10*) with the dose-limiting toxicity being myelosuppression (*11*). Oxaliplatin is active in colorectal cancer and has supplanted carboplatin and cisplatin as the largest selling platinum therapeutic. Despite its success, the most frequently encountered dose-limiting toxicity of this agent is acute onset neurotoxicity which is observed in approximately 90% of patients, while 10−15% of patients suffer from cumulative sensory neuropathy (*12*).

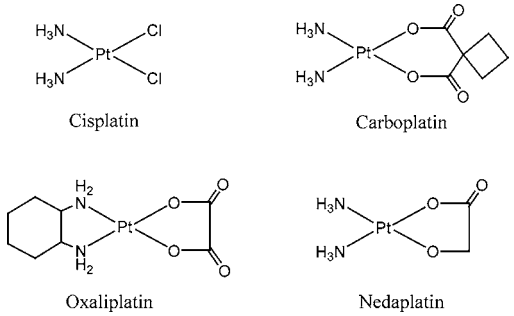

Figure 1. Structures of cisplatin, carboplatin, oxaliplatin, and nedaplatin.

In order to improve the therapeutic index of platinum agents, Access Pharmaceuticals has used a rational drug design approach, based on the principles of polymer drug delivery, to develop a polymer-linked DACH-platinum chemotherapeutic, AP5346. The biodistribution of soluble macromolecules is governed extensively by their ability to penetrate endothelial layers. As growing tumors establish their own blood supply, they develop pathological neovasculature whose blood vessels are frequently hyperpermeable to circulating macromolecules and small particulates. In addition to this enhanced permeability, tumor tissue often has limited lymphatic and/or capillary drainage, so the macromolecules can be trapped and concentrated in tumors (extensively reviewed in ref 13). If a chemotherapeutic agent is coupled to a suitable polymer or other

* Corresponding author. E-mail: paul.sood@accesspharma.com. Phone: 214 905 5100. Fax: 214 905 5101.

10.1021/bc0600517 CCC: $33.50 © 2006 American Chemical Society
Published on Web 08/15/2006

macromolecular carrier *via* a biodegradable linker, then such carriers have the potential of increasing the concentration of the chemotherapeutic agent within the tumor tissue. As a result of these characteristics, concentrations of polymer−drug conjugates in tumor tissue can reach levels some 10−100 times higher than that produced by administration of the free drug (*14*). This effect has been termed the "enhanced permeability and retention" (EPR) effect (*15*). In addition, the intrinsic cytotoxicity of the native drug is often substantially diminished when the drug is chemically linked to the polymer. This also reduces the systemic toxicity of the polymer−drug conjugate relative to the native drug.

The concept of linking a platinum agent to the water-soluble, biocompatible copolymer, *N*-(2-hydroxypropyl)methacrylamide (HPMA), was initially developed at the School of Pharmacy, University of London (*16*). The first HPMA-based chemotherapeutic drug conjugate to enter clinical trials was an HPMA−doxorubicin conjugate named PK1 (*17*). An analogue of PK1, named PK2, is also under clinical evaluation (*18*). Additional poly(HPMA)-based drug (camptothecin and paclitaxel) conjugates have also been investigated (*19, 20*). Generally for HPMA polymer platinum constructs, conjugates are synthesized by copolymerization of HPMA monomer with another monomer unit containing an oligopeptide side chain. The latter moiety contains an activated group such as a paranitrophenoxy unit, which can be substituted with a chelating ligand. This terminus to the oligopeptide is then further reacted with a platinum reagent to form the polymer−platinum construct (*21*). In other synthetic methodologies, cyclic polyphosphazene is polymerized to form a linear polyphosphazene backbone unit to which a linker-glutamate chelator moiety is then attached (*22*). This is subsequently reacted with a platinum agent to form the drug−polymer entity. A review of current polymer−platinum drug syntheses was described by Siegmann-Louda and Carraher (*23*).

The polymer-linked DACH−platinum agent AP5346 is a further example of an HPMA-based polymer therapeutic which was designed to deliver more platinum-containing drug to the tumor than can be achieved by conventional small molecule platinum agents. It consists of a hydrophilic polymer backbone linked by a tripeptide to a chelated platinum (II) species. The structure is denoted as poly(HPMA)-GGG-Ama═Pt═1*R*,2*R*-DACH, where HPMA denotes the polymer backbone, GGG denotes the tripeptide glycyl-glycyl-glycine, and the Ama═Pt═1*R*,2*R*-DACH denotes the *N*,*O*-amidomalonate═Pt-(1*R*,2*R*)-diaminoclyclohexane chelate. Preclinical data for AP5346 shows that it repeatedly exhibits superior tumor growth inhibition in numerous cell lines than oxaliplatin (*24*, *25*). This paper describes the AP5346 manufacturing procedure and characterization methods developed prior to the initiation of clinical trials, and details of an improved synthetic procedure.

EXPERIMENTAL PROCEDURES

Materials. Commercial reagents and solvents were purchased from the following sources: Pyridine (Fisher), ethanol (absolute, Aaper Alcohol), ethyl acetate (HPLC grade, Fisher), diethyl ether (ACS, Fisher), acetone (HPLC grade, Fisher), AIBN (Aldrich, recrystallized from dichloromethane), triethylamine (Aldrich), Bio-Rex MSZ 501 D resin (Bio-Rad), $DACHPt(NO_3)_2$ (Strem).

Instrumentation. NMR spectra were recorded on a Bruker AVANCE300 multinuclear NMR spectrometer resonating at 300.131 MHz for ^1H and 64.354 MHz for ^{195}Pt. A Bruker Variable Temperature unit held samples at a constant temperature of 300 K. ^1H NMR samples were prepared by dissolving 20 ± 5 mg of material in 0.7 mL of D_2O and then filtering the sample into a 5 mm NMR tube. ^1H resonances were referenced to TMSP at 0 ppm. ^{195}Pt NMR samples were prepared by dissolving 100 ± 5 mg of AP5346 in 0.7 mL of 93/7 H_2O/D_2O and filtering the sample into a 5 mm NMR tube. ^{195}Pt resonances were externally referenced to Na_2PtCl_6 at 0 ppm. Spectra were obtained using a broadband observe 5 mm probe with *z*-axis gradient capability. ^1H spectra were acquired using the standard Bruker pulse program *zg30* with 16 scans in 25 K data points over a 3.592 kHz spectral width (3.5 s acquisition time). For ^{195}Pt NMR experiments the 90° pulse width was calculated from the 360° pulse width using the Na_2PtCl_6 sample with the transmitter on resonance. The transmitter power was set to give a 90° pulse of ca. 10 μs. For samples of AP5346 the transmitter offset (o1p) was placed midway between the N,O- and N,N-chelates at −2550 ppm. The Bruker pulse program *zgmultiscan* was modified to execute a very short delay time (set at d1 = 2 ms) followed by a hard 90° pulse. The experiment was run in increments of 20 000 scans (ns = 20 000) over a 130 kHz sweep width (9 ms acquisition time). A loop counter parameter l3 = 100 was incorporated such that the initial iteration of 20 000 scans was repeated 90 times to give an accumulated number of 2 000 000 scans (the FIDs from each iteration were automatically combined and Fourier transformed to produce the frequency domain spectrum). The FIDs of AP5346 samples were processed to determine what peaks were present and the percent of the N,O-chelate relative to the total area of all integrated peaks. To these ends the following steps were taken with the exponential line broadening set at 150 Hz. The line broadening was selected prior to Fourier transform of the FID and may be increased or decreased appropriately to obtain the best resolved spectrum. First, the FID was left-shifted, Fourier transformed, and phased. This step was repeated until the baseline was flat. Second, a polynomial baseline correction was applied to the spectrum. Finally, the integral values were set such that the total of the integrated peaks was 100 which produced a convenient percent ratio of chelates. ^1H and ^{195}Pt NMR were used to determine both identity and purity of AP5346. For identity, the former indicates the presence of HPMA and MA-Gly-Gly-Gly-derived subunits while the latter shows the chelation environment of the platinum complexes and the chelate ratio. ^1H NMR was used to determine the percent of impurities with fixed or nonexchangeable hydrogen atoms such as ethanol and isopropyl alcohol. ^{195}Pt NMR was used to verify purity in that no less than 90% of the integrated peaks correspond to the amido-malonato-N,O-chelate.

A Viscotek TriSec Model 302 gel permeation chromatography (GPC) instrument was used to determine molecular weight distribution as reported by the M_w, M_n, and polydispersity index (PDI) of AP5346. The system consists of an HPLC pump with an autosampler, a refractive index detector, and a column oven set at 40 °C. Three PL Aquagel-OH mixed bed columns (one 70 × 7.5 mm guard column and two 300 × 7.5 mm analytical columns with 8 μm particles) were used. The mobile phase consists of 35/65 $MeOH/H_2O$ with 10 mM $LiClO_4$ and was pumped at 1.0 mL/min. The columns were calibrated with PEO/PEG standards (∼1.5 to 205 kD) and results fit to a fourth order polynomial of $\log(M_p)$ vs RT^{-1}. The sample was dissolved in mobile phase to give a ∼1 mg/mL solution of which 100 μL was injected. The standards and sample were run in triplicate. The reported values for M_w, M_n, and PDI represent the average of the three determinations.

Inductively coupled plasma-atomic emission spectroscopy (ICP-AES) was used for the determination of platinum in two identity analyses and one purity analysis. The identity tests were the determination of %Pt in AP5346 and the %Pt released from the polymer system at 3 and 24 h in PBS at 38 °C. The purity test was the determination of the %free Pt in pure water at ambient temperature. While release of low molecular weight platinum species within the tumor extracellular fluid or the

malignant cell itself is probably required for anticancer activity, the pharmaceutical constraints of a drug product mandate that the platinum complex remains bound to the polymer prior to administration and that release of platinum from AP5346 be minimal while in systemic circulation. The release of platinum species from the polymer carrier of AP5346 is of interest for both pharmaceutical and physiological reasons. From a pharmaceutical perspective, the release of platinum from AP5346 is a fundamental chemical characteristic, and it is a requirement of a pharmaceutical product that this property remain within a narrow range for all batches of the manufactured product.

The %Pt was determined by accurately weighing 15 ± 0.1 mg of AP5346 into each of three 20 mL scintillation vials. An accurately weighed quantity of 20 g of 3% HNO_3 was added to each vial and the mixture was vortexed to give a homogeneous sample. Platinum standards at 0, 30, and 60 ppm were prepared from a dilution of a 1000 ppm certified Pt standard in 3% HNO_3. The emission at 214.42 nm of the samples and standards were detected. From these standards a calibration curve was generated from which the amount of platinum in the sample was calculated. The results from the three samples were averaged and reported as the %Pt.

The %Pt released at 3 and 24 h from a PBS solution at 38 °C was determined by weighing 42 ± 0.1 mg of AP5346 into a 50 mL Corning centrifuge tube. Sufficient PBS solution (Sigma Chemicals: 120 mM NaCl, 2.7 mM KCl, 10 mM sodium phosphate salts, pH ~7.4) was added to make a ~2 mg/mL solution, and the mixture was vortexed to homogeneity. The solution was placed in an oven at 38 °C. After 3 h a 2.5 mL aliquot was transferred to each of three prewashed Centricon YM-3 (Millipore Corporation, 3 kDa NMWCO) ultracentrifugation devices. The charged devices were spun down at 38 °C and 4100 rpm for 90 min. After 24 h at 38 °C three additional prewashed Centricon YM-3 devices were similarly charged and centrifuged. A sample for the total Pt content is prepared by diluting 200 μL of the stock solution with 4 mL of the HNO_3/PBS solution. The six filtrates were transferred into 7 mL scintillation vials containing 4.0 mL of a 3% HNO_3/PBS solution from which a calibration curve was generated. The Pt concentration of the stock solution and the 3 and 24 h samples were determined from the emission at 214.42 nm. The %Pt released at 3 and 24 h is calculated from the ratio of the Pt content in the filtrates relative to the stock solution. The average of the three samples at each timepoint was reported.

The %free Pt of AP5346 was determined in pure water at ambient temperature. The method used was similar to that described above for 3 and 24 h release rates in PBS except the stock solution was allowed to stand for 1 h before being centrifuged. In this case, however, the calibration curve is generated using 0, 5, and 10 ppm Pt standards. The free Pt was a combination of (i) unbound small molecule Pt species, (ii) small molecule Pt species released from the polymer, and (iii) Pt attached to lower molecular weight polymer chains which have breached the membrane.

The sodium, chloride and phosphate (as phosphorus) contents were determined by elemental analysis by Desert Analytics, Tucson, AZ. These values represent the extent to which salts used in the synthesis have been removed. The sodium analysis also provides details regarding the purity of AP5346, which is a sodium salt and should contain one sodium per amidomalonato-bound platinum. This equates to a theoretical %Na of around 1%.

Tangential Flow Filtration (TFF). AP5346 was purified by an ultrafiltration technique called tangential flow filtration (TFF). This technique, where the filtered solution is pumped tangentially to the membrane, utilizes the large difference in molecular weights for the separation between AP5346 and any small molecules or ions. The TFF membranes retain large molecules and allow the small molecule or salt impurities to pass through. The retained solution is called the retentate, and the filtered solution is called the permeate or filtrate. Water for injection (WFI) quality water is used to make up the water that appears in the permeate. When seven or more volumes of permeate relative to the initial retentate volume have been collected, the concentration of small impurities have been reduced to <0.1% of their initial concentration. Because the AP5346 material is within the same size range as endotoxins, only WFI quality water was used in the preparation and in the TFF purification steps.

Initial AP5346 General Synthesis. The preclinical procedure for the synthesis of AP5346 is depicted in Figure 2. In the first step the "ONp polymer" was synthesized from two monomers using a known literature method (*26*). This material was then converted to the aminomalonate-containing polymer (the "Ame-polymer"), hydrolyzed, and platinated with subsequent purification to produce AP5346.

ONp-Polymer Synthesis. An oven-dried 10 L media bottle containing a magnetic stir bar, a three-port cap, a Teflon sparging tube, and under an $Ar_{(g)}$ flow was charged with acetone (4.7 L), MA-GG-ONp (75.2 g, 0.23 mol, 1 equiv), and HPMA (369.4 g, 2.6 mol, 11 equiv). Ar was sparged through the vigorously stirring mixture to remove oxygen for 90 min. A solution of AIBN (25.6 g, 0.16 mol, 0.7 equiv) in acetone (0.2 L) was added to the reaction mixture. Sparging with Ar was continued for an additional 90 min. The bottle was sealed from the Ar flow and heated at 50 °C for 48 h (no stirring).

After 48 h a white precipitate had formed on the bottom of the bottle and it was collected *via* centrifugation. The polymer precipitate was washed with acetone (3 × 250 mL) and diethyl ether (3 × 250 mL) and centrifuged after each wash. The supernatant was decanted and discarded each time. The polymer was dried *in vacuo* to afford 336 g of white product (76% yield).

Conversion From ONp- to Ame-Polymer. An oven-dried 10 L media bottle containing a magnetic stir bar, a septum cap, and under an Ar flow was charged with pyridine (3 L), glycylamidomalonate trifluoroacetic acid salt (TFA-Gly-Ame) (147.3 g, 0.43 mol, 2.8 equiv), and triethylamine (64.5 g, 0.64 mol, 4.1 equiv). Once a homogeneous solution was achieved, poly(HPMA)-GG-ONp (298 g, 0.15 mol, 1 equiv) was added slowly while maintaining vigorous stirring. After 2.5 h, a sample was analyzed *via* HPLC to determine the concentration of free and total *p*-nitrophenol. Once the analysis indicated 100% free, the reaction mixture was heated for an additional 2 h at 40 °C to ensure completion.

The polymer was precipitated by adding ethyl acetate/diethyl ether (6/1) (7 × total volume) to the vigorously stirring polymer solution. The precipitated polymer was collected *via* centrifugation, washed with Et_2O (2 × 250 mL), and centrifuged after each wash. The supernatant was decanted and discarded each time. The polymer was dried *in vacuo*.

A 10 L media bottle was charged with ethanol (2 L), and with vigorous stirring the polymer was added slowly. Once the polymer was in solution, the stirring was stopped, and prewashed (with ethanol) Bio-Rex MSZ 501D Resin (1 kg) was added. After 2.5 h the resin was removed *via* filtration and thoroughly washed with ethanol. All washings and filtrate were combined. The polymer was precipitated by adding ethyl acetate/diethyl ether (10/1) (6 × total volume) to the vigorously stirring polymer solution. The precipitated polymer was collected *via* centrifugation, washed with Et_2O (3 × 250 mL), and centrifuged after each wash. The supernatant was decanted and discarded each time. The polymer was dried *in vacuo* to afford 291 g (93% yield) of pure Ame-polymer.

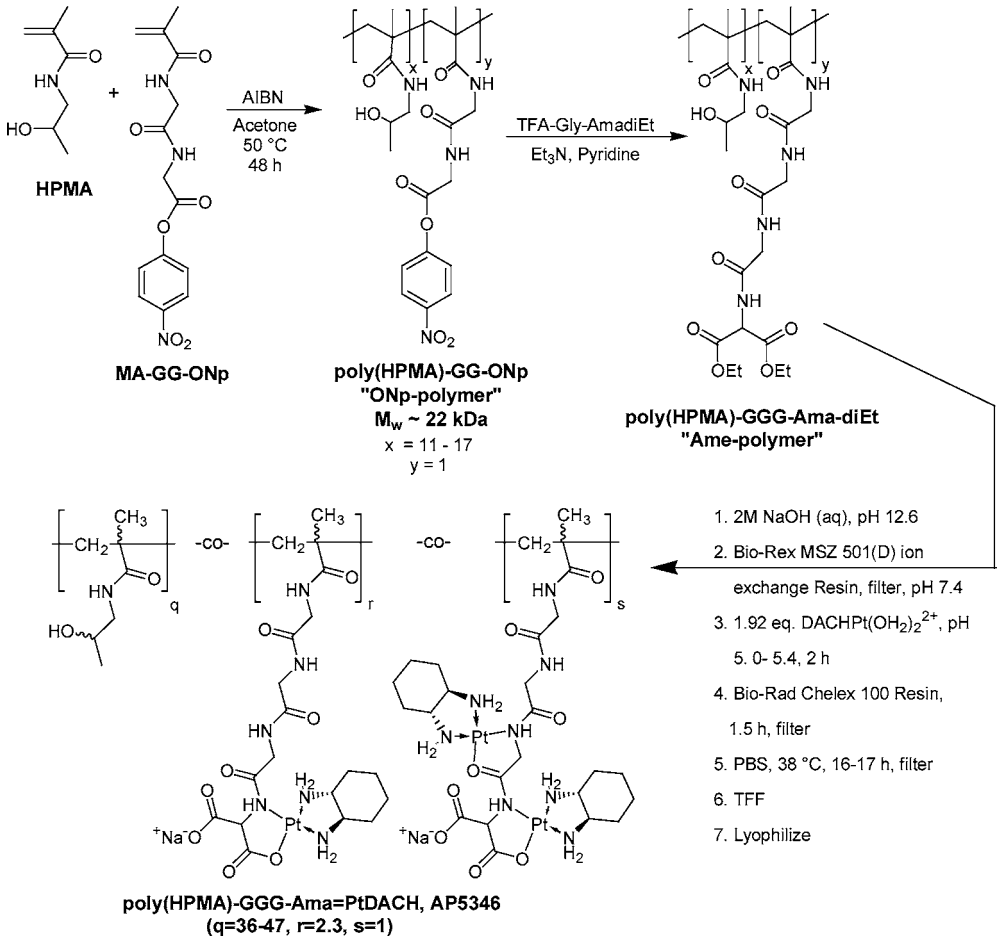

Figure 2. Initial synthesis of AP5346.

Conversion from Ame-Polymer to AP5346 (initial method). A 100 mL media bottle containing a stir bar was charged with $DACHPtCl_2$ (2.16 g, 5.69 mmol), $AgNO_3$ (1.88 g, 11.13 mmol), and 40 mL water. 5% HNO_3 was added until pH < 2 was reached, the vessel wrapped in foil, and the mixture was stirred in a 70 C water bath for 15 h. It was then cooled in an ice−water bath (0 to 5 °C) and the precipitate removed by filtration through a 0.22 μm GP Express PLUS PES Membrane Steritop device. The filtrate containing $DACHPt(OH_2)_2$ was then analyzed by ICP: 24736 mg Pt/L (99.6%).

A 100 mL media bottle containing a stir bar was charged with poly(HPMA)-GGG-Ame (5.00 g, 2.65 mmol Ame) and Milli-Q water (37 mL). The pH was raised to 12.6 by the addition of 2 M NaOH (3.4 mL) and the solution stirred for 30 min. Ion-exchange resin (5.00 g) was added and the mixture filtered when pH dropped below 7. The filtrate was adjusted to pH 7.4 using 2 M NaOH, and $DACHPt(OH_2)_2$ (40.1 mL, 5.08 mmol of a 24,736 mg Pt/L solution) was added. The reaction mixture was readjusted to pH 5.4 and stirred at 5.0−5.4 for 2 h, and then Chelex resin (3.0923 g) added with stirring for 90 min. The resin was filtered off and the resulting solution diluted to 133 mL (3.75 wt. %). It was then made 110 mM in chloride and 80 mmol in phosphate by addition of NaCl (0.8550 g, 14.63 mmol), $NaH_2PO_4 \cdot H_2O$ (0.2936 g, 2.1276 mmol), and $Na_2HPO_4 \cdot 7\ H_2O$ (2.2818 g, 8.5119 mmol). After dissolution of the salts, pH was 7.25. This was adjusted to 7.4 using 2 M NaOH, and the solution warmed to 38 °C and then placed in a 38 °C oven for 17 h. The mixture was filtered to remove a small amount of yellow precipitate, and the filtrate was purified by tangential flow filtration (7 permeate volumes collected). Lyophilization yielded the product as a tan solid (4.3451 g, 78%).

Improved Method of AP5346 Synthesis. The improved synthesis of AP5346 is depicted in Figure 3. A detailed breakdown of the process is shown although abbreviated structures have been used (the carbonyl of the third glycyl unit is included). The final AP5346 is structurally identical to that in Figure 2. The same Ame-polymer precursor is used; however, the formation of $DACHPt(OH_2)_2$ and AP5346 are somewhat different.

Conversion from Ame-Polymer to AP5346 (improved method). A 50 mL media bottle containing a stir bar was wrapped in foil and charged with $DACHPt(NO_3)_2$ (1.3965 g, 3.2231 mmol) and water (13 mL). 5% HNO_3 (100 μL) was added, the vessel capped, and the mixture stirred in a 70 °C water bath for 1 h. The platinating solution was cooled to room-temperature prior to use.

A 100 mL media bottle containing a stir bar was charged with Ame-polymer (5.00 g, 2.5330 mmol Ame) and water (28.3 mL). Upon dissolution of the polymer, 2 M NaOH (3.10 mL, 6.2 mmol) was added to the stirred polymer solution and the pH rose to 12.6 where it was maintained for 30 min. The solution was then taken to pH 7.4 by the slow addition of 5% HNO_3 (~3 mL) and then filtered through a 0.22 μm GP Express PLUS PES Membrane Steritop device. The platinating solution was then added with vigorous stirring. The pH dropped to 4.8 and was raised to 5.2 using 2 M NaOH. The solution was then stirred for 2 h with the pH held constant using a Mettler DL25 autotitrator loaded with 500 mM NaOH. The pH was adjusted to 7.4 using 2 M NaOH and placed in a 38 °C water bath and pH held constant at 7.4 for 17 h with stirring. The clear, pale yellow solution was filtered through a Steritop device and purified by TFF (five permeates collected). It was made 200

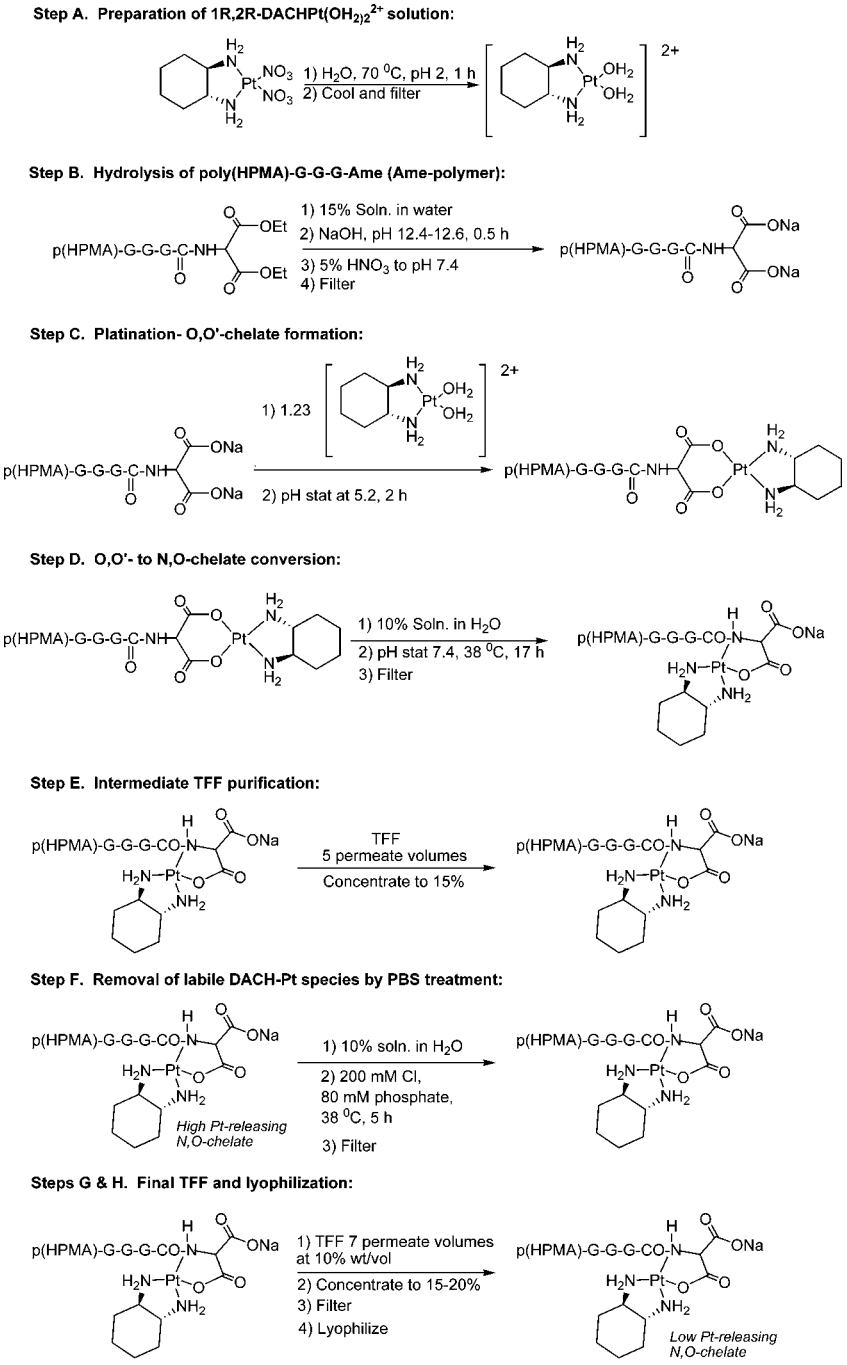

Figure 3. Improved synthesis of AP5346.

mM in chloride and 80 mM in phosphate by addition of NaCl (0.5844 g, 10.00 mmol), $NaH_2PO_4 \cdot H_2O$ (0.1104 g, 0.8000 mmol), and $Na_2HPO_4 \cdot 7H_2O$ (0.78 g, 3.2000 mmol). The solution was diluted to 50 mL (10.00 wt. %) and stirred. After dissolution of the salts, the pH was 7.1. The pH was raised to 7.4 and the solution filtered and quickly heated to 38 °C. The vessel was then placed in a 38 °C water bath for 4.5 h with no stirring. The clear solution was filtered through a Steritop device, purified by TFF (seven permeates collected), and lyophilized to yield a tan solid (4.3920 g, 75%).

RESULTS AND DISCUSSION

The initial preparation of AP5346 from its Ame-polymer precursor is a four-part process with subsequent purification and lyophilization steps. While no intermediates are isolated, two *in situ* purifications are performed. The platinating solution of the dinitrato salt of $DACHPt(OH_2)_2^{2+}$ is prepared by heating a stirring mixture of $DACHPtCl_2$ and $AgNO_3$ with a trace of nitric acid. The nitric acid and heating steps are performed to prevent any μ-hydroxo Pt species forming. Slightly less than 2 equiv of $AgNO_3$ are used otherwise the filtered solution becomes cloudy with slow forming AgCl.

Saponification of the Ame-polymer at pH 12.6 was found by ^1H NMR to proceed very quickly (complete within a few minutes). To remove any non-polymer-bound ions that would allow nonproductive electrostatic interactions with the platinating species, the solution was neutralized using mixed bed ion-exchange resin.

The saponified polymer solution was combined with the platinating solution at pH 7.4. This pH was chosen to give a combined reaction mixture with a pH of approximately 5. This pH control was important because at high pH levels the diaqua

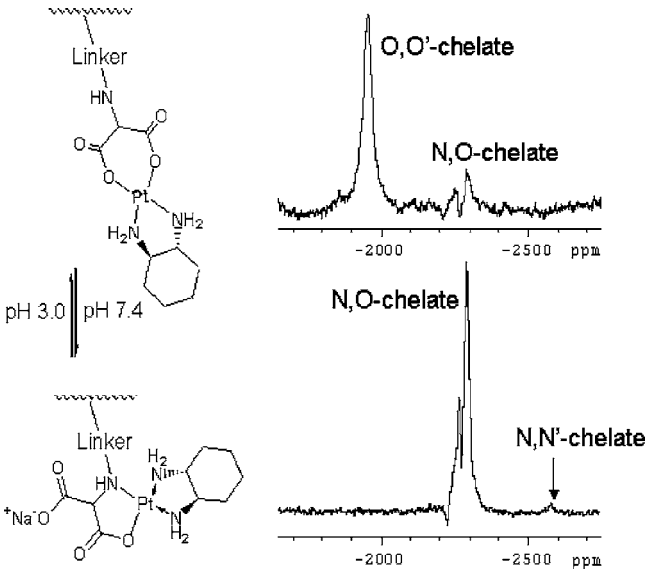

Figure 4. ^{195}Pt NMR of the conversion of O,O′-chelate to AP5346 N,O-chelate by the initial method.

platinum species (pK_{a1} = 5.4, pK_{a2} = 7.2 at 27 °C) (*27*) becomes significantly deprotonated, yielding the less reactive mono- or unreactive dihydroxo species. The pH was kept above 3 to ensure that no decarboxylation (pH < 2) takes place. A pH near 5 was preferred so that a high proportion of the amidomalonate groups are doubly deprotonated (pK_a values of approximately 2.8 and 5.6) (*28*). Thus, at a pH of approximately 5.0−5.4, the predominate Pt species will be the reactive DACHPt$(OH_2)_2^{2+}$, decarboxylation is avoided, and the amidomalonate is at least singly deprotonated with a substantial fraction of the doubly deprotonated species. These factors are all seen to facilitate the desired chelate formation and inhibit undesired or unproductive side reactions. The solution of the saponified polymer was treated with almost 2 equiv of the platinating solution. Several stoichiometries were tested and this value was chosen as it resulted in materials with the most desirable biological activity. A reaction time of 2 h was found to be ample for formation of the predominately O,O′-chelate solution.

Before proceeding to the O,O′- to N,O-chelate conversion step, the reaction mixture was treated with a metal chelating ion-exchange resin (Chelex Resin, biotech grade). Since the O,O′- to N,O− chelate conversion was performed in 110 mM NaCl and since remaining DACHPt$(OH_2)_2^{2+}$ converts to the poorly soluble DACHPtCl_2 at this concentration, the Chelex resin was used to scavenge any remaining free platinum species. This resin does not allow the polymer platinum conjugate to penetrate because it has a nominal molecular weight cutoff (NMWCO) of 1 kDa. Treatment for 90 min was sufficient to remove any such Pt species as confirmed by ICP analysis.

The filtered solution of mostly O,O′-chelate (approximately 85% O,O′-, 15% N,O-) was converted *in situ* to the N,O-species, as described, in PBS at pH 7.4 and 38 °C. These salts were chosen for their general biocompatibility. The chloride concentration is close to physiological, and it is expected and desired that any labile platinum species under such concentrations would be lost in the chelate conversion. The phosphate quantity was chosen not only to give well buffered solutions but also to account for the fact that some may also react with any free Pt species (*29*). A ^{195}Pt NMR depiction of the chelate conversion is shown in Figure 4.

While O,O′- to N,O-chelate conversion is essentially 100% at pH 7.4, it is interesting to note that the O,O′-chelate can be re-formed by treatment of the AP5346 N,O-chelate solution at pH 3 at 38 °C. After 3 h under these conditions a mixture of 85% O,O′-, 15% N,O- can be obtained. Furthermore, when the mixture of mainly O,O′- and some N,O-chelate (prior to PBS treatment for conversion to N,O-species) is treated *in situ* at pH 3 (38 °C, 3 h), the platinum converts almost entirely back to the O,O-form. Greater than 98% O,O-chelate was achieved. Increasing the reaction time did not increase the percentage of O,O′. Sohn and co-workers have recently reported on the difficulty in isolation of isomerically pure amino dicarboxylate Pt (II) complexes (*30*). They were however able to isolate a pure O,O′-chelate by utilizing N-substituted small molecule glutamates, where formation of the N,O- species was blocked. These structures were confirmed by ^{195}Pt NMR spectroscopy. In further work, the same authors report O,O′-chelates of glycyl-L-glutamate bound to polyphosphazene polymer backbones (*22*). No ^{195}Pt NMR data of these materials were obtained. The O,O′-structures were assigned based upon the fact that the glycyl-L-glutamates are also N-substituted, and as such, rearrangement to form the N,O-chelate would also be blocked in these systems. Other workers report O,O′-isomers of linear, aliphatic polyamide carriers, also with an N-substituted site adjacent to the suggested chelate structure (*31*). Again, no ^{195}Pt NMR data was obtained, and the O,O′-structure assigned based upon ^{1}H NMR spectra. The reported polymer-based O,O′-chelate structures are shown in Figure 5.

However, we have previously shown (*32*) by ^{195}Pt NMR that in polymer systems containing linkers which incorporate N-substituted moieties, the formation of the N,O-chelate is easily achieved. These studies were performed on a cisplatin type analog of AP5346, containing a GFLG-amidomalonato linker-chelate system. In fact, this N,O-isomer is preferred at higher pHs, while the pure O,O′ chelate could only be formed in two ways; by taking a solution of the N,O-species to low pH, or by forming the initial O,O′-/N,O-chelate mixture after platination and treating this in situ at pH 3.0 − 3.5 for 1 h, to form 100% O,O′-chelate. Results of the pH studies starting from 100% N,O-chelate are shown in Table 1.

Taking this data into account it is very likely that the reported O,O′-structures of Sohn (*22*) and Neuse (*31*), neither of which were confirmed by ^{195}Pt NMR, do in fact contain significant quantities of N,O-chelates, as strict pH control must be employed to isolate pure samples of either isomer. The N,O-materials are the thermodynamic products of such reactions, and the smaller ring sizes compared to the larger ring sizes of their respective O,O-analogues (kinetic products) makes their formation more favorable. The free amine tethered to the backbone in the structure reported by Neuse is also very likely to bind platinum.

As the O,O′-chelate form is more labile than the N,O-chelate, conversion back to the O,O-chelate is the reason for the increased rate of platinum release observed as pH is lowered. This characteristic enables safe transit of the conjugate in its N,O form during systemic circulation, with the low pH environment of the tumor activating increasing platinum release from the macromolecular carrier.

Purification of the AP5346 crude product was performed by TFF using a polyethersulfone (PES) membrane with a 5 kDa NMWCO. A TFF-based purification was chosen rather than preparative SEC because it is linearly scalable from mg to multi-kilogram amounts. Concentration of the purified solution to 10% w/v followed by lyophilization produces a cake of the drug substance. Less concentrated solutions produced a material which was difficult to handle due to static.

For the future synthesis of AP5346 drug substance, a more cost-effective and scaleable process were sought for both polymer manufacture and platination. Both mixed bed and Chelex ion exchange resins are expensive and elimination of these resins would be advantageous. An improvement of the reaction yields in terms of weight and/or platinum was important

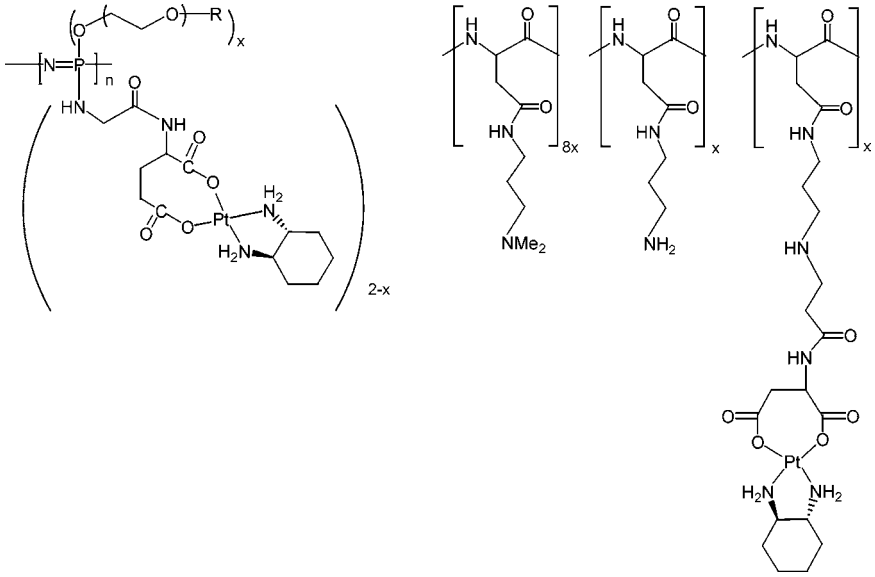

Figure 5. Reported polymer-based O,O′-chelate structures.

Table 1. Effects of pH on the p(HPMA)-GFLG-Ama═Pt(NH$_3$)$_2$ Chelate

	starting from 100% N,O-chelate p(HPMA)-GFLG-Ama═Pt(NH$_3$)$_2$							
	pH 3.0−3.5		pH 4.0−4.5		pH 5.0−5.5		pH 6.0−6.5	
time	O,O-	N,O-	O,O-	N,O-	O,O-	N,O-	O,O-	N,O-
1 h	98	2	45	55	6	94	0	100
5 h	100	0	56	44	15	85	0	100
20 h	100	0	68	32	19	81	0	100

because of the high cost of platinum. Last, a more concentrated process to allow for larger scale-up was considered to be necessary.

The formation of the DACHPt(OH$_2$)$_2^{2+}$ platinating solution for the improved synthesis was achieved by heating DACHPt-(NO$_3$)$_2$ in low pH water for 1 h. The diaqua species readily forms, and there was no need for overnight heating, filtration, and in-process testing for platinum concentration by ICP as there was in the initial method. Additionally, significantly less platinum was used (approximately 40% reduction), while obtaining the same quantities of platinum in the final product. The saponified polymer solution was prepared in the same way in both processes; however, neutralization was performed using 5% HNO$_3$ in place of the more expensive mixed bed ion-exchange resin. Upon combination of these solutions the pH was held constant at 5.2 for 2 h using an autotitrator loaded with NaOH. In this process, however, the resulting (mainly) O,O′-chelate solution was converted to the N,O-chelate by merely increasing the pH to 7.4 and heating at 38 °C for 17 h. In the initial synthesis, where a large excess of platinum was used, the same process was performed by overnight heating in PBS. The high chloride concentration prevented a significant quantity of platinum from binding to the polymer. In contrast, the lack of PBS in the improved chelate conversion process resulted in the reduction of the amount of platinum used, such that all or most of the platinum which was added binds to the polymer. Therefore there was no need for the addition of Chelex resin for removal of excess free platinum. Isolation and analysis of the N,O-chelate at this stage of the synthesis shows that by ^{1}H and ^{195}Pt NMR, this N,O-chelate is identical to the final AP5346 product. However, 3 and 24 h platinum release rates, determined by ICP, were outside the specifications. This shows that NMR spectroscopy of polymer platinum conjugates alone cannot be used to ensure reproducibility of the pharmaceutical product. Consequently this solution was purified by TFF, followed by short treatment with PBS (200 mM Cl$^-$, 80 mM PO$_4^{3-}$) at 38 °C for 4.5 h, and then subjected to a second TFF. It is believed that the short PBS treatment causes rearrangement and/or removal of small concentrations of highly labile Pt species to produce the lower Pt releasing species. The resulting solution was lyophilized to produce an AP5346 product which was identical to the initial material.

Table 2. Identity and Purity Specifications for AP5346 Drug Substance

analysis	result
Identity Specification	
^{1}H NMR spectroscopy	conforms to reference spectrum
^{195}Pt NMR spectroscopy	not less than two peaks in the range −2200 to −2350 ppm, with the main peak appearing at −2290 ± 10 ppm, and the next most distinct peak appearing at −2260 ± 10 ppm
% Pt (wt/wt)	determine and report
% water	NMT 14%
% Pt (dry weight)	10.5 ± 2.2%
% Pt Released at 3 h	NMT 1.5%
% Pt Released at 24 h	NMT 4.5%
M_w (by SEC)	25 kDa ± 8 kDa
M_n (by SEC)	17 kDa ± 6 kDa
SEC peak shape	monomodal distribution
Purity Specification	
^{1}H NMR spectroscopy	
for ethanol	NMT 1.0% ethanol
for other protonated impurities	NMT 1.0% total other impurities
^{195}Pt NMR spectroscopy	the integral of peaks in the range −2000 to −2350 ppm is not less than 90% of total
% small Pt species	NMT 0.8%
% Na	determine and report
% Cl	NMT 0.2%
% P	NMT 0.2%

In order for a batch of AP5346 to be deemed appropriate for clinical use it must conform to a set of carefully chosen specifications. The identity and purity specifications for AP5346 drug substance are listed in Table 2.

Despite the differences in the syntheses, the initial and improved methods produce AP5346 drug substance with very comparable data, all of which conforms to the specifications in Table 1. A large number of batches of AP5346 have been prepared to date, and it was found that the analytical results for these batches of drug substance usually appear within a relatively

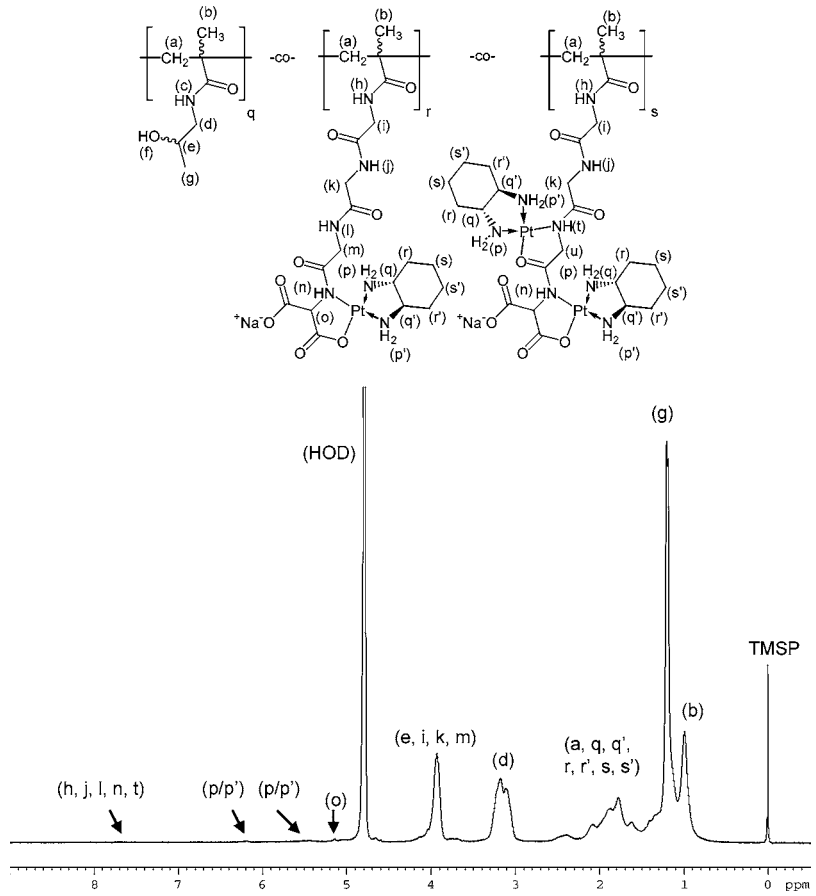

Figure 6. ^{1}H NMR spectrum and assignments of AP5346 in D_2O.

Table 3. ^{1}H NMR Chemicals Shifts, Assignments, and Peak Appearance for AP5346 in D_2O

chemical shift in D_2O (ppm)	assignment	peak appearance and number of hydrogens
0.99	(b)	br s, 3H
1.19−1.20	(g)	d, 3H
1.51−2.67	(a, q, q′, r, r′, s, s′)	br unresolved envelope, 14H
2.75−3.50	(d)	2 br peaks, 2H
3.64−4.30	(e, i, k, m)	unresolved envelope, 7H
4.78	HOD peak	sharp s
5.15	(o)	s, mostly exchanged out, 1H
5.35	(p, p′)	br peak, mostly exchanged out, 2H
6.10	(p, p′)	br peak, mostly exchanged out, 2H
7.30−8.30	(h, j, l, n, t)	br peak, mostly exchanged out, 2H

narrow range inside those specifications. The platinum release rates at 3 and 24 h are normally in the range of 1.00−1.30 and 3.00−3.80, respectively. Molecular weight analyses typically afford weight average molecular weights (M_w) and number average molecular weights (M_n) of 23 ± 3 and 14 ± 2 kDa, respectively. The % small Pt species (free platinum) is usually found to be less than 0.3%. Percent Pt is dependent on the amount of chelators present in any starting sample of Ame polymer but falls comfortably within the specification range. Elemental analyses for Cl and P only ever show trace amounts of these elements, which are significantly below the specification limit. The product is isolated by lyophilzation, and water content is determined by Karl Fischer titration.

Both methods of AP5346 syntheses produce materials which are identical by ^{1}H NMR spectroscopy. A representative spectrum of material from the improved synthesis is shown in Figure 6, and peak assignments for identity purposes are listed in Table 3.

It is known that small molecule impurities in a polymer therapeutic can be effectively quantified by ^{1}H NMR (*33*). This is possible because for most spin 1/2 nuclei in small, rapidly tumbling molecules, T_1 (longtitudinal relaxation time) and T_2 (transverse relaxation time) have the same value. The faster motion leads to slower relaxation and narrower line widths. Conversely for a polymer system such as AP5346, which tumbles more slowly in solution, T_2 is often very much shorter than T_1, leading to broad linewidths. This means that very low quantities of small molecule impurities in an AP5346 sample will have sufficiently large signal-to-noise ratio to readily allow their observation by ^{1}H NMR. Such impurities can be detected to below 0.1%.

Chemical shifts in ^{195}Pt NMR spectroscopy are very sensitive to the nature of the coordinating donor atoms. Assignments in ^{195}Pt spectra of AP5346 were made based on the literature precedents of Gibson (*34*) and Margerum (*35*). As shown in Figure 4, the main signal is the N,O-chelate at ∼ −2290 ppm. A small and controllable amount of the N,N′-chelate appears at ∼ −2600 ppm. ^{195}Pt NMR spectra of the initial and improved AP5346 syntheses are identical.

In Figure 2 it is shown that some PtDACH has bound to a glycine residue on the linker which connects the amidomalonato chelate to the polymer backbone. If one considers a sample of the Ame-polymer precursor, a known quantity of amidomalonato chelating groups must be present. This quantity corresponds to a theoretical platinum content, assuming that each group chelates one PtDACH moiety. The platinum contents in materials from both initial and improved syntheses were found to be approximately 1.2 times the theoretical value of platinum saturated amidomalonato chelators. It has been shown (*36*) using ^{15}N enriched glycyl linker groups that this "extra" platinum is located on the terminal glycine group as depicted in Figure 2. This work also seemingly suggests that the amidomalonato H atom and the terminal glycyl do not deprotonate on formation of the N,O-chelate. Deprotonation of amides upon coordination

to platinum has been studied previously (*37*). A detailed study of the AP5346 construct and related polymer-linker-chelate structures by ^{15}N PENDANT NMR, with ^{15}N enriched linkers and platinum bound ammines is in progress.

CONCLUSIONS

The syntheses of poly(HPMA)-GGG-Ama═Pt═1*R*,2*R*-DACH (AP5346) by the initial and improved routes, and the methods of analysis of the drug substances are described. It is shown that these substances can be characterized spectroscopically and furthermore that the material derived from an improved synthesis is identical to the initial material.

ACKNOWLEDGMENT

We thank Dr. N. Rao Ummaneni and Dan Nguyen of Access Pharmaceuticals, Inc., for their syntheses of the monomers used for the production of the Ame-polymer precursor to AP5346.

LITERATURE CITED

(1) Rosenberg, B., Van Camp, L., and Krigas, T. (1965) Inhibition of cell division in Escherichia coli by electrolysis products from a platinum electrode. *Nature 205*, 698−699.

(2) Weiss, R. B., and Christian, M. C. (1993) New cisplatin analogues in developement. A review. *Drugs 46*, 360−377.

(3) Natile, G., and Coluccia, M. (2001) Current status of trans-platinum compounds in cancer therapy. *Coord. Chem. Rev. 216*−*217*, 383−410 and references cited therein.

(4) Jones, A. L., Hill, A. S., Soukop, M., Hutcheon, A. W., Cassidy, J., Kaye, S. B., Sikora, K., Carney, D. N., and Cunningham, D. (1991) Comparison of dexamethasone and ondansetron in the prophylaxis os emesis induced by moderately emetogenic chemotherapy. *Lancet 338*, 483−487.

(5) Smith, D. B., Newlands, E. S., Rustin, G. J. S., Begent, R. H. J., Howells, N., McQuade, B., and Bagshawe, K. D. (1991) Comparison of ondansetron plus dexamethasone as antiemetic prophylaxis during cisplatin-containing chemotherapy. *Lancet 338*, 487−490.

(6) Cubeddu, L. Z., Horrmann, I. S., Fuenmayor, N. T., and Finn, A. L. (1990) Efficacy of ondansetron (GR38032F) and the rold of seratonin in cisplatin-induced nausea and vomiting. *N. Engl. J. Med. 322*, 810−816.

(7) Marty, M., Pouillart, P., Scholl, S., Droz, J. P., Azab, M., Brion, N., Pujade-Lauriane, E., Paule, B., Paes, D., and Bons, J. (1990) Comparison of the 5-hydroxytryptamine$_3$ (serotonin) antagonist ondansetron (GR38032F) with high-dose metoclopramide in the control of cisplatin-induced emesis. *N. Engl. J. Med. 322*, 816−821.

(8) Ito, K., Adachi, S., Itani, Y., Koyama, M., Hori, K., Chin, R., Shintani, M., Beppu, K., Kawai, S., and Saito, K. (1999) A dose finding study of nedaplatin and cyclophosphamide for patients with gynecological malignancies. *Jpn. J. Clin. Oncol. 29*, 299−302.

(9) Hambley, T. W. (1997) The influence of structure on the activity and toxicity of Pt anti-cancer drugs. *Coord. Chem. Rev. 166*, 181−223.

(10) Reedijk, J. (1996) Increased understanding in platinum antitumour chemistry. *Chem. Commun.* 801−806.

(11) Calvert, A. H., Newell, D. R., Gumbrell, L. A., O'Reilly, S., Burnell, M., Boxall, F. E., Siddik, Z. H., Judson, I. R., Gore, M. E., and Wiltshaw, E. (1989) Carboplatin dosage: prospective evaluation of a simple formula based on renal function. *J. Clin. Oncol. 7*, 1748−1756.

(12) Gamelin, E., Gamelin, L., Bossi, L., and Quasthoff. S. (2002) Clinical aspects and molecular basis of oxaliplatin neurotoxicity: current management and development of preventative measures. *Semin. Oncol. 29* (suppl 15), 21−23.

(13) Seymour, L. W. (1992) Passive tumor targeting of soluble macromolecules and drug conjugates. *Crit. Rev. Ther. Drug Carrier Syst. 9* (2), 135−187.

(14) Duncan, R. (1997) Polymer therapeutics for tumour specific delivery. *Chem. Ind.* (London), 262−264.

(15) Matsumura, Y., and Maeda, H. (1986) A new concept for macromolecular therapeutics in cancer chemotherapy: mechanism of tumoritropic accumulation of proteins and the antitumor agent SMANCS. *Cancer Res. 46* (12*)*, 6387−6392.

(16) Gianasi, E., Wasil, M., Evagorou, E. G., Keddle, A., Wilson, G., Duncan, R. (1999) HPMA copolymer platinates as novel antitumor agents: *in vitro* properties, pharmacokinetics and antitumor activity *in vivo. Eur J Cancer 35* (6*)*, 994−1002.

(17) Vasey, P. A., Kaye, S. B., Morrison, R., Twelves, C., Wilson, P., Duncan, R., Thomson, A. H., Murray, L. S., Hilditch, T. E., Murray, T., Burtles, S., Fraier, D., Cassidy, J., and Frigerio, E. (1999) Phase I clinical and pharmacokinetic study of PK1 [N-(2-hydroxypropyl)-methacrylamide copolymer doxorubicin]: first member of a new class of chemotherapeutic agents- drug-polymer conjugates. *Clin. Cancer. Res. 5* (1*)*, 83−94.

(18) Julyan, P. J., Seymour, L. W., Ferry, D. R., Daryani, S., Boivin, C. M., Doran, J., David, M., Anderson, D., Christodoulou, C., Young, A. M., Hesslewood, S., and Kerr, D. J. (1999) Preliminary clinical study of the distribution of HPMA copolymers bearing doxorubicin and galactosamine. *J. Controlled Release 57*, 281−290.

(19) Caiolfa, V. R., Zamai, M., Fiorino, A., Frigerio, E., Pellizzoni, C., d'Argy, R., Ghiglieri, A., Castelli, M. G., Farao, M., Pesenti, E., Gigli, M., Angelucci, F., and Suarato, A. (2000) Polymer bound camptothecin: initial biodistribution and antitumor activity studies. *J. Controlled Release 65*, 105−119.

(20) Meerum Terwogt, J. M., ten Bokkel Huinink, W. W., Schellens, J. H., Schot, M., Mandjes, I. A., Zurlo, M. G., Rocchetti, M., Rosing, H., Koopman, F. J., and Beijnen, J. H. (2001) Phase I clinical and pharmacokinetic study of PNU 166945, a novel water-soluble polymer-conjugated prodrug of paclitaxel. *Anticancer Drugs 12*, 315−323.

(21) Duncan, R., Evagorou, E. G., Buckley, R. G., and Gianasi, E. (1999) Polymer Platinum Compounds. US Patent 5,965,118.

(22) Jun, Y. J., Kim, J. I., Jun, M. J., and Sohn, Y. S. (2005) Selective tumor targeting by enhanced permeability and retention effect. Synthesis and antitumor activity of polyphosphazene-platinum (II) conjugates. *J. Inorg. Biochem. 99*, 1593−1601.

(23) Siegmann-Louda, D. W., and Carraher, C. E., Jr., (2004) Polymeric platinum containing drugs in the treatment of cancer. *Macromolecules Containing Metal and Metal-like Elements, Volume 3: Biomedical Applications*, pp 119−191, Wiley, New York.

(24) Thurmond, K. B., II, McEwan, J., Moro, D. G., Rice, J. R., Russell-Jones, G., St. John, J. V., Sood, P., Stewart, D. R., and Nowotnik, D. P. (2005) Targeted and non-targeted polymer drug delivery systems. *ACS Symposium Series 923* (*Polymer Drug Delivery Volume I* − *Particulate Drug Carriers*), pp 137−154, Chapter 10, American Chemical Society, Washington, DC.

(25) Rice, J. R., Gerberich, J. L., Nowotnik, D. P., and Howell, S. B. (2006) Preclinical efficacy and pharmacokinetics of AP5346, a novel DACH-platinum tumor-targeting drug delivery system. *Clin. Cancer Res. 12*, 2248−2254.

(26) Rejmanova, P., Labsky, J., and Kopecek, J. (1977) Aminolyses of monomeric and polymeric 4-nitrophenyl esters of N-methacryloamino acids. *Makromol. Chem. 178*, 2159−2168.

(27) Berners-Price, S., Frenkiel, T. A., Frey, U., Ranford, J. D., and Sadler, P. J. (1992) Hydrolysis products of cisplatin: pKa determinations via [^1H, ^{15}N] NMR spectroscopy. *J. Chem. Soc., Chem. Commun.* 789−791.

(28) This estimation is based on the pK_as of malonic acid with $pK_{a1} = 2.9$ and $pK_{a2} = 5.7$. With the electron withdrawing effects of the amide group, the pK_as are expected to be lower that those for malonic acid.

(29) Appleton, T. (1984) Reactions of platinum (II) aqua complexes. 1. Multinuclear (^{195}Pt, ^{15}N, ^{31}P) NMR study of reactions between the cis-diamminediaquaplatinum (II) cation and the oxygen donor ligands hydroxide, perchlorate, nitrate, sulfate, phosphate and acetate. *Inorg. Chem. 23*, 3514−3521.

(30) Yeong-Sang, K., Song, R., Chung, H. C., Jun, M. J., and Sohn, Y. S. (2004) Coordination modes vs antitumor activity: synthesis and antitumor activity of novel platinum (II) complexes of N-substituted amino dicarboxylic acids. *J. Inorg. Biochem. 98*, 98−104.

(31) Smit, A., Snyman, J. R., Neuse, E. W., Bohm, L., and van Rensburg, C. E. J. (2005) Evaluation of cisplatin and a novel platinum polymer conjugate for drug toxicity and drug distribution in mice. *Anti-Cancer Drugs 16*, 501−506.

(32) Sood, P., Stewart, D. R., Nowotnik, D. P., Shevchuk, S. V., and Thurmond, K. B., II (2004) O,O′-Amidomalonate and N,O-amidomalonate platinum complexes. US Patent Appl. US 2004/0175387 A1.

(33) Pinciroli, V., Rizzo, V., Angelucci, F., Tato, M., and Vigevani, A. (1997) ^{1}H NMR characterization of methacrylamide polymer conjugates with the anti-cancer drug doxorubicin. *Magn. Reson. Chem. 35*, 2−8.

(34) Gibson, D., Rosenfeld, A., Apfelbaum, H., and Blum, J. (1990) Multinuclear (^{195}Pt, ^{15}N, ^{13}C) NMR studies of the reactions between cis-diaminediaquaplatinum (II) Complexes and aminomalonate. *Inorg. Chem. 29*, 5125−5129.

(35) Kirvan, G. E., and Margerum, D. W. (1985) Formation and NMR spectra of platinum (II)-tripeptide complexes. *Inorg. Chem. 24*, 3017−3021.

(36) Sood, P., Thurmond, K. B., II, and Shevchuk, S. V. Unpublished work.

(37) Nagao, N., Kobayashi, T., Takayama, T., Koike, Y., Ono, Y., Watanabe, T., Mikami, T., Suzuki, M., Matumoto, T., and Watabe, M. (1997) Platinum (II) complexes with diglycine: X-ray crystal structure, ^{15}N NMR spectra, and growth-inhibitory activity against mouse meth A solid tumor in vivo. *Inorg. Chem. 36*, 4195−4201.

BC0600517

HIV-1 Tat Peptide Immunoconjugates Differentially Sensitize Breast Cancer Cells to Selected Antiproliferative Agents That Induce the Cyclin-Dependent Kinase Inhibitor p21$^{WAF-1/CIP-1}$

Meiduo Hu,[†,§] Judy Wang,[†] Paul Chen,[†] and Raymond M. Reilly*[,†,‡,§]

Division of Nuclear Medicine, University Health Network, Toronto, Department of Medical Imaging, University of Toronto, Toronto, and Department of Pharmaceutical Sciences, University of Toronto, Toronto, ON, Canada. Received March 3, 2006; Revised Manuscript Received July 6, 2006

In this study, we evaluated the ability of anti-p21 antibodies conjugated to 17-mer peptides [GRKKRRQRRRP-PQGYGC] harboring the membrane-translocating and nuclear import sequences [underlined] of HIV-1 tat protein to inhibit the cyclin-dependent kinase inhibitor, p21$^{WAF-1/Cip-1}$ (p21) and differentially sensitize MDA-MB-468 and MCF-7 human breast cancer (BC) cells to the antiproliferative effects of treatments that induce or do not induce p21. BC cells were treated with increasing concentrations of epidermal growth factor (EGF; 0.5−10 nM), the topoisomerase I inhibitor, camptothecin (CPT; 0.1−4 μM), or increasing doses of γ-radiation (2−20 Gy). Western blot was used to evaluate p21 expression. The effect of treatment on cell cycle distribution was studied. Growth inhibition was measured by the WST-1 assay. Expression of p21 was increased in MDA-MB-468 cells treated with EGF or CPT but not by γ-irradiation. MCF-7 cells exhibited p21 upregulation following exposure to CPT and γ-radiation but not EGF. EGF caused cell cycle arrest in G_1 phase for MDA-MB-468 cells. CPT caused G_1-phase arrest in MDA-MB-468 cells and prolonged S phase in MCF-7 cells. γ-Radiation caused an increase in cells in G_2/M phase for MDA-MB-468 and MCF-7. MDA-MB-468 cells were growth-inhibited by EGF, CPT, and γ-radiation. MCF-7 cells were growth-stimulated by EGF and inhibited by CPT and γ-radiation. Combining EGF with tat-anti-p21 immunoconjugates (ICs) amplified the growth-inhibitory effect on MDA-MB-468 cells 1.2-fold to 2.3-fold, but had no effect on the growth stimulation of MCF-7 cells by EGF. Tat-anti-p21 ICs sensitized MCF-7 cells 1.4-fold to γ-radiation but had no effect on the growth of γ-irradiated MDA-MB-468 cells. Tat-anti-p21 ICs sensitized both MDA-MB-468 and MCF-7 cells 1.7-fold to CPT. We conclude that tat-anti-p21 ICs are promising sensitizers for cytotoxic cancer therapies and that their sensitization is dependent on treatment-related p21 expression. This general approach could potentially be extended to other growth-regulatory molecules that are associated with tumor growth and progression.

INTRODUCTION

The cyclin-dependent kinase inhibitor, p21$^{WAF-1/CIP-1}$ (p21) protects cells from potentially lethal DNA damage by arresting cell cycle progression to facilitate DNA repair (*1*, *2*). p21 binds and inactivates CDK-4/Cyclin-D and CDK-2/Cyclin-E complexes, blocking G_1/S-phase cell cycle transition (*3*). CDK-2/Cyclin-A complexes required for transition through G_2/M phase are also inhibited by p21 (*4*). Furthermore, p21 has an anti-apoptotic function mediated through its phosphorylation by Akt (*5*, *6*). p21 may also promote apoptosis under certain conditions (*4*, *7*). It has been suggested that the cell cycle arrest function of p21 exists in cells with an intact p21-dependent checkpoint (*7*), whereas cells in which this checkpoint is defective may undergo p21-mediated apoptosis due to unfaithful repair of DNA damage (*5*, *8*, *9*). Many cancer therapeutics (e.g., chemotherapy and γ-radiation) cause reproductive cell death by inflicting DNA damage (*7*). Strategies to interfere with the DNA-protective function of p21 could amplify the cytotoxicity of these agents. Several approaches have been explored to attenuate p21 function in cells (*6*). Many of these have relied on antisense oligodeoxynucleotides (ODNs) to interfere with the translation of p21 mRNA into functional protein. In one study, 21-mer antisense ODNs complementary to p21 mRNA promoted apoptosis in serum-starved T47D or MCF-7 human breast cancer (BC) cells (*5*). In another report, 20-mer antisense ODNs directed against p21 mRNA converted growth arrest to apoptosis in γ-irradiated HCT 116 human colon cancer cells (*9*). These strategies are limited, however, by the well-known delivery barriers faced by DNA-based therapeutics (*10*). Furthermore, there is post-transcriptional regulation of p21 which may uncouple the expression of p21 mRNA and protein, thus potentially diminishing the effectiveness of any antisense ODN strategy (*11*).

In this study, we describe for the first time an alternative approach for inhibiting the function of p21 in cancer cells that employs anti-p21 antibodies conjugated to 17-mer synthetic peptides derived from HIV-1 virus transactivator of transcription (tat) protein. These peptides (GRKKRRQRRRPPQGYGC) harbor the polyarginines required for cell membrane penetration and the nuclear-localizing sequence (underlined) of the full-length tat protein. The construction of these tat-anti-p21 immunoconjugates (ICs) was recently reported (*12*, *13*). Tat-anti-p21 ICs penetrated MDA-MB-468 BC cells and were imported into the nucleus, where they functionally attenuated the ability of p21 to promote G_1/S-phase arrest caused by exposure of these cells to epidermal growth factor (EGF) (*13*). Nuclear translocation was important because the ability of p21 to mediate cell cycle arrest has been found to be associated mainly with its nuclear distribution (*14*).

* Address correspondence to Raymond M. Reilly, Ph.D., Leslie Dan Faculty of Pharmacy, University of Toronto, 144 College Street, Toronto, Ontario, Canada M5S 3M2. Tel.: (416) 946-5522. FAX: (416) 978-8511. E-mail: raymond.reilly@utoronto.ca.

[†] University Health Network.

[‡] Department of Medical Imaging, University of Toronto.

[§] Department of Pharmaceutical Sciences, University of Toronto.

10.1021/bc060053r CCC: $33.50 © 2006 American Chemical Society
Published on Web 08/23/2006

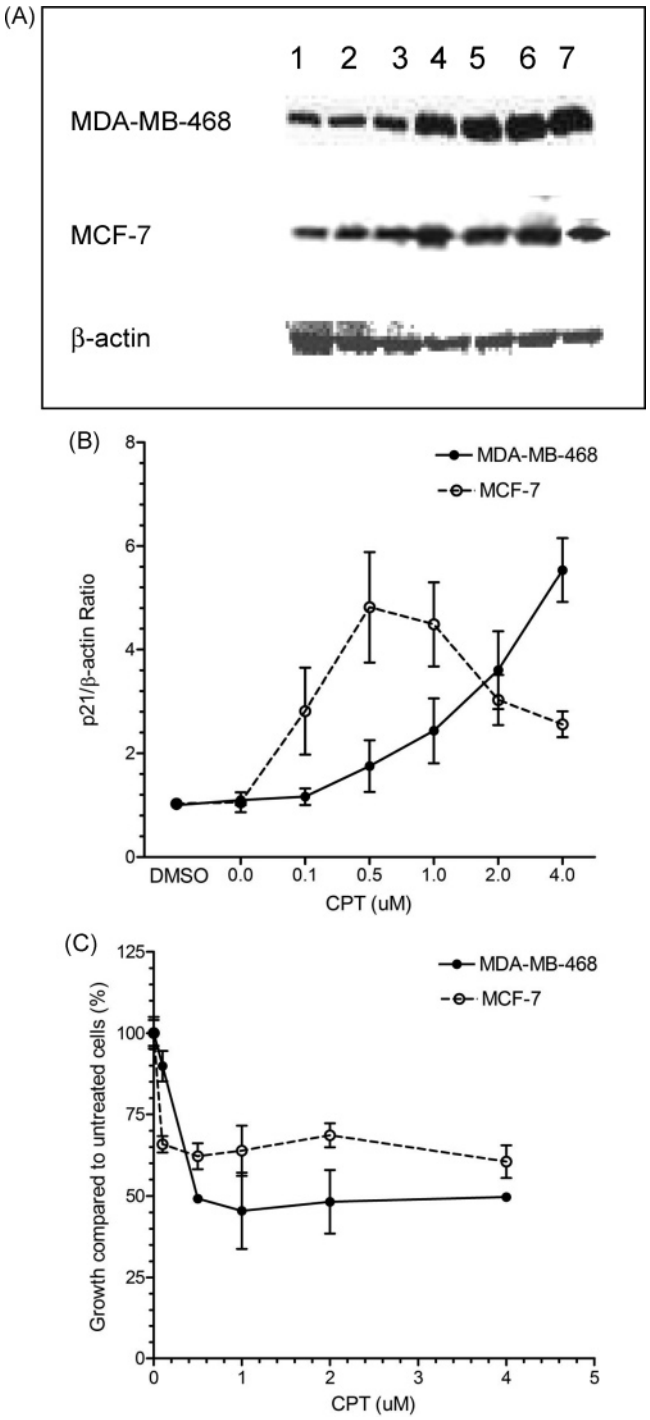

Figure 1. (A) Effect of exposure of MDA-MB-468 or MCF-7 human breast cancer cells for 24 h to increasing concentrations of camptothecin (CPT) on the expression of p21. Lane 1, DMSO-treated cells; Lanes 2−7 are cells treated with 0.0, 0.1, 0.5, 1, 2, or 4 μM of CPT, respectively. (B) The p21/β-actin ratio in the cells was evaluated by Western blot. (C) Effect of CPT exposure of MDA-MB-468 or MCF-7 cells on cell growth measured colorimetrically using the WST-1 assay. Cell growth of treated cells at 24 h was expressed as a percentage relative to that of untreated cells. Data shown are the mean ± sem of three replicate determinations.

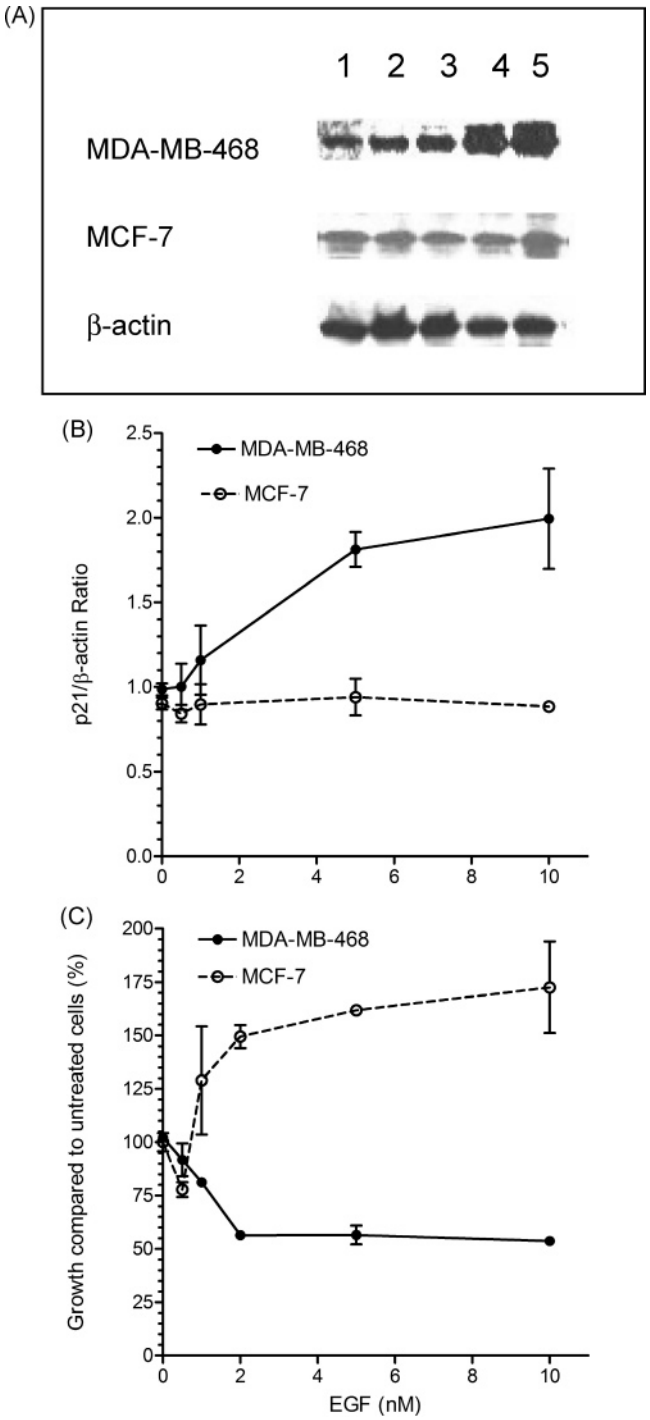

Figure 2. (A) Effect of exposure of MDA-MB-468 or MCF-7 human breast cancer cells for 24 h to increasing concentrations of EGF on the expression of p21. Lanes 1−5 are cells treated with 0.0, 0.5, 1, 5, or 10 nM of EGF, respectively. (B) The p21/β-actin ratio in the cells was evaluated by Western blot. (C) Effect of EGF exposure of MDA-MB-468 or MCF-7 cells on cell growth measured colorimetrically using the WST-1 assay. Cell growth of treated cells at 24 h was expressed as a percentage relative to that of untreated cells. Data shown are the mean ± sem of three replicate determinations.

For the current studies, two human BC cells that broadly represent two clinically relevent BC phenotypes were chosen. MDA-MB-468 cells have a mutated p53 gene (*15*), are estrogen-receptor (ER) negative, and display overexpression of EGF receptors (EGFR; $1-2 \times 10^6$ receptors/cell) (*16*). MCF-7 cells have wild-type p53, are ER-positive, and display a 100-fold lower level of EGFR on their surface (*15*). To determine if tat-anti-p21 ICs could differentially sensitize these BC cells to the growth-inhibitory effects of agents that induce p21, we selected EGF, camptothecin (CPT), and γ-radiation as treatments for these studies. Although EGF is a mitogenic peptide growth factor for MCF-7 cells, it paradoxically has growth-inhibitory effects on MDA-MB-468 cells that are mediated by its induction of p21 causing cell cycle arrest in the G_1/S phase (*16*, *17*). Camptothecin (CPT) is a topoisomerase I inhibitor in the same

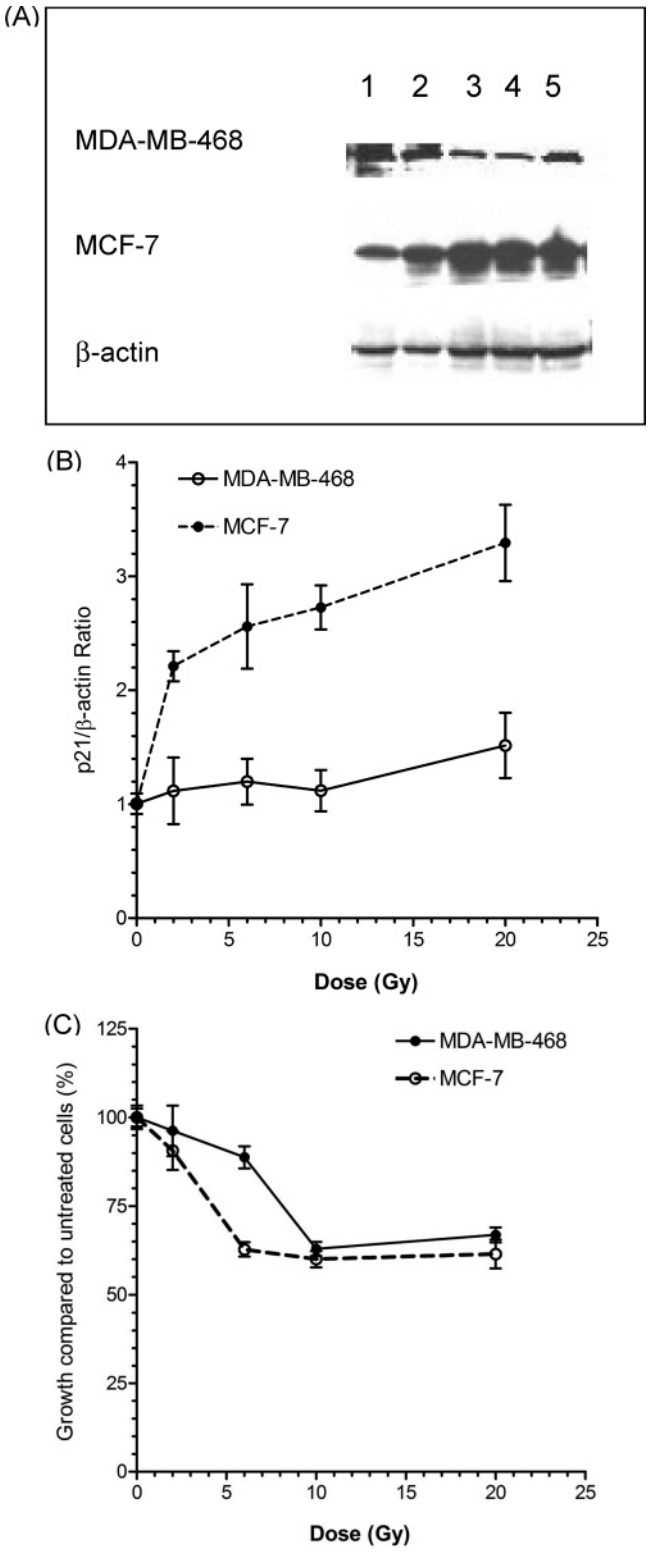

Figure 3. (A) Effect of exposure of MDA-MB-468 or MCF-7 human breast cancer cells to increasing doses of γ-radiation on the expression of p21. Lanes 1−5 are cells treated with 0, 2, 6, 10, and 20 Gy, respectively. (B) The p21/β-actin ratio in the cells was evaluated by Western blot. (C) Effect of γ-irradiation of MDA-MB-468 or MCF-7 cells on cell growth measured colorimetrically using the WST-1 assay. Cell growth of treated cells at 8 h was expressed as a percentage relative to that of untreated cells. Data shown are the mean ± sem of three replicate determinations.

class as the chemotherapeutic agents, ironotecan and topotecan. CPT has been reported to induce p21 in MDA-MB-468 and in MCF-7 cells (*15*). γ-Radiation is a standard treatment for locoregional control of BC; its effects on p21 expression are dependent on wild-type p53 expression by cells (*18*). Our objectives were (i) to fully characterize the effects of treatment of MDA-MB-468 and MCF-7 cells on p21 expression; (ii) to study the effects of p21 induction on cell cycle distribution; and (iii) to correlate p21 induction with the sensitization observed following coexposure to tat-anti-p21 ICs.

EXPERIMENTAL PROCEDURES

Breast Cancer Cells. MDA-MB-468 and MCF-7 human BC cells were obtained from the American Type Culture Collection (ATCC, Manassas, VA) and were cultured in Dulbecco's minimal essential medium (DMEM, Ontario Cancer Institute, Toronto, ON) supplemented with 10% fetal calf serum (FCS, Sigma Chemical Co., St. Louis, MO), containing 100 units/mL penicillin, 100 μg/mL streptomycin, 4 mM glutamine, and 400 μM sodium pyruvate, at 37 °C in an atmosphere of 5% of carbon dioxide (CO_2).

Treatment of Breast Cancer Cells. MDA-MB-468 and MCF-7 BC cells were seeded into 60-mm culture dishes (Nolge Nunc Internationa, Roskilde, Denmark) at a density of 6×10^5 cells per dish and cultured overnight. The cells were then treated with increasing concentrations of CPT (Sigma-Aldrich, St. Louis, MO) (0.1−4 μM) or EGF (Upstate Biotechnology, Lake Placid, NY) (0.5−20 nM). CPT was initially dissolved in dimethylsulfoxide (DMSO) at a concentration of 4 mM and stored at −20 °C. CPT was diluted in DMEM to the desired concentration immediately before use. The final concentration of DMSO in the cell culture was <0.1% (v/v), which has been shown to be nontoxic to cells (*19*). Treated and control untreated cells were harvested at 24 h after treatment by scraping them into 1 mL of 150 mM sodium chloride (AstraZeneca Canada, Inc., Mississauga, ON) and centrifuging at 350*g* for 5 min. Cells were treated with γ-radiation (2−20 Gy) delivered over 2−22 min, depending on the dose required, by a cell irradiator (model GC40-E, MDS-Nordion, Kanata, ON). These cells were harvested at 8 h postirradiation. Cell pellets were lysed in 50 μL E7 buffer consisting of 0.1% sodium dodecylsulfonate (SDS, Bio-Rad Laboratories, Hercules, CA), 1% sodium deoxycholate (Sigma), and 1% Triton X-100 (Bio-Rad Laboratories) in 10 mM Tris-HCL (Sigma)/150 mM sodium chloride (Sigma) pH 7.4 containing proteinase inhibitor (Roche, Montreal, PQ). Protein concentrations were estimated using the Bio-Rad Protein Assay kit (Bio-Rad Laboratories).

Dose-Dependent Induction of p21 Expression. Cell lysates were analyzed by Western Blot to evaluate the dose-dependent induction of p21 expression. Briefly, sodium dodecylsulfonate polyacrylamide gel electrophoresis (SDS-PAGE) was performed under reducing conditions on 10 μL (10 μg) of cell lysates on a 4−20% Tris HCL gradient Ready-Gel (BioRad, Mississauga, ON). Electrophoresed proteins were transferred to a nitrocellulose membrane (Trans-Blot, BioRad) using 25 mM Tris, 192 mM glycine, pH 8.3 buffer. The membranes were blocked overnight with 5% skimmed milk (Nestle Canada, Inc., North York, ON) or 5% bovine serum albumin (BSA) in Tris-buffered saline (TBS: 150 mM sodium chloride, 20 mM Tris-HCL, and 0.1% Tween-20, pH 7.6), rinsed with TBS, and probed at 37 °C for 45 min with 1 μg/mL of mouse anti-p21 antibodies (Oncogene Research, Cedarlane Laboratories, Mississauga, ON) or 1 μg/mL of goat polyclonal anti-β-actin antibodies (Santa Cruz Biotechnology, Santa Cruz, CA). The membranes were rinsed with TBS, then incubated at 37 °C for 45 min with a 1:1500 dilution of goat anti-mouse IgG-horseradish peroxidase (HRP) secondary antibodies (Sigma) in the case of the p21 blots or rabbit anti-goat IgG-HRP antibodies (Sigma) in the case of β-actin blots. Reactive bands were detected using the ECL enhanced chemiluminescence kit (NEN Life Science Products,

Table 1. Effect of Treatments on Cell Cycle Distribution of MDA-MB-468 and MCF-7 Cells[a]

	MDA-MB-468					MCF-7				
	untreated	DMSO[b]	CPT[c] (1 μM)	EGF[d] (10 nM)	γ-radiation (20 Gy)	untreated	DMSO	CPT (1 μM)	EGF (10 nM)	γ-radiation (20 Gy)
G_0/G_1	53.9%	52.1%	71.3%	71.7%	44.9%	50.2%	49.5%	29.2%	50.2%	35.3%
S	25.6%	21.5%	19.8%	16.3%	15.1%	39.0%	35.6%	62.8%	34.3%	4.2%
G_2/M	20.5%	26.4%	8.9%	12.0%	40.0%	10.8%	14.9%	8.0%	15.5%	60.5%

[a] At 24 h after treatment, cell cycle distribution was determined by flow cytometry by staining with propidium iodide. [b] DMSO: dimethylsulfoxide. [c] CPT: camptothecin. [d] EGF: epidermal growth factor.

Boston, MA) and visualized by exposure to Kodak BioMax film (Kodak, Rochester, NY). The intensities of p21 and β-actin bands were quantified by gel densitometry (LabWorks Analysis software, UVP, Inc., Upland, CA).

Effects of p21 Expression on Cell Cycle Distribution. The effect of p21 expression on cell cycle distribution was determined by flow cytometry. At 24 h after exposure to CPT or EGF and 8 h after γ-radiation, MDA-MB-468 or MCF-7 cells were recovered by trypsinization and rinsed with 150 mM sodium chloride/10 mM sodium phosphate pH 7.6 (PBS), then fixed in 70% ethanol (Sigma) overnight. Fixed samples were rinsed with PBS, resuspended, and stained with 10 μg/mL propidium iodide (PI) (Sigma) and 200 units of RNAse A (Sigma) in PBS. Stained samples were analyzed on a FACScan flow cytometer (BD Bioscience, Sat Jose, CA). The percentage of cells in G_1, S, and G_2/M phase were quantified using the *Modfit* software program (Verity Software House, Topsham, ME).

WST Cell Proliferation Assay. Eight thousand cells treated with CPT, EGF, or γ-radiation were cultured in wells of 96-well plates. At 8 or 24 h after treatment, 1/10 (v/v) of WST-1 (Roche) was added into each well. Two hours after incubation, the plates were read at a wavelength of 450 nm (690 nm as the reference wavelength) using an ELISA plate reader (EL_X 800, Bio-Tek Instruments, Inc., Winooski, VT). Absorbance in the wells containing treated cells was expressed as a percentage of control wells containing untreated cells. Triplicate measurements were performed at each concentration of CPT, EGF, or dose of γ-radiation.

Treatment Sensitization Effects of Tat-anti-p21 ICs. BC cells were exposed to 1 μM CPT or 10 nM EGF for 24 h in DMEM containing 10% FCS for CPT or serum-free DMEM for EGF followed by incubation with 5 μM tat-anti-p21 ICs, 5 μM unmodified anti-p21 antibodies, or normal saline (control) for 4 h. We previously found that internalization of these tat-anti-p21 ICs labeled with ^{123}I by MDA-MB-468 cells was saturable above 5−8 μM and nuclear uptake was saturable above 5 μM (*12*). Similar studies were performed for MDA-MB-468 or MCF-7 cells exposed to 10 Gy of γ-radiation. Following γ-irradiation, BC cells were cultured for 8 h in DMEM containing 10% FCS, then incubated for 4 h with 5 μM tat-anti-p21 ICs, 5 μM unmodified anti-p21 antibodies, or normal saline (control). The cellular uptake and nuclear importation of tat-anti-p21 ICs, unmodified anti-p21 antibodies, or tat peptides labeled with ^{123}I (5 μM) in MDA-MB-468 and MCF-7 cells were measured as previously reported (*12, 13*).

Statistical Analyses. Data were expressed as mean ± sem. Statistical comparisons were made by Student's *t*-test and one-way ANOVA, and post-testing was performed using Bonferroni Multiple Comparisons Test using *Prism* v. 3.02 software (GraphPad Software, Inc., San Diego, CA). Statistical significance was defined as $p < 0.05$.

RESULTS

Dose-Dependent Induction of p21 Expression. Western blot showed that the p21/β-actin ratio in MDA-MB-468 cell lysates increased in direct proportion to CPT exposure (0.1−4 μM) (Figure 1). The maximum p21/β-actin ratio (5.54 ± 0.62) occurred at a concentration of 4 μM of CPT and was significantly higher than that in cells exposed to DMSO-containing buffer without CPT (1.10 ± 0.09) or untreated cells (0.99 ± 0.02). Treatment of MCF-7 cells with CPT for 24 h also increased p21 levels (Figure 1). The maximum p21/β-actin ratio (5.29 ± 0.14) occurred at 0.5−1 μM CPT and was significantly higher than for MCF-7 cells treated with DMSO-containing buffer without CPT (1.06 ± 0.19) or for untreated cells (1.03 ± 0.01). The p21/β-actin ratio decreased in MCF-7 cells above CPT concentrations of 1 μM (Figure 1). Treatment of MDA-MB-468 cells with EGF for 24 h caused a concentration-dependent increase in p21 expression (Figure 2). The maximum p21/β-actin ratio was observed at 5 nM EGF (1.8 ± 0.1) to 10 nM EGF (2.0 ± 0.3) and was significantly higher than for untreated cells (1.0 ± 0.1; $p < 0.05$). In contrast, there was no effect of EGF on p21 expression in MCF-7 cells (Figure 2). The p21/β-actin ratio in MCF-7 cells exposed to 5 nM EGF (0.84 ± 0.12) or 10 nM EGF (0.79 ± 0.10) was not significantly different than for untreated cells (0.90 ± 0.04; $p > 0.05$). Exposure of BC cells to γ-radiation increased p21 expression up to threefold in MCF-7 cells, but there was no significant change in p21 expression in γ-irradiated MDA-MB-468 cells (Figure 3).

Effects of p21 Expression on Cell Cycle Distribution. Induction of p21 by CPT caused an increase in the proportion of MDA-MB-468 cells in G_0/G_1 phase and a decrease in the proportion of cells in G_2/M phase compared to cells exposed to DMSO-containing buffer without CPT or untreated cells (Table 1). Induction of p21 by CPT in MCF-7 cells decreased the proportion of cells in G_0/G_1 phase and increased the fraction of cells in S phase, possibly due to G_2/M-phase transition block. Induction of p21 by EGF in MDA-MB-468 cells caused an increase in the fraction of MDA-MB-468 cells in G_0/G_1 phase compared to untreated cells (Table 1). The proportion of MDA-MB-468 cells in G_0/G_1 phase increased from 54% to 72% following exposure to 10 nM EGF, whereas there was no change in the G_0/G_1-phase fraction for EGF-exposed MCF-7 cells. Exposure of BC cells to 20 Gy of γ-radiation caused a twofold increase in MDA-MB-468 cells in G_2/M phase (40.0% versus 20.5%; Table 1), whereas exposure of MCF-7 cells caused a five-to-sixfold increase in the G_2/M-phase fraction (60.5% versus 10.8%).

WST Cell Proliferation Assay. Treatment of BC cells with CPT (up to 4 μM) caused a 1.6-fold to 2-fold decrease in the growth of MDA-MB-468 cells over 24 h, whereas a 1.6-fold decreased growth rate of MCF-7 cells was observed (Figure 1). These results were comparable to those previously reported for BC cells exposed to CPT (*15, 20*). Treatment with EGF (0 to 10 nM) caused a 2-fold decrease in the growth of MDA-MB-468 cells over 24 h, whereas a 2-fold increased growth of MCF-7 cells was observed (Figure 2). Despite the lack of p21 induction in MDA-MB-468 cells, these cells were nevertheless growth-inhibited by γ-radiation (Figure 3), although they were less sensitive than MCF-7 cells, particularly at lower doses (<10 Gy). For example, the growth of MDA-MB-468 cells relative to unexposed cells follow-

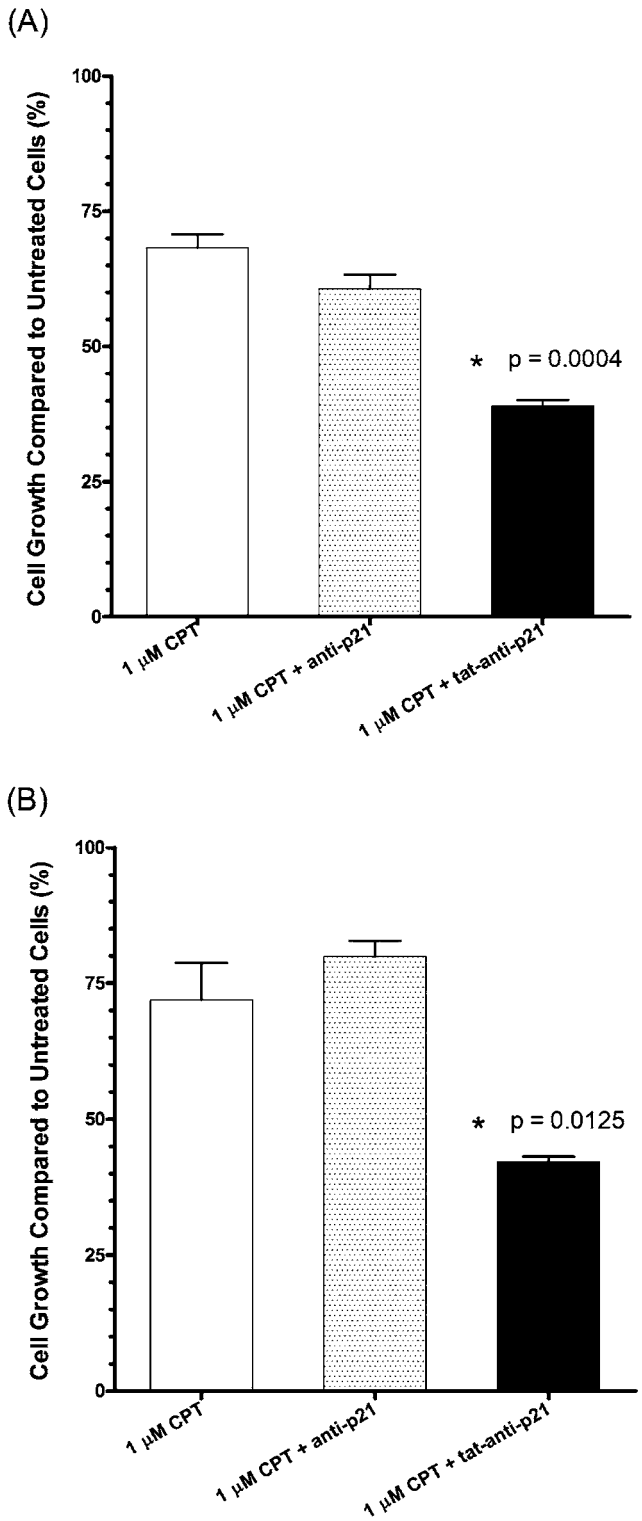

Figure 4. (A) Effect of exposure of MDA-MB-468 human breast cancer cells for 24 h to 1 μM CPT or 1 μM CPT followed by incubation with 5 μM anti-p21 antibodies or 5 μM tat-anti-p21 ICs on cell growth over 4 h measured colorimetrically using the WST-1 assay. (B) Effect of exposure of MCF-7 human breast cancer cells to 1 μM CPT followed by incubation with 5 μM anti-p21 antibodies or 5 μM tat-anti-p21 ICs or on cell growth. Cell growth is expressed as a percentage relative to that of untreated cells. Data shown are the mean ± sem of three replicate determinations. Statistical significance is indicated by the asterisk and *p*-value.

ing treatment with 6 Gy of γ-radiation was 88.7 ± 3.1% compared to 62.7 ± 2.0% for MCF-7 cells ($p = 0.002$). These results were consistent with the growth inhibitory effects of γ-radiation on MDA-MB-468 (*21*) and MCF-7 cells (*21, 22*).

Table 2. Effect of Incubation Time with EGF on Sensitization of Growth Inhibition by Tat-anti-p21 Immunoconjugates (ICs)[a]

	incubation time		
	24 h	48 h	72 h
10 nM EGF	72.5 ± 1.8%	40.1 ± 0.2%	16.5 ± 1.6%
10 nM EGF + anti-p21 antibodies	70.4 ± 0.1%	39.9 ± 4.1%	16.5 ± 0.8%
10 nM EGF + tat-anti-p21 ICs	60.9 ± 0.4%[b]	21.1 ± 1.8%[b]	7.1 ± 0.7%[b]
sensitization effect[c] (fold)	1.2-fold	1.9-fold	2.3-fold

[a] Cells were treated with 10 nM EGF for 24, 48, or 72 h, then exposed/not exposed to tat-anti-p21 ICs or unmodified anti-p21 antibodies for 4 h. Cell growth was measured colorimetrically using the WST-1 assay. Values shown are the percentage growth relative to control untreated cells (mean ± sem; $n = 3$). [b] Significantly different ($p < 0.05$) from cells treated with 10 nM EGF alone or 10 nM EGF + tat-anti-p21 antibodies. [c] Sensitization effect (fold) was calculated by dividing the growth of cells treated with 10 nM EGF + tat-anti-p21 ICs by that for cells treated with 10 nM EGF alone.

Treatment Sensitization Effects of Tat-anti-p21 ICs. The growth of MDA-MB-468 cells exposed to 1 μM CPT followed by tat-anti-p21 ICs relative to untreated cells was 39.0 ± 1.1% compared to 68.2 ± 2.5% for cells treated with CPT alone ($p = 0.0004$; Figure 4). The growth of MDA-MB-468 cells treated with 1 μM CPT and unmodified anti-p21 antibodies was 64.6 ± 2.6% relative to untreated cells. Tat-anti-p21 ICs also caused significant sensitization of MCF-7 cells to the effects of 1 μM CPT (42.1 ± 0.9% vs 71.9 ± 6.8%, respectively; $p = 0.0125$; Figure 4). Cotreatment with unmodified anti-p21 antibodies did not alter the growth inhibitory effects of CPT in MCF-7 cells (71.9 ± 6.8% vs 79.9 ± 2.9%; $p > 0.05$).

The growth of MDA-MB-468 cells exposed to EGF and tat-anti-p21 ICs relative to untreated cells was 60.9 ± 0.4% compared to 72.5 ± 1.8% for cells treated with EGF alone ($p = 0.003$; Figure 5). Although the sensitization factor was relatively low (1.2-fold), it increased with longer times of incubation with EGF. The sensitization factor increased to 1.9-fold at 48 h to 2.3-fold at 72 h of incubation with 10 nM EGF (Table 2.). There was no significant effect of tat-anti-p21 ICs on the growth of EGF-exposed MCF-7 cells relative to untreated cells (154.8 ± 4.6% vs 153.0 ± 2.4%, respectively; $p = 0.739$; Figure 5). In each case, EGF stimulated the growth of MCF-7 cells, irrespective of their exposure to tat-anti-p21 ICs. Cotreatment with unmodified anti-p21 antibodies did not change the growth of BC cells exposed to EGF: 70.4 ± 0.04% and 146.5 ± 3.8% compared to untreated cells for MDA-MB-468 and MCF-7, respectively.

Growth of MDA-MB-468 cells exposed to γ-radiation and tat-anti-p21 ICs relative to untreated cells was 73.6 ± 4.0% compared to 68.2 ± 1.9% for cells exposed to γ-radiation alone ($p = 0.291$; Figure 6). In contrast, the growth of MCF-7 cells was diminished significantly from 71.0 ± 1.3% for cells treated with γ-radiation alone to 51.4 ± 4.6% for cells treated with γ-radiation combined with tat-anti-p21 ICs relative to untreated cells ($p = 0.0154$; Figure 6). Cotreatment with unmodified anti-p21 antibodies did not significantly change the growth of BC cells exposed to γ-radiation: 74.2 ± 1.4% and 72.3 ± 1.4%, respectively; $p > 0.05$. There were no significant differences in cellular uptake or nuclear uptake of tat-anti-p21 ICs labeled with ^{123}I in MDA-MB-468 or MCF-7 cells (Table 3). The uptake of ^{123}I-tat-anti-p21 ICs by MDA-MB-468 cells was 27.9 ± 4.3% compared to 22.4 ± 1.3% for MCF-7 cells ($p > 0.05$). Nuclear importation of

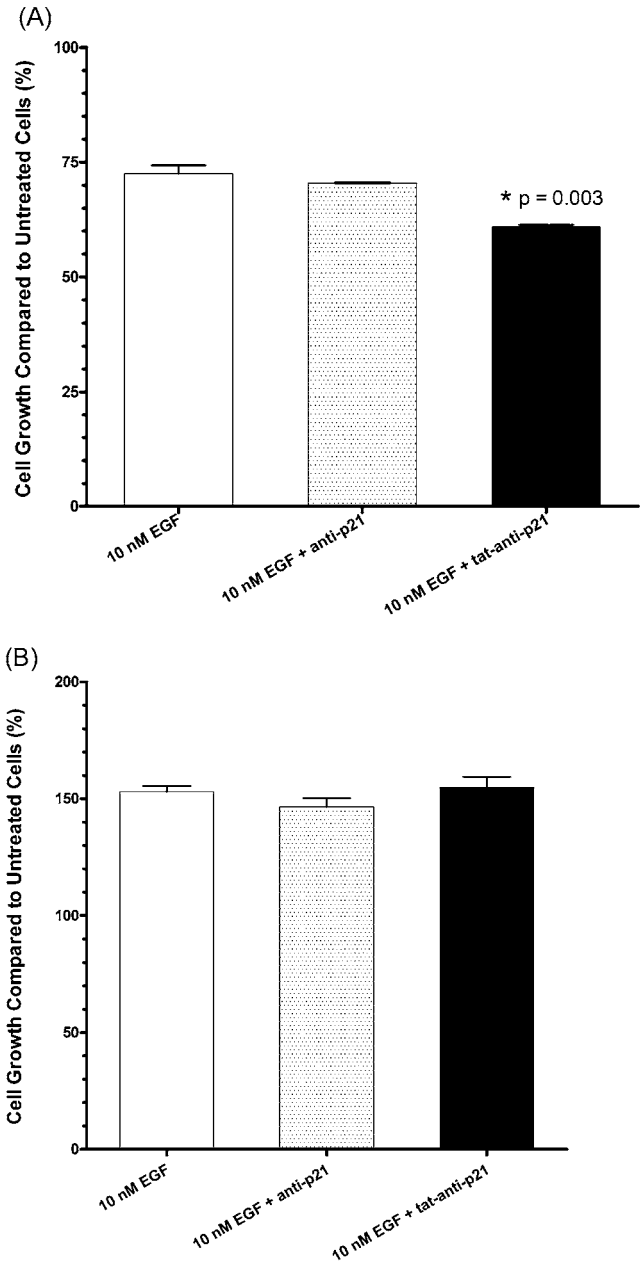

Figure 5. (A) Effect of exposure of MDA-MB-468 human breast cancer cells for 24 h to 10 nM EGF or 10 nM EGF followed by incubation with 5 μM anti-p21 antibodies or 5 μM tat-anti-p21 ICs on cell growth over 4 h measured colorimetrically using the WST-1 assay. (B) Effect of exposure of MCF-7 human breast cancer cells to 10 nM EGF followed by incubation with 5 μM anti-p21 antibodies or 5 μM tat-anti-p21 ICs or on cell growth. Cell growth is expressed as a percentage relative to that of untreated cells. Data shown are the mean $\pm$ sem of three replicate determinations. Statistical significance is indicated by the asterisk and *p*-value.

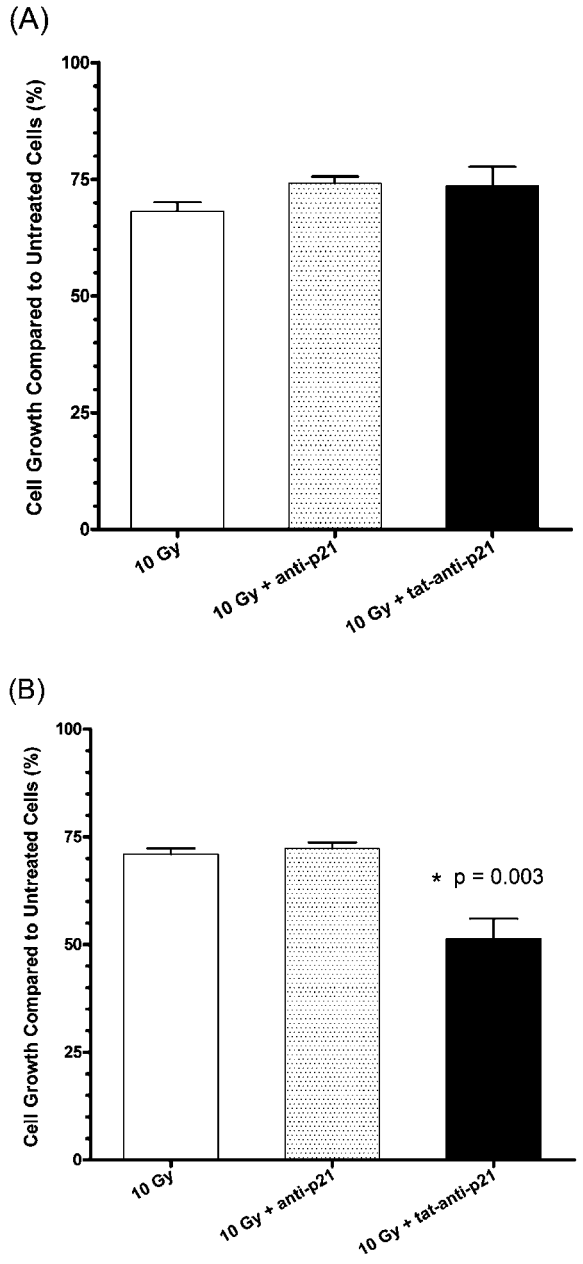

Figure 6. (A) Effect of exposure of MDA-MB-468 human breast cancer cells to 10 Gy of γ-radiation followed by incubation with 5 μM anti-p21 antibodies or 5 μM tat-anti-p21 ICs on cell growth over 4 h measured colorimetrically using the WST-1 assay. (B) Effect of exposure of MCF-7 human breast cancer cells to 10 Gy of γ-radiation, then incubation with 5 μM anti-p21 antibodies or 5 μM tat-anti-p21 ICs on cell growth. Cell growth is expressed as a percentage relative to that of untreated cells. Data shown are the mean $\pm$ sem of three replicate determinations. Statistical significance is indicated by the asterisk and *p*-value.

^{123}I-tat-anti-p21 ICs was 68.4 $\pm$ 9.3% in MDA-MB-468 and 71.6 $\pm$ 2.3% in MCF-7 cells, respectively. Accumulation of ^{123}I-labeled tat-anti-p21 ICs in cells or nuclei was similar to that of ^{123}I-tat peptides (Table 3). However, cell penetration and nuclear uptake of unmodified ^{123}I-anti-p21 antibodies were threefold and tenfold lower than those of ^{123}I-tat-anti-p21 ICs (Table 3).

DISCUSSION

In this study, we investigated for the first time the ability of tat-anti-p21 ICs to differentially sensitize BC cells to the growth-inhibitory effects of EGF, CPT, or γ-radiation. Tat peptides have been found useful for insertion of many different types of proteins and biomolecules into cells (*23*, *24*). In particular, tat peptides have been employed to insert p53 (*25*) as well as the cyclin-dependent kinase inhibitors, $p27^{Kip1}$ (*26*) or $p16^{INK4a}$ (*27*) into cells in order to restore normal growth regulatory function. The results of this study now extend these findings to the application of tat peptides for insertion of antibodies into cancer cells that have the ability to interfere with cell-protective mechanisms that limit the effectiveness of cytotoxic therapies. The construction and characterization of tat-IgG ICs were described in earlier reports by our group (*12*, *13*). In one of these studies (*13*), we showed that tat-anti-p21 ICs penetrated MDA-MB-468 cells and were translocated to the nucleus, where

Table 3. Cell Penetration and Nuclear Uptake of ^{123}I-Labeled Tat-anti-p21 Immunoconjugates (ICs), Anti-p21 Antibodies, or Tat Peptides by MDA-MB-468 or MCF-7 Cells

	MDA-MB-468 cells			MCF-7 cells		
	^{123}I-tat-anti-p21 ICs	^{123}I-anti-p21 antibodies	^{123}I-tat peptides	^{123}I-tat-anti-p21 ICs	^{123}I-anti-p21 antibodies	^{123}I-tat peptides
cell penetration	27.9 ± 4.3%[a]	9.7 ± 2.9%	26.9 ± 4.2%	22.3 ± 1.3%	7.9 ± 0.7%	19.1 ± 2.6%
nuclear uptake	59.7 ± 8.6%[b]	5.2 ± 0.3%	63.0 ± 7.3%	70.2 ± 7.4%	4.6 ± 1.0%	66.4 ± 5.7%

[a] Percentage (mean ± sem; $n = 3$) of radioactivity internalized into breast cancer cells after incubation for 4 h at 37 °C with ^{123}I-labeled tat-anti-p21 ICs, unmodified anti-p21 antibodies or tat peptides. [b] Percentage (mean ± sem; $n = 3$) of internalized radioactivity that was associated with cell nucleus. There were no significant differences in cell penetration or nuclear uptake of ^{123}I-tat-anti-p21 ICs by MDA-MB-468 or MCF-7 cells.

they attenuated the ability of p21 to mediate G_1-S-phase arrest in EGF-exposed cells. MDA-MB-468 cells exposed to 8 μM tat-anti-p21 ICs had a significantly decreased proportion of cells in G_1 phase compared to EGF-treated cells (46.1 ± 0.7% vs 81.9 ± 0.7%, respectively; $p < 0.001$); in fact, the proportion of cells in G_1 phase approached that of untreated MDA-MB-468 cells (25.8 ± 0.2%).

The sensitization by tat-anti-p21 ICs of BC cells to the growth-inhibitory effects of EGF, CPT, or γ-radiation were directly correlated with induction of p21 expression by these treatments. MDA-MB-468 cells were growth-inhibited by EGF, which was associated with higher levels of p21 and an increased proportion of cells in G_0/G_1 phase (Table 1). The antiproliferative effects of EGF were enhanced 1.2-fold to 2.3-fold by tat-anti-p21 ICs, depending on the incubation time of the cells with EGF (24 to 72 h; Table 2). Induction of p21 in MDA-MB-468 cells by EGF is mediated by a p53-independent mechanism, since these cells harbor a p53 mutation (*15*). In contrast, MCF-7 cells were growth-stimulated by EGF and did not exhibit increased p21 induction or a change in their cell cycle distribution. Cotreatment of MCF-7 cells with tat-anti-p21 ICs and EGF had no significant effect on their growth. Similar but complementary results were found for MDA-MB-468 and MCF-7 cells treated with γ-radiation. In this case, γ-irradiation increased p21 expression in MCF-7 cells (which have wild-type p53) (*15*) but not in p53-mutant MDA-MB-468 cells. Both MDA-MB-468 and MCF-7 cells showed an increase in the proportion of cells G_2/M phase and were growth-inhibited by γ-radiation. However, only in MCF-7 cells in which p21 was induced did tat-anti-p21 ICs provide a 1.4-fold significant sensitization of the growth-inhibitory effects of γ-radiation. Finally, exposure to CPT increased p21 levels in both MDA-MB-468 and MCF-7 cells, causing G_0/G_1-phase arrest in the case of MDA-MB-468 cells and an increase in the S-phase fraction for MCF-7 cells (possibly due to G_2/M-phase block). In this example, tat-anti-p21 ICs sensitized MDA-MB-468 and MCF-7 cells equivalently 1.7-fold. This differential sensitization to treatments that induce p21 by tat-anti-p21 ICs was not due to differences in cellular penetration or nuclear localization between MDA-MB-468 or MCF-7 cells, since these were virtually identical (Table 3). Unmodified anti-p21 antibodies did not sensitize BC cells to the growth-inhibitory effects of EGF, CPT, or γ-radiation (Figures 4−6). Moreover, in an earlier study, we demonstrated that nonspecific tat-mouse IgG ICs had no significant effect on G_1/S-phase arrest caused by exposure of MDA-MB-468 cells to EGF. The proportion of EGF-treated MDA-MB-468 cells in G_1 phase was 82.1 ± 0.7% and 81.9 ± 0.7% with/without cotreatment with tat-mouse IgG, respectively ($p > 0.05$). These results clearly showed that tat peptides were required for delivery of anti-p21 ICs to the nucleus of BC cells and that these ICs sensitize the cells to the growth-inhibitory effects of agents that induce p21 expression.

Our findings suggest that combining tat-anti-p21 ICs with cytotoxic agents is a promising area of research which may improve the effectiveness of anti-cancer therapy. The magnitude of sensitization observed for BC cells in this study ranged from 1.2-fold in the case of EGF (but increased to 2.3-fold with a 72 h incubation period) to 1.4-fold for CPT and 1.7-fold for γ-radiation. The ultimate clinical usefulness of this level of sensitization cannot be determined at this stage, but these orders of magnitude are similar to those previously reported for other well-known sensitizers. For example, in one study (*28*), the IC_{50} for γ-irradiation of colon cancer cells was 2.27 Gy, but this was reduced to 1.61 Gy following incubation with the radiosensitizer, 5-FU. This represents a 1.4-fold sensitization. A serious challenge in cancer treatment is the development of chemotherapy-resistant strains as a consequence of inadequate sterilization of tumor cells (*29*). Therefore, enhancement of cytotoxic potency using tat-anti-p21 ICs as illustrated in this study could potentially lessen the risk of treatment failure. Moreover, the approach could potentially be extended to functional inhibition of other key cell cycle regulatory proteins (e.g., p53, $p27^{Kip-1}$), inhibitors of apoptosis (e.g., bcl-2) or transcription factors (e.g., myc) that have been implicated in the progression of cancer (*30*−*32*). It is feasible to deliver these tat-anti-p21 ICs in vivo to human tumors. Recently, we showed that ^{123}I-labeled tat-anti-p21 ICs injected i.v. (tail vein) in athymic mice implanted s.c. with MDA-MB-468 xenografts localized preferentially in tumors that were injected intratumorally with EGF to induce p21 compared to control tumors that received saline injections (3.1 ± 0.4% i.d./g vs 1.8 ± 0.2% i.d./g, respectively; $p < 0.05$) (*13*). We have confirmed that these and other tat-immunoglobulin ICs labeled with ^{123}I penetrated cells in tumors (and normal tissues) and were imported into the nucleus of cells in vivo. Therefore, in summary, we believe that tat-anti-p21 ICs are promising as potential sensitizers for the treatment of tumors with those agents that induce p21 expression.

CONCLUSIONS

We conclude that tat-anti-p21 ICs sensitized BC cells to the antiproliferative agents of EGF, CPT, or γ-radiation and that this sensitization was dependent on the differential ability of these agents to induce p21 expression in the cells. Due to the central role of p21 in causing cell cycle arrest and/or promoting apoptosis in cells exposed to DNA-damaging agents, tat-anti-p21 ICs offer the potential to amplify the antiproliferative effects of cytotoxic therapy on cancer cells. This approach, if successful, could ultimately lessen the risk of treatment failure and the development of resistant tumor strains and could be extended to inhibit other cell growth regulatory molecules.

ACKNOWLEDGMENT

This study was supported by grants from the Canadian Breast Cancer Research Alliance with funds from the Canadian Cancer Society to R.M.R and a Predoctoral Traineeship Award from the U.S. Army Breast Cancer Research Program (DAMD 17-02-1-0598) to M.H.

LITERATURE CITED

(1) Parker, L. P., Wolf, J. K., and Price, J. E. (2000) Adenoviral-mediated gene therapy with Ad5CMVp53 and Ad5CMVp21 in combination with standard therapies in human breast cancer cell lines. *Ann. Clin. Lab. Sci. 30*, 395−405.

(2) Gorospe, M., Crieli, C., Wang, X., Seth, P., Capogrossi, M. C., and Holbrook, N. J. (1997) p21(Waf1/Cip1) protects against p53-mediated apoptosis of human melanoma cells. *Oncogene 14*, 929−935.

(3) Niculescu, A. B., 3rd., Chen, X., Smeets, M., Hengst, L., Prives, C., and Reed, S. I. (1998) Effects of p21(Cip1/Waf1) at both the G1/S and the G2/M cell cycle transition: pRb is a critical determinant in blocking DNA replication and in preventing endoreduplication. *Mol. Cell. Biol. 18*, 629−643.

(4) Dulic, V., Stein, G. H., Far, D. F., and Reed, S. I. (1998) Nuclear accumulation of p21Cip1 at the onset of mitosis: a role at the G2/M-phase transition. *Mol. Cell. Biol. 18*, 546−557.

(5) Fan, Y., Borowsky, A. D., and Weiss, R. H. (2003) An antisense oligodeoxynucleotide to p21(Waf1/Cip1) causes apoptosis in human breast cancer cells. *Mol. Cancer Ther. 2*, 773−782.

(6) Weiss, R. H. (2003) p21Waf1/Cip1 as a therapeutic target in breast and other cancers. *Cancer Cell 4*, 425−429.

(7) Waldman, T., Zhang, Y., Dillehay, L., Yu, J., Kinzler, K., Vogelstein, B., and Williams, J. (1997) Cell-cycle arrest versus cell death in cancer therapy. *Nat. Med. 3* (9), 1034−1036.

(8) Waldman, T., Lengauer, C., Kinzler, K. W., and Vogelstein, B. (1996) Uncoupling of S phase and mitosis induced by anticancer agents in cells lacking p21. *Nature (London) 381*, 713−716.

(9) Tian, H., Wittmack, E. K., and Jorgensen, T. J. (2000) p21WAF1/CIP1 antisense therapy radiosensitizes human colon cancer by converting growth arrest to apoptosis. *Cancer Res. 60*, 679−684.

(10) Stein, C. A. (1999) Two problems in antisense biotechnology: in vitro delivery and the design of antisense experiments. *Biochim. Biophys. Acta. 1489*, 45−52.

(11) Butz, K., Geissen, C., Ulmann, A., Zentgraf, H., and Hoppe-Sevler, F. (1998) Uncoupling of p21WAF1/CIP1/SDI1 mRNA and protein expression upon genotoxic stress. *Oncogene 17*, 781−787.

(12) Hu, M., Chen, P., Wang, J., Chan, C., Scollard, D. A., and Reilly, R. (2006) Site-specific conjugation of HIV-1 tat peptides to IgG: a potential route to construct radioimmunoconjugates for targeting intracellular and nuclear epitopes in cancer. *Eur. J. Nucl. Med. Mol. Imaging 33*, 301−310.

(13) Hu, M., Chen, P., Wang, J., Deborah, S., Vallis, K., and Reilly, R. (2006) ^{123}I-labeled HIV-1 tat peptide radioimmunoconjugates are imported into the nucleus of human breast cancer cells and functionally interact in vitro and in vivo with the cyclin-dependent kinase inhbitor, p21WAF-1/Cip-1. *Eur. J. Nucl. Med. Mol. Imaging*, in press.

(14) Barbareschi, M., Caffo, O., Doglioni, C., Fina, P., Marchetti, A., Buttitta, F., Leek, R., Morelli, L., Leonardi, E., Bevilacqua, G., Dalla Palma, P., and Harris, A. L. (1996) p21WAF1 immunohistochemical expression in breast carcinoma: correlations with clinicopathological data, oestrogen receptor status, MIBI expression, p53 gene and protein alterations and relapse-free survival. *Br. J. Cancer 74*, 208−215.

(15) Liu, W., and Zhang, R. (1998) Upregulation of p21WAF1/CIP1 in human breast cancer cell lines MCF-7 and MDA-MB-468 undergoing apoptosis induced by natural product anticancer drugs 10-hydroxycamptothecin and camptothecin through p53-dependent and independent pathways. *Int. J. Oncol. 12*, 793−804.

(16) Filmus, J., Pollak, M. N., Cailleau, R., and Buick, R. N. (1985) MDA-468, a human breast cancer cell line with a high number of epidermal growth factor (EGF) receptors, has an amplified EGF receptor gene and is growth inhibited by EGF. *Biochem. Res. Commun. 128*, 898−905.

(17) Thomas, T., Balabhadrapathruni, S., Gardner, C. R., Hong, J., Faaland, C. A., and Thomas, T. J. (1999) Effects of epidermal growth factor on MDA-MB-468 breast cancer cells: alterations in polyamine biosynthesis and the expression of p21/CIP1/WAF1. *J. Cell. Physiol. 179*, 257−266.

(18) Artuso, M., Esteve, A., Bresil, H., Vuillaume, M., and Hall, J. (1995) The role of the Ataxia telangectasia gene in the p53, WAF1/CIP1(p21)-, and GADD45-mediated response to DNA damage produced by ionizing radiation. *Oncogene 11*, 1427−1435.

(19) Jones, C. B., Clements, M. K., Wasi, S., and Daoud, S. S. (1997) Sensitivity to camptothecin of human breast carcinoma and normal endothelial cells. *Cancer Chemother. Pharmacol. 40*, 475−483.

(20) Wang, J. A., Fan, S., Yuan, R. Q., Ma, Y. X., Meng, Q., Goldberg, I. D., and Rosen, E. M. (1999) Ultraviolet radiation down-regulates expression of the cell-cycle inhibitor p21WAF1/CIP1 in human cancer cells independently of p53. *Int. J. Radiat. Biol. 75*, 301−316.

(21) Zhang, Z., Wang, H., Prasad, G., Li, M., Yu, D., Bonner, J. A., Agrawal, S., and Zhang, R. (2004) Radiosensitization by antisense anti-MDM2 mixed-backbone oligonucleotide in in vitro and in vivo human breast cancer models. *Clin. Cancer Res. 10*, 1263−1273.

(22) Coco Martin, J. M., Balkenende, A., Vershoor, T., Lallemand, F., and Michalides, R. (1999) Cyclin D1 overexpression enhances radiation-induced apoptosis and radiosensitivity in a breast tumour cell line. *Cancer Res. 59*, 1134−1140.

(23) Richard, J. P., Melikov, K., Vives, E., Ramos, C., Verbeure, B., Gait, M. J., Chernomordik, L. V., and Lebleu, B. (2003) Cell-penetrating peptides. A reevaluation of the mechanism of cellular uptake. *J. Biol. Chem. 278* (1), 585−590.

(24) Wadia, J. S., and Dowdy, S. F. (2005) Transmembrane delivery of protein and peptide drugs by TAT-mediated transduction in the treatment of cancer. *Adv. Drug Delivery Rev. 57*, 579−596.

(25) Snyder, E. L., Meade, B. R., Saenz, C. C., and Dowdy, S. F. (2004) Treatment of terminal peritoneal carcinomatosis by a transducible p53-activating peptide. *PLoS Biol. 2*, E36.

(26) Nagahara, H., Vocero-Akbani, A. M., Snyder, E. L., Ho, A., Latham, D. G., Lissy, N. A., Becker-Hapak, M., Ezhevsky, S. A., and Dowdy, S. F. (1998) Transduction of full-length TAT fusion proteins into mammalian cells: TAT-p27Kip1 induces cell migration. *Nat. Med. 4* (12), 1449−1452.

(27) Zezula, J., Casaccia-Bonnefil, P., Ezhevsky, S. A., Osterhout, D. J., Levine, J. M., Dowdy, S. F., Chao, M. V., and Koff, A. (2001) p21cip1 is required for the differentiation of oligodendrocytes independently of cell cycle withdrawal. *EMBO Rep. 2*, 27−34.

(28) Kjellstrom, J., Kjellen, E., and Johnsson, A. (2005) In vitro sensitization by oxaliplatin and 5-fluorouracil in a human colon cancer cell line. *Acta Oncol. 44*, 687−693.

(29) Mealey, K. L., Barhoumi, R., Burghardt, R. C., Safe, S., and Kochevar, D. T. (2002) Doxorubicin induces expression of P-gp in MCF-7 breast carcinoma cells. *Antimicrob. Agents Chemother. 46*, 755−61.

(30) Reed, J. C. (1995) Regulation of apoptosis by bcl-2 family proteins and its role in cancer and chemoresistance. *Curr. Opin. Oncol. 7*, 541−546.

(31) Hollstein, M. D., Sidransky, D., Vogelstein, B., and Harris, C. C. (1991) p53 mutations in human cancers. *Science 253*, 49−53.

(32) Brodeur, G. M., Seeger, R. C., Schwab, M., Varmus, H. E., and Bishop, J. M. (1984) Amplification of N-myc in untreated human neuroblastomas correlates with advanced disease stage. *Science 224*, 1121−1124.

BC060053R

A Method To Optimize PEG-Coating of Red Blood Cells

Sameereh Hashemi-Najafabadi,[†] Ebrahim Vasheghani-Farahani,*[,†] Seyed Abbas Shojaosadati,[†] Mohammad Javad Rasaee,[‡] Jonathan K. Armstrong,[§] Mostafa Moin,[||] and Zahra Pourpak[||]

Biotechnology Group, Chemical Engineering Department, Tarbiat Modares University, Tehran, P. O. Box 14115-143, I. R. Iran, Medical Biotechnology Department, Faculty of Medical Sciences, Tarbiat Modares University, Tehran, P. O. Box 14115-331, I. R. Iran, Department of Physiology and Biophysics, Keck School of Medicine, University of Southern California, Los Angeles, California 90033, and Immunology, Asthma and Allergy Research Institute, Children Medical Center, Tehran University of Medical Sciences, Tehran, P. O. Box 14185-863, I. R. Iran Received March 7, 2006; Revised Manuscript Received June 26, 2006

Alloimmunization to donor blood group antigens remains a significant problem in transfusion medicine. A proposed method to overcome donor−recipient blood group incompatibility is to mask the blood group antigens by the covalent attachment of poly(ethylene glycol) (PEG) to the red blood cell (RBC) membrane. Despite much work in the development of PEG-coating of RBCs, there is a paucity of data on the optimization of the PEG-coating technique; it is the aim of this study to determine the optimum conditions for PEG coating using a cyanuric chloride reactive derivative of methoxy-PEG as a model polymer. Activated PEG of molecular mass 5 kDa was covalently attached to human RBCs under various reaction conditions. Inhibition of binding of a blood-type specific antiserum (anti-D) was employed to evaluate the effect of the PEG-coating, quantified by hemocytometry and flow-cytometry. RBC morphology was examined by light and scanning electron microscopy. Statistical analysis of experimental design together with microscopy results showed that the optimum PEGylation conditions are pH = 8.7, temperature = 14 °C, and reaction time = 30 min. An optimum concentration of reactive PEG could not be determined. At high polymer concentrations (>25 mg/mL) a predominance of type III echinocytes was observed, and as a result, a concentration of 15 mg/mL is the highest recommended concentration for a linear PEG of molecular mass 5 kDa.

INTRODUCTION

The immunological response to transplanted allogeneic tissue and cells has been a significant barrier in both organ transplantation and blood transfusion. The most common example of allogeneic cell exposure is the use of red blood cells (RBCs) in transfusion. The cell surface serves as an important biological interface and biochemical barrier. The extreme complexity of proteins, carbohydrates, and lipids comprising the cell surface serves as the primary loci for tissue rejection. For blood banking, following Landsteiner's discovery of the ABO blood group antigens on RBCs a century ago (*1*), the major cause of this immune reaction had been identified. Blood samples from donor and recipient were each tested and classified into one of the four phenotypes, O, A, B, or AB, which allowed the donor and recipient phenotypes to be matched. Since this initial discovery, there are currently over 200 different known antigens (*2*). In most transfusions, ABO and D (Rhesus) blood typing is sufficient to identify appropriate donors. More often, problems are encountered in individuals who receive multiple transfusions, such as patients with sickle cell anemia and thalassemia. In such patients, alloimmunization against minor RBC antigens can make it nearly impossible to identify appropriate blood donors (*3*−*5*).

* To whom correspondence should be addressed. Tel.: +98-21-8 8005040; Fax: +98-21-88005040. E-mail: evf@modares.ac.ir.

[†] Biotechnology Group, Chemical Engineering Department, Tarbiat Modares University.

[‡] Medical Biotechnology Department, Faculty of Medical Sciences, Tarbiat Modares University.

[§] University of Southern California.

[||] Tehran University of Medical Sciences.

More than 20 years ago, Abuchowski et al. developed a technique to modify proteins by the covalent attachment of poly(ethylene glycol) (PEG). They showed that PEG-modified bovine albumin was less immunogenic than its unmodified counterpart (*6*, *7*).

The covalent attachment of PEG is now commonly used to modify a variety of proteins, enzymes, drugs, and artificial surfaces (*8*−*12*). Despite these applications, RBCs have only recently been considered for use as substrate for PEG modification. An overview of PEG-coating of RBCs by Fisher (*13*) summarizes the development of the field, and Lublin (*14*) reviewed the potential for PEG-coated RBCs as a component for the future creation of a safe, "universal" blood. The PEG-coating of RBCs provides a protective shell around the RBC that potentially excludes large molecules, such as antibodies, but does not appear to inhibit the passage of small molecules, such as glucose and oxygen (*13*).

Several reactive derivatives of methoxy-PEG (mPEG) have been used to covalently attach mPEG to the surface of RBCs (*15*−*18*). All of these reactive derivatives preferentially target epsilon amino acids (almost exclusively lysine residues) on the extracellular surface of the plasma membrane (*13*, *19*). All cells can be readily modified using cyanuric chloride activated PEG with only slight variations in pH, temperature, and time. Cyanuric chloride's strengths as a coupling agent include the malleability of its chemistry, the efficacy in membrane protein modification, and the chemical stability of the modified proteins (*20*).

Despite the development of this technology to PEG-coat RBCs, optimization of the reaction conditions has not been thoroughly investigated. In this study, RBCs were coated with a reactive cyanuric chloride mPEG derivative of 5 kDa

10.1021/bc060057w CCC: $33.50 © 2006 American Chemical Society
Published on Web 08/05/2006

molecular mass. The effects of process variables (polymer concentration, temperature, time, and pH) were investigated. Full factorial design and Taguchi analysis were employed to identify the optimum reaction conditions for PEGylation of RBCs. To assess the effectiveness of the PEG-coating, inhibition of agglutination by blood-type specific antisera was measured, using a hemocytometer to count the remaining single RBCs. In addition, the hemocytometery data were confirmed by flow cytometric analysis of fluorescein-labeled anti-D binding to PEG-coated RBCs. Finally, the morphology of PEG-RBCs was studied by light microscopy and scanning electron microscopy (SEM).

EXPERIMENTAL PROCEDURES

Reagents. Methoxy-poly(ethylene glycol) of 5 kDa molecular mass, triethanolamine (TEA), and fluorescein isothiocyanate (FITC) were purchased from Sigma (St. Louis, MO). Cyanuric chloride (2,4,6-trichloro-1,3,5-triazine), benzene, anhydrous sodium carbonate, D-glucose, sodium chloride, and potassium chloride were obtained from Merck-Schuchardt (Darmstadt, Germany). Cyclohexane was purchased from Roth (Karlsruhe, Germany). Packed Rh-positive RBCs were obtained from Iranian Blood Transfusion Organization. Anti-D was purchased from CinnaGen Inc. (Tehran, Iran).

Polymer Derivatization. Derivatization of 5 kDa mPEG with cyanuric chloride was performed using a modification of the method described by Abuchowski et al. (*6*). Briefly, 5 g of vacuum-dried mPEG (overnight at 80 °C) was dissolved in 40 mL of hot anhydrous benzene, cooled to 15 °C, and then slowly added to a solution of cyanuric chloride in benzene (5-fold molar excess). One gram of anhydrous sodium carbonate was then added. The mixture was stirred for 48 h at 15 °C under an atmosphere of dry nitrogen, and then the sodium carbonate was removed by vacuum filtration. The PEG derivative was precipitated with anhydrous cyclohexane, collected by vacuum filtration, and then resuspended in benzene. This process was repeated five times to remove any unreacted cyanuric chloride (*21*). The product was then dried under vacuum, using a freeze dryer system (Zirbus Technology, Vaco 5), and stored at −70 °C, under vacuum, until use (*22*).

Coating of Red Blood Cells with mPEG. Packed Rh-positive RBCs were resuspended to a 10% hematocrit in TEA buffer (30 mM TEA, 110 mM NaCl, 4 mM KCl, 5 mM D-glucose). A fresh cold stock solution of the derivatized polymer was prepared in 0.9% NaCl, containing 1 mM HCl, and appropriate volumes were immediately added to the RBC suspensions to yield a final polymer concentration of 5−45 mg/mL; an equivalent volume of buffer was added to the control samples. This acidic solution retards hydrolysis of the reactive PEG derivative prior to exposure to the RBCs; since only small volumes of the stock solution were added, the final pH of the suspensions remained unaltered. The samples were incubated with gentle mixing under various conditions (pH, temperature, time, and polymer concentration, defined in subsequent sections). After two washes with isotonic phosphate buffer solution (PBS, pH = 7.4) at 200 g for 10 min, packed RBCs were prepared for evaluation of the polymer coating (*23*).

RBC Agglutination by Anti-D. Inhibition of anti-D mediated agglutination was employed to assess the effectiveness of the polymer coating. Four hundred microliters of a control or PEGylated RBC (Rh-positive) suspension (6% hematocrit in isotonic saline) (*24*) was mixed with a solution of anti-D in PBS with a known concentration (ratio of anti-D: PBS = 1:3) and were incubated with a gentle mixing at room temperature for 30 min. The RBC s were then centrifuged at 200*g* for 1 min. One microliter of the pellet was re-suspended in 1 mL of PBS (0.1% hct), and then using a dye exclusion test with trypan blue (viable cells remained uncolored, dead cells showed blue color) and light microscopic system (Nikon, E200), nonagglutinated viable free cells were counted using a hemocytometer (Improved Neubauer Ruling). The Improved Neubauer Ruling is a 3 by 3 mm (9 mm^2) grid, subdivided into nine secondary squares, each 1 by 1 mm (1 mm^2). The smallest squares in the center of the grid have an area of 1/400 mm^2 and are arranged in groups of 16. Single free erythrocytes in five of the 25 sections of 16 small squares of the hemocytometer (four corner sections and the center square) were counted, which is equal to the number of free erythrocytes in 0.02 μL of suspension. For determination of free cells per 1 mL of RBCs at 100% hct, the number of counted free cells per 0.02 μL at 0.1% hct was multiplied by 5×10^7. The higher the number of free cells, the greater the effectiveness of RBC PEGylation.

Table 1. Selected Experimental Variables with Corresponding Values at Two Levels for Full Factorial Design

variable	low level (1)	high level (2)
A: temperature of reaction (°C)	4	25
B: time of reaction (min)	30	60
C: mPEG concentration (mg/mL)	5	45
D: pH of TEA buffer	8	9.5

Flow Cytometry. Labeling of anti-D with FITC was achieved by following the procedure described by Coligan et al. (*25*). Fluorescein-labeled anti-D was added to a dilute suspension of RBCs in PBS. The ratio of fluorescein-labeled anti-D to RBCs, obtained by titration, was high to prevent agglutination (60 μL of 0.1% hematocrit in PBS, added to 200 μL of fluorescein-labeled anti-D solution with a protein concentration of 0.16 mg/mL). The samples were incubated for 30 min at room temperature in the dark with gentle mixing, centrifuged, and washed twice with PBS at 500*g* for 2 min. The labeled cells were then resuspended in 1 mL of PBS. The fluorescence intensity of FITC-anti-D labeled PEG-cells was measured using a FACSTAR PLUS flow cytometer (Becton Dickinson, San Jose, CA). Ten thousand cells were counted for each sample (*23*). The fluorescence intensity of FITC-anti-D labeled cells was recorded for each sample and expressed as a ratio to the intensity of FITC-anti-D labeled control (uncoated) cells. The lower this ratio, the greater the effectiveness of RBC PEGylation.

Microscopy. The morphology of PEG-RBCs and control (uncoated) RBCs at physiological pH was studied by SEM (XL 30, Philips, Netherlands). The procedure described by Kayden and Bessis (*26*) to prepare RBCs for SEM was followed. Additionally, RBCs were suspended in compatible plasma and the RBC morphology examined by light microscopy at 40 × magnification.

Design of Experiments. Statistically designed experiments are highly efficient in that they give a fixed amount of information with much less effort than the classical one-variable-at-a-time approach, and many of them give additional information about interactions between variables. Factorial and fractional-factorial experiments are the most powerful (statistical) techniques in research, and well chosen fractional-factorials are particularly economical in assessing multivariable systems (*27*).

Full Factorial at Two Levels. The first step (using the Yates Table) was to identify which variables have the largest effects on the PEGylation reaction. Selection of these factors was based on previous studies in literature for RBC PEGylation. The evaluated variables were temperature and time of PEGylation reaction, polymer concentration, and pH of TEA buffer (Table 1).

Taguchi Design. We have employed Taguchi statistical technique to study the impact of multiple variables on single outputs (prevention of agglutination and antibody binding). In this technique, the results of the experiments are analyzed to achieve one or more of the following three objectives: (1) To

Table 2. Selected Experimental Variables with Corresponding Values at Three Levels for Taguchi Design

variable	first level (1)	second level (2)	third level (3)
A: temperature of reaction (°C)	4	14	25
B: mPEG concentration (mg/mL)	5	25	45
C: pH of TEA buffer	8	8.7	9.5

Table 3. Yates Table Analysis of a 2^4 Full Factorial Design (Four Variables in Two Levels)

trial	TC[a]	temp (A) (°C)	time (B) (min)	concn (C) (mg/mL)	pH (D)	response[b] $\times 10^{-7}$	*F*-value[c]
1	l	4	30	5	8	55	-
2	a	25	30	5	8	100	160.33
3	b	4	60	5	8	60	0.01
4	ab	25	60	5	8	100	39.47
5	c	4	30	45	8	70	115.12
6	ac	25	30	45	8	125	12.79
7	bc	4	60	45	8	65	1.58
8	abc	25	60	45	8	135	1.13
9	d	4	30	5	9.5	95	22.43
10	ad	25	30	5	9.5	75	15.70
11	bd	4	60	5	9.5	50	0.23
12	abd	25	60	5	9.5	100	30.35
13	cd	4	30	45	9.5	125	17.27
14	acd	25	30	45	9.5	125	0.23
15	bcd	4	60	45	9.5	90	1.58
16	abcd	25	60	45	9.5	175	0.01

[a] Treatment combination: The low level of any variable is denoted by l, and the high level of any variable is denoted by its lower-case letter. [b] Each value is the average number of free cells, per 1 mL suspension, for each test with two replicates. [c] $SS_x = (f^2_x)/N$, which f_x is the amount in the final column of Yates analysis corresponding to x (not presented here) and N is the total number of treatment combinations with their replications (*32*), $MS_x = SS_x/ø_x$, which $ø_x$ is the degree of freedom corresponding to x, TSS $= \Sigma y^2_i - (\Sigma y_i)^2/N = 36311.75 \times 10^{14}$, y_i is the result, RSS $=$ TSS $- \Sigma SS_x$ $= 1338 \times 10^{14}$, error degree of freedom ($ø$) $= 16$, residual error variance $=$ RSS/$ø$ $= 83.60 \times 10^{14}$, *F*-value $= MS_x$/(residual error variance), *F*-critical ($ø_1 = 1$, $ø_2 = 16$) $= 8.575$ (obtained from standard table).

establish the best or the optimum condition for a product or a process. (2) To estimate the contribution of individual factors. (3) To estimate the response under the optimum conditions.

The optimum condition is identified by studying the main effects of each of the factors. The process involves minor arithmetic manipulation of the numerical results. The main effects indicate the general trend of the influence of the factors.

If a systematic, sequential approach to experimental design is adopted, it is usually sufficient to restrict the design to two-level experiments. Sometimes, however, it is advantageous to work at three levels or more. The usual reason for employing either of these techniques is that a maximum or minimum is being approached. This design estimates the nonlinear (quadratic) effects (*28*).

To obtain the optimum condition for PEGylation of RBCs, an L_{27} array of Taguchi (*28*) for three variables at three levels was designed. The variables and their corresponding values are presented in Table 2. This design was also employed to compare the hemocytometry results with the flow cytometry data. All experiments with RBCs were performed in duplicate unless stated otherwise.

RESULTS

The results and statistical analysis for full factorial design (using Yates Table) at two levels are presented in Table 3. All the responses are presented as the number of viable free cells per 1 mL of packed cells. An increase in the number of free cells for PEGylated versus control (uncoated) RBCs shows that the PEG-RBCs were protected against agglutination. By comparison the obtained *F*-values with a critical $F_{(1,16)}$ value of 8.575 (obtained from the *F*-Table) (*27*), it is apparent that three variables (temperature, polymer concentration, and pH) and their interactions have *F*-values greater than critical *F*. Hence they were selected as important factors for PEGylation of RBCs. The effect of reaction time was less important. In fact after 30 min, the reaction was complete and any further increase in incubation time did not have a significant effect on the responses. As a result, the reaction time was fixed at 30 min to study the effect of other variables on the extent of PEGylation.

Table 4. An L_{27} Taguchi Array for RBC PEGylation

trial	temp (°C)	concn (mg/mL)	pH	response[a] $\times 10^7$	response[b]
1	4	5	8	65	0.82
2	4	5	8.7	90	0.83
3	4	5	9.5	90	0.84
4	4	25	8	130	0.80
5	4	25	8.7	135	0.71
6	4	25	9.5	150	0.77
7	4	45	8	125	0.79
8	4	45	8.7	120	0.71
9	4	45	9.5	120	0.76
10	14	5	8	140	0.64
11	14	5	8.7	120	0.55
12	14	5	9.5	195	0.64
13	14	25	8	195	0.51
14	14	25	8.7	200	0.47
15	14	25	9.5	205	0.51
16	14	45	8	170	0.49
17	14	45	8.7	210	0.38
18	14	45	9.5	165	0.62
19	25	5	8	150	0.52
20	25	5	8.7	135	0.70
21	25	5	9.5	160	0.53
22	25	25	8	180	0.59
23	25	25	8.7	180	0.52
24	25	25	9.5	130	0.45
25	25	45	8	175	0.45
26	25	45	8.7	155	0.53
27	25	45	9.5	110	0.45

[a] Each value is the average number of free cells, per 1 mL suspension for each test with two replicates. [b] Each value is the average mean fluorescence intensity ratio of FITC labeled anti-D cells of PEG-RBCs versus control (uncoated) RBCs, for each test with two replicates.

The obtained results, using an L_{27} array of Taguchi, with both data from cell counting and flow cytometry methods are presented in Table 4. The main effects of the experimental variables on the number of free single RBCs and also the mean fluorescence intensity ratio of FITC-anti-D labeled cells of PEG-RBCs versus control (uncoated) RBCs, as two indicators of the extent of PEGylation, are shown in Figures 1 and 2, respectively. These figures show the effect of one variable, when the others vary. Each point in each curve presents an average of the obtained responses from 9 duplicate experiments (18 experiments). These figures show that the optimum temperature and pH of reaction medium are 14 °C and pH $=$ 8.7, respectively. But the optimum polymer concentration, obtained by cell counting and flow cytometry methods, was 25 and 45 mg/mL, respectively.

The morphology of control (uncoated) and PEG-coated RBCs (5, 10, 15, 25, and 45 mg/mL of activated mPEG) that were prepared under optimum conditions (30 min, 14 °C and pH $=$ 8.7) and then returned to a physiological pH with PBS (pH $=$ 7.4) are presented in Figure 3 (images from SEM). RBC morphology was classified according to Bessis (*29*). At 5 mg/mL, type I echinocytes were observed with a few cells of echinocyte type II or III. At 10 mg/mL, type II echinocytes predominate with some cells of type I still observable. At 15 mg/mL, an equal amount of type II and III echinocytes were observed, and at 25 and 45 mg/mL only type III echinocytes existed. Light microscopic examination of RBCs suspended in compatible plasma confirmed the SEM observations.

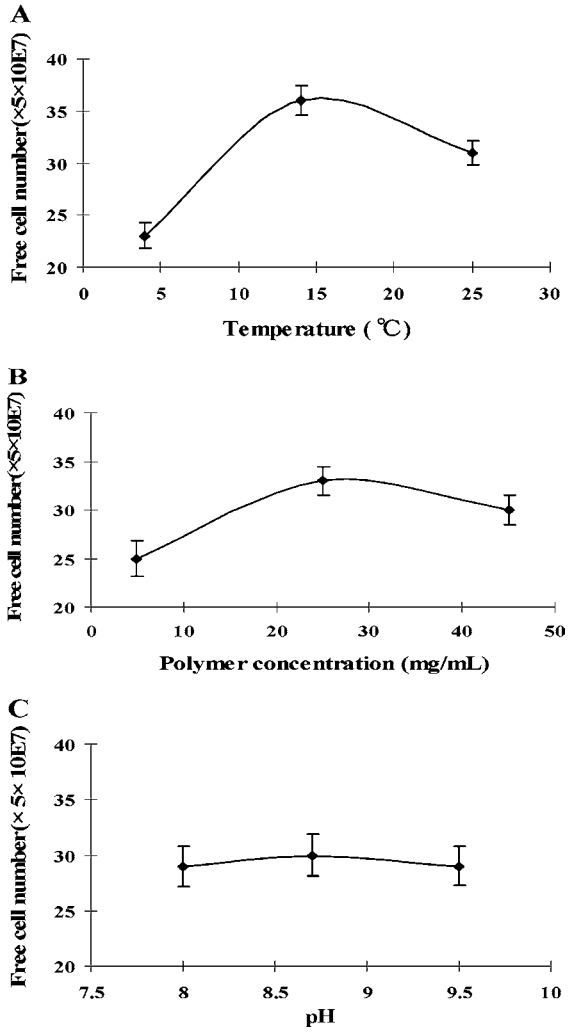

Figure 1. The effect of different factors on free cell (nonagglutinated cell) number. Shown are the effect of (A) temperature of reaction, (B) polymer concentration, and (C) pH of TEA buffer.

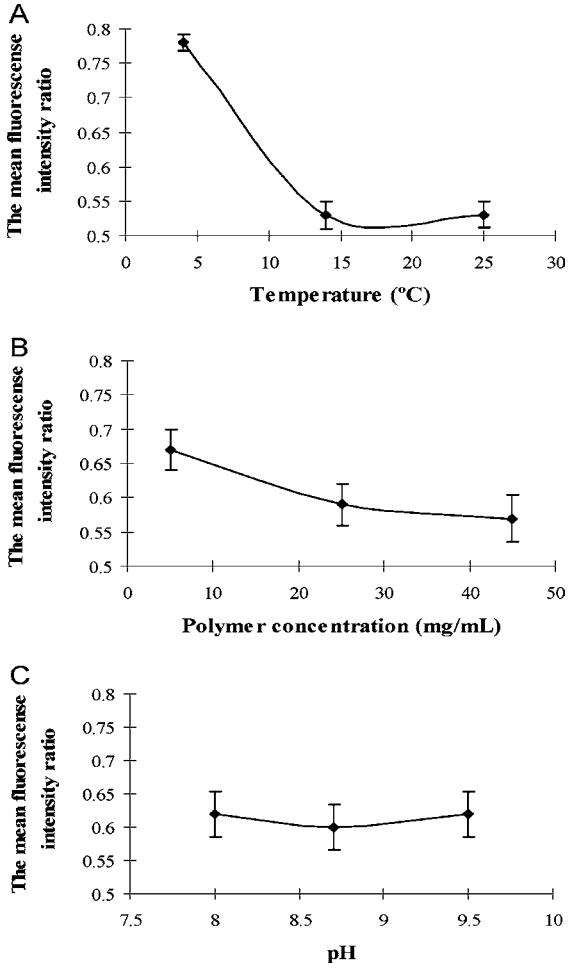

Figure 2. The effect of different factors on the mean fluorescence intensity ratio of PEG-RBCs versus control (uncoated) RBCs incubated with FITC labeled anti-D. Shown are the effect of (A) temperature of reaction, (B) polymer concentration, and (C) pH of TEA buffer.

DISCUSSION

The selection of the levels of factors for optimization were based on the range given in the literature. Jackson et al. (*30*) showed that pH = 9.2 is effective for coupling a cyanuric chloride activated mPEG to a protein. Other researchers used an elevated pH (pH = 8−9.2) for coupling an activated PEG with RBCs (*23*, *31*, *32*). The range of 30−60 min and 4−25 °C for the time and temperature of RBC PEGylation, respectively, have also been used.

Fisher (*13*) in his review noted that at polymer concentrations below 1 mM (5 mg/mL), the 5 kDa-activated mPEG is not very effective for masking antigens. Higher concentrations up to 50 mg/mL (10 mM) have also been used (*16*, *32*), but some abnormality in the morphology of RBCs was reported. Light microscopic examination of linear mPEG 5 kDa-coated RBCs in autologous plasma showed marked echinocytosis above a mPEG concentration of 2 mM (*33*) and poor *in vivo* survival of mPEG 5 kDa-coated RBCs has been observed by others in the mouse model at a concentration of 0.6mM and above (*31*). More effective antigen masking and maintenance of discocytic morphology was achieved with reactive derivatives of branched PEGs (*33*).

SEM and light microscopy results from our work presented here show that a polymer concentration of 15 mg/mL is the highest recommended level for PEGylation using a linear PEG of molecular mass 5 kDa. Above this concentration only type III echinocytes existed. RBCs of echinocyte type I and II may circulate in the host body, but cells of echinocyte type III would not circulate, because such cells are not deformable and hence would tend to get trapped in the microcirculation (*34*). Therefore the optimum concentration, 25 mg/mL, obtained by the cell counting method, and 45 mg/mL, obtained by the flow cytometry method, cannot be selected as optimum concentrations due to the loss of discocytic morphology.

The observation of increasing echinocytosis with increasing reactive PEG concentration is solely related to the presence of PEG on the cell surface, and not exposure to high pH, as all control cells showed normal discocytic morphology after returning to a physiological pH. For the purposes of the work undertaken here, it was reasonable to select a linear PEG of molecular mass 5 kDa, as this is the most commonly used PEG derivative. It is possible that PEGs of larger molecular mass or of different geometry may sustain discocytic RBC morphology, while being effective antigen masking agents (*33*), but investigation into these variables was beyond the scope of the current study.

During the incubation period at elevated pH, virtually no lysis (<1%) was observed in either the control or mPEG-modified RBCs. Indeed even mPEG concentration of up to 45 mg/mL yielded no significant lysis during RBC derivatization. Scott et al. showed that high polymer concentrations (>30 mg/mL) resulted in significant lysis after 24 h of incubation at 37 °C (but not at lower temperatures and times) (*32*).

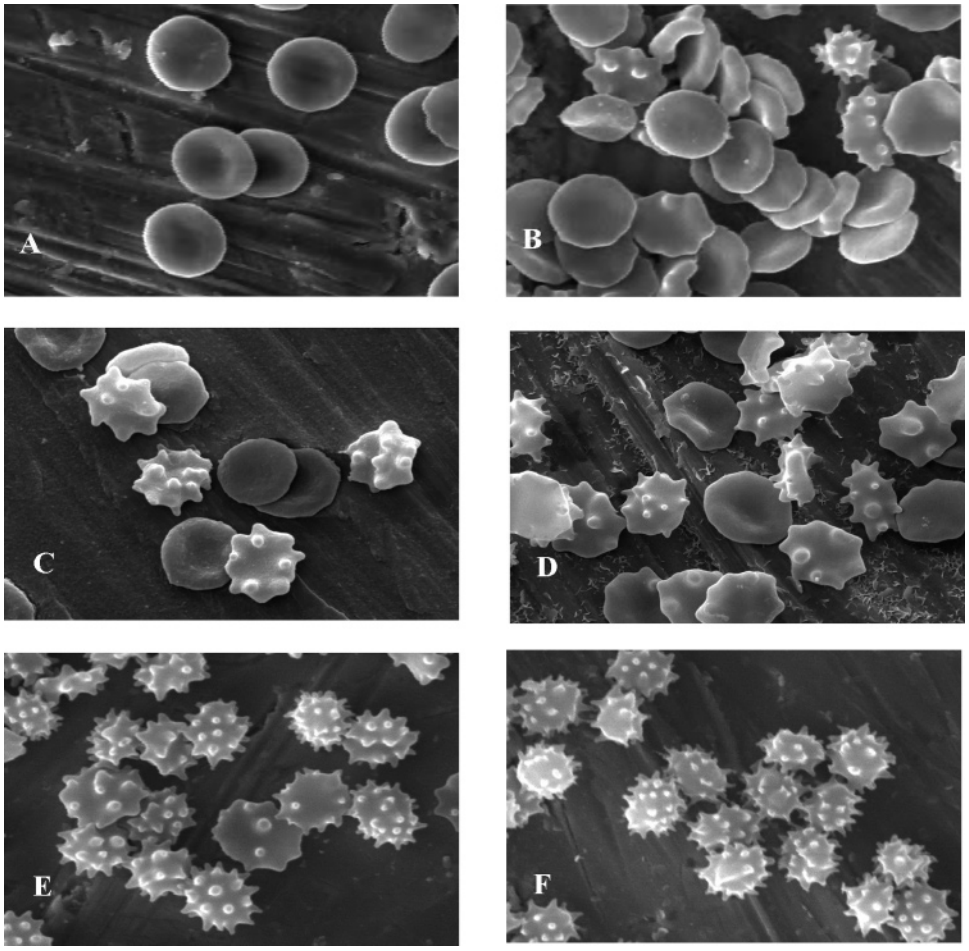

Figure 3. The morphology of mPEG-derivatized RBCs (3000×). The reactive mPEG 5kDa incubation concentrations are (A) 0 mg/mL control (uncoated), (B) 5 mg/mL, (C) 10 mg/mL, (D) 15 mg/mL (E) 25 mg/mL, and (F) 45 mg/mL.

The optimum temperature and pH of reaction medium, obtained by Taguchi design, are 14 °C and pH = 8.7. At 4 °C the rate of reaction is low, and more time is required for completion of the reaction. At temperatures higher than 20 °C, the activated polymer may show a less active form (*30*) that suggests a moderate temperature is more favorable. As mentioned earlier, a pH >7.0 is required for reaction of the PEG derivative with primary amine residues.

It can be seen that the optimum conditions at which the number of free cells was maximum, and the fluorescence intensity ratio of FITC-anti-D bound cells of the PEG-RBCs versus control (uncoated) RBCs was at a minimum, as shown in Table 4, are very similar to those deduced from Figures 1 and 2. It shows that agglutination between RBCs decreased and the corresponding number of free cells increased with increasing PEG concentration. Also as a result of RBC coating by mPEG, attachment of FITC labeled-anti-D to RBCs decreased and the corresponding ratio of mean fluorescence intensity of the PEG-RBCs versus control (uncoated) RBCs was decreased. It is worth mentioning that inhibition of agglutination does not necessarily indicate that antibody binding was inhibited relative to uncoated cells and may merely reflect the physical prevention of Igs bridging between cells. However, inhibition of agglutination does facilitate a way to quantify the PEG-coating of RBCs and is sufficient to determine the optimum conditions for PEGylating. Direct measurement of inhibition of anti-D binding to PEG-RBCs by flow cytometric analysis, using a FITC-labeled anti-D, demonstrates that the polymer coating does prevent antibody binding.

Cyanuric chloride-activated mPEG-5 kDa was covalently attached to human RBCs, and the optimum (best) conditions for this reaction were determined by different methods of experimental design. The optimum pH of TEA buffer, temperature, and reaction time were pH = 8.7, 14 °C, and 30 min, respectively. An optimum polymer concentration could not be determined by the methods employed here; however, a maximum concentration of 15 mg/mL, as the best condition, is recommended for a cyanuric chloride derivative of mPEG 5 kDa due to the observation of increasing echinocytosis with increasing concentration. Finally, concerning the good agreement between the results from hemocytometry and flow cytometry analyses, it can be concluded that the cell counting method is a simple and suitable technique to assess RBC PEGylation.

ACKNOWLEDGMENT

This work was supported by grants from the Ministry of Science, Research and Technology, and Tehran University of Medical Sciences. The authors also wish to thank Iranian Blood Transfusion Organization for providing the packed Rh-positive RBCs.

LITERATURE CITED

(1) Landsteiner, K. (1901) Uber agglutinationserscheinungen normalen menslichen blutes. *Wien. Klin. Wochenschr. 14,* 1132−1134.

(2) Reid, M. E., and Lomas-Francis, C. (1997) *The Blood Group Antigen Facts Book,* pp 19−395, Academic Press, London, UK.

(3) Castro, O., Sandler, S. G., Houston-Yu, P., and Rana, S. (2002) Predicting the effect of transfusing only phenotype-matched RBCs to patients with sickle cell disease: theoretical and practical implications. *Transfusion 42,* 684−690.

(4) Rosse, W. F., Gallagher, D., Kinney, T. R., Castro, O., Dosik, H., Moohr, J., Wang, W., and Levy, P. S. (1990) Transfusion and alloimmunization in sickle cell disease: the cooperative study of sickle cell disease. *Blood 76*, 1431−1437.

(5) Vichinsky, E. P., Earles, A., Johnson, R. A., Hoag, M. S., Williams, A., and Lublin, B. (1990) Alloimmunization in sickle cell anemia and transfusion of racially unmatched blood. *New Engl. J. Med. 322*, 1617−1621.

(6) Abuchowski, A., Es, T. V., Palczuk, N. C., and Davis, F. F. (1977) Alteration of immunological properties of bovine serum albumin by covalent attachment of polyethylene glycol. *J. Biol. Chem. 252*, 3578−3581.

(7) Abuchowski, A., McCoy, J. R., Palczuk, N. C., Es, T. V., and Davis, F. F. (1977) Effect of covalent attachment of polyethylene glycol on immunogenicity and circulating life of bovine liver catalase. *J. Biol. Chem. 252*, 3582−3586.

(8) Harris, J. M., and Zalipsky, S. (1997) *Poly(ethylene glycol): Chemistry and Biological Applications*, ACS Symposium Series, pp 1−13, American Chemical Society, Washington DC.

(9) Greenwald, R. B., Choe, Y. H., McGuire, J., and Conover, C. D. (2003) Effective drug delivery by PEGylated drug conjugates. *Adv. Drug Delivery Rev. 55*, 217−250.

(10) Hershfield, M. S. (1995) PEG-ADA replacement therapy for adenosine deaminase deficiency: an update after 8.5 years. *Clin. Immunol. Immunopathol. 76*, S228−S232.

(11) Keating, M. J., Holmes, R., Lerner, S., and Ho, D. H. (1993) L-asparaginase and PEG asparaginase−past, present, and future. *Leuk. Lymphoma 10*, 153−157.

(12) Thanou, M., and Duncan, R. (2003) Polymer-protein and polymer-drug conjugates in cancer therapy. *Curr. Opin. Invest. Drugs 4*, 701−709.

(13) Fisher, T. C. (2000) PEG-coated red blood cells − simplifying blood transfusion in the new Millennium? *Immunohematology 16*, 37−46.

(14) Lublin, D. M. (2000) Universal RBCs. *Transfusion 40*, 1285−1289.

(15) Armstrong, J. K., Meiselman, H. J., and Fisher, T. C. (1997) Covalent binding of poly(ethylene glycol) to the surface of red blood cells inhibits aggregation and reduces low-shear blood viscosity. *Am. J. Hematol. 56*, 26−28.

(16) Hortin, G. L., Lok, H. T., and Huang, S. T. (1997) Progress toward preparation of universal donor red cells. *Artif. Cells, Blood Substitutes, Immobilization Biotechnol. 25*, 487−491.

(17) Jeong, S. T., and Byun, S. M. (1996) Decreased agglutinability of methoxy-polyethylene glycol attached red blood cells: significance as a blood substitute. *Artif. Cells, Blood Substitutes, Immobilization Biotechnol. 24*, 503−511.

(18) Scott, M. D., and Chen, A. M. (2004) Beyond the red cell: PEGylation of other blood cells and tissues. *Transfus. Clin. Biol. 11*, 40−46.

(19) Chen, A. M., and Scott, M. D. (2001) Current and future applications of immunological attenuation via PEGylation of cells and tissue. *BioDrugs 15*, 833−847.

(20) Scott, M. D., and Murad, K. L. (1998) Cellular camouflage: fooling the immune system with polymers. *Curr. Pharm. Des. 4*, 423−438.

(21) Armstrong, J. K., Meiselman, H. J., and Fisher, T. C. (1999) Evidence against macromolecular "bridging" as the mechanism of red blood cell aggregation induced by nonionic polymers. *Biorheology 36*, 433−437.

(22) Sabolovic, D., Sestier, C., Perrotin, P., Guillet, R., Tefit, M., and Boynard, M. (2000) Covalent binding of polyethylene glycol to the surface of red blood cells as detected and followed up by cell electrophoresis and rheological methods. *Electrophoresis 21*, 301−306.

(23) Blackall, D. P., Armstrong, J. K., Meiselman, H. J., and Fisher, T. C. (2001) Polyethylene glycol-coated red blood cells fail to bind glycophorin A-specific antibodies and are impervious to invasion by the Plasmodium falciparum malaria parasite. *Blood 97*, 551−556.

(24) Bradley, A. J., Murad, K. L., Regan, K. L., and Scott, M. D. (2002) Biophysical consequences of linker chemistry and polymer size on stealth erythrocytes: size dose matter. *Biochim. Biophys. Acta 1561*, 147−158.

(25) Coligan, J. E., Kruisbeek, A. M., Margulies, D. H., Shevach, E. M., and Strober, W. (1991) *Current Protocols in Immunology*, vol. 1, John Wiley & Sons, Inc., New York.

(26) Kayden, H. J., and Bessis, M. (1970) Morphology of normal erythrocyte and acanthocyte using nomarski optics and the scanning electron microscope. *J. Hematol. 35*, 427−436.

(27) Davies, L. (1993) *Efficiency in Research, Development, and Production: the Statistical Design and Analysis of Chemical Experiments*, pp 1−88, The Royal Society of Chemistry, Cambridge.

(28) Roy, R. K. (1990) *A Prime on the Taguchi Method*, pp 1−155, Van Nostrand Reinhold, New York.

(29) Bessis, M. (1973) *Red Cell Shape: Physiology, Pathology, Ultrastucture*, pp 1−25, Springer-Verlag, New York.

(30) Jackson, C. C., Charlton, J. L., Kuzminski, K., Lang, G. M., and Sehon, A. H. (1987) Synthesis, isolation and characterization of conjugates of ovalbumin with monomethoxypolyethylene glycol using cyanuric chloride as the coupling agent. *Anal. Biochem. 165*, 114−127.

(31) Murad, K. L., Mahany, K. L., Brugnara, C., Kuypers, F. A., Eaton, J. W., and Scott, M. D. (1999) Structural and functional consequences of antigenic modulation of red blood cells with methoxypoly(ethylene glycol). *Blood 93*, 2121−2127.

(32) Scott, M. D., Murad, K. L., Koumpouras, F., Talbot, M., and Eaton, J. W. (1997) Chemical camouflage of antigenic determinants: stealth erythrocytes. *Proc. Natl. Acad. Sci. U.S.A. 94*, 7566−7571.

(33) Fisher, T. C., Armstrong, J. K., Meiselman, H. J., Leger, R. M., and Garratty, G. (2000) "Second generation" poly(ethylene glycol) surface coatings for red blood cells. *Transfusion 40*, 119S.

(34) Poraicu, D., Sandor, S., and Menessy, I. (1983) Decrease of red blood cell filterability seen in intensive care II. Red blood cell crenation in-vivo as morphological evidence of increased red cell viscosity in low flow states. *Resuscitation 10*, 305−316.

BC060057W

Structure−Activity Relationships of ^{111}In- and ^{99m}Tc-Labeled Quinolin-4-one Peptidomimetics as Ligands for the Vitronectin Receptor: Potential Tumor Imaging Agents

Thomas D. Harris,*[,†] Shirley Kalogeropoulos,[†] Tiffany Nguyen,[†] Gregory Dwyer,[†] D. Scott Edwards,[†] Shuang Liu,[†,‡] Judit Bartis,[†,§] Charles Ellars,[†,||] Dave Onthank,[†] Padmaja Yalamanchili,[†] Stuart Heminway,[†] Simon Robinson,[†] Joel Lazewatsky,[†] and John Barrett[†]

Discovery Research, Bristol-Myers Squibb Medical Imaging, 331 Treble Cove Road, N. Billerica, Massachusetts 01862.
Received March 12, 2006; Revised Manuscript Received May 19, 2006

The integrin receptor $\alpha_v\beta_3$ is overexpressed on the endothelial cells of growing tumors and on some tumor cells themselves. Radiolabeled $\alpha_v\beta_3$ antagonists have demonstrated potential application as tumor imaging agents and as radiotherapeutic agents. This report describes the total synthesis of eight new HYNIC and DOTA conjugates of receptor $\alpha_v\beta_3$ antagonists belonging to the quinolin-4-one class of peptidomimetics, and their radiolabeling with ^{99m}Tc (for HYNIC) and ^{111}In (for DOTA). Tethering of the radionuclide−chelator complexes was achieved at two different sites on the quinolin-4-one molecule. All such derivatives maintained high affinity for receptor $\alpha_v\beta_3$ and high selectivity versus receptors $\alpha_{IIb}\beta_3$, $\alpha_v\beta_5$, $\alpha_5\beta_1$. Biodistribution of the radiolabeled compounds was evaluated in the c-neu Oncomouse mammary adenocarcinoma model. DOTA conjugate ^{111}In-**TA138** presented the best biodistribution profile. Tumor uptake at 2 h postinjection was 9.39% of injected dose/g of tissue (%ID/g). Activity levels in selected organs was as follows: blood, 0.54% ID/g; liver, 1.94% ID/g; kidney, 2.33% ID/g; lung, 2.74% ID/g; bone, 1.56% ID/g. A complete biodistribution analysis of ^{111}In-**TA138** and the other radiolabeled compounds of this study are presented and discussed. A scintigraphic imaging study with ^{111}In-**TA138** showed a clear delineation of the tumors and rapid clearance of activity from nontarget tissues.

INTRODUCTION

Integrins are a large family of transmembrane heterodimeric glycoprotein cell surface receptors formed by associations between α and β subunits. Integrins are important facilitators of cell−cell and cell−matrix interactions and are also involved in cell signaling events (*1*). The central role that integrins play in facilitating migration and adhesion of cells on the extracellular matrix have made integrins an important area of study in cancer metastasis and angiogenesis research (*2*−*4*). The integrin $\alpha_v\beta_3$, or vitronectin receptor, recognizes several extracellular proteins through the Arg-Gly-Asp (RGD) sequence, including vitronectin, fibronectin, fibrinogen, laminin, thrombospondin, collagen, von Willebrand factor, osteopontin, and bone sialoprotein I. This receptor is generally expressed at low levels on epithelial cells and on mature endothelial cells but is highly upregulated on the neovasculature found in tumors and in wound repair (*5*−*7*). This differential expression has made the vitronectin receptor a promising target in antiangiogenic research (*8*). For example, antagonists of integrin $\alpha_v\beta_3$ have been demonstrated to inhibit tumor angiogenesis and disrupt metastasis in a number of models (*9*−*13*). However, recent work has shown that knockout mice lacking β_3 integrins, rather than showing the expected inhibition of tumor growth, produce larger and more highly vascularized tumors (*14*). Clearly, the exact mechanism by which vitronectin receptor antagonists inhibit angiogenesis is not fully understood. In addition to expression on neovasculature, there is an upregulation in the expression of integrin $\alpha_v\beta_3$ on certain tumor cells present in clinical tissue specimens, including tumors of the kidney, breast, and prostrate, melanoma, and squamous carcinoma (*15*−*18*).

These literature reports suggest that integrin $\alpha_v\beta_3$ can be exploited as a target for selective localization of diagnostic and therapeutic radiopharmaceuticals in the vicinity of malignant tumors. The technical feasibility of imaging tumors by targeting integrin $\alpha_v\beta_3$ was first demonstrated using radiolabeled cyclic RGD peptide $\alpha_v\beta_3$ antagonists. Haubner and co-workers have described the selective tumor uptake of cyclic RGD peptides labeled with ^{125}I for SPECT imaging, and ^{18}F for PET imaging in melanoma-bearing and osteosarcoma-bearing mice (*19*, *20*). van Hagen and co-workers have described the internalization of an ^{111}In-labeled peptide in isolated human cancers, and tumor uptake in a rat tumor model in vivo (*21*). At BMS Medical Imaging we have shown that in the c-neu Oncomouse model, cyclic RGD peptide dimers give superior tumor uptake and retention compared to the cyclic monomeric peptides (*22*). This dimer effect has been confirmed by the groups of Oyen and Boerman at the University Medical Center Nijmegen using BALB/c mice growing OVCAR-3 xenografts (*23*). The use of radiolabeled peptides to image tumor angiogenesis has recently been reviewed (*24*).

While many radiolabeled peptides have demonstrated potential as tumor imaging agents, none have been able to combine the high tumor uptake and retention, and low uptake in nontarget tissues, required of a radiotherapeutic agent. We reasoned that peptidomimetics having high affinity and selectivity for integrin $\alpha_v\beta_3$ offered the best opportunity to deliver diagnostically and therapeutically useful quantities of radionuclides to tumors while minimizing dose to nontarget organs. Antagonists to integrin $\alpha_v\beta_3$ have potential applications in the control of pathological angiogenesis, and a wide variety of structurally novel $\alpha_v\beta_3$

* To whom correspondence should be addressed. Phone: 978-671-8266. Fax: 978-436-7500. E-mail: thomas.d.harris@bms.com.

† Bristol-Myers Squibb Medical Imaging.

‡ Present address: Division of Nuclear Pharmacy, Purdue University, West Lafayette, IN.

§ Present address: ArQule, Woburn, MA.

|| Present address: Molecular Insight, Cambridge, MA.

10.1021/bc060063s CCC: $33.50 © 2006 American Chemical Society
Published on Web 08/08/2006

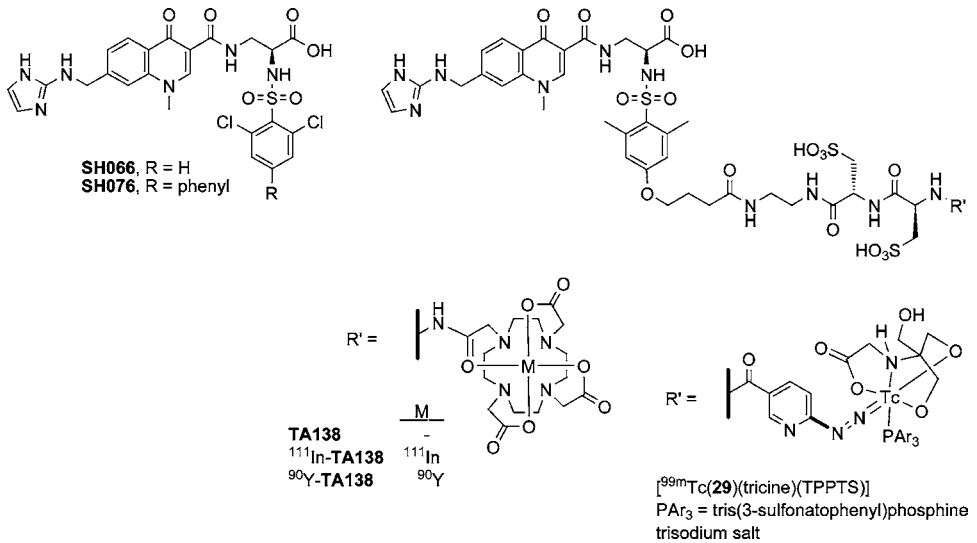

Figure 1. Structures of lead quinolin-4-one vitronectin receptor antagonist **SH066**, DOTA derivatives **TA138**, ^{111}In-**TA138**, and ^{90}Y-**TA138**, and HYNIC derivative [^{99m}Tc(**29**)(tricine))(tris{3-sulfonatophenyl}phosphine trisodium salt)].

peptidomimetic antagonists have been reported in recent years (*8*, *13*, *25*−29). The disubstituted quinolin-4-one system (e.g., **SH066**, Figure 1) developed by DuPont Pharmaceuticals was of particular interest to us. This series uses a quinolin-4-one central ring system to constrain the conformation and to serve as a scaffold on which to attach basic and acid groups that mimic the guanidine and carboxylate groups of the RGD sequence. The most active members of this series use 2-aminoimidazole and 2,3-diaminopropionate (DAP) arylsulfonamides as guanidine and carboxylate mimics, respectively. The structure−activity-relationship (SAR) for this series indicated excellent affinity for integrin $\alpha_v\beta_3$ and good selectivity versus integrin $\alpha_{IIb}\beta_3$ (*30*). The para position of the arylsulfonamide group is very tolerant of substitution and is also readily accessible synthetically, making it ideally suited as a site at which to tether a radionuclide−chelator complex. We also viewed the quinolin-4-one ring nitrogen as a potential site of derivatization. This combination of synthetic accessibility and favorable receptor selectivity made the quinolin-4-one system the ideal platform for our studies. In a preliminary publication we described the biodistribution and imaging properties of ^{111}In-**TA138**, a DOTA-conjugated quinolin-4-one integrin $\alpha_v\beta_3$ antagonists (Figure 1) (*31*). In the c-neu Oncomouse model, ^{111}In-**TA138** shows tumor uptake higher than any of the peptides reported above, while maintaining relatively low uptake in critical nontarget organs such as kidneys and bone marrow. Furthermore, in the same model, we have demonstrated a therapeutic effect using ^{90}Y-**TA138** (Figure 1) (*31*). More recently, the targeting biomolecule portion of **TA138** has been used to direct paramagnetic nanoparticles to angiogenic sites for magnetic resonance imaging (*32*, *33*). The potential applications of these molecules have also been broadened to include imaging of vascular remodeling following myocardial infarction (*34*, *35*). Herein we report the complete details of the synthesis of **TA138** and eight analogues, along with receptor affinity and biodistribution data of the radiolabeled analogues. The structural parameters investigated include attachment of tethers at two different sites on the parent quinolin-4-one structure, the use of two different radionuclide chelators (DOTA and HYNIC as shown in Figure 1), the use of two different imaging radionuclides (^{111}In and ^{99m}Tc), and the use of different pharmacokinetic modifiers (PKMs).

EXPERIMENTAL SECTION

General Experimental. All reactions were performed under a dry nitrogen atmosphere. All chemicals and solvents (reagent grade) were used as supplied from the vendors cited without further purification, unless otherwise noted. 3-((*tert*-butoxy)-carbonylamino)propyl bromide and 4,7,10-trioxa-1,13-tridecanediamine were purchased from Fluka. *tert*-Butyloxycarbonyl (Boc) amino acids and other starting amino acids were obtained from Bachem Inc., Bachem Biosciences Inc. (Philadelphia, PA), or Advanced ChemTech (Louisville, KY). 2-(1*H*-Benzotriazol-1-yl)-1,1,3,3-tetramethyluronium hexafluorophosphate (HBTU) and benzotriazol-1-yl-oxy-tris-pyrrolidinophosphonium hexafluorophosphate (PyBOP) were purchased from Advanced ChemTech. *N*-Methylmorpholine (NMM), *m*-cresol, trimethylacetyl chloride, 1,2,4-triazole, stannous chloride dihydrate, biphenyl-4,4′-disulfonyl chloride, and tris(3-sulfonatophenyl)-phosphine trisodium salt (TPPTS) were purchased from Aldrich Chemical Co. Tricine was obtained from Research Organics, Inc. Technetium-99m-pertechnetate ($^{99m}TcO_4^-$) was obtained from a DuPont Pharma ^{99}Mo/^{99m}Tc Technelite generator. ^{111}Indium chloride (Indichlor) was obtained from Amersham Medi-Physics, Inc. ^{177}Lutetium chloride was obtained from the University of Missouri Research Reactor (MURR). Ethyl acetate, chloroform ($CHCl_3$), methanol (MeOH), acetonitrile (ACN), dichloromethane (DCM), ethyl ether, acetone, and hydrochloric acid (HCl) were obtained from Baker. Anhydrous dimethylformamide (DMF), acetonitrile (ACN), pyridine, triethylamine (TEA), and diisopropylethylamine (DIEA) were obtained from Aldrich in SureSeal bottles. Absolute ethanol was obtained from Quantum Chemical Corp. Merck silica gel, grade 9385, 230−400 mesh, 60 Å, was used for flash chromatography. DOTA(O*t*-Bu)$_3$OH was obtained from Macrocyclics, Dallas, TX. Other reagents were obtained from Lancaster Synthesis, Inc., Aldrich Chemical Co, or Fluka Chemical Corp.

^{1}H NMR spectra were recorded on a Bruker Avance DRX (600 MHz) spectrometer. Chemical shifts are reported in ppm from tetramethylsilane with the residual solvent resonance resulting from incomplete deuteration as the internal standard ($CDCl_3$: δ 7.25 ppm, ACN-d_3: δ 1.95 ppm, DMSO-d_6: δ 2.50 ppm). Data are reported as follows: chemical shift, multiplicity (s = singlet, d = doublet, t = triplet, q = quartet, quin = quintet, b = broad, m = multiplet), coupling constants, and integration. ^{13}C NMR spectra were recorded on a Bruker Avance DRX (150 MHz) with complete proton decoupling. Chemical shifts are reported in ppm from tetramethylsilane with the solvent as the internal reference ($CDCl_3$: δ 77.0 ppm, ACN-d_3: δ 118.1 ppm, DMSO-d_6: δ 39.5 ppm). Low-resolution mass spectrometry was performed on an Agilent Technologies 1100 Series LC/MS ESI-

MS. High-resolution mass spectrometry was performed on a Ionspec Ultima FTMS; ESI-MS (positive mode). Melting points were determined using a Thomas-Hoover melting point apparatus and are uncorrected.

Benzyl 3-(2-(2-(3-Aminopropoxy)ethoxy)ethoxy)propylcarbamate (2). A solution of 4,7,10-trioxa-1,13-tridecanediamine (**1**) (158 mL, 0.72 mol), TEA (16.7 mL, 0.12 mol), and MeOH (300 mL) in peroxide-free THF (1000 mL) was placed in a 3 L three-neck flask fitted with a mechanical stirrer, thermometer, and addition funnel with nitrogen line. The addition funnel was charged with a solution of benzyl chloroformate (17.1 mL, 0.12 mol) in peroxide-free THF (1000 mL). The contents of the flask were cooled below 5 °C. The contents of the addition funnel were added to the flask with rapid stirring over 4 h while keeping the temperature below 5 °C. The solution was stirred an additional 30 min and concentrated to give a thick syrup. This syrup was taken up in saturated NaCl (1800 mL) and 10% Na_2CO_3 (200 mL) and extracted with ether (3 × 1.0 L). The combined ether extracts were washed with saturated NaCl (500 mL), dried ($MgSO_4$), and concentrated to give a pale yellow oil (36.74 g). Flash chromatography on a 7 × 29 cm silica gel column (DCM:MeOH:TEA, 20:15:0.5) gave **2** as a colorless syrup (19.14 g, 45%). ^{1}H NMR ($CDCl_3$): 7.33−7.25 (m, 5H), 5.59 (s, 1H), 5.06 (s, 2H), 3.62−3.45 (m, 12H), 3.32−3.25 (m, 2H), 2.74 (t, J = 6.7 Hz, 2H), 1.75 (quin, J = 6.0 Hz, 2H), 1.67 (quin, J = 6.4 Hz, 2H), 1.33 (s, 2H). MS (ESI): *m*/*z* 355.4 (M + H); HRMS: Calcd for $C_{18}H_{31}N_2O_5$ (M + H): 355.2233; Found: 355.2222.

(*S*)-Methyl 3-(*tert*-Butoxycarbonylamino)-2-(4′-(*N*-(3-oxo-1-phenyl-2,8,11,14-tetraoxa-4-azaheptadecan-17-yl)sulfamoyl)-biphenyl-4-ylsulfonamido)propanoate (3). Biphenyl-4,4′-disulfonyl chloride (2.64 g, 7.5 mmol, freshly recrystallized from $CHCl_3$) and DCM (200 mL) were placed in a 500 mL three-neck flask fitted with a thermometer, addition funnel, and nitrogen line. The addition funnel was charged with a solution of compound **2** (1.77 g, 5.0 mmol) and DIEA (0.87 mL, 5.0 mmol) in DCM (40 mL). The contents of the flask were cooled below 5 °C. The contents of the addition funnel were added to the flask with rapid stirring over 3 h while keeping the temperature of the flask below 5 °C. The addition funnel was charged with a solution of *N*-β-Boc-L-α,β-diaminopropionic acid methyl ester hydrochloride (2.55 g, 10 mmol) and DIEA (3.8 mL, 22 mmol) in DCM (25 mL). This solution was added to the flask with stirring at 5 °C over 15 min and stirred at ambient temperature for an additional 20 h. The reaction solution was washed consecutively with 0.1 N HCl (100 mL) and water (2 × 100 mL), dried ($MgSO_4$), and concentrated to give a viscous oil (5.79 g). Flash chromatography on a 5 × 21 cm silica gel column (85:15 EtOAc:hexanes, followed by 100% EtOAc) gave a colorless amorphous solid. Recrystallization from toluene (85 mL) gave the title compound as a colorless solid (2.52 g, 59%). MP: 104.5−106.5 °C; ^{1}H NMR ($CDCl_3$): δ 8.00−7.90 (m, 4H), 7.72−7.64 (m, 4H), 7.46−7.24 (m, 5H), 5.96−5.88 (m, 1H), 5.86−5.73 (m, 1H), 5.41 (s, 1H), 5.16−5.00 (m, 3H), 4.15−4.02 (m, 1H), 3.68−3.39 (m, 17H), 3.34−3.22 (m, 2H), 3.13−3.03 (m, 2H), 1.80−1.62 (m, 4H), 1.39 (s, 9H); ^{13}C NMR ($CDCl_3$): δ 170.2, 156.5, 156.1, 143.9, 143.0, 140.4, 139.4, 136.7, 128.4, 128.1, 128.0, 127.9, 127.9, 127.8, 127.3, 80.1, 70.6, 70.5, 70.2, 70.1, 70.0, 69.6, 66.5, 56.1, 52.9, 43.2, 42.4, 39.3, 29.4, 28.5, 28.2. MS (ESI): *m*/*z* 868.3 (M + NH_4); HRMS: Calcd for $C_{39}H_{55}N_4O_{13}S_2$ (M + H): 851.3207; Found: 851.3226.

(*S*)-Methyl 3-(1-Methyl-4-oxo-7-((1-trityl-1*H*-imidazol-2-ylamino)methyl)-1,4-dihydroquinoline-3-carboxamido)-2-(4′-(*N*-(3-oxo-1-phenyl-2,8,11,14-tetraoxa-4-azaheptadecan-17-yl)sulfamoyl)biphenyl-4-ylsulfonamido)propanoate (6). Compound **3** (748 mg, 0.88 mmol) was dissolved in 25:75 TFA:DCM (15 mL) and allowed to stand at ambient temperature for 15 min. The TFA was removed under vacuum, and the resulting amber oil was taken up in 50:50 ACN:water (50 mL) and treated portion wise with Bio-Rad AG 3-X4 resin, free amine form, to raise the pH from 2 to 6. The resin was removed by filtration and the filtrate was lyophilized to amine **4** as a sticky pale yellow foam.

In a separate flask, 1-methyl-4-oxo-7-((1-trityl-1*H*-imidazol-2-ylamino)methyl)-1,4-dihydroquinoline-3-carboxylic acid (**5**) (*36*) (432 mg, 0.80 mmol), TEA (0.33 mL), and HBTU (364 mg, 0.96 mmol) were dissolved in anhydrous DMF (25 mL). The resulting solution was stirred at ambient temperature for 10 min and combined with a solution of compound **4** in anhydrous DMF (15 mL). The DMF was removed under vacuum after 18 h to give a viscous yellow oil. This oil was taken up in EtOAc (175 mL), washed consecutively with water (25 mL), saturated $NaHCO_3$ (50 mL), and saturated NaCl (25 mL), dried ($MgSO_4$), and concentrated to give a viscous yellow oil. Purification by flash chromatography on a 7 × 25 cm silica gel column using a $CHCl_3$:EtOAc:MeOH step gradient (47:47:6, 46:46:8, 60:30:10) gave compound **6** as a pale yellow solid (510 mg, 50%). MP: 136−140 °C. MS (ESI): *m*/*z* 1273.4 (M + H); HRMS: Calcd for $C_{68}H_{73}N_8O_{13}S_2$ (M + H): 1273.4738; Found: 1273.4730.

(*S*)-3-(1-Methyl-4-oxo-7-((1-trityl-1*H*-imidazol-2-ylamino)-methyl)-1,4-dihydroquinoline-3-carboxamido)-2-(4′-(*N*-(3-oxo-1-phenyl-2,8,11,14-tetraoxa-4-azaheptadecan-17-yl)-sulfamoyl)biphenyl-4-ylsulfonamido)propanoic Acid (7). Compound **6** (295 mg, 0.232 mmol) was dissolved in a mixture of peroxide-free THF (12 mL), water (1.8 mL), and 3 N LiOH (1.2 mL) and stirred at ambient temperature for 30 min. The THF was removed under vacuum, and the resulting mixture was dissolved in $CHCl_3$ (75 mL) and water (50 mL). The aqueous layer was adjusted to pH 3 with 0.5 N HCl, and the layers were thoroughly mixed. The aqueous layer was extracted with additional $CHCl_3$ (2 × 25 mL). The combined $CHCl_3$ extracts were washed with saturated NaCl (50 mL), dried ($MgSO_4$), and concentrated to give the title compound as a pale yellow solid (291 mg, 100%). MS (ESI): *m*/*z* 1259.3 (M + H); HRMS: Calcd for $C_{67}H_{71}N_8O_{13}S_2$ (M + H): 1259.4582; Found: 1259.4610.

(*S*)-3-(7-((1*H*-Imidazol-2-ylamino)methyl)-1-methyl-4-oxo-1,4-dihydroquinoline-3-carboxamido)-2-(4′-(*N*-(3-(2-(2-(3-aminopropoxy)ethoxy)ethoxy)propyl)sulfamoyl)biphenyl-4-ylsulfonamido)propanoic Acid (8). Compound **7** (279 mg, 0.222 mmol) was dissolved in degassed TFA (30 mL) and treated with Et_3SiH (0.424 mL, 2.66 mmol). The solution was heated at 70 °C for 1 h and concentrated to a viscous oil. This oil was dissolved in water (20 mL) and washed with ether (2 × 20 mL). The combined ether washings were back-extracted with water (10 mL). The combined water extracts were diluted with an equal volume of ACN and treated with Bio-Rad AG 3-X4 resin, free amine form, to raise the pH from 4 to 6. The resin was removed by filtration and the filtrate was lyophilized to give the title compound as a colorless solid (220 mg). MS (ESI): *m*/*z* 883.4 (M + H), 442.5 (M + 2H); HRMS: Calcd for $C_{40}H_{51}N_8O_{11}S_2$ (M + H): 833.3118; Found: 833.3118.

(*S,E*)-3-(7-((1*H*-Imidazol-2-ylamino)methyl)-1-methyl-4-oxo-1,4-dihydroquinoline-3-carboxamido)-2-(4′-(*N*-(1-oxo-1-(6-(2-(2-sulfobenzylidene)hydrazinyl)pyridin-3-yl)-6,9,12-trioxa-2-azapentadecan-15-yl)sulfamoyl)biphenyl-4-ylsulfonamido)propanoic Acid Trifluoroacetic Acid Salt (10). A solution of compound **8** (15 mg, 0.0135 mmol), TEA (0.007 mL), and sodium (*E*)-2-((2-(5-carboxypyridin-2-yl)hydrazono)-methyl)benzenesulfonate (*37*) (**9**) (9.0 mg, 0.0204 mmol) in anhydrous DMF (2.5 mL) was allowed to stand at ambient temperature for 22 h. The DMF was removed under vacuum and the glassy solid was dissolved in 20% ACN and purified

by preparative HPLC on a Vydac C-18 column (22 × 250 mm) using 0.1% TFA in water for 5 min followed by a 2.52%/min gradient of 0−63% ACN containing 0.1% TFA at a flow rate of 20 mL/min. The main product peak eluting at 21.2 min was collected and lyophilized to give **10** as a colorless powder (3.5 mg, 20%). MS (ESI): *m*/*z* 1186.7 (M + H); HRMS: Calcd for $C_{53}H_{60}N_{11}O_{15}S_3$ (M + H): 1186.3432; Found: 1186.3410.

(*S*)-*tert*-Butyl 2,2′,2″-(10-(16-(4′-(*N*-(3-(7-((1*H*-imidazol-2-ylamino)methyl)-1-methyl-4-oxo-1,4-dihydroquinoline-3-carboxamido)-1-methoxy-1-oxopropan-2-yl)sulfamoyl)biphenyl-4-ylsulfonamido)-2-oxo-7,10,13-trioxa-3-azahexadecyl)-1,4,7,10-tetraazacyclododecane-1,4,7-triyl)triacetate Tris(trifluoroacetic Acid) Salt (11). A solution of compound **6** (68 mg, 0.0534 mmol) and Et_3SiH (0.051 mL, 0.32 mmol) in degassed TFA (5.0 mL) was stirred at 70 °C for 1 h and concentrated to dryness. The resulting amber oil was dissolved in anhydrous DMF (2 mL) and treated with TEA until basic to pH paper. A solution of DOTA(O*t*-Bu)$_3$OH (46 mg, 0.080 mmol) in anhydrous DMF (1.0 mL) was added, followed by HBTU (24 mg, 0.064 mmol), and the solution was stirred at ambient temperature for 3 h. The DMF was removed under vacuum, and the residue was dissolved in 50% ACN and purified by preparative HPLC on a Vydac C-18 column (22 × 250 mm) using a 2.1%/min gradient of 0−63% ACN containing 0.1% TFA at a flow rate of 20 mL/min. The main product peak eluting at 23.8 min was collected and lyophilized to give compound **11** as a colorless powder (16 mg, 17%). MS (ESI): *m*/*z* 1451.7 (M + H); HRMS: Calcd for $C_{69}H_{103}N_{12}O_{18}S_2$ (M + H): 1451.6954; Found: 1451.698.

(*S*)-2,2′,2″-(10-(16-(4′-(*N*-(2-(7-((1*H*-imidazol-2-ylamino)-methyl)-1-methyl-4-oxo-1,4-dihydroquinoline-3-carboxamido)-1-carboxyethyl)sulfamoyl)biphenyl-4-ylsulfonamido)-2-oxo-7,10,13-trioxa-3-azahexadecyl)-1,4,7,10-tetraazacyclododecane-1,4,7-triyl)triacetic Acid Bis(trifluoroacetic Acid) Salt (12). Compound **11** (16 mg, 0.00893 mmol) was dissolved in a mixture of peroxide-free THF (1.0 mL), water (0.115 mL), and 3 N LiOH (0.075 mL) and stirred at ambient temperature for 24 h. The reaction was concentrated to give an oily solid. This solid was dissolved in 50% ACN and purified by preparative HPLC on a Vydac C-18 column (22 × 250 mm) using a 2.52%/min gradient of 0−63% ACN containing 0.1% TFA at a flow rate of 20 mL/min. The main product peak eluting at 24.0 min was collected and lyophilized to give a colorless powder (6.0 mg). This solid was dissolved in degassed TFA (2.0 mL) and Et_3SiH (0.050 mL), stirred at 70 °C for 4.5 h, and concentrated to dryness. The resulting oil was dissolved in 25% ACN and purified by preparative HPLC on a Vydac C-18 column (22 × 250 mm) using a 1.5%/min gradient of 0−45% ACN containing 0.1% TFA at a flow rate of 20 mL/min. The main product peak eluting at 19.0 min was collected and lyophilized to give the bis-TFA salt of **12** as a colorless powder (2.0 mg, 15%). MS (ESI): *m*/*z* 1269.5 (M + H), 635.5 (M + 2H), 424.3 (M + 3H); HRMS: Calcd for $C_{56}H_{77}N_{12}O_{18}S_2$ (M + H): 1269.4920; Found: 1269.4950.

Ethyl 4-(3,5-Dimethylphenoxy)butanoate (13). Sodium metal (17.12 g, 0.744 mol) was added to anhydrous EtOH (350 mL) and stirred until dissolved. 3,5-Dimethylphenol was added, and the solution was stirred 15 min at ambient temperature. Ethyl 4-bromobutyrate (58.7 mL, 0.41 mol) was added, and the solution was stirred at ambient temperature for 28 h. The EtOH was removed under vacuum, and the oily solid was partitioned between water (1 L) and EtOAc (500 mL). The aqueous layer was extracted with additional EtOAc (500 mL). The combined EtOAc extracts were washed consecutively with saturated $NaHCO_3$ (300 mL) and saturated NaCl (300 mL), dried ($MgSO_4$), and concentrated to give an amber liquid. This liquid was vacuum fractionally distilled through a 15 cm Vigreux column. The main fraction was collected from 91 to 117 °C/6 mmHg (lit. (*38*) BP 141 °C/2 mmHg) to give compound **13** as a colorless liquid (77.77 g, 89%). ^{1}H NMR ($CDCl_3$): δ 6.59 (s, 1H), 6.52 (s, 2H), 4.16 (q, J = 7.16 Hz, 2H), 3.98 (t, J = 6.14 Hz, 2H), 2.49 (t, J = 7.34 Hz, 2H), 2.28 (s, 6H), 2.11−2.07 (m, 2H), 1.26 (t, J = 7.16 Hz, 3H). Anal. Calcd for $C_{14}H_{20}O_3$: C,71.16; H, 8.53; Found: C,71.35; H, 8.59.

4-(3,5-Dimethylphenoxy)butanoic Acid (14). Compound **13** (75.52 g, 0.320 mol) and KOH pellets (38.5 g, 0.584 mol) were dissolved in absolute EtOH (1.5 L) and heated at reflux for 3 h. The solution was concentrated to a colorless solid, which was taken up in water (2.0 L) and washed with ether (2 × 750 mL). The aqueous layer was adjusted to pH 1 with concd HCl (55 mL), and the resulting oily precipitate was extracted into EtOAc (2 × 500 mL). The combined EtOAc extracts were washed consecutively with water (300 mL) and saturated NaCl, dried ($MgSO_4$), and concentrated to give a colorless solid (64.13 g). Recrystallization from hexanes (500 mL) gave compound **14** as a colorless solid (59.51 g, 89%). MP: 66−68.5 °C (lit. (*38*) MP 69−70 °C); ^{1}H NMR ($CDCl_3$): δ 11.70 (bs, 1H), 6.59 (s, 1H), 6.52 (s, 2H), 3.99 (t, J = 6.06 Hz, 2H), 2.57 (t, J = 7.29 Hz, 2H), 2.28 (s, 6H), 2.12−2.08 (m, 2H). Anal. Calcd for $C_{12}H_{16}O_3$: C, 69.21; H, 7.74; Found: C, 69.23; H, 7.40.

4-(4-(Chlorosulfonyl)-3,5-dimethylphenoxy)butanoic Acid (15). A solution of compound **14** (20.8 g, 0.100 mol) in $CHCl_3$ (100 mL) was cooled to 0 °C and treated with chlorosulfonic acid (36 mL, 0.54 mol) dropwise and with rapid stirring while keeping the temperature of the reaction at 0 °C. The resulting gelatinous mixture was stirred an additional 10 min and poured onto an ice/water mixture (600 mL). The resulting solid precipitate was collected by filtration, washed with water (3 × 75 mL), and dried under vacuum to give **15** as a colorless solid (12.52 g, 41%). MP: 114−115 °C (with dec); ^{1}H NMR ($CDCl_3$): δ 13.84 (bs, 1H), 6.50 (s, 2H), 3.91 (t, J = 6.48 Hz, 2H), 2.48 (s, 6H), 2.32 (t, J = 7.32 Hz, 2H), 1.89−1.84 (m, 2H). IR (KBr cm^{-1}): 1705 (s), 1370 (s), 1175 (s). MS (ESI): *m*/*z* 305.1 (M − H).

(*S*)-4-(4-(*N*-(3-(*tert*-Butoxycarbonylamino)-1-methoxy-1-oxopropan-2-yl)sulfamoyl)-3,5-dimethylphenoxy)butanoic Acid (16). A solution of (*S*)-methyl 2-amino-3-(*tert*-butoxycarbonylamino)propanoate hydrochloride (568 mg, 2.10 mmol) and DIEA (0.73 mL, 4.2 mmol) in DCM (5 mL) was cooled to 0 °C and treated with a suspension of compound **15** (656 mg, 2.10 mmol) in DCM (20 mL) in small portions over a 15 min period. The reaction was stirred at ambient temperature for 18 h. The reaction was diluted with DCM (100 mL) and washed with water (3 × 75 mL). The organic phase was dried ($MgSO_4$), and concentrated to give crude product (698 mg), which was purified by preparative HPLC on a Vydac C-18 column (50 × 250 mm) using a 0.96%/min gradient of 18−58.5% ACN containing 0.1% TFA at a flow rate of 80 mL/min. The main product fraction eluting at 23.8 min was collected, adjusted to pH 3 using 1 N NaOH, partially concentrated to remove ACN, and extracted with DCM (2 × 100 mL). The DCM extracts were dried ($MgSO_4$) and concentrated to give compound **16** as a colorless solid (297 mg, 29%). ^{1}H NMR ($CDCl_3$): δ 6.61 (s, 2H), 5.66 (d, J = 7.2 Hz, 1H), 4.90 (s, 1H), 4.03 (bs, 2H), 3.86 (bs, 1H), 3.59 (s, 3H), 3.49 (bs, 2H), 2.62 (s, 6H), 2.58−2.51 (m, 2H), 2.18−2.07 (m, 2H), 1.41 (s, 9H). MS (ESI): *m*/*z* 489.4 (M + H); HRMS: Calcd for $C_{21}H_{33}N_2O_9S$ (M + Na): 511.1726, Found: 511.1747. Anal. Calcd for $C_{21}H_{32}N_2O_9S$: C, 51.62; H, 6.61; N, 5.74; Found: C, 51.47; H, 6.27; N, 5.48.

(*S*)-Methyl 2-(4-(4-(2-(Benzyloxycarbonylamino)ethylamino)-4-oxobutoxy)-2,6-dimethylphenylsulfonamido)-3-(*tert*-butoxycarbonylamino)propanoate (17). A solution of compound **16** (369 mg, 0.756 mmol), DIEA (0.52 mL, 3.0 mmol), and HBTU (315 mg, 0.832 mmol) in anhydrous

DMF (14 mL) was stirred at ambient temperature for 5 min, treated with benzyl *N*-(2-aminoethyl)carbamate hydrochloride (192 mg, 0.832 mmol), and stirred an additional 1 h. The DMF was removed under vacuum, and the oily residue was taken up in EtOAc (150 mL), washed consecutively with 0.1 N HCl (40 mL), water (40 mL), and saturated NaCl (40 mL), dried ($MgSO_4$), and concentrated to give a colorless viscous oil. Flash chromatography on a 3 × 16 cm silica gel column (EtOAc) gave the title compound as a colorless viscous oil (450 mg, 89.6%). ^{1}H NMR ($CDCl_3$): δ 7.34−7.27 (m, 5H), 6.58 (s, 2H), 6.31 (bs, 1H), 5.86 (bs, 1H), 5.36 (bs, 1H), 5.14−5.03 (m, 3H), 3.96 (t, J = 6.0 Hz, 2H), 3.88−3.83 (m, 1H), 3.56 (s, 3H), 3.47−3.25 (m, 6H), 2.59 (s, 6H), 2.31 (t, J = 6.9 Hz, 2H), 2.05 (p, J = 6.6 Hz, 2H), 1.39 (s, 9H); ^{13}C NMR ($CDCl_3$): δ 172.9, 170.5, 160.6, 157.3, 155.9, 141.8, 136.3, 128.5, 128.2, 128.0, 116.6, 79.9, 66.9, 55.5, 52.8, 43.1, 40.9, 40.3, 32.4, 28.2, 24.9, 23.3. MS (ESI): *m*/*z* 687.3 (M + Na), 665.4 (M + H); HRMS: Calcd for $C_{31}H_{45}N_4O_{10}S$ (M + H): 665.2856; Found: 665.2883.

(*S*)-Methyl 2-(4-(4-(2-(Benzyloxycarbonylamino)ethylamino)-4-oxobutoxy)-2,6-dimethylphenylsulfonamido)-3-(1-methyl-4-oxo-7-((1-trityl-1*H*-imidazol-2-ylamino)methyl)-1,4-dihydroquinoline-3-carboxamido)propanoate (19). Compound **17** (420 mg, 0.632 mmol) was dissolved in 25:75 DCM:TFA (20 mL) and allowed to stand at ambient temperature for 10 min. The solution was concentrated, and the resulting viscous oil was dissolved in 50% ACN and lyophilized to give compound **18** as a colorless solid (437 mg, 102%). MS (ESI): *m*/*z* 565.3 (M + H). In a separate flask a solution of 1-methyl-4-oxo-7-((1-trityl-1*H*-imidazol-2-ylamino)methyl)-1,4-dihydroquinoline-3-carboxylic acid (702 mg, 1.30 mmol), DIEA (0.678 mL, 3.90 mmol), and HBTU (542 mg, 1.43 mmol) in anhydrous DMF (60 mL) was stirred at ambient temperature for 10 min and treated with compound **18** (881 mg, 1.30 mmol). After 75 min the DMF was removed under vacuum and the resulting oil was purified by HPLC on a Vydac C-18 column (50 × 250 mm) using a 1.24%/min gradient of 18−67.5% ACN containing 0.1% TFA at a flow rate of 80 mL/min. A peak eluting at 18.9 min was lyophilized to give unreacted 1-methyl-4-oxo-7-((1-trityl-1*H*-imidazol-2-ylamino)methyl)-1,4-dihydroquinoline-3-carboxylic acid (308 mg). The main product peak eluting at 23.7 min was lyophilized to give compound **19** as a colorless solid (890 mg, 63.0%). ^{1}H NMR (1:1 CD_3CN:D_2O): δ 8.50 (s, 1H), 8.18 (d, J = 8.3 Hz, 1H), 7.70 (s, 1H), 7.51−7.25 (m, 15H), 7.25−7.12 (m, 5H), 6.97 (s, 1H), 6.58 (d, J = 2.3 Hz, 1H), 6.34 (s, 2H), 6.32 (d, J = 8.5 Hz, 1H), 5.09 (s, 2H), 4.65 (s, 2H), 4.29−4.23 (m, 1H), 3.88 (s, 3H), 3.80−3.50 (m, 7H), 3.41−3.28 (m, 4H), 2.61 (s, 6H), 2.26−2.11 (m, 2H), 1.92−1.76 (m, 2H). MS (ESI): *m*/*z* 1087.4 (M + H); 845.3 (M + H − Tr); HRMS: Calcd for $C_{60}H_{63}N_8O_{10}S$ (M + H): 1087.4388; Found: 1087.440.

(*S*)-2-(4-(4-(2-Aminoethylamino)-4-oxobutoxy)-2,6-dimethylphenylsulfonamido)-3-(1-methyl-4-oxo-7-((1-trityl-1*H*-imidazol-2-ylamino)methyl)-1,4-dihydroquinoline-3-carboxamido)propanoic Acid (21). A solution of compound **19** (468 mg, 0.431 mmol) in MeOH (100 mL) was hydrogenolyzed over 10% Pd/C (95 mg) at 60 psi for 1 h. The catalyst was removed by filtration through Celite, and the filtrate was concentrated to give compound **20** as a pale amber oil (405 mg, 98.7%). MS (ESI): *m*/*z* 953.3 (M + H), 711.3 (M + H − trityl). A mixture of **20** (956 mg, 1.004 mmol), peroxide-free THF (35 mL), water (5.3 mL), and 3 N LiOH (3.53 mL, 10.6 mmol) was stirred at ambient temperature for 1 h, and adjusted to pH 5−6 using 1 N HCl (10 mL). The THF was removed under vacuum causing a gummy yellow solid to precipitate. The water layer was removed by decantation, and the solid was washed with water (15 mL). The solid was dried under vacuum to give compound **21** as a dry yellow solid (324 mg, 80%). ^{1}H NMR (DMSO-d_6): δ 10.03 (t, J = 5.7 Hz, 1H), 8.70 (s, 1H), 8.16 (t, J = 5.7 Hz, 1H), 8.06 (d, J = 8.4 Hz, 1H), 7.42−7.30 (m, 11H), 7.17−7.10 (m, 6H), 6.75 (d, J = 8.4 Hz, 1H), 6.58 (s, 2H), 6.51 (d, J = 1.8 Hz, 1H), 6.30 (d, J = 1.8 Hz, 1H), 4.35 (d, J = 6.4 Hz, 2H), 4.04 (t, J = 6.0 Hz, 1H), 3.86 (s, 3H), 3.87−3.49 (m 6H), 3.26−3.12 (m, 2H), 2,60 (t, J = 6.4 Hz, 2H), 2.54 (s, 6H), 2.17 (t, J = 6.5 Hz, 2H), 1.86 (t, J = 6.5 Hz, 2H); ^{13}C NMR (DMSO-d_6): δ 175.0, 171.8, 171.4, 164.2, 159.7, 149.5, 148.4, 145.9, 141.4, 140.8, 139.6, 129.4, 128.1, 127.7, 125.6, 123.8, 122.7, 116.5, 116.1, 115.0, 110.5, 73.1, 67.0, 66.6, 46.6, 45.8, 40.9, 38.2, 36.1, 31.6, 25.1, 24.4, 22.9. MS (ESI): *m*/*z* 939.3 (M + H, 40); 697.3 (M + H − Trt, 100); HRMS: Calcd for $C_{51}H_{55}N_8O_8S$ (M + H): 939.3864; Found: 939.3845.

(*S*)-2-(4-((*R*)-2,2-Dimethyl-4,7,12-trioxo-6-(sulfomethyl)-3-oxa-5,8,11-triazapentadecan-15-yloxy)-2,6-dimethylphenylsulfonamido)-3-(1-methyl-4-oxo-7-((1-trityl-1*H*-imidazol-2-ylamino)methyl)-1,4-dihydroquinoline-3-carboxamido)propanoic Acid (22). A solution of Boc-L-cysteic acid (175 mg, 0.60 mmol), DIEA (0.208 mL, 1.20 mmol), and PyBOP (250 mg, 0.480 mmol) in anhydrous DMF (5.0 mL) was stirred at ambient temperature for 17 min, and added to a solution of compound **21** (375 mg, 0.400 mmol) and DIEA (0.070 mL, 0.400 mmol) in anhydrous DMF (4.0 mL). The resulting solution was stirred at ambient temperature for 45 min and concentrated under vacuum to give an amber oil. This oil was purified by HPLC on a Vydac C-18 column (50 × 250 mm) using a 0.29%/min gradient of 31.5−43.2% ACN containing 0.1% TFA at a flow rate of 80 mL/min. The main product peak eluting at 22.0 min was lyophilized to give compound **22** as a colorless solid (430 mg, 90%). MS (ESI): *m*/*z* 1190.3 (M + H), 948.3 (M + H − Trt); HRMS: Calcd for $C_{59}H_{68}N_9O_{14}S_2$ (M + H): 1190.4327; Found: 1190.431.

(*S*)-2-(4-(4-(2-((*R*)-2-Amino-3-sulfopropanamido)ethylamino)-4-oxobutoxy)-2,6-dimethylphenylsulfonamido)-3-(1-methyl-4-oxo-7-((1-trityl-1*H*-imidazol-2-ylamino)methyl)-1,4-dihydroquinoline-3-carboxamido)propanoic Acid (23). A solution of compound **35** (430 mg, 0.362 mmol) in 50:50 TFA:DCM (15 mL) was allowed to react at ambient temperature for 10 min and concentrated under vacuum. The resulting amber oil was taken up in 50% ACN (50 mL) and lyophilized to give **23** as a pale yellow solid (398 mg, 100%). ^{1}H NMR (MeOH- d_4): δ 8.49 (s, 1H), 8.19 (d, J = 8.4 Hz, 1H), 7.60 (s, 1H), 7.51−7.45 (m, 9H), 7.37−7.30 (m, 6H), 7.08 (d, J = 2.7 Hz, 1H), 6.81 (d, J = 2.7 Hz, 1H), 6.58 (d, J = 8.4 Hz, 1H), 6.23 (s, 2H), 4.68 (d, J = 4.9 Hz, 2H), 4.38−4.35 (m, 1H), 4.26−4.22 (m, 1H), 3.98 (s, 3H), 3.94−3.89 (m, 1H), 3.65−3.60 (m, 1H), 3.47−3.37 (m, 4H), 3.29−3.24 (m, 1H), 3.23−3.18 (m, 3H), 3.13−3.08 (m, 2H), 2.58 (s, 6H), 1.90−1.86 (m, 2H); ^{13}C NMR (MeOH-d_4): δ 177.4, 175.6, 173.6, 168.6, 167.2, 161.3, 150.0, 147.9, 143.7, 142.8, 141.5, 140.7, 131.3, 131.0, 130.0, 128.1, 127.8, 124.6, 119.5, 117.3, 116.8, 113.6, 111.5, 77.9, 68.1, 56.1, 51.9, 51.8, 47.7, 47.4, 42.5, 42.2, 40.7, 39.5, 33.5, 27.4, 26.4, 23.8. MS (ESI): *m*/*z* 1090.3 (M + H), 848.2 (M + H − Trt); HRMS: Calcd for $C_{54}H_{60}N_9O_{12}S_2$ (M + H): 1090.3808; Found: 1090.381.

(*S*)-2-(4-((6*R*,9*R*)-2,2-Dimethyl-4,7,10,15-tetraoxo-6,9-bis(sulfomethyl)-3-oxa-5,8,11,14-tetraazaoctadecan-18-yloxy)-2,6-dimethylphenylsulfonamido)-3-(1-methyl-4-oxo-7-((1-trityl-1*H*-imidazol-2-ylamino)methyl)-1,4-dihydroquinoline-3-carboxamido)propanoic Acid (24). A solution of Boc-L-cysteic acid (37.0 mg, 0.128 mmol), DIEA (0.040 mL, 0.228 mmol), and PyBOP (53.0 mg, 0.102 mmol) in anhydrous DMF (1.0 mL) was stirred at ambient temperature for 15 min, and added to a solution of compound **23** (93.0 mg, 0.0854 mmol) and DIEA (0.045 mL, 0.256 mmol) in anhydrous DMF (3.0 mL). The resulting solution was stirred at ambient temperature

for 1.5 h and concentrated to a viscous amber oil. The product was purified by HPLC on a Vydac C-18 column (50 × 250 mm) using a 0.68%/min gradient of 18−45% ACN containing 0.1% TFA at a flow rate of 80 mL/min. The main product peak eluting at 36.4 min was lyophilized to give compound **24** as a colorless solid (94.0 mg, 82%). MS (ESI): *m*/*z* 1341.2 (M + H), 1099.1 (M + H − Trt), 999.1 (M + H − Trt-Boc).

(*S*)-2-(2,6-Dimethyl-4-((4*R*,7*R*)-2,5,8,13-tetraoxo-4,7-bis(sulfomethyl)-1-(4,7,10-tris(2-*tert*-butoxy-2-oxoethyl)-1,4,7,10-tetraazacyclododecan-1-yl)-3,6,9,12-tetraazahexadecan-16-yloxy)phenylsulfonamido)-3-(1-methyl-4-oxo-7-((1-trityl-1*H*-imidazol-2-ylamino)methyl)-1,4-dihydroquinoline-3-carboxamido)propanoic Acid (26). A solution of compound **24** (90.0 mg, 0.0672 mmol) in 50:50 TFA:DCM (10.0 mL) was allowed to react at ambient temperature for 10 min and concentrated under vacuum to give amine **38** as an amber oil. MS (ESI): *m*/*z* 1241.3 (M + H), 999.3 (M + H − Trt); HRMS: Calcd for $C_{57}H_{65}N_{10}O_{16}S_3$ (M + H): 1241.3742; Found: 1241.375. A solution of DOTA(O*t*-Bu)$_3$OH (123 mg, 0.134 mmol), DIEA (0.092 mL, 0.538 mmol), and PyBOP (52.4 mg, 0.101 mmol) in anhydrous DMF (1.5 mL) was stirred at ambient temperature for 15 min and added to a solution of amine **25** (90.0 mg, 0.0672 mmol) and DIEA (0.046 mL, 0.269 mmol) in anhydrous DMF (1.5 mL). The DMF was removed under vacuum after 1 h, and the resulting amber oil was purified by HPLC on a Vydac C-18 column (50 × 250 mm) using a 0.288%/min gradient of 30.6−45% ACN containing 0.1% TFA at a flow rate of 80 mL/min. The main product peak eluting at 25.8 min was lyophilized to give compound **26** as a colorless solid (92.0 mg, 76%). MS (ESI): *m*/*z* 1795.6 (M + H), 1553.5 (M + H − Trt); HRMS: Calcd for $C_{85}H_{115}N_{14}O_{23}S_3$ (M + H): 1795.7422; Found: 1795.744.

2,2′,2″-(10-((4*R*,7*R*)-16-(4-(*N*-((*S*)-2-(7-((1*H*-Imidazol-2-ylamino)methyl)-1-methyl-4-oxo-1,4-dihydroquinoline-3-carboxamido)-1-carboxyethyl)sulfamoyl)-3,5-dimethylphenoxy)-2,5,8,13-tetraoxo-4,7-bis(sulfomethyl)-3,6,9,12-tetraazahexadecyl)-1,4,7,10-tetraazacyclododecane-1,4,7-triyl)triacetic Acid (TA138). A solution of compound **26** (89.0 mg, 0.0496 mmol) in 97:3 TFA:Et$_3$SiH (10.0 mL) was heated at 70 °C for 30 min and concentrated under vacuum. The resulting oily solid was purified by HPLC on a Vydac C-18 column (50 × 250 mm) using a 0.45%/min gradient of 4.5−22.5% ACN containing 0.1% TFA at a flow rate of 80 mL/min. The main product peak eluting at 19.5 min was lyophilized to give compound **TA138** as a colorless fluffy solid (65.0 mg, 94.6%). ^{1}H NMR (DMSO-d_6): δ 12.24 (s, 2H), 9.90 (t, J = 6.0 Hz, 1H), 8.76 (bs, 1H), 8.62−8.61 (m, 1H), 8.52 (s, 1H), 8.36 (d, J = 6.3 Hz, 1H), 8.32 (d, J = 8.2 Hz, 1H), 8.13−8.05 (m, 1H), 7.92 (d, J = 9.1 Hz, 1H), 7.86 (s, 1H), 7.75−7.82 (m, 1H), 7.66−7.45 (m, 3H), 6.97 (s, 2H), 6.27 (s, 2H), 4.72 (d, J = 5.2 Hz, 2H), 4.62 (q, J = 7.0 Hz, 1H), 4.39 (q, J = 6.0 Hz, 1H), 4.13−4.00 (m, 3H), 3.97 (s, 3H), 3.93−3.80 (m, 2H), 3.80−3.69 (m, 3H), 3.69−3.77 (m, 11H), 3.77−2.81 (m, 18H), 2.46 (s, 6H), 2.07 (t, J = 7.5 Hz, 2H), 1.70−1.61 (m, 2H); ^{13}C NMR (DMSO-d_6): δ 175.2, 172.2, 172.1, 170.3, 169.5, 164.8, 159.5, 148.6, 147.0, 143.2, 140.9, 140.1, 130.2, 126.7, 126.5, 124.2, 118.1, 116.2, 116.0, 114.3, 113.9, 112.4, 110.4, 67.0, 55.0, 54.7, 54.0, 53.0, 51.7, 51.3, 51.1, 50.6, 49.0, 46.0, 41.3, 40.5, 38.8, 38.3, 31.6, 24.8, 23.2. MS (ESI): *m*/*z* 1385.4 (M + H); HRMS: Calcd for $C_{54}H_{77}N_{14}O_{23}S_3$ (M + H): 1385.4448; Found: 1385.442.

(*S*)-3-(7-((1*H*-Imidazol-2-ylamino)methyl)-1-methyl-4-oxo-1,4-dihydroquinoline-3-carboxamido)-2-(4-(4-(2-((*R*)-2-((*R*)-2-amino-3-sulfopropanamido)-3-sulfopropanamido)ethylamino)-4-oxobutoxy)-2,6-dimethylphenylsulfonamido)propanoic Acid (27). A solution of compound **24** (75.0 mg, 0.0560 mmol) in 97:3 TFA:Et$_3$SiH (10.0 mL) was heated at 70 °C for 30 min and concentrated under vacuum. The resulting oily solid was purified by HPLC on a Dynamax C-18 column (21.6 × 250 mm) using a 0.45%/min gradient of 4.5−22.5% ACN containing 0.1% TFA at a flow rate of 20 mL/min. The main product peak eluting at 28.5 min was lyophilized to give compound **27** as a colorless fluffy solid (41.0 mg, 73.3%). MS (ESI): *m*/*z* 999.2 (M + H); HRMS: Calcd for $C_{38}H_{51}N_{10}O_{16}S_3$ (M + H): 999.2647; Found: 999.263.

Sodium (*E*)-2-((2-(5-Carboxypyridin-2-yl)hydrazono)methyl)benzenesulfonate (28). A suspension of 6-hydrazinonicotinic acid (*39*) (0.994 g, 6.5 mmol) and sodium 2-formylbenzenesulfonate (1.84 g, 8.84 mmol) in DMF was stirred at ambient temperature for 3 h. The resulting homogeneous solution was concentrated and the residue was triturated with MeOH (3 × 25 mL) to give the title compound as a colorless solid (1.40 g, 63%). MS (ESI): *m*/*z* 344.3 (M + Na, 27), 322.2 (M + H, 100); HRMS: Calcd for $C_{13}H_{12}N_3O_5S$ (M + H): 322.0498; Found: 322.0511.

(*S*)-3-(7-((1*H*-Imidazol-2-ylamino)methyl)-1-methyl-4-oxo-1,4-dihydroquinoline-3-carboxamido)-2-(2,6-dimethyl-4-((3*R*,6*R*)-1,4,7,12-tetraoxo-1-(6-((*E*)-2-(2-sulfobenzylidene)hydrazinyl)pyridin-3-yl)-3,6-bis(sulfomethyl)-2,5,8,11-tetraazapentadecan-15-yloxy)phenylsulfonamido)propanoic Acid (29). A solution of sodium (*E*)-2-((2-(5-carboxypyridin-2-yl)hydrazono)methyl)benzenesulfonate (17.2 mg, 0.050 mmol), PyBOP (19.5 mg, 0.0375 mmol), and DIEA (26 μL, 0.150 mmol) in anhydrous DMF (1.0 mL) was stirred at ambient temperature for 30 min and added to a solution of **27** (25 mg, 0.025 mmol) and DIEA (26 μL, 0.150 mmol) in anhydrous DMF (1.5 mL). The solution was stirred at ambient temperature for 4 h and concentrated under reduced pressure. The resulting residue was purified by HPLC on a Higgins Clipeus C-18 column (20 × 250 mm) using a 0.56%/min gradient of 4.5−27% ACN containing 0.1% formic acid at a flow rate of 15 mL/min. The main product peak eluting at 27.5 min was lyophilized. The resulting solid was repurified by HPLC on the same column using a 0.45%/min gradient of 4.5−22% ACN containing 10 mmol NH_4OAc, pH 7 at a flow rate of 15 mL/min. The main product peak eluting at 28.0 min was lyophilized to give **29** as a colorless fluffy solid (10.4 mg, 32.0%). MS (ESI): *m*/*z* 1302.2 (M + H, 44), 651.7 (2M + H, 100); HRMS: Calcd for $C_{51}H_{60}N_{13}O_{20}S_4$ (M + H): 1302.2960; Found: 1302.2951.

(*R*)-3-(Bis(allyloxy)phosphoryl)-2-(*tert*-butoxycarbonylamino)propanoic Acid (30). A solution of *N*-(*tert*-butoxycarbonyl)-L-serine β-lactone (*40*) (198 mg, 1.06 mmol) in diallyl-(trimethylsilyl)phosphite (*41*) (1.98 g, 8.46 mmol) was heated at 70 °C for 50 h. Excess phosphite was removed under high vacuum with heating. The resulting oil was dissolved in EtOAc (20 mL), washed with water (20 mL), dried (Na_2SO_4), and concentrated to give 190 mg of crude product. Purification by flash chromatography on a 2.0 × 13.5 cm silica gel column using a DCM:MeOH:HOAc (95:5:1) mobile phase gave **30** as a pale yellow oil (71 mg, 19%). ^{1}H NMR ($CDCl_3$): δ 5.98−5.88 (m, 2H), 5.75 (bs, 1H), 5.41−5.33 (m, 2H), 5.26 (d, J = 10.4 Hz, 2H), 2.56−2.43 (m, 2H), 1.44 (s, 9H); ^{13}C NMR ($CDCl_3$): δ 176.1, 155.3, 132.4, 118.6, 80.2, 66.9, 49.1, 28.3, 20.6; ^{31}P NMR ($CDCl_3$): δ 28.6. MS (ESI): *m*/*z* 350.4 (M + H).

(*S*)-2-(4-((*R*)-6-((diallyloxyphosphoryl)methyl)-2,2-dimethyl-4,7,12-trioxo-3-oxa-5,8,11-triazapentadecan-15-yloxy)-2,6-dimethylphenylsulfonamido)-3-(1-methyl-4-oxo-7-((1-trityl-1*H*-imidazol-2-ylamino)methyl)-1,4-dihydroquinoline-3-carboxamido)propanoic Acid (31). A solution of compound **30** (75.0 mg, 0.215 mmol), DIEA (0.100 mL, 0.861 mmol), and HBTU (68.0 mg, 0.179 mmol) in anhydrous DMF (4.0 mL) was stirred at ambient temperature for 20 min and added to a solution of compound **21** (134 mg, 0.143 mmol) and DIEA

(0.050 mL, 0.287 mmol) in anhydrous DMF (4.0 mL). The resulting solution was stirred at ambient temperature for 60 min and concentrated to a viscous yellow oil. The product was purified by HPLC on a Higgins C-18 column (20 × 250 mm) using a 0.30%/min gradient of 36−54% ACN containing 0.1% TFA at a flow rate of 15 mL/min. The main product peak eluting at 36.9 min was lyophilized to give compound **31** as a colorless solid (130 mg, 72%). MS (ESI): *m*/*z* 1270.4 (M + H, 100), 1028.3 (M + H − Trt, 55).

(*S*)-2-(4-((6*R*,9*R*)-6,9-Bis((diallyloxyphosphoryl)methyl)-2,2-dimethyl-4,7,10,15-tetraoxo-3-oxa-5,8,11,14-tetraazaoctadecan-18-yloxy)-2,6-dimethylphenylsulfonamido)-3-(1-methyl-4-oxo-7-((1-trityl-1*H*-imidazol-2-ylamino)methyl)-1,4-dihydroquinoline-3-carboxamido)propanoic Acid (33). A solution of compound **31** (151 mg, 0.117 mmol) in 50:50 TFA:DCM (10.0 mL) was allowed to react at ambient temperature for 10 min and concentrated under vacuum to give amine **32** as an amber oil. This oil was dissolved in anhydrous DMF (3 mL) and made basic (pH 10) with DIEA. In a separate flask, a solution of compound **30** (65.0 mg, 0.186 mmol), DIEA (0.100 mL, 0.861 mmol), and HBTU (56.0 mg, 0.148 mmol) in anhydrous DMF (4.0 mL) was stirred at ambient temperature for 20 min and added to the above solution of compound **32**. The resulting solution was stirred at ambient temperature for 60 min and concentrated to a viscous yellow oil. The product was purified by HPLC on a Dynamax C-18 column (41 × 250 mm) using a 0.45%/min gradient of 36−54% ACN containing 0.1% TFA at a flow rate of 80 mL/min. The main product peak eluting at 32.7 min was lyophilized to give compound **33** as a colorless solid (121 mg, 69%). ^{1}H NMR ($CDCl_3$): δ 10.4 (s, 1H), 8.51 (s, 1H), 8.06 (s, 1H), 7.96 (s, 1H), 7.80 (s, 1H), 7.62 (s, 1H), 7.48−7.30 (m, 9H), 7.22−7.04 (m, 6H), 6.94 (s, 1H), 6.54−6.23 (m, 4H), 5.88 (s, 1H), 5.95−5.62 (m, 4H), 5.38−5.28 (m, 4H), 5.27−5.21 (m, 4H), 4.90 (s, 1H), 4.73−4.59 (m, 4H), 4.59−4.19 (m, 8H), 4.37−4.28 (m, 1H), 4.03 (s, 1H), 3.88−3.64 (m, 7H), 3.38−3.23 (m, 4H), 2.60 (s, 6H), 2.57−2.20 (m, 6H), 1.94 (s, 2H), 1.42 (s, 9H). MS (ESI): *m*/*z* 1501.5 (M + H, 100), 1259.4 (M + H − Trt, 45), 1159.2 (M + H − Trt-Boc, 8); HRMS: Calcd for $C_{74}H_{91}N_{10}O_{18}P_2S$ (M + H): 1501.5631; Found: 1501.570.

(*S*)-2-(2,6-Dimethyl-4-((4*R*,7*R*)-2,5,8,13-tetraoxo-4,7-bis((diallyloxyphosphoryl)methyl)-1-(4,7,10-tris(2-*tert*-butoxy-2-oxoethyl)-1,4,7,10-tetraazacyclododecan-1-yl)-3,6,9,12-tetraazahexadecan-16-yloxy)phenylsulfonamido)-3-(1-methyl-4-oxo-7-((1-trityl-1*H*-imidazol-2-ylamino)methyl)-1,4-dihydroquinoline-3-carboxamido)propanoic Acid Bis(Trifluoroacetic Acid) Salt (35). A solution of compound **33** (88.3 mg, 0.0588 mmol) in 50:50 TFA:DCM (10.0 mL) was allowed to react at ambient temperature for 15 min and concentrated under vacuum to give amine **34** as a viscous yellow oil. This oil was dissolved in anhydrous DMF (2.0 mL) and made basic (pH 10) with DIEA. In a separate flask, a solution of DOTA(O*t*-Bu)$_3$OH (50.5 mg, 0.0883 mmol), DIEA (0.008 mL), and HBTU (26.8 mg, 0.0707 mmol) in anhydrous DMF (2.0 mL) was stirred at ambient temperature for 15 min and added to a solution of amine **34**. HPLC analysis at 60 min indicated a slow rate of reaction. Additional DOTA(O*t*-Bu)$_3$OH (30.0 mg, 0.0524 mmol) was preactivated in a separate flask by combining it with DIEA (0.005 mL) and HBTU (15.0 mg, 0.0396 mmol) in DMF (1.5 mL) at ambient temperature for 15 min. The preactivated DOTA ester was added to the main reaction solution. After an additional 60 min, the solution was concentrated to give a viscous amber oil. The product was purified by HPLC on a Dynamax C-18 column (41 × 250 mm) using a 0.90%/min gradient of 36−63% ACN containing 0.1% TFA at a flow rate of 80 mL/min. The main product, eluting as a broad peak from 21 to 25 min was lyophilized to give compound **35** as a colorless solid (37 mg, 29%). MS (ESI): *m*/*z* 1714.1 (M + H − Trt, 8), 978.9 (M + 2H, 13), 857.7 (M + 2H − Trt, 100); HRMS: Calcd for $C_{97}H_{133}N_{14}O_{23}P_2S$ (M + H): 1955.8786; Found: 1955.887.

2,2′,2″-(10-((4*R*,7*R*)-16-(4-(*N*-((*S*)-2-(7-((1*H*-Imidazol-2-ylamino)methyl)-1-methyl-4-oxo-1,4-dihydroquinoline-3-carboxamido)-1-carboxyethyl)sulfamoyl)-3,5-dimethylphenoxy)-2,5,8,13-tetraoxo-4,7-bis(phosphonomethyl)-3,6,9,12-tetraazahexadecyl)-1,4,7,10-tetraazacyclododecane-1,4,7-triyl)triacetic Acid (36). A solution of compound **35** (35.6 mg, 0.0163 mmol) in anhydrous THF (4.0 mL) was treated with morpholine (0.025 mL, 0.273 mmol) and tetrakis(triphenylphosphine)palladium ($(\phi_3P)_4Pd$) (4.6 mg, 0.004 mmol), and the reaction was stirred at ambient temperature. After 1.5 h, additional morpholine (25 μL) and catalyst (4.6 mg) were added, and the mixture was stirred an additional 4.5 h. The mixture was filtered through Celite, and the filtrate was concentrated to give the crude intermediate bis-phosphonic acid as a dark amber oil (68.2 mg). MS (ESI): *m*/*z* 1792.2 (M + H, 10), 1554.0 (M + H − Trt, 22), 777.7 (M + 2H, 100). A solution of the crude intermediate(66.7 mg, 0.037 mmol) in 97:3 TFA:Et_3SiH (5.0 mL) was heated at 70 °C for 1 h. The mixture was filtered through Celite, and the filtrate was concentrated to give a dark amber oil. The product was purified by HPLC on a Higgins Clipeus C-18 column (21 × 250 mm) using a 0.45%/min gradient of 4.5−22.5% ACN containing 0.1% TFA at a flow rate of 15 mL/min. The main product, eluting at 33 min was lyophilized to give the title compound as a colorless solid (4.5 mg, 20%). MS (ESI): *m*/*z* 1385.8 (M + H, 18), 693.5 (M + 2H, 100); HRMS: Calcd for $C_{54}H_{78}N_{14}O_{23}P_2S$ (M + H): 1385.4560; Found: 1385.465.

Ethyl 7-Bromo-1-(3-(*tert*-butoxycarbonylamino)propyl)-4-oxo-1,4-dihydroquinoline-3-carboxylate (38). A mixture of ethyl 7-bromo-4-oxo-1,4-dihydroquinoline-3-carboxylate (**37**) (*36*) (6.28 g, 0.0212 mol), 3-((*tert*-butoxy)carbonylamino)propyl bromide (30.3 g, 0.127 mol), and anhydrous K_2CO_3 (12.5 g, 0.904 mol) in anhydrous DMF (200 mL) was stirred at 60 °C for 4 h and then at ambient temperature for 72 h. The DMF was removed under vacuum, and the resulting oily solid was dissolved in EtOAc (500 mL). The EtOAc solution was washed consecutively with water (500 mL), saturated $NaHCO_3$ (500 mL), and saturated NaCl (500 mL), dried ($MgSO_4$), and concentrated to give a red oil. This oil was taken up in EtOAc (250 mL) and cooled, causing a solid precipitate to form. This precipitate was collected by filtration, washed with cold EtOAc, and dried to give **38** as a colorless solid (6.25 g, 65%). MP: 140−142 °C; ^{1}H NMR ($CDCl_3$): δ 8.49 (s, 1H), 8.39 (d, J = 8.6 Hz, 1H), 7.58 (s, 1H), 7.53 (d, J = 8.6 Hz, 1H), 4.72 (bs, 1H), 4.39 (q, J = 7.1 Hz, 2H), 4.20 (t, J = 7.6 Hz, 2H), 3.28−3.24 (m, 2H), 2.10−2.06 (m, 2H), 1.46 (s, 9H), 1.40 (t, J = 7.1 Hz, 3H). MS (ESI): *m*/*z* 455.2. (M + H); HRMS: Calcd for $C_{20}H_{26}BrN_2O_5$ (M + H): 453.1025; Found: 453.1028.

Ethyl 1-(3-(*tert*-Butoxycarbonylamino)propyl)-4-oxo-7-vinyl-1,4-dihydroquinoline-3-carboxylate (39). A solution of **38** (2.98 g, 6.60 mmol) in toluene (50 mL) at 100 °C was treated with $(\phi_3P)_4Pd$ (152 mg, 0.132 mmol). After 5 min the mixture was treated with tributyl(vinyl)tin (1.93 mL, 6.60 mmol) and stirred 4.5 h at 100 °C and 18 h at ambient temperature. Additional tributyl(vinyl)tin (0.386 mL) and $(\phi_3P)_4Pd$ (152 mg) were added, and the mixture was heated at 100 °C for an additional 17 h. The toluene was removed under vacuum, and the solid residue was triturated with ether to give **39** as a pale green solid (1.67 g, 63%). MP: 133−135 °C; ^{1}H NMR ($CDCl_3$): δ 8.52 (d, J = 8.4 Hz, 1H), 8.51 (s, 1H), 7.55 (d, J = 8.4 Hz, 1H), 7.38 (s, 1H), 6.88−6.82 (m, 1H), 5.97 (d, J = 17.4 Hz, 1H), 5.51 (d, J = 10.8 Hz, 1H), 4.75 (bs, 1H), 4.42 (q, J = 7.2 Hz, 2H), 4.27 (t, J = 7.8 Hz, 2H), 3.6−3.25 (m, 2H), 2.16−2.11 (m, 2H), 1.49 (s, 9H), 1.45 (t, J = 7.2 Hz,

3H). MS (ESI): *m*/*z* 401.3 (M + H); HRMS: Calcd for $C_{22}H_{29}N_2O_5$ (M + H): 401.2076; Found: 401.2075.

Ethyl 1-(3-(*tert*-Butoxycarbonylamino)propyl)-7-formyl-4-oxo-1,4-dihydroquinoline-3-carboxylate (40). A solution of **2** (1.50 g, 3.75 mmol) in dioxane (119 mL) and water (39 mL) was treated with a solution of OsO_4 (19.6 mg, 0.077 mmol) in dioxane (0.600 mL) and stirred at ambient temperature for 5 min. Sodium periodate (2.40 g, 11.2 mmol) was added, and the solution was stirred at ambient temperature for 2 h. The solvents were removed under vacuum, and the residue was taken up in DCM (500 mL). The DCM solution was washed consecutively with water (500 mL) and saturated NaCl (500 mL), dried ($MgSO_4$), and concentrated to give **40** as an orange oily solid (1.52 g, 100%). ^{1}H NMR ($CDCl_3$): δ 10.17 (s, 1H), 8.68 (d, J = 8.2 Hz, 1H), 8.64 (s, 1H), 8.01 (s, 1H), 7.88 (d, J = 8.2 Hz, 1H), 4.82 (bs, 1H), 4.41−4.35 (m, 4H), 3.28 (s, 2H), 2.15−2.07 (m, 2H), 1.45 (s, 9H), 1.41 (t, J = 7.1 Hz, 3H). MS (ESI): *m*/*z* 403.3 (M + H); HRMS: Calcd for $C_{21}H_{27}N_2O_6$ (M + H): 403.1870; Found: 403.1875.

Ethyl 1-(3-(*tert*-Butoxycarbonylamino)propyl)-4-oxo-7-((1-trityl-1*H*-imidazol-2-ylamino)methyl)-1,4-dihydroquinoline-3-carboxylate (41). A solution of **40** (544 mg, 1.35 mmol) and 2-amino-1-(triphenylmethyl)imidazole (*42*) (456 mg, 1.35 mmol) in toluene (60 mL) was heated at reflux for 5 h with azeotropic removal of water. The solution was cooled, treated with $Na(OAc)_3BH$ (1.14 g, 5.38 mmol), and stirred at ambient temperature for 18 h. The mixture was diluted with EtOAc (400 mL), washed consecutively with water (500 mL) and saturated NaCl (500 mL), dried ($MgSO_4$), and concentrated to give an orange solid. This solid was dissolved in 50% ACN and purified by preparative HPLC on a Vydac C-18 column (50 × 250 mm) using a 0.60%/min gradient of 18−52% ACN containing 0.1% TFA at a flow rate of 49 mL/min. The main product peak eluting at 30.8 min was collected and lyophilized to give **41** as a pale yellow solid (407 mg, 60%). MS (ESI): *m*/*z* 712.4 (M + H); HRMS: Calcd for $C_{43}H_{46}N_5O_5$ (M + H): 712.3499; Found: 712.3485.

1-(3-(*tert*-Butoxycarbonylamino)propyl)-4-oxo-7-((1-trityl-1*H*-imidazol-2-ylamino)methyl)-1,4-dihydroquinoline-3-carboxylic Acid (42). A mixture of **41** (997 mg, 1.40 mmol), water (7.3 mL), 3 N LiOH (3.5 mL), and THF (50 mL) was stirred at ambient temperature for 3 h. The THF was removed under vacuum, and the resulting mixture was dissolved in $CHCl_3$ (500 mL) and water (100 mL). The aqueous layer was adjusted to pH 3 with 1.0 N HCl, and the layers were thoroughly mixed. The organic layer was washed consecutively with water (500 mL) and saturated NaCl (500 mL), dried ($MgSO_4$), and concentrated to give **42** as a pale yellow solid (998 mg). MP: 153−160 °C; ^{1}H NMR ($CDCl_3$): δ 14.83 (s, 1H), 8.76 (s, 1H), 8.68 (s, 1H), 8.24 (d, J = 6 Hz, 1H), 7.49−7.35 (m, 9H), 7.12−7.10 (m, 6H), 6.82 (s, 1H), 6.52 (s, 1H), 6.24 (d, J = 6 Hz, 1H), 5.75 (bs, 1H), 4.87−4.83 (m, 2H), 4.77 (bs, 1H), 4.51 (t, J = 9 Hz, 2H), 3.38 (s, 2H), 2.23 (s, 2H), 1.42 (s, 9H). MS (ESI): *m*/*z* 684.3 (M + H); HRMS: Calcd for $C_{41}H_{42}N_5O_5$ (M + H): 684.3186; Found: 684.3181.

(*S*)-Methyl 3-(1-(3-(*tert*-Butoxycarbonylamino)propyl)-4-oxo-7-((1-trityl-1*H*-imidazol-2-ylamino)methyl)-1,4-dihydroquinoline-3-carboxamido)-2-(2,4,6-trimethylphenylsulfonamido)propanoate (44). A solution of **42** (300 mg, 0.437 mmol), TEA (0.243 mL, 1.75 mmol), and HBTU (230 mg, 0.606 mmol) in anhydrous DMF (4 mL) was stirred at ambient temperature for 5 min. A solution of methyl (2S)-3-amino-2-(((2,4,6-trimethylphenyl)sulfonyl)amino)propanoate hydrochloride (**43**) (*36*) (184 mg, 0.637 mmol) in anhydrous DMF (3 mL) was added, and the solution was stirred at ambient temperature for 2 h. The solution was diluted with EtOAc (200 mL) and washed consecutively with water (2 × 50 mL), saturated $NaHCO_3$ (50 mL), and saturated NaCl (50 mL), dried ($MgSO_4$), and concentrated to give a viscous amber oil. Purification by flash chromatography on a 2.5 × 24 cm silica gel column using a EtOAc:MeOH step gradient (98:2, 95:5, 75:25) gave **44** as a pale yellow oil (330 mg, 78%). MS (ESI): *m*/*z* 966.6 (M + H); HRMS: Calcd for $C_{54}H_{60}N_7O_8S$ (M + H): 966.4224; Found: 966.4224.

(*S*)-3-(7-((1*H*-Imidazol-2-ylamino)methyl)-1-(3-aminopropyl)-4-oxo-1,4-dihydroquinoline-3-carboxamido)-2-(2,4,6-trimethylphenylsulfonamido)propanoic Acid Bis(trifluoroacetic Acid) Salt (46). A solution of **44** (51 mg, 0.052 mmol), water (0.27 mL), and 3 N LiOH (0.13 mL) in MeOH (2.0 mL) was allowed to stand at ambient temperature for 3.5 h and concentrated under vacuum. The resulting solid was dissolved in water (10 mL) and adjusted to pH 3 with 1.0 N HCl. The aqueous mixture was extracted with DCM (2 × 30 mL). The combined DCM extracts were washed with saturated NaCl (30 mL), dried ($MgSO_4$), and concentrated to give intermediate carboxylic acid **45** as a colorless solid (72 mg). MS (ESI): *m*/*z* 952.5 (M + H); HRMS: Calcd for $C_{53}H_{58}N_7O_8S$ (M + H): 952.4067; Found: 952.4056.

A solution of **45** and Et_3SiH (0.042 mL, 0.26 mmol) in degassed TFA (2 mL) was heated at 70 °C for 2.5 h and concentrated to give an amber oil. This oil was dissolved in water (25 mL) and washed with ether (2 × 15 mL). The combined ether washings were back-extracted with water (15 mL). The combined aqueous extracts were lyophilized to give **46** as a colorless powder (34 mg, 78%). MS (ESI): *m*/*z* 610.4 (M + H); HRMS: Calcd for $C_{29}H_{36}N_7O_6S$ (M + H): 610.2448; Found: 610.2462.

(*S*,*E*)-3-(7-((1*H*-Imidazol-2-ylamino)methyl)-4-oxo-1-(3-(6-(2-(2-sulfobenzylidene)hydrazinyl)nicotinamido)propyl)-1,4-dihydroquinoline-3-carboxamido)-2-(2,4,6-trimethylphenylsulfonamido)propanoic Acid Trifluoroacetic Acid Salt (47). A solution of **46** (13.7 mg, 0.0163 mmol), TEA (0.015 mL, 0.108 mmol), and sodium (*E*)-2-((2-(5-carboxypyridin-2-yl)-hydrazono)methyl)benzenesulfonate (*37*) (**9**) (8.2 mg, 0.0186 mmol) in anhydrous DMF (2.0 mL) was allowed to stand at ambient temperature for 24 h. The DMF was removed under reduced pressure and the resulting amber oil was dissolved in 50% ACN and purified by preparative HPLC on a Vydac C-18 column (22 × 250 mm) using 0.1% TFA in water for 5 min followed by a 2.52%/min gradient of 0−63% ACN containing 0.1% TFA at a flow rate of 20 mL/min. The main product peak eluting at 21.4 min was collected and lyophilized to give **47** as a colorless powder (12.5 mg, 74.7%). MS (ESI): *m*/*z* 913.3 (M + H); HRMS: Calcd for $C_{42}H_{45}N_{10}O_{10}S_2$ (M + H): 913.2761; Found: 913.2751.

(*S*)-Methyl 3-(1-(2,2-Dimethyl-4,20,23-trioxo-3,9,12,15-tetraoxa-5,19,24-triazaheptacosan-27-yl)-4-oxo-7-((1-trityl-1*H*-imidazol-2-ylamino)methyl)-1,4-dihydroquinoline-3-carboxamido)-2-(2,4,6-trimethylphenylsulfonamido)propanoate (49). A solution of **44** (46.1 mg, 0.477 mmol) in 50:50 TFA:DCM (2.0 mL) was stirred for 15 min at ambient temperature and concentrated to give a yellow oil. This oil was dissolved in anhydrous DMF (1.0 mL) and made basic with TEA. In a separate flask, *N*-Boc-*N*′-succinimidyl-4,7,10-trioxatridecane-1,13-diamine (**48**) (*43*) (26.1 mg, 0.062 mmol), TEA (0.014 mL, 0.099 mmol), and HBTU (27.7 mg, 0.074 mmol) were dissolved in anhydrous DMF (1.0 mL). The resulting solution was allowed to react for 5 min and combined with the DMF solution from the TFA deprotection reaction. The combined solutions were allowed to stand at ambient temperature for 20 min and concentrated under vacuum. The resulting oil was dissolved in 50% ACN and purified by preparative HPLC on a Vydac C-18 column (22 × 250 mm) using a 1.8%/min gradient of 18−72% ACN containing 0.1% TFA at a flow rate of 20

mL/min. The main product peak eluting at 26.8 min was collected and lyophilized to give **49** as a colorless powder (44.5 mg, 68%). MS (ESI): *m*/*z* 1268.6 (M + H); HRMS: Calcd for $C_{68}H_{86}N_9O_{13}S$ (M + H): 1268.6065; Found: 1268.6070.

(*S*,*E*)-3-(7-((1*H*-Imidazol-2-ylamino)methyl)-4-oxo-1-(1,17,20-trioxo-1-(6-(2-(2-sulfobenzylidene)hydrazinyl)pyridin-3-yl)-6,9,12-trioxa-2,16,21-triazatetracosan-24-yl)-1,4-dihydroquinoline-3-carboxamido)-2-(2,4,6-trimethylphenylsulfonamido)propanoic Acid Trifluoroacetic Acid Salt (52). A solution of **49** (31.1 mg, 0.0227 mmol), 3 N LiOH (0.091 mL), and water (0.117 mL) in MeOH (1.30 mL) was stirred at ambient temperature for 8.5 h. The MeOH was removed under vacuum, and the aqueous mixture was diluted with water (30 mL) and adjusted to pH 4 with 1.0 N HCl. The resulting aqueous mixture was extracted with DCM (2 × 50 mL). The combined DCM extracts were washed with saturated NaCl (50 mL), dried ($MgSO_4$), and concentrated to give carboxylic acid **50** as a colorless solid (24.6 mg, 86%). Compound **50** (24.6 mg, 0.0194 mmol) was taken up in TFA (2.0 mL) and Et_3SiH (0.016 mL, 0.097 mmol) and heated at 70 °C for 3 h. Concentration give a yellow solid, which was dissolved in water (50 mL) and washed with ether (2 × 25 mL). The aqueous layer was lyophilized to give free amine **51** as a pale yellow solid (20.7 mg, 93%). MS: *m*/*e* 912.5 (M + H). A solution of **51** (15.5 mg, 0.0136 mmol), TEA (10 μL, 0.0746 mmol), and succinimide ester **9** (8.0 mg, 0.0182 mmol) in anhydrous DMF (2.0 mL) was allowed to stand at ambient temperature for 24 h. The DMF was removed under vacuum and the resulting yellow oil was dissolved in 50% ACN and purified by preparative HPLC on a Vydac C-18 column (22 × 250 mm) using 0.1% TFA in water for 5 min followed by a 2.5%/min gradient of 0−63% ACN containing 0.1% TFA at a flow rate of 20 mL/min. The main product peak eluting at 21.7 min was collected and lyophilized to give **52** as a colorless powder (7.2 mg, 40%). MS (ESI): *m*/*z* 1215.5 (M + H); HRMS: Calcd for $C_{56}H_{71}N_{12}O_{15}S_2$ (M + H): 1215.4603; Found: 1215.4580.

(*S*)-2,2′,2″-(10-(2-(3-(7-((1*H*-Imidazol-2-ylamino)methyl)-3-(2-carboxy-2-(2,4,6-trimethylphenylsulfonamido)ethylcarbamoyl)-4-oxoquinolin-1(4*H*)-yl)propylamino)-2-oxoethyl)-1,4,7,10-tetraazacyclododecane-1,4,7-triyl)triacetic Acid Trifluoroacetic Acid Salt (54). A solution of DOTA(O*t*-Bu)$_3$OH (89 mg, 0.0974 mmol), DIEA (0.103 mL, 0.607 mmol), and HBTU (28.0 mg, 0.0735 mmol) in anhydrous DMF (1.0 mL) was stirred at ambient temperature for 15 min and treated with a solution of compound **46** (30.0 mg, 0.0358 mmol) in anhydrous DMF (1.0 mL). The DMF was removed under vacuum after 3 h, and the residue was purified by HPLC on a Vydac C-18 column (22 × 250 mm) using a 1.1%/min gradient of 18−72% ACN containing 0.1% TFA at a flow rate of 20 mL/min. The main product peak eluting at 17.5 min was lyophilized to give DOTA conjugate **53** as a colorless solid (48.0 mg, 65.0%). MS (ESI): *m*/*z* 1164.7 (M + H). A solution of **53** (48.0 mg, 0.0375 mmol) in 95:5 TFA:Et_3SiH (2.1 mL) was stirred at 50 °C for 2 h. The solution was concentrated under vacuum and the oily residue was purified by HPLC on a Vydac C-18 column (22 × 250 mm) using a 1.2%/min gradient of 0−36% ACN containing 0.1% TFA at a flow rate of 20 mL/min. The main product peak eluting at 18.6 min was lyophilized to give **54** as a colorless solid (25.7 mg, 58.7%). MS (ESI): *m*/*z* 996.5 (M + H); HRMS: Calcd for $C_{45}H_{62}N_{11}O_{13}S$ (M + H): 996.4249; Found: 996.4278.

(*R*)-1-(3-(7-((1*H*-Imidazol-2-ylamino)methyl)-3-((*S*)-2-carboxy-2-(2,4,6-trimethylphenylsulfonamido)ethylcarbamoyl)-4-oxoquinolin-1(4*H*)-yl)propylamino)-1-oxo-3-sulfopropan-2-aminium Trifluoroacetate (55). A solution of compound **46** (105 mg, 0.125 mmol), the *N*-hydroxysuccinimide ester of Boc-L-cysteic acid (*44*) (146 mg, 0.467 mmol), and DIEA (0.120 mL, 0.69 mmol) in anhydrous DMF (1.5 mL) was stirred at ambient temperature for 24 h. The DMF was removed under vacuum and the resulting solid residue was purified by HPLC on a Vydac C-18 column (22 × 250 mm) using a 0.68%/min gradient of 9−36% ACN containing 0.1% TFA at a flow rate of 20 mL/min. The main product peak eluting at 30.3 min was lyophilized to give Boc-cysteic acid conjugate **54** as a colorless solid (73.0 mg, 67.9%). MS (ESI): *m*/*z* 861.3 (M + H). A solution of **54** (70.0 mg, 0.0814 mmol) in 2:1 DCM:TFA (1.5 mL) was allowed to react at ambient temperature for 30 min. The solution was concentrated under vacuum and the amber oil was dissolved in 50% ACN (25 mL) and lyophilized to give **55** as a colorless solid (70.8 mg, 99.5%). MS (ESI): *m*/*z* 761.2 (M + H); HRMS: Calcd for $C_{32}H_{41}N_8O_{10}S_2$ (M + H): 761.2387; Found: 761.2393.

2,2′,2″-(10-(2-((*R*)-1-(3-(7-((1*H*-Imidazol-2-ylamino)methyl)-3-((*S*)-2-carboxy-2-(2,4,6-trimethylphenylsulfonamido)-ethylcarbamoyl)-4-oxoquinolin-1(4*H*)-yl)propylamino)-1-oxo-3-sulfopropan-2-ylamino)-2-oxoethyl)-1,4,7,10-tetraazacyclododecane-1,4,7-triyl)triacetic Acid Trifluoroacetic Acid Salt (57). A solution of DOTA(O*t*-Bu)$_3$OH (20.8 mg, 0.0228 mmol), DIEA (0.006 mL, 0.034 mmol), and HBTU (6.5 mg, 0.0171 mmol) in anhydrous DMF (0.5 mL) was stirred at ambient temperature for 5 min and treated with a solution of compound **55** (10.0 mg, 0.0114 mmol) and DIEA (6 μL, 0.034 mmol) in anhydrous DMF (0.5 mL). Stirring was continued at ambient temperature for 24 h, and the reaction was diluted with water (3.0 mL), treated with concentrated ammonium hydroxide (3 μL), and stirred an additional 10 min. The solution was adjusted to pH 3 using 0.1 N HCl (6.0 mL) and diluted further with 10% ACN (5.5 mL). This solution was purified directly by HPLC on a Vydac C-18 column (22 × 250 mm) using a 0.68%/min gradient of 9−36% ACN containing 0.1% TFA at a flow rate of 20 mL/min. The main product peak eluting at 36.0 min was lyophilized to give DOTA conjugate **56** as a colorless solid (12.0 mg, 68.3%). MS (ESI): *m*/*z* 1315.6 (M + H). A solution of conjugate **56** (12.0 mg, 0.00778 mmol) in 95:5 TFA:Et_3SiH (1.0 mL) was stirred at ambient temperature for 18 h. The solution was concentrated under vacuum, and the oily residue was purified by HPLC on a Vydac C-18 column (22 × 250 mm) using a 1.2%/min gradient of 0−36% ACN containing 0.1% TFA at a flow rate of 20 mL/min. The main product peak eluting at 21.1 min was lyophilized to give **57** as a colorless solid (8.1 mg, 76%). MS (ESI): *m*/*z* 1147.3 (M + H); HRMS: Calcd for $C_{48}H_{67}N_{12}O_{17}S_2$ (M + H): 1147.4189; Found: 1147.418.

$\alpha_v\beta_3$-ELISA (Biotin-Vn) Adhesion Assay. Polystyrene ELISA plates (Costar #3590) were coated with a solution of human $\alpha_v\beta_3$ receptor (Chemicon) (500 ng/mL) in binding buffer (50 mM tris, 100 mM NaCl, 2 mM $CaCl_2$, 1 mM $MgCl_2$, pH 7.4) using 100 uL per well for 1 h at ambient temperature. The plates were rinsed three times with wash buffer (binding buffer with 0.05% Tween 20 and 1% BSA). Nonspecific binding was blocked by the addition of blocking buffer (150 uL per well) for 1 h at ambient temperatures. Human vitronectin (Chemicon) was biotinylated with sulfo-biotin-NHS (Pierce Chemical Co.) by a previously reported procedure (*45*). Solutions of the test agents were prepared using 10 nM biotinylated-n vitronectin. Test solutions (100 μL) were transferred to the ELISA plate, and the plate was incubated for 30 min at ambient temperature. Following the incubation, solution was removed from the wells, and the wells were rinsed three times with 150 uL of wash buffer. Following the washing, a solution (100 μL) of goat anti-biotin antibody alkaline phosphatase conjugate (Sigma, #A-7064) was added to each well and incubated for 1 h at ambient temperature. Solutions were removed, and the wells were rinsed with wash buffer (3 × 150 μL). A phosphatase substrate solution

was prepared by dissolving a phosphatase substrate tablet (Sigma) in 90:10 H_2O:diethanolamine. Phosphatase substrate solution (100 μL) was added to each well, and the plate was incubated for 30 min at ambient temperature. Absorbance was read on a spectrophotometer (μQuant Microplate Spectrophotometer, Bio-Tek Instruments Inc, Winooski, Vermont) at 410 nm. Nonspecific binding was subtracted from each data point, percent inhibition was calculated for each concentration of test agent, and IC_{50} values were derived.

General Procedure for ^{99m}Tc−Radiolabeling of HYNIC Conjugates. A vial containing the HYNIC conjugate (20 μg), tricine (1.0 mg), TPPTS (7.0 mg), and mannitol (20 mg) was sealed with a Teflon-coated serum stopper and aluminum crimp. A syringe was used to add a 0.9% saline solution (0.5 mL) containing 50 mCi of $^{99m}TcO_4^-$. The vial was placed in a boiling water bath for 10 min and allowed to cool to room temperature. Radiochemical purity was checked by a combination of instant thin-layer chromatography (ITLC) on silica gel strips (Gelman Sciences, Inc., Ann Arbor, MI) developed in a mobile phase of MeOH:acetone:saline, and RP-HPLC with a C18 column (Zorbax Rx-C18, 5 μm particle size, 80 Å pore size, 4.6 × 250 mm) on an Agilent 1100 HPLC system equipped with an in-line radio detector, using a 0.5%/min gradient of 10−20% ACN containing 25 mM ammonium acetate, pH 7.2, at a flow rate of 1.0 mL/min. The radiochemical purity was determined by the area percent of the product peak in the radio-HPLC method minus the area percent of insoluble ^{99m}Tc-colloid determined by the TLC method. Any compounds having a radiolabeling efficiency <95% were purified by RP-HPLC using the above column and mobile phase conditions. Gradients were modified as necessary to give the required separation. The desired product fractions were concentrated on a rotary evaporator, and the product was reconstituted in 0.9% saline for the animal studies. All complexes used in the biodistribution studies had an RCP >95%.

General Procedure for ^{111}In-Radiolabeling of DOTA Conjugates. The procedure for preparation of ^{111}In-DOTA complexes has been described in detail elsewhere (*26*, *46*). Briefly, the DOTA conjugate (200 μg), sodium gentisate (1.5 mg), and 0.5 M ammonium acetate, pH 6.0 (3.0 mL), were added to a 10 cm^3 glass vial, and the vial was sealed with a Teflon-coated serum stopper and aluminum crimp. The solution was degassed by vacuum pump for 1 min. A solution of 4.0−5.0 mCi $^{111}InCl_3$ in 0.05 N HCl (10−20 μL) was added to the vial, and the reaction solution was heated at 100 °C for 5 min and analyzed by HPLC and ITLC as described above. Purification, if required, was by the above procedure. All complexes used in the biodistribution studies had an RCP >95%.

^{177}Lu-36. The title compound was prepared in 98% RCP using a procedure developed for the preparation of ^{177}Lu-**TA138** (*47*).

In Vivo Biodistribution Study. c-neu Oncomouse Model. The mice used in this program were obtained from an in-house breeding program. Mice were used when tumors were 5−20 mm in size, as determined with digital caliper. Animals were anesthetized intramuscularly with 0.1 mL of ketamine/acepromazine (1.8 mL saline, 1.0 mL ketamine, and 0.2 mL acepromazine) prior to dosing and tissue sampling. Groups of mice (n = 3/group) were injected via the tail vein with either ^{111}In-DOTA conjugate (2 mCi/Kg in 0.1 mL) or [^{99m}Tc(HYNIC conjugate)(TPPTS)(tricine)] (2 mCi/kg in 0.1 mL). Mice were euthanized and dissected at 2 h pi. Selected tissues were removed, weighed, and counted on an LKB gamma counter. Raw radioactivity data was corrected for background and tested for quantitation limits according to the literature method.[48] Results are expressed as the percentage injected dose per gram of tissue (%ID/g). Since the c-neu Oncomouse spontaneously develops tumors in the mammary glands, most mice had more than one tumor. Each tumor was sampled and counted separately, and radioactive uptake for the tumors was then averaged to obtain an overall representation of tumor uptake. Biodistribution data are shown in Table 2, and tumor/organ ratios are shown in Table 3.

RESULTS

Synthesis of tethers on the DAP sulfonamide. Radionuclide−chelator complexes were tethered to the DAP arylsulfonamide moiety using two synthetic strategies. The first of these strategies employed a short diamino-PEG tether linked to DAP via the 4,4′-biphenyl moiety, as shown in Scheme 1 for the synthesis of **10**. 4,7,10-Trioxa-1,13-tridecanediamine (**1**) was converted to mono-Cbz derivative **2** in 45% yield using benzyl chloroformate in THF. Tethered DAP arylsulfonamide **3** was prepared from **2** in a single vessel, two-step condensation procedure in which freshly recrystallized biphenyl-4,4′-disulfonyl chloride was condensed first with **2**, and then with (*S*)-methyl 2-amino-3-(*tert*-butoxycarbonylamino)propanoate hydrochloride. Flash chromatography and recrystallization, followed by treatment with TFA to remove the Boc group gave a 59% overall yield of **4**. Conjugation with quinolin-4-one carboxylic acid **5**, prepared by the procedure of Wityak et al. (*36*), gave a 50% yield of **6**. All protecting groups were removed in a two step sequence of ester saponification using LiOH in THF, followed by treatment with TFA:Et_3SiH at 70 °C to give **8**. Conjugation with HYNIC succinimide ester **9** gave the TFA salt of **10** in 20% yield after reverse phase HPLC purification.

Compound **12**, the DOTA analogue of **10**, was prepared from compound **6** by the procedure depicted in Scheme 2. Treatment of **6** with TFA:Et_3SiH, followed by an HBTU-mediated conjugation to DOTA tri-*tert*-butyl ester gave **11** in 17% purified yield. Final deprotection consisted of ester saponification using aqueous LiOH in THF, followed by treatment with TFA:Et_3-SiH. The final purified yield of **12** was 15%, calculated as the bis-TFA salt.

The second strategy used to tether radionuclide−chelator complexes to DAP arylsulfonamides is shown in Scheme 3 for the synthesis of DOTA conjugate **TA138**. 4-(3,5-Dimethylphenoxy)butyric acid (**14**) was prepared in 79% yield from 3,5-dimethylphenol by alkylation with ethyl 4-bromobutyrate, followed by ester saponification using KOH in EtOH. Chlorosulfonation followed by conjugation of the resulting sulfonyl chloride to (*S*)-methyl 2-amino-3-(*tert*-butoxycarbonylamino)-propanoate afforded DAP arylsulfonamide **16** in 12% yield. The carboxylic acid of **16** was conjugated to benzyl *N*-(2-aminoethyl)carbamate using HBTU to give a 90% yield of **17**. Removal of the Boc protecting group using TFA and conjugation of the resulting amine to quinolin-4-one carboxylic acid **5** afforded a 57% yield of **19**. Hydrogenolysis over Pd/C removed the Cbz protecting group, and ester saponification using LiOH gave **21** in 79% yield. Two Boc-Csa(Na)-OH pharmacokinetic modifiers were added in stepwise fashion by preactivation with PyBOP to give **24** in 74% yield. Cleavage of the Boc protecting group from **24** was followed by refunctionalization of the resulting amine with preactivated DOTA tri-*tert*-butyl ester. Global deprotection using TFA:Et_3SiH gave **TA138** in 72% yield.

The HYNIC analogue of **TA138** was prepared as shown in Scheme 4. Treatment of compound **24** with 97:3 TFA:Et_3SiH removed the trityl and Boc protecting groups to give **27** in 73% yield. Conjugation of **27** with sodium (*E*)-2-((2-(5-carboxypyridin-2-yl)hydrazono)methyl)benzenesulfonate (**28**) gave **29** in 32% yield.

The cysteic acid pharmacokinetic modifiers of **TA138** were replaced with 3-phosphonoalanine as described in Scheme 5 to

Scheme 1. Synthesis of HYNIC Conjugate 10[a]

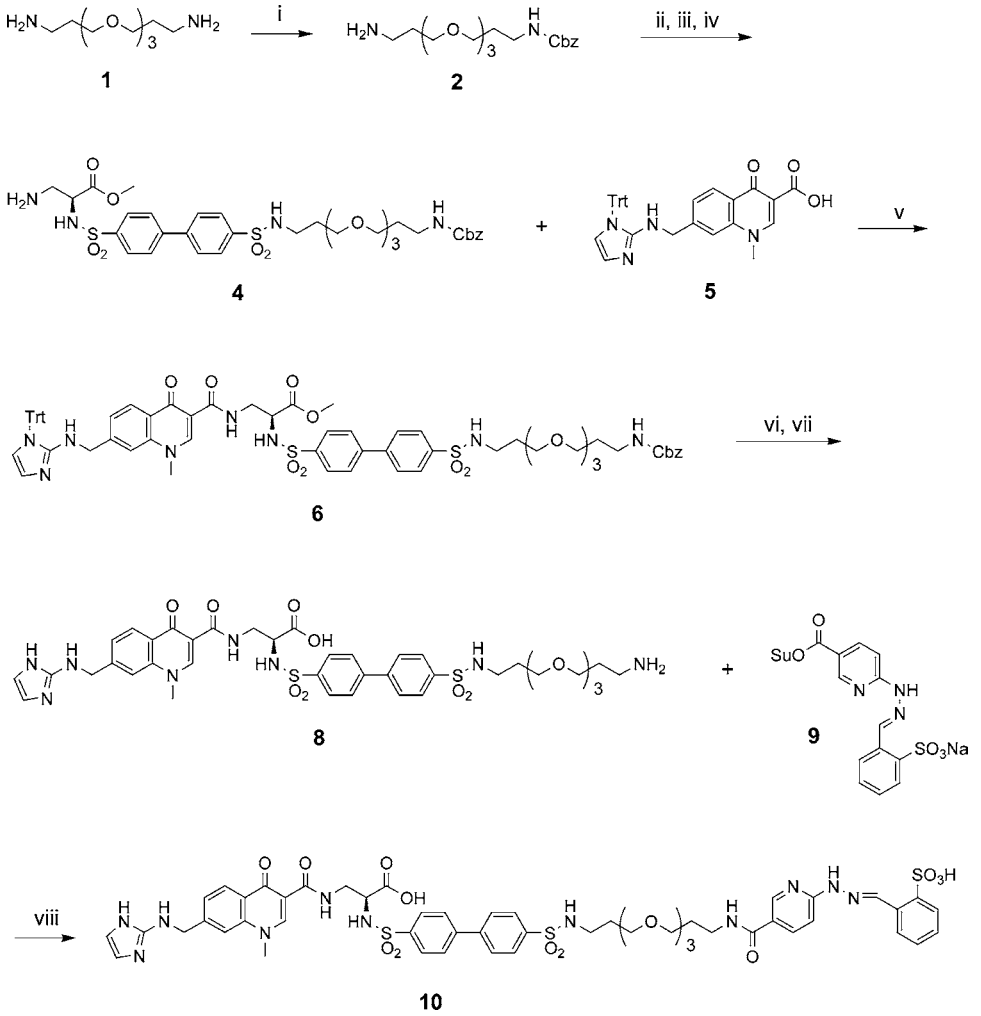

[a] Reagents: i) Cbz-Cl, THF/MeOH, TEA, 5 °C, 45%; ii) biphenyl-4,4′-disulfonyl chloride, DCM, DIEA, 5 °C; iii) (*S*)-methyl 2-amino-3-(*tert*-butoxycarbonylamino)propanoate hydrochloride, DIEA, DCM, 59%; iv) TFA, DCM; v) HBTU, TEA, DMF, 50%; vi) 3 N LiOH, THF, 100%; vii) TFA, Et_3SiH, 70 °C; viii) TEA, DMF, 20%.

Scheme 2. Synthesis of DOTA Conjugate 12[a]

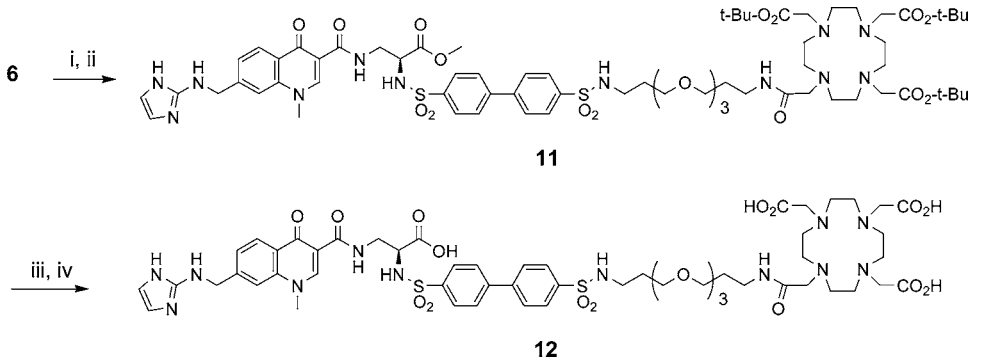

[a] Reagents: i) TFA, Et_3SiH, 70 °C; ii) DOTA(O*t*-Bu)$_3$−OH, HBTU, TEA, DMF, 17%; iii) 3 N LiOH, THF; iv) TFA, Et_3SiH, 70 °C, 15%.

give **36**. Orthogonally protected amino acid **30** was prepared from *N*-(*tert*-butoxycarbonyl)-L-serine β-lactone and diallyl-(trimethylsilyl)phosphite by a procedure analogous to that published by Lohse and Felber (*41*). Two of these phosphonic acid PKMs were added in stepwise fashion in 50% overall yield using the procedures described for **TA138** to give compound **33**. Boc protecting group cleavage was followed by conjugation to DOTA tri-*tert*-butyl ester. Final global deprotection was accomplished in two steps using $(\phi_3P)_4Pd$ and morpholine, followed by treatment with TFA:Et_3SiH. Overall yield of **36** for these final four steps was 5.8%.

Synthesis of Tethers on the Quinolin-4-one Ring Nitrogen. The quinolin-4-one ring nitrogen was alkylated with an aminopropyl tether as shown for HYNIC conjugate **47** in Scheme 6. Ethyl 7-bromo-4-oxo-1,4-dihydroquinoline-3-carboxylate (**37**) was alkylated using K_2CO_3 and a 6-fold excess of 3-((*tert*-butoxy)carbonylamino)propyl bromide in DMF at 60 °C. A liquid−liquid partitioning of the reaction mixture and crystallization from EtOAc gave compound **38** in 65% yield. Vinylation of **38** using tributyl(vinyl)tin and $(\phi_3P)_4Pd$ gave a 63% yield of compound **39**. Oxidation of the vinyl group using sodium periodate and a catalytic amount of osmium tetroxide,

Scheme 3. Synthesis of DOTA Conjugate TA138[a]

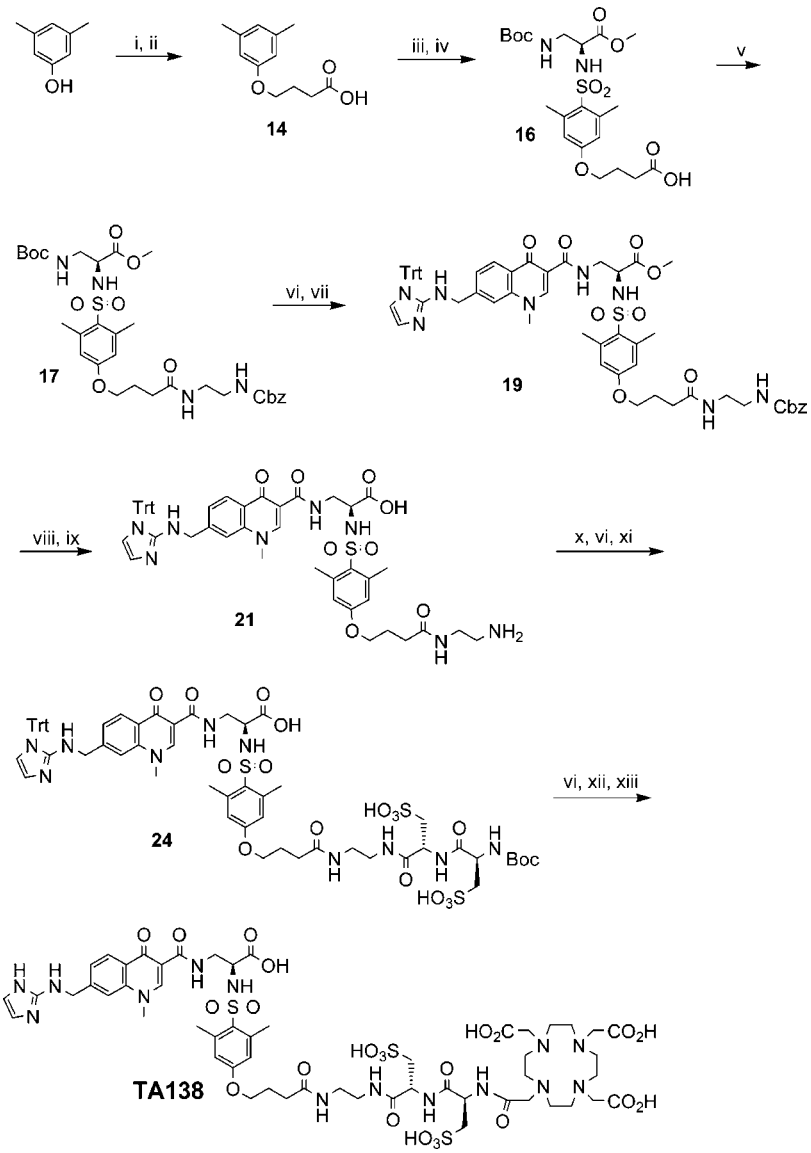

[a] Reagents: i) NaOEt, ethyl 4-bromobutyrate, EtOH, 89%; ii) KOH, EtOH, 89%; iii) chlorosulfonic acid, $CHCl_3$, 41%; iv) (*S*)-methyl 2-amino-3-(*tert*-butoxycarbonylamino)propanoate, DCM, 29%; v) benzyl *N*-(2-aminoethyl)carbamate, HBTU, DIEA, DMF, 90%; vi) TFA, DCM; vii) **5**, HBTU, DIEA, DMF, 63%; viii) H_2, 10% Pd/C, MeOH, 99%; ix) 3 N LiOH, THF, 80%; x) Boc-Csa(Na)-OH, PyBOP, DIEA, DMF; xi) Boc-Csa(Na)-OH, PyBOP, DIEA, DMF, 74%; xii) DOTA(O*t*-Bu)$_3$-OH, PyBOP, DIEA, DMF, 76%; xiii) TFA, Et_3SiH, 70 °C, 95%.

followed by reductive amination using 2-amino-1-(triphenylmethyl)imidazole and $Na(OAc)_3BH$, and saponification using LiOH gave a 60% purified yield of **42**. Conjugation of **42** with DAP arylsulfonamide **43** gave compound **44** in 78% purified yield. All protecting groups were removed in a two-step sequence consisting of ester saponification using LiOH in MeOH, followed by treatment with TFA:Et_3SiH to give a 90% yield of **46** as the bis-TFA salt. Conjugation with HYNIC succinimide ester **9** gave the TFA salt of **47** in 75% yield after reverse phase HPLC purification.

N-Boc-*N*′-succinimidyl-4,7,10-trioxatridecane-1,13-diamine (**48**), previously described by Trester-Zedlitz et al. (*43*), was used to extend the aminopropyl tether of **47**, as shown in Scheme 7. The aminopropyl tether of quinolin-4-one **44** was unmasked using TFA, and the resulting amine was conjugated to **48** using HBTU to give **49** in 68% yield. Ester saponification using LiOH, cleavage of the Boc and trityl protecting groups with TFA:Et_3-SiH, and conjugation with HYNIC succinimide ester **9** gave **52** in 32% yield.

Two DOTA analogues of **47** were prepared according to the procedures in Scheme 8. Conjugation of quinolin-4-one **46** with preactivated DOTA tri-*tert*-butyl ester, followed by protecting group cleavage gave the bis-TFA salt of **54** in 59% yield. Conjugation of quinolin-4-one **46** with the *N*-hydroxysuccinimide ester of Boc-L-cysteic acid, followed by TFA deprotection conditions, gave amine **55** in 68% yield. Conjugation of **55** with preactivated DOTA tri-*tert*-butyl ester, followed by protecting group cleavage gave the TFA salt of **57** in 52% yield.

Receptor Binding Assays. Affinity assays toward four integrin receptors were used to measure the potency and selectivity of the chelator conjugates described here. Our principle receptor $\alpha_v\beta_3$ assay was an ELISA (biotin-Vn) adhesion assay as described in the Experimental Section. The 293β_3-fibrinogen ($\alpha_v\beta_3$-mediated) adhesion assay, and the platelet aggregation $\alpha_{IIb}\beta_3$ assay have been described in detail by Wityak et al. (*42*). The human SKBR3 cell-vitronectin ($\alpha_v\beta_5$-mediated) adhesion assay and the human lymphocyte (Jurkat)-fibronectin ($\alpha_5\beta_1$-mediated) adhesion assay have been described in detail by Harris et al. (*26*). The affinity data in Table 1 shows that all compounds measured have high affinity toward receptor $\alpha_v\beta_3$, with IC_{50} values <5 nM in an ELISA assay. They also show excellent selectivity versus receptors $\alpha_{IIb}\beta_3$, $\alpha_v\beta_5$, and

Scheme 4. Synthesis of HYNIC Conjugate 29[a]

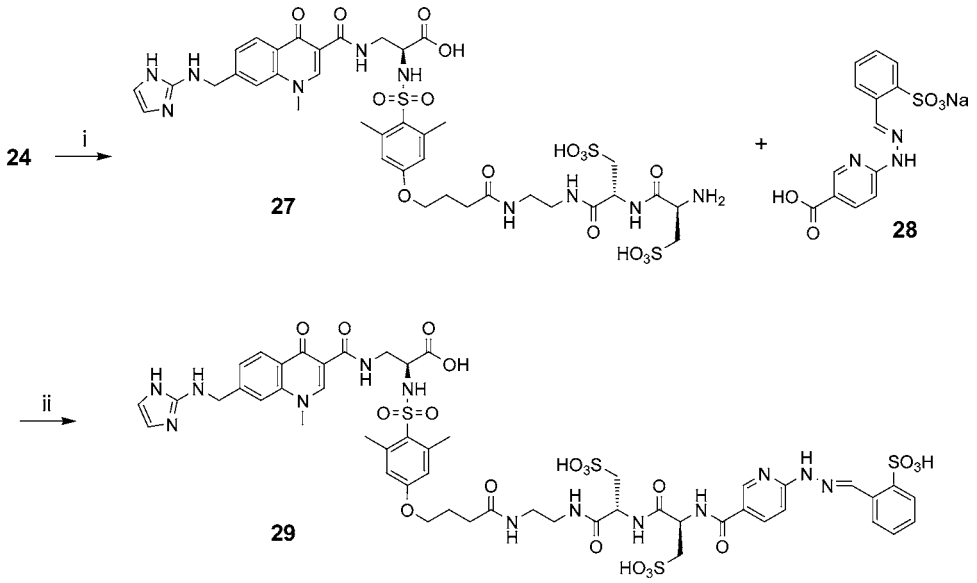

[a] Reagents: i) TFA, Et_3SiH, 70 °C, 73.3%; ii) PyBOP, DIEA, DMF, 32.0%.

Scheme 5. Synthesis of DOTA Conjugate 36[a]

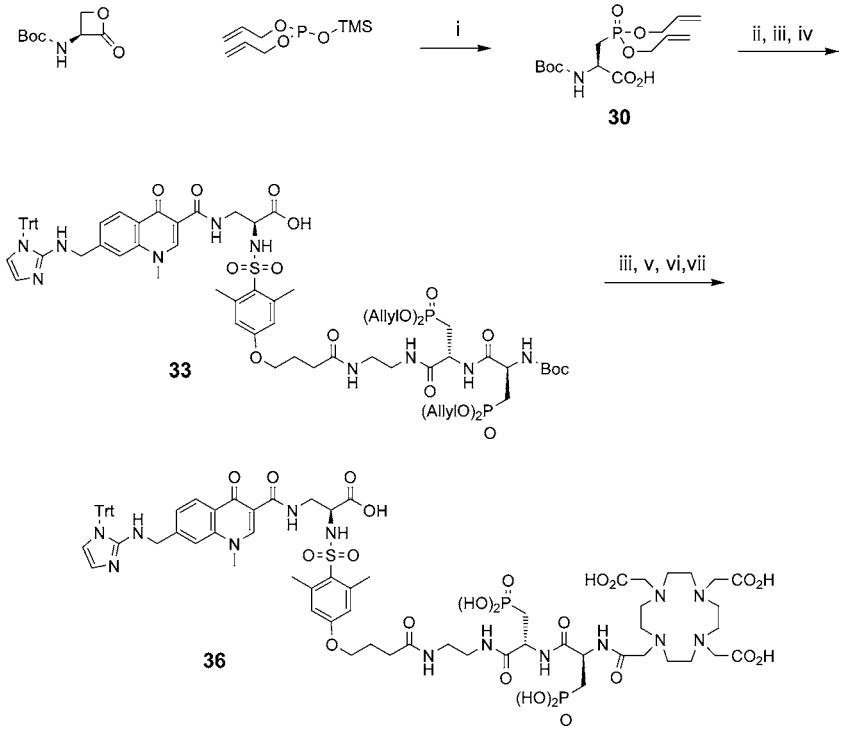

[a] Reagents: i) 70 °C, 19%; ii) **21**, HBTU, DIEA, DMF, 72%; iii) TFA, DCM; iv) **30**, HBTU, DIEA, DMF, 69%; v) DOTA(O*t*-Bu)$_3$−OH, HBTU, DIEA, DMF, 29%; vi) (ϕ_3P)$_4$Pd, morpholine, THF; vii) TFA, Et_3SiH, 70 °C, 20%.

$\alpha_5\beta_1$. Affinity and selectivity are nearly identical to parent compound **SH066** and nonradioactive complex ^{89}Y-**TA138**.

Radiolabeling. HYNIC conjugates **10**, **47**, and **52** formed stable ternary complexes with ^{99m}Tc using tricine and TPPTS as coligands, and they were isolated in >95% radiochemical purity (RCP). However, HYNIC conjugate **29** gave very poor radiochemical yields under the same conditions, and we were unable to purify it to a sufficiently high level to carry it into the biodistribution studies. The DOTA conjugates were our primary focus in this program, and no effort was made to optimize the labeling procedure for **29**. DOTA conjugates **12**, **TA138**, and **57** formed stable complexes with ^{111}In and these complexes were isolated in >95% RCP. The nonradioactive complex ^{89}Y-**TA138** was prepared in high yield and purity as previously reported (*47*). DOTA conjugate **36** failed to form a stable complex with ^{111}In. However, we were able to prepare the analogous ^{177}Lu-**36** complex in 98% RCP using a previously reported procedure (*47*), and this complex was used in the biodistribution studies described below.

In Vivo Biodistribution Study. The biodistribution properties of the compounds in this study were evaluated in the c-neu Oncomouse mammary adenocarcinoma model. The HYNIC conjugates were evaluated as ternary complexes with ^{99m}Tc using tricine and TPPTS as coligands (see, for example, the structure in Figure 1). For unknown reasons, HYNIC conjugate **29** gave an unusually low yield of the radiolabeled product, and we were unable to purify it sufficiently to carry out the biodistribution study. The DOTA conjugates were evaluated as

Scheme 6. Synthesis of HYNIC Conjugate 47[a]

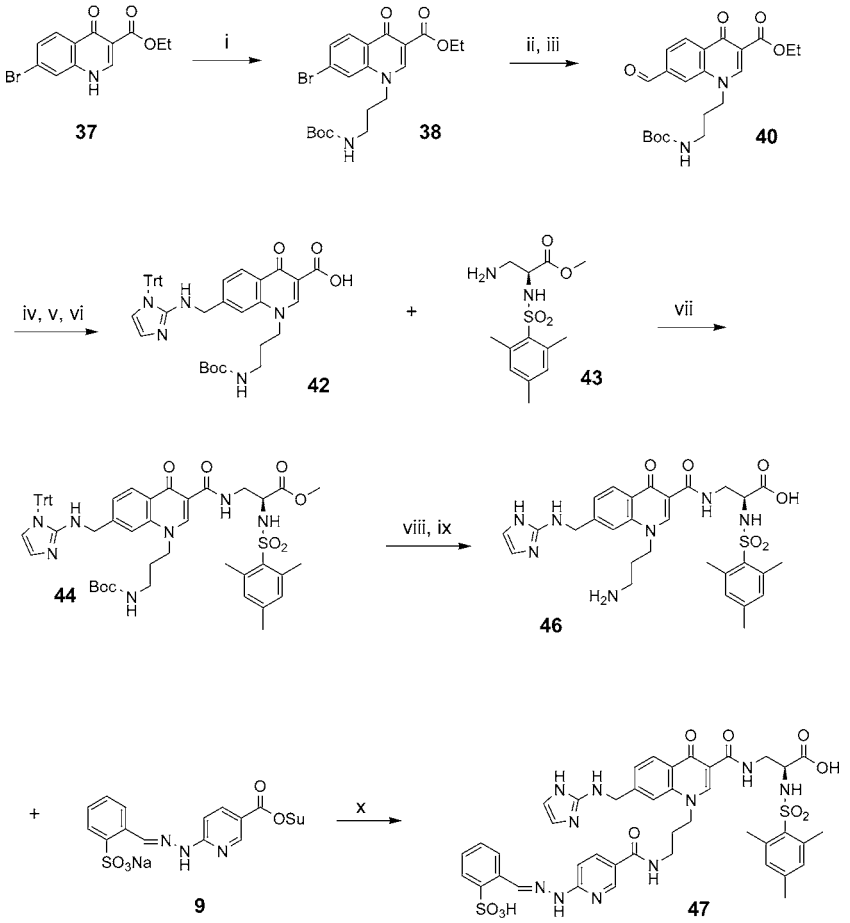

[a] Reagents: i) 3-((*tert*-butoxy)carbonylamino)propyl bromide, K_2CO_3, DMF, 60 °C, 65%; ii) $(\phi_3P)_4Pd$, tributyl(vinyl)tin, toluene, 100 °C, 63%; iii) OsO_4, $NaIO_4$, dioxane, H_2O, 100%; iv) 2-amino-1-(triphenylmethyl)imidazole, toluene, $-H_2O$; v) $Na(OAc)_3BH$, 60%; vi) 3 N LiOH, THF; vii) HBTU, TEA, DMF, 78%; viii) 3 N LiOH, MeOH; ix) TFA, Et_3SiH, 70 °C, 90%; x) TEA, DMF, 75%.

Scheme 7. Synthesis of HYNIC Conjugate 52[a]

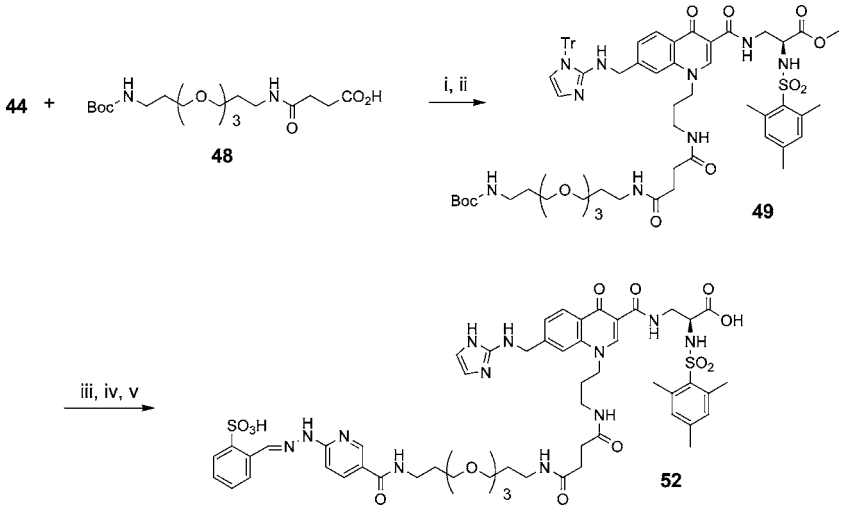

[a] Reagents: i) TFA, DCM; ii) **48**, HBTU, DIEA, DMF, 68%; iii) 3 N LiOH, MeOH, 86%; iv) TFA, Et_3SiH, 70 °C, 93%; v) **9**, TEA, DMF, 40%.

the ^{111}In complexes, except for **36**, which was evaluated at the ^{177}Lu complex. All compounds were administered at 2 mCi/Kg of body weight. Mice were euthanized and dissected at 2 h postinjection (pi), and activity in the organs and tumors was counted on a gamma counter. The data are presented in Table 2 and expressed as % of injected dose/gram of tissue (%ID/g). These data show that the agents are excreted primarily via the kidneys, with only ^{99m}Tc-**47** showing high bile activity (354% ID/g) and slightly elevated liver activity (7.10% ID/g). The relatively low blood activity indicates rapid blood clearance for all agents. Uptake was universally low in muscle, heart, eyes, spleen, bone, and stomach, and slightly elevated for most agents in colon and uterus. Tumor uptake was rapid for all agents and ranged from a low value of 2.95% ID/g for ^{111}In-**12** to a high of 11.8% ID/g for ^{111}In-**57**. Kidney uptake also covered a broad range of 2.33% ID/g for ^{11}In-**TA138** to 16.0% ID/g for ^{99m}Tc-

Scheme 8. Synthesis of DOTA Conjugates 54 and 57[a]

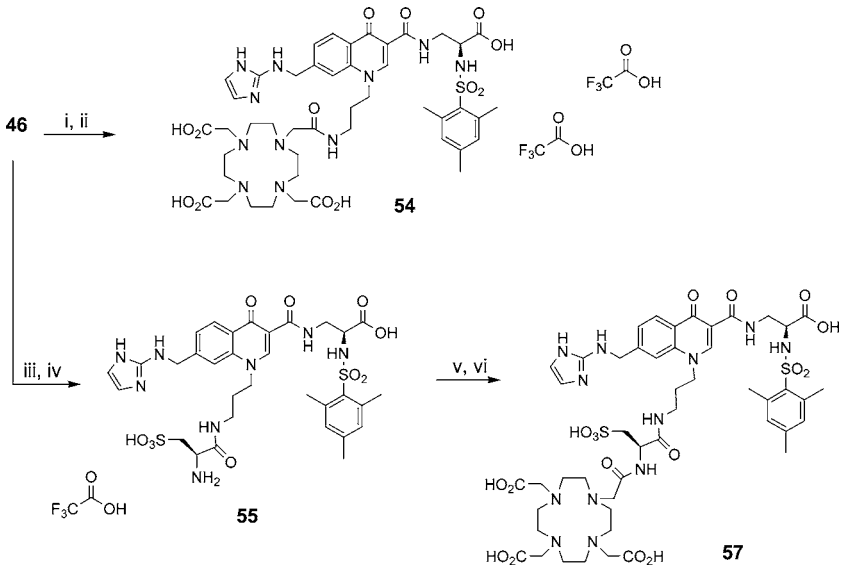

[a] Reagents: i) DOTA(O*t*-Bu)$_3$-OH, HBTU, DIEA, DMF; ii) TFA, Et$_3$SiH, 70 °C, 59%; iii) Boc- Csa(Na)-OSu, DIEA, DMF, 67.9%; iv) TFA, DCM, 99.5%; v) DOTA(O*t*-Bu)$_3$-OH, HBTU, DIEA, DMF, 68%; vi) TFA, Et$_3$SiH, 70 °C, 76%.

Table 1. In Vitro Receptor Affinity of Quinolin-4-one−Chelator Conjugates

	IC$_{50}$, nM (± SEM)[a]				
compd	$\alpha_v\beta_3$ (ELISA)	$\alpha_v\beta_3$ (293β_3)	$\alpha_{IIb}\beta_3$ (PRP[b])	$\alpha_v\beta_5$ (SKB)	$\alpha_5\beta_1$ (Jurkat)
SH066[c]	ND[d]	11 ± 3	2000	2100	>10000
10	3.0		>10000	>1000	>10000
12	2.0		4348		
TA138[c]	1.0	12 ± 3	>10000	>10000	>10000
^{89}Y-**TA138**[c]	ND[d]	18 ± 5	37000	11300 ± 1300	40300 ± 8700
36	ND[d]	140 ± 21			
29	ND[d]	27 ± 5		6700 ± 1200	>10000
47	3.0		>10000		>10000
52	0.5		2800 ± 600		2600 ± 400
54	0.7		7900 ± 1500	>1000	>10000
57	0.4		8150 ± 1100		

[a] Performed in triplicate. [b] Platelet rich plasma. [c] See ref 31. [d] Not determined.

52. Lung activity was low for all agents except ^{99m}Tc-**52**, which, at 37.4% ID/g, was more than 9-fold higher than the next highest compound.

DISCUSSION

Chemistry. Our goal in this program was to develop radiopharmaceuticals capable of delivering useful quantities of imageable and therapeutic radionuclides to tumors. The choice of a radionuclide chelator was guided by our desire to use a single targeting platform for both imaging and radiotherapeutic applications. This led us to the macrocyclic chelator DOTA as our principle chelator. In this way a complex with an imageable isotope (e.g., ^{111}In) could be used to accurately predict the biodistribution of a complex with a nonimageable therapeutic isotope (e.g., ^{90}Y). This strategy has recently been confirmed in a bioequivalence study comparing ^{111}In and ^{90}Y complexes of receptor $\alpha_v\beta_3$ antagonist−DOTA conjugates (*46*). The radionuclide having the most useful nuclear properties for SPECT imaging is ^{99m}Tc, which, unfortunately, does not form stable complexes with DOTA. 6-Hydrazinylnicotinic acid (HYNIC) is one of the best chelators for ^{99m}Tc, forming stable complexes with a variety of coligands in aqueous solutions at very low ligand concentrations (*49*). We therefore also prepared a small number of HYNIC conjugates, and evaluated them as the ternary ^{99m}Tc complexes using tricine and TPPTS as coligands. Complexes in this report represented as ^{99m}Tc-**XX** are understood to be these ternary complexes. Second, DOTA and HYNIC complexes have very different structures (see Figure 1), suggesting the possibility that they may exhibit very different biodistribution and pharmacokinetic properties. The HYNIC conjugates were synthesized with the hydrazinyl group protected as a hydrazone of 2-formylbenzenesulfonic acid. We have previously shown that such hydrazones prevent reaction of HYNIC conjugates with trace quantities of aldehydes and ketones found in the research and manufacturing environment (*37*). The hydrazone protecting group is spontaneously hydrolyzed during the radiolabeling procedure. The sulfonic acid group is not essential to this protection strategy but serves to improve water solubility in the radiolabeling solution.

The use of an α-*N*-(arylsulfonyl)diaminopropanoic acid unit as a carboxylate mimetic is a common structural theme in vitronectin receptor antagonist research. The *N*-methylquinolin-4-one system reported by Wityak and co-workers (*30*, *36*) employs DAP phenylsulfonamide and DAP biphenylsulfonamide carboxylate mimetics as shown in Figure 1. The presence of the phenyl group at the 4-position of the phenylsulfonamide did not impart an increase in affinity for $\alpha_v\beta_3$ or any increased selectivity versus other integrins when compared to the phenylsulfonamides. However, it suggested to us that the 4-position would be an ideal site at which to place a radionuclide−chelator complex. In addition, the biphenyl system suggested a synthetically easy route into a tethered analogue of **SH066**. Using biphenyl-4,4′-disulfonyl chloride and PEG diamine **2**, we were able to assemble the tethered DAP arylsulfonamide in a single-

Table 2. Biodistribution of Radiolabeled Receptor $\alpha_v\beta_3$ Antagonists, c-neu Oncomouse Mammary Adenocarcinoma Model at 2 h (PI)

	organ uptake expressed as % ID/g (± SEM)[a]							
	^{99m}Tc-Hynic complexes[b]			^{111}In-DOTA complexes[c]				
organ	**10**	**47**[d]	**52**	**12**	**TA138**[e,f]	**54**	**57**	**36**[g]
blood	1.28 (0.18)	1.28	3.85 (0.15)	4.46 (0.65)	0.54 (0.04)	1.82 (0.29)	1.35 (0.20)	0.41 (0.04)
eyes	0.35 (0.05)	0.32	0.43 (0.08)	0.40 (0.10)	0.42 (0.03)	0.52 (0.04)	0.34 (0.11)	0.32 (0.04)
muscle	1.16 (0.38)	0.61	0.97 (0.05)	0.79 (0.06)	0.55 (0.11)	0.74 (0.24)	0.89 (0.42)	0.46 (0.15)
liver	2.74 (0.25)	7.10	2.12 (0.12)	3.61 (0.51)	1.94 (0.11)	1.34 (0.16)	1.98 (0.18)	2.00 (0.18)
kidney	3.63 (0.28)	4.37	16.0 (0.57)	9.86 (1.11)	2.33 (0.14)	6.08 (0.78)	4.04 (0.48)	4.46 (0.99)
bile	2.42 (1.14)	354	0.20 (0.02)	ND[h]	0.55 (0.14)	7.30 (0.88)	1.86 (0.01)	0.36 (0.11)
spleen	2.30 (0.36)	2.37	2.08 (0.58)	2.46 (0.45)	1.80 (0.22)	1.27 (0.20)	2.34 (0.37)	3.17 (0.50)
heart	0.63 (0.09)	0.94	1.58 (0.13)	1.15 (0.10)	0.68 (0.05)	0.96 (0.15)	0.90 (0.13)	0.66 (0.06)
lung	2.17 (0.80)	2.84	37.4 (3.01)	2.53 (0.41)	2.74 (0.40)	2.34 (0.38)	3.17 (0.47)	3.94 (0.49)
urine	126 (8.73)	190.2	78.0 (65.0)	212 (56.4)	233 (61.8)	160 (64.0)	424 (253)	499 (51.0)
stomach	3.19 (0.35)	2.13	1.23 (0.41)	1.55 (0.26)	2.23 (0.21)	1.36 (0.23)	2.99 (0.75)	3.49 (0.79)
colon	3.25 (0.69)	5.47	2.36 (0.11)	1.86 (1.06)	3.84 (0.64)	2.90 (0.47)	6.10 (1.28)	8.59 (0.73)
uterus	ND[h]	5.91	7.64 (1.77)	4.05 (0.74)	4.70 (0.74)	5.68 (0.51)	10.1 (2.14)	9.36 (1.40)
bone	ND[h]	ND[h]	ND[h]	1.50 (0.16)	1.56 (0.19)	1.03 (0.18)	1.22 (0.06)	2.29 (0.29)
tumor	7.50 (0.98)	9.55	8.35 (0.54)	2.95 (0.78)	9.39 (0.62)	6.63 (0.71)	11.8 (1.11)	11.5 (1.08)

[a] Values are the average of three animals unless noted otherwise. [b] Ternary complexes with tricine and TPPTS coligands as shown in Figure 1, 2 mCi/Kg. [c] 2 mCi/Kg. [d] $N = 1$. [e] $N = 7$. [f] See ref 31. [g] Lu-177 complex, 2 mCi/Kg. [h] Not determined.

vessel, two-step condensation procedure, as shown in Scheme 1. With the proper molar ratios of reactants and careful control of addition, we were able to achieve a 59% purified yield of **4**, after removal of the Boc group. The condensation of **4** with quinolin-4-one carboxylic acid **5** used standard HBTU coupling conditions to give a 50% purified yield of **6**. All protecting groups were removed prior to conjugation with HYNIC. This strategy was guided by the concern that the hydrazone protecting group on HYNIC would react under the deprotection conditions. Reaction of fully deprotected tethered quinolin-4-one (**8**) with HYNIC succinimide ester **9** gave a 20% yield of **10** after purification. The reasons for the low yield are not fully understood, but it was observed by LC/MS that succinimide ester **9** reacts with **8** to give a transient *N*-acylimidazole byproduct.

The DOTA analogue of **10** was prepared by the procedures shown in Scheme 2. The trityl and Cbz protecting groups were removed from compound **6** using TFA/Et_3SiH, but the methyl ester was left intact for the conjugation reaction with DOTA tri-*tert*-butyl ester. Again, we saw evidence by LC/MS for the formation of *N*-acylimidazole byproducts during the conjugation reaction. In addition, the ester saponification was not as clean as we had come to expect with this system. The overall yield of DOTA conjugate **12** after final deprotection and purification was only 15%. The optimum deprotection/chelator conjugation strategy was realized with **TA138**, as described in Scheme 3.

While the DAP biarylsulfonamides described above offered a synthetically easy means of introducing a radionuclide complex, we felt that phenylsulfonamides such as **SH066** might provide improved biodistribution and pharmacokinetic properties because of their lower lipophilicity. In addition, we felt that our original use of a simple PEG tether as a pharmacokinetic modifier (PKM) provided only a small reduction in lipophilicity, and cysteic acid was selected as a second generation PKM. The high polarity of the sulfonic acid group offers a much larger PKM effect than PEG tethers, and because it is an unnatural amino acid it is less likely to undergo metabolic degradation. In addition, cysteic acid does not require side chain protection during conjugation reactions. This can increase solubility in the dipolar aprotic solvents typically used in amide bond forming reactions, as well as in the mobile phases used in reverse-phase HPLC.

3,5-Dimethylphenol was converted to carboxylic acid **14** in high yield by a combination of Williamson ether synthesis and ester saponification. Chlorosulfonation of **14** proceeded in high regioselectivity, and the small amount of unwanted isomer was removed by recrystallization from $CHCl_3$ to give a 41% yield of the desired chlorosulfonation product (**15**). This compound slowly decomposes, even when stored desiccated in the freezer, and should be used within a few days or weeks. Reaction of **15** with (*S*)-methyl 2-amino-3-(*tert*-butoxycarbonylamino)propanoate gave a 29% yield of DAP sulfonamide **16**. This reaction was very sensitive to reaction conditions, and considerable effort was expended investigating parameters such as reaction temperature, mode and rate of addition of reactants, and base used to neutralize the HCl byproduct. The principle side reaction observed was bis-conjugate **58** shown in Figure 2. Presumably this forms as a result of exchange of chloride between the sulfonyl and carboxyl groups. Curiously, we did not observe mono-conjugate **59**. Conversion of **16** to **19** proceeded in high yield. For the remaining conjugation and deprotection reactions, we elected to leave the trityl imidazole-protecting group in place but remove the methyl ester. This decision was based in part on our experiences with **10** and **12** but also on a preliminary experiment, not shown here, in which ester saponification was carried out after conjugation of the two cysteic acids and DOTA. This resulted in the formation of multiple, closely spaced, isomeric product peaks on LC/MS analysis. Presumably, these

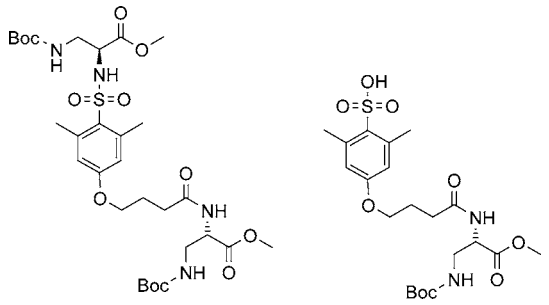

58 **59**

Figure 2. Side product **58**, formed during the synthesis of DAP arylsulfonamide **16**.

isomers are the result of epimerization at the DAP and cysteic acid residues. The two cysteic acids were added to **21** in stepwise fashion by preactivation with PyBOP to give **24** in 74% overall yield. Conjugation to DOTA tri-*tert*-butyl ester proceeded in 76% yield, and final global deprotection and purification gave a 95% yield of **TA138**.

Intermediate **24** was fully deprotected, and the resulting amine was used to prepare the HYNIC analogue of **TA138** as shown in Scheme 4. An initial conjugation reaction with HYNIC succinimide ester **9**, not shown, gave no reaction. We hypothesized that this was due to electronic repulsion between the sulfonate side chains of the cysteic acid residues and the sulfonate group on the HYNIC hydrazone. Replacing succinimide ester **9** with the more reactive HOBt ester formed by preactivation with PyBOP produced a slow conjugation reaction and a 32% isolated yield of **29**.

3-Phosphonoalanine also appeared to have great potential as a PKM. Like cysteic acid it is highly hydrophilic and is an unnatural amino acid. Lohse and Felber have shown that 3-(bis-(allyloxy)phosphono)alanine can be incorporated into peptides using standard Fmoc solid-phase synthesis methodology (*41*). Incorporation of 3-phosphonoalanine by our existing synthetic strategies required the analogous Boc-protected amino acid (**30** in Scheme 5). An Arbuzov reaction between *N*-(*tert*-butoxycarbonyl)-L-serine β-lactone and diallyl(trimethylsilyl)phosphite gave **30** in 19% yield. Two of these PKMs were incorporated into intermediate **21** in 69% yield using chemistry completely analogous to that used to prepare **TA138**. Conjugation to DOTA tri-*tert*-butyl ester was accomplished in 29% yield, and the final two-step deprotection to remove the trityl, Boc, and allyl groups gave a 20% purified yield of **36**. To our knowledge this is the first example of a phosphonic acid being introduced into a radiopharmaceutical for the sole purpose of modifying pharmacokinetics.

The original SAR of the quinolin-4-one class of vitronectin receptor antagonists used the same *N*-methylquinolin-4-one template for all compounds in the series. Variation at the quinolin-4-one ring nitrogen was not examined. However, a comparison of the structure of **SH066** with other classes of integrin $\alpha_v\beta_3$ antagonists suggested that receptor $\alpha_v\beta_3$ would tolerate radionuclide-chelator complexes on the quinolin-4-one ring nitrogen. Synthetically, this was a less attractive option than use of the arylsulfonamide position because the tether is locked in very early in the synthesis, thus limiting the ability to quickly examine alternate tethers. But having two potential sites of derivatization was viewed as a distinct advantage of the quinolin-4-one class. We chose to use the relatively short aminopropyl tether shown in Scheme 6 as the basis for all compounds in this class. Further elaboration of this tether near the end of the synthesis would allow an examination of parameters such as tether length and lipophilicity while avoiding a lengthy resynthesis.

The aminopropyl tether was introduced by alkylation of **37** using K_2CO_3 and a 6-fold excess of 3-((*tert*-butoxy)carbonylamino)propyl bromide in DMF at 60 °C. The large excess of bromide was required to compensate for the γ-lactamization side-reaction. The remaining steps in the synthesis of **44** followed the procedures as described by Wityak and Tobin (*36*) for the synthesis of the *N*-methylquinolin-4-one system, and yields were good to excellent. Complete deprotection of **44**, followed by conjugation with HYNIC succinimide ester **9**, gave **47** in 75% yield. The effect of tether length was explored by the addition of a *N*-succinimidy-PEG spacer as shown in Scheme 7. The conjugation reactions with both the additional spacer and HYNIC succinimide ester **9** proceeded in moderate yields to give **52**. The syntheses of two DOTA conjugates tethered to the quinolin-4-one ring nitrogen are shown in Scheme 8. Conjugation of DOTA directly to the aminopropyl tether of intermediate **46** gave, after deprotection, **54**, the DOTA analogue of **47**. The effect of a cysteic acid PKM on pharmacokinetics was evaluated by conjugation of Boc-cysteic acid to **46**, followed by conjugation to DOTA to give compound **57**.

Receptor Affinity and Selectivity. The receptor binding properties of the compounds in this study were evaluated in a series of integrin receptor assays that included receptors $\alpha_v\beta_3$, $\alpha_{IIb}\beta_3$, $\alpha_v\beta_5$, and $\alpha_5\beta_1$. Receptor $\alpha_v\beta_3$ affinity was determined in an ELISA assay using isolated vitronectin receptors and in a whole-cell assay using human 293 cells engineered to overexpress the $\alpha_v\beta_3$ receptor. Relative selectivity of antagonism of the $\alpha_v\beta_3$ receptor versus the $\alpha_{IIb}\beta_3$ receptor was determined by comparing these data with the IC_{50} values obtained for inhibition of platelet aggregation in a human platelet-rich-plasma (PRP) assay. Similarly, selectivity versus receptor $\alpha_v\beta_5$ was obtained in a human SKBR3 cell-vitronectin adhesion assay, and selectivity versus receptor $\alpha_5\beta_1$ was obtained in a human lymphocyte (Jurkat cells)-fibronectin adhesion assay. Receptor affinity data for parent quinolin-4-one **SH066**, **TA138**, and ^{89}Y-**TA138** were previously reported (*31*). The data are reproduced in Table 1 to allow comparison with the eight new compounds. The data in Table 1 show that all compounds screened have high affinity for $\alpha_v\beta_3$ in the ELISA assay, with IC_{50} values of 0.4−3.0 nM. Parent quinolin-4-one **SH066** was evaluated in the 293β_3-fibrinogen assay, and by using **TA138** as a crossover point, one can see that tethering the chelators at either the arylsulfonamide or quinolin-4-one ring nitrogen had virtually no effect on $\alpha_v\beta_3$ affinity. This confirmed our original belief that both of these positions would be tolerant of modification and also confirmed that only a short tether is required to avoid steric and electronic interactions between the receptor and the radionuclide chelator. It is especially interesting that the highly charged cysteic acid PKM is well tolerated, despite the use of the relatively short *N*-(2-aminoethyl)-4-oxobutanamide spacer of **TA138** and the even shorter aminopropyl spacer of **57**. All compounds displayed good selectivity for $\alpha_v\beta_3$ versus the other integrin receptors in the panel, with selectivity ranging from a low of 333-fold (compound **10**, $\alpha_v\beta_5$) to a high of 20 375-fold (compound **57**, $\alpha_{IIb}\beta_3$). Receptor affinity of nonradioactive complex ^{89}Y-**TA138** is nearly identical to free ligand **TA138**.

In Vivo Biodistribution. The c-neu Oncomouse mammary adenocarcinoma model was the principle in vivo model used in this study. The c-neu Oncomouse is a spontaneous tumor-bearing mouse that carries an activated c-neu oncogene driven by a mouse mammary tumor virus (MMTV) promoter. Transgenic mice uniformly expressing the MMTV/c-neu gene develop mammary adenocarcinomas 4 to 8 months postpartum that involve the entire epithelium in each gland. The ideal biodistribution and pharmacokinetic profile for a radiopharmaceutical is one of rapid and high uptake in the target tissue, followed by rapid clearance from nontarget tissues, and renal excretion. Such

Table 3. Tumor/Organ Ratios of Radiolabeled Receptor $\alpha_v\beta_3$ Antagonists, c-neu Oncomouse Mammary Adenocarcinoma Model at 2 h (PI)

	^{99m}Tc-Hynic complexes[a]			^{111}In-DOTA complexes[b]				
organ	**10**	**47**	**52**	**12**	**TA138**	**54**	**57**	**36**[c]
blood	5.86	7.45	2.17	0.661	17.4	3.64	8.73	28.4
eyes	21.4	30.0	19.3	7.38	22.4	12.8	34.7	35.8
muscle	6.47	15.6	8.59	3.73	17.1	8.90	13.2	24.8
liver	2.74	1.35	3.94	0.817	4.83	4.94	5.96	5.77
kidney	2.07	2.18	0.522	0.299	4.04	1.09	2.92	2.58
bile	3.10	0.023	41.5	ND[d]	17.1	0.908	6.32	31.8
spleen	3.26	4.02	4.01	1.20	5.21	5.24	5.02	3.63
heart	11.9	10.2	5.28	2.56	13.8	6.92	13.2	17.4
lung	3.46	3.36	0.223	1.17	3.43	2.83	3.72	2.93
stomach	2.35	4.49	6.79	1.90	4.22	4.89	3.94	3.30
colon	2.31	1.75	3.54	1.59	2.45	2.29	1.93	1.34
uterus	ND[d]	1.62	1.09	0.728	2.00	1.17	1.16	1.23
bone	ND[d]	ND[d]	ND[d]	1.97	6.01	6.45	9.68	5.04

[a] Ternary complexes with tricine and TPPTS coligands as shown in Figure 1, 2 mCi/kg. [b] 2 mCi/kg. [c] Lu-177 complex, 2 mCi/kg. [d] Not determined.

a profile minimizes radiation burden to the patient while minimizing background signal in imaging studies. All agents in this study showed rapid clearance from the general musculature, heart, eyes, spleen, bone, and stomach, and differences in total tracer uptake in these organs were small (Table 2). Blood clearance was generally fast for all agents with blood levels at 2 h PI in the range of 0.54% ID/g for ^{111}In-**TA138** to 4.46% ID/g for ^{111}In-**12**. Tumor uptake ranged from a low value of 2.95% ID/g for ^{111}In-**12** to a high of 11.8% ID/g for ^{111}In-**57**. Kidney uptake in the current study ranged from a low of 2.33% ID/g for ^{111}In-**TA138** to a high of 16.0% ID/g for ^{99m}Tc-**52**. Using tracer levels in tumor, blood, and kidney, we eliminated ^{99m}Tc-**52** (high kidney and blood), ^{111}In-**12** (high kidney and blood, low tumor), and ^{111}In-**54** (high kidney) from further consideration. The very high lung uptake of ^{99m}Tc-**52** (37.4% ID/g) was interesting and quite unexpected. Why the addition of the *N*-succinimidyl-PEG spacer to ^{99m}Tc-**47** should produce such a spike in lung uptake is unknown. The very high liver and bile uptake of ^{99m}Tc-**47** was sufficient to eliminate it from further consideration, while ^{99m}Tc-**10** was eliminated based on slightly higher liver and bile uptake, and tumor uptake lower than the remaining agents. The three remaining agents are all DOTA complexes, and they all have anionic PKMs (cysteic acid for ^{111}In-**TA138** and ^{111}In-**57**, and the phosphonic acid isostere of aspartic acid for ^{111}In-**36**). The failure of the radiolabeling of **29**, the HYNIC analogue of **TA138**, prevented us from assessing the relative contribution of the chelators and PKMs on biodistribution and pharmacokinetics. There is little question that the anionic PKMs in this study increase the hydrophilicity of these agents, and we believe they also contribute to lower kidney uptake. The average kidney uptake for these three agents (3.61% ID/g) is lower than the average for the entire group of DOTA complexes (5.35% ID/g) and also lower than the average of all agents in this study (6.21% ID/g). It has been reported that negatively charged molecules exhibit reduced renal uptake as a result of reduced nonspecific binding on the negatively charged membranes of renal tubular cells (*50*). The three remaining agents show excellent tumor uptake of 9.39% ID/g for ^{111}In-**TA138**, 11.8% ID/g for ^{111}In-**57**, and 11.5% ID/g for ^{111}In-**36**. While the absolute tumor uptake of ^{111}In-**TA138** is slightly lower than in the other two agents, ^{111}In-**TA138** is considered to be superior based on lower absolute uptake in kidneys, stomach, colon, and uterus and better tumor/organ ratios for these nontarget organs. See Table 3 for all tumor/organ ratios. The kidney uptake is especially important because this is considered to be the critical nontarget organ in therapeutic applications of these agents. The excellent biodistribution properties of ^{111}In-**TA138** are confirmed visually in the scintigraphic images shown in Figure 3. The images were acquired using a previously published procedure (*31*). Even relatively small tumors are clearly visible 2 h pi. The rapid clearance of background activity and the generally low level of activity in the GI track are also apparent in the images.

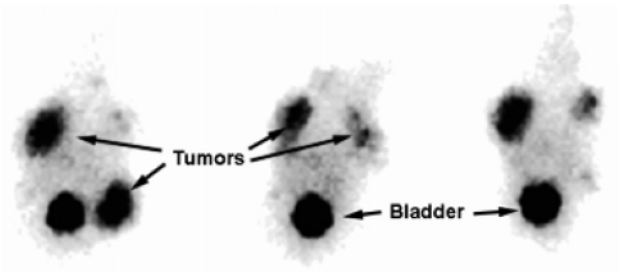

Figure 3. Representative scintigraphic images of ^{111}In-**TA138**, 2 mCi/Kg, c-neu Oncomouse mammary adenocarcinoma model, 2 h pi.

CONCLUSIONS

In the present work we have described synthetic methodology for tethering radionuclide−chelator complexes to two different positions on the quinolin-4-one class of receptor $\alpha_v\beta_3$ antagonists. A panel of integrin receptor affinity assays have shown that both of these positions, the para position of the DAP arylsulfonamide and the quinolin-4-one ring nitrogen, are very tolerant of derivatization, with no loss of receptor $\alpha_v\beta_3$ affinity and no loss of selectivity versus three other integrin receptors. Introduction of anionic, hydrophilic PKMs such as cysteic acid leads to a hydrophilic tracer with increased blood clearance and lower uptake in nontarget organs, without a reduction in tumor uptake. The complex ^{111}In-**TA138** is the superior imaging agent in this study, providing the best combination of tumor uptake and tumor/organ ratios. ^{111}In-**TA138** may be a valuable tool in patient selection, staging of disease, and the monitoring of therapy for solid tumors throughout the body.

ACKNOWLEDGMENT

The authors thank Jeffrey Bogart, John Pietryka, and Neal Williams for analytical support.

LITERATURE CITED

(1) van der Flier, A., and Sonnenberg, A. (2001) Function and Interactions of Integrins. *Cell Tissue Res. 305*, 285−298.
(2) Mizeiewski, G. J. (1999) Role of Integrins in Cancer: Survey of Expression Patterns. *Proc. Soc. Exp. Biol. Med. 222*, 124−138.
(3) Hood, J. D., and Cheresh, D. A. (2002) Role of Integrins in Cell Invasion and Migration. *Nat. Rev. Cancer 2*, 91−100.
(4) Tucker, G. C. (2002) Inhibitors of Integrins. *Curr. Opin. Pharm. 2*, 394−402.
(5) Clark, R. A., Tonnesen, M. G., Gailit, J., and Cheresh, D. A. (1996) Transient Functional Expression of $\alpha_v\beta_3$ on Vascular Cells During Wound Repair. *Am. J. Pathol. 148*, 1407−1421.
(6) Max, R., Gerritsen, R. R. C. M., Nooijen, P. T. G. A., Goodman, S. L., Sutter, A., Keilholz, U., Ruiter, D. J., and De Waal, M. W. (1997) Immunohistochemical Analysis of Integrin $\alpha_v\beta_3$ Expression on Tumor-Associated Vessels of Human Carcinomas. *Int. J. Cancer 71*, 320−324.
(7) Christofidou-Solomidou, M., Bridges, M., Murphy, G. F., Albelda, S. M., and DeLisser, H. M. (1997) Expression and Function of Endothelial Cell α_v Integrin Receptors in Wound-Induced Human Angiogenesis in Human Skin/SCID Mice Chimeras. *Am. J. Pathol. 151*, 975−983.
(8) Coleman, P. J., and Duong, L. T. (2002) Ligands to the Integrin Receptor $\alpha_v\beta_3$. *Expert Opin. Ther. Pat. 12*, 1009−1021.
(9) Brooks, P. C., Montgomery, M. P., Rosenfeld, M., Reisfeld, R. A., Hu, T., Klier, G., and Cheresh, D. A. (1994) Integrin $\alpha_v\beta_3$ Antagonists Promote Tumor Regression by Inducing Apoptosis of Angiogenic Blood Vessels. *Cell 79*, 1157−1164.

(10) Brooks, P. C., Stõmblad, S., Klemke, R., Visscher, D., Sarkar, F. H., and Cheresh, D. A. (1995) Anti-integrin $\alpha_v\beta_3$ Blocks Human Breast Cancer Growth and Angiogenesis in Human Skin. *J. Clin. Invest. 96*, 1815−1822.

(11) Kerr, J. S., Wexler, R. S., Mousa, S. A., Robinson, C. S., Wexler, E. J., Mohamed, S., Voss, M. E., Devenny, J. J., Czerniak, P. M., Gudzelak, A., Jr., and Slee, A. M. (1999) Novel Small Molecule α_v Integrin Antagonists: Comparative Anti-Cancer Efficacy with Known Angiogenesis Inhibitors. *Anticancer Res. 19*, 959−968.

(12) Kumar, C. C., Malkowski, M., Yin, Z., Tanghetti, E., Yaremko, B., Nechuta, T., Varner, J., Liu, M., Smith, E. M., Neustadt, B., Presta, M., and Armstrong, L. (2001) Inhibition of Angiogenesis and Tumor Growth by SCH221153, a Dual $\alpha_v\beta_3$ and $\alpha_v\beta_5$ Integrin Receptor Antagonist. *Cancer Res. 61*, 2232−2238.

(13) Kerr, J. S., Mousa, S. A., and Slee, A. M. (2001) $\alpha_v\beta_3$ Integrin in Angiogenesis and Restenosis. *Drug News Perspect. 14*, 143−150.

(14) Reynolds, L. E., Wyder, L., Lively, J. C., Taverna, D., Robinson, S. D., Huang, X., Sheppard, D., Hynes, R. O., and Hodivala-Dilke, K. M. (2002) Enhanced Pathological Angiogenesis in Mice Lacking β_3 Integrin or β_3 and β_5 Integrins. *Nat. Med. 8*, 27−34.

(15) Mizejewski, G. J. (1999) Role of Integrins in Cancer: Survey of Expression Patterns. *Proc. Soc. Exp. Biol. Med. 222*, 124−138.

(16) Liapis, H., Flath, A., and Kitazawa, S. (1996) Integrin $\alpha_v\beta_3$ Expression by Bone-Residing Breast Cancer Metastases. *Diag. Mol. Pathol. 5*, 127−135.

(17) Wechsel, H. W., Petri, E., Feil, G., Nelde, H. J., Bichler, K. H., and Loesr, W. (1999) Renal Cell Carcinoma: Immunohistological Investigation of Expression of the Integrin $\alpha_v\beta_3$. *Anticancer Res. 19*, 1529−1532.

(18) Zheng, D., Woodard, A. S., Fornaro, M., Tallini, G., and Languino, L. R. (1999) Prostatic Carcinoma Cell Migration via Integrin $\alpha_v\beta_3$ Is Modulated by a Focal Adhesion Kinase Pathway. *Cancer Res. 59*, 1655−1664.

(19) Haubner, R., Wester, H.-J., Burkhart, F., Senekowitsch-Schmidtke, R., Weber, W., Goodman, S. L., Kessler, H., and Schwaiger, M. (2001) Glycosylated RGD-Containing Peptides: Tracer for Tumor Targeting and Angiogenesis Imaging with Improved Biokinetics. *J. Nucl. Med. 42*, 326−336.

(20) Haubner, R., Kuhnast, B., Mang, C., Weber, W. A., Kessler, H., Wester, H.-J., and Schwaiger, M. (2004) [^{18}F]Galacto-RGD: Synthesis, Radiolabeling, Metabolic Stability, and Radiation Dose Estimates. *Bioconjugate Chem. 15*, 61−69.

(21) van Hagen, P. M., Breeman, W. A. P., Bernard, H. F., Schaar, M., Mooij, C. M., Srinivasan, A., Schmidt, M. A., Krenning, E. P., and de Jong, M. (2000) Evaluation of a Radiolabeled Cyclic DTPA-RGD Analogue for Tumor Imaging and Radionuclide Therapy. *Int. J. Cancer 8*, 186−198.

(22) Rajopadhye, M., Harris, A. R., Nguyen, H., Overoye, K. L., Bartis, J., Edwards, D. S., Liu, S., Onthank, D., and Barrett, J. A. (2000) The Synthesis and Evaluation of the ^{99m}Tc and ^{111}In Complexes of Cyclic RGD Peptide Antagonists of the Integrin $\alpha_v\beta_3$. *J. Nucl. Med. 41*, 259P.

(23) Janssen, M., Oyen, W. J. G., Massuger, L. F. A. G., Frielink, C., Dijkgraaf, I., Edwards, D. S., Radjopadhye, M., Corstens, F. H. M., and Boerman, O. C. (2002) Comparison of a Monomeric and Dimeric Radiolabeled RGD-Peptide for Tumor Targeting. *Cancer Biother. Radiopharm. 17*, 641−646.

(24) Haubner, R., and Wester, H.-J. (2004) Radiolabeled Tracers for Imaging of Tumor Angiogenesis and Evaluation of Anti-Angiogenic Therapies. *Curr. Pharm. Des. 10*, 1439−1455.

(25) Kerr, J. S., Slee, A. M., and Mousa, S. A. (2000) Small Molecule α_v Integrin Antagonists: Novel Anticancer Agents. *Exp. Opin. Invest. Drugs 9*, 1271−1279.

(26) Duggan, M. E., and Hutchinson, J. H. (2000) Ligands to the Integrin Receptor $\alpha_v\beta_3$. *Exp. Opin. Ther. Pat. 10*, 1367−1383.

(27) Miller, W. H., Keenan, R. M., Willette, R. N., and Lark, M. W. (2000) Identification and in vivo Efficacy of Small-Molecule Antagonists of Integrin $\alpha_v\beta_3$ (the Vitronectin Receptor). *Drug Discuss. Today 5*, 397−408.

(28) Pitts, W. J., Wityak, J., Smallheer, J. M., Tobin, W., Jetter, J. W., Buynitsky, J. S., Harlow, P. P., Solomon, K. A., Corjay, M. H., Mousa, S. A., Wexler, R. R., and Jadhav, P. K. (2000) Isoxazolines as Potent Antagonists of the Integrin $\alpha_v\beta_3$. *J. Med. Chem. 43*, 27−40.

(29) Henry, C., Moitessier, N., and Chapleur, Y. (2002) Vitronectin Receptor − $\alpha_v\beta_3$ Integrin − Antagonists: Chemical and Structural Requirements for Activity and Selectivity. *Mini Rev. Med. Chem. 2*, 531−542.

(30) Wityak, J. Personal communication.

(31) Harris, T. D., Kalogeropoulos, S., Nguyen, T., Liu, S., Bartis, J., Ellars, C., Edwards, D. S., Onthank, D., Silva, P., Yalamanchili, P., Robinson, R., Lazewatsky, J., Barrett, J., and Bozarth, J. (2003) Design, Synthesis, and Evaluation of Radiolabeled Integrin $\alpha_v\beta_3$ Receptor Antagonists for Tumor Imaging and Radiotherapy. *Cancer Biother. Radiopharm. 18*, 627−641.

(32) Winter, P. M., Caruthers, S. D., Kassner, A., Harris, T. D., Chinen, L. K., Allen, J. S., Lacy, E. K., Zhang, H., Robertson, J. D., Wickline, S. A., and Lanza, G. M. (2003) Molecular Imaging of Angiogenesis in Nascent Vx-2 Rabbit Tumors Using a Novel $\alpha_v\beta_3$−Targeted Nanoparticle and 1.5 T Magnetic Resonance Imaging. *Cancer Res. 63*, 5838−5843.

(33) Schmieder, A. H., Winter, P. M., Caruthers, S. D., Harris, T. D., Williams, T. A., Allen, J. S., Lacy, E. K., Zhang, H., Scott, M. J., Hu, G., Robertson, J. D., Wickline, S. A., and Lanza, G. M. (2005) Molecular MR Imaging of Melanoma Angiogenesis with $\alpha_v\beta_3$−Targeted Paramagnetic Nanoparticles. *Magn. Reson. Med. 53*, 621−627.

(34) Sadeghi, M. M., Krassilnikova, S., Zhang, J., Gharaei, A. A., Fassaei, H. R., Esmailzadeh, L., Kooshkabadi, A., Edwards, S., Yalamanchili, P., Harris, T. D., Sinusas, A. J., Zaret, B. L., and Bender, J. R. (2004) Detection of Injury-Induced Vascular Remodeling by Targeting Activated $\alpha_v\beta_3$ Integrin In Vivo. *Circulation 110*, 84−90.

(35) Meoli, D. F., Sadeghi, M. M., Krassilnikova, S., Bourke, B. N., Giordano, F. J., Dione, D. P., Su, H., Edwards, D. S., Liu, S., Harris, T. D., Madri, J. A., Zaret, B. L., and Sinusas, A. J. (2004) Noninvasive imaging of myocardial angiogenesis following experimental myocardial infarction. *J. Clin. Invest. 113*, 1684−1691.

(36) Wityak, J., and Tobin, A, E. (1998) Preparation of Novel Integrin Receptor Antagonists. U.S. Patent 6,130,231.

(37) Harris, T. D., Sworin, M., Williams, N., Rajopadhye, M., Damphousse, P. R., Glowacka, D., Poirier, M. J., and Yu, K. (1999) Synthesis of Stable Hydrazones of a Hydrazinonicotinyl-Modified Peptide for the Preparation of ^{99m}Tc-Labeled Radiopharmaceuticals. *Bioconjugate Chem. 10*, 808−814.

(38) Badilescu, I. I. (1975) Heterocyclic compounds. III. Cyclization of Ring-Substituted γ-Phenoxybutyric Acids by PPA [Polyphosphoric Acid] to 2,3-Dihydro-1-benzoxepin-5(4H)-ones. *Rev. Roum. Chim. 20*, 761−774.

(39) Abrams, M. J., Juweid, M., TenKate, C. I., Schwartz, D. A., Hauser, M. M., Gaul, F. E., Fuccello, A. J., Rubin, R. H., Strauss, H. W., and Fischman, A. J. (1990) Technetium-99m-human Polyclonal IgG Radiolabeled via the Hydrazinonicotinamide Derivative for Imaging Focal Sites of Infection in Rats**.** *J. Nucl. Med. 31*, 2022−2028.

(40) Arnold, L. D., Kalantar, T. H., and Vederas, J. C. (1985) Conversion of Serine to Stereochemically Pure β-Substituted α-Amino Acids via β-Lactones. *J. Am. Chem. Soc. 107*, 7105−7109.

(41) Lohse, P. A., and Felber, R. (1998) Incorporation of a Phosphonic Acid Isostere of Aspartic Acid into Peptides Using Fmoc-Solid-Phase Synthesis. *Tetrahedron Lett. 39*, 2067−2070.

(42) Pitts, W. J., Wityak, J., Smallheer, J. M., Tobin, A. E., Jetter, J. W., Buynitsky, J. S., Harlow, P. P., Solomon, K. A., Corjay, M. H., Mousa, S. A., Wexler, R. R., and Jadhav, P. K. (2000) Isoxazolines as Potent Antagonists of the Integrin $\alpha_v\beta_3$. *J. Med. Chem. 43*, 27−40.

(43) Trester-Zedlitz, M., Kamada, K., Burley, S. K., Fenyo, D., Chait, B. T., and Muir, T. W. (2003) A Modular Cross-Linking Approach for Exploring Protein Interactions. *J. Am. Chem. Soc. 125*, 2416−2425.

(44) Hubbuch, A., Danho, W., and Zahn, H. (1979) Synthesis of *N*-Protected Cysteic Acid Derivatives and Their Activated Esters. *Liebigs Ann. Chem.*, 776−783.

(45) Charo, I. F., Nannizzi, F., Smith, J. W., and Cheresh, D. A. (1990) The Vitronectin Receptor $\alpha_v\beta_3$ Binds Fibrinectin and Acts in Concert with $\alpha_5\beta_1$ in Promoting Cellular Attachment and Spreading on Fibronectin. *J. Cell Biol. 111*, 2795−2800.

(46) Onthank, D. C., Liu, S., Silva, P. J., Barrett, J. A., Harris, T. D., Robinson, S. P., and Edwards, D. S. (2004) ^{90}Y and ^{111}In Complexes of a DOTA-Conjugated Integrin $\alpha_v\beta_3$ Receptor Antagonist: Different but Biologically Equivalent. *Bioconjugate Chem. 15*, 235−241.

(47) Liu, S., Harris, T. D., Ellard, C. E., and Edwards, D. S. (2003) Anaerobic ^{90}Y- and ^{177}Lu-Labeling of a DOTA-Conjugated Nonpeptide Vitronectin Receptor Antagonist. *Bioconjugate Chem. 14*, 1030−1037.

(48) Currie, L. A. (1968) Limits for Qualitative Detection and Quantitative Determination. *Anal. Chem. 40*, 586−593.

(49) Edwards, D. S., Liu, S., Barrett, J. A., Harris, A. R., Looby, R. J., Ziegler, M. C., Heminway, S. J., and Carroll, T. R. (1997) New and Versatile Ternary Ligand System for Technetium Radiopharmaceuticals: Water Soluble Phosphines and Tricine as Coligands in Labeling a Hydrazinonicotinamide-Modified Cyclic Glycoprotein IIb/IIIa Receptor Antagonist with ^{99m}Tc. *Bioconjugate Chem. 8*, 146−154.

(50) Behr, T. M., Goldenberg, D. M., and Becker, W. (1998) Reducing the Renal Uptake of Radiolabeled Antibody Fragments and Peptides for Diagnosis and Therapy: Present Status, Future Prospects and Limitations. *Eur. J. Nucl. Med. 25*, 201−212.

BC060063S

Transferrin-Loaded *nido*-Carborane Liposomes: Tumor-Targeting Boron Delivery System for Neutron Capture Therapy

Yusuke Miyajima,[†] Hiroyuki Nakamura,*[,†] Yasuhiro Kuwata,[‡] Jong-Dae Lee,[†] Shinichiro Masunaga,[§] Koji Ono,[§] and Kazuo Maruyama*[,‡]

Department of Chemistry, Faculty of Science, Gakushuin University, Tokyo 171-8588, Department of Biopharmaceutics, School of Pharmaceutical Science, Teikyo University, Kanagawa 199-0195, and Research Reactor Institute, Kyoto University, Osaka 590-0494, Japan. Received March 13, 2006; Revised Manuscript Received July 8, 2006

The *nido*-carborane lipid **2** as a double-tailed boron lipid was synthesized from heptadecanol in five steps. The lipid **2** formed stable liposomes at 25% molar ratio toward DSPC with cholesterol. Transferrin was able to be introduced on the surface of boron liposomes (Tf(+)−PEG−CL liposomes) by the coupling of transferrin to the PEG−CO_2H moieties of Tf(−)−PEG−CL liposomes. The biodistribution of Tf(+)−PEG−CL liposomes, in which ^{125}I-tyraminyl inulins were encapsulated, showed that Tf(+)−PEG−CL liposomes accumulated in tumor tissues and stayed there for a sufficiently long time to increase tumor/blood concentration ratio, although Tf(−)−PEG−CL liposomes were gradually released from tumor tissues with time. A boron concentration of 22 ppm in tumor tissues was achieved by the injection of Tf(+)−PEG−CL liposomes at 7.2 mg/kg body weight boron in tumor-bearing mice. After neutron irradiation, the average survival rate of mice not treated with Tf(+)−PEG−CL liposomes was 21 days, whereas that of the treated mice was 31 days. Longer survival rates were observed in the mice treated with Tf(+)−PEG−CL liposomes; one of them even survived for 52 days after BNCT.

INTRODUCTION

Boron neutron capture therapy (BNCT) was first proposed as a binary approach to cancer treatment in 1936 (*1*). This therapy is based on the capture reaction of thermal neutrons using nonradioactive ^{10}B, which produces an α-particle and a lithium-7 nuclei ion with approximately 2.4 MeV. These high-linear-energy transfer particles dissipate their kinetic energy before traveling one cell diameter (5−9 μm) in biological tissues, ensuring their potential for precise cell killing (*2*−*4*). Their destructive effect is highly observed in boron-loaded tissues. Therefore, the successful treatment of cancer by BNCT demands the selective and marked accumulation of ^{10}B in malignant tumor tissues. The amount of ^{10}B required to obtain fatal tumor cell damage has been calculated to be more than 30 μg/g of tumor tissue, owing to the low contact probability between thermal neutrons and ^{10}B (*5*). Therefore, the marked accumulation and selective delivery of boron into tumor tissues are the most important requirements to achieve an effective BNCT of cancers. Although mercaptoundecahydrododecaborate (BSH) (*6*, *7*) and L-4-dihydroxyboronylphenylalanine (L-BPA) (*8*, *9*) have been utilized for BNCT, new boron-10 carriers that deliver an adequate concentration of ^{10}B atoms to tumors should be developed to achieve a potent and extensive cancer therapy (*10*). Recent promising approaches that meet this requirement entail the use of small boron molecules (*2*) and boron-conjugated biological complexes, such as monoclonal antibodies (*11*−*17*), epidermal growth factors (*18*−*21*), and carborane oligomers (*22*−*26*).

We have developed a new type of target-sensitive liposome-bearing polyethylene glycol (PEG), in which antibodies or specific ligands are coupled with PEG chains (*27*−*33*). PEG units have a heightened effect of a prolonged residence time in the circulation and escaping ability from reticulo-endothelial-system (RES) uptake (*34*, *35*), resulting in an enhanced vascular permeability in solid tumor tissues (*36*). Furthermore, transferrin (Tf)-loaded PEG liposomes are internalized into tumor cells by receptor-mediated endocytosis and taken up into endosome-like intracellular vesicles (*37*). This phenomenon is due to a higher Tf receptor concentration in tumor cells than that in normal cells (*38*−*40*). We have applied the selective delivery by and cell-entry mechanism of Tf−PEG liposomes in the boron delivery system for BNCT. In this system, boron compounds are encapsulated in liposomes and delivered to tumor tissues. Tf−PEG liposomes encapsulating BSH achieve sufficient therapeutic ^{10}B concentrations in solid tumor tissues in colon 26 tumor-bearing mice (e.g., 35.5 μg/g in tumor tissue) and inhibit tumor cell growth (*41*).

As an alternative boron delivery system, a system involving the accumulation of boron in the liposomal bilayer is highly potent, because drugs can be encapsulated into the vacant inner cell of a liposome. Therefore, boron and drugs may be simultaneously delivered to tumor tissues for BNCT and chemotherapy of cancer. Hawthorne and co-workers first introduced *nido*-carborane into the amphiphile **1** as a hydrophilic part (Figure 1) and examined liposomal boron delivery in mice using **1** and distearoylphosphatidylcholine (DSPC) (*42*, *43*). We designed the *nido*-carborane lipid **2** (CL), which has a double-tailed moiety conjugated with *nido*-carborane as a hydrophilic function, and communicated the successful synthesis of **2** (Scheme 1) and the stable vesicle formation determined by transmission electron microscopy analysis (*44*). Here, we developed of transferrin-loaded *nido*-carborane PEG liposomes (Tf(+)−PEG−CL liposomes) from **2** and found that Tf(+)−PEG−CL liposomes accumulate in tumor tissues for a prolonged time in tumor-bearing mice, thereby affecting the survival of such mice after neutron irradiation.

* To whom correspondence should be addressed. Phone: +81-3-3986-0221. Fax: +81-3-5992-1029. E-mail: hiroyuki.nakamura@gakushuin.ac.jp.

[†] Gakushuin University.

[‡] Teikyo University.

[§] Kyoto University.

10.1021/bc060064k CCC: $33.50 © 2006 American Chemical Society
Published on Web 08/10/2006

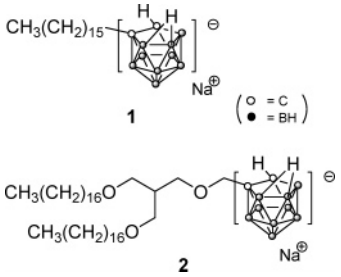

Figure 1. Structures of *nido*-carborane lipids.

Scheme 1[a]

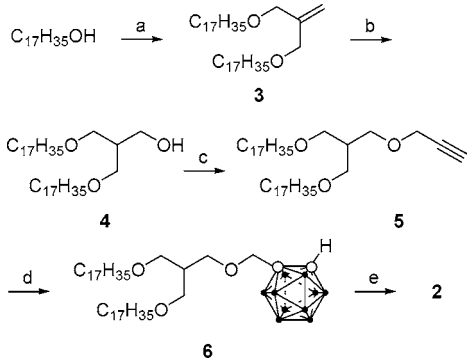

[a] Reagents: (a) (1) NaH, THF, (2) $CH_2{=}C(CH_2Cl)_2$, 93%; (b) (1) $BH_3{\cdot}Me_2S$, (2) H_2O_2, NaOH, 71%; (c) (1) NaH, THF, (2) propargyl bromide, 58%; (d) $B_{10}H_{14}$, CH_3CN, toluene, 80%; (e) NaOMe, MeOH, 57%.

MATERIALS AND METHODS

General. ^{1}H NMR and ^{13}C NMR spectra were measured on JEOL JNM-AL 300 (300 MHz) and VARIAN UNITY-INOVA 400 (400 MHz) spectrometers. Chemical shifts in the ^{1}H and ^{13}C NMR spectra were expressed in parts per million (ppm, δ units), and coupling constant was expressed in units of hertz (Hz). IR spectra were measured on a Shimadzu FTIR-8200A spectrometer. Analytical thin-layer chromatography (TLC) was performed on glass plates (Merck Kieselgel 60 F_{254}, layer thickness 0.2 mm). Column chromatography was performed on silica gel (Merck Kieselgel 70−230 mesh). All reactions were carried out under argon atmosphere using standard Schlenk techniques. Most chemicals and solvents were of analytical grade and used without further purification. Human iron-saturated transferrin (Holo-Tf) was purchased from Sigma. (St. Louis, MO). Distearoylphosphatidylcholine (DSPC) (COATSOME MC-8080), DSPE−PEG−OMe (DSPE-020C), and DSPE−PEG−O−$(CH_2)_5CO_2H$ (DSPE-034GC) were supplied by Nippon Oil and Fats (Tokyo, Japan). The average molecular weights of DSPE-020C and DSPE-034GC were 2136 and 3133, respectively, and their polydispersities were 1.03 and 1.04, respectively, as measured by gel permeation chromatography. ^{125}I-Tyraminyl inulin was synthesized as described previously (*30*, *31*).

3-Heptadecyloxy-2-heptadecyloxymethyl-1-propene (3). To a NaH (16.0 g, 0.34 mol) suspension in THF (100 mL) was added hexadecanol (26.9 g, 0.105 mol) in THF (100 mL) dropwise at 0 °C under Ar. The reaction temperature was increased to room temperature, and the reaction mixture was stirred for 4 h. The mixture was again cooled to 0 °C, and 2-chloromethyl-3-chloro-1-propene (5.5 mL, 47.6 mmol) was added dropwise. The reaction mixture was stirred at room temperature for 1 h and then refluxed for 89 h. The reaction was quenched with saturated aqueous NH_4Cl solution (50 mL), and the mixture was extracted with ether, washed with saturated aqueous NaCl solution, dried over anhydrous $MgSO_4$, and then concentrated. Purification by silica gel column chromatography (hexane/ethyl acetate = 50:1) gave **3** (25.1 g, 44.3 mmol, 93% yield) as a white solid: ^{1}H NMR ($CDCl_3$, 400 MHz) δ 5.14 (s, 2H), 3.94 (s, 4H), 3.38 (t, J = 6.8 Hz, 4H), 1.55 (m, 4H), 1.23 (brs, 56H), 0.86 (t, J = 7.2 Hz, 6H); ^{13}C NMR ($CDCl_3$, 100 MHz) δ 143.3, 113.3, 71.5, 70.6, 31.9, 29.7, 29.7, 29.6, 29.5, 29.4, 26.2, 22.7, 14.1; IR (KBr) 2916, 2848, 2804, 2731, 1666, 1473, 1380, 1109, 1078, 1045, 1010 cm^{-1}; HRMS (ESI) m/z $(M + Na)^+$ calcd for $C_{38}H_{76}O_2Na$ 587.5743, found 587.5795.

3-Heptadecyloxy-2-heptadecyloxymethylpropane-1-ol (4). To a solution of **3** (18.1 g, 31.9 mmol) in THF (300 mL) was added $BH_3{\cdot}Me_2S$ (31.9 mmol) dropwise at 0 °C under Ar. The reaction temperature was increased to room temperature, and the reaction mixture was stirred for 6 h. The mixture was again cooled to 0 °C, and an aqueous NaOH solution (3 M, 100 mL) was added. The reaction mixture was stirred at 0 °C for 24 h, and then, H_2O_2 (30%, 100 mL) was added. After 12 h at room temperature with stirring, K_2CO_3 (5.0 g) was added, and the mixture was extracted with ether, washed with saturated aqueous NaCl solution, dried over anhydrous $MgSO_4$, and then concentrated. The residue was passed through a short column chromatograph on SiO_2 with hexane/ethyl acetate (30:1). Recrystallization from hexane gave **4** (13.3 g, 22.8 mmol, 71% yield) as a colorless crystal: ^{1}H NMR ($CDCl_3$, 400 MHz) δ 3.74 (t, J = 5.2 Hz, 2H), 3.50 (m, 4H), 3.38 (t, J = 5.2 Hz, 4H), 2.07 (quint, J = 5.6 Hz, 1H), 1.53 (t, J = 6.4 Hz, 4H), 1.23 (brs, 56H), 0.86 (t, J = 6.8 Hz, 6H); ^{13}C NMR ($CDCl_3$, 100 MHz) δ 71.8, 71.2, 65.1, 41.4, 32.1, 29.9, 29.8, 29.7, 29.6, 26.3, 22.9, 14.3; IR (KBr) 3328, 2839, 2744, 1471, 1377, 1313, 1232, 1213, 1191, 1116, 1041 cm^{-1}; HRMS (ESI) m/z $(M + Na)^+$ calcd for $C_{38}H_{78}O_3Na$ 605.5848, found 605.5816.

3-Heptadecyloxy-2-heptadecyloxymethyl-1-propargyloxypropane (5). To a NaH (1.03 g, 25.7 mmol) suspension in THF (20 mL) was added **4** (3.0 g, 5.2 mmol) in THF (15 mL) dropwise at 0 °C under Ar. The temperature was increased to room temperature, and the reaction mixture was stirred for 3 h. The mixture was again cooled to 0 °C, and propargyl bromide (1.6 mL, 15.4 mmol) was added dropwise. The reaction mixture was stirred at room temperature for 20 h. The reaction was quenched with saturated aqueous NH_4Cl solution (20 mL), and the mixture was extracted with ether, washed with saturated aqueous NaCl solution, dried over anhydrous $MgSO_4$, and then concentrated. Purification by silica gel column chromatography (hexane/ethyl acetate = 30:1) gave **5** (1.87 g, 3.0 mmol, 58% yield) as a yellow solid: ^{1}H NMR ($CDCl_3$, 400 MHz) δ 4.41 (d, J = 2.4 Hz, 2H), 3.55 (d, J = 6.0 Hz, 2H), 3.43 (d, J = 6.4 Hz, 4H), 3.38 (t, J = 6.4 Hz, 4H), 2.39 (s, 1H), 2.14 (m, 1H), 1.52 (t, J = 6.8 Hz, 4H), 1.24 (brs, 56H), 0.87 (t, J = 6.8 Hz, 6H); ^{13}C NMR ($CDCl_3$, 100 MHz) δ 74.2, 71.4, 69.2, 69.0, 58.6, 40.4, 32.1, 29.9, 29.8, 29.7, 29.6, 26.4, 22.9, 14.3; IR (KBr) 3249, 2912, 2848, 2798, 1508, 1473, 1458, 1359, 1087 cm^{-1}; HRMS (ESI) m/z $(M + Na)^+$ calcd for $C_{41}H_{80}O_3Na$ 643.6005, found 643.5989.

(3-Heptadecyloxy-2-heptadecyloxymethyl-1-propoxy)methyl-*o*-carborane (6). The mixture of **5** (0.61 g, 0.99 mmol), decaborane (0.15 g, 1.2 mmol), and acetonitrile (1.56 mL, 29.6 mmol) in toluene (20 mL) was stirred under reflux condition for 6 h. The solvent was removed under reduced pressure, and the residue was purified by silica gel column chromatography (hexane/ethyl acetate = 30:1) to give **6** (0.61 g, 0.83 mmol, 80% yield) as a white solid: ^{1}H NMR ($CDCl_3$, 400 MHz) δ 3.97 (brs, 1H), 3.51 (d, J = 5.6 Hz, 2H), 3.40−1.40 (m, 10H), 2.09 (quint, J = 6.0 Hz, 1H), 1.51 (t, J = 6.8 Hz, 4H), 1.24 (brs, 56H), 0.86 (t, J = 6.8 Hz, 6H); ^{13}C NMR ($CDCl_3$, 100 MHz) δ 72.3, 71.6, 70.4, 68.9, 57.7, 40.4, 32.1, 29.9, 29.8, 29.7, 29.6, 26.4, 22.9, 14.3; IR (KBr) 2918, 2850, 2572, 1465, 1377, 1112, 1095, 1012 cm^{-1}; MS (MALDI) m/z $(M + Na)^+$ $C_{41}H_{90}O_3B_{10}Na$ 763.8.

(3-Heptadecyloxy-2-heptadecyloxymethyl-1-propoxy)methyl-*o*-*nido*-carborane sodium salt (2). The mixture of **6** (0.92 g, 1.25 mmol) and NaOMe (0.68 g, 12.5 mmol) in MeOH (15 mL) was stirred under reflux condition for 14 h. The reaction mixture was diluted with water (20 mL), extracted with ethyl acetate, washed with saturated aqueous NaCl solution, dried over anhydrous $MgSO_4$, and then concentrated. Purification by silica gel column chromatography (gradient from hexane/ethyl acetate = 30:1 to ethyl acetate only) gave **2** (0.56 g, 0.72 mmol, 57% yield) as a white solid: ^{1}H NMR ($CDCl_3$, 400 MHz) δ 3.77(d, J = 5.6 Hz, 2H), 3.52 (m, 6H), 3.40 (t, J = 6.4 Hz, 4H), 2.09 (m, 1H), 1.54 (m, 4H), 1.24 (brs, 56H), 0.87 (t, J = 6.8 Hz, 6H); ^{13}C NMR ($CDCl_3$, 100 MHz) δ 41.05, 32.31, 29.93, 29.87, 29.57, 26.02, 22.90, 14.32; IR (KBr) 3419, 3251, 2850, 2520, 1714, 1614, 1456, 1373 cm^{-1}; MS (MALDI) m/z $(M + Na)^+$ $C_{41}H_{89}O_3B_9Na_2$ 774.8.

Preparation of Calcein Encapsulated CL and PEG−CL Liposomes. CL and PEG−CL liposomes were prepared from DSPC, CH, and CL (1:1:X = 0−1, molar ratio) or DSPC, CH, DSPE−PEG−OMe, and CL (1:1:0.12:X = 0−1, molar ratio) by the reverse-phase evaporation (REV) method (*44*). The representative procedure for the preparation of 25% CL containing the PEG−CL liposome is shown as follows: A mixture of DSPC (118 mg), CH (47 mg), DSPE−PEG−OMe (56 mg), and CL (29 mg) were dissolved in 2 mL of chloroform/diisopropylether mixture (1:1, v/v) in a round-bottom flask. An aqueous solution of calcein (100 mM, 2 mL) was added to the lipid solution to form an emulsion. The volume ratio of the aqueous phase to the organic phase was maintained at 1:2. The emulsion was sonicated for 1 min, and then, the organic solvent was removed under vacuum in a rotary evaporator at 37 °C while being broken down repeatedly to obtain a suspension of liposomes. The liposomes obtained were subjected to extrusion 10 times through a polycarbonate membrane of 100-nm pore size, using an extruder device (Lipex Biomembrane, Canada) thermostated at 60 °C. Purification was accomplished by ultracentrifuging at 200 000*g* for 20 min at 4 °C (Hitachi CS120, S100AT5 rotor), and the pellets obtained were resuspended in PBS buffer. Liposome size was measured with an electrophoretic light scattering spectrophotometer (ELS-700, Otsuka Electroics, Tokyo). The size distribution of CL (25−100%) containing the PEG−CL liposome was indicated in Figure 1 in the Supporting Information.

Stability of CL and PEG−CL Liposomes in Fetal Bovine Serum. The calcein-encapsulated CL and PEG−CL liposomes were added to a fetal bovine serum (FBS) (volume ratio of FBS/vesicle solution = 9:1), and the mixture was incubated at 37 °C with stirring. The fluorescence intensity of the FBS solution was measured at 0−24 h using an excitation wavelength of 490 nm with emission wavelength of 520 nm. The fluorescence intensity was also measured at each fraction after degradation of liposomes by the addition of a 5% aqueous solution of Triton X-100 to the FBS solution.

Conjugation of Transferrin on Surface of Tf(−)−PEG−CL Liposomes. Tf(−)−PEG−CL liposomes were prepared from DSPC, CH, DSPE−PEG−OMe, DSPE−PEG−O−$(CH_2)_5CO_2H$, and CL (molar ratio 1:1:0.11:0.021:0.25) according to the procedure described above. In the case of ^{125}I-tyraminyl inulin encapsulation, the Tf(−)−PEG−CL liposomes were prepared using an aqueous solution containing ^{125}I-tyraminyl inulin (500 μg lipid/200 μL), which was obtained according to the reported procedure (*46*). Tf(+)−PEG−CL liposomes were prepared by the coupling of transferrin to the PEG−CO_2H moieties of Tf(−)−PEG−CL liposomes as previously reported (*33*). Briefly, to 1 mL of Tf(−)−PEG−CL liposomes (5.8 μmol lipid) in 1.25 mL Mes buffer (10 mM Mes/150 mM NaCl, pH 5.5), 21 μmol of EDC and 28 μmol of S-NHS were added, and the mixture was incubated for 15 min at room temperature. The mixture was loaded into a Sephadex G25 column equilibrated with Mes buffer, and liposome fractions were collected. Transferrin (1 mg) in a NaCl solution (150 mM) with PBS (final 250 μL, pH 7.4) was then added to the liposome solution, and the mixture was incubated for 3 h at room temperature with gentle stirring. Purification was accomplished by ultracentrifugation at 200 000*g* for 20 min at 4 °C, and the pellets obtained were resuspended in 2 mL of PBS. Tf(+)−PEG−CL liposomes obtained were converted into the diferric form by treatment with $FeCl_3$−nitriloacetic acid solution (250 mM, 20 μL, pH 7.4). After the reaction, the suspension was purified by ultracentrifugation and resuspended in PBS.

Biodistribution of Tf(+)−PEG−CL and Tf(−)−PEG−CL Liposomes in Tumor-Bearing Mice. Biodistribution studies were performed using male BALB/c mice (6 weeks old, 16−18 g, Nihon SLC). Tumor-bearing mice were prepared by inoculating sc a suspension (5×10^6 cells) of colon 26 cells directly into their back. The mice were kept on regular mouse diet and water, and maintained under a standard light/dark cycle in an ambient atmosphere. These experiments were performed when the tumor was 7−9 mm in diameter. ^{125}I-Tyraminyl inulin solution was encapsulated in the liposomes, and 100 μL of liposomes was injected into the mice (3 per group) via the tail vein. At selected time intervals after administration, the mice were lightly anesthetized, bled via the retro-orbital sinus, sacrificed by cervical dislocation, and dissected. Their organs were excised, and their ^{125}I content was estimated by a liquid scintillation counter.

BNCT for Tumor-Bearing Mice Using Tf(+)−PEG−CL Liposomes. Tumor-bearing mice were prepared by inoculating sc a suspension (5×10^6 cells) of colon 26 cells directly into their left thigh. Tf(+)−PEG−CL liposomes, which were prepared from the ^{10}B-enriched *nido*-carborane lipid **2**, was injected into colon 26 tumor-bearing mice (18−22 g; 8 per group) via a tail vein at a dose of 7.2 mg ^{10}B/kg (720 ppm of ^{10}B concentration; 200 μL of liposome solution). Seventy-two hours after iv injection, 4 mice in each group were sacrified by cervical dislocation and dissected. Organs were excised, and a ^{10}B concentration in each organ was determined by prompt γ-ray spectroscopy. At the same time, the other 4 mice in each group were anesthetized with sodium pentobarbital solution and placed in an acrylic mouse holder (Iuchi, Tokyo), where their whole bodies except the tumor-implanted leg were shielded with acrylic resin. The mice were irradiated in the KUR atomic reactor for 37 min at a rate of 2×10^{12} neutrons/cm^2. The antitumor effect of BNCT was evaluated on the basis of the survival of the mice. All protocol were approved by the Institutional Animal Care and Use Committee in Kyoto University.

RESULTS AND DISCUSSION

Synthesis of Double-Tailed *nido*-Carborane Lipid 2. The synthetic route of *nido*-carborane lipid **2** is shown in Scheme 1. The reaction of 2 equiv of heptadecanol with 3-chloro-2-chloromethyl-1-propene using NaH as base gave the diether **3** in 93% yield, and the hydroboration of **3** gave the corresponding alcohol **4** in 71% yield. The alcohol **4** was converted into the propargyl ether **5** in 48% yield by the treatment with propargyl bromide, and the decaborane coupling of **5** was carried out in the presence of acetonitrile in toluene under reflux condition to give the corresponding *o*-carborane **6** in 80% yield. The degradation of the carborane cage by the treatment with sodium methoxide in methanol afforded the *nido*-carborane lipid **2** (CL) in 57% yield.

Stability of CL and PEG−CL Liposomes in FBS. PEG units conjugated on the surface of liposomes are important for a prolonged residence time in the circulation and escaping ability

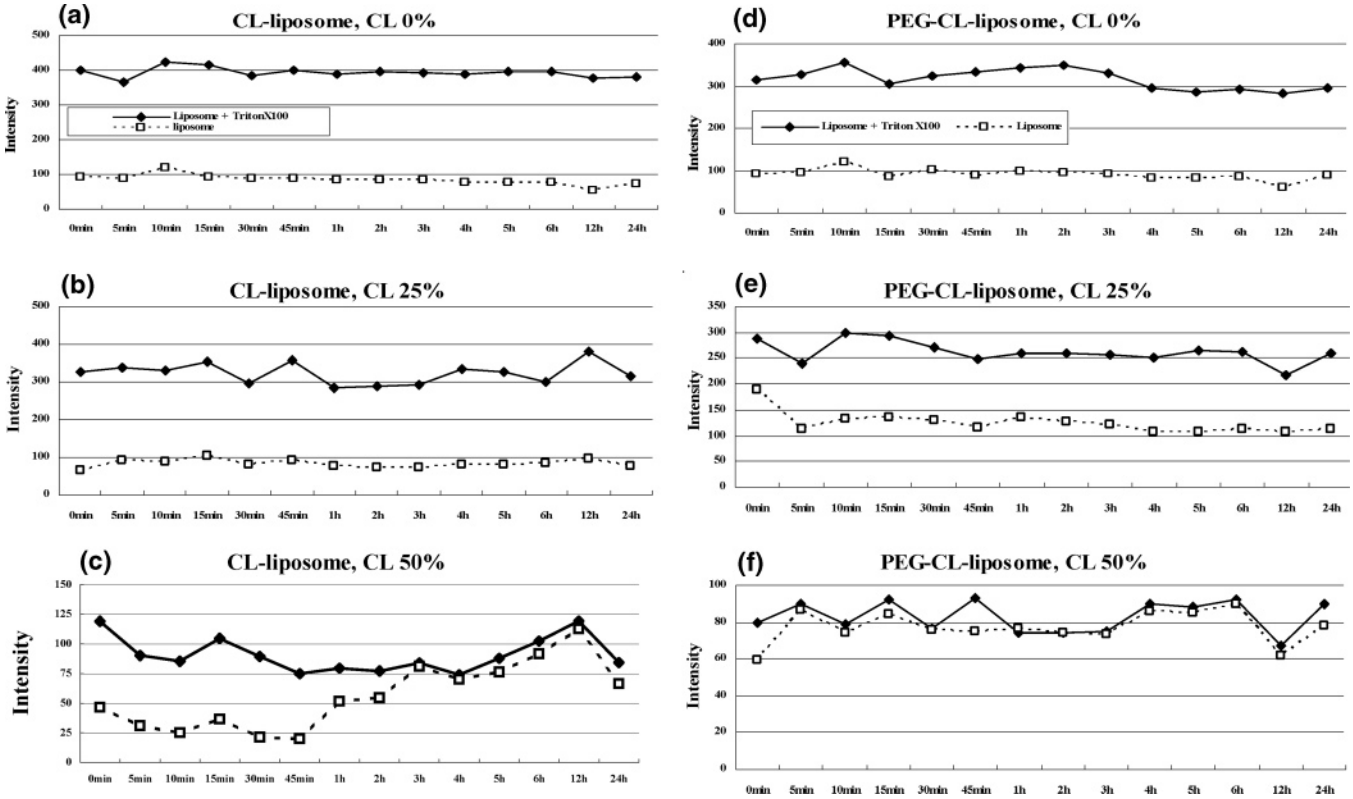

Figure 2. Fluorescence intensities of calcein-encapsulated CL and PEG−CL liposomes in fetal bovine serum (FBS). The white plots show the fluorescence intensity of the FBS solution, and the black plots show that of the solution after destruction of liposomes by the addition of Triton X-100. The difference in fluorescence intensity between the black and white plots indicates calcein release from liposomes.

from RES uptake, promoting the extravasation of the liposomes into the solid tumor tissue on liposomal drug delivery system. Therefore, we first investigated the stability of calcein-encapsulated CL and PEG unit-conjugated CL liposomes in FBS. To FBS was added a liposome solution (the volume ratio of FBS/liposome solution = 9:1) and incubated at 37 °C with stirring. The fluorescence of the FBS solutions was measured at 0−24 h. The results are shown in Figure 2. Fluorescence intensity is plotted on the vertical axis, and incubation time is plotted on the horizontal axis. The white plots show the fluorescence intensity of the FBS solution containing liposomes, and the black plots show that of the solution after destruction of liposomes by the addition of Triton X-100. In the case of liposomes with 0% and 25% CL (Figure 2a,b), no increase in the fluorescence intensity of the FBS solutions was observed within 24 h. However, the fluorescence intensity of the liposome with 50% CL increased after 1 h of incubation at 37 °C with stirring (Figure 2c). A similar tendency was observed in the case of the PEG liposomes, and the fluorescence intensity of the PEG liposomes with 50% CL increased even after 5 min of incubation (Figure 2d−f). These results indicate that the liposomes containing 25% of CL were stable in the FBS solution at 37 °C at least for 24 h and that liposomes with higher than 50% CL lead to an unstable liposomal formation. The increased rate of fluorescence intensity after the treatment with Triton X-100 may be associated with the amounts of calceins encapsulated in liposomes. Comparison of the increased rates of fluorescence intensity between PEG−CL liposome solutions and CL liposome solutions after treatment with Triton X-100 shows that the latter is relatively higher (Figure 2a−c vs d−f). This means that the PEG functional group would lower the capacity of calcein encapsulation in liposomes. Therefore, the higher CL content of the liposomes led not only to instability in liposome formation but also suppressed calcein encapsulation.

Biodistribution of Tf(−)−PEG−CL and Tf(+)−PEG−CL Liposomes in Tumor-Bearing Mice. Liposomes, in which ^{125}I-tyraminyl inulins were encapsulated, were injected intravenously into colon 26 tumor-bearing mice. At selected time intervals after administration, the mice were lightly anesthetized, bled via the retro-orbital sinus, killed by cervical dislocation, and dissected. Their organs were excised, and their ^{125}I content was estimated using a liquid scintillation counter. The time-dependent distributions of Tf(−)−PEG−CL and Tf(+)−PEG−CL liposomes in various tissues are shown in Figure 3. The rapid clearance of Tf(−)−PEG−CL and Tf(+)−PEG−CL liposomes was observed in the blood, lung, and kidney after 3 h of injection. In general, PEGylated liposomes possess a longer circulation time compared to nonstealth liposomes (*34, 35*). We examined the effect of CL on the circulation time of PEGylated liposomes and found that CL influenced a stealth property of the PEG−CL liposome (see Figure 4 in Supporting information). The enhanced accumulation of Tf(+)−PEG−CL liposomes in comparison with Tf(−)−PEG−CL liposome accumulation was observed in the spleen within 72 h. Tf(+)−PEG−CL liposomes accumulated in the liver and tumor gradually, whereas Tf(−)−PEG−CL liposomes were released from those organs 72 h after injection, although percentage doses of these liposomes were similar 24 h after injection. Surprisingly, more than 1.5% of the total dose injected accumulated in tumor tissues. This enhanced accumulation of Tf(+)−PEG−CL liposomes may reflect marked receptor-mediated endocytosis after binding to tumor cells (*37*). Since enhanced accumulation in tumor tissues and a high tumor/blood ratio were observed 72 h after the administration of Tf(+)−PEG−CL liposomes, we next investigated the ^{10}B distribution and BNCT effect in tumor-bearing mice.

^{10}B Concentration in Various Organs 72 h after Injection of Tf−PEG−CL Liposome. ^{10}B-enriched Tf(+)−PEG−CL liposomes were injected into tumor-bearing mice, in which colon

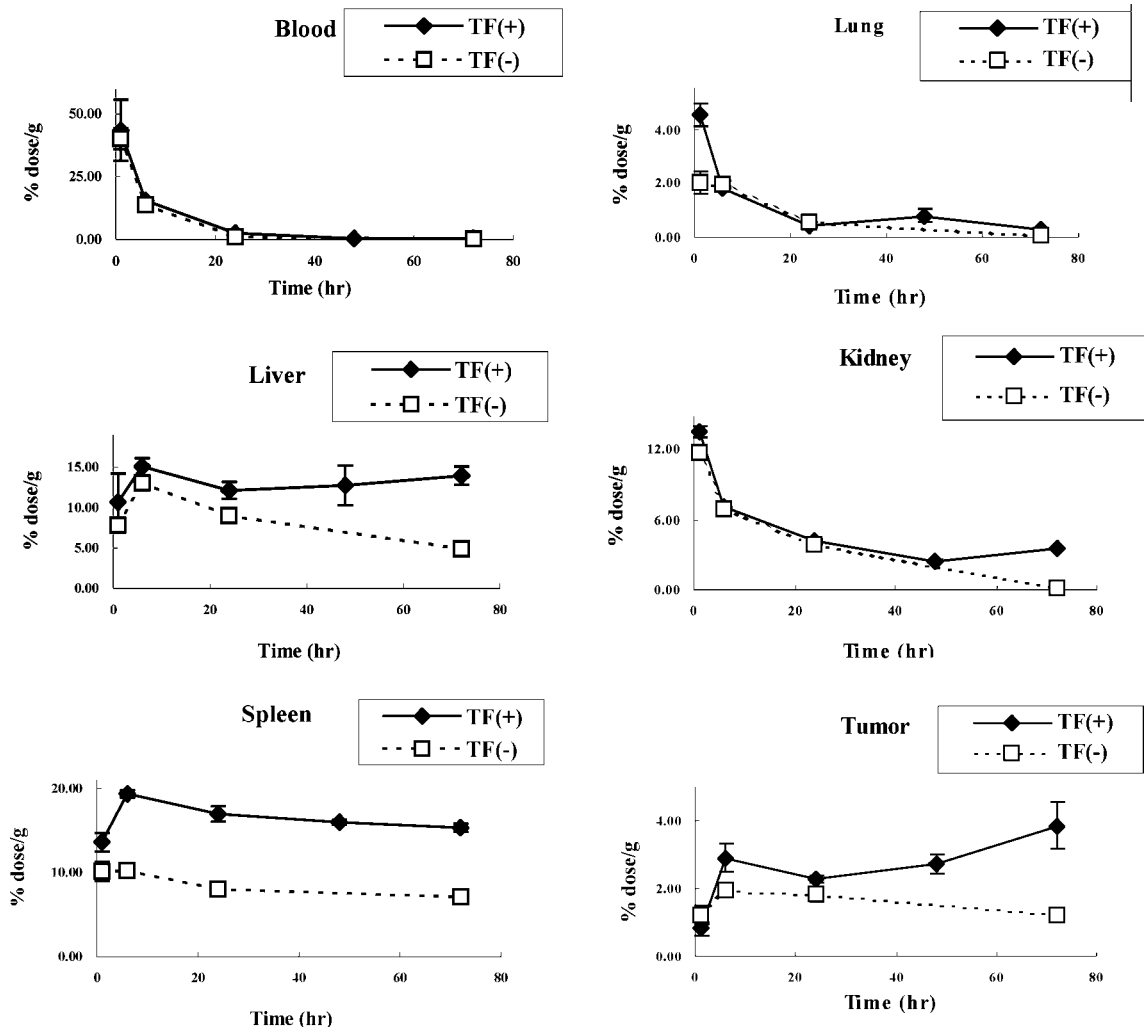

Figure 3. Time course of biodistribution of Tf(−)−PEG−CL liposome (TF(−)) and the Tf(+)−PEG−CL liposome (TF(+)). Liposomes encapsulating ^{125}I-tyraminyl inulin (500 g lipid/200 μL) were injected into male BALB/c mice (7 weeks old, weighing 20−25 g) via the tail vein. The distribution of liposomes was measured by determining the radioactivity of each tissue. The percent dose/per gram in each tissue is plotted on the vertical axis, and the time (h) after administration is plotted on the horizontal axis.

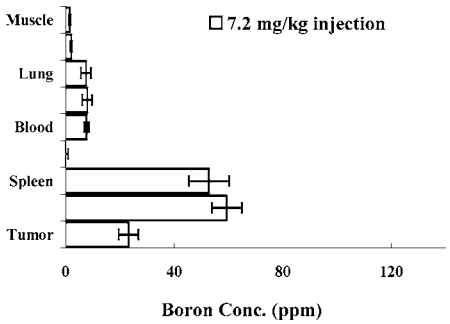

Figure 4. ^{10}B concentration in various tissues 72 h after injection of Tf(+)−PEG−CL liposomes into tumor-bearing mice. ^{10}B-enriched Tf(+)−PEG−CL liposomes were injected into tumor-bearing mice, in which colon 26 cells were transplanted into the left thigh, via the tail vein at a dose of 7.2 mg ^{10}B/kg (200 μL of liposome solution).

26 cells were transplanted into their left thigh, via the tail vein at a dose of 7.2 mg ^{10}B/kg (200 μL of a liposome solution). Seventy-two hours after administration, ^{10}B concentration in each organ was measured by prompt γ-ray spectroscopy. The results are shown in Figure 4. No boron accumulation was observed in the muscle, heart, and brain; however, the boron concentrations in the lung, kidney, and blood were approximately 10 ppm. Since no accumulation of Tf(+)−PEG−CL liposomes labeled with ^{125}I-tyraminyl inulin was observed, as shown in Figure 3, it is considered that the ^{10}B concentrations detected in such organs may be due to the accumulation of the *nido*-carborane lipid **2**, which was caused by the degradation of the parent liposomes. Enhanced accumulation of ^{10}B was observed in the spleen and liver, and this does not conflict with the result of the biodistribution of Tf(+)−PEG−CL liposomes as shown in Figure 3. A high level of ^{10}B concentration (22 ppm) in the tumor was observed in tumor tissues 72 h after the administration of Tf(+)−PEG−CL liposomes. Previously, we reported that BSH-encapsulated Tf(+)−PEG liposomes (*40*) accumulated in tumor tissues at 35.5 ppm ^{10}B concentration 72 h after administration of 35 mg/kg body weight ^{10}B. Therefore, ^{10}B delivery to tumor tissues by Tf(+)−PEG−CL liposomes would be more efficient in comparison with that by BSH-encapsulated Tf(+)−PEG liposomes. In both cases, the conjunction of transferrin to the surface of liposomes is essential for the enhanced and prolonged accumulation of ^{10}B in tumor tissues.

Survival of Tumor-Bearing Mice after BNCT. Besides the determination of ^{10}B concentration in various organs, the mice were anesthetized with sodium pentobarbital solution 72 h after the administration of Tf(+)−PEG−CL liposomes and placed in an acrylic mouse holder, where their whole bodies, except their tumor-implanted leg, were shielded with acrylic resin. Neutron irradiation was carried out for 37 min at a rate of 2×10^{12} neutrons/cm^2 in the KUR atomic reactor. The antitumor

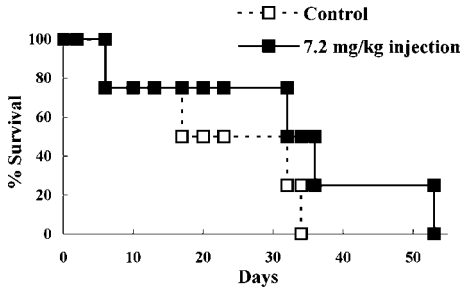

Figure 5. Survival curve of tumor-bearing mice after neutron irradiation for 37 min in KUR atomic reactor. The mice were injected with 7.2 mg ^{10}B/kg of the Tf(+)−PEG−CL liposome and incubated for 72 h before irradiation. Control indicates survival rates of tumor-bearing mice after neutron irradiation without administration of Tf(+)−PEG−CL liposomes.

effect of BNCT was evaluated on the basis of the survival of the mice, as shown in Figure 5. All the nontreated mice did not survive after 32 days of neutron irradiation, and their average survival rate was 21 days. Long survival rates were observed in the mice treated with Tf(+)−PEG−CL liposomes; one of them even survived for 52 days after neutron irradiation. The average survival rate of the treated mice was 31 days.

CONCLUSION

We succeeded in the synthesis of the double-tailed boron lipid **2**, which forms a stable liposome at 25% molar ratio toward DSPC with cholesterol. Transferrin was able to be conjugated to the surface of boron liposomes (Tf(+)−PEG−CL liposomes) by the coupling of transferrin to the PEG−CO_2H moieties of PEG(−)−CL liposomes. A biodistribution experiment on Tf(+)−PEG−CL liposomes, in which ^{125}I-tyraminyl inulins were encapsulated, showed that Tf(+)−PEG−CL liposomes accumulate in tumor tissues and stay there for a sufficiently long time to increase tumor/blood concentration ratio, although Tf(−)−PEG−CL liposomes were gradually released from tumor tissues with time. A ^{10}B concentration of 22 ppm was achieved by injection with Tf(+)−PEG−CL liposomes at 7.2 mg ^{10}B/kg in tumor-bearing mice. Although no complete cure of the tumor was observed after neutron irradiation, prolonged survivals of the mice were observed. The current boron delivery system uses the accumulation of boron in the liposomal bilayer instead of in the inner cell of liposomes. It is noted that the inner cells of a liposome are still vacant; therefore, it is envisioned that drugs can be encapsulated into the Tf(+)−PEG−CL liposome. In this system, boron and drugs can be simultaneously delivered to tumor tissues. The current investigation and liposomal delivery of the double-tailed boron lipid **2** possesses a dual-mode vehicle for BNCT and chemotherapy of cancer.

Supporting Information Available: Size distributions of PEG−CL liposomes, analysis of the conjugation of transferrin to liposomes, size distributions of Tf(−)−PEG−CL liposome and Tf(+)−PEG−CL liposome, and effect of CL on the circulation time and accumulation of PEG-conjugated liposomes in various tissues in mice. This material is available free of charge via the Internet at http://pubs.acs.org.

LITERATURE CITED

(1) Locher, G. L. (1936) Biological effects and the therapeutic possibilities of neutrons. *Am. J. Roentgenol. 36*, 1.

(2) Soloway, A. H., Tjarks, W., Barnum, B. A., Rong, F.-G., Barth, R. F., Codogni, I. M., and Wilson, J. G. (1998) The Chemistry of Neutron Capture Therapy. *Chem. Rev. 98*, 1515−1562.

(3) Barth, R. F., Soloway, A. H., and Fairchild, R. G. (1990) Boron neutron capture therapy of cancer. *Cancer Res. 50*, 1061−1070.

(4) Hawthorne, M. F. (1993) The role of chemistry in the development of boron neutron capture therapy of cancer. *Angew. Chem., Int. Ed. Engl. 32*, 950−984.

(5) Barth, R. F., Soloway, A. H., Fairchild, R. G., and Brugger, R. M. (1992) Boron neutron capture therapy for cancer. *Cancer 70*, 2995−3007.

(6) Soloway, A. H., Hatanaka, H., and Davis, M. A. (1967) Penetration of brain and brain tumor. VII. Tumor-binding sulfhydryl boron compounds. *J. Med. Chem. 10*, 714−717.

(7) Nakagawa, Y., and Hatanaka, H. (1997) Boron neutron capture therapy: Clinical brain tumor studies. *J. Neuro-Oncol. 33*, 105−115.

(8) Synder, H. R., Reedy, A. J., and Lennarz, W. J. (1958) Synthesis of aromatic boronic acids. Aldehyde boronic acids and a boronic acid analog of tyrosine. *J. Am. Chem. Soc. 80*, 835−835.

(9) Mishima, Y., Ichihashi, M., Hotta, S., Honda, C., Yamamura, K., and Nakagawa, T. (1989) New thermal neutron capture therapy for malignant melanoma: Melanogenesis-seeking ^{10}B molecule-melanoma cell interaction from in vitro to first clinical trial. *Pigment Cell Res. 2*, 226−234.

(10) Kato, I., Ono, K., Sakurai, Y., Ohmae, M., Maruhashi, A., Imahori, Y., Kirihata, M., Nakazawa, M., and Yura, Y. (2004) Effectiveness of BNCT for recurrent head and neck malignancies. *Appl. Radiat. Isot. 61*, 1069−1073.

(11) Goldenberg, D. M., Sharkey, R. M., Primus, F. J., Mizusawa, E. A., and Hawthorne, M. F. (1984) Neutron-capture therapy of human cancer: In vivo results on tumor localization of boron-10-labeled antibodies to carcinoembryonic antigen in the GW-39 tumor model system. *Proc. Natl. Acad. Sci. U.S.A. 81*, 560−563.

(12) Alam, F., Soloway, A. H., McGuire, J. E., Barth, R. F., Carey, W. E., and Adams, D. (1985) Dicesium *N*-succinimidyl 3-(undecahydro-*closo*-dodecaboranyldithio)propionate, a novel heterobifunctional boronating agent. *J. Med. Chem. 28*, 522−525.

(13) Alam, F., Soloway, A. H., and Barth, R. F. (1989) Boron containing immunoconjugates for neutron capture therapy of cancer and for immunocytochemistry. *Antibody, Immunoconjugates, Radiopharm. 2*, 145−163.

(14) Barth, R. F., Alam, F., Soloway, A. H., Adams, D. M., and Steplewski, Z. (1986) Boronated monoclonal antibody 17-1A for potential neutron capture therapy of colorectal cancer *Hybridoma 5*, S43−S50.

(15) Chen, C.-J., Kane, R. R., Primus, F. J., Szalai, G., Hawthorne, M. F., and Shively, J. E. (1994) Synthesis and characterization of oligomeric *nido*-carboranyl phosphate diester conjugates to antibody and antibody fragments for potential use in boron neutron capture therapy of solid tumors. *Bioconjugate Chem. 5*, 557−564.

(16) Liu, L., Barth, R. F., Adams, D. M., Soloway, A. H., and Reisfeld, R. A. (1996) Critical evaluation of bispecific antibodies as targeting agents for boron neutron capture therapy of brain tumors. *Anticancer Res. 16*, 2581−2588.

(17) Pak, R. H., Primus, F. J., Rickard-Dickson, K. J., Ng, L. L., Kane, R. R., and Hawthorne, M. F. (1995) Preparation and properties of *nido*-carborane-specific monoclonal antibodies for potential use in boron neutron capture therapy for cancer. *Proc. Natl. Acad. Sci. U.S.A. 92*, 6986−6990.

(18) Andersson, A., Andersson, J., Burgman, J.-O., Capala, J., Carlsson, J., Conde, H., Crawford, J., Graffmann, S., Grusell, E., and Holmberg, A. (1992) In *Progress in Neutron Capture Therapy for Cancer* (Allen, B. J., Moore, D. E., and Harrington, B. V., Eds.) p 41, Plenum Press, New York.

(19) Gedda, L., Olsson, P., and Carlsson, J. (1996) Development and in vitro studies of epidermal growth factor−dextran conjugates for boron neutron capture therapy. *Bioconjugate Chem. 7*, 584−591.

(20) Capala, J., Barth, R. F., Bendayan, M., Lauzon, M., Adams, D. M., Soloway, A. H., Fenstermaker, R. A., and Carlsson, J. (1996) Boronated epidermal growth factor as a potential targeting agent for boron neutron capture therapy of brain tumors. *Bioconjugate Chem. 7*, 7−15.

(21) Yang, W., Barth, R. F., Adams, D. M., and Soloway, A. H. (1997) Intratumoral delivery of boronated epidermal growth factor for neutron capture therapy of brain tumors. *Cancer Res. 57*, 4333−4339.

(22) Cai, J., Soloway, A. H., Barth, R. F., Adams, D. M., Hariharan, J. R., Wyzlic, I. M., and Radcliffe, K. (1997) Boron-containing polyamines as DNA targeting agents for neutron capture therapy of brain tumors: Synthesis and biological evaluation. *J. Med. Chem. 40*, 3887−3896.

(23) Sood, A., Shaw, B. R., and Spielvogel, B. F. (1990) Boron-containing nucleic acids. 2. Synthesis of oligodeoxynucleoside boranophosphates. *J. Am. Chem. Soc. 112*, 9000−9001.

(24) Fulcrand-El Kattan, G., Lesnikowski, Z. J., Yao, S., Tanious, F., Wilson, W. D., and Schinazi, R. F. (1994) Carboranyl oligonucleotides. 2. Synthesis and physicochemical properties of dodecathymidylate containing 5-(*o*-carboran-1-yl)-2′-deoxyuridine. *J. Am. Chem. Soc. 116*, 7494−7501.

(25) Kane, R. R., Drechsel, K., and Hawthorne, M. F. (1993) Automated syntheses of carborane-derived homogeneous oligophosphates: reagents for use in the immunoprotein-mediated boron neutron capture therapy (BNCT) of cancer. *J. Am. Chem. Soc. 115*, 8853−8854.

(26) Nakanishi, A., Guan, L., Kane, R. R., Kasamatsu, H., and Hawthorne, M. F. (1999) Toward a cancer therapy with boron-rich oligomeric phosphate diesters that target the cell nucleus. *Proc. Natl. Acad. Sci. U.S.A. 96*, 238−241.

(27) Klibanov, A., Maruyama, K., Beckerleg, A. M., Torchilin, V. P., and Hung, L. (1991) Activity of amphipathic poly(ethylene glycol) 5000 to prolong the circulation time of liposomes depends on the liposome size and is unfavorable for immunoliposome binding to target. *Biochim. Biophys. Acta 1062*, 142−148.

(28) Maruyama, K., Takizawa, T., Yuda, T., Kennel, S., Huang, L., and Iwatsuru, M. (1995) Targetability of novel immunoliposomes modified with amphipathic polyethyleneglycols conjugated at their distal terminals to monoclonal antibodies. *Biochem. Biophys. Acta 1234*, 74−80.

(29) Maruyama, K., Takahashi, N., Tagawa, T., Nagaike, K., and Iwatsuru, M. (1997) Immunoliposomes bearing polyethyleneglycol-coupled Fab' fragment show prolonged circulation time and high extravasation onto target solid tumors in vivo. *FEBS Lett. 413*, 177−180.

(30) Wu, M. S., Robbins, J. C., Bugianesi, R. L., Ponpipom, M. M., and Shen, T. Y. (1981) Modified in vivo behavior of liposomes containing synthetic glycolipids. *Biochem. Biophys. Acta 674*, 19−26.

(31) Maruyama, K., Unezaki, S., Takahashi, N., and Iwatsuru, M. (1993) Enhanced delivery of doxorubicin to tumor by long-circulating thermosensitive liposomes and local hyperthermia. *Biochim. Biophys. Acta 1149*, 209−216.

(32) Maruyama, K., Takizawa, T., Takahashi, N., Tagawa, T., Nagaike, K., and Iwatsuru, M. (1997) Targeting efficiency of PEG-immunoliposomes-conjugated antibodies at PEG terminals. *Adv. Drug Delivery Rev. 24*, 235−242.

(33) Ishida, O., Maruyama, K., Tanahashi, H., Iwatsuru, M., Sasaki, K., Eguchi, M., and Yanagie, H. (2001) Liposomes bearing polyethyleneglycol coupled transferrin with intracellular targeting property to the solid tumors in vivo. *Pharm. Res. 18*, 1042−1048.

(34) Mumtaz, S., Ghosh, P. C., and Bachhawat, B. K. (1991) Design of liposomes for circumventing the reticuloendothelial cells. *Glycobiology 1*, 505−510.

(35) Vaage, J., Mayhew, E., Lasic, D., and Martin, F. (1992) Therapy of primary and metastatic mouse mammary carcinomas with doxorubicin encapsulated in long circulating liposomes. *Int. J. Cancer 51*, 942−948.

(36) Wu, J., Akaike, T., and Maeda, H. (1998) Modulation of enhanced vascular permeability in tumors by a bradykinin antagonist, a cyclooxygenase inhibitor, and a nitric oxide scavenger. *Cancer Res. 58*, 159−165.

(37) Iinuma, H., Maruyama, K., Okinaga, K., Sasaki, K., Sekine, T., Ishida, O., Ogiwara, N., Johkura, K., and Yonemura, Y. (2002) Intracellular targeting therapy of cisplatin-encapsulated transferrin-polyethylene glycol liposome of peritoneal dissemination of gastric cancer. *Int. J. Cancer 99*, 130−137.

(38) Wargner, E., Curiel, D., and Cotton, M. (1994) Delivery of drugs, proteins and genes into cells using transferrin as a ligand for receptor-mediated endocytosis. *Adv. Drug Delivery Res. 14*, 177−180.

(39) Huebers, H. A., and Finch, C. A. (1987) The physiology of transferrin and transferrin receptors. *Physiol. Rev. 67*, 520−582.

(40) Aisen, P. (1994) The transferrin receptor and the release of iron from transferrin. *Adv. Exp. Med. Biol. 365*, 31−40.

(41) Maruyama, K., Ishida, O., Kasaoka, S., Takizawa, T., Utoguchi, N., Shinohara, A., Chiba, M., Kobayashi, H., Eriguchi, M., and Yanagie, H. (2004) Intracellular targeting of sodium mercaptoundecahydrododecaborate (BSH) to solid tumors by transferrin-PEG liposomes, for boron neutron-capture therapy (BNCT). *J. Controlled Release 98*, 195−207.

(42) Feakes, D. A., Shelly, K., and Hawthorne, M. F. (1995) Selective boron delivery to murine tumors by lipophilic species incorporated in the membranes of unilamellar liposomes. *Proc. Natl. Acad. Sci. U.S.A. 92*, 1367−1370.

(43) Watson-Clark, R. A., Banquerigo, M. L., Shelly, K., Hawthorn, M. F., and Brahn, E. (1998) Model studies directed toward the application of boron neutron capture therapy to rheumatoid arthritis: Boron delivery by liposomes in rat collagen-induced arthritis. *Proc. Natl. Acad. Sci. U.S.A. 95*, 2531−2534.

(44) Nakamura, H., Miyajima, Y., Takei, T., Kasaoka, T., and Maruyama, K. (2004) Synthesis and vesicle formation of a *nido*-carborane cluster lipid for boron neutron capture therapy. *Chem. Commun.* 1910−1911.

(45) Szoka, F., and Papahadjopoulos, D. (1978) Procedure for preparation of liposomes with large internal aqueous space and high capture by reverse-phase evaporation. *Proc. Natl. Acad. Sci. U.S.A. 75*, 4194−4198.

(46) Sommerman, E. F., Pritchard, P. H., and Cullis, P. R. (1984) ^{125}I labeled inulin: a convenient marker for deposition of liposomal contents in vivo. *Biochim. Biophys. Res. Commun. 122*, 319−324.

BC060064K

Carbohydrate-Appended 3-Hydroxy-4-pyridinone Complexes of the $[M(CO)_3]^+$ Core (M = Re, ^{99m}Tc, ^{186}Re)

Cara L. Ferreira,[†,‡] Simon R. Bayly,[†,‡] David E. Green,[†] Tim Storr,[†] Cheri A. Barta,[†] Jennifer Steele,[†] Michael J. Adam,*[,‡] and Chris Orvig*[,†]

Medicinal Inorganic Chemistry Group, Department of Chemistry, University of British Columbia, 2036 Main Mall, Vancouver, British Columbia V6T 1Z1, Canada, and TRIUMF, 4004 Wesbrook Mall, Vancouver, British Columbia, V6T 2A3, Canada. Received April 6, 2006; Revised Manuscript Received June 13, 2006

This work describes the use of 3-hydroxy-4-pyridinone ligands for binding the $[M(CO)_3]^+$ core (M = Re, Tc) in the context of preparing novel Tc(I) and Re(I) glucose conjugates. Five pyridinone ligands bearing pendent carbohydrate moieties, H**L**$^{1-5}$, were coordinated to the $[M(CO)_3]^+$ core on the macroscopic scale (M = Re) and on the tracer scale (M = ^{99m}Tc, ^{186}Re). On the macroscopic scale the complexes, Re**L**$^{1-5}(CO)_3(H_2O)$, were thoroughly characterized by mass spectrometry, IR spectroscopy, UV−visible spectroscopy, elemental analysis, and 1D/2D NMR spectroscopy. Characterization confirmed the bidentate coordination of the pyridinone and the pendent nature of the carbohydrate and suggests the presence of a water molecule in the sixth coordination site. In preliminary biological evaluation, both the ligands and complexes were assessed as potential substrates or inhibitors of hexokinase, but showed no activity. Labeling via the $[^{99m}Tc(CO)_3(H_2O)_3]^+$ precursor gave the tracer species ^{99m}Tc**L**$^{1-5}(CO)_3(H_2O)$ in high radiochemical yields. Similar high radiochemical yields when labeling with ^{186}Re were facilitated by in situ preparation of the $[^{186}Re(CO)_3(H_2O)_3]^+$ species in the presence of H**L**$^{1-5}$ to give ^{186}Re**L**$^{1-5}(CO)_3(H_2O)$. Stability challenges, incubating ^{99m}Tc**L**$^{1-5}(CO)_3(H_2O)$ in the presence of excess cysteine and histidine, confirmed complex stability up to 24 h.

INTRODUCTION

Because glucose is a major energy source for the body, especially for the heart and brain, the ability to monitor cell glucose metabolism has found utility in a myriad of areas of medicine (*1*). In the use of positron emission tomography, [^{18}F]-2-deoxy-2-fluoro-D-glucose (FDG) is the preeminent radiotracer used to image glucose metabolism (*2*) and is an important tool in cardiology (*3*) and neurology (*1*, *2*). As well, FDG is used in oncology as a tumor marker, due to the elevated level of glucose metabolism in many tumor types (*1*, *4*). Unfortunately, the radioisotope used in FDG, ^{18}F, is cyclotron-produced and has a short half-life ($t_{1/2}$ = 1.8 h), significantly limiting the availability of the radiotracer. Hence, there is much interest in developing FDG-like radiopharmaceuticals that are less expensive and more accessible. As well, no analogue of FDG that can be used in radiotherapy is currently available.

In developing a more accessible radiotracer, ^{99m}Tc is an optimal radioisotope to consider; ^{99m}Tc is already used in over 90% of nuclear medicine scans and is generator-produced, making it inexpensive and widely available (*5*). The physical properties of ^{99m}Tc ($t_{1/2}$ = 6.01 h, γ = 142.7 keV) are ideal for imaging with single photon emission computed tomography (SPECT), the infrastructure for which is already available in most major hospitals. In addition, the third row congener of Tc, Re, has relatively similar chemistry to that of Tc and has two particle-emitting radioisotopes of interest for therapy: ^{186}Re ($t_{1/2}$ = 3.68 d, β^- = 1.07 MeV, γ = 137 keV) and ^{188}Re ($t_{1/2}$ = 16.98 h, β^- = 2.12 MeV, γ = 155 keV). Clearly, the development of an FDG analogue which incorporates ^{99m}Tc could have a significant impact on health care cost and availability, while using the same methods to develop a Re-FDG analogue has potential for targeted radiotherapy. As well, the investigation of radiolabled carbohydrates in general has wider potential applications, such as imaging of tumor specific lectins or in investigating other biological processes where carbohydrates and carbohydrate conjugates play a central role.

Research to combine the accessibility and ideal nuclear properties of ^{99m}Tc with the biological properties and applications of FDG has led several groups to develop ^{99m}Tc glucose conjugates (*6*−*16*). The initial investigations of these radiometal carbohydrate conjugates suffered from poor characterization (*8*, *12*) or from undesirable bonding interactions between the carbohydrate and metal (*7*, *17*, *18*). More recently, well characterized ligands and complexes have been prepared, the ligands radiolabeled in high yields, and the complexes shown to be highly stable (*9*, *11*, *14*−*16*). Also, in vivo studies of a few of these compounds have shown promising biodistribution results and tumor uptake (*8*, *12*), although the mechanism of uptake does not appear to mimic that of FDG or glucose. Although nonradioactive Re compounds are commonly used as a surrogate for ^{99m}Tc on the macroscopic scale and as a standard for identifying the analogous ^{99m}Tc complexes, only two ^{186}Re glucose conjugates have been reported (*14*, *17*). Further research is needed to develop glucose conjugates of ^{99m}Tc, ^{186}Re, and ^{188}Re with high stability and optimal biological properties. In the development of ^{99m}Tc and $^{186/188}$Re glucose conjugates, the $[M(CO)_3]^+$ core is of interest due to its stability, small size, and well-studied chemistry (*19*−*27*). The $[M(CO)_3]^+$ core is kinetically inert due to the metal ion +1 oxidation state and low spin d^6 electron configuration, which is further stabilized by the facial and strongly back-bonding CO ligands. The compact core is advantageous in retaining biological activity when labeling small molecules such as glucose. Alberto and co-workers have pioneered the chemistry and radiochemistry

* Corresponding authors. E-mail: adam@triumf.ca (M.J.A.); orvig@chem.ubc.ca (C.O.).

† University of British Columbia.

‡ TRIUMF.

10.1021/bc060085e CCC: $33.50 © 2006 American Chemical Society
Published on Web 08/10/2006

Chart 1. Structures of FDG, $[Tc(CO)_3(H_2O)_3]^+$, and a 3-Hydroxy-4-pyridinone

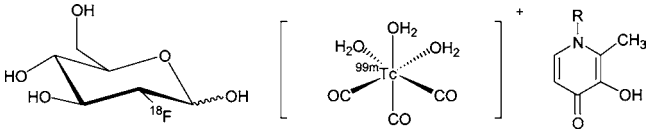

of this core and have developed a commercially available kit preparation of the $[^{99m}Tc(CO)_3(H_2O)_3]^+$ species (*25*). The three aqua ligands, each trans to a CO ligand, are labilized for substitution by various chelates functionalized with the biomolecule of interest (*19*−*21*, *24*, *26*). The $[^{188}Re(CO)_3(H_2O)_3]^+$ analogue has also been described (*22*, *23*).

Different chelating derivatives have been studied with the $[M(CO)_3]^+$ core, to optimize stability, labeling, and the physical properties of the products. Both bidentate and tridentate ligands have been investigated with a broad range of hard and/or soft bases as binding groups, including amine (*20*, *21*, *26*, *28*−*33*), thiol/thioether (*28*, *30*, *31*, *34*, *35*), thiourea (*36*), carboxylate (*9*, *30*, *37*), imine (*38*, *39*), phosphine (*40*), carborane (*13*, *41*), and cyclopentadienyl (*42*−*45*) ligands. Most of these ligands can be efficiently labeled via the $[^{99m}Tc(CO)_3(H_2O)_3]^+$ precursor and form highly stable complexes of varying charge and lipophilicity. Aromatic amines and borderline bases are considered among the best binding functionalities for this core (*21*, *33*) but do not neutralize the 1+ charge of the metal center.

A highly useful class of chelators that has not been studied with the $[M(CO)_3]^+$ system are the 3-hydroxy-4-pyrdinones, small, monanionic, bidentate O,O-chelators with a high affinity for a variety of metal ions. These chelators can be easily functionalized via the ring nitrogen. 3-Hydroxy-4-pyridinones have similar basicity to aromatic amines but can neutralize the charge of a 1+ metal center, such as Re(I) and Tc(I). Stable complexes with Re/Tc(V) (*46*) and (IV) (*47*) with 3-hydroxy-4-pyridinones have been reported. 3-Hydroxy-4-pyridnones have also been used to chelate a large number of other metals, both hard and soft acids, including V (*48*), Fe (*48*, *49*), Co (*50*), Cu (*51*, *52*), Mn (*53*), Zn (*54*), Pb (*54*), Rh (*55*), Ru (*55*, *56*), Ir (*55*), Al (*49*, *57*, *58*), Ga,(*49*, *57*−*60*), In (*57*, *59*), U (*61*), and Gd (*62*).

Recently we reported the synthesis of pyridinone bearing pendent glucose derivatives (Figure 1) and the neutral Ga and In tris complexes of these ligands as potential imaging agents (*59*). With the $[M(CO)_3]^+$ core, the pyridinone ligand is expected to form a stable neutral complex. When labeling a small neutral biomolecule such as glucose, a neutral complex may better retain the biological properties of the biomolecule compared to a cationic complex. In this work, we investigate the utility of the aforementioned pyridinone ligands bearing pendent glucose derivatives as chelates for the $[M(CO)_3]^+$ core. The resulting neutral complexes were fully characterized on the macroscopic scale, as well as prepared on the tracer level with both ^{99m}Tc and ^{186}Re. Preliminary evaluation of the complexes as potential radiopharmaceuticals is also reported.

EXPERIMENTAL SECTION

Materials. $[NEt_4]_2[Re(CO)_3Br_3]$ (*64*) $[Re(CO)_3(H_2O)_3]Br$ (*27*) and H**L**$^{1-5}$ (*59*, *63*) were prepared as reported in the literature. $Re(CO)_5Br$ was purchased from Strem Chemicals (Newburyport, MA). The Isolink boranocarbonate Kits were a gift from Mallinckrodt Inc. Saline solutions of $Na^{99m}TcO_4$ and $Na^{186}ReO_4$ were obtained from Vancouver Coastal Health-UBC Hospital and MDS Nordion Inc., respectively. All other chemicals were purchased from Sigma Aldrich and used without further purification. Water was deionized, purified (Barnstead D9802 and D9804 cartridges), and distilled with a Corning MP-1 Mega-Pure Still. All solvents were HPLC grade and purchased from Fisher. N_2 gas was acquired from Praxair. Thin layer chromatography (TLC) was performed using silica TLC plates with aluminum backing (Merck), and silica column chromatography was performed using silica from Silicycle (Quebec City, PQ). All NMR solvents were purchased from Cambridge Isotope Laboratories.

^1H NMR spectra were recorded on Bruker AV-300 or AV-400 instruments at 300.13, or 400.21 MHz, respectively. The NMR spectra were calibrated with the deuterated solvent used in each case, and $^1H-^1H$ COSY, $^1H-^{13}C$ HMQC, and HMBC HETCOR 2D NMR spectra were used to aid in the characterization of the compounds. Infrared spectra were recorded on an ATI Mattson Galaxy Series FTIR 5000 spectrophotometer as thin films on NaCl plates or as KBr discs. Mass spectra were obtained on either a Kratos Concept II H32Q instrument (Cs^+, LSIMS) or a Macromass LCT (electrospray, ES-MS). Elemental analysis was performed at the University of British Columbia Chemistry Department by Mr. M. Lakha (Carlo Erba analytical instrument). UV−visible spectra and hexokinase inhibition assays were run on a Hewlett-Packard model HP8453 diode array spectrophotometer, equipped with a kinetics software package. Purification by semipreparative HPLC was done on a Water Xterra RP C18 column (7 μm, 19 × 300 mm) using a Waters WE 600 HPLC system equipped with a 2478 dual wavelength absorbance UV detector and the Empower software package. Verification of radiolabeled products was done by HPLC analysis on a Phenomenex Hydro-Synergi C18 RP column using a Wellchrom Knauer K1001 system equipped with a K-2501 UV absorption detector, a Kapintek radiometric well counter, and Peak simple software.

Preparations of Re(L$^{1-5}$)(CO)$_3$(H$_2$O). Method A. A 1:1 stoichiometric mixture of $Re(CO)_5Br$ and H**L**$^{1-5}$ was dissolved in borate buffer (10−20 mL, 20 mM, pH 9), stirred, and heated at 75 °C for 30 min. The solvent was removed using a rotary evaporator to yield a white solid. The reaction was quantitative by ^1H NMR spectroscopy.

Method B. A 1:1 stoichiometric mixture of $[Et_4N]_2[Re(CO)_3Br_3]$ and H**L**$^{1-5}$ was dissolved in methanol (10−20 mL) and refluxed for 2 h. The solvent was removed using a rotary evaporator to yield a white solid.

Method C. A 1:1 stoichiometric mixture of $[Re(CO)_3(H_2O)_3]Br$ and H**L**$^{1-5}$ was dissolved in methanol (10−20 mL) and refluxed for 2 h. The solvent was removed using a rotary evaporator and pure product was obtained by recrystallization, column chromatography, or semipreparative HPLC.

Experimental for the Preparation of Re(L$^{1-5}$)(CO)$_3$(H$_2$O) by Method C. *fac*-(Aqua)tri(carbonyl)(1-{*N*-[*p*-benzyl β-D-glucopyranoside]ethanamide}-2-methyl-3-oxy-4(1*H*)-pyridinato)rhenium(I), (ReL^1(CO)$_3$(H$_2$O)). The title compound was prepared from H**L**^{1} (127 mg, 0.291 mmol) and $[Re(CO)_3(H_2O)_3]Br$ (119 mg, 0.294 mmol) in methanol (20 mL). The product was purified by semipreparative HPLC (30 mL/min gradient method 95% water 5% methanol to 100% methanol over 30 min) with the product collected between 11.5 and 12.5 min. Solvent was removed by rotary evaporation and the resulting white solid dried in vacuo overnight (90 mg, 44%). ^1H NMR ($CD_3OD:D_2O$ 1:1, 400 MHz): δ 2.48 (s, 3H, C13-CH_3), 3.35−3.57 (m, 4H, *H*2, *H*3, *H*4, *H*5), 3.72 (dd, 1H, *H*6a, $^3J_{5,6}$ = 5.63 Hz, $^2J_{6a,6b}$ = 12.2 Hz), 3.89 (d, 1H, *H*6b, J = 10.51 Hz), 4.98 (d, 1H, *H*1, $^3J_{1,2}$ = 7.22 Hz), 5.12 (s, 2H, *H*12), 6.68 (d, 1H, *H*16, $^3J_{16,17}$ = 6.55 Hz), 7.12 (d, 2H, *H*8, *H*8′, $^3J_{8,9}$ = 8.87 Hz), 7.46 (d, 2H, *H*9, *H*9′, $^3J_{8,9}$ = 9.05 Hz), 7.59 (d, 1H, *H*17, $^3J_{16,17}$ = 6.54 Hz). $^{13}C\{H\}$ NMR ($CD_3OD:D_2O$ 1:1, 75 MHz): δ 11.68 (C13-*C*H$_3$), 56.2 (*C*12), 60.69, (*C*6), 69.69 (*C*4), 73.21 (*C*2), 76.58 (*C*3), 76.99 (*C*5), 100.72 (*C*1), 109.15 (*C*16), 116.57 (*C*8, *C*8′). 120.49 (*C*9,*C*9), 132.56 (*C*10), 134.55 (*C*13), 135.09 (*C*17), 158.65 (*C*14), 164.34 (*C*11), 174.06 (*C*15), 199.28,

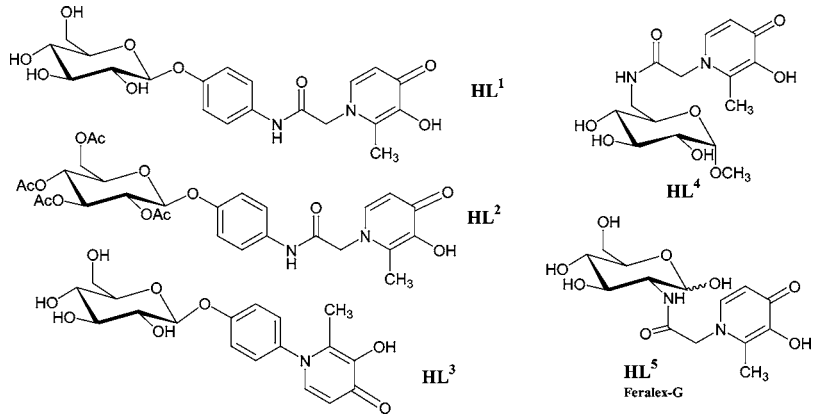

Figure 1. Structures of carbohydrate-appended pyridinone ligands (*59*, *63*).

199.99, 200.32 (3 *C*O).). IR (KBr disc, cm^{-1}): 3393 (br) (νOH), 2013 (vs), 1884 (vs) (ν(*fac*-Re(CO)$_3$)), 1686 (m), 1545 (s), (ν(CONH)), 1605 (s), (ν(CO)), 1508 (s), 1478 (s), (aryl), 1358 (s), 1285 (m), 1227 (m, br) (δ(OH)), 1073 (s, br), (ν(COH)), 835 (m), (para-substituted benzene). UV−visible spectrum (H_2O): λ_{max}/nm (ϵ_{max}/L M^{-1} cm^{-1}) = 319 (6.2×10^3), 276 (1.2×10^4). MS (ESI+): *m*/*z* (relative intensity) = 729, 727 ([M − H_2O+Na]$^+$, 100). MS (ESI-): *m*/*z* (relative intensity)= 706, 704 ([M − H_2O]$^-$, 75). Anal. Calcd for $C_{23}H_{25}N_2O_{13}Re$: C, 38.18; H, 3.50; N, 3.87. Found: C, 38.00; H, 3.90; N, 4.20.

***fac*-(Aqua)tri(carbonyl)(1-{*N*-[*p*-benzyl (2,3,4,6-tetra-*O*-acetyl-β-D-glucopyranoside)]ethanamide}-2-methyl-3-oxy-4(1*H*)-pyridinato)rhenium(I), (ReL^2(CO)$_3$(H_2O)·CH_3OH).** The title compound was prepared by refluxing H**L^2** (61 mg, 0.10 mmol) and [Re(CO)$_3$(H_2O)$_3$]Br (40 mg, 0.10 mmol) in methanol (8 mL). The product was purified by alumina column chromatography eluting with 100% methanol. The fractions containing product were reduced on a rotary evaporator. To remove any alumina present from the column, the residual solid was dissolved in ethyl acetate and passed through a 0.22 μm syringe. The solvent was removed using a rotary evaporator to yield the product as a white solid, which was dried under reduced pressure overnight (57 mg, 65%). ^{1}H NMR (CD_3OD: CD_3CN 1:1, 400 MHz): δ 2.01, 2.02, 2.05, 2.06 (4s, 12H, COOCH_3), 2.42 (s, 3H, C13-CH_3), 4.17 (m, 1H, *H*5), 4.29 (d, 1H, *H*6a, $^2J_{6a,6b}$ = 12.32 Hz), 4.42 (dd, 1H, *H*6b, $^3J_{5,6b}$ = 5.16 Hz, $^2J_{6a,6b}$ = 12.32 Hz), 4.99 (s, 2H, *H*12), 5.06−5.22 (m, 2H, *H*2, *H*4), 5.29 (d, 1H, *H*1, $^3J_{1,2}$ = 7.89 Hz), 5.37 (t, 1H, *H*3, $^3J_{3,4}$ = 9.45 Hz), 6.62 (d, 1H, *H*16, $^3J_{16,17}$ = 6.55 Hz), 7.04 (d, 2H, *H*8, *H*8′, $^3J_{8,9}$ = 8.38 Hz), 7.50 (d, 1H, *H*17, $^3J_{16,17}$ = 6.70 Hz), 7.53 (d, 2H, *H*9, *H*9′, $^3J_{8,9}$ = 8.38 Hz). ^{13}C{H} (CD_3OD: CD_3CN 1:1, 75 MHz): δ 12.30 (C9*C*H$_3$), 20.75 (4 COO*C*H$_3$), 57.7 (*C*12), 62.86 (*C*6), 69.39 (*C*4), 72.20 (*C*2), 72.82 (*C*5), 73.54 (*C*3), 99.80 (*C*1), 111.05 (*C*16), 118.26 (*C*8), 122.50 (*C*9), 134.43 (*C*10), 136.44 (*C*17), 137.36 (*C*13), 154.70 (*C*7), 159.44 (*C*14), 165.77 (*C*11), 170.93, 171.06, 171.41, 171.92 (4 *C*OOCH$_3$), 174.1 (*C*15), 199.1, 199.2, 199.4 (3 *C*O). IR (NaCl plate, cm^{-1}): 2012, 1883 (ν(*fac*-Re(CO)$_3$), 1754 (ν(COOCH$_3$)), 1692 (ν(CONH)). MS (ESI+): *m*/*z* (relative intensity) = 897, 895 ([M − H_2O +Na]$^+$, 80). MS (ESI-): *m*/*z* (relative intensity) = 873, 871 ([M − H_2O − 1]$^-$, 100). Anal. Calcd for $C_{31}H_{33}N_2O_{17}Re$·CH_3OH: C, 42.43; H, 3.89; N, 3.09. Found: C, 42.26; H, 4.05; N, 3.27.

***fac*-(Aqua)tri(carbonyl)(1-{*p*-benzyl β-D-glucopyranoside}-2-methyl-3-oxy-4(1*H*)-pyridinato)rhenium(I) Hemihydrate (ReL^3(CO)$_3$(H_2O)·0.5H_2O).** The title compound was prepared from H**L^3** (154 mg, 0.406 mmol) and [Re(CO)$_3$(H_2O)$_3$]Br (164 mg, 0.406 mmol) in methanol (20 mL). The product was purified by recrystallization from hot methanol, yielding a white solid that was dried in vacuo overnight (95 mg, 36%). ^{1}H NMR (CD_3OD:D_2O 1:1, 400 MHz): δ 2.16 (s, 3H, C11-CH_3), 3.48 (t, 1H, *H*4, $^3J_{3,4}$ = 9.14 Hz), 3.57−3.60 (m, 3H, *H*2, *H*3, *H*5), 3.76 (dd, 1H, *H*6a, $^2J_{6a,6b}$ = 12.34 Hz, $^3J_{5,6}$ = 5.79 Hz), 3.92 (d, 1H, *H*6b, *J* = 10.81), 5.12 (d, 1H, *H*1, $^3J_{1,2}$ = 7.16 Hz), 6.73 (d, 1H, *H*14, $^3J_{14,15}$ = 6.85 Hz), 7.29 (d, 2H, *H*8, *H*8′, $^3J_{8,9}$ = 8.68 Hz), 7.36 (2H, *H*9, *H*9′, $^3J_{8,9}$ = 8.99 Hz), 7.58 (d, 1H, *H*15, $^3J_{14,15}$ = 6.35 Hz). ^{13}C{H} NMR (CD_3OD:D_2O, 75 MHz): δ 14.05 (*C*H$_3$), 62.49 (*C*6), 71.31 (*C*4), 74.82 (*C*2), 77.94 (*C*3), 78.34 (*C*5), 102.14 (*C*1), 111.21 (*C*14), 118.69 (*C*8, *C*8′), 133.21 (*C*9, *C*9′), 135.78 (*C*11), 135.86 (*C*15), 137.68 (*C*10), 159.26 (*C*7), 159.86 (*C*12), 175.61 (*C*13), 199.06, 199.45, 199.82 (3 *C*O). IR (KBr disc, cm^{-1}): 3311(br) (νOH), 2025 (vs), 1907 (vs) (ν(*fac*-Re(CO)$_3$)), 1609 (s), (ν(CO)), 1538 (s), 1505 (s), 1478 (s) (aryl), 1362 (s), 1306 (m), 1240 (m, br) (δ(OH)), 1044 (s, br), 1072 (s), 1018 (s), (ν(COH)), 817 (s), (para-substituted benzene). UV−visible spectrum (H_2O): λ_{max}/nm (ϵ_{max}/L M^{-1} cm^{-1}) = 214 (3.3×10^4), 318 (1.1×10^4). MS (ESI +): *m*/*z* (relative intensity) = 672, 670 ([M − H_2O + Na]$^+$, 100), 650, 648 ([M − H_2O + 1]$^+$). Anal. Calcd for $C_{21}H_{22}NO_{12}Re$·0.5H_2O: C, 37.33; H, 3.43; N, 2.07. Found: C, 37.41; H, 3.50; N, 2.38.

***fac*-(Aqua)tri(carbonyl)(1-{*N*-[methyl 6-amino-6-deoxy-α-D-glucopyranoside] ethanamide}-2-methyl-3-oxy-4(1*H*)-pyridinato)rhenium(I), (ReL^4(CO)$_3$(OH_2)).** The title compounds was prepared using H**L^4** (123 mg, 0.343 mmol) and [Re(CO)$_3$-(H_2O)$_3$]Br (139 mg, 0.344 mmol) in methanol (10 mL), and the product was purified by semipreparative HPLC. ^{1}H NMR (CD_3OD:D_2O 1:1, 400 MHz): δ 2.39 (s, 3H, C9-CH_3), 3.22 (t, 1H, *H*4, $^3J_{3,4}$ = 9.25 Hz), 3.41 (s, 3H, OCH_3), 3.44 (m, 1H, *H*6a), 3.48 (dd, 1H, *H*2, $^3J_{1,2}$ = 3.66 Hz), 3.59−3.71 (m, 3H, *H*3, *H*5, *H*6b), 4.7 (d, 1H, *H*1, $^3J_{1,2}$ = 3.66 Hz), 4.99 (s, 2H, *H*8), 6.68 (d, 1H, *H*12, $^3J_{12,13}$ = 6.74 Hz), 7.56 (d, 1H, *H*13, $^3J_{12,13}$ = 6.93 Hz). ^{13}C{H} NMR (CD_3OD:D_2O 1:1, 75 Mz): δ 12.53 (C9-*C*H$_3$), 41.37 (*C*6), 55.94 (O*C*H$_3$), 57.79 (*C*8), 70.86 (*C*5), 70.90 (*C*4), 70.96 (*C*2), 74.12 (*C*3), 100.50 (*C*1), 111.81 (*C*12), 137.1 (*C*13), 138.5 (*C*9), 158.00 (*C*10), 169.1 (*C*7), 174.23 (*C*11), 199.06, 198.80, 198.30 (3 *C*O). IR (KBr disc, cm^{-1}): 3393 (br) (νOH), 2016 (vs), 1891 (vs) (ν(*fac*-Re(CO)$_3$)), 1676 (m), 1546 (s) (ν(CONH)), 1610 (s) (ν(CO)), 1343 (m), 1284 (m) (δ(OH)), 1058 (s, br) (ν(COH)). UV−visible spectrum (H_2O): λ_{max}/nm (ϵ_{max}/L M^{-1} cm^{-1}) 318 (6.1×10^3), 273 (9.0×10^3). MS (ESI+): *m*/*z* (relative intensity) = 651, 649 ([M − H_2O + Na]$^+$, 100), 629, 627 ([M − H_2O + 1]$^+$, 20). Anal. Calcd for $C_{18}H_{23}N_2O_{12}Re$: C, 33.49; H, 3.59; N, 4.34. Found: C, 33.12; H, 3.50; N, 3.90.

***fac*-(Aqua)tri(carbonyl)(1-{N-[2-amino-2-deoxy-D-glucopyranose]ethanamide}-2-methyl-3-oxy-4(1*H*)-pyridinato)rhenium(I) Hydrate, (ReL^5(CO)$_3$(OH_2)·H_2O).** The title compound was prepared from H**L^5** (167 mg, 0.485 mmol) and [Re(CO)$_3$-(H_2O)$_3$]Br (196 mg, 0.485 mmol) in a mixture of methanol (10

Scheme 1. Preparation and Structures of M(L$^{1-5}$)(CO)$_3$(H$_2$O) (M = Re, ^{99m}Tc, ^{186}Re), and M = Re Structures Showing Numbering Scheme for NMR Studies

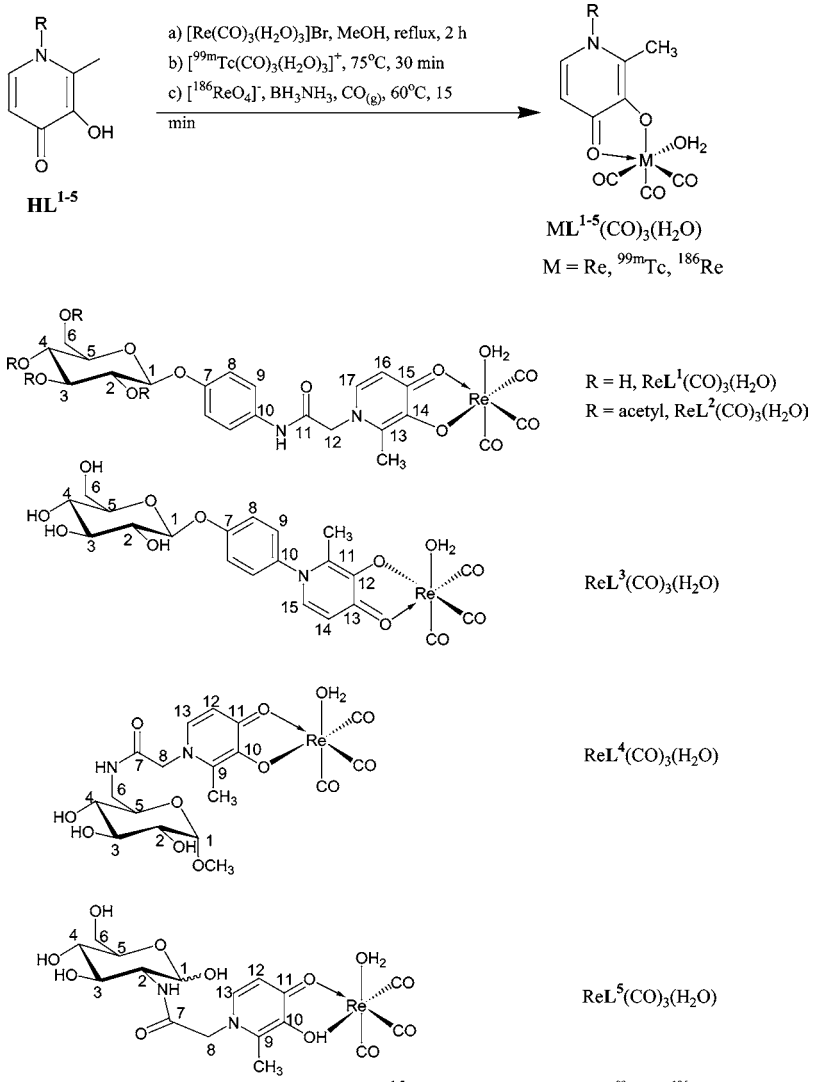

mL) and water (1 mL). The product was purified by one of two methods. The product was either allowed to precipitate from methanol (<2 mL), filtered out and washed with cold methanol or eluted from a silica column with 4:1 dichloromethane: methanol (R_f = ~0.2), and obtained by reducing the volume of product-containing fractions on a rotary evaporator. Both methods yielded a white solid that was dried in vacuo overnight (98 mg, 32%). ^{1}H NMR (CD_3OD:D_2O 1:1, 400 MHz): δ 2.39 (s, 3H, COOC*H*$_3$ α), 2.40 (s, 3H, COOC*H*$_3$ β), 3.40−3.46 (m, 3H, *H*3, *H*4β), 3.55 (m, 1H, *H*5β), 3.67 (m, 1H, *H*2β), 3.70−3.88 (m, 6H, *H*4α, *H*5α, *H*6), 3.90 (dd, 1H, *H*2α, $^3J_{1,2} \equiv$ 3.6 Hz, $^3J_{2,3}$ = 6.9 Hz), 4.71 (d, 1H, *H*1β, $^3J_{1,2}$ = 8.4 Hz), 4.99 (s, 2H, *H*8β), 5.01 (s, 2H, *H*8α), 5.18 (d, 1H, *H*1α, $^3J_{1,2}$ = 3.66 Hz), 6.67 (d, 2H, *H*12, $^3J_{12,13}$ = 6.86 Hz), 7.56 (2 overlapping dd, 2H, *H*13, $^3J_{12,13}$ = 6.85 Hz). ^{13}C{H} NMR (CD_3OD:D_2O 1:1, 75 MHz): δ 12.48 (C9*C*H$_3$$\beta$), 12.54 (C9*C*H$_3$), 55.72 (*C*2), 57.83 (*C*8), 58.11 (*C*2β), 58.37 (C8β), 62.03 (*C*6), 62.15 (*C*6β), 71.42 (*C*3β), 71.66 (*C*3), 72.11 (*C*5), 72.84 (*C*4), 75.14 (*C*5β), 77.44 (*C*4β), 92.00 (*C*1), 96.12 (*C*1β), 111.52 (*C*13), 137.11 (*C*12β), 137.18 (*C*12), 144.35 (*C*9), 158.19 (*C*10), 174.40 (*C*11), 198.98,199.15, 199.38 (3 *C*O). IR (KBr disc, cm^{-1}): 3394 (br) (νOH), 2016 (vs), 1891 (vs) (ν(*fac*-Re(CO)$_3$)), 1677 (m), 1546 (s) (ν(CONH)), 1610 (s) (ν(CO)), 1344 (m), 1284 (m) (δ(OH)), 1058 (s, br) (ν(COH)). UV−visible spectrum (H_2O): λ_{max}/nm (ϵ_{max}/L M^{-1} cm^{-1}) = 318 (8.3 × 10^3), 263 (9.9 × 10^3). MS (ESI+): *m*/*z* (relative intensity) = 637, 635 ([M − H_2O + Na]$^+$, 100). Anal. Calcd for $C_{17}H_{21}N_2O_{12}Re\cdot H_2O$: C, 31.43; H, 3.57; N, 4.31. Found: C, 31.23; H, 3.91; N, 4.14.

Solid-state Structure Determination for HL^5. Needle crystals of H**L**^{5} were grown by slow evaporation of a methanol solution, mounted on glass fibers and cooled to 173 K. Data sets were collected on a Bruker X8 APEX diffractometer using graphite-monochromated Mo Kα radiation (λ = 0.71073 Å). Data were collected and integrated using the Bruker SAINT (*65*) software package and corrected for Lorentz and polarization effects as well as for absorption (SADABS) (*66*). The structure was solved by direct methods (SIR92) (*67*). Non-hydrogen atoms were refined anisotropically, while hydrogen atoms were added but not refined. Final refinement was completed using SHELXL-97 (*68*).

Measurement of Phosphorylation of HL$^{1-5}$ by Hexokinase. The ligands H**L**$^{1-5}$ were qualitatively tested as substrates for hexokinase. Each compound (10 L, 10^{-2} M) in 30 mM triethanolamine buffer (pH = 6) was added to 1 mL of the assay mixture, which contained 100 U/L hexokinase, 1 mM ATP, and 4 mM $MgCl_2$ all dissolved in 30 mM triethanolamine buffer (pH = 6). After incubating for 10 min or 24 h, the assay mixture was analyzed by analytical HPLC, using 30 mM KH_2PO_4 buffer as the solvent. The compound was determined to be a substrate of hexokinase if the HPLC chromatogram showed the disappearance of ATP (retention time 7.0 min) and the appearance of the ADP (retention time 9.8 min).

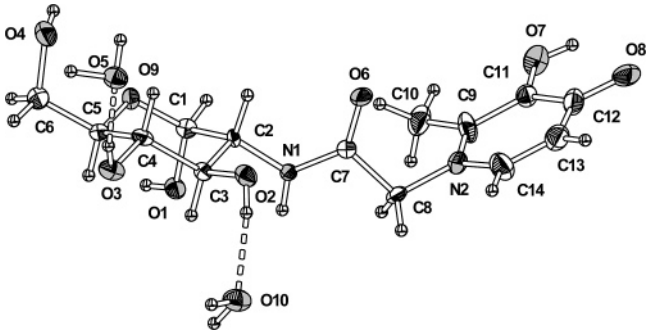

Figure 2. Structure of H**L**^{5} showing atom labeling scheme (50% thermal probability ellipsoids).

Table 1. Selected Bond Lengths (Å) and Angles (deg) in HL^5

N1−C2	1.457(4)	C2−N1−C7	123.3(3)
N1−C7	1.327(4)	N1−C7−O6	125.9(3)
O6−C7	1.222(4)	N1−C7−C8	113.3(3)
O7−C11	1.368(4)	O7−C11−C12	120.7(4)
O8−C12	1.260(4)	O8−C12−C11	120.4(3)

Inhibition of Hexokinase Glucose Phosphorylation by HL$^{1-5}$ and Re(L$^{1-5}$)(CO)$_3$(H$_2$O). The pro-ligands and their complexes were tested for their capacity to inhibit glucose phosphorylation by hexokinase. In a cuvette, 500 μL glucose (HK) assay kit (Sigma) was pipetted into a solution (750 μL) containing the pro-ligand or complex (final concentration 10^{-3}-10^{-4} M), and glucose, or just glucose alone (final concentration 10^{-4} M). The final total volume was 1250 μL. The solution was monitored by UV−visible spectroscopy at 340 nm every 30 s for 10 min to determine the reaction rate. The reaction rates with and without the pro-ligand or complex were compared to determine if each could inhibit the phosphorylation of glucose by hexokinase.

^{186}Re Radiolabelling. A sealed vial containing 3.5 mg of BH_3·NH_3 was purged with CO gas for 10 min. A solution containing 400 μL of 10^{-3} M solution of H**L**$^{1-5}$ in PBS, 100 μL of 100 MBq of $[^{186}ReO_4]^-$ in saline, and 4.5 μL of 85% H_3PO_4 was added to the vial. A syringe to compensate for any gas evolution was attached to the vial, and the vial was heated at 60 °C for 15 min. Radiochemical yield of ^{186}Re(**L**$^{1-5}$)(CO)$_3$(H$_2$O) was determined by HPLC using Re(**L**$^{1-5}$)(CO)$_3$(H$_2$O) as a standard.

RESULTS AND DISCUSSION

The 3-hydroxy-4-pyridinone moiety is a bifunctional chelate that deprotonates and binds as a monoanionic bidentate ligand, forming a stable 5-membered ring with the metal center. Simple functionalization of the nitrogen of the pyridinone ring gives a remarkable spectrum of ligand designs. In this work we examined the binding of five pyridinone based ligands bearing pendent carbohydrates (*59*). The glucose derivatives are tethered to the pyridinone binding moiety through the C1, C2, or C6 position with linkers of varying length. The solid-state structure of one of the ligands, H**L**^{5}, is reported, and confirms several salient points (Figure 2, Table 1). The structure diagram clearly shows the distance of the glucose derivative, in this case glucosamine, from the pyridinone moiety, suggesting that the carbohydrate will not interact with the metal center upon complexation. As well, the glucosamine moiety is in the common chair conformation. To retain biological activity, minimal hindrance or modification of the glucose derivative is ideal. As H**L**^{5} has one of the shortest tether lengths between the glucose and binding moieties, it can by hypothesized that none of the ligands used in this study will have direct metal-carbohydrate interaction. Although both anomers of the glucosamine are seen in the NMR spectra, (*59*) only one anomer is observed in the crystal lattice, due to preferential crystallization.

The Re**L**$^{1-5}$(CO)$_3$(H$_2$O) complexes were prepared in high yield by three different methods (Scheme 1). Preparation from Re(CO)$_5$Br required a basic buffer system and heating with the ligand, while preparation from $[NEt_4]_2[Re(CO)_3Br_3]$ and $[Re(CO)_3(H_2O)_3]Br$, which have labile Br^- and H_2O ligands respectively, only required heating. All methods were stoichiometric and quantitative as monitored by ^{1}H NMR spectroscopy. Preparation from $[Re(CO)_3(H_2O)_3]Br$ resulted in minimal side-products and was consequently the method of choice, as purification posed difficulties due to the polar nature of the complexes. In cases where recrystallization was not successful and solvent limitations excluded silica and alumina chromatography, semipreparative reverse phase HPLC was used. After purification, yields were between 30−65%.

All complexes were thoroughly characterized by the usual techniques. Electrospray mass spectrometry gave characteristic pairs of peaks with the correct isotopic pattern for Re (^{187}Re 62.6%, ^{185}Re 37.4%). In all cases the H_2O ligand proposed to occupy the sixth coordination site was not observed in the MS. The mass-to-charge ratios observed corresponded to $[M - H_2O + H]^+$ or $[M - H_2O + Na]^+$ for positive ES-MS, and $[M - H_2O - H]^-$ for negative ES-MS. Other peaks corresponding to the free ligand were observed, but are due to fragmentation, as no free ligand is observed in the NMR spectra of the crude or purified complexes. Elemental analysis confirmed the bulk composition of the complexes and included in every case the one water molecule proposed to occupy the sixth coordination site. Most complexes had more than just one water molecule associated with the solid product, common for carbohydrate containing compounds and also observed in the solid-state structure of H**L**^{5} (Figure 2). IR spectroscopy contained similar vibrational frequencies as the ligands, with additional peaks diagnostic of the carbonyl stretches. Three peaks for the carbonyl stretches are expected due to the low symmetry of each compound, one at 2025−2013 cm^{-1} and another at 1907−1883 cm^{-1}, with the broader latter peak attributable to two peaks overlapping.

Both ^{1}H and ^{13}C NMR spectroscopy confirmed the solution structures of the complexes of particular relevance, as radiolabeling is done exclusively in solution. The pendent nature of the carbohydrate groups after complexation was confirmed by the small shifts in carbohydrate-associated ^{1}H and ^{13}C NMR resonances, < 0.02 and 1 ppm, respectively (Figure 3). Large coordination-induced shifts (CIS) would be expected if any of the carbohydrate hydroxyl groups directly interacted with the metal ion. Shifts in the ^{1}H NMR spectra were observed for the pyridinone moiety, confirming binding. For all the complexes, the resonance associated with the hydrogen on the carbon atom adjacent to the binding ketone functionality shifted downfield 0.17−0.19 ppm (Figure 3). In the ^{13}C NMR spectra, the CISs were clearly observed for the carbon atoms bound to the coordinating oxygen atoms, as expected for bidentate chelation. For the ketone carbon, a downfield shift of 3.3−4.7 ppm confirms the dative bond, while the large downfield shift of 12−14.7 ppm for the adjacent hydroxyl carbon verifies the covalent metal oxygen bond. The three CO ligands were also observed in the ^{13}C NMR spectra, but the water molecule associated with the sixth coordination site was not observed in the ^{1}H NMR spectra, possibly due to exchange with the deuterated solvent (water and/or methanol).

Radiolabeling of H**L**$^{1-5}$ with ^{99m}Tc and ^{186}Re was simple, fast and high yielding. For ^{99m}Tc, the $[^{99m}Tc(CO)_3(H_2O)_3]^+$ precursor was heated with excess ligand in PBS to give >95% yield for all ligands except H**L**^{2} (Table 2, Figure 4). The lower yield for H**L**^{2} is due to its lower water solubility. The Isolink

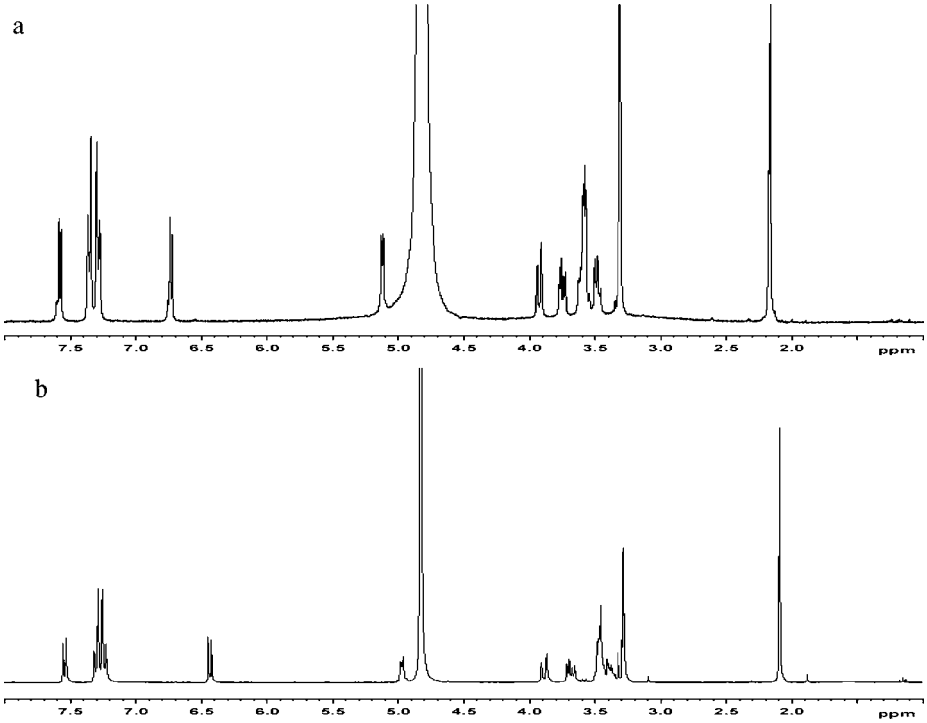

Figure 3. ^{1}H NMR spectra (400 MHz, CD_3OD:D_2O 1:1) of H**L**^{3} (a) and Re**L**$^{3}(CO)_3(H_2O)$ (b).

Table 2. Identification Methods and Radiochemical Yields for the Preparation of M(L^{1-5})$(CO)_3(H_2O)$ M = ^{99m}Tc, ^{186}Re

ligand	HPLC method[a]	UV (254 nm) detected RT of standard/min	radiation detected RT/min (radiochemical yield)	
			^{99m}Tc	^{186}Re
H**L**^{1}	70% A 30% B	9.5	9.2 (97.7 ± 0.5)	9.5 (99 ± 0.1)
H**L**^{2}	TLC method[b]	0.7[b]	0.7[b] (87)	0.7[b] (70)
H**L**^{3}	50% A 50% B	7.4	7.0 (96 ± 3)	7.3 (89 ± 3)
H**L**^{4}	70% A 30% B	9.9	9.8 (95 ± 2)	9.9 (99.1 ± 0.3)
H**L**^{5}	50% A 50% B	7.0	6.9 (96.3 ± 2)	6.9 (91 ± 2)

[a] HPLC run on Synergi 4 μm C-18 Hydro RP analytical column, isocratic 1 mL/min, solvent A: 0.1% w/w trifluoracetic acid in water, solvent B: methanol. [b] TLC run on silica plates, developing with 80% ethyl acetate and 20% methanol, analyzed with UV Lamp or RadioTLC. RT given is retention factor.

kits are found to be unsuitable for the preparation of the analogous ^{186}Re precursor, although alternative methods have been used to prepare $[^{188}Re(CO)_3(H_2O)_3]^+$ in good yields (80−90%) (*23*). Although Tc and Re have somewhat similar chemistry, Re is easier to oxidize, and thus reoxidation to perrhenate is facile, especially in basic media with extended heating. Preparing $[^{186}Re(CO)_3(H_2O)_3]^+$ as described in the literature (*14*, *17*) followed by incubation at a 75 °C for 10−30 min gave radiochemical yields <85%, with perrhenate as the major side product. To obtain the same high labeling yields for ^{186}Re as were achieved for ^{99m}Tc, several modifications were necessary. The best method was a one-pot preparation wherein the Re precursor is formed in the presence of the ligand, facilitating quick chelation of the precursor and shorter heating times to minimize reoxidation. The one-pot preparation is optimal for radiopharmaceutical synthesis and gave unprecedented radiochemical yields, for the $[^{186}Re(CO)_3^+]$ core, as high as 99% (Table 2, Figure 4). Again, H**L**^{2} labeled at lower yields due to low ligand solubility. For both ^{99m}Tc and ^{186}Re, the radiolabeled complexes were identified and radiochemical yields determined by either HPLC or TLC using the nonradioactive Re complexes for comparison. At tracer level concentrations of the radiolabeled complexes other characterization methods are precluded.

To assess the stability of the radiolabeled compounds, the ^{99m}Tc labeled species were challenged with an excess of cysteine or histidine, potential metal binding amino acids ubiquitous in vivo. All complexes were stable out to 24 h, suggesting that they would be appropriate for radiopharmaceutical applications

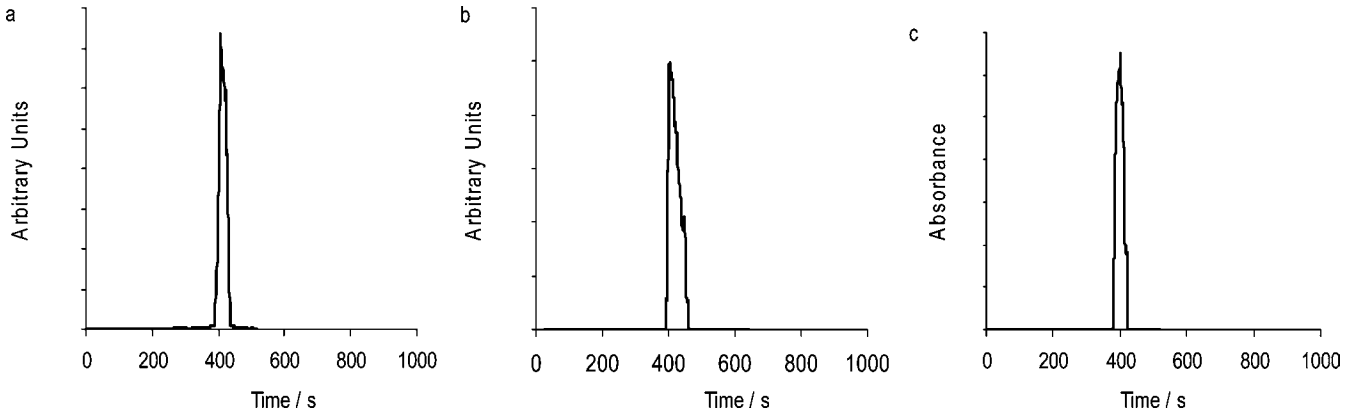

Figure 4. HPLC traces for labeling of H**L**^{5} (a) ^{186}Re(**L**^{5})$(CO)_3(H_2O)$ radiation trace, (b) ^{99m}Tc(**L**^{5})$(CO)_3(H_2O)$ radiation trace, (c) Re(**L**^{5})$(CO)_3(H_2O)$ UV trace.

Table 3. Percentage $^{99m}Tc(L^{1-5})(CO)_3(H_2O)$ Remaining Intact Determined by HPLC after 1, 4, and 24 h in 10^{-3} M Solution of Cysteine or Histidine at 37 °C

	cysteine			histidine		
ligand	1 h	4 h	24 h	1 h	4 h	24 h
H**L**^{1}	99 ± 7	99 ± 6	97 ± 3	95 ± 7	95 ± 3	71 ± 8
H**L**^{3}	99 ± 1	97 ± 2	79 ± 1	99 ± 3	97 ± 2	77 ± 6
H**L**^{4}	99 ± 1	99 ± 1	95 ± 5	99 ± 2	99 ± 4	75 ± 6
H**L**^{5}	99 ± 1	99 ± 1	81 ± 8	98 ± 1	96 ± 3	93 ± 5

(Table 3). At the 1 and 4 h time points, little decomposition was observed in all cases, with >95% of the complex remaining intact. At 24 h some decomposition was observed, mainly due to substitution of the amino acid for the ligand, but >70% of the complex was still intact regardless of which complex was challenged. High stability under these conditions has been reported for other $[^{99m}Tc(CO)_3]^+$ complexes of bidentate ligands, (*15*) but does not obviate the possibility of unfavorable binding of the complex to plasma proteins (*19*).

The optimal imaging properties of FDG partially stem from its unique interaction with hexokinase (HK), the first enzyme in glucose metabolism. FDG is a substrate for HK (*69*), which phosphorylates the sugar at the 6 position, but is not a substrate for the subsequent enzyme in the metabolism pathway. Instead, FDG becomes trapped in the cell and accumulates, resulting in higher resolution imaging than if FDG perfectly mimicked glucose (*1*). Hence, one of the potential targets for the Tc-glucose conjugates, reported herein, is the hexokinase enzyme. Each of the ligands and/or complexes was tested as potential substrates or inhibitors of HK. The free ligands were evaluated as substrates of HK, by monitoring the conversion of ATP to ADP in the presence of ligand and HK; none of ligands were substrates. To determine if other interaction between HK and the ligands could be observed, inhibition studies were completed by monitoring the affect of each ligand on the rate of glucose (the natural HK substrate) conversion. The rate was monitored using a secondary enzyme conversion which is coupled to the conversion of NAD^+ to NADH which can be quantitatively monitored by UV spectroscopy. At the concentrations tested, no inhibitory activity was observed. Other groups have noted inhibition activity of similar Re-carbohydrate complexes, even when no activity was observed for the ligand (*11*). Thus, the complexes Re**L**$^{1-5}(CO)_3(H_2O)$ were also tested for inhibition of HK, but no activity was observed at the concentration tested for the complexes either. At higher concentrations, absorptions of the ligand chromophore interfere with the assay, limiting accuracy at higher concentration for which the ligands or complexes may show activity. Further studies with other potential targets, such as glucose transporters, may show different results.

CONCLUSIONS

This work adds to the type of bifunctional chelates that have been studied with the popular $[M(CO)_3]^+$ core (M = Re, Tc) and broadens the scope of Tc-glucose conjugates. The complexes are well characterized and confirm the pendent nature of the carbohydrate, the bidentate chelation of the pyridinone, and the presence of a water molecule in the sixth coordination site. High yield labeling of the pyridinone-based ligands with both ^{99m}Tc and ^{186}Re was achieved. The one-vial, one-step labeling of ^{186}Re at such high yields is unprecedented and could be easily developed into a kit preparation. Only limited progress of Re labeling with the $[Re(CO)_3]^+$ core has been reported to date, especially with the ^{186}Re isotope, despite its radiotherapeutic potential. All ^{99m}Tc complexes proved to be reasonably stable up to 24 h when challenged with cysteine or histidine solutions, although further stability challenges in plasma and with the ^{186}Re complexes are needed to confirm that the complexes will be stable in vivo. Mixed ligand 2 + 1 complexes, where a second monodentate ligand is added, could be investigated to mask the sixth coordination site and increase the stability of the complexes. This second monodentate ligand would also allow systematic modification of the properties of the complex. Finally, the ligands and complexes were evaluated as potential substrates or inhibitors of the glucose metabolism enzyme hexokinase. Unfortunately, no substrate or inhibitory activity was observed at the concentrations tested. These compounds may still have potential as imaging and therapy agents, if they interact with glucose transporters (some of which are highly expressed in certain tumor types) or if they can accumulate in tumors via another pathway as observed for other promising Tc-glucose conjugates (*8*).

ACKNOWLEDGMENT

Acknowledgment is made to Mallinckrodt Inc. for the donation of Isolink Kits, to Vancouver Coastal Health-UBC Hospital for $[^{99m}TcO_4]^-$, to MDS Nordion Inc. for $[^{186}ReO_4]^-$ and for sponsoring an Industrial Postgraduate Scholarship (C. L. F.), to the Natural Sciences and Engineering Research Council of Canada (NSERC) for a Strategic Grant, an Industrial Postgraduate Scholarship (C.L.F.), a Post-graduate Scholarship (T.S.), and an Undergraduate Research Award (J. S.), and to UBC for a University Graduate Fellowship (C.A.B).

Supporting Information Available: Select HPLC radiation and UV traces for the cyteine/histidine challenge experiments and X-ray crystallography data. This material is available free of charge via the Internet at http://pubs.acs.org.

LITERATURE CITED

(1) Beuthien-Baumann, B., Hamacher, K., Oberdorfer, F., and Steinbach, J. (2000) Preparation of fluorine-18 labelled sugars and derivatives and their application as tracer for positron-emission-tomography. *Carbohydr. Res. 327*, 1107−1118.

(2) Krohn, K. A., Mankoff, D. A., Muzi, M., Link, J. M., and Spence, A. M. (2005) True tracers: comparing FDG with glucose and FLT with thymidine. *Nucl. Med. Biol. 32*, 663−671.

(3) Segall, G. (2002) Assessment of myocardial viability by positron emission tomography. *Nucl. Med. Commun. 23*, 323−330.

(4) Czernin, J. (2002) Clincal application of FDG-PET in oncology. *Acta Med. Aust. 5*, 162−170.

(5) Dilworth, J. R., and Parrott, S. J. (1998) The biomedical chemistry of technetium and rhenium. *Chem. Soc. Rev. 27*, 43−55.

(6) Banerjee, S. R., Babich, J. W., and Zubieta, J. (2006) A new bifunctional amino acid chelator targeting the glucose transporter. *Inorg. Chim. Acta 359*, 1603−1612.

(7) Duatti, A., Marchi, A., Magon, L., Deutsch, E., and Bertolasi, V. (1987) Synthesis and structure of an amino sugar-schiff base complex of technetium (V) containing salicyladehyde in an unusual coordination mode. *Inorg. Chem. 26*, 2182−2186.

(8) Yang, D. J., Kim, C.-G., Schechter, N. R., Azhdarinia, A., Yu, D.-F., Oh, C.-S., Bryant, J. L., Won, J.-J., Kim, E. E., and Podoloff, D. A. (2003) Imaging with ^{99m}Tc ECDG targeted at the multifunctional glucose transport system: feasibility study with rodents. *Radiology 226*, 465−473.

(9) Petrig, J., Schibli, R., Dumas, C., Alberto, R., and Schubiger, P. A. (2001) Derivatization of glucose and 2-deoxyglucose for transition metal complexation: substitution reactions with organometallic ^{99m}Tc and Re prescursors and fundamental NMR investigation. *Chem. Eur. J. 7*, 1868−1873.

(10) Dumas, C., Petrig, J., Frei, L., Spingler, B., and Schibli, R. (2005) Functionalization of glucose at C-3 for transition metal coordination: organo-rhenium complexes with carbohydrate skeletons. *Bioconjugate Chem. 16*, 421−428.

(11) Schibli, R., Dumas, C., Petrig, J., Spadola, L., Scapozza, L., Garcia-Garayoa, E., and Schubiger, P. A. (2005) Synthesis and *in vitro* characterization of organometallic rhenium and technetium

glucose complexes against GLUT 1 and hexokinase. *Bioconjugate Chem. 16*, 105−112.
(12) Ozker, K., Collier, B. D., Lindner, D. J., Kabasakal, L., Liu, Y., Krasnow, A. Z., Hellman, R. S., Edwards, S. D., Bourque, C. R., and Crane, P. D. (1999) Biodistribution of ^{99m}Tc-labelled 5-thio-D-glucose. *Nuclear Med. Commun. 20*, 1055−1058.
(13) Sobgbein, O. O., Green, A. E. C., Schaffer, P., Chankalai, R., Lee, E., Healy, B. D., Morel, P., and Valliant, J. F. (2005) Synthesis of ortho- and meta-Re(I)-metallocarboranes in water. *Inorg. Chem. 44*, 9574−9584.
(14) Storr, T., Fisher, C. L., Mikata, Y., Yano, S., Adam, M. J., and Orvig, C. (2005) A glucosamine-dipicolylamine conjugate of ^{99m}Tc(I) and ^{186}Re(I) for use in imaging and therapy. *Dalton Trans.* 654−655.
(15) Storr, T., Obata, M., Fisher, C. L., Bayly, S. R., Green, D. E., Brudziñska, I., Mikata, Y., Patrick, B. O., Adam, M. J., Yano, S., and Orvig, C. (2005) Novel carbohydrate-appended metal complexes for potential use in molecular imaging. *Chem. Eur. J. 11*, 195−203.
(16) Storr, T., Sugai, Y., Barta, C. A., Mikata, Y., Adam, M. J., Yano, S., and Orvig, C. (2005) Carbohydrate-appended 2, 2′-dipicolylamine metal complexes as potential imaging agents. *Inorg. Chem. 44*, 2698−2075.
(17) Bayly, S. R., Fisher, C. L., Storr, T., Adam, M. J., and Orvig, C. (2004) Carbohydrate conjugates of molecular imaging and radiotherapy: ^{99m}Tc(I) and ^{186}Re(I) tricarbonyl complexes of N-(2′-hydroxybenzyl)-2-amino-2-dexoy-D-glucose. *Bioconjugate Chem. 15*, 923−926.
(18) Klüfers, P., Krotz, O., and O*β*berger, M. (2002) Oxorhenium(V) complexes of carbohydrate ligands. *Eur. J. Inorg. Chem.* 1919−1923.
(19) Schibli, R., Bella, R. L., Alberto, R., Garcia-Garayoa, E., Ortner, K., Abram, U., and Schubiger, P. A. (2000) Influence of denticity of ligand systems on the *in vitro* and *in vivo* behaviour of ^{99m}Tc(I)-tricarbonyl complexes: a hint for the future functionalization of biomoecules. *Bioconjugate Chem. 11*, 345−351.
(20) Häfliger, P., Mundwiler, S., Ortner, K., Spingler, B., and Alberto, R. (2005) Structure, stability, and biodistribution of cationic $[M(CO)_3]^+$ (M = Re, ^{99}Tc, ^{99m}Tc) complexes with tridentate amine ligands. *Synth. React. Inorg. Metal-Org. Nano-Metal Chem. 35*, 27−34.
(21) Rattat, D., Eraets, K., Cleynhens, B., Knight, H., Fonge, H., and Verbruggen, A. (2004) Comparison of tridentate ligands in competition experiments fro their ability to form a $[^{99m}Tc(CO)_3]$ complex. *Tetrahedron Lett. 45*, 2531−2534.
(22) Schibli, R., Schwarzbach, R., Alberto, R., Ortner, K., Schmalle, H., Dumas, C., Egli, A., and Schubiger, P. A. (2002) Steps toward high specific activity labeling of biomolecules for therapeutic applications: prepartion of precursor $[^{188}Re(H_2O)_3(CO)_3]^+$ and synthesis of tailor-made bifunctional ligand systems. *Bioconjugate Chem. 13*, 750−756.
(23) Park, S. H., Seifert, S., and Pietzsch, H.-J. (2006) Novel and efficient preparation of precursor $[^{188}Re(OH_2)_3(CO)_3]^+$ for the labeling of biomolecules. *Bioconjugate Chem. 17*, 223−225.
(24) Alberto, R., Pak, J. K., Staveren, D. v., Mundwiler, S., and Benny, P. (2004) Mono-, bi-, or tridentate ligands? The labeling of peptides with ^{99m}Tc-carbonyls. *Biopolymers 76*, 324−333.
(25) Alberto, R., Schibli, R., Egli, A., and Schubiger, P. A. (1998) A novel organometallic aqua complex of technetium for the labeling of biomolecules: synthesis of $[^{99m}Tc(OH_2)_3(CO)_3]^+$ from $[^{99m}TcO_4]^-$ in aqueous solution and its reaction with a bifunctional ligand. *J. Am. Chem. Soc. 120*, 7987−7988.
(26) Alberto, R., Schibli, R., Waibel, R., Abram, U., and Schubiger, A. P. (1999) Basic aqueous chemistry of $[M(OH_2)_3(CO)_3]^+$ (M = Re, Tc) directed towards radiopharmaceutical application. *Coord. Chem. Rev. 99*, 901−919.
(27) Lazarova, N., James, S., Babich, J., and Zubieta, J. (2004) A convenient synthesis, chemical characterization and reactivity of $[Re(CO)_3(H_2O)_3]Br$: the crystal and molecular structure of $[Re(CO)_3(CH_3CN)_2Br]$. *Inorg. Chem. Commun. 7*, 1023−1026.
(28) Banerjee, S. R., Levadala, M. K., Lazarova, N., Wei, L., Valliant, J. F., Stephenson, K. A., Babich, J. W., Maresca, K. P., and Zubieta, J. (2002) Bifunctional single amino acid chelates for labeling biomolecules with the $\{Tc(CO)_3\}^+$ and $\{Re(CO)_3\}^+$ cores. Crystal and molecular structures of $[ReBr(CO)_3(H_2NCH_2C_5H_4N)]$, $[Re(CO)_3\{(C_5H_4NCH_2)_2NH\}]Br$, $[Re(CO)_3\{(C_5H_4NCH_2)_2NCH_2CO_2H\}]Br$, $[Re(CO)_3\{X(Y)NCH_2CO_2CH_2CH_3\}]Br$ (X = Y = 2-pyridylmethyl; X = 2-pyridylmethyl, Y = 2-(1-methylimidazoyl)methyl; X = Y = 2-(1-methylimidazoyl)methyl), $[ReBr(CO)_3\{(C_5H_4NCH_2)NH(CH_2C_4H_3S)\}]$, and $[Re(CO)_3\{(C_5H_4NCH_2(N(CH_2C_4H_3S)CH_2CO_2)\}]$. *Inorg. Chem. 41*, 6417−6425.
(29) Pak, J. K., Benny, P., Spingler, B., Ortner, K., and Alberto, R. (2003) N-Functionalization of metal and organic protected L-histidine for a highly efficient, direct labeling of biomolecules with $[Tc(OH_2)_3(CO)_3]^+$. *Chem. Eur. J. 9*, 2053−2061.
(30) Staveren, D. E. v., Benny, P. D., Waibel, R., Kurz, P., Pak, J. K., and Alberto, R. (2005) S-Functionalized cysteine: powerful ligands for the labelling of bioactive molecules with triaquatricarbonyltechnetium-99m(1+)($[^{99m}Tc(OH_2)_3(CO)_3^+]$. *Helv. Chim. Acta 88*, 447−459.
(31) Vitor, R. F., Alves, S., Correia, J. D. G., Paulo, A., and Santos, I. (2004) Rhenium(I) and technetium(I) tricarbonyl complexes anchored by bifunctional pyrazole-diamine and pyrazole-dithioether chelators. *J. Organomet. Chem. 689*, 4764−4774.
(32) Hamzavi, R., Happ, T., Weitershaus, K., and Metzler-Nolte, N. (2004) The use of 3, 3-bis(2-imidazolyl) propionic acid (bip-OH) as a new chelating ligand for $Re(CO)_3$ and Ru complexes: formation of organometallic PNA oligomers with $(bip)Re(CO)_3$ and their interaction with complementary DNA. *J. Organomet. Chem. 689*, 4745−4750.
(33) Alberto, R., Schibli, R., and Schubiger, P. A. (1999) First application of *fac*-$[^{99m}Tc(OH_2)_3(CO)_3]^+$ in biorganometallic chemistry: design, structure, and in vitro binding affinity of a 5-HT_{1A} receptor ligand labeled with ^{99m}Tc. *J. Am. Chem. Soc. 121*, 6076−6077.
(34) He, H., Lipowska, M., Xu, X., Taylor, A. T., Carlone, M., and Marzilli, L. G. (2005) $Re(CO)_3$ complexes synthesized via an improved preparation of aqueous *fac*-$[Re(CO)_3(H_2O)_3]^+$ as an aid in assessing ^{99m}Tc imaging agents. Structural characterization and solution behaviour of complexes with thioether-bearing amino acids as tridentate ligands. *Inorg. Chem. 44*, 5437−5446.
(35) Lazarova, N., Babich, J., Valliant, J., Schaffer, P., James, S., and Zubieta, J. (2005) Thiol- and thioether-based bifunctional chelates for the $\{M(CO)_3\}^+$ core (M = Tc, Re). *Inorg. Chem. 44*, 6763−6770.
(36) Braband, H., and Abram, U. (2004) Tricarbonyl complexes of rhenium(I) and technetium(I) with thiourea derivatives. *J. Organomet. Chem. 689*, 2066−2072.
(37) Schibli, R., Netter, M., Scapozza, L., Birringer, M., Schelling, P., Dumas, C., Schoch, J., and Schubiger, P. A. (2003) First organometallic inhibitors for human thymidine kinase: synthesis and in vitro evaluation of rhenium(I) and technetium(I)-tricarbonyl complexes of thymidine. *J. Organomet. Chem. 668*, 67−74.
(38) Frantz, S., Fiedler, J., Hartenbach, I., Schleid, T., and Kaim, W. (2004) A complete series of tricarbonylhalidorhenium(I) complexes $(abpy)Re(CO)_3(Hal)$, (Hal = F, Cl, Br, I; apby = 2, 2′-azobispyridine: structures, spectroeletrochemistry, and EPR of reduced forms. *J. Organomet. Chem. 689*, 3031−3039.
(39) Grewe, J., Hagenbach, A., Stromburg, B., Alberto, R., Vazquel-Lopez, E., and Abram, U. (2002) Tricarbonyl complexes of rhenium-(I) with acetylpyridine benzoylhydrazone and related ligands. *Z. Anorg. Allg. Chem. 629*, 303−311.
(40) Palma, E., Correia, J. D. G., Domingos, A., Santos, I., Alberto, R., and Spies, H. (2004) Rhenium and technetium tricarbonyl complexes anchored by 5-HT_{1A} receptor-binding ligands containing P, O/N donor atom sets. *J. Organomet. Chem. 689*, 4811−4819.
(41) Songbein, O. O., Merdy, P., Morel, P., and Valliant, J. F. (2004) Preparation of Re(I)- and Tc(I)-metallocarboranes in water under weakly basic conditions. *Inorg. Chem. 43*, 3032−3034.
(42) Bernard, J., Ortner, K., Spingler, B., Pietzsch, H.-J., and Alberto, R. (2003) Aqueous synthesis of derivatized cyclopentadienyl complexes of technetium and rhenium directed toward radiopharmaceutical application. *Inorg. Chem. 42*, 1014−1022.
(43) Masi, S., Top, S., Boubekeur, L., Jaouen, G., Mundwiler, S., Spingler, B., and Alberto, R. (2004) Direct synthesis of tricarbonyl-(cyclopentadienyl)rhenium and tricarbonyl(cyclopentadienyl)technetium units from ferrocenyl moieties - preparation of 17-ethynylestradiol derivatives bearing a tricarbonyl(cyclopentadienyl)technetium group. *Eur. J. Inorg. Chem.* 2013−2017.
(44) Saidi, M., Seifert, S., Kretzschmar, M., Bergmann, R., and Pietzsch, H.-J. (2004) Cyclopentadienyl tricarbonyl complexes of

^{99m}Tc for the *in vivo* imaging of the serotonin 5-HT_{1A} receptor in the brain. *J. Organomet. Chem. 689*, 4739−4744.
(45) Spradau, T. S., and Katzenellenbogen, J. A. (1998) Preparation of cyclopentadienyltricarbonylrhenium complexes using a double-ligand transfer reaction. *Organometallics 17*, 2009−2017.
(46) Luo, H., Rettig, S. J., and Orvig, C. (1993) Rhenium(V) and technetium(V) complexes of bidentate (O, O) monobasic 3-oxy-4-pyronato and -4-pyridinonato ligands. X-ray structures of *cis*-bromobis(3-methyl-2-oxy-4-pyronato)oxorhenium(V), tetra-*n*-butlyammonium tribromo(3-methyl-2-oxy-4-pyronato)oxorhenate(V), and tetra-*n*-butylammonium trichloro(3-methyl-2-oxy-4-pyronato)oxotechnetate(V). *Inorg. Chem. 32*, 4491−4497.
(47) Edwards, D. S., Liu, S., Poirier, M. J., Zhang, Z., Webb, G. A., and Orvig, C. (1994) Characterization of tris(N-substituted-2-methyl-3-hydroxy-4-pyridinonato)technetium(IV) cations. *Inorg. Chem. 33*, 5607−5609.
(48) Katoh, A., Taguchi, K., Saito, R., Fujisawa, Y., Takino, T., and Sakurai, H. (2003) Oxovanadiumcomplexes of N-substituted 3-hydroxy-2-methyl-4(1H)-pyridinone: synthesis, spectroscopic characterization, and insulin-mimetic activity. *Heterocycles 60*, 1147−1159.
(49) Sanots, M. A., Gil, M., Gano, L., and Chaves, S. (2005) Bifunctional 3-hydroxy-4-pyridinone derivatives as potential pharmaceuticals: synthesis, complexation with Fe(III), Al(III), Ga(III) and in vivo evaluation with ^{67}Ga. *J. Biol. Inorg. Chem. 10*, 564−580.
(50) Burgess, J., Fawcett, J., Llewellyn, M. A., Parsons, S. A., and Russell, D. R. (2000) Tris-[3-hydroxy-1, 2-dimethyl-pyridin-4(1H)-onato]cobalt(III). *Transition Met. Chem. 25*, 541−546.
(51) Tanaka, K., Tengeiji, A., Kato, T., Toyama, N., Shiro, M., and Shionoya, M. (2002) Efficient incorporation of copper hydroxypyridinone base pair in DNA. *J. Am. Chem. Soc. 124*, 12494−12498.
(52) El-Jammal, A., Howell, P. L., Turner, M. A., Lin, N., and Templeton, D. M. (1994) Copper complexation by 3-hydroxypyridin-4-one iron chelators: structural and iron competition studies. *J. Med. Chem. 37*, 461−466.
(53) Hsieh, W.-Y., and Liu, S. (2004) Synthesis, characterization and structures of $Mn(DMHP)_3 \cdot 12H_2O$ and $Mn(DMHP)_2Cl \cdot 0.5H_2O$. *Inorg. Chem. 44*, 2031−2038.
(54) Ahmed, S. I., Burgess, J., Fawcett, J., Parsons, S. A., Russell, D. R., and Laurie, S. H. (2000) The structures of bis-maltolato-zinc(II) and bis(3-hydroxy-1, 2-dimethyl-4-pyridinato)zinc(II) and lead(II). *Polyhedron 19*, 129−135.
(55) Lang, R., Palborn, K., Severin, T., and Severin, K. (1999) Halfsandwich complexes of ruthenium(II), rhodium(III) and iridium-(III) with N-substituted 3-hydroxy-2-methyl-4-pyridone ligands. *Inorg. Chim. Acta 294*, 62−67.
(56) Kennedy, D. C., Wu, A., Patrick, B. O., and James, B. R. (2005) Tris(pyronato)-and tris(pyridonato)-ruthenium(III) complexes and solution NMR studies. *Inorg. Chem. 44*, 6529−6535.
(57) Nelson, W. O., Rettig, S. J., and Orvig, C. (1988) Lipophilic coordination compounds: aluminum, gallium, and indium complexes of 1-aryl-3-hydroxy-2-methyl-4-pyridinones. *Inorg. Chem. 30*, 509−515.
(58) Nelson, W. O., Karpishin, T. B., Rettig, S. J., and Orvig, C. (1988) Aluminum and gallium compounds of 3-hydroxy-4-pyridinones: synthesis, characterization, and crystallography of biologically active complexes with unusual hydrogen bonding. *Inorg. Chem. 27*, 1045−1051.
(59) Green, D. E., Ferreira, C. L., Stick, R. V., Patrick, B. O., Adam, M. J., and Orvig, C. (2005) Carbohydrate-bearing 3-hydroxy-4-pyridinato complexes of gallium(III) and indium(III). *Bioconjugate Chem. 16*, 1597−1609.
(60) Zhang, Z., Lyster, D., Webb, G. A., and Orvig, C. (1992) Potential gallium-67 radiopharmaceuticals for myocardial imaging: tris(1-aryl-3-hydroxy-2-methyl-4-pyridnonato)gallium(III) complexes. *Nucl. Med. Biol. 19*, 327−335.
(61) Drouza, C., Gramlich, V., Sigalas, M. P., Pashalidis, I., and Keramidas, A. D. (2004) Synthesis, structure, and solution dynamices of UO_2^{2+}-hydroxy ketone compounds $[UO_2(ma)_2(H_2O)]$ and $[UO_2(dpp)(Hdpp)_2(H_2O)]ClO_4$ [ma = 3-hydroxy-2-methyl-4-pyrone, Hddp = 3-hydroxy-1, 2-dimethyl-4(1*H*)-pyridone]. *Inorg. Chem. 43*, 8336−8345.
(62) Xu, J., Churchill, D. G., Botta, M., and Raymond, K. N. (2004) Gadolinium(III) 1, 2-hydroxypyridonate-based complexes: towards MRI contrast agents of high relaxtivity. *Inorg. Chem. 43*, 5492−5494.
(63) Kruck, T. P. A., and Burrow, T. E. (2002) Synthesis of feralex a novel aluminum/iron chelating compound. *J. Inorg. Biochem. 88*, 19−24.
(64) Alberto, R., Egli, A., Abram, U., Hegetschweiler, K., Gramlich, V., and Schubiger, P. A. (1994) Synthesis and reactivity of $[NEt_4][ReBr_3(CO)_3]$. Formation and structural characterization of the clusters $[NEt_4][Re_3(m^3\text{-}OH)(\mu\text{-}OH)_3(CO)_9]$ and $[NEt_4][Re_2(\mu\text{-}OH)_3(CO)_6]$ by alkaline titration. *J. Chem. Soc., Dalton Trans.* 2815−2820.
(65) *SAINT* (1999), Bruker AXS Inc.: Madison WI.
(66) *SADABS* (1999), Bruker AXS Inc.: Madison, WI.
(67) Altomare, A., Burla, M. C., Camalli, M., Cascarano, G. L., Giocavazzo, C., Guagliardi, A., Moliterni, A. G. G., Polidori, G., and Spagna, R. (1999) SIR92. *J. Appl. Crystallogr. 32*, 115−119.
(68) *SHELXL*. (1997), Bruker AXS Inc.: Madison, WI.
(69) Bessell, E. M., Foster, A. B., and Wood, J. H. W. (1972) The use of deoxyfluoro-D-glucopyranose and related compounds in the study of yeast hexokinase specificity. *Biochem. J. 128*, 199−204.

BC060085E

Chemical Conjugate TMV−Peptide Bivalent Fusion Vaccines Improve Cellular Immunity and Tumor Protection

Alison A. McCormick,* Tina A. Corbo, Sherri Wykoff-Clary, Kenneth E. Palmer, and Gregory P. Pogue

Large Scale Biology Corporation, 3333 Vacavalley Parkway, Suite 1000, Vacaville, California 95688. Received May 12, 2006; Revised Manuscript Received July 17, 2006

Chemical conjugation of CTL peptides to tobacco mosaic virus (TMV) has shown promise as a molecular adjuvant scaffold for augmentation of cellular immune responses to peptide vaccines. This study demonstrates the ease of generating complex multipeptide vaccine formulations using chemical conjugation to TMV for improved vaccine efficacy. We have tested a model foreign antigen target—the chicken ovalbumin-derived CTL peptide (Ova peptide), as well as mouse melanoma-associated CTL epitopes p15e and tyrosinase-related protein 2 (Trp2) peptides that are self-antigen targets. Ova peptide fusions to TMV, as bivalent formulations with peptides encoding additional T-help or cellular uptake via the integrin−receptor binding RGD peptide, showed improved vaccine potency evidenced by significantly enhanced numbers of antigen-reactive T cells measured by in vitro IFNγ cellular analysis. We measured the biologically relevant outcome of vaccination in protection of mice from EG.7-Ova tumor challenge, which was achieved with only two doses of vaccine (~600 ng peptide) given without adjuvant. The p15e peptide alone or Trp2 peptide alone, or as a bivalent formulation with T-help or RGD uptake epitopes, was unable to stimulate effective tumor protection. However, a vaccine with both CTL peptides fused together onto TMV generated significantly improved survival. Interestingly, different bivalent vaccine formulations were required to improve vaccine efficacy for Ova or melanoma tumor model systems.

INTRODUCTION

Peptides derived from cancer antigens have been used for more than a decade as cheap, safe, and easy-to-manufacture vaccines that stimulate target-specific immunogenicity (*1*−*6*). Peptide vaccines, typically given as single agents mixed with adjuvant, are taken up by antigen-presenting cells (APC) at the site of injection, and, by processes not well-understood, are cross presented on MHC class I to naive T cells (*7*, *8*). However, peptide vaccines have generally shown limited efficacy in a series of disappointing clinical trials. Although immune responses may be detectible in patients immunized with peptide-based vaccines (*9*−*12*), the functional activation of antigen-presenting cells, induction of antigen-specific $CD4^+$ and $CD8^+$ cells (*13*, *14*), is not sufficient to mediate subsequent tumor clearance or disease regression in the majority of treated patients (*13*, *15*, *16*). Much effort has been made to understand why peptide vaccines have limited efficacy, and new generations of peptide vaccine formulations are being tested with the hopes that they will overcome the limitations of previous peptide−adjuvant formulations.

The importance of the context of antigen presentation to achieve appropriate immune stimulation, especially for self-antigens and breaking tolerance, has led to a recent understanding that vaccines composed of peptides or whole protein antigens generally do not sufficiently stimulate APC activation (recently reviewed in (*17*)). Resulting T-cell responses are often only transient and subject to T-regulatory mechanisms that eliminate antigen-specific reactivity (*18*, *19*). There has been significant effort, therefore, to improve peptide antigen-specific responses by a number of different mechanisms that improve antigen delivery to APCs. First, by using a pathogen to deliver the antigen, by bacterial (*20*, *21*), yeast (*22*), viral vector, or virus-like particle delivery (*23*−*26*). These approaches take advantage of particulate antigen uptake and improved cellular targeting and activation of professional APCs, such as dendritic cells (DCs). Virus expression in mammalian cells and VLP manufacturing, however, are still production-limited processes (*27*). Direct DC pulsing has also proven successful but requires generation of patient-specific DC, which remains costly (*28*). Another method to improve immunogenicity is by association of poorly immunogenic antigens to toxins (*29*−*31*), cytokines (*32*), T-helper epitopes (*33*−*35*), or peptides that improve uptake by APCs (*36*). We have melded two approaches to improve peptide antigen efficacy, by chemically conjugating peptides to the surface of a virus to create a chimeric virus particle, as well as by formulating bivalent fusions with toxin-derived peptides, T-helper epitopes, or peptides that improve uptake.

We have explored the use of the tobacco mosaic virus as an ideal peptide antigen carrier, because it provides an easily manipulated scaffold of >2100 uniform coat proteins that are 17 KDa in size. TMV also contains a +strand RNA that only transcribes in plants, but which may still engage innate antiviral immunity and activate important signaling molecules like Toll-like receptor 7, and thereby stimulate immune activation (*37*−*39*). Many studies have shown that fusions of B-cell epitopes to TMV stimulate high levels of antibody titers, and more recently high levels of tumor-protective CTL responses (*40*). TMV is easily produced on the kilogram scale from infected plants, with low cost of goods, and has shown an excellent safety profile in preclinical tests because it is produced without animal or bacterial byproducts. Using TMV as a CTL peptide antigen carrier by chemical conjugation, we have improved vaccine efficacy by bivalent fusions with toxin-derived peptides, T-helper epitopes, or peptides that improve uptake. We report that, in two different murine tumor models, representing foreign (Ova) and self (melanoma) antigens, bivalent vaccine preparations stimulate significantly improved immune responses, as measured by interferon gamma (IFNγ) secreting cells and survival from lethal tumor challenge. Interestingly, different

* E-mail: alison.mccormick@myifp.com. Office: 707-469-2384. Fax: 707-446-3917.

10.1021/bc060124m CCC: $33.50 © 2006 American Chemical Society
Published on Web 08/22/2006

Table 1. TMV Conjugation Reactions: Theoretical and Observed Masses in Daltons

conjugate name	peptide sequence	1295.10 SPDP mass	peptide mass	expected mass	observed MALDI-TOF
1295.10 + LC-SPDP				18353.5	18356.0
1295.10 + LC-SPDP + Ova	SIINFEKLc	18353.5	1065.3	19418.8	19423.9
1295.10 + LC-SPDP + E7	DRAHYNIVTFc	18353.5	1337.6	19691.1	19690.0
1295.10 + LC-SPDP + TT	QYIKANSKFIGITELKKc	18353.5	1827.8	20181.3	20185.0
1295.10 + LC-SPDP + RGD	SGRGDSGc	18353.5	736.7	19090.2	19091.6
1295.10 + LC-SPDP + p15e	KSPWFTTLc	18353.5	1082.6	19436.1	19431.4
1295.10 + LC-SPDP + trp2	SVYDFFVWLc	18353.5	1279.5	19633.0	19629.6

formulations are required for Ova or melanoma-effective tumor protective immunity. Peptide antigen delivery on TMV, using less that 1 μg per dose, stimulates these protective immune responses in murine models indicating that this approach has promise for improving the efficacy of clinically relevant peptide vaccines without sacrificing safety.

MATERIALS AND METHODS

Vaccine Production. Chemical conjugation of peptides to TMV required the introduction of a surface-reactive lysine at the N-terminus. In these experiments, a well-characterized lysine-modified TMV (TMV-lys) was used (*30*; M_1 EPMK S_2-YS) that expresses a single reactive lysine (K) residue on the surface of the TMV virion (1295.10; (*41*)). The virus was expressed by transient infection of plants and purified as previously described (*40*−*42*). Purified 1295.10 TMV-lys virus was primed with a 20-fold molar excess of the heterobifunctional linker sulfo-LC-SPDP (hereafter SPDP; Pierce, Rockfold, IL) in PBS/0.05 M EDTA. After dialysis to remove free SPDP, Ova, melanoma p15e, or melamona Trp2 peptide (>95% pure; BioMer Technology, Concord, CA) was added at a 10-fold molar excess and reacted at room temperature overnight (sequences are listed in Table 1). Resulting vaccines, Ova, p15e, or Trp2, were subsequently dialyzed and analyzed by matrix-assisted laser desorption/ionization time-of-flight (MALDI-TOF) mass spectroscopy using a Voyager-DE STR Biospectrometry Workstation (Applied Biosystems, Foster City CA) (*40*, *41*). Mass calculations were based on the combined amino acid masses of peptide and TMV-SPDP, determined by *General Protein/Mass Analysis for Windows* software (GPMAW) version 5.0 (Lighthouse Data, Denmark). Differences between expected and observed masses were within MALDI-TOF error of measurement (0.05%; Table 1). Sodium dodecyl sulfate polyacrylamide gel electrophoresis (SDS-PAGE) (10−20% Tris-Glycine; Invtrogen) and densitometry analysis (BioRad, Hercules, CA; *Quantity One* software) were used to confirm the extent of purity and >90% peptide conjugation efficiency.

Bivalent vaccine formulations were prepared by two methods. First, for most conjugations where peptide sizes were distinguishable by either SDS-PAGE or MALDI-TOF (TT, RGD, E7), 50/50 peptide mixtures were added directly to SPDP-activated TMV and evaluated for approximately 40−45% conjugation of each peptide. In some cases, peptide ratios were adjusted to balance conjugation ratios. For p15e bivalent formulation with Trp2 peptide, where peptide sizes are nearly identical, p15e peptide was added in limiting amounts to generate a TMV conjugate at 50% loading efficiency. Then, Trp2 peptide was added, and on the basis of the reduction of unconjugated TMV coat protein to ∼5%, Trp2 peptide conjugation at ∼45% was confirmed by SDS-PAGE (by the reduction in unconjugated TMV band) and by MALDI-TOF analyses (Table 1).

Vaccination. C57b/6 mice (Harlan Sprague Dawley, Indianapolis, IN) were housed at Antibodies, Inc. (Davis, CA), according to guidelines established in the *Care and Use of Animals*, and protocols were performed according to IACUC approval. Typically, 10 to 15 mice per group were given a 100−200 μL subcutaneuous (s.c.) injection of 10 or 15 μg protein with or without 25 μg of unmethylated CpG oligonucleotide (TCTCCCAGCGTGCGCCAT; (*43*)) having a stabilized phosphorothioate backbone (Oligo's Etc., Inc, Watsonville OR). Vaccines were typically administered at two-week intervals.

ELISpot Analysis of IFNγ T-Cell Secretion. Interferon-γ enzyme-linked immunospot (IFNγ ELISpot) analysis was carried out using an antibody kit, according to manufacturer's instructions (BD/Pharmingen) using membrane filter plates (Millipore, Bedford, MA), and as previously described in detail (*40*). Briefly, single cell suspensions of 2×10^5 spleen cells from each group were plated in 200 μL RPMI complete media with 10^{-5} M Ova SIINFEKL peptide, or 10^{-6} M Ova SIINFEKL peptide, or 10^{-5} M p15e (KSPWFTTL) or Trp2 (SVYDFFVWL) peptides, using a β-gal control (DAPIYTNV (*44*)) for all experiments. PMA/Ionomycin (2.5/250 ng/mL; Sigma, St. Louis, MO) treatment was used as a positive control. Cells were incubated for 22 h at 37 °C in a 5% CO_2 incubator, stained with an IFNγ−horseradish peroxidase (HRP) conjugate, and then developed for HRP reactivity according to the antibody manufacturer's instructions. IFNγ secreting cells were measured as positive spots (intensity, 7−255; size, 22−5000; gradient, 1−90) that were counted on an ELISpot reader (AID, Strasbourg, Germany), and normalized to 10^6 cells after background subtraction (irrelevant peptide stimulation, typically less than 10 spots per 10^6 cells).

Tumor Challenge. EG.7-Ova cells (ATTC, Manassas, VA (*45*)) were grown from a master cell bank for one week and maintained between 0.2 and 2×10^6 cells per milliliter in RPMI complete media. On the day of the tumor challenge, cells were washed three times in Hanks buffered saline solution (HBSS; Invtirogen/Gibco), counted (Vicell XR; Beckman Coulter, Fullerton, CA), and diluted to 2×10^6 cells/mL. 2×10^5 cells in 100 μL final volume (stored on ice until administration) were used to inoculate mice s.c. on the back. All mice showed a single subcutaneous bubble of fluid under the skin, without leakage. B16F1 cells (*46*) were grown in DMEM high glucose with 10% FCS, Glutamax, Pen/strep, Hepes, pyruvate, and nonessential amino acids (Invitrogen/Gibco). B16F1 cells were maintained for one week prior to challenge at ∼20−80% confluence, removed by Trypsin/EDTA treatment for 3 min at room temperature, washed extensively, counted, and resuspended at 5×10^5 cells/mL for delivery of 5×10^4 cells s.c. in 100 μL final volume.

Tumor appearance was monitored by eye for 8−10 days until visible signs of tumor formation were evident. Then, calipers were used to measure the longest and widest point until tumor size was in excess of 2.0 cm^2 or 1.5 cm^2, for Ova or B16 tumors, respectively, at which point animals were euthanized by CO_2 asphyxiation according to IACUC protocol. Tumor volume and survival curve comparison statistics were plotted in *GraphPad Prism 4.0* using Kaplan−Meier log rank analysis.

RESULTS

Chemical conjugate vaccines were prepared using Ova SIINFEKL peptide alone, or as bivalent vaccines combining Ova with T-helper epitopes HPV E7 (*47*, *48*)) or Tetanus toxoid

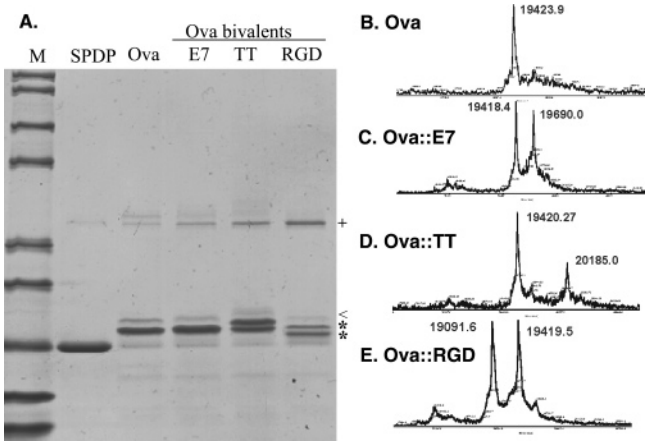

Figure 1. Qualification of TMV Ova conjugate vaccines. (A) SDS-PAGE analysis of SPDP conjugates of Ova peptides, and helper or uptake peptides, to TMV. Monovalent formulation (Ova) or bivalent formulations (::) with E7, tetanus (TT), or RGD uptake peptides are shown as final vaccine formulations, with approximately 45% Ova and 45% additional peptides in bivalent vaccines, compared to 90% conjugation of Ova alone. Single (*) and double (<) peptide additions to TMV are evident, as are TMV dimers (+). (B−E) Mass analysis by MALDI-TOF of each vaccine formulation confirms the presence of both peptides at the correct expected mass shift for monovalent or bivalent formulations, with a minimum of unconjugated free coat protein.

P2 (*49*−*51*)), or with an integrin RGD-binding domain, known to confer cellular uptake on macromolecules (*52*, *53*) and DC targeting of fiber knob modified adenovirus for improved cancer immunotherapy (*54*, *55*). Peptide sequence, mass, as well as expected and observed TMV conjugation mass for each vaccine are described in Table 1. As shown in Figure 1, vaccines were composed of TMV particles with >90% of the coat proteins conjugated with peptide and, to the extent possible, were composed of equal mixtures of Ova and additional epitopes. SDS-PAGE analysis indicates the degree of conjugation and relative percentage of Ova (Figure 1A). Ova peptide conjugation alone results in a clear size shift of TMV coat protein migration compared to TMV-SPDP alone under nonreducing conditions (*). Small amounts of Ova peptide dimers (<) and coat protein multimers (+) are also evident in less than 5% of conjugates. Ova bivalents with E7, though not clearly visible by SDS-PAGE, are evident in more definitive mass analysis (1C). Ova bivalents with tetanus toxoid (TT) and RGD peptides are clearly visible as larger and smaller shifts, respectively, based on peptide length differences (**). Mass analysis by MALDI-TOF (Figure 1B−E) confirms the presence of each correct full-length peptide fusion. The symbol (::) indicates the use of the reducible bond chemical linker to join both epitopes onto the same virus particle.

Vaccination of mice (10−20 μg TMV, normalized for the delivery of 600 ng Ova peptide per dose) was first carried out on a three-dose biweekly schedule with CpG adjuvant, and the results are shown in Figure 2. By IFNγ ELISPot analysis, Ova peptide stimulation of spleen cells from each vaccine group shows that all groups had high levels of activation, especially for a protein antigen (>500 IFN secreting cells, reported as spots per 10^6 spleen cells; Figure 2A) with a nearly 50% increase in the Ova::E7 group at >800 IFNγ spots per 10^6 cells and almost 400% more activated cells in the Ova::RGD bivalent group at

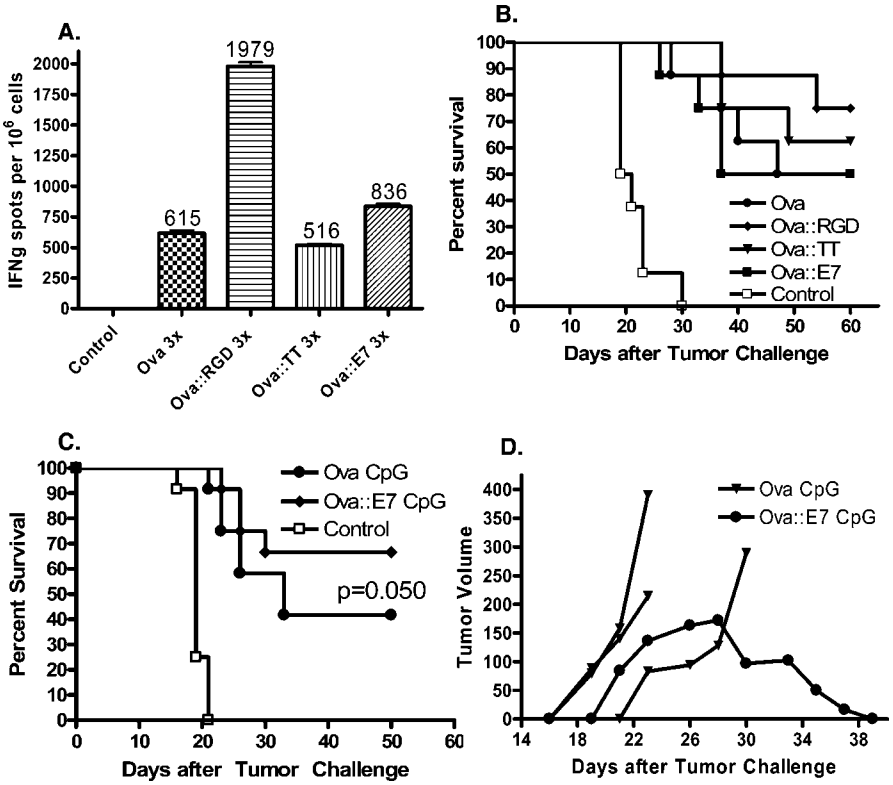

Figure 2. In vivo analysis of vaccine Ova TMV vaccine potency (with CpG DNA adjuvant) by IFNγ ELISpot and EG.7-Ova tumor challenge after three or two doses. (A) Nine days after 3 biweekly s.c. doses of 10 μg Ova TMV vaccines given with 25 μg CpG adjuvant, mice were sacrificed, and 2×10^5 single suspensions of spleen cells were tested on antibody-coated membranes for Ova-specific peptide reactivity (SIINFEKL; 10^{-6} M) after 22 h stimulation by IFNγ ELISpot. Error bars represent variation between 12-well replicates. (B) One day later, the remaining 10 animals were challenged with a lethal dose of 2×10^5 EG.7-Ova tumor cells given s.c., and the tumor area was monitored by the longest and widest caliper measurements after the onset of visible tumor. Mice were euthanized when the area exceeded 2.0 cm^2, and the time of death after tumor challenge recorded; long-term survivors were tumor-free. *GraphPad Prism 4.0* software was used to plot survival curves, and Kaplan−Meier analysis was used to determine significant difference (log-rank, $p = 0.05$). (C) EG.7-Ova survival results after two doses of the same vaccines, given with CpG adjuvant. Only Ova::E7 was statistically improved in comparison to the Ova monovalent control ($p = 0.05$); both groups were better than the control ($p < 0.0001$). (D) Tumor regression was observed in one Ova::E7 mouse, compared to Ova alone.

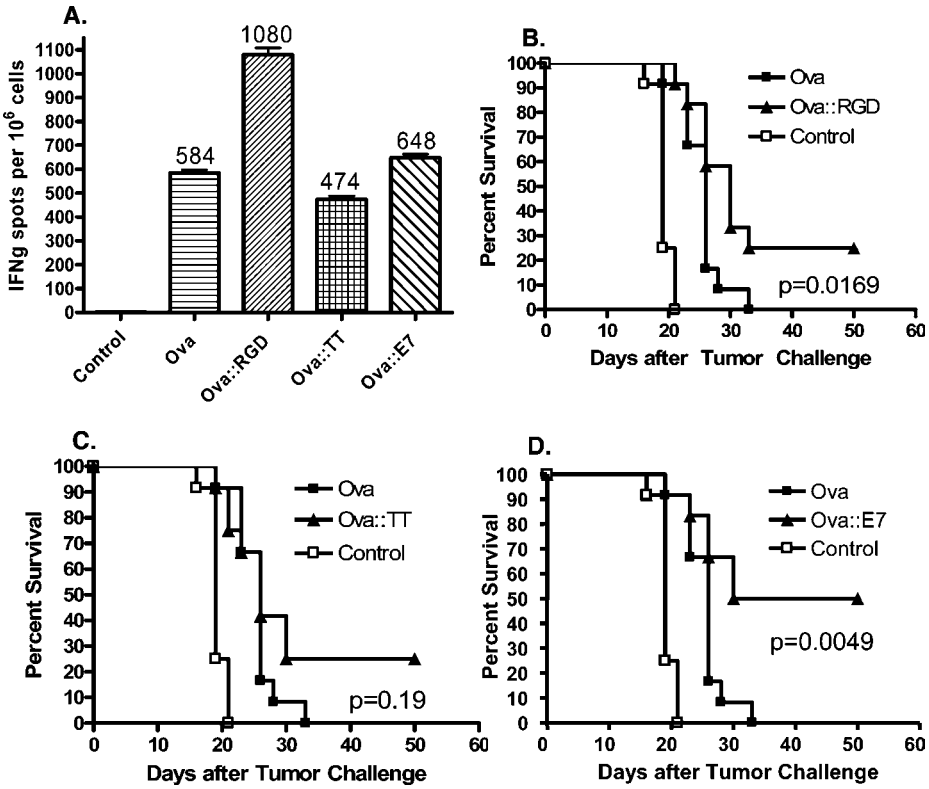

Figure 3. In vivo analysis of vaccine Ova TMV vaccine potency (no adjuvant) by IFNγ ELISpot and EG.7-Ova tumor challenge after two doses. (A) Nine days after two biweekly s.c. doses of 10 μg Ova TMV vaccines given without adjuvant, mice were sacrificed and tested for Ova-specific peptide reactivity (SIINFEL; 10^{-6} M) after 22 h stimulation by IFNγ ELISpot. (B−D) One day later, the remaining 12 animals were challenged with a lethal dose of 2×10^5 EG.7-Ova tumor cells given s.c., and the tumor area was monitored by the longest and widest caliper measurements after the onset of visible tumor and analyzed as in Figure 2. (B) Ova::RGD vaccine stimulated significantly improved survival compared to Ova TMV alone ($p = 0.0169$). (C) Ova::TT vaccine stimulated similar survival compared to Ova TMV alone ($p = 0.19$). (D) Ova::RGD vaccine stimulated significantly improved survival compared to Ova TMV alone ($p = 0.0049$).

nearly 2000 IFNγ spots per 10^6 cells. Ova::TT group had slightly lower numbers of activated cells. When the remaining mice in these groups were challenged with a lethal dose of Ovalbumin expressing EG.7-Ova tumor cells, all vaccine groups had significantly improved survival compared with the control ($p < 0.0001$; Figure 2B), with approximately 50−75% long-term survivors that were tumor-free. Previous experiments confirmed that animals immunized with TMV alone or TMV mixed with an equivalent dose of peptide (unlinked) showed similar survival kinetics compared with PBS controls (data not shown). Although Ova::RGD had the highest IFNγ activation in vitro and the highest percentage of survivors in vivo, this group was statistically similar to all other vaccine groups, including Ova−TMV given as a monovalent vaccine. Such data suggest an immune response threshold has been achieved after vaccination that protects the majority of mice from tumor lethality.

To discriminate between vaccine compositions, we administered only two immunizations normalized to deliver 600 ng of Ova peptide/dose, given with 25 μg CpG DNA adjuvant. All vaccine groups had high levels of IFN secretion by ELISpot analysis (data not shown), and all vaccine groups showed significantly improved tumor protection compared to the PBS control ($p > 0.0001$). Only one group, Ova::E7 CpG, showed improved survival compared with the monovalent Ova−TMV conjugate vaccine (Figure 2C; $p = 0.05$). Also of note, one animal in the Ova::E7 CpG group formed a visible tumor that regressed and was eliminated (Figure 2D), unlike tumors in mice vaccinated with the monovalent Ova−TMV. The figure shows tumor growth curves that are typically observed in three animals that received the Ova monovalent vaccine (triangles), in comparison with the single Ova:E7 vaccine recipient (closed circles), in which we observed clear regression of the tumor. In our experience, and on the basis of a lack of similar findings using the EG.7-Ova tumor model in the literature, peptide-vaccine-induced regression of an established tumor is unprecedented.

To further discriminate between vaccine potencies, we increased the stringency of the challenge. The same groups (as above) were vaccinated in parallel two times without CpG adjuvant. As shown in Figure 3A, in vitro analysis of cellular immunity by IFNγ ELISpot still demonstrated high levels of peptide-stimulated cells in all groups after only two immunizations, with greater than 500 IFNγ secreting (spot forming) cells per 10^6 splenocytes in the Ova−TMV group. Again, there were significantly higher numbers of activated cells in both the Ova::RGD and Ova::E7 groups compared with the monovalent vaccine, and fewer activated cells in the Ova::TT group. These results were remarkably similar to what we measured in an independent analysis after three doses with adjuvant (Figure 2A). A subsequent challenge by Ova expressing EG.7-Ova tumor cells indicates that all vaccine groups showed significantly improved tumor survival patterns in comparison with the control ($p < 0.0001$). However, two doses of the Ova−TMV monovalent conjugate vaccine only generated a significant delay in survival compared to the control, but no long-term survivors. The bivalent Ova::RGD vaccine group, with the highest level of IFNγ secreting cell numbers, performed better than Ova−TMV alone ($p = 0.0169$), with 25% long-term survivors. Ova::TT bivalent vaccine, that stimulated the lowest numbers of IFNγ secreting cells, performed no better than Ova−TMV 2× ($p = 0.19$) even though there were 25% long-term survivors. Ova::E7 outperformed Ova−TMV ($p = 0.0049$) with 50% long-term survivors. The responses of animals immunized with the Ova::RGD and Ova::E7 in the absence of adjuvant confirms the

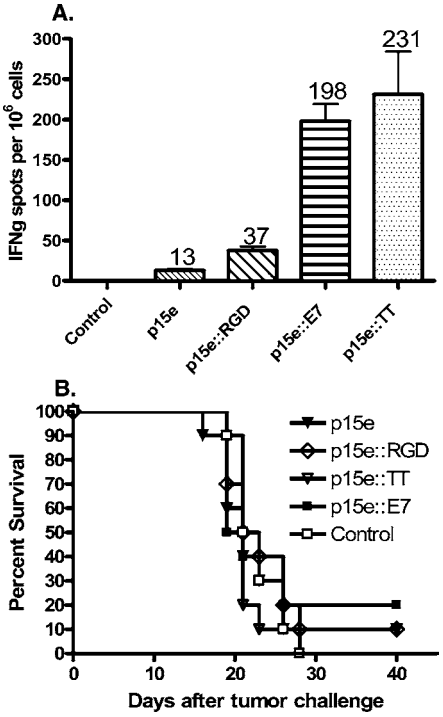

Figure 4. In vivo testing of p15e bivalent vaccine formulation efficacy by IFNγ ELISpot and by B16 tumor challenge. Three doses of 15 μg monovalent p15e vaccine, or peptide equivalent, was given on a biweekly schedule with 25 μg CpG adjuvant. (A) Nine days after the last vaccine, mice were sacrificed, and 2×10^5 single suspensions of spleen cells were tested on antibody-coated membranes for p15e specific peptide reactivity (KSPWFTTL; 10^{-5} M) after 22 h stimulation, by IFNγ ELISpot. (B) One day later, the remaining 10 animals were challenged with a lethal dose of 5×10^4 B16F1 melanoma tumor cells given s.c., and the tumor area was monitored by the longest and widest caliper measurements after the onset of visible tumor. Animals were euthanized when tumor area exceeded 1.5 cm_2; long-term survivors were tumor-free. Survival analysis was completed as in Figure 2.

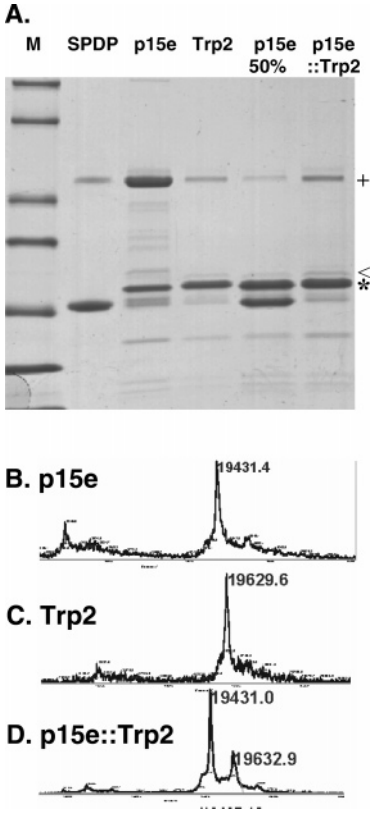

Figure 5. Qualification of TMV melanoma antigen conjugate vaccines. (A) SDS-PAGE analysis of SPDP conjugates of 15e or Trp2 peptides, and helper or uptake peptides, to TMV. Monovalent formulation (p15e or Trp2) or bivalent formulations (::) of p15e with Trp2 peptides combined are shown as final vaccine formulations, with approximately 45% p15e and 45% additional peptides in bivalent vaccines, compared to 90% conjugation of p15e or Trp2 alone. Single (*) and double (<) peptide additions to TMV are evident, as are TMV dimers (+). P15e and Trp2 peptides are of similar mass, so staged addition, first with p15e (50%) then with Trp2, was carried out. (B−D) Mass analysis by MALDI-TOF of each vaccine formulation confirms the presence of peptides fused to TMV with the correct expected mass shift for monovalent or bivalent formulations, with a minimum of unconjugated free coat protein. MALDI-TOF is qualitative, but not quantitative, for peptide addition.

improved efficacy associated with bivalent vaccine formulations when Ova peptide is presented on TMV.

In order to broaden the application of bivalent vaccine formulations, we also tested similar combinations of helper and uptake antigens in combination with a melanoma self-antigen peptide, p15e (*56*). Vaccines were formulated and qualified essentially as described for Ova bivalent vaccines, using SDS-PAGE and densitometry to gauge conjugation efficiency and MALDI-TOF mass analysis to confirm the presence of epitopes (data not shown). After three 15 μg biweekly s.c. vaccinations (~900 ng of peptide) with 25 μg CpG adjuvant, mouse splenocytes were tested for IFNγ secretion by ELISpot. Functionality of the immune response was measured by monitoring survival after challenging vaccinated animals with B16 melanoma tumor. Interestingly, for p15e bivalent vaccinations, p15e::RDG stimulated the lowest number of IFNγ secreting cells, while p15e::E7 and p15e::TT bivalents stimulated high levels of peptide-activated cell numbers after 22 h stimulation with 10^{-5} M p15e peptide (Figure 4A). After s.c. challenge with a lethal dose of B16F1 melanoma tumor cells, there were one or two tumor-free long-term survivors in all vaccine groups, but surprisingly, none of the p15e vaccine formulations provided improved protection compared to the control (Figure 4B).

In addition to testing bivalent formulations with helper or uptake peptides, we also tested the concept of delivering bivalent vaccines prepared from two different melanoma tumor-associated antigens, p15e and Trp 2 protein (*56*). Formulations of monovalent vaccines (p15e or Trp2 alone), mixtures of monovalent vaccines (p15e + Trp2), or bivalent conjugates (p15e::Trp2) were qualified as shown in Figure 5A. The majority of the species have one peptide addition (*), with a minor component of two peptide additions (<) or TMV coat multimers (+). TMV:p15e conjugates, as shown in some reactions, produce a higher proportion of coat multimers, possibly due to the presence of a second reactive lysine in the peptide. Because the p15e and Trp2 conjugation peptides were not sufficiently different in mass to resolve by SDS-PAGE (Figure 5B,C), staged conjugation, first with p15e, then with Trp2, was carried out to ensure approximately equal quantities of both peptides onto SPDP activated TMV, and the presence of the peptide was confirmed by MALDI-TOF (Table 1, Figure 5D).

Bivalent T-cell peptide vaccines were given s.c. three times with CpG adjuvant at 15 μg TMV dose, and mixed monovalent and bivalent conjugate vaccines were given at an equivalent p15e peptide dose each. After three immunizations, mice were tested for protection against tumor challenge in the B16F1 challenge model as described previously (Figure 4).

As shown in Figure 6A, monovalent formulations did not improve survival as compared with the negative control. This was the case, even though tumor dose did not yield fully penetrant lethality (one long-term survivor at 60 d post-challenge). As shown in Figure 6B, the mixture of two monovalent vaccines increased the number of tumor-free long-term survivors to 30% compared with the negative control, but

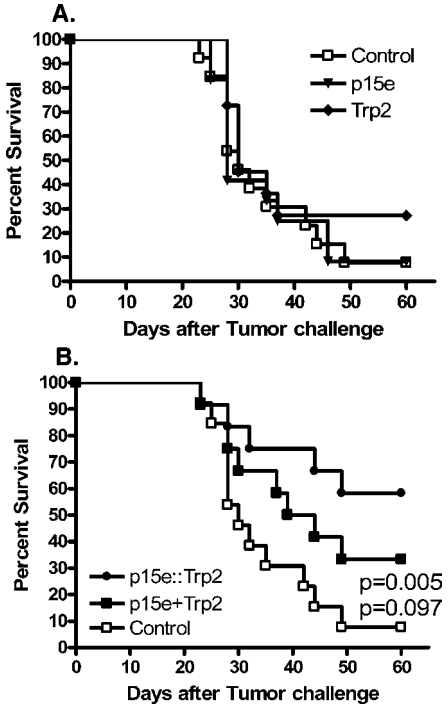

Figure 6. In vivo analysis of alternative TMV melanoma vaccine potency after B16 tumor challenge. After three 15 μg immunizations with 25*g* CpG adjuvant on a biweekly schedule, 12 mice were challenged with a lethal dose of 5×10^4 B16F1 tumor cells. After the appearance of visible tumor, the area was measured by calipers at the longest and widest points, and mice were sacrificed when the tumor area exceeded 1.5 cm^2; long-term survivors were tumor-free. With the time of death after tumor challenge recorded, *GraphPad Prism 4.0* software was used to plot survival curves, and Kaplan−Meier analysis was used to determine significant difference (log-rank, $p = 0.05$). Tumor penetrance was 91.6%, as 1 out of 12 challenged mice did not develop tumor. (A) Monovalent p15e and Trp2 vaccine formulations generated survival similar to the control. (B) Bivalent formulations of p15e with Trp2, either as mixed TMV vaccines (+) or as bivalent formulation on the same TMV (::), were tested. Both groups demonstrated long-term survivors, but only the bivalent formulation significantly improved survival compared to the control (**::** $p = 0.008$ compared to + $p = 0.097$).

this was not significantly different than the control ($p = 0.097$). In contrast, the p15e::Trp2 bivalent vaccine showed statistically improved survival ($p = 0.005$) compared with the control group, with 60% animals among the tumor-free long-term survivor group.

DISCUSSION

These data collectively demonstrate the ease of vaccine formulation and qualification (Figures 1 and 5), and the utility of combining helper, uptake, and additional T-cell targets onto a TMV virus scaffold, to improve Ovalbumin and melanoma specific vaccines. We feel that the flexible nature of the platform allows the rapid assembly of qualified target peptides into a format that has demonstrated active uptake in mammalian lymphocytes (*40*) and effective delivery of peptides in a context that stimulates effective cellular immunity at very low doses of antigen. In these studies, 600 ng of Ova peptide was delivered as a bivalent TMV vaccine with an equivalent dose of RGD, TT, or E7 peptides. In experiments where animals received three doses, given with CpG adjuvant, improvements in overall survival were evident for bivalent vaccine formulations, but none were significantly better than Ova−TMV alone (Figure 2A). When only two doses were given with adjuvant, only Ova::E7 demonstrated improved survival compared with the monovalent Ova vaccine coadministered with CpG adjuvant ($p = 0.05$; Figure 2B), and one animal in this group was actually able to reverse tumor growth after it was 1.5 cm $\times$ 1.1 cm in area (Figure 2C). In a previous study (*40*), we were able to show that after two immunizations on day one and day eight after tumor challenge, Ova−TMV vaccinated mice were protected in comparison to controls, so there is evidence in both experiments that TMV fusions may stimulate therapeutic efficacy. It will be interesting to test whether bivalent formulations can also improve vaccine potency in the presence of pre-existing tumor compared with Ova−TMV.

Using a different immunization approach to increase stringency, we also compared survival in bivalent vaccine groups given only two doses without adjuvant. We measured improved immunogenicity by increased levels of peptide-specific IFNγ secreting cells for Ova::RGD and Ova::E7 bivalent fusions (Figure 3A). These groups also had significantly improved protective immunity to the EG.7-Ova tumor challenge. Overall survival greater than 50% was measured for Ova::E7 vaccines given without adjuvant, which was similar to survival given with CpG DNA (compare Figure 3D Ova E7 to Figure 2A Ova 2x CpG).

These data indicate that TMV can be a very effective antigen delivery scaffold, and more importantly, we could replace adjuvant by formulating Ova conjugate vaccines with T-help or RGD uptake peptides. This is a 1000-fold improvement in efficacy compared to early studies with unconjugated Ova peptide, where 100 μmol doses of peptide were typically given in CFA/IFA adjuvant, in addition to 3 day CpG priming (*35*). It is also the first report, to our knowledge, of T-cell mediated immunogenicity and tumor protection from a synthetic peptide chemical conjugate vaccine given without adjuvant. Similar improvements have been demonstrated by ex-vivo pulsing of DC cells; however, we argue that, because we have previously demonstrated that TMV−antigen is efficiently taken up by DC and other important APCs, we hypothesize that the efficacy improvements we have shown are most likely due to improved in vivo DC uptake and activation, and the potential contribution of $CD4^+$ T help.

Although the helper and uptake peptides were chosen on the basis of their ability to augment immunogenicity in other vaccine applications, it is interesting to note that the ability of each peptide to augment immunogenicity in the context of self or foreign antigen fusions to TMV is quite distinct. E7, a heterologous helper epitope, and RGD, an uptake enhancer, both augment Ova::TMV vaccine immunogenicity, but not p15e self-antigen immunogenicity. It may be that because there is no pre-existing tolerance to Ova, modest improvements in vaccine potency are measurable by increased cellular activation and survival from tumor challenge but are insufficient to overcome immune tolerance.

In our second set of data, we tested similar bivalent TMV vaccine compositions using self-antigen peptides relevant to the murine B16 melanoma model. Although effective for the Ova model, we found in our first experiment that RGD, TT, and E7 bivalent vaccines with the T-cell antigen derived from p15e provided no survival advantage or long-term survival (Figure 4B) even though all p15e bivalent formulations increased the number of peptide-activated IFNγ secreting cells (Figure 4A). Although suggestive of immune induction, there was no strong correlation between IFNγ ELISpot data and tumor protection in either Ova or melanoma studies, indicating that there may be either a threshold of activated cells or a qualitative difference within activated cells, which correlates with survival. Further testing with other relevant ELISpot capture antigens, such as Granzyme B, may improve correlation strength.

Because data presented in Figure 5B did not show improved immunogenicity of p15e bivalent vaccine formulations, we also

created a bivalent vaccine composed of T-cell peptide antigens derived from two different overexpressed melanoma antigens, p15e and Trp2. Immune efficacy would be at least additive if both antigens stimulated cellular immunity independently, minimizing tumor escape from immune surveillance. Figure 6B demonstrates that two T-cell epitopes combined are indeed superior to single antigen fusions given alone, with the best formulation p15e::Trp2 providing 50% protection against tumor challenge. Interestingly, this group also had a single animal with melanoma antigen-specific autoimmunity, as measured by injection-site hair and skin depigmentation (data not shown), which was not evident in other groups in this experiment.

These results collectively demonstrate that TMV is an effective, easily qualified vaccine carrier for stimulating peptide-specific cellular immunity both for single and multipeptide fusions. Peptide vaccines are still being used actively in many recent oncology-related clinical trials (*57*−*65*) as well as in other health applications (*66*, *67*), primarily because these antigens are well-defined and have significant safety advantages. Additional studies have also used KLH conjugation for augmented T-help (*23*), but many obstacles exist in qualifying KLH−peptide conjugates, which has limited widespread clinical use. Our approach to chemically conjugating peptides directly to TMV (which in many animal studies has not induced any toxicity) may allow for stringent vaccine qualification, as well as greatly enhanced immune targeting and antigen delivery to antigen-presenting cells and improved potency, while still maintaining safety. Co-conjugation of additional stimulatory or T-helper epitopes or by generating multiepitope T-cell targets is also easily facilitated using these methods. That multiepitope melanoma vaccines have also recently been tested clinically (*10*, *68*, *69*) supports the further exploration of this type of multivalent vaccine formulation. We feel that TMV could provide superior antigen delivery of current clinically relevant peptides for future clinical use.

LITERATURE CITED

(1) Slingluff, C. L., Jr., Engelhard, V. H., and Ferrone, S. (2006) Peptide and dendritic cell vaccines. *Clin. Cancer Res. 12*, 2342s−2345s.

(2) Berzofsky, J. A., Oh, S., and Terabe, M. (2005) Peptide vaccines against cancer. *Cancer Treat. Res. 123*, 115−136.

(3) Disis, M. L., Salazar, L. G., and Knutson, K. L. (2004) Peptide-based vaccines in breast cancer. *Breast Dis. 20*, 3−11.

(4) Brinkman, J. A., Fausch, S. C., Weber, J. S., and Kast, W. M. (2004) Peptide-based vaccines for cancer immunotherapy. *Expert Opin. Biol. Ther. 4*, 181−198.

(5) Celis, E., Sette, A., and Grey, H. M. (1995) Epitope selection and development of peptide based vaccines to treat cancer. *Semin. Cancer Biol. 6*, 329−336.

(6) Livingston, P. O. (1992) Construction of cancer vaccines with carbohydrate and protein (peptide) tumor antigens. *Curr. Opin. Immunol. 4*, 624−629.

(7) Guermonprez, P., and Amigorena, S. (2005) Pathways for antigen cross presentation. *Springer Semin. Immunopathol. 26*, 257−271.

(8) Ackerman, A. L., Kyritsis, C., Tampe, R., and Cresswell, P. (2003) Early phagosomes in dendritic cells form a cellular compartment sufficient for cross presentation of exogenous antigens. *Proc. Natl. Acad. Sci. U.S.A. 100*, 12889−12894.

(9) Lazoura, E., and Apostolopoulos, V. (2005) Rational peptide-based vaccine design for cancer immunotherapeutic applications. *Curr. Med. Chem. 12*, 629−639.

(10) Rosenberg, S. A., Sherry, R. M., Morton, K. E., Yang, J. C., Topalian, S. L., Royal, R. E., Kammula, U. S., Restifo, N. P., Hughes, M. S., Schwarz, S. L., Ngo, L. T., Mavroukakis, S. A., and White, D. E. (2006) Altered CD8(+) T-cell responses when immunizing with multiepitope peptide vaccines. *J. Immunother. 29*, 224−231.

(11) Perambakam, S., Hallmeyer, S., Reddy, S., Mahmud, N., Bressler, L., Dechristopher, P., Mahmud, D., Nunez, R., Sosman, J. A., and Peace, D. J. (2005) Induction of specific T cell immunity in patients with prostate cancer by vaccination with psa146-154 peptide. *Cancer Immunol. Immunother*. 1−10.

(12) Yajima, N., Yamanaka, R., Mine, T., Tsuchiya, N., Homma, J., Sano, M., Kuramoto, T., Obata, Y., Komatsu, N., Arima, Y., Yamada, A., Shigemori, M., Itoh, K., and Tanaka, R. (2005) Immunologic evaluation of personalized peptide vaccination for patients with advanced malignant glioma. *Clin. Cancer Res. 11*, 5900−5911.

(13) Rosenberg, S. A., Sherry, R. M., Morton, K. E., Scharfman, W. J., Yang, J. C., Topalian, S. L., Royal, R. E., Kammula, U., Restifo, N. P., Hughes, M. S., Schwartzentruber, D., Berman, D. M., Schwarz, S. L., Ngo, L. T., Mavroukakis, S. A., White, D. E., and Steinberg, S. M. (2005) Tumor progression can occur despite the induction of very high levels of self/tumor antigen-specific CD8+ T cells in patients with melanoma. *J. Immunol. 175*, 6169−6176.

(14) Knutson, K. L., and Disis, M. L. (2005) Tumor antigen-specific T helper cells in cancer immunity and immunotherapy. *Cancer Immunol. Immunother. 54*, 721−728.

(15) Mocellin, S., Rossi, C. R., Nitti, D., Lise, M., and Marincola, F. M. (2003) Dissecting tumor responsiveness to immunotherapy: The experience of peptide-based melanoma vaccines. *Biochim. Biophys. Acta 653*, 61−71.

(16) Fuessel, S., Meye, A., Schmitz, M., Zastrow, S., Linne, C., Richter, K., Lobel, B., Hakenberg, O. W., Hoelig, K., Rieber, E. P., and Wirth, M. P. (2006) Vaccination of hormone-refractory prostate cancer patients with peptide cocktail-loaded dendritic cells: Results of a phase I clinical trial. *Prostate 66*, 811−821.

(17) Gajewski, T. F. (2006) Identifying and overcoming immune resistance mechanisms in the melanoma tumor microenvironment. *Clin. Cancer Res. 12*, 2326s−2330s.

(18) Chattopadhyay, S., Mehrotra, S., Chhabra, A., Hegde, U., Mukherji, B., and Chakraborty, N. G. (2006) Effect of CD4+CD25+ and CD4+CD25- T regulatory cells on the generation of cytolytic T cell response to a self but human tumor-associated epitope in vitro. *J. Immunol. 176*, 984−990.

(19) Antony, P. A., Piccirillo, C. A., Akpinarli, A., Finkelstein, S. E., Speiss, P. J., Surman, D. R., Palmer, D. C., Chan, C. C., Klebanoff, C. A., Overwijk, W. W., Rosenberg, S. A., and Restifo, N. P. (2005) Cd8+ T cell immunity against a tumor/self-antigen is augmented by CD4+ T helper cells and hindered by naturally occurring T regulatory cells. *J. Immunol. 174*, 2591−2601.

(20) Mayr, U. B., Walcher, P., Azimpour, C., Riedmann, E., Haller, C., and Lubitz, W. (2005) Bacterial ghosts as antigen delivery vehicles. *Adv. Drug Deliv. Rev. 57*, 1381−1391.

(21) Yoshimura, K., Jain, A., Allen, H. E., Laird, L. S., Chia, C. Y., Ravi, S., Brockstedt, D. G., Giedlin, M. A., Bahjat, K. S., Leong, M. L., Slansky, J. E., Cook, D. N., Dubensky, T. W., Pardoll, D. M., and Schulick, R. D. (2006) Selective targeting of antitumor immune responses with engineered live-attenuated listeria monocytogenes. *Cancer Res. 66*, 1096−1104.

(22) Franzusoff, A., Duke, R. C., King, T. H., Lu, Y., and Rodell, T. C. (2005) Yeasts encoding tumour antigens in cancer immunotherapy. *Expert Opin. Biol. Ther. 5*, 565−575.

(23) Gathuru, J. K., Koide, F., Ragupathi, G., Adams, J. L., Kerns, R. T., Coleman, T. P., and Livingston, P. O. (2005) Identification of dhbcag as a potent carrier protein comparable to KLH for augmenting muc1 antigenicity. *Vaccine 23*, 4727−4733.

(24) Boisgerault, F., Moron, G., and Leclerc, C. (2002) Virus-like particles: A new family of delivery systems. *Expert Rev. Vaccines 1*, 101−109.

(25) Chackerian, B., Lenz, P., Lowy, D. R., and Schiller, J. T. (2002) Determinants of autoantibody induction by conjugated papillomavirus virus-like particles. *J. Immunol. 169*, 6120−6126.

(26) Storni, T., Lechner, F., Erdmann, I., Bachi, T., Jegerlehner, A., Dumrese, T., Kundig, T. M., Ruedl, C., and Bachmann, M. F. (2002) Critical role for activation of antigen-presenting cells in priming of cytotoxic T cell responses after vaccination with virus-like particles. *J. Immunol. 168*, 2880−2886.

(27) Pattenden, L. K., Middelberg, A. P., Niebert, M., and Lipin, D. I. (2005) Towards the preparative and large-scale precision manufacture of virus-like particles. *Trends Biotechnol. 23*, 523−529.

(28) Banchereau, J., Ueno, H., Dhodapkar, M., Connolly, J., Finholt, J. P., Klechevsky, E., Blanck, J. P., Johnston, D. A., Palucka, A. K., and Fay, J. (2005) Immune and clinical outcomes in patients

with stage IV melanoma vaccinated with peptide-pulsed dendritic cells derived from CD34+ progenitors and activated with type I interferon. *J. Immunother. 28*, 505−516.
(29) Liao, C. W., Chen, C. A., Lee, C. N., Su, Y. N., Chang, M. C., Syu, M. H., Hsieh, C. Y., and Cheng, W. F. (2005) Fusion protein vaccine by domains of bacterial exotoxin linked with a tumor antigen generates potent immunologic responses and antitumor effects. *Cancer Res. 65*, 9089−9098.
(30) Kreitman, R. J. (2004) Confirmation and prevention of targeted toxicity by a recombinant fusion toxin. *Mol. Cancer Ther. 3*, 1691−1692.
(31) Eriksson, K., Fredriksson, M., Nordstrom, I., and Holmgren, J. (2003) Cholera toxin and its β subunit promote dendritic cell vaccination with different influences on th1 and th2 development. *Infect. Immun. 71*, 1740−1747.
(32) Ahlers, J. D., Belyakov, I. M., and Berzofsky, J. A. (2003) Cytokine, chemokine, and costimulatory molecule modulation to enhance efficacy of HIV vaccines. *Curr. Mol. Med. 3*, 285−301.
(33) Steinaa, L., Rasmussen, P. B., Wegener, A. M., Sonderbye, L., Leach, D. R., Rygaard, J., Mouritsen, S., and Gautam, A. M. (2005) Linked foreign T-cell help activates self-reactive ctl and inhibits tumor growth. *J. Immunol. 175*, 329−334.
(34) Dell, K., Koesters, R., and Gissmann, L. (2006) Transcutaneous immunization in mice: Induction of T-helper and cytotoxic T lymphocyte responses and protection against human papillomavirus-induced tumors. *Int. J. Cancer 118*, 364−372.
(35) Lu, J., Higashimoto, Y., Appella, E., and Celis, E. (2004) Multiepitope trojan antigen peptide vaccines for the induction of antitumor ctl and th immune responses. *J. Immunol. 172*, 4575−4582.
(36) Yano, A., Onozuka, A., Asahi-Ozaki, Y., Imai, S., Hanada, N., Miwa, Y., and Nisizawa, T. (2005) An ingenious design for peptide vaccines. *Vaccine 23*, 2322−2326.
(37) Schwarz, K., Storni, T., Manolova, V., Didierlaurent, A., Sirard, J. C., Rothlisberger, P., and Bachmann, M. F. (2003) Role of toll-like receptors in costimulating cytotoxic T cell responses. *Eur. J. Immunol. 33*, 1465−1470.
(38) Lund, J. M., Alexopoulou, L., Sato, A., Karow, M., Adams, N. C., Gale, N. W., Iwasaki, A., and Flavell, R. A. (2004) Recognition of single-stranded RNA viruses by toll-like receptor 7. *Proc. Natl. Acad. Sci. U.S.A. 101*, 5598−5603.
(39) Diebold, S. S., Kaisho, T., Hemmi, H., Akira, S., and Reis e Sousa, C. (2004) Innate antiviral responses by means of tlr7-mediated recognition of single-stranded RNA. *Science 303*, 1529−1531.
(40) McCormick, A. A., Corbo, T. A., Wykoff-Clary, S., Nguyen, L. V., Smith, M. L., Palmer, K. E., and Pogue, G. P. (2006) *Vaccine*, in press, Jul 5; Epub ahead of print.
(41) Smith, M. L., Lindbo, J. A., Dillard-Telm, S., Brosio, P. M., Lasnik, A. B., McCormick, A. A., Nguyen, L. V., and Palmer, K. E. (2006) Modified tobacco mosaic virus particles as scaffolds for display of protein antigens for vaccine applications. *Virology 348*, 475−488.
(42) Palmer, K. E., Benko, A., Doucette, S. A., Cameron, T. I., Foster, T., Hanley, K. M., McCormick, A. A., McCulloch, M., Pogue, G. P., Smith, M. L., and Christensen, N. D. (2006) Protection of rabbits against cutaneous papillomavirus infection using recombinant tobacco mosaic virus containing l2 capsid epitopes. *Vaccine 24*, 5516−5525.
(43) Weiner, G. J., Liu, H. M., Wooldridge, J. E., Dahle, C. E., and Krieg, A. M. (1997) Immunostimulatory oligodeoxynucleotides containing the cpg motif are effective as immune adjuvants in tumor antigen immunization. *Proc. Natl. Acad. Sci. U.S.A. 94*, 10833−10837.
(44) Overwijk, W. W., Surman, D. R., Tsung, K., and Restifo, N. P. (1997) Identification of a kb-restricted ctl epitope of β-galactosidase: Potential use in development of immunization protocols for "self" antigens. *Methods 12*, 117−123.
(45) Moore, M. W., Carbone, F. R., and Bevan, M. J. (1988) Introduction of soluble protein into the class I pathway of antigen processing and presentation. *Cell 54*, 777−785.
(46) Briles, E. B., and Kornfeld, S. (1978) Isolation and metastatic properties of detachment variants of b16 melanoma cells. *J. Natl. Cancer Inst. 60*, 1217−1222.
(47) Tindle, R. W., Fernando, G. J., Sterling, J. C., and Frazer, I. H. (1991) A "public" T-helper epitope of the e7 transforming protein of human papillomavirus 16 provides cognate help for several e7 b-cell epitopes from cervical cancer-associated human papillomavirus genotypes. *Proc. Natl. Acad. Sci. U.S.A. 88*, 5887−5891.
(48) Zwaveling, S., Ferreira Mota, S. C., Nouta, J., Johnson, M., Lipford, G. B., Offringa, R., van der Burg, S. H., and Melief, C. J. (2002) Established human papillomavirus type 16-expressing tumors are effectively eradicated following vaccination with long peptides. *J. Immunol. 169*, 350−358.
(49) Panina-Bordignon, P., Tan, A., Termijtelen, A., Demotz, S., Corradin, G., and Lanzavecchia, A. (1989) Universally immunogenic T cell epitopes: Promiscuous binding to human mhc class II and promiscuous recognition by T cells. *Eur. J. Immunol. 19*, 2237−2242.
(50) Men, Y., Gander, B., Merkle, H. P., and Corradin, G. (1996) Induction of sustained and elevated immune responses to weakly immunogenic synthetic malarial peptides by encapsulation in biodegradable polymer microspheres. *Vaccine 14*, 1442−1450.
(51) Lund, L. H., Andersson, K., Zuber, B., Karlsson, A., Engstrom, G., Hinkula, J., Wahren, B., and Winberg, G. (2003) Signal sequence deletion and fusion to tetanus toxoid epitope augment antitumor immune responses to a human carcinoembryonic antigen (cea) plasmid DNA vaccine in a murine test system. *Cancer Gene Ther. 10*, 365−376.
(52) Dickerson, E. B., Akhtar, N., Steinberg, H., Wang, Z. Y., Lindstrom, M. J., Padilla, M. L., Auerbach, R., and Helfand, S. C. (2004) Enhancement of the antiangiogenic activity of interleukin-12 by peptide targeted delivery of the Cytokine++ to $\alpha v\beta 3$ integrin. *Mol. Cancer Res. 2*, 663−673.
(53) Schraa, A. J., Kok, R. J., Botter, S. M., Withoff, S., Meijer, D. K., de Leij, L. F., and Molema, G. (2004) Rgd-modified anti-CD3 antibodies redirect cytolytic capacity of cytotoxic T lymphocytes toward $\alpha v\beta 3$-expressing endothelial cells. *Int. J. Cancer 112*, 279−285.
(54) Okada, N., Iiyama, S., Okada, Y., Mizuguchi, H., Hayakawa, T., Nakagawa, S., Mayumi, T., Fujita, T., and Yamamoto, A. (2005) Immunological properties and vaccine efficacy of murine dendritic cells simultaneously expressing melanoma-associated antigen and interleukin-12. *Cancer Gene Ther. 12*, 72−83.
(55) Liu, Y., Ye, T., Sun, D., Maynard, J., and Deisseroth, A. (2004) Conditionally replication-competent adenoviral vectors with enhanced infectivity for use in gene therapy of melanoma. *Hum. Gene Ther. 15*, 637−647.
(56) Zeh, H. J., III, Perry-Lalley, D., Dudley, M. E., Rosenberg, S. A., and Yang, J. C. (1999) High avidity ctls for two self-antigens demonstrate superior in vitro and in vivo antitumor efficacy. *J. Immunol. 162*, 989−994.
(57) Tagawa, S. T., Cheung, E., Banta, W., Gee, C., and Weber, J. S. (2006) Survival analysis after resection of metastatic disease followed by peptide vaccines in patients with stage IV melanoma. *Cancer 106*, 1353−1357.
(58) Roberts, J. D., Niedzwiecki, D., Carson, W. E., Chapman, P. B., Gajewski, T. F., Ernstoff, M. S., Hodi, F. S., Shea, C., Leong, S. P., Johnson, J., Zhang, D., Houghton, A., and Haluska, F. G. (2006) Phase 2 study of the g209-2m melanoma peptide vaccine and low-dose interleukin-2 in advanced melanoma: Cancer and leukemia group b 509901. *J. Immunother. 29*, 95−101.
(59) Bocchia, M., Gentili, S., Abruzzese, E., Fanelli, A., Iuliano, F., Tabilio, A., Amabile, M., Forconi, F., Gozzetti, A., Raspadori, D., Amadori, S., and Lauria, F. (2005) Effect of a p210 multipeptide vaccine associated with imatinib or interferon in patients with chronic myeloid leukaemia and persistent residual disease: A multicentre observational trial. *Lancet 365*, 657−662.
(60) Noguchi, M., Itoh, K., Yao, A., Mine, T., Yamada, A., Obata, Y., Furuta, M., Harada, M., Suekane, S., and Matsuoka, K. (2005) Immunological evaluation of individualized peptide vaccination with a low dose of estramustine for hla-a24+ hrpc patients. *Prostate 63*, 1−12.
(61) Uemura, H., Fujimoto, K., Tanaka, M., Yoshikawa, M., Hirao, Y., Uejima, S., Yoshikawa, K., and Itoh, K. (2006) A phase I trial of vaccination of ca9-derived peptides for hla-a24-positive patients with Cytokine-refractory metastatic renal cell carcinoma. *Clin. Cancer Res. 12*, 1768−1775.
(62) Peoples, G. E., Gurney, J. M., Hueman, M. T., Woll, M. M., Ryan, G. B., Storrer, C. E., Fisher, C., Shriver, C. D., Ioannides, C. G., and Ponniah, S. (2005) Clinical trial results of a her2/neu (e75)

vaccine to prevent recurrence in high-risk breast cancer patients. *J. Clin. Oncol. 23*, 7536−7545.

(63) Weihrauch, M. R., Ansen, S., Jurkiewicz, E., Geisen, C., Xia, Z., Anderson, K. S., Gracien, E., Schmidt, M., Wittig, B., Diehl, V., Wolf, J., Bohlen, H., and Nadler, L. M. (2005) Phase I/II combined chemoimmunotherapy with carcinoembryonic antigen-derived hla-a2-restricted cap-1 peptide and irinotecan, 5-fluorouracil, and leucovorin in patients with primary metastatic colorectal cancer. *Clin. Cancer Res. 11*, 5993−6001.

(64) Carbone, D. P., Ciernik, I. F., Kelley, M. J., Smith, M. C., Nadaf, S., Kavanaugh, D., Maher, V. E., Stipanov, M., Contois, D., Johnson, B. E., Pendleton, C. D., Seifert, B., Carter, C., Read, E. J., Greenblatt, J., Top, L. E., Kelsey, M. I., Minna, J. D., and Berzofsky, J. A. (2005) Immunization with mutant p53- and k-ras-derived peptides in cancer patients: Immune response and clinical outcome. *J. Clin. Oncol. 23*, 5099−5107.

(65) Fong, L., Hou, Y., Rivas, A., Benike, C., Yuen, A., Fisher, G. A., Davis, M. M., and Engleman, E. G. (2001) Altered peptide ligand vaccination with flt3 ligand expanded dendritic cells for tumor immunotherapy. *Proc. Natl. Acad. Sci. U.S.A. 98*, 8809−8814.

(66) Bourdette, D. N., Edmonds, E., Smith, C., Bowen, J. D., Guttmann, C. R., Nagy, Z. P., Simon, J., Whitham, R., Lovera, J., Yadav, V., Mass, M., Spencer, L., Culbertson, N., Bartholomew, R. M., Theofan, G., Milano, J., Offner, H., and Vandenbark, A. A. (2005) A highly immunogenic trivalent T cell receptor peptide vaccine for multiple sclerosis. *Mult. Scler. 11*, 552−561.

(67) Audran, R., Cachat, M., Lurati, F., Soe, S., Leroy, O., Corradin, G., Druilhe, P., and Spertini, F. (2005) Phase I malaria vaccine trial with a long synthetic peptide derived from the merozoite surface protein 3 antigen. *Infect. Immun. 73*, 8017−8026.

(68) Valmori, D., Dutoit, V., Ayyoub, M., Rimoldi, D., Guillaume, P., Lienard, D., Lejeune, F., Cerottini, J. C., Romero, P., and Speiser, D. E. (2003) Simultaneous CD8+ T cell responses to multiple tumor antigen epitopes in a multipeptide melanoma vaccine. *Cancer Immun. 3*, 15.

(69) Slingluff, C. L., Jr., Petroni, G. R., Yamshchikov, G. V., Hibbitts, S., Grosh, W. W., Chianese-Bullock, K. A., Bissonette, E. A., Barnd, D. L., Deacon, D. H., Patterson, J. W., Parekh, J., Neese, P. Y., Woodson, E. M., Wiernasz, C. J., and Merrill, P. (2004) Immunologic and clinical outcomes of vaccination with a multiepitope melanoma peptide vaccine plus low-dose interleukin-2 administered either concurrently or on a delayed schedule. *J. Clin. Oncol. 22*, 4474−4485.

BC060124M

Gene Carriers Based on Hexanediol Diacrylate Linked Oligoethylenimine: Effect of Chemical Structure of Polymer on Biological Properties

Julia Kloeckner,[†] Stefano Bruzzano,[‡] Manfred Ogris,[†] and Ernst Wagner*[,†]

Department of Pharmacy, Center of Drug Research, Pharmaceutical Biology-Biotechnology, Ludwig Maximilian University, Butenandtstrasse 5-13, D-81377 Munich, Germany, and Fraunhofer Institute for Applied Polymer Research, Geiselbergstrasse 69, D-14476 Potsdam-Golm, Germany. Received May 23, 2006; Revised Manuscript Received July 28, 2006

Two biodegradable polycations based on hexanediol diacrylate linked oligoethylenimine (OEI) were synthesized by applying different reaction temperatures, 20 °C (LT-OEI-HD) and 60 °C (HT-OEI-HD). Their structural properties were analyzed by NMR, FTIR, and SEC/MALLS (size exclusion chromatography coupled with multiangle laser light scattering detection). Reaction temperature strongly influenced molecular weight and ester/amide ratio and thus resulted in polycations with different biological activities and degradation profiles. LT-OEI-HD was an ester-based polycation of 8.7 kDa which degraded rapidly at pH 7 and pH 9 respectively. HT-OEI-HD had a molecular weight of 26.6 kDa, was mainly based on amides, and degraded more slowly than LT-OEI-HD. Both polymers mediated gene transfer as efficiently as linear polyethylenimine of 22 kDa in two cell lines while being less toxic at their optimal conjugate/plasmid (C/P) ratios. LT-OEI-HD needed higher C/P ratios for gene delivery; however, it was significantly less toxic than HT-OEI-HD.

INTRODUCTION

Clinical application of nonviral gene delivery is still limited by poor gene transfer efficiency and side effects of available transfection agents. Since high transfection activity of commonly used nondegradable polycations usually comes along with a pronounced acute cytotoxicity (*1*, *2*) and an unknown risk of long-term effects after accumulation, there is an urgent need to develop biocompatible and biodegradable polycations with high gene transfer activity.

Currently, many research groups generate biodegradable polycations by cross-linking nontoxic low molecular weight monomers or oligomers with linkers containing labile bonds. Besides disulfide linkages (*3*, *4*), phosphoesters (*5*−*7*), phosphoramidates (*8*), phosphazenes (*9*), or imine linkages (*10*), all types of carbon ester bonds were utilized for the design of degradable polymers (*11*−*17*). In general, linear cationic polyester polymers are reported to degrade fast in aqueous solution (*11*); hence cross-linked poly(amino esters) have been generated to prolong degradation (*18*, *19*). The synthesis of mixed ester/amide polymers is another approach to obtain advantageous degradation profiles (*20*, *21*).

Recently we designed a library of degradable polycations based on oligomerized polyamines (*22*). Cell culture screening revealed polymerized derivatives of 800 Da oligoethylenimine (OEI800) as efficient gene carriers. Similar polymers were previously reported by Gosselin et al. (*3*) and Forrest et al. (*23*). One of the polymers, OEI-HD, i.e., OEI800 cross-linked with equimolar amounts of hexanediol diacrylate (HD), could compete with the "golden standard" linear polyethylenimine of 22 kDa (PEI22) in terms of gene delivery while being less toxic (*22*). Our synthesis of OEI-HD was performed at 60 °C for 4 days in order to obtain a high degree of polymerization. The reaction conditions promoted ester aminolysis and generated the polymer HT-OEI-HD which is predominantly based on amide bonds. Pack and co-workers (*23*) previously had generated a similar but ester-based polymer using different reaction conditions (45 °C for 6 h).

Herein we report an ester-based analogue LT-OEI-HD, synthesized at lower temperature (20 °C), and compare it with the original HT-OEI-HD. Both polymers were analyzed with regard to structural properties and their potential as gene carriers. Despite differences in molecular weight and ester content, the novel LT-OEI-HD has similar DNA binding efficiency as HT-OEI-HD. However, differences were noticed in terms of degradation kinetics, transfection activity, and toxicity. Importantly, when applied at optimum polymer/DNA ratio, the novel gene carrier mediated gene delivery as efficiently as PEI22 and HT-OEI-HD while being significantly less toxic.

MATERIALS AND METHODS

Chemicals and Reagents. Dimethylsulfoxide puriss. (DMSO) was obtained from Fluka (Fluka Chemie GmbH, Deisenhofen, Germany). Oligoethylenimine with an average molecular mass of 800 Da (OEI800), 1,6-hexanediol diacrylate, and branched PEI with an average molecular mass of 25 kDa (PEI25) were obtained from Sigma-Aldrich (Munich, Germany). Linear PEI with an average molecular mass of 22 kDa (PEI22) is available from Polyplus Transfections (Strasbourg, France). PEI22 was also synthesized by acid-catalyzed deprotection of poly(2-ethyl-2-oxazoline) (50 kDa, Aldrich) in analogous form as described in Brissault et al. (*24*). Gel-filtrated PEI was used as a 1 mg/mL stock solution neutralized with HCl. Plasmid pCMVLuc (*Photinus pyralis* luciferase under control of the CMV enhancer/promoter) as described in Plank et al. (*25*) was produced endotoxin-free by Elim Biopharmaceuticals (San Francisco, CA) or Aldevron (Fargo, ND).

Spectroscopy. ^{1}H NMR spectra were recorded at 500 MHz in d_3-MeOH on an Eclipse +500 spectrometer from JEOL, Tokyo, Japan. FTIR spectroscopy was conducted with a FT-IR Paragon 1000 spectrometer from Perkin-Elmer, Boston, MA, using KBr pellets.

Synthesis of High-Temperature Polymer HT-OEI-HD. OEI800 (1.93 mL; 400 mg/mL in DMSO) was mixed at

* To whom correspondence should be addressed. Phone: ++49-89-2180-77841. Fax: ++49-89-2180-77798. E-mail: ernst.wagner@cup.uni-muenchen.de.

[†] Ludwig Maximilian University.

[‡] Fraunhofer Institute for Applied Polymer Research.

10.1021/bc060133v CCC: $33.50 © 2006 American Chemical Society
Published on Web 09/06/2006

equimolar ratio with 0.73 mL of HD (300 mg/mL in DMSO) and reacted for 4 days at 60 °C with constant shaking. Prior to purification, polymer samples were diluted 1:4 with H_2O_{dd} and the pH was immediately adjusted to pH 6 (with concentrated aqueous HCl). The diluted unpurified polymer was dialyzed via a Spectra/Por membrane (molecular mass cutoff 3.5 kDa; Spectrum Medical Industries, Inc., California) for 48 h against 4 L of water at 4 °C. After 24 h, water was exchanged against 4 L of fresh water. Synthesis and purification resulted in 157 mg of lyophilized OEI-HD (yield 16%). According to NMR analysis (see below), the molar ratio of hexanediol residues to OEI was 0.5:1; within the hexanediol linker, the ratio of diester to monoester was 20:80.

^{1}H NMR (500 MHz, d_3-MeOH): $\delta = 4.1$ (m, COOCH_2 ester linker, 4^aH, diester, 2^bH, monoester), 3.53 (m, 2^bH, HOCH_2, monoester), 2.6−3.5 (br m, 80H, NCH_2, of OEI ethylenes and NCH_2CH_2COO linker) 1.66 (m, 4^aH, COOCH$_2$CH_2 diester, 2^bH, monoester), 1,52 (m, 2^bH, HOCH$_2$CH_2 monoester), 1.38 (m, 4^{a+b}H, −OCH$_2$CH$_2$CH_2 linker). Integrals: a+b (linker in total), 50% of OEI protons; a (diester), 10%; b (monoester), 40%. FTIR spectroscopy (KBr pellet) showed formation of amide bonds (1638 cm^{-1}) and a weak signal of remaining ester bonds (1718 cm^{-1}).

Synthesis of Low-Temperature Polymer LT-OEI-HD. Four milliliters of OEI800 stock (400 mg/mL in DMSO) was mixed at equimolar ratio with 1.51 mL of HD stock (300 mg/mL in DMSO) and reacted for 4 days at 20 °C with constant shaking. Purification was performed as described above and resulted in 224 mg of lyophilized LT-OEI-HD (yield 11%). According to NMR analysis (see below), the molar ratio of hexanediol residues to OEI was 1.25:1; within the hexanediol linker, the ratio of diester to monoester was 50:50.

LT-OEI-HD: ^{1}H NMR (500 MHz, d$_3$-MeOH) $\delta = 4.1$ (m, COOCH_2 ester linker, 4^aH, diester, 2^bH, monoester), 3.54 (m, 2^bH, HOCH_2, monoester), 2.6−3.5 (br m, 80H, NCH_2, of OEI ethylenes and NCH_2CH_2COO linker), 1.66 (m, 4^aH, COOCH$_2$CH_2 diester, 2^bH, monoester), 1.54 (m, 2^bH, HOCH$_2$CH_2 monoester), 1.40 (m, 4^{a+b}H, −OCH$_2$CH$_2$CH_2 linker). Integrals: a+b (linker in total), 125% of OEI protons; a (diester), 62%; b (monoester), 62%. FTIR spectroscopy (KBr pellet) clearly showed strong ester signals (1725 cm^{-1}).

Size Exclusion Chromatography with Multidetection. The samples were analyzed by size exclusion chromatography (SEC) (Degasser SCM 400, isocratic pump P1000 and auto sampler AS 1000 from Spectra Physics, Egelsbach, Germany; TSK columns (polyglycidyl(meth)acrylate gel) PWH-Guard (7.5 × 37 mm, 12 μm) + G-Oligo-PW0 (7.5 × 300 mm, 6 μm) up to 3×10^3 g/mol (PEG) by Toso Haas, Stuttgart, Germany) linked with a multidetection system (viscosimeter η/Δn-1003 from WGE Dr. Bures, Dallgow, Germany; multiangle laser light scattering (MALLS) detector Dawn DSP, 632.8 nm, cell type K5; 18 detectors from 22.5° up to 147° from Wyatt, Woldert, Germany; OPTILAB DSP interferometric refractometer, 632.8 nm, cell type P10 from Wyatt, Woldert, Germany; UV−vis detector UV 2000 by Spectra Physics, Egelsbach, Germany; software Astra 4.7 from Wyatt, Woldert, Germany). The accuracy and repeatability of the determined molar masses is about ±10 and ±3%, respectively. A mixture of 0.2 mol/L Na_2SO_4 and 1% (w/w) acetic acid in deionized water was used as eluent. The flow rate was 1.0 mL/min at 20 °C using a sample loop of 100 μL and sample concentrations of 1 to 4 g/L.

The refractive index increment of a branched polyethyleneimine standard was determined by the means of interferometric measurements (ScanRef; Polymer Standards Service, Mainz, 633 nm, 20 °C). For this purpose, polyethylenimine (molecular mass ∼ 50 000 Da, 37% aqueous solution from Aldrich) was ultrafiltrated (Minisette, Omega cutoff 10 kDa from Pall Gelman), freeze-dried, and afterward solved in the eluent. A value of dn/dc = 0.195 mL/g was found. Molar masses determined for HT-OEI-HD and LT-OEI-HD samples were compared to those of commercially available branched PEIs (Lupasol G100, 5000 Da, and G20, 1300 Da).

For use in some gene transfer studies, fractions of HT-OEI-HD were chromatographically separated as described above and samples F1 and F2 were concentrated via macroseparators (Omega 3k (PALL), 4000 rpm, 20 min). The procedure was accomplished 5 times, and resulting sample solutions were analyzed again by SEC.

Degradation of HT-OEI-HD and LT-OEI-HD. Degradation was studied with polymer stocks (5 mg/mL, pH 7) incubated for 5, 10, and 15 days at 37 °C in an Eppendorf Thermomixer (500 rpm). Solutions with a pH of 5 and 9 were prepared by adding the appropriate amount of HCl and NaOH, respectively. After incubation, the pH was adjusted to pH 7. Sample aliquots were analyzed by SEC on a Sephadex G25 (10/30) with 150 mM NaCl as eluent and a flow rate of 1 mL/min. Sample detection was carried out at 210, 220, and 240 nm, and degradation rates were calculated by integrating the AUC (area under the curve) of the main polymer peak.

Ethidium Bromide (EtBr) Exclusion Assay. Aliquots of OEI-HD, LT-OEI-HD, PEI22, or PEI25 were added sequentially to a DNA solution (20 μg/mL) in either HBG (Hepes buffered glucose; 20 mM Hepes pH 7.3 plus 5% w/v glucose) or HBS (Hepes buffered saline; 20 mM Hepes pH 7.3 plus 150 mM NaCl) containing 400 ng/mL EtBr, and the decrease of fluorescence was measured in a Varian Cary Eclipse fluorescence spectrophotometer (Varian, Mulgrave, Australia). EtBr/DNA fluorescence (λex 510 nm, λem 590 nm) was set to 100% prior to addition of polycation.

DNA Polyplex Formation. Plasmid DNA encoding luciferase was condensed with standard PEI or biodegradable polymers at various conjugate/plasmid (C/P) ratios (w/w). C/P = 1 presents a N/P ratio = 5.3 for HT-OEI-HD, N/P = 4.9 for LT-OEI-HD, and N/P = 7.6 for PEI. DNA/polycation polyplexes were prepared at a final DNA concentration of 20 μg/mL as described in ref *26*. Briefly, indicated amounts of plasmid DNA and polycation were each diluted in either HBS or HBG and rapidly mixed by pipetting. Polyplexes were allowed to stand for at least 20 min at RT before use.

Cell Culture. Cell culture media, antibiotics, and fetal calf serum (FCS) were purchased from Invitrogen GmbH (Karlsruhe, Germany). All cultured cells were grown at 37 °C in 5% CO_2 humidified atmosphere. Stock cultures were grown in the absence of antibiotics. B16F10 murine melanoma cells (kindly provided by I. J. Fidler, Texas Medical Center, Houston, TX) and murine neuroblastoma Neuro2A cells (ATCC CCI-131) were cultured in DMEM (1 g of glucose/L) supplemented with 10% FCS.

Luciferase Reporter Gene Expression. For standard transfection screenings cells were seeded in 96-well plates (TPP, Trasadingen, Switzerland) at a density of 10^4 cells (Neuro2A cells) or 5×10^3 cells (B16F10 cells) in 100 μL of culture medium per well. During transfection and for the following incubation before analysis, 100 units/mL penicillin, 100 μg/mL streptomycin, and 10% FCS were present in the medium. Transfection complexes with indicated amounts of DNA (pCMVLuc) were added directly to the cells. Complex-containing medium was removed 4 h after transfection, 100 μL of fresh medium was added, and gene expression was measured after 24 h.

Cell lysis and measurement of luciferase was performed as described previously (*2*). Two nanograms of recombinant luciferase (Promega, Mannheim) corresponds to 10^7 light units.

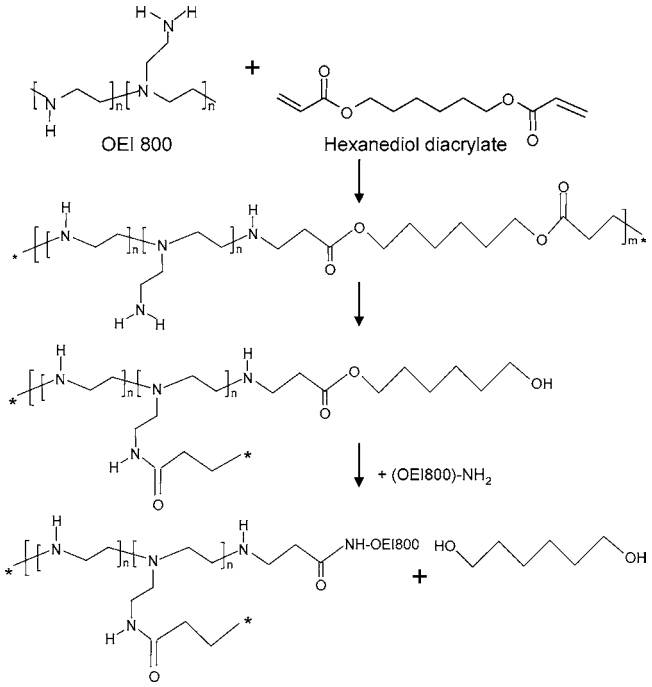

Figure 1. Synthesis of HT-OEI-HD and LT-OEI-HD. The HD (hexanediol diacrylate) linker reacts with primary and secondary amines of oligoethylenimine (OEI) to form amine bonds. At elevated temperature, amino groups of the OEI unit attack ester bonds, resulting in mixed ester/amide-based oligomers. With time, aminolysis of the esters releases the hexanediol moiety from the polymer, resulting in amide-linked derivatives of oligoethylenimine.

Metabolic Activity of Transfected Cells. Cells were grown (96-well plate) and treated with different amounts of DNA complexes as described in Luciferase Reporter Gene Expression. Metabolic activity of each well was determined by using a methylthiazoletetrazolium (MTT)/thiazolyl blue assay: To each well was added 10 μL of a 5 mg/mL solution of MTT in sterile PBS buffer (phosphate buffered saline; 150 mM NaCl buffered with 15 mM phosphate pH 7.4). Cells were incubated at 37 °C for 2 h, medium was removed, and the samples were frozen at −80 °C for at least 2 h. One hundred microliters of DMSO was added and samples were incubated at 37 °C for 30 min with constant shaking. Optical absorbance was measured at 590 nm (reference wavelength 630 nm) using a micro plate reader (Spectrafluor Plus, Tecan Austria GmbH, Grödig, Austria), and cell viability was expressed as a percent relative to untreated control cells.

RESULTS

Synthesis of OEI-HD Polymers. The 1,6-hexanediol diacrylate (HD) linker reacts with polyamines by Michael addition to either primary or secondary amines, generating ester-based polymers. In a following reaction, free amino groups may convert ester-containing polymers into amide derivatives by aminolysis of the esters **(**Figure 1). This side reaction depends on reaction temperature and the availability of supplementary free amines. In order to circumvent ester aminolysis and to generate mostly ester-containing polymers, a new OEI-HD derivative was synthesized at low temperature. The synthesis of LT-OEI-HD was carried out for 4 days at 20 °C instead of 60 °C (HT-OEI-HD). Polymers were purified by dialysis using a 3.5 kDa molecular mass cutoff membrane.

Polymer structures were analyzed by FTIR spectroscopy. LT-OEI-HD contained ester bonds (1725 cm^{-1}). In contrast, FTIR spectra of HT-OEI-HD showed only a weak signal of remaining ester bonds (1718 cm^{-1}) and the formation of amide bonds (1638 cm^{-1}). ^1H NMR confirmed the presence of ester bonds

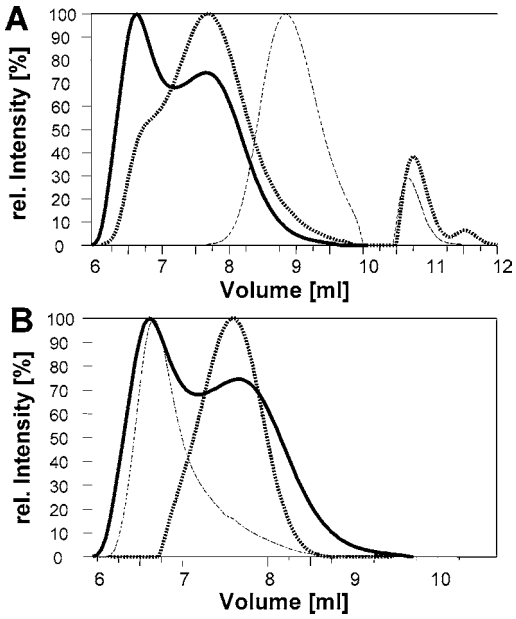

Figure 2. Fractionation and molar mass determination of polymers by SEC/MALLS. (A) SEC traces of the precursor OEI800 (dashed line) and its derivatives LT-OEI-HD (spotted line) and HT-OEI-HD-1 (solid line). Relative intensities of the refractive index detector signal are shown. Both derivatives show broad molar mass distributions, and higher molecular fractions eluting close to the column's exclusion limit (<6.7 mL) are not separated. (B) SEC traces of the standard HT-OEI-HD-1 (solid line) and its two fractions of higher (dashed line with spots) and lower (spotted line) molar masses.

in the product. Although FTIR spectra indicated extensive ester aminolysis in case of HT-OEI-HD, both polymers (HT-OEI-HD and LT-OEI-HD) clearly showed the protons belonging to methylene groups of the linker. The hexanediol chain of the HD linker was still present in both polymers, although the ratio between linker and OEI was very different. In the case of LT-OEI-HD, a molar ratio of linker to OEI of 1.25 was found, with 0.6 molar equiv of hexanediol linker preserved as diester. For the HT-OEI-HD polymer, a molar ratio of linker to OEI of 0.5 was found, with only 0.1 molar equiv of the hexanediol diester, as 80% of the linker was found converted into the monoester.

Molar Mass Determination and Polymer Fractionation. Polymer molar mass was analyzed by aqueous size exclusion chromatography (SEC) linked with a MALLS (multiangle laser light scattering) system, employing 0.2 M Na_2SO_4 + 1% HAc as eluent. Samples of different molar masses were successfully separated on a TSK-Gel Guard + G-Oligo-PW column (Figure 2). The elution profiles of HT-OEI-HD, LT-OEI-HD, and the precursor OEI800 are shown in Figure 2A. The ratio of RI (refractive index) and UV (254 nm) detection signals remained basically constant during the separation, demonstrating the same chemical composition of the polymer fractions. Absolute molar mass was determined with a MALLS detector and compared to commercially available low molecular weight PEIs **(**Table 1**)**. LT-OEI-HD had an average molar mass of 8.7 kDa, whereas HT-OEI-HD had a higher average molar mass of 26.6 kDa. The detected d*n*/d*c* of 0.21 mL/g correlated well with the d*n*/d*c* of the PEI reference (d*n*/d*c*(PEI) = 0.195 mL/g at 633 nm). Using the same SEC methodology, HT-OEI-HD was separated into two fractions F1 and F2, with average molar masses of 45.6 kDa and 9.5 kDa, respectively (Figure 2B and Table 1).

Polymer Toxicity and Degradation. Cytotoxic properties of a polycation usually correlate with the molecular weight. A decrease in molecular weight upon biological degradation should result in reduced toxicity of the polymer. Therefore, cytotoxicity of intact HT-OEI-HD and LT-OEI-HD was compared. In addition, cytotoxicity of the corresponding degradation products

Table 1. Molecular Mass Determination by SEC/MALLS[a]

	recovery (%)	Vp (mL)	Eta (mL/g)	Mp^{LS} (kDa)	Mw^{LS} (kDa)
PEI 1.3 kDa	93	8.41	4,4	2.3	2.4
PEI 5.0 kDa	92	7.79	6,7	7.5	7.4
OEI800 (pre-oligomer)	90	8.84		0.8	
HT-OEI-HD	100	7.65	11.6	7.4	26.6
fraction 1[b]		6.62		23.1	45.6
fraction 2[c]		7.61		4.7	9.5
LT-OEI-HD	90	7.71	11,5	4.6	8.7

[a] Vp: elution volume at peak maximum. Eta: bulk intrinsic viscosity. Mp: molar mass at peak maximum measured via static light scattering. Mw: mass average molar mass via static light scattering. [b] F1: fraction of higher molar mass. [c] F2: fraction of lower molar mass.

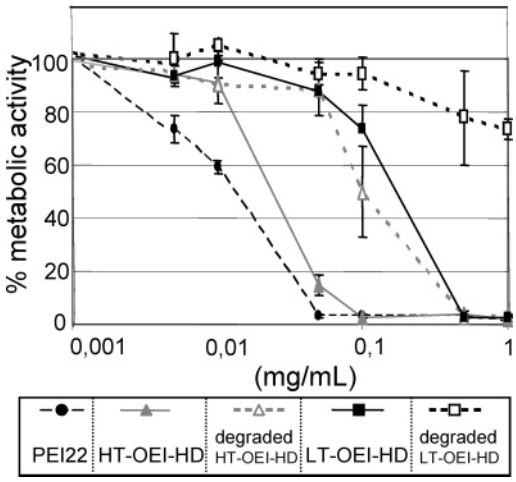

Figure 3. Cytotoxicity induced by OEI-HD polymers. HT-OEI-HD and LT-OEI-HD (5 mg/mL) were incubated at pH 9 for 5 days at 37 °C. B16F10 cells (5000 cells/well) were incubated with various concentrations of hydrolyzed and untreated polymer. After 4 h, polymer-containing medium was exchanged, and 24 h later, metabolic activity was determined by the MTT assay. Metabolic activity is presented as mean values of triplicates.

was determined. For this purpose, B16F10 cells were incubated with various amounts of free polymer for 4 h. After 24 h, the metabolic cell activity was determined by MTT assay and compared to untreated control cells. At a high polymer concentration of 50 μg/mL, PEI22 and HT-OEI-HD decreased metabolic activity down to 3% (PEI22) and 15% (HT-OEI-HD), whereas cells that were treated with the same amount of LT-OEI-HD retained 88% of their metabolic activity **(**Figure 3**)**.

For the degradation studies, both polymers were treated in aqueous solutions at pH 5, 7, and 9 at 37 °C for 5 to 15 days as described in Materials and Methods. The results of size exclusion chromatography (SEC) demonstrated that LT-OEI-HD was reduced to 68% ± 2% (pH 5), 51% ± 3% (pH 7), and 38% ± 3% (pH 9) of original polymer after 5 days of hydrolysis. As expected, HT-OEI-HD was less susceptible to hydrolysis since degradation could barely be observed after 5 days. Ten days of hydrolysis resulted in 94% ± 1% (pH 5), 77% ± 1% (pH 7), and 72% ± 2% (pH 9) of original polymer.

Interestingly, although the degradation of HT-OEI-HD was limited, it was sufficient to significantly reduce the toxicity (Figure 3) when the polymer was applied at lower doses (5−50 μg/mL). However, concentrations above 500 μg/mL strongly disturbed viability and resulted in 2−3% metabolic activity. After hydrolysis of LT-OEI-HD the degraded fragments exhibited negligible toxicity even at polymer concentrations up to 1000 μg/mL.

DNA Binding and Polyplex Formation. Next, the two OEI-HD polymers were evaluated for their ability to form DNA complexes. EtBr exclusion experiments demonstrated that DNA

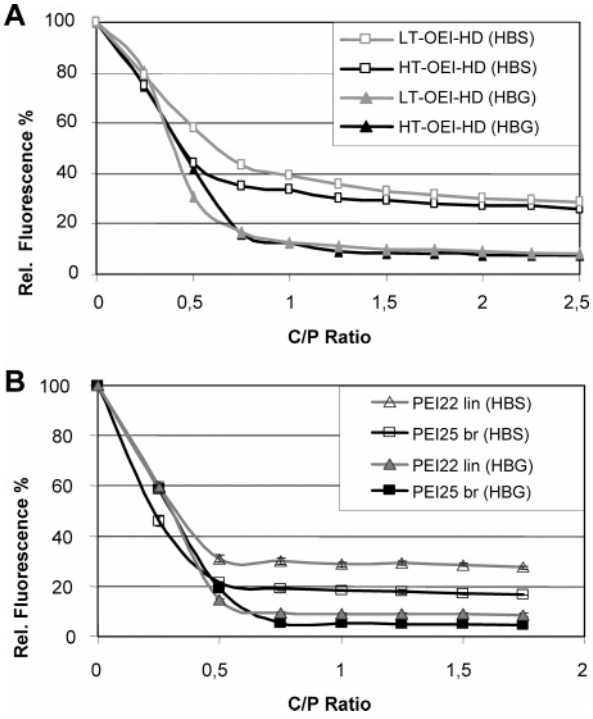

Figure 4. DNA binding and complex density of HT-OEI-HD and LT-OEI-HD. DNA complexes of HT-OEI-HD and LT-OEI-HD (A) or linear PEI22 and branched PEI25 (B) were formed in the presence of EtBr in either HBG or HBS, and inhibition of EtBr/DNA fluorescence was monitored as described in Materials and Methods. Measurements were performed in duplicate.

binding activity was not affected by differences of molecular weight or ester/amide content. Both polymers possessed similar DNA binding affinities (Figure 4A). In salt-free buffer (Hepes buffered glucose), the EtBr exclusion profiles were very similar to the profiles of linear PEI22 and branched PEI25 **(**Figure 4B**)**. In physiological salt-containing buffer (Hepes buffered sodium chloride), affinities of the OEI-HD polymers and PEI22 were comparable but slightly lower than for PEI25. Analogous trends of complexation and polyplex stability were observed using the agarose gel retardation assay. In the case of HT-OEI-HD as well as for LT-OEI-HD, DNA was completely retarded at C/P 1 (data not shown).

Reporter Gene Expression and Toxicity of HT-OEI-HD and LT-OEI-HD Polyplexes. Neuro2A cells were transfected with either HT-OEI-HD or LT-OEI-HD in order to investigate how structural differences will influence transfection efficiency and cytotoxicity of polyplexes. At C/P 2, HT-OEI-HD achieved maximal reporter gene expression **(**Figure 5A**)**, which decreased with increasing amount of polymer due to rising cytotoxicity **(**Figure 5B**)**. Although higher charge ratios (C/P 8) were needed for optimal gene delivery, LT-OEI-HD polyplexes were able to mediate gene transfer as efficiently as HT-OEI-HD without reducing the metabolic activity of transfected cells.

In order to verify these biological effects on a second cell line, different DNA concentrations were tested on B16F10 cells **(**Figure 5C**)**. According to previous experiments, HT-OEI-HD polyplexes prepared at C/P 2 were as efficient as PEI22. Polyplexes of LT-OEI-HD prepared at C/P 4 had efficiency similar to that of standard PEI polyplexes. With regard to toxicity, PEI22 and HT-OEI-HD exhibited pronounced toxicity even at low DNA concentrations, whereas LT-OEI-HD did not influence the metabolic activity of B16F10 cells at these concentrations **(**Figure 5D**)**. Generally, B16F10 cells were more sensitive than Neuro2A cells when treated with polyplexes. Metabolic activity determined 24 h after transfection was reduced by PEI22 to less than 20% of the nontransfected control

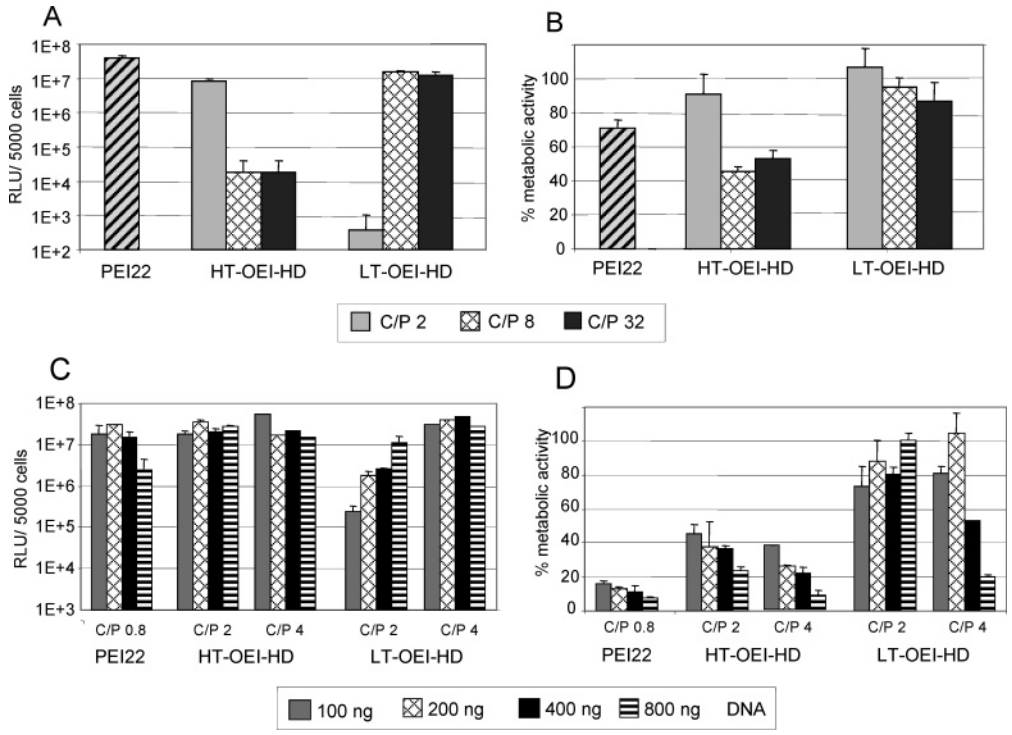

Figure 5. Reporter gene expression and toxicity after transfection with OEI-HD polymers. Neuro2a cells were transfected with polyplexes consisting of 200 ng (2 μg/mL DNA) of pCMVLuc complexed with HT-OEI-HD or LT-OEI-HD in HBS (A and B). B16F10 cells were transfected with 100−800 ng (1−8 μg/mL DNA) of pCMVLuc complexed with HT-OEI-HD or LT-OEI-HD at C/P 2 and 4 in HBS (C and D). Control PEI22 polyplexes were prepared at C/P 0.8 in HBS. Luciferase activity (A and C) and metabolic activity (MTT assay) (B and D) are presented as mean values + SD of triplicates.

cells **(**Figure 5D**)**. When cells were transfected with C/P 2 polyplexes containing 800 ng of DNA, HT-OEI-HD reduced metabolic activity down to 22% while cells transfected with LT-OEI-HD polyplexes maintained 100% of their metabolic activity. Cell viability was only affected by LT-OEI-HD when high doses of polymer and DNA were applied. Transfection with 400 ng of DNA and 1.6 μg of polymer (corresponding to C/P 4) resulted in 54% metabolic activity, which dropped to 20% at the maximal DNA dose.

Transfection Efficiency of Fractionated HT-OEI-HD. According to SEC analysis, HT-OEI-HD showed a broader molecular weight distribution with a higher average molecular mass of 26.6 kDa. To find out whether the larger or the smaller fraction is more efficient than the other, fractions F1 and F2 were collected and analyzed separately with regard to their gene transfer efficiency. B16F10 cells were transfected with HT-OEI-HD (nonpurified), fraction 1 (F1), fraction 2 (F2), and LT-OEI-HD **(**Figure 6A**)**. While standard OEI-HD reached maximal reporter gene expression at C/P 4, both F1 and F2 needed higher C/P ratios for efficient gene delivery. At C/P 8, F1 resulted in luciferase expression equivalent to that of PEI22 and HT-OEI-HD, whereas F2 was effective only at C/P 16. Neither of the purified fractions was more effective than the unpurified polymer. At the current stage the reasons for this remain unclear. It is also noteworthy that there was a difference between LT-OEI-HD and F2, although both polymers possessed similar molecular weight. LT-OEI-HD mediated efficient gene transfer at all analyzed C/P ratios and achieved maximal reporter gene expression at C/P 8 whereas F2 was characterized by poor transfection activity at low C/P ratios.

A clear correlation between molecular weight and toxicity was observed for all polymers **(**Figure 6B**)**. Cell viability decreased rapidly when cells were transfected with HT-OEI-HD or F1 polyplexes, while low molecular weight polymers (LT-OEI-HD and F2) were far less toxic.

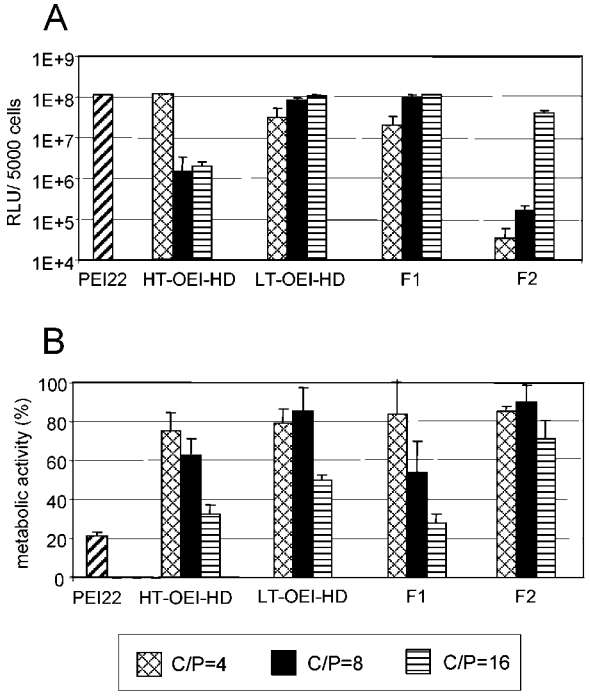

Figure 6. Reporter gene expression and toxicity of HT-OEI-HD after fractionation by SEC/MALLS. B16F10 cells were transfected with 200 ng (2 μg/mL DNA) of pCMVLuc complexed with HT-OEI-HD (nonpurified), LT-OEI-HD (8.7 kDa), HT-OEI-HD fraction 1 (53 kDa), and fraction 2 (8.1 kDa) at C/P 4 (gray bars), C/P 8 (patterned bars), and C/P 16 (black bars) in HBS. Control PEI 22 polyplexes were prepared at C/P 0.8. Luciferase activity (A) and metabolic activity (MTT assay) (B) are presented as mean values + SD of triplicates.

DISCUSSION

Previously we reported an OEI-HD polymer with high potential as a gene carrier (*22*). In contrast to a previously

published (*23*) analogous polymer, our synthesized polymer was predominantly based on amide bonds due to ester aminolysis as a result of a higher reaction temperature. Since structural properties impact both transfection activity and toxicity (*27*, *28*), we aimed to modify the synthesis protocol in order to generate faster degrading ester-based polymers (*23*) and compare them side-by-side with the amide-based polymers. Ideally, such OEI-HD ester derivatives should exhibit equivalent transfection efficiency while being less toxic.

The novel OEI-HD analogue, namely, LT-OEI-HD, was synthesized at 20 °C instead of 60 °C. According to FT-IR and NMR analysis, LT-OEI-HD largely had the predicted ester structure whereas HT-OEI-HD contained mainly amides with few esters left. Moreover, partial diester degradation was observed by the appearance of protons belonging to the methylene groups adjacent to hydroxyl groups; HT-OEI-HD lost 80% of hexanediol residue due to ester aminolysis. This demonstrates that high reaction temperature promoted inter- or intramolecular ester aminolysis.

In consideration of these structural differences, the ester-based LT-OEI-HD should be degraded under hydrolytic conditions, whereas the amide bonds of HT-OEI-HD should be more stable. Degradation studies at pH 5, 7, and 9 revealed that hydrolysis of both polymers were accelerated with increasing pH. Moreover, during the analyzed period of time (15 days), only slight alterations (∼30% degradation) were observed for HT-OEI-HD. This slow amide hydrolysis of HT-OEI-HD was in accordance with results previously reported by Kissel and his group. Their copolymer poly(ethylene-*co*-L-lactamide-*co*-succinamide) degraded via base-catalyzed hydrolytic cleavage of amide bonds over months (*20*).

Hydrolysis of LT-OEI-HD was confirmed by a rapid decrease of original polymer. After 5 days, more than 60% of LT-OEI-HD was cleaved into smaller fragments when incubated at pH 7 or pH 9. Incubation at pH 5 resulted in significantly slower degradation of LT-OEI-HD within the first 15 days. These data are in accordance with degradation profiles observed for hyperbranched poly(amino esters) (*17*). They explained rapid degradation at pH 7.4 and slow-going hydrolysis at pH 5.1 by the fact that at pH 7.4 a higher fraction of unprotonated amino groups in the polymer catalyzes the hydrolysis of ester groups.

Nevertheless, it was not yet clear whether these changes in polymer integrity would have any effect on cytotoxicity. To elucidate the impact of polymer degradation on toxicity, we analyzed metabolic activity of cells treated with either original or partially degraded polymer. In fact, moderate changes in molecular weight distribution that seemed unimportant with regard to SEC data had significant impact on the cytotoxicity of polymers. Even HT-OEI-HD-induced toxicity (which was very significant at high polymer concentrations) was strongly reduced after 5 days of hydrolysis. Degradation of the less toxic LT-OEI-HD resulted in nontoxic oligomer fragments. It should be noted that cytotoxicity induced by free polymers gives a worst case estimate for the interaction with cells and tissues (*27*, *29*). Toxicity of nonviral vectors usually decreases when polymers are complexed to DNA (*2*).

Apart from ester aminolysis, the chosen reaction conditions provoked a high degree of polymerization in the case of HT-OEI-HD, whereas LT-OEI-HD should have a significantly lower molecular weight. SEC/MALLS analysis of OEI-HD-based polymers confirmed the influence of reaction temperature on the degree of polymerization. As expected, the molecular weight of LT-OEI-HD was significantly lower than that of HT-OEI-HD. Synthesis at 20 °C (4 days) generated 8.7 kDa polymers, and a reaction temperature of 60 °C (4 days) resulted in polymers with a molecular mass of 26.6 kDa.

With regard to chemical structure, molecular weight, and degradation kinetics, we expected differences in polyplex stability, gene transfer activity, and cytotoxicity (*30*). Ester conversion into amide bonds reduces the number of potentially charge-bearing amines. On the other hand, high molecular weight and the presence of various secondary amines might provide enough positive charges for efficient DNA condensation.

While DNA-binding activity was similar for HT-OEI-HD and LT-OEI-HD, their biological activities showed significant differences. HT-OEI-HD mediated high transfection levels at low C/P ratios and was characterized by a rapid decrease in cell viability at high polymer concentrations. Furthermore, free HT-OEI-HD polymer induced erythrocyte aggregation; this can be easily explained by its higher molecular weight. In contrast, the lower molecular weight LT-OEI-HD did not interact with erythrocytes and was applied at high concentrations without inducing HT-OEI-HD-analogue toxicity. However, more polymer was needed for efficient gene transfer.

It is important to note that both polymers exceeded the "golden standard" PEI22 in terms of transfection efficiency/toxicity profile when applied at optimal doses.

Fractionation of HT-OEI-HD by SEC/MALLS resulted in a large fraction of 46 kDa and a small fraction of 9.5 kDa. The high molecular weight fraction was decisive for transfection activity as well as for cytotoxicity, and the low molecular weight fraction displayed low cytotoxicity similar to LT-OEI-HD, but far lower transfection activity.

In conclusion, we have shown the high impact of synthesis conditions on structural features of a polymer. Differences in molecular weight and degradability strongly influence gene transfer activity and cytotoxicity. Importantly, degradation of ester/amide-based OEI-HD polymers results in strongly reduced toxicity which is highly desirable with regard to long-term in vivo application. We demonstrated that both amide-based HT-OEI-HD and the ester-based LT-OEI-HD possess great potential as efficient gene carriers.

ACKNOWLEDGMENT

We thank Olga Brück for skillful assistance in preparing the manuscript and Wolfgang Rödl for helpful discussions. This work was in part funded by the Deutsche Forschungsgemeinschaft SFB 486 "Nanoman" and by the European Community FP6 network project "GIANT".

LITERATURE CITED

(1) Moghimi, S. M., Symonds, P., Murray, J. C., Hunter, A. C., Debska, G., and Szewczyk, A. (2005) A two-stage poly(ethylenimine)-mediated cytotoxicity: implications for gene transfer/therapy. *Mol. Ther. 11*, 990−995.

(2) Boeckle, S., von Gersdorff, K., van der Piepen, S., Culmsee, C., Wagner, E., and Ogris, M. (2004) Purification of polyethylenimine polyplexes highlights the role of free polycations in gene transfer. *J. Gene Med. 6*, 1102−1111.

(3) Gosselin, M. A., Guo, W., and Lee, R. J. (2001) Efficient gene transfer using reversibly cross-linked low molecular weight polyethylenimine. *Bioconjugate Chem. 12*, 989−994.

(4) Read, M. L., Singh, S., Ahmed, Z., Stevenson, M., Briggs, S. S., Oupicky, D., Barrett, L. B., Spice, R., Kendall, M., Berry, M., Preece, J. A., Logan, A., and Seymour, L. W. (2005) A versatile reducible polycation-based system for efficient delivery of a broad range of nucleic acids. *Nucleic Acids Res. 33*, e86.

(5) Wang, J., Mao, H. Q., and Leong, K. W. (2001) A novel biodegradable gene carrier based on polyphosphoester. *J. Am. Chem. Soc. 123*, 9480−9481.

(6) Wang, J., Zhang, P. C., Mao, H. Q., and Leong, K. W. (2002) Enhanced gene expression in mouse muscle by sustained release of plasmid DNA using PPE-EA as a carrier. *Gene Ther. 9*, 1254−1261.

(7) Zhao, Z., Wang, J., Mao, H. Q., and Leong, K. W. (2003) Polyphosphoesters in drug and gene delivery. *Adv. Drug Deliv. Rev. 55*, 483−499.
(8) Wang, J., Gao, S. J., Zhang, P. C., Wang, S., Mao, H. Q., and Leong, K. W. (2004) Polyphosphoramidate gene carriers: effect of charge group on gene transfer efficiency. *Gene Ther. 11*, 1001−1010.
(9) de Wolf, H. K., Luten, J., Snel, C. J., Oussoren, C., Hennink, W. E., and Storm, G. (2005) In vivo tumor transfection mediated by polyplexes based on biodegradable poly(DMAEA)-phosphazene. *J. Controlled Release 109*, 275−287.
(10) Kim, Y. H., Park, J. H., Lee, M., Kim, Y. H., Park, T. G., and Kim, S. W. (2005) Polyethylenimine with acid-labile linkages as a biodegradable gene carrier. *J. Controlled Release 103*, 209−219.
(11) Lim, Y., Choi, Y. H., and Park, J. (1999) A Self-Destroying Polycationic Polymer: Biodegradable Poly(4-hydroxy-L-proline ester). *J. Am. Chem. Soc. 121*, 5633−5639.
(12) Lim, Y. B., Han, S. O., Kong, H. U., Lee, Y., Park, J. S., Jeong, B., and Kim, S. W. (2000) Biodegradable polyester, poly[alpha-(4-aminobutyl)-L-glycolic acid], as a non-toxic gene carrier. *Pharm. Res. 17*, 811−816.
(13) Anderson, D. G., Lynn, D. M., and Langer, R. (2003) Semi-Automated Synthesis and Screening of a Large Library of Degradable Cationic Polymers for Gene Delivery. *Angew. Chem., Int. Ed. 42*, 3153−3158.
(14) Akinc, A., Anderson, D. G., Lynn, D. M., and Langer, R. (2003) Synthesis of poly(beta-amino ester)s optimized for highly effective gene delivery. *Bioconjugate Chem. 14*, 979−988.
(15) Anderson, D. G., Peng, W., Akinc, A., Hossain, N., Kohn, A., Padera, R., Langer, R., and Sawicki, J. A. (2004) A polymer library approach to suicide gene therapy for cancer. *Proc. Natl. Acad. Sci. U.S.A. 101*, 16028−16033.
(16) Anderson, D. G., Akinc, A., Hossain, N., and Langer, R. (2005) Structure/property studies of polymeric gene delivery using a library of poly(beta-amino esters). *Mol. Ther. 11*, 426−434.
(17) Zhong, Z., Song, Y., Engbersen, J. F., Lok, M. C., Hennink, W. E., and Feijen, J. (2005) A versatile family of degradable non-viral gene carriers based on hyperbranched poly(ester amine)s. *J. Controlled Release 109*, 317−329.
(18) Lim, Y. B., Kim, S. M., Suh, H., and Park, J. S. (2002) Biodegradable, endosome disruptive, and cationic network-type polymer as a highly efficient and nontoxic gene delivery carrier. *Bioconjugate Chem. 13*, 952−957.
(19) Kim, T. I., Seo, H. J., Choi, J. S., Yoon, J. K., Baek, J. U., Kim, K., and Park, J. S. (2005) Synthesis of biodegradable cross-linked poly(beta-amino ester) for gene delivery and its modification, inducing enhanced transfection efficiency and stepwise degradation. *Bioconjugate Chem. 16*, 1140−1148.
(20) Petersen, H., Merdan, T., Kunath, K., Fischer, D., and Kissel, T. (2002) Poly(ethylenimine-co-L-lactamide-co-succinamide): a biodegradable polyethylenimine derivative with an advantageous pH-dependent hydrolytic degradation for gene delivery. *Bioconjugate Chem. 13*, 812−821.
(21) Thomas, M., Ge, Q., Lu, J. J., Chen, J., and Klibanov, A. M. (2005) Cross-linked small polyethylenimines: while still nontoxic, deliver DNA efficiently to mammalian cells in vitro and in vivo. *Pharm. Res. 22*, 373−380.
(22) Kloeckner, J., Wagner, E., Ogris, M. Degradable gene carriers based on oligomerized polyamines. *Eur. J. Pharm. Sci.*, in press, DOI: 10.1016/j.ejps.2006.08.002.
(23) Forrest, M. L., Koerber, J. T., and Pack, D. W. (2003) A degradable polyethylenimine derivative with low toxicity for highly efficient gene delivery. *Bioconjugate Chem. 14*, 934−940.
(24) Brissault, B., Kichler, A., Guis, C., Leborgne, C., Danos, O., and Cheradame, H. (2003) Synthesis of linear polyethylenimine derivatives for DNA transfection. *Bioconjugate Chem. 14*, 581−587.
(25) Plank, C., Zatloukal, K., Cotten, M., Mechtler, K., and Wagner, E. (1992) Gene transfer into hepatocytes using asialoglycoprotein receptor mediated endocytosis of DNA complexed with an artificial tetra-antennary galactose ligand. *Bioconjugate Chem. 3*, 533−539.
(26) Kircheis, R., Kichler, A., Wallner, G., Kursa, M., Ogris, M., Felzmann, T., Buchberger, M., and Wagner, E. (1997) Coupling of cell-binding ligands to polyethylenimine for targeted gene delivery. *Gene Ther. 4*, 409−418.
(27) Fischer, D., Bieber, T., Li, Y., Elsasser, H. P., and Kissel, T. (1999) A novel non-viral vector for DNA delivery based on low molecular weight, branched polyethylenimine: effect of molecular weight on transfection efficiency and cytotoxicity. *Pharm. Res. 16*, 1273−1279.
(28) Fischer, D., Li, Y., Ahlemeyer, B., Krieglstein, J., and Kissel, T. (2003) In vitro cytotoxicity testing of polycations: influence of polymer structure on cell viability and hemolysis. *Biomaterials 24*, 1121−1131.
(29) Dubruel, P., Dekie, L., Christiaens, B., Vanloo, B., Rosseneu, M., Van De, K. J., Mannisto, M., Urtti, A., and Schacht, E. (2003) Poly-l-glutamic acid derivatives as multifunctional vectors for gene delivery. Part B. Biological evaluation. *Biomacromolecules 4*, 1177−1183.
(30) Kunath, K., von Harpe, A., Fischer, D., Petersen, H., Bickel, U., Voigt, K., and Kissel, T. (2003) Low-molecular-weight polyethylenimine as a non-viral vector for DNA delivery: comparison of physicochemical properties, transfection efficiency and in vivo distribution with high-molecular-weight polyethylenimine. *J. Controlled Release 89*, 113−125.

BC060133V

Synthesis and Characterization of Immunogens Based on Calix[4]arene-crown-6 for the Generation of Antibodies Directed Towards Cesium Ions

Samir Safi, Zouhair Asfari, Laurence Ehret-Sabatier, Maurice Leroy, and Agnès Hagège*

Laboratoire de Chimie Analytique et Minérale, UMR 7178 ULP/CNRS/IN2P3 (LC4), ECPM, 25 rue Becquerel, F-67087 Strasbourg Cedex, France. Received April 26, 2006; Revised Manuscript Received July 18, 2006

With the aim of generating antibodies directed towards cesium, a calix[4]arene-crown-6 in the 1,3-alternate conformation bearing an *N*-hydroxysuccinimide function was synthesized. The calixarene was coupled to bovine serum albumin using different calixarene/protein ratios, and cesium was loaded. Conjugates were characterized using trinitrobenzenesulfonic acid derivatization, matrix assisted laser desorption ionisation−mass spectrometry (MALDI-TOF-MS), and inductively coupled plasma-mass spectrometry (ICP-MS). Targeted lysines were determined after enzymatic cleavage followed by MALDI-TOF-MS, and a progressive targeting related to lysines accessibility was observed.

INTRODUCTION

The ability to rapidly monitor metals in the environment and in bodily fluids is of fundamental importance. For that purpose, antibody-based sensors seem to provide an interesting solution for rapid, in situ assessment of metal contamination. The key point of an immunoanalysis is the design of the hapten. In the case of metal immunoanalysis, the hapten consists of a complex formed between the metal to be analyzed and a receptor which will be coupled later to a carrier protein. Antibodies directed toward metal chelates, such as EDTA or DTPA, have already been reported (*1*−*5*). However, the use of such chelating agents does not allow a clear differentiation between the various bound metals. Indeed, Blake et al. (*1*, *4*, *6*) reported the production of false positives with Hg(II) when using antibodies directed toward Cd(II). Moreover, strong interferences appeared in the presence of Mn(II) and In(III). The use of more selective ligands should permit circumvention of these selectivity limitations.

Calixcrowns represent an interesting class of compounds with a three-dimensional cavity that show unique complexing properties toward alkali, alkaline earth, and ammonium cations (*7*). Numerous calix[4]arenes-crown-6 have been synthesized, and their ability to selectively complex cesium has been reported (*8*−*10*).

The coupling of such hydrophobic molecules with proteins has been poorly documented. Bryant et al. (*11*) reported the synthesis of a noncovalent calix[4]arene−Gd^{III}−albumin complex. Reinhoudt et al. (*12*) realized the synthesis of immunogens based on ^{225}Ac−calix[4]arene complexes and showed that the low solubility of the calixarene in water did not allow an efficient coupling via an isothiocyanate function. It has been noted that the use of a calixarene bearing a masked thiol function leads to an albumin connected with five calixarenes.

We have reported in a previous work the synthesis of a series of calix[4]arenes -crown-5 and -crown-6 bearing COOH and OH groups for a potential use in alkali metal immunoanalysis (*13*). In this paper, we report the synthesis of both a calix[4]-arene-crown-6-based hapten with an activated NHS ester and its BSA conjugates. The characterization of the conjugates was accomplished by both spectrophotometric and mass spectrometric methods to determine the coupling ratios and by enzymatic digestion followed by MALDI-TOF-MS to localize the linked haptens. Cesium loading was performed and its incorporation rate was determined by ICP-MS.

Scheme 1

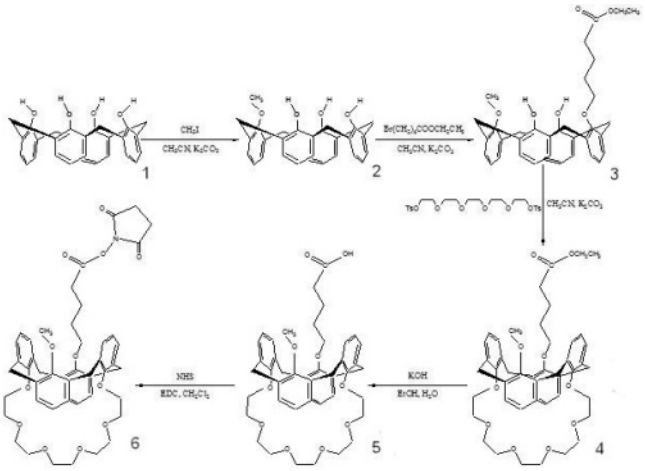

EXPERIMENTAL PROCEDURES

Materials and Methods. Melting points were determined with a Büchi 500 apparatus in a capillary sealed under nitrogen. ^{1}H NMR (300 MHz) spectra were recorded with a Bruker Avance spectrometer in the absence of an internal standard. FAB mass spectra were obtained with a VG Autospec and MALDI-TOF mass spectra with an Ultraflex (or a Reflex) instrument (Bruker). PlasmaQuad 3 ICP-MS (Thermo-Elemental) was used as an elemental detector for cesium quantification. Absorbance was measured on an HP8453E spectrophotometer. Microanalyses were performed at the Service de Microanalyse of the Institut de Chimie de Strasbourg. All reagents were purchased from Sigma at the highest purity available.

Hapten Synthesis. The synthetic pathway is illustrated in Scheme 1.

Monomethoxy-calix[4]arene ***1***. Calix[4]arene (5.10 g, 12.0 mmol) and K_2CO_3 (0.87 g, 6.3 mmol) were dissolved in acetonitrile (350 mL) and stirred for 1 h at room temperature under a nitrogen atmosphere. Methyl iodide (1.14 g, 12.0 mmol) was then added, and the reaction mixture was refluxed for 4

* Corresponding author. Fax +33. 3. 90.24.27.25; E-mail: hagegea@ecpm.u-strasbg.fr.

10.1021/bc060109h CCC: $33.50 © 2006 American Chemical Society
Published on Web 09/07/2006

days. After cooling down to room temperature, the solvent was removed under reduced pressure. The residue was dissolved in CH_2Cl_2 and acidified with 1 N HCl. The organic phase was dried over Na_2SO_4, filtered, and then concentrated. After purification by chromatography (SiO_2, eluent: CH_2Cl_2), the calixarene derivative **1** (2.26 g) was recovered in a 43% yield as a white solid. Analytical data for compound **1**: Mp = 272 °C. ^{1}H NMR (300 MHz, $CDCl_3$): 9.70 (s, 1H, ArO*H*), 9.36 (s, 2H, ArO*H*), 7.27−7.01 (m, 8H, ArH_{meta}), 6.90 (t, 1H, J = 7.5 Hz, ArH_{para}), 6.70 (t, 3H, J = 7.5 Hz, ArH_{para}), 4.39 (d, 2H, J = 13.0 Hz, ArCH_2Ar), 4.29 (d, 2H, J = 13.0 Hz, ArCH_2Ar), 4.15 (s, 3H, OCH_3), 3.49 (d, 2H, J = 13.0 Hz, ArCH_2Ar), 3.48 (d, 2H, J = 13.0 Hz, ArCH_2Ar). Anal. Found: C, 79.38; H, 5.89. Calcd for $C_{29}H_{26}O_4$: C, 79.43; H, 5.97.

*1-(Ethyl-5-oxavalerate), 3-methoxy-calix[4]arene **2**.* Monomethoxy-calix[4]arene **1** (3.51 g, 8.0 mmol) and K_2CO_3 (0.57 g, 4.2 mmol) were dissolved in acetonitrile (200 mL) and stirred for 1 h at room temperature under a nitrogen atmosphere. Ethyl-5-bromovalerate (1.67 g, 8.0 mmol) was then added, and the mixture was refluxed for 5 days. The solvent was evaporated, and the residue obtained was solubilized in CH_2Cl_2, and K_2CO_3 was neutralized with 1 N HCl. The organic phase was dried over Na_2SO_4, filtered, and then concentrated. After purification by chromatography (SiO_2, eluent: CH_2Cl_2/acetone, 98/2), compound **2** (3.08 g) was recovered in a 68% yield as a white solid. Analytical data for compound **2**: Mp = 162−163 °C. ^{1}H NMR (300 MHz; $CDCl_3$): 7.76 (s, 2H, ArO*H*), 6.98 (d, 4H, J = 7.5 Hz, ArH_{meta}), 6.81 (d, 4H, J = 7.5 Hz, ArH_{meta}), 6.67−6.55 (m, 4H, ArH_{para}), 4.24 (d, 2H, J = 13.0 Hz, ArCH_2Ar), 4.21 (d, 2H, J = 13.0 Hz, ArCH_2Ar), 4.09 (q, 2H, J = 7.0 Hz, COOCH_2CH$_3$), 3.94 (t, 2H, J = 7.0 Hz, ArOCH_2), 3.91 (s, 3H, ArOCH_3), 3.31 (d, 2H, J = 13.0 Hz, ArCH_2Ar), 3.30 (d, 2H, J = 13.0 Hz, ArCH_2Ar), 2.44 (t, 2H, J = 7.0 Hz, CH_2COOCH$_2$CH$_3$), 1.99−1.97 (m, 4H, ArOCH$_2$CH_2CH_2), 1.20 (t, 3H, J = 7.0 Hz, COOCH$_2$CH_3). Anal. Found: C, 76.05; H, 6.86. Calcd for $C_{36}H_{38}O_6$: C, 76.30; H, 6.75.

*1-(Ethyl-5-oxavalerate), 3-methoxy-calix[4]arene-crown-6 **3**.* 1-(Ethyl-5-oxavalerate), 3-methoxy-calix[4]arene **2** (1.13 g, 2.0 mmol) and K_2CO_3 (2.76 g, 20.0 mmol) were dissolved in acetonitrile (300 mL) and stirred for 1 h at room temperature under a nitrogen atmosphere. Penta(ethylene glycol)ditosylate (1.15 g, 2.0 mmol) was then added, and the mixture was refluxed for 10 days. After evaporation of the solvent, the residue was solubilized in CH_2Cl_2, and K_2CO_3 was neutralized with 1 N HCl. The organic phase was dried over Na_2SO_4, filtered, and then concentrated. After purification by chromatography (SiO_2, eluent: CH_2Cl_2/acetone, 90/10), compound **3** (0.74 g) was recovered in a 48% yield as a yellow viscous liquid. Analytical data for compound **3**: ^{1}H NMR (300 MHz; $CDCl_3$): 7.39 (d, 2H, J = 7.5 Hz, ArH_{meta}), 7.10 (d, 2H, J = 7.5 Hz, ArH_{meta}), 6.95−6.92 (m, 4H, ArH_{meta}), 6.54−6.40 (m, 4H, ArH_{para}), 4.26 (d, 4H, J = 13.0 Hz, ArCH_2Ar), 4.23−4.18 (m, 2H, COOCH_2-CH$_3$), 3.95−3.85 (m, 2H, ArOCH_2), 3.79−3.35 (m, 20H, OCH_2CH_2O), 3.24 (s, 3H, ArOCH_3), 3.12 (d, 4H, J = 13.0 Hz, ArCH_2Ar), 2.45−2.41 (m, 2H, CH_2COOCH$_2$CH$_3$), 1.94−1.75 (m, 4H, ArOCH$_2$CH_2CH_2), 1.31 (t, 3H, J = 7.0 Hz, COOCH$_2$-CH_3). Anal. Found: C, 68.72; H, 7.49. Calcd for $C_{46}H_{56}O_{10}$·2H$_2$O: C, 68.63; H, 7.51.

*1-(5-Oxavaleric acid), 3-methoxy-calix[4]arene-crown-6 **4**.* 1-(Ethyl-5-oxavalerate), 3-methoxy-calix[4]arene-crown-6 **3** (0.31 g, 0.4 mmol) and KOH (1.00 g, 17.0 mmol) were dissolved in a mixture of EtOH/H_2O 50/50 (50 mL) and refluxed for 3 h. After evaporation of the solvents, the residue was dissolved in CH_2Cl_2 and acidified with 1 N HCl. The organic phase was dried over Na_2SO_4, filtered, and then concentrated. After purification by chromatography (SiO_2, CH_2Cl_2/acetone, 80/20), compound **4** (0.28 g) was recovered in a 96% yield as a white viscous liquid. Analytical data for compound **4**: ^{1}H NMR (300 MHz; $CDCl_3$): 7.34 (d, 2H, J = 7.5 Hz, ArH_{meta}), 7.05 (d, 2H, J = 7.5 Hz, ArH_{meta}), 6.90−6.85 (m, 4H, ArH_{meta}), 6.53−6.46 (m, 4H, ArH_{para}), 4.24 (d, 4H, J = 13.0 Hz, ArCH_2Ar), 4.03−3.93 (m, 2H, ArOCH_{2-}CH$_2$), 3.80−3.62 (m, 20H, OCH_2CH_2O), 3.20 (s, 3H, ArOCH_3), 3.08 (d, 4H, J = 13.0 Hz, ArCH_2Ar), 2.45 (t, 2H, J = 7.0 Hz, CH_2COOH), 1.89−1.67 (m, 4H, CH_2CH_2CH$_2$COOH). Anal. Found: C, 67.72; H, 7.63. Calcd for $C_{44}H_{52}O_{10}$·2H$_2$O: C, 68.02; H, 7.26.

*1-(N-succinimide-5-oxavalerate), 3-methoxy-calix[4]arene-crown-6 **5**.* 1-(5-Oxavaleric acid), 3-methoxy-calix[4]arene-crown-6 (0.59 g, 0.8 mmol), NHS (*N*-hydroxysuccinimide) (0.19 g, 1.6 mmol), and EDC [3-ethyl-3-(3-dimethylaminopropyl)-carbodiimide] (0.31 g, 1.6 mmol) were dissolved in CH_2Cl_2 (50 mL), and the mixture was stirred overnight at room temperature under a nitrogen atmosphere. After purification by chromatography (SiO_2, eluent: CH_2Cl_2/acetone, 90/10), the activated ester **5** (0.40 g) was recovered in a 60% yield as a white solid. Analytical data for compound **5**: Mp = 86−87 °C. ^{1}H NMR (300 MHz; $CDCl_3$): 7.28 (d, 2H, J = 7.5 Hz, ArH_{meta}), 6.99 (d, 2H, J = 7.5 Hz, ArH_{meta}), 6.87−6.78 (m, 4H, ArH_{meta}), 6.43−6.41 (m, 4H, ArH_{para}), 4.18 (d, 4H, J = 13.0 Hz, ArCH_2-Ar), 3.63 (s, 2H, ArOCH_2), 3.63−3.46 (m, 20H, OCH_2CH_2O), 3.14 (s, 3H, ArOCH_3), 3.02 (d, 4H, J = 13.0 Hz, ArCH_2Ar), 2.75 (broad s, 4H, NHS), 2.61 (t, 2H, J = 7.0 Hz, CH_2-COONHS), 1.85−1.79 (m, 4H, CH_2CH_2CH$_2$COONHS). Anal. Found: C, 68.70; H, 6.43. Calcd for $C_{48}H_{55}O_{12}N$: C, 68.80; H, 6.61. MS (FAB$^+$): m/z = 876.6 (MK$^+$), m/z = 855.6 (MNH$_4^+$).

Conjugation of Compound 5 and Characterization of the Immunogens. To 1 mL of a BSA solution (4 mg/ mL, Sigma 96%) in 25 mM sodium borate buffer at pH 9.2 were added 100 μL of DMF containing compound **5** at various concentrations. Final **5**/BSA ratios of 10:1, 30:1, and 50:1 (mol/mol) were used. The mixtures were vortexed and incubated overnight at 4 °C. These solutions were stored at 2 °C without purification.

Spectrophotometric Method. A modified version of Habeeb's TNBS (2,4,6-trinitrobenzenesulfonic acid) assay (*14*) was used. 20 μL aliquots of the crude mixtures were diluted 40 times in 0.1 M sodium borate buffer pH 9.2. Standard solutions of glycine (2−9 μg/mL) in 0.1 M sodium borate buffer were also prepared. To 1 mL of the conjugation mixture or the glycine standards were added 500 μL of a 0.01% TNBS in a 0.1 M sodium borate buffer, and incubation was performed at 42 °C for 2 h. 500 μL of 10% (w/w) SDS and 250 μL of 1 N HCl were then added, and the absorbance was measured at 335 nm.

Mass Spectrometric Method. After removing the low molecular weight compounds with size exclusion micro Bio-Spin 6 columns (Bio-rad) at 1000 g for 4 min, the extent of conjugation was determined by MALDI-TOF-MS. The matrix was prepared from a saturated solution of α-cyano-4-hydroxycinnamic acid in 50% acetonitrile and diluted twice in 0.1% TFA in 30% acetonitrile. The samples and the matrix solution were mixed in equal amounts (0.5 μL each) and added on the stainless steel probe. The samples were allowed to dry at room temperature. The data were acquired in the linear mode.

Enzymatic Digestion. SDS-PAGE of BSA and its conjugates (10:1, 30:1, 50:1) was performed according to Laemmli (*15*). Purified solutions (37.2 μg protein /mL) were diluted twice in Laemmli sample buffer (2X) and heated at 90 °C for 5 min. 10 μL of samples were loaded on minigels (10 × 8 cm 7% total acrylamide). Molecular markers covering a molecular weight range between 6.5 and 205 kDa were used for molecular mass estimation. Migration was performed at 150 V for 90 min. Coomassie blue R250 staining and destaining were done using the standard developing protocol supplied by the manufacturer. Protein bands corresponding to BSA were excised and washed

with 200 μL water, then dehydrated with 200 μL 25 mM NH_4HCO_3 in 50% acetonitrile, then with 100% acetonitrile. Gel pieces were rehydrated in 50 μL of dithiothreitol (25 mM in NH_4HCO_3 buffer), and proteins were reduced for 20 min at 56 °C. The residual liquid was removed, and 50 μL of freshly prepared iodoacetamide (55 mM in NH_4HCO_3 buffer) was added. Samples were incubated for 20 min at room temperature in the dark. The residual iodoacetamide was eliminated by washing and the samples dehydrated. Finally, gel pieces were rehydrated for 5 min at room temperature in 20 μL of either 12.5 ng/μL trypsin (Promega, Sequence Grade Modified) or 10 ng/μL of endoproteinase Glu-C (Sigma) in 25 mM NH_4HCO_3 and then overlaid with a minimum amount of 25 mM NH_4HCO_3 to keep them immersed during the digestion. The mixture was incubated overnight at 37 °C. Afterward, peptides were extracted by addition of 80 μL of 60% acetonitrile in 5% HCOOH and sonication for 10 min. The resulting peptide extracts were directly analyzed by MALDI-TOF-MS in reflector mode. The calibration was performed in internal mode using fragments from trypsin autolysis with monoisotopic $[M - H]^+$ at *m*/*z* 842.510 and 2211.105.

Cesium Binding. To 500 μL of BSA and conjugates solutions (4 mg protein/mL), various amounts of solid $CsNO_3$ (4−21 mg) were added. The solutions were mixed for 5 days at room temperature. 50 μL of each solution was then purified by micro Bio-Spin 6 columns (Bio-rad) at 1000 g for 4 min. Prior to ICP-MS analysis, the samples were diluted 200 times in ultrapure water. Nebulization of samples was performed by means of a concentric nebulizer (flow rate: 1 mL min^{-1}). ICP conditions were the following: nebulization gas flow rate 0.75 L min^{-1}, outer gas flow rate 13.5 L min^{-1}, auxiliary gas flow rate 1.8 L min^{-1}. Detection of cesium was performed at $m/z = 133$. Plasma power was set to 1350 W and detector voltage to −2700 V. Ion lens voltages were adjusted to maximize the signals of analytes.

RESULTS AND DISCUSSION

For the generation of antibodies directed against cesium, we synthesized immunogens via the covalent attachment of calix[4]arene-crown-6 haptens to a BSA molecule. For that purpose, we synthesized the first calixarene bearing an activated ester function. This approach ensures stable crosslinking and prevents the interprotein coupling during the conjugation process.

Conjugation of the Calixarene 5. The bioconjugates presented in this paper are based on a succinimide ester that is commonly used for reactive amine crosslinking, but the ester hydrolysis is a limiting factor. To bypass this problem, the pH must be controlled. Two buffers were tested for the coupling: a phosphate buffer (pH 7.5) and a borate buffer (pH 9.2). A higher pH was shown to favor the nucleophilic attack to the detriment of the ester hydrolysis, and pH 9.2 was thus used in further experiments. The conjugation reaction gave a stable coupling ratio as determined by the spectrophotometric method after 5 h. As calixarene **5** is not soluble in pure water, coupling conditions with BSA were also optimized by varying the DMF ratio (for the 50:1 mixture). As it was found that using more than 10% of DMF did not improve the conjugation, this final DMF ratio was adopted for the conjugate synthesis.

Characterization of the Conjugates. As the hapten density governs both quantity and affinity of the antibodies produced (*16*−*18*), it is of fundamental importance to characterize the different immunogens. Although the calixarene derivatives contain UV chromophores absorbing at 270 nm, the determination of the extent of conjugation using direct UV measurements was impossible. Indeed, the conjugation led to modifications of the amino acid environment which induces changes in the BSA spectrum. So, alternative methods, namely, mass spectrometry and free lysines titration, were used.

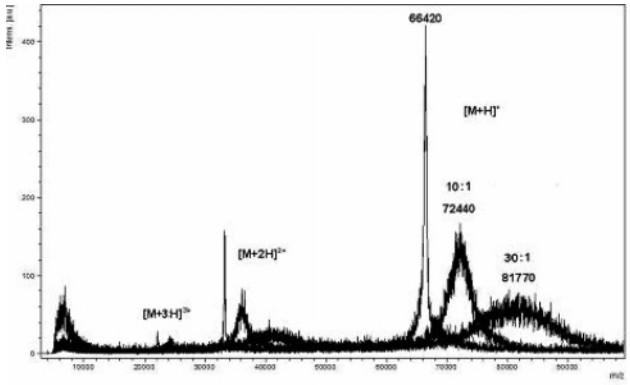

Figure 1. Mass spectra of BSA and conjugates. Values are indicated in *m*/*z*.

Table 1. Determination of Coupling Ratios Using MALDI-TOF and TNBS Methods

Calixarene **5**:BSA (mol/mol) ratio	average number of haptens[a] (mol/mol BSA)	
	MS analysis	TNBS analysis
10 :1	8 ± 2	8 ± 6
30 :1	19 ± 1	21 ± 1
50 :1		36 ± 2

[a] Standard deviations were determined from different conjugation experiments.

MALDI-MS techniques are considered an accurate tool for protein and peptide analysis (*19*, *20*). Figure 1 presents the mass spectra obtained for the BSA and its conjugates. The MALDI-TOF-MS analyses of conjugates showed that the molecular weights of the conjugates increased when increasing calixarene/BSA ratios. These mass shifts correspond to an increased coupling of calixarene moieties. The average number of coupled calixarenes was determined by calculating the mass shift between the peaks' maxima. A loss of resolution and less efficient ionization were also observed when the hapten density increases. Such behavior was previously observed by Bolbach et al. (*21*). The inability to detect the molecular ion of the conjugate when a calixarene-to-BSA ratio of 50:1 was used might be due to the high density of haptens.

The spectrophotometric method allows the determination of the available lysine residues. On the native BSA, the number of free lysines was found to be 57, while the BSA sequence actually contains 59 (*22*). The standard deviation was found to be less than 5%, except for low extents of conjugation for which this determination was found to be inaccurate.

Results obtained with both methods are given in Table 1. The results are in good agreement between TNBS and MALDI-TOF-MS methods. The coupling process was proven to be reproducible when comparing the results of various sets. As expected, the increase of calixarenes added to the BSA solution led to an increase in the hapten density, and 60% of the initial free lysines were modified.

Determination of the Targeted Lysines. Chappey et al. (*23*) found that the specificity of monoclonal antibodies depends on the structure of the hapten and on its coupling sites to the carrier protein. Attempts to localize calixarene coupling sites were then conducted by enzymatic digestion of BSA conjugates followed by MS analysis. Mass fingerprints were compared between BSA and the conjugates (10:1, 30:1, 50:1), and reduction in the intensity of peaks observed in the control sample and appearance of new peaks were examined as being indications of site modification. For the 10:1 conjugate (Figure 2), two peaks were strongly affected after conjugation with **5** (*m*/*z* 789.47, 1639.94). In parallel, appearance of peaks (*m*/*z* 1511.82, 2362.27) with observed masses corresponding to an attachment of one calix-

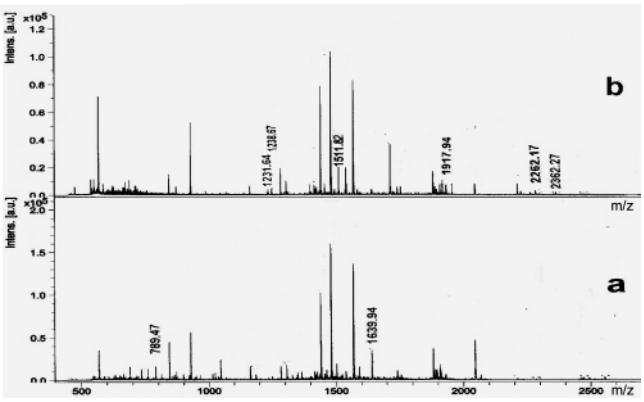

Figure 2. MALDI-TOF-MS after tryptic cleavage of native BSA (a) and 10:1 conjugate (b). Monoisotopic values (*m*/*z*) of reduced and appearing peptides are indicated.

Table 2. Monoisotopic Masses of Peptide Fragments Appearing after Tryptic Digestion of 10:1 Conjugate

sequence of the tryptic peptide	residue number	calculated mass (*m*/*z*)	observed mass in the 10:1 conjugate	Δ*m*/*z*
HKPK	558−561	509.32	1231.64	722.32
QIKK	545−548	516.35	1238.67	722.32
LVTDLTK	257−263	789.47[a]	1511.82	722.35
CASIQKFGER	223−232	1195.59	1917.94	722.35
LCVLHEKTPVSEK	483−495	1539.82	2262.17	722.35
KVPQVSTPTLVEVSR	437−451	1639.94[a]	2362.27	722.36

[a] Peptides affected by the coupling found in the native mass spectrum.

arene moiety (calculated Δ*m*/*z* = 722.34) confirmed the modification of these peptides (Table 2). Interestingly, the detection of the modified peptide LVTDLTK (at *m*/*z* 1511.82) indicates that the functionalization of the lysine side chain does not fully preclude trypsin cleavage after this residue. In addition, four other peaks appeared after conjugation, which could correspond to modified BSA tryptic peptides (*m*/*z* 1231.64, 1238.67, 1917,94, 2262.17; Table 2). These peaks were not detected in the native BSA spectrum. Another digestion with endoproteinase Glu-C was performed. The disappearance in the 10:1 conjugate spectrum (not shown) of three peptides corresponding to sequences 254−267, 544−554, and 555−565 reinforced the results found after tryptic digestion (targeting of sequences 257−263, 545−548, 558−561). The results obtained from these two digestions led to the proposition of six targeted peptide regions after conjugation with calixarene **5**. When comparing these results to the protein 3D model (www.rcsb.org), it was found that only accessible surface lysines were affected by the coupling process.

By increasing the calixarene/BSA ratio to 30, all targeted lysines in the 10:1 conjugate remained modified. In addition, additional reductions in the intensity of peaks observed in the control sample and appearance of new peaks were observed. The same behavior was noticed when increasing this ratio from 30 to 50. We can thus assume that the coupling process follows a given order that could be related to the accessibility of the different lysines.

Cesium Binding. The quantity of cesium nitrate was varied from 4 to 21 mg in order to keep the Cs/calixarene **5** (mol/mol) ratio constant and equal to 100. The amount of bound cesium was determined using ICP-MS (Table 3). A control experiment indicates the presence of no more than 0.5 mol of Cs^+ per mole of native BSA. This was due to a partial retention capacity of the desalting column in the presence of a large excess of cesium. An increase of the incorporated cesium was noted with an increased coupling ratio. However, in all cases, around

Table 3. Determination of Cesium Binding to Different BSA Conjugates

coupling ratio (**5** : BSA)	average number of cesium[a,b] (mol/mol BSA)	percentage of loaded calixarenes[b]
10:1	1.70 ± 0.04	25.3 ± 0.6
30:1	4.4 ± 0.4	22 ± 2
50:1	6.7 ± 0.2	19.8 ± 0.6

[a] The blank value was subtracted. [b] The standard deviations were calculated from ICP/MS measurements performed in triplicate for each conjugate.

22% of the calixarene cavities were occupied by cesium. Increasing the cesium ratio (up to 1000) led to an increase to a maximum of 35%. This relatively low density of incorporated cesium may however not represent a limiting factor in antibodies production. Furthermore, the loading capacity was found to be reproducible when comparing results for various sets of 50:1 conjugate.

In conclusion, to get an optimum calixarene/BSA ratio for immunization, a series of conjugates was synthesized and characterized by mass spectrometry and free lysines titration. It was demonstrated that the proposed procedure allows the coupling of hydrophobic haptens in a reproducible way. Moreover, the coupling ratio can be simply tuned by varying the calixarene concentration. Some hapten coupling locations were also identified by accurate mass measurements. These data will be used to correlate both epitope density and hapten location to the immune response.

Cesium was proven to be complexed by such conjugates. However, further studies will be carried out in order to evaluate the stability of such immunogens in sera, particularly toward the potassium concentration, and immunization will also be performed.

ACKNOWLEDGMENT

This work was supported by a grant to S.S. from the French ministry of research and higher education. The authors would like to thank C. Vidaud (SBTN, CEA, and Marcoule, France) for helpful discussions, and the LSMBO (UMR 7178, Strasbourg) for MS facilities.

LITERATURE CITED

(1) Blake, D. A., Chakrabarti, P., Khosraviani, M., Hatcher, F. M., Westhoff, C. M., Goebel, P., Wylie, D. E., and Blake, R. C. (1996) Metal binding properties of a monoclonal antibody directed toward metal-chelate complexes. *J. Biol. Chem. 271*, 27677−27685.

(2) Blake, R. C., Pavlov, A. R., and Blake, D. A. (1999) Automated kinetic exclusion assays to quantify protein binding interactions in homogeneous solution. *Anal. Biochem. 272*, 123−134.

(3) Chakrabarti, P., Hatcher, F. M., Blake, R. C., Ladd, P. A., and Blake, D. A. (1994) Enzyme immunoassay to determine heavy metals using antibodies to specific metal-EDTA complexes: optimization and validation of an immunoassay for soluble indium. *Anal. Biochem. 217*, 70−75.

(4) Jones, R. M., Yu, H., Delehanty, J. B., and Blake, D. A. (2002) Monoclonal antibodies that recognize minimal differences in the three-dimensional structures of metal−chelate complexes. *Bioconjugate Chem. 13*, 408−415.

(5) Khosraviani, M., Blake, R. C., Pavlov, A. R., Lorbach, S. C., Yu, H., Delehanty, J. B., Brechbiel, M. W., and Blake, D. A. (2000) Binding properties of a monoclonal antibody directed toward lead−chelate complexes. *Bioconjugate Chem. 11*, 267−277.

(6) Khosraviani, M., Pavlov, A. R., Flowers, G. C., and Blake, D. A. (1998) Detection of heavy metals by immunoassay: Optimization and validation of a rapid, portable assay for ionic cadmium. *Environ. Sci. Technol. 32*, 132−147.

(7) Casnati, A., Ungaro, R., Asfari, Z., and Vicens, J. (2001) Crown ethers derived from calix[4]arenes. In *Calixarenes 2001* (Asfari, Z.,

Bohmer, V., Harrowfield and Vicens, J., Eds) pp. 365−384, chapter 20, Kluwer Academic Publishers, Dordrecht.
(8) Asfari, Z., Bressot, C., Vicens, J., Hill, C., Dozol, J. F., Rouquette, H., Eymard, S., Lamare, V., and Tournois, B. (1995) Doubly crowned calix[4]arenes in the 1,3-alternate conformation as cesium-selective carriers in supported liquid membranes. *Anal. Chem. 67*, 3133−3139.
(9) Casnati, A., Pochini, A., Ungaro, R., Ugozzoli, F., Arnaud, F., Fanni, S., Schwing, M. J., Egberink, R. J. M., de Jong, F., and Reinhoudt, D. N. (1995) Synthesis, complexation, and membrane transport studies of 1, 3-alternate calix[4]arene-crown-6 conformers: A new class of cesium selective ionophores. *J. Am. Chem. Soc.* 117, 2767−2777.
(10) Arnaud-Neu, F., Asfari, Z., Souley, B., and Vicens, J. (1996) Binding properties of calix[4]-bis-crowns towards alkali cations. *New J. Chem. 20*, 456−463.
(11) Bryant, L. H., Jr., Yordanov, A. T., Linnoila, J. J., Brechbiel, M. W., and Frank, J. A. (2000) First noncovalently bound calix[4]arene-GdIII-albumin complex. *Angew. Chem., Int. Edit. 39*, 1641−1643.
(12) Grote Gansey, M. H., de Haan, A. S., Bos, E. S., Verboom, W., and Reinhoudt, D. N. (1999) Conjugation, immunoreactivity, and immunogenicity of calix[4]arenes; model study to potential calix-[4]arene-based $Ac3^{+}$ chelators. *Bioconjugate Chem. 10*, 613−623.
(13) Duta, M., Asfari, Z., Hagege, A., Thuery, P., and Leroy, M., (2004) Synthesis and complexation studies of various precursors based on calix[4]arene-crown-5 and -6 for the immunoanalysis of potassium and caesium Ions. *Supramol. Chem. 16*, 205−215.
(14) Habeeb, A. F. (1966) Determination of free amino groups in proteins by trinitrobenzenesulfonic acid. *Anal. Biochem. 14*, 328−336.
(15) Laemmli, U. K. (1970) Cleavage of structural proteins during the assembly of the head of bacteriophage T4. *Nature (London) 227*, 680−685.
(16) Klaus, G. G., and Mitchell, G. F. (1974) The influence of epitope density on the immunological properties of hapten-protein conjugates. II. The in vivo and in vitro metabolism of heavily and lightly conjugated protein. *Immunology 27*, 699−710.
(17) Klaus, G. G., and Cross, A. M. (1974) The influence of epitope density on the immunological properties of hapten-protein conjugates. III. Induction of hapten-specific tolerance by heavily and lightly hapten-substituted serum albumin. *Scand. J. Immunol. 3*, 797−808.
(18) Klaus, G. G., and Cross, A. M. (1974) The influence of epitope density on the immunological properties of hapten-protein conjugates. I. Characteristics of the immune response to hapten-coupled albumen with varying epitope density. *Cell. Immunol. 14*, 226−241.
(19) Karas, M., Bahr, U., Ingendoh, A., Nordhoff, E., Stahl, B., Strupat, K., Hillenkamp, F. (1990) Principles and applications of matrix-assisted UV-laser desorption/ionization mass spectrometry. *Anal. Chim. Acta 241*, 175−185.
(20) Fenselau, C. (1997) MALDI MS and strategies for protein analysis. *Anal. Chem. 69*, 661A−665A.
(21) Gourlaouen, N., Bolbach, G., Florentin, D., Gonnet, F., Marquet, A. (1998) Characterization of protein-hapten conjugates by mass spectrometry. *C. R. Acad. Sci., Série IIc*, 35−40.
(22) Dayhoff, M.O. (1976) *Atlas of Protein Sequence and Structure*, vol. 5, suppl. 2, National Biomedical Foundation, Washington, DC.
(23) Chappey, O. N., Sandouk, P., Scherrmann, J. M. (1992) Monoclonal antibodies in hapten immunoassays, *Pharm. Res. 9*, 1375−1379.

BC060109H

Directing Quadruplex-Stabilizing Drugs to the Telomere: Synthesis and Properties of Acridine−Oligonucleotide Conjugates

Joan Casals,[†] Laurent Debéthune,[†] Karine Alvarez,[†] Antonina Risitano,[‡] Keith R. Fox,*[,‡] Anna Grandas,[†] and Enrique Pedroso*[,†]

Departament de Química Orgànica, Facultat de Química, Universitat de Barcelona, Martí i Franquès 1-11, E-08028 Barcelona, Spain, and School of Biological Sciences, University of Southampton, Bassett Crescent East, Southampton SO16 7PX, U.K. Received July 3, 2006; Revised Manuscript Received August 10, 2006

Conjugates containing quadruplex-stabilizing acridines linked to oligonucleotides that are complementary to the G-rich human telomere sequence were synthesized. Acylation of 3,6-diaminoacridine followed by two Michael reactions provided derivatives suitable for conjugation, which were coupled to resin-linked amine-modified oligonucleotides by activating the carboxyl group with pentafluorophenyl 4-nitrobenzenesulfonate. After deprotection with aqueous ammonia at room temperature, conjugates incorporating different acridines, linkers, and oligonucleotide sequences were obtained. These were tested for their ability to stabilize intramolecular DNA quadruplexes that are based on the human telomeric repeat sequence $(GGGTTA)_n$.

INTRODUCTION

Telomerase is an enzyme that extends telomere sequences after DNA replication, and it is active in most cancer cells, but not in somatic cells. The enzyme is a ribonucleoprotein that uses an RNA template to elongate the telomeric single-stranded overhang, which has the sequence $(TTAGGG)_n$ in humans (*1*−*4*). It has been hypothesized that folding of this G-rich strand into an intramolecular quadruplex prevents interaction with the complementary RNA of telomerase and consequently interferes with the elongation of telomeres by telomerase in cancer cells (*5*−*11*).

Several classes of compounds, including anthraquinones, acridines, porphyrins, fluorenones, and other polycyclic aromatic molecules have been reported to bind to and stabilize DNA quadruplexes and possess telomerase-inhibiting properties (*12*−*18*). However, these aromatic molecules also behave as DNA intercalators and interact with double-stranded DNA as well as with G-quadruplexes. As a result, their potential use as anticancer drugs is limited by their cytotoxicity.

The parent aromatic compounds have been extensively modified to favor interaction with quadruplex rather than duplex structures (*19*−*23*). An alternative means of increasing the specificity might be to direct the aromatic drug to telomeric DNA by covalently attaching it to an oligonucleotide that is complementary to the G-rich telomere strand. This manuscript describes the preparation of a small library of such acridine−oligonucleotide conjugates and examines their interaction with intramolecular DNA quadruplexes.

EXPERIMENTAL PROCEDURES

3,6-Bis(acryloylamide)acridine, 1. A suspension of 2.5 g (10 mmol) of proflavine hydrochloride in acryloyl chloride (70 mL) was refluxed for 4 h. Then, the solid was filtered and washed with ether (4 × 25 mL). Purification of this solid by silica gel column chromatography eluting with acetone and increasing amounts of MeOH (0−30%) and TEA[1] (0−5%) afforded 2.3 g of 3,6-bis(acryloylamide)−acridine (80% yield). R_f (acetone/TEA 8:2) = 0.66. ^{1}H NMR (DMSO-d_6, 200 MHz) δ (ppm): 11.62 (s, 2H, NH), 9.50 (s, 1H, H-9), 8.88 (s, 2H, H-4,5), 8.28 (d, J = 9.2 Hz, 2H, H-1,8), 7.90 (d, J = 9.2 Hz, 2H, H-2,7), 6.70 (dd, J_{trans} = 17 Hz, J_{cis} = 10 Hz, 2H, COC**H$_A$**=CH$_B$H$_C$), 6.38 (dd, J_{trans} = 17 Hz, J_{gem} = 1 Hz, 2H, COCH$_A$=C**H$_B$**H$_C$), 5.90 (dd, J_{cis} = 10 Hz, J_{gem} = 1 Hz, 2H, COCH$_A$=CH$_B$**H$_C$**). ^{13}C-RMN (DMSO-d_6, 63 MHz) δ (ppm): 160.8 (NHCO), 146.6 (C-9), 137.6 (C-11,12), 132.4 (C-3,6), 128.7 (CH=), 126.3 (=CH$_2$), 124.8 (C-1,8), 119.7 (C-10,13), 117.3 (C-2,7), 111.6 (C-4,5). MALDI-TOF MS (positive mode, linear, DHB): m/z 318.72, $[M + H]^+$, calcd mass for $C_{19}H_{15}N_3O_2$ 317.34.

General Procedure for the Synthesis of Derivatives 2. To a stirred solution of **1** in EtOH (250 mL/g of **1**) was added dropwise a solution of the cyclic secondary amine (0.5 eq) in the same solvent (4 mL/mmol amine), and the mixture was reacted overnight (room temperature). The solvent was removed at reduced pressure, and the product was purified by silica gel column chromatography eluting with acetone and increasing amounts of MeOH (0−10%) and TEA (0−5%).

2a. 55% yield; R_f (DCM/MeOH 7:3) = 0.23. ^{1}H NMR (acetone-d_6, 200 MHz) δ (ppm): 11.20 (s, 1H, N**H**), 9.88 (s, 1H, N**H**), 8.76 (s, 1H, H-9), 8.67 (1H, H-4), 8.54 (s, 1H, H-5), 8.01 (d, J = 9 Hz, 2H, H-1,8), 7.78 (d, J = 9 Hz, 1H, H-2), 7.65 (d, J = 9 Hz, 1H, H-7), 6.47 (m, 2H, C**H$_A$**=C**H$_B$**H$_C$), 5.77

* Corresponding authors. (E.P.) Email: epedroso@ub.edu. Phone: + 34 93 403 4824. (K.R.F.) Email K.R.Fox@soton.ac.uk. Phone: +44 (0)23 8059 4374. Fax: +44 (0)23 8059 4459.

[†] Universitat de Barcelona.

[‡] University of Southampton.

[1] ACN = acetonitrile; Bz = benzoyl; CNE = 2-cyanoethyl; CPG = controlled pore glass; DCC = *N*,*N*′-dicyclohexylcarbodiimide; DCM = dichloromethane; DHB = dihydroxybenzoic acid; DIEA = *N*-ethyldiisopropylamine; DMF = *N*,*N*-dimethylformamide; DMSO = dimethylsulfoxide; DMT = 4,4′-dimethoxytrityl; Fmoc = 9-fluorenylmethoxycarbonyl; HATU = *N*-[(dimethylamino)-1*H*-1,2,3-triazolo[4,5-*b*]pyridin-1-yl-methylene]-*N*-methylmethanaminium hexafluorophosphate *N*-oxide; HOBT = 1-hydroxybenzotriazole; MALDI = matrix-assisted laser desorption ionization; MMT = 4-methoxytrityl; NMP = *N*-methylpyrrolidone; PFNB = 1,2,3,4,5-pentafluorophenyl 4-nitrobenzenesulfonate; PS = polystyrene-*co*-1%-divinylbenzene; PyAOP = (7-azabenzotriazol-1-yloxy)trispyrrolidinophosphonium hexafluoroposphate; PyBOP = (benzotriazol-1-yloxy)trispyrrolidinophosphonium hexafluoroposphate; TCA = trichloroacetic acid; TEA = triethylamine; TFA = trifluoroacetic acid; TOF = time of flight.

10.1021/bc060194t CCC: $33.50 © 2006 American Chemical Society
Published on Web 09/02/2006

(dd, J_{cis} = 9 Hz, J_{gem} = 1.8 Hz, CH_A=$CH_B\mathbf{H_C}$), 2.8−2.4 (m, 6H, $COCH_2C\mathbf{H_2}N(C\mathbf{H_2}CH_2)_2CH_2$), 2.2−1.9 (m, 2H, $COC\mathbf{H_2}$-CH_2N), 1.8−1.4 (m, 6H, $N(CH_2\mathbf{CH_2})_2\mathbf{CH_2}$). ^{13}C NMR (DMSO-$d_6$, 63 MHz) δ (ppm): 169.7 (NH**C**O−acryloyl), 164.4 (NH-**C**OCH_2), 149.9 (C-11), 141.6 (C-9), 141.3 (C-12), 136.1 (C-1,8), 132.2 (C-3), 129.8 (C-6), 129.7 (CH=**C**H_2), 128.2 (C-10), 123.1 (**C**H=CH_2), 123.0 (C-13), 122.9 (C-4), 120.7 (C-5), 114.7 (C-2), 113.8 (C-7), 63.7 ($\mathbf{C}H_2N(\mathbf{C}H_2CH_2)_2CH_2$), 29.6 ($CO\mathbf{C}H_2$), 24.3 ($N(CH_2\mathbf{C}H_2)_2CH_2$), 19.8 ($N(CH_2CH_2)_2\mathbf{C}H_2$). MALDI-TOF MS (positive mode, linear, DHB): *m*/*z* 403.72, $[M + H]^+$, calcd mass for $C_{24}H_{26}N_4O_2$ 402.49.

2b. 40% yield; R_f (DCM/MeOH 7:3) = 0.1. ^{1}H NMR (CD_3-OD, 200 MHz) δ (ppm): 8.78 (s, 1H, H-9), 8.59 (1H, H-4), 8.54 (s, 1H, H-5), 8.03 (d, J = 9 Hz, 2H, H-1,8), 7.90 (d, J = 9 Hz, 1H, H-2), 7.73 (d, J = 9 Hz, 1H, H-7), 7.65 (m, 2H, $C\mathbf{H_A}$=$C\mathbf{H_B}H_C$), 5.77 (dd, J_{cis} = 9 Hz, J_{gem} = 1.8 Hz, CH_A=$CH_B\mathbf{H_C}$), 3.01 (t, 2H, $COC\mathbf{H_2}CH_2N$), 2.75 (m, 6H, $COCH_2C\mathbf{H_2}N$-$(C\mathbf{H_2}CH_2)_2CH_2$), 1.9 (m, 6H, $N(CH_2\mathbf{CH_2})_2\mathbf{CH_2}$). ^{13}C NMR (DMSO-$d_6$, 63 MHz) δ (ppm): 164.8 (NH**C**O−acryloyl, NH**C**OCH_2), 147.3 (C-9), 139.1 (C-11,12), 135.1 (C-3,6), 129.8 (**C**H=CH_2), 128.3 (CH=**C**H_2), 127.6 (C-1,8), 122.0 (C-10,-13), 119.0 (C-2,7), 112.8 (C-4,5), 67.2 ($CH_2N(\mathbf{C}H_2CH_2)_2$), 52.8 ($\mathbf{C}H_2N(CH_2CH_2)_2$), 50.3 ($CO\mathbf{C}H_2CH_2N$), 22.2 ($N(CH_2\mathbf{C}H_2)_2$). MALDI-TOF MS (positive mode, linear, DHB): *m*/*z* 390.13, $[M + H]^+$, calcd mass for $C_{23}H_{24}N_4O_2$ 388.46.

General Procedure for the Synthesis of Asymmetrically Substituted Acridines 3. 2 (250−300 mg) was reacted with a 2- to 3-fold molar excess of either L-proline or isonipecotic acid in MeOH (1 mL/10 mg of **2**, approximately) for 6 h at room temperature (rt). Removal of the solvent in vacuo was followed by chromatographic purification.

3a. Purification by silica gel column chromatography eluting with acetone and increasing amounts of MeOH (0−20%) and TEA (0−5%); 62% yield; anal HPLC (C8 column, gradient from 5% to 35% of B in 15 min, A = 0.045% TFA in H_2O, B = 0.036% of TFA in ACN): t_R = 9.2 min. ^{1}H NMR (CD_3OD, 200 MHz) δ (ppm): 8.55 (s, 1H, H-9), 8.29 (s, 1H, H-4), 8.26 (s, 1H, H-5), 7.9−7.7 (m, 2H, H-1,8), 7.7−7.5 (m, 2H, H-2,7), 4.32 (t, J = 4.4 Hz, 1H, NC**H**COOH), 4.08−3.80 (m, 2H, CH_2-$NCH(COOH)C\mathbf{H_2}$), 3.3−2.8 (m, 10H, CH_2N). ^{13}C NMR (CD_3-OD, 63 MHz) δ (ppm): 175.3 (COOH), 171.2 and 170.1 (NHCO), 150.2 (C-9), 141.1 (C-11,12), 140.2 (C-3,6), 129.7 (C-1,8), 123.0 (C-10,13), 120.7 (C-5,4), 114.5 (C-2,7), 68.2 (N**C**HCOOH), 54.4 ($COCH_2CH_2N\mathbf{C}H_2$), 54.0 ($N(\mathbf{C}H_2)_2$), 50.6 ($\mathbf{C}H_2NHCOOH$), 43.0 ($\mathbf{C}H_2N(CH_2)_2$), 34.2 ($CO\mathbf{C}H_2CH_2$-NHCOOH), 29.5 ($CO\mathbf{C}H_2CH_2N(CH_2)_2$), 25.6 (NCHCOO-H**C**$H_2$), 24.0 ($NCH_2\mathbf{C}H_2CH_2CHCOOH$), 23.9 ($N(CH_2\mathbf{C}H_2)_2$). MALDI-TOF MS (positive mode, linear, DHB): *m*/*z* 519.15 $[M + H]^+$, calcd mass for $C_{29}H_{35}N_5O_4$ 517.62.

3b. Purification by reversed-phase medium-pressure liquid cromatography on a C18-filled column, gradient from 0% to 35% of B (A = 0.1% TFA in H_2O, B = 0.1% TFA in ACN); 80% yield; anal HPLC (C8 column, gradient from 5% to 35% of B in 15 min, A = 0.045% TFA in H_2O, B = 0.0036% of TFA in ACN): t_R = 8.0 min. ^{1}H NMR (CD_3OD, 200 MHz) δ (ppm): 9.44 (s, 1H, H-9), 8.87 (m, 2H, H-4,5), 8.32 (d, J = 3.8 Hz, 1H, H-1), 8.27 (d, J = 3.8 Hz, 1H, H-8), 7.66−7.74 (m, 2H, H2−7), 4.33 (dd, J_1 = 9.4 Hz, J_2 = 6.2 Hz, 1H, NC**H**COOH), 3.6−3.94 (m, 10H, CH_2N), 3.07−3.15 (m, 4H, $COC\mathbf{H_2}CH_2N$), 2.48−2.67 (m, 2H, $NCH_2CH_2C\mathbf{H_2}CHCOOH$), 2.00−2.30 (m, 6H, $NCH_2C\mathbf{H_2}$). ^{13}C NMR (CD_3OD, 63 MHz) δ (ppm): 168.1 (COOH), 167.3 and 167.0 (NHCO), 143.9 (C-9), 143.6 (C-11,12), 139.9 (C-3,6), 128.8 (C-1,8), 119.9 (C-10,13), 118.6 (C-5,4), 102.0 (C-2,7), 65.9 (N**C**HCOOH), 52.8 ($COCH_2CH_2N\mathbf{C}H_2$), 52.0 ($N(\mathbf{C}H_2)_2$), 48.3 ($\mathbf{C}H_2N(CH_2)_2$), 47.8 ($\mathbf{C}H_2NHCOOH$), 30.2 ($CO\mathbf{C}H_2CH_2NHCOOH$), 30.0 ($CO\mathbf{C}H_2$-$CH_2N(CH_2)_2$), 26.0 ($NCHCOOH\mathbf{C}H_2$), 20.5 ($NCH_2\mathbf{C}H_2CH_2$-CHCOOH), 20.4 ($N(CH_2\mathbf{C}H_2)_2$). MALDI-TOF MS (positive mode, linear, DHB): *m*/*z* 504.49 $[M + H]^+$, calcd mass for $C_{28}H_{33}N_5O_4$ 503.59.

3c. Purification by reversed-phase medium-pressure liquid cromatography on a C18-filled column, gradient from 5% to 50% of B (A = 0.1% TFA in H_2O, B = 0.1% TFA in ACN); 94% yield; anal HPLC (C8 column, gradient from 5% to 35% of B in 15 min, A = 0.045% TFA in H_2O, B = 0.0036% of TFA in ACN): t_R = 9.1 min. ^{1}H NMR (CD_3OD, 200 MHz) δ (ppm): 9.48 (s, 1H, H-9), 8.62 (s, 2H, H-4,5), 8.37 (d, J = 9.3 Hz, 2H, H-1,8), 7.72 (dd, J_1 = 9.3 Hz, J_2 = 1.5 Hz, 2H, H-2,7), 3.75−3.85 (m, 8H, $N(C\mathbf{H_2}CH_2)_2$), 3.3−3.4 (m, 4H, $COCH_2C\mathbf{H_2}N$), 3.1−3.3 (m, 4H, $COC\mathbf{H_2}CH_2N$), 2.9 (m, 1H, C**H**COOH), 1.9−2.5 (m, 8H, $N(CH_2C\mathbf{H_2})_2$). ^{13}C NMR (D_2O, 63 MHz) δ (ppm): 176.5 (COOH), 169.6 and 169.4 (NHCO), 144.3 (C-9), 144.2 (C-11,12), 139.0 (C-3,6), 130.0 (C-1,8), 120.2 (C-10,13), 119.9 (C-5,4), 102.9 (C-2,7), 53.8 (**C**HCOOH), 51.7 ($N(\mathbf{C}H_2CH_2)_2$-CHCOOH), 51.3 ($N(\mathbf{C}H_2CH_2)_2$), 49.5 ($\mathbf{C}H_2N(CH_2CH_2)_2$-CHCOOH), 49.3 ($\mathbf{C}H_2N(CH_2CH_2)_2$), 37.5 ($CO\mathbf{C}H_2CH_2N$), 24.8 ($N(CH_2\mathbf{C}H_2)_2CHCOOH$), 22.0 ($N(CH_2\mathbf{C}H_2)_2$). MALDI-TOF MS (positive mode, linear, DHB): *m*/*z* 518.17 $[M + H]^+$, calcd mass for $C_{29}H_{35}N_5O_4$ 517.62.

3,6-Bis[3-N-(L-prolyl)propionamide]acridine, ***3d***. To a solution of 250 mg (0.78 mmol) of **1** in EtOH (200 mL) was added a solution of L-proline (907 mg, 10 equiv) in the minimal amount of MeOH, and the mixture was stirred for 24 h at rt. Removal of the solvent was followed by HPLC purification using a preparative C4 column (gradient from 10% to 40% of B in 1 h, A = 10 mM NH_4AcO, B = ACN). 46% yield; anal HPLC (C8 column, gradient from 10% to 35% of B in 20 min, A = 0.045% TFA in H_2O, B = 0.036% TFA in ACN): t_R = 11.9 min. ^{1}H NMR (CD_3OD, 200 MHz) δ (ppm): 8.73 (s, 1H, H-9), 8.33 (s, 2H, H-4,5), 7.95 (d, J = 9 Hz, 2H, H-1−8), 7.68 (dd, J_1 = 9 Hz, J_2 = 1.8 Hz, 2H, H-2,7), 4.10 (m, 2H, NC**H**COOH), 3.95−4.01 (m, 2H, $COCH_2CH_2NC\mathbf{H_2}$), 3.70 (t, J = 6 Hz, 4H, $COCH_2C\mathbf{H_2}N$), 3.27−3.34 (m, 2H, $COCH_2CH_2NC\mathbf{H_2}$), 3.09 (t, J = 6 Hz, 4H, $COC\mathbf{H_2}CH_2N$), 2.00−2.60 (m, 8H, $NCH_2C\mathbf{H_2}C\mathbf{H_2}$-CHCOOH). ^{13}C NMR ($CD_3OD$, 63 MHz) δ (ppm): 171.0 (COOH), 169.6 (NHCO), 150.0 (C-9), 140.9 (C-11,12), 135.8 (C-3,6), 129.7 (C-1,8), 123.0 (C-5,4), 120.7 (C-10,13), 114.6 (C-2,7), 69.0 (N**C**HCOOH), 54.8 ($COCH_2CH_2N\mathbf{C}H_2$), 50.8 ($COCH_2\mathbf{C}H_2N$), 33.4 ($CO\mathbf{C}H_2CH_2N$), 29.5 ($NCH(COOH)\mathbf{C}H_2$), 23.9 ($NCH_2\mathbf{C}H_2CH_2CHCOOH$). MALDI-TOF MS (positive mode, linear, DHB): *m*/*z* 549.76 $[M + H]^+$, calcd mass for $C_{29}H_{33}N_5O_6$ 547.60.

HO-[protected oligonucleotide]−Resin, 7. The amine-substituted polystyrene-1%-divinylbenzene support suitable for oligonucleotide synthesis (loading below 0.25 mmol/g) was obtained by partial acylation of the amine groups of *p*-methylbenzhydrylamine resin (0.70 mmol/g). This was achieved by reaction with 0.35 equiv of Fmoc-alanine and DCC in a DCM/DMF mixture (9:1) for 1 h at rt. The resin was then filtered and washed with DMF, DCM, and MeOH and dried overnight in a desiccator. An aliquot of Fmoc-Ala-resin was treated with 20% piperidine in DMF to remove the Fmoc group, and the amount of 9-fluorenylmethylpiperidine formed was quantified spectrophotometrically. The loading was 0.17 mmol/g, suitable for oligonucleotide synthesis. The resin was swelled in DCM/DMF, and the remaining free amines were capped by acetylation (reaction with Ac_2O for 10 min + 10 additional min after the addition of DIEA, 10 equiv of each reagent). The Fmoc group of the total of Fmoc-Ala-resin was removed by treatment with 20% piperidine/DMF (3 + 10 min, followed by DMF washings).

Nucleotide resins were synthesized by reacting 5′-*O*-DMT-T-succinate or 5′-*O*-DMT-dA^{Bz}-succinate (3 equiv, previously prepared by reaction between the DMT-protected nucleoside and succinic anhydride in pyridine) (*24*) with H-Ala-resin in

the presence of DCC (3 equiv) for 4 h at room temperature in a DCM/DMF mixture. The absence of unreacted amines was assessed by the ninhydrin test (*25*).

DMT-T-Succinate. R_f (DCM/MeOH 9:1) = 0.1. ^{1}H NMR ($CDCl_3$, 200 MHz) δ (ppm): 9.8 (s, 1H, N**H**), 7.59 (s, 1H, H-6), 6.6−7.4 (m, 14H, Ar-H), 6.38 (t, 1H, H-1′), 5.45 (m, 1H, H-3′), 4.18 (m, 1H, H-4′), 3.77 (s, 6H, Ar-OCH_3), 3.44 (m, 2H, H-5′/5″), 2.2−2.8 (m, 6H, OCO**CH_2**C**H_2**COOH, H-2′/2″), 1.36 (s, 3H, Ar-CH_3).

DMT-dA^{Bz}-Succinate. R_f (DCM/MeOH 9:1) = 0.1. ^{1}H NMR ($CDCl_3$, 200 MHz) δ (ppm): 8.68 (s, 1H, H-8), 8.15 (s, 1H, H-2), 6.98−7.4 (m, 14H, Ar-H), 6.40 (t, 1H, H-1′), 5.42 (m, 1H, H-3′), 4.22 (m, 1H, H-4′), 3.66 (s, 6H, Ar-OCH_3), 3.36 (m, 2H, H-5′/5″), 2.50−3.00 (m, 6H, OCO**CH_2**C**H_2**COOH, H-2′/2″).

Oligonucleotides were automatically assembled (DNA synthesizer: ABI 380B) on aliquots of H-Ala-resin at the 5-μmol scale, using phosphite triester procedures slightly modified for compatibility with polystyrene supports (*26*, *27*) and the 5′-*O*-DMT−3′-*O*-phosphoramide derivatives of dT, dA^{Bz}, and dC^{Ac}.

H_2N−Linker−Oligonucleotide−Resin, 8. The 5′ end of the resin-linked oligonucleotide was derivatized by reaction with the commercially available phosphoramidite derivatives of amine-protected linkers L_3 (see below), L_5, and L_6 (MMT−NH−linker−O(OCNE)$NiPr_2$; see structures in Scheme 3) using standard phosphite triester methodology. For the preparation of conjugate **4f**, linker L_{18} was first introduced by reaction of the corresponding oligonucleotide resin with commercially available DMT−[*O*-$(CH_2)_2$]$_6$−*O*-P(OCNE)$NiPr_2$, and this was followed by incorporation of the L_5-containing derivative. Assembly of the target linker−oligonucleotide was assessed, in all cases, by treating aliquots of the linker−oligonucleotide−resin with concentrated aqueous ammonia for 6 h at room temperature and analysis of the crude by MALDI-TOF MS (negative mode).

MMT−NH−CH_2-CH_2-CH_2-OH. 3-Aminepropan-1-ol (7 mL, 93 mmol) was reacted with MMT−Cl (2 g, 0.1 equiv) in anhydrous pyridine for 3 days (room temperature). The solvent was removed at reduced pressure, and the crude was dissolved in DCM and washed with a 10% aq citric acid solution and brine. Purification was accomplished by silica gel column chromatography, eluting with hexanes and increasing amounts of DCM (5−100%) in the presence of 2% TEA (58% yield). R_f (DCM/hexanes/TEA 79:19:2) = 0.4. ^{1}H NMR ($CDCl_3$, 200 MHz) δ (ppm): 6.77−7.44 (m, 14H, Ar-H), 3.88 (t, J = 5.2 Hz, 2H, C**H_2**OH), 3.78 (s, 1H, OH), 2.40 (t, J = 5.2 Hz, 2H, NHC**H_2**), 1.7 (m, J = 5.2 Hz, 2H, CH_2C**H_2**CH_2); anal HPLC t_R = 12.8 min (C18, gradient from 50% to 100% of B in 30 min; A, 10 mM NH_4OAc in H_2O; B, ACN).

MMT−NH−L_3−P(OCNE)$NiPr_2$. Phosphitylation of the free hydroxyl group of MMT−NH−CH_2-CH_2-CH_2-OH was accomplished by overnight reaction with P(OCNE)$(NiPr_2)_2$ (3 equiv) and tetrazole (0.7 equiv) in anhydrous ACN (room temperature). After removal of the solvent, the product was dissolved in DCM, washed with saturated aq $NaHCO_3$ and brine, dried and evaporated to dryness, and used without further purification (^{31}P NMR ($CDCl_3$, 120 MHz) δ 144.9 ppm); anal HPLC t_R = 28.6 min (C18, gradient from 50% to 100% of B in 30 min; A, 10 mM NH_4OAc pH = 7; B, ACN).

Synthesis of the Conjugates 4. 1,2,3,4,5-pentafluorophenyl 4-nitrobenzenesulfonate was prepared as previously described (*28*). The MMT−NH−linker−oligonucleotide−resin (5 μmol) was transferred from the automatic DNA synthesizer reactor into a 5-mL polypropylene syringe fitted with a polyethylene disc. The MMT group was removed by subsequent treatments with the standard detritylation solution (3% TCA/DCM) until no color corresponding to the monomethoxytrityl cation was observed, which was followed by washing with DCM.

A mixture of the carboxyl-derivatized acridine (**3**) to be coupled (5 equiv with respect to resin-bound amines), PFNB (5 equiv), DIEA (25 equiv), and a catalytic amount of HOBt was dissolved in 250 μL of a 0.8 M solution of LiCl in DMF/NMP, and, after 15 min for carboxyl group preactivation, it was added to the linker−oligonucleotide−resin. After 2.5 h at room temperature with stirring, the resin was filtered, washed (DMF, DCM, and MeOH) and dried, and treated with 2 mL of a 1:1 mixture of concentrated aqueous NH_3/dioxane for 6 h at room temperature. The filtrate and washings (H_2O, MeOH) were collected, and the acridine−oligonucleotide conjugate was purified by reversed-phase medium-pressure liquid chromatography (Vydac C18, 20 × 2 cm column, gradient from 0% to 100% of B, A = 10 mM NH_4AcO, B = [65% (10 mM NH_4AcO) + 35% (ACN/H_2O 1:1)], 600 mL of each solvent). Homogeneity of the collected fractions was assessed by reversed-phase HPLC analysis (C18, gradient from 5% to 35% of B in 15 min, A = 10 mM aq NH_4AcO, B = ACN/H_2O 1:1), and characterization was carried out by MALDI-TOF MS (negative mode, reflector, 2,4,6-trihydroxyacetophenone).

4a. 11% yield; t_R: 13.7 min, *m/z* 3007.44 [M − H]$^-$ (calcd mass for the neutral molecule, $C_{111}H_{146}N_{32}O_{52}P_8$ 3008.32).

4b. 14% yield; t_R: 12.1 min, *m/z* 2980.10 [M − H]$^-$ (calcd mass for the neutral molecule, $C_{108}H_{140}N_{32}O_{53}P_8$ 2982.24).

4c. 2% yield; t_R: 11.2 min, *m/z* 3023.77 [M − H]$^-$ (calcd mass for the neutral molecule, $C_{109}H_{140}N_{32}O_{55}P_8$ 3026.25).

4d. 9% yield; t_R: 11.4 min, *m/z* 2993.18 [M − H]$^-$ (calcd mass for the neutral molecule, $C_{109}H_{142}N_{32}O_{53}P_8$ 2996.27).

4e. 1% yield; t_R: 12.4 min, *m/z* 2964.64 [M − H]$^-$ (calcd mass for the neutral molecule, $C_{108}H_{140}N_{32}O_{52}P_8$ 2966.24).

4f. 31% yield; t_R: 12.6 min, *m/z* 3319.97 [M − H]$^-$ (calcd mass for the neutral molecule, $C_{120}H_{165}N_{32}O_{62}P_9$ 3326.54).

4g. 2% yield; t_R: 12.5 min, *m/z* 2994.81 [M − H]$^-$ (calcd mass for the neutral molecule, $C_{109}H_{141}N_{31}O_{54}P_8$ 2997.25).

4h. 1% yield; t_R: 11.3 min, *m/z* 3027.48 [M − H]$^-$ (calcd mass for the neutral molecule, $C_{110}H_{141}N_{37}O_{50}P_8$ 3029.31).

4i. 2% yield; t_R: 11.9 min, *m/z* 3013.28 [M − H]$^-$ (calcd mass for the neutral molecule, $C_{109}H_{139}N_{37}O_{50}P_8$ 3015.28).

Fluorescence Melting Experiments. Fluorescence melting curves were determined using a Roche LightCycler as previously described (*29*−*31*) with excitation and detection wavelengths of 488 and 520 nm, respectively. The final concentration of the intramolecular quadruplex-forming oligonucleotide was 0.25 μM, in a total volume of 20 μL, dissolved in 50 mM potassium phosphate pH 7.4. Samples were first denatured by heating from 30 to 95 °C at a rate of 0.1 °C.s^{-1}. These were maintained at 95 °C for 5 min and annealed by cooling to 30 °C at 0.1 °C per second. The fluorescence was recorded during both the melting and annealing phases. Although the slowest heating rate for the LightCycler is 0.1 °C.s^{-1}, curves at lower rates of heating were obtained by raising the temperature in 1 °C increments, leaving the samples for 2 min between each temperature rise.

RESULTS AND DISCUSSION

Synthesis of the Acridine−Oligonucleotide Conjugates. Conjugates were designed so as to have the general structure shown in Scheme 1a. The aromatic moiety of the conjugates was expected to stabilize G-quadruplex structures and promote their formation, while the oligonucleotide chain was added to impart selectivity for the telomeric region. Acridines were chosen for the aromatic moiety of the conjugate since, when this work started, some of the most effective telomerase inhibitors reported were derivatives of 3,6-diaminoacridine (proflavin) with the two amines acylated with 3-(dialkylamine)-propionyl groups. The commercial availability and low price of proflavin also made it an advantageous starting material. We

Scheme 1. Schematic Representation of Acridine−Oligonucleotide Conjugates (a), and Retrosynthetic Analysis (b)

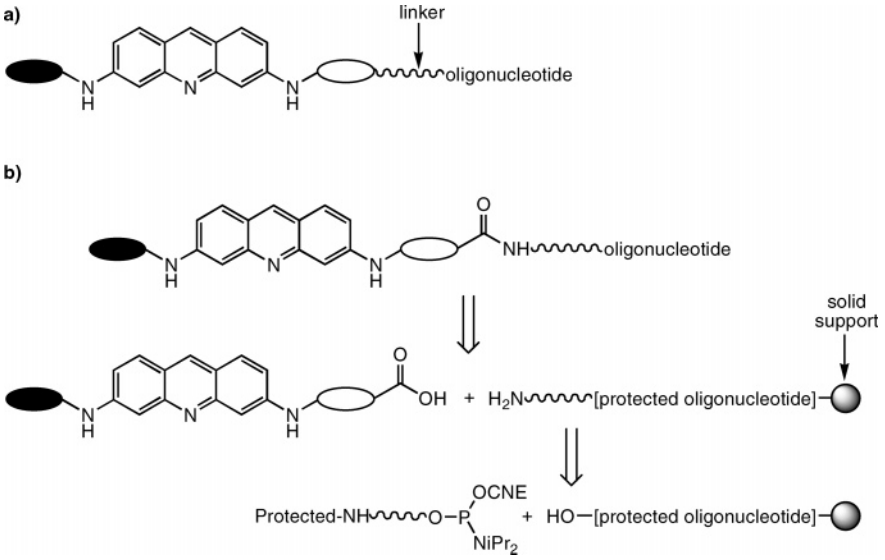

Scheme 2. Synthesis of the Asymmetrically Substituted Acridine Derivatives

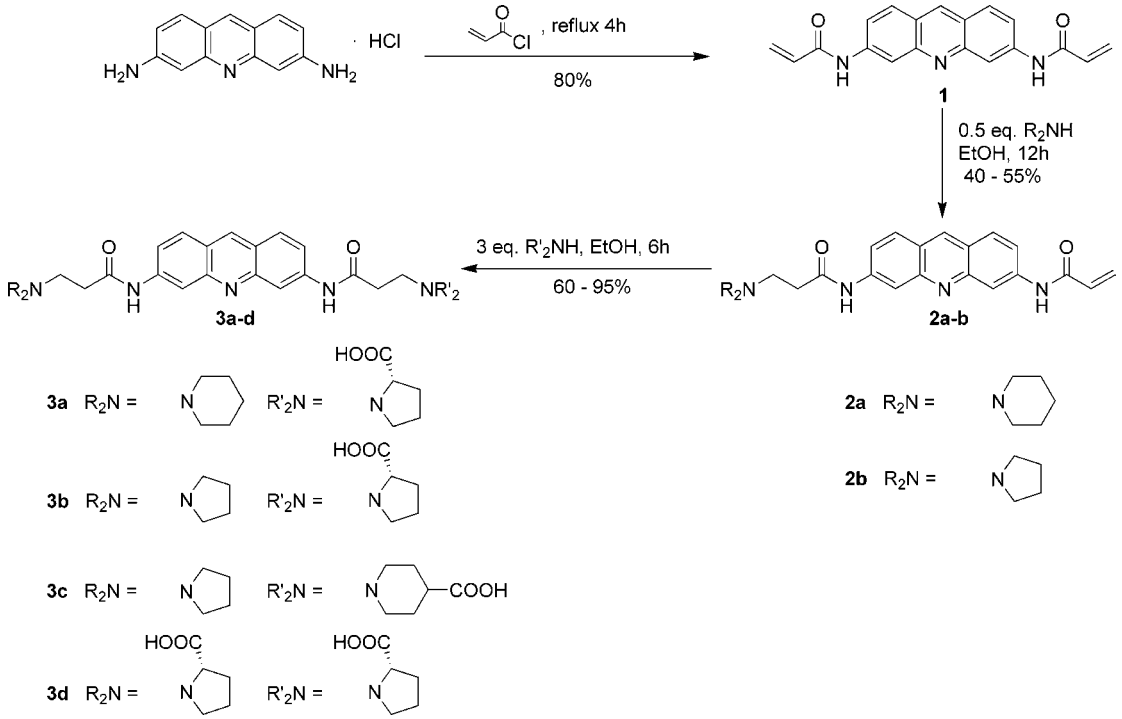

reasoned that it would be convenient to keep the same basic structure as that of the acridine derivatives that have been shown to be telomerase inhibitors (*14*). Although the two amines of proflavin have to be transformed into 3-(dialkylamino)propionamides, only one of these groups has to be derivatized to allow conjugation to the linker−oligonucleotide (Scheme 1b). Commercially available acridine phosphoramidite derivatives could not be used since their acridine rings are not suitably modified, while acridines that exhibit telomerase-inhibiting properties typically possess alkylamino side chains.

The conjugates were synthesized taking advantage of solid-phase procedures. Thus, the oligonucleotide was assembled, and its free end was modified with a suitable linker on a solid support, where the key conjugation was also carried out. An amide bond seemed a sensible choice to covalently link the two moieties. Amides are stable and can be obtained by exploiting a variety of reagents developed for peptide synthesis. In addition, amine groups are easy to add to oligonucleotide chains.

The synthesis of the asymmetrically substituted acridines was not straightforward. Attempts based on the selective protection of one of the amines of proflavin either failed or afforded the final product in very low yields. The acridines used in the conjugation reactions were synthesized from 3,6-diacryloylproflavin (**1**), which was prepared by reacting proflavin with an excess of acryloyl chloride (Scheme 2). The symmetry of the system was broken with the first Michael addition. Reaction of 3,6-diacryloylproflavine with piperidine or pyrrolidine afforded 3-(3-piperidinopropionyl)- or 3-(3-pyrrolidinopropionyl)-6-acryloylproflavin (**2a** or **2b**), respectively. The target carboxyl-derivatized acridines, **3**, were obtained after addition of proline or isonipecotic acid (isonipecotic = 4-piperidinecarboxylic) to **2**. Treatment of 3,6-diacryloylproflavin with an excess of proline afforded the symmetrical biscarboxylate **3d**.

Three oligonucleotide sequences were assembled using the standard phosphite triester methodology (phosphoramidite derivatives of dT, dA^{Bz}, and dC^{Bz}). Two were complementary to

Scheme 3. Side Reactions Taking Place at the Final Deprotection Step when the Ammonia Treatment Was Carried Out at 55 °C, Shown Here for Conjugate 4a

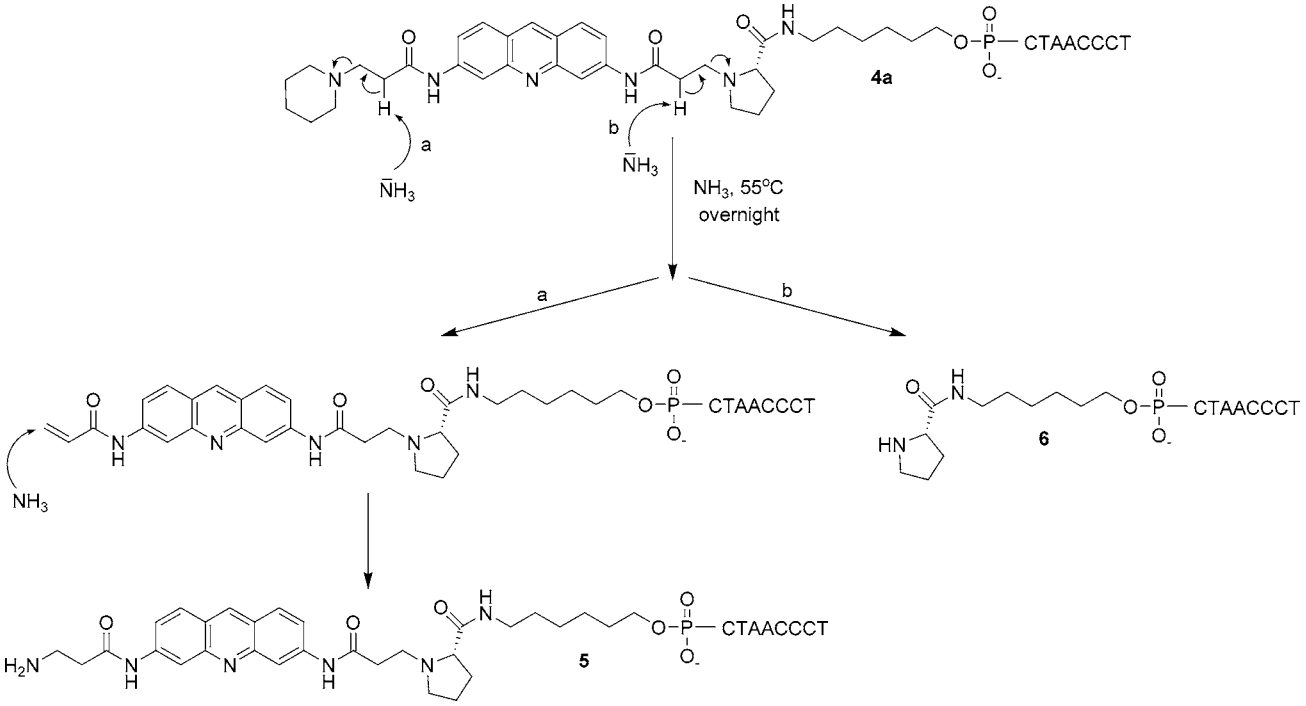

Scheme 4. Synthesis Scheme for the Preparation of the Conjugates

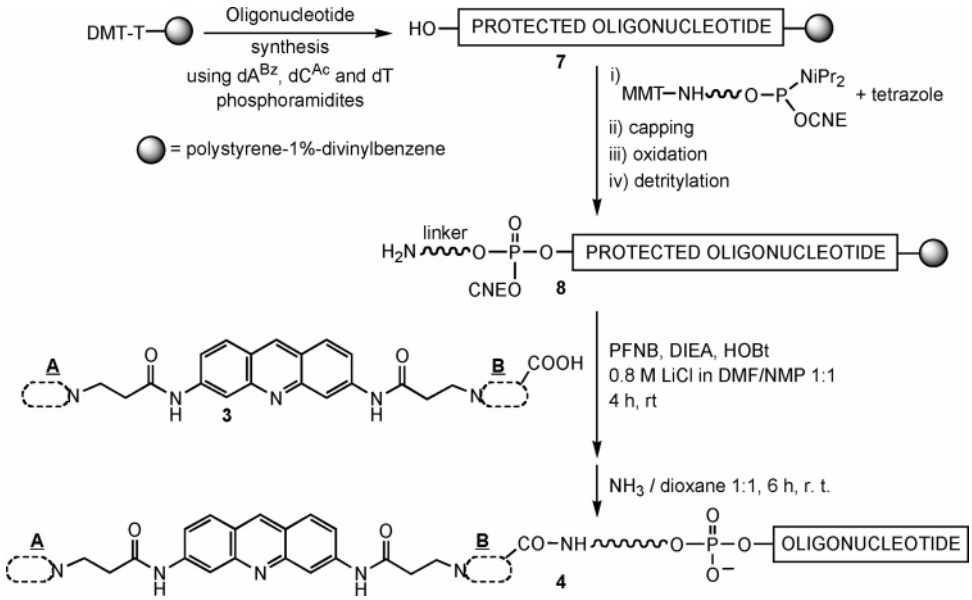

the single-stranded telomeric DNA (dCTAACCCT and dAACCCTAA) and the third, which contained the same bases randomized, was used as a control (dTCACTCAT). The 5′ end of resin-linked oligonucleotides was subsequently derivatized with an amine linker. The linker had to be long and flexible enough to allow the acridine to interact with the quadruplex structure and the oligonucleotide to hybridize with the single-stranded telomeric DNA. Linkers of different lengths containing either alkyl or ethylene glycol chains were used. The latter, more polar linkers were expected to facilitate the approach of the conjugate to the polyanionic DNA chains.

In the first conjugation experiments, the carboxyl group of the acridine derivative was activated using either *N*,*N*′-diisopropylcarbodiimide and 1-hydroxybenzotriazole, (benzotriazol-1-yloxy)trispyrrolidinophosphonium hexafluoroposphate (PyBOP) in the presence of DIEA, or (7-azabenzotriazol-1-yloxy)-trispyrrolidinophosphonium hexafluoroposphate (PyAOP) and DIEA. Although a large excess of acylating reagent was reacted with the H_2N−linker−oligonucleotide−CPG (2 h, rt), coupling yields were either 0% or below 10%.

Incorporation of the acridine moiety was controlled by treating an aliquot of conjugate−resin with concentrated aqueous ammonia and analyzing the crude by reversed-phase HPLC and MALDI-TOF MS. Detection of linker−oligonucleotide and/or acetyl−linker−oligonucleotide indicated that the coupling had not gone to completion. The origin of the acetyl−linker−oligonucleotide was not clear, but acetylation of amines has also been found to take place during the elongation of peptides on resin-linked oligonucleotides (*32*).

These experiments also showed that the deprotection conditions had to be fine-tuned. Since standard nucleobase protecting groups (A^{Bz}, C^{Bz}) had been used for oligonucleotide assembly,

Table 1.

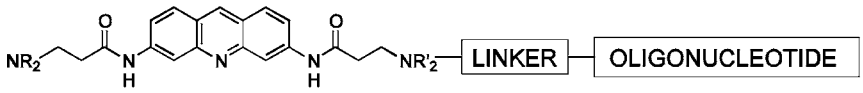

Conjugate	R_2NH	R'_2NH	Linker	Sequence
4a	Piperidine	Proline	L6	5' CTAACCCT 3'
4b	Pyrrolidine	Proline	L5	5' CTAACCCT 3'
4c	Proline	Proline	L5	5' CTAACCCT 3'
4d	Pyrrolidine	Isonipecotic acid	L5	5' CTAACCCT 3'
4e	Piperidine	Proline	L3	5' CTAACCCT 3'
4f	Pyrrolidine	Proline	L5 - L18	5' CTAACCCT 3'
4g	Pyrrolidine	Proline	L5	5' TCACTCAT 3'
4h	Pyrrolidine	Isonipecotic acid	L5	5' AACCCTAA 3'
4i	Pyrrolidine	Proline	L5	5' AACCCTAA 3'

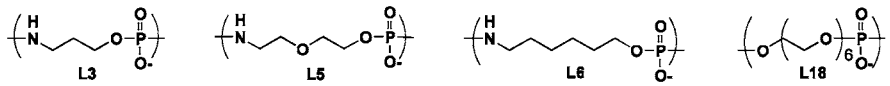

deprotection was carried out by overnight reaction with concentrated aqueous ammonia at 55 °C. Analysis of the crude product showed that the target conjugate (**4a**) was accompanied by a conjugate (**5**) in which the piperidine ring had been replaced by an amine group and proline−linker−oligonucleotide conjugate (**6**). **5** and **6** derive from the two possible reversed Michael reactions, with subsequent addition of ammonia to the acryloyl group in the case of **5** (Scheme 3).

Since we have previously obtained the best results in the synthesis of nucleopeptides and peptide−oligonucleotide conjugates using a polystyrene-1%-divinylbenzene copolymer rather than controlled pore glass (*33*, *34*), the linker−oligonucleotide moiety was resynthesized on a polystyrene matrix, and the PyAOP-mediated acylation reaction was repeated in the same conditions as on controlled pore glass. The yield of the conjugation step was slightly higher (17%) and somewhat better when *N*-[(dimethylamino)-1*H*-1,2,3-triazolo[4,5-*b*]pyridin-1-ylmethylene]-*N*-methylmethanaminium hexafluorophosphate *N*-oxide (HATU) was used to activate the carboxyl group (28% after 4 h). 1,2,3,4,5-Pentafluorophenyl 4-nitrobenzenesulfonate (*28*, *35*) was the reagent that finally allowed the conjugation reaction to attain acceptable yields (50−55%; for conditions, see below).

Finally, the target conjugates (**4**) were synthesized using the procedure outlined in Scheme 4. Oligonucleotides were assembled on an amine-derivatized polystyrene-1%-divinylbenzene support, replacing the phosphoramidite derivative of C^{Bz} by that of C^{Ac}. Linkers L_3, L_5, and L_6 (see structures in Table 1) were then introduced by coupling the corresponding monomethoxytritylamine phosphoramidite derivatives to the free 5′-hydroxyl group of the oligonucleotide (**7**), followed by capping and oxidation of the phosphite to phosphate. The longest linker, L_5-L_{18}, was introduced by subsequently coupling a hydroxyl-protected phosphoramidite (L_{18}) and an amine-protected phosphoramidite (L_5). The monomethoxytrityl amine-protecting group was removed using the same mild acid reagent commonly used to eliminate the DMT groups, and the carboxyl-derivatized acridine moiety was coupled to **8** by reaction with PFNB and DIEA (molar ratio with respect to polymer-bound amine groups 10:10:25), in the presence of catalytic amounts of HOBt. A 0.8 M solution of LiCl in a 1:1 mixture of *N*,*N*-dimethylformamide and *N*-methylpyrrolidone was used as the solvent, and the reaction was left to proceed for 4 h at room temperature. In spite of using these conditions, coupling yields remained below the expected value in some conjugation reactions.

Permanent protecting groups were removed by treatment of the conjugate resin with a 1:1 ammonia/dioxane mixture for 6 h at room temperature. In these conditions, the presence of impurities such as **5** and **6** was virtually nonexistant. Conjugates were purified by reversed-phase liquid chromatography and characterized by MALDI-TOF mass spectrometric analysis.

Interaction with Intramolecular Quadruplexes. We examined the interaction of these acridine−oligonucleotide conjugates with quadruplex-forming oligonucleotides that contain the human telomeric repeat sequences $(GGGTTA)_n$. These model oligonucleotides had to be designed to allow the formation of quadruplex structures as well as hybridization of the oligonucleotide portion of the conjugate. The quadruplex-forming sequence has to contain at least four GGG repeats, so the basic $(GGGTTA)_3GGG$ sequence was extended to offer a single-stranded arm suitable for duplex formation with the conjugates.

Information on quadruplex stabilization by the conjugates was obtained from thermal denaturation studies, in which an increase in the melting temperature of the quadruplex indicates a stabilizing effect. The thermal stability of the quadruplex was evaluated using a fluorescence-based method (*29*) which allows melting temperatures to be determined with high sensitivity using a small amount of material. In these experiments, the quadruplex-forming oligonucleotides are labeled at one end (5′) with a fluorophore (F, fluorescein) and at the other (3′) end with a quencher (Q, methyl red). When the quadruplex is folded, these groups are in close proximity, and the fluorescence is quenched. When the quadruplex melts, these groups become separated, and there is a large increase in fluorescence.

Conjugate−oligonucleotide interactions were studied using three different model oligonucleotides containing 5 or 6 GGG tracts: F-TGGGTTAGGGTTAGGGTTAGGGTTAGGG-Q (**OL-1**), F-TGGGTTAGGGTTAGGGTTAGGGTTAGGGTTAGGG-Q (**OL2**), and AGGGTTAGTTTT-Q-GGGTTAGGGTTAGGGT-TAGGG-Q (**OL3**), in which F and Q stand for the fluorophore and the quencher, respectively. **OL1** and **OL2** can adopt different structures, depending on which G tracts are part of the folded quadruplex and which are in the single-stranded overhang (Scheme 5). For **OL1**, only one of the structures

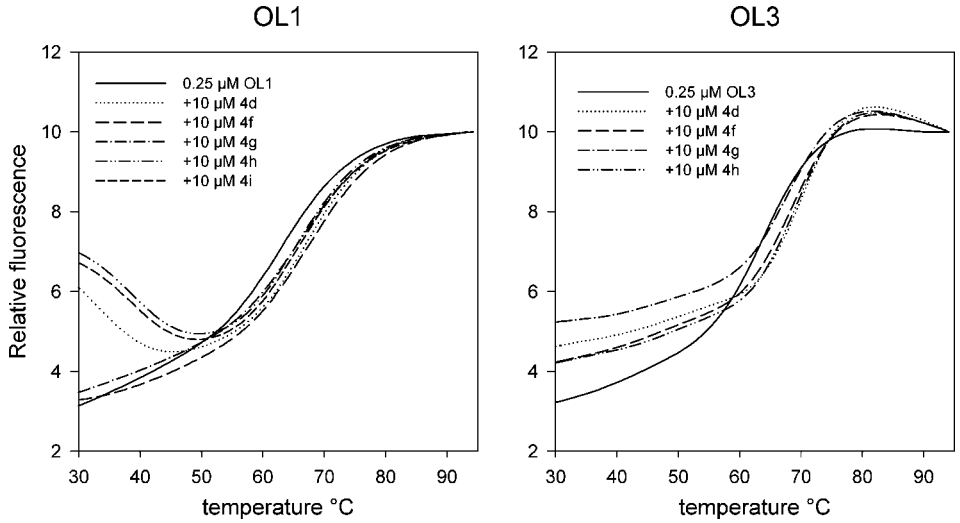

Figure 1. Fluorescence melting curves showing the effects of oligonucleotide−acridine conjugates (10 μM) on the melting of **OL1** (left-hand panel) and **OL3** (right-hand panel). The quadruplex concentration was 0.25 μM in each case, and the reactions were performed in 50 mM potassium phosphate pH 7.4. For **OL1**, the heating rate was 0.1 °C.s^{-1}; this was reduced to 0.5 °C.min^{-1} for **OL3**.

Scheme 5. Possible Structures for the Intramolecular Quadruplexes Adopted by (a) OL1, (b) OL2, and (c) OL3

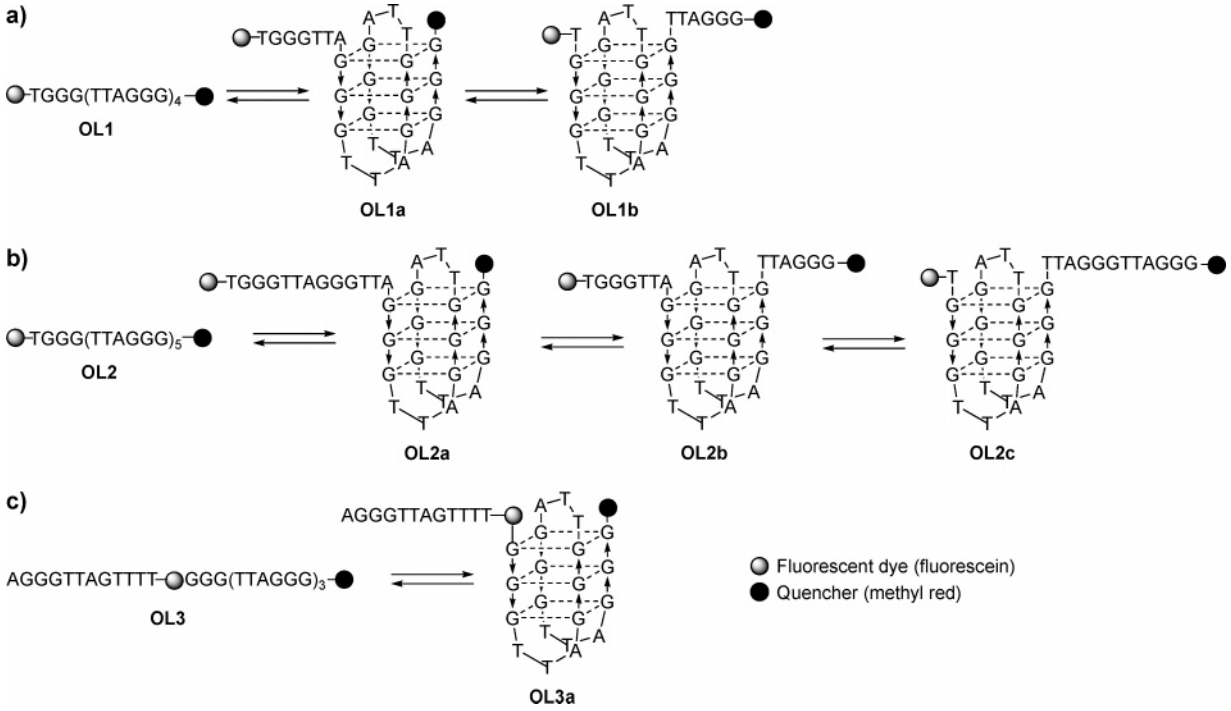

(**OL1a**, Scheme 5a) will allow the oligonucleotide moiety of the conjugates to interact with the complementary telomeric sequence. Two of the conformations of **OL2 (OL2a** and **OL2b**, Scheme 5b) are appropriate for interaction with the acridine conjugates. **OL3** was designed so that only one quadruplex structure can be formed (Scheme 5c), where the "core" quadruplex system and the single-stranded telomeric sequence are more separated than in the other model oligonucleotides.

In these melting experiments, the quadruplex-forming oligonucleotide concentration was 0.25 μM, and the concentration of the conjugates ranged between 2 and 10 μM. Representative melting curves in the presence and absence of different conjugates are shown in Figure 1. The changes in the melting temperatures of the quadruplexes (ΔT_m) produced by the conjugates are summarized in Table 2.

Examination of the data in Table 2 shows that all the conjugates stabilize quadruplex structures, and the increases in melting temperature (T_m) depend on their concentration, as expected. Inspection of the melting profiles of oligonucleotide **OL1** (Figure 1) shows that, in some cases, the transition between the folded G-quadruplex and the single-stranded form is accompanied by another transition, with a reversed profile at lower temperatures. This curve corresponds to melting of the

Table 2.

	G-quadruplex-forming oligonucleotides						
	OL1	OL2			OL3		
conjugate	10 μM	2 μM	5 μM	10 μM	2 μM	5 μM	10 μM
4a	4.3	1	2	3	2	3.5	4
4b	3.8			1	1.5	3	3.5
4c				0.5			2
4d	5.1	0.5	2	4	2	3	6.5
4e				0.5			0.5
4f	4.7		1.5	4.5	2	3	4.5
4g	3.2		1	1.5	1.5	2.5	4
4h	2.6			2	1.5	2.5	5.5
4i	2.7			0.5		1.5	2

duplex that is formed between the conjugated oligonucleotide and the single-stranded arm of **OL1**. Its reversed profile is explained by suggesting that hybridization shields the fluorophore and prevents energy transfer to the quencher. This curve was not observed when thermal denaturation experiments were carried out with **OL1** either alone, as expected, or in the presence of conjugates **4e**, **4f**, and **4g**. The oligonucleotide sequence in **4g** is not complementary to that of the telomere; this conjugate was synthesized as a control, and as expected, it does not display the reverse profile at low temperatures. Duplex formation does not occur with conjugates **4e** and **4f**. Since the main difference between these and the other conjugates is the length of the spacer linking the aromatic and oligonucleotide moieties of the conjugate, we surmise that duplex formation is hampered by the shortest and longest linkers. Linkers L5 and L6 (8 and 9 atoms long, respectively) thus seem to be the best for allowing duplex formation. Similar results were found with **OL2** with respect to duplex formation. In **OL3**, the relative position of the fluorophore and the quencher is different and is such that melting of the duplex is not observed.

Since the main purpose of this work was to add telomere-hybridizing properties to quadruplex-stabilizing molecules, these results confirm that our goal has been achieved. Our acridine−oligonucleotide conjugates can interact both with quadruplex structures and with the single-stranded telomeric sequence.

From a quantitative point of view, the quadruplex stabilization provided by the conjugates is not very high. Nevertheless, it has to be taken into consideration that **OL1** and **OL2** exist in equilibrium between three or four different structures (see Scheme 5). The T_m data therefore represent averages of the interaction with the different conformations, some of which cannot bind the conjugates. Only **OL3** adopts a single quadruplex structure, and the highest ΔT_ms were observed between this oligonucleotide and conjugates **4d** and **4h**. The complexes formed by the other conjugates and **OL3** displayed similar or slightly higher than those formed with **OL1**, which are higher than those formed with **OL2**. These results suggest that the apparent stabilization of the quadruplex by the acridine conjugate improves if the number of available conformations is lower.

CONCLUSIONS

We have developed a methodology for synthesizing a small library of acridine−oligonucleotide conjugates, making use of acylation and Michael reactions to modify the aromatic moiety, and of amide formation for the conjugation reaction. Conditions for the final deprotection of the conjugate were also established. The thermal denaturation experiments demonstrated that the acridine ring of the conjugates interacts with and stabilizes the quadruplex structures. The conjugated oligonucleotide hybridizes with the complementary single-stranded telomeric DNA to impart selectivity to the aromatic moiety. The best results were obtained with conjugate **4d**, in which the acridine ring is flanked by pyrrolidine and isonipecotic acid units and linked to oligonucleotide CTAACCCT by a bis(ethylene glycol) linker (L5).

ACKNOWLEDGMENT

This work was supported by funds from the European Union (HPRN-CT-2002-00175), the Spanish Ministerio de Educación y Ciencia (grant CTQ2004-8275-C02-01), and the Generalitat de Catalunya (2005SGR-693 and Centre de Referència de Biotecnologia).

LITERATURE CITED

(1) Blackburn, E. H. (1991) Structure and function of telomeres. *Nature (London) 350*, 569−573.

(2) Greider, C. W. (1996) Telomere length regulation. *Annu. Rev. Biochem. 65*, 337−365.

(3) Cech, T. R. (2000) Life at the end of the chromosome: telomeres and telomerase. *Angew. Chem., Int. Ed. 39*, 34−43.

(4) Blackburn, E. H. (2001) Switching and signaling at the telomere. *Cell 106*, 661−673.

(5) Zahler, A. M., Williamson, J. R., Cech, T. R., and Prescott, D. M. (1991) Inhibition of telomerase by G-quartet DNA structures. *Nature (London) 350*, 718−720.

(6) Mergny, J. L., and Hélène, C. (1998) G-quadruplex DNA: A target for drug design. *Nat. Med. 4*, 1366−1367.

(7) Han, H., and Hurley, L. H. (2000) G-quadruplex DNA: a potential target for anti-cancer drug design. *Trends Pharm. Sci. 21*, 136−142.

(8) Kelland, L. R. (2000) Telomerase inhibitors: targeting the vulnerable end of cancer? *Anti-Cancer Drugs 11*, 503−513.

(9) Neidle, S. (2000) Targeting the end of DNA. *Chem. Br. 36*, 27−29.

(10) Mergny, J. L., Riou, J. F., Mailliet. P., Teulade-Fichou, M. P., and Gilson, E. (2002) Natural and pharmacological regulation of telomerase. *Nucleic Acids Res. 30*, 839−865.

(11) Neidle, S., and Parkinson, G. (2002) Telomere maintenance as a target for anticancer drug discovery. *Nat. Rev. Drug. Discovery 1*, 383−393.

(12) Sun, D., Thompson, B., Cathers, B. E., Salazar, M., Kerwin, S. M., Trent, J. O., Jenkins, T. C., Neidle, S., and Hurley, L. H. (1997) Inhibition of human telomerase by a G-quadruplex-interactive compound. *J. Med. Chem. 40*, 2113−2116.

(13) Perry, P. J., Reszka, A. P., Wood, A. A., Read, M. A., Gowan, S. M., Dosanjh, H. S., Trent, J. O., Jenkins, T. C., Kelland, L. R., and Neidle, S. (1998) Human telomerase inhibition by regioisomeric disubstituted amidoanthracene-9,10-diones. *J. Med. Chem. 41*, 4873−4884.

(14) Harrison, R. J., Gowan, S. M., Kelland, L. R., and Neidle, S. (1999) Human telomerase inhibition by substituted acridine derivatives. *Bioorg. Med. Chem. Lett. 9*, 2463−2468.

(15) Wheelhouse, R. T., Sun, D., Han, H., Han, F. X., and Hurley, L. H. (1998) Cationic porphyrins as telomerase inhibitors: the interaction of tetra-(*N*-methyl-4-pyridyl)porphine with quadruplex DNA. *J. Am. Chem. Soc. 120*, 3261−3262.

(16) Perry, P. J., Read, M. A., Davies, R. T., Gowan, S. M., Reszka, A. P., Wood, A. A., Kelland, L. R., and Neidle, S. (1999) 2,7-Disubstituted amidofluorenone derivatives as inhibitors of human telomerase. *J. Med. Chem. 42*, 2679−2684.

(17) Fedoroff, O. Y., Salazar, M., Han, H., Chemeris, V. V., Kerwin, S. M., and Hurley, L. H. (1998) NMR-based model of a telomerase-inhibiting compound bound to G-quadruplex DNA. *Biochemistry 37*, 12367−12374.

(18) Shin-ya, K., Wierzba, K., Matsuo, K., Ohtani, T., Yamada, Y., Furihata, K., Hayakawa, Y., and Seto, H. (2001) Telomestatin, a novel telomerase inhibitor from *Streptomyces anulatus*. *J. Am. Chem. Soc. 123*, 1262−1263.

(19) Read, M., Harrison, R. J., Romagnoli, B., Tanious, F. A., Gowan, S. H., Reszka, A. P., Wilson, W. D., Kelland, L. R., and Neidle, S. (2001) Structure-based design of selective and potent G quadruplex-mediated telomerase inhibitors. *Proc. Natl. Acad. Sci. U.S.A. 98*, 4844−4849.

(20) Koeppel, F., Riou, J. F., Laoui, A., Mailliet, P., Arimondo, P. B., Labit, D., Petitgenet, O., Hélène, C., and Mergny, J. L. (2001) Ethidium derivatives bind to G-quartets, inhibit telomerase and act as fluorescent probes for quadruplexes. *Nucleic Acids Res. 29*, 1087−1096.

(21) Gowan, S. M., Heald, R., Stevens, M. F. G., and Kelland, L. R. (2001) Potent inhibition of telomerase by small-molecule pentacyclic acridines capable of interacting with G-quadruplexes. *Mol. Pharmacol. 60*, 981−988.

(22) Riou, J. F., Guittat, L., Mailliet, P., Laoui, A., Renou, E., Petitgenet, O., Mégnin-Chanet, F., Hélène, C., and Mergny, J. L. (2002) Cell senescence and telomere shortening induced by a new series of specific G-quadruplex DNA ligands. *Proc. Natl. Acad. Sci. U.S.A. 99*, 2672−2677.

(23) Harrison, R. J., Cuesta, J., Chessari, G., Read, M. A., Basra, S. K., Reszka, A. P., Morrell, J., Gowan, S. H., Incles, C. M., Tanious,

F. A., Wilson, W. D., Kelland, L. R., and Neidle, S. (2003) Trisubstituted acridine derivatives as potent and selective telomerase inhibitors. *J. Med. Chem. 46*, 4463−4476.

(24) Atkinson, T., and Smith, M. (1984) Solid-phase synthesis of oligodeoxyribonucleotides by the phosphite-triester method. In *Oligonucleotide Synthesis. A Practical Approach* (Gait, M. J., Ed.), pp 35−81, IRL Press, Oxford, U.K.

(25) Kaiser, E., Colescott, R. L., Bossinger, C. D., and Cook, P. I. (1970) Color test for detection of free terminal amino groups in solid-phase synthesis of peptides. *Anal. Biochem. 34*, 595−598.

(26) Bardella, F., Giralt, E., and Pedroso, E. (1990) Polystyrene-supported synthesis by the phosphite triester approach - an alternative for the large-scale synthesis of small oligodeoxyribonucleotides. *Tetrahedron Lett. 31*, 6231−6234.

(27) Montserrat, F. X., Grandas, A., Eritja, R., and Pedroso, E. (1994) Criteria for the economic large-scale solid-phase synthesis of oligonucleotides. *Tetrahedron 50*, 2617−2622.

(28) Pudhom, K., and Vilaivan, T. (1999) Synthesis of aryl esters of protected amino acids from aryl sulfonates. *Tetrahedron Lett. 40*, 5939−5942.

(29) Darby, R. A. J., Sollogoub, M., McKeen, C., Brown, L., Risitano, A., Brown, N., Barton, C., Brown, T., and Fox, K. R. (2002) High throughput measurement of duplex, triplex and quadruplex melting curves using molecular beacons and the LightCycler. *Nucleic Acids Res. 29*, e39.

(30) Risitano, A., and Fox, K. R. (2003) Stability of intramolecular DNA quadruplexes: comparison with DNA duplexes. *Biochemistry 42*, 6507−6513.

(31) Risitano, A., and Fox, K. R. (2004) Influence of loop size on the stability of intramolecular DNA quadruplexes. *Nucleic Acids Res. 32*, 2598−2606.

(32) Zaramella, S., Yeheskiely, E., and Stromberg, R. (2004) A method for solid-phase synthesis of oligonucleotide 5′-peptide-conjugates using acid-labile α-amino protections. *J. Am. Chem. Soc. 126*, 14029−14035.

(33) Robles, J., Beltrán, M., Marchán, V., Pérez, Y., Travesset, I., Pedroso, E., and Grandas, A. (1999) Towards nucleopeptides containing any trifunctional amino acid. *Tetrahedron 55*, 13251−13264.

(34) Marchán, V., Rodríguez-Tanty, C., Estrada, M., Pedroso, E., and Grandas, A. (2000) Alternative procedures for the synthesis of methionine-containing peptide-oligonucleotide hybrids. *Eur. J. Org. Chem.* 2495−2500.

(35) Pudhom, K., and Vilaivan, T. (2000) Pentafluorophenyl 4-nitrobenzenesulfonate as a peptide coupling reagent. *Synth. Commun. 31*, 61−70.

BC060194T

TECHNICAL NOTES

Efficient Synthesis of an Aldehyde Functionalized Hyaluronic Acid and Its Application in the Preparation of Hyaluronan−Lipid Conjugates

Dipali Ruhela, Kareen Riviere, and Francis C. Szoka, Jr.*

Departments of Pharmaceutical Chemistry and Biopharmaceutical Sciences, School of Pharmacy, University of California at San Francisco, San Francisco, CA 94143-0446. Received March 22, 2006; Revised Manuscript Received June 26, 2006

An efficient method to synthesize hyaluronan oligosaccharide lipid conjugates is described. This strategy is based on the introduction of a double bond in the glucuronic acid of the hyaluronic acid (HA), by the biodegradation of HA with hyaluronate lyase, followed by the generation of a free aldehyde group at the nonreducing end of hyaluronic acid via ozonolysis and the subsequent reduction of the generated ozonide. The resulting aldehyde-functionalized HA is then coupled to dipalmitoyl phosphatidylethanolamine (DPPE) using reductive amination chemistry. This methodology can be extended to link molecules such as biotin, polymers, or proteins to HA for numerous applications in drug delivery and in the creation of biocompatible materials for tissue repair and engineering.

INTRODUCTION

Hyaluronic acid (HA) is a high molecular weight linear polysaccharide which is composed of a simple repeating disaccharide unit of D-glucuronic acid (GlcA) and *N*-acetyl-D-glucosamine (GlcNAc) linked through a β 1,3-glycosidic bond (Figure 1). The disaccharides are in turn linked to each other through a β 1,4-glycosidic bond. HA is found in the extracellular matrix and is the main ligand for CD44, a type 1 transmembrane glycoprotein that is overexpressed in many cancers.

HA has numerous applications in tissue repair and engineering and in gene and drug delivery. Cross-linked HA has been used as a biomaterial for cartilage repair (*1*). For gene delivery applications, HA−DNA microspheres and a DNA−HA matrix have been used for the controlled release of DNA and are adaptable for site specific targeting (*2*, *3*). Various HA conjugates have been tested for targeting drugs to CD44. HA−Taxol and HA−HPMA−Doxorubicin, both synthesized from high molecular weight HA, have been shown to have an increased uptake by tumor cells and therefore have a potential to target drugs selectively to tumors (*4*, *5*). Both high molecular (*6*, *7*) and low molecular (*8*) weight HA−lipid conjugates have been shown to successfully target liposomes to CD44 expressing cancers and to increase cell killing both in vitro and in vivo. However, certain liver receptors specifically recognize high molecular weight HA and rapidly clear it from the systemic circulation (*9*). In addition, high molecular weight HA may not be ideal since the frequency of attachment between HA and the conjugated drug is often unknown. Therefore, HA conjugates having small, defined oligosaccharides may avoid clearance by the liver while still preferentially target CD44-overexpressing tumor cells. Understanding the significance of oligomer length for receptor binding is important for furthering drug targeting studies using HA.

Several HA oligosaccharides, having different lengths and modified sequences, have been synthesized over the past decade (*10*), but there are no published studies of well-defined lipooligosaccharides. Reductive amination chemistry has been used to conjugate HA with lipids (*11*, *12*), polymers (*13*), and a fluorescent tag (*14*). In our ongoing efforts to synthesize lipooligosaccharides, we have designed a more efficient strategy for the synthesis of HA−lipid conjugates of defined length. In this paper, we summarize the results of a methodology, which is based on the generation of a free aldehyde group at the nonreducing end of hyaluronic acid (HA) via enzymatic digestion of high molecular weight HA using hyaluronate lyase, ozonolysis, and the subsequent reduction of the generated ozonide. The aldehyde is much more reactive than the hemiacetal so the resulting functionalized hyaluronic acid is easily coupled to DPPE through the aldehyde rather than via the reducing end using an equimolar concentration of the lipid.

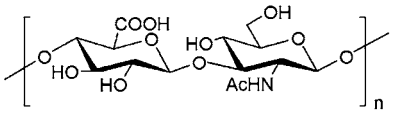

Figure 1. Disaccharide repeat unit of HA.

EXPERIMENTAL PROCEDURES

Enzymatic Digestion of HA. Sodium hyaluronate (Genzyme Biosurgery, Cambridge, MA) was dissolved in digest buffer (200 mM NaCl and 50 mM sodium acetate, adjusted to pH 6.0) at a concentration of 200 mg/40 mL, and stirred at room temperature for 1 day. To 40 mL of dissolved HA, 4000 U of hyaluronate lyase (*Streptomyces hyalurolyticus*, Sigma, St. Louis, MO) was added and allowed to incubate for 4 h at 37 °C. The enzyme was inactivated by immersing the flask in boiling water for 10 min, and the contents were lyophilized.

Size Exclusion Chromatography. The resulting white powder was dissolved in 1 mL of 0.05 M NH_4HCO_3 buffer, filtered through a 0.45 μm filter, and loaded via a sample injector onto a 50 mm × 100 cm Bio-Gel Column (Biorad P-30, medium grade, 300 g). The column was equilibrated in 0.05 M NH_4-

* Corresponding author. E-mail: szoka@cgl.ucsf.edu.

10.1021/bc0600721 CCC: $33.50 © 2006 American Chemical Society
Published on Web 07/29/2006

Scheme 1

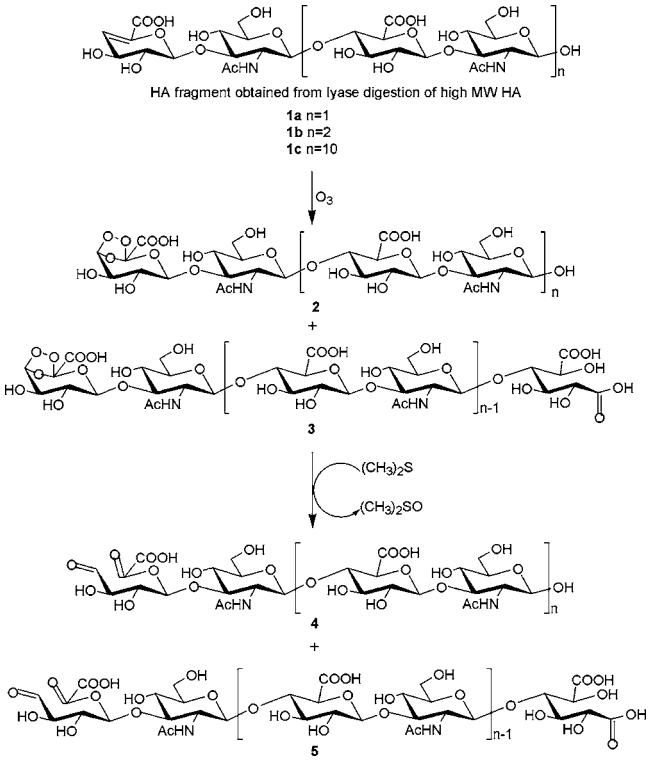

HCO_3. The first 450 mL of eluate was not collected. Thereafter, fractions of 8 mL each were collected, and their absorbances were read at 232 nm. Fractions containing HA−oligomers were pooled as individual length oligomers, lyophilized, redissolved in H_2O, and lyophilized again to remove residual ammonium bicarbonate salt. The masses of the oligomers were confirmed by MALDI-TOF. The separation profile and the MALDI-TOF results are shown in the Supporting Information.

Ozonolysis/Reduction of the HA Oligomers (Scheme 1). The HA oligomer (**1**) was dissolved in a mixture of $(CH_3)_2SO$, H_2O and CH_3OH. The solution was cooled to −78 °C and ozone was bubbled into the solution via a sintered glass pipet until a pale blue color persisted. This treatment yielded ozonide (**2**) and ozonide (**3**). Oxygen was then bubbled through the solution to remove the excess ozone until the solution became colorless. After the addition of dimethyl sulfide, the solution was allowed to stir at room temperature for 2 h to reduce the ozonides to yield products **4** and **5**. This mixture was thoroughly dried and used immediately for coupling.

Synthesis of the Lipooligosaccharide (Scheme 2). The crude mixture of **4** and **5** was resuspended in a suitable combination of $(CH_3)_2SO$ and CH_3OH. To this, 1.05 equiv of DPPE (Avanti Polar Lipids, Alabaster, AL) in CH_3OH-$CHCl_3$ was added, and the mixture was stirred at 60 °C for 2 h. Thereafter, a 50-fold molar excess of freshly prepared reducing agent solution (1% w/v of $NaCNBH_3$ (Aldrich, St. Louis, MO) in $CHCl_3/CH_3OH$ (1:1 by volume) containing 0.1% CH_3COOH) was added in five portions in 1 h increments. The resulting yellow solution was then allowed to stir at 60 °C for 2 days to yield the HA_n−DPPE conjugate (**6**), which contains DPPE at the nonreducing end, and the HA_{n-1}−DPPE conjugate (**7**), which bears DPPE on the nonreducing residue and contains a lactone at the other end. The solvent was evaporated under vacuum. The residue was resuspended in a modest amount of water and repeatedly precipitated (three times) in acetone to remove excess $NaCNBH_3$. The resultant pellet was then resuspended in minimal $CHCl_3/CH_3OH/H_2O$ (65:25:4 by volume) and loaded onto a prepacked Biotage silica column. The column was first washed with $CHCl_3$, and then a gradient program of $CHCl_3/CH_3OH/H_2O$ was run to elute the two products separately. The purified conjugates were characterized by MALDI-TOF, as shown in Table 1.

The HA_4−DPPE conjugate was fully characterized by NMR using pyridine-d_5/DCl/CD_3OD/$CDCl_3$ in a volume ratio of 1:1:2:10 (*16*). ^1H NMR (400 MHz) with characteristic peaks: δ 5.2 (1H, H-1α), 4.39 (d, 2H, H-1′β, H-1″), 4.36 (d, 2H, H-1‴β, H-1′α), 4.32 − 4.11 (20H, sugar ring protons), 3.81−3.29 (12H, sugar ring protons), 2.25−1.29 (56H, methylene protons of DPPE), 2.01 (6H, $NHCOCH_3$), 1.56 (4H, $NHCH_2CH_2$), 0.87 (6H, terminal CH_3 of DPPE). The spectra for HA_4−DPPE and HA_6−DPPE are in the Supporting Information.

Synthesis of a Biotinylated Conjugate of 1c. As an extension to our study, we synthesized a biotinylated conjugate of HA using this strategy. For this purpose, compound **1c** was subjected to ozonolysis/reduction with $(CH_3)_2S$ as mentioned above. The product was then conjugated with biotinylated diaminopyridine (BAP) using $NaCNBH_3$. The crude product was loaded onto a column, packed with AG1X2 resin (formate form), and equilibrated with 10 mM ammonium acetate. The product was then eluted from the column with 250 mM ammonium acetate and analyzed for absorbance at 210 nm. The salt was removed by dialysis against water, and the product was lyophilized to afford a light yellowish powder. A portion of this product was then loaded onto a streptavidin−agarose column in parallel with a control experiment where free HA_{12} (**1c**) was loaded onto a separate column.

RESULTS AND DISCUSSION

Conventionally, HA derivatives are directly prepared from oligomers obtained by enzymatic digestion of high molecular weight HA with hyaluronidase. Alternatively, high molecular weight HA can be digested with hyaluronate lyase, an endo-hexosaminidase whose catalytic activity introduces an α,β unsaturated carboxylic acid moiety at the nonreducing end of the oligomers. We decided to exploit this unique double bond on HA for the synthesis of small, well-defined HA−lipid conjugates. The double bond can efficiently be cleaved and converted to an aldehyde functionality via ozonolysis and subsequent reductive workup. Previously, Weingarten and Thiem (*17*) have synthesized aldehyde functionalized carbohydrate derivatives by first introducing a functionality, containing a double bond, on the sugar which was then efficiently converted to a free aldehyde via ozonolyis. Coupling of amino acids with this aldehyde functionalized carbohydrate by reductive amination led to novel carbohydrate−amino acid conjugates. However, in our case, we can generate a double bond within the HA oligomer directly by digestion with hyaluronate lyase. Ozone-assisted cleavage of this double bond can then generate a free aldehyde functionality which can be easily coupled to proteins and phospholipid amino groups by reductive amination. To test our hypothesis, we carried out this sequence of reactions on small HA oligomers and characterized the products formed.

In order to obtain well defined, small HA oligomers, ranging from 4−12 sugar residues containing a double bond at the nonreducing end (having the structure β-D-4en-thrHexA-(1→3)-[β-D-GlcNAc-(1→4)-β-D-GlcA]$_n$-(1→3)-D-GlcNAc), we followed a published procedure by Price et al. (*15*). High molecular weight HA was digested with hyaluronate lyase to yield hyaluronan fragments ranging from 4 to 12 saccharides in length. The oligomers were separated on a size exclusion column and analyzed for their absorbance at 232 nm.

The tetrasaccharide and hexasaccharide thus obtained were subjected to ozonolysis/ reduction with $(CH3)_2S$. This treatment cleanly cleaved the terminal double bond and generated a free aldehyde functionality at the nonreducing end of the oligomer.

Scheme 2

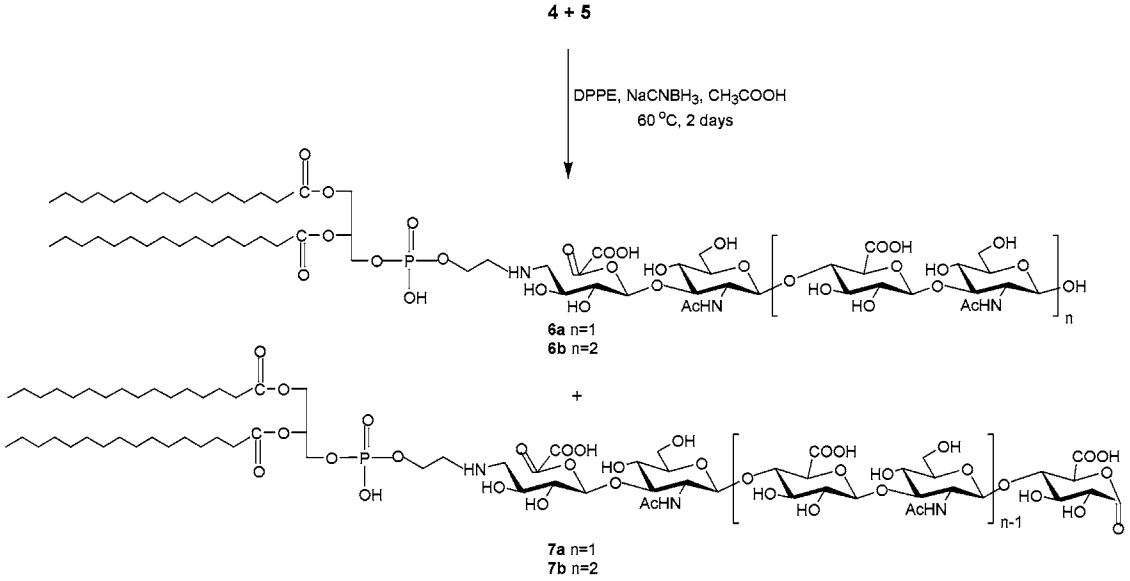

Table 1. MALDI-TOF MS (Positive Mode) Results for HA_n−DPPE Conjugates

starting compound	product	expected MW	observed MW
1a	**6a**	1464.3	1487.5 ($M + Na^+$)
	7a	1259.1	1260.3 ($M + H^+$)
1b	**6b**	1843.3	1866.3 ($M + Na^+$)
	7b	1638.1	1639.2 ($M + H^+$)

Ozonolysis of the oligomers (Scheme 1) yielded the corresponding ozonide (**2**) and ozonide (**3**) which resulted from the electrophilic attack of ozone on HA to liberate the anomeric carbon of the second sugar residue from the reducing end of the oligomer, via ozone catalyzed hydrolysis of the β 1,3-glycosidic bond. It has been previously reported that ozone can preferentially oxidize β-D-glycosidic linkages in unprotected carbohydrates and generate fragments of various repeat lengths (*18*, *19*). As illustrated in Scheme 1, controlled exposure of the carbohydrate to ozone yielded a mixture of even (compound **4**) and odd (compound **5**) numbered HA fragments, containing a free aldehyde functionality, from the same oligomer.

The resulting aldehyde functionalized HA oligomers were coupled to DPPE using reductive amination chemistry (Scheme 2) in a mixture of aprotic solvents ($CHCl_3$ and CH_3OH). The reaction with the HA_4 oligomer yielded the products **6a** and **7a**, and similarly the products **6b** and **7b** were obtained from HA_6. One-step purification of **6** and **7** by silica column chromatography afforded pure HA_n−DPPE and HA_{n-1}−DPPE conjugates. The products were analyzed by MALDI, and the correct masses for the even (**6a** and **6b**) and odd (**7a** and **7b**) lipooligosaccharides were obtained, as shown in Table 1.

HA_4−DPPE and HA_6−DPPE were also characterized by ^1H NMR. The NMR spectra showed characteristics peaks for both oligosaccharides and DPPE in the correct ratio. Furthermore, we observed the H-1α proton at δ 5.2 for HA_4−DPPE, which indicates that the anomeric proton at the reducing end of the tetrasaccharide is still intact. This confirms that DPPE is linked to HA via the nonreducing end. Due to line broadening and low resolution, we could not observe the peak for the anomeric proton in HA_6−DPPE. This line broadening is commonly encountered in the analysis of glycolipids, which have a tendency to self-associate in solution.

We also synthesized a biotinylated derivative of HA_{12} using this strategy. We purified the crude product by running the reaction mixture through an AG1X2 resin-packed column. We analyzed the fractions by reading their absorbance in the region of 210−250 nm. The product was then loaded onto a streptavidin−agarose column in parallel with a control experiment where free HA_{12} (**1c**) was loaded onto a separate column. Eluate from the control column showed absorbance in the region of 210−250 nm, which is characteristic of a sugar. In contrast, the eluate from the experimental column gave a baseline absorbance in this range, indicating that the conjugate qualitatively bound to the column via biotin−streptavidin interactions.

We have demonstrated a facile synthetic approach for preparing HA derivatives. This approach generates a free aldehyde on HA that can readily react with equimolar amounts of lipids containing an amino functionality. This route is more efficient in comparison to the conjugation at the reducing end of the sugar. In addition, we can synthesize a series of conjugates containing even and odd number sugar residues, which can have potential significance in certain applications where oligomer length is critical. Although this approach is quite efficient, it seems to be more suited for small length oligomers because of the difficulty in controlling the side reaction (the fragmentation of the larger oligosaccharides) that is caused by ozone-assisted hydrolysis of the glycoside bonds. The HA−lipid conjugates thus generated are currently being evaluated for their properties as targeting ligands and also as potential candidates to mask the surface of the liposomes and microspheres from nonspecific interactions with biological proteins and cells.

ACKNOWLEDGMENT

We wish to thank Dr. Paul Ortiz de Montellano for generously allowing us to use the ozonator in his laboratory, Joshua Park for synthesizing BAP, and Michael S. Cohen for assistance in performing the NMR analysis. We thank Dr. Joon Sig Choi for preliminary studies on hyaluronate lyase digestion of HA. We gratefully acknowledge the financial support from the National Institutes of Health (GM61851-01A1) and the Department of Defense (DAMD17-01-1-0192). Thanks are also extended to the UCSF Mass Spectrometry Facility (A. L. Burlingame, Director) supported by NIH NCRR RR01614.

Supporting Information Available: Size exclusion profile, MALDI-TOF results, and ^1H NMR spectra. This material is available free of charge via the Internet at http://pubs.acs.org.

LITERATURE CITED

(1) Nettles, D. L., Vail, T. P., Morgan, M. T., Grinstaff, M. W., and Setton, L. A. (2004) Photocrosslinkable hyaluronan as a scaffold for articular cartilage repair. *Ann. Biomed. Eng. 32*, 391−397.

(2) Yun, Y. H., Goetz, D. J., Yellen, P., and Chen, W. (2004) Hyaluronan microspheres for sustained gene delivery and site-specific targeting. *Biomaterials 25*, 147−157.

(3) Kim, A., Checkla, D. M., Dehazya, P., and Chen, W. (2003) Characterization of DNA-hyaluronan matrix for sustained gene transfer. *J. Controlled Release 90*, 81−95.

(4) Luo, Y., Ziebell, M. R., and Prestwich, G. D. (2000) A hyaluronic acid-taxol antitumor bioconjugate targeted to cancer cells. *Biomacromolecule*s *1*, 208−218.

(5) Luo, Y., Bernshaw, N. J., Lu, Z. R., Kopecek, J., and Prestwich, G. D. (2002) Targeted delivery of doxorubicin by HPMA copolymer-hyaluronan bioconjugates. *Pharm. Res. 19*, 396−402.

(6) Peer, D., and Margalit, R. (2004) Loading mitomycin C inside long circulating hyaluronan targeted nano-liposomes increases its antitumor activity in three mice tumor models. *Int. J. Cancer 108*, 780−789.

(7) Peer, D., and Margalit, R. (2004) Tumor-targeted hyaluronan nanoliposomes increase the antitumor activity of liposomal doxorubicin in syngeneic and human xenograft mouse tumor models. *Neoplasia 6*, 343−353.

(8) Eliaz, R. E., and Szoka, F. C. (2001) Liposome-encapsulated doxorubicin targeted to CD44: a strategy to kill CD44-overexpressing tumor cells. *Cancer Res. 61*, 2592−2601.

(9) Harris, E. N., Weigel, J. A., and Weigel, P. H. (2004) Endocytic function, glycosaminoglycan specificity, and antibody sensitivity of the recombinant human 190-kDa hyaluronan receptor for endocytosis. *J. Biol. Chem. 279*, 36201−36209.

(10) Karst, N. A., and Linhardt, R. J. (2003) Recent chemical and enzymatic approaches to the synthesis of glycosaminoglycan oligosaccharides. *Curr. Med. Chem. 10*, 1993−2031.

(11) Oohira, A., Kushima, Y., Tokita, Y., Sugiura, N., Sakurai, K., Suzuki, S., and Kimata, K. (2000) Effects of lipid-derivatized glycosaminoglycans (GAGs), a novel probe for functional analyses of GAGs, on cell-to-substratum adhesion and neurite elongation in primary cultures of fetal rat hippocampal neurons. *Arch. Biochem. Biophys. 378*, 78−83.

(12) Sugiura, N., Sakurai, K., Hori, Y., Karasawa, K., Suzuki, S., and Kimata, K. (1993) Preparation of lipid-derivatized glycosaminoglycans to probe a regulatory function of the carbohydrate moieties of proteoglycans in cell-matrix interaction. *J. Biol. Chem. 268*, 15779−15787.

(13) Asayama, S., Nogawa, M., Takei, Y., Akaike, T., and Maruyama, A. (1998) Synthesis of novel polyampholyte comb-type copolymers consisting of a poly (L-lysine) backbone and hyaluronic acid side chains for a DNA carrier. *Bioconjugate Chem. 9*, 476−481.

(14) Calabro, A., Benavides, M., Tammi, M., Hascall, V. C., and Midura, R. J. (2000) Microanalysis of enzyme digests of hyaluronan and chondroitin/dermatan sulfate by fluorophore-assisted carbohydrate electrophoresis (FACE). *Glycobiology 10*, 273−281.

(15) Price, K. N., Tuinman, A., Baker, D. C., Chisena, C., and Cysyk, R. L. (1997) Isolation and characterization by electrospray-ionization mass spectrometry and high-performance anion-exchange chromatography of oligosaccharides derived from hyaluronic acid by hyaluronate lyase digestion: observation of some heretofore unobserved oligosaccharides that contain an odd number of units. *Carbohydr. Res. 303*, 303−311.

(16) Wang, Y., and Hollingsworth, R. I. (1995) A solvent system for the high-resolution proton nuclear magnetic resonance spectroscopy of membrane lipids. *Anal. Biochem. 225*, 242−251.

(17) Weingarten, S., and Thiem, J. (2003) Facile formation of novel carbohydrate-amino acid conjugates by reductive amination. *Synlett. 7*, 1052−1054.

(18) Wang, Y., Hollingsworth, R. I., and Kasper, D. L. (1998) Ozonolysis for selectively depolymerizing polysaccharides containing β-D-aldosidic linkages. *Proc. Natl. Acad. Sci. 95*, 6584−6589.

(19) Wang, Y., Hollingsworth, R. I., and Kasper, D. L. (1999) Ozonolytic depolymerization of polysaccharides in aqueous solution. *Carbohydr. Res. 319*, 141−147.

BC0600721

An Intramolecular Cyclization Reaction Is Responsible for the in Vivo Inefficacy and Apparent pH Insensitive Hydrolysis Kinetics of Hydrazone Carboxylate Derivatives of Doxorubicin

Cameron C. Lee,[†] Andrew T. Cramer,[†] Francis C. Szoka, Jr.,[‡] and Jean M. J. Fréchet*[,†]

Department of Chemistry, University of California, Berkeley, California 94720-1460, and Department of Pharmaceutical Chemistry, University of California, San Francisco, California 94143-0446. Received May 5, 2006; Revised Manuscript Received June 23, 2006

Contradictory reports concerning the pH sensitive hydrolysis kinetics of certain hydrazone carboxylates of doxorubicin have appeared in this journal (Kaneko et al., *Bioconjugate Chem.* **1991**, *2*, 133. Padilla De Jesús et al., *Bioconjugate Chem.* **2002**, *13*, 453). Since the pH stability of the drug−carrier linkage in macromolecular prodrugs has a significant bearing on pharmacological efficacy, the hydrolysis kinetics of low molecular weight and polymeric doxorubicin hydrazone carboxylates were therefore reinvestigated. As observed previously, the conjugates readily release native doxorubicin at pH 5. Unexpectedly, in neutral buffer the hydrazone carboxylate conjugates do not release native doxorubicin, but instead rapidly release a doxorubicin derivative substituted at C-9 by 3,6-dihydro-1,3,4-oxadiazin-2-one with first-order kinetics ($t_{1/2}$ = 2.5 h). The proposed intramolecular cyclization reaction involving doxorubicin's C-14 hydroxyl and the carboxylate-substituted hydrazone rationalizes the seemingly anomalous hydrolysis kinetics seen for hydrazone carboxylate linked doxorubicin, and provides a possible explanation for the poor antitumor activity exhibited by polymer−doxorubicin conjugates utilizing this specific type of linkage.

INTRODUCTION

Drug delivery systems for the potent antineoplastic doxorubicin commonly rely on the use of a cleavable linkage between drug and carrier so that the drug may access the cell nucleus (*1*), although nuclear localization is not a prerequisite for cytotoxicity (*2*). For tumor-targeted drug delivery to be most effective the drug should only be released once the drug carrier has localized within the diseased tissue, and therefore premature release of the drug while circulating in the serum must be minimized. Linkages based on enzymatically labile peptides or acid-labile amides and hydrazones are the most commonly utilized means of covalent attachment between doxorubicin and a carrier (*3*, *4*).

Hydrazones, formed by condensation of the C-13 ketone of doxorubicin with a hydrazide, have been used for attaching the drug to antibodies (*5*, *6*) and polymers (*7*, *8*). Hydrazones are hydrolytically labile, with hydrolysis occurring at an accelerated rate at acidic pH. Acid-triggered prodrug conversion can be beneficial for tumor targeted drug delivery because (a) the extracellular environment of many tumors is mildly acidic (*9*) and (b) delivery of doxorubicin via an endocytic pathway, which can overcome multidrug resistance, involves trafficking via mildly acidic endosomes and lysosomes (*10*). Willner (*6*) and Ulbrich (*8*) have studied the influence of hydrazide structure on the rate of doxorubicin hydrazone hydrolysis in some depth. Curiously, Willner reported that the hydrolysis kinetics of the doxorubicin hydrazone **1** derived from hydrazine carboxylate **2** (Scheme 1) lacked pH sensitivity, with the rates of doxorubicin release at pH 4.5, 5.0, and 7.4 being essentially identical. Such behavior was not observed for hydrazones prepared from an acyl hydrazide, a semicarbazide, or a thiosemicarbazide; the authors offered no explanation for this apparent anomaly. We recently utilized a hydrazone carboxylate linkage very similar to **1** for the conjugation of doxorubicin to the end groups of a PEO−polyester dendrimer hybrid **3** (Scheme 2) (*11*, *12*). While we too found that the hydrazone carboxylate was hydrolyzed at acidic pH, in contrast to Willner's observation we reported that very little hydrolysis occurred under neutral conditions; at the time we failed to notice the discrepancy between our and Willner's results.

Our attempts at chemotherapy utilizing the doxorubicin-functionalized PEO−polyester dendrimer hybrids **3** and **4** (Scheme 2) in murine subcutaneous tumor models (B16F10 and C26) were largely unsuccessful in spite of substantial intratumoral concentrations of both polymer and drug (*13*, *14*, *15*). Unable to explain this lack of antitumor efficacy, we reexamined our system and the literature, and upon further review of the literature (especially Willner's report) we became suspicious of the hydrazone carboxylate linkage. Strengthening this suspicion was our observation that chemotherapy with PEO−dendrimer hybrid **5** (Scheme 2) provided a significantly enhanced tumor response relative to **4** (unpublished results). In polymer **5**, doxorubicin was attached via acyl hydrazone linkages, while in polymer **4**, doxorubicin was attached via hydrazone carboxylate linkages. We therefore investigated the hydrolysis kinetics of hydrazone carboxylate linked and acyl hydrazone linked doxorubicin from the polymers.

The release of drug from polymers **4** and **5** at 37 °C was monitored chromatographically. Polymers were dissolved in pH 5.0 and 7.4 buffers, and aliquots of the solutions were removed periodically for chromatographic analysis. The hydrolysis product of polymer **5** at pH 5.0 eluted at 14.2 min, coeluting with a doxorubicin hydrochloride standard. Under these conditions, the concentration of free doxorubicin in solution increased steadily with the half-maximum reached between 4 and 6 h. Only a small amount (<5%) of the same compound was released after 48 h at pH 7.4, consistent with previous reports (*6*, *7*, *8*). For polymer **4**, two unresolved peaks were observed in the

* Corresponding author. Tel: (510) 643-3077. Fax: (510) 643-3079. E-mail: frechet@berkeley.edu.

[†] University of California, Berkeley.

[‡] University of California, San Francisco.

10.1021/bc060117y CCC: $33.50 © 2006 American Chemical Society
Published on Web 09/07/2006

Scheme 1. Hydrazone Carboxylate 1

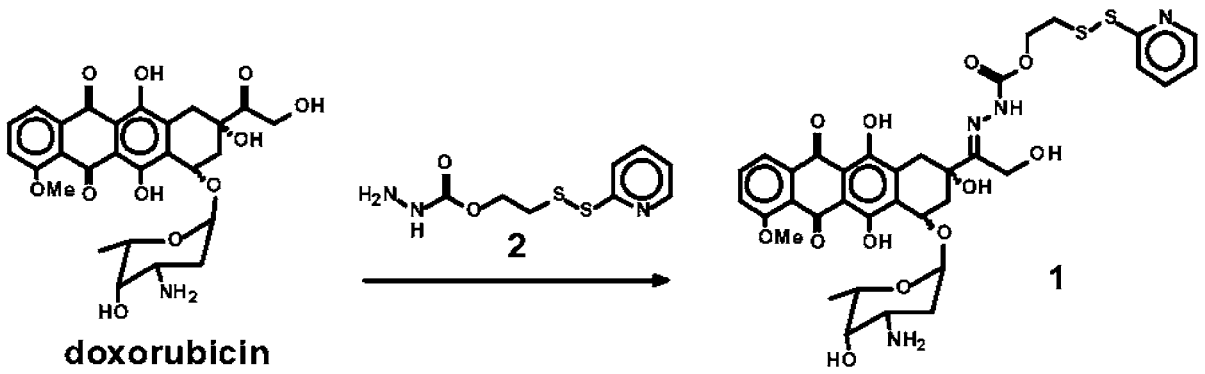

Scheme 2. Polymer−Doxorubicin Conjugates 3−5

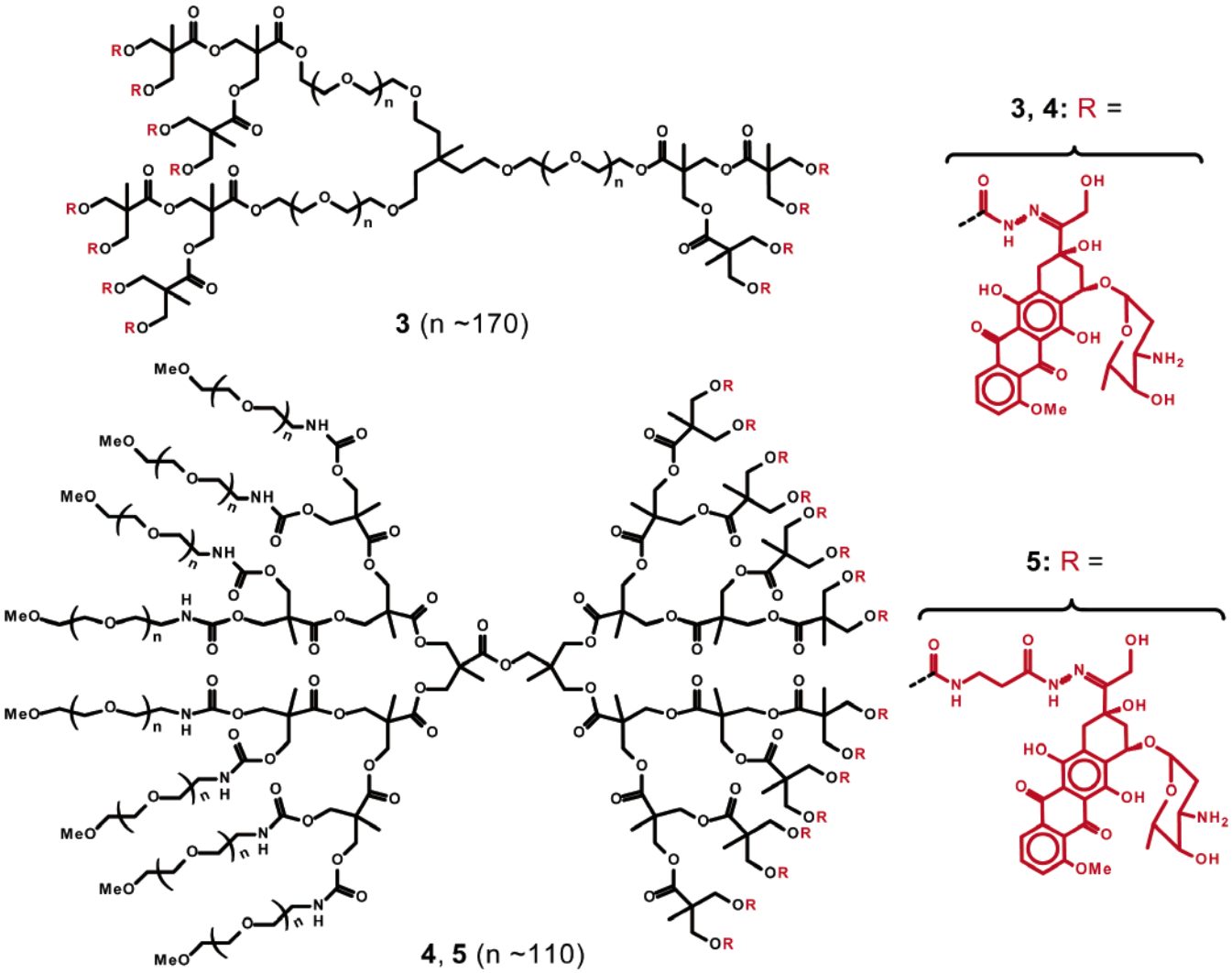

chromatogram during incubation at pH 5.0 (t_R = 14.2 min (major) and ~ 15 min (minor)), with the first peak coeluting with doxorubicin (Figure 1). The total peak area increased monotonically over time, reaching its half-maximum between 4 and 6 h. A single peak was observed upon incubation at pH 7.4, the elution time of which did not correspond to that of doxorubicin (t_R = 15.4). The area of this peak increased rapidly and reached its maximum value after 4 h, although the peak area decreased slowly over the next 48 h. We attribute the decrease in peak area to poor solubility of the released compound at pH 7.4, since we have also observed that doxorubicin hydrochloride is sparingly soluble in pH 7.4 phosphate buffers.

A quantity of the product eluting at 15.4 min suitable for characterization purposes was obtained by first synthesizing the hydrazone carboxylate **6**. As with **4**, conversion of compound **6** to the new product was >95% within 12 h upon incubation at 37 °C in a 100 mM NH_4OAc pH 7.0 buffer (the product remained soluble under these conditions). A plot of the area of **6** versus time determined chromatographically was best fit by a single inverse exponential function, indicating first-order reaction kinetics with a half-life of 2.5 h. The identity of the product was elucidated using mass spectrometry. The mass spectrum obtained was dominated by four major peaks at 584, 455, 437, and 419 *m*/*z*. We concluded that the highest mass peak was the singly protonated parent ion and was a doxorubicin

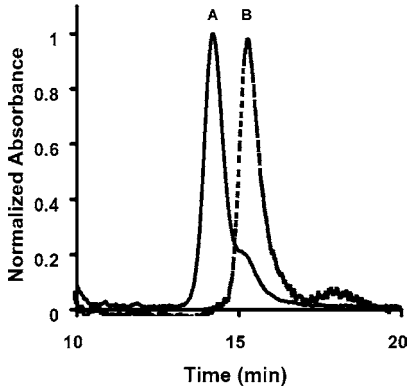

Figure 1. Normalized SEC chromatograms (λ_{abs} = 490 nm) for the products released from doxorubicin conjugate **4** after 24 h of incubation at 37 °C in aqueous solutions buffered at pH 5.0 (trace A) or pH 7.4 (trace B).

derivative, since the peaks at 455, 437, and 419 were 129, 147, and 165 *m*/*z* units below the parent ion, respectively, consistent with fragment ions resulting from the loss of daunosamine and two subsequent dehydrations. The parent ion is 40 mass units heavier than doxorubicin, and thus we have tentatively assigned its structure as a dihydrooxadiazinone cyclization product **7** resulting from intramolecular nucleophilic attack of the C-14 hydroxyl of doxorubicin on the carbonyl group of the hydrazone carboxylate linker (Scheme 3). Support for this type of reaction product is provided by a number of reports on the base-promoted cyclization of hydrazone carboxylates derived from α-hydroxy ketones (*16*, *17*, *18*).

Additional evidence for the dihydrooxadiazinone rearrangement product was provided by its ^{1}H NMR spectrum, which in most regards was identical to that of the starting material **6** but lacked the benzyl proton resonances and displayed a downfield shift of the C-14 methylene proton signal from 4.60 ppm in **6** (4.71 ppm in doxorubicin (*19*)) to 5.07 ppm in **7**, consistent with acylation of the C-14 hydroxyl. The absence of an upfield C-14 methylene proton resonance in the NMR spectrum of **7** indicates that the reaction was selective for the C-14 hydroxyl over the C-9 hydroxyl. This and the fact that the rearrangement occurs under such mild reaction conditions imply that the C-14 hydroxymethyl and carboxylate substituents of the imine are syn to each other in **4** and **6**, satisfying the geometrical requirements for nucleophilic attack by the C-14 hydroxyl (*16*, *18*). The cyclization selectivity seen for the primary hydroxyl of this α,α′-bishydroxyhydrazone is consistent with results reported by Kamernitskii et al. in their work with hydrazone derivatives of steroids with corticoid side chains (*17*). While the exclusive participation of the C-14 hydroxyl in this side reaction suggests that hydrazone carboxylate prodrugs of anthracyclines such as daunorubicin and idarubicin that lack C-14 hydroxyl groups would display normal hydrazone hydrolysis kinetics, rearrangement involving the C-9 hydroxyl to the spirocyclic dihydrooxadiazinone derivatives remains a possibility.

We contend that the dramatic difference in in vivo activity observed for the polymer−drug conjugates **4** and **5** can be explained by the relatively rapid loss of drug from **4** at physiological pH. If the drug is lost in transit before an effective dose of polymer−drug conjugate is delivered to the tumor, the targeting ability of the polymer is lost and the treatment rendered ineffective. While we have not explicitly determined the in vitro or in vivo activity of **7** alone, it is also possible that **7** is less potent than doxorubicin. However, even if **7** were an active chemotherapeutic, free doxorubicin (which is active in vitro against the tumor models utilized here) is not highly active against these tumor models in vivo without utilization of a carrier, and therefore, the rapidly released free **7** would likely be ineffective as well (*20*, *21*).

We believe that our previously published drug release results for polymer−drug conjugate **3** were affected by the analytical technique we had used (*12*). Our prior conclusions were based on data collected utilizing chromatographic conditions that may not be ideal for the analysis of doxorubicin. In the current study, we have used an acidic mobile phase for chromatography, which aids in the solubilization and elution of the hydrophobic and weakly basic drug doxorubicin; in contrast, our previous work made use of a neutral pH mobile phase. As doxorubicin is not as soluble in neutral phosphate buffers, it is possible that elution under neutral conditions could have led to strong retention or precipitation of doxorubicin within the column.

We also believe that Willner's previously published data for doxorubicin release from hydrazone carboxylate **1** at neutral pH may have been affected (*6*). While the release kinetics data may be accurate, the release rate reported at neutral pH probably represents the rate of release for the dihydrooxadiazinone cyclization product **7** derived from **1**, but not doxorubicin itself.

MATERIALS AND METHODS

Materials. Unless otherwise noted, reagents and solvents were obtained from commercial suppliers and used without further purification. Polymer **4** contained 9.25% doxorubicin by weight and was prepared as previously reported (*14*). Polymer **5** contained 9.94% doxorubicin by weight; its synthesis will be reported in a forthcoming publication.

Characterization. NMR spectra were recorded on a Bruker DRX 500 MHz instrument with MeOH as the internal standard (3.31 ppm). All chemical shifts are reported in parts per million.

Scheme 3. Intramolecular Cyclization of 6 to 7

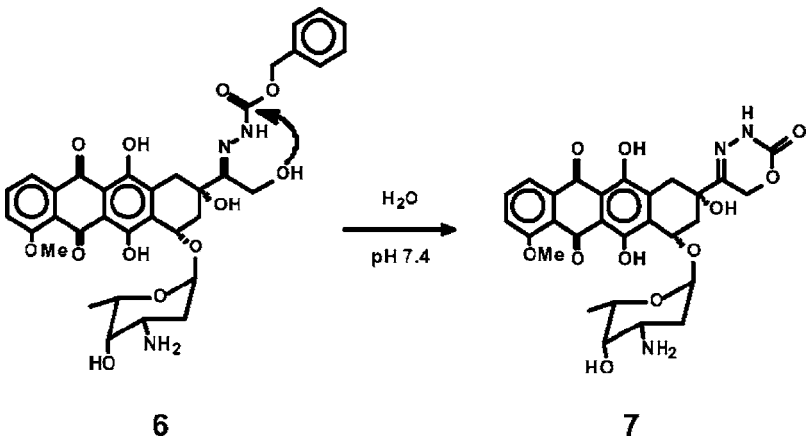

Low- and high-resolution electrospray ionization mass spectrometry (ESI-MS) was performed at the UC Berkeley Mass Spectrometry Facility and Stanford University Mass Spectrometry Laboratory, respectively.

Chromatography: Drug Release from Polymers 4 and 5. Release of drug from polymers **4** and **5** at 37 °C was measured with an HPLC system composed of a Waters 2695 separations module (sample compartment maintained at 37.0 ± 3.0 °C), a Waters 996 photodiode array detector (λ = 490 nm), and a Shodex OHpak SB-804 HQ SEC column. An isocratic flow rate of 1.0 mL/min was used with a mobile phase composed of 70%/30%/0.05% water/acetonitrile/formic acid ($t_{R,DOX}$ = 14.2 min). Polymer−drug conjugates were dissolved at concentrations of 1.0 mg/mL in aqueous solutions buffered at pH 5.0 (50 mM acetate) and pH 7.4 (50 mM phosphate). Analysis commenced immediately after dissolution utilizing the above HPLC method with samples (25 μL) withdrawn periodically over a period of 48 h.

Chromatography: Drug Release from Compound 6. The conversion of **6** to **7** at 37 °C was measured with an HPLC system composed of a Waters 2695 separations module (sample compartment maintained at 37.0 ± 3.0 °C), a Waters 996 photodiode array detector (λ = 490 nm), and a Waters Symmetry C18 column (3.5 μm, 2.1 × 150 mm). The following HPLC method was employed at a flow rate of 0.3 mL/min ($t_{R,6}$ = 12.9 min, $t_{R,7}$ = 8.9 min): 0−5 min, linear gradient of 100:0.05 water:formic acid to 70:30:0.05 water:acetonitrile:formic acid; 5−15 min, held at 70:30:0.05 water:acetonitrile:formic acid; 15−18 min, linear gradient of 70:30:0.05 water:acetonitrile:formic acid to 100:0.05 water:formic acid. Hydrazone **6** was dissolved in distilled water (0.16 mg/mL) and diluted with an equal volume of 100 mM aqueous NH_4OAc (pH = 7.0). Analysis commenced immediately utilizing the above HPLC method with samples (25 μL) withdrawn periodically over a period of 16 h.

Benzyloxycarbonyl Hydrazone of Doxorubicin (6). Doxorubicin hydrochloride (5 mg, 9 μmol), trifluoroacetic acid (1 μL, 11 μmol), and an excess of benzyloxycarbonyl hydrazide trifluoroacetate (∼30 mg, ∼ 108 μmol) were combined in anhydrous methanol (0.5 mL) and stirred in the dark at rt overnight. The product was precipitated upon addition of diethyl ether, and the resulting red solid was isolated by gravity filtration and washed with more diethyl ether. The product was extracted from the filter paper with methanol and concentrated in vacuo to yield the product as a red solid (5 mg, 70%). ^{1}H NMR (500 MHz, CD_3OD, δ): 1.29 (d, J = 6.5 Hz, 3H), 1.88 (dd, J_1 = 4.0 Hz, J_2 = 12.7 Hz, 1H), 2.02 (dt, J_1 = 4.0 Hz, J_2 = 12.7 Hz, 1H), 2.37 (br m, 2H), 3.12 (br m, 2H), 3.55 (m, 1H), 3.64 (br s, 1H), 4.01 (s, 3H), 4.25 (m, 1H), 4.60 (AB, J = 15 Hz, 2H), 5.15 (br s, 1H), 5.21 (s, 2H), 5.45 (br s, 1H), 7.2−7.5 (m, 5H), 7.54 (d, J = 8.3 Hz, 1H), 7.81 (t, J = 8.3 Hz, 1H), 7.93 (d, J = 8.3 Hz, 1H). MS-ESI m/z (relative intensity): 692 (100%), 563 (24%), 545 (42%).

9-Dihydrooxadiazinone Doxorubicin (7). Hydrazone **6** was dissolved in distilled water (1.6 mg/mL), diluted with an equal volume of 100 mM aqueous NH_4OAc (pH = 7.0), and stirred in the dark at 37 °C for 24 h (at this concentration, some of the product precipitated from solution during the course of the reaction). The reaction mixture was then frozen and lyophilized. The red solid that remained was dissolved in a small amount of methanol, precipitated from diethyl ether, and isolated by centrifugation. ^{1}H NMR (500 MHz, CD_3OD, δ): 1.31 (d, J = 6.5 Hz, 3H), 1.87 (dd, J_1 = 3.8 Hz, J_2 = 12.6 Hz, 1H), 2.02 (dt, J_1 = 3.8 Hz, J_2 = 12.6 Hz, 1H), 2.30−2.45 (m, 2H), 3.10 (br s, 2H), 3.52 (m, 1H), 3.65 (br s, 1H), 4.02 (s, 3H), 4.24 (m, 1H), 5.07 (br s, 2H), 5.12 (br s, 1H), 5.47 (br s, 1H), 7.56 (d, J = 7.9 Hz, 1H), 7.83 (t, J = 7.9 Hz, 1H), 7.93 (d, J = 7.9 Hz, 1H). MS-ESI m/z (relative intensity): 584 (13%), 455 (6%), 437 (100%), 419 (21%). HRMS-ESI: $[M + H]^+$ calcd for $C_{28}H_{30}N_3O_{11}$ 584.1880, found 584.1869; $[M + Na]^+$ calcd for $C_{28}H_{29}N_3O_{11}Na$ 606.1700, found 606.1699.

ACKNOWLEDGMENT

Financial support of this research by the National Institutes of Health (GM 65361 and EB 002047) is acknowledged with thanks.

LITERATURE CITED

(1) Kratz, F., Warnecke, A., Schmid, B., Chung, D. E., and Gitzel, M. (2006) Prodrugs of anthracyclines in cancer chemotherapy. *Curr. Med. Chem. 13*, 477−523.

(2) Tritton, T. R., and Yee, G. (1982) The anticancer agent adriamycin can be actively cytotoxic without entering cells. *Science 217*, 248−250.

(3) Kratz, F., Beyer, U., and Schütte, M. T. (1999) Drug-polymer conjugates containing acid-cleavable bonds. *Crit. Rev. Ther. Drug Carrier Syst. 16*, 245−288.

(4) Ulbrich, K., and Šubr, V. (2004) Polymeric anticancer drugs with pH-controlled activation. *Adv. Drug Delivery Rev. 56*, 1023−1050.

(5) Greenfield, R. S., Kaneko, T., Daues, A., Edson, M. A., Fitzgerald, K. A., Olech, L. J., Grattan, J. A., Spitalny, G. L., and Braslawsky, G. R. (1990) Evaluation in vitro of adriamycin immunoconjugates synthesized using an acid-sensitive hydrazone linker. *Cancer Res. 50*, 6600−6607.

(6) Kaneko, T., Willner, D., Monkovíc, I., Knipe, J. O., Braslawsky, G. R., Greenfield, R. S., and Vyas, D. M. (1991) New hydrazone derivatives of adriamycin and their immunoconjugates—a correlation between acid stability and cytotoxicity. *Bioconjugate Chem. 2*, 133−141.

(7) Rodrigues, P. C. A., Beyer, U., Schumacher, P., Roth, T., Fiebig, H. H., Unger, C., Messori, L., Orioli, P., Paper, D. H., Mülhaupt, R., and Kratz, F. (1999) Acid-sensitive polyethylene glycol conjugates of doxorubicin: Preparation, in vitro efficacy and intracellular distribution. *Bioorg. Med. Chem. Lett. 7*, 2517−2524.

(8) Etrych, T., Chytil, P., Jelínková, M., Říhová, B., and Ulbrich, K. (2002) Synthesis of HPMA copolymers containing doxorubicin bound via a hydrazone linkage. Effect of spacer on drug release and in vitro cytotoxicity. *Macromol. Biosci. 2*, 43−52.

(9) Gerweck, L. E., and Seetharaman, K. (1996) Cellular pH gradient in tumor versus normal tissue: Potential exploitation for the treatment of cancer. *Cancer Res. 56*, 1194−1198.

(10) Nori, A., and Kopecek, J. (2005) Intracellular targeting of polymer-bound drugs for cancer chemotherapy. *Adv. Drug Delivery Rev. 57*, 609−636.

(11) Ihre, H. R., Padilla de Jesús, O. L., Szoka, F. C., and Fréchet, J. M. J. (2002) Polyester dendritic systems for drug delivery applications: Design, synthesis, and characterization. *Bioconjugate Chem. 13*, 443−452.

(12) Padilla de Jesús, O. L., Ihre, H. R., Gagne, L., Fréchet, J. M. J., and Szoka, F. C. (2002) Polyester dendritic systems for drug delivery applications: In vitro and in vivo evaluation. *Bioconjugate Chem. 13*, 453−461.

(13) Padilla de Jesús, O. L. (2003) Ph.D. Dissertation, University of California, Berkeley, CA.

(14) Gillies, E. R. (2004) Ph.D. Dissertation, University of California, Berkeley, CA.

(15) Gillies, E. R., Dy, E., Fréchet, J. M. J., and Szoka, F. C. (2005) Biological evaluation of polyester dendrimer:poly(ethylene oxide) "bow-tie" hybrids with tunable molecular weight and architecture. *Mol. Pharm. 2*, 129−138.

(16) Rosenblum, M., Nayak, V., DasGupta, S. K., and Longroy, A. (1963) Synthesis of dihydrooxadiazinones and study of geometrical isomerism in α-ketol carbethoxyhydrazones. *J. Am. Chem. Soc. 85*, 3874−3878.

(17) Kamernitskii, A. V., Turuta, A. M., Korobov, A. A., and Istomina, Z. I. (1987) Transformation of corticoid side-chain of steroids into 1′,3′,4′-oxadiazine ring E. *Russ. Chem. Bull. 36*, 161−163.

(18) Kamernitskii, A. V., Turuta, A. M., Istomina, Z. I., and Korobov, A. A. (1987) Alkaline cyclization of carboethoxyhydrazones of 21-

hydroxy-20-ketosteroids to 17-β-(1′,3′,4′-oxadiazin-2′-ones) and its correlation with the geometry of the hydrazone fragment. *Russ. Chem. Bull. 36*, 173−175.

(19) McLennan, I. J., Lenkinski, R. E., and Yanuka, Y. (1985) A nuclear magnetic resonance study of the self-association of adriamycin and daunomycin in aqueous solution. *Can. J. Chem. 63*, 1233−1238.

(20) Huang, S. K., Mayhew, E., Gilani, S., Lasic, D. D., Martin, F. J., and Papahadjopoulos, D. (1992) Pharmacokinetics and therapeutics of sterically stabilized liposomes in mice bearing C-26 colon carcinoma. *Cancer Res. 52*, 6774−6781.

(21) Seymour, L. W., Ulbrich, K., Steyger, P. S., Brereton, M., Subr, V., Strohalm, J., and Duncan, R. (1994) Tumor tropism and anticancer efficacy of polymer-based doxorubicin prodrugs in the treatment of subcutaneous murine B16F10 melanoma. *Br. J. Cancer 70*, 636−641.

BC060117Y

NOVEMBER/DECEMBER 2006
Volume 17, Number 6

© *Copyright 2006 by the American Chemical Society*

Bioconjugate Chemistry

COMMUNICATIONS

PEG-Assisted DNA Solubilization in Organic Solvents for Preparing Cytosol Specifically Degradable PEG/DNA Nanogels

Hyejung Mok and Tae Gwan Park*

Department of Biological Sciences, Korea Advanced Institute of Science and Technology, Daejeon, 305-701, Korea. Received May 6, 2006; Revised Manuscript Received September 26, 2006

DNA was dissolved in selected organic solvents in the presence of poly(ethylene glycol) (PEG). Nanoscale PEG/DNA complex (∼100 nm) was produced in dimethylsulfoxide (DMSO) phase. Using a thiol-functionalized six-arm branched PEG for DNA solubilization, the PEG/DNA nanocomplex was cross-linked through the formation of disulfide linkages between the thiol groups, resulting in the production of stable PEG/DNA nanogels in aqueous solution. DNA release from the nanogels could be modulated by changing the concentration of an external reducing agent. The released plasmid DNA from the nanogels maintained intact structural integrity and exhibited appreciable gene transfection efficiency. The PEG/DNA nanogels could be potentially applied for gene therapy including DNA vaccination.

DNA is a highly charged macromolecule that is extremely difficult to solubilize in organic solvents. The direct solubilization of DNA in organic solvents is expected to broaden its therapeutic and diagnostic applications such as gene therapy and DNA-based sensing (*1, 2*). Cationic amphiphiles such as lipids, polymers, and surfactants have been commonly used to solubilize DNA in organic solvents by forming polyelectrolyte complex nanoparticles (*3*−*5*). Negatively charged DNA upon addition of positively charged amphiphile molecules is condensed by electrostatic interactions, and the resultant complex nanoparticles with hydrophobic ion-pairing could be solubilized to some extent in various organic solvents. DNA/cation complex nanoparticles formed in an aqueous solution have been widely used to transfer exogenous genes to cells via endocytosis (*6*−*12*). Use of chemically modified and synthesized cationic lipids and polymers as nonviral gene carriers still has serious cytotoxic problems in clinical applications, although they are much safer than their viral counterparts (*13*). In this communication, we demonstrate that nonionic and biocompatible poly(ethylene glycol) (PEG) can make DNA soluble in selected polar organic solvents by forming a nanoscale complex, probably resulting from hydrogen bonding between DNA and PEG. A thiol-functionalized multiarm PEG derivative was used to solubilize DNA in an organic solvent and to produce cross-linked PEG/DNA complex nanogels applicable for gene therapy. The resultant thiol-cross-linked PEG nanogels encapsulating plasmid DNA released DNA only in a reduced condition, such as an intracellular environment, by cleaving the S−S linkage.

To solubilize DNA in organic solvents, green fluorescent protein (GFP) plasmid DNA or salmon sperm DNA was desalted by ethanol precipitation (*14*). Varying amounts of PEG (Mw 3350) were mixed with 1 mg of salmon sperm DNA in deionized water and then freeze-dried. The lyophilized PEG/DNA mixture was dissolved in various organic solvents at a PEG/DNA weight ratio of 15. As shown in Figure 1a, it can be

* Corresponding author. Tel: +82-42-869-2621; fax: +82-42-869-2610. E-mail address: tgpark@kaist.ac.kr (T.G. Park).

10.1021/bc060119i CCC: $33.50 © 2006 American Chemical Society
Published on Web 10/27/2006

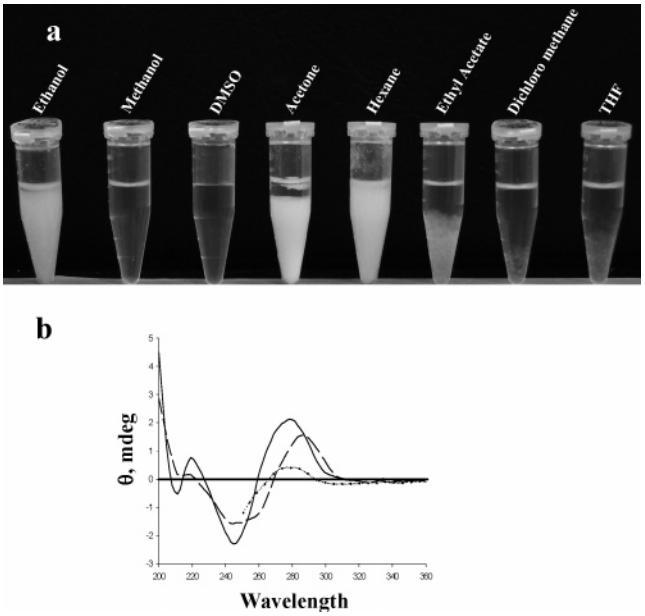

Figure 1. (a) Photograph of DNA solubilization in various organic solvents. (b) Circular dichroism spectra of plasmid DNA in DW (solid line), PEG/plasmid DNA complex (weight ratio PEG/DNA = 15) in DMSO (dotted line), and PEG/plasmid DNA in methanol (dashed line).

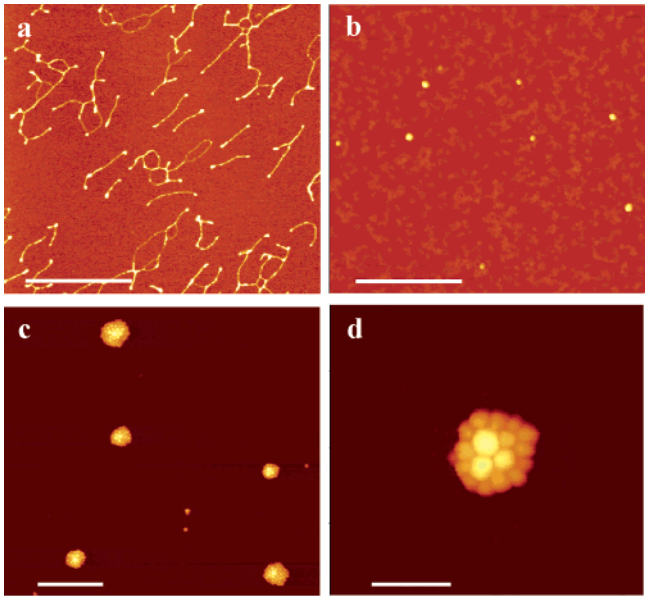

Figure 2. AFM images of (a) plasmid DNA in water, (b) PEG/DNA nanocomplex (PEG/DNA weight = 15) in DMSO, and (c,d) cross-linked PEG/DNA nanogels in water. Scale bars: (a−c) = 1 μm, (d) = 250 nm.

seen that DNA exhibits different extents of solubilization depending on organic solvents, but it is completely dissolved in methanol, dimethylsulfoxide (DMSO), and dimethylformamide (DMF). The DNA solubility in DMSO was determined by measuring the concentration of DNA in the supernatant after centrifugation at 14 000 rpm. Since the PEG/DNA nanocomplexes were spontaneously formed in DMSO without showing any turbidity, they could not be spun down. As shown in Figures S1−2 (Supporting Information), almost 100% transmittance and 100% solubility values were attained for PEG/DNA nanocomplexes dispersed in DMSO. When testing the effect of PEG/DNA weight ratio on the DNA solubilization in DMSO, the transmittance value reached 97.1 ± 1.0% at a PEG/DNA weight ratio of 5. Thus, we defined that plasmid DNA was soluble in a state of nanoparticulate in the DMSO phase. In circular dichroism (CD) spectra as shown in Figure 1b, it can be seen that a positive ellipticity peak of plasmid DNA solubilized in DMSO and methanol exhibits a red-shift while maintaining a duplex helical structure, indicating that DNA in organic solvents was in a highly compacted and collapsed state (*3*, *15*).

The state of DNA in the DMSO phase was visualized with atomic force microscopy. Figure 2a,b shows the conformation of DNA in water and DMSO in the presence of PEG (PEG/DNA weight ratio = 15), respectively. Figure S3 (Supporting Information) shows DNA conformation in DMSO at the PEG/DNA weight ratio of 1. Plasmid DNA in water is in a relaxed and stretched form with a contour length of ∼1 μm in water, but in DMSO containing PEG, it is collapsed and dispersed in a nanoscale of ∼100 nm. PEG is known to condense protein or DNA in an aqueous solution when PEG is added at a higher concentration above 7 w/v % (*16*, *17*). The effect of concentrated PEG on the DNA condensation in the aqueous phase occurs mainly via dehydrating water molecules from dissolved DNA, which results in DNA aggregation and precipitation. In this work, co-lyophilized PEG and salt-free DNA were dissolved together in an organic DMSO phase to produce individually well dispersed PEG/DNA complex nanoparticles. This indicates that the shrunken and compact DNA conformation in DMSO is likely due to the formation of hydrogen bonding between PEG and DNA. Previously, it was reported that nonionic polymers such as poly(*N*-vinylpyrrolidone) could interact with DNA by hydrogen bonding to form complex nanoparticles in an aqueous solution (*18*, *19*). It is conceivable that an oxygen atom in the ether linkage of the PEG chain can interact with −NH in the base of DNA by hydrogen bonding in an aprotic solvent such as DMSO. When redissolved in water, DNA regained its original conformation and stretched form as shown in Figure 2a, suggesting that water molecules broke up the hydrogen bonds between PEG and DNA. To prepare stable PEG nanogels containing DNA inside, a thiol-functionalized six-arm branched PEG derivative was used to condense plasmid DNA in DMSO, and then −SH groups present in the PEG/DNA nanocomplex were covalently cross-linked by a maleimide-functionalized crossinker, dithio-bis-maleimidoethane (DTME) (Scheme 1). Although air-induced and/or DMSO-induced oxidation of thiol groups also resulted in the disulfide cross-linking reaction (*20*, *21*), a bifunctional DTME cross-linker was used to facilitate the formation of PEG/DNA nanogels with more controllable cross-linking density. Plasmid DNA containing polyelectrolyte complex nanoparticles (polyplexes) cross-linked with disulfide bonds that are cleavable to cytosolic reductive conditions have been reported previously (*22*, *23*). The polyplexes formed between DNA and cationic polymers bearing −SH groups were cross-linked via disulfide linkages to stabilize the structure for improve gene transfection efficiency. In this study, plasmid DNA was first condensed with a thiol-functionalized multiarm PEG to form polyplexes in organic solvent and then free −SH groups in PEG cross-linked to form stable plasmid DNA encapsulating PEG nanogels in an aqueous solution without using any cytotoxic polycationic condensing agents.

The resultant PEG/DNA nanogels were spherical and very stable in aqueous solution (Figure 2c,d and Figure S4 (Supporting Information)). When the molar ratio of DTME/PEG-SH was adjusted at 15, the average size was 315.4 ± 91.3 nm (polydispersity 0.12 ± 0.06) and the surface charge value was −16.3 ± 2.8 mV, as determined by dynamic light scattering method. Under this condition, about 80% of the −SH groups were cross-linked as analyzed with Ellman's assay for free thiol groups (21.6 ± 13.6%). The amount of encapsulated DNA in the PEG nanogels was 5.3 ± 0.9% (w/w). The size of −S−S− cross-linked PEG nanogels could be readily controlled by varying the molar ratio of DTME/PEG-SH (Figure 3a).

Scheme 1. Schematic of PEG-assisted DNA Solubilization in Organic Solvent and Preparation of PEG/DNA Nanogels[a]

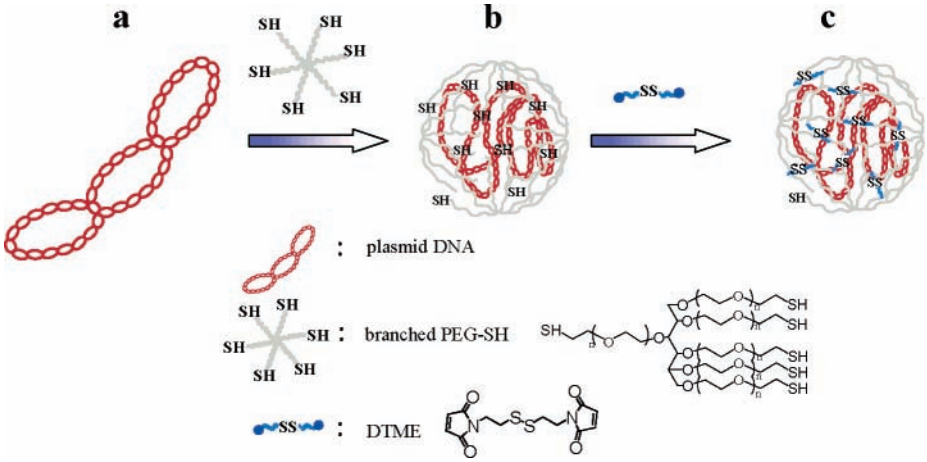

(a) Plasmid DNA in water; (b) PEG/DNA nanocomplex in DMSO; and (c) stable DTME cross-linked PEG/DNA nanogel in water.

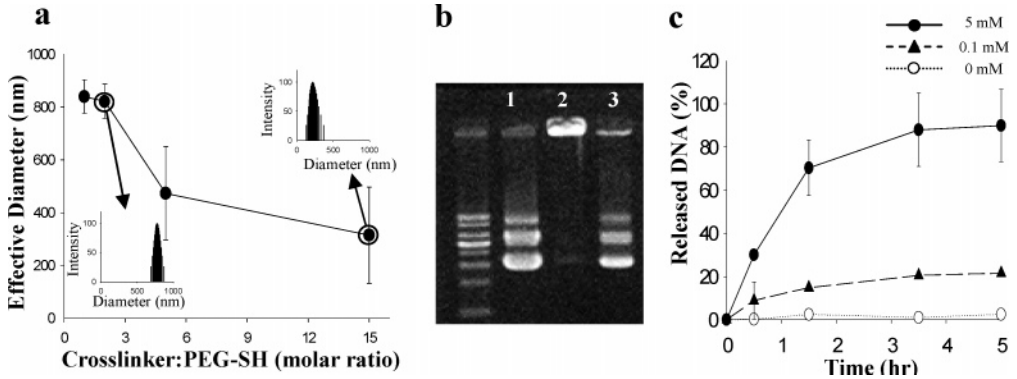

Figure 3. (a) Diameter of PEG nanogels at various molar concentrations of cross-linker, (b) gel retardation assay, and (c) DNA release profiles from PEG nanogels at various GSH concentrations of 0 (○), 0.1 (▲), and 5 (●) mM.

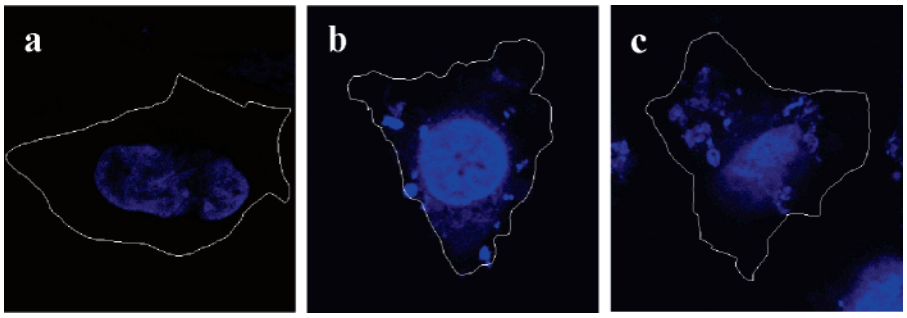

Figure 4. Confocal microscopy images of uptaken PEG nanogels within HeLa cells after (a) 0 h, (b) 1 h, and (c) 5 h post-transfection.

To prove that plasmid DNA was indeed encapsulated within cross-linked PEG nanogels, gel retardation assay was performed before and after treating a reducing agent, 100 mM dithiothreitol (DTT). Figure 3b shows that DNA encapsulated within PEG nanogels is primarily located in the loading zone (lane 2), but after treating with DTT for cleaving −S−S− linkage, supercoiled, circular, and linear DNA fractions appear in an intact form in the agarose gel (lane 3), in the same manner as those of naked plasmid DNA (lane 1). This suggests that no structural and conformational damage to DNA occurred during encapsulation, cross-linking, and degradation processes of PEG nanogels. To examine whether the PEG/DNA nanogels were degradable in an intracellular reduced environment where the concentration of glutathione (GSH) is maintained at 1−8 mM (*24*), they were exposed to 5 mM of glutathione (GSH). Figure 3c exhibits DNA release profiles from PEG/DNA nanogels at GSH concentrations of 0 (open circle), 0.1 (closed triangle), and 5 mM (closed circle). At a GSH concentration of 5 mM, the PEG nanogels released the encapsulated DNA almost completely after 4 h incubation. In contrast, at lower GSH concentrations, they were very stable without releasing DNA. This suggests that, in an extracellular condition, PEG/DNA nanogels maintained their structural integrity, but in a reductive cytosolic environment, they completely degraded and dissolved with subsequent release of entrapped DNA in the cytosol.

To prove that plasmid DNA was released from PEG nanogels in an intracellular environment, PEG/DNA nanogels were transfected to HeLa cells. To enhance the extent of cellular uptake, a positively charged KALA peptide was coated on the surface. The KALA peptide has a fusogenic effect to induce destabilization of endosomal membrane after endocytosis (*19*). To visualize DNA within the cells, intracellular DNA was stained with DAPI (4′,6-diamidino-2-phenylindole) dye, a double-strand DNA-specific marker. As shown in Figure 4, DNA is still collapsed after 1 h, but it appears to be more diffusive after 5 h in a cytosol area. This indicates that DNA release from PEG nanogels can be modulated in response to a reductive cellular environment. The transfected cells exhibited

appreciable GFP protein expression as shown in Figure S5 (Supporting Information), but the level of GFP transfection efficiency was still lower than those of commercially available transfection agents (Lipofectamine or PEI-based formulations). Thus, PEG/DNA nanogels would be usefully applied for locally delivering naked DNA in ischemic, muscular, and mucosal tissue sites. Naked plasmid DNA has been successfully administered to those tissues to treat various genetic diseases (*25*).

In conclusion, we demonstrate for the first time that plasmid DNA can be solubilized in selected polar organic solvents in the presence of PEG without using cationic polymers and surfactants. PEG-assisted DNA solubilization in organic solvents enabled plasmid DNA to be encapsulated within degradable PEG nanogels cross-linked via disulfide linkages. DNA release from the nanogels could be triggered upon exposure to reductive environments. The current formulation strategy of DNA is expected to have a wide range of applications for gene therapy including DNA vaccine.

ACKNOWLEDGMENT

This study was supported by the National Research Laboratory program from the Ministry of Science and Technology, Republic of Korea.

Supporting Information Available: Detailed materials and methods. This material is available free of charge via the Internet at http://pubs.acs.org.

LITERATURE CITED

(1) Li, X., Gartner, Z. J., Tse, B. N., and Liu, D. R. (2004) Translation of DNA into synthetic N-acyloxazolidines. *J. Am. Chem. Soc. 126*, 5090−5092.

(2) Nam, J. M., Park, S. J., and Mirkin, C. A. (2002) Bio-barcodes based on oligonucleotide-modified nanoparticles. *J. Am. Chem. Soc. 124*, 3820−3821.

(3) Ganguli, M., Jayachandran, K. N., and Maiti, S. (2004) Nanoparticles from cationic copolymer and DNA that are soluble and stable in common organic solvents. *J. Am. Chem. Soc. 126*, 26−27.

(4) Bromberg, L. E., and Klibanov, A. M. (1994) Detergent-enabled transport of proteins and nucleic acids through hydrophobic solvents. *Proc. Natl. Acad. Sci. U.S.A. 91*, 143−147.

(5) Sergeyev, V. G., Pyshkina, O. A., Lezov, A. V., Mel'nikov, A. B., Ryumtwev, E. I., Zezin, A. B.m and Kabanov, V. A. (1999) DNA complexed with oppositely charged amphiphile in low-polar organic solvents. *Langmuir 15*, 4434−4440.

(6) Jeong, J. H., Kim, S. H., Kim, S. W., and Park, T. G. (2005) Polyelectrolyte complex micelles composed of c-raf antisense oligodeoxynucleotide-poly(ethylene glycol) conjugate and poly(ethylenimine): effect of systemic administration on tumor growth. *Bioconjugate Chem. 16*, 1034−1037.

(7) Jeong, J. H., Lee, M., Kim, W. J., Yockman, J. W., Park, T. G., Kim, Y. H., and Kim, S. W. (2005) Anti-GAD antibody targeted non-viral gene delivery to islet beta cells. *J. Controlled Release 107*, 562−570.

(8) Kim, S. H., Mok, H., Jeong, J. H., Kim, S. W., and Park, T. G. (2006) Comparative evaluation of target-specific GFP gene silencing efficiencies for antisense ODN, synthetic siRNA, and siRNA plasmid complexed with PEI-PEG-FOL conjugate. *Bioconjugate Chem. 17*, 241−244.

(9) Chittimalla, C., Zammut-Italiano, L., Zuber, G., and Behr, J. P. (2005) Monomolecular DNA nanoparticles for intravenous delivery of genes. *J. Am. Chem. Soc. 127*, 11436−11441.

(10) Vinogradov, S. V., Batrakova, E. V., and Kabanov, A. V. (2004) Nanogels for oligonucleotide delivery to the brain. *Bioconjugate Chem. 15*, 50−60.

(11) McAllister, K., Sazani, P., Adam, M., Cho, M. J., Rubinstein, M., Samulski, R. J., and DeSimone, J. M. (2002) Polymeric nanogels produced via inverse microemulsion polymerization as potential gene and antisense delivery agents. *J. Am. Chem. Soc. 124*, 15198−15207.

(12) Akinc, A., Lynn, D. M., Anderson, D. G., and Langer, R. (2003) Parallel synthesis and biophysical characterization of a degradable polymer library for gene delivery. *J. Am. Chem. Soc. 125*, 5316−5323.

(13) Kunath, K., von Harpe, A., Fischer, D., Petersen, H., Bickel, U., Voigt, K., and Kissel, T. (2003) Low-molecular-weight polyethylenimine as a non-viral vector for DNA delivery: comparison of physicochemical properties, transfection efficiency and in vivo distribution with high-molecular-weight polyethylenimine. *J. Controlled Release 89*, 113−125.

(14) Liang, H., Harries, D., and Wong, G. C. (2005) Polymorphism of DNA-anionic liposome complexes reveals hierarchy of ion-mediated interactions. *Proc. Natl. Acad. Sci. U.S.A. 102*, 11173−11178.

(15) Burton, P. D. and Marcos, F. M. (1973) Experimental differential light-scattering correction to the circular dichroism of bacteriophage T2. *Proc. Natl. Acad. Sci. U.S.A. 70*, 255−259.

(16) Goodrich, G. P., Helfrich, M. R., Overberg, J. J., and Keating, C. D. (2004) Effect of macromolecular crowding on DNA:Au nanoparticle bioconjugate assembly. *Langmuir 20*, 10246−10251.

(17) Lerman, L. S. (1971) A transition to a compact form of DNA in polymer solutions. *Proc. Nat. Acad. Sci. U.S.A. 68*, 1886−1890.

(18) Mumper, R. J., Duguid, J. G., Anwer, K., Barron, M. K., Nitta, H., and Rolland, A. P. (1996) Polyvinyl derivatives as novel interactive polymers for controlled gene delivery to muscle. *Pharm. Res. 13*, 701−709.

(19) Lim, D. W., Yeom, Y. I., and Park, T. G. (2000) Poly(DMAEMA-NVP)-b-PEG-galactose as gene delivery vector for hepatocytes. *Bioconjugate Chem. 11*, 688−695.

(20) Yiannios, C. N., and Karabinos, J. V. (1963) Oxidation of thiols by dimethyl sulfoxide. *J. Org. Chem. 28*, 3246−3248.

(21) Tam, J. P., Wu, C., Liu, W., and Zhang, J. (1991) Disulfide bond formation in peptides by dimethyl sulfoxide. Scope and applications. *J. Am. Chem. Soc. 113*, 6657−6662.

(22) Miyata, K., Kakizawa, Y., Nishiyama, N., Harada, A., Yamasaki, Y., Koyama, H., and Kataoka, K. (2004) Block catiomer polyplexes with regulated densities of charge and disulfide cross-linking directed to enhance gene expression. *J. Am. Chem. Soc. 126*, 2355−2361.

(23) Kakizawa, Y., Harada, A., and Kataoka, K. (1999) Environment-sensitive stabilization of core-shell structured polyion complex micelle by reversible cross-linking of the core through disulfide bond. *J. Am. Chem. Soc. 121*, 11247−11248.

(24) Okamoto, T., Akaike, T., Sawa, T., Miyamoto, Y., van der Vliet, A., and Maeda, H. (2001) Activation of matrix metalloproteinases by peroxynitrite-induced protein S-glutathiolation via disulfide S-oxide formation. *J. Biol. Chem. 276*, 29596−29602.

(25) Jia, Z., and Danko, I. (2005) Long-term correction of hyperbilirubinemia in the gunn rat by repeated intravenous delivery of naked plasmid DNA into muscle. *Mol. Ther. 12*, 860−866.

BC060119I

Bionanoconjugation via Click Chemistry: The Creation of Functional Hybrids of Lipases and Gold Nanoparticles

Jennifer L. Brennan,[†,⊥] Nikos S. Hatzakis,[‡] T. Robert Tshikhudo,[†] Nijole Dirvianskyte,[§] Valdemaras Razumas,[§] Shamkant Patkar,[∥] Jesper Vind,[∥] Allan Svendsen,[∥] Roeland J. M. Nolte,[‡] Alan E. Rowan,*[,‡] and Mathias Brust*[,†]

Centre for Nanoscale Science, Department of Chemistry, University of Liverpool, Liverpool, L69 7ZD, U.K., Institute for Molecules and Materials, Radboud University Nijmegen, Toernooiveld 1, 6525 ED Nijmegen, The Netherlands, Institute of Biochemistry, Mokslininku 12, LT-08662 Vilnius, Lithuania, and Novozymes A/S, Smørmosevej 25, DK-2880, Bagsvaerd, Denmark. Received April 21, 2006; Revised Manuscript Received July 31, 2006

A simple and versatile method for the preparation of functional enzyme−gold nanoparticle conjugates using "click" chemistry has been developed. In a copper-catalyzed 1,2,3-triazole cycloaddition, an acetylene-functionalized *Thermomyces lanuginosus* lipase has been attached to azide-functionalized water-soluble gold nanoparticles under retention of enzymatic activity. The products have been characterized by gel electrophoresis and a fluorometric lipase activity assay. It is estimated that the equivalent of approximately seven fully active lipase molecules are attached to each nanoparticle.

The integration of biological with nonbiological materials and structures in functional devices is an interdisciplinary multiscale task of great practical importance (*1*). Its main challenge often lies in understanding and controlling the interface between biological and nonbiological materials on the molecular scale. The attachment of functional biomolecules to nonbiological nanoparticles, which is of relevance, for example, to biosensors, drug and gene delivery, tissue engineering, and the manipulation and study of single biomolecules, creates such an interface at the smallest possible scale (*1*−*9*). Here, we present a versatile preparative route to gold nanoparticle bioconjugates, which uses lipase enzymes as covalently attached biofunctional components. Only very few examples of covalently linked enzyme−gold nanoparticle conjugates have been reported (*10*−*14*), while most approaches rely on the nonspecific attachment of enzymes to nanoparticles (*15*−*20*). We now introduce the use of click chemistry (*21*−*26*) for the facile covalent coupling of adequately functionalized nanoparticles and enzymes to each other, utilizing the copper(I)-catalyzed 1,2,3-triazole formation between azides and terminal acetylenes. Click chemistry is appealing due to its dependability, specificity, and compatibility with both organic and aqueous reaction systems (*23*−*26*). As a result of this approach, the attachment of acetylene-functionalized lipase molecules to azide-functionalized gold nanoparticles under retention of enzymatic activity is demonstrated. The binding of lipase to nanoparticles via this reaction has been demonstrated by agarose gel electrophoresis and by the lipase activity of the purified conjugates.

Azide-functionalized gold nanoparticles were prepared by treating standard, citrate-stabilized gold hydrosols (*27*, *28*) with an aqueous solution of ligand **1** to directly yield thiolate-capped, azide-functionalized particles (AzNPs; Scheme 1), which were

Scheme 1. Functionalization of Gold Nanoparticles with 1, and Linking of Lipase to These Nanoparticles Using Click Chemistry

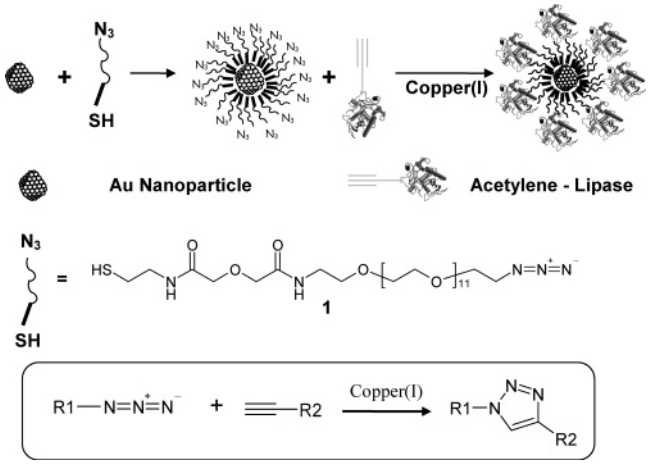

purified by repeated centrifugation and redispersion in water. They exhibit a characteristic plasmon absorption band at 523 nm, and their size is that of the original citrate-stabilized particles, 14 ± 1 nm (by TEM; Supporting Information). The number of capping ligands per nanoparticle can be estimated as 2250 ± 190 from the experimental gold, sulfur, carbon, hydrogen, and nitrogen content of the product and assuming an average nucleation number on the order of 85 000 gold atoms per particle (*29*). The particles are extremely stable and can be centrifuged, dried, and resuspended in aqueous solution several times without significant loss of material. They are stable for up to 3 months when stored at 4 °C in the dark in deionized water. Metal nanoparticles in biological systems always require ligand protection to prevent them from aggregating in the relatively high salt environment of biological buffers. As long as these ligands are reasonably short, i.e., within the limit of approximately half the diameter of the metal core, they do not affect the optical biosensing ability (distance probes) of the particles. While larger ligands may indeed prevent significant color changes upon particle aggregation, biosensing based on

* m.brust@liv.ac.uk (M.B.), a.rowan@science.ru.nl (A.E.R.).
† Centre for Nanoscale Science.
‡ Institute for Molecules and Materials.
§ Institute of Biochemistry.
∥ Novozymes A/S.
⊥ Present address: Biomedical Diagnostics Institute, Dublin City University, Dublin 9, Ireland.

10.1021/bc0601018 CCC: $33.50 © 2006 American Chemical Society
Published on Web 09/15/2006

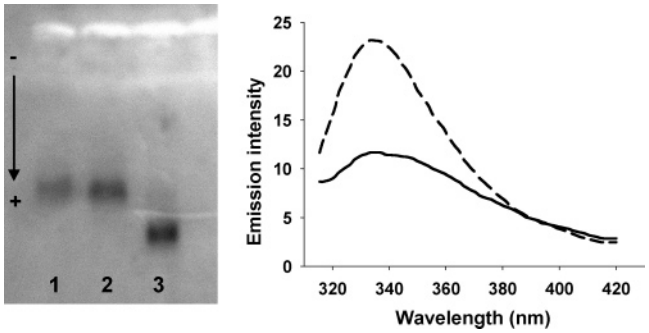

Figure 1. LHS: 1.5% agarose gel electrophoresis of AzNPs after click reaction with acetylene−lipase and following purification to remove excess lipase and copper salt. Lane 1: AzNPs. Lane 2: AzNPs reacted with acetylene−lipase without copper catalyst (blank). Lane 3: AzNPs reacted with acetylene−lipase with copper catalyst. RHS: Fluorometric lipase assay emission spectra recorded after 1 min (solid line) and 5 min (dashed line) of incubation with lipase-labeled AzNPs.

light scattering or photothermal effects is still possible (*2*−*4*). The particles described here are indeed compatible with biological buffers, tolerating salt concentrations up to 0.2 M before aggregation occurs. These properties are attributed to the structure of the ligand derived from **1**, containing a thiolate group for strong bonding to the gold nanoparticle surface and a water-soluble oligo(ethylene glycol) portion, which should also prevent denaturation of covalently bound enzymes and reduce nonspecific binding of enzymes to the particles (*30*, *31*).

These AzNPs were clicked to acetylene-functionalized lipase molecules (Scheme 1). The lipase was a 30 000 Da globular recombinant protein of fungal origin (*Thermomyces lanuginosus*), genetically altered to express only one solvent-accessible surface lysine residue (*32*, *33*). This lysine was modified using standard carbodiimide coupling chemistry (*34*) to yield a lipase with a freely accessible acetylene moiety.[1] This acetylene labeling step is facile to achieve on any protein with accessible lysines, for example, enzymes such as glucose oxidase (*34*), horseradish peroxidase (*35*), or alkaline phosphatase (*36*). Where no accessible lysines exist, standardized reagents and protocols are available to introduce amine groups without significant loss of biological activity, via modification of carboxyl or sulfhydryl amino acid functional groups or the carbohydrates of glycoproteins (*36*).

The acetylene-labeled lipase was clicked to gold nanoparticles by incubating an excess of lipase and Cu(I) catalyst with the nanoparticle suspensions at room temperature for 3 days. Although prolonged reaction times are required, this novel approach is very appealing, since no byproducts are formed. Following extensive purification by centrifugation to remove excess lipase and copper catalyst, the products were analyzed by gel electrophoresis (1.5% agarose gel, 100 V, 60 min). Figure 1 shows a gel comparing the purified reaction product (lane 3) to two control samples of as-prepared AzNPs (lane 1) and AzNPs treated with lipase in the absence of the Cu(I) catalyst (lane 2), respectively. The result indicates qualitatively the successful formation of protein−nanoparticle conjugates by click chemistry. The higher mobility of the reaction product in lane 3 is due to the covalent attachment of negatively charged lipase molecules to the gold particles. The increase in negative charge overcompensates here the effect of the increased hydrodynamic radius of the particles. The identical mobility of the two different control samples indicates the absence of nonspecifically bound lipase in the sample that has been exposed to the enzyme solution. While such nonspecific binding is usually quite common (*31*, *37*), and can indeed also be observed in our system (Supporting Information, Figure S3), this experiment demonstrates that the purification method used here is sufficient to remove all nonspecifically bound protein from the nanoparticle surface.

[1] Note that, while we have chosen here to site-specifically acetylate our enzyme, this is not a requirement to achieve click chemistry bioconjugation and simply depends on the desired application for the bioconjugate material.

Table 1. Supernatant Activity Tests during Removal of Unbound Lipase from Nanoparticle Samples Using Centrifugation[a]

sample	activity ($\times 10^{-3}$ U mL^{-1})[c]
wash 1[b]	224.57
wash 2	67.06
wash 3	3.77
wash 4	0.72
wash 5	0.39
wash 6	0.00
wash 7	0.00
wash 8	0.00
blank NPs[d]	0.00
lipase-labeled NPs	1.82

[a] Nanoparticles are washed until no activity is measured in the last three wash supernatants. [b] Refers to supernatant removed from nanoparticle pelleted by centrifugation. [c] 1 activity unit (U) is equivalent to 1 μmol of 5-OH-indole liberated per minute. [d] Lipase reacted with nanoparticle without copper catalyst.

To investigate whether the bound lipases retain their activity, the lipase-labeled and blank AzNP samples were tested using a modified fluorometric lipase activity assay (*38*). In the presence of lipase, a newly synthesized nonfluorescent ester, 5-*O*-palmitoylindole, is cleaved to a highly fluorescent 5-*OH*-indole product (λ_{max} 333 nm, synthesis in Supporting Information). Product emission is monitored at intervals of 1 and 5 min after sample addition. Activity is expressed as activity units per milliliter (U mL^{-1}), with 1 unit equivalent to 1 μmol of 5-*OH*-indole liberated per minute. Emission spectra for the lipase-labeled AzNP sample (Figure 1) demonstrate the observed increase in emission when the sample is incubated with substrate. Enzymatic activity is therefore retained when lipase is bound to the AzNP, with an enzyme activity of 1.82×10^{-3} U mL^{-1}. On the basis of the calibration curve of lipase activity versus lipase concentration for the free enzyme (Supporting Information), the measured activity of the hybrids corresponds to an average loading of seven lipase molecules per nanoparticle. This is valid only under the assumption that enzymatic activity is neither increased nor decreased upon attachment to the particles. As expected, zero activity is observed for the blank NP sample. Lipase activity assays were also performed on the supernatants from the centrifugation/washing procedure used to purify the AzNP samples, to ensure that all unbound lipase was removed from the nanoparticle suspensions. Table 1 shows the drop in supernatant lipase activity to zero as the particles are repeatedly cleaned, indicating the absence of solution free lipase in the system.

In conclusion, we have introduced the use of click chemistry for the conjugation of biomaterials to metal nanoparticles. Employing water-soluble, azide-functionalized gold nanoparticles and an acetylene-functionalized lipase as "clickable" precursor units has resulted in a new hybrid nanomaterial consisting of active lipase molecules covalently attached to the PEGylated ligand shell of a gold nanoparticle. Importantly, the coupling chemistry used here is very general and independent of the chemical nature of the nanoscopic subunits. This will allow the creation of similar composites containing a range of different biomolecular functionalities, which in the future may be used in applications such as biosensing, molecular electronics, catalysis, and controlled delivery.

ACKNOWLEDGMENT

The authors thank the European Union (BIOSCOPE, NMP4-CT-2003−505211) and Project AuTEK for financial support, and Stephen Apter for the elemental analysis.

Supporting Information Available: Experimental procedures, synthesis of all new compounds, transmission electron micrographs, fast protein liquid chromatography characterization of acetylene-labeled *T. lanuginosus*, an agarose gel of unpurified nanoparticle−lipase conjugates, and a calibration curve of lipase activity vs lipase concentration for acetylene-labeled *T. lanuginosus* lipase. This material is available free of charge via the Internet at http://pubs.acs.org.

LITERATURE CITED

(1) Langer, R., and Tirrell, D. A. (2004) Designing materials for biology and medicine. *Nature (London) 428*, 487−492.
(2) Pellegrino, T., Kudera, S., Liedl, T., Munoz, H. A., Manna, L., and Parak, W. J. (2005) On the development of colloidal nanoparticles towards multifunctional structures and their possible use for biological applications. *Small 1*, 48−63.
(3) Rosi, N. L., and Mirkin, C. A. (2005) Nanostructures in biodiagnostics. *Chem. Rev. 105*, 1547−1562.
(4) Parak, W. J., Gerion, D., Pellegrino, T., Zanchet, D., Micheel, C., Williams, S. C., Boudreau, R., Le Gros, M. A., Larabelle, C. A., and Alivisatos, A. P. (2003) Biological applications of colloidal nanocrystals. *Nanotechnology 14*, R15−R27.
(5) Kayser, O., Lemke, A., and Hernandez-Trejo, N. (2005) The impact of nanobiotechnology on the development of new drug delivery systems. *Curr. Pharm. Biotechnol. 6*, 3−5.
(6) Caruso, F. (2001) Nanoengineering of particle surfaces. *Adv. Mater. 13*, 11−22.
(7) Alivisatos, A. P. (2004) The use of nanocrystals in biological detection. *Nat. Biotechnol. 22*, 47−52.
(8) Parak, W. J., Pellegrino, T., and Plank, C. (2005) Labelling of cells with quantum dots. *Nanotechnology 16*, R9−R25.
(9) Proupin-Perez, M., Cosstick, R., Liz-Marzan, L. M., Salgueirino-Maceira, V., and Brust, M. (2005) Studies on the attachment of DNA to silica-coated nanoparticles through a Diels-Alder reaction. *Nucleosides, Nucleotides Nucleic Acids 105*, 1075−1079.
(10) Abad, J. M., Mertens, S. F. L., Pita, M., Fernandez, V. M., and Schiffrin, D. J. (2005) Functionalization of thioctic acid-capped gold nanoparticles for specific immobilization of histidine-tagged proteins. *J. Am. Chem. Soc. 127*, 5689−5694.
(11) Liobashevski, O., Chegel, V. I., Patolsky, F., Katz, E., and Willner, I. (2004) Enzyme-catalyzed bio-pumping of electrons into Au-nanoparticles: a surface plasmon resonance and electrochemical study. *J. Am. Chem. Soc. 126*, 7133−7143.
(12) Aubin-Tam, M. E., and Hamad-Schifferli, K. (2005) Gold nanoparticle−cytochrome *c* complexes: the effect of nanoparticle ligand charge on protein structure. *Langmuir 21*, 12080−12084.
(13) Aubin, M. E., Morales, D. G., and Hamad-Schifferli, K. (2005) Labelling ribonuclease S with a 3 nm Au nanoparticle by two-step assembly. *Nano Lett. 5*, 519−522.
(14) Simonian, A. L., Good, T. A., Wang, S.-S., and Wild, J. R. (2005) Nanoparticle-based optical biosensors for the direct detection of organophosphate chemical warfare agents and pesticides. *Anal. Chim. Acta 534*, 69−77.
(15) Ha, T. H., Jeong, J. Y., and Chung, B. H. (2005) Immobilization of hexa-arginine tagged esterase onto carboxylated gold nanoparticles. *Chem. Commun.* 3959−3961.
(16) Tom, R. T., and Pradeep, T. (2005) Interaction of azide ion with hemin and cytochrome *c* immobilized on Au and Ag nanoparticles. *Langmuir 21*, 11896−11902.
(17) Stonehuerner, J. G., Zhao, J., O'Daly, J. P., Crumbliss, A. L., and Henkens, R. W. (1992) Comparison of colloidal gold electrode fabrication methods: the preparation of a horseradish peroxidase enzyme electrode. *Biosens. Bioelectron. 7*, 421−428.
(18) Keating, C. D., Kovaleski, K. M., and Natan, M. J. (1998) Protein: colloid conjugates for surface-enhanced raman scattering: stability and control of protein orientation. *J. Phys. Chem. B 102*, 9404−9413.
(19) Mandal, S., Phadthare, S., Sastry, M. (2005) Interfacing biology with nanoparticles. *Curr. Appl. Phys. 5*, 118−127.
(20) Fisher, N. O., McIntosh, C. M., Simard, J. M., and Rotello, V. M. (2005) Inhibition of chymotrypsin through surface binding using nanoparticle-based receptors. *Proc. Nat. Acad. Sci. U.S.A. 99*, 5018−5023.
(21) Rostovstev, V. V., Green, L. G., Fokin, V. F., and Sharpless, K. B. (2002) A stepwise Huisgen cycloaddition process: copper(I)-catalyzed regioselective "ligation" of azides and terminal alkynes. *Angew. Chem., Int. Ed. 41*, 2596−2599.
(22) Hatzakis, N. S., Engelkamp, H., Velonia, K., Hofkens, J., Christianen, P. C. M., Svendsen, A., Patkar, S. A., Vind, J., Maan, J. C., Rowan, A. E., and Nolte, R. J. M. (2006) Synthesis and single enzyme activity of a clicked lipase-BSA hetero-dimer. *Chem. Commun. 19*, 2012−2014.
(23) Helms, B., Mynar, J. L., Hawker, C. J., and Frechet, J. M. J. (2004) Dendronized linear polymers via "click chemistry". *J. Am. Chem. Soc. 126*, 15020−15021.
(24) Fleming, D. A., Thode, C. J., Williams, M. E. (2006) Triazole cycloaddition as a general route for functionalization of Au nanoparticles. *Chem. Mater. 18*, 2327−2334.
(25) Parrish, B., Breitenkamp, R. B., and Emrick, T. (2005) PEG- and peptide-grafted aliphatic polyesters by click chemistry. *J. Am. Chem. Soc. 127*, 7404−7410.
(26) Joralemon, M. J., O'Reilly, R. K., Hawker, C. J., and Wooley, K. L. (2005) Shell click-crosslinked (SCC) nanoparticles: a new methodology for synthesis and orthogonal functionalization. *J. Am. Chem. Soc. 127*, 16892−16899.
(27) Turkevich, J., Stevenson, P. C., and Hillier, J. (1951) A study of the nucleation and growth processes in the synthesis of colloidal gold. *Discuss. Faraday Soc. 11*, 55−57.
(28) Frens, G. (1973) Controlled nucleation for regulation of particle-size in monodisperse gold suspensions. *Nat. Phys. Sci. 241*, 20−22.
(29) Yang, W., Chen, M., Knoll, W., and Deng, H. (2002) Synthesis of hexanedithiolate/decanethiolate mixed monolayer protected gold clusters and scanning tunneling microscope induced patterning on the clusters/Au(111) surface. *Langmuir 18*, 4124−4130.
(30) Prime, K. L., and Whitesides, G. M. (1993) Adsorption of proteins onto surfaces containing end-attached oligo(ethylene oxide) - a model system using self-assembled monolayers. *J. Am. Chem. Soc. 115*, 10714−10721.
(31) Zheng, M., and Huang, X. (2004) Nanoparticles comprising a mixed monolayer for specific bindings with biomolecules. *J. Am. Chem. Soc. 126*, 12047−12054.
(32) Svendsen, A. (2000) Lipase protein engineering. *Biochim. Biophys. Acta 1543*, 223−238.
(33) Valincius, G., Ignatjev, I., Niaura, G., Kazemekaite, M., Talaikyte, Z., Razumas, V., and Svendsen, A. (2005) Electrochemical method for the detection of lipase activity. *Anal. Chem. 77*, 2632−2636.
(34) Hermanson, G. T. (1996) *Bioconjugate Techniques*, p 170, Academic Press, New York.
(35) O'Brien, A. M., O'Fágáin, C., Nielsen, P. F., and Welinder, K. G. (2001) Location of crosslinks in chemically stabilized horseradish peroxidase: implications for design of crosslinks. *Biotechnol. Bioeng. 76*, 277−284.
(36) Ghosh, S. S., Kao, P. M., McCue, A. W., and Chappelle, H. L. (1990) Use of maleimide−thiol coupling chemistry for efficient synthesis of oligonucleotide−enzyme conjugate hybridization probes. *Bioconjugate Chem. 1*, 71−76.
(37) Hong, R., Emrick, N. O., Verna, A., Goodman, C. M., Emrick, T., and Rotello, V. M. (2004) Control of protein structure and function through surface recognition by tailored nanoparticle scaffolds. *J. Am. Chem. Soc. 126*, 739−743.
(38) Guilbault, G. G., and Hieserman, J. (1969) Fluorometric substrate for sulfatase and lipase. *Anal. Chem. 41*, 2006−2009.

BC0601018

ARTICLES

Synthesis and Characterization of Insulin−Transferrin Conjugates

Nikhil J. Kavimandan,[†] Elena Losi,[†,⊥] Jeffrey J. Wilson,[§] Jennifer S. Brodbelt,[§] and Nicholas A. Peppas*[,†,‡]

Department of Chemical Engineering, University of Texas at Austin, Austin, Texas 78712, Department of Biomedical Engineering, University of Texas at Austin, Austin, Texas 78712, and Department of Chemistry and Biochemistry, University of Texas at Austin, Austin, Texas, 78712. Received November 29, 2005; Revised Manuscript Received July 19, 2006

Receptor-mediated endocytosis can be exploited for improving the transcellular delivery of therapeutic proteins. Insulin conjugated to transferrin by forming disulfide bonds has been shown to improve insulin oral bioavailability in diabetic rats. We are developing a combination strategy involving complexation hydrogels as delivery vehicles for insulin−transferrin conjugates. The complexation hydrogels developed in our laboratory have been shown to be promising carriers for oral delivery of proteins and peptides. Integrating the strategies based on the complexation hydrogels and insulin−transferrin conjugates may prove to be a novel approach for oral delivery of insulin and other therapeutic proteins. In this work, electrospray ionization mass spectrometry (ESI-MS) was used to study the modification of insulin during its reaction with transferrin. The stability of the conjugated insulin to enzymatic degradation was also studied. ESI-MS studies confirmed the site-specific modifications of insulin. The transferrin conjugation of insulin was also shown to increase the stability of insulin to enzymatic degradation.

INTRODUCTION

Complexation hydrogels developed in our laboratory have emerged as one of the most promising methods for orally delivering therapeutic proteins (*1*−*3*). These hydrogels are hydrogen bonding, copolymer networks of poly(methacrylic acid) grafted with poly(ethylene glycol), henceforth designated as P(MAA-*g*-EG) hydrogels. Their pH-responsive behavior resulting from the hydrogen-bonding complexation/decomplexation characteristics makes them ideal carriers for oral delivery of proteins, such as insulin. Insulin entrapped inside the polymer network is protected in the harsh gastric environment before it is released in the upper small intestine, from which it is absorbed into the systemic circulation. Further, the polymer network can inhibit the activity of Ca^{2+}-dependent proteolytic enzymes. Both in vitro and in vivo studies with insulin-loaded polymer carriers have demonstrated the efficacy of these hydrogels as vehicles for oral administration of insulin (*1*, *4*, *5*).

One of the other effective strategies for enhancing bioavailability of proteins exploits the receptor-mediated endocytotic pathway used by the cells for selective and efficient uptake of specific macromolecules required for various cell processes. By coupling proteins and peptides to ligands that can recognize specific receptors on the epithelial cells, transcellular delivery of macromolecular biopharmaceuticals may be achieved. Since only those molecules that are conjugated to the ligands are transcytosed, this process eliminates potential side effects associated with the unspecific transport via the paracellular pathway.

Transferrin is a widely investigated protein for enhancing the cellular uptake of therapeutic agents. It is a naturally occurring protein involved in iron transport. Absorptive uptake of the iron-bound transferrin has been used to enhance the transcytosis of therapeutic agents and drug carriers across polarized cells such as the epithelial cells (*12*, *13*) and the endothelial cells (*6*−*9*). Transferrin receptor (TfR)-mediated cellular uptake has also been explored for targeted delivery of anticancer drugs, proteins, and therapeutic genes into primary proliferating malignancies (*10*, *11*).

In one promising application of TfR-mediated drug delivery, Shen and co-workers (*12*, *13*) recently demonstrated improved efficacy of orally administered insulin by conjugating insulin with transferrin through disulfide linkages (*12*). Shah and Shen (*13*) showed that insulin conjugated to transferrin via disulfide linkages can be transported across enterocytes-like Caco-2 cells. Further, Xia et al. (*12*) showed that orally administered insulin−transferrin conjugate exhibited a slow but prolonged hypoglycemic effect compared to that of the native human insulin in streptozotocin-induced diabetic rats. One important consideration relating to the use of TfR-conjugated proteins for improved oral bioavailability is that the TfR is primarily present in the basolateral membrane of the epithelial cells (*14*). This may limit the desired apical to basolateral transcytosis of the conjugated molecule. Despite this limitation, successful studies conducted by Shen and co-workers have demonstrated that insulin and granulocyte-colony stimulating factor (GCSF) conjugated to transferrin were transported across Caco-2 cell monolayers (*13*, *15*). Transcytosis experiments with radiolabeled insulin demonstrated 15-fold (apical-to-basolateral) and 5-fold (basolateral-to-apical) increases in insulin transport compared with unmodified insulin across Caco-2 cells (*13*). This transport was TfR-mediated because it was efficiently inhibited by unlabeled Tf (*13*). This indicates that the distribution of the TfRs on the apical side may be sufficient to cause significant enhancement in the transport of insulin across the epithelial cell barrier.

* Corresponding author. Tel: 512-471-6644. E-mail: peppas@che.utexas.edu.

[†] Department of Chemical Engineering.

[⊥] Permanent address: Pharmaceutical Department, University of Parma, Parma 43100, Italy.

[§] Department of Chemistry and Biochemistry.

[‡] Department of Biomedical Engineering.

10.1021/bc050344k CCC: $33.50 © 2006 American Chemical Society
Published on Web 09/14/2006

In our laboratory, we are developing a delivery system consisting of the complexation hydrogels acting as delivery vehicles for insulin−transferrin conjugates. The use of P(MAA-*g*-EG)-based microparticles as delivery vehicles for the insulin−transferrin conjugates may constitute a superior transmucosal delivery system for insulin. The system may improve the efficacy of oral insulin administration since (i) insulin in the conjugated form may be further protected from enzymatic degradation due to steric hindrance created by the conjugated transferrin, (ii) owing to the potential of complexation hydrogels to act as mucoadhesive carriers, most of the conjugate will be released within the localized microenvironment of the small intestine's filamentous brush border creating a high local concentration of the conjugate, (iii) the conjugate will have larger residence time in the small intestine, and (iv) the insulin−transferrin conjugate can cross the intestinal barrier by TfR-mediated transcellular pathway, which may further increase the efficiency of insulin absorption.

In this work, we discuss the synthesis of insulin−transferrin conjugates, analysis of the intermediate products, and characterization of the reaction products. Detailed analysis of the insulin modification reaction and determination of stability to enzymatic degradation of the conjugated insulin are important steps in developing the proposed combination strategy.

EXPERIMENTAL SECTION

Materials. The heterobifunctional cross-linker succinimidyl 3-(2-pyridyldithio)propionate (SPDP) and dithiothreitol (DTT) were purchased from Pierce (Rockford, IL). Dimethylmaleic anhydride (DMMA) was purchased from Sigma-Aldrich (Chemie, Steinheim, Germany). Bovine insulin, trypsin, and 4-phenylspiro[furan-2(3*H*),1′-phthalan]-3,3′-dione (fluorescamine) were purchased from Sigma (St. Louis, MO). Float-a-Lyzer dialysis tubings were purchased from Spectrum Laboratories (Rancho Dominguez, CA). Slide-A-Lyzer mini dialysis units, D-Salt Dextran desalting columns and immobilized trypsin, TPCK, were purchased from Pierce Biotechnology, Inc. (Rockford, IL). *N*-Ethylmaleimide (NEM) was obtained from MP Biomedicals (Aurora, OH). C18 ZipTips were purchased from Millipore (Billerica, MA).

Synthesis of Insulin−Transferrin Conjugates. The protein conjugation method described here has been developed by Carlsson et al. (*16*) and was modified for preparation of insulin−transferrin conjugates by Shah and Shen (*13*). Insulin (Ins) was conjugated to transferrin (Tf) through disulfide linkages using SPDP, according to the method described by Shah and Shen (*13*) with some modifications as described below.

Insulin Modification by DMMA (Step I). Insulin was reacted with (DMMA) to block the primary amine groups at the N-terminal ends of the insulin chains, which can potentially react with SPDP (Figure 1A). A sample of 25 mg of bovine insulin was added to a solution containing 1.5 mL of 1 N HCl and 3 mL of phosphate-buffered saline (PBS) solution (pH 6.9). After completely dissolving insulin, the pH of the solution was adjusted to 6.9 by addition of 1.5 mL of 1 N NaOH solution. Dissolved insulin was then reacted with 3.5 mg of DMMA under constant stirring for 0.5 h. The pH of the solution was maintained at 6.8 to 6.9 by addition of 1 M Na_2CO_3 solution. Reaction with DMMA was repeated two more times so that a total of 10.5 mg of DMMA was added to insulin at the controlled pH of 6.8−6.9. A micro-pH meter (IQ Scientific Instruments, San Diego, CA) was used to monitor the pH of the solution during the reaction. The reaction mixture was transferred to Float-a-Lyzer dialysis tubings (MWCO 3500) and dialyzed against PBS buffer (pH 6.9) for 24 h to remove unreacted DMMA.

Insulin Modification with SPDP (Step II). Following dialysis, the DMMA-modified insulin was reacted with SPDP to introduce disulfide bonds at primary amine group of lysine at the B29 position of insulin (Figure 1B). The pH of modified insulin solution was raised to 9.0 by addition of 1 M Na_2CO_3 and 6.0 mg of SPDP dissolved in 150 μL of dimethyl formamide (DMF) was added to this solution. The reaction was constantly stirred at 4 °C for 2 h. The pH of the reaction was maintained at 8.8−9.0 during the course of the reaction.

The modified insulin was then dialyzed against PBS buffer (pH 8.0) for 24 h to remove unreacted SPDP reagent. To measure the average number of moles of 2-pyridyl disulfide groups attached per mole of insulin (PDP/Ins ratio), 700 μL of Ins−PDP solution was reduced by 25 mM DTT. PDP-modified protein on reduction with DTT releases of 2-pyridinethione chromophore, which can be quantitated by measuring the absorbance at 343 nm (A_{343}). A molar extinction coefficient of 8.08×10^3 M^{-1} cm^{-1} at 343 nm ($\epsilon_{343,2-TP}$) and 5.10×10^3 $M^{-1}cm^{-1}$ at 280 nm ($\epsilon_{280,2-TP}$) was used for the calculations (*16, 17*). Protein concentration was determined by measuring the absorbance at 280 nm (A_{280}). The molar extinction coefficient of 5.8×10^3 M^{-1} cm^{-1}at 280 nm was used for insulin. A sample of 40 μL of DTT-reduced modified insulin solution was diluted to 700 μL, and the absorbance was measured in triplicate at 343 and 280 nm with a microplate reader (Synergy HT, Bio-Tech Instruments, Winooski, VT). The PDP/protein ratio was determined by the following formula.

$$\text{PDP/protein} = \frac{A_{343}\epsilon_{280,\text{protein}}}{(A_{280}\epsilon_{343,2-TP} - A_{343}\epsilon_{280,2-TP})} \quad (1)$$

Transferrin Modification with SPDP (Step III). Transferrin was dissolved in 4 mL of phosphate buffer (pH 7.0, 30 mM) at a concentration of 20 mg/mL. Four-fold molar excess of SPDP dissolved in 100 μL of DMF and added to the transferrin solution under constant stirring. The reaction mixture was stirred for 2 h at 4 °C. The modified transferrin was then dialyzed (MWCO 50000) against phosphate buffer (pH 8.0, 30 mM, 3 mM EDTA) for 24 h to remove unreacted SPDP reagent. Following dialysis, entire transferrin solution was reduced by 25 mM DTT for 1 h to generate thiol-containing transferrin, Tf-SH (Figure 1C). The PDP/Tf modification ratio was determined by using molar extinction coefficient of 93.0×10^3 M^{-1} cm^{-1} at 280 nm ($\epsilon_{280,Tf}$) as described above.

Conjugation of Modified Proteins (Step IV). The reaction solution from step III containing Tf-SH was immediately purified by elution on D-Salt Dextran desalting columns (MWCO 5000). Four columns were connected in series to achieve the desired purification. Phosphate buffer (pH 8.0, 30 mM, 3 mM EDTA) was used to elute the protein from the columns. Fractions with A_{280} values greater than 0.2 were collected.

Purified Tf-SH was then reacted with Ins−PDP (Figure 1D) in a molar ratio of 1:2 of Tf-SH/Ins−PDP. To follow the progress of the reaction, 40 μL of the reaction samples was withdrawn at predetermined time intervals and diluted to 700 μL with phosphate buffer. Reaction of each mole of insulin with Tf-SH is accompanied by the release of 1 mol of 2-pyridinethione. Hence, A_{343} values of the samples were measured with a microplate reader to determine the concentration of 2-pyridinethione. To determine the average number of moles of insulin attached to 1 mol transferrin (Ins/Tf ratio), concentration of the 2-pyridinethione was divided by transferrin concentration in the samples. When approximately 2 mol of 2-pyridinethione were released per mole of transferrin, the reaction was stopped by addition of 4 mg of NEM to prevent further cross-linking of transferrin molecules via oxidation of unreacted thiols (*13*). Following the reaction, the conjugate was purified by dialysis

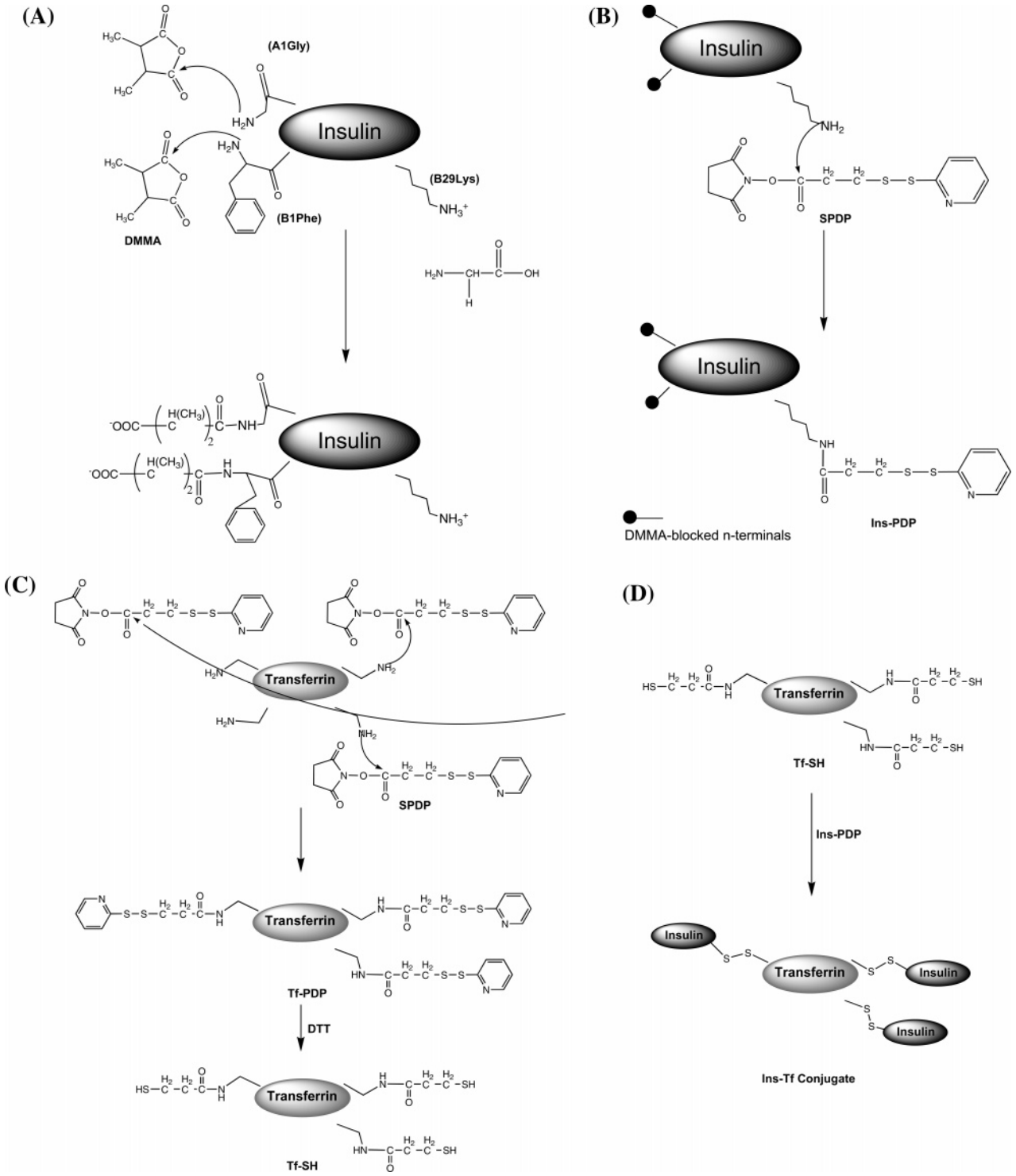

Figure 1. (A) Conjugation reaction, step I (DMMA blocking of the N-terminal amine groups). DMMA reaction with insulin at pH of 6.8−6.9. Only the primary amines at the N-terminal are deprotonated and are able to react with DMMA. Most of the primary amines at B29 lysine residue are protonated and do not react with DMMA. (B) Conjugation reaction, step II (SPDP reaction with DMMA-modified insulin). SPDP reacts with DMMA-modified insulin at pH 9.0 to form insulin−PDP. (C) Conjugation reaction, step III (SPDP modification of transferrin). SPDP reacts with transferrin at pH 7.0 to form Tf−PDP. The modification ratio can be controlled by altering the amount of SPDP reacted with transferrin. Purified Tf−PDP is then reacted with DTT to generate free thiol groups on transferrin (Tf-SH). (D) Conjugation reaction, step IV (Ins−PDP reaction with Tf−SH). Purified Tf−SH reacts with Ins−PDP obtained from step II to form Ins−Tf conjugate.

(MWCO 25 000) against phosphate buffer (pH 8.0, 30 mM, 3 mM EDTA) until no free insulin was detected in the solution by HPLC. Total protein concentration of the final purified conjugate solution was determined by Quick Start Bradford assay (Bio-Rad Laboratories, Hercules, CA) using BSA or unmodified transferrin as a reference standard (*18*).

Analysis of the Insulin Modification Reaction. Modifications of the primary amines of insulin due to DMMA reaction (step I) and SPDP modification (step II) were studied by quantitatively measuring the amount of free primary amine groups of the protein using fluorescamine assay and by identifying the sites of insulin modification by mass spectrometry. This was important since improper modifications of the protein may lead to decrease in its bioactivity (*19*).

Fluorescamine Assay for Measurement of Free Amine Groups of Insulin. A primary amine assay utilizing fluores-

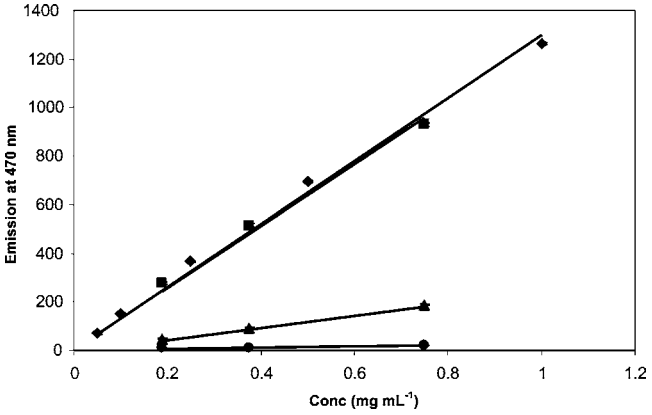

Figure 2. Fluorescamine assay for determination of free amine groups of insulin. Fluorescamine (50 μL of 1.08 mM) in acetone was added to 150 μL of protein samples in a microplate reader: insulin standard (◆), unmodified insulin (■), DMMA-modified insulin (▲), or SPDP-modified insulin (●). The fluorescence associated with the samples was measured with a microplate reader. Excitation was at 390 nm and emission at 470 nm. Error bars are smaller than the symbols; $n = 3$.

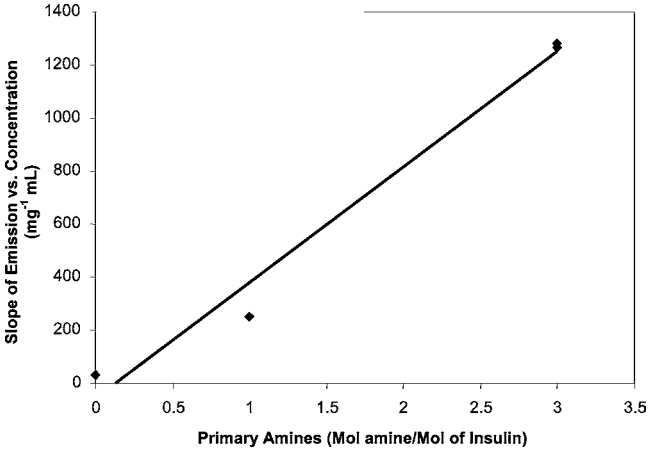

Figure 3. Fluorescamine assay for determination of free amine groups of insulin. Slopes of the linear relationship between emission at 470 nm and concentration for various insulin samples (Figure 2) plotted against the expected number of moles of free amine groups per mole of insulin.

camine was performed to estimate insulin primary amine modification by DMMA and by SPDP. Fluorescamine stock solution (1.08 mM) was prepared by dissolving 0.9 mg of fluorescamine in 3 mL of acetone. Insulin standard solutions were prepared containing 0.05, 0.1, 0.25, 0.5, 1, and 2 mg/mL native, unmodified insulin in PBS buffer. Fifty microliters of fluorescamine stock solution was added to 150 μL of insulin standard solutions in 96 well plates, and the fluorescence measurements were performed a microplate reader (*20*). The excitation wavelength for measurements was 390 nm, and the emission wavelength was 470 nm. A standard curve of emission at 470 nm (Em470) vs insulin concentration (mg/mL) was prepared (Figure 2).

Samples were taken from the modification reaction before modification with DMMA (after step I), after purification of the DMMA-modified insulin, and after purification of the SPDP-modified insulin intermediate (after step II). The concentrations of the samples were adjusted to account for the dilution caused by dialysis of the modified intermediate products, so the final concentration in all the samples was 0.75 mg/mL. A plot of Em470 vs concentration (mg/mL) was prepared for all three samples. The slopes of standard curve and plots for three samples were calculated and plotted against the expected number of moles of free amines present per mole of insulin samples (Figure 3).

Mass Spectrometry Analysis of the Insulin Modification Reaction. Sample aliquots were taken before and after the DMMA and SPDP modification steps. Dialysis of each aliquot was performed with Slide-A-Lyzer Mini Dialysis units (3500 MWCO) against 0.5 L of deionized water with triethylamine (TEA) at pH 7.5 for 30 min. The dialysis was repeated before dilution for ESI-MS analysis. SPDP-modified insulin was first dialyzed than digested with immobilized trypsin beads treated with 0.1 M ammonium acetate buffer (pH 8.5) for 18 h at 37 °C. The trypsin digest samples were desalted and concentrated with C_{18} ZipTips. ESI-MS and MS^n experiments were performed on an LCQ Duo quadrupole ion trap mass spectrometer (ThermoFinnigan, San Jose, Ca). All the samples were diluted to 10 μM and run at 3 μL/min for ESI-MS analysis in 99/1/1 methanol/water/TEA (MeOH/H_2O/TEA) by volume for negative mode or 99/1/1 methanol/water/acetic acid (MeOH/H_2O/HoAc) by volume for the positive mode unless otherwise noted. All the chemicals were purchased from Sigma (St. Louis, MO) without any further purification unless otherwise noted.

HPLC Analysis of the Insulin−Transferrin Conjugates. A reversed phase HPLC method was established for analysis of the conjugates to be used in quantification of the conjugates in later studies. The same method was used for measurement of insulin and transferrin concentrations. The HPLC system was a Waters 2695 Alliance separation module (Waters, Milford, MA) equipped with Waters 2487 Dual λ absorbance detector (Waters, Milford, MA). All the data were collected utilizing the Millenium Software Empower Application. A Symmetry300 C4 column (particle size 5 μm, 3.9 mm i.d. $\times$ 150 mm length) (Milford, MA) was used for the separations. The solvents used for the analysis were solvent A (water, 0.1% trifluoroacetic acid (TFA)) and solvent B (HPLC-grade acetonitrile, 0.08% TFA). The mobile phase for the analysis consisted of a linear gradient of 70% of solvent A to 40% of solvent A in 6 min. The gradient was controlled by the Empower software. The column temperature was set at 40 °C. The flow rate of the mobile phase was set at 0.6 mL/min, and the peaks were detected at 215 nm.

Analysis of Stability of the Insulin−Transferrin Conjugates to Enzymatic Degradation. The degradation profile of the conjugates was studied in comparison with insulin and transferrin in the presence of trypsin, a major proteolytic enzyme present in the intestine. The enzyme solution was prepared by dissolving trypsin in 50 mM phosphate buffer solution with pH of 7.4 and ionic strength of 154 mM. Insulin and transferrin stock solutions were prepared in the reaction buffer. Conjugate solution was diluted with the reaction buffer to achieve desired concentration. All the solutions were prewarmed at 37 °C for 15 min. The protein and the trypsin concentrations in the stock solutions were adjusted so that after adding trypsin solution to the insulin, transferrin, and conjugate stock solutions, the initial protein concentration in the reaction mixture was 1 mg/mL and the trypsin concentration was 3.2 mg/mL. At time $t = 0$, trypsin stock solution was added to insulin, transferrin, and the conjugate solutions at 37 °C under continuous mixing. Samples (50 μL) were withdrawn at predetermined time intervals, and the enzyme activity in the samples was stopped by addition of 50 μL of ice-cold acetic acid solution (50% (v/v) acetic acid in DI water). The samples were then analyzed by HPLC as described previously. Degradation rate constants were determined from the slope of the semilog plot of the percentage of initial protein remaining vs time.

RESULTS AND DISCUSSION

Synthesis of Insulin−Transferrin Conjugates. Insulin was conjugated to transferrin using SPDP, a heterobifunctional, cleavable cross-linker that reacts with primary amines and sulfhydryl groups (*21*) (Figure 1). Upon SPDP reaction with

the accessible primary amines of a protein, a mixed disulfide is formed that has free 2-pyridyldithio groups, which can react with free sulfhydryl groups from other proteins. This results in formation of conjugates of different proteins (heteroconjugates) without unwanted cross-reaction products such as the homoconjugates of individual proteins. This cross-linker is especially applicable to this research since the disulfide linkages are inherently unstable in the plasma (*22*). Hence disulfide linkages linking the two proteins may be cleaved once the conjugate reaches systemic circulation (*18*, *23*, *24*). Xia et al. (*12*) showed that free insulin was released within 5 min of incubation of the insulin−transferrin conjugates with rat liver slices. Free insulin was also detected in the rat serum 4 h after oral administration of the insulin−transferrin conjugates (*12*).

Step I of the conjugation involves modification of the N-terminal primary amines of insulin by reaction with DMMA. Insulin has three primary amine moieties: at A1-glycine (A1Gly), at B1-phenylalanine (B1Phe), and at B29-lysine (B29-Lys) (Figure 7). All the primary amines can potentially react with SPDP reagent at a pH where most of the amine groups are deprotonated so that the $-NH_2$ group can act as a nucleophile and react with the electron-deficient carbon atom of the succinimidyl group of SPDP. However, Lindsay and Shall (*25*) reported that acetylation of insulin at the A1Gly position resulted in decrease in the biological activity of insulin. Hence insulin modifications involving primary amines are usually directed to either B1Phe or B29Lys positions. In this work, SPDP modification was carrier out at the B29 lysine group of insulin. Hence it was necessary to block the N-terminal primary amines before reacting insulin with SPDP. This was done by reacting insulin with DMMA at a controlled pH of 6.8−6.9 (*12*). At this pH, most of the terminal amine groups were in their deprotonated state and were able to react with DMMA through nucleophilic attack. However, since the pH was about two units below the pK_a of the lysine residue, most of the lysine residues remained unreacted. The DMMA modification of insulin is acid-labile and the amino acid residues can be regenerated by making the solution slightly acidic.

SPDP modification of the purified intermediate from step I was carried out at the pH of 9.0 to generate the Ins−PDP intermediate. The modification was measured by UV spectroscopy after reducing a small aliquot of purified Ins−PDP with 25 mM DTT. The modification ratio (PDP/Ins) calculated from eq 1 was approximately 1:1. Modification ratio for transferrin (PDP/Tf) was approximately 4:1.

After reduction of the Tf−PDP intermediate to generate thiol-containing transferrin (Tf-SH), the intermediate was purified by size exclusion chromatography. Two moles of Ins−PDP were then added per mole of Tf-SH. When added, Ins−PDP was almost entirely reacted releasing 2 mol of 2-pyridinethio per mole of transferrin; the reaction was stopped by addition of NEM to prevent cross-linking of the Ins−Tf conjugates due to oxidation of excess −SH on insulin-conjugated transferrin. The conjugation ratio of 2:1 Ins/Tf was chosen since excessive modification of transferrin by insulin attachment will result in a bulky complex, which may adversely affect the diffusion characteristics of the conjugate in the polymer network reducing loading and release efficiencies of the conjugate.

Little or no insulin was detected in the reaction mixture by HPLC at the end of the reaction. The conjugate was extensively dialyzed to remove any unreacted residual insulin. The concentration of purified conjugate was determined using Bradford assay (*18*). Because many proteins have nearly identical response curve in this assay, the methods can be applied widely using a single set of standards (*18*). BSA and transferrin were used as standards to calculate the concentration of conjugate in the purified conjugate solution.

Analysis of the Insulin Modification Reaction. Cellular studies performed by Shah and Shen (*13*) showed that conjugate molecules containing up to three insulin molecules per molecule of transferrin were able to be transported across the Caco-2 cell monolayers by a transcellular mechanism. This means that the SPDP modification of the surface-exposed lysine residues of transferrin did not decrease its ability to bind the transferrin receptors on the cell surfaces nor inhibit transport across the cell monolayers by receptor-mediated transcytosis. However, improper modification of insulin by DMMA or SPDP may result in inhibition of its physiological activity. Hence sites of modification of insulin were verified here by fluorescamine assay and mass spectrometry analysis of the insulin modified by step I (DMMA modification) and step II (SPDP modification).

Fluorescamine Assay for Quantification of the Primary Amine Groups. Fluorescamine, a nonfluorescent compound, reacts rapidly with primary amines in proteins, such as the terminal amino groups and the ϵ-amino groups of lysine residues, to form fluorophors, which are excited at 390 nm and fluoresce at 475 nm (*26*). The reaction is completed in 100−500 ms, and excess reagent is quickly hydrolyzed to nonfluorescent products. The fluorescent product is stable for several hours.

Figure 2 shows the plot of Em470 vs concentration for insulin standards, unmodified insulin (before step I), DMMA-modified insulin (after step I), and SPDP-modified insulin (after step II). As can be seen from the figure, the calibration plots for standard curve and unmodified insulin overlap and have comparable slopes. The slopes of the curves are greatly reduced after DMMA modification, indicating that the number of free amino groups per mole of insulin has decreased. Fluorescence values for corresponding concentrations of the SPDP-modified insulin are even lower indicating that the SPDP-modified derivative of insulin had fewer amino groups that are free to react with fluorescamine than the DMMA-modified insulin.

Ideally, PDP−insulin should not react with fluorescamine since a successfully modified insulin molecule should not have any free amino groups. But in actual reaction, some unreacted amino groups are to be expected that can react with fluorescamine to form the fluorophors. The slopes of the calibration plots from Figure 2 were proportional to the expected number of free amino groups per mole of insulin for various samples (Figure 3), indicating that the decrease in fluorescence correlated well with the conversion of free amino groups into intermediates that were unreactive toward fluorescamine.

This was an important finding since it established that the primary amines were indeed being converted into intermediates owing to DMMA and SPDP modifications. However this assay did not provide much information about the reaction site specificity of the modification agents. Hence, mass spectrometry analysis was performed on the insulin intermediates to confirm the modifications and to evaluate the specificity of the reagents for reaction with the primary amines.

Mass Spectrometry Analysis of the Insulin Modifications. Figure 4 shows the mass spectrum of unmodified bovine insulin in the negative ESI mode. The mass to charge ratio (m/z) for the −4 charge state is 1432.2 corresponding to the molecular weight of 5732.8 Da. Figure 5 shows the ESI mass spectrum for DMMA-modified insulin sprayed from a 99/1/1 MeOH/H_2O/TEA solution. As seen from the mass spectrum, the 1:1 and 2:1 DMMA/insulin species are major products, and there is a minor amount of unreacted insulin apparent. Importantly, no peaks corresponding to the 3:1 derivative of insulin were found, supporting that nonspecific modification of insulin did not occur and consistent with restriction of the modification sites to the two N-terminal amines (A- and B-chains). The ESI-mass

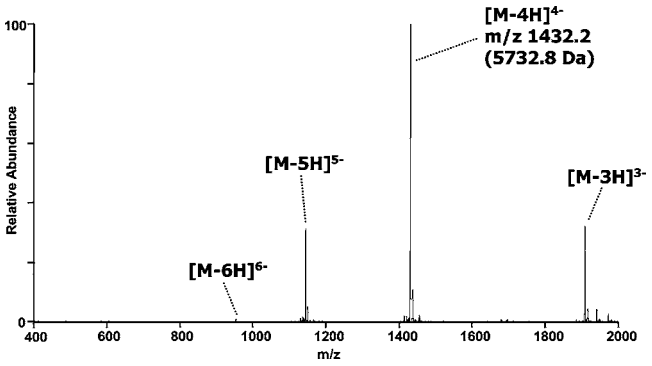

Figure 4. ESI-mass spectrum of unmodified bovine insulin showing various charge states. The −4 charge state at *m*/*z* 1432.2 corresponds to a species with a molecular weight of 5732.8 Da. The spectrum was obtained in 99/1/1 MeOH/H_2O/TEA by volume.

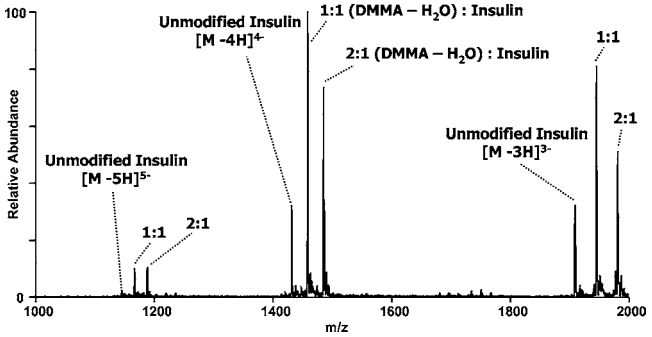

Figure 5. ESI-mass spectrum of the DMMA-modified bovine insulin in 99/1/1 MeOH/H_2O/TEA by volume. The stoichiometry values (1:1 or 2:1) represent the number of (DMMA−H_2O) modifications per insulin molecule. The −4 charge state of the 2:1 (DMMA−H_2O)/insulin species is observed at *m*/*z* 1486.3.

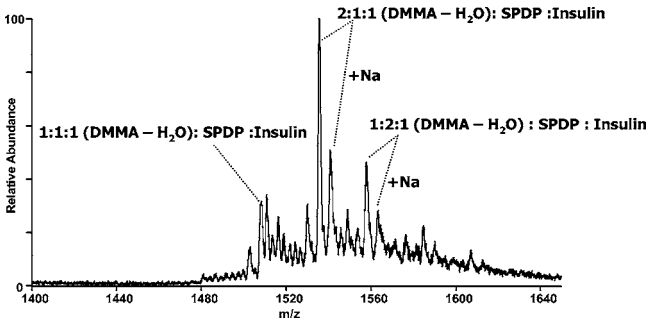

Figure 6. ESI-mass spectrum of the SPDP-modified bovine insulin (−4 charge state) in 99/1/1 MeOH/H_2O/TEA by volume. The $[M - 4H]^{4-}$ and $[M - 5H + Na]^{4-}$ ions of the 2:1:1 DMMA/insulin/PDP species are observed at *m*/*z* 1535.6 and 1540.9, respectively. Other minor peaks are attributed to various degrees of metal adduction from the ESI process.

spectrum of the SPDP-modified insulin intermediate is shown in Figure 6. The 2:1:1 DMMA/insulin/PDP species is identified at *m*/*z* 1535.6 and is shown to be the major reaction product from the mass spectrum.

To further pinpoint the sites of DMMA and SPDP modifications of insulin, ESI-MS was used to analyze the DMMA/SPDP−insulin product mixture after trypsin digestion. Figure 7 summarizes the potential sites of DMMA and SPDP modifications and the amide bonds expected to be cleaved by trypsin. Trypsin can cleave insulin at the amide bond between the B22Arg and B23Gly residues, yielding a 43 amino acid peptide (Ins-43) containing both the A- and B-chain N-termini and a smaller eight amino acid peptide (Ins-8) containing the B-chain C-terminus of insulin. The trypsin cleavage site between B29Lys and B30Ala is not accessible since the normally protonated side

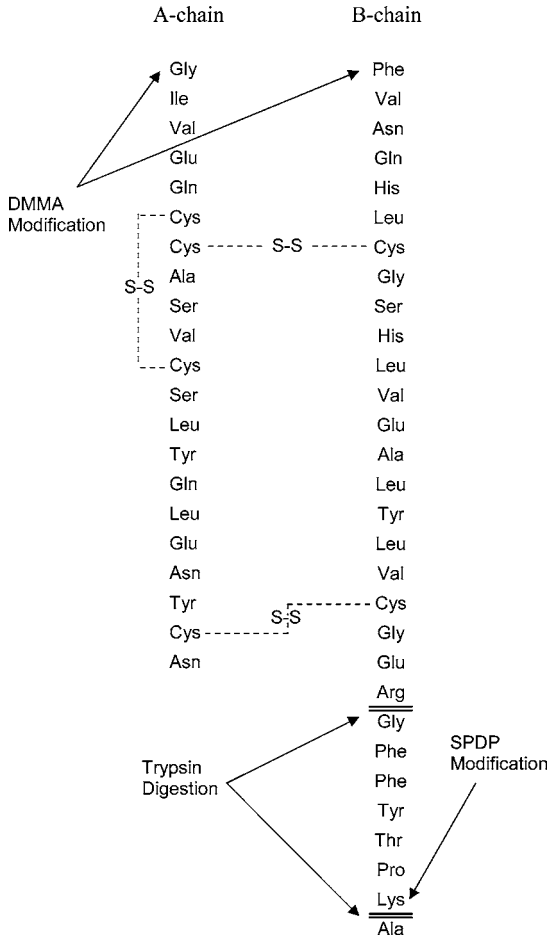

Figure 7. Insulin primary structure showing modification sites of DMMA and SPDP and sites of trypsin digestion.

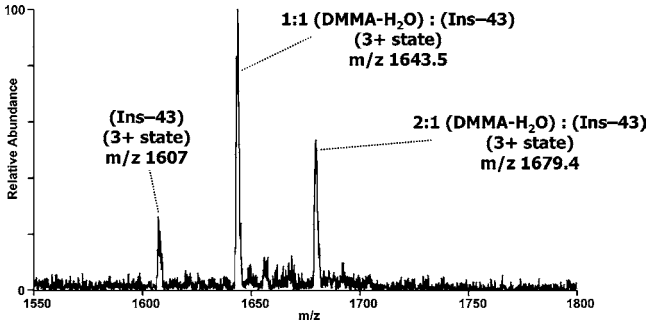

Figure 8. Expansion of the ESI-mass spectrum of the +3 charge state region for the larger peptide formed after trypsin digestion of modified insulin (Ins-43). The spectrum was obtained in 50/50/1 H_2O/MeOH/HoAc by volume. No peak for the PDP derivative of Ins-43 was identified in the mass spectrum.

chain of lysine, which signals tryptic cleavage, is blocked by the PDP modification. The two resulting tryptic peptides were structurally characterized by tandem mass spectrometry. Figure 8 shows the ESI-mass spectrum of the Ins-43 tryptic peptide (+3 charge state). As expected, peaks corresponding to both 1:1 and 2:1 DMMA/In-43 were identified in the mass spectrum, but no peaks were found for the corresponding PDP attachment to Ins-43, which would be observed at *m*/*z* 1672.7, 1708.3, or 1744.0 depending on the degree of DMMA modification. This confirms that the PDP did not attach to the N-terminal primary amines of the A or B chains.

Collisional activated dissociation (CAD), a method used to provide structural information based on the fragmentation pattern of a selected ion in the gas phase, was used for further

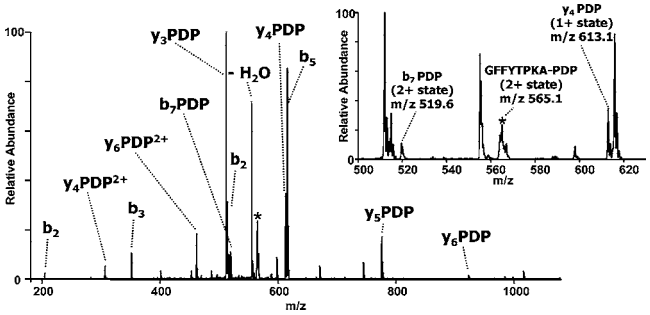

Figure 9. ESI-MS/MS spectrum of the smaller peptide (*m*/*z* 565.1, Ins-8) formed after trypsin digestion of modified insulin. The insert shows the expanded region from the middle portion of the spectrum, which contains two key diagnostic ions, $(b_7\text{-PDP})^{2+}$ at *m*/*z* 519.6, and $(y_4\text{-PDP})^{1+}$ at *m*/*z* 613.1.

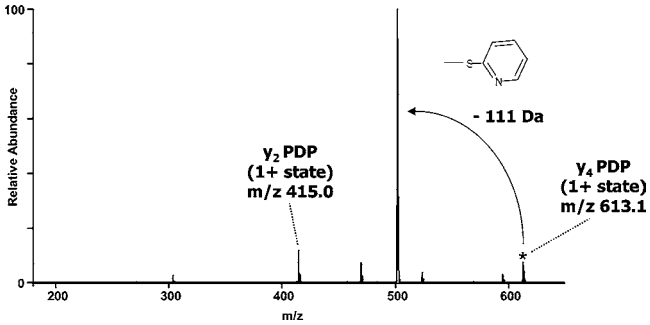

Figure 10. ESI-MS^3 spectrum of the y_4-PDP peptide fragment at *m*/*z* 613.1. The y_2-PDP fragment is observed at *m*/*z* 415.0; this ion combined with the observation of b_7-PDP in Figure 9 provides confirmation of the B29Lys position as the specific site of modification. The major peak at *m*/*z* 502 is the loss of the thiopyridyl moiety from the PDP modification.

characterization of the smaller of the two tryptic peptides (Ins-8). The ESI tandem mass spectrum for the eight amino acid peptide, Ins-8, is shown in Figure 9. The parent ion at *m*/*z* 565 corresponds to diprotonated Ins-8 with a single PDP modification and is consistent with the synthetic strategy outlined in Figure 1B and the predicted product shown in Figure 7. An array of b and y sequence ions is observed, which confirms the amino acid sequence of the Ins-8 species, and the sequence ions that are mass-shifted by 197 Da indicate the incorporation of the PDP group. From the series of fragments generated by CAD, two critical sequence ions were identified: y_4 (TPKA)−PDP and b_7 (GFFYTPK)−PDP (see inset of Figure 9), with each one containing the B-chain 29Lys residue. The *m*/*z* values of these two key sequence ions confirm the presence of PDP in both species and thus narrow the possible PDP modification sites to the residues B27Thr, B28Pro, and B29Lys because these are the only amino acids common to the two sequence ions and the Ins-8 precursor. Further dissociation of the selected y_4 (TPKA)−PDP species via a second stage of CAD yields the y_2 (KA)−PDP ion at *m*/*z* 415.0 as shown in Figure 10, along with the dominant loss of the thiopyridyl moiety, 111 Da, from the PDP group of the y_4 (TPKA)−PDP parent ion, which results in the abundant ion at *m*/*z* 502. The presence of y_2 (KA)−PDP species from this MS^3 experiment and the b_7 (GFFYTPK)−PDP species from the prior MS/MS experiment confirms B29Lys as the sole site of PDP modification because it is the only amino acid found in both species. All other peaks observed in these mass spectra support this modification site without contradiction.

The data from mass spectrometry and the fluorescamine assay together provide evidence that the SPDP modification is primarily at B29Lys and the DMMA modification sites are A1Gly and B1Phe. These are important results since improper

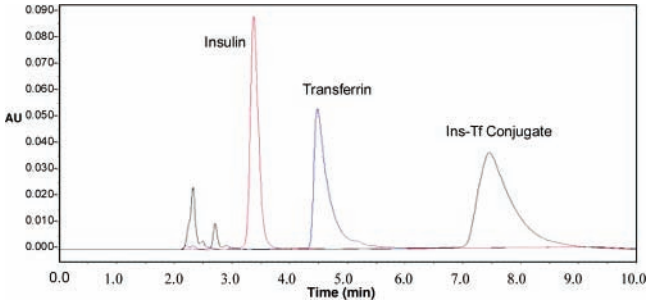

Figure 11. HPLC chromatograms of insulin, transferrin, and insulin−transferrin conjugate. The mobile phase for the analysis consisted of a linear gradient of 70% of solvent A to 40% of solvent A in 6 min. A Symmetry300 C4 column (particle size 5 μm, 3.9 mm i.d. × 150 mm length) was used for the separation.

modification may result in reduction or complete loss of insulin activity.

HPLC Analysis of the Insulin−Transferrin Conjugates. Figure 11 shows the HPLC chromatogram for insulin, transferrin, and the purified conjugate. The insulin eluted from the C4 column due to the applied gradient with a retention time of approximately 3.4 min, where as the transferrin and the conjugates eluted at around 4.5 and 7.5 min respectively. More importantly, the chromatogram of the purified conjugate did not show any peak for transferrin or insulin (data not shown), indicating that the conjugate was essentially pure and did not contain either of the unmodified proteins.

Analysis of the Stability of Insulin−Transferrin Conjugates to Enzymatic Degradation. Intact insulin−transferrin conjugate has been shown to reach systemic circulation in diabetic rats (*12*). In these studies, insulin and insulin−transferrin conjugates were orally administered in diabetic rats in a 30 mg/mL $NaHCO_3$ solution to neutralize the gastric acidity and to protect digestion of proteins in the stomach (*12*). However there was no mechanism to reduce the degradation of insulin or the conjugate in the intestinal milieu. Even in the absence of such a mechanism, the conjugate was able to reach the systemic circulation without being completely degraded. This provides an indirect evidence of the increased stability of the conjugated insulin against tryptic and chymotryptic attack. However this improvement in the stability of the conjugate in enzyme solution has not been demonstrated experimentally.

Hence in this study, the degradation profiles of insulin, transferrin, and the conjugate were evaluated in a solution containing trypsin based on HPLC analysis. As can be seen from Figure 12, most of the insulin degraded due to tryptic attack within 15−20 min of incubation, whereas transferrin was significantly more stable at the same enzyme concentrations. The conjugate degraded at a faster rate as compared to transferrin but was more stable than the unmodified insulin. The degradation rate constants were calculated from the slopes of the semilog plot of the percentage of initial protein remaining vs time at early time points (Figure 13 and Table 1). The degradation rate constant calculated was 21.1×10^{-3} min^{-1} for insulin and 0.73×10^{-3} and 6.17×10^{-3} min^{-1} for transferrin and the conjugate, respectively. These data indicated that the stability of insulin was significantly increased due to its conjugation with transferrin. This may be one of the important factors contributing to the observed hypoglycemic effect of the orally administered conjugates (*12*). Although the reasons behind the observed increase in stability of the conjugate are not clearly understood, this may be due to the shielding effect of the transferrin, which limits enzymatic degradation of insulin. Transferrin has been shown to be resistant to tryptic and chymotryptic digestion (*13*). Thus the large transferrin molecule

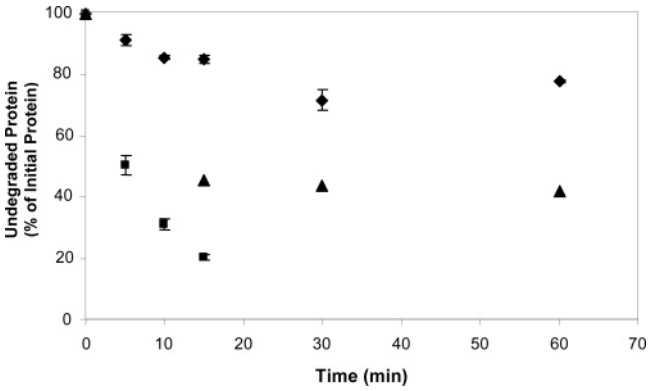

Figure 12. Protein degradation profiles in the presence of trypsin. Initial protein concentration in the reaction was 1 mg/mL, and the trypsin concentration was 3.2 mg/mL. The total reaction volume was 5 mL, and the pH was 7.4. Samples (50 μL) were withdrawn at different time intervals, and the trypsin activity in the samples was stopped by addition of equal volumes of 50% acetic acid solution. For insulin (■) and transferrin (◆) samples, $n = 3$; for the conjugate (▲) sample, $n = 1$.

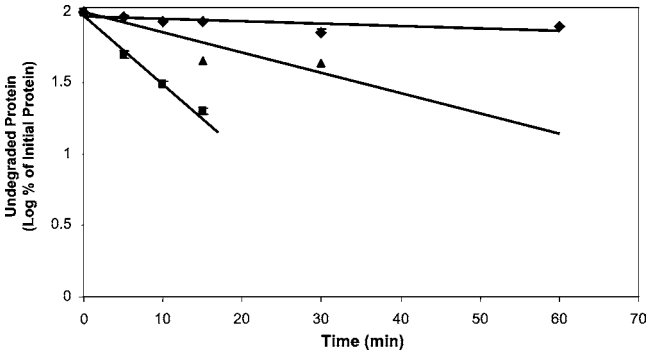

Figure 13. Semilog plot of % protein remaining vs time (min). Initial protein concentration in the reaction was 1 mg/mL, and the trypsin concentration was 3.2 mg/mL. The total reaction volume was 5 mL, and the pH was 7.4. Samples (50 μL) were withdrawn at different time intervals, and the trypsin activity in the samples was stopped by addition of equal volumes of 50% acetic acid solution. For insulin (■) and transferrin (◆) samples, $n = 3$; for the conjugate (▲) sample, $n = 1$.

Table 1. Degradation Rate Constants for Insulin, Transferrin, and Conjugate in the Presence of Trypsin[a]

protein sample	slope (min^{-1})	degradation rate constant (K), (min^{-1}) $\times 10^3$
insulin	−0.0486	21.10
transferrin	−0.0017	0.73
conjugate	−0.0142	6.17

[a] Rate constants were calculated from the slopes of semilog plot of % undegraded protein protein remaining vs time at early time points (Figure 13).

may stabilize the conjugated insulin against enzymes by creating a hindrance for the enzymatic attack.

CONCLUSIONS

An insulin−transferrin conjugate was synthesized by site-specific modification of insulin and modification of transferrin by a heterobifunctional cross-linker. Proper modification of the insulin molecule, which is critical to its physiological function, was verified through fluorescence photometry and mass spectrometry. The conjugation resulted in a macromolecular heteroconjugate consisting of two insulin molecules and one transferrin molecule. Insulin in the conjugated form exhibited enhanced stability against proteolytic attack. The insulin−transferrin conjugates synthesized here exhibit beneficial characteristics for oral delivery applications. This system when used in conjunction with the complexation hydrogels developed in our laboratory may result in a efficacious system for oral delivery of insulin.

ACKNOWLEDGMENT

This work was supported by NIH Grant R01 EB00024613 A2 to N.A.P., the Fletcher S. Pratt Foundation, NSF Grant CHE-0315337 and Welch Foundation Grant F1155 to J.S.B., and the NSF/IGERT program through Grant D6E-03333080 to N.A.P., J.S.B. and J.J.W.

LITERATURE CITED

(1) Lowman, A. M., Morishita, M., Kajita, M., Nagai, T., and Peppas, N. A. (1999) Oral delivery of insulin using pH-responsive complexation gels. *J. Pharm. Sci. 88*, 933−937.
(2) Morishita, M., Lowman, A. M., Takayama, K., Nagai, T., and Peppas, N. A. (2002) Elucidation of the mechanism of incorporation of insulin in controlled release systems based on complexation polymers. *J. Controlled Release 81*, 25−32.
(3) Lowman, A. M., and Peppas, N. A. (1997) Analysis of the complexation/decomplexation phenomena in graft copolymer networks. *Macromolecules 30*, 4959−4965.
(4) Lopez, J. E., and Peppas, N. A. (2004) Effect of poly(ethylene glycol) molecular weight and microparticle size on oral insulin delivery from P(MAA-g-EG) microparticles. *Drug Dev. Ind. Pharm. 30*, 497−504.
(5) Lopez, J. E., and Peppas, N. A. (2004) Cellular evaluation of insulin transmucosal delivery. *J. Biomater. Sci., Polym. Ed. 15*, 385−396.
(6) Gosk, S., Vermehren, C., Storm, G., and Moos, T. (2004) Targeting anti-transferrin receptor antibody (OX26) and OX26-conjugated liposomes to brain capillary endothelial cells using in situ perfusion. *J. Cereb. Blood Flow Metab. 24*, 1193−1204.
(7) Vinogradov, S. V., Batrakova, E. V., and Kabanov, A. V. (2004) Nanogels for oligonucleotide delivery to the brain. *Bioconjugate Chem. 15*, 50−60.
(8) Burdo, J. R., Antonetti, D. A., Wolpert, E. B., and Connor, J. R. (2003) Mechanisms and regulation of transferrin and iron transport in a model blood-brain barrier system. *Neuroscience 121*, 883−890.
(9) Bickel, U., Yoshikawa, T., and Pardridge, W. M. (2001) Delivery of peptides and proteins through the blood-brain barrier. *Adv. Drug Delivery Rev. 46*, 247−279.
(10) Qian, Z. M., Li, H., Sun, H., and Ho, K. (2002) Targeted drug delivery via the transferrin receptor-mediated endocytosis pathway. *Pharmacol. Rev. 54*, 561−587.
(11) Li, H., and Qian, Z. M. (2002) Transferrin/transferrin receptor-mediated drug delivery. *Med. Res. Rev. 22*, 225−250.
(12) Xia, C. Q., Wang, J., and Shen, W. C. (2000) Hypoglycemic effect of insulin-transferrin conjugate in streptozotocin-induced diabetic rats. *J. Pharmacol. Exp. Ther. 295*, 594−600.
(13) Shah, D., and Shen, W. C. (1996) Transcellular delivery of an insulin-transferrin conjugate in enterocyte-like Caco-2 cells. *J. Pharm. Sci. 85*, 1306−1311.
(14) Lim, C. J., and Shen, W. C. (2005) Comparison of monomeric and oligomeric transferrin as potential carrier in oral delivery of protein drugs. *J. Controlled Release 106*, 273−286.
(15) Widera, A., Bai, Y., and Shen, W. C. (2004) The transepithelial transport of a G-CSF−transferrin conjugate in Caco-2 cells and its myelopoietic effect in BDF1 mice. *Pharm. Res. 21*, 278−284.
(16) Carlsson, J., Drevin, H., and Axen, R. (1978) Protein thiolation and reversible protein-protein conjugation. N-Succinimidyl 3-(2-pyridyldithio)propionate, a new heterobifunctional reagent. *Biochem. J. 173*, 723−737.
(17) Stuchbury, T., Shipton, M., Norris, R., Malthouse, J. P., Brocklehurst, K., Herbert, J. A., and Suschitzky, H. (1975) A reporter group delivery system with both absolute and selective specificity for thiol groups and an improved fluorescent probe containing the 7-nitrobenzo-2-oxa-1, 3-diazole moiety. *Biochem. J. 151*, 417−432.
(18) Bradford, M. M. (1976) A rapid and sensitive method for the quantitation of microgram quantities of protein utilizing the principle of protein-dye binding. *Anal. Biochem. 72*, 248−254.

(19) Mei, H., Yu, C., and Chan, K. K. (1999) NB1-C16-insulin: site-specific synthesis, purification, and biological activity. *Pharm. Res. 16*, 1680−1686.
(20) Lorenzen, A., and Kennedy, S. W. (1993) A fluorescence-based protein assay for use with a microplate reader. *Anal. Biochem. 214*, 346−348.
(21) Garnett, M. C. (2001) Targeted drug conjugates: principles and progress. *Adv. Drug Delivery Rev. 53*, 171−216.
(22) Melton, R. G., and Sherwood, R. F. (1996) Antibody-enzyme conjugates for cancer therapy. *J. Natl. Cancer Inst. 88*, 153−165.
(23) Saito, G., Swanson, J. A., and Lee, K. D. (2003) Drug delivery strategy utilizing conjugation via reversible disulfide linkages: role and site of cellular reducing activities. *Adv. Drug Delivery Rev. 55*, 199−215.
(24) Thorpe, P. E., Wallace, P. M., Knowles, P. P., Relf, M. G., Brown, A. N., Watson, G. J., Knyba, R. E., Wawrzynczak, E. J., and Blakey, D. C. (1987) New coupling agents for the synthesis of immunotoxins containing a hindered disulfide bond with improved stability in vivo. *Cancer Res. 47*, 5924−5931.
(25) Lindsay, D. G., and Shall, S. (1971) The acetylation of insulin. *Biochem. J. 121*, 737−745.
(26) Udenfriend, S., Stein, S., Bohlen, P., Dairman, W., Leimgruber, W., and Weigele, M. (1972) Fluorescamine: a reagent for assay of amino acids, peptides, proteins, and primary amines in the picomole range. *Science 178*, 871−87.

BC050344K

Evaluation of RGD-Targeted Albumin Carriers for Specific Delivery of Auristatin E to Tumor Blood Vessels

Kai Temming,[§,†,*] Damon L. Meyer,[⊥] Roger Zabinski,[⊥] Eli C. F. Dijkers,[#] Klaas Poelstra,[†] Grietje Molema,[||] and Robbert J. Kok[†,‡]

Department of Pharmacokinetics and Drug Delivery, University Center for Pharmacy, University of Groningen, Groningen, The Netherlands; Medical Biology Section, Department of Pathology and Laboratory Medicine, University Medical Center Groningen, Groningen, The Netherlands; Department of Nuclear Medicine and Molecular Imaging, University Medical Center Groningen, Groningen, The Netherlands; KREATECH Biotechnology B.V., Amsterdam, The Netherlands; and Seattle Genetics, Bothell, Washington 98021. Received April 10, 2006; Revised Manuscript Received September 26, 2006

Induction of apoptosis in endothelial cells is considered an attractive strategy to therapeutically interfere with a solid tumor's blood supply. In the present paper, we constructed cytotoxic conjugates that specifically target angiogenic endothelial cells, thus preventing typical side effects of apoptosis-inducing drugs. For this purpose, we conjugated the potent antimitotic agent monomethyl-auristatin-E (MMAE) via a lysosomal cleavable linker to human serum albumin (HSA) and further equipped this drug−albumin conjugate with cyclic c(RGDfK) peptides for multivalent interaction with $\alpha_v\beta_3$-integrin. The RGD-peptides were conjugated via either an extended poly(ethylene glycol) linker or a short alkyl linker. The resulting drug-targeting conjugates RGDPEG−MMAE−HSA and RGD-MMAE−HSA demonstrated high binding affinity and specificity for $\alpha_v\beta_3$-integrin expressing human umbilical vein endothelial cells (HUVEC). Both types of conjugates were internalized by endothelial cells and killed the target cells at low nM concentrations. Furthermore, we observed RGD-dependent binding of the conjugates to C26 carcinoma. Upon i.v. administration to C26-tumor bearing mice, both drug-targeting conjugates displayed excellent tumor homing properties. Our results demonstrate that RGD-modified albumins are suitable carriers for cell selective intracellular delivery of cytotoxic compounds, and further studies will be conducted to assess the antivascular and tumor inhibitory potential of RGDPEG−MMAE−HSA and RGD-MMAE−HSA.

INTRODUCTION

Excessive angiogenesis, the formation of new blood vessel out of pre-existing capillaries, is a prominent feature during the pathogenesis of cancer. Solid tumors rely on angiogenesis to guarantee a continuous supply of oxygen and nutrients. Vascular-directed therapies are therefore extensively investigated for combating cancer (*1*). Induction of apoptosis in endothelial cells is one way to destroy tumor vessels. However, most cytotoxic compounds are neither selective for endothelial cells in general nor for angiogenic endothelial cells. As a consequence, they produce severe side effects limiting their applicability in cancer therapy. We propose targeting of the antimitotic agent monomethyl auristatin E (MMAE) to angiogenic blood vessels in tumor tissue. MMAE, a synthetic analogue of the natural product dolastatin 10, is a potent inhibitor of tubulin polymerization in dividing cells (*2*, *3*). Previously, MMAE has been conjugated via a valine−citrulline linker to monoclonal antibodies (mAb) for drug targeting purposes (*3*−*6*). The valine−citrulline linker is highly stable in serum but is cleaved by lysosomal enzymes like cathepsin B after internalization of the conjugate by target cells (*7*, *8*, *9*). We now present a novel type of MMAE conjugate, in which the drug is bound via the valine−citrulline linker to human serum albumin (HSA). HSA is readily available in gram amounts and can serve as a natural and therefore biocompatible and biodegradable carrier with a lower polydispersity than any artificial polymeric carrier. Selectivity for angiogenic endothelial cells is introduced into the albumin backbone by conjugation of multiple cyclic RGD-peptides, which bind to $\alpha_v\beta_3$-integrin (*10*). We applied either a short alkyl linker to introduce a maximum of RGD-peptide or an extended polyethylene glycol linker to infer an increased circulation time and shielding of the modified albumin from the immune system. The $\alpha_v\beta_3$-integrin target receptor is expressed in high amounts on angiogenic endothelium, but expression is minimal on quiescent endothelial cells and highly limited in other healthy tissues. The restricted expression profile and the good accessibility of endothelial cells make it an ideal target for drug delivery purposes (*11*). We have previously described that RGD-equipped carriers bind with high avidity to proliferating endothelial cells, and that they are internalized and lysosomally degraded (*12*−*14*).

In the present study, we first describe the synthesis and characterization of the two types of RGD-equipped MMAE−albumin conjugates. Second, we report on the binding, uptake and cell killing properties of the conjugates, and we compared the tumor vasculature homing potential in C26 tumor bearing mice.

MATERIALS AND METHODS

Synthesis and Purification of MMAE−HSA. HSA (Sanquin, Amsterdam, The Netherlands) was thiolated with 2-iminothiolane (2-IT) at pH 8, 37 °C. Thiolation was monitored by DTNB of PD10-purified analytical samples. When the desired

* Corresponding author. E-mail: k.temming@rug.nl. Tel: +31 50 363 7627. Fax: +31 50 363 3247.

§ KREATECH Biotechnology B.V.

† Pharmacokinetics and Drug Delivery.

⊥ Seattle Genetics.

Department of Nuclear Medicine and Molecular Imaging.

|| Medical Biology Section, Department of Pathology and Laboratory Medicine.

‡ Present affiliation: Department of Pharmaceutics, Utrecht Institute for Pharmaceutical Sciences, University of Utrecht, The Netherlands.

10.1021/bc060087z CCC: $33.50 © 2006 American Chemical Society
Published on Web 10/17/2006

thiolation level was reached (4.1 SH/albumin), the modified albumin was purified over a G25 gel filtration desalting column. The thiol/albumin mole ratio was determined by measuring the thiol concentration with Ellman's assay and the albumin concentration by UV absorbance at 280 nm. Thiolated albumin was treated with a 20% excess (over measured thiols) of MC−val-cit−PAB−MMAE. Ellman's assay was performed on the reaction mixture to ensure complete alkylation. Excess maleimide-drug-linker was quenched, and removed with solid-phase resin-bound-DTT (BioVectra cat. #3505), and the product was purified by gel filtration chromatography.

Characterization of MMAE−HSA. The concentration of the MMAE−HSA conjugates was measured using the BCA assay kit from Pierce. The MMAE−HSA conjugate was analyzed by size exclusion chromatography for percentage of monomer using a Tosoh Bioscience TSKgel G3000SW (7.8 cm × 30 cm, 5 μm) size exclusion chromatography (SEC) column. The conjugates were more than 91% monomer. To check for residual drug-linker, a sample of conjugate was treated with MeOH and separated in a microconcentrator to precipitate the protein, and the supernatant was analyzed by reverse phase (RP) HPLC (Synergi C12 column with a linear gradient from 5 mM ammonium phosphate, pH 7, to 100% acetonitrile). No free drug-linker was detectable, compared to spiked controls and a standard curve with a quantitation limit of <0.5% of bound drug. The MMAE−HSA conjugates were tested for endotoxin contaminant using BioWhitaker-Cambrex LAL QCL-1000 kit. Endotoxin was below the limit of detection (~0.2 EU/mg).

The drug to HSA ratio was estimated by treating 300 μg of conjugate with cathepsin B to release free MMAE from the MC−val-cit−PAB linker. The protein was removed by precipitation with TCA/MeOH, heated at 37 °C for 10 min and centrifuged at high speed to pellet. The released drug in the supernatant was analyzed by RP-HPLC as described above for drug-linker and quantitated by comparison to a standard curve. The drug/albumin values agreed closely (±5%) with the thiol/albumin ratios determined prior to conjugation. A change in the OD250/OD280 ratio commensurate with the conjugation of PAB-containing moieties qualitatively corroborated the measured drug load. Thereafter MMAE−HSA was subjected to MALDI-TOF analysis. HSA and MMAE−HSA were dissolved in 50:50:0.1 methanol:water:acetic acid at a concentration of 1 mg/mL. 1 μL was mixed with 1μL of matrix (20 mg/mL sinapinic acid in 60:40:0.1 water:acetonitrile:trifluoroacetic acid), transferred onto a stainless steel sample holder, and dried before being introduced into a Voyager-DE PRO workstation (Applied Biosystems). Mass spectra were obtained by averaging the signals from 100 laser shots. Correction of data was performed using BSA as a control. Average molecular weights received by MALDI-TOF analysis were used to calculate differences in mass of HSA to MMAE−HSA.

Synthesis of RGDPEG−MMAE−HSA. MMAE−HSA (59.1 nmol) dissolved in PBS was incubated with a 50-fold molar excess of vinylsulfone-poly(ethylene glycol)-*N*-hydroxysuccinimide ester (VNS-PEG-NHS; Nektar, AL; 20 mg/mL in water, 2.96 μmol), which was added dropwise. The mixture was protected from light with aluminum foil and incubated for 1h at room temperature while gently shaking on a spiramix. Meanwhile, the RGD−peptide c(RGDf(ϵ-*S*-acetylthioacetyl)K) (Ansynth Service, Roosendaal, The Netherlands) was dissolved at 10 mg/mL in a 1:4 acetonitrile/water mixture. The peptide (3.25 μmol) was added dropwise to the reaction mixture at a peptide to protein molar ratio of 55:1, after which hydroxylamine was added to a final concentration of 50 mM. Reaction was carried out over night at room temperature while protected from light. Remaining VNS groups were quenched by addition of cysteine (3.25 μmol; 55-fold molar excess over the amount of HSA), after which the product was dialyzed against PBS and finally purified by SEC using a Superdex200 column on an Äkta System (GE Healthcare, Uppsala, Sweden). The final product RGDPEG−MMAE−HSA was stored at −20 °C. A control conjugate RADPEG−MMAE−HSA was prepared according to the same protocol with the control peptide c(RADf(ϵ-*S*-acetylthioacetyl)K).

Synthesis of RGD−MMAE−HSA. MMAE−HSA (59.1 nmol) dissolved in PBS was incubated with a 22-fold molar excess of iodoacetic acid *N*-hydroxysuccinimide ester (SIA-linker; Sigma, St. Louis, MO; 10 mg/mL in DMF, 1.3 μmol), which was added dropwise. The mixture was protected from light with aluminum foil and incubated for 1 h at room temperature while gently shaking on a spiramix. RGD−peptide (1.48 μmol) was added in a mole:mole ratio of 25:1 followed by hydroxylamine addition as described above. Reaction was carried out within 6 h at room temperature while protected from light. Products are purified by dialyzing three times against PBS using Slide-A-Lyzer dialysis cassettes (Pierce, MWCO 10 kDa). The final products RGD−MMAE−HSA and the control conjugate RAD−MMAE−HSA were stored at −20 °C.

Characterization of RGDPEG−MMAE−HSA and RGD−MMAE−HSA. Protein content of synthesis products was estimated by BCA protein assay kit (Pierce). Both the intermediate and final products were subjected to analytical SEC to reveal increase in size, purity, and grade of aggregation. SDS-PAGE (12%, Ready Gel; Bio-Rad, Veenendaal, The Netherlands) and Western blotting were performed to corroborate covalent binding of the RGD−peptide. Duplicate gels were either stained for protein (Coomassie Brilliant Blue staining) or blotted on a PVDF membrane (Roche, Mannheim, Germany). The membrane was blocked with BSA and subsequently incubated with an in-house prepared rabbit anti-RGD antiserum (*12*). The signal was amplified with a polyclonal goat anti rabbit IgG conjugated with horse radish peroxidase (GARPO, DAKO). Peroxidase was visualized by incubation with 3-amino-9-ethylcarbazole (AEC, Sigma). The amount of RGDPEG and RGD bound per HSA was determined by MALDI-TOF analysis, as explained earlier in this section.

Cells. HUVEC were obtained from the UMCG Endothelial Cell Facility. Primary isolates were cultured in 1% gelatin-coated tissue culture flasks (Costar, Cambridge, MA) at 37 °C under 5% CO_2/95% air. The culture medium, hereafter referred to as EC medium, consisted of RPMI 1640 (BioWittaker, Verviers, Belgium) supplemented with 20% heat inactivated fetal calf serum (Integro, Zaandam, The Netherlands), 2 mM L-glutamine (Invitrogen, Breda, The Netherlands), 5 U/mL heparin (Leo Pharmaceutical Products, Weesp, The Netherlands), 100 U/mL penicillin (Yamanouchi Pharma, Leiderdorp, The Netherlands, 100 μg/mL streptomycin (Radiumfarma-Fisiopharma, Italy), and 50 μg/mL EC growth factor supplement extracted from bovine brain. After attaining confluence, cells were detached from the surface by trypsin EDTA (0.5/0.2 mg/mL in PBS) treatment and split in 1:3 ratio. Cells were used up to passage four. C26 mouse carcinoma cells were cultured under the same conditions as described for HUVEC, in DMEM medium (Gibco) containing 10% fetal calf serum.

Endothelial Cell Binding Affinity of RGD-Equipped Conjugates. Binding affinity of RGDPEG−MMAE−HSA and RGD−MMAE−HSA to $\alpha_v\beta_3$-integrin expressed on the surface of HUVEC was determined by competitive binding studies using ^{125}I-labeled echistatin as radioligand for $\alpha_v\beta_3$-integrin (*15*). Echistatin was radiolabeled using the chloramine T method (*16*). On the day of the experiment, ^{125}I-echistatin was purified using a PD-10 column (GE Healthcare). Confluent monolayers of HUVEC in a 24-well plate (Costar) were incubated with 100 000 cpm ^{125}I-echistatin in the presence of serial dilutions of the

conjugates in binding buffer (50 mM Tris-HCl, pH 7.4, 150 mM NaCl, 1 mM $CaCl_2$, 1 mM $MgCl_2$, 1 mM $MnCl_2$ and 1% BSA) at 4 °C for 4 h (*13*). Subsequently, the supernatant was harvested, and cells were washed three times with binding buffer and lysed with 1 M NaOH. Radioactivity was counted in a Packard RIASTAR multiwell gamma counter (GMI). Data were analyzed by nonlinear regression using the GraphPad Prism program (GraphPad Software Inc).

Binding Specificity of RGD-Equipped Conjugates to Endothelial Cells and Tumor Cells. HUVEC were incubated with ^{125}I-radiolabeled RGDPEG−MMAE−HSA and RGD−MMAE−HSA, which had been radiolabeled using the chloramine T method, and purified on the day of the experiment. Radiochemical purity as determined by trichloroacetic acid precipitation was above 96%, and specific activity was respectively 690 kBq/μg and 570 kBq/μg. Confluent monolayers of HUVEC in 24-well plates were incubated with 100 000 cpm of radiolabeled conjugate in presence of excess of c(RGDfK)-Ata (10 μM), C(RADfK)-Ata (10 μM), and RGD−HSA (0.5 μM) in binding buffer. Cell-bound radioactivity was harvested and counted as described above.

Both radiolabeled conjugates were also incubated with confluent C26 carcinoma cells in the absence and presence of an excess of c(RGDfK)-Ata (10 μM). Incubation conditions and analysis of cell-bound radioactivity were as describe above.

Uptake of RGD-Equipped Conjugates into Endothelial Cells. HUVEC were incubated with ^{89}Zr-radiolabeled RGD-PEG−MMAE−HSA or RGD−MMAE−HSA to determine uptake of the products. The ^{89}Zr-radiolabel will remain trapped inside the cells after degradation of the carrier, in contrast to the ^{125}I-radiolabel. For radiolabeling, 3.7 nmol RGDPEG−MMAE−HSA or RGD−MMAE−HSA was mixed with 18.6 nmol of the chelator TFP-N-succinyldesferal-Fe (desferal) at pH 8.5. After an incubation period of 30 min, the reaction mixture was purified on a Hitrap desalting column (GE Healthcare). UV absorbance at 430 nm was used to assess conjugation of Fe^{3+}-containing desferal. Fe^{3+} was replaced with radioactive ^{89}Zr at pH 6.8 as described (*17*), and the product was purified using a centricon filter unit (MWCO 10 kDa; Millipore, Billerica, MA). Radiochemical purity was 96% or higher, as determined by trichloroacetic acid precipitation, and specific activity was 17.75 MBq/mg and 2.1 MBq/mg for RGDPEG−MMAE−HSA and RGD−MMAE−HSA. Confluent cell layers were incubated with 250 000 cpm ^{89}Zr-RGDPEG−MMAE−HSA or 50 000 cpm ^{89}Zr-RGD−MMAE−HSA at either 4 °C or 37 °C for 4 and 8 h. Supernatant and cell associated radioactivity were harvested as described above, and radioactivity was counted on a 1282 COMPUGAMMA CS (Perkin-Elmer, Boston, MA).

***In Vitro* Killing Efficacy of RGD-Equipped Conjugates.** HUVEC were plated on 96-well plates (Costar) at 5000 cell/well and exposed to a graded titration of RGDPEG−MMAE−HSA and RGD−MMAE−HSA. RAD-equipped conjugates were tested at a concentration of 1 and 10 μg/mL. After 72 h of incubation, cell viability was determined by MTS cell viability assay (Promega, Madison, WI) (*18*). Absorption was measured on a Thermomax microplate reader (Molecular Devices, Sunnyvale, CA) at 490 nm after 2 h of incubation at 37 °C. Data were analyzed by nonlinear regression using GraphPad Prism.

Tumor Accumulation of RGD-Equipped Conjugates in Subcutaneous C26 Tumor Model. All animal experiments were performed according to the national law on animal experiments and were approved by the Animal Ethics Committee of the University of Groningen. Upon arrival, male Balb/C mice were housed in a temperature-controlled room with a 12 h light/dark cycle and offered ad libitum intake of tap water

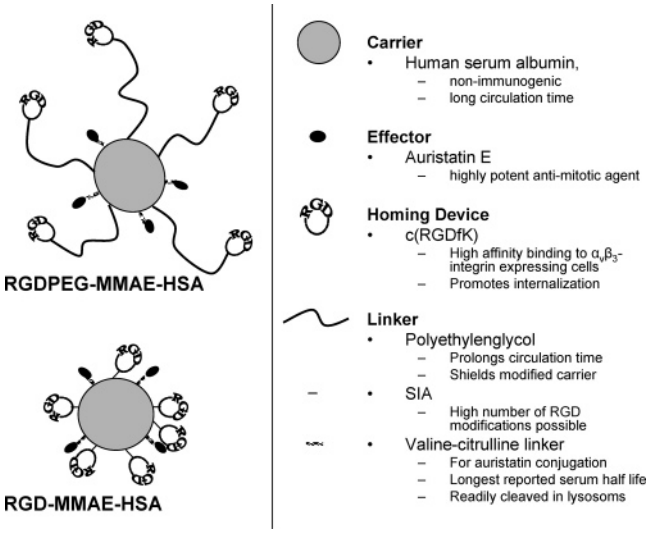

Figure 1. Schematic representation of RGD-equipped MMAE−albumin conjugates.

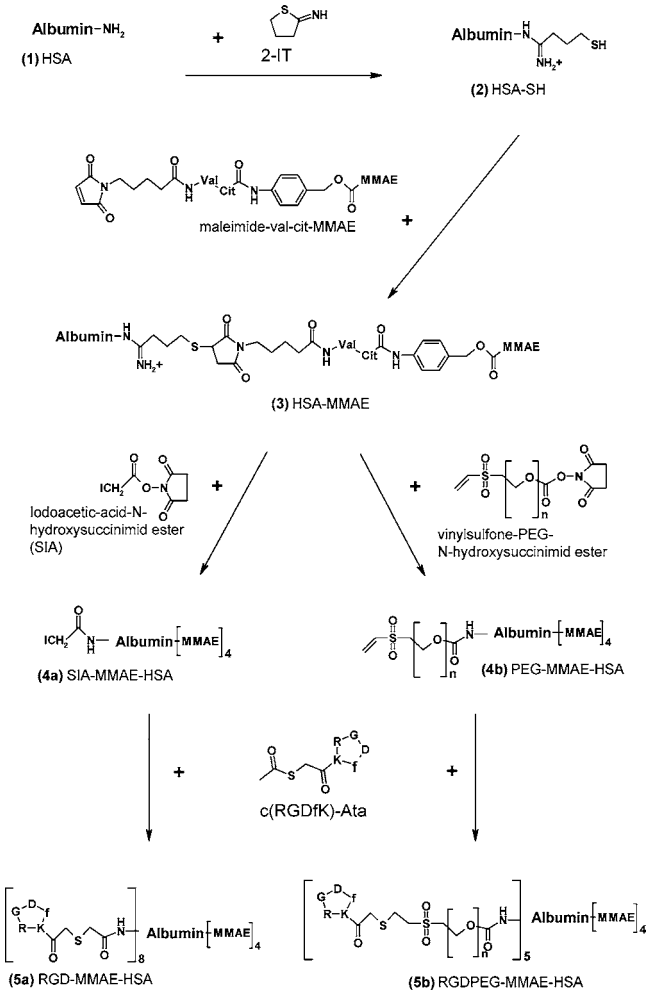

Figure 2. Reaction scheme for the synthesis of RGDPEG-MMAE−HSA and RGD−MMAE−HSA.

and standard rodent chow. Mice were anesthetized by Forene (Abbott B.V. Hofddorp, The Netherlands) inhalation in combination with N_2O (600 mL/min) and O_2 (300 mL/min). C26 murine colon carcinoma cells (1×10^6) were inoculated subcutaneously in the flank of the mice and allowed to grow to a size of approximately 8 × 8 mm. Thereafter a single dose of 30 μg of RGDPEG−MMAE−HSA or RGD−MMAE−HSA was injected in the penis vein under Forene/N_2O/O_2 anesthesia.

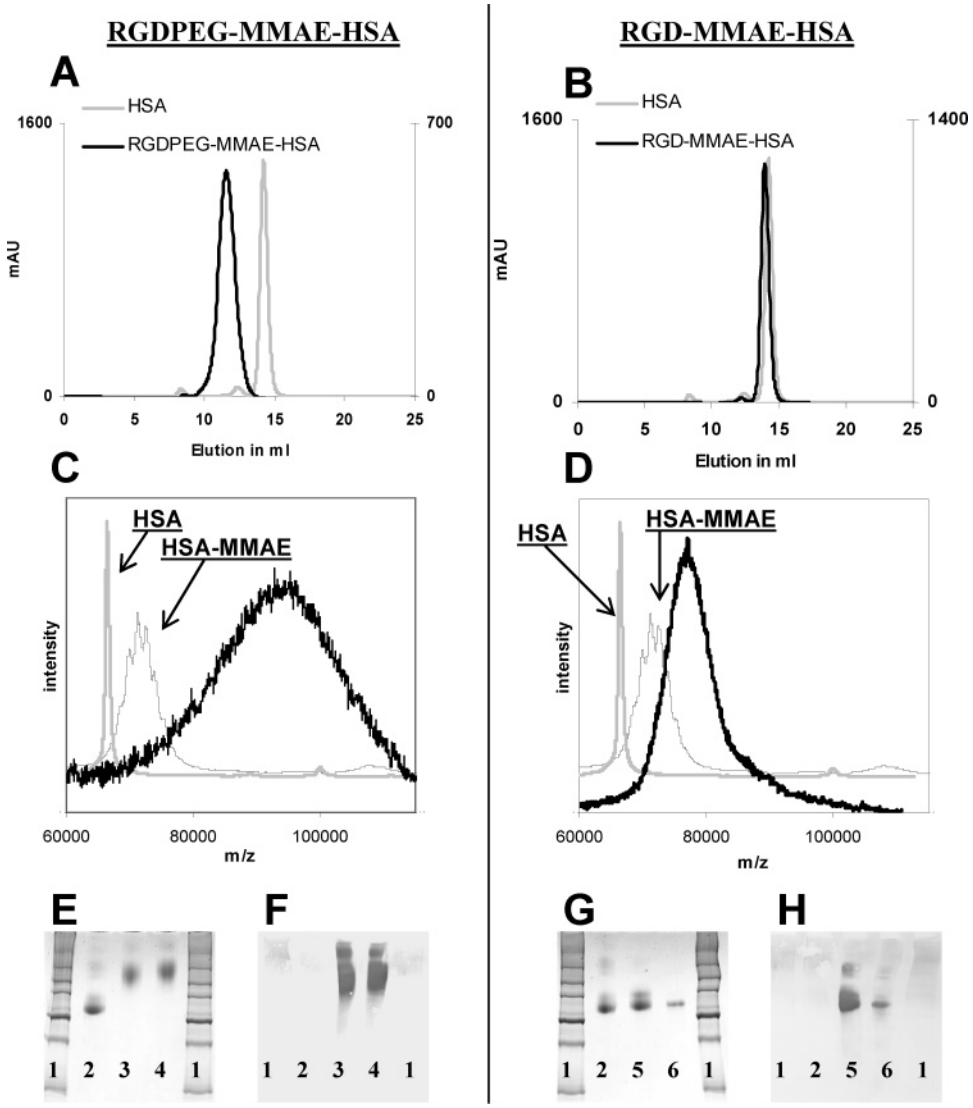

Figure 3. A,B: Size exclusion chromatography of RGDPEG-MMAE−HAS (A) and RGD−MMAE−HSA (B) revealed increase in size due to coupling of RGD−peptide via a PEG-linker (A) or a short alkyl linker (B). No aggregates had been formed. C,D: MALDI-TOF has been used to estimate molecular weight of RGDPEG-MMAE−HSA (C) and RGD−MMAE−HSA (D). HSA and MMAE−HSA are shown for comparison. E−H: SDS-PAGE (E, G) had been performed with a molecular weight marker (*1*), MMAE−HSA (*2*), RGDPEG-MMAE−HSA (*3*), RGDPEG−HSA (*4*), RGD−MMAE−HSA (*5*), and RGD−HSA (*6*). Identical gels have been blotted on a membrane and were immunostained using anti-RGD antibody (F, H).

Mice were sacrificed at 3 h after injection or at 24 h after injection. Tumor, liver, kidney, and spleen were collected and snap frozen in liquid nitrogen.

Immunohistochemical Detection of Conjugates. Cryostat sections (5 μm) prepared from tumor, liver, kidney, and spleen were fixed in acetone and stained for the presence of the conjugates. For this purpose, a rabbit anti-HSA antibody was applied to the sections in a 1:1500 dilution. After removal of endogenous peroxidase activity, staining was amplified with a peroxidase-conjugated goat anti-rabbit IgG (GARPO, DAKO) followed by a peroxidase-conjugated rabbit anti-goat IgG (RAGPO, DAKO). Peroxidase was visualized by incubation with 3-amino-9-ethylcarbazole (AEC, Sigma), and sections were counterstained with Mayers hematoxylin (Merck, Darmstadt, Germany) according to standard laboratory protocols.

Colocalization of conjugates with either tumor endothelium or tumor cells was investigated by fluorescent immunohistochemistry. Deposited conjugate was stained by rabbit anti-HSA antibody (1:1000 dilution), followed by secondary staining with FITC-conjugated goat anti-rabbit IgG (DAKO). Nuclei were stained using 4′-6-Diamidino-2-phenylindole (DAPI, Sigma). Nuclei of endothelial cells and tumor cells were discriminated by phenotypical differences (endothelial nuclei are flattened, as compared to big tumor cell nuclei).

Table 1. Characterization of Drug-Targeting Conjugates by MALDI-TOF

	number of modifications per HSA		
	MMAE	RGDPEG or RGD	MW in kDa
RGDPEG-MMAE−HSA	4.1	5.4	94.5
RGDPEG−HSA	-	7.1	96.1
RGD−MMAE−HSA	4.1	7.6	77.3
RGD−HSA	-	13.2	76.2

RESULTS

Synthesis and Characterization. We developed RGD-equipped auristatin conjugates that are directed to $\alpha_v\beta_3$-integrin on angiogenic endothelium (Figure 1). These drug-targeting conjugates were prepared by coupling MMAE and RGD or RGDPEG to an albumin backbone (Figure 2). Both, HPLC and MALDI-TOF analysis demonstrated an average of four MMAE per albumin (Table 1, Figure 3). RP-HPLC revealed that the products did not contain free drug or linker molecules. The short

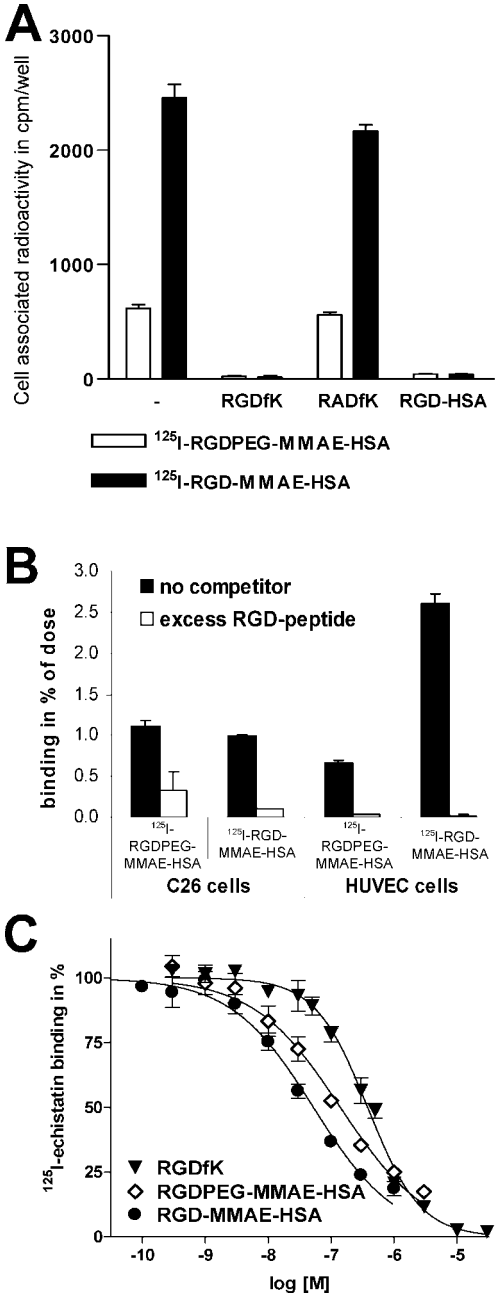

Figure 4. Binding properties of drug-targeting conjugates. **(**A**)** Binding specificity was tested by coincubation of radiolabeled drug-targeting conjugates with excess of c(RGDfK)-Ata (10 μM), c(RADfK)-Ata (10 μM), and RGD−HSA (0.3 μM) on $\alpha_v\beta_3$-expressing HUVEC. **(**B**)** Radiolabeled drug-targeting conjugates were incubated with C26 carcinoma cells and HUVEC. Specificity of binding was determined by conincubation with excess of c(RGDfK)-Ata (10 μM). **(**C**)** Binding affinity is detected by competition between ^{125}I-echistatin and increasing concentrations of drug-targeting conjugates for $\alpha_v\beta_3$-integrin on HUVEC. Concentrations are expressed in mol/L.

SIA linker allowed more RGD to be coupled per HSA compared to the extended PEG linker. Furthermore, RGD numbers were higher in conjugates prepared with parental albumin, not equipped with MMAE (Table 1). SEC analysis demonstrated an increase in size due to the modification, especially for PEGylated products (Figure 3). In addition, it was shown that little aggregation of products occurred, comparable to aggregation found for nonmodified HSA. Aggregation hampered further use of drug-targeting conjugates only when drug loads of eight MMAE per albumin were tested (data not shown). Coupling of RGD−peptide onto the distal end of PEG was demonstrated by anti-RGD western blot. Both products as well as their

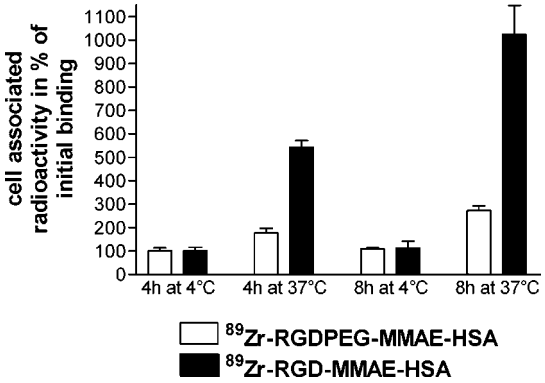

Figure 5. ^{89}Zr-RGDPEG-MMAE−HSA and ^{89}Zr-RGD−MMAE−HSA were incubated with HUVEC at 4 and 37 °C for 4 or 8 h to determine uptake of the drug-targeting conjugates.

Table 2. Binding and Cell Killing Potency of Drug-targeting Conjugates

		binding		fold
	RGD−peptides per HSA	EC_{50} in nM	IC_{50} in nM	increase vs RGD
RGDPEG-MMAE−HS A	5.4	41.1	141	2.7
RADPEG-MMAE−HS A		>150[a]	>1000[a]	-
RGDPEG−HSA	7.1		18.6	21
RGD−MMAE−HSA	7.6	6.64	52.6	7.3
RAD−MMAE−HSA		>150[a]	>300[a]	-
RGD−HSA	13.2		5.90	65
c(RGDfK)-Ata			382	1

[a] Highest tested concentration.

respective control products RGDPEG−HSA and RGD−HSA were positively stained by anti-RGD antibody, while MMAE−HSA was not stained (Figure 3).

Binding Specificity of RGD-Equipped Conjugates to Endothelial Cells and C26 Carcinoma Cells. Binding specificity was evaluated using ^{125}I-labeled drug-targeting conjugates. Both conjugates bound to $\alpha_v\beta_3$-integrin expressing HUVEC and could be completely displaced by excess of RGD−peptide or RGD−HSA but not by RAD−peptide (Figure 4A). This demonstrated that binding was mediated exclusively by the introduced RGD-moiety. Remarkably, a 4 times higher binding of ^{125}I-RGD−MMAE−HSA than of ^{125}I-RGDPEG−MMAE−HSA was observed. Both conjugates bound also to C26 cells but in contrast to HUVEC no difference in the quantity of binding could be detected. Binding to C26 cells was as well mediated by the introduced RGD-moiety, as could be concluded from the complete displacement by RGD−peptide (Figure 4B).

Binding Affinity of RGD-Equipped Conjugates to Endothelial Cells. Binding affinity of drug-targeting conjugates was determined in competition experiments with the known $\alpha_v\beta_3$-integrin ligand ^{125}I-echistatin as shown in Figure 4C. Both conjugates displaced ^{125}I-echistatin in the low nanomolar range, with the binding affinity of RGD−MMAE−HSA being higher than of RGDPEG−MMAE−HSA. The respective control conjugate RGDPEG−HSA and RGD−HSA displayed higher affinities (Table 2). All conjugates possessed an increased affinity for $\alpha_v\beta_3$-integrin as compared to the single c(RGDfK) peptide. Furthermore, a clear relationship was observed between the average number of RGD/albumin and affinity for the target cells. The observation that multivalent RGD-carriers bind with higher affinity than monovalent carriers has been made before (*12, 19, 20*).

Uptake of RGD-Equipped Conjugates into Endothelial Cells. Drug-targeting conjugates were labeled with ^{89}Zr to study intracellular uptake. ^{89}Zr, captured by the chelator desferal, is highly stable, and its hydrophilicity will lead to its entrapment

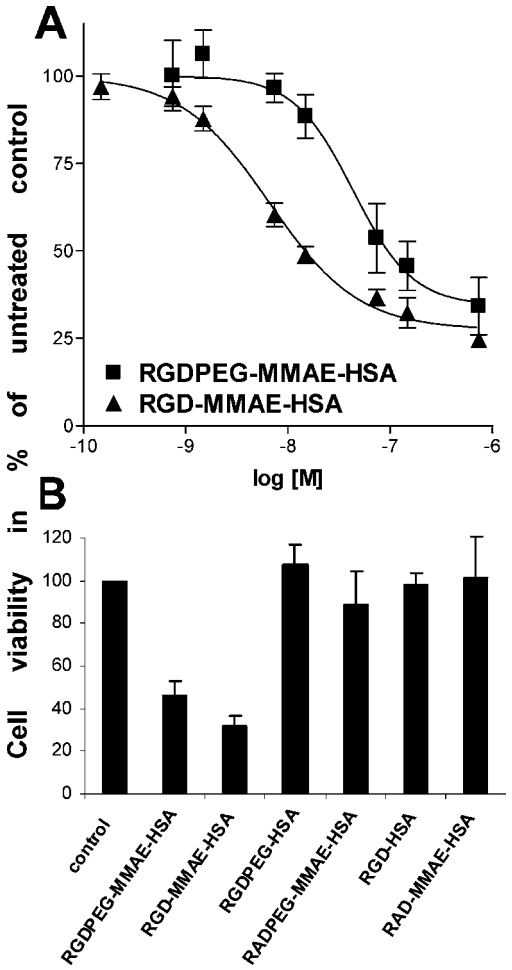

Figure 6. **(A)** HUVEC have been incubated with increasing concentrations of drug-targeting conjugates to determine killing efficacy. Concentrations are expressed in mol/L. (EC_{50}s: RGDPEG-MMAE−HSA 41 nM; RGD−MMAE−HSA 6.6 nM). **(B)** Viability of HUVEC treated with 150 nM of drug targeting and control conjugates.

inside the cells after degradation of the carrier (*21*, *22*). As such, it is an ideal label for uptake studies since this will prevent redistribution of the radiolabel. In spite of all previous modifications, we were able to attach 1.2 (RGDPEG−MMAE−HSA) and 0.9 (RGD−MMAE−HSA) desferal per conjugate. ^{89}Zr labeled conjugates were incubated with HUVEC at 4 °C and 37 °C degrees. Energy dependent uptake processes take place at 37 °C, at which more cell associated radioactivity was found than at 4 °C (Figure 5), at which these processes are inhibited. The cell-associated radioactivity increased further upon longer incubation at 37 °C but not at 4 °C. Taken together, these results indicated uptake of the drug-targeting conjugates via an active process. Uptake was more pronounced for ^{89}Zr-RGD−MMAE−HSA than for ^{89}Zr-RGDPEG−MMAE−HSA (black versus white bars).

***In Vitro* Killing Efficacy of RGD-Equipped Conjugates.** Monomethyl auristatin E has been shown to inhibit the polymerization of tubulin in dividing cells and thus to induce apoptosis (*3*). To study the effect of intracellularly delivered MMAE, HUVEC were exposed for 72 h to serial dilutions of both drug-targeting conjugates and their respective control. Regression analysis of the concentration−cytotoxicity curves in Figure 6A revealed EC_{50}s (effective concentrations) of 44 nM for RGDPEG−MMAE−HSA and 6.6 nM for RGD−MMAE−HSA. In contrast, the RAD-containing control conjugates and the control conjugates without MMAE showed no effect at concentration as high as 150 nM (Figure 6B).

Preliminary *In Vivo* Evaluation. To determine whether the RGD-equipped drug carriers accumulate in the tumor endothelium, we administered RGDPEG−MMAE−HSA and RGD−MMAE−HSA to C26 murine colon carcinoma-bearing mice. Anti-HSA staining of sections of organs and tumors showed the presence of both conjugates in the tumor, 3 h after injection (Figure 7A,F). In contrast, hardly any drug-targeting conjugate was found in the spleen and kidneys. A clear staining was detected in the liver. Higher magnification revealed the presence of the drug-targeting conjugates in the hepatic sinusoids, not confined to any sinusoidal cell type.

This distribution pattern changed after 24 h. RGD−MMAE−HSA could not be detected in any of the three control organs (Figure 7H−J) while a clear accumulation in the tumor could be detected (Figure 7G). RGDPEG−MMAE−HSA was also absent in kidneys and spleen but showed some residual staining in the liver (Figure 7C−E), apart from the pronounced tumor accumulation (Figure 7B).

To identify which cell types had accumulated the auristatin−albumin conjugates, we investigated the colocalization of the albumins with either endothelial cells or tumor cells. Since endothelial cells display typically flattened nuclei in contrast to bigger nuclei for C26 cells, DAPI nuclear staining could be used to discriminate between vasculature and tumor cells. Figure 8 shows the typical fluorescent staining for cell nuclei (blue) and HSA (green) of a tumor 24 h after injection of RGD−MMAE−HSA (8A) and RGDPEG−MMAE−HSA (8B). A blood vessel with two typically flattened endothelial nuclei is pointed out by red arrows, while some of the larger tumor cell nuclei are indicated by yellow arrows. HSA was found along the vessel wall, but also colocalized with tumor cells within the tumor mass.

DISCUSSION

Immunotoxins are an attractive strategy to kill specific cell types without affecting other cells in the body. Typically, such conjugates have been prepared by conjugating cytotoxic agents to antibodies (*23*). We now report on a different type of target-cell specific toxin containing conjugate, in which RGD−peptides facilitate recognition of angiogenic endothelial cells (Figure 1). The RGD-motif is a highly conserved receptor binding ligand and allows studying RGD-equipped drug targeting in different species without further modification of the homing ligand. This is not possible for antibodies that commonly are species specific. RGD-equipped albumin conjugates are a versatile platform that can be readily modified with drugs and tailored with other moieties such as PEG. HSA functions in this context as a monomeric polymer featuring low immunogenicity, high biocompatibility, and excellent biodegradability. Furthermore, renal filtration of drug is prevented by the high molecular size of albumin enabling prolonged exposure of the target cells to the conjugates. Here we report the development of RGD−MMAE−HSA and RGDPEG−MMAE−HSA, in which MMAE−HSA is equipped with RGD−peptide via a short alkyl linker or via an extended PEG linker (Figure 2). MALDI-TOF analysis of synthesis products demonstrated that both conjugates were modified with multiple RGD−peptides. It has been recognized that RGD-based drug-targeting conjugates need to be equipped with multiple RGD−peptides in order to obtain optimal binding to and uptake into the target cell (*11*, *24*) and current research focuses on various multivalent carriers for delivery of therapeutic or diagnostic agents (*25*−*29*). The presently developed drug-targeting conjugates both demonstrated multivalent binding, as they bind with higher affinity than single RGD−peptide, and they are also taken up, thus fulfilling these criteria. However, application of the short alkyl linker resulted in a higher average RGD/carrier ratio than the PEG linker. As a consequence,

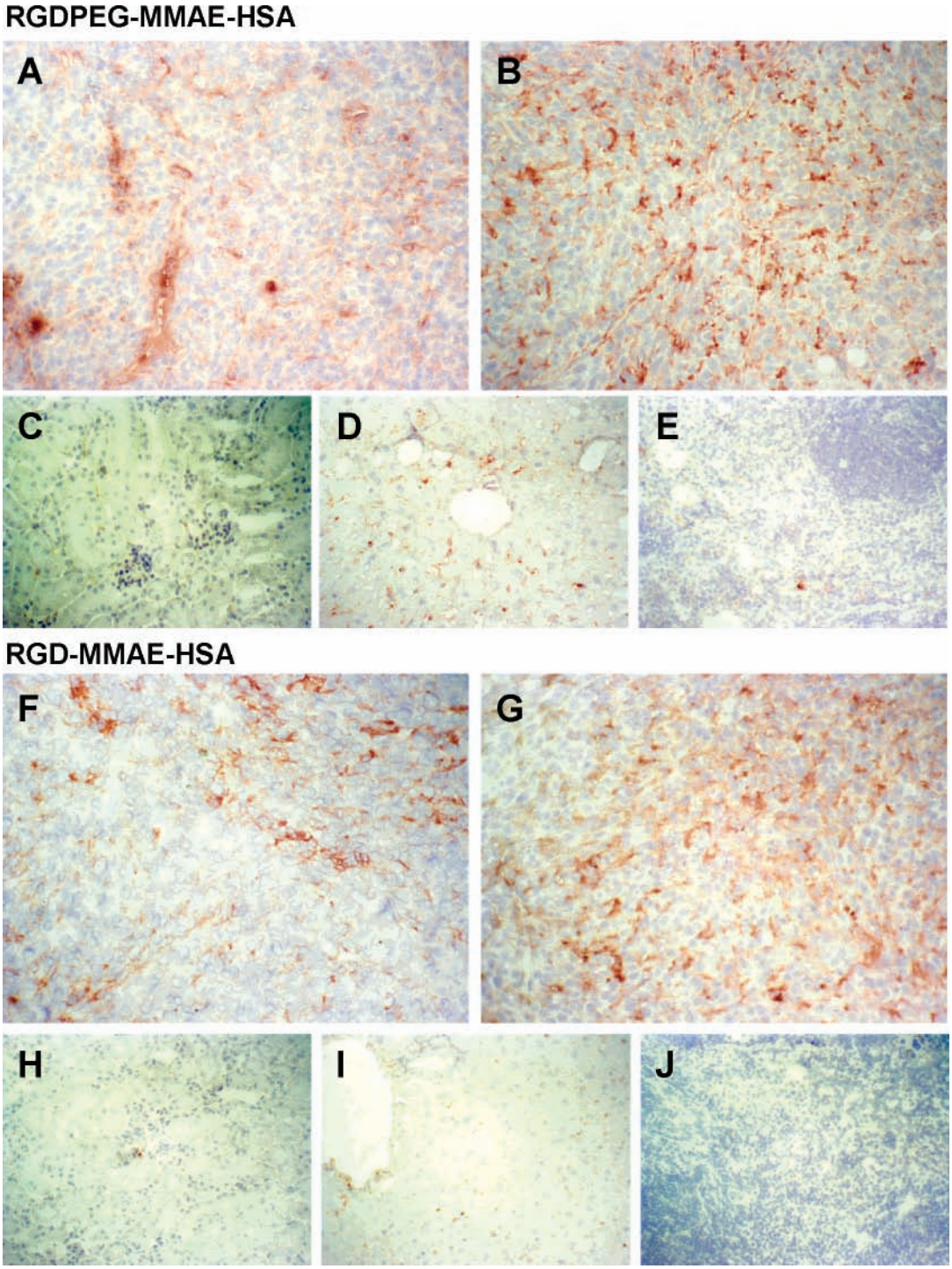

Figure 7. C26 tumor bearing mice had been injected with either 30 μg RGDPEG-MMAE−HSA (A-E) or RGD−MMAE−HSA (F−J). Sections were stained with rabbit antiHSA antibody. Both drug-targeting conjugates localized in C26 tumors 3 h (A, F) and 24 h (B, G) after i.v. administration. Sections of kidney (C, H), liver (I), and spleen (E, J) at 24 h time point are stained negative. All pictures are taken at magnification of 200×; C−E and H−J are reduced to 45% of the size of A, B, F, and G.

RGD−MMAE−HSA bound with higher affinity and in higher quantity to $\alpha_v\beta_3$-expressing HUVEC than RGDPEG−MMAE−HSA. We did not fractionate our products further into batches with a narrow RGD/HSA ratio, and it can be conceived that individual RGDPEG−MMAE−HSA with high RGD loading will bind stronger to the target cells. Another explanation for the difference in affinity might be a different spatial presentation of RGD−peptides due to the extended PEG linker, or differences in hydrophobicity between the two linkers.

In line with the observed higher affinity and higher uptake efficiency, RGD−MMAE−HSA demonstrated superior EC_{50} in cell killing as compared to the PEGylated conjugates. This result was corroborated upon testing of RGD−MMAE−HSA bearing an average of six MMAE molecules but less RGD−peptides per carrier, since only little improvement in EC_{50} was found (data not shown). Taken together, these data indicate that a high number of RGD−peptides and efficient internalization is more important than a high drug load.

Both drug-targeting conjugates demonstrated efficient killing of the target cells at nanomolar concentrations. The EC_{50} values (Table 2) are in a similar range as EC_{50} values of MMAE modified antibodies against E-selectin (*6*), CD20 on non-Hodgkin's lymphoma (*4*), TMEFF2, a plasma membrane protein overexpressed in prostate cancer (*5*), and the glycoprotein NMB

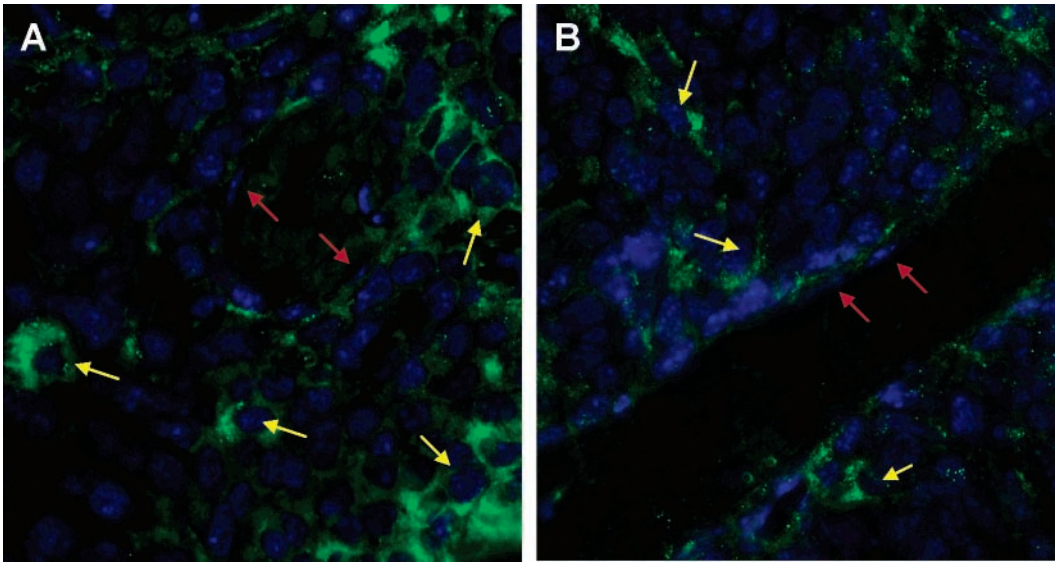

Figure 8. Colocalization of auristatin−albumin conjugates with tumor vasculature and tumor cells. C26 tumor section of RGDPEG-MMAE−HSA (A) and RGD−MMAE−HSA (B) treated mice (24 h postinjection) were stained with DAPI (blue) to visualize endothelial cells (flattened nuclei) or tumor cells (big nuclei). Accumulated conjugate was visualized by anti-HSA staining (green). Red arrows point at the typically flattened nuclei of endothelial cells and identify a blood vessel, colocalizing with HSA. Examples for tumor cells nuclei that colocalize with HSA are pointed out using yellow arrows. Magnification 400×.

found on melanoma (*30*). *In vitro* cell killing assays showed that a fraction of the cells survived treatment with highest concentrations of immunoconjugates (*6*, *31*, *5*). Identical observations were made for our RGD-based conjugates. Most likely, this fraction represented not dividing cells, which therefore do not respond to MMAE.

The short alkyl linker was chosen to modify MMAE−HSA with a maximum of RGD−peptides but the extended PEG linker was chosen for its known ability to shield the modified HSA, to prolong circulation time, and to increase passive targeting by the enhanced permeability and retention (EPR) effect (*32*, *33*). These advantages cannot be detected in in vitro assays. In the C26 tumor bearing mice, both conjugates accumulated to a similar extent in the tumors in time, with a stronger and more widespread localization for the conjugates after 24 h compared to localization at 3 h. At the later time point, kidney, liver, and spleen were almost devoid of drug-targeting conjugates. Thus, the concentration of drug-targeting conjugate increased in the tumor, and at the same time the concentration in organs decreased. Mitra et al. (*34*) reported similar findings in which a RGD-equipped polymer accumulated in the course of 3 days in prostate tumors.

RGDPEG−MMAE−HSA was still detectable in the liver 24 h after injection. A possible explanation for this might be a longer circulation time and delayed degradation compared to RGD−MMAE−HSA due to the PEG moiety. A remarkably strong staining at both time points and for both conjugates was observed in tumor tissue. It is important to note that not a tracer dose but a therapeutic dose (30 μg/ mouse) was given, thus reflecting the distribution pattern during treatment. In the future experiments, we will use the here prepared ^{89}Zr-labeled conjugates in combination with positron emission tomography (PET) to gain more insight in organ distribution of RGD-equipped drug−albumin conjugates. In those studies, tumor accumulation of RGD-based carriers will also be compared to carriers that accumulate in tumors by enhance-permeability retention (EPR), such as for instance the above presented RAD-modified albumins. ^{89}Zirkonium captured by the chelator desferal is the ideal label for these studies, as it is highly stable, hydrophilic enough to prevent redistribution, and equipped with a half-life that allows PET scans for longer than 48 h.

The preliminary distribution data of our product indicated that the accumulation in the tumor was widespread and did not reflect a vascular staining pattern. Fluorescent staining of nuclei demonstrated colocalization of the conjugates with both endothelial cells and tumor cells. We therefore investigated binding of ^{125}I-labeled conjugates to C26 tumor cells. Indeed, both RGDPEG−MMAE−HSA and RGD−MMAE−HSA bound to C26 cells and were displaceable by coincubation with an excess of free RGD−peptide. This indicated that binding was mediated via the RGD−peptide to C26 carcinoma cells, and binding presumable took place via $\alpha_v\beta_3$-integrin or related α_v integrins. Thus angiogenic endothelium and tumor cells were both targeted in the chosen tumor model, explaining the staining pattern. An $\alpha_v\beta_3$-integrin-expressing tumor is likely to be more responsive than a $\alpha_v\beta_3$-integrin-negative tumor. Although this may perturbate the selectivity of the RGD-equipped conjugates for the tumor vasculature per se, this will even enhance the potential antitumor effects of the compounds. Similarly, many of the studies employing RGD−peptides for either imaging or drug delivery have been conducted in tumor models that express $\alpha_v\beta_3$ integrin at the tumor cells (*11*).

In conclusion, two types of RGD-equipped auristatin−albumin conjugates have been developed, demonstrating the versatility of such a targeting approach. Both drug-targeting conjugates displayed excellent binding and cell killing properties, and strongly accumulate in a C26 tumor in mice. These results indicate that RGD-mediated targeting of auristatin E is a promising strategy for delivery of a proapoptotic payload to tumor vasculature and carcinoma cells and a valid alternative to current immunoconjugates. In the future pharmacokinetics and tumor growth inhibition of these promising compounds will be evaluated in detail.

ACKNOWLEDGMENT

J. H. Pol from the Department of Nuclear Medicine is kindly acknowledged for radiolabeling of proteins, H. E. Moorlag from the Endothelial Cell Facility UMCG for skillful isolation and culturing of HUVEC, and Annemiek van Loenen-Weemaes for assistance with animal experiments. We also acknowledge Prof.

G. A. M. S. van Dongen and Ir. L. R. Perk of the VU Medical Center for providing the desferal labeling technology. This work was made possible by grants from Marie Curie (HPMI-CT-2002-00218) and SenterNovem (TSGE1083).

LITERATURE CITED

(1) Ferrara, N., and Kerbel, R. S. (2005) Angiogenesis as a therapeutic target. *Nature (London) 438*, 967−974.

(2) Pettit, G. R. (1997) The dolastatins. *Fortschr. Chem. Org. Naturst. 70*, 1−79.

(3) Doronina, S. O., Toki, B. E., Torgov, M. Y., Mendelsohn, B. A., Cerveny, C. G., Chace, D. F., DeBlanc, R. L., Gearing, R. P., Bovee, T. D., Siegall, C. B., Francisco, J. A., Wahl, A. F., Meyer, D. L., and Senter, P. D. (2003) Development of potent monoclonal antibody auristatin conjugates for cancer therapy. *Nat. Biotechnol. 21*, 778−784.

(4) Law, C. L., Cerveny, C. G., Gordon, K. A., Klussman, K., Mixan, B. J., Chace, D. F., Meyer, D. L., Doronina, S. O., Siegall, C. B., Francisco, J. A., Senter, P. D., and Wahl, A. F. (2004) Efficient elimination of B-lineage lymphomas by anti-CD20-auristatin conjugates. *Clin. Cancer Res. 10*, 7842−7851.

(5) Afar, D. E., Bhaskar, V., Ibsen, E., Breinberg, D., Henshall, S. M., Kench, J. G., Drobnjak, M., Powers, R., Wong, M., Evangelista, F., O'Hara, C., Powers, D., DuBridge, R. B., Caras, I., Winter, R., Anderson, T., Solvason, N., Stricker, P. D., Cordon-Cardo, C., Scher, H. I., Grygiel, J. J., Sutherland, R. L., Murray, R., Ramakrishnan, V., and Law, D. A. (2004) Preclinical validation of anti-TMEFF2-auristatin E-conjugated antibodies in the treatment of prostate cancer. *Mol. Cancer Ther. 3*, 921−932.

(6) Bhaskar, V., Law, D. A., Ibsen, E., Breinberg, D., Cass, K. M., DuBridge, R. B., Evangelista, F., Henshall, S. M., Hevezi, P., Miller, J. C., Pong, M., Powers, R., Senter, P., Stockett, D., Sutherland, R. L., von Freeden-Jeffry, U., Willhite, D., Murray, R., Afar, D. E., and Ramakrishnan, V. (2003) E-selectin up-regulation allows for targeted drug delivery in prostate cancer. *Cancer Res. 63*, 6387−6394.

(7) Sanderson, R. J., Hering, M. A., James, S. F., Sun, M. M., Doronina, S. O., Siadak, A. W., Senter, P. D., and Wahl, A. F. (2005) In vivo drug-linker stability of an anti-CD30 dipeptide-linked auristatin immunoconjugate. *Clin. Cancer Res. 11*, 843−852.

(8) Dubowchik, G. M., Mosure, K., Knipe, J. O., and Firestone, R. A. (1998) Cathepsin B-sensitive dipeptide prodrugs. 2. Models of anticancer drugs paclitaxel (Taxol), mitomycin C and doxorubicin. *Bioorg. Med. Chem. Lett. 8*, 3347−3352.

(9) Dubowchik, G. M., Firestone, R. A., Padilla, L., Willner, D., Hofstead, S. J., Mosure, K., Knipe, J. O., Lasch, S. J., and Trail, P. A. (2002) Cathepsin B-labile dipeptide linkers for lysosomal release of doxorubicin from internalizing immunoconjugates: model studies of enzymatic drug release and antigen-specific in vitro anticancer activity. *Bioconjugate Chem. 13*, 855−869.

(10) Pierschbacher, M. D., and Ruoslahti, E. (1984) Cell attachment activity of fibronectin can be duplicated by small synthetic fragments of the molecule. *Nature (London*) *309*, 30−33.

(11) Temming, K., Schiffelers, R. M., Molema, G., and Kok, R. J. (2005) RGD-based strategies for selective delivery of therapeutics and imaging agents to the tumour vasculature. *Drug Resist. Updates 8*, 381−402.

(12) Kok, R. J., Schraa, A. J., Bos, E. J., Moorlag, H. E., Asgeirsdottir, S. A., Everts, M., Meijer, D. K., and Molema, G. (2002) Preparation and functional evaluation of RGD-modified proteins as alpha(v)-beta(3) integrin directed therapeutics. *Bioconjugate Chem. 13*, 128−135.

(13) Schraa, A. J., Kok, R. J., Berendsen, A. D., Moorlag, H. E., Bos, E. J., Meijer, D. K., de Leij, L. F., and Molema, G. (2002) Endothelial cells internalize and degrade RGD-modified proteins developed for tumor vasculature targeting. *J. Controlled Release 83*, 241−251.

(14) Schraa, A. J., Kok, R. J., Botter, S. M., Withoff, S., Meijer, D. K., de Leij, L. F., and Molema, G. (2004) RGD-modified anti-CD3 antibodies redirect cytolytic capacity of cytotoxic T lymphocytes toward alphavbeta3-expressing endothelial cells. *Int. J. Cancer. 112*, 279−285.

(15) Kumar, C. C., Nie, H., Rogers, C. P., Malkowski, M., Maxwell, E., Catino, J. J., and Armstrong, L. (1997) Biochemical characterization of the binding of echistatin to integrin alphavbeta3 receptor. *J. Pharmacol. Exp. Ther. 283*, 843−853.

(16) Hunter, W. M., and Greenwood, F. C. (1962) Preparation of iodine-131 labelled human growth hormone of high specific activity. *Nature (London*) *194*, 495−496.

(17) Verel, I., Visser, G. W., Boellaard, R., Stigter-van, Walsum, M., Snow, G. B., and van Dongen, G. A. (2003) 89Zr immuno-PET: comprehensive procedures for the production of 89Zr-labeled monoclonal antibodies. *J. Nucl. Med. 44*, 1271−1281.

(18) Alley, M. C., Scudiero, D. A., Monks, A., Hursey, M. L., Czerwinski, M. J., Fine, D. L., Abbott, B. J., Mayo, J. G., Shoemaker, R. H., and Boyd, M. R. (1988) Feasibility of drug screening with panels of human tumor cell lines using a microculture tetrazolium assay. *Cancer Res. 48*, 589−601.

(19) Schraa, A. J., Kok, R. J., Moorlag, H. E., Bos, E. J., Proost, J. H., Meijer, D. K., de Leij, L. F., and Molema, G. (2002) Targeting of RGD-modified proteins to tumor vasculature: a pharmacokinetic and cellular distribution study. *Int. J. Cancer. 102*, 469−475.

(20) Thumshirn, G., Hersel, U., Goodman, S. L., and Kessler, H. (2003) Multimeric cyclic RGD peptides as potential tools for tumor targeting: solid-phase peptide synthesis and chemoselective oxime ligation. *Chemistry 9*, 2717−2725.

(21) Verel, I., Visser, G. W., Boerman, O. C., van Eerd, J. E., Finn, R., Boellaard, R., Vosjan, M. J., Stigter-van, Walsum, M., Snow, G. B., and van Dongen, G. A. (2003) Long-lived positron emitters zirconium-89 and iodine-124 for scouting of therapeutic radioimmunoconjugates with PET. *Cancer Biother. Radiopharm. 18*, 655−661.

(22) Perk, L. R., Visser, G. W., Vosjan, M. J., Stigter-van, Walsum, M., Tijink, B. M., Leemans, C. R., and van Dongen, G. A. (2005) (89)Zr as a PET surrogate radioisotope for scouting biodistribution of the therapeutic radiometals (90)Y and (177)Lu in tumor-bearing nude mice after coupling to the internalizing antibody cetuximab. *J. Nucl. Med. 46*, 1898−1906.

(23) Wu, A. M., and Senter, P. D. (2005) Arming antibodies: prospects and challenges for immunoconjugates. *Nat. Biotechnol. 23*, 1137−1146.

(24) Wester, H. J., and Kessler, H. (2005) Molecular targeting with peptides or peptide-polymer conjugates: just a question of size? *J. Nucl. Med. 46*, 1940−1945.

(25) Temming, K., Lacombe, M., Schaapveld, R. Q. J., Orfi, L., Keri, G., Poelstra, K., Molema, G., and Kok, R. J. (2006) Rational Design of RGD-albumin conjugates for targeted delivery of the VEGF-R kinase inhibitor PTK787 to angiogenic endothelium. *ChemMedChem 11*, Epub ahead of print, DOI: 10.1002/cmdc.200600201.

(26) Temming, K., Lacombe, M., van der Hoeven, P., Prakash, J., Gonzalo, T., Dijkers, E. C. F., Orfi, L., Keri, G., Poelstra, K., Molema, G., and Kok, R. J. (2006) Delivery of the p38 MAPkinase inhibitor SB202190 to angiogenic endothelial cells: development of novel RGD-equipped and pegylated drug-albumin conjugates using platinum(II) based drug linker technology. *Bioconjugate Chem.* Epub ahead of print.

(27) Toublan, F. J., Boppart, S., and Suslick, K. S. (2006) Tumor targeting by surface-modified protein microspheres. *J. Am. Chem. Soc. 128*, 3472−3473.

(28) Kim, W. J., Yockman, J. W., Jeong, J. H., Christensen, L. V., Lee, M., Kim, Y. H., and Kim, S. W. (2006) Anti-angiogenic inhibition of tumor growth by systemic delivery of PEI-g-PEG-RGD/pCMV-sFlt-1 complexes in tumor-bearing mice. *J. Controlled Release 114*, 381−388.

(29) Shukla, R., Thomas, T. P., Peters, J., Kotlyar, A., Myc, A., and Baker, J. R., Jr. (2005) Tumor angiogenic vasculature targeting with PAMAM dendrimer-RGD conjugates. *Chem. Commun. (Camb.*) 5739−5741.

(30) Tse, K. F., Jeffers, M., Pollack, V. A., McCabe, D. A., Shadish, M. L., Khramtsov, N. V., Hackett, C. S., Shenoy, S. G., Kuang, B., Boldog, F. L., MacDougall, J. R., Rastelli, L., Herrmann, J., Gallo, M., Gazit-Bornstein, G., Senter, P. D., Meyer, D. L., Lichenstein, H. S., and LaRochelle, W. J. (2006) CR011, a fully human monoclonal antibody-auristatin E conjugate, for the treatment of melanoma. *Clin. Cancer Res. 12*, 1373−1382.

(31) Francisco, J. A., Cerveny, C. G., Meyer, D. L., Mixan, B. J., Klussman, K., Chace, D. F., Rejniak, S. X., Gordon, K. A., DeBlanc,

R., Toki, B. E., Law, C. L., Doronina, S. O., Siegall, C. B., Senter, P. D., and Wahl, A. F. (2003) cAC10-vcMMAE, an anti-CD30-monomethyl auristatin E conjugate with potent and selective antitumor activity. *Blood 102*, 1458−1465.

(32) Tanaka, T., Shiramoto, S., Miyashita, M., Fujishima, Y., and Kaneo, Y. (2004) Tumor targeting based on the effect of enhanced permeability and retention (EPR) and the mechanism of receptor-mediated endocytosis (RME). *Int. J. Pharm. 277*, 39−61.

(33) Caliceti, P., and Veronese, F. M. (2003) Pharmacokinetic and biodistribution properties of poly(ethylene glycol)-protein conjugates. *Adv. Drug Delivery Rev. 55*, 1261−1277.

(34) Mitra, A., Mulholland, J., Nan, A., McNeill, E., Ghandehari, H., and Line, B. R. (2005) Targeting tumor angiogenic vasculature using polymer-RGD conjugates. *J. Controlled Release 102*, 191−201.

BC060087Z

Multiblock Reducible Copolypeptides Containing Histidine-Rich and Nuclear Localization Sequences for Gene Delivery

Devika Soundara Manickam and David Oupický*

Department of Pharmaceutical Sciences, Wayne State University, Detroit, Michigan 48202. Received April 23, 2006; Revised Manuscript Received September 3, 2006

Polyplexes sensitive to redox potential gradients represent promising gene delivery vectors. High molecular weight polypeptides containing disulfide bonds in the backbone were synthesized by an oxidative copolymerization of a histidine-rich peptide (HRP) and a nuclear localization sequence (NLS) peptide. The synthetic approach allowed an easy synthesis of reducible copolypeptides (rCPP) with different relative contents of the HRP and NLS sequences. Cytotoxicity and transfection activity of rCPP-based DNA polyplexes were evaluated in vitro. In comparison with control polyethylenimine (PEI), only minimum toxic effects of rCPPs were observed on the metabolic activity and membrane integrity of human endothelial cells. These findings are predominantly ascribed to favorable structural features like lower charge density and higher chain rigidity of the rCPPs compared to PEI and also to a reductive intracellular and plasma membrane degradation. Transfection activity in all tested cell lines increased with increasing content of the HRP sequence in the rCPPs, while no clearly measurable effect of the NLS sequence was found.

INTRODUCTION

Polyelectrolyte complexes of nucleic acids with polycations (polyplexes) are investigated as promising delivery vectors for a variety of nucleic acid therapeutics. In particular, polyplexes capable of responding to environmental changes or stimuli by altering their properties and behavior promise a significant improvement of the efficacy of the delivery process. One of the several microenvironmental features, which could be exploited for improving the efficiency of nucleic acid delivery, is the redox potential gradient existing between extracellular environment and various subcellular organelles in normal as well as pathological states. The existence of such gradients has been exploited by incorporating disulfide bonds into the structure of a variety of delivery vectors to provide them with a capability to release the therapeutic cargo selectively in the subcellular reducing space (*1*−*5*).

The easy intracellular reversibility of disulfide bonds in redox-sensitive polyplexes proved to be a highly advantageous feature for delivering a variety of nucleic acids, including plasmid DNA, mRNA, antisense oligonucleotides, and siRNA. Delivery of plasmid DNA has been by far the most investigated application of the redox-sensitive polyplexes. A number of studies in a variety of cell lines showed transfection activities comparable to or better than those observed for polyethylenimine (PEI) and/or commercially available lipid formulations (*6*−*10*). The benefits of intracellular reduction of disulfides in the redox-sensitive polyplexes for efficient delivery of nucleic acids have been demonstrated also for mRNA, siRNA, and antisense oligonucleotides (*4*, *11*).

Redox-sensitive polyplexes based on cationic peptides are attractive vectors because of the possibility of combining DNA condensation capability with an inherent biological activity of the peptides (*12*−*14*). Here, we synthesized reducible copolypeptides (rCPP) composed of two cationic peptide sequences that should provide the copolymers with endosomal buffering capability and nuclear localization capability. It is hypothesized that the combination of the two features in a single carrier will improve the overall efficiency of the gene delivery process. The copolypeptides are synthesized by an oxidative polycondensation using an engineered histidine-rich peptide (HRP) and a nuclear localization sequence (NLS) derived from the SV40 virus. The copolypeptides show minimal cytotoxicity and transfection activity comparable to or better than control PEI polyplexes.

EXPERIMENTAL PROCEDURES

Materials. Peptides, NLS (CGAGPKKKRKVC, Mr 1274), and HRP (CKHHHKHHHKC, Mr 1431) were custom-synthesized by Sigma-Genosys. Branched PEI (25 000 g/mol), poly-L-lysine (PLL, 240 000 g/mol), dithiothreitol (DTT), chloroquine, genistein (Gen) and bafilomycin A1 (Baf.A1) were from Sigma-Aldrich. Plasmid DNA vectors, gWiz high-expression luciferase (gWiz-Luc) containing luciferase reporter gene, and gWiz high-expression GFP (gWiz-GFP) containing enhanced green fluorescent protein reporter gene were from Aldevron (Fargo, ND). Dulbecco's modified Eagle medium (DMEM), fetal bovine serum (FBS), and Roswell Park Memorial Institute 1640 (RPMI 1640) medium were from Invitrogen. All other chemicals were obtained from Fisher Scientific unless otherwise noted.

Synthesis of Reducible Copolypeptides. The rCPPs were synthesized by DMSO-mediated oxidative polycondensation described previously (*15*). Five rCPPs were prepared using NLS and HRP peptides at different molar ratios in the reaction mixture. Relative content of the NLS and HRP peptides in the synthesized copolypeptides was determined by amino acid analysis (Michigan State University Macromolecular Core) using the average ratio of histidine residues of HRP to valine and alanine residues of NLS peptide. The concentration of the polypeptides in solution was estimated from the amino acid analysis by adding L-norleucine as an internal standard.

Formulation of DNA Polyplexes. DNA solution (20 μg/mL) in 10 mM HEPES buffer (pH 7.4) was used to prepare complexes with PEI, and DNA solution in 30 mM sodium acetate buffer (pH 5) was used to prepare polyplexes with rCPPs at the desired N/P mixing ratio (*c*(basic amino acid residues of a peptide or amino groups of PEI)/*c*(DNA phosphates)) and mixed by vigorous vortexing for 10 s.

* To whom correspondence should be addressed. E-mail: oupicky@wayne.edu.

10.1021/bc060104k CCC: $33.50 © 2006 American Chemical Society
Published on Web 10/20/2006

Hydrodynamic Radius and ζ Potential Determination. The determination of hydrodynamic diameters and ζ potentials of polyplexes was performed using ZetaPlus Particle Size and Zeta Potential analyzer (Brookhaven Instruments Inc.) as described previously (*14*).

Salt Dissociation Assay. Polyplexes were formulated as described above and incubated in 25 mM DTT for 1 h at 37 °C. Then, increasing concentration of NaCl (0−1 M) was added and samples were loaded onto 0.8% agarose gel containing 0.5 μg/mL ethidium bromide and run for 90 min at 120 V in 0.5× TBE buffer. The amount of DNA released from the polyplexes at a given NaCl concentration was analyzed using Kodak 1D image analysis software.

Cell Lines. Murine melanoma cell line B16F10, mouse mammary tumor cell line 4T1, human cervical cancer cell line HeLa, human breast carcinoma MCF-7, and African green monkey kidney fibroblasts COS-7 were obtained from ATCC. Human endothelial cell line EA.hy926, derived by a fusion of human umbilical vein endothelial cells with a lung carcinoma A549, was a kind gift from Dr. Edgell (University of North Carolina). B16F10, HeLa, EA.hy926, and COS-7 were maintained in DMEM and MCF-7 and 4T1 in RPMI 1640. Both media were supplemented with 4 mM L-alanyl-L-glutamine and 10% FBS.

Cytotoxicity Evaluation. Cytotoxicity of rCPPs and control PEI in EA.hy926 cells were determined by MTS and LDH assays using commercially available kits. The MTS assay was performed using the CellTiter 96 aqueous cell proliferation assay (Promega). Twenty-thousand cells seeded in a 96-well plate 2 days before the experiment were incubated with increasing concentration of the polycations in 150 μL of DMEM/FBS. The medium was removed after 16 h and replaced with a mixture of 100 μL of fresh DMEM and 20 μL of MTS reagent solution. The cells were incubated for 1 h at 37 °C in a CO_2 incubator. The absorbance of each sample was then measured at 505 nm to determine cell viability. The results are expressed as the mean percentage cell viability relative to untreated cells ± SD. The cytotoxicity of the polycations was also determined by a CytoTox 96 nonradioactive cytotoxicity assay, an assay that measures LDH release from damaged cells. EA.hy926 cells were incubated with increasing concentrations of the polycations in DMEM/FBS lacking phenol red. After 2 h of incubation at 37 °C, the medium was removed and centrifuged at 250*g* at 4 °C for 5 min. An amount of 50 μL of the supernatant was diluted with 50 μL of DMEM/FBS without phenol red. The LDH substrate (50 μL) was added to each sample and incubated for 30 min in the dark. An amount of 50 μL of the stop solution was added to each sample, and the absorbance was measured at 490 nm. The maximum LDH release was quantified by freeze−thaw lysis of untreated cells followed by medium processing as described above. The results are expressed as the mean % LDH release ± SD.

Transfection Efficiency in Vitro. Transfection activity was tested using polyplexes prepared as described above at the indicated N/P ratio. All transfection studies were performed in 48-well plates with cells plated 24 h before transfection at a seeding density of 30 000 cells per well using previously described protocols (*10*, *14*). On a day of transfection, the cells were incubated with the complexes in 150 μL of FBS-supplemented media or medium lacking FBS as indicated. After 3 h of incubation, the transfection mixture was completely removed and the cells were cultured for an additional 24 h in fresh media supplemented with 10% FBS prior to analysis of reporter gene expression. Transfections in the presence of chloroquine and Baf.A1 were performed in the same way except that the drug was added to the culture medium before addition of the polyplexes. Caveolae inhibition experiments were conducted by preincubating the cells for 30 min with the respective inhibitor or combination of inhibitors (200 μM genistein, 100 nM bafilomycin A1) before the addition of polyplexes. The inhibitors were present in the transfection medium throughout the 3 h of incubation. The luciferase transfection results are expressed as relative light units (RLU) per milligram of cellular protein ± SD of triplicate experiments. The GFP transfection results are expressed as the percentage of GFP-positive cells determined by flow cytometry ± SD of triplicate experiments.

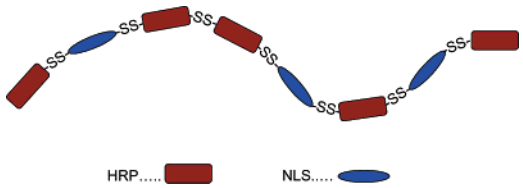

Figure 1. Schematic representation of the multiblock reducible copolypeptides (rCPP).

Table 1. Composition and Molecular Weight of Multiblock Reducible Copolypeptides (rCPP)

polycation	% HRP in reaction	% HRP in polymer[a]	M_w
rCPP-A	0	0	∼100 000
rCPP-B	25	27	
rCPP-C	50	52	∼60 000
rCPP-D	75	80	
rCPP-E	100	100	∼200 000

[a] Determined from amino acid analysis.

RESULTS

Synthesis of rCPP and Characterization of rCPP/DNA Polyplexes. To combine two functional peptides into a single polymeric carrier, multiblock reducible copolypeptides were synthesized by randomly connecting HRP and NLS peptides via disulfide bonds into a linear polypeptide chain (Figure 1). Mild oxidation of the terminal Cys residues with DMSO was used as described in our earlier work (*14*, *15*). Five different compositions of the rCPP were prepared by varying the amount of the NLS and HRP peptides in the polycondensation reaction (Table 1). Amino acid analysis was used to determine the relative content of the two peptides in the rCPPs. Molecular weights of selected rCPPs were estimated by size exclusion chromatography and were found to range from ∼60 000 to ∼200 000 (Table 1). The ability of the rCPP polycations to condense DNA was confirmed by ethidium bromide exclusion (data not shown) and gel retardation assays (Figure 2a). All rCPPs were able to fully condense DNA in buffers at pH 7.4 and 5 at N/P ratios of ≥2. Hydrodynamic size and ζ potential of the rCPP polyplexes were measured by dynamic light scattering using optimized polyplex compositions determined in the transfection assay (Table 2). All rCPPs formed polyplexes with sizes and ζ potentials fully comparable to those of control PEI. The sensitivity of the rCPP/DNA polyplexes to reducing environment was tested by following the polyplex dissociation with NaCl (*16*). No detectable dissociation was observed under nonreducing conditions up to 1 M NaCl (Figure 2b, data shown for rCPP−C/DNA only). Reduction of the disulfide bonds in rCPP-C in 25 mM DTT resulted in the polyplex dissociation already starting in ∼0.3 M NaCl.

Cytotoxicity of rCPP Polycations. The cytotoxicity of the rCPP polycations was evaluated using MTS and LDH assays in human endothelial cells (Figure 3). The results show that the rCPP polycations exhibit only a negligible cytotoxicity in the MTS assay after 16 h of incubation in the concentration range 0−300 μg/mL, while control PEI shows an IC_{50} value less than 10 μg/mL (Figure 3a). The LDH release assay, which was used to estimate the early-stage cytotoxicity associated with

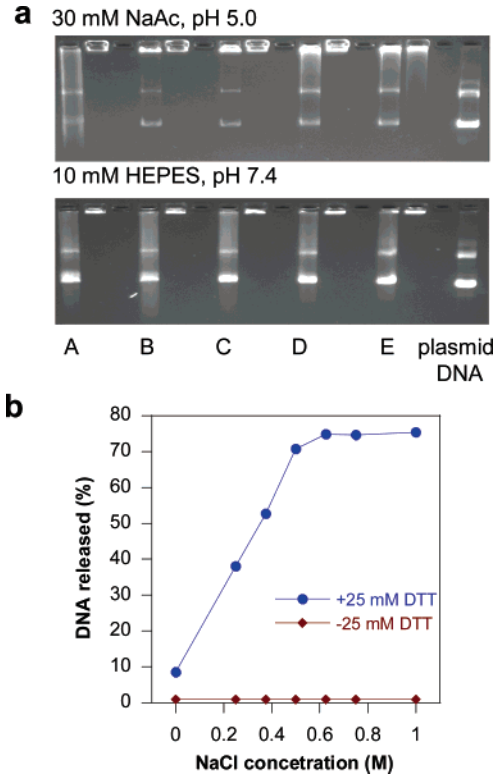

Figure 2. (a) DNA condensation by rCPPs. Polyplexes were prepared at N/P ratios of 0.5 and 2.0 (left and right lanes) in 30 mM sodium acetate buffer (pH 5.0) (upper panel) and 10 mM HEPES buffer (pH 7.4) (lower panel). (b) Salt dissociation of rCPP-C/DNA polyplexes under reducing conditions of 25 mM DTT.

Table 2. Molecular Parameters of rCPP-Based DNA Polyplexes[a]

polycation	hydrodynamic diameter (nm)	ζ potential (mV)
rCPP-A	105 ± 3	47 ± 1
rCPP-B	125 ± 1	49 ± 4
rCPP-C	145 ± 2	43 ± 1
rCPP-D	135 ± 1	46 ± 1
rCPP-E	96 ± 1	55 ± 1
PEI	115 ± 1	47 ± 5

[a] The polyplexes were formulated at optimum molar mixing ratios. Results are presented as the mean ± SD ($n = 3$).

plasma membrane disruption, shows results similar to the MTS data. When the LDH is measured after 2 h of incubation with the polycations, PEI exhibits a similar IC_{50} value as in case of the MTS assay. The rCPPs show minimal LDH release at concentrations below 100 μg/mL, but unlike in the MTS assay considerable cytotoxicity is observed at the highest concentration (300 μg/mL) tested (Figure 3b). Light transmission micrographs were obtained after a 16 h incubation of the cells with the polycations to directly document the differential effects of PEI and rCPP on the human endothelial cells (Figure 3c). The images show the cells incubated with the rCPP polycations as healthy, attached to the surface, and of similar appearance as untreated cells. The cells incubated with PEI, on the other hand, show clear signs of toxicity indicated by changed morphology and a large number of rounded and detached cells.

Transfection Activity of rCPP/DNA Polyplexes. Initial transfection experiments were conducted to determine the optimum N/P ratio for each rCPP/DNA formulation to achieve maximum transgene expression levels in B16F10 cells (Figure 4). The N/P ratio that resulted in maximum luciferase expression was then used in all subsequent experiments. The N/P dependence of the transfection activity is mostly influenced by the content of the pH-buffering HRP peptide. For example, transfection activity of rCPP-B with 27% of HRP gradually decreases with increasing N/P ratio, while the activity of rCPP-E (100% HRP) peaks at N/P = 8 and then slowly declines, similar to the control PEI/DNA.

The transfection activity of the optimized rCPP/DNA formulations was further tested in a panel of six cell lines (Figure 5). A general trend of gradual increase in the transfection activity with increasing content of HRP is observed in all the cell lines. The best performing rCPP-E polyplexes exhibit between 2- and 7-fold higher transfection activity than control PEI polyplexes depending on the cell line. It is worth noting that the difference between the lowest and the highest observed transfection is almost 5 orders of magnitude. Similar results were obtained across the same panel of cell lines in GFP transfection experiments (data not shown).

The effect of chloroquine on the luciferase reporter expression of the rCPP/DNA polyplexes is plotted in Figure 6a as a chloroquine enhancement ratio ([RLU/mg protein with chloroquine]/[RLU/mg protein without chloroquine]). In fast-growing B16F10 cells, the presence of 100 μM chloroquine results in an almost 10000-fold increase in the transfection activity of rCPP-A, which consists of 100% NLS and thus lacks any buffering capability. As expected, increasing the HRP content in the polypeptides leads to a decrease in the potentiation of the transfection activity by chloroquine. The two other cell lines tested show a slightly different pattern of chloroquine effect, with maximum enhancement seen for rCPP-C/DNA polyplexes. Complementary results are obtained for the GFP reporter plasmid in B16F10 cells (Figure 6b).

The dependence of transfection activity of polyplexes on pH-buffering capability of the polypeptides was examined by conducting transfections in the presence of Baf.A1, a potent inhibitor of vacuolar ATPases (Figure 7). It has been reported that, depending on the cell line used, the transfection activity of PEI can be reduced 7- to 74-fold in the presence of 175 nM Baf.A1 (*17*). Unexpectedly, rCPP-A polyplexes that lack any buffering capability exhibited almost a 1000-fold increase in the transfection activity in the presence of 100 nM Baf.A1 in B16F10 cells (Figure 7a). A decreasing effect of Baf.A1 on transfection enhancement is observed when moving from rCPP-A to rCPP-E. The transfection activity of control PEI/DNA increased almost 2-fold under the same conditions. Baf.A1 has a smaller but similar enhancing effect on the transfection of rCPP-A polyplexes in HeLa cells (Figure 7b). A 2- to 4-fold, statistically insignificant, increase in the transfection activity of the remaining four rCPP polyplexes is observed in the presence of 10% FBS and 175 nM Baf.A1 (Figure 7b). There was a 2-fold decrease in the transfection activity of control PEI, which is in close agreement with the results reported previously (*17*). Unlike HeLa and B16F10 cells, Baf.A1 has no enhancing effect on the transfection activity of rCPP polyplexes in MCF-7 cells (Figure 7c).

In experiments conducted in the absence of FBS (Figure 7d–f), Baf.A1 causes the expected decrease of transfection activity of polyplexes capable of endosomal pH buffering. Especially in the HeLa and MCF-7 cells, the Baf.A1 effect is directly correlated with the content of HRP (Figure 7e,f). For example, the decrease in the transfection activity of rCPP-E polyplexes in HeLa cells is almost 2 orders of magnitude. In addition, Baf.A1 has a more pronounced effect on the transfection activity of rCPP-E than PEI polyplexes. No significant differences were observed in the transfection activity of control PLL polyplexes in the presence and absence of Baf.A1 (data not shown). In B16F10 cells, the enhancing effect of Baf.A1 was preserved for polyplexes with no (rCPP-A) or minimum buffering capability (rCPP-B) (Figure 7d). There was almost a 10-fold increase in the transfection activity of rCPP-A. In agreement with the

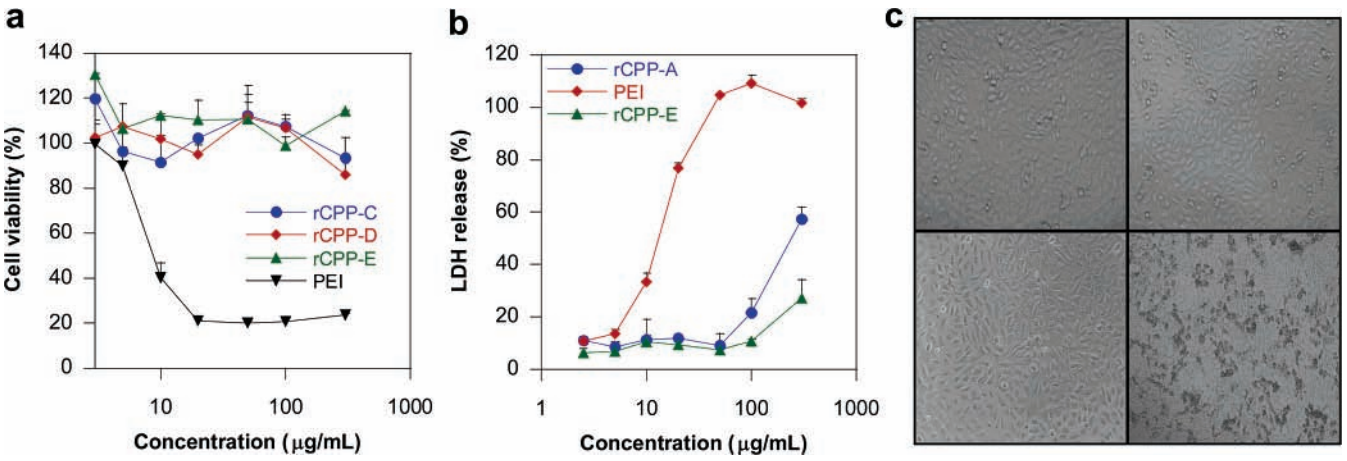

Figure 3. Cytotoxicity evaluation in human endothelial EA.hy926 cells. (a) Metabolic activity was measured by MTS assay following 16 h of incubation of the cells with the polycations (mean ± SD, $n = 3$). (b) Membrane toxicity was measured by LDH release assay after 2 h of incubation of the cells with the polycations (mean ± SD, $n = 3$). (c) Light transmission micrographs of the cells after 16 h of incubation with the polycations (upper left, rCPP-E; upper right, rCPP-C; lower left, rCPP-D; lower right, PEI).

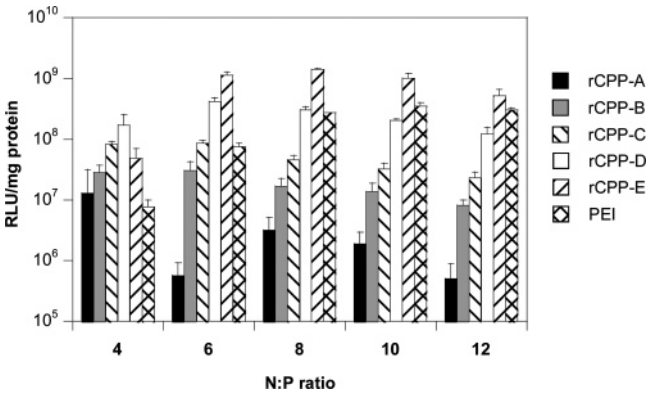

Figure 4. Influence of N/P ratio on transfection activity of rCPP/DNA in B16F10 cells. Results are shown as mean relative light units (RLU) of luciferase per milligram of cellular protein ± SD ($n = 3$).

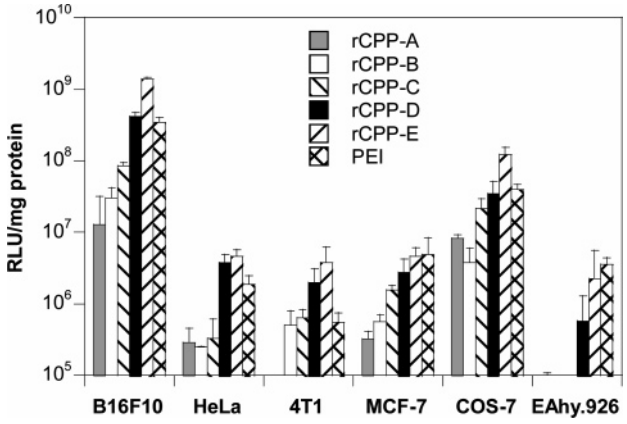

Figure 5. Transfection activity of optimized rCPP/DNA in a panel of cell lines. Luciferase activity was measured after 24 h. Results are shown as mean RLU per milligram of cellular protein ± SD ($n = 3$).

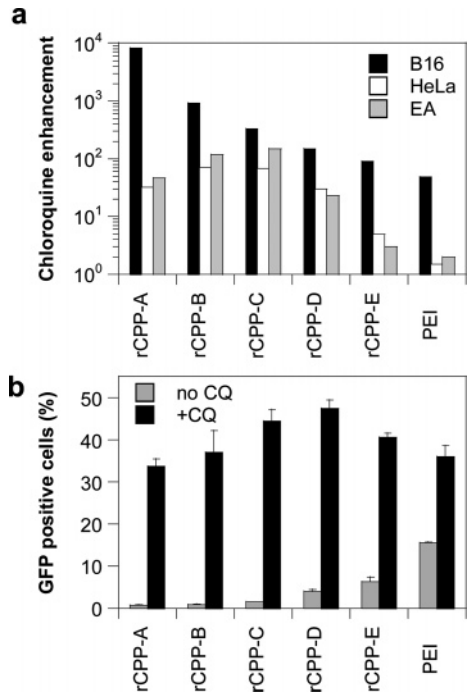

Figure 6. Effect of chloroquine on transfection activity of rCPP/DNA: (a) chloroquine-induced enhancement of luciferase expression; (b) effect of chloroquine on eGFP expression in B16F10 cells ($n = 3$).

original expectations, polycations with significantly higher buffering capabilities (rCPP-D and rCPP-E) demonstrated a decrease in the transfection activity of the polyplexes in the presence of Baf.A1, 3- and 5-fold, respectively.

Since the effects of Baf.A1 in B16F10 cells showed a strong dependence on the presence or absence of serum, we conducted transfections using medium supplemented with gradually increasing concentrations of bovine serum albumin (BSA) (Figure 8a). The results show that in the presence of Baf.A1, rCPP-A with no buffering capability exhibits a gradual increase in the transfection activity with increasing concentration of BSA in the incubation medium and rCPP-E with the maximum buffering capability among the tested compositions shows no significant increase. Additional transfection studies were conducted to further probe the unexpected effect of Baf.A1 on the activity of rCPP-A polyplexes. It has been reported that cellular uptake of polyplexes proceeds via a clathrin- or caveolae-dependent endocytic pathway (*18*). To determine an involvement of an alternative endocytosis pathway, caveolae inhibition studies were carried out using genistein, a specific inhibitor of tyrosine kinase involved in receptor-induced formation of caveolae (Figure 8b) (*19*, *20*). In the presence of Baf.A1, there was a 100-fold increase in transfection activity of rCPP-A polyplexes, an 8-fold increase in the case of rCPP-C polyplexes, while no effect was observed for rCPP-E polyplexes (Figure 8b). Unlike Baf.A1, genistein had no marked effect on the transfection activity of the NLS-containing rCPP polyplexes, but it led to a decrease of transfection activity of rCPP-E polyplexes. It has been

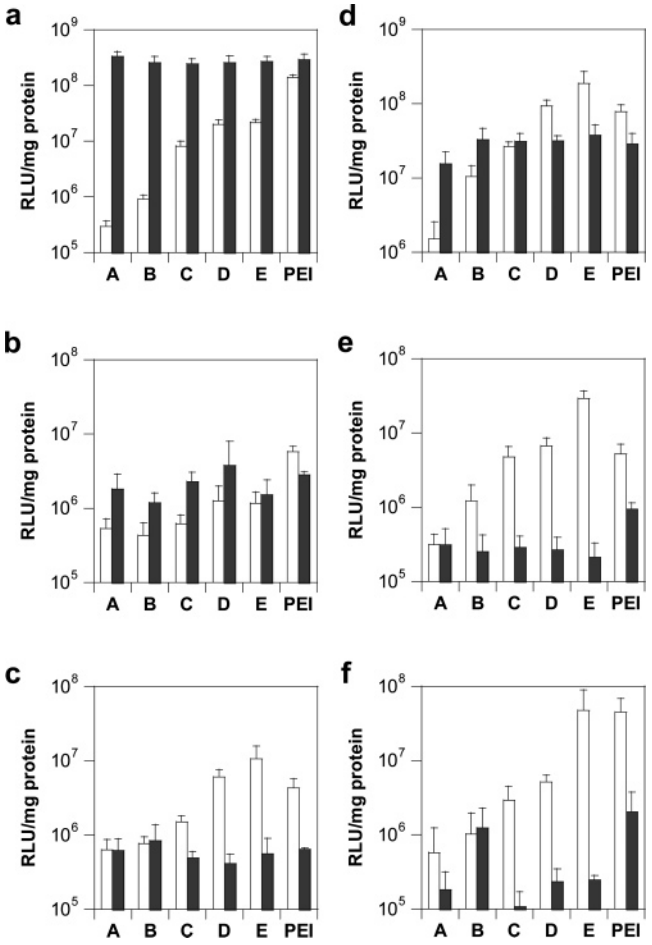

Figure 7. Effect of Baf.A1 on transfection activity of rCPP polyplexes. Transfections were performed in the presence (a) or absence (d) of 10% FBS in B16F10 cells, in the presence (b) or absence (e) of 10% FBS in HeLa cells, and in the presence (c) or absence (f) of 10% FBS in MCF-7 cells. Luciferase activity was measured after 24 h, and results are shown as mean RLU per milligram of cellular protein and SD from triplicate samples (empty bars, absence of Baf.A1; solid bars, presence of Baf.A1).

reported that transfection activity of polyplexes is mediated by both clathrin-dependent and caveolae-dependent endocytosis pathways whereas lipoplex transfection is mediated only by the clathrin endocytosis pathway and is unaffected by inhibiting the caveolae endocytosis pathway (*18*). DOTAP lipoplexes were therefore included as a control (not shown) to verify if the observed decrease in the transfection activity of rCPP-E polyplexes in the presence of genistein was due to inhibition of the caveolae endocytosis pathway. The transfection activity of DOTAP lipoplexes was not affected by genistein, confirming published observations (*18*). Treatment of cells with both genistein and Baf.A1 prevented the Baf.A1-induced increase in the transfection activity of rCPP-A polyplexes. The transfection activity of NLS-containing (rCPP-A and rCPP-C) polyplexes was almost equal to levels mediated in inhibitor-free conditions. However, there was a significant decrease in the transfection activity of rCPP-E polyplexes in the presence of both genistein and Baf.A1.

DISCUSSION

Polyplexes sensitive to redox potential gradients represent promising gene delivery vectors because of a favorable safety profile and flexibility for use in delivery of a wide range of nucleic acids. Reducible polypeptides used in the preparation of such polyplexes are typically based on a single peptide

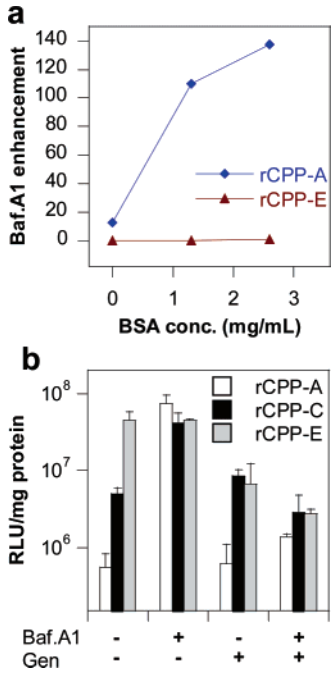

Figure 8. (a) Effect of BSA on Baf.A1-induced enhancement of luciferase expression in B16F10 cells (Baf.A1 enhancement = [RLU/mg with Baf.A1]/[RLU/mg without Baf.A1]). (b) Effect of Baf.A1 and caveolae inhibitor genistein (Gen) on the transfection activity of polyplexes in B16F10 cells. Luciferase activity was measured after 24 h, and results are shown as mean RLU per milligram of cellular protein and SD from triplicate samples.

sequence and are prepared either by DNA-template polymerization or by DMSO-mediated polycondensation (*7*, *11*, *14*, *21*). The only example of a reducible polypeptide composed of several peptides of different amino acid sequences was reported by Rice et al. and used the DNA-template polymerization (*22*). Here, we use a polycondensation approach to demonstrate the feasibility of synthesizing reducible sequential polypeptides consisting of two peptides with distinct biological functions (Figure 1). This approach represents a viable alternative of preparing high molecular weight repetitive polypeptides with a better control over the amino acid sequence and molecular weight than traditional chemical synthesis and an easier alternative to polypeptide synthesis using genetic engineering methods, which provide the ultimate control over the properties of polypeptides (*23*).

Peptide selection for the synthesis of rCPPs was based on recognizing the importance of endosomal escape and nuclear transport for the efficacy of DNA polyplexes. To enable endosomal escape of the polyplexes, HRP peptide containing histidyl residues capable of buffering in the endo/lysosomal pH range was used. The sequence of the HRP peptide was selected on the basis of previous findings that high His content is required for efficient transfection (*7*, *24*). Two trihistidyl blocks were separated by lysyl residues to improve DNA binding capability. To provide the polyplexes with potential nuclear localization capability, NLS peptide was used that was derived from the importin α binding SV40 T antigen sequence (*13*, *25*). Neither of the two peptides used here requires a free terminus for their activity. In cases where the N- or C-terminus of a peptide is required for its activity, a single Cys residue can be placed at the opposite end and used in the oxidative polycondensation scheme as an end-capping functionality. The copolymerization proceeded readily for all five HRP/NLS ratios tested and resulted in the formation of high molecular weight linear polypeptides. No information could be obtained about the distribution of the HRP and NLS blocks in the polypeptides. The fact that the content of the two peptides in rCPP is close to that in the

reaction mixture (Table 1) suggests similar reactivity of both peptides, and therefore, it is likely that HRP and NLS blocks are randomly distributed in the rCPPs.

As expected, the HRP-containing rCPPs exhibited better DNA condensation ability at slightly acidic pH of 5 because of higher protonation levels of the His residues. The principle of the redox sensitivity of rCPP/DNA polyplexes was demonstrated in cell-free conditions by determining the concentration of NaCl required to dissociate the polyplexes in reducing and non-reducing environment. It is assumed that the disulfide bonds in the backbone of the rCPP chains are cleaved in the reducing environment of DTT. The resultant short cationic HRP and NLS peptide residues then display lower affinity to the DNA and allow subsequent dissociation of the polyplexes at lower NaCl concentration. The concentration of NaCl required to dissociate the polyplexes is directly related to the affinity between DNA and polycations, which in turn depends, among other factors, on the molecular weight of the polycations (*16*, *26*). Because of the cooperative nature of polycation binding to DNA, the molecular weight dependence of the dissociating NaCl concentration is especially strong in the low-to-medium molecular weight range of the polycations and is therefore highly suitable to follow the degradation of rCPPs in the polyplexes. The observed NaCl concentration required to dissociate the polyplexes in reducing conditions (~0.3 M) was close to that of polyplexes based on control small peptides, confirming that reduction of the disulfide bonds of the rCPPs proceeds readily in the polyplexes.

Cellular delivery of intact nucleic acids is not the only goal in designing a successful delivery vector. The vector should be able to accomplish this without negatively affecting normal functions of the cell. The toxicity of polycations like PEI and their DNA polyplexes has been reported by a number of investigators in both in vitro and in vivo experiments. The studies suggest two types of cytotoxic action of PEI. The first type of toxicity originates from compromised plasma membrane integrity and occurs in the early stages of incubating the cells with PEI. The first phase of the cytotoxic activity of PEI is then followed by apoptosis caused by PEI-induced channel formation in the mitochondrial membrane (*27*, *28*). Structural features that most affect the way polycations interact with cells include charge density, molecular weight, molecular flexibility, and type of charged center. Rigid molecules have more difficulties attaching to the membranes than flexible molecules. Therefore, high cationic charge densities and highly flexible polymers, such as PEI, are expected to cause greater cytotoxic effects than those with low cationic charge density and more rigid chains. We have hypothesized that intracellular degradation of rCPP into short cationic fragments will significantly reduce the cytotoxicity because of the dependence of polycation toxicity on the molecular weight. The results obtained from the MTS assay, which measures metabolic activity of cells, seem to confirm the hypothesis because no significant toxicity was observed for any of the tested rCPPs up to 300 μg/mL, while PEI showed $IC_{50} \approx 10$ μg/mL.

To further assess the short-term acute cytotoxicity of rCPPs, studies were performed to measure the amount of LDH released in the early stages of incubation. It is expected that during the early stages of incubation, the plasma membrane disruption by extracellular polycations will be the main contributing factor to the observed LDH release. Even though the reducible polycations are not degraded in the cell culture medium, their acute toxicity measured in the LDH assay is minimal when compared to control PEI. Only at the highest rCPP concentrations (300 μg/mL) do the levels of LDH release suggest substantial membrane perturbation. Because of the strong dependence of polycation toxicity on their molecular weight, it is important to analyze possible cellular sites of rCPP degradation before drawing any conclusions. The intracellular reduction of disulfide bonds of rCPPs is most likely mediated by small redox molecules like glutathione (GSH), either alone or with the help of redox enzymes. GSH is the most abundant intracellular sulfhydryl present in millimolar concentrations inside the cell but only in micromolar concentrations in the blood plasma (*29*). The intracellular glutathione concentration is an additive function of both the oxidized (GSSG) and the reduced forms (GSH) of glutathione. The glutathione concentration and redox ratio (GSH/GSSG) are different in the various subcellular compartments, with the lowest redox potential in the cell usually found in the nucleus, where it is required for DNA synthesis and DNA repair as well as to maintain a number of transcription factors in a reduced state. The concentration of GSH has been reported to be about 4 mM in the cytoplasm and about 20 mM in the nucleus (*30*, *31*). The subcellular distribution of GSH suggests that intracellular reduction of disulfide bonds will proceed preferentially in the cytoplasm and nucleus. Even though some evidence also suggests the possibility of endosomal and lysosomal reduction of disulfide bonds (*32*), a recent report indicates that both the endosomal and lysosomal environments are oxidizing and that disulfide bond reduction proceeds rather inefficiently (*33*). Despite the oxidizing nature of the extracellular environment, the presence of redox-active sulfhydryl groups in numerous proteins on the cellular plasma membrane suggests that at least the microenvironment of the cell surface can also support redox reactions in and between certain surface proteins (*34*, *35*).

On the basis of our data and the above analysis, we assume that the reduced cytotoxicity of the rCPP polycations observed in the MTS assay is due to the intracellular reduction of the disulfide bonds resulting in short fragments with decreased binding affinity to membranes, nucleic acids, and vital proteins inside the cell. The limited ability of rCPPs to damage cell membrane and release the LDH is predominantly due to favorable (compared to PEI) structural features such as lower charge density and higher chain rigidity. It might be also possible that plasma membrane reduction of rCPPs contributes to their favorable cytotoxic properties. To enable more direct and unambiguous evaluation of the contribution of disulfide bond reduction to the cytotoxicity of reducible polycation, reducible and nonreducible polycations with similar chemical structures should be used instead of comparing peptide-based polycations with PEI. Such studies are currently underway in our lab using reducible and nonreducible forms of poly(L-lysine) (*15*).

One of the disadvantages in employing short bioactive cationic peptides as carriers in gene delivery lies in their nonspecific interactions with nucleic acids, which can hinder their biological activity. Polyplexes formed using short cationic peptides also show less efficient transfection (*7*) and are less stable because of the less prominent cooperative effect (*16*). These major limitations in utilizing bioactive peptides can be overcome by the use of reversible polymeric forms of the peptides, such as demonstrated here. Analysis of the transfection data of the rCPP/DNA polyplexes reveals that of the two peptides used in rCPP synthesis, HRP is more important than NLS for the transfection activity. The activity increases in all cell lines with increasing content of HRP. The increase in transfection activity of HRP-rich polyplexes with increasing N/P ratio suggests an important contribution of the free polypeptides to the polyplex activity (*36*). It was expected that an optimum HRP/NLS composition might exist at which maximum transfection activity would be observed. The results, however, suggest no clearly measurable effect of an NLS role in the rCPP/DNA activity. The apparent lack of NLS contribution to enhanced activity of the rCPP may be explained by several factors. The

NLS activity in DNA polyplexes is limited, as suggested by numerous reports demonstrating only modest enhancing effect on the transfection (*25*, *37*−*39*). The large size of the plasmid DNA and the large particle size of the polyplexes might be another factor, which limits the nuclear delivery. The notion that the size of the nucleic acid may play a role in the nuclear transport of polyplexes is supported by recent findings that rCPP containing the NLS sequence (rCPP A, B, C, D) can mediate nuclear delivery of siRNA (*40*). Yet another reason for the apparent lack of NLS effect on the rCPP activity may lie in the loss of NLS sequences from the surface of the polyplexes in the reducing environment of cytosol by the cleavage of the disulfide bonds. Finally, it may be possible that even if a small increase in efficiency of nuclear delivery mediated by the NLS is achieved, it may not manifest itself by a significant enhancement of reporter gene expression (*41*, *42*).

The contribution of the buffering capability of HRP to the overall transfection activity of rCPP polyplexes was tested by conducting the experiments in the presence of chloroquine and Baf.A1. The lysosomotropic activity of chloroquine is known to preferentially enhance activity of polyplexes based on polycations with no buffering potential, and as such, the chloroquine-mediated enhancement of transfection can serve as a measure of the importance of the buffering component in the polyplexes. This is clearly documented especially in the fast-growing B16F10 cells where the chloroquine enhancement ratio decreases with increasing HRP content. In the other two cell lines tested, the same effect is observed only in the three rCPPs with the highest HRP content. To complement the chloroquine data, we conducted the transfection experiments also in the presence of the inhibitor of vacuolar type H^+ ATPases, Baf.A1. Since polycations with pH buffering properties require exposure to an acidic environment for their activity (*43*), inhibition of the vacuolar ATPases by Baf.A1 should inhibit activity of the polyplexes based on such polycations (*17*). Dependent on the cell line and conditions used, our data show great qualitative and quantitative differences in the effect of Baf.A1 on the transfection activity of rCPP polyplexes. When the experiments were conducted under our standard transfection conditions (i.e., in the presence of 10% FBS), only the results in MCF-7 cells confirm the expected effect of Baf.A1 and show a significant decrease of levels of transgene expression for polyplexes with high HRP content and control PEI polyplexes (Figure 7c). Qualitatively different results are observed in B16F10 cells where a large increase of luciferase expression induced by Baf.A1 is observed, especially for rCPP with no or limited buffering capability, while no significant effect is seen for control PEI (Figure 7a). Most previous studies on the effects of Baf.A1 on transfection activity of polyplexes were conducted in serum-free conditions. Under serum-free conditions in B16F10 cells (Figure 7d), we observed that Baf.A1 exhibited the expected effect on the transfection activity of rCPP/DNA polyplexes in compositions containing comparatively higher amounts of the HRP peptide (D and E), which was compatible with a mechanism of action that depends on proton capture during the acidification process during endocytosis. Also, in HeLa and MCF-7 (Figure 7e,f), Baf.A1 demonstrated the expected effect on transfection activity of rCPP/DNA complexes compatible with the mechanism mentioned above. In all three cell lines, Baf.A1 decreases the luciferase expression of the polyplexes with the highest HRP content. The effect is best shown in HeLa and MCF-7 cells, while the data obtained in B16F10 cells are less clear and a Baf.A1-mediated increase of luciferase expression is still observed for rCPP-A even in serum-free conditions. This effect seems to be at least partially dependent on the amino acid sequence of the NLS peptide because no effect of such magnitude was observed for similar nonbuffering reducible polypeptides based on CKKKK-KKKKKKC or CGRKKRRQRRRGC peptides (data not shown). In addition, Baf.A1 caused no increase in cellular uptake of the polyplexes in B16F10 (data not shown). As shown in Figure 7, the Baf.A1 effect on the activity of rCPP-A polyplexes in B16F10 cells is strongly associated with the presence of serum. To determine if there is a specific component of the serum responsible for the observed effect, we have conducted the experiment in the presence of bovine serum albumin (BSA) (Figure 8a). Increasing the albumin concentration leads to increased transfection induced by Baf.A1 in rCPP-A polyplexes but has almost no effect on rCPP-E polyplexes. As reported previously, Baf.A1 is toxic to the B16F10 cells and causes significant levels of apoptotic cell death at 100 nM (*44*). To limit the adverse toxic effects of Baf.A1, control experiments were also conducted at 20 nM Baf.A1. In the presence of 10% FBS, the observed results showed similar effects of Baf.A1 on the transfection activity of rCPP-A demonstrated by ∼75-fold increase of luciferase expression (data not shown). The data obtained with the caveolae inhibitor genistein (Figure 8b) seem to suggest that Baf.A1 treatment may redirect at least some of the NLS-containing polyplexes to a caveolae-mediated uptake mechanism. Since this mechanism of cellular uptake avoids routing to the lysosomal degradative environment, it may be possible that avoidance of the lysosomal degradation of the polyplexes may be the reason for the observed Baf.A1 effect (*45*). It should be noted, however, that detailed understanding of the unexpected behavior of the NLS-containing polyplexes in the presence of Baf.A1 is not available at this moment and further detailed investigation of this phenomenon is beyond the scope of this manuscript.

CONCLUSION

In conclusion, the present studies demonstrate that reducible multiblock copolypeptides can be readily synthesized by an oxidative polycondensation. This synthetic approach allows an effective control of the relative content of individual building blocks of the copolypeptides, which is demonstrated here on the copolypeptides of the histidine-rich and NLS peptides. As such, this versatile approach should be suitable for generation of chemical libraries of copolypeptides consisting of a variety of bioactive peptide sequences. By use of the reducible copolypeptides, polyplexes sensitive to redox potential gradients can be formulated as promising gene delivery vectors. In comparison with control polyethylenimine, only minimum toxic effects of rCPPs are observed on the metabolic activity and membrane integrity of human endothelial cells. These findings are explained by a reductive intracellular and plasma membrane degradation and lower charge density and higher chain rigidity of the rCPPs than PEI. Transfection activity in all tested cell lines increases with increasing content of the HRP sequence in the rCPPs, while no clearly measurable effect of the NLS sequence is found. Overall, we believe that reducible co-polypeptides possess a number of advantageous features to make them an attractive tool for gene delivery.

ACKNOWLEDGMENT

This work was supported by NIH Grant CA109711. We thank David Bassett for help with FACS analysis and Harender Bisht and Yezi You for help with the polypeptide characterization.

LITERATURE CITED

(1) Tang, F. X., and Hughes, J. A. (1999) Use of dithiodiglycolic acid as a tether for cationic lipids decreases the cytotoxicity and increases transgene expression of plasmid DNA in vitro. *Bioconjugate Chem. 10,* 791−796.

(2) Byk, G., Wetzer, B., Frederic, M., Dubertret, C., Pitard, B., Jaslin, G., and Scherman, D. (2000) Reduction-sensitive lipopolyamines as a novel nonviral gene delivery system for modulated release of DNA with improved transgene expression. *J. Med. Chem. 43*, 4377−4387.

(3) Chittimalla, C., Zammut-Italiano, L., Zuber, G., and Behr, J. P. (2005) Monomolecular DNA nanoparticles for intravenous delivery of genes. *J. Am. Chem. Soc. 127*, 11436−11441.

(4) Oishi, M., Hayama, T., Akiyama, Y., Takae, S., Harada, A., Yamasaki, Y., Nagatsugi, F., Sasaki, S., Nagasaki, Y., and Kataoka, K. (2005) Supramolecular assemblies for the cytoplasmic delivery of antisense oligodeoxynucleotide: polyion complex (PIC) micelles based on poly(ethylene glycol)-SS-oligodeoxynucleotide conjugate. *Biomacromolecules 6*, 2449−2454.

(5) Saito, G., Swanson, J. A., and Lee, K. D. (2003) Drug delivery strategy utilizing conjugation via reversible disulfide linkages: role and site of cellular reducing activities. *Adv. Drug Delivery Rev. 55*, 199−215.

(6) Miyata, K., Kakizawa, Y., Nishiyama, N., Harada, A., Yamasaki, Y., Koyama, H., and Kataoka, K. (2004) Block catiomer polyplexes with regulated densities of charge and disulfide cross-linking directed to enhance gene expression. *J. Am. Chem. Soc. 126*, 2355−2361.

(7) McKenzie, D. L., Smiley, E., Kwok, K. Y., and Rice, K. G. (2000) Low molecular weight disulfide cross-linking peptides as nonviral gene delivery carriers. *Bioconjugate Chem. 11*, 901−909.

(8) McKenzie, D. L., Kwok, K. Y., and Rice, K. G. (2000) A potent new class of reductively activated peptide gene delivery agents. *J. Biol. Chem. 275*, 9970−9977.

(9) Balakirev, M., Schoehn, G., and Chroboczek, J. (2000) Lipoic acid-derived amphiphiles for redox-controlled DNA delivery. *Chem. Biol. 7*, 813−819.

(10) Read, M. L., Bremner, K. H., Oupicky, D., Green, N. K., Searle, P. F., and Seymour, L. W. (2003) Vectors based on reducible polycations facilitate intracellular release of nucleic acids. *J. Gene Med. 5*, 232−245.

(11) Read, M. L., Singh, S., Ahmed, Z., Stevenson, M., Briggs, S. S., Oupicky, D., Barrett, L. B., Spice, R., Kendall, M., Berry, M., Preece, J. A., Logan, A., and Seymour, L. W. (2005) A versatile reducible polycation-based system for efficient delivery of a broad range of nucleic acids. *Nucleic Acids Res. 33*, e86.

(12) Ogris, M., Carlisle, R. C., Bettinger, T., and Seymour, L. W. (2001) Melittin enables efficient vesicular escape and enhanced nuclear access of nonviral gene delivery vectors. *J. Biol. Chem. 276*, 47550−47555.

(13) Zanta, M. A., Belguise-Valladier, P., and Behr, J. P. (1999) Gene delivery: A single nuclear localization signal peptide is sufficient to carry DNA to the cell nucleus. *Proc. Natl. Acad. Sci. U.S.A. 96*, 91−96.

(14) Soundara Manickam, D., Bisht, H. S., Wan, L., Mao, G., and Oupicky, D. (2005) Influence of TAT-peptide polymerization on properties and transfection activity of TAT/DNA polyplexes. *J. Controlled Release 102*, 293−306.

(15) Oupicky, D., Parker, A. L., and Seymour, L. W. (2002) Laterally stabilized complexes of DNA with linear reducible polycations: Strategy for triggered intracellular activation of DNA delivery vectors. *J. Am. Chem. Soc. 124*, 8−9.

(16) Reschel, T., Konak, C., Oupicky, D., Seymour, L. W., and Ulbrich, K. (2002) Physical properties and in vitro transfection efficiency of gene delivery vectors based on complexes of DNA with synthetic polycations. *J. Controlled Release 81*, 201−217.

(17) Kichler, A., Leborgne, C., Coeytaux, E., and Danos, O. (2001) Polyethylenimine-mediated gene delivery: a mechanistic study. *J. Gene Med. 3*, 135−144.

(18) Rejman, J., Bragonzi, A., and Conese, M. (2005) Role of clathrin- and caveolae-mediated endocytosis in gene transfer mediated by lipo- and polyplexes. *Mol. Ther. 12*, 468−474.

(19) Akiyama, T., Ishida, J., Nakagawa, S., Ogawara, H., Watanabe, S., Itoh, N., Shibuya, M., and Fukami, Y. (1987) Genistein, a specific inhibitor of tyrosine-specific protein kinases. *J. Biol. Chem. 262*, 5592−5595.

(20) Parton, R. G., Joggerst, B., and Simons, K. (1994) Regulated internalization of caveolae. *J. Cell Biol. 127*, 1199−1215.

(21) Park, Y., Kwok, K. Y., Boukarim, C., and Rice, K. G. (2002) Synthesis of sulfhydryl cross-linking poly(ethylene glycol)-peptides and glycopeptides as carriers for gene delivery. *Bioconjugate Chem. 13*, 232−239.

(22) Kwok, K. Y., Park, Y., Yang, Y., McKenzie, D. L., Liu, Y., and Rice, K. G. (2003) In vivo gene transfer using sulfhydryl cross-linked PEG-peptide/glycopeptide DNA co-condensates. *J. Pharm. Sci. 92*, 1174−1185.

(23) Haider, M., Megeed, Z., and Ghandehari, H. (2004) Genetically engineered polymers: status and prospects for controlled release. *J. Controlled Release 95*, 1−26.

(24) Putnam, D., Gentry, C. A., Pack, D. W., and Langer, R. (2001) Polymer-based gene delivery with low cytotoxicity by a unique balance of side-chain termini. *Proc. Natl. Acad. Sci. U.S.A. 98*, 1200−1205.

(25) Bremner, K. H., Seymour, L. W., Logan, A., and Read, M. L. (2004) Factors influencing the ability of nuclear localization sequence peptides to enhance nonviral gene delivery. *Bioconjugate Chem. 15*, 152−161.

(26) Schindler, T., and Nordmeier, E. (1997) The stability of polyelectrolyte complexes of calf-thymus DNA and synthetic polycations: Theoretical and experimental investigations. *Macromol. Chem. Phys. 198*, 1943−1972.

(27) Godbey, W. T., Wu, K. K., and Mikos, A. G. (2001) Poly(ethylenimine)-mediated gene delivery affects endothelial cell function and viability. *Biomaterials 22*, 471−480.

(28) Moghimi, S. M., Symonds, P., Murray, J. C., Hunter, A. C., Debska, G., and Szewczyk, A. (2005) A two-stage poly(ethylenimine)-mediated cytotoxicity: implications for gene transfer/therapy. *Mol. Ther. 11*, 990−995.

(29) Jones, D. P., Carlson, J. L., Samiec, P. S., Sternberg, P., Jr., Mody, V. C., Jr., Reed, R. L., and Brown, L. A. (1998) Glutathione measurement in human plasma. Evaluation of sample collection, storage and derivatization conditions for analysis of dansyl derivatives by HPLC. *Clin. Chim. Acta 275*, 175−184.

(30) Hwang, C., Lodish, H. F., and Sinskey, A. J. (1995) Measurement of glutathione redox state in cytosol and secretory pathway of cultured cells. *Methods Enzymol. 251*, 212−221.

(31) Hwang, C., Sinskey, A. J., and Lodish, H. F. (1992) Oxidized redox state of glutathione in the endoplasmic reticulum. *Science 257*, 1496−1502.

(32) Saito, G., Amidon, G. L., and Lee, K. D. (2003) Enhanced cytosolic delivery of plasmid DNA by a sulfhydryl-activatable listeriolysin O/protamine conjugate utilizing cellular reducing potential. *Gene Ther. 10*, 72−83.

(33) Austin, C. D., Wen, X., Gazzard, L., Nelson, C., Scheller, R. H., and Scales, S. J. (2005) Oxidizing potential of endosomes and lysosomes limits intracellular cleavage of disulfide-based antibody−drug conjugates. *Proc. Natl. Acad. Sci. U.S.A. 102*, 17987−17992.

(34) Jiang, X. M., Fitzgerald, M., Grant, C. M., and Hogg, P. J. (1999) Redox control of exofacial protein thiols/disulfides by protein disulfide isomerase. *J. Biol. Chem. 274*, 2416−2423.

(35) Sahaf, B., Heydari, K., Herzenberg, L. A., and Herzenberg, L. A. (2005) The extracellular microenvironment plays a key role in regulating the redox status of cell surface proteins in HIV-infected subjects. *Arch. Biochem. Biophys. 434*, 26−32.

(36) Boeckle, S., von Gersdorff, K., van der Piepen, S., Culmsee, C., Wagner, E., and Ogris, M. (2004) Purification of polyethylenimine polyplexes highlights the role of free polycations in gene transfer. *J. Gene Med. 6*, 1102−1111.

(37) van der Aa, M., Koning, G. A., d'Oliveira, C., Oosting, R. S., Wilschut, K. J., Hennink, W. E., and Crommelin, D. J. A. (2005) An NLS peptide covalently linked to linear DNA does not enhance transfection efficiency of cationic polymer based gene delivery systems. *J. Gene Med. 7*, 208−217.

(38) Boulanger, C., Di Giorgio, C., and Vierling, P. (2005) Synthesis of acridine-nuclear localization signal (NLS) conjugates and evaluation of their impact on lipoplex and polyplex-based transfection. *Eur. J. Med. Chem. 40*, 1295−1306.

(39) Akita, H., Tanimoto, M., Masuda, T., Kogure, K., Hama, S., Ninomiya, K., Futaki, S., and Harashima, H. (2006) Evaluation of the nuclear delivery and intra-nuclear transcription of plasmid DNA condensed with micro (mu) and NLS-micro by cytoplasmic and nuclear microinjection: a comparative study with poly-L-lysine. *J. Gene Med. 8*, 198−206.

(40) Howard, K. A., Liu, X., Oupicky, D., Besenbacher, F., and Kjems, J. (2005) Short interfering RNA delivery and gene silencing using polymeric nanocarrier systems. *J. Biotechnol. 118*, S76−S76.

(41) Varga, C. M., Tedford, N. C., Thomas, M., Klibanov, A. M., Griffith, L. G., and Lauffenburger, D. A. (2005) Quantitative comparison of polyethylenimine formulations and adenoviral vectors in terms of intracellular gene delivery processes. *Gene Ther. 12*, 1023−1032.

(42) Hama, S., Akita, H., Ito, R., Mizuguchi, H., Hayakawa, T., and Harashima, H. (2006) Quantitative comparison of intracellular trafficking and nuclear transcription between adenoviral and lipoplex systems. *Mol. Ther. 13*, 786−794.

(43) Forrest, M. L., and Pack, D. W. (2002) On the kinetics of polyplex endocytic trafficking: implications for gene delivery vector design. *Mol. Ther. 6*, 57−66.

(44) Ancans, J., and Thody, A. J. (2000) Activation of melanogenesis by vacuolar type H(+)-ATPase inhibitors in amelanotic, tyrosinase positive human and mouse melanoma cells. *FEBS Lett. 478*, 57−60.

(45) Pelkmans, L., Kartenbeck, J., and Helenius, A. (2001) Caveolar endocytosis of simian virus 40 reveals a new two-step vesicular-transport pathway to the ER. *Nat. Cell Biol. 3*, 473−483.

BC060104K

Fabrication of Cell-Based Arrays Using Micropatterned Alkanethiol Monolayers for the Parallel Silencing of Specific Genes by Small Interfering RNA

Hiroyuki Fujimoto, Satoru Yoshizako, Koichi Kato, and Hiroo Iwata*

Institute for Frontier Medical Sciences, Kyoto University, 53 Kawahara-cho, Shogoin, Sakyo-ku, Kyoto 606-8507, Japan.
Received April 23, 2006; Revised Manuscript Received September 19, 2006

The emergence of small interfering RNA (siRNA) opened a new opportunity to study gene functions in a genome. However, large-scale loss-of-function analyses further require cell-based high-throughput methods that allow simultaneous silencing of the huge number of genes by siRNA. In this study, we aim at fabricating the cell-based siRNA arrays that facilitate parallel introduction of multiple siRNAs into cultured mammalian cells. The siRNA arrays were prepared using surface chemical processes including the micropatterning of a self-assembled monolayer and the layer-by-layer assembly of siRNA and cationic lipid. We examined the feasibility of the siRNA array for the sequence-specific gene silencing in an array format. Furthermore, the effects of siRNA loading and culture period after transfection were studied to optimize cell-based assays on the siRNA arrays. The results obtained in this study demonstrated that our method provides the siRNA arrays with spatial specificity in gene silencing, which will serve to obtain a quantitative data set from the cell-based screens on siRNA arrays.

INTRODUCTION

Small interfering RNA (siRNA) have recently been recognized as a powerful tool for analyzing gene functions in mammalian cells (*1*). When introduced into cytoplasm, double-stranded RNA of ~21 nucleotides triggers RNA interference (RNAi) by which specific genes having homologous sequences are transiently silenced to yield mutants. The abnormal phenotypes caused by RNAi provide the biological readouts from which we can infer the functions of particular genes. Recently, we have gained deep insights into the cellular mechanism involved in siRNA-triggered gene silencing (*2, 3*), while advances in siRNA technology opened a new opportunity to study gene functions genome-wide (*4*−*7*).

The genome-wide RNAi screens require several methodological arrangements: A library of siRNA clones must be implemented to cover the huge number of genes. Efficient cell reporting systems are further needed to monitor phenotypic alterations on living cells. In addition, it is practically important especially for high-throughput screens to develop efficient and flexible platforms that permit parallel introduction of siRNA clones into living cells. Because the number of genes has reached a few tens of thousands, this is not straightforward by conventional microplate formats. To solve this problem, a number of groups have developed the cell-based arrays that allow parallel introduction of multiple siRNAs into cultured mammalian cells (*8*−*11*).

The idea of cell-based arrays for large-scale genetic screens was derived from the pioneering study by Ziauddin and Sabatini (*12*). In that study, expression constructs for defined cDNAs were printed together with cationic lipid and gelatin onto a glass slide in an array format. It was shown that, when cultured directly on the slide, cells were successfully transfected with released DNA to express individual cDNAs within the defined areas. This technology was immediately extended to the parallel transfection of siRNA into living cells (*8*−*11, 13*). In most cases, siRNA arrays were fabricated in a similar way to the plasmid DNA array as mentioned above, but simply replacing DNA with siRNA.

Although early studies (*8*−*11, 13*) succeeded in demonstrating the feasibility of the cell-based arrays for RNAi screens, further improvements are considered necessary to obtain quantitative and accurate data for finding out specific phenotypes from a large data set. First of all, it is obvious that low transfection efficiency would make experimental data difficult to interpret. Other important factors include deviation of transfection efficiency between different siRNAs on separate spots on a single array. Such deviation would make it difficult to distinguish small difference in phenotypic readouts, such as fluorescent intensity in an assay combined with a reporter system using mutants with green fluorescent protein (GFP). In addition, the efficiency of gene silencing at the different regions within a single spot is also a matter of utmost concern in quantitative analysis. Because the extent of gene silencing is expressed as a reduction rate of protein expression in total transfected cells, siRNA should be introduced to the cells on precisely restricted regions and, at the same time, homogenously to the entire cells over the spot.

Here, we present our attempts to fabricate cell-based siRNA arrays using surface chemical processes including the micropatterning of a self-assembled monolayer (SAM) (*14*−*16*) and the layer-by-layer (LBL) assembly (*17*) of siRNA and cationic lipid. In our previous study, cell-based arrays for the efficient overexpression of defined cDNAs were successfully fabricated using the LBL process on the micropatterned SAM (*18*). It was demonstrated that these processes provide an effective way to reproducibly introduce plasmid DNA into cells at the restricted regions on the array. The present study is therefore the extension of our outstanding method for the array-based loss-of-function assays using siRNA. In this study, photoassisted micropatterning of SAM was employed to create an array of small anionic dots on a glass substrate. The array was then utilized as a platform for loading siRNA with cationic lipid and plasmid DNA by the LBL process to obtain siRNA arrays. We examined the feasibility of our siRNA arrays for the sequence- and site-specific gene silencing. Furthermore, the effects of siRNA loading and culture period after transfection were studied to

* Corresponding author. E-mail: iwata@frontier.kyoto-u.ac.jp Tel & Fax: +81-75-751-4119.

10.1021/bc060105c CCC: $33.50 © 2006 American Chemical Society
Published on Web 10/19/2006

optimize cell-based assays on the siRNA arrays. We show that the method used in this study provides the siRNA arrays with spatial specificity in gene silencing, which will serve to obtain a quantitative data set from the cell-based screens on siRNA arrays.

EXPERIMENTAL SECTION

Preparation of Patterned SAM. A glass plate ($22 \times 26 \times 0.5$ mm^3, Matsunami Glass Industries, Ltd., Osaka, Japan) was immersed in piranha solution (7:3, v/v 96% H_2SO_4/30% H_2O_2) for 5 min at room temperature to remove impurities and then washed with 2-propanol and MilliQ water. Thin layers of chromium (thickness: 1 nm) and gold (thickness: 49 nm) were sequentially deposited onto the purified glass plate in a continuous process with a vacuum evaporator (V-KS200, Osaka Vacuum Instruments, Osaka, Japan) operated at a pressure of $3-4 \times 10^{-4}$ Pa. Immediately after deposition, the plate was immersed in 1 mM 1-hexadecanethiol (Tokyo Kasei Kogyo Co., Tokyo, Japan) solution in ethanol at room temperature for 24 h to allow the formation of a methyl-terminated SAM (CH_3-SAM) on gold. The plate was washed with ethanol and water to remove unreacted alkanethiols, and dried under a stream of dried N_2 gas.

For micropattterning, the glass plate having a CH_3-SAM was radiated by ultraviolet light through a photomask (*15*). The photomask was made of a quartz plate deposited with a thick chromium layer having 5×5 circular holes with a diameter of 1 mm. The SAM surface was overlaid with the photomask and irradiated with ultraviolet light through the photomask from an ultrahigh-pressure mercury lamp (500 W, Optical Modulex SX-UI500HQ, Ushio Inc., Osaka, Japan). After 2 h irradiation, the plate was washed with ethanol and water to remove photocleaved alkanethiols and immediately immersed in a 1 mM solution of 11-mercapto-1-undecanoic acid (Aldrich Chemical Co., Milwaukee, WI) in ethanol. The plate was kept in the solution for 2 h at room temperature to allow the formation of a carboxylic acid terminated SAM (COOH-SAM) within the UV-radiated spots. Finally, the plate was washed with ethanol and water to remove unreacted alkanethiols and dried under a stream of N_2 gas.

siRNA and Plasmid DNA. Synthetic siRNAs of 21 or 22 nucleotides were purchased from Qiagen, Hilden, Germany, and Dharmacon, Inc., Colorado, U.S.A.: Specific siRNA for enhanced GFP (EGFP-siRNA): sense, 5′-GCAAGCUGACCCUGAAGUUCAU-3′; antisense, 5′-GAACUUCAGGGUCAGCUUG CCG-3′ (Qiagen). For *Discosoma* sp. red fluorescent protein (DsRed-siRNA): sense, 5′-AGUUCCAGUACGGCUCCAAUU-3′; antisense, 5′-UUGGAGCCGUACUGGAACUUU-3′ (Dharmacon). Nonspecific siRNA (control-siRNA): sense, 5′-UUCUCCGAACGUGUCACGUdTdT-3′; antisense, 5′-ACGUGACACGUUCGGAGAAdTdT-3′ (Qiagen). EGFP-siRNA conjugated with rhodamine at the 3′-end (EGFP-siRNA-Rho): sense, 5′-GCAAGCUGACCCUG AAGUUCAU-3′; antisense, 5′-GAACUUCAGGGUCAGCUUGCCG-3′ (Qiagen).

Plasmids used were pEGFP-C1 and pDsRed2-C1 (Clontech Laboratories, Palo Alto, CA), which encoded, respectively, EGFP and DsRed, under the control of the immediate early promoter of human cytomegalovirus. We refer to these plasmids as pEGFP and pDsRed, respectively. These plasmids were amplified in *Escherichia coli* DH5α and purified using a Plasmid Maxiprep Kit (Qiagen). A rhodamine labeled plasmid, pGeneGrip Rhodamine/GFP, was purchased from Gene Therapy Systems, California, and used as received.

Loading of siRNA and Plasmid DNA. The outline of array preparation is shown in Scheme 1. Opti-MEM (Gibco Life Technologies, Grand Island, NY), containing siRNA (0−20 μg/mL) and plasmid DNA (10 μg/mL), and lipofectAMINE2000

Scheme 1. Loading of siRNA by LBL Assembly To Individual Dots on the Micropatterned SAM[a]

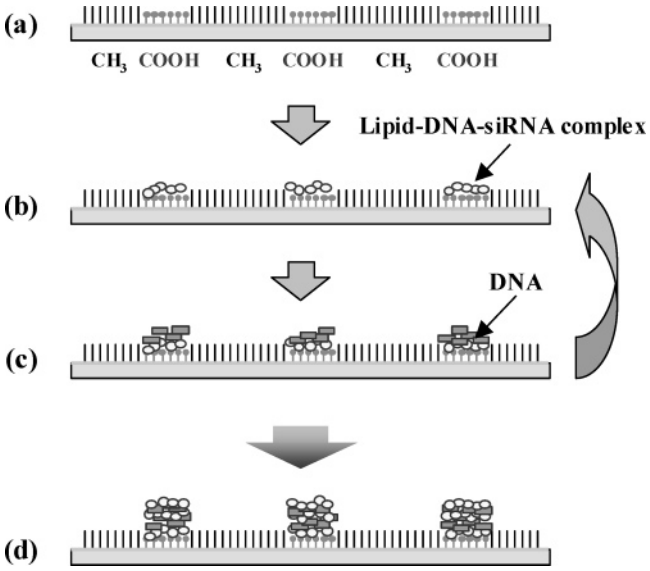

[a] (a) Micropatterned alkanethiol SAM. (b) Adsorption of LDR complex. (c) Adsorption of plasmid DNA. The procedures (b) and (c) were repeated to obtain a siRNA-loaded array (d).

(30 μg/mL; Invitrogen Corp., Carlsbad, CA) was prepared and kept at room temperature for 20 min to form an electrolyte complex between the anionic nucleic acids (siRNA and plasmid DNA) and the cationic lipid. We refer hereafter to this lipid−DNA−RNA complex as LDR complex. The solution (approximately 200 nL) of LDR complex was manually pipetted to COOH-terminated dots on the patterned SAM and kept for 5 min to adsorb the complex to the dot surface. After aspiration of the LDR complex solutions, 200 nL of a plasmid DNA solution (10 μg/mL) in Opti-MEM was then pipetted to the LDR-adsorbed dots and kept for 5 min to adsorb DNA to the dots. These procedures were repeated to form a multilayer consisting of LDR−DNA−LDR−DNA−LDR. Finally, the entire surface of the array was washed with PBS and immediately used for further experiments without drying.

To determine the amount of plasmid DNA and siRNA loaded to the dots, either the rhodamine conjugate of plasmid DNA (pGeneGrip Rhodamine/GFP) or siRNA (EGFP-siRNA-Rho) was loaded to the patterned SAM together with unlabeled siRNA or plasmid DNA, respectively, in the same manner as described above. The dots were observed with a fluorescence stereomicroscope (MZ FLIII, Leica, Switzerland) equipped with a cooled-CCD camera (ORCA-ER; Hamamatsu Photonics K.K., Shizuoka, Japan). A fluorescence intensity was measured for the entire area within a single dot using an AQUA-Lite digital imaging software (Hamamatsu Photonics). The fluorescence intensity was converted to the amount of DNA or siRNA using a calibration curve obtained by depositing the rhodamine-labeled DNA and siRNA of known amount to a dot. The data was expressed as mean ± standard deviation for $n = 5$.

Gene Silencing on siRNA Array. Human embryonic kidney cell, HEK293, was obtained from Health Science Research Resources Bank, Tokyo, Japan, and grown in minimal essential medium (MEM; Gibco) containing 10% fetal bovine serum (FBS), 100 U/mL penicillin, and 0.1 mg/mL streptomycin at 37 °C under 5% CO_2. The cells were harvested by trypsin treatment and suspended in antibiotics-free MEM with or without 10% FBS. The siRNA-loaded array was placed in a 35-mm Petri dish, and the cells were seeded onto the array at a density of 6.7×10^4 cells/cm^2. The cells were incubated at 37 °C under 5% CO_2 to allow cell adhesion and cotransfection of plasmid DNA and siRNA. Then, the medium was replaced

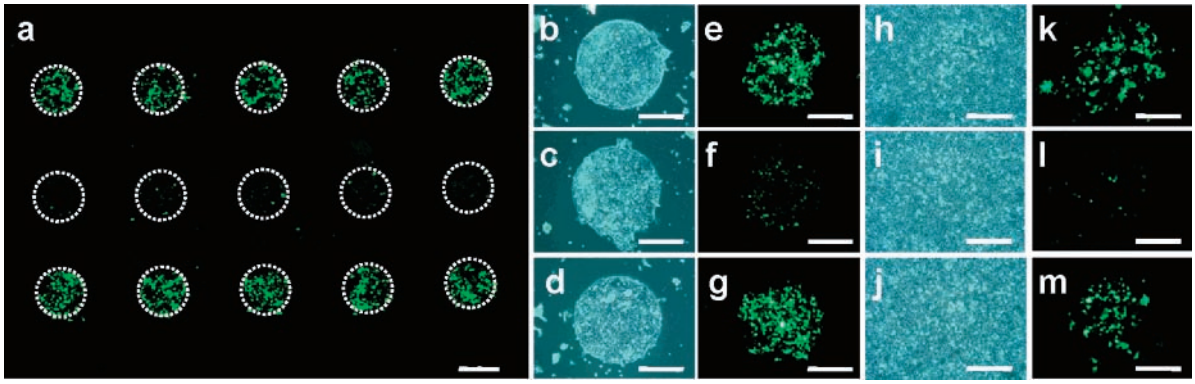

Figure 1. Gene silencing on the siRNA array. (a) Fluorescent image of the array on which HEK293 cells were seeded in the presence of FBS. The images were recorded 48 h after cell seeding. The position of dots is indicated in the image with dotted circles. (b−m) Higher-magnification images of selected dots. Cells were seeded in (b−g) the presence and (h−m) the absence of FBS. Phase contrast (b−d, h−j) and the corresponding fluorescent (e−g, k−m) images are shown for three cases: (top) pEGFP alone, (middle) pEGFP + EGFP-siRNA, (bottom) pEGFP + control-siRNA. Bar = (a) 1 mm, (b−m) 500 μm.

with a fresh MEM containing 10% FBS and antibiotics 6 h (for cells seeded without FBS) or 24 h (for cells seeded with FBS) after cell seeding. During culture, cells were observed with an epifluorescence microscope (Olympus, Tokyo, Japan). The fluorescence intensity of EGFP or DsRed was measured 48 h after cell seeding for the entire area of a dot using a fluorescence stereomicroscope (MZ FLIII, Leica). The efficiency of gene silencing (suppression efficiency) was determined according to the following equation

$$\text{Suppression efficiency (\%)} = [1 - (I_{\text{specific}}/I_{\text{control}})] \times 100$$

where I_{specific} is the fluorescent intensity of EGFP measured for the dot on which plasmid DNA and the specific siRNA were cotransfected, and I_{control} is that for the dot on which either of the plasmids were cotransfected with control siRNA. All the data presented in this paper were the average of three independent experiments.

RESULTS

Preparation of siRNA Array. The photoassisted patterning of CH_3-SAM and the subsequent formation of COOH-SAM within the radiated areas gave rise to the patterned SAM which possessed hydrophilic dots (COOH-SAM) surrounded by the hydrophobic regions (CH_3-SAM). Thanks to the difference in hydrophilicity, a liquid droplet pipetted was readily positioned to the hydrophilic dot. This feature served to confine siRNA to the dots, and eventually to produce well-formatted siRNA arrays.

Our previous study (*18*) revealed that the complex consisting of plasmid DNA and excess cationic lipid (lipofectAMINE2000) was attracted by the negatively charged surface of COOH-SAM through electrostatic interactions. From an analogy to the previous observation, it is plausible that the LDR complex employed in this study adsorbed ionically to the COOH-SAM surface. Similarly, alternate adsorption of LDR complex (cationic assembler) and free plasmid DNA (anionic assembler) is expected to produce a multilayer comprising siRNA, plasmid DNA, and cationic lipid. The amount of adsorbed siRNA and plasmid DNA reached, respectively, 38 ± 11 ng/cm^2 and 150 ± 67 ng/cm^2, when determined for a multilayer formed using 1 μg/mL siRNA solution after 5 adsorption procedures, i.e., a multilayer with LDR−DNA−LDR−DNA−LDR.

Sequence-Specific Gene Silencing on siRNA Array. Figure 1 shows the representative results of sequence-specific gene silencing on the siRNA-loaded array. When seeded in the presence of FBS, adhesion of HEK293 cells were restricted to the dots (Figure 1b−d), probably due to preferential adsorption of abundant serum proteins such as albumin and globulin onto hydrophobic regions between dots (*19*−*22*), which might suppress cell adhesion to these areas. The cell adhesion within dots may be promoted by the cationic nature of the uppermost surface, because the LBL process was always ended with the LDR complex. The typical number of cells was approximately 2500 cells per dot under the conditions employed here. EGFP expression was observed on the dots loaded with the EGFP-coding plasmid but lacking siRNA (5 dots on the upper line in Figure 1a) with a similar extent between the spots. Cells on the dots with both plasmid and control siRNA (5 dots on the bottom line in Figure 1a) also expressed EGFP, indicating the insignificant effect of nonspecific siRNA on protein synthesis. In contrast, a lower level of EGFP expression was observed on the dots with EGFP-coding plasmid and EGFP-siRNA (5 dots on the middle line in Figure 1a), indicating the suppression of EGFP synthesis. The fluorescence intensities were determined to be 0.19 ± 0.09 (EGFP-siRNA), 2.30 ± 0.31 (control-siRNA), and 2.36 ± 0.86 (no siRNA). The observed small deviations denote the reproducibility of transfection. These results suggested that both plasmid and siRNA were transferred from the array into the cells to reproducibly silence EGFP synthesis in sequence- and region-specific manners.

Similar to the case in which cells were seeded in the presence of FBS, sequence- and region-specific gene silencing was observed in the absence of FBS (Figure 1h−m). In the absence of FBS, however, cells adhered and grew on the entire surface of the array.

In order to gain deeper insights into the interactions operated in the LBL process, an amine-terminated SAM (NH_2-SAM) having a positively charged surface was used instead of a COOH-SAM. When the LDR complex (lipid/pEGFP/control siRNA) was adsorbed as the first assembler to obtain five-layered LDR−DNA composites, EGFP was expressed in HEK293 cells to a lower extent compared to the case with COOH-SAM (Supporting Information Figure S1), indicating that the combination of the COOH-SAM having an anionic surface and the LDR complex plays an important role in efficient transfection. This finding supports our hypothesis that the LDR complex bares cationic charges and that electrostatic interactions are predominant forces operated in the LBL assembly process. It seems that the cationic NH_2-SAM surface inefficiently attracts the LDR complex with the same sign of charges.

To clarify the mechanism by which the array functions, two different plasmids, pEGFP and pDsRed, were used respectively as a component of the LDR complex and anionic assembler, or vice versa. GFP-siRNA and control siRNA were used as a RNA component in the LDR complex. As shown in Figure 2, the plasmid contained in the LDR complex was efficiently expressed

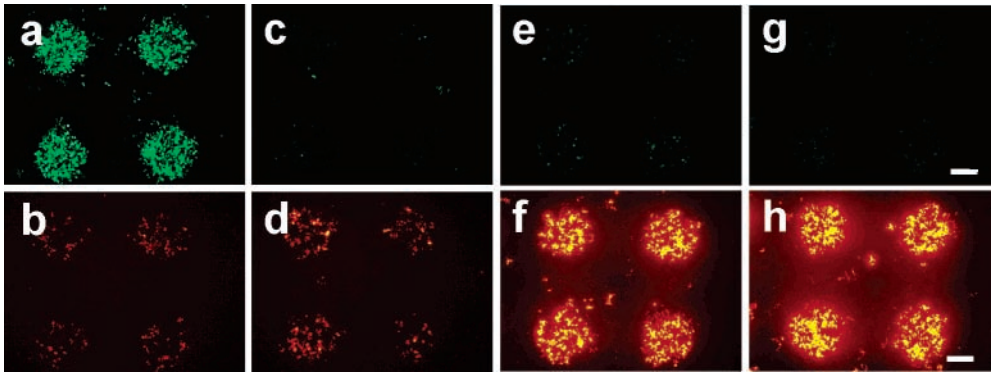

Figure 2. Fluorescent images of HEK293 cells transfected on siRNA arrays prepared from different compositions of siRNAs and plasmid DNAs. Plasmid DNA: (a−d) LDR; pEGFP, D; pDsRed, (e−h) LDR; pDsRed, D; pEGFP. siRNA: (a,b,e,f) control-siRNA, (c,d,g,h) GFP-siRNA. Bar = 500 μm.

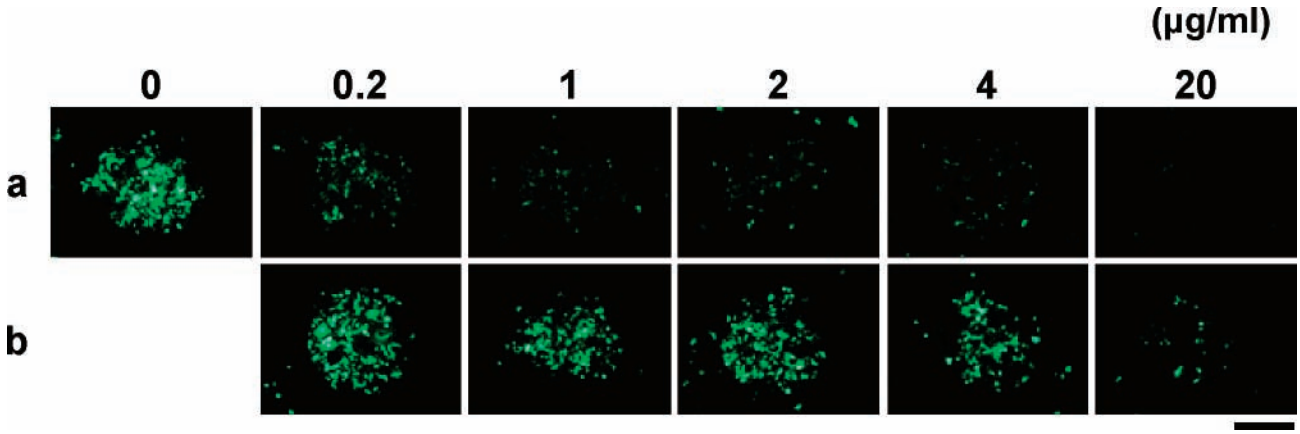

Figure 3. Fluorescent images showing the effect of siRNA loading on the silencing of EGFP expression. EGFP-siRNA (a) and control siRNA (b) were cotransfected with pEGFP. The concentration of siRNA used in the preparation of LDR complex is indicated above the corresponding photographs. Bar = 500 μm.

in the cells (Figure 2a,f), but that used as an anionic assembler was not (Figure 2b,e). The expression of GFP was efficiently suppressed by the GFP-siRNA incorporated to the LDR complex (Figure 2c,g). The DsRed expression was not influenced by GFP-siRNA, as expected (Figure 2d,h). These results demonstrate that plasmid contained in the LDR complex is transfected more efficiently than that used as an anionic assembler.

Attempts were further made to examine the feasibility of the SAM array for silencing endogenous targets. The LBL assembly was conducted using the complex consisting of GFP-siRNA and the lipid as cationic assembler and GFP-siRNA as anionic assembler. HEK293 cells stably transformed with GFP gene were plated to the array. It was found that the expression of GFP was efficiently reduced in a sequence-specific manner (data not shown).

Effect of siRNA Loading. Figure 3 shows the effect of siRNA loading on the suppression of EGFP expression. The LDL complex was prepared using different concentrations of siRNA together with the fixed concentration of plasmid DNA and cationic lipid. As is seen from the series of fluorescent images, silencing by specific siRNA (Figure 3a) was evident at a siRNA concentration of 0.2 μg/mL with a suppression efficiency of 76%. The highest suppression efficiency (=90%) was achieved at a siRNA concentration of more than 1.0 μg/mL. When a siRNA solution of relatively high concentration (>4 μg/mL, Figure 3b) was used, EGFP expression was impaired in the cells transfected with both EGFP-specific and control siRNAs. This is partly because of nonspecific inhibition of protein synthesis by highly concentrated exogeneous RNA (*23*). Another factor that affects EGFP expression may be altered charge balance in the LDR complex, which would affect introduction of plasmid DNA into cells. These results suggest that the most efficient, sequence-specific gene silencing can be achieved with 1.0−2.0 μg/mL siRNA under the experimental conditions employed here, while nonspecific effects are insignificant.

Time Dependence of Gene Silencing. As shown in Figure 4a, EGFP expression on the dots without siRNA and with control siRNA increased during the initial 4 days after cell seeding in the presence of FBS, reached the maximal expression level at day 4, and then gradually decreased afterward, most likely due to plasmid metabolism (*24*). In contrast, a low level of EGFP expression was observed on the dots loaded with EGFP-siRNA throughout the culture period. The highest suppression was achieved 48 h after cell seeding, with a suppression efficiency of 91% compared to the fluorescence intensity determined at the same time points for cells transfected with control siRNA. Similar time dependence was observed in the experiments in which cells were seeded in the absence of FBS (Figure 4b): The highest efficiency of gene silencing (80−90% compared to the results with control siRNA) was achieved after 48 h of culture on the array. When control siRNA was transfected, the expression of EGFP was lower in the absence of serum than in the presence of serum (open bars in Figure 4a,b). Although we do not have a clear explanation for this result at this moment, the composition of lipid/siRNA/DNA might not be optimal for transferring pEGFP under the serum-free condition. However, we also cannot rule out the possibility that control siRNA might cause nonspecific inhibition particularly in the absence of serum.

Parallel and Dual Silencing. We examined the feasibility of the array method for the parallel experimentation in which

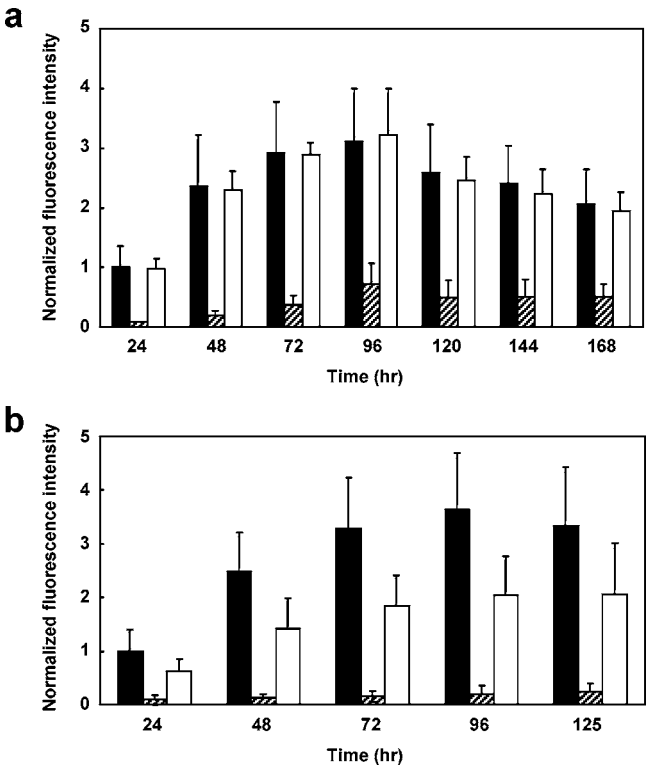

Figure 4. Time dependence of EGFP expression on the siRNA array. Cells were seeded in (a) the presence and (b) the absence of FBS (see Materials and Methods for details). Fluorescent intensities measured on the dots at various time points were normalized by that of control dot (no siRNA transfected) at 24 h. Closed bar: no siRNA transfected. Hatched bar: transfected with EGFP-siRNA. Open bar: transfected with control siRNA. The data are expressed as mean ± standard deviation for $n = 3$.

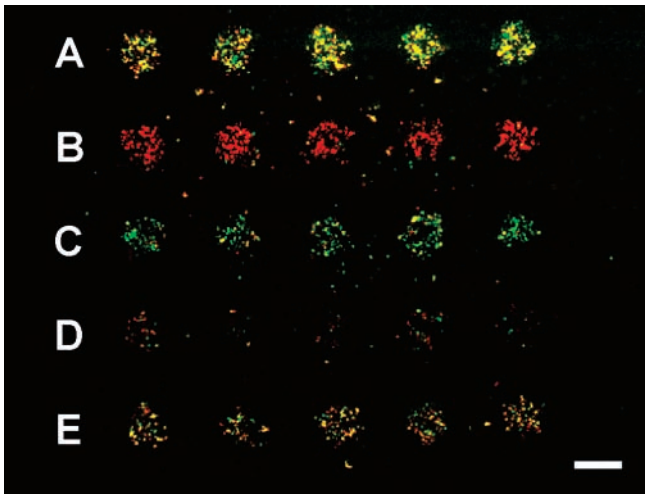

Figure 5. Parallel and dual silencing of gene expression on the siRNA array. The fluorescent images acquired using an interference filter for EGFP and DsRed were pseudo-colored and merged. Two plasmids, pEGFP and pDsRed, were loaded to all the dots (a) without any siRNA or together with (b) EGFP-siRNA, (c) DsRed-siRNA, (d) EGFP-siRNA plus DsRed-siRNA, and (E) control siRNA. Bar = 500 μm.

two different siRNAs are introduced separately to the cells on different dots on a single array. In addition, attempts were made to simultaneously introduce different siRNAs to the cells on a single dot. The result is shown in Figure 5. All the dots were loaded with both plasmids, pEGFP and pDsRed. The siRNAs used here (EGFP-siRNA and DsRed-siRNA) were specific for the distinct sequences in the respective cDNA, and hence are not expected to interfere with each other. As shown in Figure 5, transfection of siRNA resulted in the reasonable gene expression profiles expected from the combinations of siRNAs and plasmids. This simple demonstration shows the feasibility of our method for use in parallel and/or dual silencing analysis on a single array platform.

DISCUSSION

In order to conduct array-based large-scale RNAi screens to distinguish peculiar phenotypes from the multitude of negative backgrounds, it is primarily important that the reliability and accuracy of phenotypic readouts are guaranteed. To realize such an assay method, we prepared cell-based siRNA arrays using processes for micropatterning and LBL assembly. As demonstrated in the present study, our siRNA arrays allowed us to silence specific genes in a spatially restricted manner, which enabled us to quantitatively determine silencing efficiency. The silencing efficiency determined for cotransfected EGFP gene reproducibly reached ca. 90% under the optimum conditions.

A key technology in our siRNA array preparation is an alkanethiol SAM that provides well-characterized functional surfaces for further modifications (*14*, *25*). In combination with micropatterning techniques, the SAM finds a great opportunity to be applied in micro- and nanobiotechnology, especially in cell-based array technology (*26*−*31*). The UV-assisted patterning process used here is a simple and reproducible technique. The flexibility in pattern size and shape is of great advantage in restricting regions for siRNA loading over other methods such as, for instance, spotting by means of robotic arrayers. Using SAM, one can readily design distinctive surface chemistry between the patterns and the surrounding areas, which consequently affords higher restrictions on the regions of siRNA loading and, in particular cases, cell adhesion.

The spots created on the SAM had an area of 0.79 mm^2 (1 mm in diameter), on which approximately 2500 HEK293 cells were grown at confluence. Although this size is rather large for the conventional microarrays, much smaller spots will probably affect the reliability of quantitative data obtained from a single spot. For a quantitative study, the spot size should be carefully optimized depending on the cells used, because the confluent density is also a subject of cell types. In micropatterning of SAM, the size as well as the density of the spot can be easily changed by appropriately designing a photomask using the standard lithography-based technique.

One of the most important requirements for siRNA arrays is that nucleotides must be transiently loaded on the array before cell seeding. They were realized in this study by employing the LBL assembly process. The surface of COOH-SAM, possessing the negative charge under neutral conditions, attracts the LDR complex probably through electrostatic interactions, because the complexes formed with siRNA, plasmid DNA, and excess cationic lipid are expected to bear net positive charge. It is likely that the adsorption of the LDR complex overcompensates to generate cationically charged surface which, in turn, attracts excess anionic DNA to generate again an anionically charged surface. These alternate adsorptions were repeated to obtain 5 layers consisting of the LDR complex and plasmid DNA. It was shown that the silencing of the EGFP expression was restricted to the cells within the dot loaded with EGFP-siRNA, whereas EGFP expression in the cells at the surrounding regions outside the dot as well as those on the neighboring dots were not affected by released EGFP-siRNA. This observation suggests that the leaching of siRNA out of the dot was not significant until cells were seeded and that the concentration of siRNA was too low to silence gene expression in the adjacent cells.

The concentration of siRNA in a solution used for LDR complex formation had a large effect on the level of gene

silencing, with the optimum concentration of 1.0 μg/mL (Figure 3). This effect is most likely due to the fact that higher concentration of siRNA gives rise to the larger loading on the dot. The loading of too much siRNA might enhance the introduction of siRNA into cells, initiating nonspecific inhibition of protein synthesis as in the case with control siRNA. However, the large amount of siRNA seems to weaken the cationic nature of the LDR complex, which in turn would retard transfection of cells with plasmid DNA, reducing the level of EGFP expression.

It was further demonstrated that the micropatterned SAM-based siRNA array allowed parallel and dual silencing of specific genes (Figure 5). Taking into account the high silencing efficiency as well as the possibility of silencing endogenous genes, the array method presented here has potential as an excellent platform for large-scale RNAi screens. Moreover, assays using the siRNA array require neither the large number of cells nor the extremely expensive robotic machine for dispensing liquid. In addition, there is no difficulty in microscopic observation of living cells with an array format, in marked contrast to the assays using the conventional microplates.

In conclusion, the siRNA arrays prepared by means of micropatterning and LBL assembly processes enable us to precisely restrict regions of gene silencing. This feature will facilitate obtaining quantitative data from cell-based RNAi screens on mammalian cells. The flexibility of array design and the capability of controlling the cell adhesion area expand the future application of the siRNA arrays.

ACKNOWLEDGMENT

This study was supported by Grants-in-Aid for Scientific Research (B) (N6.15310090), Ministry of Education, Culture, Sports, Science and Technology (MEXT), and Kobe Cluster, the Knowledge-Based Cluster Creation Project, MEXT.

Supporting Information Available: Details of experimental procedures and results (Figure S1) for gene silencing on the siRNA array prepared using a micropatterned NH_2-SAM. This material is available free of charge via the Internet at http://pubs.acs.org.

LITERATURE CITED

(1) Elbashir, S. M., Harborth, J., Lendeckel, W., Yalcin, A., Weber, K., and Tuschl, T. (2001) Duplexes of 21-nucleotide RNAs mediate RNA interference in cultured mammalian cells. *Nature (London) 411*, 494−498.

(2) Hammond, S. M., Caudy, A. A., and Hannon, G. J. (2001) Post-transcriptional gene silencing by double-stranded RNA. *Nat. Rev. Genet. 2*, 110−119.

(3) Leung, R. K., and Whittaker, P. A. (2005) RNA interference: from gene silencing to gene-specific therapeutics. *Pharmacol. Ther. 107*, 222−239.

(4) Boutros, M., Kiger, A. A., Armknecht, S., Kerr, K., Hild, M., Koch, B., Hass, S. A., Paro, R., and Perrimon, N. (2004) Genome-wide RNAi analysis of growth and viability in *Drosophila* cells. *Science 303*, 832−835.

(5) Ashrafi, K., Chang, F. Y., Watts, J. L., Fraser, A. G., Kamath, R. S., Ahringer, J., and Ruvkun, G. (2003) Genome-wide RNAi analysis of *Caenorhabditis elegans* fat regulatory genes. *Nature (London) 421*, 268−272.

(6) Chi, J. T., Chang, H. Y., Wang, N. N., Chang, D. S., Dunphy, N., and Brown, P. O. (2003) Genomewide view of gene silencing by small interfering RNAs. *Proc. Natl. Acad. Sci. U.S.A. 100*, 6343−6346.

(7) Zheng, L., Liu, J., Batalov, S., Zhou, D., Orth, A., Ding, S., and Schultz, P. G. (2004) An approach to genomewide screens of expressed small interfering RNAs in mammalian cells. *Proc. Natl. Acad. Sci. U.S.A. 101*, 135−140.

(8) Kumar, R., Conklin, D. S., and Mittal, V. (2004) High-throughput selection of effective RNAi probes for gene silencing. *Gemone Res. 13*, 2333−2340.

(9) Silva, J. M., Mizuno, H., Brady, A., Lucito, R., and Hannon, G. J. (2004) RNA interference microarrays: high-throughput loss-of-function genetics in mammalian cells. *Proc. Natl. Acad. Sci. U.S.A. 101*, 6548−6552.

(10) Mousses, S., Caplen, N. J., Cornelison, R., Weaver, D., Basik, M., Hautaniemi, S., Elkahioun, A. G., Lotufo, R. A., Choudary, A., Dougherty, E. R., Suh, E., and Kallioniemi, O. (2004) RNAi microarray analysis in cultured mammalian cells. *Genome Res. 13*, 2341−2347.

(11) Yoshikawa, T., Uchimura, E., Kishi, M., Funeriu, D. P., Miyake, M., and Miyake, J. (2004) Transfection microarray of human mesenchymal stem cells and on-chip siRNA gene knockdown. *J. Controlled Release 96*, 227−232.

(12) Ziauddin, J., and Sabatini, D. M. (2001) Microarrays of cells expressing defined cDNAs. *Nature (London) 411*, 107−110.

(13) Wheeler, D. B., Bailey, S. N., Guertin, D. A., Carpenter, A. E., Higgins, C. O., and Sabatini, D. M. (2004) RNAi living-cell microarrays for loss-of-function screens in *Drosophila melanogaster* cells. *Nat. Methods 1*, 1−6.

(14) Bain, C. D., Troughton, E. B., Tao, Y.-T., Evall, J., Whitesides, G. M., and Nuzzo, R. G. (1989) Formation of monolayer films y the spontaneous assembly of organic thiols from solution onto gold. *J. Am. Chem. Soc. 111*, 321−335.

(15) Tarlov, M. J., Burgess, D. R. F., and Gillen, G. (1993) UV photopatterning of alkanethiolate monolayers self-assembled on gold and silver. *J. Am. Chem. Soc. 115*, 5305−5306.

(16) Huang, J., Dahlgren, D. A., and Hemminger, J. C. (1994) Photopatterning of self-assembled alkanethiolate monolayers on gold: A simple monolayer photoresist utilizing aqueous chemistry. *Langmuir 10*, 626−628.

(17) Decher, G. (1997) Fuzzy nanoassemblies: Toward layered polymeric multicomposites. *Science 277*, 1232−1237.

(18) Yamauchi, F., Kato, K., and Iwata, H. (2004) Micropatterned, self-assembled monolayers for fabrication of transfected cell microarrays. *Biochem. Biophys. Acta 1672*, 138−147.

(19) Lopez, G. P., Albers, M. W., Schreiber, S. L., Carroll, R., Peralta, E., and Whitesides, G. M. (1993) Convenient methods for patterning the adhesion of mammalian cells to surfaces using self-assmbled monolayers of alkanethiols on gold. *J. Am. Chem. Soc. 115*, 5877−5878.

(20) Cooper, E., Wiggs, R., Hutt, D. A., Parker, L., Leggett, G. J., and Parker, T. L. (1997) Rates of attachment of fibroblasts to self-assembled monolayers formed by the adsorption of alkylthiols onto gold surfaces. *J. Mater. Chem. 7*, 435−441.

(21) Haddow, D. B., France, R. M., Short, R. D., MacNeil, S., Dawson, R. A., Leggett, G. J., and Cooper, E. (1999) Comparison of proliferation and growth of human keratinocytes on plasma copolymers of acrylic acid/1, 7-octadiene and self-assembled monolayers. *J. Biomed. Mater. Res. 47*, 379−387.

(22) McClary, K. B., Ugarova, T., and Grainger, D. W. (2000) Modulating fibroblast adhesion, spreading, and proliferation using self-assembled monolayer films of alkylthiolates on gold. *J. Biomed. Mater. Res. 50*, 428−439.

(23) Persengiev, S. P., Zhu, X., Green, M. R. (2004) Nonspecific, concentration-dependent stimulation and repression of mammalian gene expression by small interfering RNAs (siRNAs). *RNA 10*, 12−18.

(24) Lechardeur, D., Sohn, K.-J., Haardt, M., Joshi, P. B., Monck, M., Graham, R. W., Beatty, B., Squire, J., O'Brodovich, H., and Lukacs, G. L. (1999) Metabolic instability of plasmid DNA in the cytosol: a potential barrier to gene transfer. *Gene Ther. 6*, 482−497.

(25) Ulman, A. (1996) Formation and structure of self-assembled monolayers. *Chem. Rev. 96*, 1533−1554.

(26) Mrksich, M., Dike, L. E., Tien, J., Ingber, D. E., and Whitesides, G. M. (1997) Using microcontact printing to pattern the attachment of mammalian cells to self-assembled monolayers of alkanethiolates on transparent films of gold and silver. *Exp. Cell Res. 235*, 305−313.

(27) Mrksich, M., and Whitesides, G. M. (1995) Patterning self-assembled monolayers using microcontact printing: A new technology for biosensors? *Trends Biotechnol. 13*, 228−235.

(28) Lopez, G. P., Biebuyck, H. A., Harter, R., Kumar, A., Whitesides, G. M. (1993) Fabrication and imaging of two-dimensional patterns of proteins adsorbed on self-assembled monolayers by scanning electron microscopy. *J. Am. Chem. Soc. 115*, 10774−10781.

(29) Nelson, B. P., Grimsrud, T. E., Liles, M. R., Goodman, R. M., and Corn, R. M. (2001) Surface plasmon resonance imaging measurements of DNA and RNA hybridization adsorption onto DNA microarrays. *Anal. Chem. 73*, 1−7.

(30) Ko, I. K., Kato, K., and Iwata, H. (2005) Antibody microarray for correlating cell phenotype with surface marker. *Biomaterials 6*, 687−696.

(31) Kato, K., Sato, H., and Iwata, H. (2005) Immobilization of histidine-tagged recombinant proteins onto micropatterned surfaces for cell-based functional assays. *Langmuir 21*, 7071−7075.

BC060105C

Cellular Uptake Mechanism of an Inorganic Nanovehicle and Its Drug Conjugates: Enhanced Efficacy Due To Clathrin-Mediated Endocytosis

Jae-Min Oh,[§] Soo-Jin Choi,[§] Sang-Tae Kim,[§] and Jin-Ho Choy*

Center for Intelligent Nano-Bio Materials, Division of Nanoscience and Department of Chemistry, Ewha Womans University, Seoul 120-750, Korea. Received May 23, 2006; Revised Manuscript Received September 4, 2006

We present the mechanism for the cellular uptake of layered double hydroxide (LDH) nanoparticles that are internalized into MNNG/HOS cells principally via clathrin-mediated endocytosis. The intracellular LDHs are highly colocalized with not only typical endocytic proteins, such as clathrin heavy chain, dynamin, and eps15, but also transferrin, a marker of the clathrin-mediated process, suggesting their specific internalization pathway. LDHs loaded with an anticancer drug (MTX−LDH) were also prepared to confirm the efficacy of LDHs as drug delivery systems. The cellular uptake of MTX was higher in MTX−LDH-treated cells than in MTX-treated cells, giving a lower IC_{50} value for MTX−LDH than for MTX only. The inhibition of the cell cycle was greater for MTX−LDH than for MTX only. This result clearly shows that the internalization of LDH nanoparticles via clathrin-mediated endocytosis may allow the efficient delivery of MTX−LDH in cells and thus enhance drug efficacy.

INTRODUCTION

Nanomaterials such as nanoparticles, nanohybrids, or nanocomposites, as well as nanoporous materials, have been widely studied in the view point of physics, chemistry, biosciences, and materials engineering (*1*−*6*). Among these nanomaterials, the use of nanoparticles as nanomedicines (*7*) for alternative drug delivery vehicles (*8*−*12*) or molecular diagnostics (*13*−*15*) has attracted much interest. Designing nanomedicines with enhanced and intentional functionalities required an understanding of the intracellular trafficking pathway of nanoparticles so that their fate in the cell can be predicted. Recently, it has been reported that certain nanoparticles, such as iron oxide and silica, as well as carbon nanotubes, are internalized in cells via the endocytic pathway (*11*, *16*−*21*). Endocytosis is a conserved process in eukaryotes by which extracellular components are taken up into cells by invagination of the plasma membrane to form vesicles that enclose these materials.

In the present study, we have used layered double hydroxide (LDH) to investigate the cellular interaction and uptake of nanoparticles, since LDH is considered as a candidate for drug delivery nanovehicles (*4*, *11*, *12*). LDHs are positively charged metal hydroxide layers in which solvated exchangeable anions are stabilized to compensate for the positive layer charges (*22*). Due to their hydrolysis behavior in acidic media and their anionic exchange capacity, LDHs are already used as antiacid and antipepsin agents (*23*). More recently, we have successfully demonstrated that the positively or neutrally charged LDHs which encapsulate anionic molecules are easily attached to the surface of a negatively charged plasma membrane, and in such a way their internalization into cells could be facilitated. Thus, LDHs may prove useful as gene or drug delivery vectors (*11*, *12*).

EXPERIMENTAL PROCEDURES

Preparation of LDHs. All reagents, $Mg(NO_3)_2{\cdot}6H_2O$, $Al(NO_3)_3{\cdot}9H_2O$, NaOH, $NaHCO_3$, methotrexate (MTX), and fluorescein 5′-isothiocyanate (FITC) were purchased from Aldrich Co. Ltd. An LDH with the formula $Mg_{0.68}Al_{0.32}(OH)_2(CO_3)_{0.16}{\cdot}0.1H_2O$ was prepared by coprecipitation at room temperature by titration to pH ∼ 9.5 with NaOH/$NaHCO_3$ solution (0.5 M/0.5 M). The obtained mixed solution was then hydrothermally treated at 100 °C for 24 h to give even particle size distribution (CO3−LDH), as described previously (*24*). LDH loaded with the anticancer drug MTX (MTX−LDH), and FITC-loaded LDH (FITC−LDH) were also prepared by respectively coprecipitation and anion exchange, as previously reported (*12*). Powdered MTX was dissolved in decarbonated water, and 0.5 M NaOH solution was added carefully to give a 0.032 M solution of MTX at pH 7. A mixed solution of $Mg(NO_3)_2{\cdot}6H_2O$ (0.032 M) and $Al(NO_3)_3{\cdot}9H_2O$ (0.016 M) was then added. The pH of the mixture was adjusted to 9.5 by NaOH titration. For FITC−LDH, a 0.032 M solution of FITC was prepared with decarbonated water and NaOH titration. LDH particles ($Mg_{0.68}Al_{0.32}(OH)_2(NO_3)_{0.32}{\cdot}0.1H_2O$) dispersed in decarbonated water were then added to the FITC solution. Both the MTX and FITC mixtures were left to stand for 48 h at room temperature. Each LDH sample (CO3−LDH, MTX−LDH, and FITC−LDH) was thoroughly washed with decarbonated water and dried in vacuum to give a powder, which was then redispersed in decarbonated water for the next step. The prepared LDHs were analyzed by powder X-ray diffraction (PXRD; Phillips PW3710 diffractometer with Ni-filtered Cu Kα radiation ($\lambda = 1.5418$ Å)) and by scanning electron microscopy (SEM; HITACHI S-4300).

Immunofluorescence/Confocal Microscopy. MNNG/HOS cells were seeded on 12-well slides (5×10^3 cells/well) and incubated with 50 μg/mL FITC−LDH for 10 min, 1, 2, or 3 h. The effects of a membrane entry inhibitor were examined by incubating the cells with 10 μg/mL chlorpromazine for 1 h at 37 °C followed by treatment with FITC−LDH as described above. The cells were washed several times with ice-cold PBS, fixed by incubation with freshly made 3% formaldehyde (containing 1.5% methanol) in PBS (pH 7.4) for 15 min, and permeabilized by incubation with 0.1% Triton X-100 in PBS for 10 min. The cells were incubated with primary antibodies against mouse clathrin, caveolin-1, eps15, dynamin, and Trans-

* Corresponding author. E-mail: jhchoy@ewha.ac.kr, Tel.: +82-02-3277-4305, Fax.: +82-02-3277-4340.

[§] Equally contributed to the work reported.

10.1021/bc0601323 CCC: $33.50 © 2006 American Chemical Society
Published on Web 10/21/2006

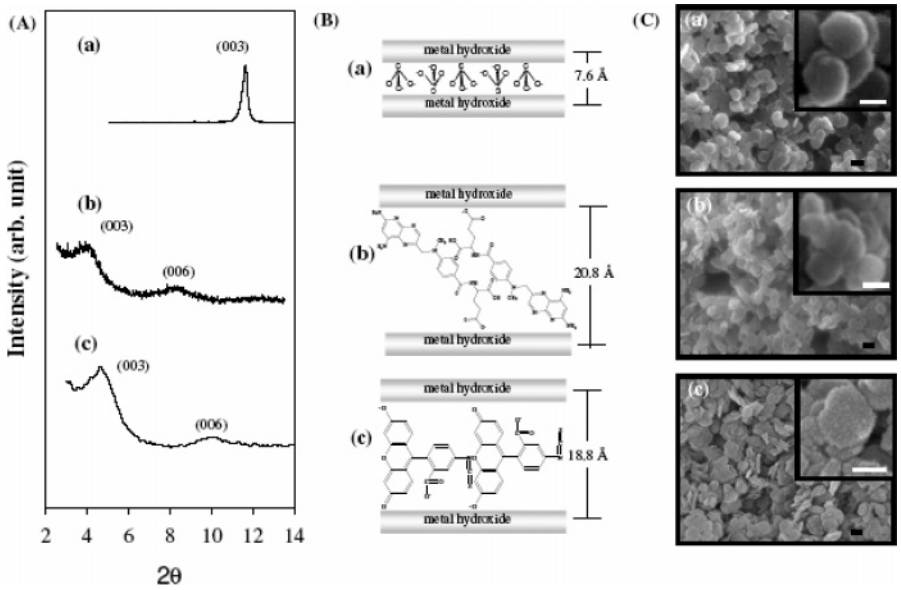

Figure 1. (A) Powder X-ray diffraction (PXRD) patterns, (B) schematic diagram of the structure, and (C) SEM images of three different LDH particles. (a) CO3−LDH (b) MTX−LDH, and (c) FITC−LDH. (Scale bars in part C represent 100 nm).

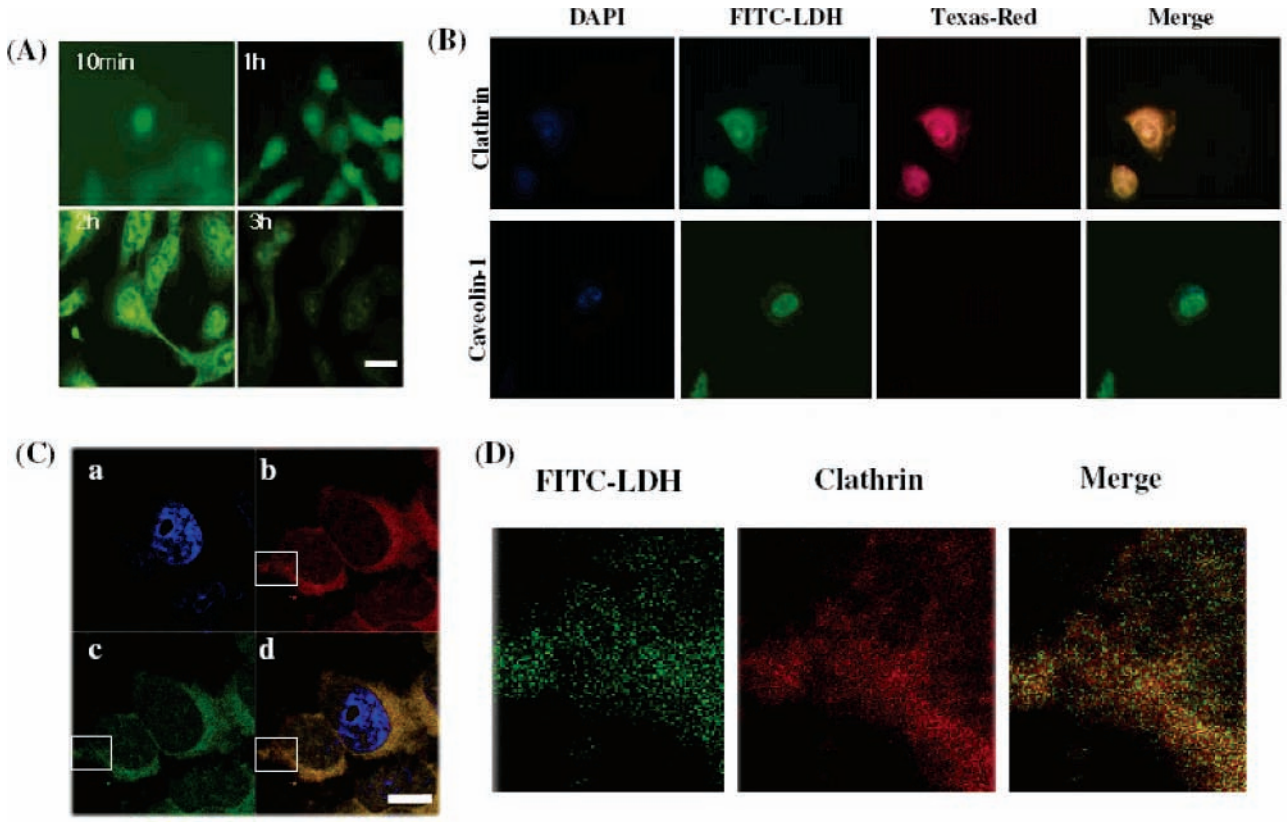

Figure 2. (A) Fluorescence microscopic images of FITC−LDH-treated MNNG/HOS cells depending on incubation time. (B) Immunofluorescence microscopic images showing the colocalization of clathrin and LDH in MNNG/HOS cells. (C) Confocal microscopy: colocalization of FITC−LDH and clathrin in MNNG/HOS cells. Localization of (a) nucleus, (b) clathrin, and (c) FITC−LDH, the merged image (d) in MNNG/HOS cells. Cells were incubated with FITC−LDH for 2 h, treated with clathrin antibodies, and stained by TR and DAPI. Scale bar represents 10 μm. (D) Magnified images of the white boxes in part C are also given. The images identify areas showing colocalization of FITC−LDH and clathrin, as shown merged in yellow.

ferrin (Tf) for 1 h, washed, and then incubated with secondary antibodies conjugated to Texas Red (TR : Molecular Probe) or Alexa fluor 594 (Molecular Probe). The cells were then stained by incubation with 2 μg/mL DAPI dye for 10 min at room temperature in the dark. The cells were washed and visualized by fluorescence microscopy using an Axioplan Zeiss microscope and photographed with a digital camera (CCD). For laser scanning confocal microscopy (LSCM), the cells were visualized using a Zeiss LSM 510 confocal microscope (Carl Zeiss Inc., Germany) equipped with Argon (488 nm) and HeNe (543 nm) lasers for fluorescence. Image acquisition and analysis was done using LSM 510 software. Each experiment was repeated three times on separate days.

MTX Quantification by HPLC. Cells (1×10^6) were seeded on a 60 mm culture dish and treated with 50 μM/mL MTX or the equivalent amount of MTX−LDH with respect to MTX

Table 1. Chemical Formula and Colloidal Properties of Each LDH Sample (MTX: $C_{20}H_{20}N_8O_5^{2-}$, FITC: $C_{21}H_{10}O_5SN^{2-}$)

sample	chemical formula	particle size (nm)[a]	zeta potential (mV)
CO3−LDH	$Mg_{0.68}Al_{0.32}(OH)_2(CO_3)_{0.16}\cdot 0.1H_2O$	136 ± 29	∼+20
MTX−LDH	$Mg_{0.68}Al_{0.32}(OH)_2(MTX)_{0.16}\cdot 0.1H_2O$	127 ± 25	∼+5.6
FITC−LDH	$Mg_{0.68}Al_{0.32}(OH)_2(FITC)_{0.16}\cdot 0.1H_2O$	147 ± 31	∼−4.9

[a] Each sample was dispersed in deionized water, and the suspension was dropped on the flat Si-wafer. After evaporating water in the oven, particles on the Si-wafer were measured by scanning electron microscopy. Fifty particles were randomly selected from SEM image, and the diameters of particles were measured. Zeta potential was measured at pH 7.

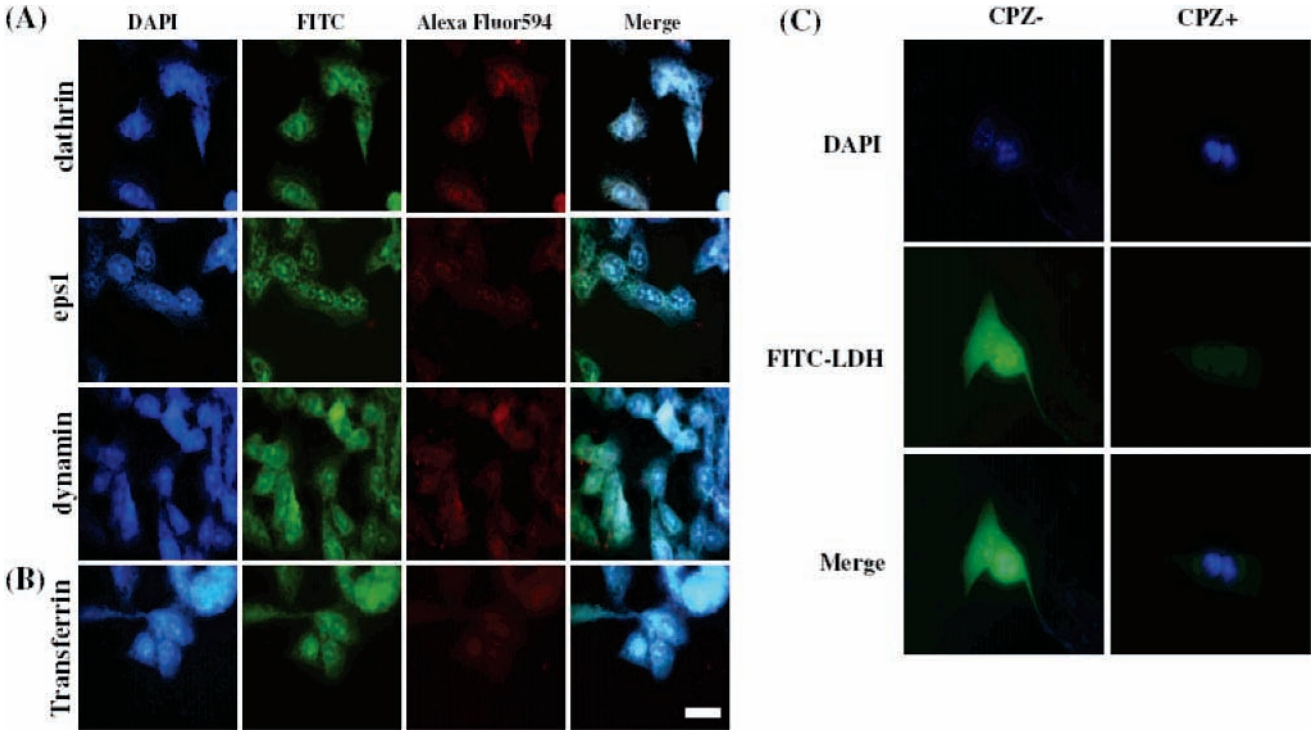

Figure 3. Colocalization of FITC−LDH with clathrin-mediated endocytic proteins and markers. FITC−LDH-treated MNNG/HOS cells were fixed and processed for immunofluorescence microscopy. (A) Fluorescence microscopic images of the cells treated with clathrin, eps15, and dynamin antibodies and then stained with secondary antibodies conjugated to Alexa Fluor 594, showing the same localization pattern. (B) Colocalization of FITC−LDH and Alexa Fluor 594-labeled Tf, a well-known marker of clathrin-mediated endocytosis. The localization of LDH and Tf clearly overlaps. Scale bars, 20 μm. (C) The effect of clathrin inhibition on the entry of LDHs in MNNG/HOS cells. The cells initially incubated with a clathrin inhibitor, CPZ, showed a considerable reduction in LDH particle uptake.

concentration. After 0.5, 1, 2, 4, 8, and 24 h, the cells were washed twice with PBS, harvested by trypsin−EDTA treatment, and cell pellets were collected by centrifugation. After the pellets were washed twice with PBS, cell lysis buffer (20 mM Tris-HCl, pH 7.5, 1% Triton X-100, 150 mM NaCl, and 1 mM EDTA) was added and the pellets were incubated on ice for 20 min followed by ultrasonication for 20 s (Sonics & Materials Inc.) The crude cell lysates were then centrifuged at 10 000*g* for 5 min. Two volumes of acetonitrile were added to the cell supernatants and mixed vigorously to precipitate proteins. After centrifugation at 10 000*g* for 3 min, four volumes of chloroform were added to the supernatant to remove lipids. The supernatants were then collected by centrifugation at 2000*g* for 10 min and analyzed by high performance liquid chromatography (HPLC). MTX was quantified by HPLC using an Agilent 1100 series HPLC system on a C18 column (Nucleosil, 250 × 4.6 mm, Alltech). The mobile phase was 0.05 M KH_2PO_4, 10% acetonitrile, pH 6.6, and flow rate was 1 mL/min. Column temperature was maintained at a constant 40 °C and MTX was detected by UV absorption at 304 nm. Each experiment was repeated three times on separate days.

In Vitro Cell Viability/Cytotoxicity Studies. Cells were seeded onto 96-well plates at a density of 5×10^3 cells/well and incubated overnight at 37 °C in a 5% CO_2 atmosphere. The medium in the wells was then replaced with the fresh medium containing nanoparticles (CO3−LDH or MTX−LDH) in a concentration range of 0 to 2 mg/mL. After 72 h, cell viability and cytotoxicity were monitored by counting viable (trypan blue excluding) cells in a hemacytometer.

Flow Cytometric Analysis of the Cell Cycle. Cells (1×10^6) were treated with indicated concentrations of drugs for 20 h. They were then harvested by trypsin treatment, washed with PBS, and fixed by incubation with cold 70% ethanol on ice for 1 h. The fixed cells were washed with PBS and incubated with PI (40 μg/mL PI, 320 μg/mL RNase-A in PBS) at 4 °C for 30 min. Flow cytometric measurement was done on a flow cytometer (FACS Calibur, Becton Dickinson BD). For each analysis, 20 000 events were monitored.

RESULTS AND DISCUSSION

We used three different kinds of LDHs in this study. Pristine LDH with a formula of $Mg_{0.68}Al_{0.32}(OH)_2(CO_3)_{0.16}\cdot 0.1H_2O$ (CO3−LDH) and fluorescein isothiocyanate (FITC)-loaded LDH (FITC−LDH) were used to check, by electron and fluorescence microscopy, the cellular uptake pathway of the drug delivery vector, LDH. LDH loaded with the anticancer drug methotrexate (MTX) (MTX−LDH) was used to confirm the increased efficacy of drug delivery by LDH encapsulation. The powder X-ray diffraction patterns showed that each LDH had a typical LDH structure (Figure 1A), and the *d*-spacing of each LDH determined was 7.6, 20.8, and 18.8 Å, respectively, upon

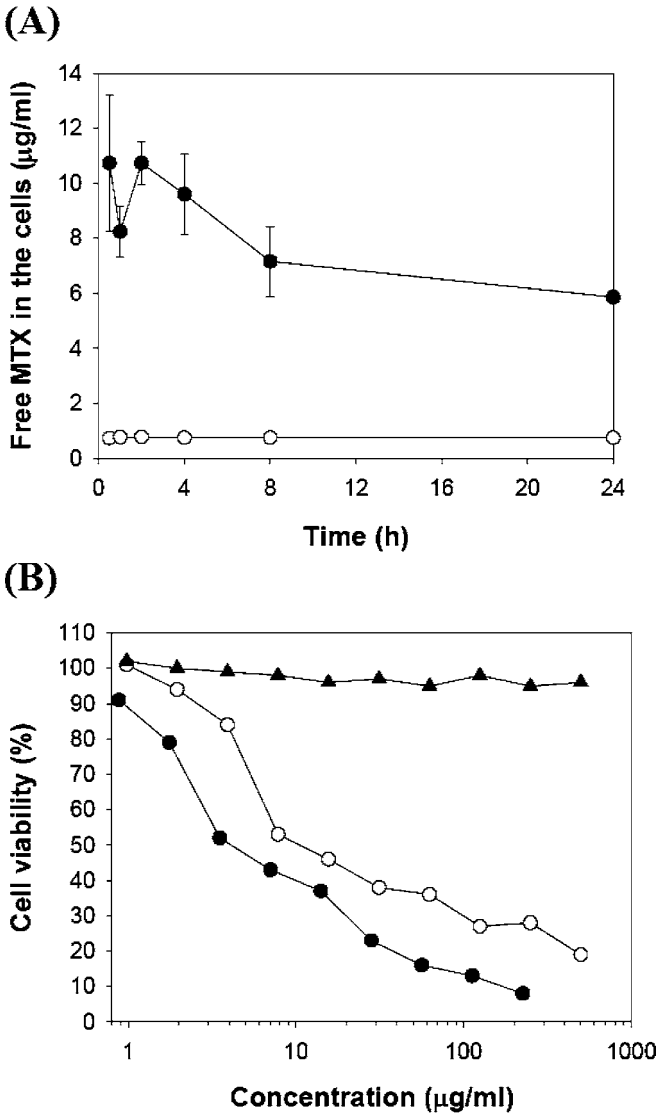

Figure 4. Cellular accumulation of free MTX molecules in MNNG/HOS cells treated with either MTX (○) or MTX−LDH (●), as quantified by HPLC analysis (see Experimental Procedures). (A). Cell viability/cytotoxicity of MNNG/HOS cells treated with LDH (▲), MTX (○), and MTX−LDH (●), as monitored by trypan blue exclusion, with respect to drug concentration (see Experimental Procedures) (B).

molecular size of interlayer anions such as CO_3^{2-}, MTX, and FITC (Figure 1B), as previously reported (*11*, *12*, *24*). The SEM results (Figure 1C) showed that all the LDH particles have characteristic hexagonal plate like morphology with uniform size. When dispersed in water (neutral pH), the particle size of approximately 150 nm was determined with narrow distribution as shown in Table 1, and the zeta potential of each colloidal LDH was positive or neutral. The LDH particle should have positive layer charge due to the isomorphous substitution of Mg^{2+} ions by Al^{3+} ions. This is the reason why negatively charged organic molecules such as MTX and FITC could be intercalated into the interlayer space of LDH. In this way, charge neutralization of the reaction could be satisfied (Table 1).

There are several possible endocytic pathways for internalizing LDH nanoparticles, such as clathrin-mediated endocytosis, caveolae-mediated endocytosis, and clathrin-caveolae-independent endocytosis. We determined the specific endocytic pathway used by the LDH nanoparticles for membrane entry by immunofluorescence and confocal microscopic studies. We used tumorogenic osteosarcoma MNNG/HOS cells treated with the fluorescent FITC−LDH to measure the intracellular fluorescence intensity with respect to time. The fluorescence microscopic images (Figure 2A) showed an increasingly strong fluorescent signal inside the cell as the incubation time increased to 2 h. For the immunofluorescence study, the cells were treated with FITC−LDH for 2 h, during which the maximum fluorescence intensity was attained, and stained with either anti-clathrin antibody or anti-caveolin-1 antibody both conjugated to TR. The immunofluorescence microscopic images showed that both the clathrin staining red fluorescence (TR) and the LDH green one (FITC) overlapped each other perfectly. Though the red immunofluorescent caveolin-1 was observed but faintly, no clear merged image could be seen when treated with the LDH fluorescence as shown in Figure 2B. MNNG/HOS cells treated with FITC−LDH and the anti-clathrin antibody showed that, as expected, FITC−LDHs were mainly located in the cytosol, with a perinuclear distribution and was highly colocalized with clathrin (Figure 2C). The magnified image (Figure 2D) revealed that the green FITC fluorescence (LDH) and the red fluorescent clathrin staining overlapped well to produce a yellow fluorescence. This result clearly suggests that clathrin-mediated endocytosis is the principal mechanism for the cellular internalization of LDH nanoparticles. Caveolae-mediated endocytosis does not appear to be responsible for LDH uptake.

We confirmed the clathrin-mediated cellular uptake of LDH nanoparticles by determining the involvement of certain accessory proteins related to clathrin-mediated endocytosis. Thus, we investigated whether FITC−LDH colocalized with typical endocytic proteins such as dynamin and eps15. Dynamin regulates endocytic vesicle formation in different endocytic pathways (*25*), and eps15 is involved in regulating clathrin-coated pit assembly (*26*). We incubated MNNG/HOS cells with FITC−LDH and stained them with antibodies against clathrin, dynamin, and eps15, with the red Alexa Fluor 594 conjugated to the secondary antibodies as the probe (Figure 3A). We found that FITC−LDH was well colocalized with clathrin, dynamin, and eps15. eps15 plays a critical role only in clathrin-mediated endocytosis by associating with the plasma membrane adaptor, the AP-2 protein (*26*), which is essential for receptor-mediated endocytosis. As a positive control, we also compared the internalization of FITC−LDH with that of Tf, which is well-known to undergo the clathrin-mediated endocytosis through the transferrin receptor (*27*). Intracellular FITC−LDH was highly colocalized with the Tf labeled with Alexa Fluor 594 (Figure 3B). This is consistent with the results seen for clathrin, dynamin, and eps15, confirming the clathrin-mediated internalization of LDH nanoparticles.

We confirmed LDH entry via clathrin-coated vesicles biochemically by studying the effect of chlorpromazine (CPZ), a clathrin inhibitor, on LDH entry. CPZ is a cationic amphiphilic drug that prevents clathrin-mediated endocytosis by disrupting the assembly of the clathrin adaptor protein at the cell surface (*28*). Thus, we incubated MNNG/HOS cells with CPZ before observing the cellular uptake of FITC−LDH. Unsurprisingly, clathrin inhibition gave rise to a considerable reduction of the uptake of the LDH particles (Figure 3C). Altogether, it is concluded that LDH nanoparticles are transported into MNNG/HOS cells principally via clathrin-mediated endocytosis.

The targeted entry of nanoparticles into cells is important in nanomedicines, as their specific intracellular delivery can considerably reduce drug toxicity and increase therapeutic effects. Drugs conjugated with a ligand that can be efficiently and specifically recognized by receptor-mediated endocytosis have been already used to deliver drugs into cells; for example, transferrin/transferrin receptor-mediated drug delivery (*29*, *30*). Thus, our results showing that LDH nanoparticles primarily select the clathrin-mediated process such as the transferrin ligand/receptor interaction for cellular entry suggest that they may prove promising as nanomedicines and drug delivery

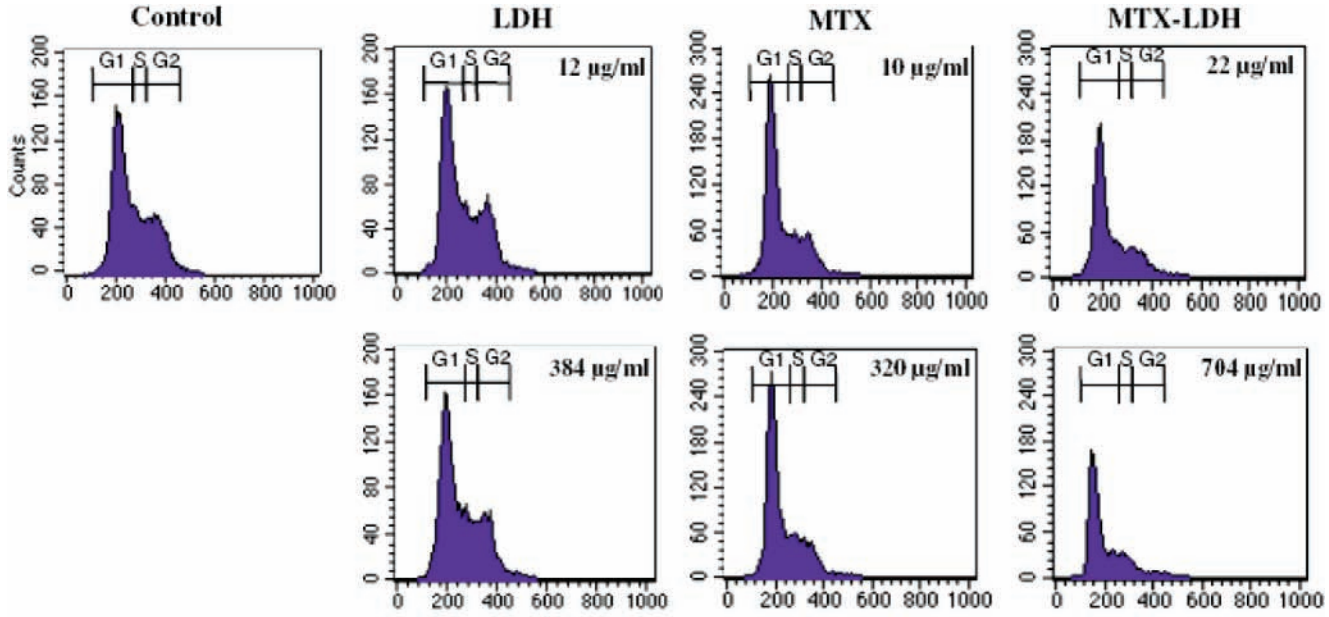

		G1 (%)	S (%)	G2 (%)
Control		50.72	25.00	24.41
LDH (µg/ml)	12	52.34	24.32	23.51
	384	55.17	24.25	20.49
MTX (µg/ml)	10	63.87	17.71	19.69
	320	66.62	17.73	15.73
MTX-LDH (µg/ml)	22	75.09	12.25	12.78
	704	85.59	9.15	5.02

Figure 5. G1 phase arrest of MNNG/HOS cells exposed to either MTX or MTX−LDH at different concentrations for 20 h. The cell cycle was studied by FACS analysis of PI-stained cells. DNA histograms are shown, with the *x*-axis representing the DNA content and the *y*-axis representing the cell number. Note that 10 and 320 μg/mL MTX are equivalent to 22 and 704 μg/mL of MTX−LDH, respectively, based on MTX content in MTX−LDH.

nanovehicles. Their intracellular trafficking mechanism may also be predicted, being transported to endosomes, and subsequently to the Golgi complex or/and lysosomes after uptake (*31*).

From our results, we would expect an enhanced internalization of the drug in vitro due to their being encapsulated in the LDH nanoparticles. Thus, we investigated the applicability of LDH nanoparticles as drug delivery nanovectors for anticancer chemotherapy using a well-known anticancer drug, MTX, a folate antagonist. MTX binds competitively and reversibly to dihydrofolate reductase and inhibits important biochemical pathways, including the syntheses of thymidine, purine, DNA, RNA, and proteins (*32*). MTX is used in patients with certain forms of leukemia, and also in patients with various malignant diseases, such as lymphoma, choriocarcinoma, osteosarcoma, and uterus, breast, lung, head, neck, and ovarian cancers. However, high doses of MTX are required because of the antifolate properties of MTX, which is one of the major disadvantages of MTX medication (*33*). Thus, new chemotherapeutic approaches are urgently needed to limit its toxic effects.

We prepared MTX−LDH and quantified the level of intracellular "free MTX in the cells" by HPLC to determine its accumulation in cells (Figure 4A). The concentration of MTX within MTX−LDH-treated cells was considerably higher than in the cells treated with MTX only at all incubation times. This result strongly suggests that in an osteosarcoma cell culture line, the clathrin-mediated endocytosis of LDH nanoparticles enhances the internalization of conjugated drug molecules. As shown in Figure 4B, MTX−LDH was more toxic than MTX only as demonstrated that the IC_{50} value of MTX−LDH in the cells was about 2.5 lower than that of MTX only which means that MTX−LDH penetrates the cell membrane more effectively than MTX only, resulting in a better efficacy. This result indicates that the drug efficacy of MTX−LDH significantly increased over MTX only, resulting from effective internalization of MTX−LDH. Furthermore, LDH alone does not influence the cell viability at levels up to 500 μg/mL (Figure 4 B).

We also investigated the effect of MTX and MTX−LDH on cell cycle distribution to confirm further the efficacy of MTX−LDH. The cell cycle consists of interphases (G1, S, and G2) and mitosis (M). During the G1 period, cells increase in size, produce RNA, and synthesize proteins for DNA formation. During the S phase, DNA replication occurs and the cells continue to grow, producing new proteins at the G2 phase. Nuclear and cytoplasmic division occurs at the M stage. We used fluorescence-activated cell sorting (FACS) analysis to study propidium iodide (PI)-stained cells treated with either MTX or MTX−LDH (Figure 5). Over 20 h, MTX and MTX−LDH treatments resulted in an accumulation of cells in the G1 phase and a decrease in the number of cells in the S and G2 phases versus control cells. This is probably due to inhibition of DNA synthesis and blockage at the G1/S boundary. However, the

inhibition of G1/S transition was more evident in MTX−LDH-treated cells than in MTX-treated cells at the same concentration (63.87% versus 75.09% at 10 μM/mL) and was considerably increased at higher concentrations of MTX−LDH. This suggests that using LDH as drug delivery vector effectively enhances MTX efficacy, consistent with above results (Figure 4A,B). LDH alone did not affect the cell cycle at concentrations between 1.5 and 384 μg/mL. The G1 checkpoint stops replication of cells with DNA damage and is involved the development of cancer. Proteins involved in the G1 checkpoint, such as p53, a tumor suppressor protein, and cyclin-dependent kinases may be targets for cancer therapeutics (*34*).

We have shown using immunofluorescence and confocal microscopy that LDH nanoparticles are internalized in MNNG/HOS cells via clathrin-mediated endocytosis. FITC−LDHs were highly colocalized with clathrin and Tf, and also clathrin-mediated endocytosis substrates, such as dynamin and eps15. We also studied the efficacy of MTX−LDH as a potential drug delivery nanovector. The cellular uptake of MTX−LDH was found to be considerably higher than that for MTX only, resulting in lower IC_{50} values and an increased inhibition of the G1 cell cycle.

LDH nanoparticles can stabilize MTX during cell permeation and intracellular trafficking by encapsulation and can release it in the cytoplasm in a stable and constant manner due to its anion exchange capacity in acidic pH. The most common endocytic pathway, the clathrin-coated pit process, for LDH uptake may contribute to the efficient delivery of MTX−LDH in the cells and thus enhance drug efficacy.

These results allow us to propose new directions in designing target-specific nanomedicine. Our research, particularly in designing drug delivery nanovehicles based on metal hydroxide nanoparticles, may provide a new strategy based on a better understanding of their cellular uptake pathways and intracellular delivery mechanism.

ACKNOWLEDGMENT

We thank Dong-Ok Kim for her help in supporting cell preparations. This work was financially supported by the SRC program of MOST/KOSEF through the Center for Intelligent Nano-Bio Materials at Ewha Womans University (grant: R11-2005-008-00000-0), and partly by MOCIE through the National R&D project for Nano Science and Technology (grant: 2005-0980-1 and 2005-0546-1).

Supporting Information Available: Supplementary data. This material is available free of charge via the Internet at http://pubs.acs.org.

LITERATURE CITED

(1) Choy, J. H., Kwon, S. J., and Park, G. S. (1998) High-T-c superconductors in the two-dimensional limit: [(Py-CnH2n + 1)-(2)HgI4]-Bi2Sr2Cam-1CumOy (m = 1 and 2). *Science 280*, 1589−1592.

(2) Choy, J. H., Jang, E. S., Won, J. H., Chung, J. H., Jang, D. J., and Kim, Y. W. (2003) Soft solution route to directionally grown ZnO nanorod arrays on Si wafer; room-temperature ultraviolet laser. *Adv. Mater. 15*, 1911-+.

(3) Usuki, A., Hasegawa, N., Kadoura, H., and Okamoto, T. (2001) Three-dimensional observation of structure and morphology in nylon-6/ clay nanocomposite. *Nano Lett. 1*, 271−272.

(4) Choy, J. H., Oh, J. M., Park, M., Sohn, K. M., and Kim, J. W. (2004) Inorganic-biomolecular hybrid nanomaterials as a genetic molecular code system. *Adv. Mater.* 16, 1181-+.

(5) Maxwell, D. J., Taylor, J. R., and Nie, S. M. (2002) Self-assembled nanoparticle probes for recognition and detection of biomolecules. *J. Am. Chem. Soc. 124*, 9606−9612.

(6) Choy, J. H., Kwak, S. Y., Park, J. S., Jeong, Y. J., and Portier, J. (1999) Intercalative nanohybrids of nucleoside monophosphates and DNA in layered metal hydroxide. *J. Am. Chem. Soc. 121*, 1399−1400.

(7) Moghimi, S. M., Hunter, A. C., and Murray, J. C. (2005) Nanomedicine: current status and future prospects. *FASEB J. 19*, 311−330.

(8) Zhao, W., Gu, J., Zhang, L., Chen, H., and Shi, J. (2005) Fabrication of Uniform Magnetic Nanocomposite Spheres with a Magnetic Core/Mesoporous Silica Shell Structure. *J. Am. Chem. Soc. 127*, 8916−8917.

(9) Andersson, J., Rosenholm, J., Areva, S., and Linden, M. (2004) Influences of material characteristics on ibuprofen drug loading and release profiles from ordered micro- and mesoporous silica matrices. *Chem. Mater. 16*, 4160−4167.

(10) Lai, C. Y., Trewyn, B. G., Jeftinija, D. M., Jeftinija, K., Xu, S., Jeftinija, S., and Lin, V. S. Y. (2003) A mesoporous silica nanosphere-based carrier system with chemically removable CdS nanoparticle caps for stimuli-responsive controlled release of neurotransmitters and drug molecules. *J. Am. Chem. Soc. 125*, 4451−4459.

(11) Choy, J. H., Jung, J. S., Oh, J. M., Park, M., Jeong, J., Kang, Y. K., and Han, O. J. (2004) Layered double hydroxide as an efficient drug reservoir for folate derivatives. *Biomaterials 25*, 3059−3064.

(12) Choy, J. H., Kwak, S. Y., Jeong, Y. J., and Park, J. S. (2000) Inorganic layered double hydroxides as nonviral vectors. *Angew. Chem., Int. Ed. 39*, 4042−4045.

(13) Portet, D., Denizot, B., Rump, E., Lejeune, J. J., and Jallet, P. (2001) Nonpolymeric coatings of iron oxide colloids for biological use as magnetic resonance imaging contrast agents. *J. Colloid Interface Sci. 238*, 37−42.

(14) Wunderbaldinger, P., Josephson, L., and Weissleder, R. (2002) Tat peptide directs enhanced clearance and hepatic permeability of magnetic nanoparticles. *Bioconjugate Chem. 13*, 264−268.

(15) Won, J., Kim, M., Yi, Y. W., Kim, Y. H., Jung, N., and Kim, T. K. (2005) A magnetic nanoprobe technology for detecting molecular interactions in live cells. *Science. 309*, 121−5.

(16) Oh, J. M., Park, M., Kim, S. T., Jung, J. Y., Kang, Y. K., Choy, J. H. (2006) Efficient delivery of anticancer drug MTX through MTX-LDH nanohybrid system. *J. Phys. Chem. Solids. 67*, 1024−1027.

(17) Berry, C. C. (2005) Possible exploitation of magnetic nanoparticle-cell interaction for biomedical applications. *J. Mater. Chem. 15*, 543−547.

(18) Xing, X., He, X., Peng, J., Wang, K., and Tan, W. (2005) Uptake of silica-coated nanoparticles by HeLa cells. *J. Nanosci. Nanotechnol. 5*, 1688−93.

(19) Kam, N. W. S., and Dai, H. J. (2005) Carbon nanotubes as intracellular protein transporters: Generality and biological functionality. *J. Am. Chem. Soc. 127*, 6021−6026.

(20) Choy, J. H., Kwak, S. Y., Park, J. S., and Jeong, Y. J. (2001) Cellular uptake behavior of [gamma-P-32] labeled ATP-LDH nanohybrids. *J. Mater. Chem. 11*, 1671−1674.

(21) Kam, N. W., Liu, Z., and Dai, H. (2006) Carbon nanotubes as intracellular transporters for proteins and DNA: an investigation of the uptake mechanism and pathway. *Angew. Chem., Int. Ed. 45*, 577−81.

(22) Vaccari, A. (1998) Preparation and catalytic properties of cationic and anionic clays. *Catal. Today 41*, 53−71.

(23) Tarnawski, A., Pai, R., Itani, R., and Wyle, F. A. (1999) The antacid Talcid adsorbs and neutralizes all proteins secreted by H. pylori including VacA cytotoxin: A new mechanism for its ulcer-healing action? *Digestion 60*, 449−455.

(24) Oh, J. M., Hwang, S. H., and Choy, J. H. (2002) The effect of synthetic conditions on tailoring the size of hydrotalcite particles. *Solid State Ionics 151*, 285−291.

(25) Sever, S., Damke, H., and Schmid, S. L. (2000) Garrotes, springs, ratchets, and whips: putting dynamin models to the test. *Traffic 1*, 385−92.

(26) Benmerah, A., Bayrou, M., Cerf-Bensussan, N., and Dautry-Varsat, A. (1999) Inhibition of clathrin-coated pit assembly by an Eps15 mutant. *J. Cell Sci. 112 (Pt 9)*, 1303−11.

(27) Singh, M. (1999) Transferrin As A targeting ligand for liposomes and anticancer drugs. *Curr. Pharm. Des. 5*, 443−51.

(28) Kirchhausen, T. (2000) Three ways to make a vesicle. *Nat. Rev. Mol. Cell. Biol. 1*, 187−98.

(29) Li, H., and Qian, Z. M. (2002) Transferrin/transferrin receptor-mediated drug delivery. *Med. Res. Rev. 22*, 225−50.

(30) Widera, A., Norouziyan, F., and Shen, W. C. (2003) Mechanisms of TfR-mediated transcytosis and sorting in epithelial cells and applications toward drug delivery. *Adv. Drug Delivery Rev. 55*, 1439−66.

(31) Medina-Kauwe, L. K., Xie, J., and Hamm-Alvarez, S. (2005) Intracellular trafficking of nonviral vectors. *Gene Ther. 12*, 1734−51.

(32) McGuire, J. J. (2003) Anticancer antifolates: current status and future directions. *Curr. Pharm. Des. 9*, 2593−613.

(33) Ackland, S. P., and Schilsky, R. L. (1987) High-dose methotrexate: a critical reappraisal. *J. Clin. Oncol. 5*, 2017−31.

(34) Shapiro, G. I., and Harper, J. W. (1999) Anticancer drug targets: cell cycle and checkpoint control. *J. Clin. Invest. 104*, 1645−53.

BC0601323

Binding, Electrochemical Activation, and Cleavage of DNA by Cobalt(II) Tetrakis-*N*-methylpyridyl Porphyrin and Its β-Pyrrole Brominated Derivative

Shivaraj Yellappa, Jaldappagari Seetharamappa,† Lisa M. Rogers, Raghu Chitta, Ram P. Singhal,* and Francis D'Souza*

Department of Chemistry, Wichita State University, 1845 Fairmount, Wichita, Kansas 67260-0051. Received June 5, 2006; Revised Manuscript Received September 26, 2006

The binding of nucleic acids by water-soluble cobalt(II) tetrakis-*N*-methylpyridyl porphyrin, (TMPyP)Co, and its highly electron-deficient derivative cobalt(II) tetrakis-*N*-methyl pyridyl-β-octabromoporphyrin, (Br_8TMPyP)Co, was investigated by UV−visible absorption, circular dichroism (CD), and electrochemical and gel electrophoresis methods. The changes of the absorption spectra during the titration of these complexes with polynucleotides revealed a shift in the absorption maxima and a hypochromicity of the porphyrin Soret bands. The intrinsic binding constants were found to be in the range of 10^5-10^6 M^{-1}. These values were higher for the more electron-deficient (Br_8TMPyP)Co. Induced CD bands were noticed in the Soret region of the complexes due to the interaction of these complexes with different polynucleotides, and an analysis of the CD spectra supported a mainly external mode of binding. Electrochemical studies revealed the cleavage of polynucleotides by (TMPyP)Co and (Br_8TMPyP)Co in the presence of oxygen preferentially at the A−T base pair region. Gel electrophoresis experiments further supported the cleavage of nucleic acids. The results indicate that the β-pyrrole brominated porphyrin, (Br_8TMPyP)Co, binds strongly and cleaves nucleic acids efficiently as compared with (TMPyP)Co. This electrolytic procedure offers a unique tool in biotechnology for cleaving double-stranded DNA with specificity at the A−T regions.

INTRODUCTION

Macrocyclic compounds that bind and cleave nucleic acids have gained importance as reagents to retrieve structural and genetic information and also to develop efficient chemical nucleases (*1*, *2*). Several metal ions and complexes have been attached to DNA-interactive groups to produce DNA chain scission. For example, Fe(II)−EDTA covalently bound to methidium as an intercalator (*3*) to oligonucleotides (*4*, *5*) and to oligopeptides/proteins (*6*, *7*) in the presence of dioxygen and a reducing agent efficiently cleaves DNA. Nuclease activity has been observed for complexes of porphyrins of Fe(III), Mn(III), Co(III), Cu(II), and Zn(II) under chemical and photochemical conditions (*2*, *8*−*17*). Hence, the porphyrin and its metal complexes have been extensively studied as models of DNA-reactive complexes (*18*, *19*). The majority of reports have concentrated on *meso*-tetra(4-*N*-methylpyridyl) porphyrin (TMPyP) and its metal complexes by spectroscopic methods. The cationic TMPyP has a high binding affinity for anionic DNA strands with association constants in the range of 10^5-10^7 M^{-1} (*20*−*22*). The DNA binding mechanism is dependent on both the sequence of the DNA strands and the structure perturbation of the porphyrin molecules (*23*, *24*). Additionally, the ionic strength of the solution is also known to influence the binding modes (*25*, *26*).

The interaction of porphyrins with DNA can occur through three types of binding modes, namely, intercalation, outside binding in the groove, and outside binding with self-stacking along the DNA surface. DNA footprinting investigations have revealed that Mn^{3+}, Fe^{3+}, Zn^{2+}, and Co^{2+} metal complexes of TMPyP bind to the A−T-rich regions of DNA in the minor groove while Ni^{2+} and Cu^{2+} complexes of TMPyP intercalate in the G−C-rich regions and bind in the A−T-rich regions by an outside binding mode (*27*, *28*). These metal derivatives of TMPyP were found to cleave DNA in the presence of oxygen and either a reducing or an oxidizing agent, namely, ascorbate, superoxide, and iodosobenzene (*27*). Fiel et al. (*29*) have reported that Fe^{III}−TMPyP can nick DNA without any added activating agent, while the studies by Praseuth et al. (*13*) have indicated that the photoactivation of Co^{III}−TMPyP (but not Mn^{III}−TMPyP) in the presence of O_2 can induce DNA cleavage. They have also demonstrated that Fe^{III}−TMPyP can degrade DNA in a few minutes without light irradiation but that the extent of degradation increased with exposure to light. The possible mechanism of the chemically activated cleavage process includes the generation of a reduced form of oxygen produced in a redox reaction of the metal ion with oxygen.

Among the different porphyrins employed for DNA binding studies, the positively charged (TMPyP)M is the most efficient in terms of binding and cleaving DNA as compared with either the neutral or negatively charged porphyrins. One way of improving the processes of binding and cleavage of DNA by porphyrins is by making the porphyrin ring more electrophilic while keeping the positive charges on the porphyrin macrocyle for its intrinsic affinity for DNA. This can be achieved by introducing one or more peripheral electron-withdrawing substituents like halogens at the β-pyrrole positions of the TMPyP macrocycle. The first part of this study addresses this issue by employing a highly electron-deficient, water-soluble β-brominated cobalt porphyrin (*30*−*32*) as a DNA binding and cleaving agent (Scheme 1).

Electrochemical methods can also be used to study binding and cleavage of DNA (*33*). Electrochemical methods offer several advantages for probing metalloporphyrin binding and DNA cleavage and can provide a useful complement to the widely used spectroscopic methods. These advantages include

* Corresponding author. Phone: (316) 978 7380. E-mail: Francis.DSouza@wichita.edu.

† On leave from the Department of Chemistry, Karnatak University, Dharwad 580003, Karnataka, India.

10.1021/bc060153x CCC: $33.50 © 2006 American Chemical Society
Published on Web 10/28/2006

Scheme 1. Structure of the Water-Soluble Cobalt Porphyrins Utilized in the Present Study

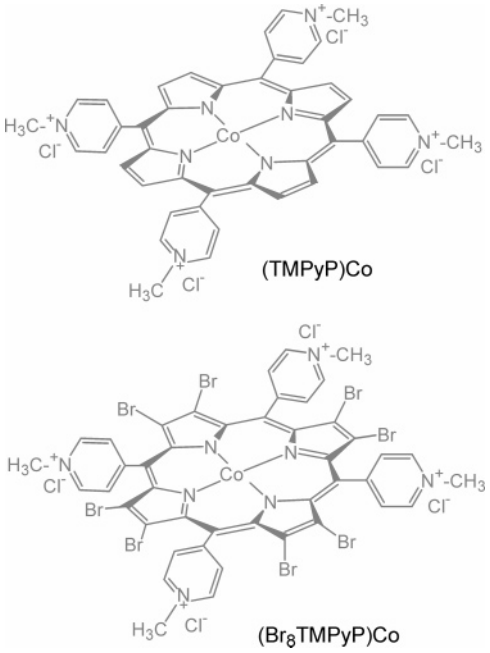

the following: (i) Metal ion complexed macrocyclic compounds that are not amenable to spectroscopic methods, either because of weak absorption bands or because of overlap of electronic transitions with those of the DNA molecule, can potentially be studied via electrochemical techniques. (ii) Multiple oxidation states of the same species as well as mixtures of several interacting species can be observed simultaneously by electrochemical methods. (iii) Equilibrium constants (*K*) for the interaction of the metal complexes with DNA can be obtained from the shifts of peak potentials. (iv) Electrochemical analysis is a cleaner method that does not require addition of a reductant and, hence, makes the analysis of the reaction products easier. (v) Electrochemical methods also offer a wider range of potentials to activate molecules with different binding specifications that may not be activated by chemical methods and may also be useful in following the formation and consumption of electroactive species to study reaction mechanisms. (vi) Finally, the activation process can be studied using metalloporphyrin- or DNA-modified electrode surfaces. The modified electrodes offer distinct advantages of requiring smaller amounts of samples and well understood surface electrochemical phenomenon. In spite of all these advantages, utilization of electrochemical techniques to study DNA interaction and cleavage has been scarce (*33*−*36*). In the present study, we have also explored electrochemical methods to activate and cleave DNA by cobalt porphyrins. As shown here, the β-pyrrole brominated porphyrin exhibits better binding and cleavage of DNA under electrochemical conditions.

EXPERIMENTAL PROCEDURES

Chemicals and Reagents. (TMPyP)Co as a tetrachloride salt was purchased from Mid-Century Chemicals Co., Illinois, and used as received, while (Br_8TMPyP)Co as tetrachloride salt was prepared by following the reported procedure (*30*). Calf thymus DNA (CT-DNA), double-stranded (ds) poly[d(G·C)] and ds poly[d(A·T)], sodium dihydrogen phosphate, sodium phosphate dibasic, and cacodylic acid were obtained from Sigma Aldrich, while phi-X174 DNA was purchased from Promega. Tris base, boric acid, and EDTA were received from Fischer Scientific Chemicals Ltd., New Jersey.

Stock solution of CT-DNA was prepared by sonication at 0−5 °C. Concentration of DNA was determined by UV absorbance at 260 nm ($\epsilon_{260} = 6.6 \times 10^3$ M^{-1} cm^{-1}). Stock solutions of ds poly[d(G·C)] and ds poly[d(A·T)] were prepared in different buffers as mentioned in the text. A 0.05 M phosphate buffer of pH 10.5 and a cacodylic buffer of pH 7.0 were used in the study. Tris−borate−EDTA buffer of pH 8.3 was used as a loading buffer in electrophoresis experiment. Stock solutions of 1 μM each of (TMPyP)Co and (Br_8TMPyP)Co were prepared separately in deionized water. High purity nitrogen was used for deaeration.

Instrumentation. Electrochemical measurements were performed on a PAR electrochemical instrument model PARSTAT 2273 (Ametek, PAR, Oak Ridge, TN). The standard cell consisted of three electrodes that include the working electrode (platinum or glassy carbon electrode), the reference electrode (Ag/AgCl/3 M KCl), and an auxiliary electrode (Pt wire). In order to obtain reproducible results, the electrodes were cleaned with soft emery paper (600 Å), polished with 0.05 μm alumina, then sonicated (ultrasound bath) for 3 min and rinsed with deionized water before making a measurement.

The CD measurements were made on a 70 JASCO-J-810 spectropolarimeter (Tokyo, Japan) using a 0.1 cm cell at 0.2 nm intervals with five scans averaged for each CD spectrum.

The absorption spectra were recorded on a double beam UV−visible spectrophotometer (Shimadzu UV-1650 PC). A quartz cell of 1.00 cm was used for measurements.

Gel electrophoresis experiments were carried out on a Mini-Sub Cell GT from Bio-Rad and Bio-Rad Power PAC 1000 as power source.

Hypochromicity and Evaluation of Binding Constant. The hypochromicity in the Soret band of the cationic porphyrins caused by their interaction with CT-DNA/ds poly[d(A·T)]/ds poly[d(G·C)] was determined by performing absorption titration experiments wherein the concentration of the metal porphyrin complex is kept constant and the concentration of nucleic acid/polynucleotide was varied in cacodylic buffer of pH 7. Absorbance values were recorded at room temperature after each successive addition of CT-DNA/ds poly[d(A·T)]/ds poly[d(G·C)] [0.25−0.3 μL of CT-DNA or 1 μL of ds poly[d(A·T)]/ds poly[d(G·C)]] to (TMPyP)Co (0.005 μM for ds poly[d(A·T)] and ds poly[d(G·C)] or 0.05 μM for CT-DNA) or (Br_8TMPyP)Co (0.083 μM for ds poly[d(A·T)] and ds poly[d(G·C)] or 0.01 μM for CT-DNA) and equilibration (ca. 0.5 min). Buffer blanks were used to compensate for the dilution effect. The percentage of hypochromicity was determined from eq 1.

$$((I_f - I_b)/I_f) \times 100 \quad (1)$$

where I_f and I_b represent the optical density of the free porphyrin complex and the mixture of free porphyrin complex and that bound to DNA/ds poly[d(A·T)]/ds poly[d(G·C)], respectively. The absorbance data were fit to a Benesi−Hildebrand plot (*37*) of $I/\Delta I$ *versus* $1/C$ to evaluate the binding constant of (TMPyP)Co/(Br_8TMPyP)Co−DNA/ds poly[d(A·T)]/ ds poly[d(G·C)].

Circular Dichroism Measurements. CD spectra of CT-DNA/ds poly[d(A·T)]/ds poly[d(G·C)] were recorded in the presence of increasing amounts of (TMPyP)Co and (Br_8TMPyP)Co complexes (0.005−0.03 μM), separately in cacodylic buffer of pH 7.

Modification of Glassy Carbon Electrode. Stock solutions of CT-DNA, ds poly[d(G·C)] and ds poly[d(A·T)] were prepared in Tris-HCl buffer of pH 7.3 containing 0.1 M NaCl. These solutions were used for making the CT-DNA and ds poly[d(A·T)]/ds poly[d(G·C)] modified electrodes. To prepare a drop-coated electrode, 5 μL of CT-DNA solution was transferred to cover the glassy carbon (GC) electrode's surface, and then warm air (about 50 °C) was blown from a distance of 10 cm to dry the electrode's surface to make a film. Later,

(TMPyP)Co/(Br_8TMPyP)Co was transferred on the DNA film modified electrode and dried by warm air. Electrochemical deposition was performed by holding the potential at a suitable reduction potential for the metalloporphyrin film. Stable GC/DNA/metalloporphyrin films can also be prepared by keeping the potential of the DNA-modified electrode at −40 mV (*versus* Ag/AgCl) in a metalloporphyrin aqueous solution as is done in consecutive cyclic voltammetry (*38*).

Solutions were thoroughly deoxygenated, unless otherwise indicated, by bubbling with nitrogen that had been previously saturated with water. During the data acquisition, a nitrogen atmosphere was maintained over the solution in the cell.

Bulk Electrolysis. In order to conserve the nucleic acid and ds poly[d(A·T)]/ds poly[d(G·C)], it becomes essential to carry-out the bulk electrolysis experiments on a small scale. A homemade microcell assembly consisting of an outer working electrode compartment and an inner compartment with a porous Vycor plug containing the reference and counter electrodes was used to electrolyze different amounts of the metalloporphyrins with phi-X174 DNA, ds poly[d(G·C)], and ds poly[d(A·T)] at a concentration of 0.6 μg. The reaction mixture was placed in the working electrode compartment. The other compartment consisted of supporting electrolyte, phosphate buffer of pH 10.5. The working solution compartment volume was maintained at 120 μL. The electrolysis was carried out in the dark for 10 h at −450 mV in the presence of (TMPyP)Co or (Br_8TMPyP)Co. During electrolysis, O_2 was bubbled into the solution. The working, counter, and reference electrodes used were Pt foil, Pt wire, and Ag/AgCl, respectively.

Gel Electrophoresis. A sample (120 μL) of either phi-X174 DNA or ds poly[d(G·C)] or ds poly[d(A·T)] each with (TMPyP)Co or (Br_8TMPyP)Co was electrolyzed for 10 h in the presence of oxygen. From this, a fraction of the reaction mixture (20 μL) containing phi-X174 DNA (0.1 μg), (TMPyP)Co (8.3 μL, 1 μM), and phosphate buffer of pH 10.5 (10 μL) was added followed by 2 μL of the loading dye (bromophenol blue dye and sucrose) into the wells of a 1% horizontal agarose gel containing 1 μg/mL ethidium bromide. The gel electrophoresis was carried out at 4 V/cm for 1 h in 89 mM Tris base, 89 mM boric acid, 2 mM EDTA buffer of pH 8.3. After electrophoresis, the DNA bands were visualized and photographed under ultraviolet light.

RESULTS AND DISCUSSION

Absorption Studies. Absorption spectroscopy is one of the convenient tools for examining the interaction between ligands and nucleic acids. The different modes of interaction of a metal complex with DNA can be studied not only by this technique but also by circular dichroism (CD) spectroscopy. Binding of (TMPyP)Co or (Br_8TMPyP)Co to native and synthetic polynucleotides induces changes of the absorption spectrum in the Soret band. The extent of the shift and hypochromism depends on the nature of the polynucleotide, the porphyrin, and the binding mode. Generally, the change is large for intercalation and small for a groove binding or stacking mode. The absorption spectra of both (TMPyP)Co and (Br_8TMPyP)Co were recorded separately in the presence of increasing amounts of nucleic acid/ds poly[d(G·C)]/ds poly[d(A·T)] in cacodylic buffer of pH 7. The representative absorption spectra of (TMPyP)Co−ds poly-[d(A·T)] and (Br_8TMPyP)Co−ds poly[d(A·T)] are shown in Figure 1, panels a and b, respectively. Upon successive addition of ds poly[d(A·T)], ds poly[d(G·C)], and CT-DNA, the Soret bands of (TMPyP)Co were red-shifted from 433.9 to 440.3 nm, from 434 to 436 nm, and from 433.5 to 437.4 nm, respectively, while in the case of (Br_8TMPyP)Co, a blue shift in Soret band was observed from 468.5 to 462.7 nm, from 467.8 to 464.7 nm, and from 469.8 to 468.2 for ds poly[d(A·T)],

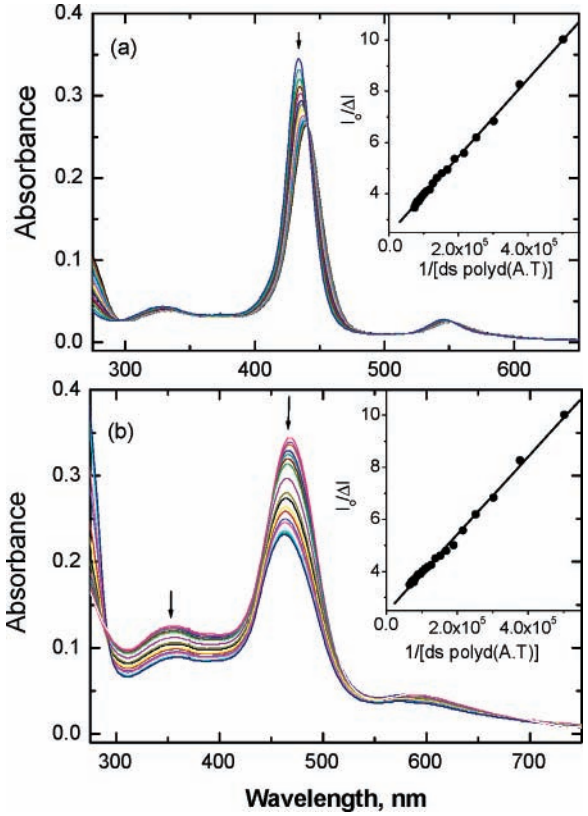

Figure 1. UV−visible spectrum of (a) (TMPyP)Co and (b) (Br_8TMPyP)Co on increasing addition of ds poly[d(A·T)] (0.004 μM each addition). The inset shows the Benesi−Hildebrand plot of $I/\Delta I$ *versus* $1/C$ constructed for the determination of binding constant.

ds poly[d(G·C)], and CT-DNA, respectively. (TMPyP)Co exhibited 9.25−13.58%, 3.71−24.18%, and 2.94−46.93% hypochromism, while (Br_8TMPyP)Co showed 3.43−6.49%, 3.50−35.0%, and 4.05−36.85% hypochromism with CT-DNA, ds poly[d(A·T)], and ds poly[d(G·C)], respectively. These results reveal that both porphyrin complexes interact with nucleic acid, ds poly[d(G·C)], and ds poly[d(A·T)].

In order to compare quantitatively the binding strength of the complexes, the intrinsic binding constants, K_b, of (TMPyP)Co and (Br_8TMPyP)Co with ds poly[d(A·T)], ds poly-[d(G·C)], and CT-DNA were determined from their spectral changes monitored in the Soret region. The intrinsic binding constants as evaluated from Benesi−Hildebrand plots (*37*) (see Figure 1 inset) were found to be 1.5×10^5, 7.0×10^5, and 8.0×10^5 M^{-1} for (TMPyP)Co and 8.0×10^5, 9.0×10^5, and 7.0×10^6 M^{-1} for (Br_8TMPyP)Co with ds poly[d(A·T)], ds poly-[d(G·C)], and CT-DNA, respectively. These results indicate that the (Br_8TMPyP)Co binds more strongly to ds poly[d(A·T)], ds poly[d(G·C)], and CT-DNA as compared with (TMPyP)Co.

Circular Dichroism Studies. Circular dichroism is a powerful technique for distinguishing the three main DNA-binding modes, namely, intercalation (negative CD), outside groove binding (positive CD), and outside stacking (bisignate CD) (*39*, *40*). The metalloporphyrin derivatives considered here do not display CD spectra in the absence of nucleic acid/ds poly[d(G·C)]/ds poly[d(A·T)], but CD spectra are induced in the Soret region when they are bound to nucleic acids/ds poly[d(G·C)]/ds poly[d(A·T)] due to the interaction between the transition moments of the achiral porphyrin and chirally arranged DNA base transitions. Representative induced CD spectra in the visible region for unbrominated and brominated cobalt porphyrins recorded in the presence of CT-DNA and ds poly[d(A·T)] are shown in Figure 2. The mole ratio of porphyrin to DNA base pairs, R value, was varied from 6.3 to 19.

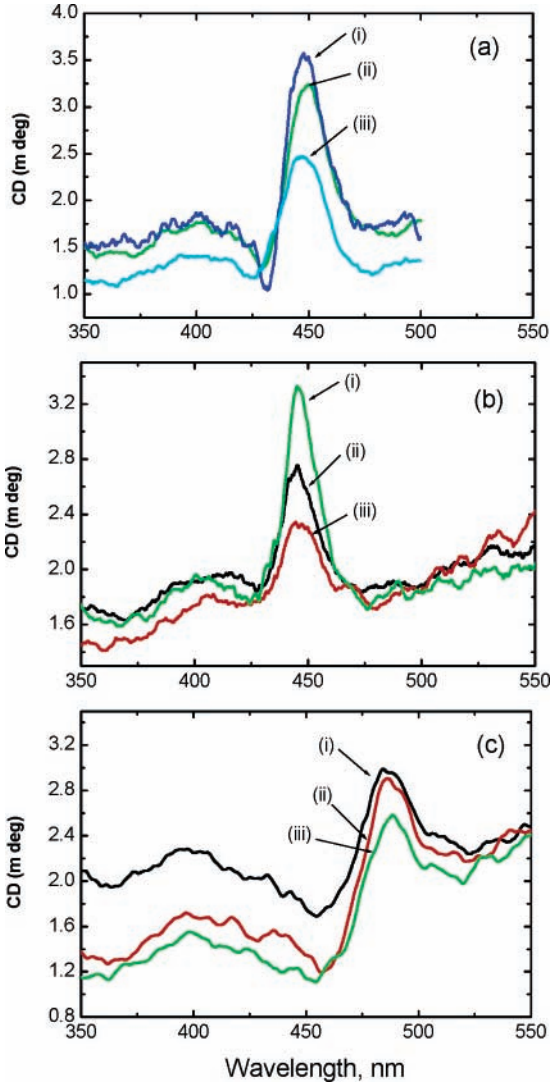

Figure 2. Circular dichroism spectrum of (a) CT-DNA interacting with (TMPyP)Co (i−iii represents 0.01 μM each addition), (b) poly[d(A·T)$_2$] interacting with (TMPyP)Co (i−iii represents 0.01 μM each addition), and (c) poly [d(A·T)$_2$] interacting with (Br_8TMPyP)Co (i−iii represents 0.01 μM each addition). All the spectra were recorded in cacodylic acid buffer at pH 7.0.

(TMPyP)Co examined in the present study displayed two positive induced CD signals in the Soret region at 402 and 447 nm in presence of CT-DNA (Figure 2a), at 400 and 444 nm in presence of ds poly[d(A·T)] DNA (Figure 2b), and at 397 and 485 nm for ds poly[d(G·C)]. The CD spectra of (Br_8TMPyP)Co exhibited positive bands at 398 and 487 nm for CT-DNA, at 398 and 485 nm for ds poly[d(A·T)] (Figure 2c), and at 397 and 483 nm for ds poly[d(G·C)]. These results reveal that the interaction is not through intercalation (*41*) but through an external binding mode at these investigated *R* values. It is important to note that although the macrocycle of the brominated cobalt porphyrin is severely distorted (up to 2 Å as estimated from computational calculations), it effectively interacts with CT-DNA/ds poly[d(A·T)].

The CD spectrum of CT-DNA (not shown) recorded in the absence of the porphyrin complex shows a positive band at 275 nm due to base stacking and a negative band at 245 nm due to helicity and is characteristic of DNA in the right-handed B form (*42*). The conformational changes observed in the UV region may be due to the effect of nucleobase or porphyrin (since porphyrin has weak absorption in the same region where the nucleobase moiety absorbs). In the presence of (TMPyP)Co or (Br_8TMPyP)Co, the negative band at 245 nm decreases while

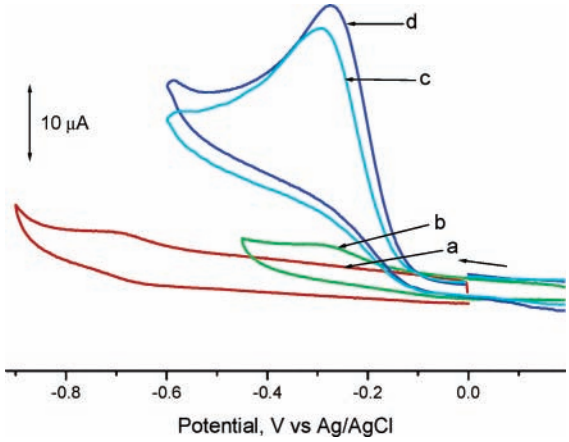

Figure 3. Cyclic voltammograms of (a) (TMPyP)Co and (b) (Br_8TMPyP) in nitrogen atmosphere and (c) (TMPyP)Co and (d) (Br_8TMPyP)Co in oxygen atmosphere. Solution composition was phosphate buffer at pH 10.5. Scan rate = 50 mV s^{-1}.

the positive band at 275 nm disappears and a negative peak appears at the same wavelength. These observations also indicate that the CT-DNA interacts with both (TMPyP)Co and (Br_8TMPyP)Co through an external binding mode. Both porphyrin complexes exhibited a strong negative band around the 280 nm region when bound to ds poly[d(A·T)] and a positive peak around 275 nm when bound to ds poly[d(G·C)]. These observations are in agreement with the reported literature (*43*).

Electrochemistry of (TMPyP)Co and (Br_8TMPyP)Co. Both cyclic voltammetry (CV) and differential pulse voltammetry (DPV) were employed to probe the binding of metalloporphyrins to DNA in solution. The selection of CV and DPV techniques is based on their different time scales (*44*). The time scale, τ, for a typical CV experiment is around 250 ms ($\tau \approx RT/(\nu F)$, R = molar gas constant, F = faraday constant, ν = scan rate, and T = temperature), while for a DPV under the same conditions, this value is 17 ms. As a result, the reversibility of heterogeneous electron-transfer kinetics will be different for these two techniques. DPV data were used to obtain quantitative information about the interaction of these metalloporphyrins with CT-DNA and phi-X174 DNA.

Figure 3 shows the cyclic voltammograms of (TMPyP)Co and (Br_8TMPyP)Co in the absence and presence of oxygen. The electroreduction behavior of these porphyrins is reversible to quasi-reversible. The potentials corresponding to the reduction processes are located at $E_{1/2} = -0.67$ and $E_{pc} = -0.29$ V vs Ag/AgCl, respectively, for (TMPyP)Co and (Br_8TMPyP)Co under the given solution conditions of pH 10.5. It is evident that the redox potentials for the brominated porphyrin are shifted positively as compared with that of the corresponding unbrominated derivative. Both metalloporphyrins reduce dioxygen as shown by the voltammograms in Figure 3c,d. In a previous study, we have shown the occurrence of a two-electron reduction leading to the formation of H_2O_2 by these porphyrins (*30*). The peak potentials for the catalytic reduction are located at $E_{pc} = -0.29$ and -0.27 V vs Ag/AgCl for (TMPyP)Co and (Br_8TMPyP)Co, respectively, while that of free O_2 is observed at -0.56 V. That is, the dioxygen reduction was easier by 20 mV by the more electron-deficient β-pyrrole brominated cobalt porphyrin. It may be mentioned here that a similar electrocatalytic reduction of dioxygen was observed when electrodes modified by drop coating the cobalt porphyrins were used.

As shown in Figure 4, DNA binding to metalloporphyrins yields diminished currents as a result of reduced diffusion of the porphyrin−DNA complex. This change is also accompanied by a shift in the redox potential values as a result of complex formation. The magnitude of this potential shift is dependent

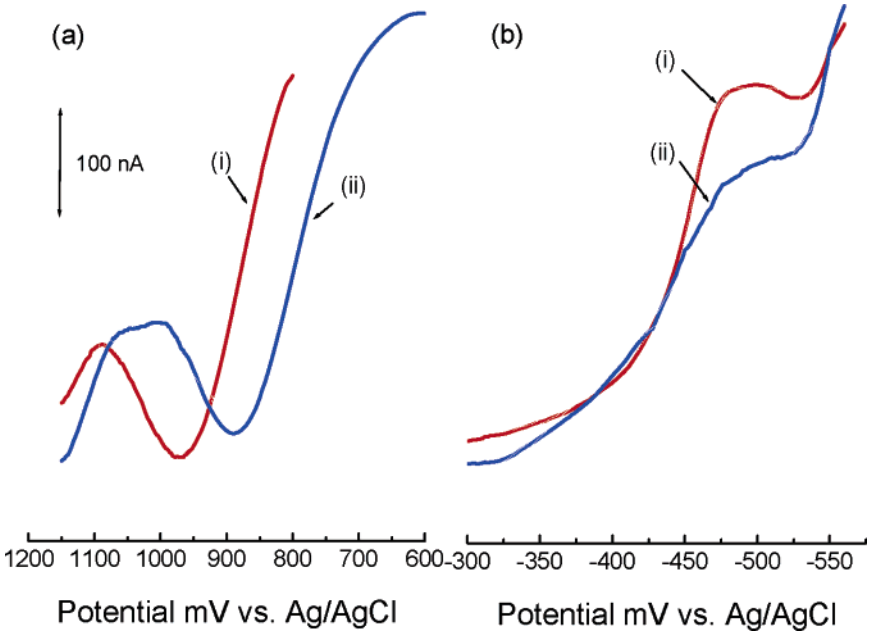

Figure 4. Differential pulse voltammograms for (a) the first oxidation and (b) the first reduction of (TMPyP)Co in the absence (curve i) and presence of ~10 equiv of calf thymus DNA (curve ii) in pH 7.4 buffer solution. Ionic strength = 0.1 M. Scan rate = 2 mV s^{-1}, pulse width = 0.50 s, and pulse height = 0.025 V.

upon the oxidation state of the metal ion. That is, a cathodic shift of ~0.1 V is observed for Co^{3+} (oxidized species) binding to DNA, while this shift is <20 mV for Co^{+} (reduced species) binding to DNA in Figure 4a,b. These results indicate a higher binding power of porphyrins having metal ions in higher oxidation state, a novel property that could be probed easily by electrochemical techniques.

DNA Cleavage by an Electrochemical Method. The DNA cleavage studies were performed by drop coating the electrode surfaces with the catalyst and DNA in order to conserve the catalyst and the substrate. In a typical cleavage experiment, a modified electrode of glassy carbon/DNA/(Br_8TMPyP)Co or (TMPyP)Co was immersed in phosphate buffer of pH 10.5, and voltammograms were recorded under nitrogen atmosphere. Thereafter the modified electrode was taken out of the solution. A stream of oxygen was bubbled through the phosphate buffer for 2 min. The electrode was then dipped into the aerated buffer, and voltammograms were recorded.

Figure 5, panels a and b, shows representative CV and DPV for (TMPyP)Co in the presence of CT-DNA in oxygen-saturated solution and (Br_8TMPyP)Co in the presence of ds poly[d(A·T)] in oxygen-saturated solution, respectively. The potential of the cyclic voltammogram was scanned, first, in the negative direction, and after crossing the potential corresponding to the catalytic reduction of dioxygen, the scan direction was changed into the positive direction. That is, oxygen was *in-situ* reduced, and its effect on the DNA cleavage was simultaneously monitored by following oxidative waves corresponding to the cleavage products. Two oxidative cleavages were noticed at the potentials of +0.72 and +1.01 V for CT-DNA (Figure 5a), at +0.73 and +1.02 V for phi-X174 DNA, and at +0.69 and +1.09 V for ds poly[d(A·T)] in presence of (TMPyP)Co and at +0.67 and +1.02 V for CT-DNA, at +0.65 and +0.99 V for phi-X174 DNA, and at +0.71 and +0.99 V for ds poly[d(A·T)] (Figure 5b) with (Br_8TMPyP)Co. Almost similar behavior was observed for rest of the nucleic acids and ds poly[d(A·T)]/cobalt porphyrins. In all of these experiments, currents of the second oxidation wave were found to be much larger than those of the first one suggesting occurrence of other oxidation processes at this potential. In order to identify the nucleobase pair of the nucleic acid at which the cleavage has

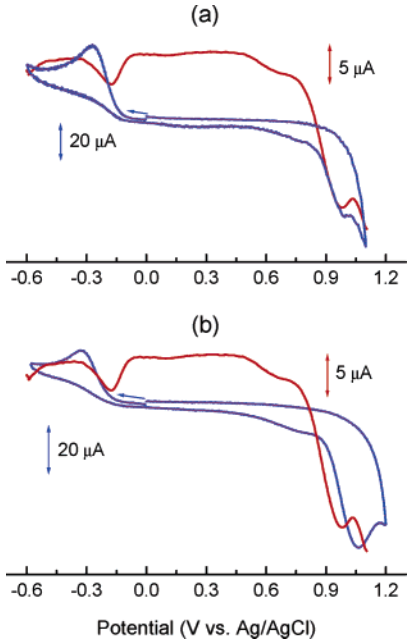

Figure 5. Cyclic (blue lines) and differential pulse (red lines) voltammograms of (a) (TMPyP)Co in the presence of CT-DNA in oxygen-saturated solution and (b) (Br_8TMPyP)Co in the presence of ds poly[d(A·T)] in oxygen-saturated solution. Conditions: phosphate buffer (pH 10.5); scan rate = 50 and 5 mV s^{-1} for CV and DPV, respectively.

occurred, in a control experiment we recorded the voltammograms by external addition of monomer nucleobases (adenine, guanine, thymine, and cytosine) into the electrochemical cell used above. Addition of adenine increased the intensity of the peak at ~0.67 V, while thymine increased the intensity of the peak at ~1.0 V suggesting that the DNA cleavage takes place at adenine and thymine base pairs. It may be mentioned here that when the potential was scanned initially in the positive direction, no wave at ~0.67 V corresponding to the oxidation of adenine was observed. However, the wave at ~1.0 V was observed with diminished currents. These results suggest that the wave at ~1.0 V may involve currents from reoxidation of

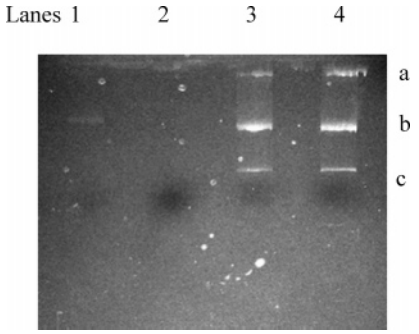

Figure 6. Electrophoresis results showing cleavage of phi-X175 DNA by electrolysis carried out in the presence of (TMPyP)Co and oxygen: Lane 1, nonelectrolyzed phi-X174 DNA, 0.1 μg; lane 2, bromophenol blue dye (2 μL); lane 3, electrolyzed plasmid phi-X174 DNA, 0.1 μg; lane 4, electrolyzed phi-X174 DNA, 0.125 μg. Conditions: agarose gel 1.0%; ethidum bromide 10 μL (1 μg/mL); potential applied = 40 V; loading dye 2 μL; electrophoresis time 1 h. Bulk electrolysis conditions: phi-X174 DNA with (TMPyP)Co and 0.05 M phosphate buffer of pH 10.5 with 10 μL of 10% of SDS at −0.45 V with continuous oxygen purging for 10 h.

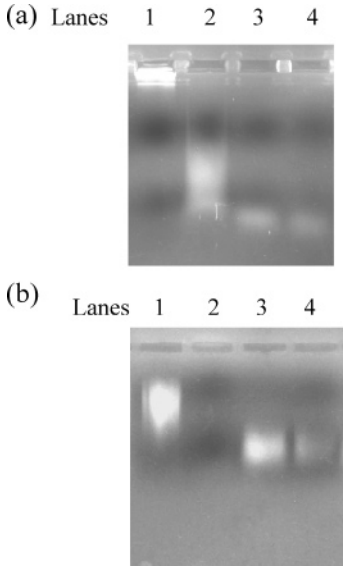

Figure 7. (a) Electrophoresis results showing cleavage of ds poly[d(A·T)] by electrolysis carried out in the presence of (TMPyP)Co and oxygen: lane 1, nonelectrolyzed ds poly[d(A·T)], 0.05 μg; lane 2, ds poly[d(A·T)], 0.075 μg, electrolyzed for 30 min; lane 3, ds poly[d(A·T)], 0.075 μg, electrolyzed for 45 min; lane 4, ds poly[d(A·T)], 0.05 μg, electrolyzed for 45 min. Conditions: agarose gel 1.0%; ethidum bromide 10 μL (1 μg/mL); potential applied = 40 V; loading dye 1 μL; electrophoresis time 1 h. (b) Electrophoresis results showing cleavage of ds poly[d(A·T)] by electrolysis carried out in the presence of (Br_8TMPyP)Co and oxygen: lane 1, nonelectrolyzed ds poly[d(A·T)], 0.05 μg; lane 2, loading dye, 2 μL; lane 3, electrolyzed [ds poly[d(A·T)], 0.075 μg, (TMPyP)Co, 1 μM, and phosphate buffer, pH 10.5; lane 4, electrolyzed [ds poly[d(A·T)], 0.075 μg, (Br_8TMPyP)Co, 1 μM, and phosphate buffer, pH 10.5. Electrolysis time = 45 min. Conditions: agarose gel 1.0%; ethidum bromide 10 μL (1 μg/mL); potential applied = 40 V; loading dye 1 μL; electrophoresis time 1 h.

the peroxide generated during the catalytic reduction of oxygen or direct oxidation of the nucleic acid and polynucleotide at this potential or both. Moreover, it was noticed that the ds poly[d(G·C)] did not show significant cleavage with (TMPyP)Co and (Br_8TMPyP)Co. That is, no peaks corresponding to guanine or cytosine were observed indicating cleavage preference over ds poly[d(A·T)] by the cobalt porphyrins. These results were further confirmed by gel electrophoresis experiments of electrolyzed ds poly[d(A·T)] and ds poly[d(G·C)] with (TMPyP)Co and (Br_8TMPyP)Co, discussed below.

In order to understand the role of the electro-active cobalt in the DNA cleavage process, control experiments were performed utilizing free-base porphyrin, (TMPyP)H_2, and zinc porphyrin, (TMPyP)Zn (zinc is an electro-inactive metal), in the presence of oxygen and DNA. Under these experimental conditions, no peak corresponding to DNA oxidation products around +0.7 V was observed suggesting the absence of DNA cleavage by these porphyrins (see Supporting Information for figures). Similarly, the electrolysis products of the above reaction mixture revealed no DNA fragments by the agorose gel electrophoresis indicating the absence of a DNA cleavage process.

Electrophoresis Study—Cleavage of DNAs and Polynucleotides. Samples containing phi-X174 DNA and (TMPyP)Co in a phosphate buffer of pH 10.5 were submitted to voltammetric electrolysis at −0.45 V for 10 h with continuous oxygen purging. Figure 6 shows the gel electrophoresis of phi-X174 DNA with (TMPyP)Co. Bromophenol blue dye (2 μL) was injected at lanes 1−4 and nonelectrolyzed DNA was injected at lane 1. At lanes 3 and 4, 0.1 and 0.125 μg of electrolyzed reaction mixture of DNA with (TMPyP)Co were injected, respectively. After gel electrophoresis experiments, though no separations of phi-X174 DNA were observed in lane 1, there was a prominent band representing a supercoiled form of DNA at position a. A dark band in lane 2 is caused by the run dye. In lanes 3 and 4, form I of DNA (supercoiled form) of phi-X174 DNA observed at position a gradually disappeared, and form II (relaxed circular form) at position b was observed. It was only when the number of single-strand breaks become sufficient that the band corresponding to form III (linear form) was seen on electrophoresis gels. Thus, the double-strand breaks in DNA responsible for these linear forms of DNA have to be considered as resulting from coincidence of two random single-strand breaks. More predominant bands were observed with larger amount of electrolyzed reaction mixture (lane 3).

Figure 7, panels a and b, shows the cleavage of ds poly[d(A·T)] by (TMPyP)Co and (Br_8TMPyP)Co, respectively. In Figure 7a, the electrolysis was carried out at the potential of −0.45 V for 30 and 45 min separately with continuous oxygen purging. A broad band was observed with the reaction mixture that was electrolyzed for 30 min indicating incomplete cleavage of ds poly[d(A·T)] by (TMPyP)Co. However, complete cleavage of ds poly[d(A·T)] was noticed with the reaction mixture electrolyzed for 45 min. Hence, the electrolysis was carried out for 45 min in all subsequent experiments. Further, the band intensity varied with the concentration of ds poly[d(A·T)] in lanes. Similar behavior was observed with ds poly[d(A·T)] in the presence of (Br_8TMPyP)Co as shown in Figure 7b. A comparison between the cleaving behavior of (TMPyP)Co and (Br_8TMPyP)Co in Figure 7b (lanes 3 and 4) clearly shows that (Br_8TMPyP)Co is as good if not better than (TMPyP)Co. Similar experiments carried out for ds poly[d(G·C)] in the presence of either (TMPyP)Co or (Br_8TMPyP)Co revealed no cleavage products corresponding to guanine or cytosine. This confirms the earlier electrochemical claim that the cleavage of phi-X174 DNA and CT-DNA occur at A·T bases but not at G·C bases.

A possible mechanism for binding and cleavage of dsDNA (natural or synthetic) by the studied cobalt porphyrins is shown in Scheme 2. The initial step involves electroreduction of cobalt porphyrin to a reduced state. Based on the electrochemical data in Figure 3, one could assign Co^{II} as the species responsible for dioxygen binding in the case of (TMPyP)Co, while a Co^{I} species is responsible for dioxygen binding in the case of (Br_8TMPyP)Co. The reduced cobalt porphyrin binds dioxygen and catalytically reduces it to hydrogen peroxide. The hydrogen peroxide thus generated reacts with the reduced cobalt porphyrins generating hydroxyl radicals, which in turn cleave the DNA/ds poly[d(A·T)] at the A·T region. Although the present

Scheme 2. Proposed Mechanism of Electrochemically Activated Cobalt Porphyrin−Dioxygen-Induced DNA Cleavage

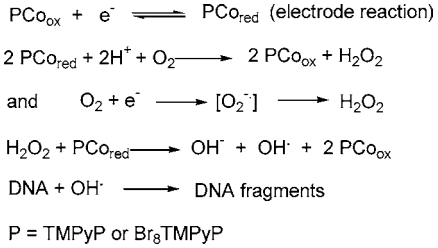

investigation could not fully explain the observed A·T selectivity, previous studies have confirmed such behavior of metalloporphyrin in the presence of chemical reducing agents (*27*, *28*). Currently, we are involved in covalently linking intercalators such as acridine to the β-brominated metalloporphyrins to probe the binding and cleavage studies by electrochemical techniques.

CONCLUSIONS

Cobalt(II) tetrakis-*N*-methylpyridyl porphyrin and its β-pyrrole brominated derivative have been successfully utilized for nucleic acid/ds poly[d(G·C)]/ds poly[d(A·T)] binding studies. UV−vis and CD studies have been carried out to determine the nature of binding between metalloporphyrin complexes and nucleic acid/ds poly[d(G·C)]/ds poly[d(A·T)]. The shift in the wavelength maxima, percent hypochromicity, and binding constant values indicate that the behavior of both cobalt porphyrins with nucleic acid/ds poly[d(G·C)]/ds poly[d(A·T)] is the same; however, the more electron-deficient brominated porphyrin binds more strongly when compared with unbrominated porphyrin. Circular dichroism studies revealed that the mode of binding is the same for both porphyrins and it is through an external binding mode. Electrochemical studies revealed that the cobalt porphyrins bind and catalytically reduce dioxygen to hydrogen peroxide and indicated that they complex with the employed nucleic acid, ds poly[d(G·C)], or ds poly[d(A·T)] as evidenced by the shift in the potentials and reduced peak currents. In the presence of dioxygen, the cobalt porphyrins electrochemically cleave nucleic acid and ds poly[d(A·T)]. Gel electrophoresis experiments were carried out to investigate the cleavage of DNA base pairs, ds poly[d(G·C)], and ds poly-[d(A·T)]. The electrochemical studies coupled with the gel electrophoresis results clearly suggest that the cleavage occurs at the A·T base pairs and not at the G·C base pairs. The procedure offers a unique tool to cleave dsDNA at A−T specific bonds in molecular biology.

ACKNOWLEDGMENT

Support from the National Institutes of Health, the Petroleum Research Fund administered by the American Chemical Society, and the West Memorial Foundation is gratefully acknowledged.

Supporting Information Available: Cyclic voltammograms of calf thymus DNA in the presence of free-base and zinc porphyrins. This material is available free of charge via the Internet at http://pubs.acs.org.

LITERATURE CITED

(1) Sigman, D. S. (1990) Chemical nucleases. *Biochemistry 29*, 9097−9105.
(2) Sashikumar, M., Munson, B. R., and Pandey, R. K. (1999) DNA interaction and photocleavage properties of porphyrins containing cationic substituents at the peripheral position. *Bioconjugate Chem. 10*, 94−102.
(3) Hertzberg, R. P., and Dervan, P. B. (1984) Cleavage of DNA with methidiumpropyl-EDTA-iron (II): reaction conditions and product analyses. *Biochemistry 23*, 3934−3945.
(4) Chu, B. C. F., and Orgel, L. E. (1985) Nonenzymic sequence-specific cleavage of single-stranded DNA. *Proc. Natl. Acad. Sci. U.S.A. 82*, 963−967.
(5) Moser, H. E., and Dervan, P. B. (1987) Sequence-specific cleavage of double helical DNA by triple helix formation. *Science 238*, 645−650.
(6) Youngquist, R. S., and Dervan, P. B. (1985) Sequence-specific recognition of B-DNA by oligo(N-Methylpyrrolecarboxamides). *Proc. Natl. Acad. Sci. U.S.A. 82*, 2565−2569.
(7) Sluka, J. P., Horvath, S. J., Bruist, M. F., Simon, M. I., and Dervan, P. B. (1987) Synthesis of a sequence-specific DNA-cleaving peptide. *Science 238*, 1129−1132.
(8) Trung, L. D., Perrouault, L., Chassignol, M., Nguyen, T. T., and Helene, C. (1987) Sequence-targeted chemical modifications of nucleic acids by complementary oligonucleotides covalently linked to porphyrins. *Nucleic Acids Res. 15*, 8643−8659.
(9) Ford, K. G., and Neidle, S. (1995) Perturbations in DNA structure upon interaction with porphyrins revealed by chemical probes, DNA footprinting and molecular modeling. *Bioorg. Med. Chem. 3*, 671−677.
(10) Fiel, R. J., Beerman, T. A., Mark, E. H., and Datta-Gupta, N. (1982) DNA strand scission activity of metalloporphyrins. *Biochem. Biophys. Res. Commun. 107*, 1067−1074.
(11) Aft, R. L., and Mueller, G. C. (1983) Hemin-mediated DNA strand scission. *J. Biol. Chem. 258*, 12069−12072.
(12) Groves, J. T., and Farrell, T. P. (1989) DNA cleavage by a metal chelating tricationic porphyrin. *J. Am. Chem. Soc. 111*, 4998−5000.
(13) Praseuth, D., Gaudemer, A., Verlhac, J. B., Kraljic, I., Sissoeff, I., and Guille, E. (1986) Photocleavage of DNA in the presence of synthetic water-soluble porphyrins. *Photochem. Photobiol. 44*, 717−724.
(14) Chatterjee, S. R., Shetty, S. J., Devasagayam, T. P. A., and Srivastava, T. S. (1997) Photocleavage of plasmid DNA by the prophyrin *meso*-tetrakis[4-(carboxymethyleneoxy)phenyl]porphyrin. *J. Photochem. Photobil. B. 41*, *128*−135.
(15) James, B. R., Meng, G. G., Posakony, J. J., Ravensbergen, J. A., Ware, C. J., and Skov, K. A. (1996) Porphyrins and metalloporphyrins: potential hypoxic agents. *Met.-Based Drugs 3*, 85−90.
(16) Krijt, J., Stranska, P., Maruna, P., Vokurka, M., and Sanitrak, J. (1997) Herbicide-induced experimental variegate porphyria in mice: Tissue porphyrinogen accumulation and response to porphyrogenic drugs. *Can. J. Physiol. Pharmacol. 75*, 1181−1196.
(17) Feng, Q, Nanqiang, L., and Yu-Yang, J. (1998) Electrochemical studies of CuTMAP interaction with DNA and determination of DNA. *Microchem. J. 58*, 39−51.
(18) Berlin, K., Jain, K. R., Simon, D. M., and Richert, C. (1998) A porphyrin embedded in DNA. *J. Org. Chem. 63*, 1527−1535.
(19) Huang, C. Z., Li, K. A., and Tong, S. H. (1996) Determination of nucleic acids by a resonance light-scattering technique with $\alpha,\beta,\gamma,\delta$-tetrakis[4-trimethyl-ammoniumyl)phenyl]porphine. *Anal. Chem. 68*, 2259−2263.
(20) Anantha, N. V., Azam, M., and Sheardy, R. D. (1998) Porphyrin binding to quadruplexed T_4G_4. *Biochemistry 37*, 2709−2714.
(21) Gray, T. A., Yue, K. T., and Marzilli, L. G. (1991) Effect of N-alkyl substituents on the DNA binding properties of *meso*-tetrakis (4-N-alkylpyridinium-4-yl)porphyrins and their nickel derivatives. *J. Inorg. Biochem. 41*, 205−219.
(22) Feng, Q., Nan-Qiang, L., and Yu-Yang, J. (1998) Electrochemical studies of NiTMpyP and interaction with DNA. *Talanta 45*, 787−793.
(23) Feng, Q., Nan-Qiang, L., and Yu-Yang, J. (1997) Electrochemical studies of porphyrin interacting with DNA and determination of DNA. *Anal. Chim. Acta. 344*, 97−104.
(24) Hudson, B. P., Sou, J., Berger, D. J., McMillin, D. R. (1992) Luminescence studies of the intercalation of Cu(TMpyP4) into DNA. *J. Am. Chem. Soc. 114*, 8997−9002.
(25) Mestre, B., Jakobs, A., Pratviel, G., and Meunier, B. (1996) Structure/nuclease activity relationships of DNA cleavers based on cationic metalloporphyrin−oligonucleotide conjugates. *Biochemistry 35*, 9140−9149.
(26) Wilson, W. D., Lynda, R., Zhao, M., Lucjan, S., and Boykin, D. (1993) The search for structure-specific nucleic acid-interactive

drugs: Effects of compound structure on RNA versus DNA interaction strength. *Biochemistry 32*, 4098−4104.
(27) Ward, B., Skorobogaty, A., and Dabrowiak, J. C. (1986) DNA cleavage specificity of a group of cationic metalloporphyrins. *Biochemistry 25*, 6875−6883.
(28) Bromley, S. D., Ward, B. W., and Dabrowiak, J. C. (1986) Cationic porphyrins as probes of DNA structure. *Nucleic Acids Res. 14*, 9133−9148.
(29) Fiel, R. J. (1989) Porphyrin-nucleic acid interactions: A Review. *J. Biomol. Struct. Dyn. 6*, 1259−1274.
(30) D'Souza, F., Deviprasad, R. G., and Hsieh, Y. Y. (1996) Synthesis and studies on the electrocatalytic reduction of molecular oxygen by non-planar cobalt(II) tetrakis- (N-methyl pyridyl)-*β*-octabromoporphyrin. *J. Electroanal. Chem. 411*, 167−171.
(31) D'Souza, F., Hsieh, Y. Y., and Deviprasad, R. G. (1998) Four-electron electrocatalytic reduction of dioxygen to water by an ion-pair cobalt porphyrin dimer adsorbed on a glassy carbon electrode. *Chem. Commun. 9*, 1027−1028.
(32) D'Souza, F., Hsieh, Y. Y., and Deviprasad, R. G. (1998) Electrochemical and spectroelectrochemical characterization of water-soluble, *β*-pyrrole-brominated cobalt porphyrins. *J. Porphyrins Phthalocyanines 2*, 429−437.
(33) Rogriguesz, M., Kodadek, T., Torres, M., and Bard, A. J. (1990) Cleavage of DNA by electrochemically activated Mn(III) and Fe(III) complexes of *meso*-tetrakis(*N*-methyl-4-pyridyniumyl)porphine. *Bioconjugate Chem. 1*, 123−131.
(34) Basile, L. A., Raphael, A. L., and Barton, J. K. (1987) Metal-activated hydrolytic cleavage of DNA. *J. Am. Chem. Soc. 109*, 7550−7551.
(35) Sequaris, J. M., and Valenta, P. (1987) AC voltammetry: A control method for the damage to DNA caused in vitro by alkylating mutagens. *J. Electroanal. Chem. 227*, 11−20 and references therein.
(36) Van Atta, R. B., Long, E. C., and Hecht, S. M. (1989) Electrochemical activation of oxygenated Fe-bleomycin. *J. Am. Chem. Soc. 111*, 2722−2724.
(37) Benesi, H. A., and Hildebrand, J. H. **(**1949) A spectrophotometric investigation of the interaction of iodine with aromatic hydrocarbons. *J. Am. Chem. Soc. 71*, 2703−2707.
(38) Armistead, P. M., and Thorp, H. H. (2000) Modification of indium tin oxide electrodes with nucleic acids: detection of attomole quantities of immobilized DNA by electrocatalysis. *Anal. Chem. 72*, 3764−3770.
(39) Pasternack, R. F. (2003) Circular dichroism and the interactions of water soluble porphyrins with DNA-a mini review. *Chirality 15*, 329−332.
(40) Dalgleish, D. G., Feil, M. C., and Peacocke, A. R. (1972) The circular dichroism of complexes of 2,7-di-tertiary-butyl proflavine with DNA. *Biopolymers 11*, 2415−2422.
(41) Qu, J., Shen, Y., Qu, X., and Dong, S. (2004) Electrocatalytic reduction of oxygen at multi-walled carbon nanotubes and cobalt porphyrin modified glassy carbon electrode, *Electroanalysis 16*, 1444−1450.
(42) Ivanov, V. I., Minchenkova, L. E., Schyolkina, A. K., and Poletayev, A. I. (1973) Different conformations of double-stranded nucleic acid in solution as revealed by circular dichroism. *Biopolymers 12*, 89−110.
(43) Yun, B. H., Jeon, S. H., Cho, T.-S., Yi, S. Y., Sehlstedt, U., and Kim, S. K. (1998) Binding mode of porphyrins to poly[d(A-T)$_2$] and poly[d(G-C)$_2$]. *Biophys. Chem. 70*, 1−10.
(44) Bard, A. J., and Faulkner, L. R. (2001) *Electrochemical Methods Fundamentals and Applications*, 2nd ed, John Wiley, New York.

BC060153X

A Comparison of the Emission Efficiency of Four Common Green Fluorescence Dyes after Internalization into Cancer Cells

Yukihiro Hama,[†] Yasuteru Urano,[‡] Yoshinori Koyama,[†] Marcelino Bernardo,[§] Peter L. Choyke,[†] and Hisataka Kobayashi*,[†]

Molecular Imaging Program, Center for Cancer Research, National Cancer Institute, National Institutes of Health, Bethesda, Maryland 20892-1088, Graduate School of Pharmaceutical Sciences, The University of Tokyo, 7-3-1 Hongo, Bunkyo-ku, Tokyo 113-0033, Japan, and Research Technology Program, Science Applications International Corporation (SAIC)-Frederick, Frederick, Maryland 21702 Received June 9, 2006; Revised Manuscript Received August 9, 2006

In vivo optical imaging to enhance the detection of cancer during endoscopy or surgery requires a targeted fluorescent probe with high emission efficiency and high signal-to-background ratio. One strategy to accurately detect cancers is to have the fluorophore internalize within the cancer cells permitting nonbound fluorophores to be washed away or absorbed. The choice of fluorophores for this task must be carefully considered. For depth of penetration, near-infrared probes are ordinarily preferred but suffer from relatively low quantum efficiency. Although green fluorescent protein has been widely used to image tumors on internal organs in mice, green fluorescent probes are better suited for imaging the superficial tissues because of the short penetration distance of green light in tissue and the highly efficient production of signal. While the fluorescence properties of green fluorophores are well-known in vitro, less attention has been paid to their fluorescence once they are internalized within cells. In this study, the emission efficiency after cellular internalization of four common green fluorophores conjugated to avidin (Av−fluorescein, Av−Oregon green, Av−BODIPY-FL, and Av−rhodamine green) were compared after each conjugate was incubated with SHIN3 ovarian cancer cells. Using the lectin binding receptor system, the avidin−fluorophore conjugates were endocytosed, and their fluorescence was evaluated with fluorescence microscopy and flow cytometry. While fluorescein demonstrated the highest signal outside the cell, among the four fluorophores, internalized Av-rhodamine green emitted the most light from SHIN3 ovarian cancer cells both in vitro and in vivo. The internalized Av-rhodamine green complex appeared to localize to the endoplasmic vesicles. Thus, among the four common green fluorescent dyes, rhodamine green is the brightest green fluorescence probe after cellular internalization. This information could have implications for the design of tumor-targeted fluorescent probes that rely on cellular internalization for cancer detection.

INTRODUCTION

In vivo optical imaging during endoscopy or surgery requires targeted fluorescence probes with high signal-to-background ratios to detect cancer on the surface of tissues such as the peritoneum or colon. Although green fluorescent protein has been used to image tumors on internal organs in mice (*1*, *2*), green fluorescent probes are ordinarily used less for in vivo imaging than near-infrared probes because of their short penetration distance within tissue; however, when the surface is being imaged, green fluorophores hold considerable advantages over fluorophores that emit at higher wavelengths due to their higher emission efficiency and the ability to distinguish them from the background autofluorescence. There is a growing list of green fluorophores available for probe development (*3*, *4*). Fluorescein, a well-established bright green fluorescence dye, is approved for human use to perform retinal angiography and therefore has advantages based on its known safety profile in humans (*5*). More recently, three other green fluorescence dyes, Oregon green (OreG), rhodamine green (RhodG), and 4,4-difluoro-4-bora-3*a*,4*a*-diaza-*s*-indacene (BODIPY; BODIPY-FL), have been developed and are commercially available (Figure 1). Each of these has similar emission spectra to that of fluorescein, and it is not immediately clear which of these agents is preferred.

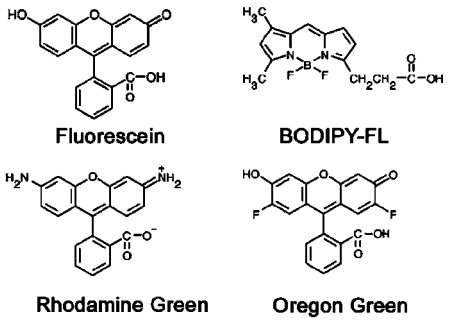

Figure 1. The chemical structures of the four green fluorescence dyes compared in this study.

In theory, one has only to look at the relative brightness of these fluorophores in vitro to determine which is the most desirable from the standpoint of optical probe development. However, it has recently been shown that there are considerable advantages if the fluorophore can be internalized within the cancer cell rather than simply remaining on its surface. For internalizing probes, noninternalized fluorophores are either washed away or absorbed, leading to a very high signal emanating from the cells and negligible background signal. For instance, when avidin-conjugated fluorescein was instilled in the peritoneum of mice bearing implanted ovarian cancers, it was either internalized within the cancers or absorbed through

* Correspondence to: Hisataka Kobayashi, M.D., Ph.D., Molecular Imaging Program, Center for Cancer Research, National Cancer Institute, NIH, Bethesda, MD 20892-1088. Phone 301-435-4086; Fax 301-402-3191. E-mail: Kobayash@mail.nih.gov.

[†] National Cancer Institute.

[‡] The University of Tokyo.

[§] SAIC-Frederick.

10.1021/bc0601626 CCC: $33.50 © 2006 American Chemical Society
Published on Web 10/17/2006

the peritoneum, making it possible to detect submillimeter cancer implants (*6*). The specific uptake of avidin was based on its affinity for asialo-receptors found in abundance on the cell surface of various cancers, especially those which can form metastatic implants in the peritoneal space such as ovarian, colorectal, gastric, and pancreatic cancers (*7*). However, it is uncertain whether the optical properties of fluorophores change in the unique chemical environment of the cell (e.g., acidic pH, oxidation, aggressive proteolysis), and it is possible that the newer dyes might yield greater signal within cancer cells than fluorescein. This could impact the detectability of minute cancer implants at a time when they are most curable. In the present study, we conjugated four widely available green fluorescent dyes to avidin to study them both in vitro and in vivo before and after uptake into ovarian cancer cells and compared their emission efficiency and brightness.

EXPERIMENTAL PROCEDURES

Synthesis of Avidin-Conjugated Green Fluorescence Dyes. Avidin was purchased from Pierce Biochemical, Inc. (Milwaukee, WI); amido-reactive fluorescein, BODIPY (BODIPY-FL), OreG, and RhodG were purchased from Molecular Probes, Inc. (Eugene, OR). At room temperature, 400 μg (5.9 nmol) of avidin in 198 μL of Na_2HPO_4 was incubated with 12 nmol (2 μL/6 mM) of isothiocyanatobenzyl−fluorescein or BODIPY−, OreG−, or RhodG−succinoimidyl ester, respectively, in DMSO for 15 min. The mixture was purified with Sephadex G50 (PD-10; GE Healthcare, Milwaukee, WI). Avidin-conjugated fluorescein, BODIPY, OreGr, and RhodG samples (Av−FITC, Av−BODIPY, Av−OreG, and Av−RhodG, respectively) were kept at 4 °C in the refrigerator as stock solutions.

The protein concentrations of Av−FITC, Av−BODIPY, Av−OreG, and Av−RhodG samples were determined with Coomassie Plus protein assay kit (Pierce Chem Co., Rockford, IL) by measuring the absorption at 595 nm with a UV−vis system (8453 Value UV-Bis system, Agilent Technologies, Palo Alto, CA) using standard solutions of known concentrations of avidin (100, 200, and 400 μg/mL). Then, the concentration of fluorescein, BODIPY, OreG, and RhodG were measured by the absorption at 497, 508, 500, and 503 nm, respectively, with a UV−vis system (8453 Value UV-Bis system, Agilent Technologies, Palo Alto, CA) to confirm the number of fluorophore molecules conjugated with each avidin molecule. By changing the concentration of avidin solution, the number of fluorophore molecules per avidin was adjusted to be approximately 0.8.

Cell Culture. An established ovarian cancer cell line SHIN3 (*8*) was used for in vitro fluorescence microscopy, flow cytometry, and in vivo optical imaging for intraperitoneal disseminated cancer implants. The cell lines were grown in RPMI 1640 medium (Gibco, Gaithersburg, MD) containing 10% fetal bovine serum (FBS) (Gibco, Gaithersburg, MD), 0.03% L-glutamine at 37 °C, 100 units/mL penicillin, and 100 μg/mL streptomycin in 5% CO_2.

Fluorescence Microscopy. SHIN3 cells (1×10^4) were plated on a cover glass bottom culture well and incubated for 16 h. Av−FITC, Av−BODIPY, Av−OreG, or Av−RhodG was added to the medium (30 μg/mL), and the cells were incubated for 1 h. Cells were washed one time with PBS, and fluorescent microscopy was then performed immediately and at 4 and 8 h after washing with PBS. Cells were incubated in RPMI 1640 medium without dyes after wash with PBS. Fluorescence microscopy was performed using an Olympus BX51 microscope (Olympus America Inc., Melville, NY) equipped with the following filters: excitation wavelength 470−490 nm, emission wavelength 515 nm long pass.

Flow Cytometry. One-color flow cytometry was performed for the assessment of fluorescing capability of Av−FITC, Av−BODIPY, Av−OreG, and Av−RhodG in SHIN3 cancer cells. SHIN3 cells (1×10^4) were plated on a 12-chamber culture well and incubated for 16 h. Av−FITC, Av−BODIPY, Av−OreG, or Av−RhodG was added to the medium (30 μg/mL), and the cells were incubated for 96 h. Cells were washed twice with PBS and incubated in RPMI 1640 medium without fluorophores. Cells were washed once with PBS, trypsinized, and flow cytometry was performed immediately and at 24 h after washing with PBS. The argon ion 488 nm laser was employed for excitation. Signals from cells were collected using a 530/30 nm band-pass filter. Cells were analyzed in a FACScan cytometer (Becton Dickinson, Franklin Lakes, NJ), and all data were analyzed using *CellQuest* software (Becton Dickinson, Franklin Lakes, NJ). The fluorescing capability of each fluorophore was referred to as mean fluorescence index (MFI).

Fluorescence Intensity of Four Dyes before Intraperitoneal Injection. To compare the fluorescing capability of the four fluorophore conjugates before intraperitoneal injection, fluorescence intensity and emission spectra of Av−BODIPY, Av−FITC, Av−OreG, and Av−RhodG were measured by the Maestro In-Vivo Imaging System (CRi, Inc., Woburn, MA) in arbitrary units. Av−BODIPY, Av−FITC, Av−OreG, and Av−RhodG (5 μg/390 μL PBS) were put in a nonfluorescent 96-well plate, and spectral fluorescence imaging was performed. The ratio of BODIPY, fluorescein, OreG, or RhodG molecules to avidin molecules was 0.8. To study the fluorescing capability under the acidic condition, 5 μg Av−BODIPY, Av−FITC, Av−OreG, and Av−RhodG were diluted in 390 μL buffer mixture consisting of sodium dihydrogen phosphate and phosphate (pH 3.3). A band-pass filter from 445 to 490 nm and a long-pass filter over 515 nm were used for emission and excitation light, respectively. The tunable filter was automatically stepped in 10 nm increments from 500 to 800 nm, while the camera captured images at each wavelength interval with constant exposure. Spectral unmixing algorithms were applied to create the unmixed image of the four green dyes distinguished from background autofluorescence. A region of interest (ROI) as large as each well was drawn to determine the fluorescence intensity as well as the emission spectra of each of the four dye conjugates in order to exclude a dye that had the emission peak different from the fluorescein peak.

Tumor Model. All procedures were carried out in compliance with the Guide for the Care and Use of Laboratory Animal Resources (1996), National Research Council, and approved by the local Animal Care and Use Committee. The intraperitoneal tumor implants were established by intraperitoneal injection of 2×10^6 cells suspended in 200 μL of PBS in female nude mice (National Cancer Institute Animal Production Facility, Frederick, MD). Experiments with tumor-bearing mice were performed at 14 days after injection of the cells.

In Vivo Spectral Fluorescence Imaging. 50 μg each of Av−BODIPY, Av−FITC, Av−OreG, and Av−RhodG were diluted in 300 μL PBS and injected into the peritoneal cavities of mice with peritoneally disseminated cancer implants. Three hours after injection of each dye, each mouse was sacrificed at a time with carbon dioxide. Immediately after sacrifice, the abdominal cavity was exposed, and the four mice, each with a different fluorophore instilled in the peritoneum, were placed side-by-side on a nonfluorescent plate to compare the fluorescence intensity of tumors simultaneously. Spectral fluorescence images were obtained using the Maestro In-Vivo Imaging System (CRi, Inc., Woburn, MA). Whole abdominal images as well as close-up peritoneal membrane images were obtained. A band-pass filter from 445 to 490 nm and a long-pass filter over 515 nm were used for emission and excitation light, respectively. The tunable filter was automatically stepped in 10 nm increments from 500 to 800 nm, while the camera captured images at each wavelength

interval with constant exposure. The spectral fluorescence images consisting of autofluorescence spectra and a spectrum from each of the four green dyes were obtained and then unmixed on the basis of their spectral patterns using commercial software (*Maestro* software, CRi, Inc., Woburn, MA). The experiment was repeated three times ($n = 3$ mice per fluorophore).

Using the unmixed fluorescence images of the peritoneal membranes, fluorescence intensity of the cancer implants was semiquantitatively compared among the four dyes. An ROI as large as the peritoneal membrane was drawn inside the bowel, and a histogram (number of pixels at specific fluorescence intensity) was created using *ImageJ* software (http://rsb.info.nih.gov/ij/plugins/mri-analysis.html). Then, a threshold was set in the fluorescence intensity above which a pixel is counted. The total number of pixels (N) within the threshold range was calculated at a threshold value of t (eq 1).

$$N_{(t)} = \sum_{i=t}^{\infty} n_{(i)} \quad (1)$$

where i is the fluorescence intensity in arbitrary units, n is the number of pixels at the fluorescence intensity of i, t is the threshold value, and N is the total number of pixels within the threshold range ($i \geq t$). The common logarithm (log) values of N were calculated and plotted as a function of t. The regression line and the correlation coefficient (r) were calculated from these data sets (t and log N) by Microsoft *Excel 2003* (Microsoft, Redmond, WA). For comparison of the fluorescing capability or the "brightness" of each dye, the slopes of the regression line were compared among the four dyes. If the absolute value of r was less than 0.9, then slope values were not included.

RESULTS AND DISCUSSION

Optical Characteristics of Avidin-Conjugated Dyes. To investigate the optical characteristics of Av−BODIPY, Av−FITC, Av−OreG, and Av−RhodG ex vivo, fluorescence intensity and emission spectra were measured under the same conditions: total dose, concentration of the solution, number of fluorophore conjugated per avidin, excitation/emission filters, and exposure time. All four spectra contained an emission peak at a wavelength of 550 nm when stepped in 10 nm increments at pH 7.4 (Figure 2a). The fluorescence intensities of Av−BODIPY, Av−FITC, Av−OreG, and Av−RhodG were 28, 238, 170, and 159 in arbitrary units, respectively (Figure 2b). Thus, ex vivo, the Av−FITC demonstrated the highest signal and the Av−BODIPY the lowest in PBS solution at pH 7.4. When these four dyes were put into the phosphate buffer at pH 3.3, the fluorescence intensities of Av−BODIPY, Av−FITC, Av−OreG, and Av−RhodG were 35, 33, 122, and 199 in arbitrary units, respectively (Figure 2b). That is, when the pH changed from 7.4 to 3.3, the fluorescence intensities of Av−BODIPY and Av−RhodG increased by 25% and 25%, respectively, although BODIPY emitted over $^1/_5$-fold less fluorescence than the other three dyes, when conjugated with avidin. In contrast, Av−FITC and Av−OreG decreased by 86% and 28%, respectively.

Intracellular Av−RhodG Demonstrates Progressive Fluorescence after Internalization. SHIN3 cells were incubated with each of the four fluorophores for 1 h, and fluorescent microscopy was then performed immediately and at 4 and 8 h after washing with PBS (Figure 3). No visual differences were seen among the different fluorophores at any of these time points except for the 8 h image obtained using Av-RhodG, which showed very bright fluorescent dots within the cytoplasm and was so intense that exposure times were halved to create the image to avoid overwhelming the dynamic range of the camera (Figure 3). The images also revealed that the Av−RhodG was clearly internalized within the endoplasmic vesicles within the cytoplasm. These data suggest that Av−RhodG behaves differently than the other three dyes regarding fluorescent intensity and the stability within the cells.

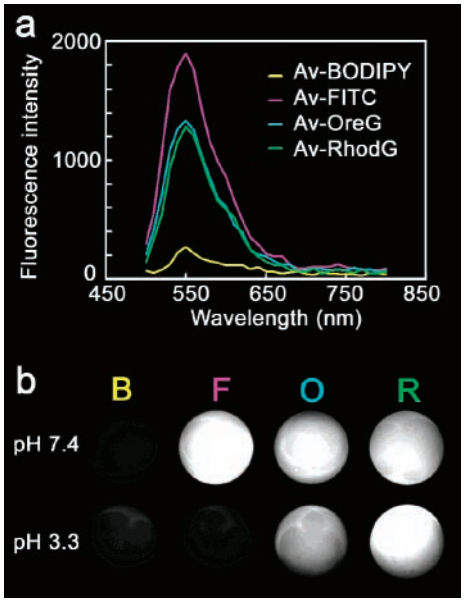

Figure 2. Optical characteristics of avidin-conjugated BODIPY, FITC, OreG, and RhodG. 5 μg Av−BODIPY, Av−FITC, Av−OreG, or Av−RhodG in 390 μL PBS (pH 7.4) or the mixture of sodium dihydrogen phosphate and phosphate (pH 3.3) were placed in a nonfluorescent 96-well plate and spectral fluorescence image was obtained. The ratio of BODIPY, FITC, OreG, or RhodG molecules to avidin was 0.8 in all cases. (a) Emission spectra. All four dyes had the same emission peak at a wavelength of 550 nm, but the fluorescence intensity was different, with Av−FITC the highest, followed by Av−OreG, Av−RhodG, and Av−BODIPY. (b) Fluorescence intensities of Av−BODIPY (B), Av−FITC (F), Av−OreG (O), and Av−RhodG (R) were 28, 238, 170, and 159, respectively, in arbitrary units (a.u.), with Av−FITC the highest and Av−BODIPY the lowest under pH 7.4. However, under the acidic condition (pH 3.3), fluorescence intensities of Av−BODIPY, Av−FITC, Av−OreG, and Av−RhodG were 35, 33, 122, and 199 (a.u.), respectively, with Av−FITC the lowest and Av−RhodG the highest.

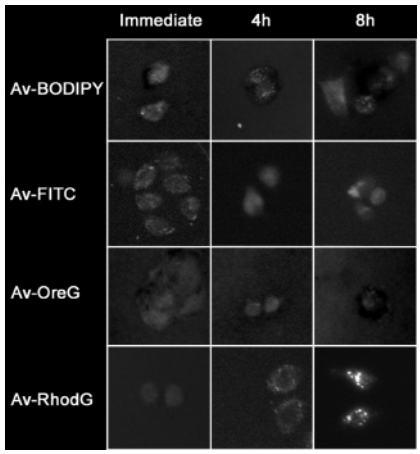

Figure 3. Serial fluorescence microscopy images of SHIN3 ovarian cancer cells. SHIN3 cells were incubated with each of the four fluorophores for 1 h, and fluorescent microscopy was then performed immediately and at 4 and 8 h after washing with PBS. Av−RhodG showed that the size of intracellular fluorescent dots as well as the fluorescence intensity progressively increased with time, while the other three dyes showed a minimal change. Original magnification: 200× Photographic exposure times: Av−BODIPY, Av−FITC, and Av−OreG (immediate, 4 h, and 8 h) = 2 s; Av−RhodG (immediate and 4 h) = 2 s; Av−RhodG (8 h) = 1 s.

Intracellular Av−RhodG Demonstrates Significantly Higher Fluorescence on FACS than Other Fluorophores. After 96

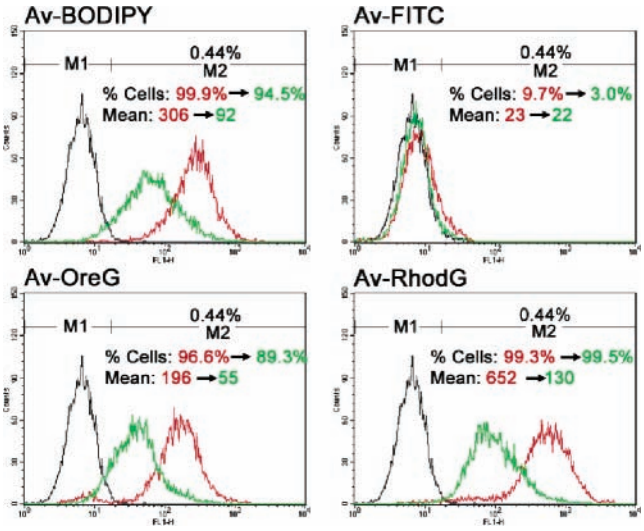

Figure 4. Histograms for flow cytometric analysis of SHIN3 cancer cells immediately (red) and at 24 h (green) after washout of each of the four green dyes as well as the control SHIN3 cells without treatment with dye (black). Samples with Av−BODIPY, Av−OreG, and Av−RhodG showed a significant rightward shift both immediately and at 24 h after washing dyes compared with the untreated control samples. Av−RhodG demonstrated the highest fluorescence both immediately (MFI 652) and 24 h after (MFI 130) washing. The percent cells in M2 increased from 0.44% to 99.9% for Av−BODIPY, 96.6% for Av−OreG, and 99.3% for Av−RhodG after 96 h incubation with each of the four dyes. Av−FITC did not show a significant rightward shift with percent cells in M2 from 0.44% to 9.7%.

h incubation with each of the fluorophores, flow cytometry was performed immediately and 24 h following washing on SHIN3 cells. Immediately after washing, Av−BODIPY, Av−OreG, and Av−RhodG showed a significant shift (>one order shift) as compared with unstained SHIN3 control cells (Figure 4). Among the four agents, Av−RhodG showed significantly higher mean fluorescence intensity (MFI) despite suboptimal excitation wavelength for Av−RhodG ($p < 0.001$). However, Av−FITC demonstrated minimal rightward shift (from 0.4% to 9.7%), and the MFI did not increase significantly. The cells were evaluated 24 h later for MFI, and Av−RhodG still demonstrated the highest fluorescence among the four fluorophores.

Av-RhodG Demonstrated the Highest Fluorescence on in Vivo Spectral Fluorescence Imaging. Three hours after intraperitoneal injection of 50 μg Av−BODIPY, Av−FITC, Av−OreG, and Av−RhodG, spectral fluorescence images of the whole abdominal cavity as well as close-up images of the peritoneal membranes were obtained by placing four mice, each with a different fluorophore, side by side on a nonfluorescent plate. Using spectral unmixing algorithm, the fluorescence signals of tumors were clearly distinguished from the autofluorescence from the intestine and the other organs. Unmixed images of the peritoneal cavities demonstrated that Av−BODIPY, Av−OreG, and Av−RhodG depicted the tumor foci; however, Av−FITC failed to visualize the tumors due to the insufficient fluorescence intensity compared to the other fluorophores at the same exposure times (Figure 5). Unmixed images of the peritoneal membranes clearly visualized lesions as small as 1 mm in diameter in all mice (Figure 5). However, the fluorescence intensity of Av−RhodG was the highest and that of Av−FITC was the lowest of all when compared visually.

To make an objective comparison of fluorescence intensity of the peritoneal implants among the four dyes, an ROI encompassing the peritoneal membrane was drawn inside the intestine using the unmixed green fluorescence image (Figure 6a), and a histogram depicting the distribution of pixel intensities was created (Figure 6b). The dynamic range of signal intensity

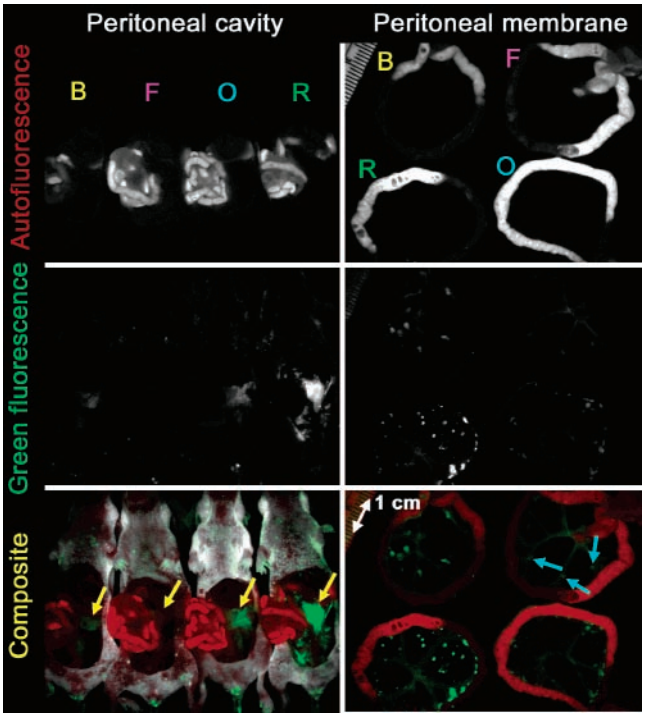

Figure 5. In vivo spectral fluorescence images of tumor-bearing mice 3 h after intraperitoneal injection with Av−BODIPY (B), Av−FITC (F), Av−OreG (O), and Av−RhodG (R). Upper: Autofluorescence image. Middle: Green dye fluorescence image. Lower: Composite image (red, autofluorescence; green, green dye fluorescence). Spectral fluorescence image of the peritoneal cavities clearly visualized the disseminated tumor foci (yellow arrows) in mice incubated with Av−BODIPY, Av−OreG, or Av−RhodG; whereas Av−FITC failed to visualize tumor foci (yellow arrow) due to insufficient fluorescence intensity. Close-up image of the peritoneal membranes demonstrates peritoneal implants histologically confirmed to be metastatic deposits as small as 1 mm in diameter in all mice including Av−FITC injected mouse (blue arrows). The fluorescence intensity of Av−RhodG was the highest, and that of Av−FITC was the lowest of all when compared visually.

in the unmixed fluorescence image was set from 1 to 256 in arbitrary units (a.u.), and the threshold value (t) was changed from 41 to 241 in increments of 10, because the background signals, such as the normal peritoneal membrane excluding tumors and the nonfluorescent plate, were mostly less than 40 (a.u.). Then, the total number of pixels (N) within the threshold range was calculated as a function of threshold (t), and a regression line was calculated in each ROI (Figure 6c). The correlation coefficients of Av−BODIPY, Av−FITC, Av−OreG, and Av−RhodG were −0.982, −0.989, −0.989, and −0.965, respectively. The slopes of Av−BODIPY, Av−FITC, Av−OreG, and Av−RhodG were −0.022, −0.056, −0.028, and −0.006, respectively. These results indicate that internalized Av−RhodG not only had the highest fluorescence, but above a specific threshold, only Av−RhodG was capable of detecting tumors. Among the other fluorophore, Av−FITC had the lowest internalized fluorescence, and Av−BODIPY and Av−OreG had intermediate fluorescence in vivo. Contrary to the preinjection fluorescence intensity, where Av−FITC was the highest (Figure 2), internalized Av−RhodG demonstrated much higher fluorescence than Av−FITC in vivo indicating that the two agents had changed fluorescence properties after internalization. With the use of Av−RhodG, submillimeter SHIN3 ovarian cancer implants on the perioneum were depicted with intense green fluorescence, which was able to overwhelm the background autofluorescence and visualize tiny tumors in close-up views without the use of the wavelength-resolved spectral imaging technique (Figure 7). On the basis of these in vitro and in vivo

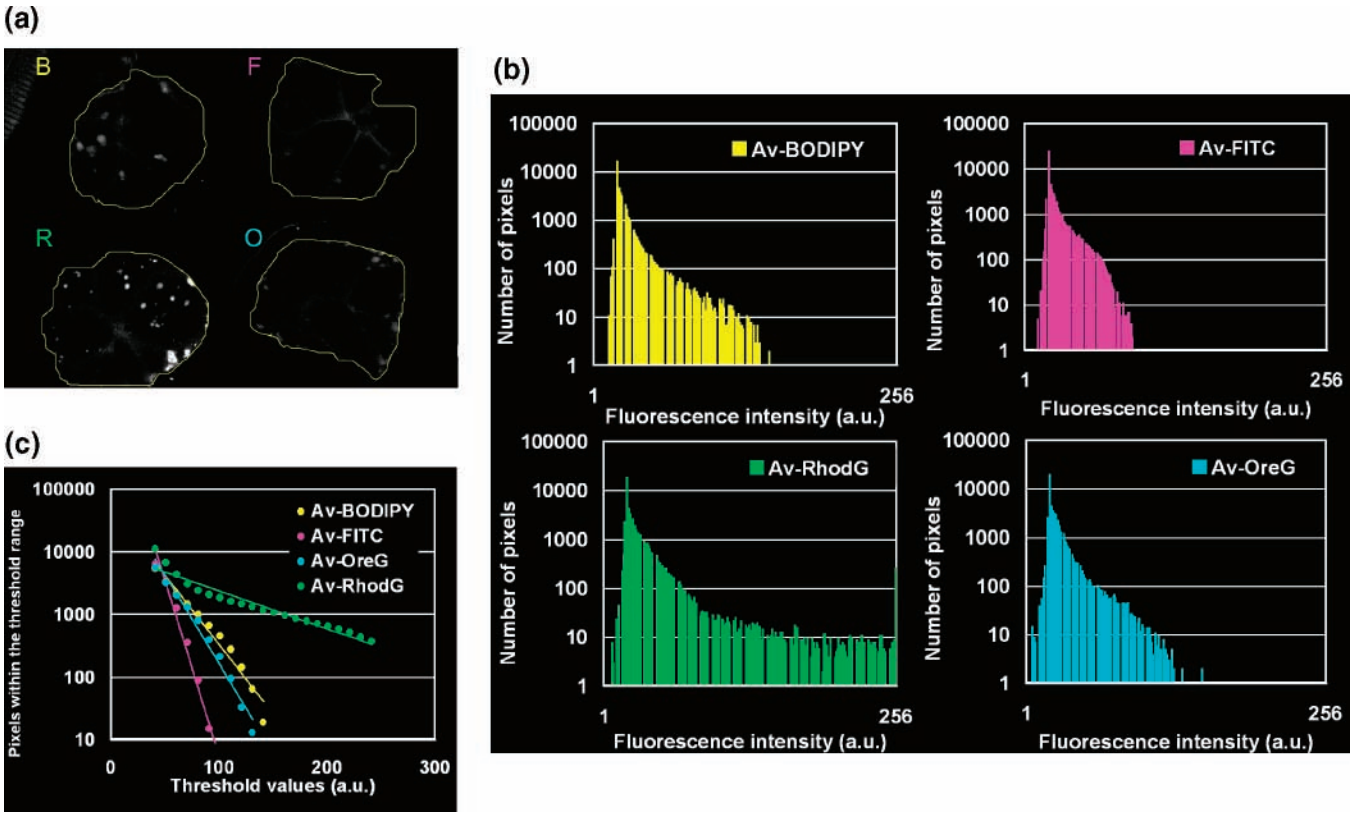

Figure 6. Semiquantitative assessment of in vivo fluorescence intensity. (a) ROI was drawn inside the intestine on the unmixed green fluorescence image (the same image as the unmixed green fluorescence image of Figure 5). B: Av−BODIPY. F: Av−FITC. O: Av−OreG. R: RhodG. (b) Histogram of fluorescence intensity of an ROI drawn on each of the peritoneal membranes instilled with 4 green dyes, Av−BODIPY, Av−FITC, Av−OreG, and RhodG. The dynamic range of the fluorescence intensity was split into 256 equal-sized bins (1−256). Then, for each bin (horizontal axis), the number of pixels from the data set that fall into each bin (vertical axis) are counted. The shape of the plot distribution ≤40 in arbitrary unit (a.u.) is almost the same among the 4 histograms. (c) Regression lines of 4 green dyes. The regression lines were calculated from the data sets (fluorescence threshold values 41−241, total number of pixels within the threshold rage 10−100 000 in common logarithm). The slopes of Av−BODIPY, Av−FITC, Av−OreG, and Av−RhodG were −0.022, −0.056, −0.028, and −0.006, respectively. Av−RhodG has the highest slope value, consistent with it being the brightest fluorophore, whereas Av−FITC had the lowest slope value, and Av−BODIPY and Av−OreG were intermediate.

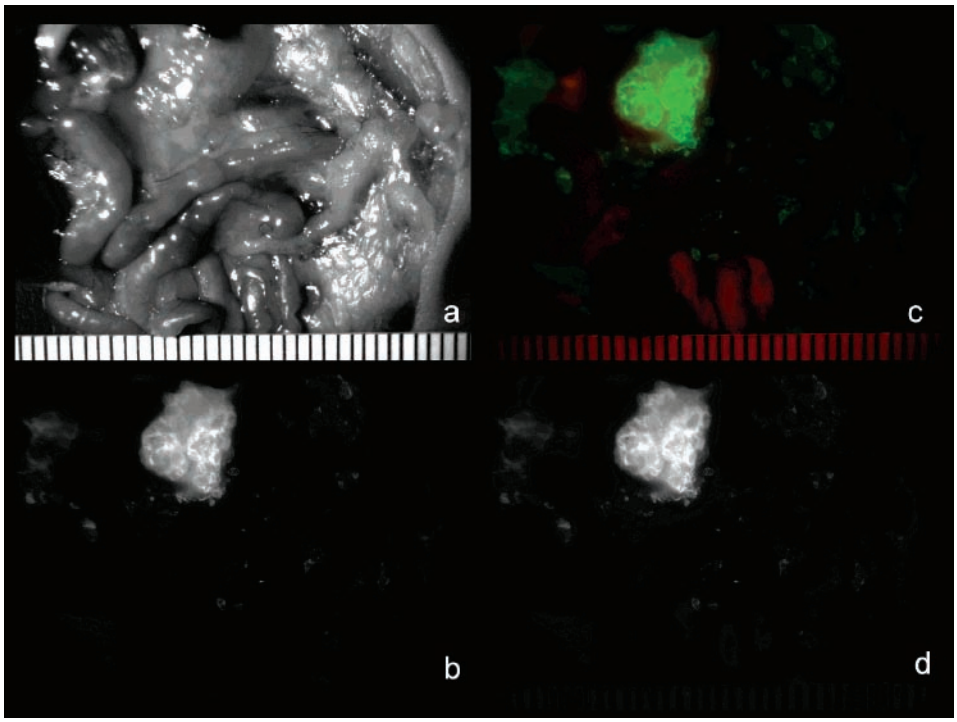

Figure 7. In vivo spectral fluorescence close-up images of a peritoneally disseminated SHIN3 ovarian cancer-bearing mouse 6 h after intraperitoneal injection with Av−RhodG. A white light image (a), a green fluorescence image (b), a composite image of green fluorescence (green) and autofluorescence (red) (c), and an uncalculated image obtained with a 545−555 nm band-pass filter. Strong green florescence derived from Av−RhodG allow visualization of SHIN3 ovarian cancer submillimeter implants in an uncalculated image taken with a 545−555 nm band-pass filter without the use of the wavelength-resolved technique (d) as well as in a spectrally calculated green fluorescence image (b).

results, Av−RhodG was considered the most compelling choice for a cellular targeting optical probe.

When the fluorescent dyes are conjugated with proteins, it is well-known that fluorescence emission of each dye is generally altered differently in each combination of dyes and proteins. Additionally, this study demonstrated that the in vivo characteristics of fluorophores, once internalized within cells, could be very different from their extracellular behavior. When four green dyes were conjugated with avidin, Av−BODIPY had the lowest signal intensity in the solution at physiological pH and remained low at acidic pH. Av−FITC, which clearly had the highest signal intensity in the solution at physiological pH, demonstrated minimal fluorescence once it was internalized, probably because of acidic pH in the endoplasmic vessicles. Conversely, Av−RhodG, which had modest fluorescence extracellularly, remain unchanged or even progressively increased in fluorescence once it had been internalized. Thus, in designing optical fluorescence probes, it is important to consider whether the agent will end up intracellular or will remain in the extracellular environment.

On the basis of its biocompatibility and efficacy, fluorescein is the most feasible green dye for clinical translation, since it has been used in clinical practice for the past three decades (*9*, *10*). Fluorescein emits in the green wavelength (fluorescence emission maximum around 520 nm) at physiological pH. However, fluorescein is known to decrease its emission signal at lower pH (*11*, *12*). Thus, when SHIN3 cancer cells were targeted by an avidin conjugate (or another targeting ligand) conjugated to a fluorophore, the agent was internalized and catabolized. The low pH conditions found within the endosome and lysosome might rapidly compromise the signal of the fluorescein, especially when we utilize a quickly internalizing ligand−receptor system such as the avidin−lectin system. The other three dyes, BODIPY, OreG, and RhodG, have been reported to emit photons in a less pH-independent fashion than fluorescein. Therefore, we hypothesized that, if pH-independent alternative dyes were used instead of pH-dependent fluorescein, we could achieve better targeting of the cancer due to the stronger signals from internalized reagents in cancer cells.

Non-FITC green fluorescent dyes were designed to resist the photobleaching associated with the fluorescein dyes (*13*, *14*). Since fluorescein is sensitive to photobleaching, RhodG and BODIPY-FL were synthesized as photobleaching-resistant alternatives to fluorescein. However, to the best of our knowledge, the changes in fluorescence in vivo and their comprehensive comparison among green fluorophores in response to internalization have not been reported. In our results, RhodG is the most suitable dye to be conjugated with quickly internalizing receptor ligands or antibodies such as avidin or trastuzumab (Herceptin) (*15*), although the exact reason why Av−RhodG was brighter than Av−OreG or Av−BODIPY-FL in the endoplasmic vesicles is still unknown.

The rate at which Av−fluorophore complexes, such as Av−RhodG, are internalized and catabolized can be determined by examining the combined fluorescence of these agents. In theory, such agents could be used to measure internalization rates, and the effect of various drugs and interventions on internalization could be measured using fluorescence to monitor the process (*16*, *17*).

CONCLUSION

Whereas Av−FITC demonstrated the brightest fluorescence in vitro, once the fluorophores were internalized, Av−RhodG demonstrated the brightest fluorescence. Chemical change in the fluorophores induced by the low pH of the lysosome/endosome is one of the likely reasons. Therefore, RhodG is a suitable fluorescence dye for internalized in vivo spectral fluorescence imaging to detect cancer.

ACKNOWLEDGMENT

This research was supported by the Intramural Research Program of the NIH, National Cancer Institute, Center for Cancer Research, and funded in part with federal funds from the National Cancer Institute, National Institutes of Health, under contract N01-CO-12400. The content of this publication does not necessarily reflect the views or policies of the Department of Health and Human Services, nor does mention of trade names, commercial products, or organizations imply endorsement by the U.S. Government.

LITERATURE CITED

(1) Yang, M., Baranov, E., Jiang, P., Sun, F. X., Li, X. M., Li, L., Hasegawa, S., Bouvet, M., Al-Tuwaijri, M., Chishima, T., Shimada, H., Moossa, A. R., Penman, S., and Hoffman, R. M. (2000) Whole-body optical imaging of green fluorescent protein-expressing tumors and metastases. *Proc. Natl. Acad. Sci. U.S.A. 97*, 1206−1211.

(2) Hoffman, R. M. (2005) The multiple uses of fluorescent proteins to visualize cancer in vivo. *Nat. Rev. Cancer 5*, 796−806.

(3) Bremer, C., Ntziachristos, V., and Weissleder, R. (2003) Optical-based molecular imaging: contrast agents and potential medical applications. *Eur. Radiol. 13*, 231−243.

(4) Ntziachristos, V., Bremer, C., and Weissleder, R. (2003) Fluorescence imaging with near-infrared light: new technological advances that enable in vivo molecular imaging. *Eur. Radiol. 13*, 195−208.

(5) Ciardella, A. P., Prall, F. R., Borodoker, N., and Cunningham, E. T., Jr. (2004) Imaging techniques for posterior uveitis. *Curr. Opin. Ophthalmol. 15*, 519−30.

(6) Hama, Y., Urano, Y., Koyama, Y., Kamiya, M., Bernardo, M., Paik, R. S., Krishna, M. C., Choyke, P. L., and Kobayashi, H. (2006) In vivo spectral fluorescence imaging of submillimeter peritoneal cancer implants using a lectin-targeted optical agent. *Neoplasia 8*, 607−612.

(7) Hama, Y., Urano, Y., Koyama, Y., Choyke, P. L., and Kobayashi, H. (2006) Targeted optical imaging of cancer cells using lectin-binding BODIPY conjugated avidin. *Biochem. Biophys. Res. Commun. 348*, 807−813.

(8) Imai, S., Kiyozuka, Y., Maeda, H., Noda, T., and Hosick, H. L. (1990) Establishment and characterization of a human ovarian serous cystadenocarcinoma cell line that produces the tumor markers CA-125 and tissue polypeptide antigen. *Oncology 47*, 177−184.

(9) Brancato, R., and Trabucchi, G. (1998) Fluorescein and indocyanine green angiography in vascular chorioretinal diseases. *Semin. Ophthalmol. 13*, 189−198.

(10) Kelley, J. S. (1977) Fluorescein angiography: techniques and toxicity. *Int. Ophthalmol. Clin. 17*, 25−33.

(11) Chen, Y., and Arriaga, E. A. (2006) Individual acidic organelle pH measurements by capillary electrophoresis. *Anal. Chem. 78*, 820−826.

(12) Sklar, L. A., Jesaitis, A. J., Painter, R. G., and Cochrane, C. G. (1982) Ligand/receptor internalization: a spectroscopic analysis and a comparison of ligand binding, cellular response, and internalization by human neutrophils. *J. Cell. Biochem. 20*, 193−202.

(13) Lichtman, J. W., and Conchello, J. A. (2005) Fluorescence microscopy. *Nat. Methods 2*, 910−919.

(14) Terasaki, M. (1989) Fluorescent labeling of endoplasmic reticulum. *Methods Cell. Biol. 29*, 125−135.

(15) Coussens, L., Yang-Feng, T. L., Liao, Y. C., Chen, E., Gray, A., McGrath, J., Seeburg, P. H., Libermann, T. A., Schlessinger, J., Francke, U., Levinson, A., and Ullrich, A. (1985) Tyrosine kinase receptor with extensive homology to EGF receptor shares chromosomal location with neu oncogene. *Science 230*, 1132−1139.

(16) Padari, K., Saalik, P., Hansen, M., Koppel, K., Raid, R., Langel, U., and Pooga, M. (2005) Cell transduction pathways of transportans. *Bioconjugate Chem. 16*, 1399−13410.

(17) Marecos, E., Weissleder, R., and Bogdanov, A., Jr. (1998) Antibody-mediated versus nontargeted delivery in a human small cell lung carcinoma model. *Bioconjugate Chem. 9*, 184−191.

BC0601626

Enzymatic Activation of Second-Generation Dendritic Prodrugs: Conjugation of Self-Immolative Dendrimers with Poly(ethylene glycol) via Click Chemistry

Anna Gopin,[†] Sharon Ebner,[‡] Bernard Attali,[‡] and Doron Shabat[†,*]

School of Chemistry, Raymond and Beverly Sackler Faculty of Exact Sciences, and Department of Physiology and Pharmacology, Sackler Faculty of Medical Sciences, Tel-Aviv University, Tel Aviv 69978 Israel. Received June 26, 2006; Revised Manuscript Received September 21, 2006

Single-triggered disassemble dendrimers were recently developed and introduced as a potential platform for a multi-prodrug. These unique structural dendrimers can release all of their tail units through a self-immolative chain fragmentation initiated by a single cleavage at the dendrimer's core. There are several examples for the bioactivation of first-generation self-immolative dendritic prodrugs. However, enzymatic activation failed for second-generation self-immolative dendrimers. The hydrophobic large molecular structure of the dendritic prodrugs results in aggregation under aqueous conditions and prevented the enzyme from reaching the triggering substrate. Here we show a simple solution for the enzymatic activation of second-generation self-immolative dendrimers. Poly(ethylene glycol) (PEG) was conjugated to the dendritic platform via click chemistry. The poly(ethylene glycol) tails significantly decreased the hydrophobic properties of the dendrimers and thereby prevented aggregate formation. We designed and synthesized a dendritic prodrug with four molecules of the anticancer agent camptothecin and a trigger that can be activated by penicillin-G-amidase. The PEG5000-conjugated, self-immolative dendritic prodrug was effectively activated by penicillin-G-amidase under physiological conditions and free camptothecin was released to the reaction media. Cell-growth inhibition assays demonstrated increased toxicity of the dendritic prodrug upon incubation with the enzyme.

INTRODUCTION

Recently, three groups, almost simultaneously, reported the design and synthesis of novel dendritic structures. These dendrimers include a trigger that initiates the fragmentation of the molecule in a self-immolative manner with the consequent release of the tail-high-group units (*1*−*3*). All three groups exploited the fact that the dendrimer skeleton can be constructed in such a way that it will disintegrate into known molecular fragments once the disintegration process has been initiated. These unique structural dendrimers can release all of their tail units through a domino-like chain fragmentation, initiated by a single cleavage at the dendrimer's core (*4*). Incorporation of drug molecules as the tail units and use of an enzyme substrate as the trigger generates a multi-prodrug unit that is activated with a single enzymatic cleavage. We have shown significant advantage in tumoral cell-growth inhibition by our single-triggered dendritic prodrugs in comparison with classic monomeric prodrugs (*5*, *6*). In another report, we designed and synthesized fully biodegradable dendrimers that disassemble through multienzymatic triggering followed by self-immolative chain fragmentation (*7*). A practical application for such multitriggered self-immolative dendrons was recently demonstrated by the concept of prodrug activation through a molecular OR logic trigger (*8*).

Two options for the triggering/activation of self-immolative dendrimers were proposed. One approach is based on chemical triggering whereas the other is based on enzymatic bioactivation. While chemical activation of first and second generation self-immolative dendrimers was achieved by all three groups, only ours successfully demonstrated the enzymatic approach with incorporation of substrate triggers for catalytic antibody 38C2 (*9*−*11*) and penicillin-G-amidase (*12*) (PGA). However, when second-generation self-immolative dendrimer were tested for enzymatic activation, no fragmentation was observed at all. We assumed that the hydrophobic structure of the dendritic prodrugs generates aggregation under aqueous conditions, which prevented the enzyme from accessing the triggering substrate (*13*). Here we report a simple solution to this problem. Enzymatic activation of second-generation self-immolative dendrimers was achieved through conjugation of poly(ethylene glycol) (PEG) to the dendritic platform via click chemistry. The PEG tails significantly decreased the hydrophobicity of the dendrimers and thereby prevented aggregate formation.

EXPERIMENTAL PROCEDURES

General. All reactions requiring anhydrous conditions were performed under argon or N_2 atmosphere. Chemicals and solvents were either A.R. grade or purified by standard techniques. Thin layer chromatography (TLC): silica gel plates Merck 60 F_{254}; compounds were visualized by irradiation with UV light and/or by treatment with a solution of 25 g phosphomolybdic acid, 10 g $Ce(SO_4)_2{\cdot}H_2O$, 60 mL concd H_2SO_4, and 940 mL H_2O, followed by heating. Flash chromatography (FC): silica gel Merck 60 (particle size 0.040−0.063 mm), eluent given in parentheses. ^{1}H NMR: Bruker AMX 200 or 400. The chemical shifts are expressed in δ relative to TMS (δ = 0 ppm) and the coupling constants J in hertz. The spectra

* Corresponding author. Tel: +972 (0) 3 640 8340. Fax: +972 (0) 3 640 9293. E-mail: chdoron@post.tau.ac.il.

† School of Chemistry.

‡ Department of Physiology and Pharmacology.

[1] Abbreviations. ACN, acetonitrile; Boc, *tert*-butoxycarbonyl; DCM, dichloromethane; DIPEA, diisopropylethyleneamine; DMAP, dimethylaminopyridine; DMF, dimethylformamide; EDC, *N*-(3-dimethylaminopropyl)-*N*′-ethylcarbodiimide; EtOAc, ethyl acetate; He, hexanes; HOBT, 1-hydroxybenzotriazole; NHS, *N*-hydroxysuccinimide; PEG, poly(ethylene glycol); PNP, *p*-nitrophenol; t_R, retention time; TBSCl, *tert*-butyldimethylsilyl chloride; TBTA, tris(1-benzyl-1*H*-[1,2,3]triazol-4-ylmethyl)amine; TFA, trifluoroacetic acid; THF, tetrahydrofuran.

10.1021/bc060180n CCC: $33.50 © 2006 American Chemical Society
Published on Web 10/17/2006

were recorded in $CDCl_3$ or CD_3OD as a solvent at room temp. All reagents, including salts and solvents, were purchased from Sigma-Aldrich. PEG_{400}-azide was received from Polypure (Norway). TBTA was received from the Sharpless laboratory (Scripps, La Jolla).

Compound 2. Commercially available 4-hydroxybenzoic acid (2.0 g, 14.5 mmol) was dissolved in DMF. Then EDC (3.3 g, 17.4 mmol), HOBT (1.0 g, 7.3 mmol), and propargyl amine (1.0 mL, 14.5 mmol) were added. The mixture was stirred overnight and monitored by TLC (EtOAc:He = 2:3). After completion of the reaction, the solvent was removed under reduced pressure. The crude product was purified by column chromatography on silica gel (EtOAc:He = 2:3) to give compound **2 (**1.8 g, 70%) in the form of yellowish oil.

^{1}H NMR (200 MHz, $CDCl_3$) δ = 7.70 (2H, d, J = 6.8 Hz); 6.81 (2H, d, J = 6.8); 4.11 (2H, d, J = 2.5); 2.71 (1H, t, J = 2.5). ^{13}C (400 MHz, $CDCl_3$) δ = 167.9, 160.6, 128.8, 124.4, 114.5, 79.5, 70.3, 28.3. MS (FAB): calculated for $C_{10}H_9NO_2$ 176.0 [M + H $^+$], found 176.0.

Compound 3. To a cool 12% NaOH (12 mL) compound **2** (1.8 g, 10.2 mmol) was added while being cooled to 0 °C. Formaldehyde 37% in water (10 mL) was added. The reaction was stirred at 55 °C for 3 days and monitored by TLC (EtOAc: MeOH = 95:5). After completion the reaction was diluted with EtOAc and washed with ammonium chloride saturated solution. The aqueous layer was washed twice with EtOAc. The combined organic layer was dried over magnesium sulfate and the solvent was removed under reduced pressure. The crude product was purified by column chromatography on silica gel (EtOAc: MeOH = 95:5) to give compound **3 (**1.9 gr, 80%) in the form of a white solid.

^{1}H NMR (200 MHz, CD_3OD) δ = 7.80 (2H, s); 4.91 (4H, s); 4.26 (2H, d, J = 2.5); 2.70 (1H, t, J = 2.5). ^{13}C (400 MHz, CD_3OD) δ = 168.1, 156.7, 126.8, 126.0, 124.4, 79.4, 70.2, 60.3, 28.3. MS (FAB): calculated for $C_{12}H_{13}NO_4$ 236.0 [M + H $^+$], found 236.0.

Compound 4. Compound **3** (713 mg, 3.0 mmol) was dissolved in DMF and cooled to 0 °C. Imidazole (408 mg, 6.0 mmol) and TBSCl (910 mg, 6.0 mmol) were added. The reaction was stirred at room temp for 2 h and monitored by TLC (EtOAc: He = 2:8). After completion, the reaction was diluted with ether and washed with ammonium chloride saturated solution. The organic layer was dried over magnesium sulfate, and the solvent was removed under reduced pressure. The crude product was purified by column chromatography on silica gel (EtOAc:He = 15:85) to give compound **4 (**1.12 g, 80%) in the form of a colorless oil.

^{1}H NMR (400 MHz, $CDCl_3$) δ = 7.57 (2H, s); 4.87 (4H, s); 4.23 (2H, dd, J = 2.5, J = 2.6); 2.17 (1H, t, J = 2.5); 0.95 (18H, s); 0.13 (12H, s). ^{13}C (400 MHz, $CDCl_3$) δ = 166.7, 156.4, 126.1, 124.5, 79.6, 71.7, 62.7, 29.6, 25.8, 25.6, 18.2, −5.5. MS (FAB): calculated for $C_{24}H_{41}NO_4Si_2$ 464.2 [M + H $^+$], found 464.2.

Compound 5. Compound **4** (1.12 g, 2.4 mmol) was dissolved in dry THF, Et_3N (1.0 mL, 7.2 mmol) was added, and the mixture was cooled to 0 °C. Then, *p*-nitrophenyl chloroformate (581 mg, 2.9 mmol) dissolved in dry THF (10 mL) was added dropwise, and the reaction was stirred for 1 h at room temp and monitored by TLC (EtOAc:He = 2:8). After completion, the reaction was filtered, the solvent was evaporated, and the crude product was purified by column chromatography on silica gel (EtOAc:He = 15:85) to give compound **5 (**1.35 g, 90%) in the form of a colorless oil.

^{1}H NMR (200 MHz, $CDCl_3$) δ = 8.43 (2H, d, J = 8.1); 8.02 (2H, s); 7.63 (2H, d, J = 8.1); 7.01 (1H, m); 4.91 (4H, s); 4.38 (2H, dd, J = 2.5, J = 2.6); 2.41 (1H, t, J = 2.5); 1.08 (18H, s); 0.29 (12H, s). ^{13}C (400 MHz, $CDCl_3$) δ = 166.4, 155.2, 149.4, 147.7, 145.5, 133.9, 132.2, 126.3, 125.3, 121.5, 79.2, 71.8, 60.3, 31.5, 25.8, 18.2, −5.5. HRMS (MALDI-TOF): calculated for $C_{31}H_{44}N_2O_8Si_2$ 651.2528 [M + Na^+], found 651.2562.

Compound 6. Compound **5** (1.5 g, 2.3 mmol) was dissolved in DMF. Mono-Boc-N,N′-dimethylethylenediamine (541 mg, 2.9 mmol) was added. The reaction was stirred at room temperature for 1 h and monitored by TLC (EtOAc:He = 1:1). After completion, the solvent was removed under reduced pressure and the crude product was purified by column chromatography on silica gel (EtOAc:He = 2:8) to give compound **6** (1.45 g, 90%) in the form of a colorless oil.

^{1}H NMR (400 MHz, $CDCl_3$) δ = 7.79 (2H, s); 6.32 (1H, m); 4.68−4.67 (4H, m); 4.27−4.25 (2H, m); 3.61−3.43 (4H, m); 3.24 (2H, s); 3.12 (1H, s); 2.96 (3H, s); 2.32 (1H, bs); 1.51−1.46 (9H, m); 0.92 (18H, s); 0.08 (12H, s). ^{13}C (400 MHz, $CDCl_3$) δ = 167.2, 153.1, 153.0, 134.6, 130.8, 125.1, 80.2, 78.8, 72.0, 59.9, 46.4, 46.1, 36.4, 35.9, 35.1, 29.8, 28.3, 25.7, 18.2, −5.5. MS (FAB): calculated for $C_{34}H_{59}N_3O_7Si_2$ 700.4 [M + Na $^+$], found 700.3.

Compound 7. Compound **6** (1.5 g, 2.2 mmol) was dissolved in 10 mL of methanol, and amberlist 15 was added. The reaction was stirred at room temperature for 2 h and monitored by TLC (EtOAc:MeOH = 95:5). After completion, the amberlist was filtered out and the solvent was removed under reduced pressure. The crude product was purified by column chromatography on silica gel (EtOAc:MeOH = 95:5) to give compound **7 (**500 mg, 56%) in the form of a white solid.

^{1}H NMR (200 MHz, CD_3OD) δ = 7.78 (2H, s); 4.57 (4H, bs); 4.25−4.23 (2H, m); 3.6−3.4 (4H, m); 3.2 (2H, s); 3.1 (1H, s); 2.96 (3H, s); 2.40 (1H, bs); 1.59−1.54 (9H, m). ^{13}C (400 MHz, CD_3OD) δ = 169.8, 158.9, 157.5, 152.1, 134.1, 130.3, 130.0, 83.2, 83.0, 74.4, 62.5, 50.3, 49.0, 38.7, 37.9, 37.6, 31.3. HRMS (MALDI-TOF): calculated for $C_{22}H_{31}N_3O_7$ 472.2015 [M + Na^+], found 472.2059.

Compound 8. Triphosgen (57 mg, 2 mmol) was dissolved in 10 mL of dry THF and was cooled to 0 °C. A mixture of *p*-nitroaniline (614 mg, 4.5 mmol) and Et_3N (622 μL, 4.5 mmol) dissolved in 20 mL dry THF was added dropwise. The reaction was stirred for 20 min, and afterward a mixture of compound **7** (400 mg, 0.9 mmol) and DMAP (274 mg, 2.3 mmol) in dry THF was added dropwise. The reaction was stirred at room temperature overnight and monitored by TLC (EtOAc:He = 1:1). After completion, the mixture was diluted with EtOAc and was washed with 1 M HCl. The organic layer was dried over magnesium sulfate, and the solvent was removed under reduced pressure. Then, the crude product was dissolved in a small amount of DCM and filtered. The filtrate was concentrated, and the product was purified by column chromatography to give compound **8** (478 mg, 68%) in the form of a yellow solid.

^{1}H NMR (400 MHz, $CDCl_3$) δ = 8.11 ppm (4H, d, J = 9 Hz); 7.9 (2H, s); 7.61 (4H, d, J = 9); 5.2 (4H, bs); 4.13 (2H, s); 3.66−3.64 (1H, m); 3.4−3.2 (4H, m); 3.2 (2H, s); 3.1 (1H, s); 2.96 (3H, s); 2.46 (1H, bs); 1.37 (9H, s). ^{13}C NMR (400 MHz, $CDCl_3$) δ = 166.2; 156.4; 155.9; 153.8; 153.5; 144.6; 142.5; 131.2; 130.2; 129.9; 129.8; 124.9; 117.8; 80.6; 79.2; 71.7; 61.6; 46.6; 45.5; 34.3; 34.0; 29.6; 28.3. HRMS (MALDI-TOF): calculated for $C_{36}H_{39}N_7O_{13}$ [M + Na^+] 800.2498; found 800.2454.

Compound 10. Previously reported compound **9** (344 mg, 0.9 mmol) was deprotected with 1 mL TFA to remove the Boc group. The excess of the acid was removed under reduced pressure, and the residue was dissolved in 1 mL DMF. Linker **12** (305 mg, 0.75 mmol) was added followed by addition of Et_3N (374 μL, 2.7 mmol). The reaction was stirred at room temperature for 1 h and monitored by TLC (EtOAc:He = 3:1). After completion, the solvent was removed under reduced

pressure, and the crude product was purified by column chromatography to give compound **10** (380 mg, 69%) in the form of a sticky foam.

^{1}H NMR (200 MHz, $CDCl_3$) δ = 7.4−7.1 ppm (11H, m); 5.11 (2H, bs); 4.5 (4H, s); 3.7 (2H, s); 3.6−3.46 (4H, m); 3.15 (1H, s); 3.01−2.93 (4H, m); 2.3 (3H, s). ^{13}C NMR (200 MHz, $CDCl_3$) δ = 169.3; 156.1; 137.6; 134.5; 133.4; 132.7; 132.4; 130.8; 130.4; 129.9; 129.6; 128.9; 127.8; 120.0; 67.2; 60.8; 47.6; 46.7; 45.2; 31.6; 21.0. HRMS (MALDI-TOF): calculated for $C_{30}H_{35}N_3O_7$ [M + Na^+] 572.2367, found 572.2349

Compound 11. Compound **10** (370 mg, 0.67 mmol) was dissolved in 10 mL of dry THF and cooled to 0 °C. Then DIPEA (692.5 mg, 5.36 mmol) was added followed by *p*-nitrophenyl chloroformate (814 mg, 4.04 mmol) and pyridine (26 mg, 0.34 mmol). The reaction was allowed to warm to room temperature and monitored by TLC (EtOAc:He = 35:65). After completion, the reaction was diluted with EtOAc and washed with 1 M HCl and with saturated $NaHCO_3$ solutions. The organic layer was dried over magnesium sulfate, and the solvent was removed under reduced pressure. The crude product was purified by column chromatography on silica gel (EtOAc:He = 35:65) to give compound **11** (547 mg, 93%) in a form of a white solid.

^{1}H NMR (200 MHz, $CDCl_3$) δ = 8.39 ppm (4H, d, J = 8); 7.52−7.39 (15H, m); 5.38 (4H, s); 5.19 (2H, s); 3.7 (2H, s); 3.6−3.46 (5H, m); 3.15 (1H, s); 3.01−2.93 (6H, m); 2.3 (3H, s). HRMS (MALDI-TOF): calculated for $C_{44}H_{41}N_5O_{15}$ [M + Na^+] 902.2491; found 902.2475

Compound 1. Compound **8** (200 mg, 0.26 mmol) was deprotected with 1 mL TFA to remove the Boc group. The excess of the acid was removed under reduced pressure, and the residue was dissolved in 1 mL DMF. Compound **11** (75 mg, 0.09 mmol) was added followed by addition of Et_3N (50 μL, 0.36 mmol). The reaction was stirred at room temperature for 1 h and was monitored by TLC (EtOAc:He = 85:15). After completion, the solvent was removed under reduced pressure, and the crude product was purified by column chromatography to give compound **1** (158 mg, 89%) in the form of a light yellow solid. ^{1}H NMR (200 MHz, $CDCl_3$) δ = 8.23−8.17 ppm (8H, m); 7.8−8.1 (4H, m); 7.7−7.6 (8H,m), 7.5−7.25 (11H, m); 5.25−4.8 (14H, m); 4.3 (4H, bs); 3.8 (2H, bs); 3.75−3.4 (14H, m); 3.25−2.8 (18H, s); 2.4 (3H, bs); 2.3 (2H, s). HRMS (MALDI-TOF): calculated for $C_{94}H_{93}N_{17}O_{31}$ [M + Na^+] 1978.6116; found 1978.6293.

Compound 15. Compound **14** (226 mg, 1.28 mmol) was dissolved in DCM. NHS (162 mg, 1.4 mmol) and EDC (269 mg, 1. 4 mmol) were added, and the mixture was stirred at room temp for 15 min and monitored by TLC (EtOAc:He = 4:6). After completion, the solvent was evaporated and the crude product was purified by column chromatography to give product **15** (310 mg, 88%) in the form of a white solid.

^{1}H NMR (200 MHz, $CDCl_3$) δ = 8.16 ppm (2H, d, J = 8.2); 7.47 (2H, d, J = 8.2); 4.4 (2H, s); 2.91 (4H, s). ^{13}C (400 MHz, $CDCl_3$) δ = 169.1; 161.4; 131.1; 131.0; 128.1; 126.9; 54.0; 25.6. HRMS (MALDI-TOF): calculated for $C_{12}H_{10}N_4O_4$ [M + Na^+] 297.0572, found 297.0572.

Compound 16. PEG_{5000}-amine (500 mg, 0.1 mmol) was dissolved in DMF. Compound **15** (42 mg, 0.15 mmol) was added. The reaction was stirred for 2 h and monitored by TLC (DCM: MeOH = 9: 1). After completion, the solvent was removed under reduced pressure and the crude product was purified by column chromatography, dissolved in water, filtered and lyophilized to give compound **16** (67%) in the form of a white powder.

^{1}H NMR (200 MHz, $CDCl_3$) δ = 7.93 ppm (2H, d, J = 8.2); 7.43 (2H, d, J = 8.2); 4.4 (2H, s); 3.8−3.2 (multiplet signal of PEG).

Compound 17. Compound **7** (300 mg, 0.67 mmol) was deprotected with 1 mL TFA to remove the Boc group. The excess of the acid was removed under reduced pressure, and the residue was dissolved in 1 mL DMF. Compound **11** (196 mg, 0.22 mmol) was added followed by addition of Et_3N (185 μL, 1.34 mmol). The reaction was stirred at room temperature overnight and monitored by TLC (EtOAc 100% then EtOAc: MeOH = 8:2). After completion, the solvent was removed under reduced pressure and the crude product was purified by column chromatography (EtOAc:MeOH = 8:2) to give compound **17** (154 mg, 54%) in the form of sticky foam.

^{1}H NMR (200 MHz, MeOD) δ = 8.04 ppm (4H, s); 7.65 (2H, m); 7.47−7.20 (9H, m); 5.2−5.0 (6H, m); 4.68−4.5 (8H, m); 4.28 (4H, d, J = 2.4); 3.78−3.61 (14H, m); 3.27 (3H, s); 3.18−3.03 (15H, m); 2.72 (2H, t, J = 2.4); 2.31−2.29 (3H, m). HRMS (MALDI-TOF): calculated for $C_{66}H_{77}N_9O_{19}$ [M + Na^+] 1322.5228; found 1322.5360.

Compound 18. Compound **17** (154 mg, 0.11 mmol) was dissolved in 10 mL of dry THF at 0 °C. Then, DIPEA (254 mg, 1.97 mmol) was added followed by *p*-nitrophenyl chloroformate (290 mg, 1.44 mmol) and pyridine (10 mg, 0.13 mmol). The reaction was allowed to warm to room temperature and monitored by TLC (EtOAc:He = 85:15). After completion, the reaction was diluted with EtOAc and washed with 1 M HCl and with saturated $NaHCO_3$ solutions. The organic layer was dried over magnesium sulfate. The solvent was removed under reduced pressure. The crude product was purified by column chromatography on silica gel (EtOAc:He = 85:15) to give compound **18** (156 mg, 69%) in the form of a white solid.

^{1}H NMR (400 MHz, $CDCl_3$) δ = 8.25 ppm (8H, d, J = 8.3); 8.0 (4H, s); 7.37−7.03 (17H, m); 5.3 (8H, bs); 5.18 (2H, s); 5.1 (6H, m); 4.28 (4H, s); 3.8−3.5 (16H, m); 3.3 (4H, s); 3.0−2.8 (16H, m); 2.3 (2H, s); 2.1−2.0 (3H, m). HRMS (MALDI-TOF): calculated for $C_{94}H_{89}N_{13}O_{35}$ [M + Na^+] 1982.5476; found 1982.5429.

Compound 20. Previously reported CPT-amine-Boc unit **19** (259 mg, 0.5 mmol) was deprotected with 1 mL TFA to remove the Boc group. The excess of the acid was removed under reduced pressure and the residue was dissolved in 1 mL DMF. Compound **18** (150 mg, 0.077 mmol) was added followed by addition of Et_3N (140 μL, 1 mmol). The reaction was stirred at room temperature overnight and was monitored by TLC (EtOAc: MeOH = 8:2). After completion, the solvent was removed under reduced pressure, and the crude product was purified by column chromatography to give compound **20** (188 mg, 75%) in the form of a yellowish solid.

^{1}H NMR (200 MHz, $CDCl_3$) δ = 8.5 ppm (4H, s); 8.32 (4H, d, J = 8.4); 8.07−8.03 (6H, m); 7.9 (6H, t, J = 7); 7.7 (6H, t, J = 7); 7.6−7.5 (2H, m); 7.4−7.2 (14H, m); 5.9−5.7 (4H, m); 5.5 (4H, m); 5.3−5.1 (19H, m); 4.3−4.2 (4H, m); 3.75−3.5 (25H, m); 3.4−3.25 (14H, m); 3.25−2.99 (25H, m); 2.8−2.75 (3H, m); 2.5−2.25 (18H, m); 1.4 (16H, s); 1.1−0.95 (12H, m). HRMS (MALDI-TOF): calculated for $C_{170}H_{173}N_{25}O_{43}$ [M + Na^+] 3275.2011, found 3275.2221.

General Procedure for the "Click Chemistry". Corresponding PEG-azide (2.2 equiv) was dissolved in DMF. Corresponding dendrimer (1 equiv) was added followed by addition of copper sulfate (0.5 equiv) and TBTA (1equiv). Then, few copper turnings were added, and the reaction was stirred overnight at room temperature. The reaction was monitored by HPLC and after completion the mixture was filtered, and the solvent was removed under reduced pressure. The crude product was purified by column chromatography on silica gel (DCM: MeOH = 9:1) to give desired product.

Compound 1a. HPLC conditions: C18 reverse phase column, λ = 348 nm, flow rate 1 mL/min, gradient program: t = 0 (30% ACN: 70% H_2O); t = 20−25 min (100% ACN).

Scheme 1. Molecular Structure of Second-Generation Self-Immolative Dendron with a Trigger Designed for Activation by PGA (red), Reporter Groups of 4-Nitroaniline (blue), and Acetylene Functional Groups (purple) for Click Conjugation

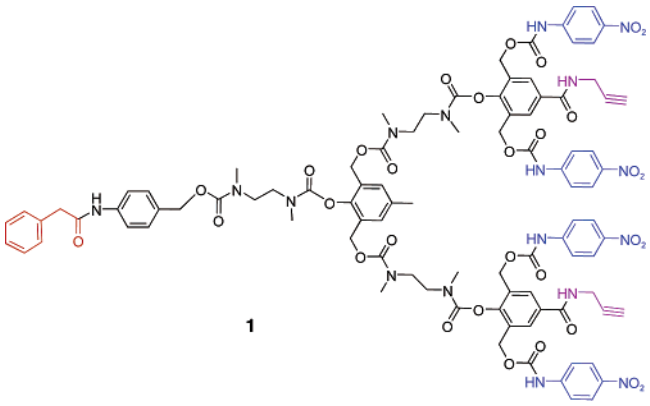

t_R(compound **1**) = 18.5 min, t_R(compound **1a**) = 15.5 min. The yield after column chromatography is 52%. HRMS (MALDI-TOF): calculated for $C_{126}H_{159}N_{23}O_{47}$ 2769.0651 [M + Na^+], found 2769.0859.

Compound 13. HPLC conditions: C18 reverse phase column, λ = 360 nm, flow rate 1 mL/min, gradient program: t = 0 (30% ACN: 70% H_2O); t = 20−25 min (100% ACN). t_R(compound **20**) = 14 min, t_R(compound **13**) = 11 min (broad peak). After the column chromatography, the product was dissolved in mixture of water:MeOH = 9:1, filtered, and lyophilized to give pure product (50.4%) in a form of a yellowish powder.

Solubility Determination. Compound **13** (2 mg) was suspended in 100 μL of distilled water. The mixture was stirred for 1 h and filtered. The concentration of the filtrate was determined by spectroscopic assay (wavelength 360 nm) with CPT solution as a reference. The observed concentration of solution was 11 mg/mL.

Cell-Growth Inhibition Assays. The human embryonic kidney HEK293 cell line was maintained in DMEM (Biological Industries, Beit Haemek, Israel) supplemented with 10% fetal calf serum, 2 mM L-glutamine, and penicillin (10 U/mL)−streptomycin (0.01 mg/mL). The human Molt3 and Jurkat leukemia cell lines were maintained in RPMI 1640 (Biological Industries, Beit Haemek, Israel) supplemented with 20% FCS, 1 mM L-glutamine, and penicillin (10 U/mL)−streptomycin (0.01 mg/mL). Cells were grown in Nunclon Flasks in a humidified atmosphere at 37 °C in 5%CO_2.

For measurements of growth inhibition by CPT and prodrug **13**, the Quick cell Proliferation Assay was used (Biovision). Briefly, Jurkat and Molt3 cells were cultured in 96-well microtiter plate at an initial density of 15 000 cells per well in a final volume of 200 μL medium. Various concentrations of the cytotoxic substance were added to the wells in triplicates, and the extent of cell proliferation was determined 3 days later using the WST-1 reagent. The WST-1 reagent is cleaved to a formazan dye via the mitochondrial dehydrogenase, and the dye produced by viable cells was quantified by measuring absorbance of the dye solution at 440 nm. HEK293 cell line proliferation was evaluated in a similar manner, except that the initial culture density was 2500 cells per well. The cytotoxicity effect of prodrug **13** was evaluated in the presence/absence of 1 μM of the enzyme PGA.

RESULTS AND DISCUSSION

Synthesis and Bioactivation of Second-Generation Dendritic Model System. In order to test our approach, we designed and synthesized second-generation dendritic molecule **1** (Scheme 1). The molecule has an enzymatic trigger that is activated by PGA (red), four reporter groups of 4-nitroaniline (blue), and two acetylene functional groups that are ready to be coupled to various PEG-azide units (purple). The synthesis of dendritic molecule **1** was achieved as illustrated in Schemes 2 and 3. 4-Hydroxybenzoic acid was coupled with propargylamine to give amide

Scheme 2. Synthesis of Intermediate Compound 8

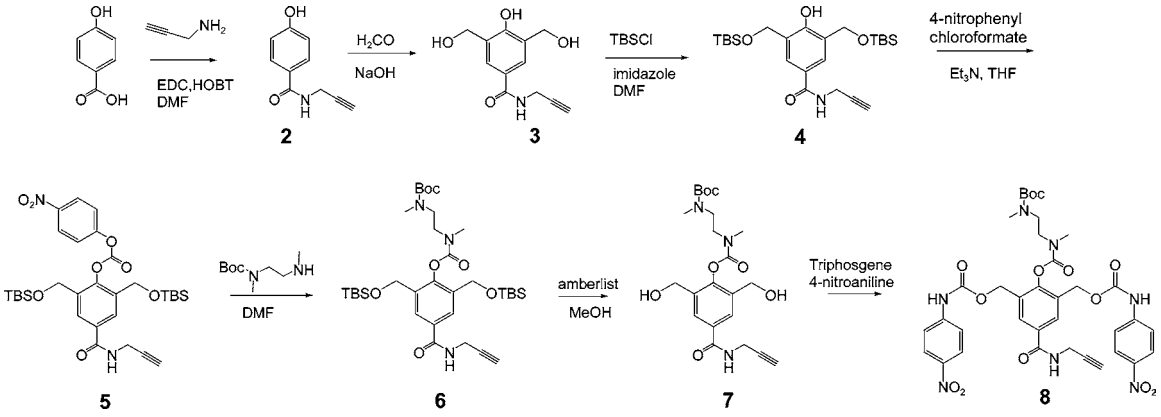

Scheme 3. Synthesis of Self-Immolative Dendritic Compound 1

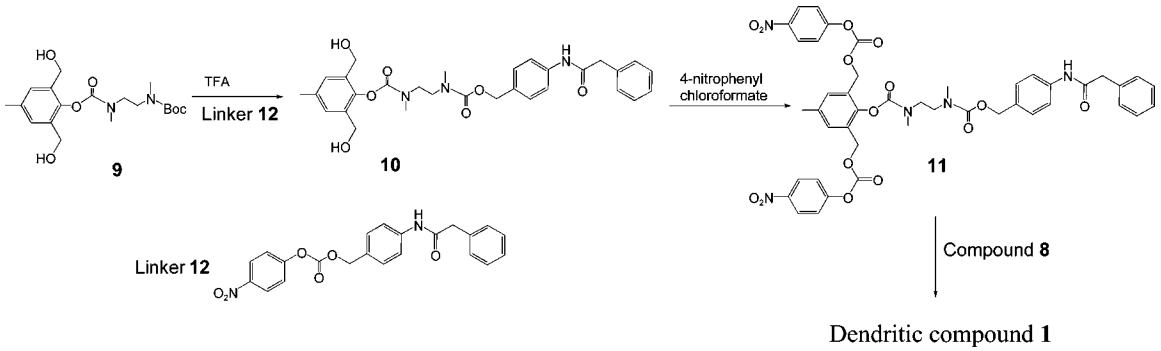

Scheme 4. Conjugation of Dendritic Molecule 1 with PEG400-azide

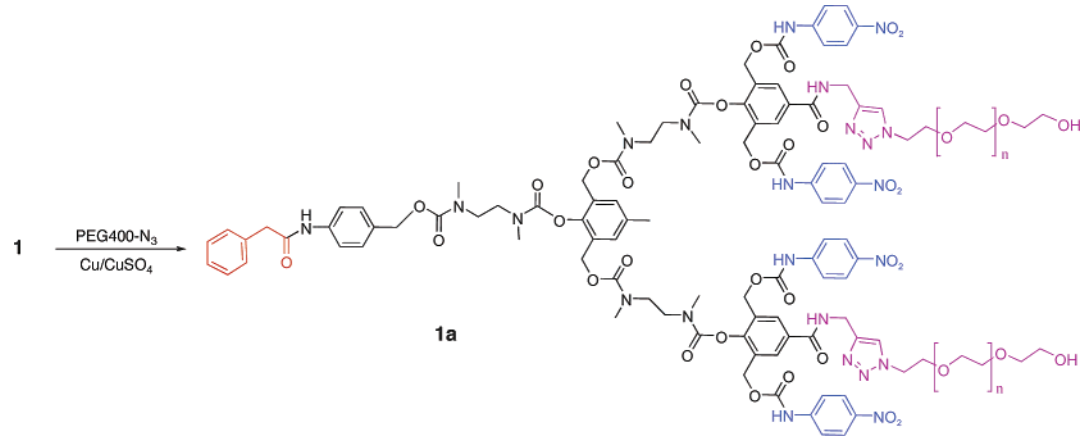

Scheme 5. Disassembly Pathway of Second-Generation Dendritic Molecule 1a Triggered by Enzymatic Activation of PGA

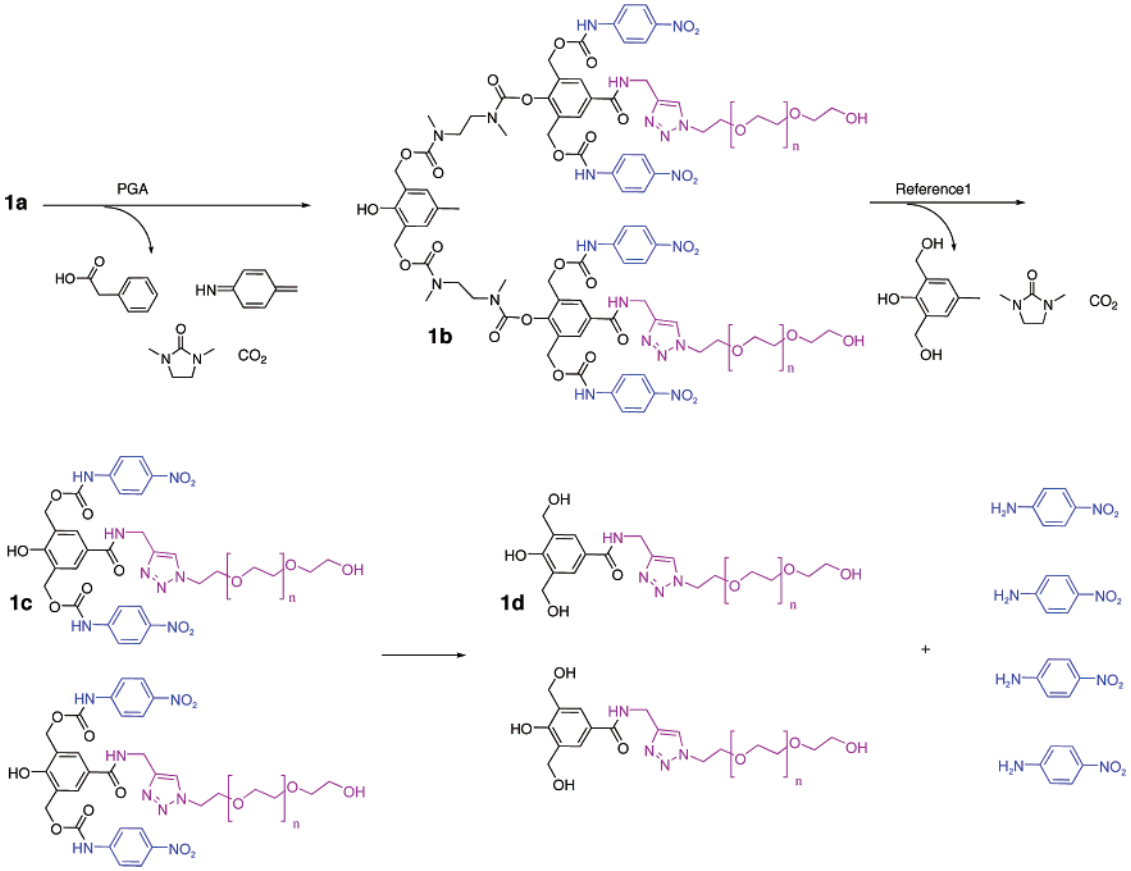

2, which was further reacted with formaldehyde under aqueous basic conditions to afford compound **3**. The latter was selectively protected with two equivalents of *tert*-butyl-dimethylsilyl chloride to generate phenol **4**, which was then activated with *p*-nitrophenyl chloroformate to give carbonate **5**. Reaction of mono-Boc-*N*,*N*′-dimethylethylenediamine with carbonate **5** afforded carbamate **6**, which was stirred with amberlist 15 in methanol to generate compound **7**. The latter was reacted with 4-nitrophenyl isocyanate (generated *in situ* from 4-nitrophenyl and triphosgene) to give compound **8**. Carbamate **9** (*1*) was then deprotected with trifluoroacetic acid (TFA) and directly reacted with linker **12** to generate compound **10**, which was activated with *p*-nitrophenyl chloroformate to give dicarbonate **11**. Compound **8** was deprotected with TFA and immediately reacted with dicarbonate **11** to afford dendritic molecule **1**.

Dendritic molecule **1** was conjugated with 2 equiv of commercially available PEG400-azide via the copper-catalyzed click reaction (*14*) to give conjugate **1a** (Scheme 4). The location of the PEG tails in the dendron's periphery was highly important for aqueous solubility during the dendritic platform fragmentation as presented in Scheme 5. The PEG tails remained attached to the dendron fragments until the reporter groups of 4-nitroaniline were released. Cleavage of the phenylacetamide group by PGA triggered the disassembly of dendron **1a** through a known self-immolative reaction sequence (*1*).

Following the enzymatic cleavage, azaquinone methide was rapidly eliminated and decarboxylation occurred, leading to internal cyclization that released a urea derivative and phenol **1b**. The latter was disassembled as previously described (*1*) to generate 2 equiv of phenol **1c**, which was further fragmented to release the four reporter groups.

In order to prepare aqueous solutions of **1** and **1a**, the compounds were initially dissolved in DMSO/Cremophor EL (4/1) and then diluted into water. The final composition of the

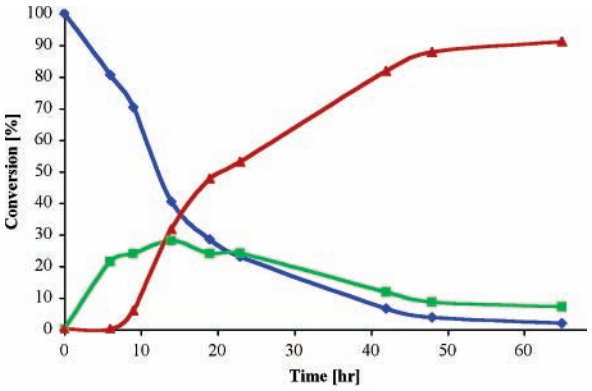

Figure 1. Bioactivation of dendron **1a** by PGA: (blue) dendron **1a**, (green) intermediates, (red) 4-nitroaniline.

solution was 10% organic and 90% aqueous. Dendritic molecules **1** and **1a** were then incubated with PGA in phosphate-buffered saline (PBS, pH 7.4) at 37 °C. Control solutions were composed of buffer without the enzyme. The sequential fragmentation illustrated in Scheme 5 was monitored by observing the disappearance of dendrons **1** or **1a** and the release of 4-nitroaniline by RP-HPLC. As expected, dendron **1** could not be activated by PGA and remained intact for 72 h (data not shown). However, dendron **1a** showed clear activation upon incubation with PGA, and its corresponding peak completely disappeared from the HPLC chromatogram as 4-nitroaniline appeared (Figure 1). No 4-nitroaniline was observed in the control experiment when dendron **1a** was incubated in the buffer without PGA.

Synthesis and Bioactivation of Second-Generation Dendritic Prodrug System. Motivated by the results obtained with the model system, we evaluated the enzymatic activation of a second-generation dendritic prodrug with camptothecin (CPT), an anticancer agent, in place of the reporter groups (dendron **13**). The antitumor activity of 20(*S*)-camptothecin, a pentacyclic plant alkaloid, was recognized more than 20 years ago. It was first isolated from the Asian tree *Camptotheca acuminata* by Wall and co-workers in 1966 (*15*). CPT exerts its antitumor activity mainly through inhibition of topoisomerase I (*16*). This enzyme, which is found in all mammals, binds preferentially to double-stranded DNA, cleaving one strand and forming an enzyme−DNA covalent bond between a tyrosine residue and the 3′ phosphate of the cleaved DNA. Drug-induced accumulation of topoisomerase I−DNA complexes was identified as an essential step in the effects of CPT, ultimately leading to cell death by apoptosis (*17*).

There are two problems associated with CPT therapy: the instability of the 20-hydroxy lactone and the insolubility of CPT in aqueous and organic media. Both the lactone ring and the 20-hydroxy group of CPT are critical for its antitumor activity. The 20-hydroxy lactone is readily hydrolyzed at neutral pH, yielding the inactive carboxylate. The 20-hydroxyl generates an intramolecular hydrogen bond with the carbonyl moiety of the lactone, accelerating the hydrolysis of the otherwise stable lactone ring. Masking of the 20-hydroxy group of CPT results in increased stability of the lactone ring, but also in reduced activity of the drug (*18*). However, a prodrug can be generated from CPT by masking the 20-hydroxyl by a chemical linker that can be selectively removed (*19*). The masking linker serves two purposes: (*1*) removal of the intramolecular hydrogen bond, resulting in a stable lactone, and (*2*) increased solubility of CPT. These circumstances make CPT an ideal drug candidate for the evaluation of our dendritic prodrug system.

Second-generation CPT dendritic prodrug **13** was prepared with a trigger that is activated by PGA and PEG5000 tails to allow sufficient aqueous solubility (Scheme 6). The synthesis

Scheme 6. Molecular Structure of Second-Generation, Self-Immolative, Dendritic CPT (blue) Prodrug with a Trigger Designed for Activation by PGA (red)

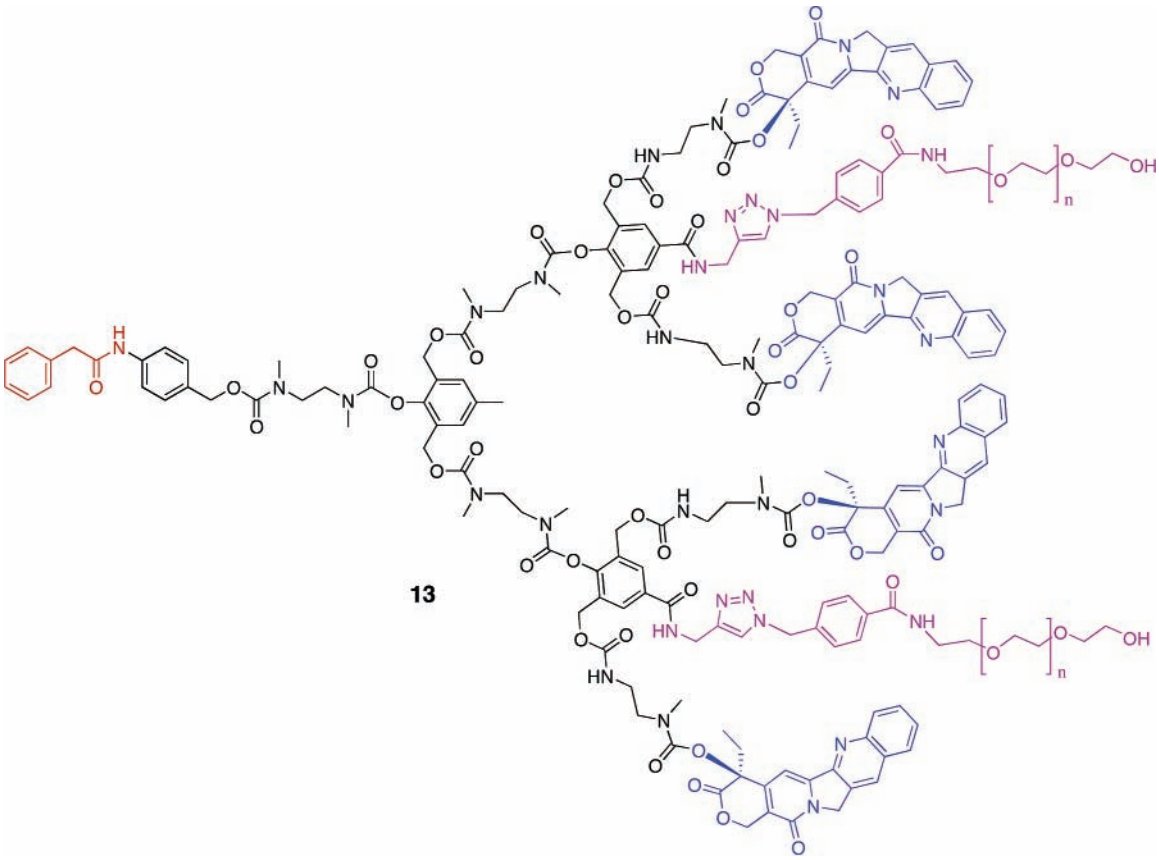

Scheme 7. Synthesis of PEG5000 Azide Derivative

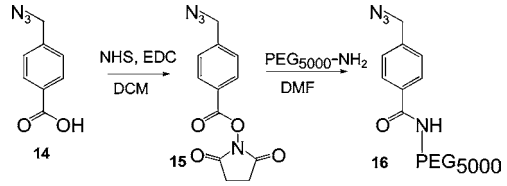

is outlined in Schemes 7 and 8. In order to conjugate PEG5000 with the dendritic platform via a click reaction, we had initially prepared a PEG-azide derivative. Hence, compound **14** was synthesized as previously reported (*20*) and its *N*-hydroxysuccinimide ester **15** was prepared (Scheme 7). The latter was reacted with commercially available PEG5000-amine to afford the PEG5000-azide derivative **16**. Then, compound **7** (Scheme 8) was deprotected with TFA and directly reacted with linker **12** to generate compound **17**, which was activated with *p*-nitrophenyl chloroformate to give tetracarbonate **18**. Four equivalents of CPT derivative **19** (prepared according to published procedure (*21*)) was reacted with **18** to afford dendritic molecule **20**. Click conjugation of azide **16** (2 equiv) with diacetylene **20** afforded conjugate **13**.

The aqueous solubility of dendritic prodrug **13** was measured as described in the experimental section and found to be over 11 mg/mL. The bioactivation of the CPT dendritic prodrugs **20** and **13** by PGA was then evaluated. The prodrugs were incubated in PBS (pH 7.4) at 37 °C with and without PGA and the release of free CPT was monitored by RP-HPLC. As in the model system described above, the PEG-conjugated prodrug **13** was efficiently activated by PGA, whereas its parent prodrug **20** (without the PEG) remained intact. The release of CPT from dendritic prodrug **13** as a function of time is plotted in Figure 2. No release was observed when prodrug **13** was incubated in the buffer without PGA.

Cell-Growth Inhibition Assays. Next we evaluated the ability of dendritic prodrug **13** to inhibit cell proliferation in

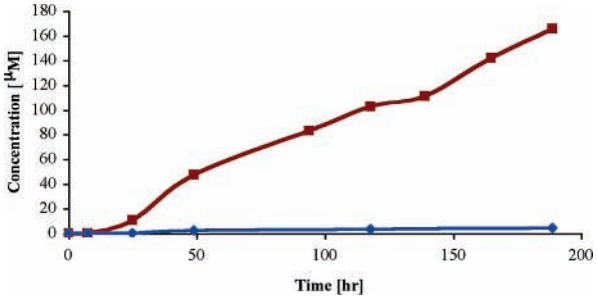

Figure 2. CPT release from dendritic prodrug **13** with PGA (red) and without PGA (blue).

Table 1. IC_{50} (nM) Values from Cell-Growth Inhibition Assays

	MOLT-3		JURKAT		HEK-293	
drug/ prodrug	IC_{50}[a]	IC_{50}[b]	IC_{50}[a]	IC_{50}[b]	IC_{50}[a]	IC_{50}[b]
CPT	2.9	2.9	3.1	3.1	12	12
pro-CPT **13**	4200	41	2000	13	4100	22

[a] Cells were incubated in medium with drug/prodrug. [b] Cells were incubated in medium with drug/prodrug + 1 μM of PGA.

the presence of PGA using three different cell lines: the human T-lineage acute lymphoblastic leukemia cell line MOLT-3, the human leukemia T cell line JURKAT, and the human kidney embryonic HEK-293 cell line. The results are summarized in Table 1, and the full data from the cell assays are presented in Figure 3. PGA effectively activated dendritic prodrug **13**, and its toxicity was significantly increased in the cell-growth inhibition assays of three cancerous cell lines. The IC_{50} of prodrug **13** was between 100- and 1000-fold less than free CPT. When PGA was added, the prodrug was activated and its toxicity approached that of free CPT. The 2−3 log difference between the drug and the prodrug cytotoxicity suggests that relatively high concentration of prodrug may be applied for tumor therapy, decreasing the negative side-effect of chemotherapeutic drugs.

Scheme 8. Synthesis of Second-Generation Dendritic Prodrug 13

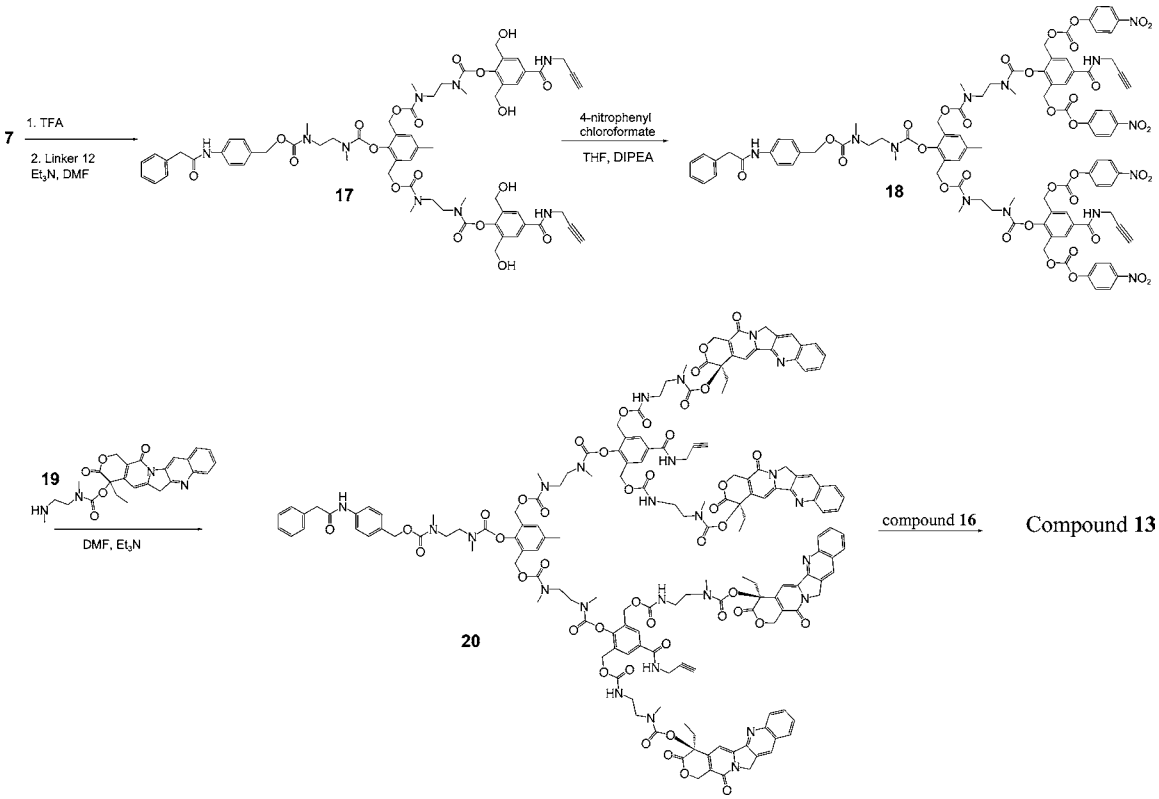

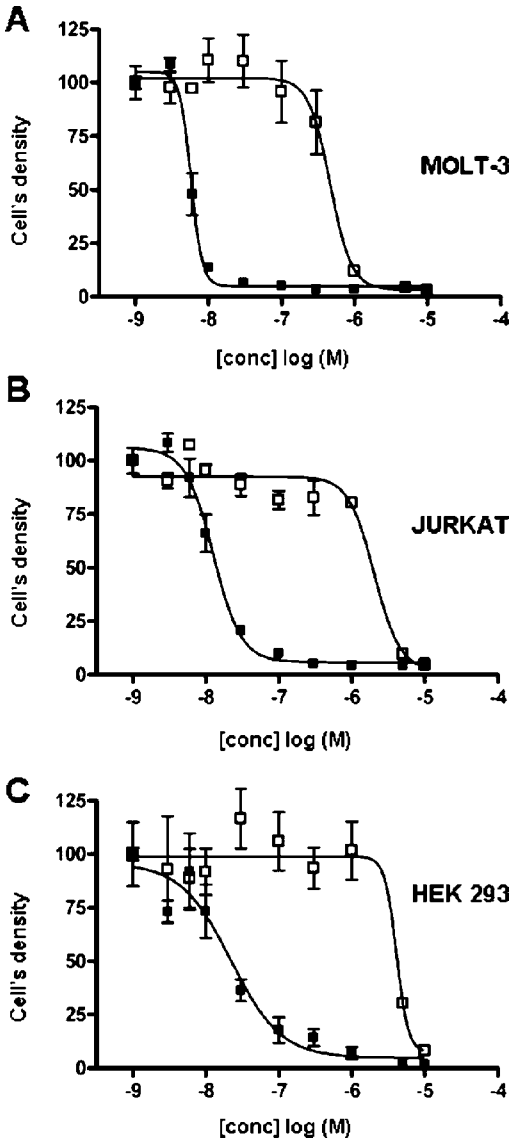

Figure 3. Growth inhibition assay of three human cancerous cell lines, with dendritic prodrug **13** in the presence (■) and absence (□) of PGA; cells were incubated for 72 h.

A dramatic 75% decrease in subcutaneous (s.c.) tumor size has been observed in mice that received a combination of intratumoral injections of activator protein (catalytic antibody 38C2) and systemic treatments with an etoposide prodrug that was 500-fold less toxic than its parent drug (*10*).

It has been previously demonstrated that PEG conjugation prevents protein precipitation by two possible mechanisms (*22*). One possibility is that the PEG group poses a steric hindrance to protein−protein association. A second possibility is that the PEG group shields hydrophobic patches on the protein. Both would significantly reduce protein aggregation and enhance solubility of hydrophobic molecules in water. In the present study even two short PEG400 oligomers were sufficient to permit access of the enzyme to substrate in the dendron's focal point and allow the bioactivation of the system. However, the PEG400 oligomers were large enough to significantly affect to dendrons' aqueous solubility. We assumed that the conjugation PEG oligomers with higher mass should achieved sufficient hydrophilicity to solubilize the dendritic prodrug system in water. Indeed, when PEG5000 was conjugated to a second-generation dendritic prodrug bearing four molecules of the hydrophobic drug CPT, the conjugate had significant aqueous solubility and PGA efficiently activated it.

CONCLUSIONS

In summary, we have demonstrated the first enzymatic activation of second-generation self-immolative dendrimers. We designed and synthesized a dendritic prodrug with four molecules of the anticancer agent camptothecin and a trigger that allows activation by PGA. Two molecules of PEG5000 were conjugated via click chemistry to the dendritic platform in order to gain aqueous solubility. The second-generation self-immolative dendritic prodrug was effectively activated by PGA under physiological conditions, and free CPT was released to the reaction media. Cell-growth inhibition assays demonstrated toxicity of the dendritic prodrug dependent upon incubation with PGA. Incorporation of a specific enzymatic substrate, cleaved by a protease that is overexpressed in tumor cells, could generate a cancer-cell-specific dendritic prodrug activation system.

ACKNOWLEDGMENT

D.S. thanks the Israel Science Foundation, the Israel Ministry of Science "Tashtiot" program, and the Israel Cancer Association for financial support.

LITERATURE CITED

(1) Amir, R. J., Pessah, N., Shamis, M., and Shabat, D. (2003) Self-immolative dendrimers. *Angew. Chem., Int. Ed. 42*, 4494−4499.
(2) de Groot, F. M., Albrecht, C., Koekkoek, R., Beusker, P. H., and Scheeren, H. W. (2003) "Cascade-release dendrimers" liberate all end groups upon a single triggering event in the dendritic core. *Angew. Chem., Int. Ed. 42*, 4490−4494.
(3) Szalai, M. L., Kevwitch, R. M., and McGrath, D. V. (2003) Geometric disassembly of dendrimers: dendritic amplification. *J. Am. Chem. Soc. 125*, 15688−15689.
(4) Flomenbom, O., Klafter, J., Amir, R. J., and Shabat, D. (2005) Dendrimer-based devices: antennae and amplifiers. *Energy Harvest. Mater*. 245−279.
(5) Haba, K., Popkov, M., Shamis, M., Lerner, R. A., Barbas, C. F., 3rd, and Shabat, D. (2005) Single-triggered trimeric prodrugs. *Angew. Chem., Int. Ed. 44*, 716−720.
(6) Shamis, M., Lode, H. N., and Shabat, D. (2004) Bioactivation of self-immolative dendritic prodrugs by catalytic antibody 38C2. *J. Am. Chem. Soc. 126*, 1726−1731.
(7) Amir, R. J., and Shabat, D. (2004) Self-immolative dendrimer biodegradability by multi-enzymatic triggering. *Chem. Commun.* 1614−1615.
(8) Amir, R. J., Popkov, M., Lerner, R. A., Barbas, C. F., 3rd, and Shabat, D. (2005) Prodrug activation gated by a molecular "OR" logic trigger. *Angew. Chem., Int. Ed. 44*, 4378−4381.
(9) Sagi, A., Rishpon, J., and Shabat, D. (2006) Amperometric assay for aldolase activity: antibody-catalyzed ferrocenylamine formation. *Anal. Chem. 78*, 1459−1461.
(10) Shabat, D., Lode, H., Pertl, U., Reisfeld, R. A., Rader, C., Lerner, R. A., and Barbas, C. F., III. (2001) In vivo activity in a catalyic antibody-prodrug system: Antibody catalyzed etoposide prodrug activation for selective chemotherapy. *Proc. Natl. Acad. Sci. 98*, 7528−7533.
(11) Shabat, D., Rader, C., List, B., Lerner, R. A., and Barbas, C. F., III. (1999) Multiple event activation of a generic prodrug trigger by antibody catalysis. *Proc. Natl. Acad. Sci. 96*, 6925−6930.
(12) Claridge, C. A., Gourevitch, A., and Lein, J. (1960) Bacterial penicillin amidase. *Nature 187*, 237−238.
(13) Shabat, D. (2006) Self-immolative dendrimers as novel drug delivery platforms. *J. Polym. Sci., Part A: Polym. Chem. 44*, 1569−1578.
(14) Rostovtsev, V. V., Green, L. G., Fokin, V. V., and Sharpless, K. B. (2002) A stepwise Huisgen cycloaddition process: copper(I)-catalyzed regioselective "ligation" of azides and terminal alkynes. *Angew. Chem., Int. Ed. 41*, 2596−2599.
(15) Wall, M. E., Wani, M. C., Cook, C. E., Palmar, K. H., McPhail, A. T., and Sim, G. A. (1966) Plant antitumor agents **I**. The isolation and structure of camptothecin, a novel alkaloidal leukemia and tumor-inhibitor from Acuminata. *J. Am. Chem. Soc. 88*, 3888−3890.

(16) Hertzberg, R. P., Caranfa, M. J., and Hecht, S. M. (1989) On the mechanism of topoisomerase I inhibition by camptothecin: evidence for binding to an enzyme−DNA complex. *Biochemistry 28*, 4629−4638.

(17) Hsiang, Y. H., Liu, L. F., Wall, M. E., Wani, M. C., Nicholas, A. W., Manikumar, G., Kirschenbaum, S., Silber, R., and Potmesil, M. (1989) DNA topoisomerase I-mediated DNA cleavage and cytotoxicity of camptothecin analogues. *Cancer Res. 49*, 4385−9.

(18) Zhao, H., Lee, C., Sai, P., Choe, Y. H., Boro, M., Pendri, A., Guan, S., and Greenwald, R. B. (2000) 20-*O*-acylcamptothecin derivatives: evidence for lactone stabilization. *J. Org. Chem. 65*, 4601−4606.

(19) Leu, Y. L., Roffler, S. R., and Chern, J. W. (1999) Design and synthesis of water-soluble glucuronide derivatives of camptothecin for cancer prodrug monotherapy and antibody-directed enzyme prodrug therapy (ADEPT). *J. Med. Chem. 42*, 3623−3628.

(20) Zhou, Z., and Fahrni, C. J. (2004) A fluorogenic probe for the copper(I)-catalyzed azide−alkyne ligation reaction: modulation of the fluorescence emission via 3(n,π)−1(π,π) inversion. *J. Am. Chem. Soc. 126*, 8862−8863.

(21) Pessah, N., Reznik, M., Shamis, M., Yantiri, F., Xin, H., Bowdish, K., Shomron, N., Ast, G., and Shabat, D. (2004) Bioactivation of carbamate-based 20(S)-camptothecin prodrugs. *Bioorg. Med. Chem. 12*, 1859−1866.

(22) Rajan, R. S., Li, T., Aras, M., Sloey, C., Sutherland, W., Arai, H., Briddell, R., Kinstler, O., Lueras, A. M., Zhang, Y., Yeghnazar, H., Treuheit, M., and Brems, D. N. (2006) Modulation of protein aggregation by poly(ethylene glycol) conjugation: GCSF as a case study. *Protein Sci. 15*, 1063−1075.

BC060180N

Copper Complex-Assisted DNA Hybridization

Gapian Bianké,[†] Valérie Chaurin,[‡] Maxim Egorov,[§] Jacques Lebreton,[§] Edwin C. Constable,[‡] Catherine E. Housecroft,[‡] and Robert Häner*,[†]

Department of Chemistry and Biochemistry, University of Bern, Freiestrasse 3, CH-3012 Bern, Switzerland, Department of Chemistry, University of Basel, Spitalstrasse 51, CH-4056 Basel, Switzerland, and Laboratoire de Synthèse Organique, UMR-CNRS 6513, University of Nantes, 44322 Nantes, France. Received June 26, 2006; Revised Manuscript Received September 12, 2006

2,2′-Bipyridine (bpy) or 1,10-phenanthroline (phen) metal-binding domains were covalently attached to oligonucleotides, and the influence of metal ions on the hybridization of the conjugates was investigated. Metal-binding domains were attached to oligonucleotides at 3′- and 5′-terminal positions, thus placing them in juxtaposed positions after hybridization to a common target strand. While the ligands alone had a positive effect (increased T_m) on hybrid stability, the duplex was further stabilized by the addition of copper(I) and/or copper(II) through the formation of a metal complex in which the two short sequences are linked through {Cu(bpy)$_2$}, {Cu(phen)$_2$}, or {Cu(bpy)(phen)} domains. The increase in T_m, due to formation of the {Cu(bpy)$_2$}, {Cu(phen)$_2$}, or {Cu(bpy)(phen)} motifs is reversed upon addition of EDTA, consistent with the stripping of copper from the ligands. The effect of metal complex formation on the duplex strength was shown to be highest if the two metal-coordinating ligand strands are placed as close to each other as possible.

INTRODUCTION

There is currently significant interest in the development of short oligonucleotides, which bind to nucleic acid targets with high selectivity as well as high affinity (*1*, *2*). Different strategies have been adopted for this purpose, including the conjugation of oligonucleotides with affinity-enhancing moieties and the synthesis of oligonucleotide analogs with enhanced binding properties (*3*, *4*). An additional approach consists of the use of molecular or supramolecular interactions in assisting the hybridization of nucleic acids (*5*−*8*). One possible type of cooperativity is coordination to metal ions to produce metal-linked oligonucleotide strands. When two short oligonucleotide sequences are coupled by coordination to a single metal center, the so-formed, metal-linked oligonucleotide will be capable of recognizing a long complementary sequence with enhanced binding characteristics. The binding of metal ions, taking place concomitantly to the hybridization process, offers a powerful and selective methodology for nucleotide recognition. It is well-known that metal ions can interact with donor atoms of both the backbone and the bases of nucleic acids, and the importance of metal ions in controlling the structure and function of nucleic acids is well-documented (*9*−*12*). Transition metal ions are also of interest in controlling and developing the molecular architecture of nucleic acids and their analogs. Metal-mediated hybridization of various types of DNA analogs has been reported (*13*−*18*), and specific modification through the incorporation of metal-binding domains has been used for the synthesis of DNA-based nanostructures (*19*−*22*). Furthermore, metal-derived hairpin mimics have been described (*23*−*25*), and different types of transition metal complexes have found applications in the context of artificial ribonucleases (*26*−*28*). Due to their compatibility with nucleic acids, metal ions are ideal candidates for the development of systems in which DNA hybridization and metal complex formation can act in a cooperative way. The feasibility of metal cooperative complex formation in assisting nucleic acid hybridization has been demonstrated by Balasubramanian and co-workers, who reported that the coordination of gadolinium(III) to two short oligonucleotides modified with iminodiacetic acid donors leads to enhanced target affinity (*8*). Important in this general context are the recent observations of Sasaki and co-workers (*29*), who showed that copper-induced dimerization of a minor groove-binding ligand increases its affinity to DNA. Stimulated by this work, we have studied the effect of copper ion complexation by metal-binding domains attached to complementary oligodeoxynucleotides in DNA hybridization. For this purpose, oligonucleotide conjugates incorporating 2,2′-bipyridine (bpy) and 1,10-phenanthroline (phen) metal-binding domains were synthesized, and the influence on the structure and stability of duplexes formed with complementary target strands in the absence and presence of copper(I) and copper(II) was investigated (illustrated in Figure 1). The findings are reported herein.

EXPERIMENTAL PROCEDURES

General. Reactions were carried out under N_2 atmosphere using distilled, anhydrous solvents. Flash column chromatography was performed using silica gel 60 (63−32 μM, Chemie Brunschwig AG). If compounds were sensitive to acid, the silica was pretreated with solvent containing 2% Et_3N. Oligonucleotides were synthesized on a 392 DNA/RNA Synthesizer (Applied Biosystems). Nucleoside phosphoramidites were from Transgenomic (Glasgow G20 OUA, Scotland); universal solid support used for the reverse synthesis was from Glen/Research (Sterling, Virginia). The solvents (CH_3CN and CH_2Cl_2) were of analytical grade from Proligo GmbH (Hamburg) and reagents (3% TCA/DCM deblock solution, 30 mg/mL activator solution, oxidizing solution, capping solutions A and B) used for the synthesis were from Transgenomic (Glasgow G20 OUA, Scotland). Experiments with EDTA involved the use of a 0.5 M aqueous EDTA stock solution (titrated to pH 8.0 with NaOH). CD experiments were performed using a Jasco J-715 spectropolarimeter with a 150 W Xe high-pressure lamp. A Jasco PDF-

* Author to whom correspondence should be addressed. Fax +41 31 631 8057. E-mail robert.haener@ioc.unibe.ch.

[†] University of Bern.

[‡] University of Basel.

[§] University of Nantes.

10.1021/bc0601830 CCC: $33.50 © 2006 American Chemical Society
Published on Web 10/18/2006

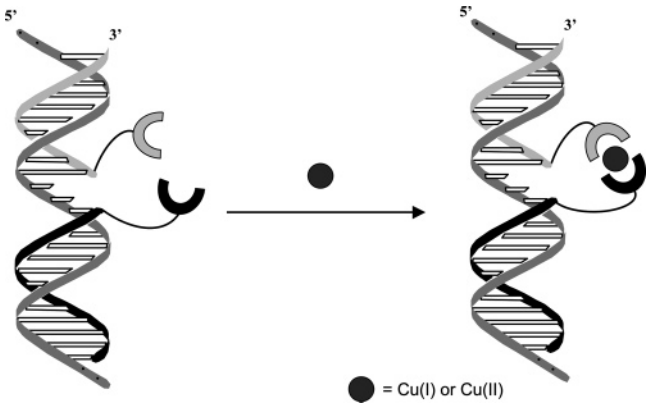

Figure 1. Illustration of copper complex-assisted DNA hybridization.

350S-Peltier unit, coupled with a Colora K5 ultrathermostat, controlled the temperature of the cell holder. All NMR spectra were measured at room temperature on a Buker AC-300 spectrometer. ^{1}H NMR spectra were recorded at 300 MHz. Chemical shifts (δ) are reported in parts per million relative to the residual undeuterated solvent ($CDCl_3$, 7.27 ppm; CD_3CN, 1.94 ppm). Coupling constants *J* are in hertz. Multiplicities are abbreviated as follows: s = singlet, d = doublet, t = triplet, q = quadruplet, m = multiplet. ^{13}C NMR spectra were recorded at 75 MHz. Chemical shifts are reported in parts per million relative to the residual nondeuterated solvent ($CDCl_3$, 77.00 ppm; CD_3CN, 1.32 ppm). ^{31}P NMR spectra were recorded at 162 MHz. Chemical shifts are reported in parts per million relative to 85% H_3PO_4 as an external standard. Electrospray ionization mass spectra (ESI-MS) were recorded on VG platform Fisons instruments.

2-Cyanoethyl (6′-Methyl-2,2′-bipyridin-6-yl)methyl *N*,*N*-Diisopropylphosphoramidite (2). Cyanoethyl *N*,*N*,*N*′,*N*′-tetraisopropylphosphoramidite (*30*) (360 mg, 1.2 mmol) was added to a mixture of **1** (200 mg, 1 mmol) and diisopropylammonium tetrazolide (171 mg, 1 mmol) in dry CH_2Cl_2 (10 mL) under a nitrogen atmosphere. The mixture was stirred at room temperature (rt) for 1 h. After evaporation of the solvent, the residue was purified by flash chromatography (hexane/EtOAc 2:1 + 2% Et_3N) to afford **2** (280 mg, 70%). ^{1}H NMR (300 MHz, CD_3CN): δ = 1.26 (m, 12H); 2.61 (s, 3H); 2.73 (m, 2H); 2.77 (m, 2H); 3.95 (m, 2H); 4.91 (m, 2H); 7.30 (d, *J* = 7.72, 1H); 7.56 (d, *J* = 7.72, 1H); 7.82 (t, *J* = 7.73, 1H); 7.95 (t, *J* = 7.73, 1H); 8.33 (d, *J* = 7.53, 1H); 8.36 (d, *J* = 7.92, 1H). ^{13}C NMR (75 MHz, CD_3CN): δ = 20.37; 20.45; 21.80; 22.39; 24.58; 24.63; 24.73; 43.19; 43.35; 47.32; 47.38; 58.52; 48.78; 66.32; 118.18; 119.64; 120.61; 123.19; 137.00; 137.42; 155.62. ^{31}P NMR (161.9 MHz, CD_3CN): δ = 148.71. ESI-MS (positive mode): *m*/*z* = 401.

2-Cyanoethyl (9-Methyl-1,10-phenanthrolin-2-yl)methyl *N*,*N*-Diisopropylphosphoramidite (4). 2-Cyanoethyl *N*,*N*,*N*′,*N*′-tetraisopropylphosphoramidite (*30*) (242 mg, 0.8 mmol) was added to a mixture of **3** (150 mg, 0.67 mmol) and diisopropylammonium tetrazolide (114 mg, 0.67 mmol) in dichloromethane (6 mL) under nitrogen atmosphere. The mixture was stirred at rt for 1 h. After concentration, the product was purified by flash column chromatography using hexane/EtOAc (1:2) + 2% Et_3N as eluant to afford **4** (214 mg, 75%). TLC (hexane/EtOAc 1:2 + 2% Et_3N): R_f = 0.7. ^{1}H NMR (300 MHz, $CDCl_3$): δ = 1.08−1.25 (m, 18H); 2.64 (t, *J* = 6.4, 3H); 2.87 (s, 3H); 3.42−357 (m, 2H); 3.63−3.71 (m, 3H); 3.82−3.94 (m, 2H); 5.08−5.27 (m, 2H); 7.45 (d, *J* = 8.29, 1H); 7.68 (s, 2H); 7.85 (d, *J* = 8.29, 1H); 8.09 (d, *J* = 8.29, 1H); 8.22 (d, *J* = 8.45, 1H). ^{13}C NMR (75 MHz, $CDCl_3$): δ = 20.38; 21.76; 22.39; 24.66; 25.96; 43.24; 47.31; 58.62; 120.45; 125.57; 126.02; 136.33; 136.83. ^{31}P NMR (161.9 MHz, $CDCl_3$): δ = 149.11.

Table 1. Oligonucleotides (targets T*n*, references R*n*, and conjugates C*n*) Used in This Study.

oligomer	sequence	mass calcd.	mass found
T0	5′-GCGGCGTCAATAACGCTGACG-3′		
T1	5′-GCGGCGTCAATAA**C**CGCTGACG-3′		
T2	5′-GCGGCGTCAATAA**CC**CGCTGACG-3′		
T3	5′-GCGGCGTCAATAA**CCC**CGCTGACG-3′		
R1	GCGACTGC-5′		
R2	3′-CGCCGCAGTTATT		
C1-bpy	3′-CGCCGCAGTTATT-**bpy**	4188	4187
C1-phen	3′-CGCCGCAGTTATT-**phen**	4213	4211
C2-bpy	**bpy**-GCGACTGC-5′	2673	2672
C2-phen	**phen**-GCGACTGC-5′	2698	2696

Oligonucleotide Synthesis and Purification. Oligonucleotides were synthesized according to the standard phosphoramidite solid-phase chemistry. The 5′-conjugated oligonucleotide sequences were elongated from the 3′-end using normal nucleoside phosphoramidites, whereas the 3′-conjugated oligonucleotide sequences were elongated from the 5′-end using universal-Q solid support (*31*) and reverse nucleoside phosphoramidites. The standard synthetic procedure ("trityl-off" mode) and standard condition (i.e., a coupling time of 90 s) were used to incorporate the phosphoramidite building blocks **2** and **4** into oligonucleotide sequences. Detachment of the oligonucleotides from the solid support and deprotection after the synthesis were performed using standard procedures (conc NH_3 solution, 55 °C, 16 h), followed by filtration through Spritzenfilter (nylon, 0.17 mm/0.45 μm, Semadeni AG). All crude oligonucleotides were purified by ion-exchange HPLC, using Tricorn column−Source 15Q 4.6/100PE−15 μm from Amersham Biosciences (Freiburg, Germany). The collected fractions were desalted over Sep-Pak cartridges (Waters, Milford, U.S.A.). Optical densities (ODs) of the purified oligonucleotides were measured at 260 nm with a NanoDrop ND-1000 spectrophotometer, and the masses determined by electrospray mass spectroscopy: VG Platform single quadrupole ESI-MS. Sequences and data are shown in Table 1.

UV Melting Experiments. If not indicated otherwise, all experiments were carried out under the following conditions: oligonucleotide concentration 1.5 μM; 10 mM phosphate buffer, pH = 7.5 (23 °C); 100 mM NaCl. For experiments with metals, 1 mM stock solutions (in milliQ-H_2O) of the following metals were used: $ZnCl_2$; $CuCl_2 \cdot 2H_2O$; $[Cu(CH_3CN)_4][PF_6]$. The latter was prepared as described in the literature (*32*). The solution of $[Cu(CH_3CN)_4][PF_6]$ was always freshly prepared, and argon bubbled through it for at least 10 min to avoid rapid oxidation of copper(I) to copper(II). This procedure was also used to degas the buffers or solution used in all the experiments involving copper(I).

Thermal denaturation experiments were performed on a Varian Cary 3e UV−vis spectrophotometer equipped with a Peltier block temperature controller, and Varian *WinUV* software was utilized to determine the melting curves at 260 nm; a heating−cooling−heating cycle in the temperature range 0−90 °C or 10−90 °C was applied with a temperature gradient of 0.5 °C/min. To avoid H_2O condensation on the UV cells at temperatures ≤20 °C, the cell compartment was flushed with N_2. Data were collected and analyzed with *Kaleidagraph* software from Synergy Software. T_m values were determined as the maximum of the first derivative of the melting curve; each T_m is the average of three independent experiments; exptl error: ±0.5 °C.

RESULTS AND DISCUSSION

Synthesis of the Phosphoramidite Building Blocks. The required phosphoramidite building blocks were obtained from

Scheme 1. Conditions: (a) $(iPr_2N)_2P(OCH_2CH_2CN)$, *N,N*-diisopropylammonium 1*H*-tetrazolide, CH_2Cl_2, rt, 1 h.

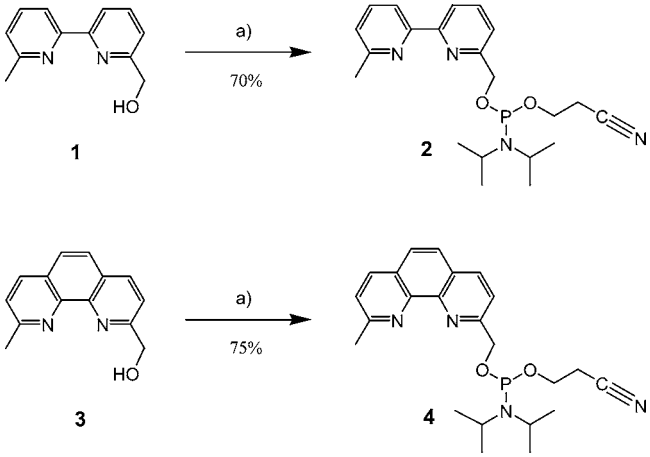

Table 2. Effect of Terminal bpy and phen Ligands on Hybrid Stability.

entry	hybrid [a]	Tm (°C)	ΔTm [b] (°C)
2-1	**T0** + **R1** + **R2**	49.0	-
2-2	**T0** + **C1-bpy** + **C2-bpy**	53.5	+ 4.5
2-3	**T0** + **C1-phen** + **C2-phen**	56.5	+ 7.5

[a] Conditions: Na_2HPO_4 (10 mM; pH = 7.5); NaCl (100 mM); oligonucleotides (1.5 μM); T_m values were determined as the first derivative of the melting curve. [b] Difference in T_m relative to reference (entry 2−1).

known precursors (*33*−*35*). Thus, 6-methyl-2,2′-bipyridine (**1**) was converted to the bpy−phosphoramidite **2** in 70% via the intermediate 6-hydroxymethyl derivative. Similarly, 2-methyl-1,10-phenanthroline (**3**) yielded the phen−phosphoramidite **4** (75%) as shown in Scheme 1.

Oligonucleotide Synthesis. The phosphoramidites **2** and **4** were incorporated into the oligonucleotides (Table 1) using standard oligonucleotide technology (*36*, *37*). The metal-binding domains were incorporated at the 5′-end of a 13-mer sequence (**C1-bpy** and **C1-phen**) and at the 3′-end of an 8-mer sequence (**C2-bpy** and **C2-phen**). For the synthesis of the **C1** conjugates, conventional deoxynucleoside phosphoramidites were used. The **C2** conjugates were synthesized using reverse phosphoramidites (*38*, *39*). Standard conditions were applied, with the exception that prolonged (5 min) coupling time was allowed for the modified building blocks to ensure maximal coupling efficiency. The **C1** conjugates were designed to be complementary to the 5′-end and the **C2** conjugates complementary to the 3′-end of the target (**T0**). Oligonucleotides **R1** and **R2** were prepared as reference oligonucleotides. Detachment of the oligonucleotides from the solid support and deprotection involved standard conditions (conc NH_3 solution, 55 °C, 16 h). Oligonucleotides were purified using ion-exchange HPLC and characterized by electron spray mass spectrometry.

Effect of bpy and phen Metal-Binding Domains on the Duplex Stability in the Absence of Metal Ions. We first examined the influence on the stability of the duplex of the bpy- and phen-modified oligonucleotides with the target complementary strand **T0** in the absence of metal ions. T_m values obtained from thermal denaturation experiments are shown in Table 2. The introduction of metal-binding domains leads to an increase in stability in comparison to the native duplex (Table 2). Thus, an increase in the T_m value of 4.5 and 7.5 °C, respectively, for bpy- (entry 2−2) and phen-modified (entry 2−3) oligonucleotide hybrids with **T0** was observed. The increase in the stability of the modified duplexes (in comparison to the unmodified duplex, which possesses a nicked sequence in the molecule structure) may be the result of stacking interaction between the two diimine ligands facing each other or between the diimine ligands and the adjacent nucleobases.

Table 3. Thermal Denaturing Experiments with bpy and phen Conjugate in the Presence and Absence of Metal.

entry	hybrid [a]	Tm (°C)	ΔTm [b] (°C)
3-1	**T0** + **C1-bpy** + **C2-bpy**	53.5	-
3-2	**T0** + **C1-bpy** + **C2-bpy** + Cu(I)	61.0	+ 7.5
3-3	**T0** + **C1-bpy** + **C2-bpy** + Cu(II)	60.5	+ 7.0
3-4	**T0** + **C1-bpy** + **C2-bpy** + Zn(II)	52.5	- 1.0
3-5	**T0** + **C1-phen** + **C2-phen**	56.5	-
3-6	**T0** + **C1-phen** + **C2-phen** + Cu(I)	61.0	+ 4.5
3-7	**T0** + **C1-phen** + **C2-bpy**	57.0	-
3-8	**T0** + **C1-phen** + **C2-bpy** + Cu(I)	61.0	+ 4.0
3-9	**T0** + **C1-bpy** + **C2-phen**	51.0	-
3-10	**T0** + **C1-bpy** + **C2-phen** + Cu(I)	61.0	+ 10.0

[a] Conditions: Na_2HPO_4(10 mM; pH = 7.5); NaCl (100 mM); oligonucleotides (1.5 μM); T_m values were determined as the first derivative of the melting curve. [b] Difference in T_m relative to the respective metal-free experiment.

Effect of Metal Coordination on Duplex Stability. We next investigated the influence of copper(I) and copper(II) salts on the stability of the modified duplexes. The thermal denaturing experiments with the modified duplex in the presence of these metal ions showed a further remarkable increase in the T_m values by the presence of copper(II) and/or copper(I) (Table 3). For the bpy conjugates (**C1**−**bpy** and **C2**−**bpy**, entries 3−2 and 3−3) an increase of approximately 7 °C was observed upon addition of either of the two metals. In aqueous solution, simple copper(I) salts are unstable with respect to oxidation or disproportionation, and copper(II) species are expected at equilibrium. However, in the case of bpy ligands bearing substituents at the 6- or 6,6′-positions or phen ligands bearing substituents at the 2- or 2,9-positions, copper(I) $\{CuL_2\}^+$ complexes are stabilized by about 3 lgK units to give water-stable copper(I) complexes (*40*−*44*). Furthermore, with 6,6′-disubstituted 2,2′-bipyridine or 2,9-disubstituted 1,10-phenanthroline ligands, reaction with copper(II) or copper(I) leads to the same copper(I) solution species. This phenomenon is discussed in detail elsewhere (*45*). On the other hand, no effect was observed with zinc(II) (Table 3, entry 3−4) as expected from the observations that (i) zinc(II) complexes of bpy and phen ligands are less stable than copper complexes following the Irving−Williams series and (ii) zinc(II) complexes of bpy ligands bearing substituents at the 6- or 6,6′- positions or phen ligands bearing substituents at the 2- or 2,9-positions are less stable than those with bpy and phen. These findings can be interpreted in terms of a common copper(I) complex and

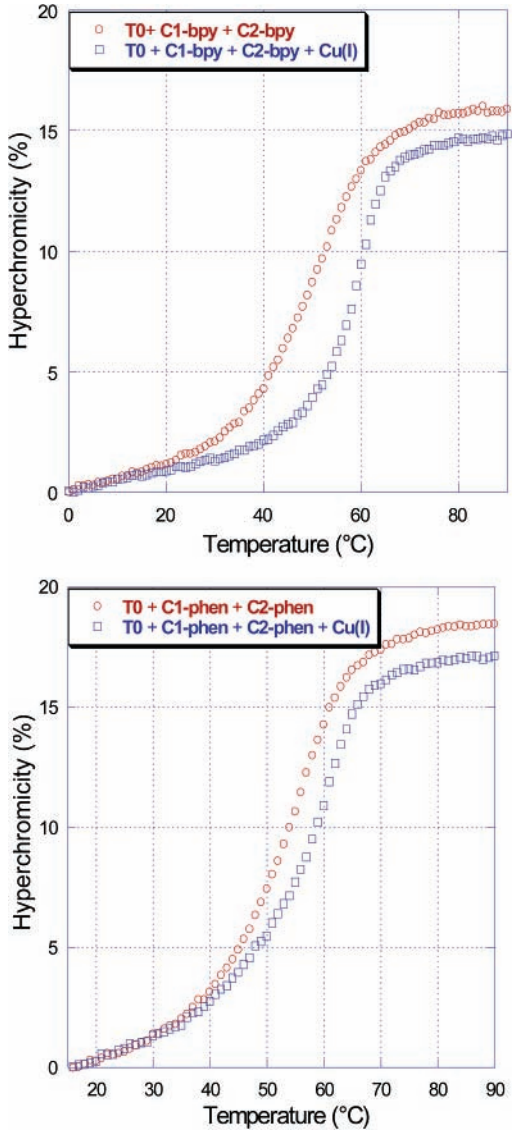

Figure 2. Thermal denaturing curves of hybrids formed by target and conjugates in the presence and absence of metals. Conditions: Na_2HPO_4 (10 mM; pH = 7.5); NaCl (100 mM); oligonucleotides (1.5 μM); heating and cooling rate, 0.5 °C/min; each of the curves shown corresponds to the second of three ramps.

minimal binding of Zn^{2+} to conjugate ligands under the experimental conditions. The phen conjugates (**C2−phen**) showed an increase of 4.5 °C in T_m upon addition of copper(I). The thermal denaturation curves for the hybrids in the absence and presence of copper(I) for both types of conjugates, i.e., bpy and phen, are shown in Figure 2. In all cases, a single transition is observed. Hyperchromicities in the presence and absence of the metals are comparable. Copper(I) and copper(II) ions interact with two bpy or phen ligands to form a stable tetrahedral $\{CuL_2\}$ species (*46*−*48*). Although initial studies utilized both copper(I) and copper(II), we subsequently only investigated interactions with copper(I). The formation of these metal complexes leads to a linking of the two conjugate strands and the formation of a single metallonucleotide strand and, hence, an increase in hybrid stability. The addition of transition metal salts had no experimentally significant influence on the T_m of any control duplex (see Supporting Information). Thus, we can rule out that the effects observed in the case of modified duplexes are due to general metal coordination to the nucleic acid—DNA and RNA are well-known to have a large variety of sites for metal interaction (*36*−*40*)—but rather to specific complex formation with the bpy and phen ligands. Formation of the copper(I) complex does not have an influence on the general B-form structure of the DNA as verified by circular dichroism analysis (see Supporting Information).

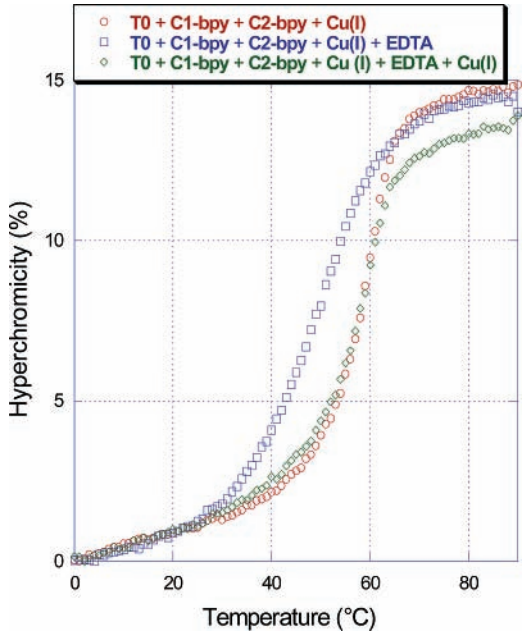

Figure 3. Thermal denaturing curves of hybrids formed by bpy conjugated duplex with consecutive metal and EDTA additions. Conditions: see Figure 2; each of the curves shown corresponds to the second of three ramps.

Effect of Mixed-Ligand Complexes on Hybrid Stability. Mixed-ligand duplexes were formed by hybridizing one bpy and one phen oligonucleotide probe to the target **T0** (Table 3, entries 3−7 and 3−9). With a difference of 6 °C between these two duplexes (57.0 °C and 51.0 °C, respectively) in the absence of metal, the stability of the mixed-ligand duplex depends considerably on the relative positions (3′ or 5′) of the bpy or phen metal-binding domains. Upon the addition of copper(I) (Table 3, entries 3−8 and 3−10), this difference between the two heteroleptic duplexes disappears (T_m = 61 °C in both cases), consistent with the formation of two very similar metal complexes. Furthermore, for both mixed-domain complexes, the hybrid stability is, not unexpectedly, very similar to that of the homocomplexes (entries 3−2 and 3−6).

Effect of EDTA on the Duplex Stabilization. Experiments involving EDTA were performed in order to test the strength of the bpy−metal complexes and the reversibility of metal-induced duplex formation. The denaturation curves are shown in Figure 3. The addition of EDTA to the metalloduplex leads to a T_m which is equal to the one obtained in the absence of metal—in other words, the copper is removed quantitatively upon treatment with the chelating ligand EDTA. The T_m value of the metal-coordinated duplex is restored upon treatment with additional copper(I) or copper(II), establishing the complete reversibility of the formation of the metal linkage between the oligonucleotides.

Influence of Gap Size at the Site of Metal-Complex Formation. In order to investigate the influence of the gap between the two metal-binding domains facing each other—at the complexation site—on duplex stability, hybridization to targets **T1**−**T3**, containing one, two, and three additional cytidines at the junction of the two complementary functionalized oligomers (Table 4), was examined. These oligonucleotides are formally derived from **T0** by sequential addition of the respective numbers of cytosines after position 13. In this way, the relative distance between the metal-binding bpy or phen

Table 4. Influence of Gap Size between the Metal Ligands on Hybrid Strength[c]

entry	hybrid [a]	Tm (°C)	ΔTm [b] (°C)
4-1	**T0** + **C1-bpy** + **C2-bpy**	53	-
4-2	**T0** + **C1-bpy** + **C2-bpy** + Cu(I)	61	+ 8
4-3	**T1** + **C1-bpy** + **C2-bpy**	55	-
4-4	**T1** + **C1-bpy** + **C2-bpy** + Cu(I)	57	+ 2
4-5	**T2** + **C1-bpy** + **C2-bpy**	55	-
4-6	**T2** + **C1-bpy** + **C2-bpy** + Cu(I)	57	+ 2
4-7	**T3** + **C1-bpy** + **C2-bpy**	56	-
4-8	**T3** + **C1-bpy** + **C2-bpy** + Cu(I)	57	+ 1

[a] Conditions: Na_2HPO_4 (10 mM, pH = 7.5); NaCl (100 mM); oligonucleotides (1.5 μM); T_m values were determined as the first derivative of the melting curve. [b] Difference in T_m relative to the metal-free reference. [c] Gap size was varied by increasing the number (0−3) of cytidine nucleotides in the target strand.

domains was gradually increased, while the total number of base pairs formed in each hybrid was kept constant. Thermal denaturing experiments were performed with the bpy conjugates **C1**−**bpy** and **C2**−**bpy**, and the results are summarized in Table 4. In the absence of copper, an elongation of the gap between the two ligands leads to a slight increase (2−3 °C) in the T_m value of the duplex. This stabilization may well be attributed to steric requirements of the bpy or phen substituents. With increasing gap size, the metal-free functionalized oligonucleotides are better accommodated with a reduction of repulsion between the metal-binding domains, and hence hybrid stability increases. Upon the addition of the metal ion, however, formation of the metal complex becomes the dominant aspect. Apparently, close proximity facilitates the coordination of the metal by the two terminal metal-binding domains. In this context, the relatively short and inflexible methylene linker further supports this interpretation of the data: the stability of the hybrids is highest if the gap is minimal, i.e., if the two metal-binding domains are juxtaposed, as is the case with target **T0**.

CONCLUSIONS

The influence of metal complex formation on hybridization of oligodeoxynucleotides was investigated. Oligonucleotides containing 3′- and 5′-linked 6′-methyl-2,2′-bipyridine- and 2-methyl-1,10-phenanthroline-derived metal-binding domains were synthesized. Pairs of oligonucleotide conjugates were designed to hybridize to a target DNA sequence, such that the two copper-binding domains are arranged head-to-head in the ternary hybrid to create an N_4 metal-binding site. Incorporation of the metal-binding domains had a positive influence on hybrid stability per se (ΔT_m = 4.5−7.5 °C). Addition of copper(I) or copper(II) sources results in the formation of metal complex and leads to substantial further stabilization (up to 10 °C increase in T_m). While the placement of the metal-free ligands had no influence on the extent of the stabilization, the stabilizing effect obtained by metal coordination was found to be distance-dependent, i.e., the largest increase is observed upon placement of the ligands as close to each other as possible. While the stability of the hybrid is substantially influenced by metal coordination, the overall B-form structure of the DNA is not affected. This study shows that hybridization of relatively short (13- and 8-mer) oligonucleotides modified with bpy or phen metal-binding domains to a complementary target DNA is assisted by formation of {$Cu(bpy)_2$}, {$Cu(phen)_2$}, or {Cu(bpy)-(phen)} metal complexes.

ACKNOWLEDGMENT

Financial support by the Swiss National Foundation (grant 20C321-101121), the University of Bern, and the University of Basel is gratefully acknowledged. This work is part of the Transnational Project CERC3 2002 (209921-101121.02).

Supporting Information Available: ^{13}C-Spectra of compounds **2** and **4**, thermal denaturation curves, control experiments (T_m values), circular dichroism spectra, and nondenaturing polyacrylamide gel electrophoresis experiments are included. This material is available free of charge via the Internet at http://pubs.acs.org/BC.

LITERATURE CITED

(1) Chan, J. H. P., Lim, S. H., and Wong, W. S. F. (2006) Antisense oligonucleotides: From design to therapeutic application. *Clin. Exp. Pharmacol. Physiol. 33*, 533−540.
(2) Chen, X. L., Dudgeon, N., Shen, L., and Wang, J. H. (2005) Chemical modification of gene silencing oligonucleotides for drug discovery and development. *Drug Discovery Today 10*, 587−593.
(3) Uhlmann, E., and Peyman, A. (1990) Antisense oligonucleotides−A new therapeutic principle. *Chem. Rev. 90*, 543−584.
(4) De Mesmaeker, A., Häner, R., Martin, P., and Moser, H. E. (1995) Antisense oligonucleotides. *Acc. Chem. Res. 28*, 366−374.
(5) Distefano, M. D., Shin, J. A., and Dervan, P. B. (1991) Cooperative binding of oligonucleotides to DNA by triple helix formation - dimerization via Watson-Crick hydrogen-bonds. *J. Am. Chem. Soc. 113*, 5901−5902.
(6) Distefano, M. D., and Dervan, P. B. (1992) Ligand-promoted dimerization of oligonucleotides binding cooperatively to DNA. *J. Am. Chem. Soc. 114*, 11006−11007.
(7) Kandimalla, E. R., Manning, A., Lathan, C., Byrn, R. A., and Agrawal, S. (1995) Design, biochemical, biophysical and biological properties of cooperative antisense oligonucleotides. *Nucleic Acids Res. 23*, 3578−3584.
(8) Horsey, I., Krishnan-Ghosh, Y., and Balasubramanian, S. (2002) Enhanced cooperative binding of oligonucleotides to form DNA duplexes mediated by metal ion chelation. *Chem. Commun.* 1950−1951.
(9) Barton, J. K., and Lippard, S. J. (1980) Heavy metal interactions with nucleic acids. In *Nucleic Acid-Metal Ion Interactions* (Spiro, T. G., Ed.) pp 31−113, John Wiley & Sons, Princeton University.
(10) Wilson, T. J., and Lilley, D. M. J. (2002) Metal ion binding and the folding of the hairpin ribozyme. *RNA 8*, 587−600.
(11) Pyle, A. M. (2002) Metal ions in the structure and function of RNA. *J. Biol. Inorg. Chem. 7*, 679−690.
(12) Göritz, M., and Krämer, R. (2005) Allosteric control of oligonucleotide hybridization by metal-induced cyclization. *J. Am. Chem. Soc. 127*, 18016−18017.
(13) Meggers, E., Holland, P. L., Tolman, W. B., Romesberg, F. E., and Schultz, P. G. (2000) A novel copper-mediated DNA base pair. *J. Am. Chem. Soc. 122*, 10714−10715.
(14) Weizman, H., and Tor, Y. (2001) 2,2′-Bipyridine ligandoside: A novel building block for modifying DNA with intra-duplex metal complexes. *J. Am. Chem. Soc. 123*, 3375−3376.
(15) Zimmermann, N., Meggers, E., and Schultz, P. G. (2002) A novel silver(I)-mediated DNA base pair. *J. Am. Chem. Soc. 124*, 13684−13685.
(16) Tanaka, K., Yamada, Y., and Shionoya, M. (2002) Formation of silver(I)-mediated DNA duplex and triplex through an alternative base pair of pyridine nucleobases. *J. Am. Chem. Soc. 124*, 8802−8803.
(17) Tanaka, K., Tengeiji, A., Kato, T., Toyama, N., and Shionoya, M. (2003) A discrete self-assembled metal array in artificial DNA. *Science 299*, 1212−1213.

(18) Zhang, L. L., and Meggers, E. (2005) An extremely stable and orthogonal DNA base pair with a simplified three-carbon backbone. *J. Am. Chem. Soc. 127*, 74−75.
(19) Stewart, K. M., Rojo, J., and McLaughlin, L. W. (2004) Ru(II) tris(bipyridyl) complexes with six oligonucleotide arms as precursors for the generation of supramolecular assemblies. *Angew. Chem., Int. Ed. 43*, 5808−5811.
(20) Stewart, K. M., and McLaughlin, L. W. (2003) Design and synthesis of DNA-tethered ruthenium complexes that self-assemble into linear arrays. *Chem. Commun.* 2934−2935.
(21) Choi, J. S., Kang, C. W., Jung, K., Yang, J. W., Kim, Y. G., and Han, H. Y. (2004) Synthesis of DNA triangles with vertexes of bis-(terpyridine)iron(II) complexes. *J. Am. Chem. Soc. 126*, 8606−8607.
(22) Mitra, D., Di Cesare, N., and Sleiman, H. F. (2004) Self-assembly of cylclic metal - DNA nanostuctures using ruthenium tris(bipyridine)-branched oligonucleotides. *Angew. Chem., Int. Ed. 43*, 5804−5808.
(23) Lewis, F. D., Helvoigt, S. A., and Letsinger, R. L. (1999) Synthesis and spectroscopy of Ru(II)-bridged DNA hairpins. *Chem. Commun.* 327−328.
(24) Czlapinski, J. L., and Sheppard, T. L. (2004) Template-directed assembly of metallosalen-DNA hairpin conjugates. *ChemBioChem 5*, 127−129.
(25) Bianké, G., and Häner, R. (2004) A metal-coordinating DNA hairpin mimic. *ChemBioChem 5*, 1063−1068.
(26) Trawick, B. N., Daniher, A. T., and Bashkin, J. K. (1998) Inorganic mimics of ribonucleases and ribozymes: From random cleavage to sequence-specific chemistry to catalytic antisense drugs. *Chem. Rev. 98*, 939−960.
(27) Häner, R., and Hall, J. (1997) The sequence-specific cleavage of RNA by artificial chemical ribonucleases. *Antisense Nucleic Acid Drug Dev. 7*, 423−430.
(28) Niittymaki, T., and Lönnberg, H. (2006) Artificial ribonucleases. *Org. Biomol. Chem. 4*, 15−25.
(29) Tanada, M., Tsujita, S., Kataoka, T., and Sasaki, S. (2006) Cu-(2+)-mediated assembly of the minor groove binders on the DNA template with sequence selectivity. *Org. Lett. 8*, 2475−2478.
(30) Bannwarth, W., and Treciak, A. (1987) A simple and effective chemical phosphorylation procedure for biomolecules. *Helv. Chim. Acta 70*, 175−186.
(31) Pon, R. T., and Yu, S. Y. (1997) Hydroquinone-O,O′-diacetic acid as a more labile replacement for succinic acid linkers in solid-phase oligonucleotide synthesis. *Tetrahedron Lett. 38*, 3327−3330.
(32) Kubas, G. J. (1979) Tetrakis(acetonitrile)copper(I) hexafluorophosphate, *Inorg. Synth. 19*, 90−92.
(33) Shaul, M., and Cohen, Y. (1999) Novel phenanthroline-containing trinuclear double-stranded helicates: Self-recognition between helicates with phenanthroline and bipyridine binding sites. *J. Org. Chem. 64*, 9358−9364.
(34) Schubert, U. S., Newkome, G. R., Goldel, A., Pemp, A., Kersten, J. L., and Eisenbach, C. D. (1998) Bipyridine building blocks for self-organization systems: First complete NMR-spectroscopic investigation of 6,6′-disubstituted 2,2′-bipyridines obtained via N-oxidation route and related reactions. *Heterocycles 48*, 2141−2148.
(35) Newkome, G. R., Theriot, K. J., Gupta, V. K., Fronczek, F. R., and Baker, G. R. (1989) Chemistry of heterocyclic-compounds. 124. Mono-α-functionalization of 2,9-dimethyl-1,10-phenanthroline. *J. Org. Chem. 54*, 1766−1769.
(36) Beaucage, S. L., and Caruthers, M. H. (1981) Deoxynucleoside phosphoramidites - a new class of key intermediates for deoxypolynucleotide synthesis. *Tetrahedron Lett. 22*, 1859−1862.
(37) Sinha, N. D., Biernat, J., McManus, J., and Köster, H. (1984) Polymer support oligonucleotide synthesis XVIII: use of beta-cyanoethyl-N, N-dialkylamino-/N-morpholino phosphoramidite of deoxynucleosides for the synthesis of DNA fragments simplifying deprotection and isolation of the final product. *Nucleic Acids Res. 12*, 4539−4557.
(38) Claeboe, C. D., Gao, R., and Hecht, S. M. (2003) 3′-Modified oligonucleotides by reverse DNA synthesis. *Nucleic Acids Res. 31*, 5685−5691.
(39) Pease, A. C., Solas, D., Sullivan, E. J., Cronin, M. T., Holmes, C. P., and Fodor, S. P. A. (1994) Light-generated oligonucleotide arrays for rapid DNA-sequence analysis. *Proc. Natl. Acad. Sci. U.S.A. 91*, 5022−5026.
(40) Smith, A. P., and Fraser, C. L. (2004) Bipyridine Ligands. In *Comprehensive Coordination Chemistry II* (McCleverty, J. A., and Meyer, T. J., Eds.) pp 1−23, Elsevier, Oxford.
(41) Luman, C. R., and Castellano, F. N. (2004) Phenanthroline Ligands. In *Comprehensive Coordination Chemistry II* (McCleverty, J. A., and Meyer, T. J., Eds.) pp 25−39, Elsevier, Oxford.
(42) Kaes, C., Katz, A., and Hosseini, M. W. (2000) Bipyridine: The most widely used ligand. A review of molecules comprising at least two 2,2′-bipyridine units. *Chem. Rev. 100*, 3553−3590.
(43) Brandt, W. W., Dwyer, F. P., and Gyarfas, E. C. (1954) Chelate complexes of 1,10-phenanthroline and related compounds. *Chem. Rev. 54*, 959−1017.
(44) James, B. R., and Williams, R. J. (1961) Oxidation-reduction potentials of some copper complexes. *J. Chem. Soc.* 2007−2019.
(45) Chaurin, V., Constable, E. C., and Housecroft, E. C. (2006) What is the coordination number of copper(II) in metallosupramolecular chemistry? *New J. Chem.*, in press.
(46) Siddique, Z. A., Yamamoto, Y., Ohno, T., and Nozaki, K. (2003) Structure-dependent photophysical properties of singlet and triplet metal-to-ligand charge transfer states in copper(I) bis(diimine) compounds, *Inorg. Chem. 42*, 6366−6378.
(47) Kickelbick, G., Reinohl, U., Ertel, T. S., Weber, A., Bertagnolli, H., and Matyjaszewski, K. (2001) Extended X-ray absorption fine structure analysis of the bipyridine copper complexes in atom transfer radical polymerization. *Inorg. Chem. 40*, 6−8.
(48) Garribba, E., Micera, G., Sanna, D., and Strinna-Erre, L. (2000) The Cu(II)-2,2′-bipyridine system revisited. *Inorg. Chim. Acta 299*, 253−261.

BC0601830

Engineering an Arginine Catabolizing Bioconjugate: Biochemical and Pharmacological Characterization of PEGylated Derivatives of Arginine Deiminase from *Mycoplasma arthritidis*

Maoliang Wang, Amartya Basu, Thomas Palm, Jack Hua, Stephen Youngster, Lisa Hwang, Hsien-Ching Liu, Xiguang Li, Ping Peng, Yue Zhang, Hong Zhao, Zhihua Zhang, Clifford Longley, Mary Mehlig, Virna Borowski, Prakash Sai, Manickam Viswanathan, Eun Jang, Gerald Petti, Sam Liu, Karen Yang, and David Filpula*

Enzon Pharmaceuticals, 20 Kingsbridge Road, Piscataway, New Jersey 08854-3969. Received July 5, 2006; Revised Manuscript Received August 31, 2006

Arginine is an important metabolite in the normal function of several biological systems, and arginine deprivation has been investigated in animal models and human clinical trials for its effects on inhibition of tumor growth, angiogenesis, or nitric oxide synthesis. In order to design an optimal arginine-catabolizing enzyme bioconjugate, a novel recombinant arginine deiminase (ADI) from *Mycoplasma arthritidis* was prepared, and multi-PEGylated derivatives were examined for enzymatic and biochemical properties in vitro, as well as pharmacokinetic and pharmacodynamic behavior in rats and mice. ADI bioconjugates constructed with 12 kDa or 20 kDa monomethoxy-poly(ethylene glycol) polymers with linear succinimidyl carbonate linkers were investigated via intravenous, intramuscular, or subcutaneous administration in rodents. The selected PEG−ADI compounds have 22 ± 2 PEG strands per protein dimer, providing an additional molecular mass of about $0.2-0.5 \times 10^6$ Da and prolonging the plasma mean residence time of the enzyme over 30-fold in mice. Prolonged plasma arginine deprivation was demonstrated with each injection route for these bioconjugates. Pharmacokinetic analysis employed parallel measurement of enzyme activity in bioassays and enzyme assays and demonstrated a correlation with the pharmacodynamic analysis of plasma arginine concentrations. Either ADI bioconjugate depressed plasma arginine to undetectable levels for 10 days when administered intravenously at 5 IU per mouse, while the subcutaneous and intramuscular routes exhibited only slightly reduced potency. Both bioconjugates exhibited potent growth inhibition of several cultured tumor lines that are deficient in the anabolic enzyme, argininosuccinate synthetase. Investigations of structure−activity optimization for PEGylated ADI compounds revealed a benefit to constraining the PEG size and number of attachments to both conserve catabolic activity and streamline manufacturing of the experimental therapeutics. Specifically, ADI with either 12 kDa or 20 kDa PEG attachments on 33% of the primary amines retained about 60% or 48% of enzyme activity, respectively; the K_m and pH profiles were nearly unchanged; IC_{50} values were diminished by less than 30%; while stability studies demonstrated full retention of activity at 4 °C for 5 months. A comparison of the enzymatic properties of a second ADI from *Pseudomonas putida* illustrated the superior characteristics of the *M. arthritidis* ADI enzyme.

INTRODUCTION

Enzymes have inherent utility as pharmaceuticals, owing to their substrate specificity, catalytic efficiency, and favored function under physiological environments (*1*−*7*). Unlike antibodies, receptors, or ligands, enzymes have the capacity to permanently alter their target, rather than merely act as its antagonist or agonist. Yet enzymes, as a drug category, have demonstrated insufficient progress in recent years, due to the considerable challenges of (*1*) identifying and manufacturing the optimal enzyme, (*2*) employing the best drug delivery formulation, and (*3*) recognizing the correct patient population whose genotype correlates with a metabolic difference which the enzyme therapy may exploit.

While the target specificity of enzymes makes them attractive drug candidates, protein therapeutics also have disadvantages including immunogenicity, limited stability and circulating life, and suboptimal biodistribution/bioavailability. Advances in drug delivery systems for protein therapeutics have increased interest in enzyme therapy as a strategy for disease management (*8, 9*). The pioneering research on the antineoplastic activity of L-asparaginase led to the establishment of this bacterial enzyme as a major component in the treatment of acute lymphoblastic leukemia—the first FDA licensed heterologous enzyme therapy for cancer (*7, 10, 11*). Asparaginase therapy exploits a difference in asparagine auxotrophy between normal and leukemic cells. Unfortunately, few tumor-specific metabolic targets have been well-established.

One promising metabolic target which has shown promise in experimental therapies for the treatment of cancer is arginine, an amino acid which plays an important role in many metabolic pathways (*12*−*14*). Arginine is a nonessential amino acid for the growth of most normal and tumor cells, which are able to convert citrulline into arginine. The apparent arginine auxotrophy of melanoma and hepatocellular carcinoma (HCC) cells may offer an effective method for selective growth inhibition by enzymatic depletion of plasma arginine (*15*−*18*). Arginine is synthesized from citrulline by two urea cycle enzymes, argininosuccinate synthetase (AS) and argininosuccinate lyase (AL). In humans, the AS gene is expressed in all normal cells and tissues except circulating humoral cells. The AS gene appears to be regulated by metabolite repression, and the cultivation of human cells in arginine free medium, supplemented with citrulline, increases the expression of AS by 3- to 150-fold (*12*). AL, the second enzyme involved in the conversion of citrulline

* Corresponding author. Tel # 732-980-4941, FAX # 732-885-2950, E-mail: david.filpula@enzon.com.

10.1021/bc060198y CCC: $33.50 © 2006 American Chemical Society
Published on Web 10/17/2006

to arginine, appears to be constitutively expressed in all tissues (*12*). Recently, it has been shown that human melanomas and hepatocellular carcinomas are frequently deficient in AS expression (*15*, *19*, *20*), which may be the underlying mechanism that rendered these cells susceptible to growth inhibition by arginine deprivation.

Arginine deiminase (ADI[1]; L-arginine iminohydrolase, EC 3.5.3.6) catalyzes the conversion of L-arginine into L-citrulline and ammonia. Although not present in humans, ADI is expressed in many microbial organisms, such as mycoplasma, yeast, bacteria, and protozoa. The best-studied of these enzymes are obtained from *Pseudomonas aeruginosa*, *Mycoplasma arginini*, and *Mycoplasma hominis* (*21*−*27*). These enzymes, as well as mammalian arginase, have been shown to be effective in inhibiting growth of cancer cell lines in vitro and in experimental tumors in rodents (*28*−*34*), as well as exhibiting antiviral effects (*35*), anti-angiogenesis activity (*36*), and decreasing nitric oxide production (*37*). Early clinical studies suggest arginine deprivation may be a significant therapy for selected carcinomas (*34*, *38*, *39*). These arginine catabolizing enzymes are not ideal therapeutics, however. Reported K_m values of 0.2−2 mM are not well matched to the task of total elimination of plasma arginine (∼100 μM), and the enzymes are not optimally active at physiological pH (*33*). Furthermore, all of these enzymes present drug delivery and immunogenicity challenges that may be addressed by bioconjugate chemistry.

PEGylation, the covalent attachment of poly(ethylene glycol) polymers to compounds, has become one of the best-validated drug delivery methods for extension of serum half-life and the reduction of immunogenicity (*1*, *9*, *40*−*47*), and at least six PEGylated protein therapeutics are now on the market (*8*). In general, activated PEG polymers reacted with primary amines have been employed in multiple attachments with catabolic enzymes and other macromolecules which recognize small substrates. Several different chain lengths of PEG have been examined with various linker chemistries in previous reports (*40*, *44*, *46*). While bioconjugates of enzymes with PEG have demonstrated some of the expected benefits in pharmacological behavior, there has been insufficient focus in bioconjugate science on first engineering a superior active pharmaceutical protein and also matching that compound to the best linkage and the preferred degree of modification.

The goals of our current studies were to develop a new arginine-catabolizing bioconjugate which would (1) demonstrate superior pharmacological properties in vivo, (2) offer a practical manufacturing process, and (3) exhibit improved stability and potency in vitro. Our work plan focused on development of a new arginine deiminase from *Mycoplasma arthritidis*. Several reports describe *M. arthritidis* ADI as a novel enzyme in this category (*48*−*50*), with a distinct physiological pH optimum, suitable activity, very low K_m, and unusual disulfide content that might be ideal as an in vivo therapeutic. We purified and characterized recombinant *M. arthritidis* ADI and employed a stable succinimidyl carbonate linker with a parsimonious PEGylation strategy to preserve enzyme activity and antitumor potency in cell culture, while achieving excellent pharmacokinetics and pharmacodynamics in rodent studies.

EXPERIMENTAL PROCEDURES

Materials. Hiload Superdex 200, Q Sepharose FF (QSFF), and Arginine Sepharose 4B resins were supplied by GE Healthcare (Piscataway, NJ), and Poros HS was supplied by Applied Biosystems (Foster City, CA). YM-100 (100 kDa MWCO) CentriPlus devices were from Millipore (Billerica, MA). Precast 4−20% Tris-glycine SDS−PAGE gels and cell culture media were obtained from Invitrogen (Carlsbad, CA). Titrisol iodine solution was obtained from EM Science (Gibbstown, NJ). 2,3-Butanedione monoxime was purchased from Alfa Aesar (Ward Hill, MA). Antipyrine and jack bean urease were supplied by Sigma. Anti-ADI rabbit serum was produced by BioSynthesis (Lewisville, TX). *P. putida* ADI (25 IU/mg) was obtained from Enzon Pharmaceuticals, Inc.

Synthesis of SC−PEG. A solution of 12 kDa mPEG-OH (12.3 g, 1.03 mmol) was azeotroped in 450 mL of toluene for 2 h while removing 150 mL of toluene/water, followed by cooling to 50 °C. To this was added triphosgene (0.31 g, 1.04 mmol) and pyridine (0.61 g, 7.6 mmol), and the mixture was stirred for 3 h at 50 °C, followed by the addition of *N*-hydroxyl succinimide (NHS, 0.36 g, 3.13 mmol) and pyridine (0.39 g, 5.0 mmol). This mixture was stirred overnight at 50 °C, followed by partial removal of the solvent by rotary evaporation under reduced vacuum and precipitation of the product with ether. The solid was collected, washed with ether, and recrystallized from DMF/IPA to yield the SC−PEG product (11.6 g, 0.97 mmol, 94%). ^{13}C NMR analysis was conducted: (75.4 MHz, $CDCl_3$) δ 168.14, 151.09, 71.54−67.95 (PEG), 56.65, 25.13. Other SC−PEG polymers with differing masses were synthesized by comparable steps (*51*).

Expression of *M. arthritidis* ADI gene in *E. coli*. *M. arthritidis* strain 14152 was obtained from the American Type Culture Collection. The ADI gene was isolated by PCR using the primer pair 5′-GGCAATCGATGTCTGTATTTGACAGTA-3′ and 5′-TGAGGATCCTTACTACCACTTAACATCTTTACG-3′ derived from the ADI sequence of *M. arginini* LBIF (GenBank Accession X54312). Thirty cycles were carried out (94 °C, 60 s; 37 °C, 180 s; 72 °C, 120 s). A single 1.2 kb fragment was cloned and sequenced and confirmed to have sequence similarity to ADI. The N-terminal region of the *M. arthritidis* gene was confirmed by inverse PCR methods. The five TGA codons in the isolated ADI gene which encode tryptophan in *Mycoplasma* were changed to TGG codons by oligonucleotide-directed mutagenesis. The gene was inserted into vector pET 27b+ (Novagen) and expressed in host BLR(DE3). The GenBank Accession Code has been assigned BD056868. DNA sequence confirmation of all ADI genes was performed on an ABI PRISM 310 Genetic Analyzer.

Purification of *M. arthritidis* ADI. Recombinant ADI was purified from inclusion bodies as described (*21*) with the following modifications. Inclusion bodies were resuspended in 6 M guanidine−HCl buffer containing 10 mM DTT and diluted 20-fold with refolding buffer containing 0.5 M arginine, and allowed to refold for at least 16 h at 4 °C. Chaotropic agent and reducing agent were then removed by diafiltration. The diafiltered ADI solution was applied to a Q Sepharose FF column which was pre-equilibrated with buffer A (20 mM sodium phosphate, pH 7.2). The loaded column was washed with 5 CV buffer A, and ADI was eluted with a 10−50% gradient of buffer B (20 mM sodium phosphate, pH 7.2, 1.0 M NaCl). The active peak fractions from QSFF were pooled and applied to an Arginine Sepharose 4B column which was pre-equilibrated with 20% buffer B. Any nonspecifically bound protein was removed from the column with 20% buffer B (5 CV), and ADI was eluted with a 20−50% gradient of buffer B.

[1] Abbreviations: ADI, arginine deiminase; AUC, area under the curve; CV, column volume; ELISA, enzyme-linked immunosorbent assay; HAc, acetic acid; HRP, horseradish peroxidase; i.m., intramuscular; i.v., intravenous; LOQ, limits of quantification; mAb, monoclonal antibody; mPEG, monomethoxy-PEG; MRT, mean retention time; MW, molecular weight; NHS, *N*-hydroxysuccinimide; PBS, phosphate-buffered saline; PD, pharmacodynamics; PEG, poly(ethylene glycol); PK, pharmacokinetics; RP, reversed phase; s.c., subcutaneous; SC, succinimidyl carbonate; SE-HPLC, size-exclusion high-performance liquid chromatography; $t_{1/2}$, serum half-life; TFA, trifluoroacetic acid; TNBS, trinitrobenzene sulfonic acid; UF/DF, ultrafiltration/diafiltration.

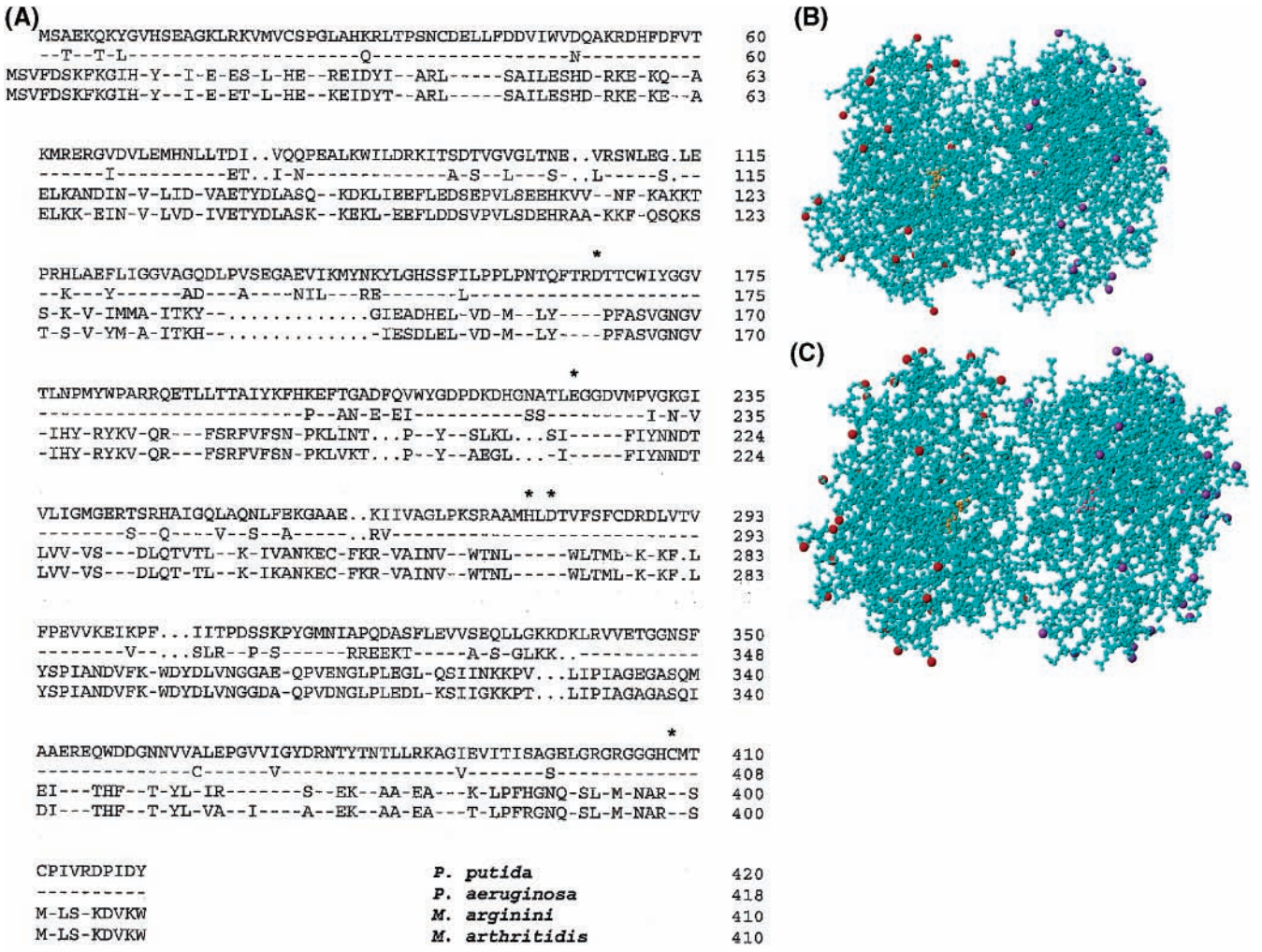

Figure 1. (A) Amino acid coding sequences of ADI from *P. putida* (U07185), *P. aeruginosa* (X14694), *M. arginini* (X54312), and *M. arthritidis* (AR112900) Putative active site catalytic residues are highlighted (*), and residues identical to the *P. putida* sequence (- - -) or residues missing in the aligned sequence (⋯) are indicated. (B) Molecular architecture of *M. arginini* ADI dimer (*23*) (PDB file name 1LXY) with lysine N-atoms highlighted by purple and red spheres in the two subunits. Citrulline covalently attached at the active site is depicted by orange and pink spheres, respectively. (C) Molecular modeling of *M. arthritidis* lysine positions based on *M. arginini* dimer structure with lysine N-atoms symbolized by purple and red spheres and the product citrulline covalently attached at the active site depicted in orange and pink spheres.

Table 1. Purification of Recombinant *M. arthritidis* ADI from Inclusion Bodies

purification step[a]	volume (mL)	protein concn (mg/mL)	total protein (mg)	specific activity (U/mg)	total activity[b] (IU)	purity[c] (%)
inclusion body solution	200	3.00	600			60.6
Q-sepharose-FF	450	0.43	198	22.0	4356	95.0
arginine sepharose	225	0.78	175	22.9	4007	99.9

[a] From 2 g of inclusion bodies. [b] 1 IU of ADI produces 1 μmol of citrulline per min at 37 °C. [c] From scanning densitometry of SDS-PAGE.

Purification and Gene Cloning of *P. putida* ADI. The ADI gene of *P. putida* ATCC 4359 was isolated by screening a genomic library of HindIII fragments in Lambda ZAP (Stratagene) with the *P. aeruginosa*-derived oligonucleotide 5′-CACTCCGAAGCCGGCAAACT-3′ as a ^{32}P-phosphorylated probe. The nonrecombinant ADI protein was also purified from the same strain to about 95% purity by published methods (*26*, *52*).

ADI Enzyme Assays. The ADI assay was modified from previous reports (*53*, *54*). The determination of citrulline (the product of ADI activity) in 96-well microplates utilized a colorimetric enzyme activity assay based on the Bagrel et al. method (*54*) using antipyrine, ferric chloride, and butanedione monoxime, which is well-suited to measure low citrulline concentrations in the range 0−0.25 mM; this assay was also used for K_m determinations. Another assay based on the Oginsky method (*53*) using only butanedione monoxime is less sensitive but better suited to measure citrulline in the range of ≥0.2−2.5 mM. Data were analyzed with *SigmaPlot*. ADI activity assays for blood plasma samples included urease (1 mg/mL) in the assay buffer (0.2 M Na phosphate, 0.2% BSA, pH = 7.3 ± 0.1) with 2.5 mM arginine. Plates were read at 490 nm, and the data were analyzed using Microsoft *Excel*.

PEGylation of ADI. The PEGylation of *M. arthritidis* ADI (1−20 mg/mL; 0.1 M sodium phosphate, pH = 8.0 ± 0.1, 145 mM NaCl) with 12 kDa PEG−SC and 20 kDa PEG−SC followed identical procedures. Reaction stoichiometries with 10-fold to 50-fold molar excess of PEG to ADI subunit were examined. The SC−PEG polymers were dissolved at a concentration of 125 mg/mL in 2 mM hydrochloric acid and added to a solution of, e.g., 5 mg/mL native ADI in 100 mM phosphate buffer. After 60 min reaction time at 22 °C, free glycine was added in 15-fold molar excess to PEG to terminate the reaction, and residual free PEG compound was removed by repeated

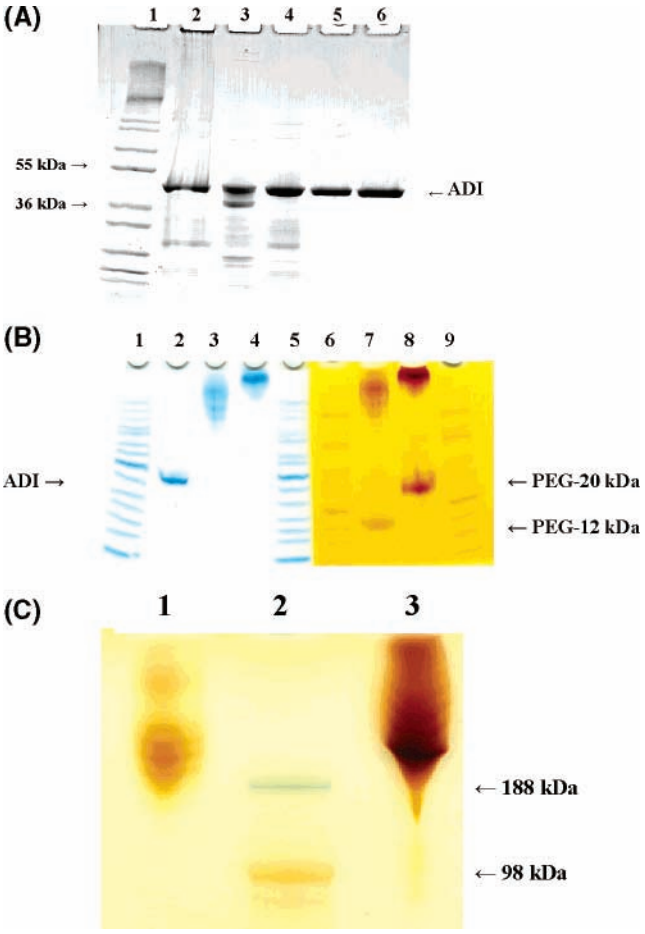

Figure 2. (A) SDS-PAGE analysis of purification steps for *M. arthritidis* ADI: lane 1, mark-12 molecular weight markers; lane 2, inclusion bodies in guanidine hydrochloride; lane 3, refolded ADI solution; lane 4, diafiltration; lane 5, eluate from QSFF; lane 6, eluate from arginine−sepharose 4B. The samples (1 μg per lane) were denatured by heating at 85 °C for 3 min in the presence of 12 mM β-mercaptoethanol. (B) SDS-PAGE (4−20%) analysis of multi-PEGylated *M. arthritidis* ADI with either 12 kDa or 20 kDa SC-PEG polymers. Lanes 1 and 5, molecular weight markers (Fermentas); lane 2, native ADI; lane 3, 12 kDa PEG−ADI; lane 4, 20 kDa PEG−ADI; lanes 6 and 9, molecular weight markers (Bio-Rad); lane 7, 12 kDa PEG−ADI; lane 8, 20 kDa PEG−ADI. Lanes 1−5 are stained with Coomassie Blue; lanes 6−9 are stained with iodine. (C) PEG staining of PEG−ADI compounds after extended run on SDS-PAGE. Lane 1, 12 kDa PEG−ADI (1 μg); lane 2, molecular weight markers (Invitrogen SeeBlue Plus2); lane 3, 20 kDa PEG−ADI (2 μg). Gel staining is with iodine to identify PEG bands.

dilution of the reaction mixture with formulation buffer and concentration using a 100 kDa molecular weight cutoff (MWCO) centrifugal filter unit. While PEGylated ADI was retained by the device, free PEG compound passed through the pores. Several rounds of dilution and concentration resulted in higher than 20 mg/mL PEGylated ADI protein that contained a minor amount (<0.1 mg/mL) of the free PEG polymer. All samples were recovered in high yield (70−90%) and filtered through a 0.22 μm filter. In some studies, PEG−ADI was purified with Superdex-200 SEC with a mobile phase of 50 mM Na phosphate, pH = 6.5, 140 mM NaCl.

Scheme 1. SC Synthesis

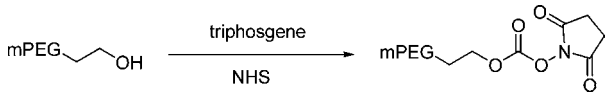

Scheme 2. Reaction of SC-PEG with Amine of Protein to Form a Urethane Linkage

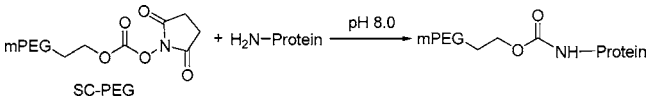

Cell Culture Studies. The cell lines used in these experiments were as follows: CCRF S-180 II (mouse sarcoma), SK-MEL-2 (human melanoma), SK-HEP-1 (human liver adenocarcinoma), PC-3 (human prostate adenocarcinoma), and KHOS/NP (human osteosarcoma), which were obtained from the American Type Culture Collection. RT-PCR analysis confirmed AS deficiency in these cells. All cells were cultured in Minimal Essential Medium with Earle's salts, supplemented with 10% (v/v) fetal bovine serum, 0.1 mM nonessential amino acids, and 1 mM sodium pyruvate. Quantitative cell proliferation assays by the MTT or Alamar Blue methods were performed with published procedures (*41*, *43*) to determine IC_{50} values. Typically, cells (2.5×10^3) in a volume of 0.1 mL of growth medium were added to each well of a 96-well plate. ADI was diluted by 2-fold serial dilutions into the growth medium (0.1 mL). The 96-well plates were incubated for 72 h at 37 °C, before dye addition, processing, and analysis using *SOFTmax PRO 4.0* template and Microsoft *Excel*.

Amino Acid Analysis. Arginine levels in mouse or rat plasma were determined by derivatization with FMOC-Cl followed by RP-HPLC with fluorescence detection using a Phenomenex Synergi Max-RP column at 40 °C. Mobile phase A was 0.1% TFA in water; mobile phase B was 0.1% TFA in 80% acetonitrile and 20% water. The limits of quantification were 2.3 μM arginine.

Analytical Characterization of ADI and PEG−ADI. Protein concentrations were determined by the bicinchoninic acid assay (BCA) (*55*) using a BSA standard and confirmed by UV absorbance at 280 nm. TNBS (*56*) and fluoresamine (*57*) assays for determination of primary amines were conducted as described. N-terminal protein sequencing was performed on PROCISE (Applied Biosystems).

IEF was conducted on Invitrogen precast vertical Novex pH 3−10 mini gels. Western blot analysis was performed with anti-ADI rabbit antiserum as a primary antibody and goat anti-rabbit HRP as a secondary antibody with a TMBM peroxidase substrate. Iodine staining (*43*) of SDS-PAGE gels was performed after gels were rinsed with distilled water and placed in 5% barium chloride solution. After 10 min of gentle mixing, the gels were again rinsed with water and placed in 0.1 M Titrisol iodine solution for color development.

Table 2. Features and Analysis of *M. arthritidis* ADI and Bioconjugates[a]

compound	sp. act. (IU/mg)	linker	PEG (%) TNBS[b]	PEG (%) Fl[b]	PEG mass (kDa)	K_m (μM)	pI	mass[c]	SEC[d] (kDa)	SDS-PAGE (kDa)	IC_{50}[e] (ng/mL)
ADI	22.9 ± 1.4	none	0	0	0	10.4	5.35	46182	92.5	46	11 ± 1
12 kDa PEG-ADI	13.6 ± 0.7	SC	32.9 ± 4.3	33.7 ± 3.5	264	8.8			>700	>200	13 ± 1
20 kDa PEG-ADI	10.9 ± 0.6	SC	33.3 ± 2.4	35.5 ± 1.3	452	11.9			>700	>200	14 ± 1

[a] The described conjugates were prepared at 17.5:1 PEG/ADI subunit reaction ratio and used in PK/PD studies. [b] PEG (%) is the fraction of available ADI amines modified by PEG and corresponds to 22 PEGs per ADI dimer for either bioconjugate. [c] LC/MS and sequence calculated mass are identical, and protein sequence analysis confirmed N-terminal methionine removal. [d] ADI is ≥98% dimer in gel filtration. [e] ADI protein concentration providing 50% inhibition of CCRF S-180 II mouse sarcoma cultures.

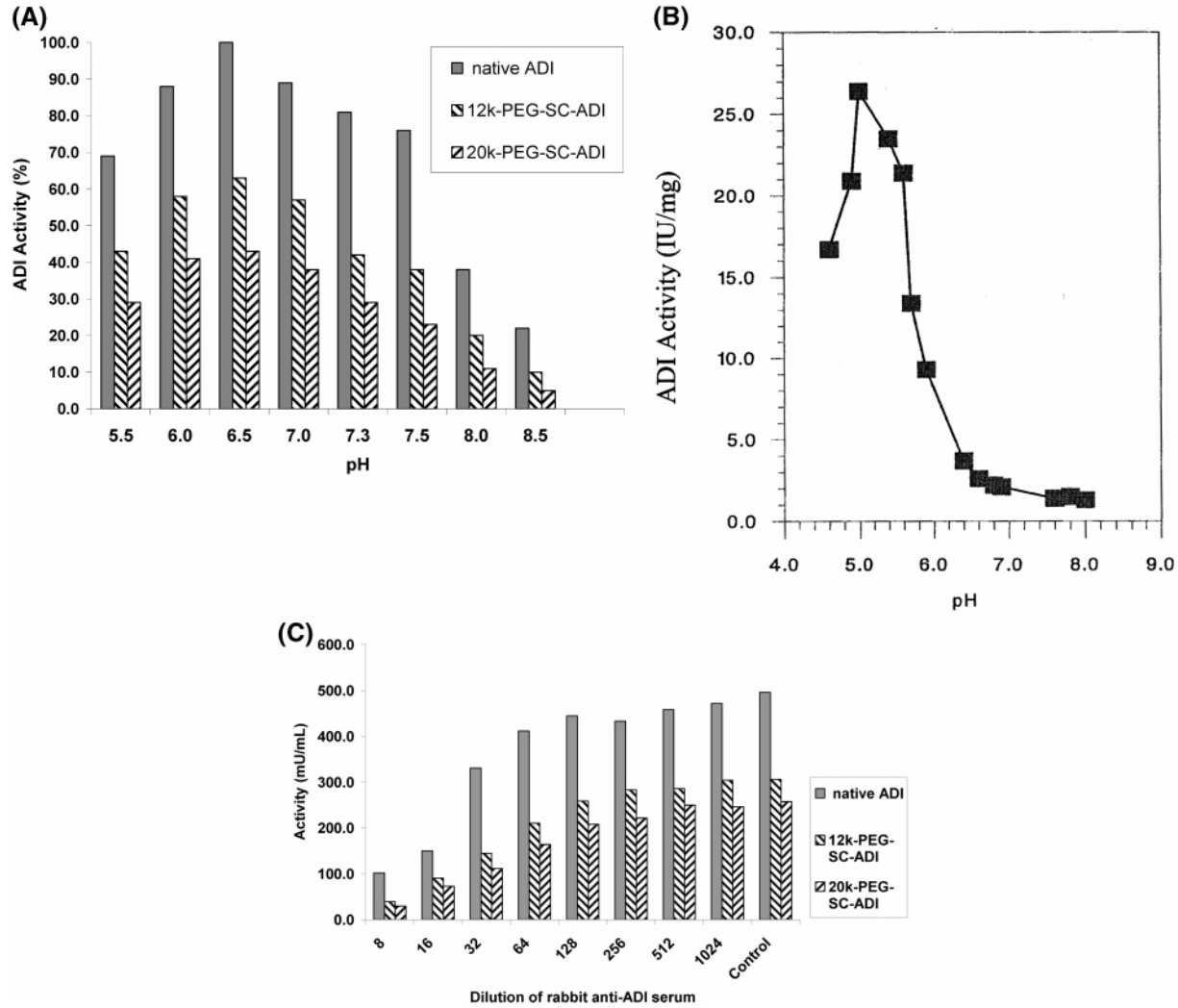

Figure 3. pH dependence of *M. arthritidis* ADI and PEG−ADI activity. (A) ADI, 12 kDa PEG−ADI, and 20 kDa PEG−ADI activity are measured at eight pH values. Values (%) are shown relative to native ADI at pH = 6.5 (100%). (B) pH profile of specific activity of *P. putida* ADI. (C) Stability studies in rat plasma for *M. arthritidis* ADI, 12 kDa PEG−ADI, and 20 kDa PEG−ADI stored at 4, 25, and 37 °C, and assayed at 10 min, 18 h, or 5 days. Relative activity is shown with 100% corresponding to the 4 °C stock solution.

Mass values of ADI were determined with liquid chromatography/mass spectrometry (LC/MS). Apparent molecular weights (Stoke radius) of the compounds were estimated using Superdex 200 HR 10/30 gel filtration column chromatography. The mobile phase was composed of 100 mM sodium phosphate, pH 6.8, at 24 °C. Evaporative light scattering detection (ELSD; Sedere, Inc.) allowed free PEG detection. Additionally, analysis of molecular masses on 4−20% SDS-PAGE gels was performed using protein and PEG−protein standards.

Pharmacokinetic Analysis of PEG−ADI in Mice and Rats. Single i.v., i.m., or s.c. injections of 5, 0.5, or 0.05 IU/mouse of ADI, 12 kDa PEG−ADI, or 20 kDa PEG−ADI were administered to female Balb/c mice on day 0. A total of 171 mice were assigned into 9 groups, with 3 mice/timepoint. The mice were bled at the following timepoints: −1 h, 1 h, 24 h, and 3, 6, 10, and 15 days. Animals were bled through cardiac puncture, and plasma samples were isolated. Plasma concentration of native or PEGylated ADI was determined by enzyme assay and by cell-based cytotoxicity assay, and plasma arginine concentration was determined by an HPLC assay. Descriptive statistics (mean, SD) and noncompartmental analysis were used to calculate pharmacokinetic parameters using *WinNonlin* version 4.0.1 (Pharsight Corp.). The pharmacokinetic parameters estimated were $AUC_{0-\infty}$ (the AUC from time 0 to infinity), C_{max} (maximum plasma concentration), T_{max} (the time to reach maximum concentration), and half-life of λ_z (first-order elimination rate constant). The $AUC_{0-\infty}$ values were calculated using the linear trapezoidal method. Statistical comparisons between data sets were performed using paired *T*-test in *Excel* software.

Rat PK analysis was conducted with similar methods. Single i.v. injection of 8, 2.5, or 0.8 IU/kg of ADI, 12 kDa PEG−ADI, or 20 kDa PEG−ADI was administered to female CD rats on day 0. The rats (3/timepoint) were bled at the following timepoints: −1 h, 1 h, 24 h, and 5, 7, 10, and 15 days. Animals were bled through retro-orbital plexus, and plasma samples were isolated for enzyme, bioassay, and HPLC analysis.

RESULTS AND DISCUSSION

Recombinant ADI from *M. arthritidis*. The gene for *M. arthritidis* ADI was cloned from the same ATCC deposit 14152 as previously used for nonrecombinant ADI characterization (*48*−*50*). We also cloned and sequenced the ADI gene from *P. putida* for an extended comparison of primary structures in the ADI family. As shown in Figure 1A, it appears that the *M. arthritidis* ADI and *P. putida* ADI sequences conform overall to previously reported ADI primary structures, with conservation also of key catalytic residues, when compared to *M. arginini* and *P. aeruginosa* ADI (86% and 84% identity, respectively, among common genus). Modeling of the exposed lysine residues

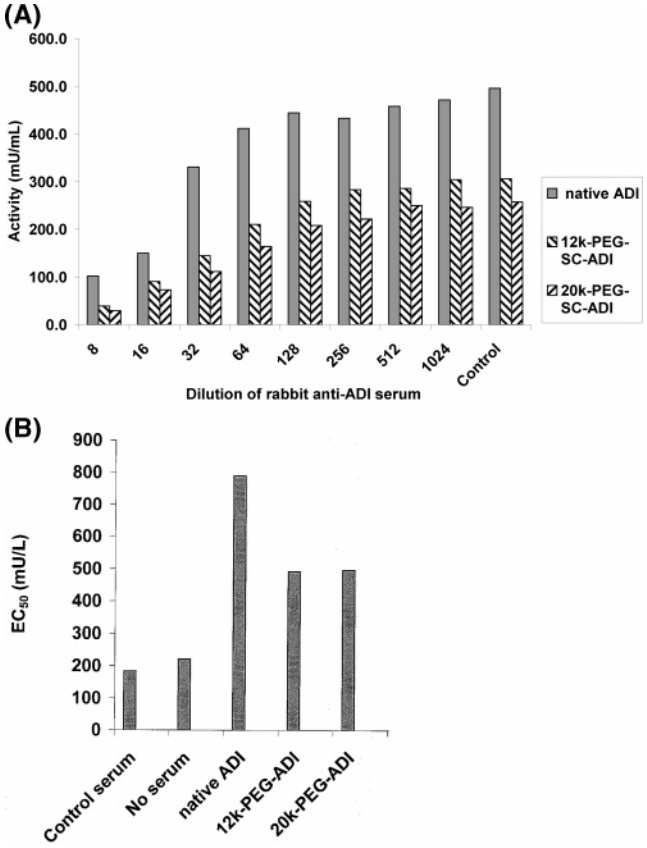

Figure 4. Neutralizing anti-ADI antibodies of rabbit antiserum raised against native *M. arthritidis* ADI. (A) Enzyme activity of ADI, 12 kDa PEG−ADI, and 20 kDa PEG−ADI were measured in the presence of increasing dilutions of rabbit antiserum. The control assay contained an 8-fold dilution of preimmunized rabbit serum. (B) Cell culture assays with ADI-sensitive tumor line CCRF S-180 II determined the EC_{50} values of ADI, 12 kDa PEG−ADI, and 20 kDa PEG−ADI using serial dilutions of the ADI compounds in the presence of a 250-fold dilution of rabbit anti-ADI serum. The control serum is from preimmunized rabbits. Control and serum-free samples contained native ADI; the PEG−ADI samples contained only conjugates; all samples included the rabbit antiserum (1:250 dilution).

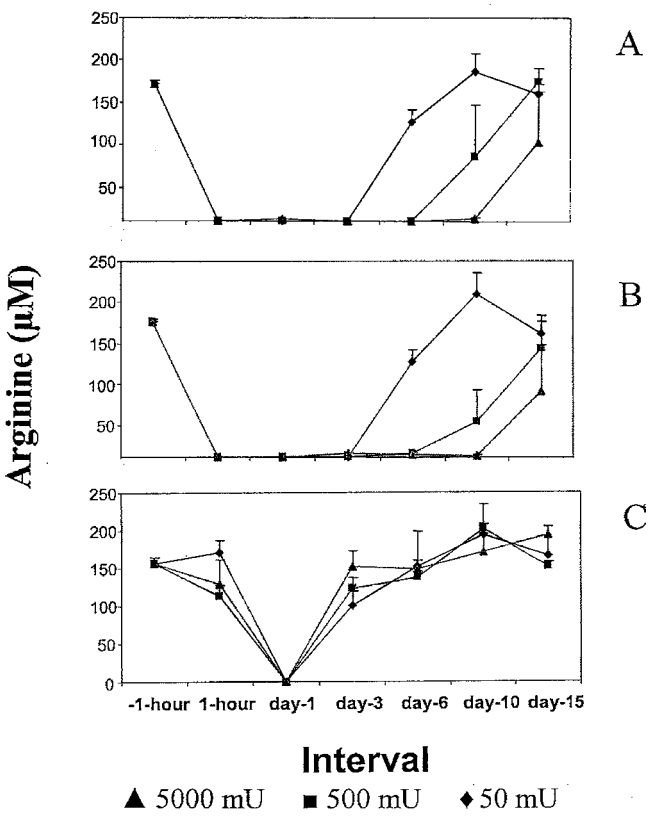

Figure 5. Pharmacodynamics of *M. arthritidis* ADI and PEG−ADI in mice following single i.v. administration. (A) 20 kDa PEG−ADI. (B) 12 kDa PEG−ADI. (C) unmodified ADI. Arginine levels in plasma (mean ± SD) are measured at the indicated durations following 5000 mU (▲), 500 mU (■), or 50 mU (♦) doses.

on the surface of *M. arginini* ADI (29 lysines/subunit; Figure 1B) or *M. arthritidis* ADI (32 lysines/subunit; Figure 1C) reveals numerous positional substitutions of the primary amines available for conjugation, and this may influence the properties of these bioconjugates. Of these four ADI proteins, the *M. arthritidis* ADI dimer has both the greatest number and the least clustering of the surface lysine residues, providing a potential advantage for conjugation. However, an understanding of biochemical properties of the enzymes will follow purification of the recombinant proteins. This was achieved as summarized in Table 1 and Figure 2A for recombinant *M. arthritidis* ADI. Specific activity of this enzyme was about 30% higher than previous preparations of recombinant *M. arginini* ADI prepared and assayed by a similar protocol (Filpula, D. Unpublished results). Moreover, the K_m of *M. arthritidis* ADI (10.4 μM) is notably lower than for any other reported ADI enzyme (*25*, *26*, *29*, *30*, *33*, *52*). Nonetheless, the *M. arthritidis* ADI clearly resides in the same structure−function design of previously described ADI. Although we used the same ATCC deposit as reported for the prior *M. arthritidis* nonrecombinant ADI characterization (*48*−*50*), we cannot exclude the possibility that there exists another modified or distinct ADI enzyme not identified in our present studies; alternatively, our current thorough studies on this recombinant enzyme may define the only ADI enzyme in this species. As summarized in Table 2, *M. arthritidis* ADI is a homodimer of 40 182 Da subunits, and its IEF-determined pI agrees with the predicted pI = 5.35 for this protein. Potent growth inhibition of cultured sarcoma (Table 2), hepatoma, and melanoma tumor cells was demonstrated. Investigations of the capacity of this enzyme to inhibit the growth of several tumor cell lines (including CCRF S-180 II, SK-MEL-2, KHOS/NP, SK-HEP-1, and PC-3) demonstrated about 50% lower IC_{50} values than for similar recombinant *M. arginini* ADI preparations (data not shown).

In comparison, we observed that *P. putida* ADI, also an apparent homodimeric enzyme, exhibited suitable specific activity (25 IU/mg) at pH 5.5. However, this enzyme was not a potent inhibitor of growth in these tumor cell lines and exhibited IC_{50} values 100- to 1000-fold higher than the *M. arthritidis* enzyme. This may be explained in part by the higher K_m value of the *P. putida* enzyme (K_m = 1.8 mM without $MgCl_2$; K_m = 0.2 mM with $MgCl_2$). However, another significant factor is the pH profile for enzyme activity of *P. putida* ADI whereby only 5−10% of enzyme activity is retained at physiological pH when compared to its pH optimum of 5.5. Therefore, the *P. putida* ADI was not successfully developed as a lead pharmaceutical in either its native or PEGylated format.

PEGylated *M. arthritidis* ADI. The development of foreign proteins as therapeutics frequently requires the employment of controlled release technology, and most frequently PEGylation (*8*). It was certain from pilot experiments that unmodified ADI protein would clear too rapidly from animals and also exhibit profound immunogenicity. Therefore, we focused our investigations on the optimal development of a PEGylated *M. arthritidis* ADI, which conserved the attractive catalytic parameters of the enzyme, while introducing the desired pharmacokinetic and pharmacodynamic features in animal models. Although multiple attachment of 5 kDa PEG polymers has been the best developed approach for pharmaceutical enzymes, such as ADAGEN and

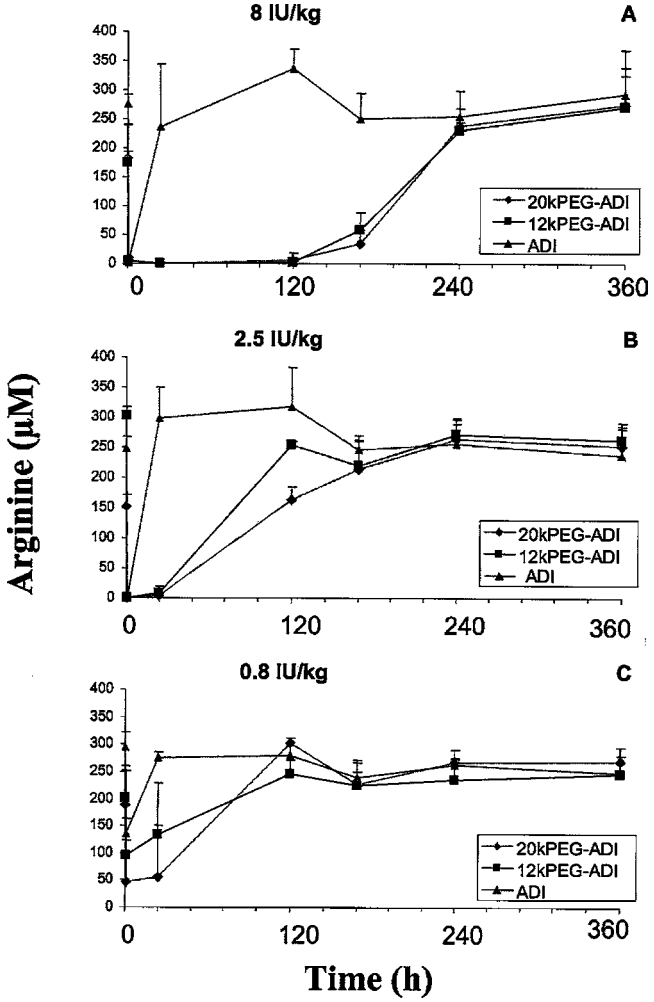

Figure 6. Pharmacodynamics of *M. arthritidis* ADI and PEG−ADI in rats following single i.v. administration. (A) 8 IU/kg dose. (B) 2.5 IU/kg dose. (C) 0.8 IU/kg dose. Arginine levels in plasma are measured at the indicated durations following injection of ADI (▲), 12 kDa PEG−ADI (■), or 20 kDa PEG−ADI (◆).

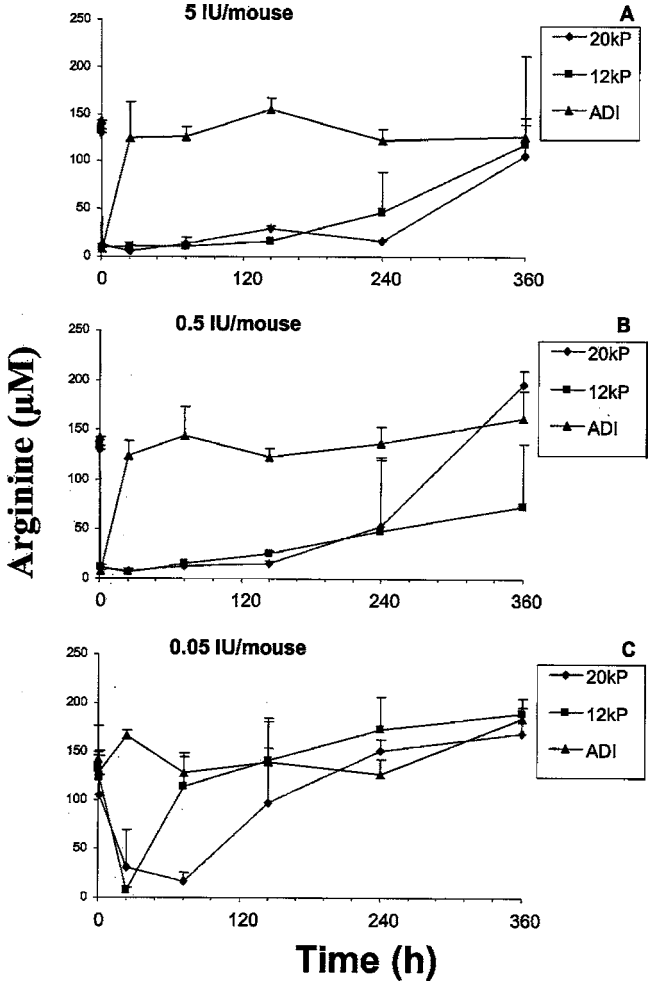

Figure 7. Pharmacodynamics of *M. arthritidis* ADI and PEG−ADI in mice following single i.m. administration. (A) 5000 mU. (B) 500 mU. (C) 50 mU. Arginine levels in plasma are measured at the indicated durations following injection of ADI (▲), 12 kDa PEG−ADI (■), or 20 kDa PEG−ADI (◆).

ONCASPAR (*10*), our studies and published reports (*27*, *31*) demonstrated a benefit to employment of larger PEG polymers to extend the PK/PD and AUC performance of the arginine-depleting compounds. Nonetheless, we wished to limit the quantities of the attached PEG to the extent possible due to process design, potency, and cost of goods considerations. Therefore, we sought to revisit the prior conclusions that multi-PEGylation of ADI with the largest PEG polymers is necessary for optimal performance. Specifically, we have undertaken a rigorous in vitro and in vivo comparative investigation of two multi-PEGylated *M. arthritidis* ADI bioconjugates having either 12 kDa PEG polymers or 20 kDa PEG polymers.

Succinimidyl carbonate (SC) linkers were chosen for this study on the basis of their confirmed chemical stability (*42*, *51*) in contrast to the hydrolytically labile succinimidyl succinate linkers employed in other PEG−ADI reports (*31*, *37*). The synthesis of SC-PEG-12 kDa or SC-PEG-20-kDa is shown in Scheme 1, while the reaction of these activated polymers with primary amines of ADI is shown in Scheme 2. The PEGylation reactions were performed at an elevated ADI concentration (5 mg/mL) and a diminished reactant stoichiometry with only 17.5:1 molar excess of activated PEG over ADI subunit, in contrast to prior conjugate studies which utilized low protein concentrations (1 mg/mL) and a 40-fold excess of activated PEG (*27*, *31*). The current approach provided complete conversion of ADI to multi-PEGylated derivatives using a manageable concentration of polymers in the reaction while retaining excellent activity as shown in Table 2. Further increases in PEG reactant concentrations provided only a marginal increase in PEG attachments, which plateau at about 40% modification of available amines, while further diminishing the specific activity of the compounds. Since both the optimized 12 kDa and 20 kDa PEG−ADI compounds exhibited about 33% modification, which was verified by both TNBS and fluoresamine methods, a direct comparison of biochemical and pharmacological performance for the conjugates is possible. SDS-PAGE analysis of the PEG−ADI preparations is also shown in Figure 2B,C which illustrate the total conversion of the protein into multi-PEGylated compounds, the degree of product heterogeneity, and the large apparent molecular weights of the bioconjugates. Figure 2B also illustrates the retention of significant amounts of free PEG (16% and 5% of the total PEG in the preparations for 20 kDa and 12 kDa reactions, respectively) following two rounds of dilution and concentration through a 100 kDa molecular weight cutoff filtration membrane. Although the free PEG can be completely removed by size exclusion chromatography, smaller PEGs prove easier to separate in standard UF/DF manufacturing processes.

Key biochemical properties are summarized in Table 2. Retention of ADI specific activity is 59% and 48% for the 12 kDa and 20 kDa PEG−ADI compounds, respectively, and K_m determinations were not notably altered by PEGylation. The improvement in PEG−ADI specific activity relative to other

examined formulations might provide an opportunity for reduced dosing of these compounds. The total PEG mass differs by nearly 200 kDa between these two PEG−ADI compounds; yet, both are enormous molecules in hydrodynamic volume as demonstrated by the size exclusion chromatography analysis. A critical measurement of the biological potency of the two PEG−ADI conjugates was performed by evaluation of the inhibitory activity in cell culture proliferation assays of several tumor cell lines known to be sensitive to arginine deprivation. For example, the IC_{50} values for native ADI and the two PEG−ADI conjugates differ by only 20−30% with the CCRF S-180 II mouse sarcoma tumor cell line (Table 2). Other sensitive tumor lines exhibited comparable results. These data confirm that the intrinsic catalytic characteristics of *M. arthritidis* ADI are well-preserved in these bioconjugates.

The pH profile for enzymatic activity may be crucial for the suitability of enzymes as successful therapeutics. Therefore, we examined these characteristics both for the native enzyme and the two PEGylated derivatives. As shown in Figure 3A, *M. arthritidis* ADI activity exhibits a broad pH range; although activity is maximal at pH 6.5, about 80% of the activity is retained at pH 7.5. The 12 kDa and 20 kDa PEG−ADI derivatives demonstrated very similar pH dependence that confirms that extensive lysine derivatization does not appear to alter the catalytic profile of the enzyme. For comparison, Figure 3B displays the determined pH dependence for *P. putida* ADI activity. Less than 10% of maximal activity remains at physiological pH for this *Pseudomonas* enzyme which is most active at pH 5.5. PEG derivatives of this ADI exhibited similar profiles (data not shown). Although enzymes with unfavorable K_m and pH profile characteristics may produce pharmacological effects, the required elevated dosing regimen discourages development of these compounds.

Since stability is another crucial concern for the PEG−ADI compounds, we investigated enzyme activity over a period of 5 months stored in PBS buffer, pH 7.4, at 4 °C. Both native ADI and PEG−ADI compounds retained full activity (±10%) for the duration of this study. Further, both PEG−ADI compounds retained full activity (±10%) in mouse plasma over a 5 day incubation at 4, 25, or 37 °C, while native ADI exhibited slight (20−30%) activity losses at 37 °C. Interestingly, the PEG−ADI compounds were not completely stable in rat plasma under the same stability parameters. As shown in Figure 3C, about half of the activity of these compounds was lost in rat plasma at 37 °C over 5 days. The root cause of this instability was not determined but may correspond to proteolysis. While these conjugates are extensively shielded with PEG polymers, the density of attachment sites may not preclude all protein−protein interactions in solution, as suggested by the molecular model in Figure 3C.

Immunogenicity is another important concern in the development and drug monitoring of protein therapeutics, including PEGylated proteins. Binding antibodies are commonly encountered, and neutralizing antibodies versus PEGylated enzymes have been investigated (*5*, *9*, *41*, *58*, *59*). It is well-established that proteins, including ADI proteins, demonstrate markedly diminished immunogenicity following PEGylation (*8*, *27*, *58*; Filpula, D. Unpublished results). We wished to address here a more specific question on the antigenicity of the PEG−ADI compounds. Rabbit antisera versus unmodified *M. arthritidis* ADI were produced with complete Freund's adjuvant. As shown in Figure 4A, at very high titers (<1:50 dilution), rabbit antibodies versus ADI are able to significantly neutralize the enzyme activity of ADI and, to a lesser extent, the activity of either PEG−ADI compound. Figure 4B shows that this effect may also be observed when bioassays of serially diluted ADI compounds are conducted with arginine requiring cell cultures

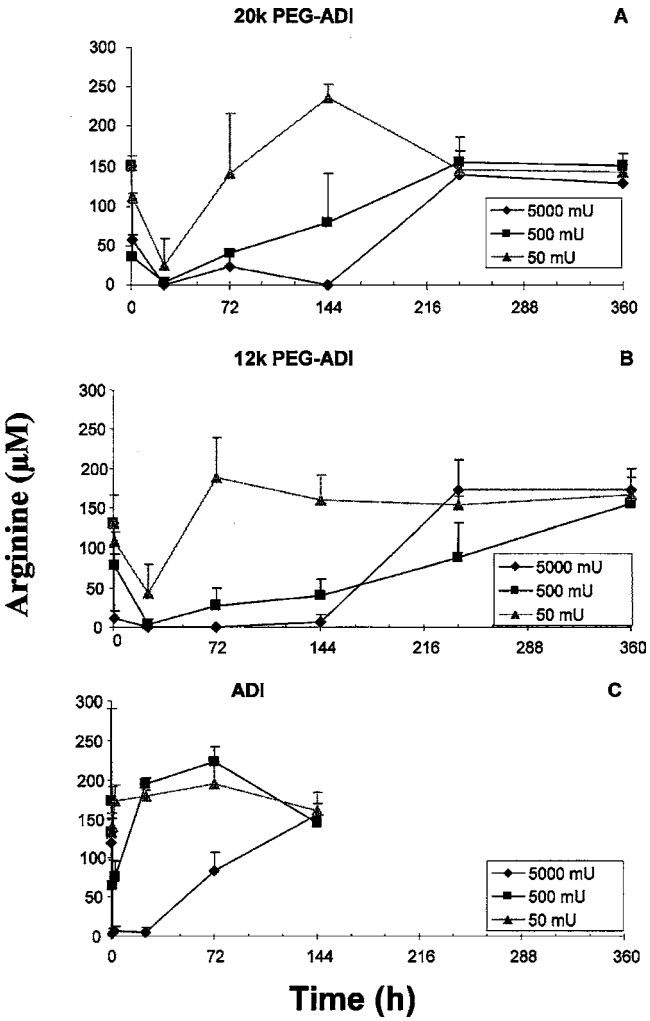

Figure 8. Pharmacodynamics of *M. arthritidis* ADI and PEG−ADI in mice following single s.c. administration. (A) 20 kDa PEG−ADI. (B) 12 kDa PEG−ADI. (C) unmodified ADI. Arginine levels in plasma are measured at the indicated durations following 5000 mU (◆), 500 mU (■), or 50 mU (▲) doses.

in the presence of a fixed concentration of neutralizing antiserum. The greater sensitivity of unmodified ADI to the antiserum compared to the conjugates reverses the slight potency advantage of the native ADI over the conjugates when measured in the absence of the antiserum, and this may suggest another benefit for the PEG−ADI compounds in an in vivo setting. In contrast, a previous study suggested neutralizing antibodies versus *M. hominis* ADI were not generated by immunization (*27*). Although the effects of neutralizing antibodies in our present study were not of high potency, these data once again illustrate that the PEGylated ADI compounds, although chemically shrouded in their molecular environment, are not expected to be totally secluded from protein−protein interactions in vivo.

Pharmacodynamics of PEG−ADI. A hallmark of the beneficial effects of PEGylation is an increased blood residency time of the bioconjugates. In order for PEG−ADI to exhibit prolonged pharmaceutical effects in therapy of oncological disease or inflammatory disorders, a potent and sustained pharmacodynamic effect is desired, whereby arginine concentrations in blood, and ultimately in the diseased tissues, are reduced to undetectable levels. We examined the pharmacodynamic potency of our experimental PEG−ADI compounds in rodent studies. As shown in Figure 5A,B, i.v. administration of 5 IU (5000 mU) of either 20 kDa PEG−ADI or 12 kDa PEG−ADI per mouse depleted plasma of detectable arginine within 1 h and maintained undetectable levels through 10 days (LOQ =

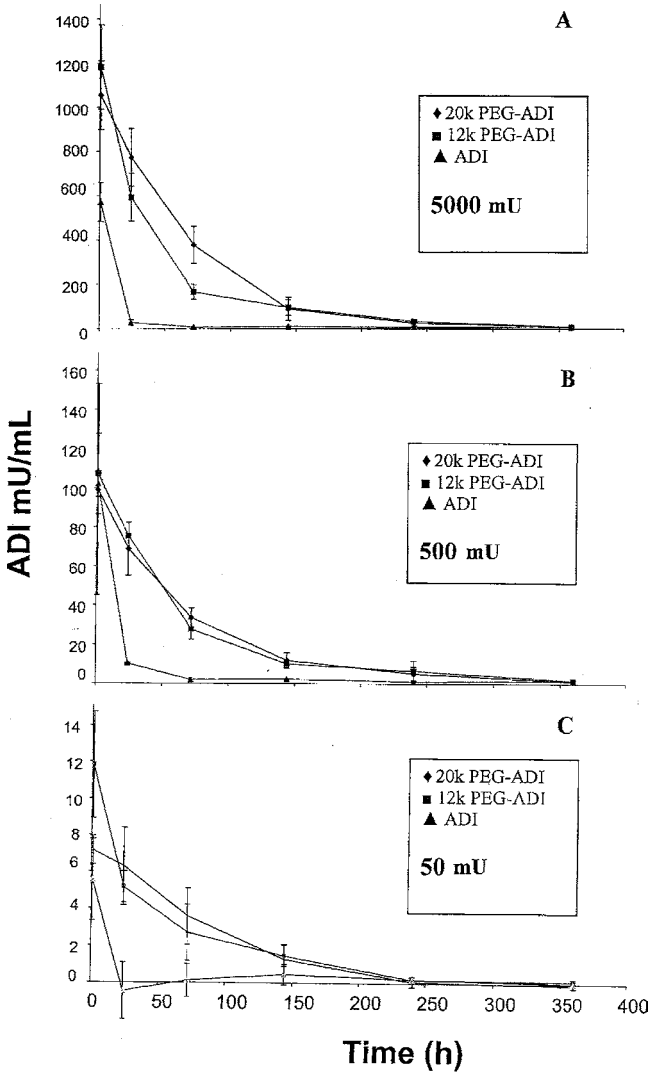

Figure 9. Pharmacokinetics of *M. arthritidis* ADI and PEG−ADI in mice following single i.v. administration. (A) 5000 mU. (B) 500 mU. (C) 50 mU. ADI concentrations (activity) in plasma (mean ± SD) are measured by enzyme assay at the indicated durations following injection of ADI (▲), 12 kDa PEG−ADI (■), or 20 kDa PEG−ADI (◆).

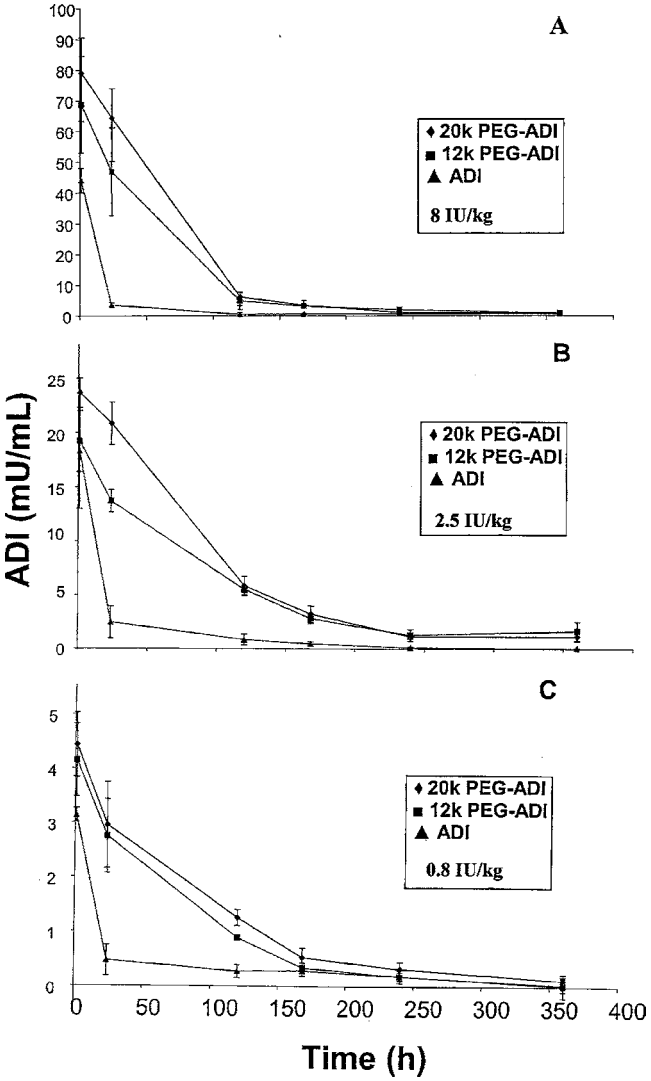

Figure 10. Pharmacokinetics of *M. arthritidis* ADI and PEG−ADI in rats following single i.v. administration. (A) 8 IU/mg dose. (B) 2.5 IU/mg dose. (C) 0.8 IU/mg dose. ADI activity in plasma is measured by enzyme assay at the indicated durations following injection of ADI (▲), 12 kDa PEG−ADI (■), or 20 kDa PEG−ADI (◆).

2.3 μM arginine in these studies). These PD effects compare favorably to prior reports with i.v. administration of other ADI formulations (*27*, *31*). The unmodified ADI protein at any dose produced only transient arginine depletion for no more than 1 day (Figure 5C; data not shown), whereas the PEG−ADI compounds suppressed arginine plasma levels in a dose-dependent manner (Figure 5A,B), with both conjugates demonstrating comparable dose−response effects. Additional studies demonstrated that the PD effects are rapid for both ADI and PEG−ADI, with elimination of all detectable plasma arginine occurring within 10 min of compound administration. Since the ADI dose was based on units of activity, the 12 kDa PEG−ADI compound produced similar PD effects at about 75% of the protein dose of the 20 kDa PEG−ADI conjugate (see Table 2).

In Figure 6, similar PD investigations were conducted in rats. Since arginine has been reported to be an essential amino acid in rats, but not mice, a reduced dosing schedule for the compounds was utilized, and no toxicity was observed in the animals under these conditions. At the highest i.v. dose (8 IU/kg = 1.6 IU/rat), both the 12 kDa and 20 kDa PEG−ADI compounds eliminated detectable arginine from plasma rapidly and sustained this condition for 5 days (Figure 6A). This dose−response study also revealed a comparability of the two conjugates at lower doses (Figure 6B,C). The necessity for PEGylation in development of this enzyme therapeutic is evident from the short-lived PD effect of unmodified ADI even at the highest dose, both in these rat studies and in all of the mouse investigations.

Administration of PEG−ADI in a clinical setting may benefit from the convenience of intramuscular (i.m.) or subcutaneous (s.c.) injection. As shown in Figure 7, the dosing schedule employed for i.v. administration in mice produced a less pronounced PD effect via i.m. administration. Although arginine levels in plasma remained severely diminished for 10 days, concentrations of this amino acid were within the limits of detection and quantitation. The 12 kDa and 20 kDa PEG−ADI again produced comparable dose-dependent PD effects. Investigation of PD effects of PEG−ADI using this same dosing schedule by s.c. administration in mice (Figure 8) revealed comparable outcomes but with two interesting differences. The s.c. route of injection of both PEG−ADI compounds did result in diminution of plasma arginine levels to essentially undetectable levels for about 6 days; however, the duration of the PD effect was actually shortened when compared to i.m. administration. These pharmacological effects may have a biological basis relating to biodistribution of the compounds under different

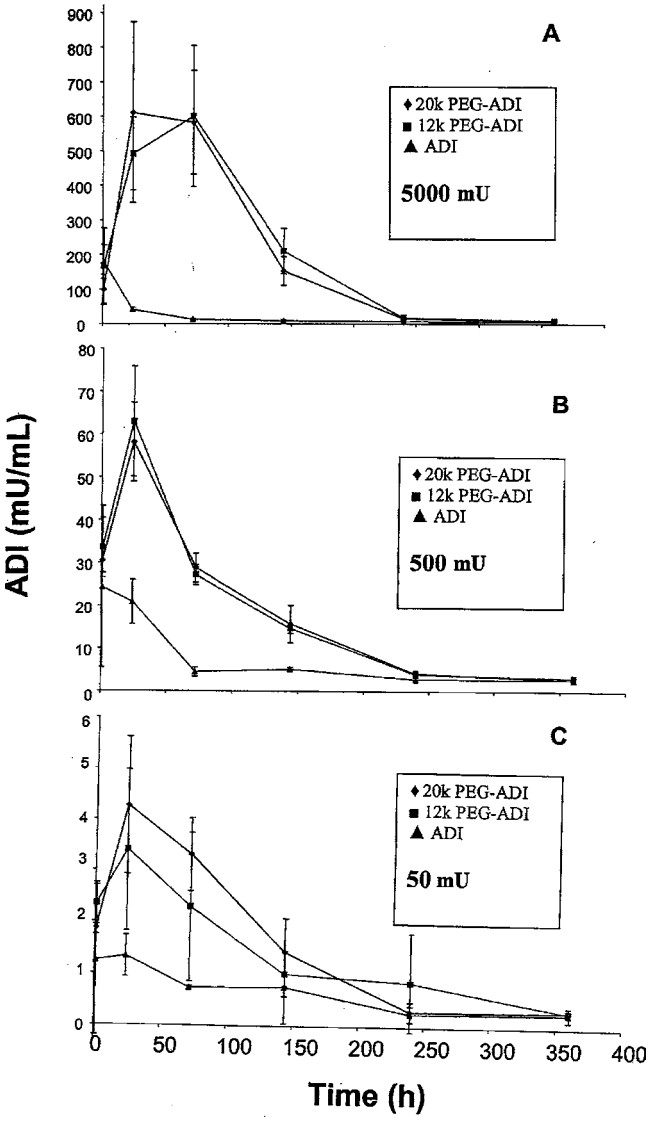

Figure 11. Pharmacokinetics of *M. arthritidis* ADI and PEG−ADI in mice following single i.m. administration. (A) 5000 mU. (B) 500 mU. (C) 50 mU. ADI activity in plasma is measured by enzyme assay at the indicated durations following injection of ADI (▲), 12 kDa PEG−ADI (■), or 20 kDa PEG−ADI (◆).

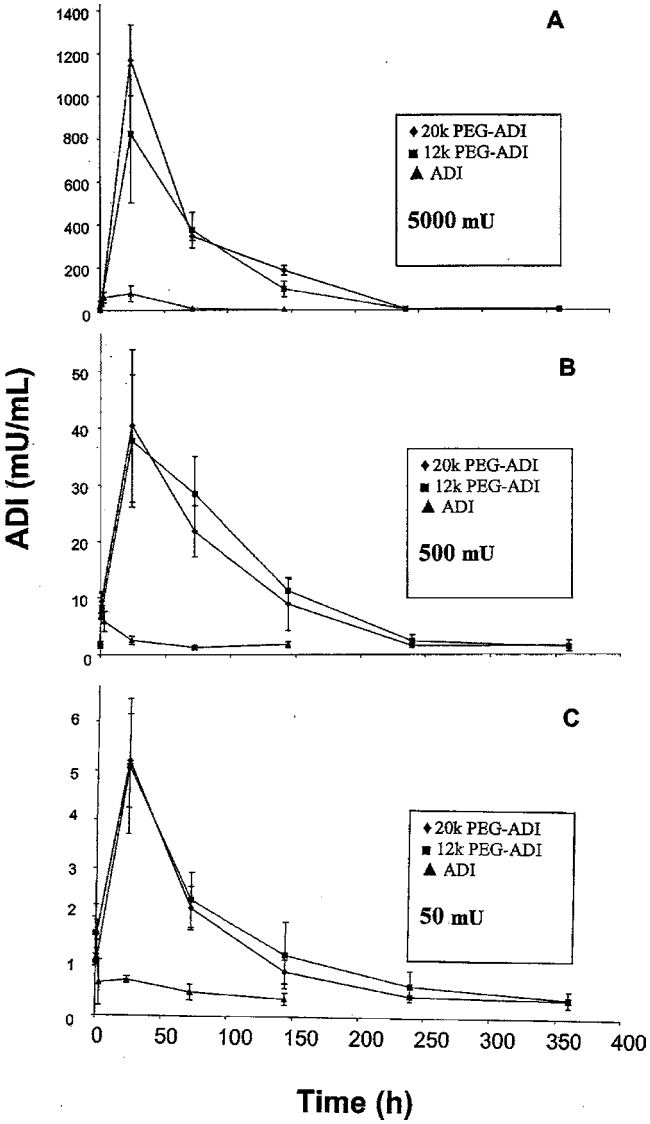

Figure 12. Pharmacokinetics of *M. arthritidis* ADI and PEG−ADI in mice following single s.c. administration. (A) 5000 mU. (B) 500 mU. (C) 50 mU. ADI activity in plasma is measured by enzyme assay at the indicated durations following injection of ADI (▲), 12 kDa PEG−ADI (■), or 20 kDa PEG−ADI (◆).

injection routes or may relate to the innate metabolism of the tissue types and biological response to compound bolus injection. Possibly arginine synthesis is stimulated in a differential manner dependent on injection site. The overall conclusion from these PD studies is that both 12 kDa and 20 kDa PEG−ADI potently catabolized arginine by each parenteral route of administration, and, as expected, i.v. administration provided the most sustained elimination of plasma arginine.

Pharmacokinetics of PEG−ADI. Completion of the pharmacological studies of *M. arthritidis* ADI and PEG−ADI compounds also required a thorough understanding of the pharmacokinetics (PK) of these compounds. Therefore, PK analyses were conducted as companion studies with the above PD investigations. Measurements of PK profiles for multi-PEGylated proteins present special challenges due to the effects of PEG polymers on physically shielding the protein. Three assays were evaluated for the PK studies. Immunoassays were determined to lack sufficient sensitivity for PEG−ADI detection. Enzyme assays were instead developed by modifying the citrulline detection method for plasma samples as described in Experimental Procedures. Finally, we also conducted, as a confirmatory though less sensitive method, bioassays of the PK samples using IC_{50} determinations for the growth inhibition of the S-180 II mouse sarcoma tumor cell line in vitro.

As shown in Figure 9, using the enzyme method, the PK profiles for the 12 kDa and 20 kDa PEG−ADI compounds following i.v. administration in mice were shown to be comparable, as anticipated from the companion PD study results shown in Figure 5. Native ADI is rapidly eliminated from circulation. Similarly, as shown in Figure 10, i.v. administration of these compounds in rats revealed comparability in PK profiles for the 12 kDa and 20 kDa PEG−ADI which correlates with PD effects (Figure 6). In this experiment, as well as the other current pharmacological studies, there was no statistically significant difference in the PK and PD effects of the two conjugates. Figures 11 and 12 record the PK profiles of the ADI and PEG−ADI compounds by i.m. and s.c. administration, respectively. An absorption phase is observed, followed by clearance, and both PEG−ADI compounds demonstrated similar PK profiles. In comparison to the corresponding PD profiles (Figures 7 and 8), the i.m.-administered PEG−ADI compounds demonstrated a similar C_{max} while exhibiting a slower elimination phase when compared to s.c. administration, which appears to correlate with the observed PD effects. When PK profiles

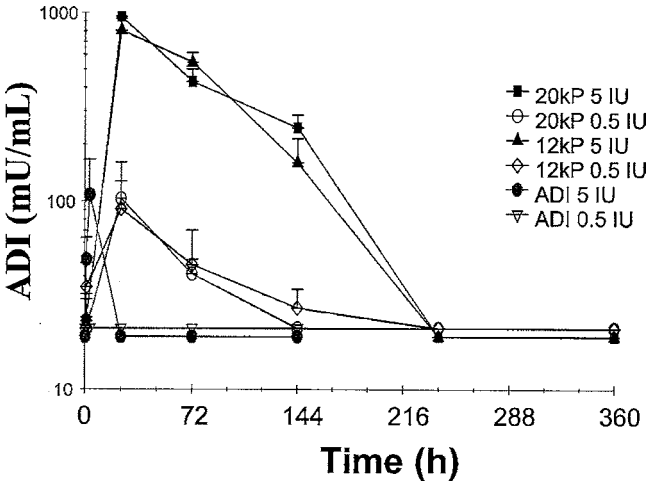

Figure 13. Pharmacokinetics via bioassay of *M. arthritidis* ADI and PEG−ADI in mice following single s.c. administration. ADI activity in plasma (mean ± SD) is measured by S-180 II cell culture growth inhibition assay at the indicated durations following injection of ADI (5 IU, ●; 0.5 IU, ▼), 12 kDa PEG−ADI (5 IU, ▲; 0.5 IU, ◇), or 20 kDa PEG−ADI (5 IU, ■; 0.5 IU, ○).

Table 3. Pharmacokinetic Parameters of ADI Compounds in Mice (5 IU/mouse)

route	HL (h)	C_{max} (IU/mL)	T_{max} (h)	AUC (h×IU/mL)	MRT (h)	CL (mL/h)	bioavailability (%)
				20k PEG−ADI			
i.v.	50.0	2.57		176.4	66.9	0.03	
i.m.	36.8	0.86	24	101.9	80.4	0.05	57.7
s.c.	63.0	0.95	24	89.4	98.7	0.06	50.7
				12k PEG−ADI			
i.v.	48.7	2.73		174.8	80.1	0.03	
i.m.	48.8	0.98	24	124.4	89.6	0.04	71.2
s.c.	50.5	0.80	24	79.7	82.4	0.06	45.6
				ADI			
i.v.	2.81	2.34	-	29.7	1.1	0.17	
i.m.	4.84	0.35	1	4.4	2.4	1.12	15.0

were examined by bioassay methods rather than enzyme assay measurements, comparable results were observed, except that the bioassay limits of quantitation allowed evaluation of only the higher two of the three doses in the dose range studies. An example of this approach is shown in Figure 13 for s.c. administration in mice, which may be compared to the enzyme method of Figure 12.

Pharmacological parameters from the mouse studies employing 5 IU doses/mouse were compiled and are presented in Table 3. Biological half-lives for the PEG−ADI compounds do not vary greatly when comparing the 12 kDa and 20 kDa derivatives or when comparing injection routes. However, PEGylation imparts nearly 10-fold increased half-life in the bioconjugates. C_{max} is about 2.5-fold higher for the PEG−ADI compounds by i.v. administration compared to the s.c. or i.m. routes. AUC values are markedly similar between the two bioconjugates and over 5-fold greater than for the unmodified ADI. Bioavailability via the i.m. route of administration appeared about 30% higher than s.c. administration in these investigations, and a suitable overall bioavailability (∼50%) was achieved for either the 20 kDa PEG−ADI or 12 kDa PEG−ADI compound.

CONCLUSIONS

We describe investigations of the physical and functional properties of a new arginine-degrading ADI enzyme from *M. arthritidis*, which exhibited most of the favored characteristics for therapy, including low K_m, high specific activity, near physiological pH optimum, prolonged stability in vitro and in vivo, together with retention of these desired properties in multi-PEGylated formulations.

Our investigations in PEGylation optimization of *M. arthritidis* ADI evaluated both in vitro and in vivo performance, and these studies provided the basis for selection of developmental drug candidates which differ in composition from most conventional and experimental PEG enzymes. Specifically, although a multi-PEGylated enzyme format is beneficial in addressing immunogenicity concerns, as illustrated by ADAGEN and ONCASPAR, employment of PEG polymers larger than 5 kDa is required to optimize PK and PD of ADI. However, in contrast to other studies (*27*, *31*), we do not observe a benefit to increasing total PEG mass to the upper limits of conjugation and polymer dimensions, although it is uncertain to what extent the use of an unstable succinimidyl succinate linker employed in prior reported studies influenced in vivo pharmacological behavior. We chose to instead construct the present conjugates with the highly stable succinimidyl carbonate linker (*42*, *51*). PD effects of multi-PEGylated ADI with either 12 kDa or 20 kDa polymers and equivalent numbers of attachments demonstrated comparable outcomes. However, the 12 kDa polymers provide advantages in processing due to reduced viscosity and easier separation on ultrafiltration/diafiltration, as well as potential cost of goods advantages, a lower protein dose, and possibly better tumor penetration. Our studies also streamlined PEGylation reaction conditions, providing a manageable amount of polymer to be consumed while still approaching maximal modification. The PD performance of the PEG−ADI compounds in eliminating detectable plasma arginine from mice for 10 days with a 5 IU single dose is outstanding for this category of enzyme conjugates (*27*−*31*). Further development of these lead compounds in preclinical studies is ongoing to determine the dosing regimen for oncological indications.

ACKNOWLEDGMENT

We thank Enzon colleagues for assistance in purification and characterization of *P. putida* ADI. Stanford Lee, Srijata Sarkar, and Alahari Arunakumari made key contributions in advancing this overall program. Dechun Wu and Yoany Lozanguiez contributed in chemical synthesis of linkers; Ramesh Chintala, Ahsen Janjua, and Magda Mendez supported the bioconjugate purifications; Qing Dong, Qing-Hong Dai, Kavitha Kumar, Michelle Boro, and Julia Zhu assisted in analytical assays. We thank Uli Grau and Gerrit Borchard for their encouragement and support and Lee Greenberger and Ivan Horak for a critical review of the manuscript.

LITERATURE CITED

(1) Abuchowski, A., Kazo, G. M., Verhoest, C. R., Van Es, T., Kafkewitz, D., Nucci, M. L., Viau, A. T., and Davis, F. F. (1984) Cancer therapy with chemically modified enzymes. I. Antitumor properties of polyethylene glycol-modified asparaginase conjugates. *Cancer Biochem. Biophys. 7*, 175−186.

(2) Wheatley, D. N. (2004) Controlling cancer by restricting arginine availability − arginine-catabolizing enzymes as anticancer agents. *Anti-Cancer Drugs. 15*, 825−833.

(3) Takakura, T., Takimoto, A., Notsu, Y., Yoshida, H., Ito, T., Nagatome, H., Ohno, M., Kobayashi, Y., Yoshioka, T., Inagaki, K., Yagi, S., Hoffman, R. M., and Esaki, N. (2006) Physicochemical and pharmacokinetic characterization of highly potent recombinant L-methionine gamma-lyase conjugated with polyethylene glycol as an antitumor agent. *Cancer Res. 66*, 2807−2814.

(4) Chan, B., Wara, D., Bastian, J., Hershfield, M. S., Bohnsack, J., Azen, C. G., Parkman, R., Weinberg, K., and Kohn, D. B. (2005) Long-term efficacy of enzyme replacement therapy for adenosine deaminase (ADA)-deficient severe combined immunodeficiency (SCID). *Clin. Immunol. 117*, 133−143.

(5) Chester, K. A., Baker, M., and Mayer, A. (2005) Overcoming the immunologic response to foreign enzymes in cancer therapy. *Expert Rev. Clin. Immunol. 1*, 549−559.

(6) Gamez, A., Sarkissian, C. N., Wang, L., Kim, W., Straub, M., Patch, M. G., Chen, L., Striepeke, S., Fitzpatrick, P., Lemontt, J. F., O'Neill, C., Scriver, C. R., and Stevens, R. C. (2005) Development of pegylated forms of recombinant *Rhodosporidium toruloides* phenylalanine ammonia-lyase for the treatment of classical phenylketonuria. *Mol. Ther. 11*, 986−989.

(7) Graham, M. L. (2003) Pegaspargase: a review of clinical studies. *Adv. Drug Delivery Rev. 55*, 1293−1302.

(8) Harris, J. M., and Chess, R. B. (2003) Effect of pegylation on pharmaceuticals. *Nat. Rev. Drug Discovery 2*, 214−221.

(9) Hershfield, M. S., Chaffee, S., Koro-Johnson, L., Mary, A., Smith, A. A., and Short, S. A. (1991) Use of site-directed mutagenesis to enhance the epitope-shielding effect of covalent modification of proteins with polyethylene glycol. *Proc. Natl. Acad. Sci. U.S.A. 88*, 7185−7189.

(10) Davis, F. F. (2003) PEG-adenosine deaminase and PEG-asparaginase. *Adv. Exp. Med. Biol. 519*, 51−58.

(11) Muller, H. J., and Boos, J. (1998) Use of L-asparaginase in childhood ALL. *Crit. Rev. Oncol. Hematol. 28*, 97−113.

(12) Jackson, M. J., Beaudet, A. L., and O'Brien, W. E. (1986) Mammalian urea cycle enzymes. *Annu. Rev. Genet. 20*, 431−464.

(13) Rodriguez, P. C., Zea, A. H., Culotta, K. S., Zabaleta, J., Ochoa, J. B., and Ochoa, A. C. (2002) Regulation of T cell receptor CD3ζ chain expression by L-arginine. *J. Biol. Chem. 277*, 21123−21129.

(14) Morris, S. M., Jr. (2006) Arginine: beyond protein. *Am. J. Clin. Nutr. 83*, 508S−512S.

(15) Sugimura, K., Ohno, T., Kusuyama, T., and Azuma, I. (1992) High sensitivity of human melanoma cell lines to the growth inhibitory activity of mycoplasmal arginine deiminase *in vitro*. *Melanoma Res. 2*, 191−196.

(16) Shen, L. J., Beloussow, K., and Shen, W. C. (2006) Modulation of arginine metabolic pathways as the potential anti-tumor mechanism of recombinant arginine deiminase. *Cancer Lett. 231*, 30−35.

(17) Sarkar, S., Arunakumari, A., Wang, M., Filpula, D., and Shorr, R. G. L. (1996) Growth inhibition of melanoma cell lines by an arginine depleting enzyme and its reversal by argininosuccinate synthetase gene overexpression. *Proc. Amer. Assoc. Cancer Res. 37*, 418−419.

(18) Wheatley, D. N., Kilfeather, R., Stitt, A., and Campbell, E. (2005) Integrity and stability of the citrulline-arginine pathway in normal and tumour cell lines. *Cancer Lett. 227*, 141−152.

(19) Shen, L. J., Lin, W. C., Beloussow, K., and Shen, W. C. (2003) Resistance to the anti-proliferative activity of recombinant arginine deiminase in cell culture correlates with the endogenous enzyme, argininosuccinate synthetase. *Cancer Lett. 191*, 165−170.

(20) Dillon, B. J., Prieto, V. G., Curley, S. A., Ensor, C. M., Holtsberg, F. W., Bomalaski, J. S., and Clark, M. A. (2004) Incidence and distribution of argininosuccinate synthetase deficiency in human cancers: a method for identifying cancers sensitive to arginine deprivation. *Cancer 100*, 826−833.

(21) Misawa, S., Aoshima, M., Takaku, H., Matsumoto, M., and Hayashi, H. (1994) High-level expression of *Mycoplasma* arginine deiminase in *Escherichia coli* and its efficient renaturation as an anti-tumor enzyme. *J. Biotechnol. 36*, 145−155.

(22) Lu, X., Galkin, A., Herzberg, O., and Dunaway-Mariano, D. (2004) Arginine deiminase uses an active-site cysteine in nucleophilic catalysis of L-arginine hydrolysis. *J. Am. Chem. Soc. 126*, 5374−5375.

(23) Das, K., Butler, G. H., Kwiatkowski, V., Clark, A. D., Jr., Yadav, P., and Arnold, E. (2004) Crystal structures of arginine deiminase with covalent reaction intermediates: implications for catalytic mechanism. *Structure 12*, 657−667.

(24) Galkin, A., Lu, X., Dunaway-Mariano, D., and Herzberg, O. (2005) Crystal structures representing the Michaelis complex and the thiouronium reaction intermediate of *Pseudomonas aeruginosa* arginine deiminase. *J. Biol. Chem. 280*, 34080−34087.

(25) Lu, X., Li, L., Wu, R., Feng, X., Li, Z., Yang, H., Wang, C., Guo, H., Galkin, A., Herzberg, O., Mariano, P. S., Martin, B. M., and Dunaway-Mariano, D. (2006) Kinetic analysis of *Pseudomonas aeruginosa* arginine deiminase mutants and alternate substrates provides insight into structural determinants of function. *Biochemistry 45*, 1162−1172.

(26) Baur, H., Luethi, E., Stalon, V., Mercenier, A., and Haas, D. (1989) Sequence analysis and expression of the arginine-deiminase and carbamate-kinase genes of *Pseudomonas aeruginosa*. *Eur. J. Biochem. 179*, 53−60.

(27) Holtsberg, F. W., Ensor, C. M., Steiner, M. R., Bomalaski, J. S., and Clark, M. A. (2002) Poly(ethylene glycol) (PEG) conjugated arginine deiminase: effects of PEG formulations on its pharmacological properties. *J. Controlled Release 80*, 259−271.

(28) Miyazaki, K., Takaku, H., Umeda, M., Fujita, T., Huang, W. D., Kimura, T., Yamashita, J., and Horio, T. (1990) Potent growth inhibition of human tumor cells in culture by arginine deiminase purified from a culture medium of a *Mycoplasma*-infected cell line. *Cancer Res. 50*, 4522−4527.

(29) Takaku, H., Takase, M., Abe, S., Hayashi, H., and Miyazaki, K. (1992) *In vivo* anti-tumor activity of arginine deiminase purified from *Mycoplasma arginini*. *Int. J. Cancer 51*, 244−249.

(30) Takaku, H., Misawa, S., Hayashi, H., and Miyazaki, K. (1993) Chemical modification by polyethylene glycol of the anti-tumor enzyme arginine deiminase from *Mycoplasma arginini*. *Jpn. J. Cancer Res. 84*, 1195−1200.

(31) Ensor, C. M., Holtsberg, F. W., Bomalaski, J. S., and Clark, M. A. (2002) Pegylated arginine deiminase (ADI-SS $PEG_{20,000mw}$) inhibits human melanomas and hepatocellular carcinomas *in vitro* and *in vivo*. *Cancer Res. 62*, 5443−5450.

(32) Beloussow, K., Wang, L., Wu, J., Ann, D., and Shen, W. C. (2002) Recombinant arginine deiminase as a potential anti-angiogenic agent. *Cancer Lett. 183*, 155−162.

(33) Takaku, H., Matsumoto, M., Misawa, S., and Miyazaki, K. (1995) Anti-tumor activity of arginine deiminase from *Mycoplasma arginini* and its growth-inhibitory mechanism. *Jpn. J. Cancer Res. 86*, 840−846.

(34) Cheng, P. N., Leung, Y. C., Lo, W. H., Tsui, S. M., and Lam, K. C. (2005) Remission of hepatocellular carcinoma with arginine depletion induced by systemic release of endogenous hepatic arginase due to transhepatic arterial embolisation, augmented by high-dose insulin: arginase as a potential drug candidate for hepatocellular carcinoma. *Cancer Lett. 224*, 67−80.

(35) Kubo, M., Nishitsuji, H., Kurihara, K., Hayashi, T., Masuda, T., and Kannagi, M. (2006) Suppression of human immunodeficiency virus type 1 replication by arginine deiminase of *Mycoplasma arginini*. *J. Gen. Virol. 87*, 1589−1593.

(36) Park, I.-S., Kang, S.-W., Shin, Y.-J., Chae, K.-Y., Park, M.-O., Kim, M.-Y., Wheatley, D. N., and Min, B.-H. (2003) Arginine deiminase: a potent inhibitor of angiogenesis and tumour growth. *Br. J. Cancer 89*, 907−914.

(37) Thomas, J. B., Holtsberg, F. W., Ensor, C. W., Bomalaski, J. S., and Clark, M. A. (2002) Enzymic degradation of plasma arginine using arginine deiminase inhibits nitric oxide production and protects mice from the lethal effects of tumour necrosis factor α and endotoxin. *Biochem. J. 363*, 581−587.

(38) Curley, S. A., Bomalaski, J. S., Ensor, C. M., Holtsberg, F. W., and Clark, M. A. (2003) Regression of hepatocellular cancer in a patient treated with arginine deiminase. *Hepato-Gastroenterology 50*, 1208−1211.

(39) Izzo, F., Marra, P., Beneduce, G., Castello, G., Vallone, P., De Rosa, V., Cremona, F., Ensor, C. M., Holtsberg, F. W., Bomalaski, J. S., Clark, M. A., Ng, C., and Curley, S. A. (2004) Pegylated arginine deiminase treatment of patients with unresectable hepatocellular carcinoma: results from Phase I/II studies. *J. Clin. Oncol. 22*, 1815−1822.

(40) Zalipsky, S. (1995) Functionalized poly(ethylene glycol) for preparation of biologically relevant conjugates. *Bioconjugate Chem. 6*, 150−165.

(41) Basu, A., Yang, K., Wang, M., Liu, S., Chintala, R., Palm, T., Zhao, H., Peng, P., Wu, D., Zhang, Z., Hua, J., Hsieh, M.-C., Zhou, J., Petti, G., Li, X., Janjua, A., Mendez, M., Liu, J., Longley, C., Zhang, Z., Mehlig, M., Borowski, V., Viswanathan, M., and Filpula, D. (2006) Structure-function engineering of interferon-β-1b for improving stability, solubility, potency, immunogenicity, and pharmacokinetic properties by site-selective mono-PEGylation. *Bioconjugate Chem. 17*, 618−630.

(42) Zhao, H., Yang, K., Martinez, A., Basu, A., Chintala, R., Liu, H.-C., Janjua, A., Wang, M., and Filpula, D. (2006) Linear and branched bicin linkers for releasable PEGylation of macromol-

ecules: controlled release in vivo and in vitro from mono- and multi-PEGylated proteins. *Bioconjugate Chem. 17*, 341−351.
(43) Yang, K., Basu, A., Wang, M., Chintala, R., Hsieh, M.-C., Liu, S., Hua, J., Zhang, Z., Zhou, J., Li, M., Phyu, H., Petti, G., Mendez, M., Janjua, H., Peng, P., Longley, C., Borowski, V., Mehlig, M., and Filpula, D. (2003) Tailoring structure-function and pharmacokinetic properties of single-chain Fv proteins by site-specific PEGylation. *Protein Eng. 16*, 761−770.
(44) Greenwald, R. B. (2001) PEG drugs: an overview. *J. Controlled Release 74*, 159−171.
(45) Greenwald, R. B., Yang, K., Zhao, H., Conover, C. D., Lee, S., and Filpula, D. (2003) Controlled release of proteins from their poly(ethylene glycol) conjugates: drug delivery systems employing 1,6-elimination. *Bioconjugate Chem. 14*, 395−403.
(46) Roberts, M. J., Bentley, M. D., and Harris, J. M. (2002) Chemistry for peptide and protein PEGylation. *Adv. Drug Delivery Rev. 54*, 459−476.
(47) Wang, M., Lee, L. S., Nepomich, A., Yang, J.-D., Conover, C., Whitlow, M., and Filpula, D. (1998) Single-chain Fv with manifold *N*-glycans as bifunctional scaffolds for immunomolecules. *Protein Eng. 11*, 1277−1283.
(48) Weickmann, J. L., and Fahrney, D. E. (1977) Arginine deiminase from *Mycoplasma arthritidis*: evidence for multiple forms. *J. Biol. Chem. 252*, 2615−2620.
(49) Weickmann, J. L., Himmel, M. E., Squire, P. G., and Fahrney, D. E. (1978) Arginine deiminase from *Mycoplasma arthritidis*: properties of the enzyme from log phase cultures. *J. Biol. Chem. 253*, 6010−6015.
(50) Smith, D. W., Ganaway, R. L., and Fahrney, D. E. (1978) Arginine deiminase from *Mycoplasma arthritidis*: structure-activity relationships among substrates and competitive inhibitors. *J. Biol. Chem. 253*, 6016−6020.
(51) Miron, T., and Wilchek, M. (1993) A simplified method for the preparation of succinimidyl carbonate polyethylene glycol for coupling to proteins. *Bioconjugate Chem. 4*, 568−569.
(52) Shibatani, T., Kakimoto, T., and Chibata, I. (1975) Crystallization and properties of L-arginine deiminase of *Pseudomonas putida*. *J. Biol. Chem. 250*, 4580−4583.
(53) Oginsky, E. (1957) Isolation and determination of arginine and citrulline. *Methods Enzymol. 3*, 639−643.
(54) Bagrel, A., Museur, G., and Siest, G. (1975) Colorimetric measurement of ornithine carbamoyl transferase activity in plasma, and results for a supposedly healthy population. *Clin. Chem. 21*, 1716−1720.
(55) Smith, P. K., Krohn, R. I., Hermanson, G. T., Mallia, A. K., Gartner, F. H., Provenzano, M. D., Fujimoto, E. K., Goeke, N. M., Olson, B. J., and Klenk, D. C. (1985) Measurement of protein using bicinchoninic acid. *Anal. Biochem. 150*, 76−85.
(56) Habeeb, A. F. (1966) Determination of free amino groups in proteins by trinitrobenzenesulfonic acid. *Anal. Biochem. 14*, 328−336.
(57) Stocks, S. J., Jones, A. J., Ramey, C. W., and Brooks, D. E. (1986) A fluorometric assay of the degree of modification of protein primary amines with polyethylene glycol. *Anal. Biochem. 154*, 232−234.
(58) Savoca, K. V., Abuchowski, A., van Es, T., Davis, F. F., and Palczuk, N. C. (1979) Preparation of a non-immunogenic arginase by the covalent attachment of polyethylene glycol. *Biochim. Biophys. Acta 578*, 47−53.
(59) Chaffee, S., Mary, A., Stiehm, E. R., Girault, D., Fischer, A., and Hershfield, M. S. (1992) IgG antibody response to polyethylene glycol-modified adenosine deaminase in patients with adenosine deaminase deficiency. *J. Clin. Invest. 89*, 1643−1651.

BC060198Y

Biologically Active Amphotericin B-Calix[4]arene Conjugates

Valérie Paquet, Andreas Zumbuehl, and Erick M. Carreira*

Laboratorium für Organische Chemie, ETH Hönggerberg, CH-8093 Zürich, Switzerland. Received July 10, 2006; Revised Manuscript Received September 24, 2006

In order to provide tools for investigations of amphotericin B ion channels, new conjugates bearing a calix[4]-arene scaffold covalently linked to four amphotericin B molecules were synthesized. These macromolecules adopt a cone conformation that mimics the structure of a transmembrane pore. The antifungal activity of the conjugates **3** and **4** was superior or similar to that of native amphotericin B, with minimal inhibitory concentration values of 0.10 and 0.25 μM, respectively. Furthermore, the hemotoxicity of the new conjugates was considerably lower (at least 10 times) than the hemotoxicity of monomeric amphotericin B. Finally, the formation of ion channels in the lipid bilayer by the amphotericin B tetramer was monitored by measuring the K^+ efflux from various liposomes.

INTRODUCTION

Over the past 50 years, amphotericin B (AmB, **1**) has remained the drug of choice against systemic fungal infections especially because of its broad spectrum of activity (*1*, *2*). However, although AmB (**1**) has been the subject of many studies, its mechanism of action has not been clearly elucidated and is still a subject of debate (*3*). The most widely accepted model refers to the formation of a barrel-stave structure in the membrane that serves as an ion channel causing electrolyte loss that ultimately leads to cell death (Figure 1) (*4*). AmB (**1**) molecules are believed to organize in a fashion such that the hydrophilic hydroxylated portion of each molecule faces the inside of the pore, forming a hydrophilic channel, while correspondingly the polyene section of the molecule interacts with the lipid bilayer by being oriented toward the outside of the channel.

Even though this model is a classic in membrane biology, both the formation sequence and the precise structure of the channel remain to be confirmed. For instance, several pore sizes have been reported where the number of AmB (**1**) molecules required to form a channel ranged from 4 to 12, albeit 8 molecules is generally accepted (*5*). Moreover, the mechanism of pore formation is sometimes described as independent of the sterol located in the membrane (ergosterol in yeast cells and cholesterol in mammalian cells) (*6*). However, it is more often asserted that channel formation is sterol-dependent, but again, the reported values for the stoichiometry between the sterol and AmB (**1**) varies considerably in the literature from 0.7 to 3.9 (*7*). Furthermore, until recently no evidence was available as to whether a single-length or a double-length barrel was formed in the membrane (*8*). The myriad of mechanistic hypotheses argues for the necessity of designing and synthesizing AmB (**1**) conjugates with the purpose of providing additional insight.

In an attempt to elucidate the nature of the structure of the AmB (**1**) channel in lipid bilayers, we sought to assemble AmB (**1**) molecules on a scaffold that would mimic a single-length ion channel structure (*9*). In such a system, AmB (**1**) molecules would be preorganized and covalently bound; consequently the number of AmB units forming the pore is clearly defined. Calixarenes were chosen because they are a class of compound that is already known to form synthetic cation channels in lipid membranes (*10*). Furthermore, calix[4]arenes are well-defined scaffolds because of their rigidity, particularly with respect to the cone shape, and practical to work with because they are readily synthesized and functionalized (*11*). Herein, we report the synthesis of a preformed AmB (**1**) channel bearing four AmB (**1**) molecules covalently bound to a calix[4]arene core (Figure 2). When compared to monomeric AmB (**1**), the novel conjugates retain the ability to induce K^+ leakage as well as antifungal activity. Investigation of the hemotoxicity also revealed that these macromolecules are 10 times less toxic than native AmB (**1**).

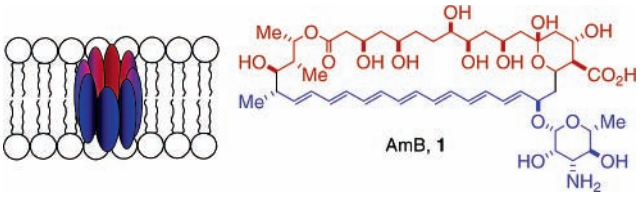

Figure 1. Barrel-stave model wherein AmB molecules form a transmembrane aqueous channel.

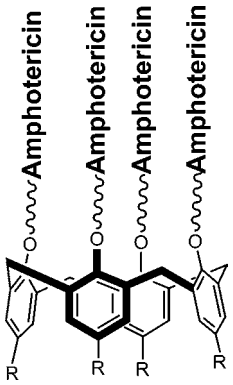

Figure 2. Amphotericin B−calix[4]arene conjugate mimicking transmembrane ion channel.

EXPERIMENTAL PROCEDURES

Susceptibility Assays. The minimal inhibitory concentration (MIC) values were determined for the *Saccharomyces cerevisiae* wild type (BY4741, a derivative of S288C) (*12*). The assays were inspired by the standard protocol approved by the National Committee of Clinical Laboratory Standards (NCCLS) but using

* To whom correspondence should be addressed. E-mail: carreira@org.chem.ethz.ch.

10.1021/bc060205i CCC: $33.50 © 2006 American Chemical Society
Published on Web 10/20/2006

Scheme 1

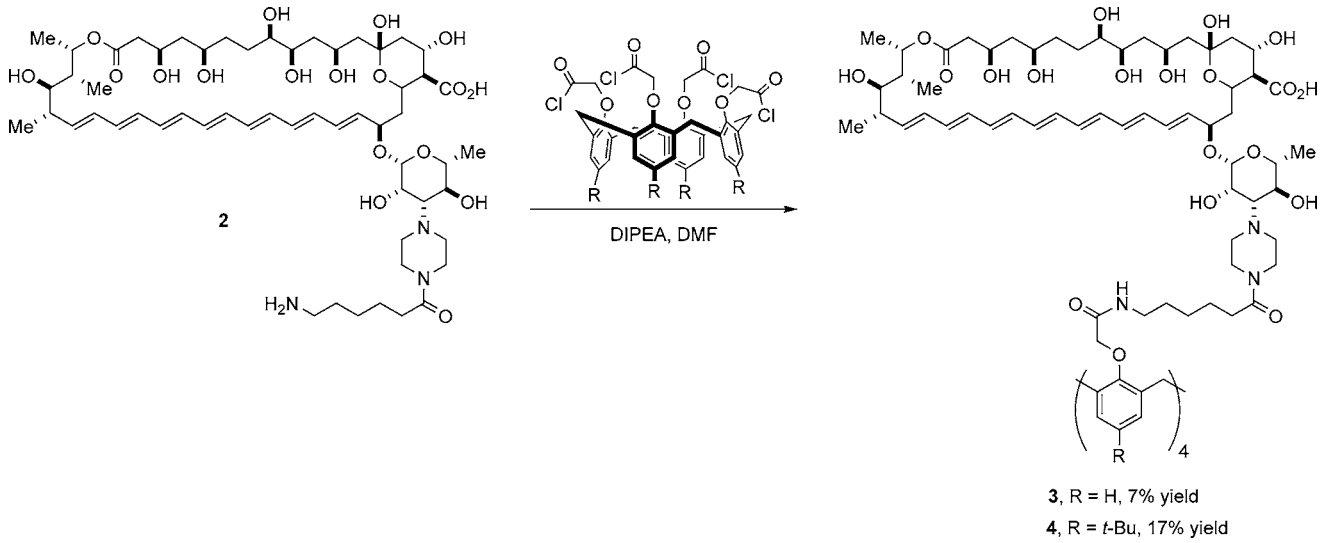

YEPD liquid medium instead of the RPMI-1640 medium (*13*). The strains were cultivated overnight in 5 mL of YEPD liquid medium at 30 °C with constant shaking. The saturated cultures were diluted to an ODB_{600B} of 0.1 (3×10^7 cells/mL). For the 24-well plate, each well was prepared by adding 1% (12 μL) of DMSO solution of the tested compound with 1% (12 μL) yeast cells solution and completed with YEPD (1.176 mL). The plates were sealed with Parafilm and then incubated for 18 h at 30 °C. The optical density was read at 600 nm using 1.5 mL cuvettes. The MIC value was defined as the drug concentration needed to inhibit growth at less than 5% compared to a drug-free culture.

Hemolytic Assays (*14*). Human blood, anticoagulated with citrate or EDTA, was centrifuged (2000*g*) at 4 °C for 10 min. The pellets were washed three times with PBS buffer (pH 7.2 with 2 g/L glucose) and then diluted to a concentration of 4% (4×10^8 cells/mL). All experiments were done in triplicate, and the total volume for the hemolysis tubes was 1.4 mL. The solutions were prepared by adding 1% (14 μL) of DMSO solution of the tested compound with 736 μL of PBS buffer and completed with 750 μL of 4% erythrocytes. After 1 h of incubation at 37 °C, the samples were centrifuged (1500*g*) at 4 °C for 5 min and the absorbance of the supernatant was measured at 560 nm. The concentration that led to 50% hemolysis (EH_{50}) was interpolated graphically. The value for the 100% hemolysis was obtained by the treatment with 100 μM AmB.

K^+ Efflux Assays. The K^+ efflux measurements were made following a procedure previously described (*15*). The appropriate liposome suspensions were prepared using POPC, cholesterol, and ergosterol. Then the liposomes were sized by extrusion through two 400, 200, and finally 100 nm pore size membranes (10 times for each pore size). The resultant "100 nm" unilamellar liposomes were dialyzed against 600 mL of 150 mM NaCl, 5 mM HEPES (pH 7.4) buffer. Afterward, the suspension was diluted with 150 mM NaCl, 5 mM HEPES (pH 7.4) buffer to 1 mM overall lipid concentration (phospholipids + sterols). For each efflux measurement 10 mL of this liposome suspension was placed in a small beaker. Potentiometric measurements were performed every second with a 16-channel electrode monitor in magnetically stirred solutions at ambient temperature. The reference electrode was a Metrohm double-junction Ag/AgCl reference electrode with 3 M KCl as the reference electrolyte and 1 M LiOAc as the bridge electrolyte. After recording the amphotericin-induced potassium efflux, liposomes were lysed by adding sodium cholate (172 mg). The resulting reading (taken after 1 h) was used to quantify the 100% K^+ release.

Table 1. MIC and EH_{50} Values for AmB (1) and Conjugates 3 and 4

compd	MIC BY4741 (μM)[a]	EH_{50} (μM)[b]
1 (AmB)	0.30	4.0
3	0.10	50
4	0.25	40

[a] Assayed with *S. cerevisiae* (BY4741) following the NCCLS protocol. See Supporting Information for details. [b] Determined according to the procedure in ref 14. EH_{50}: concentration causing 50% hemoglobin release in human erythrocytes. MIC: minimal inhibitory concentration.

RESULTS AND DISCUSSION

Our group has previously reported the synthesis of a readily accessible piperazine linker as a synthetic anchor for the conjugation of various entities to AmB (**1**), such as fluorescein (*15*). On the basis of this approach, we envisioned the use of the AmB derivative **2** in a series of amide coupling reactions with a calix[4]arene precursor bearing several acyl chloride functionalities (Scheme 1). This synthetic route conveniently allows the use of natural and unprotected AmB (**1**) because the four coupling reactions are chemoselective. The yields reported correspond to pure single isomers of the calixarene AmB conjugates as shown. The conical shape of the calix[4]arene scaffold is preserved throughout the synthesis because it was fixed during a prior alkylation step (*16*). The conical conformation in the final products was also confirmed by the symmetry found in the aromatic region of the ^1H NMR spectra of the conjugates **3** and **4**.

After the isolation of conjugates **3** and **4**, we could then examine if such a preorganized macromolecular arrangement of AmB (**1**) molecules would display biological activity. First, to evaluate the antifungal activities of **3** and **4**, the minimal inhibitory concentrations (MIC, the concentration needed to inhibit growth at less than 5% compared to a drug-free culture) against *Saccharomyces cerevisiae* were determined (Table 1). Interestingly, there was no diminution in the antifungal activity observed for the conjugates in comparison to native AmB (**1**). In fact, both MIC values for **3** and **4** (0.10 and 0.25 μM, respectively) were slightly better than for monomeric AmB (**1**) (MIC = 0.30 μM). These results are consistent with the ion channel mechanism because the AmB conjugate that mimics pore structure retains good antifungal activity. However, they do not rule out completely the possibility of other mechanisms

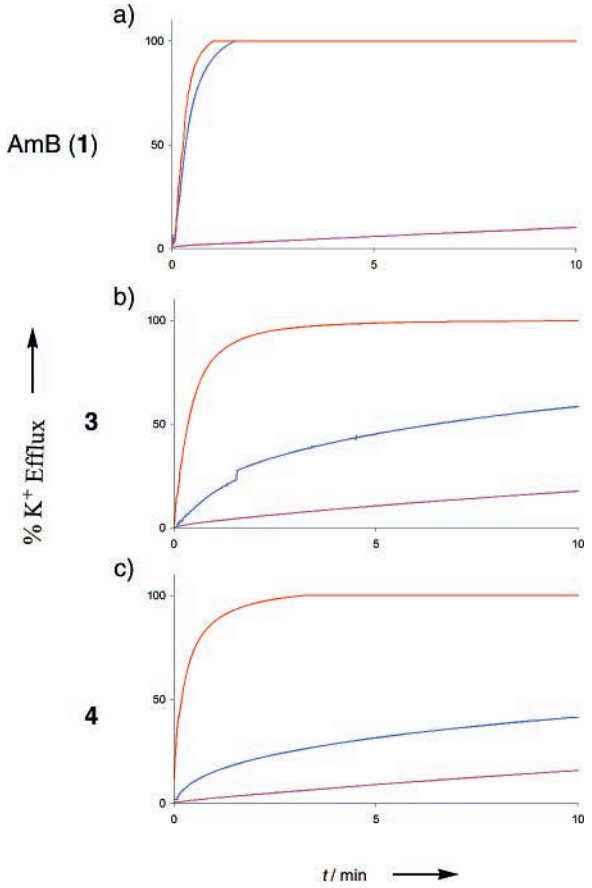

Figure 3. K^+ efflux from vesicles ($LUVET_{100}$) prepared from 1-palmitoyl-2-oleoyl-*sn*-glycero-3-phosphocholine (POPC) (pink line), POPC with 13% ergosterol (red line), and POPC with 30% cholesterol (blue line) caused by AmB (**1**), **3**, and **4**, added in DMSO to a suspension of vesicles to give a final concentration of 1.0 μM (a−c).

such as internalization, membrane disruption, and peroxidation. However, in contrast to the prevailing models, which call for 8−12 AmB staves, it would seem that a large number of AmB (**1**) molecules are not required to form an active ion channel because an arrangement containing only four AmB (**1**) units is sufficient to preserve activity in the calixarene that forms the basis of our study.

The toxicity of the AmB (**1**) derivatives toward erythrocytes was next examined (Table 1), for which an EH_{50} value (the concentration of an agent that causes 50% hemoglobin release) can be measured using an established assay (*14*). AmB derivative **3** ($EH_{50} = 50\ \mu$M) was 10 times less toxic than AmB (**1**) ($EH_{50} = 4.0\ \mu$M), while **4** displayed even less toxicity ($EH_{50} = 40\ \mu$M). Previous observations have shown that AmB aggregates were more toxic for mammalian cells than the corresponding monomer. However, our results suggest that the spatial arrangement of the complex might be an important factor for controlling the toxicity, with head-to-tail complexes showing higher toxicity than head-to-head complexes such as seen in this communication (*17*).

Differential interactions between ergosterol found in fungal membranes and cholesterol in mammalian cells and the concurrent membrane preorganization are often considered the basis for the selectivity of AmB (**1**) as an antifungal agent. A convenient assay for studying the channel formation process involves the measurement of induced K^+ efflux in liposomes (*18*). We then studied the ability of derivatives **3** and **4** to lead to K^+ efflux from large unilamellar vesicles (LUVs) prepared from POPC (1-palmitoyl-2-oleoyl-*sn*-glycero-3-phosphocholine) admixed with sterols, mimicking conditions found in natural biomembranes (Figure 3) (*19*). In accordance with the MIC values previously observed, all compounds rapidly induce complete K^+ efflux from vesicles containing ergosterol (red line). The channel formation process seems unaffected by the nature of the substituent distally substituted on the calixarene because both conjugates **3** and **4** retain the ability to induce K^+ leakage in the same fashion as a free monomeric AmB (**1**) molecule. However, derivatives **3** and **4** caused significantly reduced efflux with cholesterol-containing vesicles (blue line), indicating improved selectivity over AmB (**1**). This superior differentiation between ergosterol and cholesterol containing lipid bilayers is consistent with the observation that compounds **3** and **4** are less hemotoxic than AmB (**1**), since the nonselective binding of AmB (**1**) in membranes incorporating ergosterol (fungal) and cholesterol (mammalian) has been considered the main cause of toxicity.

In conclusion, the first preorganized AmB single-length ion channels based on a calix[4]arene scaffold were synthesized. Conjugates **3** and **4** not only are as active as native AmB (**1**) against *S. cerevisiae* but also retain the ability to induce K^+ leakage from vesicles, suggesting an efficient channel formation in the membrane. The fact that these molecules are active is unusual, as previous assumptions have called for 8−12 AmB molecules per channel, while the compounds reported herein consist of only 4 AmB units. Moreover, the minimal hemotoxicity observed for these tetramers is noteworthy. Finally, molecular architectures such as AmB−calix[4]arene discussed herein can serve as an interesting starting point for transmembrane pore models.

ACKNOWLEDGMENT

We acknowledge Oliver Scheidegger from LOC Mass Spectrometry Service for mass measurements. This work was supported by internal ETH Grant TH 0-20201-04 and by a postdoctoral fellowship from NSERC (Canada).

Supporting Information Available: Experimental procedures and compound characterization data for all compounds. This material is available free of charge via the Internet at http://pubs.acs.org.

LITERATURE CITED

(1) (a) Donovick, R., Gold, W., Pagano, J. F., Stout, H. A. (1955) Amphotericins A and B, antifungal antibiotics produced by a streptomycete. I. In vitro studies. *Antibiot. Annu. 3*, 579−586. (b) Hartsel, S. C., Bolard, J. (1996) Amphotericin B: new life for an old drug. *Trends Pharmacol. Sci. 12*, 445−449. (c) Gallis, H. A., Drew, R. H., Pickard, W. W. (1990) Amphotericin B: 30 years of clinical experience. *Rev. Infect. Dis. 12*, 308−329. (d) Lemke, A., Kiderlen, A. F., Kayser, O. (2005) Amphotericin B. *Appl. Microbiol. Biotechnol. 68*, 151−162. (e) Brajtburg, J., Bolard, J. (1996) Carrier effects on biological activity of amphotericin B. *Clin. Microbiol. Rev. 9*, 512−531.

(2) Wu, W., Wieckowski, S., Pastorin, G., Benincasa, M., Klumpp, C., Briand, J.-P., Gennaro, R., Prato, M., Bianco, A. (2005) Targeted delivery of amphotericin B to cells by using functionalized carbon nanotubes. *Angew. Chem., Int. Ed. 44*, 6358−6362.

(3) (a) Brajtburg, J., Powderly, W. G., Kobayashi, G. S., Medoff, G. (1990) Amphotericin B: current understanding of mechanisms of action. *Antimicrob. Agents Chemother. 34*, 183−188. (b) Fujii, G., Chang, J.-E., Coley, T., Steere, B. (1997) The formation of amphotericin B ion channel in lipid bilayers. *Biochemistry 36*, 4959−4968. (c) Resat, H., Baginski, M. (2002) Ion passage pathways and thermodynamics of the amphotericin B membrane channel. *Eur. Biophys. J. 31*, 294−305. (d) Gruszecki, W. I., Gagos, M., Herec, M., Kernen, P. (2003) Organization of antibiotic amphotericin B in model lipid membranes. A mini review. *Cell. Mol. Biol. Lett. 8*, 161−170. (e) Odds, F. C., Brown, A. J. P., Gow, N. A. R. (2003) Antifungal agents: mechanisms of action. *Trends Microbiol. 11*, 272−279.

(4) De Kruijff, B., Demel, R. A. (1974) Polyene antibiotic−sterol interactions in membranes of *Acholeplasma laidlawii* cell and lecithin liposomes. III. Molecular structure of the polyene antibiotic−cholesterol complexes. *Biochim. Biophys. Acta 339*, 57−70.

(5) (a) Andreoli, T. E. (1974) The structure and function of amphotericin B cholesterol pores in lipid bilayer membranes. *Ann. N.Y. Acad. Sci. 235*, 448−468. (b) Moreno-Bello, M., Bonilla-Marin, M., Gonzalez-Beltran, C. (1988) Distribution of pore sizes in black lipid membranes treated with nystatin. *Biochim. Biophys. Acta. 944*, 97−100. (c) Bonilla-Marin, M., Moreno-Bello, M., Ortega-Blake, I. (1991) A microscopic electrostatic model for the amphotericin B channel. *Biochim. Biophys. Acta 1061*, 65−77.

(6) Hartsel, S. C., Benz, S. K., Peterson, R. P., Whyte, B. S. (1991) Potassium-selective amphotericin B channels are predominant in vesicles regardless of sidedness. *Biochemistry 30*, 77−82.

(7) (a) De Kruijff, B., Gerritsen, W. J., Oerlemans, A., van Dijck, P. W., Demel, R. A., van Deenen, L. L. (1974) Polyene antibiotic−sterol interactions in membranes of *Acholesplasma laidlawii* cells and lecithin liposomes. II. Temperature dependence of the polyene antibiotic−sterol complex formation. *Biochim. Biophys. Acta 339*, 44−56. (b) Hartsel, S. C., Hatch, C., Ayenew, W. (1993) How does amphotericin B work? Studies on model membrane systems. *J. Liposome Res. 3*, 377-408. (c) Milhaud, J., Ponsinet, V., Takashi, M., Michels, B. (2002) Interactions of the drug amphotericin B with phospholipid membranes containing or not ergosterol: new insight into the role of ergosterol. *Biochim. Biophys. Acta 1558*, 95−108.

(8) Matsuoka, S., Ikeuchi, H., Matsumori, N., Murata, M. (2005) Dominant formation of a single-length channel by amphotericin B in dimyristoylphosphatidylcholine membrane evidence by $^{13}C-^{31}P$ rotation echo double resonance. *Biochemistry 44*, 704−710.

(9) For synthetic studies in which the polyene subunit was replaced with a biaryl bis, see the following. Rogers, B., Selsted, M. E., Rychnovsky, S. D. (1997) Synthesis and biological evaluation of non-polyene analogs of amphotericin B. *Bioorg. Med. Chem. Lett. 7*, 3177−3182.

(10) (a) De Mendoza, J., Cuevas, F., Prados, P., Meadows, E. S., Gokel, G. W. (1998) A synthetic cation-transporting calix[4]arene derivative active in phospholipid bilayers. *Angew. Chem., Int. Ed. 37*, 1534−1537. (b) Yoshino, N., Satake, A., Kobuke, Y. (2001) An artificial ion channel formed by a macrocyclic resorcin[4]arene with amphiphilic cholic acid ether groups. *Angew. Chem., Int. Ed. 40*, 457−459. (c) Maulucci, N., De Riccardis, F., Botta, C. B., Casapullo, A., Cressina, E., Fregonese, M., Tecilla, P., Izzo, I. (2005) Calix[4]-arene−cholic acid conjugates: a new class of efficient synthetic ionophores. *Chem. Commun. 10*, 1354−1356.

(11) Gutsche, C. D. (1998) Calixarenes revisited. In *Monographs in Supramoleular Chemistry* (Stoddart, J. F., Ed.) Royal Society of Chemistry, Cambridge, U.K.

(12) Brachmann, C. B.; Davies, A.; Cost, G. J.; Caputo, E.; Li, J.; Hieter, P.; Boeke, J. D. (1998) Designer deletion strains derived from *Saccharomyces cerevisiae* S288C: A useful set of strains and plasmids for PCR-mediated gene disruption and other applications. *Yeast 14*, 115−132.

(13) (1995) *Reference Method for Broth Dilution Antifungal Susceptibility Testing of Yeast, M27-A2, Approved Standard*, 2nd ed. Vol. 22, Number 15, National Committee of Clinical Laboratory Standards: Wayne, PA.

(14) Kinsky, S. C., Avruch, J., Permutt, M., Rogers, H. B. (1962) The lytic effect of polyene antifungal antibiotics on mammalian erythrocytes. *Biochem. Biophys. Res. Commun. 9*, 503−507.

(15) Zumbuehl, A., Jeannerat, D., Martin, S. E., Sohrmann, M., Stano, P., Vigassy, T., Clark, D. D., Hussey, S. L., Peter, M., Peterson, B. R., Pretsch, E., Walde, P., Carreira, E. M. (2004) An amphotericin B−fluorescein conjugate as a powerful probe for biochemical studies of the membrane. *Angew. Chem., Int. Ed. 43*, 5181−5185.

(16) (a) Gutsche, C. S., Levine, J. A. (1982) Calix[4]arenes. 6. Synthesis of a functionalizable calix[4]arene in a conformationally rigid cone conformation. *J. Am. Chem. Soc. 104*, 2652−2653. (b) Casnati, A., Ting, Y., Berti, D., Fabbi, M., Pochini, A., Ungaro, R., Sciotto, D., Lombardo, G. G. (1993) Synthesis of water soluble molecular receptors from calix[4]arenes fixed in the cone conformation. *Tetrahedron 49*, 9815−9822.

(17) (a) Hartsel, S. C., Bauer, E., Kwong, E. H., Wasan, K. M. (2001) The effect of serum albumin on amphotericin B aggregate structure and activity. *Pharm. Res. 9*, 1305−1309. (b) Szlinder-Richert, J., Mazerski, J., Cybulska, B., Grzybowska, J., Borowski, E. (2001) MFAME, *N*-methyl-*N*-D-fructosyl amphotericin B methyl ester, a new amphotericin B derivative of low toxicity: relationship between self-association and effects on red blood cells. *Biochim. Biophys. Acta 1528*, 15−24. (c) Janknegt, R., de Marie, S., Bakker-Woudenberg, I. A., Crommelin, D. J. (1992) Liposomal and lipid formulations of amphotericin B. *Clin. Pharmacol. 4*, 279−291. (d) Bolard, J., Legrand, P., Heitz, F., Cybulska, B. (1991) One-sided action of amphotericin B on cholesterol-containing membranes is determined by its self-association in the medium. *Biochemistry 23*, 5707−5715.

(18) Zumbuehl, A., Stano, P., Heer, D., Walde, P., Carreira, E. M. (2004) Amphotericin B as a potential probe of the physical state of vesicle membranes. *Org. Lett. 6*, 3683−3686.

(19) Paquet, M.-J., Fournier, I., Barwicz, J., Tancrède, P., Auger, M. (2002) The effects of amphotericin B on pure and ergosterol- or cholesterol-containing dipalmitoylphosphatidylcholine bilayers as viewed by ^{2}H NMR. *Chem. Phys. Lipids. 119*, 1−11.

BC060205I

Dendrimer Versus Linear Conjugate: Influence of Polymeric Architecture on the Delivery and Anticancer Effect of Paclitaxel

Jayant J. Khandare,[†] Sreeja Jayant,[†] Ajay Singh,[‡] Pooja Chandna,[†] Yang Wang,[†] Nicholi Vorsa,[‡] and Tamara Minko*,[†]

Department of Pharmaceutics, Rutgers, The State University of New Jersey, Piscataway, New Jersey 08854, and Department of Plant Biology and Pathology, The State University of New Jersey, New Brunswick, New Jersey 08854. Received August 1, 2006; Revised Manuscript Received September 25, 2006

The relative difference in polymeric architectures of dendrimer and linear bis(poly(ethylene glycol)) (PEG) polymer in conjugation with paclitaxel has been described. Paclitaxel, a poorly soluble anticancer drug, was covalently conjugated with PAMAM G4 hydroxyl-terminated dendrimer and bis(PEG) polymer for the potential enhancement of drug solubility and cytotoxicity. Both conjugates were characterized by ^{1}NMR, HPLC, and MALDI/TOF. In addition, molecular conformations of dendrimer, bis(PEG), paclitaxel, and its polymeric conjugates were studied by molecular modeling. Hydrolysis of the ester bond in the conjugate was analyzed by HPLC using esterase hydrolyzing enzyme. In vitro cytotoxicity of dendrimer, bis(PEG), paclitaxel, and polymeric conjugates containing paclitaxel was evaluated using A2780 human ovarian carcinoma cells. Cytotoxicity increased by 10-fold with PAMAM dendrimer−succinic acid−paclitaxel conjugate when compared with free nonconjugated drug. Data obtained indicate that the nanosized dendritic polymer conjugates can be used with good success as anticancer drug carriers.

INTRODUCTION

Paclitaxel (Taxol) is a diterpenoid obtained from the bark of the pacific yew tree *Taxus brevifolia* (*1*) and is one of the most promising chemotherapeutic agents acclaimed by the National Cancer Institute (*2*). The drug promotes tubulin polymerization by forming a hyperstabilized structure, disrupting the normal tubule dynamics essential in cellular division, thereby inducting cell death (*3*). Due to low aqueous solubility of paclitaxel (about 0.3 μg/mL), numerous attempts are being made to increase solubility of the drug using various formulations and prodrug conjugates (*4*−*8*). Among the latter, poly(ethylene glycol) (PEG) prodrugs have been the most promising, providing for an increased aqueous solubility, enhanced pharmacological activity, lowered systemic toxicity, reduced immunogenicity, and prolonged plasma lifetime. Greenwald et al. proposed several relatively high molecular weight PEG prodrugs to render paclitaxel more soluble and increase its systemic circulation time (*9*).

Various polymers with different architectures have been used for the delivery of therapeutic agents (*10*−*19*). Only a few of these polymers, such as *N*-(2-hydroxypropylmethacrylamide) (HPMA), PEG, and poly(glutamic acid) (PGA), and their polymeric prodrug conjugates have shown promise in clinical applications for the delivery of anticancer drugs. Among these, only PGA is a biodegradable polymer. In the case of PEG and HPMA copolymers, molecular weights have been limited to 40 kDa to ensure their renal elimination (*20*).

Recently, novel branched polymers (e.g., dendrimers) have been introduced as carriers of therapeutic agents. Such branched carriers are characterized by *nanosized*, monodispersed peripheral multiend sites that allows for conjugation of multiple drug molecules per one molecule of the carrier. In addition, dendrimers possess unique characteristics including specific shape, branch length-to-density ratio, and surface functionality, which distinguish them from conventional linear polymers (*21*−*23*). Moreover, these polymers have entered into therapeutics with successful human clinical (Phase I) trials, namely, dendrimer-based nanopharmaceuticals (VivaGel), nanodiagnostics (Stratus), DNA delivery vectors (Superfect), and other drug delivery/polyvalency prototypes (*24*).

Many attempts have been made to improve the solubility of the highly water insoluble paclitaxel using formulations, surfactants, PEGylated polymers, Cremophor, solid dispersions, micro-nanoparticles, and complexation with cyclodextrins (*25*). Another strategy involves prodrug conjugation using small molecules or polymers as solubilizing entities at either C2′primary or C7 secondary hydroxyl positions in paclitaxel (*26*−*30*). Such conjugates can potentially improve aqueous solubility of the drug and thereby enhance its antitumor activity. However, polymeric carriers with different architectures have not been compared on the similar experimental conditions in order to assess the effectiveness of the various architectural elements in the delivery of anticancer drug by the carrier (i.e., by linear or branched).

The present work is aimed at comparing the ability of carriers with two different polymeric architectures, i.e., (a) polyamidoamine (PAMAM) G4 hydroxyl-terminated dendrimer and (b) conventional linear PEG polymer to deliver anticancer drug paclitaxel. Paclitaxel was covalently conjugated with bis-(carboxymethyl) PEG and dendrimer by the condensation method. To study the cellular entry dynamics by confocal microscopy, fluorescent probe fluoroisothiocynate (FITC) was covalently conjugated with paclitaxel, polymers, and polymeric conjugates containing paclitaxel. Conjugates were characterized by ^{1}HNMR, MALDI/TOF, and HPLC methods. The rate of hydrolysis of the ester bond in the conjugates was analyzed by

* To whom correspondence should be addressed: Tamara Minko, Ph.D., Department of Pharmaceutics, Ernest Mario School of Pharmacy, Rutgers, The State University of New Jersey, 160 Frelinghuysen Road, Piscataway, NJ 08854−8020. Phone: 732-445-3831 x 214. Fax: 732-445-3134. Email: minko@rci.rutgers.edu.

[†] Department of Pharmaceutics.

[‡] Department of Plant Biology and Pathology.

10.1021/bc060240p CCC: $33.50 © 2006 American Chemical Society
Published on Web 10/20/2006

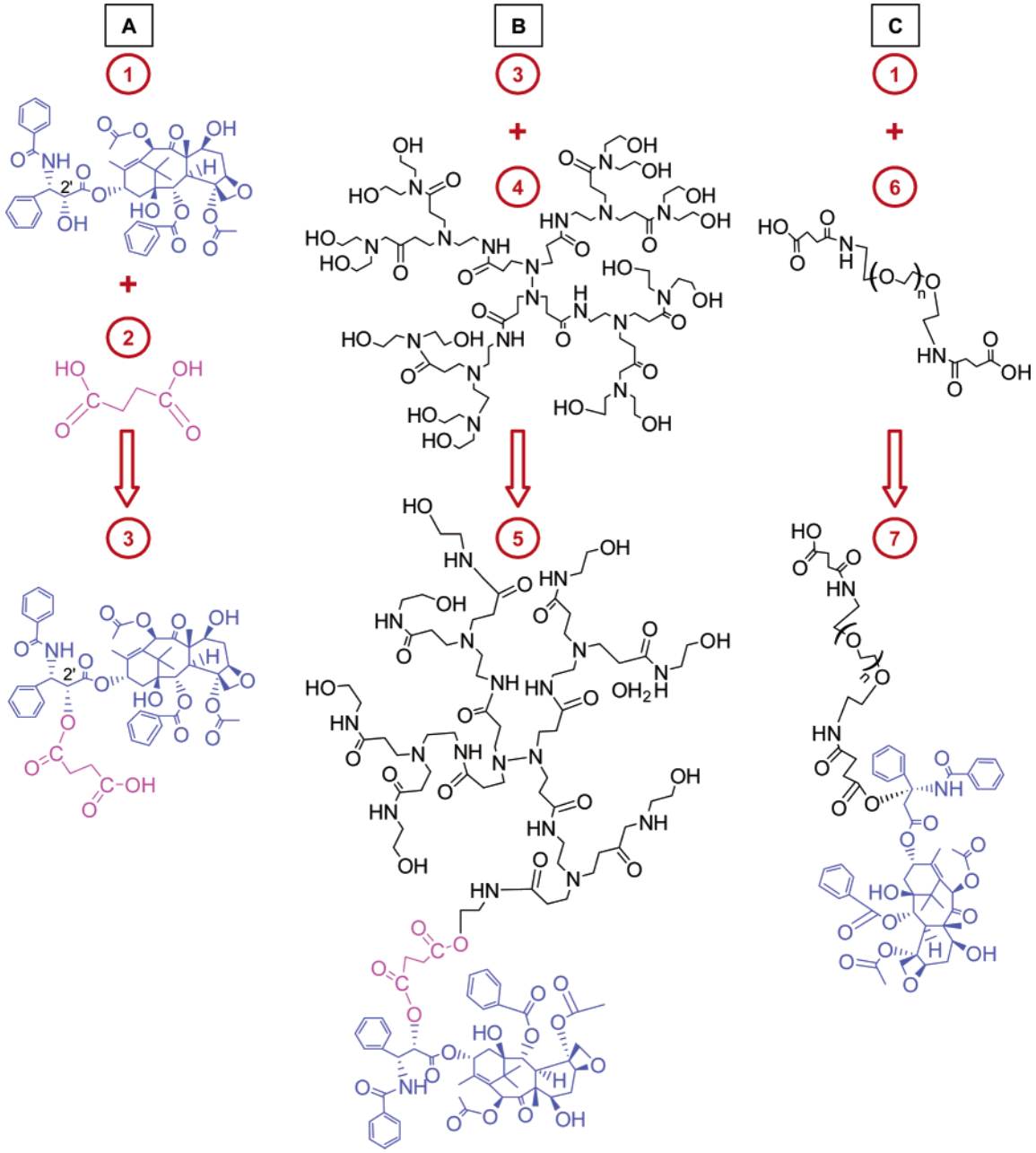

Figure 1. Synthesis of conjugates. (A) Paclitaxel (**1**) was first bound to succinic acid (**2**, SA) forming paclitaxel−SA conjugate (**3**). (B) PAMAM G4 hydroxyl-terminal dendrimer (**4**) was further coupled with paclitaxel−SA conjugate (**3**) to form paclitaxel−dendrimer conjugate (**5**). (C) bis-(PEG) (**6**) was joined with paclitaxel (**1**) to yield PEG−paclitaxel conjugate (**7**).

HPLC using esterase enzyme. In addition, polymers and conjugates with paclitaxel were studied for molecular conformations by the molecular modeling method. In vitro cytotoxicity (IC_{50}) of the conjugates was evaluated.

EXPERIMENTAL SECTION

Materials. Paclitaxel (M_w ~853.9 Da) was obtained from Sigma Chemical Co. (Atlanta, GA); α,ω-bis(2-carboxyethyl)-poly(ethylene glycol) (M_w ~10 000 Da) and fluorescein isothiocyanate (FITC) were obtained from Fluka (Allentown, PA). PAMAM−G4-OH (M_w ~14 279 Da, 64 end groups) dendrimers, *N*,*N*-diisopropylethylamine (DIEA), 4-(methylamino)pyridine (DMAP), and succinic acid (SA) were purchased from Sigma-Aldrich (St. Louis, MO). *N*-(3-dimethylaminopropyl)-*N*-ethylcarbodiimide HCl (EDC.HCl) was purchased from Fluka. Dialysis membrane of the molecular weight cutoff of 3500 Da (Spectra Pore), dimethyl sulfoxide (DMSO), dimethyl formamide (DMF), dichloromethane (DCM) acetone, ethanol, and diethyl ether were purchased from Fischer Scientific. Jupiter C5 column was purchased from Phenomenex (Torrance, CA).

Cell Line. The human ovarian carcinoma A2780 cell line was obtained from Dr. T. C. Hamilton (Fox Chase Cancer Center, PA). Cells were cultured in RPMI 1640 medium (Sigma Chemical Co., St. Louis, MO) supplemented with 10% fetal bovine serum (FBS) (HyClone, Logan, UT). Cells were grown at 37 °C in a humidified atmosphere of 5% CO_2 (v/v) in air. All experiments were performed on cells in the exponential growth phase.

Synthesis of Paclitaxel−Succinic acid (SA) Conjugate (Figure 1A). SA (**2**) is a bis(carboxylic acid) moiety and is reacted on an equimolar basis with the hydroxyl group in paclitaxel (**1**) to form a paclitaxel−SA conjugate (**3**), leaving one free carboxyl group for further conjugation with hydroxyl-terminal dendrimer. Briefly, paclitaxel (10.0 mg, 0.0118 mM)

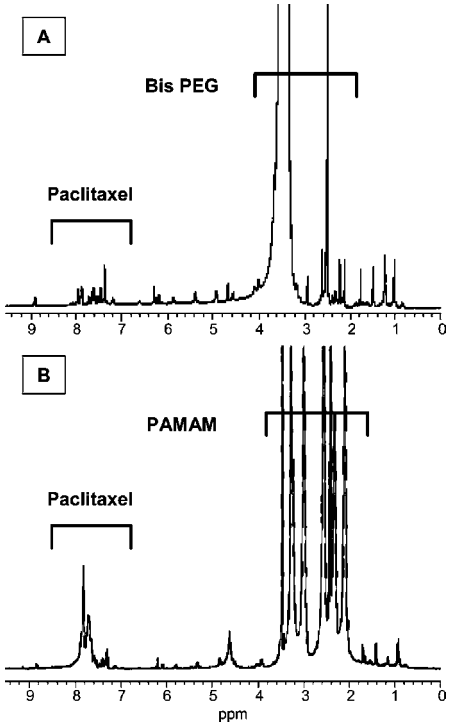

Figure 2. Proton nuclear magnetic resonance (^{1}H NMR) spectra of bis(PEG)−paclitaxel conjugate (A) and paclitaxel−SA−PAMAM dendrimer conjugate (B). ^{1}H NMR spectra were recorded on 400 MHz spectrophotometer using DMSO-d_6 as a solvent.

and succinic acid (1.4 mg, 0.0118 mM) were dissolved in 3.0 mL of anhydrous DMSO and 10.0 mL of anhydrous DCM. To the resulting mixture, *N*-(3- dimethylaminopropyl)-*N*-ethylcarbodiimide HCl (EDC.HCl, 2.30 mg, 0.0118 mM) and DMAP (1.0 mg) were used as a catalyst. The reaction was carried out with continuous stirring for 24 h at room temperature. The resulting solution was filtered to remove dicyclohexilurea (DCU) obtained as a byproduct during the reaction. Paclitaxel−SA conjugate (**3**) was precipitated using diethyl ether and dried under vacuum.

Synthesis of PAMAM-G4−Succinic Acid−Paclitaxel Conjugate (Figure 1B). Conjugation of succinic acid to paclitaxel resulted in the formation of monocarboxylic acid conjugate (**3**), which was further conjugated with hydroxyl groups in PAMAM-G4-OH dendrimer (**4**). Briefly, dendrimer (88 mg, 0.0061 mM) and paclitaxel−succinic acid conjugate (**3**) (6.0 mg, 0.0061 mM) were dissolved in 4.0 mL of anhydrous DMSO and 10.0 mL of anhydrous DCM. The mole ratio of dendrimer to paclitaxel−SA conjugate was maintained at 1:1. EDC.HCl (1.2 mg, 0.0062 mM) was added as a coupling agent, and DMAP (1.0 mg) was used as a catalyst. The reaction was stirred continuously for 24 h at room temperature. The resulting solution was filtered to remove DCU, and the filtrate was dialyzed extensively with anhydrous DMSO using dialysis membrane of molecular weight cutoff of 2000 Da for 24 h to remove unreacted paclitaxel−SA conjugate and EDC.HCl. Further, the conjugate was purified by size exclusion chromatography to remove unreacted paclitaxel−SA conjugate and excess EDC.HCl. Conjugate was dried under vacuum at room temperature. ^{1}H NMR was recorded in DMSO-d_6 on a 400 MHz NMR spectrophotometer and characterized for the peaks of dendrimer and paclitaxel (Figure 2B). Dendrimer, bis(PEG), and paclitaxel conjugates were analyzed for molecular mass by MALDI/TOF (Figure 3A,B) and HPLC (Figure 3D−F).

Synthesis of α,ω-Bis((2-carboxyethyl)PEG)−Paclitaxel Conjugates (Figure 1C). α,ω-Bis($PEG_{10\,000}$)−citric acid (**6**) containing carboxyl end groups at the terminals was coupled with hydroxyl groups in paclitaxel to form an ester conjugate (**1**). Briefly, bis((2-carboxyethyl)PEG) (50 mg, 0.005 mM) and paclitaxel (4.2 mg, 0.005 mM) were dissolved in 5.0 mL of anhydrous dimethylformamide (DMSO) and 15 mL of anhydrous dichloromethane (DCM). To this solution, 1-[3-(dimethylaminopropyl]-3-ethylcarbodiimide HCl (EDC.HCl, 1.0 mg, 0.0052 mM) was added as a coupling agent and 4-(methylamino)pyridine (DMAP, 0.5 mg, 0.004 mM) was used as a catalyst. The reaction solution was stirred continuously for 24 h at room temperature. The reaction yields formation of carbodiimide urea, which was removed by filtration. The conjugate was purified to remove unreacted paclitaxel and EDC.HCl by the dialysis method using a Spectra/Por membrane (M_w cutoff ∼2000 Da) in DMSO as a solvent. After the additional purification by size exclusion chromatography, α,ω-bis((2-carboxyethyl)PEG−paclitaxel conjugate was dried under vacuum at room temperature. ^{1}H NMR spectra were recorded in DMSO-d_6 on a 400 MHz NMR spectrophotometer and characterized for the peaks of bis(PEG) polymer and paclitaxel (Figure 2A). In addition, the molecular mass was measured by MALDI/TOF (Figure 3C) and characterized by HPLC (Figure 3F).

FITC Labeling of Bis(PEG), PAMAM Dendrimer, Free Paclitaxel, PEG−Paclitaxel, and PAMAM Dendrimer−SA−Paclitaxel Conjugates. FITC possesses carboxyl as well as hydroxyl groups for chemical conjugation with either hydroxyl or carboxyl group-possessing compounds. The reacting components were used in the following proportions: carboxyl-terminated bis(PEG) (60.0 mg, 0.006 nM) and FITC-OH (2.33 mg, 0.006 nM); PAMAM dendrimer (45 mg, 0.0032 nM) and FITC (5.0 mg, 0.0128 nM); paclitaxel (5.0 mg, 0.0058 nM) and FITC (2.28 mg, 0.0058 nM); PEG−paclitaxel conjugate (27 mg, 0.0025 nM) and FITC (1.0 mg, 0.0025 nM); PAMAM dendrimer−SA−paclitaxel conjugate (25 mg, 0.00163 nM) and FITC (2.5 mg, 0.0064 nM). All the components were dissolved separately in a round-bottom flask, and anhydrous DMSO and dichloromethane (DCM) were added. EDC.HCl was added with equivalent moles of FITC to be conjugated, and the reaction was carried out for 24 h at room temperature. Urea salt was precipitated and removed by filtration. All the FITC-labeled components (except paclitaxel−FITC conjugate) were dialyzed extensively using anhydrous DMSO (dialysis membrane of molecular weight cutoff of 2000 Da) for 24 h to remove unreacted FITC and EDC.HCl. Further, the conjugates were purified using size exclusion chromatography to remove unreacted FITC and excess EDC.HCl. All the conjugates were precipitated three times in acetone to remove free FITC.

HPLC. Quantitative evaluations of individual samples were obtained using Water Empower HPLC consisting of an in-line degasser, a 600E multisolvent delivery pump, a 717plus autosampler, and a Photodiode array detector 996. The separations were performed using a Jupiter column (C5, 4.6 × 250, 5−300 A) from Phenomenex (Torrance, CA). Two solvent systems were used. Solvent system A consisted of 99.9% water with pH 3.5 (adjusted with formic acid) and 10% methanol. Solvent B consisted of 20% water with pH 3.5 (adjusted with formic acid), 20% methanol, and 60% acetonitrile. The flow rate was maintained at 1 mL/min using step gradients of 0 min solvent A 100%; 10 min solvent A 100%; 20 min solvent A 0%, and 30 min solvent A 0%, 32 min solvent A 100%. The spectra were recorded ranging from 210 to 600 nm at 1.5 nm step. The spectra of each peak were superimposed with corresponding spectra and retention times. Only peaks which showed no more than 1.0% difference were used for integration and evaluation. Twenty microliters of each sample and standard were injected. The stock solutions (1 mg/mL) of analyzed substances were prepared using methanol as a solvent. The calibration standards of paclitaxel (0.24 mg/mL to 0.000296 mg/

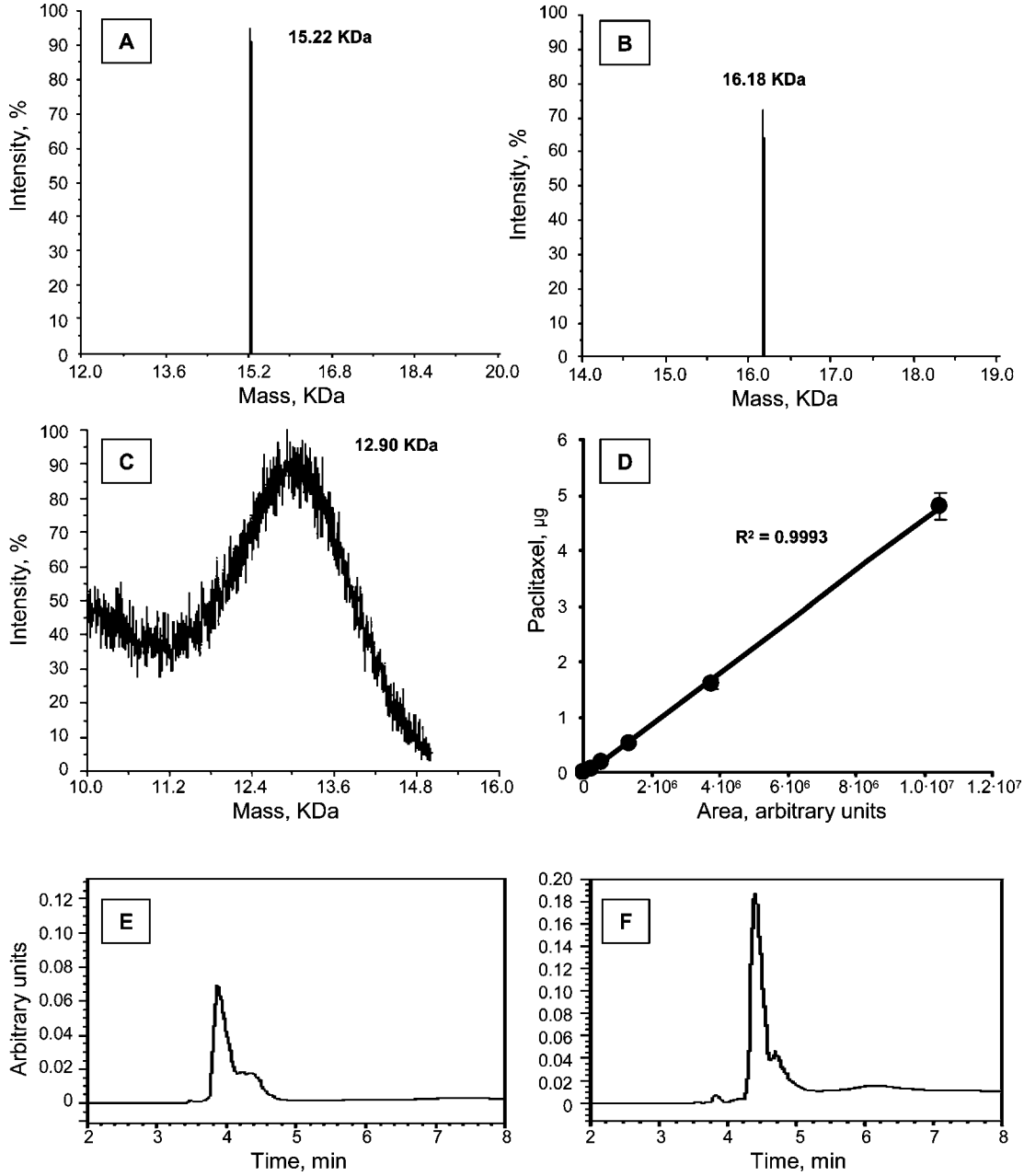

Figure 3. Characterization of synthesized polymer conjugates. Mass of PAMAM G4 OH dendrimer (A, 15.22 KDa), paclitaxel−SA−PAMAM dendrimer (B, 16, 18 KDa) and paclitaxel−bis(PEG) conjugates (C, 12.90 KDa) were measured by MALDI/TOF (Voyager De-Pro) system using sinapinic acid (3,5-dimethoxy-4-hydroxycinnamic acid) as a matrix. The total mass of the components indicate the appropriate formation of the paclitaxel conjugates. Calibration curve for paclitaxel (D) and typical HPLC chromatograms (E,F) of paclitaxel−SA−PAMAM dendrimer conjugate and PEG−paclitaxel conjugate, respectively. Peaks from 3.5 to 5 min retention time indicate the formation of high molecular weight conjugates.

mL) were prepared by serial dilution to achieve the nominal concentrations in reaction mass and hydrolyzed reaction mass.

Release of Paclitaxel from the Conjugates. The release of drug from the conjugates was assessed by HPLC method using esterase as hydrolyzing enzyme at pH 7.4. The standard curve of paclitaxel (Figure 3D) was obtained in a special series of HPLC experiments and used for calculating drug release from the conjugates. The data are presented as a percentage of total bound of paclitaxel, which is released from the conjugates (Figure 5).

Molecular Modeling. The studies were focused on analysis of conformational structures, energy minima, and molecular dynamics of bis(PEG) polymer, PAMAM dendrimer, free paclitaxel, and paclitaxel containing polymeric conjugates. The chemical structures were built using *ChemDraw 9.0 Pro* (Cambrigesoft Corp., Cambridge, MA). Free PEG and its bioconjugate with paclitaxel were built to represent seven ethylene repeat ($-CH_2-O-CH_2-$) units. The settings for energy minima and molecular dynamics were of the order reported by us earlier: 1.000 step interval, 2.0 fs; frame interval, 10 fs; terminated after 10 000 steps; heating/cooling rate, 1.000 kcal/atom/ps; target temperature, 300 K. Distance between the first and last carbon atom was measured for the molecular dynamics structures of bis(PEG) and its conjugation with paclitaxel. *RasTop* molecular visualization software (Philippe Valadon, San Diego, CA) was used for obtaining lengths of free drug, polymer, and its conjugates.

Cellular Internalization (Confocal Microscopy). Cellular internalization of FITC-labeled PEG−polymer, dendrimer, paclitaxel, PEG−paclitaxel, and PAMAM−dendrimer−paclitaxel conjugates was studied by confocal microscopy. To assess intracellular distribution of the substances, six optical sections, known as a *z*-series, were scanned sequentially along the vertical (*z*) axis from the top to the bottom of the cell.

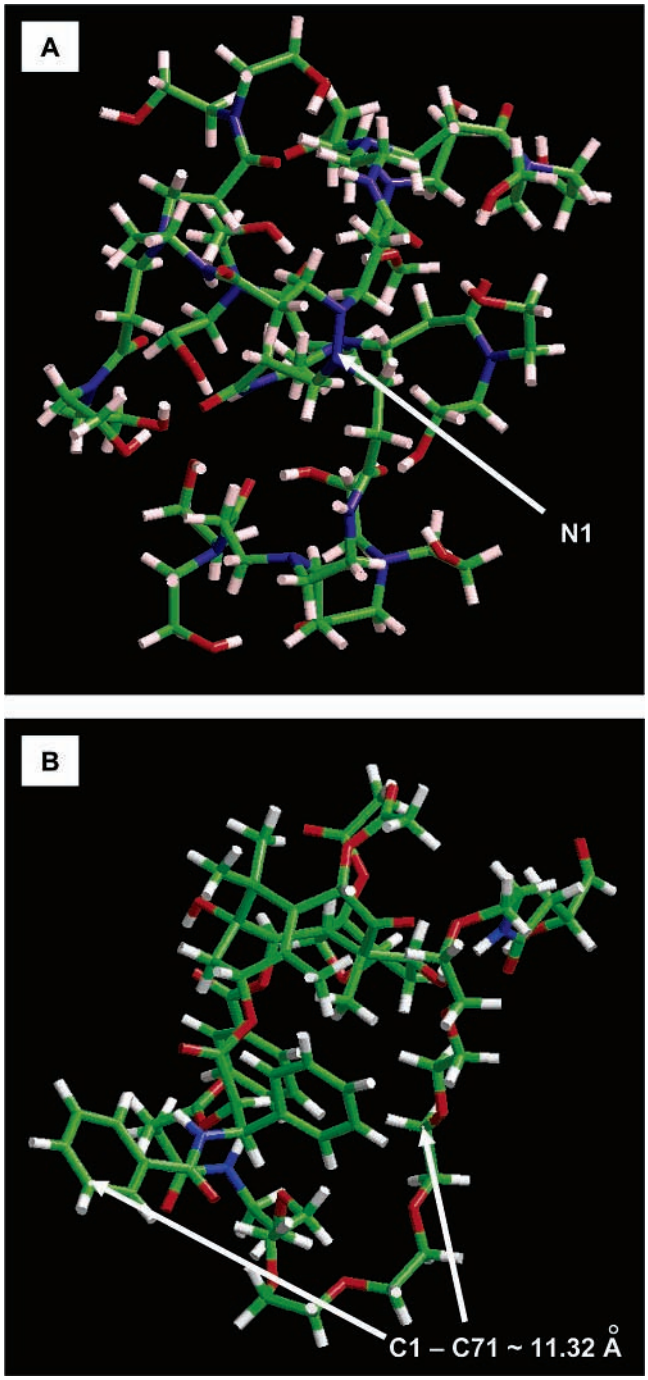

Figure 4. Molecular modeling studies of paclitaxel−SA−PAMAM dendrimer (A) and PEG−paclitaxel conjugate (B). Polymeric structures were built in *Chemdraw* software and allowed to undergo conformational stabilization for energy minima. The stabilized structure of PEG−paclitaxel conjugate was exported to *RasTop* software to estimate the distances between the first and last carbon atoms (here, C1−C71). The distance was measured to be 11.32 Å for energy-minimized molecule.

In Vitro Cytotoxicity. The cytotoxicity of paclitaxel conjugates and free paclitaxel was assessed by using a modified MTT (3-(4,5-dimethylthiazol-2-yl)-2,5-diphenyltetrazolium bromide) assay as previously described (*31*, *32*). To measure cytotoxicity, cells were separately incubated in a microtiter plate with different concentrations of free paclitaxel, PEG−paclitaxel, and PAMAM dendrimer−paclitaxel conjugates. Control cells received an equivalent volume of fresh medium. The duration of incubation was 24 h. On the basis of these measurements, IC_{50} doses of free paclitaxel and its polymeric conjugates (the concentrations of active ingredients necessary to inhibit the cell growth by 50%) were calculated. A decrease in the IC_{50} dose indicates an increase in drug toxicity.

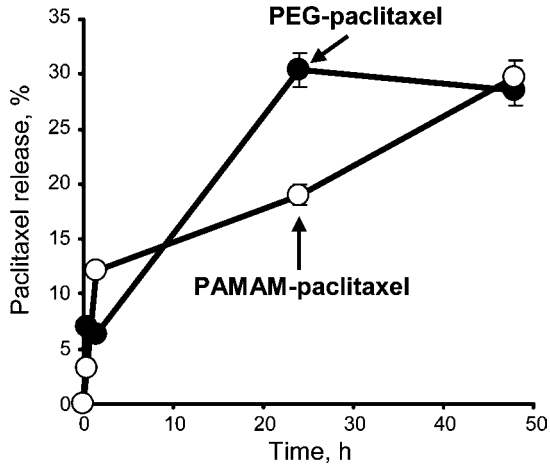

Figure 5. A release profile of paclitaxel from the conjugates determined by HPLC after enzymatic hydrolysis using esterase as the enzyme at pH 7.4. After 24 h, the release of paclitaxel in the PEG conjugate was observed to be 30%. In the case of paclitaxel−SA−PAMAM dendrimer conjugate, the 30% release of the drug was achieved after 48 h, indicating slower release.

Statistics. All in vitro experiments were performed in quadruplicate. The results are expressed as mean ± SD from 4−8 independent measurements. Statistical analysis was performed as a one-way analysis of variance (ANOVA) and comparisons among groups were performed by independent sample *t*-tests.

RESULTS

Synthesis and Characterization of Paclitaxel Conjugates. α,ω-Bis(PEG)−paclitaxel and dendrimer−SA−paclitaxel conjugates were prepared by using EDC.HCl as a coupling agent. Conjugates were purified by membrane dialysis using the molecular weight cutoff method and by size exclusion chromatography. Each of the conjugates was characterized by ^{1}H NMR on 400 MHz spectrophotometer. Proton peaks arising from paclitaxel, bis(PEG), and PAMAM dendrimer were analyzed (Figure 2A,B), and the peak area was integrated and compared for the conjugation ratio (integration values not shown in proton spectra). Both the conjugates and free paclitaxel were further analyzed and characterized by HPLC. In addition, the masses of the PAMAM dendrimer, bis(PEG) polymer, and their conjugates having paclitaxel were characterized by MALDI/TOF. FITC was covalently labeled with paclitaxel, polymers, and their paclitaxel conjugates, for evaluating cellular dynamics using confocal microscopy.

NMR Peaks Characterization and Estimation of Conjugation Ratios. *PEG−Paclitaxel Conjugate.* ^{1}H NMR spectrum (Figure 2A) showed the broad peaks from 3.2 to 3.9 ppm indicating protons for $-CH_2CH_2O-$ in bis(PEG) polymer. A peak at 8.85 ppm shows the presence of two hydrogen atoms arising from the phenyl ring in paclitaxel at the C2′ position (*33*). Proton peaks from δ 3.2 to 3.9 ppm corresponded to PEG and have the integrated peak area of 639 arbitrary units (integration values not shown in proton spectra). Bis(PEG) polymer with molecular weight 10 000 Da has approximately 257 protons in this region. So, each proton corresponds to a value of 2.49 units (639/257). On the other hand, a peak at δ 8.85 ppm corresponds to a value of 0.025 units for a single proton in the phenyl ring of paclitaxel (integration for value ∼0.05/2 = 0.025). Therefore, the ratio of protons of PEG to paclitaxel is inferred to be around 0.99.

Dendrimer−SA−Paclitaxel Conjugate. ^{1}H NMR spectrum (Figure 2B) showed the multiplets between δ 2.0 and 3.6 ppm

corresponding to the presence of 985 protons of CH_2 of PAMAM-G4-OH (integration values not shown in the proton NMR spectra) (*34*). On the other hand, a peak at 8.85 ppm showed the presence of two hydrogen atoms on the phenyl ring in paclitaxel at the C2′ position. The integrated peak areas for protons in dendrimer and paclitaxel are 104.17 and 0.18, respectively. Since the value for each proton in dendrimer and paclitaxel corresponds to 0.105 and 0.09, respectively (i.e., 104.17/985 = 0.105 and 0.18/2 = 0.09), the ratio of paclitaxel molecules per dendrimer is ~0.857 (0.09/0.105 = 0.857). The proton NMR provides evidence for the formation of PEG−paclitaxel and PAMAM dendrimer−paclitaxel conjugates.

Characterization of Conjugates. *MALDI/TOF* (Figure 3A−C). Masses of PAMAM-G4-OH dendrimer, paclitaxel−SA−PAMAM dendrimer, and paclitaxel−bis(PEG) conjugates were measured by MALDI/TOF Voyager DE-Pro system (Applied Biosystems, Foster City, CA) using sinapinic acid (3,5-dimethoxy-4-hydroxycinnamic acid) as a matrix. The molecular masses were found to be 15.22 KDa for PAMAM-G4-OH dendrimer (Figure 3A), 16, 18 KDa for paclitaxel−SA−PAMAM dendrimer (Figure 3B), and 12.90 KDa for paclitaxel−bis(PEG) conjugate (Figure 3C). The total mass of the compounds indicates formation of the paclitaxel conjugates. In addition, HPLC data confirmed the peaks between 3.5 and 5 min (Figure 3E,F) indicating high molecular weight conjugate formation for both PAMAM−SA−paclitaxel and PEG−paclitaxel.

HPLC. In this study, we used HPLC for analysis of paclitaxel in conjugates and free form. Quantification of free and polymer-bound paclitaxel was achieved using the reverse-phase HPLC method preceded by C5 column (4.6 × 250, 5−300 A, Phenomenex, Torrance, CA). Paclitaxel has an absorbance spectrum with the maximum at 280 nm allowing quantitative determination of polymer−drug conjugates. The use of the C5 column improved the retention time of polymer-bound paclitaxel when compared with C18 and C8 columns (Figure 3E,F). The chromatogram represents the broad peak which may arise from conjugation formed at primary as well as secondary hydroxyl positions. The stability of the bond in paclitaxel−polymer conjugates was investigated by measuring the release of free paclitaxel in stock solution. The conjugates were stored at 4 and −20 °C for 1 month, and no significant release of free drug was observed. In addition, the release of paclitaxel from the conjugates after enzymatic hydrolysis was determined using esterase as enzyme at pH 7.4 (Figure 5). Data obtained showed that about 30% of paclitaxel were released from PEG−paclitaxel conjugate after 24 h of incubation. In contrast, less than 20% of the drug was released after 24 h of incubation from PAMAM−SA−paclitaxel dendrimer, reaching 30% only after 48 h of the experiment. Although dendrimer−SA−paclitaxel conjugate has two ester sites for hydrolysis (Figure 1A,B), its enzymatic degradation was slower when compared with PEG conjugate, which has only one ester site (Figure 1C). This may be a result of specific nanosized dendrimer architecture which exhibits higher steric hindrance for esterase degradation at macromolecular ester sites when compared with linear PEG conjugate.

Enhanced Aqueous Solubility of Paclitaxel Using Dendritic and PEG Conjugates. Both of these polymers increased aqueous solubility of the drug. Solubility was higher for dendrimer−paclitaxel conjugate when compared to PEG−paclitaxel conjugates. While the aqueous solubility of paclitaxel is limited to 0.3μg/mL, the solubility of paclitaxel−bis(PEG) conjugate was observed to be 2.5 mg/mL. Moreover, the solubility for PAMAM−paclitaxel conjugate was further improved and was found to be 3.2 mg/mL.

Molecular Modeling Studies. We compared the structural stability of the linear PEG polymer with the well-defined molecular structure of PAMAM dendrimer, built structures, and evaluated the energy minima and molecular dynamics of paclitaxel, bis(PEG), PAMAM dendrimer, and polymeric conjugates containing paclitaxel. An example of molecular modeling of PAMAM dendrimer is shown in Figure 4. The energy minima conformational distance for paclitaxel was observed to be 8.24 Å (C1 to C47, the figure not shown). On the other hand, the molecular dynamics structure showed a distance of 7.99 Å (figure not shown). Energy minima conformation for paclitaxel−SA−PEG conjugate (Figure 4B) was observed to be 11.32 Å (C1 to C71). On the other hand, the molecular conformation of PAMAM dendrimer was found to be more stable than that of its paclitaxel conjugate, indicating conformational bulkiness of the resulting conjugate due to addition of the drug (Figure 4A).

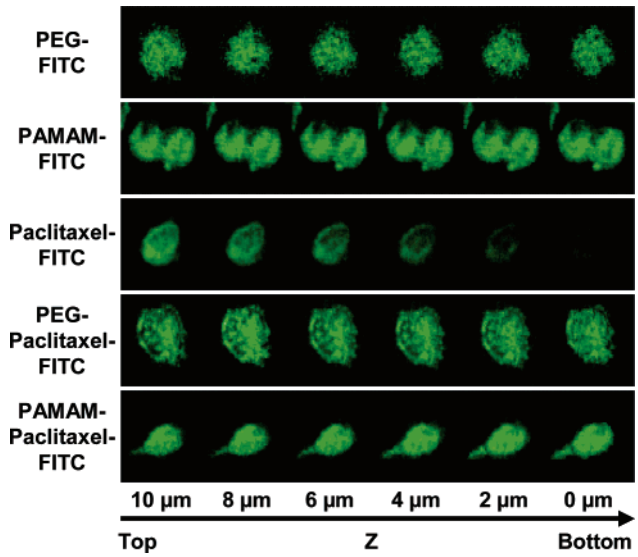

Figure 6. Confocal microscopy fluorescent images of human A2780 ovarian carcinoma cells incubated for 24 h with FITC-labeled substances (*z*-series, from the top of the cell to the bottom).

Cellular Localization of Labeled FITC Having Bis(PEG) and Dendrimer with Paclitaxel. Theoretically, high molecular weight drug conjugates could adhere to the surface of cancer cells and erroneously be visualized on microscopic images as internalized within cells. To exclude such errors, we analyzed the distribution of FITC-labeled polymers, polymer−drug conjugates, and free paclitaxel in different cellular layers from the upper to the lower of the fixed cell using confocal fluorescent microscopy (*z*-sections, Figure 6). In these experiments, the studied components were labeled with FITC and incubated with A2780 human ovarian carcinoma cells. The cells were fixed and subjected to confocal microscopy. The *z*-sections of single cells showed the homogeneous and uniform distribution of labeled polymers with or without paclitaxel. In contrast, the distribution of free paclitaxel inside the cancer cell was highly inhomogeneous both within the one layer and through different layers of a single cell. Free paclitaxel accumulated mainly in the cytoplasm near the plasma membrane and predominantly on the top of the cell in the place of cellular contact with the medium containing the drug (the bottom surface of the cell was attached to the flask wall). These data suggest that both linear PEG polymer and PAMAM dendrimer enhance the penetration of paclitaxel into cancer cells, resulting in a more homogeneous drug distribution inside the single cells.

In Vitro Cytotoxicity. Conjugation of paclitaxel to linear PEG polymer and PAMAM dendrimer substantially influenced its cytotoxicity (Figure 7). While linear PEG−paclitaxel conjugate showed more than 25-fold lower toxicity (IC_{50} dose increased), PAMAM−dendrimer−paclitaxel conjugate showed

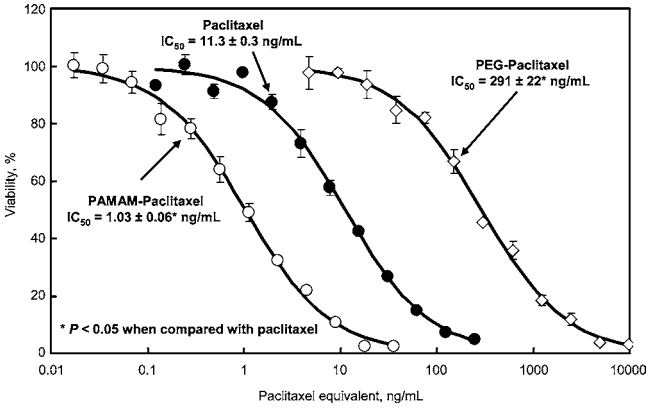

Figure 7. In vitro cytotoxicity of free paclitaxel, PEG−paclitaxel, and paclitaxel−SA−PAMAM dendrimer conjugates toward A2780 human ovarian carcinoma cells. PAMAM−SA dendrimer substantially enhances toxicity of paclitaxel by decreasing the dose of the drug required to kill 50% of cells (IC_{50} dose). Means ± SD are shown. *$P < 0.05$ when compared with free paclitaxel.

significantly ($P < 0.05$) higher toxicity (IC_{50} dose was more them 10 times lower) when compared with free drug.

DISCUSSION

Polymeric architecture, molecular weight, and molecular charge play important roles in delivering drugs (*35*). This is especially true when the polymeric materials have linear, branched, and graft architectures. In addition, such polymers exhibit high steric hindrance for cellular internalization and might often result in delayed cellular entry. For instance, PEGylated adenovirus vectors exhibit longer plasma half-life when compared with free adenovirus, and their entry into cells has been prevented by steric hindrance by poly(ethylene glycol) (PEG) chains (*36*). Moreover, linear PEG polymer may possess higher polydispersity, and theoretical size may range greater than 300−500 nm even for lower molecular weight polymer. In contrast, hyperbranched polymers, e.g., dendrimers, due to their well-defined monodispersity (PI ≈ 1.0), controlled architecture, nanosize (20−40 nm), and shape, are often considered most promising vehicles for the delivery of drugs, proteins, and other therapeutic agents (*21*, *37*−*39*). Dendrimers in conjugation with FITC have been reported to achieve rapid cellular entry even in 5 min (*34*). Dendrimers have unique architecture, as they are prepared through controlled synthetic methods: either by divergent or convergent method having control over the branching architecture. Therefore, in a short time, they have emerged as the most promising drug delivery carriers. In this work, we compared the difference in delivery ability of these polymers with the conventional linear PEG polymers.

Conjugation of a low-solubility drug with high-solubility polymers bears an additional advantage of forming a prodrug with enhanced aqueous solubility. Such soluble prodrugs further increase the bioavailability of the drug and therefore have a potential to enhance its activity (cytotoxicity in the case of an anticancer drug). Recently, polyglycerol dendrimers (PGDs) with 4−5 generations were used to investigate the effect of dendritic architecture and its generation on the aqueous solubilization of paclitaxel (*7*). It was shown that the increase in the paclitaxel solubility by PGDs was dependent on the dendrimer generation. In the present study, both polymers increased the aqueous solubility of the drug. However, the increase in the solubility was higher for the dendrimer−paclitaxel conjugate when compared with the PEG−paclitaxel conjugate. The aqueous solubility of paclitaxel−bis(PEG) was equal to 2.5 mg/mL, while that of PAMAM−SA−paclitaxel conjugate was 3.2 mg/mL. The aqueous solubility of free paclitaxel was about 0.3 μg/mL. Such a dramatic enhancement in paclitaxel solubility allowed dissolving of conjugates in buffer for our in vitro cytotoxicity studies, while the free drug was dissolved in ethanol.

Besides solubility and size, the bioavailability and anticancer activity of conjugated drug substantially depend on the type of bond between the drug and a carrier. Specific spacers are often used to control the rate of drug release from the conjugate. We used succinic acid as a spacer to bind paclitaxel to PAMAM dendrimer. SA is a bis functional carboxylic acid and therefore can be conjugated with hydroxyl groups in paclitaxel, thereby resulting in forming an ester bond with the drug, and yet leaves one free carboxyl group for further conjugation with another component. Paclitaxel−SA conjugate was coupled with hydroxyl-terminal PAMAM dendrimer to obtain dendrimer−SA−paclitaxel conjugate. In the past, the role of bis functional spacers (e.g., glutaric acid) has been established in increasing the reactivity of the low-reactivity drugs with the hyperbranched polymers (*34*). Additionally, bis functional spacers such as succinic acid may decrease the steric hindrance for conjugation with polymers, especially with the hyperbranched polymers, due to crowded functional groups (*34*). This is especially important when the dendrimer conjugate is expected to obtain a high payload of drug in the conjugate. It should be noted that, in the present conjugation reaction, two ester bonds are formed, i.e., one with the drug and another with the dendrimer, thereby providing two sites for hydrolysis to release the free drug. It is expected that free paclitaxel will be released from the conjugated drug following hydrolysis of this bond after internalization of the whole complex into the cancer cell. On the other hand, α,ω-bis($PEG_{10\,000}$) polymer contains carboxyl end groups at the terminals and therefore can be coupled directly with 2′ hydroxyl groups in paclitaxel. Although the bis(PEG) polymer consists of two reactive sites, only one molecule of paclitaxel was coupled using equivalent moles of drug and EDC.HCl as a condensing agent. It has been reported in the past that the most suitable position for structural conjugation in paclitaxel is either C2′ or C7′ hydroxyl (*33*). It has been well-realized that usually the primary hydroxyl C2′ site is a more active site than the secondary hydroxyl C7′ site due to less steric hindrance, and esterification is preferentially formed at C2′. However, it is possible to form more than one conformation of the conjugates reacting either at C2′ or at C7′. The second free carboxyl group available on the bis(PEG)−paclitaxel conjugate was utilized for coupling with the hydroxyl group in FITC, allowing for visualization of the conjugate by fluorescent/confocal microscopy.

A polymer and its reaction with bulkier drug molecules undergo steric hindrance due to higher molecular mass and unstable conformations (*35*). The net result may lead to lower yields or may even form by-products through incomplete conjugation reactions with free and unreacted drug and polymer chains. Prodrug conjugation reactions may be studied using modeling through the conformations and minima energies. In addition, the reactivity of both polymers as well as drugs could be increased by incorporating spacer molecules. One of the objectives of the present study was to compare the structural stability of the linear PEG polymer with well-defined, monodispersed PAMAM dendrimers. In the past, polymeric conformations with a glycine spacer have been evaluated using modeling studies to estimate the spacer length and molecule stability (*40*, *41*). More recently, few studies suggest applications of modeling in prodrug bioconjugates, involving incorporation of spacers and strategies to reduce the steric hindrance in prodrug synthesis (*42*). The author has demonstrated steric hindrance associated with conjugation of an anticancer drug with PEG polymer by a molecular modeling method to determine

the most suitable bicarboxylic amino acid that possesses the least steric hindrance.

Recently, we reported molecular structures of bis(PEG) polymer with multiple copies of the drug camptothecin (CPT) using molecular modeling tools (*40*). The minima represented the minimum energies (kcal) indicating the degree of conformational freedom for (a) seven repeating units of bis(PEG) polymeric chain conjugate, (b) generation 2 hydroxyl-terminated PAMAM dendrimer, and (c) its conjugate with paclitaxel. The minimum-energy conformational distance for paclitaxel was observed to be 8.24 Å (C1 to C47). On the other hand, the molecularly dynamic structure showed a distance of 7.99 Å. The minimum-energy conformation for paclitaxel−SA−PEG conjugate was observed to be 11.32 Å (C1 to C71). On the other hand, molecular confirmation of PAMAM dendrimer was found to be more stable than its paclitaxel conjugate, indicating conformational bulkiness of the resulting conjugate due to addition of the drug. Previously, we reported the results of molecular modeling studies which support our synthetic strategies in selecting reactive peptides, polymers, drugs, and spacers to reduce steric hindrance, especially prodrug conjugates involving multiple components (*35*, *40*).

Although conjugation of paclitaxel to both traditional PEG polymer and PAMAM G4−SA dendrimer improve the bioavailability of the drug, the influence of the conjugation on anticancer activity of paclitaxel depended on the type of drug carrier. Conjugation to PEG polymer significantly decreased the toxicity of paclitaxel. In fact, the IC_{50} dose of PEG−paclitaxel conjugate was more than 25 higher when compared with free drug. Such a decrease in anticancer activity might be explained by the increase in molecular mass of the whole complex, which in turn changed the mechanism of the cellular internalization of PEG−paclitaxel polymer from diffusion (free drug) to endocytosis. In contrast, conjugation of paclitaxel to PAMAM G4−SA dendrimer substantially enhanced cytotoxicity of the drug leading to the decrease in the IC_{50} dose more than 10-fold when compared with free drug.

CONCLUSIONS

Taken together, the data obtained suggest that PAMAM G4−SA dendrimer represents a promising vehicle for intracellular delivery of low-solubility drugs such as paclitaxel. The developed dendrimer provides both cytoplasmic and nuclear delivery of therapeutics and enhances anticancer activity of paclitaxel.

ACKNOWLEDGMENT

This work was supported by National Institutes of Health grant CA100098 from the National Cancer Institute.

LITERATURE CITED

(1) Wani, M. C., Taylor, H. L., Wall, M. E., Coggon, P., and McPhail, A. T. (1971) Plant antitumor agents. VI. The isolation and structure of taxol, a novel antileukemic and antitumor agent from Taxus brevifolia. *J. Am. Chem. Soc. 93*, 2325−2327.

(2) Singla, A. K., Garg, A., and Aggarwal, D. (2002) Paclitaxel and its formulations. *Int. J. Pharm. 235*, 179−192.

(3) Wall, M. E., and Wani, M. C. (1996) Camptothecin and taxol: from discovery to clinic. *J. Ethnopharmacol. 51*, 239−253; discussion 253−254.

(4) Dorr, R. T. (1994) Pharmacology and toxicology of Cremophor EL diluent. *Ann. Pharmacother. 28*, S11−14.

(5) Feng, X., Yuan, Y. J., and Wu, J. C. (2002) Synthesis and evaluation of water-soluble paclitaxel prodrugs. *Bioorg. Med. Chem. Lett. 12*, 3301−3.

(6) Fjallskog, M. L., Frii, L., and Bergh, J. (1993) Is Cremophor EL, solvent for paclitaxel, cytotoxic? *Lancet 342*, 873.

(7) Ooya, T., Lee, J., and Park, K. (2004) Hydrotropic dendrimers of generations 4 and 5: synthesis, characterization, and hydrotropic solubilization of paclitaxel. *Bioconjugate Chem. 15*, 1221−1229.

(8) Rowinsky, E. K., Eisenhauer, E. A., Chaudhry, V., Arbuck, S. G., and Donehower, R. C. (1993) Clinical toxicities encountered with paclitaxel (Taxol). *Semin. Oncol. 20*, 1−15.

(9) Greenwald, R. B., Gilbert, C. W., Pendri, A., Conover, C. D., Xia, J., and Martinez, A. (1996) Drug delivery systems: water soluble taxol 2′-poly(ethylene glycol) ester prodrugs-design and in vivo effectiveness. *J. Med. Chem. 39*, 424−431.

(10) Allen, T. M., and Cullis, P. R. (2004) Drug delivery systems: entering the mainstream. *Science 303*, 1818−1822.

(11) Choi, Y., Thomas, T., Kotlyar, A., Islam, M. T., and Baker, J. R., Jr. (2005) Synthesis and functional evaluation of DNA-assembled polyamidoamine dendrimer clusters for cancer cell-specific targeting. *Chem. Biol. 12*, 35−43.

(12) Conover, C. D., Linberg, R., Gilbert, C. W., Shum, K. L., and Shorr, R. G. (1997) Effect of polyethylene glycol conjugated bovine hemoglobin in both top-load and exchange transfusion rat models. *Artif. Organs 21*, 1066−1075.

(13) Dharap, S. S., Wang, Y., Chandna, P., Khandare, J. J., Qiu, B., Gunaseelan, S., Sinko, P. J., Stein, S., Farmanfarmaian, A., and Minko, T. (2005) Tumor-specific targeting of an anticancer drug delivery system by LHRH peptide. *Proc. Natl. Acad. Sci. U.S.A. 102*, 12962−12967.

(14) Duncan, R. (2003) The dawning era of polymer therapeutics. *Nat. Rev. Drug Discovery 2*, 347−360.

(15) Kitchens, K. M., El-Sayed, M. E., and Ghandehari, H. (2005) Transepithelial and endothelial transport of poly (amidoamine) dendrimers. *Adv. Drug Delivery Rev. 57*, 2163−2176.

(16) Kopecek, J., Kopeckova, P., Minko, T., Lu, Z. R., and Peterson, C. M. (2001) Water soluble polymers in tumor targeted delivery. *J. Controlled Release 74*, 147−158.

(17) Maeda, H. (2001) The enhanced permeability and retention (EPR) effect in tumor vasculature: the key role of tumor-selective macromolecular drug targeting. *Adv. Enzyme Regul. 41*, 189−207.

(18) Putnam, D. (2006) Polymers for gene delivery across length scales. *Nat. Mater. 5*, 439−451.

(19) Wang, C., Ge, Q., Ting, D., Nguyen, D., Shen, H. R., Chen, J., Eisen, H. N., Heller, J., Langer, R., and Putnam, D. (2004) Molecularly engineered poly(ortho ester) microspheres for enhanced delivery of DNA vaccines. *Nat. Mater. 3*, 190−196.

(20) Vicent, M. J., and Duncan, R. (2006) Polymer conjugates: nanosized medicines for treating cancer. *Trends Biotechnol. 24*, 39−47.

(21) Gurdag, S., Khandare, J., Stapels, S., Matherly, L. H., and Kannan, R. M. (2006) Activity of dendrimer−methotrexate conjugates on methotrexate-sensitive and -resistant cell lines. *Bioconjugate Chem. 17*, 275−283.

(22) Patri, A. K., Myc, A., Beals, J., Thomas, T. P., Bander, N. H., and Baker, J. R., Jr. (2004) Synthesis and in vitro testing of J591 antibody−dendrimer conjugates for targeted prostate cancer therapy. *Bioconjugate Chem. 15*, 1174−1181.

(23) Svenson, S., and Tomalia, D. A. (2005) Dendrimers in biomedical applications−reflections on the field. *Adv. Drug Delivery Rev. 57*, 2106−2129.

(24) Tomalia, D. A., and Frechet, J. M. (2005) Introduction to "Dendrimers and dendritic polymers". *Progr. Polym. Sci. 30*, 217−219.

(25) Sweetana, S., and Akers, M. J. (1996) Solubility principles and practices for parenteral drug dosage form development. *PDA J. Pharm. Sci. Technol. 50*, 330−342.

(26) Deutsch, H. M., Glinski, J. A., Hernandez, M., Haugwitz, R. D., Narayanan, V. L., Suffness, M., and Zalkow, L. H. (1989) Synthesis of congeners and prodrugs. 3. Water-soluble prodrugs of taxol with potent antitumor activity. *J. Med. Chem. 32*, 788−792.

(27) Li, C., Yu, D. F., Newman, R. A., Cabral, F., Stephens, L. C., Hunter, N., Milas, L., and Wallace, S. (1998) Complete regression of well-established tumors using a novel water-soluble poly(L-glutamic acid)-paclitaxel conjugate. *Cancer Res. 58*, 2404−2409.

(28) Vyas, D. M., Ueda, Y., Wong, H., Matiskella, J. D., Hauck, S., Mikkilineni, A. B., Farina, V., Rose, W. C., and Casazza, A. M. (1995) Phosphate-activated prodrugs of paclitaxel. In *Taxane anticancer agents: Basic science and current status* (Chen, T. T.,

Ojima, I., and Vyas, D. M., Eds.) pp 124−137, American Chemical Society, Washington, DC.
(29) Zhang, X., Li, Y., Chen, X., Wang, X., Xu, X., Liang, Q., Hu, J., and Jing, X. (2005) Synthesis and characterization of the paclitaxel/MPEG-PLA block copolymer conjugate. *Biomaterials 26*, 2121−2128.
(30) Zhao, Z., Kingston, D. G. I., and Crosswell, A. R. (1991) Modified taxols, 6. Preparation of water-soluble prodrugs of taxol. *J. Nat. Prod. 54*, 1607−1611.
(31) Minko, T., Kopeckova, P., and Kopecek, J. (1999) Chronic exposure to HPMA copolymer-bound adriamycin does not induce multidrug resistance in a human ovarian carcinoma cell line. *J. Controlled Release 59*, 133−148.
(32) Pakunlu, R. I., Wang, Y., Tsao, W., Pozharov, V., Cook, T. J., and Minko, T. (2004) Enhancement of the efficacy of chemotherapy for lung cancer by simultaneous suppression of multidrug resistance and antiapoptotic cellular defense: novel multicomponent delivery system. *Cancer Res. 64*, 6214−6224.
(33) Shi, Q., Wang, H. K., Bastow, K. F., Tachibana, Y., Chen, K., Lee, F. Y., and Lee, K. H. (2001) Antitumor agents 210. Synthesis and evaluation of taxoid-epipodophyllotoxin conjugates as novel cytotoxic agents. *Bioorg. Med. Chem. 9*, 2999−3004.
(34) Khandare, J., Kolhe, P., Pillai, O., Kannan, S., Lieh-Lai, M., and Kannan, R. M. (2005) Synthesis, cellular transport, and activity of polyamidoamine dendrimer−methylprednisolone conjugates. *Bioconjugate Chem. 16*, 330−337.
(35) Khandare, J. J., and Minko, T. (2006) Polymer drug conjugates: Progress in polymeric prodrugs. *Prog. Polym. Sci. 31*, 359−397.
(36) Eto, Y., Gao, J. Q., Sekiguchi, F., Kurachi, S., Katayama, K., Maeda, M., Kawasaki, K., Mizuguchi, H., Hayakawa, T., Tsutsumi, Y., Mayumi, T., and Nakagawa, S. (2005) PEGylated adenovirus vectors containing RGD peptides on the tip of PEG show high transduction efficiency and antibody evasion ability. *J. Gene Med. 7*, 604−612.
(37) Grainger, D., and Okano, T. (2003) Biomedical micro- and nanotechnology. *Adv. Drug Delivery Rev. 55*, 311−313.
(38) Kono, K., Liu, M., and Frechet, J. M. (1999) Design of dendritic macromolecules containing folate or methotrexate residues. *Bioconjugate Chem. 10*, 1115−1121.
(39) Morgan, M. T., Carnahan, M. A., Immoos, C. E., Ribeiro, A. A., Finkelstein, S., Lee, S. J., and Grinstaff, M. W. (2003) Dendritic molecular capsules for hydrophobic compounds. *J. Am. Chem. Soc. 125*, 15485−15489.
(40) Khandare, J. J., Chandna, P., Wang, Y., Pozharov, V. P., and Minko, T. (2006) Novel polymeric prodrug with multivalent components for cancer therapy. *J. Pharmacol. Exp. Ther. 317*, 929−937.
(41) Paranjpe, P. V., Chen, Y., Kholodovych, V., Welsh, W., Stein, S., and Sinko, P. J. (2004) Tumor-targeted bioconjugate based delivery of camptothecin: design, synthesis and in vitro evaluation. *J. Controlled Release 100*, 275−292.
(42) Schiavon, O., Pasut, G., Moro, S., Orsolini, P., Guiotto, A., and Veronese, F. M. (2004) PEG-Ara-C conjugates for controlled release. *Eur. J. Med. Chem. 39*, 123−133.

BC060240P

Antibody Linking to Atomic Force Microscope Tips via Disulfide Bond Formation

A. S. M. Kamruzzahan, Andreas Ebner, Linda Wildling, Ferry Kienberger, Christian K. Riener, Christoph D. Hahn, Philipp D. Pollheimer, Peter Winklehner, Martin Hölzl, Bernd Lackner,† Daniela M. Schörkl, Peter Hinterdorfer, and Hermann J. Gruber*

Institute of Biophysics and Institute of Organic Chemistry, J. Kepler University, Altenberger Str. 69, A-4040 Linz, Austria.
Received August 16, 2006; Revised Manuscript Received September 29, 2006

Covalent binding of bioligands to atomic force microscope (AFM) tips converts them into monomolecular biosensors by which cognate receptors can be localized on the sample surface and fine details of ligand−receptor interaction can be studied. Tethering of the bioligand to the AFM tip via a ∼6 nm long, flexible poly(ethylene glycol) linker (PEG) allows the bioligand to freely reorient and to rapidly "scan" a large surface area while the tip is at or near the sample surface. In the standard coupling scheme, amino groups are first generated on the AFM tip. In the second step, these amino groups react with the amino-reactive ends of heterobifunctional PEG linkers. In the third step, the 2-pyridyl-S-S groups on the free ends of the PEG chains react with protein thiol groups to give stable disulfide bonds. In the present study, this standard coupling scheme has been critically examined, using biotinylated IgG with free thiols as the bioligand. AFM tips with PEG-tethered biotin-IgG were specifically recognized by avidin molecules that had been adsorbed to mica surfaces. The unbinding force distribution showed three maxima that reflected simultaneous unbinding of 1, 2, or 3 IgG-linked biotin residues from the avidin monolayer. The coupling scheme was well-reproduced on amino-functionalized silicon nitride chips, and the number of covalently bound biotin-IgG per μm^2 was estimated by the amount of specifically bound ExtrAvidin−peroxidase conjugate. Coupling was evidently via disulfide bonds, since only biotin-IgG with free thiol groups was bound to the chips. The mechanism of protein thiol coupling to 2-pyridyl-S-S-PEG linkers on AFM tips was further examined by staging the coupling step in bulk solution and monitoring turnover by release of 2-pyridyl-SH which tautomerizes to 2-thiopyridone and absorbs light at 343 nm. These experiments predicted 10^3-fold slower rates for the disulfide coupling step than actually observed on AFM tips and silicon nitride chips. The discrepancy was reconciled by assuming 10^3-fold enrichment of protein on AFM tips via preadsorption, as is known to occur on comparable inorganic surfaces.

INTRODUCTION

Microscopy of biomolecules and subcellular structures has made invaluable contributions to modern bioscience. While this field wasoriginally dominated by electron microscopy, the invention of atomic force microscopy (AFM)[1] has opened new fields of investigation, because AFM can operate in aqueous solution under physiological conditions of ionic strength, pressure, and temperature (for a review, see ref 1) and thereby reveal submolecular details not resolved by electron microscopy (*2*). Moreover, the AFM tip can be converted into a specific biosensor by stable attachment of a bioligand which has the ability to specifically bind to a complementary molecule on the biological specimen which is scanned by this functionalized AFM tip. The bioligand can itself be a biomolecule (antibody, hormone, single- or double-strand nucleic acid, etc.) or a synthetic molecule or whatever structure that is being recognized by a complementary molecule on the surface of the biological sample to be studied. In single molecule recognition force microscopy (SMRFM), specific binding of the ligand on the tip to a single immobile target molecule is followed by specific unbinding when the tip moves on (*3*, *4*), and the unbinding occurs with a defined force that is highly dependent on the biochemical state of the interacting molecules; thus, unique mechanistic details can be revealed by single molecule force spectroscopy (*5*).

Linear PEG chains have frequently been used to attach one or a few sensor molecules to an AFM tip, because the PEG itself is chemically and physically inert and it allows for rapid and free reorientation of the sensor molecule when the AFM tip approaches the surface (*6*−*15*). Thus, even a single sensor molecule on the tip can recognize its cognate molecule on the target surface with up to 25% probability in one force−distance cycle with 50−200 nm amplitude and 1 s cycle time (*16*). Furthermore, the 6−8 nm long PEG linker between the tip and the probe molecule facilitates data analysis in SMRFM, because the nonlinear elasticity of PEG allows for easy discrimination

* Corresponding author. At the Institute of Biophysics in Linz. Phone: +43 (732) 2468-9271. Fax: +43 (732) 2468-9270. E-mail: hermann.gruber@jku.at.

† Institute of Organic Chemistry.

[1] Abbreviations: AFM, atomic force microscope (or microscopy); APTES, 3-aminopropyltriethoxysilane; biotin-cap-NHS, *N*-succinimidyl 6-(*N*-biotinoylamino)-hexanoate; biotin-IgG, goat IgG derivatized with biotin-cap-NHS; biotin-IgG-SATP, goat IgG derivatized with both biotin-cap-NHS and SATP (see Figure 10S in the Supporting Information); biotin-PEG-NHS, analogous to PDP-PEG-NHS in Figure 2, with biotin in place of the PDP group; BSA, bovine serum albumin; DMF, *N*,*N*-dimethylformamide; DMSO, dimethylsulfoxide; EAP, ExtrAvidin-peroxidase; EDTA, ethylene diamine-*N*,*N*,*N*′,*N*′-tetraacetic acid; ELISA, enzyme-linked immunosorbent assay; G-SH, glutathion; IgG, immunoglobulin G; NH_2-PEG-NH_2, *O*,*O*′-bis(2-aminopropyl)poly(ethylene glycol) 800; NH_2-PEG-COOH, *N*-glutaryl derivative of NH_2-PEG-NH_2; NHS, *N*-hydroxysuccinimide; OPD, *o*-phenylenediamine·2HCl; PBS, phosphate-buffered saline; PDP-, 3-(2-pyridyl)-dithiopropionyl group; PDP-PEG-BSA, BSA derivatized with ∼1 PDP-PEG- per BSA; PDP-PEG-COOH and PDP-PEG-NHS, see Figure 2; PEG, poly(ethylene glycol); Pyr-S-S-PEG-NHS, see Figure 3; SATP, *N*-succinimidyl 3-(acetylthio)-propionate; SPDP, *N*-succinimidyl 3-(2-pyridyldithio)-propionate; SMRFM, single molecule recognition force microscopy; TEA, *N*,*N*,*N*-triethylamine; TSTU, *N*,*N*,*N*′,*N*′-tetramethyl-*O*-(*N*-succinimidyl)-uronium tetrafluoroborate.

10.1021/bc060252a CCC: $33.50 © 2006 American Chemical Society
Published on Web 10/26/2006

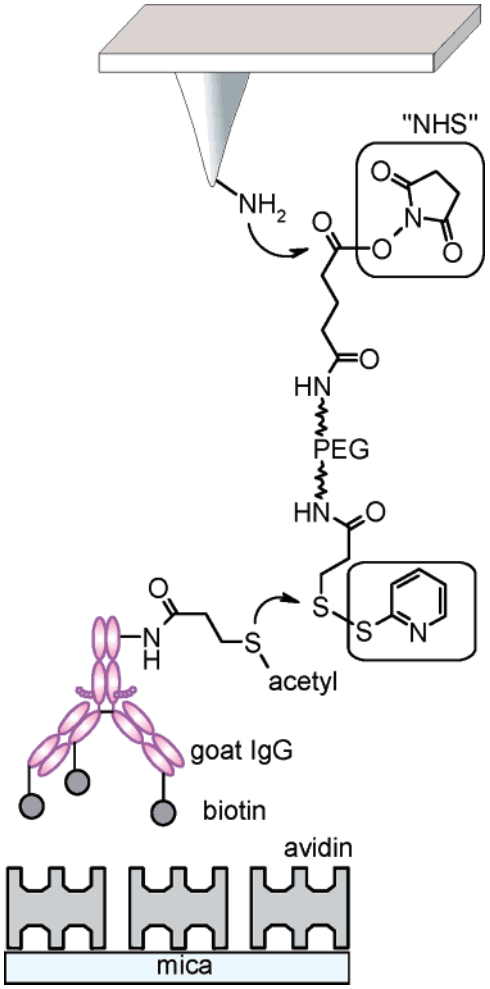

Figure 1. Schematic representation of the testing system for tip−antibody linking via disulfide bond formation. In the first step, the crosslinker PDP-PEG-NHS reacts with an amino group on the tip, with concomitant loss of the NHS leaving group. Hydroxylamine-induced de-acetylation of the SATP group on the antibody exposes a free SH group which reacts with the 2-pyridyldithio group on the free crosslinker end. When brought into contact with avidin-covered mica, the biotin residues on the model antibody showed reversible binding to, and unbinding from, immobilized avidin.

of specific unbinding events which are preceded by nonlinear PEG stretching from nonspecific tip adhesion (*16*−*18*). Moreover, 6−8 nm long PEG linkers are indispensable for a new method in which surface topography and a map of recognition sites are simultaneously acquired in one fast surface scan (*19*−*21*). Finally, the PEG-linked sensor molecule appears to regularly escape the danger of being crushed between tip and sample surface in each force−distance cycle, as is deduced from preservation of single sensor molecules over many thousands of cycles.

Our standard method of tip functionalization (*9*, *10*) involves three steps (see Figure 1): (i) generation of NH_2 groups on the silicon nitride tip, (ii) attachment of a heterobifunctional PEG linker with one end by amide bond formation, and (iii) linking of a sulfhydryl-containing sensor molecule to the outer end of the PEG tentacle on the tip by disulfide bond formation. The first two steps have been analyzed and optimized in a recent model study (*16*) in which the third step had been eliminated by using a PEG linker already carrying a bioligand (*d*-biotin) on its outer end. With respect to the first step, gas-phase aminosilanization with APTES or silanol group esterification with ethanolamine hydrochloride proved to be equally suitable to create a sufficient number of grafting sites for attachment of up to $2 \times 10^3\ \mu m^{-2}$ PEG-biotin tentacles on silicon nitride chips, as estimated from specific binding of ExtrAvidin−peroxidase with colorimetric peroxidase quantitation, using OPD and hydrogen peroxide as chromogenic substrates. When using the same functionalization conditions for AFM tips, the tip-bound PEG-biotin tentacles exhibited a binding probability of 10−20% to a dense monolayer of avidin on mica, i.e., about 10−20% of the force distance cycles showed a specific unbinding event, and specificity was proven by block with *d*-biotin.

In the present study, the third step of tip functionalization (attachment of an antibody molecule to the outer end of a tip-bound PEG linker) has been investigated in detail, using biotinylated goat IgG as a model antibody (see Figure 1). Besides biotin residues, the IgG molecule needed to carry protected thiols (*S*-acetylated thiopropionyl residues). These were deprotected in situ with hydroxylamine to allow for disulfide bond formation with the pyridine-S-S group on the outer end of PEG on the AFM tip (see Figure 1). The interaction of tip-tethered biotin-IgG with mica-bound avidin was studied with SMRFM, and the specificity of interaction was demonstrated by specific block with *d*-biotin. In parallel, silicon nitride chips were functionalized in the same sequence, and chip-tethered biotin-IgG was measured by specific binding of ExtrAvidin−peroxidase which was quantified by enzymatic color production from chromogenic substrates. In addition, the kinetics of disulfide bond formation between a thiolated protein and a PDP-PEG linker in bulk solution was monitored spectrophotometrically, and valuable clues on the mechanism of protein coupling to tip-bound PEG tentacles were obtained.

EXPERIMENTAL PROCEDURES

Materials. Analytical-grade materials were used as long as they were commercially available. The starting materials were of highest available purity. NH_2-PEG-COOH and PDP-PEG-NHS were synthesized as described (*22*), using multistep extraction for purification of PDP-PEG-COOH (see Supporting Information). Muscovite mica sheets were supplied by Christine Gröpl Elektronenmikroskopie (Tulln, Austria). Si_3N_4 measuring tips were bought from Veeco Instruments (Dourdan, France) and Si_3N_4 chips from Wacker-Chemitronic GmbH (Germany). Pyr-S-S-PEG-NHS was purchased from Polypure (Oslo, Norway).

Protein Modifications. Biotin-IgG and biotin-IgG-SATP were prepared by reacting goat IgG (10 mg/mL in buffer D) with a 10-fold excess of biotin-cap-NHS (from a 66 mM stock solution in DMSO), lowering the pH to 7.5, and adding a 10-fold excess of SATP (from a 66 mM stock solution in DMSO), followed by removal of unbound reagent by gel filtration in buffer A (100 mM NaCl, 50 mM NaH_2PO_4, 1 mM EDTA, pH 7.5 adjusted with NaOH), as described in the Supporting Information.

Functionalization of AFM Tips with PEG Linkers and Antibodies. AFM tips (Si_3N_4) were amino-functionalized as described before, using the room-temperature method for reaction with ethanolamine hydrochloride (*16*). Attachment of the PEG linkers (Pyr-S-S-PEG-NHS or PDP-PEG-NHS; see Figures 1 and 2) was accomplished by incubating the tip for 2 h with 1 mg/mL (or 10 mg/mL, as indicated) of PEG linker in chloroform containing 0.5% (v/v) of triethylamine. After rinsing with chloroform, the tip was stored in a desiccator for less than 5 days. For coupling of antibody, 40 μL of biotin-IgG-SATP (2.2 mg/mL) was mixed with 380 μL of buffer A and 80 μL of 500 mM hydroxylamine reagent (500 mM hydroxylamine hydrochloride, 25 mM EDTA, titrated to pH 7.5 with Na_2CO_3) (*9*). Tips with PEG linkers were immersed in this solution for 1 h, washed in buffer A (2×) and PBS (2×) and stored in PBS at 4 °C until used (up to 3 days). Detailed descriptions of all steps can be found in the Supporting Information.

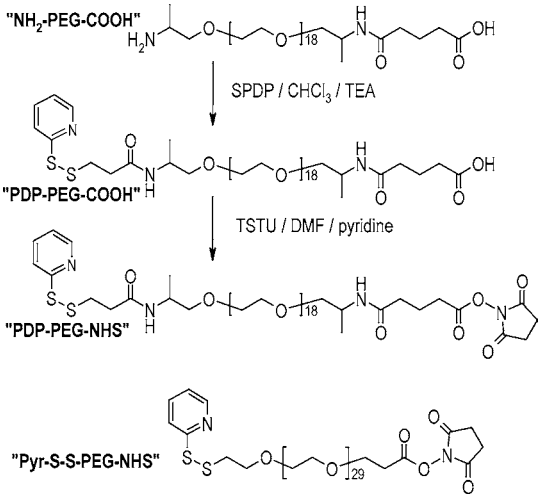

Figure 2. Synthesis of PDP-PEG-NHS from NH_2-PEG-COOH and structural comparison with the commercial crosslinker Pyr-S-S-PEG-NHS.

Monitoring of Single Unbinding Events between Tip-Bound Biotin-IgG and Mica-Bound Avidin by Force Spectroscopy. Avidin (1 mg/mL in PBS, 150 mM NaCl, 5 mM NaH_2PO_4, pH 7.4 adjusted with NaOH) was diluted with 9 volumes of water and adsorbed to freshly cleaved mica. After 15 min, the substrate was rinsed with a 1/9 mixture of PBS and water and imaged in PBS. Force measurements with biotin-IgG-functionalized AFM tips were performed in the fluid cell of a commercial AFM (Pico-SPM, Molecular Imaging, Phoenix, AZ) using a Nanoscope IIIA controller (Digital Instruments, Santa Barbara, CA). Force−distance cycles (conventional force calibration mode) were recorded at a 1 Hz vertical scan rate and 300 nm *z*-range. The measurements were done in PBS at a constant trace and retrace velocity of 100 nm/s. The spring constants of the levers were determined by the thermal noise method (*23*, *24*). Further details can be found in the Supporting Information.

Functionalization of Silicon Nitride Chips with Amines, PEG Linkers, and Biotin-IgG-SATP, and Quantitative Assay for Chip-Bound Biotin-IgG-SATP. Silicon nitride chips were precut, weighed for calculation of the effective surface area, precleaned, and amino-functionalized in a DMSO solution of ethanolamine hydrochloride (16 h), using the room-temperature method (*16*). After washing in DMSO (3×) and ethanol (3×), the chips were dried with nitrogen and derivatized with Pyr-S-S-PEG-NHS or PDP-PEG-NHS exactly as described above for AFM tips. After binding of the PEG linkers, the chips were washed in chloroform (3×), dried with nitrogen, and placed in a plastic petri dish. Biotin-IgG-SATP (2.2 mg/mL) or biotin-IgG (3.2 mg/mL) was mixed with buffer A and 500 μL hydroxylamine reagent to adjust final concentrations of 0.5 mg/mL for IgG and 50 mM for hydroxylamine, and 50 μL of this solution was pipetted onto the surface of each chip. The petri dishes were covered with a lid and incubated for 60 min. The chips were removed and washed in buffer A (3 × 10 min) and PBS (3 × 10 min).

For quantification of chip-bound biotin-IgG-SATP or biotin-IgG, most of the buffer was removed from the chips and they were placed on Teflon plates (prewashed with ethanol and dried well) which were lying in disposable petri dishes. Unblocked EAP reagent (50 μL, prepared by dilution of commercial EAP solution, Sigma/Austria, with 19 volumes of PBS containing 0.5% Tween 20) was placed on each chip and incubated in the closed chamber for 60 min. In parallel controls, 50 μL portions of blocked EAP reagent were used which contained 1 mM of biotin in addition. The chips were removed and washed in PBS containing 0.5% Tween 20 (3 × 10 min) and PBS (3 × 10 min). For measurement of chip-bound ExtrAvidin−peroxidase, 3 mL of citrate buffer (50 mM citric acid, pH adjusted to 5.5) containing OPD (0.8 mg/mL) was mixed with 30 μL of 3% H_2O_2 and stirred in a photometer cuvette. The chip was immersed in the cuvette for 1 min and then stored in the same buffer while reading A_{490}. In the case of small absorbance values, the chip was reimmersed in the cuvette for a longer time period. The amount of enzyme on the chip was calculated by comparison with calibration series in which known amounts of soluble enzyme were added to the chromogenic mixture and color production was also monitored over defined time intervals. A detailed description can be found in the Supporting Information.

RESULTS AND DISCUSSION

Syntheses of PDP-PEG-NHS, SPDP, and Biotin-cap-NHS. The synthesis of PDP-PEG-NHS followed our standard scheme (Figure 2), i.e., the general precursor NH_2-PEG-COOH was first acylated with SPDP, yielding the intermediate PDP-PEG-COOH, the carboxyl function of which was activated as NHS ester to give PDP-PEG-NHS (*22*). The published procedure has often been reproduced with good success, but in some batches, complete removal of unreacted and/or hydrolyzed SPDP from the intermediate PDP-PEG-COOH has been a problem. Now, this problem has been eliminated by a multistep extraction procedure, as described in the Supporting Information. In addition, the published procedures for synthesis of SPDP have been optimized for reliability and convenience, and the same applies to the synthesis of biotin-cap-NHS (see Supporting Information).

Since PDP-PEG-NHS is not commercially available, a comparable commercial linker (Pyr-S-S-PEG-NHS, purchased from Polypure, Oslo, Norway; see Figure 2) was tested in the same way as PDP-PEG-NHS. As shown in the Supporting Information (Figure 14S), it gave very similar results and thus appears well-suited for AFM tip functionalization by the scheme shown in Figure 1.

Recognition Force Microscopy with AFM Tip-Bound Biotin-IgG and Mica-Bound Avidin. In a preceding model study on AFM tip functionalization (*16*), the amino-functionalized tips were reacted with the NHS ester function of biotin-PEG-NHS, resulting in tip-bound PEG tentacles which already carried a specific bioligand (biotin) on their outer ends. The ligand function of tip-bound biotin residues was particularly easy to study by SMRFM, because the complementary acceptor protein (avidin) can easily be immobilized on mica by electrostatic adsorption (*16*), as exemplified in Figure 3. Due to the high density of avidin on the surface, the probability for specific recognition of tip-tethered biotin by an immobilized avidin molecule in a single approach-and-retraction cycle was found to be ≤20% (*16*). It is important to take into account the published correction note of reference (*16*), according to which a very low salt concentration (e.g., 15 mM NaCl as used here) is required for rapid adsorption of positively charged avidin (isoelectric pH ∼10; see ref 25) to the negatively charged mica surface (*26*), in contrast to lysozyme (isoelectric pH ∼11.2; see ref 27) which quickly adsorbs to mica in PBS (*11*). Once the avidin monolayer is formed, however, it can be exposed to PBS (150 mM NaCl) without dissociation of avidin (*16*).

In the present study, the previous model system was modified to study the tethering of antibodies, rather than biotin residues, to AFM tips via long, flexible PEG linkers. We adhered to our standard coupling scheme for antibody coupling (*9*) but used biotinylated IgG in place of some specific antibody (see Figure 1). As a consequence, we could take advantage of the well-known rupture force of the avidin−biotin bond and of specific block with minute concentrations of *d*-biotin (*16*, *28*, *29*).

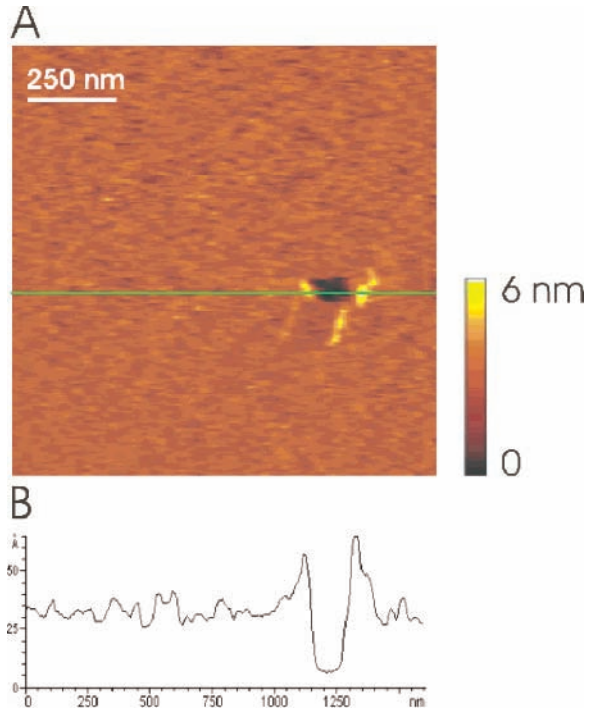

Figure 3. Topographical image of a dense avidin monolayer on mica support, formed by incubation (15 min) of freshly cleaved mica in 15 mM NaCl containing 0.1 mg/mL of avidin. Before the image in panel A was taken (at a force of 200 pN), a small rectangular area (100 nm × 100 nm) was scraped free of avidin with high force (10 nN) in order to expose bare mica. The straight line in panel A indicates the location of the cross section shown in panel B. The height of the avidin monolayer was observed to be 3−4 nm.

Consequently, IgG was statistically labeled with both biotin and SATP, resulting in at least 5 biotin and at least 5 protected thiol groups per IgG (see Supporting Information). The acetyl protecting groups on the latter were removed with hydroxylamine, liberating free thiols which reacted with the 2-pyridyl-S-S group on the tip-bound PEG linker (see Figure 1) to form a stable disulfide bond, with concomitant loss of 2-mercaptopyridine ("leaving group").

Tips with such PEG-linked biotin-IgG were tested for function by repeated approach to, and retraction from, mica densely covered with a monolayer of avidin (see Figure 3), measuring the repulsive and attractive forces by SMRFM. Typical results are shown in Figure 4. The vertical distance between tip and support is plotted on the *X*-axis and cantilever deflection on the *Y*-axis. Before plotting, the deflection amplitudes had been converted into force values after having measured the spring constant of the cantilever (see legend to Figure 4). Panel A shows a force−distance cycle with a specific unbinding event. The gray, dotted trace was measured during cantilever approach. Upon contact (at distance = 0 nm), the cantilever starts to bend upward. The constant slope shows that the cantilever obeys Hook's law, and the same is true for retraction to the point of zero force (solid, black trace) which again occurs at a vertical distance of 0 nm. Upon further retraction, however, the cantilever is bent downward until the force acting on the cantilever has reached −55 pN. At this point, the connection between the tip and the mica substrate suddenly breaks and the cantilever jumps back to the resting position, where it remains during further retraction.

The vertical jump from −55 pN to zero force can be attributed to the sudden unbinding of one biotin residue (of tip-bound biotin-IgG) from mica-bound avidin, for the following reasons: (i) Under identical conditions, the same unbinding force had previously been measured for tip-bound biotin and immobilized avidin, or vice versa (*16*, *28*). (ii) The nonlinear bending of the cantilever before the unbinding event is known to reflect the nonlinear elasticity of the PEG tether (*18*). (iii) The probability of observing such an unbinding event in one force−distance cycle was reduced from 44% in the absence of biotin to 3.0% in the presence of *d*-biotin, resulting in mostly "event-free" force−distance cycles, as shown in panel C. (iv) In the absence of *d*-biotin, the unbinding force distribution showed a maximum at 59 pN (solid line in panel D), which is the typical value expected for the avidin−biotin bond at the applied loading rate (*16*, *28*). In the presence of biotin, however, no such prominent peak was observed in the force distribution profile. (v) Specific unbinding events (as in panel A) were easily differentiated from direct tip−substrate adhesion (shown in panel B). While specific unbinding was preceded by the nonlinear stretching of PEG (solid line in panel A), the cantilever showed only linear deflection before rupture of direct adhesion (black

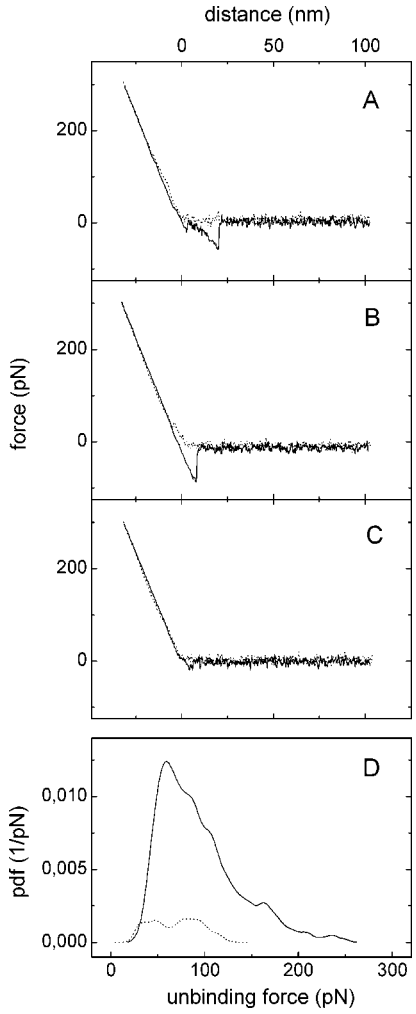

Figure 4. Force measurements of single avidin−biotin interactions. The tip was functionalized with PDP-PEG_{800}-NHS and with biotin-IgG-SATP, and avidin was irreversibly adsorbed to mica, as depicted in Figure 1. The piezo movement in the approach-and-retraction cycles was ±300 nm in 1 s and the force constant of the cantilever was 17 pN/nm, thus the loading rate was 10.2 nN/s. (A) Example of a force−distance cycle showing specific avidin−biotin unbinding in the absence of *d*-biotin. Unbinding occurred at a rupture force of 56 pN. (B) Example of a force−distance cycle in which the tip was directly stuck to the mica substrate by electrostatic adhesion. (C) Example of a force−distance cycle performed in the presence of free *d*-biotin (0.1 mg/mL). (D) Probability density function (pdf) of the unbinding forces observed in 435 out of 980 force−distance cycles (solid line). In the presence of free *d*-biotin (dotted line), only 29 out of 980 force−distance cycles appeared to reflect specific unbinding.

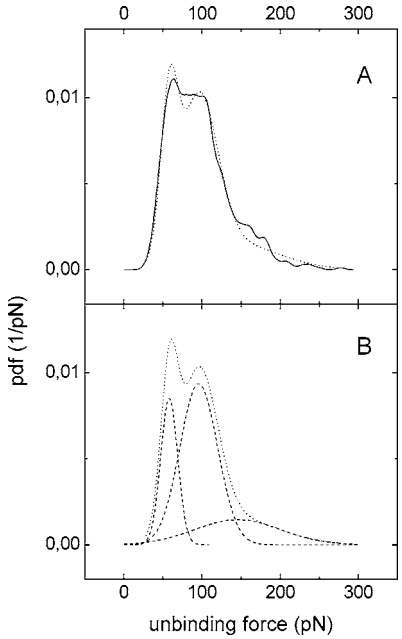

Figure 5. Multicomponent analysis of the unbinding force distribution obtained with the identical tip as used in Figure 4. (A) The solid curve is the unbinding force distribution from 643 recognition events obtained with the same tip as used in Figure 4D but in another location on the avidin-covered mica. The dotted line is a fit as explained in B. (B) The experimental profile (i.e., the solid line in (A)) was fitted by the sum of three Gaussian peaks with the force maxima 58 pN, 96 pN, and 150 pN (dashed lines). For an easier comparison between experiment (A) and mathematical fit (B), the sum of the three Gaussian components (dotted line) is shown both in (B) and in (A).

solid line in panel B), with the same slope as observed in the contact region of the gray dotted line panel B.

The AFM tip used in Figure 4 was moved to another spot of the avidin-covered mica, and another 999 force−distance cylces were acquired. The force distribution of the 208 unbinding events seen on site no. 2 (not shown) was added to the force distribution of the 435 unbinding events seen on site no. 1, which is shown in Figure 4 (panel D, solid line). The sum of the two force distributions is depicted in Figure 5 (panel A, solid line). It could well be fitted to the sum (dotted line in panel A and B) of three individual Gaussian peaks (dashed curves in panel B). The three Gaussian curves were found to peak at 58 pN, 96 pN, and 150 pN. The large width of the third curve is likely to result from implicit inclusion of a fourth curve with an even higher force maximum in the actual data. The amplitude of this putative component, however, was too small for explicit fitting. Since the 58 pN value is known to be the typical unbinding force of a single biotin residue from avidin, the peak maxima at 96 and 150 pN probably reflect the simultaneous unbinding of two or three biotin residues, respectively, from immobilized avidin molecules. The two or three biotin residues may have been located on a single tip-bound IgG or on two different tip-bound biotin-IgG molecules, albeit the latter situation seems less likely to cause such simultaneous unbinding events with twice or thrice the unbinding force of one avidin−biotin bond. In any case, Figure 5 can be taken as additional confirmation for successful tip−PEG-IgG linking by the scheme in Figure 1 and for proper function of the functionalized tip.

Imitation of AFM Tip Functionalization by Analogous Functionalization of Silicon Nitride Chips for Semiquantitative Analysis of Efficiency. In our preceding model study on the linking of biotin-PEG-NHS to amino-functionalized AFM tips (*16*), the AFM data were complemented with parallel macroscopic experiments in which silicon nitride chips (same material as the tips) were amino-functionalized and reacted with biotin-PEG-NHS. The chip-bound biotin-PEG residues were then quantified with the help of a conjugate between avidin and a marker enzyme (ExtrAvidin−peroxidase), similar as in other solid phase assays such as ELISA. By analogy, we have now reacted amino-functionalized silicon nitride chips with PDP-PEG-NHS and subsequently coupled biotin-IgG-SATP via disulfide bond formation, thereby also simulating AFM tip functionalization (see Figure 1) on a macroscopic scale (see Figure 15S in the Supporting Information for a schematic illustration of these steps, as well as of the quantification of bound biotin-IgG).

The covalently bound probe molecules (biotinylated IgG) were again labeled with ExtrAvidin−peroxidase, the amount of which was estimated from its enzymatic activity, i.e., from the rate of color production in a solution containing OPD and H_2O_2 when the chip was immersed in a stirred solution (3 mL) for a defined time interval (1 min, or several minutes if the response was low). The measured absorbance increase (A_{490}) per minute was compared to the absorbance increase measured with a known number of ExtrAvidin−peroxidase molecules in the total assay volume in order to calculate the number of enzymes bound on the chip (expressed as sites/μm^2; see Table 1).

Admittedly, ExtrAvidin−peroxidase is not a stoichiometric conjugate of one avidin and one enzyme molecule; therefore, the supplier's specifications were used to estimate the number of aggregates, both in the calibration series with ExtrAvidin−peroxidase in bulk solution and in the samples with chip-bound ExtrAvidin−peroxidase. Due to the high number of biotin-binding sites per aggregate, one aggregate can bind many PEG-linked biotin residues within reach; thus, the number of bound avidin−enzyme conjugates is expected to level off at higher numbers of binding sites per μm^2.

Nonspecific adsorption of ExtrAvidin−peroxidase was measured in the presence of *d*-biotin and subtracted from the total amount of ExtrAvidin−peroxidase bound in the absence of *d*-biotin to calculate the extent of specific binding (see Table 1). Moreover, 0.5% of Tween-20 was used to minimize the extent of nonspecific binding of ExtrAvidin−peroxidase.

As can be seen from Table 1, both the commercial linker Pyr-S-S-PEG-NHS and our standard linker PDP-PEG-NHS gave similar densities of specific binding sites for ExtrAvidin−peroxidase. Moreover, the concentration of PEG linker had little influence on the number of linkers bound to the amino-functionalized surface. The last two lines represent a separate data set with a new batch of amino-functionalized chips in which a critical control was included to prove that binding of biotin-IgG-SATP was indeed accomplished by disulfide bond formation (as indicated in Figure 1), rather than by some unknown mechanism. For this purpose, biotin-IgG was used in place of biotin-IgG-SATP, i.e., without the protected thiol (3-[acetylthio]-propionyl) functions shown in Figure 1. As can be seen from the last two lines of Table 1, the binding of biotin-IgG was indeed crucially dependent on the presence of SATP residues on IgG, since biotin-IgG-SATP was bound at a high density, whereas no detectable amount of simple biotin-IgG was bound on chips from the same batch of amino-functionalization.

In conclusion, the marker enzyme assay previously used to "count" the number of biotin-PEG tentacles on amino-functionalized silicon nitride chips also proved useful for examination of covalent binding of a thiolated protein to chips with covalently bound pyridine-S-S-PEG tentacles on a semiquantitative scale. Specific binding to biotin residues was easily discriminated from nonspecific binding, the extent of which was low anyway, and coupling was fully dependent on a free thiol; thus, the protein was indeed bound by the coupling scheme shown in Figure 1 and not via some unknown mechanism.

Table 1. Tethering of Antibodies to Silicon Nitride Chips via PEG Linkers[a]

linker type	[linker] (mg/mL)	antibody	total sites (μm^{-2})	nonspecific sites (μm^{-2})	specific sites (μm^{-2})
Pyr-S-S-PEG-NHS	10	biotin-IgG-SATP	2800 ± 100	90	2700 ± 200
	1	biotin-IgG-SATP	2800 ± 100	110	2700 ± 200
PDP-PEG-NHS	10	biotin-IgG-SATP	2900 ± 100	110	2800 ± 200
	1	biotin-IgG-SATP	1900 ± 100	170	1700 ± 200
PDP-PEG-NHS	1	biotin-IgG-SATP	2100 ± 300	130	2000 ± 400
	1	biotin-IgG	130 ± 40	120	0 ± 100

[a] The chip surface was amino-functionalized with ethanolamine hydrochloride and reacted with the NHS-ester function of the PEG linker molecule (see Figure 1). For coupling of protein, the chips were incubated in aqueous solutions of biotin−IgG−SATP or biotin−IgG and washed. The number of biotinylated IgG molecules per μm^2 surface was estimated from the amount of bound ExtrAvidin−peroxidase and measured in the absence (total sites) or presence (nonspecific sites) of free *d*-biotin.

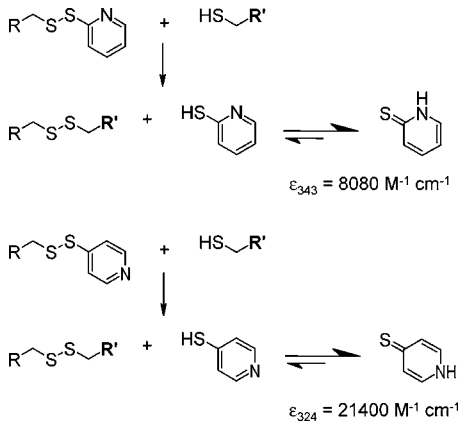

Figure 6. Reaction of 2-pyridyldithio or 4-pyridyldithio groups with aliphatic thiols, yielding stable disulfides and 2- or 4-mercaptopyridine which are quickly converted into 2- or 4-thiopyridone, respectively, by tautomerism. The latter have intense UV absorption bands in the near UV region (343 and 324 nm, respectively).

Hypothesis on Protein Preadsorption as the Main Accelerator of Protein Coupling to AFM Tips. Having demonstrated that protein coupling to silicon nitride surfaces with 2-pyridyl-S-S-PEG tentacles is indeed via disulfide bond formation (see previous paragraphs and Table 1), it was of interest to compare the observed disulfide coupling on surfaces with the rate of disulfide bond formation between a thiol component and a second component which carried 2-pyridyl-S-S groups (*30*). As shown in Figure 6, this reaction can easily be followed spectrophotometrically because it is accompanied by release of 2-mercaptopyridine, which quickly tautomerizes into 2-thiopyridone which has an absorption maximum at 343 nm (molar extinction coefficient $\epsilon_{343} = 8080\ M^{-1}\ cm^{-1}$) (*31*). By analogy, 4-pyridyldithio groups release 4-thiopyridone, which has an absorption maximum at 324 nm ($\epsilon_{324} = 21\,400\ M^{-1}\ cm^{-1}$) (*32*).

For monitoring of disulfide bond formation in bulk solution, a quartz cuvette with 1 cm light path was filled with buffer A (pH 7.5, same as used for disulfide coupling to AFM tips and silicon nitride chips) containing an excess of a pyridyldithio component (e.g., 80 μM), and this solution was continuously stirred. Disulfide bond formation was started by sudden addition of a small quantity of thiol component (e.g., at 20 μM final concentration), and the time course of 2- or 4-thiopyridone release was monitored by the change in A_{343} or A_{324}, respectively, as exemplified in the Supporting Information (Figure 8S). Table 2 lists the pairs of thiol components (third column) and pyridyldithio components (second column) for which the reaction rate was determined in the way described above. The data were analyzed as described in the Supporting Information, in order to estimate the bimolecular kinetic constant k_2 for each of these pairs.

For easier understanding of the results, the k_2 values were used to predict half-time values ($t_{1/2}^{calc}$, last two columns of Table 2) of the apparent monoexponential time course of pyridyldithio component turnover if it is reacted with a large excess of thiol component. In one model situation, the concentration of the thiol excess component is assumed to be 1 mM (next-to-last column in Table 2); in the other model situation, the thiol concentration is assumed to be 1 μM (last column in Table 2).

The first three lines of Table 2 show that the reaction rate is only weakly influenced if 2-mercaptoethanol is replaced by a BSA carrying 3-mercaptopropionyl residues. However, comparison with line 11 shows that the reaction is dramatically slowed down if the 2-pyridyl-S-S group is also linked to BSA via the short propionyl spacer. In the first three lines of Table 2, charge effects are absent since the pyridyldithio component is uncharged at the pH of the reaction (7.5). In contrast, the reaction of cationic 2-(2-pyridyldithio)-ethylamine (line 4) with anionic BSA-SH is accelerated by electrostatic attraction. By the same rationale, the reaction is decelerated by electrostatic repulsion between anionic pyridyldithiopropionate (2- and 4-isomer, lines 5 and 6) and the negatively charged protein.

Line 7 describes the reaction of BSA-SH with 2-pyridyl-S-S-PEG_{800}-COO^-. It is of particular interest since the latter is almost identical with PDP-PEG-NHS, which we have used to link thiolated protein to AFM tips (see Figures 1 and 2). As can be seen from a comparison of line 5 with line 7, the PEG_{800} linker did not slow down the reaction with a thiolated protein. Rather, the reaction was even accelerated by a factor of 2, which is attributed to elimination of electric repulsion by the long PEG_{800} spacer (line 7). The same effect of PEG chain length is seen in the corresponding set of with 4-pyridyldithio groups (lines 6 and 8), taking into account the usual observation that 4-pyridylditho groups are somewhat more reactive (*33*).

Most interesting for the purpose of this study is the comparison between line 7 and line 9 (or line 8 and line 10 for the corresponding 4-isomers). In line 7, the 2-pyridyl-S-S group sits on one end of a PEG_{800} chain, the other end of which is free to diffuse in solution; whereas in line 9, the other end of the PEG chain (1 kDa) is anchored on the relatively large BSA molecule (65 kDa). This difference caused a deceleration by a factor of <10, and the same was observed with the 4-isomers (lines 8 and 10). It is therefore justified to assume that a similar reaction rate should hold for disulfide bond formation between a thiolated protein (which is in excess) and a single 2-pyridyl-S-S-PEG_{800} tentacle that is anchored on the apex of an AFM tip. In this situation, the predicted monoexponential time course no longer means actual turnover but instead the probability that the single 2-pyridyl-S-S-PEG reacts with a thiolated protein. In this study, we applied 0.2 mg/mL of biotin-IgG-SATP for disulfide bond formation with the AFM tip which corresponds to a molar concentration of 1.4 μM. Taking into account the slower diffusion of biotin-IgG-SATP (150 kDa), we can assume the *calculated* half-time to be similar to that given in line 9 for 1 μM of BSA-SH ($t_{1/2}^{calc} = 5$ days). In reality, however, disulfide coupling has proven quite successful in the time

Table 2. Kinetics of Disulfide Bond Formation between PDP Groups and Free Sulfhydryls Attached to Various Kinds of Molecules[a]

line	pyridyldithio component (minute concentration)	thiol component (in excess, 1 mM or 1 mM)	$t_{1/2}^{calc}$ at excess of 1 mM	$t_{1/2}^{calc}$ at excess of 1 μM
1	2-pyridyl-S-S-CH_2-CH_2-OH	HO-CH_2-CH_2-SH	0.3 min	5 h
2	4-pyridyl-S-S-CH_2-CH_2-OH	HO-CH_2-CH_2-SH	0.1 min	2 h
3	2-pyridyl-S-S-CH_2-CH_2-OH	BSA-SH	0.7 min	11 h
4	2-pyridyl-S-S-CH_2-CH_2-NH_3^+	BSA-SH	0.07 min	1 h
5	2-pyridyl-S-S-CH_2-CH_2-COO^-	BSA-SH	2 min	1 d
6	4-pyridyl-S-S−CH_2-CH_2-COO^-	BSA-SH	1 min	1 d
7	2-pyridyl-S-S-PEG_{800}-COO^-	BSA-SH	1 min	1 d
8	4-pyridyl-S-S-PEG_{800}-COO^-	BSA-SH	0.5 min	8.3 h
9	2-pyridyl-S-S-PEG_{800}-CO−NH-BSA	BSA-SH	7 min	5 d
10	4-pyridyl-S-S-PEG_{800}-CO−NH-BSA	BSA-SH	2 min	1 d
11	2-pyridyl-S-S-propionyl-NH-BSA	BSA-SH	1 h	60 d
12	2-pyridyl-S-S-propionyl-NH-BSA	G-SH	4 min	3 d

[a] After mixing of the components, the rate of disulfide bond formation was monitored in a UV−vis spectrophotometer via release of 2-thiopyridone (at 343 nm, $\epsilon_{343} = 8080\ M^{-1}\ cm^{-1}$) (*28*) or 4-thiopyridone (at 324 nm, $\epsilon_{324} = 21400\ M^{-1}\ cm^{-1}$) (*32*), and the kinetic parameters were calculated, as described in the Supporting Information.

window of 1 h, both on the AFM tip (see Figure 4) and on silicon nitride chips (see Table 1), even at 0.2 μM IgG (30 μg/mL) (*7*, *9*−*11*, *14*, *15*). On the basis of the kinetic data from bulk solution (see Table 2), the half-time for coupling of 0.2 μM IgG to a 2-pyridyl-S-S-PEG tentacle on the AFM tip should be 1 month, not to speak of the five half-times needed to reach 97% probability for coupling.

The big discrepancy between the slow disulfide coupling in bulk solution when working at 1 μM thiolated protein (Table 2) and efficient coupling to AFM tips and silicon nitride chips (Table 1) within 1 h allows for two alternate explanations: The uneasy hypothesis would mean that our actual success of biotin-IgG-SATP coupling to AFM tips and silicon nitride chips were not via disulfide coupling but by some other mechanism. The more favorable explanation means that some additional mechanism is in operation which greatly accelerates coupling of thiolated proteins to 2-pyridyl-S-S-PEG tentacles on AFM tips.

Fortunately, the first hypothesis can be dismissed on the following grounds: (i) The last two lines of Table 1 demonstrate without any doubt that the coupling to chip-bound 2-pyridyl-S-S-PEG tentacles is solely via disulfide bond formation, since only biotin-IgG-SATP but not simple biotin-IgG was covalently bound. (ii) All specific unbinding events (as in Figure 4A) were preceded by the typical nonlinear stretching behavior of the PEG linker (*18*); thus, the ligand molecule (biotin-IgG) necessarily must have been bound to the outer end of the PEG linker. (iii) Before coupling of protein, the outer end of the PEG had been a 2-pyridyl-S-S group, which is known for its exceptionally high selectivity for thiol over amino groups (*34*) (also exemplified by very slow reaction with 10 mM ethanolamine, even at pH 8.6 and 37 °C; see Figure 1B in ref 35). (iv) The number of lysine residues per IgG (∼80 to 90) (*36*) is only 1 order of magnitude higher than the number of deprotected SATP groups per IgG (>5; see Supporting Information) which is by far too little to override the much higher reactivity of deprotected SATP groups for 2-pyridyl-S-S functions.

From the previous paragraph, it is concluded that incubation of tips or chips with 2-pyridyl-S-S-PEG tentacles with micromolar concentrations of biotin-IgG-SATP actually results in disulfide coupling as depicted in Figure 1 (and Figure 15S in the Supporting Information). Consequently, the unexpectedly high rate of coupling to surface-bound 2-pyridyl-S-S-PEG tentacles at micromolar protein concentrations must be caused by some catalytic effect which accelerates coupling by about 3 orders of magnitude in comparison to bulk solution kinetics. As explained in the following, preadsorption of protein to the tip/chip surface must be assumed as the only plausible effect which appears to enrich the effective protein concentration from micromolar in bulk solution to millimolar at the site of action, i.e., next to a tip/chip-bound PEG linker.

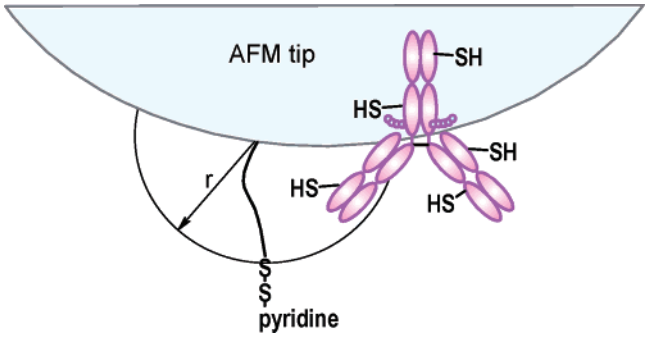

Figure 7. Model for acceleration of antibody linking to tip-bound PDP-PEG tentacles, due to preadsorption of protein next to the PEG linker. The free end of a 6 nm long, surface-bound PEG linker can reach all locations in a hemisphere with $r = 6$ nm. One particle per hemisphere (450 nm^3) corresponds to a formal concentration of 3 mM. Tip radius, antibody dimensions, and PEG length were drawn roughly to scale.

As depicted in Figure 7, the 2-pyridyl-S-S group on the outer end of a tip-bound PEG_{800} chain can reach every point in a hemisphere with the radius $r \approx 6$ nm (*16*−*18*). The volume of this hemisphere is ∼450 nm^3; consequently, the concentration of a single 2-pyridyl-S-S group per hemisphere corresponds to a formal concentration of ∼3 mM. The next question concerns the effective concentration of protein within the hemisphere. As long as proteins only transiently collide with the surface and continue to diffuse, the concentration of protein will be similar to that in bulk solution, i.e., micromolar. However, the surface of the tip used in SMRFM usually consists of superficially oxidized silicon nitride (or silicon), which is known to get largely covered with protein when in contact with a protein solution, with desorption being induced only upon washing with protein-free buffer (*27*, *37*, *38*). In addition, amino-functionalization causes coverage of the tip surface with organic material (detected by AFM imaging) (*16*), which is known for enhanced protein adsorption (*39*). Moreover, amino-functionalization induces some cationic charges which are known to further promote protein adsorption (*39*). In conclusion, it is safe to assume that the amino-functionalized AFM tip will get largely covered with protein when immersed in buffer with micromolar protein concentrations. Consequently, at least one IgG molecule should be adsorbed near each individual PEG linker on the tip (see Figure 7), and the effective protein thiol concentration next to the PEG linker should be at least 1 mM, taking into account the number of at least 5 SATP residues per IgG (see Supporting Information) which compensates for the large dimensions of the IgG molecule.

With an effective protein thiol concentration of >1 mM within reach of each tip-bound PEG chain having been estimated, Table 2 can again be consulted for prediction of the

time course of disulfide coupling between the protein thiol and the 2-pyridyl-S-S-PEG on the tip. As argued before, line 9 describes that situation in bulk solution which is closest to the situation on the AFM tip (Figure 7). For >1 mM thiol component, a half-time of <7 min can be assumed for protein coupling to the AFM tip. This finally explains why the majority of AFM tips actually gets functionalized within 1 h with at least one IgG molecule per tip when using the coupling scheme shown in Figure 1, even when the bulk solution contains only micromolar concentrations of IgG, as used in typical applications (*7*, *9*−*11*, *14*, *15*).

In conclusion, preadsorption of protein next to the pyridine-S-S-PEG tentacle on the tip surface appears to be the key parameter which helps to raise protein concentration even from submicromolar concentrations in bulk solution to millimolar concentration at the site of linking (see Figure 7). This is the only plausible hypothesis which can explain why coupling of a thiol protein to a 2-pyridyl-S-S-PEG linker on an AFM tip (Figure 1 and Figure 7) takes 1 h only, rather than months, as would have been predicted for a collisional mechanism of coupling (as in Table 2) when reacting at micromolar protein concentrations.

The above model has important consequences for practical application. It warns against mixing of the thiol protein with excess of non-thiol protein, e.g., for the sake of physical stabilization during storage or freezing. The non-thiol protein is likely to be equally preadsorbed and over-represented next to the surface-bound PEG linkers, thereby inhibiting coupling of thiol protein to the PEG linker. Another warning is that preadsorption will not occur with many small thiol ligands, in which case higher concentrations and/or longer reaction times will be required. At the same time, there is an upper limit for the concentration of a small thiol ligand which should be observed: Too-high concentrations and/or too-long reaction times will obviously cause the coupling product "ligand-S-S-PEG-tip" to be attacked by another HS-ligand, resulting in release of "ligand-S-S-ligand" from "HS-PEG-tip". The question is which concentration of a small ligand-SH will ensure coupling without subsequent cleavage. Fortunately, the last line of Table 2 allows estimation of the concentration and reaction time needed for collisional coupling of a small thiol ligand. Line 12 reports a half-time of 4 min for coupling of 1 mM glutathion (G-SH, a small tripeptide) to 2-pyridyl-S-S-PEG_{800}-BSA, which resembles coupling to PEG_{800} on the AFM tip. Incubation for five half-times (20 min) at 1 mM small ligand thiol concentration, therefore, should be appropriate for a 97% probability of coupling to 2-pyridyl-S-S-PEG on the AFM tip. Accordingly, 200 min or longer times will be required when working at 100 μM or lower ligand thiol concentrations. Although these numbers are meant as rough estimates, they still appear helpful to choose reasonable starting conditions from which tip functionalization can further be optimized in a particular case.

CONCLUSIONS

In this study, the coupling of a thiolated antibody to 2-pyridyl-S-S-PEG_{800} linkers on AFM tips and silicon nitride chips was demonstrated by use of biotin-IgG-SATP in place of some specific antibody. Accordingly, SMRFM experiments were performed with avidin as a partner molecule, which was particularly easy to immobilize on mica by electrostatic adsorption (*16*). The observed unbinding events were easily assigned to rupturing of single avidin−biotin bonds, because (i) the unbinding force was the same as previously measured under the same loading rate (*16*, *28*) and (ii) binding was efficiently blocked by low concentrations of free biotin. Blocking with such a small molecule appears more convincing than by addition of protein which might be suspected to block an AFM tip by nonspecific adsorption. In conclusion, tip-bound biotin-IgG-SATP and mica-bound avidin appear particularly suited as a start-up and testing system in SMRFM, due to simplicity, low cost, and easy differentiation between specific and nonspecific data.

Blocking with free biotin was also employed to distinguish specific from nonspecific binding of ExtrAvidin−peroxidase to biotin-IgG-SATP which had been coupled to 2-pyridyl-S-S-PEG_{800} linkers on silicon nitride chips. Specific binding indicated a density of $\sim$2000 μm^{-2} for chip-bound biotin-IgG-SATP, which nicely explained the observation that 1−2 functional antibodies were typically found on the apex of a functionalized AFM tip (*16*). Tethering of antibodies to silicon nitride tips by the scheme shown in Figure 1 was thus reproduced on silicon nitride chips in a semiquantitative way, and the disulfide coupling step was proven, because only biotin-IgG *with* free thiols was able to couple at all.

Finally, the mechanism of thiol protein coupling to tip-bound 2-pyridyl-S-S-PEG_{800} linkers was elucidated by staging the coupling reaction in bulk solution and measuring the reaction rates photometrically. Surprisingly, the coupling of micromolar protein was $\sim 10^3$-fold slower in bulk solution than on tips or chips. The only conceivable reason to explain $\sim 10^3$-fold faster coupling on the surfaces was found in preadsorption of protein next to the surface-bound PEG linkers which raises the effective protein concentration from micromolar (or lower) in bulk solution to millimolar on the surface. Taken together, the insights from this study provide for a rational approach to biofunctionalization of scanning probes with single molecules.

ACKNOWLEDGMENT

We are indebted to Prof. Norbert Müller for use of spectrometer facilities. This work was supported by the Austrian Research Funds (projects P-15295) and by EU project "Tips4Cells".

Supporting Information Available: Modified syntheses of SPDP, PDP-PEG-NHS, and biotin-cap-NHS. Preparation of buffers, reagent stock solutions, biotin-IgG, and biotin-IgG-SATP. Procedures for functionalization of AFM tips and silicon nitride chips with ethanolamine hydrochloride, PEG linkers, and biotin-IgG-SATP. Procedure for quantification of chip-bound biotin-IgG-SATP. Procedure for preparation of avidin monolayers on mica and force microscopy with tip-bound biotin-IgG-SATP. Force microscopy data obtained with the commercial crosslinker Pyr-S-S-PEG-NHS. Preparation of the thiol and disulfide components in Table 2 and spectrophotometric measurement of thiol−disulfide exchange kinetics. Schematic illustration of silicon nitride chip functionalization and quantification of bound biotin-IgG with ExtrAvidin−peroxidase. This material is available free of charge via the Internet at http://pubs.acs.org.

LITERATURE CITED

(1) Hörber, J. K. H., and Miles, M. J. (2003) Scanning probe evolution in biology. *Science 302*, 1002−1005.
(2) Scheuring, S., Müller, D. J., Ringler, P., Heymann, J. B., and Engel, A. (1999) Imaging streptavidin 2D crystals on biotinylated lipid monolayers at high resolution with the atomic force microscope. *J. Microsc. 193*, 28−35.
(3) Hinterdorfer, P., and Dufrene, Y. F. (2006) Detection and localization of single molecular recognition events using atomic force microscopy. *Nat. Methods 3*, 347−355.
(4) Kienberger, F., Ebner, A., Gruber, H. J., and Hinterdorfer, P. (2006) Molecular recognition imaging and force spectroscopy of single biomolecules. *Acc. Chem. Res. 39*, 29−36.
(5) Nevo, R., Stroh, C. M., Kienberger, F., Kaftan, D., Brumfeld, V., Elbaum, M., Reich, Z., and Hinterdorfer, P. (2003) A molecular

switch between alternative conformational states in the complex of Ran and importin β_1. *Nat. Struct. Biol. 10*, 553−557.
(6) Avci, R., Schweitzer, M., Boyd, R. D., Wittmeyer, J., Steele, A., Toporski, J., Beech, W., Arce, F. T., Spangler, B., Cole, K. M., and McKay, D. S. (2004) Comparison of antibody-antigen interactions on collagen measured by conventional immunological techniques and atomic force microscopy. *Langmuir 20*, 11053−11063.
(7) Baumgartner, W., Hinterdorfer, P., Ness, W., Raab, A., Vestweber, D., Schindler, H., and Drenckhahn, D. (2000) Cadherin interaction probed by atomic force microscopy. *Proc. Natl. Acad. Sci. U.S.A. 97*, 4005−4010.
(8) Bonanni, B. Kamruzzahan, A. S. M., Bizzarri, A. R., Rankl, C., Gruber, H. J., Hinterdorfer, P., and Cannistraro, S. (2005) Single molecule recognition between cytochrome C 551 and gold-immobilized azurin by force spectroscopy. *Biophys. J. 89*, 2783−2791.
(9) Hinterdorfer, P., Baumgartner, W., Gruber, H.J., Schilcher, K., and Schindler, H. (1996) Detection and localization of individual antibody-antigen recognition events by atomic force microscopy. *Proc. Natl. Acad. Sci. U.S.A. 93*, 3477−3481.
(10) Hinterdorfer, P., Schilcher, K., Baumgartner, W., Gruber, H. J., and Schindler, H. (1998) A mechanistic study of the dissociation of individual antibody-antigen pairs by atomic force microscopy. *Nanobiology 4*, 177−188.
(11) Raab, A., Han, W., Badt, D., Smith-Gill, S. J., Lindsay, S. M., Schindler, H., and Hinterdorfer, P. (1999) Antibody recognition imaging by force microscopy. *Nat. Biotechnol. 17*, 902−905.
(12) Ros, R., Schwesinger, F., Anselmetti, D., Kubon, M., Schafer, R., Plückthun, A., and Tiefenauer, L. (1998) Antigen binding forces of individually addressed single-chain Fv antibody molecules. *Proc. Natl. Acad. Sci. U.S.A. 95*, 7402−7405.
(13) Strunz, T., Oroszlan, K., Schafer, R., and Güntherodt, H. J. (1999) Dynamic force spectroscopy of single DNA molecules. *Proc. Natl. Acad. Sci. U.S.A. 96*, 11277−82.
(14) Wielert-Badt, S., Hinterdorfer, P., Gruber, H. J., Lin, J.-T., Badt, D., Wimmer, B., Schindler, H., and Kinne, R. K.-H. (2002) Single molecule recognition of protein binding epitopes in brush border membranes by force microscopy. *Biophys. J. 82*, 2767−2774.
(15) Willemsen, O. H., Snel, M. M. E., van der Werf, K. O., Gruber, H. J., Hinterdorfer, P., Schindler, H., van Kooyk, Y., de Grooth, B. G., Greve, J., and Figdor, C. G. (1999) Simultaneous height and adhesion imaging of antibody-antigen interactions by atomic force microscopy. *Biophys. J. 75*, 2220−2228.
(16) Riener, C. K., Stroh, C. M., Ebner, A., Klampfl, C., Gall, A. A., Romanin, C., Lyubchenko, Y. L., Hinterdorfer, P., and Gruber, H. J. (2003) Simple test system for single molecule recognition force microscopy. *Anal. Chim. Acta 479*, 59−75.
(17) Kienberger, F., Kada, G., Gruber, H. J., Pastushenko, V. P., Riener, C. K., Trieb, M., Knaus, H.-G., Schindler, H., and Hinterdorfer, P. (2000) Recognition force spectroscopy studies of the NTA-His_6 bond. *Single Mol. 1*, 59−65.
(18) Kienberger, F., Pastushenko, V. P., Kada, G., Gruber, H. J., Riener, C. K., Schindler, H., and Hinterdorfer, P. (2000) Static and dynamic properties of single poly(ethylene glycol) molecules investigated by force microscopy. *Single Mol. 1*, 123−128.
(19) Ebner, A., Kienberger, F., Kada, G., Stroh, C. M., Geretschläger, M., Kamruzzahan, A. S. M., Wildling, L., Johnssohn, W. T., Ashcroft, B., Nelson, J., Lindsay, S. M., Gruber, H. J., and Hinterdorfer, P. (2005) Localization of single avidin-biotin interactions using simultaneous topography and molecular recognition imaging. *ChemPhysChem. 6*, 897−900.
(20) Stroh, C. M., Ebner, A., Geretschläger, M., Freudenthaler, G., Kienberger, F., Kamruzzahan, A. S. M., Smith-Gill, S. J., Gruber, H. J., and Hinterdorfer, P. (2004) Simultaneous topography and recognition imaging using force microscopy. *Biophys. J. 87*, 1981−1990.
(21) Stroh, C. M., Wang, H., Bash, R., Ashcroft, B., Nelson, J., Gruber, H., Lohr, D., Lindsay, S. M., and Hinterdorfer, P. (2004) Single-molecule recognition imaging microscopy. *Proc. Natl. Acad. Sci. U.S.A. 101*, 12503−12507.
(22) Riener, C. K., Kienberger, F., Hahn, C. D., Buchinger, G. M., Egwim, I. O. C., Haselgrübler, T., Ebner, A., Romanin, C., Klampfl, C., Lackner, B., Prinz, H., Blaas, D., Hinterdorfer, P., and Gruber, H. J (2003) Heterobifunctional crosslinkers for tethering single ligand molecules to scanning probes. *Anal. Chim. Acta 497*, 101−114.
(23) Hutter, J., and Bechhoefer, J. (1993) Calibration of atomic-force microscope tips. *Rev. Sci. Instrum. 64*, 1868−1873.
(24) Butt, H. J., and Jaschke, M. (1995) Calculation of the thermal noise in atomic force microscopy. *Nanotechnology 82*, 1−7.
(25) Green, N. M. (1990) Avidin and Streptavidin. *Methods Enzymol. 184*, 51−67.
(26) Pericet-Camara, R., Papastavrou, G., and Borkovec, M. (2004) Atomic force microscopy study of the adsorption and electrostatic self-organization of poly(amidoamine) dendrimers on mica. *Langmuir 20*, 3264−3270.
(27) Kondo, A., and Higashitani, K. (1992) Adsorption of model proteins with wide variation in molecular properties on colloidal particles. *J. Colloid Interface Sci. 150*, 344−351.
(28) De Paris, R., Strunz, T., Oroszlan, K., Güntherodt, H.-J., and Hegner, M. (2000) Force spectroscopy and dynamics of the biotin-avidin bond studied by scanning force microscopy. *Single Mol. 1*, 285−290.
(29) Florin, E. L., Moy, V. T., and Gaub, H. E. (1994) Adhesion forces between individual ligand-receptor pairs. *Science 264*, 415−417.
(30) Riener, C. K. (1998) Diploma Thesis at the University of Linz, Austria.
(31) Leserman, L. D., Machy, P., and Barbet, J. (1984) Covalent coupling of monoclonal antibodies and protein A to liposomes: Specific interactions with cells in vitro and in vivo. *Liposome Technology* (G. Gregoriadis, Ed.) Vol. 3, pp 29−40, CRC Press, Boca Raton, FL.
(32) Riener, C. K., Kada, G., and H. J. Gruber (2002) Quick measurement of protein sulfhydryls with Ellman's reagent and with 4,4′-dithiodipyridine. *Anal. Bioanal. Chem. 373*, 266−276.
(33) Grimshaw, C. E., Whistler, R. L., and Cleland, W. W. (1979) Ring opening and closing rates for thiosugars. *J. Am. Chem. Soc. 101*, 1521−1532.
(34) Carlsson, J., Drevin, H., and Axen, R. (1978) Protein thiolation and reversible protein-protein conjugation. *Biochem. J. 173*, 723−737.
(35) Haselgrübler, T., Amerstorfer, A., Schindler, H., and Gruber, H. J. (1995) Synthesis and application of a new poly(ethylene glycol) derivative for the crosslinking of amines with thiols. *Bioconjugate Chem. 6*, 242−248.
(36) Dorner, M. M., Bassett, E. W., Beiser, S. M., Kabat, E. A., and Tanenbaum, S. W. (1967) Studies on human antibodies: V. Amino acid composition of antidextrans of the same and of different specificities from several individuals. *J. Exp. Med. 125*, 823−831.
(37) Fitzpatrick, H., Luckham, P. F., Eriksen, S., and Hammond, K. (1992) Use of X-ray photoelectron spectroscopy to study protein adsorption to mica surfaces. *J. Colloid Interface Sci. 149*, 1−9.
(38) Sevastianov, V. I., Kulik, E. A., and Kalinin, I. D. (1991) The model of continuous heterogeneity of protein-surface interactions for human serum albumin and human immunoglobulin G adsorption onto quartz. *J. Colloid Interface Sci. 145*, 191−206.
(39) Andrade, J. D., Hlady, V., Wie, A.-P., Ho, C.-H., Lea, A. S., Jeon, S. I., Lin, Y. S., and Stroup, E. (1992) Proteins at interfaces: principles, multivariate aspects, protein resistant surfaces, and direct imaging and manipulation of adsorbed proteins. *Clin. Mater. 11*, 67−84.

BC060252A

Photocrosslinking/Label Transfer: A Key Step in Mapping Short α-Neurotoxin Binding Site on Nicotinic Acetylcholine Receptor

Pascal Kessler,* Robert Thai, Fabrice Beau, Jean-Luc Tarride, and André Ménez

CEA, DSV, DIEP, Gif-sur-Yvette, F-91191, France. Received June 19, 2006; Revised Manuscript Received August 23, 2006

We developed a novel radioactive short bifunctional photoprobe, which could be coupled through a cleavable bond to an engineered cysteinyl residue on an analogue of a nicotinic acetylcholine receptor-specific α-neurotoxin. This cysteine was put on the tip of loop II in place of Arg33, a major residue for the interaction with the receptor. To facilitate the purification of the nAChR labeled subunits, we tagged the ligand with a desthiobiotin moiety. After irradiation of the photosensitive toxin−nAChR complex, gel electrophoresis showed that most of the radioactivity was attached to the α subunit (59%), followed by the γ subunit (28%), with the δ subunit (13%) being less labeled. On a preparative scale, the labeled subunits were purified on streptavidin beads before separation on SDS-PAGE. "In-gel" CNBr cleavage of the labeled α subunit followed by Edman degradation of the purified peptides showed that αTyr190 and αTyr198 were the most labeled residues, with a less important labeling on αCys192. We believe that the novel photoactivatable probe will be of great use to identify key residues of ligands interacting with macromolecules.

INTRODUCTION

With relation to the discovery of soluble acetylcholine binding proteins (AChBP's[1]) in various snails, the recent past has been quite rich in structure descriptions of complexes between nicotinic ligands and the surrogate of the acetylcholine receptor. These data brought new insights on the interactions between agonists/antagonists and their intrinsic acetylcholine protein target. X-ray crystallography of complexes between AChBP and agonists, such as nicotine, carbamylcholine (*1*), epibatidine, or lobeline (*2*) showed that the critical C loop, classically harbored by α-subunits on nAChRs, wraps these ligands, occluding the binding site. In contrast to these data, structures of complexes with peptidic antagonists, such as α-conotoxin ImI (*2*), α-conotoxin PnIA (*3*), or α-cobratoxin (*4*) showed a more or less extended C loop, its position depending on the steric hindrance of the antagonist.

Three finger curaremimetic snake α-neurotoxins can be divided into long-chain and short-chain toxins. α-Bungarotoxin and α-cobratoxin belong to the first group, which binds with high affinity to the neuronal α7 receptor and to AChBP. Crystals and X-ray data of a complex between AChBP and α-cobratoxin have been obtained recently by Bourne and colleagues (*4*), revealing an unpredicted conformation of the toxin-bound AChBP, especially of loop C on the α subunit.

NmmI, erabutoxin-a, NTII, and the α-neurotoxin of *Naja nigricollis* belong to the short-chain group, which is specific to the muscle-type nAChR. This family of toxins do not bind with high affinity to AChBP (*4*, *5*), and no structure of a complex with AChBP has ever been published. However, by checking the ability of making ternary complexes between nAChR, streptavidin, and biotinylated analogues of *Naja nigricollis* α-neurotoxin, it was concluded that short and long curaremimetic toxins share a similar overall topology of interaction when bound to nicotinic receptors (*6*). Moreover, by comparing the structure of the α-cobratoxin−AChBP complex to data obtained by double mutant cycle analysis of a muscle nAChR and the short-chain α-neurotoxin NmmI (*7*, *8*), Bourne and colleagues suggested that NmmI binds at the subunit interface of the muscle-type nAChR in a somewhat different orientation than α-cobratoxin, with Arg33 acting as a pivot. More recently, an in silico study suggested that the way of entry into the nAChR binding pocket of the second loop of NTII, another short-chain α-neurotoxin, differs from that of α-cobratoxin (*9*).

In order to test these proposals, we mapped the binding area of the tip of the second loop of a short-chain α-neurotoxin on the acetylcholine receptor by photoaffinity labeling. Unfortunately, with such ligands, this technique almost never led to the characterization of the labeled residues on the targeted protein, due essentially to the noncleavable nature of the covalent bond linking the photoprobe to the toxin. Actually, a labeled residue could only be characterized once (*10*), when the radioactive label was transferred from the ligand to the receptor. However, the 16.5 Å long linker did not lead to a precise mapping of the binding site. To overcome this drawback, we designed here a novel short bifunctional tritiated aryldiazonium photoprobe.

This paper describes the synthesis of the photoprobe followed by its coupling, through a cleavable disulfide bond, to an engineered cysteinyl residue at the putative pivotal position 33 of an analogue of a short-chain α-neurotoxin. Photoaffinity experiments, using this new toxin photoprobe in complex with nAChR on *Torpedo marmorata* membranes, showed a preferential labeling of the α and γ subunits compared to the δ subunit. Edman degradation of the α-subunit-labeled peptides showed that αTyr190, αTyr198, and, to a lesser extent, αCys192 reacted with the photoprobe. Our results reinforce the idea that long and short α-neurotoxins bind to their receptors in a similar manner, at least with the critical Arg33 residue.

* Address correspondence to: Pascal Kessler, CEA, DSV, DIEP, Bâtiment 152, courrier N*o* 24, Gif-sur-Yvette, F-91191, France. Tel. 33-1-69-08-40-74; Fax. 33-1-69-08-90-71; E-mail: pascal.kessler@cea.fr.

[1] The abbreviations used are as follows: nAChR, nicotinic acetylcholine receptor; AChBP, acetylcholine binding protein; SDS, sodium dodecyl sulphate; DTT, dithiothreitol; TCEP, Tris-carboxyethylphosphine; HATU, *N*-[(dimethylamino)-1*H*-1,2,3-triazolo[4,5-*b*]pyridin-1-ylmethylene]-*N*-methylmethanaminium hexafluorophosphate *N*-oxide; dtb, desthiobiotin; dtb-R33C, *Naja nigricollis* N-terminal-desthiobiotinylated α-neurotoxin cysteine analogue; dtb-R33C-ArN_2^+, *Naja nigricollis* N-terminal-desthiobiotinylated α-neurotoxin cysteine analogue harboring an aryldiazonium salt at position 33; R33C-DABD, α-neurotoxin cysteine analogue harboring a diaminobenzenediazonium salt at position 33.

10.1021/bc060175j CCC: $33.50 © 2006 American Chemical Society
Published on Web 10/19/2006

EXPERIMENTAL PROCEDURES

For the sake of clarity, we decided to use erabutoxin numbering for the amino acids of *Naja nigricollis* α-neurotoxin as we did in previous papers (*6*, *11*, *12*).

Peptide synthesis was achieved on an Applied Biosystems 433 apparatus. The Fmoc-protected amino acids were obtained from Novabiochem or Advanced Chemtech. All the chemicals were of the highest purity commercially available. Live *Torpedo marmorata* were purchased from the Station Biologique d'Arcachon (France). Western blots were carried out using Advance-ECL from Amersham Biosciences. Monoclonal antibodies mAb140, mAb155, and mAb165 were a generous gift of Dr. Tzartos (Hellenic Pasteur Institute, Athens). Goat anti-rat IgG peroxidase $F(ab')_2$ fragment (H + L) conjugate was purchased from Jackson ImmunoResearch Laboratories (West Grove, PA). Synthesis of *Naja nigricollis* R33C toxin analogue was achieved as described earlier (*11*). Electrospray mass spectrometry was achieved on a Quattro II from Micromass. NMR spectra were recorded on a Bruker Avance 250 MHz. Melting points were taken on a Kofler device. The irradiating device was composed of a 1000 W mercury lamp (Osram), an aperture, and a series of lenses focusing the polychromatic light to a monochromator (Jobin-Yvon), after which a series of lenses focused the monochromatic light to a thermostatic quartz cuvette containing the nAChR. The light intensity was measured with a radiometer IL1700 (International Light, Newburyport, MA). Each experiment involving photoactivatable compounds was done under sodium light, safe for aryldiazonium derivatives.

2-Hydroxymethyl-6-iodo-4-nitrophenol (1). 2-Hydroxy-5-nitrobenzoic acid (10.2 g, 55.7 mmol) was selectively reduced with BH_3-THF (2.2 equiv) in dry THF (150 mL), at reflux for 1 h. The borates were solvolyzed in dry MeOH, added to destroy the excess of borane. The mixture was evaporated to dryness. The residue was then solubilized again in dry MeOH, evaporated to dryness, and dissolved in a mixture of $MeOH/H_2O$ (200 mL/50 mL). After treatment with Na_2CO_3 (1.5 g), ICl (1 equiv) was added. The mixture was stirred for half an hour and then acidified with citric acid. Iodine was reduced with an excess of sodium thiosulphate. The mixture was then concentrated and extracted with EtOAc. The organic phase was washed with water and brine, dried over $MgSO_4$, and purified by silica gel chromatography (gradient: *n*-hexane 7/EtOAc 3 to *n*-hexane 5/EtOAc 5), giving orange oil, which was crystallized in $CHCl_3$. The final yield was 14 g (85%) of orange needles, mp 87 °C. ^{1}H NMR (acetone-d_6): δ (ppm) 4.97 (s, 2H), 5.58 (s_{broad}, 1H), 8.15 (d, $J = 2.7$ Hz, 1H), 8.50 (d, $J = 2.7$ Hz, 1H), 10.07 (s_{broad}, 1H). ^{13}C NMR (acetone-d_6): δ (ppm) 61.8, 83.6, 123.0, 127.0, 133.2, 141.1, 160.8. Anal. ($C_7H_6INO_4$) calcd %: C 28.50, H 2.05, N 4.75, I 43.02. Found %: C 28.74, H 2.06, N 4.72, I 43.11.

1-Iodo-2-methoxy-3-[(4-methoxyphenyl)diphenylmethoxymethyl]-5-nitrobenzene (2). Compound (**1**) (1.475 g, 5 mmol) was dissolved in pyridine (10 mL) with (4-methoxyphenyl)-diphenylmethoxymethyl chloride (2.4 g, 1.5 equiv) and heated to 65 °C for 1.5 h. The mixture was then evaporated, and the residue was dissolved in EtOAc and washed with H_2O, a saturated solution of NH_4Cl, and a 10% citric acid solution. The organic phase was dried over $MgSO_4$ and evaporated. The residue was taken in DMF (20 mL). Following the addition of $NaHCO_3$ (2.35 g, 28 mmol) and CH_3I (2 mL, 32 mmol), the mixture was stirred for 1 day, after which it was concentrated and taken into EtOAc. The organic phase was washed with water and brine, dried over $MgSO_4$, and purified by silica gel chromatography (eluent: *n*-hexane 95/EtOAc 5), yielding a white solid (2.33 g, 80%), mp 143 °C. ^{1}H NMR ($CDCl_3$): δ (ppm) 3.65 (s, 3H), 3.79 (s, 3H), 4.33 (s, 2H), 6.85 (dd, $J =$ 6.8 Hz, $J = 2.1$ Hz, 2H), 7.24−7.52 (m, 12H), 8.45 (d, $J = 2.7$ Hz, 1H), 8.55 (d, $J = 2.7$ Hz, 1H). ^{13}C NMR ($CDCl_3$): δ (ppm) 55.2, 60.7, 61.3, 87.5, 91.0, 113.3, 124.7, 127.2, 128.0, 128.3, 130.3, 133.5, 134.7, 135.0, 143.9, 144.6, 158.8, 162.3. Anal. ($C_{28}H_{24}INO_5$) calcd %: C 57.84, H 4.16, N 2.41, I 21.83. Found %: C 57.77, H 4.77, N 2.48, I 21.98.

{3-Iodo-4-methoxy-5-[(4-methoxyphenyl)diphenylmethoxymethyl]phenyl}carbamic Acid *tert*-Butyl Ester (3). Nitro compound (**2**) (1.63 g, 2.5 mmol) was selectively reduced with an excess of fresh NaSH, xH_2O (8 g) in a mixture of MeOH (50 mL) and THF (20 mL), under reflux for 2 h. After an evaporation step, the product was dissolved in EtOAc, washed with water and brine, and dried over $MgSO_4$. The amine was then taken in THF (10 mL) and protected with ditertiobutyldicarbonate (1.1 g, 2 equiv) at 50 °C, overnight. Finally, it was purified by silica gel chromatography (eluent: *n*-hexane 9/EtOAc 1), yielding 1.24 g of a white powder (76.5%), mp 201 °C. ^{1}H NMR (acetone-d_6): δ (ppm) 1.51 (s, 9H), 3.52 (s, 3H), 3.80 (s, 3H), 4.20 (s, 2H), 6.92 (dd, $J = 6.8$ Hz, $J = 2.2$ Hz, 2H), 7.26−7.58 (m, 12H), 7.89 (d, $J = 2.6$ Hz, 1H), 8.17 (d, $J = 2.6$ Hz, 1H), 8.55 (s_{broad}, 1H). ^{13}C NMR (acetone-d_6): δ (ppm) 28.5, 55.5, 61.4, 61.9, 80.4, 87.8, 91.7, 114.0, 120.2, 127.8, 128.1, 128.7, 129.2, 131.2, 134.1, 136.2, 138.2, 145.5, 153.1, 153.7, 159.8. Anal. ($C_{33}H_{34}INO_5$) calcd %: C 60.83, H 5.26, N 2.15, I 19.48. Found %: C 60.98, H 5.30, N 2.18, I 19.57.

(3-Hydroxymethyl-5-iodo-4-methoxyphenyl)carbamic Acid *tert*-Butyl Ester (4). Compound (**3**) (1.55 g, 2.4 mmol) was dissolved in THF (50 mL), and the mixture was diluted with H_2O (10 mL) and AcOH (50 mL) and refluxed for 3 h. The solvents were evaporated, and the product was purified by silica gel chromatography (gradient: *n*-hexane 8/EtOAc 2 to *n*-hexane 7/EtOAc 3), yielding a colorless oil which turned to a white solid (641 mg, 71%), mp 146 °C. ^{1}H NMR ($CDCl_3$): δ (ppm) 1.50 (s, 9H), 3.17 (s_{broad}, 1H), 3.75 (s, 3H), 4.65 (s, 2H), 6.87 (s_{broad}, 1H), 7.27 (d, $J = 2.6$ Hz, 1H), 7.80 (d, $J = 2.6$ Hz, 1H). ^{13}C NMR ($CDCl_3$): δ (ppm) 28.2, 60.7, 61.4, 80.8, 91.5, 119.5, 128.4, 135.0, 135.8, 152.7, 152.8. Anal. ($C_{13}H_{18}INO_4$) calcd %: C 41.17, H 4.78, N 3.69, I 33.47. Found %: C 41.27, H 4.87, N 3.71, I 33.59.

Thioacetic Acid *S*-(5-*tert*-butoxycarbonylamino-3-iodo-2-methoxybenzyl) Ester (5). Methanesulfonyl chloride (107 μL, 1.5 equiv) was added to a mixture of compound (**4**) (350 mg, 0.92 mmol) and Et_3N (195 μL, 1.5 equiv) in dry THF (10 mL) and stirred for 15 min. A mixture of thioacetic acid (294 μL, 4 equiv) and Et_3N (570 μL, 4 equiv) in EtOAc (3 mL) was added to the mesylate, and the solution was stirred for 1 h, at room temperature. After concentration, the residue was dissolved in EtOAc and washed with water and brine, dried over $MgSO_4$, and purified by silica gel chromatography (eluent: *n*-hexane 9/EtOAc 1), yielding 345 mg (85.5%) of yellowish oil. ^{1}H NMR ($CDCl_3$): δ (ppm) 1.50 (s, 9H), 2.35 (s, 3H), 3.80 (s, 3H), 4.13 (s, 2H), 6.49 (s_{broad}, 1H), 7.18 (d, $J = 2.6$ Hz, 1H), 7.88 (d, $J = 2.6$ Hz, 1H). ^{13}C NMR ($CDCl_3$): δ (ppm) 28.2, 28.5, 30.2, 61.4, 80.7, 91.6, 121.0, 128.6, 131.6, 135.7, 152.5, 153.3, 195.0. Anal. ($C_{15}H_{20}INO_4S$) calcd %: C 41.20, H 4.61, N 3.20, I 29.02, S 7.33. Found %: C 40.47, H 4.56, N 3.10, I 27.75, S 7.34.

Thioacetic Acid *S*-(5-*tert*-butoxycarbonylamino-2-methoxybenzyl) Ester (6). Iodide (**5**) (490 mg, 1.12 mmol) was hydrogenated ($P(H_2) = 2$ bar) for 1 h in EtOAc (10 mL) in the presence of Pd black (1.3 g) and Et_3N (700 μL). The mixture was filtered and washed with water and brine, dried over $MgSO_4$, and purified by silica gel chromatography (eluent: *n*-hexane 9/EtOAc 1), yielding 240 mg (69%) of colorless oil. ^{1}H NMR ($CDCl_3$): δ (ppm) 1.50 (s, 9H), 2.31 (s, 3H), 3.81 (s, 3H), 4.09 (s, 2H), 6.40 (s_{broad}, 1H), 6.77 (d, $J = 8.8$ Hz, 1H), 7.19 (d, $J = 2.7$ Hz, 1H), 7.34 (dd, $J = 8.8$ Hz, $J = 2.7$ Hz, 1H). ^{13}C NMR ($CDCl_3$): δ (ppm) 28.2, 28.3, 30.3, 55.8, 80.2, 110.9, 119.4, 121.7, 126.2, 131.1, 153.1, 153.4, 195.7. Anal.

($C_{15}H_{21}NO_4S$) calcd %: C 57.85, H 6.80, N 4.50, S 10.30. Found %: C 57.50, H 6.91, N 4.42, S 10.58.

[4-Methoxy-3-(pyridin-2-yldisulfanylmethyl)phenyl]carbamic Acid *tert*-Butyl Ester (7). Thioacetate (**6**) (102 mg, 0.33 mmol) was solvolyzed in a mixture of dry MeOH (4 mL) and NaOMe (80 mg, 4 equiv) for 4 h, at room temperature. The fraction of disulfide formed during the methanolysis was then reduced with TCEP (100 mg, 1 equiv) dissolved in a mixture of H_2O (1 mL) and pyridine (600 μL). 2,2′-Dithiopyridine (480 mg, 6.6 equiv) was then added to this mixture and stirred overnight. After evaporation, the residue was dissolved in EtOAc and washed with water and brine and dried over $MgSO_4$. The product was purified by silica gel chromatography (eluent: CH_2Cl_2 97/EtOAc 3), yielding 98 mg (79%) of a white powder, mp 122 °C. MS (ES-MS): $M + H^+ = 379.2$ [$C_{18}H_{22}N_2O_3S_2$ (378.5)]. ^{1}H NMR ($CDCl_3$): δ (ppm) 1.50 (s, 9H), 3.81 (s, 3H), 4.01 (s, 2H), 6.26 (s_{broad}, 1H), 6.75 (d, $J = 8.8$ Hz, 1H), 6.98−7.04 (m, 1H), 7.09 (d, $J = 2.7$ Hz, 1H), 7.25 (m, 1H), 7.49−7.55 (m, 1H), 7.60 (dd, $J = 8.8$ Hz, $J = 2.7$ Hz, 1H), 8.40 (d, $J = 4.0$ Hz, 1H). ^{13}C NMR ($CDCl_3$): δ (ppm) 28.3, 38.5, 55.7, 80.1, 110.9, 119.2, 119.7, 120.2, 122.0, 125.1, 131.1, 136.7, 149.1, 153.0, 153.3, 160.6. Anal. ($C_{18}H_{22}N_2O_3S_2$) calcd %: C 57.11, H 5.86, N 7.40, S 16.94. Found %: C 57.01, H 5.92, N 7.40, S 16.91. UV: $\lambda_{max} = 287$ nm, $\epsilon = 5900$ $M^{-1}.cm^{-1}$.

4-Methoxy-3-(pyridin-2-yldisulfanylmethyl)benzenediazonium Trifluoroacetate (8). The aromatic amine of compound (**7**) (19 mg, 50 μmol) was deprotected in trifluoroacetic acid (2 mL) for 15 min. The mixture was cooled down to about 0 °C, and sodium nitrite (1.1 equiv) dissolved in water (100 μL) was added dropwise. The solution was evaporated to dryness, taken into H_2O, and purified by reverse-phase HPLC on a Vydac C4 preparative column (22 × 250 mm; flow rate 15 mL.min^{-1}; linear gradient: 0% B to 10% B in 5 min, then isocratic at 10% B. A: H_2O, 0.1% TFA. B: CH_3CN) yielding aryldiazonium (**8**) (26%). MS (ES-MS): $M = 262.87$ ($M - N_2$) [$C_{13}H_{12}N_3S_2^+$ (290.4)]. ^{1}H NMR (CD_3OD): δ (ppm) 4.09 (s, 3H), 4.11 (s, 2H), 7.20−7.23 (m, 1H), 7.42 (d, $J = 9.3$ Hz, 1H), 7.66−7.75 (m, 2H), 8.33−8.35 (m, 1H), 8.38 (d, $J = 2.6$ Hz, 1H), 8.49 (dd, $J = 9.3$ Hz, $J = 2.6$ Hz, 1H). ^{13}C NMR (CD_3OD): δ (ppm) 37.1, 58.6, 103.0, 115.1, 121.8, 122.8, 131.2, 135.3, 137.5, 139.2, 150.3, 160.4, 160.9, 161.5, 169.3.

[4-Methoxy-3-(pyridin-2-yldisulfanylmethyl)-5-[^{3}H]-phenyl]carbamic Acid *tert*-Butyl Ester (7bis). Iodide (**5**) (44 mg, 0.1 mmol) was hydrogenated ($P(^3H_2) = 2$ bar) for 1 day in EtOAc (1 mL) in the presence of Pd black (120 mg) and Et_3N (60 μL). The mixture was centrifuged and the catalyst washed with EtOAc (5 mL). The organic phase was concentrated to 1 mL and purified by thin layer silica gel chromatography (eluent: *n*-hexane 8/EtOAc 2), yielding 18 mg (58%) of colorless oil, coeluting on TLC with the equivalent non-radioactive compound (**6**). The tritiated derivative was then dissolved in dry MeOH and reacted with an excess of NaOMe (15 mg) for 3 h, at room temperature. The mixture was then buffered by adding 75 μL of pyridine in 150 μL H_2O. Treatment with an excess of TCEP (20 mg) reduced the formed disulfide. An excess of 2,2′-dithiopyridine (60 mg) was then added to this mixture, which was evaporated after 10 min. The remaining oil was diluted in 1.5 mL CH_3CN and 750 μL H_2O and purified by HPLC on a Vydac C18 analytical column (4.8 × 250 mm; flow rate 1 mL.min^{-1}; isocratic: 55% B. A: H_2O without TFA. B: CH_3CN), yielding 61% of pure radioactive product (**7bis**). It coeluted with the non-radioactive compound on HPLC, and their ^{1}H NMR spectra were identical. However, as expected, the integration of the proton in the ortho position of the methoxy group in **7bis** corresponded to about 40% of the expected value on the non-radioactive compound, due to the replacement of part of the proton by tritium. Its radioactive specificity (12.5 Ci.mmol^{-1}) was determined by UV spectroscopy ($\lambda_{max} = 287$ nm, $\epsilon = 5900$ $M^{-1}.cm^{-1}$) and β-counting and corresponded to the proton integration in ^{1}H NMR. This compound was stable for months in a $^1/_4$ mixture of $CDCL_3$/toluene, in liquid N_2.

4-Methoxy-3-(pyridin-2-yldisulfanylmethyl)-5-[^{3}H]-benzenediazonium Trifluoroacetate (8bis). The aromatic amine of compound **7bis** (3 μmol) was deprotected in trifluoroacetic acid (500 μL) for 2 h. The mixture was cooled down to about 0 °C, and sodium nitrite (1.1 equiv) dissolved in water (10 μL) was added. The solution was evaporated to dryness, taken into H_2O, and purified by reverse-phase HPLC on a bondasorb C18 (10 μm) analytical column (4.8 × 250 mm; flow rate 1 mL.min^{-1}; linear gradient: 0% B to 40% B in 20 min. A: H_2O, 0.01% TFA. B: CH_3CN) yielding aryldiazonium (**8bis**) (25%). The pure tritiated compound coeluted on a C18 column (conditions mentioned above) with the same non-radioactive derivative and had identical UV spectra. The concentrated HPLC fraction of compound **8bis** was stable for months in liquid N_2. UV: $\lambda_{max} = 313$ nm, $\epsilon = 20\,000$ $M^{-1}.cm^{-1}$; the molar absorption coefficient was determined using the radioactive compound **8bis**, by correlating its UV spectrum and its radioactive specificity (12.5 Ci.mmol^{-1}).

N-Terminal Modification of *Naja nigricollis* R33C Toxin Analogue with Desthiobiotin. After the automated peptide synthesis of the precursor of *Naja nigricollis* R33C toxin analogue (*11*), 6-fmoc-aminohexanoic acid was coupled to the N-terminus of the peptide still linked to the resin, using a standard HATU/diisopropylethylamine overnight activation in *N*-methylpyrrolidone. The fmoc group was released by piperidine treatment. Desthiobiotin was then coupled in the same way than the aminohexanoic linker. After deprotection for 1.5 h in TFA/triisopropylsilane/water (9/0.5/0.5), the peptide was precipitated in cold terbutyl ethyl ether and centrifuged. The pellet was dissolved in 10% acetic acid overnight. The linear peptide was purified as described earlier (*11*) and then refolded at 10 μM, in Tris-HCl 100 mM, pH 7.8, oxidized DTT 5 mM, for 1 day. Purification was carried out as described earlier (*11*) and afforded pure dtb-R33C toxin analogue, which was checked by electrospray mass spectrometry. $M_{calcd} = 7043.2$; $M_{found} = 7043.0$.

Coupling of Aryldiazonium Salt (8bis) to dtb-R33C. A solution of 1.3 mg (190 nmol) of dtb-R33C in 250 μL of 1.6 M sodium citrate buffer (pH 2.2) was mixed, under rapid stirring, with 2.2 equiv of diazonium (**8bis**) diluted in 250 μL of the same buffer. The mixture was allowed to stand at room temperature in the dark for 1 day. The toxin derivative [^{3}H]-dtb-R33C-ArN_2^+ was then purified by HPLC on a Vydac C4 analytical column (4.8 × 250 mm; flow rate 1 mL.min^{-1}; linear gradient: 10% B to 10% B in 10 min, then 10% to 18% B in 6 min, then 18% to 24% B in 19 min. A: H_2O, 0.1% TFA. B: CH_3CN), and checked by electrospray mass spectrometry. M_{calcd} (dtb-R33C-ArN_2^+) = 7222.25; $M_{found} = 7222.35$. UV: $\lambda_{max} = 314$ nm, $\epsilon = 20\,000$ $M^{-1}.cm^{-1}$; toxin concentration was determined by acidic hydrolysis and subsequent quantification of the contained amino acids.

Preparation of nAChR-Rich Membranes. nAChR-rich membranes from the electric tissue of *Torpedo marmorata* were prepared as previously described (*13*). The concentration of acetylcholine binding sites was typically between 0.9 and 1.4 nmol per milligram of proteins.

Analytical Scale Photolabeling. *Torpedo* membranes (2 μM, 500 pmol α-bungarotoxin sites) were incubated in $NaPO_4$ 250 mM, pH 6.9, at room temperature in the dark for 15 min with [^{3}H]-dtb-R33C-ArN_2^+ (0.95 equiv). The mixture was then stirred in a quartz cuvette and irradiated at 323 nm (200 μW.cm^{-2}) for 10 min, at 10 °C. The size of the light beam was approximately 2 mm × 12 mm. For protection experiments,

Scheme 1. Synthesis of the Aryldiazonium Salts (8) and (8bis)[a]

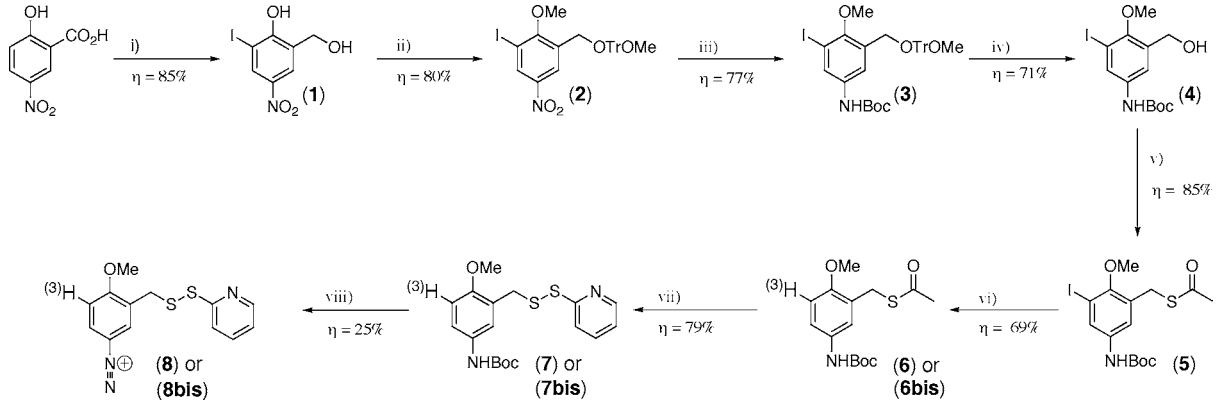

[a] Reagents and conditions: (i) (a) BH_3-THF, (b) Na_2CO_3, ICl, MeOH/H_2O; (ii) (a) ClTrOMe, pyridine, 100 °C, (b) CH_3I, $NaHCO_3$, DMF; (iii) (a) NaSH, MeOH/THF, reflux, (b) *tert*-butyl dicarbonate; (iv) (a) THF, H_2O, AcOH; (v) (a) CH_3SO_2Cl, Et_3N, THF, (b) CH_3COSH/Et_3N, THF; (vi) H_2 or $^3H_2$ (2 bar), Pd black; (vii) (a) NaOMe, MeOH, (b) TCEP, (c) 2,2′-dithiodipyridine; (viii) TFA, $NaNO_2$. Yields are given for non-radioactive products.

membranes were incubated with 20 equiv of α-bungarotoxin at room temperature for 1 h, before adding the tritiated photoactivatable toxin analogue. Following irradiation, the membranes were centrifuged at 22 000 g for 30 min, at 4 °C, and the pellets were solubilized in Laemmli buffer to be run on a 10% SDS-PAGE. The gels were then transferred to PVDF-membranes, which were exposed to a *β*-imager in order to visualize the labeled bands. These bands were compared to the one obtained by Western blotting of the same PVDF-membranes with mAbs 155, 165, and 140, which are specific for the α, *γ*, and *δ* subunits, respectively.

Preparative Scale Photolabeling and Isolation of the Labeled α Subunit. Large quantities of torpedo membranes (30 nmol) were irradiated in the same conditions as for analytical scale experiments, except that the size of the light beam was 5 mm × 12 mm, and the energy was equal to 300 $\mu W.cm^{-2}$. Following irradiation, the membrane suspension was centrifuged at 22 000 g for 30 min, at 25 °C, and the pellet solubilized in buffer A (Tris-HCl 50 mM, pH 8, LiDS 1%, LiCl 2 M). The mixture was then centrifuged as described before. The supernatant was poured onto streptavidin Sepharose beads (Amersham Biosciences), equilibrated with buffer A. The beads were washed with buffer A (2 × 10 mL) and with Tris 50 mM pH8, SDS 0.2% (3 × 10 mL). The labeled subunits were then recovered by incubating the beads twice (2 mL and 1 mL) in buffer B (Tris-HCl 2M pH 8, SDS 0.2%, biotin 50 mM) at 70 °C for 30 min. The subunits were reduced with TCEP (20 mM) at 25 °C overnight, and the sulfydryls were blocked with iodoacetamide (35 mM) at 25 °C for 15 min. The mixture was concentrated on centricon-30 and washed with Tris-HCl 20 mM pH 7. The solubilized and labeled subunits were subjected to 10% SDS-PAGE. The gel was covered with a dry PVDF-membrane for 15 min, which enabled the location of the radioactive bands after exposing the membrane on a *β*-imager (Beta Imager 2000 from Biospace). The labeled subunits could then be excised from the gel without any staining. The gel fraction containing the α-subunit was cut into small pieces, transferred to an Eppendorf tube, and washed twice with a 50% aqueous solution of CH_3CN (2 × 1 mL) for 10 min.

"In Gel" CNBr Cleavage of the α Subunit and Peptide Purification. Cleavage of the α subunit and extraction of the labeled peptides were done as described in Grutter et al. (*14*), except that extraction of the peptides from the gel was carried out only with a mixture of H_2O − 0.1% TFA/CH_3CN (50/50). The extract was purified on a Vydac C4 narrow-bore column by HPLC (2.1 × 250 mm; flow rate 0.2 $mL.min^{-1}$; linear gradient: 5% B to 5% B in 10 min, then 5% to 25% B in 10 min, then 25% to 35% B in 155 min, then 35% to 100% B in 30 min, then 100% to 100% B in 15 min, then 100% to 5% B in 5 min. A: H_2O, 0.1% TFA. B: 70% CH_3CN, 30% *n*-propanol, 0.095% TFA). UV absorbance was monitored at 220 nm. Fractions (400 μL) were collected, and aliquots were counted for radioactivity.

Peptide Sequencing. HPLC fractions were concentrated (speedvac) and loaded onto a biobrene-pretreated filter of the sequencer. Automated Edman degradation was performed on an Applied Biosystems Procise sequencer. The HPLC output from each cycle was collected and counted for radioactivity quantification.

RESULTS

Synthesis of the Bifunctional Photoprobe (8bis) (Scheme 1). The aryldiazonium salt (**8**) was synthesized in fourteen steps, with an overall yield of about 4%. A radioactive version was obtained by treating the aryliodide (**5**) with tritium gas leading to the thioacetate (**6bis**). Its radioactive specificity was 12.5 $Ci.mmol^{-1}$. The main secondary reaction observed in this step (radioactive or not) was the concomitant desulfurization of (**5**). The methanolysis of the thioacetate (**6bis**) followed by the reduction of the formed disulfide and the dithiopyridinylation of the thiol were made one-pot. We thus obtained the precursor (**7bis**) of the bifunctional photoprobe (**8bis**). This precursor was kept in a mixture of toluene and chloroform (4/1) in liquid nitrogen and was stable for months. Diazotization of (**7bis**) led to the aryldiazonium salt (**8bis**), which was purified by HPLC. After concentration, the HPLC fractions were stable for months in liquid nitrogen.

As was the case for a previous non-radioactive bifunctional photoprobe (*12*), this novel tritiated molecule carries an aryldiazonium salt, which can be photodecomposed at wavelengths which are safe for proteins (above 300 nm). Consistent with earlier data (*15*), replacing the dimethylamino group on the para position of the diazonium moiety (*12*) by a methoxy group (this work) shifted the maximal wavelength from 391 to 313 nm.

Coupling of the Bifunctional Photoprobe to dtb-R33C. We synthesized a previously described analogue of the α-neurotoxin of *Naja nigricollis* (*11*) in which Arg33, at the tip of loop II, is replaced by a cysteine residue (Figure 1). This residue was shown to be a major hot spot for the interaction with the nAChR (*16*). Following automated peptide synthesis, we coupled manually a desthiobiotin through an aminohexanoic linker to the N-terminus of the peptide, in order to enable a prepurification of labeled subunits on streptavidin beads. In contrast to biotin, desthiobiotin binds reversibly to streptavidin (*17*), a huge advantage in such a study, as it enables the recovery of the purified labeled subunits.

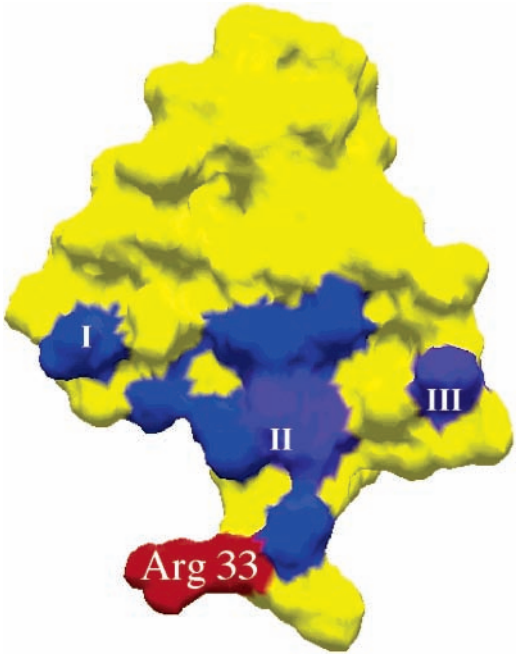

Figure 1. *Naja nigricollis* α-neurotoxin. The structure has been taken from Zinn-Justin et al. (*33*). The molecular surface has been represented in yellow, showing the binding surface in blue and highlighting the critical Arg33 residue in red on tip of loop II. Note that the numbering of the residue corresponds to erabutoxin numbering.

We tried to couple the unique free cysteine of the refolded toxin to our bifunctional photoprobe at the same conditions as previously described for the achievement of R33C-DABD (*12*). Unfortunately, we obtained a mixture of the expected product and a molecule derived from the attack of the cysteine thiolate on the diazonium moiety (data not shown). This undesired reaction showed that, in the absence of light, the methoxy group renders the *p*-diazonium moiety more sensitive to nucleophilic attack than the dimethylamino group did. Lowering the pH from 7 to 4.5, during such coupling reaction, accelerates the disulfide exchange on the pyridyl disulfide, by protonation of the pyridine nitrogen (*18*). As the pK_a value of 2,2′-pyridyl disulfide is 2.45 (*18*), we observed that decreasing the pH to 2.2 enabled the expected reaction to happen with the robust snake toxin, without any side reaction but with longer reaction times, as the cysteine residue is almost fully protonated.

The maximum wavelengths of the obtained toxin photoprobe and of the initial bifunctional photoprobe (**8 bis**) were almost identical (Figure 2). This aryldiazonium toxin was stable for months in acidic conditions (HPLC fractions) in liquid nitrogen in the dark. However, the stability of the diazonium group at physiological pH (half-life = 5 h at 17 °C in 250 mM sodium phosphate, pH 6.9, in the dark, data not shown) was not sufficient for equilibrium binding experiments in order to determine the inhibition constant of the modified toxin on the torpedo receptor. Nevertheless, a similar but more stable modified toxin (R33C-DABD), in which only the *p*-methoxy group on the bifunctional photoprobe was replaced by a *p*-dimethylamino moiety (*12*), showed an almost wild-type affinity for the nicotinic receptor.

This novel toxin photoprobe had various specific characteristics (Scheme 2). The desthiobiotin tag enables purification of the labeled subunits of the nAChR. The disulfide bond, linking the toxin to the radioactive photoprobe, can easily be reduced, allowing the release of the toxin at will after photolabeling and, therefore, the transfer of radioactivity from the ligand to the receptor. This feature facilitates the purification and the analysis of the labeled peptides (*10*), as we have then to deal with standard labeling with a small non-peptidic molecule. The length

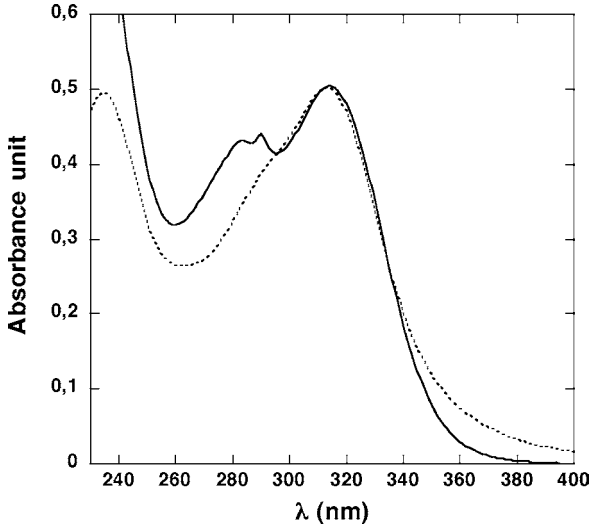

Figure 2. UV/visible spectrum of compound (**8**) (·····) and dtb-R33C-ArN_2^+ in water (—).

Scheme 2. Coupling of Aryldiazonium Salt (8bis) to dtb−R33C

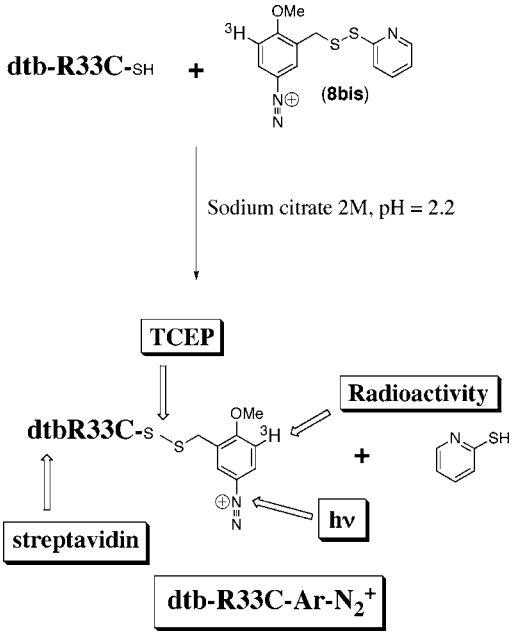

(8.5 Å) between the α-carbon attached to the photosensitive moiety and the reactive carbon on the arylcation, produced by UV irradiation, is almost as short as the replaced arginine residue, enabling a precise mapping of the binding site. It is also positively charged, therefore probably being a better mime than standard azido, diazirine, and benzophenone photoprobes on position 33 of the toxin.

Photolabeling of *Torpedo marmorata* Membranes. The nAChR was irradiated in the presence of about 1 equiv of photosensitive toxin (dtb-R33C-ArN_2^+) at 323 nm, which is farther from the protein absorption band than the maximum wavelength of the photoprobe (314 nm). However, at this wavelength, the molar absorption coefficient is still close to the highest (Figure 2).

For analytical experiments, labeled membranes were centrifuged, and the pellets taken in Laemmli buffer and run on a 10% SDS-PAGE. The gel was then transferred onto a PVDF-membrane. Once dry, the latter was exposed on a β-imager (Figure 3). Mainly four bands could be seen for the pellet dissolved in nonreducing Laemmli buffer (lane 5). Their apparent molecular weights were consistent with those of the

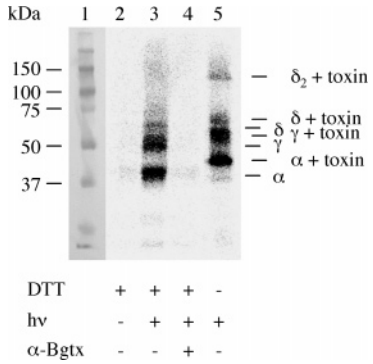

Figure 3. Detection of the nAChR labeled subunits by β-imaging. *Torpedo* membranes (2 μM α-bungarotoxin sites) were incubated with dtb-R33C-ArN_2^+ (0.95 equiv) and irradiated at 323 nm for 10 min, at 10 °C (see Experimental Procedures). Following irradiation, the membrane suspension was centrifuged at 22 000 g for 20 min at 4 °C, and the pellets solubilized in Laemmli sample buffer and run on 10% SDS-PAGE. Lane 1, molecular weight markers; lane 2, nonirradiated nAChR−photoprobe complex; lane 3, nAChR irradiated in the presence of dtb-R33C-ArN_2^+; lane 4, nAChR, preincubated with a large excess of α-bungarotoxin (20 equiv) and irradiated in the presence of dtb-R33C-ArN_2^+; samples corresponding to lanes 1−4 were dissolved in reducing Laemmli buffer; lane 5, nAChR irradiated in the presence of dtb-R33C-ArN_2^+ (nonreducing Laemmli buffer). After SDS-PAGE, the proteins were transferred to a PVDF-membrane and exposed to a β-imager.

α, γ, and δ subunits coupled to a toxin molecule, with the highest weight being consistent with the dimer δ_2 coupled to at least one toxin molecule. These two bands for the δ subunit show that, as is often the case, a mixture of monomers and dimers of nAChR were present in the torpedo membranes used. Three radioactive bands (lane 3) could be observed for the pellet dissolved in reducing Laemmli buffer. Their apparent molecular weights (38, 56, and 65 kDa) were consistent with those of the α, γ, and δ subunits, as expected after reduction of the disulfide bond linking the toxin to the receptor, leaving the radioactive probe on the receptor side.

The labeling yield was determined on a similar polyacrylamide gel, which was cut in 1 mm pieces and counted for $[^3H]$-radioactivity. The band at 38 kDa was the most labeled (59% of the total labeling, 7.6% of the added toxin), due probably, in part, to the presence of two α subunits, followed by the band at 56 kDa (28% of the total labeling, 3.2% of the added toxin), with the last one being the band at 65 kDa, which was the least labeled subunit (13% of the total labeling, 1.2% of the added toxin). As expected, controls (i) with no irradiation of the toxin−receptor complex (lane 2) or (ii) with preincubation of the nAChR with an excess of α-bungarotoxin before the addition of dtb-R33C-ArN_2^+ (lane 4) showed no incorporation of radioactivity, demonstrating the total specificity of photolabeling.

Desthiobiotin coupled to the N-terminus of the toxin analogue enabled purification on streptavidin beads of the whole set of labeled subunits (data not shown). Photolabeled membrane pellets were solubilized and denatured in lithium dodecyl sulfate, in order to purify the subunits covalently linked to the toxin by affinity chromatography on streptavidin Sepharose beads. Lithium chloride and lithium dodecyl sulfate were chosen instead of the sodium salts for solubility reasons, as sodium dodecyl sulfate precipitates rapidly in the presence of a high concentration of sodium chloride in buffers. Unexpectedly, recovery of the labeled subunits was not efficient enough when the disulfide bond linking the toxin to the irradiated photoprobe was directly reduced on the beads. To be quantitative, it required many repetitive reducing steps, preventing the recovery of the labeled subunits in a small volume. This was also the case when the beads were only incubated with an excess of biotin at room temperature. Thus, after many washings, the labeled subunits

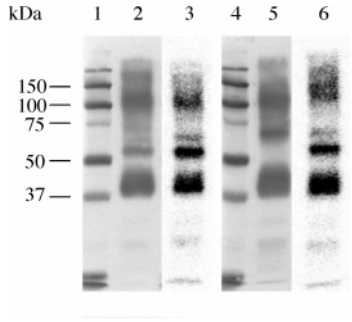

Figure 4. Labeling specificity of dtb-R33C-ArN_2^+. After irradiation, the solubilized dtb-toxin-nAChR covalent complex was purified on streptavidin Sepharose beads and run on SDS-PAGE, using reducing Laemmli buffer. The proteins were then transferred from the gel to another PVDF-membrane, which was incubated with mAb155 + mAb165 or mAb155 + mAb140 to visualize the α and γ, respectively, the α and δ subunits of the *Torpedo* nAChR (see Experimental Procedures). Lanes 1 and 4, prestained molecular weight markers; lane 2, immunoblot with mAb155 + mAb165 (α + γ); lane 3, β-imaging of lane 2; lane 5, immunoblot with mAb155 + mAb140 (α + δ); lane 6, β-imaging of lane 5.

were recovered by heating the beads at 70 °C in the presence of an excess of biotin, and then reduced and alkylated. The radioactivity was hence transferred from the ligand to the subunits by release of the toxin from the photoprobe. The labeled subunits were then separated by 10% SDS-PAGE.

On an analytical scale, the polyacrylamide gel was transferred on a PVDF-membrane, which was then exposed on a β-imager, followed by a Western blot with monoclonal antibodies mAb155, mAb165, and mAb140 directed against the α, γ, and δ subunits, respectively. This blot coupled to the $[^3H]$-image demonstrated unambiguously that the labeled bands were indeed the formerly cited subunits (Figure 4). As expected, no labeling of the β subunit was observed. However, a varying amount of aggregates could be observed by β-imaging as well as by Western blotting. These aggregates depended on the quality of the torpedo membrane preparation but might also form in part during the treatment of the streptavidin beads at 70 °C.

On a preparative scale (30 nmol of binding sites), the affinity purified subunits were run on three 1.5-mm-thick one-well SDS-PAGE. The labeled subunits were detected without any staining. Actually, we covered the gel for about 15 min with a dry PVDF-membrane. This contact was sufficient to transfer enough molecules to be detected on a β-imager. Superimposing this image to the gel enabled cutting of the labeled subunits.

Characterization of the Labeled Residues on the α Subunit. The gel fractions corresponding to the α subunit were digested "in-gel" with CNBr as described earlier (*14*). The extracted peptides were purified by HPLC on a Vydac C4 narrow-bore column (Figure 5). One major radioactive peak could be observed (fractions 39 to 44) corresponding to many poorly separated UV-detected peaks.

The 4 fractions containing most of the radioactivity (**40**, **41**, **42**, and **43)** were analyzed separately by sequential Edman degradation for ^3H and mass release on 28 cycles (Figure 6). For fraction **40**, 4 peptides beginning at αTrp118 (I_o = 124 pmol, R = 86%), αGlu172 (first 6 residues detected, I_o = 73 pmol, R = 58%), αLys179 (I_o = 81 pmol, R = 88%), and αVal405 (I_o = 45 pmol, R = 74%) could be detected. For fraction **41**, five peptides from the nAChR α-subunit were detected: the first sequence began at αTrp118 (I_o = 50 pmol, R = 92%), the second at αLys145 (I_o = 41 pmol, R = 79%), the third at αGlu172 (first 20 residues detected, I_o = 39 pmol, R = 83%), the fourth at αLys179 (I_o = 70 pmol, R = 88%), and the fifth at αPro309 (I_o = 55 pmol, R = 87%). For fraction **42**, 4 peptides beginning at αGlu172 (first 25 residues detected,

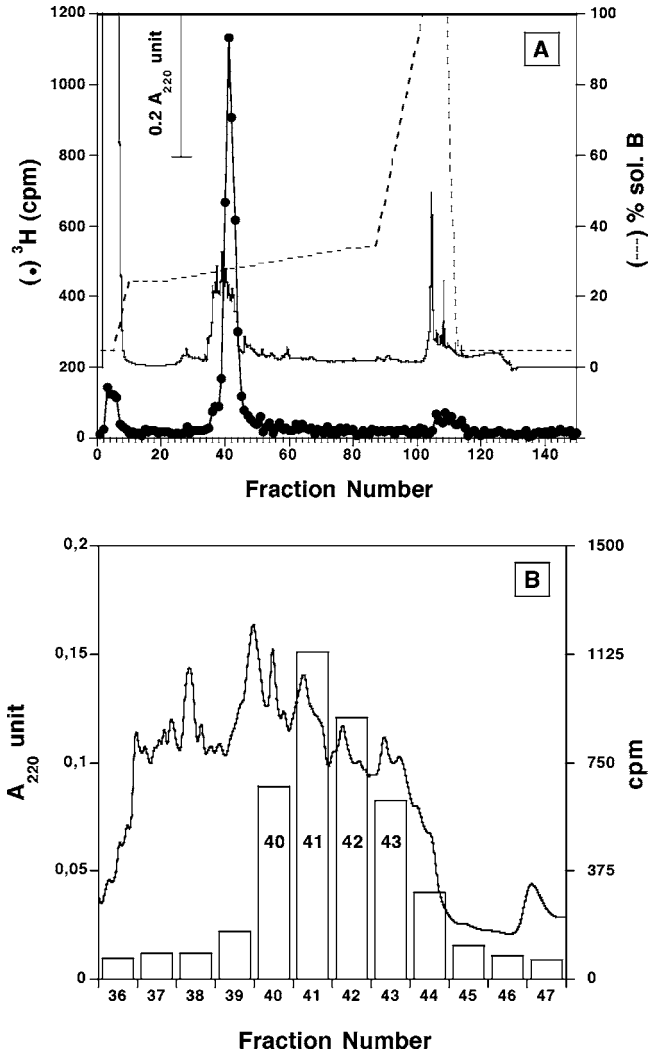

Figure 5. Reversed-phase HPLC of CNBr digests of the labeled α-subunit. *Torpedo* membranes (30 nmol, 2 μM α-bungarotoxin sites) were irradiated at 323 nm (300 μW.cm^{-2}) for 10 min, at 10 °C in the presence of [^{3}H]-dtb-R33C-ArN_2^+ (0.95 equiv). Following irradiation, the membrane suspension was centrifuged (22 000 g for 30 min, 25 °C), and the pellet solubilized in buffer A (Tris-HCl 50 mM, pH 8, LiDS 1%, LiCl 2 M). The labeled subunits were prepurified by affinity chromatography on streptavidin Sepharose beads (Amersham Biosciences) (6 mL), and the disulfide bonds were then reduced with TCEP and the cysteine blocked with iodoacetamide (see Experimental Procedures). The mixture was then concentrated on centricon-30 and subjected to 10% SDS-PAGE (three 1.5-mm-thick minigels). The labeled subunits were then excised from the gel, cut into small pieces, and cleaved "in gel" with CNBr. The extracted peptides were purified on a Vydac C4 narrow-bore column (2.1 × 250 mm; flow rate, 0.2 mL.min^{-1}; linear gradient, 5% B to 5% B in 10 min, then 5% to 25% B in 10 min, then 25% to 35% B in 155 min, then 35% to 100% B in 30 min, then 100% to 100% B in 15 min, then 100% to 5% B in 5 min. A: H_2O, 0.1% TFA. B: 70% CH_3CN, 30% *n*-propanol, 0.095% TFA). UV absorbance was monitored at 220 nm. Fractions (400 μL) were collected, and aliquots were counted for radioactivity in a scintillation counter. (A) (-----) Gradient profile, (—) UV profile, (-●-) [^{3}H] profile. (B) Zoom between fractions 36 and 47; (—) UV profile; ^{3}H profile has been represented as a histogram.

I_o = 28 pmol, R = 89%), αLys179 (I_o = 63 pmol, R = 87%), αPro309 (I_o = 116 pmol, R = 85%), and αLys330 (I_o = 35 pmol, R = 91%) were detected. For fraction **43**, 3 peptides from the α-subunit were detected: the first primary sequence began at αGlu172 (first 10 residues detected, I_o = 24 pmol, R = 93%), a second at αLys179 (I_o = 57 pmol, R = 87%), and a third at αLys330 (I_o = 75 pmol, R = 86%).

As can be seen, the two unique peptides common to fractions **40**, **41**, **42**, and **43** extend from αGlu172 and αLys179 and harbor the critical C loop of the α-subunit, which occludes the ligand binding site and wraps agonists. However, only the peptide extending from αLys179 could be detected during the 28 cycles; the other peptide was already undetectable from cycles 7 and 11 for fractions **40** and **43**, respectively. The 4 fractions also share 2 common positions of radioactive release, on cycles 12 and 20, corresponding to αTyr190 and αTyr198, respectively, on the peptide extending from αLys179. A third radioactive amino acid could be detected at cycle 14 for fractions **42** and **43**, corresponding to αCys192 on the same peptide, as αAla343, which belongs to the peptide extending from αLys330, is cytoplasmic. As observed in fractions **40**, **41**, and **42**, a very faint labeling could be seen on cycle 19 which might correspond to αTyr190 on the peptide beginning at αGlu172. Such an increase in radioactive detection was also visible on cycle 21, in fractions **42** and **43**, and might correspond to αCys192 on the same peptide.

It must be noted that a small radioactive peak was repeatedly detected at the third cycle. It would correspond to a faint labeling of αTyr181 on the peptide starting at αLys179 or of αGly174 on the peptide starting at αGlu172, which seems unreasonable considering their orientation and their distance to the ligand binding site (*19*). Moreover, repetitive experiments showed that the intensity of this peak was always low and not related to the intensity of the peaks at positions 12, 14, and 20 (data not shown). Further studies are necessary to explain its presence. Hence, the labeled residues are unambiguously primarily αTyr190, followed by αTyr198, with αCys192 being less labeled.

DISCUSSION

Despite numerous photolabeling experiments of the muscle-type nicotinic acetylcholine receptor with α-neurotoxins in these past decades (*10*, *20*−*29*), no labeled residue belonging to the toxin-binding site could be characterized. The only success (*10*) managed a label-transfer technique with a commercial derivative. However, the linker between the photoactivatable moiety and the toxin was, at that time, too long to explore the binding site.

Recently, we described the synthesis of a novel short cleavable photoactivatable probe with dual functionality, which can be selectively linked to any natural or engineered cysteinyl residue in peptides or proteins through a disulfide bond (*12*). This probe was coupled to a synthetic analogue of *Naja nigricollis* α-neurotoxin, in which a cysteine residue replaced Arg33 on the tip of loop II (Figure 1). Chemical synthesis of this toxin analogue allowed modification on a critical position, which could not be modified using wild-type toxins. This new photosensitive toxin analogue efficiently coupled to the receptor α subunit, but unfortunately, we could not get through the characterization of the labeled residues, as the synthesis of a radioactive version of this probe appeared impossible.

We developed here a novel aryldiazonium photoprobe, in which a *p*-methoxy group replaced the stabilizing *p*-dimethylamino moiety (Scheme 1). This modification enabled the synthesis of a bifunctional cleavable tritiated photoactivatable probe via an iodinated derivative. The aryldiazonium salt showed long stability when stored in acidic conditions. The use of tritium makes it safe against irradiation and radioactively stable for years. However, the pH needed for coupling the aryldiazonium to the ligand restricts its use to acid-stable ligands. To our knowledge, no commercial molecule is shorter than 14 Å (compared to 8 Å here), and only one other short radioactive photocrosslinking/label-transfer probe was described (*30*). It harbors a benzophenone photosensitive moiety, is radioiodinatable, and has about the same length than our probe, but is more bulky. However, the authors did not get through the character-

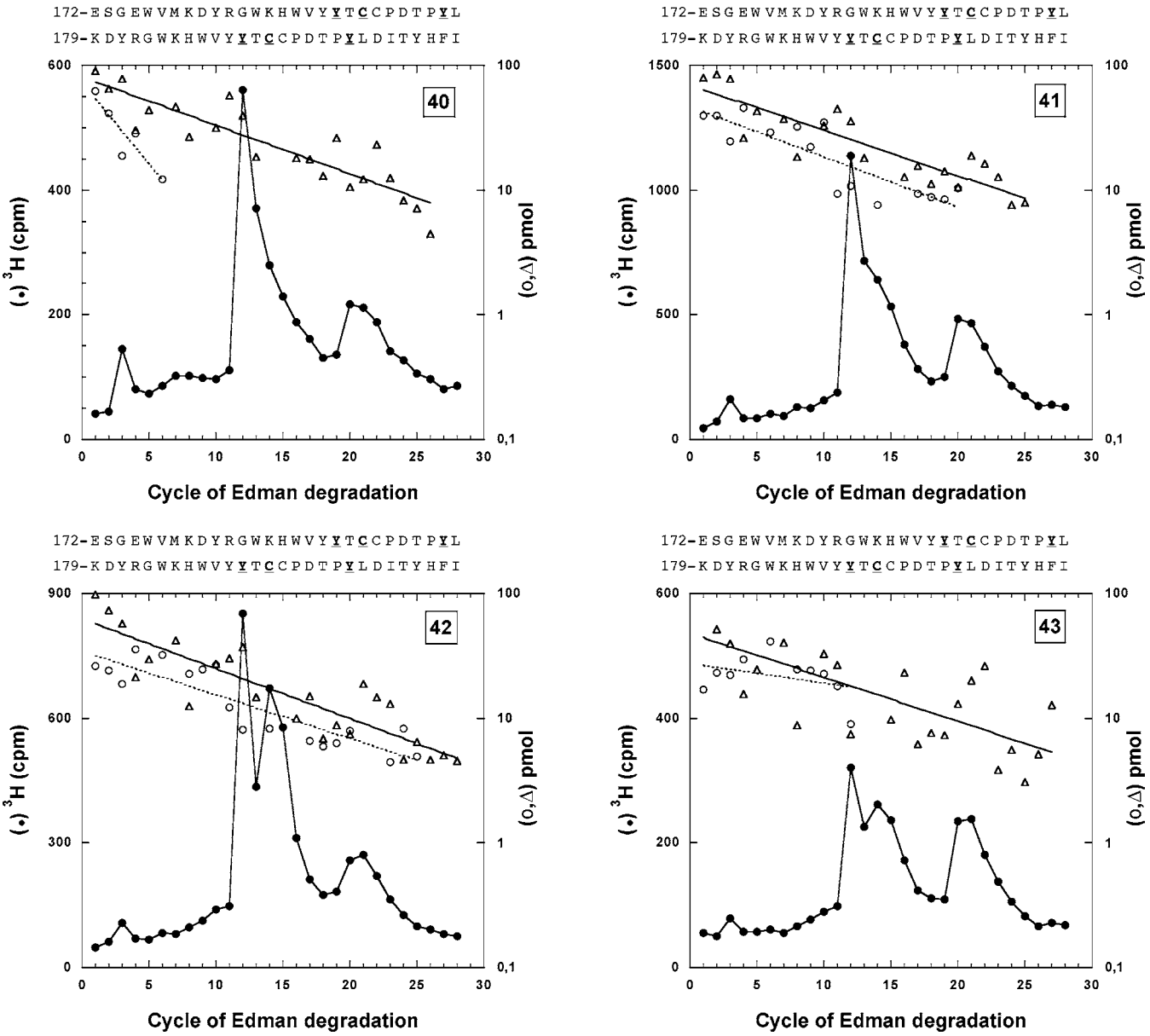

Figure 6. Identification of nAChR α-subunit amino acids photolabeled by [^{3}H]-dtb-R33C-ArN_2^+: ^{3}H and mass release at each cycle upon sequential Edman degradation of HPLC fractions **40**, **41**, **42**, and **43** (see Figure 5B). For fraction **40**, 2.6×10^4 cpm was loaded on the filter. After 28 cycles, 16% of the radioactivity (4200 cpm) remained on the filter and 17% (4300 cpm) was recovered. Four peptides from the nAChR α-subunit were detected: the first primary sequence began at αTrp118 (I_o = 124 pmol, R = 86%), a second at αGlu172 (I_o = 73 pmol, R = 58%), a third at αLys179 (I_o = 81 pmol, R = 88%), and a fourth at αVal405 (I_o = 45 pmol, R = 74%). For fraction **41**, 4.4×10^4 cpm was loaded on the filter. After 28 cycles, 17% of the radioactivity (7500 cpm) remained on the filter and 18% (7,800 cpm) was recovered. Five peptides from the nAChR α-subunit were detected: the first primary sequence began at αTrp118 (I_o = 50 pmol, R = 92%), a second at αLys145 (I_o = 41 pmol, R = 79%), a third at αGlu172 (I_o = 39 pmol, R = 83%), a fourth at αLys179 (I_o = 70 pmol, R = 88%), and a fifth at αPro309 (I_o = 55 pmol, R = 87%). For fraction **42**, 3.5×10^4 cpm was loaded on the filter. After 28 cycles, 14% of the radioactivity (4800 cpm) remained on the filter and 16% (5800 cpm) was recovered. Four peptides from the nAChR α-subunit were detected: the first primary sequence began at αGlu172 (I_o = 28 pmol, R = 89%), a second at αLys179 (I_o = 63 pmol, R = 87%), a third at αPro309 (I_o = 116 pmol, R = 85%), and a fourth at αLys330 (I_o = 35 pmol, R = 91%). For fraction **43**, 2.4×10^4 cpm was loaded on the filter. After 28 cycles, 14% of the radioactivity (3300 cpm) remained on the filter and 15% (3600 cpm) was recovered. Three peptides from the nAChR α-subunit were detected: the first primary sequence began at αGlu172 (I_o = 24 pmol, R = 93%), a second at αLys179 (I_o = 57 pmol, R = 87%), and a third at αLys330 (I_o = 75 pmol, R = 86%). The mass release curves were only represented for the two unique common peptides to fractions **40**, **41**, **42**, and **43** extending from αGlu172 and αLys179. Their primary sequences are shown on top of the figures. Labeled residues are indicated in bold underlined characters.

ization of the labeled residues. Our probe showed also good labeling yields and is potentially dual, as the aryldiazonium moiety can be changed easily in an arylazido group, just by working in buffers containing sodium azide (*12*).

The aryldiazonium photoprobe was subsequently coupled to a previously described (*11*) cysteine analogue of *Naja nigricollis* α-neurotoxin, through a cleavable disulfide bond. Moreover, to facilitate the purification of the labeled subunits, we tagged the N-terminus of the toxin with desthiobiotin. Assembly on the same toxin probe of a tag and a cleavable disulfide bond linking the toxin to a radioactive photoprobe allowed us to characterize for the first time the labeled residues of the toxin-binding site on the α subunit of the nAChR.

This tagged photoactivatable toxin labeled the torpedo nicotinic acetylcholine receptor with a 12% overall yield on the α (7.6%), γ (3.2%), and δ (1.2%) subunits, showing a small preference for the α subunit (3.8% on one α subunit at least). This may be due in part to the presence on this subunit of a higher number of aromatic amino acids, which are preferentially targeted by the arylcation formed through irradiation of an

aryldiazonium moiety. Edman degradation of purified CNBr fragments of the α subunit showed that three residues (αTyr190, αTyr198, and αCys192) were labeled. They all belong to the C loop, which wraps the agonists and occludes the binding site. They also belong to the group of residues labeled by another aryldiazonium antagonist named DDF (*31*, *32*). But, in contrast to DDF, no labeling of αTrp149 could be detected, as we did not see any radioactive peak on cycle five when the CNBr fragments of HPLC fraction **41**, containing a sequence beginning at αLys145, were submitted to Edman degradation.

αTyr190, αCys192, and αTyr198 are located at less than 10 Å from the toxin backbone at position 33, as the reactive carbon of the photoprobe is located at about 8.5 Å, at most, from the Cys33 α-carbon. This is about the length of residue Arg33, meaning that the labeled residues are in close contact to Arg33 in the receptor/wild-type toxin complex. Our data corroborate double mutant cycle analysis with another short toxin (NmmI) (*8*), showing the proximity of αTyr190 and αTyr198 to Arg33. Notably, our results, obtained with a short α-neurotoxin, also fit well to the structure of the complex between a long neurotoxin and AChBP (*4*), where the shortest distances between the α-carbon of Arg33 and the side chains of the equivalent residues of αTyr190, αCys192, and αTyr198 on AChBP are close to 4−6 Å. This confirms a similar binding mode for short and long neurotoxins, at least at position 33, where the arginine residue may possibly act as a pivot. In contrast, our results do not agree with the recently proposed model of interaction between the short toxin NTII and the nAChR (*9*) in which the orientation of the toxin would hardly allow the labeling of αTyr190 and αCys192.

In a prospective way, if we suppose that short- and long-chain toxins bind in a similar manner, the AChBP/α-cobratoxin complex structure may also give a possible explanation of the different labeling yields between the γ and δ subunits, as (i) the common Trp55 would be too far away (>11 Å) to be labeled and (ii) γTyr116, which would be located as close to Arg33 as the three labeled α residues, is replaced by the nonaromatic δThr119, which is not a preferential target of aryldiazonium photoprobes. However, these conclusions need further work in the characterization of the γ- and δ-subunit labeled residues.

The novel cleavable photoprobe described in this paper may be of great use for photocrosslinking/label transfer experiments between macromolecules and peptidic ligands. The literature shows no general rule to choose the best photosensitive moiety, when a photoaffinity labeling experiment on a given ligand−receptor complex is planned. Therefore, two and potentially three radioactive label transfer probes with various reactivity are welcome in the "photocrosslinking/label transfer kit".

ACKNOWLEDGMENT

We thank Dr. Tzartos for a generous gift of monoclonal antibodies directed against the nAChR subunits and Gilles Mourier for technical support and fruitful discussion on peptide synthesis.

NOTE ADDED AFTER ASAP PUBLICATION

This manuscript was released ASAP on October 19, 2006 with missing information in the list of authors. The correct version was posted on October 25, 2006.

LITERATURE CITED

(1) Celie, P. H., van Rossum-Fikkert, S. E., van Dijk, W. J., Brejc, K., Smit, A. B., and Sixma, T. K. (2004) Nicotine and carbamylcholine binding to nicotinic acetylcholine receptors as studied in AChBP crystal structures. *Neuron 41*, 907−914.

(2) Hansen, S. B., Sulzenbacher, G., Huxford, T., Marchot, P., Taylor, P., and Bourne, Y. (2005) Structures of Aplysia AChBP complexes with nicotinic agonists and antagonists reveal distinctive binding interfaces and conformations. *EMBO J. 24*, 3635−3646.

(3) Celie, P. H., Kasheverov, I. E., Mordvintsev, D. Y., Hogg, R. C., van Nierop, P., van Elk, R., van Rossum-Fikkert, S. E., Zhmak, M. N., Bertrand, D., Tsetlin, V., Sixma, T. K., and Smit, A. B. (2005) Crystal structure of nicotinic acetylcholine receptor homolog AChBP in complex with an alpha-conotoxin PnIA variant. *Nat. Struct. Mol. Biol. 12*, 582−588.

(4) Bourne, Y., Talley, T. T., Hansen, S. B., Taylor, P., and Marchot, P. (2005) Crystal structure of a Cbtx-AChBP complex reveals essential interactions between snake alpha-neurotoxins and nicotinic receptors. *EMBO J. 24*, 1512−1522.

(5) Smit, A. B., Syed, N. I., Schaap, D., van Minnen, J., Klumperman, J., Kits, K. S., Lodder, H., van der Schors, R. C., van Elk, R., Sorgedrager, B., Brejc, K., Sixma, T. K., and Geraerts, W. P. M. (2001) A glia-derived acetylcholine-binding protein that modulates synaptic transmission. *Nature (London) 411*, 261−268.

(6) Teixeira-Clerc, F., Ménez, A., and Kessler, P. (2002) How do short neurotoxins bind to a muscular-type nicotinic acetylcholine receptor? *J. Biol. Chem. 277*, 25741−25747.

(7) Ackermann, E. J., Ang, E. T. H., Kanter, J. R., Tsigelny, I., and Taylor, P. (1998) Identification of pairwise interactions in the α-neurotoxin-nicotinic acetylcholine receptor complex through double mutant cycles. *J. Biol. Chem. 273*, 10958−10964.

(8) Malany, S., Osaka, H., Sine, S. M., and Taylor, P. (2000) Orientation of alpha-neurotoxin at the subunit interfaces of the nicotinic acetylcholine receptor. *Biochemistry 39*, 15388−15398.

(9) Mordvintsev, D. Y., Polyak, Y. L., Levtsova, O. V., Tourleigh, Y. V., Kasheverov, I. E., Shaitan, K. V., Utkin, Y. N., and Tsetlin, V. I. (2005) A model for short alpha-neurotoxin bound to nicotinic acetylcholine receptor from *Torpedo californica*: Comparison with long-chain alpha-neurotoxins and alpha-conotoxins. *Comput. Biol. Chem. 29*, 398−411.

(10) Machold, J., Utkin, Y., Kirsch, D., Kaufmann, R., Tsetlin, V., and Hucho, F. (1995) Photolabeling reveals the proximity of the α-neurotoxin binding site to the M2 helix of the ion channel in the nicotinic acetylcholine receptor. *Proc. Natl. Acad. Sci. U.S.A. 92*, 7282−7286.

(11) Michalet, S., Teixeira, F., Gilquin, B., Mourier, G., Servent, D., Drevet, P., Binder, P., Tzartos, S., Ménez, A., and Kessler, P. (2000) Relative spatial position of a snake neurotoxin and the reduced disulfide bond alpha (Cys192-Cys193) at the alpha gamma interface of the nicotinic acetylcholine receptor. *J. Biol. Chem. 275*, 25608−25615.

(12) Teixeira-Clerc, F., Michalet, S., Menez, A., and Kessler, P. (2003) A cysteine-linkable, short cleavable photoprobe with dual functionality to explore protein−protein interfaces. *Bioconjugate Chem. 14*, 554−562.

(13) Saitoh, T., Oswald, R., Wennogle, L. D., and Changeux, J. P. (1980) Conditions for the selective labelling of the 66 000 Dalton chain of the acetylcholine receptor by the covalent non-competitive blocker 5-azido-[^{3}H]-Trimethisoquin. *FEBS Lett. 116*, 30−36.

(14) Grutter, T., Ehret-Sabatier, L., Kotzyba-Hibert, F., and Goeldner, M. (2000) Photoaffinity labeling of *Torpedo* nicotinic receptor with the agonist [^{3}H]DCTA: identification of amino acid residues which contribute to the binding of the ester moiety of acetylcholine. *Biochemistry 39*, 3034−3043.

(15) Kieffer, B., Goeldner, M., and Hirth, C. (1981) Aryldiazonium salts as photo-affinity labelling reagents for proteins. *J. Chem. Soc., Chem. Comm.* 398−399.

(16) Pillet, L., Trémeau, O., Ducancel, F., Drevet, P., Zinn Justin, S., Pinkasfeld, S., Boulain, J.-C., and Ménez, A. (1993) Genetic engineering of snake toxins. Role of invariant residues in the structural and functional properties of a curaremimetic toxin, as probed by site-directed mutagenesis. *J. Biol. Chem. 268*, 909−916.

(17) Hirsch, J. D., Eslamizar, L., Filanoski, B. J., Malekzadeh, N., Haugland, R. P., and Beechem, J. M. (2002) Easily reversible desthiobiotin binding to streptavidin, avidin, and other biotin-binding proteins: uses for protein labeling, detection, and isolation. *Anal. Biochem. 308*, 343−357.

(18) Brocklehurst, K., and Little, G. (1972) Reactivities of the various protonic states in the reactions of papain and of L-cysteine with 2,2′- and with 4,4′-dipyridyl disulphide: evidence for nucleophilic reactivity in the un-ionized thiol group of the cysteine-25 residue of papain

occasioned by its interaction with the histidine-159-asparagine-175 hydrogen-bonded system. *Biochem. J. 128*, 471−474.
(19) Unwin, N. (2005) Refined structure of the nicotinic acetylcholine receptor at 4A resolution. *J. Mol. Biol. 346*, 967−989.
(20) Hucho, F. (1979) Photoaffinity derivatives of α-*Naja naja siamensis* toxin. *FEBS Lett. 103*, 27−32.
(21) Witzemann, V., Muchmore, D., and Raftery, M. A. (1979) Affinity-directed cross-linking of membrane-bound acetylcholine receptor polypeptides with photolabile α-bungarotoxin derivatives. *Biochemistry 18*, 5511−5518.
(22) Ovchinnikov, Y., Grishin, E., and Tsetlin, V. (1984) Photoactivatable neurotoxins in studying membrane receptors. *Tetrahedron 40*, 521−528.
(23) Chatrenet, B., Trémeau, O., Bontemps, F., Goeldner, M. P., Hirth, C. G., and Ménez, A. (1990) Topography of toxin-acetylcholine receptor complexes by using photoactivatable toxin derivatives. *Proc. Natl. Acad. Sci. U.S.A. 87*, 3378−3382.
(24) Kreienkamp, H. J., Utkin, Y. N., Weise, C., Machold, J., Tsetlin, V. I., and Hucho, F. (1992) Investigation of ligand-binding sites of the acetylcholine receptor using photoactivatable derivatives of neurotoxin II from *Naja naja oxiana*. *Biochemistry 31*, 8239−8244.
(25) Hervé, M., Pillet, L., Humbert, P., Trémeau, O., Ducancel, F., Hirth, C., and Ménez, A. (1992) Role and environment of the conserved Lys27 of snake curaremimetic toxins as probed by chemical modifications, site-directed mutagenesis and photolabelling experiments. *Eur. J. Biochem. 208*, 125−131.
(26) Machold, J., Weise, C., Utkin, Y., Tsetlin, V., and Hucho, F. (1995) The handedness of the subunit arrangement of the nicotinic acetylcholine receptor from *Torpedo californica*. *Eur. J. Biochem. 234*, 427−430.
(27) Machold, J., Weise, C., Utkin, Y. N., Franke, P., Tsetlin, V. I., and Hucho, F. (1995) A new class of photoactivatable and cleavable derivatives of neurotoxin II from *Naja naja oxiana*. Synthesis, characterisation, and application for affinity labelling of the nicotinic acetylcholine receptor from *Torpedo californica*. *Eur. J. Biochem. 228*, 947−954.
(28) Utkin, Y. N., Krivoshein, A. V., Davydov, V. L., Kasheverov, I. E., Franke, P., Maslennikov, I. V., Arseniev, A. S., Hucho, F., and Tsetlin, V. I. (1998) Labeling of *Torpedo californica* nicotinic acetylcholine receptor subunits by cobratoxin derivatives with photoactivatable groups of different chemical nature at Lys23. *Eur. J. Biochem. 253*, 229−235.
(29) Kasheverov, I., Zhmak, M., Chivilyov, E., Saez-Brionez, P., Utkin, Y., Hucho, F., and Tsetlin, V. (1999) Benzophenone-type photoactivatable derivatives of alpha-neurotoxins and alpha-conotoxins in studies on *Torpedo* nicotinic acetylcholine receptor. *J. Recept. Signal Transduction Res. 19*, 559−571.
(30) Guo, L. W., Hajipour, A. R., Gavala, M. L., Arbabian, M., Martemyanov, K. A., Arshavsky, V. Y., and Ruoho, A. E. (2005) Sulfhydryl-reactive, cleavable, and radioiodinatable benzophenone photoprobes for study of protein−protein interaction. *Bioconjugate Chem. 16*, 685−693.
(31) Dennis, M., Giraudat, J., Kotzyba-Hibert, F., Goeldner, M., Hirth, C., Chang, J. Y., Lazure, C., Chrétien, M., and Changeux, J. P. (1988) Amino acids of the *Torpedo marmorata* acetylcholine receptor α-subunit labeled by a photoaffinity ligand for the acetylcholine binding site. *Biochemistry 27*, 2346−2357.
(32) Galzi, J. L., Revah, F., Black, D., Goeldner, M., Hirth, C., and Changeux, J. P. (1990) Identification of a novel amino acid α-tyrosine 93 within the cholinergic ligands-binding sites of the acetylcholine receptor by photoaffinity labeling. *J. Biol. Chem. 265*, 10430−10437.
(33) Zinn Justin, S., Roumestand, C., Gilquin, B., Bontems, F., Ménez, A., and Toma, F. (1992) Three-dimensional solution structure of a curaremimetic toxin from *Naja nigricollis* venom: a proton NMR and molecular modeling study. *Biochemistry 31*, 11335−11347.

BC060175J

Site-Specific Attachment of Polyethylene Glycol-like Oligomers to Proteins and Peptides

Yoann Marsac,† Janina Cramer,† Diana Olschewski, Kirill Alexandrov, and Christian F. W. Becker*

Max-Planck Institute of Molecular Physiology, Department of Physical Biochemistry, Otto-Hahn Str. 11, 44227 Dortmund, Germany. Received July 3, 2006; Revised Manuscript Received October 2, 2006

Modification of proteins with polymers is a viable method to tune protein properties, e.g., to render them more water-soluble by using hydrophilic polymers. We have utilized precision-length, polyethylene glycol-based oligomers carrying a thioester moiety in transthioesterification and native chemical ligation reactions with internal and N-terminal cysteine residues in proteins and peptides. These reactions lead to uniquely modified proteins with an increased solubility in chaotrope- and detergent-free aqueous systems. Polymer modification of internal cysteines is fully reversible and allows generation of stable protein−polymer conjugates for enzymatic manipulations as demonstrated by proteolytic cleavage of a protein construct that was only soluble in buffers incompatible with protease activity before polymer modification. The permanent polymer modification of a Rab protein at its N-terminal cysteine produced a fully active Rab variant that was efficiently prenylated. Thus, PEGylation of prenylated proteins might be a viable route to increase water solubility of such proteins in order to carry out experiments in detergent- and lipid-free systems.

INTRODUCTION

Polymer modifications of proteins have become a major focus of protein drug development (*1*, *2*). The attachment of polymers such as polyethylene glycol (PEG) to side chain groups of certain amino acids improves the behavior of proteins with regard to their biomedical properties. These modifications lead to an increase in solubility, which enhances bioavailability, help to resist proteolytic degradation, reduce immunogenicity, and prolong plasma circulation times (*3*, *4*). However, PEG modifications are desirable not only for certain medicinal applications for the above-mentioned reasons, but also for functional analysis of proteins in biophysical or biochemical studies. Site-selective and reversible attachment of polymers leads to proteins with new properties with regard to their aggregation propensity or their propensity to absorb to glass or plastic surfaces. Proteins modified with polymers could help to overcome experimental limitations when proteins are needed at specific concentrations well beyond their solubility in aqueous systems. This point is of special interest whenever integral membrane proteins or membrane-attached proteins are used in solution-based assays that do not allow the use of detergents or liposomes (*5*). Furthermore, such solubilizing modifications can help to process peptides and proteins in proteolytic digests and other enzyme-based assays that otherwise cannot be used due to their limited solubility in chaotrope-free buffers.

Additionally, the introduction of such polymers increases the hydrodynamic radius of proteins and might facilitate separation from smaller impurities by dialysis or ultrafiltration (*6*). Biophysical probes can be attached to proteins by exploiting the polymers as inert linker molecules that can be uniquely modified with diverse functionalities.

A variety of methods for the amino acid specific modification of proteins and peptides has been suggested that allow the irreversible as well as the reversible modification of specific residues such as lysine and cysteine by using chemistry that leads to secondary amines, thioethers, or disulfides (*7*−*9*). Recently, a procedure was introduced that leads to site-specific PEGylation of native disulfide bonds by bisalkylation of the two thiol groups involved (*10*). However, thioester chemistry has experienced only very limited use for side chain modification of proteins, even though this type of chemistry is heavily used in protein synthesis via native chemical and expressed protein ligation, as well as by nature for posttranslational attachment of lipid groups (*11*, *12*). During NCL and EPL, a nucleophilic attack of the thiol group of a cysteine residue with an unblocked amino group leads to an initial transthioesterification of a thioester-containing compound, which can be a small molecule or a large protein. Upon formation of this intermediate, the amino group is in close proximity to the thioester and can easily undergo a rearrangement to form an amide bond via a 5-membered transition state (Scheme 1B). This reaction is driven by the final S-to-N acyl shift that leads to the formation of an amide bond between the two reaction partners and can be exploited to attach non-natural groups such as PEG-based polymers to the N- and C-termini of proteins via a stable amide bond. Generally, an excess of exogenous thiols such as thiophenol, mercaptoethanesulfonic acid (Mesna), or, as recently suggested, 4-mercaptophenyl acetic acid MPAA (*13*) has to be added to the reaction mixture in order to form reactive thioester species, keep the cysteine residues in a reduced state, and reverse transthioesterification with internal cysteine residues (Scheme 1A). Such transthioesterification reactions lead to the attachment of thioester species to unblocked thiol groups of internal cysteines in peptides and proteins and have been observed for reactions with small molecule thioesters (*14*, *15*). Therefore, thioester bond formation with thiol groups of cysteine side chains can potentially be used to selectively modify peptides and proteins. These thioester bonds are stable at physiological and acidic pH and have been utilized in chemical protein synthesis to successfully link peptide segments (*16*, *17*).

* Correspondence should be addressed to: Christian F.W. Becker, Max-Planck Institute of Molecular Physiology, 44227 Dortmund, Germany. Phone: +49 231 1332312, Fax: +49 231 1332399, Email: christian.becker@mpi-dortmund.mpg.de.

† These authors contributed equally to this work.

10.1021/bc0601931 CCC: $33.50 © 2006 American Chemical Society
Published on Web 11/01/2006

Scheme 1. Reactions of Polymer Thioesters with Cysteine Residues in Peptides and Proteins[a]

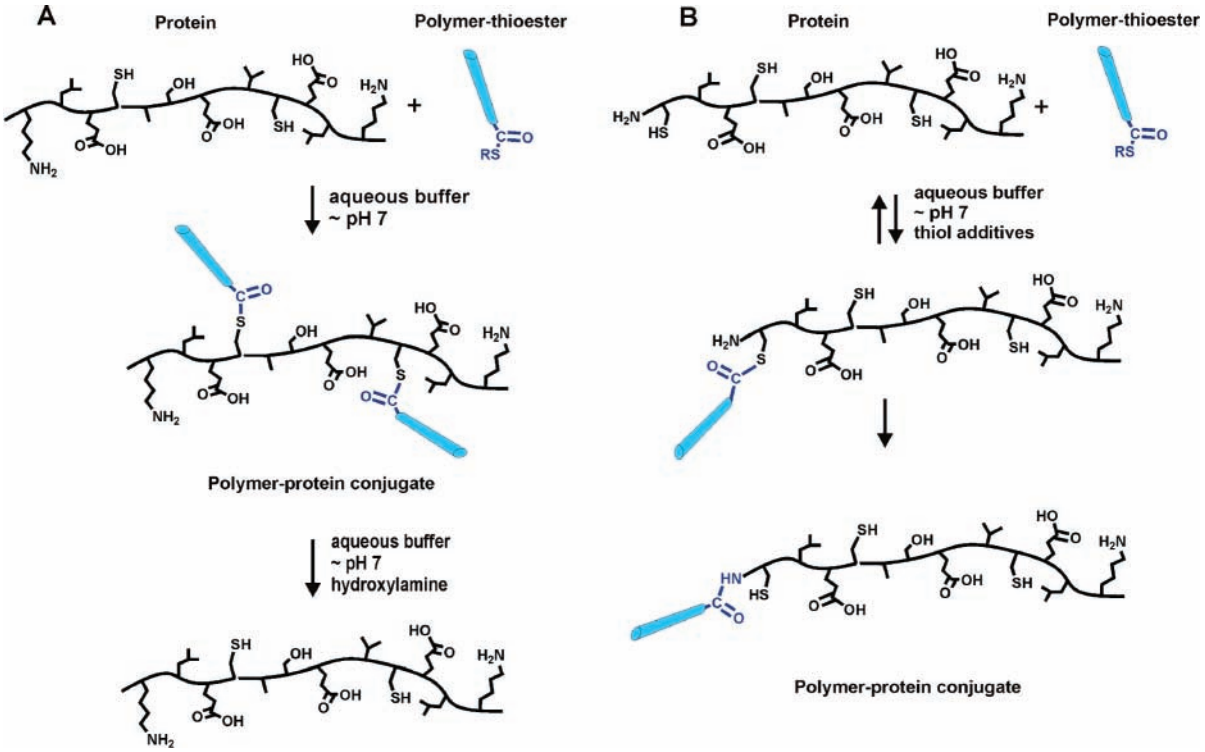

[a] (A) Reaction with internal thiol groups to form reversibly polymer-modified polypeptides. Polymer modifications can be removed by treatment with a strong nucleophile or at pH > 8.5. (B) Native chemical ligation reaction of polymer thioester with an N-terminal cysteine residue to give an irreversibly polymer modified protein/peptide.

EXPERIMENTAL PROCEDURES

Materials. *tert*-Butyloxycarbonyl (Boc)-protected amino acids, 2-(1*H*-benzotriazol-1-yl)-1,1,3,3-tetramethyluronium hexafluorophosphate (HBTU), and the Boc-amino acyl-OCH_2-phenylacetamidomethyl resins were purchased from Novabiochem (Schwalbach). Trifluoroacetic acid was from Roth (Karlsruhe). Hydrogen fluoride was obtained from Merck (Darmstadt). All other chemicals were obtained from Sigma-Aldrich at the highest purity available.

Peptide Synthesis. Solid-phase peptide synthesis was performed on a custom-modified 433A peptide synthesizer from Applied Biosystems, using Boc-chemistry, *in situ* neutralization, and HBTU activation protocols (*18*). The peptides were deprotected and simultaneously cleaved from the resin using anhydrous HF. Subsequently, they were precipitated with ether, and the crude products were dissolved in 50% aqueous acetonitrile (0.1% TFA) and lyophilized. The peptide segments were purified by RP-HPLC on a C4-column from Vydac (Hesperia, CA) using linear gradients of solution B (acetonitrile with 0.08% trifluoroacetic acid) in solution A (water with 0.1% trifluoroacetic acid). The elution of the peptide was monitored at 214 nm.

Polymer Synthesis. Polyethylene glycol polyamide oligomers (PPOs) were synthesized on SASRIN resin (Bachem) starting with the coupling of succinic anhydride (10 equiv) in the presence of *N*,*N*-dimethyl-4-aminopyridine (10 equiv) for 30 min. The resin was washed with dimethylformamide (DMF) and treated with a 0.5 M of 1,1′-carbodiimidazole in DMF for 30 min and then washed with DMF. (4,7,10)-Trioxa-1,13-tridecanediamine (TTD) was activated with a 0.5 M 1-hydroxybenzotriazole (HOBT) solution in DMF and added to the resin for 30 min. After washing the resin with DMF, another succinic anhydride unit was added to the resin activated with 0.5 M HOBT solution and diisopropylethylamine (DIEA) for 30 min. Further extension of the oligomer chain was achieved as described. For synthesis of the thioester, after drying the resin, *tert*-butyl mercaptoacetate (4 equiv) and 1,3-diisopropylcarbodiimide (4 equiv) were combined in DMF in a solid-phase vessel. After one night, the PPO−resin was washed by DMF (1 min) and CH_2Cl_2 (1 min) and then dried in vacuo for cleavage. Different conditions of cleavage reaction were attempted: For R = H, a 95/5 TFA/H_2O mixture was used for 15 min to deprotect the *tert*-butyl group and cleave the thioPEG from the resin. For R = *tert*-butyl, the CH_2Cl_2/TFA 97/3 mixture used for 20−30 min led to efficient cleavage of the PPO from the resin without deprotection of *tert*-butyl.

HPLC and Mass Spectrometry. HPLC analysis of PPOs and peptides was performed on an analytical RP-C4-column (Vydac) at a flow rate of 1 mL/min over 30 min with a gradient from 5% to 65% (v/v) buffer B (CH_3CN + 0.08% TFA) in buffer A (H_2O + 0.1% TFA). Peak areas were used to determine peptide concentrations in solution. Polyethylene glycol polyamide oligomer and peptide/protein masses were determined by electrospray ionization mass spectrometry on an LCQ Advantage Max (Finnigan) operating in positive ion mode. The molecular masses were deconvoluted from the charged ion spectra.

PPO Modifications. *N-Terminal Modification.* Peptides and proteins with N-terminal cysteines were dissolved in HEPES or NaPi buffered solutions (pH ∼7.5) at concentrations of 100 μM up to 1 mM and a solution containing 15 equiv TCEP (tris-(2-carboxyethyl)phosphine hydrochloride), 80 equiv Mesna (sodium 2-mercaptoethanesulfonate), and 10 equiv PPO−thioester was added. The reaction mixture was gently agitated overnight at room temperature.

Modification of Internal Cysteine Side Chains. Peptides and proteins with internal cysteines were dissolved in HEPES or NaPi buffered solutions (pH ∼7.5) at concentrations of 30 μM up to 1 mM. 15 equiv of TCEP and a 5−10-fold excess of PPO thioester over every sulfhydryl group was added. The reaction

Scheme 2. Synthesis Scheme and Structure of Precision-Length Polymer Thioesters Used in Peptide and Protein Modification Reactions

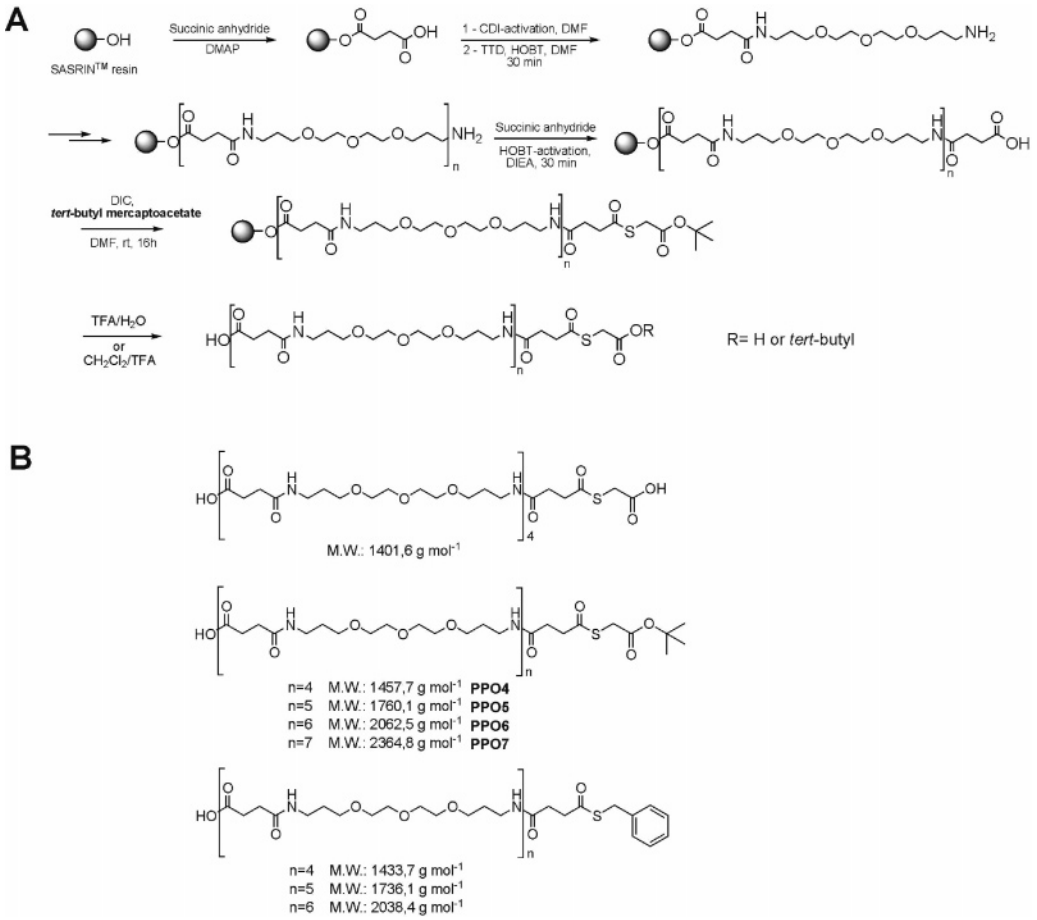

mixture was incubated overnight at room temperature. Excess PPO_n was removed either by RP-HPLC for peptides or by dialysis using a 10 kDa molecular weight cutoff. If necessary, buffers containing 6 M guanidine were used to solubilize peptides and proteins.

PPO Removal with BME and Hydroxylamine. A 50 mM hydroxylamine solution (NaPi buffered at pH ~7.5) was added to the PPO-modified protein or peptide to adjust a final hydroxylamine concentration of 12.5 mM. The reaction mixture was gently shaken and incubated at room temperature. Complete conversion was achieved between 1 and 5 h, depending on the protein/peptide used. Similar results were obtained by treating PPO-modified protein or peptide with 50 equiv of BME for 1 to 4 h at room temperature and gentle shaking.

Protein Expression. The coding sequences for Tev_Ras_Mxe (H-Ras, aa 51−180 with an N-terminal His-tag and a Tev site) and Tev_PrP (mouse Prion protein, aa 134−232 with an N-terminal His-tag and a Tev site), respectively, were cloned into the pTXB3-vector (New England Biolabs) and expressed in *E. coli* BL21(DE3) RIL as fusion proteins with the *GyrA* intein from *Mycobacterium xenopis* and a chitin-binding domain.

Protein expression was induced with IPTG. The cells were harvested by centrifugation and lysed in a M110S Microfluidizer (Microfluids Corporation, Newton). Cell debris and insoluble proteins were removed by centrifugation, and the supernatant was loaded onto Ni-NTA superflow matrix (Qiagen) for purification. Tev_PrP and Tev_Ras_Mxe were deposited in inclusion bodies during expression and had to be dissolved in 6 M guanidine prior to Ni-NTA purification.

Expression Rab6. Expression and purification of recombinant Rab6 containing an N-terminal cysteine residue instead of methionine was described elsewhere (*14*).

TEV Digest. PPO_7-modified His_8TEV_PrP134−232 was dialyzed into a buffer consisting of 1 M urea, 50 mM NaPi, 0.5 mM EDTA, and 1 mM TCEP. Proteolysis was achieved with an addition of $^1/_{60}$ equiv of TEV protease for 16 h at RT. Removal of TEV protease and the cleaved-off N-terminal protein segment was achieved by Ni-NTA purification.

Prenylation Assay. Time course of fluorescence change upon prenylation catalyzed by RabGGTase (0.02 μM) on Rab6:REP-1 complex (6 μM) in the presence of NBD−FPP (4 μM) at 37 °C was monitored by a change in fluorescence excited at 479 nm and recorded at 520 nm. Assay conditions: 50 mM HEPES, pH 7.2, 50 mM NaCl, 5 mM DTE, 2 mM $MgCl_2$, 10 μM GDP.

RESULTS AND DISCUSSION

Here, we report the use of polyethylene glycol-like oligomers equipped with a thioester moiety in native chemical ligation reactions with N-terminal cysteine residues as well as in transthioesterification reactions with cysteine side chains within proteins to generate stable protein−thioester species (Scheme 1).

The polyethylene glycol polyamide oligomers (PPO) were synthesized by stepwise solid-phase synthesis using (4,7,10)-trioxa-1,13-tridecanediamine (TTD) and succinic anhydride as building blocks. Discrete oligomers and polymers composed of these building blocks have been used as inert peptide linkers and solubilizing modifications as well as enhancers of pharmacokinetic properties of protein pharmaceuticals (6, *19*, *20*). The obtained PPOs were furnished with a variety of thioesters and varied in length from 3 to 7 TTD subunits and therefore from 1154 to 2365 Da in molecular weight (Scheme 2). All of them were produced in high yields (50−75%) and with excellent

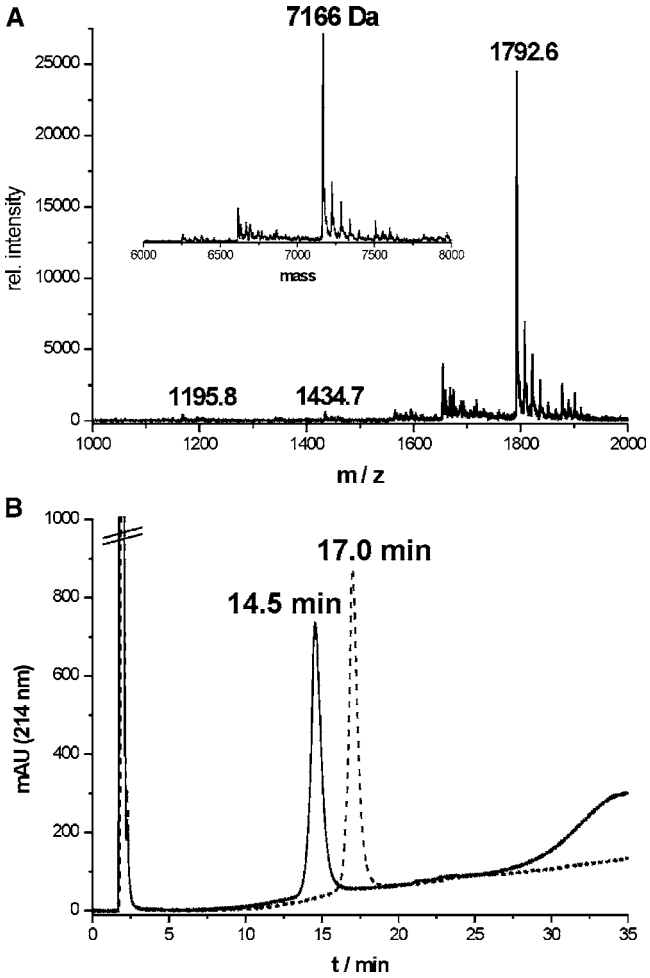

Figure 1. (A) Electrospray-MS of PPO_7-modified RBD96−131 (calculated molecular mass: 7165 Da). (B) HPLC chromatograms of RBD96−131 (dashed line) and PPO_7-modified RBD96−131 (solid line) using a RP-C4 analytical column and a gradient of 5% to 65% acetonitrile (+0.08% TFA) in water (+0.1% TFA).

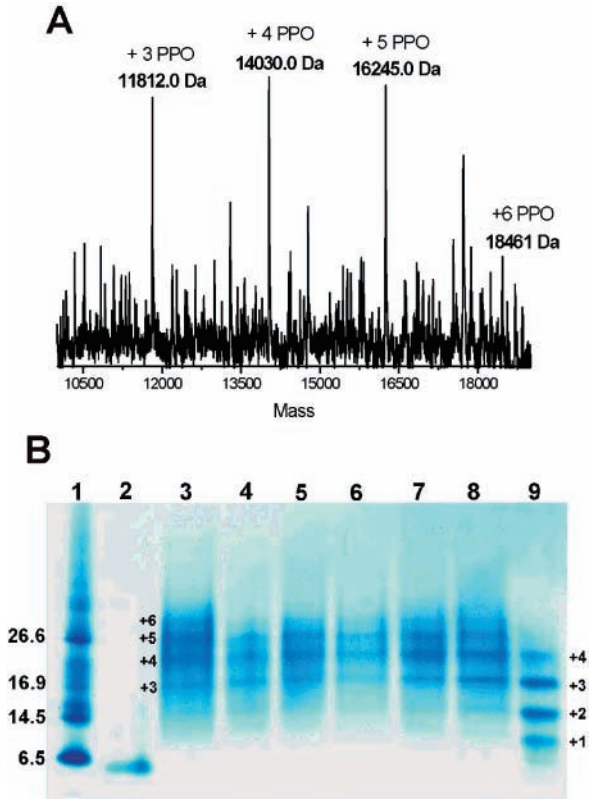

Figure 2. Polymer modification of a 45 amino acid human β-defensin3 (hBD-3) peptide that contains 6 internal cysteine residues for polymer modification. (A) ESI-MS of the polymer-modified hBD-3 indicates modification with 3, 4, 5, and 6 PPO_7 units, respectively. (B) Stability of the PPO-modified hBD-3. Coomassie-stained SDS-PAGE of PPO_7-modified hBD-3; lane 1, polypeptide marker; lane 2, hBD-3; lane 3; PPO_7-modified hBD-3 showing a mixture of conjugates containing $(PEG_7)_n$−peptide species with $n = 2$, 3, 4, 5, and 6; lane 4, PPO_7-modified hBD-3 at pH 4.0 after 2 days at 22 °C; lane 5, PPO_7-modified hBD-3 at pH 5.0 after 2 days at 22 °C; lane 6, PPO_7-modified hBD-3 at pH 6.0 after 2 days at 22 °C; lane 7, PPO_7-modified hBD-3 at pH 7.0 after 2 days at 22 °C; lane 8, PPO_7-modified h-BD3 at pH 8.0 after 2 days at 22 °C; lane 9, PPO_7-modified h-BD3 at pH 9.0 after 2 days at 22 °C.

purity of ∼92−95%. Formation of mercaptoacetate, *tert*-butyl-mercaptoacetate, and benzylmercaptane thioesters was achieved on the solid support by treatment with mercaptoacetate, *tert*-butyl mercaptoacetate, or benzylmercaptane, respectively, in the presence of DIC (*21*). Closely related polyethylene glycol (PEG)−thioesters are commercially available and could, in principle, be used in a similar way as described below. However, since these commercially available PEG−thioesters are polymerization products and therefore not monodisperse, characterization of the resulting protein−polymer conjugates would be more difficult.

Modified Peptides. The obtained PPO thioesters were initially tested in native chemical ligation reactions with a N-terminal cysteine containing synthetic peptide mimicking the last 36 amino acids of the Ras-binding domain (RBD) of cRaf1 kinase (*22*, *23*). The reactions were highly specific and produced the peptide carrying one polymer modification at its N-terminus (Figure 1A). A typical peptide−oligomer conjugate consisting of the RBD peptide and PPO_7 exhibited a 10-fold increase in solubility in chaotrope-free aqueous systems (0.5 mg/mL compared to 0.05 mg/mL) and a distinct change toward a lower retention time on a RP-C4 column (Figure 1B). This indicates the increase in hydrophilicity induced by the attached PPO_7.

To demonstrate that sulfhydryl groups of internal cysteine residues are accessible to transthioesterification reactions, we chose a 45 amino acid long fully reduced synthetic human β-defensin (hBD-3, 45 amino acids) (*24*) that contains 6 internal cysteine residues. After 12 h incubation at room temperature of PPO_7 with hBD-3, a mixture of different PPO_7-modified species was obtained that exhibits an ambivalent solubility behavior with high water solubility as well as a dramatically increased solubility in organic solvents such as ethanol and tetrahydrofurane (Figure 2). The hBD-3−PPO_7 conjugates were used to study the stability of the thioester linkage between the polymers and the peptide. After up to 24 h at RT and at pH values ranging from 4.0 up to 8.0, no significant thioester hydrolysis was found. However, at a pH above 8.5, a shift to hBD-3 species with less PPO_7 moieties attached was observed, which leads to the conclusion that thioester hydrolysis above pH 8 is accelerated (Figure 2B). In the presence of low concentrations of thiols such as Mesna and DTT (0.5 to 2 mM) that, in principle, can undergo transthioesterification reactions with the polymer−protein thioester conjugate, only very slow removal of polymer modifications was observed. Efficient removal was achieved by addition of strong nucleophiles such as hydroxylamine that lead to release of the polymers and produces unmodified peptide after 1 to 5 h at RT. Hydrolysis of the thioester bonds at pH > 8.5 as well as treatment with thiols was slower and led to less homogeneous samples. Since the PPO modifications are stable at conditions commonly used for biochemical and biophysical analysis of proteins but can be easily removed with protein-friendly reagents, this approach for the (transient) PEGylation of proteins could prove to be a highly

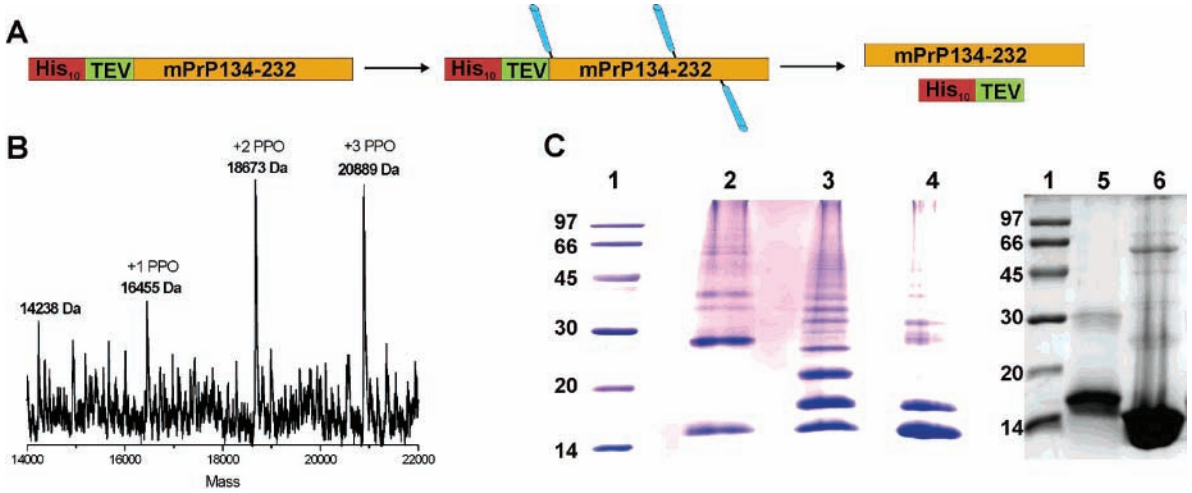

Figure 3. Characterization of PPO-modified Tev_PrP. (A) Polymer modification reaction followed by protease cleavage and removal of polymers. (B) Deconvoluted mass spectrum of PEG-modified TEV_PrP (M = 14 235 Da, 3 Cys) after 16 h of reaction with 5 equiv/Cys of PPO_7 thioester in denaturating buffer (6 M GdmCl, 50 mM Tris pH 8.0). (C) Coomassie-stained SDS-PAGE of TEV_PrP PEGylation reaction; lane 1, protein marker; lane 2, TEV_PrP; lane 3, crude PEGylation showing a mixture of conjugates containing $(PEG_7)_n$−protein species with n = 0, 1, 2, and 3; lane 4, incubation of PPO_7-modified Tev_PrP diluted 10-fold with 50 mM hydroxylamine in 6 M GdmCl, 100 mM sodium phosphate, pH 7.2 for 2 h; lane 5, TEV_PrP; lane 6: PrP134−232 after treatment with TEV protease.

valuable tool for purification and analysis of otherwise insoluble proteins. It should be noted that the different polymer thioester species exhibited a marked difference in reactivity with the *tert*-butylmercaptoacetate thioester giving the most efficient labeling yields when compared to the mercaptoacetate and benzylmercaptane thioester polymers. This behavior is difficult to explain but might be due to favorable electronic and steric conditions of the *tert*-butylmercaptoacetate thioester, which render this variant more reactive.

Modified Proteins. As a first application, we chose a segment of the mouse Prion protein comprising residues 134−232 with an N-terminal octa-histidine tag and a TEV protease cleavage site that in our experience was difficult to solubilize and handle (Figure 3) (*25*, *26*). This protein construct contains three cysteine residues that are available for reaction with thioester-tagged polymers. The transthioesterification reaction was carried out under denaturing conditions by using a 5-fold excess of polymer over every cysteine residue in the protein and yielded polymer-modified protein (Figure 3A). These modifications could be removed by a brief treatment with hydroxylamine (1 h at RT). The mixture of Tev_PrP modified with 1, 2, or 3 PEGs respectively was easily transferred into buffer conditions (1 M urea at pH 8) that allowed proteolytic removal of the N-terminal His-tag and protease recognition site with excellent yields. In contrast to this behavior, the non-polymer-modified counterpart could only be solubilized at high chaotrope concentrations (6 M Gdn or 8 M urea), which prevents enzymatic processing of the target protein. A brief treatment (1 h at RT) with hydroxylamine gave the desired PrP134−232 with an overall yield of 60% (Figure 3B).

Similar modification experiments were performed with a Tev_Ras51−180_GyrA construct with an N-terminal hexahistidine tag, a TEV-protease site, and a C-terminal fusion to the GyrA intein of *Mycobacterium xenopi* (*27*, *28*). This protein contains 7 internal cysteines and was modified with PPO_7 using similar conditions as described above (data not shown). The resulting protein−polymer conjugate could be transferred into low chaotrope buffer as well, even though it did not solubilize as efficiently as the PrP construct. However, modification of proteins containing multiple internal cysteine residues appears to be incomplete in most cases. This problem cannot be easily overcome by increasing the amount of PPO−thioester and might be related to secondary structure effects and/or formation of disulfide bonds under the reaction conditions used. The addition of phosphine-based reducing agents during the modification reaction might help to overcome this problem, as well as the use of strongly denaturing conditions that could be induced by heating of the reaction mixture or addition of denaturing detergents.

The procedure described here establishes access to transiently polymer modified proteins that are, prior to polymer modification, insoluble in chaotrope-free buffers. We demonstrate that the solubilized PPO−protein conjugates can be processed by specific proteases. Furthermore, removal of the polymer modifications is efficient and provides an unaltered polypeptide chain that could again form essential disulfide bonds during oxidative refolding.

Modified Rab Protein. Rab proteins are central regulators of vesicular transport and are involved in vesicular budding, targeting, and fusion (*29*). These proteins are attached to their resident membranes by virtue of C-terminal geranylgeranyl group(s). This modification is attached posttranslationally to one or two C-terminal cysteine residues by Rab geranylgeranyl transferase (RabGGTase) (*30*). RabGGTase is a multimeric enzyme consisting of catalytic α/β heterodimer and an accessory factor termed Rab escort protein (REP). REP functions as a molecular chaperone that delivers newly synthesized Rab proteins to the catalytic α/β heterodimer and then upon catalysis delivers the prenylated protein to the target membrane. Central to the function of REP protein is its ability to maintain in solution otherwise insoluble lipidated RabGTPases (*31*). In order to study the interaction of Rab GTPases and other prenylated proteins with their interaction partners and membranes, it would be very desirable to obtain them soluble in prenylated form without the native chaperones attached to them. We surmise that this could be achieved by site-selective PEGylation. This approach would provide a protein−PPO conjugate with a well-defined molecular structure and a potentially increased solubility in water.

Initial attempts to modify Rab proteins with commercially available PEGs functionalized with maleimide groups did not produce any site-specifically modified proteins and always interfered with subsequent prenylation assays, since sulfhydryl groups are nonspecifically modified by this reaction and, in particular, the C-terminal cysteine residues were no longer available for prenyl transfer. In order to circumvent this problem, we applied the above-described procedure that leads to reversible

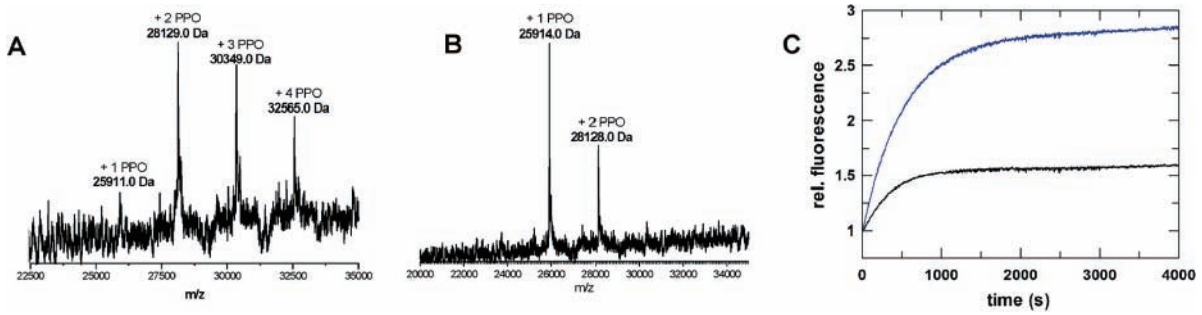

Figure 4. PPO_7 modification of Rab6 and its use in a prenylation assay. (A) Deconvoluted ESI-MS of PPO_7-modified Rab6 prior to hydroxylamine treatment. (B) Deconvoluted ESI-MS of PPO_7-modified Rab6 after hydroxylamine treatment (1 h at RT). (C) Kinetics of prenylation of Rab6 (black) and PPO_7-modified Rab6 (blue) with NBD-labeled farnesylpyrophosphate (NBD-Fpp) in the presence of RabGGTase and Rep1.

PPO modification of internal cysteine residues and nonreversible PPO attachment to N-terminal cysteines.

Rab6 is a well-studied Rab GTPase involved in control of vesicular trafficking from early endosomes to the trans-Golgi network, through the Golgi apparatus, and from the Golgi to the endoplasmatic reticulum, and appears to be involved in a complex network of protein−protein interactions (*32*). We used its recombinant variant that contains 3 cysteine residues with 1 positioned at the N-terminus and 2 within the last 3 C-terminal amino acids (*14*). The protein was treated with 10 equiv of PPO_7 under conditions that kept all cysteines in a reduced state and in the absence of any additional thiol. After 16 h incubation at 4 °C, we observed a complete conversion Rab6 to product carrying 2, 3, and 4 PPO_7 moieties (Figure 4A). The observed polymer modification pattern was stable for several hours, and the protein could be stored for up to 3 days at 4 °C without detectable changes. However, incubation of the PPO_7-modified Rab6 with β-mercaptoethanol at pH 8.0 or hydroxylamine for 1 h at 4 °C efficiently removed the PPO_7 moieties from the C-terminal cysteine residues. Following this treatment, the major fraction of Rab6 contained 1 PPO_7 unit attached to its N-terminus via an amide bond. The other PPO_7 units, bound to the protein via a thioester bond, were removed by transthioesterification with BME or by nucleophilic attack of the strong nucleophile hydroxylamine (Figure 4B). A small fraction of Rab6 still carried a second PPO_7 unit, but subsequent prenylation experiments demonstrated that this modification did not interfere with prenyl transfer onto the C-terminal cysteine residues of Rab6.

In vitro prenylation assays were carried out in the presence of a fluorescently labeled (NBD) farnesyl pyrophosphate analog as the limiting substrate for the prenyl transfer reaction and with PPO_7-modified Rab6 as well as with unmodified Rab6 (*33*). In both cases, isoprenoid transfer was observed, as evidenced by an increase of NBD fluorescence over time. Similar rates were observed for PPO_7-modified Rab6 and unmodified Rab6, but a large increase in overall fluorescence intensity (amplitude) was found for PPO_7-modified Rab6 (Figure 4C). This effect could be explained either by a change in the NBD environment in prenylated, PPO_7-modified Rab6 when compared to the prenylated wild-type protein or by release of the prenylated, PPO_7-modified Rab6 from the ternary complex with RabGGTase and REP-1 due to an increased solubility of the prenylation product. However, further evidence is needed to confirm either one of these two explanations.

CONCLUSIONS

Site-selective PEGylation of proteins via amide bond formation and reversible modification by transthioesterification are valuable tools for the production of defined protein−polymer structures that carry a chemically inert solubilization helper. Such conjugates have proven useful in converting peptides and proteins that can only be solubilized under strongly denaturing conditions into protein−polymer conjugates that can be enzymatically processed under rather mild conditions. The solubilizing polymers are easily removed subsequent to any protein manipulation and allow the recovery of desired native protein segments for further studies. Native disulfide bonds in proteins can remain intact during the polymer modification reaction, and such disulfides will not be modified. Reducing conditions can be applied to the polymer−protein conjugates; however, reducing agent carrying a free thiol group led to transthioesterification and, depending on the concentration, to slow or fast polymer removal.

Rab6, N-terminally modified with PPO_7, was fully active in prenylation experiments when compared to wild-type protein.

The high selectivity of the described modification reactions and the resulting well-defined molecular structures in combination with the freedom to introduce a variety of orthogonal reactive groups into the polymers render this approach highly interesting for targeting protein−polymer conjugates to specific cells, surfaces, or nanoparticles.

ACKNOWLEDGMENT

The authors are thankful to Ralf Seidel for providing the expression plasmid of TevRas51-166 and to Jörg Tatzelt for the mPrP gene. We are also grateful to Yoawen Wu for help with the prenylation assay, and we would like to thank Martin Engelhard and Roger Goody for continuous support. This work was funded in part by the VCI (C.F.W.B.), grant DFG AL 484/5-2, and grant I/77 977 of the Volkswagen foundation to K.A.

LITERATURE CITED

(1) Kochendoerfer, G. G. (2005) Site-specific polymer modification of therapeutic proteins. *Curr. Opin. Chem. Biol. 9*, 555−560.

(2) Harris, J. M., and Chess, R. B. (2003) Effect of pegylation on pharmaceuticals. *Nat. Rev. Drug Discovery 2*, 214−221.

(3) Delgado, C., Francis, G. E., and Fisher, D. (1992) The uses and properties of PEG-linked proteins. *Crit. Rev. Ther. Drug Carrier Syst. 9*, 249−304.

(4) Mehvar, R. (2000) Modulation of the pharmacokinetics and pharmacodynamics of proteins by polyethylene glycol conjugation. *J. Pharm. Pharm. Sci. 3*, 125−136.

(5) Becker, C. F. W., Strop, P., Bass, R. B., Hansen, K. C., Locher, K. P., Ren, G., Yeager, M., Rees, D. C., and Kochendoerfer, G. G. (2004) Conversion of a mechanosensitive channel protein from a membrane-embedded to a water-soluble form by covalent modification with amphiphiles. *J. Mol. Biol. 343*, 747−758.

(6) Kochendoerfer, G. G., Chen, S. Y., Mao, F., Cressman, S., Traviglia, S., Shao, H., Hunter, C. L., Low, D. W., Cagle, E. N., Carnevali, M., Gueriguian, V., Keogh, P. J., Porter, H., Stratton, S. M., Wiedeke, M. C., Wilken, J., Tang, J., Levy, J. J., Miranda, L. P., Crnogorac, M. M., Kalbag, S., Botti, P., Schindler-Horvat, J., Savatski, L., Adamson, J. W., Kung, A., Kent, S. B., and Bradburne,

J. A. (2003) Design and chemical synthesis of a homogeneous polymer-modified erythropoiesis protein. *Science 299*, 884−887.
(7) Veronese, F. M., Sacca, B., de Laureto, P. P., Sergi, M., Caliceti, P., Schiavon, O., and Orsolini, P. (2001) New PEGs for peptide and protein modification, suitable for identification of the PEGylation site. *Bioconjugate Chem. 12*, 62−70.
(8) Woghiren, C., Sharma, B., and Stein, S. (1993) Protected thiol polyethylene-glycol - a new activated polymer for reversible protein modification. *Bioconjugate Chem. 4*, 314−318.
(9) Pomroy, N. C., and Deber, C. M. (1999) Conjugation of polyethylene glycol via a disulfide bond confers water solubility upon a peptide model of a protein transmembrane segment. *Anal. Biochem. 275*, 224−230.
(10) Shaunak, S., Godwin, A., Choi, J. W., Balan, S., Pedone, E., Vijayarangam, D., Heidelberger, S., Teo, I., Zloh, M., and Brocchini, S. (2006) Site-specific PEGylation of native disulfide bonds in therapeutic proteins. *Nat. Chem. Biol. 2*, 312−313.
(11) Dawson, P. E., Muir, T. W., Clark-Lewis, I., and Kent, S. B. H. (1994) Synthesis of proteins by native chemical ligation. *Science 266*, 776−779.
(12) Muir, T. W. (2003) Semisynthesis of proteins by expressed protein ligation [Review]. *Annu. Rev. Biochem. 72*, 249−289.
(13) Johnson, E. C. B. and Kent, S. B. H. (2006) Insights into the mechanism and catalysis of the native chemical ligation reaction. *J. Am. Chem. Soc. 128*, 6640−6646.
(14) Kushnir, S., Marsac, Y., Breitling, R., Granovsky, I., Brok-Volchanskaya, V., Goody, R. S., Becker, C. F. W., and Alexandrov, K. (2006) Rapid production of functionalized recombinant proteins: marrying ligation independent cloning and in vitro protein ligation. *Bioconjugate Chem. 17*, 610−617.
(15) Schuler, B., and Pannell, L. K. (2002) Specific labeling of polypeptides at amino-terminal cysteine residues using Cy5-benzyl thioester. *Bioconjugate Chem. 13*, 1039−1043.
(16) Muir, T. W., and Kent, S. B. (1993) The chemical synthesis of proteins. *Curr. Opin. Biotechnol. 4*, 420−427.
(17) Kent, S. (2003) Total chemical synthesis of enzymes. *J. Pept. Sci. 9*, 574−593.
(18) Schnölzer, M., Alewood, P., Jones, A., Alewood, D., and Kent, S. B. H. (1992) In situ neutralization in Boc-chemistry solid phase peptide synthesis. Rapid, high yield assembly of difficult sequences. *Int. J. Pept. Protein Res. 40*, 180−193.
(19) Rose, K., and Vizzavona, J. (1999) Stepwise solid-phase synthesis of polyamides as linkers. *J. Am. Chem. Soc. 121*, 7034−7038.
(20) Becker, C. F., Oblatt-Montal, M., Kochendoerfer, G. G., and Montal, M. (2004) Chemical synthesis and single channel properties of tetrameric and pentameric TASPs (template-assembled synthetic proteins) derived from the transmembrane domain of HIV virus protein u (Vpu). *J. Biol. Chem. 279*, 17483−17489.
(21) Tolbert, T. J. and Wong, C. H. (2002) New methods for proteomic research: Preparation of proteins with N-terminal cysteines for labeling and conjugation. *Angew. Chem. 41*, 2171−2174.
(22) Becker, C. F., Hunter, C. L., Seidel, R. P., Kent, S. B., Goody, R. S., and Engelhard, M. (2001) A sensitive fluorescence monitor for the detection of activated Ras: total chemical synthesis of site-specifically labeled Ras binding domain of c-Raf1 immobilized on a surface. *Chem. Biol. 8*, 243−252.
(23) Sydor, J. R., Herrmann, C., Kent, S. B., Goody, R. S., and Engelhard, M. (1999) Design, total chemical synthesis, and binding properties of a [Leu-91- N^1-methyl-7-azaTrp]Ras-binding domain of c-Raf-1. *Proc. Natl. Acad. Sci. U.S.A. 96*, 7865−7870.
(24) Harder, J., Bartels, J., Christophers, E., and Schroder, J. M. (2001) Isolation and characterization of human β-Defensin-3, a novel human inducible peptide antibiotic. *J. Biol. Chem. 276*, 5707−5713.
(25) Kapust, R. B., Tozser, J., Fox, J. D., Anderson, D. E., Cherry, S., Copeland, T. D., and Waugh, D. S. (2001) Tobacco etch virus protease: mechanism of autolysis and rational design of stable mutants with wild-type catalytic proficiency. *Protein Eng. 14*, 993−1000.
(26) Locht, C., Chesebro, B., Race, R., and Keith, J. M. (1986) Molecular cloning and complete sequence of prion protein cDNA from mouse brain infected with the scrapie agent. *PNAS 83*, 6372−6376.
(27) Becker, C. F., Seidel, R., Jahnz, M., Bacia, K., Niederhausen, T., Alexandrov, K., Schwille, P., Goody, R. S., and Engelhard, M. (2006) C-terminal fluorescence labeling of proteins for interaction studies on the single-molecule level. *Chembiochem 7*, 891−895.
(28) Telenti, A., Southworth, M., Alcaide, F., Daugelat, S., Jacobs, W. R., Jr., and Perler, F. B. (1997) The *Mycobacterium xenopi* GyrA protein splicing element: characterization of a minimal intein. *J. Bacteriol. 179*, 6378−6382.
(29) Zerial, M., and McBride, H. (2001) Rab proteins as membrane organizers. *Nat. Rev. Mol. Cell Biol. 2*, 107−117.
(30) Casey, P. J., and Seabra, M. C. (1996) Protein prenyltransferases. *J. Biol. Chem. 271*, 5289−5292.
(31) Andres, D. A., Seabra, M. C., Brown, M. S., Armstrong, S. A., Smeland, T. E., Cremers, F. P., and Goldstein, J. L. (1993) cDNA cloning of component A of Rab geranylgeranyl transferase and demonstration of its role as a Rab escort protein. *Cell 73*, 1091−1099.
(32) Darchen, F., and Goud, B. (2000) Multiple aspects of Rab protein action in the secretory pathway: focus on Rab3 and Rab6. *Biochimie 82*, 375−384.
(33) Dursina, B., Reents, R., Delon, C., Wu, Y., Kulharia, M., Thutewohl, M., Veligodsky, A., Kalinin, A., Evstifeev, V., Ciobanu, D., Szedlacsek, S. E., Waldmann, H., Goody, R. S., and Alexandrov, K. (2006) Identification and specificity profiling of protein prenyltransferase inhibitors using new fluorescent phosphoisoprenoids. *J. Am. Chem. Soc. 128*, 2822−2835.

BC0601931

Impact of PKM Linkers on Biodistribution Characteristics of the ^{99m}Tc-Labeled Cyclic RGDfK Dimer

Shuang Liu,* Zhengjie He, Wen-Yuan Hsieh, Young-Seung Kim, and Young Jiang

School of Health Sciences, Purdue University, 550 Stadium Mall Drive, West Lafayette, Indiana 47907. Received July 31, 2006; Revised Manuscript Received September 27, 2006

This report describes synthesis of three new cyclic RGDfK peptide conjugates, HYNIC−PKM−SU016 (PKM = E, K and PEG4) and in vivo evaluation of the impact of PKM linkers on biodistribution characteristics of their ternary ligand complexes [^{99m}Tc(HYNIC−PKM−SU016)[1](tricine)(TPPTS)] in athymic nude mice bearing the MDA-MB-435 human breast cancer xenografts. Results from biodistribution studies show that PKM linkers have minimal impact on the integrin $\alpha_v\beta_3$ binding capability of radiotracers. Even though they have different charges under physiological conditions, all three linkers (E, K, and PEG4) are able to reduce the uptake of ^{99m}Tc-labeled E[c(RGDfK)]$_2$ in blood, kidneys, liver, and lungs, and increase target-to-background (*T*/*B*) ratios at >30 min postinjection. E and K may have advantages over PEG4 due to a combination of relatively low liver uptake and high tumor/liver and tumor/lung ratios of ternary ligand complexes [^{99m}Tc(HYNIC−PKM−SU016)(tricine)-(TPPTS)] (PKM = E and K).

INTRODUCTION

For the past several years, we and others have been using multimeric cyclic RGD peptides, such as E[c(RGDfK)]$_2$ (SU016), to develop integrin $\alpha_v\beta_3$-targeted radiotracers for imaging rapidly growing and metastatic tumors (*1*−*11*). The RGD peptide serves as "vehicles" to carry radionuclide (^{99m}Tc, ^{18}F, and ^{64}Cu) to the integrin $\alpha_v\beta_3$ overexpressed on tumor cells and activated endothelial cells of the tumor neovasculature. ^{99m}Tc is the choice of radionuclide for single photon emission computed tomography (SPECT) and planar imaging due to its optimal nuclear properties (half-life, abundance, and energy of γ photons) and easy availability at low cost (*12*−*14*). For the ^{99m}Tc-labeling, 6-hydrazinonicotinic acid (HYNIC) has been used as a bifunctional coupling agent, while tricine and a water-soluble phosphine or pyridine analog are used as coligands to prepare ternary ligand ^{99m}Tc complexes [^{99m}Tc(HYNIC−SU016)(tricine)(L)] (L = ISONIC (isonicotinic acid), TPPTS (trisodium triphenylphosphine-3,3′,3″-trisulfonate, and PDA (2,5-pyridinedicarboxylic acid)) (*1*−*3*).

Recently, we studied the effect of coligands on biodistribution characteristics of ternary ligand complexes [^{99m}Tc(HYNIC−SU016)(tricine)(L)] (Figure 1; L = ISONIC, TPPTS, and PDA) in athymic nude mice bearing MDA-MB-435 human breast cancer xenografts (*2*). It was found that the coligand has a significant impact on the radiotracer excretion kinetics from nontumor organs, such as liver and lungs, while maintaining their tumor targeting capability. Similar results were observed for [^{99m}Tc(HYNIC−SU016)(tricine)(L)] (L = TPPTS and ISONIC) and [^{99m}Tc(HYNIC−SU016)(EDDA)] (EDDA = ethylenediamine-*N*,*N*′-diacetic acid) in BALB/c mice bearing human U87MG glioma xenografts (*3*). Among several radiotracers evaluated, [^{99m}Tc(HYNIC−SU016)(tricine)(TPPTS)] shows a great potential as a new radiotracer for imaging the integrin $\alpha_v\beta_3$-positive tumors.

It is highly desirable for the radiotracer to clear from noncancerous organs, such as liver and lungs, so that a high target-to-background (*T*/*B*) ratio can be achieved and clinically useful images of tumor can be obtained in a short period of time. In the past several years, a variety of pharmacokinetic modifying (PKM) linkers have been used to improve excretion kinetics of radiolabeled cyclic RGD peptides. For example, a sugar moiety was used to increase *T*/*B* ratios of the ^{125}I- and ^{18}F-labeled cyclic RGD peptides (*15*−*20*). Small peptides sequences, such as di(cysteic acid), Asp$_3$, and Ser$_3$, have been used to improve blood clearance and to minimize liver accumulation of radiolabeled nonpeptide integrin $\alpha_v\beta_3$ antagonists (*21*, *22*) and ^{18}F-labeled c(RGDfK) (*23*, *24*). The hexaethylene glycol (HEG) linker has been used in the ^{18}F-labeled RGDfE dimer and tetramer (*11*, *12*, *23*, *24*). It was reported that introduction of the polyethylene glycol (PEG) linker can improve not only tumor uptake but also excretion kinetics of ^{125}I- and ^{18}F-labeled c(RGDyK) and ^{64}Cu-labeled E[c(RGDyK)]$_2$ (*25*−*28*). PKM linkers and their applications to improve the excretion kinetics of radiolabeled small biomolecules have been reviewed recently (*13*, *24*, *29*−*31*).

To explore the impact of PKM linkers on tumor uptake and excretion kinetics of the ^{99m}Tc-labeled E[c(RGDfK)]$_2$, we have prepared three HYNIC conjugates, HYNIC−PKM−SU016 (Figure 1; PKM = glutamic acid (E), lysine (K), and PEG4), and their ternary ligand complexes [^{99m}Tc(HYNIC−PKM−SU016)(tricine)(TPPTS)] (PKM = E, K, and PEG4). These three PKM linkers were chosen due to their different charge under physiological conditions. In this report, we present synthesis and in vivo evaluation of biodistribution characteristics of complexes [^{99m}Tc(HYNIC−PKM−SU016)(tricine)(TPPTS)] (PKM = E, K, and PEG4) in athymic nude mice bearing MDA-MB-435 human breast cancer xenografts. The main objective of this study is to select an optimal PKM linker (E, K, or PEG4) for the ^{99m}Tc-labeled small biomolecules, which is very

* To whom correspondence should be addressed. School of Health Sciences, Purdue University, 550 Stadium Mall Drive, West Lafayette, IN 47907. Phone: 765-494-0236; Fax 765-496-1377; Email: lius@pharmacy.purdue.edu.

[1] Abbreviations: HYNIC = 6-hydrazinonicotinamide; PKM = pharmacokinetic modifier; E = glutamic acid; K = lysine; PEG4 = 15-amino-4,7,10,13-tetraoxapentadecanoic acid; SU016 = Glu(cyclo{Lys-Arg-Gly-Asp-D-Phe})-cyclo{Lys-Arg-Gly-Asp-D-Phe}; and TPPTS = trisodium triphenylphosphine-3,3′,3″-trisulfonate.

10.1021/bc060235l CCC: $33.50 © 2006 American Chemical Society
Published on Web 11/01/2006

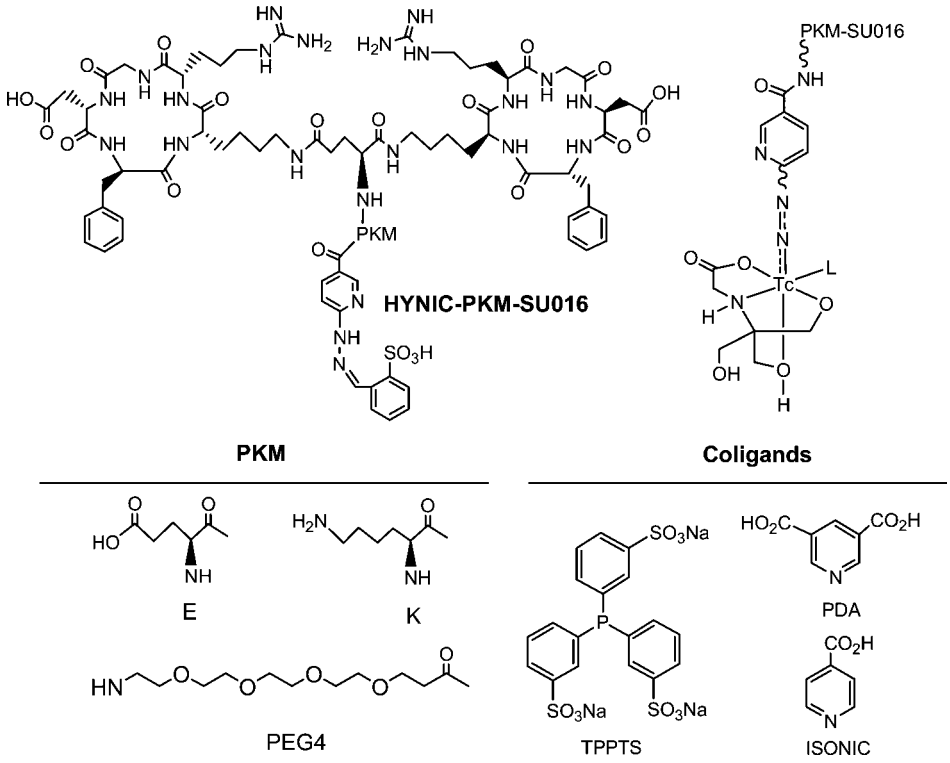

Figure 1. Structures of HYNIC−PKM−SU016 conjugates and their ternary ligand complexes [^{99m}Tc(HYNIC−PKM−SU016)(tricine)(TPPTS)] (PKM = E, K, and PEG4).

important in successful development of target-specific radiopharmaceuticals.

EXPERIMENTAL SECTION

Materials. Dicyclohexylcarbodiimide (DCC), *N*-hydroxysuccinimide (NHS), succinic acid, trisodium triphenylphosphine-3,3′,3″-trisulfonate (TPPTS), and tricine were purchased from Sigma-Aldrich (St. Louis, MO). Boc-Glu(OSu)OH and lys(Boc)-OH were from Bachem Biosciences, Inc. (Prussia, PA). The Boc-protected PEG4 was obtained from Quanta BioDesign, Ltd. (Powell, OH). Cyclic pentapeptide, c(RGDfK), was obtained from Peptides International, Inc. (Louisville, KY). The cyclic RGDfK dimer, E[c(RGDfK)]$_2$ (SU016), was prepared according to the procedure described in our previous communication (*2*). Sodium succinimidyl 6-(2-(2-sulfonatobenzaldehyde)hydrazono)-nicotinate (HYNIC−NHS) was prepared according to literature procedure (*32*). Na^{99m}TcO$_4$ was obtained from a DuPont Pharma ^{99}Mo/^{99m}Tc generator, N. Billerica, MA.

Instrument and Methods. The ^{1}H NMR data were obtained using a Bruker ARX 300 MHz FT NMR spectrometer and chemical shifts as δ are reported in ppm relative to TMS. Mass spectral data were collected on a Finnigan LCQ classic mass spectrometer, School of Pharmacy, Purdue University. The semi-prep HPLC method (method 1) used a LabAlliance semi-prep HPLC system equipped with a UV/vis detector (λ = 254 nm) and Zorbax C_{18} semi-prep column (9.4 mm × 250 mm, 100 Å pore size) for peptide purification. The flow rate was 2.5 mL/min. The mobile phase was isocratic with 90% solvent A (0.1% acetic acid in water) and 10% solvent B (0.1% acetic acid in acetonitrile) at 0−5 min, followed by a gradient mobile phase going from 90% solvent A and 10% solvent B at 5 min to 60% solvent A and 40% solvent B at 20 min. The radio-HPLC method (method 2) used the LabAlliance HPLC system equipped with a β-ram IN-US detector and Zorbax C_{18} column (4.6 mm × 250 mm, 300 Å pore size). The flow rate was 1 mL/min. The mobile phase was isocratic with 90% solvent A (25 mM ammonium acetate buffer, pH = 5.0) and 10% solvent B (acetonitrile) at 0−2 min, followed by a gradient mobile phase going from 10% solvent B at 2 min to 15% solvent B at 5 min and to 20% solvent B at 20 min. The ITLC method used GelmanSciences silica-gel paper strips and a 1:1 mixture of acetone and saline as eluant. By this method, ^{99m}Tc complexes migrate to the solvent front, while ^{99m}TcO$_4^-$ and [^{99m}Tc]colloid remain at the origin.

Boc−E(OBu-t)−SU016. To a solution of Boc−E(OBu-t)−NHS (8.0 mg, 0.02 mmol) in DMF (1.0 mL) was added diisopropylethylamine (DIEA) to adjust pH of the reaction mixture to 8.0−8.5. SU016 (13.8 mg, 0.01 mmol) was added, and the resulting mixture was stirred for 30 min. The reaction was stirred at room temperature overnight, and the pH was maintained at 8.0−8.5 with DIEA. The crude product was dissolved in 2 mL of 0.5 N NH_4OAc buffer (pH = 7.0) and was purified by HPLC (method 1). The fraction at ∼16 min was collected. Lyophilization of the collected fractions afforded Boc−E(OBu-t)−SU016. The yield was 10 mg (∼60%). ESI-MS (positive mode): m/z = 1603.9 for $[M + H]^+$ (1603.82 calcd. for $[C_{73}H_{111}N_{20}O_{21}]^+$).

E−SU016. Boc−E(OBu-t)−SU016 (10 mg) was treated with 1.0 mL of trifluoroacetic acid (TFA), and the resulting mixture was stirred at room temperature for 30 min. Excess TFA was removed. The crude product was dissolved in 0.5 N NH_4OAc buffer (pH = 7.0) and purified by HPLC (method 1). The fraction at ∼11 min was collected. Lyophilization of the combined collections afforded E−SU016. The yield was 6.4 mg (∼71%). ESI-MS (positive mode): m/z = 1447.5 for $[M + H]^+$ (1447.70 calcd. for $[C_{64}H_{95}N_{20}O_{19}]^+$).

HYNIC−E−SU016. HYNIC−NHS (1.3 mg, 3 μmol) and E−SU016 (3.1 mg, 2 μmol) were dissolved in 1.0 mL of DMF. The mixture was stirred at room temperature for 12 h with pH being maintained at 8.0−8.5. The resulting mixture was subjected to HPLC purification (method 1). The fraction at ∼14 min was collected. Lyophilization of the collected fractions afforded HYNIC−E−SU016 as a white powder. The yield was

2.0 mg (~60%). ESI-MS (positive mode): m/z = 1750.5 for $[M + H]^+$ (1750.74 calcd. for $[C_{77}H_{103}N_{23}O_{23}S]^+$).

HYNIC−K(Boc)OH. To a solution of HYNIC−NHS (200 mg, 0.5 mmol) in 10 mL of DMF were added K(Boc)OH (123 mg, 0.5 mmol) and triethylamine (~60 μL, 0.5 mmol). The mixture was stirred at room temperature for 24 h. After filtration, the filtrate was evaporated to dryness. The residue was washed with diethyl ether. The crude product was purified by HPLC (method 1). Fractions at ~14 min were collected. Lyophilization of the combined collections gave an off-white powder. The yield was 200 mg (~73%). ^{1}H NMR (DMSO-d_6, chemical shifts in ppm relative to TMS): 1.34 (s, 9H, Boc group); 1.36 (m, 4H, CH_2); 1.78 (m, 2H, CH_2); 2.90 (q, 2H, *CH*$_2$NH-Boc); 4.35 (m, H, *CH*); 6.75 (t, 1H, *NH*-Boc); 7.10−8.50 (m, 8H, aromatic); 8.52 (s, 1H, =*CH*); 8.75 (bs, 1H, *NH*CO); and 11.90 (s, 1H, *NH*N=CH). ESI-MS (positive mode): m/z = 550.2 for $[M + H]^+$ (549.19 calcd. for $[C_{24}H_{32}N_5O_8S]^+$).

HYNIC−K(Boc)−NHS. To a solution of HYNIC−K(Boc)-OH (170 mg, 0.31 mmol) and NHS (41 mg, 0.36 mmol) in DMF (5 mL) was added DCC (74 mg, 0.36 mmol). The mixture was stirred at room temperature for 24 h. To the mixture was added 100 μL of acetic acid, and the solution was stirred for 5 h. After filtration, the filtrate was evaporated to dryness. The residue was dissolved in CH_2Cl_2 (10 mL), and the mixture was filtered to remove insoluble solid. To the filtrate was added 20 mL diethyl ether to give an off-white precipitate, which was collected, washed with diethyl ether, and dried under vacuum. The yield was 165 mg (~82%). ^{1}H NMR (DMSO-d_6, chemical shifts in ppm relative to TMS): 1.35 (s, 9H, Boc group); 1.50 (m, 4H, *CH*$_2$); 1.80 (m, 2H, *CH*$_2$); 3.32 (m, 2H, *CH*$_2$NH-Boc); 4.30 (m, 1H, *CH*); 7.20−8.10 (m, 8H, aromatic); 8.30 (t, 1H, *NH*-Boc); 8.58 (d, 1H, *NH*CO); 9.00 (s, 1H, =*CH*); and 11.31 (s, 1H, *NH*). ESI-MS (positive mode): m/z = 647.2 for $[M + H]^+$ (647.21 calcd. for $[C_{28}H_{35}N_6O_{10}S]^+$).

HYNIC−K(Boc)−SU016. HYNIC−K(Boc)−NHS (1.3 mg, 2 μmol) and SU016 (3.1 mg, 2 μmol) were dissolved in 1.0 mL of anhydrous DMF. The pH was maintained at 8.0−8.5 with DIEA, and the reaction mixture was stirred at room temperature for 12 h. After addition of 2 mL of 0.5 M NH_4OAc buffer (pH = 7.0), the product was isolated by HPLC (method 1). The fraction at ~16 min was collected. Lyophilization of the combined collections afforded the expected product, HYNIC−K(Boc)−SU016. The yield was 6.4 mg (~60%). ESI-MS (positive mode): m/z = 1849.9 for $[M + H]^+$ (1849.85 calcd. for $[C_{83}H_{117}N_{24}O_{23}S]^+$).

HYNIC−K−SU016. HYNIC−K(Boc)−SU016 (2 mg) was treated with 1.0 mL of TFA, and the mixture was stirred at room temperature for ~30 min. Excess TFA was removed under vacuum. The residue was dissolved in 3 mL of 0.5 N NH_4OAc buffer (pH = 7.0). The product was purified by HPLC (method 1). Lyophilization of the collected fractions at ~11 min afforded the expected product, HYNIC−K−SU016. The yield was 1.2 mg (~63%). ESI-MS (positive mode): m/z = 1749.9 for $[M + H]^+$ (1749.78 calcd. for $[C_{78}H_{109}N_{24}O_{21}S]^+$).

Boc−PEG4−SU016. To a solution of Boc−PEG4−OH (5.5 mg, 0.015 mmol) in 1 mL of DMF were added NHS (3.5 mg, 0.03 mmol) and DCC (6.2 mg, 0.03 mmol). After the mixture was stirred at room temperature for 2 h, SU016 (26.3 mg, 0.02 mmol) was added into the mixture above. The pH was adjusted to 8.0−8.5 using DIEA (~8 μL). The reaction mixture was stirred at room temperature overnight. To the reaction mixture was added 3 mL of 0.5 M NH_4OAc buffer (pH = 7.0). The cloudy solution was filtered, and the filtrate was subjected to HPLC purification (method 1). The fraction at ~14 min was collected. Lyophilization of the combined fractions afforded Boc−PEG4−SU016. The yield was 7.5 mg (~30%). ESI-MS (positive mode): m/z = 1665 for $[M + H]^+$ (1665.85 calcd. for $[C_{75}H_{117}N_{20}O_{23}]^+$).

PEG4−SU016. Boc−PEG4−SU016 (10 mg, 6 μmol) was treated with TFA (3.0 mL) at room temperature for 30 min. The TFA was removed under the reduced pressure. The residue was dissolved in 2 mL of ammonium acetate buffer (pH = 7.0) and was then purified by HPLC to afford the expected product PEG4−SU014. The yield was 7.0 mg (~74%). ESI-MS (positive mode): m/z = 1565.2 for $[M + H]^+$ (1565.80 calcd. for $[C_{70}H_{109}N_{20}O_{21}]^+$).

HYNIC−PEG4−SU016. In a 5 cm^3 vial, HYNIC−NHS (1.3 mg, 3 μmol) and PEG4−SU016 (3.0 mg, 2 μmol) were mixed with 1 mL of anhydrous DMF. After the mixture was stirred at room temperature for 10 min, the pH was adjusted to 8.0−8.5 with DIEA. The reaction mixture was stirred for 6 h at room temperature, and was then mixed with 3 mL of 0.5 M NH_4OAc buffer (pH = 7.0). The resulting solution was subjected to HPLC purification. The desired product HYNIC−PEG4−SU016 was collected after lyophilization. The yield was 2.0 mg (~54%). ESI-MS (positive mode): m/z = 1869.0 for $[M + H]^+$ (1868.83 calcd. for $[C_{83}H_{118}N_{23}O_{25}S]^+$).

General Procedure for Preparation of Ternary Ligand ^{99m}Tc Complexes: [^{99m}Tc(HYNIC−PKM−SU016)(tricine)-(TPPTS)] (PKM = E, K, and PEG4). To a 5 cm^3 vial filled with 1.0 mL solution (pH = 4.8) containing 5 mg of TPPTS, 6.5 mg of tricine, 40 mg of mannitol, 38.5 mg of disodium succinate hexahydrate, and 12.7 mg of succinic acid were added 0.2 mL of the solution containing HYNIC−PKM−SU016 (100 μg/mL in water) and 0.3 mL of Na[^{99m}TcO$_4$] solution (30−100 mCi/mL) in saline. The vial was heated at 100 °C for 20 min in a lead-shielded water bath. After radiolabeling, the vial was placed back into the lead pig and allowed to stand at room temperature for 5−10 min. A sample of the resulting solution was analyzed by the radio-HPLC (method 2) and TLC. The radiochemical purity (RCP) was >95%. The [^{99m}Tc]colloid was minimal (<0.5%) using the non-$SnCl_2$ formulation.

Dose Preparation for Animal Studies. For biodistribution studies, ternary ligand complexes [^{99m}Tc(HYNIC−PKM−SU016)(tricine)(TPPTS)] (PKM = E, K, and PEG4) were first prepared and then purified by radio-HPLC (method 2). Volatiles in the HPLC mobile phases were completely removed under the reduced pressure. Doses were made by dissolving the HPLC-purified radiotracer in saline to give a concentration of ~10 μCi/mL. Each tumor-bearing mouse was administered intravenously 0.1 mL of the prepared dose solution.

Determination of Log *P* Values. Log *P* values of ternary ligand ^{999m}Tc complexes [^{99m}Tc(HYNIC−PKM−SU016)-(tricine)(TPPTS)] (PKM = E, K, and PEG4) were determined using the following procedure: the radiotracer was prepared and purified by HPLC (method 2). Volatiles were completely removed under the reduced pressure. The residue was dissolved in a mixture of equal volume (3 mL/3 mL) *n*-octanol and 25 mM phosphate buffer (pH = 7.4). After stirring vigorously for 20−25 min, the mixture was centrifuged for 5 min at a speed of 8000 rpm. Samples (in triplets) from *n*-octanol and aqueous layers were obtained and were counted in a γ counter (Beckman Gama 8000). The partition coefficient was calculated using the following equation: P = (activity concentration in *n*-octanol)/(activity concentration in aqueous layer). The log *P* values were reported as an average of three different measurements plus the standard variation.

Animal Studies. Biodistribution and metabolism studies were performed using the athymic nude mice bearing MDA-MB-435 human breast cancer xenografts in compliance with NIH animal experiment guidelines (*Principles of Laboratory Animal Care*, NIH Publication No. 86-23, revised 1985). The animal

Chart 1. Synthesis of HYNIC-Conjugated Cyclic RGDfK Conjugates

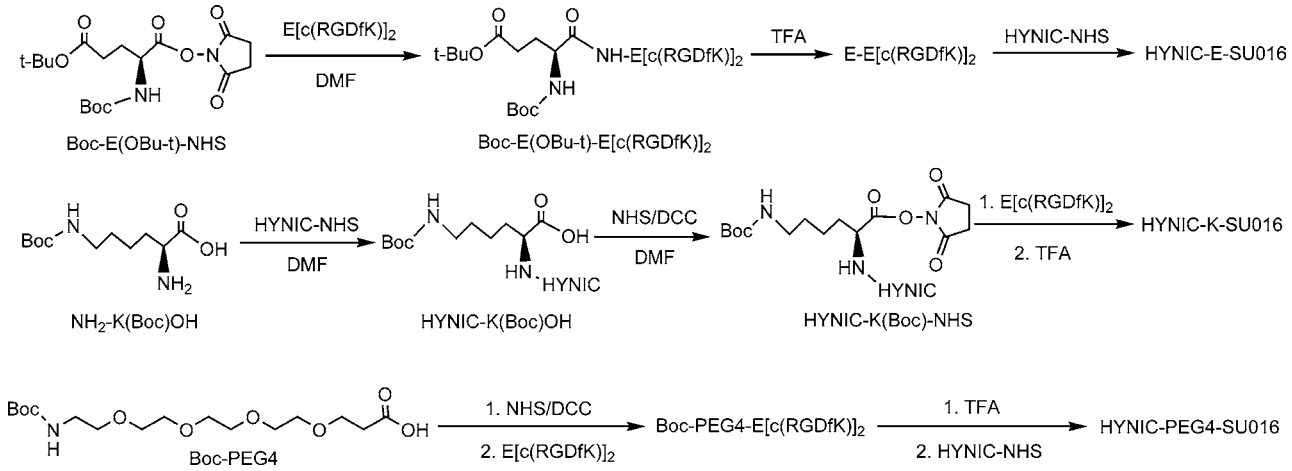

protocol for animal studies has been approved by the Purdue University Animal Care and Use Committee (PACUC).

Tumor-Bearing Mice. Female athymic nu/nu mice were purchased from Harlan (Indianapolis, IN) at 4−5 weeks of age. Tumor cells were grown at 37 °C in minimal essential medium (alpha modification) containing 3.7 g of sodium bicarbonate/L, and 10% fetal bovine serum v/v, in a humidified atmosphere of 5% carbon dioxide. The nude mice were implanted with ∼5 × 10^6 cells of MDA-MB-435 estrogen-receptor-negative human breast cancer cells into the mammary fat pad. Four weeks after inoculation, animals were used for biodistribution and metabolism studies.

Biodistribution. Sixteen tumor-bearing mice (20−25 g) were anesthetized with IP injection of Ketamine (40−100 mg/kg) and Xylazine (2−5 mg/kg). Once the animal was in the surgical plane of anesthesia, as noted by lack of pain response, the radiotracer (∼1 μCi) dissolved in 0.1 mL saline was administered via the tail vein. Four animals were sacrificed by exsanguinations and opening of thoracic cavity at 5, 30, 60, and 120 min postinjection. Organs (tumor, blood, brain, eyes, spleen, lungs, liver, kidneys, muscle, and intestine) were excised, washed with saline, weighed, and counted on a γ counter. The organ uptake was calculated as a percentage of the injected dose per organ (% ID/organ) and a percentage of the injected dose per gram of wet tissue (% ID/g).

Metabolism. Two tumor-bearing mice were used for each radiotracer. Each tumor-bearing mouse was administered the radiotracer at a dose of 100 μCi/mice. Urine samples were collected at 2 h postinjection by manual void and were mixed with equal volume of acetonitrile. The mixture was centrifuged at 8000 rpm. The supernatant was collected and filtered through a 0.20 μm Millex-LG syringe-driven filter unit to remove any precipitate and large proteins. The filtrate was analyzed by radio-HPLC. Feces samples were collected at ∼120 min postinjection. The sample was suspended in a mixture of 50% acetonitrile aqueous solution, and the resulting mixture was vortexed for 5−10 min. After centrifuging at 8000 rpm for 5 min, the supernatant was collected and passed through a 0.20 μm Millex-LG syringe-driven filter unit. The filtrate was analyzed by radio-HPLC.

Data and Statistical Analysis. The biodistribution data and *T*/*B* ratios are reported as an average plus the standard variation based on the results from four animals at each time point. Comparison between two different radiotracers was also made using the one-way ANOVA test. The level of significance was set at $p = 0.05$.

RESULTS

HYNIC−PKM−SU016 Conjugates. HYNIC−E−SU016 was prepared (Chart 1) by conjugation of Boc−E(OBu-t)−NHS with 1 equiv of E[c(RGDfK)]$_2$ (SU016), followed by deprotection of the Boc-protecting group in TFA, and conjugation with HYNIC−NHS in DMF. HYNIC−K−SU016 was prepared (Chart 1) by conjugation of HYNIC−NHS with 1 equiv of K(Boc)OH, followed by activation of the carboxylic group in HYNIC−K(Boc)OH, conjugation of HYNIC−K(Boc)−NHS with SU016 in DMF, and deprotection of the Boc-protecting group. For HYNIC−PEG4−SU016 (Chart 1), Boc−PEG4 was first activated to form the activated ester Boc−PEG4−NHS, which was then allowed to react with SU016 to afford Boc−PEG4−SU016. The Boc-protecting group was removed by treating Boc−PEG4−SU016 with anhydrous TFA. Conjugation of PEG4−SU016 with HYNIC−NHS in DMF produced HYNIC−PEG4−SU016. The HYNIC−PKM−SU016 (PKM = E, K, and PEG4) conjugates were purified by a semi-prep HPLC method. Their HPLC purity was >95% before being used for the ^{99m}Tc-labeling.

Radiochemistry. [^{99m}Tc(HYNIC−PKM−SU016)(tricine)-(TPPTS)] (PKM = E, K, and PEG4) were prepared according to Chart 2. TPPTS was chosen as the coligand due to the high solution stability of its ternary ligand ^{99m}Tc complexes (*1*−*4*) and the availability of the non-$SnCl_2$ formulation (*33*−*35*). The radiochemical purity (RCP) of all three radiotracers was >95% with minimal amount (<0.5%) of [^{99m}Tc]colloid using non-$SnCl_2$ formulation. It was also found that all three radiotracers remained stable in 25 mM ammonium acetate buffer (pH = 5) for more than 12 h, which is consistent with the results obtained from our previous studies (*1*, *2*).

All three radiotracers were analyzed by the same HPLC method (method 2). Figure 2 shows their representative HPLC chromatograms in the kit matrix. Small radioimpurities were formed during the radiolabeling process. No identification was made for these radioimpurities. The HPLC retention times for [^{99m}Tc(HYNIC−E−SU016)(tricine)(TPPTS)], [^{99m}Tc(HYNIC−K−SU016)(tricine)(TPPTS)] and [^{99m}Tc(HYNIC−PEG4−SU016)(tricine)(PDA)] were 12.2, 15.0, and 13.5 min, respectively, under identical chromatographic conditions. It is interesting to note that [^{99m}Tc(HYNIC−K−SU016)(tricine)(TPPTS)] shows two peaks, which are often observed for ternary ligand complexes [^{99m}Tc(HYNIC−biomolecule)(tricine)(TPPTS)] due to chirality of the Tc chelate and presence of chiral center(s) in the targeting biomolecule (*35*−*38*). However, [^{99m}Tc(HYNIC−E−SU016)(tricine)(TPPTS)] and [^{99m}Tc(HYNIC−PEG4−SU016)(tricine)(TPPTS)] both show one radiometric peak under the same chromatographic conditions (Figure 2). Attempts to separate the two diastereomers in [^{99m}Tc(HYNIC−E−SU016)-(tricine)(TPPTS)] and [^{99m}Tc(HYNIC−PEG4−SU016)(tricine)-(TPPTS)] were not successful. It is obvious that the introduction

Chart 2. Synthesis of Ternary Ligand ^{99m}Tc Complexes

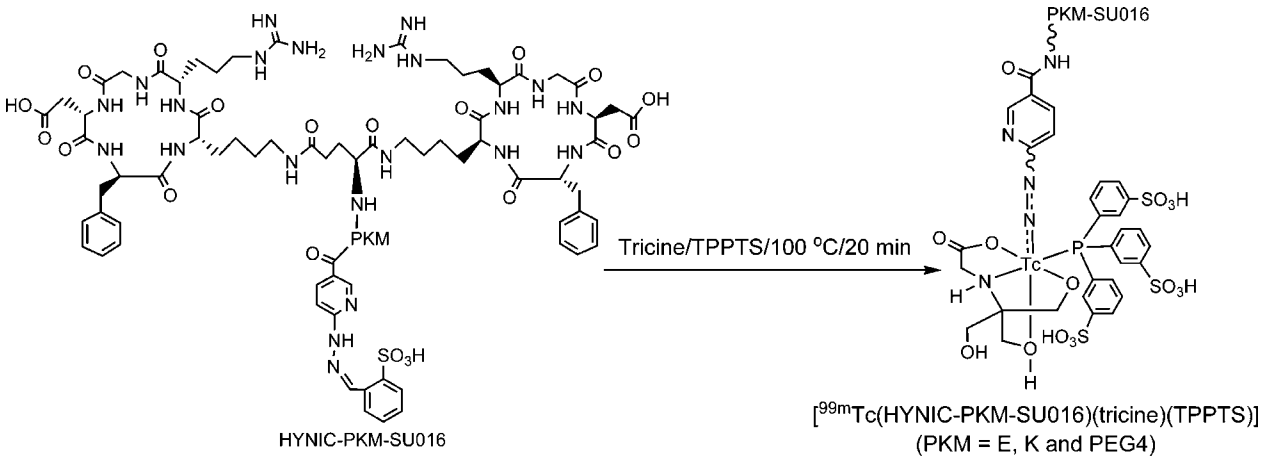

of E or PEG4 linker between HYNIC and E[c(RGDfK)]$_2$ makes it much more difficult to separate these two diastereomers.

To further explore the linker effect on lipophilicity of ternary ligand complexes [^{99m}Tc(HYNIC−PKM−SU016)(tricine)-(TPPTS)] (PKM = E, K, and PEG4), we also determined their partition coefficients (*P* values) in an equal volume mixture of *n*-octanol and 25 mM phosphate buffer (pH = 7.4). The log *P* values are −3.13 ± 0.20, −3.41 ± 0.14, and −3.56 ± 0.16 for [^{99m}Tc(HYNIC−E−SU016)(tricine)(TPPTS)], [^{99m}Tc(HYNIC−K−SU016)(tricine)(TPPTS)], and [^{99m}Tc(HYNIC−PEG4−SU016)(tricine)(TPPTS)], respectively. As expected, complexes [^{99m}Tc(HYNIC−PKM−SU016)(tricine)(TPPTS)] (PKM = E, K, and PEG4) are more hydrophilic than [^{99m}Tc(HYNIC−SU016)(tricine)(TPPTS)] (log *P* = −2.66 ± 0.25) (*2*). There is no significant difference in log *P* values of all three new radiotracers within experimental error, even though their HPLC retention times suggest that [^{99m}Tc(HYNIC−E−SU016)(tricine)-(TPPTS)] might be more hydrophilic than [^{99m}Tc(HYNIC−K−SU016)(tricine)(TPPTS)] and [^{99m}Tc(HYNIC−PEG4−SU016)-(tricine)(TPPTS)] (Figure 2).

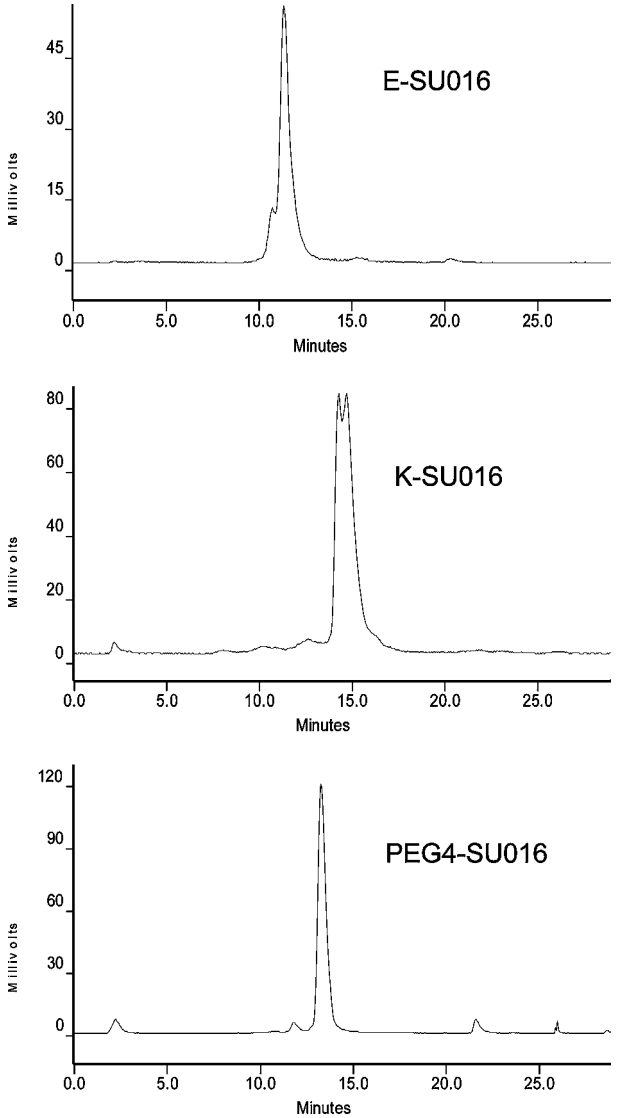

Figure 2. Radio-HPLC chromatograms of [^{99m}Tc(HYNIC−E−SU016)-(tricine)(TPPTS)] (top), [^{99m}Tc(HYNIC−K−SU016)(tricine)(TPPTS)] (middle), and [^{99m}Tc(HYNIC−PEG4−SU016)(tricine)(TPPTS)] (bottom) in the kit matrix.

Biodistribution Characteristics. For biodistribution studies, all three radiotracers were purified by HPLC to remove excess "unlabeled" HYNIC−PKM−SU016 conjugate that may compete with the radiotracer in binding to the integrin $\alpha_v\beta_3$. Biodistribution data for complexes [^{99m}Tc(HYNIC−PKM−SU016)(tricine)(TPPTS)] (PKM = E, K, and PEG4) are summarized in Supporting Information Tables 1−3, respectively. Figure 3 shows direct comparison of their tumor uptake and excretion kinetics from blood, liver, and kidneys at 5, 30, 60, and 120 min postinjection. The *T*/*B* ratios in selected organs are illustrated in Figure 4. The biodistribution data and *T*/*B* ratios for [^{99m}Tc(HYNIC−SU016)(tricine)(TPPTS)] were obtained from our previous studies (*2*).

In general, [^{99m}Tc(HYNIC−PKM−SU016)(tricine)(TPPTS)] (PKM = K and PEG4) have the tumor uptake (3−4% ID/g) very similar to that of [^{99m}Tc(HYNIC−SU016)(tricine)(TPPTS)] (Figure 3). Their tumor uptake remains constant over the 2 h study period. The tumor uptake of [^{99m}Tc(HYNIC−E−SU016)-(tricine)(TPPTS)] is comparable to that of [^{99m}Tc(HYNIC−PKM−SU016)(tricine)(TPPTS)] (PKM = K and PEG4) and [^{99m}Tc(HYNIC−SU016)(tricine)(TPPTS)] over the first 30 min, but it increases from 4.07 ± 0.19% ID/g at 30 min postinjection to 6.33 ± 0.55% ID/g at 60 min postinjection and remains almost unchanged between 60 and 120 min postinjection. Compared to [^{99m}Tc(HYNIC−SU016)(tricine)(TPPTS)], all three new radiotracers show faster clearance from blood, liver, muscle, lungs, and kidneys (Supporting Information Tables 1−3). As a result, there is a steady increase in *T*/*B* ratios over the 2 h study period. Among the three radiotracers evaluated in this study, [^{99m}Tc(HYNIC−K−SU016)(tricine)(TPPTS)] has the best tumor/liver and tumor/lung ratios at 120 min postinjection, while [^{99m}Tc(HYNIC−E−SU016)(tricine)(TPPTS)] has the best tumor/blood and tumor/muscle ratios (Figure 4). The tumor/muscle ratio of [^{99m}Tc(HYNIC−PEG4−SU016)(tricine)(TPPTS)]

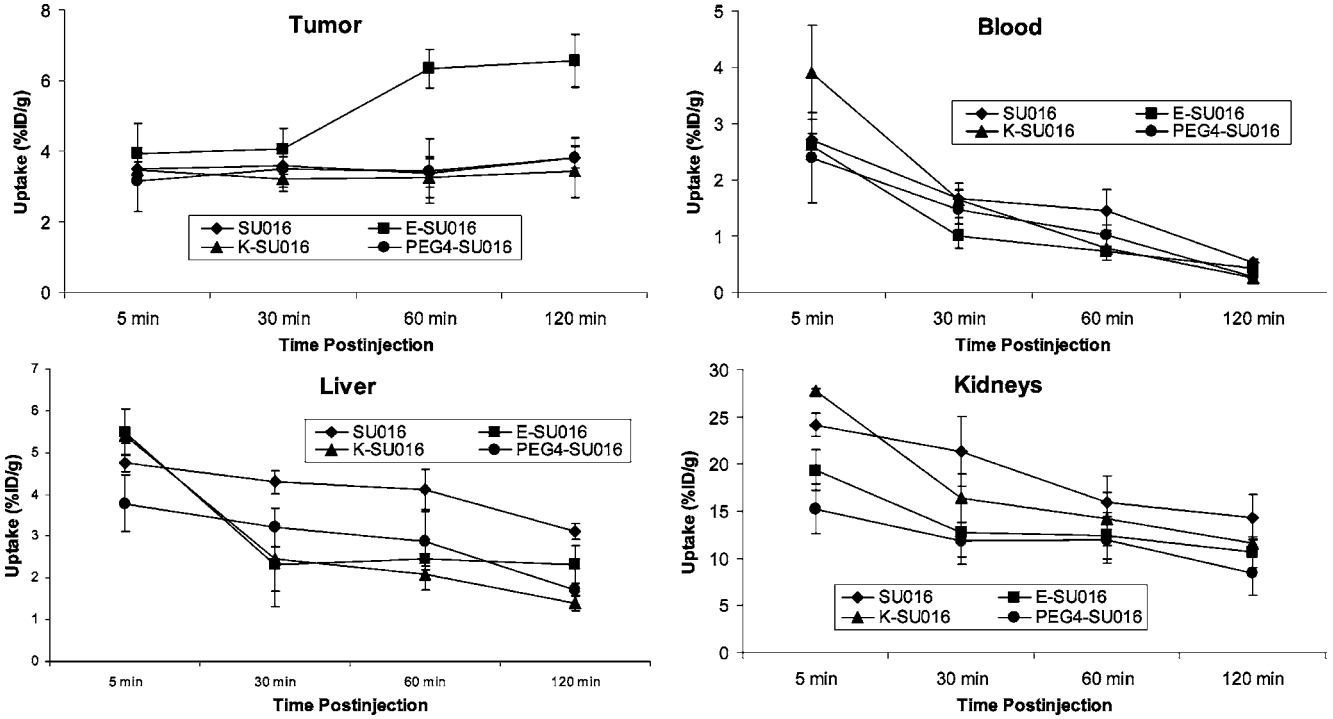

Figure 3. Comparison of organ uptake (% ID/g) among [^{99m}Tc(HYNIC−SU016)(tricine)(TPPTS)], [^{99m}Tc(HYNIC−E−SU016)(tricine)(TPPTS)], [^{99m}Tc(HYNIC−K−SU016)(tricine)(TPPTS)], and [^{99m}Tc(HYNIC−PEG4−SU016)(tricine)(TPPTS)] in athymic nude mice bearing MDA-MB-435 human breast cancer xenografts.

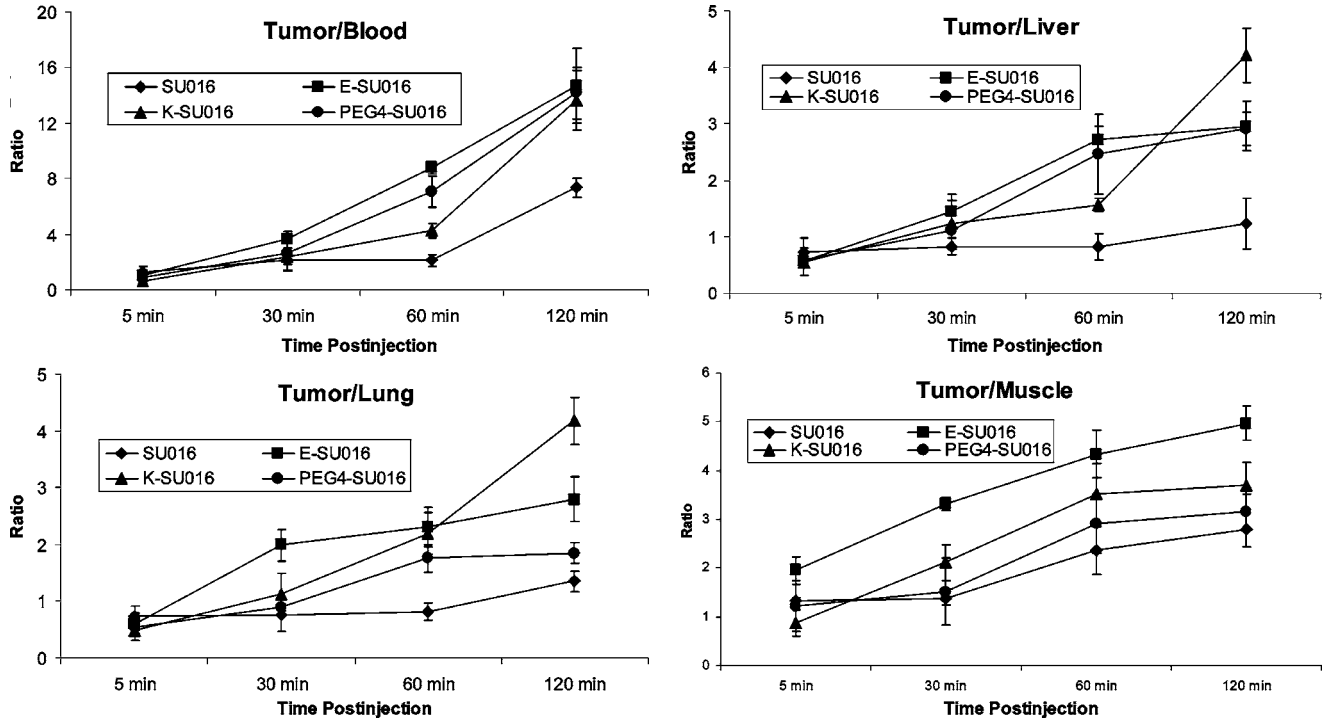

Figure 4. Comparison of *T*/*B* ratios among [^{99m}Tc(HYNIC−SU016)(tricine)(TPPTS)], [^{99m}Tc(HYNIC−E−SU016)(tricine)(TPPTS)], [^{99m}Tc(HYNIC−K−Su016)(tricine)(TPPTS)], and [^{99m}Tc(HYNIC−PEG4−SU016)(tricine)(TPPTS)] in athymic nude mice bearing MDA-MB-435 human breast cancer xenografts.

are almost the same as that of [^{99m}Tc(HYNIC−SU016)(tricine)-(TPPTS)]. Its tumor/liver ratio is comparable to that of [^{99m}Tc(HYNIC−PEG4−SU016)(tricine)(TPPTS)] within experimental error over the 2 h study period.

Metabolism. We performed metabolism studies on all three new radiotracers using athymic tumor-bearing nude mice. Since they are excreted from renal and hepatobiliary (to a much lesser degree) routes, we tried to collect samples from both feces and urine and determine if these radiotracers retain their chemical integrity at 2 h postinjection. Figure 5 shows radio-HPLC chromatograms of [^{99m}Tc(HYNIC−PKM−SU016)(tricine)-(TPPTS)] (PKM = E, K, and PEG4) in the urine at 120 min postinjection. It is quite clear that these three radiotracers have different metabolic patterns. For example, [^{99m}Tc(HYNIC−E−SU016)(tricine)(TPPTS)] had no significant metabolism (<1.0%) over the 2 h study period. The percentage of "metabolized component" (at ∼3 min) for [^{99m}Tc(HYNIC−K−SU016)-(tricine)(TPPTS)] was <10% at 120 min postinjection, and

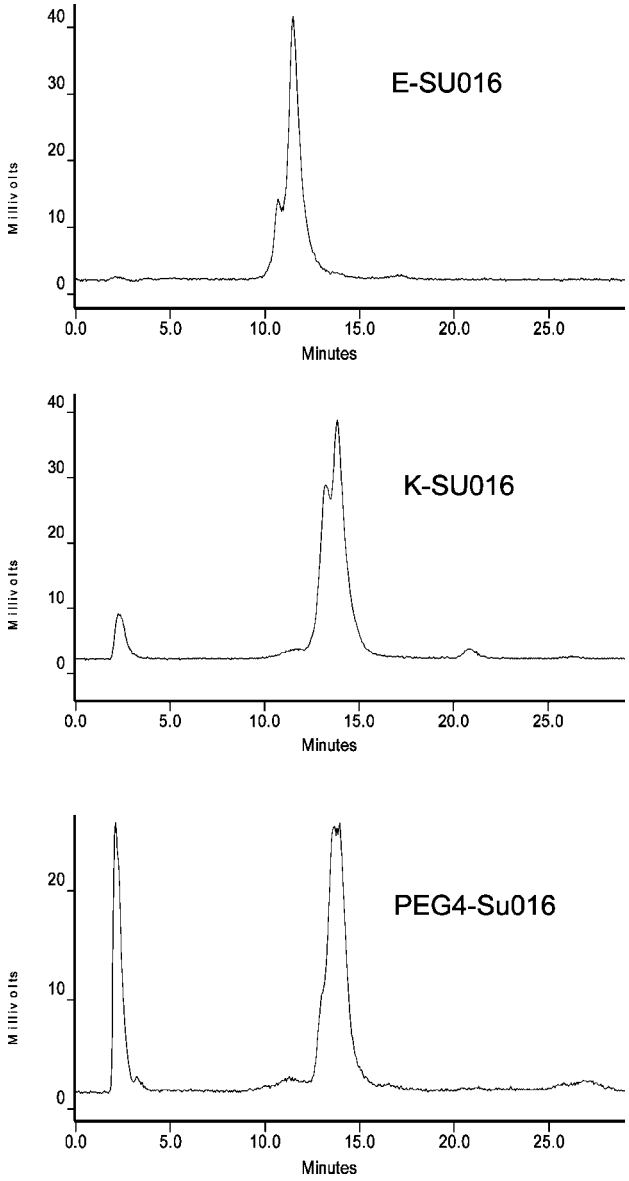

Figure 5. Radio-HPLC chromatograms of [^{99m}Tc(HYNIC−E−SU016)(tricine)(TPPTS)] (top), [^{99m}Tc(HYNIC−K−SU016)(tricine)(TPPTS)] (middle), and [^{99m}Tc(HYNIC−PEG4−SU016)(tricine)(TPPTS)] (bottom) in the urine at 120 min postinjection. Each tumor-bearing mouse was administered 100−120 μCi of radiotracer. Two tumor-bearing mice were used for each radiotracer.

>70% of [^{99m}Tc(HYNIC−PEG4−SU016)(tricine)(TPPTS)] remained intact over 2 h postinjection (Figure 5). The presence of two overlapped peaks in the HPLC chromatogram of [^{99m}Tc(HYNIC−PEG4−SU016)(tricine)(TPPTS)] is probably due to chromatographic artifact. We also tried to extract radioactivity from feces samples, but the activity level in feces samples was so low that we were unable to detect either intact ternary ligand ^{99m}Tc complexes or their metabolites.

DISCUSSION

For a new integrin $\alpha_v\beta_3$-targeted radiotracer to be successful, it should be able to have a high tumor uptake with diagnostically useful *T*/*B* ratios in a short period of time (*28*, *29*). Since most high-incidence tumors (namely, lung, colorectal, and breast cancers metastatic to the lymphatic system) occur in the torso, it is necessary to avoid radioactivity accumulation in the gastrointestinal tract, which may interfere with interpretation of tumor activity in the abdominal region. Therefore, efforts have been directed toward optimization of excretion kinetics so that the radiotracer has a fast clearance from nontumor organs (such as blood, liver, and lungs) while maintaining its high tumor uptake.

There are several approaches to increase the renal clearance of radiotracers (*13*, *29*, *30*). These include (*1*) the use of hydrophilic amino acid residues in targeting biomolecules; (*2*) the use of hydrophilic chelators or coligands for the ^{99m}Tc-labeling; and (*3*) the use of charged PKM linkers between the ^{99m}Tc-chelator and the targeting biomolecule (namely, E[c(RGDfK)]$_2$ or SU016 in this study). Incorporation of different amino acid residues into small biomolecules, such as cyclic RGD pentapeptides, often leads to alteration of their receptor-binding affinity. Thus, it is common to use PKM linkers and chelators or coligands to modify pharmacokinetics of radiotracers while keeping the cyclic pentapeptide framework intact so that the integrin $\alpha_v\beta_3$ binding affinity is not adversely affected.

Recently, we examined the coligand effect on biodistribution characteristics of [^{99m}Tc(HYNIC−SU016)(tricine)(L)] (L = ISONIC, TPPTS, and PDA) in athymic nude mice bearing MDA-MB-435 human breast cancer xenografts and found that the coligand has a significant impact on excretion kinetics of the ^{99m}Tc-labeled E[c(RGDfK)]$_2$ from blood, liver, and lungs (*2*). In this study, we studied the impact of three PKM linkers (E, K, and PEG4) on lipophilicity, tumor uptake, and excretion kinetics of the ^{99m}Tc-labeled E[c(RGDfK)]$_2$. It was found that all three radiotracers [^{99m}Tc(HYNIC−PKM−SU016)(tricine)-(TPPTS)] (PKM = E, K, and PEG4) (log P = −3.13 ± 0.20, −3.41 ± 0.14, and −3.56 ± 0.16, respectively) are more hydrophilic than [^{99m}Tc(HYNIC−SU016)(tricine)(TPPTS)] (log P = −2.66 ± 0.25). On the basis of biodistribution characteristics, it seems that PKM linkers have minimal impact on tumor-targeting capability, as indicated by their similar tumor uptake (Figure 3). Even though they may have different charges under physiological conditions, all three PKM linkers (E, K, and PEG4) are able to reduce the uptake of ^{99m}Tc-labeled E[c(RGDfK)]$_2$ in blood, liver, and lungs and increase their *T*/*B* ratios, particularly at >60 min postinjection (Figure 4). E and K are especially useful to minimize radioactivity accumulation in liver and lungs.

Small peptides in blood plasma are filtered through glomerular capillaries in the kidneys and subsequently reabsorbed by proximal tubular cells by carrier-mediated endocytosis. The membranes of renal tabular cells contain negatively charged sites to which the positively charged groups, such as guanidine moieties in cyclic RGD peptides, are expected to bind. In this respect, the negatively charged small peptides, such as E, can be used as PKM linkers to reduce renal uptake of ^{99m}Tc-labeled E[c(RGDfK)]$_2$ since the extra carboxylic groups are expected to be deprotonated under physiological conditions. In this way, the interaction between membranes of renal tabular cells and the positively charged guanidine groups in E[c(RGDfK)]$_2$ can be minimized, thereby reducing renal uptake of the ^{99m}Tc-labeled E[c(RGDfK)]$_2$. This assumption is supported by the lower kidney uptake of [^{99m}Tc(HYNIC−E−SU016)(tricine)(TPPTS)] than that of [^{99m}Tc(HYNIC−SU016)(tricine)(TPPTS)] (Figure 3). The use of negatively charged E linker also decreases the radiotracer accumulation in blood and liver (Figure 3), which results in high tumor/blood and tumor/liver ratios for [^{99m}Tc-(HYNIC−E−SU016)(tricine)(TPPTS)] (Figure 4). Similar results were also reported for ^{99m}Tc−DKCK−c(RGDfK) (*39*). Therefore, the negatively charged PKM linkers are particularly useful to enhance the radiotracer elimination from the body without prolonged retention in kidneys.

Harris et al. reported the use of a PEG4 linker to improve *T*/*B* ratios of the ^{99m}Tc-labeled nonpeptide integrin $\alpha_v\beta_3$ antagonists (*21*, *22*). Chen et al. also found that introduction of

the PEG linker (Mw = 2000 or 3400 Da) can improve tumor uptake and excretion kinetics of the radiolabeled RGD peptides (*25*−*28*). In this study, we found that the PEG4 linker significantly enhances the radiotracer excretion from blood, liver, and kidneys. Among three radiotracers evaluated in this study, [^{99m}Tc(HYNIC−PEG4−SU016)(tricine)(TPPTS)] has the lowest kidney uptake (Figure 3). Even though PEG linkers are neutral, they are useful tools for optimization of pharmacokinetic parameters of target-specific radiotracers.

Extensive metabolic degradation has been observed for the ^{99m}Tc-labeled c(RGDfK) (*39*), [^{99m}Tc(HYNIC−SU016)(tricine)-(TPPTS)] (*2*), and the ^{64}Cu-labeled c(RGDfK) tetramer (*7*). In this study, we found that all three radiotracers have a different degree of metabolism. For example, [^{99m}Tc(HYNIC−E−SU016)-(tricine)(TPPTS)] has little metabolism (<1.0%), while [^{99m}Tc-(HYNIC−K−SU016)(tricine)(TPPTS)] has <10% metabolism during the 2 h study period. The majority (>70%) of [^{99m}Tc-(HYNIC−PEG4−SU016)(tricine)(TPPTS)] remained intact at 2 h postinjection (Figure 5). Since all three radiotracers used in this study share the same Tc chelate and the same cyclic RGDfK dimer, the difference in their metabolic patterns is likely related to the PKM linker.

The pharmacokinetic requirement for an optimal radiotracer depends largely on its medical applications (diagnostic or therapeutic). For therapeutic radiopharmaceuticals, the high uptake in kidneys and prolonged kidney retention of radiotracers will impose a serious challenge for the radiolabeled cyclic RGD peptides (*12*, *30*, *31*). For tumor imaging, however, the most important factor in selecting an optimal radiotracer is its excretion kinetics from the liver and lungs (*29*, *30*). Although all three linkers are able to increase the excretion rate of ^{99m}Tc-labeled E[c(RGDfK)]$_2$ from nontumor organs, E and K may have advantages over PEG4 due to a combination of low liver uptake and high tumor/liver and tumor/lung ratios (Figure 4) of [^{99m}Tc(HYNIC−PKM−SU016)(tricine)(TPPTS)] (PKM = E and K).

CONCLUSION

In this report, we described the in vivo evaluation of biodistribution characteristics of complexes [^{99m}Tc(HYNIC−PKM−SU016)(tricine)(TPPTS)] (PKM = E, K, and PEG4) in nude mice bearing MDA-MB-435 human breast cancer xenografts. The results from biodistribution studies show that excretion kinetics of the ^{99m}Tc-labeled E[c(RGDfK)]$_2$ can be modified with various PKM linkers. The fact that [^{99m}Tc-(HYNIC−PKM−SU016)(tricine)(TPPTS)] (PKM = E, K, and PEG4) have a tumor uptake comparable to that of [^{99m}Tc-(HYNIC−SU016)(tricine)(TPPTS)] during the 2 h study period suggests that changing PKM linkers has no adverse effect on the integrin $\alpha_v\beta_3$ binding capability of the ^{99m}Tc-labeled E[c(RGDfK)]$_2$. Among the three linkers, E and K linkers are especially useful in minimizing the radioactivity accumulation in liver and lungs. For other ^{99m}Tc-labeled small biomolecules, the choice of PKM linker must be confirmed by their distribution characteristics.

ACKNOWLEDGMENT

Authors would like to thank Lee Ann Grote, Carol Dowell, and Cheryl Anderson from the Department of Veterinary Clinical Sciences, Purdue University, for their assistance with biodistribution studies. This work is supported, in part, by research grants: BCTR0503947 (S.L.) from Susan G. Komen Breast Cancer Foundation, AHA0555659Z (S.L.) from the Greater Midwest Affiliate of American Heart Association, R21 EB003419−02 (S.L.) from National Institute of Biomedical Imaging and Bioengineering (NIBIB), and R21 HL083961−01 (S.L.) from National Heart, Lung, and Blood Institute (NHLBI).

Supporting Information Available: Supplementary Tables 1−3. This material is available free of charge via the Internet at http://pubs.acs.org.

LITERATURE CITED

(1) Liu, S., Edwards, D. S., Ziegler, M. C., Harris, A. R., Hemingway, S. J., and Barrett, J. A. (2001) ^{99m}Tc-Labeling of a hydrazinonicotinamide-conjugated vitronectin receptor antagonist useful for imaging tumors. *Bioconjugate Chem. 12*, 624−629.

(2) Liu, S., Hsieh, W. Y., Kim, Y. S., and Mohammed, S. I. (2005) Effect of coligands on biodistribution characteristics of ternary ligand ^{99m}Tc complexes of a HYNIC-conjugated cyclic RGDfK dimer. *Bioconjugate Chem. 16*, 1580−1588.

(3) Jia, B., Shi, J., Yang, Z., Xu, B., Liu, Z., Zhao, H., Liu, S., and Wang, F. (2006) ^{99m}Tc-labeled cyclic RGDfK dimer: initial evaluation for SPECT imaging of glioma integrin $\alpha_v\beta_3$ expression. *Bioconjugate Chem. 17*, 1069−1076.

(4) Liu, S., Hsieh, W.-Y., Jiang, Y., Kim, Y.-S, Sreerama, S. G., Chen, X. Y., Jia, B., and Wang, F. Evaluation of a ^{99m}Tc-labeled cyclic RGD tetramer for non-invasive imaging integrin $\alpha_v\beta_3$-positive breast cancer. *J. Nucl. Med.* Submitted.

(5) Chen, X. Y., Liu, S., Hou, Y. P., Tohme, M., Park, R., Bading, J. R., and Conti, P. S. (2004) MicroPET imaging of breast cancer $\alpha_v\beta_3$-integrin expression with ^{64}Cu-labeled dimeric RGD peptides. *Mol. Imaging Biol. 6*, 350−359.

(6) Chen, X. Y., Tohme, M., Park, R., Hou, Y., Bading, J. R., and Conti, P. S. (2004) MicroPET imaging of breast cancer α_v-integrin expression with ^{18}F-labeled dimeric RGD peptide. *Mol. Imaging 3*, 96−104.

(7) Wu, Y., Zhang, X. Z., Xiong, Z. M., Cheng, Z., Fisher, D. R., Liu, S., Gambhir, S. S., and Chen, X-Y. (2005) MicroPET imaging of glioma α_v-integrin expression using ^{64}Cu-labeled tetrameric RGD peptide. *J. Nucl. Med. 46*, 1707−1718.

(8) Janssen, M. L., Oyen, W. J. G., Dijkgraaf, I., Massuger, L. F., Frielink, C., Edwards, D. S., Rajopadyhe, M., Boonstra, H., Corsten, F. H., and Boerman, O. C. (2002) Tumor targeting with radiolabeled $\alpha_v\beta_3$ integrin binding peptides in a nude mouse model. *Cancer Res. 62*, 6146−6151.

(9) Janssen, M., Oyen, W. J. G., Massuger, L. F. A. G., Frielink, C., Dijkgraaf, I., Edwards, D. S., Rajopadyhe, M., Corsten, F. H. M., and Boerman, O. C. (2002) Comparison of a monomeric and dimeric radiolabeled RGD-peptide for tumor targeting. *Cancer Biother. Radiopharm. 17*, 641−646.

(10) Poethko, T., Schottelius, M., Thumshirn, G., Herz, M., Haubner, R., Henriksen, G., Kessler, H., Schwaiger, M., and Wester, H.-J. (2004) Chemoselective pre-conjugate radiohalogenation of unprotected mono- and multimeric peptides via oxime formation. *Radiochim. Acta 92*, 317−327.

(11) Thumshirn, G., Hersel, U., Goodman, S. L., and Kessler, H. (2003) Multimeric cyclic RGD peptides as potential tools for tumor targeting: solid-phase peptide synthesis and chemoselective oxime ligation. *Chem.—Eur. J. 9*, 2717−2725.

(12) Liu, S., and Edwards, D. S. (2002) Fundamentals of receptor-based diagnostic metalloradiopharmaceuticals. *Top. Curr. Chem. 222*, 259−278.

(13) Liu, S. (2004) The role of coordination chemistry in development of target-specific radiopharmaceuticals. *Chem. Soc. Rev. 33*, 1−18.

(14) Liu, S., and Edwards, D. S. (1999) ^{99m}Tc-labeled small peptides as diagnostic radiopharmaceuticals. *Chem. Rev. 99*, 2235−2268.

(15) Haubner, R., Wester, H. J., Senekowitsch-Schmidtke, R., Diefenbach, B., Kessler, H., Stöcklin, G., and Schwaiger, M. (1999) RGD-peptides for tumor targeting: biological evaluation of radioiodinated analogs and introduction of a novel glycosylated peptide with improved biokinetics. *J. Labelled Compd. Radiopharm. 40*, 383−385.

(16) Haubner, R., Wester, H.-J., Reuning, U., Senekowtisch-Schmidtke, R., Diefenbach, B., Kessler, H., Stöcklin, G., and Schwaiger, M. (1999) Radiolabeled $\alpha_v\beta_3$ integrin antagonists: a new class of tracers for tumor imaging. *J. Nucl. Med. 40*, 1061−1071.

(17) Haubner, R., Wester, H. J., Burkhart, F., Senekowtisch-Schmidtke, R., Weber, W., Goodman, S. L., Kessler, H., and Schwaiger, M. (2001) Glycosylated RGD-containing peptides: tracer for tumor targeting and angiogenesis imaging with improved biokinetics. *J. Nucl. Med. 42*, 326−336.

(18) Haubner, R., Wester, H. J., Weber, W. A., Mang, C., Ziegler, S. I., Goodman, S. L., Senekowtisch-Schmidtke, R., Kessler, H., and Schwaiger, M. (2001) Noninvasive imaging of $\alpha_v\beta_3$ integrin expression using ^{18}F-labeled RGD-containing glycopeptide and positron emission tomography. *Cancer Res. 61*, 1781−1785.

(19) Beer, A. J., Haubner, R., Goebel, M., Luderschmidt, S., Spilker, M. E., Webster, H.-J., Weber, W. A., and Schwaiger, M. (2005) Biodistribution and pharmacokinetics of the $\alpha_v\beta_3$-selective tracer ^{18}F-Galacto-RGD in cancer patients. *J. Nucl. Med. 46*, 1333−1341.

(20) Haubner, R., Weber, W. A., Beer, A. J., Vabuliene, E., Reim, D., Sarbia, M., Becker, K.-F., Goebel, M., Hein, R., Wester, H.-J., Kessler, H., and Schwaiger, M. (2005) Noninvasive visualization of the activated $\alpha_v\beta_3$ integrin in cancer patients by positron emission tomography and [^{18}F]Galacto-RGD. *PLOS Med. 2 e70*, 244−252.

(21) Harris, T. D., Kalogeropoulos, S., Nguyen, T., Liu, S., Bartis, J., Ellars, C., Edwards, D. S., Onthank, D., Yalamanchili, P., Robinson, S. P., Lazewatsky, J., and Barrett, J. A. (2003) Design, synthesis and evaluation of radiolabeled integrin $\alpha_v\beta_3$ antagonists for tumor imaging and radiotherapy. *Cancer Biother. Radiopharm. 18*, 627−641.

(22) Onthank, D. C., Liu, S., Silva, P. J., Barrett, J. A., Harris, T. D., Robinson, S. P., and Edwards, D. S. (2004) ^{90}Y and ^{111}In complexes of a DOTA-conjugated integrin $\alpha_v\beta_3$ receptor antagonist: Different but biologically equivalent. *Bioconjugate Chem. 15*, 235−241.

(23) Haubner, R., and Wester, H. R. (2004) Radiolabeled tracers for imaging of tumor angiogenesis and evaluation of anti-angiogenic therapies. *Curr. Pharm. Des. 10*, 1439−1455.

(24) Poethko, T., Thumshirn, G., Hersel, U., Rau, F., Haubner, R., Schwaiger, M., Kessler, H., and Wester, H. J. (2003) Improved tumor uptake, tumor retention and tumor/background ratios of pegylated RGD multimers. *J. Nucl. Med. 44*, 46P.

(25) Chen, X. Y., Park, R., Shahinian, A. H., Tohme, M., Khankaldyyan, V., Bozorgzadeh, M. H., Bading, J. R., Moats, R., Laug, W. E., and Conti, P. S. (2004) ^{18}F-labeled RGD peptide: initial evaluation for imaging brain tumor angiogenesis. *Nucl. Med. Biol. 31*, 179−189.

(26) Chen, X. Y., Park, R., Shahinian, A. H., Bading, J. R., and Conti, P. S. (2004) Pharmacokinetics and tumor retention of ^{125}I-labeled RGD peptide are improved by PEGylation. *Nucl. Med. Biol. 31*, 11−19.

(27) Chen, X. Y., Sievers, E., Hou, Y., Park, R., Tohme, M., Bart, R., Bremner, R., Bading, J. R., and Conti, P. S. (2005) Integrin $\alpha_v\beta_3$-targeted imaging of lung cancer. *Neoplasia 7*, 271−279.

(28) Chen, X. Y. (2006) Multimodality imaging of tumor integrin $\alpha_v\beta_3$ expression. *Mini-Rev. Med. Chem. 6*, 227−234.

(29) Liu, S., Robinson, S. R., and Edwards, D. S. (2003) Integrin $\alpha_v\beta_3$ directed radiopharmaceuticals for tumor imaging. *Drugs Future 28*, 551−564.

(30) Liu, S. (2006) Radiolabeled multimeric cyclic RGD peptides as integrin $\alpha_v\beta_3$-targeted radiotracers for tumor imaging. *Mol. Pharm. 3*, 472−487.

(31) Liu, S., and Edwards, D. S. (2001) Bifunctional chelators for therapeutic lanthanide radiopharmaceuticals. *Bioconjugate Chem. 12*, 7−34.

(32) Harris, T. D., Sworin, M., Williams, N., Rajopadhye, M., Damphousse, P. R., Glowacka, D., Poirier, M. J., and Yu, K. (1999) Synthesis of stable hydrazones of a hydrazinonicotinyl-modified peptide for the preparation of ^{99m}Tc-labeled radiopharmaceuticals. *Bioconjugate Chem. 10*, 808−814.

(33) Liu, S., Edwards, D. S., Harris, A. R., Ziegler, M. C., Poirier, M. J., Ewels, B. A., DiLuzio, W. R., and Hui, P. (2001) Towards developing a non-$SnCl_2$ formulation for RP444: a new radiopharmaceutical for thrombus imaging. *J. Pharm. Sci. 90*, 114−123.

(34) Liu, S., Edwards, D. S., Williams, N. E., and Harris, A. R. (2002) ^{99m}Tc-labeling of a hydrazinonictotinamide-conjugated LTB_4 receptor antagonist useful for imaging infection and inflammation. *Bioconjugate Chem. 13*, 881−886.

(35) Liu, S. (2005) 6-Hydrazinonicotinamide derivatives as bifunctional coupling agents for ^{99m}Tc-labeling of small biomolecules. *Top. Curr. Chem. 252*, 117−153.

(36) Edwards, D. S., Liu, S., Barrett, J. A., Harris, A. R., Looby, R. J., Ziegler, M. C., Heminway, S. J., and Carroll, T. R. (1997) A new and versatile ternary ligand system for technetium radiopharmaceuticals: water soluble phosphines and tricine as coligands in labeling a hydrazino nicotinamide-modified cyclic glycoprotein IIb/IIIa receptor antagonist with ^{99m}Tc. *Bioconjugate Chem. 8*, 146−154.

(37) Liu, S., Edwards, D. S., and Harris, A. R. (1998) A novel ternary ligand system for ^{99m}Tc-labeling of hydrazinonicotinamide-modified biologically active molecules using imine-N containing heterocycles as coligands. *Bioconjugate Chem. 9*, 583−595.

(38) Liu, S., Edwards, D. S., Harris, A. R., Heminway, S. J., and Barrett, J. A. (1999) Technetium complexes of a hydrazinonicotinamide-conjugated cyclic peptide and 2-hydrazinopyridine: Synthesis and characterization. *Inorg. Chem. 38*, 1326−1335.

(39) Haubner, R., Bruchertseifer, F., Bock, M., Schwaiger, M., Wester, H. J. (2004) Synthesis and biological evaluation of ^{99m}Tc-labeled cyclic RGD peptide for imaging integrin $\alpha_v\beta_3$ expression. *Nuklearmedizin 43*, 26−32.

BC060235L

Influence of Carrier Proteins on the Immunologic Response to Haptenic Antitetrodotoxin Vaccine

Qin-Hui Xu,* Xiu-Nan Zhao, Jun-Ping Cheng, Chang-Hua Wei, Qin-Hua Zhang, and Kang-Tai Rong

Beijing Institute of Pharmacology and Toxicology, 27 Taiping Road, Beijing 100850, P.R. China. Received April 4, 2006; Revised Manuscript Received August 29, 2006

Tetrodotoxin (TTX) is a haptenic, highly toxic neurotoxin with no specific antidote available yet. Anti-TTX vaccine is being studied for antitoxin development. The effectiveness of the carrier protein in eliciting TTX-specific antibody response was comparatively studied. TTX was conjugated to *Tachypleus tridentatus* hemocyanin (TTH), *Limulus polyphemus* hemocyanin (LPH), tetanus toxoid (TT), diphtheria toxoid (DT), and bovine serum albumin (BSA) chemically to form artificial antigens TTH−TTX, LPH−TTX, TT−TTX, DT−TTX, and BSA−TTX, respectively, with which BALB/c mice were immunized, and the antibody response and antitoxic efficacy were detected. The serum anti-TTX antibody response and antitoxic efficacy varied markedly with adopted carrier protein. TTH−TTX elicited the best and BSA−TTX the worst TTX-specific antibody response. The proportion of the immunized mice surviving a 3× lethal dose (LD) dose of TTX challenge was 92%, 75%, 42%, 8%, and 0% for TTH−, TT−, LPH−, DT−, and BSA−TTX conjugates, respectively. The rank order of total efficacy of carrier protein for both anti-TTX antibody response and antitoxic effect was TTH > TT > LPH > DT > BSA. As a result of formaldehyde treatment in coupling of TTX carriers, the relative immunogenicity of TTX *vs* carrier, that is, the ratio of TTX- to carrier-specific antibody response, evidently varied with respective carrier adopted, in a rank order of TT > BSA > TTH > DT > LPH. The results suggest that the carrier protein used in haptenic TTX vaccine is greatly important in eliciting potent anti-TTX antibody, and both TTH and TT are the preferred carriers for development of excellent experimental TTX vaccine.

INTRODUCTION

A small molecular chemical is immunologically inert. So it has to be chemically modified by covalent linking to a large molecular weight carrier protein (CP)[1] to form an artificial antigen before it can act as an immunogen (*1*−*6*). The selection of the carrier molecule of the haptenic vaccine is paramount for the successful production of hapten-specific antibody, although special research on selection of CP for a haptenic vaccine is very rare (*7*, *8*).

Tetrodotoxin (TTX), mainly found in the organs of puffer fish, is one of the highly toxic haptenic neurotoxins. TTX blocks diffusion of sodium through the sodium channel, preventing depolarization and propagation of action potentials in nerve cells. Poisoning with TTX usually occurs after ingestion of improperly prepared TTX-containing puffer fish in China and Japan where the puffer fish is considered a delicacy. Death in seriously poisoned humans often occurs from respiratory failure (*9*−*11*). Management of clinical TTX poisoning disease is often difficult, and the main treatment is meticulous supportive care, but it is usually inefficient in serious cases. So far no specific antidote for TTX poisoning has been available (*12*, *13*). Immunological protection, especially the passive immunotherapy of antitoxin, has been considered as a unique measure capable of conquering TTX diseases; studies in this field have been published with varying degrees of success (*14*−*19*). As a first stage to producing a potential anti-TTX antitoxin for treating victims, a chemo-experimental vaccine of TTX that could highly effectively protect animals from TTX intoxication has been developed (*20*−*22*), and a preliminary attempt of passive immunization research for TTX has been performed (*23*) in our lab.

The purpose of this report is to present an anterior research on the selection of CP in anti-TTX experimental vaccine in order to obtain a potent antibody response and then excellent antitoxic effect from TTX vaccine and further to develop a potential anti-TTX antitoxin. Five experimental vaccines constructed by coupling TTX to different proteins have been compared in their immunogenic potency and antitoxic efficacy in mice, the possible cause for the effect differences among vaccines has been analyzed experimentally, and the optimal carriers adopted in TTX vaccine have been validated.

MATERIALS AND METHODS

Materials. TTX (M_r 319.3) was purchased from Fisheries Research Institute of Hebei Province (Qinhuangdao, China); the product was prepared by freeze-drying the original solution containing citrate buffer with pH 4.8−4.9 and with purity of 98%. Bovine serum albumin (BSA, M_r 67 000) and *Limulus polyphemus* hemocyanin (LPH, M_r 3 300 000) were purchased from Sigma; diphtheria toxoid (DT, M_r 63 000) and tetanus toxoid (TT, M_r 67 000) were obtained from Changchun Institute of Biological Products (Changchun, China); *Tachypleus tridentatus* hemocyanin (TTH) with molecular weight of 3 000 000 Da by ultracentrifugation analysis was prepared by our lab. All these proteins were lyophilized.

Mice. Female BALB/c mice, aged 6−8 weeks, Grade II, Certificate No. SCXK 2003-001, were obtained from the Institute of Jing-Feng Medical Laboratory Animals (IJM) (Beijing, China) and were housed under standard laboratory conditions and fed *ad libitum* diet and water. All animal study

* Corresponding author. Tel: +86-10-6687-4609. Fax: +86-10-6821-1656. E-mail address: xuqh_bj@yahoo.com.

[1] Abbreviations: BSA, bovine serum albumin; CP, carrier protein; DT, diphtheria toxoid; ELISA, enzyme-linked immunosorbent assay; K_{ap}, apparent affinity; LPH, *Limulus polyphemus* hemocyanin; PBS, phosphate-buffered saline; TT, tetanus toxoid; TTH, *Tachypleus tridentatus* hemocyanin; TTX, tetrodotoxin.

10.1021/bc060083u CCC: $33.50 © 2006 American Chemical Society
Published on Web 11/02/2006

procedures were approved by the Center on Experimental Animal Care and Research from our Institute.

Preparation of Artificial Antigen. TTX was conjugated to CP via formaldehyde as the coupling agent to form artificial antigen as described previously with modification (*22*−*24*). Briefly, 1 mg of lyophilized TTX was dissolved in 1 mL of distilled water to yield an aqueous solution consisting of citrate buffer, pH 4.9. CP (8 mg), that is, TTH, TT, LPH, DT, or BSA, was dissolved in 2.0 mL of 20 mM phosphate-buffered saline (PBS) (pH 6.8), and TTX solution was added to yield a weight ratio of TTX to CP of 1:8. Then formaldehyde was added up to final concentration of 1.5%. The reagents were thoroughly mixed and slowly shaken in a 30 °C water bath for 72 h, and then dialyzed for 48 h at 4 °C against six 1 L changes of PBS (pH 7.2) to remove residual free TTX. TTX−CP conjugates, that is, TTH−TTX, TT−TTX, LPH−TTX, DT−TTX, and BSA−TTX, were obtained, and conjugate aliquots were stored at −20 °C before use. In addition, the formal-treated control CPs, that is, f−TTH and f−BSA, were prepared by the above procedure with omission of TTX.

Immunization of Mice. Mice were randomly divided into groups of 12 and immunized intraperitoneally (ip) with 50 μg of TTX−CP, emulsified by mixing it with an equal volume of complete Freund's adjuvant. Booster immunizations were administered at the 15th day after the primary immunization (d15), d30, d55, d85, d115, and d150 with 50 μg of TTX−CP per injection, emulsified in incomplete Freund's adjuvant or in saline solution alternatively. Each mouse received a total of 350 μg of artificial antigen in terms of the amounts of CP. In addition, mice were immunized with representative CPs instead, that is, DT, TT, and TTH, according to the same scheme acting as control.

Determination of TTX-Specific Antibody Response. The antisera were collected on schedule during the immunization and the TTX challenge course by tail-bleeding and stored at −20 °C until tested. Antibody quality, expressed by parameters antibody titer and apparent affinity, was tested as described before (*22*, *23*). Briefly, test antigen BSA−TTX, at a concentration of 2 μg/mL, 100 μL/well, was coated onto 96-well microtiter plates for detection of antibody against all TTX conjugates except BSA−TTX itself, and instead, TTX−DT was used for detection of TTX−BSA, in order to avoid the false positive reaction from the antibody against CP of immunogen reacting on the same CP in test antigen. DT−TTX acting as test antigen was certified essentially identical with BSA−TTX in preliminary experiments.

The antisera were tenfold serially diluted in PBS (pH 7.2) containing 1% BSA, and the antibody reactivity with test antigen (BSA−TTX or DT−TTX) was detected by enzyme-linked immunosorbent assay (ELISA). TTX-specific antibody level was expressed as antibody titer (**n**). The **n** value was defined as the logarithm of specimen dilution at which the positive reaction was certificated as a result of $A_{490\ nm}$ read on a Bio-Rad model 550 microplate reader (Bio-Rad), exceeding those in normal mice sera control 3-fold.

Apparent affinity (K_{ap}) was assayed by competition-inhibited enzyme immunoassay. Briefly, the mixtures of a series of molar concentrations of TTX solution and antibody specimens in fixed dilutions ranging from 10^2−10^5 were incubated with test antigen at 37 °C for 0.5 h. Then anti-TTX antibody reactivity was determined as above, and IC_{50}, the TTX concentration (M) inhibiting 50% of antibody binding activity to test antigen, was calculated. The apparent affinity, K_{ap}, was defined as the negative logarithm of IC_{50} ($K_{ap} = pIC_{50}$).

Determination of CP-Specific Antibody Response. CP-specific antibody in antisera was determined by ELISA procedure same as the above by a modification of using respective CP alone, that is, TT, DT, or TTH, instead of BSA−TTX or DT−TTX conjugate as a test antigen.

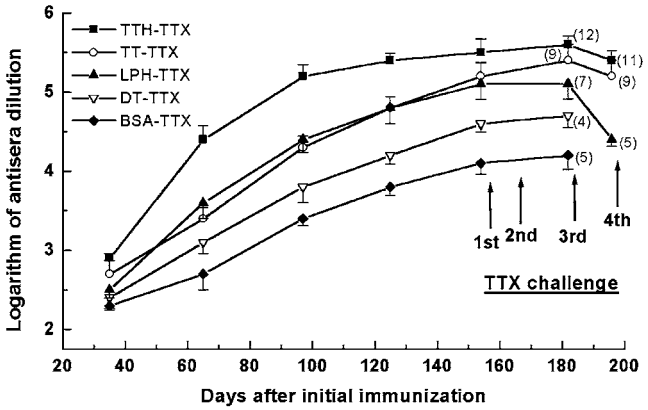

Figure 1. Comparison of the dynamic course of TTX-specific antibody level among TTX vaccines. BALB/c mice in groups were immunized with different TTX−carrier conjugates, and the antiserum specimens were prepared on schedule, initially at day 35 after initial immunization. Antibody titer (**n**), defined as the negative logarithm of the final dilution of antisera at which positive antibody reactivity appeared, was detected by ELISA procedure and expressed as mean ± SEM, $n = 12$ per group initially, and thereafter the survival number is indicated otherwise in parentheses.

Calculation of Relative Immunogenicity of TTX *vs* CP. The relative immunogenicity of TTX *vs* CP was reflected by relative antibody response intensity and expressed as the ratio of TTX- to carrier-specific antibody response in $A_{490\ nm}$ read assayed as above.

TTX Challenge Experiment. To compare the antitoxic effect of different CP−TTX vaccines, 12 immunized mice from each group were challenged repeatedly with 1× lethal dose (LD) of TTX for the first challenge at d157, 2×LD for the second at d167, 3×LD for the third at d183, and 4×LD for the fourth at d198. Referring to a previous report (*25*), a dose of 13.5 μg/kg of TTX in 10 mL/kg of normal saline solution was defined as 1×LD of TTX intraperitoneal (ip) challenge for female BALB/c mice in this study. The survivals were determined 24 h after TTX exposure, and the lethal time in the case of decedents was recorded.

Statistical Analysis. All replicate data were expressed as mean ± S.E.M. The differences among groups were determined by using Student's *t*-test, and $P < 0.05$ was considered significant as compared with the corresponding control.

RESULTS

Comparison of the Dynamic Course of TTX-Specific Antibody Level among Different Vaccines. The circulating TTX-specific antibody level (**n**) was increased gradually within 3−6 months (Figure 1). Among the five TTX vaccines, the quickest antibody-raising rate occurred in the TTH−TTX group; a moderate rate occurred in both the TT− and LPH−TTX groups; a slower rate occurred in the DT−TTX group; and the slowest rate occurred in the BSA−TTX group. A 3-month period for TTH group but a 5−6-month period for the others was necessary for the antibody titer to ascend to its top level. As a result, the antibody titer difference between the highest in the TTH−TTX and the lowest in the BSA−TTX group approximated two units of **n** value during the antibody-raising course. The **n** value from the fourth assay (d125) exemplified in Table 1 statistically differed from each other for all paired comparisons between groups, except TT−TTX *vs* LPH−TTX. The sequence of final antibody level magnitude was accordant with the antibody-raising rate, keeping rank as TTH−, TT−/LPH−, DT−, and BSA−TTX groups (Figure 1). After repeated

Table 1. Comparison of the Antibody Level among TTX Vaccines with Different Carrier Proteins

		statistical significance of difference between groups[b]				
immunogen	titer (**n**)[a]	BSA−TTX	DT−TTX	LPH−TTX	TT−TTX	TTH−TTX
TTH−TTX	5.4 ± 0.1	***	***	*	**	
TT−TTX	4.8 ± 0.1	***	**	†		
LPH−TTX	4.8 ± 0.2	***	*			
DT−TTX	4.2 ± 0.1	*				
BSA−TTX	3.8 ± 0.1					

[a] Antisera were collected at day 125 after initial immunization. The titer (**n**) was detected as note in Figure 1 and expressed as mean ± SEM, $n = 12$ per group. [b] Asterisks and daggers indicated statistical significance of difference in **n** values: † $P > 0.05$, * $P < 0.05$, ** $P < 0.01$, and *** $P < 0.001$, compared with each other group by *t*-test.

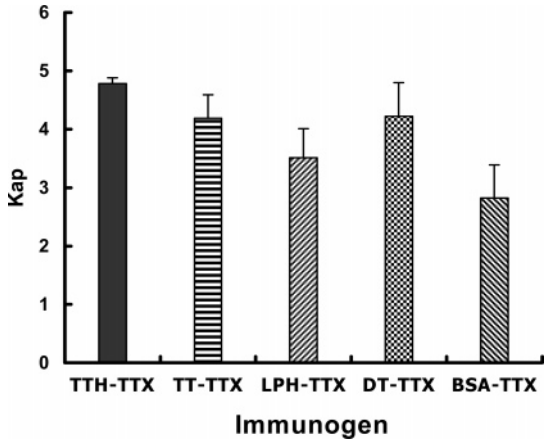

Figure 2. Comparison of TTX-specific antibody affinity among TTX vaccines. Antisera were prepared before the first TTX challenge in groups. Apparent affinity, K_{ap}, defined as the negative logarithm of IC_{50}, the TTX concentration (M) inhibiting 50% of antisera binding activity to test antigen ($K_{ap} = pIC_{50}$), was tested by competition-inhibited enzyme immunoassay procedure and expressed as mean ± SEM, $n = 12$ per group.

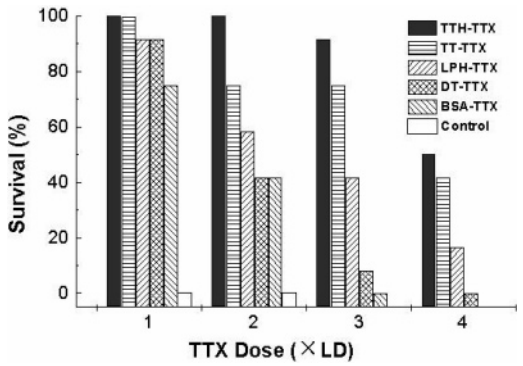

Figure 3. Comparison of antitoxic efficiency among TTX vaccines. Immunized mice in groups of 12 were intraperitoneally challenged repeatedly with 1×LD of TTX for the first challenge at the 157th day after initial immunization (d157), 2×LD for the second at d167, 3×LD for the third at d183, and 4×LD for the fourth at d198. All control mice, uninoculated or inoculated with TTH or TT alone, died of 1×LD ($n = 22$) and 2×LD ($n = 6$) TTX challenge; 1×LD = 13.5 μg/kg, in 10 mL/kg of normal saline. The survivors were counted 24 h after TTX exposure.

TTX challenges, the antibody level declined slightly in both the TTH and TT vaccines and sharply in the LPH vaccine, while all mice in the DT− and BSA−TTX groups had died off, implying that the circulating antibody had been neutralized by TTX *in vivo* (Figure 1). No TTX-specific antibody certainly was detected in the sera from mice immunized with CP alone.

Comparison of Antibody Affinity among TTX Vaccines. The apparent affinity (K_{ap}) for TTX-specific antibody, assayed before the first TTX challenge, also varied with CP adopted in these vaccines (Figure 2). The difference between the highest in the TTH−TTX and the lowest in BSA−TTX group was as high as approximately two units of K_{ap} value; the average magnitude of K_{ap} sequenced basically same as that of antibody level with the exception of the DT−TTX group, which showed slightly higher K_{ap} value. In the TTH−TTX group, a lower standard deviation of K_{ap} value implied that the antibody affinity matured more rapidly and then more readily tended to uniformity than in other four vaccines.

Comparison of Antitoxic Efficacy among TTX Vaccines. TTX challenge experiments began at d157 when the antibody level in all tested groups approximately approached the top level and was repeated at intervals of 10−16 days with gradually increasing doses (Figure 3). The majority of the immunized mice were able to tolerate more than one TTX exposure. The group TTH−TTX showed the most excellent effect, all mice surviving a 2×LD single dose and the majority surviving increasing TTX doses, and the group TT−TTX showed a slightly lower effect, all surviving a 1×LD single TTX dose. In turn, LPH−TTX presented a moderate antitoxic potency, the majority surviving 1×LD and the survival rate descending sharply with the increasing TTX doses. The DT−TTX showed a poorer effect; and especially, the BSA−TTX showed the poorest effect, none surviving the 3×LD TTX dose. The survival proportion of the immunized mice, for example, challenged with a single TTX dose of 3×LD, was 92%, 75%, 42%, 8%, and 0% for TTH−, TT−, LPH−, DT−, and BSA−TTX, respectively. The group sequence in anti-TTX poisoning effect was approximately consistent with that for both antibody-raising rate and antibody level (Figure 1), that is, in the order TTH, TT, LPH, DT, and BSA carrier. All control mice, uninoculated or immunized with TTH or TT alone, died of 1× or 2×LD TTX exposure.

Table 2. Comparison of Lethal Time for Victims among TTX Vaccines

immunogen	number of mice	TTX dose[a] (×LD)	lethal time[b] (min)
uninoculated control	12	1	13 ± 2
	6	2	5 ± 0
TTH or TT control	10	1	10 ± 1
TTH−TTX	6	3−4	22 ± 3*,‡
TT−TTX	7	2−4	56 ± 26*,†
LPH−TTX	10	1−4	20 ± 6
DT−TTX	12	1−4	21 ± 4†
BSA−TTX	12	1−3	10 ± 1

[a] The animals were challenged as described in Figure 3. [b] Lethal times are means ± SEM. *$P < 0.05$ vs control of 1×LD and †$P < 0.05$, ‡$P < 0.01$ vs BSA−TTX by *t*-test.

In addition, the decedents in all groups except BSA−TTX, especially in TTH− and TT−TTX groups, survived longer than those in control groups, even those who were challenged with higher TTX doses, whereas the victims in the BSA−TTX group behaved almost the same as the control (Table 2).

Influence of Formaldehyde Treatment of CP on Its Antigenicity. In an attempt to explain the cause of the difference in TTX-antibody response among TTX vaccines, the influence of formaldehyde treatment in coupling of TTX−CP on CP

Table 3. Cross-reactivity ($A_{490\ nm}$) of Anti-CP Antisera against CP and CP−TTX Conjugate[a]

	anti-CP antisera eliciting immunogen[c]		
test antigen[b]	TT ($n = 10$)	DT ($n = 8$)	TTH ($n = 9$)
BSA	−	−	−
f−BSA	−	−	−
DT	−	0.38 ± 0.02	−
LPH	−	−	0.73 ± 0.04
TT	0.68 ± 0.05	−	−
TTH	−	−	0.94 ± 0.05
f−TTH	−	−	0.15 ± 0.01‡
DT−TTX	−	0.42 ± 0.02	−
LPH−TTX	−	−	1.11 ± 0.12 **
TT−TTX	0.36 ± 0.05**	−	−
TTH−TTX	−	−	0.98 ± 0.06

[a] $A_{490\ nm}$ values are means ± SEM; n indicates the number of specimens tested. **$p < 0.01$ vs respective CP and ‡$p < 0.01$ vs TTH, by t-test; − denotes a value of $A_{490\ nm} < 0.1$, same as that in normal mice sera control. [b] f−BSA and f−TTH refer to formaldehyde-treated BSA and TTH, the procedure being the same as the preparation of CP−TTX conjugates by omission of TTX. [c] Antisera, collected at day 120 from mice immunized with CP, were tested by ELISA procedure at a dilution of 1:1000.

antigenicity and the cross-antigenicity between CPs have been assayed using mice antisera elicited by three representative CPs, that is, TT, DT, and TTH (Table 3). The anti-TT antisera reacted with TT−TTX far more weakly than with TT alone, whereas both anti-TTH and anti-DT antisera reacted similarly with their respective TTX conjugates and CP alone. Moreover, the anti-TTH antisera reacted very weakly with f−TTH, a product from aggregation of TTH molecules by formaldehyde treatment. These results indicated that the change of antigenicity for CP involved in the TTX conjugate due to formaldehyde treatment varied markedly, that is, significant loss in the case of TT and negligible change in DT and TTH, and that formaldehyde might bring on the loss of most antigenicity in free TTH but had negligible effect on TTH involved in its TTX conjugate.

In addition, except anti-TTH antisera, which reacted with LPH and LPH−TTX, no positive cross-reaction occurred between individual anti-CP antisera and unrelated CP, implying that only TTH and LPH may share common antigenicity.

Cross-Reactivity of Anti-TTX Vaccine Antisera to CP and TTX. To compare the relative immunogenicity of TTX *vs* CP in individual TTX vaccines, both CP-specific and TTX-specific antibodies contained in antisera were measured by the ELISA procedure (Table 4). The antisera elicited by the TT−TTX vaccine strongly reacted with TTX ligand but weakly with TT carrier. Similarly, the anti-TTH−TTX antisera reacted very strongly with TTX but considerably less strongly with TTH, and anti-BSA−TTX antisera moderately to TTX but negligibly to BSA. In contrast, the antisera against both LPH−TTX and DT−TTX reacted with the respective CPs more strongly than with TTX. Furthermore, the antisera from both TTH−TTX and LPH−TTX obviously cross-reacted each other, whether the CP was in a free or coupled state, which was somewhat consistent with the case of anti-TTH antisera being cross-reactive to LPH or LPH−TTX (Table 3).

Based on these data, the relative intensity of anti-TTX to anti-CP antibody response was analyzed (Table 5). The ratio of TTX- to CP-specific antibody response ranks in sequence of TT−, BSA−, TTH−, DT−, and LPH−TTX vaccine.

DISCUSSION

It is considered that proteins of large molecular size and originating from outside the mammalian order are strongly immunogenic and could be preferred as CPs of haptenic vaccine. Among the proteins studied, both TTH and LPH are excellent immunogenic agents themselves (*26*−*28*) and have been effectively used as carriers of other haptenic poisons (*29*, *30*); TT and DT have been clinically used as active immunizing agents for a long time; BSA has the advantage of being easily available in pure form and proven to be an effective carrier (*4*, *31*, *32*), whereas some reports showed it being a weak carrier in other poison conjugates (*33*, *34*).

The present research showed that the anti-TTX antibody response elicited by TTX vaccines varied greatly with vaccine-

Table 4. Cross-Reactivity ($A_{490\ nm}$) of Antisera Elicited by TTX Vaccines to Both Haptenic TTX and CP[a]

	antisera-eliciting immunogen				
test antigen	BSA−TTX ($n = 8$)	DT−TTX ($n = 9$)	LPH−TTX ($n = 10$)	TT−TTX ($n = 12$)	TTH−TTX ($n = 12$)
BSA−TTX	0.75 ± 0.15	0.66 ± 0.14	1.02 ± 0.15	1.20 ± 0.08	1.69 ± 0.07
DT−TTX	0.57 ± 0.10	1.94 ± 0.19	0.93 ± 0.18	1.36 ± 0.06	1.90 ± 0.08
LPH−TTX	†	†	1.72 ± 0.14	†	2.52 ± 0.12
TT−TTX	†	†	†	1.27 ± 0.08	†
TTH−TTX	†	†	1.50 ± 0.05	†	1.56 ± 0.09
BSA	0.20 ± 0.02	−	−	−	−
DT	−	1.12 ± 0.15	−	−	−
LPH	−	−	1.85 ± 0.11	−	1.66 ± 0.12
TT	−	−	−	0.25 ± 0.02	−
TTH	−	−	1.17 ± 0.07	−	1.20 ± 0.10
f−TTH	−	−	−	−	0.18 ± 0.02

[a] Cross-reactivity was assayed by ELISA procedure in which antisera were diluted 1000-fold with PBS containing 1% BSA (pH 7.2). The results ($A_{490\ nm}$) are means ± SEM; the control value of nonspecific binding of normal mice sera (1:1000) to test antigens was 0.09 ± 0.00, $n = 22$. †, not detected; − denotes a value of $A_{490\ nm} < 0.1$, same as that in normal mice sera control. No TTX-antibody reaction was detected from antisera from control mice inoculated with TTH or TT alone ($n = 12$). f−TTH refers to formaldehyde-treated TTH.

Table 5. Analysis for Relative Intensity of Antibody Reaction to TTX and CP

	antisera-eliciting immunogen				
	BSA−TTX	DT−TTX	LPH−TTX	TT−TTX	TTH−TTX
reactivity to CP[a]	±/+	+++	++++	+	+++
reactivity to TTX[a]	++	++	+++	+++	++++
reactivity ratio of TTX/CP[b]	4.3 ± 1.0	0.8 ± 0.2	0.5 ± 0.1	5.0 ± 0.4	1.6 ± 0.1
sequence of ratio[c]	2	4	5	1	3

[a] The grade of intensity was defined according to data in Table 4: ±, $A_{490\ nm} < 0.2$; +, $0.2 < A_{490\ nm} < 0.5$; ++, $0.5 < A_{490\ nm} < 1.0$; +++, $1.0 < A_{490\ nm} < 1.5$; ++++, $A_{490\ nm} > 1.5$. [b] The reactivity ratio means the ratio of TTX-specific antibody reaction with test antigen in which the CP was different from that in immunogen vs CP-specific antibody reaction with respective CP alone. Values are means ± SEM; $n = 8$−12 per group. [c] The numbers denote the sequence of ratios listed above, indicating relative potency of TTX-specific antibody response as $1 > 2 > 3 > 4 > 5$.

constituting CP species. The TTH−TTX was excellent, showing strong antibody response and high antitoxic efficacy; the TT−TTX was just slightly inferior to TTH−TTX in turn; the DT−TTX showed a weak immune effect and some toxic side effects; and the BSA−TTX showed poor immune response. The LPH−TTX vaccine showed only a moderate anti-TTX effect, although LPH is also macromolecular and shares common antigenicity with TTH, as proved by cross-reactivity to anti-TTH antisera (Table 3). Previous reports demonstrated that only 46% of the amino acid sequence of the N-terminal segment of the LPH molecule is identical with that of the α-chain of TTH (*35*, *36*) and that their characteristics are different in ultracentrifugation, chromatography, electrophoresis, electron microscopy, and immunogenicity (*26*−*28*, *37*, *38*). These differences in structure and characteristics might be responsible for their different effect in application to TTX vaccines. Consequently, TTH chiefly and also TT were selected as optimal CP candidates and approved by further study (*22*).

The antitoxic potency for all TTX vaccines was basically consistent with the respective antibody response. The highest antibody quality induced the best antitoxic efficacy in TTH−TTX; the lowest antibody response produced the poorest antitoxic potency in BSA−TTX. This fact demonstrated that the antibody response was consequentially the basis of the antitoxic effect. The results also suggested that an early quick antibody response must result in a higher final circulating antibody level and quicker affinity maturation.

Usually the CP involved in an artificial antigen conjugate may be more immunogenic than the hapten, and the conjugate could induce inhomogeneous antisera containing both CP- and hapten-specific antibodies. So the binary antitoxic sera, for example, against both TT or DT and TTX, would be possibly elicited by immunization with TT− or DT−TTX conjugates. Nevertheless, the results in this study showed that the relative intensity of antibody response to CP and to TTX varied with CP species used in the vaccine (Table 5). Animals responded strongly to the TTX ligand but weakly to the TT carrier for the TT vaccine. Similarly, higher TTX/CP antibody response ratio appeared both in the TTH vaccine, very powerful response, and in the BSA vaccine, very weak response. But, in a contrary mode, a stronger response to CP than to TTX was observed in DT and LPH vaccines. The phenomenon that the immunogenicity of some proteins involved in artificial antigens was inferior to that of haptenic TTX is interesting and inexplicable yet. Whether it is true for other CP−hapten conjugates remains to be studied. The experiments on cross-reactivity of anti-CP antisera showed that formaldehyde treatment caused the majority of antigenicity of free TTH to be lost. Probably some immunologically active group becomes inactive because of intra- and intermolecule cross-linking (*39*, *40*). But, in the case of the TTX−CP conjugate coupled via formaldehyde, the change in CP antigenicity varied according to adoptive protein species, decreasing for TT, invariable for TTH, and increasing for DT and LPH (Table 3). This was even consistent with and thereby might be able partially to interpret the sequence of TTX/CP antibody response ratios (Table 5). The decrease of CP antigenicity might be beneficial to the prominence of anti-TTX antibody response. This imbalance of immune response against CP and TTX may be one of the direct causes of diverse TTX-specific antibody production. There is much more to be learned whether and how the species and structure of CPs bring on different haptenic stimulus properties. This first work will serve as a basis for further elucidation of influences of CP on haptenic vaccine.

The classical coupling technique of TTX to proteins by formaldehyde treatment in which amino groups of proteins were cross-linked with guanidyl groups of the TTX molecule (*24*, *41*) was to some extent reversible; thereby the free toxin resulting from possible decomposition during the storage, management, or even after injection would poison animals as indicated by the early case of paralytic shellfish poison (*24*). By virtue of improvement of preparation and storage of vaccine, all TTX vaccines except DT−TTX showed no perceivable side effects. The majority of mice in the DT−TTX group became thin ($P < 0.01$ *vs* control), developed sag and lackluster hair, and quivered, whereas no visible side effects were found in mice immunized with DT itself. The results suggested that the side effects were induced by the DT vaccine; perhaps it might release free toxin more easily than other CP conjugates by reversible decomposition. The variability in rates of decomposition might be very different from protein to protein.

In conclusion, The TTX vaccines constructed with various CPs brought on obviously different TTX- to CP-specific antibody response ratios. The CP functionally affected the TTX-specific antibody intensity and then the antitoxic effect. The rank order of total efficacy of CP for these respects is TTH > TT > LPH > DT > BSA. Both TTH and TT were selected as optimal CP candidates for a TTX vaccine because of their excellent TTX-specific antibody-eliciting capacity and few side effects. The use of optimal CP may be able greatly to improve the effect of an anti-TTX vaccine and be beneficial to anti-TTX antitoxin research.

ACKNOWLEDGMENT

This work was supported by both the ninth and tenth Five-year Plan Foundation of Military Medical Science, the Chinese P.L.A. The authors are highly grateful to Dr. Z. G. Xue for her help with preparation of TTH and to Prof. Y. F. Ren for critical review of this manuscript.

LITERATURE CITED

(1) Erlanger, B. F. (1973) Principles and methods for the preparation of drug protein conjugates for immunological studies. *Pharmacol. Rev. 25*, 271−280.

(2) Erlanger, B. F. (1980) The preparation of antigenic hapten−carrier conjugates: A survey. *Methods Enzymol. 70A*, 85−104.

(3) Chu, F. S., Lau, H. P., Fan, T. S., and Zhang, G. S. (1982) Ethylendiamine modified bovine serum albumin as protein carrier in the production of antibody against mycotoxins. *J. Immunol. Methods 5*, 73−78.

(4) Makela, O., and Seppala, I. J. T. (1986) Haptens and Carriers. *Handbook of Experimental Immunology in four volumes, 4th ed., Volume 1: Immunochemistry* (Weir, D. M., Ed.) Chapter 3, Blackwell Scientific Publications, Oxford, U.K..

(5) Pauillac, S., Naar, J., Branaa, P., and Chinain, M. (1998) An improved method for the production of antibodies to lipophilic carboxyl hapten using small amount of hapten−carrier conjugate. *J. Immunol. Methods 220*, 105−114.

(6) Johnson, J. K., Cerasolim, D. M., and Lenz, D. E. (2005) Role of immunogen design in induction of soman-specific monoclonal antibodies. *Immunol. Lett. 96*, 121−127.

(7) Naim, J. O., and van Oss, C. J. (1991) The generation of antibody in mice to tuftsin: a naturally occurring phagocytosis stimulating tetrapeptide. *Immunol. Invest. 20*, 351−364.

(8) De Silva, B. S., Egodage, K. L., and Wilson, G. S. (1999) Purified protein derivative (PPD) as an immunogen carrier elicits high antigen specificity to haptens. *Bioconjugate Chem. 10*, 496−501.

(9) Jin, P. G., and Xu, H. X. (1999) Analysis of food poisoning death in 1983−1997 yrs in Zhejiang Province. *Zhejiang Yufang Yixue - Zhejiang Prev. Med. (Chin.) 11*, 20−21.

(10) Chen, W. H. (2001) The decennary food poisoning in island city and measure of prevention and cure. *Chin. J. Health Inspect. 8*, 61−63.

(11) How, C. K., Chern, C. H., Huang, Y. C., Wang, L. M., and Lee, C. H. (2003) Tetrodotoxin poisoning. *Am. J. Emergency Med. 21*, 51−54.

(12) Smith, J. I. (1992) Symptoms and treatment of common seafood poisonings. *Handbook of natural toxins, volume 7: Food poisoning* (Tu, A. T., Ed.) pp 401−414, Marcel Dekker Inc., New York, Basel, Hong Kong.

(13) White, J., Warrell, D., Eddleston, M., Currie, B. J., Whyte, I. M., and Isbister, G. K. (2003) Clinical toxinology-where are we now? *J. Toxicol., Clin. Toxicol. 42*, 263−276.

(14) Hout, R., Armstrong, D. L., and Chanh, T. C. (1989) Protection against nerve toxicity by monoclonal antibodies to the sodium channel blocker tetrodotoxin. *J. Clin. Invest. 83*, 1821−1826.

(15) Kaufman, B., Wright, D. C., Ballou, W. R., and Monheit, D. (1991) Protection against tetrodotoxin and saxitoxin intoxication by a cross-protective rabbit anti-tetrodotoxin antiserum. *Toxicon 2*, 581−587.

(16) Fukiya, S., and Matsumur, K. (1992) Active and passive immunization for tetrodotoxin in mice. *Toxicon 30*, 1631−1634.

(17) Miao, X. F., Gao, Q. B., and Song, J. J. (1993) Preparation and characteristic of monoclonal antibodies against tetrodotoxin. *Acad. J. Second Mil. Med. Univ. (Chin.) 14*, 540−544.

(18) Matsumura, K. (1995) A monoclonal antibody against tetrodotoxin that reacts to the active group for the toxicity. *Eur. J. Pharmacol. Environ. Toxicol. Pharmacol. 29*, 41−45.

(19) Rivera, V. R., Poli, M. A., and Bignami, G. S. (1995) Prophylaxis and treatment with a monoclonal antibody of tetrodotoxin poisoning in mice. *Toxicon 33*, 1231−1237.

(20) Xu, Q. H., Rong, K. T., Yun, L. H., Wei, C. H., Gao, L. S., and Huang, K. (2003) New artificial antigen for tetrodotoxin and its high efficiency on antitoxic effect. *Mianyixue Zazhi-Immunol. J. (Chin.) 19*, 424−428.

(21) Xu, Q. H., Rong, K. T., Yun, L. H., Wei, C. H., Huang, K., and Gao, L. S. (2003) An experimental vaccine against tetrodotoxin with longer term of validity. *U.S. Chin. J. Microbiol. Immunol. 5*, 44−49.

(22) Xu, Q. H., Zhao, X. N., Wei, C. H., and Rong, K. T. (2005) Immunologic protection of anti-tetrodotoxin vaccines against lethal activities of oral tetrodotoxin challenge in mice. *Int. Immunopharmacol. 5*, 1213−1224.

(23) Xu, Q. H., Wei, C. H., Huang, K., and Rong, K. T. (2005) Toxin-neutralizing effect and activity-quality relationship for mice tetrodotoxin-specific polyclonal antibodies. *Toxicology 206*, 439−448.

(24) Johnson, H. M., Frey, P. A., Angelotti, R., Campbell, J. E., and Lewis, K. H. (1964) Haptenic properties of paralytic shellfish poison conjugated to proteins by formaldehyde treatment. *Proc. Soc. Exp. Biol. Med. 117*, 425−430.

(25) Xu, Q. H., Huang, K., Gao, L. S., Zhang, H., and Rong, K. T. (2003) Toxicity of tetrodotoxin towards mice and rabbits. *Weisheng Yanjiu − J. Hyg. Res. 32*, 371−374.

(26) Lamy, J., Lamy, J., Weill, J., Bonaventura, J., Bonaventura, C., and Brenowitz, M. (1979) Immunological correlates between the multiple hemocyanin subunits of *Limulus polyphemus* and *Tachypleus tridentatus. Arch. Biochem. Biophys. 196*, 324−339.

(27) Ellerton, H. D., Ellerton, N. F., and Robinson, H. A. (1983) Hemocyanins- a cuurent perspective. *Prog. Biophys. Mol. Biol. 41*, 143−248.

(28) Chen, X. S., Wu, T. A., and Wang, D. Y. (1984) Studies on the horseshoe crab (*Tachypleus tridentatus*) hemolymph. I. Separation and immunogencity of hemocyanin. *Dongwuxue Yanjiu-Zool. Res.* (*Chin.*) *5*, 105−107.

(29) Wang, G., Xu, Q., Ma, Z., Rong, K., and He, F. (1999) Production and identification of anti-paraoxon monoclonal antibodies. *Weisheng Yanjiu − J. Hyg. Res. 28*, 321−323.

(30) Xu, Q. H., Zhao, Y. M., and Rong, K. T. (2003) Preparation of monoclonal antibodies against neurotoxic agent raised from an organophosphorus hapten and its characterization. *Xibao Yu Fenzi Mianyixue Zazhi - Chin. J. Cell. Mol. Immunol. 19*, 172−175.

(31) Schmidt, D. H., and Butler, V. P. (1971) Immunological protection against digoxin toxicity. *J. Clin. Invest. 50*, 866−871.

(32) Moran, E., O'Keeffe, M., O'Connor, R., Larkin, A. M., Murphy, P., and Clynes, M. (2002) Methods of generation of monoclonal antibodies to the very small drug hapten, 5-benzimidazolecarboxylic acid. *J. Immunol. Methods 271*, 65−75.

(33) Ragelis, E. P. (1985) Report on seafood toxins. *J. Assoc. Off. Anal. Chem. 68*, 252−254.

(34) Grognet, J. M., Ardouin, T., Istin, M., Vandais, A., Noel, J. P., Rima, G., Satge, J., Pradel, C., Sentenac-Roumanou, H., and Lion, C. (1993) Production and characterization of antibodies directed against organophosphorus nerve agent VX. *Arch. Toxicol. 7*, 66−71.

(35) Nemoto, T., and Takagi, T. (1981) The amino acid sequence of the amino-terminal cyanogen bromide fragment of *Tachypleus tridentatus* hemocyanin alpha chain. *Biochim. Biophys. Acta 670*, 79−83.

(36) Yokota, E., and Riggs, A. F. (1984) The structure of the hemocyanin from the horseshoe crab, *Limulus polyphemus.* The amino acid sequence of the largest cyanogen bromide fragment. *J. Biol. Chem. 259*, 4739−4749.

(37) Liu, L., Wang, H. M., Hung, L. S., Li, M. F., and Ku, K. Y. (1979) Hemocyanins: electron microscopy and their conjugation with other molecules. *Shiyan Shengwu Xuebao - Acta Biol. Exp. Sin. (Chin.) 12*, 1−3.

(38) Hong, S. G., Hu, Y. C., Li, Q. F., Xia, C. W., and Li, X. Q. (1997) Studies on hemocyanin of the horseshoe crab, *Tachypleus tridentatus. Xiamen Daxue Xuebao (Ziran Kexue Ban)-J. Xiamen Univ. (Nat. Sci.) (Chin.) 36*, 763−768.

(39) Fraenkel-Conrat, H., and Olcott, H. S. (1948) Reaction of formaldehyde with proteins. VI. Cross-linking of amino groups with phenol, imidazol or indole groups. *J. Biol. Chem. 174*, 827−843.

(40) Metz, B., Jiskoot, W., Hennink, W. E., Crommelin, D. J. A., and Kersten, G. F. A. (2003) Physicochemical and immunochemical techniques predict the quality of diphtheria toxoid vaccines. *Vaccine 22*, 156−167.

(41) Fraenkel-Conrat, H., and Olcott, H. S. (1948) The reaction of formaldehyde with proteins. V. Cross-linking between amino and primary amide or guanidyl groups. *J. Am. Chem. Soc. 70*, 2673−2684.

BC060083U

Biotin Reagents for Antibody Pretargeting. 7. Investigation of Chemically Inert Biotinidase Blocking Functionalities for Synthetic Utility

D. Scott Wilbur,* Donald K. Hamlin, and Ming-Kuan Chyan

Department of Radiation Oncology, University of Washington, Seattle, Washington 98195. Received April 6, 2006; Revised Manuscript Received August 10, 2006

An investigation was conducted to evaluate three biotin derivatives designed to block biotinidase cleavage of the biotinamide bond. Difficulties in multistep syntheses of molecules containing *tert*-butyl protected hydroxymethyl and carboxylate groups positioned α to a biotinamide bond led to the investigation of alternative biotinidase-blocking moieties that do not require protection and deprotection. The targeted biotin derivatives contained serine-*O*-methyl ether, 2-aminobutyric acid, and valine moieties conjugated to the biotin carboxylate functionality. Those derivatives were further modified with a radioiodinated aryl ring to study their biotinidase stability. As a comparison to previously studied biotin derivatives, radioiodinated versions of biotin conjugates that contained (a) no biotinidase stabilizing group, (b) an *N*-methyl (sarcosine) stabilizing group, (c) an α-carboxylate (aspartate) stabilizing group and hydroxymethyl (serine) stabilizing group were also prepared and tested. When tested in human serum, all of the radioiodinated biotinidase-stabilized biotin derivatives had <1% biotinamide cleavage. Thus, under the conditions studied, all of the tested biotinidase blocking moieties appeared to be equal with regards to protection from biotinidase cleavage. Further testing of the biotin derivatives included a HPLC assay to determine their relative dissociation from recombinant streptavidin (rSAv). The dissociation of cyanocobalamin (CN-Cbl) adducts of biotin−serine-*O*-methyl ether, biotin−aminobutyric acid, and biotin−valine were compared with the CN-Cbl adduct of biotin−sarcosine. The relative rates of dissociation found were biotin−sarcosine−CN-Cbl > biotin−valine−CN-Cbl > biotin−serine-*O*-methyl ether−CN-Cbl > biotin−aminobutyric acid−CN-Cbl. Due to the high cost of serine-*O*-ethyl ether (and its N-Boc derivative) and difficulty in syntheses of its biotin derivatives, that adduct is not an attractive candidate for application to compounds used in vivo. The higher lipophilicity and diminished binding of the biotin−valine adduct also makes its use in vivo less attractive. Thus, the biotin−aminobutyric acid adduct appears to be the best candidate for incorporation into biotin derivatives used in vivo, as it simplifies the synthetic procedures, has low cost, and provides effective blocking of biotinidase while retaining high binding affinity.

INTRODUCTION

This laboratory has been involved in the development of radiohalogenated biotin derivatives for therapy of cancer using the monoclonal antibody-based "pretargeting" approach (*1*−*3*). As part of those studies, we have investigated structural requirements in biotin derivatives to block the activity of the enzyme biotinidase (*4*−*7*). Biotinidase functions in a biotin salvage pathway, where it cleaves the biotinamide bond in the biotin−lysine adduct biocytin, which is present from peptidase degradation of biotin-containing carboxylases and histones (*8*, *9*). Biotinidase may also function as a biotin carrier (*10*) to transfer biotin to other proteins such as histones (*11*, *12*). The biotinamide cleavage by biotinidase is not specific for biocytin, as it occurs with biotin conjugates of other alkyl and aromatic amino compounds. This nonspecificity has allowed the development of colorimetric assays with *p*-aminobenzoic acid and aminoquinoline adducts of biotin (*13*), and radiometric assays with biotin adducts of *p*-[^{14}C]aminobenzoic acid (*14*) and [^{125}I]-iodotyramine (*15*), for measuring bioactivity of biotinidase in clinical assays. Indeed, biotinidase may not be highly specific for biotin adducts either, as data has been published which indicates that it can cleave structurally similar desthiobiotinyl-*p*-aminobenzoic acid (*16*) and lipoic acid−lysine adducts (*8*, *17*, *18*).

* Address correspondence to: D. Scott Wilbur, Ph.D., Department of Radiation Oncology, University of Washington, Box 359658, 325 Ninth Ave., Seattle, WA 98104, Phone: 206-341-5437, FAX: 206-341-5438, E-mail: dswilbur@u.washington.edu.

The nonspecific nature of the cleavage of biotinamide bonds in biotin conjugates has made it imperative that biotin derivatives employed in vivo be designed in a manner that blocks the enzyme activity. For this reason, a number of investigators (*19*−*21*), including ourselves (*22*, *23*), have studied biotin conjugates for use in pretargeting applications which have structural features designed to block biotinidase action. Our studies initially followed the lead reported by other investigators in which it was found that the *N*-methylglycine (sarcosine) adduct of biotin fully blocked the action of biotinidase (*24*). However, we felt it was important that the high binding affinity of biotin with avidin or streptavidin be retained, so competitive binding studies were conducted with biotin. From those studies, some biotin adducts were identified which were stable to biotinidase and retained the high binding affinity of the biotin−(strept)avidin system (as measured by a slow dissociation rate). The biotin adducts identified contained either a carboxylate (e.g., biotin−aspartate, biotin−lysine, biotin−cysteine) or hydroxymethyl (e.g., biotin−serine) on the carbon α to the biotinamide bond (*25*).

Subsequently, we have conducted a number of synthetic studies incorporating aspartate, lysine, and serine in the targeted biotin-containing compounds. In most synthetic studies, biotin−aspartate or biotin−lysine was used, and the biotinidase-blocking carboxylate was protected as a *tert*-butyl ester. Unfortunately, unwanted side reaction products were obtained with the *t*-Bu ester protecting group. The problems encountered in synthetic procedures led us to investigate alternate biotinidase blocking

10.1021/bc060084m CCC: $33.50 © 2006 American Chemical Society
Published on Web 10/28/2006

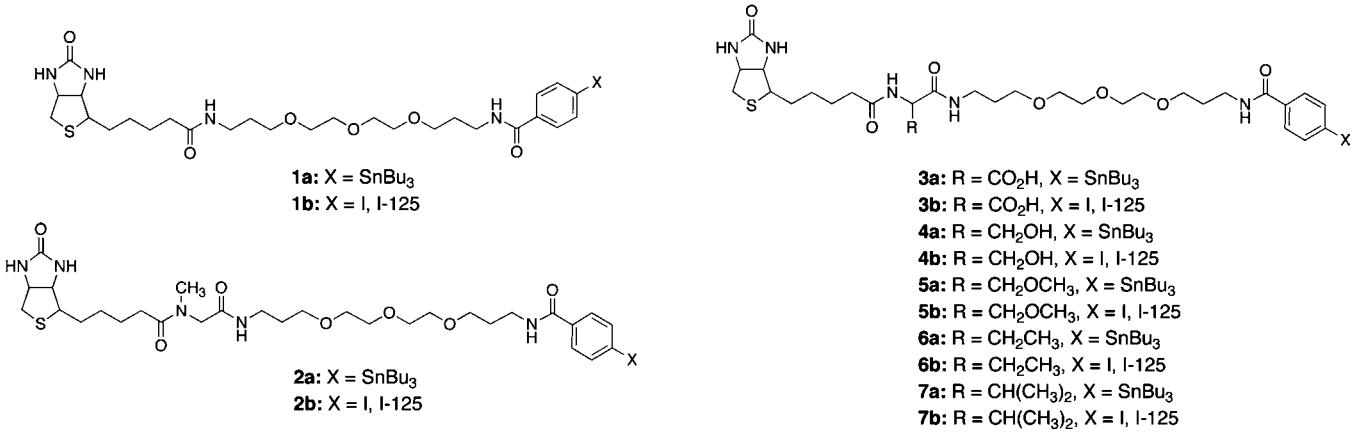

Figure 1. Radioiodinated biotin derivatives and precursors prepared for evaluation in the biotinidase assay.

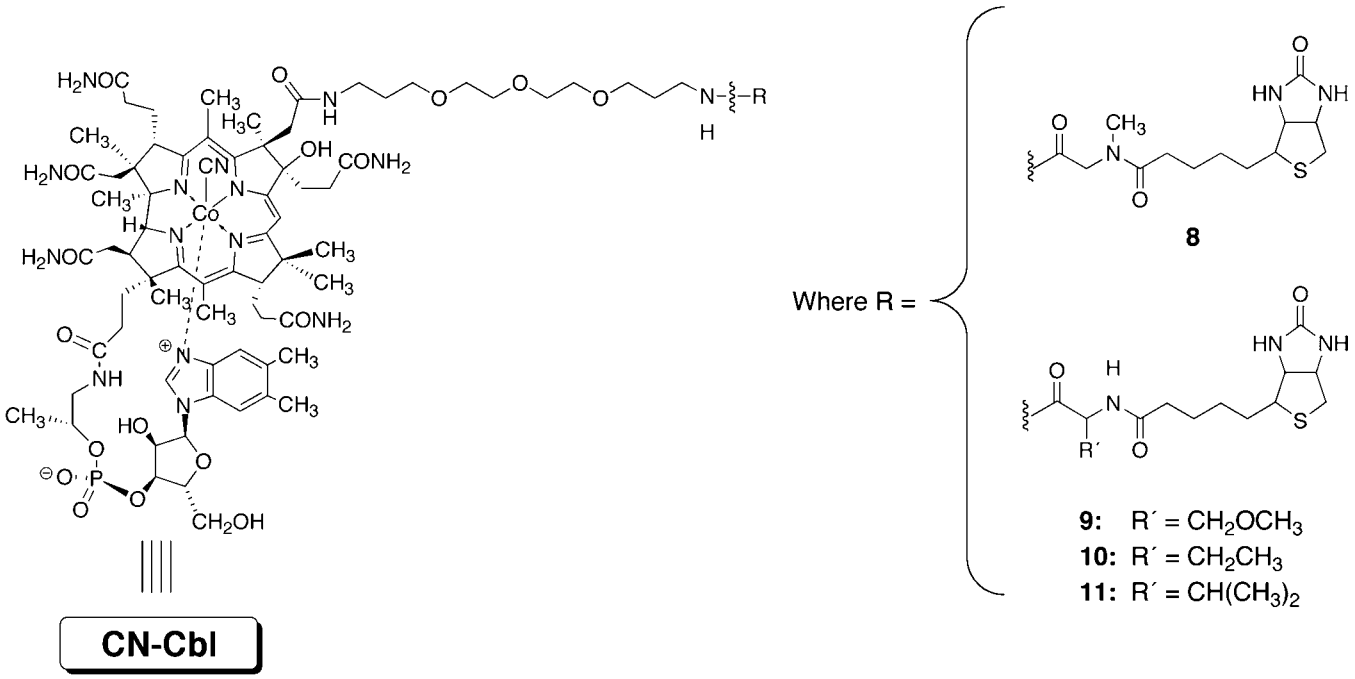

Figure 2. Cyanocobalamin adducts of biotin derivatives prepared for evaluation in the biotin dissociation assay.

groups that are chemically inert or functionalized in a manner that a protecting group does not have to be removed after the synthesis. The studies focused on three biotin−amino acid conjugates that have steric, but nonreactive, functional groups α to the biotinamide bond. The biotin derivatives were synthesized and evaluated for biotinidase stability and binding with streptavidin. The derivatives studied included biotin conjugates of (a) L-serine-methyl ether, (b) D,L-2-aminobutyric acid and (c) L-valine, which contain methyl hydroxymethyl, ethyl and isopropyl functional groups (respectively) α to the biotinamide functionality.

Stability of the biotin−amino acid conjugates toward biotinidase cleavage in human serum was evaluated by preparing radioiodinated biotin derivatives from arylstannyl-biotin derivatives (*22*, *23*). The structures of the biotin derivatives prepared, radioiodinated, and evaluated are shown in Figure 1. Changes in the binding affinity of two of the three biotin−amino acid adducts with recombinant streptavidin (rSAv) was evaluated using a size-exclusion HPLC assay (*26*). In that assay, relative rates of dissociation of biotin derivatives from rSAv can be observed after challenge with a large excess of biotin. The assay required preparation of CN-Cbl conjugates shown in Figure 2. The preparation of biotin derivatives, radioiodination of biotin−arylstannanes, and evaluation of radioiodinated biotin derivatives in the biotinidase assay and biotin−CN-Cbl derivatives in the HPLC dissociation assay are described herein.

EXPERIMENTAL PROCEDURES

General. Most chemicals were purchased from Sigma-Aldrich Corporation (St. Louis, MO, and Milwaukee, WI) as analytical grade and were used without further purification. Boc-serine(Me)-OH DCHA salt was obtained from Bachem Bioscience Inc. (King of Prussia, PA). Biotin *N*-hydroxysuccinimide ester, **11**, was obtained as a gift from Quanta BioDesign, Ltd (Powell, OH). Solvents for HPLC analysis were obtained as HPLC grade and were filtered (0.2 μm) prior to use. Silica gel chromatography was conducted with 70−230 mesh 60 Å silica gel (Aldrich Chemical Co.). Microcon-30 centrifugation concentrators were obtained from Amicon (Beverly, MA). Melting

[1] Abbreviations: Av, avidin; BSA, bovine serum albumin; CN-Cbl, cyanocobalamin; cpm, counts per minute; DCHA, dicyclohexylammonium salt; EDC, 1-[3-(dimethylamino)propyl]-3-ethylcarbodiimide; HOHgBz, hydroxymercuribenzoic acid; NCS, *N*-chlorosuccinimide; NHS, *N*-hydroxysuccinimide; PBS, phosphate-buffered saline; rt, room temperature; rSAv, recombinant streptavidin; SAv, streptavidin; t-Boc, *tert*-butyloxycarbonyl; TFA, trifluoroacetic acid; TFP, tetrafluorophenyl; TFP-OTFA, tetrafluorophenyl trifluoroacetate.

points were obtained in open capillary tubes on a Mel-Temp II apparatus with a Fluke 51 K/J electronic thermometer and are uncorrected.

Spectral Analyses. ^{1}H NMR were obtained on either a Bruker AV 300 (300 MHz) or Bruker AV 500 (500 MHz) instrument. Chemical shifts are expressed as ppm using tetramethylsilane as internal standard (δ = 0.0 ppm). High-resolution mass spectral (HRMS) data were obtained on a Bruker APEX III 47e Fourier transform mass spectrometer using electrospray ionization. For analysis, the samples were dissolved in 50/50 MeOH/H_2O and were introduced by an integral syringe infusion pump (Cole Parmer Series 74900).

Radioactive Materials. Standard methods for safely using radionuclides of iodine were employed (*27*). Na[^{125}I]I was purchased from Perkin-Elmer Life Sciences (Billerica, MA) as high pH, high concentration solutions in 0.1 N NaOH. Measurement of ^{125}I was accomplished on the Capintec CRC-15R or a Capintec CRC-6A Radioisotope Calibrator. Radioactive samples were counted in a Wallac 1480 Wizard Gamma Counter (Perkin-Elmer Life and Analytical Services, Wellesley, MA).

Chromatography. HPLC separations of nonradioactive compounds were obtained on Hewlett-Packard quaternary 1050 gradient pumping system with a variable wavelength UV detector (254 nm) and a Varex ELSD MKIII evaporative light-scattering detector. Analysis of the HPLC data were conducted on Hewlett-Packard HPLC ChemStation software. All reactions were monitored by HPLC. Reversed-phase HPLC chromatography was carried out using an Alltech Altima C-18 column (5 μm, 250 mm × 4.6 mm) using a gradient solvent system at a flow rate of 1 mL/min. A gradient of MeOH and H_2O/0.1% HOAc was used. Starting with 40% MeOH, the initial solvent mixture was held for 2 min, the gradient was increased to 100% MeOH over the next 10 min, and then held at 100% MeOH for 8 min. Retention times (t_R) under these conditions for biotin conjugates are provided with the compound experimental.

HPLC separations of radioiodinated biotin derivatives were conducted using a gradient system consisting of a HP 1050 quaternary pump, a Waters Model 481 UV detector (254 nm), and a Beckman model 170 radioisotope detector. The separations were obtained using HPLC conditions described for Gradient I, above, except water was used in the place of the H_2O/0.1% HOAc.

Size-exclusion HPLC analyses used in the rSAv binding (dissociation) experiments were conducted on a system consisting of a Hewlett-Packard 1050 Multiple Wavelength Detector (280 and 362 nm), isocratic pump, and a Waters Protein-Pak 300SW glass column. The mobile phase was an aqueous solution containing 50 mM potassium phosphate (pH 6.8), 300 mM NaCl, 1 mM EDTA, and 1 mM NaN_3. A flow rate of 1.0 mL/min was used. Retention time for rSAv and bound biotin−cyanocobalamin derivatives was 10.5 min and free biotin−cyanocobalamin derivatives was 14.0 min.

The following compounds were prepared as previously described: **1a**, **1b**, [^{125}I]**1b**, **2a**, **2b**, [^{125}I]**2b** (*22*); **3a**, **3b**, [^{125}I]-**3b**, **4a**, **4b** [^{125}I]**4b** (*23*); **8** (*26*); **18** (*28*); **25**, **26** (*22*); **27** (*26*).

General Procedure for Synthesis of Biotin−Amino Acid−Trioxatridecanediaminebenzamide Adducts, 5a/b−7a/b. A quantity of **19**, **20**, or **21** was dissolved in neat TFA (3−5 mL) and stirred at room temperature for 10 min. Then the TFA was evaporated under a stream of argon. The amine **22**, **23**, or **24** (TFA salt) was washed with EtOAc (3 × 20 mL) and dried under vacuum for 2 h. The crude amine TFA salt was dissolved in a solution of anhydrous DMF (10 mL) and Et_3N (0.25 mL, 1.79 mmol), and then 1.3 equiv of the *p*-tri-*n*-butylstannylbenzoate TFP ester **25** or *p*-iodobenzoate TFP ester **26** was added and stirred at room temperature for 10 min to 1 h. The volatile materials were removed under vacuum. The residue was purified by a silica gel column (1.5 cm × 25 cm), eluting with a mixture of MeOH/EtOAc to give the desired product **5a**, **5b**, **6a**, **6b**, **7a**, or **7b**.

2-(*N*-Biotinoyl)-1-(*N*′-(13′-*p*-(tri-*n*-butylstannyl)benzoylamino)-4′,7′,10′-trio xatridecanamino)-L-serine-*O*-methyl Ether, 5a. Following the general procedure (stirring for 30 min), **5a** was obtained after silica gel chromatography (20% MeOH/EtOAc) as a colorless solid in 87% yield, mp = 137−139 °C. ^{1}H NMR 300 MHz (CD_3OD): δ 0.91 (t, J = 7.3 Hz, 9H), 1.13 (t, J = 8.1 Hz, 4H), 1.32−1.51 (m, 10H), 1.55−1.81 (m, 14H), 1.88−1.96 (m, 2H), 2.32 (t, J = 7.3 Hz, 2H), 2.73 (d, J = 12.5 Hz, 1H), 2.92−2.99 (m, 1H), 3.19−3.35 (m, 4H), 3.37 (s, 3H), 3.49−3.54 (m, 4H), 3.56−3.71 (m, 9H), 4.33 (dd, J = 4.4, 7.9 Hz, 1H), 4.49−4.54 (m, 2H), 7.59 (d, J = 8.2 Hz, 2H), 7.78 (d, J = 8.2 Hz, 2H). HRMS (ES^+) calcd for $C_{43}H_{75}N_5NaO_8SSn$ $(M + Na)^+$: 964.4256. Found: 964.4274. HPLC: t_R = 16.7 min.

2-(*N*-Biotinoyl)-1-(*N*′-(13′-*p*-iodobenzoylamino)-4′,7′,10′-trioxatridecaneam ino)- L-serine-*O*-methyl Ether, 5b. Following the general procedure (stirring for 1 h), **5b** was obtained after silica gel chromatography (40% MeOH/EtOAc) as a colorless solid in 83% yield, mp = 152−154 °C. ^{1}H NMR 300 MHz (CD_3OD): δ 1.34 (t, J = 7.3 Hz, 3H), 1.41−1.52 (m, 2H), 1.56−1.82 (m, 5H), 1.86−1.95 (m, 2H), 2.32 (t, J = 7.3 Hz, 2H), 2.73 (d, J = 12.6 Hz, 1H), 2.94 (dd, J = 5.0, 12.6 Hz, 1H), 3.24 (q, J = 7.3 Hz, 3H), 3.33−3.35 (m, 2H), 3.37 (s, 3H), 3.47−3.54 (m, 3H), 3.56−3.70 (m, 9H), 4.33 (dd, J = 4.4, 8.0 Hz, 1H), 4.49−4.54 (m, 2H), 7.60 (d, J = 8.5 Hz, 2H), 7.87 (d, J = 8.5 Hz, 2H). HRMS (ES^+) calcd for $C_{31}H_{48}IN_5NaO_8S$ $(M + Na)^+$: 800.2166. Found: 800.2157. HPLC: t_R = 11.9 min.

2-(*N*-Biotinoyl)-1-(*N*′-(13′-*p*-(tri-*n*-butylstannyl)benzoylamino)-4′,7′,10′-trio xatridecanamino)aminobutyramide, 6a. Following the general procedure (stirring for 30 min), **6a** was obtained after silica gel chromatography (15% MeOH/EtOAc) as a colorless solid in 91% yield, mp = 130−132 °C. ^{1}H NMR 300 MHz (CD_3OD): δ 0.90−0.99 (m, 10H), 1.14 (t, J = 8.1 Hz, 4H), 1.32−1.51 (m, 10H), 1.55−1.83 (m, 14H), 1.86−1.96 (m, 2H), 2.29 (t, J = 7.3 Hz, 2H), 2.72 (d, J = 12.4 Hz, 1H), 2.94 (dd, J = 5.0, 12.9 Hz, 1H), 3.19−3.35 (m, 6H), 3.51 (t, J = 6.1 Hz, 4H), 3.56−3.70 (m, 9H), 4.16−4.24 (m, 1H), 4.32 (dd, J = 4.4, 7.9 Hz, 1H), 4.51 (dd, J = 4.4, 7.9 Hz, 1H), 7.59 (d, J = 8.3 Hz, 2H), 7.77 (d, J = 8.3 Hz, 2H). HRMS (ES^+) calcd for $C_{43}H_{75}N_5NaO_7SSn$ $(M + Na)^+$: 948.4307. Found: 948.4302. HPLC: t_R = 16.8 min.

2-(*N*-Biotinoyl)-1-(*N*′-(13′-*p*-iodobenzoylamino)-4′,7′,10′-trioxatridecanam ino)aminobutyramide, 6b. Following the general procedure (stirring for 10 min), **6b** was obtained after silica gel chromatography (30% MeOH/EtOAc) as a colorless solid in 88% yield, mp = 80−82 °C. ^{1}H NMR 300 MHz (CD_3OD): δ 0.96 (t, J = 7.5 Hz, 3H), 1.41−1.51 (m, 2H), 1.55−1.83 (m, 8H), 1.86−1.97 (m, 2H), 2.29 (t, J = 7.3 Hz, 2H), 2.72 (d, J = 12.5 Hz, 1H), 2.95 (dd, J = 5.0, 12.7 Hz, 1H), 3.19−3.35 (m, 4H), 3.50 (q, J = 6.4 Hz, 4H), 3.56−3.69 (m, 9H), 4.19 (dd, J = 5.9, 8.3 Hz, 1H), 4.32 (dd, J = 4.5, 7.9 Hz, 1H), 4.52 (dd, J = 4.5, 7.9 Hz, 1H), 7.60 (d, J = 8.6 Hz, 2H), 7.87 (d, J = 8.6 Hz, 2H). HRMS (ES^+) calcd for $C_{31}H_{48}IN_5NaO_7S$ $(M + Na)^+$: 784.2217. Found: 784.2205. HPLC: t_R = 12.2 min.

2-(*N*-Biotinoyl)-1-(*N*′-(13′-*p*-(tri-*n*-butylstannyl)benzoylamino)-4′,7′,10′-trio xatridecanamino)-L-valine, 7a. Following the general procedure (stirring for 30 min), **7a** was obtained after silica gel chromatography (15% MeOH/EtOAc) as a colorless solid in 89% yield, mp = 134−136 °C. ^{1}H NMR 300 MHz (CD_3OD): δ 0.92 (t, J = 7.4 Hz, 6H), 0.97 (dd, J = 2.6, 6.5 Hz, 6H), 1.14 (t, J = 8.0 Hz, 3H), 1.34 (t, J = 7.3 Hz, 6H), 1.39−1.51 (m, 4H), 1.55−1.82 (m, 10H), 1.87−1.96 (m, 2H),

1.99−2.11 (m, 1H), 2.30 (t, J = 7.3 Hz, 2H), 2.72 (d, J = 12.9 Hz, 1H), 2.94 (dd, J = 5.0, 12.7 Hz, 1H), 3.24 (q, J = 7.3 Hz, 6H), 3.29−3.35 (m, 4H), 3.51 (t, J = 6.4 Hz, 4H), 3.55−3.70 (m, 9H), 4.11 (dd, J = 1.8, 7.7 Hz, 1H), 4.32 (dd, J = 4.4, 7.9 Hz, 1H), 4.51 (dd, J = 4.4, 7.9 Hz, 1H), 7.58 (d, J = 8.2 Hz, 2H), 7.77 (d, J = 8.2 Hz, 2H). HRMS (ES$^+$) calcd for $C_{44}H_{77}N_5NaO_7SSn$ (M + Na)$^+$: 962.4463. Found: 962.4453. HPLC: t_R = 16.8 min.

2-(*N*-Biotinoyl)-1-(*N*′-(13′-*p*-iodobenzoylamino)-4′,7′,10′-trioxatridecanam ino)-L-valine, 7b. Following the general procedure (stirring for 10 min), **7b** was obtained after silica gel chromatography (15% MeOH/EtOAc) as a colorless solid in 85% yield, mp = 144−146 °C. ^{1}H NMR 300 MHz (CD_3OD): δ 0.97 (dd, J = 2.9, 6.7 Hz, 6H), 1.41−1.51 (m, 2H), 1.56−1.82 (m, 6H), 1.87−1.95 (m, 2H), 1.97−2.11 (m, 1H), 2.31 (t, J = 7.3 Hz, 2H), 2.73 (d, J = 12.6 Hz, 1H), 2.95 (dd, J = 5.0, 12.7 Hz, 1H), 3.19−3.35 (m, 4H), 3.51 (q, J = 6.3 Hz, 4H), 3.56−3.70 (m, 9H), 4.11 (dd, J = 1.8, 7.8 Hz, 1H), 4.32 (dd, J = 4.5, 7.9 Hz, 1H), 4.52 (dd, J = 4.5, 7.9 Hz, 1H), 7.60 (d, J = 8.7 Hz, 2H), 7.87 (d, J = 8.7 Hz, 2H). LRMS (ES$^+$) calcd for $C_{32}H_{51}IN_5O_7S$ (M + H)$^+$: 776.2554. Found: 776.2563. HPLC: t_R = 12.6 min.

General Procedure for Synthesis of Biotin−Cyanocobalamin Derivatives 9, 10, and 11. To a solution of 48 μmol biotin amino acid adduct **15**, **16**, or **17**, and Et_3N (9 μL, 64 μmol) in anhydrous DMF (2 mL), at room temperature was added 48 μmol trifluoroacetate tetrafluorophenyl ester (TFP-OTFA). The mixture was stirred at room temperature for 0.5 h, and then 32 μmol of the cyanocobalamin-trioxadiamine adduct **27** was added. That mixture was stirred at room temperature for 0.5 h, and EtOAc (15 mL) was added and stirred for an additional 5 min. The crude product was filtered, washed with EtOAc (3 × 10 mL), and then purified by TLC plate (RP-18 F_{254S}, 20 × 20, Merck) eluting with 1:1 MeOH/H_2O.

Biotin−Serine-OMe−Cyanocobalamin Conjugate, 9. Following the general procedure, **9** was obtained as a red solid in 40% yield, mp 183−186 °C. ^{1}H NMR 500 MHz (CD_3OD): d −.49 (s, 3H), 1.23 (s, 6H), 1.28−1.42 (m, 6H), 1.49 (s, 3H), 1.63−1.86 (m, 10H), 1.91 (s, 6H), 1.95−2.26 (m, 6H), 2.29 (d, J = 3.4 Hz, 6H), 2.33−2.42 (m, 6H), 2.50 (s, 3H), 2.59 (s, 6H), 2.63 (s, 3H), 2.85−2.97 (m, 2H), 3.10−3.30 (m, 6H), 3.37 (2xs, 3H), 3.41−3.45 (m, 3H), 3.52−3.71 (m, 14H), 3.79 (dd, J = 3.7, 12.7 Hz, 1H), 3.93 (dd, J = 3.6, 12.6 Hz, 1H), 4.09−4.22 (m, 2H), 4.32−4.38 (m, 1H), 4.50−4.54 (m, 1H), 6.08 (s, 1H), 6.31 (d, J = 3.0 Hz, 1H), 6.54 (s, 1H), 7.17 (s, 1H), 7.28 (s, 1H). HRMS (ES$^+$) calcd for $C_{87}H_{129}CoN_{18}Na_2O_{22}PS$ (M−H+2Na)$^+$: 1945.8115. Found: 1945.8079. HPLC: t_R = 7.8−7.9 min.

Biotin−2-Aminobutyrate−Cyanocobalamin Conjugate, 10. Following the general procedure, **10** was obtained as a red solid in 90% yield, mp 196−199 °C. ^{1}H NMR 300 MHz (CD_3OD): δ 0.48 (s, 3H), 0.96−1.03 (m, 3H), 1.22 (s, 3H), 1.28 (d, J = 5.5 Hz, 3H), 1.34 (t, J = 7.3 Hz, 2H), 1.40 (d, J = 5.7 Hz, 6H), 1.49 (s, 3H), 1.59−1.82 (m, 8H), 1.91 (s, 2H), 1.97−2.26 (m, 10H), 2.30 (s, 6H), 2.41 (s, 1H), 2.51 (s, 3H), 2.53−2.61 (m, 2H), 2.64 (s, 3H), 2.69 (s, 6H), 2.75−3.19 (m, 5H), 3.24 (q, J = 7.3 Hz, 2H), 3.30−3.38 (m, 2H), 3.41−3.46 (m, 2H), 3.52−3.73 (m, 9H), 3.79 (dd, J = 4.5, 12.8 Hz, 1H), 3.94 (dd, J = 3.1, 12.5 Hz, 1H), 3.91−3.97 (m, 1H), 4.08−4.22 (m, 3H), 4.31−4.35 (m, 1H), 4.51 (dd, J = 4.5, 8.0 Hz, 1H), 4.65−4.74 (m, 2H), 6.07 (s, 1H), 6.31 (d, J = 2.8 Hz, 1H), 6.54 (s, 1H), 7.17 (s, 1H), 7.28 (s, 1H), 7.85 (s, 1H); LRMS (ES$^+$) calcd for $C_{87}H_{130}N_{18}O_{21}PSCoNa$ (M + Na)$^+$: 1907.8. Found: 1907.9. HPLC: t_R = 8.5 min.

Biotin−Valine−Cyanocobalamin Conjugate, 11. Following the general procedure, **11** was obtained as a red solid in 86% yield, mp 200−203 °C. ^{1}H NMR 300 MHz (CD_3OD): δ 0.48 (s, 3H), 0.97 (dd, J = 2.8, 6.9 Hz, 6H), 1.17−1.29 (m, 6H), 1.41 (d, J = 8.7 Hz, 6H), 1.49 (s, 3H), 1.60−1.84 (m, 8H), 1.87−2.12 (m, 10H), 2.19 (s, 1H), 2.22−2.26 (m, 1H), 2.29 (s, 6H), 2.50 (s, 3H), 2.55−2.60 (m, 2H), 2.63 (s, 3H), 2.90 (s, 6H), 3.15 (t, J = 6.4 Hz, 3H), 3.25 (t, J = 7.2 Hz, 3H), 3.32−3.35 (m, 2H), 3.41 (s, 6H), 3.45 (s, 3H), 3.51−3.72 (m, 9H), 3.84−3.96 (m, 3H), 4.09−4.23 (m, 3H), 4.31−4.39 (m, 1H), 4.50−4.58 (m, 1H), 4.68−4.76 (m, 1H), 6.07 (s, 1H), 6.31 (d, J = 2.8 Hz, 1H), 6.54 (s, 1H), 7.17 (s, 1H), 7.28 (s, 1H), 7.85 (s, 1H); LRMS (ES$^+$) calcd for $C_{88}H_{133}N_{18}O_{21}PSCo$ (M + H)$^+$: 1899.9. Found: 1899.9. HPLC: t_R = 9.1 min.

General Procedure for Synthesis of Biotin−Amino Acid Adducts, 15−17. A quantity of the amino acid **12** (see below), **13**, or **14** dissolved in a solution of water (15 mL) and sodium hydrogen carbonate (0.50 g, 6.24 mmol), then biotin *N*-hydroxysuccinimide ester (0.71 g, 2.08 mmol) and acetone (15 mmol) were added respectively. The resultant solution was stirred at room temperature for 16 h, then the solution was evaporated to dryness under vacuum. The residue was redissolved in water (50 mL), and the aqueous solution was acidified to pH 2.0 by 1 N HCl. The white precipitate was filtered, washed with water (300 mL), and dried under vacuum to afford the compound **15**, **16** or **17**.

***N*-Biotinoyl-L-serine-*O*-methyl Ether, 15.** *N*-(*tert*-Butoxycarbonyl)-L-serine-*O*-methyl ether DCHA salt (1.0 g, 2.50 mmol) was used rather than 12. To prepare 12, the tBoc protected amino acid was dissolved in neat trifluoroacetic acid (3 mL) and stirred at rt for 10 min. After volatile materials were removed under a stream of argon, the residue was washed with ethyl acetate (3 × 20 mL), then dried under vacuum for 1 h. The dried residue was used directly in the synthesis. Following the general procedure, 15 was obtained as a colorless solid in 81% yield, mp = 245−247 °C. ^{1}H NMR 300 MHz (D_2O/NaOD): d 1.39−1.50 (m, 2H), 1.56−1.81 (m, 4H), 2.35 (t, J = 7.4 Hz, 2H), 2.79 (d, J = 13.4 Hz, 1H), 3.01 (dd, J = 5.0, 13.1 Hz, 1H), 3.33−3.39 (m, 1 H), 3.37 (s, 3H), 3.73−3.75 (m, 2H), 4.40 (2xd, J = 4.1, 4.3 Hz, 1 H), 4.44 (dd, 4.3, 8.0 Hz, 1H), 4.62 (dd, J = 4.3, 8.0 Hz, 1H). HRMS (ES$^+$) calcd for $C_{14}H_{23}N_3NaO_5S$ (M + Na)$^+$: 368.1256. Found: 368.1259. HPLC 4.4 min.

***N*-Biotinoyl-2-aminobutyric Acid, 16.** Following the general procedure, **16** was obtained as a colorless solid in 95% yield, mp 216−218 °C dec. ^{1}H NMR 500 MHz (DMSO-d_6): δ 0.87 (t, J = 7.2 Hz, 3H), 1.27−1.37 (m, 2H), 1.41−1.65 (m, 4H), 1.66−1.74 (m, 1H), 2.10−2.14 (m, 2H), 2.56, 2.59 (2xs, 2H), 2.80, 2.83 (2xd, J = 5.0 Hz, 1H), 3.07−3.12 (m, 1H), 4.07−4.14 (m, 2H), 4.31 (dd, J = 4.3, 8.0 Hz, 1H), 6.35 (s, 1H), 6.40 (s, 1H), 8.02 (s, 1H). HRMS (ES$^+$) calcd for $C_{14}H_{24}N_3O_4S$ (M + H)$^+$: 330.1488. Found: 330.1493. HPLC: t_R = 6.5 min.

***N*-Biotinoyl-L-valine, 17.** Following the general procedure, **17** was obtained as a colorless solid in 86% yield, mp 207−209 °C dec [lit. 215−216 °C] (*29*). ^{1}H NMR 300 MHz (DMSO-d_6): δ 0.87 (d, J = 6.8 Hz, 6H), 1.24−1.38 (m, 2H), 1.40−1.68 (m, 4H), 1.97−2.08 (m, 1H), 2.16 (t, J = 7.2 Hz, 2H), 2.57 (d, J = 12.5 Hz, 1H), 2.82 (dd, J = 5.0, 12.4 Hz, 1H), 3.06−3.12 (m, 2H), 4.10−4.15 (m, 2H), 4.30 (dd, J = 5.1, 7.8 Hz, 1H), 6.38 (d, J = 15.9 Hz, 2H), 7.91 (d, J = 8.5 Hz, 1H). HRMS (ES$^+$) calcd for $C_{15}H_{26}N_3O_4S$ (M + H)$^+$: 344.1644. Found: 344.1645. HPLC: t_R = 8.1 min.

General Procedure for Syntheses of Biotin−Amino Acid−Trioxadiamine Adducts, 19−21. To a solution containing 0.7 mmol of **15**, **16** or **17** and 1-[3-(dimethylamino)propyl]-3-ethylcarbodiimide hydrochloride (0.9 mmol) in anhydrous DMF (8 mL) was added 0.9 mmol of **18**. The reaction was stirred at room temperature for 4 h to 5 days. After that period, DMF was removed under vacuum and the crude residue was purified

by silica column (1.5 cm × 25 cm) eluted with a MeOH/EtOAc mixture to obtain **19**, **20**, or **21**.

2-(*N*-Biotinoyl)-1-(*N*′-(13′-*tert*-butoxycarbonylamino)-4′,7′,-10′-trioxatrideca neamino)-L-serine-*O*-methyl Ether, 19. Following the general procedure (stirring for 5 d), **19** was obtained after silica gel chromatography (40% MeOH/EtOAc) as a colorless solid product in 77% yield, mp 142−144 °C. ^{1}H NMR 300 MHz (CD_3OD): δ 1.49 (s, 9H), 1.62−1.92 (m, 8H), 1.96−2.04 (m, 1H), 2.33−2.45 (m, 2H), 2.77 (d, J = 12.8 Hz, 1H), 2.99 (dd, J = 4.8, 12.8 Hz, 1H), 3.14−3.20 (m, 4H), 3.24−3.38 (m, 3H), 3.41 (s, 3H), 3.55−3.61 (m, 4H), 3.63−3.75 (m, 9H), 4.38 (dd, J = 4.5, 7.7 Hz, 1H), 4.52−4.59 (m, 2H). HRMS (ES^+) calcd for $C_{29}H_{53}N_5NaO_9S$ $(M + Na)^+$: 670.3462. Found: 670.3449. HPLC: t_R = 11.0 min.

2-(*N*-Biotinoyl)-1-(*N*′-(13′-*tert*-butoxycarbonylamino)benzoylamino)-4′,7′,10′-trioxatri-decaneamino)aminobutyramide, 20. Following the general procedure (stirring for 4 h), **20** was obtained after silica gel chromatography (20% MeOH/EtOAc) as a colorless solid in 83% yield, mp 125−127 °C. ^{1}H NMR 300 MHz (CD_3OD): δ 0.99 (t, J = 7.3 Hz, 3H), 1.47 (s, 9H), 1.60−1.87 (m, 10H), 2.31 (t, J = 7.2 Hz, 2H), 2.74 (d, J = 12.6 Hz, 1H), 2.96 (dd, J = 4.9, 12.8 Hz, 1H), 3.16 (t, J = 7.9 Hz, 2H), 3.21−3.35 (m, 4H), 3.52−3.57 (m, 4H), 3.60−3.69 (m, 9H), 4.17−4.25 (m, 1H), 4.34 (dd, J = 5.0, 7.9 Hz, 1H), 4.53 (dd, J = 5.0, 7.9 Hz, 1H). HRMS (ES^+) calcd for $C_{29}H_{53}N_5NaO_8S$ $(M + Na)^+$: 654.3513. Found: 654.3505. HPLC: t_R = 11.4 min.

2-(*N*-Biotinoyl)-1-(*N*′-(13′-*tert*-butoxycarbonylamino)benzoylamino)-4′,7′,10′-trioxatri-decaneamino)-L-valine, 21. Following the general procedure (stirring for 16 h), **20** was obtained after silica gel chromatography (15% MeOH/EtOAc) as a colorless solid in 88% yield, mp 133−135 °C. ^{1}H NMR 300 MHz (CD_3OD): δ 1.08 (dd, J = 2.3, 6.7 Hz, 6H), 1.56 (s, 9H), 1.69−1.94 (m, 8H), 2.10−2.22 (m, 1H), 2.41 (t, J = 7.3 Hz, 2H), 2.83 (d, J = 12.8 Hz, 1H), 3.05 (dd, J = 4.9, 12.8 Hz, 1H), 3.25 (t, J = 6.8 Hz, 2H), 3.30−3.46 (m, 4H), 3.62−3.67 (m, 4H), 3.70−3.78 (m, 9H), 4.21 (dd, J = 1.8, 7.8 Hz, 1H), 4.43 (dd, J = 4.9, 7.8 Hz, 1H), 4.62 (dd, J = 4.9, 7.8 Hz, 1H). HRMS (ES^+) calcd for $C_{30}H_{56}N_5O_8S$ $(M + H)^+$: 646.3850. Found: 646.3856. HPLC: t_R = 11.9 min.

Radioiodination. To 100 μL of a 1 mg/mL solution of **5a**, **6a**, or **7a** was added 1−5 μL of Na[^{125}I]I in 0.1 N NaOH, followed by 15 μL of a 1 mg/mL solution of *N*-chlorosuccinimide in MeOH/5% HOAc. After 5 min, 15 μL of a 1 mg/mL aqueous sodium metabisulfite solution was added. The reaction mixture was then drawn into a syringe for purification by HPLC. The radioiodinated [^{125}I]**5b**, [^{125}I]**6b**, or [^{125}I]**7b** was obtained from the HPLC effluent, collecting the peak that had a retention time 0.2 min later than the nonradioactive **5b**, **6b**, or **7b** (this compensation is made due to the difference in UV and radioactivity detectors).

2-(*N*-Biotinoyl)-1-(*N*′-(13′-*p*-[^{125}I]iodobenzoylamino)-4′,7′,-10′-trioxatrideca neamino)-L-serine-*O*-methyl Ether, [^{125}I]-5b. This compound was obtained in 13% isolated radiochemical yield.

2-(*N*-Biotinoyl)-1-(*N*′-(13′-*p*-iodobenzoylamino)-4′,7′,10′-trioxatridecaneam ino)amino-butyramide, 6b. This compound was obtained in 39% isolated radiochemical yield.

2-(*N*-Biotinoyl)-1-(*N*′-(13′-*p*-iodobenzoylamino)-4′,7′,10′-trioxatridecaneam ino)-L-valine, 7b. This compound was obtained in 19% isolated radiochemical yield.

Biotinidase Cleavage Assay. The same experimental conditions were used as previously reported (*22*). Briefly; the radiolabeled biotin derivative (isolated from HPLC effluent) was diluted to obtain approximately 500 000 cpm per 10 μL in a well counter. To each set of three 0.5 mL aliquots of diluted serum (1:10 with 20 mM phosphate buffer, pH 6.8) was added 10 μL of the HPLC purified radiolabeled biotin derivative in MeOH. Each tube was lightly vortexed and placed in a 37 °C heating block. After the desired time (e.g., 2 h), the vials were removed and 40 μL of 2 mM 4-(hydroxymercuri)benzoic acid (HOHgBz), sodium salt in H_2O, was added to inhibit biotinidase. To that solution was added an excess of rSAv (40 μL; 0.24 mg), and it was incubated at 37 °C for another 30 min. A 200 μL aliquot of each triplicate sample was transferred to a Microcon-30 filter and centrifuged at 3000*g* for 10 min. The material remaining on the filter was washed with 4 × 100 μL phosphate buffer, concentrating by centrifugation each time. The top and bottom (containing filtrate and washes) of the Microcon-30 were counted in a gamma counter. The ratio of nonbound counts (bottom) to the total counts (top and bottom) was calculated to determine the percent of the biotin derivative that had been cleaved. As a control, this procedure was repeated as above except that the 4-(hydroxymercuri)benzoic acid was added prior to the radiolabeled biotin derivative to inhibit biotinidase activity.

HPLC Biotin Derivative Dissociation Measurements. The same experimental conditions were used as previously reported (*26*). Briefly, to 400 μL of a 0.5 mg/mL solution of rSAv (200 μg; 3.8 nmol) in a microcentrifuge vial was added ∼4 equiv (16 nmol) of a biotin conjugate (**8**, **9**, or **10**) dissolved in 20 μL of a 10% aqueous DMSO solution. The rSAv/biotin derivative mixture was incubated for 1 h at room temperature, and 100 μL of the solution was injected onto the SE-HPLC column and eluted to assay binding. To the remaining avidin/biotin derivative solution was added 60 μL of a 0.575 mg/mL solution of biotin (34.5 μg; 141 nmol) in 10% aqueous DMSO. That solution was incubated for 1 h, and 100 μL was removed for analysis by HPLC. The remaining solution was incubated for an additional 2−3 h, and then another 100 μL was removed and analyzed by HPLC.

RESULTS

Synthesis of Biotin Derivatives. Biotin derivatives that contain an unprotected biotinamide bond (**1a/b**), a *N*-methyl-substituted biotinamide bond (**2a/b**), a carboxylate α to the biotinamide bond (**3a/b**), and a hydroxymethyl group α to the biotinamide bond (**4a/b**) were prepared as previously described (*23*). The synthetic route to obtain biotin derivatives that contain a methoxymethyl (**5a/b**), an ethyl (**6a/b**), or an isopropyl (**7a/b**) group α to the biotinamide bond is shown in Scheme 1. 2-Aminobutyric acid, **13**, and valine, **14**, are commercially available, but the serine-*O*-methyl ether, **12**, was not readily obtained, so an alternate, the N-*t*-Boc protected derivative, was used instead. The *t*-Boc protecting group was readily removed to provide **12**, and all three amino acids (**12**, **13**, **14**) were conjugated with biotin *N*-hydroxysuccinimidyl ester to give the desired adducts in 81−95% yields. The resulting biotin derivatives **15**, **16**, and **17** were coupled with mono-*t*-Boc protected trioxadiamine, **18**, to provide adducts **19**, **20**, and **21** in 77−88% yields. Deprotection of **19**, **20**, and **21** was essentially quantitative in neat trifluoroacetic acid (TFA) to provide the free amine derivatives **22**, **23**, and **24**. The biotin−amine derivatives were used without isolation in reactions with benzoate esters **25** and **26**. Iodobenzamide derivatives **5b**, **6b**, and **7b**, used as HPLC standards, were prepared in 83−88% yield by reaction of *p*-iodobenzoate tetrafluorophenyl (TFP) ester **26** with **22**, **23**, or **24** (respectively). Similarly, the stannylbenzoate-containing biotin derivatives **5a**, **6a**, and **7a**, used as intermediates for radioiodination, were prepared in 87−91% yields by reaction of the tri-*n*-butylstannylbenzoate TFP ester, **25**, with **22**, **23**, or **24**.

Four biotin−cyanocobalamin derivatives (**8**, **9**, **10**, **11**) were prepared for evaluation of their relative binding with rSAv.

Scheme 1. Synthetic Route for Preparation of Iodinated and Radioiodinated Biotin Derivatives 5b, 6b, and 7b[a]

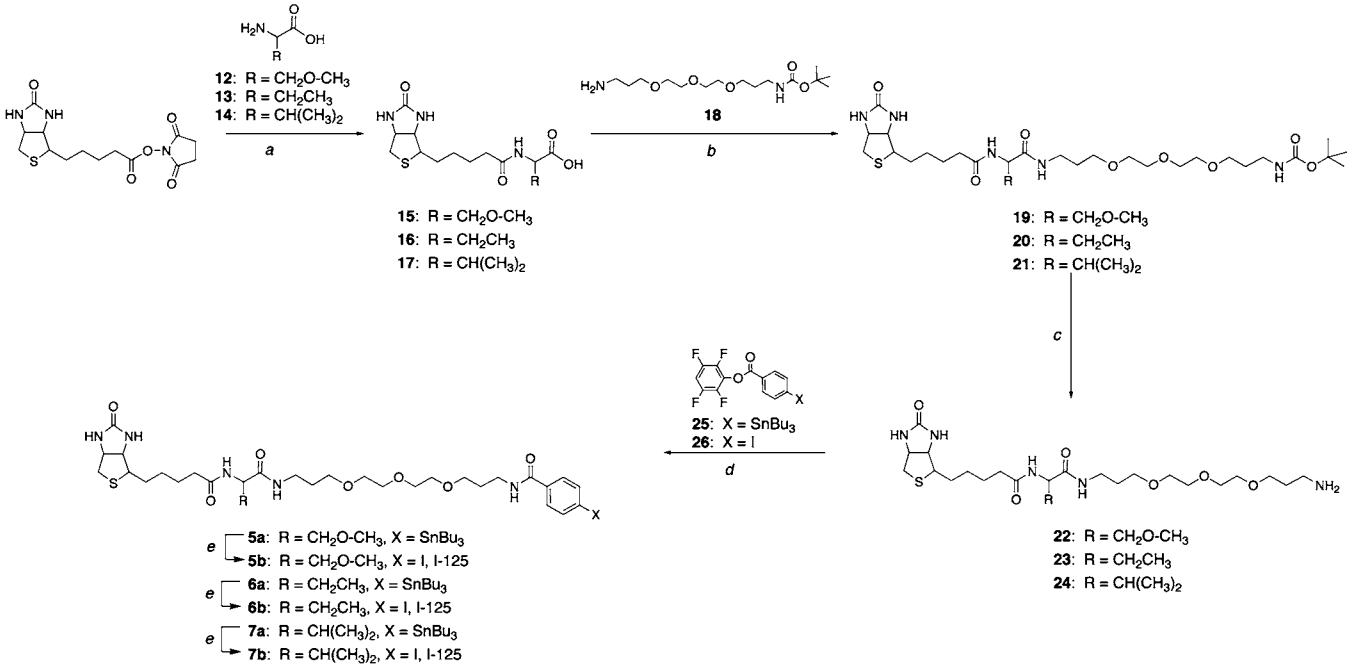

[a] (a) H_2O, Na_2CO_3, **12**, **13**, or **14**, acetone, rt, 16 h; (b) DMF, EDC, **15**, **16**, or **17**, 4 h to 5 d; (c) TFA, rt, 10 min; (d) DMF, Et_3N, **25** or **26**, rt, 10 min to 1 h; (e) MeOH/5% HOAc, **5a**, **6a**, or **7a**, NCS, 2 min.

Scheme 2. Reaction for Preparation of Biotin−Cyanocobalamin Derivatives 9, 10, and 11[a]

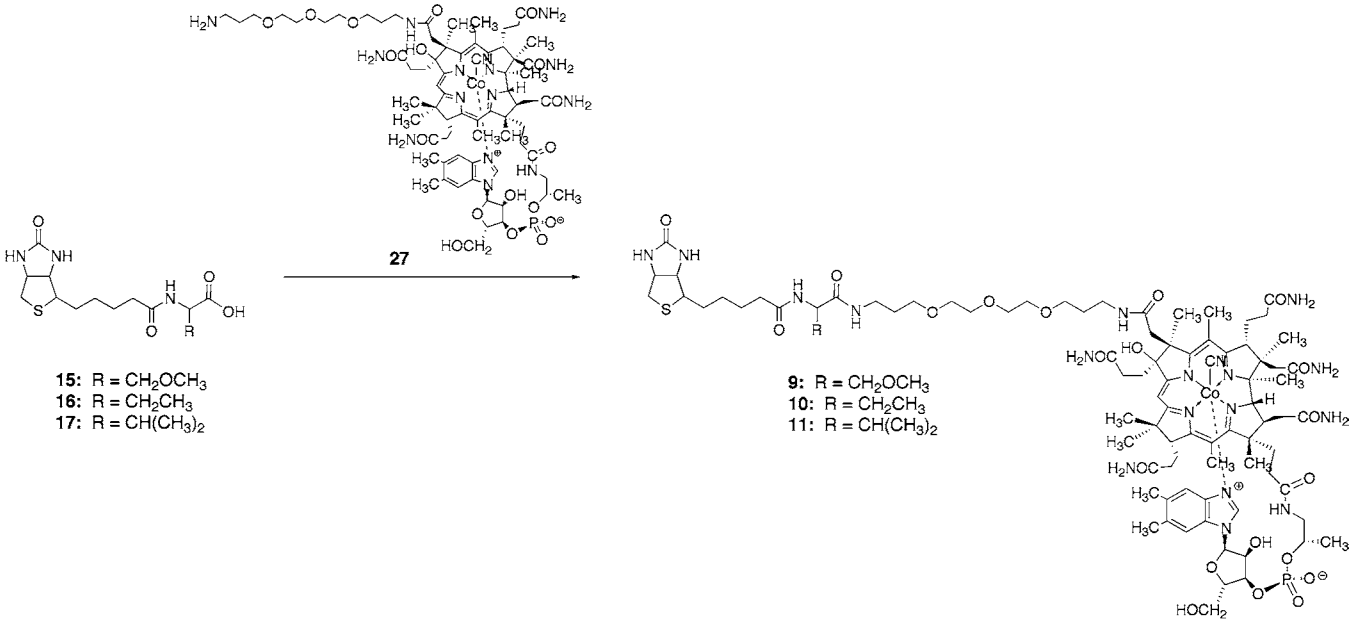

[a] (a) DMF, **15**, **16**, or **17**, TFP-OTFA, rt, 0.5 h; (b) **27**, rt, 30 min.

Biotin cyanocobalamin **8** was prepared as previously described (*26*). Biotin−cyanocobalamin derivatives **9**, **10**, and **11** were prepared using the same synthetic route, as shown in Scheme 2. Reaction of biotin adducts **15**, **16**, and **17** with trifluoroacetate tetrafluorophenyl ester (TFA-OTFP) to form the corresponding biotin TFP esters in situ, followed by reaction with the trioxadiamine adduct of cyanocobalamin **27** provided **9**, **10**, and **11** in 40%, 90%, and 86% yield (respectively). Cyanocobalamin derivative **27** was prepared by reaction of 1,13-diamino-4,7,-10-trioxatridecane as previously described (*26*).

Radioiodination of Biotin Derivatives. The radioiodinated derivatives [^{125}I]**1b**, [^{125}I]**2b**, [^{125}I]**3b**, [^{125}I]**4b**, [^{125}I]**5b**, [^{125}I]-**6b**, and [^{125}I]**7b** were prepared in 13−80% yield from the corresponding tri-*n*-butylstannylbenzamide derivatives **1a**, **2a**, **3a**, **4a** **5a**, **6a**, or **7a** in MeOH/1% HOAc using *N*-chlorosuccinimide (NCS) as the oxidant as previously described (*22*, *23*). The radioiodinated derivatives were purified by collection from the HPLC effluent. Identification was accomplished by co-injection of the isolated radioiodinated derivative with the HPLC standards. The radiochemical yields were not optimized, as only a small amount of material was required for the biotinidase evaluations.

Assessment of Biotinidase Activity. In this study, as in our previous studies, incubation of the radioiodinated samples in a 1 to 10 dilution of fresh human serum was used to assess biotinidase activity. Cleavage of the biotinamide bond is demonstrated as a lack of binding of radioactivity with rSAv. In the experiment, parallel sets of triplicate samples (for most

Table 1. Estimates of Biotinamide Cleavage in Biotin Derivatives[a]

compound no. [blocking group]	% bound[b] (serum)	% bound[c] (serum+HOHgBz)	% cleaved[d] by biotinidase
1b [H]	8.34 ± 0.50	98.52 ± 0.41	91.5
2b [N-CH_3]	96.93 ± 0.07	97.76 ± 0.23	0.8
3b [CO_2H]	92.47 ± 0.04*	92.57 ± 0.14	0.1
4b [CH_2OH]	86.92 ± 0.07	87.13 ± 0.07	0.2
5b [CH_2OCH_3]	90.57 ± 0.21	91.43 ± 0.05*	0.9
6b [CH_2CH_3]	92.92 ± 0.10	93.42 ± 0.10	0.5
7b [$CH(CH_3)_2$]	91.84 ± 0.31	91.66 ± 0.16	0.0

[a] Values were obtained from percent [^{125}I]iodophenyl-biotin derivative bound to rSAv after incubation with human serum or human serum treated with 4-(hydroxymercuri)benzoic acid (HOHgBz). All % bound values represent the percentage of total radioactivity remaining in a Microcon-30 centrifugation unit (bound with rSAv or nonspecifically bound) after repeated (3×) centrifugations/washes at 2000 rpm for 5 min. Values are an average of three analyses ± SD, except those denoted by * which are from two analyses. Human serum was obtained on the day of the experiments. [b] Radiolabeled biotin was placed in 10% human serum for 2 h at 37 °C, rSAv was added, and an aliquot was spun in Microcon-30 centrifugation unit. [c] Radiolabeled biotin was placed in HOHgBz-treated 10% human serum for 2 h at 37 °C, rSAv was added, and an aliquot was spun in a Microcon-30 centrifugation unit. [d] Percentages are derived from the formula (100 − [% bound for noninhibited/% bound after HOHgBz inhibition] × 100]). Values for percent biotinamide cleaved that are less than 1% may be reflective of experimental error and not actual biotinidase cleavage.

compounds) either were treated with the sulfhydryl-reactive HOHgBz to block biotinidase activity (as a control) or were untreated to measure biotinidase cleavage. All samples were incubated at 37 °C for 2 h, then samples previously untreated with HOHgBz were treated with that reagent to quench the enzyme activity. Following that, rSAv was added to all samples and they were incubated at 37 °C for 30 min. Ultrafiltration was then conducted on each sample using Microcon-30 filters to separate the rSAv-bound radioactivity from the nonbound radioactivity. The results obtained are shown as percent bound radioactivity in Table 1. The control group (serum + HOHgBz) provides a value for the amount of radiolabeled biotin that will bind with rSAv under the conditions of the study. In theory, this value should be 100%, but other factors may cause a decrease in the binding of the radiolabeled biotin derivatives with rSAv. One such factor is production of biotin sulfoxide under the radioiodination conditions (*30*). To assess the percent biotinamide bond cleaved, the percent bound values obtained after incubation with serum is subtracted from the control binding values (serum + HOHgBz). At least 90% of the unprotected biotinamide bond in **1b** was cleaved by biotinidase, demonstrating the activity of the enzyme. All of the other samples evaluated had less than 1% cleaved, indicating that they are very stable to biotinidase activity. It is likely that the <1% values are within experimental error and all samples are stable to biotinidase over the time period (2 h) of the study.

Biotin Derivative Dissociation Assay. The results of the competitive binding assay conducted with biotin−CN-Cbl derivatives **8**, **9**, **10**, and **11** are shown in Table 2. The values at $t = 0$ in theory should be 100%. An attempt was made to have a small excess (i.e., > 4 equiv) of the biotin−cyanocobalamin reagent prior to the competitive reaction so that both protein-bound activity and free biotin derivative could be seen on the chromatogram (UV trace). Thus, the percent bound values observed at $t = 0$ are less than 100%. It should be noted that the variance in free biotin−CN-Cbl will potentially askew the values at the later time points, so caution must be used in comparing data between studies. However, the data in Table 2 clearly show the differences in dissociation of the biotin−CN-Cbl derivatives tested. The *N*-methylbiotinamide derivative **8** was included in the assay as a control to compare with the rates of dissociation of **9**, **10**, and **11**. The data indicate that the release of the α-isopropyl (biotin−valine) derivative **11** is slower than

Table 2. Percent Biotin−Cyanocobalamin Derivatives 8, 9, 10, and 11 Bound with rSAv before and after Challenged by a Large Excess of Biotin[a]

compound no. [blocking group]	$t = 0$ (%)[b]	$t = 1$ h (%)	$t = 3$ h (%)	$t = 5$ h (%)
8 [N-CH_3]	86	42	11	4
8 [N-CH_3][c]	100	53	15	4
9 [CH_2OCH_3][c]	89	77	56	47
10 [CH_2CH_3]	95	86	74	62
11 [$CH(CH_3)_2$]	93	65	42	32

[a] Biotin derivative (4+ equiv) was incubated for 1 h with rSAv ($t = 0$), 50 equiv of biotin was added, and aliquots of the mixture were taken at 1, 3, and 5 h for analysis by size exclusion HPLC. Samples were covered from light and kept at room temperature during the experiment. Values from $t = 0$ are not 100% due to an excess of the reagent being present. [b] Percent values were obtained from analysis of peak areas from size exclusion HPLC chromatograms. UV traces were obtained for 280 and 362 nm, where the protein and vitamin B_{12}, respectively, have strong absorbances. The % bound values were obtained from the 362 nm traces and represent the [area of protein-bound peak divided by the area of protein bound peak + free biotin derivative] × 100. [c] Analysis of binding run at a separate time from cyanocobalamin derivatives **8**, **9**, and **10**. Cyanocobalamin derivative **8** was run a second time as control.

the N-Me (biotin−sarcosine) derivative **8**, but is faster than the α-methylmethyl ether and the smaller α-ethyl derivative **10** (i.e., dissociation rates are: **8** > **11** > **9** > **10**).

DISCUSSION

Animals and humans have significant amounts of biotinidase in serum and tissues (*8*), raising the possibility that biotinylated compounds used in vivo will be degraded (biotin released) before the intended binding with avidin or streptavidin can occur. For this reason, all of the biotin derivatives prepared for in vivo application in our laboratory incorporate biotinidase-stabilizing functionalities as a precautionary measure to assure that no cleavage (release) of the biotin occurs. It should be noted that there may be in vivo applications where biotinidase stabilization is not required, or even desirable. For example, in some applications, modification for biotinidase stabilization may impart undesirable properties to biotinylated molecules, such as increasing the lipophilicity. Additionally, there may be instances where biotinidase cleavage offers an advantage for blood and tissue clearance, particularly if an avidin or streptavidin binding of the biotinylated compound postinjection is not required. Another example where biotinidase stabilization may not be required is in vivo use of biotinylated proteins such as monoclonal antibodies. In studies of biotinylated antibodies in this laboratory no difference was observed in avidin column capture of monoclonal antibodies biotinylated with biotinidase stabilized or nonstabilized biotin reagents after subjecting to human serum (unpublished results). These results do not necessarily indicate that biotinidase is incapable of acting on biotinylated antibodies, but rather that the rate of cleavage from the (usual) multi-biotinylated protein is slow enough that the biotinylated protein can be captured on an avidin column after incubation in serum. In fact, published data suggests that intact proteins can be debiotinylated by biotinidase (*9*), and biotinidase stabilizing groups can block the cleavage (*31*).

It became apparent in our early studies that biotinidase-blocking functional groups were essential for optimal pretargeting of therapeutic radionuclides. In those studies, we identified biotin conjugates that contain carboxylate and hydroxymethyl functionalities on the carbon α to the biotinamide bond as derivatives of choice for in vivo application (*25*). However, later synthetic studies to prepare dendrimers and dendrons with multiple biotin conjugates containing these functionalities were fraught with difficulties. Importantly, in some examples, unexpected side reactions prevailed, and in other

examples, removal of the *t*-Bu protecting group was problematic. Further, the cost of the protected amino acids (e.g., aspartate *t*-Bu ester and serine-*O*-*t*-Bu ether) used in the syntheses was perceived as a potential roadblock to their widespread application. These shortcomings led us to consider alternate biotinidase-blocking functionalities that were inert to most chemical transformations and could be obtained at a lower cost.

A primary goal of the studies was to identify biotinidase-blocking moieties that were inert to most reaction conditions, such that they did not have to be protected and deprotected in the syntheses of targeted biotin derivatives. We reasoned that it was best to incorporate functional groups just large enough to block the biotinidase without dramatically affecting avidin/streptavidin binding or other properties of the conjugates. A nonreactive derivative previously tested had a methyl group α to the biotinamide bond. Unfortunately, the methyl group did not fully block biotinidase cleavage, only decreased its rate of cleavage. Since it appeared that the α-methyl group was not large enough to fully block biotinidase activity, slightly larger nonreactive functional groups adjacent to the biotinamide were sought. We chose to incorporate 2-aminobutyric acid and valine as biotin adducts as those amino acid adducts have either an ethyl or isopropyl group α to the biotinamide bond. The ethyl and isopropyl group are inert to most reaction conditions and are similar in steric size of a hydroxymethyl and carboxylate functionality (respectively), which have been previously shown to be stable to biotinidase activity. We also chose to include the biotin adduct of serine-*O*-methyl ether in the study, as it is nonreactive under most reaction conditions and has a similar steric size but would be expected to be less lipophilic.

Radioiodinated derivatives of the serine-*O*-methyl ether, 2-aminobutyric acid, and valine adducts of biotin, ([^{125}I]**5b**, [^{125}I]-**6b**, and [^{125}I]**7b**) were prepared and evaluated in a biotinidase assay. As controls, radioiodinated derivatives of biotin without an amino acid blocking group ([^{125}I]**1b**) or containing the amino acids sarcosine, aspartate, and serine ([^{125}I]**2b**, [^{125}I]**3b**, [^{125}I]-**4b**) were also prepared and tested. All of the biotin derivatives containing an amino acid conjugated with the biotin carboxylate were found to be very stable toward biotinidase cleavage (Table 1). On the basis of the theory that blockage of the enzyme is controlled by steric bulk, one might expect the steric isopropyl group in valine to block biotinidase more effectively. However, under the conditions studied there was essentially no difference between the compounds. More concentrated serum samples or longer incubation times may be required to determine if there are small differences in the biotinidase-blocking capacity of the various derivatives. It should be noted that biotin derivatives of interest for our studies have a very short half-life in blood (i.e., 4 min in α-phase and 1 h in *β*-phase (*33*)], making the 2 h incubation time adequate to assess their in vivo use. Biotin derivatives of molecules that have long biological half-lives in blood may require further studies of biotinidase stability.

In addition to biotinidase stability, we believe it is very important to retain the high binding affinity in the biotin derivatives used in vivo to alleviate the potential for displacement from streptavidin by endogenous biotin (*34*, *35*). While there are methods for decreasing biotin concentrations in blood, it appears that some biotin will always be present to compete for the biotin-binding pockets on SAv. To assess the relative retention of biotin derivatives bound with rSAv, a simple size-exclusion HPLC assay has been developed (*26*). In that assay, 4 equiv of a biotin−CN-Cbl derivative are bound with rSAv and then challenged with a large excess (50 equiv) of biotin. Under these conditions, any biotin−CN-Cbl derivative that is dissociated will be replaced with biotin. Thus, the relative rate of dissociation of a biotin derivative can be estimated by the quantity of free biotin−CN-Cbl derivative versus rSAv-bound biotin−CN-Cbl derivative. The use of biotin−CN-Cbl derivatives makes HPLC analysis possible, as UV detection of the protein can be measured at 280 nm and the biotin−cyanocobalamin derivative at 362 nm, where there is very little absorption by the protein. Significant differences in the rate of dissociation were measured between the biotin derivatives (Table 2). As in previous studies, nearly all biotin−sarcosine-CN-Cbl, **8**, is displaced within 5 h at room temperature. The biotin−valine−CN-Cbl, **11**, has the second fastest rate of dissociation, with the biotin−serine-*O*-methyl ether−CN-Cbl, **9**, a little slower, and the biotin−2-aminobutyric acid−CN-Cbl, **10**, having the slowest dissociation. It is interesting to note that the rate of dissociation correlates with the steric bulk of the substituent on the carbon α to the biotinamide bond. While the differences in amount of biotin−amino acid adduct dissociated by 5 h is fairly large, this may not be important for in vivo application. Indeed, it is likely that all three new biotin derivatives would provide adequate binding to be useful in most in vivo applications. This statement is made based on the fact that highly successful pretargeting of rSAv conjugates on tumors in vivo has been accomplished with a biotin−sarcosine derivative (*36*), which has the fastest dissociation from SAv out of the compounds studied.

CONCLUSION

Problems encountered in prior studies employing *t*-Bu protected hydroxyl and carboxylate biotinidase stabilizing groups led to this investigation to develop alternate biotinidase stabilizing functionalities. In the investigation, new functionalized biotin derivatives were targeted that retained criteria set previously, i.e., that they effectively block biotinidase while retaining high binding affinity with rSAv but had the additional criteria that they (*1*) are chemically inert, (*2*) do not require protection/deprotection in the syntheses, and (*3*) have a low cost such that they can be applied widely. While all three of the biotin−amino acid derivatives tested were found to be stable to biotinidase, the cost of serine-*O*-methyl ether and difficulties encountered in syntheses using it makes that derivative less attractive than the 2-aminobutyric acid and valine adducts. The data obtained indicate that biotin−valine adduct could be used for in vivo studies, but higher lipophilicity and faster dissociation than that of the 2-aminobutyric acid adduct make it a second choice. The low cost and high binding affinity of the biotin−2-aminobutyric acid derivative make it particularly attractive for development of reagents to be used in vivo. While there is little doubt that other untested functional groups can also provide biotinidase blockage, it seems likely that a relatively small number would meet all of the criteria set. It is anticipated that a majority of our subsequent synthetic studies with biotin derivatives will incorporate the 2-aminobutyric acid moiety to block biotinidase.

ACKNOWLEDGMENT

We are grateful for the financial support provided by the Department of Energy, Medical Applications and Biophysical Research Division, OHER (DE-FG03-98ER62572), and National Cancer Institute, NIH (5 RO1 CA113431). We thank Quanta BioDesign (Powell, OH) for providing the biotin *N*-hydroxysuccinimide ester as a gift.

LITERATURE CITED

(1) Goodwin, D. A., and Meares, C. F. (1997) Pretargeting: General Principles. *Cancer (Suppl.) 80*, 2675−2680.
(2) Zhu, H., Jain, R. K., and Baxter, L. T. (1998) Tumor Pretargeting for Radioimmunodetection and Radioimmunotherapy. *J. Nucl. Med. 39*, 65−76.
(3) Stoldt, H. S., Aftab, F., Chinol, M., Paganelli, G., Luca, F., Testori, A., and Geraghty, J. G. (1997) Pretargeting Strategies for Radio-

immunoguided Tumour Localisation and Therapy. *Eur. J. Cancer 33*, 186−192.
(4) Wright, L. D., Driscoll, C. A., and Boger, W. P. (1954) Biocytinase, an enzyme concerned with hydrolytic cleavage of biocytin. *Proc. Soc. Exp. Biol. Med. 86*, 335−7.
(5) Wolf, B., Hymes, J., and Heard, G. S. (1990) *Biotinidase Methods Enzymol. 184*, 103−111.
(6) Oizumi, J., and Hayakawa, K. (1993) Biocytin-specific 110-kDa biotinidase from human serum. *Clin. Chim. Acta. 215*, 63−71.
(7) Hymes, J., Fleischhauer, K., and Wolf, B. (1997) Biotinidase in Serum and Tissues. *Methods Enzymol. 279*, 422−434.
(8) Pispa, J. (1965) Animal Biotinidase. *Ann. Med. Expl. Biol. Fenniae 43*, 3−40.
(9) Ballard, T. D., Wolff, J., Griffin, J. B., Stanley, J. S., van Calcar, S., and Zempleni, J. (2002) Biotinidase catalyzes debiotinylation of histones. *Eur. J. Nutr. 41*, 78−84.
(10) Chauhan, J., and Dakshinamurti, K. (1988) Role of Human Serum Biotinidase as Biotin-Binding Protein. *Biochem. J. 256*, 265−270.
(11) Stanley, C. M., Hymes, J., and Wolf, B. (2004) Identification of alternatively spliced human biotinidase mRNAs and putative localization of endogenous biotinidase. *Mol. Genet. Metab. 81*, 300−12.
(12) Zempleni, J. (2005) Uptake, localization, and noncarboxylase roles of biotin. *Annu. Rev. Nutr. 25*, 175−96.
(13) Hayakawa, K., Yoshikawa, K., Oizumi, J., and Yamauchi, K. (1997) Determination of Biotinidase Activity with Biotinyl-6-aminoquinoline as Substrate. *Methods Enzymol. 279*, 435−442.
(14) Wolf, B., and McVoy, J. S. (1983) A sensitive radioassay for biotinidase activity: deficient activity in tissues of serum biotinidase-deficient individuals. *Clin. Chim. Acta 135*, 275−281.
(15) Livaniou, E., Kakabakos, S. E., Evangelatos, S. A., Evangelatos, G. P., and Ithakissios, D. S. (1997) Determination of Serum Biotinidase Activity with Radioiodinated Biotinylamide Analogs. *Methods Enzymol. 279*, 442−451.
(16) Chauhan, J., and Dakshinamurti, K. (1986) Purification and Characterization of Human Serum Biotinidase. *J. Biol. Chem. 261*, 4268−4275.
(17) Nilsson, L., and Kagedal, B. (1994) Lipoamidase and biotinidase activities in the rat: tissue distribution and intracellular localization. *Eur. J. Clin. Chem. Clin. Biochem. 32*, 501−9.
(18) Nilsson, L., and Kagedal, B. (1993) Co-purification of human serum lipoamidase and biotinidase: evidence that the two enzyme activities are due to the same enzyme protein. *Biochem. J. 291* (Pt 2), 545-51.
(19) Gustavson, L. M., Srinivasan, A., Fritzberg, A. R., Reno, J. M., and Axworthy, D. B. (1994) NeoRx Corporation, US Patent 5,283,-342.
(20) Rosebrough, S. F. (1993) Plasma Stability and Pharmacokinetics of Radiolabeled Deferoxamine-Biotin Derivatives. *J. Pharmacol. Exp. Ther. 265*, 408−415.
(21) Foulon, C. F., Alston, K. L., and Zalutsky, M. R. (1998) Astatine-211-Labeled Biotin Conjugates Resistant to Biotinidase for Use in Pretargeting Radioimmunotherapy. *Nucl. Med. Biol. 25*, 81−88.
(22) Wilbur, D. S., Hamlin, D. K., Pathare, P. M., and Weerawarna, S. A. (1997) Biotin reagents for antibody pretargeting. Synthesis, radioiodination and in vitro evaluation of water soluble, biotinidase resistant biotin derivatives. *Bioconjugate Chem. 8*, 572−584.
(23) Wilbur, D. S., Hamlin, D. K., Chyan, M. K., Kegley, B. B., and Pathare, P. M. (2001) Biotin reagents for antibody pretargeting. 5. Additional studies of biotin conjugate design to provide biotinidase stability. *Bioconjugate Chem. 12*, 616−23.
(24) Axworthy, D. B., Theodore, L. J., Gustavson, L. M., and Reno, J. M. (1997) NeoRx Corporation, US Patent 5,608,060.
(25) Wilbur, D. S., Chyan, M.-K., Pathare, P. M., Hamlin, D. K., Frownfelter, M. B., and Kegley, B. B. (2000) Biotin Reagents for Antibody Pretargeting. 4. Selection of Biotin Conjugates for in Vivo Application Based on Their Dissociation Rate from Avidin and Streptavidin. *Bioconjugate Chem. 11*, 569−583.
(26) Wilbur, D. S., Pathare, P. M., Hamlin, D. K., Frownfelter, M. B., Kegley, B. B., Leung, W. Y., and Gee, K. R. (2000) Evaluation of biotin-Dye conjugates for use in an HPLC assay to assess relative binding of biotin derivatives with avidin and streptavidin. *Bioconjugate Chem. 11*, 584−98.
(27) Wilbur, D. S., Hamlin, D. K., Vessella, R. L., Stray, J. E., Buhler, K. R., Stayton, P. S., Klumb, L. A., Pathare, P. M., and Weerawarna, S. A. (1996) Antibody fragments in tumor pretargeting. Evaluation of biotinylated Fab′ colocalization with recombinant streptavidin and avidin. *Bioconjugate Chem. 7*, 689−702.
(28) Wilbur, D. S., Hamlin, D. K., Buhler, K. R., Pathare, P. M., Vessella, R. L., Stayton, P. S., and To, R. (1998) Streptavidin in antibody pretargeting. 2. Evaluation of methods for decreasing localization of streptavidin to kidney while retaining its tumor binding capacity. *Bioconjugate Chem. 9*, 322−330.
(29) Bhuniya, S., Park, S. M., and Kim, B. H. (2005) Biotin-amino acid conjugates: an approach toward self-assembled hydrogelation. *Org. Lett. 7*, 1741−4.
(30) Wilbur, D. S., Hamlin, D. K., and Chyan, M.-K. (2005) Addition of Methionine to Radiohalogenation Reactions of Biotin Derivatives Decreases Formation of Biotin Sulfoxide by Oxidants. *J. Labelled Compd. Radiopharm. 48*, S305 (abstract).
(31) Bogusiewicz, A., Mock, N. I., and Mock, D. M. (2005) A biotin-protein bond with stability in plasma. *Anal. Biochem. 337*, 98−102.
(32) Visintin, C., Aliev, A. E., Riddall, D., Baker, D., Okuyama, M., Hoi, P. M., Hiley, R., and Selwood, D. L. (2005) Membrane receptor probes: solid-phase synthesis of biotin-Asp-PEG-arvanil derivatives. *Org. Lett. 7*, 1699−702.
(33) Fritzberg, A. R., Beaumier, P. L., Bottino, B. J., and Reno, J. M. (1994) Approaches to improved antibody- and peptide-mediated targeting for imaging and therapy of cancer. *J. Controlled Release 28*, 167−173.
(34) Rusckowski, M., Fogarasi, M., Fritz, B., and Hnatowich, D. J. (1997) Effect of Endogenous Biotin on the Applications of Streptavidin and Biotin in Mice. *Nucl. Med. Biol. 24*, 263−268.
(35) Wang, H., and Pevsner, J. (1999) Detection of endogenous biotin in various tissues: novel functions in the hippocampus and implications for its use in avidin-biotin technology. *Cell Tissue Res. 296*, 511−6.
(36) Theodore, L. J., Fritzberg, A. R., Schultz, J. E., and Axworthy, D. B. (2000) Evolution of a Pretarget Radioimmunotherapeutic Regimen. In *Radioimmunotherapy of Cancer* (Abrams, P. G., and Fritzberg, A. R., Eds.) pp 195-221, Marcel Dekker, New York.

BC060084M

Amino Acid Conjugated Sophorolipids: A New Family of Biologically Active Functionalized Glycolipids

Abul Azim,[†] Vishal Shah,[†] Gustavo F. Doncel,[‡] Nicholas Peterson,[†] Wei Gao,[†] and Richard Gross*[,†]

NSF I/UCR Center for Biocatalysis and Bioprocessing of Macromolecules, Polytechnic University, Six Metrotech Center, Brooklyn, New York 11201, and CONRAD, Department of Obstetrics and Gynecology, Eastern Virginia Medical School, Norfolk, Virginia, 23507. Received April 17, 2006; Revised Manuscript Received September 23, 2006

Sophorolipids (SLs) are extra cellular glycolipids produced by *Candida bombicola* ATCC 22214 when grown in the presence of glucose and fatty acids. These compounds have a disaccharide head group connected to a long-chain hydroxyl−fatty acid by a glycosidic bond. To explore structure−activity of modified SLs, a new family of amino acid−SL derivatives was prepared. Synthesized analogs consist of amino acids linked by amide bonds formed between their α-amino moiety and the carboxyl group of ring-opened SL fatty acids. Their preparation involved the following: (i) hydrolysis of a natural SL mixture with aqueous alkali to give SL free acids, (ii) coupling of free acids to protected amino acids using dicarbodiimide, and (iii) removing amino acid carboxyl protecting groups. These conjugates were evaluated for their antibacterial, anti-HIV, and spermicidal activity. All tested analogs showed antibacterial activity against both gram +ve and gram −ve organisms. Leucine-conjugated SL was most efficient. For example, the minimum inhibitory concentrations (MIC) for *Moraxella* sp. and *E. coli* were 0.83 and 1.67 mg/mL, respectively. Among the alkyl esters of amino acid conjugated SLs, the ethyl ester of leucine−SLs was most active. Against *Moraxella* sp., *S. sanguinis*, and *M. imperiale*, MIC values are 7.62×10^{-4}, 2.28×10^{-3} and 1.67 mg/mL, respectively. All compounds displayed virus-inactivating activity with 50% effective concentrations (EC_{50}) below 200 μg/mL. The EC_{50} of leucine−SL ethyl ester was 24.1 μg/mL, showing that it is more potent than commercial spermicide nonoxynol-9 ($EC_{50} \approx 65$ μg/mL).

INTRODUCTION

Sophorolipids (SLs) are glycolipids produced by the yeast *Candida bombicola* when cultured on carbohydrate and lipidic substrates. Structurally, SLs are composed of dimeric sophorose (2′-*O*-*β*-D-glucopyranosyl-*β*-D-glucopyranose) linked to the hydroxyl group at the penultimate position of, most often, a monounsaturated C18 fatty acid (*1*). First described by Gorin et al. (*2*), SLs exist as mixtures of eight major components (lactone and acid forms) with varying degrees of acetylation at the 6′- and 6″-positions of the sophorose moiety (Chart 1).

Our ongoing research with SLs and their derivatives have shown that they have immense potential as therapeutic agents that can function as septic shock antagonists (*3*), anticancer agents (*4*), and antibacterial (*5*), antiviral (*6*, *7*), spermicidal (*6*, *7*), and antifungal agents (*8*). However, more structural derivatives of SLs are needed to better define structural−biological activity relationships and thereby enhance SL efficacy and its spectrum of action.

Attempts have been made to perform in vivo modifications of SL structure during biosynthesis. Selective feeding during fermentations of lipophilic substrates such as alkanes and fatty acids did bring about changes in the sophorolipid structure (*9*−*11*). Although this approach is promising, thus far it has affected a change in only a small fraction of the SLs produced.

Thus far, in vitro modification of SLs has been most successful. Earlier reports from our laboratories described SL modifications by chemoenzymatic strategies (*12*, *13*). Bisht et al. synthesized several alkyl esters of SLs using sodium alkoxide/alkanol mixtures under reflux conditions. The resulting

Chart 1. Structures of Sophorolipids Produced by *Candida bombicola*

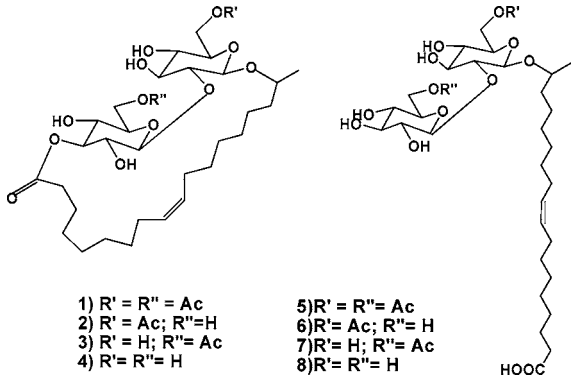

SL alkyl esters were subjected to Novozyme 435 catalyzed acylation in anhydrous THF to furnish C-6′ and C-6″ acylated compounds in high yields with excellent chemoselectivity (*13*). Singh et al. synthesized SL−amide derivatives by lipase-catalyzed amidation of SL ethyl ester in dry THF. Amines used included phenethylamine, tyramine, and 2-(*p*-tolyl)ethylamine (*12*). Recently, Nunez et al. reported the synthesis of galactose conjugated SL ester. They successfully transesterified SL methyl ester with 1,2-3,4-di-*O*-isopropylidene-D-galactopyranose in THF using an immobilized lipase catalyst (*14*).

In this paper, a new family of SL derivatives consisting of SL−amino acid and SL−amino acid ethyl ester conjugates were prepared by linking the α-NH_2 group of amino acids to the carboxyl terminus of SL fatty acids. These compounds were assayed to ascertain their antibacterial, anti-HIV, and spermicidal activities. The results of this work provide important insights that expand our knowledge of SL structure−bioactivity relationships.

* Corresponding author. Phone: 718-260-3024. Fax: 718-260-3075. Email: rgross@poly.edu.

[†] Polytechnic University.

[‡] Eastern Virginia Medical School.

10.1021/bc060094n CCC: $33.50 © 2006 American Chemical Society
Published on Web 10/31/2006

Scheme 1. (i) DCC, DCM/DMF (4:1), RT, 24 hr; (ii) 13 → 14, TFA/DCM, 0 °C, 30 min; (iii) Pd/C ethanol, H_2

9) R= $CH_2COOCH_2C_6H_5$,R"= $CH_2C_6H_5$, R'=-CH=CH(**Aspartic**)
10) R=CH_2OH,R"=$CH_2C_6H_5$,R'=-CH=CH(**Serine**)
11) R=$CH_2CH(CH_3)_2$,R"=$CH_2C_6H_5$,R'=-CH=CH(**Leucine**)
12) R=$CH_2C_6H_5$,R"=$CH_2C_6H_5$,R'=-CH=CH(**phenylalanine**)
13) R=$CH_2CH_2COOC(CH_3)_3$,R"= $C(CH_3)_3$,R'=-CH=CH(**Glutamic**)
14) R=CH_2CH_2COOH,R"=H,R'=-CH=CH (**glutamic**)
15) R=CH_2COOH,R"=H,R'=CH_2-CH_2(**Aspartic**)
16 R=CH_2OH,R"=H,R'=-CH-CH(**Serine**)
17) R=$CH_2CH(CH_3)_2$,R"=H,R'=CH_2-CH_2(**leucine**)
18) R=CHC_6H_5,R"=H,R'=CH_2-CH_2(**phenylalanine**)
19)R=CHC_6H_5,R"=C_2H_5,R'=-CH=CH(**phenylalanine**)
20)R=$CH_2CH(CH_3)_2$,R"=C_2H_5 ,R'=-CH=CH(**leucine**)
21)R= H, R"= CH_3,R'= -CH=CH(**Glycine**)

EXPERIMENTAL SECTION

General Chemicals and Procedures. Anhydrous solvents, methylene chloride, *N*,*N*-dimethylformamide, hydrochloride form of carboxyl group protected amino acids, dicyclohexylcarbodiimide (DCC), 1-hydroxybenzotriazole (HOBt), and 4-(dimethylamino)pyridine (DMAP) were purchased from Aldrich Chemical Company in the highest available purity and were used as received unless otherwise noted. Amino acid alkyl ester hydrochlorides were converted to the free-amine form by treatment with an equivalent amount of *N*-methylmorpholine. All liquid reagents were transferred by syringe under N_2 atmosphere. Proton (^{1}H) NMR spectra were recorded on Bruker-300 and Varian 400 M spectrometers at 300 and 400 MHz, respectively. Carbon (^{13}C) NMR spectra were recorded on a Bruker-300 spectrometer at 75 MHz. Chemical shifts are reported in parts per million downfield from 0.00 ppm using trimethylsilane (TMS) as the internal standard. Coupling constants are expressed in hertz (Hz). Column chromatographic separations were conducted with silica gel 60 (Aldrich Chemical Co.). Analytical thin layer chromatography (TLC) were performed on Merck silica gel $^{60}F_{254}$ plates. The spots were developed by spraying with α-naphthol/sulfuric acid (for 100 mL solution, 500 mg of α-naphthol in 5% sulfuric acid solution in ethanol) detecting system. IR spectra were recorded using a Perkin-Elmer FT-IR 1600 series. The samples were dissolved in THF and deposited as thin films on KBr discs. Optical rotations were determined at 598 nm on a Perkin-Elmer 241 digital polarimeter with a 2 dm cell. Values of $[\alpha]_D$ are given in units of 10^{-1} deg cm^2 g^{-1}.

Sophorolipids Synthesis. SLs were synthesized by fermentation of *Candida bombicola* (*12*, *13*). The fermentation media contained glucose (100 g), yeast extract (10 g), urea (1 g), and oleic acid (40 g) per 1000 mL water. After 10 day fermentations, SLs were extracted three times with ethyl acetate. The extracts were pooled and the solvent removed. The resulting product was washed with hexane to remove residual fatty acids.

Isolation of SL-COOH (structure 8). Acidic SLs were synthesized from the natural mixture by alkaline hydrolysis following a literature procedure (*12*, *13*). The hydrolyzed SLs were acidified, the solution was cooled in an ice bath, and the precipitate was further purified by silica gel column chromatography using a chloroform/methanol gradient (3:22 to 4:22, v/v). The product was identified by NMR and LC-MS, which were identical to previously published spectra.

General Procedure for DCC Coupling of SL-COOH (structure 8) with C-Terminal Protected Amino Acids (structures 9−13, 19−21). Amino acid alkyl ester hydrochloride (1 mmol) was suspended in a 4:1 mixture of DCM/DMF (15 mL). The hydrochloride salt was neutralized with *N*-methylmorpholine (1 mmol, 108 μL) and stirred for 15 min giving a clear solution. SL-COOH (**8**, 622 mg, 1 mmol), HOBt (135 mg, 1 mmol), DCC (1.2 mmol, 244 mg), and DMAP (0.1 mmol, 12 mg) were then added to the clear solution. Stirring was continued at room temperature for 24 h. Water (2 mL) was added, and the reaction was stirred for an additional 10 min. Filtration of DCU followed by solvent evaporation gave a transparent syrup which was diluted with ethyl acetate and subsequently washed with cold 0.1 N HCl (20 mL). The ethyl acetate layer was dried over $MgSO_4$, filtered, and concentrated. Purification was performed by flash chromatography to give the desired compounds in 72−78% yields.

Removal of *tert*-Butyl Protecting Group. A solution of **13** (500 mg, 0.58 mmol) in 10 mL CH_2Cl_2/TFA (7:3) was stirred at 0 °C for 30 min. After completion of the reaction, the solution was concentrated under vacuum and twice evaporated with anhydrous toluene to give **14** (380 mg, 87% yield).

Removal of Benzyl Protection and Hydrogenation of cis Double Bond. A solution of **9−12** in 5 mL dry ethanol was stirred at room temperature under H_2 atmosphere in the presence of 10% pd/C (50 mg) for 72 h. Reaction progress was monitored by TLC, and on completion, the solids were removed from the reaction mixture by passing it through a celite pad. The filtrate was concentrated by rotoevaporation under vacuum to give compounds **15−18** in quantitative yields.

Liquid Chromatography−Mass Spectrophotometry Analysis of SLs. A Waters ZQ LC/MS system was used for analysis and identification of individual sophorolipids and amino acid conjugated sophorolipids. The system includes 2795 Alliance HT separation module, 2996 photodiode array detector, and

Waters (Micromass) ZQ 2000 online mass detector. Separation was carried out on a 250 × 4.6 mm polymeric reversed-phase PLRP-S column (particle size 8 μm, pore size 1000 Å, Polymer Laboratories). The water/acetonitrile mobile phase was programmed as follows: 60% water to 50% water in 20 min, then 60% water for 5.0 min (re-equilibration). The HPLC eluent (1 mL/min) was split at the outlet of the column by means of a zero-dead-volume tee splitter to introduce eluent to PDA detector and mass spectrometer. LC-MS was operated with an atmospheric pressure chemical ionization (APCI) probe in positive ion mode. Probe and source temperature were set to 450 and 50 °C, respectively. Cone voltage, corona current, and nebulizer gas flow were set at 60 V, 0.66 μA, and 300 L/h, respectively. Sophorolipids were detected in scan mode with a scan duration of 2.0 s, interscan delay of 0.1 s, and scan range 170−850 *m*/*z*. Data acquisition and mass spectrometric evaluation were performed with *MassLynx Software 4.0*. The samples for LC/MS were dissolved in 50:50 acetonitrile/water at a concentration of 40−200 μg/mL and were passed through a 0.45 μm PTFE filter before injection.

17-L-[(2′-O-β-D-glucopyranosyl-β-D-glucopyranosyl)oxy]-*cis*-9-octadecenoic Acid (structure 8). $[\alpha]_D^{25} = -12.8$ (c = 0.0104 g/mL in MeOH); IR [KBr plate, cm^{-1} (% *T*)] 3378, 2924, 2853, 1702, 1550, 1412, 1074, 722, 626. ^{1}H NMR (CH_3OH-d_4): 5.35 (2H, m, H-9 and H-10), 4.63 (1H, d, J = 8.1 Hz, H-1″), 4.44 (1H, d, J = 7.5 Hz, H-1′), 3.82−3.87 (3H, m, H-6′b, H-6″b, and H-17), 3.63−3.68 (3H, m, H-6′a, H-6″a, and H-5″), 3.53−3.58 (2H, m, H-2′ and H-3′), 3.21−3.41 (5H, m, H-3″, H-2″, H-4″, H-4′, and H-5′), 2.27 (2H, t, J = 7.3 Hz, H-2), 2.03−2.05 (4H, m, H-8 and H-11), 1.57−1.62 (4H, m, H-3 and H-16), 1.30−1.46 (16H, m, H-4−7 and H-12−15), 1.24 (3H, d, J = 6.0 Hz, H-18).^{13}C NMR (CH_3OH-d_4): 178.42 (C═O), 130.84, 130.93 (CH═CH), 104.70 (C-1″), 102.76 (C-1′), 81.96, 78.89, 78.36, 78.27, 77.82, 77.78, 75.90, 71.82, 70.52, 63.14, 62.81, 37.85, 35.17, 30.94, 30.85, 30.80, 30.43, 30.33, 30.27, 30.20, 28.18, 28.14, 26.28, 26.19, 21.94 (C-18). LC/APCI-MS: R_t 4.2 min, *m*/*z* 645.39 $[M + Na]^+$; 4.6 min, *m*/*z* 645.41-$[M + Na]^+$.

Aspartic Acid-*N*-{17-L-[(2′-O-β-D-glucopyranosyl-β-D-glucopyranosyl)-oxy]-*cis*-9-octadecenamide}dibenzyl Ester (Structure 9). $[\alpha]_D^{25} = -14.7$ (c = 0.0112 g/mL in MeOH); IR [KBr plate, cm^{-1} (% T)] 3357, 2925, 2853, 2360, 1741, 1650, 1543, 1377, 1227, 1169, 1078, 894. ^{1}H NMR (CH_3OH-d_4): 7.30−7.39 (10H, m, $-CH_2C_6H_5 \times 2$), 5.34(2H, m, H-9 and H-10), 5.09 and 5.12 (4H, 2s, $-CH_2C_6H_5 \times 2$), 4.84 (1H, overlapping triplet with HDO peak, CONHC*H*), 4.63 (1H, d, J = 8.1 Hz, H-1″), 4.44 (1H, d, J = 7.5 Hz, H-1′), 3.81−3.87 (3H, m, H-6′b, H-6″b, and H-17), 3.62−3.68 (3H, m, H-6′a, H-6″a, and H-5″), 3.35−3.58 (4H, m, H-2′, H-3′, H-3″, and H-2″), 3.21−3.33 (3H, m, H-4″, H-4′, and H-5′), 2.90 (2H, dd, J = 7.2 and 11.7 Hz CH_2 protons from aspartic acid moiety), 2.15 (2H, t, J = 7.2 Hz, H-2), 2.03−2.05 (4H, m, H-8 and H-11), 1.59−1.65 (4H, m, H-3 and H-16), 1.30−1.46 (16H, m, H-4−7 and H-12−15), 1.24 (3H, d, J = 6.3 Hz, H-18).^{13}C NMR (CH_3OH-d_4): 176.05, 171.83 and 171.59 (CO × 3), 137.04, 136.84, 130.76, 129.22, 129.45, 104.57 (C-1″ or C-1′), 102.57 (C-1″ or C-1′), 81.84 (C-2′), 79.55, 79.11, 78.70, 78.12, 75.70, 71.66, 71.34, 68.21, 67.25, 63.00, 62.66, 37.68, 36.98, 36.66, 30.73, 30.12, 26.75, 26.16, 21.89 (C-18). LC/APCI-MS: R_t 15.4 min, *m*/*z* 940.56 $[M + Na]^+$ and 16.9 min, 940.56 $[M + Na]^+$.

Serine-*N*-{17-L-[(2′-O-β-D-glucopyranosyl-β-D-glucopyranosyl)oxy]-*cis*-9-octadecenamide} Benzyl Ester (structure 10). $[\alpha]_D^{25} = -6.8$ (c = 0.0128 g/mL in MeOH); IR [KBr plate, cm^{-1} (% T)] 3561, 2920, 2849, 2390, 1713, 1624, 1537, 1414, 1242, 1148, 1077, 786. ^{1}H NMR (CH_3OH-d_4): 7.32−7.34 (5H, m, $CH_2C_6H_5$), 5.36 (2H, m, H-9 and H-10), 5.18 (2H, s, $CH_2C_6H_5$), 4.63 (1H, d, J = 8.1 Hz, H-1″), 4.56 (1H, t, J = 4.5 Hz, NHC*H*$COOCH_2C_6H_5$), 4.45 (1H, d, J = 7.5 Hz, H-1′), 3.79−3.93 (5H, m, CH_2OH from serine, H-6′b, H-6″b, and H-17), 3.58−3.69 (3H, m, H-6′a, H-6″a, and H-5″), 3.35−3.58 (4H, m, H-2′, H-3′, H-3″, and H-2″), 3.21−3.33 (3H, m, H-4″, H-4′, and H-5′), 2.26 (2H, t, J = 7.2 Hz, H-2), 2.03−2.04 (4H, m, H-8 and H-11), 1.57−1.62 (4H, m, H-3 and H-16), 1.31−1.46 (16H, m, H-4−7 and H-12−15), 1.24 (3H, d, J = 6.3 Hz, H-18).^{13}C NMR (CH_3OH-d_4): 176.55, 171.83, 137.25, 129.57, 129.93, 129.15, 104.76 (C-1″ or C-1′), 102.73 (C-1″ or C-1′), 82.09 (C-2′), 78.82, 78.27, 77.83, 75.92, 71.86, 71.58, 68.05, 63.14, 62.85, 56.38, 37.82, 36.85, 30.84, 30.38, 30.25, 28.19, 26.89, 26.27, 21.92 (C-18). LC/APCI-MS: R_t 5.5 min, *m*/*z* $[M + Na]^+$ 822.51 and 6.1 min, *m*/*z* 822.49 $[M + Na]^+$.

Leucine-*N*-{17-L-[(2′-O-β-D-glucopyranosyl-β-D-glucopyranosyl)oxy]-*cis*-9-octadecenamide} Benzyl Ester (structure 11). $[\alpha]_D^{25} = -7.5$ (c = 0.0160 in MeOH).^{1}H NMR (CH_3OH-d_4): 7.30−7.36 (5H, m, $CH_2C_6H_5$), 5.36 (2H, m, H-9 and H-10), 5.14 (2H, s, $CH_2C_6H_5$), 4.63 (1H, d, J = 8.1 Hz, H-1″), 4.38−4.50 (1H, m, NHC*H*$COOCH_2C_6H_5$), 4.45 (1H, d, J = 7.5 Hz, H-1′), 3.82−3.87 (3H, m, H-6′b, H-6″b, and H-17), 3.58−3.69 (3H, m, H-6′a, H-6″a, and H-5″), 3.35−3.58 (4H, m, H-2′, H-3′, H-3″, and H-2″), 3.21−3.33 (3H, m, H-4″, H-4′, and H-5′), 2.21 (2H, t, J = 7.2 Hz, H-2), 2.03−2.04 (4H, m, H-8 and H-11), 1.58−1.68 (7H, m, $CH_2CH(CH_3)_2$, H-3 and H-16), 1.31−1.46 (16H, m, H-4−7 and H-12−15), 1.24 (3H, d, J = 6.3 Hz, H-18), 0.93 and 0.89 (6H, 2d, J = 6 Hz each, $CH_2CH(CH_3)_2$).^{13}C NMR (CH_3OH-d_4): 176.86, 174.47, 137.70, 129.51, 130.15, 130.76, 104.76, 102.73, 82.34, 79.28, 78.67, 78.63, 78.14, 76.28, 72.20, 71.89, 63.48, 63.17, 52.46, 42.21, 38.23, 37.82, 31.21, 30.86, 30.64, 27.38, 27.01, 26.71, 26.50, 23.90, 22.34, 22.12. LC/APCI-MS: R_t 14.4 min, *m*/*z* 848.94 $[M + Na]^+$ and 13.02 min, *m*/*z* 848.91 $[M + Na]^+$.

Phenylalanine-*N*-{17-L-[(2′-O-β-D-glucopyranosyl-β-D-glucopyranosyl)oxy]-*cis*-9-octadecenamide} Benzyl Ester (structure 12). $[\alpha]_D^{25} = -34.8$ (c = 0.0117 in MeOH). ^{1}H NMR (CH_3OH-d_4): 7.28−7.36 (5H, m, $CH_2C_6H_5$), 7.15−7.25 (5H, m, C_6H_5), 5.36 (2H, m, H-9 and H-10), 5.12 (2H, s, $CH_2C_6H_5$), 4.69−4.74 (1H, t, merging with HDO signal, NHC*H*$COOCH_2C_6H_5$), 4.63 (1H, d, J = 8.1 Hz, H-1″), 4.45 (1H, d, J = 7.5 Hz, H-1′), 3.82−3.86 (3H, m, H-6′b, H-6″b, and H-17), 3.58−3.69 (3H, m, H-6′a, H-6″a, and H-5″), 3.35−3.47 (4H, m, H-2′, H-3′, H-3″, and H-2″), 3.21−3.33 (3H, m, H-4″, H-4′, and H-5′), 2.98−2.93 (2H, m, $C_6H_5CH_2$ phenylalanine moiety), 2.15 (2H, t, J = 7.2 Hz, H-2), 2.03−2.03 (4H, m, H-8 and H-11), 1.44−1.65 (7H, m, $CH_2CH(CH_3)_2$, H-3 and H-16), 1.33−1.40 (16H, m, H-4−7 and H-12−15), 1.24 (3H, d, J = 6.3 Hz, H-18). ^{13}C NMR (CH_3OH-d_4): 176.67, 173.34, 138.58, 137.48, 131.29, 130.68, 128.29, 129.99, 129.75, 105.11 (C-1″ or C-1′), 103.05 (C-1″ or C-1′), 82.55, 79.12, 78.62, 78.09, 76.26, 72.16, 71.98, 68.38, 65.87, 63.43, 63.15, 55.71, 44.85, 38.75, 38.19, 37.18, 31.23, 30.76, 30.59, 28.60, 27.33, 26.67, 22.27. LC/APCI-MS: R_t 14.3 min, *m*/*z* 882.59 $[M + Na]^+$ and 15.7 min, *m*/*z* 882.56 $[M + Na]^+$.

Glutamic Acid-*N*-{17-L-[(2′-O-β-D-glucopyranosyl-β-D-glucopyranosyl)oxy]-*cis*-9-octadecenamide} *tert*-Butyl Ester (structure 13). $[\alpha]_D^{25} = -13.3$ (c = 0.0125 g/mL in MeOH). IR [KBr plate, cm^{-1} (% T)] 3347, 2927, 2854, 2360, 1731, 1650, 1593, 1540, 1368, 1255, 1154, 1074, 894. ^{1}H NMR (CH_3OH-d_4): 5.34 (2H, m, H-9 and H-10), 4.63 (1H, d, J = 8.1 Hz, H-1″), 4.44 (1H, d, J = 7.5 Hz, H-1′), 4.30 (1H, dd, J = 5.4 and 9.6 Hz, CONHC*H*), 3.81−3.87 (3H, m, H-6′b, H-6″b, and H-17), 3.62−3.68 (3H, m, H-6′a, H-6″a, and H-5″), 3.35−3.58 (4H, m, H-2′, H-3′, H-3″, and H-2″), 3.21−3.33 (3H, m, H-4″, H-4′, and H-5′), 2.31 (2H, t, J = 7.5 Hz, CH_2 protons from glutamic acid moiety), 2.15 (2H, t, J = 7.2 Hz, H-2), 2.03−2.11 (5H, m, CH_a from γ methylene of glutamic acid moiety, H-8 and H-11), 1.80−1.90 (1H, m, CH_b from β methylene of

glutamic acid moiety), 1.59−1.65 (4H, m, H-3 and H-16), 1.45 and 1.46 (18H, 2s, C(CH_3)$_3$ × 2), 1.30−1.48 (16H, m, H-4−7 and H-12−15), 1.24 (3H, d, J = 6.3 Hz, H-18). ^{13}C NMR (CH_3-OH-d_4): 176.38, 173.66 and 172.65 (C═O × 3), 130.87, 104.71 (C-1″ or C-1′), 102.74 (C-1″ or C-1′), 82.85, 81.90 (C-2′), 78.84, 78.30, 77.82, 75.91, 71.83, 71.34, 63.13, 62.79, 53.71, 37.83, 36.81, 30.84, 30.29, 28.35, 28.31, 28.19, 27.86, 27.00, 26.61, 26.27, 26.16, 21.93 (C-18). LC/APCI-MS: R_t 10.9, m/z 886.62 [M + Na]$^+$ and 12.2 min, m/z 886.60 [M + Na]$^+$.

Glutamic-*N*-{17-L-[(2′-*O*-*β*-D-glucopyranosyl-*β*-D-glucopyranosyl)oxy]-*cis*-9-octadecenamide} Acid (structure 14). $[\alpha]_D^{25} = -12.3$ (c = 0.0121 g/mL in MeOH). ^{1}H NMR (CH_3-OH-d_4): 5.35 (2H, m, H-9 and H-10), 4.63 (1H, d, J = 8.1 Hz, H-1″), 4.43−4.60 (2H, m, CONHCHCOOH, H-1′), 3.82−3.87 (3H, m, H-6′b, H-6″b, and H-17), 3.62−3.68 (3H, m, H-6′a, H-6″a, and H-5″), 3.35−3.58 (4H, m, H-2′, H-3′, H-3″, and H-2″), 3.21−3.34 (3H, m, H-4″, H-4′, and H-5′), 2.40 (2H, t, J = 7.5 Hz, CH_2 protons from glutamic acid moiety), 2.25 (2H, t, J = 7.2 Hz, H-2), 2.18−2.22 (1H, m, CH_a from β methylene of glutamic acid moiety), 1.89−2.04 (5H, m, CH_b from β methylene of glutamic acid moiety H-8 and H-11), 1.59−1.70 (4H, m, H-3 and H-16), 1.30−1.48 (16H, m, H-4−7 and H-12−15), 1.25 (3H, d, J = 6.3 Hz, H-18). ^{13}C NMR (CH_3OH-d_4): 176.38, 175.0 and 174.32 (C═O × 3), 130.89, 104.74 (C-1″ or C-1′), 102.74 (C-1″ or C-1′), 82.05, 78.86, 78.29, 77.80, 75.92, 71.86, 71.57, 65.19, 63.15, 62.82, 44.00, 37.84, 36.86, 31.29, 30.85, 30.38, 30.27, 28.19, 27.89, 26.92, 26.28, 21.93 (C-18). LC/APCI-MS: R_t 2.9 min, m/z 774.54 [M + Na]$^+$ and 4.1 min, m/z 774.57 [M + Na]$^+$.

Aspartic-*N*-{17-L-[(2′-*O*-*β*-D-glucopyranosyl-*β*-D-glucopyranosyl)oxy]octadecanamide} Acid (structure 15). $[\alpha]_D^{25} = -5.7$ (c = 0.1050 in MeOH). ^{1}H NMR (CH_3OH-d_4): 4.80−4.87 (1H, overlapping multiplet with HDO signal, CONHCH-COOH), 4.63 (1H, d, J = 8.1 Hz, H-1″), 4.45 (1H, d, J = 7.5 Hz, H-1′), 3.81−3.89 (3H, m, H-6′b, H-6″b, and H-17), 3.62−3.68 (3H, m, H-6′a, H-6″a, and H-5″), 3.35−3.55 (4H, m, H-2′, H-3′, H-3″, and H-2″), 3.21−3.35 (3H, m, H-4″, H-4′, and H-5′), 2.80 (2H, dd, J = 6.6 and 9.3 Hz CH_2 protons from aspartic acid), 2.23 (2H, t, J = 7.2 Hz, H-2), 1.59−1.74 (4H, m, H-3 and H-16), 1.30−1.46 (24H, m, H-4−15), 1.24 (3H, d, J = 6.3 Hz, H-18). ^{13}C NMR (CH_3OH-d_4): 176.12 (CONH), 174.39 and 174.52 (CO × 2), 104.57 (C-1″ or C-1′), 102.57 (C-1″ or C-1′), 82.02 (C-2′), 78.87, 78.34, 77.80, 75.92, 71.86, 71.57, 63.13, 62.82, 37.84, 37.29, 36.90, 34.78, 30.79, 30.23, 26.88, 26.78, 26.31, 26.08, 21.91 (C-18). LC/APCI-MS: R_t 2.8 min, m/z 762.39 [M + Na]$^+$ and 3.1 min, 762.55 [M + Na]$^+$.

Serine-*N*-{17-L-[(2′-*O*-*β*-D-glucopyranosyl-*β*-D-glucopyranosyl)oxy]octadecanamide} (structure 16). $[\alpha]_D^{25} = -10.4$ (c = 0.0156 g/mL in MeOH). ^{1}H NMR (CH_3OH-d_4): 4.60 (1H, d, J = 8.1 Hz, H-1″), 4.45 (1H, t, J = 4.28 Hz, NHCHCOOH), 4.40 (1H, d, J = 7.5 Hz, H-1′), 3.74−3.88 (5H, m, CH_2OH from serine, H-6′b, H-6″b, and H-17), 3.58−3.69 (3H, m, H-6′a, H-6″a, and H-5″), 3.35−3.58 (4H, m, H-2′, H-3′, H-3″, and H-2″), 3.16−3.33 (3H, m, H-4″, H-4′, and H-5′), 2.26 (2H, t, J = 7.2 Hz, H-2), 1.57−1.62 (4H, m, H-3 and H-16), 1.31−1.46 (24H, m, H-4−15), 1.21 (3H, d, J = 6.3 Hz, H-18). ^{13}C NMR (CH_3OH-d_4): 176.82, 173.89, 105.04 (C-1″ or C-1′), 103.11 (C-1″ or C-1′), 82.30 (C-2′), 79.29, 78.65, 78.14, 76.28, 72.20, 71.89, 63.47, 63.36, 56.43, 8.23, 37.27, 31.17, 30.32, 30.67, 27.24, 26.68, 22.29 (C-18). LC/APCI-MS: R_t 2.4 min, m/z [M + Na]$^+$ 734.76 and 3.2 min, m/z 734.78 [M + Na]$^+$.

Leucine-*N*-{17-L-[(2′-*O*-*β*-D-glucopyranosyl-*β*-D-glucopyranosyl)oxy]octadecanamide} (structure 17). $[\alpha]_D^{25} = -8.2$ (c = 0.0151 g/mL in MeOH). IR [KBr plate, cm^{-1} (% T)] 3352, 2924, 2853, 2390, 1713, 1644, 1538, 1466, 1235, 1163, 1077, 720. ^{1}H NMR (CH_3OH-d_4): 4.58 (1H, d, J = 8.1 Hz, H-1″), 4.40 (1H, d, J = 7.5 Hz, H-1′), 4.34−4.40 (1H, m, NHCH-COOH), 3.78−3.86 (3H, m, H-6′b, H-6″b, and H-17), 3.57−3.64 (3H, m, H-6′a, H-6″a, and H-5″), 3.36−3.53 (4H, m, H-2′, H-3′, H-3″, and H-2″), 3.19−3.33 (3H, m, H-4″, H-4′, and H-5′), 2.18 (2H, t, J = 7.2 Hz, H-2), 1.54−1.67 (7H, m, $CH_2CH(CH_3)_2$, H-3 and H-16), 1.31−1.46 (24H, m, H-4−15), 1.19 (3H, d, J = 6.3 Hz, H-18), 0.90 and 0.87 (6H, 2d, J = 6.0 Hz each, $CH_2CH(CH_3)_2$). ^{13}C NMR (CH_3OH-d_4): 176.86, 176.76, 105.07, 103.11, 82.35, 79.28, 78.67, 78.63, 78.14, 76.28, 72.20, 71.89, 63.49, 63.17, 52.46, 42.05, 38.24, 37.24, 31.22, 30.86, 30.64, 27.39, 27.01, 26.71, 26.50, 23.90, 22.34, 22.25. LC/APCI-MS: R_t 3.2 min, and 3.9 min, m/z 760.64 [M + Na]$^+$.

Phenylalanine-*N*-{17-L-[(2′-*O*-*β*-D-glucopyranosyl-*β*-D-glucopyranosyl)oxy]octadecanamide} (structure 18). $[\alpha]_D^{25} = -11.3$ (c = 0.0142 g/mL in MeOH). IR [KBr plate, cm^{-1} (% T)] 3416, 2917, 2849, 2390, 1730, 1643, 1542, 1468, 1238, 1158, 1080, 864. ^{1}H NMR (CH_3OH-d_4): 7.13−7.17 (5H, m, C_6H_5 from phenylalanine), 4.54−4.56 (2H, m, H-1″ and NHCHCOOH), 4.35 (1H, d, J = 7.5 Hz, H-1′), 3.82−3.86 (3H, m, H-6′b, H-6″b, and H-17), 3.58−3.69 (3H, m, H-6′a, H-6″a, and H-5″), 3.35−3.47 (4H, m, H-2′, H-3′, H-3″, and H-2″), 3.21−3.33 (3H, m, H-4″, H-4′, and H-5′), 3.02 (2H, m, CH_2 phenylalanine moiety), 2.15 (2H, t, J = 7.2 Hz, H-2), 1.50−1.52 (4H, m, H-3 and H-16), 1.33−1.40 (24H, m, H-4−15), 1.21(3H, d, J = 6.3 Hz, H-18). ^{13}C NMR (CH_3OH-d_4): 176.56, 175.71, 139.05, 130.63, 129.78, 128.11, 105.06, 103.12, 82.33, 79.25, 78.63, 78.17, 72.20, 71.92, 65.52, 63.47, 63.15, 58.71, 44.35, 38.83, 38.22, 37.27, 31.17, 30.82, 30.48, 27.28, 26.68, 22.28. LC/APCI-MS: R_t 2.8 min, m/z 794.62 [M + Na]$^+$ and 3.2 min, m/z 794.60 [M + Na]$^+$.

Phenylalanine-*N*-{17-L-[(2′-*O*-*β*-D-glucopyranosyl-*β*-D-glucopyranosyl)oxy]-*cis*-9-octadecanamide} Ethyl Ester (structure 19). $[\alpha]_D^{25} = -8.6$ (c = 0.0152 g/mL in MeOH). IR [KBr plate, cm^{-1} (% T)] 3331, 2925, 2854, 2360, 1738, 1650, 1603, 1542, 1454, 1376, 1172, 1074, 1034. ^{1}H NMR (CH_3OH-d_4): 7.29−7.19 (5H, m, C_6H_5 from phenylalanine), 5.35 (2H, m, H-9 and H-10), 4.68−4.62 (2H, m, H-1″ and NHCHCOOH), 4.44 (1H, d, J = 7.5 Hz, H-1′), 4.13 (2H, q, J = 7.2 Hz, OCH_2-CH_3), 3.82−3.87 (3H, m, H-6′b, H-6″b, and H-17), 3.58−3.69 (3H, m, H-6′a, H-6″a, and H-5″), 3.35−3.47 (4H, m, H-2′, H-3′, H-3″, and H-2″), 3.21−3.33 (3H, m, H-4″, H-4′, and H-5′), 3.02 (2H, t, J = 5.1 Hz, CH_2 phenylalanine moiety), 2.15 (2H, t, J = 7.2 Hz, H-2), 2.03−2.05 (4H, m, H-8 and H-11), 1.44−1.65 (4H, m, H-3 and H-16), 1.33−1.40 (16H, m, H-4−7 and H-12−15), 1.24−1.26 (6H, m, OCH_2CH_3 and H-18). ^{13}C NMR (CH_3OH-d_4): 176.57, 173.63, 138.68, 131.23, 130.59, 129.84, 128.22, 105.08, 103.11, 82.37, 79.25, 78.71, 78.65, 78.21, 76.27, 72.21, 71.90, 63.50, 63.15, 62.71, 55.58, 38.82, 37.09, 31.29, 31.20, 30.77, 30.71, 30.56, 30.46, 28.55, 27.26, 26.63, 22.28. LC/APCI-MS: R_t 8.9 min, m/z 820.87 [M + Na]$^+$ and 10.0 min, m/z 820.87 [M + Na]$^+$.

Leucine-*N*-{17-L-[(2′-*O*-*β*-D-glucopyranosyl-*β*-D-glucopyranosyl)oxy]-*cis*-9-octadecanamide} Ethyl Ester (structure 20). $[\alpha]_D^{25} = -6.4$ (c = 0.0181 g/mL in MeOH). IR [KBr plate, cm^{-1} (% T)] 3316, 2927, 2855, 2360, 1737, 1649, 1560, 1446, 1375, 1266, 1196, 1087, 940, 857. ^{1}H NMR (CH_3OH-d_4): 5.34−5.38 (2H, m, H-9 and H-10), 4.65 (1H, d, J = 7.8 Hz, H-1″), 4.41−4.48 (2H, m, NHCHCOOCH$_2$CH$_3$ and H-1′), 4.18 (2H, q, OCH_2CH_3), 3.88−3.84 (3H, m, H-6′b, H-6″b, and H-17), 3.71−3.64 (3H, m, H-6′a, H-6″a, and H-5″), 3.36−3.55 (4H, m, H-2′, H-3′, H-3″, and H-2″), 3.19−3.33 (3H, m, H-4″, H-4′, and H-5′), 2.04−2.06 (4H, m, H-8 and H-11), 2.18 (2H, t, J = 7.2 Hz, H-2), 1.54−1.67 (7H, m, $CH_2CH(CH_3)_2$, H-3 and H-16), 1.31−1.46 (16H, m, H-4−7 and H-12−15), 1.24−1.30 (6H, m, OCH_2CH_3 and H-18), 0.93 and 0.97 (6H, 2d, J = 6.0 Hz each, $CH_2CH(CH_3)_2$). ^{13}C NMR (CH_3OH-d_4): 176.82, 174.78, 131.32, 131.24, 105.10, 103.11, 82.42, 79.23, 78.69, 78.63, 78.20, 78.14, 76.28, 72.23, 71.90, 63.53, 63.19,

62.63, 52.48, 41.80, 38.22, 37.14, 31.32, 31.22, 30.80, 30.74, 30.66, 30.59, 27.38, 26.66, 26.45, 23.78, 22.36, 22.28. LC/APCI-MS: R_t 7.7 min, *m*/*z* 786.79 $[M + Na]^+$ and 8.7 min, *m*/*z* 786.89 $[M + Na]^+$.

Glycine-*N*-{17-L-[(2′-*O*-*β*-D-glucopyranosyl-*β*-D-glucopyranosyl)oxy]-*cis*-9-octadecenamide} Methyl Ester (structure 21). $[\alpha]_D^{25} = -8.6$ ($c = 0.0136$ g/mL in MeOH). IR [KBr plate, cm^{-1} (% T)] 3357, 2925, 2853, 1741, 1650, 1543, 1377, 1227, 1169, 1078, 894. ^{1}H NMR (CH_3OH-d_4): 5.36 (2H, m, H-9 and H-10), 4.63 (1H, d, $J = 8.1$ Hz, H-1″), 4.45 (1H, d, $J = 7.5$ Hz, H-1″), 3.92 (2H, s, $NHCH_2COOCH_3$), 3.81−3.87 (3H, m, H-6′b, H-6″b, and H-17), 3.72 (3H, s, $NHCH_2COOCH_3$), 3.63−3.74 (3H, m, H-6′a, H-6″a, and H-5″), 3.35−3.58 (4H, m, H-2′, H-3′, H-3″, and H-2″), 3.21−3.33 (3H, m, H-4″, H-4′, and H-5′), 2.25 (2H, t, $J = 7.2$ Hz, H-2), 2.03−2.05 (4H, m, H-8 and H-11), 1.59−1.65 (4H, m, H-3 and H-16), 1.30−1.46 (16H, m, H-4−7 and H-12−15), 1.24 (3H, d, $J = 6.3$ Hz, H-18).^{13}C NMR (CH_3OH-d_4): 176.83, 171.99, 130.95, 130.90 (*C*H═*C*H), 104.85, 102.73, 82.27 (C-2′), 79.08 (C-17), 78.68, 78.64 (C-3″ and C-5′), 78.26, 78.16 (C-3′ and C-5″), 76.29 (C-2″), 72.28, 72.01 (C-4″ and C-4′), 63.54, 63.24 (C-6′ and C-6″), 52.93 (OCH_3), 42.26 ($NHCH_2COOCH_3$), 38.18, 37.16, 31.26, 31.17, 30.96, 30.75, 30.67, 30.57, 28.54, 27.19, 26.62, 22.25 (C-18). LC/APCI-MS: R_t 4.1 min, *m*/*z* 716.38 $[M + Na]^+$ and 4.3 min, *m*/*z* 716.38 $[M + Na]^+$.

Antimicrobial Assay. To determine antimicrobial activities, *Escherichia coli*, *Bacillus subtilis*, *Salmonela cholerasesuis*, *Microbacterium imperiale* (obtained from ATCC, U.S.A.), *Moraxella* sp., *Streptococcus agalactiae*, and *Streptococcus sanguinis* (obtained as gift cultures from Dr. Maja Nowakowski, SUNY downstate medical center, NY) were used.

The minimum inhibitory concentrations (MIC) of the amino acid conjugated SLs were determined by the broth serial dilution method performed in 96-well microtiter plates. A stock solution of SL (15 mg/mL) was prepared in 200 mg/mL sucrose solution (pH 9.0). Cultures were grown o/n and diluted to 0.1 OD before experiments. Serial dilutions (50 μL) of each sample were made in the broth, and plates incubated at 30 °C. After 18−24 h, the plates were examined for growth of the organisms. The concentration that inhibited more then 90% growth of the organism was record as the MIC. Positive control (cells plus medium) and negative control (medium only) were performed with each experiment. Percent inhibition was calculated by comparing the experimental readings with the positive control. Three replicates were performed for each SL derivative against each test organism.

Spermicidal Assay. The spermicidal activity of SLs was evaluated using a modification of the method by Sander and Cramer (*15*). Semen samples were collected from normal donors by masturbation, allowed to liquefy at room temperature, and assessed for motility. The protocol was approved by the Eastern Virginia Medical School Institutional Review Board. Stock solutions, typically 10 mg/mL, were prepared in DMSO. Serial 2-fold dilutions in 0.9% NaCl of test compounds were incubated with semen aliquots for 30 s. Motility was evaluated under the microscope during the first incubation and after dilution in buffer and further incubation for 1 h. Only those dilutions that immobilized 100% of the spermatozoa pass the test. Results were expressed as minimum effective concentrations (MEC or ED100).

HIV Inactivation Assay. Anti-HIV activity was evaluated by incubating serial dilutions of the SL compounds with HIV-1 (IIIB) and CD4/*β*-galactosidase-expressing HeLa cells for 2 h in 12-well plates (*16*). After this incubation, virus and compounds were washed away, and the cells were resuspended and cultured in fresh RPMI 1640 medium supplemented with 10% fetal bovine serum for 48 h at 37 °C and 5% CO_2. These cells express *β*-galactosidase under the control of the HIV long terminal repeat (LTR). Thus, expression of this enzyme is linked to HIV infection. After the 48 h incubation, cells were washed in PBS, and *β*-galactosidase activity was measured using the Galacto-Star *β*-galactosidase reporter gene assay (Applied Biosystems, Foster City, CA). Briefly, the cells were lysed and their contents incubated with Galacto-Star substrate. Chemiluminescence was quantified in a luminometer. Cells incubated with virus and no compounds provided values representing 100% infection. Fifty percent effective concentrations (EC_{50}) were calculated using a linear regression model.

RESULTS AND DISCUSSION

Synthesis. SL mixture produced by the fermentation of *C. bombicola* on glucose/oleic acid contains at least fourteen different compounds that exist mainly in the lactonic and acidic forms. These compounds also have a variable degree of acetylation at the primary hydroxyl groups at 6′ and 6″ positions. The aliphatic component of SLs is composed of 17-hydroxyoleic acid that exists in hydrogenated and non-hydrogenated forms. To free carboxylic groups of lactonic sophorolipids as well as to reduce natural sophorolipid mixture heterogeneity, alkaline hydrolysis was performed according to a published procedure (*17*). During alkaline hydrolysis, acetate groups of sophorose units were removed with concomitant opening of the lactonic ring to give 17-L-[(2′-*O*-*β*-D-glucopyranosyl-*β*-D-glucopyranosyl)oxy]-*cis*-9-octadecenoic acid (SL-COOH, **8**). The downfield shift (δ 3.66) for the C-1 carbon of **8** (δ 178.42), when compared to the cyclic form (δ 174.76), confirmed that opening of the lactonic ring occurred (*18*). All peaks due to carbohydrate protons match well with other ring-open derivatives synthesized in the past and for which rigorous assignments had been made using ^{1}H−^{1}H COSY NMR and DEPT 135 experiments (*12*, *13*). Finally, before conjugation, purity of the SL-COOH was determined by LC/APCI (*m*/*z* 645.39 and 645.41). Two peaks of the same mass at different retention times were observed. This is attributed to attachment of dimeric sophorose to the hydroxyl group at either the penultimate or terminal fatty acid carbon where the later is the minor component (*19*).

The free carboxylic group was used as a handle to anchor various amino acids using DCC coupling. The coupling was performed without protecting free hydroxyl groups of sophorose moieties. SL-COOH is sparingly soluble in DCM; however, addition of anhydrous DMF renders the compound completely soluble, yielding a homogeneous solution. Conjugation of amino acids to sophorolipids was confirmed by identifying relevant NMR signals of the amino acid moiety. For example, coupling of dibenzylaspartic ester to SL-COOH gave a double doublet at 2.90 ppm (2H) that corresponds to the aspartate methylene of the side chain. Furthermore, ^{13}C NMR showed three peaks in the carbonyl region, two at 171.83 and 171.59 ppm due to esters and one at 176.05 ppm due to newly formed amide. Deprotection of sophorolipid−amino acid conjugates with benzyl ester protecting groups was performed in dry ethanol by hydrogenation over Pd/C. This method resulted in both the removal of benzyl ester groups and the reduction of cis double bonds of the SL fatty acid moiety. Removal of *tert*-butyl protecting groups was carried out in DCM/TFA at 0 °C. Performing this reaction under mild acidic conditions avoided the hydrolysis of anomeric linkages of SLs.

To further broaden the range of SL−amino acid conjugates for bioactivity studies, amino acid ethyl esters were coupled to SL-COOH. SL−amino acid conjugates where the amino acid carboxylate groups are ethyl esters increases compound hydrophobicity relative to its corresponding carboxylate salt form. Furthermore, introduction of ethyl esters was not considered problematic, since liberation of ethanol by metabolism gives readily metabolized byproducts.

Table 1. Antimicrobial Activity of Different Amino Acid Conjugated SLs

SL sample	**14**	**15**	**16**	**17**	**18**	**19**	**20**	**21**	MAEE-SL[a]
Culture	Minimal Inhibitory Concentration (mg/mL)								
E. coli	0.56	5	5	1.67	5	>5	>5	>5	5
B. subtilis	>7.5	>7.5	>7.5	5	>7.5	5	1.67	1.67	0.06
Moraxella sp.	1.67	5	7.5	0.83	5	5	0.000762	NA	0.02
S. cholerasesuis	>7.5	>7.5	>7.5	5	>7.5	>5	>5	>5	5
S. agalactiae	5	5	5	5	>7.5	1.67	ND[b]	5	0.007
S. sanguinis	>7.5	>7.5	5	2.5	7.5	5	0.00228	0.56	ND[b]
M. imperiale	>7.5	>7.5	5	5	>7.5	>5	1.67	5	ND[b]

[a] MAEE-SL = ethyl 17-L-([2′-*O*-*β*-D-glucopyranosyl-*β*-D-glucopyranosyl]oxy)-*cis*-9-octadecenoate-6′,6″-diacetate. The compound was synthesized using protocol described elsewhere.[13] [b] ND = not determined.

This family of new SL−amino acid conjugates was assessed to understand structure−bioactivity relationships by performing studies of antibacterial, anti-HIV, and spermicidal activity.

Biological Activity. Biosurfactants represent an emerging class of important compounds in biomedical science that offer antifungal, antibacterial, antimycoplasmal, and antiviral properties (*20*). The proposed primary mechanism of action of these surfactants is membrane lipid order perturbation, which compromises the viability of microorganisms (*21*). Some amino acid conjugated SLs display bactericidal and virucidal activity. However, none of these compounds are significantly spermicidal, showing a certain degree of membrane specificity in their lytic action.

Antibacterial Activity. All tested analogues showed antibacterial activity against both gram +ve and gram −ve organisms (Table 1). Comparing the efficiencies of amino acid conjugated SLs shows that leucine-conjugated SL is most efficient with MIC of 5 mg/mL or less for all seven of the organisms tested. MIC for *Moraxella* sp. was 0.83 mg/mL, and for *E. coli*, it was 1.67 mg/mL. This derivative was also the most effective of those tested against *B. subtilis* and *S. sanguinis* (5 mg/mL and 2.5 mg/mL, respectively). Among the alkyl esters of amino acid conjugated SLs, the ethyl ester of leucine−SLs was most active. It is also the most effective compound of those evaluated against *Moraxella* sp., *S. sanguinis*, and *M. imperiale* with MIC values of 7.62×10^{-4}, 2.28×10^{-3}, and 1.67 mg/mL, respectively. In earlier studies by our laboratory, monoacetylated ethyl ester SL (MAEE-SL) was identified as an efficient antibacterial compound.[5] After comparing the activity of ethyl ester leucine−SL to that of MAEE-SL, it is evident that ethyl ester−leucine SL is more potent against *Moraxella* sp. However, the antibacterial activity of MAEE relative to ethyl ester−leucine SL was higher against the other microorganisms tested. Therefore, future experiments will be directed toward preparing amino acid−SLs whose sophorose head group contains various extents of acetylation.

Anti-HIV Activity. As shown in Table 2, all compounds displayed virus inactivating activity with 50% effective concentrations (EC_{50}) below 200 μg/mL. Comparing potencies of amino acid conjugated SLs and their alkyl esters showed that esterified derivatives were more effective than corresponding non-esterified compounds. The ethyl ester of leucine-conjugated SL was most potent with an EC_{50} of 24.1 μg/mL. This analogue was more potent than the commercial spermicide nonoxynol-9, which displays virucidal anti-HIV activity with an $EC_{50} \approx$ 65 μg/mL. Dimethyl sulfoxide (DMSO) did not display antiviral activity at the concentrations present in the tested compound dilutions.

Spermicidal Activity. Spermicidal activity was measured using a modified Sander−Cramer test. None of the compounds displayed significant spermicidal activity beyond that shown by the solvent (DMSO) control. In contrast, nonoxynol-9 (N-9) and MAEE, included as positive controls, revealed the minimum effective concentration (MEC) values of around 300 and 500 μg/mL, respectively.

Table 2. Anti-HIV and Spermicidal Activity of Different Amino Acid Conjugated SLs

SL sample	anti-HIV activity EC_{50} (μg/mL)	spermicidal activity MEC*a* (mg/mL)
14	194.9	ND[e]
15	182.3	7.5 ± 1.0
16	177.4	7.5 ± 1.0
17	116.9	7.0 ± 1.1
18	148.7	6.7 ± 1.0
19	65.9	5.8 ± 0.8
20	24.1	7.5 ± 1.0
21	92	9.2 ± 0.8
MAEE	ND[e]	0.5 ± 0.04
DMSO[c]	>1000[b]	7.5 ± 1.0[b]
N-9[d]	ND[e]	0.339 ± 0.057

[a] Minimum effective concentration. [b] Solute equivalent concentration. [c] Dimethyl sulfoxide. [d] Nonoxynol-9. [e] Not determined.

SUMMARY OF RESULTS

By changing the amino acid from hydrophilic (L-glutamic, L-aspartic, L-serine) to hydrophobic (L-phenylalanine, L-leucine), improved antimicrobial properties were achieved. The leucine-conjugated SL ethyl ester derivative was the most potent bactericidal and HIV-1 virucidal compound studied herein. Nevertheless, the potency of this analog must be further enhanced before it can be considered as an important candidate for advanced therapy. The results of structure−activity relationships from this work provide important guidance in how to engineer SL derivatives to achieve effective new therapeutics. Work is in progress to determine how the length of leucine alkyl esters conjugated to SL, and acetylating sophorose head groups of amino acid−SL conjugates, modulates SL biological properties.

Supporting Information Available: NMR spectra. This material is available free of charge via the Internet at http://pubs.acs.org.

LITERATURE CITED

(1) Davila, A. M., Marchal, R., Monin, N., and Vandecastelle, J. P. (1993) Identification and determination of individual sophorolipids in fermentation products by gradient elution high-performance chromatography and evaporative light scattering and UV detection. *J. Chromatogr. 648*, 139−149.

(2) Gorin, A. P. J., Spencer, J. F. T., and Tulloch, A. P. (1961) Hydroxy fatty acid glycosides of sophorose from *Torulopsis magnoliae. Can. J. Chem. 39*, 846−895.

(3) Kandil, E., Zhang, H., Schulze, R., Dresner, L., Nowakowski, M., Gross, R., and Zenilman, M. E. (2003) Sophorolipids block lethal effects of septic shock. *J. Am. Coll. Surg. 197*, S40−41.

(4) Gross, R., Guilmanov, V., and Scholz, C. (1999) Glycolipids from *torulopsis bombicola*: biosynthesis, lipase-selective modification and anti-cancer activity. Book of abstracts, 217th ACS national meeting.

(5) Gross, R., and Shah, V. (2003) Antibacterial properties of various forms of sophorolipids. U.S. Patent Application PCT/US2003/035871.

(6) Gross, R., Shah, V., and Gustavo, D. (2004) Spermicidal and virucidal properties of various forms of sophorolipids. U.S. Patent Application 10/804778.

(7) Shah, V., Doncel, G. F., Seyoum, T., Eaton, K. M., Zalenskaya, I., Hagver, R., Azim, A., and Gross, R. (2005) Sophorolipids: novel glycolipid preventive agents for conception and sexual transmission. *Antimicrob. Agents Chemother. 49*, 4093−4100.

(8) Gross, R., and Shah, V. (2004) Antifungal activity of various forms of sophorolipids. U.S. Patent Application 11/020683.

(9) Zhou, Q.-H., and Kosaric, N. (1995) Utilization of canola oil and lactose to produce biosurfactant with *Candida bombicola. J. Am. Oil Chem. Soc. 72*, 67−71.

(10) Davila, A. M., Marchal, R., and Vandecasteele, J. P. (1992) Kinetics and balance of fermentation free from product inhibition: sophorose lipid production by *Candida bombicola. Appl. Microbiol. Biotechnol. 38*, 6−11.

(11) Cavalero, D. A., and Cooper, D. G. (2003) The effect of medium composition on the structure and physical state of sophorolipids produced by *Candida bombicola* ATCC 22214. *J. Biotechnol. 103*, 31−41.

(12) Singh, S. K., Felse, A. P., Nunez, A., Foglia, T. A., and Gross, R. A. (2003) Regioselective enzyme-catalyzed synthesis of sophorolipid esters, amides, and multifunctional monomers. *J. Org. Chem. 68*, 5466−5477.

(13) Bisht, K. S., Gross, R. A., and Kaplan, D. L. (1999) Enzyme-mediated regioselective acylations of sophorolipids. *J. Org. Chem. 64*, 780−789.

(14) Nunez, A., Folgia, T. A., and Ashby, R. (2003) Enzymatic synthesis of galactopyanose sophorolipid fatty acid ester. *Biotechnol. Lett. 25*, 1291−1297.

(15) Savle, P. S., Doncel, G. F., Bryant, S. D., Hubieki, M. P., Robinette, R. G., and Gandour, R. D. (1999) Acylcarnitine analogues as topical, microbicidal spermicides. *Bioorg. Med. Chem. Lett. 9*, 2545−2548.

(16) Krebs, F. C., Miller, S. R., Malamud, D., Howett, M. K., and Wigdahl, B. (1999) Inactivation of human immunodeficiency virus type 1 by nonoxynol-9, C31G, or an alkyl sulfate, sodium dodecyl sulfate. *Antiviral Res. 43*, 157−173.

(17) Tulloch, A. P., Hill, A., and Spencer, J. F. T. (1968) Structure and reaction of lactonic and acidic sophorosides of 17-hydroxyoctadecenoic acid. *Can. J. Chem. 46*, 3337−3351.

(18) Rau, U., Heckmann, R., Wray, V., and Lang, S. (1999) Enzymatic conversion of a sophorolipid into a glucose lipid. *Biotechnol. Lett. 21*, 973−977.

(19) Cavalero, D. A., and Cooper, D. G. (2003) The effect of medium composition on the structure and physical state of sophorolipids produced by *Candida bombicola* ATCC 22214. *J. Biotechnol. 103*, 31−41.

BC060094N

Synthesis and in Vitro Evaluation of Glutamide-Containing Cationic Lipids for Gene Delivery

Vijaya Gopal,[†] Tekkatte K. Prasad,[‡,§] Nalam M. Rao,*[,†] Makoto Takafuji,[‡] Mohammed M. Rahman,[‡] and Hirotaka Ihara*[,‡]

Centre for Cellular and Molecular Biology, Uppal Road, Hyderabad, India 500 007, and Department of Applied Chemistry and Biochemistry, Faculty of Engineering, Kumamoto University, 2-39-1 Kurokami, Kumamoto, Japan, 860-8555. Received April 22, 2006; Revised Manuscript Received July 20, 2006

A novel series of cationic amphiphiles based on dialkyl glutamides with cationic pyridinium head group were synthesized as potential gene delivery agents. Four cationic lipids with glutamide as linker and varying chain lengths were tested for their transfection efficiency in three cell lines. The DNA−lipid complexes were characterized for their ability to bind to DNA, protection from nuclease digestion, size, ζ-potential, and toxicity. All four lipids demonstrated efficient transfection in MCF-7, COS, and HeLa cells, and the reporter gene expression was much higher with DOPE as the helper lipid in the formulation when compared to cholesterol. Among these 14-carbon lipids, lipid **2** has shown the highest transfection efficiency, complete protection of DNA from nuclease digestion, and low toxicity. Interestingly, lipid **2** has also shown remarkable enhancement in transfection in the presence of serum.

INTRODUCTION

Carriers that can deliver nucleic acids into cells have immense potential to investigate the properties of gene sequences and in gene therapy (*1*−*4*), and broadly fall into viral and nonviral classes. Among the nonviral carriers, the successful strategies are mainly based on cationic lipids, cationic peptides, or polymers and cationic dendrimers (*5*). Cationic lipids have several advantages including simplicity of method, clinical grade manufacturing, lack of ability to elicit immune response, and capacity to carry large fragments of DNA (*6*, *7*). Several clinical trials employing cationic lipids are in progress (*8*).

Cationic lipids are amphiphilic in nature and carry a positive charge at physiological pH (*9*, *10*). The cationic nature of the lipids allows them to bind to the nucleic acids and also to the negatively charged cell membrane. Besides being cationic, the long hydrophobic moiety of these lipids allows self-assembly into vesicles to entrap the nucleic acids, thus protecting DNA from nucleases (*9*). The synthesis, chemistry, and biology of the cationic lipids have been extensively reviewed (*10*−*15*). Essentially, a cationic lipid has a cationic head group that is connected to a hydrophobic moiety by a linker. Glycerol, with ether or ester bonds with fatty acids, is the most popular linker, though other groups such as phosphonates and aromatic groups have also been used (*16*). We report here the synthesis and transfection efficiencies of cationic lipids based on glutamic acid as the linker. These glutamide-derived dialkyl lipids form self-assembled lamellar and non-lamellar structures based on intermolecular hydrogen bonding among amide moieties (*17*−*20*). Four cationic pyridinium amphiphiles with different alkyl chain lengths (C12 to C18) with glutamide as a linker were synthesized. The physical properties of these lipids have been characterized and were tested for their DNA binding and transfection ability in the presence of serum on three cell lines.

* Corresponding authors. Tel +91-40-27192552; Fax +91-40-27160311, E-mail: madhu@ccmb.res.in (N.M.R.). TEL/FAX +81-96-342-3662, E-mail: ihara@kumamoto-u.ac.jp (H.I.).

[†] Centre for Cellular and Molecular Biology.

[‡] Kumamoto University.

[§] Present address: Department of Biochemistry and Molecular Biophysics, Columbia University, 650 West, 168th Street, BB-536, New York, NY-10032. Phone: 1-212-342-2943 (O); 1-212-568-7232 (R).

EXPERIMENTAL PROCEDURES

Plasmid/Chemicals. pCMV.SPORT-β-gal plasmid, Lipofectamine, and Lipofectin were purchased from Invitrogen. DOTAP, cholesterol, and DOPE were purchased from Avanti Polar Lipids, Inc. Dulbecco's Modified Eagle's Medium (DMEM) and cholesterol was obtained from Sigma Chemicals, U.S.A. All other reagents used were of high-quality grade.

Preparation of Liposomes. The methods employed here have been described earlier (*21*, *22*). In the preparation of lipid−DNA complex (Lipoplex) cationic lipids were either mixed with DOPE or cholesterol as the helper lipid. Liposomes were prepared at 1:1 (mol/mol) ratio of cationic lipid and helper lipid, by drying the chloroform stock solutions in 1.5 mL glass tubes under nitrogen gas. Tubes were dried under vacuum to remove traces of chloroform for about 2 h. Sterile MilliQ was added to dried lipid film and hydrated overnight by incubating the tubes at 55 °C in water bath. The sample was vortexed for about 3 min and sonicated using a microprobe until the solution became clear.

Cell Culture. MCF-7, COS-1, and HeLa cells were maintained in DMEM containing 10% fetal bovine serum and 500 μg/mL penicillin, 600 μg/mL streptomycin, and 1 mg/mL kanamycin.

Cell Transfections. For quantitating the transient transfections in cell lines, the β-gal activity was measured 24 h after the transfections (*23*). Lipoplexes with different lipid/DNA charge ratios were prepared by mixing different amounts of liposomes with plasmid DNA (0.3 μg per well) in DMEM and incubated at room temperature for about 15 min. Complexes were incubated with cells for about 3 h, after which lipoplex-containing medium was replaced with 10% serum containing DMEM medium. After 24 h, the medium was removed, and cells were washed with PBS and lysed with 50 μL lysis buffer (250 mM Tris-HCl pH 8.0 containing 0.5% NP40) for 10 min at room temperature. Cell lysate was used for protein estimation

10.1021/bc0601020 CCC: $33.50 © 2006 American Chemical Society
Published on Web 10/04/2006

by Lowry's method and 50 μL was used for the β-galactosidase activity. Absorbance at 410 nm was read in a SPECTRA Max ELISA plate reader. β-Galactosidase activity was calculated from a standard graph constructed from commercial β-galactosidase enzyme. β-Galactosidase activity was normalized against milligrams of cell protein. For transient transfections done in the presence of varying serum concentrations, CLDC was prepared in the absence of serum, and serum was added to the complex at the required final concentration, after which they were added to the cells. Data is represented as β-gal activity per well (~20 000 cells).

Binding of Lipid to DNA and DNaseI Protection Assay. pCMVβ-gal was complexed with cationic lipids at charge ratios varying from 0.3:1 to 3:1 (lipid/DNA) in order to measure the DNA binding ability and, second, to evaluate the susceptibility of the DNA in these complexes to DNaseI digestion. In a typical binding assay, 0.6 nmol of DNA was complexed with lipids in MQ water to obtain the above charge ratios and incubated for 25 min at room temperature (RT) prior to electrophoresis on an agarose gel. For the DNaseI protection assay, the complexes were prepared in 0.5× PBS (pH 7.5). Subsequently, the complexes were treated with 0.2 units of DNaseI and incubated at RT for 20 min, followed by heat inactivation at 60 °C for 7 min. The reactions were then halted with EGTA added to a final concentration of 30 mM. Lipids from the lipoplex were extracted with a phenol−chloroform mixture. Equal volumes of the aqueous phase was treated with DNA loading dye and electrophoresed on a 0.8% agarose gel in TAE buffer at a constant voltage (80 V). The gel was stained with ethidium bromide postelectrophoresis and the bands visualized on a transilluminator.

Cytotoxicity Assay. MCF-7 cells were grown in 96-well plates at about 70% confluency (*24*). After incubating the lipoplexes with the cells for 3 h, the lipoplexes were removed from the well, washed once with PBS, and replaced with 100 μL of DMEM containing 10% serum and antibiotics per well. To this, 100 μL of MTT (5 mg/mL in PBS) solution was added to each well, and the cells were incubated in the incubator for additional 2 h. At the end of 2 h, the medium was removed, and 100 μL of DMSO/methanol (1:1 vol/vol) was added per well. The plate was gently rocked and kept at room temperature for 5 min and then read at 540 nm in the SPECTRA Max ELISA plate reader. Data were represented as percentage cell viability.

Lipoplex Size. The sizes of lipoplexes were measured by photon correlation spectroscopy on a Zeta sizer 3000HSA (Malvern, U.K.) in DMEM and HEPES buffer, pH 7.4, using a sample refractive index of 1.59 and a viscosity of 0.89. The system was calibrated by using the 200/5 nm polystyrene polymer (Duke Scientific Corporation, Palo Alto, CA).

Synthesis of Lipids. Structures and the synthesis scheme of glutamide-derived lipids having cationic pyridinium head groups with different alkyl chain lengths are shown in Figure 1. The synthesis processes of lipid **1** are given below.

N′,N″-Didodecyl-N-benzyloxycarbonylglutamide (2C12-Gln-(Z)). *N*-Benzyloxycarbonylglutamic acid (Glu(Z)) (7.0 g, 25 mmol), *n*-dodecylamine (12 mL, 53 mmol), and triethylamine (8.9 g, 63 mmol) were dissolved in THF (400 mL) (*23*). The solution was cooled to 0 °C, and diethylphosphorocyanidate (DEPC) (10 mL, 64 mmol) was added to the solution and stirred for 1 h at this temperature. After stirring for 1 day at room temperature, the solution was concentrated in vacuo, and the residue was dissolved in 350 mL of chloroform. The solution was washed with 10% $NaHCO_3$, 0.1 mol/L HCl, and water. The solution was dried over Na_2SO_4, concentrated, and finally recrystallized from ethanol, which gave a white solid powder: yield 10.7 g (68%, 17 mmol); mp 141−143 °C; FT-IR (KBr)/3287, 2917, 2850, 1686, 1637, and 1539 cm^{-1}; ^1H NMR

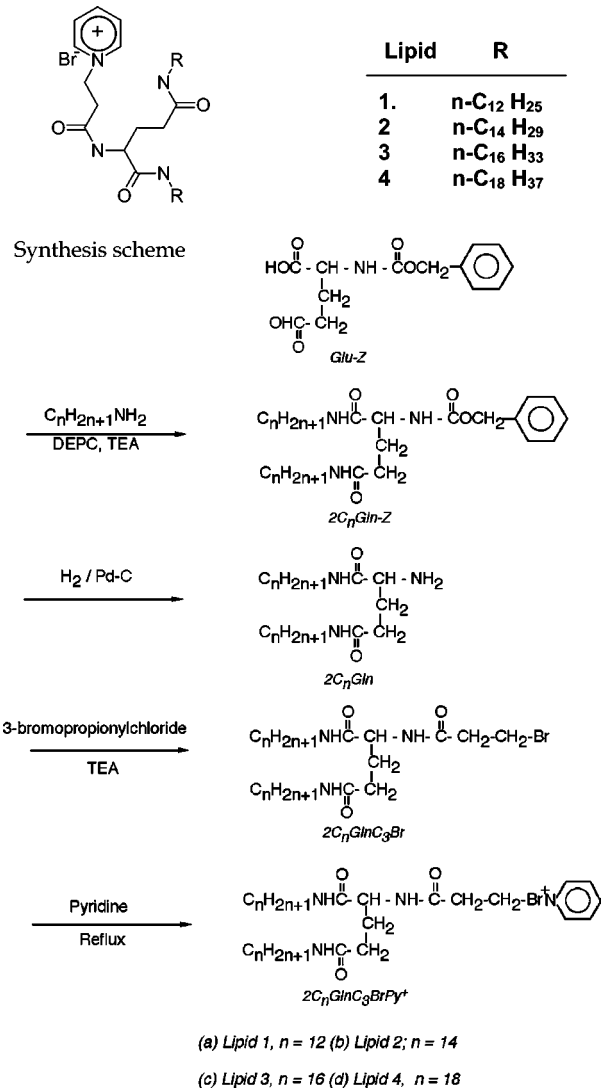

Figure 1. Structures and the synthesis scheme of the glutamide lipids used in this study.

($CDCl_3$) δ 0.862−0.896 (t, 6H, C*H*$_3$), 1.257 (m, 36H, CH_3-(CH_2)$_9$), 1.486 (m, 4H, C*H*$_2$CH$_2$NHC(=O)), 1.980 (m, ^1H, C*HC*H$_2$), 2.091 (m, 1H, C*HC*H$_2$), 2.297 (m, 2H, C*HCH$_2$-C*H*$_2$C(=O)), 3.221 (m, 4H, C*H*$_2$NHC(=O)), 4.144 (m, 1H, C**H*), 5.098 (s, 2H, C*H*$_2$Ph), 7.328 (s, 5H, C$_6$*H*$_5$). Anal. Found: H, 10.9; C, 71.8; N, 6.75; Calcd. for $C_{37}H_{65}N_3O_4$: H, 10.9; C, 72.1; N, 6.82.

N′,N″-Didodecylglutamide (2C$_{12}$-Gln). 2C$_{12}$-Gln(Z) (10.0 g, 16 mmol) was dissolved in 400 mL ethanol with heating, and Pd carbon (1 g) was added to the solution. H_2 gas was bubbled slowly into the solution for 10 h at 60 °C. Pd carbon was removed by filtration. The solution was concentrated, recrystallized from methanol, and dried in vacuo to give a white solid powder: yield 6.76 (88%, 14 mmol); mp 117.0−118.5 °C; FT-IR (KBr)/3318, 2934, 2874, 1647, and 1553 cm^{-1}; ^1H NMR ($CDCl_3$) δ 0.88 (t, 6H, C*H*$_3$), 1.26 (m, 36H, CH_3(C*H*$_2$)$_9$), 1.50 (m, 4H, C*H*$_2$CH$_2$NHC(=O)), 1.95 (m, 2H, C*HC*H$_2$CH$_2$C-(=O)), 2.31 (m, 2H, C*HCH$_2$C*H*$_2$C(=O)), 3.23 (m, 4H, C*H*$_2$-NHC(=O)), 3.41 (m, 1H, C**H*). Anal. Found: H, 12.2; C, 72.1; N, 8.74. Calcd. for $C_{29}H_{59}N_3O_2$: H, 12.3; C, 72.3; N, 8.72.

N′,N″-Didodecyl-N-bromopropionylglutamide (2C$_{12}$-GlnC$_3$Br). 2C$_{12}$-Gln (1.45 g, 3.0 mmol) was dissolved in THF (100 mL); 3-bromopropionylchloride (0.77 g 4.5 mmol) and triethylamine (0.91 g, 9.0 mmol) were also added into the solution. The solution was cooled to 0 °C and stirred for 1 h at this temperature. After being stirred for 1 day at room temperature,

Table 1. Elemental Analysis and Average Mass of Different Glutamide-Derived Cationic Lipids

	elemental analysis		average mass (MALDI-TOF-MS)	
	calculated	found	calculated	found
		Lipid **1**		
C%	63.8	63.5		
N%	8.0	7.95	615.9	616.9
H%	9.7	9.75		
		Lipid **2**		
C%	65.4	64.0		
N%	7.4	7.3	672.0	673.4
H%	10.0	9.8		
		Lipid **3**		
C%	66.8	65.9		
N%	6.9	6.8	728.2	730.2
H%	10.3	10.5		
		Lipid **4**		
C%	68.1	67.0		
N%	6.4	6.3	784.3	785.5
H%	10.6	10.7		

the solution was concentrated, and the residue was dissolved in chloroform. The solution was washed with 10% $NaHCO_3$, 0.1 mol/L HCl, and water. The solution was dried over Na_2SO_4, concentrated, and finally recrystallized from ethyl acetate, which gave a white solid powder: yield 0.93 g (49%, 1.51×10^{-3} mol); mp 164−166 °C; FT-IR (KBr)/3316, 2933, 2875, 1648, and 1555 cm^{-1}; ^1H NMR ($CDCl_3$) δ 0.73 (t, 6H, CH_3), 1.23 (m, 36H, $CH_3(CH_2)_9$), 1.33 (m, 2H, C*HC$H_2$$CH_2$C(=O)), 1.43 (m, 4H, C$H_2CH_2$NH), 2.43 (m, 2H, C*$HCH_2CH_2$C(=O)), 2.83 (t, 2H, C(=O)C$H_2CH_2Br^-$), 2.93 (m, 4H, CH_2CH_2NH), 3.28 (t, 2H, C(=O)$CH_2CH_2Br^-$), 4.73 (m, 1H, C*H). Anal. Found: H, 10.3; C, 63.1; N, 6.94. Calcd. for $C_{32}H_{62}N_3O_3Br$: H, 10.13; C, 62.32; N, 6.81.

*N′,N″-Didodecyl(pyridinium-N-propionyl)glutamide Bromide ($2C_{12}$-GlnC$_3$Py$^+$Br$^-$), Lipid **1**.* $2C_{12}$-$GlnC_3Br$ (0.50 g, 0.81 mmol) was dissolved in 50 mL of pyridine and stirred at reflux temperature for 2 days. After cooling to room temperature, a white crystal appeared, and unreacted pyridine was removed by filtration. The white crystal was dissolved in methanol and filtered. The white crystals in this step were dried in vacuo: yield 0.31 g (54%, 0.44 mmol); mp 180−182 °C; FT-IR (KBr)/3295, 2928, 2865, 1650, and 1541 cm^{-1}; ^1H NMR (CD_3OD) δ 0.87−0.91 (t, 6H, CH_2), 1.28 (m, 36H, $(CH_2)_3(CH_2)_9$), 1.47 (m, 4H, CH_2CH_2C(=O)), 1.80−1.85 (m, 2H, C*HCH_2CH_2C(=O)), 1.94−1.99 (t, 2H, C*HCH_2CH_2C(=O)), 2.16−2.20 (t, 2H, C(=O)C$H_2CH_2Py^+$), 3.02−3.04 (t, 2H, C(=O)$CH_2CH_2Py^+$), 3.13−3.15 (m, 4H, CH_2CH_2C(=O)), 4.19−4.22 (m, 1H, C*H), 8.07−8.10 (m, 2H, pyridine ring), 8.56−8.60 (t, 1H, pyridine ring), 8.98−9.00 (d, 2H, pyridine ring). Anal. Found: H, 9.85; C, 62.8; N, 7.75. Calcd. for $C_{37}H_{67}N_4O_3Br$: H, 9.70; C, 63.86; N, 8.05. The others (lipids **2**, **3**, and **4**) were also synthesized, and the structures of the compounds in each step were characterized using procedures employed in the synthesis of lipid **1**. The results of elemental analysis, melting points, and MALDI-TOF-MS data for all four lipids are provided in Table 1.

RESULTS AND DISCUSSION

DNA Binding of the Lipids 1−4. To quantify the binding strength of the four lipids to DNA, the lipid-bound DNA was separated from the free or unbound DNA by agarose gel electrophoresis. Figure 2 shows that, in phosphate-buffered saline (PBS), complete binding of DNA was observed with all four lipids when the helper lipid was DOPE. With cholesterol as the helper lipid, only lipids **1** and **4** has shown complete binding, while the binding of lipids **2** and **3** to DNA was comparatively lower. Also, the presence of lipid at charge ratio of 2:1 was sufficient to achieve complete binding. However, when the complexes were prepared in water, all the lipids bind DNA strongly, indicating an ionic basis of DNA interaction with the cationic lipids (data not reported).

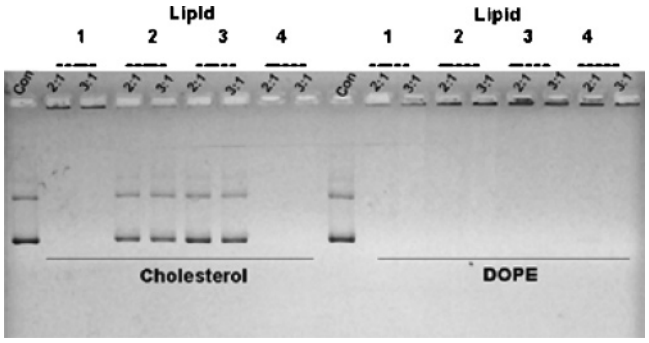

Figure 2. Binding of DNA with lipids **1**−**4**/0.8% agarose gel electrophoresis of plasmid pCMVβ-gal complexed with lipids **1**−**4** at two charge ratios, i.e., 2:1 and 3:1. The helper lipid is either cholesterol or DOPE. Free DNA was loaded in the first well and the tenth well.

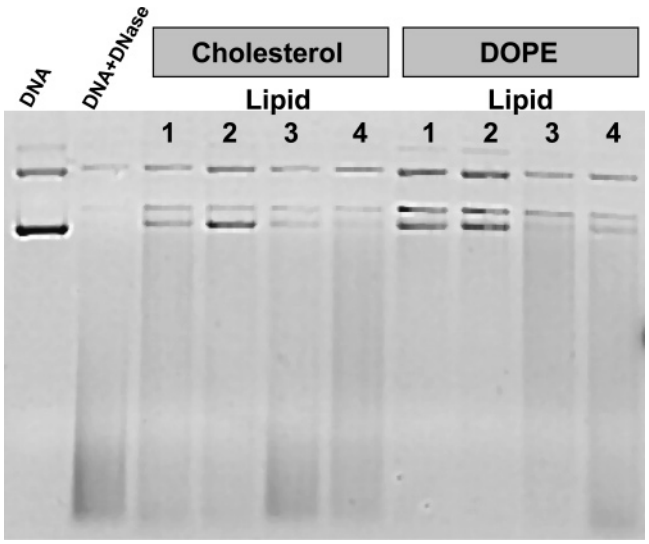

Figure 3. Sensitivity of DNA in lipid−DNA complexes to DNaseI/0.8% agarose gel electrophoresis of lipid−DNA complexes treated with DNaseI. Lane 1: Control plasmid pCMVβ-gal. Lane 2: Control DNA + DNaseI. Lanes 3−6: Lipids **1**−**4** with cholesterol as the co-lipid at 3:1 lipid/DNA. Lanes 7−10: Lipids **1**−**4** with DOPE as the co-lipid at 3:1 lipid/DNA.

In addition to the DNA binding assay, the susceptibility of bound DNA to DNaseI was performed to assess the protective ability of the lipid. Presence of DOPE as helper lipid offers better protection of DNA from DNase I digestion compared to cholesterol (Figure 3). Although all the eight formulations showed protection to DNA from DNaseI treatment to some extent, complete protection was seen only with lipid **2** with either of the helper lipids. Lipid **1** also showed compete protection with DOPE alone but not with cholesterol as the helper lipid.

Size of the Lipoplexes Prepared with Lipids 1−4 and Plasmid DNA. Transfection efficiency of lipoplexes was known to depend strongly on the size and the surface charge of the lipoplex (*25*, *26*). We measured these parameters on lipoplexes with DOPE as the helper lipid in DMEM, since this medium is relevant to the transfection protocol. The data presented in Table 2 demonstrate that the size of the complex increases with the increase in charge ratio with all four lipids. Chain length of the lipid does not influence the size of the complex with varying charge ratios, though longer chain-length lipids have resulted in vesicles of larger size. Surface charge as measured by ζ-potential has negative values across all the lipids and at all

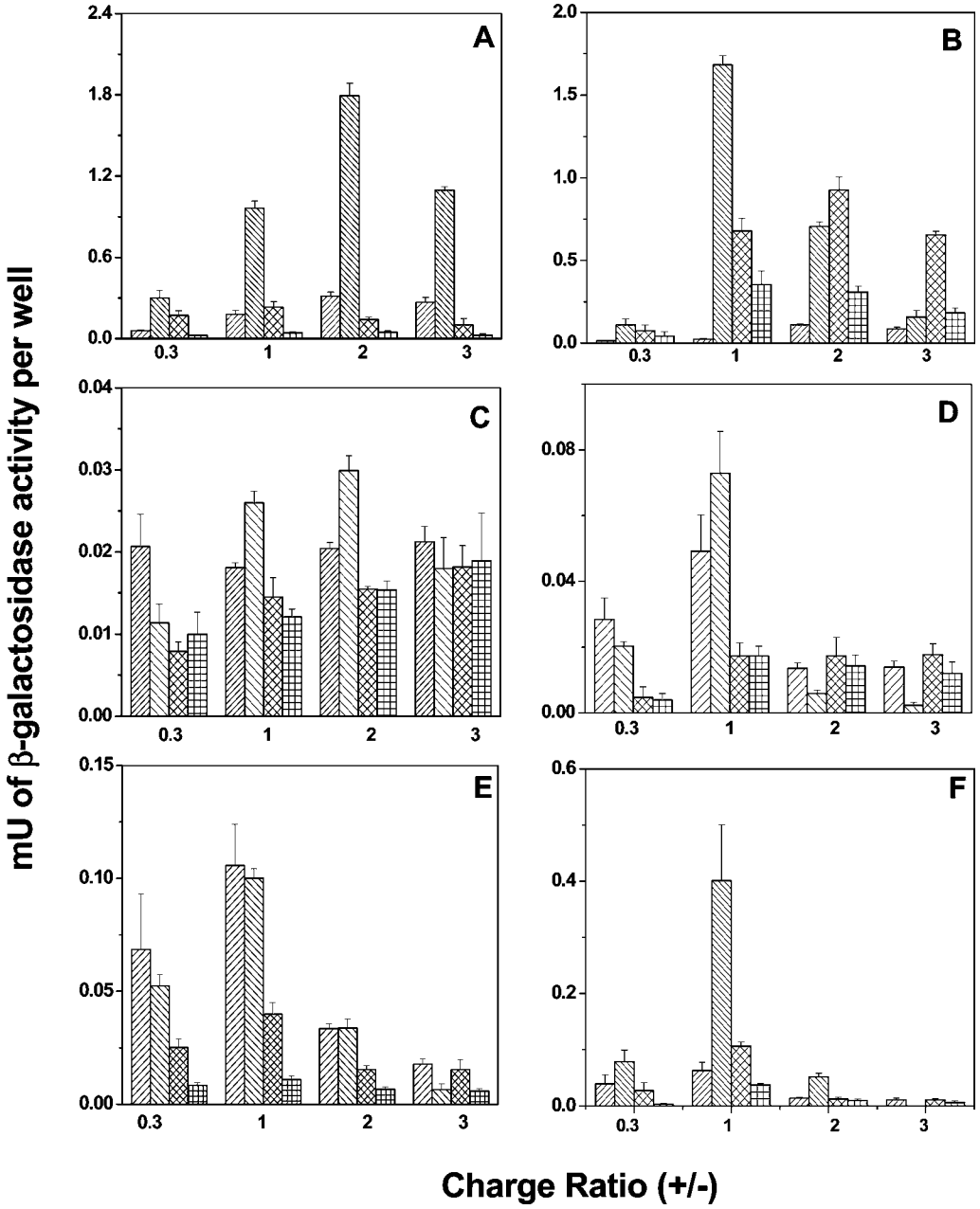

Figure 4. Transfection efficiencies of lipids **1**−**4** on MCF-7 (A, B), HeLa (C, D), and COS (E, F) cell lines. The four lipids were tested with either cholesterol (A, C, E) or DOPE (B, D, F) as the helper lipid. Bar fills are as follows: Lipid **1**, left slanting lines; lipid **2**, right slanting lines; lipid **3**, angled mesh; and lipid **4**, square mesh.

Table 2. Size of the Lipoplexes of Lipids 1−4:

charge ratio (±)	size, nm			
	0.3	1	2	3
lipid **1**	214 ± 4.7	242 ± 1.5	361 ± 14.7	956 ± 65.5
lipid **2**	267 ± 6.3	894 ± 592	367.7 ± 24	1036 ± 109
lipid **3**	441 ± 25	719 ± 52	1379 ± 41	2043 ± 91
lipid **4**	489 ± 13	561 ± 39	913 ± 60	1426 ± 113

charge ratios except in the case of **1** at 3:1 charge ratio (data not reported). Generally, lipoplexes achieve maximum size when the net charge is zero, and the size decreases when the particle is either net positive or net negative (*27*−*29*). The net charge with glutamide lipids even at 3:1 charge ratio was negative in DMEM, suggesting charge neutralization did not occur at these charge ratios. Though the cationic charge is far in excess compared to the charge on the nucleic acids, the negative ζ-potential indicates that components of the medium DMEM may bind to the complexes and render them anionic. However, if the potential measurements were made in water, the potential was found to be positive above a 1:1 charge ratio (data not reported).

Transfection Studies with Lipids 1−4. We have tested the four dialkyl pyridinium glutamides for their transfection efficiencies with two helper lipids in three different cell lines, viz., MCF7, COS, and HeLa. Since non-cationic lipid additives in the formulations were known to enhance the transfection efficiency, we have used either DOPE or cholesterol as the helper lipid to investigate if the transfection efficiency is helper-lipid-dependent (*30*). Since the transfection efficiency depends on the ratio of the positive "lipid" charges to negative phosphate charges in the DNA, we have also tested the efficiency at various charge ratios (*23*). The reporter gene expression as measured by monitoring β-galactosidase activity is shown in Figure 4A−F to compare transfection efficiency among the three cell lines. MCF-7 cells showed maximum transfection compared to COS and HeLa cells. Between the two helper lipids, DOPE enhanced

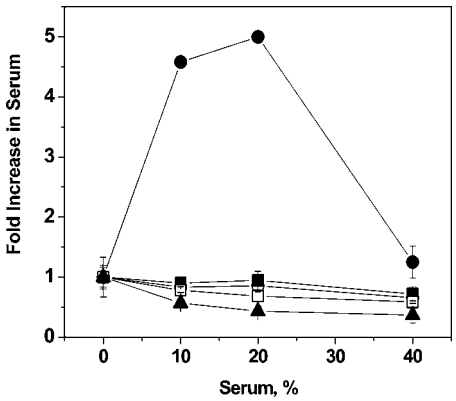

Figure 5. Transfection efficiency of lipid **2** in MCF-7 cells in the presence of serum. Transfection efficiency (fold increase) of lipid **2** + DOPE (●), with varying concentrations of serum compared with Lipofectamine (1 mg/mL) used at 1 μL (■), 2 μL (□), 4 μL (▲), and 8 μL (○) with 0.9 μg of DNA.

transfection in COS and HeLa cell lines compared to cholesterol; however, such differences were not apparent in the MCF-7 cell line where both the helper lipids elicited similar transfection efficiencies. Though the optimum charge ratio was dependent on the lipids and also on cell lines, a charge ratio of approximately 1:1 or 2:1 was found to be optimal. Very high (3:1) or low (0.3:1) charge ratios were not effective in transfection (*31*). Lipid **2** showed maximum transfection in all three cell lines at a 1:1 charge ratio with DOPE as the helper lipid. The observed maximum transfection with a 14-carbon lipid is in agreement with the reported literature that a 12- to 16-carbon length hydrophobic domain is optimally suited for transfection (*25*, *32*). Lack of transfection with shorter-chain lipids was suspected to be due to poor vesicle-forming abilities and toxicity to the cells. Long-chain lipids would probably result in stable and rigid vesicles unsuitable for transfection. Some lipids were reported to be efficient when the chain length was 18-carbon (*16*).

Transfection Efficiency in the Presence of Serum. Serum stability of the lipoplexes is very important for their in vivo efficacies (*33*, *34*). We have tested the transfection efficiency of lipids, initially in the presence of 10% serum, and found that only lipid **2** shows significant transfection efficiencies in the presence of serum (Figure 5). The other lipids showed decreased transfection efficiency in the presence of serum (data not shown). Serum contains nucleases, which would degrade the plasmid DNA, and also contains several proteins, including albumin, which would reduce the cell association properties of the lipoplex (*35*). We further tested lipid **2** with both the helper lipids in MCF-7 cells, in the presence of 0−40% serum along with a commercial transfecting agent Lipofectamine (Figure 5). We observed nearly a 5-fold increase in the transfection efficiency with lipoplexes with lipid **2** and DOPE in the presence of 20% serum (Figure 5). Unlike the small decrease in transfection efficiency observed with Lipofectamine, the transfection efficiency of lipid **2** has in fact enhanced by 5-fold in the presence of serum. Such increases in transfection efficiency by cationic lipids in the presence of serum have not been reported to our knowledge. This suggests that lipid **2** demonstrates a very interesting stability to serum and also a serum-mediated enhancement of transfection efficiency.

Toxicity of the Formulations on MCF-7. Since toxicity of the formulations to the cells is critical for transfection, we have tested the viability of MCF-7 cells in the presence of formulations prepared with the four lipids along with two helper lipids. Lipoplexes with cholesterol were found to be very toxic to the cell by decreasing the cell viability by more than 50% even at

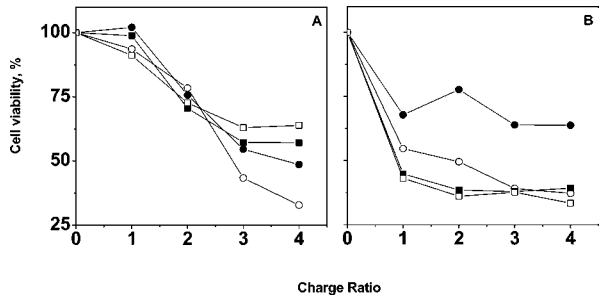

Figure 6. Cytotoxicity of lipids **1**−**4** on MCF-7 cells. Toxicity, measured as percent viability, was evaluated with lipids **1** (●), **2** (○), **3** (■), and **4** (□) with DOPE (A) and cholesterol (B) as helper lipids. The absorption values obtained using reduced formazon with cells in the absence of lipids were taken to be 100.

a 1:1 charge ratio. In comparison, DOPE marginally affects the viability at a 1:1 charge ratio and by 20% at a 2:1 charge ratio (Figure 6).

Four dialkyl glutamides of varying chain lengths were synthesized and characterized. The data presented here demonstrate that these lipids efficiently transfect three cell lines tested in this study. These lipids have significant binding to DNA at charge ratios above 2:1 when the helper lipid in the formulation is DOPE. In line with this observation, the DNaseI protection was also higher in the presence of DOPE compared to cholesterol. Cholesterol apparently does not form stable lipoplexes strongly for occluding the DNA inside the lipoplex. Even at a 3:1 charge ratio, the lipoplexes have a net negative charge leading to a continuous increase in size. Among the four lipids, lipid **2** with DOPE as the helper lipid shows very promising transfection efficiencies on all three cell lines tested. The efficiency of the cationic lipids with chain length in the range 12−16 carbons in length is well-documented, and often 14-carbon-length lipids are most efficient among several cationic lipids with differing chemistries (*15*). The balance between the stability of the liposome in the medium and the readiness of the liposome to release the DNA is important for good transfection efficiency (*36*). Short-chain lipids may not result in stable liposomes, and long-chain lipids may form very stable particles for release of the DNA. Lipid **2** with DOPE as the helper lipid has good DNA binding ability, provides DNaseI protection, and is also less toxic. All these properties together elicited high transfection efficiencies. The converse is true with cholesterol in most of the cases. The size of the lipoplexes does not show any correlation with the transfection efficiency, indicating that factors in addition to size play a role in lipoplex and cell interactions. The role of biophysical properties of the lipid−DNA complex in its association and uptake by cells is still poorly understood (*37*, *38*). The remarkable enhancement of transfection of lipoplexes prepared with lipid **2** in the presence of serum suggests the potential of this lipid for in vivo transfections.

Tetraalkyldiglutamides with long spacers were synthesized by alkylating the free amino group into tertiary amine (*39*). These lipids with charge on the glutamate, called as lipopeptides, were shown to transfect cells with efficiencies lower than Lipofectin on 293 cells. Pyridinium head groups have been made popular with the publication of the Saint series of lipids, though the pyridinium was bonded to a linker at C3 and an R group was attached to the nitrogen (*40*−*42*). Cationic lipids with a heterocyclic trimethylpyridinium as the polar head linked to two alkyl chains via a propyl group have shown good transfection in both in vitro and in vivo experiments (*43*). Unlike the Saint lipids, in the lipids described here, the pyridine is N-linked to the linker, i.e., glutamic acid. Dialkyl glutamides were tested for their ability to form supramolecular structures due to the presence of a chiral center (*19*). The intermolecular hydrogen

bonding among the amide moieties of the lipids contributes to self-assembly and thus stabilizes the liposome (*17*, *44*). As a linker molecule, glutamic acid offers a synthetic flexibility to design various cationic lipids. To the best of our knowledge, this is the first report where dialkyl glutamides have been shown to transfect several cell lines efficiently.

CONCLUSIONS

Four cationic lipids based on glutamide as a linker were synthesized. Formulations with DOPE as the helper lipid show excellent transfection in three different cell lines. Although DNA binding and protection from nuclease, size, or surface potential measurements of lipoplexes of these lipids show variation, there is no apparent correlation with their transfection abilities. Very remarkably, one of the lipids, lipid **2,** demonstrates enhanced transfection in the presence of serum, suggesting its physiological relevance and suitability for in vivo applications.

LITERATURE CITED

(1) Audouy, S., and Hoekstra, D. (2001) Cationic lipid-mediated transfection in vitro and in vivo. *Mol. Membr. Biol. 18*, 129−143.

(2) Banerjee, R., Das, P. K., Srilakshmi, G. V., Chaudhuri, A., and Rao, N. M. (1999) Novel series of non-glycerol-based cationic transfection lipids for use in liposomal gene delivery. *J. Med. Chem. 42*, 4292−4299.

(3) Banerjee, R., Mahidhar, Y. V., Chaudhuri, A., Gopal, V., and Rao, N. M. (2001) Design, synthesis, and transfection biology of novel cationic glycolipids for use in liposomal gene delivery. *J. Med. Chem. 44*, 4176−4185.

(4) Cavazzana-Calvo, M., Lagresle, C., Hacein-Bey-Abina, S., and Fischer, A. (2005) Gene therapy for severe combined immunodeficiency. *Annu. Rev. Med. 56*, 585−602.

(5) Chesnoy, S., and Huang, L. (2000) Structure and function of lipid-DNA complexes for gene delivery. *Annu. Rev. Biophys. Biomol. Struct. 29*, 27−47.

(6) Ciani, L., Ristori, S., Salvati, A., Calamai, L., and Martini, G. (2004) DOTAP/DOPE and DC-Chol/DOPE lipoplexes for gene delivery: zeta potential measurements and electron spin resonance spectra. *Biochim. Biophys. Acta 1664*, 70−79.

(7) Davis, M. E. (2002) Non-viral gene delivery systems. *Curr. Opin. Biotechnol. 13*, 128−131.

(8) Davis, M. E. (2002) Non-viral gene delivery systems. *Curr. Opin. Biotechnol. 13*, 128−131.

(9) Elouahabi, A., and Ruysschaert, J. M. (2005) Formation and intracellular trafficking of lipoplexes and polyplexes. *Mol. Ther. 11*, 336−347.

(10) Hope, M. J., Mui, B., Ansell, S., and Ahkong, Q. F. (1998) Cationic lipids, phosphatidylethanolamine and the intracellular delivery of polymeric, nucleic acid-based drugs. *Mol. Membr. Biol. 15*, 1−14.

(11) Ihara, H., Takafuji, M., and Sakurai, T. (2004) Self-assembled nano fibers. *Encyclopedia of Nanosciences and Nanotechnology* pp 473−495, Vol 9, American Scientific Publishers, Stevenson Ranch, CA.

(12) Ihara, H., Yoshikai, K., Takafuji, M., Hirayama, K., and Yamada, J. (1991) Stabilization of enhanced chirality from pyrene-containing L-glutamide lipid in methyl methacrylate by photo-induced polymerization. *Jpn. J. Polym. Sci. Technol. 48*, 327−334.

(13) Ihara, H., Yoshitake, M., Hirayama, K., and Yamada, K. (1992) Lipid membrane analogues: Formation of highly oriented structures and their phase separation behaviour in benzene. *J. Chem. Soc., Chem. Commun. 17*, 1244−1245.

(14) Ihara, H., Takafuji, M., Sakurai, T., Katsumoto, M., Ushijima, N., Shirosaki, T., and Hachisako, H. (2003) Novel self-assembling organogelators by combination of a double chain-alkylated L-glutamide and a polymeric head group. *Org. Biomol. Chem. 1*, 3004−3006.

(15) Ilies, M. A., Johnson, B. H., Makori, F., Miller, A. D., Seitz, W. A., Thompson, E. B., and Balaban, A. T. (2005) Pyridinium cationic lipids in gene delivery: an in vitro and in vivo comparison of transfection efficiency versus a tetraalkylammonium congener. *Arch. Biochem. Biophys. 435*, 217−226.

(16) Kay, M. A., Glorioso, J. C., and Naldini, L. (2001) Viral vectors for gene therapy: the art of turning infectious agents into vehicles of therapeutics. *Nat. Med. 7*, 33−40.

(17) Kay, M. A., Glorioso, J. C., and Naldini, L. (2001) Viral vectors for gene therapy: the art of turning infectious agents into vehicles of therapeutics. *Nat. Med. 7*, 33−40.

(18) Koynova, R., and MacDonald, R. C. (2005) Lipid transfer between cationic vesicles and lipid-DNA lipoplexes: effect of serum. *Biochim. Biophys. Acta 1714*, 63−70.

(19) Laxmi, A. A., Vijayalakshmi, P., Kaimal, T. N., Chaudhuri, A., Ramadas, Y., and Rao, N. M. (2001) Novel non-glycerol-based cytofectins with lactic acid-derived head groups. *Biochem. Biophys. Res. Commun. 289*, 1057−1062.

(20) Laxmi, A. A., Vijayalakshmi, P., Kaimal, T. N., Chaudhuri, A., Ramadas, Y., and Rao, N. M. (2001) Novel non-glycerol-based cytofectins with lactic acid-derived head groups. *Biochem. Biophys. Res. Commun. 289*, 1057−1062.

(21) Li, S., and Huang, L. (2000) Nonviral gene therapy: promises and challenges. *Gene Ther. 7*, 31−34.

(22) Martin, B., Sainlos, M., Aissaoui, A., Oudrhiri, N., Hauchecorne, M., Vigneron, J. P., Lehn, J. M., and Lehn, P. (2005) The design of cationic lipids for gene delivery. *Curr. Pharm. Des. 11*, 375−394.

(23) Medina-Kauwe, L. K., Xie, J., and Hamm-Alvarez, S. (2005) Intracellular trafficking of nonviral vectors. *Gene Ther. 12*, 1734−1751.

(24) Miller, A. D. (1998) Nonviral liposomes. *Angew. Chem., Int. Ed Engl. 37*, 1768−1785.

(25) Miller, A. D. (2004) Nonviral liposomes. *Methods Mol. Med. 90*, 107−137.

(26) Nishikawa, M., and Huang, L. (2001) Nonviral vectors in the new millennium: delivery barriers in gene transfer. *Hum. Gene Ther. 12*, 861−870.

(27) Prasad, T. K., Rangaraj, N., and Rao, N. M. (2005) Quantitative aspects of endocytic activity in lipid-mediated transfections. *FEBS Lett. 579*, 2635−2642.

(28) Rao, N. M., and Chaudhuri, A. (2002) Non-glycerol based lipofectins for gene delivery. *Cell Mol. Biol. Lett. 7*, 296.

(29) Rejman, J., Oberle, V., Zuhorn, I. S., and Hoekstra, D. (2004) Size-dependent internalization of particles via the pathways of clathrin- and caveolae-mediated endocytosis. *Biochem. J. 377*, 159−169.

(30) Ross, P. C., and Hui, S. W. (1999) Lipoplex size is a major determinant of in vitro lipofection efficiency. *Gene Ther. 6*, 651−659.

(31) Ross, P. C., and Hui, S. W. (1999) Lipoplex size is a major determinant of in vitro lipofection efficiency. *Gene Ther. 6*, 651−659.

(32) Shi, F., Nomden, A., Oberle, V., Engberts, J. B., and Hoekstra, D. (2001) Efficient cationic lipid-mediated delivery of antisense oligonucleotides into eukaryotic cells: down-regulation of the corticotropin-releasing factor receptor. *Nucleic Acids Res. 29*, 2079−2087.

(33) Simberg, D., Weiss, A., and Barenholz, Y. (2005) Reversible mode of binding of serum proteins to DOTAP/cholesterol lipoplexes: a possible explanation for intravenous lipofection efficiency. *Hum. Gene Ther. 16*, 1087−1096.

(34) Singh, R. S., Mukherjee, K., Banerjee, R., Chaudhuri, A., Hait, S. K., Moulik, S. P., Ramadas, Y., Vijayalakshmi, A., and Rao, N. M. (2002) Anchor dependency for non-glycerol based cationic lipofectins: mixed bag of regular and anomalous transfection profiles. *Chemistry 8*, 900−909.

(35) Smyth, T. N. (2003) Cationic liposomes as in vivo delivery vehicles. *Curr. Med. Chem. 10*, 1279−1287.

(36) Takafuji, M., Ishiodori, A., Yamada, T., Sakurai, T., and Ihara, H. (2004) Stabilization of enhanced chirality from pyrene-containing L-glutamide lipid in methyl methacrylate by photo-induced polymerization. *Chem. Commun. (Cambridge, U.K.)* 1122−1123.

(37) Templeton, N. S. (2002) Cationic liposome-mediated gene delivery in vivo. *Biosci. Rep. 22*, 283−295.

(38) Venkata, S. G., Sen, J., Chaudhuri, A., Ramadas, Y., and Madhusudhana, R. N. (2002) Anchor-dependent lipofection with non-glycerol based cytofectins containing single 2-hydroxyethyl head groups. *Biochim. Biophys. Acta 1559*, 87−95.

(39) Verma, I. M., and Weitzman, M. D. (2005) Gene therapy: twenty-first century medicine. *Annu. Rev. Biochem. 74*, 711−738.
(40) Yew, N. S., and Scheule, R. K. (2005) Toxicity of cationic lipid-DNA Complexes. *Adv. Genet. 53PA*, 189−214.
(41) Yi, S. W., Yune, T. Y., Kim, T. W., Chung, H., Choi, Y. W., Kwon, I. C., Lee, E. B., and Jeong, S. Y. (2000) A cationic lipid emulsion/DNA complex as a physically stable and serum-resistant gene delivery system. *Pharm. Res. 17*, 314−320.
(42) Zabner, J., Fasbender, A. J., Moninger, T., Poellinger, K. A., and Welsh, M. J. (1995) Cellular and molecular barriers to gene transfer by a cationic lipid. *J. Biol. Chem. 270*, 18997−19007.
(43) Zhdanov, R. I., Elkadi, A., Moskovtsev, A. A., Sebyakin, Y. L., Larin, A. S., Muranov, A. V., and Khokhlov, A. R. (2004) The dependence of the efficiency of gene transfer with the use of lipoplexes based on new dicationic lipids on their structure. *Dokl. Biochem. Biophys. 398*, 261−264.
(44) Zuhorn, I. S., Kalicharan, R., and Hoekstra, D. (2002) Lipoplex-mediated transfection of mammalian cells occurs through the cholesterol-dependent clathrin-mediated pathway of endocytosis. *J. Biol. Chem. 277*, 18021−18028.

BC0601020

Improving the Antigenicity of sTn Antigen by Modification of Its Sialic Acid Residue for Development of Glycoconjugate Cancer Vaccines

Jian Wu and Zhongwu Guo*

Department of Chemistry, Wayne State University, 5101 Cass Avenue, Detroit, Michigan 48202. Received April 22, 2006; Revised Manuscript Received September 20, 2006

Sialyl Tn (sTn) antigen is a sialylated disaccharide abundantly expressed by many tumors. To search for effective cancer immunotherapies based on sTn antigen, we designed and synthesized a series of unnatural *N*-acyl derivatives of sTn and studied their immunological properties. For this purpose, an efficient method was developed to synthesize the natural and unnatural forms of sTn antigen and their protein conjugates. The resultant glycoconjugates were used to immunize C57BL/6 mice, and the immune response was assessed by enzyme-linked immunosorbent assay (ELISA). Whereas the keyhole limpet hemocyanin (KLH) conjugate of sTn elicited low levels of IgM antibodies, the KLH conjugates of *N*-*iso*-butanoyl sTn and *N*-phenylacetyl sTn, especially the latter, induced high titers of antigen-specific IgG antibodies, showing a T-cell-dependent response that is critical for the antitumor activity. The results suggest that the modified forms of sTn, especially *N*-phenylacetyl sTn, have improved antigenicity and promising immunological properties for use as cancer vaccines.

INTRODUCTION

Many tumors express certain unique carbohydrates termed tumor-associated carbohydrate antigens (TACAs), and the TACAs are closely correlated with cancer cell adhesion and metastasis (*1*, *2*). TACAs are also useful molecular targets in the design and development of novel strategies for cancer diagnosis and therapy, such as cancer vaccines (*3*−*9*). Among numerous TACAs identified (*2*−*5*), sialyl Tn antigen (sTn, Figure 1), an *O*-linked disaccharide [NeuAcα(2→6)GalNAc], is of particular interest. First, sTn is relatively tumor-specific. Even though sTn antigen is richly expressed on a number of tumors, such as breast, prostate, colorectal, and ovarian cancer (*10*−*13*), it is rarely observed on normal tissues. Second, the expression of sTn has been identified as an independent indicator for poor prognosis of cancer (*11*−*14*). Consequently, sTn antigen and relevant mucins that are aberrantly glycosylated with sTn have been extensively investigated for the immunotherapy of cancer (*15*−*20*). The protein conjugates of sTn antigen could indeed elicit humoral immune response that showed remarkable specificity for cancer cells (*21*). The keyhole limpet hemocyanin (KLH) conjugate of sTn antigen (*19*, *20*) has been developed and tested as a therapeutic vaccine (Theratope) for treatment of metastatic breast cancer (*22*, *23*). Unfortunately, at the Phase III clinical trial Theratope failed to meet the endpoints of time-to-disease progression and overall survival rate (*23*), which was largely because it cannot induce strong T-cell-mediated immune response in patients. In fact, most natural TACAs elicit IgM antibodies rather than IgG antibodies (*24*), while T-cell dependent IgG response is critical for immunotherapy of cancer (*25*, *26*). The problem of the lack of a T-cell-dependent immune response to TACAs has severely hindered further progress of TACA-based cancer vaccines.

To overcome such problems, our group has recently developed a novel strategy for immunotherapy (*27*), which is based on metabolic engineering of cell surface *N*-acetylneuraminic acid (Neu5Ac) (*28*, *29*). The concept is to immunize cancer patients with a synthetic vaccine made of an artificial *N*-acyl derivative of a natural sialyl TACA. After a specific immune response is established, the patients will be treated with correspondingly *N*-acylated D-mannosamine to induce the expression of this artificial antigen on tumor cells in place of the natural TACA. The provoked immune system will then eliminate the bioengineered tumors. As sTn antigen contains a sialic acid residue at its nonreducing end, we anticipated that the new strategy should be applicable to it for the development of useful cancer immunotherapy.

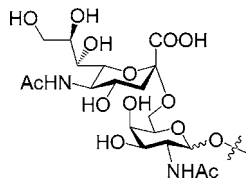

Figure 1. The structure of sTn antigen.

For the new strategy to work, an important condition is an effective vaccine that can induce a T-cell-dependent immune response. The other condition is a method that can effectively bioengineer tumor cells (*30*). The main aim of this work is to study the influence of chemical modification of the sialic acid residue of sTn on its antigenicity and to identify a derivative that may be used as a vaccine to induce robust T-cell-dependent immune responses. For this purpose, we have synthesized the natural and unnatural *N*-acyl derivatives of sTn, linked them to KLH, and studied the immunological properties of the resultant glycoconjugates.

EXPERIMENTAL PROCEDURES

2-Azidoethyl *O*-[Methyl 4,7,8,9-tetra-*O*-acetyl-3,5-dideoxy-5-trifluoroacetamido-D-*glycero*-α-D-*galacto*-non-2-ulopyranosylonate]-(2→6)-*O*-2-acetamido-2-deoxy-*β*-D-galactopyranoside (16). A mixture of **14** (400 mg, 1.21 mmol), **15** (700 mg, 1.21 mmol), and activated molecular sieves (4 Å, 2.0 g) in anhydrous acetonitrile (5.0 mL) was stirred at rt for 2 h under an atmosphere of argon. After the mixture was cooled to −35 °C, *N*-iodosuccinamide (NIS) (1.1 g, 4.84 mmol) and triflic acid (TfOH) (53 μL, 0.61 mmol) were added with stirring. The mixture was kept at −35 °C for 30 min and then diluted with

* Corresponding author. Tel.: 313-577-2557; fax: 313-577-8822; e-mail: zwguo@chem.wayne.edu.

10.1021/bc060103s CCC: $33.50 © 2006 American Chemical Society
Published on Web 10/26/2006

DCM (20 mL). The solid material was filtered off and washed with DCM (10 mL). The combined filtrates were washed with aqueous $Na_2S_2O_3$ (20%) and water. The organic phase was dried over Na_2SO_4 and concentrated under reduced pressure. The residue was purified on a silica gel column (EtOAc/hexane 2:1) to give a mixture of α-/β-disaccharide (680 mg, 65%, α/β 4:1) as a white foamy solid. $R_f = 0.19$ (EtOAc/hexane 2:1); HR FABMS (*m*/*z*): cacld for $C_{33}H_{46}F_3N_5NaO_{18}$ ($M + Na^+$) 880.2688, found 880.2685. This mixture was directly used in the next step of the reaction without further purification.

A solution of the above product (600 mg, 0.7 mmol) in 65% $HOAc/H_2O$ (v/v, 6 mL) was stirred at 60 °C for 1.5 h. Thin layer chromatography (TLC) showed the complete consumption of the starting material. The mixture was concentrated and coevaporated with toluene (3 × 5 mL). The residue was purified by flash column chromatography (DCM/MeOH 18:1) to afford compound **16** (420 mg, 70%) as a white solid ($R_f = 0.27$, DCM/MeOH 12:1) and its β-anomer (100 mg, 17%, $R_f = 0.32$, DCM/MeOH 12:1). Compound **16**: $[\alpha]_D$ −42.4 (*c* 1.0, $CHCl_3$); ^{1}H NMR ($CDCl_3$, 600 MHz): δ 6.72 (d, *J* 9.6 Hz, 1H), 6.17 (d, *J* 3.6 Hz, 1H), 5.37−5.26 (m, 2H), 5.21 (dd, *J* 7.8, 1.8 Hz, 1H), 4.99−4.93 (m, 1H), 4.50 (d, *J* 8.4 Hz, 1H, H-1), 4.36 (dd, *J* 12.6, 3.0 Hz, 1H), 4.27 (dd, *J* 10.8, 2.4 Hz, 1H), 4.10 (dt, *J* 10.8, 3.6 Hz, 1H), 4.00 (dd, *J* 12.6, 6.6 Hz, 1H), 3.98−3.93 (m, 2H), 3.82 (s, 3H), 3.79−3.67 (m, 6H), 3.59−3.54 (m, 1H), 3.28 (dt, *J* 13.2, 3.0 Hz, 1H), 2.91 (s, 1H), 2.63 (dd, *J* 12.6, 4.2 Hz, 1H, H-3′e), 2.15, 2.14, 2.05, 2.03, 2.01 (5s, 5 × 3H, Ac), 1.96 (t, *J* 12.6 Hz, 1H, H-3′a). HR FABMS (*m*/*z*) calcd for $C_{30}H_{42}F_3N_5O_{18}$ ($M + H^+$) 818.2555, found 818.2552.

***N*-{2-*O*-{[Methyl 4,7,8,9-tetra-*O*-acetyl-3,5-dideoxy-5-trifluoroacetamido-D-*glycero*-α-D-*galacto*-non-2-ulopyranosylonate]-(2→6)-*O*-2-acetamido-2-deoxy-β-D-galactopyranosyl}-ethyl} 4-Pentenamide (17).** A solution of **16** (330 mg, 0.404 mmol) in MeOH (15 mL) was stirred with 10% Pd/C under a H_2 atmosphere at rt for 1 h. After the catalyst was filtered off, to the filtrate that contained glycosyl amine was added 4-pentenoic anhydride. The mixture was stirred at rt overnight. The solution was condensed, and the crude product was purified by flash chromatography (DCM/MeOH 10:1) to afford compound **17** (270 mg, 80%) as a white solid. $R_f = 0.19$ (DCM/MeOH 12:1). $[\alpha]_D$ −39.5 (*c* 1.0, $CHCl_3$); ^{1}H NMR ($CDCl_3$, 600 MHz): δ 7.08 (d, *J* 9.0 Hz, 1H), 6.99 (d, *J* 5.4 Hz, 1H), 6.41 (s, 1H), 5.86−5.78 (m, 1H, CH_2=C<u>H</u>-), 5.38−5.32 (m, 1H), 5.25 (dd, *J* 7.8, 1.2 Hz, 1H), 5.08 (d, *J* 16.8 Hz, 1H, C<u>H</u>$_2$=CH-), 5.02 (d, *J* 10.2 Hz, 1H, C<u>H</u>$_2$=CH-), 4.98 (dt, *J* 11.4, 4.2 Hz, 1H), 4.50 (d, *J* 8.4 Hz, 1H, H-1), 4.39 (dd, *J* 12, 1.8 Hz, 1H), 4.31 (dd, *J* 10.8, 1.8 Hz, 1H), 4.04−3.98 (m, 2H), 3.94 (d, *J* 3.6 Hz, 1H), 3.88−3.74 (m, 7H), 3.70−3.64 (m, 3H), 3.26−3.20 (m, 1H), 2.65 (dd, *J* 12.6, 4.8 Hz, 1H, H-3′e), 2.41−2.36 (m, 2H), 2.33−2.28 (m, 2H), 2.16, 2.15, 2.09, 2.03, 2.02 (5s, 5 × 3H, Ac), 1.96 (t, *J* 12.6 Hz, 1H, H-3′a). HR FABMS (*m*/*z*) calcd for $C_{35}H_{50}F_3N_3NaO_{19}$ ($M + Na^+$) 896.2888, found 896.2896.

Compounds 18−21. To a stirred solution of **17** (220 mg, 0.252 mmol) in methanol (10 mL) was added a sodium methoxide solution in methanol (0.1 M, 1.8 mL). After the mixture was stirred at rt for 5 h, it was neutralized with Amberlite IR-120 (H^+) resin. The resin was filtered off and washed with methanol. The filtrate and washings were combined and concentrated to a small volume (ca. 10 mL), to which was added an aqueous NaOH solution (1 N, 3 mL). After the reaction finished within 24 h, as indicated by TLC, the mixture was neutralized with diluted HCl to pH 7. Then, the reaction mixture was concentrated in a vacuum to give the fully deprotected disaccharide, which was directly used in the next step. $[\alpha]^{20}_D$ −23.2 (c 1.0, MeOH); ^{1}H NMR (D_2O, 600 MHz): δ 5.86−5.78 (m, 1H, CH_2=C<u>H</u>-), 5.04 (dd, *J* 17.4, 1.8 Hz, 1H, C<u>H</u>$_2$=CH-), 4.97 (dd, *J* 10.2, 1.8 Hz, 1H, C<u>H</u>$_2$=CH-), 4.33 (d, *J* 8.4 Hz, 1H, H-1), 3.94−3.76 (m, 6H), 3.74−3.46 (m, 8H), 2.81 (t, *J* 9.6 Hz, 1H), 2.76 (dd, *J* 12.6, 4.8 Hz, 1H, H-3′e), 2.36−2.24 (m, 4H), 1.97 (s, 3H, C<u>H</u>$_3$CONH), 1.55 (t, *J* 12.0 Hz, 1H, H-3′a). HR FABMS (*m*/*z*) calcd for $C_{24}H_{40}N_3Na_2O_{14}$ ($M + Na^+$) 640.2306, found 640.2324.

To a solution of the above product (40 mg, 0.065 mmol) in MeOH (6 mL) was added an acyl anhydride (Ac_2O 0.1 mL, Pr_2O 0.12 mL, *i*Bu_2O 0.14 mL, or $PhAc_2O$ 100 mg). After the reaction finished within 4 h, as indicated by TLC, the mixture was condensed under reduced pressure. The residue was purified on a Biogel P-2 column with H_2O as the eluent. Fractions containing the expected product were combined and freeze-dried to afford *N*-acyl sTn derivatives **18−21.**

***N*-{2-*O*-{[5-Acetamido-3,5-dideoxy-D-*glycero*-α-D-*galacto*-non-2-ulopyranosylonic acid]-(2→6)-*O*-2-acetamido-2-deoxy-β-D-galactopyranosyl}-ethyl} 4-Pentenamide (18).** ^{1}H NMR (D_2O, 600 MHz): δ 5.75−5.67 (m, 1H, CH_2=C<u>H</u>-), 4.94 (d, *J* 17.4 Hz, 1H, C<u>H</u>$_2$=CH-), 4.89 (d, *J* 9.6 Hz, 1H, C<u>H</u>$_2$=CH-), 4.29 (d, *J* 8.4 Hz, 1H, H-1), 3.83−3.71 (m, 5H), 3.68 (t, *J* 10.2 Hz, 1H,), 3.63−3.47 (m, 7H), 3.43 (dd, *J* 9.0, 1.2 Hz, 1H), 3.27−3.16 (m, 2H), 2.58 (dd, *J* 12.0, 4.2 Hz, 1 H, H-3′e), 2.24−2.16 (m, 4 H), 1.89, 1.88 (2s, 2 × 3H, C<u>H</u>$_3$CONH), 1.55 (t, *J* 12.6 Hz, 1H, H-3′a). HR ESIMS (*m*/*z*) calcd for $C_{26}H_{42}N_3Na_2O_{15}$ ($M + Na^+$) 682.2406, found 682.2407.

***N*-{2-*O*-{[5-Propanoylamido-3,5-dideoxy-D-*glycero*-α-D-*galacto*-non-2-ulopyranosylonic acid]-(2→6)-*O*-2-acetamido-2-deoxy-β-D-galactopyranosyl}-ethyl} 4-Pentenamide (19).** ^{1}H NMR (D_2O, 600 MHz): δ 5.75−5.67 (m, 1H, CH_2=C<u>H</u>-), 4.94 (dd, *J* 16.8, 1.8 Hz, 1H, C<u>H</u>$_2$=CH-), 4.89 (dd, *J* 10.2, 1.8 Hz, 1H, C<u>H</u>$_2$=CH-), 4.29 (d, *J* 8.4 Hz, 1H, H-1), 3.83−3.71 (m, 5H), 3.68 (t, *J* 10.2 Hz, 1H,), 3.63−3.47 (m, 7H), 3.41 (dd, *J* 9.0, 1.8 Hz, 1H), 3.27−3.16 (m, 2H), 2.59 (dd, *J* 12.6, 4.8 Hz, 1 H, H-3′e), 2.24−2.16 (m, 4 H), 2.15 (q, *J* 7.8 Hz, 2H, CH_3C<u>H</u>$_2$CO), 1.88 (s, 3H, C<u>H</u>$_3$CONH) 1.55 (t, *J* 12.6 Hz, 1H, H-3′a), 0.97 (t, *J* 7.8 Hz, 3H, C<u>H</u>$_3$CH$_2$CO). HR ESIMS (*m*/*z*) calcd for $C_{27}H_{44}N_3Na_2O_{15}$ ($M + Na^+$) 696.2562, found 696.2566.

***N*-{2-*O*-{[5-(2-Methylpropanoylamido)-3,5-dideoxy-D-*glycero*-α-D-*galacto*-non-2-ulopyranosylonic acid]-(2→6)-*O*-2-acetamido-2-deoxy-β-D-galactopyranosyl}-ethyl} 4-Pentenamide (20).** ^{1}H NMR (D_2O, 600 MHz): δ 5.75−5.67 (m, 1H, CH_2=C<u>H</u>-), 4.94 (dd, *J* 16.8, 1.8 Hz, 1H, C<u>H</u>$_2$=CH-), 4.89 (dd, *J* 10.2, 1.8 Hz, 1H, C<u>H</u>$_2$=CH-), 4.29 (d, *J* 9.0 Hz, 1H, H-1), 3.84−3.46 (m, 13H), 3.39 (dd, *J* 9.0, 1.8 Hz, 1H), 3.27−3.16 (m, 2H), 2.59 (dd, *J* 12.6, 4.2 Hz, 1 H, H-3′e), 2.39 (m, 1H, Me_2CHCO), 2.24−2.16 (m, 4H), 1.88 (s, 3H, CH_3CONH) 1.55 (t, *J* 12.6 Hz, 1H, H-3′a), 0.97, 0.96 (2d, 2 × 3H, *J* 6.6 Hz, Me_2CHCO). HR ESIMS (*m*/*z*) calcd for $C_{28}H_{46}N_3Na_2O_{15}$ ($M + Na^+$) 710.2719, found 710.2719.

***N*-{2-*O*-{[5-Phenylacetamido)-3,5-dideoxy-D-*glycero*-α-D-*galacto*-non-2-ulopyranosylonic acid]-(2→6)-*O*-2-acetamido-2-deoxy-β-D-galactopyranosyl}-ethyl} 4-Pentenamide (21).** ^{1}H NMR (D_2O, 600 MHz): δ 7.29−7.18 (m, 5H), 5.74−5.66 (m, 1H, CH_2=C<u>H</u>-), 4.94 (dd, *J* 17.4, 1.2 Hz, 1H, C<u>H</u>$_2$=CH-), 4.89 (dd, *J* 10.2, 1.2 Hz, 1H, C<u>H</u>$_2$=CH-), 4.28 (d, *J* 8.4 Hz, 1H, H-1), 3.84−3.46 (m, 15H), 3.37 (dd, *J* 11.4, 6.0 Hz, 1H), 3.26−3.16 (m, 2H), 2.59 (dd, *J* 12.6, 4.8 Hz, 1 H, H-3′e), 2.21−2.16 (m, 4H), 1.88 (s, 3H, CH_3CONH) 1.53 (t, *J* 12.6 Hz, 1H, H-3′a). HR ESIMS (*m*/*z*) calcd for $C_{32}H_{46}N_3Na_2O_{15}$ ($M + Na^+$) 758.2719, found 758.2710.

Compounds 22−25. Ozone was bubbled into individual solutions of **18−21** (20 mg) in MeOH (10 mL) at −78 °C until a blue color appeared. The solutions were kept at −78 °C for another 10 min, and then nitrogen was introduced to remove the remaining ozone. After Me_2S (0.5 mL) was added at −78 °C, the resultant solutions were allowed to warm to rt over a period of 1 h and stand for another 1 h before it was condensed

in vacuum. The crude products were purified on a Biogel P-2 column using distilled water as the eluent to give aldehydes **22**−**25** as white solids, which were used in the following conjugation reactions without further purification.

***N*-{2-*O*-{[5-Acetamido-3,5-dideoxy-D-*glycero*-α-D-*galacto*-non-2-ulopyranosylonic acid]-(2→6)-*O*-2-acetamido-2-deoxy-β-D-galactopyranosyl}-ethyl} 4-Oxo-butanamide (22).** ^{1}H NMR (D_2O, 600 MHz): δ 4.89 (t, *J* 6.0 Hz, 1H, -CH(OH)$_2$), 4.30 (d, *J* 8.4 Hz, 1H, H-1), 3.44 (d, *J* 9.0 Hz, 1H), 2.70 (t, *J* 6.6 Hz, 1H), 2.59 (dd, *J* 12.6, 4.8 Hz, 1 H, H-3′e), 2.50−2.38 (m, 1H), 2.27−2.16 (m, 1H), 1.88 (s, 6H, CH_3CONH), 1.78−1.68(m, 1H), 1.54 (t, *J* 12.0 Hz, 1H, H-3′a).

***N*-{2-*O*-{[5-Propanoylamido-3,5-dideoxy-D-*glycero*-α-D-*galacto*-non-2-ulopyranosylonic acid]-(2→6)-*O*-2-acetamido-2-deoxy-β-D-galactopyranosyl}-ethyl} 4-Oxo-butanamide (23).** ^{1}H NMR (D_2O, 600 MHz): δ 5.24 (t, *J* 6.0 Hz, 1H, -CH(OH)$_2$), 4.29 (d, *J* 8.4 Hz, 1H, H-1), 3.41 (d, *J* 8.4 Hz, 1H), 3.28−3.18 (m, 1H), 2.59 (dd, *J* 12.6, 4.8 Hz, 1 H, H-3′e), 2.50−2.41(m, 1H), 2.29−2.22 (m, 2H), 2.15 (q, *J* 7.8 Hz, 2H, $CH_3C\underline{H}_2CO$), 1.89 (s, 3H, CH_3CONH), 1.78−1.73(m, 1H), 1.54 (t, *J* 12.6 Hz, 1H, H-3′a), 0.97 (t, *J* 7.8 Hz, 3H, $C\underline{H}_3CH_2CO$).

***N*-{2-*O*-{[5-(2-Methylpropanoylamido)-3,5-dideoxy-D-*glycero*-α-D-*galacto*-non-2-ulopyranosylonic acid]-(2→6)-*O*-2-acetamido-2-deoxy-β-D-galactopyranosyl}-ethyl} 4-Oxo-butanamide (24).** ^{1}H NMR (D_2O, 600 MHz): δ 5.24 (t, *J* 3.0 Hz, 1H, -CH(OH)$_2$), 4.28 (d, *J* 8.4 Hz, 1H, H-1), 3.39 (d, *J* 9.0 Hz, 1H), 3.28−3.18 (m, 1H), 2.59 (dd, *J* 12.6, 4.2 Hz, 1 H, H-3′e), 2.50−2.19 (m, 4H), 1.89 (s, 3H, CH_3CONH), 1.80−1.71 (m, 1H), 1.55 (t, *J* 12.0 Hz, 1H, H-3′a), 0.97, 0.96 (2d, 2 × 3H, *J* 6.6 Hz, Me_2CHCO).

***N*-{2-*O*-{[5-Phenylacetamido)-3,5-dideoxy-D-*glycero*-α-D-*galacto*-non-2-ulopyranosylonic acid]-(2→6)-*O*-2-acetamido-2-deoxy-β-D-galactopyranosyl}-ethyl} 4-oxo-butanamide (25).** ^{1}H NMR (D_2O, 600 MHz): δ 7.30−7.17 (m, 5H), 5.23 (t, *J* 3.6 Hz, 1H, -CH(OH)$_2$), 4.27 (d, *J* 8.4 Hz, 1H, H-1), 3.38 (dd, *J* 12.0, 6.6 Hz, 1H), 3.24−3.16 (m, 2H), 2.59 (dd, *J* 12.6, 4.8 Hz, 1 H, H-3′e), 2.49−2.40 (m, 1H), 2.34−2.18 (m, 2H), 1.89 (s, 3H, CH_3CONH), 1.80−1.70 (m, 1H), 1.54 (t, *J* 12.6 Hz, 1H, H-3′a).

General Procedure for the Coupling between 22 and 25 and KLH or Human Serum Albumin (HSA). A solution of **22**, **23**, **24**, or **25** (8 mg), KLH or HSA (6 mg), and $NaBH_3CN$ (6 mg) in 0.1 M $NaHCO_3$ (0.2 mL, pH 7.5−8.0) was allowed to stand at rt in the dark for 3 days with occasional shaking. The reaction mixture was then loaded onto a Biogel A0.5 column (1 × 15 cm) and eluted with 0.1 M phosphate buffered saline (PBS) buffer (I = 0.1, pH = 7.8). The fractions containing the glycoconjugate, characterized by a bicinchoninic acid (BCA) assay for proteins and by the Svennerholm method for sialic acid, were combined and dialyzed against distilled water for 2 days. It was then lyophilized to give a white powder of the expected glycoconjugates **4**−**11** (5−6 mg).

Analysis of the Carbohydrate Loading Levels of the Glycoconjugates (*31*, *32*). After the solution of an exactly weighed sample of the glycoconjugate (0.5 mg) in distilled water (1.0 mL) was mixed with the resorcinol reagent (2.0 mL), the mixture was heated in a boiling water bath for 30 min. It was cooled to rt, and to this mixture was then added an extraction solution (1-butanol acetate and 1-butanol, 85:15 v/v, 3.0 mL). The mixture was shaken vigorously before it was allowed to stand still for ca. 10 min to allow the organic layer to separate well from the inorganic layer. The organic layer was transferred to a 1.0-cm cuvette, and its absorbance at 580 nm was determined by an UV−vis spectrometer, using a blank organic solution as the control. The sialic acid content of the glycoconjugate was determined against a calibration curve created with the standard NeuNAcyl (Acyl = Ac, Pr, iBu, PhAc) solutions analyzed under the same condition. The carbohydrate loading of each glycoconjugate was calculated according to the following equation.

$$N\text{-Acyl sTn loading (\%)} = \frac{\text{amount of sialic acid (mg) in the sample}}{\text{weight of the glycoconjugate sample (mg)}} \times \frac{\text{molecular weight of sTn}}{\text{molecular weight of sialic acid}} \times 100\%$$

Immunization of Mice. Five female C57BL/6 mice at the age of 8 weeks (Jackson Laboratories, Bar Harbor, ME) were immunized for each sTn−KLH conjugate. Immunizations were intraperitoneal with the glycoconjugate containing 2 μg of carbohydrate in 200 μL of saline mixed with 200 μL of MPL/TDM Ribi adjuvant (Sigma Chemical, St. Louis, MO) following the manufacturer's protocol. The mice were boosted with identical immunizations on days 15 and 22 following the initial immunization. The mice were bled by tail vein prior to the initial immunization on day 0 and after immunization on day 14 and day 31. Bleed was clotted to obtain sera, which were stored at −80 °C.

Protocols for Enzyme-Linked Immunosorbent Assay (ELISA) Analysis. ELISA plates were first treated with 100 μL solution of KLH or the HSA conjugate of sTn or sTn derivatives (1 μg/mL 0.1 M bicarbonate buffer) overnight at 4 °C, followed by washing with PBS. Pooled sera from each group of mice were diluted 1:300 to 1:72900 in serial half-log dilutions in PBS with 0.02% azide and incubated overnight in the coated ELISA plates (100 μL/well). The plates were then washed and incubated with 1:1000 dilution of alkaline phosphatase linked anti-κ, anti-IgM, or anti-IgG2a antibodies or with a 1:2000 dilution of anti-IgG1 or anti-IgG3 antibodies (Southern Biotechnology, Buckingham, AL) for 1 h at rt. Plates were washed and developed with PNPP substrate for colorimetric readout using a BioRad 550 plate reader at 405 nM wavelength.

For titer analysis, optical density (OD) values were plotted against dilution values, and a best-fit line was obtained. The equation of this line was employed to calculate the dilution value at which an OD of 0.5 was achieved, and the antibody titer was calculated at the inverse of this dilution value.

RESULTS AND DISCUSSION

In the design of sTn analogues, we focused on the modification of the sialic acid residue because previous studies have demonstrated that cells can be readily bioengineered to express unnatural sialic acids following the uptake of *N*-acyl mannosamines as biosynthetic precursors (*30*, *33*−*36*). The sTn derivatives synthesized and studied in this work were *N*-propionyl sTn (sTnNPr, **1**), *N*-*iso*-butanoyl sTn (sTnN*i*Bu, **2**), and *N*-phenylacetyl sTn (sTnNPhAc, **3**) (Figure 2). The same *N*-acyl derivatives of sialic acid proved to be more antigenic than Neu5Ac itself (*37*); therefore, we expected that **1**, **2**, and **3** would be better antigens than sTn. On the other hand, it has been reported that *N*-propionyl and *N*-phenylacetyl mannosamines could efficiently glycoengineer tumor cells (*30*, *31*). It is thus reasonable to expect the feasibility of achieving glycoengineered modification of sTn on tumors by these functional groups, which is necessary for the new immunotherapeutic strategy. Consequently, if certain glycoconjugates designed above show desired immunological properties, they will have great potential for use as vaccines in the exploration of new cancer immunotherapies.

To form effective vaccines, sTn and its *N*-acyl derivatives were coupled to a carrier protein. We chose KLH for this purpose, since KLH has shown useful immunological properties (*15*, *38*). Alternatively, to avoid the detection of antibodies

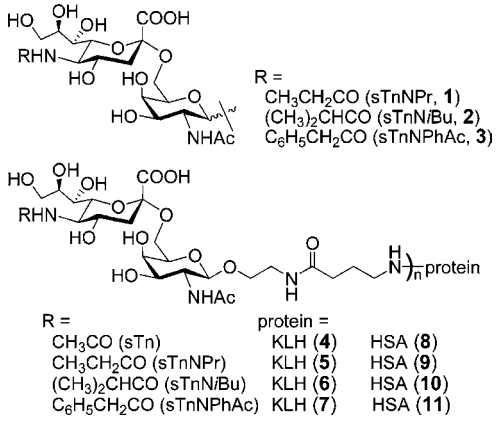

Figure 2. Structures of *N*-modified sTn antigens and the glycoconjugate vaccines studied.

specific for KLH in ELISA, HSA was employed as the carrier protein of the capture reagents. The antigens and carrier proteins were coupled together by a convenient and efficient method based on the pentenoyl group (*39*). An additional advantage of this coupling method is that the linker itself does not cause an immune response (*40*).

The synthesis of natural sTn antigen, its unnatural *N*-acyl derivatives, and their protein conjugates is outlined in Scheme 1. The glycosyl acceptor **14** was prepared from D-galactosamine (**12**) after a series of transformations including conversion of **12** into a 2-azidoethanol glycoside **13** followed by complete *O*-deacetylation and then selective protection of the 3,4-hydroxyl groups as an acetonide. A major issue in this synthetic scheme is the sialylation reaction, which is one of the most difficult glycosylation reactions in carbohydrate chemistry. We used the method of Boons and co-workers (*41*) to achieve this transformation, in which an *N*-trifluoroacetyl derivative of neuraminic acid was employed as the glycosyl donor to offer the desired α-glycoside. The trifluoroacetyl group as a protecting group was easily removable to facilitate N-deprotection and subsequent modification with various acyl groups, offering a highly convergent route to the target structures. Thus, after the required sialyl donor **15** was prepared from Neu5Ac following a literature procedure (*41*), it was used to glycosidate **14** using *N*-iodosuccinamide (NIS) and triflic acid (TfOH) as the promoters. This reaction afforded the disaccharide in a good yield (65%) and a reasonable stereoselectivity (α/β: 4/1), but the two anomers were almost inseparable by column chromatography. However, we found that after the acetonide was removed, the diol products were easily separated to afford pure **16**. The α-configuration of its sialic acid was determined by the unique, downfield-shifted NMR signal of H-3e (δ 2.63, compared to δ 2.35 of β-linked sialic acid), which was further confirmed by structural analysis of subsequent products. Compound **16** was then converted into *N*-acyl derivatives of sTn and linked to the carrier proteins.

The pentenoyl group used to couple carbohydrate antigens to carrier proteins was introduced upon selective reduction of the azido group to form a primary amine and then selective acylation of the amino group with pentenoic anhydride. The product **17** was a common intermediate in the synthesis of sTn and its *N*-acyl derivatives. The *N*-trifluoroacetyl group and all *O*-acetyl groups were selectively removed by treatments with a methanolic solution of NaOMe and a methanolic aqueous solution of NaOH, in the presence of an *N*-pentenoyl group. To the exposed amino group were then regioselectively introduced acyl groups in methanol by reactions with acetic, propionic, *iso*-butyric, and phenylacetic anhydrides to afford **18**−**21**, respectively. These products were purified on a Biogel P2 column. Their identity and purity were supported by NMR

Scheme 1[a]

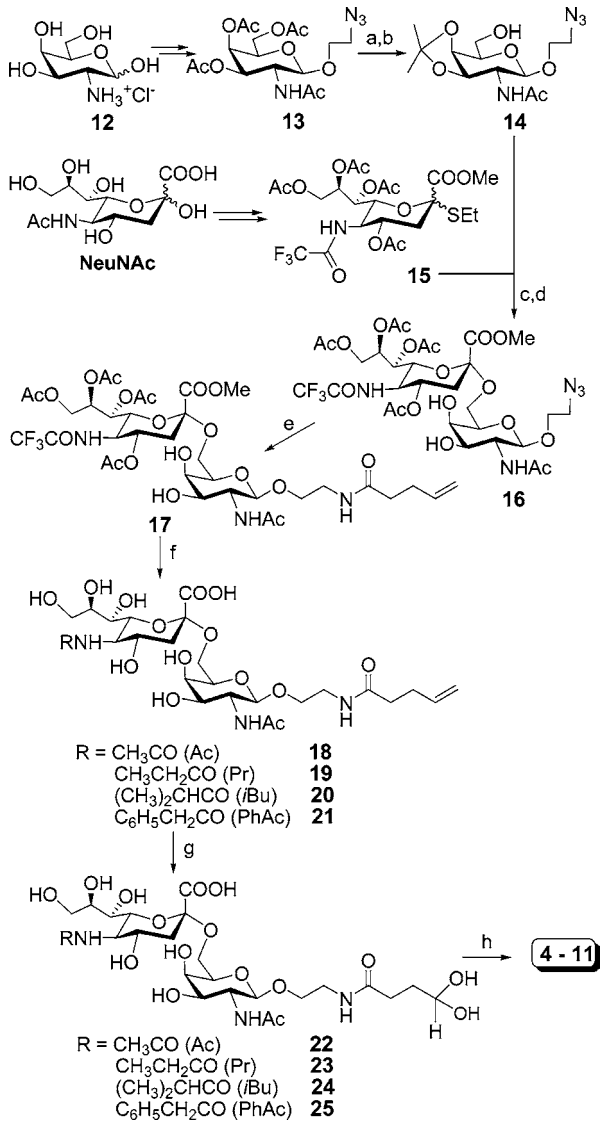

[a] Reagents and conditions: (a) NaOMe, MeOH, 99%; (b) dimethoxypropane, *p*-TsOH, DMF, 65 °C, 90%; (c) NIS, TfOH, MS 4 Å, MeCN, −35 °C, 65%; (d) 60% HOAc, 65 °C, 87%; (e) 10% Pd/C, H_2, MeOH, 1 h; then 4-pentenoic anhydride, overnight, 80%; (f) 0.1 N MeONa/MeOH; then 1 N NaOH, 24 h; finally various anhydrides, rt, >95%; (g) O_3, MeOH, −70 °C, 0.5 h; then Me_2S, to rt, 2 h, 85−90%; (h) KLH or HSA, $NaBH_3CN$, 0.1 N $NaHCO_3$, rt in dark, 3 days.

and HR MS. At this stage, the α-configuration of sialic acid was further confirmed by a downfield-shifted H-3e NMR signal (δ 2.59) compared to the β-anomer (δ < 2.40).

Finally, sTn and its derivatives were coupled to the carrier proteins by a two-step procedure (*39*). First, **18**−**21** were treated with ozone in methanol to selectively oxidize their carbon−carbon double bond and produce hydrated aldehydes **22**−**25** that were purified on a Biogel P2 column. The ^1H NMR spectra of **22**−**25** clearly showed the hydrated aldehyde signal at δ 5.2, whereas the signals of protons linked to carbon−carbon double bond disappeared completely. Next, **22**−**25** were coupled to the carrier proteins, KLH and HSA, by reductive amination carried out in a 0.1 M $NaHCO_3$ buffer in the presence of $NaBH_3CN$. The sTn derivatives **22**−**25** were employed in excess, and the unreacted **22**−**25** were readily separated from the glycoconjugate products on a Biogel A0.5 column. Fractions containing the glycoconjugate, which was the first eluted component, were combined and dialyzed against distilled water. Freeze drying of the aqueous solution afforded glycoconjugates **4**−**11** as white fluffy solids.

Table 1. Antigen Loading Level of the Glycoconjugates

	KLH conjugates				HSA conjugates			
sample	**4**	**5**	**6**	**7**	**8**	**9**	**10**	**11**
loading (%)	8	10	9	10	11	14	10	13

The sialic acid contents of resultant glycoconjugates **4**−**11** were analyzed by the Svennerholm method (*32*). The contents were converted into carbohydrate loading levels according to the equation presented in Experimental Procedures. As shown in Table 1, the coupling reactions yielded glycoconjugates containing 8−13% (w/w) of carbohydrates. The loading level of HSA conjugates was slightly higher than that of KLH conjugates, which might be determined by the property of carrier proteins. Nevertheless, the level of antigen loading in these glycoconjugates is typical for glycoconjugate vaccines.

The immunological properties of glycoconjugates **4**−**7** as vaccines were studied in C57BL/6 mice. For immunizations, each glycoconjugate containing ca. 2 μg of carbohydrates mixed with MPL/TDM Ribi adjuvant (*42*) was injected intraperitoneally in mice. These mice were then boosted with the same glycoconjugate on day 15 and day 22 following the initial immunization. On day 14 and day 31, animal sera were withdrawn and pooled with respect to the individual group and date. The titer of total antigen-specific antibody or a specific antibody isotype including IgM, IgG1, IgG2a, and IgG3 of the pooled sera was assessed by ELISA.

In ELISA, plate wells were first coated with a derivatized sTn−HSA conjugate or KLH alone as the capture antigen and then treated with the pooled day −1, day 14, or day 31 sera of five immunized mice in a glycoconjugate group. Pooling the sera of immunized mice in each group gave a mean serum antibody concentration. Antibodies captured by the coating antigen on plates were detected with goat anti-mouse kappa light chain specific and horseradish peroxidase (HRP) conjugated antibody, which would reflect about 95% of the total antibody response (*26*). Using sTn−HSA conjugates as the capture antigens allowed us to detect antibodies that were specific for the modified sTn component of KLH conjugates without detection of anti-KLH antibodies. The assays using KLH as the capture antigen served as a positive control, since KLH is well established as a strong immunogen to elicit high titers of antibodies. The sera obtained after the primary immunization, namely, obtained on day 14, gave low ELISA titers, so only the ELISA data of sera obtained on day 31 are presented and discussed in detail here.

Figure 3A shows the total antibody titers with the OD plotted against pooled sera dilutions. Figure 3B gives the normalized titer analysis data (Experimental Procedures) which can quantify more accurately the antigenicity of the glycoconjugates. Although all of the tested glycoconjugates **4**−**7** were immunogenic, sTnNPhAc gave obviously the highest level of antigen-specific antibodies, and the natural sTn antigen gave the lowest concentration of sTn-specific antibodies. There was essentially no binding of preimmune serum to various sTn−HSA conjugates.

Figure 4 shows the titers of different isotypes of antibodies. All glycoconjugates produced relatively equivalent concentrations of IgM antibodies (panel A), but a significant difference was observed with IgG responses. Panel B reveals that the tested glycoconjugates induced low levels of IgG1 antibody, but sTnNPhAc and sTnN*i*Bu induced significant amounts of IgG2a antibodies (panel C). IgG3 titers (panel D) showed a hierarchy similar to that of antigenicity in Figure 3B.

Finally, we also examined the reactivity of antisera from modified sTn-immunized mice to the HSA conjugate of natural sTn (Figure 5). The antisera of sTnNPr and sTnN*i*Bu showed low binding titers, indicating some cross reactivity to sTn. Since

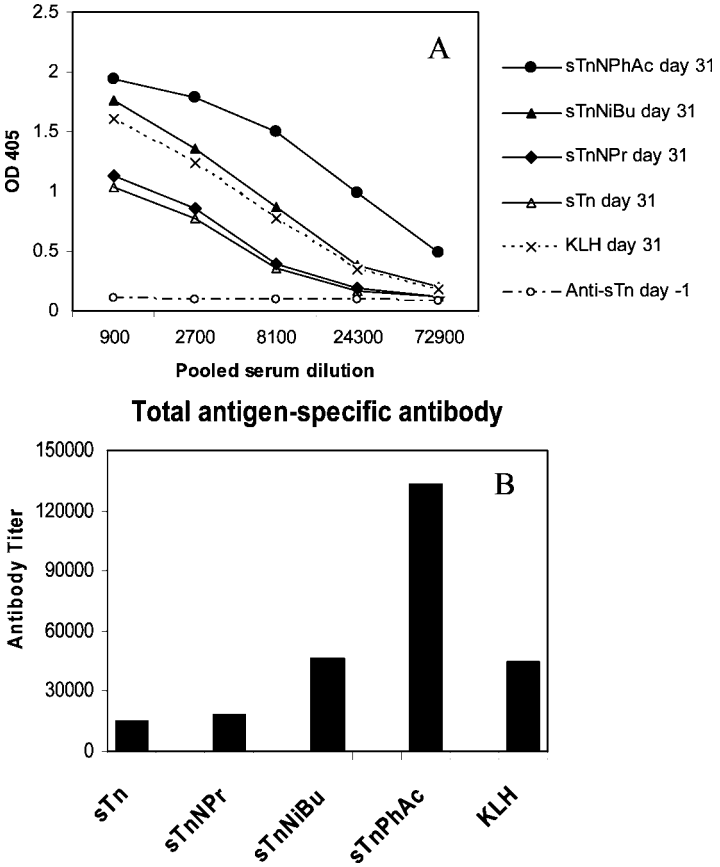

Figure 3. Antigen-specific total antibody contents in sera analyzed by ELISA. (A) Each line represents the antibody level in serum pooled from a group of five mice. Anti-sTn and anti-derivatized sTn antibody levels were obtained from mice immunized with glycoconjugates **4**−**7**. Anti-KLH antibody level was obtained from mice immunized with sTn, and anti-sTn antibody level of preimmune serum was obtained from the same group and used as the negative control (equivalent results were obtained from other groups). Error bars are smaller than the symbol width. (B) Normalized ELISA data of total antibodies. A best-fit line was obtained by plotting OD values against dilution values, and the equation of this line was used to calculate the dilution value at which an OD of 0.5 was achieved.

sTn is relatively tumor-specific, this cross reactivity may not have a major impact on normal tissues. In fact, under certain conditions the synthetic vaccines with improved immunological properties, combined with the cross reactivity of their immune responses to native sTn antigen as well as the unique presentation of sTn on tumor cells, may be useful for cancer immunotherapy. However, sTnNPr-KLH and sTnN*i*Bu-KLH are definitely not the ideal vaccines for our new strategy of cancer immunotherapy, due to the cross reactivity and relatively poor antigenicity. In contrast, the reactivity of sTnNPhAc sera to sTn was too low to be detected. This result suggests that the immune response induced by sTnNPhAc was specific.

Above ELISA data suggest that chemical modifications of sTn antigen could improve its antigenicity, which is consistent with the conclusions about other TACAs (*27*, *37*, *40*, *43*, *44*). Moreover, sTnNPhAc proved to be the most antigenic among the sTn derivatives investigated. Most importantly, although the natural sTn antigen induced exclusively IgM antibodies (Figures 3 and 4), sTnNPhAc induced significant titers of IgG antibodies, which indicates a T-cell-dependent immune response, such as antibody isotype switching, antibody affinity maturation, immunological memory, and the induction of cell-mediated cytotoxicity (*6*, *25*, *26*). The switch to T-cell-dependent immune response is important for the antitumor activity of cancer vaccines (*45*). The reasons for the antigenicity improvement of

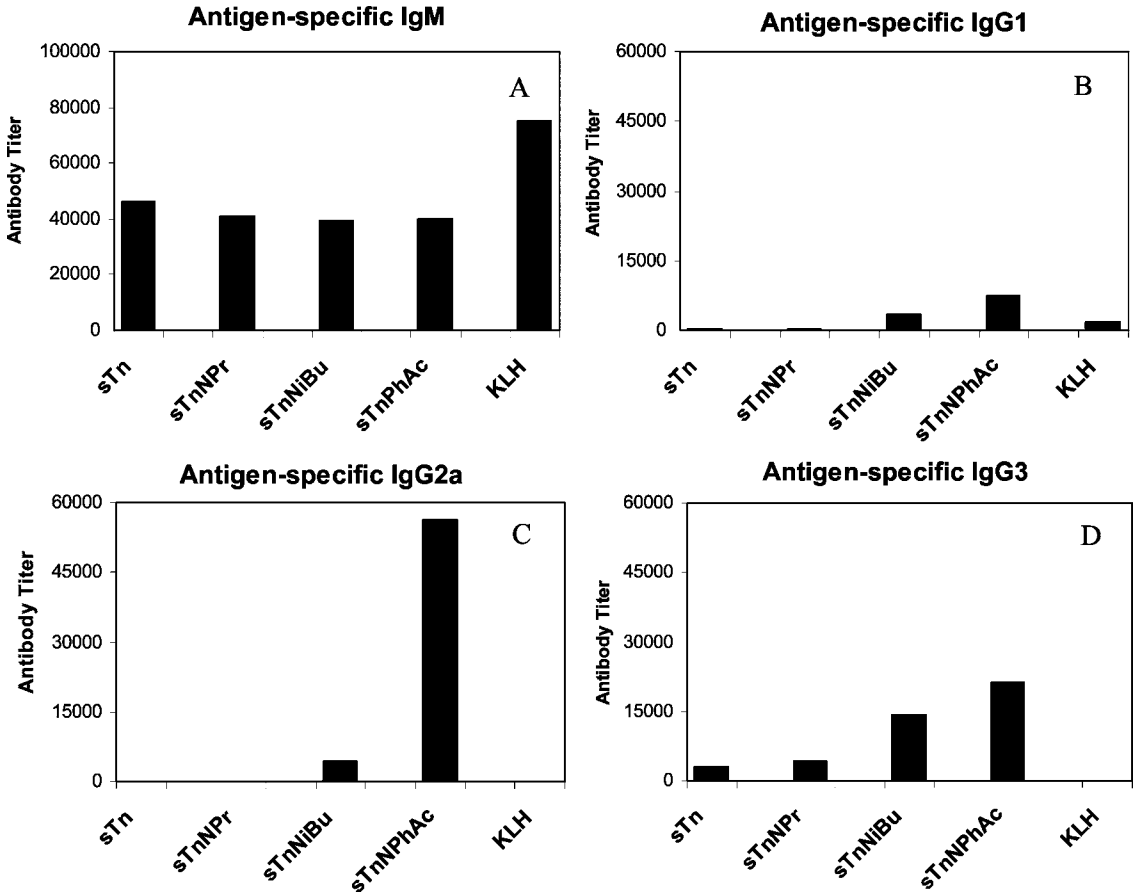

Figure 4. (A−D) Titer analysis of different isotypes of antigen-specific antibodies determined by ELISA assay. Each represents the titer in pooled serum obtained on day 31 after primary and booster immunizations from five replicate animals.

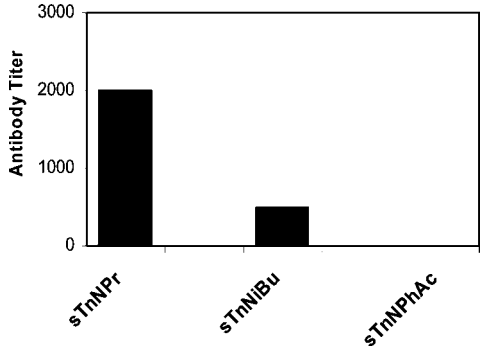

Figure 5. Titer analysis of the cross reactivity determined by ELISA. Each bar represents total anti-sTn reactivity in pooled sera from five replicate animals immunized with a derivatized sTn−KLH conjugate.

modified forms of sTn antigen and their capability to stimulate T-cell-dependent immune responses are not clear, but we think that the significant difference of the structure and chemical properties of sTnPhAc compared to native sTn, especially the increased hydrophobicity of the former, may play a critical role. For instance, this may facilitate the recognition and binding of sTnNPhAc by the immune system and immune cells. ELISA data of the reactivity of antisera obtained from mice immunized with modified sTn−KLH conjugates to native sTn antigen revealed that sTnNPhAc sera had essentially no cross reaction. This may well suggest that when being used as cancer vaccines the sTnNPhAc conjugate would cause no or relatively low autoimmune reactions. This result may be explained by the significant structural difference between the phenylacetyl group in sTnNPhAc and the acetyl group in native sTn. The high antigenicity of sTnNPhAc−KLH combined with its relatively low potential to cause autoimmune reactions makes it an excellent vaccine.

In summary, this paper has established an expedient method for synthesizing N-modified derivatives of sTn antigen and their protein conjugates. After careful analysis of the immunological properties of the synthetic glycoconjugates, we identified sTnNPhAc−KLH as a promising candidate for being developed into a functional cancer vaccine, not only because sTnNPhAc is highly antigenic, but also because it can induce IgG immune responses that are critical for the antitumor applications (*25, 26*). An effective glycoconjugate vaccine based on sTnNPhAc combined with the fact that cancer cell surface Neu5Ac can be readily and effectively engineered by *N*-phenylacetyl-D-mannosamine may provide a solution to the problem of immune tolerance to sTn and may be used for the immunotherapy of cancer, such as breast cancer, which expresses high levels of sTn antigen,

ACKNOWLEDGMENT

This work was supported by an NIH/NCI research grant (1R01 CA95142). The authors thank Dr. Clifford Harding, Dr. Peter Chefalo, and Ms. Nancy Nagy for allowing the use of their lab space and equipment for this study, as well as for their stimulating discussion and generous assistance with the immunological experiments.

Supporting Information Available: Additional experimental procedures and selected NMR spectra. This material is available free of charge via the Internet at http://pubs.acs.org.

LITERATURE CITED

(1) Hakomori, S. (1991) Possible functions of tumor-associated carbohydrate antigens. *Curr. Opin. Immunol. 3,* 646−653.

(2) Hakomori, S., and Zhang, Y. (1997) Glycosphingolipid antigens and cancer therapy. *Chem. Biol. 3*, 97−104.
(3) Reisfeld, A. R., and Cheresh, D. A. H. (1987) Human tumor antigens. *Adv. Immunol. 40*, 323−377.
(4) Ben-Efraim, S. (1999) One hundred years of cancer immunotherapy: a critical appraisal. *Tumor Biol. 20*, 1−24.
(5) Ragupathi, G. (1998) Carbohydrate antigens as targets for active specific immunotherapy. *Cancer Immunol. Immunother. 46*, 82−87.
(6) Danishefsky, S. J., and Allen, J. R. (2000) From the laboratory to the clinic: A retrospective on fully synthetic carbohydrate-based anticancer vaccines. *Angew. Chem. Int. Ed. 39*, 837-863.
(7) Hellstrom, K. E., Gladstone, P., and Hellstrom, I. (1997) Cancer vaccines: Challenges and potential solutions. *Mol. Med. Today* 286-290.
(8) Chen, C.-H., and Wu, T.-C. (1998) Experimental vaccine strategies for cancer immunotherapy. *J. Biomed. Sci. 5*, 231−252.
(9) Livingston, P. O. (1992) Construction of cancer vaccines with carbohydrate and protein tumor antigens. *Curr. Opin. Immunol. 4*, 624−629.
(10) Yonezawa, S., Tachikawa, T., and Sato, E. (1992) Sialosyl-Tn antigens. Its distribution in normal human tissues and expression in adenocarcinoma. *Am. J. Clin. Pathol. 98*, 167−174.
(11) Itzkowitz, S. H., Bloom, E. J., and Kim, Y. S. (1990) Sialosyl-Tn. A novel mucin antigen associated with prognosis in colorectal cancer patients. *Cancer 66*, 1960−1966.
(12) Kobayashi, H., Terao, T., and Kawashima, Y. (1992) Serum sialyl Tn as an independent predictor of poor prognosis in patients with epithelial ovraian cancer. *J. Clin. Oncol. 10*, 95−101.
(13) Leivonen, M., Nordling, S., Lundin, J., and Haglund, C. (2001) sTn and prognosis in breast cancer. *Oncology 61*, 299−305.
(14) Nakagoa, T., Sawai, T., and Tsuji, T. (2002) Predictive factors for preoperative serum levels of sialyl Lewis(x), sialyl Lewis(a) and sialyl sTn antigens in gastric cancer patients. *Anticancer Res. 22*, 451-458.
(15) Adluri, S., Helling, F., Ogata, S., and Livingston, P. O. (1995) Immunogenicity of synthetic TF-KLH and sTn-KLH conjugates in colorectal carcinoma patients. *Cancer Immunol. Immunother. 41*, 185−192.
(16) Livingston, P. O., Zhang, S., and Lloyd, K. O. (1997) Carbohydrate vaccines that induce antibodies against cancer. 1. Rationale. *Cancer Immunol. Immunother. 45*, 1−9.
(17) Ragupathi, G., Koganty, R. R., Qiu, D., Lloyd, K. O., and Livingston, P. O. (1998) A novel and efficient method for synthetic carbohydrate conjugate vaccine preparation: synthesis of sialyl Tn-KLH conjugate using a 4-(4-N-maleimidomethyl) cyclohexane-1-carboxyl hydrazide (MMCCH) linker arm. *Glycoconjugate J. 15*, 217−221.
(18) Ragupathi, G., Howard, L., Cappello, S., Koganty, R., and Livingston, P. O. (1999) Vaccines prepared with sialyl-Tn and sialyl-Tn trimers using the 4-(4-maleimidomethyl)cyclohexane-1-carboxyl hydrazide linker group result in optimal antibody titers against ovine submaxillary mucin and sialyl-Tn-positive tumor cells. *Cancer Immunol. Immunother. 48*, 1−8.
(19) MacLean, G. D., Reddish, M., Koganty, R. R., Wong, T., and Longenecker, B. M. (1993) Immunization of breast cancer patients using a synthetic sialyl-Tn glycoconjugate plus Detox adjuvant. *Cancer Immunol. Immunother. 36*, 215−222.
(20) Miles, D. W., Towlson, K. E., Graham, R., Reddish, M., Longenecker, B. M., and Rubens, R. D. (1996) A randomized phase II study of sialyl-Tn and DETOX-B adjuvant with or without cyclophosphamide pretreatment for the active specific immunotherapy of breast cancer. *Br. J. Cancer 74*, 1292−1296.
(21) Sørensen, A. L., Reis, C. A., Tarp, M. A., Mandel, U., Ramachandran, K., Sankaranarayanan, V., Schwientek, T., Graham, R., Taylor-Papadimitriou, J., Hollingsworth, M. A., Burchell, J., and Clausen, H. (2006) Chemoenzymatically synthesized multimeric Tn/STn MUC1 glycopeptides elicit cancer-specific anti-MUC1 antibody responses and override tolerance. *Glycobiology 16*, 96−107.
(22) Holmberg, L. A., Oparin, D. V., Gooley, T., Lilleby, K., Bensinger, W., Reddish, M. A., MacLean, G. D., Longenecker, B. M., and Sandmaier, B. M. (2000) Clinical outcome of breast and ovarian cancer patients treated with high-dose chemotherapy, autologous stem cell rescue and Theratope STn-KLH cancer vaccine. *Bone Marrow Transplant. 25*, 1233−1241.
(23) Holmberg, L., and Sandmaier, B. (2004) Vaccination with Theratope (sTn-KLH) as treatment for breast cancer. *Expert Rev. Vaccines 3*, 655−663.
(24) Livingston, P. O. (1995) Approaches to augmenting the immunogenicity of melanoma gangliosides: from the whole melanoma cells to ganglioside-KLH conjugate vaccines. *Immunol. Rev. 145*, 147−156.
(25) Casadevall, A., and Pirofski, L. A. (2003) Antibody-mediated regulation of cellular immunity and the inflammatory response. *Trends Immunol. 24*, 474−478.
(26) Goldsby, R. A., Kindt, T. J., Osborne, B. A., and Kuby, J. (2003) Antibodies: Structure and Function. In *Fundamental Immunology*, pp 76−105, W. H. Freeman and Company, New York.
(27) Liu, T., Guo, Z., Yang, Q., Sad, S., and Jennings, H. J. (2000) Biochemical engineering of surface α(2-8)polysialic acid for immunotargeting cancer cells. *J. Biol. Chem. 275*, 32832−32836.
(28) Kayser, H., Geile, C. C., Paul, C., Zeitler, R., and Reutter, W. (1992) Incorporation of N-acyl-2-amino-2-deoxy-hexoses into glycosphingolipids of pheochromocytoma cell line PC12. *FEBS Lett. 301*, 137−140.
(29) Mahal, K. L., Yarema, K. J., and Bertozzi, C. R. (1997) Engineering chemical reactivity on cell surfaces through oligosaccharide biosynthesis. *Science 276*, 1125−1128.
(30) Chefalo, P., Pan, Y., Nagy, N., Harding, C., and Guo, Z. (2006) Effective metabolic engineering of GM3 on tumor cells by *N*-phenylacetyl-D-mannosamine. *Biochemistry 45*, 3733−3739.
(31) Pan, Y., Ayani, T., Nadas, J., and Guo, Z. (2004) Accessibility of N-acyl derivatives of D-mannosamine to *N*-acetylneuraminic acid aldolase. *Carbohydr. Res. 339*, 2091−2100.
(32) Svennerholm, L. (1957) Estimation of sialic acids. II. Colorimetric resorcinol-hydrochloric acid method. *Biochim. Biophys. Acta 24*, 604−611.
(33) Keppler, O. T., Stehling, P., Herrmann, M., Kayser, H., Grunow, D., Reutter, W., and Pawlita, M. (1995) Biosynthetic modulation of sialic acid-dependent virus-receptor interactions of two primate polyoma viruses. *J. Biol. Chem. 270*, 1308−1314.
(34) Tangvoranuntakul, P., Gagneux, P., Diaz, S., Bardor, M., Varki, N., Varki, A., and Muchmore, E. (2003) Human uptake and incorporation of an immunogenic nonhuman dietary sialic acid. *Proc. Natl. Acad. Sci. U.S.A. 100*, 12045−12050.
(35) Kim, E. J., Sampathkamur, S.-G., Jones, M. B., Rhee, J. K., Baskaran, G., Goon, S., and Yarema, K. J. (2004) Characterization of the metabolic flux and apoptotic effects of O-hydroxyl and N-acyl-modified *N*-acetylmannosamine (ManNAc) analogs in Jurkat (human T-lymphoma-derived) cells. *J. Biol. Chem. 279*, 18342−18352.
(36) Mahal, L. K., and Bertozzi, C. R. (1997) Engineering cell surfaces: fertile ground for molecular landscaping. *Chem. Biol. 4*, 415−422.
(37) Chefalo, P., Pan, Y. B., Nagy, N., Harding, C. V., and Guo, Z. (2004) Preparation and immunological studies of protein conjugates of *N*-acylneuraminic acids. *Glycoconjugate J. 20*, 407−414.
(38) MacLean, G. D., Miles, D. W., Rubens, R. D., Reddish, M. A., and Longenecker, B. M. (1996) Enhancing the effect of Theratope STn-KLH cancer vaccine in patients with metastatic breast cancer by pretreatment with low-dose intravenous cyclophosphamide. *J. Immunother. Emphasis Tumor Immunol. 19*, 309−316.
(39) Xue, J., Pan, Y., and Guo, Z. (2002) Neoglycoprotein cancer vaccines: Synthesis of an azido derivative of GM3 and its efficient coupling to proteins through a new linker. *Tetrahedron Lett. 43*, 1599−1602.
(40) Pan, Y. B., Chefalo, P., Nagy, N., Harding, C. V., and Guo, Z. (2005) Synthesis and immunological properties of N-modified GM3 antigens as therapeutic cancer vaccines. *J. Med. Chem. 48*, 875−883.
(41) De Meo, C., Demchenko, A. V., and Boons, G.-J. (2001) A stereoselective approach for the synthesis of α-sialosides. *J. Org. Chem. 66*, 5490−5497.
(42) Evans, J. T., Cluff, C. W., Johnson, D. A., Lacy, M. J., Persing, D. H., and Baldridge, J. R. (2003) Enhancement of antigen-specific immunity via the TLR4 ligands MPL adjuvant and Ribi. 529. *Expert Rev. Vaccine 2*, 219−229.
(43) Ritter, G., Boosfeld, E., Calves, M. J., Oettgen, H. F., Old, L. J., and Livingston, P. O. (1990) Antibody response after immunization with ganglioside GD3, GD3 lactones, GD3 amide and GD3

gangliosidol in the mouse. GD3 lactone I induces antibodies reactive with human melanoma. *Immunobiology 182*, 32.

(44) Krug, L. M., Ragupathi, G., Ng, K. K., Hood, C., Jennings, H. J., Guo, Z., Kris, M. G., Miller, V., Pizzo, B., Tyson, L., Baez, V., and Livingston, P. O. (2004) Vaccination of small cell lung cancer patients with polysialic acid or N-propionylated polysialic acid conjugated to keyhole limpet hemocyanin. *Clin. Cancer Res. 10*, 916−923.

(45) Lanzavecchia, A. (1985) Antigen-specific interaction between T and B cells. *Nature 314*, 537−539.

BC060103S

Rigid Linkers for Bioactive Peptides

Josef Vagner,[†] Heather L. Handl,[‡] Yasunari Monguchi,[†] Umasish Jana,[†] Lucinda J. Begay,[†] Eugene A. Mash,[†] Victor J. Hruby,[†,‡] and Robert J. Gillies*[,‡]

Department of Chemistry, University of Arizona, Tucson, Arizona 85721, and Department of Biochemistry and Molecular Biophysics, Arizona Cancer Center, Tucson, Arizona 85724. Received June 5, 2006;
Revised Manuscript Received August 18, 2006

Rigid linkers of variable length were used to connect two high-affinity Nle[4]-D-Phe[7]-α-melanocyte stimulating hormone (NDP-α-MSH) or two low-affinity MSH(4) ligands. The linked peptides were synthesized by solid-phase methods. Control experiments indicate there is little or no effect of these linkers on NDP-α-MSH or MSH-(4) binding to the human melanocortin 4 receptor (hMC4R). Tethering two high-affinity ligands gave no binding enhancement, while tethering two low-affinity ligands resulted in binding enhancement that decreased with increased linker length. Furthermore, for the low-affinity ligands, the enhancement of affinity is inversely proportional to the estimated molecular moments of inertia. These results are consistent with a model wherein binding is enhanced when the rate of ligand reattachment to the receptor is fast relative to the rate of ligand diffusion.

INTRODUCTION

Early diagnosis is critical to the successful treatment of many human cancers. Noninvasive methods for early detection depend on the availability of nontoxic reagents that can seek out and selectively bind to cancer cells and report their existence and location by molecular imaging (*1*, *2*). We are engaged in a program to develop reagents that target human cancers that presently are difficult to detect, such as melanoma and pancreatic cancer. Our strategy involves linking together reporter moieties and ligands that bind to cell surface receptors that are expressed in cancer cells (*3*). The resulting multivalent molecules could display enhanced affinity for the targeted cells (*4*, *5*).

Factors that must be considered in designing linkers for bioactive multimeric ligands include the distance that must be spanned, availability, and ease of use. The distance that must be spanned between targeted receptors on the cell surface will vary depending on the number, kind, and mobility of the receptors, but it is expected to greatly exceed the typical dimensions of small molecules (*6*). Several small molecule linkers connected in series will therefore be necessary to span the distance between receptors. For peptide ligands, linkers should terminate in amine and/or carboxylic acid functional groups to facilitate incorporation by solid-phase peptide synthesis. Both flexible linkers (*7*, *8*) and rigid linkers (*9*) are of interest. Each new linker must be validated as noninterfering with the binding of the ligand. We report herein the use of rigid linkers **1**−**4** (Figure 1), which are of variable length (*10*) to join two "high-affinity" or two "low-affinity" α-melanocyte stimulating hormone (α-MSH) peptide ligands (*11*−*16*), and evaluations of the bioactivities of these linker-spliced peptides.

EXPERIMENTAL PROCEDURES

Materials and Methods. The *N*-9-fluorenylmethyloxycarbonyl (Fmoc) derivative **5** (Figure 1) was purchased from Torviq (Niles, MI). The *N*-trifluoroacetamide (TFA) derivatives **6**−**8** (Figure 1) were prepared as previously described (*17*). Other *N*-α-Fmoc-protected amino acids and Rink amide resin were purchased from SynPep (Dublin, CA) or from Novabiochem (San Diego, CA). *O*-[1*H*-6-Chlorobenzotriazol-1-yl)(dimethylamino)methylene]uranium hexafluorophosphate *N*-oxide (HCTU), 1-hydroxybenzotriazole (HOBt), and 6-chloro-1-hydroxybenzotriazole (HOCt) were purchased from IRIS Biotech (Marktredwitz, Germany). For the *N*-α-Fmoc-protected amino acids, the following side-chain protecting groups were used: Arg(N^{γ}-2,2,4,6,7-pentamethyldihydrobenzofuran-5-yl sulfonyl); Glu(O^{γ}-*t*Bu); His(N^{im}-triphenylmethyl); Lys(N^{ϵ}-*tert*-butyloxycarbonyl); Ser(*O*-*t*Bu); Trp(N^{i}-*tert*-butyloxycarbonyl). Peptide synthesis solvents, reagents, and acetonitrile for HPLC were reagent grade, were acquired from VWR (West Chester, PA) or Sigma-Aldrich (Milwaukee, WI), and were used without further purification unless otherwise noted. Solid-phase synthesis was performed in fritted syringes using a Domino manual synthesizer obtained from Torviq (Niles, MI).

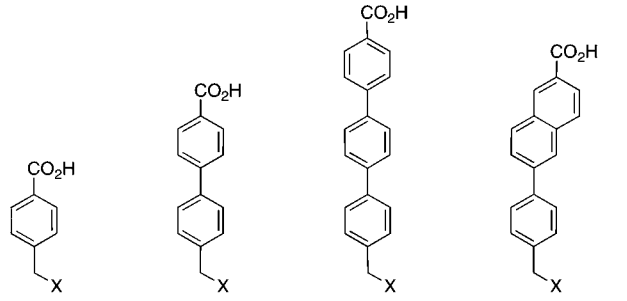

Figure 1. Rigid amino acid linkers **1**−**4** and *N*-protected derivatives **5**−**8**.

Purification of peptide products was achieved on a Waters 600 HPLC using a reverse-phase column (Vydac C-18, 15−20 m, 22 × 250 mm). Peptide products were eluted with a linear gradient of CH_3CN/0.1% CF_3CO_2H at a flow rate of 5.0 mL/min. Separation was monitored at 230 and 280 nm. The purity of the final peptide products was checked by TLC and by analytical PR-HPLC using a Waters Alliance 2695 separation

* Address correspondence to Prof. Robert J. Gillies, Department of Biochemistry and Molecular Biophysics, Arizona Cancer Center, P. O. Box 245024, Tucson, Arizona 85724-5024. Email gillies@email.arizona.edu; phone (520) 626-5050; FAX (520) 626-5051.

[†] University of Arizona.

[‡] Arizona Cancer Center.

10.1021/bc060154p CCC: $33.50 © 2006 American Chemical Society
Published on Web 09/28/2006

Scheme 1. Solid-phase Synthesis of Compounds 9−11 Containing Linked NDP-α-MSH Ligands and Control Compounds 12−14.

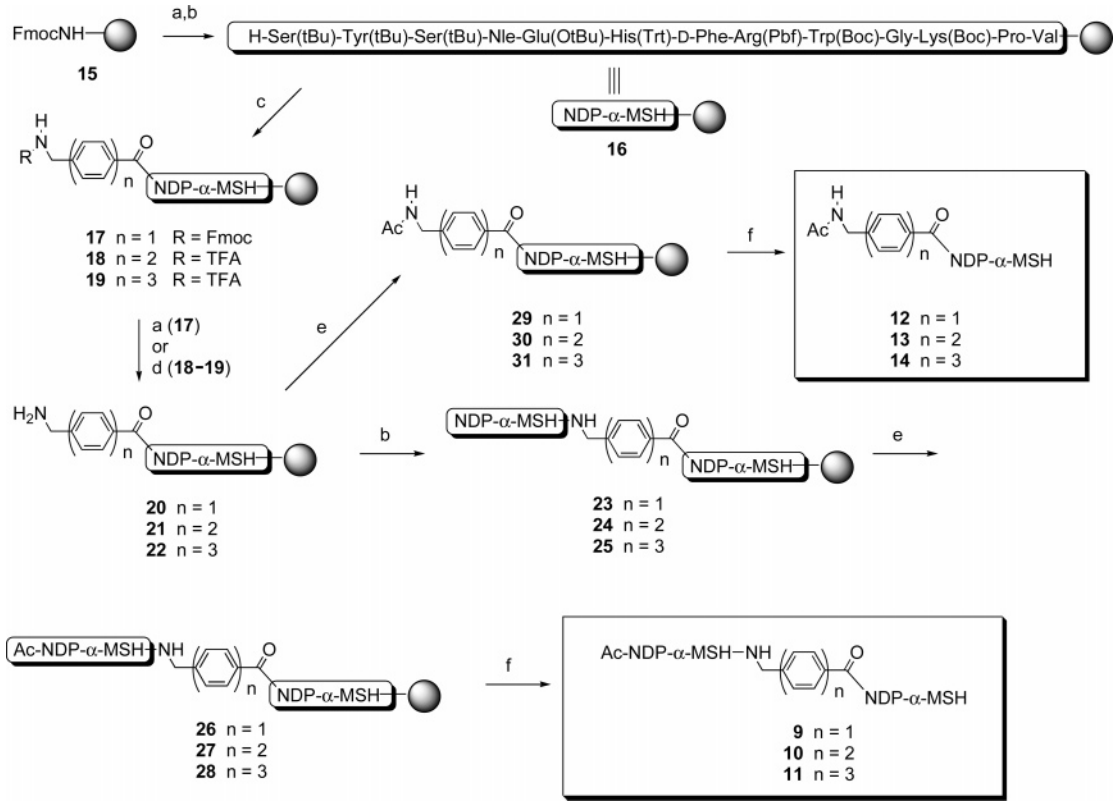

Reagents and conditions: (a) piperidine. (b) Fmoc/*t*Bu solid-phase synthesis (Refs 18 and 19). (c) *N*-protected linker (**5**, **6**, or **7**), HOCt-DIC, DMF. (d) THF/MeOH/N_2H_4 (70/15/15). (e) pyridine/Ac_2O (50/50). (f) CF_3CO_2H/$HSCH_2CH_2SH$/PhSMe/H_2O (91/3/3/3).

model with a Waters 2487 dual wavelength detector (220 and 280 nm) on a reverse-phase column (Waters Symmetry 4.6 × 75 mm, 3.5 μm). Peptide products were eluted with a linear gradient of 60% aqueous MeCN/0.1 M NH_4OAc or MeCN/0.1% CF_3CO_2H at a flow rate of 1.0 mL/min. Size exclusion chromatography was performed on a borosilicate glass column (2.6 × 250 mm, Sigma, St. Louis, MO) filled with medium-sized Sephadex G-25 or G-10. The compounds were eluted with an isocratic flow of 1.0 M aqueous AcOH.

Structures were characterized by ESI (Finnigan, Thermoquest LCQ ion trap instrument) or MALDI-TOF (Bruker Rexlex-III, α-cyanocinnamic acid as a matrix). For internal calibration, an appropriate mixture of standard peptides was used with an average resolution of 8000−9000.

Solid-Phase Synthesis (*18*−*19*)**.** Rink resin was washed with DMF, and the *N*-Fmoc protecting group was removed with 50% piperidine in DMF (1 × 2 min and 1 × 20 min). The resin was washed successively with DMF, 1.0 M HOBt in DMF, and DMF, and the next *N*-α-Fmoc amino acid was coupled using preactivated 0.3 M HOCt ester in THF (3 equiv of *N*-α-Fmoc amino acid, 3 equiv of HOCt, and 3 equiv of DIC). The resin slurry was stirred for 2 h or until the bromophenol test became negative. If the test failed, the resin was washed with DMF, and the amino acid was coupled again by the HCTU/2,4,6-lutidine procedure (0.3 M solution of 3 equiv of *N*-α-Fmoc amino acid, 3 equiv of HCTU, and 6 equiv of 2,4,6-lutidine in DMF) for 3 h or until the Kaiser test was negative. If a positive Kaiser test was observed after the second coupling, the resin was washed with DMF and any reactive amine groups capped by treatment with 50% Ac_2O in pyridine for 10 min.

After the first peptide segment had been assembled on the solid support (e.g., see Scheme 1), an N-protected linker (**5**, **6**, **7**, or **8**) was attached to the free N-terminal amine using the coupling methods previously described. The resin was then split into two portions. The first portion of the resin was treated either with 50% piperidine in DMF to remove the Fmoc protecting group or with 15% anhydrous N_2H_4 plus 15% MeOH in THF at room temperature for 6 h to remove the trifluoroacetyl protecting group, from the N-terminus of the resin-bound linker. The conditions for TFA cleavage were defined by an empirical study (see Table 1 and the accompanying discussion). The free amine was acetylated using 50% Ac_2O in pyridine for 10 min and the [peptide + linker] cleaved off the resin. A cleavage cocktail (10 mL per 1 g of the resin) consisting of CF_3CO_2H (91%), H_2O (3%), $HSCH_2CH_2SH$ (3%), and PhSMe (3%) was injected into the resin, and the mixture was stirred at room temperature for 3 h. The solution was filtered off, the resin was washed with CF_3CO_2H (2 × 3 min), the liquid phases were concentrated under a stream of nitrogen, and the product was precipitated using cold Et_2O. The peptide pellets were washed three times with cold Et_2O, lyophilized, purified, and characterized as described above. For the second portion of the resin, removal of the N-terminal Fmoc or TFA was carried out, and assembly of the second peptide segment was completed using the methods previously described. Following incorporation of the last amino acid, the N-terminal protecting group was removed and the free amine acetylated using 50% Ac_2O in pyridine for 10 min. The resin was then thoroughly washed with DMF and CH_2Cl_2, the [peptide + linker + peptide] was cleaved off the resin using the cleavage cocktail, and the product purified as described above. Mass spectral and HPLC characterization data for the peptide products are given in Table 2 and are discussed later.

Biological Assays. Ligand binding was evaluated using a previously described lanthanide-based binding assay (*20*). HEK293 cells overexpressing the human melanocortin 4 receptor (hMC4R) were used to assess ligand binding (*21*). The coding region of the hMC4R gene was expressed in pcDNA3.1 (Invitrogen, Carlsbad, California). HEK293/hMC4R cells were grown in Dulbecco's Modified Eagle Medium (DMEM) supple-

Table 1. Optimization of *N*-TFA Cleavage Using Resin 34[a]

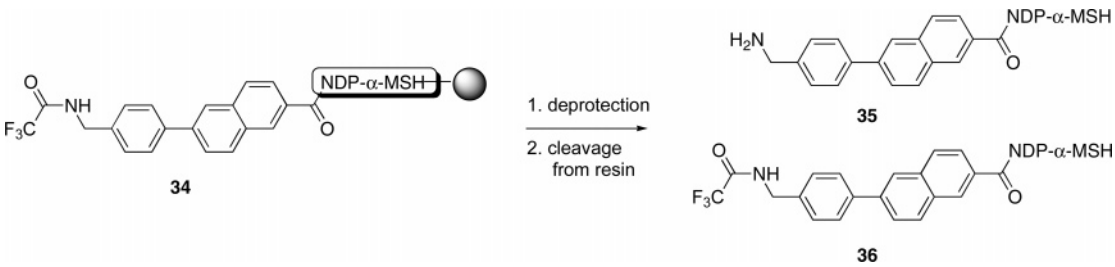

entry	conditions	time (min)	yields (%)[b] 35	36	impurity[c]
1	10% piperidine, 10% H_2O in DMF	30	0	100	0
2	0.6 M potassium silanolate in THF	30	0	100	0
3	15% N_2H_4 in DMF	75	9	91	0
4	15% N_2H_4 in DMF	180	34	64	2
5	15% N_2H_4, 15% MeOH in THF	300	100	0	0
6	15% N_2H_4, 15% MeOH in THF	180	99	>1	0
7	15% N_2H_4, 15% MeOH in THF	75	78	22	0
8	15% N_2H_4, 15% MeOH in THF	10	15	85	0
9	3% N_2H_4, 15% MeOH in THF	75	3	97	0
10	15% 0.5 M LiOH, 15% MeOH in THF	180	49	0	51
11	15% 0.5 M CsOH, 15% MeOH in THF	180	40	0	60

[a] NDP-α-MSH Rink resin **34** (30 μL of resin slurry in THF) was placed into a small fritted 2 mL syringe and washed with an *N*-TFA cleavage solvent mixture. After the treatment, the resin was washed with THF and CH_2Cl_2, and the peptide was cleaved off the resin and side-chain protecting groups removed as described in the Materials and Methods section. The peptide was then dissolved in 30% aqueous MeCN and analyzed by HPLC using a linear MeCN/0.1% CF_3CO_2H aqueous gradient (10% to 40% in 30 min) at a flow rate of 1.0 mL/min. [b] Yields were determined as ratios of peak areas at 280 nm on HPLC analyses; product **35** had a retention time of 16.1 min, and product **36** had a retention time of 24.2 min. [c] Unidentified impurities.

Table 2. Analytical Data for Synthetic Compounds

Ac-NDP-α-MSH-linker-NDP-α-MSH-NH_2					Ac-linker-NDP-α-MSH-NH_2				
	mass spectrum[a]			HPLC[b]		mass spectrum[a]			HPLC[b]
compd	ion	calcd	obsd	k'	compd	ion	calcd	obsd	k'
9	$(M+3)^{3+}$	1122.896	1122.90	18.13	**12**	$(M+2)^{2+}$	890.4446	890.40	15.11
10	$(M+2)^{2+}$	1721.860	1721.81	20.24	**13**	$(M+2)^{2+}$	995.4462	995.40	22.69
11	$(M+3)^{3+}$	1173.592	1173.50	22.43	**14**	$(M+2)^{2+}$	993.4618	993.91	27.11
32	$(M+4)^{4+}$	873.9417	873.94	21.35	**33**	$(M+3)^{3+}$	653.9693	653.98	25.25
Ac-MSH(4)-linker-MSH(4)-NH_2					Ac-linker-MSH(4)-NH_2				
	mass spectrum[a]			HPLC[b]		mass spectrum[a]			HPLC[b]
compd	ion	calcd	obsd	k'	compd	ion	calcd	obsd	k'
37	$(M+1)^{1+}$	1445.705	1445.911	9.16	**41**	$(M+1)^{1+}$	819.3976	819.40	7.05
38	$(M+1)^{1+}$	1521.737	1522.176	10.77	**42**	$(M+1)^{1+}$	895.4289	895.41	9.65
39	$(M+1)^{1+}$	1597.768	1597.910	13.00	**43**	$(M+1)^{1+}$	971.4603	971.65	13.13
40	$(M+1)^{1+}$	1571.752	1571.833	12.03	**44**	$(M+1)^{1+}$	945.4445	945.48	11.66

[a] MS found molecular peaks $(M+1)^{1+}$, $(M+2)^{2+}$, $(M+3)^{3+}$, and $(M+4)^{4+}$. One diagnostic peak is listed here for each compound. [b] Peptides were eluted with a linear MeCN/0.1% CF_3CO_2H aqueous gradient (10% to 40% in 30 min) at a flow rate of 1.0 mL/min.

mented with 10% fetal bovine serum (FBS). Cells were plated in Black & White Isoplates (Wallac, 1450−583) at a density of 12 000 cells/well and were allowed to grow for 3 days. On the day of the experiment, media was aspirated from all wells. Ligands of interest were diluted in binding buffer [DMEM, 1 mM 1,10-phenanthroline, 200 mg/L bacitracin, 0.5 mg/L leupeptin, 0.3% bovine serum albumin (BSA)] to result in final dilutions ranging from 10 μM to 4 pM. Eu-labeled NDP-α-MSH was used at a final concentration of 10 nM. 50 μL of the ligand of interest and 50 μL of Eu-NDP-α-MSH were added to each well, and plates were incubated for 40 min at 37 °C. Following the incubation, cells were washed four times with Wash Buffer (50 mM Tris-HCl, 0.2% BSA, 30 mM NaCl) using Molecular Devices SkanWasher. Enhancement solution (Perkin-Elmer, 1244−105) was added (100 μL/well), and the plates were incubated for 30 min at 37 °C prior to reading. The plates were read on a Wallac VICTOR[3] instrument using the standard Eu time-resolved fluorescence (TRF) measurement (340 nm excitation, 400 μs delay, and emission collection for 400 μs at 615 nm). Competition curves were analyzed with GraphPad *Prism* software using the sigmoidal dose−response classical equation for nonlinear regression analysis. Each data point represents the average of at least four samples, with the error bars indicating standard error of the mean.

RESULTS

Solid-Phase Synthesis. The synthesis of compounds **9**−**11** consisting of two linked "high-affinity" NDP-α-MSH ligands connected in a head-to-tail fashion by linkers **1**−**3** is depicted in Scheme 1. Also depicted is the synthesis of control compounds **12**−**14** which are composed of a single "high-affinity" NDP-α-MSH ligand and an N-terminally acylated linker.

The tridecapeptide NDP-α-MSH was constructed on PS−Rink resin (**15**, initial loading 0.17 mmol/g, 1% DVB). Resin

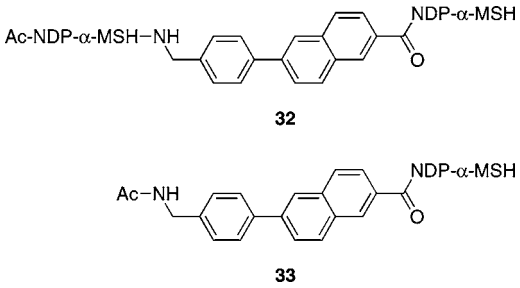

Figure 2. Dimeric and monomeric NDP-α-MSH compounds **32** and **33**.

16 retained all side-chain protecting groups. The N-protected linkers **5**−**7** were coupled to the N-terminus of **16**, giving resins **17**−**19**. The *N*-Fmoc group of **17** was cleaved by treatment with piperidine, and the *N*-TFA groups of **18** and **19** were cleaved by treatment with 15% hydrazine and 15% methanol in THF. The resulting resins **20**−**22** were each split into two portions. For the synthesis of **9**−**11**, the free amine groups of resins **20**−**22** were coupled with Fmoc−valine and solid-phase peptide synthesis continued to completion of the second NDP-α-MSH sequence, giving resins **23**−**25**. The peptide was then capped by N-acetylation, giving resins **26**−**28**. Simultaneous side-chain deprotection and cleavage of the peptides from the Rink resin was effected using a mixture of trifluoroacetic acid, 1,2-ethanedithiol, thioanisole, and water (91/3/3/3) that produced the desired compounds **9**−**11**. For the synthesis of **12**−**14**, resins **20**−**22** were terminally N-acetylated to give resins **29**−**31**. Treatment of these resins with the $CF_3CO_2H/HSCH_2CH_2SH/PhSMe/H_2O$ cocktail effected simultaneous side-chain deprotection and cleavage of the peptides from the resin, producing compounds **12**−**14**. Compounds **32** and **33** (Figure 2) that incorporate the phenylnaphthyl linker **4** were similarly prepared (see Scheme S1 in the Supporting Information).

N-TFA derivatives **6**−**8** were employed instead of the corresponding Fmoc derivatives of **2**−**4**, since this enhanced the solubility of these more hydrophobic linkers under the conditions employed for solid-phase synthesis.

The intermediate resin **34** was used to establish conditions for the cleavage of the TFA protecting group from resin-bound linkers (Table 1). Published conditions (*22*) for *N*-ϵ-trifluoroacetyl group deprotection in peptides (aqueous piperidine) gave poor results (Table 1, entry 1). DMF suppressed the cleavage of the *N*-ϵ-trifluoroacetyl group (entries 1, 3, and 4). Optimal conditions developed for the removal of the TFA protecting group from the resin-bound linker were treatment with 15% N_2H_4 and 15% MeOH in THF for 5 h at room temperature (entry 5).

A similar synthetic strategy was employed to synthesize molecules **37**−**40** containing linked "low-affinity" MSH(4) ligands (His-D-Phe-Arg-Trp; see Schemes S2 and S3 in the Supporting Information) and the corresponding controls **41**−**44** (Figure 3).

All products from solid-phase syntheses were purified by reverse-phase C_{18} preparative HPLC and were characterized by analytical HPLC, ESI-MS, and/or MALDI-TOF. Characterization data are listed in Table 2.

Biological Assays. Shown in Figure 4 are representative results from a competition binding assay, described in Handl et al. (*20*) This figure shows the reduction of Eu-NDP-α-MSH binding in the presence of increasing concentrations of compounds **10** and **13**. From these data, IC_{50} values were calculated as the concentration of test ligand that reduced Eu-NDP-α-MSH binding by 50%. These values can be quantitatively related to K_d by correcting for the ratio of the Eu-NDP-α-MSH concentration relative to its K_d (*11*). Similar data sets were obtained multiple times for all compounds. Table 3 lists the IC_{50} values (averaged over *n* experiments) for the dimeric and monomeric complexes of NDP-α-MSH and MSH(4). Compounds **9**−**11** and **32** contained dimeric NDP-α-MSH ligands, compounds **37**−**40** contained dimeric MSH(4) ligands, and compounds **12**−**14**, **33**, and **41**−**44** were the corresponding monomeric ligand controls. This table also shows the fold increase in avidity as the ratio of IC_{50} for the dimeric ligands relative to the corresponding monomeric ligands.

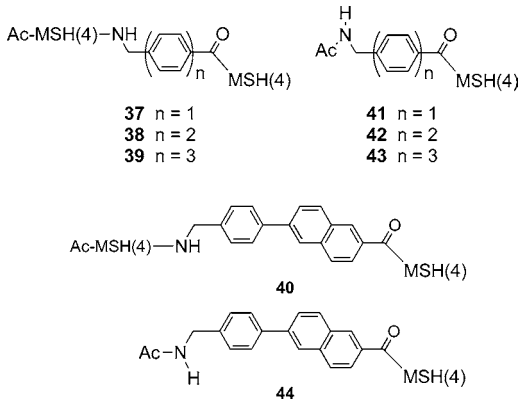

Figure 3. Dimeric and monomeric MSH(4) compounds **37**−**44**.

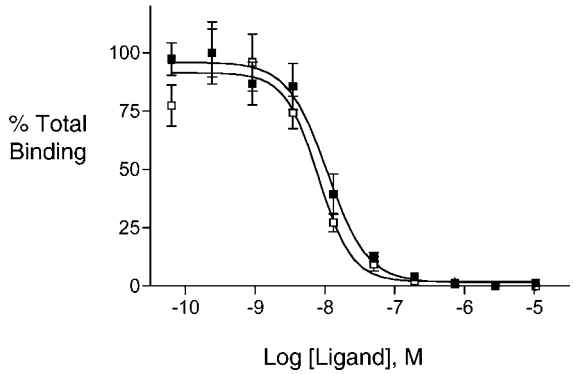

Figure 4. Representative ligand binding curves generated through competitive ligand binding analysis compare the binding affinities of ligands **10** (□) and **13** (■). The calculated IC_{50} for **10** is 8 nM with an R^2 value = 0.91 and for **13** 10 nM with an R^2 value = 0.93.

Table 3. Competitive Binding of Linked NDP-α-MSH and MSH(4) Ligands to hMC4R

compound	monomer/ dimer	linker[a]	IC_{50}	*n*[b]	fold increase
NDP-α-MSH		none	5.6 ± 0.2 nM	3	
9	D	Ph	3.5 ± 2.2 nM	4	1.4
12	M	Ph	5.0 ± 1.2 nM	4	
10	D	BP	5.6 ± 3.5 nM	5	0.9
13	M	BP	5.2 ± 5.2 nM	5	
11	D	TP	8.4 ± 2.9 nM	5	2.0
14	M	TP	16.5 ± 14.7 nM	5	
32	D	PN	3.7 ± 0.9 nM	5	1.1
33	M	PN	3.9 ± 1.2 nM	4	
MSH(4)		none	2.1 ± 0.8 μM	3	
37	D	Ph	0.1 ± 0.05 μM	4	22.9
41	M	Ph	1.8 ± 0.2 μM	4	
38	D	BP	0.6 ± 0.2 μM	4	4.8
42	M	BP	2.8 ± 1.1 μM	4	
39	D	TP	2.6 ± 1.0 μM	4	1.9
43	M	TP	5.0 ± 3.6 μM	5	
40	D	PN	0.5 ± 0.2 μM	4	3.2
44	M	PN	1.5 ± 0.7 μM	4	

[a] Ph = phenyl linker **1**; BP = biphenyl linker **2**; TP = terphenyl linker **3**; and PN = phenylnaphthyl linker **4**. [b] The IC_{50} value given is the average of *n* independent binding experiments, each done in quadruplicate.

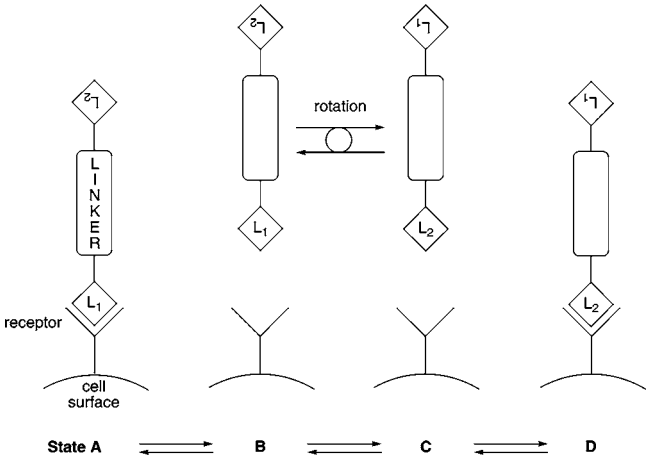

Figure 5. Binding of Linked MSH Ligands to hMC4R. **State A**: L_1 is bound, L_2 is unavailable for binding. **State B**: $L_1$and L_2 are unbound, L_1 is positioned for binding. **State C**: $L_1$and L_2 are unbound, L_2 is positioned for binding. **State D**: L_2 is bound, L_1 is unavailable for binding. **State E**: Compound is dissociated from cell surface (not shown).

DISCUSSION

The IC_{50} values for the [linker + NDP-α-MSH] control compounds **12**, **13**, and **33** were virtually the same as the IC_{50} for the parental NDP-α-MSH ligand. Similarly, the IC_{50} values for the [linker + MSH(4)] control compounds **41**, **42**, and **44** were very close to the IC_{50} for the parental MSH(4) ligand. These results indicate that attachment of the phenyl, biphenyl, and phenylnaphthyl linkers to the NDP-α-MSH and MSH(4) ligands had little or no effect on the binding of either ligand to hMC4R. In contrast, control compounds **14** and **43** that incorporate the terphenyl linker showed modest (3-fold and 2-fold, respectively) increases in IC_{50}. These results indicate that attachment of the terphenyl linker diminishes slightly NDP-α-MSH and MSH(4) ligand binding affinity to hMC4R.

The expected statistical halving of the IC_{50} for compounds that contain two ligands was observed only for terphenyl-containing NDP-α-MSH compounds **11** and **14** and for MSH-(4) compounds **39** and **43**. This is consistent with the observation that terphenyl-containing compounds bind less well to hMC4R. Tight binding in the cases of **9**, **10**, and **33**, presumably due to slow off-rates for the NDP-α-MSH ligand, effectively removes tethered, unbound ligands from the ligand pool (Figure 5), implying that states B, C, and D are insignificant. Poorer binding of the terphenyl-containing compounds **11** and **14** permits observance of statistical halving of the IC_{50} for these compounds (Figure 5), implying that states B, C, and D are significant.

A greater than stoichiometric increase in affinity for the hMC4R is observed relative to controls for compounds **37**, **38**, and **40** that contain two of the more weakly binding MSH(4) ligands joined by noninterfering linkers. This increase in affinity is inversely correlated (Figure 6) with an estimation of the molecular moments of inertia (I_M) calculated using eq 1 where *M* is the compound molecular weight and *R* is the linker length measured from one benzylic carbon to the other.

$$I_M = MR^2/2 \quad (1)$$

Compound **39** that incorporates the terphenyl linker is displaced from the best-fit line, possibly due to its inherently poorer binding to hMC4R. The existence of this correlation is consistent with a competition between diffusion of the compound away from the receptor (to give state E in Figure 5) and rotation of the compound necessary for presentation of the second ligand to the receptor (equilibration of states B and C).

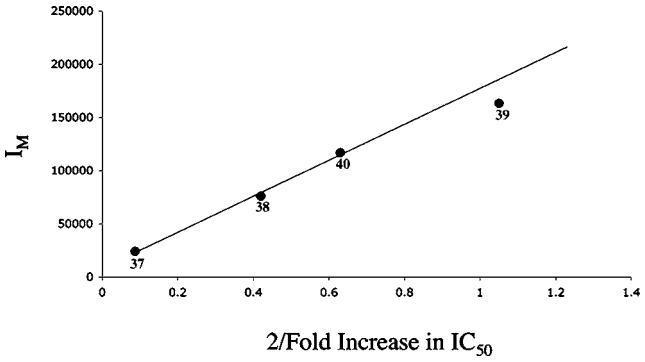

Figure 6. Inverse correlation of compound binding affinity and linker length.

The greater the moment of inertia, the longer this rotation will take, leading to an increased probability of diffusion away from the cell surface before rebinding (to states A and D) can occur.

CONCLUSION

Low- and high-affinity forms of melanocortin ligands were attached to rigid linkers in either monomeric or dimeric forms. Binding affinities of these ligands were tested in whole cells expressing the hMC4 receptor using a sensitive competition assay based on detection of lanthanide (europium) with time-resolved fluorescence. Consistent with previous results, addition of linkers resulted in a reduction in binding affinity that was dependent on the size of the linker. Notably, the short phenyl and biphenyl linkers did not adversely affect binding affinities of monomeric ligands. Also consistent with previous results, there was an increase in binding affinity in dimers compared to the corresponding monomers, and the increase was inversely related to the calculated moment of inertia for the molecules. We interpret these results to indicate that the increased affinity of dimers was due to increased local concentrations of ligand, also known as the statistical effect of Kiessling (*5*). Somewhat surprisingly, this enhancement of dimers was only observed for the low-affinity MSH(4) ligands and not for the high-affinity NDP-α-MSH ligands. We interpret this to suggest that the statistical effect enhancement is critically dependent on a low-affinity ligand, with potentially faster on-rates relative to the rate of diffusion.

ACKNOWLEDGMENT

This work was supported by NIH grants R33 CA 95944 and RO1 CA 97360.

Supporting Information Available: Additional synthetic schemes and details of the solid-phase synthesis and compound characterization. This material is available free of charge via the Internet at http://pubs.acs.org/BC.

LITERATURE CITED

(1) Gillies, R. J., Hoffman, J. M., Lam, K. S., Menkens, A. E., Piwnica-Worms, D. R., Sullivan, D. C., and Weissleder, R. (2005) Meeting Report: High-Throughput Technologies for In Vivo Imaging Agents *Molecular Imaging 4*, 98−103.

(2) Gillies, R. J., and Hruby, V. J. (2003) Expression-driven Reverse Engineering of Targeted Imaging and Therapeutic Agents. *Expert Opin. Ther. Targets 7*, 137−139.

(3) Handl, H. L., Vagner, J., Han, H., Mash, E., Hruby, V. J., and Gillies, R. J. (2004) Hitting Multiple Targets with Multimeric Ligands. *Expert Opin. Ther. Targets 8*, 565-586.

(4) Mammen, M., Chio, S.-K., and Whitesides, G. M. (1998) Polyvalent Interactions in Biological Systems: Implications for Design and Use of Multivalent Ligands and Inhibitors. *Angew. Chem. Int. Ed. 37*, 2754−2794.

(5) Kiessling, L. L., Gestwicki, J. E., and Strong, L. E. (2000) Synthetic Multivalent Ligands in the Exploration of Cell-surface Interactions. *Curr. Opin. Chem. Biol. 4*, 696−703.

(6) Small molecule dimensions are on the order of ten Angstroms, while the distance between receptors is on the order of tens to hundreds of Angstroms; see Tron, L.; Szollosi, J., Szabo, G., Jr., Matyus, L., and Damjanovich, S. (1984) Cell Surface Dynamics and Distance Relationship of Integral Membrane Proteins. *Symposia Biologica Hungarica. 26*, 307−328.

(7) Vagner, J., Handl, H. L., Gillies, R. J., and Hruby, V. J. (2004) Novel Targeting Strategy Based on Multimeric Ligands for Drug Delivery and Molecular Imaging: Homooligomers of α-MSH. *Bioorg. Med. Chem. Lett. 14*, 211−215.

(8) Raju, N., Ranganathan, R. S., Tweedle, M. F., and Swenson, R. E. (2005) A New Dendrimer Scaffold for Preparing Dimers or Tetramers of Biologically Active Molecules. *Tetrahedron Lett. 46*, 1463−1465.

(9) Maison, W., Frangioni, J. V., and Pannier, N. (2004) Synthesis of Rigid Multivalent Scaffolds Based on Adamantane. *Org. Lett. 6*, 4567−4569.

(10) Distances between the benzylic carbon atoms: **1**, 5.8 Å; **2**, 10.0 Å; **3**, 14.3 Å; and **4**, 12.2 Å; determined using AM1 in Spartan '02 v1.0.4e.

(11) The "high-affinity" ligand employed here was based on NDP-α-MSH (Ser-Tyr-Ser-Nle-Glu-His-D-Phe-Arg-Trp-Gly-Lys-Pro-Val); see References 12 and 13. The "low-affinity" ligand employed was based on the minimal active sequence for full agonist activity of α-MSH (His-D-Phe-Arg-Trp); see References 14-16.

(12) Sawyer, T. K., Sanfilippo, P. J., Hruby, V. J., Engel, M. H., Heward, C. B., Burnett, J. B., and Hadley, M. E. (1980) 4-Norleucine, 7-D-phenylalanine-α-melanocyte-stimulating Hormone: A Highly Potent α-Melanotropin with Ultralong Biological Activity. *Proc. Natl. Acad. Sci. U.S.A. 77*, 5754−5758.

(13) Hadley, M. E., Anderson, B., Heward, C. B., Sawyer, T. K., and Hruby, V. J. (1981) Calcium-dependent Prolonged Effects on Melanophores of [4-Norleucine, 7-D-phenylalanine]-α-melanotropin. *Science 213*, 1025−1027.

(14) Hruby, V. J., Wilkes, B. C., Hadley, M. E., Al-Obeidi, F., Sawyer, T. K., Staples, D. J., DeVaux, A. E., Dym, O., Castrucci, A. M., Hintz, M. F., Riehm, J. P., and Rao, K. R. (1987) α-Melanotropin: the Minimal Active Sequence in the Frog Skin Bioassay. *J. Med. Chem. 30*, 2126−2130.

(15) de Lauro Castrucci, A. M., Hadley, M. E., Sawyer, T. K., Wilkes, B. C., Al-Obiedi, F., Staples, D. J., DeVaux, A. E., Dym, O., Hintz, M. F., Riehm, J. P., Rao, K. R., and Hruby, V. J. (1989) Alpha-melanotropin: the Minimal Active Sequence in the Lizard Skin Bioassay. *Gen. Comp. Endocrinol. 73*, 157−163.

(16) Haskell-Luevano, C., Hendrata, S., North, C., Sawyer, T. K., Hadley, M. E., Hruby, V. J., Dickinson, C., and Gantz, I. (1997) Discovery of Prototype Peptidomimetic Agonists at the Human Melanocortin Receptors MC1R and MC4R. *J. Med. Chem. 40*, 2133−2139.

(17) Monguchi, Y., Vagner, J., Handl, H. L., Jana, U., Begay, L. J., Hruby, V. J., Gillies, R. J., and Mash, E. A. (2005) Design, Synthesis, and Validation of Rigid Linkers for Bioactive Peptides. *Tetrahedron Lett. 46*, 7589−7592.

(18) Merrifield, R. B. (1963) Solid Phase Peptide Synthesis. I. The Synthesis of a Tetrapeptide. *J. Am. Chem. Soc. 85*, 2149−2154.

(19) Hruby, V. J., and Meyer, J. -P. (1998) Chemical Synthesis of Peptides. In "Bioorg. Chem.: Peptides and Proteins"; Hecht, S. M., Ed.; Oxford Univ. Press: New York, 1998; pp. 27−64.

(20) Handl, H. L., Vagner, J., Yamamura, H. I., Hruby, V. J., and Gillies, R. J. (2004) Lanthanide-based time-resolved fluorescence of in cyto ligand-receptor interactions. *Anal. Biochem. 330*, 242−250.

(21) The hMC4R vector was originally received from Dr. Ira Gantz; see Gantz, I., Miwa, H., Konda, Y., Shimoto, Y., Tashiro, T., Watson, S. J., DelValle, J., and Yamada, T. (1993) Molecular Cloning, Expression, and Gene Localization of a Fourth Melanocortin Receptor. *J. Biol. Chem. 268*, 15174−15179.

(22) Goldberger, R. F., and Anfinsen, C. B. (1962) The Reversible Masking of Amino Groups in Ribonuclease and Its Possible Usefulness in the Synthesis of the Protein. *Biochemistry 1*, 401−405.

BC060154P

Influence of the Linker on the Biodistribution and Catabolism of Actinium-225 Self-Immolative Tumor-Targeted Isotope Generators

Christophe Antczak, Jaspreet S. Jaggi, Clare V. LeFave, Michael J. Curcio, Michael R. McDevitt, and David A. Scheinberg*

Department of Molecular Pharmacology and Chemistry, Memorial Sloan Kettering Cancer Center, New York, New York 10021. Received June 7, 2006; Revised Manuscript Received August 24, 2006

Current limitations to applications of monoclonal antibody (mAb) targeted isotope generators in radioimmunotherapy include the low mAb labeling yields and the nonspecific radiation of normal tissues by nontargeted radioimmunoconjugates (RIC). Radiotoxicity occurs in normal organs that metabolize radiolabeled proteins and peptides, primarily liver and kidneys, or in radiosensitive organs with prolonged exposure to the isotope from the blood, such as the bone marrow. Actinium-225 nanogenerators also have the problem of released α-emitting daughters. We developed two new bifunctional chelating agents (BCA) in order to address these issues. Thiol−maleimide conjugation chemistry was employed to increase the efficiency of the mAb radiolabelings by up to 8-fold. In addition, one bifunctional chelating agent incorporated a cleavable linker to alter the catabolism of the α-particle-emitting mAb conjugate. This linker was designed to be sensitive to cathepsins to allow release and clearance of the chelated radiometal after internalization of the radioimmunoconjugate into the cell. We compared the properties of the cleavable conjugate (mAb−DOTA−G3FC) to noncleavable constructs (mAb−DOTA−NCS and mAb−DOTA−SH). The cleavable RIC was able to release 80% of its radioactive payload when incubated with purified cathepsin B. The catabolism of the constructs mAb−DOTA−G3FC and mAb−DOTA−NCS was investigated in vitro and in vivo. RIC integrity was retained at 85% over a period of 136 h in mouse serum in vivo. Both conjugates were degraded over time inside HL-60 cells after internalization and in mouse liver in vivo. While we found that the rates of degradation of the two RICs in those conditions were similar, the amounts of the radiolabeled product residues were different. The cleavable mAb−DOTA−G3FC conjugate yielded a larger proportion of fragments below 6kDa in size in mouse liver in vivo after 12 h than the DOTA−NCS conjugate. Biodistribution studies in mice showed that the mAb−DOTA−G3FC construct yielded a higher liver dose and prolonged liver retention of radioactivity compared to the mAb−DOTA−NCS conjugate. The accumulation in the liver seemed to be in part caused by the maleimide functionalization of the antibody, since the noncleavable mAb−DOTA−SH maleimide-functionalized control conjugate displayed the same biodistribution pattern. These results provide an insight into the catabolism of RICs, by demonstrating that the release of the radioisotope from a RIC is not a sufficient condition to allow the radioactive moiety to clear from the body. The excretion mechanisms of radiolabeled fragments seem to constitute a major limiting step in the chain of events leading to their clearance.

INTRODUCTION

In hematopoietic malignancies, the accessibility of tumor cells in the blood, marrow, spleen, and lymph nodes enables rapid targeting of specific antibodies. Several antigens have been identified that allow selective targeting of neoplastic hematopoietic cells while sparing other necessary hematopoietic lineage and progenitor cells. One of the most suitable targets for myeloid leukemias is CD33, an antigen whose expression is restricted to myelogenous leukemias and myeloid progenitor cells. This marker is absent from other normal tissues or ultimate bone marrow stem cells (*1*−*4*). The antibody HuM195, humanized version of the antibody M195 directed against CD33, has been developed and characterized by our group (*5*). M195 showed targeting to leukemia cells in humans (*6*) with the majority of the bound IgG being internalized into target cells in vivo (*7*, *8*). On the basis of this biology and pharmacokinetics, it has been proposed that mAb tagged with short-lived nuclides emitting short-ranged, high linear energy transfer (LET) α particles may be effective in therapy (*9*). These short-ranged particles may be capable of single-cell kill while sparing bystanders. High LET α-emitters used in radioimmunotherapy include bismuth-212 (*10*−*12*) and -213 (*13*−*15*), astatine-211 (*16*), and actinium-225. This latter isotope is an in vivo isotope generator, in that it has a long (10 day) half-life and decays via α-emission through three short-lived atoms, each of which yields an α particle (*12*, *14*). Previous work in our laboratory led to the synthesis, purification, and analysis of ^{225}Ac stably bound to the IgG via a bifunctional macrocyclic chelator DOTA (1,4,-7,10-tetraazacyclodoecane-1,4,7,10-tetraacetic acid) (*15*). These constructs specifically killed leukemia and cancer cells at becquerel (picocurie) levels in vitro. Injection of rodents bearing disseminated human lymphoma or solid carcinoma with single courses of the constructs at kilobecquerel (nanocurie) levels induced tumor regression and prolonged survival in a substantial fraction of animals without toxicity (*15*, *17*, *18*).

A first limitation to the use of targeted ^{225}Ac isotope generators is the poor yield of labeled antibody (*19*). Chelation of Ac-225 stably under physiological conditions requires the use the macrocyclic chelator DOTA with all four carboxylic groups available (Antczak et al., unpublished data). However, heating to 60 °C is necessary for complete and stable ^{225}Ac chelation by DOTA, a condition that is unsuitable for retention of mAb function (*19*). Therefore, a two-step procedure was developed to label the antibodies (*19*). The first step consisted

* Corresponding author. D.A. Scheinberg, 1275 York Avenue, Box 531. Tel: 646-888-2190. Fax: 646-422-0296. E-mail: d-scheinberg@ski.mskcc.org.

10.1021/bc060156+ CCC: $33.50 © 2006 American Chemical Society
Published on Web 10/27/2006

Scheme 1. Bifunctional Chelating Agents

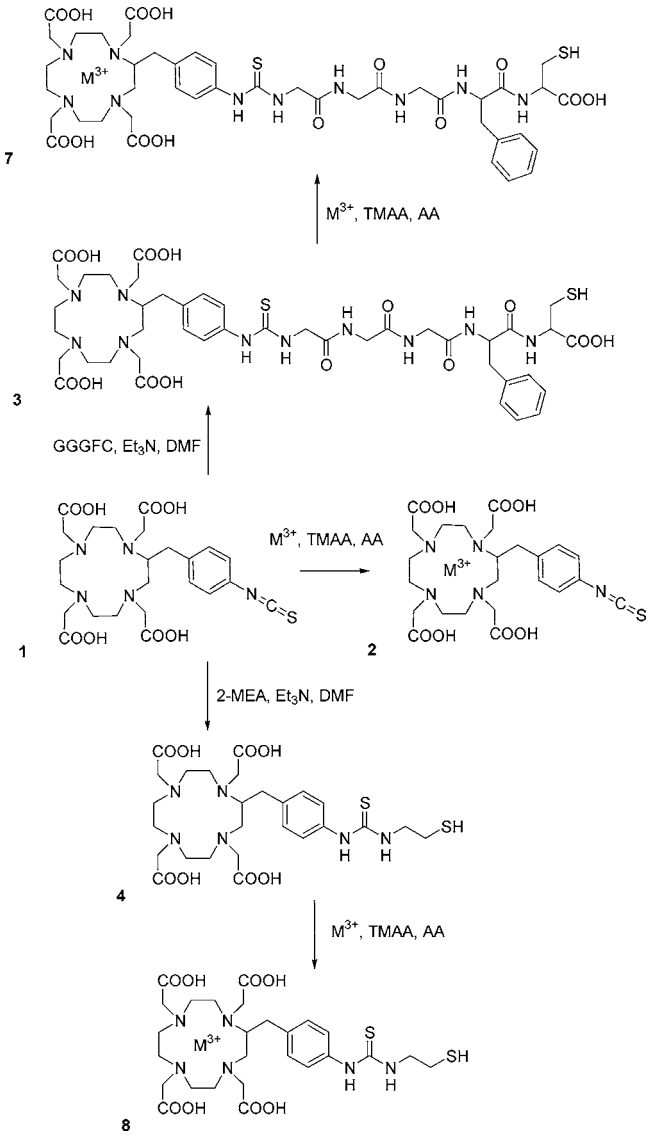

of the chelation of ^{225}Ac by the bifunctional chelating agent DOTA−NCS **1** (Scheme 1). A low-yield second step of the process was the reaction of the ^{225}Ac−DOTA−NCS **2** with the IgG. HPLC studies showed that the first step largely degrades the isothiocyanate moiety required for the labeling of the antibody in the second step, thus reducing product yields (data not shown). Therefore, we based our new BCAs on novel thiol-based BCAs following the assumption that thiol groups would be more stable than isothiocyanates during the first step of the labeling process.

Another limitation to a more general application of tumor-targeted ^{225}Ac nanogenerators is the excessive radiation of normal tissues by the RIC. With the exception of antibodies targeting leukemias, most (>99%) of the injected antibody dose remains circulating in the blood or is not associated with the target tumor. The prolonged circulation time of untargeted antibodies, typically days to weeks, results in radiation exposure of normal organs that catabolize or retain proteins and peptides, primarily liver and kidneys (*20*, *21*). In the case of in vivo generators, an additional major potential obstacle to their safe use is the sequential release of three unchelated α-emitting daughter atoms following initial decay of the generator. Uptake into organs such as the kidney or the liver could induce toxicity (*22*).

One attractive approach to overcome the long circulation time of untargeted radioimmunoconjugates is the development of BCAs that allow conditional release of the chelated radioactive payload. The introduction of a cleavage site in the linkage between the radiochelate and the mAb is meant to permit the release of a low molecular weight radiochelate from its carrier mAb and its subsequent rapid clearance once the radioconjugate has accumulated in metabolizing organs. The chelated radiometal then rapidly clears the body through the kidneys, thereby reducing toxicity. This strategy has been attempted using disulfide, ester, tartramide, and peptide bonds (*23*, *24*). An optimal linker should (1) link the carrier mAb to the radiochelator without impairing the functionality of either, (2) provide a stable linkage in circulation, and (3) degrade under specific conditions. Stability in circulation has proven to constitute a particularly important factor for success using this strategy. Perhaps for this reason, peptide linkers, which are usually more stable than esters and disulfides in serum, have been most successful in RICs and in the design of antibody−drug conjugates (ADC) (*25*, *26*). The most extensively studied peptide linkers are sensitive to cathepsins. More precisely, ADCs incorporating the dipeptide valine−citrulline have been shown to enter the target cells and migrate to the lysosomes, where they release their drug specifically under the action of cysteine proteases (*27*).

The most advanced strategy for the release of a radionuclide from a RIC is the one followed by DeNardo et al., based on cathepsin-sensitive peptide linkers. On the basis of the hypothesis that intrahepatocyte cathepsins are responsible for most of the protein metabolism in hepatic lysosomes, a BCA was designed to incorporate a specific cathepsin B cleavage site. Even though human tumors express cathepsin B (*28*), studies from DeNardo et al. have demonstrated that the dose achieved at the xenograft after treatment with four cathepsin B labile radioconjugates was comparable to that achieved with a noncleavable control. This remained true for two different antibodies and for two human maligancies (an adenocarcinoma and a lymphoma) (*29*). The cathepsin B-sensitive conjugate glycylglycylglycyl-L-*p*-isothiocyanatophenylalanine-Lym-1 demonstrated great stability in human serum. This cleavable construct was compared to a noncleavable construct in human breast cancer xenografts, and a 30−70% decrease in the liver dose and a slightly increased tumor dose was observed (*29*, *30*). In patients with prostate and breast cancer, the pharmacokinetics and tumor dose were similar for both cleavable and noncleavable RICs, except for about a 30% decrease in the mean dose to the liver with the cleavable linker (*31*). In another clinical study with patients with breast and prostate cancer, the liver dose was consistantly lower with the cleavable RIC compared to a noncleavable conjugate, while the tumor dose was not significantly affected by the linker (*32*). Therefore, we applied a cathepsin-sensitive linker strategy to the ^{225}Ac nanogenerators.

EXPERIMENTAL PROCEDURES

Radionuclides, Reagents, and Monoclonal Antibodies. The ^{225}Ac was obtained from Oak Ridge National Laboratory (Oak Ridge, TN) as a nitrate salt. The ^{225}Ac salt was dissolved in 0.15 M Optima grade HCl (Fisher Scientific, Pittsburgh, PA). Metal-free water (MFW) used for this and all other solutions was obtained from a Purelab Plus system (US Filter Corp., Lowell, MA) and was sterile filtered. The parent ^{225}Ac activity was measured when it was in secular equilibrium with its daughters using a drop well dose calibrator (CRC-17; E.R. Squibb and Sons, Inc., Princeton, NJ) set at 775 and the reading multiplied by 5.

The chelating agent DOTA−NCS **1**, 2-(*p*-isothiocyanatobenzyl)-1,4,7,10-tetraazacyclododecane-1,4,7,10-tetracetic acid, was obtained from Macrocyclics (Dallas, TX). The heterobifunctional linker LC-SMCC and 2-mercaptoethylamine (2-MEA)

were provided by Pierce (Rockford, IL). Chemicals used in the radiolabeling and purification steps were ACS reagent grade or better. Dithiothreitol (DTT), tetramethylammonium acetate (TMAA), L-ascorbic acid (AA), sodium carbonate (Na_2CO_3), dimethylformamide (DMF), triethylamine (Et_3N), trishydroxymethylaminomethane hydrochloride (Tris-HCl), Triton X-100, trifluoroacetic acid (TFA), acetonitrile (CH_3CN), and ethylenediamine tetraacetic acid (EDTA) were obtained from Sigma-Aldrich (Saint Louis, MO). Sulfur-35 radiolabeled cysteine was provided by Perkin-Elmer (Wellesley, MA). Bovine spleen cathepsin B (E.C. 3.4.22.1), was obtained from Sigma-Aldrich. The protease inhibitor cocktail was provided by Roche Diagnostics Gmbh (Mannheim, Germany). The cation exchange resin Sephadex C-25 was purchased from Amersham Biosciences (Piscataway, NJ). Human serum albumin (HSA) (Swiss Red Cross, Bern, Switzerland) and 0.9% NaCl (Abbott Laboratories, North Chicago, IL) were used as received. A 10DG desalting column (Bio-Rad, Hercules, CA) was used for RIC purification.

The cell line HL-60 was obtained from the ATCC (catalog #CCL-240) and was cultured following the ATCC recommendations. The humanized murine monoclonal antibody HuM195 directed against the cell surface myelomonocytic differentiation antigen CD33 was generously provided by Protein Design Laboratories (Sunny View, CA). The mouse monoclonal antibody SJ25C1 directed against the CD19 antigen present on human B lymphocytes was provided by the monoclonal antibody core facility of the Sloan-Kettering Institute.

HPLC. Reversed-phase HPLC was performed using a Beckman Coulter System Gold Bioessential HPLC, equipped for analytical studies with a Varian C18 Inertsil ODS-3 5 μ 250 $\times$ 4.6 mm column, and with a Varian C18 Inertsil ODS-3 5 μ 250 $\times$ 10 mm column for semipreparative runs. Detection of the peaks was performed using a Beckman Coulter 168 diode array detector at 220 nm. Data was analyzed using the system's 32 Karat software.

Synthesis of 3-Mercapto-2-(3-phenyl-2-{2-[2-(2-{3-[2-*p*-(1,4,7,10-tetraazacyclododecane-1,4,7,10-tetraacetic acid)-benzyl]thioureido}acetylamino)acetylamino]acetylamino}-propionylamino)propionic Acid (*3*). To a solution of peptide GGGFC (16.5 mg, 37.6 μmol) and Et_3N (22 μL, 219.1 μmol) in dry DMF, a solution of DOTA−NCS **1** (17.2 mg, 31.3 μmol) in dry DMF was slowly added. After 1 h reaction at room temperature, the product DOTA−G3FC **3** was purified by semipreparative reversed-phase HPLC. The mobile phases consisted of A, 0.1% (v/v) trifluoroacetic acid (TFA) in water, and B, 0.1% TFA in acetonitrile (CH_3CN). The reaction mixture was solubilized in mobile phase A and injected for a 30-min run at 5.0 mL/min at room temperature. The column was previously equilibrated in eluent A with 5% eluent B. The gradient was 5−20% B in 20 min, 20−90% B in 10 min. After lyophilization, the desired product **3** was isolated as a white powder (26.5 mg, 26.8 μmol, 86% yield) and stored under vacuum. Analytical HPLC using the same gradient gave a single peak. HRMS (ESI): *m*/*z* 496.1860 $[M + 2H]^{++}$; calcd for $C_{42}H_{58}N_{10}O_{14}S_2$ 990.3575; found 990.3563.

Synthesis of 2-*p*-(2-mercaptoethylthioureido)benzyl-(1,4,-7,10-tetraazacyclododecane-1,4,7,10-tetraacetic acid) (*4*). To a solution of 2-mercaptoethylamine (2-MEA) (1.3 mg, 11.5 μmol) and Et_3N (1.8 μL, 17.9 μmol) in dry DMF was slowly added a solution of DOTA−NCS **1** (4 mg, 7.3 μmol) in dry dimethylformamide (DMF). After 1 h reaction at room temperature, the product **4** was purified by semipreparative reversed-phase HPLC as previously described for compound **3**. After lyophilization, the desired compound **4** was isolated as a white powder (3.9 mg, 6.19 μmol, 85% yield) and stored under vacuum. Analytical HPLC using the same gradient gave a single peak. HRMS (ESI): *m*/*z* 629.2434 $[M + H]^{+}$; calcd for $C_{26}H_{40}N_6O_8S_2$ 628.2349; found 628.2356.

Functionalization and Characterization of Maleimide−Antibodies. The heterobifunctional linker LC-SMCC (0.375 mg, 833 nmol) was solubilized just prior to use in DMSO and added to 1 mL of the antibody solution in PBS (5 mg, 33.3 nmol). The pH was adjusted to 7.0 by adding a few microliters of a 200 mM Na_2CO_3 solution to the reaction mixture, and the reaction was carried out over 2 h at 24 °C. The modified antibody was purified by size-exlusion chromatogaphy (10-DG desalting column, Bio-Rad) in degassed PBS EDTA 5 mM, pH 6.4. Protein concentration was performed using Microcon YM-50 centrifugal filter devices (Millipore) in order to reach 3−5 mg/mL. The protein concentration was determined using the Bradford assay (Bio-Rad) before storage at −80 °C. The extent of maleimide functionalization was determined by trace-labeling with ^{35}S-labeled cysteine. The antibody solution in PBS EDTA 5 mM, pH 6.4 (100 μL, 0.3 mg, 2 nmol) was mixed with cysteine (0.07 mg, 400 nmol) containing trace amounts of ^{35}S-cysteine. The pH was adjusted to 7.0 by adding a few microliters of a 200 mM Na_2CO_3 solution, and after 30 min at room temperature, the protein was purified from the low molecular weight content by size-exclusion chromatography. After determination of the protein concentration, an aliquot was counted in a β scintillation counter (Beckman LS6000 IC), and by comparison with an aliquot of the ^{35}S-cysteine/cold cysteine solution, the total amount of cysteine bound to the protein was calculated. Using the protein concentration, the amount of maleimide residues per antibody was determined.

Preparation of Radioimmunoconjugates. The chelation of the radiometal during the first step to yield the chelates **2**, **7**, and **8** was performed as follows. All the reagent solutions were degassed by sonication under vacuum just prior to use. Depending on the scale of the subsequent conjugation reaction, a few microliters of $^{225}Ac(NO_{3)3}$ dissolved in 0.15 M HCl or $^{111}InCl_3$ at 0.1 mCi/mL were added to 50 μL of 2 M tetramethylammonium acetate (TMAA). To this solution was added 20 μL of 150 g/L ascorbic acid (AA) as a radioprotectant and 50−500 μL of the BCA solubilized at 1−10 mg/mL in freshly degassed metal-free water (MFW). If necessary, another 50 μL of the TMAA solution was added in order to reach pH 5.5. The pH was checked by testing an aliquot of the reaction mixture using pH test papers in the appropriate range (Micro Essential Laboratory, Inc., NY). The reaction mixture was incubated under argon at 60 °C over 30 min. The percentage of incorporation of the radiometal by the chelate was determined by loading 1−2 μL of the reaction mixture onto a 1 mL cation exchange resin (Sephadex C-25) equilibrated with 0.9% saline and eluting the column two times with 3 mL of saline. The eluate was collected, and the activity of the eluate and the column measured immediately for ^{111}In and when in equilibrium with its decay products in the case of ^{225}Ac. Chelated radiometals elute, whereas the free radiometals are retained on the column.

The second step of the labeling was achieved by adding 100 μL to 1 mL of the unmodified or maleimide-functionalized antibody in solution with 5 mM EDTA (3−5 mg/mL) to the reaction mixture. The pH was brought to 8.5 by adding a few microliters of a 200 mM Na_2CO_3 solution. The conjugation was allowed to proceed for 150 min at 37 °C. Purification of the conjugate was performed using a 10-DG desalting column using saline with 1% HSA as the mobile phase.

Characterization of the Radioimmunoconjugates. The radiochemical purity of the RICs was determined by instant TLC in triplicate (SG TLC plates; Gelman Sciences Inc., Ann Arbor, MI) using 10 mM EDTA as the mobile phase. The strips were analyzed immediately to detect ^{111}In or allowed to sit overnight before measuring ^{225}Ac. Analysis was performed using a gas

ionization detector (Ambis 4000; Ambis, San Diego, CA). The R_f of the radiolabeled antibody was 0, and both the free metal species and metal chelates were characterized by an R_f of 1.

The immunoreactivity of the purified RICs was determined by incubating the radiolabeled antibodies with AL67 (CD33-positive) or Daudi (CD33-negative) cells. First, cells were washed twice with ice-cold PBS and then blocked by incubation on ice with 2% rabbit serum. Then, 8 ng of the RICs of 1% HSA in PBS was added to 2.5×10^7 AL67 cells or 5×10^6 Daudi cells and incubated on ice for 30 min in a final volume of 20 μL. The cells were washed twice with ice-cold PBS, and the washes were saved and counted along with the cells after 20 h.

Radiometal Release by Cathepsin B and in Vitro Serum Stability. The cleavable RIC SJ25C1-DOTAG3FC **11** was used for these studies. Assay conditions were chosen to approximate the lysosomal medium. A stock solution of bovine spleen cathepsin B was prepared by dissolving the lyophilized solid at 15 U/mL in the cathepsin buffer, which consisted of 50 mM sodium acetate, 1 mM EDTA, pH 4.5. The enzyme was activated just prior use by incubation at 37 °C with 50 mM DTT for 30 min. The assay was performed at 37 °C using 25 μg conjugate, and the final enzyme concentration was 1.5 U/mL in a total volume of 150 μL. The control cathepsin buffer experiment was run in exactly the same conditions except no enzyme was added. The serum stability experiment was conducted at 37 °C with fresh human or mouse (Balb/c) serum prepared in the laboratory. The final serum concentration was 64% in saline, pH 7.6. The radiometal release was assessed by TLC. Preliminary studies using sodium hydroxide as the mobile phase allowed us to determine that the radiometal was released in a chelated form ($R_f = 1$). Kinetic studies were later performed by TLC using 10 mM EDTA as the mobile phase. The protein-bound ^{225}Ac was measured at $R_f = 0$ and expressed as a percentage of the total activity of the strip at equilibrium. Mean values and standard deviations were calculated from triplicate TLC experiments.

Animal Studies. Female Balb/c mice 10 weeks of age were obtained from Taconic (Germantown, NY). The studies were conducted according to the NIH Guide for the Care and Use of Laboratory Animals and were approved by the Institutional Animal Care and Use Committee at Memorial Sloan Kettering Cancer Center.

The mice were anesthetized and then injected i.v. (via the retroorbital venous plexus) with 0.5 μCi labeled antibody. The injected volume was 100 μL. Animals were sacrificed at different time points after injection by carbon dioxide asphyxiation, and the liver was removed. In addition, for the biodistribution studies, samples of blood (by cardiac puncture) and kidneys were removed. The organs were washed in distilled water, dried on gauze, and weighed, and the activities of ^{221}Fr (185−250 keV window) and ^{213}Bi (360−480 keV window) were measured using a γ counter (COBRA II, Packard Instrument Company, Meriden, CT). Samples of the injectate were used as decay correction standards. Percentage injected dose of ^{225}Ac per gram of tissue weight (% ID/g) was calculated for each animal at the time of sacrifice, using the equation described previously (*33*). The mean % ID/g was determined for each experimental group.

Radiometal Release in Cultured Cells and in Vivo. Assessment of RIC integrity was performed by protein A assay. The protein A resin (protein A sepharose CL-4B resin, Amersham Biosciences, Piscataway, NJ) was used according to the directions provided by the supplier. The beads were washed 3 times in PBS before use. For each experiment, a 100-fold excess of beads was used compared to the calculated amount of protein A necessary to bind the estimated amount of antibody.

For the cell internalization experiment, 2×10^6 HL-60 cells per milliliter were incubated for 30 min in RPMI 1640 with 10% fetal bovine serum with 30 ng of conjugate **9** or **11** labeled with ^{225}Ac in a total of 6 mL on ice. Each experiment was conducted in duplicate, and data values were averaged. After 2 washes with cold media, the cells were resuspended at 1×10^6 cells per milliliter in fresh media and incubated at 37 °C. At different time points, the cells were washed 2 times with cold media, and the pellet was lysed for 30 min at 4 °C in 100 mM NaCl, 10 mM Tris-HCl buffer, pH 8.0, containing 1% Triton and supplemented with the Roche protease inhibitor cocktail. The protein A resin in suspension in PBS was then added to the cell lysate, and the suspension was agitated for 30 min at 4 °C. The resin was then separated from the supernatant by quick centrifugation and washed 2 times. The radioactivity was measured in scintillation liquid using a β counter. The activity in the washes was negligible, and the activity associated to the beads was at least 25-fold superior to background. The antibody-bound activity was expressed as the percentage of the activity bound to the beads compared to the total activity found in the supernatant and associated with the resin.

For the in vivo radiometal release experiments, the constructs **9** or **11** labeled with ^{225}Ac (0.1 mCi in saline 1% HSA) were injected ip to two groups of three Balb/c female mice. At different time points, the isolated livers were homogenized on ice in 10 mL of 10 mM Tris-HCL buffer at pH 8.0 containing 0.25 M sucrose and 1% Triton X-100, supplemented with the Roche protease inhibitor cocktail. After pelleting at 12 000 g at 4 °C for 10 min, the supernatant was submitted to the protein A beads assay as described above. In order to estimate the size of the antibody fragments carrying the radiolabel, the liver extracts were submitted to size-exclusion chromatography using 10-DG columns (Bio-Rad), which have a 6 kDA molecular weight cutoff. This type of column was previously calibrated in the laboratory using the following method. Fractions collected after the purification of the RIC HuM195−DOTA−NCS labeled with ^{225}Ac were analyzed by size-exclusion HPLC to determine the volume corresponding to the elution of high molecular weight molecules. The same protocol was later used to analyze the radiolabeled components of the liver homogenates, allowing separation of the high (>6 kDa) and low (<6 kDa) molecular weight content.

RESULTS

Design and Synthesis of the Bifunctional Chelating Agents. In order to achieve high labeling yields, we based our conjugation strategy on thiol/maleimide chemistry, because thiols would be resistant to the conditions used during the ^{225}Ac chelation step. Since all four carboxylic groups of DOTA need to be available for stable ^{225}Ac chelation, we decided to use the bifunctional DOTA−NCS **1** macrocyclic chelator as the starting material for the synthesis of the new linkers, because its *p*-benzylisothiocyanate moiety is directly linked to the macrocycle backbone rather than to one of the carboxylic groups.

We used a cathepsin B-sensitive linker in the design of our self-immolative nanogenerators on the basis that cathepsin B is a prominent enzyme implicated in the catabolism of proteins in the liver (*29*−*31, 34*). The cleavable BCA DOTA−glycyl-glycylglycyl−L-*p*-isothiocyanatophenylalanine used by DeNardo et al. was shown to be cleaved by cathepsin B before the phenylalanine residue (*35*). This residue was bound to the antibody through a thiourea moiety in the para position of the benzyl moiety. We hypothesized that this nonpeptidic bond was not required for recognition by the enzyme cathepsin B, and instead, we incorporated to our linker a regular phenylalanine residue. A terminal cysteine residue was added in order to provide the reactive thiol for conjugation to the maleimide-

Scheme 2. Radioimmunoconjugates

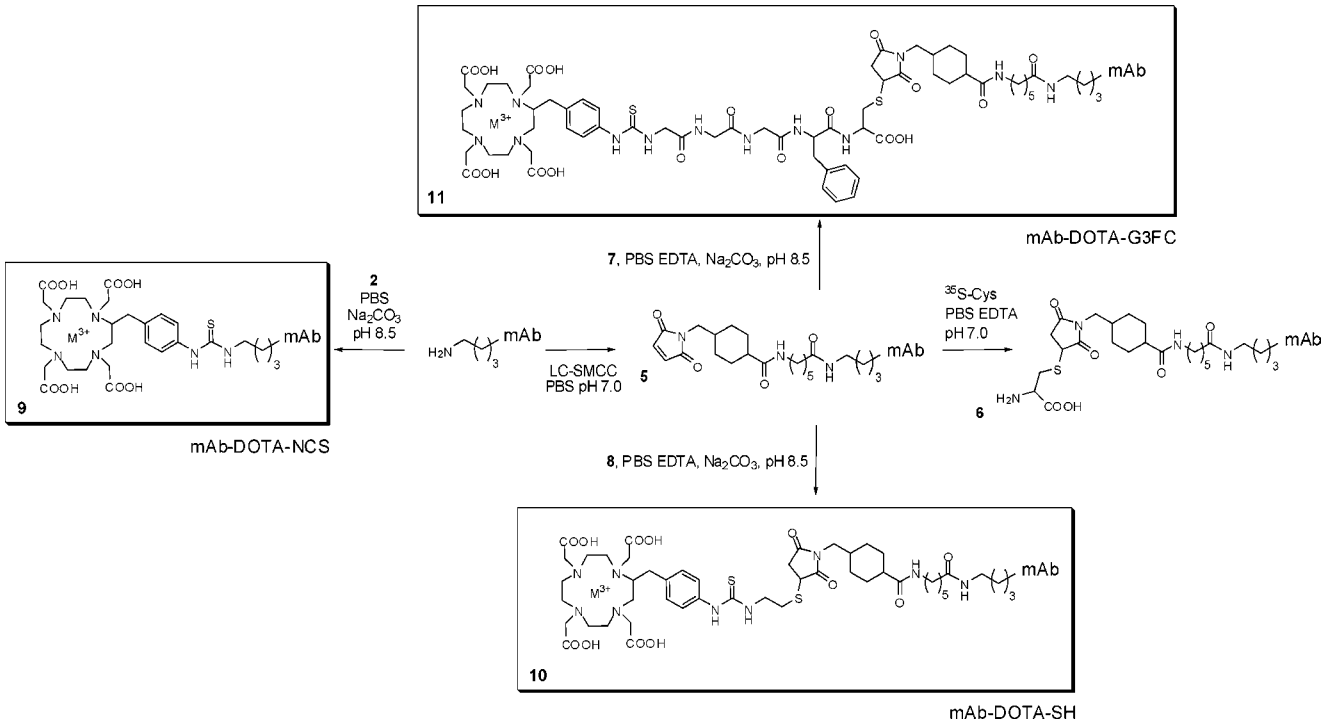

functionalized antibody. The synthesis of our cleavable BCA required a single step consisting of coupling the pentapeptide GGGFC to DOTA−NCS (Scheme 1). This was achieved in anhydrous DMF in the presence of triethylamine with a 86% yield; the resulting product DOTA−G3FC **3** was purified by semipreparative reversed-phase HPLC. Similarly, we synthesized the noncleavable control BCA DOTA−SH **4** by coupling DOTA−NCS with 2-mercaptoethylamine (2-MEA), with a 85% yield.

Preparation of the Radioimmunoconjugates. Our thiol−maleimide conjugation strategy requires the functionalization of the antibody with a maleimide moiety, which was readily achieved through the use of the commercially available bifunctional linker LC-SMCC (Scheme 2). The long chain (LC) version of this reagent was preferred in order to reduce the possible steric hindrance provided by the proximity of the antibody, therefore allowing maximum accessibility of the enzyme cathepsin to the linker. The protocol allowed derivatization of the antibody with a reproducible amount of maleimides. A 25-fold molar excess of LC-SMCC per antibody yielded about 8 mol maleimide per mole of HuM195 antibody (7.7 ± 0.9; $n = 8$). Purification of the functionalized antibody **5** was achieved by size-exclusion chromatography. This functionalization method was successfully applied to two different antibodies: HuM195 and SJ25C1. Using similar conditions as the one optimized for HuM195 led to the functionalization of SJ25C1 with a reproducible amount of about eight maleimide moieties per antibody. The degree of maleimide functionalization was assessed by ^{35}S-cysteine labeling of an aliquot of the prepared batch of antibody (Scheme 2). Specific activity was determined on the product, allowing determination of the number of of available maleimides per antibody. The storage buffer (freshly degassed PBS with 5 mM EDTA) at pH 6.4 was chosen because the slightly acidic pH is necessary for the stability of the construct. Upon storage at −80 °C in PBS/EDTA at pH 6.4, the functionalized mAbs suffered little loss of their maleimide moiety (1−9% over a period of 6 months). The presence of EDTA and the degassing are important for the second step, in order to prevent the oxidation of the reactive thiol on the BCAs **7** and **8**.

The chelation efficiencies of ^{225}Ac by the newly synthesized BCAs to yield the chelates **7** and **8** were similar to those obtained with DOTA−NCS **1**. Metal chelation efficiency was typically 95% to >99% when using a ^{225}Ac/DOTA ratio of 1:5000 or greater.

The noncleavable, control RIC mAb−DOTA−NCS **9** (*15*, *19*) was prepared using the commercially available BCA DOTA−NCS **1**. After completion of the first step, the reaction of **2** with the antibody afforded the RIC **9** with a radiochemical yield of 5−10%. Its radiochemical purity was typically 90% or greater. Previous studies have shown that an average of 5.4 DOTA per antibody are attached (*19*).

The conjugate mAb−DOTA−SH (**10**) (Scheme 2) was prepared using the novel, noncleavable BCA DOTA−SH (**4**). We optimized the conditions of the maleimide/thiol conjugation during the second step using the ^{225}Ac chelate DOTA−SH **8**. Increasing the pH up to 8.5 increased the radiochemical yields by up to 2-fold compared to pH 6.8. Similarly, incubating the reaction mixture at 37 °C instead of room temperature increased the efficiency by a factor of 1.8. The stoichiometry of the reaction also constituted an important parameter in the reaction, since using 0.5 mol equiv of BCA **8** per maleimide instead of a 2:1 DOTA−SH/maleimide ratio increased the radiochemical yield by another 2-fold. When combined, these parameters allowed the labeling of antibodies with ^{225}Ac through the noncleavable BCA **8** with radiochemical yields ranging from 30% to 40%. The purity of those constructs was 93% and greater, as assessed by thin layer chromatography (TLC). When applied to the labeling of antibodies with the cleavable BCA **7** and ^{225}Ac, those conditions afforded the same range of yields and purities.

Characterization of the RICs in Vitro. The immunoreactivity of the three different constucts HuM195−DOTA−NCS **9**, HuM195−DOTA−SH **10**, and HuM195−DOTAG3FC **11** labeled with ^{225}Ac were tested on the CD33-positive AL67 cells. All conjugates were active with immunoreactivities of 93%, 87%, and 82%, respectively. The amount of construct bound to the control CD33-negative Daudi cells ranged between 1% and 2%. Therefore, neither the maleimide functionalization of the mAb HuM195 nor its coupling to the newly synthesized

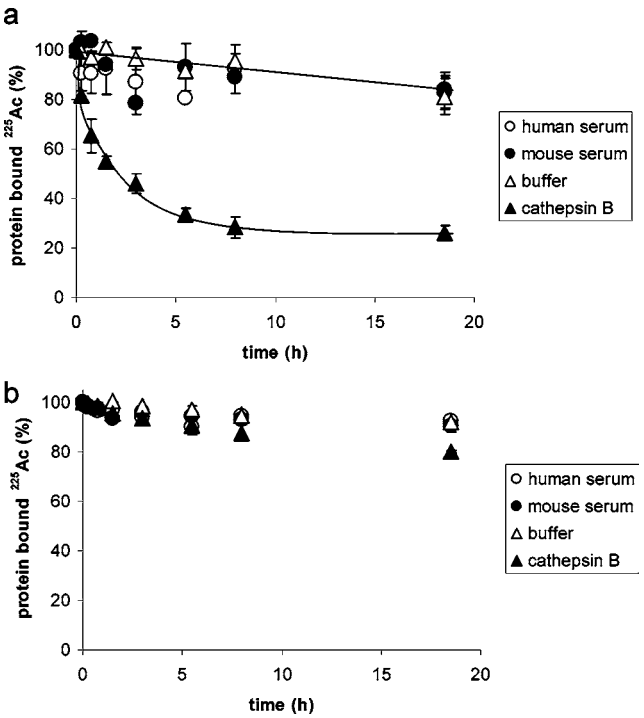

Figure 1. (a) Cathepsin B-mediated release of chelated ^{225}Ac from the cleavable RIC SJ25C1−DOTA−G3FC **11**. (b) Stability of the noncleavable RIC SJ25C1−DOTA−NCS **9**. The release of the radiometal from the conjugates was measured at 37 °C and assessed by thin layer chromatography.

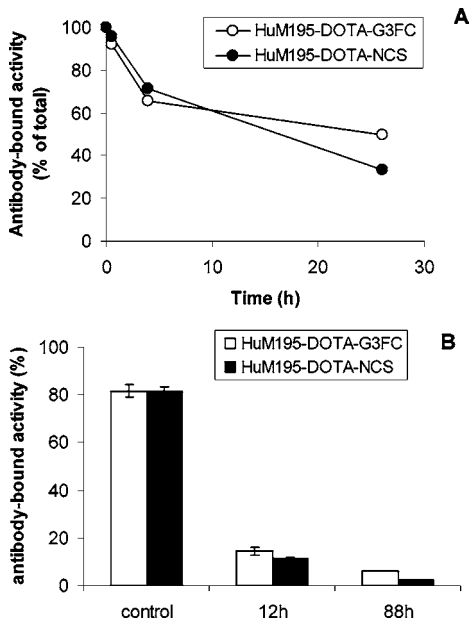

Figure 2. Comparison of ^{225}Ac release from HuM195−DOTA−G3FC **11** and HuM195−DOTA−NCS **9** after HL-60 cell internalization in vitro (A) or in mouse liver in vivo (B). The antibody-bound activity was measured after cell homogenization by using protein A beads.

BCAs significantly affected the immunoreactivity or specificity of the antibody in vitro.

The next step in the evaluation of the cleavable construct mAb−DOTA−G3FC **11** consisted of verifying the recognition of the inserted linker as a substrate of cathepsin B in vitro. As assessed by TLC, the construct released ^{225}Ac in a chelated form over time when incubated with purified cathepsin B at 37 °C (Figure 1a). The drug cleavage half-life was about 150 min, and up to 80% of its radioactive payload was released within 7 h. As a control, the RIC was incubated in the cathepsin buffer without cathepsin B, in order to test whether the acidic conditions (pH 4.5) were responsible for the degradation of the linker. No significant radioisotope release was observed within 10 h, indicating that the cleavage of the linker was cathepsin-dependent (Figure 1b). We showed that the cathepsin is cleaving the linker, rather than the IgG backbone by conductiong another control, which consisted of analyzing the noncleavable conjugate SJ25C1−DOTA−NCS **9** in the same conditions (Figure 1b). Only about 10% of the conjugated radiometal was released within 10 h, demonstrating that the degradation observed with the construct SJ25C1−DOTAG3FC **11** was linker-dependent and did not result of antibody metabolism by cathepsin B during that time frame.

The observed degradation of the RIC SJ25C1−DOTAG3FC in mouse and human serum was lower than 20% over 20 h at 37 °C, indicating that it was stable in these conditions (Figure 1a). When the in vitro cleavage of the cathepsin-sensitive RIC mAb−DOTA−G3FC (made with either the HuM195 antibody (data not shown) or the mouse SJ25C1 antibody) was tested, no difference in the degradation rate between the two constructs was observed. This indicated that the source of the antibody seemed not to interfere with the enzymatic cleavage of the DOTA−G3FC BCA.

We wanted to investigate whether the self-immolative RIC mAb−DOTA−G3FC was susceptible to degradation after cell internalization in vitro. For this purpose, we compared the fates of the cleavable HuM195−DOTA−G3FC **11** and of the noncleavable HuM195−DOTA−NCS **9**, each labeled with ^{225}Ac, in target HL-60 cells. After specific binding at 4 °C and internalization at 37 °C, both RICs were degraded inside the cells over time, as demonstrated by the increasing failure of the labeled construct to bind protein A beads (Figure 2A). The rates of degradation of both RICs were similar. This result suggested that both the noncleavable RIC HuM195−DOTA−NCS **9** and the cathepsin-sensitive RIC HuM195−DOTA−G3FC **11** are susceptible to protein catabolism after cell internalization, presumably inside the lysosomes. As the kinetics of loss of binding to protein A were similar, it appeared that both constructs were submitted to a protease activity that separated the radiolabel from the Fc portion of the IgG.

Characterization of the RICs in Vivo. A protein A bead assay was run on the serum of mice injected with the same constructs labeled with ^{111}In. The experiment showed that all three conjugates were stable in mouse serum in vivo, since between 80% and 85% of the serum activity was antibody-bound after 136 h.

The catabolism of the three RICs labeled with ^{225}Ac was investigated in vivo after iv injection in mice. Mouse livers from untreated animals were homogenized at different time points, and the integrity of the RICs was assessed using the protein A bead assay (Figure 2B). As a control, the intact RICs were mixed with a liver homogenate suplemented with a cocktail of protease inhibitors. In these control conditions, 80% of both RICs were able to bind the protein A beads. In contrast, at 12 and 88 h after injection, both RICs were significantly degraded, since their ability to recognize the beads was reduced to about 10%. Similar to the in vitro observation with HL-60 cells, both constructs had their radiolabel separated from a functional Fc at the same rate.

In order to estimate the sizes of the fragments carrying the radiolabel, at 12 h after injection, we passed the liver extracts through a size-exclusion column (10-DG). This analysis revealed that 84% (±3%) of the radioactivity was bound to fragments smaller than 6 kDa for the cleavable RIC, whereas those fragments represented only 62% (±3%) for the noncleavable RIC HuM195−DOTA−NCS.

We then compared the biodistribution in mice of ^{225}Ac after injection of the cleavable RIC HuM195−DOTA−G3FC **11** or

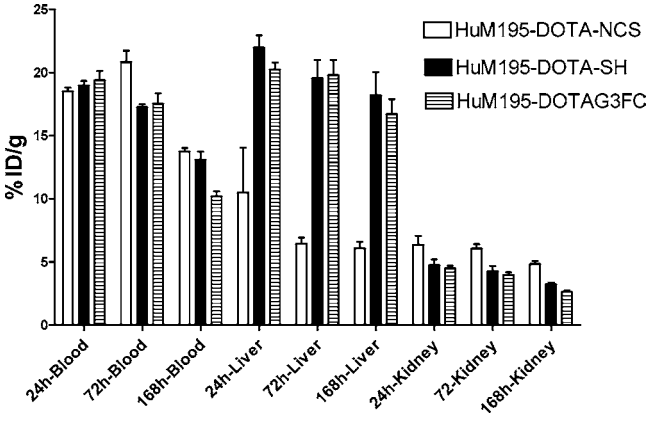

Figure 3. Comparison of the biodistribution in mice of the RICs HuM195−DOTA−NCS **9**, HuM195−DOTA−SH **10**, and HuM195−DOTA−G3FC **11** labeled with ^{225}Ac.

of the noncleavable RIC HuM195−DOTA−NCS **9** (Figure 3). For this study, we included another noncleavable control construct: HuM195−DOTA−SH **10**. The antibody in the latter conjugate was functionalized with maleimides the same way the degradable RIC **11** was, but the BCA DOTA−SH **4** used for its labeling is not sensitive to cathepsins. The biodistribution study revealed that all three constructs cleared from the blood in a similar way, approaching 10−14% of the injected dose at 168 h. A striking difference, however, was seen in the accumulation into the liver. Both the noncleavable HuM195−DOTA−SH and the cleavable HuM195−DOTA−G3FC constructs yielded a 2-fold higher liver accumulation at 24 h compared to the noncleavable HuM195−DOTA−NCS conjugate. Their slow clearance from the liver eventually yielded a 3-fold higher liver uptake at 168 h. The kidney accumulation for the two maleimide-functionalized constructs **10** and **11** was slightly lower, probably related to the increased liver uptake. Clearance was observed over time for all constructs.

DISCUSSION

This report describes the synthesis of two new BCAs that allow markedly improved yields for the labeling of antibodies with ^{225}Ac. By using the newly synthesized BCAs, chelation yields of 95% to >99% and labeling yields of up to 40% were routinely observed. This result constitutes a dramatic improvement compared to the typical yields using the isothiocyanate-functionalized macrochelator DOTA−NCS **2**, which average 5−10% (*19*). This difference is likely to be attributable to the sensitivity to hydrolysis of DOTA−NCS during the chelating step of ^{225}Ac at 60 °C. This hypothesis was in part confirmed by an HPLC stability study, which showed a half-life of DOTA−NCS of 30 min in those conditions (data not shown). We therefore demonstrate here that thiol/maleimide chemistry constitutes an alternative conjugation method that is preferrable when a high radiochemical yield is needed with ^{225}Ac. The yields might be further improved with additional process development and optimization.

The pharmacology of an in vivo isotope generator is complex. The three α-emitting daughters of ^{225}Ac pose a potential threat to injected patients if the elements cannot be controlled and cleared quickly. Strategies to decrease exposure to RICs of nontarget organs include antibody engineering, pretargeting, extracorporeal depletion, and cleavable conjugates (*25*). In this article, we describe the design of a self-immolative tumor-targeted isotope nanogenerator. Our intent was to develop a RIC capable of generating four high LET α particles at the tumor site, whose radioactive payload can be enzymatically disarmed in order to reduce damage to normal tissues should the RIC not target. The DOTA−G3FC BCA **3** incorporates a cleavage site for the enzyme cathepsin B allowing release of the radiometal from the carrier antibody in a chelated, safe form. The specific degradation of the linker by purified cathepsin B was demonstrated. The chemical half-life of the linker in those conditions was 150 min, whereas no significant radiometal release was observed during that time frame with buffer only. Furthermore, this peptide link proved to be stable in circulation in vivo, since the cleavable RIC HuM195−DOTA−G3FC **11** labeled with ^{225}Ac was found intact in mouse serum 136 h after injection.

When we investigated the fate of the cleavable RIC **11** after internalization in cultured HL-60 cells, we discovered that its rate of degradation (as measured by retention of the isotope on protein A-beads, which requires an intact Fc portion for binding) was similar to the noncleavable control construct **9**. This result was confirmed in vivo in the liver homogenate experiment. A rapid degradation of both constructs occurs in mouse liver, leaving less than 20% conjugate intact 12 h after injection. The nature of the degradation, however, cannot be determined by this assay. Other groups have reported that radiolabled antibodies are processed after cell internalization. Geissler at al. have shown that following cell surface binding, different radiolabeled antibodies are internalized and degraded in the lysosome (*36*, *37*). When injected in vivo, a large fraction of a radiolabeled murine antibody against a tumor glycoprotein accumulated in the liver. Its liver uptake is mediated by its Fc portion (*38*). The same authors observed the conversion in the liver of the ^{111}In−DTPA RIC into small radiolabeled fragments, presumably ^{111}In−DTPA bound to one or a few amino acids. This hypothesis was confirmed by several groups who identified the in vivo metabolite of different ^{111}In−DTPA−NCS labeled proteins as indium−DTPA−lysine (*39*−*41*). Therefore, it is likely that the noncleavable control construct HuM195−DOTA−SCN **9** undergoes a similar process, explaining the degradation we observed after cell internalization in vitro and in the liver in vivo.

On the basis of the protein A assay, the kinetics of degradation observed for the cleavable RIC **11** and the noncleavable construct **9** were similar within the studied time frame. However, the protein A assay does not provide information regarding the way the radiolabeled antibody was degraded, other than reporting the separation of the radiolabel from a functional Fc end of the IgG. We could therefore not rule out the possibility that the degradation of both constructs was qualitatively different and that the cathepsin-sensitive linker was degraded in addition to the catabolism of the antibody. For this reason, we investigated the size of the radiolabeled fragments in the liver. At 12 h after injection, the proportion of small radiolabeled fragments (<6 kDa) was significantly greater for the cleavable construct, suggesting that additional processing of the linker had occurred. It is also likely that a more significant difference may be observed at earlier time points. Indeed, a study using comparable cathepsin-sensitive RICs demonstrated processing of the radiolabeled conjugates in mice liver as early as 30 min postinjection. In particular, a RIC with a linker incorporating the sequence Gly-Phe-Gly showed little radioactivity associated with the intact antibody and most of the activity associated with the low molecular weight fragments in a gel filtration chromatography experiment after hepatic catabolism (*42*). Similar to our findings, a study was recently published that describes the unexpected activity of a control immunoconjugate not designed to be able to release an active drug (*43*). Drug release from this conjugate was shown to take place through mAb degradation. Taken together, these results suggest that the G3FC linker in the cathepsin-sensitive RIC **11** was cleaved in vivo and that catabolism of the antibody backbone took place for both the

cleavable and noncleavable constructs at the same time, obscuring the linker degradation.

When we investigated the biodistribution of the cathepsin-sensitive construct HuM195−DOTA−G3FC **11** in mice, we observed its accumulation in the liver, leading to 2- to 3-fold higher liver uptake compared to the noncleavable construct HuM195−DOTA−NCS **9**. A different noncleavable control construct HuM195−DOTA−SH **10** induced a similar liver accumulation of ^{225}Ac in the liver. Since the antibody in this conjugate was functionalized by maleimides the same way as the cleavable construct **11**, it is likely that the functionalization of HuM195 with LC-SMCC was responsible for its increased uptake. It was recently demonstrated that drug-load stoichiometry can significantly influence immunoconjugate pharmacokinetics (*44*). It is also known that the pI of an antibody or antibody fragment affects its biodistribution (*45*−*47*). Therefore, a difference in the number of modifed lysines between the constructs could account for different drug loading and a different overall charge of the conjugates, which could explain the difference in behaviors in vivo. Presumably, about eight lysines were modified during maleimide functionalization, which is comparable to the number of lysines derivatized with DOTA−NCS (*8*−*10*) using our protocols. However, we cannot rule out the possibility that the resulting amount of maleimides after reaction with LC-SMCC does not reflect the number of modified lysines, because some maleimide hydrolysis may have occurred. Another explanation for the different fate in vivo of the two noncleavable constructs could be a different localization of the radiochelate on the antibody due to the different chemistries used. Catabolism of the conjugates could then produce different labeled fragments, with nonsimilar excretion properties. The decreased kidney accumulation consistently observed for the two maleimide-functionalized constructs **10** and **11** probably resulted from to the increased liver uptake.

Although the cleavable construct HuM195−DOTA−G3FC **11** was demonstrated to be extensively catabolized, the organ distribution profile of the cleavable construct and of the noncleavable control conjugate HuM195−DOTA−SH **10** were similar. Both constructs showed prolonged retention of the radioactivity in the liver. The lack of accelerated liver isotope clearance by the cathepsin-sensitive linker on the cleavable construct raises questions about the fate of the radioconjugate once inside the liver. We speculate that the accumulation of ^{225}Ac in the liver, which was associated with the treatment with conjugate **11**, is the result of an absence of secretion of the radiolabeled metabolites, rather than an absence of cleavage. Lysosomes are known to be highly selective with respect to the release of molecules in the cytoplasm, and accumulation of certain compounds like weak bases results (*48*). Differences in the catabolism of different radiolabels on antibodies have been observed previously (*8*). Several authors have reported the accumulation of RIC metabolites in the liver (*38*) or in their lysosomes (*39*). Furthermore, not all cathepsin-sensitive linkers in RICs resulted in accelerated liver clearance. For example, while the previously described Ala-Leu-Ala-Leu peptide was beneficial in a daunorubicin conjugate (*49*), the linker did not significantly increase the liver clearance of a ^{111}In-labeled antibody (*50*). The authors concluded that the chelates were cleaved off in the liver but were trapped there (*50*). The difference in biodistribution with the previously reported result (*49*) was attributed to the different method used to attach the linker to the antibody, the different number of chelates, and possibly different positions of attachment. In another study, Meares et al. synthesized various peptide-derivatized DOTA compounds and selected the best substrates for cathepsin B and D (*51*, *52*). The most efficiently cleaved peptide sequences in vitro were not the linkers leading to the best clearance of the liver in vivo (*29*). This result most likely could be explained by the absence of correlation between rate of linker degradation by purified cathepsin and rate of liver clearance, which depends on other catabolic steps.

Together, these results show that cleavage of a linker by cathepsins is not necessarily the limiting step in the clearance of a self-immolative RIC. We postulate that the catabolism and release of the radiolabeled fragments from liver constitutes a major limiting step in the clearance of RIC metabolites. Therefore, similar cathepsin-sensitive linkers, for example, those reported here and those described by DeNardo et al., could display different biodistributions. Additional support for this hypothesis is derived from work with similar BCAs used to label F(ab′)2 antibody fragments with copper, in which slight modifications in the linker structure dramatically influenced the biodistribution and clearance of the radiometal (*42*). A better understanding of those mechanisms is required for the design of successful self-immolative RIC.

ACKNOWLEDGMENT

Christophe Antczak is a Lymphoma Research Foundation Fellow. David A. Scheinberg is Doris Duke distinguished scientist. The authors thank Dr. Darren Veach, Dr. George Sukenick, Ms. Sylvi Rusli, and Ms. Anna Dudkina for helpful assistance with compounds characterization. This work was supported in part by the NIH grants R01-CA 55349 and CA 33049, the Joseph LeRoy and Ann C. Warner fund, the Lymphoma Foundation, the William and Alice Goodwin Commonwealth Foundation for Cancer Research, and the Sloan Kettering Experimental Therapeutics Center. Actinium-225 was purified at Oak Ridge National Laboratory and was provided by Actinium Pharmaceuticals, Inc.

LITERATURE CITED

(1) Scheinberg, D. A., Tanimoto, M., McKenzie, S., Strife, A., Old, L. J., and Clarkson, B. D. (1989) Monoclonal antibody M195: a diagnostic marker for acute myelogenous leukemia. *Leukemia 3*, 440−5.

(2) Tanimoto, M., Scheinberg, D. A., Cordon-Cardo, C., Huie, D., Clarkson, B. D., and Old, L. J. (1989) Restricted expression of an early myeloid and monocytic cell surface antigen defined by monoclonal antibody M195. *Leukemia 3*, 339−48.

(3) Bernstein, I. D., Singer, J. W., Andrews, R. G., Keating, A., Powell, J. S., Bjomson, B. H., Cuttner, J., Najfeld, V., Reaman, G., Raskind, W.; Sutton, D. M. C., and Fialkow, P. J. (1987) Treatment of acute myeloid leukemia cells in vitro with a monoclonal antibody recognizing a myeloid differentiation antigen allows normal progenitor cells to be expressed. *J. Clin. Invest. 79*, 1153−9.

(4) Griffin, J. D., Linch, D., Sabbath, K., Larcom, P., and Schlossman, S. F. (1984) A monoclonal antibody reactive with normal and leukemic human myeloid progenitor cells. *Leuk. Res. 8*, 521−34.

(5) Co, M. S., Avdalovic, N. M., Caron, P. C., Avdalovic, M. V., Scheinberg, D. A., and Queen, C. (1992) Chimeric and humanized antibodies with specificity for the CD33 antigen. *J. Immunol. 148*, 1149−54.

(6) Scheinberg, D. A., Lovett, D., Divgi, C. R., Graham, M. C., Berman, E., Pentlow, K., Feirt, N., Finn, R. D., Clarkson, B. D., Gee, T. S., Larson, S. M., Octtgen, H. F., and Old, L. J. (1991) A phase I trial of monoclonal antibody M195 in acute myelogenous leukemia: specific bone marrow targeting and internalization of radionuclide. *J. Clin. Oncol. 9*, 478−90.

(7) Scheinberg, D. A., and Strand, M. (1982) Leukemic cell targeting and therapy by monoclonal antibody in a mouse model system. *Cancer Res. 42*, 44−9.

(8) Scheinberg, D. A., and Strand, M. (1983) Kinetic and catabolic considerations of monoclonal antibody targeting in erythroleukemic mice. *Cancer Res. 43*, 265−72.

(9) Scheinberg, D. A., Strand, M., and Gansow, O. A. (1982) Tumor imaging with radioactive metal chelates conjugated to monoclonal antibodies. *Science 215*, 1511−3.

(10) Geerlings, M. W., Kaspersen, F. M., Apostolidis, C., and van der Hout, R. (1993) The feasibility of 225Ac as a source of alpha-particles in radioimmunotherapy. *Nucl. Med. Commun. 14*, 121−5.
(11) Kaspersen, F. M., Bos, E., Doornmalen, A. V., Geerlings, M. W., Apostolidis, C., and Molinet, R. (1995) Cytotoxicity of 213Bi- and 225Ac-immunoconjugates. *Nucl. Med. Commun. 16*, 468−76.
(12) Macklis, R. M., Lin, J. Y., Beresford, B., Atcher, R. W., Hines, J. J., and Humm, J. L. (1992) Cellular kinetics, dosimetry, and radiobiology of alpha-particle radioimmunotherapy: induction of apoptosis. *Radiat. Res. 130*, 220−6.
(13) Vriesendorp, H. M., Quadri, S. M., Andersson, B. S., and Dicke, K. A. (1996) Hematologic side effects of radiolabeled immunoglobulin therapy. *Exp. Hematol. 24*, 1183−90.
(14) McDevitt, M. R., Barendswaard, E., Ma, D., Lai, L., Curcio, M. J., Sgouros, G., Ballangrud, A. M., Yang, W. H., Finn, R. D., Pellegrini, V., Geerlings, M. W., Jr., Lee, M., Brechbiel, M. W., Bander, N. H., Cordon-Cardo, C., and Scheinberg, D. A. (2000) An alpha-particle emitting antibody ([213Bi]J591) for radioimmunotherapy of prostate cancer. *Cancer Res. 60*, 6095−100.
(15) McDevitt, M. R., Ma, D., Lai, L. T., Simon, J., Borchardt, P., Frank, R. K., Wu, K., Pellegrini, V., Curcio, M. J., Miederer, M., Bander, N. H., and Scheinberg, D. A. (2001) Tumor therapy with targeted atomic nanogenerators. *Science 294*, 1537−40.
(16) Zalutsky, M. R., and Vaidyanathan, G. (2000) Astatine-211-labeled radiotherapeutics: an emerging approach to targeted alpha-particle radiotherapy. *Curr. Pharm. Des. 6*, 1433−55.
(17) Borchardt, P. E., Yuan, R. R., Miederer, M., McDevitt, M. R., and Scheinberg, D. A. (2003) Targeted actinium-225 in vivo generators for therapy of ovarian cancer. *Cancer Res. 63*, 5084−90.
(18) Miederer, M., McDevitt, M. R., Borchardt, P., Bergman, I., Kramer, K., Cheung, N. K., and Scheinberg, D. A. (2004) Treatment of neuroblastoma meningeal carcinomatosis with intrathecal application of alpha-emitting atomic nanogenerators targeting disialoganglioside GD2. *Clin. Cancer Res. 10*, 6985−92.
(19) McDevitt, M. R., Ma, D., Simon, J., Frank, R. K., and Scheinberg, D. A. (2002) Design and synthesis of 225Ac radioimmunopharmaceuticals. *Appl. Radiat. Isot. 57*, 841−7.
(20) Andrew, S. M., Perkins, A. C., Pimm, M. V., and Baldwin, R. W. (1988) A comparison of iodine and indium labelled anti CEA intact antibody, F(ab)2 and Fab fragments by imaging tumour xenografts. *Eur. J. Nucl. Med. 13*, 598−604.
(21) Pimm, M. V., Perkins, A. C., and Baldwin, R. W. (1985) Differences in tumour and normal tissue concentrations of iodine- and indium-labelled monoclonal antibody. II. Biodistribution studies in mice with human tumour xenografts. *Eur. J. Nucl. Med. 11*, 300−4.
(22) Jaggi, J. S., Seshan, S. V., McDevitt, M. R., LaPerle, K., Sgouros, G., and Scheinberg, D. A. (2005) Renal tubulointerstitial changes after internal irradiation with alpha-particle-emitting actinium daughters. *J. Am. Soc. Nephrol. 16*, 2677−89.
(23) Kukis, D. L., Novak-Hofer, I., and DeNardo, S. J. (2001) Cleavable linkers to enhance selectivity of antibody-targeted therapy of cancer. *Cancer Biother. Radiopharm. 16*, 457−67.
(24) Quadri, S. M., and Vriesendorp, H. M. (1998) Effects of linker chemistry on the pharmacokinetics of radioimmunoconjugates. *Q. J. Nucl. Med. 42*, 250−61.
(25) Wu, A. M., and Senter, P. D. (2005) Arming antibodies: prospects and challenges for immunoconjugates. *Nat. Biotechnol. 23*, 1137−46.
(26) Sanderson, R. J., Hering, M. A., James, S. F., Sun, M. M., Doronina, S. O., Siadak, A. W., Senter, P. D., and Wahl, A. F. (2005) In vivo drug-linker stability of an anti-CD30 dipeptide-linked auristatin immunoconjugate. *Clin. Cancer Res. 11*, 843−52.
(27) Sutherland, M. S., Sanderson, R. J., Gordon, K. A., Andreyka, J., Cerveny, C. G., Yu, C., Lewis, T. S., Meyer, D. L., Zabinski, R. F., Doronina, S. O., Senter, P. D., Law, C. L., and Wahl, A. F. (2006) Lysosomal trafficking and cysteine protease metabolism confer target-specific cytotoxicity by peptide-linked anti-CD30-auristatin conjugates. *J. Biol. Chem. 281*, 10540−7.
(28) Berquin, I. M., and Sloane, B. F. (1996) Cathepsin B expression in human tumors. *Adv. Exp. Med. Biol. 389*, 281−94.
(29) DeNardo, G. L., DeNardo, S. J., Peterson, J. J., Miers, L. A., Lam, K. S., Hartmann-Siantar, C., and Lamborn, K. R. (2003) Preclinical evaluation of cathepsin-degradable peptide linkers for radioimmunoconjugates. *Clin. Cancer Res. 9*, 3865S−72S.
(30) DeNardo, G. L., Kroger, L. A., Meares, C. F., Richman, C. M., Salako, Q., Shen, S., Lamborn, K. R., Peterson, J. J., Miers, L. A., Zhong, G. R., and DeNardo, S. J. (1998) Comparison of 1,4,7,10-tetraazacyclododecane-N,N′,N″,N‴-tetraacetic acid (DOTA)-peptide-ChL6, a novel immunoconjugate with catabolizable linker, to 2-iminothiolane-2-[p-(bromoacetamido)benzyl]-DOTA-ChL6 in breast cancer xenografts. *Clin. Cancer Res. 4*, 2483−90.
(31) DeNardo, S. J., DeNardo, G. L., Yuan, A., Richman, C. M., O'Donnell, R. T., Lara, P. N., Kukis, D. L., Natarajan, A., Lamborn, K. R., Jacobs, F., and Siantar, C. L. (2003) Enhanced therapeutic index of radioimmunotherapy (RIT) in prostate cancer patients: comparison of radiation dosimetry for 1,4,7,10-tetraazacyclododecane-N,N′,N″,N‴-tetraacetic acid (DOTA)-peptide versus 2IT-DOTA monoclonal antibody linkage for RIT. *Clin. Cancer Res. 9*, 3938S−44S.
(32) Richman, C. M., Denardo, S. J., O'Donnell, R. T., Yuan, A., Shen, S., Goldstein, D. S., Tuscano, J. M., Wun, T., Chew, H. K., Lara, P. N., Kukis, D. L., Natarajan, A., Meares, C. F., Lamborn, K. R., and DeNardo, G. L. (2005) High-dose radioimmunotherapy combined with fixed, low-dose paclitaxel in metastatic prostate and breast cancer by using a MUC-1 monoclonal antibody, m170, linked to indium-111/yttrium-90 via a cathepsin cleavable linker with cyclosporine to prevent human anti-mouse antibody. *Clin. Cancer Res. 11*, 5920−7.
(33) Mirzadeh, S., Kuman, K., and Gansow, O. A. (1993) The chemical fate of ^{213}Bi-DOTA formed by β-decay of ^{212}Pb(DOTA)2-. *Radiochim. Acta 60*, 1−10.
(34) Barrett, A. J., and Kirschke, H. (1981) Cathepsin B, cathepsin H, and cathepsin L. *Methods Enzymol. 80*, 535−61.
(35) Li, M., and Meares, C. F. (1993) Synthesis, metal chelate stability studies, and enzyme digestion of a peptide-linked DOTA derivative and its corresponding radiolabeled immunoconjugates. *Bioconjugate Chem. 4*, 275−83.
(36) Geissler, F., Anderson, S. K., and Press, O. (1991) Intracellular catabolism of radiolabeled anti-CD3 antibodies by leukemic T cells. *Cell. Immunol. 137*, 96−110.
(37) Geissler, F., Anderson, S. K., Venkatesan, P., and Press, O. (1992) Intracellular catabolism of radiolabeled anti-mu antibodies by malignant B-cells. *Cancer Res. 52*, 2907−15.
(38) Jones, P. L., Brown, B. A., and Sands, H. (1990) Uptake and metabolism of 111In-labeled monoclonal antibody B6.2 by the rat liver. *Cancer Res.* 50, 852s−856s.
(39) Duncan, J. R., and Welch, M. J. (1993) Intracellular metabolism of indium-111-DTPA-labeled receptor targeted proteins. *J. Nucl. Med. 34*, 1728−38.
(40) Franano, F. N., Edwards, W. B., Welch, M. J., and Duncan, J. R. (1994) Metabolism of receptor targeted 111In-DTPA-glycoproteins: identification of 111In-DTPA-epsilon-lysine as the primary metabolic and excretory product. *Nucl. Med. Biol. 21*, 1023−34.
(41) Rogers, B. E., Franano, F. N., Duncan, J. R., Edwards, W. B., Anderson, C. J., Connett, J. M., and Welch, M. J. (1995) Identification of metabolites of 111In-diethylenetriaminepentaacetic acid-monoclonal antibodies and antibody fragments in vivo. *Cancer Res. 55*, 5714s−5720s.
(42) Novak-Hofer, I., Zimmermann, K., and Schubiger, P. A. (2001) Peptide linkers lead to modification of liver metabolism and improved tumor targeting of copper-67-labeled antibody fragments. *Cancer Biother. Radiopharm. 16*, 469−81.
(43) Doronina, S. O., Mendelsohn, B. A., Bovee, T. D., Cerveny, C. G., Alley, S. C., Meyer, D. L., Oflazoglu, E., Toki, B. E., Sanderson, R. J., Zabinski, R. F., Wahl, A. F., and Senter, P. D. (2006) Enhanced activity of monomethylauristatin F through monoclonal antibody delivery: effects of linker technology on efficacy and toxicity. *Bioconjugate Chem. 17*, 114−24.
(44) Hamblett, K. J., Senter, P. D., Chace, D. F., Sun, M. M., Lenox, J., Cerveny, C. G., Kissler, K. M., Bernhardt, S. X., Kopcha, A. K., Zabinski, R. F., Meyer, D. L., and Francisco, J. A. (2004) Effects of drug loading on the antitumor activity of a monoclonal antibody drug conjugate. *Clin. Cancer Res. 10*, 7063−70.
(45) Khawli, L. A., Glasky, M. S., Alauddin, M. M., and Epstein, A. L. (1996) Improved tumor localization and radioimaging with chemically modified monoclonal antibodies. *Cancer Biother. Radiopharm. 11*, 203−15.

(46) Kim, I., Kobayashi, H., Yoo, T. M., Kim, M. K., Le, N., Han, E. S., Wang, Q. C., Pastan, I., Carrasquillo, J. A., and Paik, C. H. (2002) Lowering of pI by acylation improves the renal uptake of 99mTc-labeled anti-Tac dsFv: effect of different acylating reagents. *Nucl. Med. Biol. 29*, 795−801.

(47) Kobayashi, H., Le, N., Kim, I. S., Kim, M. K., Pie, J. E., Drumm, D., Paik, D. S., Waldmann, T. A., Paik, C. H., and Carrasquillo, J. A. (1999) The pharmacokinetic characteristics of glycolated humanized anti-Tac Fabs are determined by their isoelectric points. *Cancer Res. 59*, 422−30.

(48) Ohkuma, S. (1987) The lysosomal proton pump. In *Lysosomes: Their Role in Protein Breakdown* (Glaumann, H., and Ballard, F., Eds.), Academic Press, New York.

(49) Trouet, A., Masquelier, M., Baurain, R., and Deprez-De Campeneere, D. (1982) A covalent linkage between daunorubicin and proteins that is stable in serum and reversible by lysosomal hydrolases, as required for a lysosomotropic drug-carrier conjugate: in vitro and in vivo studies. *Proc. Natl. Acad. Sci. U.S.A. 79*, 626−9.

(50) Studer, M., Kroger, L. A., DeNardo, S. J., Kukis, D. L., and Meares, C. F. (1992) Influence of a peptide linker on biodistribution and metabolism of antibody-conjugated benzyl−EDTA. Comparison of enzymatic digestion in vitro and in vivo. *Bioconjugate Chem. 3*, 424−9.

(51) Peterson, J. J., Pak, R. H., and Meares, C. F. (1999) Total solid-phase synthesis of 1,4,7,10-tetraazacyclododecane-N,N′,N″,N‴-tetraacetic acid-functionalized peptides for radioimmunotherapy. *Bioconjugate Chem. 10*, 316−20.

(52) Peterson, J. J., and Meares, C. F. (1999) Enzymatic cleavage of peptide-linked radiolabels from immunoconjugates. *Bioconjugate Chem. 10*, 553−7.

BC060156+

Triplex Staples: DNA Double-Strand Cross-Linking at Internal and Terminal Sites Using Psoralen-Containing Triplex-Forming Oligonucleotides

Hong Li,[†] Victoria J. Broughton-Head,[‡] Guomei Peng,[†] Vicki E. C. Powers,[†] Matthew J. Ovens,[‡] Keith R. Fox,[‡] and Tom Brown*[,†]

School of Chemistry, University of Southampton, Highfield, Southampton SO17 1BJ, U.K., School of Biological Sciences, University of Southampton, Bassett Crescent East, Southampton SO16 7PX, U.K. Received June 29, 2006; Revised Manuscript Received August 10, 2006

A method has been developed to attach 4′-(hydroxymethyl)-4,5′,8-trimethylpsoralen to the 5 position of thymine bases during solid-phase oligonucleotide synthesis. UV irradiation of triplex-forming oligonucleotides (TFOs) containing internally attached psoralens produces photoadducts at TpA steps within target duplexes, thus relaxing the constraints on selection of psoralen target sequences. Photoreaction of TFOs containing two psoralens, located at the 5′- and 3′-ends, has been used to create double-strand cross-links (triplex staples) at both termini of the TFO. Such complexes have no free single-stranded ends. TFOs containing 4′-(hydroxymethyl)-4,5′,8-trimethylpsoralen, 3-methyl-2-aminopyridine, and 5-(3-aminoprop-2-ynyl)deoxyuridine formed photoadducts with target duplexes under near-physiological conditions.

INTRODUCTION

Triplex-forming oligonucleotides (TFOs) bind in a sequence-specific manner to the major groove of double-stranded DNA (dsDNA). In the parallel motif, hydrogen bonds are formed with purine bases in the oligopurine strand through T•AT and C^+•GC Hoogsteen interactions, whereas in the antiparallel motif, A•AT, T•AT, and G•GC reverse Hoogsteen triplets are formed (*1*−*3*). TFOs can be used to modulate gene expression and as molecular tools to cause strand cleavage (*4*). They are also powerful tools for causing site-specific chemical damage at selected DNA sequences, thereby introducing mutations (*5*, *6*). Parallel triplexes are more stable than the antiparallel variants, but the affinity of the third strand for the duplex is relatively low at physiological pH due to the requirement for protonation of the third strand cytosine (*7*, *8*). Parallel TFOs constructed from normal bases are therefore not suitable for use in vivo.

Psoralens are bifunctional photo-cross-linking agents that have been used as probes of nucleic acid structure and function (*9*). When attached to the termini of TFOs as shown in Scheme 1 (structure **1**), psoralens intercalate into the neighboring duplex and stabilize the triple-stranded complex (*10*). Irradiation at 365 nm induces a [2 + 2] cycloaddition reaction between the intercalated psoralen and pyrimidine bases in the duplex to form adducts with one or both strands, principally at TpA steps (*11*, *12*). The 3,4-double bond of the pyrone ring and the 4′,5′-double bond on the furan ring of psoralen are involved (*10*). Double-strand cross-linking only occurs if the furan moiety undergoes reaction first (*9*). Such cross-links can inhibit replication and transcription by preventing opening of the double helix, and psoralen-modified oligonucleotides have been proposed as tools in molecular biology and as potential therapeutic agents (*13*, *14*).

The attachment of psoralen to the termini of TFOs limits the choice of duplex target, as efficient double-strand cross-linking requires a TpA step just outside the triplex binding site. This constraint could be relaxed if cross-linking was possible at TpA sites within the triplex binding site. With this in mind, we have studied the DNA binding and photochemical cross-linking properties of TFOs that contain an internal psoralen tethered to a uracil as shown in Scheme 1 (structure **2**). We have also synthesized a TFO containing two psoralens, one at the 5′-end (**1**) and one at the 3′-end (**2**) and have investigated its interactions with a duplex target. This double psoralen-labeled TFO acts as a triplex staple.

EXPERIMENTAL PROCEDURES

Materials. All reagents were purchased from Aldrich, Avocado, or Fluka and used without purification with the exception of the following solvents, which were purified by distillation: methanol (over iodine and magnesium), tetrahydrofuran (over sodium wire and benzophenone), dichloromethane, *n*-diisopropylethylamine, pyridine, and triethylamine (over calcium hydride). All reactions were carried out under an argon atmosphere using oven-dried glassware with purified and distilled solvents. Column chromatography was carried out under pressure using Fisher Scientific DAVISIL 60A (35−70 μm) silica. Thin layer chromatography was performed using Merck Kieselgel 60 F24 (0.22 mm thickness, aluminum backed). Compounds were visualized by ultraviolet light at 254 nm or by staining with 10% phosphomolybdic acid in ethanol (A′), or anisaldehyde (B′).

^{1}H NMR and ^{13}C NMR spectra were measured on a Bruker AC300 spectrometer or a Bruker DPX400 spectrometer. Chemical shifts are given in parts per million relative to tetramethylsilane, and *J* values in hertz. Multiplicities of ^{13}C signals were determined using the DEPT spectral editing technique and are described as s (quartenary carbon), d (CH), t (CH_2), and q (CH_3). Assignment was also aided by COSY (^{1}H−^{1}H), HMQC, and HMBC experiments. ^{31}P NMR spectra were recorded on a Bruker AV300 spectrometer at 121 MHz or 162 MHz on a Bruker DPX400 spectrometer and were externally referenced to 85% phosphoric acid in D_2O.

Low-resolution mass spectra were recorded by electrospray on a Fisons VG platform instrument in acetonitrile or a Waters

* Corresponding author: Professor Tom Brown, School of Chemistry, University of Southampton, Highfield, Southampton SO17 1BJ, U.K. Tel. +44 23 8059 2974. Fax: +44 238059 2991. E-mail: tb2@soton.ac.uk.

[†] School of Chemistry.

[‡] School of Biological Sciences.

10.1021/bc0601875 CCC: $33.50 © 2006 American Chemical Society
Published on Web 10/27/2006

Scheme 1. Strategies for Introducing Psoralen into TFOs (1) at the 5′-end and (2) Internally and 3′ [a]

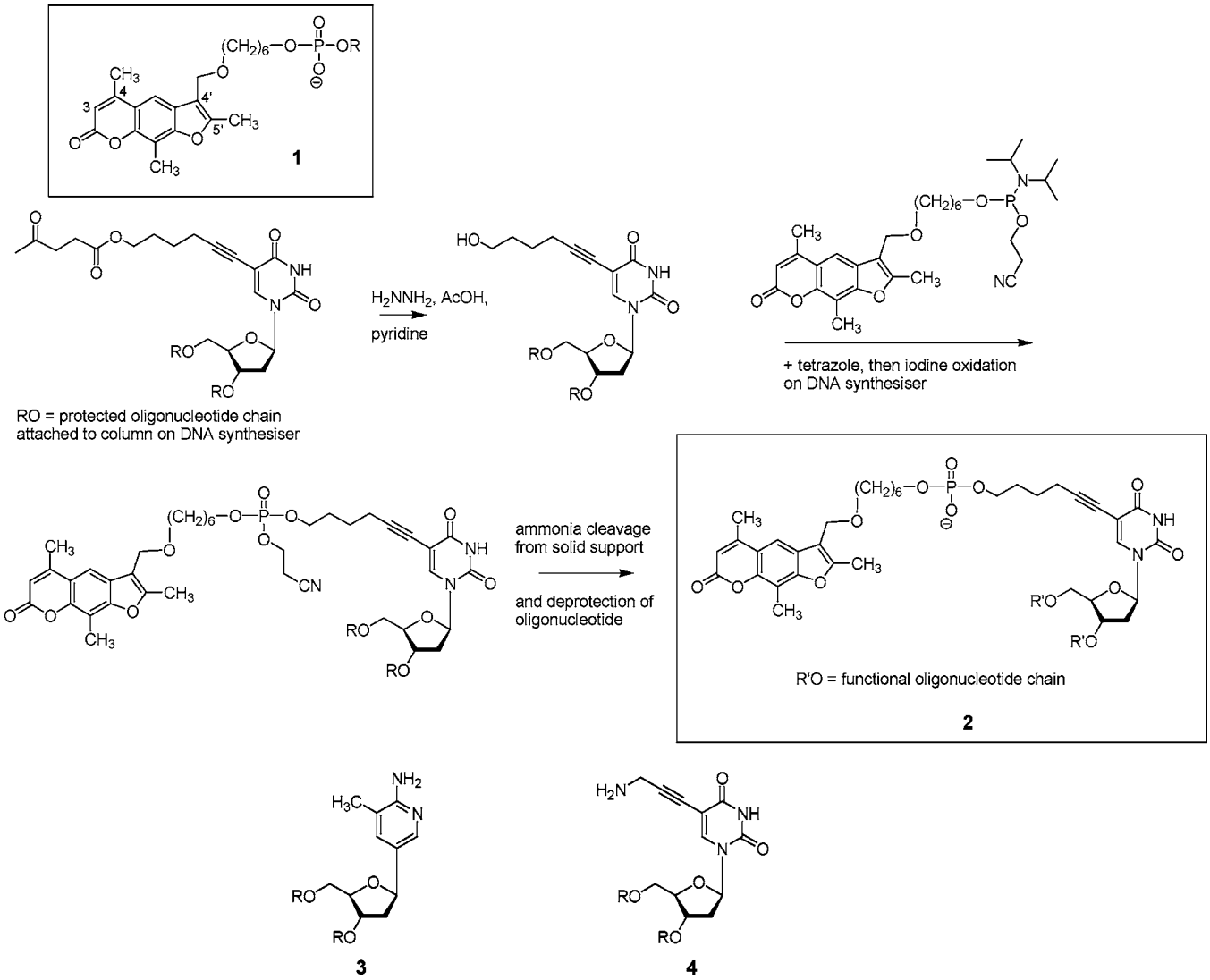

[a] **1**, 6[4′-(hydroxymethyl)-4,5′,8-trimethylpsoralen]hexyl-1-phosphate attached to the 5′-end of an oligonucleotide; **2**, 6[4′-(hydroxymethyl)-4,5′,8-trimethylpsoralen]hexyl-1-phosphate attached to 5-(hex-5-ynyl)-2′-deoxyuridine in an oligonucleotide strand. Nucleoside analogues for triplex stabilization; **3**, 3-methyl-2-aminopyridine-2′-deoxyriboside; **4**, 5-(3-aminoprop-2-ynyl)deoxyuridine.

ZMD quadrupole mass spectrometer in methanol or water (HPLC grade). High-resolution mass spectra were recorded in acetonitrile, methanol, or water (HPLC grade) by electrospray on a Bruker APEX III FT-ICR mass spectrometer. Oligonucleotides were analyzed by MALDI-TOF MS using a ThermoBioAnalysis Dynamo MALDI-TOF mass spectrometer in positive ion mode using internal T_n standards.

Hex-5-ynyl-4-oxopentanoate. Levulinic acid (1.05 mL, 10.2 mmol) was added to a solution of dicyclohexyl carbodiimide (2.1 g, 10.2 mmol) in dichloromethane (10 mL). The slurry was stirred for 10 min at room temperature before adding further dichloromethane (10 mL), 5-hexyn-1-ol (0.55 mL, 5.1 mmol), and 4-dimethylaminopyridine (62 mg, 0.5 mmol). The reaction was stirred at room temperature for 2 h and filtered to remove dicyclohexylurea. The filtrate was washed with saturated sodium bicarbonate, 10% citric acid, and saturated potassium chloride, dried over sodium sulfate, filtered, and the solvent evaporated in vacuo. Purification by column chromatography (9.5:0.5 toluene/ethyl acetate) gave the title compound as a colorless oil in quantitative yield. R_f (9:1 toluene/ethyl acetate, A′) 0.43; δ_H (400 MHz, $CDCl_3$) 4.09 (2H, t, $J = 6.5$ Hz, **H**^{6}), 2.73 (2H, t, $J = 6.5$ Hz, **H**^{8}), 2.56 (2H, t, $J = 6.5$ Hz, **H**^{7}), 2.22 (2H, td, $J = 6.5$, 2.5 Hz, **H**^{4}), 2.18 (3H, s, C**H**$_3$), 1.94 (1H, t, $J = 2.5$ Hz, **H**^{6}), 1.71−1.78 (2H, m, **H**^{2}), 1.55−1.62 (2H, m, **H**^{3}); δ_C (100 MHz, $CDCl_3$) 206.6 (s, **C**O**)**, 172.9 (s, **C**O), 84.0 (s, **C**^{5}), 68.8 (d, **C**^{6}), 64.2 (t, **C**^{1}), 38.1 (t, **C**^{8}), 30.0 (q, **C**H_3), 28.1 (t, **C**^{7}), 27.8 (t, **C**^{2}), 25.0 (t, **C**^{3}), 18.2 (t, **C**^{4}); *m/z* LRMS [ES^+, MeOH] 219 ($M + Na^+$, 100%); *m/z* HRMS [ES^+, MeOH] found 415.2092 ($2M + Na^+$) $C_{22}H_{32}O_6Na$ requires 415.2090.

5′-*O*-(4,4′-Dimethoxytrityl)-5-(hex-5-ynyl-4-oxopentanoyl)-2′-deoxyuridine. 5′-*O*-(4,4′-Dimethoxytrityl)-5-iodo-2′-deoxyuridine (2.60 g, 3.96 mmol) was dissolved in anhydrous dimethylformamide (20 mL). Cu^I iodide (302 mg, 1.59 mmol) and triethylamine (5.52 mL, 39.6 mmol) were added, followed by hex-5-ynyl 4-oxopentanoate (1.72 g, 8.72 mmol) in dimethylformamide (5.0 mL). The reaction mixture was stirred under an argon atmosphere in the dark for 10 min before adding $Pd(PPh_3)_4$ (0.92 g, 0.79 mmol), then left to stir for a further 12 h in the dark at room temperature. The solvent was then removed in vacuo, and the residue partitioned between dichloromethane and saturated potassium chloride. The organic layer was washed with water, dried over sodium sulfate, filtered, and the solvent removed in vacuo. Purification by column chromatography (4:1 ethyl acetate/hexane, 1% pyridine) gave the title compound as a pale yellow foam (2.33 g, 81%). R_f (7:3 ethyl acetate/hexane, B′) 0.45; δ_H (400 MHz, d_6-DMSO) 11.6 (1H, s, N**H**), 7.91 (1H, s, **H**^{6}), 7.25−7.71 (9H, m, C**H**^{Ar}), 6.92 (4H, d, $J = 8.5$ Hz, C**H**^{Ar}), 6.16 (1H, t, $J = 6.5$ Hz, **H**^{11}), 5.34 (1H, d, $J = 4.5$ Hz,

O**H**$^{3'}$), 4.32 (1H, bs, **H**$^{3'}$), 3.94 (1H, app t, J = 6.5 Hz, **H**$^{4'}$), 3.77 (6H, s, OC**H**$_3$), 1.55 (1H, dt, J = 14.5, 6.5 Hz, **H**$^{2'}$), 1.35 (1H, dt, J = 15.0, 7.0 Hz, **H**$^{2'}$); δ_C (400 MHz, d_6-DMSO) 206.7 (s, **C**O), 172.2 (s, **C**O), 161.6 (s, **C**O), 158.0 (s, **C**O), 149.3, 144.7 (s, **C**^{Ar}), 141.9 (d, **C**H^6), 135.5, 129.6, 129.6, 128.8, 128.6, 128.1, 127.8 (d, **C**H^{Ar}), 127.6 (s, **C**^{Ar}), 113.1 (d, **C**H^{Ar}), 99.2 (s, **C**), 92.9 (s, **C**^{8}), 85.8 (d, **C**H$^{4'}$), 84.8 (d, **C**H$^{1'}$), 72.4 (s, **C**^{7}), 70.4 (d, **C**H$^{3'}$), 63.3 (t, $^{5'}$**C**H$_2$), 55.0 (q, O**C**H$_3$), 40.0 (t, ^{14}**C**H$_2$), 37.4 (t, ^{12}**C**H$_2$), 29.5 (q, **C**H$_3$), 27.5 (t, ^{13}**C**H$_2$), 27.3 (t, ^{10}**C**H$_2$), 24.4 (t, ^{11}**C**H$_2$), 18.3 (t, $^{2'}$**C**H$_2$); *m*/*z* LRMS [ES$^+$, MeCN] 747 (M + Na$^+$, 100%); *m*/*z* HRMS [ES$^+$, MeCN] found 747.2870 (M + Na$^+$) $C_{41}H_{44}N_2O_{10}Na$ requires 747.2888.

5′-*O*-(4,4′-Dimethoxytrityl)-5-(hex-5-ynyl-4-oxopentanoyl)-2′-deoxyuridine-3′-*O*-(2-cyanoethyl-*N*,*N*-disopropyl)phosphoramidite. 5′-*O*-(4,4′-Dimethoxytrityl)-5-(hex-5-ynyl-4-oxopentanoyl)-2′-deoxyuridine (2.28 g, 3.15 mmol) was dissolved in distilled tetrahydrofuran (20 mL) under argon. *N*,*N*-Diisopropylethylamine (1.4 mL, 7.87 mmol) was added, followed by 2-cyanoethyl-*N*,*N*-diisopropylchlorophosphoramidite (0.77 mL, 3.46 mmol). The reaction mixture was left to stir at room temperature for 1 h, then transferred under argon (with degassed ethyl acetate washings, 2 × 20 mL) into a separating funnel containing degassed ethyl acetate (10 mL). This mixture was washed with saturated potassium chloride (20 mL), dried over sodium sulfate, filtered, and the solvent removed in vacuo. Purification by silica gel column chromatography (7:3 ethyl acetate/hexane, 1% pyridine, under argon pressure) gave the product as a colorless foam (2.49 g, 86%). This was dissolved in anhydrous acetonitrile and filtered through a Millipore Millex-FH syringe filter (0.45 μm, 25 mm diameter). The solvent was removed under reduced pressure, and the monomer was dissolved in freshly distilled dichloromethane. Aliquots of 100 μmol were transferred to monomer reagent bottles and dried in a desiccator overnight under high vacuum before being stored under a slight positive pressure of argon at −20 °C. R_f (4:1 ethyl acetate/hexane, B′) 0.5, 0.45 (diastereomers); δ_P (121 MHz, d_6-DMSO) 148.8, 148.4; *m*/*z* LRMS [ES$^+$, MeCN] 947 (M + Na$^+$, 100%); *m*/*z* HRMS [ES$^+$, MeCN] found 947.3978 (M + Na$^+$) $C_{50}H_{61}N_4O_{11}PNa$ requires 947.3967.

Oligonucleotide Synthesis and Purification. Standard DNA phosphoramidites, solid supports, and additional reagents were purchased from Link Technologies or Applied Biosystems, Ltd. The psoralen C6 phosphoramidite was purchased from Glen Research, Inc. All oligonucleotides were synthesized on an Applied Biosystems 394 automated DNA/RNA synthesizer using a 1.0 μmol phosphoramidite cycle of acid-catalyzed detritylation, coupling, capping, and iodine oxidation. Normal monomers (A, G, C, and T) were allowed to couple for 25 s and all other monomers for an additional 300 s. Stepwise coupling efficiencies and overall yields of monomers with DMT protection were determined by measuring trityl cation conductivity and in all cases were >98.0%.

The deprotection mixture for cleavage of the levulinoyl group from the lev dU monomer was prepared by adding hydrazine monohydrate (30.3 μL) to a stirred solution of distilled pyridine and acetic acid (4:1, 2.5 mL). Deprotection was achieved as follows: An empty 1 mL luer tipped syringe was fitted to one end of the column and a 1 mL luer tipped syringe filled with the deprotection mixture to the other end. The mixture was slowly pushed through the column from one syringe to the other and the process repeated every 3 min. After 12 min, the deprotection solution was removed by syringe, and the column was washed with acetonitrile (6 × 1 mL). It was then returned to the DNA synthesizer for addition of the psoralen C6 phosphoramidite.

Table 1. Oligonucleotide Sequences[a]

Duplexes	
5'-TCA**T**AGAGAA**TA**AAGA**TA**TAGGC-3'	5
3'-AGT**AT**CTCTT**AT**TTCT**AT**ATCCG-5'	6
TFOs	
5'-TCTCTTGTTTCT-3'	7
5'-**Pso**-TCTCTTGTTTCT-3'	8
5'-TCTCTTGTTTC**T**^{Pso}-p-3'	9
5'-**Pso**-TCTCTTGTTTC**T**^{Pso}-p-3'	10
5'-TCTCTTG**T**^{Pso}TTCT-3'	11
5'-**Pso**-TMTMTPGPTPMT-3'	12
5'-**Pso**-TMTMTPGPTPM**T**^{Pso}-prop-3'	13

[a] Oligonucleotides **5**·**6** form the duplex that contains the target site for the TFOs. The TpA steps in the target are shown in bold, and the binding site for the TFOs is underlined. Pso indicates 5′-psoralen (4′-(methoxyhexyl)-4,5′,8-trimethylpsoralen), while **T**^{Pso} corresponds to 5-(6-*O*-levulinoylhex-1-ynyl)-2′-deoxyuridine attached psoralen via an extended hexynyl linker. M and P correspond to 3-methyl-2-aminopyridine-2′-deoxyriboside and 5-(3-aminoprop-2-ynyl)deoxyuridine, respectively. **9** and **10** contain a 3′-phosphate, while **13** has a propanol attached to the 3′-phosphate.

Cleavage of the oligonucleotides from the solid support was carried out in a mixture of *t*-butylamine, methanol, and water (1:1:2) at room temperature for 20 h.

The sequences of the oligonucleotides used in this work are shown in Table 1

Oligonucleotide Purification. Purification of oligonucleotides was carried out by reversed-phase HPLC on a Gilson system using an ABI Aquapore column (C8), 8 mm × 250 mm, pore size 300 Å, controlled by *Gilson 7.12* software. The following protocol was used: Run time 30 min, flow rate 3 mL per minute. Binary system: time in minutes (% buffer B); 0 (0); 3 (0); 5 (20); 22 (100); 25 (100); 27 (0); 30 (0). Elution buffer A: 0.1 M ammonium acetate, pH 7.0. Buffer B: 0.1 M ammonium acetate with 50% acetonitrile pH 7.0 (modified oligomers). Buffer B: 0.1 M ammonium acetate with 25% acetonitrile pH 7.0 (unmodified oligomers). Elution was monitored by ultraviolet absorption at 295 nm (unmodified oligomers) or 305 nm (psoralen-containing oligomers). After HPLC purification, oligonucleotides were desalted using disposable NAP 10 Sephadex columns (Pharmacia) using the manufacturer's instructions, aliquoted into Eppendorf tubes, and stored at −20 °C in distilled deionized water.

Ultraviolet Melting Experiments. UV melting experiments were performed on a Varian Cary 400 Scan UV−visible spectrophotometer, in Hellma SUPRASIL synthetic quartz, 10 mm path length cuvettes, monitoring at 260 nm, at a 1 μM concentration of duplex strands and 10 μM of TFO, in a volume of 1.5 mL. The sample chamber was flushed with air pumped through a desiccant to prevent condensation of atmospheric water on the cells. Samples were prepared as follows: The third strand and duplex were mixed in a 2 mL Eppendorf tube, then lyophilized before resuspending in 1.5 mL of the appropriate buffer solution (50 mM sodium acetate at pH 5.0 containing 200 mM NaCl or 10 mM sodium phosphate at pH 7.0 or 7.5, containing 200 mM NaCl and 1 mM EDTA). The samples were then filtered into the cuvettes with Kinesis regenerated cellulose 13 mm, 0.45 μM syringe filters. Following an initial heating and cooling cycle (20−80−5 °C at 10 °C/min) to ensure uniform annealing of the strands, the UV−melting curves were recorded for three consecutive heating and cooling cycles (20 °C to 80 °C to 20 °C at 0.5 °C/min). Melting curves were then repeated over the triplex melting range at a slower rate of heating and cooling (0.12 °C/min) to eliminate hysteresis.

Fluorescence Measurements. Fluorescence measurements were carried out using a Perkin-Elmer LS 50B luminescence spectrometer. The samples were irradiated for 1 h using a 6 W

Table 2. Thermal Stability (T_m, °C) and Cross-Linking (%) of Triplexes Formed between Psoralen-Linked Oligonucleotides and Duplex 5·6[a]

	T_m (°C)		(% cross-linking after 60 min)			
			purine strand labeled		pyrimidine strand labeled	
TFO	before irradiation	after 60 min irradiation	monoadduct	bis-adduct	monoadduct	bis-adduct
7	25, 56	25, 56	0.0	0.0	0.0	0.0
8	33, 56	58, >75	1.3 ± 0.2	73.4 ± 1.8	7.4 ± 0.4	75.5 ± 2.6
9	30, 56	59, >75	7.2 ± 1.6	68.2 ± 2.3	6.4 ± 2.7	63.6 ± 0.2
10	42, 56		0.4 ± 0.1	73.6 ± 4.6	0.5 ± 0.2	76.8 ± 0.8
11	25, 56	57, 75	10.2 ± 2.5	24.9 ± 5.4	2.2 ± 0.4	31.0 ± 4.2

[a] The reactions were performed in 50 mM sodium acetate pH 5.0 containing 200 mM NaCl.

UVGL-58 Mineralight lamp at 365 nm, with readings taken after 1, 2, 4, 10, 15, 30, and 60 min. The excitation wavelength for psoralen was 340 nm, the slit width was 4 nm, and the scan speed was 120 nm/min. Solutions were prepared using buffer solutions as mentioned above; the concentration of the TFO was 5 μM, and the concentration of the duplex was 25 μM.

Cross-Linking and Gel Electrophoresis. Synthetic oligonucleotides were radiolabeled at the 5′-end using [γ-^{32}P]ATP and polynucleotide kinase. Each radiolabeled oligonucleotide was annealed to its unlabeled complementary strand to generate a duplex in which one strand is labeled. Triplexes were prepared with radiolabeled oligonucleotide duplex (approximately 1 nM) and TFO (10 μM) in a total volume of 30 μL in 50 mM sodium acetate at pH 5.0, containing 200 mM NaCl, or 10 mM sodium phosphate at pH 7.0 or 7.5, containing 200 mM NaCl and 1 mM EDTA, and were incubated at 20 °C for 1 h before cooling on ice for 30 min. The samples (30 μL) were added to a 96-well plate on ice and irradiated with UV light (365 nm) at a distance of 2 cm for various times. At each time point, 4.5 μL was removed and added to 4 μL of 80% formamide containing 10 mM EDTA, 10 mM NaOH, and 0.2% (w/v) bromophenol blue. Samples were heated to 100 °C for 3 min, before rapidly cooling on ice and loading onto a 14% polyacrylamide gel containing 8 M urea. Polyacrylamide gels (40 cm long and 0.3 mm thick) were run at 1500 V for 2 h and then fixed in 10% (v/v) acetic acid. These were transferred to Whatman 3MM paper and dried under vacuum at 86 °C for 1 h. The dried gels were subjected to phosphorimaging using a Molecular Dynamics Storm phosphorimager. The intensity of bands was estimated using *ImageQuant* software. For each reaction, the amounts of monoadduct and bisadduct were expressed as a percentage of total radiolabeled DNA in the lane.

RESULTS AND DISCUSSION

Oligonucleotides. A 23-mer duplex (**5·6**) was used as a target for the psoralen-linked TFOs (**7**−**13**) (Table 1, in which the 12-base pair TFO binding site is underlined). This duplex contains three 5′-TpA-3′ sites (shown in bold) for psoralen cross-linking. These are located at the 5′-end, the center, and the 3′-end of the TFO binding site. Several TFOs with the same sequence but with different points of psoralen attachment were synthesized by automated solid-phase methods. In TFOs **7**−**11**, cytosine is used for recognizing GC base pairs and thymine for recognizing AT. The internal TA inversion is recognized using guanine forming a G.TA triplet. In TFO **8**, psoralen was attached at the 5′-end using 4′-(methoxyhexyl)-4,5′,8-trimethylpsoralen phosphoramidite (Pso C6) from Glen Research, Inc., (**1**, Scheme 1) in the final step of oligonucleotide assembly.

Psoralen was attached internally or at the 3′-end as follows: The modified nucleoside, 5-(6-*O*-levulinoylhex-1-ynyl)-2′-deoxyuridine, was introduced during oligonucleotide synthesis at the desired position as a phosphoramidite monomer. This is similar to a previously reported monomer 5-(*N*(6)-*O*-levulinoyl-1-aminohexyl)-3(*E*)acrylamido)-2′-deoxyuridine (*15*), but an alkynyl group has been introduced to stabilize triplexes (*16*). After oligonucleotide assembly, the levulinoyl group was removed by treatment of the solid support with hydrazine. The column was returned to the DNA synthesizer, and Pso C6 phosphoramidite was coupled to the free hydroxyl group of the modified thymine base (**2**, Scheme 1). The synthetic strategy for incorporating the psoralen internally (and 3′) in the TFO is outlined in Scheme 1. For TFO **9** and TFO **11**, the 5′-end of the TFO was capped with acetic anhydride and *N*-methylimidazole on the DNA synthesizer prior to levulinoyl deprotection to prevent double attachment. TFO **9** and TFO **10** were synthesized using phosphate solid support, which produces an oligonucleotide with a 3′-phosphate group. Subsequently, (in TFO **13**) this was changed for a 3′-hydroxypropylphosphate due to concerns that the bis-hydroxyethylsulfonyl linkage used to introduce a 3′-phosphate might be slightly labile during levulinoyl deprotection. All oligonucleotides were prepared on a 1.0 μmol scale on an ABI 394-08 synthesizer using cyanoethyl phosphoramidite chemistry. They were deprotected in a mixture of *t*-butylamine, methanol, and water (1:1:2) at room temperature for 20 h, then purified by reversed-phase HPLC (*17*). Characterization was carried out by MALDI-TOF mass spectrometry (*18*) (Supporting Information).

UV-Melting Studies. The interaction of unlabeled TFO **7** and psoralen-linked oligonucleotides **8**−**11** with the duplex DNA target **5·6** were initially studied by ultraviolet melting at pH 5.0, and the results are shown in the first two columns of Table 2. In the absence of any TFO, duplex **5·6** gave a single transition with a T_m of 56 °C, whereas in the presence of the unmodified control TFO **7** (without attached psoralen), two transitions were observed, the lower of which (25 °C) was due to triplex melting and the higher (56 °C) to duplex melting. Significant increases in thermal stability were observed for psoralen-labeled TFOs **8**−**10**, even before UV-irradiation. The increase in T_m was 8 °C for the 5′-labeled TFO (**8**), 5 °C for the 3′-labeled sequence (**9**), and 17 °C for the 5′−3′double label (**10**). The very large increase in T_m caused by the latter is particularly striking, suggesting that the psoralens are intercalated at both duplex−triplex junctions and produce a powerful cooperative enhancement of binding to this target. TFO **11**, containing a single internally attached psoralen, did not increase the T_m relative to the unmodified TFO **7**, either because intercalation did not occur or because internal intercalation does not increase triplex stability. These triplexes were then irradiated with UV light (365 nm, for up to 60 min at 0 °C) and subjected to further melting studies. In all cases except the unlabeled control, the melting curves were totally transformed (e.g., Figure 1, TFO **11**). After irradiation, the transition due to dissociation of the TFO disappeared. A minor transition, corresponding to that of the residual duplex, was present around 56 °C, and a new high-temperature transition was observed, which presumably reflects melting of the cross-linked triplex. Shorter irradiation times produced intermediate melting profiles with a significant transition at 55 °C and a high-melting species around 75 °C. It is known that short exposure of psoralen triplexes to UV light leads to the formation of monoadducts between the

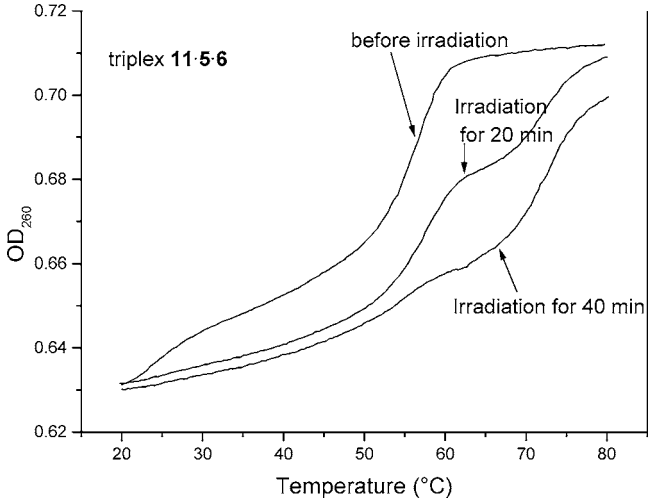

Figure 1. UV-melting profiles for the complex between TFO **11** and duplex **5·6.** The reaction was performed in 50 mM sodium acetate, 200 mM NaCl, pH 5.0. The duplex concentration was 1 μM, and the TFO concentration was 10 μM.

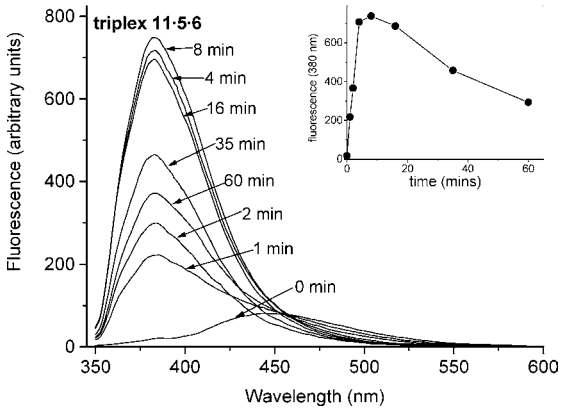

Figure 2. Fluorescence emission spectra of TFO **11** when complexed with duplex **5·6** after various emission times. The reaction was performed in 50 mM sodium acetate pH 5.0 containing 200 mM NaCl. The duplex concentration was 5 μM with a TFO concentration of 1 μM. The inset shows the time-dependent fluorescence intensity at 380 nm.

TFO and a single strand of the DNA target, and further irradiation converts these to bis-adducts (*13*). The changes in the UV-melting curves after irradiation of triplexes **8·5·6** and **9·5·6** were similar to those observed for triplex **11·5·6**. Interestingly, no melting transitions were observed after UV-irradiation of triplex **10·5·6** (Supporting Information). In this case, the psoralen moieties at both ends of the TFO can form double-strand cross-links with the duplex to produce a very stable species (a triplex staple) with no free ends to initiate the triplex melting processes. Such a species might have the added advantage of being resistant to enzymic degradation in vivo. These thermal stability measurements suggest that internally linked psoralen, as well as psoralen attached at the 3′- and 5′-ends of a TFO, can form photoreaction products with the duplex target.

Fluorescence Studies. Further proof of cross-linking between the intercalated psoralen and its target can be obtained from fluorescence measurements (*19*). TFO **11**, containing an internally attached psoralen, exhibited a weak fluorescence emission spectrum between 380 and 600 nm with maximum at 460 nm (Figure 2). Upon hybridization with the target duplex **5·6**, the intensity of the psoralen fluorescence dropped slightly, while the λ_{max} shifted from 460 to 450 nm due to fluorescence quenching of the excited state of the intercalated dye by the DNA bases. After irradiation at 365 nm to promote cross-linking, the fluorescence at 450 nm declined, and a new intense peak appeared at 380 nm due to formation of the monoadduct. Further irradiation produced a decline in fluorescence intensity due to the conversion of the monoadducts to bis-adducts (*19*). Fluorescence experiments with the other psoralen modified triplexes produced similar results. The final fluorescence intensity at 380 nm was lowest for the complex formed with TFO **8·5·6**, suggesting that the 5′-modification produces the greatest conversion to the bis-cross-linked adduct (Supporting Information).

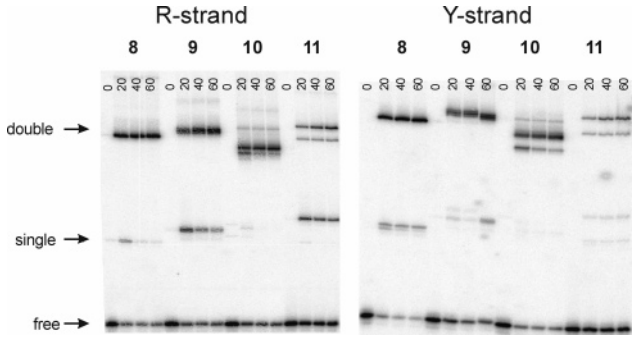

Figure 3. UV-induced cross-linking of the psoralen-linked oligonucleotides to duplex **5·6**. The target duplex was labeled on either the purine (**5**) or pyrimidine (**6**) strand. The reactions were performed in 50 mM sodium acetate pH 5.0 containing 200 mM NaCl. The concentration of the third strand was 10 μM; this was equilibrated with the duplex (approximate concentration 1 nM) for 1 h at 20 °C before irradiating for 0, 20, 40, and 60 min. The samples were then denatured and run on a 14% polyacrylamide gel containing 8 M urea. "free", "single", and "double" indicate the presence of a single DNA strand, the adduct(s) between the TFO and one strand of the duplex, and the adduct(s) between the TFO and both strands of the duplex, respectively.

Gel Electrophoresis. The propensity of psoralen-labeled TFOs to form double-strand cross-links with target duplexes was further investigated by gel-retardation analysis (*20*). One strand of the duplex was labeled at the 5′-end with [^{32}P] phosphate, and after irradiation at 365 nm, the reaction products were analyzed by denaturing polyacrylamide gel electrophoresis. Figure 3 shows the time dependence of typical experiments with TFOs **8**−**11**, and the relative intensities of the bands is shown in Table 2. With TFO **8**, the usual pattern of retarded bands is produced when the duplex is labeled on either the purine or pyrimidine strands (*20*). The lower retarded species corresponds to the monoadduct, with the TFO cross-linked to the labeled strand, while the upper (slower) band corresponds to the bis-adduct in which the TFO is linked to both strands of the duplex. The slower bis-adduct is the predominant species, and it increases with irradiation time. On the labeled purine strand, the intensity of the band due to the monoadduct decreases with longer irradiation times, suggesting that this is converted to the bis-adduct. In contrast, with the labeled pyrimidine strand, there are two monoadduct bands, the most intense of which remains constant and does not diminish with longer irradiation times. The banding pattern for the purine strand is consistent with previous observations that the furan side of the psoralen first reacts with the purine-labeled strand and that this initial cycloaddition product undergoes a second reaction involving the 3,4-double bond on the pyrone moiety of psoralen to produce the bis-adduct (*10, 21*). If the first reaction were to involve the pyrone 3,4-double bond, then this monoadduct could not be converted to the bis-adduct by further photolysis. In contrast, the small amount of stable monoadduct formed with the pyrimidine-labeled strand must correspond to reaction with the pyrone 3,4-bond, and this is not converted to the bis-adduct on further irradiation. The lower of the two pyrimidine monoadduct bands disappears with prolonged irradiation, suggesting that there is some degree of initial cross-linking of the furan moiety

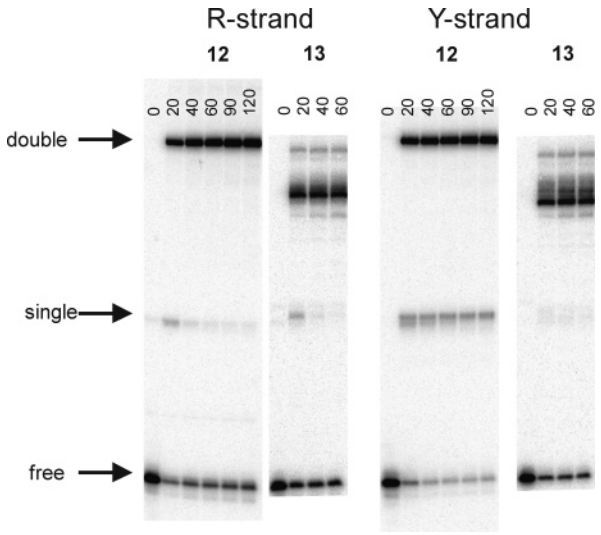

Figure 4. UV-induced cross-linking of psoralen-linked TFOs **12** and **13** to duplex **5·6**. The target duplex was labeled on either the purine-containing (**5**) or pyrimidine-containing (**6**) strand. The reactions were performed in 10 mM sodium phosphate pH 7.0 containing 200 mM NaCl and 1 mM EDTA. The concentration of the third strand was 10 μM; this was equilibrated with the duplex for 1 h at 20 °C before irradiating for 0, 20, 40, 60, and 120 min. The samples were then denatured and run on a 14% polyacrylamide gel containing 8 M urea. "free", "single", and "double" indicate the presence of a single DNA strand, the adduct(s) between the TFO and one strand of the duplex, and the adduct(s) between the TFO and both strands of the duplex, respectively.

of psoralen to the pyrimidine strand followed by cross-linking of the pyrone moiety to the purine strand. This complexity arises from the fact that there are two possible intercalation modes for psoralen at TpA sites. A similar effect is observed with TFOs **9**−**11**, though the yield of the fully cross-linked bis-adduct is lower. TFO **10**, containing two psoralen moieties, produced a more complicated pattern of cross-linked species. It is likely that the most intense band in the lanes for TFO **10** in both gels is due to a 5′,3′-double cross-link, whereas the band just below this arises from a 5′-double, 3′-single cross-link, which is almost completely converted to the upper band over the time course of the experiment. The very weak high running band has the same mobility as the double cross-links for TFOs **8**, **9**, and **11** and is probably due to a double cross-link at one end of the TFO and no cross-linking at the other end. This could arise from a minor intramolecular photoreaction between psoralen and a thymine base in the TFO, which renders the psoralen inert to reaction with the duplex. Indeed, TFO **10** has a 5′-thymine adjacent to psoralen. In TFOs **8**, **9**, and **11**, such a species would not be observed, as the inactivated TFOs would fail to interact with the duplex. Surprisingly, TFO **11** also produces a complex pattern of retarded bands, suggesting that this single central psoralen can react at more than one location, and this is the only case where a stable monoadduct is formed with the purine strand of the duplex.

Similar experiments were also performed with oligonucleotides in which the central psoralen was tethered by different length linkers (not shown). When psoralen C2 phosphoramidite was used in place of psoralen C6 in TFO **11**, only 0.5% double-strand cross-linking was observed after 60 min irradiation. A longer linker was then produced by synthesizing a TFO with hexaethylene glycol inserted between the oligonucleotide and Pso C6; this also produced a low level of cross-linking (4% double-strand cross-linking after 60 min irradiation).

These experiments were performed at pH 5.0 to ensure protonation of the third strand cytosine and therefore the formation of stable triplexes. No significant cross-linking was observed at pH 6.0 or 7.0. For nonbiological applications, e.g., in nanotechnology, TFOs can be used at low pH to reversibly attach functionality to double-stranded DNA scaffolds. However, in most biological applications, triplexes have to be stable under physiological conditions. We therefore prepared two psoralen-labeled TFOs containing modified bases (TFOs **12** and **13**) and investigated their photoreaction at pH 7.0. 3-Methyl-2-amino-pyridine-2′-deoxyriboside (M) (**3**, Scheme 1) (*22*, *23*) recognizes GC at elevated pH and 5-(3-aminoprop-2-ynyl)deoxyuridine (P) (**4**, Scheme 1) (*16*, *24*) produces stable recognition of AT. The results of experiments with these oligonucleotides at pH 7.0 are shown in Figure 4, and the relative cross-linking at pH 7.0 and 7.5 is presented in Table 3. As expected, these modified TFOs produce efficient cross-linking at pH 5.0 (not shown), which is also evident at pH 7.0 and higher.

Table 3. Cross-Linking (%) of Triplexes Formed between Psoralen-Linked Oligonucleotides Containing Modified Bases and Duplex 5·6[a]

	purine strand labeled		pyrimidine strand labeled	
TFO	monoadduct	bis-adduct	monoadduct	bis-adduct
		pH 7.0		
12	0.7 ± 0.1	80.9 ± 0.6	9.5 ± 0.5	83.2 ± 2.4
13	0.6 ± 0.2	52.9 ± 4.7	0.6 ± 0.2	60.8 ± 4.1
		pH 7.5		
12	0.8 ± 0.3	41.9 ± 13.9	4.4 ± 0.8	41.8 ± 7.2
13	0.2 ± 0.2	7.2 ± 3.3	0.0	11.3 ± 6.0

[a] The reactions were performed in 10 mM sodium phosphate pH 7.0 or 7.5, containing 200 mM NaCl and 1 mM EDTA and were irradiated for 60 min.

CONCLUSIONS

This new methodology provides a means for covalently attaching psoralen to any thymine within a triplex-forming oligonucleotide. This relaxes some of the constraints on selection of TFO target sequences. By using psoralen derivatives in combination with nucleotide analogues, triplex-directed double-stranded psoralen photoadduct formation can be achieved under near-physiological conditions.

ACKNOWLEDGMENT

This work was supported by grants from the European Union and the BBSRC.

Supporting Information Available: Additional experimental data. This material is available free of charge via the Internet at http://pubs.acs.org.

LITERATURE CITED

(1) Fox, K. R. (2000) Targeting DNA with triplexes. *Curr. Med. Chem. 7*, 17−37.

(2) Beal, P. A., and Dervan, P. B. (1991) Second structural motif for recognition of DNA by oligonucleotide-directed triple-helix formation. *Science 251*, 1360−1363.

(3) Radhakrishnan, I., Delossantos, C., and Patel, D. J. (1991) Nuclear magnetic resonance structural studies of intramolecular purine.purine.pyrimidine DNA triplexes in solution - base triple pairing alignments and strand direction. *J. Mol. Biol. 221*, 1403−1418.

(4) Moser, H. E., and Dervan, P. B. (1987) Sequence-specific cleavage of double helical DNA by triple helix formation. *Science 238*, 645−650.

(5) Faria, M., and Giovannangeli, C. (2001) Triplex-forming molecules: from concepts to applications. *J. Gene. Med. 3*, 299−310.

(6) Knauert, M. P., and Glazer, P. M. (2001) Triplex forming oligonucleotides: sequence-specific tools for gene targeting. *Hum. Mol. Genet. 10*, 2243−2251.

(7) Lavelle, L., and Fresco, J. R. (1995) UV spectroscopic identification and thermodynamic analysis of protonated third strand deoxycytidine residues at neutrality in the triplex $d(C^+\text{-}T)_6$:[$d(A\text{-}G)_6.d(C\text{-}T)_6$]; evidence for a Proton Switch. *Nucleic Acids Res. 23*, 2692−2705.

(8) Singleton, S. F., and Dervan, P. B. (1992) Influence of pH on the equilibrium association constants for oligodeoxyribonucleotide-directed triple helix formation at single DNA sites. *Biochemistry 31*, 10995−11003.

(9) Cimino, G. D., Gamper, H. B., Isaacs, S. T., and Hearst, J. E. (1985) Psoralens as photoactive probes of nucleic-acid structure and function - organic chemistry, photochemistry and biochemistry. *Annu. Rev. Biochem. 54*, 1151−1193.

(10) Takasugi, M., Guendouz, A., Chassignol, M., Decout, J. L., Lhomme, J., Thuong, N. T., and Hélène, C. (1991) Sequence-specific photoinduced cross-linking of the two strands of double-helical DNA by a psoralen covalently linked to a triple helix-forming oligonucleotide. *Proc. Natl. Acad. Sci. U.S.A. 88*, 5602−5606.

(11) Ping, Y. H., and Rana, T. M. (2005) Mechanism of site-specific psoralen photoadduct formation in triplex DNA directed by psoralen-conjugated oligonucleotides. *Biochemistry 44*, 2501−2509.

(12) Giovannangeli, C., Thuong, N. T., and Hélène, C. (1992) Oligodeoxynucleotide-directed photoinduced cross-linking of HIV proviral DNA via triple-helix formation. *Nucleic Acids Res. 20*, 4275−4281.

(13) Besch, R., Giovannangeli, C., Schuh, T., Kammerbauer, C., and Degitz, K. (2004) Characterization and quantification of triple helix formation in chromosomal DNA. *J. Mol. Biol. 341*, 979−989.

(14) Shahid, K. A., Majumdar, A., Alam, R., Liu, S. T., Kuan, J. Y., Sui, X. F., Cuenoud, B., Glazer, P. M., Miller, P. S., and Seidman, M. M. (2006) Targeted cross-linking of the human beta-globin gene in living cells mediated by a triple helix forming oligonucleotide. *Biochemistry 45*, 1970−1978.

(15) Lyttle, M. H., Walton, T. A., Dick, D. J., Carter, T. G., Beckman, J. H., and Cook, R. M. (2002) New reagents and methods for the synthesis of internal and 3′-labeled DNA. *Bioconjugate Chem. 13*, 1146−1154.

(16) Bijapur, J., Keppler, M. D., Bergqvist, S., Brown, T., and Fox, K. R. (1999) 5-(1-propargylamino)-2′-deoxyuridine (U^p): a novel thymidine analogue for generating DNA triplexes with increased stability. *Nucleic Acids Res. 27*, 1802−1809.

(17) Brown, T., and Brown, D. J. S. (1992) Purification of synthetic DNA. *Methods Enzymol. 211*, 20−35.

(18) Langley, G. J., Herniman, J. M., Davies, N. L., and Brown, T. (1999) Simplified sample preparation for the analysis of oligonucleotides by matrix-assisted laser desorption/ionisation time-of-flight mass spectrometry. *Rapid Commun. Mass Spectrom. 13*, 1717−1723.

(19) Song, P. S., and Tapley, K. J. (1979) Photochemistry and photobiology of psoralens. *Photochem. Photobiol. 29*, 1177−1197.

(20) Yeung, A. T., Jones, B. K., and Chu, C. T. (1988) Photoreactivities and thermal-properties of psoralen cross-links. *Biochemistry 27*, 3204−3210.

(21) Bates, P. J., Laughton, C. A., Jenkins, T. C., Capaldi, D. C., Roselt, P. D., Reese, C. B., and Neidle, S. (1996) Efficient triple helix formation by oligodeoxyribonucleotides containing alpha- or beta-2-amino-5-(2-deoxy-D-ribofuranosyl)pyridine residues. *Nucleic Acids Res. 24*, 4176−4184.

(22) Cassidy, S. A., Slickers, P., Trent, J. O., Capaldi, D. C., Roselt, P. D., Reese, C. B., Neidle, S., and Fox, K. R. (1997) Recognition of GC base pairs by triplex forming oligonucleotides containing nucleosides derived from 2-aminopyridine. *Nucleic Acids Res. 25*, 4891−4898.

(23) Hildbrand, S., Blaser, A., Parel, S. P., and Leumann, C. J. (1997) 5-substituted 2-aminopyridine C-nucleosides as protonated cytidine equivalents: Increasing efficiency and selectivity in DNA triple-helix formation. *J. Am. Chem. Soc. 119*, 5499−5511.

(24) Sollogoub, M., Darby, R. A. J., Cuenoud, B., Brown, T., and Fox, K. R. (2002) Stable DNA triple helix formation using oligonucleotides containing 2′-aminoethoxy,5-propargylamino-U. *Biochemistry 41*, 7224−7231.

BC0601875

Synthesis and in Vitro Biological Evaluation of Mannose-Containing Prodrugs Derived from Clinically Used HIV-Protease Inhibitors with Improved Transepithelial Transport

Dominique Roche,[†] Jacques Greiner,[†] Anne-Marie Aubertin,[‡] and Pierre Vierling*[,†]

Laboratoire de Chimie des Molécules Bioactives et des Arômes, UMR 6001 CNRS, Université de Nice Sophia-Antipolis, Parc Valrose, F-06108 Nice Cédex 2, France, and INSERM U74, Institut de Virologie, 3 rue Koeberlé, F-67000 Strasbourg, France. Received July 12, 2006; Revised Manuscript Received September 22, 2006

In an approach to improve the pharmacological properties, safety and pharmacokinetic profiles, and their penetration into HIV reservoirs or sanctuaries, and consequently, the therapeutic potential of the current protease inhibitors (PIs) used in clinics, we investigated the synthesis of various mannose-substituted saquinavir, nelfinavir, and indinavir prodrugs, their in vitro stability with respect to hydrolysis, anti-HIV activity, cytotoxicity, and permeation through a monolayer of Caco-2 cells used as a model of the intestinal barrier. Mannose-derived conjugates were prepared in two steps, in good yields, by condensing an acid derivative of a protected mannose with the PIs, followed by deprotection of the sugar protecting group. With respect to hydrolysis, these PI prodrugs are chemically stable with half-life times in the 50−60 h range that are compatible with an in vivo utilization aimed at improving the absorption/penetration or accumulation of the prodrug in specific cells/tissues and liberation of the active free drug inside HIV-infected cells. These stabilities correlate closely with the low in vitro anti-HIV activity measured for those prodrugs wherein the coupling of mannose to the PIs was performed through the peptidomimetic PI's hydroxyl. Importantly, mannose conjugation to the PIs was further found to improve the absorptive transepithelial transport of saquinavir and indinavir but not of nelfinavir across Caco-2 cell monolayers, by contrast to glucose conjugation which had the opposite effect. The mannose-linked prodrugs of saquinavir and indinavir display therefore a most promising therapeutic potential provided that bioavailability, penetration into the HIV infected macrophages, and HIV-reservoirs of these PIs are improved.

INTRODUCTION

Combination therapy against AIDS using two types of inhibitors, HIV reverse transcriptase and protease inhibitors (PIs), has been remarkably successful in reducing viral load below the threshold of detectability and increasing T4 lymphocytes, leading to a decline in morbidity and mortality (*1*). However, despite these improvements, viral replication in infected patients persists, indicating the existence of reservoirs or sanctuaries for the virus, such as the lymphatic system and central nervous system (*2*−*4*), wherein the antivirals, and more particularly the PIs, do not penetrate at an inhibitory level (*5*, *6*).

To reduce total body viral replication, alternatives are to develop new more efficient PIs or to improve the pharmacological properties, safety and pharmacokinetic profiles, and, consequently, the therapeutic potential of the PIs already used in clinics. Aiming at this latter goal, we adopted the very efficient prodrug approach (*7*−*14*). This approach has been widely used for improving HIV reverse transcriptase inhibitors (*8*, *15*, *16*). It also has been applied to PIs (*9*, *17*−*19*), and successful results were obtained with the disclosure of the recently FDA-approved fosamprenavir, a phosphate ester prodrug of amprenavir (*20*−*24*). However, a number of shortcomings have still to be overcome for the PIs. Among others, the generation of "modified" PIs should display higher water solubility, increased bioavailability (plasma concentration, blood circulation time), and/or improved delivery into HIV sanctuaries. One should also be able with these "modified" PIs to (i) circumvent their inactivation resulting from their in vivo binding to mainly the plasma α_1-acid glycoprotein, (ii) limit their rapid metabolization and inactivation by the liver cytochrome P450 enzymes (mainly the 3A4 isoform), and/or (iii) inhibit their possible transport by the multi-drug-resistant P-glycoprotein (P-gp) responsible for their limited oral bioavailability and brain penetration (*25*, *26*).

In continuation of our previous studies that already showed the benefit of the prodrug approach (*27*−*30*), one of the remaining challenge is the targeting of HIV reservoirs and particularly the lymphatic system. It is well-known that macrophages and dendritic cells are professional antigen presenting cells, unique in their ability to initiate naive T cells, and primary targets for HIV-1 infection. The regeneration of these cells is of particular interest for helping the immune system to overcome the virus. Macrophages and dendritic cells abundantly express mannose receptors (*31*−*33*). Thus, receptor-mediated PIs transfer via mannose receptor offers a versatile tool for targeting PIs toward these cells (*34*−*37*). Therefore, we tagged PIs used in clinics, saquinavir (Saq), indinavir (Ind), and nelfinavir (Nelf), with a mannose residue. Although for successful and efficient targeting one should conjugate these entities to multivalent cluster glycoside moieties to obtain high-affinity ligands for the mannose receptor, as reported by several groups (*31*−*33*), we connected nevertheless the PIs to only a single and/or two mannose residues (in the case of indinavir and nelfinavir). Indeed, recognition of low molecular weight mannosides, even of monomers, by the mannose receptor was shown to be possible, albeit weak (*38*). This could be nevertheless sufficient to improve their absorption/penetration or accumulation into those reservoirs of HIV. Moreover, the development of cluster glycoside structures is a highly demanding and challenging strategy, leading to high-molecular weight compounds. This

* To whom correspondence should be addressed.
[†] UMR 6001 CNRS, Université de Nice Sophia-Antipolis, Parc Valrose.
[‡] INSERM U74, Institut de Virologie.

10.1021/bc060210m CCC: $33.50 © 2006 American Chemical Society
Published on Web 11/01/2006

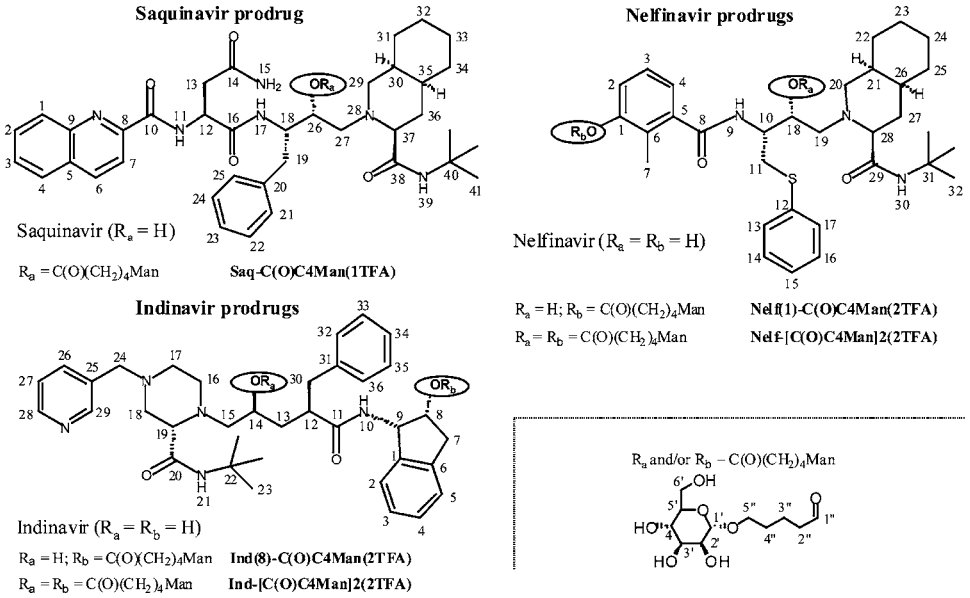

Figure 1. Chemical structures and code names of the mannose-containing protease inhibitor (PI = saquinavir, indinavir, and nelfinavir) prodrugs described in this study and atom numbering used in the description of their NMR spectra.

constitutes a drawback when the use of such high-value prodrugs as oral therapeutics against AIDS is contemplated and is also a reason for selecting mannose monovalent/divalent PI conjugates. The PI and mannose moieties were linked together through a hydrolyzable ester function. As esterases are ubiquitous in cells, in vivo hydrolysis of the ester prodrugs is expected to release the active parent drug. Although the mannose receptor tolerates ligands with large substituents at the mannose C-1 anomeric position (*39*), a spacer between the PI and mannose units was nevertheless introduced for the modulation of the chemical and biological stability of the prodrugs and for the accessibility of mannose, thus allowing a better recognition by its cellular receptors. For synthetic purposes, and as the impact of the anomeric mannosyl carbon atom on its recognition by the cellular receptor is not well established, the mannose unit was joined to the spacer through a glycoside bond of α/β configuration. This should further preserve its recognition (*39*−*42*).

This paper is dedicated to the synthesis of various mannose-derived PI prodrugs (Figure 1), their chemical stability with respect to hydrolysis under physiological conditions, and their in vitro anti-HIV activity. Using an in vitro model (i.e., Caco-2 cell monolayer) that mimics the human intestinal epithelium, we report also on their transepithelial transport. All these features are some of the prerequisites for further in vitro and in vivo investigations, including binding to and uptake into mannose receptor expressing cells and reservoirs of HIV, and pharmacokinetic studies.

EXPERIMENTAL PROCEDURES

Chemical Section. *General.* Unless otherwise indicated, the reactions were performed under anhydrous nitrogen using dry solvents and reagents. Anhydrous solvents were prepared by standard methods. Chlorotrimethylsilane, 2,2-dimethoxypropane, 1-(3-dimethylaminopropyl)-3-ethyl-carbodiimide hydrochloride (EDC), 4-dimethylaminopyridine (DMAP), lithium hydroxide, pyridine, triethylamine, *p*-toluenesulfonic acid (*p*-TsOH), and *N*,*O*-bis(trimethylsilyl)acetamide *δ*-valerolactone were purchased from Aldrich, and ammonium iodide, 2-chloropyridine, 2,6-dimethylpyridine, diphenyl sulfoxide, iodotrimethylsilane, mannose, 2-methoxypropene, trifluoroacetic acid (TFA), and trifluoromethanesulfonic anhydride were from Fluka. All these materials were used without further purification. Saquinavir, indinavir, and nelfinavir (as their methanesulfonate salt or sulfate salt) were a gift from Hoffmann-La Roche, E. Merck, and Agouron, respectively, and were deprotonated prior to their use in the synthetic processes ($CHCl_3$ or EtOAc extraction of the free base from a $NaHCO_3$ or Na_2CO_3 10% solution of the antiprotease).

Using previously described procedures, methyl 5-hydroxypentanoate was quantitatively prepared by the acid-catalyzed transesterification of *δ*-valerolactone with methanol (*43*, *44*). Because of its easy relactonization, the product was used without purification immediately after preparation [R_f 0.63 (AcOEt); ^{1}H NMR ($CDCl_3$): δ 3.80 (s, 1 H, OH), 3.38 (s, 3 H, OCH_3), 3.31 (t, *J* 6.1 Hz, 2 H, H-5), 2.07 (t, *J* 7.3, 2 H, H-2), 1.49−1.21 (m, 4 H, H-3, H-4); ^{13}C NMR ($CDCl_3$): δ 173.91 (C-1), 61.2 (C-5), 51.0 (OCH_3), 33.2 (C-2′), 31.4 (C-4), 20.8 (C-3)].

2,3;4,6-Di-*O*-isopropylidene-α-D-mannopyranoside **3α** (HO-ManP) was prepared from D-mannose in three steps consisting of the synthesis of benzyl α-D-mannopyranoside, then protection as the benzyl 2,3;4,6-di-*O*-isopropylidene-α-D-mannopyranoside, then benzyl deprotection (nearly 55% yields), as described in the literature (*45*−*47*) [R_f 0.26 (7:3 hexane-AcOEt); ^{1}H NMR (DMSO-d_6): δ 6.47 (s, 1 H, OH), 5.13 (s, 1H, H-1′), 4.70 (dd, 1 H, *J* 5.9, *J* 3.6 Hz, H-3′), 4.44 (d, 1H, *J* 5.9 Hz, H-2′), 4.24 (∼ q, 1 H, *J* 6.4, 5.8 Hz, H-5′), 4.01 (dd, 1 H, *J* 6.4, 3.6 Hz, H-4′), 3.96 (dd, 1 H, *J* 8.3, *J* 6.4 Hz, H-6′a), 3.82 (dd, 1 H, *J* 8.3, *J* 5.8 Hz, H-6′b), 1.34, 1.32, 1.26, and 1.23 (4 s, 12 H, CH_3C); ^{13}C NMR (DMSO-d_6): δ 111.3 and 107.9 ($CH_3\underline{C}$), 100.4 (C-1′), 85.5 (C-2′), 79.4 (C-3′), 79.2 (C-4′), 72.8 (C-5′), 65.9 (C-6′), 26.6, 25.7, 25.2, and 24.3 ($\underline{C}H_3$C)].

If not specified, column chromatography purifications were carried out on Silica Gel 60 (E. Merck, 70−230 mesh). The purity of all new compounds was checked by TLC, NMR, MS, and HPLC. TLC analyses were performed on precoated Silica Gel F254 plates (E. Merck) with detection by UV and by charring with 50% methanol−sulfuric acid solution, ninhydrin or $KMnO_4$. HPLC analyses of the synthesized prodrugs (flow of 1 mL/min) were performed using a HP1100 apparatus using a Lichrospher 100 RP-18 (5 μm) column (250 × 3.2 mm) with gradient A: H_2O-CH_3CN (v:v) 0.1% TFA gradient as eluent (from 80:20 to 0:100) over 30 min; UV detection at 210 nm. With these conditions, retention times (R_t) of indinavir, nelfinavir, and saquinavir are 10.4, 10.8, and 15.3 min, respectively. ^{1}H, ^{13}C, and ^{19}F NMR spectra were recorded with a Brucker AC 200 or AC 500 spectrometer at 200 (or 500), 50.3 (or 125.8),

and 188.3 MHz, respectively. Chemical shifts (δ) are given in ppm relative to the signal (i) of remaining $CHCl_3$ (δ 7.26) for ^1H, (ii) of $CDCl_3$ (δ 77.16) for ^{13}C, or of remaining water for ^1H (δ 4.87) and CD_3OD for ^{13}C (δ 49.00) when recorded in CD_3OD. Concerning the description of the prodrug NMR spectra, the atoms of the PI part are depicted as C-x and H-y, whereas those of the sugar part are depicted as C-x′ and H-y′ according to their standard nomenclature numbering and those of the linker part are depicted as C-x″ and H-y″ (see Figure 1 for numbering). COSY $^1H/^1H$, $^1H/^{13}C$ NMR correlation (on Brucker AC 500 spectrometer), ^{13}C DEPT, and/or mass spectrometry data fully confirm the signal assignments and structure of the isolated materials. The mannose-deprotected target compounds consisted of TFA salts, and the TFA anion quantification was assessed by ^{19}F NMR using 3,3,3-trifluoroethanol as an internal standard. Electron-spray ionization mass spectra (ESI-MS) were run on a Finnigan MAT TSQ 7000 apparatus equipped with an atmospheric pressure ionization source. This method used in positive mode gives either M^+, $[M + H]^+$ and/or $[M + Na]^+$ signals.

Syntheses. *Methoxycarbonylbutyl-α-D-mannopyranoside, **7α,β** and **7α**.* D-Mannose (5.0 g, 25 mmol) and *N,O*-bis(trimethylsilyl)acetamide (30 mL, 125 mmol) in anhydrous CH_2Cl_2 were stirred at room temperature for 12 h. The reaction mixture was evaporated under reduced pressure. The resulting mixture diluted in Et_2O (100 mL) was washed with 5% aq HCl, saturated aq $NaHCO_3$, and water. The organic layer was dried over Na_2SO_4 and concentrated giving a mixture of trimethylsilyl 2,3,4,6-tetra-*O*-trimetylsilyl-D-mannopyranoside **6α,β** as an oil (15 g, α:β = 79:21) [R_f 0.82 (CH_2Cl_2); ^1H NMR ($CDCl_3$): δ 4.88 (m, 1 H, H-1α); 4.62 (m, 0.27 H, H-1β); ^{13}C NMR ($CDCl_3$): δ 95.8 (C-1α), 95.7 (C-1β)]. Freshly distilled iodotrimethylsilane (1.5 mL, 11.0 mmol) was added to a solution of **6α,β** (5 g, 2.13 mmol) in dry CH_2Cl_2 (100 mL). After the sample was stirred at room temperature for 45 min, tetrabutylammonium iodide (6.75 g, 10.7 mmol) was added and stirred for 15 min more before adding a CH_2Cl_2 solution (50 mL) containing methyl 5-hydroxypentanoate (2.35 g, 16 mmol) and 2,6-lutidine (1.25 mL, 16 mmol). The reaction mixture was stirred at room temperature for 6 h, and then desilylation was performed in 30 min with MeOH (200 mL). After addition of Et_3N, the resulting solution was concentrated and purified by column chromatography (9:1 CH_2Cl_2-MeOH) affording **7α,β** as a yellow solid (2.3 g, 30% with α:β = 60:40).

R_f 0.56 (9:1 CH_2Cl_2-MeOH); ^1H NMR ($CDCl_3$): δ 5.15 (bs, 3 H, 3 OH), 4.78 (s, 0.6 H, H-1′α), 4.60 (s, 1 H, OH), 4.48 (s, 0.4 H, H-1′β), 4.10−3.72 (m, 5 H, H-2′, H-3′, H-4′, H-6′), 3.64 (s, 3 H, OCH_3), 3.64−3.18 (m, 3 H, H-5′, H-5″), 2.31 (t, *J* 7.1 Hz, 2 H, H-2″), 1.62 (m, 4 H, H-3″, H-4″); ^{13}C NMR ($CDCl_3$): δ 174.2 (C-1″), 100.2 (C-1′α,β), 77.4 (C-5′β), 74.0 (C-3′β), 72.5 (C-5′α), 71.6 (C-2′β), 71.3 (C-3′α), 71.0 (C-2′α), 69.4 (C-5″β), 67.3 (C-5″α), 66.4 (C-4′α), 66.3 (C-4′β), 61.0 (C-6′α,β), 51.7 (OCH_3), 33.8 (C-2″), 28.9 (C-4″), 21.7 (C-3″). ESI-MS (positive mode): $(M + Na)^+ = 316.9$ in agreement with the mass calculated for $M = C_{12}H_{22}O_8$ (294.13).

The same experimental procedure when applied to 1.0 g of **6α,β** gave, after several purifications by column chromatography (9:1 CH_2Cl_2-MeOH), **7α** as a yellow solid (0.46 g, 30%). R_f 0.56 (9:1 CH_2Cl_2-MeOH); ^1H NMR ($CDCl_3$): δ 5.06 (bs, 1 H, OH), 5.03 (bs, 1 H, OH), 4.95 (bs, 1 H, OH), 4.79 (s, 1 H, H-1′), 4.49 (bs, 1 H, OH), 3.94−3.88 (m, 3 H, H-2′, H-3′, H-6′a), 3.80−3.73 (m, 2 H, H-4′, H-6′b), 3.65 (bs, 4 H, H-5″a, OCH_3), 3.47 (m, 1 H, H-5′), 3.39 (m, 1 H, H-5″b), 2.32 (t, *J* 7.1 Hz, 2 H, H-2″), 1.66−1.57 (m, 4 H, H-3″, H-4″); ^{13}C NMR ($CDCl_3$): δ 174.2 (C-1″), 100.2 (C-1′), 72.4 (C-5′), 71.7 (C-3′), 71.1 (C-2′), 67.3 (C-5″), 66.4 (C-4′), 61.1 (C-6′), 51.7 (OCH_3), 33.8 (C-2″), 28.9 (C-4″), 21.8 (C-3″); ESI-MS (positive mode): $(M + Na)^+ = 316.9$ in agreement with the mass calculated for $M = C_{12}H_{22}O_8$ (294.13).

*2,3,4,6-Di-O-isopropylidene-1-(4-methoxycarbonylbutyl)-α-D-mannopyranoside, **4α**. Path A.* Trifluoromethanesulfonic anhydride (24 μL, 0.16 mmol) was added to a solution of **3α** (30 mg, 0.11 mmol) and diphenyl sulfoxide (65 mg, 0.32 mmol) in a mixture of 1:3 toluene−dichloromethane (4 mL) at −78 °C, and stirred for 5 min, then at −40 °C for 1 h. Chloropyridine (54 μL, 0.57 mmol) and methyl 5-hydroxypentanoate (43.6 mg, 0.33 mmol) were then added successively. The resulting solution was stirred at −40 °C for 1 h, at 0 °C for 30 min, and finally at 23 °C for 1 h before the addition of excess Et_3N (153 μL, 1.09 mmol). The solution diluted with CH_2Cl_2 (50 mL) was successively washed with saturated aq Na_2CO_3 and saturated aq NaCl. The organic layer was dried over Na_2SO_4 and concentrated, and the residue was purified by column chromatography (gradient elution: 10:0 to 1:1 hexane−ethyl acetate) to afford **4α** as a white solid (10 mg, 4%).

Path B. p-Toluenesulfonic acid (*p*-TsOH) (20 mg, 0.1 mmol) was added to a solution of **7α** (0.5 g, 1.70 mmol) and 2-methoxypropene (0.64 mL, 6.7 mmol) solubilized in CH_2Cl_2 (20 mL). After the sample was stirred for 6 h at room temperature, the resulting solution was made neutral with $NaHCO_3$ (8.4 mg, 0.1 mmol) and concentrated, and purification by column chromatography (98:2 CH_2Cl_2-AcOEt) afforded compound **4α** (400 mg, 63%).

R_f 0.71 (98:2 CH_2Cl_2-AcOEt); ^1H NMR ($CDCl_3$): δ 4.89 (s, 1 H, H-1′), 4.08−4.04 (m, 2 H, H-2′, H-3′), 3.81−3.57 (m, 7 H, H-4′−6′, OCH_3), 3.50−3.41 (m, 1 H, H-5″a), 3.37−3.27 (m, 1 H, H-5″b), 2.25 (t, *J* 7.0 Hz, 2 H, H-2″), 1.70−1.52 (m, 4 H, H-3″, H-4″), 1.44, 1.41, 1.32, and 1.25 (4 s, 12 H, CH_3C); ^{13}C NMR ($CDCl_3$): δ 173.6 (C-1″), 109.2 and 99.5 ($CH_3\underline{C}$), 97.7 (C-1′), 76.0 (C-2′), 74.8 (C-3′), 72.7 (C-5′), 67.2 (C-5″), 62.0 (C-6′), 61.2 (C-4′), 51.4 (OCH_3), 33.5 (C-2″), 28.7 (C-4″), 29.0, 28.1, 26.1, and 18.7 ($\underline{C}H_3C$), 21.6 (C-3″).

*2,3;4,6-Di-O-isopropylidene-1-(4-methoxycarbonylbutyl)-α,β-D-mannopyranoside, **4α,β**.* The same experimental procedure described above in path B for the preparation of **4α**, when applied to *p*-TsOH (86 mg, 0.5 mmol), **7α,β** (2.30 g, 7.82 mmol) and 2-methoxypropene (2.94 mL, 30.7 mmol) gave, after purification by column chromatography, compound **4α,β** (2.08 g, 71% with α:β = 53:47). R_f 0.71 (98:2 CH_2Cl_2-AcOEt); ^1H NMR ($CDCl_3$): δ 4.96 (s, 0.6 H, H-1′α), 4.89 (s, 0.4 H, H-1′β), 4.13−4.07 (m, 2 H, H-2′), 3.91−3.83 (m, 1 H, H-6′a), 3.79−3.65 (m, 7 H, H-3′, H-4′β, H-5′α, H-6′b, H-5″a, OCH_3), 3.58−3.49 (m, 1 H, H-4′α, H-5′β), 3.46−3.38 (m, 1 H, H-5″b), 2.32 (t, *J* 7.0 Hz, 2 H, H-2″), 1.92−1.80 (m, 2 H, H-3″), 1.73−1.59 (m, 2H, H-4″), 1.52, 1.49, 1.40 and 1.32 (4 s, 12 H, CH_3C); ^{13}C NMR ($CDCl_3$): δ 174.0 (C-1″), 109.5 and 99.8 ($CH_3\underline{C}$), 98.9 (C-1′β), 97.9 (C-1′α), 76.2 (C-3′β), 76.1 (C-2′α), 75.0 (C-3′α, C-2′β), 72.9, 72.8 (C-5′α, C-4′β), 67.4 (C-5″), 62.2 (C-6′α,β), 61.4, 61.3 (C-4′α, C-5′β), 51.6 (OCH_3), 33.8 (C-2″), 28.9 (C-4″), 29.1, 28.3, 26.2, and 18.8 ($\underline{C}H_3C$), 21.8 (C-3″).

*2,3;4,6-Di-O-isopropylidene-1-(4-carboxybutyl)-α-D-mannopyranoside, **5α**.* A 1 N LiOH aq solution (2 mL) was added to **4α** (200 mg, 0.53 mmol) in THF (2 mL) cooled at 0 °C. After 12 h at room temperature, the resulting solution was made neutral with 1 N HCl. After evaporation of THF, the product was extracted with CH_2Cl_2, dried over Na_2SO_4, filtered, and concentrated. **5α** was obtained almost quantitatively as a colorless oil (187 mg, 98%); R_f 0.38 (96:4 CH_2Cl_2−AcOEt); ^1H NMR (CD_3OD): δ 4.94 (s, 1 H, H-1′), 4.11 (d, *J* 5.7 Hz, 1 H, H-2′), 4.01 (dd, *J* 7.6, 5.7 Hz, 1 H, H-3′), 3.82−3.64 (m, 4 H, H-4′−6′), 3.50−3.38 (m, 2 H, H-5″), 2.28 (t, *J* 6.9 Hz, 2 H, H-2″), 1.58−1.55 (m, 4 H, H-3″, H-4″), 1.43 (s, 6 H, CH_3C), 1.26, and 1.24 (2 s, 6 H, CH_3C); ^{13}C NMR (CD_3OD): δ 177.6

(C-1″), 110.4 and 100.8 (CH_3**C**), 99.1 (C-1′), 77.5 (C-2′), 76.2 (C-3′), 74.1 (C-5′), 68.4 (C-5″), 63.0 (C-6′), 62.6 (C-4′), 34.8 (C-2″), 29.9 (C-4″), 29.4, 28.4, 26.5, and 19.2 (**C**H_3C), 22.9 (C-3″).

*2,3;4,6-Di-O-isopropylidene-1-(4-carboxybutyl)-*α,β*-*D*-mannopyranoside,* ***5α,β***. The same experimental procedure as described above for the preparation of **5α**, when applied to ***4α,β*** (2.0 g, 5.35 mmol) gave ***5α,β*** (1.77 g, 92%) as a white solid; R_f 0.38 (96:4 CH_2Cl_2-AcOEt); ^{1}H NMR (CD_3OD): δ 4.09 (dd, *J* 5.5, 2.3 Hz, 1 H, H-2′), 4.00 (m, 1 H, H-6′a), 3.81−3.36 (m, 7 H, H-4′−5′, H-6′b, H-5″), 2.13 (m, 2 H, H-2″), 1.59−1.50 (m, 4 H, H-3″, H-4″), 1.32, 1.28, 1.26, 1.20 (4s, 12 H, CH_3C); ^{13}C NMR (CD_3OD): δ 180.4 (C-1″), 110.5 and 100.9 (CH_3*C*), 100.1 (C-1′ *β*), 99.1 (C-1′α), 77.6 (C-3′ *β*), 77.4 (C-2′α), 76.3 (C-3′α, C-2′ *β*), 74.2, 74.1 (C-5′α, C-4′ *β*), 68.8 (C-5″), 63.1 (C-6′α,*β*), 62.6, 62,5 (C-4′α, C-5′*β*), 38.9 (C-2″), 30.5 (C-4″), 29.4, 28.4, 26.5, 24.3, 19.1 and 18.4 (**C**H_3C), 24.4 (C-3″).

Nelf(1)-C(O)C4Man and Nelf-[C(O)C4Man]2. General Esterification Method. EDC (101 mg, 0.53 mmol) was added to a solution of ***5α,β*** (190 mg, 0.53 mmol), DMAP (65 mg, 0.53 mmol), and nelfinavir (300 mg, 0.53 mmol) in CH_2Cl_2 (10 mL) at 0 °C. Then, the mixture was stirred for 15 min at 0 °C then for 19 h at room temperature. The reaction mixture was washed, and the organic layer was dried over Na_2SO_4 filtered, and evaporated under reduced pressure. Then, the residue was chromatographed three times on silica gel (100:0 to 98:2 CH_2Cl_2-EtOH) to give Nelf(1)-C(O)C4ManP (130 mg, 27% with α:*β* = 55:45) and Nelf-[C(O)C4ManP]2 (80 mg, 12% with α:*β* = 55:45) as white solids.

Nelf(1)-C(O)C4ManP. R_f 0.79 (92:8 CH_2Cl_2-EtOH); ^{1}H NMR (CD_3OD): δ 7.55 (m, 2 H, H-13, H-17), 7.40 (d, *J* 7.5 Hz, 1 H, H-4), 7.36−7.33 (m, 3 H, H-3, H-14, H-16), 7.23 (m, 1 H, H-15), 7.15 (m, 1 H, H-2), 5.09 (s, 0.6 H, H-1′α), 4.90 (d, *J* 2.2 Hz, 0.4 H, H-1′*β*), 4.51 (m, 1H, H-10), 4.35 (dd, *J* 2.5, *J* 6.1 Hz, 0.4 H, H-2′*β*), 4.25 (d, *J* 5.7 Hz, 0.6 H, H-2′α), 4.21 (m, 0.4 H, H-3′*β*), 4.09 (m, 2 H, H-3′α, H-5′*β*, H-18), 3.97−3.79 (m, 3.6 H, H-5′α, H-6′α*β*, H-5″aα*β*), 3.72−3.46 (m, 3.6 H, H-4′α, H-5″bα*β*, H-11), 3.35 (m, 0.4 H, H-4′*β*), 3.08 (d, *J* 11.5 Hz, 1 H, H-20a), 2.73 (t, *J* 7.1 Hz, 2 H, H-2″), 2.65 (m, 2 H, H-19a, H-28), 2.31 (s, 3 H, H-7), 2.22 (m, 2 H, H-19b, H-20b), 2.07−1.55 (m, 16 H, H-3″, H-4″, H-21−27), 1.43−1,35 (m, 12 H, 4 CH_3C), 1.21 (m, 9 H, H-32); ^{13}C NMR (CD_3OD): δ 176.0 (C-8), 173.0 (C-1″), 172.3 (C-29), 150.9 (C-1), 140.0 (C-5), 137.5 (C-12), 130.6 (C-13, C-17), 129.9 (C-14, C-16), 129.4 (C-6), 127.5 (C-3), 126.9 (C-15), 126.0 (C-4), 124.5 (C-2), 111.7, 110.3, 100, 7, 100.6, (CH_3*C*), 99.8 (C-1′*β*), 99.0 (C-1′α), 77.5 (C-3′*β*), 77.4 (C-2′α), 76.1 (C-3′α), 75.6 (C-2′*β*), 73.9 (C-5′α), 73.4 (C-5′*β*), 70.9 (C-28), 70.3 (C-18), 70.1 (C-5″*β*), 68.3 (C-5″α), 66.8 (C-4′*β*), 63.6 and 63.0 (C-6′α*β*), 62.6 (C-4′α), 60.3 (C-20), 59.5 (C-19), 54.3 (C-10), 51.7 (C-31), 37.4 (C-21), 35.4 (C-11), 35.0 (C-26), 34.5 (C-2″), 32.0 (C-27), 30.0 and 29.8 (C-4″α*β*), 28.9 (C-32), 31.6, 27.4, 27.0, and 21.6 (C-22−25), 29.5, 28.9, 28.5, 27.9, 26.6, 26.4, 19.2 and 19.3 (**C**H_3C), 22.8 (C-3″α*β*), 13.6 (C-7).

Nelf-[C(O)C4ManP]2. R_f 0.89 (92:8 CH_2Cl_2−EtOH); ^{1}H NMR (CD_3OD): δ 7.58 (m, 2 H, H-13, H-17), 7.42 (m, 1H, H-4), 7.40−7.26 (m, 3 H, H-3, H-14, H-16), 7.16 (m, 1 H, H-2), 5.47 (m, 1 H, H-18), 5.10 (s, 0.6 H, H-1′α), 5.06 (s, 0.6 H, H-1′α), 4.93 (d, *J* 1.1 Hz, 0.4 H, H-1′*β*), 4.90 (bs, 0.4 H, H-1′*β*), 4.68 (m, 1H, H-10), 4.38 (m, 0.8 H, H-2′*β*), 4.28−4.06 (m, 6 H, H-2′α, H-3′α*β*, H-5′*β*), 3.99−3.73 (m, 7.2 H, H-5′α, H-6′α*β*, H-5″aα*β*), 3.68−3.46 (m, 5.2 H, H-4′α, H-5″bα*β*, H-11), 3.35 (m, 0.8 H, H-4′*β*), 3.08 (d, *J* 11.1 Hz, 1 H, H-20a), 2.76 (m, 3 H, H-2″ext, H-19b), 2.66 (d, *J* 10.8 Hz, 1 H, H-28), 2.44 (m, 2 H, H-2″int), 2.30 (m, 5 H, H-7, H-19b, H-20b), 2.09−1.23 (m, 44 H, H-3″, H-4″, H-21−27, 8 CH_3C), 1.19 (s, 9 H, H-32); ^{13}C NMR (CD_3OD): δ 175.8 (C-8), 174.0 (C-1″int), 172.8 (C-29), 171.7 (C-1″ext), 150.9 (C-1), 140.0 (C-5), 136.8 (C-12), 131.1, 130.6 (C-13, C-17), 129.9 and 129.8 (C-14, C-16), 129.1 (C-6), 127.5 (C-3), 127.2 (C-15), 125.8 (C-4), 124.5 (C-2), 111.6, 110.4, 100.7, and 100.6 (CH_3*C*), 99.7 (C-1′*β*), 98.94 and 98.89 (C-1′α), 77.5 (C-3′*β*), 77.3 (C-2′α), 76.1 (C-3′α), 75.6 (C-2′*β*), 73.9 (C-5′α), 73.3 (C-5′*β*), 72.23 and 72.14 (C-18α*β*), 70.7 (C-28), 70.1 (C-5″*β*), 68.3 (C-5″α), 66.8 (C-4′*β*), 63.6, 62.9 (C-6′α*β*), 62.5 (C-4′α), 60.3 (C-20), 56.5 (C-19), 52.0 (C-10), 51.8 (C-31), 37.3 (C-21), 35.8 (C-11), 35.0 (C-26), 34.7 and 34.4 (C-2″int,ext), 32.0 (C-27), 29.9 and 29.7 (C-4″α*β*), 28.9 (C-32), 31.6, 27.4, 27.0, and 21.7 (C-22−25), 29.5, 28.9, 28.5, 28.0, 26.6, 26.4, 19.3 and 19.2 (**C**H_3C), 22.79 and 22.76 (C-3″α*β*), 13.6 (C-7).

Nelf(1)-C(O)C4Man. General Deprotection Method. Nelf-(1)-C(O)C4ManP (100 mg, 0.11 mmol) in a 1:9 TFA-CH_2Cl_2 v/v mixture (10 mL) was stirred for 2 h at room temperature. The residue obtained after evaporation of the solvents was purified by chromatography (10:0 to 4:1 CH_2Cl_2-MeOH) to give Nelf(1)-C(O)C4Man (2TFA) (105 mg, 90% with α:*β* = 58:42) as a white solid; R_f 0.46 (4:1 CH_2Cl_2-MeOH); R_t 17.2 min (gradient A); ^{1}H NMR (CD_3OD): δ 7.45−7.41 (m, 2 H, H-13, H-17), 7.31−7.03 (m, 6 H, H-2−4, H-14−16), 4.73 (d, *J* 3.4 Hz, 0.6 H, H-1′α), 4.49 (s, 0.4 H, H-1′*β*), 4.25 (m, 1H, H-10), 4.13−3.40 (m, 12 H, H-2′-6′α*β*, H-5″α*β*, H-11, H-18, H-20a), 3.22 (m, 1 H, H-20a), 2.82−2.60 (m, 4 H, H-2″, H-19a, H-28), 2.19 (s, 3 H, H-7), 2.05−1.24 (m, 16 H, H-3″, H-4″, H-19b, H-20b, H-21−27), 1.16 (s, 9 H, H-32); ^{13}C NMR (CD_3OD): δ 173.4 (C-8), 173.2 (C-1″), 172.3 (C-29), 151.1 (C-1), 140.0 (C-5), 137.5 (C-12), 130.9 (C-13, C-17), 130.1 (C-14, C-16), 129.5 (C-6), 127.6 (C-3), 127.3 (C-15), 126.1 (C-4), 124.8 (C-2), 101.6 (C-1′*β*), 101.5 (C-1′α), 78.1 (C-5′*β*), 75.1 (C-3′*β*), 74.5 (C-5′α), 72.6 (C-2′*β*), 72.5 (C-3′α), 72.2 (C-2′α), 70.2 (C-18, C-28), 70.0 (C-5″*β*), 68.5 (C-4′α), 68.4 (C-4′*β*), 68.1 (C-5″α), 62.7 (C-6′α), 62.6 (C-6′*β*), 59.8 (C-20), 58.3 (C-19), 54.3 (C-10), 52.2 (C-31), 36.8 (C-21), 35.5 (C-11), 34.5 (C-2″), 34.3 (C-26), 31.7 (C-27), 29.9 (C-4″α*β*), 28.8 (C-32), 31.1, 27.2, 26.5, and 21.6 (C-22−25), 22.9 and 22.7 (C-3″α*β*), 13.6 (C-7). ESI-MS: *m*/*z* 830.4 $[M + H]^+$, in agreement with the calculated mass for [M] = $C_{43}H_{63}N_3O_{11}S$ (829.42).

Nelf-[C(O)C4Man]2. Deprotection of Nelf-[C(O)C4ManP]2 (14 mg, 0.008 mmol) afforded after purification by chromatography (10:0 to 4:1 EtOAc−MeOH) Nelf-[C(O)C4Man]2 (2TFA) (13 mg, 92% with α:*β* = 60:40) as a white solid; R_f 0.25 (4:1 CH_2Cl_2-MeOH); R_t 16.1 min (gradient A); ^{1}H NMR (CD_3OD): δ 7.56 (m, 2 H, H-13, H-17), 7.41−7.23 (m, 5 H, H-3, H-4, H-14-16), 7.14 (m, 1 H, H-2), 5.43 (m, 1 H, H-18), 4.83 (s, 0.6 H, H-1′α), 4.78 (s, 0.6 H, H-1′α), 4.58 (s, 0.4 H, H-1′*β*), 4.56 (s, 0.4 H, H-1′*β*), 4.64 (m, 1H, H-10), 4.05−3.45 (m, 19 H, H-11, H-2′α*β*, H-3′α*β*, H-4′α, H-5′α*β*, H-6′α*β*, H-5″α*β*), 3.26 (m, 0.8 H, H-4′*β*), 3.05 (d, *J* 11.1 Hz, 1 H, H-20a), 2.71 (m, 4 H, H-19b, H-28, H-2″ext), 2.42−2.28 (m, 4 H, H-19b, H-20b, H-2″int), 2.24 (m, 3 H, H-7,), 2.07−1.33 (m, 18 H, H-21−27, H-3″, H-4″), 1.16 (m, 9 H, H-32); ^{13}C NMR (CD_3OD): δ 176.1 (C-8), 174.4 (C-1″int), 173.2 (C-29), 172.2 (C-1″ext), 151.2 (C-1), 140.2, 137.0 (C-5, C-12), 131.2 (C-13, C-17), 130.0 (C-14, C-16), 129.1 (C-6), 127.7 (C-3), 127.4 (C-15), 125.9 (C-4), 124.7 (C-2), 101.6 (C-1′*β*), 100.7 (C-1′α), 78.1 (C-5′*β*), 75.1 (C-3′*β*), 74.8 (C-5′α), 74.6 (C-2′*β*), 74.5 (C-3′α), 72.6 (C-2′α), 72.2 (C-18), 70.8 (C-28), 70.1, 70.0 (C-5″*β*), 68.5 (C-4′α), 68.4 (C-4′*β*), 68.1 (C-5″α), 62.6 (C-6′α), 62.5 (C-6′*β*), 60.3 (C-20), 56.5 (C-19), 52.2 (C-10), 52.0 (C-31), 37.6 (C-21), 35.5 (C-11), 35.2 (C-26), 34.8, 34.5 (C-2″), 32.1 (C-27), 30.0, 29.9 (C-4″α*β*), 28.8 (C-32), 31.8, 27.5, 27.2, 21.7 (C-22−25), 22.9, 22.7 (C-3″α*β*), 13.5 (C-7).

ESI-MS: *m/z* 1092.5 $[M + H]^+$, 1114.5 $[M + Na]^+$, in agreement with the calculated mass for [M] = $C_{54}H_{81}N_3O_{18}S$ (1091.52).

Saq-C(O)C4ManP. The general esterification method applied to **5α,β** (160 mg, 0.45 mmol), DMAP (55 mg, 0.45 mmol), saquinavir (300 mg, 0.45 mmol), and EDC (86 mg, 0.45 mmol) afforded, after workup and purification by chromatography on silica gel (100:0 to 98:2 CH_2Cl_2-MeOH), Saq-C(O)C4ManP (320 mg, 71% with α:β = 64:36) as a white solid; R_f 0.72 (98:2 CH_2Cl_2-MeOH) ^{1}H NMR (CD_3OD): δ 8.46 (d, *J* 8.5 Hz, 1 H, H-6), 8.17 (d, *J* 8.5 Hz, 1 H, H-7), 8.14 (d, *J* 8.6 Hz, 1 H, H-1), 8.00 (d, *J* 8.5 Hz, 1 H, H-4), 7.83 (m, 1 H, H-2), 7.69 (m, 1 H, H-3), 7.25 (d, *J* 7.2 Hz, 2 H, H-21, H-25), 7.04 (m, 2 H, H-22, H-24), 6.90 (m, 1 H, H-23), 5.33 (m, 1 H, H-26), 5.00 (s, 0.6 H, H-1′α), 4.90 (m, 1 H, H-12), 4.84 (d, *J* 2.4 Hz, 0.4 H, H-1′*β*), 4.46 (m, 1 H, H-18), 4.30 (dd, *J* 2.5, *J* 6.1 Hz, 0.4 H, H-2′*β*), 4.17 (m, 0.6 H, H-2′α), 4.14 (m, 0.4 H, H-3′*β*), 4.05 (m, 0.6 H, H-3′α), 3.99 (m, 0.4 H, H-5′*β*), 3.89−3.68 (m, 3.6 H, H-5′α, H-6′α*β*, H-5″aα*β*), 3.53 (m, 1 H, H-4′α, H-5″b*β*), 3.45 (m, 0.6 H, H-5″bα), 3.26 (m, 0.4 H, H-4′*β*), 3.06 (dd, *J* 14.0, *J* 3.5 Hz, 1 H, 19a), 3.00 (d, *J* 11.5 Hz, 1 H, H-29a), 2.80−2.66 (m, 5 H, H-13, H-19b, H-27a, H-37), 2.41 (m, 3 H, H-2″, H-27b), 2.24 (m, 1 H, H-29b), 2.04−1.32 (m, 28 H, H-3″, H-4″, H-30−36, 4 CH_3C), 1.36 (s, 9 H, H-41); ^{13}C NMR (CD_3OD): δ 175.0, 174.7 (C-14, C-16, C-1″), 172.3 (C-38), 166.1 (C-10), 150.3 (C-8), 147.8 (C-9), 139.3 (C-20), 138.9 (C-6), 131.5 (C-2), 130.8 (C-5), 130.7 (C-1), 130.3 (C-21, C-25), 129.4 (C-3), 129.2 (C-22, C-24), 129.0 (C-4), 127.2 (C-23), 119.7 (C-7), 111.7, 110.4, 100.8, 100.7 (CH_3C), 100.0 (C-1′*β*), 99.1 (C-1′α), 77.7 (C-3′*β*), 77.5 (C-2′α), 76.3 (C-3′α), 75.8 (C-2′*β*), 74.7 (C-26), 74.1 (C-5′α), 73.6 (C-5′*β*), 70.9 (C-37), 70.3 (C-5″*β*), 68.4 (C-5″α), 67.0 (C-4′*β*), 63.7 (C-6′*β*), 63.0 (C-6′α), 62.6 (C-4′α), 59.9 (C-29), 56.8 (C-27), 53.0 (C-12), 52.0 (C-40), 51.5 (C-18), 38.0 (C-13), 37.0 (C-30), 35.5 (C-19), 34.9 (C-2″), 34.8 (C-35), 31.8 (C-36), 30.1 and 30.0 (C-4″α*β*) 29.0 (C-41), 31.4, 27.1 (2C), and 22.0 (C-31−34), 29.5, 28.4, 28.0, 26.5, 26.4, 19.3, and 19.2 (CH_3C), 22.63 and 22.59 (C-3″α*β*).

Saq-C(O)C4Man. Deprotection of Saq-C(O)C4ManP (150 mg, 0.15 mmol) led, after chromatography (10:0 to 4:1 EtOAc-MeOH), to Saq-C(O)C4Man (1TFA) (149 mg, 95% with α:β = 64:36) as a white solid; R_f 0.23 (9:1 EtOAc-MeOH); R_t 16.7 min (gradient A); ^{1}H NMR (CD_3OD): δ 8.52 (d, *J* 8.5 Hz, 1 H, H-6), 8.20 (d, *J* 8.4 Hz, 1 H, H-7), 8.19 (d, *J* 7.8 Hz, 1 H, H-1), 8.05 (d, *J* 8.2 Hz, 1 H, H-4), 7.88 (m, 1 H, H-2), 7.74 (m, 1 H, H-3), 7.26 (d, *J* 7.5 Hz, 2 H, H-21, H-25), 7.06 (t, 2 H, *J* 7.5 Hz, H-22, H-24), 6.91 (m, 1 H, H-23), 5.33 (m, 1 H, H-26), 4.92 (t, *J* 13.0 Hz, 1 H, H-12), 4.78 (d, *J* 1.5 Hz, 0.6 H, H-1′α), 4.55 (s, 0.4 H, H-1′*β*), 4.48 (dt, *J* 10.7, *J* 1.4 Hz, 1 H, H-18), 3.92−3.38 (m, 7.6 H, H-2′α*β*, H-3′α*β*, H-4′α, H-5′α*β*, H-6′α*β*, H-5″α*β*), 3.26 (m, 0.4 H, H-4′*β*), 3.05 (m, 2 H, 19a, H-29a), 2.74 (m, 5 H, H-13, H-19b, H-27a, H-37), 2.41 (m, 3 H, H-27b, H-2″), 2.26 (m, 1 H, H-29b), 2.04−1.32 (m, 16 H, H-30−36, H-3″, H-4″), 1.37 (s, 9 H, H-41); ^{13}C NMR (CD_3OD): δ 175.0, 174.9 (C-14, C-16, C-1″), 172.4 (C-38), 166.2 (C-10), 150.3 (C-8), 148.0 (C-9), 139.3 (C-20), 139.0 (C-6), 131.6 (C-2), 130.9 (C-5), 130.8 (C-1), 130.3 (C-21, C-25), 129.5 (C-3), 129.2 (C-22, C-24), 129.0 (C-4), 127.2 (C-23), 119.7 (C-7), 101.7 (C-1′*β*), 101.5 (C-1′α), 77.7 (C-5′*β*), 75.2 (C-3′*β*), 74.6 (C-5′α, C-26), 72.6 (C-2′*β*), 72.5 (C-2′α), 72.2 (C-2′α), 70.8 (C-37), 70.2 (C-5″*β*), 68.6, 68.5 (C-4′α*β*), 68.1 (C-5″α), 62.8 (C-6′α), 62.7 (C-6′*β*), 59.9 (C-29), 56.8 (C-27), 53.1 (C-12), 52.0 (C-40), 51.5 (C-18), 38.0 (C-13), 37.1 (C-30), 35.5 (C-19), 34.9 (C-2″), 34.8 (C-35), 31.8 (C-36), 30.0 (C-4″), 29.0 (C-41) 31.8, 31.0, 31.4, 27.1, and 22.0 (C-31−34), 22.7 and 22.6 (C-3″). ESI-MS: *m/z* 933.5 $[M + H]^+$, 955.5 $[M + Na]^+$, in agreement with the calculated mass for [M] = $C_{49}H_{68}N_6O_{12}$ (932.49).

Ind(8)-C(O)C4ManP and [Ind-[C(O)C4ManP]2]. The general esterification method applied to **5α,β** (176 mg, 0.49 mmol), DMAP (71 mg, 0.58 mmol), indinavir (300 mg, 0.49 mmol), and EDC (112 mg, 0.58 mmol) afforded, after workup and three successive chromatographies on silica gel (10:0 to 98:2 CH_2Cl_2-EtOH) Ind(8)-C(O)C4ManP (102 mg, 22% with α:β = 52:48) and Ind-[C(O)C4ManP]2 (95 mg, 15% with α:β = 62:38) as white solids.

Ind(8)-C(O)C4ManP. R_f 0.58 (92:8 CH_2Cl_2-EtOH); ^{1}H NMR (CD_3OD): δ 8.51(s, 1 H, H-29), 8.47 (d, *J* 4.8 Hz, 1 H, H-28), 7.84 (d, *J* 7.6 Hz, 1 H, H-26), 7.43 (dd, *J 7.6, J* 4.8 Hz, 1 H, H-27), 7.29−7.19 (m, 9 H, H-2−5, H-32−36), 5.60 (d, *J* 5.1 Hz, 1 H, H-9), 5.40 (m, 1 H, H-8), 4.96 (s, 0.5 H, H-1′α), 4.77 (s, 0.5 H, H-1′*β*), 4.26 (dd, *J* 6.0, *J* 2.2 Hz, 0.5 H, H-2′*β*), 4.16−4.13 (m, 1 H, H-2′α, H-3′*β*), 4.05−3.98 (m, 1 H, H-3′α, H-5′*β*), 3.89−3.72 (m, 3 H, H-2′α, H-6′α*β*, H-5″a*β*, H-14), 3.64 (m, 0.5 H, H-5″aα), 3.59 (s, 2 H, H-24), 3.52−3.47 (m, 1 H, H-4′α, H-5″b*β*), 3.39 (m, 0.5 H, H-4′*β*), 3.29−3.20 (m, 2 H, H-7a, H-19), 3.10−2-97 (m, 4 H, H-7b, H-12, H-18a, H-30a), 2.88 (m, 0.5 H, H-5″bα), 2.75−2.66 (m, 3 H, H-16a, H-17a, H-30b), 2.50−2.35 (m, 5 H, H-15, H-16b, H-17b, H-18b), 2.20 (m, 2 H, H-2″), 2.11 (m, 1 H, H-13a), 1.67−1.55 (m, 4 H, H-3″, H-4″), 1.54−1.33 (m, 13 H, H-13b, CH_3C), 1.33 (s, 9 H, H-23); ^{13}C NMR (CD_3OD): δ 177.6 (C-11), 174.3, (C-1″), 172.9 (C-20), 150.7 (C-29), 149.0 (C-28), 141.6 (C-31), 140.7, 140.6 (C-1, C-6), 139.1 (C-26), 135.0 (C-25), 130.1 (C-32, C-36), 129.4 (C-33, C-35), 129.1 (C-2), 128.0 and 127.3 (C-3, C-4), 125.9 (C-34), 125.0 (C-5), 124.8 (C-27), 111.6, 110.4, 100.7, and 100.6 (CH_3*C*), 99.8 (C-1′*β*), 98.9 (C-1′α), 77.6 (C-3′*β*), 77.3 (C-2′α), 76.7 (C-8), 76.1 (C-3′α), 75.6 (C-2′*β*), 74.0 (C-5′α), 73.4 (C-5′*β*), 70.2 (C-5″*β*), 68.3 (C-5″α), 68.2 (C-4′*β*), 67.6 (C-14), 66.8 (C-19), 63.6 (C-15), 63.2, 62.9 (C-6′α*β*), 62.5 (C-4′α), 60.4 (C-24), 56.5 and 53.1 (C-16, C-17), 56.4 (C-9), 52.1 (C-22), 51.9 (C-18), 46.1 (C-12), 40.6 (C-30), 38.5 (C-13), 38.2 (C-7), 34.5 (C-2″), 29.9 and 29.8 (C-4″α*β*), 29.0 (C-23), 29.4, 28.4, 28.0, 26.4, and 19.2 (*C*H_3C), 22.5 and 22.4 (C-3″α*β*).

Ind-[C(O)C4ManP]2. R_f 0.79 (9.2:0.8 CH_2Cl_2-EtOH); ^{1}H NMR (CD_3OD): δ 8.53 (s, 1 H, H-29), 8.49 (d, *J* 3.9 Hz, 1 H, H-28), 7.85 (d, *J* 7.9 Hz, 1 H, H-26), 7.46 (dd, *J* 7.7, *J* 4.9 Hz, 1H, H-27), 7.41 (s, 1 H, H-21), 7.32−7.25 (m, 10 H, H-2−5, H-10, H-32−36), 5.66 (m, 1 H, H-9), 5.52 (m, 1 H, H-8), 5.21 (m, 1 H, H-14), 5.04 (s, 0.6, H-1′αint), 4.98 (s, 0.6 H, H-1′αext), ∼4.87 (hindered by water H-1′αint), 4.78 (1s, 0.4 H, H-1′αext), 4.34 (dd, *J* 6.0, *J* 2.5 Hz, 0.4 H, H-2′*β*), 4.27 (dd, *J* 6.0, *J* 2.4 Hz, 0.4 H, H-2′*β*), 4.22−3.99 (m, 4 H, H-2′α*β*, H-3′α*β*), 3.95−3.65 (m, 8 H, H-5′α*β*, H-6′α*β*, H-5″aα*β*), 3.60 (s, 2 H, H-24), 3.58−3.39 (m, 3.2 H, H-4′α, H-5″bα*β*), 3.55−3.25 (m, 2 H, H-7a, H-19), 3.04−2.90 (m, 4.4 H, H-7b, H-12, H-18a, H-30a, H-4′*β*), 2.77−2.20 (m, 13 H, H-13a, H-15, H-16, H-17, H-18b, H-30b, H-2″), 1.79−1.36 (m, 33 H, H-13b, H-3″, H-4″, CH_3C), 1.34 (s, 9 H, H-23); ^{13}C NMR (CD_3OD): δ 177.4 (C-11), 174.6 (C-1″int), 174.2 (C-1″ext), 172.4 (C-20), 150.6 (C-29), 148.9 (C-28), 141.3 (C-31), 141.7, 140.0 (C-1, C-6), 138.9 (C-26), 134.8 (C-25), 129.9 (C-32, C-36), 129.3 (C-33, C-35), 129.1 (C-2), 128.0, 127.4 (C-3, C-4), 125.7 (C-34), 125.0 (C-5, C-27), 111.6, 110.3, 100.7, and 100.6 (CH_3*C*), 99.78 and 99.70 (C-1′α), 98.83 and 98.77 (C-1′*β*), 77.5 (C-3′*β*), 77.3 (C-2′α), 76.75 and 76.71 (C-8), 76.0 (C-3′α), 75.5 (C-2′*β*), 73.8 (C-5′α), 73.3 (C-5′*β*), 70.84 and 70.77 (C-14), 70.24 and 70.16 (C-5″*β*), 68.29 and 68.19 (C-5″α), 68.1 (C-4′*β*), 66.7 (C-19), 63.5 and 62.9 (C-6′α*β*), 62.4 (C-4′α), 60.4 (C-24), 59.6 (C-15), 56.4 (C-9), 56.3 (C-18), 52.9 and 51.9 (C-16, C-17), 51.5 (C-22), 45.0 (C-12), 40.5 (C-30), 38.2 (C-7), 34.9 (C-13), 34.7 and 34.5 (C-2″), 30.0, 29.8, and 29.7 (C-4″), 29.0 (C-23), 29.4, 28.4, 28.0, 26.4, and 19.2 (**C**H_3C), 22.5 and 22.4 (C-3″α*β*).

Ind(8)-C(O)C4Man. Deprotection of Ind(8)-C(O)C4ManP (90 mg, 0.09 mmol) yielded, after chromatography (10:0 to 4:1 EtOAc−MeOH), Ind(8)-C(O)C4Man (2TFA) (90 mg, 91% with α:β = 58:42) as a white solid. R_f 0.62 (7:3 EtOAc−MeOH); R_t 9.5 min (gradient A); ^{1}H NMR (CD_3OD): δ 8.52−8.44 (m, 2 H, H-28, H-29), 7.86 (d, *J* 7.9 Hz, 1 H, H-26), 7.43 (m, 1 H, H-27), 7.30−7.15 (m, 9 H, H-2−5, H-32−36), 5.50 (d, *J* 4.8 Hz, 1 H, H-9), 5.30 (m, 1 H, H-8), 4.63 (s, 0.6 H, H-1′α), 4.33 (s, 0.4 H, H-1′β), 4.00−2.55 (m, 25 H, H-7, H-12, H-14−19, H-24, H-30, H-2′-6′, H-5″), 2.11 (m, 2 H, H-2″), 1.88 (m, 1 H, H-13a), 1.49 (m, 5 H, H-3″, H-4″, H-13b), 1.24 (s, 9 H, H-23); ^{13}C NMR (CD_3OD): δ 177.5 (C-11), 174.6, 174.5 (C-20, C-1″), 150.8 (C-29), 149.5 (C-28), 141.5 (C-31), 140.9, 140.5 (C-1, C-6), 139.9 (C-26), 135.0 (C-25), 130.1 (C-32, C-36), 129.4 (C-33, C-35), 129.2 (C-2), 128.1, 127.5 (C-3, C-4), 125.9 (C-34), 125.5 (C-5), 125.0 (C-27), 101.6 (C-1′α), 101.4 (C-1′β), 78.1 (C-5′β), 76.8 (C-8), 75.1 (C-3′β), 74.5 (C-5′α), 72.6 (C-2′β), 72.4 (C-3′α), 72.1 (C-2′α), 70.0 (C-5″β), 68.4 (C-4′$\alpha\beta$), 68.0 (C-5″α), 67.2 (C-14), 66.4 (C-19), 62.7 and 62.6 (C-6′$\alpha\beta$, C-15), 59.3 (C-24), 58.3 and 54.7 (C-16, C-17), 56.6 (C-9), 52.5 (C-22), 51.3 (C-18), 45.8 (C-12), 40.5 (C-30), 38.2 and 38.4 (C-7, C-13), 34.6 (C-2″), 29.9, 29.8 (C-4″$\alpha\beta$), 28.7 (C-23), 22.6, 22.4 (C-3″$\alpha\beta$). ESI-MS: *m*/*z* 876.4 $[M + H]^+$, 898.5 $[M + Na]^+$, in agreement with the calculated mass for [M] = $C_{47}H_{65}N_5O_{11}$ (875.47).

Ind-[C(O)C4Man]2. Deprotection of Ind-[C(O)C4ManP]2 (80 mg, 0.06 mmol) led, after chromatography (10:0 to 4:1 EtOAc-MeOH), to Ind-[C(O)C4Man]2 (2TFA) (78 mg, 95% with α:β = 60:40) as a white solid; R_f 0.48 (7:3 EtOAc−MeOH); R_t 9.0 min (gradient A); ^{1}H NMR (CD_3OD): δ 8.50 (m, 2 H, H-28, H-29), 7.85 (d, *J 7.7* Hz, 1 H, H-26), 7.45 (s, 1 H, H-21), 7.38 (m, 1H, H-27), 7.29−7.22 (m, 10 H, H-2−5, H-10, H-32−36), 5.62 (d, *J* 4.8 Hz, 1 H, H-9), 5.48 (m, 1 H, H-8), 5.16 (m, 1 H, H-14), 4.76 (1s, 0.6 H, H-1′αint), 4.71 (1s, 0.6 H, H-1′αext), 4.51 (1s, 0.4 H, H-1′βint), 4.39 (1s, 0.4 H, H-1′βext), 3.94−3.41 (m, 19.2 H, H-2′$\alpha\beta$, H-3′$\alpha\beta$, H-4′α, H-5′$\alpha\beta$, H-6′$\alpha\beta$, H-5″$\alpha\beta$, H-15, H-24), 3.26−3.17 (m, 2 H, H-7a, H-19), 3.00−2.87 (m, 4.8 H, H-4′β, H-7b, H-12, H-18a, H-30a), 2.72−2.39 (m, 13 H, H-2″, H-13a, H-15, H-16, H-17, H-18b, H-30b), 1.72−1.53 (m, 9 H, H-3″, H-4″, H-13b), 1.30 (s, 9 H, H-23); ^{13}C NMR (CD_3OD): δ 177.4 (C-11), 175.1 (C-1″int), 174.7 (C-1″ext), 172.8 (C-20), 150.9 (C-29), 149.0 (C-28), 141.5 (C-31), 141.1, 140.3 (C-1, C-6), 139.3 (C-26), 132.4 (C-25), 130.2 (C-32, C-36), 129.5 (C-33, C-35), 129.3 (C-2), 128.2, 127.6 (C-3, C-4), 125.9 (C-34), 125.3 (C-5, C-27), 101.68, 101.60, 101.56, and 101.48 (C-1′α and C-1′β), 78.22 and 78.16 (C-5′β), 76.9 (C-8), 75.31 and 75.23 (C-3′β), 74.62 and 74.55 (C-5′α), 72.68, 72.65, 72.56, and 72.48 (C-2′β, C-3′α), 72.2 (C-2′α), 71.1 (C-14), 70.1 and 70.0 (C-5″β), 68.65, 68.61, and 68.51 (C-19, C-4′$\alpha\beta$), 68.1 and 68.0 (C-5″α), 62.9, 62.8, and 62.7 (C-6′$\alpha\beta$), 60.4 (C-24), 59.9 (C-15), 56.8 (C-9), 56.3 (C-18), 53.1, and 52.1 (C-16, C-17), 51.8 (C-22), 45.2 (C-12), 40.7 (C-30), 38.3 (C-7), 35.1 (C-13) 34.9 and 34.7 (C-2″), 30.1 and 30.0 (C-4″$\alpha\beta$), 29.0 (C-23), 22.8, 22.6, and 22.5 (C-3″$\alpha\beta$). ESI-MS: *m*/*z* 1138.5 $[M + H]^+$, 1160.6 $[M + Na]^+$, in agreement with the calculated mass for [M] = $C_{58}H_{83}N_5O_{18}$ (1137.57).

Biological Section. *Materials.* 1-Pentanesulfonic acid sodium salt, sodium acetate trihydrate, and acetonitrile were high-performance liquid chromatography (HPLC) grade. Foetal bovine serum (FBS), Dulbecco's phosphate buffered saline (DPBS), penicillin−streptomycin solution (5000 U/mL:5000 μg/mL), trypsin-EDTA 0.25% solution (2.5 g trypsin and 0.2 g EDTA in 1 L DPBS), D-(+)-glucose, and *N*-[2-hydroxyethyl]-piperazine-*N*-ethanesulfonic acid (HEPES) were purchased from Sigma Chemical (St Quentin Fallavier, France). Dulbecco's modified eagle's medium (DMEM) and nonessential amino acids DMEM 100× (NEAA) were purchased from Gibco-Life Technologies (Cergy-Pontoise, France). Transport Medium (TM) consisted of DPBS containing 25 mM glucose and 10 mM HEPES (pH 7.4). Cell culture medium consisted of DMEM supplemented with 20% foetal bovine serum, 1% NEAA, and 2% penicillin−streptomycin.

HPLC Conditions for Chemical Stability and Transport Experiments. All HPLC analyses used for chemical stability and transport experiments were performed using a HP1100 apparatus with a Lichrospher 100 RP-18 (5 μm)-packed column (250 × 3.2 mm) with a flow rate of 1 mL/min. The isocratic mobile phase consisted of $CH_3COONa{\cdot}3H_2O$ (15 mM) and $CH_3(CH_2)_4SO_3Na$ (15 mM), 5 mM pH 6 buffer and CH_3CN: 59:41 for Ind, Ind(8)-C(O)C4Man and Ind-[C(OC4Man]2, 41:59 for Saq and Saq-C(O)C4Man, and 45:55 for Nelf, Nelf(1)-C(O)C4Man and Nelf(1)-[C(O)C4Man]2. The prodrugs and/or drugs were detected by measuring their UV absorption at 210 (Ind, Nelf, and their derivatives) or 254 nm (Saq and its derivative) and the signals (peak integration) were interpreted by the software provided. Under their respective HPLC conditions, the retention times measured for the different compounds were of 4.9 min for Ind, 3.5 min for Ind(8)-C(O)C4Man, 3.3 min for Ind-[C(OC4Man]2, 5.6 min for Saq, 5.0 min for Saq-C(O)C4Man, 12.5 min for Nelf, 5.2 min for Nelf(1)-C(O)C4Man, 4.8 min for Nelf-[C(OC4Man]2. The prodrug and/or drug concentration was determined from HPLC calibration curves. These curves were established under the same HPLC conditions, using standard calibrated prodrug and drug solutions that were prepared in the same hydrolysis medium as the sample under investigation. The calibration curves were linear (correlation coefficients from 0.9993 to 0.9998) in a concentration range of 0.4 to 1143 μM for Ind and its prodrugs, 0.1 to 300 μM for Saq and its prodrug, and 0.1 to 301 μM for Nelf and its prodrugs, the lower limit corresponding to the limit of detection that can be quantified with accuracy. Above the lower concentration limit, the analytical method was reproducible.

Hydrolysis. Hydrolysis experiments were performed by incubating 20 mL of a DMEM-MeOH solution (pH 7.3) of the prodrug (250 μg/mL) at 37 °C with stirring. The amount of MeOH (v/v) in these solutions was 4% for Ind(8)-C(O)C4Man, 5% for Ind-[C(OC4Man]2, 3% for Saq-C(O)C4Man, and 5% for Nelf(1)-C(O)C4Man. Hydrolysis was followed by HPLC monitoring of either the disappearance of the prodrug and appearance of the parent drug by injecting 40 μL of the solution onto the HPLC column (for HPLC conditions see above). Plots of $\ln([\text{prodrug}]_o - [\text{prodrug}(t)])$ and of $\ln[\text{drug}(t)]$ against time were linear within the concentration range studied, indicating that the hydrolysis is a first-order process with respect to the prodrug. The half-lives of hydrolysis ($t_{1/2}$) were measured, when possible, or calculated from these plots; $t_{1/2}$ is related to the slope, *K*, of these curves by the relation $t_{1/2} = (\ln 2)/K$.

Caco-2 Cell Monolayers. Caco-2 cells, clone TC7, were kindly provided by Dr. A. Zweibaum (INSERM U178, Villejuif, France). The cells were routinely maintained in 75 cm^2 culture flasks at 37 °C in an atmosphere containing 5% CO_2 and 95% relative humidity. Cells were split every 7 days at a density of 1.5×10^6 cells/flask. For the transepithelial transport experiments, Caco-2 cells (passage 60−65) were harvested with trypsin-EDTA and seeded on Anopore membrane inserts (0.2 μm pore diameter, 25 mm diameter; Nunc, Roskilde, Denmark) at a density of 5×10^5 cells/insert (cm^2). Apical (AP) and basolateral (BL) chamber volumes were maintained at 2 mL. Culture medium was changed every 3−4 days and cells were used for the experiments between days 14 and 27 post-seeding. Monolayer formation was monitored by measurement of trans-epithelial electrical resistance (TEER) using a Millicel ERS apparatus (Millipore).

Transport Experiments. Before the transepithelial transport experiments, the Caco-2 monolayers were rinsed twice with the transport medium (TM) (both chambers) and preincubated for 30 min in the TM. After this equilibration period, the monolayer integrity was checked by measuring its TEER. For the transport experiments, only monolayers displaying TEER values above 176 Ω·cm^2 and for which TEER values fell by less than 15% from the value measured at the end of the equilibration period were used. Under these conditions, the age of the cell monolayer within the 14−27 day's postseeding range did not affect the transport results. Transport was initiated by replacing the TM in the AP or in the BL "donor" compartment with 2 mL of the drug or prodrug solution. AP and BL chamber volumes were maintained at 2 mL. The test solutions were prepared by mixing a known amount of TM with a concentrated MeOH stock solution of the drug or prodrug under investigation to reach a final concentration of the drug or prodrug in the 230−300 μM, 280 μM, and 252−344 μM range for the indinavir, saquinavir, and nelfinavir derivatives, respectively (the exact concentrations used for each derivative are given in the figures showing their transepithelial transport). The final MeOH concentration in the drug or prodrug solutions in contact with the monolayers never exceeded 3% MeOH (TEER monitoring and transport experiments have shown that MeOH at concentrations up to 5% did not affect cell monolayer integrity during the 3-h period of transport experiment nor the amount of drug and/or prodrug transported, respectively). 200 μL samples were withdrawn from the "acceptor" compartment (opposite to the addition "donor" chamber) every 1 h over a period of 3 h and replaced by the same amount of fresh transport medium to maintain the same volume. The dilution was taken into account for the calculations. To prevent hydrolysis of the prodrugs, all these samples were stored at 4 °C awaiting prodrug and/or parent drug HPLC-analysis (see above section: HPLC conditions). At the end of the experiments (3 h), samples were also taken from the "donor" compartment for HPLC analysis, and the monolayers were checked for integrity by measuring TEER values. The concentrations of the prodrug and parent drug that were measured in the donor and acceptor chamber at the end of the transport experiment indicated that no nonspecific adsorption on glass or on plastic had occurred. The experiments for which TEER has decreased by more than 8% from the value measured at the beginning of the experiment were discarded. Transport was expressed as a percentage of the initial amount added to the donor compartment. All flux experiments were conducted at least in triplicate in the AP to BL and BL to AP directions. If possible, a concentration of the prodrug in the donor chamber the closest to that of the parent drug was preferred, but solubility issues of the prodrug (which needed in some cases the use of MeOH) and detection issues of the prodrug and/or parent drug in the acceptor chamber were also considered for the selection of the prodrug concentration.

Data Analysis for the Transport Experiments. The apparent permeability coefficients P_{app} (cm/s) were calculated by linear regression analysis on the time course plot of amount of (pro)-drug transported from equation $P_{app} = k(V_D/A)$, where k is the slope of the linear curve $\ln(C_t/C_o) = -kt$, C_t being the (pro)-drug concentration in the receiver chamber at time t, C_o is the initial concentration in the donor chamber, A is the membrane surface area (4.52 cm^2), and V_D is the volume of the donor chamber (2 cm^3). These calculations were performed for each transport experiment, and the values that are reported in Table 3 represent the means (±SD) of at least three independent experiments.

RESULTS AND DISCUSSION

Synthesis. The mannose-derived PI prodrugs shown in Figure 1 were prepared in two steps by condensing the saquinavir, indinavir, or nelfinavir with the key acid synthon **5α,*β***, a protected mannosylated derivative, followed by deprotection of the sugar protecting group (Scheme 1). Owing to the difficulties to prepare large amounts of pure **5α** or **5*β***, the synthon **5** was used as a mixture of α/*β* anomers. The esterification (first step) of the PI hydroxyl(s) was the limiting step. Indeed, the deacetalation of the protected mannose unit in the various saquinavir, indinavir, or nelfinavir was performed with 90−95% yields. Note that all the mono- and diester PI-prodrugs were isolated as mixtures of α,*β*-D-mannose anomers (see below).

Concerning saquinavir, acylation of its unique hydroxyl was performed in 71% yield using conventional EDC/DMAP as coupling reagent (*48*). Concerning indinavir and nelfinavir, which both contain two hydoxyls, and in line with previous work (*27*−*29*), a stochastic esterification, one to one equivalent, was preferred instead of a more tedious and time-consuming protection/deprotection strategy of one of these two hydoxyls. The stochastic esterification led into the formation of a mixture of mainly the monoester and diester resulting from the esterification of the C1-hydroxyl of nelfinavir and C8-hydroxyl of indinavir, and of both hydroxyls, respectively. Only tiny amounts (less than 2%) of the monoesters corresponding to the esterification of the C18-hydroxyl of nelfinavir and C14-hydroxyl of indinavir were detected. In the case of indinavir and nelfinavir esters, monoester versus diester formation was favored but only slightly by contrast with what we noticed for all nelfinavir or indinavir prodrugs synthesized so far, using the same reaction conditions (*27*−*29*). Indeed, acylation of indinavir (respectively nelfinavir) with acid **5α,*β*** led to a 1.5:1 (respectively 2.2:1) mixture of monoester Ind(8)-C(O)C4ManP (respectively Nelf-(1)-C(O)C4ManP) and diester Ind-[C(O)C4ManP]2 (respectively Nelf-[C(O)C4ManP]2). By contrast, and as reported elsewhere, reaction of indinavir with 1,2:5,6-di-*O*-isopropylidene-3-*O*-(4-carboxybutyl)-α-D-glucofuranose, a close analogue of the mannosylated acid **5α,*β***, produced a 4:1 mixture of the monoester and diester adducts (*29*). Deprotection of the mannose unit in the saquinavir, indinavir, or nelfinavir conjugates was performed using aqueous TFA and afforded almost quantitatively the target Saq-C(O)C4Man(TFA), Ind(8)-C(O)C4Man(2TFA), Ind-[C(O)-C4ManP]2(2TFA), Nelf(1)-C(O)C4Man(2TFA), and Nelf-[C(O)-C4ManP]2(2TFA) prodrugs, respectively.

Concerning the synthesis of the starting mannose-derived building block **5** and owing to the presence of several hydroxyl groups on mannose with close reactivity, protection/deprotection steps were needed to prepare this key synthon. Moreover, as this synthon was linked to the PI via an ester linkage, the use of protecting groups for the sugar part that are labile under basic conditions was precluded. Therefore, we selected the isopropylidene acid-labile acetal protection, which has further been shown to be highly compatible for similar glucosylated derivatives (*29*). To the best of our knowledge, examples of glycosylation with saccharides containing a 2,3-isopropylidene protecting group used as a glycoside donor are few (*49*−*54*), and only one concerns the mannopyranose moiety (*53*). In our hands, this latter strategy failed. Indeed, the glycosylation of methyl 5-hydroxypentanoate with 2,3;4,6-di-*O*-isopropylidene α-D-mannopyranose derivative **3α** (HO-ManP) (Scheme 1, path A) gave the target molecule **4α** in 4% yield only.

To overcome this drawback, another strategy was attempted where the diisopropylidene protection was performed after the glycosylation step using a more conventional procedure (Scheme 1, path B). The glycosylation was achieved using the very labile trimethylsilyl group as transient intermediate protecting group adapting a process described in literature for the preparation of an analogous mannosylated derivative (*55*). The transitory persilylated mannopyanose **6α,*β*** (obtained as a 80:20 α/*β*

Scheme 1. Synthetic Pathway to the Mannose-Containing Prodrugs of Saquinavir, Indinavir, and Nelfinavir[a]

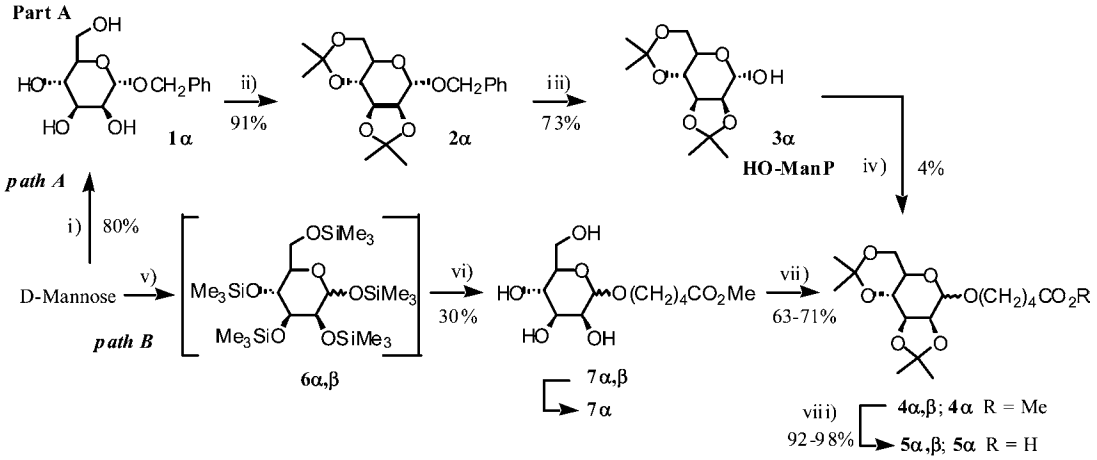

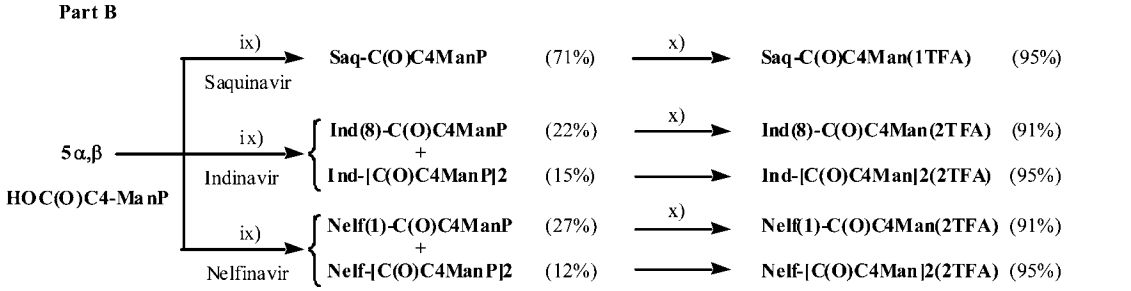

[a] (i) $PhCH_2OH$ (reactive and solvent), *p*-TsOH; (ii) 2,2-dimethoxypropane, acetone, *p*-TsOH; (iii) H_2/Pd/C, 2:2:1 THF/EtOH/H_2O; (iv) $HO(CH_2)_4CO_2Me$, Ph_2SO, $(CF_3SO_2)_2O$, 2,6-dimethylpyridine; (v) $MeC[=NSi(Me)_3]OSiMe_3$, CH_2Cl_2, rt or Me_3SiCl, $(Me_3Si)_2NH$, pyridine, rt; (vi) (a) Me_3SiI, NH_4I, CH_2Cl_2, rt, (b) $HO(CH_2)_4CO_2Me$, rt, (c) MeOH; (vii) 2-methoxypropene, *p*-TsOH, CH_2Cl_2; (viii) 1 M LiOH, THF; (ix) EDC/DMAP, CH_2Cl_2; (x) TFA, CH_2Cl_2.

Scheme 2. Chemical Structures and Code Names of the Antiprotease Inhibitor (PI = Saquinavir, Indinavir, and Nelfinavir) Prodrugs Already Published[a]

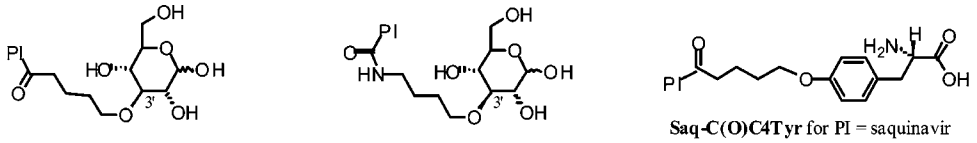

Saq-C(O)C4Glc for PI = saquinavir
Ind(8)-C(O)C4Glc for PI = indinavir
Nelf(18)-C(O)NC4Glc for PI = nelfinavir
Saq-C(O)C4Tyr for PI = saquinavir
Ind(8)-C(O)C4Tyr for PI = indinavir
Nelf(1)-C(O)C4Tyr for PI = nelfinavir

[a] Refs *28* and *29*.

anomeric mixture, according to ^1H NMR) was prepared from D-mannose using either *N,O*-bis(trimethylsilyl)acetamide in dichloromethane or a mixture of chlorotrimethylsilane and 1,1,1,3,3,3-hexamethyldisilazane in pyridine, the former conditions being preferred. Then, action of iodotrimethylsilane gave the in situ persilylated mannopyranosyl iodide which, by reaction with methyl 5-hydroxypentanoate followed by desilylation, afforded methyl ester **7α,*β*** in 30% yield as a 60:40 α/*β* mixture according to ^1H NMR (see below). Pure **7α** could be separated and isolated from this mixture after several column chromatographies. The acetalation protection was then performed by action of 2-methoxypropene on **7α,*β*** giving **4α,*β*** in 71% yield. Saponification released almost quantitatively the acid intermediate **5α,*β*** (20% overall yield from D-mannose). In the same way, the anomeric material **5α** was obtained from **7α**.

The chemical structures of (i) all protected and deprotected PI prodrugs, which consist into mixtures of α,*β*-D-mannose anomers, (ii) anomeric mixtures of **4α,*β*/5α,*β*/7α,*β***, and (iii) pure **4α**/**5α**/**7α** were unambiguously ascertained by ^1H,^{13}C NMR and mass spectrometry. That each of the protected and deprotected PI prodrugs consisted of a mixture of α,*β*-D-mannose anomers was shown by the presence of anomeric H-1α and H-1*β* singlets in approximately 64:36 to 52:48, which are close to that of the 53:47 protected material **4α,*β***, and of anomeric C-1α and C-1*β* resonances in its ^1H and ^{13}C NMR spectrum, respectively (see Table 1). The α/*β* assignment was attested by comparison of these NMR signals with those collected for pure **4α**, **5α**, and anomeric **4α,*β*** or **5α,*β*** mixtures (see Table 1) and by comparison with the ^1H (*55*−*57*) and ^{13}C NMR data for similar derivatives (*55*, *56*, *58*). For instance, the α and *β* configurations of **4** are confirmed by the anomeric H-1α and H-1*β* singlets at 4.96 and 4.89 ppm, respectively, the C-13α and C-13*β* resonances determined by 2D experiments being at 97.9 and 98.9 ppm, respectively (*55*, *59*). The variations of α:*β* ratios of the various protected and deprotected PI prodrugs were essentially due to the purification steps which were performed by column chromatography.

That formation of the monoesters occurred on the C-26 saquinavir, C-8 indinavir, and C-1 nelfinavir hydroxyls is also unambiguously established by ^1H and ^{13}C NMR. As expected, the resonances of the corresponding H-26 (respectively H-8) proton and C-26 (respectively C-8) carbon atoms of the saquinavir (respectively indinavir) derivative, are deshielded ($|\Delta\delta| = 1.25-1.38$ ppm and $|\Delta\delta| = 3.7-7.6$ ppm, respectively) in comparison with those of the parent PI. For nelfinavir, acylation of its aromatic C-1 hydroxyl resulted in the shielding ($|\Delta\delta| = 5.9$ ppm) of the C-1 carbon resonance (*60*, *61*), as expected for phenyl esters. Furthermore, the resonances of the

Table 1. α:β Anomer Ratio of the Mannosylated Starting Building Blocks 4/5 and PI-Prodrugs, and NMR Data of Their Anomeric H- and C-Atom Signals[a]

compound	α:β ratio	H-1′α[b]	H-1′β[b]	C-1′α	C-1′β
4α	100:0	4.89		97.7	
4α,β	53:47	4.96	4.89	97.9	98.9
5α	100:0	4.94		99.1	
5α,β		*c*	*c*	99.1	100.1
Saq-C(O)C4ManP	64:36	5.00	4.84 (d, *J* 2.4)	99.1	100.0
Saq-C(O)C4Man	64:36	4.78 (d, *J* 1.5)	4.55	101.5	101.7
Ind(8)-C(O)C4ManP	52:48	4.96	4.77	98.9	99.8
Ind(8)-C(O)C4Man	58:42	4.63	4.33	101.6	101.4
Ind-[C(O)C4ManP]2[d]	62:38	5.04 (C-14)	4.87 (C-14)	99.78 (C-14)	98.83 (C-14)
		4.98 (C-8)	4.78 (C-8)	99.70 (C-8)	98.77 (C-8)
Ind-[C(O)C4Man]2[d]	60:40	4.76 (C-14)	4.51 (C-14)	101.68[e]	101.56[e]
		4.71 (C-8)	4.39 (C-8)	101.60[e]	101.48[e]
Nelf(1)-C(O)C4ManP	55:45	5.09	4.90 (d, *J* 2.2)	99.0	99.8
Nelf(1)-C(O)C4Man	58:42	4.73 (d, *J* 3.4)	4.49	101.5	101.6
Nelf-[C(O)C4ManP]2[f]	55:45	5.10	4.93 (d, *J* 1.1)	98.94	99.7
		5.06	4.90	98.89	
[Nelf-C(O)C4Man]2[f]	60:40	4.83	4.58	100.7	101.6
		4.78	4.56		

[a] δ in ppm, *J* in Hz. [b] Singlet unless otherwise stated. [c] Hindered by the residual peak of water. [d] C-8/C-14 means that the mannosylated residues are connected to the indinavir C-8/C-14 atom, respectively. [e] Could not be assigned to the indinavir C-8 or C-14 connecting position [f] Could not be assigned to the nelfinavir C-1 or C-18 connecting position.

H-14/C-14 indinavir and H-18/C-18 nelfinavir atoms bearing the remaining "free" hydroxyl and of their vicinal β-carbon atoms are almost not affected. These resonances are deshielded in the diesters, confirming that acylation of the two hydroxyls of indinavir and nelfinavir has occurred. All these trends are in line with those reported for the C-14/C-8 indinavir and C-18/C-1 nelfinavir prodrugs (*27*−*29*).

Concerning the protected and deprotected diester prodrugs derived from indinavir or nelfinavir, their $^{1}H/^{13}C$ NMR spectra are very complex. This is due to the presence of four isomers consisting of the α/α-, α/β-, β/α-, and β/β- connection of the mannose moiety to each of the two hydroxyl groups of the PI. Indeed, their $^{1}H/^{13}C$ NMR spectra exhibit four signals for the α/β anomeric H/C atoms, two sets for each of the C14α/β- and C8-α/β-indinavir (respectively, C18- and C1-nelfinavir) α/β-anomers, as expected (see Table 1).

Mannose-deprotection is confirmed among others by the absence of the characteristic isopropylidene resonances in the NMR spectra of the isolated deprotected PI prodrugs.

Biological Activity and Chemical Stability. The saquinavir hydroxyl, the indinavir C-14 but not the C-8 hydroxyl, and the nelfinavir C-18 but not the C-1 hydroxyl, are involved in the peptidomimetic noncleavable transition state isostere responsible for the protease inhibitory potency of saquinavir, indinavir, and nelfinavir, respectively (*62*). Therefore, it is most important that these hydroxyls be accessible for antiviral activity. In the previous studies dedicated to the ester prodrugs of saquinavir, indinavir, and nelfinavir (*27*, *28*), a close correlation between their anti-HIV activity and the hydrolysis of their acylated "peptidomimetic" hydroxyl, hence the liberation of the active free drug during the time of incubation, was found: the faster the hydrolysis, the closer the anti-HIV activity level to that of the respective parent drug. Concomitantly, the level of HIV inhibition was very low for the prodrugs for which hydrolysis and release of this peptidomimetic hydroxyl was very slow. On the other hand, no correlation was found between the hydrolysis rate of the acylated C-8 indinavir prodrugs (C-8 hydroxyl is not part of the transition state isostere) and their anti-HIV activity (*27*). The HIV inhibition levels and cytotoxicities of D-mannose-containing saquinavir, indinavir, and nelfinavir prodrugs (as their TFA salt) were evaluated in vitro in CEM-SS and MT4 cells against HIV-1 according to published procedures (*63*−*65*). The data are collected in Table 2 together with those of saquinavir and nelfinavir (*66*) (as their methanesulfonate salt), and indinavir (as its sulfate salt).

The sensitivity to hydrolysis of the mannose prodrugs was checked using the same hydrolysis protocol as that described in previous studies from our laboratory. These hydrolysis experiments were performed in a pH 7.3 buffer at 37 °C and in the absence of serum, cells and virus using a prodrug concentration in the 476−1015 μM range. All compounds were hydrolyzed within a close interval of time, their hydrolysis $t_{1/2}$ being comprised between 30 and 60 h (Table 2). These results are close to those established for glucose prodrug analogues containing the same spacer with the striking exception of the glucose analogue Saq-C(O)C4Glc (Scheme 2) which was found to be quite unstable ($t_{1/2}$ = 3 h) (*29*). No obvious explanation may be found for the higher resistance to hydrolysis of the mannosylated saquinavir conjugates as compared with the glucosylated one.

The anti-HIV efficiency of saquinavir, indinavir, and nelfinavir is substantially reduced when D-mannose is conjugated to the peptidomimetic hydroxyl of these protease inhibitors as well as to the hydroxyl of indinavir and nelfinavir, which is not part of the transition state isostere. This is illustrated by the large *R* values (from ≥44 to 1060), which correspond to the ratio of the IC_{50} of the PI prodrug versus that of the parent PI (see Table 2). The lower anti-HIV activities of these PI prodrugs reflect to some extent their relative stabilities with respect to hydrolysis during the 4 day time-span of the antiviral assays.

Considering the sole masking of the "non-peptidomimetic hydroxyl" C-8 of indinavir and C-1 of nelfinavir, this modified also drastically the antiviral activity of nelfinavir ($R \sim 170$ and ~ 120 for Nelf(1)-C(O)C4Man) but not that of indinavir ($R \sim 7$ and ~ 12 for Ind(8)-C(O)C4Man). The activity found for this latter prodrug is in the same range than that of its glucose analogue, Ind(8)-C(O)C4Glc (Scheme 2) (*29*). These data indicate likely that C-8 indinavir conjugates themselves may possess an antiviral activity, which is lower than that of indinavir, and that the hydrolysis rate may also, to some extent, contribute to increasing their intrinsic antiviral potency. In addition, it appears that the nature of the substituent at the other end of the C(O)C4 spacer linked to the non-peptidomimetic C-8 indinavir or C-1 nelfinavir hydroxyl is also of importance for the anti-HIV activity. Indeed, anti-HIV activity is increasing along the mannose, glucose, and tyrosine series (Scheme 2), with these derivatives displaying comparable chemical stability ($t_{1/2}$ in the 40−60 h range, Table 2).

Transepithelial Transport. There is currently a considerable interest in increasing the intestinal absorption of the HIV

Table 2. Anti-HIV Activity (IC_{50}) and Cytotoxicity (CC_{50}) Data for Mannosylated Saquinavir, Indinavir and Nelfinavir Prodrugs[a] in CEM-SS and MT-4 Cell Cultures Infected with HIV-1 LAI and HTLV IIIB, Respectively, Together with Their Hydrolysis Half-Life ($t_{1/2}$), as Compared with Glucose- and Tyrosine-Based Analogous Prodrugs[b]

compound[c]	IC_{50} (nM)	R[d]	IC_{50} (nM)	R[d]	CC_{50} (M)	CC_{50} (M)	$t_{1/2}$[e] hydrolysis (h)
	CEM-SS		MT-4		CEM-SS	MT-4	
Saquinavir*	9		18		$>10^{-5}$	$>10^{-5}$	
Saq-C(O)C4Man	484	~54	2165	~120	$>5\times10^{-5}$	$>5\times10^{-5}$	50
Indinavir**	≤10		22		$>10^{-4}$	$>10^{-4}$	
Ind(8)-C(O)C4Man	71	≥7	263	~12	$>10^{-4}$	$>10^{-4}$	50
Ind-[C(OC4Man]2	440	≥44	2233	~102	$>5\times10^{-5}$	$>5\times10^{-5}$	60
Nelfinavir*	2[f]						
Nelf(1)-C(O)C4Man	339	~170	240	120	$>5\times10^{-5}$	$>5\times10^{-5}$	48
Nelf-[C(OC4Man]2	2120	~1060	$>CC_{50}$		$>5\times10^{-5}$	$>5\times10^{-5}$	*g*
Saq-C(O)C4Tyr[i]	39	~4	160	~9			40
Saq-C(O)C4Glc[j]	<11	~1	62	3.4			3
Ind(8)-C(O)C4Tyr[h,i]	9	≥1	47	4.7			50
Ind(8)-C(O)C4Glc[j]	48	≥5	190	9			*k*
Nelf(1)-C(O)C4Tyr[i]	21	~10	193				60

[a] These data reflect the amount of parent drug released during the 4-day period of the experiments. [b] See Scheme 2 for the structures of glucose (Glc) and tyrosine (Tyr) prodrugs. *, as its mesylate and **, sulfate salt. [c] Prodrugs are tested as their TFA salt. [d] R is the ratio of the prodrug IC_{50} to that of its parent compound. [e] $t_{1/2}$, which corresponds to the time at which 50% of hydrolysis is observed, has been determined from hydrolysis experiments performed by incubating the prodrugs in a pH 7.3 DMEM solution at 37 °C. [f] Data from ref *66*. [g] Not tested. [h] Data from ref *27*. [i] Data from ref *28*. [j] Data from ref *29*. [k] 5% of hydrolysis in 3 h of incubation in the transepithelial transport assay across Caco-2 cell monolayers (culture cell media close to those used for hydolysis experiments) (data from ref *30*).

Table 3. Percentages of Prodrug and PI Transport Across a Monolayer of Caco-2 Cells from the Donor Chamber after 3 h of Experiment and Apparent Permeability Coefficients P_{app}

		absorptive direction (AP to BL)		secretion direction (BL to AP)	
compound[a]	conc in donor chamber (μM)	percent (±SD) in receiver chamber	P_{app} (±SD) (cm/s, $\times10^{-8}$)	percent (±SD) in receiver chamber	P_{app} (±SD) (cm/s, $\times10^{-8}$)
Saquinavir*	9.4	2.6 (0.4)	110 (31)	10.3 (1.9)	398 (117)
Saq-C(O)C4Man	280	6.8 (0.3)	321 (73)	43.1 (0.4)	1622 (36)
Indinavir**	175	2.6 (0.3)	103 (10)	38 (2)	1550 (234)
Ind(8)-C(O)C4Man	300	14.3 (2.5)	526 (66	17.9 (0.6)	662 (25)
Ind-[C(OC4Man]2	230	19 (2.3)	761 (71)	23.5 (2.6)	947 (102)
Nelfinavir*	8	2.7 (1.1)	103 (66)	6.3 (1.4)	251 (68)
Nelf(1)-C(O)C4Man	344	nd[c]		nd	
Nelf-[C(OC4Man]2	247	nd		nd	
Saq-C(O)C4Glc[b]	12.5	nd		22.1 (7.4)	950 (720)
Ind(8)-C(O)C4Glc[b]	265	2.7 (1.3)	66 (31)	6.2 (1.5)	251 (110)
Nelf(18)-C(O)NC4Glc[b]	29	1.6 (0.2)	44 (6)	8.5 (0.8)	339 (51)
Nelf(1)-C(O)C4Tyr[b]	15	nd		nd	

[a] *, as its mesylate $MeSO_3H$ and **, sulfate salt. Prodrugs are tested as their TFA salt. [b] Data from ref *30*; see Scheme 2 for the structures of glucose (Glc) and tyrosine (Tyr) prodrugs. [c] nd = not detected, i.e., below the detection limit which is 0.4, 0.1, and 0.1 μM for the indinavir, saquinavir, and nelfinavir derivatives, respectively.

protease inhibitors and in reducing their recognition by the efflux P-gp carrier (*67*, *68*) which is a possible reason for their poor or variable uptake from the intestinal lumen into the blood circulation. In this regard, esterase-rich and efflux carrier-expressing Caco-2 cell line monolayers are widely accepted in vitro models of the intestinal epithelium for screening drug and prodrug candidates and thus for evaluating prodrug approaches for enhanced intestinal drug absorption (*69*−*73*). This human cell line forms indeed polarized monolayers, which have been shown to express most of the enzymatic, functional, and morphologic characteristics of the intestinal mucosa (*69*, *74*). They express, on the apical side of the monolayer, efflux carrier systems, such as the multidrug-resistant P-gp, which is responsible for the limited oral bioavailability and brain penetration of the protease inhibitors (*67*, *68*). Caco-2 cell line monolayers have already been used in numerous studies to characterize the permeation of various drugs and prodrugs, including indinavir, saquinavir, and nelfinavir (*67*, *68*) and prodrugs deriving therefrom which have been developed in our laboratory (*30*).

Translocation of the various mannosylated protease inhibitor prodrugs across Caco-2 cell monolayers was evaluated at a concentration where they are soluble. Transepithelial electrical resistance after confluence has been used to monitor the integrity of the cell layer (*75*). Translocation was then initiated by adding the test solution to the apical (AP) or basolateral (BL) side of the monolayer (donor chamber). Investigation of the transport across the polarized Caco-2 cell monolayer in the absorptive AP to BL direction and in the secretory BL to AP one constitutes a mean of evaluating the influence of P-gp and related efflux carriers which are located on the AP side of the monolayer. As Caco-2 cells are also rich in esterases, the hydrolysis of the ester prodrugs during their permeation across Caco-2 monolayers was carefully checked. Only the prodrugs were detected either in the donor or acceptor chamber, indicating that no hydrolysis occurred during the transport experiments.

The results of the bidirectional transport studies of D-mannose conjugated prodrugs and of their parent protease inhibitor are presented in Figure 2 (which illustrates the transport profiles) and Table 3. This table collects the percentages of (pro)drug that have been transported after the 3 h experiment and the apparent permeability coefficients P_{app} that were calculated from the slope of a plot of the cumulative receiver concentration with time. In addition, the P_{app} of mannose-conjugated derivatives are presented in Figure 3 in comparison with those of the closely related glucose-conjugated ones (*29*, *30*).

The bidirectional transport results of D-mannose-conjugated prodrugs were very contrasting depending on the PI concerned. Moreover, they contrast also very strongly with those reported for their D-glucose analogues (*30*). Most importantly, the mannosylated saquinavir and indinavir (but not nelfinavir)

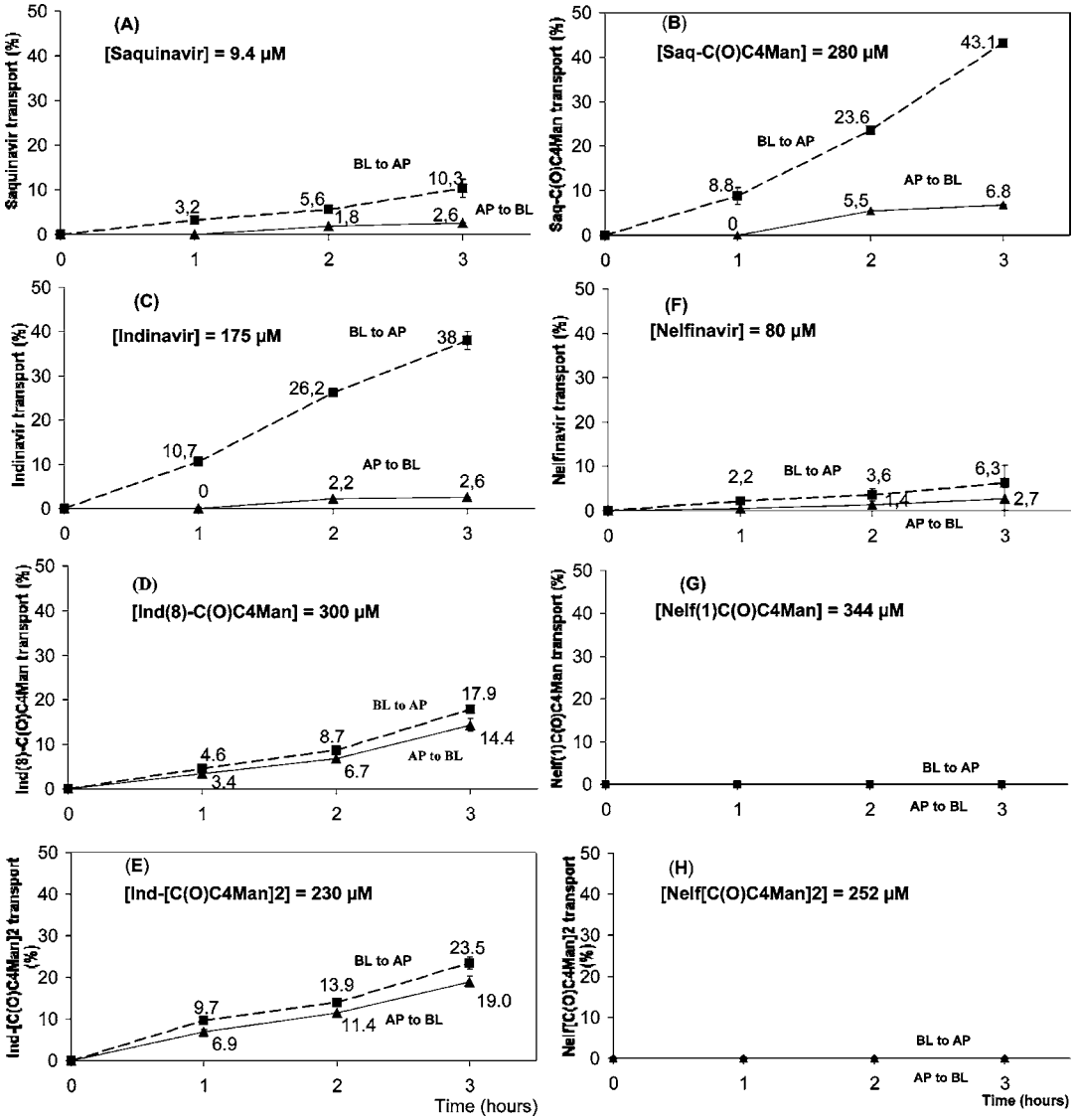

Figure 2. Bidirectional transepithelial transport across a monolayer of Caco-2 cells of mannose-conjugates of PIs (panels B, D, E, G, H) in comparison with their parent drugs (panels A, C, F) (data from ref *30*). Absorptive translocation [apical (AP) to basolateral (BL) compartment]: filled lozenges. Secretory translocation (BL to AP): filled squares. The results are expressed as prodrug transport percentages versus time. The percentage values represent the ratios of (pro)drug concentration in receiver vs donor chamber × 100. The initial concentration of the prodrug in the donor compartment is indicated on each panel. Results are means ± SD from three experiments. All incubations were performed at 37 °C and pH 7.4.

prodrugs were found to display very promising transport profiles that could improve the intestinal absorption of these two protease inhibitors.

Concerning the saquinavir derivative (Figure 2B), Saq-C(O)-C4Man showed an asymmetric permeation profile indicating that, as its parent PI, it is substrate of the apically localized efflux P-gp carrier (*67*, *68*). This highly asymmetric permeation profile was already observed for the D-glucose conjugate analogues [(i.e., Saq-C(O)C4Glc and Saq-C(O)NC4Glc (Scheme 2))]. However, it is noteworthy that the permeation of Saq-C(O)-C4Man in the absorptive AP to BL direction is significantly much higher than those of its glucose analogues for which no transport across the Caco-2 cell monolayer was observed (Table 3 and Figure 3). In comparison with that of its parent drug, permeation of Saq-C(O)C4Man is enhanced in the two directional transport: ∼3-fold in the absorptive AP to BL direction and ∼4-fold in the secretory BL to AP efflux (Table 3, Figure 2A). These absorptive and secretory transport enhancements are not only attributable to a lower affinity of the efflux carriers for this conjugate but also to an active transport mechanism involving a mannose carrier system located at the brush border side of the Caco-2 cell monolayer, if present. It could also arise from an improvement of passive permeation. However, this seems unlikely since conjugation of mannose to saquinavir induced a hydrophilicity increase, though tiny, as shown by the slight decrease of HPLC mobility and logP coefficient[76] (Table 4).

For the indinavir prodrugs, the monoester and diester conjugates, Ind(8)-C(O)C4Man and Ind-[C(OC4Man]2, presented similar and almost superimposable absorptive and secretory permeation profiles (Figure 2D,E). It appears also that, as for saquinavir, conjugation of indinavir to D-mannose improves substantially the absorptive permeation of indinavir (Figure 2C) across Caco-2 cell monolayers (∼5- and 7-fold increase, respectively), by contrast to its conjugation to D-glucose (Table 3 and Figure 3). It is further noticeable that the secretory permeations of these indinavir prodrugs are lower than that of indinavir, indicating that conjugation of D-mannose to indinavir decreases its passive diffusion, as expected from an increase of its hydrophilicity[76] (see Table 4). Therefore, the absorptive transport enhancements are more likely attributable to a substantial decrease of their efflux owing to a lower affinity

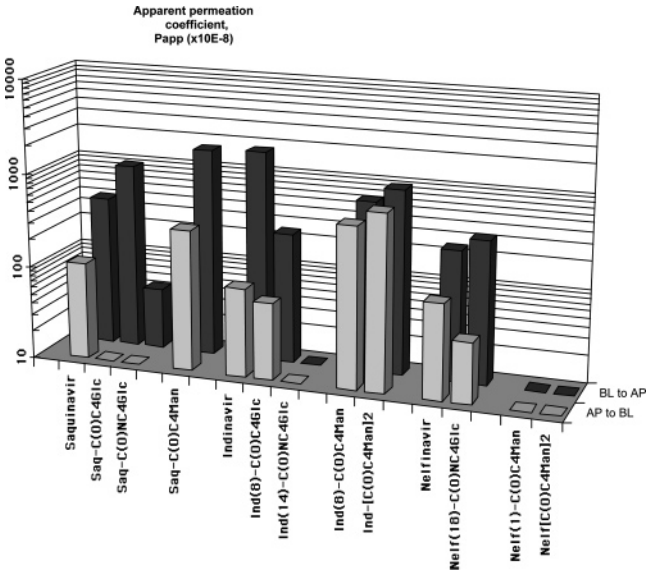

Figure 3. Caco-2 cell monolayer apparent permeation coefficients (P_{app}) in the absorptive (AP to BL; gray bars) and secretion (BL to AP; dark gray bars) direction of indinavir, saquinavir, nelfinavir, and of their mannose conjugates displayed in Scheme 1, and of their glucose conjugates (data from ref *30*), structures in Scheme 2.

Table 4. HPLC Mobility and LogP Data of PIs and Prodrugs

compound[a]	HPLC mobility[a] (in min)	log P[b]
Saquinavir	5.6	4.727 (4.73)[c]
Saq-C(O)C4Man	5.0	4.218
Indinavir	4.9	3.681 (3.68)[c]
Ind(8)-C(O)C4Man	3.5	3.216
Ind-[C(OC4Man]2	3.3	2.062
Nelfinavir	12.5	5.842 (5.84)[c]
Nelf(1)-C(O)C4Man	5.2	4.490
Nelf-[C(OC4Man]2	4.8	3.659

[a] Determined on a HP1100 apparatus with a Lichrospher 100 RP-18-packed column. The isocratic mobile phase consisted of a pH 6 buffer/CH_3CN mixture (41:59 for saquinavir and its prodrug; 59:41 for indinavir and its two prodrugs; 45:55 for nelfinavir and its two prodrugs (for more details, see experimental section). [b] Calculated using Chem 3D Ultra 8.0, CambridgeSoft, Cambridge, MA. [c] Data taken from ref 76 and calculated using CQSAR program.

of the efflux carriers for these conjugates and/or to an active transport mechanism involving a mannose carrier system located at the brush border side of the Caco-2 cell monolayer, if present. Such an absorptive transport improvement was already detected for valine conjugates of indinavir (*30*).

Concerning the mannose-nelfinavir prodrugs, the conjugation of D-mannose to nelfinavir, Nelf(1)-C(O)C4Man and Nelf-[C(OC4Man]2, was highly detrimental to its permeation across the Caco-2 cell monolayers. No detectable transport, at least above the detection limit for nelfinavir derivatives (0.1 μM), was observed whatever the AP to BL or BL to AP directional transport (Figure 2F−H). A similar behavior was also found for Nelf(1)-C(O)C4Tyr (*30*) (Table 3, Scheme 2), a tyrosine analogue prodrug of Nelf(1)-C(O)C4Man. However, it is in sharp contrast with a D-glucose analogue prodrug, i.e., Nelf-(18)-C(O)NC4Glc (Table 3, Figure 3, Scheme 2), for which transport in both direction was observed. These results indicate that the mannose-nelfinavir conjugates are not recognized and actively transported by a mannose carrier system, if present on the Caco-2 cells. The absence of any secretory transport supports further that conjugation of D-mannose to nelfinavir reduces drastically its passive permeation, as expected from an increase of its hydrophilicity. This is indeed reflected by the substantial much larger decrease of HPLC mobility and logP coefficient observed for nelfinavir (which of the three PIs investigated is the most lipophilic) than for saquinavir and indinavir[76] (Table 4).

CONCLUSION

Mannose-derived conjugates were prepared in two steps, in good yields, by condensing an acid derivative of the appropriate protected mannose with the PI, followed by deprotection of the sugar protecting group. With respect to hydrolysis, these PI prodrugs are chemically stable with half-life times in the 50−60 h range that are further compatible with an in vivo utilization aimed at improving the absorption/penetration or accumulation of the prodrug in specific cells/tissues and liberation of the active free drug inside HIV-infected cells. These stabilities correlate closely with the low in vitro anti-HIV activity measured for those prodrugs wherein the coupling of mannose to the PIs was performed through the peptidomimetic PI's hydroxyl. Ind(8)-C(O)C4Man, wherein the coupling of the mannosylated residue was performed onto the non-peptidomimetic PI hydroxyl, displayed a quite high antiviral activity and stability, indicating that this prodrug is also to some extent an antiviral drug by itself. Mannose conjugation to the PIs was further found to improve the absorptive transepithelial transport of saquinavir and indinavir, but not of nelfinavir, across Caco-2 cell monolayers used as a model of the intestinal barrier. These data indicate also that the conjugation of mannose to saquinavir and indinavir could constitute a mean to improve their intestinal absorption. It is noteworthy that mannose conjugation improved the absorptive transepithelial transport of saquinavir and indinavir by contrast to glucose conjugation which had the opposite effect. The mannose-linked prodrugs of saquinavir and indinavir display therefore a most promising therapeutic potential provided that bioavailability, penetration into the HIV infected macrophages and HIV-reservoirs of these PIs are improved. Further work aimed at a better understanding of the impact of D-mannose on the absorptive transepithelial transport of the PIs and of the transport mechanism of the mannosylated PI prodrugs, and at evaluating their uptake by macrophages is under progress and will be reported in due course.

ACKNOWLEDGMENT

This work was supported by research funds provided by the Fondation de la Recherche Médicale (Sidaction), the Agence Nationale de la Recherche sur le SIDA (ANRS) and the Centre National de la Recherche Scientifique (CNRS) and by a Conseil Régional de la Martinique grant (D.R.).

LITERATURE CITED

(1) Gulick, R. M. (2002) Protease inhibitors: clinical efficacy. *Infect. Dis. Ther. 25*, 179−236.
(2) Blankson, J. N., Persaud, D., and Siliciano, R. F. (2002) The challenge of viral reservoirs in HIV-1 infection. *Annu. Rev. Med. 53*, 557−593.
(3) Chun, T.-W., and Fauci, A. S. (1999) Latent reservoirs of HIV: obstacles to the eradication of virus. *Proc. Natl. Acad. Sci. U.S.A. 96*, 10958−10961.
(4) Chun, T.-W., Stuyver, L., Mizell, S. B., Ehler, L. A., Mican, J. A. M., Baseler, M., Lloyd, A. L., Nowak, M. A., and Fauci, A. S. (1997) Presence of an inducible HIV-1 latent reservoir during highly active antiretroviral therapy. *Proc. Natl. Acad. Sci. U.S.A. 94*, 13193−13197.
(5) Li, X., and Chan, W. K. (1999) Transport, metabolism and elimination mechanisms of anti-HIV agents. *Adv. Drug Deliv. Rev. 39*, 81−103.
(6) Taylor, S., and Pereira, A. (2000) Penetration of HIV-1 protease inhibitors into CSF and semen. *HIV Med. 1*, 18−22.

(7) Bickel, U., Yoshikawa, T., and Pardridge, W. M. (2001) Delivery of peptides and proteins through the blood-brain barrier. *Adv. Drug Deliv. Rev. 46*, 247−279.
(8) Calogeropoulou, T., Detsi, A., Lekkas, E., and Koufaki, M. (2003) Strategies in the design of prodrugs of anti-HIV agents. *Curr. Top. Med. Chem. 3*, 1467−1495.
(9) Vierling, P., and Greiner, J. (2003) Prodrugs of HIV protease inhibitors. *Curr. Pharm. Des. 9*, 1755−1770.
(10) Wang, W., Jiang, J., Ballard, C. E., and Wang, B. (1999) Prodrug approaches to the improved delivery of peptide drugs. *Curr. Pharm. Des. 5*, 265−287.
(11) Denny, W. A. (2001) Prodrug strategies in cancer therapy. *Eur. J. Med. Chem. 36*, 577−595.
(12) Denny, W. A. (2003) Prodrugs for gene-directed enzyme-prodrug therapy (suicide gene therapy). *J. Biomed. Biotechnol. 2003*, 48−70.
(13) Yatvin, M. B., Li, W., Meredith, M. J., and Shenoy, M. A. (1999) Improved uptake and retention of lipophilic prodrug to improve treatment of HIV. *Adv. Drug Deliv. Rev. 39*, 165−182.
(14) Niculescu-Duvaz, I., Friedlos, F., Niculescu-Duvaz, D., Davies, L., and Springer, C. J. (1999) Prodrugs for antibody- and gene-directed enzyme prodrug therapies (ADEPT and GDEPT). *Anticancer Drug Des. 14*, 517−538.
(15) Tan, X., Chu, C. K., and Boudinot, F. D. (1999) Development and optimization of anti-HIV nucleoside analogs and prodrugs: A review of their cellular pharmacology, structure-activity relationships and pharmacokinetics. *Adv. Drug Deliv. Rev. 39*, 117−151.
(16) Wiebe, L. I., and Knaus, E. E. (1999) Concepts for the design of anti-HIV nucleoside prodrugs for treating cephalic HIV infection. *Adv. Drug Deliv. Rev. 39*, 63−80.
(17) Gunaseelan, S., Debrah, O., Wan, L., Leibowitz, M. J., Rabson, A. B., Stein, S., and Sinko, P. J. (2004) Synthesis of poly(ethylene glycol)-based saquinavir prodrug conjugates and assessment of release and anti-HIV-1 bioactivity using a novel protease inhibition assay. *Bioconjugate Chem. 15*, 1322−1333.
(18) Jain, R., Agarwal, S., Majumdar, S., Zhu, X., Pal, D., and Mitra, A. K. (2005) Evasion of P-gp mediated cellular efflux and permeability enhancement of HIV-protease inhibitor saquinavir by prodrug modification. *Int. J. Pharm. 303*, 8−19.
(19) Luo, S., Kansara, V. S., Zhu, X., Mandava, N. K., Pal, D., and Mitra, A. K. (2006) Functional characterization of sodium-dependent multivitamin transporter in MDCK-MDR1 cells and its utilization as a target for drug delivery. *Mol. Pharm. 3*, 329−339.
(20) Gatell, J. M. (2001) From amprenavir to GW433908. *J. HIV Ther. 6*, 95−99.
(21) Sorbera, L. A., Martin, L., Castaner, J., and Castaner, R. M. (2001) Fosamprenavir. Anti-HIV HIV protease inhibitor. *Drugs Future 26*, 224−231.
(22) Chapman, T. M., Plosker, G. L., and Perry, C. M. (2004) Fosamprenavir: a review of its use in the management of antiretroviral therapy-naive patients with HIV infection. *Drugs 64*, 2101−2124.
(23) Becker, S., and Thornton, L. (2004) Fosamprenavir: advancing HIV protease inhibitor treatment options. *Exp. Opin. Pharmacother. 5*, 1995−2005.
(24) Furfine, E. S., Baker, C. T., Hale, M. R., Reynolds, D. J., Salisbury, J. A., Searle, A. D., Studenberg, S. D., Todd, D., Tung, R. D., and Spaltenstein, A. (2004) Preclinical pharmacology and pharmacokinetics of GW433908, a water-soluble prodrug of the human immunodeficiency virus protease inhibitor amprenavir. *Antimicrob. Agents Chemother. 48*, 791−798.
(25) Flexner, C. W. (2002) Pharmacology and drug interactions of HIV protease inhibitors. *Infect. Dis. Ther. 25*, 139−159.
(26) Fromm, M. F. (2000) P-glycoprotein: A defense mechanism limiting oral bioavailability and CNS accumulation of drugs. *Int. J. Clin. Pharmacol. Ther. 38*, 69−74.
(27) Farese-Di Giorgio, A., Rouquayrol, M., Greiner, J., Aubertin, A.-M., Vierling, P., and Guedj, R. (2000) Synthesis and anti-HIV activity of prodrugs derived from saquinavir and indinavir. *Antivir. Chem. Chemother. 11*, 97−110.
(28) Gaucher, B., Rouquayrol, M., Roche, D., Greiner, J., Aubertin, A.-M., and Vierling, P. (2004) Prodrugs of HIV protease inhibitors-saquinavir, indinavir and nelfinavir-derived from diglycerides or amino acids: synthesis, stability and anti-HIV activity. *Org. Biomol. Chem. 2*, 345−357.
(29) Rouquayrol, M., Gaucher, B., Greiner, J., Aubertin, A.-M., Vierling, P., and Guedj, R. (2001) Synthesis and anti-HIV activity of glucose-containing prodrugs derived from saquinavir, indinavir and nelfinavir. *Carbohydr. Res. 336*, 161−180.
(30) Rouquayrol, M., Gaucher, B., Roche, D., Greiner, J., and Vierling, P. (2002) Transepithelial Transport of Prodrugs of the HIV Protease Inhibitors Saquinavir, Indinavir, and Nelfinavir Across Caco-2 Cell Monolayers. *Pharm. Res. 19*, 1704−1712.
(31) Barratt, G., and Schuber, F. (1993) Targeting of liposomes with mannose-terminated ligands, in *Liposome Technology*, 2nd Ed. (Gregoriadis, G. Ed.) Vol. 3, pp 199−218, CRC, Boca Raton, U.S.A.
(32) Molema, G., Jansen, R. W., Pauwels, R., de Clercq, E., and Meijer, D. K. (1990) Targeting of antiviral drugs to T4-lymphocytes. Anti-HIV activity of neoglycoprotein-AZTMP conjugates in vitro. *Biochem. Pharmacol. 40*, 2603−2610.
(33) Bolmstedt, A. J., O'Keefe, B. R., Shenoy, S. R., McMahon, J. B., and Boyd, M. R. (2001) Cyanovirin-N defines a new class of antiviral agent targeting N-linked, high-mannose glycans in an oligosaccharide-specific manner. *Mol. Pharmacol. 59*, 949−954.
(34) Ferkol, T., Perales, J. C., Mularo, F., and Hanson, R. W. (1996) Receptor-mediated gene transfer into macrophages. *Proc. Natl. Acad. Sci. U.S.A. 93*, 101−105.
(35) Linehan, S. A., Martinez-Pomares, L., and Gordon, S. (2000) Macrophage lectins in host defence. *Microb. Infect. 2*, 279−288.
(36) Martinez-Pomares, L., Linehan, S. A., Taylor, P. R., and Gordon, S. (2001) Binding properties of the mannose receptor. *Immunobiology 204*, 527−535.
(37) Diebold, S. S., Plank, C., Cotten, M., Wagner, E., and Zenke, M. (2002) Mannose receptor-mediated gene delivery into antigen presenting dendritic cells. *Somat. Cell Mol. Genet. 27*, 65−74.
(38) Grandjean, C., Angyalosi, G., Loing, E., Adriaenssens, E., Melnyk, O., Pancre, V., Auriault, C., and Gras-Masse, H. (2001) Novel hyperbranched glycomimetics recognized by the human mannose receptor: quinic or shikimic acid derivatives as mannose bioisosteres. *ChemBioChem 2*, 747−757.
(39) Lee, R. T., Ichikawa, Y., Fay, M., Drickamer, K., Shao, M., and Lee, Y. C. (1991) Ligand-binding characteristics of rat serum-type mannose-binding protein (MBP-A). Homology of binding site architecture with mammalian and chicken hepatic lectins. *J. Biol. Chem. 266*, 4810−4815.
(40) Gouyette, C., Neumann, J. M., Fauve, R., and Huynh-Dinh, T. (1989) 6- and 1- Substituted mannosyl phosphotriesters as lipophilic macrophage-targeted carriers of antiviral nucleosides. *Tetrahedron Lett. 30*, 6019−6022.
(41) Muller, C. D., and Schuber, F. (1989) Neo-mannosylated liposomes: synthesis and interaction with mouse Kupffer cells and resident peritoneal macrophages. *Biochim. Biophys. Acta 986*, 97−105.
(42) Park, K.-H., Sung, W. J., Kim, S., Kim, D. H., Akaike, T., and Chung, H.-M. (2005) Specific interaction of mannosylated glycopolymers with macrophage cells mediated by mannose receptor. *J. Biosci. Bioeng. 99*, 285−289.
(43) Frappier, F., Audinot, M., Beaucourt, J. P., Sergent, L., and Lukacs, G. (1982) Mechanism of the backbone rearrangement of amino steroids. A carbon-13 and tritium nuclear magnetic resonance spectroscopic study of isoconessine, neoconessine and the corresponding polydeuterated and polytritiated species. *J. Org. Chem. 47*, 3783−3785.
(44) Huckstep, M., Taylor, R. J. K., and Caton, M. P. L. (1982) A convenient method of preparing the leukotriene precursor methyl 5-oxopentanoate. *Synthesis* 881−882.
(45) Bashyal, B. P., Fleet, G. W. J., Gough, M. J., and Smith, P. W. (1987) Synthesis of the α-mannosidase inhibitors swainsonine [(1S,2R,8R,8aR)-1,2,8-trihydroxyoctahydroindolizine] and 1,4-dideoxy-1,4-imino-D-mannitol from mannose. *Tetrahedron 43*, 3083−3093.
(46) Winnik, F. M., Carver, J. P., and Krepinsky, J. J. (1982) Syntheses of model oligosaccharides of biological significance. 2. Synthesis of a tetramannoside and of two lyxose-containing trisaccharides. *J. Org. Chem. 47*, 2701−2707.
(47) Chung, S.-K., and Moon, S.-H. (1994) Synthesis and biological activities of (4,6-di-*O*-phosphonato-β-D-mannopyranosyl)- methylphosphonate as an analog of 1L-myo-inositol 1,4,5-trisphosphate. *Carbohydr. Res. 260*, 39−50.

(48) Bodanszky, M., and Bodanszky, A. (1984) *The Practice of Peptide Synthesis*, Springer-Verlag, Berlin.

(49) Dasser, M., Chretien, F., and Chapleur, Y. (1990) A facile and stereospecific synthesis of L-glycero-D-manno-heptose and some derivatives. *J. Chem. Soc., Perkin Trans. 1*, 3091−3094.

(50) Maeda, H., Matsumoto, S., Koide, T., and Ohmori, H. (1998) Dehydroxy substitution reactions of the anomeric hydroxy groups in some protected sugars initiated by anodic oxidation of triphenylphosphine. *Chem. Pharm. Bull. 46*, 939−943.

(51) Marra, A., Scherrmann, M.-C., Dondoni, A., Casnati, A., Minari, P., and Ungaro, R. (1994) Sugar calixarenes: synthesis of calix[4]arenes with *O*-glycosyl substituents at upper and lower edges. *Angew. Chem., Int. Ed. Engl. 33*, 2479−2481.

(52) McAdam, D. P., and Stick, R. V. (1988) The treatment of some carbohydrate alcohols and diols with *N*-dibromomethylene-*N*,*N*-dialkylammonium bromides: a synthesis of glycosyl bromides. *Aust. J. Chem. 41*, 563−573.

(53) Nguyen, H. M., Poole, J. L., and Gin, D. Y. (2001) Chemoselective iterative dehydrative glycosylation. *Angew. Chem., Int. Ed. 40*, 414−417.

(54) Stepowska, H., and Zamojski, A. (1994) A convenient preparation of 5-benzyl ethers of D-gluco- and D-manno-furanose derivatives. *Carbohydr. Res. 265*, 133−137.

(55) Ferrieres, V., Roussel, M., Gelin, M., and Plusquellec, D. (2001) A new approach to a disaccharidic hapten containing a galactofuranosyl entity. *J. Carbohydr. Chem. 20*, 855−865.

(56) Nguyen, H. M., Chen, Y., Duron, S. G., and Gin, D. Y. (2001) Sulfide-mediated dehydrative glycosylation. *J. Am. Chem. Soc. 123*, 8766−8772.

(57) Chretien, F., Chapleur, Y., Castro, B., and Gross, B. (1980) Alkyloxytris(dimethylamino)phosphonium salts. Part 21. Anomeric hydroxy-group activation of 2,3:4,6-di-*O*-isopropylidene-α-D-mannopyranose, thioglycosylation, and glycosylation. *J. Chem. Soc., Perkin Trans. 1*, 381−384.

(58) Bock, K., and Pedersen, C. (1983) Carbon-13 nuclear magnetic resonance spectroscopy of monosaccharides. *Adv. Carbohydr. Chem. Biochem. 41*, 27−66.

(59) Sugawara, T., Irie, K., Iwasawa, H., Yoshikawa, T., Okuno, S., Watanabe, H. K., Kato, T., Shibukawa, M., and Ito, Y. (1992) Synthesis of omega-(methoxycarbon)alkyl and 9-(methoxycarbonyl)-3,6-dioxanonyl glycopyranosides for the preparation of carbohydrate-protein conjugates. *Carbohydr. Res. 230*, 117−149.

(60) Sequin, U. (1981) Carbon-13 NMR spectral differences between corresponding methyl esters, phenyl esters and 2-substituted chromones. *Helv. Chim. Acta 64*, 2654−2664.

(61) Schuster, I. I. (1985) A carbon-13 NMR study of electronic effects in the hydrogen bonding of trifluoroacetic acid with substituted benzenes, 1- and 2-substituted naphthalenes, and 9-substituted anthracenes in chloroform. *J. Org. Chem. 50*, 1656−1662.

(62) Lebon, F., and Ledecq, M. (2000) Approaches to the design of effective HIV-1 protease inhibitors. *Curr. Med. Chem. 7*, 455−477.

(63) Pauwels, R., Balzarini, J., Baba, M., Snoeck, R., Schols, D., Herdewijn, P., Desmyter, J., and De Clercq, E. (1988) Rapid and automated tetrazolium-based colorimetric assay for the detection of anti-HIV compounds. *J. Virol. Methods 20*, 309−321.

(64) Genu-Dellac, C., Gosselin, G., Puech, F., Henry, J. C., Aubertin, A. M., Obert, G., Kirn, A., and Imbach, J. L. (1991) Systematic synthesis and antiviral evaluation of α-L-arabinofuranosyl and 2′-deoxy-α-L-erythro-pentofuranosyl nucleosides of the five naturally occurring nucleic acid bases. *Nucleosides Nucleotides 10*, 1345−1376.

(65) Moog, C., Wick, A., Le Ber, P., Kirn, A., and Aubertin, A.-M. (1994) Bicyclic imidazo derivatives, a new class of highly selective inhibitors for the human immunodeficiency virus type 1. *Antiviral Res. 24*, 275−288.

(66) West, M. L., and Fairlie, D. P. (1995) Targeting HIV-1 protease: a test of drug-design methodologies. *Trends Pharmacol. Sci. 16*, 67−74.

(67) Kim, R. B., Fromm, M. F., Wandel, C., Leake, B., Wood, A. J. J., Roden, D. M., and Wilkinson, G. R. (1998) The drug transporter P-glycoprotein limits oral absorption and brain entry of HIV-1 protease inhibitors. *J. Clin. Invest. 101*, 289−294.

(68) Aungst, B. J., Nguyen, N. H., Bulgarelli, J. P., and Oates-Lenz, K. (2000) The influence of donor and reservoir additives on Caco-2 permeability and secretory transport of HIV protease inhibitors and other lipophilic compounds. *Pharm. Res. 17*, 1175−1180.

(69) Artursson, P. (1991) Cell cultures as models for drug absorption across the intestinal mucosa. *Crit. Rev. Ther. Drug Carrier Syst. 8*, 305−330.

(70) Augustijns, P., Annaert, P., Heylen, P., Van den Mooter, G., and Kinget, R. (1998) Drug absorption studies of prodrug esters using the Caco-2 model: evaluation of ester hydrolysis and transepithelial transport. *Int. J. Pharm. 166*, 45−53.

(71) Annaert, P., Gosselin, G., Pompon, A., Benzaria, S., Valette, G., Imbach, J. L., Naesens, L., Hatse, S., De Clercq, E., Van Den Mooter, G., Kinget, R., and Augustijns, P. (1998) Comparison of the disposition of ester prodrugs of the antiviral agent 9-(2-phosphonylmethoxyethyl)adenine [PMEA] in Caco-2 monolayers. *Pharm. Res. 15*, 239−245.

(72) Artursson, P., Palm, K., and Luthman, K. (2001) Caco-2 monolayers in experimental and theoretical predictions of drug transport. *Adv. Drug Deliv. Rev. 46*, 27−43.

(73) Gres, M.-C., Julian, B., Bourrie, M., Meunier, V., Roques, C., Berger, M., Boulenc, X., Berger, Y., and Fabre, G. (1998) Correlation between oral drug absorption in humans, and apparent drug permeability in TC-7 cells, a human epithelial intestinal cell line: comparison with the parental Caco-2 cell line. *Pharm. Res. 15*, 726−733.

(74) Gan, L. S., Eads, C., Niederer, T., Bridgers, A., Yanni, S., Hsyu, P. H., Pritchard, F. J., and Thakker, D. (1994) Use of Caco-2 cells as an in vitro intestinal absorption and metabolism model. *Drug Dev. Ind. Pharm. 20*, 615−631.

(75) Lu, S., Gough, A. W., Bobrowski, W. F., and Stewart, B. H. (1996) Transport properties are not altered across Caco-2 cells with heightened TEER despite underlying physiological and ultrastructural changes. *J. Pharm. Sci. 85*, 270−273.

(76) Bhhatarai, B., and Garg, R. (2005) From SAR to comparative QSAR: role of hydrophobicity in the design of 4-hydroxy-5,6-dihydropyran-2-ones HIV-1 protease inhibitors. *Bioorg. Med. Chem. 13*, 4078−4084.

BC060210M

A Bioconjugate Approach toward Squalamine Mimics: Insight into the Mechanism of Biological Action

Wen-Hua Chen,[†] Xue-Bin Shao,[†] Robert Moellering,[‡] Christine Wennersten,[‡] and Steven L. Regen*[,†]

Department of Chemistry, Lehigh University, Bethlehem, Pennsylvania 18015, and Infectious Disease, BIDMC, Harvard Institutes of Medicine, 77 Avenue Louis Pasteur, Boston, Massachuestts 02115. Received July 19, 2006; Revised Manuscript Received July 20, 2006

A short and efficient synthesis has been devised for a family of squalamine mimics, based on the use of cholic acid, deoxycholic acid, lithocholic acid, putrescine, and spermine as starting materials. Those mimics that contain two facially amphiphilic sterol−spermidine conjugates show strong antibacterial activity against a broad spectrum of Gram-positive bacteria; their corresponding activities against a broad spectrum of Gram-negative bacteria are relatively moderate. Larger mimics, containing four such sterol−spermidine conjugates, exhibit very weak activities. Reversal of the pendent spermidine moiety and a putrescine linkage on the A- and D-rings had little consequence on the antibacterial activity for the most active of the squalamine mimics, which contained two sterol−polyamine units; similar results were obtained with squalamine mimics made from only one sterol unit. Detailed structure−activity measurements, in combination with kinetic studies carried out using liposomes as model membranes, support a mechanism of action involving noncovalent dimers as ion transporting species, most probably via the formation of pores or channels.

INTRODUCTION

The emergence of multidrug-resistant microorganisms, such as methicillin-resistant *Staphylococcus aureus* and vancomycin-resistant *Enterococcus*, has prompted major efforts aimed at developing new classes of antibiotics (*1*−*6*). Squalamine, a compound that has been isolated from the stomach of the dogfish shark, possesses an unusual chemical structure that consists of a spermidine moiety that is attached to a sterol backbone (Chart 1) (*7*−*9*). The fact that it exhibits significant activity against Gram-negative and Gram-positive bacteria has led to the proposal that squalamine is likely to play a role in the immune defense system of the dogfish shark (*7*). It has also stimulated interest in such structures as therapeutic agents (*9*).

In previous work, we have shown that the placement of pendent spermidine and sulfate groups on the A- and D-rings can be reversed in a closely related sterol (i.e., **1**) with retention of significant antibacterial activity (Chart 1) (*10*). Using a bioconjugate approach toward even simpler analogues (e.g., **2**), we also found that the sulfate group is not essential for strong antibiotic activity (*11*, *12*). Although the mechanism of action of these squalamine mimics is not presently known, the fact that *subinhibitory* concentrations of **2** significantly enhance the activity of rifampin against Gram-negative bacteria suggested that they may act at the membrane level (*11*). Previous studies of **1** in model systems have lent support for the notion that such compounds are membrane-active agents. Specifically, a kinetic analysis of the activity of **1**, in discharging pH gradients across liposomal membranes, supports a model in which monomers of **1** are in equilibrium with transport-active dimers; they also imply that this equilibrium strongly favors the monomeric form (*13*, *14*). In this previous investigation, we also postulated that **1** may be operating via a H^+/Cl^- symport mechanism (*13*). In Figure 1, we provide a stylized illustration of two hypothetical transport-active dimers that could shuttle HCl across lipid bilayers. In model "A", two U-shaped forms of a sterol−polyamine conjugate lie side-by-side in a thinned region of a lipid bilayer. In model "B", one U-shaped conjugate lies adjacent to a second one in the adjoining monolayer to form a contiguous pathway for HCl transport across the bilayer.

In the work reported herein, we have carried out a detailed structure−activity investigation using a family of "connected" sterol−polyamine conjugates. Our primary aim was to gain further insight into the probable mechanism of biological action of this general class of compounds. For this purpose, we have used a design strategy that is related to one that we have previously employed in constructing "molecular umbrellas"; that is, bioconjugates derived from two or more naturally occuring facial amphiphiles (*15*−*17*). Conjugate **3** is a generalized structure that is illustrative of the types of molecular umbrellas that we have previously reported (Chart 2).

EXPERIMENTAL PROCEDURES

General Methods. ^{1}H NMR spectra were recorded in either CD_3OD or $CDCl_3$ using a Bruker 500 spectrometer and the solvent as a reference. MALDI-TOF mass spectra were recorded on a DE-STR mass spectrometer. Silica gel 60 (Fluka, particle size 0.035−0.070 mm, 220−440 mesh) was used for all column chromatographic purifications. Thin-layer chromatography (TLC) was performed on glass plates that were precoated with silica gel containing a fluorescence indicator (Whatman). Detection on TLC was made by use of 10% sulfuric acid in water, iodine, ninhydrin solution and UV (254 or 365 nm). All reagents and chemicals were obtained from commercial sources and used as received unless noted otherwise. *N*-Methyldeoxycholamide was prepared according to the reported procedures (*18*).

Synthesis of 8a. To a solution of cholic acid (1.0 g, 2.45 mmol) and *N*-hydroxylsuccinimide (324 mg, 2.81 mmol) in anhydrous THF (5 mL) was added DCC (759 mg, 3.68 mmol). The resulting mixture was stirred at room temperature for 6 h, filtered, and concentrated under reduced pressure. The residue was dissolved in $CHCl_3$ (100 mL) and washed with saturated aqueous $NaHCO_3$ (100 mL), water (100 mL), and brine (100

* Corresponding author. E-mail: slr0@lehigh.edu.
[†] Lehigh University.
[‡] Harvard Institutes of Medicine.

10.1021/bc060220n CCC: $33.50 © 2006 American Chemical Society
Published on Web 10/27/2006

Chart 1

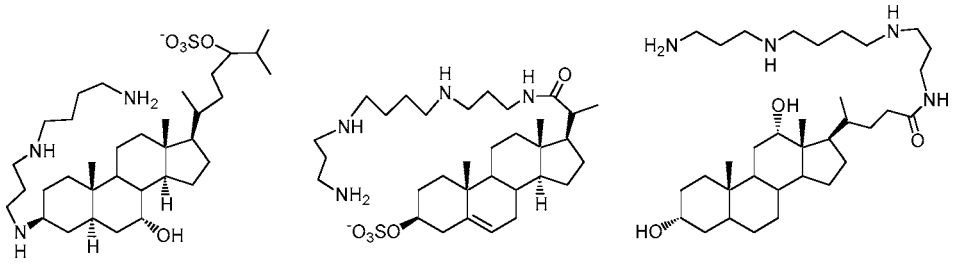

mL). The organic layer was dried over anhydrous sodium sulfate and concentrated under reduced pressure to give crude cholic acid *N*-succinimidyl ester (1.20 g). To a solution of spermine (750 mg) in $CHCl_3$ (10 mL) was added dropwise a solution of the above crude ester in $CHCl_3$ (15 mL) over 20 min. The resulting mixture was stirred at room temperature overnight and then concentrated under reduced pressure. The obtained residue was dissolved in methanol (15 mL), and a solution of di-*tert*-butyl carbonate (3.24 g, 4 equiv) in methanol (10 mL) was added dropwise at 0 °C. The reaction mixture was warmed to room temperature and continued to stir at room temperature for 3 h. After concentration under reduced pressure, the obtained residue was purified by chromatography on a silica gel column ($CHCl_3$/MeOH, 10/1, v/v) to give **8a** (1.37 g, 67%) having ^{1}H NMR (CD_3OD, 500 MHz) δ 3.94 (s, 1 H), 3.78 (s, 1 H), 3.36 (m, 1 H), 3.20−3.15 (m, 10 H), 3.02 (t, J = 6.72 Hz, 2 H), 2.29−2.24 (m, 3 H), 2.10 (m, 1 H), 2.00−0.91 (m, 61 H), 0.70 (s, 3 H). MALDI-TOF MS: m/z 915 ($[M + Na]^+$).

Synthesis of 8b. Compound **8b** was synthesized from deoxycholic acid (1.0 g, 2.55 mmol) using procedures similar to those used for the preparation of **8a** except that $CHCl_3$/MeOH (20/1, v/v) was used as an eluting solvent. The desired product (1.61 g, 72%) had ^{1}H NMR (CD_3OD, 500 MHz) δ 3.95 (s, 1 H), 3.52 (m, 1 H), 3.20−3.14 (m, 10 H), 3.03 (t, J = 6.74 Hz, 2 H), 2.24 (m, 1 H), 2.11 (m, 1 H), 1.89−0.92 (m, 65 H), 0.70 (s, 3 H). MALDI-TOF MS: m/z 899 ($[M + Na]^+$).

Synthesis of 9a. To a solution of **8a** (725 mg, 0.81 mmol) in a 16 mL of a mixture of $CHCl_3$/CH_3CH/ Et_3N (1/1/1.2, v/v/v) was added di-(*N*-succinimidyl)carbonate (DSC, 937 mg, 3.65 mmol). After stirring at 45 °C for 3 h, the reaction mixture was diluted with $CHCl_3$ (100 mL), washed with water (100 mL × 2) and dried over anhydrous sodium sulfate. Concentration under reduced pressure and drying under vacuum afforded residue (796 mg) that was used immediately in the subsequent reaction. To a solution of the residue in anhydrous DMF (5 mL) was added a solution of putrescine (22 mg, 0.25 mmol) and 4-methylmorpholine (1.0 mL). The resulting mixture was stirred at room temperature overnight and concentrated under reduced pressure. The residue was then partitioned between H_2O (150 mL) and $CHCl_3$ (150 mL). The organic layer was separated and dried over anhydrous sodium sulfate. After the solvent was removed under reduced pressure, the residue was purified by chromatography on a silica gel column ($CHCl_3$/CH_3OH, 15/1, v/v) to give **9a** (350 mg, 73%) having ^{1}H NMR (CD_3OD, 500 MHz) δ 4.35 (m, 2 H), 3.95 (s, 2 H), 3.79 (s, 2 H), 3.21−3.15 (m, 20 H), 3.06−3.01 (m, 8 H), 2.39−2.36 (m, 2 H), 2.26−2.24 (m, 4 H), 2.10 (m, 2 H), 2.00−0.92 (m, 126 H), 0.70 (s, 6 H). MALDI-TOF MS: m/z 1949 ($[M + Na]^+$).

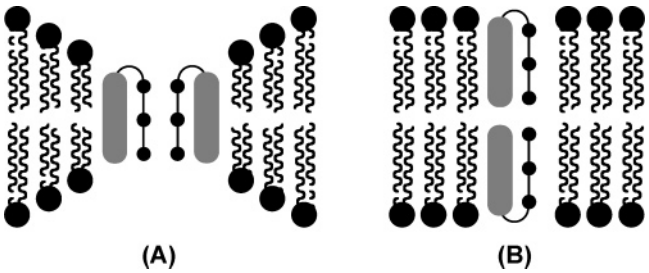

Figure 1. Stylized illustration showing hypothetical transport active dimers made from sterol−polyamine conjugates where (A) two monomers lie side-by-side in a thinned region of the lipid bilayer, and (B) two monomers are adjacent to one another in adjoining leaflets.

Chart 2

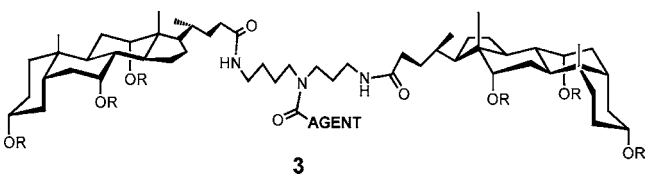

Synthesis of 9b. Compound **9b** was synthesized from **8b** (635 mg, 0.72 mmol) and putrescine (19 mg, 0.22 mmol) using procedures similar to those used for the preparation of **9a** except that $CHCl_3$/MeOH (30/1, v/v) was used as an eluting solvent. The desired product (240 mg, 59%) had ^{1}H NMR ($CDCl_3$, 500 MHz) δ 4.45 (m, 2 H), 3.88 (s, 2 H), 3.13−2.92 (m, 28 H), 2.17 (m, 2 H), 2.02 (m, 2 H), 1.80−0.81 (m, 134 H), 0.57 (s, 6 H). MALDI-TOF MS: m/z 1917 ($[M + Na]^+$).

Synthesis of 4a. To a solution that was prepared from **9a** (125 mg) in dichloromethane (2.0 mL) at 0 °C was added trifluoroacetic acid (2.0 mL). The reaction mixture was then stirred at room temperature for 12 h and concentrated under reduced pressure. The residue was dissolved in methanol (5 mL), adjusted to pH 10 with concentrated ammonium hydroxide and stirred at room temperature for 30 min. After concentration under reduced pressure, the residue was dissolved in water (5.0 mL) and dialyzed against pure water (250 mL, Micro Dispo-Dialyzer, MWCO 500) for 48 h. Concentration under reduced pressure and drying under vacuum gave **4a** (85 mg, *ca* 100%) having ^{1}H NMR (CD_3OD, 500 MHz) δ 4.35 (s, 2 H), 3.95 (s, 2 H), 3.79 (s, 2 H), 3.27 (t, J = 6.42 Hz, 4 H), 3.12 (t, J = 7.62 Hz, 4 H), 3.07−2.98 (m, 20 H), 2.40−0.92 (m, 80 H), 0.70 (s, 6 H). MALDI-TOF MS: m/z 1326 ($[M + H]^+$).

Synthesis of 4b. Compound **4b** was prepared from **9b** (85 mg) using procedures similar to those used in the synthesis of **4a**, affording 56 mg (100%) of product having ^{1}H NMR (CD_3OD, 500 MHz) δ 4.49 (s, 2 H), 3.96 (s, 2 H), 3.27 (t, J = 6.51 Hz, 4 H), 3.12−2.97 (m, 24 H), 2.28 (m, 2 H), 2.15−2.05 (m, 6 H), 1.88−0.93 (m, 76 H), 0.70 (s, 6 H). MALDI-TOF MS: m/z 1294 ($[M + H]^+$).

Synthesis of 10. To a solution of deoxycholic acid methyl amide (708 mg, 1.75 mmol) in 16 mL of a mixture of $CHCl_3$/CH_3CH/Et_3N (1/1/1.2, v/v/v) was added DSC (2.01 g, 7.85 mmol). After stirring at 45 °C for 3 h, the reaction mixture was concentrated under reduced pressure. The residue was then partitioned between H_2O (150 mL) and $CHCl_3$ (150 mL). The organic layer was separated, washed with water, and dried over anhydrous magnesium sulfate. Concentration under reduced

pressure and drying under vacuum gave crude product (725 mg, 1.33 mmol) which was used in the subsequent reaction without further purification. To a solution of the above crude product (500 mg) in anhydrous DMF (5 mL) was added a solution of tri-Boc protected spermine (688 mg, 1.37 mmol) and 4-methylmorpholine (1.0 mL) in anhydrous DMF (5.0 mL). The resulting mixture was stirred at 50 °C overnight and concentrated under reduced pressure. The obtained residue was partitioned between H_2O (150 mL) and $CHCl_3$ (150 mL). The organic layer was separated and dried over anhydrous sodium sulfate. After the solvent was removed under reduced pressure, the residue was purified by chromatography on a silica gel column ($CHCl_3$/CH_3OH, 15/1, v/v) to give **10** (699 mg, 43%) having ^{1}H NMR ($CDCl_3$, 500 MHz) δ 4.48 (s, 1 H), 3.88 (s, 1 H), 3.14−3.00 (m, 12 H), 2.68 (s, 3 H), 2.15−2.13 (m, 1 H), 2.02−2.00 (m, 1 H), 1.75−0.82 (m, 65 H), 0.59 (s, 3 H). MALDI-TOF MS: *m*/*z* 957 ([M + Na]$^+$).

Synthesis of 5. To a solution that was prepared from **10** (100 mg) in dichloromethane (1.0 mL) at 0 °C was added trifluoroacetic acid (1.0 mL). The reaction mixture was then stirred at room temperature overnight and concentrated under reduced pressure. The resulting residue was dissolved in methanol (5 mL), adjusted to pH 10 with concentrated ammonium hydroxide, and stirred at room temperature for 30 min. After concentration under reduced pressure, the residue was purified by chromatography on a silica gel column (CH_3OH/NH_4OH, 2/1, v/v) to give **5** (59 mg, 87%) having ^{1}H NMR (CD_3OD, 500 MHz) δ 4.50 (m, 1 H), 3.95 (s, 1 H), 3.16 (t, J = 6.65 Hz, 2 H), 2.85 (t, J = 6.98 Hz, 2 H), 2.78 (t, J = 7.16 Hz, 2 H), 2.75−2.72 (m, 6 H), 2.69 (s, 3 H), 2.21 (m, 1 H), 2.08 (m, 1H), 1.89−0.94 (m, 38 H), 0.70 (s, 3 H). MALDI-TOF MS: *m*/*z* 635 ([M + H]$^+$).

Synthesis of 11a. To a solution of cholic acid methyl ester (1.50 g, 3.55 mmol) in a 16 mL of a mixture of $CHCl_3$/CH_3CH/Et_3N (1/1/1.2, v/v/v) was added DSC (3.58 g, 14.0 mmol). After the mixture was stirred at 45 °C for 3 h, the product mixture was diluted with $CHCl_3$ (100 mL) and washed with water. The organic layer was then dried over anhydrous sodium sulfate and concentrated under reduced pressure. The residue was purified by column chromatography [silica gel, $CHCl_3$/CH_3CO_2Et (1/1, v/v)] to give 1.40 g (70%) of product having ^{1}H NMR (CD_3OD, 500 MHz) δ 4.57 (s, 1 H), 3.99 (s, 1 H), 3.86 (s, 1 H), 3.66 (s, 3 H), 2.82 (s, 4 H), 2.38−2.21 (m, 2 H), 1.94−0.91 (m, 28 H), 0.69 (s, 3 H).

Synthesis of 11b. Compound **11b** was prepared from deoxycholic acid methyl ester (2.00 g, 4.92 mmol) using procedures similar to that used in the preparation of **11a**, except that $CHCl_3$/CH_3CO_2Et (3/1, v/v) was employed as an eluting solvent. The desired product (1.71 g, 62%) had ^{1}H NMR (CD_3OD, 500 MHz) δ 4.70 (s, 1 H), 3.98 (s, 1 H), 3.66 (s, 3 H), 2.82 (s, 4 H), 2.35−2.24 (m, 2 H), 2.04−0.92 (m, 30 H), 0.69 (s, 3 H).

Synthesis of 11c. Compound **11c** was prepared from lithocholic acid methyl ester (2.50 g, 6.40 mmol) using procedures similar to that used in the preparation of **11a** except that $CHCl_3$/CH_3CO_2Et (10/1, v/v) was used as an eluting solvent. The desired product (2.78 g, 82%) had ^{1}H NMR ($CDCl_3$, 500 MHz) δ 4.69 (s, 1 H), 3.64 (s, 3 H), 2.80 (s, 4 H), 2.33−2.19 (m, 2 H), 2.01−0.88 (m, 32 H), 0.62 (s, 3 H).

Synthesis of 12a. To a solution of **11a** (1.40 g, 2.56 mmol) in anhydrous DMF (5 mL) and DIPEA (0.83 mL, 5 mmol) was added tri-Boc protected spermine (1.30 g, 2.5 mmol). After stirring for 12 h at 50 °C, under a nitrogen atmosphere, the product mixture was concentrated under reduced pressure. The residue was then dissolved in $CHCl_3$ (100 mL), washed with water, dried over anhydrous sodium sulfate, and concentrated under reduced pressure. Purification by column chromatography [silica gel, $CHCl_3$/CH_3CO_2Et (1/2, v/v)] afforded 1.69 g (71%) of the desired product having ^{1}H NMR (CD_3OD, 500 MHz) δ 4.35 (s, 1 H), 3.94 (s, 1 H), 3.79 (s, 1 H), 3.63 (s, 3 H), 3.21 (br, 8 H), 3.06−3.02 (m, 4 H), 2.37−2.26 (m, 4 H), 1.97−0.92 (m, 61 H), 0.70 (s, 3 H). MALDI-TOF MS: *m*/*z* 974 ([M + Na]$^+$).

Synthesis of 12b. Compound **12b** was prepared from **11b** (1.64 g, 3.08 mmol) in a manner that was similar to that described for the synthesis of **12a**, except that $CHCl_3$/CH_3CO_2Et (3/1, v/v) was used as an eluting solvent. The desired product (2.90 g, 98%) had ^{1}H NMR (CD_3OD, 500 MHz) δ 4.50 (s, 1 H), 3.95 (s, 1 H), 3.64 (s, 3 H), 3.20 (br, 8 H), 3.07−2.99 (m, 4 H), 2.35−2.25 (m, 2 H), 1.89−0.94 (m, 65 H), 0.70 (s, 3 H). MALDI-TOF MS: *m*/*z* 958 ([M + Na]$^+$).

Synthesis of 12c. Compound **12c** was prepared from **11c** (1.37 g, 2.66 mmol) in a manner that was similar to that described for the synthesis of **12a**, except that $CHCl_3$/CH_3CO_2Et (10/1, v/v) was used as an eluting solvent. The desired product (1.96 g, 83%) had ^{1}H NMR ($CDCl_3$, 500 MHz) δ 4.57 (s, 1 H), 3.63 (s, 3 H), 3.27−3.06 (m, 12 H), 2.32−2.19 (m, 2 H), 1.95−0.87 (m, 67 H), 0.63 (s, 3 H).

Synthesis of 13a. To a solution of **12a** (2.30 g, 2.42 mmol) in methanol (30 mL) was added an aqueous Na_2CO_3 solution (10 wt %, 10 mL). The mixture was refluxed until thin layer chromatographic analysis showed the complete disappearance of the starting material. The product mixture was then acidified to pH 3 with dilute HCl at 0 °C and extracted with $CHCl_3$ (3 × 50 mL). The combined organic phase was dried over anhydrous sodium sulfate and concentrated under reduced pressure. The residue was then purified by column chromatography [silica gel, $CHCl_3$/MeOH (6/1, v/v)] to give 1.64 g (70%) of product having ^{1}H NMR (CD_3OD, 500 MHz) δ 4.38 (s, 1 H), 3.95 (s, 1 H), 3.79 (s, 1 H), 3.21 (br, 8 H), 3.07−3.01 (m, 4 H), 2.34−2.15 (m, 4 H), 2.00−0.93 (m, 61 H), 0.71 (s, 3 H). MALDI-TOF MS: *m*/*z* 960 ([M + Na]$^+$).

Synthesis of 13b. Compound **13b** was synthesized from **12b** (2.76 g, 2.95 mmol) in a manner that was similar to that used in the preparation of **13a** except that LiOH was used as the base and $CHCl_3$/CH_3CO_2Et (12/1, v/v) was used as an eluting solvent to give 2.03 g (73%) of product having ^{1}H NMR (CD_3OD, 500 MHz) δ 4.50 (s, 1 H), 4.00 (s, 1 H), 3.20 (br, 8 H), 3.08−3.00 (m, 4 H), 2.31−2.21 (m, 2 H), 1.90−0.94 (m, 65 H), 0.71 (s, 3 H). MALDI-TOF MS: *m*/*z* 944 ([M + Na]$^+$).

Synthesis of 13c. Compound **13c** was synthesized from **12c** (1.96 g, 2.13 mmol) in a manner that was similar to that used in the preparation of **13a** except that LiOH was used as the base and $CHCl_3$/CH_3CO_2Et (20/1, v/v) was used as an eluting solvent. The desired product (1.47 g, 83%) had ^{1}H NMR ($CDCl_3$, 500 MHz) δ 4.57 (s, 1 H), 3.25−3.00 (m, 12 H), 2.38−2.24 (m, 2 H), 1.93−0.86 (m, 67 H), 0.63 (s, 3 H). MALDI-TOF MS: *m*/*z* 928 ([M + Na]$^+$).

Synthesis of 14a. To a solution that was made from **13a** (400 mg, 0.42 mmol) and 3-hydroxy-4-oxo-3,4-dihydro-1,2,3-benzotriazine (DHBT, 86 mg, 0.53 mmol) in anhydrous DMF (5 mL) was added DCC (130 mg, 0.63 mmol). The mixture was stirred at room temperature for 3 h. A solution of putrescine (17.8 mg, 0.20 mmol) and DMAP (100 mg) in anhydrous DMF (1.0 mL) was then added, and the mixture was stirred for 12 h. After the solution was concentrated under reduced pressure, the resulting residue was partitioned between water (50 mL) and $CHCl_3$ (50 mL), and the aqueous phase then extracted with $CHCl_3$ (3 × 50 mL). The combined organic phase was washed with water (100 mL) and dried over anhydrous sodium sulfate. Removal of solvent under reduce pressure and purification by column chromatography [silica gel, $CHCl_3$/MeOH (13/1, v/v)] afforded 228 mg (59%) of **14a** having ^{1}H NMR (CD_3OD, 500 MHz) δ 4.38 (s, 2 H), 3.95 (s, 2 H), 3.79 (s, 2 H), 3.21 (m, 20 H), 3.07−

3.01 (m, 8 H), 2.35−0.93 (m, 134 H), 0.70 (s, 6 H). MALDI-TOF MS: *m*/*z* 1949 ([M + Na]$^+$).

Synthesis of 14b. Compound **14b** was synthesized from **13b** (500 mg, 0.54 mmol) and putrescine (17 mg, 0.19 mmol) using procedures similar to those used for the preparation of **14a**, except that $CHCl_3$/MeOH (25/1, v/v) was used as an eluting solvent. The desired product (200 mg, 53%) had ^{1}H NMR (CD_3OD, 500 MHz) δ 4.50 (s, 2 H), 3.94 (s, 2 H), 3.19−3.16 (m, 20 H), 3.07−3.03 (m, 8 H), 2.38−0.93 (m, 138 H), 0.66 (s, 6 H). MALDI-TOF MS: *m*/*z* 1917 ([M + Na]$^+$).

Synthesis of 14c. Conjugate **14c** was synthesized from **13c** (320 mg, 0.35 mmol) and putrescine (15 mg, 0.17 mmol) using procedures similar to those used for the preparation of **14a** except that $CHCl_3$/MeOH (50/1, v/v) was used as an eluting solvent. The desired product (234 mg, 74%) had ^{1}H NMR ($CD_3OD/CDCl_3$, 500 MHz) δ 4.43 (s, 2 H), 3.15−2.94 (m, 28 H), 2.15 (m, 2 H), 1.97−0.79 (m, 140 H), 0.52 (s, 6 H). MALDI-TOF MS: *m*/*z* 1885 ([M + Na]$^+$).

Synthesis of 6a. To a solution that was prepared from **14a** (100 mg) in dichloromethane (2.0 mL) at 0 °C was added trifluoroacetic acid (2.0 mL). The reaction mixture was then stirred at room temperature for 12 h and concentrated under reduced pressure. The residue was dissolved in methanol (5 mL), adjusted to pH 9−10 with concentrated ammonium hydroxide, and stirred at room temperature for 30 min. After concentration under reduced pressure, the residue was dissolved in water (5.0 mL) and dialyzed against pure water (250 mL, Micro DispoDialyzer, MWCO 500) for 48 h. Concentration under reduced pressure and drying under vacuum gave 70 mg (100%) of **5a** having ^{1}H NMR (CD_3OD, 500 MHz) δ 4.38 (s, 2 H), 3.95 (s, 2 H), 3.79 (s, 2 H), 3.18−3.01 (m, 28 H), 2.40−0.93 (m, 80 H), 0.70 (s, 6 H). MALDI-TOF MS: *m*/*z* 1326 ([M + H]$^+$).

Synthesis of 6b. Compound **6b** was prepared from **14b** (117 mg) using procedures similar to those used in the synthesis of **6a**, affording 76 mg (100%) of product having ^{1}H NMR (CD_3OD, 500 MHz) δ 4.52 (s, 2 H), 3.96 (s, 2 H), 3.20−3.17 (m, 8 H), 3.03−2.93 (m, 20 H), 2.23 (m, 2 H), 2.00−0.88 (m, 82 H), 0.70 (s, 6 H). MALDI-TOF MS: *m*/*z* 1294 ([M + H]$^+$).

Synthesis of 6c. Compound **6c** was prepared from **14c** (130 mg) using procedures similar to those used for the synthesis of **6a**, affording 86 mg (100%) of product having ^{1}H NMR (CD_3OD, 500 MHz) δ 4.52 (s, 2 H), 3.20−3.00 (m, 28 H), 2.21 (m, 2 H), 2.09−0.95 (m, 86 H), 0.68 (s, 6 H). MALDI-TOF MS: *m*/*z* 1262 ([M + H]$^+$).

Synthesis of 15a. To a solution that was prepared from **13a** (1.60 g, 1.71 mmol) and DHBT (500 mg, 3.06 mmol) in anhydrous DMF (5 mL) was added DCC (610 mg, 2.97 mmol). After the mixture was stirred at room temperature for 4 h, spermine (61 mg, 0.30 mmol) and Et_3N (0.5 mL) were added. The reaction mixture was stirred for an additional 12 h and filtered. Concentration of the filtrate under reduced pressure gave a residue that was dissolved in methanol (20 mL). To this solution was then added an aqueous Na_2CO_3 solution (10 wt %, 5 mL). This solution was stirred at room temperature for 1 h and added, dropwise, into water. The resulting precipitate was collected by filtration and purified by column chromatography [silica gel, $CHCl_3$/MeOH (10/1, v/v)] to give 468 mg (40%) of product having ^{1}H NMR (CD_3OD, 500 MHz) δ 4.34 (s, 4 H), 3.94 (s, 4 H), 3.78 (s, 4 H), 3.34 (m, 8 H), 3.28 (br, 4 H), 3.19 (m, 32 H), 3.08−2.96 (m, 16 H), 2.36−0.69 (m, 268 H), 0.63 (s, 12 H). MALDI-TOF MS: *m*/*z* 3901 ([M + Na]$^+$).

Synthesis of 15b. Compound **15b** was prepared from **13b** (1.95 g, 2.12 mmol) and spermine (76 mg, 0.38 mmol) in a manner that was similar to that used in the preparation of **15a**, except that $CHCl_3$/MeOH (15/1, v/v) was used as an eluting solvent. The desired product (141 mg, 10%) had ^{1}H NMR (CD_3OD, 500 MHz) δ 4.48 (s, 4 H), 3.93 (s, 4 H), 3.32 (m, 8 H), 3.28 (br, 4 H), 3.17 (m, 32 H), 3.04−3.00 (m, 16 H), 2.36−0.92 (m, 276 H), 0.67 (s, 12 H). MALDI-TOF MS: *m*/*z* 3839 ([M + Na]$^+$).

Synthesis of 15c. Compound **15c** was prepared from **13c** (650 mg, 0.72 mmol) and spermine (33 mg, 0.16 mmol) in a manner that was similar to that used in the preparation of **15a** except that $CHCl_3$/MeOH (50/1, v/v) was used as an eluting solvent. The desired product (422 mg, 69%) had ^{1}H NMR (CD_3OD, 500 MHz) δ 4.51 (s, 4 H), 3.35 (m, 8 H), 3.20 (m, 36 H), 3.09−3.01 (m, 16 H), 2.25−0.97 (m, 284 H), 0.70 (s, 12 H).

Synthesis of 7a. To a cooled solution (0 °C) that was made from **15a** (60 mg) and dichloromethane (1.0 mL) was added trifluoroacetic acid (1.0 mL). The reaction mixture was then stirred at room temperature for 12 h and concentrated under reduced pressure. The residue was dissolved in methanol (5 mL), adjusted to pH 9−10 with concentrated ammonium hydroxide, and stirred at room temperature for 30 min. Removal of solvent under reduced pressure gave a residue, which was dissolved in water (5.0 mL) and dialyzed against pure water (250 mL, Micro DispoDialyzer, MWCO 500) for 48 h. Concentration under reduced pressure and drying under vacuum afforded 44 mg (100%) of the desired product having ^{1}H NMR (CD_3OD, 500 MHz) δ 4.38 (s, 4 H), 3.95 (s, 4 H), 3.79 (s, 4 H), 3.34 (m, 8 H), 3.18−3.12 (m, 20 H), 3.03 (br, 16 H), 2.38−0.93 (m, 160 H), 0.70 (s, 12 H). MALDI-TOF MS: *m*/*z* 2700 ([M + Na]$^+$).

Synthesis of 7b. Compound **7b** was prepared from **15b** (70 mg) using a procedure that was similar to that used for the synthesis of **7a**. The desired product (48 mg, 100%) had ^{1}H NMR (CD_3OD, 500 MHz) δ 4.52 (s, 4 H), 3.96 (s, 4 H), 3.34 (m, 8 H), 3.19−3.10 (m, 20 H), 3.03 (br, 16 H), 2.25−0.94 (m, 168 H), 0.70 (s, 12 H). MALDI-TOF MS: *m*/*z* 2636 ([M + Na]$^+$).

Synthesis of 7c. Compounds **7c** was prepared from **15c** (175 mg) using a procedure that was similar to that used for the synthesis of **7a**. The desired product (117 mg, 100%) had ^{1}H NMR (CD_3OD, 500 MHz) δ 4.52 (s, 4 H), 3.34 (m, 8 H), 3.19−3.10 (m, 20 H), 3.03 (br, 16 H), 2.24−0.96 (m, 176 H), 0.69 (s, 12 H). MALDI-TOF MS: *m*/*z* 2550 ([M + H]$^+$).

Partitioning between 1-Octanol and Water. A given conjugate (1 mg) was partitioned between an equal volume of water (1 mL) and 1-octanol (1 mL) at room temperature and allowed to equilibrate over 10 h. The aqueous and organic phases were then separated, and aliquots (5 μL) of each phase were deposited onto a thin layer chromatography plate, dried, and stained (ninhydrin solution). The density of each spot was analyzed by densitometry and used to calculate the partition coefficient P according to the equation $P = \log[\text{conjugate}]_{1-\text{octanol}}/[\text{conjugate}]_{\text{water}}$.

pH Discharge Measurements. Typically, 1-palmitoyl-2-oleoyl-*sn*-glycero-3-phosphatidylglycerol (POPG) (0.5 mL, 20 mg/ mL in chloroform) was transferred to a pyrex test tube. While rotating the tube, the organic solvent was removed under a stream of nitrogen, resulting in a thin lipid film. The last traces of solvent were then removed under reduced pressure (25 °C, 12 h, <0.2 Torr). To the dried film was added 1.0 mL of a 0.1 mM pyranine in 25 mM HEPES buffer (pH 7.0, 50 mM NaCl), and the mixture was vortexed for 1 min. The dispersion was then incubated for 5 min, followed by another 1 min of vortexing and 20 min of incubation at ambient temperature. The sample was subjected to five freeze/thaw cycles (77 K/325 K), followed by sequential extrusion through a 400 nm Nuclepore membrane (10 times) and a 200 nm membrane (10 times). After extrusion, the dispersion was incubated at room temperature for 1.25 h. The non-entrapped pyranine was removed via gel filtration (Sephadex G-25, 1 × 32 cm, eluting with 25 mM HEPES buffer (pH 7.0, 50 mM NaCl)).

Chart 3

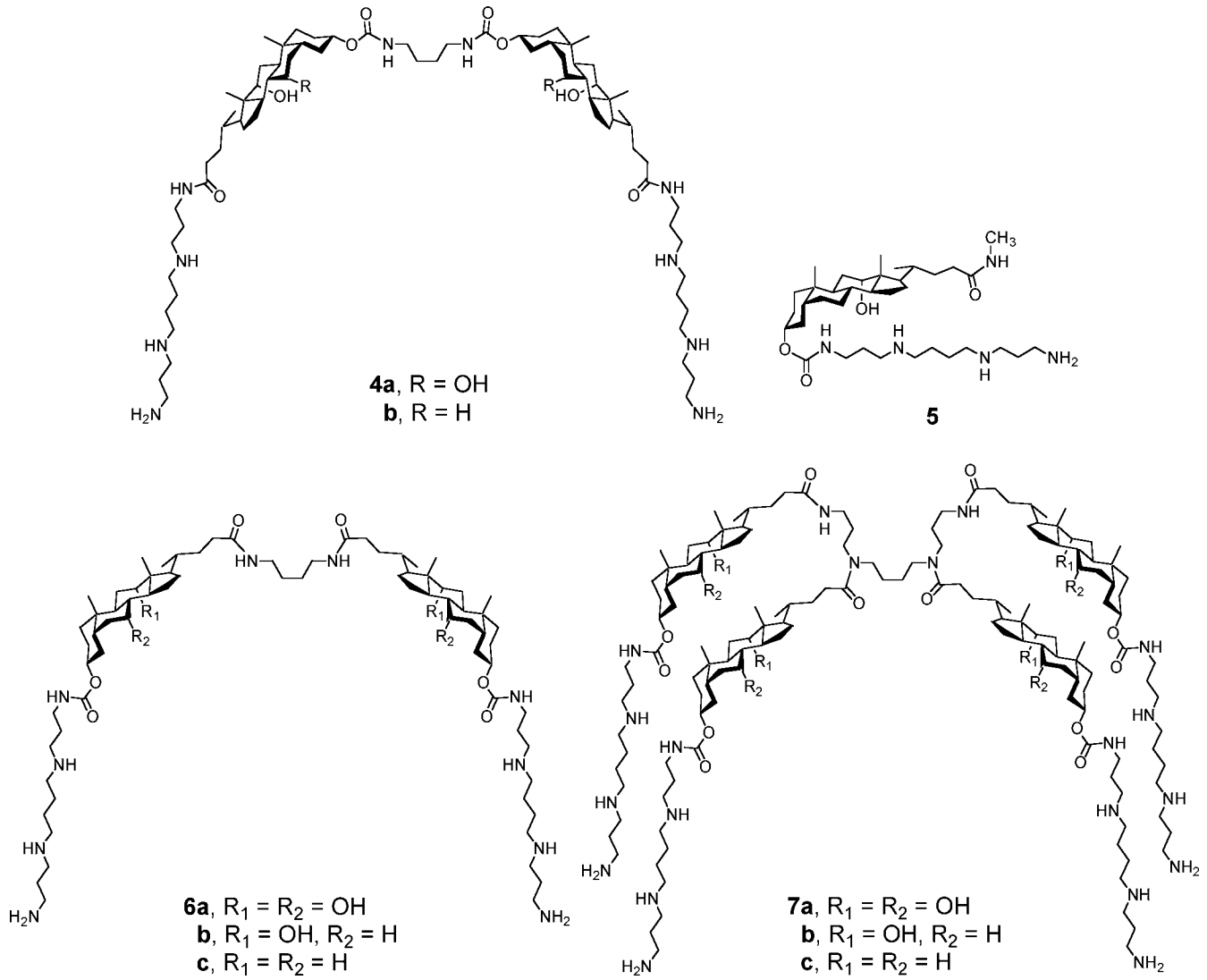

The vesicle dispersion (0.3 mL) was added to 1.7 mL of a 25 mM HEPES buffer (pH 8.0, 50 mM NaCl) that contained the desired amount of sterol−spermine conjugate. The appearance of fluorescence intensity was then monitored as a function of time (λ_{ex} 460 nm, em 510 nm, $\lambda_{ex}/\lambda_{em}$ 2.5 nm/2.5 nm) on a Perkin-Elmer Luminescence Spectrometer LS50B. After 60 min, an aqueous solution of Triton X-100 (50 μL, 5 wt %) was added. Pseudo first-order rate constants for pH discharge were calculated from the change in the fluorescence intensity of pyranine as a function of time using a curve-fitting procedure.

Determination of Minimum Inhibitory Concentrations (MICs). Bacteria used in this study were recent clinical isolates from the Beth Israel Deaconess Medical Center or Massachusetts General Hospital in Boston, with the following exceptions: Strains 1, 20, 24, 28, and 32 were standard strains from the American Type Culture Collection; strain 25 was a clinical isolate from Boston in 1969; strain 29 was a recent clinical isolate from New York and strain 31 was isolated in Spain.

Antimicrobial susceptibilities were done by the agar dilution method, incorporating Mueller-Hinton II agar (Becton, Dickenson, & Co., Sparks, MD) (*20*). Inocula of approximately 10^4 colony-forming units (CFU) per spot were applied with a multiprong replicator, and the plates were examined for growth after overnight incubation in room air at 35 °C.

RESULTS

Molecular Design. In this investigation, we sought to devise short and efficient syntheses of a family of squalamine mimics, using fully biogenic starting materials. With this goal in mind, the specific synthetic targets that were chosen were conjugates **4a**, **4b**, **5**, **6a**, **6b**, **6c**, **7a**, **7b**, and **7c** (Chart 3). In essence, **4a** and **4b** are molecular umbrella-like analogues of **2**, in which two facially amphiphilic sterol−spermidine units have been connected through their A-ring. Comparison of **4a** with **4b**, bearing two and one hydroxyl groups on the α-face of the sterols, respectively, provides a means for judging the importance of facial hydrophilicity on antibacterial activity. Comparison of **6a** and **6b** with **4a** and **4b**, respectively, having the putrescine linkages and the pendent spermidine groups reversed, addresses the question of specificity; that is, if receptors were involved in their biological action, then it is highly unlikely that they would have similar activities. In addition, we sought to address this same question in monomeric squalamine mimics, by comparing the activities of **2** with a carbamate analog (i.e., **5**), in which the pendent spermidine unit is placed at the A-ring instead of the D-ring. Conjugate **6c** represents a control compound since it is devoid of facial amphiphilicity and molecular umbrella character. Finally, conjugates **7a**, **7b**, and **7c**, which can be viewed as larger versions of **6a**, **6b**, and **6c**, were chosen as synthetic targets to determine how the presence

Scheme 1

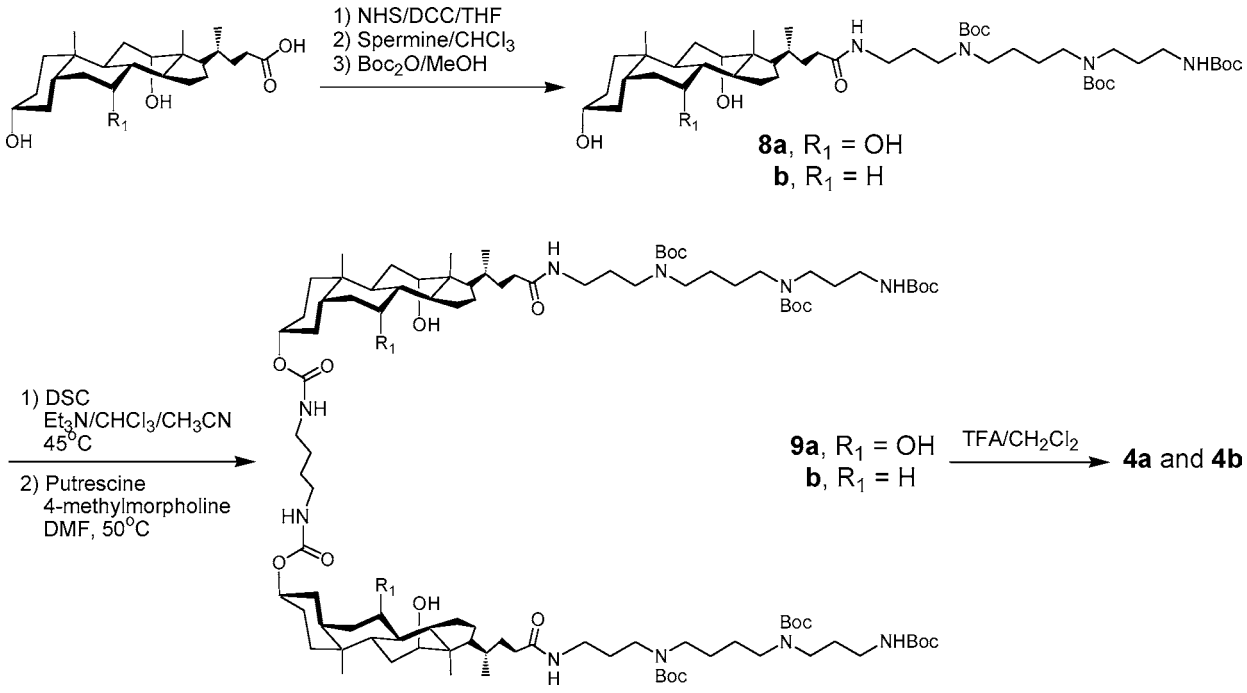

Scheme 2

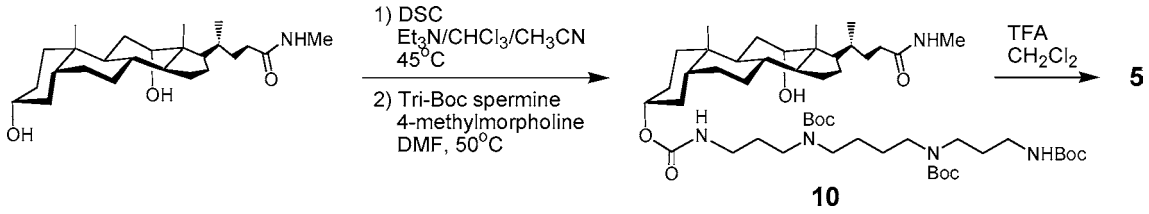

Scheme 3

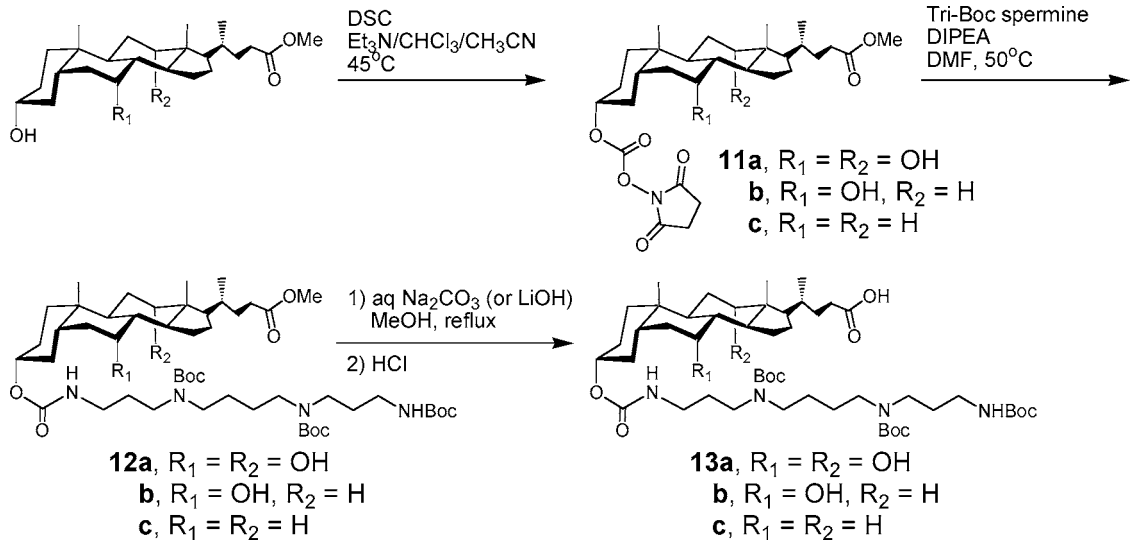

of additional facially amphiphilic-spermidine units influences the antibacterial properties of such squalamine mimics.

Molecular Synthesis. The general synthetic route that was used to prepare **4a** and **4b** is outlined in Scheme 1. In essence, both conjugates can be prepared via "two-pot" syntheses. Thus, monoacylation of spermine by cholic acid or deoxycholic acid, followed by Boc-protection of the remaining amino groups (one pot), afforded **8a** and **8b**. Subsequent activation of the C-3 hydroxyl group with di-(*N*-succinimidyl) carbonate (DSC) and condensation with putrescine (second pot) yielded **9a** and **9b**, which upon deprotection gave the desired conjugates **4a** and **4b**, respectively. The synthesis of **5** was readily accomplished by activating the C-3 hydroxyl group of deoxycholic acid methyl amide with DSC, condensing the product with tri-Boc-protected spermine to give **10**, followed by deprotection (Scheme 2).[18,19]

The syntheses of **6a**, **6b**, and **6c** were carried out using the strategies that are outlined in Scheme 3 and Scheme 4. In brief, the C-3 hydroxyl group of the methyl ester of cholic acid, deoxycholic acid, or lithocholic acid was activated by reaction with DSC to give **11a**, **11b**, and **11c**, followed by condensation with tri-Boc-protected spermine to yield **12a**, **12b**, and **12c** (Scheme 3) (*19*). Mild hydrolysis with Na_2CO_3 or LiOH and

Scheme 4

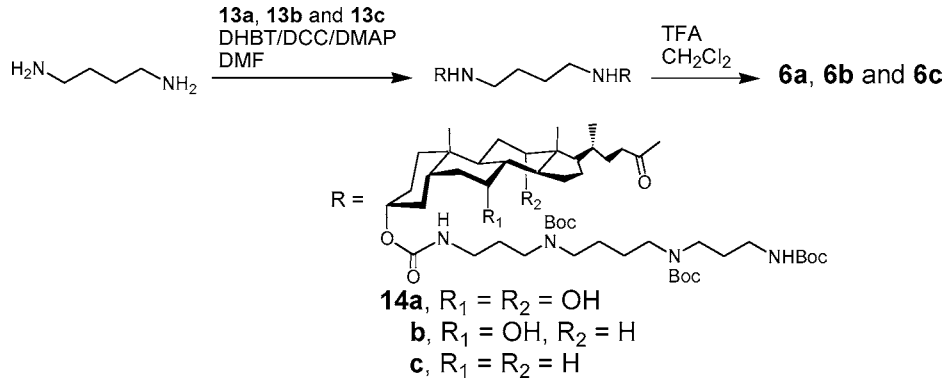

Scheme 5

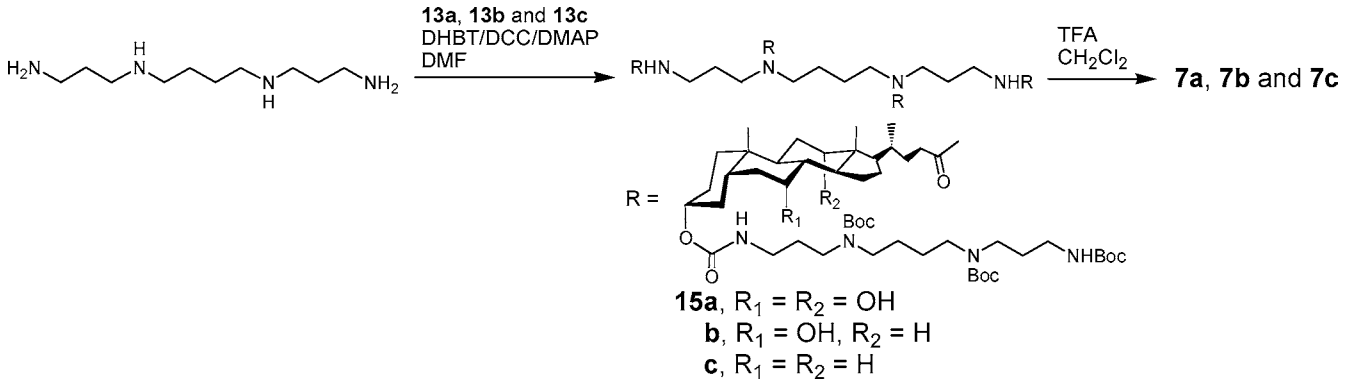

acidification with HCl then afforded **13a**, **13b**, and **13c**. These sterols were then used to fully acylate putrescine to give **14a**, **14b**, and **14c** (Scheme 4). Finally deprotection with trifluoroacetic acid afforded the desired conjugates **6a**, **6b**, and **6c**.

A similar sequence of reactions was used to prepare **7a**, **7b**, and **7c**. In this case, spermine was exhaustively acylated with **13a**, **13b**, and **13c** (Scheme 5). Finally deprotection with trifluoroacetic acid afforded the desired conjugates **7a**, **7b**, and **7c**.

Activity in Discharging pH Gradients. To determine whether dimeric squalamine mimics are capable of discharging pH gradients across lipid bilayers, we examined the ability of **6a**, **6b**, and **6c** to eliminate a pH differential across vesicle membranes derived from 1-palmitoyl-2-oleoyl-*sn*-glycero-3-phosphatidylglycerol (POPG). For this purpose, a pH-sensitive dye (pyranine, pK_a = 7.2) was entrapped within large unilamellar vesicles (200 nm diameter, extrusion) and used as a fluorescence-responsive reporter of pH changes within the vesicle interior (*13*). Figure 2 shows the action of each of these conjugates on liposomal dispersions containing an internal pH of 7.0 and an external aqueous phase of pH of 8.0. In each case, apparent first-order kinetics was observed for the pH discharge. Of these three conjugates, **6a**, having the greatest facial hydrophilicity showed the highest activity. Further examination of the activity of **6a** was then carried out using varying mole percentages of the conjugate with a fixed liposome concentration. A plot of pseudo-first-order rate constants (k_{obsd}) versus the mol % of **6a** in the dispersion is presented in Figure 3. The solid line that appears in this figure represents a nonlinear least-squares fit of the data according to $k_{obsd} = k_0 + k_2(\text{mol \% } \mathbf{6a})^n/K$, where k_o is the background rate of pH discharge in the absence of the conjugate, and K is the dissociation constant of an aggregate composed of n molecules of **6a**, through which ions may pass. As discussed elsewhere, the basic assumptions that underlie this kinetic analysis are (i) that the conjugate exists primarily in its monomeric form, and (ii) the conconcentration of the conjugate in the membrane can be approximated by its *analytical* concentration; that is, its total concentration that is present in the dispersion (*13*). The fact that n is found to be equal to 1.93 implies that dimers of **6a** are the transport-active species. It also suggests, a priori, that such compounds might have biological activities that are comparable to those of **1** and **2** and that only a small percentage of **6a** is in its active-noncovalent, dimeric form.

Antibacterial Properties. Table 1 summarizes the antibacterial activities that were determined for squalamine mimics **2**, **4a**, **4b**, **5**, **6a**, **6b**, **6c**, **7a**, **7b**, and **7c** against a broad series of Gram positive and Gram negative bacteria. Similar to what we have observed previously, **2** was found to have significant activity against most of the microorganisms tested. Conjugate **5**, having the pendent spermidine moiety located at the C-3

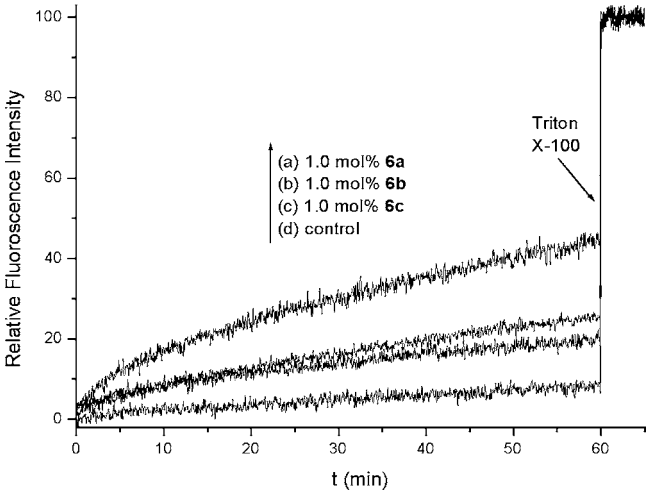

Figure 2. Discharge of a pH gradient (23 °C) across POPG-based liposomal membranes with an internal compartment containing 0.1 mM pyranine (pH 7.0) and an external aqueous phase of pH of 8.0 in the presence of (a) 1.0 mol % **6a**, (b) 1.0 mol % **6b**, and (c) 1.0 mol % **6c**; (d) a control experiment in which **6a** was not added to the dispersion.

Table 1. Antibacterial Activities of Squalamine Mimics 2, 4a, 4b, 5, 6a, 6b, 6c, 7a, 7b, and 7c.

		MIC (μg/ mL)									
	bacteria[a]	**2**	**5**	**4a**	**4b**	**6a**	**6b**	**6c**	**7a**	**7b**	**7c**
					Gram Negative						
1	*E. coli* A6974 ATCC 25922	16	32	32	256	64	64	> 256	256	> 256	> 256
2	*E. coli* A9745 ESBL+	16	32	32	256	64	64	> 256	256	> 256	> 256
3	*E. coli* A9746 ESBL+	128	128	32	256	64	64	> 256	256	> 256	> 256
4	*Klebsiella pneumoniae* A9747 ESBL+	128	128	32	> 256	64	64	> 256	256	> 256	> 256
5	*Klebsiella pneumoniae* A9748 ESBL+	128	128	32	> 256	64	64	> 256	> 256	> 256	> 256
6	*Klebsiella pneumoniae* A9022	32	32	32	256	16	64	> 256	256	> 256	> 256
7	*Acinetobacter* spp. A8968	8	8	8	128	16	32	> 256	128	256	> 256
8	*Acinetobacter* spp. A8969	32	128	32	256	64	128	> 256	256	> 256	> 256
9	*Pseudomonas aeruginosa* A9749	8	16	128	> 256	128	256	> 256	> 256	> 256	> 256
10	*Pseudomonas aeruginosa* A9750	16	32	128	> 256	128	256	> 256	> 256	> 256	> 256
11	*Pseudomonas aeruginosa* A9751	8	16	128	256	128	256	> 256	> 256	> 256	> 256
					Gram Positive						
12	group A *Streptococcus* A9164	2	4	8	64	8	32	> 256	> 256	256	> 256
13	group A *Streptococcus* A9165	1	2	8	64	4	16	> 256	256	256	> 256
14	group A *Streptococcus* A9166	1	2	8	32	8	16	> 256	256	256	> 256
15	coag. neg. *Staphylococcus* A9233 OxS	1	2	2	16	4	8	128	32	64	> 256
16	coag. neg. *Staphylococcus* A9234 OxR	2	2	8	32	16	16	256	64	128	> 256
17	coag. neg. *Staphylococcus* A7828 LinR	0.5	0.5	2	16	2	8	128	32	256	> 256
18	*Staphylococcus aureus* A8347 MSSA	4	8	4	64	16	32	256	128	256	> 256
19	*Staphylococcus aureus* A8349 MSSA	4	4	4	64	8	32	256	128	256	> 256
20	*Staphylococcus aureus* A3257 ATCC 29213	4	4	8	64	16	32	256	128	256	> 256
21	*Staphylococcus aureus* A8115 MSSA	4	4	8	64	16	32	256	128	> 256	> 256
22	*Staphylococcus aureus* A8816 MRSA	8	16	16	128	64	32	> 256	256	256	> 256
23	*Staphylococcus aureus* A5948 MRSA 32	2	4	8	32	8	32	256	128	256	> 256
24	*Enterococcus faecium* A3250 ATCC 19434	16	64	8	64	16	64	> 256	256	256	> 256
25	*Enterococcus faecium* A326	16	16	4	64	16	32	> 256	128	256	> 256
26	*Enterococcus faecium* A6349 vanA, LinR	32	64	16	64	32	32	> 256	256	> 256	> 256
27	*Enterococcus faecium* A902 vanD	8	16	8	64	16	64	256	128	256	> 256
28	*Enterococcus faecalis* A3256 ATCC 29212	16	16	16	128	64	32	> 256	> 256	> 256	> 256
29	*Enterococcus faecalis* A763	128	128	64	128	256	128	> 256	> 256	> 256	> 256
30	*Enterococcus faecalis* A1005	32	64	64	128	128	64	> 256	> 256	> 256	> 256
31	*Enterococcus faecalis* A401 vanA	64	128	64	128	128	64	> 256	> 256	> 256	> 256
32	*Enterococcus faecalis* A3279 ATCC 51299	128	128	64	128	256	64	> 256	> 256	> 256	> 256

[a] Abbreviations: ESBL+, extended spectrum β-lactamase producer; OxS/R, susceptible/resistant to oxacillin; LinR, resistant to linezolid; MRSA, methicillin resistant *S. aureus*; MSSA, susceptible to methicillin; vanA, vancomycin resistant due to acquisition of vanA gene; vanD, vancomycin resistant due to acquisition of vanD gene.

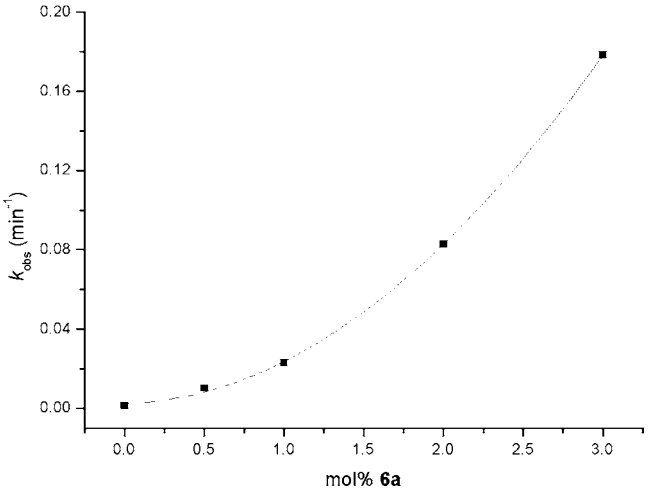

Figure 3. Plot of k_{obsd} versus (mol % **6a**) in POPG liposomes. The solid line represents a nonlinear least-squares fit of the data according to $k_{obsd} = k_0 + k_2(\text{mol \% } \mathbf{6a})^n/K$, where $n = 1.93$.

position of the A-ring, had antibacterial activities that were very similar to that of **2**. Squalamine mimic, **4a**, also had activities that were similar to that of **2**. Removal of the C-7 hydroxyl groups in both sterols (i.e., **4b**), which reduced its degree of facial hydrophilicity, showed a general decrease in activity. Similar removal of the C-7 hydroxyls, on going from **6a** to **6b**, also resulted in a general decrease in activity, but this change was only modest. In addition, conjugates **6a** and **6b** showed activities that were similar to those of **4a** and **4b**, respectively. Removal of facial amphiphilicity, in the case of **6c**, eliminated nearly all antibacterial activity. Finally, the larger squalamine mimics, **7a** and **7b**, showed relatively poor antibacterial activity. Removal of facial amphiphilicity within this series of conjugates (i.e., **7c**) resulted in the complete elimination of antibacterial activity. An analysis of the hydrophobic/hydrophilic balance for **6a** and **7a**, using conventional 1-octanol/water partition coefficients, *P*, where *P* is defined in eq 1, showed that **7a** was significantly more hydrophilic; that is, the values of *P* for **7a** and **6a** were -0.93 and -0.54, respectively.

$$P = \log(\text{conjugate})_{1-\text{octanol}}/(\text{conjugate})_{\text{water}} \qquad (1)$$

DISCUSSION

Four possible modes of action that seem most probable for this class of antibiotics, include (i) competitive binding to a specific receptor on a membrane surface, (ii) complexation with a protein or DNA in the cytoplasm, (iii) a carrier mechanism in which the conjugate shuttles ions across the membrane in both directions via an umbrella mechanism, and (iv) channel or pore formation in the plasma membrane. Taken together, all of our data point toward a mechanism that involves the formation of channels or pores. The fact that antibacterial activity is largely independent of the placement of the pendent polyamine chain at the A- or the D-ring (i.e., **2** versus **5**, **4a** versus **6a**, and **4b** versus **6b**) argues, strongly, against binding to a specific receptor. Additionally, the substantial loss in activity on going from **6a** to **7a**, together with the greater hydrophilicity of **7a** (the *P* values indicate 1-octanol/water partition coefficients that differ by a factor of ca. 2.5) argues against complexation within

the cytoplasm as being responsible for antibacterial activity. In particular, if the site of action were located in the cytoplasm, then the more hydrophilic conjugate, **7a**, would be expected to have greater apparent activity since less of it would be partitioned into the plasma membrane. An additional argument against complexation is the fact that **7a** has four sterol−polyamine units and **6a** has only two. One might expect, therefore, that **7a** would be a stronger complexing agent and exhibit greater activity due to cooperative forces, which is clearly not the case. The fact that the umbrella-like dimers and tetramers are not more active than the monomeric mimics of squalamine also argues against a carier mechanism of ion transport. Within each subclass (**4a** versus **4b**; **6a** versus **6b**, and **7a** versus **7b**), the general trend that we have observed is that the presence of both the C-7 and C-12 hydroxyl groups leads to higher activities as compared with analogues having only C-12 hydroxyls. This finding parallels, exactly, what we have observed in model systems, where **6a** exhibited greater activity in discharging a pH gradient relative to **6b**. Taken together, these results support the premise that these conjugates function as antibiotics by acting at the membrane level, most probably via the formation of pores or channels.

The fact that dimers of **6a** appear to be the species that are responsible for promoting pH discharge across liposomal membranes can also account for a level of antibiotic activity that is comparable with that found for monomeric mimics of squalamine. Thus, in both cases, the majority of the monomeric and dimeric squalamine mimics are present in the bacterial membrane in nonaggregated, inactive forms, and only a small fraction are appropriately clustered to promote ion transport. At the same time, these results suggest that the active species may not be of the type that are illustrated in Figure 1. In particular, one can envision an alternate structure in which both monomers fully span the bilayer but lie antiparallel. Here, the hydrophilic face of each sterol lies across from the polyamine moiety of a neighboring conjugate. If this structure is correct, then one might expect that head-to-tail dimers could be more active than the head-to-head (molecular umbrella-like) dimers reported herein. The reason for the relatively low activity of those conjugates bearing four sterols and four pendent spermine moieties (i.e., **7a**, **7b**, and **7c**) is not presently clear. One possibility is that adverse steric interactions with peripheral proteins may inhibit their effective insertion into the plasma membrane.

CONCLUSIONS

Short and efficient syntheses have been devised for the preparation of a series of dimeric mimics of squalamine. Those mimics having relatively high facial hydrophilicity exhibit generally strong antibacterial properties, especially toward Gram-positive bacteria. Structure−activity studies, along with kinetic measurements for pH discharge in model membranes, have provided inferential evidence, which point toward a mechanism of action that involves membrane perturbation, most probably pore or channel formation. The fact that dimeric mimics of squalamine have molecular umbrella-like features raises the intriguing possibility that their biodistribution may be quite different than squalamine, itself, or monomeric mimics of squalamine. Whether such differences can improve their therapeutic potential, however, remains to be established.

ACKNOWLEDGMENT

We are grateful to the National Science Foundation (CHE-0345248) for support of this research.

LITERATURE CITED

(1) Armstrong, D., New, H., Peterson, S. L., and Tomasz, A. (1995) The prospects of treatment failure in the chemotherapy of infectious diseases in the 1990s. *Microb. Drug Resist. 1*, 1−4.

(2) Wood, M. J., and Moellering, R. C., Jr. (2003) Microbial resistance: bacteria and more. *Clin. Infect. Dis. 36* (Suppl. 1), S2-3.

(3) Zinner, S., Wise, R., and Moellering, R. C., Jr. (2001) Maximizing antimicrobial efficacy, minimizing antimicrobial resistance: A paradigm for the new millennium. *Clin. Infect. Dis. 33* (Suppl. 3), S107-S260.

(4) Spellberg, B., Powers, J. H., Brass, E. P., Miller, L. G., and Edwards, J. E., Jr. (2004) Trends in antimicrobial drug development: implications for the future. *Clin. Infect. Dis. 38*, 1279−1286.

(5) McDonald, L. C. (2006) Trends in antimicrobial resistance in health care-associated pathogens and effect on treatment. *Clin. Infect. Dis. 42* (suppl 2), S65-71.

(6) Courvalin, P. (2005) Antimicrobial drug resistance: prediction is very difficult, especially about the future. *Emerg. Infect. Dis. 11*, 1503−1506.

(7) Moore, K. S., Wehrli, S., Roder, H., Rogers, M., Forrest, J. N., Jr., McCrimmon, D., and Zasloff, M. (1993) Squalamine: an aminosterol antibiotic from the shark. *Proc. Natl. Acad. Sci. U.S.A. 90*, 1354−1358.

(8) Brunel, J. M., Salmi, C., Loncle, C., Vidal, N., and Letourneux, Y. (2005) Squalamine: a polyvalent drug of the future? *Curr. Cancer Drug Targets. 5*, 267−272.

(9) Moriarity, R. M., Tuladhar, S. M., Guo, L., and Wehrli, S. (1994) Synthesis of. squalamine. A steroidal antibiotic from the shark. *Tetrahedron Lett. 35*, 8103−8106.

(10) Sadownik, A., Deng, G., Janout, V., Regen, S. L., Bernard, E. M., Kikuchi, K., and Armstrong, D. (1995) Rapid construction of a squalamine mimic. *J. Am. Chem. Soc. 117*, 6138−6139.

(11) Kikuchi, K., Bernard, E. M., Sadownik, A., Regen, S. L., and Armstrong, D. (1997) Antimicrobial activities of squalamine mimics. *Antimicrob. Agents Chemother. 41*, 1433−1438.

(12) For a series of papers involving sterol-based polyamine antibiotics, see: (a) Savage, P. B. (2002) Design, synthesis and characterization of cationic peptide and steroid antibiotics. *Eur. J. Org. Chem.* 759−768. (b) Brunel, J. M., and Letourneux, Y. (2003) Recent advances in the synthesis of spermine and spermidine analogues of the shark aminosterol squalamine. *Eur. J. Org. Chem.* 3897−3907. (c) Salunke, D. B., Hazra, B. G., and Pore, V. S. (2003) Bile acid-polyamine conjugates as synthetic ionophores. *Arkivoc.* 115−125. (d) Kichler, A., Leborgne, C., Savage, P. B., and Danos, O. (2005) Cationic steroid antibiotics demonstrate DNA delivery properties. *J. Controlled Release 7*, 174−182. (e) Ding, B., Yin, N., Liu, Y., Cardenas-Garcia, J., Evanson, R., Orsak, T., Fan, M., Turin, G., and Savage, P. B. (2004) Origins of cell selectivity of cationic steroid antibiotics. *J. Am. Chem. Soc. 126*, 13642−13648. (f) Ding, B., Taotofa, U., Orsak, T., Chadwell, M., and Savage, P. B. (2004) Synthesis and characterization of peptide-cationic steroid antibiotic conjugates. *Org. Lett. 6*, 3433−3436. (g) Ding, B., Guan, Q., Walsh, J. P., Boswell, J. S., Winter, T. W., Winter, E. S., Boyd, S. S., Li, C., and Savage, P. B. (2002) Correlation of the antibacterial activities of cationic peptide antibiotics and cationic steroid antibiotics. *J. Med. Chem. 45*, 663−669. (h) Guan, Q., Li, C., Schmidt, E. J., Boswell, J. S., Walsh, J. P., Allman, G. W., and Savage, P. B. (2000) Preparation and characterization of cholic acid-derived antimicrobial agents with controlled stabilities. *Org. Lett. 2*, 2837−2840. (i) Willemen, H. M., de Smet, L. C. P. M., Koudijs, A., Stuart, M. C. A., Heikamp-de Jong, I. G. A. M., Marcelis, A. T. M., and Sudholter, E. J. R. (2002) Micelle formation and antimicrobial activity of cholic acid derivatives with three permanent ionic head groups. *Angew. Chem., Int. Ed.* 41, 4275−4277.

(13) Merrit, M., Lanier, M., Deng, G., and Regen, S. L. (1998) Sterol-polyamine conjugates as synthetic ionophores. *J. Am. Chem. Soc. 120*, 8494−8501.

(14) For reviews of synthetic ionophores, see: (a) Matile, S. (2004) Recent Synthetic Ion Channels and Pores. *Tetrahedron 60*, 6405−6435. (b) Gokel, G. W., and Mukhopadhyay, A. (2001) Synthetic models of cation-conducting channels. *Chem. Soc., Rev. 30*, 274−286. (c) Kobuke, Y. (1997) *Advances in Supramolecular Chemistry* (Gokel, G. W., Ed.) Vol 4, pp 163−210, JAI Press, Greenwich, CT.

(d) Fyles, T. M.; van Straaten-Nijenhuis, W. F. (1996) *Comprehensive Supramolecular Chemistry* (Reinhoudt, D. N., Ed.) Vol. 10, pp 53−77, Elsevier Science, Amsterdam.

(15) Janout, V., Jing, B., and Regen, S. L. (2005) Molecular umbrella-assisted transport of an oligonucleotide across cholesterol-rich phospholipid bilayers. *J. Am. Chem. Soc. 127*, 15862−15870.

(16) Janout, V., and Regen, S. L. (2005) A Needle and thread approach towards bilayer transport: permeation of a molecular umbrella-oligonucleotide conjugate across a phospholipid membrane. *J. Am. Chem. Soc. 127*, 22−23.

(17) Janout, V., Staina, I. V., Bandyopadhyay, P., and Regen, S. L. (2001) Evidence for an umbrella mechanism of bilayer transport. *J. Am. Chem. Soc. 123*, 9926−9927.

(18) Fini, A., Fazio, G., Roda, A., Bellini, A. M., Mencini, E., and Guarneri, M. (1992) Basic cholane derivatives. XI: comparison between acid and basic derivatives. *J. Pharm. Sci. 81*, 726−730.

(19) Blagbrough, I. S., Al-Hadithi, D., and Geall, A. J. (2000) Cheno-, urso-, and deoxycholic acid spermine conjugates: relative binding affinities for calf thymus DNA. *Tetrahedron. 56*, 3439−3447.

(20) National Committee for Clinical Laboratory Standards. 2003. 6th ed. NCCLS document M7-A6. National Committee for Clinical Laboratory Standards, Wayne, PA.

BC060220N

Facile Synthesis of Multivalent Nitrilotriacetic Acid (NTA) and NTA Conjugates for Analytical and Drug Delivery Applications

Zhaohua Huang,[†] Joshua I. Park,[†] Douglas S. Watson,[§] Peter Hwang,[‡] and Francis C. Szoka, Jr.*[,†]

Departments of Pharmaceutical Chemistry and Biopharmaceutical Sciences, School of Pharmacy, University of California at San Francisco, San Francisco, California 94143-0446, and Department of Biochemistry and Biophysics, School of Medicine, University of California at San Francisco, San Francisco, California 94143-2240. Received July 20, 2006; Revised Manuscript Received October 3, 2006

High-affinity nitrilotriacetic acids (NTA) have great potential in the molecular manipulation of His-tagged proteins. We have developed a facile method to synthesize multivalent NTA and its conjugates. Starting with appropriately protected lysine, we synthesized the mono-NTA synthons functionalized with either an amino group or a carboxylic group. We then obtained tri-NTA through the condensation of the amino NTA and the carboxylic NTA. Using amino tri-NTA as the key intermediate, we synthesized a series of tri-NTA conjugates with a variety of functional units including biotin, dialkyl, fluorescein, and a hydroxybenzimidate moiety. The biotin−tri-NTA was employed to convert a Biacore streptavidin chip into a high-affinity tri-NTA chip. The equilibrium dissociation constants of tri-NTA/His-tagged protein complexes measured by surface plasmon resonance are in the 20 nM range. Histidine-(6)-tagged yeast cytosine deaminase (His6-yCD) was incorporated onto the liposome surface by the lipid−tri-NTA conjugate without any activity loss. Fluorescein−tri-NTA formed a stable 1:1 complex with His6-yCD without significant fluorescence quenching. Specific tri-NTA derivatives for the radiolabeling and coupling of two His-tagged proteins to each other are described. Thus, we have added to the toolbox a number of high-affinity tri-NTA adaptors for the manipulation of His-tagged molecules.

INTRODUCTION

Generic chemical tools are highly sought for the selective and efficient modification of recombinant proteins. Nitrilotriacetic acid (NTA) has become a commonly used reagent for the purification of His-tagged proteins since the introduction of immobilized metal-affinity chromatography (IMAC) (*1*, *2*). Although the binding affinity of mono-NTA (K_D ca. 10 μM) (*3*, *4*) fulfills the need of IMAC, the molecular-level manipulation of His-tagged proteins requires tighter association to form stable complexes at low concentrations often found in biological systems. Theoretically, three NTAs will form exactly three coordination pairs with the hexahistidine (His6) tag, and provide sufficient binding affinity to form a tight NTA−protein complex. Indeed, multivalent NTAs have higher binding affinity (K_D ca. 20 nM) toward His-tagged proteins than mono-NTA (*5*). In the work of Lata and colleagues, tri-NTA had significantly higher affinity toward His-tagged proteins than bis-NTA, but tetra-NTA provided no additional binding advantage over tri-NTA. Thus, tri-NTA is a good choice for a multivalent adaptor to join a functional moiety to His6 recombinant proteins. We sought to develop an efficient method to synthesize tri-NTA conjugates and to use them for the analysis and modification of His-tagged proteins for use in diagnostic and delivery systems.

While mono-NTA has been mostly used in the purification of His-tagged proteins, it has also been applied to other manipulations of His-tagged proteins such as surface immobilization (*6*−*9*), biosensor detection (*10*−*12*), and fluorescence labeling (*3*, *13*, *14*). Multivalent NTA derivatives are better suited for these applications due to the stronger binding affinity. Recently, ditetradecylamine−tri-NTA (NTA_3−DTDA) was used to introduce His-tagged monoclonal antibody fragment onto a liposome surface for tumor immunotherapy (*15*). The synthesis of NTA_3−DTDA was not disclosed in this paper or in a later related publication (*16*). In the course of our present work, some fluorophore−tri-NTA conjugates have been reported for the specific and stable labeling of His-tagged proteins (*17*). Quantitative labeling was achieved with fluorophore−tri-NTA, while the fluorophore−mono-NTA-protein complex was hardly detectable. However, the load of Ni(II) on the fluorophore−tri-NTA resulted in significant fluorescence quenching due to possible electron and energy transfer (*18*, *19*). In this paper, we report the facile synthesis of a series of tri-NTA conjugates with improved yields. We illustrate a few examples of their applications for the creation of a modified Biacore surface and for the attachment of a His-tagged enzyme to the liposome surface.

EXPERIMENTAL PROCEDURES

General. H-Lys(Z)-OtBu.HCl was from BACHEM (Torrance, CA). Fluorescein−PEG-NHS was from Nektar, Inc. (Huntsville, AL). Phospholipids were purchased from Avanti Polar Lipids (Alabaster, AL). Phosphate buffered silane (PBS) was from UCSF Cell Culture Facility. Other reagents were from Aldrich (Milwaukee, WI). ^{1}H NMR (400 MHz) spectra were recorded on a Varian 400 MHz instrument. Chemical shifts are expressed as parts per million using tetramethylsilane as internal standard. *J* values are in hertz. MALDI-TOF mass spectra were obtained at the Mass Spectrometry Facility, University of California, San Francisco. TLC analyses were performed on 0.25-mm silica gel F_{254} plates. High-performance flash chromatography (HPFC) was carried out on a Biotage (Charlottesville, VA) Horizon HPFC system with pre-packed silica gel columns (60 Å, 40−63 μm). Unless noted otherwise, the ratios describing the composition of solvent mixtures represent relative volumes.

Compound ***1***. To a suspension of H-Lys(Z)-OtBu.HCl (14.64 g, 39.5 mmol) in DMF (300 mL) were added *tert*-butyl

* Corresponding author. Tel: (415) 476-3895; Fax: (415) 476-0688; E-mail: szoka@cgl.ucsf.edu.

[†] School of Pharmacy.

[§] Joint Graduate Group in Bioengineering, University of California at San Francisco and Berkeley, San Francisco, CA 94143.

[‡] School of Medicine.

10.1021/bc0602228 CCC: $33.50 © 2006 American Chemical Society
Published on Web 10/27/2006

bromoacetate (23.3 mL, 158 mmol) and diisopropylethylamine (33.7 mL, 198 mmol) under nitrogen. The reaction mixture was stirred overnight at 55 °C. The volatiles were evaporated under reduced pressure at 60 °C. The slurry residue was extracted with hexane−ethyl acetate (3:1) three times (200 mL × 3). The combined extracts were then concentrated and purified by high-performance flash chromatography (HPFC) with programmed elution gradient (25−40% ethyl acetate in hexane). Yield: 19.7 g, 88.3% with respect to (wrt) H-Lys(Z)-OtBu.HCl. TLC: $R_f = 0.46$ in hexane−ethyl acetate (3:1). ^{1}H NMR ($CDCl_3$), δ 1.42 (s, 18H); 1.45 (s, 9H); 1.53 (m, 4H); 1.62 (m, 2H); 3.20 (m, 2H); 3.31 (t, $J = 7.2$, 1H); 3.44 (dd, $J = 16$, 8.4, 4H); 5.08 (s, 2H); 7.34 (m, 5H). MALDI-MS calcd for $C_{30}H_{49}N_2O_8^+$ $[M + H]^+$ 565.35, found 565.39.

*Compound **2***. To a solution of **1** (15 g, 26.5 mmol) in methanol (200 mL) under nitrogen were added 10% Pd/C (1 g) and ammonium formate (13.6 g, 216 mmol) solution in 10 mL water and 90 mL methanol sequentially. The reaction mixture was vigorously stirred for 3 h under nitrogen at 40 °C. Pd/C was filtered off over celite, and the filtrate was evaporated under reduced pressure. The residual ammonium formate was removed by repeated evaporation with ethanol. The crude product was then purified by HPFC (10−18% methanol in chloroform). Yield: 10.5 g, 91.8% wrt **1**. TLC: $R_f = 0.5$ in chloroform−methanol (6:1). ^{1}H NMR ($CDCl_3$), δ 1.44 (s, 18H); 1.45 (s, 9H); 1.63 (m, 6H); 2.87 (t, $J = 7.2$, 2H); 3.29 (t, $J = 7.6$, 1H); 3.44 (dd, $J = 17.2$, 9.2, 4H). MALDI-MS calcd for $C_{22}H_{42}N_2O_6^+$ $[M + H]^+$ 431.35, found 431.30.

*Compound **3**.* To a solution of **1** (7 g, 12.3 mmol) in chloroform (40 mL) were added trifluoroacetic acid (TFA) (20 mL) and triisopropylsilane (1 mL). The reaction mixture was stirred at 23 °C and monitored by TLC. After 3 h, methanol (10 mL) and water (5 mL) were added to the reaction mixture. The volatiles were evaporated under reduced pressure. The residue was dried azeotropically with toluene and triturated with anhydrous ether. The white precipitate was collected and dried over high vacuum. Yield: 4.36 g, 89% wrt **1**. TLC: $R_f = 0.06$ in chloroform−methanol−water (65:25:4). ^{1}H NMR (MeOH-d_4), δ 1.48−1.53 (m, 4H); 1.66 (m, 1H); 1.78 (m, 1H); 3.15 (m, 2H); 3.45 (t, $J = 12.8$, 1H); 3.63 (dd, $J = 18$, 9.6, 4H); 5.08 (s, 2H); 7.36 (m, 5H). MALDI-MS calcd for $C_{18}H_{24}N_2NaO_8^+$ $[M + Na]^+$ 419.14, found 419.11.

*Compound **4***. To a solution of **3** (2.33 g, 5.87 mmol) in anhydrous DMF (50 mL) were added *N*-hydroxysuccinimide (NHS) (4.05 g, 35.22 mmol), 4,4-dimethylaminopyridine (DMAP) (1 g), and dicyclohexylcarbodiimide (DCC) (7.25 g, 35.22 mmol). The reaction was kept at 23 °C for 5 h, then a solution of **2** (11.37 g, 26.42 mmol) and anhydrous diisopropylethylamine (3 mL) in anhydrous methanol-free chloroform (25 mL) was added. After 24 h reaction, the mixture was filtered and the filtrate was evaporated to dryness under reduced pressure. The residue was loaded onto column and purified by HPFC (0−4% methanol in chloroform). Yield: 9 g, 93.8% wrt **3**. TLC: $R_f = 0.84$ in chloroform−methanol (9:1). ^{1}H NMR ($CDCl_3$), δ 1.44 (s, 54H); 1.46 (s, 27H); 1.53 (m, 16H); 1.63 (m, 8H); 3.20−3.31 (m, 12H); 3.44 (m, 16H); 5.08 (s, 2H); 7.34 (m, 5H).

*Compound **5***. To a solution of **4** (9 g, 5.5 mmol) in 95% methanol (120 mL) under nitrogen were added 10% Pd/C (0.69 g) and ammonium formate (4 g, 63.4 mmol) solution in 4 mL water and 20 mL methanol sequentially. The reaction mixture was vigorously stirred for 3 h under nitrogen at 40 °C. Pd/C was filtered off over celite, and the filtrate was evaporated under reduced pressure. The residual ammonium formate was removed by repeated evaporation with toluene. The crude product was then purified by HPFC (4−10% methanol in chloroform). Yield: 7.2 g, 90.6% wrt **4**. TLC: $R_f = 0.48$ in chloroform−methanol (9:1). ^{1}H NMR ($CDCl_3$), δ 1.44 (s, 54H); 1.46 (s, 27H); 1.53 (m, 8H); 1.63 (m, 8H); 1.78 (m, 4H); 1.94 (m, 4H); 3.20−3.31 (m, 12H); 3.44 (m, 16H). MALDI-MS calcd for $C_{77}H_{144}N_9O_{23}^+$ $[M + H + NH_4OOCH]^+$ 1563.04, found 1563.07.

*Compound **6***. To a solution of biotin (2.44 g, 10 mmol) in DMF (130 mL) were added NHS (1.38 g, 12 mmol), DMAP (0.2 g), and DCC (2.88 g, 14 mmol). The reaction was kept at 23 °C overnight, and the precipitate was filtered off. Then, 4,7,10-trioxatridecane diamine (22 mL, ca. 100 mmol) and diisopropylethylamine (5 mL) were added to the filtrate. After 16 h reaction, the volatiles were evaporated at reduced pressure, and the residue was triturated with diethyl ether (250 mL). The solid was dissolved in chloroform (150 mL) and filtered again. The filtrate was then evaporated and triturated with diethyl ether. The crude solid product was dissolved in the minimum amount of chloroform and purified by HPFC (chloroform to chloroform−methanol−ammonia, 65:35:5). Yield: 2.2 g, 49.2% wrt biotin. TLC: $R_f = 0.44$ in chloroform−methanol−ammonia (65:35:5). ^{1}H NMR ($CDCl_3$), δ 1.44 (m, 2H); 1.65 (m, 2H); 1.77 (m, 6H); 2.19 (t, $J = 7.2$, 2H); 2.60 (br, 2H); 2.72 (m, 2H); 2.85 (m, 2H); 3.15 (m, 1H); 3.34 (m, 2H); 3.55−3.63 (m, 12H); 4.30 (m, 1H); 4.49 (m, 1H); 5.47 (br, 1H); 6.37 (br, 1H); 6.96 (br, 1H). MALDI-MS calcd for $C_{40}H_{39}N_4O_5S^+$ $[M + H]^+$ 447.27, found 447.21.

*Compound **7***. To a solution of **6** (2.2 g, 4.92 mmol) in dry, ethanol-free chloroform (50 mL) was added succinic anhydride (1 g, 5 mmol) and anhydrous diisopropylethylamine (3 mL). The reaction mixture was stirred at 23 °C for 18 h, and evaporated to dryness. The residue was triturated with diethyl ether (100 mL) and purified by HPFC (chloroform to chloroform−methanol−ammonia, 65:25:4). Yield: 2.1 g, 78% wrt **6**. TLC: $R_f = 0.24$ in chloroform−methanol−ammonia (65:25:4). ^{1}H NMR ($CDCl_3$), δ 1.45 (m, 2H); 1.69−1.77 (m, 8H); 2.20 (t, $J = 7.2$, 2H); 2.48 (m, 2H); 2.66 (m, 2H); 2.92 (m, 2H); 3.04 (m, 2H); 3.17 (m, 1H); 3.35 (m, 2H); 3.55−3.63 (m, 12H); 4.35 (m, 1H); 4.51 (m, 1H); 6.61 (br, 1H); 6.87 (br, 1H); 6.99 (br, 1H). MALDI-MS calcd for $C_{24}H_{43}N_4O_8S^+$ $[M + H]^+$ 547.28, found 547.30.

*Compound **8***. To a solution of **7** (0.53 g, 0.97 mmol) in dry, methanol-free chloroform (15 mL), were added NHS (167.3 mg, 1.46 mmol), DMAP (50 mg), and DCC (300 mg, 1.46 mmol). The mixture was stirred at 23 °C for 3 h, and a solution of **5** (1.45 g, 0.97 mmol) in dry, ethanol-free chloroform (15 mL) was added. After overnight reaction, the precipitate was filtered off, and the filtrate was concentrated under reduced pressure. The residue was purified by HPFC (0−10% methanol in chloroform). Yield: 1.42 g, 72.2% wrt **7**. TLC: $R_f = 0.19$ in chloroform−methanol (9:1).^{1}H NMR ($CDCl_3$), δ 1.46 (m, 83H); 1.53−1.78 (m, 32H); 2.15 (m, 2H); 2.44 (m, 2H); 2.62 (m, 2H); 2.83 (m, 2H); 3.15−3.40 (m, 45H); 4.34 (m, 1H); 4.54 (m, 1H).

*Biotin−tri-NTA (**9**)*. To a solution of **8** (1.34 g, 0.637 mmol) in chloroform (27 mL) were added triisopropylsilane (2 mL) and TFA (9 mL). After 3 h reaction at 23 °C, the volatiles were evaporated at reduced pressure, and the residue was precipitated from 50 mL diethyl ether at −20 °C. The precipitate was dissolved in methanol, evaporated, and precipitated from ether again. The solid was then collected and dried over high vacuum. Yield: 0.88 g, 90.9% wrt **8**. ^{1}H NMR ($CDCl_3$), δ 1.45−1.80 (m, 34H); 2.20 (t, $J = 7.2$, 2H); 2.46 (m, 2H); 2.67 (m, 2H); 2.92 (m, 2H); 3.0−3.40 (m, 33H); 3.45−3.71 (m, 12H); 4.31 (m, 1H); 4.50 (m, 1H). MALDI-MS calcd for $C_{64}H_{107}N_{12}O_{28}S^+$ $[M + H]^+$ 1523.71, found 1523.77.

*Compound **10***. To a solution of dioctadecylamine (4.95 g, 9.48 mmol) in dichloromethane (100 mL) were added succinic anhydride (1.9 g, 2 equiv) and anhydrous triethylamine (12 mL). The reaction mixture was stirred at 23 °C overnight in the dark.

The mixture was then extracted consecutively with hydrochloric acid (1 M, 100 mL) and water (100 mL × 2), and dried over anhydrous sodium sulfate, filtered, and evaporated. The crude product was recrystallized from acetone (ca. 50 mL) twice. Yield: 5.0 g, 85% wrt dioctadecylamine. TLC: $R_f = 0.5$ in chloroform−methanol (9:1). ^{1}H NMR ($CDCl_3$), δ 0.89 (t, $J =$ 6.8, 6H); 1.26 (m, 60H); 1.54 (m, 4H); 2.68 (m, 4H); 3.23 (t, $J = 8.4$, 2H); 3.32 (t, $J = 8.0$, 2H). MALDI-MS calcd for $C_{40}H_{80}NO_3^+$ $[M + H]^+$ 622.62, found 622.64.

*Compound **11***. This compound was synthesized according to the same method as **8** but using **10** as the acid substrate. The crude product was purified by HPFC (0−4% methanol in chloroform). Yield: 86.3% wrt **10**. TLC: $R_f = 0.6$ in chloroform−methanol (9:1). ^{1}H NMR ($CDCl_3$), δ 0.89 (t, $J = 6.8$, 6H); 1.26 (m, 60H); 1.44 (s, 54H); 1.46 (s, 27H); 1.53−1.80 (m, 28H); 2.50 (t, $J = 6.8$, 2H); 2.61 (t, $J = 6.8$, 2H); 3.17−3.31 (m, 16H); 3.44 (m, 16H).

*DOD−tri-NTA (**12**)*. Compound **12** was synthesized according to the same method as **9** but using **11** as the substrate. The crude product was extracted with hexane twice at −20 °C and repeatedly dried with methanol, then dried over high vacuum. Yield: 90.8% wrt **11**. ^{1}H NMR (MeOH-d_4), δ 0.90 (t, $J = 6.8$, 6H); 1.28 (m, 60H); 1.48−1.80 (m, 28H); 2.68 (m, 4H); 3.17−3.34 (m, 16H); 3.44−3.70 (m, 16H). MALDI-MS calcd for $C_{80}H_{144}N_9O_{23}^+$ $[M + H]^+$ 1599.04, found 1599.10.

*Compound **13***. To a solution of fluorescein−PEG-NHS (500 mg, Mw 2000, ca. 0.25 mmol) in dry, ethanol-free chloroform (20 mL) was added **5** (0.38 g, 0.25 mmol) and diisopropylethylamine (anhydrous, 1 mL). The reaction mixture was purged with argon and stirred in the dark at 23 °C overnight. The volatiles were evaporated under reduced pressure, and the residue was purified by HPFC (2−9% methanol in chloroform). Yield: 215 mg, 25% wrt fluorescein−PEG-NHS. TLC: $R_f =$ 0.21 in chloroform−methanol (9:1). ^{1}H NMR ($CDCl_3$), δ 1.44 (s, 54H); 1.46 (s, 27H); 1.53−1.78 (m, 26H); 2.44 (t, $J = 6.4$, 2H); 3.24 (m, 14H); 3.45 (m, 16H); 3.60 (m, 180H); 6.59−6.78 (m, 5H); 7.05 (m, 1H); 7.64 (m, 3H).

*Fluorescein−tri-NTA (**14**)*. This compound was synthesized according to the same method as **9** but using **13** as the substrate. Yield: 90% wrt **13**. ^{1}H NMR ($CDCl_3$), δ 1.53−1.78 (m, 26H); 2.46 (t, $J = 6.4$, 2H); 3.06−3.31 (m, 14H); 3.48 (m, 16H); 3.60 (m, 180H); 6.51−6.80 (m, 5H); 7.06 (m, 1H); 7.64 (m, 3H). MALDI-MS calcd for $C_{155}H_{265}N_{10}O_{72}S^+$ $[M + H]^+$ 3450.84, found 3450.80.

*Compound **15***. Methyl *p*-hydroxybenzimidate hydrochloride (0.308 g, 1.65 mmol) and **5** (0.5 g, 0.33 mmol) were placed in dry, ethanol-free chloroform (15 mL). Upon the addition of diisopropylethylamine (1 mL), the reaction mixture turned clear. The reaction was kept at 23 °C overnight. Then, chloroform−water (40 mL/40 mL) was added to the mixture, and the oil layer was washed with water (40 mL) again. The organic layer was evaporated and purified by HPFC (10−70% methanol in chloroform). Yield: 332 mg, 62.2% wrt **5**. TLC: $R_f = 0.63$ in chloroform−methanol (4:1). ^{1}H NMR ($CDCl_3$), δ 1.44 (s, 54H); 1.46 (s, 27H); 1.53−1.78 (m, 24H); 3.16−3.30 (m, 12H); 3.45 (m, 16H); 6.59 (m, 2H); 7.42 (m, 2H); 8.01 (br, 2H). MALDI-MS calcd for $C_{83}H_{144}N_9O_{22}^+$ $[M + H]^+$ 1619.05, found 1619.02.

*Compound **16***. This compound was synthesized according to the same method as **9** but using **15** as the substrate. Yield: 93% wrt **15**. ^{1}H NMR (MeOH-d_4), δ 1.55−1.89 (m, 24H); 3.24 (m, 12H); 3.50 (m, 16H); 6.97 (m, 2H); 7.65 (m, 2H). MALDI-MS calcd for $C_{47}H_{72}N_9O_{22}^+$ $[M + H]^+$ 1114.48, found 1114.42.

*Compound **17***. 3,6,9-Trioxaundecanoic diacid (110 mg, 0.495 mmol) was azeotropically dried with toluene and then dissolved in dry, ethanol-free chloroform (20 mL). To this solution were added NHS (125.3 mg, 1.09 mmol), DMAP (50 mg), and DCC (224.3 mg, 1.09 mmol). The reaction was kept at 23 °C for 1 h, then **5** (1.63 g, 1.09 mmol) with additional dicyclohexylcarbodiimide (224.3 mg, 1.09 mmol) in dry ethanol-free chloroform (15 mL) was added to the reaction mixture. The reaction was left at 23 °C overnight. The precipitate was filtered off, and the filtrate was evaporated at reduced pressure. The crude product was purified by HPFC (0−5% methanol in chloroform). Yield: 0.97 g, 61.5% wrt 3,6,9-trioxaundecanoic diacid. ^{1}H NMR ($CDCl_3$), δ 1.44 (s, 54H); 1.46 (s, 27H); 1.52−1.88 (m, 48H); 3.24 (m, 24H); 3.45 (m, 32H); 3.70 (m, 8H); 3.98 (m, 4H).

*Compound **18***. This compound was synthesized according to the same method as **9** but using **17** as the substrate. Yield: 95% wrt **17**. ^{1}H NMR (MeOH-d_4), δ 1.49−1.80 (m, 48H); 3.24 (m, 24H); 3.45−3.71 (m, 40H); 4.00 (m, 4H). MALDI-MS calcd for $C_{88}H_{142}N_{16}NaO_{47}^+$ $[M + Na]^+$ 2197.91, found 2197.96.

Cloning, Expression, and Purification of His-yCD. The yeast cytosine deaminase gene was amplified by a polymerase chain reaction using Pfu Ultra DNA polymerase (Stratagene, La Jolla, CA), pORF-fcy::fur plasmid (InvivoGen, San Diego, CA) as a template, a 5′ primer designed to include NdeI restriction site and a 6x-histidine tag followed by a thrombin cleavage site sequence (5′-CTCGT**CATATG**CATCATCACCACCATCACCTGGTGCCACGCGGTAGTGTCACAGGAGGCATGGC-3′), and a 3′ primer including XhoI restriction site and a stop codon (5′-GCTCGT**CTCGAG**TTACTCCCCAATGTCCTCAAAC-3′). The amplified gene and pET41 bacterial expression vector (Novagen; San Diego, CA) were digested with NdeI and XhoI restriction enzymes (New England Biolabs; Beverly, MA) and ligated together using T4 ligase (New England Biolabs; Beverly, MA). The ligated plasmid, pET41-HY, was transformed into DH5α *E. coli* cells (Invitrogen; Carlsbad, CA). The DNA sequence of purified pET41-HY plasmid was verified (SeqWrite DNA Technology Services; Houston, TX).

Expression and purification of His-yCD from *E. coli* were accomplished following published protocols (*20*, *21*). To express His6-yCD, purified pET41-HY plasmid was transformed into BL21-Codon Plus (DE3)-RIPL *E. coli* cells (Stratagene; La Jolla, CA). For a large-scale expression, the cells were grown in 1 L of LB culture medium containing 30 μg/mL kanamycin and 50 μg/mL chloramphenicol at 35 °C until the $OD_{600\ nm}$ reached 0.6−0.8, and the protein expression was induced by adding 0.5 mM isopropyl β-D-1-thiogalactopyranoside (IPTG) supplemented with 0.5 mM zinc acetate. The protein was expressed overnight at 23 °C with constant shaking at 200 rpm.

To purify His-yCD, the IPTG-induced cells were harvested by centrifugation at 6000 × *g* at 4 °C for 30 min. The cell pellet was resuspended in 20 mL of the lysis buffer containing 300 mM NaCl, 20 mM Tris-Cl, 40 mM imidazole, 0.2% Triton X-100, and 0.5 mM PMSF protease inhibitor. After one freeze−thaw cycle, the cells were lysed by lysozyme and sonication treatments on ice−water bath. The cell lysate was further treated with DNase I and RNase A, and it was centrifuged at 10 000 × *g* for 45 min at 4 °C. 1 mM DTT was added to the supernatant fraction and filtered through a 0.4 μm membrane. The filtered supernatant fraction was applied to HisTrap FF affinity column (Amersham Biosciences; Piscataway, NJ) pre-equilibrated with 300 mM NaCl, 20 mM Tris-Cl, pH 8.0, 40 mM imidazole at the flow rate of 1 mL/min. Then, the column was washed with a 15-column volume of the equilibration buffer, and the bound protein was eluted with the elution buffer containing 300 mM NaCl, 20 mM Tris-Cl, pH 8.0, and 500 mM imidazole. The eluates were pooled together and applied to HiPrep Sephacryl S-100HR 16/60 size exclusion column (Amersham Biosciences) equilibrated with 50 mM NaCl and 25 mM Tris-Cl, pH 8.0, at 4 °C. The column was operated at the flow rate of 0.5 mL/min, and 2 mL was collected for each fraction. $OD_{280\ nm}$ was

measured to obtain the fractions containing His6-yCD. On average, 30 mg of highly pure His6-yCD was obtained from a liter of culture using this method. The purity of His6-yCD was confirmed by SDS-PAGE analysis (see Supporting Information).

Surface Plasmon Resonance (SPR). The binding affinity of tri-NTA and His-tagged proteins was determined by SPR using an upgraded Biacore 1000 instrument (Piscataway, NJ). His6-yCD was freshly prepared as mentioned above, and the molecular weight of the dimer in the solution is ca. 36 KDa. HIP1R is a homolog of the Huntington protein HIP1, an adaptor protein for membrane transport. His6-tagged HIP1R is a generous gift from Jeremy Wilbur (University of California, San Francisco, Department of Biochemistry and Biophysics). His6-tagged HIP1R forms dimer in the solution with a molecular weight of 22 KDa. Tris-HCl buffer (50 mM NaCl, 20 mM Tris-HCl, 0.005% Tween 80, pH 8.0) served as the instrument running buffer and was used in the preparation and dilution of all samples. The streptavidin-coated SA sensor chip is from Biacore (Piscataway, NJ). The chip was pre-rinsed with 1 M NaCl, followed by 50 mM NaOH, then primed with Tris-HCl buffer, and coated with tri-NTA by flowing 100 nM biotin-PEO3-tri-NTA at 20 μL/min for 1 min to capture a 50 RU response. Various concentrations of the His-tagged HIP1R protein were injected to flow over the tri-NTA surface, according to an automated program cycle of the following sequence: (1) activation of tri-NTA with Ni(II), (2) protein injection, (3) Ni(II) removal with 0.3 M EDTA, and (4) rinse with 0.25% SDS for baseline regeneration. For the reference control, the same program cycle was used, except that no Ni(II) was provided in the first step. Both sample and control measurements were run in duplicate. The crude data were processed with the manufacturer-supplied *Biaevaluation 3.2 RC1* software, and the kinetic parameters were obtained by fitting the experimental curves with 1:1 Langmuir binding model.

Load of His6-Tagged yCD on Liposomes. Liposomes were prepared by sonication and extrusion as described by Szoka et al. (*22*). Briefly, a solution of given lipids was added to a depyrogenated borosilicate glass tube and evaporated under reduced pressure at room temperature to form a lipid film. The tube was placed under high vacuum overnight to remove residual solvent. Films were hydrated in 1 mL HEPES buffer (20 mM HEPES, 140 mM NaCl, pH 8.0) with intermittent vortex. Tubes containing the lipid suspension were then filled with argon, sealed, and sonicated at 23 °C for 5 min. The resultant liposomes were extruded 11 times through a 100 nm polycarbonate membrane (Nucleopore; Pleasanton, CA) with a hand-held extruder (Avestin; Ontario, Canada). The tri-NTA containing formulation (DOD−tri-NTA/POPC/Chol, 5:57:38, molar ratio) was used to bind to His-tagged yCD, and the POPG formulation (POPG/POPC/Chol, 22.5:46.5:31, molar ratio) with a similar negative charge density to the tri-NTA formulation was used as a negative control. To load the NTA head groups with Ni(II), liposomes were incubated with 5 mM $NiCl_2$ at 4 °C for 15 min with stirring. Excess Ni(II) was removed by immediately passing the liposomes down a 1 × 20 cm Sepharose 4B column under gravity flow. In some experiments, a tri-NTA-containing formulation without Ni(II) was also used as a negative control. The final phospholipid concentration was determined by the method of Bartlett (*23*). Liposome size and ζ potential were measured using a Zetasizer 3000 (Malvern, U.K.).

The ability of NTA liposomes to bind His-tagged yCD was assessed. Liposomes containing 1 μmol total lipids were incubated with 180 μg His6-yCD in 0.49 mL HEPES buffer at 4 °C for 1 h with magnetic stirring. For tri-NTA-containing lipids, this yielded a 10:1 molar ratio of DOD−tri-NTA/His6-yCD. After 1 h incubation, samples were immediately passed down a 1 × 20 cm Sepharose 4B column under gravity flow. Liposomes eluted in the void volume. The absorbance of eluted fractions at 220 nm was measured with a NanoDrop spectrophotometer (NanoDrop; Wilmington, DE). For liposome-containing fractions, phospholipid concentration was determined by the method of Bartlett. Protein concentration was determined by the CBQCA assay (Molecular Probes; Eugene, OR).

Enzyme Activity Assay. Cytosine deaminase assay was performed using the methods described by Senter et al. (*24*). Briefly, a stock solution of 50 mM 5-fluorocytosine (5-FC) was prepared in 1 × PBS. Then, 5 mM 5-FC and His6-yCD liposomes in 1 × PBS were incubated together at 37 °C. An aliquot (20 μL) of the reaction mixture was removed at given time point, and quenched by 0.1 N HCl in 1 × PBS (980 μL). The amount of 5-fluorouracil (5-FU) formed in the reaction was determined by measuring the UV absorbance at 255 and 290 nm.

Fluorescent Labeling of His-yCD. Fluorescein−tri-NTA was incubated with excessive $NiCl_2$ for 15 min at 23 °C in the dark and chromatographed on a Sephacryl S-100 HR column (1 × 20 cm) to remove the excessive Ni(II). Then, the Ni(II)-loaded fluorescein−tri-NTA was incubated with His6-yCD at a given molar ratio. The mixture was separated on a Sephacryl S-100 HR column (1 × 20 cm). Fractions were monitored at both 220 nm (protein) and 492 nm (fluorescein). When fluorescein−tri-NTA was in excess, the fractions of the first peak were pooled and analyzed by absorbance at 280 nm (protein) and 492 nm (fluorescein). All solutions were prepared in 20 mM HEPES, 150 mM NaCl, pH 8.0 buffer.

Fluorescence Spectra. The fluorescence spectra were recorded on a Spex Fluorolog fluorometer (Edison, NJ) with 1.25 mm excitation and emission slits. Fluorescein−tri-NTA was dissolved in pH 7.4 PBS and diluted to 7.5 μM for the measurement of absorption (E_m: 518 nm) and emission (E_x: 492 nm) spectra. Then, the stock solution was mixed with 3 mol equiv of $NiCl_2$ and diluted to 7.5 μM for the fluorescence spectra measurement. For fluorescein-labeled His-yCD, the concentration of fluorescein was determined by absorbance (492 nm) first, then the emission spectra of both protein and fluorescein−tri-NTA were measured at the same concentration.

RESULTS

Synthesis of NH_2-tri-NTA(*t*-Bu)$_3$. The synthetic steps for building NH_2-tri-NTA(*t*-Bu)$_3$ are shown in Scheme 1. In the initial step, H-Lys(Z)-OtBu.HCl was converted to **1** by introducing two more *tert*-butyl acetate groups on the α-nitrogen. Selective removal of the protective groups from **1** led to the first generation of NTA dendrons with either an amino group (**2**) or three carboxylic groups (**3**). The coupling of **2** and **3** afforded the fully protected dendrimer **4**. The key intermediate (**5**) was obtained after the removal of Cbz group by catalytic transfer hydrogenation.

Synthesis of Biotin−tri-NTA As shown in Scheme 2, the reaction of activated biotin with excessive 4,7,10-trioxatridecane diamine gave **6** in a moderate yield. Then, the carboxylic group was introduced through the amino group by reaction with succinic anhydride. Compound **8** was obtained by the coupling of **7** and **5**. The removal of *tert*-butyl groups from **8** led to biotin−tri-NTA (**9**) in a good yield.

Synthesis of DOD−tri-NTA. The synthetic strategy (Scheme 3) is similar to the synthesis of **9.** First, dioctadecylamine was transformed to the acid derivative (**10**) using succinic anhydride. Then, **10** was activated,and coupled to **5**, affording **11**. Finally, *tert*-butyl groups were cleaved from **11**, and DOD−tri-NTA (**12**) was obtained in good overall yield.

Synthesis of Fluorescein−tri-NTA. The synthesis of **14** is straightforward (Scheme 4). The direct reaction of commercially available fluorescein−PEG2000-NHS and **5** led to **13** in 25% yield after the removal of unreacted PEG by HPFC. The removal

Scheme 1. Synthesis of NH_2-tri-NTA(*t*-Bu)$_3$

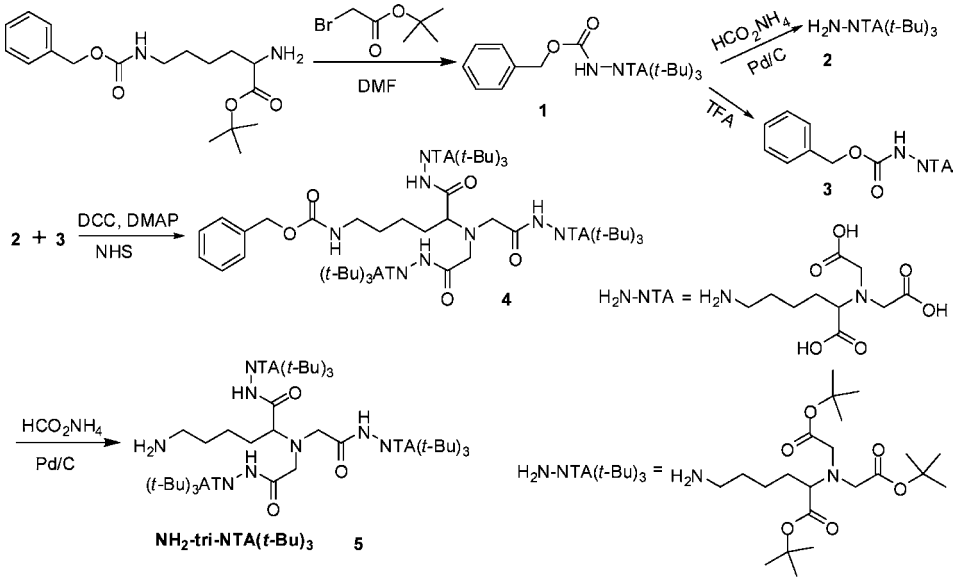

Scheme 2. Synthesis of Biotin−tri-NTA

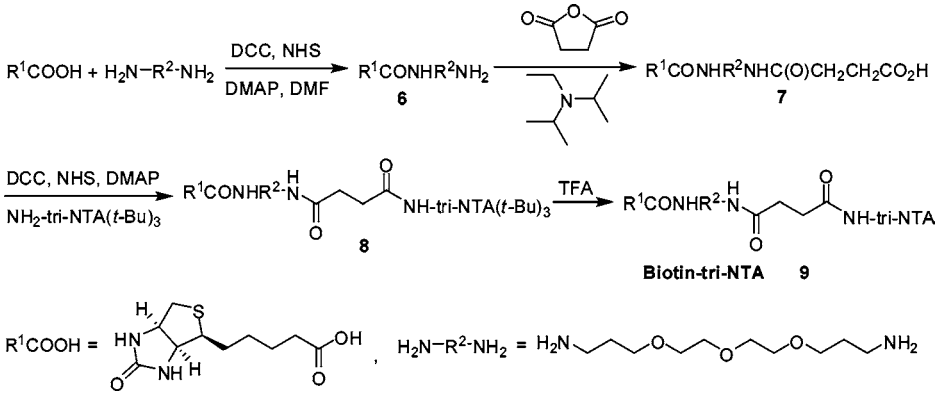

Scheme 3. Synthesis of DOD−tri-NTA

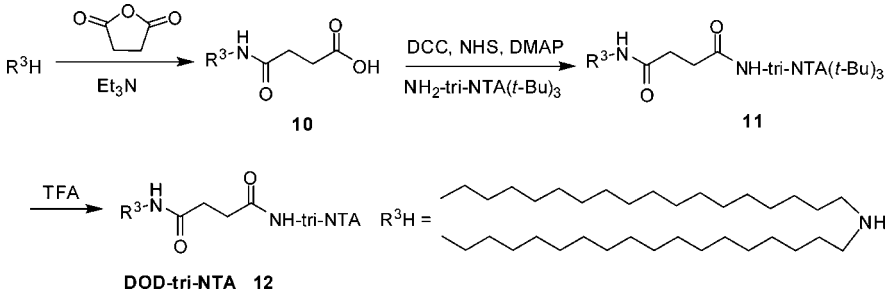

Scheme 4. Synthesis of Fluorescein−tri-NTA

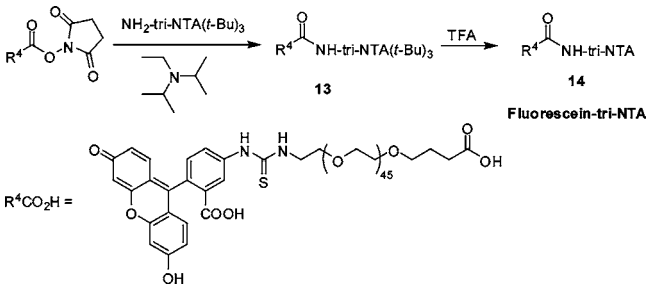

of *tert*-butyl group from **13** gave the desired product fluorescein−tri-NTA (**14**).

Synthesis of 16. As shown in Scheme 5, the reaction of NH_2-tri-NTA(*t*-Bu)$_3$ with excessive methyl *p*-hydroxybenzimidate afforded **15** in 62.2% yield. Compound **16** was obtained in high yield after the treatment of **15** with TFA.

Synthesis of 18. This molecule was synthesized following a similar method to **9** (Scheme 6). Trioxaundecanoic diacid was first activated with NHS using DCC and DMAP. Then, the activated ester was treated with slightly excessive **5**, affording **17** in moderate yield. The cleavage of *tert*-butyl groups with TFA gave the final product **18** in high yield.

Binding Constants. We synthesized biotin−tri-NTA as a bridging reagent to allow the use of standard streptavidin Biacore chip to anchor His6-containing protein and peptide to the chip. These proteins could then be used as receptors for probing protein−ligand interactions. In order to minimize surface crowding (*25*), we coated the SA chip with a very low density (50 response units, about 0.005 ng/mm) of biotin−tri-NTA. Signal from nonspecific interactions of His-tagged protein with

Scheme 5. Synthesis of 16

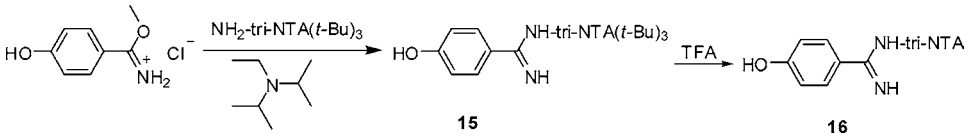

Scheme 6. Synthesis of 18

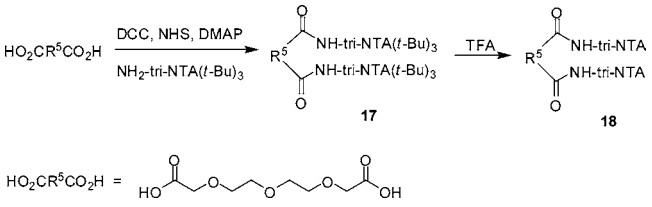

Table 1. Binding Parameters of Tri-NTA/His-Tagged Proteins

	HIP1R				yCD
concn (nM)	200	300	500	750	50
K_a (1/Ms)	8.65×10^4	1.66×10^5	2.16×10^5	1.89×10^5	4.04×10^5
K_d (1/s)	2.88×10^{-3}	3.43×10^{-3}	3.92×10^{-3}	4.32×10^{-3}	2.17×10^{-3}
K_D (M)	3.33×10^{-8}	2.06×10^{-8}	1.81×10^{-8}	2.28×10^{-8}	5.37×10^{-9}
χ^2 [a]	0.609	0.226	1.42	3.03	0.232

[a] The χ^2 value represents the sum of squared differences between the experimental data and the fit data at each point. It was used to evaluate the quality of fit between the experimental data and the binding model.

Table 2: Liposome Diameter and ζ Potential

	POPG[a]	NTA[b]	NTA + Ni[c]	NTA−yCD[d]
diameter (nm)	104.3 ± 0.8	91.5 ± 1.5	139.6 ± 4.6	105.6 ± 2.9
ζ potential (mV)	−29.6 ± 12.7	−37.2 ± 12.3	−24.2 ± 4.6	−24.6 ± 8.4

[a] POPG liposomes: POPG/POPC/Chol, 22.5:46.5:31. [b] Tri-NTA liposomes: DOD−tri-NTA/POPC/Chol, 5:57:38. [c] Ni(II) loaded tri-NTA liposomes. [d] Tri-NTA liposomes with His6-yCD engrafted on the surface.

the prepared tri-NTA surface was removed by subtracting the response on the control surface (inactivated tri-NTA). After appropriate processing of the raw data (e.g., alignment, zeroing, and reference subtraction), the tri-NTA/His-tagged protein interaction data were fitted to a simple 1:1 Langmuir model. The kinetic parameters of the interaction at various concentrations are listed in Table 1. The χ^2 value represents the sum of squared differences between the experimental data and the fit data at each point. The χ^2 value and residual plots (not shown) indicated a satisfactory fit between the experimental data and the binding model. For His-tagged HIP1R, the computed equilibrium dissociate constant (K_D) was around 20 nM (18−33 nM). The K_D of tri-NTA/His-tagged yCD (5.4 nM) is similar to that of HIP1R, albeit slightly lower. A difference may be expected due to varying accessibility of His6 tags in their different protein structure contexts.

His6-yCD-NTA Liposomes. DOD−tri-NTA was readily incorporated into the liposome bilayer. The particle diameters and ζ potentials of all the liposomes are summarized in Table 2. The presence of DOD−tri-NTA in the liposome formulation led to a negative surface charge on the liposomes at pH 8.0. The incorporation of Ni(II) into the NTA−lipid resulted in a less-negative surface charge and larger particle diameter. The diameter change of Ni(II)-loaded liposomes may be attributed to partial aggregation due to the reduced surface charge and possible cross-linking through the relatively weak NTA-Ni(II)-NTA interaction (*26*). When His6-yCD was incubated with Ni(II)-NTA-containing liposomes for 1 h and the preparation applied to the size exclusion column, His6-yCD was associated with liposome peak (first peak), and the free protein peak was not detectable (Figure 1). Enzymatically active yCD was detected in the liposome fractions. His6-yCD on the liposome surface caused the particle diameter to drop to around 105 nm

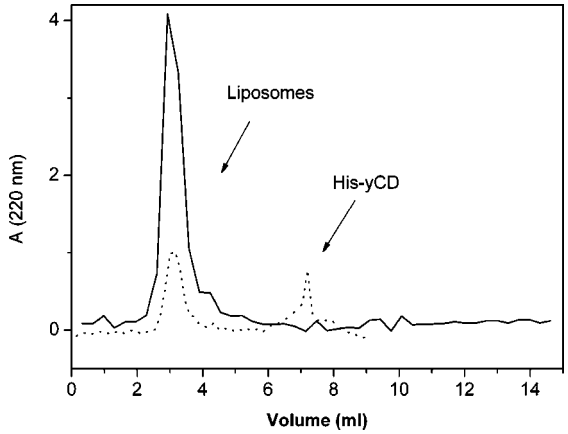

Figure 1. Incorporation of His6-yCD on the surface of tri-NTA liposome. The absorbance was monitored at 220 nm. Solid line: chromatogram of Ni(II) loaded tri-NTA liposome (excess) + His6-yCD. Dotted line: chromatogram of POPG liposome (excess) + His6-yCD. First peak: liposomes. Second peak: His6-yCD.

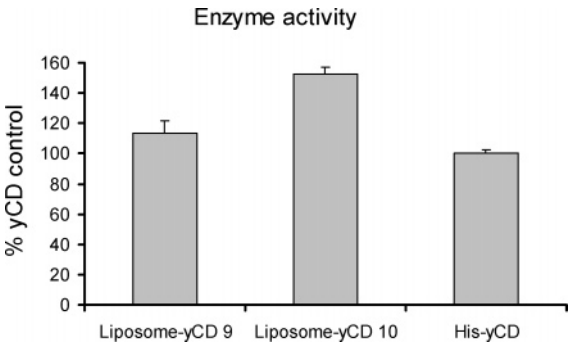

Figure 2. Relative enzyme activity of liposomal yCD. The enzyme activity was normalized with respect to the activity of yCD control. Liposome-yCD 9 and 10 are the major fractions of yCD bound on liposomes collected from size exclusion column.

and had no significant influence on the surface charge. When His6-yCD was incubated with POPG control liposomes for 1 h and passed down a Sepharose 4B column, two separate chromatographic peaks were evident. No protein was detected in the liposome peak (first peak), and enzymatically active protein was found in the second peak. Similar results were also obtained in experiments using tri-NTA liposomes without Ni(II) as an additional negative control. Liposome-associated protein was only detected on the Ni(II)-loaded tri-NTA liposomes (Supporting Information Figure S2).

Enzyme Activity of Liposomal yCD. The activity of liposomal yCD to convert 5-FC to 5-FU was measured, calculated as the rate of production of 5-FU (mM/min) per milligram of protein, and normalized with respect to the activity of free His6-yCD (Figure 2). Two liposomal yCD fractions showed a similar order of activity as that of free yCD. The slight increase in activity of liposome-associated yCD may be due to the interference of the liposome lipid on the protein concentration measurement rather than a surface-induced increase in enzyme activity.

Fluorescent Labeling of His6-yCD. We sought to confirm that fluorescein−tri-NTA could be used to noncovalently label His6-containing proteins. The absorption and emission spectra

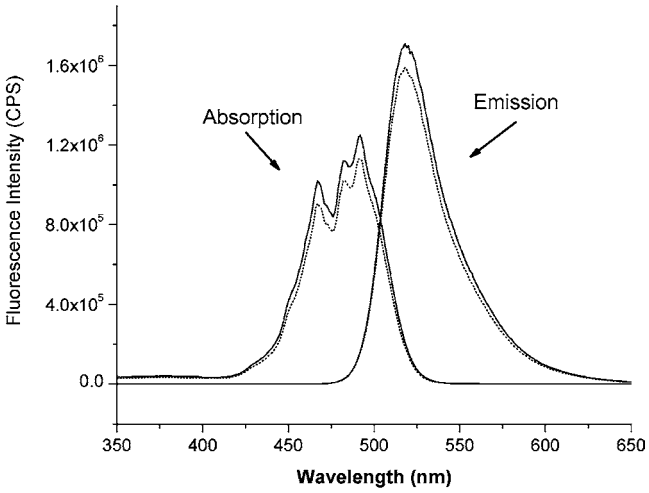

Figure 3. Fluorescence spectra of fluorescein−tri-NTA. Solid line: without Ni(II). Dotted line: Ni(II) loaded. Spectra were recorded at same concentration of fluorescein.

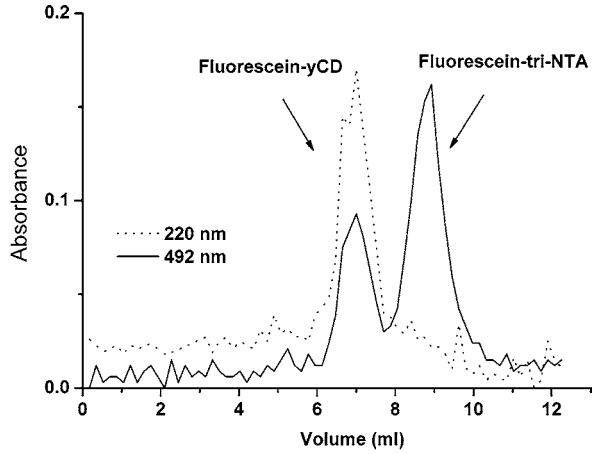

Figure 4. Fluorescent labeling of His6-yCD. His6-yCD was mixed with excessive Ni(II) loaded fluorescein−tri-NTA, then passed down a Sephacryl S-100 HR column. Absorbance of fractions was monitored at both 220 nm (protein) and 492 nm (fluorescein). First peak: fluorescein−NTA-yCD conjugate. Second peak: free fluorescein−tri-NTA.

of fluorescein−tri-NTA were measured with or without Ni(II) (Figure 3). The incorporation of Ni(II) resulted in slight decrease of both absorption and emission intensity. When His6-yCD was incubated with excess fluorescein−tri-NTA-Ni(II), two distinct peaks were obtained from the column (Figure 4). The first peak was detectable at both 220 nm (protein) and 492 nm (fluorescein). The second peak was only detectable at 492 nm, corresponding to excess fluorescein−tri-NTA-Ni(II). When excess His6-yCD was used, there was no free fluorescein−tri-NTA, and only the first peak (His6-yCD bound fluorescein) was detectable (data not shown). The absorbance analysis of the purified fluorescein−yCD conjugate showed a 1:1 (fluorescein/His6) composition. Thus, His6-yCD was quantitatively labeled with fluorescein−tri-NTA-Ni(II), and stable 1:1 conjugate was obtained after column separation. No significant fluorescence quenching was observed on the fluorescein−NTA-yCD conjugate (spectra not shown).

DISCUSSION

A number of groups have documented the great potential of multivalent NTAs in the handling of His-tagged molecules (*5*, *15*). The broad application of this type of noncovalent interaction will depend upon the ease of synthesis of the multivalent NTA and the ability to prepare a variety of multivalent NTA conjugates in high yield. Our strategy is to build NH_2-tri-NTA-(t-Bu)$_3$ as the key intermediate first and introduce specific functionality into the conjugate later. This strategy provided a general way to construct a variety of tri-NTA molecules. The presence of *tert*-butyl ester group provided NH_2-tri-NTA(t-Bu)$_3$ good organic solvent solubility and less polarity, which made the synthesis and purification of the tri-NTA conjugates much easier compared with the synthesis of tri-NTA conjugates containing multiple unprotected carboxylic groups (*5*). Furthermore, the lysine-based dendritic structure branched each mono-NTA unit seven atoms apart, which might allow a more flexible binding of NTA to His-tag that favors the formation of a stable complex.

Biotin−tri-NTA was designed and synthesized for the modification of streptavidin sensor chips so that the interaction between tri-NTA and His-tagged molecules can be measured by SPR. The inclusion of a short polyethylene oxide spacer provided good solubility and flexibility. This bifunctional adaptor can be used in many other applications where a conversion between streptavidin/biotin interaction and tri-NTA/His-tag interaction is desired. The PEO spacer could be adjusted to fit the application. Although both HIP1R and yCD form dimers in the solution and have the potential to cross-link with tri-NTA, the kinetic data showed good fits with the simple 1:1 Langmuir binding model. We avoided the potential complexity of an avidity effect due to the binding of two subunits of the His-tagged protein by the experimental conditions used here: low surface capacity, relatively high flow rate, and low concentration of analyte.

An advantage of the tri-NTA chip is that it can retain strong affinity at very low surface capacity due to the low equilibrium dissociation constant. Similar affinity can be achieved in a mono-NTA chip only at a high surface density (*12*). At high surface densities, analysis of the binding efficiency is complicated due to mass transport, surface crowding, and possible avidity effect (*25*).

Due to the low equilibrium dissociation rate, tri-NTA is a promising tool for the noncovalent modification of His-tagged proteins. Fluorescent labeling is a powerful technique for the study of biomacromolecules. We have shown that fluorescein−tri-NTA forms a stable complex with His6-yCD without significant fluorescent quenching. The coordination of Ni(II) with NTA dramatically quenches the fluorescence of NTA-associated fluorophore and the effect is distance-dependent (*17*). The PEG2000 spacer between fluorescein and tri-NTA shielded not only the influence of Ni(II) on fluorescein but also the influence of protein on fluorescence. The removal of excessive Ni(II) can be easily achieved by size exclusion chromatography in the presence of PEG2000 spacer. Thus, fluorescein−tri-NTA is an ideal molecule for the noncovalent yet reversible labeling of His-tagged proteins and a good example for making other similar fluorophores.

There is also a demand for an efficient yet mild method to radiolabel proteins without damaging the protein activity. In the traditional method, the radiolabeling chemistry is done directly on the protein, and there is always a risk of activity loss. Since His-tag technology has been widely adopted in the engineering of recombinant proteins, the use of radioactive tri-NTA as a noncovalent way of labeling protein could be a good choice. We have designed and synthesized compound **16** as a potential tool for this purpose. The beauty of this method is we can always iodinate **16** first (*27*), then conjugate it with His-tagged protein, avoiding the direct exposure of protein to the harsh iodination conditions. The use of **16** for radiolabeling His-tagged proteins is under investigation, and we will publish it elsewhere later.

To enable the noncovalent cross-linking of two different proteins to the same carrier, we have synthesized **18** as a bifunctional tri-NTA with a short polyethylene oxide spacer. This molecule could be used to form fusion proteins by attaching different His-tagged proteins at each end. It provides a shortcut to creating fusion proteins that are difficult to engineer or manufacture by the traditional recombinant methods.

Mono-NTA lipids have been used to attach His-tagged proteins to monolayers (*4*, *28*) and also liposomes (*29*). However, the affinity of the proteins to a mono-NTA lipid was not high enough to keep the protein from dissociating from the liposomal surface during separation of liposome-bound protein from nonattached protein (*29*). The introduction of tri-NTA lipid has solved the problem (*5*, *16*). The synthesis of DOD−tri-NTA introduced here is efficient. Although van Broekhoven and coworkers clearly recognized the importance of multivalent binding to attach a protein to a liposome, they did not reveal the synthesis of NTA_3−DTDA in detail (*15*, *16*). The Tampe group has discussed the synthesis of mono-NTA−lipid conjugates and the multi-NTA−fluorophore conjugates, but has not yet published the use of multivalent NTA to attach proteins to the liposome surface. As a proof of the concept, we synthesized DOD−tri-NTA and used it as an adaptor to attach His6-yCD to the liposome surface, and demonstrated complete retention of enzyme activity. Multiple proteins could be attached to the same liposome surface. Using the tri-NTA liposome as a surface to attach different proteins permits one to use a single liposome to explore the effect of a wide range of ratios of multiple proteins without having to do chemistry for each combination. As others have noted (*5*, *16*), this provides a toolbox to create combinatory arrays of proteins and other molecules such as PEG. His-tagged targeting molecules could be incorporated on the liposome surface by the same method.

We have demonstrated a practical method to synthesize the lysine-based dendron NH_2-tri-NTA(*t*-Bu)$_3$ and its derivatives. The applications of multivalent NTAs have been anticipated by others (*5*), but we provide a facile chemical synthesis to accelerate their use in biotechnology applications and drug delivery.

ACKNOWLEDGMENT

This work was supported by NIH EB003008 and GM61851. D. Watson is supported by a U.S. Department of Homeland Security Graduate Fellowship, administered by the Oak Ridge Institute for Science and Education under U.S. Department of Energy contract number DE-AC05-00OR22750. The opinions expressed herein do not necessarily reflect the policies and views of DHS, DOE, or ORISE. We thank Jeremy Wilbur for the generous gift of HIP1R protein. Thanks are also extended to the UCSF Mass Spectrometry Facility (A.L. Burlingame, Director) supported by NIH NCRR RR01614.

Supporting Information Available: The SDS-PAGE analysis of purified His6-yCD and the analysis of liposome associated His6-yCD. This material is available free of charge via the Internet at http://pubs.acs.org.

LITERATURE CITED

(1) Porath, J., Carlsson, J., Olsson, I., and Belfrage, G. (1975) Metal chelate affinity chromatography, a new approach to protein fractionation. *Nature (London) 258*, 598−599.

(2) Gaberc-Porekar, V., and Menart, V. (2005) Potential for using histidine tags in purification of proteins at large scale. *Chem. Eng. Technol. 28*, 1306−1314.

(3) Kapanidis, A. N., Ebright, Y. W., and Ebright, R. H. (2001) Site-specific incorporation of fluorescent probes into protein: hexahistidine-tag-mediated fluorescent labeling with (Ni(2+):nitrilotriacetic acid (n)-fluorochrome conjugates. *J. Am. Chem. Soc. 123*, 12123−12125.

(4) Dorn, I. T., Neumaier, K. R., and Tampe, R. (1998) Molecular recognition of histidine-tagged molecules by metal-chelating lipids monitored by fluorescence energy transfer and correlation spectroscopy. *J. Am. Chem. Soc. 120*, 2753−2763.

(5) Lata, S., Reichel, A., Brock, R., Tampe, R., and Piehler, J. (2005) High-affinity adaptors for switchable recognition of histidine-tagged proteins. *J. Am. Chem. Soc. 127*, 10205−10215.

(6) Sigal, G. B., Bamdad, C., Barberis, A., Strominger, J., and Whitesides, G. M. (1996) A self-assembled monolayer for the binding and study of histidine-tagged proteins by surface plasmon resonance. *Anal. Chem. 68*, 490−497.

(7) Schmid, E. L., Keller, T. A., Dienes, Z., and Vogel, H. (1997) Reversible oriented surface immobilization of functional proteins on oxide surfaces. *Anal. Chem. 69*, 1979−1985.

(8) Schmitt, L., Ludwig, M., Gaub, H. E., and Tampe, R. (2000) A metal-chelating microscopy tip as a new toolbox for single-molecule experiments by atomic force microscopy. *Biophys. J. 78*, 3275−3285.

(9) Xu, C., Xu, K., Gu, H., Zhong, X., Guo, Z., Zheng, R., Zhang, X., and Xu, B. (2004) Nitrilotriacetic acid-modified magnetic nanoparticles as a general agent to bind histidine-tagged proteins. *J. Am. Chem. Soc. 126*, 3392−3393.

(10) Gershon, P. D., and Khilko, S. (1995) Stable chelating linkage for reversible immobilization of oligohistidine tagged proteins in the BIAcore surface plasmon resonance detector. *J. Immunol. Methods 183*, 65−76.

(11) Nieba, L., Nieba-Axmann, S. E., Persson, A., Hamalainen, M., Edebratt, F., Hansson, A., Lidholm, J., Magnusson, K., Karlsson, A. F., and Pluckthun, A. (1997) BIACORE analysis of histidine-tagged proteins using a chelating NTA sensor chip. *Anal. Biochem. 252*, 217−28.

(12) Altin, J. G., White, F. A., and Easton, C. J. (2001) Synthesis of the chelator lipid nitrilotriacetic acid ditetradecylamine (NTA-DTDA) and its use with the IAsys biosensor to study receptor-ligand interactions on model membranes. *Biochim. Biophys. Acta 1513*, 131−148.

(13) Goldsmith, C. R., Jaworski, J., Sheng, M., and Lippard, S. J. (2006) Selective labeling of extracellular proteins containing polyhistidine sequences by a fluorescein-nitrilotriacetic acid conjugate. *J. Am. Chem. Soc. 128*, 418−9.

(14) Guignet, E. G., Hovius, R., and Vogel, H. (2004) Reversible site-selective labeling of membrane proteins in live cells. *Nat. Biotechnol. 22*, 440−444.

(15) van Broekhoven, C. L., Parish, C. R., Demangel, C., Britton, W. J., and Altin, J. G. (2004) Targeting dendritic cells with antigen-containing liposomes: a highly effective procedure for induction of antitumor immunity and for tumor immunotherapy. *Cancer Res. 64*, 4357−65.

(16) van Broekhoven, C. L., and Altin, J. G. (2005) The novel chelator lipid 3(nitrilotriacetic acid)-ditetradecylamine (NTA(3)-DTDA) promotes stable binding of His-tagged proteins to liposomal membranes: potent anti-tumor responses induced by simultaneously targeting antigen, cytokine and costimulatory signals to T cells. *Biochim. Biophys. Acta 1716*, 104−116.

(17) Lata, S., Gavutis, M., Tampe, R., and Piehler, J. (2006) Specific and stable fluorescence labeling of histidine-tagged proteins for dissecting multi-protein complex formation. *J. Am. Chem. Soc. 128*, 2365−2372.

(18) Richmond, T. A., Takahashi, T. T., Shimkhada, R., and Bernsdorf, J. (2000) Engineered metal binding sites on green fluorescence protein. *Biochem. Biophys. Res. Commun. 268*, 462−465.

(19) Varnes, A. W., Dodson, R. B., and Wehry, E. L. (1972) Interactions of transition-metal ions with photoexcited states of flavins. Fluorescence quenching studies. *J. Am. Chem. Soc. 94*, 946−950.

(20) Ko, T. P., Lin, J. J., Hu, C. Y., Hsu, Y. H., Wang, A. H., and Liaw, S. H. (2003) Crystal structure of yeast cytosine deaminase. Insights into enzyme mechanism and evolution. *J. Biol. Chem. 278*, 19111−19117.

(21) Ireton, G. C., Black, M. E., and Stoddard, B. L. (2003) The 1.14 A crystal structure of yeast cytosine deaminase: evolution of nucleotide salvage enzymes and implications for genetic chemotherapy. *Structure 11*, 961−972.

(22) Szoka, F., Olson, F., Heath, T., Vail, W., Mayhew, E., and Papahadjopoulos, D. (1980) Preparation of unilamellar liposomes of intermediate size (0.1−0.2 μmol) by a combination of reverse phase evaporation and extrusion through polycarbonate membranes. *Biochim. Biophys. Acta 601,* 559−71.
(23) Bartlett, G. R. (1959) Phosphorus assay in column chromatography. *J. Biol. Chem. 234*, 466−468.
(24) Senter, P. D., Su, P. C., Katsuragi, T., Sakai, T., Cosand, W. L., Hellstrom, I., and Hellstrom, K. E. (1991) Generation of 5-fluorouracil from 5-fluorocytosine by monoclonal antibody-cytosine deaminase conjugates. *Bioconjugate Chem. 2*, 447−451.
(25) Myszka, D. G. (1999) Improving biosensor analysis. *J. Mol. Recognit. 12*, 279−284.
(26) Tareste, D., Pincet, F. R., Brellier, M., Mioskowski, C., and Perez, E. (2005) The binding energy of two nitrilotriacetate groups sharing a nickel ion. *J. Am. Chem. Soc. 127*, 3879−3884.
(27) Larwood, D. J., and Szoka, F. C., Jr. (1984) Synthesis, characterization, and in vivo disposition of iodinatable polyethylene glycol drivatives: differences in vivo as a function of chain length. *J. Labelled Compd. Radiopharm. 21*, 603−614.
(28) Dietrich, C., Schmitt, L., and Tampe, R. (1995) Molecular-organization of histidine-tagged biomolecules at self-assembled lipid interfaces using a novel class of chelator lipids. *Proc. Natl. Acad. Sci. U.S.A. 92*, 9014−9018.
(29) Van, Broekhoven, C. L., and Altin, J. G. (2001) A novel system for convenient detection of low-affinity receptor-ligand interactions: chelator-lipid liposomes engrafted with recombinant CD4 bind to cells expressing MHC class II. *Immunol. Cell Biol. 79*, 274−84.

BC0602228

Preparation and Biological Characterization of Isomeric ^{188}Re(V) Oxocomplexes with Tetradentate S_4 Ligands Derived from *meso*-Dimercaptosuccinic Acid for Labeling of Biomolecules

Sepp Seifert,* Tobias Heinrich, Christian Jentschel, Christian Smuda, Ralf Bergmann, and Hans-Juergen Pietzsch

Forschungszentrum Rossendorf, Institut für Radiopharmazie, PF 510 119, D-01314 Dresden, Germany. Received July 27, 2006; Revised Manuscript Received September 15, 2006

A new type of tetradentate S_4 ligand has been synthesized by bridging two molecules of *meso*-2,3-dimercaptosuccinic acid for stable binding and easy conjugation of rhenium-188 to tumor targeting structures. The stereoisomeric tetrathiolato S_4 ligands form very robust anionic five-coordinated oxorhenium(V) and oxotechnetium(V) complexes. Two routes for the preparation of the ^{188}Re(V) oxocomplexes with $(iBu)_2N(O)C-C(SH)C(SH)C(O)NH(CH_2)_3NH(CH_2)_3NHC(O)C(SH)C(SH)C(O)N(iBu)_2$ (ligand **1**) and its hydrophilic crown ether derivative (ligand **2**) were tested and optimized. Several isomers were separated by HPLC from the preparation solutions and characterized *in vitro* and *in vivo*. The identity of the species obtained was determined by comparison with the HPLC profiles of reference $^{185/187}$Re analogues and $^{99/99m}$Tc complexes which were characterized by ESI-MS. All of them were absolutely stable in rat and human plasma solutions. Challenge experiments with cysteine corroborated the high inertness of the isomers toward ligand exchange reactions. Various *in vivo* samples, taken off at different times from blood, intestine, and urine of rats, confirmed the high *in vivo* stability of the $^{188}Re-S_4$ complexes. Biodistribution studies using male Wistar rats were performed and exhibited a high uptake and fast clearance from the liver of the more lipophilic cis and trans isomers of complex **I** (log $P_{o/w}$ between 1.5 and 1.7), whereas the isomers of the hydrophilic complex **II** (log $P_{o/w}$ about -1.75) were rapidly excreted *via* the renal and the hepatobiliary pathway. The low level of activity in the stomach confirms good *in vivo* stability. Thus, these new $^{188}Re-S_4$ complexes fulfill the requirements for a stable and high specific activity labeling of biomolecules with rhenium-188.

INTRODUCTION

Rhenium-188 ($E_{\beta max} = 2.1$ MeV, $t_{1/2} = 16.9$ h) is an attractive radionuclide for developing therapeutic radiopharmaceuticals due to its favorable nuclide properties and its daily availability from commercial $^{188}W/^{188}Re$ generators in high specific activity (*1*−*3*). Besides the therapeutic usefulness of ^{188}Re, the emission of the 155 keV gamma photon is an additional advantage since the biodistribution of ^{188}Re-labeled agents can be evaluated *in vivo* with a gamma camera. A further advantage of using rhenium-188 as a therapeutic radionuclide is the chemical analogy with technetium-99m, which is the most widely used radioisotope in gamma camera imaging. Both radionuclides are obtained as sodium permetalates by elution of the generator with 0.9% saline. Because $Na^{188}ReO_4$ constitutes the starting material for the preparation of ^{188}Re radiopharmaceuticals, any synthetic procedure must comprise an appropriate reduction step required to change the metal oxidation state from +7 to lower values and to allow the formation of complexes between the metal and some selected ligand. To improve the potencies of rhenium-188, tumor-specific substances must be developed to accumulate the radioactive compound in the tumor and to spare healthy tissue from radiation. This can be achieved by linking a radionuclide-bearing chelate to a target-seeking biomolecule. Various chelate systems coordinating the metal at different oxidation states are currently under investigation for stable labeling of biomolecules according to the bifunctional approach (*4*−*8*). At oxidation state +5, ligands of the "N_2S_2" or "N_3S" type (e.g., *9*−*11*) are used. They bind rhenium rapidly to form stable pentacoordinate complexes with oxorhenium(V). Unfortunately, chelate complexes of ^{188}Re often degrade much more rapidly than the ^{99m}Tc analogues, which are limiting the further development of rhenium-based therapeutic agents.

To overcome this stability problem, we developed a tetradentate S_4 ligand system derived from *meso*-dimercaptosuccinic acid (DMSA), which forms very robust oxorhenium(V) complexes (*12*). Two isomers have been fully characterized both in solid and solution states and found to adopt the expected square-pyramidal coordination geometry. The equatorial plane is formed by four thiolate sulfur atoms, whereas the oxygen occupies the apical position. The orientation of the metal oxo group is exo in relation to the carbamido groups in both isomers (Figure 1).

In the present study, we describe preparation routes for the lipophilic complex **I** (no carrier added and carrier added ^{99m}Tc−S_4 **I** and carrier-free $^{188}Re-S_4$ **I**) and the hydrophilic $^{188}Re-S_4$ complex **II** (Figure 2).

While the preparation of the ^{99m}Tc(V) oxocomplex succeeded in one step in alkaline solution with propylene glycol as an ancillary ligand (*13*), attempts to prepare the corresponding ^{188}Re complex by direct reduction of perrhenate, according to the preparation of $[^{188}ReO(DMSA)_2]^-$ (*14*), failed. However, the preparation was successful using conditions described by Bolzati et al. (*15*). This procedure differs from that commonly applied to the reduction of pertechnetate or perrhenate by the presence of two additional reagents (oxalate ions as ancillary ligand and γ-cyclodextrin as host molecule). Beside this improved preparation method, we also tested an indirect preparation route. Recently, we have reported the preparation of ^{188}Re(V) oxocomplexes by a combined reoxidation/ligand exchange reaction starting from ^{188}Re(III)−EDTA (*16*). The formation of the precursor complex and the subsequent preparation of the desired ^{188}Re(V) complexes may be performed under mild conditions

* Corresponding author. Tel: +49 351 260 2442. Fax: +49 351 260 3232. E-mail: s.seifert@fz-rossendorf.de.

10.1021/bc0602331 CCC: $33.50 © 2006 American Chemical Society
Published on Web 10/17/2006

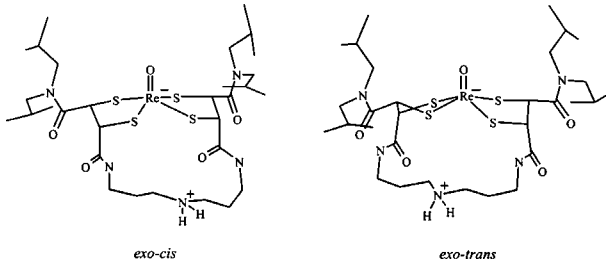

Figure 1. Molecular structures of the exo-cis (left) and one exo-trans (right) isomer of the Re−S_4 complex **I**.

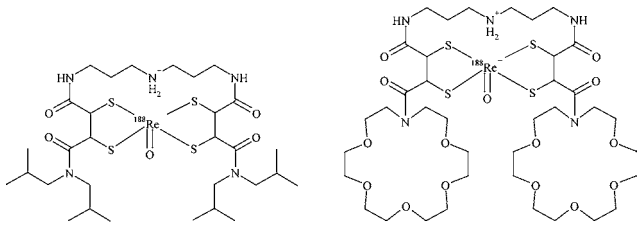

Figure 2. Chemical structures of the ^{188}Re−S_4 complexes **I** and **II**.

and consequently allows the labeling of sensitive biomolecules coupled to bidentate or tetradentate chelators.

Beside various preparation methods, we report on the *in vitro* and *in vivo* behavior of the two ^{188}Re−S_4 complexes **I** and **II** and their isolated isomers.

EXPERIMENTAL PROCEDURES

Materials and Methods. All solvents and commercially available substances were of reagent grade and used without further purification. The tetradentate S_4 ligand **1** has been synthesized by bridging two molecules of *N*,*N*′-diisobutyl-2,3-dimercaptosuccinamide with *N*-(3-aminopropyl)propane-1,3-diamine (*12*). Ligand **2** was prepared in an analogous way, starting from 4-nitrophenyl 2,2-dimethyl-5-(1,4,7,10,13-pentaoxa-16-azacyclooctadecan-16-ylcarbonyl)-1,3-dithiolane-4-carboxylate. $Na^{99m}TcO_4$ was obtained from a ^{99}Mo/^{99m}Tc generator (Mallinckrodt, Petten, The Netherlands), and $Na^{188}ReO_4$ was eluted from a ^{188}W/^{188}Re generator (Oak Ridge National Laboratories, Oak Ridge, TN). Thin-layer chromatography (TLC) and high performance liquid chromatography (HPLC) analyses were performed for controlling the identity, the radiochemical purity, and the stability of the preparations. For controlling the ^{188}Re−EDTA preparations by TLC, silica gel strips (Kieselgel 60, Merck) were used and developed with mobile phases of acetone and water. RP-18 strips and mixtures of acetonitrile and water (80/20 to 20/80) were used as mobile phases for analyzing the final ^{188}Re−S_4 complex preparations. The strips were scanned with a TLC radioanalyzer (Rita, raytest Isotopenmessgeräte GmbH, Straubenhardt, Germany). HPLC analyses were performed on a Perkin-Elmer device consisting of a Turbo LC System with a quaternary pump (Series 200 LC Pump), a Programmable Absorbance Detector Model 785A (Perkin-Elmer Instruments GmbH, Rodgau-Jügesheim, Germany), and a homemade γ-ray detector (well-type NaI(Tl) crystal). HPLC analyses were carried out with a Zorbax 300SB-C18 column (5 μm, 250 × 4.6 mm, Agilent) using a gradient eluant of acetonitrile (A) with 0.1% TFA/water (B) with 0.1% TFA, linear gradient elution (**I**): 0−20 min 40 to 50% A, 5 min 50 to 90% A, 10 min 90% A; linear gradient elution (**II**): 0−5 min 0 to 20% A, 30 min 20 to 25% A, 5 min 25 to 100% A, 10 min 100% A; flow rate 1 mL/min. The effluent from the column was monitored by UV absorbance at 254 nm for Re reference complexes or γ-ray detection for the ^{99m}Tc and ^{188}Re complexes. The separation of the isomers was performed with a semipreparative Zorbax 300SB-C18 column (5 μm, 250 × 9.4 mm, Agilent) using the same linear gradient elution and a flow rate of 4 mL/min. For separation of the $^{99/99m}$Tc complexes the HPLC system started with 50% of A from 0 to 20 min followed by a linear gradient 50% A/50% B to 100% B from 20 to 25 min. The gradient remained at 100% B for 6 min before switching back to 50% A. Mass spectrometric analyses were carried out on a Micromass Tandem Quadrupole Mass Spectrometer (Quattro LC) operating in the MS mode. Mass spectral data were recorded at the negative and positive ESI mode using a cone voltage between 20 and 150 V. About 0.01 mg of the sample dissolved in 1.0 mL methanol/water (50/50) was infused at a flow rate of 5 μL/min.

Synthesis of Nonradioactive Reference Rhenium Complexes I and II. To a solution of 1 equiv of tetrabutylammonium tetrachlorooxorhenate(V) in dry methanol was added slowly a solution of 1 equiv of the corresponding S_4 ligand **1** or **2** dissolved in dry methanol and stirred at room temperature under nitrogen. The crude product was purified and separated by preparative HPLC yielding single isomers. The cis and the trans isomer of **I** was already intensively described (*12*).

Two different isomers of complex **II** could be separated by preparative HPLC and characterized by ESI-MS.

HPLC: $t_R(\mathbf{II^1}) = 10.9$ min, $t_R(\mathbf{II^2}) = 11.5$ min (0−12 min, 20−30% A; 12−15 min, 30−40% A; 15−20 min, 40−90% A; 20−22 min, 90% A).

II^1 MS: pos. ESI: $[M + H]^+$, *m*/*z* 1151.2, $[M + Na]^+$, *m*/*z* 1173.3; neg. ESI: $[M - H]^-$, *m*/*z* 1148.4.

II^2 MS: pos. ESI: $[M + H]^+$, *m*/*z* 1151.0, $[M + Na]^+$, *m*/*z* 1172.8; neg. ESI: $[M - H]^-$, *m*/*z* 1148.2.

The mixture of isomers was characterized by NMR. ^{1}H NMR (CD_3OD)/399.95 MHz: δ = 1.64−1.85 (m, 4H, 2 CH_2CH_2-CH_2), 2.70−3.23 (m, 8H, $CH_2NH_2CH_2$, 2 CH_2NH), 3.51−3.82 (m, 48 H, 24 CH_2), 3.92−4.03 (m, 2H, 2 C*H*S), 4.66−4.72 (m, 2H, 2 C*H*S), the ammonium and amide protons were not detected.

Preparation of No-Carrier-Added and Carrier-Added ^{99m}Tc−S_4 Complex I. To 0.5 mg of the S_4 ligand **1** dissolved in 0.1 mL of methanol and 0.2 mL of propylene glycol were added 0.1 mL of pertechnetate eluate and 0.2 mL of 1 M NaOH. After addition of 0.5 mg of stannous chloride dissolved in 0.2 mL of methanol, the reaction solution was allowed to stand for 10 min at room temperature. Carrier-added preparations for ESI-MS analyses were performed with 20 μL of a 0.005 M $K^{99}TcO_4$ solution (0.1 μmol) which was added to the eluate. The isomers were separated by HPLC before mass analyses; MS: pos. ESI: $[M + H]^+$, *m*/*z* 794.4; neg. ESI: $[M - H]^-$, *m*/*z* 792.3.

Synthesis Procedure for the ^{188}Re Complexes. *^{188}Re−S_4 Complex I. Method 1*. Following the procedure developed by the Duatti group (*15*) for the preparation of ^{188}Re(V)−DMSA, which was optimized for the tetradentate S_4 ligand **1**, a mixture of 1.0 mL of perrhenate eluate (50−500 MBq) and 0.2 mL of ethanol, containing 5 mg of oxalic acid, 5 mg of γ-cyclodextrin, 5 mg of ascorbic acid, and 0.05−0.1 mg of S_4 ligand **1**, was reduced by adding 0.1−1.0 mg of stannous chloride dissolved in 0.1 mL of 0.1 N HCl. The reaction was completed by heating at 50 °C for 30 min. Radiochemical yield: 90−93% (HPLC and TLC, all isomers). For stability and biodistribution studies, the isomers were separated by semipreparative HPLC. After neutralization of the isomer fraction, the organic eluants were evaporated *in vacuo*, and the complexes were redissolved in saline and 20% of propylene glycol. Finally, the desired radioactive concentration was adjusted by dilution with saline. The identity of the species obtained was confirmed by comparison with the HPLC profiles of reference $^{185/187}$Re analogues.

^{188}Re-EDTA. A 2−3 mL volume of perrhenate eluate from a ^{188}W/^{188}Re generator (50−500 MBq/mL) were added together with 0.05 mL of 1 M HCl to a kit vial containing 5 mg of EDTA, 5 mg of mannitol, and 1.0 mg of $SnCl_2$ in freeze-dried form under nitrogen. After 20−30 min at room temperature, the complex formation was finished. Radiochemical yield: >95% (TLC).

Method 2. To 1.0 mL of the acidic ^{188}Re−EDTA solution, 0.25 mg of the S_4 ligand **1** dissolved in 0.5 mL of ethanol was added, and the reaction solution was heated at 50 °C for 30 min. Radiochemical yield: 65−75% (HPLC).

*^{188}Re−S_4 Complex **II**. Method 1*. Using 0.005−0.01 mg of the hydrophilic ligand **2**, the preparation of complex **II** may be performed in aqueous solution with the same amounts of ancillary ligands and reducing agent. The reaction is completed within 30 min at 50 °C. Radiochemical yield: 90−94% (HPLC and TLC, all isomers).

Both complexes can be prepared using a kit formulation, in which the ligand is stabilized in the form of a stannous complex. The kit vial contains 5 mg each of oxalic acid, γ-cyclodextrin, and ascorbic acid, 10−50 μg of the Sn−S_4 complex, and 1.0 mg of $SnCl_2$ in freeze-dried form and under nitrogen. For the reconstitution not more than 1.5 mL of [^{188}Re]perrhenate eluate must be added.

Method 2. To 1.0 mL of the acidic ^{188}Re−EDTA solution was added 0.25 mg of the S_4 ligand **2** dissolved in 0.5 mL of water, and the reaction solution was heated at 50 °C for 30 min. Yield: 60−70% (HPLC).

Determination of Partition Coefficients. Partition coefficients of the separated isomers of the ^{188}Re−S_4 complexes were determined by shake-flask method by mixing 0.5 mL of the complex solution (0.1 M phosphate buffer pH 7.4 with 20% propylene glycol) and 0.5 mL of octanol and shaking for 5 min. After centrifugation, aliquots of both phases were counted and the partition coefficient calculated. The measurement was repeated three times.

Stability Studies. For *in vitro* stability studies, 0.5 mL of 0.1 M phosphate buffer solution of pH 7.4 as well as rat and human plasma (diluted 1:1 with 0.1 M phosphate buffer) were incubated with each separated isomer of ^{188}Re−S_4 complexes **I** and **II** at 37 °C for 1, 2, 24, and 48 h. The reoxidation to perrhenate was determined by TLC. The pH-stability of the cis and trans isomer was determined in aqueous solutions containing 20% propylene glycol at pH 2, 7, and 9. The samples were analyzed by HPLC after 1, 4, 24, and 48 h. Ligand exchange (challenge) experiments were performed in 0.01 M solution of cysteine at 37 °C for 2 h and analyzed by HPLC. The *in vivo* stability of ^{188}Re−S_4 complexes was studied using rat arterial blood samples, kidneys, urine, and intestine samples at various time points (1−10 min, 1 h, 2 h) after injection of 30 MBq of ^{188}Re−S_4 complex. To precipitate the blood cells and proteins, 0.15 mL of ethanol was added to 0.10 mL of the supernatants obtained after centrifugation (11000*g*, 3 min) of the samples. After cooling at −60 °C for 5 min and repeated centrifugation, the supernatants were analyzed by HPLC and TLC.

Biodistribution Studies. The animal studies were carried out according to the relevant national regulations using male Wistar rats (5−6 weeks old). About 0.5 mL of the ^{188}Re complex solution (0.5 MBq) was injected into the tail vein under slight ether anesthesia. After the injection, the rats were sacrificed by heart puncture 5 and 60 min as well as 24 and 48 h postinjection (pi). Selected organs were isolated for weighing and counting. The activity concentration in the tissue of organs was calculated in terms of percentage of injected total activity (dose) per gram tissue (% ID/g) or injected dose per organ (% ID/organ).

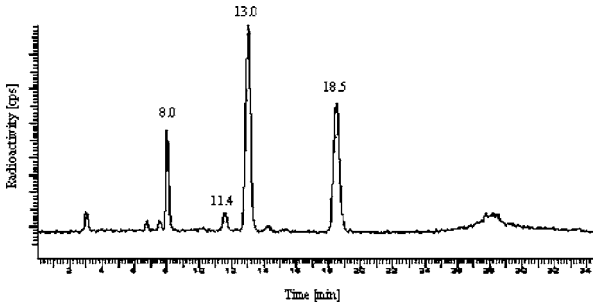

Figure 3. HPLC pattern of a $^{99/99m}$Tc−S_4 preparation used for separation of isomers; RP-18 column (Zorbax 300, 5 μm, 9.4 × 250 mm), acetonitrile/0.1% TFA (A)//water/0.1% TFA (B), (50/50) for 20 min, than in 5 min to 90% A, 6 min at 90% A; flow rate 4.0 mL/min.

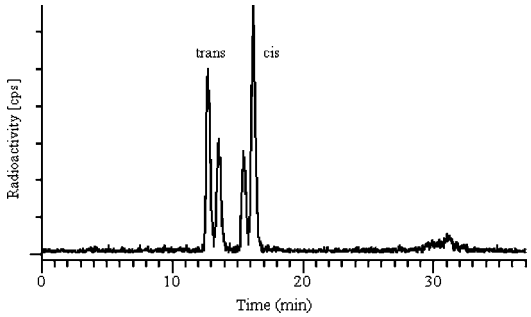

Figure 4. HPLC pattern of an ^{188}Re−S_4 **I** preparation according to method 1 with 0.05 mg of ligand and 60 min heating at 50 °C.

RESULTS AND DISCUSSION

Synthesis and Characterization of ^{99m}Tc and ^{188}Re Complexes. The preparation of the ^{99m}Tc complex **I** succeeded in high yields in slightly alkaline solution. The reaction products were analyzed by HPLC and ESI-MS. For that reason, carrier-added preparations were performed which resulted in the same HPLC pattern as no-carrier-added preparations. Using optimized HPLC conditions, the following chromatogram was obtained (Figure 3). It shows a mixture of isomers which was eluted between 8 and 19 min. The main products were identified by comparison of their retention times with those of isolated cold rhenium isomers (not shown). They represent the exo-trans (13.0 min) and the exo-cis (18.5 min) isomers of the Tc−S_4 complex **I**. For the compounds which were eluted at 8.0 and 11.4 min, the same masses of m/z = 794.4 ($[M + H]^+$) and 792.3 ($[M-H]^-$) were found as for both exo isomers. It may be concluded that the corresponding endo isomers may also be formed under the special reaction conditions.

The preparation of the desired ^{188}Re−S_4 complexes was performed by two different reaction routes. According to method 1, the direct reduction of perrhenate in the acidic solution of the S_4 ligand and ancillary ligands, perrhenate was completely reduced within 30 min at 50 °C or 60 min at room temperature by 1.0 mg of stannous chloride. Using 1.0 mg of S_4 ligand **1**, more than 30% of an unknown ^{188}Re product was formed which was eluted in HPLC at about 31 min. The percentage of this impurity decreased when the ligand amount was reduced. Less than 10% was still formed using 0.05−0.01 mg of the S_4 ligand (Figure 4). Under these conditions, the reduction was completed after 60 min at 50 °C in a total volume of not more than 1.5 mL. Because of the high lipophilicity of the S_4 ligand **1** and the resulting ^{188}Re complex **I**, the preparation had to be carried out in aqueous/alcoholic solution.

As demonstrated for the corresponding ^{99m}Tc complex isomers, the exo-cis and exo-trans isomer of the ^{188}Re−S_4 complex **I** was determined by comparison of retention times with those of cold rhenium reference isomers.

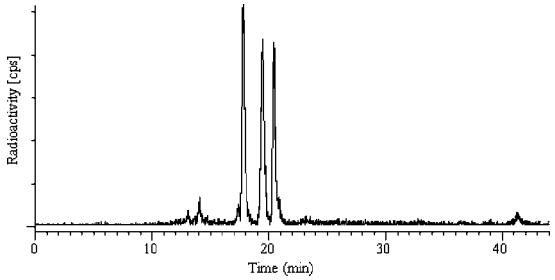

Figure 5. HPLC pattern of $^{188}Re-S_4$ complex **II** prepared according to method 1 with 0.01 mg of ligand 2 and 1.0 mg $SnCl_2$ by 30 min heating at 50 °C.

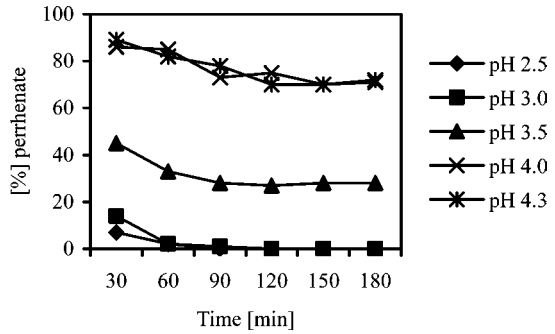

Figure 6. Decrease of perrhenate yield in the reaction solution as measure of formation of complex **II** in dependence on pH (50 °C, 1.0 mg $SnCl_2$).

Table 1. Logarithms of Partition Coefficients of $^{188}Re-S_4$ Complex Isomers between Octanol and 0.1 M Phosphate Buffer of pH 7.4 (mean ± SD, $n = 5$)

complex/isomer	log $P_{o/w}$, pH 7.4
I/trans	1.56 ± 0.03
I/cis	1.73 ± 0.04
II/1	−1.72 ± 0.05
II/2	−1.86 ± 0.04
II/3	−1.71 ± 0.03

The preparation of complex **I** according to method 2 resulted in lower yields of the $^{188}Re-S_4$ complex. In contrast to the preparation of $^{188}Re(V)$−DMSA, which was formed in neutral solution in yields of >95% using the same ^{188}Re−EDTA preparation as starting complex (*16*), the $^{188}Re-S_4$ complex requires acidic solution for the formation. The four isomers known from method 1 were also observed in method 2 preparations. The conformation of the two other isomers, which were eluted between the trans and the cis isomer, remains unknown, because they were only observed in solutions of very low concentrations of the radiometals. Probably, rhenium-188 and technetium-99m form complexes with the meso as well as the racemic bridged ligands. That would result in six isomers according to the following Scheme 1.

In contrast to the non-radioactive rhenium complex preparations, in which only the exo complexes were detected, the carrier-free ^{188}Re preparations seem to result in the formation of the exo and endo complexes, respectively. Three assumed isomers were separated by HPLC, when the $^{188}Re-S_4$ complex **II** with the crown ether S_4 ligand **2** was analyzed (Figure 5).

Two of the three peaks found in HPLC analyses of carrier-free preparations could be assigned to the two isomers which were separated by HPLC of cold reference rhenium complex **II** preparations. These isolated fractions $\mathbf{II^1}$ and $\mathbf{II^2}$ showed the same *m*/*z* values in positive and negative ESI-MS analyses. As already observed for complex **I**, more than two isomers were also detected in preparations of $^{188}Re-S_4$ complex **II**. In accordance with findings made for the optimum preparation of $^{188}Re-S_4$ **I**, diminishing of ligand quantity also resulted in higher

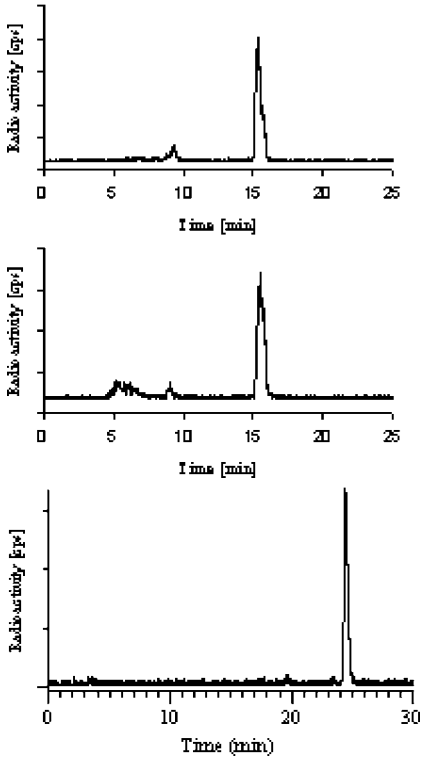

Figure 7. HPLC patterns of *in vivo* samples of the cis isomer of complex **I** (top: intestine, 2 h pi; middle: urine, 2 h pi), and isomer 2 of complex **II** (bottom: urine, 1 h pi).

Table 2. Biodistribution of the Cis and Trans Isomers of Complex I after Intravenous Administration in Wistar Rats ($n = 5$) at 5 and 60 min pi (% ID/g ± SD)

	cis [% ID/g ± SD]		trans [% ID/g ± SD]	
tissue	5 min	60 min	5 min	60 min
blood	0.85 ± 0.15	0.09 ± 0.00	3.34 ± 0.90	0.44 ± 0.13
liver	3.42 ± 0.28	1.30 ± 0.14	3.50 ± 0.68	0.88 ± 0.10
kidneys	0.53 ± 0.15	0.10 ± 0.03	1.51 ± 0.14	0.23 ± 0.04
intestine[a]	47.12 ± 8.41	80.64 ± 1.02	26.16 ± 5.51	66.14 ± 2.83
spleen	2.66 ± 0.56	2.41 ± 0.41	1.29 ± 0.16	0.70 ± 0.21
pancreas	0.15 ± 0.03	0.03 ± 0.01	0.42 ± 0.07	0.14 ± 0.02
lungs	0.92 ± 0.08	0.40 ± 0.04	1.43 ± 0.09	0.58 ± 0.12
stomach[a]	0.54 ± 0.22	0.53 ± 0.04	0.65 ± 0.19	0.58 ± 0.09
thyroid[a]	0.03 ± 0.01	0.01 ± 0.00	0.08 ± 0.03	0.03 ± 0.01
heart	0.31 ± 0.05	0.05 ± 0.00	0.96 ± 0.16	0.21 ± 0.08
femur	0.16 ± 0.02	0.04 ± 0.00	0.36 ± 0.04	0.13 ± 0.03
brain	0.04 ± 0.02	0.01 ± 0.01	0.08 ± 0.02	0.01 ± 0.00
muscle	0.10 ± 0.02	0.04 ± 0.02	0.16 ± 0.03	0.10 ± 0.02

[a] % ID/organ.

yields of the desired complex isomers. While 15−20% of the lipophilic impurities ($t_R = 41$ min) were formed when the preparations were carried out with 0.5−0.1 mg of ligand **2**, only 3−5% was found in HPLC using the very low amounts of 0.02−0.005 mg of ligand **2** for preparation.

On the basis of these results, a kit formulation for the preparation of the $^{188}Re-S_4$ complexes was developed. The low amounts of the sensitive tetrathiolate ligands could be stabilized as stannous complexes. Between 10 μg (complex **II**) and 50 μg (complex **I**) of the $Sn-S_4$ complex was found to be sufficient for optimum labeling yields of 90−94%.

Surprisingly, it is possible to clearly diminish the amount of the reducing agent $SnCl_2$. For a complete reduction of 100−1000 MBq of [^{188}Re]perrhenate, 0.1 mg or even 0.05 mg of $SnCl_2$ per vial was sufficient. The complex formation succeeded quickly and completely in an acidic solution of pH 1.5−2.0. However, the reduction of perrhenate was delayed when the pH of the reaction solution was increased (Figure 6). Despite

Scheme 1.

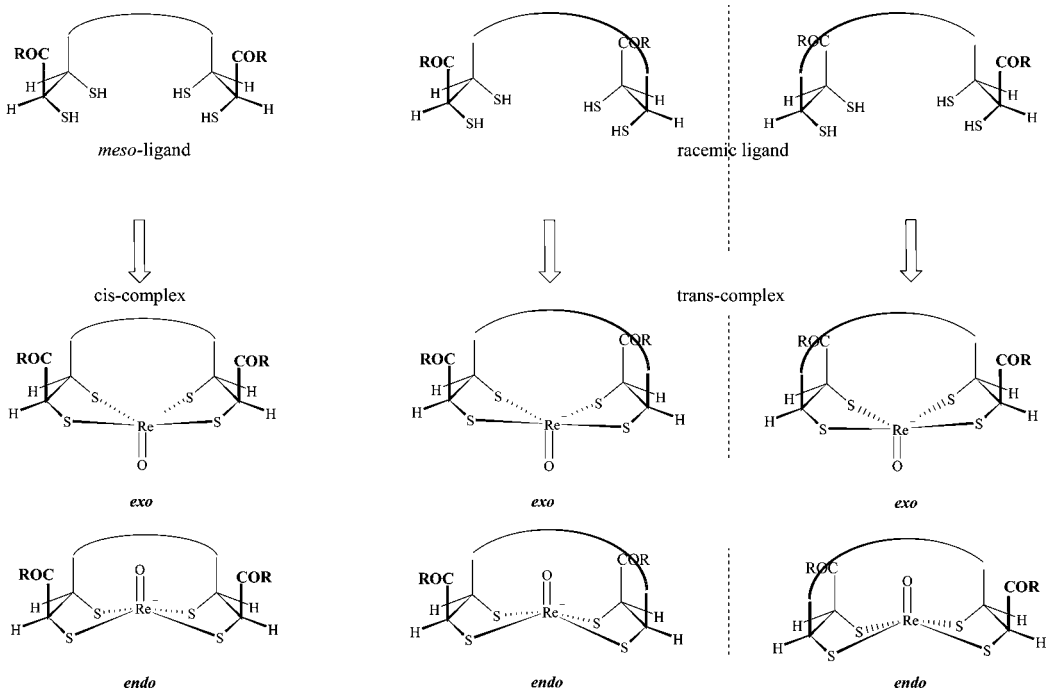

Table 3. Biodistribution of the Isomers 1, 2, and 3 of Complex II after Intravenous Administration in Wistar Rats ($n = 5$) at 5 and 60 min pi (% ID/g ± SD)

	isomer 1 [% ID/g ± SD]		isomer 2 [% ID/g ± SD]		isomer 3 [% ID/g ± SD]	
tissue	5 min	60 min	5 min	60 min	5 min	60 min
blood	0.18 ± 0.04	0.01 ± 0.00	0.44 ± 0.07	0.05 ± 0.00	0.61 ± 0.08	0.05 ± 0.01
liver	1.56 ± 0.33	0.03 ± 0.01	0.87 ± 0.10	0.12 ± 0.03	0.83 ± 0.05	0.09 ± 0.02
kidneys	0.60 ± 0.13	0.10 ± 0.02	1.82 ± 0.46	0.32 ± 0.01	2.13 ± 0.38	0.38 ± 0.05
intestine[a]	33.56 ± 3.74	57.99 ± 6.82	16.33 ± 3.45	41.49 ± 4.39	10.22 ± 2.55	25.29 ± 2.28
spleen	0.05 ± 0.01	0.01 ± 0.00	0.13 ± 0.02	0.03 ± 0.01	0.14 ± 0.01	0.05 ± 0.03
pancreas	0.12 ± 0.07	0.04 ± 0.06	0.26 ± 0.12	0.12 ± 0.04	0.21 ± 0.04	0.17 ± 0.13
lungs	0.16 ± 0.02	0.01 ± 0.00	0.36 ± 0.05	0.05 ± 0.01	0.43 ± 0.04	0.05 ± 0.00
stomach[a]	1.32 ± 0.29	0.87 ± 0.94	2.25 ± 1.75	5.56 ± 1.50	0.78 ± 0.37	0.91 ± 0.62
thyroid[a]	0.02 ± 0.01	0.00 ± 0.00	0.05 ± 0.01	0.03 ± 0.02	0.05 ± 0.01	0.01 ± 0.00
heart	0.07 ± 0.02	0.00 ± 0.00	0.18 ± 0.01	0.03 ± 0.00	0.22 ± 0.03	0.02 ± 0.00
femur	0.08 ± 0.02	0.01 ± 0.00	0.18 ± 0.02	0.03 ± 0.00	0.25 ± 0.03	0.03 ± 0.00
brain	0.01 ± 0.00	0.01 ± 0.00	0.02 ± 0.00	0.01 ± 0.01	0.02 ± 0.01	0.00 ± 0.00
muscle	0.05 ± 0.01	0.02 ± 0.02	0.13 ± 0.03	0.10 ± 0.09	0.12 ± 0.01	0.02 ± 0.00

[a] % ID/organ.

the high excess of 1.0 mg of $SnCl_2$, no complete reduction was reached within several hours, when the pH of the solution was higher than 3.

These results, which were observed for both preparations, could be improved using the kit formulation mentioned above. Under the special conditions and an additional portion of 15 mg of oxalic acid a complete reduction of perrhenate within 3 h was still possible at pH 3.5.

For further characterization of the $^{188}Re-S_4$ complex **I** its cis and trans isomers were separated by HPLC. Using optimized HPLC conditions, the trans isomer was earlier eluted than the cis isomer. The observed difference in retention time was confirmed by octanol/water distribution studies at pH 7.4 performed with both isomers. As shown in Table 1, the cis isomer is more lipophilic. As expected, complex **II** exhibits a strong hydrophilic behavior caused by the crown ether groups of ligand **2**. A successful separation of the isomers was only possible using a very smooth gradient for HPLC analysis. In accordance, nearly similar octanol/water distribution data were determined for the three isomers of complex **II**.

***In Vitro* Stability of $^{188}Re-S_4$ Complexes.** The stability of the ^{188}Re complexes toward reoxidation to perrhenate was investigated with the isolated isomers in phosphate buffer solution of pH 7.4, in rat plasma, and in human plasma at 37 °C for 48 h. Only minor reoxidation (<3%) of the metal center to $^{188}ReO_4^-$ could be observed in phosphate buffer solution during this time. Moreover, the isomers were absolutely stable in rat and human plasma solutions. Both isomers of complex **I** were also stable against isomerization at pH 2, 7, and 9. The challenge experiments with cysteine corroborated the high stability of the cis and trans isomers. They were completely inert toward ligand exchange in the cysteine solution. The isomers of complex **II** were stable in acidic and neutral solutions. At pH values higher than 8 they were converted to unknown products which were eluted in HPLC between 12 and 15 min. These products were also observed as impurities in low yields in the reaction solution (Figure 5).

***In Vivo* Stability and Biodistribution.** Samples of rat plasma, urine, kidneys, and contents of intestine were analyzed by HPLC and TLC 1 and 2 h postinjection of the isomers. Neither perrhenate nor other metabolites were observed in plasma samples of complexes **I** and **II**. However, some metabolites were detected in the intestine and the urine samples of the cis and the trans isomers of complex **I** (Figure 7a and 7b). In both samples a more lipophilic product was observed which was eluted at about 9.5 min. Additionally, perrhenate

and other hydrophilic products were found in the urine samples. Between 60 and 70% of the total injected dose of complex **I** was found in the intestine 2 h postinjection. Considering the predominant hepatobiliary excretion pathway of complex **I**, it can be concluded that only a very low part of the administered ^{188}Re complex is reoxidized *in vivo*. There are no differences concerning the *in vivo* stability between the cis and the trans isomers. That applies to the isomers of complex **II** too. Because of their high hydrophilicity they were excreted *via* the renal and the hepatobiliary pathway. Therefore, urine samples were analyzed by HPLC (Figure 7c). No perrhenate was detected in the urine samples. That demonstrates again the high *in vivo* stability of the ^{188}Re−S_4 complexes.

Biodistribution studies in male Wistar rats were performed with the cis and trans isomers of complex **I** and the three isomers of complex **II** to investigate their organ uptake and excretion pathways. Generally, a fast clearance of radioactivity within 1 h from significant organs and the blood was observed. As shown in Table 2, the lipophilic isomers of complex **I** were preferentially excreted *via* the hepatobiliary pathway. Meanwhile, no increase of radioactivity was found in the stomach indicating high *in vivo* stability of the cis and trans isomers, respectively. In contrast to complex **I**, the hydrophilic isomers of complex **II** were excreted *via* the kidneys as well as the hepatobiliary pathway. The concentration of the isomers 2 and 3 in the kidneys was around three times higher than that of isomer 1. Correspondingly, the concentration of isomer 1 in the liver was higher than the concentration of isomers 2 and 3. All three isomers exhibited a remarkable high in vivo stability. The observed differences in the elimination behavior could hence be due to varying affinities to plasma proteins, the transport to the elimination organs, or other parts of the biological system. This has to be further investigated.

CONCLUSIONS

Two routes for carrier-free preparations of a new type of ^{188}Re−S_4 complexes were studied and the reaction conditions were optimized. A kit formulation was developed which contains only microgram amounts of the S_4 ligand stabilized in the form of a stannous complex. The ^{188}Re−S_4 complexes were found to be stable toward reoxidation and ligand exchange *in vitro* and *in vivo*. Their charge and lipophilicity may be controlled by various possibilities to introduce functional groups. The bridging amine group of the ligand framework makes available a reactive position for coupling biomolecules to the chelate. Summarizing, it can be concluded that the new ^{188}Re−S_4 complexes offer the possibility of stable and high specific activity labeling of biomolecules for therapeutic application.

LITERATURE CITED

(1) Knapp, F. F. (1998) Rhenium-188—a generator-derived radioisotope for cancer therapy. *Cancer Biother. Radiopharm. 13*, 337−349.

(2) Knapp, F. F., Beets, A. L., Guhlke, S., Zamora, P. O., Bender, H., Palmedo, H., and Biersack, H.-J. (1997) Availability of rhenium-188 from the alumina-based tungsten-188/rhenium-188 generator for preparation of rhenium-188-labeled radiopharmaceuticals for cancer treatment. *Anticancer Res. 17*, 1783−1796.

(3) Jeong, J. M., and Chung, J.-K. (2003) Therapy with ^{188}Re labeled radiopharmaceuticals: an overview of promising results from initial clinical trials. *Cancer Biother. Radiopharm. 5*, 707−717.

(4) Alberto, R., Schibli, R., Angst, D., Schubiger, P. A., Abram, U., Abram, S., and Kaden, T. A. (1997) Application of technetium and rhenium carbonyl chemistry to nuclear medicine. *Trans. Met. Chem. 22*, 597−601.

(5) Schibli, R., Schwarzbach, R., Alberto, R., Ortner, K., Schmalle, H., Dumas, C., Egli, A., and Schubiger, P. A. (2002) Steps toward high specific activity labeling of biomolecules for therapeutic application: preparation of precursor $[^{188}Re(H_2O)_3(CO)_3]^+$ and synthesis of tailor-made bifunctional ligand systems. *Bioconjugate Chem. 13*, 750−756.

(6) Boschi, A., Bolzati, C., Uccelli, L., and Duatti, A. (2003) High-yield synthesis of the terminal ^{188}Re≡N multiple bond from generator-produced $[^{188}ReO_4]^-$. *Nucl. Med. Biol. 30*, 381−387.

(7) Seifert, S., Künstler, J.-U., Schiller, E., Pietzsch, H.-J., Pawelke, B., Bergmann, R., and Spies, H. (2004) Novel procedures for preparing ^{99m}Tc complexes with tetradentate/monodentate coordination of varying lipophilicity and adaption to ^{188}Re analogues. *Bioconjugate Chem. 15*, 856−863.

(8) Schiller, E., Seifert, S., Tisato, F., Refosco, F., Kraus, W., Spies, H., and Pietzsch, H.-J. (2005) Mixed-ligand rhenium-188 complexes with tetradentate/monodentate NS_3/P ('4+1') coordination: relation of structure with antioxidation stability. *Bioconjugate Chem. 16*, 634−643.

(9) Davison, A., Jones, A. G., Orvig, C., and Sohn, M. (1981) A new class of oxotechnetium (5+) chelate complexes containing a $TcON_2S_2$ core. *Inorg. Chem. 20*, 1629−1632.

(10) Rao, T. N., Adhikesavalu, D., Camerman, A., and Fritzberg, A. R. (1990) Technetium(V) and rhenium(V) complexes of 2, 3-bis-(mercaptoacetamido)propanoate: chelate ring stereochemistry and influence on chemical and biological properties. *J. Am. Chem. Soc. 112*, 5798−5804.

(11) Guhlke, S., Schaffland, A., Zamora, P. O., Sartor, J., Diekman, D., Bender, H., Knapp, F. F., and Biersack, H.-J. (1998) ^{188}Re- and ^{99m}Tc-MAG_3 as prosthetic groups for labeling amines and peptides: approaches with pre- and postconjugate labeling. *Nucl. Med. Biol. 25*, 621−631.

(12) Heinrich, T., Kraus, W., Pietzsch, H.-J., Smuda, C., and Spies, H. (2005) A novel rhenium chelate system derived from dimercaptosuccinic acid for the selective labeling of biomolecules. *Inorg. Chem. 44*, 9930−9937.

(13) Seifert, S., Gupta, A., Syhre, R., Spies, H., and Johannsen, B. (2001) Ligand-exchange reaction of labile "3+1" ^{99m}Tc(V) complexes with SH group-containing proteins. *Appl. Radiat. Isot. 54*, 637−644.

(14) Blower, P. J., Lam, A. S. K., O' Doherty, M. J., Kettle, A. G., Coakley, A. J., and Knapp, F. F., Jr. (1998) Pentavalent rhenium-188 dimercaptosuccinic acid for targeted radiotherapy: synthesis and preliminary animal and human studies. *Eur. J. Nucl. Med. 25*, 613−621.

(15) Bolzati, C., Boschi, A., Uccelli, L., Duatti, A., Franceschini, R., and Piffanelli, A. (2000) An alternative approach to the preparation of ^{188}Re radiopharmaceuticals from generator-produced $[^{188}ReO_4]^-$: efficient synthesis of ^{188}Re(V)-*meso*-2, 3-dimercaptosuccinic acid. *Nucl. Med. Biol. 27*, 309−314.

(16) Seifert, S., and Pietzsch, H.-J. (2006) The ^{188}Re(III)-EDTA complex—a multipurpose starting material for the preparation of relevant ^{188}Re complexes under mild conditions. *Appl. Radiat. Isot. 64*, 223−227.

BC0602331

TECHNICAL NOTES

Multiplex Analysis with Peptide-Encoded Beads

Nuria Sanvicens, Paul Galvin,† and Thomas G. Cotter*

Cell Development and Disease Laboratory, Department of Biochemistry, Bioscience Research Institute, University College, Cork, and Tyndall National Institute, University College Cork, Lee Maltings, Prospect Row, Cork, Ireland.
Received January 17, 2006; Revised Manuscript Received July 3, 2006

Paramagnetic beads have considerable potential as identification tags in biological analysis. For example, magnetic sensor-based arrays using the magnetic field generated by paramagnetic beads to test hybridization between interacting molecules have attracted widespread interest in recent years. However, application of paramagnetic beads as identification tags is still limited, since they do not permit differentiation between samples for multiplex analysis. Here, we report the application of a novel encoding of paramagnetic beads with peptide sequences. This strategy allows DNA samples labeled with peptide-encoded paramagnetic beads to be identified by the selective enzymatic cleavage of each peptide cross-linker.

INTRODUCTION

Paramagnetic beads have been extensively used for the preparation, separation, transportation, and detection of biological molecules such as DNA, due to their efficiency, simplicity, and low cost (*1*−*4*). More recently, paramagnetic particles have also been used as labels for target DNA in microarray applications, where, in the presence of an external magnetic field, the field from the paramagnetic bead labels can be detected using an array of integrated magnetic sensors (e.g., giant magnetoresistance (GMR) sensors), thereby enabling the detection of DNA hybridization (*5*−*8*). However, the range of applications that can utilize paramagnetic beads has been limited due to the difficulty of distinguishing between different particles based on magnetic properties, and hence, they do not permit differentiation between samples for multiplexed analysis (e.g., parallel analysis of a test and control sample in a single reaction as is done using different fluorophores for gene expression analysis). Therefore, methods are required that enable paramagnetic bead based assays to be multiplexed. In this report, paramagnetic beads have been encoded using different peptide sequences, which are each cleavable by a specific enzyme. This novel approach based on an enzymatic cleavage methodology enables differentiation between beads (and hence samples). Using this approach, we have labeled oligonucleotides with different peptide-encoded paramagnetic beads. Subsequent identification of each oligonucleotide was possible through selective enzymatic cleavage of peptide cross-linkers from the paramagnetic beads.

EXPERIMENTAL PROCEDURES

Chemicals and Oligonucleotides. EDC (1-ethyl-3-(3-dimethylaminopropyl)-carbodiimide), sulfo-NHS (sulfo-*N*-hydroxysuccinimide), PDITC (4-phenylenediisothiocyanate), 3-aminopropyltrimethoxysilane, proteinase K, and organic solvents were purchased from Sigma Chemical Co. (Poole, U.K.). Oligonucleotides were obtained from MWG Biotech (Ebersberg, Germany). Chymotrypsin was purchased from Calbiochem (La Jolla, CA).

Target DNA Labeling with Peptide-Tagged Paramagnetic Beads. Preparation of peptide-tagged paramagnetic beads to was done as follows: 1 μm paramagnetic beads (Roche; Roche Diagnostics Ltd., Sussex, U.K.) coated with streptavidin were washed in twice their volume of PBS (phosphate-buffered saline) buffer giving a final concentration of 5 mg/mL. A magnetic separator was used to remove the beads from solution. Then, 2 pmol of a biotin-terminated oligonucleotide (sequences used were GGGG (peptide G) and GGFG (peptide F); Bachem UK Ltd., Merseyside, U.K.) were added for every 1 μL of bead solution, and the mixture was allowed to react for 2 h at room temperature while rotating at a speed of 30 rpm. Following the conjugation of the peptide to the beads, the free carboxylic end of the peptide was activated by means of EDC chemistry as follows: 20 pmol EDC and 20 pmol sulfo-NHS were added into the bead solution for every picamole of peptide, and the resulting mixture was shaken for 3 h at room temperature. Subsequently, labeling of target DNA with peptide-tagged paramagnetic beads was done as follows: a 1:50 dilution of the solution containing the activated peptide-tagged beads was prepared in 0.15 M borate buffer pH 8.5, and 4 μM of target DNA were added into it and the mixture allowed to react for 3 h at room temperature while rotating at a speed of 30 rpm.

Specificity Studies of Oligonucleotide Attachment onto the Peptide-Tagged Bead Surface. Studies were done using oligonucleotide F. Fluorescence intensity was compared between blank solutions containing beads, peptide-encoded tagged beads (peptide G), and samples containing oligonucleotide F modified with cy3 and labeled with peptide-tagged paramagnetic beads (peptide/oligonucleotide ratios 1:1, 1:2.5, 1:5, and 1:10). Fluorescence intensity was measured at 560 nm (excitation at 510 nm) with a FlexStation II instrument (Molecular Devices, Wokingham, U.K.) at room temperature.

* To whom correspondence should be addressed. Prof. Thomas G Cotter, Cell Development and Disease Laboratory, Department of Biochemistry, Bioscience Research Institute, University College, Cork, Ireland. E-mail: t.cotter@ucc.ie, Phone: +353 21 490 1321, FAX: +353 21 490 1377.

† Tyndall National Institute.

10.1021/bc060008j CCC: $33.50 © 2006 American Chemical Society
Published on Web 10/25/2006

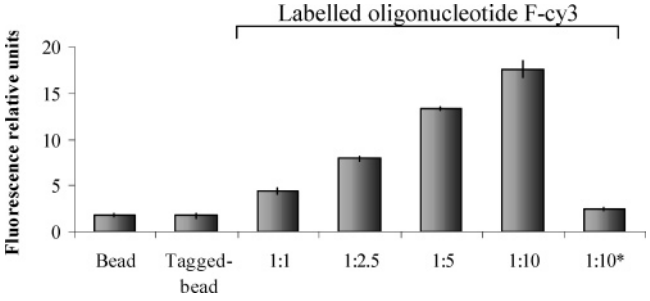

Figure 1. Specific binding of a 20mer oligonucleotide to peptide-encoded beads. Fluorescence studies demonstrated specific binding of oligonucleotide F-cy3 (5′-GTGACTTCCCCTAAATATAA-3′; modifications: 5′ amino-modifier C12 and 3′ Cy3) to paramagnetic beads encoded with peptide G. A peptide/oligonucleotide ratio of 1:10 rendered the maximum coupling yield with no indication of nonspecific binding (coupling in sample 1:10* was performed without EDC and supho-NHS). The data shown represent mean ± SD (standard deviation) of three independent experiments.

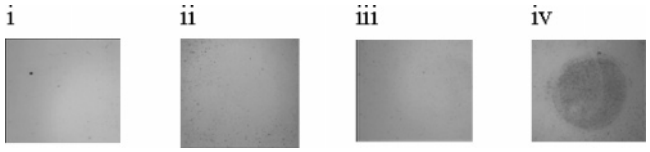

Figure 2. Hybridization and control experiments with peptide-encoded paramagnetic beads. Oligonucleotides G and F were labeled with peptide-encoded beads (G). Substrate contained the oligonucleotide comp-F, which is complementary to oligonucleotide F but not to G. Examples where (i) substrate has no oligonucleotide on it, (ii) beads have no oligonucleotide but the substrate does, (iii) the substrate and the peptide-encoded beads have noncomplementary oligonucleotide sequences (comp-F and G, respectively), and (iv) the substrate and the peptide-encoded beads have complementary oligonucleotide sequences (comp-F and F, respectively). Figures are representative of an experiment performed in triplicate. Images were acquired using a Zeiss Axioskop II Plus epi-fluorescence microscope equipped with an Optronics DEI-750 CCD camera and appropriate filter sets.

Surface Functionalization. Deposition and covalent immobilization of synthetic DNA probes onto the array surface involved substrate cleaning and deposition of a silane anchor layer, followed by the addition of a PDITC homobifunctional linker molecule, to facilitate the covalent binding of the oligonucleotides (see Scheme 2). Substrates were cleaned by sonication in trichlorethylene (10 min), immersion in acetone at 50 °C (10 min), sonication in isopropyl alcohol (10 min), followed by drying in N_2. For deposition of the anchor layer, 3-aminopropyltrimethoxysilane (3% v/v) was reacted with the free hydroxyl groups on the surface by sonication in ambient temperature using a in a 95:5 methanol/water solution, then sequentially rinsed in methanol and water and dried in N_2. Following this, substrates were cured at 120 °C (15 min). Covalent attachment of the amino-terminated oligonucleotide probes was mediated by activation of the amino silanated substrates with a PDITC homobifunctional crosslinker. For this, the amino silanated substrates were immersed in a 40 mL solution of 1 mM PDITC in 10% v/v anhydrous pyridine/dimethylformamide (DMF, 2 h), followed by thorough sequential rinsing with DMF and dichloroethane, and then drying in N_2.

Oligonucleotide Probe Patterning and Immobilization over Functionalized Substrate. Deposition of unlabeled amino modified oligonucleotide comp-F was performed using a Staedtler technical drawing pin to print 0.5 mL of a 4 μM oligonucleotide solution in 1% *N*,*N*-diisopropylethylamine Tris-HCl buffer. Substrates were then placed in a humid atmosphere at 37 °C overnight. After immobilization, substrates were washed in a 0.1% SDS solution at 60 °C (10 min) and dried in N_2. Following this, substrates were immersed in 0.1% milk PBS buffer for 2 h to deactivate any remaining unreacted surface-bound isothiocyanate groups to prevent nonspecific binding of target DNA or beads during hybridization. Finally, substrates were rinsed thoroughly in water and dried in N_2.

DNA Hybridization. A solution comprising 5 mg/mL of paramagnetic bead-labeled target DNA suspended in 20 μL hybridization buffer (3× SSPE) was introduced onto the array surface. Hybridization was carried out at room temperature for 3 h. Substrate surface was then rinsed with deionized water to remove nonspecifically bound beads, so that only beads immobilized by selective hybridization of target DNA to complementary probes remained.

Enzyme Studies. Cleavage and Removal of Beads. Release of the beads attached to oligonucleotide F through peptide F was done using chymotrypsin, which specifically cleaves the sequence containing phenylalanine while leaving the sequence containing glycine intact (beads tagged with the peptide G remain attached to oligonucleotide F). A solution containing 200 ng of chymotrypsin was prepared in 100 M Tris 10 mM $CaCl_2$ buffer (pH 7.8). Then, 20 μL of the enzyme solution was added onto the chip surface and incubated for 3 h at 37 °C. Following this, the substrate surface was rinsed with deionized water to remove cleaved beads, so that only beads attached to oligonucleotide F through peptide G remained. Selective release of beads attached through peptide F was then visualized by fluorescence imaging. Subsequently, beads attached to oligonucleotide F through peptide G were released using the peptidase proteinase K. For this purpose, a saturated solution of proteinase K was prepared in 100 M Tris 10 mM $CaCl_2$ buffer (pH 7.8). Then, 20 μL of the enzyme solution were added onto the substrate surface and incubated for 3 h at 37 °C. Subsequently, the surface was rinsed with deionized water to remove the remaining beads. Selective release of beads attached through peptide G was then visualized by fluorescence imaging. Images were acquired using an Axioskop II Plus epi-fluorescence microscope equipped with an optronics DEI-750 CCD camera and appropriate filter sets. Imagines were analyzed using *Image Pro Express* software (Media Cybernetics).

RESULTS AND DISCUSSION

Paramagnetic beads were encoded by coating them with one of two different peptide sequences: G or F (Scheme 1, step 1). Each peptide comprised a 4 amino acid sequence with the amino end modified with a biotin molecule (Table 1). In this manner, attachment of the peptides to the surface of streptavidin-coated paramagnetic beads was done by means of a biotin−streptavidin conjugation. In a second step, oligonucleotides were labeled with the peptide-encoded beads. This step comprised the attachment of the oligonucleotide containing a 5′-amino group (Table 1) to the free carboxylic end of the specific amino acid sequence of the peptide-encoded bead using carbodiimide chemistry in a buffered solution (Table 2). In this manner, the peptide remained as a cross-linker between the bead and the target DNA sequence (Scheme 1, step 2). To control the number of DNA oligonucleotide molecules per peptide-encoded bead and to minimize nonspecific attachment onto the bead surface, we optimized the peptide/oligonucleotide ratio in the coupling reaction to 1:10. Figure 1 illustrates how a 1:10 peptide/oligonucleotide ratio yielded the maximum fluorescence intensity from all the proportions assayed. Lack of fluorescence in a sample, in which the coupling reaction of oligonucleotide F modified with cy3 onto the beads had been done without EDC and sulfo-NHS, confirmed specific attachment of the oligonucleotide onto the bead surface. Peptide/oligonucleotide ratios higher than 1:10 rendered nonspecific attachment of the oligonucleotide onto the bead surface (data not shown).

Specific hybridization of target DNA labeled with peptide-encoded paramagnetic beads to the complementary DNA

Scheme 1. Scheme of the Strategy for Labeling and Differencing DNA Oligonucleotide Target Sequences with Peptide-encoded Paramagnetic Beads[a]

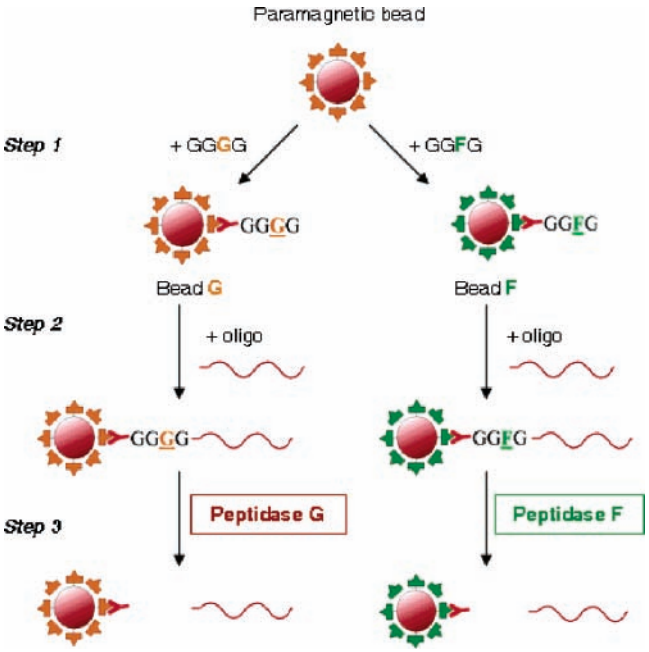

[a] The first step comprises encoding paramagnetic beads with different peptide sequences (G or F in the example). In a subsequent step, DNA oligonucleotide targets are labeled with peptide-encoded paramagnetic beads. In this manner, the peptide sequence remains as a cross-linker between the bead and the target oligonucleotide. Then, each target DNA oligonucleotide can be selectively recognized by cleavage of the peptide sequence with a specific peptidase (peptidase F will cleave peptide F but not G). This strategy allows multiplexed analysis in paramagnetic bead based assays.

Table 1. Sequences of Peptides and DNA Oligonucleotides[a]

name	sequence
Peptide G	Bt-GGGG-COOH
Peptide F	Bt-GGFG-COOH
Oligonucleotide G	5′-GTACTCTATTTGTAGGTTCTTACGT−3′
Oligonucleotide F	5′-GTGACTTCCCCTAAATATAA−3′ Modification: 5′ amino-modifier C12
Oligonucleotide comp-F	5′-TTA TAT TTA GGG GAA GTC AC−3′ Modification: 5′ amino-modifier C12

[a] Bt, biotin; comp, complementary.

Table 2. Scheme of Labeling a DNA Oligonucleotide Sequence with Peptide-Encoded Paramagnetic Beads[a]

1	Bead-SA + Bt-G-COOH → Bead-**SA-Bt**-G-COOH
2	Bead-SA-Bt-G-COOH + oligonucleotide F-NH_2 → Bead-SA-Bio-G-**CONH**-oligonucleotide-F

[a] SA, streptavidin; Bt, biotin.

sequence attached onto an array surface was investigated. Surface functionalization and oligonucleotide patterning and immobilization over the substrate were carried out as previously described (*9*) (see Scheme 2). Control studies were performed to investigate nonspecific interaction onto the substrates of target DNA labeled with peptide-encoded beads. Furthermore, hybridization conditions were optimized to achieve specific hybridization of target oligonucleotide (F) to complementary sequences (oligonucleotide comp-F). A concentration of beads of 5 mg/mL produced the best results. We found higher concentrations of beads to produce nonspecific binding onto the substrate and lower concentrations to render poor density of bead spots. Under the optimized conditions, assays were carried out in which either the substrate (Figure 2i) or the beads (Figure 2ii) did not bear DNA. Control experiments demonstrated that nonspecific binding was minimal. As illustrated in Figure 2, bead spots were only distinctly observed when the oligonucleotide attached to the bead was complementary to the one on the substrate (noncomplementary oligonucleotide G, Figure 2iii; complementary oligonucleotide F, Figure 2iv).

Scheme 2. Scheme of the Surface Functionalization, Oligonucleotide Immobilization, and Hybridization of Complementary Probe Labeled with Peptide-Encoded Paramagnetic Beads

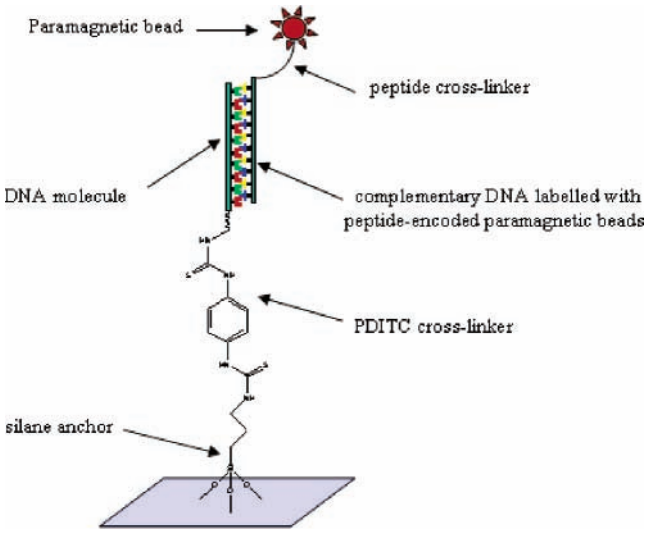

The peptidase chymotrypsin selectively hydrolyzes peptide sequences at bonds involving the carboxyl group of aromatic L-amino acids such as phenylalanine (F). Therefore, we chose chymotrypsin as the peptidase for releasing paramagnetic beads tagged with peptide F. Since chymotrypsin does not cleave nonaromatic L-amino acids such as glycine (G), paramagnetic beads encoded with the peptide G should remain unaffected after chymotrypsin treatment. Then, for releasing of beads cross-linked with peptide G, we chose the general peptidase proteinase K. Studies to evaluate the enzymatic activity of chymotrypsin and proteinase K were performed on glass slides, in which for simplification oligonucleotide probes labeled with peptide-encoded fluorescent tags were immobilized. Under these conditions, concentration of enzyme, reaction time, and temperature were optimized to achieve maximum activity and selectivity toward each peptide sequence (Figure 3). Subsequently, selective cleavage of peptide-encoded paramagnetic beads from target oligonucleotides by a specific peptidase was investigated. Oligonucleotide F encoded with either beads G or F was hybridized to oligonucleotide comp-F attached onto the substrate surface. In a first step, substrates were treated with chymotrypsin, which only removed beads encoded with peptide F (Figure 4a). Under these conditions, beads encoded with peptide G remained unaltered on the substrate surface. Subsequent treatment with proteinase K cleaved the beads encoded with peptide G. Neither treatment with chymotrypsin nor treatment with proteinase K affected the density of beads on the control spot (beads with no peptide linker). Therefore, our results demonstrate that the enzymatic cleavage approach allows the selective removal of the beads from the substrate surface.

CONCLUSIONS

This report proposes a strategy for encoding paramagnetic beads by labeling them with different peptide sequences. It has been demonstrated that samples labeled with encoded paramagnetic beads can be subsequently identified by the selective enzymatic cleavage of each peptide cross-linker. Using this approach, we have been able to differentiate between beads

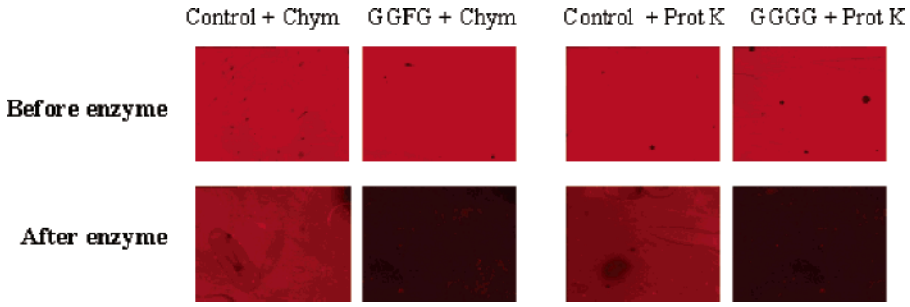

Figure 3. Selective cleavage of fluorophores from glass surface. Oligonucleotide F labeled with peptide-tagged fluorophores (fluorophore is streptavidin, Alexa Fluor; Bio Sciences, Ltd., Dun Laoghaire, Ireland) was immobilized onto a glass surface as described in the Experimental Procedures section. Conditions were optimized for selective recognition and hydrolysis of peptide F and peptide G by chymotrypsin and proteinase K, respectively. Both chymotrypsin and proteinase K successfully removed the fluorophores encoded with peptide F and G, respectively, from the glass surface resulting in a significant decrease of fluorescence, while only a slight lost of fluorescence was observed in controls (fluorophores without the peptide). Images were acquired using a Zeiss Axioskop II Plus epi-fluorescence microscope equipped with an Optronics DEI-750 CCD camera and appropriate filter sets.

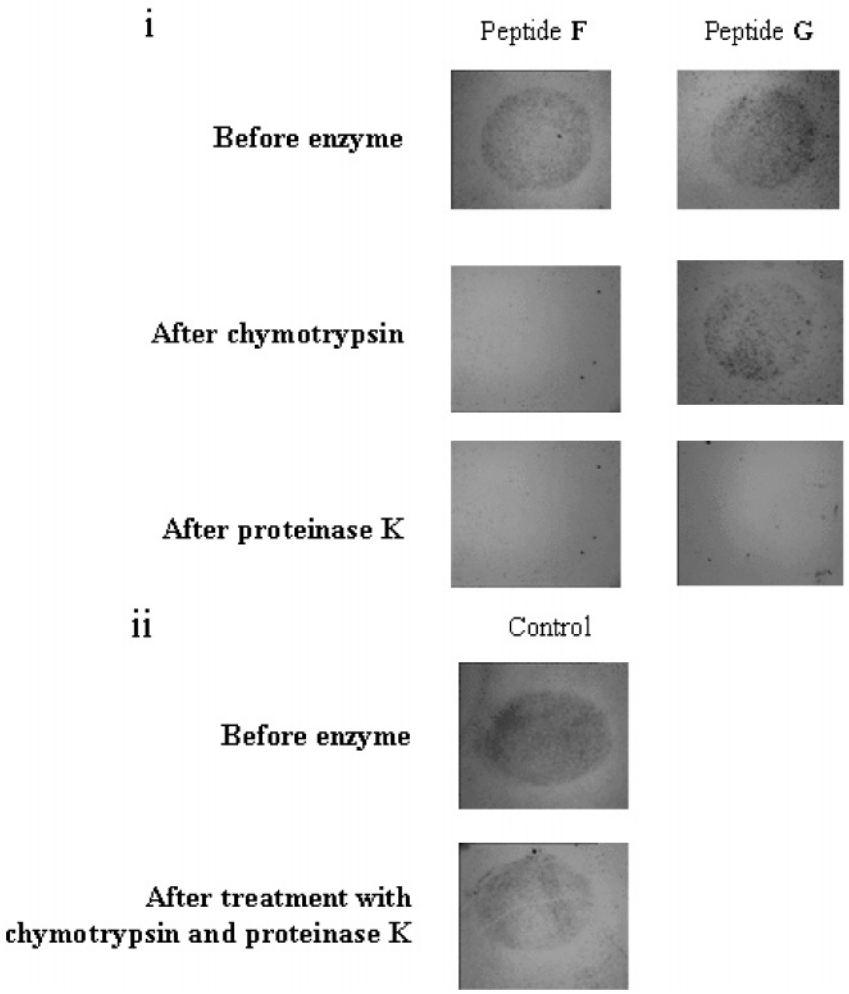

Figure 4. Demonstration of selective enzymatic cleavage of peptide-encoded paramagnetic beads, where oligonucleotide comp-F was immobilized onto the substrate surface by means of covalent chemistry. (i) Hybridization with Oligonucleotide F labeled with peptide-encoded paramagnetic beads (i.e., Bead F or Bead G) was then performed. In a first step, release of the beads encoded with Peptide F was done using chymotrypsin where beads tagged with Peptide G and control beads (beads with no peptide cross-linker) remained intact. Subsequently, beads encoded with Peptide G were released using the generic enzyme, Proteinase K. In this manner, selective enzymatic cleavage of the peptide linkers enabled differentiation between beads, and thereby enabled differentiation between the attached oligonucleotides. Figures are representative of an experiment done in triplicate. (ii) Controls were done with Oligonucleotide F labeled with paramagnetic beads with no peptide cross-linker. Images were acquired using a Zeiss Axioskop II Plus epi-fluorescence microscope equipped with an Optronics DEI-750 CCD camera and appropriate filter sets

encoding different target DNA oligonucleotides. Interestingly, this strategy is not restricted to encoding of paramagnetic beads, but it can also be used to label supports of any nature (for example, nanocrystals, gold nanoparticles, glass beads). While some micro- and nanoparticles are distinguishable on the basis of different colors (or if fluorescent, on the basis of different excitation and emission spectra), the sensitivity achievable with sensor systems necessary to enable color imaging is typically

much less than that achievable with equivalent monochrome technology. Therefore, the present methodology can be employed to increase the multiplicity in any kind of biological assay. Moreover, in addition to the possibility of simultaneous analysis of multiple samples, this approach allows modulation of the bead characteristics by introducing a large number of distinguishable sequences. Brust and co-workers have already reported that functionalized peptide binding to nanoparticle permits introducing multiple functionalities onto gold nanoparticles (*10*). We contemplate that properties related to hydrophobicity and charge of the encoded beads could also be modulated in a controlled manner by modifying the nature and the number of the nonrelevant amino acids comprising the peptide sequence. Undoubtedly, this would have an impact on the hybridization efficiency. This approach could also be adapted to create dynamic substrates, in which the surface properties could be selectively modified in a spatial manner, by patterning of different molecules that would be tethered to the substrate by different peptide sequences, and by subsequent selective cleavage of molecules in an ordered manner.

ACKNOWLEDGMENT

This study was supported by funds from the European Union (contract number QLK3-CT-2001-01982).

LITERATURE CITED

(1) Isalan, M., Santori, M., Gonzalez, C., and Serrano, L. (2005) *Nat. Methods 2*, 113−118.
(2) Brzeska, M., Panhorst, M., Kamp, P., Schotter, J., Reiss, G., Puhler, A., Becker, A., and Bruckl, H. (2004) *J. Biotechnol. 112*, 25−33.
(3) Scherfer, C., Karlsson, C., Loseva, O., Bidla, G., Goto, A., Havemann, J., Dushay, M., and Theopold, U. (2004) *Curr. Biol. 14*, 625−629.
(4) Wang, Z., and Jones, M. (2003) *Methods Mol. Biol. 221*, 25−31.
(5) Fan, Z., Mangru, S., Granzow, R., Heaney, P., Ho, W., Dong, Q., and Kumar, R. (1999) *Anal. Chem. 71*, 4851−4859.
(6) Edelstein, R., Tamanaha, C., Sheehan, P., Miller, M., Baselt, D., Whitman, L., and Colton, R. (2000) *Biosens. Bioelectron. 14*, 805−813.
(7) Graham, D., Ferreira, H., and Freitas, P. (2004) *Trends Biotechnol. 22*, 455−462.
(8) Lagae, L., Wirix-Speetjens, R., Liu, C., Laureyn, W., De Boeck, J., Borghs, G., Galvin, P., Graham, D., Ferreira, H., Freitas, P., Amaral, M., and Clarke, L. (2005) *IEE Proceedings, Part G: Circuits, Devices and Systems 152*, 393−400.
(9) Manning, M., Harvey, S., Galvin, P., and Redmond, G. (2003) *Mater. Sci. Eng. C 23* 347−351.
(10) Wang, Z., Levy, R., Fernig, D., and Brust, M. (2005) *Bioconjugate Chem. 16*, 497−500.

BC060008J

Synthesis of Fluorescent Analogs of α-Conotoxin MII

Vijay A. Vishwanath[†] and J. Michael McIntosh*[,‡]

Interdepartmental Program in Neuroscience and Departments of Psychiatry and Biology, University of Utah, Salt Lake City, Utah 84112. Received June 9, 2006; Revised Manuscript Received August 23, 2006

α-Conotoxins (α-CTxs) are small peptides that are competitive inhibitors of nicotinic acetylcholine receptors (nAChRs) and have been used to study the kinetics of nAChRs. α-CTx MII, from the venom of *Conus magus*, has been shown to potently block both rat α3β2 and rat chimeric α6/α3β2β3 cloned nAChRs expressed in *Xenopus* oocytes. Tetramethylrhodamine (TMR), Bodipy FL, Alexa Fluor 488, and terbium chelates (TbCh) are fluorescent molecules that can be reacted with the N-terminus of the conopeptide to produce fluorescent conjugates. TMR and Bodipy FL were individually conjugated to α-CTx MII using different succinimidyl ester amine labeling reactions resulting in the formation of carboxamide conjugates. Alexa Fluor 488 succinimidyl ester conjugation reaction yielded low amounts of conjugate. TbCh was also individually reacted with the N-terminus of MII using the isothiocyanate conjugation reaction resulting in the formation of a thiourea conjugate. The conjugates were purified using reverse-phase high-pressure liquid chromatography (RP-HPLC) and their masses verified by matrix-assisted laser desorption-ionization with time-of-flight mass spectroscopy (MALDI-TOF MS). When tested on target nAChRs expressed in *Xenopus* oocytes, TMR−MII, Bodipy FL−MII, and TbCh−MII potently blocked the response to acetylcholine with slow off-rate kinetics. These fluorescent conjugates can be used to localize specific subtypes of neuronal nAChRs or ligand-binding sites within receptors in various tissue preparations; additionally, they may also be used to study conformational changes in receptors using fluorescence or lanthanide-based resonance energy transfer.

INTRODUCTION

The venom of *Conus* (cone snail) contains diverse pharmacologically active peptides (*1*). Conotoxins are disulfide-rich peptide toxins that act at ligand-gated ion channels and voltage-gated ion channels. α-Conotoxins (α-CTxs) are small peptides that competitively inhibit nicotinic acetylcholine receptors (nAChRs) and have been used extensively to study and differentiate specific subtypes of nAChRs. Some α-CTxs also bind with different affinities to the individual acetylcholine-binding sites on nAChRs. α-CTxs are thus ligands of choice to study localization, differentiation, and kinetics of specific subtypes of nAChRs (*2*−*5*). α-CTxs may act on either muscle or neuronal nAChRs (*2*−*5*). Most α-CTxs generally have four cysteines, with disulfide connectivities between the first and third cysteines and between the second and fourth cysteines. On the basis of the number of residues in between successive cysteine residues in a two-loop framework, the α-CTxs that act on neuronal nAChRs are further classified into α4/7, α4/3, or α4/4 framework peptides (*5*). α-CTx MII, isolated from the venom of *Conus magus*, is a peptide that has sixteen amino acid residues, with four residues in the first loop and seven residues in the second loop, making it a prototypical α4/7 framework peptide (*6*). The peptide sequence and characteristic disulfide linkage of α-CTx MII are shown in Figure 1. α-CTx MII specifically blocks α3- and α6-containing cloned nAChRs expressed in *X. laevis* oocytes (*6*−*9*). ^{125}I-α-CTx MII has been used to label α3- and α6-containing nAChRs in autoradiography assays (*10*, *11*). Striatal α6-containing nAChRs have been implicated in Parkinson's disease (*12*, *13*). Fluorescent analogs of α-CTx MII would thus provide a novel tool to explore the functional neuroanatomy of α3- and α6-containing nAChRs in the central nervous system.

Fluorophores are functional fluorescent groups that absorb energy of a specific wavelength and emit the energy at a different specific wavelength. Fluorescence labeling, when used in conjunction with a sensitive imaging device (such as a confocal microscope) provides a direct method to visualize molecular interactions with high precision and resolution. An external energy source (like a laser) excites photons, and a photon's energy can be absorbed by a fluorophore creating an excited, unstable electronic singlet state, following which the excited molecules drop to the lowest vibrational energy level within the electronic excited state and then to the ground state. When a fluorophore molecule falls from the excited state to the ground state, the energy of the emitted photon is often emitted at a characteristic wavelength (*14*). A fluorophore can be chemically attached to a nonfluorescent molecule like a peptide (*15*) to produce novel fluorescent conjugate molecules (Scheme 1). Tetramethylrhodamine (TMR) (*16*), Bodipy FL (*17*), Alexa Fluor 488 (*18*), and terbium chelates (TbChs) (*19*) are fluorescent molecules (available as succinimidyl ester, sulfosuccinimidyl ester, carboxylic acid−succinimidyl ester, and isothiocyanate, respectively) that can be reacted with the N-terminus of the conopeptide to produce fluorescent conjugates (Figure 1). Herein, we report the successful synthesis and purification of three different fluorescent analogs of α-CTx MII, namely, TMR−MII, Bodipy FL−MII, and TbCh−MII. The use of conjugation reaction to synthesize fluorescent analogs of conotoxins is particularly appealing because the bond between the fluorophore and peptide is stable to routine storage conditions. The masses of these fluorescent analogs were measured and verified. They were then tested on *X. laevis* oocytes that heterologously expressed rat α6/α3β2β3 nAChRs.

* J. Michael McIntosh, Dept. Biology, University of Utah, 257 South 1400 East, Salt Lake City, UT 84112-0840. Tel. 801-585-3622; Fax 801-585-5010. E-mail: mcintosh.mike@gmail.com.

[†] Interdepartmental Program in Neuroscience.

[‡] Departments of Psychiatry and Biology.

10.1021/bc060163y CCC: $33.50 © 2006 American Chemical Society
Published on Web 10/21/2006

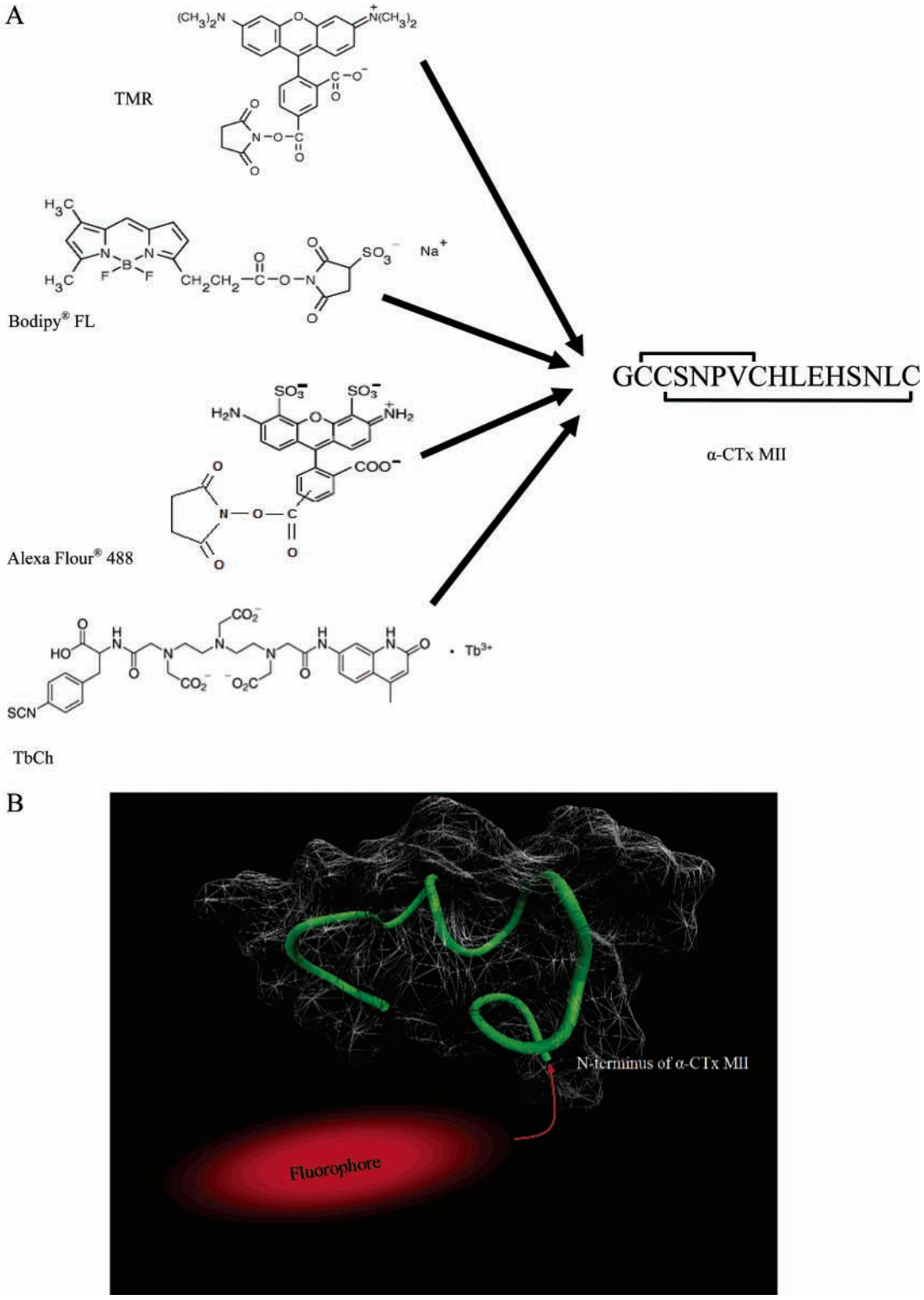

Figure 1. A. The chemical structures of TMR, Bodipy FL, Alexa Fluor 488, and TbCh fluorophores (left) and the peptide sequence and disulfide connectivity of α-CTx MII (right). The conjugation reaction involves interaction of the fluorophores with the free α-amine of the α-CTx MII N-terminus. B. Three-dimensional structure of α-CTx MII with fluorophore being conjugated to the free α-amine of the N-terminus of α-CTx MII.

EXPERIMENTAL PROCEDURES

Materials. TMR, Bodipy FL, and Alexa Fluor 488 (catalog nos. C2211, D6140, and A20000, respectively) were obtained from Molecular Probes, Inc. (Eugene, OR). TbChs (catalog no. P3055) was obtained from PanVera LLC (Madison, WI).

Synthesis and Folding of α-CTx MII. α-CTx MII was synthesized as described earlier (*6*). Briefly, the synthesis was done on an amide resin using Fmoc (*N*-(9-fluorenyl)methoxycarbonyl) chemistry and standard side protection, except on cysteine residues, that were protected in pairs with *S*-trityl on the first and third cysteine residues and *S*-acetamidomethyl on the second and fourth cysteine residues. Following removal from the resin and precipitation, the peptides were folded using a two-step oxidation process using potassium ferricyanide and iodine.

Conjugation Reaction. The dye and the conopeptide were mixed in fixed ratios in the presence of an alkaline buffer, like

Scheme 1. Experimental Design: Synthesis of Fluorescent Analogs of α-CTx MII.

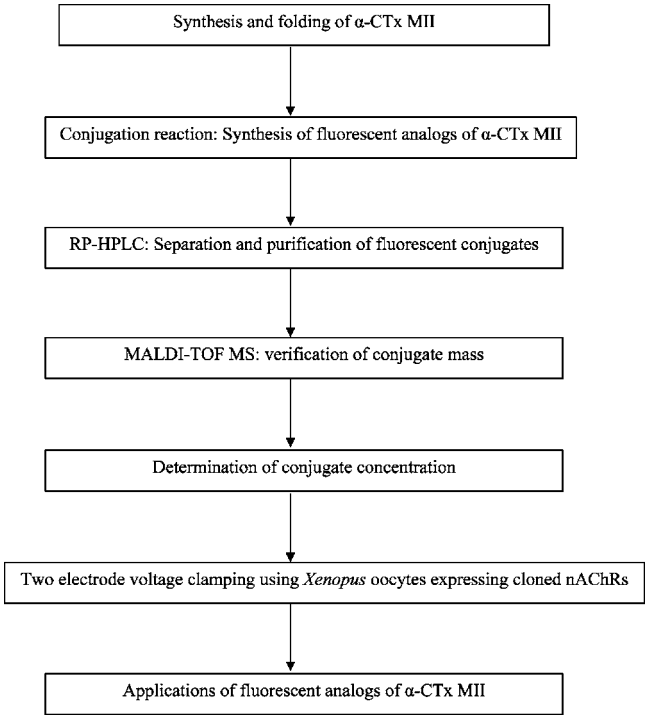

sodium bicarbonate or sodium borate, to enable the conjugation process. The following measures helped in obtaining a higher labeling yield:

(i) The reaction had 3 to 4 molar excesses of dye per toxin peptide.

(ii) The pH of the reaction was kept alkaline (pH range 7.0−8.5).

(iii) The reaction was carried out at room temperature for 1 h and stored overnight at 4 °C.

Acylating reagents are susceptible to degradation in the presence of water molecules, with the rate increasing as the pH increases. Since most of the buffers do contain water molecules, the three measures listed above help in reducing the degradation of the reactants (*14*). The photosensitive dye was protected from UV light throughout the experiments (*15*). There was minimal light exposure during the conjugation reaction and the purification of the conjugated peptides.

RP-HPLC. Analytical reverse-phase high-pressure liquid chromatography (RP-HPLC) with a diode array detector was used to separate the conjugated products from the unconjugated reactants. The analysis and separation of the conjugated products was done on an analytical RP-HPLC using buffers A (0.1% trifluoroacetic acid) and B (0.092% trifluoroacetic acid, 60% acetonitrile) on a Vydac C18 column. The samples tested included the unconjugated parent peptide, unconjugated dye, and the conjugation reaction mixture. The buffer gradients used to purify TMR−MII, Bodipy FL−MII, Alexa Fluor−MII, and TbCh−MII were 25% to 60% B60 in 35 min, 2% to 95% B60 in 40 min, 2% to 70% B60 in 60 min, and 0% to 80% B60 in 40 min, respectively, at a flow rate of 1 mL/min.

The eluents corresponding to the various peaks in the chromatogram were collected, quantitated, and lyophilized. The absorbance of the eluent peak corresponding to the conjugate at 220 nm (A_{220}) and 280 nm (A_{280}) and the emission maximum of the fluorophore (A_{EM}) were measured. Following purification of TbCh−MII using RP-HPLC, the terbium center of the chelate was reconstituted by adding 1.1 equiv of $TbCl_3$ to the purified conjugate.

Mass Spectrometry. The conjugation process was verified by measuring the mass of the conjugates using matrix-assisted laser desorption-ionization with time-of-flight mass spectroscopy (MALDI-TOF MS).

Oocyte Expression and Electrophysiology. When injected with appropriate β nAChR subunits, rat α6 nAChR subunits do not express successfully in *X. laevis* oocytes (*7*, *9*), but they can be functionally expressed as a chimeric receptor with amino acids 1 to 237 of rat α6 nAChR subunit protein linked to amino acids 233 to 499 of the rat α3 nAChR subunit protein (*7*). cRNA was transcribed in vitro, injected in *X. laevis* oocytes, and electrophysiological recording using two-electrode voltage-clamp configuration (model OC-725B; Warner Instrument, Hamden, CT) was done as described previously (*7*). Briefly, 5 ng cRNA of each subunit was injected into stage V *X. laevis* oocytes and incubated at 18 °C. After 3 days, the oocytes were voltage-clamped at −70 mV in a 30 μL cylindrical Sylgard recording chamber perfused with ND96A buffer (96.0 mM NaCl, 2.0 mM KCl, 1.8 mM $CaCl_2$, 1.0 mM $MgCl_2$, 1 μM atropine, and 5 mM HEPES, pH 7.1−7.5) and pulsed with acetylcholine (ACh) every minute. The fluorescent analogs were applied for 5 min in a static bath, followed by monitoring of responses to ACh pulses. Nonspecific adsorption of peptide was reduced by including 0.1 mg/mL bovine serum albumin in buffer and toxin solutions.

RESULTS AND DISCUSSION

Fluorophores. The use of fluorophores to label ligand peptide molecules produces a novel ligand analog that can functionally help in understanding and visualizing receptor−ligand interactions (*14*). TMR, Bodipy FL, and Alexa Fluor 488 are organic fluorophores; TMR has an absorbance maximum of 555 nm and emission maximum of 580 nm, Bodipy FL has an absorbance maximum of 505 nm and emission maximum of 513 nm, and Alexa Fluor 488 has an absorbance maximum of 494 nm and emission maximum of 519 nm. TbChs (a kind of lanthanide chelates) are good alternatives to conventional organic fluorophores because of their distinct structural and spectral characteristics. Structurally, the amine-reactive TbChs used to label peptides are made up of a diethylene triamine pentaacetate (DTPA) chelate with a carbostyril 124 (CS124) antenna and an isothiocyanate functional group. The CS124-DTPA-based terbium chelates have an absorbance maximum of 340 nm, and the emission spectrum has four distinct peaks at 490, 546, 585, and 620 nm. The reaction between the TbCh isothiocyanate and the peptide N-terminus free α-amine results in the formation of a thiourea conjugate.

Conjugation Reaction. α-CTx MII is a prototypical α4/7 α-conotoxin that is composed of 16 amino acid residues. Other important structural characteristics of α-CTx MII are (a) the C-terminal α-carboxyl group of α-CTx MII is amidated, (b) the backbone structure conformation of α-CTx MII is determined by the disulfide bonds, and (c) there are no lysines in the α-CTx MII peptide sequence (*6*). Amine-reactive fluorescent moieties are ideal functional groups that can be conjugated to the N-termini of small peptides. Most commercially available amine-reactive fluorophore moieties are acylating reagents that form carboxamides, thioureas, or sulfonamides upon reaction with amines (*15*). Amine reactive moieties generally react with (a) the free α-amine at the N-terminus or (b) lysine's ϵ-amino group in a peptide. The free α-amine at the peptide N-terminus usually has a pK_a of ∼7 making it selective to modification at near-neutral pH. If the peptide contains lysine in its sequence, the ϵ-amino group of lysine will also be labeled at pH of 8.5 to 9.5 (*14*). Succinimidyl and sulfosuccinimidyl esters of dyes are commonly used in conjugation reactions to label peptides, because they form carboxamide products containing stable

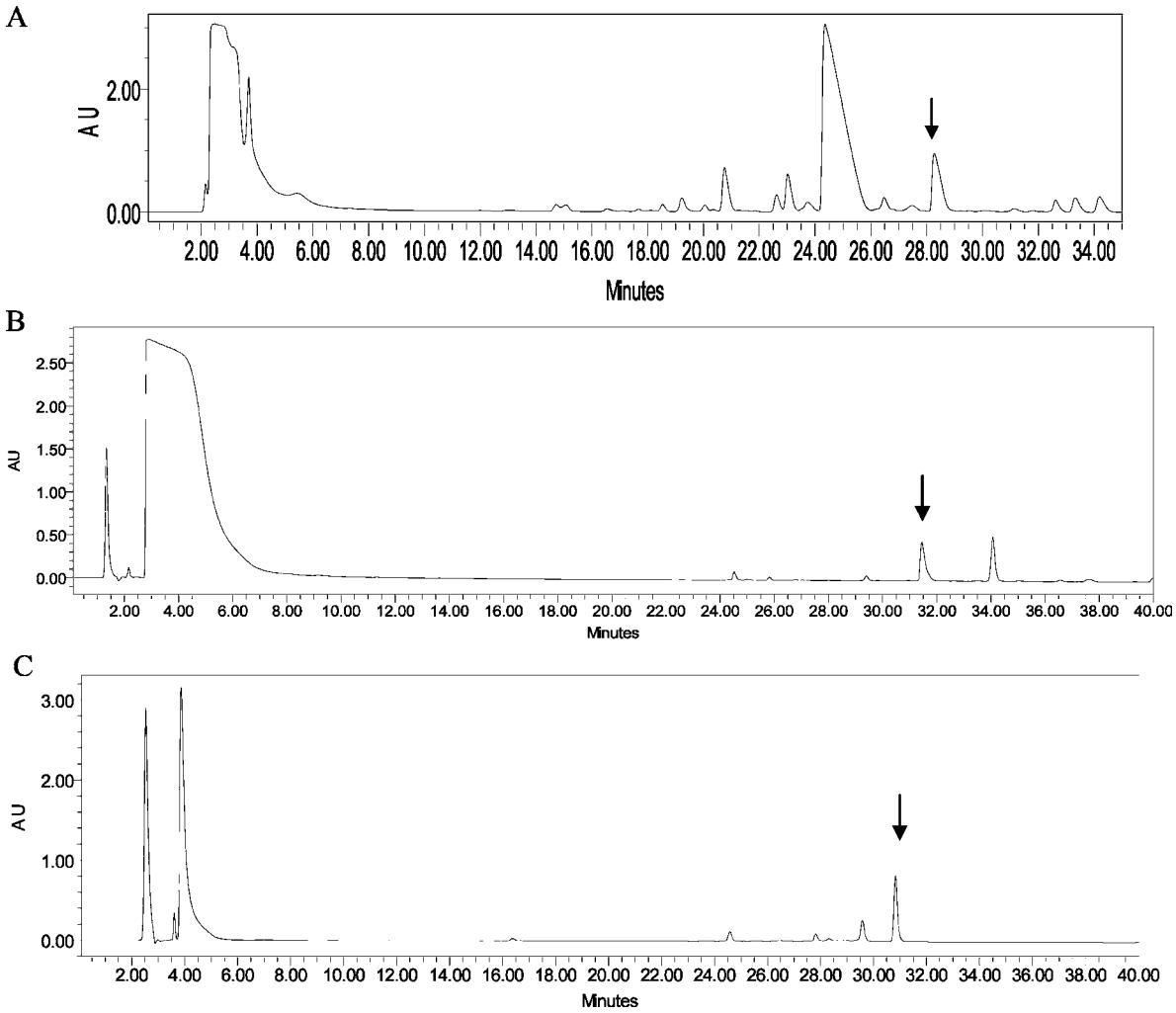

Figure 2. Analysis of the TMR (A), Bodipy FL (B), and TbCh (C) conjugation reaction samples at wavelength 220 nm. Black arrows indicate respective conjugates in each HPLC chromatogram.

amide bonds between the dye molecules and the peptides. An alternative labeling strategy involves the use of thiol reactive fluorescent moieties, which would be unsuitable for labeling α-CTxs because of the characteristic disulfide connectivities between the cysteines.

Since there are no lysines in the peptide sequence of α-CTx MII, only the N-terminus free α-amine reacts with the succinimidyl esters of TMR and Alexa Fluor 488, the sulfosuccinimidyl ester of Bodipy FL or the isothiocyanate group of TbCh to form fluorescent α-CTx MII analogs. The amount of conjugate yield from the conjugation reaction, using only a few nanomoles of peptide, depends on (i) reaction buffer pH, (ii) reaction temperature, (iii) duration of reaction, and (iv) dye-to-peptide molar ratio (*15*). All of the above factors were altered to determine optimal conditions for each conjugation reaction.

Purification and Quantification of the Fluorescent Conjugates. Analysis of the RP-HPLC chromatogram indicated four distinct peaks, two of which corresponded to the unreacted dyes, one of which corresponded to the unreacted toxin, and the other peak corresponding to the fluorescent conjugate. The peak areas for the conjugates provide estimates of the efficiency of the labeling reaction. When calculating the concentration of the fluorescent conjugates, the contribution of the dye to the absorbance of the conjugate (A_{280}) was corrected using published values of correction factors and extinction coefficients for each of the fluorophores. The conjugate yield was 28−40% of the parent peptide added in the reaction. The TMR−MII conjugation reaction was the most efficient with the conjugate yield close to 40% under optimal conditions. The Bodipy FL−MII conjugate was easier to purify because the unconjugated reactants showed distinct peaks on the RP-HPLC chromatogram and could be more discernibly differentiated on the basis of their absorbance analysis (Figure 2). Alexa Fluor 488 conjugation reaction produced a very low conjugate yield that could not be further improved by altering the reaction conditions (see Supporting Information). The other fluorescent analogs were purified and tested on cloned nAChRs expressed in *X. laevis* oocytes.

Verification of Masses of Fluorescent Conjugates. Since α-CTx MII has a mass of 1710.6 Da (*6*) and the molecular masses of TMR, Bodipy FL, and TbCh are 527.53, 491.2, and 909.14 Da (*16*, *17*, *19*), respectively, the fluorescent conjugates must have masses approximately in the range 1900−2500 Da (equal to the sum of the mass of a single molecule of each fluorophore and the molecular mass of α-CTx MII minus the mass of the byproduct, if present, after accounting for the new bonds being formed during the conjugation reaction). The monoisotopic masses of TMR−MII, Bodipy FL−MII, and TbCh−MII were observed to be 2122.52 (calculated 2122.79), 1984.86 (calculated 1984.75), and 2465.17 (calculated 2464.86), respectively.

Activity of the Fluorescent Conjugates. The lyophilized eluent fractions that were confirmed by MALDI-TOF MS to be fluorescent α-CTx MII conjugates were then tested on rat α6/α3β2β3 nAChRs expressed in *X. laevis* oocytes using two-electrode voltage clamping. All fluorescent analogs of α-CTX MII blocked rat α6/α3β2β3 nAChRs with slow off-rate kinetics

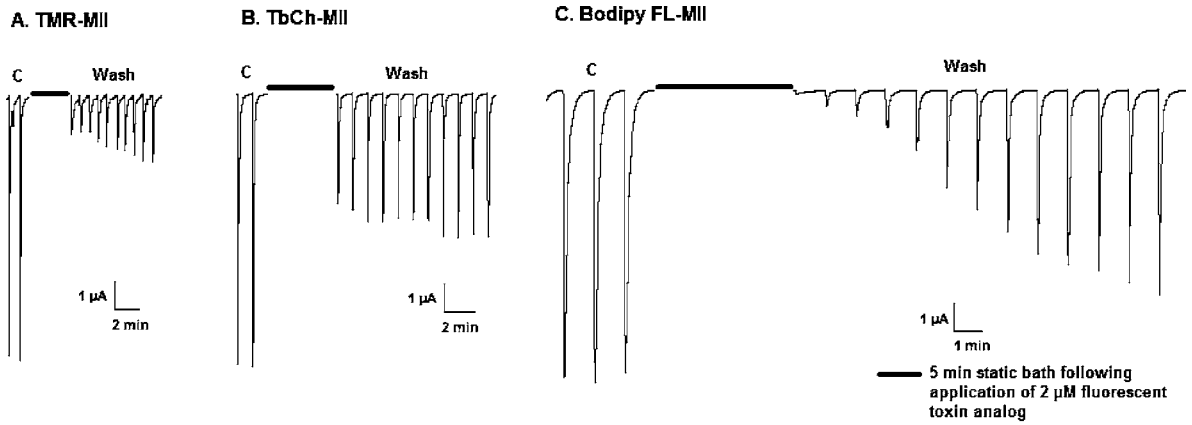

Figure 3. Kinetics of toxin block. 2 μM fluorescent analogs of α-CTx MII were applied to *X. laevis* oocytes expressing rat α6/α3β2β3 nAChRs. TMR-MII (A), TbCh-MII (B), and Bodipy FL-MII (C) at 2 μM were bath-applied for 5 min, and the toxin unblock kinetics were monitored by applying 1 s pulses of ACh every minute. C, control pulses.

similar to that of α-CTx MII (Figure 3). 2 μM of Bodipy FL−MII was found to be more potent on rat α6/α3β2β3 nAChRs than the same concentration of TMR−MII or TbCh−MII. TMR−MII was further investigated by testing its potency on α3β2 nAChRs expressed in *X. laevis* oocytes (see Supporting Information). When compared to the parent peptide, the fluorescent analogs of α-CTx MII exhibited ∼45−60-fold decrease in affinity toward the target receptors. The fluorescent analogs of α-CTx MII have not exhibited dissociation following long storage times (n = 60 days).

Limitations. There are certain limitations in the above-described synthesis of fluorescent conjugates of α-CTxs. The conjugation reaction is an efficient method of labeling the N-termini of α-CTxs that have no lysines in their peptide sequences. In the presence of lysine(s) in the peptide sequence of an α-CTx, the lysine can be selectively labeled by increasing the pH of the conjugation reaction buffer. Alternatively, selective deprotection of the lysine residue after fluorophore conjugation could be utilized. If lysine is not critical to toxin activity, a mutant version of the toxin (where the lysines have been substituted by alanines) may be used for labeling. The other limitation in the function of these conjugates is the ∼45−60-fold loss in affinity toward the target receptors, which might be overcome by the insertion of a spacer between the fluorophore and the peptide.

CONCLUSION

We have synthesized three different fluorescent analogs of α-CTx MII after optimizing the conditions for each conjugation reaction. These fluorescent analogs have the expected masses and retain activity against target receptors with off-rates comparable to that of the parent peptide. They can be used to localize target neuronal nAChRs including α3β2 and α6* nAChRs in the central nervous system.

There may be other applications of these fluorescent α-CTx MII analogs. Both Bodipy FL−MII and TMR−MII are organic fluorophore-conjugated molecules with the emission spectrum of Bodipy FL overlapping the absorbance spectrum of TMR, making them a probable donor−acceptor pair for fluorescence resonance energy transfer (FRET). FRET has been used to quantify distances in the range 1−10 nm between two fluorophore molecules and study conformational changes following interaction between receptors and ligands (*20*). TbCh−MII is a conjugate that holds the terbium ion in the chelate and acts as a donor to conventional organic fluorophores like TMR in lanthanide-based resonance energy transfer (LRET) (*21*). LRET is a modification of the FRET technique that has the advantages of reducing problems of background luminescence and accurately measuring larger distance ranges (>10 nm). LRET has been used to study conformational changes in *Shaker* potassium channels (*22*), interactions of proteins dystrophin and actin in muscle cells (*23*), and conformational changes following DNA−protein interactions (*24*).

Fluorescent analogs of α-CTx MII have been used in preliminary studies to localize α6-containing receptors in specific anatomical regions of mouse brain using confocal microscopy (*25*, *26*). Other α-conotoxins could also be fluorescently labeled to increase the number of fluorescent ligand probes for specific subtypes of nAChRs. Thus, fluorescent analogs of α-conotoxins represent a novel class of functional tools that may aid in our understanding of receptor localization and in the study of receptor conformational changes, kinetics, and neuroanatomy.

ACKNOWLEDGMENT

This work was supported by NIH grant MH53631 (to J.M.M). MALDI-MS was performed by W. Low and R. Kaiser of the Salk Institute. The authors thank Dr. Doju Yoshikami for technical advice and Dr. Layla Azam for RNA used in *X. laevis* oocyte injections.

Supporting Information Available: Additional information about (a) synthesis of Alexa Fluor 488−MII and (b) testing of TMR−MII on *X. laevis* oocytes expressing α3β2 nAChRs. This material is available free of charge via the Internet at http://pubs.acs.org.

NOTE ADDED AFTER ASAP PUBLICATION

This manuscript published ASAP on October 21, 2006 with a missing character in the sequence of the peptide in Figure 1. The correct version was posted on October 31, 2006.

LITERATURE CITED

(1) Terlau, H., and Olivera, B. M. (2004) *Conus* venoms: a rich source of novel ion channel-targeted peptides. *Physiol. Rev. 84*, 41−68.
(2) McIntosh, J. M., Gardner, S., Luo, S., Garrett, J. E., and Yoshikami, D. (2000) Conus peptides: novel probes for nicotinic acetylcholine receptor structure and function. *Eur. J. Pharmacol. 393*, 205−208.
(3) McIntosh, J. M., and Jones, R. M. (2001) Cone venom-from accidental stings to deliberate injection. *Toxicon 39*, 1447−1451.
(4) McIntosh, J. M., Santos, A. D., and Olivera, B. M. (1999) *Conus* peptides targeted to specific nicotinic acetylcholine receptor subtypes. *Annu. Rev. Biochem. 68*, 59−88.
(5) Janes, R. W. (2005) α-Conotoxins as selective probes for nicotinic acetylcholine receptors. *Curr. Opin. Pharmacol. 5*, 280−292.

(6) Cartier, G. E., Yoshikami, D., Gray, W. R., Luo, S., Olivera, B. M., and McIntosh, J. M. (1996) A new α-conotoxin which targets α3β2 nicotinic acetylcholine receptors. *J. Biol. Chem. 271*, 7522−7528.

(7) McIntosh, J. M., Azam, L., Staheli, S., Dowell, C., Lindstrom, J. M., Kuryatov, A., Garrett, J. E., Marks, M. J., and Whiteaker, P. (2004) Analogs of α-conotoxin MII are selective for α6-containing nicotinic acetylcholine receptors. *Mol. Pharmacol. 65*, 944−952.

(8) Harvey, S. C., McIntosh, J. M., Cartier, G. E., Maddox, F. N., and Luetje, C. W. (1997) Determinants of specificity of α-conotoxin MII on α3β2 neuronal nicotinic receptors. *Mol. Pharmacol. 51*, 336−342.

(9) Kuryatov, A., Olale, F., Cooper, J., Choi, C., and Lindstrom, J. (2000) Human α6 AChR subtypes: subunit composition, assembly, and pharmacological responses. *Neuropharmacology 39*, 2570−2590.

(10) Whiteaker, P., McIntosh, J. M., Luo, S., Collins, A. C., and Marks, M. J. (2000) ^{125}I-α-Conotoxin MII identifies a novel nicotinic acetylcholine receptor population in mouse brain. *Mol. Pharmacol. 57*, 913−925.

(11) Champtiaux, N., Han, Z. Y., Bessis, A., Rossi, F. M., Zoli, M., Marubio, L., McIntosh, J. M., and Changeux, J. P. (2002) Distribution and pharmacology of α6-containing nicotinic acetylcholine receptors analyzed with mutant mice. *J. Neurosci. 22* (4), 1208−1217.

(12) Quik, M., and McIntosh, J. M. (2006) Striatal α6* nicotinic acetylcholine receptors: potential targets for Parkinson's disease therapy. *J. Pharmacol. Exp. Ther. 316* (2), 481−489.

(13) Quik, M. (2004) Smoking, nicotine and Parkinson's disease. *Trends Neurosci. 27* (9), 561−568.

(14) Haugland, R. P. (2002) *Handbook of Fluorescent Probes and Research Chemicals*. Ninth Edition. Molecular Probes (Invitrogen), Eugene, OR.

(15) Hermanson, G. T. (1996) *Bioconjugate Techniques*; Academic Press, Inc., New York.

(16) Molecular Probes, Invitrogen. Tetramethylrhodamine (TMR), S. E., catalog no. C2211.

(17) Molecular Probes, Invitrogen. Bodipy F. L., catalog no. D6140.

(18) Molecular Probes, Invitrogen. Alexa Fluor 488. catalog no. A20000.

(19) PanVera. LRET Terbium labeling reagents catalog no. P3055.

(20) Periaswamy, A. (2001) Fluorescence resonance energy transfer microscopy: a mini review. *J. Biomed. Opt. 6*, 287−291.

(21) Selvin, P. R. (2002) Principles and biophysical applications of lanthanide-based probes *Annu. Rev. Biophy. Biomol. Struct. 31*, 275−302.

(22) Cha, A., Snyder, G. E., Selvin, P. R., and Bezanilla, F. (1999) Atomic scale movement of the voltage sensing region in a potassium channel measured via spectroscopy *Nature (London) 402*, 809−813.

(23) Root, D. D. (1997) In situ molecular association of dystrophin with actin revealed by sensitized emission immuno-resonance energy transfer. *Proc. Natl. Acad. Sci. U.S.A. 94*, 5685−5690.

(24) Heyduk, E., and Heyduk, T. (1999) Architecture of a complex between the sigma 70 subunit of *Escherichia coli* RNA polymerase and the nontemplate strand oligonucleotide. Luminescence resonance energy transfer study. *J. Biol. Chem. 274*, 3315−3322.

(25) Vishwanath, V. A., and McIntosh, J. M. (2004) Synthesis and applications of fluorescent conjugates of α-conotoxins. Program no. 624.15, *2004 Abstract Viewer and Itinerary Planner*, San Diego: Society for Neuroscience, San Diego.

(26) Vishwanath, V. A. and McIntosh, J. M. (2005) Labeling of α-conotoxin MII with fluorophore Cy3. Program no. 722.20, *2005 Abstract Viewer and Itinerary Planner*, Society for Neuroscience, Washington, DC, 2005.

BC060163Y

A Rapid and Versatile Method to Label Receptor Ligands Using "Click" Chemistry: Validation with the Muscarinic M1 Antagonist Pirenzepine

Dominique Bonnet,*[,†] Brigitte Ilien,*[,‡] Jean-Luc Galzi,[‡] Stéphanie Riché,[†] Cyril Antheaune,[§] and Marcel Hibert[†]

Département de Pharmacochimie de la Communication Cellulaire, Département Récepteurs et Protéines Membranaires, and IFR85, Service commun de RMN, Institut Gilbert Laustriat, UMR 7175-LC1 ULP/CNRS, Faculté de Pharmacie de Strasbourg, 74 Route du Rhin, 67401 Illkirch, France. Received May 29, 2006; Revised Manuscript Received July 28, 2006

Tagged biologically active molecules represent powerful pharmacological tools to study and characterize ligand−receptor interactions. However, the labeling of such molecules is not trivial, especially when poorly soluble tags have to be incorporated. The classical method of coupling usually necessitates a tedious final purification step to remove the excess of reagents and to isolate tagged molecules. To overcome this limitation, Cu(I)-catalyzed 1,3-dipolar cycloaddition, referred to as "click" chemistry, was evaluated as a tool to facilitate the access to labeled molecules. In order to validate the approach, we focused our attention on the incorporation of a fluorophore (Lissamine Rhodamine B), a nonfluorescent dye (Patent Blue VF), or biotin into a muscarinic antagonist scaffold derived from pirenzepine. The reaction performed in acetonitrile/water, in the presence of $CuSO_4$ and Cu wire, allowed us to obtain three novel pirenzepine derivatives with high purity and in good yield. No coupling reagents were needed, and the quasi-stoichiometric conditions of the reaction enabled the straightforward isolation of the final product by simple precipitation and its use in bioassays. The affinity of the compounds for the human M1 muscarinic receptor fused to EGFP was checked under classical radioligand and FRET binding conditions. The three pirenzepine constructs display a nanomolar affinity for the M1 receptor. In addition, both dye-labeled derivatives behave as potent acceptors of energy from excited EGFP with a very high quenching efficiency.

INTRODUCTION

Biomolecules bearing a biotin tag or dye labels represent useful pharmacological tools for studying receptors (*1*). Biotinylated compounds, together with their streptavidin partner, can be used in a wide variety of bioanalytical applications, such as affinity chromatography, affinity cytochemistry, and immunoassays (*2*), and also as biosensors for drug development (*3*) or for receptor purification (*4*). Fluorescent drug molecules allow the visualization of their receptor target at the single-cell level (*5*, *6*). More generally, these molecules are used as tracers in binding assays where they represent a safe and versatile alternative to radioligands, thus eliminating issues related to handling and disposal of radioactive materials (*7*). Recently, Ilien et al. reported on the synthesis of a series of fluorescent derivatives of the muscarinic M1 antagonist pirenzepine and on their binding properties at an enhanced green fluorescent protein (EGFP)−human M1 receptor chimera, examined through fluorescence resonance energy transfer (FRET) (*8*, *9*). Among these ligands, Lissamine Rhodamine B-labeled pirenzepine **1a** (Figure 1) displayed both a nanomolar affinity and the highest FRET efficiency. In a subsequent article, these authors provided evidence that pirenzepine derivatives labeled with a nonfluorescent dye, such as Patent Blue VF in compound **1b,** were useful tools to improve the reliability of FRET-based binding assays when performed at high probe concentrations (*10*).

Several methods are currently available to label biomolecules such as peptides or small organic molecules (*11*). However, most of these methods suffer from several limitations: (1) Activated tags are generally provided in small quantities suitable for biochemical applications, but amounts typically required for synthetic organic chemistry are prohibitively expensive. (2) To ensure good solubility of both partners, the coupling step has to be carried out in high boiling point solvents such as DMF or DMSO. This renders the final workup, i.e., the isolation of the labeled molecule, more difficult. (3) Excess of one of the partners is generally used to drive the reaction to completion. This makes final purification more tedious, as the excess of both reagents and coupling agents have to be removed. (4) Last but not least, the labeling is not chemoselective and other nucleophile groups have to be protected before performing the

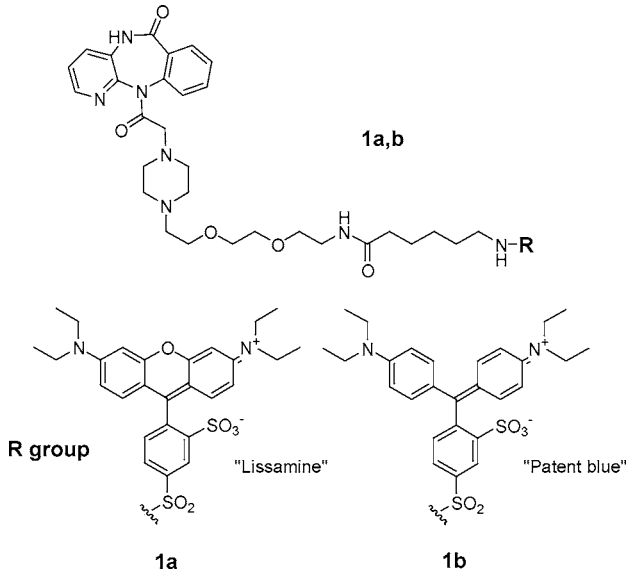

Figure 1. Chemical structures of fluorescent (Lissamine Rhodamine B-labeled; **1a**) and nonfluorescent (Patent Blue VF-labeled; **1b**) pirenzepine derivatives as described in refs 9 and 10.

* To whom correspondence should be addressed. Phone: +33(0)390244236. Fax: +33(0)390244310. E-mail: dominique.bonnet@pharma.u-strasbg.fr or ilien@esbs.u-strasbg.fr.

† Département de Pharmacochimie de la Communication Cellulaire.

‡ Département Récepteurs et Protéines Membranaires.

§ IFR85, Service commun de RMN.

10.1021/bc060140j CCC: $33.50 © 2006 American Chemical Society
Published on Web 10/19/2006

coupling reaction. Therefore, the numerous difficulties associated with the preparation of such molecules prompted us to develop a novel method to ensure rapid, low-cost, and chemoselective labeling of biomolecules.

Herein, we describe a simple and efficient method, referred to as "click" chemistry, to label a small ligand with various tags (such as biotin, Lissamine Rhodamine B, or Patent Blue VF) using Cu(I)-catalyzed 1,3-dipolar cycloadditions. After optimization on a model reaction, the method was successfully applied to the synthesis of three novel pirenzepine (an M1 selective muscarinic antagonist) derivatives **14a**−**c**, with high yield and purity. An important issue was the impact of the triazole link on the biological activity of these ligands. Therefore, their binding properties at the muscarinic M1 receptor were examined through classical [^{3}H]-NMS competition experiments and through FRET-based saturation assays using the EGFP-(Δ17)hM1 chimera (*8*). Affinity parameters (K_i and K_d values) were determined and compared to those previously reported for the parent molecules **1a** and **1b**. Maximal amplitudes for EGFP fluorescence extinction, achieved at saturating concentrations of **14a** and **14b**, allowed the estimation of the efficiency of the energy transfer process promoted by their interaction with the receptor.

EXPERIMENTAL PROCEDURES

General. All chemicals were obtained from commercial suppliers and used without further purification. Lissamine Rhodamine B sulfonyl chloride and D(+)biotin were purchased from Acros and Avocado, respectively. 6-(Boc-amino)caproic acid *N*-succinimidyl ester **6** and 11-azido-3,6,9-trioxaundecan-1-amine were from Fluka and benzotriazole-1-yl-oxy-tris-(pyrrolidino)phosphonium hexafluorophosphate (PyBOP) was supplied from Novabiochem. Compounds **9** and **13** were prepared as previously described in the literature (*9*, *10*). Silica gel 60F 254 plates for thin-layer chromatography (TLC) were purchased from Merck. Column chromatographic separations were carried out by flash chromatography using silica gel (Merck) with a particle size of 0.040−0.063 mm. ^{1}H NMR spectra were recorded at 200 or 300 MHz on a Bruker Advance spectrometer. Chemicals shifts are given in parts per million and coupling constants (*J*) in hertz. Analytical RP-HPLC separations were performed on a C18 Symmetry Shield column (4.6 × 150 mm) using a linear gradient of eluent B in eluent A (0−100% B in 30 min, flow rate 1 mL.min^{-1}, detection at 220 and 254 nm) and a linear gradient of eluent D in eluent C (0−100% D in 60 min, flow rate 0.8 mL.min^{-1}, detection at 220 and 254 nm). The following buffers were used: (eluent A) water containing 0.1% TFA; (eluent B) acetonitrile containing 0.1% TFA; (eluent C) water containing 0.1% HFBA; (eluent D) MeOH containing 0.1% HFBA. ESI-TOF (electrospray ionization time-of-flight) spectra were recorded on a Perseptive Biosystem Mariner 5155 spectrometer. The *m*/*z* range 200−2100 was scanned using an ion-spray voltage of 4500 V. The nozzle was ranged between 30 and 60 V.

***N*-(2-{2-[2-(2-Azidoethoxy)-ethoxy]-ethoxy}-ethyl)-4-nitrobenzamide 2.** 11-azido-3,6,9-trioxaundecan-1-amine (200 μL, 1 mmol) was dissolved in CH_2Cl_2 and Et_3N (210 μL, 1.5 mmol). 4-Nitrobenzoyl chloride (226 mg, 1.2 mmol) dissolved in CH_2Cl_2 was added to the solution. The resulting mixture was stirred for 4 h at room temperature. The crude reaction was then diluted with CH_2Cl_2 and washed with 10% citric acid solution and brine. The organic layer was dried over Na_2SO_4, filtered, and concentrated under reduced pressure. Compound **2** was isolated by column chromatography (CH_2Cl_2/CH_3OH 98/2) to afford a yellow oil (281 mg, 77%); R_f = 0.35 (CH_2Cl_2/MeOH 98/2); ^{1}H NMR ($CDCl_3$, 300 MHz) δ 8.28 (d, *J* = 8.4 Hz, 2H), 7.98 (d, *J* = 7.1 Hz, 2H), 3.95−3.35 (m, 14H), 3.35 (t, 4.8 Hz, 2H); ^{13}C NMR ($CDCl_3$, 75 MHz) δ 165.7, 149.8, 140.5, 128.6, 123.9, 70.9, 70.7, 70.5, 70.2, 69.8, 50.9, 40.3; ES-MS MW calcd 368.14 *m*/*z*, found 390.17 [M + Na]$^+$; RP-HPLC purity >90%.

2 (and 4)-[6-(diethylamino)-3-(diethyliminio)-3*H*-xanthen-9-yl]-5 (or 3)-({[6-oxo-6-(prop-2-ynylamino)hexyl]amino}-sulfonyl)benzenesulfonate 3. To a solution of 6-(Boc-amino)-caproic acid *N*-succinimidyl ester (200 mg, 0.61 mmol) in a CH_2Cl_2/DMF (1/2) mixture were added propargylamine (62 μL, 0.91 mmol) and Et_3N (94 μL, 0.66 mmol). The resulting solution was stirred at room temperature overnight and then diluted with CH_2Cl_2 and washed with 10% citric acid solution, 10% aqueous Na_2CO_3, and brine. The organic layer was dried over Na_2SO_4, filtered, and concentrated under reduced pressure to give a white powder which was further purified through a short column of silica gel (CH_2Cl_2/CH_3OH 97/3) to afford compound **7** in 76% yield (125 mg). R_f = 0.38 (CH_2Cl_2/MeOH 97/3); ES-MS MW calcd 268.4, *m*/*z* found 291.2 [M + Na]$^+$. Compound **7** (100 mg, 0.37 mmol) was treated with a CH_2Cl_2/TFA (1/1) mixture for 20 min at room temperature. Following TFA removal under reduced pressure, the resulting deprotected compound **8** (yellow oil) was dissolved in CH_2Cl_2/DMF (5/1) mixture containing Et_3N (250 μL) and cooled at 0 °C. Lissamine Rhodamine B sulfonyl chloride (165 mg, 0.28 mmol) was added in portions over 20 min. The solution was allowed to warm up to room temperature and stirred overnight. The crude mixture was concentrated under reduced pressure. Compounds **3a** (para isomer) and **3b** (ortho isomer) were isolated by flash chromatography with a step gradient from 5% to 10% MeOH in CH_2Cl_2 and obtained as a red dark solid: **3a** (89 mg, 44%,); R_f = 0.37 (CH_2Cl_2/MeOH 93/7); ^{1}H NMR ($CDCl_3$/CD_3OD 9/1, 300 MHz) δ 8.57 (d, *J* = 1.8 Hz, 1H), 7.94 (dd, *J* = 1.8 and 8.1 Hz, 1H), 7.18 (d, *J* = 8.1 Hz, 1H), 7.04 (d, *J* = 9.6 Hz, 2H), 6.75 (dd, *J* = 2.1 and 9.6 Hz, 2H), 6.63 (d, *J* = 2.1 Hz, 2H), 3.80 (d, *J* = 2.5 Hz, 2H), 3.25 (bs, 1H), 2.95 (t, *J* = 6.6 Hz, 2H), 2.10−2.08 (m, 3H), 1.51−1.38 (m, 4H), 1.31−1.14 (m, 14H); ^{13}C NMR ($CDCl_3$/CD_3OD 9/1, 75 MHz) δ 175.7, 159.4, 158.5, 157.1, 147.8, 144.3, 135.2, 134.2, 132.0, 129.4, 128.2, 115.6, 115.2, 97.3, 72.4, 47.8, 47.4, 44.4, 37.1, 31.1, 30.6, 30.1, 27.4, 26.6, 13.9, 10.0; MW calcd 708.88, *m*/*z* found 731.36 [M + Na]$^+$; RP-HPLC purity >95%. **3b** (53 mg, 27%); R_f = 0.30 (CH_2Cl_2/MeOH 93/7); δ 8.44 (d, *J* = 1.7 Hz, 1H), 8.13 (dd, *J* = 1.7 and 7.8 Hz, 1H), 7.19 (d, *J* = 7.8 Hz, 1H), 7.01 (d, *J* = 9.4 Hz, 2H), 6.77 (dd, *J* = 2.4 and 9.4 Hz, 2H), 6.65 (d, *J* = 2.5 Hz, 2H), 3.82 (d, *J* = 2.5 Hz, 2H), 3.23 (bs, 1H), 3.03 (q, *J* = 7.5 Hz, 8H), 2.75 (t, *J* = 6.6 Hz, 2H), 2.11 (t, *J* = 2.5 Hz, 2H), 2.10−2.05 (m, 2H), 1.42−0.75 (m, 18H); ^{13}C NMR ($CDCl_3$/CD_3OD 9/1, 75 MHz) δ 175.7, 159.4, 157.3, 154.4, 150.7, 134.1, 133.5, 131.4, 127.6, 119.6, 115.6, 110.0, 99.0, 97.7, 72.7, 47.9, 47.6, 44.5, 37.2, 31.2, 30.2, 29.5, 27.5, 26.4, 14.0, 10.1; ES-MS MW calcd 708.88, *m*/*z* found 731.33 [M + Na]$^+$; RP-HPLC purity >95%.

2-{[4-(diethylamino)phenyl][4-(diethyliminio)cyclohexa-2,5-dien-1-ylidene] methyl}-5- ({[6-oxo-6-(prop-2-ynylamino)-hexyl]amino}sulfonyl)benzenesulfonate 4. A solution of aqueous lithium hydroxide hydrate 1 N (89 μL, 89.7 μmol) was added at room temperature to methyl 6-(4-[(4-diethylamino-phenyl)(4-diethylimino-2,5-cyclohexadien-1ylidene)methyl]-3-sulfo-1-phenylsulfonamido)hexanoate **9** (20 mg, 29.7 μmol) dissolved in dioxane. The mixture was stirred overnight at room temperature or 10 min at 80 °C using microwave irradiation. Dioxane was removed under reduced pressure, and water was added. The mixture was washed with CH_2Cl_2, acidified with a 1 M $KHSO_4$ solution, and extracted with CH_2Cl_2. Organic layers were combined and concentrated under pressure to give acid **10** which was used as crude material in the next step.

Crude acid **10** was dissolved in DMF with propargylamine (3 μL, 38.6 μmol). PyBOP (16 mg, 29.7 μmoles) was added, followed by DIEA (16 μL, 89.1 μmol). The resulting mixture was stirred at room temperature overnight. DMF solvent was removed under reduced pressure, and the crude material was purified by column chromatography (CH_2Cl_2/MeOH 95/5) to afford compound **4** as a blue powder (17.3 mg, 83%). R_f = 0.35 (CH_2Cl_2/MeOH 95/5); ^{1}H NMR ($CDCl_3$/CD_3OD 9:1, 300 MHz) δ 8.54 (d, *J* = 1.5 Hz, 1H), 7.88 (dd, *J* = 1.5 and 7.7 Hz, 1H), 7.33 (d, *J* = 9.5 Hz, 4H), 7.12 (d, *J* = 7.8 Hz, 1H), 6.72 (d, *J* = 9.5 Hz, 4H), 4.21 (d, *J* = 3.4 Hz, 1H), 3.84 (brd, *J* = 2.5 Hz, 2H), 3.58−3.48 (m, 8H), 2.98 (t, *J* = 6.5 Hz, 2H), 2.14−2.07 (m, 3H), 1.53−1.18 (m, 18H); ^{13}C NMR ($CDCl_3$/CD_3OD 9:1, 75 MHz) 174.1, 155.4, 147.0, 142.8, 140.9, 132.0, 131.2, 129.0, 128.4, 127.9, 127.4, 127.1, 126.8, 113.4, 46.1, 45.1, 43.0, 35.8, 29.8, 28.8, 26.0, 25.2, 12.8. ES-MS MW calcd 694.9, *m*/*z* found 717.4 $[M + Na]^+$; RP-HPLC purity >95%.

5-[(4*R*)-2-oxohexahydro-1*H*-thieno[3,4-*d*]imidazol-4-yl]-*N*-prop-2-ynylpentanamide 5. D(+)biotin (50 mg, 205 μmol) was dissolved in DMF in presence of DIEA (107 μL, 615 μmol). Propargylamine (28 μL, 410 μmol) was added, followed by PyBOP (106 mg, 205 μmol). After overnight stirring at room temperature, DMF solvent was removed under reduced pressure. The crude material was then purified by column chromatography on silica gel (CH_2Cl_2/MeOH 9/1) to get compound **5** as a white powder (35 mg, 60%). R_f = 0.24 (CH_2Cl_2/MeOH 9/1); ^{1}H NMR (CD_3OD, 200 MHz) δ 4.56−4.52 (m, 1H), 4.37−4.31 (m, 1H), 3.99 (d, *J* = 2.5 Hz, 2H), 3.32−3.22 (m, 1H), 2.97 (dd, *J* = 6.0 Hz, 12.0 Hz, 1H), 2.74 (d, *J* = 11.4 Hz, 1H), 2.61 (t, *J* = 2.5 Hz, 1H), 2.26 (*t*, *J* = 7.2 Hz, 2H), 1.84−1.40 (m, 6H); ^{13}C NMR (CD_3OD, 75 MHz) δ 176.4, 166.9, 81.5, 72.9, 64.2, 62.4, 57.8, 41.8, 37.3, 30.5, 30.3, 30.2, 27.5; ES-MS MW calcd 281.38, *m*/*z* found 304.15 $[M + Na]^+$.

General Procedure for the Preparation of Triazoles: **Synthesis of Compound 12.** Azido **2** (4.1 mg, 11.2 μmol) and alkyne **3a** (9.6 mg, 13.5 μmol) were dissolved in 9/1 acetonitrile/water mixture (600 μL) in presence of $CuSO_4$ (solution 26.7 μM, 40 μL, 1.11 μmol) and Cu wire (68 mg). The solution was stirred overnight at 30 °C, the solvent removed, and the crude material purified by column chromatography (CH_2Cl_2/MeOH 9/1). Compound **12** (9.0 mg, 75%) was obtained as a red solid. R_f = 0.28 (CH_2Cl_2/MeOH 9/1); ^{1}H NMR ($CDCl_3$/CD_3OD 9:1, 200 MHz) δ 8.62 (s, 1H), 8.13 (d, *J* = 8.5 Hz, 2H), 7.95 (m, 3H), 7.20 (d, *J* = 7.8 Hz, 1H), 7.07 (d, *J* = 9.3 Hz, 2H), 6.75 (d, *J* = 9.3 Hz, 2H), 6.59 (d, *J* = 1.9 Hz, 2H), 4.39−4.33 (m, 4H), 3.75 (t, *J* = 4.6 Hz, 2H), 3.60−3.33 (m, 18H), 2.95 (t, *J* = 4.6 Hz, 2H), 2.77 (bs, 1H), 2.35−1.93 (m, 4H), 1.6−1.0 (m, 18H); ^{13}C NMR (CD_3OD, 50 MHz) δ 158.1, 155.8, 133.8, 133.0, 130.5, 128.9, 128.0, 127.0, 123.8, 114.3, 114.0, 95.9, 70.6, 70.3, 69.7, 46.2, 43.1, 40.2, 12.7; ES-MS MW calcd 1075.4, *m*/*z* found 1076.6 $[M + H]^+$, 1098.6 $[M + Na]^+$; RP-HPLC purity >95%.

Compound 14a. The same procedure as that described above for compound **12** was used starting from azido **13** (4.7 mg, 9.5 μmol) and alkyne **3a** (8.0 mg, 11.3 μmol). After 4 h at 30 °C, triazole **14a** (8.9 mg, 78%) was isolated by column chromatography on silica gel (CH_2Cl_2/MeOH 9:1/NH_4OH 1% in water) as a red solid. R_f = 0.21; RP-HPLC purity >95%; HRMS calcd for $C_{60}H_{75}N_{12}O_{11}S_2$ 1203.5114, found 1203.5156.

Compound 14b (5.0 mg, 70%, blue solid) was obtained by reacting azido **13** (3 mg, 6.0 μmol) and alkyne **4** (5.3 mg, 7.5 μmol) at 30 °C for 4 h and subsequent purification by column chromatography (CH_2Cl_2/MeOH 9:1/NH_4OH 1% in water). R_f = 0.27; RP-HPLC purity >95%; HRMS calcd for $C_{60}H_{77}N_{12}O_{10}S_2$ 1189.5322, found 1189.5298.

Compound 14c (5.9 mg, 92%, white solid) was obtained by reacting azido **13** (4.2 mg, 8.5 μmol) and alkyne **5** (3.0 mg, 10.6 μmol) following the same experimental conditions as for **14b**. R_f = 0.15 (CH_2Cl_2/MeOH 9:1/NH_4OH 1% in water); RP-HPLC purity >95%; HRMS calcd for $C_{37}H_{50}N_{11}O_6S$ 776.3661, found 776.3631.

Construction and Expression of the Chimeric hM1 Receptor. The human M1 muscarinic receptor with a truncated N-terminus fused to EGFP, referred to as EGFP-(Δ17)hM1, was obtained and stably expressed in HEK 293 cells as previously reported (*8*).

[^{3}H]-NMS Binding Assays. Competition experiments were performed using intact EGFP-(Δ17)hM1 expressing cells (60 000 cells) suspended in 1 mL HEPES/BSA buffer (10 mM HEPES, 137.5 mM NaCl, 1.25 mM $MgCl_2$, 1.25 mM $CaCl_2$, 6 mM KCl, and 10 mM glucose, pH 7.4; supplemented with 1 mg.mL^{-1} bovine serum albumin). Incubation proceeded at 20 °C for 22 h in the presence of 100−150 pM [^{3}H]-NMS ([^{3}H]-*N*-methylscopolamine) of various concentrations of compounds to be tested or of 4 μM atropine for nonspecific binding measurement. K_i values of competitors were calculated from IC_{50} values, using the Cheng and Prusoff relationship (*12*) and taking a K_d value of 90 pM for the radioligand.

Spectroscopy. UV−visible absorbance spectroscopy was performed with a Cary 1E (Varian) spectrophotometer. Absorption spectra for compounds, diluted in MeOH, were recorded in the 450−750 nm wavelength range. Fluorescence measurements were made using a SPEX Fluorolog 2 (Jobin Yvon Horiba) spectrofluorimeter equipped with a 450 W Xe lamp. Data were stored using the DM3000 software provided with the spectrofluorimeter.

FRET-Based Binding Measurements. EGFP-(Δ17)hM1 cells (1 × 10^6 cells), suspended in 1 mL HEPES/BSA buffer, were incubated with increasing concentrations of fluorescent ligand, in the absence or presence of 10 μM atropine to assess the specificity of the signal. Equilibrium was allowed to proceed for 22 h at 20 °C. Thereafter, the incubation medium was transferred to a 1 mL thermostated (21 °C) quartz cuvette with magnetic stirring and recorded for fluorescence intensity at 510 nm (excitation set at 470 nm). Occupancy curves were generated by plotting amplitudes for fluorescence extinction as a function of ligand concentration as previously described (*10*). K_d values and maximal FRET amplitudes were from data fitting to the empirical Hill equation derived for saturation. Efficiency of fluorescence energy transfer (*E*) was defined as the fractional decrease in specific EGFP fluorescence due to ligand binding as previously reported (*8*).

RESULTS AND DISCUSSION

Chemistry. The generation of (1,2,3)-triazoles through 1,3-dipolar cycloadditions of alkynes to azides, which belongs to a group of reactions referred to as "click chemistry" (*13*), proceeds at room temperature in the presence of copper(I) as a catalyst (*14*). Among various applications, this reaction has enabled the selective modification of virus particles (*15*), nucleic acids (*16*), and proteins (*17*) in biological environments.

In the first part of the study, the potential of this method for the labeling of bioactive molecules was examined using the azido model **2** and alkynes derived from Lissamine Rhodamine B **3**, Patent Blue VF **4**, and biotin **5** (Scheme 1).

Alkyne **3** was obtained in three steps starting from commercially available 6-(Boc-amino)caproic acid *N*-succinimidyl ester **6**. Substitution of ester with propargylamine gave access to alkyne **7** that was subsequently deprotected in the presence of TFA. Resulting amine **8** was reacted with Lissamine Rhodamine B sulfonyl chloride (commercially available as a mixture of ortho and para isomers) in CH_2Cl_2/DMF mixture in the presence of Et_3N and 4-dimethylaminopyridine (DMAP) to afford **3** as a mixture of ortho **3a** and para **3b** isomers (1:1.6

Scheme 1. Routes for Preparation of Alkyne Derivatives 3−5[a]

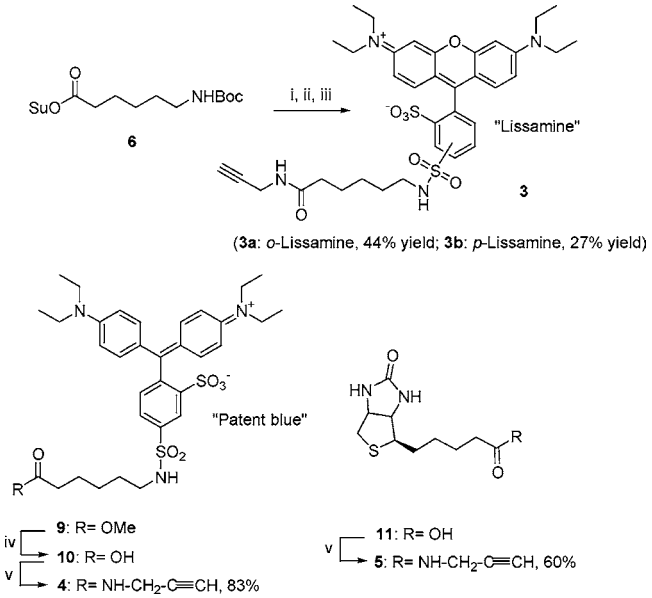

[a] Legend: (i) propargylamine, CH_2Cl_2/DMF, Et_3N, rt, 16 h; (ii) TFA/CH_2Cl_2 (1:1), rt, 20 min; (iii) Lissamine sulfonyl chloride, CH_2Cl_2/DMF (5:1), Et_3N/DMAP, 0 °C, 15 min then rt, overnight; (iv) LiOH, dioxane/H_2O, 40 °C, 16 h or microwave irradiation (80 °C, 10 min); (v) propargylamine, PyBOP, DIEA, DMF, rt, overnight.

Scheme 2. Model Reaction to Optimize Cu(I)-Catalyzed 1,3-Dipolar Cycloaddition

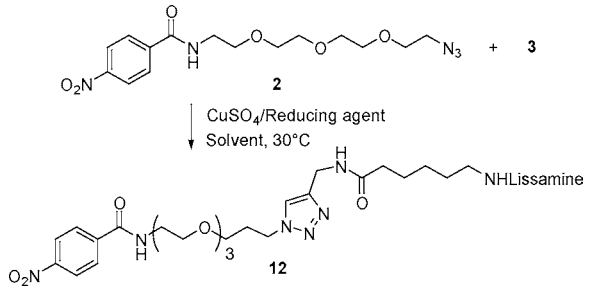

ratio, respectively, as shown by ^{1}H NMR and RP-HPLC analysis (*18*)). Column chromatography on silica gel allowed the separation of both isomers **3a** and **3b** obtained in a 44% and 27% overall yield, respectively.

Alkyne **4** was prepared starting from Patent Blue VF methyl ester **9** (*10*). In an attempt to obtain **4** in one step, aminolysis of **9** with an excess of propargylamine was tried and found to be inefficient, regardless of the solvent, the temperature, and the presence or absence of a catalytic amount of cyanide anion (*19*). Compound **4** was finally obtained in two steps. Ester **9** was first hydrolyzed in the presence of LiOH in a dioxane/water mixture at 40 °C overnight, leading quantitatively to acid **10**. Interestingly, hydrolysis was dramatically accelerated by using microwave irradiation (80 °C, 10 min). Crude acid **10** was then coupled with propargylamine following PyBOP in situ activation to provide **4** in 83% overall yield.

Finally, alkyne derived from biotine **5** was obtained by coupling propargylamine with D(+)biotin using PyBOP activation in DMF at 40 °C in 60% yield after purification on silica gel (Scheme 1).

With alkynes **3**−**5** in hand, "click" reaction efficacy was evaluated with the model azido **2** and the alkyne derived from Lissamine **3**. The reaction was conducted in the presence of $CuSO_4$ and of a reducing agent to generate Cu(I) species in polar solvents at 30 °C (Scheme 2). The influence of key parameters such as the nature of the reducing agent and the solvent on the formation of the triazole derivative **12** was carefully investigated. RP-HPLC yields were determined following overnight stirring at 30 °C (Table 1).

Table 1. Optimization of the Synthesis of Triazole 12.

entry	solvent	reducing agent	RP-HPLC yield of **12**[a] (%)
1	EtOH/$H_2$0 (1:1)	TCEP	0
2	EtOH/$H_2$0 (1:1)	ascorbic acid	30
3	EtOH/$H_2$0 (1:1)	Cu wire	38
4	EtOH/$H_2$0 (9:1)	Cu wire	68
5	MeOH/$H_2$0 (9:1)	Cu wire	59
6	tBuOH/$H_2$0 (9:1)	Cu wire	65
7	ACN/$H_2$0 (9:1)	Cu wire	90
8	ACN/$H_2$0 (1:1)	Cu wire	74

[a] Yields were approximated by RP-HPLC and calculated using the ratio of surface area of reactant species to surface area of product species (see experimental procedures for RP-HPLC conditions).

Scheme 3. Novel Pirenzepine Derivatives Obtained Using "Click" Chemistry

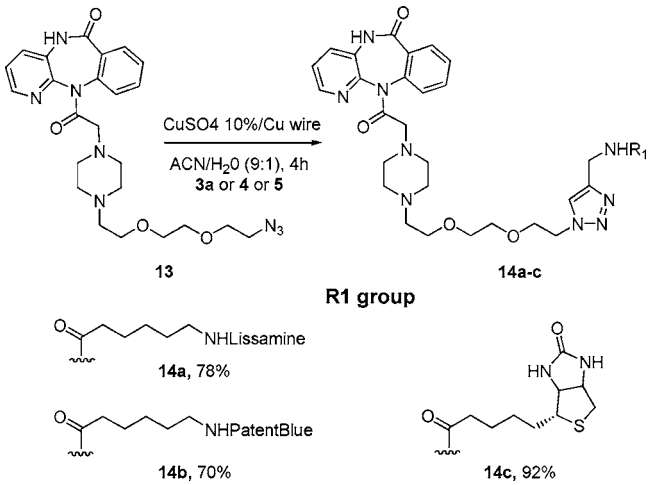

In our hands, the classical experimental conditions described in the literature (*14*), i.e., EtOH/H_2O (1:1) mixture in the presence of tris(carboxyethyl)phosphine (TCEP), failed (entry 1). Replacement of phosphine by ascorbic acid or Cu wire allowed an improvement of RP-HPLC yields from 30% to 38% (entries 2 and 3). The nature of the solvent and the ratio of water were found to be crucial for the reaction (entries 4−8), with the best result (90%) being obtained by using an acetronitrile (ACN)/water (9:1) mixture (entry 7). Using these conditions, compound **12** was isolated in 75% overall yield.

The scope and limitations of the method were further investigated by considering the incorporation of Lissamine Rhodamine B, but also of Patent Blue and of sparsely soluble biotin onto pirenzepine (Scheme 3). The azido pirenzepine derivative **13** was synthesized as previously described (*9*). 1,3-Dipolar cycloaddition was performed in the presence of 1.2 equiv of alkyne **3a** (para isomer), 0.1 equiv of $CuSO_4$, and Cu wire in an acetonitrile/water (9:1) mixture. Completion of the reaction was observed after only 4 h stirring at 30 °C. Thus, compound **14a** was isolated by column chromatography in 78% yield.

Similar results were obtained with alkynes derived from Patent Blue VF leading to the corresponding labeled pirenzepine **14b** in 70% isolated yield. Finally, the "click" reaction of alkyne **13** with azido-derived biotin **5** was found to be particularly clean and rapid, since conjugate **14c** was isolated in 92% yield following 4 h at 30 °C.

It is noteworthy that, owing to the excellent purity of the crude mixture, labeled compounds could be used directly for

Scheme 4. Synthesis of Fluorescent Labeled Pirenzepine 1a[a]

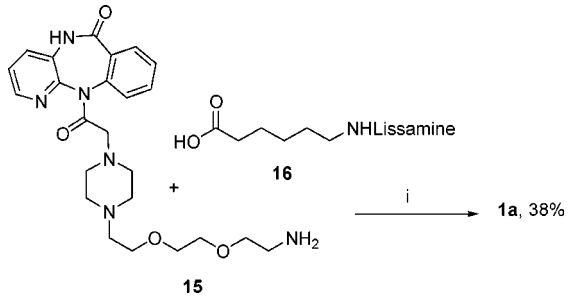

[a] Legend: (i) PyBOP, DIEA, DMF, 30 °C, 4 h.

Table 2. Binding Properties of Compounds 14a−c at the Muscarinic M1 Receptor.

		fluorescence resonance energy transfer[b]		
compound	[^{3}H]NMS binding[a] K_i (nM)	K_d (nM)	amplitude (%)	efficiency E
pirenzepine	7.1			
1a	46	18.7	48	0.68
1b	189	30	37	0.52
14a[c]	30	20	55	0.78
14b	16.3	11	46	0.65
14c	49			

[a] K_i values are from competition experiments performed in duplicate using [^{3}H]-NMS as the radioligand. The K_i value reported for compound **1b** (tested against [^{3}H]-QNB) is from ref 10. [b] Values listed for compounds **1a** and **1b** are, respectively, from refs 9 and 10. Other values are from a typical experiment performed in duplicate. [c] Only the para isomer was considered.

biological evaluation without any additional purification. Cu wire is simply picked up from the solution with tweezers, the crude product is diluted in water, and the resulting precipitate washed to remove $CuSO_4$. The use of metal resin scavengers, such as Chelex resin (Bio-Rad), may be regarded as an alternative process to get rid of Cu^{2+} (*20*).

To highlight the efficiency of the "click" reaction versus traditional coupling, pirenzepine amine **15** obtained by reduction of azido **13** (*10*) was reacted with 1.2 equiv of acid **16** (*21*) following PyBOP in situ activation in DMF (Scheme 4). After 4 h at 30 °C, this control experiment resulted in a low conversion of starting materials involving a tedious final purification by RP-HPLC to isolate Lissamine-labeled pirenzepine **1** in modest 38% yield (vs 78% for "click" reaction).

This first part of the study highlighted the efficiency of the "click" process to easily access the novel pirenzepine-labeled derivatives **14a−c**. The reaction is rapid, insensitive to water, and almost quantitative regardless of the nature and the solubility of tags incorporated. Interestingly, the absence of coupling reagents and quasi-stoichiometric conditions, combined with the use of an acetonitrile/water mixture, allow the isolation of the final labeled products by simple precipitation.

The main issue of the second part of the work was to check whether the triazole moiety was compatible with high-affinity binding of the pirenzepine derivatives to the muscarinic M1 receptor, a G protein-coupled receptor belonging to the bioamine group whose binding domain is deeply buried in the receptor protein.

Pharmacological Study of Novel Pirenzepine Derivatives 14a−c. Ligand binding affinity at equilibrium was evaluated through competition (conventional [^{3}H]NMS assay) and saturation (FRET-based assay) experiments, using the EGFP-(Δ17)hM1 chimera (*8*).

Binding parameters are listed in Table 2 and may be compared to those determined for pirenzepine and for the two parent ligands **1a** and **1b**, under similar experimental conditions.

The three novel pirenzepine derivatives retain nanomolar affinities for [^{3}H]-NMS binding sites. The Lissamine Rhodamine B conjugate **14a** exhibits a K_i value similar to that of its parent molecule **1a**, while the Patent Blue derivative **14b** displays a significantly higher affinity than **1b** (which has been tested against [^{3}H]-QNB; (*10*)). The introduction of the small biotine substituent in **14c**, as compared to the more voluminous dyes in **14a** and **14b**, does not lead to appreciable affinity changes. Thus, neither the incorporation of a triazole ring within the spacer nor the exchange of a large chromophore for a smaller moiety are detrimental to high-affinity binding of the compounds to the hM1 receptor.

For all tested molecules, similar affinity rank order and parameter values were determined from competition-type ([^{3}H]-NMS binding) or from saturation-type (FRET) equilibrium experiments. A subtle but constant increase in affinity is however noted for the compounds when tested for their ability to behave as energy acceptors from excited EGFP. Such a feature has been already reported, and was even exacerbated, when [^{3}H]-QNB- and FRET-derived binding affinity constants for a series of dye derivatives of pirenzepine were compared (*9*, *10*). Most probably, these variations stem from differences in the physicochemical properties of the ligands.

A surprising finding was the apparent increase in maximal extinction amplitude afforded at saturating micromolar concentrations of **14a** and **14b**, as compared to **1a** and **1b**, respectively. These changes cannot be attributed to modifications in EGFP-(Δ17)hM1-expressing cell properties, as a control Bodipy-pirenzepine derivative (Bo(10)PZ), taken at 200 nM, provided here a maximal extinction amplitude of 44.8%, in perfect agreement with previous determinations (*8*, *9*). Moreover, the muscarinic specificity of the FRET signal achieved at high probe concentrations was verified by the full protective (competitive) effect of 10 μM atropine. As far as identical dyes (Lissamine Rhodamine B for **1a** and **14a**; Patent Blue for **1b** and **14b**) and identical EGFP-fused receptors (FRET donor) are concerned, it is tempting to suggest that an increase in maximal extinction amplitude reflects an increase in FRET efficiency. Indeed, the efficiency of fluorescence energy transfer (E) is defined as the fractional decrease in EGFP fluorescence due to ligand binding and is expressed by $E = 1 - F_{DA}/F_D$, where F_{DA} and F_D are the specific donor fluorescence emission values in the presence or the absence of saturating concentrations of ligand, respectively (*8*). According to the Förster equation, $R = R_0(1/E - 1)^{1/6}$ (*21*, *22*), with a Förster radius R_0 value set as a constant, an increase in FRET efficiency is clearly linked to a shortening of the actual distance R which separates the EGFP donor from the acceptor dye. It is thus possible that the triazole ring allows a reorientation of the ligand chromophore within the receptor and its projection toward an external domain, closer to EGFP. Though such a possibility deserves further investigations, similar distance shortenings (close to 3.5 Å) could be estimated when using triazole-containing probes instead of their more flexible original analogues.

An alternate explanation is to consider that, owing to the presence of the triazole ring within the spacer, the ligand chromophore would no longer adopt a random orientation of its absorption transition dipoles relative to those of donor emission. Such a possibility is difficult to verify and would affect the estimation of the Förster radius value, R_0, that specifies the theoretical distance separating a given donor−acceptor pair for 50% energy transfer efficiency. Altogether, these results indicate that the substitution of an amide bond to a small and rigid 1,4-triazole ring within the spacer connecting pirenzepine to the label is not deleterious for binding. Furthermore, this may be considered an interesting way to shorten the separation between FRET partners, i.e., between the donor (EGFP) and the acceptor

(dye moiety of the ligand), and to further increase the sensitivity in detecting the formation of ligand−receptor complexes.

CONCLUSION

In this paper, we describe a versatile and convenient method to facilitate the labeling of the small pirenzepine ligand with either a fluorescent probe, a nonfluorescent dye, or biotin. Cu(I)-catalyzed 1,3-dipolar cycloaddition, performed in partially aqueous media, is rapid, chemo- and regioselective, and leads to the formation of a stable triazole connection. The three new probes exhibit a nanomolar affinity for EGFP(Δ17)-hM1 receptors, indicating that the triazole link does not perturb binding to M1 receptors. It is also compatible with FRET-based binding assays. "Click" chemistry may thus be regarded as a convenient method to tag GPCR ligands with different probes useful for various applications. For instance, these three novel pharmacological tools will be involved in studies aimed at crystallizing muscarinic M1 receptor. Fluorescent and colored ligands will be used to detect and quantify correctly folded receptors. The biotinylated derivative will be used to prepare affinity chromatography columns necessary to the ultimate purification of functional M1 receptor.

ACKNOWLEDGMENT

This work was supported by the Centre National de la Recherche Scientifique, the Université Louis Pasteur, the European Community's Sixth Framework Program (grant LSHB-CT-2003-503337). We thank Pascale Buisine (IFR85) for ES-MS analyses, Aziz Chenaf for participating in the binding assay experiments, and Line Bourel for proofreading the manuscript.

LITERATURE CITED

(1) Baindur, N., and Triggle, D. (1994) Concepts and progress in the development and utilization of receptor-specific fluorescent ligands. *J. Med. Res. Rev. 14*, 591−664.

(2) Wilcheck, M., and Bayer, E. (1998) The avidin-biotin complex in bioanalytical applications. *Anal. Biochem. 171*, 1−32.

(3) Sakai, T., Naidenko, O., Iijima, H., Kronenberg, M., and Koezuka, Y. (1999) Syntheses of biotinylated alpha-galactosylceramides and their effects on the immune system and CD1 molecules. *J. Med. Chem. 42*, 1836−1841.

(4) Honda, T., Janosik, T., Honda, Y., Han, J., Liby, K. T., Williams, C. R., Couch, R. D., Anderson, A. C., Sporn, M. B., and Gribble, G. W. (2004) Design, synthesis, and biological evaluation of biotin conjugates of 2-cyano-3, 12-dioxooleana-1, 9(11)-dien-28-oic acid for the isolation of the protein targets. *J. Med. Chem. 47*, 4923−4932.

(5) Hegener, O., Jordan, R., and Häberlein, H. (2004) Dye-labeled benzodiazepines: Development of small ligands for receptor binding studies using fluorescence correlation spectroscopy. *J. Med. Chem. 47*, 3600−3605.

(6) Hess, S. T., Huang, S., Heikal, A. A., and Webb, W. W. (2002) Biological and chemical applications of fluorescence correlation spectroscopy: a review. *Biochemistry 41*, 697−705.

(7) Middleton, R. J., and Kellam, B. (2005) Fluorophore-tagged GPCR ligands. *Curr. Opin. Chem. Biol. 9*, 517−525.

(8) Ilien, B., Franchet, C., Bernard, P., Morisset, S., Weill, C. O., Bourguignon, J.-J., Hibert, M., and Galzi, J.-L. (2003) Fluorescence resonance energy transfer to probe human M1 muscarinic receptor structure and drug binding properties. *J. Neurochem. 85*, 768−778.

(9) Tahtaoui, C., Parrot, I., Klotz, P., Guillier, F., Galzi, J.- L., Hibert, M., and Ilien, B. (2004) Fluorescent pirenzepine derivatives as potential bitopic ligands of the human M1 muscarinic receptor. *J. Med. Chem. 47*, 4300−4315.

(10) Tahtaoui, C., Guillier, F., Klotz, P., Galzi, J.-L., Hibert, M., and Ilien, B. (2005) On the use of nonfluorescent dye labeled ligands in FRET-based receptor binding studies. *J. Med. Chem. 48*, 7847−7859.

(11) Montalbetti, C. A. G. N., and Falque, V. (2005) Amide bond formation and peptide coupling. *Tetrahedron 61*, 10827−10852.

(12) Cheng, Y.-C., and Prusoff, W. H. (1973) Relationship between the inhibition constant (K1) and the concentration of inhibitor which causes 50 per cent inhibition (I50) of an enzymatic reaction. *Biochem. Pharmacol. 22*, 3099−3108.

(13) Kolb, H. C., Finn, M. G., and Sharpless, K. B. (2001) Click chemistry: diverse chemical function from a few good reactions. *Angew. Chem., Int. Ed. 40*, 2004−2021.

(14) Rostovtsev, V. V., Green, L. G., Vokin, V. V., and Sharpless, K. B. (2002) A stepwise Huisgen cycloaddition process: Copper(I)-catalyzed regioselective "ligation" of azides and terminal alkynes. *Angew. Chem., Int. Ed. 41*, 2596−2599.

(15) Wang, Q., Chan, T. R., Hilgraf, R., Fokin, V. V., Sharpless, K. B., and Finn, M. G. (2003) Bioconjugation by copper(I)-catalyzed azide-alkyne [3 + 2] cycloaddition. *J. Am. Chem. Soc. 125*, 3192−3193.

(16) Seo, T. S., Li, Z., Ruparel, H., and Ju, J. (2003) Click chemistry to construct fluorescent oligonucleotides for DNA sequencing. *J. Org. Chem. 68*, 609−612.

(17) Link, A. J., and Tirrell, D. A. (2003) Cell surface labeling of *Escherichia coli* via copper(I)-catalyzed [3+2] cycloaddition. *J. Am. Chem. Soc. 125*, 11164−11165.

(18) Corrie, J. E. T., Davis, C. T., and Eccleston, J. F. (2001) Chemistry of sulforhodamine amine conjugates. *Bioconjugate Chem. 12*, 186−184.

(19) Hoegberg, T., and Ulff, B. (1984) Stereoconservative reductive methyl- and dimethylamination of isomeric 3,3-diarylpropenals. Synthetic and mechanistic studies on control of the stereochemistry. *J. Org. Chem. 49*, 4209−4214.

(20) Greenberg, R. R., and Kingston, H. M. (1983) Trace element analysis of natural water samples by neutron activation analysis with chelating resin. *Anal. Chem. 55*, 1160−1165.

(21) Förster, T. (1948) Zwischenmolekulare energiewanderung und fluoreszenz. *Ann. Phys. (Leipzig) 2*, 55−75.

(22) Lakowicz, J. R. (1999) *Principles of fluorescence spectroscopy.* Kluwer Academic/Plenum Press, New York.

(23) Lefevre, C., Chol Kang, H., Haugland, P. R., Malekzadeh, N., Arttamangkul, S., and Haugland, P. R. (1996) Texas Red-X and rhodamine Red-X, new derivatives of sulforhodamine 101 and lissamine rhodamine B with improved labeling and fluorescence properties. *Bioconjugate Chem. 7*, 482−489.

BC060140J

A Solvent-Free Method for Isotopically or Radioactively Labeling Cyclodextrins and Cyclodextrin-Containing Polymers

Ryan K. Zeidan,[†] Stacey A. Kalovidouris,[§] Thomas Schluep,[§] Robert Fazio,[#] Robert Andresini,[#] and Mark E. Davis*[,†]

Division of Chemistry and Chemical Engineering, California Institute of Technology, Pasadena California, 91125, Insert Therapeutics, 129 N. Hill Avenue, Suite 104, Pasadena, California 91106, and Vitrax, 660 S. Jefferson Street, Unit E, Placentia, California 92870. Received July 12, 2006; Revised Manuscript Received September 20, 2006

A method for installing a distinguishable label onto cyclodextrins or cyclodextrin-containing polymers is reported. Cyclodextrins (CD) and cyclodextrin-containing polymers are exposed to labeled (^{2}H or ^{14}C) ethylene oxide (EO) vapor and the alcohol groups on the CD ring open the EO to give ether-linked labeled methylenes and a terminal alcohol. This method provides for the incorporation of an easily tracked and quantified label without the use of solvents or purification steps. The method can be generalized for use with materials that contain nucleophiles other than alcohols, e.g., amines.

INTRODUCTION

Cyclodextrin-containing compounds and materials are becoming more widespread in drug delivery applications due to commercial availability, ability to form inclusion complexes, biocompatibility, and other unique chemical properties that contribute to their ease of chemical functionalization (*1*). Cyclodextrins do not contain chromophores or fluorophores in the parent structure and thus create difficulties in monitoring by spectrophotometric methods. Herein, a robust and general method to incorporate labels (deuterium or ^{14}C) to cyclodextrin compounds simply and without solvents or purification is described that utilizes the reactivity of sugars with ethylene oxide vapor. This labeling method is also applicable to other sugar-containing molecules as well as any material bearing a reactive nucleophile group. The ability to incorporate radioactive isotopes such as ^{14}C provides for materials that can be used for pharmacokinetic and pharmacodynamic studies (tritium labels, for example, may be lost from material in vivo (*2*)). The addition of the EO to the CD does not change the total amount of alcohol groups and just inserts a two-methylene spacer onto the sugar. Thus, there is minimal differences in the physicochemical properties from the parent CD.

LeMaistre and Seymour (*3*) reported that the reaction of sucrose in aqueous sodium hydroxide solution with ethylene oxide occurred in high yield. However, there are no reports of the reaction of EO with CD. Here, we react individual CDs and CD-containing polymers with EO.

EXPERIMENTAL SECTION

General. Deuterated ethylene oxide was obtained as a gas from Sigma Aldrich. β-cyclodextrin was obtained from Wacker.

Labeling with Ethylene Oxide-d_4. β-Cyclodextrin (50 mg) was dried at 100 °C under vacuum for 12 h overnight in order to completely remove residual water (water reacts with ethylene oxide to form ethylene glycol if not removed). After drying, the solid β-cyclodextrin sample was then allowed to cool to RT. The lecture bottle with ethylene oxide-d_4 was then attached to the reaction flask, and gas was flowed over the material for 2 min at 17 psi. The reaction vessel was then placed under vacuum to remove unreacted ethylene oxide-d_4. The resulting white solid was then analyzed by ESI-MS to test for EO incorporation. Deuterium NMR experiments were performed also to confirm the presence of the EO incorporation.

Labeling with ^{14}C Ethylene Oxide. The cyclodextrin-containing polymer conjugate of camptothecin, IT-101 (*4*−*7*) (1.6 g), was reacted with 1 mmol ethylene oxide [1,2-^{14}C], 50 mCi/mmol, under anhydrous conditions. Ethylene oxide, [1,2-^{14}C] was generated from bromoethanol, [1,2-^{14}C] under basic conditions, dried, and vacuum transferred into a 50 mL glass pressure vessel containing IT-101. The resultant mixture, at approximately 0.5 atm, was allowed to incubate for 4 days. The excess ethylene oxide, [1,2-^{14}C] was removed by vacuum transfer, and no further workup was performed. The specific activity was measured by gravimetric assay to be 1.01 μCi/mg. Yield 1440 μCi, remaining a light yellow solid.

RESULTS AND DISCUSSION

The reaction of dried β-CD with ethylene oxide-d_4 (EO-d_4) was carried out with vapor EO (Figure 1). Ethylene oxide-d_4 has a mass of 48 and for each EO-d_4 that reacts with the β-CD a corresponding increase in mass should be detectable by ESI/MS.

The resulting solid product after exposure to EO-d_4 was analyzed by ESI/MS to observe the amount of labeling that has occurred. When the β-CD is not dried in advance, there is only a trace of EO incorporation (see Supporting Information), as residual water reacts with EO to give ethylene glycol. The same experiment was then carried out with β-CD that was dried at 100 °C for 24 h prior to use and then treated with EO-d_4 for 5 min. The resulting ESI/MS data are shown in Figure 2. It is clear that there are observable species in the mass spectrum that correspond to various levels of ethylene oxide incorporation into the β-CD. The parent peak at 1157.4 corresponds to [M + Na] for the parent β-CD. The corresponding peak for 1 addition of EO is at [M + Na] = 1205.4 and is clearly present. The corresponding peaks for 2, 3, 4, and 5 EO additions are also observed, as well as trace peaks corresponding to 6 and 7 additions at *m*/*z* of 1445 and 1493. The distribution of labeled products is also very clearly an exponentially decreasing trend

* Corresponding author. E-mail: mdavis@cheme.caltech.edu.
[†] California Institute of Technology.
[§] Insert Therapeutics.
[#] Vitrax.

10.1021/bc060211e CCC: $33.50 © 2006 American Chemical Society
Published on Web 10/31/2006

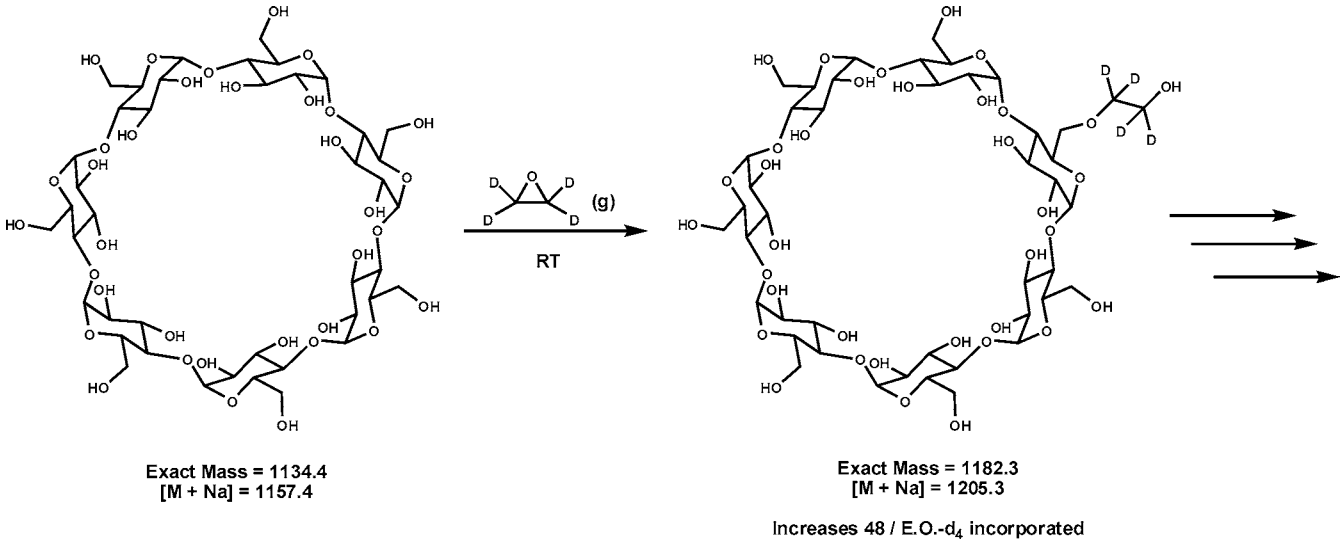

Figure 1. Schematic of reaction of β-cyclodextrin with ethylene oxide-d_4.

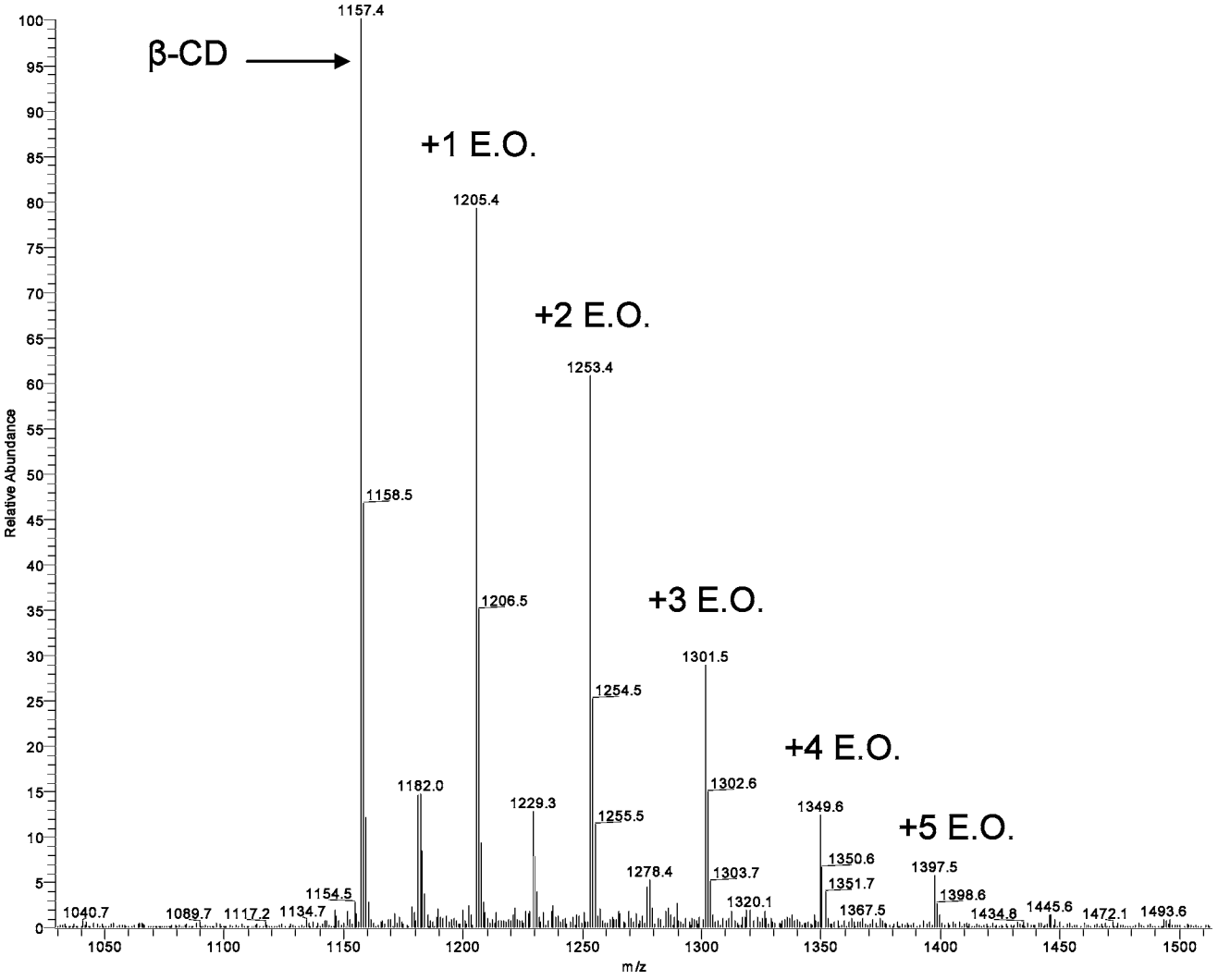

Figure 2. ESI/MS analysis of labeled β-CD.

as the *m*/*z* increases to values indicative of highly labeled species. By using shorter exposure time and lower reaction temperatures, less EO-d_4 is incorporated (see Supporting Information).

There is a need to incorporate radioactive labels into materials that can be used for in vivo studies. A major concern when labeling materials is whether or not the labeling significantly alters the material properties from those of the parent compound. Incorporation of EO into CDs does alter the properties of the labeled compound from those of the parent CD (unlike placing the label in the sugar itself). However, the consequences of the slight differences in properties may be significantly outweighed by the ease in the labeling methodology with EO; especially for CD-containing materials.

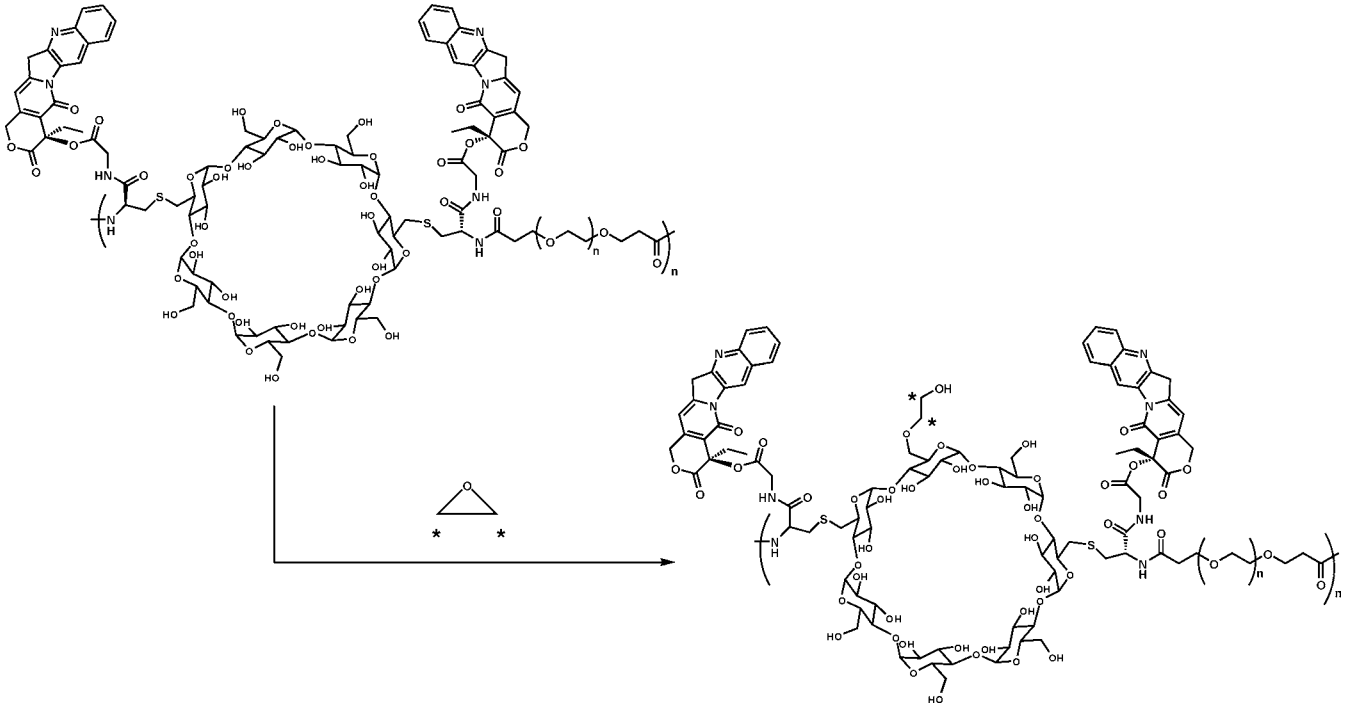

Figure 3. Schematic of radioactively labeled EO reaction with IT-101.

Radiolabeled ^{14}C ethylene oxide would be expected to react with β-CD in a manner similar to the EO-d_4. The radioactivity of the resulting material could be quantified to evaluate the level of incorporation of EO and provide for straightforward analysis if used in vivo. To illustrate the methodology on β-CD containing polymer, we used IT-101 (*4*−*7*), a linear, water soluble cyclodextrin-containing polymer that is conjugated with camptothecin (Figure 3) to react with ^{14}C ethylene oxide.

IT-101 was exposed to radiolabeled ^{14}C ethylene oxide, and the resulting material was analyzed for radioactivity to quantify the extent of labeling. Note that in this case the drying step was carried out at room temperature to prevent polymer−conjugate decomposition. This drying step is sufficient to show that no radioactively labeled ethylene glycol is formed (see Supporting Information). The labeled IT-101 contained 1.01 mCi/mg of radioactivity that corresponds to ca. 1.5 EO molecules added per polymer chain. The labeling was performed in the absence of solvents on the polymer conjugate, and when the "hot" IT-101 is dissolved in water it forms particles with average size of 43 nm (analysis was performed by The Southwest Research Institute). This size is consistent with published data of IT-101 that is not radiolabeled (*4*−*7*). These data suggest that substantial levels of radiolabel can be incorporated into IT-101 and its properties not significantly modified from the parent compound. Animal studies using radiolabeled IT-101 are in progress and will be reported at a later time.

In summary, a simple and efficient method for labeling cyclodextrin-containing materials without the use of solvents or purification is described through reaction with ethylene oxide, and this methodology is applicable to any materials bearing nucleophilic sites. When using radiolabeled ethylene oxide, an accurately quantifiable labeling method is achieved and it allows for the preparation of radiolabeled materials for in vivo studies.

Supporting Information Available: Experimental details. This material is available free of charge via the Internet at http://pubs.acs.org.

LITERATURE CITED

(1) Davis, M. E., and Brewster, M. E. (2004) Cyclodextrin-based pharmaceutics: Past, present, future. *Nat. Rev. Drug Discovery 3*, 1023−1035.

(2) Beumer, J. H., Beijnen, J. H., and Schellens, J. H. (2006) Mass balance studies, with a focus on anticancer drugs. *Clin. Pharmacokinet. 45*, 33−58.

(3) LeMaistre, J. W., and Seymour, R. B. (1948) The Reaction of Sucose with Ethylene Oxide. *J. Org. Chem. 13*, 782−785.

(4) Cheng, J. J., Khin, K. T., Jensen, G. S., Liu, A., and Davis, M. E. (2003) Synthesis of Linear, Beta-Cyclodextrin-Based Polymers and Their Camptothecin Conjugates. *Bioconjugate Chem. 14*, 1007−1017.

(5) Cheng, J. J., Khin, K. T., and Davis, M. E. (2004) Antitumor Activity of β-Cyclodextrin Polymer−Camptothecin Conjugates *Mol. Pharm. 1*, 183−193.

(6) Schluep, T., Cheng, J. J., Kim, K. T., and Davis, M. E. (2006) Pharmacokinetics and biodistribution of the camptothecin-polymer conjugate IT-101 in rats and tumor-bearing mice. *Cancer Chemother. Pharmacol. 57*, 654−662.

(7) Schluep, T., Hwang, S. J., Cheng, J. J., Heidel, J. D., Bartlett, D. W., and Davis, M. E. (2006) Preclinical Efficacy of the Camptothecin-Polymer Conjugate IT-101 in Multiple Cancer Models. *Clin. Cancer Res. 12*, 1606−1614.

BC060211E